

# The Effect of Preoxidation and Meniscus Shape on the Hydrogen-Platinum Anode of a Molten-Carbonate Fuel Cell

James T. Cobb, Jr.<sup>1</sup> and Lyle F. Albright

School of Chemical Engineering, Purdue University, Lafayette, Indiana

## ABSTRACT

Electrochemical phenomena in a hydrogen-oxygen fuel cell were studied at 723°K for the three-phase region on smooth platinum anode sheets, partially immersed in a eutectic mixture of lithium, sodium, and potassium carbonates. The meniscus shape varied with the composition of the gas phase and the potential of the anode. A platinum oxide surface was formed on the anode either by a preoxidation technique or by contacting the platinum with gaseous oxygen. A platinized surface, obtained by reduction with hydrogen of this surface, resulted in immediate large increases in current (activation), but the current slowly decreased with time (deactivation). Temporary increases in current were observed as the contact angle suddenly increased as the electrolyte film drained from the anode. The molten-carbonate film, obtained during raising the anode, was apparently relatively impermeable to hydrogen.

The current density at a selected polarization or voltage can be substantially increased through a smooth platinum anode completely submerged in an aqueous electrolyte by preoxidizing the anode surface (1, 2). The platinized surface, produced by the reduction of the oxide layer, slowly "recrystallizes," and the current density decreases toward its value before pre-oxidation. A similar effect is found on a smooth hydrogen-platinum anode partially immersed in an aqueous electrolyte (3).

On a smooth, partially immersed hydrogen-platinum anode, only well-developed menisci (formed by good wetting of the anode by the electrolyte) have been reported. However, evidence exists of variations in the contact angle on several other metal surfaces, partially immersed in aqueous solutions and exposed to various atmospheres and potentials (4-6). Changes in the contact angle have also been observed when the atmosphere was changed around sessile drops of molten sodium disilicate and molten lithium metaborate on smooth platinum surfaces at 1273°K (7, 8).

When a well-developed meniscus is present on an electrode partially immersed in an aqueous electrolyte, a film extends above the meniscus and over 75% of the current results from the transfer of the hydrogen through it (9-11). Migration of hydrogen along the surface of the anode has been shown to be insignificant under these conditions (9, 11). However, the possibility of significant bulk diffusion through the anode material of a high-temperature (723°-973°K) fuel cell has been postulated (12).

The present investigation concerned itself with these phenomena on a platinum anode partially immersed in a eutectic mixture of lithium, sodium, and potassium carbonates at 723°K. The effects of (a) preoxidation, (b) changes in composition of the gas phase, and (c) resistances to hydrogen transfer through an electrolyte film were investigated in regard to the current density through the anode and on the contact angle made by the molten salt with the anode.

**Equipment.**—The fuel cell used is shown schematically in Fig. 1. A 1:1:1 by weight mixture of lithium, sodium, and potassium carbonates (item 1) filled a 2500 ml Vycor beaker (item 2) to a depth of 12.5 cm. The salt was prepurified by melting and skimming the salt, then reducing metallic ions with a magnesium metal strip. An inverted 800 ml glass beaker (item 3) was

immersed approximately 2.5 cm in the salt and served as the fuel chamber. It was supported by three 6 mm glass tubes. Two of these tubes (items 4 and 5) extended to within 2.5 cm of the top of the fuel chamber. One was the gas inlet and the other the gas outlet. A fourth tube, fused shut on the end, contained a chromel-alumel thermocouple, which was placed at the salt surface either just outside the fuel chamber or inside the chamber about 2.5 cm from the anode (item 7).

The glass tube (item 6), which supported the anode, contained a No. 16 B&W gauge Nichrome wire, spot welded to a 12.5 cm length of No. 20 B&W gauge platinum wire, which in turn was spot welded to the anode. The anodes were 4 x 4 cm squares of 0.0125 cm thick platinum sheets. Before use, they were cleaned for a few minutes in cold, concentrated HF. The position of the anode could be altered using a finely adjustable screw support device. Glass tubes and wire connections similar to those of the anode were provided for two platinum-air electrodes (one, the cathode; the other, the reference electrode) (items 8, 9, 10, and 11).

This cell assembly was positioned inside an electric oven (item 12), which had two 6.25 cm square windows, one in the front wall and the other in the back wall. A focused beam of light was directed through the back window. Visual reading of the contact angle allowed only approximate values (0°, 15°, 30°, 60°, and 90°) to be reported. The electric oven was covered with insulation which is not shown in Fig. 1.

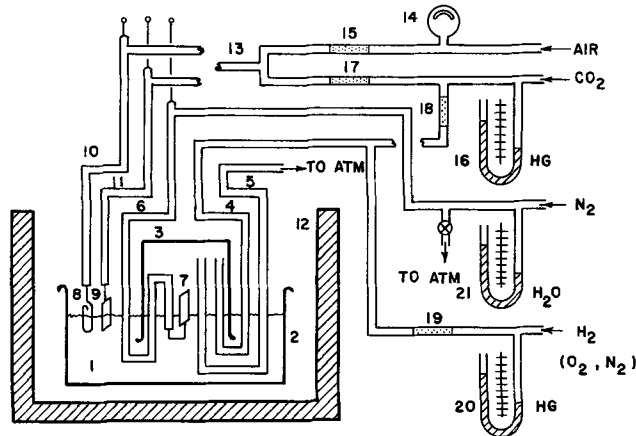


Fig. 1. Fuel cell and gas feed system

<sup>1</sup> Present address: U. S. Naval Weapons Center, China Lake, California.

A dry, metered mixture of about 6% CO<sub>2</sub> and 94% air was fed to the cathode and reference electrode through their support tubes (items 10, 11, 13, 14, 15, 16, and 17). Hydrogen, oxygen, nitrogen, carbon dioxide, and mixtures of these gases could be fed to the fuel chamber (items 4, 5, 16, 18, 19, 20, and 21). As a rule, the gas chamber contained about 10% carbon dioxide and 90% hydrogen.

A variable potential was applied to the anode by means of a set of wet cells connected across a voltage divider. The anode potential, with respect to the reference electrode, was measured using a combination of an L&N Type K potentiometer, a Rubicon galvanometer, and an Eppley standard cell. The current passing through the anode was measured using a Triplet Model 630 VOM meter.

*Contact angles and menisci.*—Advancing and receding contact angles are most commonly defined in a system where the entire mass of the liquid is in motion relative to the solid, *i.e.*, a drop of water running down a window pane or an electrode being raised from or lowered into an electrolyte. In the case of the experiments involving a stationary sessile drop or a meniscus on a stationary vertical plate, there was no movement of the bulk liquid with respect to the solid and so there was no classical advancing or receding contact angle. Only increasing or decreasing contact angles (which may have been related to receding and advancing contact angles, respectively) could be observed.

A meniscus whose contact angle is 0° has a film extending above it up the surface of the solid. No three-phase line was present, only a three-phase region at the top of the film. Once a finite contact angle appeared, then a three-phase line became well-defined at the top of the meniscus.

*Effect of atmosphere on contact angle.*—With hydrogen gas above the electrolyte in the beaker (item 3), the contact angle between a partially immersed platinum anode and the electrolyte was approximately 90° at open circuit conditions. The potential was -0.94v. As the hydrogen was replaced with nitrogen, the potential slowly rose, but the contact angle remained constant. After 5 hr the nitrogen was replaced by oxygen. Within several minutes, the potential had risen to a constant value of 0.08v and the contact angle had decreased to about 15°.

*Preoxidation of anode.*—A preoxidation procedure was used in which the anode was maintained briefly at a high potential (0.0-0.3v), and then returned to a lower one (usually -0.5v). Higher currents and changes of the contact angle were observed after preoxidation. Potentiostatic current-voltage curves had characteristics different from those found by Will (13), who did not mention any preoxidation effects. For example, a slightly roughened platinum anode partially immersed in the electrolyte at open circuit had a reference potential of -0.93v and an initial contact angle of about 90°. The potential was then adjusted in steps to -0.8, -0.6, -0.4, -0.2, and 0.0v in two sequences as shown in Fig. 2. The current tended to drop slightly with time after the potential was adjusted upward and to rise slightly with time after the potential was adjusted downward. In each case, the potential was maintained constant for 10 min, and the current was recorded at the end of this time.

When a potential of -0.20v was impressed, the contact angle of the meniscus changed to around 60°; at 0.00v, the angle became 0°. The meniscus height, measured with a cathetometer, was 0.40 cm. As the potential was lowered back to its open-circuit value, the contact angle slowly increased to 60°. After several hours at open circuit, the contact angle had increased to just under 90°. The current was significantly increased after preoxidation at 0.00v, as is seen in the second half of curve 2 of Fig. 2. Such an increase in

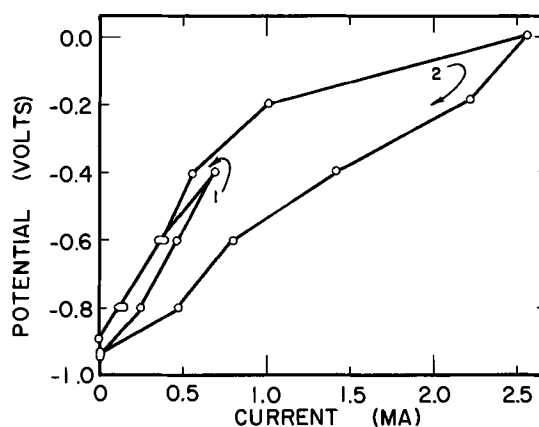


Fig. 2. Polarization of a platinum anode showing the effect of preoxidation.

current was also observed in several other current-voltage curves, obtained in a similar manner.

The relationship between the conditions of preoxidation and the increase in activity of the anode following preoxidation was studied. Two series of runs were made with partially immersed anodes, in which the voltage was switched back and forth between -0.50v and 0.10v holding the potential steady at each value for 2 min. This operation was repeated several times and the current at the end of each 2-min interval was recorded, as shown in Fig. 3. Curves 1a and 1b are for a slightly roughened anode; curves 2a and 2b for a smooth one. The (a) portion of each curve indicates the values obtained at -0.50v; the (b) portion shows the data at 0.10v. The contact angle for the first point on the (a) portions was about 90°. For all the other points of the four curves, it was 0°. The current at -0.50v through both anodes increased by a factor of 1.8 in the interval of 2-6 min. This current was somewhat lower at 10 min, then gradually increased for the remainder of the 30-min experiment. At 0.10v, a sharp drop in current through both anodes (curves 1b and 2b) by a factor of about 0.7 was observed between the data points at 4 min and at 8 min. This drop in current was followed by a gradual increase until the very end of the experiment when a second drop in current seemed to be starting.

The rate at which the larger currents, following preoxidation, decreased was found to depend on the conditions of preoxidation. The data for curve 1 of Fig. 4 were obtained at an emergence height of 2.65 cm (*i.e.*, height that the top edge of the anode was above the undisturbed electrolyte surface), beginning with a relatively inactive surface (contact angle about 90°, current 0.71 ma, volts -0.5). Preoxidation was obtained using a potential of 0.10v for 1 min, from -1 to

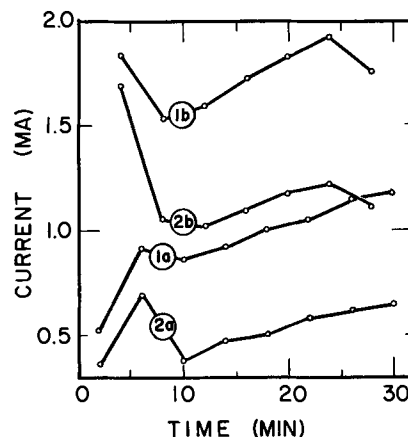


Fig. 3. Increase in current with time of preoxidation on a platinum anode.



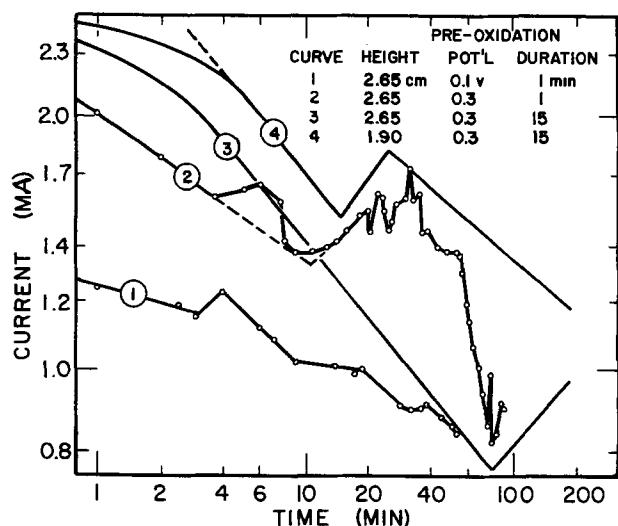


Fig. 4. Deactivation of a platinum anode following preoxidation

0 min on the abscissa (not shown). During this period, the contact angle changed to about  $60^\circ$ . At the end of this 1-min period, the external driving potential was removed temporarily to allow the cell potential to drop to  $-0.50$ v. The external driving potential was then reapplied, and the  $-0.50$ v cell potential was maintained for the next 55 min. The current decreased in general rather steadily during this period from about 1.25 to 0.82 ma. The contact angle remained at  $60^\circ$  during this entire period.

Curve 2 of Fig. 4 describes the behavior of an anode, also at 2.65 cm, which was preoxidized using a higher potential (0.3v for 1 min) then returned to  $-0.50$ v. A minute after preoxidation, the current was 2.0 ma. It decreased rapidly for 5 min, after which it rose slightly for 2 min, then fell rapidly to 1.38 ma at about 10 min after preoxidation. During the first 2 min of this initial 10-min period, the contact angle remained at  $0^\circ$ . For the last 8 min, ripples began to appear at the top of the meniscus. These ripples apparently were caused by the presence along the meniscus top of a number of small regions in which the meniscus was receding. The apparent contact angle increased to perhaps  $10^\circ$  or  $20^\circ$ , and thus a well-defined three-phase line was visible. The ripples were still apparent until 20 min, when the contact angle was around  $30^\circ$ . For the next 10 min, the contact angle continued to increase sporadically along the top of the meniscus. At 30 min, it averaged at about  $60^\circ$ . During this entire 20-min period, the current was generally increasing, although its value fluctuated significantly over short periods of time, as indicated by the data points shown on Fig. 4. Once the contact angle reached  $60^\circ$ , it remained there for the next 60 min. During this period, the current fell with some fluctuations from 1.74 to 0.82 ma.

The general increase in current by a factor of between 1.2 and 1.7 from curve 1 to curve 2 of Fig. 4 is attributed to the increase in the potential of the pre-oxidation process. Apparently the degree of oxidation and possibly the type of oxide on the platinum was different in each case.

Curves 3 and 4 of Fig. 4 and curve 1 of Fig. 5 were obtained on anodes at different emergence heights, which were preoxidized for even longer periods of time (15 min) at 0.30v and then returned to  $-0.50$ v. The generally higher current of curve 4 of Fig. 4 and lower current of curve 1 of Fig. 5 were apparently caused by the difference in the past history of the various portions of the anode surface at the three-phase region in each case. All three curves exhibited a temporary increase in current as rippling became noticeable (see Table I). The data points are not shown in these curves in order to maintain clarity. In general, there were fewer short-term current fluctua-

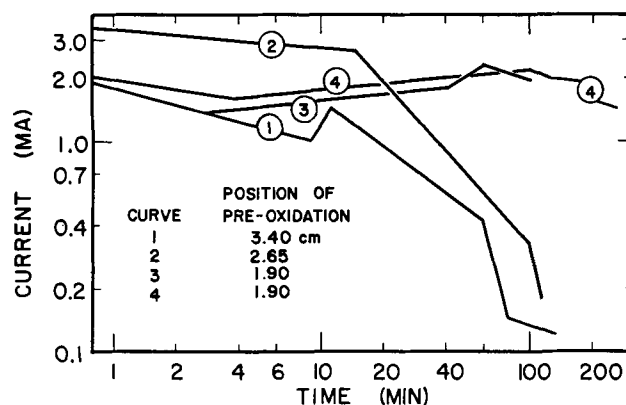


Fig. 5. Deactivation of a platinum anode following preoxidation

tions than observed in curve 2 of Fig. 4. Curves 2 and 4 of Fig. 4 indicate that the rate of deactivation in the time period before ripples appear is a function of the length and potential of preoxidation.

Raising the anode from one partially immersed position to another immediately after preoxidation tended to give immediately higher currents and/or increased currents over relatively long periods of time. The effect of this raising is shown in curves 2, 3, and 4 of Fig. 5. In each case, the anode was raised to an emergence height of 3.4 cm (i.e., to a position where 3.4 cm of the anode was above the undisturbed electrolyte surface) immediately following preoxidation for 15 min at 0.30v. The position of preoxidation is indicated in the legend. After raising, the potential was maintained at  $-0.50$ v, and the current was observed for several hours.

The current increases depended on the distance that the anode was raised (as comparisons of curve 1 of Fig. 5 with curves 2, 3, and 4 indicate). The currents were higher when the anode was raised 0.75 cm as compared to those currents through the stationary anode. For the anodes raised 1.5 cm (curves 3 and 4), the higher currents remained for significantly longer periods of time than those through the stationary anode or through the anode raised 0.75 cm, although during the initial 20 min curves 3 and 4 were below curve 2. The contact angle behavior during the periods covered by each of the curves of Fig. 5 is also shown in Table I. In general, raising the anode after preoxidation lengthened the duration of both the lower contact angles and higher currents.

#### Current Distribution Profile

The current obtained as a function of the emergence height was investigated using an anode which had been preoxidized for 10 min (while completely submerged). Curve 1 of Fig. 6 records the current which was obtained when the anode was raised 0.05 cm every 2 min to an emergence height of 1.15 cm. The top of this anode was not quite horizontal so that its top edge did not rise completely above the level of the undisturbed salt surface until 0.4 cm. The current, which was 0.32 ma at complete submergence, increased very slowly during the initial 0.4 cm to a value of 0.40 ma. The current then increased rapidly for the next 0.6 cm with several small halts before reaching 1.00

Table I. Contact angles during time periods (in minutes) described by various curves of Fig. 4 and 5

Figure	Curve	$0^\circ$	Ripples	$30^\circ$	$60^\circ$	$90^\circ$
4	1					1-55
4	2	1-2	2-20	20-30	30-90	
4	3	1-45	45-130	130-165		
4	4	1-2	2-11	11-20	20-195	
5	1	1-4	5-14	15-23	24-135	
5	2	1-7	8-13	14-24	24-76	80-128
5	3	1-64	70-109			
5	4	1-64	70-174	220-255	267-1485	

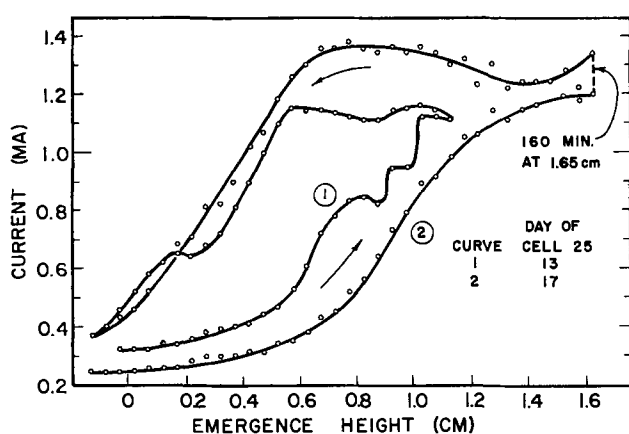


Fig. 6. Change in current through a platinum anode being raised and lowered.

cm emergence. Here the current leveled out at about 1.12 ma. The contact angle was  $0^\circ$  during the entire period of raising.

After 4 min at an emergence height of 1.15 cm the anode was slowly lowered to complete submergence, again at 0.05 cm intervals every 2 min. The contact angles at various heights were as follows

1.15 to 1.10 cm—	$0^\circ$
1.05 to 1.00 cm—	$30^\circ$
0.95 to 0.75 cm—	$60^\circ$
0.70 to 0.10 cm—	$90^\circ$

At 0.10 cm the lowest part of the top edge of the anode became completely covered with electrolyte. The upper edge was not completely submerged until  $-0.15$  cm had been reached. The current remained fairly constant at about 1.13 ma during lowering down to 0.50 cm. Only then did the current begin to decrease as lowering continued. The current reached a value of 0.37 ma at  $-0.15$  cm.

A similar procedure was followed using an anode which had been preoxidized, raised, and lowered several times before the data, shown in curve 2 of Fig. 6, were taken. In this case the anode was raised to 1.65 cm and held there for 160 min before lowering was begun. The current during raising was 0.1–0.3 ma smaller than corresponding points on curve 1. The contact angle of the meniscus remained at  $0^\circ$ . During lowering, the current rose slightly and plateaued at about 1.35 ma until a height of 0.65 cm was reached. There the current began to drop. Its values were about 0.10 ma above the corresponding values of curve 1 at positions down to 0.20 cm and then about the same below that point. The contact angle did not rise above  $30^\circ$  during lowering until a height of 0.65 cm was reached. Below 0.65 cm on the lowering portion of the curve, the contact angle rose to around  $60^\circ$ .

## Discussion of Results

### The Platinum Surface

The results of this investigation imply that three basic surface structures were present at various times and positions on the platinum anodes described above. The first of these was smooth platinum covered with sorbed hydrogen (denoted Pt-H) in the potential range  $-1.0$ v to approximately  $-0.30$ v. The second was smooth platinum covered with sorbed oxygen (denoted Pt-O) in the potential range  $-0.20$  to  $0.30$ v. Finally, there was essentially smooth platinum covered by a thin platinized layer (denoted Pt\*) also in the potential range  $-1.0$  to  $-0.30$ v. Such surfaces have been postulated as occurring on platinum surfaces by previous investigators (1, 8, 2). These three surfaces help explain many of the results presented above.

The  $90^\circ$  contact angle on a stationary anode in a hydrogen atmosphere is attributed to the presence of

the Pt-H surface at the three-phase boundary. The  $0^\circ$  contact angle is attributed to the Pt-O surface obtained from a Pt-H surface either by increasing the anode potential or changing the atmosphere to oxygen. The second of these methods shows that the change in contact angle from  $90^\circ$  to  $0^\circ$  is caused by a change in the chemical and physical, but not necessarily electrical, structure of the surface. Chemical changes of the surface affect the roughness (14) and surface tension (15, 8) of the surface. Pask (8) has discussed his results in light of these effects.

When hydrogen replaced oxygen in the atmosphere above the anode, or the potential was reduced below  $-0.20$ v (depending on which method was used to produce the Pt-O surface), the platinum oxide was reduced either directly, by diffusion of hydrogen along the surface or through the anode material, or by a small electrochemical "corrosion-type" cell on the anode surface. The rapid return of the potential to  $-0.50$ v, as noted in Fig. 4 and 5, indicates that the entire Pt-O surface is rapidly reduced. The slow return of the contact angle to high values, in spite of this rapid potential change, supports the hypothesis of the platinized surface (Pt\*). The high degree of roughness, supposedly possessed by such a surface, should be sufficient, according to Johnson and Dettre (14), to maintain a low contact angle.

The activation by preoxidation techniques of a platinum anode for low-temperature cells has previously been reported to be caused by the thin platinum layer of the Pt\* surface (1). However, no mention was made of changes in the meniscus shape as were noted in the present study. Platinized surfaces, however, presumably contain considerably more active catalytic sites than an atomically smooth surface; each site may also be more "active". The slow increase in contact angle, plus the decrease in current following preoxidation, strongly indicate that recrystallization of the platinized surfaces occurs slowly with time to form smooth surfaces again. The observed contact angle on a surface should increase as the surface roughness decreases (15, 14). However, the increase in contact angle will be slower than the roughness decrease, since the electrolyte is receding from the platinum surface (14). Thus, lower currents may be observed at the same contact angle with receding than with advancing menisci.

### The Electrolyte Film

The results of this investigation also imply that any film of molten salt electrolyte above the meniscus region on the electrode is less pervious to transfer of reactants or of products to or from the anode surface than aqueous electrolyte films in low-temperature cells (13). In the present cell, hydrogen as fuel was transferred from the gas phase to the anode; the products, steam and carbon dioxide, were transferred from the anode to the gas phase. Based on molecular size considerations, transfer of the products might be more controlling than the transfer of the small hydrogen molecules.

When an activated anode was raised even relatively slowly, a film of electrolyte was pulled up on the previously submerged portions of the anode. The results of Fig. 6, especially curve 2, show that the presence of this film during raising may cause a current decrease of up to 1 ma from the value observed after the film has drained away. When a film is present, the three-phase region is at the top of this film. The ohmic resistance of the film increases the over-all ohmic resistance of the cell (11), thus lowering the current. There is insufficient transport of reactants or products across the film to counter the removal of the reaction sites to the top of the film.

When a film is present, as is always true to some extent, the resistance to ion transport in this film causes lower potentials toward the top of the film during preoxidation. Thus the upper portions of the anode

should not be as heavily oxidized, and thereafter platinized.

The sudden increase in current on stationary anodes, recorded in curves 2, 3, and 4 of Fig. 4 and in curve 1 of Fig. 5 is attributed to the drop of the three-phase region into the more heavily platinized regions below the top of the original well-developed meniscus. In addition, there was a simultaneous increase in the length of the three-phase region (when rippling appeared.)

Further indication of the nature of the electrolyte film is seen in curves 2, 3, and 4 of Fig. 5. When the anode was raised immediately after preoxidation, the reaction region again remained at a relatively well-defined three-phase region at the top of the film. Very soon (probably fractions of a minute) after preoxidation, this reaction region began to move down, because of film drainage, into a highly-oxidized region on the anode, thus explaining the lack of a sharp, upward increase in the current in these three cases. The fact that a higher initial current was obtained from the anode, which was raised only 0.75 cm, indicated that the film in this case was thick enough to support good currents at a reaction site about 0.35 cm above the top of the meniscus. Only when the anode was raised 1.60 cm after preoxidation did the ionic resistance in the film (mentioned before) lower the initial current. In this case, as the film thinned and drained away, the current slowly increased until the three-phase region reached the top of the meniscus about an hour following preoxidation. The contact angle was also increasing during this time.

When the anode was slowly lowered into the electrolyte and the contact angle of the advancing electrolyte increased up to 30°, the current, as observed in both curves 1 and 2 of Fig. 6, remained constant at its maximum value, or even rose slightly, until an emergence height of 0.50 cm. From this observation, it seems clear that diffusion of hydrogen along the electrolyte/solid interface or through the anode material itself from the Pt-H surface just above the three-phase region is the chief avenue of hydrogen to the reaction site.

Although platinum was the only material used for the anode, it is probable that results similar to those obtained in this investigation might be found with other types of anodes, such as nickel or palladium.

### Conclusions

1. Platinum anodes immersed in a molten carbonate eutectic mixture at 723°K are activated by a preoxi-

dation technique; the platinum surface is first oxidized and then reduced by hydrogen to platinized surfaces. Higher currents are obtained with platinized surfaces.

2. The contact angle between the 723°K molten carbonate eutectic mixture and a stationary, inactive platinum anode is around 90°. During preoxidation it decreases to 0°. The contact angle slowly changes to 90° during deactivation. If the hydrogen atmosphere above a stationary inactive anode is replaced by oxygen, the contact angle again becomes 0° and the height of the meniscus 0.40 cm.

3. At 723°K hydrogen diffuses mainly to the reaction site by a combination of diffusion along the interface of platinum and molten carbonates and/or diffusion through the bulk platinum.

4. Hydrogen apparently does not diffuse in appreciable amounts through the 723°K molten-carbonate film which may be present above the meniscus.

### Acknowledgment

This work was supported by the Indiana Gas Association.

Manuscript received Aug. 29, 1966; revised manuscript received Sept. 7, 1967.

Any discussion of this paper will appear in a Discussion Section to be published in the December 1968 JOURNAL.

### REFERENCES

1. W. C. French and T. Kuwana, *J. Phys. Chem.*, **68**, 1279 (1964).
2. S. Shibata, *Bull. Chem. Soc. Japan*, **36**, 525 (1963).
3. H. J. Davitt, Personal communication (1965).
4. M. Bonnemay, G. Bronoel, and E. Levart, *Compt. rend.*, **257**, 3394 (1963).
5. M. J. Sparnaay, *Surface Sci.*, **1**, 213 (1964).
6. H. C. Weber, H. P. Meissner, and D. A. Sama, *This Journal*, **109**, 994 (1962).
7. B. S. Ellefson and N. W. Taylor, *J. Am. Ceram. Soc.*, **21**, 205 (1938).
8. J. A. Pask and R. M. Fulrath, *ibid.*, **45**, 592 (1962).
9. R. P. Iczkowski, *This Journal*, **111**, 1078 (1964).
10. T. Katan, E. A. Grens II, and R. M. Turner, *Preprints of Papers, Symposium on Fuel Cell Systems*, 31 (1963).
11. F. G. Will, *This Journal*, **110**, 152 (1963).
12. E. Gorin and H. L. Recht, *Fuel Cells*, **1**, 109 (1960).
13. F. G. Will, *This Journal*, **110**, 145 (1963).
14. R. E. Johnson, Jr., and R. H. Dettre, *Adv. Chem. Series*, **43**, 112 (1964).
15. A. W. Adamson and I. Ling, *Ibid.*, **43**, 57 (1964).

## The Anodic Oxidation of Manganese Oxides in Alkaline Electrolytes

Hong Y. Kang and Charles C. Liang\*

P. R. Mallory & Co., Inc., Laboratory for Physical Science, Burlington, Massachusetts

### ABSTRACT

Manganese dioxide electrodes are discharged in electrolytes of 1M to 10M KOH and immediately reoxidized anodically. The efficiency of the oxidation, determined by chemical analysis as well as subsequent cathodic reduction, is a function of the concentration of KOH and decreases as the KOH concentration increases from 1M to 10M KOH. In 1M KOH, MnO<sub>2</sub> is reduced to a species tentatively identified as an active form of manganese (III) oxide, which can be efficiently reoxidized to MnO<sub>2</sub>. In 10M KOH, however, MnO<sub>2</sub> is reduced first to manganese (III) oxide and subsequently to manganese (II) oxide. This manganese (II) oxide can be recharged only to an inactive form of manganese (III) oxide which is not reoxidized efficiently to MnO<sub>2</sub>.

The cathodic reduction of manganese dioxide in alkaline electrolytes has been investigated by a number of authors (1-5). Kozawa and co-workers (1, 2)

studied the discharge process of electrodeposited manganese dioxide on spectroscopic grade graphite rods in pure KOH solutions in the absence of the zinc electrode. Boden *et al.* (3), Cahoon and Kover (4), and

\* Electrochemical Society Active Member.

Bell and Huber (5) investigated the same process for the pressed  $\text{MnO}_2$ -graphite electrode with and without zinc electrodes present. Kozawa *et al.* (1, 2) observed a two step reduction while other authors (3, 5) observed a three stage reduction in their systems.

The manganese dioxide electrode of rechargeable batteries (6-11) has also received some attention. Koval and Vorobeva (11) studied the anodic oxidation of a mixture of manganese oxide and nickel or iron hydroxide in alkaline electrolytes. They found that the efficiency of the oxidation of the electrode ranged from 6 to 20% and was dependent on the nature of the anion in the manganese salt used for the preparation of the electrode. However, no attempt was made by these authors to analyze and identify the products of the oxidation.

In view of the growing interest in the manganese dioxide-alkaline system in the secondary battery field, it was desirable to investigate the electrochemical behavior of the discharged manganese dioxide electrode. In the present work, electrodeposited manganese dioxide on graphite was first cathodically reduced in pure KOH solutions, then the anodic oxidation of the reduced electrode was studied under various conditions. The presence of a Zn electrode or ZnO in the KOH solution was avoided to eliminate any additional complications in interpreting the data.

### Experimental

**Preparation of the  $\text{MnO}_2$  electrode.**—Manganese dioxide was electrodeposited on 3.2 mm diameter spectroscopic graphite rods (AGKSP). The electrodeposition conditions were similar to those used by Nichols (12). Electrodes were plated at an apparent current density of 2 ma/cm<sup>2</sup> for 1500 sec from a solution containing 50g of  $\text{MnSO}_4 \cdot \text{H}_2\text{O}$  and 65g of  $\text{H}_2\text{SO}_4$  per liter at  $80^\circ \pm 1^\circ\text{C}$ . The electrodeposited manganese dioxide electrodes were washed thoroughly with distilled water and were kept in distilled water for at least 48 hr before use. From the chemical analysis by the method described below,  $6.0 \pm 0.3$  mg of  $\text{MnO}_2$  per electrode were obtained giving  $1.97 \pm 0.02$  for the  $x$  value in  $\text{MnO}_x$ .

**Constant current experiments.**—The manganese dioxide electrodes were discharged and charged in KOH solutions. A platinum wire was used as the counter electrode in an H-cell with a sintered glass frit separating the two compartments. The discharge and charge processes were carried out at room temperature ( $25^\circ \pm 1^\circ\text{C}$ ) at constant current densities supplied by an E/M Model C614 constant current power supply. The working electrode potential during the electrolysis was measured against a Hg/HgO electrode in the same solution as the electrolyte by means of an E-H Model 250 electrometer. The potential-time curves were recorded by a Varian G-14 recorder. All the potentials reported in this paper are referred to the Hg/HgO electrode immersed in KOH of the same concentration as the electrolyte.

**Chemical analyses of the electrodes.**—The oxidation state of manganese on the electrode was determined from the chemical analysis as follows: The sample electrode was put in 50 ml of 6N HCl containing approximately 1g of KI. The HCl solution was well de-aerated in advance by bubbling argon through it. The bubbling was continued until the manganese oxides on the electrode were completely dissolved. The oxidation power of the sample, *i.e.*, the amount of manganese oxides that oxidized iodide was then measured by a titration of the liberated  $\text{I}_2$  with a standard 0.10N  $\text{Na}_2\text{S}_2\text{O}_3$  solution using a microburet. After the titration, the total content of manganese in the solution was determined by the colorimetric analysis of the permanganate produced from the oxidation of  $\text{Mn}^{++}$  by  $\text{KIO}_4$  (13). The  $x$  value in  $\text{MnO}_x$  was calculated

from the total manganese content and the oxidizing power.

**X-ray diffraction.**—The manganese dioxide electrodes which had been subjected to discharge and recharge under various conditions were washed with distilled water until free from hydroxide ion. The electrodes were then dried in a vacuum oven at  $60^\circ\text{--}70^\circ\text{C}$  for about 18 hr prior to the x-ray analyses. Debye-Scherrer x-ray powder photographs of the samples were made using standard techniques (Fe  $K\alpha$  radiation).

### Results and Discussion

Manganese dioxide electrodes were discharged in various KOH solutions at a constant current density to a potential of  $-1.0\text{v}$ , whereupon the current was immediately reversed and the electrodes were charged anodically to various potentials. The current density used in these experiments were ranged from 0.2 to 2 ma/cm<sup>2</sup> of apparent surface area. The electrodes were then removed from the solution, and the oxidation state of manganese on each electrode was determined. The oxidation states of manganese thus determined were compared with those based on the total charge involved in the electrochemical process. Results of these comparisons are shown in Tables I and II. The recharge efficiency, expressed as the fraction of oxidized manganese to the total amount of oxidizable manganese, is also shown in the tables. These results indicate clearly that the rechargeability of the electrode was affected by the concentration of the KOH solution. The higher the concentration of the electrolyte the more difficult it was to reoxidize the electrode to manganese (IV) oxide. It also can be seen from Table II, in the range of current density studied, the general pattern of the electrochemical behavior was not affected by the current density.

It is also noted in Table I that when the manganese dioxide electrode was cathodized to the potential of  $-1.0\text{v}$  the oxidation state of manganese on the electrode or the depth of discharge differed in different KOH solutions. This is in agreement with the observations made by Kozawa and Yeager (1). The reduction of manganese (IV) stopped at manganese (III) when

Table I. Effect of KOH concentration on the recharge efficiency of the discharged manganese dioxide electrode at an apparent current density of 1 ma/cm<sup>2</sup>

KOH concentration, M	Anodization time at 1 ma/cm <sup>2</sup> sec	Potential at the end of charge volt (vs. Hg/HgO)	X in $\text{MnO}_x$		Per cent <sup>3</sup> $\text{MnO}_2$ recovery efficiency	Per cent <sup>4</sup> Mn in electrolyte
			Analytical	Calculated <sup>1</sup>		
1	0	Initial <sup>4</sup>	1.51	1.52	—	0
	850	0.2	1.74	1.78	50.0	0
	1100	0.4	1.85	1.89	73.9	0
	1300	0.6	1.93	1.96	91.3	0
2	0	Initial	1.45	1.43	—	0
	900	0.2	1.70	1.73	48.1	0
	1300	0.4	1.81	1.88	69.2	0
	1500	0.6	1.89	1.95	84.6	0
4	0	Initial	1.35	1.32	—	0
	1100	0.2	1.64	1.75	46.8	0
	1500	0.4	1.76	1.84	66.1	0
	1800	0.6	1.78	1.91	69.4	5
6	0	Initial	1.24	1.26	—	0
	1300	0.2	1.56	1.70	42.1	0
	1700	0.4	1.71	1.79	61.8	0
	1900	0.6	1.72	1.94	63.2	5
10	0	Initial	1.14	1.15	—	4
	650	-0.3	1.24	1.24	12.0	4
	1300	0.2	1.52	1.59	41.9	5
	1600	0.2	1.62	1.69	57.8	10
	1800	0.4	1.68	1.79	65.1	17
	1900	0.55	1.65	1.87	61.4	20

<sup>1</sup> Calculated on the basis of the total charge (current  $\times$  time) involved in discharge and recharge, and the total amount of Mn in the electrode

<sup>2</sup> Fraction of oxidized manganese to the total amount of manganese oxidizable to  $\text{MnO}_2$ .

<sup>3</sup> Fraction of manganese in the electrolyte at the end of each electrolysis to the total amount of manganese initially present.

<sup>4</sup> Initial state of the electrode is that obtained by cathodically discharging the original  $\text{MnO}_2$  electrode to  $-1.0\text{v}$  (vs. Hg/HgO) in each KOH solution.

Table II. Recharge efficiency of the discharged manganese dioxide electrode at different current densities

Apparent current density, ma/cm <sup>2</sup>	KOH Concentration, M	Anodization time, sec	Cut-off potential volt (vs. Hg/HgO)	X in MnO <sub>2</sub>		Per cent <sup>3</sup> MnO <sub>2</sub> recovery efficiency
				Analytical	Calculated <sup>1</sup>	
0.2	1	0	Initial <sup>3</sup>	1.51	1.52	—
		4500	0.2	1.77	1.79	56.5
		5600	0.4	1.85	1.90	73.9
	10	6600	0.6	1.95	1.98	95.6
		0	Initial	1.14	1.15	—
		6700	0.2	1.52	1.60	45.8
2.0	1	9000	0.4	1.65	1.79	61.5
		10500	0.6	1.65	1.93	61.5
		0	Initial	1.51	1.52	—
	10	410	0.2	1.70	1.77	41.3
		540	0.4	1.82	1.88	67.4
		600	0.6	1.89	1.93	82.6
900	0	Initial	1.14	1.15	—	
	590	0.2	1.45	1.55	37.4	
	850	0.4	1.63	1.71	59.1	
900	0.6	1.60	1.83	55.4		

<sup>1</sup> Calculated on the basis of the total charge involved in discharge and recharge, and the total amount of Mn in the electrode.

<sup>2</sup> Fraction of oxidized manganese to the total amount of oxidizable manganese.

<sup>3</sup> The initial state of the electrode is that obtained by cathodically discharging the original MnO<sub>2</sub> electrode to -1.0v (vs. Hg/HgO) at 1 ma/cm<sup>2</sup> in each KOH solution.

the manganese dioxide electrode was discharged to -1.0v in 1M KOH or to -0.4v in 10M KOH. Further reduction from manganese (III) to manganese (II) occurred when the discharge was carried out in 10M KOH to the potential of -1.0v. It was concluded by these authors (1) that the second step discharge from manganese (III) to manganese (II) occurred through the dissolution of manganese (III) oxide in 10M KOH followed by reduction of Mn(III) in solution to Mn(II) and reprecipitation of manganese (II) in solution to solid manganese (II) oxide. The absence of the second step reduction in dilute KOH solutions was explained as the result of insolubility of manganese (III) oxide in dilute solutions (14).

In addition, the different KOH concentrations resulted in distinctive potential-time curves. This is well illustrated by Fig. 1 where two typical curves, viz., one for 10M and another for 1M KOH, are shown. The dotted lines show the second discharge curves following the anodic oxidation. It is seen that in 10M KOH the recharge curve showed two plateaus whereas in 1M KOH no distinct plateau appeared in the re-

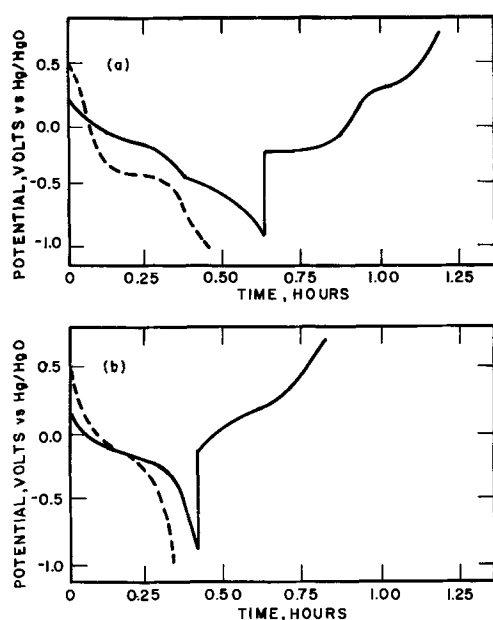


Fig. 1. Potential-time curves of the manganese dioxide electrode at a constant current density of 1 ma/cm<sup>2</sup>; (a) in 10M KOH; (b) in 1M KOH. — First discharge and charge; - - - second discharge.

charge curve. Distinctive characteristics in different KOH solutions can be observed for the second discharge curves also. In 10M KOH the second discharge curve differed pronouncedly from the first discharge curve, indicating that the preceding recharge to the original manganese (IV) state was not efficient. On the other hand, in 1M KOH the second discharge curve was similar to the first one, indicating that the preceding recharge was efficient.

The different behavior patterns of manganese oxides during their anodic oxidation in different KOH solutions may be attributed either to the effect of KOH concentration on the oxidation or to the depth of discharge at the initial point of the anodization. The observations shown in Fig. 2 seem to support the latter case. Figure 2a and 2b show the cases where the re-oxidation of the discharged manganese dioxide electrode was started from the manganese (III) state. Figure 2c shows the recharge curve in 1M KOH when the initial oxidation state of manganese was the manganese (II) state. These time-potential curves clearly indicate that when the recharge following the discharge was carried out in the same solution the KOH concentration affected the anodic oxidation of the discharged manganese dioxide electrode only in that it brought about different depths of discharge. The depth of discharge at the initial point of the anodic oxidation determined the characteristics of the charge process. The chemical analyses of the oxidation states of manganese in these cases (Fig. 2) also supported the conclusion that the depth of discharge was responsible for the different behavior patterns during the anodic oxidation. For instance, when the recharge was started from manganese (II) state, even if it was carried out in 1M KOH (Fig. 2c), the oxidation state of manganese at the end of anodization was about the same as that for the case of 10M KOH.

A necessary consequence of the above conclusion is that the manganese (III) oxide produced from the cathodic reduction of manganese dioxide was more

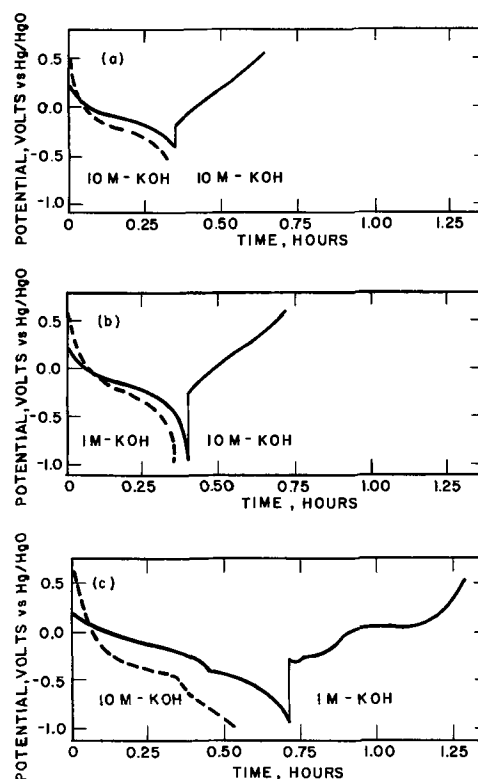


Fig. 2. Potential-time curves of the MnO<sub>2</sub> electrode at 1 ma/cm<sup>2</sup>; (a) Both discharge and charge in 10M KOH. (b) Discharge in 1M KOH, recharge in 10M KOH. (c) Discharge in 10M KOH, recharge in 1M KOH. — First discharge and charge; - - - second discharge.

active to the anodic reoxidation than the manganese (III) oxide formed by the anodic oxidation of manganese (II) oxide. Indeed either in 10M KOH or in 1M KOH the anodic oxidation beyond manganese (III) oxide was inefficient when the initial material of the oxidation was manganese (II) oxide. While manganese (III) oxide from the cathodic reduction of manganese dioxide was efficiently reoxidized to manganese dioxide in either 10M KOH or 1M KOH.<sup>1</sup>

Attempts to distinguish the two forms of electrochemically different manganese (III) oxide employing the x-ray diffraction technique were not successful because both the samples showed similar x-ray patterns corresponding to  $\gamma$ -Mn<sub>2</sub>O<sub>3</sub>. However, it was also found that both forms of manganese (III) oxide including the originally active one were inactive to the anodic oxidation to manganese dioxide after they were subjected to the washing and drying processes of the sample preparation for the x-ray analysis. Evidently, one or both of the manganese (III) oxides changed in crystal structure during the sample preparation, with a corresponding change in electrochemical behavior. Hence, in the present paper, the differentiation between the two forms of manganese (III) oxide is made primarily on the basis of electrochemical data.

It was proposed by Kozawa *et al.* (1, 2) that the mechanism of the first step discharge of MnO<sub>2.0</sub> to MnO<sub>1.5</sub> is a homogeneous phase reduction and that the product of this step is  $\alpha$ -MnOOH. In the present work it was found that the anodic oxidation was always efficient whenever the preceding discharge of the manganese dioxide electrode was stopped at the point where one could expect  $\alpha$ -MnOOH to be produced. Therefore, it seems logical to conclude that the active manganese (III) oxide which can be efficiently reoxidized to manganese dioxide was  $\alpha$ -MnOOH. Both  $\gamma$ -MnO<sub>2</sub> and  $\alpha$ -MnOOH have the same rhombic crystal structure. And since the mechanism of the cathodic reduction of  $\gamma$ -MnO<sub>2</sub> to  $\alpha$ -MnOOH is a homogeneous phase reaction, it is probable that the anodic oxidation of  $\alpha$ -MnOOH to  $\gamma$ -MnO<sub>2</sub> was a homogeneous phase process also.

The two forms of manganese (III) oxide may differ only in physical properties which lead, *e.g.*, to differences in the contact areas between the depolarizer and the conductor, or in chemical reactivity and identity with its consequences. Differences probably exist between the physical properties of the two forms of the oxide in view of the different paths leading to the two oxides. The active form was produced from  $\gamma$ -MnO<sub>2</sub> through a homogeneous phase reduction, and the inactive form was produced from  $\gamma$ -MnO<sub>2</sub> after it had undergone such processes as (a) a first step reduction, (b) a second step reduction which included (i) dissolution of manganese (III) oxide, (ii) solution reduction, and (iii) reprecipitation of manganese (II), and (c) reoxidation of manganese (II) oxide which may include again dissolution and reprecipitation. These processes most likely resulted in changes in the contact areas between the oxide and the substrate, in the particle size of the oxide, and in the site of deposition of the oxide. However, the electrochemical similarities between the electrodeposited manganese dioxide electrodes and the pressed manganese dioxide-graphite pellet electrodes suggested that these physical conditions alone could not be the decisive cause for the distinctive electrochemical behavior patterns of two forms of manganese (III) oxide.

This leaves the possibility that the two forms of the oxide differed in chemical identity. If this were the case, a possible chemical identity of the inactive form, among others, is  $\gamma$ -Mn<sub>2</sub>O<sub>3</sub> according to the x-ray dif-

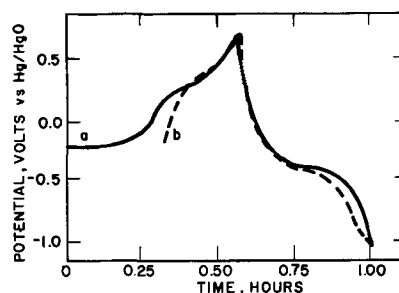


Fig. 3. Potential-time curves (charge and discharge) at 1 ma/cm<sup>2</sup> in 10M KOH. (a) — Electrodeposited MnO<sub>2</sub> electrode discharged to -1.0v (vs. Hg/HgO); (b) - - - -  $\gamma$ -Mn<sub>2</sub>O<sub>3</sub> electrode made from the electrodeposited MnO<sub>2</sub> electrode by discharging it to manganese (II) oxide, then charging it to manganese (III) oxide, and washing and drying; it was identified by x-ray analysis.

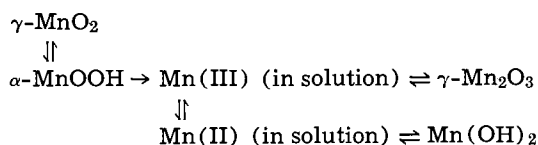
fraction patterns discussed in the previous section. The data in Fig. 3 support this conclusion. In this series of experiments, the electrochemical behaviors of the  $\gamma$ -Mn<sub>2</sub>O<sub>3</sub> electrode and that of the inactive Mn(III) oxide electrode were compared. The  $\gamma$ -Mn<sub>2</sub>O<sub>3</sub> electrode could be prepared according to either of the following procedures.

1. An electrodeposited MnO<sub>2</sub> electrode was cathodized to -1.0v then anodized to 0.2v in 10M KOH. After the electrochemical treatment, the electrode was washed thoroughly and dried at about 60°C.

2. An electrodeposited MnO<sub>2</sub> electrode was cathodized to -1.0v in 10M KOH. The reduced electrode was then taken out of the solution and subjected to air oxidation for at least 8 hr.

Chemical analyses showed that the empirical formula of the manganese oxide in these electrodes was MnO<sub>1.5±0.02</sub> and the x-ray diffraction patterns proved that these were indeed  $\gamma$ -Mn<sub>2</sub>O<sub>3</sub> electrodes. The potential-time curves for the anodic oxidation and the subsequent cathodic reduction of the  $\gamma$ -Mn<sub>2</sub>O<sub>3</sub> are shown by the dotted curves in Fig. 3. When the electrode was anodized to +0.6v where the evolution of O<sub>2</sub> began to be visible, the oxidation state of manganese was analytically determined as 3.2 ± 0.04. These results clearly indicated that  $\gamma$ -Mn<sub>2</sub>O<sub>3</sub> could not be efficiently oxidized to MnO<sub>2</sub> under the experimental conditions. This fact was also shown by the subsequent discharge curve. Most of the discharge process occurred at the potential near -0.4v where MnO<sub>1.5</sub> to MnO took place. When the potential-time curves for the anodization and subsequent cathodization of the Mn(II) oxide electrode (solid line in Fig. 3) were compared with those of the  $\gamma$ -Mn<sub>2</sub>O<sub>3</sub> electrode, it revealed that they were superimposable after the Mn(II) oxide electrode reached -0.2v where the manganese oxide became Mn(III) oxide. Based on the similarity of the electrochemical behaviors of these Mn(III) oxides, it is suggested that the manganese (III) oxide produced during the anodic oxidation of manganese (II) oxide in 10M KOH was most likely  $\gamma$ -Mn<sub>2</sub>O<sub>3</sub>. In view of the fact that  $\gamma$ -Mn<sub>2</sub>O<sub>3</sub> and Mn(OH)<sub>2</sub> have different crystal structure and that both Mn(OH)<sub>2</sub> and Mn<sub>2</sub>O<sub>3</sub> dissolve in 10M KOH, the anodic oxidation of the manganese (II) oxide to the manganese (III) oxide probably involved dissolution, solution oxidation, and reprecipitation.

In summary, the electrochemical cycle of reduction-oxidation of the manganese dioxide in 10M KOH is postulated to comprise:



<sup>1</sup> We shall refer the manganese (III) oxide which can be efficiently reoxidized to manganese dioxide as active form and the one which cannot be efficiently reoxidized to manganese dioxide as inactive form. Notice that both of these manganese (III) oxides are active to the cathodic reduction to manganese (II) oxide.

The first step oxidation of  $Mn(OH)_2$  to manganese (III) oxide may involve the dissolution of manganese (II), its solution oxidation to manganese (III) followed by the precipitation of manganese (III). The precipitated form of manganese (III) is thought to be  $\gamma\text{-Mn}_2\text{O}_3$  which is inactive to further oxidation. When the discharge process of  $\gamma\text{-MnO}_2$  is stopped at the end of the first step the reoxidation of the product manganese (III) oxide which is  $\alpha\text{-MnOOH}$  is efficient. Also, once manganese (III) dissolves in KOH solution, reprecipitation to  $\alpha\text{-MnOOH}$  seems to be inhibited.

#### Acknowledgment

The authors wish to express their thanks to Dr. P. Bro and Dr. R. G. Selim for their helpful discussions, to Mr. L. B. Griffiths for the x-ray diffraction measurements, and to Mr. G. H. Boyle for his help in preparing the graphs.

Manuscript received July 19, 1967; revised manuscript received Sept. 5, 1967. This paper was presented at the Chicago Meeting, Oct. 15-19, 1967 as Abstract No. 40.

Any discussion of this paper will appear in a Discussion Section to be published in the December 1968 JOURNAL.

#### REFERENCES

1. A. Kozawa and J. F. Yeager, *This Journal*, **112**, 959 (1965).
2. A. Kozawa and P. W. Powers, *ibid.*, **113**, 870 (1966).
3. D. Boden, C. J. Venuto, D. Wisler, and R. B. Wylie, *ibid.*, **114**, 415 (1967).
4. N. C. Cahoon and M. P. Kover, *ibid.*, **106**, 745 (1959).
5. G. S. Bell and R. Huber, *ibid.*, **111**, 1 (1964).
6. L. F. Urry, U. S. Pat., 3, 024,297 (1962).
7. L. F. Urry, U. S. Pat. 3,053,701 (1962).
8. K. V. Kordesch, U. S. Pat. 3,113,050 (1963).
9. G. R. Drengler, U. S. Pat. 3,226,260 (1965).
10. A. F. Daniel, J. J. Murphy, and J. M. Hovendon, "Batteries," Vol. 1, p. 169, D. H. Collins, Editor, McMillan Co., New York, (1963).
11. I. I. Koval and V. N. Vorobeva, *Vestnik Elektropromyshlennosti*, **4**, 47 (1958) (AD No. 243823, translated by G. Kinner).
12. G. W. Nichols, *Trans. Electrochem. Soc.*, **62**, 392 (1932).
13. L. F. Hamilton and S. G. Simpson, "Quantitative Chemical Analysis," p. 477, McMillan Co., New York (1964).
14. A. Kozawa, T. Kalnoki-Kiss, and J. F. Yeager, *This Journal*, **113**, 405 (1966).

## The Chemistry and Crystallography of Basic Antimony Sulfates

H. E. Hintermann\*<sup>1</sup> and C. J. Venuto\*

*ESB Incorporated, The Carl F. Norberg Research Center, Yardley, Pennsylvania*

#### ABSTRACT

The system  $Sb_2O_3\text{-SO}_3\text{-H}_2O$  has been investigated in the  $H_2SO_4$ -molarity range  $0 < M < 12.7$ . Five distinct basic antimony sulfates, previously unreported, have been identified. The chemistry and crystallography of these salts have been established and their ranges of stability in  $H_2SO_4$  determined at room temperature and at the boiling point of the acid. Earlier experimental findings suggesting large amounts of bound crystallization water in these compounds have been disproved.

The ternary system  $Sb_2O_3\text{-SO}_3\text{-H}_2O$  has not been studied extensively. The few reports providing substantial data are those published by Adie (1) in 1890 and more recently by the Russian workers Tananaev and Mizetskaya (2) and Veller and Sobol (3). The results reported on the chemical composition of the basic antimony sulfates are inconsistent and contradictory. The system is of theoretical and practical interest, however, since solutions of antimony or antimony trioxide in sulfuric acid are widely used in analytical procedures and in industry for producing a variety of antimony compounds and more recently in the development of a new battery system (4). This latter application has stimulated a more thorough study of the  $Sb_2O_3\text{-SO}_3\text{-H}_2O$  system at medium and low sulfuric acid concentrations.

The chemical compositions and crystal structures are well established for the two modifications of  $Sb_2O_3$ , i.e., Valentinite (orthorhombic) and Senarmontite (cubic) and for the normal sulfate  $Sb_2(SO_4)_3$  (5, 6). The composition of the basic sulfates, derived from  $Sb_2(SO_4)_3$  as a hydrolysis product or produced by reacting  $Sb_2O_3$  with polyhydrated sulfuric acid,  $H_2SO_4 \cdot x H_2O$ , are uncertain. According to a comprehensive treatise on this subject (7), the normal sulfate  $Sb_2(SO_4)_3$  is obtained in  $H_2SO_4 \cdot 1 H_2O$ . By hydrolyzing this salt in cold water  $2Sb_2O_3 \cdot SO_3$  is formed, by

hydrolyzing it in hot water  $7Sb_2O_3 \cdot 2SO_3$ . In the acid range  $H_2SO_4 \cdot 2H_2O$  (12.3M) to  $H_2SO_4 \cdot 4H_2O$  (8.7M)  $Sb_2O_3 \cdot H_2O$  is said to be formed at room temperature while  $Sb_2O_3$  is formed on heating. Further dilution leads to the precipitation of hydrated antimony trioxide  $Sb_2O_3 \cdot 3H_2O$ .

The Russian investigators (2, 3) obtained an even larger number of basic antimony sulfates by hydrolysis of the  $Sb_2(SO_4)_3$ . At concentrations lower than 8.6-10.7M  $H_2SO_4$ , compounds like  $Sb_2(SO_4)_3 \cdot y H_2O$  are formed at room temperature with  $y$  being 5 or 10, and compounds like  $Sb_2O_3 \cdot x SO_3 \cdot y H_2O$  at 100° and 155°C with  $x/y$  ratios of 2.5/24, 6/23, 20/100, 28/93, and 31/13, respectively.

The primary purpose of the Russian work was the determination of the solubility limits of trivalent antimony in aqueous sulfuric acid of various concentrations, rather than to investigate the composition of the solid phases formed during the reaction. The authors themselves regard the results of the proposed stoichiometry of the reported basic antimony sulfates as only an approximation. Hence not much accurate information exists on the chemical composition of basic antimony sulfates and none on their crystallography.

#### Experimental

The  $Sb_2O_3\text{-SO}_3\text{-H}_2O$  system requires a long time to reach equilibrium condition, i.e., several months at

<sup>1</sup> Present address: Laboratoire Suisse de Recherches Horlogères, Neuchâtel, Suisse.

\* Electrochemical Society Active Member.



room temperature and several days at boiling temperature of the solution. If equilibrium conditions are not attained, mixtures of basic sulfates will result and will make subsequent chemical analyses inaccurate. This is one possible source of error to explain the lack of consistency in the results of previous workers. In addition, once formed, the solid equilibrium reaction product is difficult to isolate from the mother solution in a pure state without further hydrolyzing it or otherwise changing it in the course of the washing procedure. Some workers (1, 3) omit washing the crystalline solid phase with any solvent at all. They attempt to remove the adherent film of mother liquid on the crystal faces by sedimentation, centrifugation, or drying between porous plates. None of these methods is effective enough, and it is obvious that the chemical analyses obtained with these procedures are inaccurate and unreliable.

We found that the high basic sulfates, produced at very low  $H_2SO_4$  concentrations, could be washed effectively with cold water and the medium and lower basic sulfates with absolute methanol, without changing the structural features of these salts. X-ray powder diffraction patterns obtained on the reaction product before and after the washing procedure proved to be a sensitive means of detecting any change in the structure, and thus the chemical composition of the original salt, due to hydrolysis or solvolysis.

The experiments were carried out with reaction mixtures of 10g  $Sb_2O_3$  in 1 liter  $H_2SO_4$  of different concentrations in the molarity range  $0 < M < 12.7$ . To obtain equilibrium conditions, the mixtures were either stored in glass stoppered Pyrex glass bottles at room temperature for 3 to 6 months or heated to the boiling point in Pyrex reaction kettles with reflux condensers for 15 to 25 days. Fisher Certified Analytical Chemicals were used. Prior to use the  $Sb_2O_3$  was dried at  $110^\circ C$  in air for 5 hr. Its x-ray diffraction pattern agreed with that published by ASTM for Senarmontite.

The equilibrium reaction products were filtered through a Gooch crucible of 8-10 $\mu$  pore size. A sample was taken from the still wet residue for x-ray powder diffraction, and some crystals were selected for single crystal analysis for use with a Weissenberg camera. They had a prismatic shape with dimensions of about 0.4 mm in one direction and 0.1 mm in the two others. The powder pattern, obtained on a Norelco diffraction unit using Nickel filtered Copper K  $\alpha$  radiation, served to establish the stability ranges of basic antimony sulfates in sulfuric acid of different molarities at room and boiling temperature of the solutions. It was used further to determine if an equilibrium state actually had been attained and a single pure phase had been formed or if the reaction product consisted of more than one solid phase. Finally, it

served a reference pattern to confirm whether the washing procedure instigated any structural changes of the salt formerly in equilibrium with its solution. Single crystals, representative of each structure type that was stable in a given acid range, were used for microscopical investigations and for the determination of the density by the wet pycnometer method using methyl-benzoate ( $\rho = 4.69 \text{ g/cm}^3$ ) at  $27^\circ C$ . The unit cell dimensions, the space group, the number of asymmetric units per unit cell, and the x-ray reflections for each structure type were established by single crystal x-ray diffraction methods.

The remaining residue was washed either in cold water or absolute methanol while still in the crucible and dried in air. Samples from this product were chemically analyzed. The solvents for  $Sb_2O_3$  found in the literature (1, 8) could not be applied to the basic antimony sulfates. These were neither completely soluble in  $NH_4Cl$ ,  $NH_4NO_3$ , nor in molten  $Na_2CO_3$ . They were soluble in HCl; however, an insoluble basic chloride precipitated simultaneously. Addition of tartaric acid almost completely prevented basic chloride formation. Nevertheless, a slight turbidity of the solution could not be avoided. All basic antimony sulfates investigated were found entirely soluble when heated in a slightly alkaline solution of  $Na_2S$  or  $(NH_4)_2S$ . Acidifying this solution with HCl precipitated antimony as  $Sb_2S_3$  which could be determined gravimetrically as such. The  $SO_4^{=}$  content was determined in the filtrate as  $BaSO_4$ , the water of hydration as the balance. The mean error of determination of Sb and  $SO_4^{=}$  carried out on blanks was smaller than  $\pm 2$  and  $\pm 4\%$ , respectively.

### Results and Discussion

From the unit cell dimensions, space group, number of asymmetric units per unit cell, and the density it was possible to calculate the molecular weight of the compound according to

$$M = \frac{a_o \cdot b_o \cdot c_o \cdot \rho}{z \cdot 1/N}$$

where  $M$  = molecular weight of one asymmetric unit in the unit cell;  $a_o$ ,  $b_o$ ,  $c_o$  = unit cell dimensions in Angstrom units ( $\text{\AA}$ );  $\rho$  = density of the pure phase in  $\text{g/cm}^3$ ;  $N$  = Avogadro's number;  $1/N = 1.6606 \cdot 10^{-24}$  = weight of g in a hypothetical atom of atomic weight 1.000; and  $z$  = number of asymmetric units in the unit cell. Combining these results with those obtained from the chemical analyses, i.e., the Sb/ $SO_3$  ratio of the molecule, the actual chemical formula of the compound could be derived. Thus five distinct basic antimony sulfates were identified in the  $H_2SO_4$  range  $0 < M < 12.7$ . These sulfates are tabulated in Table I together with some crystallographic, chem-

Table I. Chemistry and crystallography of basic antimony sulfates

Structure type	A	B	C	D	E
Crystal system	Orthorhombic	Orthorhombic	Orthorhombic	Orthorhombic	Orthorhombic
Space group	$Pm\bar{m}n-D_{2h}^{13}$	$Pm\bar{m}n-D_{2h}^{13}$	$Pm\bar{m}n-D_{2h}^{13}$	$Pm\bar{m}n-D_{2h}^{13}$	$Pm\bar{m}n-D_{2h}^{13}$
Asymmetric units	4	8	4	4	8
Unit cell dim, $\text{\AA}$ .	$a_o$ 14.83	$a_o$ 14.26	$a_o$ 12.03	$a_o$ 13.23	$a_o$ 15.35
	$b_o$ 11.42	$b_o$ 14.16	$b_o$ 18.89	$b_o$ 16.21	$b_o$ 14.61
	$c_o$ 5.80	$c_o$ 8.98	$c_o$ 6.00	$c_o$ 13.50	$c_o$ 9.23
Unit cell vol, $\text{cm}^3$	$0.982280 \cdot 10^{-21}$	$1.813256 \cdot 10^{-21}$	$1.363480 \cdot 10^{-21}$	$2.895210 \cdot 10^{-21}$	$2.069952 \cdot 10^{-21}$
Density, $\text{g/cm}^3$	$4.30 \pm 0.05$	$4.82 \pm 0.05$	$5.16 \pm 0.05$	$4.87 \pm 0.05$	$4.69 \pm 0.05$
Weight of unit cell, g	$4.22380 \cdot 10^{-21}$	$8.73989 \cdot 10^{-21}$	$7.03965 \cdot 10^{-21}$	$14.10 \cdot 10^{-21}$	$9.811573 \cdot 10^{-21}$
Multiple of M, cU	2544.0	5264.0	4240.0	8500	5909.51
Actual M	636.0	658.0	1060.0	2125	738.69
Observed % Sb	71.5	72.8	70.8	65.5	65.3
Observed % $SO_4^{=}$	14.5	14.1	18.5	23.7	25.8
Observed Sb/ $SO_4^{=}$	3.99:1	3.96:1	3.02:1	2.16:1	1.999:1
Derived chem. formula	$Sb_2O_3 \cdot [(SbO)_2SO_4]$ or $2Sb_2O_3 \cdot SO_3$	$Sb_2O_3 \cdot [(SbO)_2SO_4]$ or $2Sb_2O_3 \cdot SO_3$	$Sb_2O_3 \cdot [(SbO)_2SO_4]_2$ or $3Sb_2O_3 \cdot 2SO_3$	$[(SbO)_2 \cdot SO_4]_6$ or $(Sb_2O_3 \cdot SO_3)_6$	$[(SbO)_2SO_4]_2$ or $(Sb_2O_3 \cdot SO_3)_2$
Theoretical M	663.11	663.11	1034.70	2229.54	743.18
Theoretical % Sb	73.5	73.5	70.6	65.5	65.5
Theoretical % $SO_4^{=}$	14.5	14.5	18.6	25.85	25.85
Theoretical Sb/ $SO_4^{=}$	4:1	4:1	3:1	2:1	2:1
BET, $\text{m}^2/\text{g}$	0.3	0.1	1.1	1.3	<0.1



Table II. Stability ranges for basic antimony sulfates in H<sub>2</sub>SO<sub>4</sub> at room temperature and the temperature of the boiling solution

Structure type formed	Proposed chemical formula	H <sub>2</sub> SO <sub>4</sub> molarity range, M		
		At room temperature	At boiling temperature	
I	—	Sb <sub>2</sub> O <sub>3</sub> , cub	0-0.4	0-0.25
II	A and/or B	Sb <sub>2</sub> O <sub>3</sub> · [(SbO) <sub>2</sub> SO <sub>4</sub> ] or 2Sb <sub>2</sub> O <sub>3</sub> · SO <sub>3</sub>	0.5-2.5	0.25-2.0
III	A	Sb <sub>2</sub> O <sub>3</sub> · [(SbO) <sub>2</sub> SO <sub>4</sub> ] or 2Sb <sub>2</sub> O <sub>3</sub> · SO <sub>3</sub>	2.6-4.2	
IV	C	Sb <sub>2</sub> O <sub>3</sub> · [(SbO) <sub>2</sub> SO <sub>4</sub> ] <sub>2</sub> or 3Sb <sub>2</sub> O <sub>3</sub> · 2SO <sub>3</sub>	4.3-6.9	2.0-6.5
V	D	[(SbO) <sub>2</sub> SO <sub>4</sub> ] <sub>6</sub> or (Sb <sub>2</sub> O <sub>3</sub> · SO <sub>3</sub> ) <sub>6</sub>	7.0-10.2	6.5-9.6*
VI	E	[(SbO) <sub>2</sub> SO <sub>4</sub> ] <sub>2</sub> or (Sb <sub>2</sub> O <sub>3</sub> · SO <sub>3</sub> ) <sub>2</sub>	10.9-12.7	10.2-12.7
—	K	Sb <sub>2</sub> (SO <sub>4</sub> ) <sub>3</sub>	—	≥17.9

\* A mixture of D and E is formed at  $9.6 < M < 10.2$ .

ical, and physical properties. The stability ranges for the basic antimony sulfates at room temperature and at the boiling point of the acid are reported in Table II.

At boiling temperatures, the basic antimony sulfates form larger crystals and purer reaction products than at room temperature. In the acid range II (Table II) seeds of the structure-type A preferentially formed at room temperature, those of the type B in the boiling acid. Thus the activation energy for the formation of nuclei of the A-type basic sulfate is smaller than for the B-type sulfate at room temperature and *vice versa* at the boiling point of the solutions. A mixture of both salts is formed at intermediate temperatures. Once nuclei of one kind are formed, however, the crystals grow in the crystal habit of the seed, independent of temperature changes that occur during the reaction. Hence the free enthalpy of formation of both salts must be very similar.

The molarity range  $12.7 < M < 15.3$  was not investigated. The normal antimony sulfate Sb<sub>2</sub>(SO<sub>4</sub>)<sub>3</sub> was obtained on heating Sb<sub>2</sub>O<sub>3</sub> in an acid 18.7M, *i.e.*, concentrated H<sub>2</sub>SO<sub>4</sub>. No experiments were carried out to hydrolyze this salt in successive steps.

In conclusion, within the sulfuric acid molarity range  $0 < M < 12.7$  none of the five sulfates isolated contains any water of crystallization. This result was

confirmed also by thermal decomposition analysis of these salts at 550°C in a He-stream. The reaction products were Sb<sub>2</sub>O<sub>4</sub>, Sb<sub>2</sub>O<sub>3</sub>, and SO<sub>2</sub> in each instance; no water was found. Earlier experimental findings suggesting large amounts of crystallization water in these sulfates are thus disproved; the water must have been just adsorbed in the form of a sulfuric acid film on the surface of the crystals not properly removed during separation. This is supported by the proposed chemical formulas of the basic antimony sulfates reported by other authors which show that the Sb/SO<sub>3</sub> ratios of compounds obtained in acid concentrations equal to ours are consistently smaller than corresponds to the formulas proposed in this work. This can be explained again in terms of adsorbed layers of dilute H<sub>2</sub>SO<sub>4</sub> at the crystal surfaces of the reaction product.

#### Acknowledgment

The authors wish to thank Dr. R. A. Schaefer for his continuous support and for permission to publish this paper, Mr. R. T. Angstadt for his contribution in the analytical chemical work, Dr. T. H. Doyne of Villanova University for the single crystal studies, and Dr. P. Rüetschi for his valuable advice during the course of this study.

Manuscript received Aug. 18, 1967.

Any discussion of this paper will appear in a Discussion Section to be published in the December 1968 JOURNAL.

#### REFERENCES

1. R. H. Adie, *J. Chem. Soc.*, **57**, 540 (1890).
2. I. V. Tananaev and I. B. Mizetskaya, *Suz. ANSSSR*, **4**, 391.
3. R. L. Veller and S. I. Sobol, *Sbornik Nauch. Trudov, Gosudarst. Nauch-Issledovatel Inst. Isvetnykh Metal*, **13**, 123 (1957).
4. P. Rüetschi, U.S. Pat. 3,265,534.
5. M. J. Buerger and S. B. Hendricks, *Z. Krist.*, **98**, 1 (1937).
6. Standard X-Ray Powder Data N.B.S. Cir. 539, Vol. III, 31 and *ibid.* Vol. XI, 6.
7. J. W. Mellor, "A Comprehensive Treatise on Inorganic and Theoretical Chemistry," Vol. IX, p 425, Longmans Green and Company, New York (1929).
8. F. P. Treadwell, "Analytische Chemie," Bd. 1,247, F. Deuticke, John Wiley & Sons, Inc., New York (1946).

## The Oxidation of Iron Single Crystals at 350°C

N. Ramasubramanian,<sup>1</sup> P. B. Sewell, and M. Cohen\*

Division of Applied Chemistry, National Research Council, Ottawa, Ontario, Canada

#### ABSTRACT

A comparison of the oxidation of (001) and (112) surface single crystals of iron at 350°C and 20 Torr oxygen has been made. The (001) oxidizes more rapidly than the (112). Cubic Fe<sub>2</sub>O<sub>3</sub> persists for a longer time on the (001) than on the (112). The orientation of the underlying magnetite remains constant on both crystals for up to 100 min. With both orientations the α-Fe<sub>2</sub>O<sub>3</sub> starts out as a highly oriented oxide, but on the (112) it becomes randomly oriented at the surface after 50 min. The oxide on the (001) is more firmly adherent than on the (112). In both cases there appears to be an intermediate layer of "γ-Fe<sub>2</sub>O<sub>3</sub>" between the Fe<sub>3</sub>O<sub>4</sub> and α-Fe<sub>2</sub>O<sub>3</sub>. The cross sections of the oxides, as revealed by replica electron microscopy, are different but typical for the two orientations.

A study of the kinetics of oxidation of the various orientations of an iron single crystal in the range of 250°-550°C and 10-760 mm oxygen has been reported by Wagner, Lawless, and Gwathmey (1). The thick-

ening of the oxide was followed by observing the interference colors, a procedure similar to that of Mehl and McCandless in their lower temperature work (2). In the temperature region studied the oxide formed is usually at least two phases, and the interference color method has certain limitations (3, 4).

<sup>1</sup> Former Post-Doctorate Fellow. Present address: Atomic Energy of Canada Ltd., Chalk River, Ontario, Canada.

\* Electrochemical Society Active Member.

In this paper the results of some experiments on the oxidations of two single crystals of iron of widely different orientation at 350°C are reported. Weight gains were sufficiently high to measure by microbalance weighing. At this temperature both a cubic oxide and  $\alpha$ -Fe<sub>2</sub>O<sub>3</sub> are formed, and the amounts of these oxides were measured by a combination of weighing and cathodic reduction. The crystal structure and orientation of the oxides were determined by reflection electron diffraction.

### Experimental

The oxidation apparatus and procedure have been described fully previously (5). All experiments were done at 350°C and a pressure of 20 Torr of oxygen. The specimens were first electropolished (6) and then brought to temperature in a vacuum of 10<sup>-5</sup> to 10<sup>-6</sup> Torr. Blank experiments showed that there was no visible change in the appearance of the specimens nor a measurable weight gain during this period. Oxygen was then admitted rapidly. The experiment was stopped by removing the furnace and cooling the quartz tube with water. Specimens were weighed before and after oxidation on a Mettler microbalance.

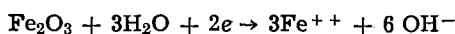
The specimens were strain-annealed Ferrovac E<sup>2</sup> single crystals. Two orientations, (001) and (112) were used. Surface areas were approximately 10 cm<sup>2</sup>.

The amount of reducible oxide was measured using the electrolytic reduction method of Oswin and Cohen (7). The solution was 0.15*N* boric acid adjusted to a pH of 7.58 with sodium borate. A current density of approximately 10-11  $\mu$ a cm<sup>-2</sup> was used and potentials are reported *vs.* the saturated calomel electrode. The amount of reducible oxide was determined both by weight loss and by a measurement of Fe<sup>++</sup> in solution.

Reflection electron diffraction was done in a G. E. diffraction apparatus using a camera length of 50 cm and an accelerating voltage of 50 kv. Replicas for electron microscopy were made using the two-stage formvar, platinum-carbon technique.

### Results

The weight gain-time curves are shown in Fig. 1. The total weight gain was determined from the difference in weight before and after oxidation. The reducible oxide was determined both by weight loss due to cathodic reduction and by colorimetric analysis of ferrous iron in solution assuming a cathodic reduction reaction of



These two numbers were then averaged. The magnetite was determined by difference.

It can be seen that both the over-all weight gain and the final rate of oxidation are higher with (001) than the (112) surfaces. In both cases there is a rapid formation of Fe<sub>2</sub>O<sub>3</sub> which then remains fairly constant in amount, while the Fe<sub>3</sub>O<sub>4</sub> increases until both oxides are approximately equal in amount at 100 min. In both cases there is a very rapid weight gain in the first 4 min. After this time the curves are approximately parabolic.

Cathodic reduction curves for the two crystals oxidized for various lengths of time are shown in Fig. 2 and 3. In both cases a definite  $\gamma$ -Fe<sub>2</sub>O<sub>3</sub> wave (-300 to -400 mv) is observed with specimens oxidized for less than 100 min. The main Fe<sub>2</sub>O<sub>3</sub> wave is that for  $\alpha$ -Fe<sub>2</sub>O<sub>3</sub> at about -600 mv. The final potential drop in all the curves is toward the Fe<sub>3</sub>O<sub>4</sub> potential. This drop is best defined for specimens which have been oxidized for the longer times. The amounts of reducible oxide as determined by both gravimetric and colorimetric analysis and the current efficiency of cathodic reduction are given in Table I.

The specimens were examined by both electron diffraction and electron microscopy after oxidation and

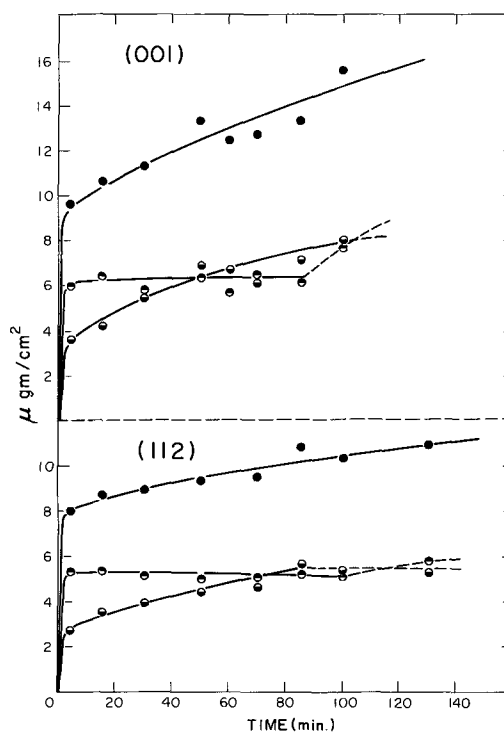


Fig. 1. Weight-gain time curves for the (001) and (112) crystals. ● Total, ○ Fe<sub>3</sub>O<sub>4</sub>, ◐ Fe<sub>2</sub>O<sub>3</sub>.

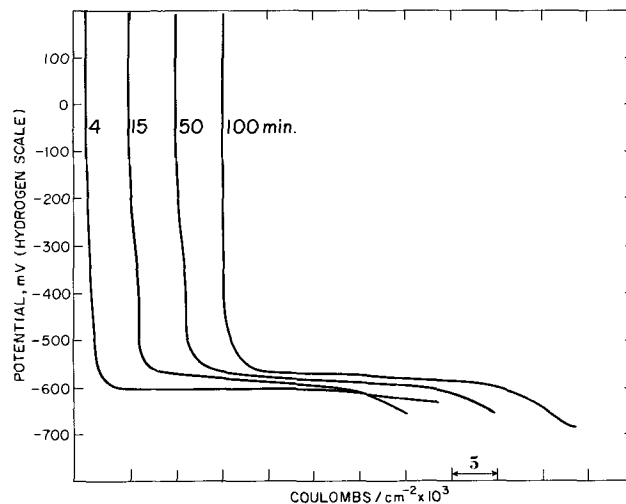


Fig. 2. Cathodic reduction curves of Fe<sub>2</sub>O<sub>3</sub> on (001) after various oxidation times.

after cathodic reduction to the magnetite, Fig. 4. Once again there was a marked difference in behavior between the two orientations. In the case of the (001) surface there was some evidence for a cubic oxide in the outer layer even after oxidation for 100 min. At 4 min the pattern was predominantly cubic. On the other hand with the (112) crystal the cubic pattern was extremely weak or had disappeared after about 15 min oxidation. Even at 4 min the diffraction pattern was predominantly that of  $\alpha$ -Fe<sub>2</sub>O<sub>3</sub>. In both cases the patterns from the magnetite layers were characteristic of a highly oriented microcrystalline material and were essentially unchanged from 4 to 100 min. The pattern from the outer  $\alpha$ -Fe<sub>2</sub>O<sub>3</sub> layer showed evidence of random orientation at longer times of oxidation, particularly with (112) crystals. The relative orientations are the same as those reported previously (8).

The topographical features of the oxides on the two orientations were also markedly different, as shown in Fig. 5 and 6. On the (001) surface the outer layer was essentially smooth at 4 min and there was some

<sup>2</sup> Ferrovac E: C—0.007%, Mn—0.0002, Si—0.0015, Cr—0.0002, Ni—0.0009, Al—0.0005, P—0.003.

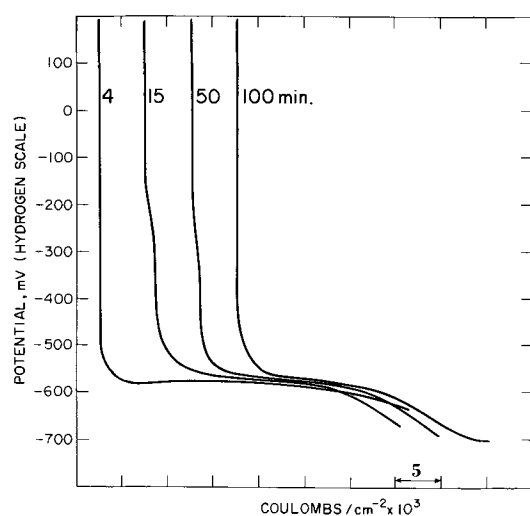


Fig. 3. Cathodic reduction curves of  $\text{Fe}_2\text{O}_3$  on (112) after various oxidation times.

roughening at 100 min. The underlying magnetite had a cross-hatch structure, similar to that observed by Laukonis (9) for thick oxide films, from the beginning. On the (112) surface both the outer and inner layers have parallel ridges which seem to become more accentuated with increased time of oxidation. These are similar to the ridges observed by Boggs (10) on some grains of polycrystalline iron oxidized under similar conditions to these. In both cases the thickness of the outer  $\text{Fe}_2\text{O}_3$  layer varied markedly over the surface. This is shown schematically in Fig. 7.

It was noted that the adherence of the underlying magnetite to the metal on the (112) surface was very poor after cathodic reduction of the  $\text{Fe}_2\text{O}_3$ . This led to some stripping of the oxide with the formvar replica. This is shown in Fig. 6 where the darker areas are  $\text{Fe}_3\text{O}_4$ . It can be seen that the oxide has the same structural characteristics as are shown by the replica.

A number of annealing experiments were made in which samples were heated at  $350^\circ\text{C}$  in a vacuum of  $10^{-5}$  Torr after oxidation was completed. There was a marked decrease in the amount of reducible oxide and very little change in the shape of the phase boundaries. Due to the scatter in the measurements no useful kinetic data could be obtained.

### Discussion

The marked effect of crystal orientation on both the over-all reaction rate and the oxide structure which was observed at  $200^\circ$  and  $260^\circ\text{C}$  (11) is even more pronounced at  $350^\circ\text{C}$ . In this work it is also seen that this difference is accompanied by distinct variations in the shape of the oxide-gas interface and the  $\text{Fe}_3\text{O}_4$ - $\text{Fe}_2\text{O}_3$  interface. The oxide on the (112) appears to be less adherent at the metal oxide interfaces than the ox-

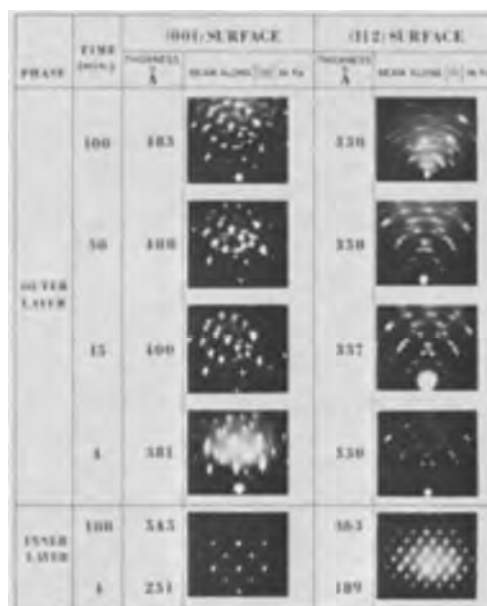


Fig. 4. Electron diffraction patterns for both surface layer and underlying magnetite on (001) and (112) after various oxidation times.

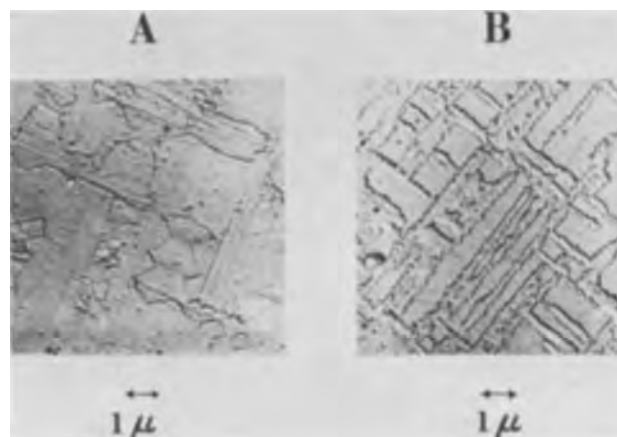


Fig. 5. Replicas of outer surface (A) and magnetite surface (B) on (001) crystal after 100 min oxidation.

ide on the (001), particularly after cathodic reduction to the magnetite. Despite these differences the general kinetics is that of very rapid oxidation in the first few minutes followed by essentially parabolic kinetics for the rest of the time. The lack of adhesion on the (112) surface may indicate the formation of voids at the oxide metal interface which, in turn, would decrease the rate of transfer of metal to the oxide and, hence, decrease the oxidation rate. This factor, combined with

Table I. Oxidation of iron single crystals, (001) and (112) surfaces, at  $350^\circ\text{C}$  in 20 mm oxygen

Time in min	Weight data in terms of oxygen, $\mu\text{g}/\text{cm}^2$							
	(001) Surface				(112) Surface			
	Total wt	Reducible oxide		Magnetite $W_{R1} + W_{R2}$ 2	Total wt	Reducible oxide		Magnetite $W_{R1} + W_{R2}$ 2
		Gravimetric $W_{R1}$	Colorimetric $W_{R2}$			Gravimetric $W_{R1}$	Colorimetric $W_{R2}$	
4	9.59	6.43	5.52	3.62	8.00	—	5.30	2.7
15	10.60	6.57	6.29	4.17	8.73	5.40	5.16	3.45
30	11.32	5.90	5.70	5.52	8.90	5.30	4.80	3.85
50	13.30	6.60	6.04	6.98	9.31	5.08	4.80	4.37
60	12.36	5.80	5.50	6.71	—	—	—	—
70	12.67	6.55	6.60	6.10	9.53	5.06	4.86	4.57
85	13.30	6.30	6.04	7.13	10.80	5.40	5.00	5.60
100	15.61	7.93	7.44	7.92	10.30	—	5.10	5.20
130	—	—	—	—	10.92	5.50	5.90	5.22

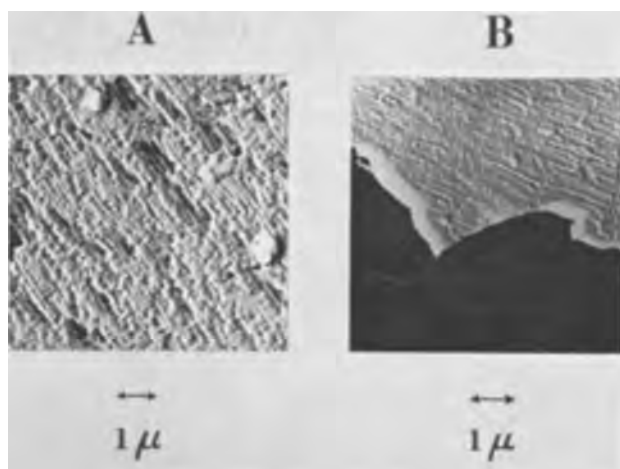


Fig. 6. Replica of outer surface (A) and magnetite surface (B) on (112) crystal after 100 min oxidation. Note dark area is transmission through stripped  $\text{Fe}_3\text{O}_4$ .

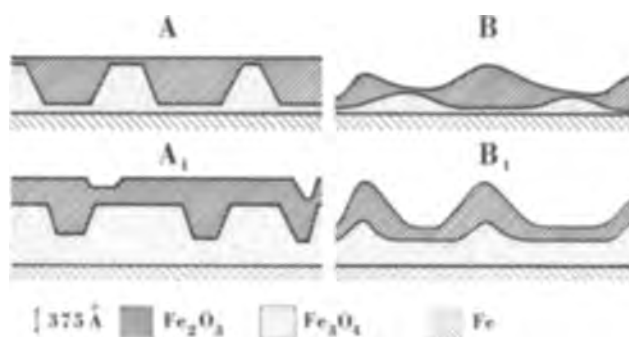


Fig. 7. Schematic of cross section through the oxides as deduced from electron micrographs, weight gains, and cathodic reduction. The  $\text{Fe}_2\text{O}_3$  layer is "cathodically reducible oxide" and would include the  $\gamma\text{-Fe}_2\text{O}_3$ . A,  $A_1$ , (001)<sub>4</sub> and 100 min; B,  $B_1$ , (112).

the uneven nature of the  $\text{Fe}_3\text{O}_4\text{-Fe}_2\text{O}_3$  boundaries renders a quantitative discussion of the diffusion rates fairly fruitless.

The cathodic reduction curves all show evidence of the presence of  $\gamma\text{-Fe}_2\text{O}_3$  as part of the "reducible oxide." This is probably not on the surface but is present at the  $\text{Fe}_3\text{O}_4\text{-Fe}_2\text{O}_3$  interface as an intermediate phase. The cathodic reduction observation is confirmed by the reflection electron diffraction. Strong spots characteristic of a cubic pattern are observed on the (001) crystal at the end of 4 min and are still discernible after 100 min of oxidation. In contrast to this no diffraction spots belonging to the cubic oxide are observed on the (112) crystal after 15 min of oxidation. This may be due to the outer layer of  $\alpha\text{-Fe}_2\text{O}_3$  on the (112) becoming too thick to allow penetration of the beam to the underlying  $\gamma\text{-Fe}_2\text{O}_3$  or to different shapes of the oxide surface on the two crystals. This difference in shape is observed by replica electron microscopy. The outer layer of oxide on the (001) is smooth, while that on the (112) has a ridgelike structure. The difference in shape of the outer layer results in a difference in penetration of the electron beam to the intermediate cubic oxide. (In the above discussion it should not be assumed that the  $\gamma\text{-Fe}_2\text{O}_3$  is a stoichiometric phase but rather something equivalent to  $\text{Fe}_{3-x}\text{O}_4$  which within some composition range has the electrochemical properties of  $\gamma\text{-Fe}_2\text{O}_3$ .)

The sharp turnover of the weight-gain time curves at around 5 min is probably related to the formation of a continuous outer layer of  $\alpha\text{-Fe}_2\text{O}_3$  of sufficient thickness to lead to a change from an oxidation rate which is controlled by cation diffusion in the cubic oxide to control by anion diffusion in the hexagonal

$\alpha\text{-Fe}_2\text{O}_3$ . As was noted in the results section both the initial and final rates of oxidation are higher on the (001) than on the (112) crystal. This may be related to two factors. First,  $\gamma\text{-Fe}_2\text{O}_3$  is a larger proportion of the reducible oxide on the (001) than on the (112). The  $\alpha\text{-Fe}_2\text{O}_3$  is therefore thinner and the final oxidation rate would be higher. The initially higher oxidation rate is related to the more difficult transformation of cubic oxide to hexagonal oxide on the (001) surface. This was also observed at lower temperatures. The second factor leading to a lowering of rate on the (112) surface is the separation which occurs at the metal-oxide interface. Cation diffusion from the metal surface outward is accompanied by vacancy diffusion toward the metal surface. If the vacancies condense to form voids at the metal surface, separation occurs between the metal and oxide. This has been observed by metallographic techniques for oxidation at higher temperatures (12). It would appear that vacancies can be destroyed at the metal-oxide interface more easily on the (001) crystal than on the (112) crystal. This may be related to the fit of the highly oriented oxide on the metal. The condensation of vacancies to form voids would decrease the oxidation rate by decreasing the effective area of the specimen for cation diffusion. The resultant lowering of the cation flow with the (112) crystal may also result in earlier formation of  $\alpha\text{-Fe}_2\text{O}_3$  as well as recrystallization of the outer  $\alpha\text{-Fe}_2\text{O}_3$  to form polycrystalline oxide. If the final rate of oxidation is controlled by the diffusion of oxygen through the outer  $\alpha\text{-Fe}_2\text{O}_3$ , then the decreased cation flow on the (112) crystal would lead to a smaller oxygen gradient in the oxide and a reduced final rate of oxidation.

The shapes of the  $\text{Fe}_3\text{O}_4\text{-Fe}_2\text{O}_3$  interface appear to be characteristic for the different orientations of underlying iron. Both Laukonis (9) and Boggs (10) have observed similar structures under slightly different conditions of oxidation. The cross-hatch structure of the magnetite surface on the (001) crystal may be related to the method of nucleation or growth of the outer  $\alpha\text{-Fe}_2\text{O}_3$ . Both oxides remain highly oriented even after 100 min of oxidation. The ridgelike structure of both the  $\text{Fe}_3\text{O}_4\text{-Fe}_2\text{O}_3$  interface and the  $\text{Fe}_2\text{O}_3$  surface may be related to the mechanism whereby stress is relieved in the growing oxide film.

With both orientations the combination of the shape of the phase boundaries and the different diffusion mechanisms in the two main oxides make it rather difficult or impossible to calculate diffusion coefficients with the data at hand. The attempt to measure cation diffusion in the magnetite layer by the annealing experiments was unsuccessful due to lack of reproducibility in the measurements.

#### Acknowledgment

The authors wish to thank Mr. E. G. Brewer for the electron microscopy.

Manuscript received May 11, 1967; revised manuscript received Sept. 7, 1967. This paper was presented at the Washington Meeting, Oct. 11-15, 1964 as Abstract No. 56.

Any discussion of this paper will appear in a Discussion Section to be published in the December 1968 JOURNAL.

#### REFERENCES

1. J. B. Wagner Jr., K. R. Lawless, and A. T. Gwathmey, *Trans. AIME*, **221**, 257 (1961).
2. R. F. Mehl and E. L. McCandless, *ibid.*, **25**, 531 (1937).
3. D. E. Davies, U. R. Evans, and J. N. Agar, *Proc. Roy. Soc.*, **A225**, 443 (1954).
4. E. J. Caule, *Corrosion Sci.*, **2**, 147 (1962).
5. E. J. Caule, K. H. Buob, and M. Cohen, *This Journal*, **108**, 829 (1961).
6. P. B. Sewell, C. D. Stockbridge, and M. Cohen, *Can. J. Chem.*, **37**, 1813 (1959).

7. H. G. Oswin and M. Cohen, *This Journal*, **104**, 9 (1957).  
 8. P. B. Sewell and M. Cohen, *ibid.*, **111**, 508 (1964).  
 9. J. V. Laukonis and R. J. Coleman, *J. Appl. Phys.*, **30**, 1364 (1959).  
 10. W. E. Boggs, R. H. Kachik, and G. E. Pellisier, *This Journal*, **112**, 539 (1965).  
 11. P. B. Sewell and M. Cohen, *ibid.*, **111**, 501 (1964).  
 12. D. Caplan and M. Cohen, *Corrosion Sci.*, **6**, 321 (1966).

## The Nucleation, Growth, and Structure of Thin Ni-P Films

J. P. Marton and M. Schlesinger

Department of Physics, University of Western Ontario, London, Ontario, Canada

### ABSTRACT

The nucleation, early growth, and structure of Ni-P on SnCl<sub>2</sub>-PdCl<sub>2</sub> activated dielectric substrates were studied. The SnCl<sub>2</sub>-PdCl<sub>2</sub> treatment was found to provide small catalytic sites on the substrate, serving as the nuclei for Ni-P growth. The average diameter of catalytic sites was estimated to be less than 10Å. The microscopic time rate of Ni-P growth on the nuclei was found to be constant and the growth to be isotropic. The resulting Ni-P deposit in the early stages of growth consists of circular islands. The surface density  $\sigma$  of islands were affected by activation. In later stages of growth, the circular Ni-P islands merged to form a continuous film. The critical film thickness at which continuity is attained is shown to be a function of  $\sigma$ . The structure of as-deposited islands, as well as that of fresh continuous film, was determined by electron diffraction to be liquidlike.

Electroless deposition of nickel on catalytic surfaces due to Brenner and Riddell (1) is well documented (1-4). The chemistry of deposition (4) and some physical properties of electroless nickel (4-6) have been reported. Deposition on dielectric (noncatalytic) surfaces has also been demonstrated (1, 2, 7). A dielectric substrate may be activated (8) by immersion in solutions of SnCl<sub>2</sub> and PdCl<sub>2</sub> for electroless nickel deposition.

Deposits from a number of electroless solutions have been determined (4) to consist of Ni and P, with 2%  $\leq P \leq 12\%$  by weight. Fresh bulk deposits were stated to have either amorphous liquidlike (5) or fine polycrystalline (6) structures. Fresh film deposits were found (9) to be in a liquidlike state. The growth and film geometry of fresh Ni-P deposits have not been reported. Other electroless films (Co-P and Ni-Fe-P) deposited on activated substrates exhibit island-type growth and agglomerated structure. Judge *et al.* (10) found a "hemispherical clumpy growth" of electroless cobalt, and the surface of electroless nickel-iron films was reported by Schmeckenbecher (11) to consist of an "agglomeration of balls." Frieze and Weil (12) reported that nucleation of electroless Co-P films occurred on isolated Pd particles, followed by lateral growth to produce a continuous film.

In our work the nucleation, growth, and structure of electroless Ni-P films on activated substrates were studied. The geometry of films at various stages of growth was determined by transmission electron microscopy and the structure by transmission electron diffraction. Activation of substrates by SnCl<sub>2</sub>-PdCl<sub>2</sub> method results in an island-type growth of Ni-P in the early stage, becoming continuous as the growth proceeds. The surface density of islands and the maximum size of islands varied with the method of activation and the wetting property of substrate surfaces. The structure of individual islands, ranging in size from 200 to 2000Å as well as that of continuous thin films (9), was found to be liquidlike.

### Experimental

Clean substrates of glass, quartz, mica, and Formvar were activated by immersion in activating solutions at room temperature. The variations in activation of

the substrates are shown in Table I. Activated substrates were immersed in electroless nickel solution for Ni-P deposition. The composition of solutions is listed in Table II. Film geometry was not affected by variations in the composition, pH, and temperature of electroless solutions; therefore only one solution of pH = 5.3 was used. Deposition temperature was adjusted to 25° ± 0.5°C, and the time of deposition was varied.

Ni-P was also deposited from the solution on electropolished solid nickel substrates and on microscope slides coated with pure nickel and palladium by vacuum evaporation. These deposits were compared with those grown on SnCl<sub>2</sub>-PdCl<sub>2</sub> activated substrates.

The mass thickness and average thickness of films was determined by weighing and by the Tolansky method (13), respectively. Deposits were prepared for electron microscopy three ways. Self-supporting Ni-P films were floated off the substrates for direct transmission and diffraction measurements; discontinuous deposits were backed by Formvar and then floated off the substrates; shadowed replicas of the surface of deposits were made. Deposits grown on

Table I. Variations in activation of substrates

Method (a)	Dip clean substrates in activating solutions listed in Table II in succession.
Method (b)	Dip clean substrates as in (a) in activating solutions modified by the addition of 10 cc/l isopropyl alcohol.
Method (c)	Dip clean substrates as in (a) in activating solutions modified by the addition of 5 cc/l Kodak "Photo-Flo."

Table II. Composition of solutions used in the experiments

Activating solutions		Electroless solution	
SnCl <sub>2</sub> solution	SnCl <sub>2</sub> 0.1 g/l HCl 0.1 cc/l	Nickel sulphate Sodium hypophosphite Sodium succinate Succinic acid	29 g/l 17 g/l 15 g/l 1.3 g/l
Rinse:	H <sub>2</sub> O at pH = 7	Solution pH	5.3
PdCl <sub>2</sub> solution	PdCl <sub>2</sub> 0.1 g/l HCl 0.1 cc/l	Solution temperature	25°C
Rinse:	H <sub>2</sub> O at pH = 7		

Formvar substrates were left on the substrates and were examined directly.

For transmission and diffraction measurements, a Philips EM75C and an AEI EM6G microscope was used respectively. Both microscopes were operated at 75 kv.

### Results and Discussion

**Nucleation and growth.**—The deposition of Ni-P on all substrates activated by method (a) in Table I, was found to be selective. Deposition appeared to start at certain points on the substrate and continue at those points only. As deposition progressed, islands formed on these nucleation points. If deposition was allowed to proceed, the islands grew in size and eventually merged to form a continuous film. Figure 1 is the transmission image of a typical deposit. Parts of the deposit are islands, other parts are already continuous. In contrast with the island-type growth, deposits that were formed on nickel substrates and on nickel and palladium coated microscope slides were homogeneous and showed no island structure. The image of a shadowed surface replica of such a deposit is reproduced in Fig. 2.

These findings show that the surface of a  $\text{SnCl}_2$ - $\text{PdCl}_2$  treated dielectric substrate is not completely activated. The activation is visualized to produce small catalytic sites dispersed on the surface, serving as the nuclei for Ni-P deposition. The sites are estimated to be less than  $30\text{\AA}$  in diameter, as they cannot be detected in the electron microscope having a point resolution of  $30\text{\AA}$ . A closer estimate of size of the catalytic sites was made indirectly. The diameter  $2r$  of the growing Ni-P islands was measured and was plotted against deposition time. This is shown in Fig. 3. The diameter of catalytic sites was estimated by extrapolation (dotted line), to be less than  $10\text{\AA}$ .

Again from Fig. 3, the microscopic time rate of Ni-P growth  $c$  ( $= dr/dt$ ) is seen to be constant. Also, the geometry of growing islands was observed to be circular in all deposits. These findings imply isotropic growth, and one expects the islands to be half spheres situated base down on the substrate. The circular geometry is shown in Fig. 4 for islands ranging in size from  $200$  to  $2000\text{\AA}$ .

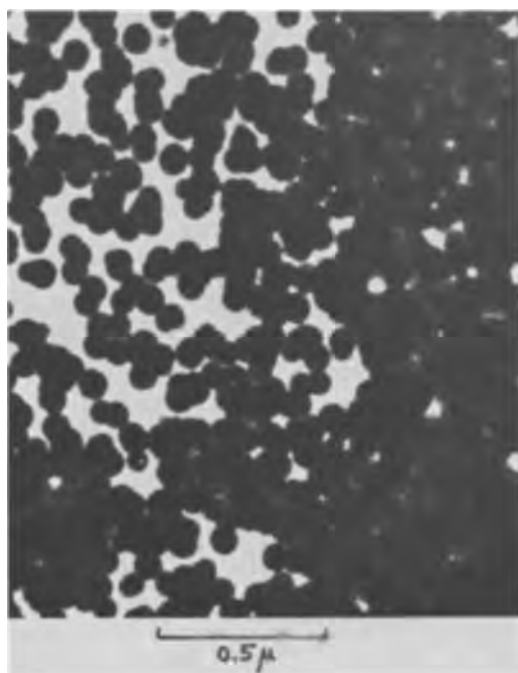


Fig. 1. Electron transmission image of a typical Ni-P deposit on  $\text{SnCl}_2$ - $\text{PdCl}_2$  activated substrate. Parts of the deposit are islands, other parts are continuous.

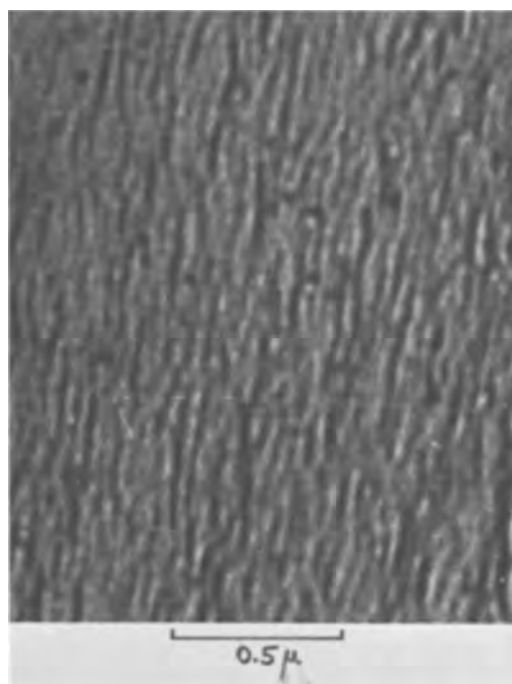


Fig. 2. Shadowed surface replica of a Ni-P deposit on a solid nickel substrate. Note the absence of islands.

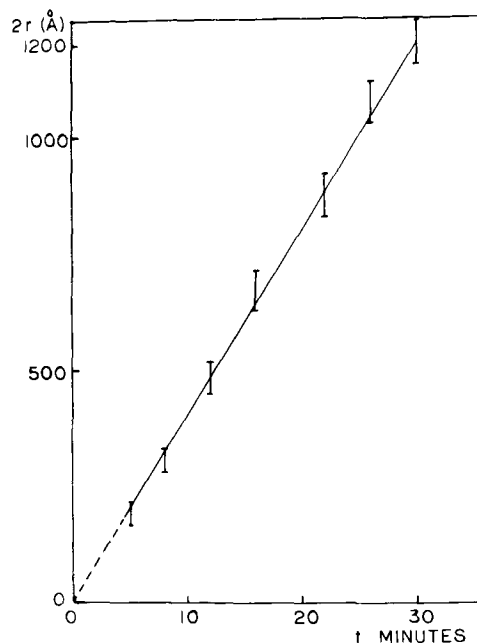


Fig. 3. Plot of diameter  $2r$  of the growing Ni-P islands against time of deposition. Rate of growth  $c = dr/dt$  is constant. Extrapolation (dashed line) at  $t = 0$  gives average size of active sites to be less than  $10\text{\AA}$ .

The number of activation sites per unit surface area  $\sigma$  was found different for different substrates. The value of  $\sigma$  ranged from  $10/\mu^2$  to  $10^4/\mu^2$ . The value of  $\sigma$  was large on substrates with hydrophilic surfaces (i.e., glass), and small on those with hydrophobic surfaces (i.e., Formvar). This is shown in Fig. 5. Figure 5a is the transmission image of sites on glass, and Fig. 5b is the image of sites on Formvar. The respective average values of  $\sigma$  are  $10^4/\mu^2$  and  $10^2/\mu^2$ . It was found possible to decrease the difference in  $\sigma$  between hydrophilic and hydrophobic surfaces by activation method (b) in Table I and to eliminate it by method (c) in Table I. In both cases the small  $\sigma$  increased and the large  $\sigma$  remained constant. Attempts to increase the value of  $\sigma$  beyond  $10^4/\mu^2$  have failed.

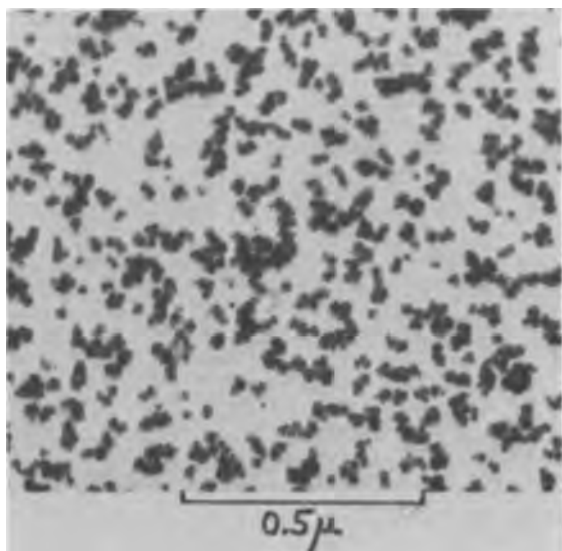


Fig. 4. Circular transmission images of islands ranging in size from 200 to 2000Å in four different deposits (a, b, c, d). The islands are visualized to be half spheres situated "base down" on the substrate in all deposits. Fig. 4a. Island size 200Å.

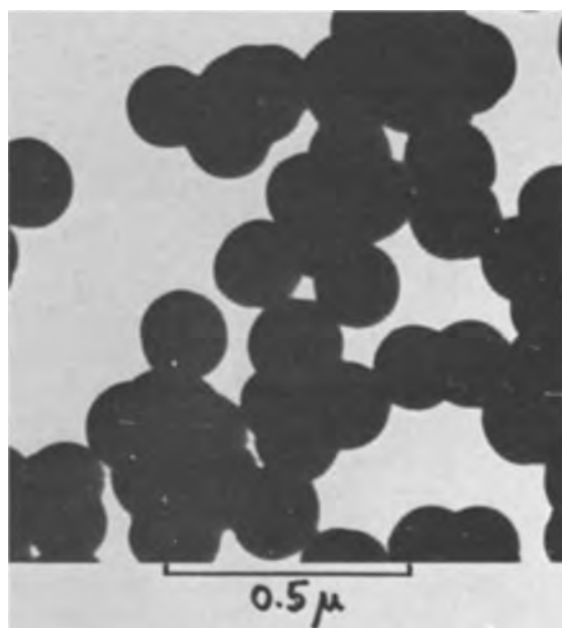


Fig. 4d. Island size 2000Å

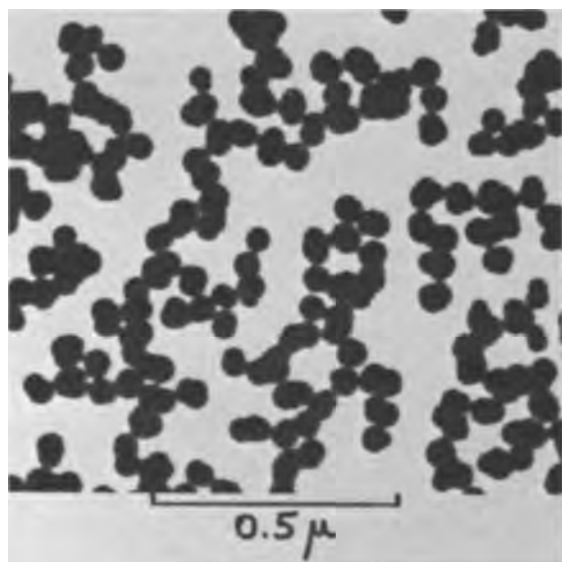


Fig. 4b. Island size 600Å

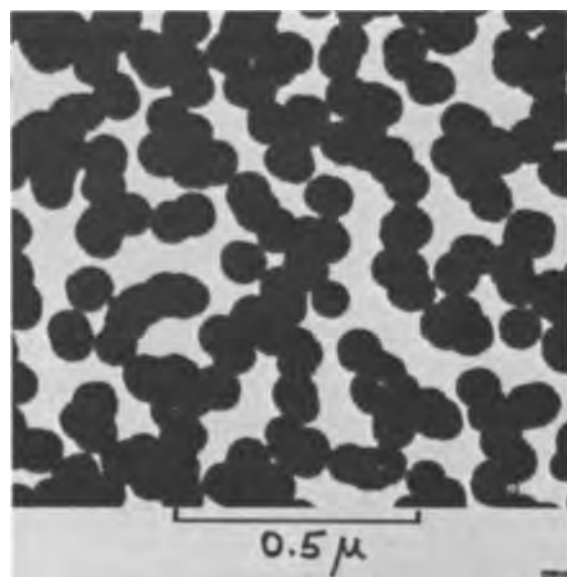


Fig. 4c. Island size 1000Å

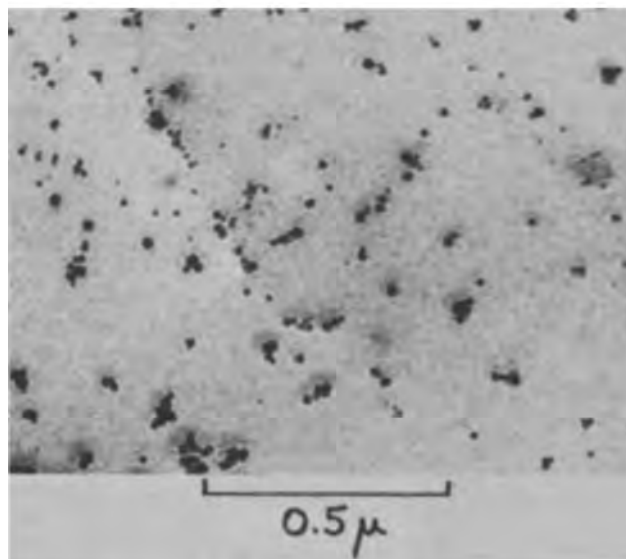
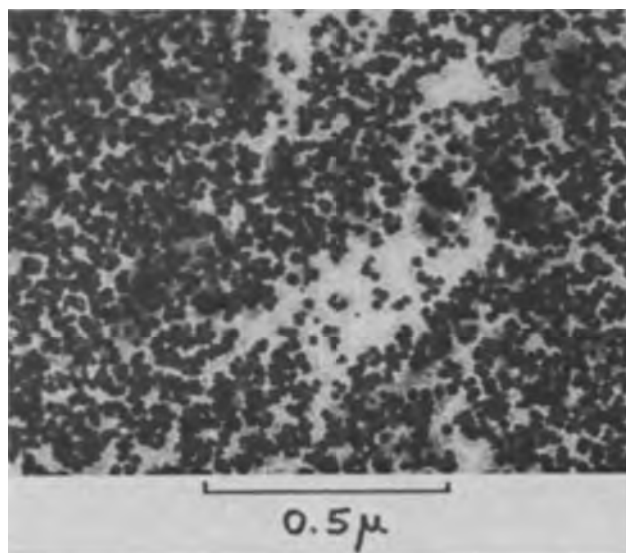


Fig. 5. Transmission images of active sites on (a) (top) glass, and (b) (bottom) Formvar substrates made visible by a slight deposit of Ni-P on them. The surface density of sites is  $10^4/\mu^2$  for glass and  $10^2/\mu^2$  for Formvar.



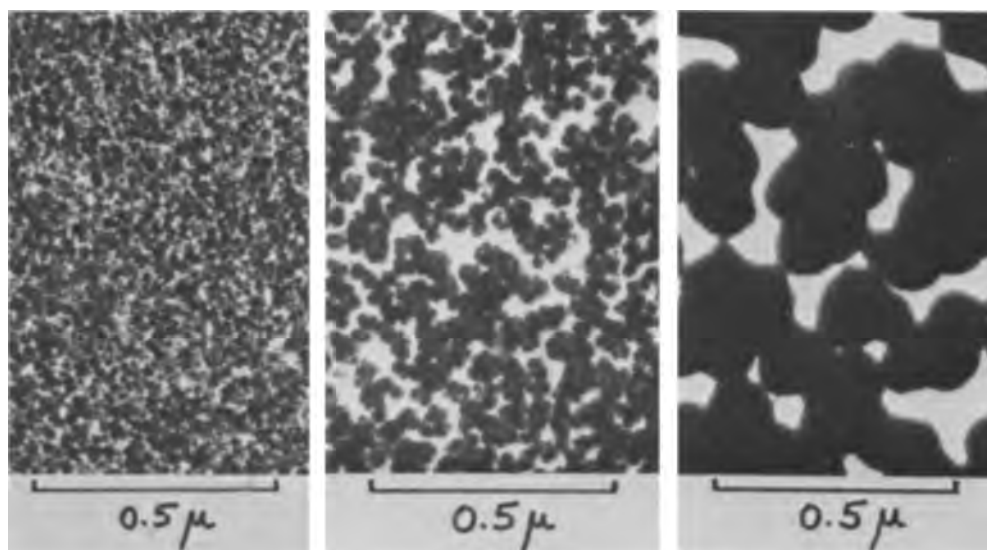


Fig. 6. Transmission images of deposits on substrates with different activation densities: (a) (left)  $10^4/\mu^2$ ; (b) (center)  $10^3/\mu^2$  and (c) (right)  $10^2/\mu^2$ . Note the dependence of film geometry on activation density.

**Film geometry.**—The natural consequence of the variation of  $\sigma$  is a variation in Ni-P film geometry. This is shown in Fig. 6 by the transmission image of three different deposits. The films were deposited on substrates with average  $\sigma$  values of  $10^4/\mu^2$  (Fig. 6a);  $10^3/\mu^2$  (Fig. 6b) and  $10^2/\mu^2$  (Fig. 6c). From the figure it is evident that  $\sigma$  is an important deposition parameter. The quantitative dependence of film growth and geometry on  $\sigma$  may be expressed<sup>1</sup> as

$$d = 2\pi\sigma ct \left( r_0^2 + r_0 ct + \frac{1}{3} c^2 t^2 \right); \quad 0 \leq t \leq (c\sqrt{\sigma\pi})^{-1} \quad [1]$$

and

$$d = 2r_0 (1 + r_0\sqrt{\sigma\pi}) - \frac{1}{3\sqrt{\sigma\pi}} + ct; \quad t \geq (c\sqrt{\sigma\pi})^{-1} \quad [2]$$

where  $d$  is the mass thickness of deposit (volume per unit surface area);  $c$  is the microscopic rate of deposition (increase of local thickness per unit time and/or  $dr/dt$ );  $\sigma$  is the activation surface density (number of active sites per unit surface area);  $2r_0$  is the diameter of active sites; and  $t$  is the time of deposition. Expression [1] describes the growth of discontinuous (island-type) films and the description of growth after continuity is attained is given by expression [2]. Transition from the former to the latter configuration occurs at  $t = (c\sqrt{\sigma\pi})^{-1}$ .

Figure 7a is the plot of expressions [1] and [2] at  $r_0 = 5\text{\AA}$ .<sup>2</sup> The dashed line represents the transition between discontinuous films (below dashed line) and continuous films (above dashed line) and the solid straight line represents a linear ( $d = ct$ ) film growth. In Fig. 7b a comparison is made between the mass thickness of growing deposits and the theoretical curves. Both solid Ni and  $\text{SnCl}_2\text{-PdCl}_2$  activated substrates were used. With  $c = 20 \text{\AA}/\text{min}$   $\sigma$  was found to range between  $10^4/\mu^2$  and  $10/\mu^2$  for the activated substrates.

**"As-deposited" structure.**—The crystal structure of fresh Ni-P deposits has been investigated in the past with somewhat conflicting results. Goldenstein *et al.* (5) determined amorphous liquidlike structure for bulk deposits by x-ray diffraction, and Graham and co-workers (6) found fresh bulk deposits to be polycrystalline by electron diffraction. The present authors (9) showed that continuous, as-deposited thin films of Ni-P are in a liquidlike state. In that work

<sup>1</sup> See Appendix.

<sup>2</sup> The variation of  $r_0$  does not influence the curves appreciably, as  $r_0$  is much smaller than  $ct$  in the range of  $ct$  considered here.

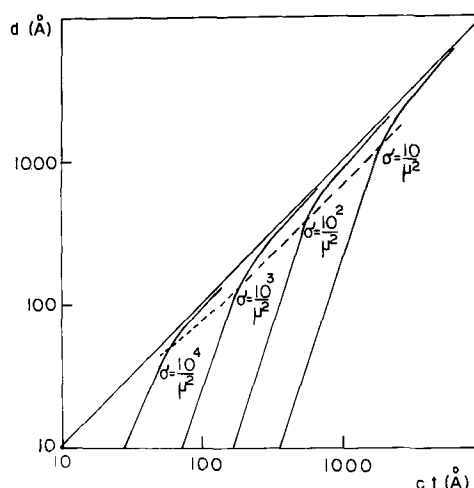


Fig. 7a. Mass thickness  $d$  of Ni-P deposits. Theoretical curves of  $d$  as a function of  $ct$  ( $c$  is rate of deposition,  $t$  is deposition time) for different activation densities  $\sigma$ . Dashed line represents transition between islands and continuous film.

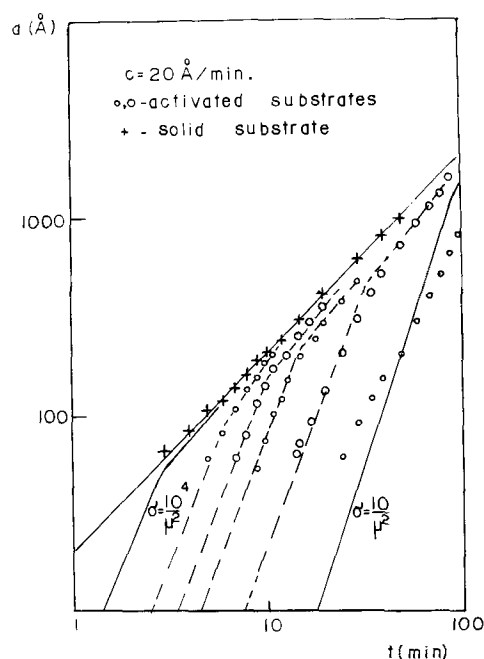


Fig. 7b. Mass thickness  $d$  of Ni-P deposits. Comparison of theoretical curves (a) and experimental values for  $c = 20 \text{\AA}/\text{min}$ . Activation density is seen to range between  $10^4/\mu^2$  and  $10/\mu^2$ .



(9) the temperature dependence of the structure of continuous films was investigated. In the present work the structural nature of as-deposited islands, ranging in size from 200 to 2000Å, as well as that of fresh continuous films of various geometry were studied.

It can be argued that, if the islands in films are single crystals, but are too small to cause proper diffraction, then the same islands grown larger would eventually reveal their crystal identity. If, however, the islands were in a liquidlike state, no size dependency should be detected in the diffraction pattern. From selected area diffraction experiments the latter case was confirmed. Islands whose size ( $2r \approx 2000\text{Å}$ ) was comparable to the effective diameter of the electron beam (8000Å) showed an identical liquidlike structure to those with 200Å diameter. The diffraction pattern of continuous films was also the same. Figure 8 is an example of the diffraction pattern of all our (thin) Ni-P deposits.

The present findings of a liquidlike structure is in apparent contradiction with the results of Graham *et al.* (6); however the difference may be explained by the difference in sample preparation. In their experiments (bulk) deposits were prepared at 90°C for many hours, whereas our (thin) samples were grown at 25°C for only a few minutes.

### Summary

It was shown that electroless deposition of Ni-P on  $\text{SnCl}_2\text{-PdCl}_2$  activated dielectric substrates is selective and that it is homogeneous on continuous catalytic surfaces. The selective deposition is due to selective activation. The  $\text{SnCl}_2\text{-PdCl}_2$  treatment produces catalytic sites on the substrate with less than 10Å diameter. The growth of Ni-P on these sites is isotropic, resulting in a spherical island-type film geometry. The surface density of catalytic sites  $\sigma$  was seen to depend on the substrate material and type of activation, with a maximum value of  $10^4/\mu^2$ . The importance of  $\sigma$  as a deposition parameter was pointed out, and its influence on film growth and geometry was shown quantitatively. Evidence of island growth of different electroless metals (10-12) suggests that the present description of nucleation, growth, and geometry may also be applicable to other electroless films deposited on activated surfaces. The structure of as-deposited Ni-P islands with variable size, as well as that of fresh continuous films, was determined to be liquidlike, and it was concluded that individual islands are not single crystals. Finally, it was suggested that different results on the structure of fresh deposits reported by other workers may have been due to differences in sample preparation.

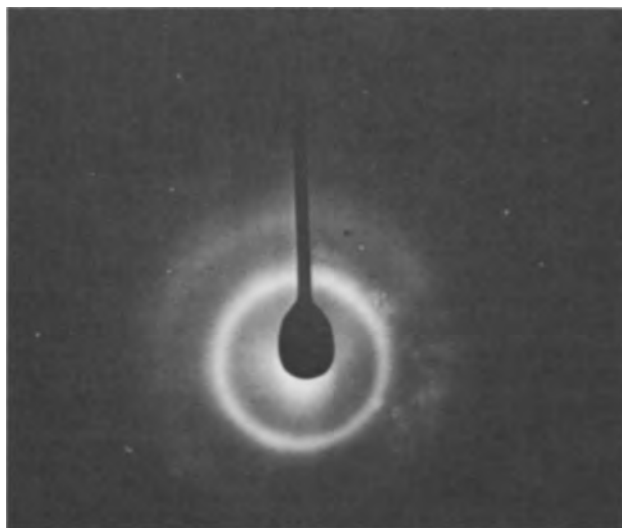


Fig. 8. Typical diffraction pattern of as-deposited Ni-P islands, and fresh thin Ni-P films (P content of 5 w/o).

### Acknowledgments

The authors wish to acknowledge the valuable assistance of Dr. J. Brown in the diffraction experiments.

The present work is part of a Ph.D. Thesis to be submitted by J. P. Marton to the Graduate Faculty of the University of Western Ontario. Work was supported in part by a Defence Research Board of Canada Grant to Welwyn Canada Limited, London, Ontario, Canada.

Manuscript received July 26, 1967; revised manuscript received Oct. 12, 1967.

Any discussion of this paper will appear in a Discussion Section to be published in the December 1968 JOURNAL.

### REFERENCES

1. A. Brenner and G. E. Riddell, *J. Research Natl. Bur. Standards*, **37**, 31 (1946); **39**, 385, (1947).
2. G. Gutzeit, W. J. Crehan, and A. Krieg, U.K. Pat. 761,556.
3. A. Brenner, *Metal Finishing*, **52**, 68 (1954).
4. A.S.T.M. Special Technical Publication No. 265 (1959).
5. A. W. Goldenstein, W. Rostoker, F. Schosberger, and G. Gutzeit, *This Journal*, **104**, 104 (1957).
6. A. H. Graham, R. W. Lindsay, and H. J. Read, *ibid.*, **112**, 401 (1965).
7. P. Baeyens (Philips Electrical Industries), U.K. Pat. 749,824.
8. E. A. Bergstrom, U.S. Pat. 2,702,253.
9. M. Schlesinger and J. P. Marton *J. Phys. Chem. Solids*, To be published.
10. J. S. Judge, J. R. Morrison, D. E. Speliotis, and G. Bate, *This Journal*, **112**, 681 (1965).
11. A. F. Schmeckenbecher, *ibid.*, **113**, 778 (1966).
12. A. S. Frieze and R. Weil, Sixth International Conference for Electron Microscopy, Kyoto (1966) p. 533.
13. S. Tolansky, "Multiple Beam Interferometry of Surfaces and Films," Clarendon Press, Oxford (1948).

### APPENDIX

Assume that the small catalytic sites are half spheres with radius  $r_0$ , situated "base-down" on the substrate. Let  $\sigma$  be the number of active half spheres per unit substrate area. Assume that the Ni-P deposition parameters (solution concentration and temperature) are constant in time, and that the density of Ni-P deposit  $\rho$  is constant. Let  $m$  be the mass of the deposit on each active island, and  $r$  be the radius of the growing half sphere. Then  $m = 2/3 \pi (r^3 - r_0^3) \rho$ , and the time rate of change of  $m$  is

$$\frac{dm}{dt} = \frac{dm}{dr} \frac{dr}{dt} = 2\pi\rho r^2 \frac{dr}{dt}$$

Since  $dr/dt = c$ , (c.f. Fig. 3), and  $r = r_0 + ct$  we get

$$dm = 2\pi\rho c (r_0 + ct)^2 dt$$

After integration

$$m = 2\pi\rho ct [r_0^2 + r_0ct + (1/3) c^2t^2]$$

Assuming an average value of  $\sigma$  on the substrate, the total mass  $M$  on the substrate with surface area  $A$  is

$$M = A\sigma 2\pi\rho ct [r_0^2 + r_0ct + (1/3) c^2t^2]$$

With the definition of the mass thickness  $d = M/A\rho$  we get

$$d(t) = 2\pi\sigma ct [r_0^2 + r_0ct + (1/3) c^2t^2] \quad [1]$$

Further assume the islands to form a close packed surface distribution on the substrate. In this configuration each island may occupy a maximum surface area of  $\sigma^{-1}$ . As the islands grow in time the base of each island spreads in the available surface area of  $\sigma^{-1}$ . After a time  $t_0$  the islands touch and begin to form a continuous film whose surface retains the hemispherical features of the islands. At time,  $t_0$ , the area of the base of each hemisphere,  $\pi r^2 \approx \sigma^{-1}$  for large values of  $\sigma$ . Since  $r = r_0 + ct$ ,  $t_0 \approx (c\sqrt{\sigma\pi})^{-1}$  for

small values of  $r_0$ . Relation [1] is therefore valid for times  $0 \leq t \leq (c\sqrt{\sigma\pi})^{-1}$ . For times longer than  $t_0$  the now-continuous film is visualized to grow at a constant macroscopic rate. This growth may be described by

$$d(t) = d(t_0) + c(t-t_0) = 2r_0(1 + r_0\sqrt{\sigma\pi}) - \frac{1}{3\sqrt{\sigma\pi}} + ct \quad [2]$$

$d(t_0)$  having been evaluated by setting  $t = t_0 = (c\sqrt{\sigma\pi})^{-1}$  in Eq. [1]. Combining [1] and [2] the final expression is

$$d(t) = \begin{cases} 2\pi\sigma ct [r_0^2 + r_0ct + (1/3)c^2t^2]; & 0 \leq t < (c\sqrt{\sigma\pi})^{-1} \\ 2r_0(1 + r_0\sqrt{\sigma\pi}) - \frac{1}{3\sqrt{\sigma\pi}} + ct; & t > (c\sqrt{\sigma\pi})^{-1} \end{cases}$$

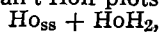
## The Holmium-Hydrogen System

F. C. Perkins and C. E. Lundin

*Metallurgy Division, Denver Research Institute, University of Denver, Denver, Colorado*

### ABSTRACT

Pressure-temperature-composition data were obtained to study the nature of the holmium-hydrogen system. A Sieverts-type apparatus was employed to perform measurements in the temperature range, 250°-950°C, in the composition range, Ho to HoH<sub>3</sub>, and at pressures from 10<sup>-4</sup> to 630 Torr. The existence of three homogeneous phases was established: holmium solid solution, the dihydride, and the trihydride phases. The limits of hydrogen solid solution in each of the phases were determined from discontinuities in the isothermal plots. Equilibrium plateau decomposition relationships were determined from van't Hoff plots in the two-phase regions



$$\log_{10} p \text{ (Torr)} = -\frac{11,520 \pm 50}{T} + 10.66 \pm 0.05$$



$$\log_{10} p \text{ (Torr)} = -\frac{4080 \pm 50}{T} + 9.12 \pm 0.09$$

The differential heats of reaction in these two regions are,  $\Delta H = -52.7 \pm 0.2$  kcal/mole of H<sub>2</sub> and  $\Delta H = -18.7 \pm 0.2$  kcal/mole of H<sub>2</sub>, respectively. The differential entropies of reaction are,  $\Delta S = -35.6 \pm 0.2$  cal/deg · mole of H<sub>2</sub> and  $\Delta S = -28.6 \pm 0.4$  cal/deg · mole of H<sub>2</sub>, respectively. Relative partial molal and integral thermodynamic quantities were calculated for the system.

The dissociation pressure equation for the holmium solid solution dideuteride plateau region was determined for comparison purposes

$$\log_{10} p \text{ (Torr)} = -\frac{11,420 \pm 60}{T} + 10.70 \pm 0.06$$

The enthalpy of reaction to form the dideuteride phase is  $\Delta H = -52.3 \pm 0.3$  kcal/mole of D<sub>2</sub>, and the entropy of reaction is  $\Delta S = -35.8 \pm 0.3$  cal/deg · mole of D<sub>2</sub>.

Rare-earth metals are characterized by the ability to absorb large quantities of hydrogen and to combine with hydrogen to form hydride phases. Previous investigations concerned with the heavy rare-earth metals at this laboratory defined the systems, erbium-hydrogen (1) and erbium-deuterium (2). The interest in these systems embraced the holmium-hydrogen system as well, because this latter system would be expected from chemical considerations to exhibit hydride phases with characteristics and thermal stabilities similar to the erbium hydrides.

The properties of the rare-earth-metal hydrogen systems have been reviewed in the literature (3-5). The holmium-hydrogen system has been outlined in one previous investigation (6). The present study was undertaken to broaden the temperature and compositional ranges of the above work and to extend the limits of thermodynamic data available for this system.

### Experimental Procedure

The experiments were conducted in a modified Sieverts apparatus. The unit incorporated a mercury diffusion pump for evacuation and a manifold to which were connected a palladium-silver hydrogen thimble,

a gas burette, a mercury manometer, a McLeod gauge (Kontes Glass Company) and a quartz reaction tube for heating to temperatures up to 950°C. High-purity hydrogen was obtained by passing hydrogen through the heated palladium-silver thimble. The 100-ml, precision gas burette was graduated to 0.1 ml divisions. Gas pressures were measured on the manometer to  $\pm 0.5$  Torr and in the McLeod gauge range (10<sup>-4</sup> to 1 Torr) to  $\pm 3\%$ . The quartz reaction tube was heated by a nichrome-wound furnace controlled to a temperature cycle of  $\pm 1^\circ\text{C}$ . Specimen temperatures in the quartz tube were measured independently by means of a chromel-alumel thermocouple located outside and adjacent to the tube at the vicinity of the specimen.

The specimen material was nuclear-grade holmium sponge, 99.9% purity, obtained from the Lunex Company. The large surface area of the sponge and the short diffusion paths permitted the attaining of equilibrium in relatively short periods of time. The typical specimen size was 0.3g.

The specimen of holmium sponge was contained in a tungsten foil boat to prevent contact with the quartz tube. At the beginning of each experiment, the system

with specimen in place was evacuated to less than  $10^{-6}$  Torr and flushed several times with high-purity hydrogen, and finally evacuated again ready for the first gas addition. The specimen was then heated under vacuum to the desired temperature and exposed to a measured batch of hydrogen. After equilibrium was attained (usually in a few hours) the pressure was measured, and the hydrogen composition of the specimen calculated. Successive batches of hydrogen were added until atmospheric pressure was reached. These data were then plotted as an isothermal curve of specimen composition (hydrogen-to-holmium atomic ratio) vs. pressure. Other isotherms were developed in the same manner. Compositions are estimated to be accurate to  $\pm 1\%$ . Preliminary experiments indicated that absorption of hydrogen by the specimen during flushing at room temperature was insignificant and did not change the specimen compositions beyond the limits of error.

The partial-pressure plateaus were determined by cycling suitably hydrided specimens through the temperature ranges of interest. At each temperature, time was permitted for equilibrium to be attained, and the pressure was recorded. The temperatures were cycled both up and down to detect nonequilibrium effects. The logarithm of pressure was plotted against the reciprocal absolute temperature, and the data were treated by a least squares computer analysis to obtain a mathematical van't Hoff relationship.

### Results and Discussion

The holmium-hydrogen system resembles the erbium-hydrogen system, which confirms the tendency for most heavy rare-earth metals to form isomorphous systems when combined with hydrogen. As hydrogen is reacted with holmium the gas is dissolved interstitially in the hexagonal close-packed lattice. On reaching saturation, additional hydrogen reacts with holmium to form the face-centered-cubic, holmium dihydride phase (lattice parameter  $a_0 = 5.165\text{\AA}$ ) (7). A further addition of hydrogen produces the holmium trihydride phase, which has a hexagonal lattice with parameters  $a_0 = 6.308\text{\AA}$ ,  $c_0 = 6.560\text{\AA}$  (8). The dihydride and trihydride phases are not stoichiometric, but exhibit compositional ranges of hydrogen solubility which broaden at high temperatures. The trihydride phase is stable only at relatively low temperatures, tending to decompose to the dihydride at temperatures above  $370^\circ\text{C}$  at atmospheric pressure.

Isothermal curves for the holmium solid solution-dihydride composition range are presented in Fig. 1, and a similar plot for the dihydride-trihydride range is presented in Fig. 2. More than 500 individual data points are represented by these curves. The points are not shown because of the small scale of the plot and the many points involved.

The isotherms can be correlated to the phases and solubility relationships of the holmium-hydrogen phase diagram. For example, as hydrogen initially is taken into solid solution in the holmium metal the gas pressure increases. As the metal becomes saturated, additional hydrogen initiates the formation of the dihydride phase, and the pressure remains constant in the two-phase region. This behavior is in accordance with the phase rule, which dictates that the appearance of a new phase is accompanied by the loss of one degree of freedom. Constant-pressure plateaus were observed at all temperatures investigated. Additions of hydrogen advancing the composition into the single phase dihydride region produce another increase in pressure. Experimental error accounts for the apparent crossing of some isothermal curves in this region. A second two-phase plateau region (Fig. 2) is observed between the dihydride and trihydride single-phase regions at lower temperatures. It is therefore seen that the extremities of the horizontal plateau lines demark the transitions in number

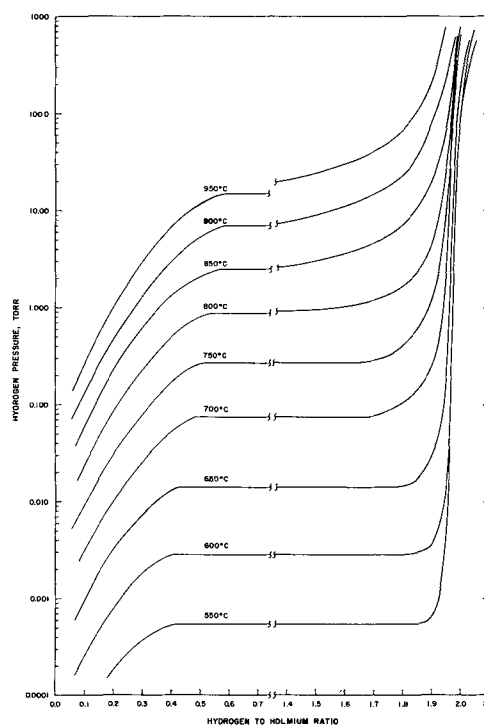


Fig. 1. Family of isotherms in the solid solution-dihydride region of the holmium-hydrogen system.

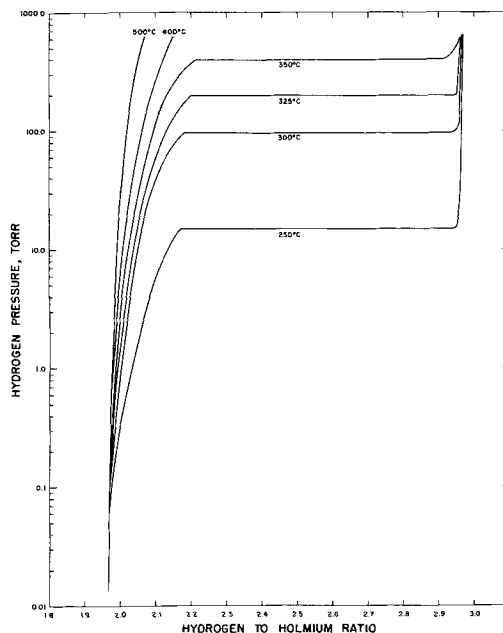


Fig. 2. Family of isotherms in the dihydride-trihydride region of the holmium-hydrogen system.

of phases and indicate the compositional solid solution limits of hydrogen in the three phases. The solubility limits of the holmium-hydrogen system are listed in Table I.

A log-log plot of composition vs. pressure for the various isotherms in the holmium solid solution region yielded straight lines with slopes approximating 2. This value confirms the validity of Sieverts' law for hydrogen in holmium. Sieverts' law states that the solubility of a diatomic gas in a metal is proportional to the square root of the pressure, implying that the gas is dissolved atomically in the metal.

A total of 78 independent determinations were made to establish dissociation pressures in the metal solid solution-dihydride plateau region as a function of temperature. Specimens were hydrided to 1.0 H/Ho ratio and cycled to temperatures between  $550^\circ$  and  $900^\circ\text{C}$ . Hysteresis effects were absent. The data were treated

Table I. Solubility boundaries in the Ho-H system

Temp, °C	Two-phase region Ho + HoH <sub>2</sub>		Two-phase region HoH <sub>2</sub> + HoH <sub>3</sub>	
	H/Ho	H/Ho	H/Ho	H/Ho
950	0.59	1.20	—	Not stable
900	0.58	1.30	—	Not stable
850	0.56	1.40	—	Not stable
800	0.53	1.50	—	Not stable
750	0.51	1.65	—	Not stable
700	0.48	1.65	—	Not stable
650	0.43	1.80	—	Not stable
600	0.40	1.85	—	Not stable
550	0.40	1.85	—	Not stable
350	—	—	2.21	2.91
325	—	—	2.20	2.95
300	—	—	2.19	2.95
250	—	—	2.17	2.95

by a least-squares computer analysis to describe the best straight line, and the following equation was obtained

$$\log_{10} p \text{ (Torr)} = -\frac{11,520 \pm 50}{T} + 10.66 \pm 0.05$$

where  $p$  = equilibrium hydrogen pressure and  $T$  = absolute temperature, Kelvin.

The plot of the log of plateau equilibrium pressure vs. reciprocal temperature is illustrated in Fig. 3. The slope of the line is related to the enthalpy of the reaction across the plateau region, and the intercept is related to the entropy of the reaction. The values for this plateau region are  $\Delta H = -52.7 \pm 0.2$  kcal/mole of H<sub>2</sub> and  $\Delta S = -35.6 \pm 0.2$  cal/deg · mole of H<sub>2</sub>.

Dissociation pressures of the holmium solid solution-deuteride plateau region were also determined over the same temperature range to detect differences, if any, caused by the isotopic effect. The procedure was the same as described, except deuterium was substituted for the hydrogen. A total of 57 equilibrium pressure points were employed in the least squares analysis, and the resulting equation is presented here

$$\log_{10} p \text{ (Torr)} = -\frac{11,420 \pm 60}{T} + 10.70 \pm 0.06$$

The enthalpy of reaction to form the dideride phase is  $\Delta H = -52.3 \pm 0.3$  kcal/mole of D<sub>2</sub>, and the entropy of reaction is  $\Delta S = -35.8 \pm 0.3$  cal/deg · mole of D<sub>2</sub>. The dissociation pressures for the deuterium plateaus are consistently higher than for the hydrogen system (see the deuterium plateau pressures plotted in Fig. 3). The entropy of reaction for the HoD<sub>2</sub> is slightly more negative than the entropy of reaction for HoH<sub>2</sub>, which is in the right direction on the basis of theoretical considerations (2).

A similar procedure was employed for the analysis of the dihydride-trihydride plateau region. In this in-

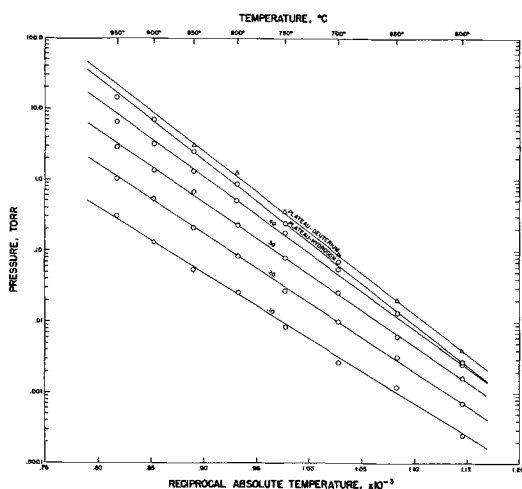


Fig. 3. Family of isopleths in the holmium-hydrogen system (included is the plateau isopleth of the holmium-deuterium system).

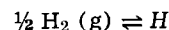
stance a total of 54 equilibrium pressures were obtained at temperatures between 200° and 350°C. The specimens were initially hydrided to a 2.8 H/Ho composition because the high equilibrium pressures above 300°C depleted the specimen of hydrogen. Specimens not containing an initial excess of hydrogen transformed completely to the dihydride phase at the higher temperatures. Long periods of time were required in order to attain equilibrium at each temperature. In general, the pressure values obtained on heating the specimen to the desired temperature were more reproducible than those obtained by cooling from a higher temperature. The pressures obtained by cooling were erratic and high. A plot of the log of plateau pressure vs. reciprocal temperature was made, and the equation obtained by computer, least-squares analysis is as follows

$$\log_{10} p \text{ (Torr)} = -\frac{4080 \pm 50}{T} + 9.12 \pm 0.09$$

The enthalpy of reaction to form the trihydride phase from the dihydride phase is  $\Delta H = -18.7 \pm 0.2$  kcal/mole of H<sub>2</sub>, and the entropy of reaction is  $\Delta S = -28.6 \pm 0.4$  cal/deg · mole of H<sub>2</sub>.

Data in the metal solid solution region were treated in this same manner. These data are presented in Fig. 3 as a series of isopleths in conjunction with the plateau data. Each solid solution isopleth was fitted by a least-squares, computer program to an equilibrium dissociation pressure equation of the van't Hoff form,  $\log_{10} p = -A/T + B$ . The equation constants,  $A$  and  $B$ , for each of the compositions are tabulated in Table II.

The solution reaction in the metal solid solution is



for which the relative partial molal free energy of solution is

$$\bar{G}_H - \frac{1}{2} G_{\text{H}_2}^0 = RT \ln p^{1/2} \text{H}_2$$

From this relationship, the Gibbs-Helmholtz equation is integrated to provide the van't Hoff form of the dissociation pressure equation

$$\log_{10} p = \frac{-2(\bar{H}_H - \frac{1}{2} H_{\text{H}_2}^0)}{2.303 RT} + \text{constant}$$

The relative partial molal enthalpy and entropy of solution in the holmium solid solution are calculated from the slope and equation constant, respectively. These quantities are tabulated in Table III.

Table II. Equilibrium dissociation pressure equations for the holmium-hydrogen system

Atomic ratio (H/Ho)	Constants in $\log_{10} p \text{ (Torr)} = -A/T + B$	
	A	B
0.10	8,840 ± 240*	6.65 ± 0.24*
0.20	9,430 ± 150	7.72 ± 0.15
0.30	9,830 ± 80	8.52 ± 0.08
0.40	10,330 ± 120	9.31 ± 0.12
Plateau region	11,520 ± 50	10.66 ± 0.05

\* Standard deviations.

Table III. Relative partial molal enthalpy and entropy for hydrogen in the holmium solid solution and two-phase region

Atomic ratio (H/Ho)	$\bar{H}_H - \frac{1}{2} H_{\text{H}_2}^0$ kcal/g-atom H	$\bar{S}_H - \frac{1}{2} S_{\text{H}_2}^0$ cal/g-atom H · deg
0.00	-19.8*	+∞
0.10	-20.2 ± 0.5	-8.6 ± 0.5
0.20	-21.6 ± 0.3	-11.1 ± 0.3
0.30	-22.6 ± 0.2	-12.9 ± 0.2
0.40	-23.7 ± 0.3	-14.7 ± 0.3
Plateau region	-26.4 ± 0.1	-17.3 ± 0.1

\* Extrapolated value.

Table IV. Integral free energies, enthalpies, and entropies of mixing in the holmium-hydrogen system at 650°C

Composition H/Ho ratio	$-\Delta G^M$ (kcal/ g-atom soln)	$-\Delta H^M$ (kcal/ g-atom soln)	$-\Delta S^M$ (cal/ deg · g-atom soln)
0	0	0	0
0.10	1.21	1.73	0.57
0.20	2.09	3.33	1.37
0.30	2.77	4.77	2.17
0.40	3.31	6.09	3.01
0.43*	3.44	6.45	3.26
1.80*	6.05	16.20	10.10

\* Solubility boundaries of the two-phase region,  $\text{Ho}_{0.88} + \text{HoH}_{1.80}$ .

The relative partial molal quantities were used to calculate the integral free energy, entropy, and enthalpy of mixing in the holmium-hydrogen system. The equation for determining the integral enthalpy of mixing per g-atom of solution is

$$\Delta H^M = \frac{1}{1 + n_{\text{H}}/n_{\text{Ho}}} \int_0^{n_{\text{H}}/n_{\text{Ho}}} (\bar{H}_{\text{H}} - \frac{1}{2} \text{H}^{\circ}_{\text{H}_2}) d(n_{\text{H}}/n_{\text{Ho}})$$

The integral entropies and free energies of mixing were obtained in the same manner. A graphical integration was necessary to determine the appropriate thermodynamic quantity for each level of  $n_{\text{H}}/n_{\text{Ho}}$ . Data are presented in Table IV for the temperature 650°C.

#### Acknowledgment

The writers are grateful for the support of the Sandia Corporation, Albuquerque, New Mexico (prime

contractor to the Atomic Energy Commission) in the conduct of this work. Appreciation is expressed for the help of Mr. Russell A. Nye, who served as laboratory technician.

Manuscript received July 27, 1967; revised manuscript received Sept. 14, 1967.

Any discussion of this paper will appear in a Discussion Section to be published in the December 1968 JOURNAL.

#### REFERENCES

1. C. E. Lundin, Final Report, Sandia Contract No. 16-2524, August 1965, accepted for publication in *Trans. AIME*.
2. C. E. Lundin, Final Report, Sandia Contract No. 16-4115, December 1966, to be published.
3. J. C. Warf and W. L. Korst, *Inorganic Chem.*, **5**, 1719 (1966).
4. W. G. Bos and K. H. Gayer, *J. Nucl. Matls.*, **18**, 1 (1966).
5. G. G. Libowitz, "The Solid State Chemistry of Binary Metal Hydrides," W. A. Benjamin, New York (1965).
6. P. M. S. Jones, J. Southall, and K. Goodhead, AWRE Report No. 0-22/64, United Kingdom Atomic Energy Authority, June 1964, (*C. A.*, **61**, 7728g, 1964).
7. A. Pebler and W. E. Wallace, *J. Phys. Chem.*, **66**, 148 (1962).
8. M. Mansmann and W. E. Wallace, *J. Phys. (Paris)*, **25**, 454 (1964).

## Chemistry of Electrical Wire Explosions in Hydrocarbons

Richard L. Johnson and Bernard Siegel

Laboratories Division, Aerospace Corporation, El Segundo, California

#### ABSTRACT

This paper describes the types and extents of high-temperature reactions that can proceed when metals are electrically exploded into atmospheres of various hydrocarbons. Pyrolyses to other hydrocarbons are readily initiated by the electrical wire explosions, forming both equilibrium and nonequilibrium products to relative extents depending on the reaction energetics and kinetics of the individual hydrocarbon reactants. A surprising aspect of these reactions is the extremely high chemical abstraction of the imparted electrical energy. The principal volatile pyrolysis product is always either acetylene or methane. Thermally labile organometallics and metal hydrides do not form in such explosions. However thermally stable metal carbides form readily during wire explosions in highly endothermic unsaturated hydrocarbons, while the saturated hydrocarbons are more inert.

The physical mechanisms of electrical wire explosions have been investigated widely (1), but it is only recently that chemists have begun to investigate the utility of this technique for chemical synthesis (2-5). An electrical wire explosion can be achieved by transferring the stored energy of a bank of capacitors to a metal conductor in a time interval so short that the energy is conserved in the conductor until explosive vaporization or liquefaction results. If the imparted electrical energy exceeds the thermodynamic heat of vaporization, it can be assumed that initially the exploded metal is mainly in the vapor state. In the presence of a surrounding gas of considerably higher total heat capacity the metal vapor will rapidly transfer energy to the surrounding gas. At this point two processes are possible. Either the cooling metal vapor will react chemically with the heated gas to form products containing metal atoms, or the heated gas molecules may react independently of the vapor by undergoing pyrolytic reactions. Al-

ternatively, if the imparted electrical energy is only sufficient to explosively liquefy the metal, one can only observe liquid-gas reactions.

Our laboratory has been engaged in an effort to determine whether conditions can be established for predicting the reaction products of wire explosions in various gases from simple thermodynamic and kinetic factors, and thus to elucidate the scope of this method of synthesizing inorganic and organic compounds. In ref. (2) we showed the effect of reaction energetics on the ultimate yield of products arising from metal explosions in sulfur hexafluoride. In ref. (6) we studied the pyrolysis of methane that is initiated by exploding a number of metals. It was shown that energy is very efficiently transferred from the exploding wire to the surrounding methane molecules, raising portions of these molecules to transient temperatures of 3200°-3500°K. At such temperatures methane is rapidly pyrolyzed to the equilibrium products, acetylene and hydrogen, the predominant volatile products which

we found experimentally. About 70% of the imparted electrical energy was absorbed chemically by the system to effect this pyrolysis. The remaining 30% of the imparted electrical energy was transferred ultimately to the reactor walls and lost to the outside environment. This wastage of energy is believed to have resulted from the rapid temperature quenching that accompanies the endothermic pyrolysis reaction, coupled with the relative inertness of methane at temperatures much below 2500°K.

In the present paper we extend the study of pyrolyses initiated by electrical wire explosions to more reactive hydrocarbons. It was desired to ascertain whether such reactants would lead to the formation of significant amounts of nonequilibrium products in cooler regions of the wire explosion, thus raising the fraction of the imparted electrical energy which is transformed to chemical energy of pyrolysis. Another objective was to ascertain which types of hydrocarbons would react chemically toward the exploding metals, forming products such as metal carbides, organometallics, or metal hydrides; it was shown in ref. (6) that methane is essentially inert in this respect.

### Experimental

**Wire explosions.**—The wire explosions were carried out in a stainless steel bomb shown in Fig. 1. This bomb was machined from a solid block to a wall thickness of  $\frac{1}{4}$  in. to withstand the anticipated shock waves from the exploding wires. The bomb is in two sections so that the wires to be exploded can be mounted conveniently. There are four O-ring seals to keep the bomb vacuum tight. The largest of these O-rings is readily seen on the circumference of the upper section. The other three O-rings, which are not visible, seal between the upper plate surface and the swagelock fittings. The bomb can be evacuated to a pressure of  $2 \times 10^{-5}$  Torr. However, since initial pressures of  $10^{-3}$  Torr produced extraneous gases at levels too low to be observed gas chromatographically within the time limits of our experiments, this level of vacuum was used frequently. Teflon insulators separate the  $\frac{1}{4}$  in. copper pole electrodes from stainless steel parts. Wires to be exploded are fastened to the lower ends of the electrodes by set screws. The distance between electrodes is  $1\frac{1}{2}$  in., and they are positioned to hold the wire  $1\frac{3}{4}$  in. from the top of the cylinder if the wire is placed linearly between the electrodes, the only position used in our experiments. The internal diameter of the bomb is 4 in., and the internal volume is 833 cc. The entire bomb assembly was connected to a vacuum line by a steel ball joint so that the bomb could be filled

with gases and volatile products could subsequently be transferred.

Two electrical discharge systems were used. For those runs in which the delivered electrical input energy was 148 or 466 joules a mechanical Jennings vacuum switch was used to discharge three 14- $\mu$ f capacitors, which were rated for a maximum of 20 kv and connected in parallel. For those runs in which the delivered energy was 2188 joules this capacitor arrangement was discharged by a GE model 7703 ignitron tube. The reported energies are those energies that were actually delivered to the reactor rather than the nominal energies stored in the capacitors. Since a considerable fraction of the nominally stored energy is lost to the external circuitry on discharging the capacitors, it was deemed necessary to determine experimentally the fraction delivered to the exploding wire. This was done by calorimetry.

Wire explosions were carried out as follows. Weighed wires were connected to the electrodes, and the reactor was then sealed and evacuated. The hydrocarbon gas was then introduced to the desired pressure, the valve closed, and the wire exploded by the firing system described above. After firing, the final gas pressure was measured and the volatiles were transferred to a sample bulb for gas chromatographic analysis. The reactor was then opened in a nitrogen atmosphere enclosure for recovery of the nonvolatile products.

The wire masses that had actually been exploded are given in Table I. These masses were determined by weighing the unexploded residues still attached to the electrodes after the wires had been fired. From high-temperature heat capacity data (7,8) we have computed the fractions of exploded wires that were either explosively liquefied or vaporized. For those runs in which 0.3g Pt was exploded, sufficient energy was imparted for vaporization of only 29.4% of the exploded material at an input energy of 466 joules, while the initially exploded Pt was completely liquid at 148 joules. In each of the experiments in which 0.01g Pt or 0.05-0.06g Al were exploded, sufficient energy had been imparted to vaporize the metal fully by a large margin. In the iron explosions there could not have been any appreciable vapor at 466 joules, but sufficient energy had been imparted in the 2188 joule runs for complete vaporization of the iron.

It might be noted that experimentation with explosions of various metals into methane had demonstrated that neither the identity of the metal nor its mass over a wide range of mass ratios affected appreciably the degree of pyrolysis or the ratios of the volatile products (6). Therefore, in studying the pyrolysis reactions of higher hydrocarbons in the present paper it was deemed unnecessary to use mass or identity of the metal as a control factor for pyrolytic reactions. Because we were primarily interested in the chemical reactions resulting from the wire explosion, rather than the electrical explosion itself, the current-time characteristics of the wire explosions were not measured routinely. However there is no question but that explosions did occur. Measurements of the rate of change of current in the conductors being exploded were carried out in this laboratory under conditions somewhat similar to many of the explosions reported herein. These data indicated that current rose to a maximum within several microseconds and then damped out to zero over periods up to 100  $\mu$ sec. Further, examination of the bomb contents after firing of the wire showed that the original wire had disappeared and the metal was found in the form of a fine powder, which was distributed relatively uniformly over all of the walls of the reactor.

**Product analysis.**—Gas chromatographic analysis of the volatiles was made on a dual-column, programmed-temperature instrument with katharometer detection, using a flow rate of 120 ml/min. For earlier runs, hydrocarbons were determined on a 6 ft x  $\frac{1}{4}$  in. column of 120/150 mesh Porapak Q, temperature programmed



Fig. 1. Exploding wire apparatus

Table I. Hydrocarbon pyrolysis data

Reactants <sup>(a)</sup>	Imparted energy <sup>(c)</sup> joules	Per cent pyrolysis <sup>(d)</sup>	Volatile products <sup>(e)</sup>				
			1st	2nd	3rd	4th	5th
Methane, 0.3g Pt	148	2.4 (1.5)	C <sub>2</sub> H <sub>2</sub> 100	C <sub>3</sub> H <sub>6</sub> 3.3	C <sub>4</sub> H <sub>4</sub> 2.4	C <sub>2</sub> H <sub>4</sub> 1.9	
Methane, 0.3g Pt	466	7.8 (2.5)	C <sub>2</sub> H <sub>2</sub> 100	C <sub>3</sub> H <sub>6</sub> 3.4	C <sub>4</sub> H <sub>4</sub> 2.0	C <sub>2</sub> H <sub>4</sub> 0.7	
Methane, 0.06g Al	2188	16.4 (18.6)	C <sub>2</sub> H <sub>2</sub> 100 <sup>(f)</sup>	C <sub>6</sub> H <sub>6</sub> 3.1	C <sub>3</sub> H <sub>4</sub> 2.8	C <sub>4</sub> H <sub>4</sub> 2.6 <sup>(e)</sup>	C <sub>2</sub> H <sub>6</sub> 2.0
Ethane, 0.3g Pt	148	3.6	C <sub>2</sub> H <sub>2</sub> 100	CH <sub>4</sub> 19	C <sub>3</sub> H <sub>6</sub> 11		
Ethane, 0.06g Al	2188	25.7 (8.2)	C <sub>2</sub> H <sub>2</sub> 100 <sup>(f)</sup>	CH <sub>4</sub> 47	C <sub>4</sub> H <sub>4</sub> 2.7 <sup>(e)</sup>	C <sub>3</sub> H <sub>6</sub> 1.7	C <sub>2</sub> H <sub>4</sub> 1.4
n-Butane, 0.3g Pt	148	2.1	C <sub>2</sub> H <sub>2</sub> 100	CH <sub>4</sub> 29	C <sub>3</sub> H <sub>6</sub> 7.4	C <sub>2</sub> H <sub>4</sub> 5.4	C <sub>2</sub> H <sub>6</sub> 2.7
Isobutane, 0.3g Pt	148	1.7	C <sub>2</sub> H <sub>2</sub> 100	CH <sub>4</sub> 54	C <sub>3</sub> H <sub>6</sub> 23	C <sub>3</sub> H <sub>8</sub> 8.0	C <sub>2</sub> H <sub>4</sub> 4.4
Isobutane, 0.3g Pt <sup>(b)</sup>	148	5.0	C <sub>2</sub> H <sub>2</sub> 100	CH <sub>4</sub> 44	C <sub>3</sub> H <sub>6</sub> 21	C <sub>3</sub> H <sub>8</sub> 7.6	C <sub>2</sub> H <sub>4</sub> 5.1
Isobutane, 0.3g Pt	466	5.7	C <sub>2</sub> H <sub>2</sub> 100	CH <sub>4</sub> 52	C <sub>3</sub> H <sub>6</sub> 18	C <sub>3</sub> H <sub>8</sub> 7.7	C <sub>2</sub> H <sub>4</sub> 2.5
Isobutane, 0.05-0.06g Al	2188	11.8 (5.4)	CH <sub>4</sub> 100	C <sub>2</sub> H <sub>2</sub> 98 <sup>(f)</sup>	C <sub>3</sub> H <sub>6</sub> 30	C <sub>3</sub> H <sub>4</sub> 0.8	C <sub>2</sub> H <sub>6</sub> 0.5
Ethylene, 0.3g Pt	148	2.8	C <sub>2</sub> H <sub>2</sub> 100	C <sub>4</sub> H <sub>4</sub> 60	CH <sub>4</sub> 3.6	C <sub>4</sub> H <sub>2</sub> 3.2	C <sub>6</sub> H <sub>6</sub> 0.2
Ethylene, 0.01g Pt	466	9.3 (1.9)	C <sub>2</sub> H <sub>2</sub> 100 <sup>(f)</sup>	C <sub>4</sub> H <sub>4</sub> 4.8	CH <sub>4</sub> 1.8	C <sub>4</sub> H <sub>2</sub> 1.5	(C <sub>6</sub> H <sub>6</sub> 0.3 C <sub>6</sub> H <sub>6</sub> 0.3)
Butadiene-1,3,0.01g Pt	466	3.9 (1.6)	C <sub>2</sub> H <sub>2</sub> 100 <sup>(f)</sup>	CH <sub>4</sub> 6.6	C <sub>3</sub> H <sub>4</sub> 2.8	C <sub>6</sub> H <sub>6</sub> 1.1	
Cyclopentadiene, 0.25g Fe	466	4.7	C <sub>2</sub> H <sub>2</sub> 100 <sup>(f)</sup>	CH <sub>4</sub> 20	C <sub>3</sub> H <sub>4</sub> 5.0	C <sub>6</sub> H <sub>6</sub> 3.9	(C <sub>4</sub> H <sub>4</sub> 2.2 C <sub>4</sub> H <sub>4</sub> 2.2)
Cyclopentadiene, 0.2g Fe	2188	8.6 (82.8)	CH <sub>4</sub> 100	C <sub>2</sub> H <sub>2</sub> 8.1 <sup>(f)</sup>	C <sub>3</sub> H <sub>6</sub> 1.1	C <sub>6</sub> H <sub>6</sub> 1.8	
Acetylene, 0.01g Pt	148	0.6 (96.3)	CH <sub>4</sub> 100	C <sub>2</sub> H <sub>2</sub> 2.9	C <sub>3</sub> H <sub>6</sub> 1.0		
Allene, 0.01g Pt	466	10.7 (86.1)	CH <sub>4</sub> 100	C <sub>2</sub> H <sub>2</sub> 14.5 <sup>(f)</sup>	C <sub>3</sub> H <sub>6</sub> 1.5	C <sub>3</sub> H <sub>4</sub> 1.5	C <sub>6</sub> H <sub>6</sub> 2.5
Propyne, 0.01g Pt	466	7.8 (89.0)	CH <sub>4</sub> 100	C <sub>2</sub> H <sub>2</sub> 19 <sup>(f)</sup>	C <sub>3</sub> H <sub>6</sub> 2.0	C <sub>3</sub> H <sub>4</sub> 2.0	C <sub>6</sub> H <sub>6</sub> 0.5

<sup>(a)</sup> Unless specified otherwise initial hydrocarbon pressures were in range 400-450 mm.

<sup>(b)</sup> Initial isobutane pressure was 100 mm.

<sup>(c)</sup> All runs except those using input energies of 2188 joules were with Jennings mechanical switch; 2188 joule runs used ignitron switch.

<sup>(d)</sup> Values listed first are for per cent decomposition to volatiles; those given in parentheses are the per cent decomposition to nonvolatile solids.

<sup>(e)</sup> Aggregate of C<sub>4</sub>H<sub>4</sub> + C<sub>4</sub>H<sub>2</sub>.

<sup>(f)</sup> In these runs small amounts of ethylene were not separated from acetylene.

<sup>(g)</sup> The products have been normalized to a scale of 100 for the most prevalent species.

from 50° to 250°C at 4°/min, and hydrogen was determined on a molecular sieve or on a column of coconut charcoal, 6 ft x ¼ in. at 50°C. In later runs all compounds were determined on a 12 ft x ¼ in. Porapak Q column, programmed, after a 4-min delay, at 4°/min from 40° to 250°C. Samples were taken from a glass bulb reservoir through a gas valve with a 5-ml sampling loop. Values reported in Table I are averages of 6 to 12 multiple runs.

In those runs where platinum alkyls were suspected nonvolatile products, the nonvolatile solids were extracted with benzene and the extract tested for a platinum compound. Similarly in the iron-cyclopentadiene explosions, the nonvolatiles were extracted with diethyl ether and the extract tested for ferrocene. Aluminum alkyls are volatile, and these were sought in the Al explosions by mass spectrometric analysis of the volatile products. Carbides were sought by x-ray diffraction. There has never been a reported platinum carbide (9), and x-ray diffraction patterns of our products failed to demonstrate the existence of a platinum carbide in those runs which involved explosions of platinum wires.

The carbon and hydrogen contents of the nonvolatile residues were obtained by the usual combustion procedure, after extraction with organic solvents for those runs in which organometallic products were sought. These residues were not investigated further. Our main purpose in determining the carbon contents was to compute the per cent decomposition of the hydrocarbons to nonvolatile solids for those wire explosions where thermochemical calculations were desired. In those runs where the over-all pyrolysis was very small an experimental uncertainty of several per cent in the gas chromatographic data prevented direct calculation of the yields from data on the lowering of the concentration of the hydrocarbon reactants. The yield of volatile products was obtained by summing carbon atoms from all the volatile product data, and the yield of nonvolatile hydrocarbons (or carbon) was obtained from the carbon content of the residues.

### Results and Discussion

**Hydrocarbon pyrolyses.**—Saturated hydrocarbons higher than methane have increasingly higher rate constants for pyrolytic reactions (10-13). Our prediction that this would lead to more complex pyrolysis products for such hydrocarbons in wire explosions, as compared to methane, with larger proportions of nonequilibrium products and lesser proportions of acetylene, is supported by the product data in Table I.

The pyrolyses of ethane and the butanes resemble that of methane in that much of the acetylene is undoubtedly formed in the 3200°-3500°K temperature range. This temperature range is undoubtedly achieved in a significant portion of the hydrocarbon molecules surrounding the exploding wire as soon as sufficient numbers of molecules abstract energy from the exploded material to reduce the very much higher temperatures that would characterize the previously smaller heated portion. In the case of hydrocarbons higher than methane, further reactions are possible when the temperature falls below even 2000°K, after temperature quenching caused by the endothermicity of acetylene formation and further heat conduction to cold regions of the surrounding gas. At these lower temperatures the speed of the over-all process requires that pyrolyses fall short of equilibrium, and one obtains the nonequilibrium products shown in Table I for the ethane, n-butane, and isobutane reactions.

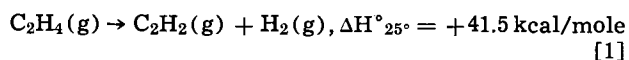
This additional reactivity at lower temperatures is reflected in the degree to which chemical energy is abstracted from the imparted electrical energy. Whereas the methane pyrolyses carried out at energy levels at 148 to 466 joules waste approximately 30% of the imparted energy, there is essentially no wasted energy in the ethane pyrolysis at 148 joules. From thermochemical data we compute that 110.7% of the imparted energy was transformed into chemical energy of pyrolysis in the ethane run. In view of the 6% uncertainty in calorimetric measurement of the imparted energy to the wire and the experimental uncertainties in the gas chromatographic analyses of products, this is believed to represent essentially complete energy abstraction. There is no conflict between these data and the apparently lower efficiencies of energy abstraction in the methane and ethane runs at 2188 joules. We have observed that the more rapid explosion that accompanies the use of an ignitron firing circuit, rather than a Jennings mechanical switch, leads to a lower degree of energy abstraction with the ignitron system. Because the latter was used in the 2188 joule runs, we compute lower values of 57.3 and 41.6%, respectively, for the degree of energy abstraction in the ethane and methane pyrolyses. However the relative efficiencies of methane and ethane extraction of electrical energy for chemical purposes remain unchanged.

Since saturated hydrocarbons are themselves exothermic, their pyrolysis to acetylene and hydrogen, or even to carbon and hydrogen, is always endothermic.



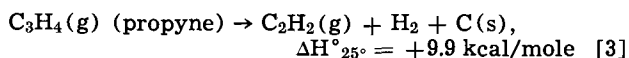
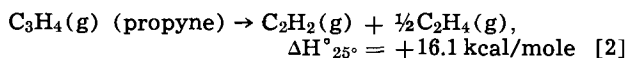
One would thus expect that the yield of pyrolysis products would be directly proportional to the imparted electrical energies in wire explosions. This is essentially verified by the data for methane and isobutane. At constant pressure, variation of the electrical energy from 148 to 466 joules, a 3.15-fold increase, leads to measured 3.25 and 3.35-fold increases in the yields of volatile products. The data for runs at 2188 joules cannot be compared with these runs because a different firing circuitry was used. Somewhat surprising is the fact that ethylene behaves similarly to the saturated hydrocarbons, both in type of products formed, and in exhibiting a 3.32-fold increase in volatile products when the input energy is increased from 148 to 466 joules. One might expect that ethylene would pyrolyze directly to graphite and hydrogen since the latter reaction is exothermic. Further, the yield of an exothermic reaction should not be directly proportional to the imparted energy.

The explanation for the ethylene data is based on reaction kinetics. It is known that the pyrolysis of ethylene to carbon and hydrogen proceeds through a mechanism that includes Eq. [1] (14); the heats of reaction cited in this paper were computed from



data in ref. (15). The relatively high endothermicity of this step increases the dependence of the type of product formed on the amount of electrical energy imparted to the exploding wire. At lower energy input levels the endothermicity of Eq. [1] reduces the over-all gas temperature to a point where acetylene is kinetically trapped and precludes the exothermic pyrolysis of acetylene to carbon and hydrogen. This should be readily overcome at higher energy levels, as is seen by the data for cyclopentadiene, which is similar to ethylene in the energetics of these pyrolytic reactions. At the higher energy level one obtains a drastically different pyrolysis. The yield approaches completion, unlike any of the pyrolyses of saturated hydrocarbons at such conditions, and the principal volatile hydrocarbon product becomes methane rather than acetylene.

This trend continues in the more highly endothermic alkyne molecules. Comparison of Eq. [1] with Eq. [2] and [3] indicates



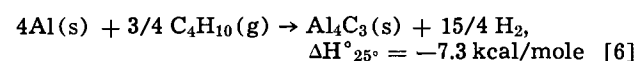
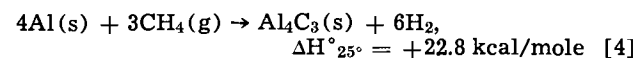
a much lesser tendency toward kinetic trapping of acetylene for wire explosions carried out in propyne (allene has very similar energetics), and explains the very high yields of pyrolysis products and volatile product distributions in propyne or allene explosions at lower energy input levels than had been required for comparable pyrolyses of cyclopentadiene. Acetylene, of course, cannot form permanently stable volatile intermediates by endothermic processes and should pyrolyze exothermically at energy input levels even lower than those required for the higher alkynes. Virtually complete pyrolysis of acetylene was observed at the lowest energy input level used in our experiments.

*Metal-hydrocarbon reactions.*—Metal alkyls were not formed by any of the explosions of aluminum or platinum into saturated hydrocarbons. The aluminum alkyls are well-known compounds, and both  $(\text{CH}_3)_4\text{Pt}$  and  $(\text{CH}_3)_6\text{Pt}_2$  have been reported to be reasonably stable compounds (16-19). A qualifying note might be added in regard to the platinum alkyls since doubt has recently been cast on the authenticity of the reported syntheses of these compounds (20). Yet it must be concluded that it appears unlikely that metal alkyls can be prepared by this technique. We

next studied the possible formation of ferrocene by iron wire explosions in cyclopentadiene. This pi-bonded organometallic compound has been reported to have an unusually high thermal stability for this class of compounds since it is not extensively decomposed even at 470°C (21). Yet ferrocene was not formed, at either 466 joules where the over-all reaction of the cyclopentadiene was relatively small or at 2188 joules where the cyclopentadiene reacted extensively.

The difficulty in preparing organometallics by the present technique can be attributed to the limited thermal stabilities of such compounds and the competing pyrolysis reactions of the hydrocarbon reactants. Similar considerations apply to thermally labile hydrides, such as  $\text{AlH}_3$ , which also did not form in these experiments.

On the other hand many metal carbides are extremely stable thermally and should be capable of synthesis by the technique described in the present paper. Although  $\text{Al}_4\text{C}_3$  was not observed in the methane explosion at 2188 joules, this carbide was observed among the products of the aluminum explosions in ethane and isobutane at 2188 joules. This was established by the presence of the x-ray diffraction spectrum characteristic of  $\text{Al}_4\text{C}_3$  in the spectrum of the nonvolatile products of the ethane and isobutane explosions and its absence in the products of the methane explosion. Yet even when  $\text{Al}_4\text{C}_3$  was found among the products of Al explosions in the higher saturated hydrocarbons, the intensities of the Al lines were considerably larger than those of  $\text{Al}_4\text{C}_3$ . Thus the reaction does not go very far toward completion, even at 2188 joules. These results reflect the energetics of Eq. [4] to [6]. Cook and Siegel showed (2) that



for kinetic reasons endothermic reactions in which the metal reacts chemically with the surrounding gas are very inefficient in abstraction of electrical energy in wire explosions. Therefore Eq. [4] could be predicted to proceed to a lesser extent than would Eq. [5] or [6], if all other conditions were equal. Further, the marginal exothermicities of Eq. [5] and [6] would indicate poor yields. On this basis the endothermic unsaturated hydrocarbons should be superior to the exothermic saturated hydrocarbons as reactants leading to metal carbide formation. This is substantiated by the ready formation of  $\text{Fe}_{20}\text{C}_9$  by iron explosions in cyclopentadiene at 2188 joules. Acetylene should be better still, and  $\text{Al}_4\text{C}_3$  was found to be a product of aluminum explosions in acetylene, at energy input levels as low as 148 joules.

*Future studies.*—The application of the exploding wire technique in a small volume bomb is particularly efficacious for the synthesis of transition metal carbides. Cook (22) of this laboratory has expanded on the results of the present study by showing that titanium wire explosions into acetylene diluted with an inert gas can lead to the preparation of TiC samples in high yield and in purity at least equal to 98.6% by weight. The general applicability of the method is indicated by the successful synthesis of  $\text{LaC}_2$ , TiC, ZrC, NbC,  $\text{Nb}_2\text{C}$ ,  $\text{Ta}_2\text{C}$ , MoC,  $\text{Mo}_2\text{C}$ , and  $\text{W}_2\text{C}$ . Although the utility of wire explosions in a small volume bomb for the synthesis of thermally labile compounds appears dim, in view of the results of the present paper, we believe that there is a possible solution to this problem. What is evidently required is the introduction of an additional mode of temperature quenching superimposed on the temperature quenching processes oc-



curing naturally in wire explosions carried out in a limited volume bomb. We are now trying to develop a technique in which the wire explosion is coupled to a device similar to a shock tube. This would provide both extra temperature quenching and longer path lengths at lower temperatures.

#### Acknowledgment

The authors gratefully acknowledge the general laboratory assistance of Miss C. G. Johnson who obtained all the gas chromatography data. Messrs. T. L. North and S. B. Mason assisted with the electrical discharge systems, while S. Hotta, P. Marsh, and E. S. Elliott obtained analytical data.

Manuscript received June 26, 1967; revised manuscript received Sept. 18, 1967.

Any discussion of this paper will appear in a Discussion Section to be published in the December 1968 JOURNAL.

#### REFERENCES

1. "Exploding Wires," W. G. Chace and H. K. Moore, Editors, Vol. 1-3, Plenum Press, New York (1959, 1962, 1964).
2. E. Cook and B. Siegel, *J. Inorg. Nucl. Chem.*, In press.
3. F. Mahieux, *Compt. rend.*, **257**, 1083 (1963).
4. M. J. Joncich, J. W. Vaughn, and B. F. Knutsen, *Can. J. Chem.*, **44**, 137 (1966).
5. M. J. Joncich and D. G. Bleu, "Exploding Wires," pp. 353-359, W. G. Chace and H. K. Moore, Editors, Plenum Press, New York (1964).
6. B. Siegel and R. L. Johnson, *A Thermal Model of Wire Explosions in Methane*, presented at the Fourth International Symposium on the Exploding Wire Phenomenon, Boston, October 1967, and will be published in the proceedings.
7. H. L. Schick, "Thermodynamics of Certain Refractory Compounds," Vol. II, Academic Press, New York (1966).
8. D. R. Stull and G. C. Sinke, "Thermodynamic Properties of the Elements," American Chemical Society, 1956.
9. W. A. Frad, Carbides, A.E.C. Report IS-722, August 1963.
10. G. B. Skinner and W. E. Ball, *J. Phys. Chem.*, **64**, 1025 (1960).
11. C. P. Quinn, *Proc. Roy. Soc. (London)*, **275A**, 190 (1963).
12. J. H. Purnell and C. P. Quinn, *ibid.*, **270A**, 267 (1962).
13. G. I. Kozlov and V. G. Knorre, *Zhur. Fiz. Khim.*, **37**, 2082 (1963).
14. G. B. Skinner and E. M. Sokolowski, *J. Phys. Chem.*, **64**, 1028 (1960).
15. F. D. Rossini, Selected Values of Properties of Hydrocarbons, API Research Project 44, Nat. Bur. Stand., 1947.
16. H. Gilman and M. Lichtenwalter, *J. Am. Chem. Soc.*, **60**, 2085 (1938).
17. R. E. Rundle and E. J. Holman, *ibid.*, **71**, 3264 (1949).
18. G. Illuminati and R. E. Rundle, *ibid.*, **71**, 3575 (1949).
19. R. E. Rundle and J. H. Sturdivant, *ibid.*, **69**, 1561 (1947).
20. F. A. Cotton and G. Wilkinson, "Advanced Inorganic Chemistry," 2nd ed., p. 1036, Interscience Publishers, Inc. New York (1966).
21. G. Wilkinson, M. Rosenblum, M. C. Whiting, and R. B. Woodward, *J. Am. Chem. Soc.*, **74**, 2125 (1952).
22. E. Cook and B. Siegel, Unpublished results.

## On the Activity of Platinum Catalysts in Solution

### II. Kinetics of the Pt-O Reaction with Hydrogen and of Pt-H Deposition Using a Double Pulse Technique

Theodore B. Warner\* and Sigmund Schuldiner\*

Naval Research Laboratory, Washington, D. C.

#### ABSTRACT

Surface coverages of oxygen and hydrogen were determined on electrodes of differing activities as a function of time and of voltage in the potential decay curve following an anodic pulse. The electrolyte was 1M H<sub>2</sub>SO<sub>4</sub> containing dissolved hydrogen. No important difference, other than rate, is found in the way Pt-O is removed from surfaces of differing activity; however, a significant difference is noted in the way hydrogen resorbs. The rate of Pt-O removal is of apparent first order in adsorbed oxygen when the initial fraction of the surface covered is about 1.0; it is zero order in adsorbed oxygen and in amount reacted when the initial surface coverage is <0.8. The rate of the decay reaction is probably not limited by mass transport of solution H<sub>2</sub> to the surface, by obstruction of active surface sites by sorbed product molecules, or by slow chemisorption of solution H<sub>2</sub> on the electrode prior to reaction with Pt-O.

In Part I of this series (1) and in a preceding paper (2), the rate of the reaction of oxygen, chemisorbed on smooth platinum, with hydrogen dissolved in 1M H<sub>2</sub>SO<sub>4</sub> and in the Pt derma (the Pt-O/hydrogen reaction) was monitored by observing potential decay on open circuit after an anodic current pulse. The purpose in Part I was to examine how different thermal or chemical treatments affected the intrinsic catalytic activity of smooth platinum, using this reaction rate as a measure of activity. It was found that this intrinsic activity could be modified by several orders of magnitude. The purpose of this work was to determine if surfaces known to have different catalytic

\* Electrochemical Society Active Member.

activities for the Pt-O/hydrogen reaction exhibited significant differences (other than rate) in the way oxygen was removed or hydrogen resorbed.

Breiter (3) has previously studied the chemical reduction of chemisorbed oxygen with H<sub>2</sub>. His results should not be compared directly with these due to important differences in experimental procedure, as previously discussed (2). Sawyer and Seo (4) have also studied this system. Their oxygen generation rates were very low, however, so the electrodes would be presumed to contain some oxygen absorbed in the lattice. The presence of such oxygen affects the hydrogen/oxygen interaction markedly (2). The oxygen

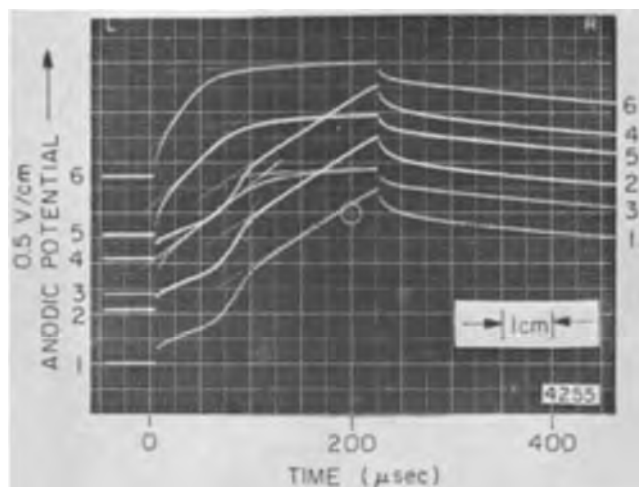


Fig. 1. Double pulse electrode polarization. First pulses (oxidation of  $H_{ad}$  followed by oxidation of  $H_2O$  to  $O_{ad}$ ) are traces 1, 2, and 4; second pulses (oxidation of  $H_2O$  to  $O_{ad}$ ) are traces 3, 5, and 6 taken after reaction ( $Pt-O_{ad} + \text{hydrogen}$ ) times of 10, 6, and 3 msec, respectively, on an electrode with a monolayer decay time of 21 msec. Current density is 2.92 amp/cm<sup>2</sup>.

generation rates used in this work were adjusted such that oxygen was deposited on the platinum surface without concurrent absorption of oxygen into the lattice.

### Experimental

Apparatus and procedures were the same as in Part I except that two precisely spaced galvanostatic pulses were used.<sup>1</sup> A Hewlett-Packard 5214L Electronic Counter (clock rate 100 kc) provided two trigger pulses separated by a time known within 1  $\mu$ sec. These pulses triggered a pulse generator (either an EH Model 132A or an Electropulse 3450D), sending two identical current pulses through the cell. The pulses were adjusted so that the first ended after a known amount, usually one monolayer, of chemisorbed oxygen atoms had been deposited on the electrode (Fig. 1). Current densities were from 2.9 to 4.5 amp/cm<sup>2</sup>.<sup>2</sup>

The anodic charging curves are conceptually divided into the usual regions, called the "H ionization region" and the "O sorption region." In the subsequent decay, the first region is called the "O removal region," and the second the "H deposition region." These regions are diagrammed in Fig. 1a of ref. (2) and they are apparent in Fig. 2 here. In the O removal region, hydrogen is reacting with the oxygen chemisorbed on the electrode. This hydrogen can come from the  $H_2$  dissolved in the bulk of the solution, from  $H_2$  bubbles at the surface and from dermasorbed H (H absorbed in the top 2 or 3 atomic layers of Pt). After a known time into the decay,  $t$ , called at different times either the "reaction time" or the "decay time," the second pulse was triggered to determine how much charge was required to bring Pt-O coverage up to one monolayer. Knowing the initial coverage and this, the amount reacted could be computed. When the voltage decayed below 0.3v, the second pulse gave both the charge required to form the oxygen region and the charge due to oxidation of adsorbed hydrogen.

It was assumed that in the oxygen regions,  $q_0 = q_{\text{measured}} - q_{dl}$ , and in the hydrogen regions,  $q_H =$

<sup>1</sup>Unless otherwise specified, potentials are given vs. the normal hydrogen electrode, all measures of precision are standard deviations of an individual measurement, and electrode areas are "true" (5) areas based on the assumption that  $q_{O+dl} = 456 \mu\text{coul/cm}^2$  when one monolayer of oxygen is deposited at a current density of 3 amp/cm<sup>2</sup>. Precision of an individual area measurement was  $\pm 3.2\%$ .

<sup>2</sup>At these current densities, the IR drop in the solution is a large fraction of the total cell voltage. The IR drop was at times removed from the display by using a Tektronix Type 547 oscilloscope with a Type 1A1 dual trace preamplifier. The rectangular pulse at the generator output was applied to input 1 and appropriately attenuated; the cell voltage was applied to input 2 and the difference signal was displayed.

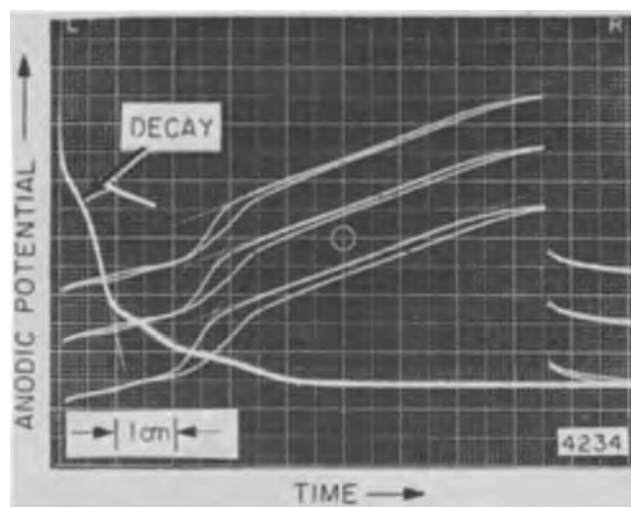


Fig. 2. Double pulse polarization of electrode on which some hydrogen had resorbed, and typical full decay curve. Pulses are 20  $\mu$ sec/cm and 0.5 v/cm; decay is 50 msec/cm and 0.2 v/cm. Reaction times between pulses were 200, 230, and 260 msec reading from bottom to top on an electrode whose  $t_0$  was 48 msec. Current density is 4.56 amp/cm<sup>2</sup>.

$q_{\text{measured}} - q_{dl}$ . For the first pulse, the significance of the various terms is well understood. For the second pulse, the assumption is made in what follows that all of the charge designated  $q_0$  went to form  $Pt-O_{ad}$  via a net 2-electron oxidation, and all charge designated  $q_H$  went to oxidize  $Pt-H$  to  $H^+$ . The validity of these assumptions will be supported later. The charge due to double layer charging was subtracted from the various  $q_{\text{measured}}$  using previously reported (5) double layer capacitance vs. potential data integrated over the potential region of interest.<sup>3</sup>

The "foot" of each charging curve in Fig. 1 (the horizontal trace to the left of time zero) gives the potential of the electrode prior to each pulse. The first of each pair of pulses started at the normal equilibrium hydrogen potential (0.000v). The foot of the second pulse then defined the potential,  $E(t)$ , in the decay from which the second pulse was taken.

Two bright platinum bead electrodes were used, one with a monolayer decay time,  $t_0$ , of  $47.8 \pm 0.5$  msec, and one with  $t_0$  of  $21.3 \pm 1.5$  msec. The monolayer decay time is the time required for the reduction of a monolayer of chemisorbed oxygen with hydrogen. The electrode areas were about 0.1 cm<sup>2</sup>. For convenience, the more active electrode (activity defined by the rate of the Pt-O/hydrogen reaction) with  $t_0 = 21$  will be termed electrode A, and the less active one, electrode L. It was important to confirm that each measurement of voltage and redeposited charge was made on an electrode whose  $t_0$  was unchanged. This was done by plotting measurements of potential vs. reaction time,  $t$ , from a number of full decay curves taken before, during, and after the double pulse studies, and then comparing these data with the voltage/time information obtained from the foot of the second pulse. The  $t_0$  for the electrodes used did not change during the course of the experiments.

### Results

**Oxygen removal region:  $Pt-O + \text{Hydrogen} = Pt + H_2O$ .**—Voltage-time relation.—To facilitate comparison of results on electrodes with different intrinsic activities, the results for each electrode have been expressed in terms of relative decay times,  $t/t_0$ , where  $t$  is the reaction time, and  $t_0$  the monolayer decay time.

<sup>3</sup>For the second pulse this treatment involved the assumption that  $q_{dl}$  (which includes a contribution from pseudocapacitance near 0.000v) under the nonsteady-state conditions prevailing was not significantly different from that measured in (5). Consideration of the physical situation prevailing shows that this is reasonable; further, the  $q_{dl}$  terms are small compared to total  $q$ .

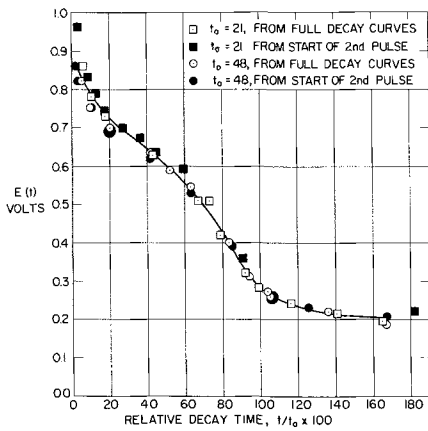


Fig. 3. Basic decay curve: potential vs. relative decay time

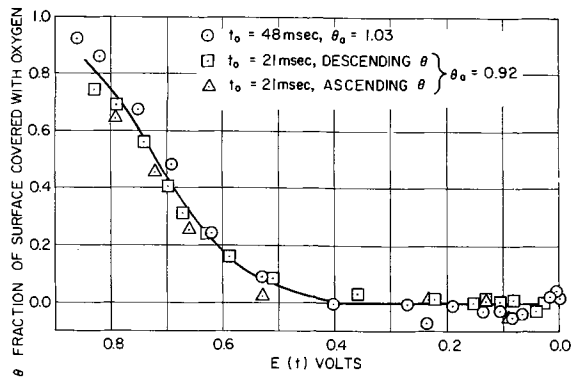


Fig. 4. Fraction of surface covered with  $O_{ad}$  vs. potential during decay. The initial coverages are denoted  $\theta_a$ .

Plots of electrode potential during the decay,  $E(t)$ , vs.  $t/t_0$  (Fig. 3) for data obtained on electrodes with  $t_0 = 21$  and  $48$  msec show no important difference nor are differences noted for the relation between voltage in the decay curve and fraction  $\theta$  of surface covered with oxygen (Fig. 4). It must be kept in mind that the actual times of reaction, however, differed by a factor of 2.2. From repeated measurements on electrodes whose  $t_0$  ranged from 17 to 180 msec, the potential at the end of the decay plateau, at  $t = t_0$  was found to be  $0.283 \pm 0.004v$ .

**Oxygen coverage vs. voltage and time.**—Let  $a$  be the initial oxygen coverage of the electrode in  $\mu\text{coul}/\text{cm}^2$  deposited by the first pulse, and let  $(a-x)$  be the coverage at any later time  $t$ . Let  $q_0$  be the amount of oxygen used in the second pulse to reform one monolayer of  $O_{ad}$ . We assume that  $q_0 + (a-x) = 420 \mu\text{coul}/\text{cm}^2$ ; i.e., the electrode is once again polarized up to the  $O_2$  evolution region when its total oxygen coverage is brought back to one monolayer. The fraction  $\theta$  of the surface covered with oxygen is

$$\theta = \frac{420 - q_0}{420} \quad [1]$$

It is necessary to maintain a clear distinction between  $a$ , the initial concentration in  $\mu\text{coul}/\text{cm}^2$  of oxygen on the surface;  $\theta_a$ , this initial concentration expressed as the fraction of Pt surface sites covered with  $O_{ad}$  ( $\theta_a = a/420 \mu\text{coul}/\text{cm}^2$ ), and  $\theta$ , the fraction of the surface covered with oxygen at time  $t$  after some of the oxygen initially deposited has reacted with hydrogen.

The results in Fig. 5 and 6 show that the relationships between  $\theta$  and  $t/t_0$  for the cases where  $\theta_a \approx 1$  and for  $0.32 \leq \theta_a \leq 0.77$  are quite different. For  $0.32 \leq \theta_a \leq 0.77$ , Fig. 6a shows that the rate of oxygen removal is zero order in the initial concentration  $a$  and in the amount reacted  $x$ . The slopes are independent of  $a$  and average  $700 \mu\text{coul}/\text{cm}^2$ . Converting into units

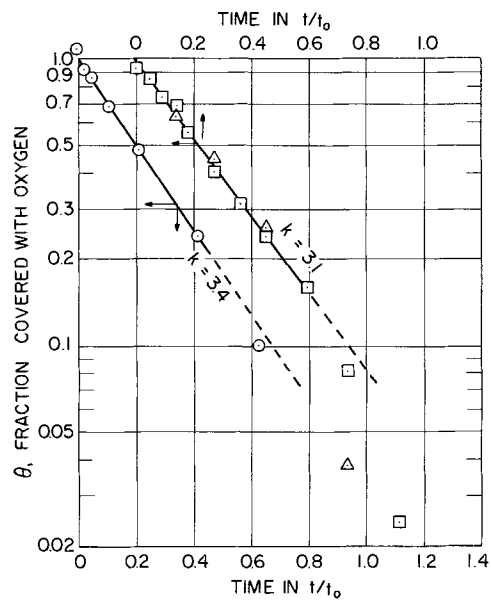


Fig. 5. Rate of removal of oxygen for case where fraction of surface initially covered is near unity. The symbols have the same meaning as in Fig. 4.

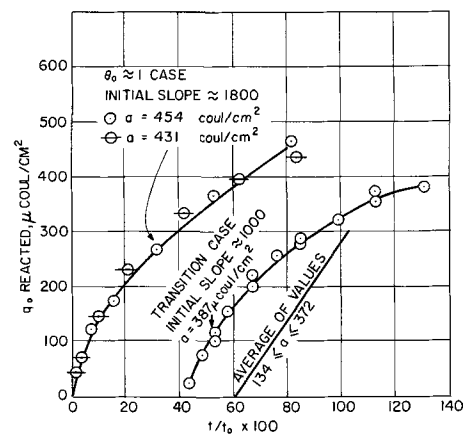
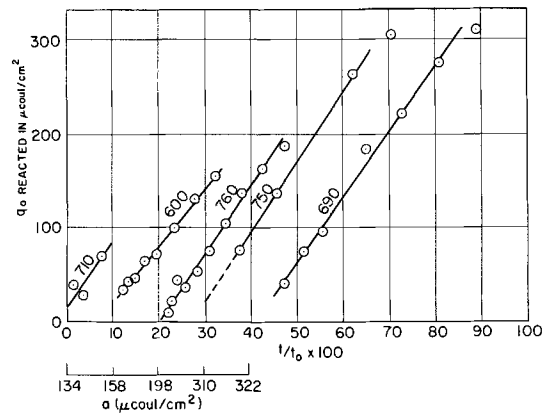


Fig. 6. (a, top) Rate of removal of oxygen for case where fraction of surface covered initially is  $< 0.8$ . The initial coverage  $a$  for each curve is indicated on abscissa below  $t/t_0 \times 100$  values. The origin of each succeeding curve is displaced 10 time units to the right of the preceding curve. The numbers on the curves represent the slopes in  $\mu\text{coul}/\text{cm}^2$ . Fig. 6 (b, bottom) Comparison of cases where  $\theta_a \approx 1$  with ones where  $\theta_a < 0.8$ . The origins for the two curves to the right have been displaced by 40 and 60 ( $t/t_0 \times 100$ ) units.

of  $\theta$ , the rate of oxygen removal is

$$\theta = \theta_a - 1.67 \frac{t}{t_0} \quad [2a]$$

However, for  $0.92 \leq \theta_a \leq 1.03$ , the rate of oxygen re-

removal is given by a first order relation

$$\theta = \exp\left(-k \frac{t}{t_0}\right) \quad [2b]$$

over the range  $1 \leq \theta \leq 0.15$  where  $k$  is the first order rate constant of about 3.2. The curves, plotted separately, show logarithmic relations; the slopes are not considered to be significantly different. (The slopes are strongly dependent on the average values used for  $t_0$  and  $q_0$  monolayer, as well as the extent to which some hydrogen may or may not be oxidized in the oxygen region.)

**Hydrogen redeposition region:**  $\text{Pt} + \text{H} = \text{Pt} - \text{H}$ .—The measured quantities were  $q_{\text{H} + \text{ad}}$ ,  $q_0 + \text{ad}$ ,  $E(t)$ , and time since the end of the first pulse,  $t$ . The time available for hydrogen sorption was taken as  $(t - t_0)$ . Since charging curves at times up to  $t = t_0$  gave little or no indication of any sorbed hydrogen, it was assumed that all hydrogen reaching the electrode up to this time was consumed in reaction with Pt-O, which was known to be present up to  $t = t_0$ . The validity of this assumption is examined in the Discussion Section. After correction for double layer charging, the resulting  $q_{\text{H}}$  vs.  $E(t)$ ,  $q_0$  vs.  $E(t)$ , and  $E(t)$  vs.  $(t - t_0)$  data are shown in Fig. 7 and 8.

### Discussion

**Hydrogen redeposition region.**—The factors that affect rate of potential decay in the Pt-O removal region exert no influence on the rate of potential change in the hydrogen resorption region. However, the amount of hydrogen found sorbed on the electrode after decay to a given potential does vary with the intrinsic activity of the electrode. The more active electrode, A, shows faster hydrogen reappearance in

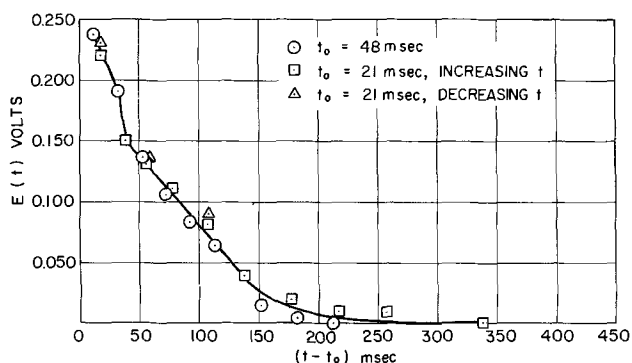


Fig. 7. Decay potential vs. time allowed for hydrogen resorption

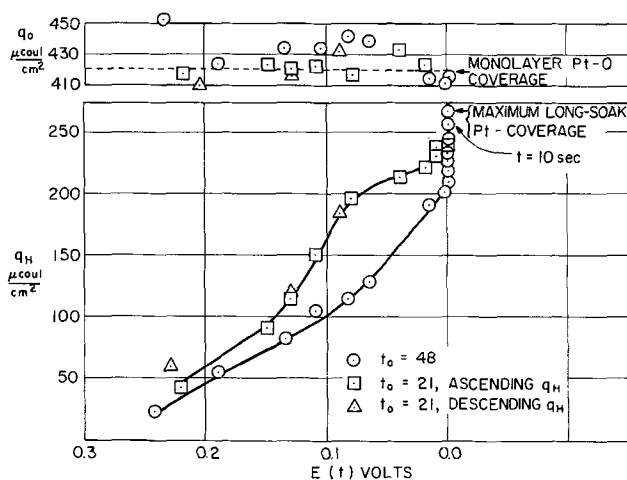


Fig. 8. Amounts of hydrogen found in the hydrogen region, and "oxygen" found in the oxygen region vs. potential attained in decay curve.

the hydrogen ionization region and no excess charge in the oxygen region whereas electrode L shows less  $q_{\text{H}}$  in a given time while the  $q_0$  measured simultaneously is anomalously high. It appears that the over-all rate of the hydrogen resorption is not greatly different in the two cases, but on L considerably more time is required for hydrogen to be sorbed in a form detected below 0.8v in a charging curve. Therefore, on L some hydrogen not yet sorbed in the usual ways is oxidized in the O sorption region, adding to the charge measured there. The slow process impeding hydrogen sorption could be either diffusion to a suitable chemisorption site, sorption of H into the derma, or the act of strong chemisorption itself. An alternate possibility is that it is not the sorption of the hydrogen that governs the potential at which it oxidized, but the kinetics of its subsequent oxidation. Then tiny amounts of unremoved oxygen in the Pt could act as a catalytic poison, impeding the oxidation of hydrogen sorbed near it. It is reasonable that the L electrode would hold oxygen more firmly in the H resorption region just as it did in the O removal region. The fact that oxygen coverage measured on L returns to the normal 1 monolayer at long times assures that no error in electrode area distorts these data.

A very long time, much greater than 10 sec, is required to cover the electrode with full steady-state H coverage, although the equivalent of one monolayer ( $210 \mu\text{coul}/\text{cm}^2$ ) is sorbed in about 0.2 sec on each electrode. This is fully consistent with the view repeatedly expressed by this Laboratory that hydrogen sorbed on the surface is present in various forms, namely, weakly and strongly bonded H and derma-sorbed hydrogen (hydrogen present in the Pt atomic layers just below the surface layer). It is probable that resorption of hydrogen into the derma is the slow process governing uptake of the last portion of the hydrogen sorbed.

The difference between A and L, which affects the rate of Pt-O<sub>ad</sub> reaction with hydrogen, also affects the manner in which hydrogen resorbs on the electrode. It does not, however, affect the  $E(t)$  vs. time relation or the over-all rate of sorption materially.

**Oxygen removal region.**—**Oxygen coverage vs. potential.**—It is apparent from Fig. 3 and 4 that the intrinsic difference between the reaction rates on the two electrodes is removed by normalization, giving voltage/time and oxygen coverage/time behaviors that are essentially the same. The data for  $0.3\text{v} > E(t) > 0.0\text{v}$  (Fig. 4), in which the oxygen coverage of L appears to drop below zero, results from the anomalously high "oxygen" coverages found in the second pulse at certain times (cf. Fig. 8 and discussion in preceding section). It appears that true zero Pt-O coverage may be more closely related to the point of inflection in the decay curve at 0.35v and  $t/t_0 = 0.90$ . Conclusions previously drawn based on comparisons of decay times would not be influenced materially by a 10% change in the decay time used.

**Rate of oxygen removal.**—The rate of oxygen removal was previously (2) shown to be zero order in hydrogen partial pressure (from 1.0 to 0.1 atm), in stirring rate (from quiescent to vigorously gas-stirred), and in amount of oxygen removed from  $\frac{1}{2}$  monolayer to 2 monolayers. Hence, mass transport of solution  $\text{H}_2$  to the surface is not rate-limiting. There is no indication that bare surface must be available for  $\text{H}_2$  to chemisorb prior to reaction with Pt-O, for the integrated rate of removal of oxygen was the same for initial coverages ranging from less than a monolayer to two monolayers (2). In this study the kinetics of the removal were essentially the same for initial coverages of 0.92 and 1.03 monolayer.

The changes observed both in reaction order and in rate when initial Pt-O concentration was less than 0.8 monolayer indicate that the mechanism of the oxygen removal reaction changes. For this reason, the cases

where the initial coverage  $\theta_a$  is less than 0.8 and where it is about 1.0 are discussed separately.

*Case where  $\theta_a < 0.8$ .*—The rate of oxygen removal is independent of  $\theta_a$  and  $x$ . This behavior is to be expected if the surface contains sites with widely differing activities, and if the over-all rate of the reaction  $v_R$  is determined by the rapid rate  $v_R^*$  at relatively few "active sites" that comprise fraction  $l$  of the surface, and that are supplied (rate of surface diffusion  $v_D$ ) as rapidly as necessary from the reservoir of oxygen atoms sorbed on the rest of the surface. Recognizing that in fact there is probably a whole spectrum of sites of differing activity on the surface, we may for simplicity consider the surface to have two kinds of sites, active and inactive (or less active), of fractions  $l$  and  $m$  with the fraction of  $l$  and  $m$  covered with oxygen being  $\theta_l$  and  $\theta_m$ . If  $l$  is quite small, say less than 0.05, and if  $v_D \gg v_R^*$ , then as long as Pt-O is still present on inactive sites,  $l$  remains fully covered until  $\theta_m$  becomes very low. Hence the rate of the reaction of the species on  $l$ , which is the only area catalytically significant, will be zero order in reactant. This model would make reasonable the very wide variations in  $v_R$  that have been observed as a result of thermally annealing or chemically etching the surfaces (1), for if  $l$  is sufficiently small, then addition or subtraction of relatively few active sites can change  $l$  substantially.

For several reasons, it is improbable that active sites are obstructed by product molecules as the reaction proceeds. First, the product will either be  $H_2O$ , the same as the solvent, or, if it is an intermediate, it is likely unstable with a short lifetime. Second, if active sites were obscured, then reaction rate would decrease with amount reacted, contrary to the data in Fig. 6. Finally, when all of the  $O_{ad}$  was reduced, the second charging curve in the O sorption region showed  $q_0 = 420 \mu\text{coul}/\text{cm}^2$ , the amount required for adsorption of 1 monolayer of  $O_{ad}$ . If during decay a significant amount of  $O_{ad}$  were reduced to a product that required only 1 electron per  $O_{ad}$  atom reformed, then recharging to full  $O_{ad}$  coverage would require  $< 420 \mu\text{coul}/\text{cm}^2$ .

*Case where  $\theta_a \approx 1.0$ .*—The rate of oxygen removal was found to be first order in oxygen coverage. The reason for this difference in reaction order and the increase in initial rate at  $a \approx 1.0$  is obscure. It is not the same sort of apparent reaction order change frequently noted in catalytic reactions, where as concentration of the reactant on the active surface increases, the reaction order decreases from unity to zero. Here, in the  $\theta_a < 0.8$  case, the active surface is thought to be fully covered at the lowest initial concentrations used, yet in the  $\theta_a \approx 1$  case the additional adsorbed oxygen somehow causes a change in the reaction order.

Tucker (6) has reported that when oxygen at  $2 \times 10^{-6}$  Torr interacts with Pt at  $400^\circ\text{C}$ , the results may be interpreted in terms of surface Pt atoms being displaced from their normal positions. If the high activity

of the oxygen generated electrochemically in this work is a sufficiently large driving force, then perhaps a related rearrangement occurs here. In such a case, at high coverages the electrode surface would be quite different from that at lower coverages and a different mechanism would be reasonable. It is also conceivable that at very high coverages, additional sites on the surface become catalytically important and hence the initial rate becomes larger. However, it is then not clear why, when coverage has declined to 0.8, the other sites do not control the course of the reaction. In such a case, a zero order reaction rate should be observed for the removal of the remaining oxygen.

### Conclusions

1. This work verifies that in  $H_2$ -saturated solution the time required for potential decay to about 0.300v, after a preceding anodic pulse, is also the time required for removal of the chemisorbed oxygen deposited by that pulse.
2. The rate of removal of  $O_{ad}$  is of apparent first order in adsorbed oxygen when the initial fraction of surface covered is about 1.0; it is zero order in adsorbed oxygen and in amount reacted when the initial fraction of surface covered is  $< 0.8$ . It is zero order in hydrogen partial pressure in both cases.
3. Several alternative rate-determining steps in the decay reaction were considered, one being the rate of surface diffusion of  $O_{ad}$  or  $H_{ad}$  to the active sites, another being the actual rate of reaction at these active sites. The latter is favored as somewhat more probable, for it appears that active sites are involved rather than the whole surface, at least for  $\theta_a < 0.8$ . Steps probably excluded as rate-limiting are: (a) mass transport of solution  $H_2$  to the surface, (b) obstruction of active surface sites by adherent product molecules, (c) chemisorption of solution  $H_2$  on electrode prior to reaction with Pt-O.
4. For electrodes of differing activities, a significant difference is found in the way hydrogen resorbs on recently stripped electrodes; no difference other than rate is found in the way the Pt-O is removed.

Manuscript received June 22, 1967; revised manuscript received Sept. 27, 1967.

Any discussion of this paper will appear in a Discussion Section to be published in the December 1968 JOURNAL.

### REFERENCES

1. T. B. Warner, S. Schuldiner, and B. J. Piersma, *This Journal*, **114**, 1120 (1967).
2. S. Schuldiner and T. B. Warner, *ibid.*, **112**, 212 (1965).
3. M. W. Breiter, *ibid.*, **109**, 425 (1962).
4. D. T. Sawyer and E. T. Seo, *J. Electroanal. Chem.*, **5**, 23 (1963).
5. S. Schuldiner and R. M. Roe, *This Journal*, **110**, 332 (1963).
6. C. W. Tucker, Jr., *J. Appl. Phys.*, **35**, 1897 (1964).

# Thermodynamic Properties of LiCl in Dimethyl Sulfoxide

William H. Smyrl and Charles W. Tobias\*

*Inorganic Materials Research Division, Lawrence Radiation Laboratory, and  
Department of Chemical Engineering, University of California, Berkeley, California*

## ABSTRACT

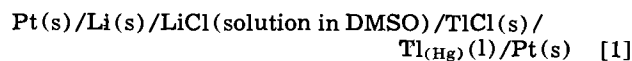
EMF measurements were performed at 25°, 30°, and 35°C on the cell



For concentrations up to 0.12M, the activity coefficients at each temperature may be represented satisfactorily by Guggenheim's extension of the Debye-Hückel equation. The partial molal Gibbs free energy, entropy and enthalpy of transfer of LiCl from DMSO to water have been calculated to be  $-4.93$  kcal/mole,  $+24.8$  cal/°K-mole and  $+2.61$  kcal/mole, respectively.

Because of its high dielectric constant and stability, dimethyl sulfoxide has been of interest as an ionizing solvent for some time (Table I). Although the chemistry of the solvent has been the subject of numerous investigations, very few thermodynamic data are available for its solutions. The only thermodynamic data which have been reported for electrolytic solutions in DMSO are some solubilities (1, 2), some acid-base equilibria (3), cryoscopic data on electrolytes in the solvent (4-6), and the heats of solution of several iodides (7). In addition, Cogley and Butler (8) have reported some qualitative thermodynamic results from measurements on the cell to be described below.

The present work is based on EMF measurements on the cell



The paucity of information relevant to the behavior of inorganic salts, and of reactive metals in nonaqueous media, as well as the potential usefulness of the solvent in voltaic cells, and in electrosynthesis, justify this choice. A halide system was chosen because of the low solubility of other salts in the solvent medium for which a reference electrode with a common anion could be found. Previous work in this laboratory established the advantages of the thallium amalgam-thallose chloride reference electrode (9). The nature of the reference electrode restricted the choice of the anion to chlorides and the metal cation to one of those rather high in the oxidation potential series. The lithium electrode was in part selected because of the opportunity to obtain direct thermodynamic measurements on a metal-metal ion couple which, along with the other alkali and alkaline earth metals, reacts spontaneously with most other ionizing solvent media. The potential usefulness of a lithium electrode in galvanic cells was also considered.

## Experimental

The vacuum-tight Pyrex cell constructed for this purpose (Fig. 1) consisted of five approximately 2-cm

diameter tubes arranged in radial positions, each connected to a central tube by 6 mm glass tubing. Reference electrodes and the counter electrodes (Li) were placed in the peripheral compartments, while the central tube served to introduce the solutions. In each experiment, two reference electrodes and three lithium electrodes were used. The cell was designed so that solutions did not come in contact with stopcocks.

The solvent (Matheson, Coleman, and Bell, spectrographic grade) was purified by distillation under reduced pressure at 80°C. The product was found to contain less than 50 ppm water by Karl Fischer titration and had a melting point of 18.58°C.

Lithium chloride (Baker and Adamson) was dried by refluxing thionyl chloride over it for 2 hr. The dried salt was stored in a vacuum desiccator under an atmosphere of dry argon.

The lithium metal (Lithium Corporation of America, 99.9%) was obtained commercially and stored under oil.

Solutions were made either by direct weighing of solute and solvent or by dilution of more concentrated solutions. The solutions were prepared and stored in a glove box under an atmosphere of dry argon. The lithium electrodes were prepared by etching the surface in an HCl solution in DMSO, carefully rinsing with solvent, and then rinsing with a portion of the solution to be used in the cell. The cell was

Table I. Selected physical properties of DMSO

		Reference
Molecular weight	78.13	†
Melting point	18.58°C	(10)
Boiling point	189.0°C	(10)
Dielectric constant, 25°C	48.05	
Density	1.0956 g/cm <sup>3</sup>	(11)
Entropy of vaporization, 189°C	25.8 cal/mole-°K	
Dipole moment	3.9 Debye	(12)
Debye-Hückel constant, 25°C	2.57 (kg/mole) <sup>1/2</sup>	
30°C	2.57 (kg/mole) <sup>1/2</sup>	
35°C	2.59 (kg/mole) <sup>1/2</sup>	

† Present work.

\* Electrochemical Society Active Member.



Fig. 1. Five-compartment cell used for emf measurements

assembled, the solution introduced, and the cell was removed from the glove box and suspended in a grounded water bath. Temperature was controlled within  $\pm 0.01^\circ\text{C}$ .

On each cell the measuring procedure began 15 min after thermal equilibrium at  $25^\circ\text{C}$  had been attained. The measurements were made with an L&N K-3 potentiometer, using carefully calibrated standard cells. The second set of measurements at  $25^\circ\text{C}$  was made 1 hr later and, if there was less than 0.1 mv difference between the readings, the temperature was raised to  $30^\circ$  and  $35^\circ\text{C}$ , respectively, where the measurements were repeated. The temperature was then reduced to  $25^\circ\text{C}$ , and another set of measurements was made. The last measurement at  $25^\circ\text{C}$  always agreed within less than 0.1 mv with the earlier measurements at  $25^\circ$  if the temperature cycle was shorter than 12 hr. The bias potential between the reference electrodes was always less than 0.05 mv and for the lithium electrodes was less than 0.1 mv.

The thallium amalgams used in the present studies were all in the concentration order of  $10^{-2}$  mole fraction thallium. The voltage of the cell [1], was "corrected" to solid thallium metal by using the emf data on thallium amalgam concentration cells of Richards and Daniels (14). The relative potentials of the amalgams employed are given in Tables II, III, and IV.

In Tables V, VI, and VII are given the results of the cell measurements at  $25^\circ$ ,  $30^\circ$ , and  $35^\circ\text{C}$ , respectively. In the first column is given the molality of LiCl in solution. The measured cell voltage,  $E$ , and the amalgam are listed in the second and third columns, respectively. The cell voltage "corrected" to solid thallium,  $E'$ , is given in the fourth column.  $E'$  is related to the standard cell potential and the solution concentration by

$$E' = E^0 - \frac{2RT}{F} \ln m_{\text{LiCl}} \gamma_{\text{LiCl}} \quad [2]$$

where both  $E^0$  and  $\gamma_{\text{LiCl}}$  are unknowns. The usual arbitrary definition is adopted: the activity coefficient of lithium chloride approaches unity as the concentration of lithium chloride approaches zero. The limiting equation proposed by Guggenheim (13) is employed to facilitate extrapolation to infinite dilution, i.e.

$$\ln \gamma_{\text{LiCl}} = -\frac{\alpha z_+ |z_-| I^{1/2}}{1 + I^{1/2}} + 2\beta_{\text{LiCl}} m_{\text{LiCl}} \quad [3]$$

Table II. Relative potentials of thallium amalgams at  $20^\circ\text{C}$

Mole fraction Tl <sup>a</sup>	Amalgam	$\mathcal{E}^b$
$9.67 \times 10^{-3}$	1	0
$9.32 \times 10^{-3}$	3	-0.00107
$1.035 \times 10^{-2}$	2	+0.00193
$9.71 \times 10^{-3}$	4	+0.00012
1		+0.14690

Table III. Relative potentials of thallium amalgams at  $30^\circ\text{C}$

Mole fraction Tl <sup>a</sup>	Amalgam	$\mathcal{E}^b$
$9.67 \times 10^{-3}$	1	0
$9.32 \times 10^{-3}$	3	-0.00107
$1.035 \times 10^{-2}$	2	+0.00199
$9.71 \times 10^{-3}$	4	+0.00012
1		+0.15091

Table IV. Relative potentials of thallium amalgams at  $40^\circ\text{C}$

Mole fraction Tl <sup>a</sup>	Amalgam	$\mathcal{E}^b$
$9.67 \times 10^{-3}$	1	0
$9.32 \times 10^{-3}$	3	-0.00111
$1.035 \times 10^{-2}$	2	+0.00203
$9.71 \times 10^{-3}$	4	+0.00012
1		+0.15483

<sup>a</sup> Calculated using molecular weights based on  $C^{12} = 12.000$ .  
<sup>b</sup> Absolute volts.

Table V. Results of cell potential measurements at  $25^\circ\text{C}$

m (moles/kg)	$E$ (volts)	Amalgam	$E'$ (volts)	$E^0$ (volts)
0.87877	2.47341	1	2.32451	2.25398
0.30177	2.52252	3	2.37255	2.26417
0.16389	2.54697	4	2.39819	2.26722
0.12450	2.55971	3	2.40974	2.26825*
0.12213	2.56064	3	2.41067	2.26843*
0.08803	2.57327	1	2.42437	2.26930*
0.08775	2.57324	1	2.42434	2.26915*
0.07592	2.57932	4	2.43054	2.26956*
0.05821	2.59230	3	2.44233	2.27055*
0.05821	2.59110	4	2.44232	2.27054*
0.02821	2.62266	4	2.47388	2.27156*
0.01775	2.64319	1	2.49429	2.27164*
0.00988	2.66970	1	2.52080	2.27163
0.00891	2.67465	1	2.52575	2.27182
0.00884	2.67500	1	2.52610	2.27180
0.00768	2.67933	2	2.53236	2.27157
0.00677	2.68436	2	2.53739	2.27072
0.00456	2.70491	1	2.55601	2.27115
0.00383	2.71131	2	2.56434	2.27075
0.00356	2.71687	1	2.56797	2.27099
0.00332	2.71830	2	2.57133	2.27060
0.00275	2.72604	2	2.57907	2.26958
0.00190	2.74340	2	2.59643	2.26900
0.00178	2.74803	1	2.59913	2.26849
0.00089	2.77455	2	2.62758	2.26288
0.00084	2.77562	2	2.62965	2.26208
0.00045	2.79921	2	2.65224	2.25358

\* Data used in least squares analysis.

Table VI. Results of cell potential measurements at  $30^\circ\text{C}$

m (moles/kg)	$E$ (volts)	Amalgam	$E'$ (volts)	$E^0$ (volts)
0.30177	2.52102	3	2.36904	2.25885
0.16389	2.54550	4	2.39471	2.26154*
0.12450	2.55880	3	2.40682	2.26296*
0.12213	2.55951	3	2.40753	2.26291*
0.07592	2.57825	4	2.42746	2.26378*
0.05821	2.59156	3	2.43958	2.26492*
0.05821	2.59039	4	2.43960	2.26494*
0.02821	2.62241	4	2.47162	2.26591*
0.00988	2.67002	2	2.52110	2.26576
0.00768	2.67988	2	2.53096	2.26575
0.00677	2.68496	2	2.53604	2.26488
0.00456	2.70393	2	2.55501	2.26489
0.00383	2.71222	2	2.56330	2.26474
0.00357	2.71765	1	2.56674	2.26478
0.00275	2.72716	2	2.57824	2.26352
0.00190	2.74477	2	2.59585	2.26315
0.00178	2.74936	1	2.59845	2.26226
0.00089	2.77639	2	2.62747	2.25661
0.00084	2.77798	2	2.62906	2.25529
0.00045	2.80111	2	2.65219	2.24679

\* Data used in least squares analysis.

Table VII. Results of cell potential measurements at  $35^\circ\text{C}$

m (moles/kg)	$E$ (volts)	Amalgam	$E'$ (volts)	$E^0$ (volts)
0.30177	2.51946	3	2.36550	2.25310
0.16389	2.54423	4	2.39148	2.25581*
0.12450	2.55773	3	2.40377	2.25726*
0.12213	2.55842	3	2.40446	2.25717*
0.07592	2.57747	4	2.42472	2.25810*
0.05821	2.59072	3	2.43676	2.25902*
0.05821	2.58964	4	2.43689	2.25915*
0.02821	2.62214	4	2.46939	2.26013*
0.00988	2.67039	1	2.51752	2.25989
0.00768	2.68038	2	2.53032	2.23987
0.00677	2.68587	2	2.53581	2.25950
0.00383	2.71319	2	2.56313	2.25679
0.00357	2.71865	1	2.56578	2.25878
0.00275	2.72829	2	2.57823	2.25747
0.00190	2.74617	2	2.59611	2.25683
0.00178	2.75068	1	2.59781	2.25603
0.00089	2.77775	2	2.62769	2.24637
0.00084	2.77939	2	2.62933	2.24515
0.00045	2.80276	2	2.65270	2.23982

\* Data used in least squares analysis.

Here,  $\alpha$  = Debye-Hückel constant,  $I$  = ionic strength =  $\frac{1}{2} \sum_i z_i^2 m_i$ , and  $\beta_{\text{LiCl}}$  = constant, independent of molality. From [2],

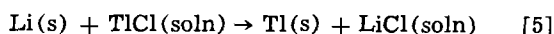
$$E' - \frac{\alpha z_+ |z_-| I^{1/2}}{1 + I^{1/2}} \left( \frac{2RT}{F} \right) + \frac{2RT}{F} \ln m = E^0 = E^0 - \frac{4RT}{F} \beta_{\text{LiCl}} m \quad [4]$$



where Eq. [4] defines  $E^o$ . The function  $E^o$  is listed in the fifth column of Tables V, VI, and VII.

By constructing a plot of  $E^o$  vs.  $m$ , according to Eq. [4], one should obtain a straight line. Extrapolating to  $m \rightarrow 0$ , one can obtain  $E^o$  and then  $\gamma_{\text{LiCl}}$ , for other concentrations at which the cell emf is measured.

$E^o$  is plotted vs. molality in Fig. 2, 3, and 4. The emf-s of the cells were found to be well behaved for concentrated solutions of lithium chloride. As the concentration is decreased, the function  $E^o$  becomes a linear function of molality. The sharp decrease of  $E^o$  at concentrations below  $2 \times 10^{-2}M$  was quite unexpected. This behavior could not be explained by random scatter of data; the decrease persisted at all three temperatures. Several independent sets of solutions, made by both methods, were used, and the data was found to be reproducible and not due to errors in solutions concentration. A reaction in the cell could not have caused this behavior because the cell voltage was constant over the period of the temperature cycle. After 12-hr the lithium electrodes became discolored, and the cell potential began to decrease steadily due to the reaction



The unexpected decrease of  $E^o$  occurred in solutions where the concentration of LiCl was approaching that of TlCl. The solubility product of TlCl in dimethyl sulfoxide is  $5 \times 10^{-7}$  (8). Since TlCl must be kept away from the lithium electrode, where it will react, a concentration gradient of TlCl exists in the cell. The cell potential will be lower than expected when there is diffusion of the sparingly soluble salt from the reference electrode. At higher concentrations of LiCl, it would be expected that the nonuniform concentration distribution would be of no effect, and the effect should become greater as the solution concentration of LiCl decreases. The departure of the potential from

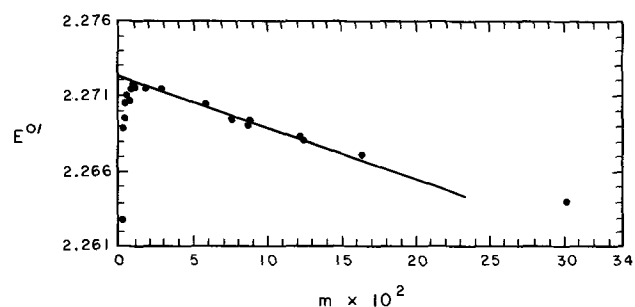


Fig. 2. Extrapolation of emf data to infinite dilution at 25°C.

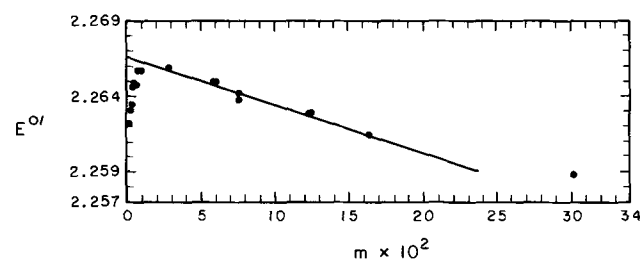


Fig. 3. Extrapolation of emf data to infinite dilution at 30°C

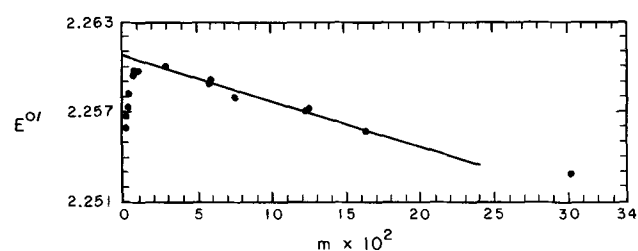
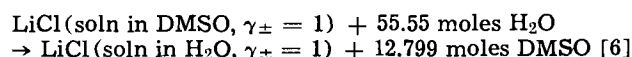


Fig. 4. Extrapolation of emf data to infinite dilution at 35°C

the linear extension of the line obtained by least squares fit of the data at higher concentrations can be, to a good approximation, explained by quantitative consideration of the effect of diffusion of TlCl (15).

With the foregoing consideration in mind, the extrapolation to infinite dilution was made by fitting a least squares line to the data in the linear region. The results of the data analysis are summarized in Table VIII for the 95% confidence level. From these results were calculated  $\Delta G^o$ ,  $\Delta H^o$ , and  $\Delta S^o$  for the cell reaction. These thermodynamic functions are given in Table IX.

The same calculations may be carried out for aqueous solutions. The quantity  $\Delta \bar{G}^o$  for the transfer at 25°C,



is found to be

$$\Delta \bar{G}^o = -4.93 \text{ kcal/mole}$$

The entropy of transfer at this temperature is calculated to be +24.8 cal/°K-mole, after correcting for the difference in partial molal volume of the two solvents.

Activity coefficients were determined as a function of concentration at the measured temperatures. Activity coefficients obtained from the smoothed data are given in Table X at rounded concentrations.

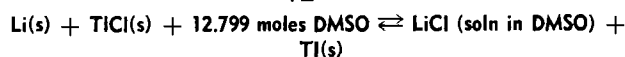
The behavior of the activity coefficient of LiCl indicates that it is a completely dissociated salt in very dilute solutions. We arrive at this interpretation from the value of  $\beta_{\text{LiCl}}$  which is positive, as in aqueous solutions. In aqueous solutions, a negative value of  $\beta$  is interpreted as an indication of ion pairing (18). Although the magnitude of  $\beta_{\text{LiCl}}$  in dimethyl sulfoxide is larger than in water, we attach less significance to the magnitude than to the sign. Further interpretation

Table VIII. Standard cell potentials at 25°, 30°, and 35°C

T (°K)	$E^o$ (volts)	$\beta_{\text{LiCl}}$ (kg/mole)
298.15	2.27234 ± 0.00045	0.325 ± 0.040
303.15	2.26685 ± 0.00072	0.298 ± 0.052
308.15	2.26083 ± 0.00064	0.286 ± 0.045

Table IX.  $\Delta G^o$ ,  $\Delta S^o$ , and  $\Delta H^o$  for the reaction

$$\gamma_{\pm} = 1$$



T (°K)	$\Delta G^o$ (kcal/mole)	$\Delta S^o$ (cal/°K-mole)	$\Delta H^o$ (kcal/mole)
298.15	-52.40 ± 0.01	-26 ± 2	-60.2 ± 0.6
303.15	-52.27 ± 0.02	-26 ± 4	-60.2 ± 0.6
308.15	-52.14 ± 0.01	-26 ± 2	-60.2 ± 0.6

Table X. Activity coefficients of lithium chloride at 25°, 30°, and 35°C

m moles/kg	-ln $\gamma_{\text{LiCl}}$		
	25°	30°	35°
0.005	0.152	0.160	0.165
0.010	0.220	0.230	0.230
0.015	0.270	0.275	0.275
0.020	0.306	0.310	0.310
0.025	0.335	0.339	0.340
0.030	0.360	0.364	0.365
0.035	0.383	0.385	0.392
0.040	0.404	0.405	0.414
0.045	0.422	0.423	0.430
0.050	0.440	0.440	0.447
0.060	0.470	0.470	0.475
0.080	0.511	0.520	0.525
0.100	0.548	0.560	0.565
0.120	0.582	0.592	0.600

must await further data on other electrolytes in dimethyl sulfoxide.

The activity coefficients from the present study (25°) are consistently higher than those reported by Dunnett and Gasser (18.5°) obtained from freezing point depression studies (4). According to our measurements, correction for temperature would increase the discrepancy. Analysis of the results of Dunnett and Gasser according to the method suggested by Brown and Prue (16)<sup>1</sup> yields a value  $\beta_{\text{LiCl}} = -2.11$ . The reasons for the disagreement with the present study are not understood. It seems possible that traces of water may have caused anomalous freezing point readings in the dilute solutions, those most important for the determination of  $\beta_{\text{LiCl}}$ . Also, the value of the cryoscopic constant (4.36) used by Dunnett and Gasser is subject to question. This value reported by Lindberg, Kenttämää, and Nissema (17) is based on cryoscopic measurements on solutions of benzene in dimethyl sulfoxide, but the most dilute solution used was 0.88M. If one used the cryoscopic constant of Skerlak *et al.* (5), *i.e.*, 3.97, for the above analysis, the value of  $\beta_{\text{LiCl}}$  becomes positive. The value of 3.97 is also consistent with the data of Lindberg *et al.*

According to the present results the free energy and entropy of transfer of LiCl from dimethyl sulfoxide to water are in the direction one would predict from the relative dielectric constant of the two solvents. Calculations of the dielectric constant effect according to the Born equation do not account quantitatively for the free energy and entropy of transfer. Similar conclusions were reached for several other solvents by Strehlow (19). The heat of transfer of LiCl from DMSO to H<sub>2</sub>O is calculated to be +2.61 kcal. This may be compared to the recent measurements of the heats of transfer of several iodides from DMSO to H<sub>2</sub>O (7), for which the heats of transfer, as expected, are larger, in the order of +10 kcal.

#### Acknowledgment

This work was supported in part by the Electrochemistry Branch Naval Ordnance Laboratory, Corona, and in part by the Atomic Energy Commission.

<sup>1</sup>In these calculations we used for the dielectric constant 49.15 (10), 18.55°C as the melting point of the solvent (4), 1.1000 g/cm<sup>3</sup> for the density (11), and 4.36 (17) for the molal cryoscopic constant.

Manuscript received Aug. 28, 1967; revised manuscript received Oct. 16, 1967. This paper was presented at the Dallas Meeting, May 7-12, 1967, as Abstract 133.

Any discussion of this paper will appear in a Discussion Section to be published in the December 1968 JOURNAL.

#### REFERENCES

1. J. Kenttämää, *Suomen Kemistilehti*, **B33**, 180 (1960).
2. C. Melendres (Dissertation), University of California, September, 1965.
3. I. M. Koltoff and T. B. Reddy, *Inorg. Chem.*, **1**, 189 (1962).
4. J. S. Dunnett and R. P. H. Gasser, *Trans. Faraday Soc.*, **61**, 922 (1965).
5. T. Skerlak, B. Ninkov, and V. Sislov, *Bull. Soc. Chim. Sarajevo*, (Yugoslavia), **11**, 34 (1962).
6. M. D. Archer and R. P. H. Gasser, *Trans. Faraday Soc.*, **62**, 3451 (1966).
7. E. M. Arnett and D. R. McKelvey, *J. Am. Chem. Soc.*, **88**, 2598 (1966).
8. D. R. Cogley and J. N. Butler, *This Journal*, **113**, 1074 (1966).
9. W. H. Smyrl and C. W. Tobias, *ibid.*, **113**, 754 (1966).
10. H. L. Schläfer and W. Schaffernicht, *Angew. Chem.*, **72**, 618 (1960).
11. R. G. LeBel and D. A. I. Goring, *J. Chem. Engr. Data*, **1**, 100 (1962).
12. F. A. Cotton and R. Francis, *J. Inorg. Nuclear Chem.*, **17**, 62 (1961).
13. E. A. Guggenheim, *Phil. Mag.*, **19**, 588 (1935).
14. T. W. Richards and F. Daniels, *J. Am. Chem. Soc.*, **41**, 1732 (1919).
15. W. H. Smyrl and C. W. Tobias, "The Effect of Diffusion of a Sparingly Soluble Salt on the EMF of a Cell without Transference," *Electrochim. Acta*, **13** (1968).
16. P. G. M. Brown and J. E. Prue, *Proc. Roy. Soc. (London)*, **A232**, 320 (1955).
17. J. J. Lindberg, J. Kenttämää, and A. Nissema, *Suomen Kemistilehti*, **B34**, 98 (1961).
18. E. A. Guggenheim, "Thermodynamics," 4th ed., p. 361, North-Holland, Amsterdam, (1959).
19. H. Strehlow, *Z. Elektrochem.*, **56**, 827 (1952).
20. W. H. Smyrl (Dissertation), University of California, Berkeley, 1966.

## Technical Note



### Effects of Probe Position on Potentiostatic Control during the Breakdown of Passivity

D. C. Mears<sup>1</sup> and G. P. Rothwell

Department of Metallurgy, University of Cambridge, Cambridge, England

The breakdown of passivity of stainless steels with the formation of brightened pits in chloride-containing solutions has received considerable attention since the observations of Brennert(1). More recently, similar breakdown of passivity has been recorded for a wide variety of passive alloys in solutions in which the anion concentration and anode potential are sufficiently high(2). It is of practical interest to assess the natural resting potential of such alloys, and to compare it

with the breakdown potential determined during the measurement of polarization curves in deaerated solutions. If the breakdown potential is considerably higher than the highest natural resting potential of an alloy in a given chloride solution, the alloy is unlikely to undergo chloride breakdown in use in that solution(3). It is essential, however, to know and to control the anode potential precisely during the polarization measurements. We have measured anode potentials simultaneously with two Luggin probes in different positions and find that electrode geometry strongly influences

<sup>1</sup>Present address: Nuffield Department of Orthopaedic Surgery, University of Oxford, Oxford, England.

the potential recorded at different points on the anode. Furthermore, prior to and during breakdown of passivity the electrode potential of the pitting region may fall rapidly to ca. 100 mv more negative than the controlled electrode potential at the passive anode surface.

Electrical analogues have also illustrated these and other problems of electrode geometry(4). Somewhat similar observations have previously been made on the localization of attack on naturally corroding specimens (5-7).

### Electrochemical Experiments

Specimens of stainless steel (18Cr-10Ni-3Mo) and of Vitallium (30Cr-5Mo, bal.Co) were prepared by masking the borders with Picien wax or Lacomit stopping-off lacquer. The anode potential was controlled potentiostatically using a Luggin probe at the center of the specimen. Additional probes were positioned at the masked edge and at the center of the specimen (Fig. 1); the pd between these two saturated calomel reference electrodes was measured using an electronic millivoltmeter. The area of the anode was ca. 1 cm<sup>2</sup>, and that of the concentric cathode ca. 10 cm<sup>2</sup>. Solutions of 0.2M and 1M sodium chloride, and 4M magnesium chloride were deaerated(8) until the specimen potential had fallen below ca. -350 mv(nhe). Potentiostatic anodic polarization curves were then measured in 50 mv, 10 min steps for both alloys, in the three solutions; at each step the pd between the two non-controlling probes was also measured.

While a specimen is passive, the pd between the probes at edge and center is negligible (< 2 mv), except during the current transient after each increase in potential, when the current initially rises, then falls due to film thickening(9), and the pd between the probes may rise to ca. 20 mv (the edge probe being positive), falling rapidly to zero. As the specimen undergoes film breakdown, the transient and steady potential differences between the two probes increase to ca. 100 mv and 40 mv, respectively. Breakdown of passivity, with the formation of hemispherical brightened pits, occurs predominantly at the masked edge of the specimen. As the anode cd increases further the pd between middle and edge probes ceases to rise, and may decrease, falling below zero in many cases. Figure 2 shows a typical polarization curve for Vitallium in 0.2M sodium chloride solution, with a probe pd/potential curve superimposed. For anode potentials below ca. 200 mv, corresponding to passive

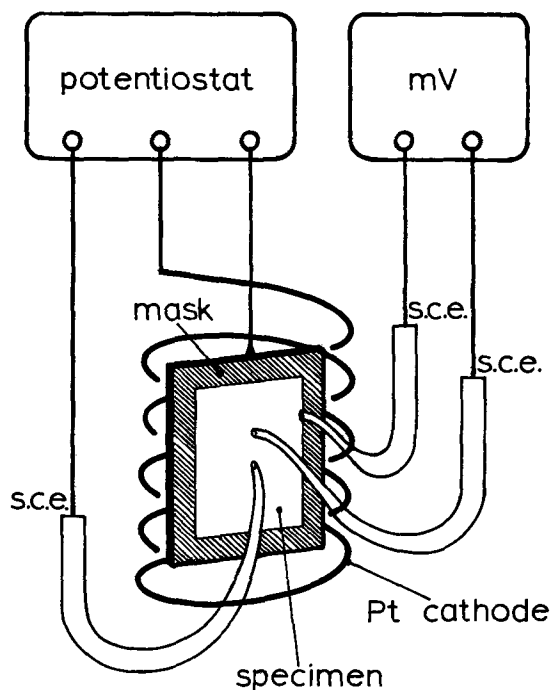


Fig. 1. Apparatus for electrochemical experiments

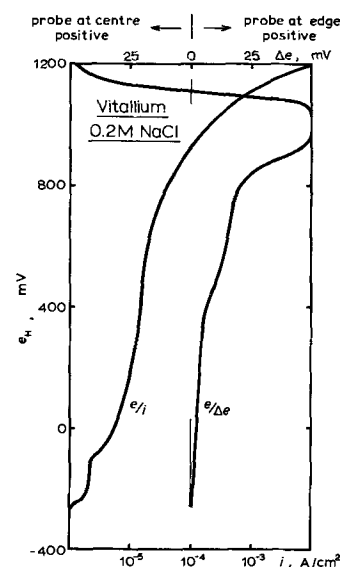


Fig. 2. Anodic polarization curve ( $e/i$ ) and curve for edge/center potential difference ( $e/\Delta e$ ) for Vitallium in 0.2M sodium chloride solution.

current densities of less than 10  $\mu\text{A}/\text{cm}^2$ , the pd between the edge and the middle is negligible. At higher potentials, rapid breakdown occurs with a large increase in current. The pd between edge and middle rises rapidly to ca. 60 mv. At still higher anode potentials, the steady pd decreases rapidly and ultimately changes sign.

The edges of some specimens were coated with Picien wax so that the wax was flush with the face of the specimen. Polarization curves and pd measurements gave results similar to those for earlier experiments.

The above experiments were repeated with the potential of the edge, rather than that of the middle controlled potentiostatically. With specimens at potentials at which they exhibit passive behavior, the pd from middle to edge is negligible. At higher anode potentials chloride breakdown occurs primarily at the center of the specimen. The probe at the middle of the specimen becomes positive to that at the edge by ca. 60 mv.

Anodic polarization curves and pd measurements were repeated in rapidly stirred solutions: breakdown of passivity occurred with random pitting, and the electrode potentials at different points on the anode differed by less than 5 mv.

### Discussion

Potential variations in natural corrosion environments have been measured by previous workers for many different systems. The work of Bianchi(10) deserves particular attention. In the present work, the polarization experiments with measurement of potential variation across the controlled anode show that electrode geometry may strongly influence the observed behavior of specimens under potentiostatic control. For specimens with surface area of ca. 1 cm<sup>2</sup> determinations of the breakdown potential may be in error by  $\pm 50$  mv; for larger specimens, greater error could occur. The site of breakdown may be altered from random pitting to preferential edge attack. Very high rates of flow tend to minimize the effects of electrode geometry and may cause a return to random pitting behavior. These effects may also be minimized when the anode and counter electrode are opposed parallel surfaces of the same extent, such as two plates or two concentric cylinders, with an insulating barrier extending perpendicularly between their ends, as has been suggested by Piontelli(11).

For film growth on a passive metal under potentiostatic conditions, in a cell giving anything other than perfect uniformity of potential, the rate of the anodic

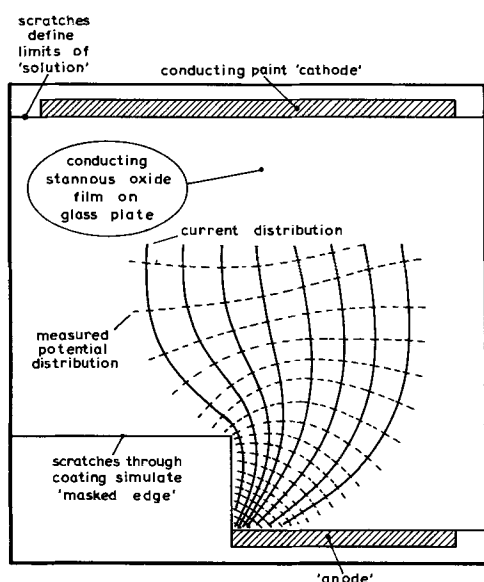


Fig. 3. Potential and current distributions for an electrical analogue of the masked edge on a passive specimen.

process is correspondingly nonuniform. Figure 3 shows the current distribution in an electrical analogue of the masked edge of a passive specimen(4). When the electrode potential, controlled by a probe at the center of the specimen is increased abruptly, the cd at the central region also increases abruptly, then decreases as the passive film thickens. At regions remote from the controlling probe, in which the current distribution leads to current densities higher than those on the bulk of the specimen, the transient cd must also be greater than that near to the probe, although the electrode potential appears to be lower (i.e., potential in the solution more positive), until the equilibrium film thickness has been reached. The transient metal dissolution and film formation processes also occur faster in these regions. This variation in rates of formation may itself lead to structural variations in the film in different regions of the specimen, and to enhanced take-up of aggressive anions into the film, leading ultimately to the observed initial breakdown in these regions. Very high rates of flow of solution then lead to more random attack by increasing the (diffusion controlled) cd near the probe during the transient period, shortening the transient and minimizing differences of potential across the specimen. Similarly, if the controlling probe is placed at the masked edge of the specimen, where the natural current distribution leads to the highest transient current densities, the effect of such transients in determining the site of breakdown is minimized, and random attack is usually observed.

After high potential breakdown of passivity in natural environments, the corrosion process is under cathodic control, and the potential in the pit decreases (b Fig. 4). Consequently, at the lowered mixed potential the pit may be gradually repassivated. If the pit becomes repassivated, the mixed potential may again rise until breakdown of passivity occurs elsewhere on the specimen. Once a pit has formed breakdown in the adjacent area is less likely because of the change in potential distribution. Random breakdown is thus observed in this case.

If the potential is under the control of a cathodic reaction which is not readily polarized, the potential at the pit site falls only slightly after the breakdown of passivity (c Fig. 4), so that adjacent, and ultimately general breakdown can ensue.

For passive specimens under potentiostatic control, with this type of nonuniform current distribution the potentiostat supplies to the center of the specimen the cd required by the anode, and to the edge areas a cd proportionally higher, as dictated by the geometry

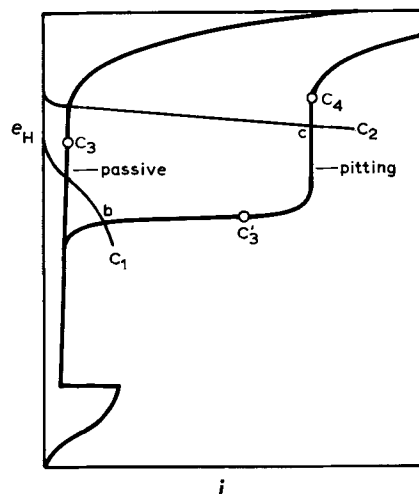


Fig. 4. Schematic anodic polarization curves for a typical passive alloy which undergoes high potential breakdown. Curve  $C_1$  represents the behavior of a natural cathode and  $C_2$  that of a less polarizable cathodic reaction. Points  $C_3$ ,  $C_3'$  represent the behavior under potentiostatic control of a system with small pits, and  $C_3$ ,  $C_4$  the behavior of the same system when the pits have become large enough to affect current distribution at the probe.

of the system. When pitting starts, provided that the total current in this area is less than that available in the distribution the pitting can proceed at its limiting cd at the same potential as the bulk of the specimen. However when the pitting area increases so that the current requirement exceeds that available, then the potential and the pitting cd fall so that the total current requirement can be maintained. Thus the electrode potential may fall during pitting to a point such as  $C_3'$  while the bulk of the specimen may be at  $C_3$ . The fact that the film resistance decreases greatly with the onset of pitting may lead to a decreased  $iR$  drop across the film, leading to a still lower measured electrode potential of the metal.

As the pitting area grows larger it may influence the current distribution at the center of the specimen. If this occurs, the pitting current may increase by drawing from the main current distribution, the potentiostat supplying more current as required to maintain the passive potential. Once the pitting current density again reaches the limiting cd, the pitting potential, which is virtually under galvanostatic control, may continue to rise toward  $C_4$ , giving ultimately the observed change in sign of the difference in potential between the pitting and passive regions. We stress therefore that potentiostatic control does not necessarily insure uniformity of potential at the surface of the working electrode.

Manuscript received Aug. 1, 1966; revised manuscript received Sept. 19, 1967.

Any discussion of this paper will appear in a Discussion Section to be published in the December 1968 JOURNAL.

#### REFERENCES

1. S. Brenner, *Korros. Metallsch.*, **12**, 46 (1936).
2. T. P. Hoar, D. C. Mears, and G. P. Rothwell, *Corros. Sci.*, **5**, 279 (1965).
3. T. P. Hoar and D. C. Mears, *Proc. Roy. Soc.*, **A294**, 486 (1966).
4. D. C. Mears, Ph.D. Thesis, University of Cambridge 1965.
5. U. R. Evans, *J. Iron St. Inst.*, **141**, 219P (1940).
6. U. R. Evans and T. P. Hoar, *Proc. Roy. Soc.*, **A137**, 343 (1932).
7. R. H. Brown and R. B. Mears, *Trans. Electrochem. Soc.*, **74**, 495 (1938).
8. D. C. Mears and G. P. Rothwell, *J. Sci. Inst.*, **42**, 446 (1965).
9. T. P. Hoar, "Anodic Behaviour of Metals" in "Modern Aspects of Electrochemistry," No. 2, J. O'M. Bockris, Editor, Butterworths, London (1954).
10. G. Bianchi, *Metallurg. ital.*, **45**, 123, 323 (1953).
11. R. Piontelli, *Z. Elektrochem.*, **59**, 778 (1955).

# Electret Phenomenological Theory Presented in Linear Systems Formalism

Donald E. Tilley

Department of Physics, Collège militaire royal de Saint-Jean, Saint-Jean, Québec, Canada

## ABSTRACT

Standard techniques for the analysis of linear systems are applied to the phenomenological theory of the electret effect, as developed by Wiseman and Feaster and extended by Perlman and Meunier. A generalized electric susceptibility is introduced which allows electret behavior at constant temperature to be characterized by two functions, the impedance and the short-circuit current. Asch's electret theory is shown to be equivalent to the assumption that the generalized susceptibility is an exponential function.

A phenomenological theory of electrets, based on Gross's two-charge theory (1) and the superposition principle used by Wiseman and Feaster (2) as well as by Perlman and Meunier (3), has been given by the author in a previous paper (4) in a form which allows a simple and unified treatment of several electret problems. In the present paper, this theory is reviewed and amplified with the presentation now given using the most familiar tool for the analysis of linear systems, the Laplace transform. Natural generalizations of the electric susceptibility and the dielectric constant are introduced, and the role of these quantities in electret phenomenological theory is emphasized. Finally, it is shown that this theory includes, as a very special case, the electret theory of Asch (5).

### Generalized Electric Susceptibility

The polarization of a dielectric with a time dependent internal electric field  $E(t)$  depends not only on the present value of the field but also on the history of the dielectric. It is convenient to regard the polarization  $P(t)$  as a sum

$$P(t) = P_i(t) + P_s(t) \quad [1]$$

where  $P_i(t)$  is the polarization which responds practically instantaneously to the applied field, and  $P_s(t)$  is the slow response that is determined by fields that have existed at all previous instants up to the time  $t$ . The method of measurement will determine in a given experiment what response should be classified as instantaneous. In any case, in a linear isotropic dielectric the fast response is given by

$$P_i(t) = \chi_i E(t) \quad [2]$$

where  $\chi_i/\epsilon_0$  is the electric susceptibility characterizing the instantaneous response. (MKS units are used throughout this paper.)

The experiments of Wiseman and Feaster (2) and of Perlman and Meunier (3) show that, at constant temperature, the polarization of Carnauba wax is a linear superposition of the contributions furnished by electric fields applied in the past. This superposition principle can be expressed in several different but equivalent ways. The formulation of the superposition principle given in this paper allows the introduction of natural generalizations of the electric susceptibility and the dielectric constant. We assume that the slow polarization response of a dielectric maintained at constant temperature can be characterized by a response function  $\chi_s(t)$  such that a field  $E(t)$  applied between the times  $T$  and  $T + dT$  produces a polarization which, at a later time  $t$ , is  $\chi_s(t-T)E(T)dT$ . The linear superposition of contributions from all previous electric fields gives the polarization

$$P_s(t) = \int_{-\infty}^t \chi_s(t-T)E(T)dT \quad [3]$$

It is assumed that  $\chi_s(t) = 0$  for  $t < 0$  and that  $\chi_s(t) \rightarrow 0$  as  $t \rightarrow \infty$ . The response function  $\chi_s(t)$  is to be determined empirically and is often assumed to be a sum of exponential decays. Equations [1]-[3] yield, for the total polarization, the expression

$$P(t) = \int_{-\infty}^{t+} \chi(t-T)E(T)dT \quad [4]$$

where

$$\chi(t) = \chi_i \delta(t) + \chi_s(t) \quad [5]$$

and  $\delta(t)$  is the Dirac delta function [ $\int_{-\infty}^{+\infty} \delta(t) = 1$

and  $\delta(t) = 0$  for  $t \neq 0$ ]. The relationship between  $\chi(t)$  and the response function  $\pi(t)$  used by previous workers (2, 3) is  $\chi(t) = d\pi/dt$ . In a pioneering paper on dielectric after-effects (6), Gross expressed the after-current as a superposition of contributions from previous voltage changes and used a response function  $\phi(t)$  which is proportional to  $\chi_s(t)$ .

It is the function  $\chi(t)/\epsilon_0$  which merits the name "the generalized electric susceptibility." The corresponding generalized dielectric constant is  $K(t)/\epsilon_0$  where

$$K(t) = \epsilon_0 \delta(t) + \chi(t) \quad [6]$$

as can be seen by examining the relationship between the electric displacement  $D(t)$  and the electric field. The electric displacement is defined by

$$D(t) = \epsilon_0 E(t) + P(t) \quad [7]$$

Now using Eq. [4], [6], and [7] we obtain

$$D(t) = \int_{-\infty}^{t+} K(t-T)E(T)dT \quad [8]$$

which shows that it is the function  $K(t)$  which enables the electric displacement to be expressed as a superposition of contributions from previous electric fields.

The convolution relationships given by Eq. [3], [4], and [8] in the time domain take on a particularly simple form when one takes either the Fourier transform or the two-sided Laplace transform to pass to the domain of complex frequency  $s$ . Since the transform of the convolution of two functions is the product of the transforms, the transform of the polarization is simply the product of the transform of the generalized electric susceptibility with the transform of the electric field.

In initial value problems, it is convenient to use the one-sided Laplace transform with the lower limit 0- (7). Using the bar notation for such transforms we define

$$\bar{E}(s) = \int_{0-}^{\infty} E(t)e^{-st}dt \quad [9]$$

It is necessary to single out the part,  $P_b(t)$ , of the slow polarization response that arises from electric fields which have existed before  $t = 0$ . Equation [3] gives

$$P_b(t) = \int_{-\infty}^{0^-} \chi_s(t-T)E(T)dT \quad [10]$$

Equations [4] and [10] now yield the simple algebraic relation between Laplace transforms

$$\bar{P}(s) = \bar{P}_b(s) + \bar{\chi}(s)\bar{E}(s) \quad [11]$$

and Eq. [5], [6], [8], and [10] give

$$\bar{D}(s) = \bar{P}_b(s) + \bar{K}(s)\bar{E}(s) \quad [12]$$

Equations [11] and [12] show that, in the complex frequency domain, except for the appearance of the term  $P_b(s)$ , the relationship between the fields and the generalized susceptibility and dielectric constant is the same as the relationship in time domain between the fields and the usual susceptibility and dielectric constant when the response is considered to be instantaneous.

#### Electret Impedance

The formalism introduced in the preceding section can be used to present the solution to the electret field equations in the familiar language of circuit analysis. At the interface of an electrode carrying a real surface charge density  $\sigma(t)$  with a dielectric within which there is an electric displacement  $D(t)$ , Gauss's law gives

$$D(t) = \sigma(t) \quad [13]$$

Differentiation of Eq. [13] yields

$$dD(t)/dt = J(t) - cE(t) \quad [14]$$

where  $J(t)$  is the conduction current density within the electrode and  $cE(t)$  is the ohmic conduction current within the dielectric.<sup>1</sup> Taking Laplace transforms we obtain from Eq. [14]

$$s\bar{D}(s) - D(0^-) = \bar{J}(s) - c\bar{E}(s) \quad [15]$$

Using Eq. [12], the solution to Eq. [14] can be written in the transparent and useful form

$$\bar{E}(s) = \bar{z}(s)[\bar{J}(s) - \bar{J}_b(s)] \quad [16]$$

where

$$\bar{z}(s) = 1/[c + s\bar{K}(s)] \quad [17]$$

and

$$\bar{J}_b(s) = s\bar{P}_b(s) - D(0^-) \quad [18]$$

The electret impedance, in the complex frequency domain, is determined by  $\bar{z}(s)$  which is seen to be a simple function of the conductivity  $c$  and the generalized dielectric constant  $\bar{K}(s)$ .

The quantity  $\bar{J}_b(s)$  is the value of  $\bar{J}(s)$  when  $\bar{E}(s) = 0$  and therefore is named the short-circuit current density. All the effects of the past history (at constant temperature) of the dielectric are included in this term. A useful expression for the evaluation of  $\bar{J}_b(s)$  is obtained by using Eq. [1], [2], [7], and [10], together with Eq. [18] to yield

$$\bar{J}_b(s) = s\bar{P}_b(s) - P_b(0^-) - [\epsilon_0 + \chi_i]E(0^-) \quad [19]$$

In Eq. [19], the quantity  $s\bar{P}_b(s) - P_b(0^-)$  is simply the Laplace transform of  $dP_b(t)/dt$ .

Several applications of Eq. [16]-[18] are given in ref. (4). An important special case arises when the generalized susceptibility function is assumed to involve a sum of two exponentials

$$\chi_s(t) = Ae^{-\alpha t} + Be^{-\beta t} \quad [20]$$

<sup>1</sup> It is assumed that the dielectric is homogeneous and that, within the dielectric, the fields  $E$ ,  $D$ ,  $P$  are uniform.

for  $t \geq 0$ . Such a function, with constants  $A$ ,  $B$ ,  $\alpha$ , and  $\beta$  determined empirically, has been found adequate to give good agreement with experimental measurement of the charge decay at constant temperature of Carnauba wax electrets (2-4). For such a  $\chi_s(t)$ , it is easy to give a simple equivalent circuit for a dielectric slab (4).

#### Asch's Theory as a Special Case

Instead of assuming a superposition principle, Asch (5) postulates that the polarization  $P_s(t)$  satisfies the first order linear differential equation

$$dP_s(t)/dt = -\alpha[P_s(t) - kE(t)] \quad [21]$$

with an initial condition,

$$P_s(0) = P_0 \quad [22]$$

It is interesting to notice that Asch's equations, Eq. [21] and [22], are equivalent to a very special case of the general theory developed in this paper, the case where  $\chi_s(t)$  is (for  $t \geq 0$ ) the single exponential function

$$\chi_s(t) = \alpha ke^{-\alpha t} \quad [23]$$

with the initial polarization given by

$$P_b(0) = P_0 \quad [24]$$

In this case Eq. [3] and [10], together with Eq. [23] and [24] yield

$$P_s(t) = e^{-\alpha t} P_0 + \int_0^t k\alpha e^{-\alpha(t-T)} E(T) dT \quad [25]$$

Now using the familiar rules for the differentiation of an integral it is easy to verify that the  $P_s(t)$  given by Eq. [25] is the solution to Asch's Eq. [21] and [22].

In applying his equations to the case of an electret which is polarized at one temperature and then cooled and maintained, for times  $t \geq 0$ , at a constant final temperature, Asch implies that the effect of the temperature change can be described very simply as follows. For a given value of the initial polarization  $P_0$  at the final temperature, the subsequent electret behavior is independent of the temperatures encountered before  $t = 0$  and therefore is the same as if the electret had been maintained always at the final temperature. With this assumption, the polarization  $P_s(t)$  given by Eq. [25] is, for  $t \geq 0$ , the common prediction of both Asch's theory and the special case of the superposition principle, Eq. [3], which arises when  $\chi_s(t)$  is the exponential function given in Eq. [23].

#### Acknowledgment

The author wishes to thank Professor M. M. Perlman for stimulating discussions and for reading the manuscript.

Manuscript received Aug. 30, 1967. This paper was presented at the Electrets Symposium at the Chicago Meeting, Oct. 15-19, 1967, as Abstract 120.

Any discussion of this paper will appear in a Discussion Section to be published in the December 1968 JOURNAL.

#### REFERENCES

1. B. Gross, *Phys. Rev.*, **66**, 26 (1944).
2. G. Wiseman and G. Feaster, *J. Chem. Phys.*, **26**, 521 (1957).
3. M. M. Perlman and J. L. Meunier, *J. Appl. Phys.*, **36**, 420 (1965).
4. D. E. Tilley, *ibid.*, **38**, 2543 (1967).
5. G. Asch, *C. R. Acad. Sci. (France)*, **256**, 5302 (1963).
6. B. Gross, *Phys. Rev.*, **57**, 57 (1940).
7. F. F. Kuo, "Network Analysis and Synthesis," p. 121, John Wiley & Sons, Inc., New York (1962).

# The Electret Effect in Ice

J. D. Cross

University of Manchester, Institute of Science and Technology, Manchester, England

## ABSTRACT

The electret behavior of polycrystalline and single crystal ice is investigated by means of measurements of the dipole moment of the samples, the currents flowing during charging and discharging, and the potential distribution within the sample. For comparison, measurements are made of the persistent dipole moment of tetradecanol, carboxylic acid C<sub>20</sub>, and paraffin wax. The results show that in these substances the build-up and decay of space charges contribute to the volume polarization.

The electret effect has been mainly studied in complex materials; although such materials have shown the electret effect very strongly their complexity is a severe hindrance to workers hoping to identify the mechanisms of the electret effect. A suitable material for a study of the mechanisms of electret formation should have a known simple structure, the normal conduction processes should be known, and it should be possible to produce samples of high purity in both polycrystalline and single crystal states. All these conditions are fulfilled by ice, and therefore it was chosen as the principal subject for this investigation. To determine the effect of internal structure on the electret effect behavior measurements were also made on samples of 1-tetradecanol, carboxylic acid C<sub>20</sub>, and paraffin wax.

## Experimental Methods

The quantities measured in this investigation were the macroscopic dipole moment of the electrets, the currents flowing during charging and discharging of the electrets, and the potential distribution within the electrets. All samples were disks 12 mm in diameter and 3 mm thick. Polycrystalline samples were made by allowing materials to solidify in a mould. Single ice crystals were grown by a method described by Jaccard (1), and disks were cut from these. All measurements were carried out at a temperature of  $-70^{\circ}\text{C}$  in a nitrogen atmosphere. In all cases the polarizing field was applied for 30 min. The water used had an impurity content of 7 ppm.

*Dipole moment measurements.*—Measurement of the macroscopic dipole moment of an unshielded electret provides a sensitive method of observing changes in the polarization of the electret without the disturbance produced by the removal and replacement of surface electrodes involved in the usual lifted electrode measurements of the surface charge. The dipole moments were measured with a torsion balance similar to that described by Cross and Hart (2).

A schematic diagram of the balance is shown in Fig. 1. The sample, in the form of a disk, is suspended by a gold ribbon between two parallel plates referred to as the field plates. The upper end of the gold ribbon is attached to a torsion head free from backlash. Mirrors  $M_1$  and  $M_2$  are used in conjunction with a lamp and scale to determine the angular position of the sample with respect to the field plates. When the sample holder is clamped the sliding electrodes can be used to apply the required polarizing field; these electrodes are withdrawn when dipole moment measurements are made.

When a potential difference is applied to the field plates the field so produced interacts with the dipole moment of the sample to produce a torque,  $\tau$ , given by  $\tau = \mu \times E$  where  $E$  is the field applied and  $\mu$  is the dipole moment of the sample. By rotating the head of the suspension on opposing torque is applied to the sample to position the axis of the sample at right

angles to the applied field. The field is then reversed, and the suspension is again rotated to position the axis of the sample at right angles to the field. Readings of the torsion head are taken for each field direction. The angular difference between these two readings is twice the angle of twist necessary to counteract the torque due to the field. The dipole moment can be calculated if the torsional properties of the suspension and the field strength are known. The suspension used had a torsion constant of 0.1 dyne cm/radian, the torsion head could be read to 1 min of arc, the applied field was 0.5 esu/cm and therefore dipole moments of approximately  $10^{-4}$  esu could be measured. To study the electret behavior of a material with this balance a sample is prepared in the form of a disk 12 mm in diameter. The sample is fitted into the holder and the sliding electrodes moved to the required position with respect to the sample, and the polarizing field is applied. After a suitable time interval the polarizing field is removed, the sliding electrodes are withdrawn, and the dipole moment is measured as described above.

*Current measurements.*—When a potential difference is applied to electrodes in contact with an electret material a current flows through the circuit. This current decreases with time to a small constant value. If the source of potential difference is removed and electrodes connected together, a current, which decreases with time, flows in the reverse direction.

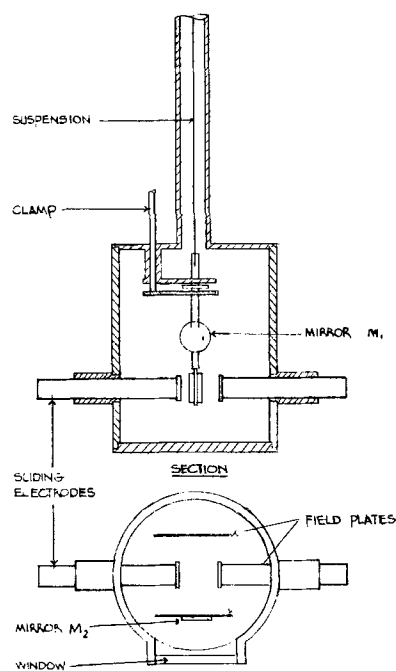


Fig. 1. Torsion balance



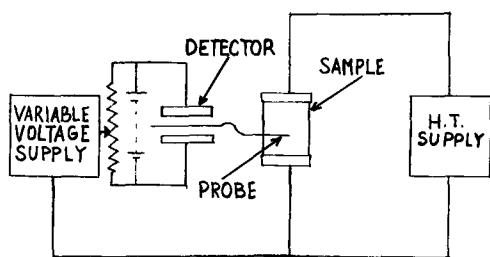


Fig. 2. Schematic diagram of the probe circuit

In this investigation measurements were made of these charging and discharging currents for polycrystalline ice.

**Potential distribution measurements.**—The potential distribution within polycrystalline ice disks, after the application of an electric field by means of electrodes on the surface, was measured by means of three platinum probes inserted at distances of 0.5, 1.3, and 2.5 mm from the cathode. The potential of the probes was determined by a null method. The circuit is shown schematically in Fig. 2. The null detector designed by Hart and Mungall (3) is essentially a robust equivalent of the string electrometer and can easily be constructed to produce a detector with extremely high leakage resistance so that off balance the current drawn by the probe is negligible and at balance there is no current drawn. The sensitivity of the detector was  $\pm 5$ v.

### Results and Discussion

Figure 3 shows the variation of the charging and discharge currents for a sample of ice electrified by applying 3 kv to brass electrodes in contact with the surface. The currents fall off with time reaching almost constant values within 6 min. The total charge liberated on discharging is approximately 150 esu. Figure 4 shows the variation with time of the dipole moment of ice electrified by applying 3 kv to brass electrodes in contact with the sample. The dipole moment corresponds always to a homocharge, the magnitude of which decreases with time. As ice has a low-frequency dielectric constant of approximately 100 the field in the region between an electrode and the sample it is nominally in contact with will be very high, and therefore a considerable amount of charge transfer is to be expected; this may therefore mask any volume effect. To avoid this, samples of ice were electrified by applying a potential difference to electrodes 1 mm from the surface of the samples. Figure 5 shows the dipole moment of ice electrified in this manner as a

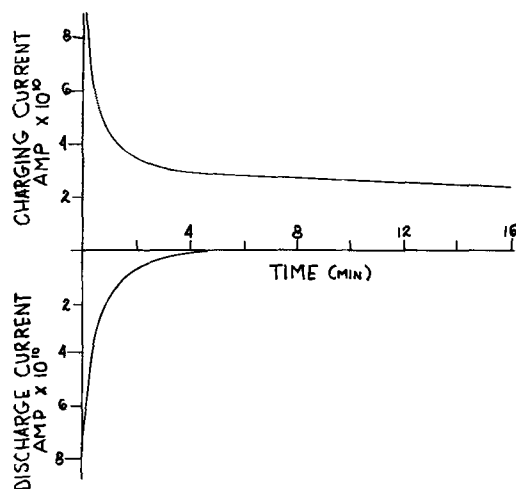


Fig. 3. Charge and discharge currents as a function of time for polycrystalline ice electrified between brass electrodes in contact with the surface: applied potential 3 kv.

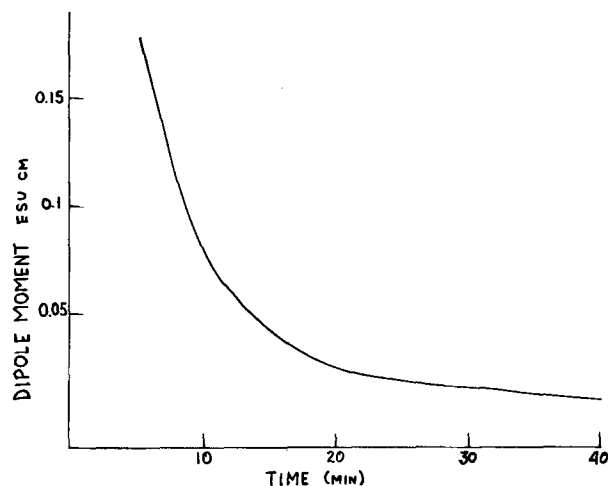


Fig. 4. Dipole moment as a function of time for polycrystalline ice electrified between brass electrodes in contact with the surface: applied potential 3 kv.

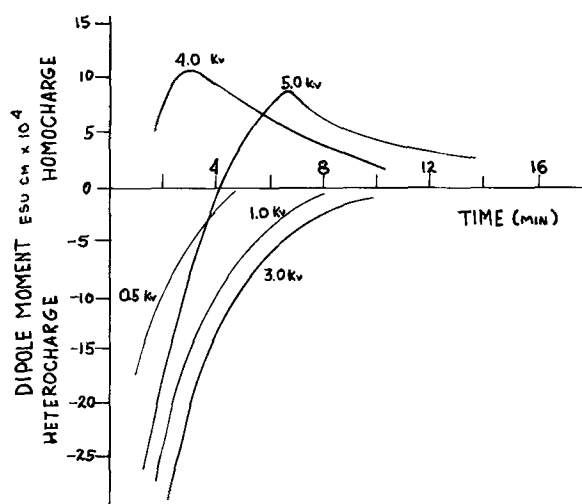


Fig. 5. Dipole moment as a function of time for polycrystalline ice electrified between electrodes 1 mm from the surface: applied potentials 0.5, 1.0, 3.0, 4.0, and 5.0 kv.

function of time after removal of the polarizing field. For applied potentials of 0.5, 1.0, and 3.0 kv the dipole moment corresponds to a volume polarization which decays to zero. For an applied potential of 4 and 5 kv the dipole moment is initially equivalent to a heterocharge, it falls to zero, rises to a maximum value in the opposite direction, and then falls slowly toward zero. This is an electret effect similar to that observed in carnauba wax, the only difference being in time scale. The behavior is explicable in terms of the two-charge theory: ice has a low frequency constant of 100 and therefore with applied potentials of 0.5, 1.0, and 3.0 kv the fields in the air gap between the electrodes and the samples are 2.5, 5.0, and 15 kv/cm, respectively. These fields are too low to cause breakdown in the gap, and therefore no surface charge is deposited, and the dipole moment is due to a heterocharge. With applied potentials of 4 and 5 kv the fields in the air gap are 20 and 25 kv/cm; enhancement by uneven surfaces will produce breakdown, and the observed dipole moment will be the resultant of the volume polarization and a real surface charge.

It should be noted that the dipole moment for samples polarized with "contact" electrodes is approximately one hundred times that for samples electrified with 1 mm air gap. This supports the suggestion that in the case of contact electrodes the high field at the dielectric-electrode interface caused a large transfer of

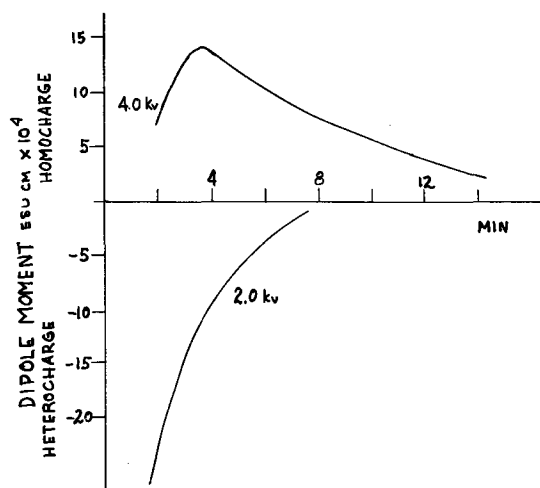


Fig. 6. Dipole moment as a function of time for single crystal ice electrified between electrodes 1 mm from the surface: applied potentials 2.0 and 4.0 kv.

charge which would have masked the volume polarization present.

Figure 6 shows the dipole moment for single crystal ice electrified between electrodes 1 mm from the surface. The behavior of the single crystal is almost identical to the polycrystalline sample.

The nature of the volume polarization has been a point of dispute in electret studies. The choice lies between a space charge mechanism, a uniform volume polarization, or a combination of the two. All measurements of the internal potential distribution with probes have shown the existence of space charges near the surfaces. X-ray studies of polarized and nonpolarized electrets have failed to show any increased ordering in the polarized electrets. From this evidence it seems that a space charge effect must exist. Objections have been made [Gerson (4)] to the apparent independent decay of a space charge in close proximity with a real surface charge of opposite polarity. This behavior can be explained by a simple model. It is necessary to assume that the surface charges are trapped so that they are not discharged by the approach of a charge carrier forming the space charge, then the situation at the moment the external field is removed is illustrated by Fig. 7. As a simplification the space charges are assumed to exist as a thin uniform layer of charge near each electrode, the charge per unit area being  $Q$ . The trapped surface charge has a density  $\sigma$  per unit area. The electric field at a point in the space charge layer is equal to  $\sigma - Q/KE_0$ , where  $K$  is the dielectric constant of the medium. For  $\sigma > Q$  the surface charge initially predominates, and the internal field holds the space charge to the surface layer. The change in dipole moment is controlled then by the decay rate of the surface charge, the dipole moment reaching zero when  $\sigma = Q$ . This is the behavior shown in Fig. 4 for the sample electrified with electrodes in contact with the sample.

If  $\sigma < Q$  the internal polarization predominates initially, and the internal field results in a migration of the space charge layers to the center of the sample. This migration reduces the contribution of the space charge to the dipole moment, causing the surface

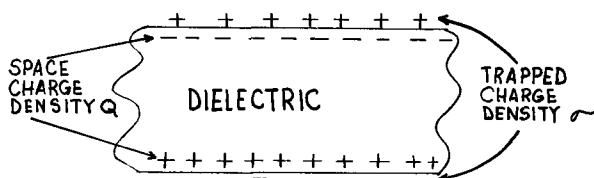


Fig. 7. Schematic diagram of a polarized electret

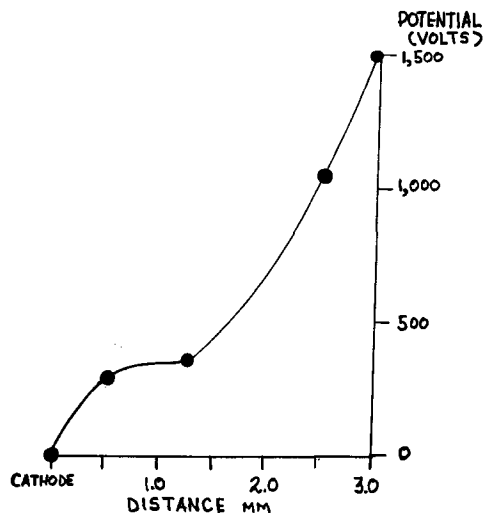


Fig. 8. Potential distribution within a 3 mm thick sample of polycrystalline ice, 30 min after the application of 1500v to electrodes on the surface.

charge to predominate. The maximum value of the positive dipole moment is reached when the space charges of opposite sign meet. From then on the change in dipole moment is controlled by the decay of surface charge. This is the behavior shown in Fig. 5 and 6 for ice samples electrified between electrodes spaced 1 mm from the surface.

The potential distribution within ice with an applied potential difference of 1.5 kv, measured by the probes, is shown in Fig. 8. The potential distribution shows the existence of a strong positive space charge near the cathode and a very weak negative space charge near the anode. This is to be expected from the theory of electrical conduction in ice proposed by Jaccard (5) in which conduction is attributed to the migration of protons and  $H_3O^+$  ions.

The main experimental evidence against a space charge mechanism is the work by Gross (6) in which measurements were made of the discharge current released when an electret, that had been cooled during polarization, was reheated. The discharge current liberated by sections cut from the electret was found to be independent of the thickness of the sections and of the position in the electret from which the section was taken. This indicated that a uniform polarization was responsible for the current. However, experiments on tetradecanol by Cross and Hart (2) showed that discharge currents are not dependent on internal polarization alone, and the results shown in Fig. 3 and 4 support this view. The surface charge on the ice electret electrified between contact electrodes completely obscures any volume effect and the decay of this major charge concentration must effect the discharge current. Measurements of the discharge current cannot be taken as evidence in favor of a uniform volume polarization unless the contributions of surface effects can be shown to be zero in that experiment.

A uniform volume polarization would arise from a mechanism such as dipole orientation or the short range movements of charges. Such mechanism should be sensitive to the internal structure of the dielectric. To check the dependence of the internal polarization on structure, samples of ice, tetradecanol, carboxylic acid  $C_{20}$ , and paraffin wax were polarized by applying a potential difference of 3 kv to electrodes 1 mm from the surfaces of the samples. The results of these measurements are shown in Fig. 9. All four materials show similar behavior, that is, a slowly diminishing dipole moment corresponding to a volume polarization, yet the structure of the materials differ widely: ice is a purely hydrogen bonded solid. In tetradecanol long hydrogen bonded chains are formed. In carboxy-

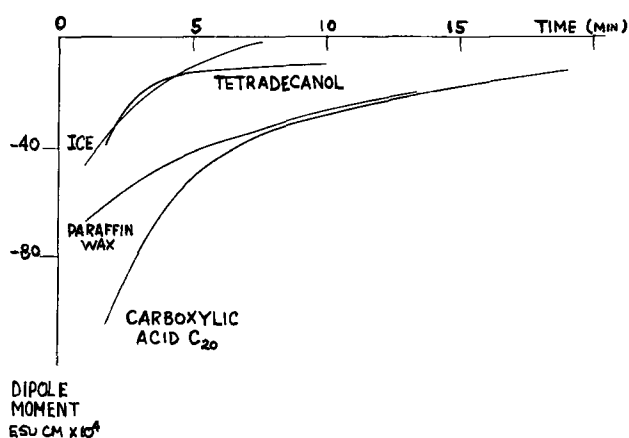


Fig. 9. Dipole moment as a function of time for ice, tetradecanol, carboxylic acid C<sub>20</sub>, and paraffin wax, electrified between electrodes 1 mm from the surface. Applied potential 3.0 kv.

lic acid C<sub>20</sub> hydrogen bonded dimmers form and in paraffin as there is no hydrogen bonding.

As the polarization is so little affected by differing structure and crystalline state it is improbable that uniform volume polarization is involved. All dielectrics used in electret studies have a finite electrical conductivity. In any dielectric with a finite electrical conductivity space charges will accumulate near the electrodes applied to the surface if there is any hindrance to the complete discharge of the charge carriers at the electrode. It is impossible to attach removable electrodes to a solid dielectric in such a way that there is perfect electrical contact over the

whole dielectric-electrode interface and, if the surface charge or dipole moment is to be measured, and hence a volume polarization detected, the electrodes must be removable. Therefore in any electret study space charges must accumulate; and in fact whenever they have been directly sought by probe techniques, as in this work and in tetradecanol by Cross and Hart (2) or in carnauba wax [Gemant (7), Antennan (8), Van der Linde (9)], they have been detected.

The conclusion to be drawn is that the persistent volume polarization in electrets must be, at least in part, due to space charges and in simple materials it is wholly due to space charges.

Manuscript received June 29, 1967; revised manuscript received ca. Sept. 27, 1967. This paper was presented at the Electrets Symposium at the Chicago Meeting, Oct. 15-19, 1967, as Abstract 125. This work was supported by a Science Research Council Grant, reference B/SR/4382.

Any discussion of this paper will appear in a Discussion Section to be published in the December 1968 JOURNAL.

#### REFERENCES

1. C. Jaccard, *Helv. Phys. Acta*, **32**, 89 (1959).
2. J. Cross and J. Hart, *Brit. J. Appl. Phys.*, **17**, 311 (1966).
3. J. Hart and A. G. Mungall, *J. Sci. Instr.*, **33**, 411 (1956).
4. R. Gerson and J. Rohrbaugh, *J. Chem. Phys.*, **23**, 2381 (1955).
5. C. Jaccard, *Ann. N. Y. Acad. Sci.*, **125**, 390 (1965).
6. B. Gross and R. J. DeMoraes, *J. Chem. Phys.*, **34**, 2061 (1962).
7. A. Gemant, *Phil. Mag.*, **20**, 929 (1935).
8. K. Antennan, *Z. Angew. Math. Phys.*, **7**, 478 (1955).
9. L. Van der Linde, *Z. Physik*, **155**, 413 (1959).

## Production and Charge Decay of Film Electrets

Martin M. Perlman<sup>1</sup>

*Department of Physics, Collège militaire royal de Saint-Jean, Saint-Jean, Québec, Canada*

and Cornelis W. Reedyk

*Northern Electric Research and Development Laboratories, Ottawa, Ontario, Canada*

#### ABSTRACT

The object of this work has been to obtain charged dielectric films, electrets, that retain their charge over periods of years when left open circuited. Such films are receiving increasing attention because of their potential use in practical devices such as condenser microphones, electrostatic recorders, air filters, etc. Procedures have been devised to form highly charged thin films and to measure their decay rates. Charge decay comparisons are made among different materials at various temperatures, charged in different ways. A procedure is developed that enables long lifetimes of electrets at room temperature to be predicted by extrapolating short charge decay times at elevated temperatures. A number of materials are identified as suitable for very long-lived electrets.

#### *Production of Electrets with a Large Net Homocharge*

The decay lifetime of the homocharge of an electret is generally much longer than that of the heterocharge. It is desirable therefore to obtain samples with a large net homocharge. The films used in this work vary in thickness between 0.25 and 5 mils. If such a film be charged in the usual way, i.e., by sandwiching between two metal electrodes, applying heat and a field, net heterocharged electrets result. If one attempts to create net homocharged samples by increasing the applied field, the film soon arcs through at a weak point, dust spot, or microscopic inhomogeneity in the surface of the electrodes.

<sup>1</sup> Consultant at Northern Electric Research and Development Laboratories, Ottawa, Ontario, Canada.

Electrets with a large net homocharge may be produced, without arcing, by inserting an appropriate dielectric between metal electrodes and film (1). The dielectric, air gaps, and film then form a 5-layer capacitor, Fig. 1. (The dielectric inserts are metallized on their surfaces remote from the film to eliminate dielectric-electrode air gaps.) The electric fields in the various layers can be determined by applying Maxwell's equations. The expression for the electric fields in the air gaps enables one to explain why electrets with a large net homocharge are obtained using dielectric inserts.

Assuming that the air gaps behave as ideal dielectrics of dielectric constant equal to unity, using the line integral law for electric field, Gauss's law, and

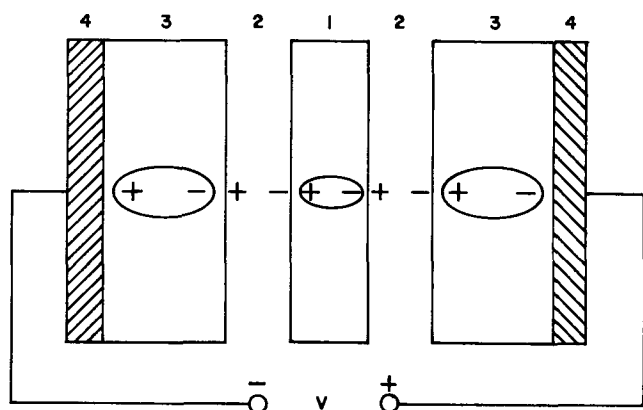


Fig. 1. Five-layer capacitor with dielectric inserts: 1, film; 2, air gaps; 3, inserts; 4, metal electrodes.

the expression connecting electric displacement, field, and polarization, one has (2)

$$E_2 = \frac{V + [d_1(P_1 - \sigma_{r1}) + 2d_3(P_3 - \sigma_{r3})]/\epsilon_0}{d_1 + 2d_2 + 2d_3} \quad [1]$$

where  $E_2$  is the field in the air gaps;  $V$  is the applied charging voltage; subscripts 1, 2, and 3 refer to the film, air gaps, and inserts, respectively;  $d$  is the thickness;  $\sigma_r$  is the real homocharge; and  $P$  is the volume polarization or heterocharge.

At  $t = 0$ , there is no homocharge, i.e.,  $\sigma_{r1} = \sigma_{r3} = 0$ . During charging, the heterocharges  $P_1$  and  $P_3$  increase, and so does the field in the gaps. Eventually, this field will exceed the breakdown strength of the air in the gap, and spray discharges (i.e., homocharge deposition) will occur, increasing  $\sigma_{r1}$  and  $\sigma_{r3}$ . The numerator in Eq. [1] then decreases, and the field in the gap falls to a value below breakdown, quenching the discharges. The heterocharge then continues to increase, and the cycle repeats.

Both heterocharge and homocharge should be present on charging with or without dielectric inserts. However, with inserts, the contribution to the field in the air gap due to the polarization of the inserts relative to that due to polarization of the film is  $2d_3P_3/d_1P_1$ . In these experiments, the latter quantity ranges between 500 and 25, since the insert is 1/16 in. thick, the films are 0.25 to 5 mils thick, and  $P_3$  and  $P_1$  are of the same order. Comparing Eq. [1] with the expression for the field in the air gaps when the inserts are not present (put  $d_3 = 0$  in the numerator of Eq. [1];  $2d_2 + 2d_3$  in the denominator is now the thickness of the air gap), one can see that the gaps will break down many more times during the course of polarization with inserts than without, and one may expect a much larger homocharge in the former case. In Fig. 2, typical voltages across the air gaps are plotted as a function of time in the two cases. Note that the breakdown frequency is much greater in the former case.  $V_0$  is the breakdown voltage of the gaps.

If one attempts to charge an ideal dielectric without inserts,  $d_3 = 0$  in the numerator of Eq. [1], the gap is  $2d_2 + 2d_3$ ,  $\sigma_{r1} = 0$  and  $P_1$  is constant; thus the field in the gap is a constant, and repetitive breakdown cannot occur. With inserts,  $P_3$  varies, and the heterocharge-homocharge cycle takes place. One can of course use a sufficiently high field to create a corona or Townsend discharge and produce homocharge on all films (ideal or not). Charging with inserts produces a large homocharge simultaneous with a volume polarization in nonideal dielectrics, which is desirable for the long-lived electrets considered here.

Most samples were charged with 6 kv applied across the electrodes for 0.5 hr at 120°C. The initial fields were of order 30 kv/cm in the films, 100 kv/cm in the air gaps, and 20 kv/cm in the inserts. Initial charges obtained were about  $5 \times 10^{-8}$  coul/cm<sup>2</sup>. All films were

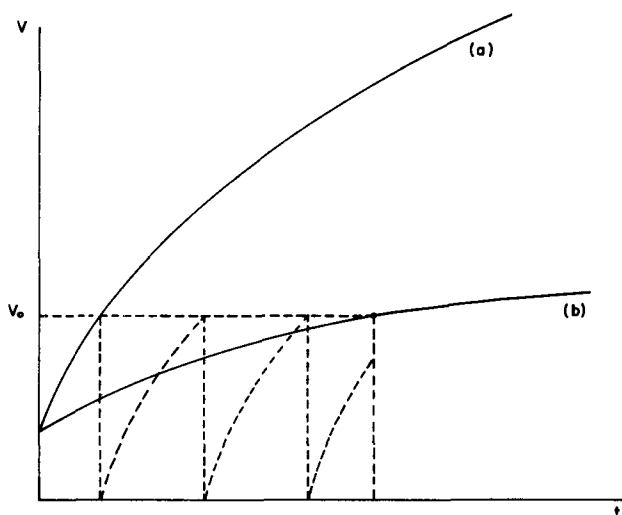


Fig. 2. Voltage  $V$  across the air gap as a function of time  $t$ ; (a) with inserts (b) with inserts replaced by air gaps.

metallized on one side and stored in microphones, with the charged surface in contact with a metallic backplate. The films were only partially shielded because the average gap between surface and backplate was of the same order as the thickness of the film.

The charges were measured by applying sound pressure to vibrate the film, displaying the output signal on a C.R.O., and applying a d-c bias across the metallized side of the film and backplate sufficient to produce zero output signal (3).

The net surface charge ( $\sigma_r - P_s$ ) and bias  $V_B$  are related by

$$(\sigma_r - P_s) = K\epsilon_0 V_B/d_1 \quad [2]$$

where  $K$  is the dielectric constant of the film, and  $\epsilon_0$  is the permittivity of free space.

#### Typical Homocharged and Heterocharged Film Electrets

All films acquired a large net homocharge when polarized using the inserts; those polarized without the inserts were mainly net heterocharge. Both homocharge and heterocharge were simultaneously present whether samples were charged with inserts or not. This is illustrated in Fig. 3 and 4. In Fig. 3, a 5-mil Mylar sample polarized without inserts had an initial bias of 1200v net heterocharge. (Values stated for the bias  $V_B$  may be converted to net surface charge density,  $\sigma_r - P_s$ , using Eq. [2] with appropriate values for dielectric constant and thickness of the films.) The charge was allowed to decay at room temperature and fell to 200v in about 20 days. The sample was then heated to 80°C to increase the rate of decay. Within 4 hr the net heterocharge decayed to zero and reversed its sign to 48v net homocharge. In Fig. 4, a 5-mil Mylar sample polarized with inserts had an initial bias of 500v net homocharge. The charge was allowed to decay

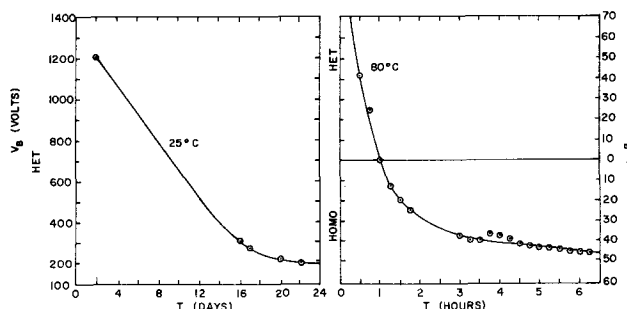


Fig. 3. Charge decay of a net heterocharged electret (5-mil Mylar charged without inserts).

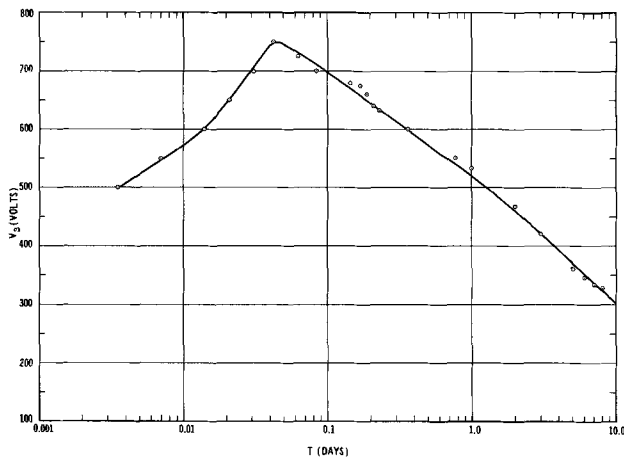


Fig. 4. Charge decay of a net homocharged electret (5-mil Mylar charged with inserts).

at 80°C. An increase in net homocharge to 750v took place in about 1 hr and then a decay over the next ten days. The initial increase in net homocharge is due to the decay of the heterocharge and is just what one expects if both heterocharge and homocharge are present in a net homocharge sample. The real homocharge in the sample polarized with inserts was at least 15 times greater than in the sample polarized without inserts.

To demonstrate that air breakdown is necessary to produce a homocharge in film electrets, a sample of 0.25-mil Mylar was polarized in a vacuum of  $10^{-5}$  Torr at room temperature. The charge was measured during the polarization process using a dissectible capacitor. A slowly increasing heterocharge was observed over a period of ten days. The sample was then heated and the net heterocharge decayed to zero, rather than reversing the sign of its charge, demonstrating that heterocharge only was present in a vacuum.

The above experiments show that we are dealing with the decay of two coexisting charges, resulting in the decay of a net surface charge, *i.e.*, with a true electret phenomenon in films.

*Charge Decay Comparisons at Various Temperatures*

Charge decay comparisons were made, both at room temperature and at elevated temperature, among many different film materials. The most interesting of the charge decay curves are those of Fig. 5, taken at room temperature. Here, the 1-mil K-1 polycarbonate<sup>2</sup> electret (4) shows no measurable charge decay over a period of 7½ months. These measurements have now been extended. The charge on K-1 polycarbonate shows no measurable decay after 1½ years of storage at room temperature. There are variations of  $\pm 6\%$  in the experimental points about an initial bias of 375v. Figure 6 compares the charge decay of various electret films at 95°C, and Fig. 7 compares K-1 polycarbonate and FEP Teflon<sup>3</sup> at 130°C.

The K-1 polycarbonate electrets are the best of all films tried. They are very long-lived and have the desired mechanical characteristics over a wide temperature range for use in our application, *i.e.*, microphones. Figures 5 and 7 show that whereas K-1 polycarbonate is longer lived than FEP Teflon at room temperature, it is slightly inferior at 130°C. FEP Teflon electrets are the next best choice. They are longer-lived than Mylar<sup>4</sup> and most other films, but tend to flow under stress at elevated temperature.

H-film<sup>5</sup> is poorer than Mylar at room temperature, but better at 95°C. Makrofol KG-polycarbonate<sup>4</sup> and

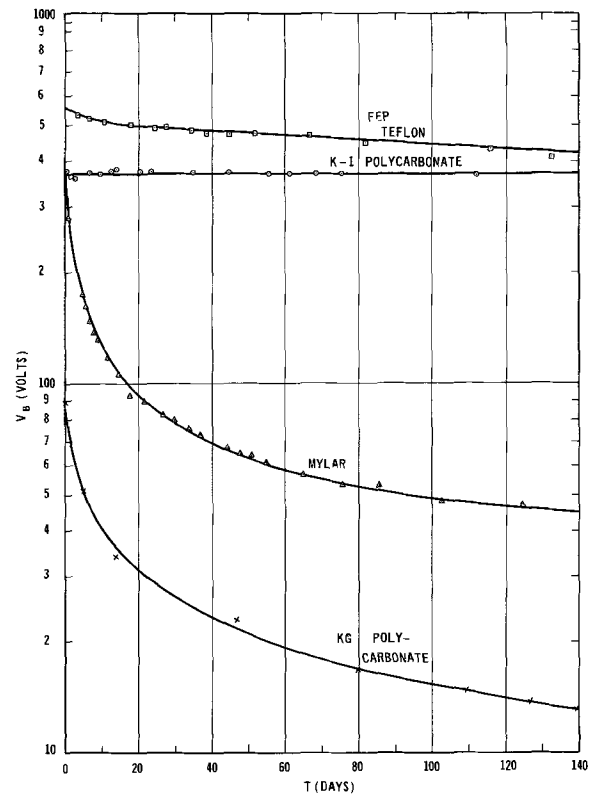


Fig. 5. Charge decay of various film materials at 25°C

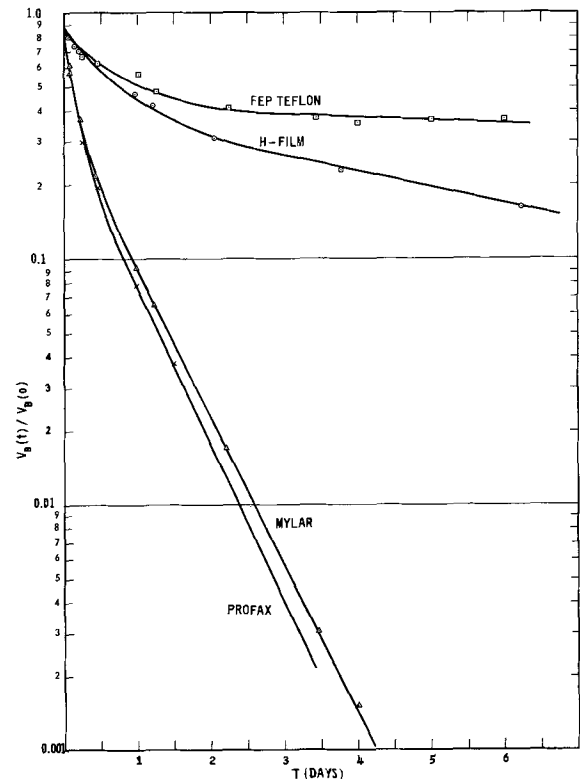


Fig. 6. Charge decay of various film materials at 95°C

Profax<sup>5</sup> form short-lived electrets. Two other films with promising electrical properties are polystyrene<sup>6</sup> and Surlyn.<sup>3</sup> While both have high volume resistivities, they have low service temperatures. Surlyn was longer-lived at room temperature than all other films, with the exception of K-1 polycarbonate. However, its

<sup>2</sup> Supplied by and registered trademark of Tennessee Eastman Co., Kingsport, Tennessee.

<sup>3</sup> Supplied by and registered trademarks of E. I. Du Pont de Nemours and Co., Wilmington, Delaware.

<sup>4</sup> Supplied by American Dielectrics Division of American Anodizing Corp., Quincy, Massachusetts.

<sup>5</sup> Supplied by and registered trademark of C.I.L. Montreal, Canada.

<sup>6</sup> Supplied by Natvar Corp., Woodbridge, New Jersey.

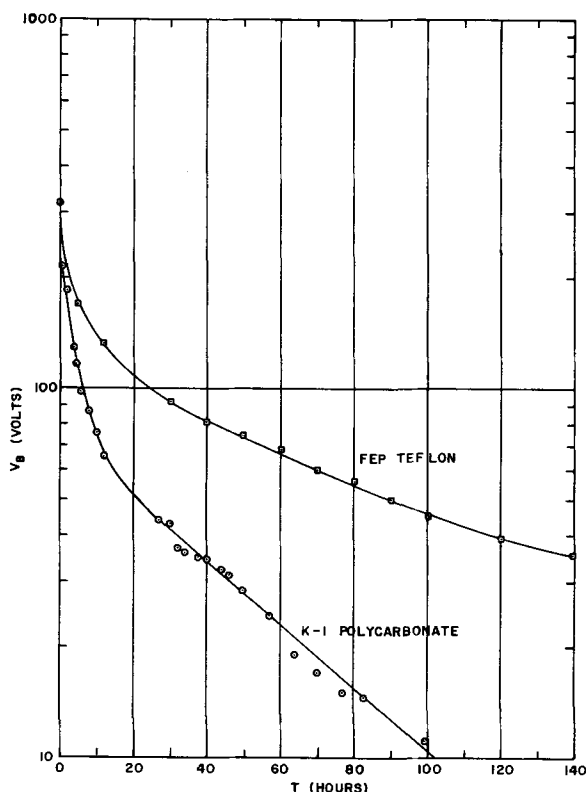


Fig. 7. Charge decay of 1 mil films at 130°C

decay just 10°C above room temperature proved to be more rapid than even that of Mylar.

#### Extrapolation Procedure on Arrhenius Plots

An extrapolation procedure on measurements of short charge decay lifetime at elevated temperature has been developed, which enables a prediction of the long lifetimes at room temperature. In many dielectrics, after decay has taken place for some time, the subsequent decay can be characterized by a single relaxation time  $T_2$ . The dependence of this time on the absolute temperature  $\theta$  is often of the form (5)

$$T_2 = \alpha e^{\epsilon/k\theta} \quad [3]$$

where  $\epsilon$  is an activation energy,  $\alpha$  is constant, and  $k$  is Boltzmann's constant. An "Arrhenius" plot of  $\ln T_2$  vs.  $1/\theta$  usually yields one or more straight lines of different slope. The change in slope takes place at the glass transition temperature.

Figure 8 shows an experimental Arrhenius plot for 1/4-mil Mylar over the temperature range 25°-100°C. Mylar has a glass transition temperature of 80°C. It is amorphous below this temperature and partly crystalline above it. Two straight lines above and below 80°C are evident. Measurements on 1-mil K-1 polycarbonate at 5 different temperatures, and on 1-mil FEP Teflon at 3 temperatures are also plotted in Fig. 8. K-1 polycarbonate is amorphous, and cannot be crystallized at any temperature (6). Thus, hopefully, one straight line can be drawn through the 5 points and extrapolated back to room temperature. This yields a useful life at room temperature in the thousands of years. As stated above, room temperature measurements on the charge of electreted K-1 polycarbonate show no measurable decay over a period of 1½ years. It should also be noted that activation energies may be determined from the slopes of the Arrhenius plots.

#### Parameters Optimizing Lifetime

A theory that relates the net surface charge of electrets to internal field and constants of the material, when the dielectric is polarized at one temperature and decays at another, is not available at present.

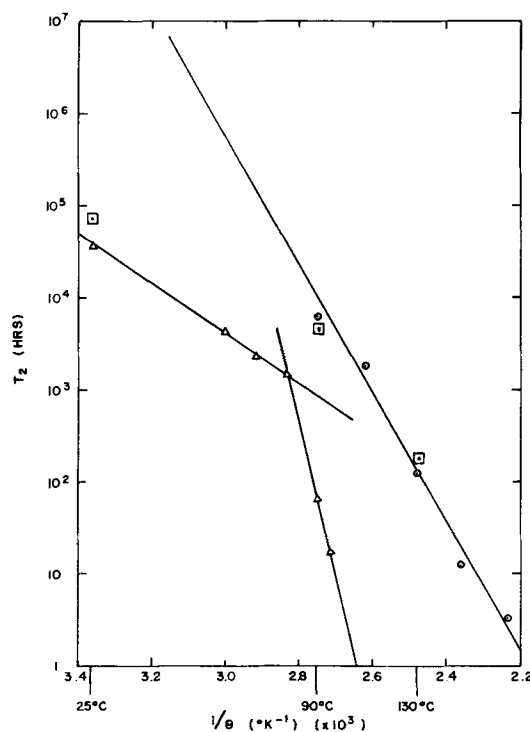


Fig. 8. Arrhenius plot of charge decay lifetimes;  $\Delta$ , 0.25 mil Mylar;  $\circ$ , 1 mil K-1 polycarbonate;  $\square$ , 1 mil FEP Teflon.

One can, however, make some guesses as to the parameters that influence lifetime.

The long charge decay lifetimes of net homocharge electrets are due to the presence of two charges of opposite polarity, each of which decays. If both homocharge and heterocharge were to decay at the same rate, the net charge, their difference, would remain constant. Thus comparable rates of decay of homocharge and heterocharge are desirable.

In net homocharge electrets the internal field during decay is in the same direction as that during charging. In general, the volume resistivity must be large ( $> \sim 10^{18}$  ohm-cm) or the homocharge would disappear by conduction in a short time unless the air gaps are zero. The internal field would then be opposite to that during charging, and the decay of the remaining heterocharge would take place in a relatively short time. Since a large resistivity implies a slow rate of decay of the homocharge, one must have a material with a comparable slowly varying polarization, for a long-lived electret.

An imperfectly shielded charged thick sample has a smaller internal field and experimentally, a longer life than a thin sample (2). Crystallinity of the material has an adverse effect on longevity. It may be possible to extend the life of the homocharge by charging under corona at high temperature to produce deep penetration and trapping, and to control the life of the heterocharge by the addition of various ionic impurities to ideal dielectrics.

#### Acknowledgment

The authors wish to thank Professor D. E. Tilley of Collège militaire royal de Saint-Jean, Saint-Jean, Québec for reading and correcting the manuscript, and P. Fatovic, M. Hutchison, and C. Lafrance of Northern Electric Research and Development Laboratories, Ottawa, Ontario for their help with the experiments. This work was supported in part by the Department of Defence Production of Canada under Contract 9PJ4-40 and in part by the Defence Research Board of Canada under Grant 5501-33.

Manuscript received Aug. 17, 1967; revised manuscript received Sept. 25, 1967. This paper was pre-

sented at the Electrets Symposium at the Chicago Meeting, Oct. 15-19, 1967, as Abstract 133.

Any discussion of this paper will appear in a Discussion Section to be published in the December 1968 JOURNAL.

#### REFERENCES

1. P. Fatovic, Fixture for Use During the Polarization of an Electret, Pat. pend.
2. M. M. Perlman and C. W. Reedyk, Northern Electric Co. Final Report on Condenser Microphone

Contract 9PJ4-40. The Department of Defence Production, Canada.

3. C. W. Reedyk and M. M. Perlman, *This Journal*, 115, 49 (1968).
4. M. M. Perlman and C. W. Reedyk, Long-lived K-1 Polycarbonate Electrets, Pat. pend.
5. P. H. Sutter and A. S. Nowick, *J. Appl. Phys.*, 34, 734 (1963).
6. R. G. Devaney, Proceedings of the Sixth Electrical Insulation Conference, Sept. 13-16 (1965).

## The Measurement of Surface Charge

Cornelis W. Reedyk

Northern Electric Research and Development Laboratories, Ottawa, Ontario, Canada

and Martin M. Perlman<sup>1</sup>

Department of Physics, Collège militaire royal de Saint-Jean, Saint-Jean, Québec, Canada

#### ABSTRACT

A new method of measuring the charge density on a dielectric surface has been developed. An electrode is vibrated in the surface field to produce a signal that is displayed on an oscilloscope, or measured with a VTVM. A bias is then applied across the vibrating and fixed electrodes sufficient to produce zero output signal. The value of this bias and a simple calculation yields the surface charge and its polarity. The method is simple, nondestructive, gives reliable results when compared with other techniques, and has few disadvantages. Measurements may be made at atmospheric pressure without fear of discharges at a wide range of surface-to-electrode gaps. The measurement of the surface charge is independent of circuit parameters.

In 1959, Gubkin *et al.* (1) reviewed various methods of measuring the charge of electrets. This paper outlines the advantages and disadvantages of the various techniques and suggests a new method that is simple and has proven to be reliable.

One of the earliest techniques is that of electrostatic induction, as in Gross (2). The electret is made the dielectric in a dissectible capacitor, whose upper electrode is moveable. To measure the surface charge, the upper electrode is grounded and lowered to induce a charge on it, and then disconnected from ground and raised to transfer this charge to a known capacitor. The voltage across this capacitor is measured and the charge calculated in a simple manner. An inherent disadvantage in the use of the dissectible capacitor is that, except for low surface charge densities, measurements must be made in vacuum to prevent discharges. The discharges in air arise because the field strength in the gap, between the surface of the dielectric and the movable upper electrode, can exceed the breakdown strength of the air, as the electrode is raised for a measurement (3). Another disadvantage is that charges are often generated on contact of the induction electrode and the dielectric (4).

Gubkin (1), Freedman (5), and also Gross (6) have suggested vibrating an electrode or rotating a wafer (10) in the field of the electret, measuring short-circuit alternating current or open-circuit voltage, and relating these quantities to surface charge. While measurements may be conveniently made at atmospheric pressure, ideal short- or open-circuit conditions can never be achieved, and the results must be corrected for circuit parameters.

The charge may of course be determined by applying heat and measuring the resultant thermal depolarization current (9), but this method destroys the sample.

Other methods such as the mechanical displacement of a moveable electrode (1), or the deflection of an electron beam (7) in the field of the electret are cumbersome and have not been widely applied.

#### New Method

In the method suggested here, an electrode is vibrated in the field of the electret to produce a signal that is displayed on an oscilloscope, or measured with a VTVM. A bias is then applied across the vibrating and fixed electrodes (Fig. 1) sufficient to produce zero output signal. The surface charge of the electret is simply related to this bias, the dielectric constant of the sample and its thickness, and is independent of the gap and electrical circuit parameters, as shown below. The polarity of the charge is identical to that of the bias. This method was first used by the authors to study the rate of decay of thin electret films in microphones, as described by Sessler and West (8). Here, an electret film, metallized on one side, was vibrated by sound, and the backplate (electrode) held fixed. The bias was applied as in Fig. 1.

#### Theory

To calculate the electric field in the air gap, apply the line integral law to the two layer capacitor of

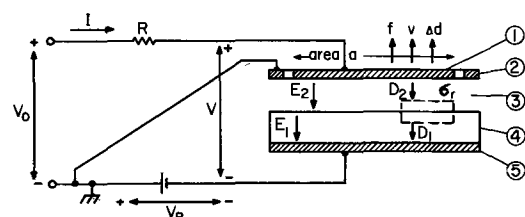


Fig. 1. Electrical circuit: 1, vibrating electrode; 2, guardring; 3, air gap  $d_2$ ; 4, dielectric  $d_1$ ,  $K$ ; 5, fixed electrode.

<sup>1</sup> Consultant, Northern Electric Research and Development Laboratories, Ottawa, Ontario, Canada.



Fig. 1, i.e.

$$d_1 E_1 + d_2 E_2 = V \quad [1]$$

where  $d_1$  and  $d_2$  are the thicknesses of sample and gap, respectively,  $E_1$  and  $E_2$  are the electric fields in sample and gap, respectively, and  $V$  is the potential difference between the electrodes. From Gauss's law, one has

$$D_1 - D_2 = \sigma_r \quad [2]$$

where  $D_1$  and  $D_2$  are the electric displacements in sample and gap, respectively, and  $\sigma_r$  is the real charge on the surface of the sample. By definition

$$D_1 = P_1 + \epsilon_0 E_1 \quad [3]$$

where  $P_1$  is the polarization response of the sample to the applied field, and  $\epsilon_0$  is the permittivity of free space. The polarization response  $P_1(t)$  is resolved into two components

$$P_1(t) = P_i(t) + P_s(t) \quad [4]$$

where  $P_s(t)$  is the component that responds slowly to changes in the internal field  $E_1(t)$ , and  $P_i(t)$  is the component that responds practically instantaneously to changes in the internal field and can be characterized by a dielectric constant  $K$ , i.e.

$$P_i(t) = \epsilon_0(K-1)E_1(t) \quad [5]$$

In the air gap,  $P_s(t) = 0$ , and thus combining Eq. [3], [4], and [5] one has

$$D_2 = \epsilon_0 E_2 \quad [6]$$

and

$$D_1 = K \epsilon_0 E_1 + P_s \quad [7]$$

Finally, combining Eq. [1], [2], [6], and [7], the field in the air gap is

$$E_2 = \frac{KV - \left( \frac{\sigma_r - P_s}{\epsilon_0} \right) d_1}{d_1 + Kd_2} \quad [8]$$

where  $(\sigma_r - P_s)$  is the net surface charge density. If now one applies a bias  $V = V_B$  so that  $E_2 = 0$ , Eq. [8] yields

$$(\sigma_r - P_s) = K \epsilon_0 V_B / d_1 \quad [9]$$

Thus the net surface charge of the sample is simply related to the bias that produces zero field in the air gap, and hence zero output signal when the upper electrode is vibrated.<sup>2</sup> The value of the net surface charge, obtained by this method, is also independent of the air gap  $d_2$ . The polarity of the net surface charge (heterocharge or homocharge) is automatically given by the polarity of  $V_B$ .

While the suggested method of measurement is completely independent of the signal voltage and current, it is useful to relate these to surface charge to obtain some idea of the orders of magnitude of the signals involved. Gubkin (1) and Sessler (8) have related the absolute value of the net surface charge to the short-circuit current amplitude and open-circuit voltage amplitude, respectively. The polarity of the charge must be determined independently.

In this paper, a harmonic analysis is made on the electrical mesh of Fig. 1. A general expression is obtained for the output voltage amplitude  $V_o$  in terms of circuit parameters. This result contains Eq. [9] and Gubkin's and Sessler's equations as special cases.

In Fig. 1, applying the principle of continuity at the vibrating electrode, one has

$$I - a \frac{\partial D_2}{\partial t} = 0 \quad [10]$$

where  $I$  is the current in the external circuit and  $a$  is the cross-sectional area of the sample.

<sup>2</sup> It is assumed that during the time the bias is applied the slowly varying polarization  $P_s$  remains constant.

The voltage  $V$  across the electrodes is

$$V = V_B + V_o - V_1 \quad [11]$$

where  $V_1 = IR$  is the voltage drop across resistance  $R$ .

The air gap  $d_2$  is given by

$$d_2 = d_{20} + x \quad [12]$$

where  $d_{20}$  is the equilibrium thickness of the gap and  $x$  is the variation about  $d_{20}$  as the electrode is vibrated.

Combining Eq. [6], [8], [10], [11], and [12], one obtains an equation relating current  $I$  to  $x$ ,  $V$ , and their time derivatives. Assuming that the variables  $x$ ,  $V_o$ ,  $V_1$  can be expanded in a Fourier series, i.e. as

$$A = \frac{1}{2} A_1 e^{j\omega t} + \frac{1}{2} A^* e^{-j\omega t} \quad [13]$$

and keeping only first order terms, one has the following solution for the fundamental frequency mode of operation

$$V_o = (R + 1/j\omega C_o)I + \frac{[V_B - (\sigma_r - P_s) d_1 / (\epsilon_0 K)] C_o v}{j\omega \epsilon_0 a} \quad [14]$$

$C_o$  is the static value of the capacitance of the system, i.e.

$$C_o = \epsilon_0 a / (d_2 + d_1 / K) \quad [15]$$

and

$$v = j\omega \Delta d \quad [16]$$

where  $v$  is the velocity of the vibrating electrode, and  $\Delta d$  is the amplitude of vibration.

There is no output signal under short-circuit or open-circuit conditions when the bias has reduced  $E_2$  to zero so that Eq. [9] applies, since then the coefficient of  $v$  in Eq. [14] is zero. The electromechanical coupling is reduced to zero, and the motion of the system is a function of the mechanical constants only.

Using Eq. [14] with  $R = 0$ ,  $V_o = V_B = 0$ ,  $I = I_o$ , one obtains the following relation between the net surface charge and the short circuit current amplitude  $I_o$ :

$$(\sigma_r - P_s) = (Kd_2/d_1 + 1)^2 d_1 I_o / (Ka\Delta d\omega) \quad [17]$$

This result agrees with Gubkin (1). Combining Eq. [9] and [17]

$$I_o/\Delta d = \epsilon_0 a \omega V_B / (d_2 + d_1/K)^2 \quad [18]$$

Using Eq. [14] with  $I = 0$ ,  $V_B = 0$ , one obtains the following relation between the net surface charge and the open-circuit voltage amplitude  $V_o$ .

$$(\sigma_r - P_s) = - (Kd_2/d_1 + 1) \epsilon_0 V_o / \Delta d \quad [19]$$

This result agrees with Sessler (8).

Combining Eq. [8] or [9] and [19]

$$V_o/\Delta d = E_2 = -V_B / (d_2 + d_1/K) \quad [20]$$

Plots of  $I_o/\Delta d$ ,  $V_o/\Delta d$  vs. gap  $d_2$  using Eq. [18] and [20] are shown in Fig. 2 and 3 for a typical polycarbonate electret film with  $K = 2.9$ ,  $d_1 = 1/4$  mil,  $V_B = 50$  v,  $a = 10$  cm<sup>2</sup>,  $f = 100$  Hz. Note that with gaps ranging from 1 to 4 mm, signals of the order of 1 to 0.3 v/mil of vibration are obtainable.

### Experimental

A preliminary apparatus (Fig. 4) was built to test this idea. It consisted of an electrode made to vibrate by alternating current fed to a solenoid. The assembly was placed over a charged sample that was metallized on one side and provision made to vary the gap  $d_2$ . The electrodes were connected to an oscilloscope, and the bias applied as in Fig. 4. Signals of the order of those predicted were observed. We verified that Eq. [9] is independent of gap (from 0 to 10 mm) and electrical circuit parameters to an accuracy of better than 1%. The charge given by Eq. [9] also agrees with that determined using a dissectible capacitor to bet-

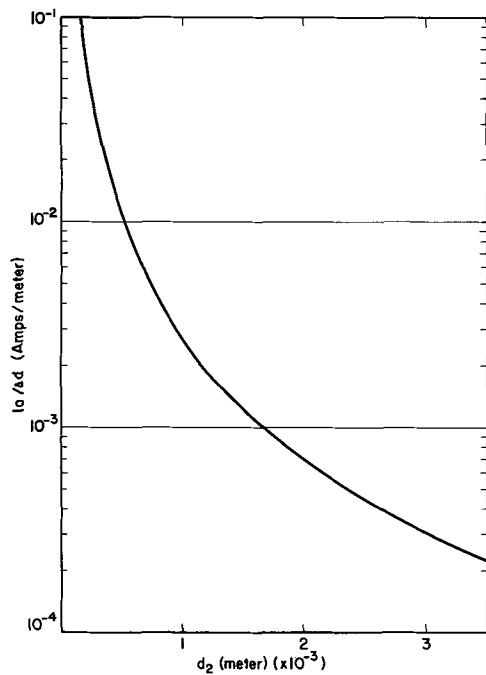


Fig. 2. Short circuit current/amplitude of vibration vs. gap

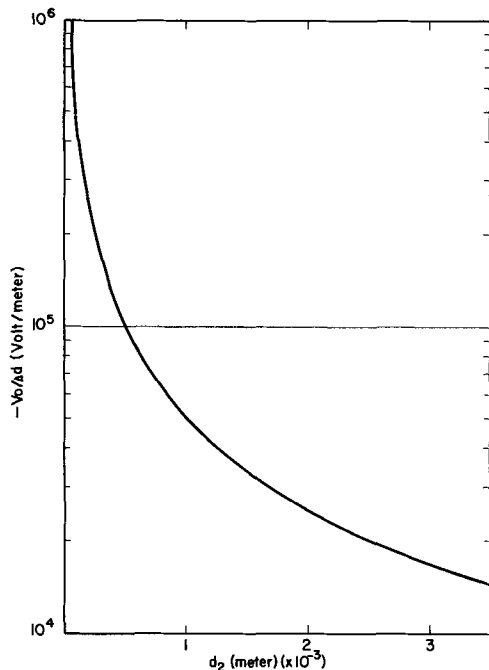


Fig. 3. Open circuit voltage/amplitude of vibration vs. gap

ter than 1%. A sturdier apparatus is shown in Fig. 5. Here, a motor drives a horizontal rod, eccentrically connected to its shaft. This motion is then translated into a vertical vibration of the upper electrode.

**Conclusions**

A new method of measuring the charge density on a dielectric surface has been developed. The method is simple, nondestructive, gives reliable results when compared with other techniques, and has few disadvantages. A voltage measurement and a simple calculation yield the surface charge and its polarity. Measurements may be made at atmospheric pressure without fear of discharges, at a wide range of gaps, and the surface charge is independent of electrical circuit parameters.

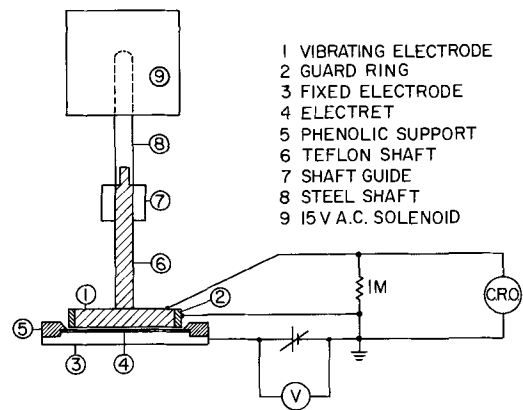


Fig. 4. Vibrating electrode apparatus

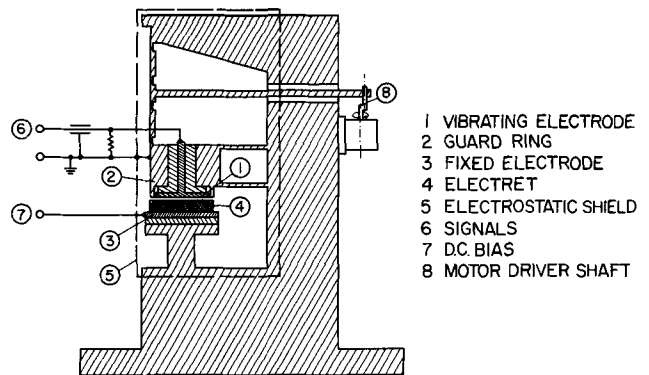


Fig. 5. Vibrating electrode apparatus

**Acknowledgments**

The authors wish to thank P. Fatovic, C. Lafrance, and B. Creswell for their help with the experiments and F. Stokes for the design of the vibrating electrode apparatus, all of Northern Electric Research and Development Laboratories, Ottawa, Ontario, Canada.

Manuscript received Sept. 5, 1967; revised manuscript received ca. Oct. 15, 1967. This paper was presented at the Electrets Symposium at the Chicago Meeting, Oct. 15-19, 1967, as Abstract 137. Work on this paper was supported in part by the Department of Defence Production of Canada under Contract 9PJ4-40 and in part by the Defence Research Board of Canada under Grant 5501-33.

Any discussion of this paper will appear in a Discussion Section to be published in the December 1968 JOURNAL.

**REFERENCES**

1. A. N. Gubkin *et al.*, *Instrum, exper. tech. (USA)*, June 1960.
2. B. Gross, *J. Chem. Phys.*, **17**, [10] Oct. 1949.
- 3a. M. M. Perlman and J. L. Meunier, *J. Appl. Phys.*, **36**, [2] Feb. 1965. b. B. Gross, *Brit. J. Appl. Phys.*, **1**, Oct. 1950.
4. G. G. Wiseman and G. R. Feaster, *J. Chem. Phys.*, **26**, [3] March 1957.
5. L. A. Freedman and L. A. Rosenthal, *Rev. Sci. Inst.*, **21**, [11] Nov. 1950.
6. B. Gross, Private communication.
7. H. Saito, *Jap. J. of Appl. Phys.*, **4**, [11], Nov. 1965.
8. G. M. Sessler and J. E. West, *J. Acoust. Soc. Am.*, **35**, 1354 (1963).
9. B. Gross and L. Ferreira Denard, *Phys. Rev.*, **67**, [7 and 8] (Apr. 1945).
10. S. Kojima and K. Kato, *J. Phys. Soc. Jap.*, **6**, 207 (1951).

# Preparation and Properties of Vanadium Dioxide Films

J. B. MacChesney, J. F. Potter, and H. J. Guggenheim

Bell Telephone Laboratories, Incorporated, Murray Hill, New Jersey

## ABSTRACT

Phase equilibria of the vanadium-oxygen system have been restudied in the composition range  $\text{VO}_2$ - $\text{V}_2\text{O}_5$  in order to establish the conditions required for stable existence of the  $\text{VO}_2$  phase. Using this knowledge, it was possible to prepare films of  $\text{VO}_2$  exhibiting transition in conductivity between semiconducting and metallic states. Films of  $\text{V}_2\text{O}_5$  were first prepared by vapor deposition of vanadyl trichloride at temperatures below  $127^\circ\text{C}$  in 1 atm of  $\text{CO}_2$ . Reduction of these to  $\text{VO}_2$  was accomplished by heating in controlled atmospheres of appropriate partial oxygen pressure at temperatures between  $500^\circ$  and  $550^\circ\text{C}$ . The resulting thin film ( $0.1$ - $1.0\mu$ ) exhibited a sharp drop (greater than two orders of magnitude) in resistance at the expected transition temperature,  $67^\circ\text{C}$ .

A flurry of interest greeted Morin's discovery in 1959 (1) of unusual semiconducting to metallic transitions in the conductivities of  $\text{VO}_2$ ,  $\text{V}_2\text{O}_3$ , and  $\text{VO}$ . Although, for a time, actively pursued by investigators intent on understanding the mechanism of the conduction anomaly, this interest was largely spent until revived recently. The recent emphasis has been directed toward utilizing this phenomenon in devices. However, difficulties have been encountered in the preparation of the  $\text{VO}_2$  phase in a form applicable to device fabrication. Although methods for the growth of single crystals had been developed (2-4), single crystals were found to be undesirable for this purpose since they tend to disintegrate on cycling through the transition temperature. On the other hand, preparation of dense, sound ceramic bodies has proved difficult (5) due to inability to sinter this oxide by conventional means. Methods for preparing thin films, probably the most desirable form for utilization of  $\text{VO}_2$  in devices, have only recently been reported (6).

In the present work the phase equilibria of the vanadium oxygen system are studied for the range of compositions between  $\text{VO}_2$  and  $\text{V}_2\text{O}_5$ . This knowledge was then utilized to reduce amorphous vanadium pentoxide films to polycrystalline vanadium dioxide films. Resistance measurements of these showed an abrupt change at the appropriate transition temperature which was comparable in magnitude to that of single crystals.

## Experimental Procedures

Although the phase relations of the vanadium oxygen system are generally known (7-10) the conditions of temperature and oxygen partial pressure necessary for the stable existence of vanadium dioxide are uncertain. Since knowledge of these parameters is indispensable to the purpose of this investigation, our first step was to determine representative oxygen isobars for the liquidus region of the diagram  $\text{VO}_2$ - $\text{V}_2\text{O}_5$ . For this study both the quenching technique and weight changes, measured by means of a recording Chevrand thermobalance, were employed. In both cases, controlled atmospheres consisting of carbon dioxide or mixtures of carbon monoxide and carbon dioxide were used. Desired mixtures were obtained using commercially available flowmeters; compositions of these were determined using a gas chromatograph (L&N Chromolax II) which had been calibrated by gas mixtures of known composition. The phase assemblage of each quenched specimen was determined by x-ray diffraction.

Thin films of crystalline  $\text{V}_2\text{O}_5$ , suitable for reduction to  $\text{VO}_2$  were prepared by vapor deposition on polished single crystal sapphire substrates. The apparatus used for deposition is shown in Fig. 1. It consists only of a bell jar with a side arm to permit intro-

duction of  $\text{CO}_2$  and a heater. Vaporization was carried out in 1 atm of  $\text{CO}_2$  by heating  $\text{VOCl}_3$  to near its boiling point while maintaining the substrates at temperatures between  $60^\circ$  and  $120^\circ\text{C}$ . Vaporization was continued until films of desired thickness (approximately  $1\mu$ ) were attained. Subsequent annealing was carried out at temperatures sufficiently below the melting point of  $\text{V}_2\text{O}_5$  to prevent the formation of a liquid phase which would separate into globules on the substrate surface. Resistance measurements of these specimens were made using indium-gallium stripes drawn on their surface as electrodes. These films were further characterized by electron microscopy, and electron and x-ray diffraction.

## Results and Discussion

We should like to preface discussion of our results by a brief description of the phase equilibria of the vanadium oxygen system. It will be appreciated that these can be studied as either a closed or an open system. Most previous studies have been made on the closed system. By this technique various mixtures of vanadium oxides whose total composition is that desired are equilibrated in sealed containers. As such, the amount of oxygen in the container is fixed, and at equilibrium the total composition of the condensed phase or phases will be essentially that of the initial mixture, with only a small pressure of oxygen present in the gas phase filling the volume of the container. Our studies have been made on the open system. Here the total composition of the condensed vanadium oxide phase assemblage changes in response to the oxygen

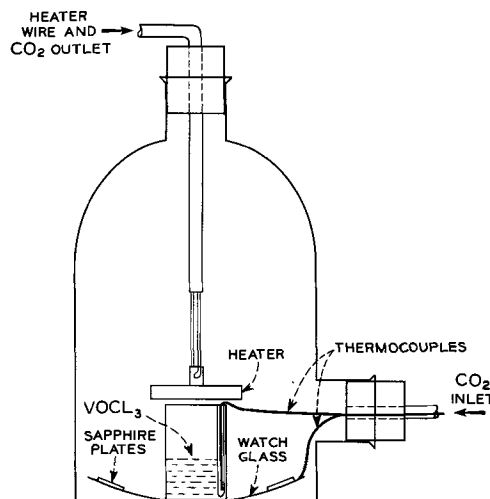


Fig. 1. Experimental apparatus used for deposition of amorphous  $\text{V}_2\text{O}_5$  coatings from  $\text{VOCl}_3$ .

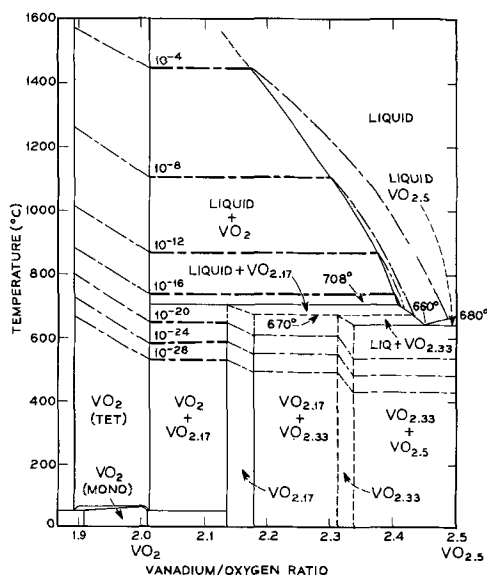


Fig. 2. Phase diagram for vanadium-oxygen system reconstructed from Kachi and Roy (10). Heavy dash-dot lines are oxygen isobars which have been determined for the Liquid + VO<sub>2</sub> and VO<sub>2</sub> + VO<sub>2.17</sub> phase regions. Estimates of the positions of those in adjoining areas of the diagram are shown by light dash-dot lines.

partial pressure of the furnace atmosphere until equilibrium is attained.

Such changes can be visualized by the use of oxygen isobars. These show the change in total composition taking place at fixed partial oxygen pressure in response to changes in temperature. In Fig. 2, a portion of the vanadium-oxygen phase diagram is shown for compositions from VO<sub>2</sub>-V<sub>2</sub>O<sub>5</sub>. The diagram is based on that of Kachi and Roy's (10), but has been modified to show the existence of VO<sub>2.33</sub> (9) and also by the imposition of representative oxygen isobars obtained from the present study. Dashed portions of these show expected trends of such curves in phase regions not extensively studied in the present work.

The significance of these isobars to the present work will become obvious if one recalls the phase rule

$$P + F = C + 2$$

where  $C$  is the number of components of a system,  $F$  is the number of degrees of freedom, and  $P$  represents the number of phases present at equilibrium.

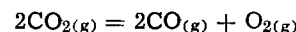
In the present system there are two components, vanadium and oxygen, so that  $P + F = 4$ . First let us consider that portion of the diagram representing a single liquid phase. At equilibrium, in addition to the condensed phase, a gas phase is present containing oxygen at a pressure of 1 atm or less. In this situation, two degrees of freedom remain so that, within limits, both temperature and oxygen partial pressure can be changed without altering the phase assemblage.

But what happens when these limits are exceeded? Specifically, what happens when the temperature or the oxygen pressure is fixed such that the composition of the system is changed so as to cross the liquidus curve separating the liquid phase region from that of crystalline VO<sub>2</sub>? Now three phases are present, and only one degree of freedom remains. In order to maintain two condensed phases (crystalline VO<sub>2</sub> and liquid) in equilibrium, the temperature and oxygen pressure can no longer be independently varied. Instead, VO<sub>2</sub> and liquid are stable only at a single oxygen partial pressure at a single temperature. In practice then, reduction of the oxygen partial pressure at fixed temperature or increasing temperature at fixed oxygen partial pressure will ultimately bring about the complete precipitation of the liquid phase as VO<sub>2</sub>. It can be shown by similar reasoning that VO<sub>2</sub> can be ob-

tained from other crystalline phases in the same manner at lower temperatures.

With this in mind we can simplify the diagram of Fig. 2 to describe more readily the conditions necessary for the stable existence of VO<sub>2</sub> at equilibrium. Since temperature and oxygen pressure are not independently variable when two condensed phases are present, the two-phase region of the diagram of Fig. 2, will become a line on the diagram of  $\log P_{O_2}$  vs.  $10^4/T$  ( $^{\circ}K^{-1}$ ). Such a diagram, Fig. 3, has been constructed from the data of the present study. Here, phase fields of VO<sub>2</sub>-liquid and VO<sub>2</sub>-VO<sub>2.17</sub> are separated by the solid line representing the conditions necessary for the existence of these phases at equilibrium. Dashed lines again are used to represent estimates of conditions giving rise to univariant equilibria involving other vanadium oxide phases.

Before proceeding to describe preparation of films it is important to point out that the oxygen pressures referred to in this discussion are calculated from the standard free energy change for the reaction



An equilibrium constant can be written for this reaction

$$K = \frac{P_{O_2} \cdot P_{CO}^2}{P_{CO_2}^2}$$

from which the oxygen partial pressure is defined by the familiar expression:

$$\begin{aligned} \Delta F^{\circ} &= -RT \ln K \\ &= -RT \ln \left( \frac{P_{CO}^2}{P_{CO_2}^2} \cdot P_{O_2} \right) \end{aligned}$$

In its evaluation, standard free energy values of Coughlin (11) were used, and experimental CO/CO<sub>2</sub> ratios were provided by gas chromatograph readings.

### Preparation of Thin Films

Vapor deposition was attempted using several halide and metallo-organic compounds of vanadium. Among these VOCl<sub>3</sub> (vanadyl trichloride) proved to be satis-

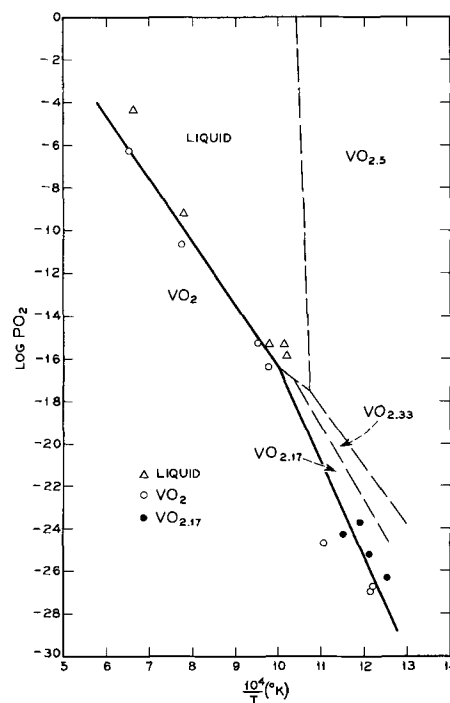
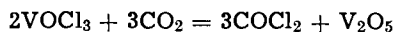


Fig. 3. Diagram of  $\log P_{O_2}$  vs.  $10^4/T^{\circ}K^{-1}$  showing boundary between VO<sub>2</sub>-liquid and VO<sub>2</sub>-VO<sub>2.17</sub> phase fields. Dashed lines are sketched to illustrate positions of phase boundaries of adjacent phases.

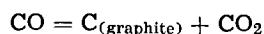
factory. Not only is its boiling point low, but also its vapor is decomposed at low temperatures to yield  $V_2O_5$ . We conceive of this decomposition taking place by the reaction



This supposition is strengthened by chromatographic analysis which found phosgene among the effluent gases.

Thin films can be deposited quite rapidly (greater than  $1\mu/hr$ ), even using the rather crude apparatus described which was not intended to optimize the rate. The films produced were amber and transparent. Electron diffraction patterns showed these films to be crystalline  $V_2O_5$ . A typical electron micrograph of the surface (Fig. 4) shows a poorly developed microstructure composed of grains between 0.01 and  $0.1\mu$ .

In reducing these films to  $VO_2$  it was found necessary to remain well below liquidus temperatures. Apparently the liquid oxide phase does not wet the sapphire surface so that the film separated into droplets on the surface whenever reduction was attempted above  $550^\circ C$ . At the same time lowering the annealing temperature very much below this temperature presents a problem. Here, at the relatively high  $CO/CO_2$  ratios needed to accomplish reduction of these films, carbon monoxide will be decomposed to graphite according to the reaction.



Thus there is a lower limit to the temperature range over which reduction can be accomplished using these gas mixtures.

After reduction under the conditions described in Table I, these films were again viewed by electron microscopy. Figure 5 shows a typical surface. Individual crystallites measuring up to  $500\text{\AA}$  can be recognized. The micrograph also shows blistering which is probably caused by release of volatile components during annealing. Talysurf measurements of this film show its thickness to range between 6500 and 9000 $\text{\AA}$ . X-ray diffraction patterns from the surface show the film to be  $VO_2$ . No other phases can be recognized.

Resistance measurements over the range of  $25^\circ$  to approximately  $100^\circ C$  are shown by Fig. 6. Here re-



Fig. 4. Electron micrograph of a  $V_2O_5$  film on sapphire at ca. 7600X.

Table I. Conditions employed in preparation of  $VO_2$  films by vapor deposition from  $VOCl_3$ , and from oxidized vanadium films

	Vaporization of $VOCl_3$			Annealing				Film thickness, $\mu$
	Substrate Temp, $^\circ C$	$VOCl_3$ Temp, $^\circ C$	Time, hr	Temp, $^\circ C$	Atmosphere $CO_2$ vol. 90	$CO$ vol. 90	Time, min.	
Fig. 6	64	134	2	526	50	50	33	0.9
Fig. 7	—	—	—	482	50	50	15	0.2

sistance (ohms/square) is plotted vs. reciprocal temperature ( $10^3/T^\circ K^{-1}$ ). It is to be observed that, on heating to  $65^\circ C$  (2.96 on the reciprocal temperature scale), there is a drop in resistance of more than three orders of magnitude. A hysteresis amounting to between  $7^\circ$  and  $8^\circ C$  is observed in the cooling curve of this figure.

Another experiment which may be of interest to persons concerned with this subject was carried out in conjunction with Rozgonyi and Polito. They prepared polycrystalline  $V_2O_5$  films of 2000 $\text{\AA}$  thickness by oxi-

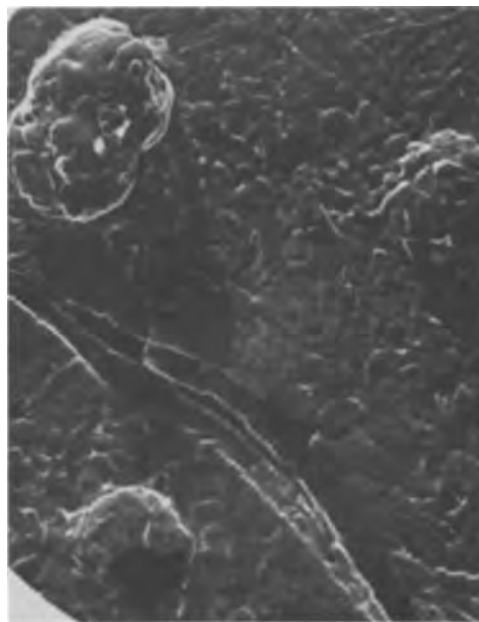


Fig. 5. Electron micrograph, at ca. 7600X, of a typical film after annealing in  $CO/CO_2$  mixture to convert it to vanadium dioxide.

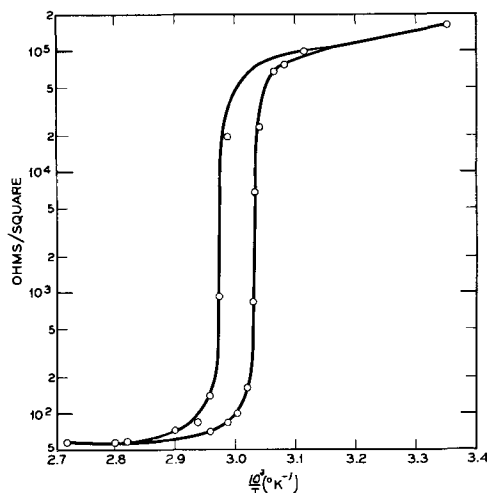


Fig. 6. Resistance vs. reciprocal temperature of vapor deposited film applied on a single crystal sapphire substrate and annealed in 1:1  $CO:CO_2$  at  $526^\circ C$ .

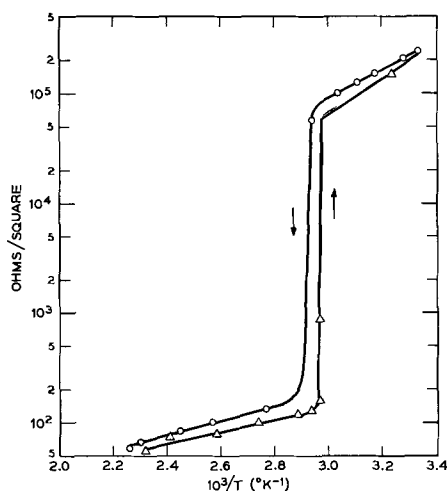


Fig. 7. Resistance vs. reciprocal temperature of a metallic vanadium film first oxidized to  $V_2O_5$  and then reduced to  $VO_2$  in a mixture of 1:1:CO:CO<sub>2</sub> at 482°C.

dizing sputtered vanadium deposits.<sup>1</sup> These were then reduced in mixtures of CO/CO<sub>2</sub> as also described in Table I. Resistance measurements for one such film are shown in Fig. 7. It will be observed that the character of the curves are similar to those shown in the preceding figure. However the transition temperature is slightly higher, 67°C (2.93 on the reciprocal temperature scale). Also it appears that the material behaves as a semiconductor both above and below the transition.

### Discussion

The reader has probably observed that we have taken some pains in our annealing experiments always to approach the  $VO_2$  phase from an oxygen rich composition. This was done to take advantage of the favorable kinetics provided by carrying out the reductions at temperatures only 100°C below the eutectic temperature in the system  $VO_2$ - $V_2O_5$ . This is also thought to provide an additional advantage by retarding the rate at which reduction of  $VO_2$  to phases of lower oxygen content takes place. We have shown in another paper (12) that reduction, even when carried out at oxygen partial pressures appreciably below that in equilibrium with  $VO_2$  phase, can still yield this phase provided that the annealing is not too prolonged.

Another comment on this work concerns the purity of vapor deposited films. After completing the work described above we performed an additional evaporation, employing the same conditions but depositing on a large graphite plate. This provided enough specimen for semiquantitative spectrographic analysis. Results given in Table II show the deposit to be contaminated. These impurities are thought not to be derived from the graphite plate, rather, we think, they result from attack by the vapor species of the nichrome heating elements and its support which were suspended in the bell jar. Obviously this can be eliminated by a different experimental arrangement. However, it is surprising that the properties of these films are not appreciably degraded by high levels of impurities. Although

<sup>1</sup> See "Preparation of Thin Films of Vanadium (Di-, Sesqui-, and Pent-) Oxide" by G. A. Rozgonyi and W. J. Polito, *This Journal*, 115, 56 (1968).

Table II. Impurity levels of vapor deposited thin films

	w/o		w/o
Aluminum	0.X	Copper	0.00X
Iron	0.0X	Titanium	0.00X
Silicon	0.0X	Lead	0.00X
Nickel	0.00X	Magnesium	0.00X low
Tin	0.00X	Manganese	0.000X low

the impurities may contribute to the slight lowering of the transition temperature of the vapor deposited films compared to that of the sputtered vanadium film, and single crystals (1), they have not drastically "smeared" the transition or affected the apparent resistivity of these films.

### Conclusions

Investigation of the phase equilibria of the vanadium-oxygen system has resulted in a further definition of the limits of temperature and oxygen pressure for the stability of the  $VO_2$  phase field. Using these data it was possible to prepare specimens exhibiting a sharp drop in resistivity characteristic of the phase transition between the monoclinic and tetragonal polymorphs of that phase.

Thin films of amorphous  $V_2O_5$  were first prepared on sapphire substrates by vapor deposition. Here,  $VOCl_3$  was vaporized by decomposing  $VOCl_3$  vapor in 1 atm of CO<sub>2</sub> and then converting this to  $VO_2$  by suitable annealing at low oxygen partial pressure. Thin films produced in this manner were shown to have electrical properties typical of the vanadium dioxide and comparable to single crystals of that phase.

### Acknowledgments

The authors are indebted to Miss S. E. Koonce for electron micrographs and to D. L. Nash for spectrographic analysis. They also wish to thank M. D. Rigerink for helpful comments on the text, and to acknowledge useful discussion with W. R. Sinclair, P. J. Fillingham, and G. A. Rozgonyi.

Manuscript received July 25, 1967. This paper was presented at the Dallas Meeting, May 7-12, 1967, as Abstract No. 19.

Any discussion of this paper will appear in a Discussion Section to be published in the December 1968 JOURNAL.

### REFERENCES

1. F. J. Morin, *Phys. Rev. Letters*, **3**, 34 (1959).
2. H. J. Guggenheim, "Solid State Physics," vol. 12, p. 209, F. Seitz and D. Turnbull, Editors, Academic Press, Inc., New York, (1961).
3. H. Sasaki, *J. Phys. Soc. Japan*, **19**, 1748 (1964).
4. P. F. Bongers, *Solid State Com.*, **3**, 275 (1965).
5. T. Ohashi and A. Watanabe, *J. Am. Ceram. Soc.*, **49**, 46 (1966).
6. S. Koide and H. Takei, *J. Phys. Soc. Japan*, **22**, 946 (1967).
7. G. Anderson, *Acta Chem. Scand.*, **8**, 1599 (1954).
8. F. Aebi, *Helv. Chim. Acta*, **31**, 8 (1948).
9. J. Tudo and G. Tridot, *Compt. rend.*, **261**, 2911 (1965).
10. S. Kachi and R. Roy, Second Quarterly Report, Materials Research Laboratory, The Pennsylvania State University, (Contract DA-28-043-AMC-01304E U. S. Army Electronics Laboratory) 1966.
11. J. P. Coughlin, U.S. Bureau of Mines Bull. #542 (1954).
12. J. B. MacChesney, J. F. Potter, and H. J. Guggenheim, *J. Am. Ceram. Soc.*, in press.

# Preparation of Thin Films of Vanadium (Di-, Sesqui-, and Pent-) Oxide

G. A. Rozgonyi and W. J. Polito

*Bell Telephone Laboratories, Incorporated, Murray Hill, New Jersey*

## ABSTRACT

Polycrystalline thin films of  $V_2O_3$ ,  $VO_2$ , and  $V_2O_5$  have been prepared in the thickness range from 500 to 4000Å. The films are obtained by a post-deposition heat-treatment of sputtered V or V-O films. The quality of the films has been studied by x-ray diffraction techniques and by measuring resistivity as a function of inverse temperature to check the magnitude of the metal to semiconductor transition. Electrically the films compare favorably with bulk crystals, and in addition the films are extremely stable during repeated cycling through the transition temperature.

Since Morin (1) reported on the metal to semiconductor transition in certain oxides there has been considerable interest in the preparation and properties of single crystals of the oxides of vanadium. Vanadium dioxide,  $VO_2$ , which gives rise to a conductivity change of up to  $10^4$  at 338°K has received the most attention (2-7) due to the very convenient transition temperature. However, for fundamental studies and some more restricted device applications vanadium sesquioxide,  $V_2O_3$ , with a conductivity change of greater than  $10^6$  at 168°K, is also of great interest (8-10). A serious problem encountered with both  $V_2O_3$  and  $VO_2$  is a tendency for bulk crystals to fracture. This fracture, plus the need for material in configurations compatible with modern device technology, has stimulated our effort to deposit thin films of the above oxides.

Previous work on thin films has been restricted to the deposition of  $VO_2$  films. The films were obtained either by vapor deposition techniques (11,12) using  $VOCl_3$  or by reactive sputtering of vanadium in argon and oxygen mixtures (13). Since difficulties have been encountered in obtaining consistently reproducible results on these films simple postdeposition annealing of films was attempted. Considerable success was achieved in obtaining uniform large area films of  $V_2O_5$  and  $V_2O_3$ , as well as  $VO_2$ , by choosing a suitable oxidizing or reducing atmosphere while treating sputtered V or V-O films.

## Apparatus and Procedures

Experimentally the vacuum system is identical to that used previously for the sputtering of ZnO (14) with the ZnO cathode replaced by  $V_2O_5$ . However, due to the complexity of the oxidation states of vanadium it was not possible to deposit crystalline films reproducibly and directly, as was accomplished with ZnO. Therefore, postdeposition treatments were devised which recrystallized the films such that their properties were comparable to bulk single crystals. Vanadium films sputtered in conventional bell jar systems were also studied. Substrate materials included single crystal sapphire and amorphous Pyrex glass slides with the best results obtained on the sapphire.

Depending on the oxide desired the films were annealed in the presence of three different flowing gases in three separate open tube furnaces. The gases were water vapor, a mixture of 90%  $N_2$ -10%  $O_2$ , and  $H_2$  which had been bubbled through water. The optimum conditions for obtaining the V-O composition of interest are presented in Table I. No attempt has been made in this study to determine the exact conditions of temperature and oxygen partial pressure necessary for the stable formation of a particular V-O phase. The choice of gas was based simply on its expected oxidizing ( $N_2$ - $O_2$ ,  $H_2O$ ) or reducing ( $H_2$ ) properties.

Attempts at varying the conditions of the wet  $H_2$  treatment to obtain a crystalline phase intermediate to  $V_2O_3$ - $V_2O_5$ , specifically  $VO_2$ , were not successful. This is consistent with the work of Gel'd *et al.* (15) who found that, although  $VO_2$  and  $V_6O_{13}$  were detected during the reduction of powders of  $V_2O_5$  in  $H_2$ , single phases of these compositions could not be formed.<sup>1</sup> In order to obtain  $VO_2$  films the water vapor treatment was used to provide a slightly oxidizing atmosphere for the sputtered V-O films. The exact composition of the thin (500-4000Å), as-sputtered films could not be determined because of the small amount of material and its amorphous nature. However, since they were sputtered in pure argon it is expected that the  $V_2O_5$  cathode material converted to  $V_2O_3 + O_2$  and that the resulting film stoichiometry was of a phase lower in oxygen than  $VO_2$ .

## Results and Discussion

The films were evaluated crystallographically by x-ray powder diffraction techniques and electrically by plotting the resistivity as a function of inverse temperature. A standard four-point probe with 0.010 in. separation was used for the resistivity measurements. Figure 1 shows the  $\rho$  vs.  $1/T$  data for the phases of interest. The metal-to-semiconductor transitions in  $V_2O_3$  and  $VO_2$  films are of the same magnitude as those reported for bulk material (1) and occur at approximately the same temperatures. The semiconductor behavior of  $V_2O_5$  films over the entire temperature range studied is also consistent for that material (2). The width of the hysteresis and the relatively soft behavior at the transition is most likely due to the polycrystalline nature of the films, and the resulting grain boundary effects, although strain introduced at the film-substrate interface, may also be important. Slight chemical inhomogeneities are also possible, and, in certain films, an extra x-ray diffraction line was observed at  $d = 2.25$ . This line could not be unequivocally assigned to any one phase, but it is suspected to be a reflection from  $VO_{1.87}$ . However, the metallic behavior and positive temperature coefficient of resistance in the high temperature regions indicate that the electrical behavior is not seriously effected by extraneous phases. X-ray photographs were taken with Ni filtered  $Cu-K_{\alpha}$  radiation at a fixed beam incidence of  $16^\circ$ , treating the polycrystalline film as if it were a powdered sample. The x-ray results are presented in Table II and compared with the ASTM data for the various phases. The grain size of all films was estimated to be less than 100Å.

The resistance of these films to fracture was checked by cycling the  $VO_2$  samples from room temperature to  $\sim 100^\circ C$  on a hot plate and dipping the  $V_2O_3$  sam-

<sup>1</sup> It should be noted that MacChesney (11) has reduced our  $V_2O_5$  films to  $VO_2$  using a  $CO/CO_2$  reducing atmosphere.



Table I. Optimum conditions for preparation of vanadium oxide films

Desired film	Initial sputtered or recrystallized film	Annealing conditions		
		Atmosphere	Temp, °C	Time, hr
V <sub>2</sub> O <sub>5</sub>	Amorphous V-O or Polycrystalline V	90% N <sub>2</sub> -10% O <sub>2</sub>	500	4
V <sub>2</sub> O <sub>3</sub>	Recrystallized V <sub>2</sub> O <sub>5</sub>	Wet H <sub>2</sub>	550	1
VO <sub>2</sub>	Amorphous V-O Recrystallized V <sub>2</sub> O <sub>5</sub> *	Water vapor	450	4

\* See (11) for details.

ples in and out of liquid nitrogen at least 12 times. The samples would undergo repeated resistance changes of  $>10^3$  ohms for VO<sub>2</sub> and  $>10^7$  ohms for V<sub>2</sub>O<sub>3</sub> as measured with a simple ohmmeter. A point-by-point measurement after the above cycling did not reveal any change in performance.

It has been demonstrated that polycrystalline films of V<sub>2</sub>O<sub>5</sub>, VO<sub>2</sub>, and V<sub>2</sub>O<sub>3</sub> can be prepared by a suitable postdeposition heat-treatment of sputtered V or V-O films. The VO<sub>2</sub> and V<sub>2</sub>O<sub>3</sub> films exhibit metallic-semiconductor behavior characteristic of bulk vanadium oxides with the added feature of stability and resistance to fracture during repeated temperature cycling. It is expected that these films will prove to be reproducible and stable samples for further investigations into the properties of vanadium oxides and the mechanism of the metal-to-semiconductor transition.

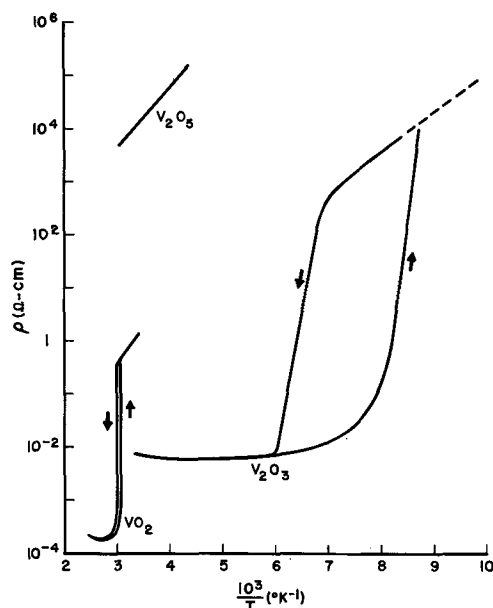


Fig. 1. Resistivity vs. reciprocal temperature for V<sub>2</sub>O<sub>5</sub>, VO<sub>2</sub>, and V<sub>2</sub>O<sub>3</sub> films. Arrows indicate direction of temperature change.

Table II. X-ray diffraction data for vanadium oxide films

Phase	ASTM index			Thin film	
	d, Å	Relative intensity	hkl	d, Å	Relative intensity, estimated
V <sub>2</sub> O <sub>5</sub>	4.38	100	001	4.4	100
	4.09	35	101	4.1	15
	3.40	90	110	3.4	80
	2.88	65	400	2.9	10
	2.76	35	011	2.8	10
	2.147	11	102	2.14	15
V <sub>2</sub> O <sub>3</sub>	1.757	30	601	1.75	20
	2.70	80	104	2.7	60
	2.47	60	110	2.45	100
	2.18	20	113	2.15	10
	1.69	100	116	1.65	40
	VO <sub>2</sub>	3.20	100	011	3.2
2.430		40	202	2.43	80
2.422		60	211		
2.139		50	212	2.13	40
2.131		50	210		
1.657		30	213	1.65	50
VO <sub>2</sub>	1.654	30	222		
	1.650	60	220, 211		

### Acknowledgment

The authors wish to thank G. Mahoney for making the four-point probe measurements, J. Sosniak and D. Hensler for providing sputtered V films, and to acknowledge helpful discussions with J. B. MacChesney, H. J. Guggenheim, G. E. Smith, and P. Fillingham.

Manuscript received July 25, 1967.

Any discussion of this paper will appear in a Discussion Section to be published in the December 1968 JOURNAL.

### REFERENCES

1. F. J. Morin, *Phys. Rev. Letters*, **3**, 34 (1959).
2. S. Kachi, T. Takada, and K. Kosuge, *J. Phys. Soc. Japan*, **18**, 1839 (1963).
3. K. Kosuge, T. Takada, and S. Kachi, *ibid.*, **18**, 318 (1963).
4. S. Minomura and H. Nagasaki, *ibid.*, **19**, 131 (1964).
5. H. Sasaki and A. Watanabe, *ibid.*, **19**, 1748 (1964).
6. P. F. Bongers, *Solid State Commun.*, **3**, 275 (1965).
7. H. J. Guggenheim, To be published.
8. G. Goodman, *Phys. Rev. Letters*, **9**, 305 (1962).
9. I. G. Austin, *Phil. Mag.*, **7**, 961 (1962).
10. D. Adler and J. Feinleib, *Phys. Rev. Letter*, **12**, 700 (1964).
11. J. B. MacChesney, J. F. Potter, and H. J. Guggenheim, *This Journal*, **115**, 52 (1968).
12. S. Koida and H. Takei, *J. Phys. Soc. Japan*, **22**, 46 (1966).
13. E. N. Fuls, D. H. Hensler, and A. R. Ross, *Appl. Phys. Letters*, **10**, 199 (1967).
14. G. A. Rozgonyi and W. J. Polito, *Appl. Phys. Letters*, **8**, 220 (1966).
15. P. V. Gel'd, S. I. Alyamovskii, and I. I. Matveenko, *Russ. J. Inorg. Chem.*, **5**, 815 (1960).

# The Measurement of Ionic Mobilities in the Anodic Oxides of Tantalum and Zirconium by a Precision Sectioning Technique

J. L. Whitton<sup>1</sup>

Research Chemistry Branch, Chalk River Nuclear Laboratories, Chalk River, Ontario, Canada

## ABSTRACT

The technique of removing thin sections of anodic oxides by vibratory polishing has been used in conjunction with implantation of anion, cation, and inert gas radiotracers to measure the mode of anodic oxide formation on Zr and Ta. The measured transport number for metal during the growth of  $Ta_2O_5$  (0.28) is in good agreement with previous work.  $ZrO_2$  is shown to grow by oxygen migration and preliminary experiments suggest that the process occurs by rapid movement of the oxygen along defects. Comparison of the movement of anion and cation radiotracers with that of an inert gas provides additional evidence that xenon and krypton may be regarded as immobile markers for use in oxidation studies.

The transport mechanism responsible for oxide film growth on metals, i.e., whether growth occurs by metal or oxygen migration or both, can best be measured by the use of inert markers. These markers can be placed initially on, or just beneath the surface of the specimen, and any change in their location, due to subsequent oxidation, is then directly related to the transport mechanism involved.

The best type of marker for thin anodic films is an inert radiotracer injected at a known depth by means of an isotope separator (the conventional embedded Pt wire method is not suitable for oxides of thicknesses less than a few microns). This radiotracer method, using  $^{125}Xe$  as the radioactive marker has been used previously [(1) and references cited therein] to study the anodic oxidation mechanisms of several "valve" metals, including Zr and Ta, the position of the Xe before and after oxidation being determined by  $\beta$ -ray spectroscopy.

A detailed pictorial illustration of the method of obtaining transport numbers from these radiotracer measurements is shown in Fig. 1. The initial location of injected Kr atoms in an oxide layer is shown. In the case where the oxide grows by oxygen migration alone, the marker atoms stay at the same distance from the outer surface; where only metal migration occurs the marker atoms remain at the same distance from the metal-oxide interface; and where a combination of metal-oxygen migration occurs, the marker atoms are buried to an intermediate depth which depends on the ratio of metal to oxygen ion mobility.

As noted in the previous work (1), the ideal marker atoms should be immobile and should not significantly change the properties of the oxide in which they are embedded. Hence, they should be: (i) uncharged, so that no movement occurs due to the applied electric field, (ii) large in size, so that diffusion within the oxide is not a significant factor, and (iii) present in trace amount, so that the macroscopic properties of the oxide remain unaltered. Inert gas isotopes, such as  $^{125}Xe$ ,  $^{133}Xe$ ,  $^{85}Kr$  etc., are expected to fulfill rather closely these requirements of the ideal marker.

Although it is difficult to devise an experiment to show unambiguously that the inert gas markers are or are not immobile, some indication of this can be expected by comparison of the behavior of inert gas atoms with that of anions and cations. This type of experiment can best be performed by injecting two or more radiotracers in the same specimen, then locating simultaneously their positions relative to each

other. The results of such experiments are reported here.

A new method of determining the locations or depth distributions of the radiotracers before and after oxidation has been used. This is a method of precise sectioning using a vibratory polisher which allows layers as thin as 20Å to be removed. As successive layers are removed, the fraction of tracer remaining is determined by measurement of the residual activity, thus providing a direct measure of the location and depth distribution of the markers.

## Experimental Method

The sectioning technique makes use of a commercial vibratory polisher<sup>2</sup> and has been described previously (2). Briefly, the specimens to be sectioned are prepared in the form of right cylinders  $\sim \frac{1}{2}$  in. diameter by  $\sim \frac{3}{4}$  in. long. These have one face mechanically polished on carborundum paper, then on successively finer diamond grit down to 0.25  $\mu m$  before being finally vibratory polished in an aqueous slurry of 0.05  $\mu m$  Linde A  $Al_2O_3$  for 72 hr. It has been shown (2) that this treatment leaves a virtually undeformed mirror-like surface.

The anodic oxide films required for the sectioning procedure were prepared by anodizing vibratory polished surfaces of Ta and Zr at 1 ma/cm<sup>2</sup>, using 0.1M

<sup>2</sup> Syntron Company, Homer City, Pennsylvania.

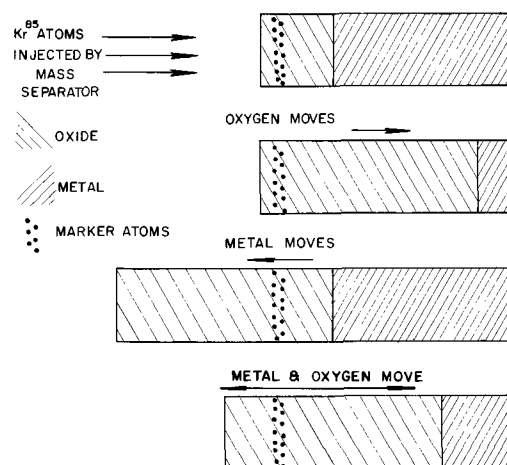


Fig. 1. A schematic representation of the effect of metal and oxygen migration on the final position of an inert marker in an oxide film.

<sup>1</sup> Present address: Department of Electrical Engineering and Electronics, The University of Liverpool, Liverpool, England.

H<sub>2</sub>SO<sub>4</sub> as the electrolyte for tantalum and saturated ammonium borate for zirconium.

The rate of removal of Ta<sub>2</sub>O<sub>5</sub> and ZrO<sub>2</sub> was calibrated by observing optically the residual oxide thickness after each layer was removed, and plotting this thickness vs. the polishing time. The oxide thicknesses were measured on a u.v. spectrophotometer, using the interference minima-oxide thickness calibration data of Young (3) for Ta<sub>2</sub>O<sub>5</sub> and of Wilkins (4) for ZrO<sub>2</sub>. The rate of removal of Ta<sub>2</sub>O<sub>5</sub> is shown in Fig. 2; the slopes correspond to a rate of 50Å/min of vibratory polishing. The ZrO<sub>2</sub> removal rate (Fig. 3) is not so uniform initially but becomes reasonably constant after the first 100Å. As the removal rate is less than 5 atom layers per minute of vibratory polishing, it is perhaps not too surprising to find that the rate differs somewhat from one experiment to the other. It means,

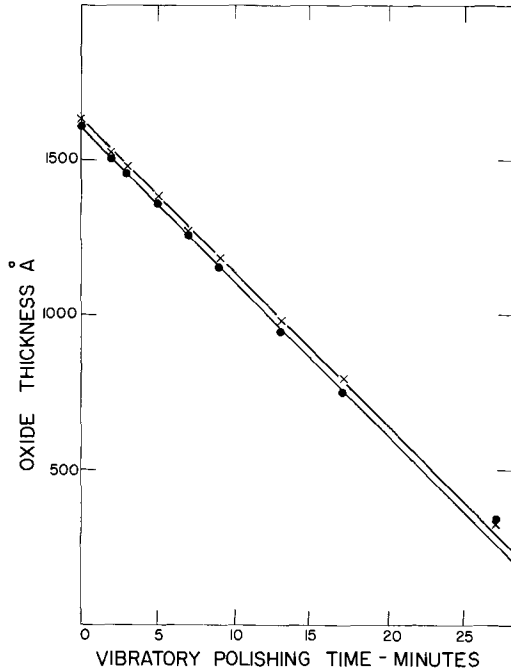


Fig. 2. Spectrophotometric calibration of sectioning method for Ta<sub>2</sub>O<sub>5</sub>: X, specimen 1; ●, specimen 2.

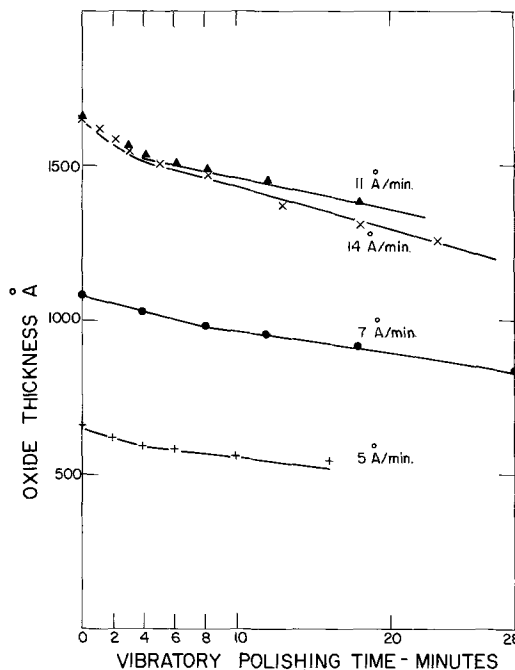


Fig. 3. Spectrophotometric calibration of sectioning method for ZrO<sub>2</sub>: Δ, X, ●, +, specimens 1, 2, 3, and 4.

however, that a more careful spectrophotometric control is required for ZrO<sub>2</sub> than for Ta<sub>2</sub>O<sub>5</sub>.

The choice of radiotracers was governed by the need to have (i) an anion, a cation, and an inert gas, (ii) such a trio having approximately the same mass so as to have the same initial depth distribution, and (iii) having activities that could be determined independently by a combination of radioactive measuring techniques.

The trio <sup>82</sup>Br, <sup>85</sup>Kr, and <sup>86</sup>Rb fulfill these requirements. Conditions (i) and (ii) are obviously met and condition (iii) also, as <sup>82</sup>Br and <sup>86</sup>Rb emit β<sup>-</sup> particles and gamma rays while <sup>85</sup>Kr is an almost pure β<sup>-</sup> emitter. These properties, therefore, make it possible for the inert gas and the anion or the inert gas and the cation to be injected in the same specimen and the precise location of each isotope determined by a combination of sectioning, measuring the β and γ activities and comparing these measurements to a standard source of each isotope.

In a typical experiment, two specimens of Ta, anodized to 20v in order to form an oxide layer ~ 400Å thick, were used. The Chalk River isotope separator (5) was utilized to inject 30 kev <sup>85</sup>Kr and <sup>86</sup>Rb into one and 30 kev <sup>85</sup>Kr and <sup>82</sup>Br into the second. The depth distributions of these embedded atoms were then measured by removing successive thin layers on the vibratory polisher and using the isotope-selective β- and γ-counting technique to determine at each stage the residual activity of both radiotracers independently.

The anodizing and injection procedure was then repeated but the oxide layer was increased to a total thickness of 1600Å (80v) before the depth distribution was measured. The depth distributions of each isotope were again obtained by β- and γ-counting.

Results and Discussion

The distribution of the three isotopes in Ta<sub>2</sub>O<sub>5</sub> before and after oxide growth is shown in Fig. 4. It is assumed at this point that Kr is a truly immobile marker, so the abscissa scale for the initial distribution (upper scale) has been displaced to make the two Kr peak positions coincide. The fraction of oxide growth by metal migration outward is then immediately seen. Of the extra 1200Å of oxide grown, 340Å are due to metal migrating outwards, and hence 860Å are due to oxygen moving inwards. This gives a transport number for the metal of 0.28 ± 0.03 in good agreement with the previous values of 0.31 ± 0.03 by β-ray spectrometry (1) and of 0.255 ± 0.004 by a chemical stripping method (6).

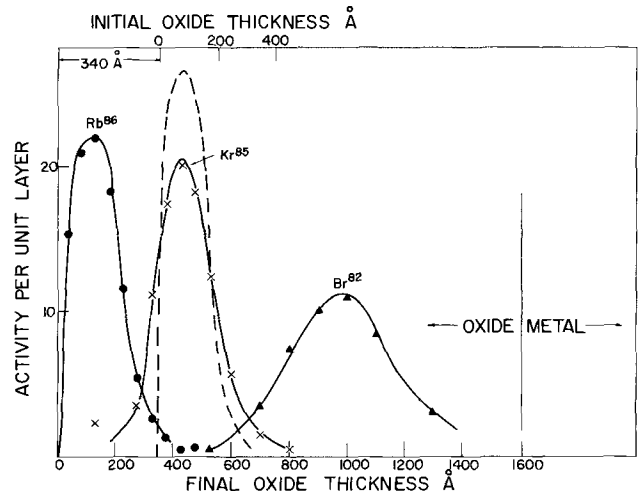


Fig. 4. Differential distribution of 30 kev <sup>86</sup>Rb, (●), <sup>85</sup>Kr (x) and <sup>82</sup>Br (Δ) in Ta<sub>2</sub>O<sub>5</sub> before (---) and after (—) additional anodizing. The abscissa scale for the initial distribution has been shifted by 340Å (upper scale) in order to make the <sup>85</sup>Kr peak positions coincide.

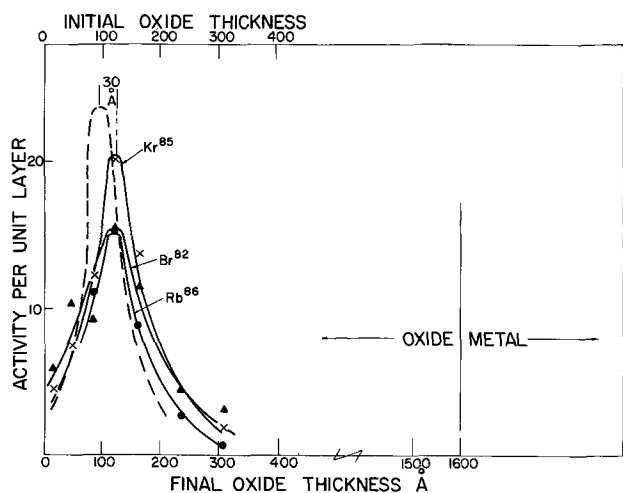


Fig. 5. Differential distribution of 30 keV  $^{86}\text{Rb}$ , ( $\bullet$ ),  $^{85}\text{Kr}$  ( $\times$ ) and  $^{82}\text{Br}$  ( $\Delta$ ) in  $\text{ZrO}_2$  before (---) and after (—) additional anodizing.

The final locations of  $^{82}\text{Br}$  and  $^{86}\text{Rb}$  indicate that bromine migrates inwards, but with two thirds the mobility of the oxygen, and that the rubidium migrates outwards with two thirds the mobility of the Ta. Qualitatively, this behavior is what would be predicted from simple chemical considerations, *viz.*, that Br migrates as an anion, and Rb as a cation. The broadening of the Br peak may be attributed to the combination of (i) a random walk broadening due to movement of the ions during oxide growth and (ii) the preferential removal of oxide from the edges of the specimen [c.f. ref. (2)].

The location of Kr, Br, and Rb in  $\text{ZrO}_2$  after anodic oxidation is shown in Fig. 5, where again the initial distribution of the three isotopes is shown by the dotted line. In this case the final distribution curves are virtually the same as the initial one (except for a slight broadening), indicating that no new oxide has been formed on the surface, and that therefore all the oxide formation is by oxygen migrating inwards. This is in agreement with the previous work (1).

However, it is interesting to note that although zirconium oxide grows almost completely by oxygen migration, the Br anion does not move appreciably as it does during the growth of tantalum oxide (Fig. 4). This would indicate that in  $\text{ZrO}_2$ , a large monovalent ion such as  $^{82}\text{Br}$  has a negligible mobility compared to the oxygen ion. An alternative possibility is that oxygen movement in  $\text{ZrO}_2$  is by way of holes, grain boundaries, defects, etc. Such a transport mechanism might not be available to the marker atoms because these are embedded uniformly at a depth of about 100 Å in the oxide lattice.

It is known that anodically formed  $\text{Ta}_2\text{O}_5$  is amorphous (7) while  $\text{ZrO}_2$  formed anodically in saturated ammonium borate is crystalline (8) and may contain defects such as holes, cracks, etc. This information strengthens the latter explanation but a more direct method of testing it would be to add  $^{82}\text{Br}$  atoms to the electrolyte and then measure their uptake into a growing  $\text{ZrO}_2$  film, and their final depth distribution within the  $\text{ZrO}_2$  layer.

Preliminary experiments of this type indicate that an appreciable amount of  $^{82}\text{Br}$  does in fact penetrate deeply into the growing  $\text{ZrO}_2$  layer. The measurements were made by first growing a 400 Å (20v) oxide in inactive electrolyte then increasing the oxide thickness to 700 Å (35v) in  $\text{Br}^-$  doped electrolyte. Sectioning and measurement of the residual  $\text{Br}^-$  activity showed that it was distributed throughout the complete oxide, old and freshly formed. The experiment was repeated but in this case the initial undoped oxide was formed to a thickness of 400 Å (20v) then immersed in the  $\text{Br}^-$  doped electrolyte at 10v. Again, on sectioning,

the  $\text{Br}^-$  was found distributed through the oxide. As a control, a 400 Å oxide was formed in inactive electrolyte then immersed in the  $\text{Br}^-$  doped electrolyte with no voltage applied. Sectioning showed that the  $\text{Br}^-$  had not penetrated into the oxide.

These results, together with the observation (Fig. 2) that none of the radiotracers moves appreciably during the anodic formation of  $\text{ZrO}_2$ , suggests that defects, holes, grain boundaries etc. may contribute significantly to the mode of oxygen movement through the growing oxide. This has been postulated previously by Cox and Roy (9) who measured the diffusion of oxygen into growing oxide films of zirconium, and concluded that the measured rates represented diffusion along easy paths which were "probably crystallite boundaries."

Additional evidence that  $\text{ZrO}_2$  grows by oxygen migration was obtained by injecting 30 keV  $^{133}\text{Xe}$  into a 400 Å  $\text{ZrO}_2$  layer, increasing the oxide thickness to 1600 Å and finally injecting 30 keV  $^{125}\text{Xe}$ . The depth distributions of the two Xe isotopes were then measured simultaneously by the sectioning technique and the separation of the gamma ray peaks of  $^{133}\text{Xe}$  (81 keV) and  $^{125}\text{Xe}$  (243 keV). Since the ranges of 30 keV  $^{125}\text{Xe}$  and  $^{133}\text{Xe}$  are virtually the same (10), their final depth distributions in  $\text{ZrO}_2$  should be identical provided that the oxide grows by oxygen migration alone. The results (Fig. 6) illustrate that the  $^{133}\text{Xe}$  and  $^{125}\text{Xe}$  have almost exactly the same location, the extent of metal ion transport, if any, being evidently less than 1%.

### Summary

The comparison of cation and anion movement with the location of krypton in the anodic oxides of tantalum and zirconium, and the measurement of different isotopes of xenon in  $\text{ZrO}_2$  has provided additional evidence that xenon and krypton are immobile markers for use in oxidation studies. The lack of measurable broadening of the krypton distribution tends to confirm this.

The transport number of metal in the anodic oxidation of tantalum has been measured as  $0.28 \pm 0.03$ , in good agreement with other workers' results. The anodic oxidation of zirconium has been shown to proceed almost entirely by oxygen migration, probably by some defect mechanism.

The technique of removing thin sections of anodic oxides by vibratory polishing has been shown to be suitable for the measurement of ionic transport numbers in  $\text{Ta}_2\text{O}_5$  and  $\text{ZrO}_2$ . This type of measurement may in principle be extended to any other metals on which coherent oxides can be formed. A large number of isotopes may be used as radiotracers as shown and, if chosen carefully, may be used simultaneously.

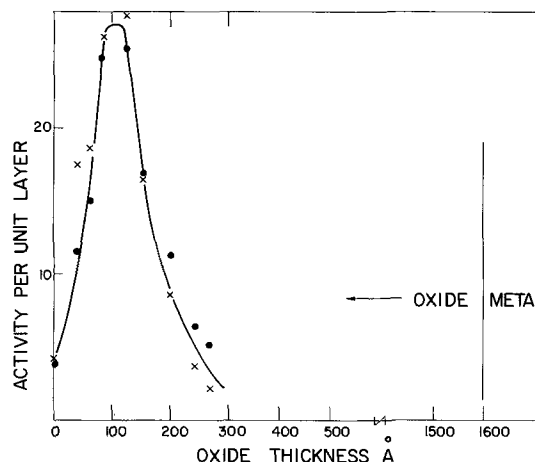


Fig. 6. Differential distribution of 30 keV  $^{133}\text{Xe}$  ( $\bullet$ ) in 400 Å and 30 keV  $^{125}\text{Xe}$  ( $\times$ ) in 1600 Å  $\text{ZrO}_2$ .

**Acknowledgment**

The author is grateful to Dr. J. A. Davies for many useful discussions and to J. P. S. Pringle for the use of his spectrophotometric calibration data.

Manuscript received July 17, 1967.

Any discussion of this paper will appear in a Discussion Section to be published in the December 1968 Journal.

**REFERENCES**

1. J. A. Davies, B. Domeij, J. P. S. Pringle, and F. Brown, *This Journal*, **112**, 675 (1965).
2. J. L. Whitton, *J. Appl. Phys.*, **36**, 3917 (1965).
3. L. Young, *Proc. Roy. Soc.*, **A244**, 41 (1958).
4. N. J. M. Wilkins, *Corrosion Science*, **5**, 3 (1965).
5. J. A. Davies, F. Brown, and M. McCargo, *Can. J. Phys.*, **41**, 829 (1963).
6. J. P. S. Pringle, Private communication.
7. P. H. G. Draper and J. Harvey, *Acta Met.*, **11**, 873 (1963).
8. J. N. Wanklyn, A.S.T.M. S.T.P. 368, 58 (1963).
9. B. Cox and C. Roy, *Electrochem. Technol.*, **4**, 121 (1966).
10. P. Jespersgaard and J. A. Davies, Private communication.

## Property Changes in Pyrolytic Silicon Nitride with Reactant Composition Changes

V. Y. Doo,\* D. R. Kerr,\* and D. R. Nichols<sup>1</sup>

*IBM Components Division, East Fishkill Facility, Hopewell Junction, New York*

**ABSTRACT**

Property changes in pyrolytic silicon nitride were investigated as a function of the reactant composition (silane:ammonia ratio). The potential of developing cracks in films deposited on silicon was greatly reduced by decreasing the ammonia injection rate. However, all films in this work with low ammonia and the films in the previous work with high ammonia were amorphous. Decreasing the ammonia injection rate increases the index of refraction and the electronic leakage while decreasing the dissolution rate (in 48% HF). The deposition rate, the dielectric constant, and the flat-band charge density are not significantly affected by the ammonia injection rate.

In pyrolytic deposition of amorphous silicon nitride films by the reaction of silane and ammonia (1-4), an excess quantity of ammonia is normally injected into the reaction chamber to ensure that the silane will react completely. The properties of the films deposited with silane:ammonia injection ratios in the range of 1:20-40 and under given conditions (temperature, deposition rate, etc.) are essentially the same (1). As the ammonia injection rate is gradually reduced to approach the silane injection rate, the ammonia becomes scarce around a silane molecule. One expects part of the silane to decompose and then be deposited on the substrate without reacting with ammonia, thus causing deficient Si-N bonds in Si<sub>3</sub>N<sub>4</sub> films. In other words, the composition of the silicon nitride films would become silicon rich, thereby affecting the film properties. This paper reports the findings on the property changes of amorphous silicon nitride films as a function of the reactant composition.

**Experimental Procedures**

The amorphous silicon nitride films were prepared by the pyrolytic reaction of silane and ammonia in a hydrogen atmosphere (1-4). The reaction occurred in a fused quartz tube in which a surface treated high-purity graphite susceptor was used to couple with an rf coil placed outside of the quartz tube. The injection rates of silane and hydrogen were maintained at 1 ml min<sup>-1</sup> and 4 liters min<sup>-1</sup>, respectively, throughout this work, while the injection of ammonia was regulated to the predetermined rate.

The substrates were n-type silicon wafers of about 1.5 ohm-cm. The wafers were chemically polished in HF-HNO<sub>3</sub> solution. Prior to deposition, the substrate surface was *in situ* cleaned by heating in hydrogen at about 1225°C. The substrate temperature was then lowered to the predetermined deposition temperature. After the substrate temperature, which varied

from 800° to 1000°C, was stabilized, the deposition of nitride film proceeded.

The film thickness of the amorphous silicon nitride was measured by the interference fringes under sodium light and checked by a Tolansky (5) interferometer. The index of refraction was determined by the differential interfringe spacing method (1) with sodium light ( $\lambda = 5900\text{\AA}$ ) on samples with the nitride films deposited on thermally oxidized silicon substrates. Estimated accuracy is  $\pm 0.05$ .

Electrical properties of the films were investigated using MIS (metal-insulator-silicon) capacitors. After deposition of the silicon nitride films (typically 6000\AA thick), circular aluminum electrodes (20 mil diameter) were evaporated to form the MIS structures. Surface charge was determined from the well-known capacitance-voltage measurement (6,7) using a frequency of 10 kHz. Dielectric constant and electronic leakage measurements were made on the same structures.

**Results and Discussion**

The structure of the pyrolytic silicon nitride films was studied by the transmission electron diffraction and electron microscopy. The results of all the films studied confirmed earlier reports (1) that the films were amorphous. A typically broadly diffused diffraction pattern is shown in Fig. 1. In one sample prepared at 800°C with the silane to ammonia injection, ratio of 1:1, however, a thin layer of fine polycrystallites was detected at the film-substrate interface. Figures 2 and 3 show the transmission electron diffraction and the transmission electron microscopy, respectively, of the polycrystalline material identified as silicon crystallites. The deposit of silicon crystallites may have been caused by the sudden surge of silane at the beginning of deposition. Other samples grown at the same substrate temperature and silane:ammonia ratio with silane injection started 15 sec after ammonia showed no evidence of the presence of polycrystalline silicon.

<sup>1</sup>Present address: Materials Research Corporation, Orangeburg, New York.

\* Electrochemical Society Active Member.

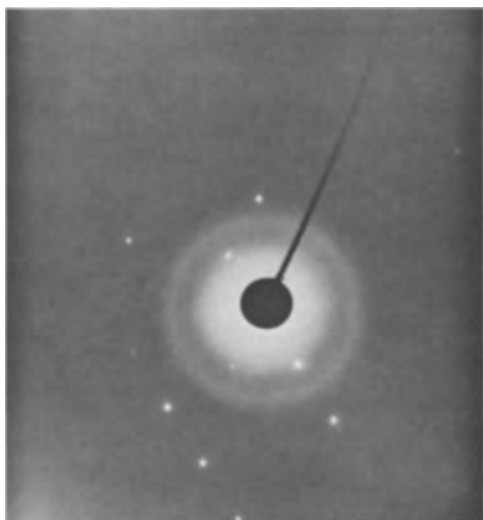


Fig. 1. Typical transmission electron diffraction pattern of pyrolytic amorphous silicon nitride. Spots are from single crystal silicon substrate.

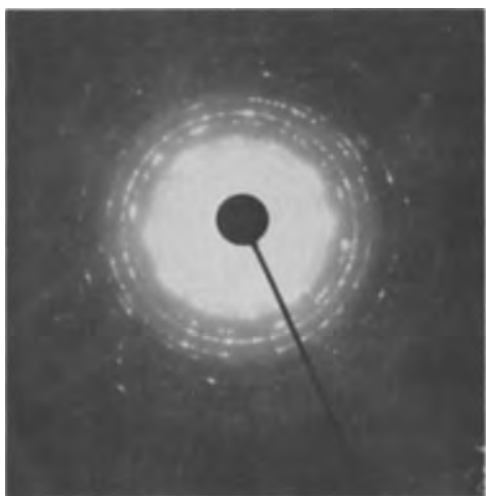


Fig. 2. Transmission electron diffraction pattern of polycrystalline silicon detected at the interface of silicon nitride-substrate.

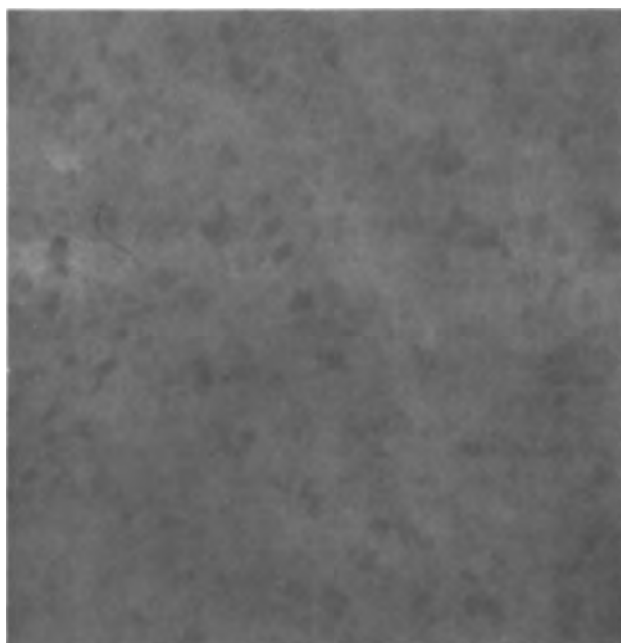


Fig. 3. Transmission electron microscopy of the same sample as Fig. 2.

Earlier work (1) reported that cracks are often observed on thick ( $>1\mu$ ) silicon nitride films grown on silicon substrates. The density of cracks increased with increasing film thickness and growth rate ( $>500\text{\AA min}^{-1}$ ). Thick silicon nitride films were grown at a silane:ammonia injection ratio of 1:40. The potential of developing cracks in silicon nitride films (on silicon) is greatly minimized for ratios of 1:1 to 1:5 even though the growth rate is a factor of three greater ( $1500\text{\AA min}^{-1}$ ) as shown in Fig. 4. These results indicate that the composition of the reactants has a profound effect on the stress and strain in the silicon nitride-silicon interface.

The growth rate of the silicon nitride is plotted as a function of the silane to ammonia injection ratio as shown in Fig. 4. Note that at a given deposition temperature, the deposition rate is practically independent of the ammonia injection rate when the silane to ammonia injection ratio is in the range of 1:1 to 1:10. The scattering of results was caused primarily by the experimental error in controlling low injection rates of the reactant gases and the error in thickness measurements.

The index of refraction of the pyrolytic silicon nitride was investigated as a function of the silane to ammonia injection ratio. In general, the index of refraction increases with decreasing ammonia injection rates at all the deposition temperatures (from  $800^\circ$  to  $1000^\circ\text{C}$ ). At the highest ammonia injection rates the refractive index was in the range 2.0-2.1. When the ammonia injection rate equals the silane injection rate, the index of refraction of the amorphous silicon nitride exceeds the index of refraction of the crystalline  $\alpha\text{-Si}_3\text{N}_4$  (RI = 2.1) (8). These results strongly indicate that the composition of the pyrolytically deposited films change gradually toward silicon rich silicon nitride as the ammonia injection rate is reduced to approach the silane injection rate. Since the film structure is amorphous, the excess silicon atoms must be dispersed randomly within the silicon nitride.

The dissolution rate of the silicon nitride in 48% HF (at room temperature) was determined. Figure 5 shows the dissolution rate plotted as a function of the silane to ammonia injection ratio. The dissolution rate of the silicon nitride films grown at a given silane to ammonia injection ratio decreases as expected with increasing deposition temperature. The  $800^\circ\text{C}$  films dissolved much faster than the  $900^\circ$  and  $1000^\circ\text{C}$  films.

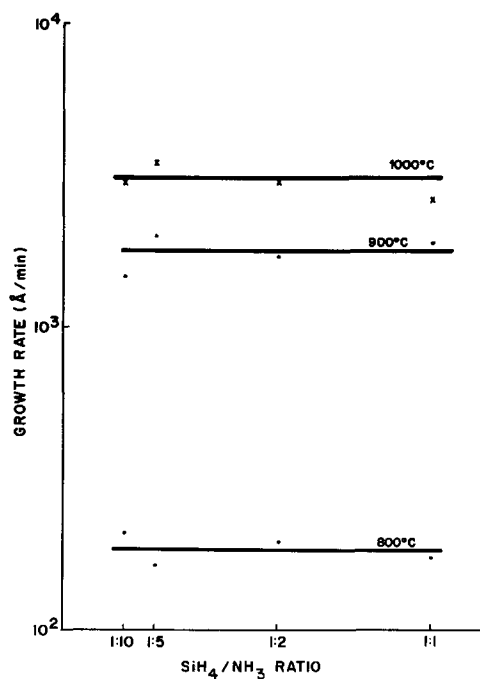


Fig. 4. Growth rate vs. silane to ammonia injection ratio

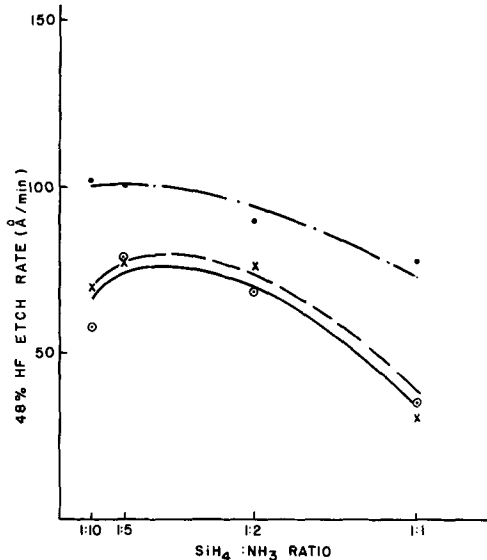


Fig. 5. Dissolution rate in 48% HF vs. silane to ammonia injection ratio. ●, 800°C films; X, 900°C films; ○, 1000°C films.

This suggests that the 800°C films are substantially less tightly bound than the 900° and 1000°C films. The dissolution rate of the films grown at a given temperature decreases with decreasing ammonia injection rate as it approaches the silane injection rate. This can be due to the film composition changing toward the silicon rich silicon nitride.

In all capacitance-voltage measurements a negative bias is required on the aluminum to observe the flat-band capacitance. Flat-band surface charge is defined by  $N_{FB} = C_N V_{FB} / q$  where  $C_N$  is the nitride film capacitance per square centimeter,  $V_{FB}$  is the flat-band bias, and  $q$  is electronic charge. In Fig. 6 the surface charge is plotted vs. silane:ammonia ratio for films deposited at 800°, 900°, and 1000°C. It is seen that the magnitude of  $N_{FB}$  varies with deposition temperature (900°C giving lowest values) but has little dependence on the silane:ammonia ratio. The surface charge has the same sign as that found with thermally grown  $SiO_2$  but is an order of magnitude larger (7). The dielectric constant of the films was obtained by measuring capacitance per square centimeter in the accumulated portion of the C-V characteristic and thickness by the Tolansky technique (5) after etching a step with HF. Uncertainties in the film thickness, electrode area, and capacitance indicate an absolute error in the dielectric constant of, at most, 3%. This permits more accurate dielectric constant measurements than

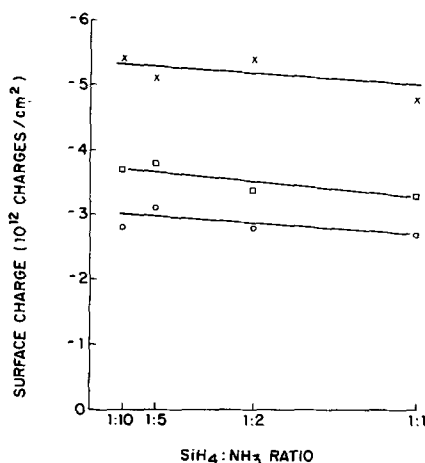


Fig. 6. Flat-band surface charge from C-V measurements on pyrolytic silicon nitride films deposited on silicon. Measurement frequency is 10 kHz. □, 800°C films; ○, 900°C films; X, 1000°C films.

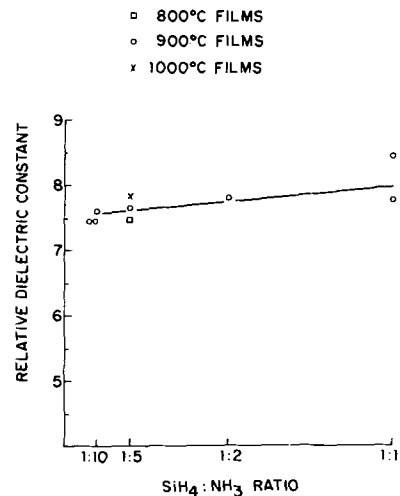


Fig. 7. Relative dielectric constant of pyrolytic silicon nitride films. Measurements are at 25°C and 10 kHz. Each data point represents an individual wafer. □, 800°C films; ○, 900°C films; X, 1000°C films.

those previously reported (1, 9). Figure 7 shows that the relative dielectric constant (measured at 10 kHz) has little dependence on the deposition temperature or the silane:ammonia ratio and approaches a value of 7.6 as the ammonia fraction increases. Dielectric constant measurements over the range 100 Hz to 1 MHz show no variation with frequency.

At high fields ( $E > 10^6$  V/cm), electronic leakage currents were observed at room temperature in the MIS devices. These currents are characterized as being reproducible between devices on a given wafer, being symmetrical with respect to polarity of the d-c bias, showing no decay with time, and having a nonohmic I-V characteristic. Note that  $\log(I/A)$  is a linear function of the square root of the applied field as shown in Fig. 8 and that doubling the field results in a current increase by several orders of magnitude. Figure 8 also shows a strong dependence of the conductivity on the silane:ammonia ratio. Increasing the ammonia fraction causes a shift of the curve to higher fields with little change of slope. Increasing the ammonia fraction beyond the 1:10 ratio causes very little additional shifting of the characteristic. The slopes of

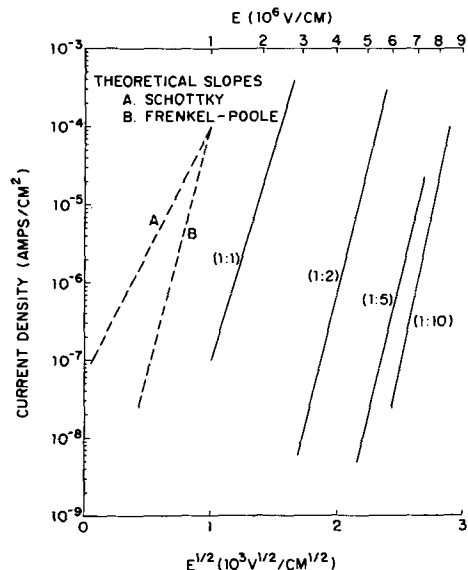


Fig. 8. Electronic leakage of pyrolytic silicon nitride films deposited at 900°C. Measurements are at 25°C, and the silane:ammonia ratios are given in parentheses on each curve. Theoretical slopes are shown for Schottky barrier injection and Frenkel-Poole emission from traps.



the curves permit a tentative identification of the conduction mechanism. Schottky barrier injection from the electrodes gives a current dependence on the field of  $I \sim \exp(q^3 E / \pi \epsilon)^{1/2} / 2kT$  where  $E$  is the field, and  $\epsilon$  is the optical dielectric constant of the insulator. A Frankel-Poole mechanism (10) in which carriers are emitted from traps in the bulk of the film gives the dependence  $I \sim \exp(q^3 E / \pi \epsilon)^{1/2} / kT$ , which has twice the slope of the Schottky equation. These theoretical slopes are shown in Fig. 8 using a dielectric constant of  $\epsilon/\epsilon_0 = 4$  (refractive index squared) and  $T = 300^\circ\text{K}$ . The slopes of the experimental curves and the symmetry with bias polarity are evidence for the bulk-limited, Frenkel-Poole mechanism. A detailed study of the conduction mechanism is being conducted.

### Conclusion

In the pyrolytic deposition of the amorphous silicon nitride films with the reaction of silane and ammonia, the film property changes were investigated as a function of the reactant composition. The reactant composition was changed by gradually reducing the ammonia injection rate while the silane injection rate was kept constant. The potential of developing cracks in silicon nitride films deposited on silicon substrates is greatly reduced by decreasing the ammonia injection rate to 1-5 times greater than the silane. However, the structure of all films in this work grown with low ammonia and in the previous work (1) with high ammonia ratios is amorphous. The index of refraction increases while the dissolution rate in 48% HF decreases with a decreasing ammonia injection rate. These results indicate that silicon nitride films grown with reduced ammonia (approaching the silane rate) are silicon rich in film composition. The electronic leakage current increases rapidly with decreasing ammonia. The film deposition rate, the dielectric constant, and the flat-band charge density are not significantly affected by the ammonia injection rate.

### Acknowledgment

The authors wish to thank Dr. S. Dash for the electron microscopy and diffraction analysis, Mr. J. R. Petrak for the electrical measurements, and Dr. G. A. Silvey for valuable discussion. This work was supported in part by the National Aeronautic and Space Administration, Electronic Research Center under Contract NAS 12-105.

Manuscript received April 19, 1967; revised manuscript received Sept. 21, 1967. This paper was presented in part at the Philadelphia Meeting of the Society, Oct. 9-14, 1966, as Abstract 146. The research reported in this paper was sponsored by the Electronics Research Center of the National Aeronautics and Space Administration under NASA Contract No. 12-105.

Any discussion of this paper will appear in a Discussion Section to be published in the December 1968 JOURNAL.

### REFERENCES

1. V. Y. Doo, D. R. Nichols, and G. A. Silvey, *This Journal*, **113**, 1279 (1966).
2. K. E. Bean, P. S. Gleim, and W. R. Runyan, Paper presented at the Philadelphia Meeting of the Society, Oct. 9-14, 1966, as Abstract 147.
3. J. H. Scott and J. A. Olmstead, *ibid.*, Abstract 151.
4. C. H. Lee, T. L. Chu, and G. A. Gruber, *ibid.*, Abstract 154.
5. S. Tolansky, "Multiple-Beam Interferometry of Surfaces and Films," Clarendon Press, Oxford, England (1948).
6. D. R. Kerr, *IBM Journal*, **8**, 385 (1964).
7. A. S. Grove, B. E. Deal, E. H. Snow, and C. T. Sah, *Solid-State Electronics*, **8**, 145 (1965).
8. W. D. Forgeng and B. F. Decker, *Trans. Met. Soc. AIME*, **47**, 343 (1958).
9. S. M. Hu, *This Journal*, **113**, 693 (1966).
10. S. M. Hu, D. R. Kerr, and L. V. Gregor, *Appl. Phys. Letters*, **10**, 97 (1967).

## Computer Programs for Quantitative and Semiquantitative Analysis with the Electron Microprobe Analyzer

S. S. So and H. R. Potts\*

Systems Development Division, International Business Machines Corporation, Endicott, New York

### ABSTRACT

A description of two FORTRAN IV computer programs is presented to simplify quantitative and semiquantitative analysis with the electron microprobe analyzer. The first program, EPMP1, determines the weight fraction of each element in a specimen from the characteristic x-ray intensity measurements of the specimen and the standards. The second program, EPMP2, calculates the relative characteristic x-ray intensities of all the elements in a specimen by assuming the composition of the specimen to be known. The correction procedure includes dead time correction, one of two background corrections (either constant background or background depending on composition), Philibert's absorption correction modified by Duncumb and Shields, one of three fluorescence corrections (either Birks', Castaing's, or Reed's), and a compound standard correction. The effects of the absorption and the fluorescence of each element in the specimen are easily seen from the output results. Versatility, efficiency, and ease of operation are emphasized in the programs.

Two FORTRAN IV computer programs<sup>1</sup> have been written to facilitate quantitative and semiquantitative analysis with the electron microprobe analyzer. The

\* Present address: IBM, Components Division, East Fishkill, New York.

<sup>1</sup> The program package is available from the IBM Program Information Department, Hawthorne, New York.

first program, EPMP1, calculates the weight fraction of each element in the specimen from the characteristic x-ray intensity measurements of the specimen and the standards. The second program, EPMP2, which is essentially the inverse of the first program, calculates the relative characteristic x-ray intensities of all

the elements in the specimen by assuming the composition of the specimen to be known.

Many correction procedures for electron microprobe analysis are available in literature (1-13). Each procedure has its merits and deficiencies, depending on the system being analyzed. Because of the complex, tedious, and time-consuming process of these correction procedures, computer techniques have been used to make proper correction for a more accurate quantitative analysis (14-18). The present programs include the following corrections: (i) dead time correction, (ii) a background correction (either constant background or background dependent on composition), (iii) Philibert's absorption correction modified by Duncumb and Shields, (iv) Birks', Castaing's, or Reed's fluorescence correction, and (v) a compound standard correction. However, there is no correction provided in the programs for the errors contributed by the following: atomic number effect, fluorescence excitation by the continuum, or contamination of the specimen and the standards.

The programs emphasize versatility and ease of operation. The large combinations of input data indicate the flexibility of the programs; this flexibility allows use of experimental data from various commercial electron microprobes. Codes for the various corrections are provided to eliminate unnecessary input data and computations; these codes thus enhance the efficiency of the programs.

### Theory of Corrections

The theory of electron microprobe analysis is based on relating the weight fraction of an element in a specimen to a ratio. This ratio is defined as the characteristic x-ray intensity generated in the specimen to that generated by a pure standard of the same element under the same experimental conditions. The characteristic x-ray intensity measured by the electron microprobe analyzer is affected by the following: finite resolving time of the detector, background x-ray spectrum, absorption of the emerging characteristics radiation in the specimen, and the fluorescence excitation by the characteristic radiations of other elements in the specimen. The program considers the previous effects in order to have an accurate quantitative analysis.

Due to the finite resolving time of the detector, the measured x-ray intensity,  $I_M$ , is less than true intensity,  $I_T$ . If the dead time,  $DT$ , is known, the program will make a dead time correction for all measured x-ray intensities as given by

$$I_T = \frac{I_M}{1 - I_M \cdot DT \cdot 10^{-6}} \quad [1]$$

where  $DT$  is in microseconds. If no dead time correction is necessary, set  $DT = 0$ , and the program will bypass above calculation.

Two types of background intensity corrections are provided in the program, the constant background and the background depending on the composition. If the continuum x-ray intensity,  $I_B$ , is small compared with the measured characteristic intensity,  $I_T$  (corrected for dead time), a constant background may be used. The corrected x-ray intensity for the  $i^{\text{th}}$  element in a matrix or the  $i^{\text{th}}$  standard element is simply given by

$$\begin{aligned} I_i &= I_T - I_B \\ I_{\text{std}} &= I_{T\text{std}} - I_{B\text{std}} \end{aligned} \quad [2]$$

However, for very small weight fractions (where the characteristic intensity approaches that of the continuum) the background intensity must be measured for each characteristic radiation and for each element in the specimen. Then the background intensity for the  $i^{\text{th}}$  element is given by

$$(I_B)_i = \sum_j W_j I_{ji} \quad [3]$$

where  $W_j$  is the weight fraction of the  $j^{\text{th}}$  element and

$I_{ji}$  is the background intensity of the  $i^{\text{th}}$  element due to the  $j^{\text{th}}$  element. The summation is carried over all the elements in the specimen.

The characteristic radiation is generated beneath the surface of the target and undergoes absorption when it emerges from the target before being detected by the spectrometer. Philibert's absorption correction (4), modified by Duncumb and Shields (11), is used in the program. The true weight fraction of the  $i^{\text{th}}$  element in the specimen, with absorption correction, is given by

$$W_i = I_{\text{rel}} \left[ \frac{F_{\text{std}}(\chi)}{F_i(\chi)} \right] \quad [4]$$

where the relative x-ray intensity,  $I_{\text{rel}}$ , is defined as the ratio of measured characteristic x-ray intensity from the specimen to that of the standard (corrected for dead time and background)

$$I_{\text{rel}} = \frac{I_i}{I_{\text{std}}} \quad [5]$$

and  $F_{\text{std}}(\chi)$  and  $F_i(\chi)$  are the absorption correction factors for the standard and the specimen, respectively. The absorption correction parameter is given by

$$F(\chi) = \frac{1}{\left(1 + \frac{\chi}{\sigma}\right) \left[1 + h \left(1 + \frac{\chi}{\sigma}\right)\right]} \quad [6]$$

where

$$\chi = \text{cosec } \psi \cos \theta \sum_j \mu_{ij} W_j \quad [7]$$

$$h = 1.2 \frac{\sum_j A_j W_j}{\left[\sum_j Z_j W_j\right]^2} \quad [8]$$

$$\sigma = \frac{2.39 \times 10^5}{V^{1.5} - V_c^{1.5}} \quad [9]$$

with  $\mu_{ij}$  as the mass absorption coefficient for characteristic radiation generated from the  $j^{\text{th}}$  element absorbed by the  $i^{\text{th}}$  element,  $\psi$  as x-ray emerging angle with respect to the surface of the target,  $\theta$  as incident electron beam angle with respect to the normal of the target,  $A$  as the atomic weight,  $Z$  as the atomic number,  $V$  as the incident electron beam potential, and  $V_c$  as the critical excitation potential. Note that the parameter  $\chi$  has been modified to account for the inclination of the target to the electron beam.

When the characteristic radiation of the  $j^{\text{th}}$  element is shorter in wavelength than the absorption edge of the  $i^{\text{th}}$  element, it is able to enhance the characteristic radiation of the  $i^{\text{th}}$  element. The true weight fraction of the  $i^{\text{th}}$  element in a specimen, with both absorption and fluorescence corrections, is then given by

$$W_i = I_{\text{rel}} \left[ \frac{F_{\text{std}}(\chi)}{F_i(\chi)} \right] \left[ \frac{1}{1 + K_{fi}} \right] \quad [10]$$

where  $K_f$  is the fluorescence correction factor. Three methods are available in the program to calculate the fluorescence correction parameter,  $K_f$ .

Birks' equation (7) is given by

$$K_{fi} = 0.6 \sum_j E_{ij} W_j \left( \frac{\mu_{ij}}{\mu_j} \right) \left( \frac{V - V_{cj}}{V - V_{ci}} \right)^{1.65} \quad [11]$$

where  $E_{ij}$  is the excitation efficiency of the  $i^{\text{th}}$  element by the characteristic radiation of the  $j^{\text{th}}$  element, and  $\mu_j$  is the mass absorption coefficient of the specimen for characteristic radiation generated from  $j^{\text{th}}$  element.

Castaing's equation (1) is given by

$$\begin{aligned} K_{fi} &= 0.5 \left( \frac{\tau_i - 1}{\tau_i} \right) \sum_{j \neq i} W_j \omega_j(K) \left( \frac{\lambda_j}{\lambda_i} \right) \left( \frac{\mu_{ij}}{\mu_j} \right) \left( \frac{A_i}{A_j} \right) \\ &\quad \cdot \left[ \frac{\ln(1+u)}{u} + \frac{\ln(1+v)}{v} \right] \end{aligned} \quad [12]$$

where

$$u = \left( \frac{\mu_i}{\mu_j} \right) \operatorname{cosec} \psi \quad [13]$$

$$v = \left( \frac{\sigma}{\mu_j} \right) \sec \theta \quad [14]$$

with  $r_i$  as the absorption edge jump ratio (12),  $\omega(K)$  as the K-shell fluorescence yield (19), and  $\lambda$  as the characteristic wavelength.

Reed's equation (9) is a modified form of Castaing's equation; it considers all cases involving K and L characteristic radiations and may be written as

$$K_{fi} = 0.5 P_{mn} \left( \frac{r_i - 1}{r_i} \right) \sum_{j \neq i} W_j \omega_j(K) \left( \frac{U_j - 1}{U_i - 1} \right)^{1.67} \cdot \left( \frac{\mu_{ij}}{\mu_j} \right) \left( \frac{A_i}{A_j} \right) \left[ \frac{\ln(1+u)}{u} + \frac{\ln(1+v)}{v} \right] \quad [15]$$

where  $P_{KK} = P_{LL} = 1$ ,  $P_{KL} = 0.24$ ,  $P_{LK} = 4.2$ , and

$$U_i = \frac{V}{V_{ci}} \quad [16]$$

If a compound of known composition is used as a standard for the  $i^{\text{th}}$  element instead of a pure standard, then the measured x-ray intensity of that element from the compound standard ( $I_{cs}$ ) must be adjusted to be equivalent to the pure standard form ( $I_{std}$ ). Namely,

$$I_{std} = \frac{I_{cs}}{\xi_i} \quad [17]$$

where the compound standard correction factor is calculated from

$$\xi_i = W_i \left[ \frac{F_i(\chi)}{F_{cs}(\chi)} \right] (1 + K_{fcs}) \quad [18]$$

to include both absorption and fluorescence effects of the compound standard.

### Programs

**Quantitative analysis.**—The first program, EPMP1, calculates the weight fraction of each element in the specimen from the characteristic x-ray intensity measurements of the specimen and the standards. Figure 1 outlines the basic operation of EPMP1. Many features are built into the program to handle various situations in data compilation. Any number of problems can be analyzed in the same run of the program by simply stacking each set of input data one after another. The program treats each set of input data as a separate analysis. However, in the analysis of a system of specimens consisting of the same elements but different compositions, the standard intensity measurements may change from one specimen measurement to another because of the stability of the electron microprobe. In this case, the input data for the successive problems may be simplified by the continuation code. Other codes are provided for dead time, background, fluorescence, and compound standard corrections to enhance the efficiency of the program. If any of these corrections are not necessary, then input data is not required for that correction and the program will bypass the execution of that correction. (See List of Input Data.)

The incident electron beam of variable energy may be inclined at any angle with respect to the target. The x-ray emerging angle may be varied from element to element in the specimen. Each element in the specimen has its own compound standard code, so that any number of compound standards may be used as the standard of the specimen. The elements in the specimen may be analyzed in any order. Furthermore, if there is an uncertainty in any of the specimen x-ray intensity measurements, that intensity may be set

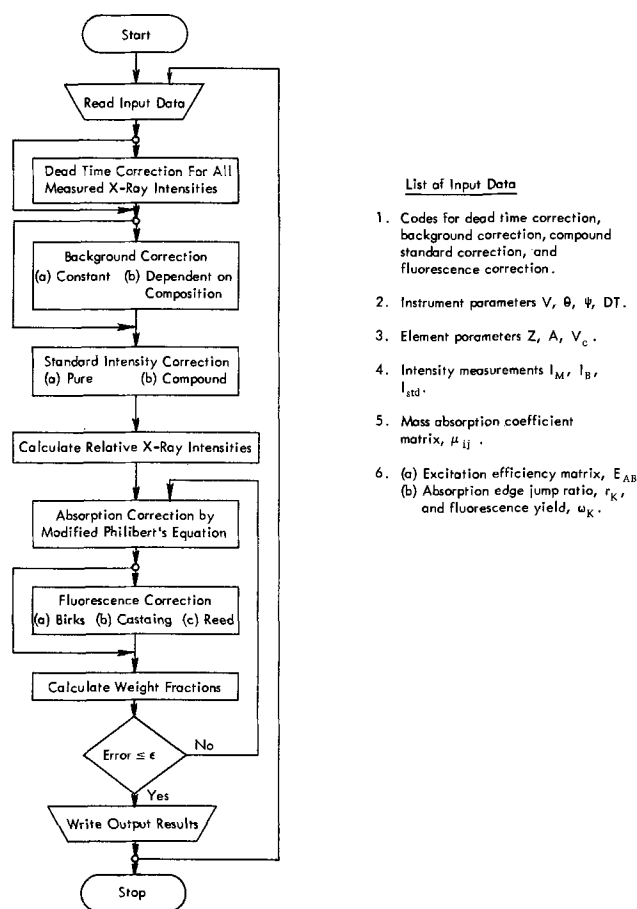


Fig. 1. Flow chart of EPMP1

to zero in the input data. The program will calculate the weight fractions of all other elements in the specimen and will set the remaining weight fraction in the specimen equal to the weight fraction of the uncertain element. This is the only case where the quantitative analysis will yield normalized weight fractions.

Note that the background (dependent on composition), absorption, fluorescence, and compound standard corrections are all dependent on the weight fractions of each element in the specimen. However, these weight fractions are the unknowns of the quantitative analysis. Therefore, the normalized relative x-ray intensities are taken as a first approximation for the weight fractions in calculating the correction terms. This is the only place where any normalization occurs in the iterative approximation. After having made the proper correction, the unnormalized weight fractions obtained from the previous approximation are then used to recalculate the correction terms for the successive approximations. This sets up the iterative procedure which is satisfied by either: (i) the successive approximations of the weight fractions do not change by more than a specified error,  $\epsilon$ , or (ii) the specified number of iterations has been reached. In the latter case, a warning message will be printed out to indicate the slow convergence or the divergence of the iterative steps.

All input data are printed out for easy reference, and they also serve as a record of the problem analyzed. In the output data, the measured relative x-ray intensity and the unnormalized weight fractions (with absorption correction or with both absorption and fluorescence corrections) are printed out. From these values, the effect of the absorption and the fluorescence of each element in the analyzed system is clearly seen. The value of the total unnormalized weight fractions gives an indication of the accuracy of the experimental data.

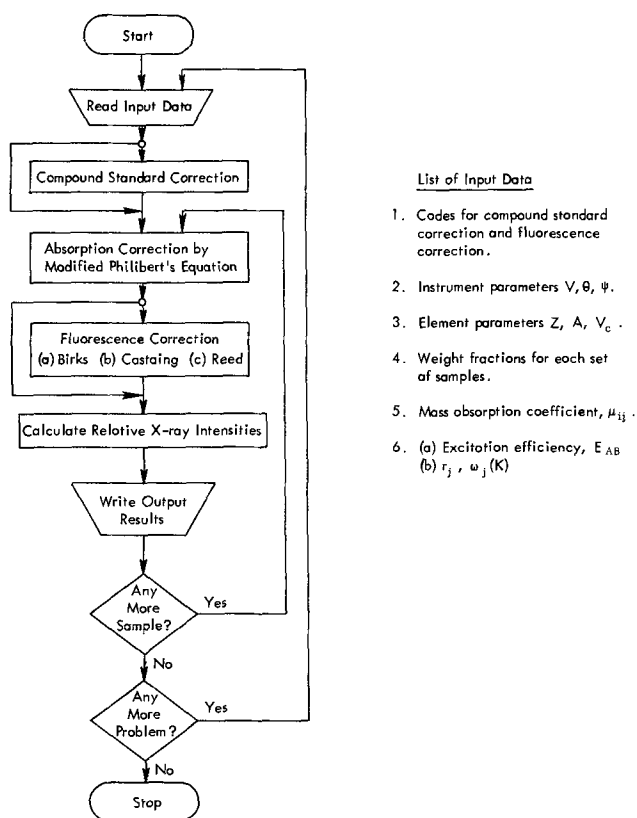


Fig. 2. Flow chart of EPMP2

**Semiquantitative Analysis.**—The second program, EPMP2, is particularly useful in a quick semiquantitative analysis, especially for binary alloys. By assuming various combinations of the weight fractions of a specimen, this program calculates the relative x-ray intensity of each element in the specimen. Figure 2 outlines the basic operation of EPMP2. The correction procedure is the same as the first program, EPMP1 (for the quantitative analysis), except no iterative approximation is necessary since the weight fractions of the specimen are assumed to be known. The calculated results may be plotted on a graph. Then, from the measured relative x-ray intensity (taken with the electron microprobe analyzer), the graph directly gives the weight fraction of that element (Fig. 3). Furthermore, it gives an indication of the degree of accuracy of the x-ray intensity measurements by noting: (i) how near the measured relative intensities approximate a vertical line, or (ii) how close the total measured relative x-ray intensity compared with the total calculated relative x-ray intensity.

### Examples

Table I and Fig. 3 are included to illustrate quantitative and semiquantitative analysis with the electron microprobe analyzer on a system of FeNi alloys over a wide range of compositions. The data<sup>2</sup> used in each alloy correspond to the averaged values of three different locations on the alloy, with ten consecutive measurements over each location. The measured relative intensities (in per cent) of Table I are calculated by Eq. [5].

By assuming various combinations of weight fractions of Fe and Ni, the relative characteristic x-ray intensities are calculated by EPMP2. These results are plotted on a graph as shown in Fig. 3. Using the values of measured, relative, characteristic x-ray intensities from Table I (column 3), Fig. 3 directly yields the weight fractions which are shown in column 4 of

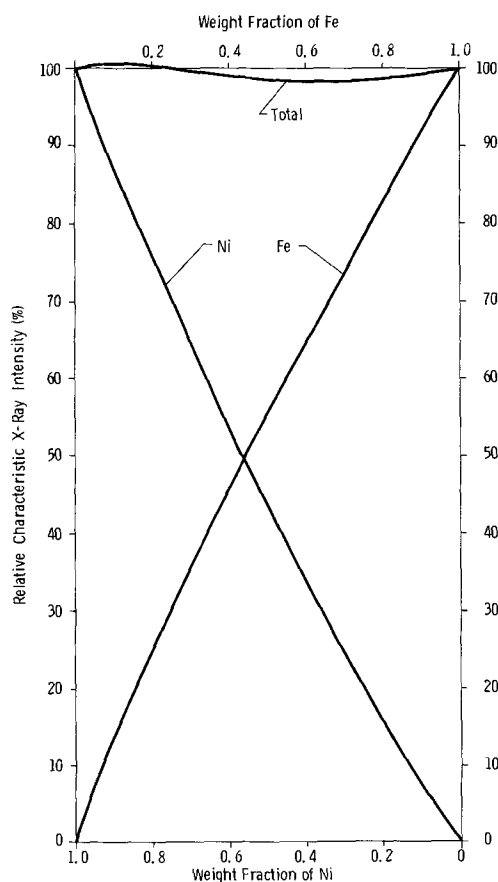


Fig. 3. Calculation of relative x-ray intensity by EPMP2 for FeNi binary alloys.

Table I. This gives a quick semiquantitative analysis of FeNi alloys. If more accurate results are required, the raw data from the electron microprobe analyzer measurements can be fed into EPMP1. Since three methods of fluorescence correction are available in the program, the differences between Birks', Castaing's, and Reed's equations are easily detected by comparing their results as shown in columns 5, 6, and 7 of Table I. The weight fractions of the FeNi alloys were determined by chemical analysis, and listed in column 8 of Table I.

By comparing column 4 of Table I with columns 5, 6, and 7, one can see that the results of EPMP2 are a good approximation to the quantitative analysis. Furthermore, by comparing columns 5, 6, and 7, one should note that the fluorescence corrections by Birks',

Table I. Quantitative analysis of FeNi alloys

Set	2	3 Measured relative intensity, %	4		6		8 Chemical analysis*
			EPMP2 Weight fraction	Weight fraction <sup>a</sup>	EPMP1 Weight fraction <sup>b</sup>	Weight fraction <sup>c</sup>	
I	Fe	14.06	0.105	0.09810	0.10005	0.10607	0.106
	Ni	86.28	0.895	0.88945	0.88988	0.89125	0.888
	Total	100.34	1.000	0.98755	0.98993	0.99732	0.994
II	Fe	43.42	0.375	0.37907	0.36623	0.37804	0.370
	Ni	54.32	0.610	0.60810	0.60635	0.60799	0.628
	Total	97.74	0.985	0.98717	0.97258	0.98603	0.998
III	Fe	49.42	0.435	0.44155	0.42675	0.43862	0.437
	Ni	48.92	0.555	0.55706	0.55525	0.55674	0.564
	Total	98.34	0.990	0.99861	0.98200	0.99536	1.001
IV	Fe	95.00	0.940	0.94693	0.94484	0.94590	0.939
	Ni	2.51	0.030	0.03278	0.03278	0.03278	0.051
	Total	97.51	0.970	0.97971	0.97762	0.97868	0.990

<sup>a</sup> Birks' fluorescence correction.

<sup>b</sup> Castaing's fluorescence correction.

<sup>c</sup> Reed's fluorescence correction.

\* G. Fisher, INCO.

<sup>2</sup> Measurements were taken by Electron Microprobe Analyzer, Model 400, Materials Analysis Company, at an electron beam voltage of 30 kv.

Table II. Correlation of relative intensities calculated from weight fractions by EPMP2 and weight fractions calculated from these intensities by EPMP1

Set	Input to EPMP2 Weight fractions		Output from EPMP2 = Input to EPMP1		Output from EPMP1	
	P	Cu	Relative inten- sity (%) <sup>*</sup>		Weight fractions <sup>*</sup>	
			P	Cu	P	Cu
1	0.1	0.9	3.71182	89.45734	0.10001	0.90000
2	0.2	0.8	7.99170	79.00667	0.20002	0.79999
3	0.3	0.7	12.97807	68.65514	0.30005	0.69999
4	0.4	0.6	18.85751	58.41150	0.40008	0.59999
5	0.5	0.5	25.88731	48.28600	0.50011	0.49999
6	0.6	0.4	34.43199	38.29140	0.59999	0.40000
7	0.7	0.3	45.02460	28.44341	0.70012	0.29999
8	0.8	0.2	58.47522	18.76149	0.80007	0.20000
9	0.9	0.1	76.07399	9.27002	0.89999	0.10000

\* Modified Philibert's absorption correction and Reed's fluorescence correction.

Castaing's, and Reed's equations differ more significantly for small weight fraction of Fe but tend to agree for larger weight fraction of Fe.

One way to check the accuracy of the iterative approximation of EPMP1 is to use the output from EPMP2 as the input of EPMP1. Then by comparing the output from EPMP1 with the original input to EPMP2, the difference gives a direct indication of the accuracy of the iterative approximation used in EPMP1. Table II illustrates this check with a system of PCu alloys. Nine sets of weight fractions of P and Cu are assumed and used in the input data to EPMP2. The relative characteristic x-ray intensities calculated by EPMP2 are then used as the input data to EPMP1. The weight fractions calculated by EPMP1 may be compared with the original assumed weight fractions. The difference, less than  $\pm 0.03\%$ , is the error of the iterative approximation of EPMP1.

Similarly, the uncertainty in any parameter of the correction procedure may be detected by varying that parameter. By comparing the output results, one gets an indication of the resultant effect on the quantitative analysis due to that particular parameter.

### Conclusions

Two FORTRAN IV computer programs have been used to facilitate quantitative and semi-quantitative analysis with the electron microprobe analyzer. These programs emphasize versatility, efficiency, and ease of operation. A primary advantage of these programs is the freedom of the user to utilize many alternative forms of correction to coincide with the data available. The efficiency of the programs is enhanced by the codes provided, so that unnecessary input data and computations are eliminated. All input data are printed out for easy reference, and they also serve as a record of the problem analyzed. From the output results, the effect of the absorption and the fluorescence of each element in the analyzed system is clearly indicated.

The over-all accuracy of the quantitative and the semiquantitative analysis with the electron microprobe analyzer is still limited by many factors. It not only depends on the system of elements being analyzed, but also depends on the correction procedures, the uncertainty in their parameter values, and the over-all experimental error. As better theories for the electron microprobe analysis are developed, the present programs can be easily modified to give more accurate results.

### Acknowledgments

The authors wish to thank Mr. H. R. MacQueen for experimental data measurements; Metropolitan New York section of The Electron Probe Analysis Society of America for supplying the FeNi specimens and the wet chemistry data on them; and Mr. J. E. Riedy for his assistance in preparing the manuscript.

Manuscript received March 28, 1967; revised manuscript received Sept. 28, 1967.

Any discussion of this paper will appear in a Discussion Section to be published in the December 1968 JOURNAL.

### REFERENCES

1. R. Castaing, Ph.D. Thesis, Univ. of Paris, 1951; O.N.E.R.A. Publication No. 55 (1952); Report No. WAL 142/59-7 (English).
2. D. B. Wittry, Univ. of S. California Engineering Center, Rept. 84-204 (1962).
3. D. M. Poole and P. M. Thomas, *J. Inst. Metals*, **90**, 228 (1962).
4. J. Philibert, "X-Ray Optics and X-Ray Microanalysis," p. 379, Pattee *et al.*, Editors, Academic Press, New York (1963).
5. G. Archard and T. Mulvey, "X-Ray Optics and X-Ray Microanalysis," p. 398, Academic Press, New York (1963).
6. M. Green, "X-Ray Optics and X-Ray Microanalysis," p. 361, Pattee *et al.*, Editors, Academic Press, New York (1963).
7. L. S. Birks, "Electron Probe Microanalysis," Interscience Publishers, New York (1964).
8. T. O. Ziebold and R. E. Ogilvie, *Anal. Chem.*, **36**, 322 (1964).
9. S. J. B. Reed, *Brit. J. Appl. Phys.*, **16**, 913 (1965).
10. R. Theisen, "Quantitative Electron Microprobe Analysis," Springer-Verlag, New York Inc. (1965).
11. P. Duncumb and P. K. Shields, "The Electron Microprobe," p. 284, McKinley *et al.*, Editors, John Wiley & Sons, Inc, New York (1966).
12. K. F. J. Heinrich, *ibid.*, p. 296.
13. J. W. Colby, *ibid.*, p. 95.
14. J. D. Brown, *Anal. Chem.*, **38**, 890 (1966).
15. J. W. Criss and L. S. Birks, "The Electron Microprobe," p. 217, McKinley *et al.*, Editors, John Wiley & Sons, Inc., New York (1966).
16. E. Davidson, W. E. Fowler, H. Neuhans, and W. G. Shequen, *ibid.*, p. 454.
17. D. R. Beaman, Second National Conference on Electron Microprobe Analysis, Boston, Mass. (1967).
18. H. E. Bishop, *Brit. J. Appl. Phys.*, **18**, 703 (1967).
19. R. W. Fink, R. C. Jopson, H. Mark and C. D. Swift, *Rev. Modern Phys.*, **38**, 513 (1966).

## Crystal Growth of a New Laser Material, Fluorapatite

R. Mazelsky,\* R. C. Ohlmann, and K. Steinbruegge

Westinghouse Electric Corporation, Research and Development Center, Pittsburgh, Pennsylvania

### ABSTRACT

Neodymium-doped calcium fluorophosphate is an efficient laser crystal. The growth method, chemistry, spectroscopy, and some pulsed laser results are presented.

The growth of laser technology has resulted in the need for crystals of large size which can perform at higher efficiencies than currently existing materials. A

\* Electrochemical Society Active Member.

material that meets these specifications is neodymium-doped calcium fluorophosphate,  $\text{Ca}_5(\text{PO}_4)_3\text{F}$ . This material doped with manganese and antimony is known to be an efficient phosphor and is, in fact, used in

fluorescent lamps. Johnson (1) has been successful in pulling large crystals of fluorapatite, pure and manganese-doped, from the melt. We have succeeded in preparing crystals by the Czochralski method which, when doped with neodymium, show laser oscillations at low threshold. This paper describes the method and apparatus for growth of the crystals and the pertinent spectroscopic data.

### Experimental

The pulling apparatus was designed such that pull rates between 1 and 40 mm/hr and rotation speeds of 10-110 rpm can be used. The furnace is surrounded by a quartz cylinder attached to the apparatus by means of a neoprene gasket and a brass flange. There are inlet holes for the introduction of appropriate atmospheres and a temperature sensing device. An iridium crucible is used to contain the fluorapatite. Insulation is provided by ½-in. thick zirconia quadrants stacked to form a cylinder. A circular zirconia plate with an access hole caps the furnace and serves as a reflector for minimizing thermal losses from the surface of the melt.

Heating is accomplished using a 30 kw motor-driven 10 kc generator, the a-c power driving water-cooled copper induction coils. It has been found that the lower frequencies give fairly uniform heating even though there are irregularities present in the iridium susceptor. Even with large irregularities no "hot spots" have been observed.

Temperature is controlled by using the output of a sapphire-light-pipe radiomatic detector and feeding it into an L&N Azar recorder controller. The voltage from the recorder controller in association with an L&N current adjusting type relay supplies the input circuit of a Norbatrol linear power controller. The Norbatrol output voltage supplies the necessary field excitation required by the 10 kc generator.

The seed holder consists of a pin vise or a water-cooled copper shaft which is threaded to accommodate a tantalum chuck. The seed is pinned to the tantalum chuck which is then threaded onto the water-cooled shaft such that the seed butts against the shaft. A schematic of the apparatus is shown on Fig. 1.

The fluorapatite crystals are grown in an argon atmosphere. The temperature at the surface of the melt as determined by optical pyrometer readings uncorrected for emissivity is 1705°C during growth. Pull rates of 3-8 mm/hr are used, and the seed crystal is rotated between 30-100 rpm. The melt is quite viscous, and the rapid rotation rate creates a visible swirl pattern on the surface of the melt.

Crystals obtained using rapid pull rates had visible feathery imperfections along the center of the boule. These were described by Johnson (1) as "opalescent inclusions." However, these "feathers" can be minimized or removed by utilizing slower pull rates in the range of 3-5 mm/hr. By using a seed crystal in which the feathers are present, it is possible to propagate these imperfections along the length of the crystal. Rapid changes in the diameter of the growing crystal results in large numbers of these imperfections. Under these conditions the preferred direction for the propagation of imperfections is along the "c" axis of the crystal. It is believed that these imperfections are associated with fluoride vacancies.

Neodymium-doped crystals can be obtained by simple substitution of neodymium for calcium in the melt. Since neodymium is a trivalent ion substituting for divalent calcium, some charge compensation is necessary. There is a self-compensating mechanism by which a fluoride ion may be replaced by an oxide ion. This can also be accomplished by the creation of a vacancy. The chemical formulas for crystals compen-

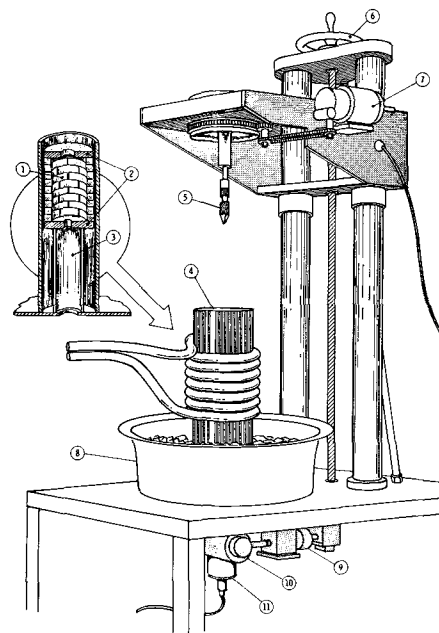
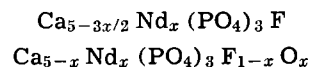


Fig. 1. Schematic of crystal puller. 1, Stabilized zirconia quadrant bricks; 2, stabilized zirconia quadrant plates; 3, stabilized zirconia quadrant cylinder; 4, 90 mm Vycor tube; 5, seed chuck; 6, manual feed; 7, rotator motor; 8, stainless steel basin; 9, electrically operated clutch; 10, pull motor; 11, sapphire rod radiomatic detector.

sated in these ways can be represented by the following



Both mechanisms are possible although it is not clear which predominates during growth.

Calcium fluorophosphate is a complicated chemical system in which it is necessary to consider at least four chemical entities,  $\text{Ca}^{+2}$ ,  $\text{PO}_4^{-3}$ ,  $\text{O}^{=}$ , and  $\text{F}^{-}$ . It is indeed fortuitous that the combination is congruently melting. The substitution of neodymium in the melt is an additional complication. Calcium fluorophosphate is prepared by combining the appropriate weights of  $\text{CaHPO}_4$ ,  $\text{CaCO}_3$ , and  $\text{CaF}_2$ . The substitution of neodymium for calcium can be accomplished by the replacement of any of these compounds with  $\text{Nd}_2\text{O}_3$ . Crystals were grown with  $\text{Nd}_2\text{O}_3$  replacing  $\text{CaCO}_3$ ,  $\text{CaF}_2$ , and combinations of the two. In all cases crystals of fair quality were obtained but they had a pronounced tendency to form color centers under ultraviolet radiation. The problem of color centers in halophosphate crystals has been discussed by Swank (2). Substitution of neodymium can also be accomplished by charge compensation; i.e.,  $\text{Na}^{+1}$ ,  $\text{Nd}^{+3}$  pairs being introduced into the divalent sites. No differences were observed in the Nd emission spectra or in the laser properties, whether the crystals were ion-compensated or allowed to self-compensate.

The segregation coefficient of neodymium in calcium fluorophosphate was determined by x-ray fluorescence analysis. Standard concentrations of neodymium in the host were prepared by solid-state reaction and analyzed. Then small crystals were grown from charges of several concentrations of neodymium varying from 0.5 to 5%. Crystals of the same concentration were pulled at different rates and analyzed to insure that the system was near equilibrium. In each case the mass of the crystals pulled were less than 1% of the total charge. The crystals, ground into powders, were analyzed for neodymium by x-ray fluorescence and compared to the standards. In this manner the concentration of neodymium in the pulled crystal as compared to the melt was determined. A plot of atomic per cent (a/o) neodymium in the melt versus atomic per cent neodym-

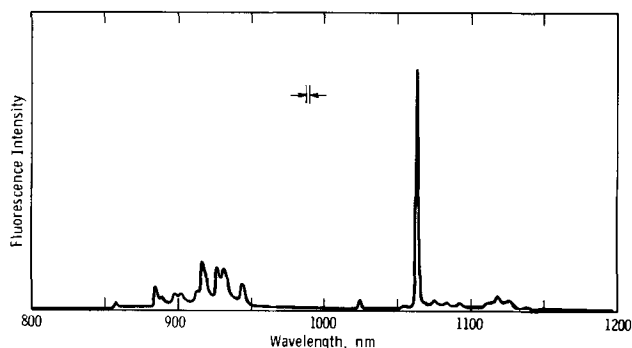


Fig. 2. Relative quanta rate of fluorescence of Nd doped  $\text{Ca}_5(\text{PO}_4)_3\text{F}$  at room temperature and 523 nm excitation. Corrected spectrum.

ium in the solid was prepared and a segregation coefficient of 0.52 was determined.

**Optical properties.**—The fluorescence spectrum of  $\text{Nd}^{3+}$  in calcium fluorophosphate at room temperature is shown in Fig. 2. This spectrum has been corrected for sensitivity so that the amplitude is proportional to quanta/sec nm. A larger fraction of the  $\text{Nd}^{3+}$  emission is present in a single line (at 10629 Å) than is found in the  $\text{Nd}^{3+}$  spectra in most other host crystals. The fluorescence decay time of the  $\text{Nd}^{3+}$  fluorescence is 180  $\mu\text{sec}$  at room temperature in a crystal containing 1 a/o neodymium by analysis.

The spectral quantum efficiency, i.e., the number of quanta emitted per unit wavelength interval for each quantum absorbed, particularly at the peak of an emission line, is an important parameter for laser materials. The room temperature line width of the principal line in calcium fluorophosphate is 6 Å, about the same as in yttrium aluminum garnet (YAG). The greater concentration of the emission in a single line in fluorapatite implies a greater spectral quantum efficiency than in YAG for the same over-all efficiency. A direct comparison of a YAG:Nd and fluorapatite:Nd crystal was made by measuring both the amount of energy absorbed and the peak emission intensity for each crystal. It was found that the spectral quantum efficiency at room temperature is  $2 \pm 0.2$

times larger for  $\text{Nd}^{3+}$  in fluorapatite than in YAG for 0.5 a/o Nd in each. This implies that the stimulated emission gain for a given rate of absorbing energy is correspondingly greater for fluorapatite than YAG. The  $\text{Nd}^{3+}$  absorption and excitation spectra are similar for the two materials although fluorapatite has broader absorption bands which are more intense in the visible region of the spectrum. One would expect, therefore, that the threshold for the fluorophosphate should be considerably less than for the same size YAG:Nd rod for the same distributed losses. This has been borne out by laser tests.

Crystals of fluorapatite with 1 a/o neodymium have been fabricated into rods 6.3 mm in diameter and 37 mm long. In the laser testing only a moderately efficient cylindrical pumping cavity was used. A typical rod was excited by a xenon flash lamp with an 800  $\mu\text{sec}$  pulse length. The laser rod had flat polished and parallel ends which were uncoated. Flat external mirrors were used as resonators. The threshold with reflectivities of 99% at one end and 35% at the other was 8 joules, a factor of two lower than YAG:Nd in the same apparatus. The crystal measured appeared of poor optical quality by visual inspection and the loss coefficient was fairly large. However, slope efficiencies in excess of 1% were obtained.

### Conclusion

Fluorapatite is by no means optimized with respect to either crystal quality or doping. However, sufficient data have been obtained to indicate potential superiority with respect to threshold and efficiency over existing crystalline lasers.

### Acknowledgment

The authors wish to acknowledge the assistance of W. E. Kramer and E. P. H. Metz, helpful discussions with Dr. R. C. Miller and A. J. Venturino, and the analytical work of J. Rudolph.

Manuscript received Aug. 23, 1967.

Any discussion of this paper will appear in a Discussion Section to be published in the December 1968 JOURNAL.

### REFERENCES

1. P. D. Johnson, *This Journal*, **108**, 159 (1961).
2. R. K. Swank, *Phys. Rev.*, **135**, 1A, 266 (1964).

## Microscopic Rates of Growth in Single Crystals Pulled from the Melt: Indium Antimonide

August F. Witt\* and Harry C. Gatos\*

Department of Metallurgy and Center for Materials Science and Engineering, Massachusetts Institute of Technology, Cambridge, Massachusetts

### ABSTRACT

Vibrations of known frequency introduced into a melt during crystal growth appear as impurity "vibrational" striations in the grown crystal. The growth-characteristics of crystal pulling under rotation (instantaneous microscopic growth rates and growth interface topography) were determined from the spacing and direction of introduced vibrational striations. It was demonstrated that periodic growth rate fluctuations (including local remelting) in the "off-facet" region are associated with rotational crystal pulling in the presence of thermal asymmetry. As a result of local remelting the average microscopic growth rate was shown to be significantly greater than the corresponding pulling rate. "Facet" growth is unaffected by rotation and proceeds at a rate which is identical with the pulling rate, although impurity heterogeneities have been identified in "facet" growth regions.

The effects of growth rates and their variations on crystalline perfection and the distribution of impurities during solidification have been treated extensively

\* Electrochemical Society Active Member.

in a large number of theoretical studies (1-7). The related experimental investigations do not provide the necessary information regarding instantaneous rates of growth and impurity concentrations (8-15). In these

investigations the instantaneous microscopic growth rates could not be directly determined. By necessity, the assumption has been made in some instances that the growth rate is equal to the pulling rate. Very often this assumption is not valid on the microscale. Thus, the formation of impurity striations (rotational and nonrotational) is generally attributed to periodic or random variations of the microscopic growth rate which imply deviations from the pulling rate. The origin of these growth rate fluctuations is attributed to short time temperature variations at the growth interface, caused by rotation of the growing crystal in a thermally asymmetric surrounding (rotational striations) (15), or alternately by random thermal convections due to unavoidable temperature gradients in the system (nonrotational striations) (12).

Recently a technique has been developed (16) which permits the determination of microscopic growth rates and the evaluation of interface morphology with high precision. This technique is presently applied to the investigation of InSb single crystal growth by the Czochralski technique.

### Experimental Procedure

A standard Czochralski crystal puller was modified to permit the introduction of vibrations with controlled and known frequency into the melt during crystal growth (Fig. 1). The incorporation of these vibrations in the form of impurity vibrational striations was achieved by doping the InSb melt with tellurium (15 mg of Te per 50g of InSb). All crystals were grown in a  $\langle 111 \rangle$  B direction (14) and subsequently cut along the growth axis to expose a (211) plane. The cut crystals were then mounted in plastic and polished. The final polish was obtained with a Linde "B" abrasive on a rotating wheel with the polishing direction parallel to that of the growth axis. It was found to be important that alumina abrasive particles be carefully removed from the InSb surface by means of a cotton pad under running water. The InSb crystal while still wet was immersed in a permanganate etchant for 2 min (17). The etched specimens were then rinsed in tap water, washed with soap, and dried in hot air. The etching process revealed impurity heterogeneities including the vibrational stri-

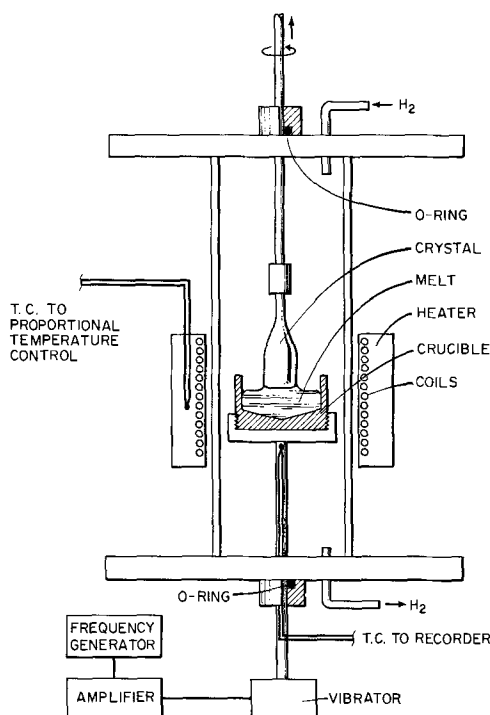


Fig. 1. Schematic representation of crystal growth arrangement

ations as elevations and depressions since the rate of etching is a function of the impurity concentration in the semiconductor. The presence of Te in InSb decreases the rate of etching. The microscopic investigation was performed with an interference contrast microscope (Normarski interferometer).

### Experimental Results and Discussion

*Effects of thermal asymmetry on rotational crystal growth.*—A recent investigation (15) of crystal growth under rotation revealed that in the presence of thermal asymmetry the instantaneous microscopic growth rate should be subject to sinusoidal fluctuations and follow the relationship

$$V = V_0 - \frac{2\pi\Delta TR}{G} \cos 2\pi Rt \quad [1]$$

where  $V$  is the instantaneous rate of growth,  $V_0$  is the pulling rate,  $\Delta T$  is the temperature variation during a  $360^\circ$  seed rotation,  $R$  is the rate of rotation,  $G$  is the temperature gradient in the melt, and  $t$  is the time.

Figure 2 is a section near the periphery of a single crystal which was pulled at a rate of 22 mm/hr and rotated at a rate of 8 rpm. The vibrational frequency was 3.5/sec. The thermal asymmetry was measured by a rotating thermocouple in the melt (without the seed present) at a distance of 6 mm from the rotational axis and was found to be  $1.8^\circ\text{C}$  for a full rotation. It is, of course, expected that the thermal asymmetry during actual growth ( $\Delta T$  in Eq. [1]) is somewhat different from the one measured. The changing spacing of the vibrational striations clearly reveals periodic growth rate changes with a periodicity of  $V_0/R$ . The so-called rotational striations (indicated by arrows) can be clearly identified here as the result of a decreased microscopic growth rate (decreased spacing in vibrational striations) which took place in the "hot" region of the thermally asymmetric melt (15). The actual in-

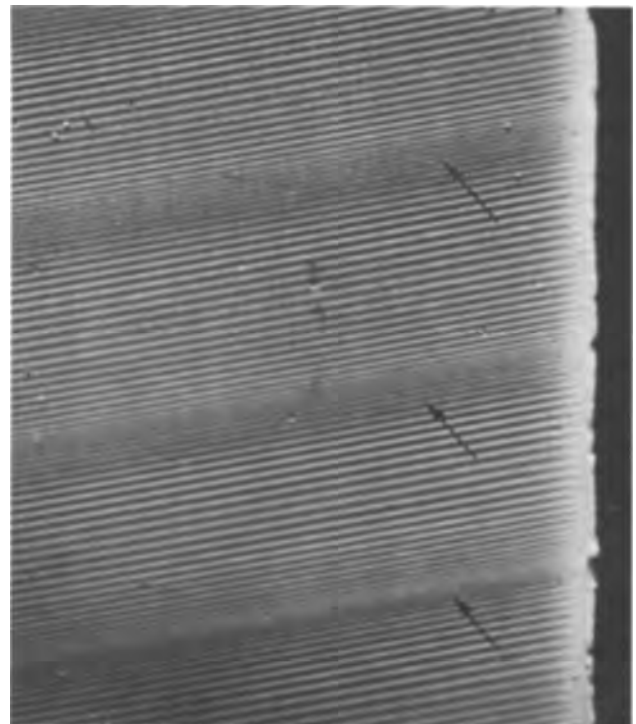


Fig. 2. Peripheral (off-facet) section of a Te doped InSb single crystal. The variations in the spacing of the vibrational striations reflect fluctuations in the microscopic rate of growth. Rotational striations appear as areas of decreased growth rate (arrows). Pulling rate 22 mm/h; rate of rotation 8 rpm; vibrational frequency 3.5/sec. Magnification ca. 600X.



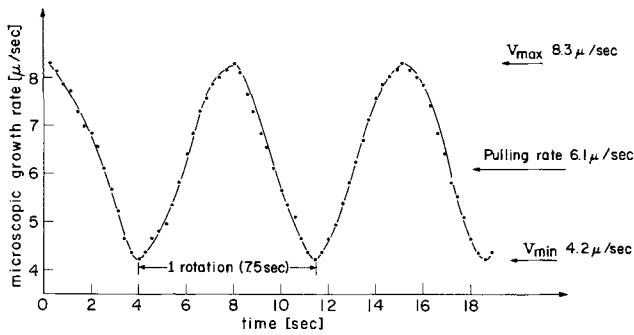


Fig. 3. Microscopic growth rates of the crystal shown in Fig. 2, as computed from the spacing of the vibrational striations measured at a distance of  $15\mu$  from the actual crystal periphery.

stantaneous growth rates, corresponding to the crystal of Fig. 2, as determined from the spacing of consecutive vibrational striations are seen in Fig. 3. The sinusoidal variations predicted in Eq. [1] are clearly shown. It should be noted that thermal conditions other than those assumed in Eq. [1] and encountered in the case of Fig. 2 can prevail in which case the variations in the microscopic rate of growth are no longer sinusoidal.

The effects of increased thermal asymmetry ( $\Delta T$   $2.4^\circ\text{C}$ ) on the microscopic growth rate during rotational pulling are depicted in Fig. 4. The small increase of  $\Delta T$  from  $1.8^\circ$  to  $2.4^\circ\text{C}$  has resulted in a change of the maximum to minimum growth velocity ratio, within one revolution, from 2.1 (Fig. 3) to 7.4. The small but readily observable change in direction of the vibrational striations in going from the minimum to the maximum spacing reflects a change in the radius of curvature of the growth interface which is greatest in the "hot" region and smallest in the "cold" region during a given revolution. This change corresponds to the continuous relocation of the growth interface which at any point in this "off facet" region (15) is determined by the exact position of the solidification isotherm.

A further increase in thermal asymmetry ( $\Delta T = 2.7^\circ\text{C}$ ) which was brought about by the lateral displacement of the tubular heating element ( $\frac{1}{8}$  in. from its original position) resulted in partial remelting of the grown crystal during rotation as shown in Fig. 5. Such a remelting phenomenon is predicted from Eq. [1] and reflects negative values of the minimum microscopic growth rates. A continuous change in the shape of the growth interface can readily be observed

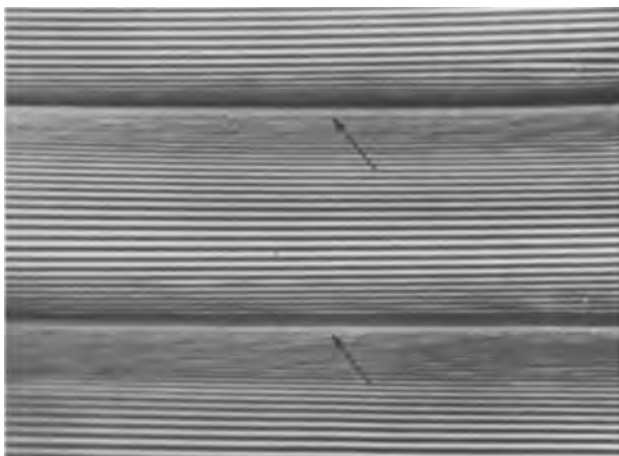


Fig. 4. InSb single crystal pulled under rotation in the presence of thermal asymmetry. Two rotational striations (arrows) can readily be observed. They reflect the onset of local remelting. Pulling rate 22 mm/hr; rate of rotation 8 rpm; vibrational frequency 8.2/sec. Magnification ca. 1320X.

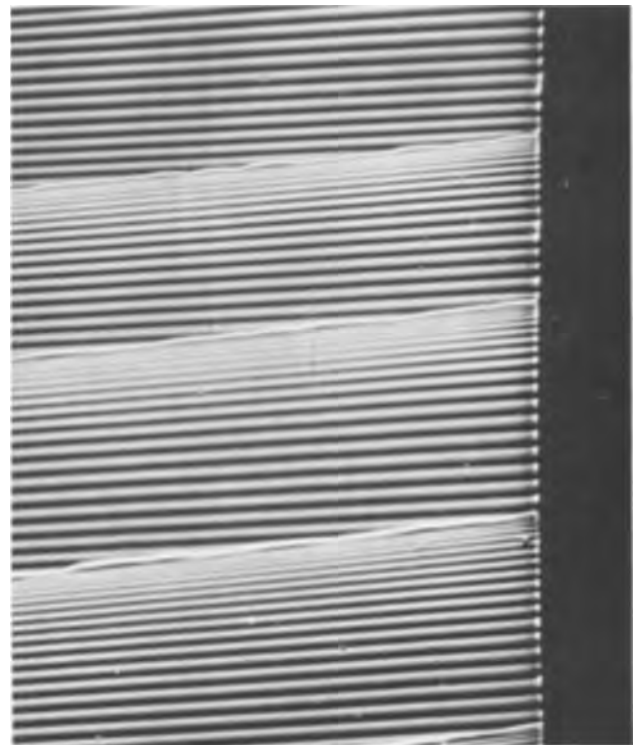


Fig. 5. Off-facet growth characteristics in InSb pulled under rotation in the presence of pronounced thermal asymmetry. The observed rotational striations are remelt lines which delineate the transitions of high to very low instantaneous growth rates (see text). The change in the direction of the vibrational striations reflects the continuous change of the radius of curvature of the growth interface during rotation. Pulling rate 22 mm/hr; rate of rotation 8 rpm; vibrational frequency 5/sec. Magnification ca. 675X.

here which is more pronounced than in Fig. 2 and 4. During a  $180^\circ$  rotation of the crystal from the hot into the cold region of the melt, the rate of growth increases steadily. This increase is accompanied by a decrease in the radius of curvature of the growth interface and reflects the relocation of the solidification isotherm deeper into the melt. Further rotation by  $180^\circ$  into the original hot region results in a steadily decreasing growth rate which, in turn, corresponds to an upward shift of the solidification isotherm. Concurrently with the growth rate decrease the radius of curvature of the growth interface increases. It can be observed that during this latter  $180^\circ$  rotation remelting takes place, i.e., the microscopic growth rate assumes negative values. Such remelting is a consequence of the fact that the rate at which the crystal is pulled from the melt is less than the rate of upward relocation of the crystal-melt interface. The resulting rotational remelt striation delineates the abrupt transition from a relatively high growth rate to a growth rate which starts at zero and increases steadily to its maximum value at the coldest point in the rotational cycle. It is apparent that for impurities with an equilibrium distribution coefficient  $k_0 < 1$ , the rotational striations constitute regions of decreased impurity concentration.

Single crystal growth in the  $\langle 111 \rangle$  direction generally leads to a more or less extensive facet formation at the growth interface. Figure 6 shows the transition region of a curved, nonsingular growth region (off-facet) to a flat singular facet region, which is reflected in the directional change of the vibrational striations. This transition is characterized by a rather abrupt change of the microscopic growth rate. While the growth rate varies continuously in the "off facet" region it assumes a constant value in the facet region which is identical to that of the macroscopic pulling rate. Obviously variations of the growth rate within

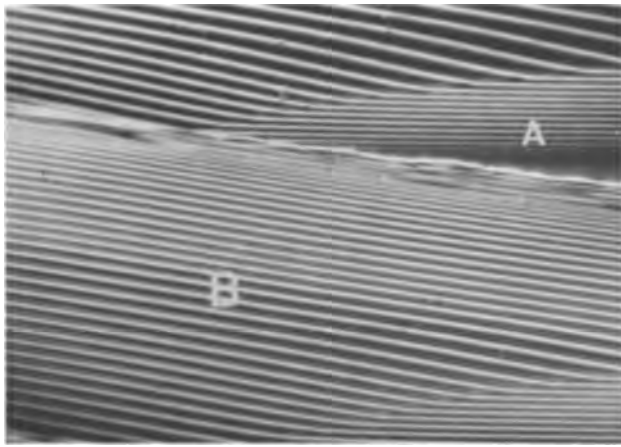


Fig. 6. Transition region of off-facet to facet growth; A facet region, B off facet region. The transition is characterized by the abrupt directional change of the vibrational striations. It can be observed that the instantaneous microscopic rate of growth varies during rotation in the off-facet region and becomes constant in the facet region. Small growth rate variations in the lower part of the facet near the off-facet region are attributed to growth on vicinal planes. Magnification ca. 1250X, oil immersion.

the facet region will result whenever significant temperature changes occur in the melt.

The interaction of remelt rotational striations with the facet results in its abrupt termination; the regrowth immediately following remelting is off facet growth (15). The interference of rotational remelting with the normal facet formation can clearly be observed in Fig. 7. This crystal was pulled at a rate of 35 mm/hr and rotated at a rate of 29 rpm. The frequency of the imposed vibrations was 6/sec. The upper part of the figure shows a section grown in the regular off

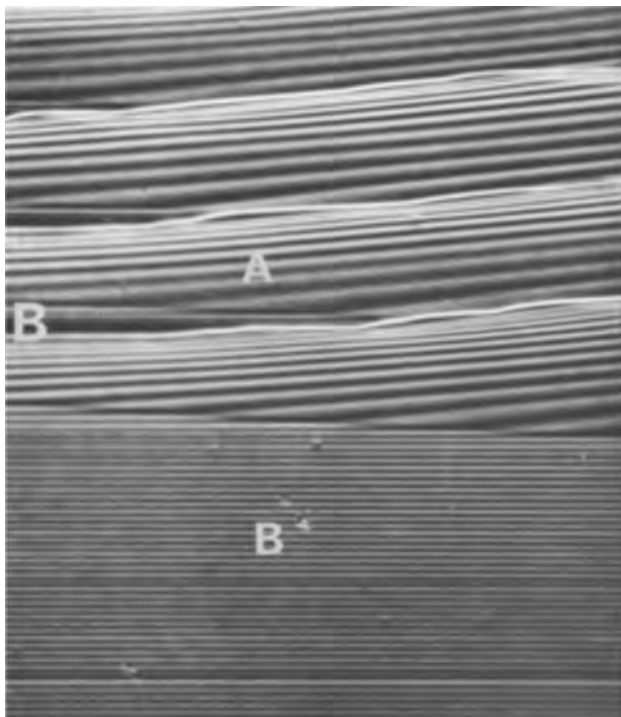


Fig. 7. Off-facet, A, and facet, B, region of an InSb single crystal. In the upper part grown under vibration, irregular growth conditions with extensive remelting are observed. Rotation has prevented the normal facet formation. Portions of the suppressed facet can be observed on the extreme left (B). After stopping rotation (lower part) the facet expands and covers the whole field shown. Pulling rate 35 mm/hr; rate of rotation 29 rpm; vibrational frequency 6/sec. Magnification ca. 500X.

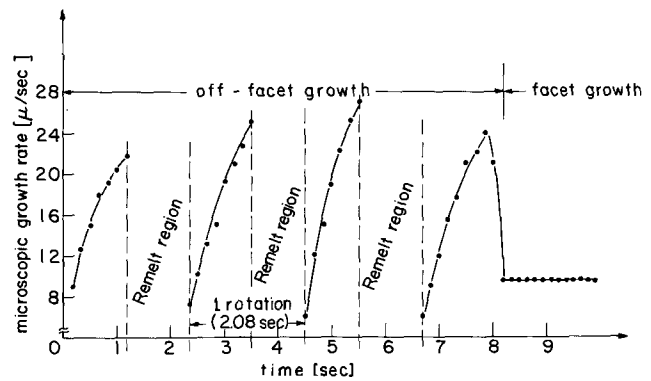


Fig. 8. Instantaneous microscopic rates of growth of the crystal shown in Fig. 7 as computed from the spacing of the vibrational striations. The duration of remelting is determined from the number of missing vibrational striations per rotation.

facet mode with the usual microscopic growth rate fluctuations and local remelting. Facet formation can barely be observed in this section since its lateral expansion is depressed by the backmelting process. Upon stopping the rotation (lower part of Fig. 7) the core or facet region expands to the right and the growth rate assumes a constant value identical with the crystal pulling rate (Fig. 8). This experimental result confirms the predicted independent and constant facet growth rate (15).

It can be clearly seen from Fig. 7 and 8 that due to local remelting the actual average microscopic growth rate is significantly greater than the pulling rate.

When, in addition to the controlled vibrations through the crucible, controlled vibrations are simultaneously introduced through the seed, then rather complex interference patterns of vibrational striations are observed in the curved, nonsingular growth sections (Fig. 9). Since this type of vibrational interference pattern is not present in the facet region, it is quite clear that singular and nonsingular planes exhibit basic differences in their growth characteristics.

It is generally assumed that off-facet growth proceeds normal to the interface without substantial kinetic supercooling since nucleation sites are provided by the curved growth interface. "Facet" growth, on the other hand, is believed to require the nucleation of growth steps (kinetic supercooling) which grow at

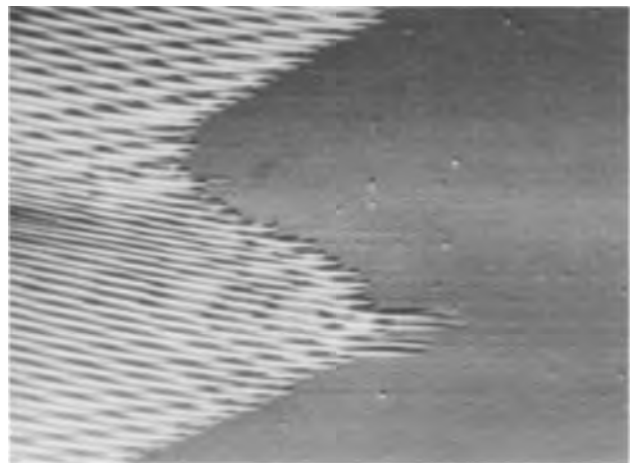


Fig. 9. Effect of the simultaneous introduction of vibrations through the crucible and the seed holder. The resulting vibrational striations exhibit pronounced interference patterns in the off-facet region. No interference patterns can be observed in the facet region. The frequency of the observed vibrational striations in the facet region shows that the seed vibrations are not incorporated in the form of vibrational striations. Magnification ca. 1000X, oil immersion.

high rates in a lateral direction. The width of individual vibrational lines in the facet region of Fig. 9 corresponds to approximately  $1000\text{\AA}$ . Thus, if facet growth proceeds by actual step growth, then, under the present experimental conditions, the step height cannot exceed  $1000\text{\AA}$  since a height in excess of this value would interfere with the formation of the observed striations. It is apparent that the present technique is uniquely suited for studies of the mechanism of facet growth.

The interference patterns of Fig. 9, which represent localized impurity concentration changes, are not caused by correspondingly localized growth rate fluctuations, since such fluctuations in rate would lead to continuous corrugations at the curved interface. Thus, the observed patterns must be attributed to localized perturbations (in the thickness and/or impurity concentration) of the interfacial boundary layer. Although vibrational interference effects are not observed in the facet region, impurity concentration changes (dark and light regions) under constant microscopic growth rate are observed as shown in Fig. 10. These concentration changes are, thus, most likely due to corresponding concentration changes in the boundary layer.

Impurity concentration changes unrelated to the microscopic growth rate are also shown in the facet region of Fig. 11. In this case controlled vibrations through the seed were intermittently superimposed to the regular vibrations as can readily be seen in the off facet region. The observed concentration changes in the facet region are apparently associated with rotational effects. It is not resolved as yet whether impurity heterogeneities in the facet grown region are due to changes in the thickness, the impurity concentration of the boundary layer, or other effects.

Growth rate fluctuations in a single crystal pulled from the melt without rotation are shown in Fig. 12. The resulting nonrotational heterogeneities are attributed to temperature fluctuations at the growth interface brought about by convective currents (14). From

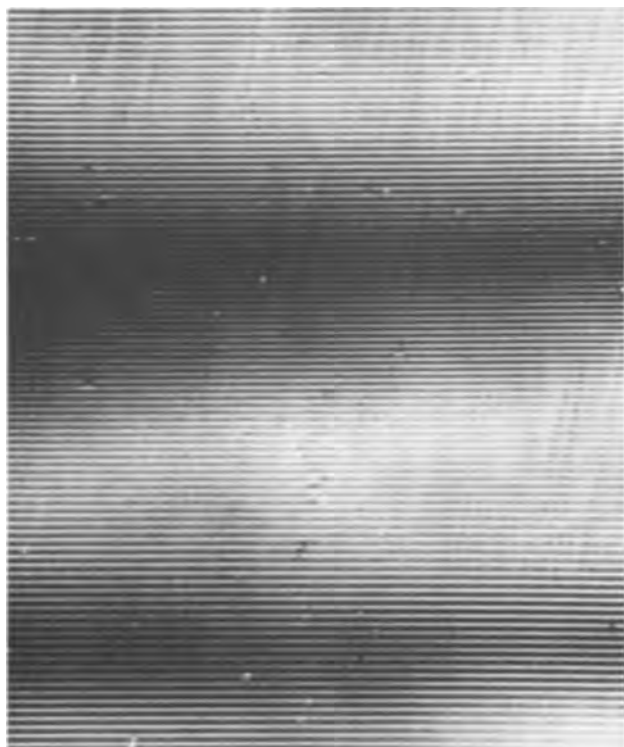


Fig. 10. Facet region in a single crystal of InSb. The observed dark regions reflect an increased impurity concentration. These impurity concentration changes are not related to growth rate changes since the spacing of vibrational striations remains constant. Magnification ca. 700X.

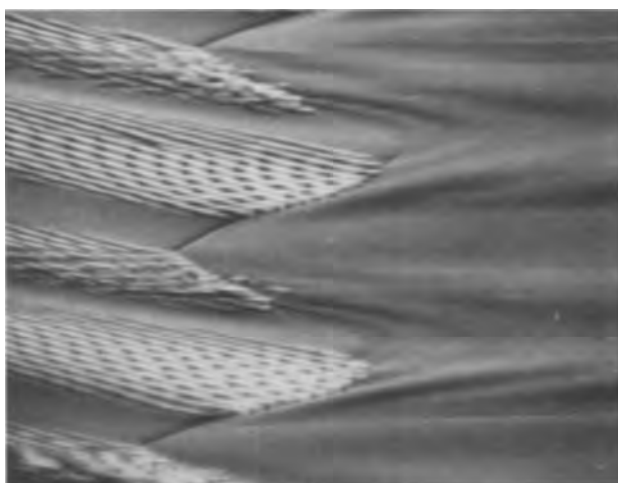


Fig. 11. Transition region (off-facet to facet) in InSb which was intermittently subjected to crucible and seed vibrations. Pronounced heterogeneities in impurity concentration are observed in the facet region. These heterogeneities exhibit the periodicity of rotation. Magnification ca. 1000X.

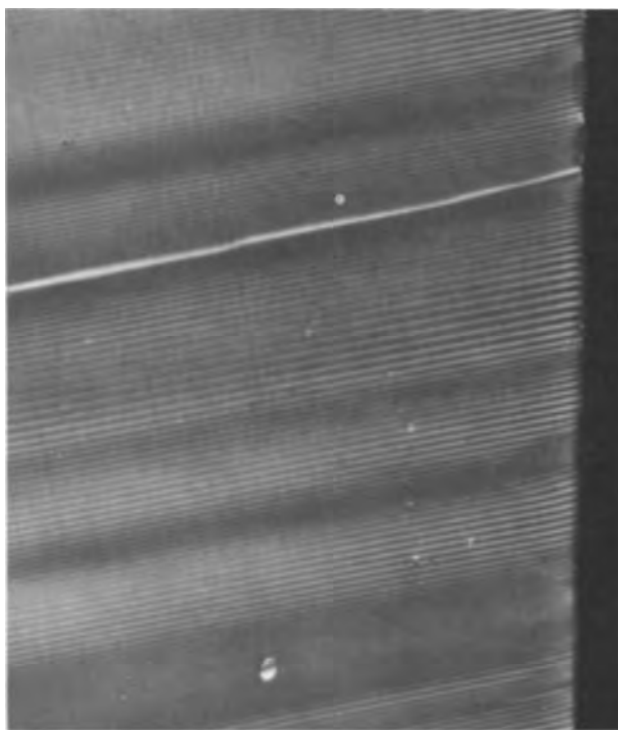


Fig. 12. Nonrotational striations in the peripheral part of an InSb single crystal. Note microscopic growth rate changes. Magnification ca. 600X.

the spacing of the vibrational striations (10/sec) and its variation it can be seen that the duration of the growth rate perturbations ranges from a fraction of a second to several seconds. It was generally observed (under the present experimental conditions) that such random growth rate fluctuations are less common in crystals pulled with rotation and could not be observed in crystals pulled under high rotational rates.

#### Summary

Microscopic rates of growth were determined in single crystals pulled from the melt by introducing vibrations of known frequency into the melt containing small amounts of impurity. Such vibrations are incorporated into the growing crystal in the form of vibrational striations. In the investigated system (InSb doped with Te) impurity heterogeneities and superimposed vibrational striations were revealed by means of

a permanganate etchant. The microscopic rates of growth and crystal-melt-interface topography were determined from the spacing and direction of the vibrational striations.

It was shown that off-facet regions (nonsingular, curved interfaces) exhibit constant and periodic growth rate fluctuations during rotational crystal pulling. The extent of the growth rate variations (at constant pulling rate) is a function of the degree of thermal asymmetry in the system. With increasing thermal asymmetry partial remelting results, i.e., the minimum microscopic growth rate assumes negative values during rotation through the hot region of the melt. The so called rotational striations were identified as the result of a decrease in the microscopic growth rate. The extent of the associated variation in impurity concentration is controlled by the rate at which the microscopic growth rate changes. Crystal growth on singular interfaces (facets) was shown to occur at a constant rate, equal to the pulling rate. Impurity heterogeneities were observed in facet regions grown under constant microscopic rate. Their origin is associated with perturbations in the boundary layer conditions.

#### Acknowledgment

This work was supported by the National Science Foundation Grant GK-1653 and by a grant from the Sloan Basic Research Fund administered by M.I.T. The authors wish to express their appreciation to Mr. C. J. Herman and Mr. W. J. Fitzgerald for their skillful laboratory assistance.

Manuscript received Aug. 17, 1967.

Any discussion of this paper will appear in a Discussion Section to be published in the December 1968 JOURNAL.

#### REFERENCES

1. J. A. Burton, R. C. Prim, and W. P. Slichter, *This Journal*, **21**, 1987 (1953).
2. R. N. Hall, *J. Phys. Chem.*, **57**, 836 (1953).
3. W. A. Tiller, K. A. Jackson, J. W. Rutter, and B. Chalmers, *Acta Met.*, **1**, 428 (1953).
4. C. Wagner, *J. Metals*, **200**, 154 (1954).
5. A. Trainor and B. E. Bartlett, *Solid State Electr.*, **2**, 106 (1961).
6. L. S. Milevskii, *Soviet Phys. Crystallography*, **6**, 193 (1961).
7. P. J. Holmes, *J. Phys. Chem. Solids*, **24**, 1239 (1963).
8. J. A. Burton, E. D. Kolb, W. P. Slichter, and J. D. Struthers, *J. Chem. Phys.*, **21**, 1991 (1953).
9. P. R. Camp *J. Appl. Phys.*, **25**, 459 (1954).
10. H. Ueda, *J. Phys. Soc. Japan*, **16**, 61 (1961).
11. K. F. Hulme and J. B. Mullin, *Solid State Electr.*, **5**, 211 (1962).
12. A. Mueller and M. Wilhelm, *Z. Naturforschung*, **19a**, 254 (1964).
13. J. R. Carruthers, *Can. Met. Quart.*, **5**, 55 (1966).
14. A. F. Witt and H. C. Gatos, *This Journal*, **113**, 808 (1966).
15. K. Morizane, A. F. Witt, and H. C. Gatos, *ibid.*, **114**, 738 (1967).
16. A. F. Witt and H. C. Gatos, *ibid.*, **114**, 413 (1967).
17. A. F. Witt, *ibid.*, **114**, 298 (1967).

## The Deposition of Silicon on Single-Crystal Spinel Substrates

P. H. Robinson\* and D. J. Dumin

RCA Laboratories, Princeton, New Jersey

#### ABSTRACT

Single crystal silicon has been epitaxially grown on (100), (110), and (111) magnesium aluminate spinel. The Hall mobilities of films grown on (111) spinel were higher than similar resistivity films grown on (100) and (110) spinel. Typical values of mobility have been 200 cm<sup>2</sup>/v-sec on 1 μm thick p-type films and 300 cm<sup>2</sup>/v-sec on 15 μm thick p-type films of 0.1 ohm-cm silicon. These mobility values represent 80-100% of the mobility expected on similar resistivity bulk silicon. The autodoping of the films by the substrate was measured and compared with the aluminum autodoping of silicon-on-sapphire films. Silicon grown on spinel was doped about an order of magnitude less than silicon-on-sapphire. The deformation of the film and substrate was found to be anisotropic and the silicon was under a compressive stress of 1-4 · 10<sup>10</sup> dynes/cm<sup>2</sup>.

Recently there has been considerable interest in the growth of silicon films on insulating substrates (1-5). The major portion of this work has been done using either single crystal sapphire or quartz as the substrate material. There have also been reports (6,7) that single crystal magnesium aluminate spinel substrates can be used for the growth of single crystal silicon.

Spinel is a solid solution of MgO and Al<sub>2</sub>O<sub>3</sub> and has a cubic crystal structure with a thermal coefficient of expansion variable with composition but lower than that of sapphire. Spinel is a good insulator which is commercially available in large flame-fusion grown single-crystal boules. This paper will describe the deposition and characterization of single-crystal silicon layers on single-crystal spinel substrates.

#### Physical Properties

The reaction used for the growth of single-crystal silicon films was the pyrolysis of silane diluted in hy-

drogen and has been described in detail (8). Electron diffraction patterns obtained have consistently been those of single-crystal oriented silicon layers and it has been found that the silicon lattice was parallel to the spinel substrate orientation, i.e., (111) silicon parallel to (111) spinel, (110) silicon parallel to (110) spinel, and (100) silicon parallel to (100) spinel, in agreement with previously reported results (6).

Sirtl (9) etching was used to reveal the number of dislocations present in the silicon layers. A typical film grown on (111) spinel and dislocation etched is shown in Fig. 1. The major growth imperfection appears to be stacking faults.

The deformation of silicon films between 2 and 25 μm thick on 0.025 and 0.050 cm thick spinel has been measured using a cross-section microscope. In all cases the deformations were anisotropic and exhibited a maximum deformation in one direction and a minimum deformation perpendicular to this direction. A

\* Electrochemical Society Active Member.

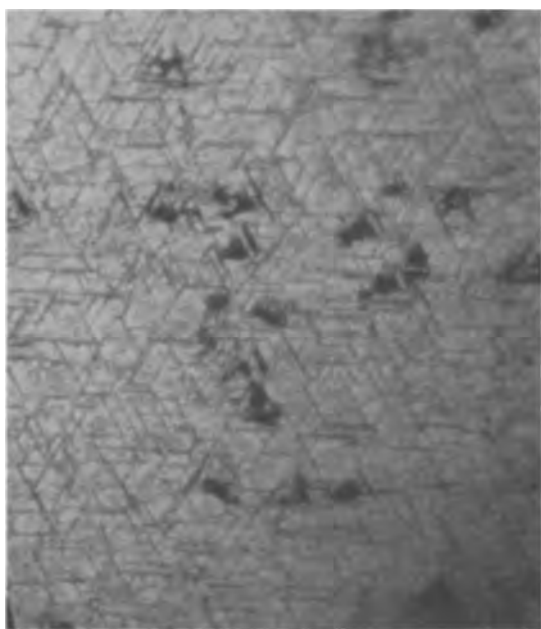


Fig. 1. Dislocation etched 15  $\mu\text{m}$  thick silicon-on-spinel film

typical plot of maximum and minimum deformation of a 5  $\mu\text{m}$  thick silicon film on 0.050 cm thick (111) oriented spinel is shown in Fig. 2. Removal of the silicon by chemical etching restored the spinel to a flat surface. This maximum deformation is about five times as large as the deformation of silicon grown on sapphire (10) and corresponds to a stress in the silicon of  $1.4 \times 10^{10}$  dynes/cm<sup>2</sup>. Measurements of silicon grown on (100) and (110) spinel substrates have yielded similar but smaller anisotropic deformations than (111) spinel. Occasionally the deformation is accompanied by cracking of the spinel substrate as well as the exsolution of  $\alpha\text{-Al}_2\text{O}_3$  from the spinel.

In an attempt to lower the deformation, 0.005 in. stripes spaced 0.050 in. on centers were etched in a 5  $\mu\text{m}$  thick film deposited on (100) spinel. The deformation measured in the direction of the stripes was small; however, the deformation perpendicular to this direction was relatively large. This is a further indication of the anisotropy in the spinel substrates used. Attempts to grow silicon on spinel through holes in a sapphire mask lead to spinel that was cracked along the edge of the deposited line.

#### Electrical Properties

Both p- and n-type silicon films have been grown via the addition of either  $\text{B}_2\text{H}_6$  or  $\text{AsH}_3$  during silicon growth on (100), (110), and (111)  $\text{MgO} \cdot 3.5 \text{Al}_2\text{O}_3$  spinel. Films between 1 and 30  $\mu\text{m}$  thick have been grown. Typical Hall mobilities measured on films 10-15  $\mu\text{m}$  thick are shown in Table I for films grown on different orientations of spinel. The films grown on (111) spinel have consistently had higher mobilities

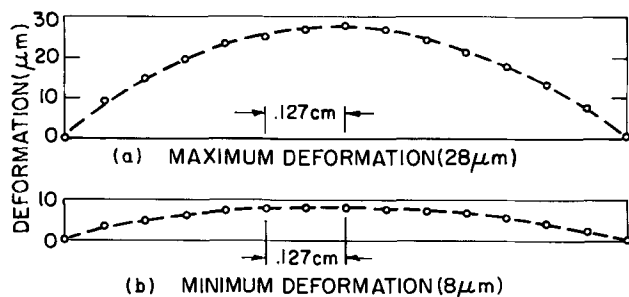


Fig. 2. Deformation of silicon-on-spinel film: (a) deformation along axis of maximum deformation; (b) deformation along axis of minimum deformation.

Table I. Hall mobility of 10-15  $\mu\text{m}$  thick silicon films grown on spinel

Spinel orientation	Hall mobility (cm <sup>2</sup> /v-sec)	Conductivity type	% of Bulk for same resistivity
(111)	250-330	p-type	80-100
(100)	162-170	p-type	48-58
(110)	50-60	p-type	16-18
(111)	410-645	n-type	53-65

than films grown on either (100) or (110) spinel. The p-type films had higher resistivity than films grown on sapphire under similar growth conditions indicating that aluminum autodoping from the substrate is less severe in silicon grown on spinel than in silicon grown on sapphire (5).

The Hall mobility and resistivity of 1-2  $\mu\text{m}$  thick silicon films grown on (100) and (111) spinel at different growth temperatures were measured and are shown in Fig. 3 and 4. The highest mobility films were grown at temperatures near 1200°C where typical values of 200 cm<sup>2</sup>/v-sec on (111) spinel and 100 cm<sup>2</sup>/v-sec on (100) spinel were obtained on p-type films. Higher Hall mobilities have been measured on thicker films indicating an improvement in silicon structure as the film grows thicker. The increase in Hall mobility with film thickness appears to be a general characteristic of heteroepitaxially grown films (11). The mobility-growth temperature curve was more sharply peaked in (111) silicon films than on (100) silicon films, similar to the behavior of (111) silicon grown on (0001) sapphire and (100) silicon grown on (1102) sapphire (12).

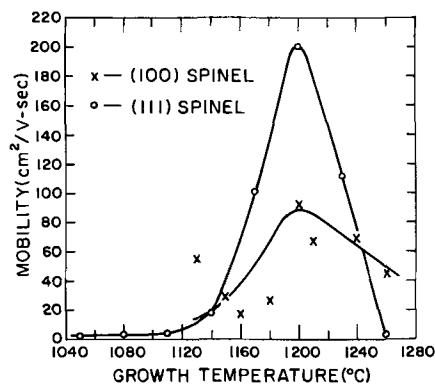


Fig. 3. Hall mobility of silicon films grown on (100) and (111) spinel as a function of growth temperature.

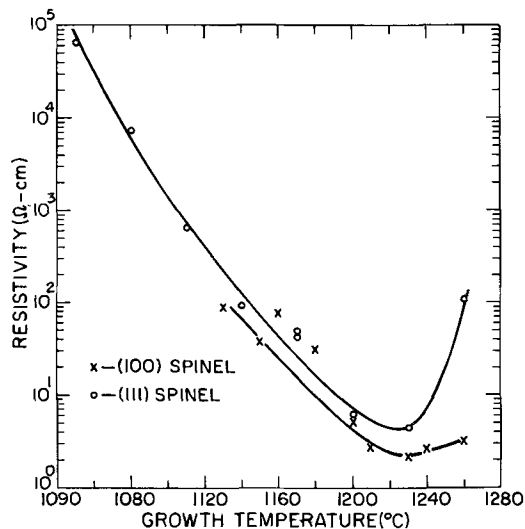


Fig. 4. Resistivity of silicon films grown on (100) and (111) spinel vs. growth temperature.

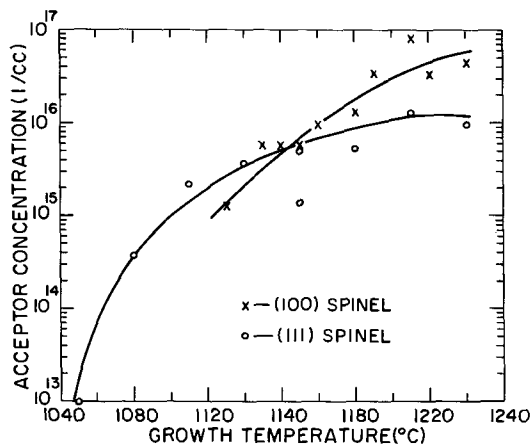


Fig. 5. Carrier concentration vs. growth temperature

Improvement in silicon crystal quality with increasing film thickness has been directly observed. Silicon films  $15\ \mu\text{m}$  thick grown on (111) spinel were polished at a  $\frac{1}{2}^\circ$  angle to the substrate. Chemical etching of the films indicated a decrease in the incidence of crystal faults as the film became thicker. Defect densities of the order of  $10^8/\text{cm}^2$  have been observed at the surface of  $5\ \mu\text{m}$  thick films.

The carrier concentration of the silicon films, as derived from the Hall data, is plotted in Fig. 5. The substrate autodoping raises the acceptor concentration in films grown at the higher temperatures, an effect previously observed in silicon grown on sapphire (5). At a given growth temperature the acceptor concentration (presumably due to aluminum) in a silicon film grown on spinel is approximately an order of magnitude less than the acceptor concentration in a similar film grown on sapphire. In silicon grown on sapphire the autodoping has been linked with the hydrogen reduction of sapphire releasing aluminum into the film. It is suspected that a similar reaction is releasing aluminum into the silicon films grown on spinel, but the cracking and exsolution of the  $\alpha\text{-Al}_2\text{O}_3$  in spinel at high temperatures have limited the high temperature experiments to determine the source of the acceptors. A comparison between the autodoping found in silicon-on-spinel films and silicon-on-sapphire films is shown in Fig. 6, where the acceptor concentration vs. growth temperature is plotted for  $2\ \mu\text{m}$  thick films grown on both spinel and sapphire.

The activation energy associated with the autodoping process has been determined from plots of accep-

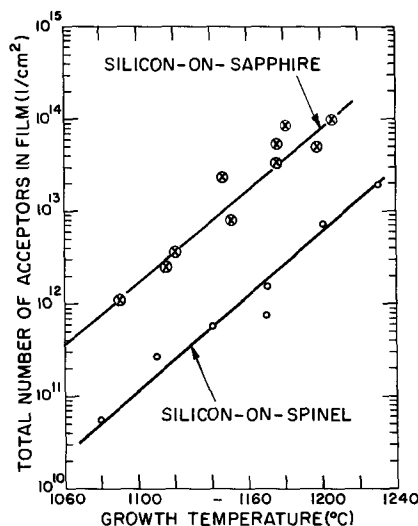


Fig. 6. Comparison of autodoping on silicon films grown epitaxially on sapphire and spinel.

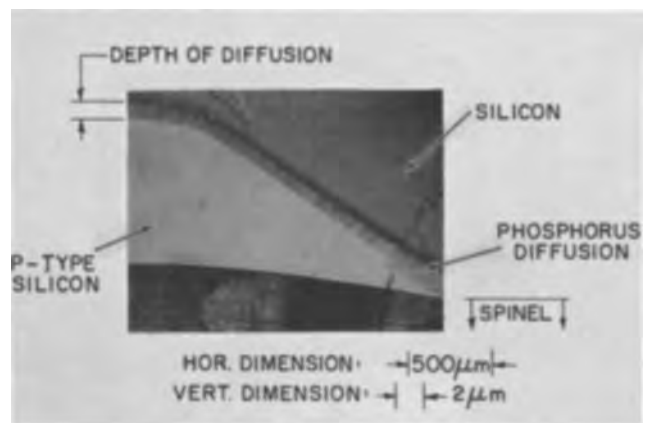


Fig. 7. Diffusion front of phosphorus into p-type silicon-on-spinel as a function of silicon thickness.

tor concentration vs. reciprocal temperature. Activation energies of 170 kcal/mol and 160 kcal/mol on (111) and (100) silicon on spinel have been measured, similar to the activation energies measured in silicon-on-sapphire films.

Diffusion of phosphorus into angle polished surfaces has led to a diffusion profile which was uniform in the thick silicon and a profile that contained diffusion spikes in the thin silicon. A photograph of a phosphorus diffusion front in p-type silicon as a function of film thickness is shown in Fig. 7 where the better quality of the thick film is evident from the sharp diffusion front obtained in the thicker section.

The diode characteristics obtained by phosphorus diffusion into silicon grown on (100) and (111) spinel have been compared with diodes made on similar resistivity bulk silicon. For silicon layers thicker than about  $8\ \mu\text{m}$  the diffusion fronts were sharp and were of the same depth as in bulk silicon. Diode breakdown voltages agreed with those predicted for bulk silicon of similar resistivity (13). The breakdowns were sharp although the reverse currents were larger than predicted (14). This could be due to the low minority carrier lifetime in these films (nano-second range) or due to high field emission in the vicinity of diffusion spikes or precipitates.

All of the work reported in this paper on the growth of silicon on spinel has been with alumina rich spinel having the composition  $\text{MgO}:\text{Al}_2\text{O}_3$ ; 1:3.0-3.5. The major difficulty with the use of alumina rich spinel as a substrate is the exsolution of  $\alpha\text{-Al}_2\text{O}_3$  at dislocations and subgrain boundaries that accompanies high temperature firing of the spinel (15). This weakens the spinel often causing severe cracking of the substrate as well as deterioration of the substrate surface.

Several (111) oriented stoichiometric spinel wafers were polished and fired in hydrogen for times up to 4 hr at  $1400^\circ\text{C}$ . X-ray and microscopic examination of these surfaces after heating showed that no exsolution of  $\alpha\text{-Al}_2\text{O}_3$  had taken place. There was also no evidence of deterioration of the spinel surface or cracking after this heating. A number of polished (111) oriented stoichiometric spinel surfaces were examined by electron diffraction techniques before and after heat treatment in hydrogen. Before heat treatment the mechanically polished stoichiometric spinel surface gave a ring type Laue pattern. Figure 8 shows the electron diffraction pattern indicating poor polycrystalline surface structure representing work damage. After heating in hydrogen at  $1500^\circ\text{C}$  for 1 hr, the surface observed by the electron diffraction pattern is shown in Fig. 9. A much better single crystal spinel surface free of work damage was produced. Microscopic examination of the spinel surface revealed that thermal etching of the spinel was responsible for this change in surface structure.

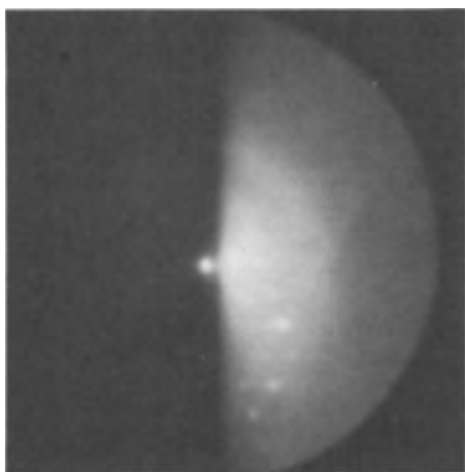


Fig. 8. Electron diffraction pattern of mechanically polished spinel wafer.

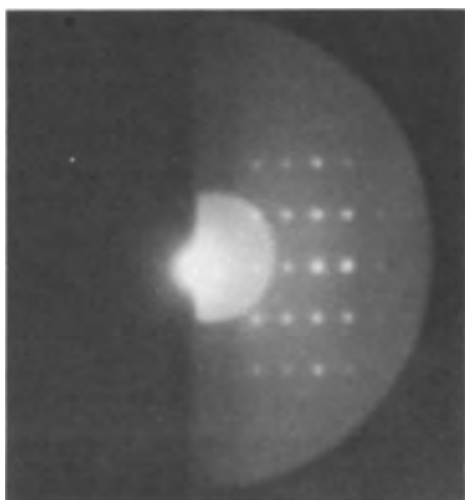


Fig. 9. Electron diffraction pattern of mechanically polished spinel wafer after heating in  $H_2$  at  $1500^\circ C$  for 1 hr.

Work is underway to investigate the electrical properties of silicon on stoichiometric spinel.

#### Summary

The electrical and mechanical properties of silicon grown on excess  $Al_2O_3$  spinel have been measured and compared to silicon films grown epitaxially on sapphire. The films grown on (111) spinel have in general both higher Hall mobilities and less autodoping than similar thickness films grown on ( $\bar{1}\bar{1}02$ ) sapphire. The films on both substrates have a highly reflective surface and in thicknesses less than 4-6  $\mu m$

can be used directly in device processing without the need for mechanical polishing. The temperature at which the highest mobility films were obtained on spinel was about  $50^\circ C$  higher than the temperature at which the highest mobility films were obtained on sapphire (12). Even at the higher growth temperature the autodoping from the substrate is less on the spinel than on the sapphire. Diodes fabricated in the silicon on spinel have yielded sharp reverse breakdown voltages of a value comparable to the breakdown found in bulk silicon.

#### Acknowledgments

The authors wish to acknowledge the technical assistance and encouragement of C. W. Mueller. The authors are also indebted to A. Kokkas for some of the exsolution experiments and to C. C. Wang for supplying the stoichiometric spinel. We also wish to thank R. Adams and R. O. Wance for sample preparation and electrical measurements. Thanks are also due to R. Smith, W. C. Roth, and E. Krieger for both x-ray and electron-diffraction analysis. Research reported in this paper was sponsored by the Air Force Avionics Laboratory, Research and Technology Division, Wright-Patterson Air Force Base, Ohio, under Contract No. F33615-67-C-1150, and RCA Laboratories, Princeton, New Jersey.

Manuscript received July 17, 1967; revised manuscript received Sept. 5, 1967.

Any discussion of this paper will appear in a Discussion Section to be published in the December 1968 JOURNAL.

#### REFERENCES

1. H. M. Manasevit and W. I. Simpson, *J. Appl. Phys.*, **35**, 1349 (1964).
2. C. W. Mueller and P. H. Robinson, *Proc. IEEE*, **52**, 1487 (1964).
3. B. A. Joyce, R. J. Bennett, R. W. Bicknell, and P. J. Etter, *Trans. Met. Soc. AIME*, **233**, 556 (1965).
4. H. M. Manasevit, Arnold Miller, F. C. Morritz, and R. Nolder, *ibid.*, **233**, 540 (1965).
5. D. J. Dumin and P. H. Robinson, *This Journal*, **113**, 469 (1966).
6. H. M. Manasevit and D. H. Forbes, *J. Appl. Phys.*, **37**, 734 (1966).
7. V. H. Seiter and C. H. Zaminer, *Z. Angew. Physik.*, **20**, 158 (1965); H. Schlotterer and C. H. Zaminer, *Phys. Stat. Sol.*, **15**, 399 (1966).
8. P. H. Robinson and C. W. Mueller, *Trans. Met. Soc. AIME*, **236**, 268 (1966).
9. E. Sirtl and A. Adler, *Z. Metallk.*, **52**, 529 (1961).
10. D. J. Dumin, *J. Appl. Phys.*, **36**, 2700 (1965).
11. B. W. Sloope and C. O. Tiller, *ibid.*, **38**, 140 (1967).
12. D. J. Dumin, *ibid.*, **38**, 1909 (1967).
13. S. M. Sze and G. Gibbons, *Appl. Phys. Lett.*, **8**, 111 (1966).
14. C. T. Sah, R. N. Noyce, and W. Shockley, *Proc. IRE*, **45**, 1228 (1957).
15. H. Saalfeld and H. Jagodzinski, *Acta. Cryst.*, **7**, 666 (1954).



# Phosphorus Concentration Profile and Phase Segregation in Phosphosilicate Glass on SiO<sub>2</sub> Films

P. F. Schmidt,\* W. van Gelder,\* and J. Drobek

Bell Telephone Laboratories, Inc., Allentown, Pennsylvania

## ABSTRACT

The phosphorus distribution in phosphorus diffused SiO<sub>2</sub> films has been determined by means of neutron activation. The general shape of the profile is in good agreement with the results by Fränz *et al.* (4), who used the P<sup>32</sup> isotope. In the phosphosilicate region occasional strong fluctuations of the P concentration were observed, usually accompanied by changes in the etch rate in 0.2N HF opposite to the expected dependence of etch rate on P concentration. The fluctuations were tentatively attributed to phase segregation in the phosphosilicate glass. Confirmation was obtained from related experiments in which polycrystalline films of composition P<sub>2</sub>O<sub>5</sub> x SiO<sub>2</sub> (and possibly P<sub>2</sub>O<sub>5</sub> x 2SiO<sub>2</sub>) were obtained and identified by electron diffraction.

The neutron activation of phosphosilicate layers on SiO<sub>2</sub> films reported here was originally undertaken in order to study the phosphorus distribution for different phosphorus diffusion and subsequent reoxidation conditions. The resulting phosphorus distributions are described.

During the course of this investigation, strong fluctuations of the phosphorus concentration in the glass region as a function of distance into the glass were discovered. It was noticed that these fluctuations often coincided with a trend of the etch rate in 0.2N HF opposite from that expected from the phosphorus concentration: the higher phosphorus concentration often corresponded to a slower etch rate, and vice versa.

These observations could be explained by assuming phase segregation in the glass, with formation of one or more of the compounds occurring in the P<sub>2</sub>O<sub>5</sub>-SiO<sub>2</sub> system according to Tien and Hummel (1), but there was no hard evidence for the correctness of this assumption except for some radioautographs which showed that slow etching regions of the glass contained indeed more phosphorus than the faster etching portions. Audley (2) has reported on the insolubility in HF of a SiO<sub>2</sub> x P<sub>2</sub>O<sub>5</sub> compound. According to Eitel (3) the system SiO<sub>2</sub>-P<sub>2</sub>O<sub>5</sub> is remarkable in that its components and the binary mixtures near them form glasses readily, while the compounds crystallize well.

Independent evidence for the occasional occurrence of a SiO<sub>2</sub>-P<sub>2</sub>O<sub>5</sub> compound in the phosphosilicate glass was obtained when a polycrystalline film, insoluble in HF, was observed to form at the interface between the phosphosilicate glass and a pyrolytic SiO<sub>2</sub> film deposited on top of the glass. Pyrolysis had been carried out at a much lower temperature (850°C) than was used for the original phosphorus diffusion (1040°C).

It was possible to isolate this polycrystalline film, and to identify by electron diffraction alpha-SiO<sub>2</sub> x P<sub>2</sub>O<sub>5</sub> as its main constituent, with possibly some admixture of 2SiO<sub>2</sub> x P<sub>2</sub>O<sub>5</sub>. The surface of the phosphosilicate layer prior to the pyrolytic SiO<sub>2</sub> deposition showed no evidence of compound formation detectable by electron diffraction or etch rate in HF.

Fränz *et al.* (4), who used the P-32 isotope in their study, also report a scatter in the phosphorus profile [Fig. 8b of ref. (4)], which appears to be outside the error of measurement; however, they did not attempt an explanation. If the cause for the fluctuation in phosphorus concentration reported by them is also phase segregation, as appears likely, then their results would indicate that neither neutron activation nor pyrolytic

deposition of SiO<sub>2</sub> are required to trigger the formation of SiO<sub>2</sub> x P<sub>2</sub>O<sub>5</sub> in the phosphosilicate glass.

It is perhaps worth noting in this context that Snow and Deal (5) describe phosphosilicate layers as "behaving as though they had a very slow dipolar polarizability. The 'dipoles' involved may be physical dipoles with a concentration of 10<sup>19</sup> cm<sup>-3</sup>, or they may be small regions of the glass occupying about 6% of the volume which polarize by interfacial polarization."

## Activation Studies

*Method.*—P-type silicon disks after oxidation and phosphorus diffusion, were subjected to neutron activation. The wafers were then etched in dilute HF to remove the oxide in controlled steps of about 100Å, and the phosphorus profile in the oxide was established by measuring the activity remaining on the slice after each etching step. The oxide thickness was measured by means of a spectrophotometer.

As stated above, strong fluctuations in phosphorus concentration were observed in the phosphosilicate region. In order to evaluate the reliability of the tracer data, a knowledge of all possible sources of error is necessary. The experimental technique used is given in the Appendix, together with a brief discussion of the uncertainties accompanying the measured parameters. A full account of the experimental method used for establishing the phosphorus concentration profile in the oxide is given in an extended appendix which is available from the authors on request. It is shown there that the fluctuations of the phosphorus concentration observed in the phosphosilicate region are far outside the error limits.

*Results.*—The over-all diffusion results are summarized in Table I. The thickness of the phosphosilicate glass is defined as that position in the oxide at which the phosphorus concentration drops steeply according to the activity data (see graphs). It can be seen that the phosphorus concentration increases with increasing temperature of diffusion, as expected. Reoxidation in steam under the conditions shown leads to a relatively small increase in glass thickness, to a slight decrease in phosphorus concentration, and to some loss of phosphorus to the ambient (total P/cm<sup>2</sup> of oxide, column 5).

Figures 1 and 2 show two typical phosphorus concentration and etch rate profiles observed in analyzing the samples listed in Table I. The profile shown in Fig. 1 (wafer 30-211), in which phosphorus concentration and etch rate vary in opposite direction at certain positions in the oxide was observed more often than the profile shown in Fig. 2, in which phosphorus concentration and etch rate vary in the same direction. The error bars shown include the contributions

\* Electrochemical Society Active Member.



Table I. Tracer data on oxidized and phosphorus diffused silicon wafers

No.	Treatment	Final oxide thickness, Å	Thickness of P <sub>2</sub> O <sub>5</sub> glass, Å	Total P/cm <sup>2</sup> of oxide	Highest conc in oxide
30-203	Ox. 900°C, 45 min	1600	1200	3.7 × 10 <sup>16</sup>	3.6 × 10 <sup>21</sup> cm <sup>-3</sup>
30-238	Diff. PBr <sub>3</sub> 1000°C, 20 min Ox. 900°C, 45 min	3350	1600	3.2 × 10 <sup>16</sup>	2.2 × 10 <sup>21</sup> cm <sup>-3</sup>
30-208	Reox. 900°C, 45 min Ox. 900°C, 90 min	2900	600	1.4 × 10 <sup>16</sup>	3.9 × 10 <sup>21</sup> cm <sup>-3</sup>
30-209	Diff. PBr <sub>3</sub> 1000°C, 10 min	2900	Lost data	1.6 × 10 <sup>16</sup>	Lost data
30-210	Same as 30-208 Ox. 900°C, 90 min	3250	800	1.3 × 10 <sup>16</sup>	3.5 × 10 <sup>21</sup> cm <sup>-3</sup>
30-211	Diff. PBr <sub>3</sub> 1000°C, 10 min Reox. 900°C, 20 min	3200	800	4.4 × 10 <sup>15</sup>	3.9 × 10 <sup>21</sup> cm <sup>-3</sup>
30-215	Same as 30-210 Ox. 900°C, 90 min	2750	450	4.4 × 10 <sup>15</sup>	1.4 × 10 <sup>21</sup> cm <sup>-3</sup>
30-216	Diff. PBr <sub>3</sub> 745°C, 45 min Ox. 900°C, 90 min	3150	600	2.9 × 10 <sup>15</sup>	2.1 × 10 <sup>20</sup> cm <sup>-3</sup>
30-221	Diff. PBr <sub>3</sub> 745°C, 45 min Reox. 900°C, 20 min	4000	1200	3.9 × 10 <sup>16</sup>	7.2 × 10 <sup>21</sup> cm <sup>-3</sup>
30-222	Ox. 1050°C, 30 min Diff. PBr <sub>3</sub> 1000°C, 20 min	4900	1600	7.2 × 10 <sup>16</sup>	3.1 × 10 <sup>21</sup> cm <sup>-3</sup>
30-223	Ox. 1050°C, 30 min Reox. 900°C, 45 min	5000	1500	3.3 × 10 <sup>16</sup>	2.6 × 10 <sup>21</sup> cm <sup>-3</sup>

from all known causes. It can be seen that the fluctuations of the phosphorus concentration in Fig. 1 are far outside the errors of measurement.

The low concentration phosphorus tail extending all the way through the oxide and into the silicon substrate<sup>1</sup> is a result of the intense neutron irradiation, and has been described in detail elsewhere (6). An interesting series of autoradiographs is shown in Fig. 3 (wafer 30-223). In addition to the large "diffusion pipe," extending all the way through the oxide, there is a triangular "hot spot," which was initially invisible (a) because it was masked by the high phosphorus concentration of the surface layers. It became visible (b) when 800Å of the oxide had been removed by etching, and then lasted for another 800Å (c) before disappearing again (d); it is thus located in the phosphosilicate glass region (cf. Table I). This triangular spot also showed up optically as a region of increased oxide thickness. If the spot were due just to a higher local concentration of phosphorus (without compound formation), one would expect an increased etch rate and therefore a locally decreased oxide thickness, i.e., the reverse of what is observed. The explanation that adsorption of some kind of protective film had occurred in the area of the triangular spot appears invalid because the oxide thickness in the area of the triangular spot did not remain constant during the series of etching steps from (b) to (c), but decreased

though at a slower rate than the rest of the oxide. Unfortunately, the opportunity was missed to examine this triangular spot by electron diffraction. It will be appreciated that the exposure times in Fig. 3 increased with each etching step, so that features well visible in the long exposure autographs would be swamped in the short exposure pictures. The size of the circular diffusion pipe in radioautographs (c) and (d) is an artifact: the "pipe" has not spread in diameter, but the image of the pipe was badly overexposed at an exposure time adequate for the rest of the wafer. The overexposure caused the diffuse lateral spreading of the image of the pipe. Wafer 30-223 was also the only wafer on which a pipe of such intensity was observed. Densitometric evaluation of the radioautographs taken from other wafers showed that the contribution by pipes is unimportant relative to the phosphorus concentration in the rest of the oxide, at least in the high phosphorus concentration region. In particular, the pipes cannot be held responsible for the fluctuations of phosphorus concentration observed in the phosphosilicate glass region.

The number 30-223 appearing in (d) of Fig. 3 is due to phosphorus decoration of dislocations generated by scribing the Si disk. The decoration disappeared when 1200Å of silicon were removed by anodic oxidation. The lighter periphery of the disks is due to preferential loss of phosphorus from the wafers during neutron irradiation; evaporation of

<sup>1</sup> In addition to some P<sub>2</sub>O<sub>5</sub> "pipes" not present on all wafers.

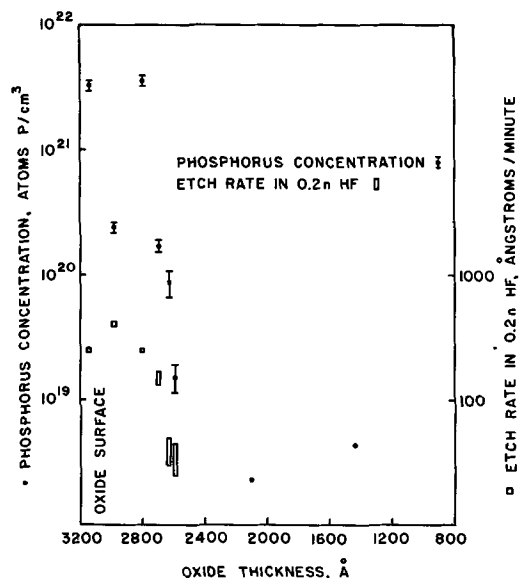


Fig. 1. Phosphorus concentration and etch rate profiles of diffused and reoxidized wafer 30-211.

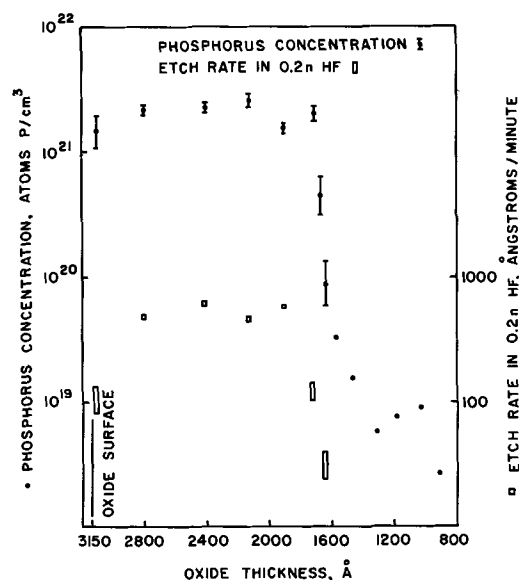


Fig. 2. Phosphorus concentration and etch rate profiles of diffused and reoxidized wafer 30-238.

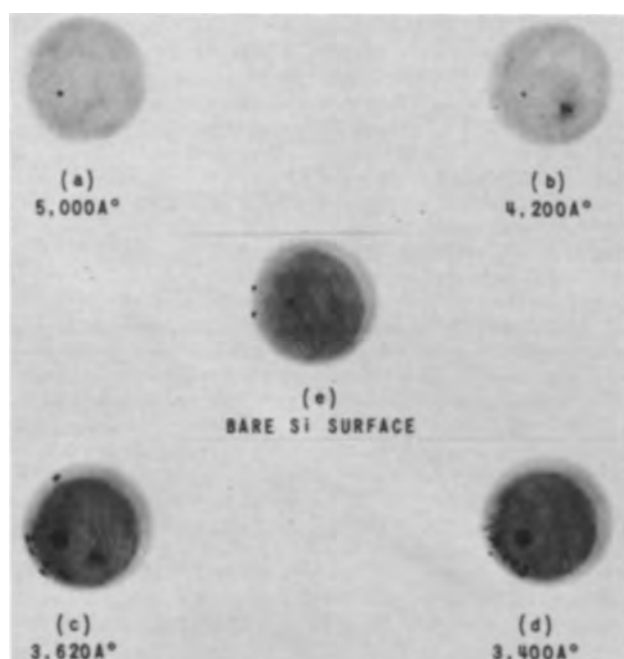


Fig. 3. Radioautographs of diffused and reoxidized wafer 30-223 at different remaining oxide thicknesses.

phosphorus from the center of the disks was suppressed by aluminum spacers inserted between each wafer.

#### Formation of a Polycrystalline Phosphosilicate Film Triggered by Pyrolytic Deposition of $\text{SiO}_2$

**Experimental.**—A number of chemically polished silicon slices, 50 ohm-cm P-type, {111} oriented, diameter 1 in., were oxidized in 100% steam of atmospheric pressure for 1 hr at 1100°C. The resulting oxide thickness was 6800Å, as determined from the wavelength position of the interference fringe minima. The slices were next phosphorus diffused in  $\text{PBr}_3$  at 1040°C for 40 min, resulting in a phosphosilicate glass layer on top of the  $\text{SiO}_2$  film. The total thickness of the dielectric layer after diffusion was 7150Å. The slices were then deposited with  $\text{SiO}_2$  at 850°C from a gas mixture consisting of 0.15%  $\text{SiCl}_4$ , 0.15%  $\text{O}_2$ , and 99.7%  $\text{H}_2$ . The total thickness after deposition of the pyrolytic  $\text{SiO}_2$  was 10,200Å. The slices were then step-etched in P-etch (14), and the remaining thickness of the dielectric layer was measured at various intervals.

Figure 4 shows that the etch rate of the oxide "sandwich" varied with depth as expected. That is, at first the etch rate was fairly constant, then increased steeply in the phosphosilicate glass region, to fall off

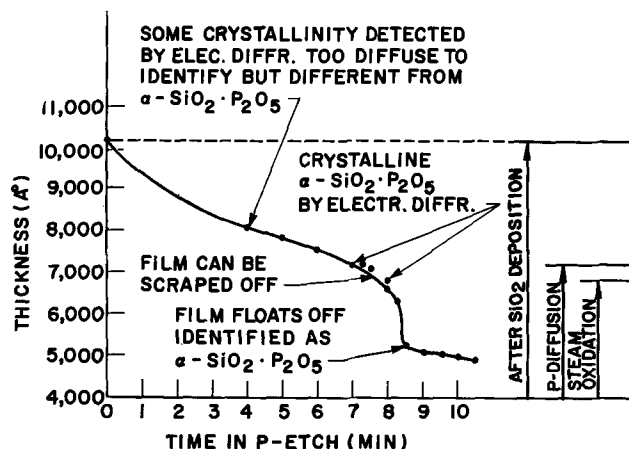


Fig. 4. Oxide thickness of sandwich vs. time in P-etch. Thermal  $\text{SiO}_2$ /phosphosilicate glass/pyrolytic  $\text{SiO}_2$ .

Table II. Comparison of electron diffraction data (this work) with the x-ray data of Tien and Hummel Identification of  $\text{SiO}_2 \times \text{P}_2\text{O}_5$  by electron diffraction

X-ray data by Tien and Hummel (1)	Data calculated from electron diffraction of HF insoluble film	
$d$ (Å)	$I/I_0$	$d$ (Å)
5.87	15	5.91
4.82	5	4.80
4.00	16	—
3.80	23	—
3.69	100	3.658 (strongest obs. refl.)
—	—	3.54*
3.38	25	3.372
3.26	5	—
3.20	38	—
3.10	7	—
2.91	6	—
2.68	4	2.69
2.59	18	2.586
2.35	2	—
2.26	5	2.24
2.22	8	2.15
2.12	6	—
2.09	5	2.085
2.05	8	2.02
2.00	4	—
1.977	8	—
1.888	3	—
1.863	3	1.844
1.824	3	—

\* 3.54 is the highest intensity  $d$ -value of  $2\text{SiO}_2 \times \text{P}_2\text{O}_5$  according to Tien and Hummel (1).

again to a low and constant value when the phosphorus concentration had become negligible.

After 8.5 min of etching, a thin film, apparently insoluble in the P-etch, floated off the surface. This film was removed from the solution and placed into buffered HF<sup>2</sup> for 3 days without dissolving. Transmission electron diffraction showed the film to be  $\alpha\text{-SiO}_2\text{-P}_2\text{O}_5$  (compare below).

No insoluble film was observed when the phosphosilicate layer was etched prior to pyrolytic  $\text{SiO}_2$  deposition. After  $\text{SiO}_2$  deposition, followed by 4 min of etching in P-etch, i.e., still in the deposited  $\text{SiO}_2$  layer, glancing-angle electron diffraction showed some crystallinity, too diffuse for identification (cf. Fig. 4). However, after 7 and 8 min of etching, electron diffraction showed the presence of  $\alpha\text{-SiO}_2\text{-P}_2\text{O}_5$ . This diffraction pattern was distinctly different from the diffuse pattern seen after 4 min of etching. It appears likely that the  $\text{SiO}_2\text{-P}_2\text{O}_5$  crystals induced conversion of  $\text{SiO}_2$  to  $\alpha$ -crystalalite which extended some distance into the pyrolytic  $\text{SiO}_2$ . It is known (7) that  $\text{SiO}_2\text{-P}_2\text{O}_5$  is highly analogous to  $\alpha$ -crystalalite and catalyzes this transformation.

After 8 min of etching there are also indications of the presence of traces of  $2\text{SiO}_2 \times \text{P}_2\text{O}_5$  (presence of the reflection  $d = 3.54\text{Å}$ , cf. Table II), according to the data by Tien and Hummel (1). At 8 min the polycrystalline film was visible under an optical microscope and could be scraped with a sharp needle.

Figures 5, 6, and 7 are a series of pictures of a slice on which the left half lagged 1 min behind in etching time compared to the right hand half. This difference in etching time was brought about by masking the left half, etching the slice for 1 min, and then removing the mask. From then on the left half always lagged behind the right half by 1 min etching time. The pictures were taken under dark field illumination at a magnification of 428x.

Figure 5 shows a polycrystalline film appearing on the right hand side after 8 min of etching, while no crystallinity is yet visible on the left hand side (etched for 7 min). The high intensity light spots on both left and right hand side should be ignored as due to either pin holes or loose particles on the surface.

Figure 6 is taken from the same area of the slice as the right hand side of Fig. 5. It was also etched for 8 min and it shows the film partly scraped by means of a sharp needle.

<sup>2</sup> 40g  $\text{NH}_4\text{F}$ , 15 cc conc HF, 60 cc  $\text{H}_2\text{O}$ .

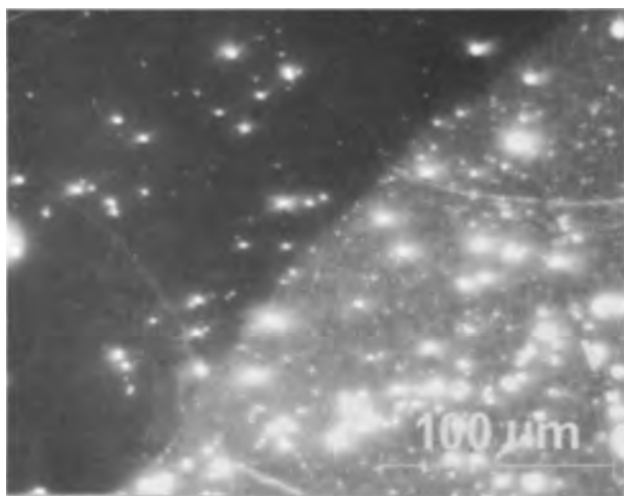


Fig. 5. Microphotograph of oxide sandwich after etching in P-etch. Right half etched for 8, left half for 7 min. Polycrystalline film visible only on right half.

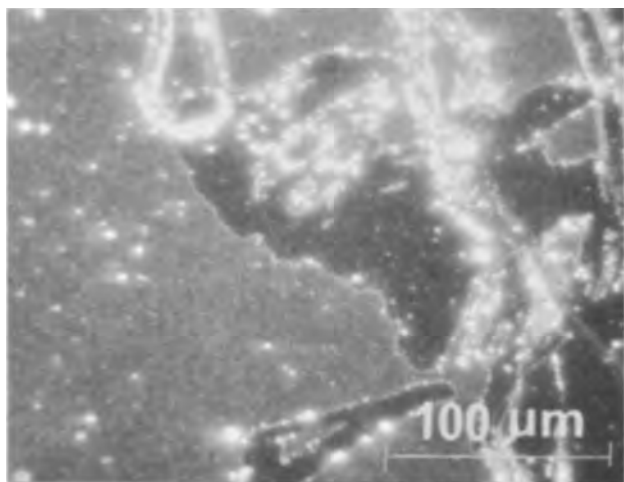


Fig. 6. Microphotograph of right half of Fig. 5, after scraping with steel needle.

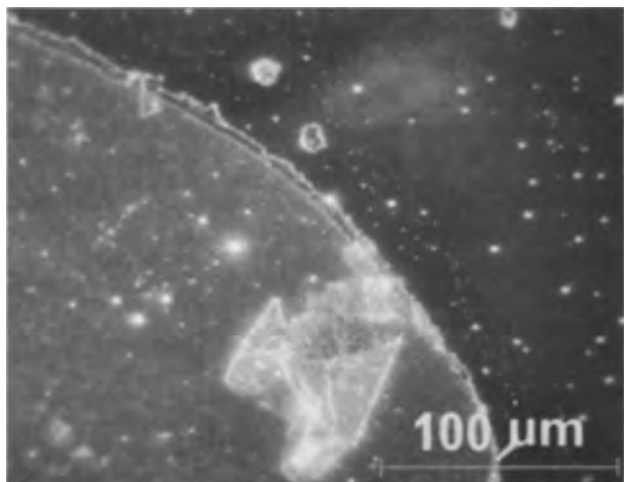


Fig. 7. Microphotograph of oxide sandwich after etching in P-etch. Right half etched for 9, left half for 8 min. Polycrystalline film has lifted from right side, but is visible on left side.

The right hand side of Fig. 7 shows an area that was etched 9 min. The film has completely lifted from this side. A part of the loose film is visible in the lower middle part of the picture. The left side of the

picture shows an area that was etched for 8 min. The polycrystalline film on this side is clearly visible and is identical in appearance with the film in Fig. 6.

#### Identification of the Film as $\alpha$ - $\text{SiO}_2 \cdot \text{P}_2\text{O}_5$ by Electron Diffraction

Electron diffraction patterns were obtained both from the isolated film (in transmission) and from the film on the surface (in reflection) after 7-8 min of etching. The patterns taken in transmission were more distinct, and are compared in Table II to the x-ray data by Tien and Hummel (1) for the low-temperature (=  $\alpha$ ) modification of  $\text{SiO}_2 \cdot \text{P}_2\text{O}_5$ . The agreement is very satisfactory. The x-ray data contain reflections which do not show up in the electron diffraction pattern because in this latter case the sample is not being rotated so that certain crystal planes do not reflect. The observed reflections, however, match their counterparts in the x-ray data quite closely. The appearance of a reflection at  $d = 3.54\text{\AA}$  may be considered as an indication that traces of  $2\text{SiO}_2 \cdot \text{P}_2\text{O}_5$  are present since this is the strongest reflection of this compound according to Tien and Hummel (1).

#### Discussion

Phase segregation is suggested by the large fluctuations in phosphorus concentration in the phosphosilicate region, and by the often opposing trends of phosphorus concentration and etch rate. The latter relationship is masked to some extent by the strong effect of the neutron irradiation on the etch rate.

The transition from phosphosilicate glass to undoped  $\text{SiO}_2$  extends over 100-200 $\text{\AA}$ . The shape of the diffusion profile in this transition region can be explained on the basis of strongly concentration dependent diffusivity. It was shown by Thurston *et al.* (8) that the diffusivity of phosphorus (pentoxide) in  $\text{SiO}_2$  at lower concentrations than corresponds to the "glass" is strongly concentration dependent and very slow, especially at lower temperatures (below 1200°C). Thus the diffusivity in the phosphosilicate glass region, according to Sah *et al.* (9), is  $2.5 \times 10^{-13} \text{ cm}^2 \text{ sec}^{-1}$  at 1100°C, but only about  $10^{-16} \text{ cm}^2 \text{ sec}^{-1}$  at the same temperature and a concentration of 3%  $\text{P}_2\text{O}_5$  in  $\text{SiO}_2$  according to Thurston *et al.* (8). The fast diffusion in the glass region thus ensures a practically flat concentration profile in the glass up to the point where the phosphorus concentration drops steeply. Reoxidation of the wafers leads to slight penetration of the phosphorus front under the given reoxidation conditions (2-400 $\text{\AA}$ ), a lowering of the maximum phosphorus concentration, and to some loss of phosphorus to the ambient (about 15% of the total originally contained in the oxide after diffusion).

Pyrolytic deposition of  $\text{SiO}_2$  leads occasionally to the formation of a polycrystalline film across the whole surface of the phosphosilicate glass, thus facilitating its detection. The details of this (catalytic) effect have not been established. The main constituent of this film has been unambiguously established as  $\text{SiO}_2 \cdot \text{P}_2\text{O}_5$ , possibly with traces of  $2\text{SiO}_2 \cdot \text{P}_2\text{O}_5$ . The ratio of  $\text{SiO}_2$  to  $\text{P}_2\text{O}_5$  in the phosphosilicate glass is about 4:1, so that formation of some  $2\text{SiO}_2 \cdot \text{P}_2\text{O}_5$  might be expected. According to Tien and Hummel, the 2:1 compound melts incongruently at 1120°C to a silica-rich liquid and  $\text{SiO}_2 \cdot \text{P}_2\text{O}_5$ . Even though the system in the present case was not heated to 1120°C, the formation of the 1:1 compound was favored.

#### Acknowledgments

The authors wish to thank V. E. Hauser for the deposition of the pyrolytic  $\text{SiO}_2$  films, and D. R. Wonsidler for help with the tracer experiments.

Manuscript received June 5, 1967; revised manuscript received Sept. 27, 1967.

Any discussion of this paper will appear in a Discussion Section to be published in the December 1968 JOURNAL.

## REFERENCES

1. T. Y. Tien and F. A. Hummel, *J. Am. Ceram. Soc.*, **45**, 422 (1962).
2. J. A. Audley, "Silica and the Silicates," pp. 9-10, Bailliere, Tindall & Cox, London (1921).
3. W. Eitel, "The Physical Chemistry of the Silicates," Univ. Chicago Press (1954).
4. I. Fränz, W. Langheinrich, and K. H. Löcherer, *Telefunken-Zeitung*, **37**, 194 (1964).
5. E. H. Snow and B. E. Deal, *This Journal*, **113**, 263 (1966); SCP and Solid State Technology, November 1966, p. 30.
6. P. F. Schmidt, *Appl. Physics Letters*, **8**, 264 (1966).
7. G. Peyronel, *Z. Kristallographie*, **95**, 274 (1936).
8. M. O. Thurston, J. C. C. Tsai, and K. D. Kang, ASTIA Report AD 261 201 (1961).
9. C. T. Sah, H. Sello, and D. A. Tremere, *J. Phys. Chem. Solids*, **11**, 288 (1959).
10. T. M. Buck, F. G. Allen, J. B. Dalton, and J. D. Struthers, *This Journal*, **114**, 862 (1967).
11. R. O. Carlson, R. N. Hall, and E. M. Pell, *J. Phys. Chem. Solids*, **8**, 81 (1959).
12. F. Reizman, *J. Appl. Phys.*, **36**, 3804 (1965); F. Reizman and W. van Gelder, *Solid State Electronics*, **10**, 625 (1967).
13. B. R. Rex and G. H. Schneer, Private communication.
14. W. A. Pliskin and R. G. Gnall, *This Journal*, **111**, 872 (1964).
15. A. Kant, J. P. Cali, and H. D. Thompson, *Anal. Chem.*, **28**, 1867 (1956).
16. Am. Inst. of Physics Handbook, 2nd edition.

## APPENDIX

*Activation Studies, Experimental*

Float-zoned 1.3 ohm-cm P-type silicon, {111} oriented, was used throughout. The wafers were mechanically lapped and polished, and then given a chemical polish to remove surface damage. Average dislocation density of the starting material was  $12,000 \text{ cm}^{-2}$  by Sirtl etch.

Table I lists the wafers according to oxidation and diffusion treatment. Oxidation was carried out in steam, diffusion was from a  $\text{PBr}_3$  source kept at  $30^\circ\text{C}$ , with part of the carrier gas bubbling through the  $\text{PBr}_3$  source. Subsequent to diffusion the wafers were cooled directly to room temperature by pulling from the furnace.

For irradiation, the wafers were wrapped in a special high purity aluminum foil, with high purity aluminum disks inserted between each Si wafer in order to insure uniformity of neutron dose throughout the charge. The wafers were irradiated for seven days at the Brookhaven National Laboratories at a flux of  $1.2 \times 10^{13} \pm 5\%$  thermal and  $1.5 \times 10^{11} \pm 10\%$  fast neutrons  $\text{cm}^{-2} \text{ sec}^{-1}$ , leading to a specific activity of 11.0 Curies per mol of phosphorus. The wafers were not intentionally cooled during neutron irradiation, and the temperature in the aluminum capsule may have risen about  $50^\circ\text{C}$  above the ambient temperature of  $250^\circ\text{C}$  at the place of irradiation.

Subsequent to irradiation the wafers were kept in storage for several weeks to permit decay of the  $\text{Na}^{24}$  beta and gamma activity (from the reaction  $\text{Al}^{27}(\text{n},\alpha)\text{Na}^{24}$ ), of the beta-activity of  $\text{Si}^{31}$  (from the reaction  $\text{Si}^{30}(\text{n},\gamma)\text{Si}^{31}$ ), and of the beta activity of  $\text{Br}^{82}$  (from the reaction  $\text{Br}^{81}(\text{n},\gamma)\text{Br}^{82}$ ). The half-lives of  $\text{Na}^{24}$ ,  $\text{Si}^{31}$ , and  $\text{Br}^{82}$  are 15.05 hr, 2.62 hr, and 35.5 hr., respectively. At the end of the investigation, when the phosphorus activity had already largely decayed, the presence of  $\text{S}^{35}$  could be detected both from its decay rate and its beta-energy spectrum.<sup>3</sup> The  $\text{S}^{35}$  was probably introduced by neutron activation of a chlorine impurity in the  $\text{PBr}_3$  source, by means of the reaction  $\text{Cl}^{35}(\text{n},\text{p})\text{S}^{35}$ .<sup>4</sup> The level of contamination with  $\text{S}^{35}$  was too low to affect the phosphorus determinations. The half-life of  $\text{S}^{35}$  is 86.7 days.

<sup>3</sup>The authors are indebted to J. D. Struthers for these measurements.

<sup>4</sup>Contamination with sulphur cannot be the cause since the observed surface concentrations of  $8 \times 10^{10} \text{ cm}^{-3}$  are above the solid solubility limit for sulphur in silicon (11).

A Nuclear-Chicago gas flow detector, model D47, operated in the Geiger tube mode, in conjunction with a Nuclear-Chicago Decade Scaler, series 8703, was used to determine the activity of the samples. Since this counting system has already 1% loss at 6000 counts/min, suitable aluminum absorbers were placed over the samples. Each time an absorber was removed or exchanged against another absorber, the ratio of the counts under the two conditions was determined. It was thus possible to calculate the counting rate in the most active conditions of the wafers (i.e., before step-wise stripping of the oxide in HF) by using the final counting rate without any absorber (i.e., when most of the activity had been etched away) as the starting point for the calculation. It is felt that no appreciable error was introduced by this procedure, since a sufficient number of counts was taken to reduce the statistical errors to insignificant values.

The detection efficiency of the detector was measured by means of a  $\text{P}^{32}$  simulated source of  $2.8 \times 10^{-5}$  millicuries (supplier: Tracerlab, Waltham, Massachusetts) calibrated against standards of the NBS.

An aluminum holder served to position either the  $\text{P}^{32}$  simulated source or the Si wafers underneath the window of the Geiger tube. Measuring conditions for source and samples were kept as nearly identical as possible. Counts were taken to 10,000 for each point in the high phosphorus concentration region, and to at least 2000 above background in the low phosphorus concentration region of the oxide films.

A Perkin-Elmer model 202 visible-uv spectrophotometer was used to measure the reflectance minima as a function of wavelength (12). Oxide film thicknesses were then calculated by assuming the same refractive index for the phosphorus-doped film as for thermal  $\text{SiO}_2$  films. This involves only a small error, of the order of 1% (4, 13); a more accurate determination of the refractive index would not have been meaningful in view of the continuously changing  $\text{SiO}_2\text{-P}_2\text{O}_5$  composition as a function of film thickness.

Radioautographs were taken with type AA x-ray film because of its sensitivity. It is, however, a double emulsion film and rather coarse grained.

The analysis consisted in principle in measuring the activity of the silicon wafers before and after successive etching of the oxide in dilute HF in order to decrease its thickness in steps of about 100Å each. The oxide from one side of the wafer was removed completely, and the wafer was measured with active side facing the window. After each etching step the oxide thickness was remeasured. On a considerable number of wafers radioautographs were taken before, during, and after stepwise dissolution of the oxide. Controlled etching of the oxide was carried out in 0.2N HF until low phosphorus concentrations were reached and the strength of the etching solution had to be increased in order to have reasonable etch rates. In the phosphosilicate glass region it was not possible to use the so-called "P-Etch" (14) because of the excessively fast etch rate caused by radiation damage to the oxide.<sup>5</sup> It was, however, noticed that the 0.2N HF solution was more sensitive to variations in phosphorus concentration than a 1.0N HF solution, and the latter in turn was more sensitive than the P-Etch. The dissolution of the oxide was usually very uniform, and only occasionally were very weak differences in local interference color detectable by the unaided eye.

The counting rates observed were converted to phosphorus concentrations by means of the relationship

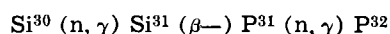
$$A = N \times f \times \sigma \times S \times e^{-\lambda t} \quad [1]$$

where  $A$  is the activity in disintegrations  $\text{sec}^{-1}$  (corrected for the detection efficiency of the system, 13.5%),  $N$  is the number of atoms of  $\text{P}^{31}$  originally present,  $f$  is the thermal neutron flux  $\text{cm}^{-2} \text{ sec}^{-1}$ ,  $\sigma$  is the capture cross section of  $\text{P}^{31}$  for thermal neutrons,  $S$  equals  $1 - e^{-\lambda t}$ ; for  $t$  equals 1 week ( $6.04 \times 10^5 \text{ sec}$ ), and the decay constant  $\lambda$  of  $\text{P}^{32} = 5.6 \times 10^{-7} \text{ sec}^{-1}$ , the saturation factor  $S = 0.28$ . The  $t$  in the exponent in Eq. [1] is the time in seconds elapsed since the end of irradiation.

Equation [1] must in principle be corrected for a

<sup>5</sup>Enhanced by a factor of  $\sim 2$  for pure  $\text{SiO}_2$  and of  $\sim 8$  for phosphosilicate glass compared to the values given in ref. (14).

background activity of  $P^{32}$  introduced by the reaction (15)



However, for phosphorus concentration above  $10^{17} \text{ cm}^{-3}$ , *i.e.*, in the phosphorus concentration range of interest here, this correction may be neglected.

#### Errors

The accuracy of the terms in Eq. [1] determines the precision with which a known disintegration rate can be converted into number of phosphorus atoms. The accuracy with which the disintegration rate is known depends on the knowledge of the collection efficiency of the measuring system. The following assumptions were made concerning these quantities: the slow neutron flux was assumed to be known to  $\pm 5\%$ ; the activation cross section of  $P^{31}$ ,  $0.19 \pm 5.2\%$  barns (16); decay constant of  $P^{32}$ , 14.30 days; accuracy of  $P^{32}$  simulated source,  $\pm 5\%$ ; statistical error inherent in the radioactive decay phenomenon was kept at 1% in the phosphosilicate glass region by taking a sufficiently large number of counts.

The phosphorus concentration profile was obtained by dividing the decrement in phosphorus activity detected on the silicon after each etching step by the thickness of the oxide slice removed. The error due to

statistical fluctuations in counting rate can be kept small, as discussed above, but the determination of the oxide slice thickness introduces a considerable error. The shift in the position of the reflectance minima from one etching step to the next can be measured to about  $\pm 15\text{\AA}$ ; since a single etching step was usually of the order of 200\AA, the error for each individual point in the phosphosilicate glass region due to this source of error is usually about 7.5%.

At the transition from the glass region to the weakly phosphorus-doped  $SiO_2$ , etch rates occasionally dropped to very low values and only 40-50\AA were removed per step. Where the experimental points in the graphs shown are very closely spaced ( $\ll 100\text{\AA}$  apart), only the general trend of the curve, rather than the absolute values of the individual points should be considered; the latter could easily be wrong by a factor of 2. The points outside the phosphosilicate region are shown only for the sake of completeness; they show very strong scatter, as is to be expected for a variety of reasons.

It is estimated that the absolute phosphorus concentrations in the phosphosilicate region are known to better than  $\pm 30\%$ , the relative phosphorus concentrations in the glass region to better than  $\pm 20\%$ , and the relative phosphorus concentrations in the low phosphorus region within a factor of about 2.

## Effects of High Phosphorus Concentration on Diffusion into Silicon

M. C. Duffy,\* F. Barson,\* J. M. Fairfield,\* and G. H. Schwutte

IBM Components Division, East Fishkill Facility, Hopewell Junction, New York

#### ABSTRACT

Phosphorus diffusion into silicon has been explored near and above the solubility limit by radiochemical profiling and compared with crystal damage by x-ray diffraction microscopy and Sirtl etch techniques. An apparent diffusion retardation has been found for very high source concentrations that results in a shallowed junction penetration for certain higher surface concentrations. The retardation phenomenon occurs over a narrow range of surface concentrations, within which diffused junctions are nonuniform, or ragged. This effect can be correlated with large amounts of crystal disorder inside the diffused area and dislocation loops outside at the peripheries. These outside loops have been found to degrade transistor gain.

Phosphorus diffusion into silicon has been very important in the semiconductor device industry because of its use in fabricating N-P junctions, especially emitters for N-P-N transistors. Nevertheless, phosphorus diffusion from high concentrations is not well understood and many anomalous effects have been reported (1-6). An additional anomaly not reported previously has been found which manifests itself in an apparent retardation of the phosphorus diffusion under some circumstances when maximum surface concentrations are involved. This anomaly can have serious consequences upon device fabrication.

The effect can best be described by outlining the conditions under which it has arisen in typical transistor fabrication procedures. In our case, phosphorus diffusion is accomplished by a two step process, a deposition and a drive-in cycle. The system and technique are similar to that used by McDonald *et al.* (6). The deposition cycle is 35 min in length at  $970^\circ\text{C}$  with a controlled amount of a phosphorus source in an ambient of nitrogen with about 2% oxygen. The drive-in cycle is 5 min in dry  $O_2$ , 30 min in steam, and 40 min in dry  $O_2$ , also at  $970^\circ\text{C}$ . After deposition only, the diffused junction depth increases with phosphorus source concentration (in the ambient gas) up to a point and, thereafter, remains constant.

Presumably this point corresponds to the solid solubility of phosphorus at the deposition temperature. After the subsequent drive-in cycle, the

junction depth initially increases with phosphorus source concentration as before, but at a certain concentration it decreases sharply as shown in Fig. 1. Also, as illustrated by the photo inserts, there is a concentration range in which the junctions are ragged, which is a serious effect for emitter diffusions. Flat junctions are obtainable above and below this ragged area, which appears to be a transition region.

An understanding of this phenomenon is important for controlling transistor fabrication procedures employing high concentration phosphorus diffusions. Other types of phosphorus diffusion techniques also result in this retardation effect at high concentrations. Furthermore, although flat emitter junctions can be made by employing phosphorus concentrations above the ragged region, certain transistor parameters are influenced and degraded (*e.g.*, gain) when the emitter diffusion is in this retarded region. Therefore, this phenomenon has been investigated with the purpose of understanding the conditions under which it arises. This report describes the investigation and discusses possible mechanisms through which the diffusion retardation and ragged junctions should occur.

#### Experimental Procedure

For this investigation, Czochralski grown silicon wafers (111) oriented and virtually dislocation free were used. They were lapped and chemically polished to remove all surface damage. Phosphorus diffusions

\* Electrochemical Society Active Member.

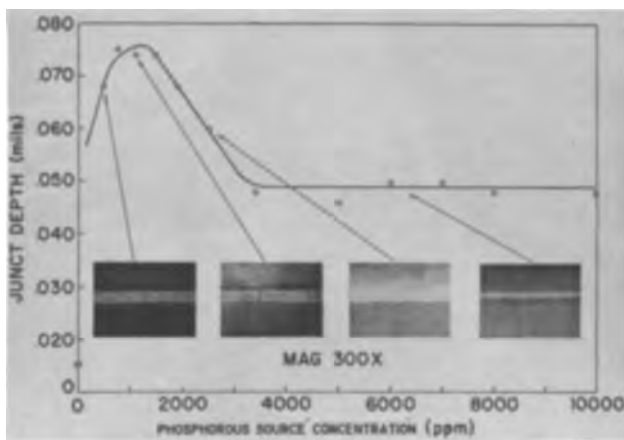


Fig. 1. Junction depth vs. phosphorus concentration; circles represent data after drive-in cycle. Photo inserts illustrate the junction depth from beveling and staining at representative points.

were done in the manner described in the introduction. Both blanket diffusions over the entire wafers and planar diffusions using standard oxide masking techniques were used; some of the planar structures were emitters of actual N-P-N transistors. Junction depths were measured by standard angle lap and copper staining techniques.

Diffused phosphorus profiles were determined on blanket diffusions by neutron activation analysis techniques similar to that employed by Tannenbaum (1) and Kooi (7). After diffusion, wafers were irradiated with neutrons to produce  $P^{32}$ . The wafers were profiled by anodizing and etching the resultant oxide to remove thin layers of silicon and employing a liquid scintillation radio-assay of the etchants to determine the amount of phosphorus atoms removed in each etching step. In some cases, the wafer itself was counted with a Geiger-Mueller type counter after each step; the two counting techniques agreed well.

The crystallographic damage of the diffused areas was determined by x-ray transmission diffraction microscopy, using the scanning oscillator technique (SOT) to record topographs of entire wafers (8); by transmission electron microscopy (9); and by Sirtl etching (10) of diffused areas. Taking advantage of the nondestructive nature of the first technique, x-ray topographs were made of both blanket and planar diffused wafers after both the deposition and the drive-in cycles. In a few cases, transmission electron microscopy was used to resolve the structure of the crystal disorder revealed by the x-ray topographs (11). Finally, diffused areas were Sirtl etched for 10-15 sec and examined for crystal disorder.

In some cases when the crystal structure around actual devices was examined, transistor gain and  $V_{be}$  were measured and correlated with the crystallographic structure of the phosphorus diffused area. If the base width is narrow compared to carrier diffusion length,  $V_{be}$  at a given low current can be used as a relative measure of total base doping (12). Since the time-temperature cycles of these diffusions were identical and the junction depths similar, small variations in  $V_{be}$  reflect similar variations in effective base width; equal  $V_{be}$ 's indicate equal base widths. For this investigation  $V_{be}$  was used only as a relative measure of effective base width and no attempt was made to relate this factor to transistor gain theoretically.

### Results and Discussion

Figure 2a illustrates the phosphorus profiles prior to drive-in for two concentrations of phosphorus, one above and the other below the ragged region. As might be expected, the profiles are similar and the junction depths are almost equal. Figure 2b shows profiles for two similar wafers after drive-in. In agreement with the junction depth measurements shown in Fig. 1,

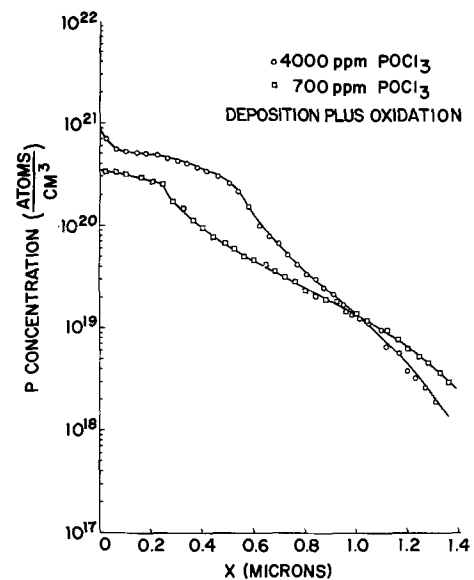
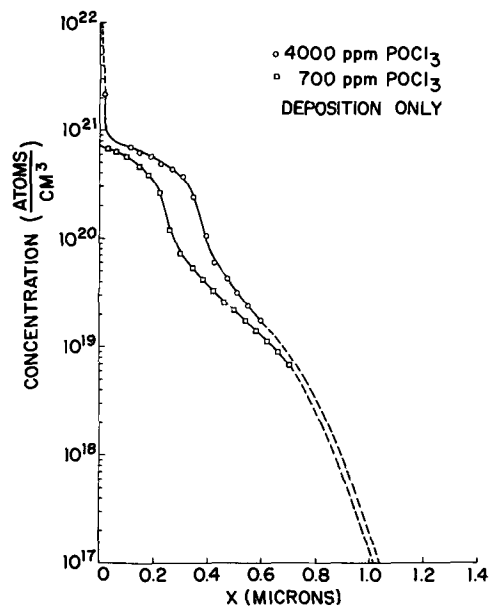


Fig. 2. Total phosphorus concentration profiles; (a) after deposition only, (b) after both deposition and drive-in.

the lower surface concentration diffused to a greater depth. Also, the concentration gradient at any depth is steeper for the higher concentration diffusion. Thus, the effective diffusion coefficient for the higher concentration appears to be reduced all along the profile.

The crystal damage in the diffused areas shows a similar relation to the process steps as the diffusion profiles in that anomalous behavior appears after the oxidizing drive-in-cycle on high concentration samples. After deposition only, the x-ray topographs show almost no evidence of dislocations or precipitation even when very high concentrations of phosphorus are used. An example of such a topograph is illustrated in Fig. 3a which shows no contrast indicative of damage. However, after drive-in, wafers deposited with high concentrations of phosphorus (*i.e.*, above the ragged region) reveal much crystal disorder as indicated by the anomalous contrast of Fig. 3b; this is the same wafer shown in Fig. 3a. It was confirmed through electron microscopy that this crystal disorder consists of dislocations and precipitates as illustrated by the electron micrographs, Fig. 3c.<sup>1</sup> On the other hand,

<sup>1</sup> It may seem surprising that no dislocations appear after deposition; however, it is possible that the rather abrupt appearance of the dislocations is the result of a threshold effect activated by the small increase in total concentration and/or an enhancement of crystal energy from the additional heat cycle and surface oxidation of the drive-in. This is supported by Shockley's model which requires a certain minimum impurity concentration for dislocation formation (see H. S. Queisser, *J. Appl. Phys.*, 32, 1776 (1961)).



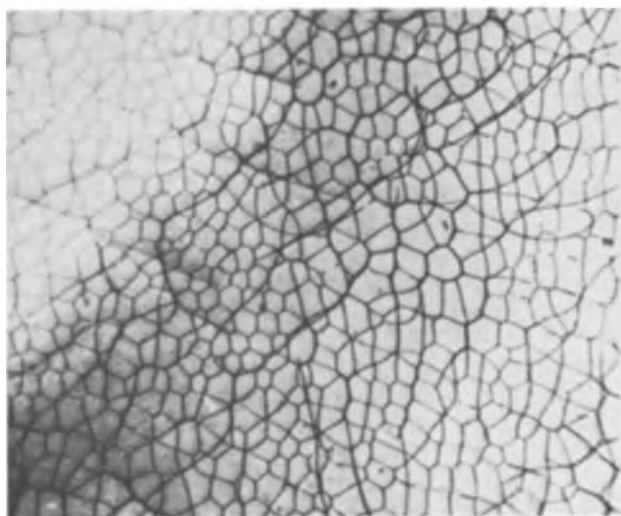


Fig. 3. X-ray topograph (SOT) and electron micrographs of blanket phosphorus diffused wafer; (a) x-ray topograph after deposition only; (b) x-ray topograph after drive-in; (c) electron micrograph illustrating dislocation networks, taken at the surface, magnification ca. 8000X.

wafers whose deposition phosphorus concentration was below the ragged region are still relatively free of crystal damage after drive-in. Wafers within the ragged region show a varied crystal disorder.

These observations are confirmed by Sirtl etching. After deposition only, the Sirtl etch technique reveals

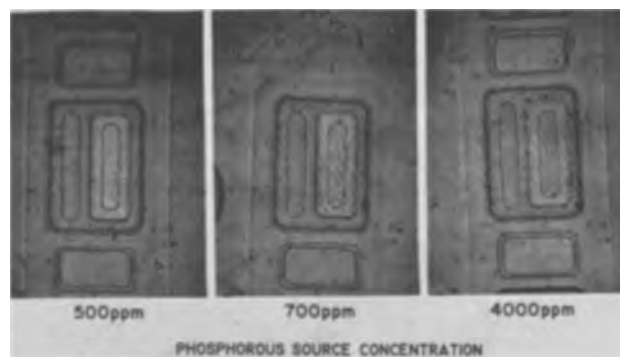


Fig. 4. Sirtl etch patterns of transistor structures with phosphorus diffused emitters. Note etch pits surrounding emitter area of unit highest phosphorus concentration. Magnification ca. 215X.

little surface structure. After drive-in, there is much crystal disorder for the wafers of higher phosphorus concentration as shown in Fig. 4. For the sample of 500 ppm phosphorus source, there is the beginnings of a "crow's foot" type pattern similar in nature to the slip lines reported by McDonald *et al.* (6) for similar types of phosphorus diffusion. As the concentration increases, the pattern becomes more dense until it resembles a general haze. Note that for the highest concentration there are a large number of etch pits surrounding the emitter. These pits result from dislocation loops that propagate for considerable distances outside of some high concentration phosphorus diffused planar structures. These dislocations have been described previously (13), and have been shown to be distinct from and often in addition to the diffusion induced dislocation networks within the diffused areas.

From the foregoing observation, it appears that the ragged junction area is a transition region in which diffusion induced dislocations and precipitates are forming. In other words, the dislocations, etc. can be directly correlated with retardation of phosphorus diffusion. When these dislocations are uniformly present or absent across a wafer, the junctions are flat. When these dislocations are not uniform, as when the phosphorus concentration is such that dislocations are just beginning to form, the diffused junctions have variable depths; or, they are ragged. This would correspond to the ragged region of Fig. 1.

The crystal damage within the diffused areas, consisting of diffusion induced dislocations and precipitation, was found to extend into the silicon for about 20-25  $\mu$ in. (or about 1/3 junction depth) as determined by combining the x-ray technique with the anodic removal of thin silicon layers. Conversely, the dislocation loops around the edges of the planar structures extend to depths of 0.5 mils (and sometimes more). Thus, the former type of damage would be confined to the emitter of a transistor, whereas the peripheral dislocation loops would extend well through the base. These dislocation loops are correlated with a reduction of transistor gain; a phenomenon presumably due to carrier recombination within the base along the dislocations. For example, consider the two device wafers, of which x-ray topographs are shown in Fig. 5. The phosphorus concentrations are just about the ragged region in both cases (Fig. 1), and all junctions are flat. However, the peripheral dislocation loops around the edges appear on only one of the wafers. Note that the geometry of the units themselves are delineated by the contrast resulting from the macroscopic elastic strains around the phosphorus diffused areas. The average  $V_{be}$  for both was 0.70v ( $\pm 0.005$ ), but the transistor gain (at 2.5 ma) of those without dislocations was  $52 \pm 3$  and of those with dislocations was  $33 \pm 5$ . This phenomenon can also be illustrated by Fig. 6 which plots transistor gain ( $\beta$ ) vs.  $V_{be}$  for units whose phosphorus concentrations in the emitters were both above and below the ragged re-

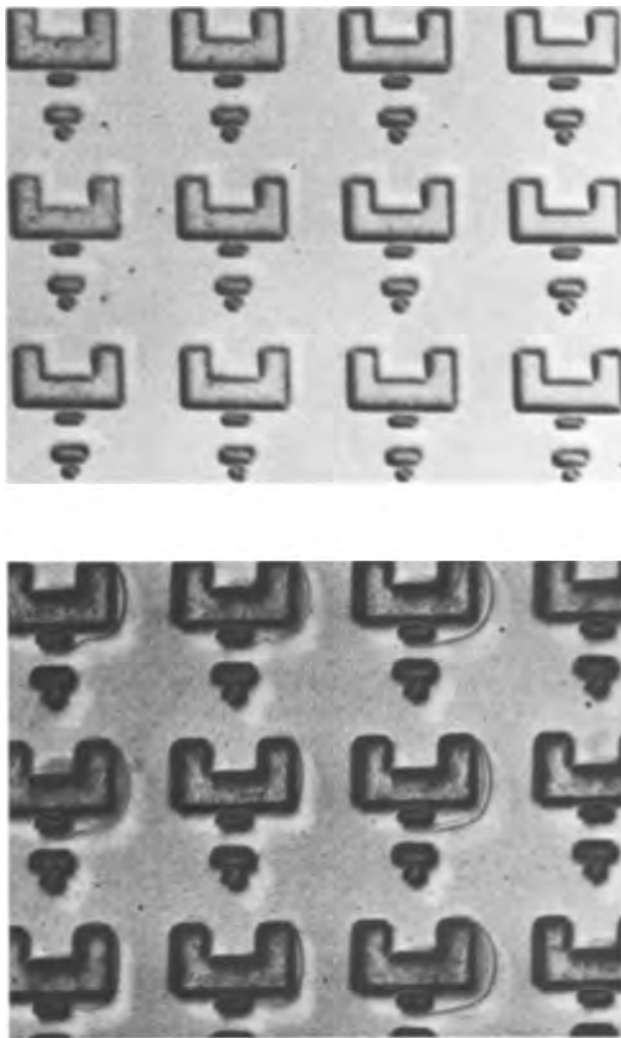


Fig. 5. X-ray topographs of device structures upon which transistor gain was subsequently measured.  $V_{be} = 0.70$  at  $I_e = 0.5$  ma: (a) devices without peripheral dislocation loops,  $\beta = 52$ ; (b) devices with dislocation loops,  $\beta = 33$ .

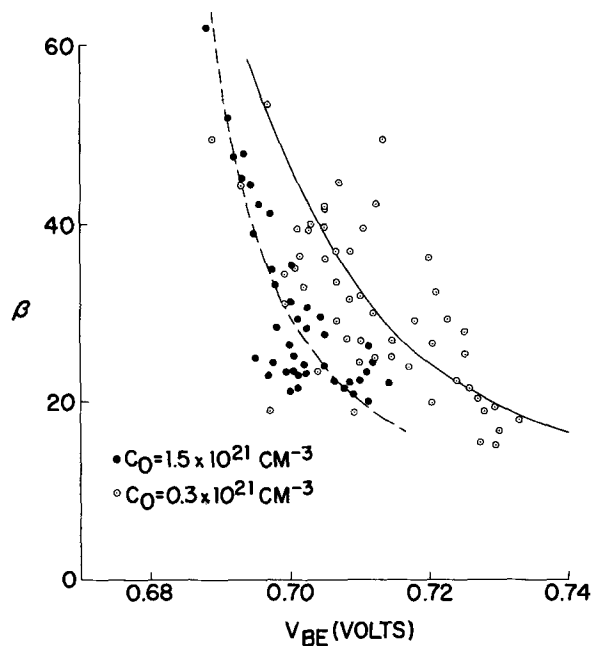


Fig. 6. Transistor gain, " $\beta$ " vs.  $V_{be}$  taken at  $I_e = 0.5$  ma for transistor made with high and low phosphorus emitter diffusions.

gion, 8000 ppm and 500 ppm, respectively. Those of higher concentration would have the peripheral dislocation loops but the others would not. It is obvious that the lower phosphorus concentration yields a higher gain for any given  $V_{be}$ .

#### Possible Mechanisms

At this time, it is not possible to establish a firm model to explain the retardation or ragged junction phenomenon; however, several possible contributory mechanisms may be discussed. As indicated above, the formation of dislocations and precipitates at high concentrations of phosphorus appears to correlate directly with the retardation of the phosphorus diffusion. This suggests a possible relation with relief of lattice strain through dislocations. The diffusing phosphorus concentration profile will introduce strains which are counterbalanced by tensile stresses of the silicon covalent bonds in the neighborhood of the profile itself (14). This strain may enhance the diffusion coefficients of the diffusing impurities. For example, Balluffi and Ruoff (15) proposed three possible mechanisms whereby diffusion is enhanced in strained lattices owing to an increased concentration of vacancies. (Phosphorus is generally believed to diffuse by vacancy exchange.) Two of their three mechanisms involve relationships of excess vacancies to moving dislocations, and the third involves merely an increase in vacancy formation rate in the bulk lattice. Now, the formation of high densities of dislocations (or precipitates) may either simply reduce the lattice strain and the strain enhanced diffusion, or it may "anchor" the dislocations at nodal points of the dislocation networks to prevent a dislocation movement. With respect to the latter possibility, Joshi and Wilhelm (9), show the existence of such nodal points in phosphorus diffusion induced dislocation networks and suggested their role in preventing dislocation movement. Thus, the diffusion induced dislocations may nullify a strain enhanced diffusion mechanism, which is operative just below the ragged junction region.

In addition, the diffusion induced dislocations and precipitates may reduce the effective mobility of the diffusing phosphorus atoms by providing precipitation sites for some phosphorus atoms. This possibility was suggested by Lawrence (16) to explain an apparent retarded phosphorus base diffusion of a PNP transistor when high concentrations of phosphorus were used as the base diffusant, and it was further discussed by Joshi and Dash. (17). However, it must be noted from Fig. 2b that the lower phosphorus concentration profile reflects a higher effective diffusion coefficient at depths well below the point at which precipitates cease.

Since high densities of dislocations correspond to the condition of retarded diffusion, any diffusion enhancement due to dislocations, or their formation, is secondary. This is reasonable since these dislocations normally lie perpendicular to the diffusion direction, see Fig. 3c, and are, thus, unlikely to provide preferential diffusion paths. Also, the formation of these dislocations need not produce a large excess of vacancies if their formation mechanism is by slip. Thus, Nicholas' model, whereby the mere formation of dislocations causes very high vacancy concentrations (3), is probably not important in our system.

#### Summary

A retardation effect of phosphorus diffusion at very high concentration is reported. This retardation is phenomenologically related to the formation of diffusion induced dislocations. It is suggested that this relation is through a reduction of strain enhanced diffusion through dislocation formation. However, precipitation at dislocations may also affect the system.

Also reported is the existence of large dislocation loops around planar structures diffused under conditions of retarded phosphorus diffusion. If these dis-



location loops occur around the emitters, they seriously reduce transistor gain.

### Acknowledgments

The authors gratefully acknowledge the help of Dr. B. Masters, under whose direction the radiochemical profiles were obtained, and Mr. B. Medvecky for virtually all of the diffusion work.

Manuscript received June 26, 1967; revised manuscript received Sept. 11, 1967. This paper was presented at the Philadelphia Meeting, Oct. 9-14, 1966, as Abstract 193. Part of this work was supported under AFCRL Contract AF 19(628)-5059, Bedford, Massachusetts.

Any discussion of this paper will appear in a Discussion Section to be published in the December 1968 JOURNAL.

### REFERENCES

1. E. Tannenbaum, *Solid State Electron.*, **2**, 123 (1961).
2. S. Maekawa, *J. Phys. Soc. Japan.*, **17**, 1592 (1962).
3. K. H. Nichols, *Solid State Electron.*, **9**, 35 (1962).
4. U. K. Subashiev, A. P. Landsman, and A. A. Kukharskii, *Soviet Phys. Solid St.*, **2**, 2406 (1961).
5. P. A. Iles and B. Leibenhaut, *Solid State Electron.*, **5**, 331 (1962).
6. R. A. McDonald, G. G. Ehlenberger, and T. R. Huffman, *ibid.*, **9**, 807 (1966).
7. E. Kooi, *This Journal*, **111**, 1383 (1964).
8. G. H. Schwuttke, *J. Appl. Phys.*, **36**, 2712 (1965).
9. M. L. Joshi and F. Wilhelm, *This Journal*, **112**, 185 (1965).
10. E. Sirtl and A. Adler, *Z. Metallkde.*, **52**, 529 (1961).
11. G. H. Schwuttke and F. Wilhelm, *Bull. Am. Phys. Soc.*, **12**, 120 (1967).
12. H. K. Gummel, *Proc. I.R.E.*, **49**, 834 (1961).
13. G. H. Schwuttke and J. M. Fairfield, *J. Appl. Phys.*, **37**, (1966); and J. E. Lawrence, *This Journal*, **113**, 819 (1966).
14. S. Prussin, *J. Appl. Phys.*, **32**, 1876 (1961).
15. R. W. Balluffi and A. L. Ruoff, *ibid.*, **34**, 1634 (1963).
16. J. E. Lawrence, *ibid.*, **37**, 4106 (1966).
17. M. L. Joshi and S. Dash, *IBM J. Research and Dev.*, **10**, 446 (1966).

## D-C Dielectric Breakdown of Amorphous Silicon Dioxide Films at Room Temperature

F. L. Worthing

*Bell Telephone Laboratories, Incorporated, Murray Hill, New Jersey*

### ABSTRACT

The dielectric breakdown properties of atmospheric pressure steam-grown silicon dioxide films, grown on fresh epitaxial layers with degenerate silicon substrates, were studied at room temperature as a function of d-c voltage, time, polarity, thickness of the oxide, and rate of change of voltage. Contact was made to the oxide by 0.025 in. diameter evaporated gold dots. The observed phenomena were found to depend basically on the polarity of the applied potential. At positive silicon potentials (gold dots negative) dielectric breakdown occurred abruptly with no detectable conduction below breakdown. Positive breakdown is not time dependent and appears to be of the type generally referred to as intrinsic or disruptive breakdown. At negative silicon potentials (gold dots positive) these films exhibited conduction in the nA range and a time dependence of dielectric breakdown. If  $t$  is the time it takes an oxide to breakdown at an applied voltage  $V$ , a linear relationship between  $V$  and  $t^{-1/4}$  is observed over a range of approximately 150v. This is an empirical relationship known as Peek's law.

Several measurements have been found useful for the comparative evaluation of silicon dioxide films developed for device passivation. One of these is dielectric breakdown strength. However, there has frequently been confusion due to discrepancies between values obtained by different methods.

The dielectric breakdown properties of silicon dioxide films were studied at room temperature as a function of d-c voltage, time, polarity, thickness of the oxide, and rate of change of voltage. The films were grown on fresh epitaxial layers of approximately 25 ohm-cm, N-type with 0.01 ohm-cm, N-type silicon substrates. Surface cleaning of the substrates prior to epitaxial deposition consisted of a solvent degrease, a 2-min HF dip, a deionized water rinse, a 15-min soak in HNO<sub>3</sub> at 80°C, and a final deionized water rinse. Oxides were grown directly on the epitaxial layers, without additional cleaning, by heating the silicon substrates in 1050°C steam at atmospheric pressure. Oxide growth time was about 1 hr (depending on the desired oxide thickness) after which the samples were air quenched. Index of refraction for the oxide films was about 1.47.

For the tests about to be described, dielectric breakdown will be arbitrarily defined as occurring at that voltage which is sufficient to produce damage resulting

in a sustained leakage current greater than 1  $\mu$ a as long as the applied voltage is maintained. An order of magnitude change in either direction for this definition would not greatly alter the values of dielectric strength reported here. After-breakdown self-healing is excluded, and a contact dot generally exhibits current greater than 0.1  $\mu$ a at any applied voltage in the same polarity.

### Sample Preparation and Measuring System

The silicon wafers used were 0.250  $\times$  0.420  $\times$  0.015 in. Various samples having oxide thicknesses ranging from 3000 to 10,000Å were used, although the most commonly used oxide thickness was 6000Å. Fifty 0.025 in. diameter gold contact dots 5000Å thick were evaporated on the oxide. The underside of the silicon substrate was electroless nickel plated to make electrical contact with the test stage. Unless otherwise noted, all samples with their contact dots were baked at 400°C for approximately 1 hr in air before breakdown tests were conducted. The gold dots were contacted by a 0.002 in. diameter gold probe.

Test equipment consisted of a Keithley Model 240 regulated high voltage power supply (accuracy  $\pm$ 1%) and a Hewlett-Packard 425A microammeter. Chart recordings were obtained from a Varian strip chart

recorder, Model G-11A, fed from the microammeter. Voltages were measured by a Keithley Model 610A electrometer. The experimental arrangement is shown in Fig. 1. In some cases voltage was applied at a constant rate by means of a motor driven potentiometer.

In defining polarities the convention will be to call the negative polarity that voltage which makes the silicon negative, or gold contact dot positive.

**Results and Discussion**

*Incipient breakdown region.*—Figure 2 shows the current-voltage characteristic of a contact dot for which the voltage was applied as a voltage ramp. The ramp was started from zero and increased at a constant rate of 10 v/min, in the negative direction, that is, with silicon negative. The start of a region which will be referred to as the "incipient breakdown region" is indicated by the increase in conduction at about 280v ( $4.7 \times 10^6$  v/cm). As application of the voltage ramp continued, conduction continued to increase more and more rapidly, until breakdown occurred at 395v ( $6.6 \times 10^6$  v/cm). Figure 3 shows the conduction pattern of a contact dot for which negative potential was again applied as a voltage ramp, increasing at the rate of 10 v/min. This time, however, the ramp was stopped at the very beginning of the "incipient breakdown region." With the resulting fixed voltage of 300v ( $5.0 \times 10^6$  v/cm) maintained on the sample conduction continued to increase, until breakdown occurred 46 min later. It was thus found convenient to define the "incipient breakdown region" as that region where the application of negative potential results in a leakage current sufficiently unstable that, with no further increase in the applied voltage, it will eventually rise continuously until breakdown occurs.

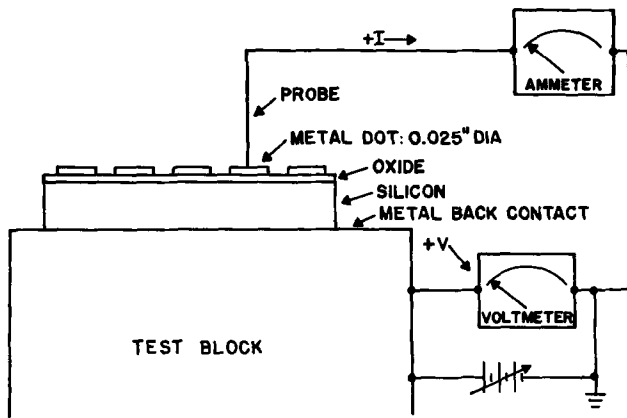


Fig. 1. Experimental arrangement for dielectric breakdown studies, shown for the case of positive silicon potential.

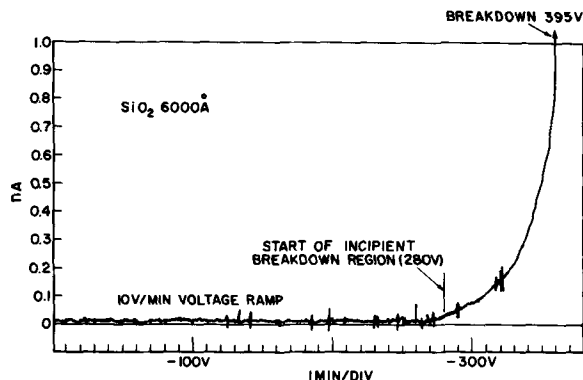


Fig. 2. Current-voltage characteristic of a contact dot for which increasing negative potential was applied to the silicon by means of a voltage ramp generator. Start of the incipient breakdown region is indicated by an increase in conduction at about 280v.

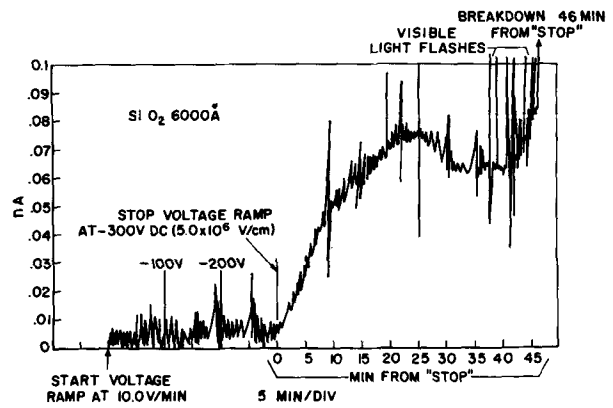


Fig. 3. Conduction pattern of a contact dot for which negative silicon potential was increased to 300v. Conduction continued to increase, with the voltage held constant, until dielectric breakdown occurred in 46 min. Note the appearance of transient current noise pulses, accompanied by visible light flashes, just prior to breakdown.

This is a characteristic feature of the conduction behavior for any fixed negative voltage in or close to the incipient breakdown region; over 100 dielectric breakdown tests were conducted in the manner described using various SiO<sub>2</sub> film samples. Thus the time required for breakdown to occur at the negative polarity is determined by the magnitude of the voltage and its rate of application prior to reaching that magnitude.

If the incipient breakdown region was approached repeatedly by the voltage ramp technique, the current instability started at a somewhat lower voltage each time and eventually breakdown occurred at about 250v ( $4.16 \times 10^6$  v/cm). This is about 150v lower than breakdowns obtained by a single continuous application of the voltage ramp. It thus appears that permanent damage was done each time the incipient breakdown region was approached, even though the current was never allowed to exceed 0.1 na. The phenomenon described here applies only to the case of silicon negative, since the incipient breakdown region is polarity dependent. The effect of lowering the breakdown strength by the previous application of stress has been noted previously by others (1). The foregoing observation would seem also to be in agreement with the theory of a constant volt-time life of insulation (2).

*Time-voltage curves.*—These experimental results show that, with negative voltages applied to the silicon, breakdown of SiO<sub>2</sub> usually is a gradual time dependent process. It is not therefore to be confused with intrinsic breakdown (to be discussed later) which would occur only as a very rapid process and for the most part at considerably higher field strengths.

In Fig. 4 each point represents time to breakdown, at negative silicon potential, for a different contact dot on the same sample. For example, the point indi-

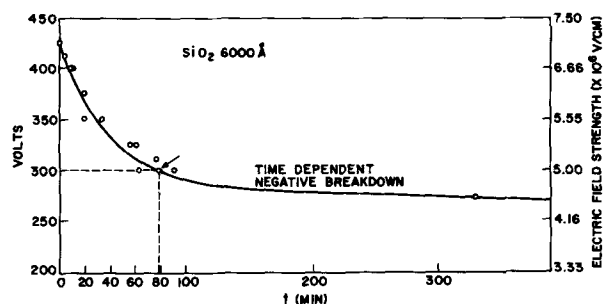


Fig. 4. Dielectric breakdown levels vs. time for negative silicon potential. Point indicated by the arrow was obtained by applying a negative potential of 300v until breakdown occurred in 78 min.

cated by the arrow was obtained by applying full stress at 300v until breakdown occurred in 78 min. ("Full stress" means that full voltage was reached in less than 1 min.) By choosing different test voltages for the various contact dots on a sample a time voltage curve is obtained. These test voltages are shown plotted against linear time. A replot of the same data is shown in Fig. 5 with the linear time scale replaced by a  $t^{-1/4}$  scale, where  $t$  is time to breakdown. The  $t^{-1/4}$  dependence is an empirical relationship known as Peek's law which may be stated as  $V = V_0 + at^{-1/4}$ , where  $V$  is breakdown voltage at any time  $t$ ,  $V_0$  is the infinite-time breakdown, and  $a$  is a constant (3). Materials for which curves obeying this law have been reported in the literature include synthetic plastics, various glasses, porcelain, and mica. (It should be noted, however, that in most of these cases there was no polarity effect, since the same electrodes were used on both sides of the insulator.) Peek's law appears to hold for d.c. only where there is some instability in conduction behavior which causes the current to tend to increase with the voltage held constant. This degradation of the dielectric with time has often been referred to in the literature as "thermal instability," although what actually happens may be gradual chemical or physical deterioration as suggested by Miller (4). The term thermal instability is used here with this qualification. Peek's law is applicable below some potential which is called the intrinsic breakdown level. In Fig. 5 the last two breakdown points, at the extreme right of the figure, fall short of the curve because they are in the intrinsic range which is not time dependent. The intrinsic level for this sample was about 410v. Time-voltage curves, similar to the one shown here, have been obtained for numerous samples with negative potentials applied over the range of 250-450v and at times ranging up to about 22 hr. These curves are reproducible on the same sample. Extrapolation of the curve of Fig. 5 to the intercept at  $t^{-1/4} = 0$  yields an infinite-time breakdown voltage ( $V_0$  of Peek's law) of about 190v ( $3.16 \times 10^6$  v/cm).

Breakdown tests have been performed, using negative potentials, while a sample was held immersed in liquid nitrogen. Negative breakdown was found to be no longer time dependent. This result shows that heating of the stressed area must have some influence on the time dependent type of negative breakdown previously described. At a sufficiently high voltage breakdown occurred instantaneously in a manner similar to that to be described for positive potentials.

**Transient current pulses.**—Rather severe transient current noise pulses are frequently observed in the incipient breakdown region. Such pulses are shown in the chart recording of Fig. 3. A number of workers have reported the unsteady nature of currents just prior to breakdown. O'Dwyer has observed that one of the characteristics of avalanche breakdown in solids

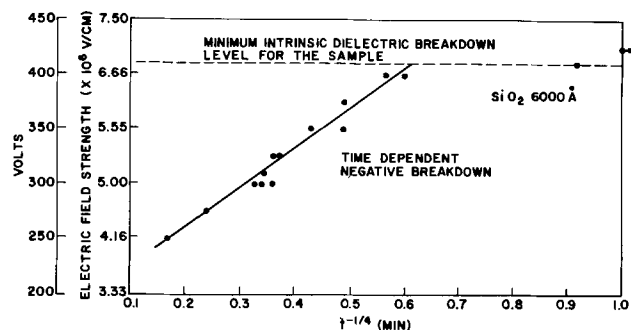


Fig. 5. Replot of the data of Fig. 4 with the linear time scale replaced by a  $t^{-1/4}$  scale, where  $t$  is time to breakdown. The last two breakdown points, at the extreme right of the figure, are not in agreement with Peek's law because they are in the intrinsic range which is not time dependent.

is that prebreakdown current will be very noisy, due to the buildup of avalanches which fail to reach the critical size (5). These pulses are randomly distributed although their magnitude increases with increasing voltage. They may appear with either fixed voltages or with voltage applied by the ramp technique.

**Light emission and surface spots.**—When the pulses described exceed approximately 10 na they are usually accompanied by visible light flashes which occur at various locations over the surface of the gold contact dot. The appearance is that of one or more pin point flashes of blue-white light, when the sample is viewed through a low power microscope in semidarkness. Where such flashes have occurred a change in the surface texture of the gold is usually observed. A portion of the surface of a gold contact dot is shown highly magnified in Fig. 6. The surface spots seen here are burned spots in the gold which indicate the location of previous flash sites. In some instances these spots are observed to have actual holes at their centers. There is evidence that these holes may extend through both the gold contact and the dielectric layer. In this respect they are apparently very similar to the self-healing breakdowns associated with weak spots in the dielectric, as recently reported by Klein and Gafni (6).

A sample on which the oxide under most of the gold contact dots had been broken down was subjected to a 20 to 1 mixture of nitrogen and chlorine gas at 800°C for 30 min (standard for all our chlorine etch studies) after the contact dots had been removed. Etch pits were found where contact dots had been located but not in the 0.024 in. margins between rows of dots.

To check the possibility that potential pinholes of the type discussed by Lopez (7) might be present within the film an ammonium fluoride-hydrofluoric acid etch was then used to reduce the oxide thickness from 6000 to 2500Å. The sample was again subjected to a hot chlorine etch for 30 min. No new etch pits developed in the margins.

As a further check for the possible presence of potential pinholes several samples were exposed to a water-amine-pyrocatechol etching system (8) at 110°C for 6 hr. This treatment removed approximately 1000Å of oxide, and the samples were found to have a negligible pinhole count. From these test results it was concluded that the oxide prior to dot evaporation was relatively free from pinholes or potential pinholes and that the reported light flashes are not caused by pinholes or potential pinholes which are detectable by chlorine or water-amine-pyrocatechol etching (9).

**Discharges.**—An obvious question concerning current pulses and flashes of the type described is whether they might be attributed to some type of discharge phenomena not occurring within the oxide itself. Possibilities include internal discharges (between the gold dot and the  $\text{SiO}_2$  or in minute voids or cavities where the gold makes poor contact with the  $\text{SiO}_2$ ), external or surface discharges (between the edges of

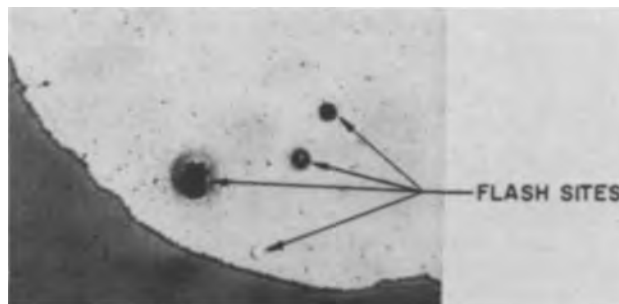


Fig. 6. A portion of the surface of a gold contact dot. Surface spots seen in this figure are burned spots in the gold which indicate the location of previous flash sites. Magnification ca. 100X.

the dot and the neighboring  $\text{SiO}_2$ ), or corona type discharges. Mason has reported that surface discharges are often 10-50 times larger than internal discharges (10).

To determine whether these flashes were occurring in voids, cavities, or areas of poor contact between the gold and the  $\text{SiO}_2$ , the dots on one sample were subjected to rapid heating which caused the formation of many tiny bubbles under each dot. Electric field strengths sufficiently high to cause appearance of the usual flashes were then applied. It was observed that the flashes did not occur under or even near the edges of a bubble.

Next the possibility was investigated that some of these flashes might be the result of surface-type discharges occurring between the gold contact dot and the neighboring oxide. The gold probe was lowered to make contact with a gold contact dot, then paraffin wax was melted over the entire surface of the dot and around the gold probe. It was found that the flashes still occurred with about the same distribution and in the same field strength range. It was further found, however, that negative breakdown was no longer time dependent. Apparently in this case the heat produced when a flash occurred melted some of the adjacent wax which in turn cooled the flash site, thus preventing thermal instability. These results, along with those previously described concerning breakdowns obtained at liquid nitrogen temperature, reinforce speculation that the negative breakdowns observed were the result of thermal instability and were not influenced by external discharge effects.

Further evidence that external discharges need not occur in the range of field strengths observed is found in work done by Austen and Whitehead (11) in which they obtained even higher field strengths in air without encountering discharges. They measured the dielectric breakdown strength of thin sheets of mica at thicknesses of the same order as the  $\text{SiO}_2$  films reported here. Their measurements were made using d-c voltage to obtain field strengths in the range of approximately  $11$  to  $16 \times 10^6$  v/cm. They confirmed the absence of discharges by separate experiments. In later work Plessner has reported similar findings for silica films (12).

**Dielectric breakdown at positive polarities.—Lack of positive conduction.**—Dielectric breakdown at positive potentials (silicon positive) is not time dependent and appears to be of an intrinsic nature, which yields the true dielectric strength of the material itself (13). This lack of time dependence is attributed to the absence of thermal instability, which in turn results from the lack of conduction below breakdown at this polarity.<sup>1</sup> In other words, in the absence of conduction, thermal instability cannot occur. Oxide specimens appear to remain indefinitely stable at positive potentials below their intrinsic dielectric breakdown levels. A typical pattern illustrating the absence of conduction and the lack of time dependence of breakdown with positive silicon potential is shown in Fig. 7. Here the voltage ramp technique was used to apply positive potential at the rate of 10 v/min. Notice the capacitance charging current of about 3 pa which ceased when the ramp was stopped at the 400v level.

This sample was known to have an intrinsic dielectric breakdown of about 410v. However, a potential only 10v below this value could be maintained for over 10 hr with no sign of increased conduction or of breakdown. After this time the voltage ramp was restarted and breakdown occurred, as predicted, at the 410v level ( $\sim 6.8 \times 10^6$  v/cm). Notice the contrast between this behavior and that of the sample shown in Fig. 3.

Conductivity and charge storage experiments, in which asymmetric conduction has been observed in

<sup>1</sup> The lowest current that could be accurately measured was around 2 pa.

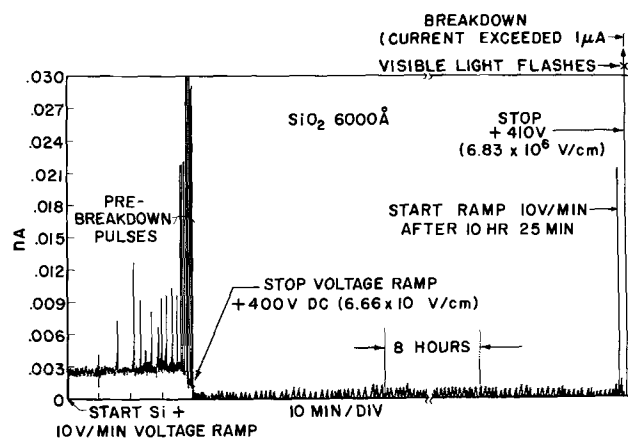


Fig. 7. Typical positive conduction pattern illustrating; (a) capacitive charging current of about 3 pa which ceased when the 10 v/min voltage ramp was stopped at the 400v level; (b) pre-breakdown noise pulses; (c) absence of conduction and lack of time dependence with a positive potential of 400v applied to the silicon for over 10 hr; (d) a positive dielectric breakdown level of 410v ( $\sim 6.8 \times 10^6$  v/cm) which was reached when the voltage ramp was restarted.

silica films at low voltage and high temperature, have been reported by (among others): Kerr, Logan, Burkhardt, and Pliskin; Ishikawa, Sasaki, Seki, and Inowaka; and by Yamin and Worthing (14). It was found that rectification occurred and that the conducting direction was with silicon negative, which is in agreement with observations reported here.

#### Voltage ramp technique and transient current pulses.

—Some samples show current pulses in the prebreakdown region with changing positive potential. An example of this may be seen in Fig. 7. Samples which show this effect will often break down about 5-10% below what has been tentatively established (by the application of fixed stresses) as an intrinsic or disruptive breakdown level, if the voltage ramp is allowed to continue.

As previously described for pulses occurring at negative potentials, these current pulses are accompanied by visible light flashes at various locations on the surface of the gold contact dot when they exceed approximately 10 na. If at any time prior to breakdown the voltage ramp is stopped and the resulting fixed voltage maintained on the sample, charging current ceases and breakdown does not occur.

#### Other contact metals and films by other methods.—

The polarity effects and the time dependence of dielectric breakdown reported have been observed for other contact metals such as aluminum and platinum.

The techniques described have been applied to the evaluation of films obtained by other methods on similar substrates.  $\text{SiO}_2$  films obtained by plasma deposition, as reported by Ligenza and Povelonis (15), were tested by the methods described. Some differences in dielectric breakdown and prebreakdown conduction levels were observed, but in general the same basic phenomena as reported for steam-grown  $\text{SiO}_2$  films were found.

**Dielectric strength of atmospheric-pressure steam-grown  $\text{SiO}_2$ .**—Approximately 50 positive dielectric breakdown tests were conducted using various  $\text{SiO}_2$  film samples. Values of intrinsic dielectric strength, derived from the observed positive breakdown potentials, ranged from about  $7 \times 10^6$  v/cm to about  $1 \times 10^7$  v/cm. These values are in general agreement with those reported in the literature for quartz and vitreous silica (16). Positive breakdown values are, in general, highly reproducible for different contact dots on the same sample. A comparison of 12 positive breakdown values, obtained using several different  $\text{SiO}_2$  film sam-

ples, showed an average dielectric strength value of  $7.03 \times 10^6$  v/cm with a standard deviation of  $0.30 \times 10^6$  v/cm. A comparison of dielectric strength values obtained using different area contact dots showed no significant area dependence. No variation in dielectric strength (volts/centimeter) with thickness of the oxide was found over the thickness range used (3000-10,000Å). Since the films were amorphous in structure, no variation of the dielectric strength with thickness was expected from Fröhlich's theory, because the mean-free paths for electrons would be too short (12).

### Summary and Conclusions

Dielectric breakdown and prebreakdown phenomena, for SiO<sub>2</sub> films on silicon, are found to depend primarily on the polarity of the applied potential. This stems from a fundamental difference in the breakdown mechanism involved. At negative silicon polarities dielectric breakdown strength bears a linear relationship to  $t^{-1/4}$ , over a range of approximately 150v, where  $t$  is time for which voltage is applied. This is attributed to conduction and thermal instability. Time-voltage curves form a convenient means for displaying this time dependence at negative potentials.

Dielectric breakdown at fixed positive potentials is not time dependent. Breakdown appears to be of an intrinsic nature which yields the true electric strength of the dielectric independent of time. This is attributed to the lack of conduction below breakdown at positive potentials and the absence of thermal instability, whether due to electrical, thermal, chemical, or other effects. The polarity effects and time dependence of breakdown reported have been observed for other contact metals, such as aluminum and platinum.

In the breakdown experiments reported, which were performed at high voltages and room temperature, it was observed that the conducting direction is with silicon negative.

Conductivity and charge storage experiments have been performed on silica films at low voltage and high temperatures. These have been reported by, among others, Kerr *et al.*, Isikawa *et al.*, and by Yamin and Worthing (14). In these experiments it was also found that rectification occurred and that the conducting direction was with silicon negative.

Light flashes are usually observed at various locations over the surface of the contact dot when transient current noise pulses exceed approximately 10 na. Since both chlorine etch tests and the water-amine-pyrocatechol etching system indicate that the oxides used were initially free of pinholes or potential pinholes, it is concluded that the light flashes are not caused by pinholes which are detectable by these etches.

Values of intrinsic electric strength, derived from observed positive breakdown potentials, range from

about 7 to  $10 \times 10^6$  v/cm. These values are in general agreement with those reported in the literature for quartz and vitreous silica. Positive breakdown values are, in general, highly reproducible for different contact dots on the same sample. No variation in dielectric strength (volts/cm) with thickness of the oxide was found over the thickness range of 3000-10,000Å.

Manuscript received Aug. 23, 1966; revised manuscript received Sept. 29, 1967. This paper was presented at the San Francisco Meeting, May 9-13, 1965, as Abstract 97.

Any discussion of this paper will appear in a Discussion Section to be published in the December 1968 JOURNAL.

### REFERENCES

1. S. Whitehead, "Dielectric Phenomena," Vol. III, "Breakdown of Solid Dielectrics," p. 248, Ernest Benn Limited, Bouverie House, London (1932).
2. D. F. Miner, "Insulation of Electrical Apparatus," p. 49, McGraw-Hill Book Co., New York (1941).
3. D. F. Miner, *ibid.*, p. 40 (1941).
4. H. N. Miller, "Nondestructive High Potential Testing," p. 17, Hyden Book Co., New York (1964).
5. J. J. O'Dwyer, "The Theory of Dielectric Breakdown of Solids," p. 12, Oxford at the Clarendon Press (1964). J. J. O'Dwyer, *Advances in Physics*, **7**, 349, (1958).
6. N. Klein and H. Gafni, *IEEE Trans. on Electron Devices*, Vol. ED-13, February 1966, pp. 281-289.
7. A. D. Lopez, *This Journal*, **113**, 89 (1966).
8. R. M. Finne and D. L. Klein, paper presented at the Toronto Meeting of the Society, May 3-7, 1964, Abstract 82.
9. J. V. Dalton, Private communication.
10. J. H. Mason, "Progress in Dielectrics," Vol. I, p. 33, John Wiley & Sons, Inc., New York (1959).
11. A. E. W. Austen and S. Whitehead, *Proc. Roy. Soc.*, **A176**, 33, (1940).
12. K. W. Plessner, *Proc. Phys. Soc.*, **60**, 243 (1948).
13. S. Whitehead, "Dielectric Breakdown of Solids," p. 5, Oxford at the Clarendon Press (1951). A. von Hippel, "Tables of Dielectric Materials," Lab for Insulation Research, MIT, Vol. II, p. 71, June 1945.
14. D. R. Kerr, J. G. Logan, P. J. Burkhardt, and W. A. Pliskin, *IBM J. Res. Developm.*, **8**, 376-384 (1964); Y. Ishikawa, Y. Sasaki, Y. Seki, and G. Inowaka, *J. of Apply. Phys.*, **34**, 867 (1963); M. Yamin and F. L. Worthing, Paper presented at the Toronto Meeting of the Society, May 3-7, 1964, Abstract 75; M. Yamin, *IEEE Trans. on Electron Devices*, Vol. ED-12, March 1965, pp. 88-96.
15. J. R. Ligenza and E. I. Povilonis, Paper presented at the Washington Meeting of the Society, Oct. 11-15, 1964, Abstract 138.
16. A. E. W. Austen and S. Whitehead, *Proc. Roy. Soc.*, **A176**, 33 (1940); A von Hippel and R. G. Maurer, *Phys. Rev.*, **59**, 820 (1941); K. J. Keller, *Physics*, **14**, 15 (1948).

# Mechanism of Branching and Kinking during VLS Crystal Growth

R. S. Wagner and C. J. Doherty

*Bell Telephone Laboratories, Incorporated, Murray Hill, New Jersey*

## ABSTRACT

The morphology of the solid-liquid interface and the contact angle configuration of the liquid alloy droplet determine the direction of growth of crystals prepared by the vapor-liquid-solid (VLS) technique. There are four different processes by which both growth kinks and branches can be formed. A change in solid-liquid interface shape during VLS caused by a lateral temperature gradient results in the formation of growth kinks. Branches are formed if the alloy droplet ruptures during the kinking sequence. A sudden increase in temperature can cause an unstable contact angle configuration. The alloy droplet may run down the side faces of the growing crystal, leading to the formation of growth kinks or branches. A sudden decrease in temperature may cause "pinching off" of small droplets from the main droplet, giving rise to branches. Finally, the codeposition of liquid-forming impurities may also lead to branch and kink formation. The proposed models have been verified experimentally for VLS growth of silicon and germanium. Crystalline defects, such as dislocations, are not essential for the branching and kinking process. It is shown that "growth shaping" during the VLS process is possible.

Many whisker crystals grown from the vapor contain growth kinks and branches. The accidental attachment of two crystals during growth, which occurs rather frequently, will not be considered in this paper. The morphology of branched and kinked crystals has been studied for germanium (1) and silicon whiskers (2). It has been found that the various segments of these crystals constitute a single crystal. For a kinked germanium crystal, the direction of growth was found to change abruptly from  $[111]$  to  $[\bar{1}\bar{1}\bar{1}]$ . Similarly, a branched silicon whisker with a  $[111]$  main direction was found to be a single crystal, the branch resulting from simultaneous growth in the  $[\bar{1}\bar{1}\bar{1}]$  direction.

Many different theories (3-7) have been proposed to explain branching and kinking during vapor-phase growth of whisker crystals. All theories assume that the whisker crystals grow by the "screw dislocation" mechanism. Branching and kinking are explained by a variation of the dislocation model involving either a climb process of the dislocation at the whisker's tip or nucleation of a branch at a dislocation intersection. However, there is no reported experimental evidence to justify any of the proposed theories. It appears rather that the observation of growth kinking and branching has led many investigators to believe that these changes in growth habit can be attributed to the operation of a screw dislocation mechanism in whisker growth.

It has been shown that the vapor-liquid-solid (VLS) (8-12) mechanism explains many features of the growth of whisker crystals. It is the purpose of this paper to show that branching, kinking, and the growth of curved crystals can also be accounted for by the VLS process. The present work is an outgrowth of an earlier investigation on the controlled growth of silicon crystals in the form of intricate patterns on silicon substrates (10). The crystals shown in Fig. 8 in ref. (10) were grown under nearly isothermal conditions using a resistance heated furnace 10 in. long. Branched or kinked whiskers did not form under these experimental conditions. At this point of the investigation, it was considered worthwhile to take motion pictures during VLS growth. For this objective, the experimental conditions had to be changed drastically. The limited working distance of the microscope required an alteration of the heating system. The resistance furnace was replaced by a 2 in. long graphite tube which served as susceptor inside the reaction tube. A considerable lateral and axial temperature

gradient in the growth zone could not be avoided. Motion pictures of VLS growth clearly showed that very frequently the crystal branched or kinked during growth. In some experiments all the crystals in an array kinked in the same direction, toward the higher temperature region. Because of the small thermal mass of the graphite susceptor, sudden changes in temperature in the growth zone could be obtained by changes in the r-f output of the generator. Such changes, whether intentional or accidental, quite often resulted in branched and kinked whiskers. Similar changes in growth morphology were obtained by sudden changes of the total gas flow through the reaction tube. These observations were studied in detail, and the results are discussed in the following sections.

The proposed models are both simple and unique, and the experimental verification is unequivocal. It will be shown that crystalline defects, such as dislocations, are not essential for the branching and kinking process. We discuss in the first part of the paper the factors which control the direction of growth of silicon crystals grown by VLS. In subsequent sections are described four different processes by which branches and growth kinks can be formed. It is shown that controlled "growth shaping" during whisker growth from the vapor phase is possible.

## Experimental

The experimental procedure for controlled VLS growth of silicon crystals has been reported previously (10). The hydrogen reduction of  $\text{SiCl}_4$  was used as the transport reaction and gold as the liquid-forming impurity. The following experimental parameters were used in this investigation. The mean temperature of crystal growth was  $1000^\circ\text{C}$ . Temperature changes which were introduced intentionally will be discussed in the appropriate sections. A temperature gradient smaller than  $3^\circ\text{C}/\text{cm}$  was used for the isothermal growth experiments. The gradient was increased to over  $40^\circ\text{C}/\text{cm}$  for nonisothermal growth. In some experiments, the gradient was further increased by focussing a high power heat source on the sides of the growing crystals. A total hydrogen flow of 300 cc/min was used with a  $\text{SiCl}_4$ -to-hydrogen mole ratio of 0.02. Preliminary experiments indicated that controlled doping during VLS growth can yield important information about the growth mechanism. It was found that the dopant, introduced in gaseous form, also preferentially enters the liquid alloy droplet at the tip of the growing crystal. Doping therefore results

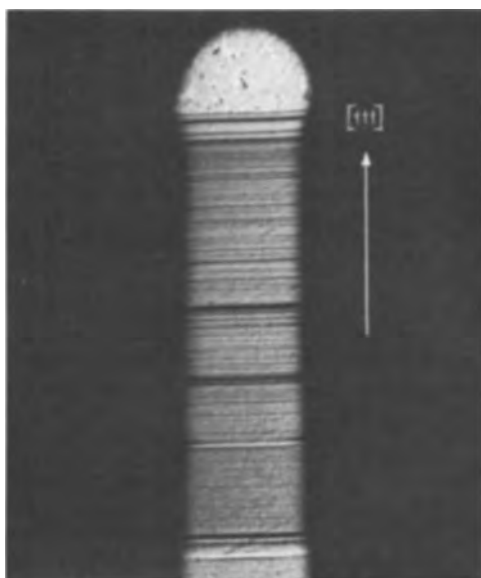


Fig. 1. Etched section of a [111] silicon crystal doped with phosphorus during isothermal growth. Magnification approximately 50X.

in clearly identifiable impurity striations which are parallel to the solid-liquid (SL) interface. These interface markers, introduced at given time intervals, permit a careful evaluation of interface transitions during branching and kinking. Ten cc/min hydrogen with a mole ratio of 0.0004  $\text{PCl}_3$  was used for the doping experiment. The duration of doping varied from 10 to 30 sec. Doped silicon crystals were sectioned parallel to the growth direction and etched with Sirtl (14) etch for about 1 to 4 min. The maximum diameter of all crystals shown in this paper is about 250-300 $\mu$ . The measured rate of VLS growth was about 1 mm/hr. A high-temperature microscope<sup>1</sup> in conjunction with a movie camera was used to record the growth of individual crystals by time-lapse photography (13). X-ray topographs by the Lang (15) technique were taken on some samples using silver radiation.

**Isothermal VLS growth.**—The majority of silicon crystals prepared by the VLS technique, under isothermal conditions, grew in a [111] direction. It has been proposed (8) that this particular growth direction arises because the solid-liquid interface is a single (111) plane. It has been shown (12) that the interface can be very stable during VLS growth; the stabilizing factor is very likely the interface kinetics. To confirm this point, a number of silicon crystals were doped with phosphorus during isothermal growth. The crystals were subsequently sectioned on a plane parallel to the growth direction and etched as shown in Fig. 1. The pronounced bands indicate the introduction of dopant during growth, whereas the fine bands are produced by fluctuations in growth rate (12). The figure clearly shows that the solid-liquid interface remains stable, parallel to a (111) plane during isothermal VLS growth. It must be concluded that layer growth occurs on this interface; the alloy droplet advances therefore perpendicular to this face in a [111] direction.

It has been reported (12) that the shape of the solid-liquid interface of a [111] crystal is not circular but triangular with rounded corners. Microscopic observation shows that the solid-liquid contact angle along the meniscus of the droplet is nonuniform during growth, being slightly larger at the rounded corners. However, such a contact angle configuration, having threefold symmetry, stabilizes the liquid droplet on the growing crystal. The effect of gravity on the con-

tact angle was found to be negligible. Crystals with diameters ranging from 50 to about 300 $\mu$  were grown in the usual way, vertically upward. Subsequently, the whole growth apparatus was rotated 90°, and the VLS growth continued in a horizontal direction to about 1 cm length. The crystals were afterwards examined in an optical goniometer and found to be straight. Similarly, x-ray reflections obtained with a Weissenberg goniometer showed that the crystals were straight and grew in a [111] direction. It is evident, however, that any force which is strong enough to change the symmetry of the solid-liquid contact angle configuration can influence the direction of growth. Although layer growth still occurs on a (111) plane under isothermal conditions, the resultant growth direction will be controlled by the liquid contact angles.

A suitable combination of interface morphology and liquid contact angle can give rise to growth directions other than [111]. For example, silicon crystals can be grown in a [110] direction as shown in Fig. 2. The doping striations show that the interface consists of two {111} planes forming a ridge configuration. If the crystals are grown at about 1050°C, the prismatic side faces are four {111} planes which are parallel to the [110] growth direction. This configuration leads to a twofold symmetry of the contact angles, stabilizing the droplet on the growing crystals. VLS-grown germanium whiskers are frequently observed with the same [110] morphology. In addition, germanium crystals also grow in the [100] direction (16). In this case, the solid-liquid interface is formed by four {111} planes in the shape of a pyramid. Another morphology has been observed both for germanium and silicon, a twinned crystal growing in a [211] direction. The shape of the interface of these crystals is similar to that one of crystals with a [110] growth direction. However, the angle between the two {111} planes is 141.06° for twinned [211] crystals and 109.48° for [110] crystals, respectively. It can be said in conclusion that the solid-liquid interface is not necessarily perpendicular to the direction of growth. The interface morphology determines the direction of growth, and unidirectional growth is only possible for a stable contact angle configuration. It will be shown in the

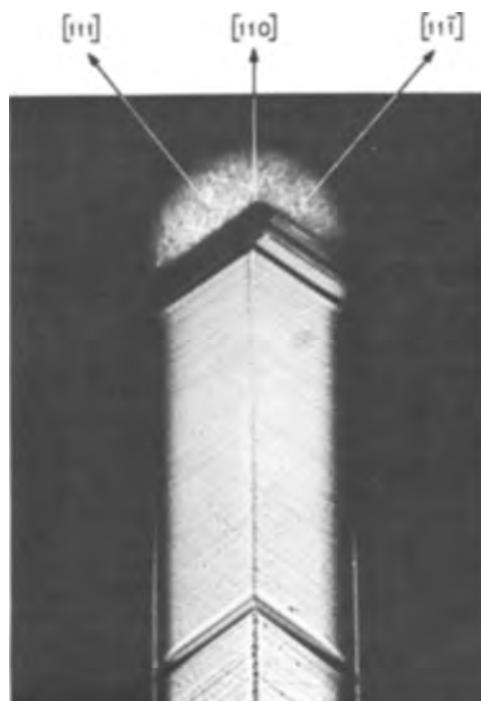


Fig. 2. Etched section of a [110] silicon crystal doped with phosphorus during isothermal growth. Magnification approximately 100X.

<sup>1</sup> American Optical long working distance microscope.



following section that a change in interface morphology during VLS growth invariably results in a change in growth direction.

**Nonisothermal growth.**—A model for branching and kinking during nonisothermal VLS growth has been proposed in a previous paper (11). The model is based on the assumption that a lateral temperature gradient can change the morphology of the SL-interface and thereby change the direction of crystal growth. The experimental verification of the proposed mechanism will be discussed in this section. The temperature conditions during VLS growth were changed from isothermal to nonisothermal. Time-lapse photography was used to obtain a permanent record of the growth sequence. The crystals were doped with phosphorus before, during, and after completion of the kinking process. Subsequently, the samples were sectioned, polished, and etched on a plane which is coplanar with the axial directions of the kinked crystal. A typical example of such an experiment is shown in Fig. 3 for a  $[111]$  to  $[\bar{1}\bar{1}\bar{1}]$  kink. In this case the kinking was caused by exposing the right side of the growing crystal to a higher temperature than the left side.

The value of using controlled doping to study successive interface positions is evident. During isothermal conditions, the crystal grew perpendicular to the  $(111)$  plane, as discussed previously. However, the introduction of a lateral temperature gradient caused a change in interface morphology. The  $(\bar{1}\bar{1}\bar{1})$  plane was partly exposed in addition to the original interface. The growth rate perpendicular to the newly formed interface is slower than on the  $(111)$  plane because it is in a region of higher temperature. The new interface grew in area at the expense of the old one until finally the  $(111)$  interface has disappeared. The liquid droplet shifts during this process from the  $(111)$  to the  $(\bar{1}\bar{1}\bar{1})$  interface. Further VLS growth proceeds in the  $[\bar{1}\bar{1}\bar{1}]$  direction. Figure 4 shows an enlargement of a  $(111)$  to  $(\bar{1}\bar{1}\bar{1})$  kink. Note that neither the  $(111)$  nor the  $(\bar{1}\bar{1}\bar{1})$  interface planes deviate from planarity during the kinking process. The macroscopic growth direction gradually changes from  $[111]$  to  $[\bar{1}\bar{1}\bar{1}]$  resulting in the growth of a curved crystal. Figure 5

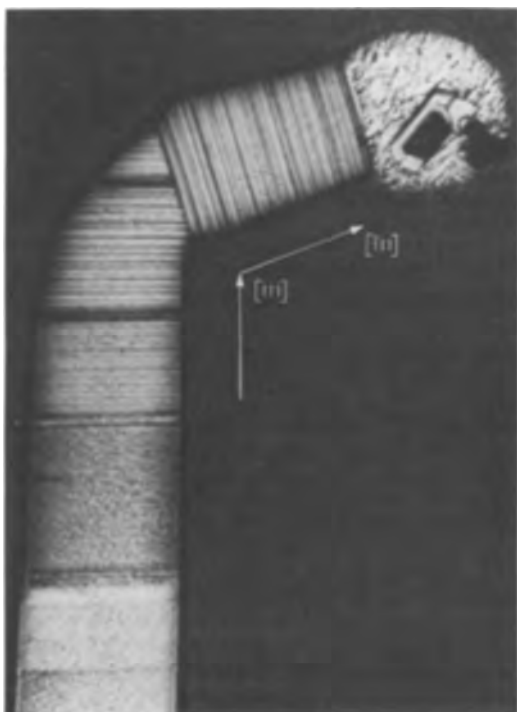


Fig. 3. Etched section of a  $[111]$  to  $[\bar{1}\bar{1}\bar{1}]$  kinked silicon crystal doped with phosphorus. Magnification approximately 100X.

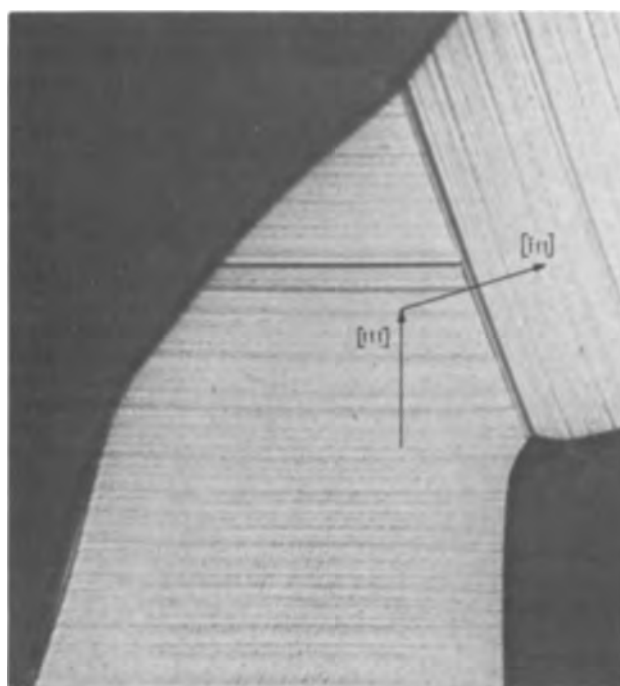


Fig. 4. Etched section of a  $[111]$  to  $[\bar{1}\bar{1}\bar{1}]$  kink. Magnification approximately 275X.

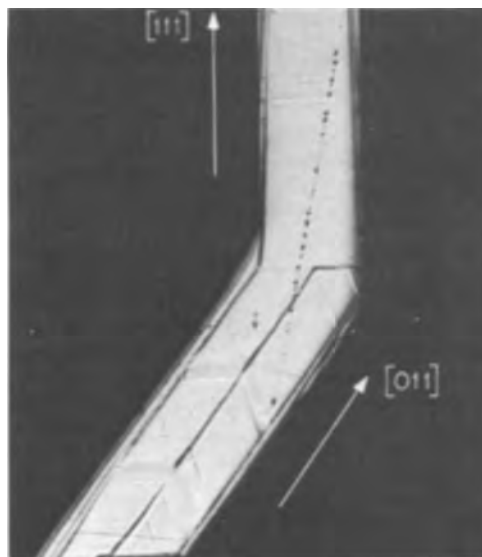


Fig. 5. Etched section of a  $[110]$  to  $[111]$  kink. Magnification approximately 50X.

shows a section of a crystal with a  $[011]$  to  $[111]$  kink. The  $[011]$  section of the crystal grew with an interface consisting of  $(111)$  and  $(\bar{1}\bar{1}\bar{1})$  planes. Again the SL interface changes in compliance with the proposed model. This sample was grown at a temperature of about  $1050^\circ\text{C}$ . The vapor-solid deposition rate becomes noticeable at this temperature (9, 12). This deposit surrounds the crystal grown by VLS. At even higher temperatures, the concave side of the kink becomes a preferred site for vapor-solid (VS) epitaxy. The true, original shape of the kink will be drastically altered by this deposit.

A small lateral temperature gradient may cause a gradual change in interface morphology. The growth direction will vary over a considerable length of the crystal, resulting in the growth of a curved whisker. Such events have been observed in a few cases. Figure 6 shows a photograph of a crystal curved during VLS growth. The liquid droplet is not supported by a single  $(111)$  interface, but rather extends downwards





Fig. 6. Curved silicon crystal photographed during nonisothermal growth. Magnification approximately 50X.

at the left side of the growing crystal. Again, a VS deposit will obscure the shape of curved crystals. At high temperatures, the deposit ultimately will tend to "straighten" such curved sections, by increasing the diameter of the crystal.

Kinking under the influence of a temperature gradient was observed for over 100 crystals. About 20 crystals were examined for the presence of crystalline defects in the kink region. Lang topographs were taken and sectioned crystals were etched as shown in Fig. 3 and 5. The majority of the samples did not contain any observable defects in the kink region. A few specimens contained islands of Au-Si entrapments which are known to give rise to the generation of defects (12). It must be concluded that crystalline defects, such as dislocations, are not essential for the reported kinking process. Entrapment of liquid alloy may occur during kinking with subsequent formation of defects during cooling.

Figure 7 shows a Lang topograph of a  $[110]$  to  $[11\bar{1}]$  kink. The crystal was grown on an imperfect  $(111)$  substrate. Some dislocations continued to grow from

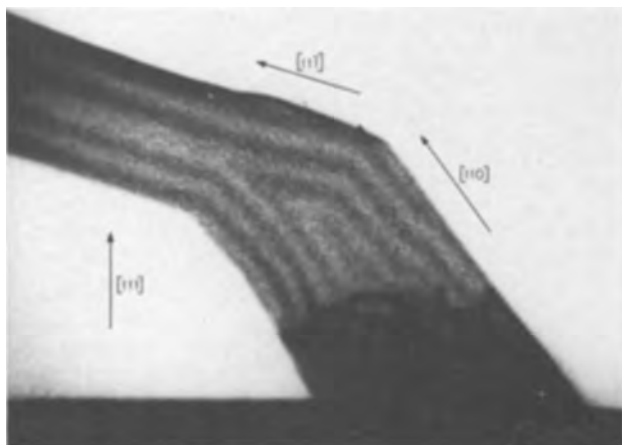


Fig. 7.  $(111)$  X-ray topograph of a  $[110]$  to  $[11\bar{1}]$  kinked silicon crystal. Magnification approximately 70X.

the substrate into the crystal. All dislocations apparently grew out of the crystal at the lower section. The remainder of the sample, including the kink, is dislocation-free. Note the occurrence of "pendellösung" fringes both in the  $[110]$  and  $[11\bar{1}]$  sections of the crystal. The shapes of the fringes in the two sections are different because the cross section of the crystal is not the same in the two regions. The cross section is diamond-shaped in the  $[110]$  region and hexagonal in the  $[11\bar{1}]$  part. The occurrence of pendellösung fringes in the kink provides additional evidence that defects are not involved in the kinking mechanism.

It is evident from Fig. 4 that the area of the SL interface changes during the kinking process. The area first increases and finally returns to its original value after completion of kinking. The change in interfacial area imposes a constraint on the contact angle of the liquid alloy droplet. The constraint frequently causes rupture of the droplet, thereby giving rise to the formation of branch crystals as shown in Fig. 8. The time-lapse sequence, taken at constant magnification, illustrates four different stages during and after the kinking sequence. The crystal was grown on a  $(111)$  substrate at about  $1050^\circ\text{C}$ . The plane of the photograph is approximately  $(110)$ . Figure 8a shows the trace of the SL interface and the droplet configuration during kinking at a time when the interfacial area is at a maximum. The kinking sequence is almost completed in Fig. 8b. The new  $\{111\}$  interface has increased considerably at the expense of the old interface. A small droplet, indicated by the arrow, has broken away from the main droplet during the transition. Figure 8c shows the interface and droplet configuration after completion of kinking. The small droplet gave rise to the growth of a branch crystal with a  $[111]$  growth direction. A later sequence of growth is shown in Fig. 8d. The effect of VS epitaxy in changing the

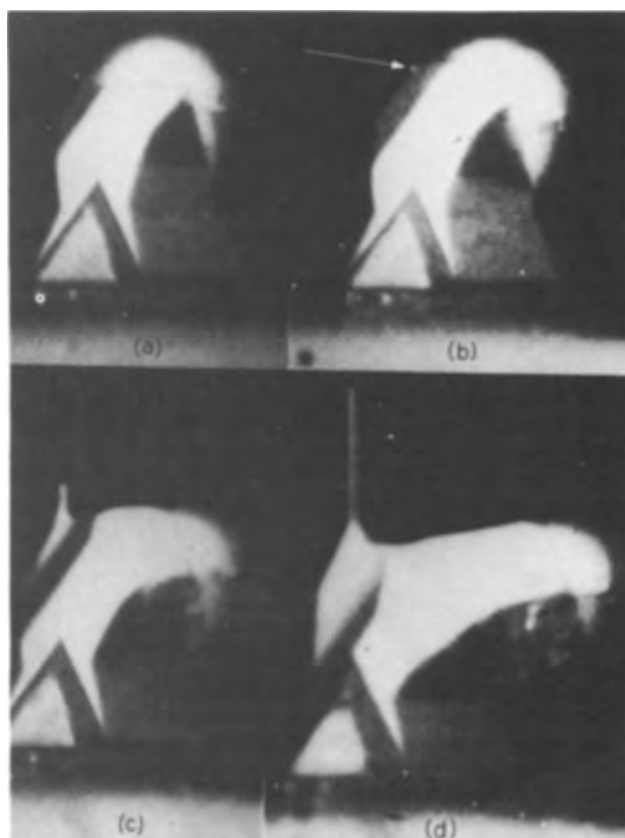


Fig. 8. Time-lapse sequence of branching and kinking caused by a lateral temperature gradient. Magnification approximately 120X.

external morphology can be seen at the base region of the small branch crystal by comparison of Fig. 8c and Fig. 8d. Some samples in which branching occurred during the kinking process were examined for perfection, both by x-ray topograph and etching. In most cases the branch and kink were found to be dislocation-free.

Generally, it is rather difficult to control the formation of a desired kink configuration under the influence of a lateral temperature gradient. Kinking can be initiated readily; however, there is little control over the shape of the liquid droplet during the transition process. The orientation of the growing crystal with respect to the isotherm is an important factor, as is evident from Fig. 3. The preferred orientation as indicated in the figure, is that in which only one plane, for example the  $(\bar{1}11)$  plane, is parallel to the isotherm. If the interface transition occurs by exposing two or even three new  $\{111\}$  planes, the droplet invariably ruptures and multiple kinking ("antler" growth) will result. A slow VLS growth rate and a small temperature gradient help to prevent a rapid interface transition which also can cause a rupture of the liquid droplet.

**Sudden increase in temperature.**—It has been shown (10) that the volume of the liquid droplet during VLS growth depends on the deposition temperature. This dependency arises from the liquidus phase relationship of the particular alloy system. This feature has been used to change the diameter of silicon crystals during VLS growth by proper changes of the deposition temperature. It has been noted that such changes must be made gradually in order to avoid instability of the liquid droplet. A sudden increase in temperature, for example, from  $1000^\circ$  to  $1100^\circ\text{C}$  in 10 sec, will usually cause instability. The volume of the droplet will increase by about 13% for such a temperature change. The amount of silicon which is required to satisfy the new phase equilibrium cannot be supplied rapidly enough from the vapor-phase reaction. As a result, the necessary amount will be dissolved from the VLS crystal. The SL interfacial area, however, remains that for the  $1000^\circ\text{C}$  growth condition. As a consequence, the liquid will bulge over the side of the crystal. It will eventually wet the side faces in order to increase the interfacial area and to satisfy a stable contact angle configuration. The individual droplets will cause formation of branch crystals or kinks as VLS growth continues. A typical example of this process is shown in the time-lapse sequence in Fig. 9. Two crystals were initially grown at  $1000^\circ\text{C}$ , then the temperature was rapidly raised to about  $1100^\circ\text{C}$ . Figure 9a shows the droplet configuration during the rise in temperature. The solid-liquid contact angle which is slightly larger than  $90^\circ$  under equilibrium conditions has noticeably increased. In Fig. 9b, taken at maximum temperature, the droplet has increased its contact area by wetting the side faces of the crystal. Subsequently, the temperature was reduced to about  $1000^\circ\text{C}$ . The next two photographs show the resulting growth morphology at different times. The liquid broke up into smaller droplets giving rise to branch growth. Numerous experiments of the kind described in Fig. 9 were performed. It was found that the only important factor is a sufficiently large, rapid increase in temperature. The temperature does not have to be returned to its starting value. A large decrease in temperature after the instability has occurred must be avoided because this may lead to nucleation of silicon crystals in the droplets, resulting in uncontrolled growth (10). The droplet configuration during the rise in temperature was observed visually in some experiments. This provides some control over the resulting droplet configuration. Figure 10 is an etched  $(0\bar{1}1)$  section of a crystal which was kinked by a controlled increase in temperature. Doping was used to

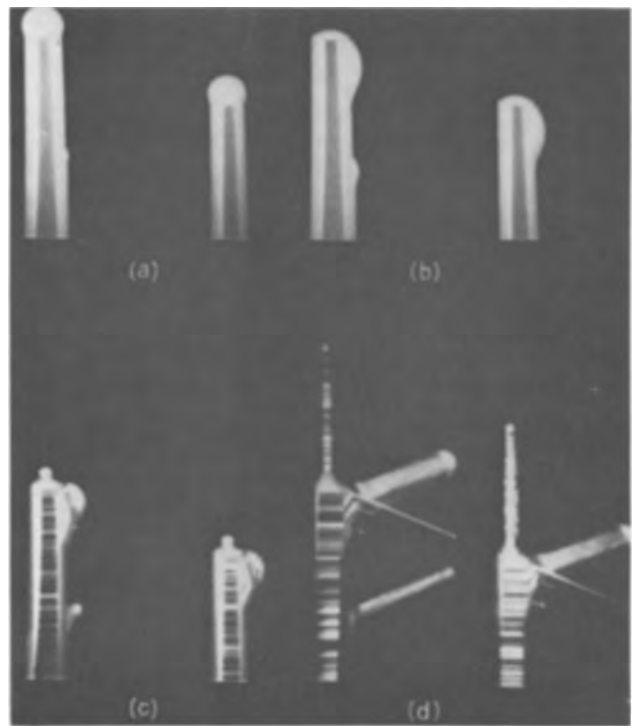


Fig. 9. Time-lapse sequence of kinking and branching caused by a sudden increase in temperature. Magnification approximately 13X.

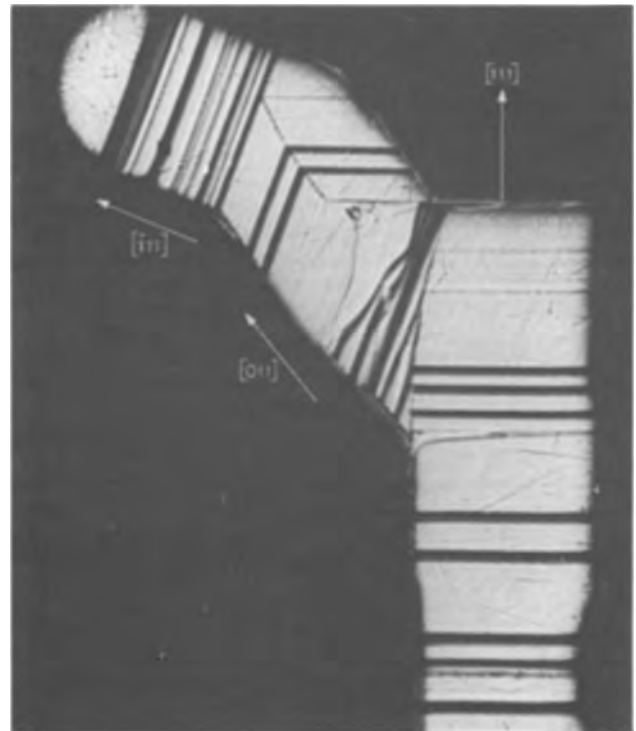


Fig. 10. Etched section of a silicon crystal kinked by a sudden increase in temperature, doped with phosphorus. Magnification approximately 100X.

mark the position of the SL interface during the growth experiment. Before raising the temperature, the droplet was on top of the  $[111]$  crystal which had grown under isothermal condition. The temperature was carefully increased until the droplet was clinging to the side of the crystal near its tip. The doping striations show that a new SL interface configuration was established. The crystal first grew in approximately a  $[011]$  direction and gradually changed to the stable

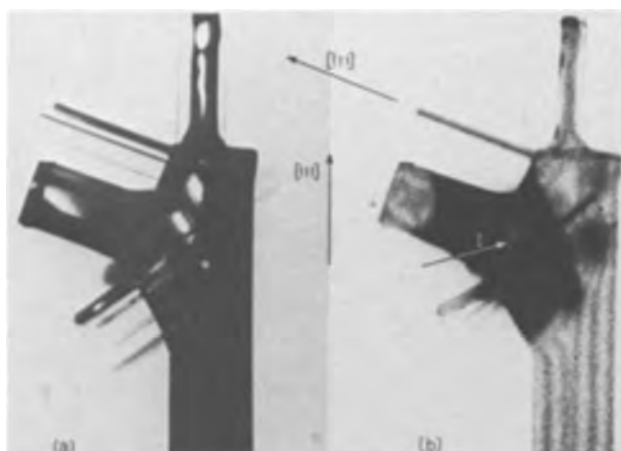


Fig. 11(a). Photograph of a branched crystal with alloy tips removed by etching. Fig. 11 (b). (111) X-ray topograph showing Au-Si entrapment. Magnification approximately 35X.

[111] direction. No dislocation etch pits could be found on this sample. Six crystals which branched or kinked by the discussed procedure were examined by x-ray topography. Entrapments of Au-Si alloy were found in four samples. Such a topograph and the actual sample are shown in Fig. 11. The hemispherical tips, composed of Au-Si alloy were removed from the crystals by etching. A significant aspect is that the crystallography of the branch and kink crystals is the same as that of the main crystal. Some of the fine crystals which can be seen on the actual sample could not be reproduced properly from the x-ray topograph. An island of Au-Si eutectic is indicated by an arrow. As usual, the inclusion gives rise to formation of defects (12).

**Sudden decrease in temperature.**—This mechanism is basically similar to the one discussed in the previous section. The volume of the liquid droplet decreases if the temperature is lowered during VLS growth. The excess of silicon freezes out of solution, by normal alloy regrowth, in order to establish the equilibrium composition. The solid-liquid contact angle, however, remains essentially constant during the change in temperature. This implies that a reduction in SL interfacial area is required to satisfy the same contact angle configuration. Therefore, a sudden decrease in temperature causes a sudden increase in growth rate because of alloy regrowth and a reduction of the diameter of the growing crystal. Small droplets frequently separate from the meniscus region of the droplet during the transition in volume. These droplets then give rise to formation of branches during subsequent VLS growth. The growth of branch crystals by this process is illustrated by the time-lapse sequence in Fig. 12. The crystal is shown in Fig. 12a during growth at about 1050°C. The temperature was subsequently decreased by 100°C in about 30 sec. Three small droplets were "pinched off" the main droplet during the transition, Fig. 12b. The last figure shows the crystal after continued VLS growth. The three branches grew in the same  $\langle 111 \rangle$  direction, although inclined to the [111] direction of the main crystal.

It has been found in many experiments that this process of branch formation can be initiated easily by a sudden drop in deposition temperature. However, there is little control over the number of branches formed. The change in temperature must be rapid enough to cause separation of small droplets from the main body of the liquid alloy. A gradual decrease in temperature only causes a reduction in diameter of the growing crystal. The deposition temperature can be gradually raised after completion of branching. However, a sudden large reduction in temperature must be avoided because this may result in nucleation of sil-

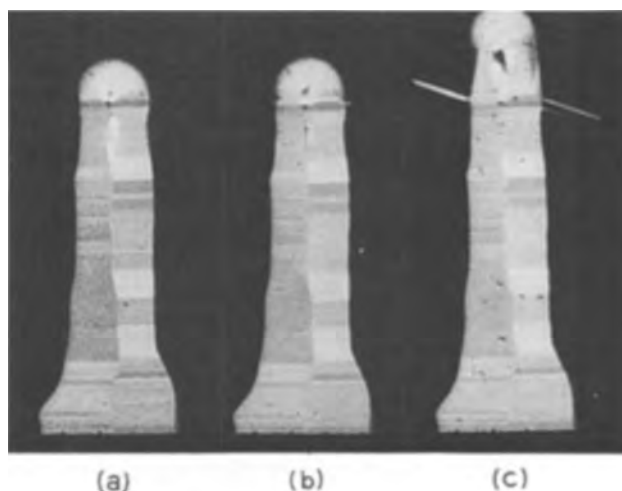


Fig. 12. Time-lapse sequence of branching caused by a sudden decrease in temperature. Magnification approximately 35X.

icon crystals in the liquid alloy. Such a large reduction may lead to uncontrolled VLS growth as shown in another paper (10).

The most common direction of the side branches is  $\langle 111 \rangle$ . The  $\langle 110 \rangle$  direction has been observed in a few cases. The diameters of the branches are usually small compared to the diameter of the main crystal. X-ray topography and etching studies indicate that the majority of the crystals are dislocation-free.

**Codeposition of liquid-forming impurities.**—The most likely process of branch and kink formation during vapor phase growth is due to codeposition of impurities. Impurities which satisfy the criteria for VLS growth may condense on an already grown whisker crystal. The transport can occur by a chemical reaction, for example, by disproportionation, or simply by an evaporation and condensation process. Such an impurity transport frequently has been observed during whisker growth of silicon or germanium using either a closed or a dynamic system. Each alloy droplet formed by this means may give rise to VLS growth of a branch crystal. The original crystal serves as substrate material. It should be emphasized that only extremely small amounts of impurities are required for this process. For example, a gold-silicon alloy droplet of about 100Å diameter can result in the growth of a silicon whisker a few millimeters long. The final morphology will be altered drastically in most cases because of VS deposition during and after VLS growth.

Many branched and kinked whisker crystals of silicon and of germanium were grown using codeposition of impurities. The experimental conditions for the growth of silicon whiskers have been described previously (2). Similar conditions were used for germanium (16). The formation of branch crystals is initiated by a sudden increase in supersaturation of liquid forming impurities in the growth zone, during or after completion of VLS growth. Numerous new alloy droplets will form and branch growth occurs. The resulting growth morphologies are similar to those in Fig. 3 and Fig. 8 in ref. (2). It is obvious that this process may not be used for controlled growth of branched and kinked crystals.

The mechanism discussed involving the codeposition of impurities probably is the most common cause of uncontrolled VLS growth. It should be noted that careful experimentation with codeposition of impurities originally lead to the discovery of the VLS mechanism (2).

### Summary

The growth direction of silicon crystals prepared by the VLS technique is determined by both the shape

of the solid-liquid interface and the contact angle configuration of the alloy droplet. Unidirectional growth can occur only if these two parameters are kept constant during growth. A necessary condition for unidirectional growth is therefore an isothermal environment. Most crystals grown under this condition grow with a single  $\{111\}$  interface in a  $\langle 111 \rangle$  direction. However, the macroscopic growth direction is not necessarily perpendicular to the growth interface. Specific interface configurations have been found where the interface consists of more than one  $\{111\}$  plane of equal area. These interfaces also form a stable contact angle configuration of the alloy droplet. The resulting growth direction is the vector sum of the individual interface growth directions.

A sufficiently large lateral temperature gradient changes the equilibrium interface, which invariably leads to a change in growth direction. A new stable interface will be formed during growth which is as parallel as possible to the isotherm. While a curved crystal is grown during the interface transition, subsequent growth is again unidirectional. Branches are formed if the alloy droplet ruptures during the kinking sequence. The likelihood of kinking for a given lateral gradient depends on the diameter of the growing crystal. It is the absolute temperature difference across the interface that causes interface transition.

Either a sudden increase or decrease in deposition temperature may introduce instability of the alloy droplet. A sudden rise in temperature causes an unstable contact angle configuration. The droplet may wet the side faces of the crystal to increase the interfacial area. The new droplet configuration results in formation of branches and or kinks. Similarly, a sudden decrease in temperature may cause pinching off of small droplets from the main droplet. These two processes of branching and kinking are more or less independent of the diameter of the growing crystal.

The most common cause of uncontrolled VLS growth of silicon or germanium was found to be the result of codeposition of liquid-forming impurities. The impurities can be transported to the reaction zone by a chemical reaction or by evaporation. Branches are formed when liquid-forming impurities condense on an already grown whisker crystal.

This investigation modifies the usual definition of a branch or kink. The terminology is unambiguous for a single kink, where the liquid droplet did not rupture during the interface transition. It is suggested

that the growth direction which is associated with the main body of the liquid be used as the criterion. If this direction changes during growth, then the crystal is kinked. This is true even if small branch crystals continue to grow in the original growth direction. If the main growth direction remains constant, then any side crystal formed by small droplets is defined as a branch.

In conclusion it is emphasized that the proposed mechanism of unidirectional growth, branching, and kinking is strictly applicable only to whisker crystals grown by the VLS process.

#### Acknowledgments

The authors are grateful to W. G. Pfann, Professor N. Kato, and S. M. Arnold for many helpful contributions.

Manuscript received July 18, 1967; revised manuscript received Oct. 4, 1967.

Any discussion of this paper will appear in a Discussion Section to be published in the December 1968 JOURNAL.

#### REFERENCES

1. R. G. Treuting and S. M. Arnold, *Acta Met.*, **5**, 598 (1957).
2. R. S. Wagner, W. C. Ellis, K. A. Jackson, and S. M. Arnold, *J. Appl. Phys.*, **35**, 2993 (1964).
3. W. W. Webb, *ibid.*, **36**, 214 (1965).
4. J. P. Hirth and F. C. Frank, *Phil. Mag.*, **3**, 1110 (1958).
5. S. Amelinckx, *ibid.*, **3**, 425 (1958).
6. F. R. N. Nabarro and P. J. Jackson, "Growth and Perfection of Crystals," p. 81, John Wiley & Sons, Inc., New York (1958).
7. S. Amelinckx, *ibid.*, p. 144.
8. R. S. Wagner and W. C. Ellis, *Appl. Phys. Letters*, **4**, 89 (1964).
9. R. S. Wagner and W. C. Ellis, *Trans. Met. Soc. AIME*, **233**, 1053 (1965).
10. R. S. Wagner and C. J. Doherty, *This Journal*, **113**, 1300 (1966).
11. R. S. Wagner, "Crystal Growth," p. 347, Pergamon Press, Oxford and New York (1967).
12. R. S. Wagner, *J. Appl. Phys.*, **38**, 1554 (1967).
13. R. S. Wagner, C. J. Doherty, and S. M. Arnold, *J. Metals*, **17**, 1031 (1965).
14. E. Sirtl and A. Adler, *Z. Metallk.*, **52**, 529 (1961).
15. A. R. Lang, *J. Appl. Phys.*, **29**, 597 (1958); **30**, 1748 (1959).
16. R. S. Wagner, Unpublished work.

## Diffusion Masking of Silicon Nitride and Silicon Oxynitride Films on Si

F. K. Heumann\* and D. M. Brown

General Electric Research and Development Center, Schenectady, New York

and E. Mets\*

General Electric Semiconductor Products Department, Auburn, New York

#### ABSTRACT

A qualitative study of the masking properties of thin ( $\leq 1500\text{\AA}$ ) silicon nitride and silicon oxynitride films on Si is presented. A range of diffusion conditions was studied for doping sources including B, P, Ga, and As. Silicon nitride was not found to be a diffusion mask for all conditions. Conditions under which it can be expected to mask are specified.

The work of Hu (1) and Doo (2) on the diffusion masking of silicon nitride films on Si showed that very thin layers ( $\leq 1200\text{\AA}$ ) of nitride would mask against B, P, As, and Ga, and might even be utilized as a

\* Electrochemical Society Active Member.

universal diffusion mask, since no masking failures were encountered in their shallow junction diffusion studies. The studies reported here using B, P, As, and Ga diffusion sources were carried out over a wide range of conditions, and although the results do in-

deed indicate that thin ( $\leq 1500\text{\AA}$ ) nitride and oxynitride films will mask for a certain set of diffusion conditions, it becomes clear that silicon nitride cannot be utilized as a universal diffusion mask. Various types of masking failures occur for temperatures and times required for deep junction diffusions.

### Experimental Techniques

Chemically etched 1 ohm-cm Si wafers were coated with nitride or oxynitride films by the pyrolysis of silane and ammonia or silane, ammonia, and nitric oxide at  $1000^\circ\text{C}$ . The volumetric gas ratios used to form these films were: ammonia/silane = 40,000/1 for nitride films and ammonia/silane/nitric oxide = 40,000/1/500 for oxynitride films. No carrier gases were used in either case. Studies of these particular glassy amorphous oxynitride films indicate an equivalent  $\text{SiO}_2$  composition of about 20% (3). The thickness of these films was varied between about 200 and  $2000\text{\AA}$  with a thickness variation over the inner  $3/4$  area of each 2.5 cm diameter wafer of only  $\pm 3\%$ . In some cases, the diffusion studies were carried out using two types of dopant sources: a semisealed quartz box diffusion using dry  $\text{N}_2$  ambient and a glass source containing the dopant element to be studied (phosphosilicate glass or borosilicate glass) and a sealed tube or capsule containing the dopant material (As, P, Ga, B) which after loading, was degassed, evacuated, and back-filled with argon. The results were determined by the following procedure: the nitride film was removed using HF and a thermoelectric probe and surface resistivity measurements were used to indicate whether there was any detectable masking failure, and masked and unmasked portions of the wafer were angle lapped and stained to give junction penetration depths into the Si.

### Results

A general summary of the results of the diffusion experiments using films of  $2000\text{\AA}$  or less are shown in Table I. In some cases, dry thermal oxides were used as control samples. In these instances no masking was evident. It must be pointed out, however, that the masking ability of oxides (and nitrides) are

extremely dependent on the chemical nature of the diffusion conditions. For instance, Thomas *et al.* (4) have shown that very thin oxide films are excellent diffusion masks against B diffusion if the diffusions are carried out under nonglass-forming conditions.

**Boron.**—Amorphous silicon nitride films of thicknesses greater than  $600\text{\AA}$  are excellent masks for temperatures up to  $1250^\circ\text{C}$  for at least 10 hr if the sealed tube system is used. In these cases, the films after diffusion etched at the normal rate of  $150\text{\AA}/\text{min}$  in concentrated 48% HF; however,  $1200^\circ\text{C}$  diffusions for 30 hr resulted in films that would not dissolve in HF even though the films still masked against boron. X-ray diffraction indicated that the films were still amorphous so the original films had not yet converted to the more dense crystalline form. This phenomenon is not understood; perhaps an insoluble B-Si-N compound was formed. Silicon oxynitride films also appear to be suitable B diffusion masks; however, the thickness required for masking is somewhat greater than that for pure nitride. For instance,  $500\text{\AA}$  of oxynitride is not thick enough to mask boron for 4 hr at  $1100^\circ\text{C}$ ;  $1000\text{\AA}$  suffices, however.

In the case of the borosilicate glass box system, it was found that at  $1100^\circ\text{C}$  nitride films of  $500\text{\AA}$  or more mask for at least 5 hr and dissolved at the normal etch rate. However, at  $1200^\circ\text{C}$ , the films failed as diffusion masks and dissolved at about 40 times the normal etch rate. This phenomenon is also not understood, but it suggests that borosilicate-nitride glass can be formed under certain diffusion conditions.

**Phosphorus.**—The results in Table I show that a  $1500\text{\AA}$  thick film of pyrolytic silicon nitride will mask against elemental phosphorus during a sealed tube diffusion at  $1100^\circ\text{C}$  for times up to 10 hr. For 4 hr at  $1200^\circ\text{C}$ ,  $1500\text{\AA}$  is apparently not thick enough, however. Experiments with these particular silicon oxynitride films indicate that  $1500\text{\AA}$  will mask phosphorus for 4 hr at  $1100^\circ\text{C}$ ; thinner films do not mask.

Silicon nitride films do not mask, however, when used in box diffusions where the source is vitrified phosphorous glass. In this case, the films become coated with phosphorus pentoxide or a phosphorous glass during the diffusion experiments and apparently rapidly convert to some kind of  $\text{Si}_3\text{N}_4\text{-P}_2\text{O}_5$  glass as

Table I.  $\text{Si}_x\text{O}_y\text{N}_z$  diffusion masking

Dopant	Diffusion system	Type of film	Thickness (Å)	Temp ( $^\circ\text{C}$ )	Time (hr)	Masked	Masked junct. depth, $\mu^*$	Unmasked junct. depth, $\mu$	Comments
B	Sealed Tube	$\text{SiO}_2$	2000	1100	4	No	6	6	Oxide control
B	Sealed Tube	$\text{Si}_3\text{N}_4$	$\geq 300$	1100	4	Yes	—	6	
B	Sealed Tube	$\text{Si}_3\text{N}_4$	$\geq 400$	1200	20	Yes	—	25	
B	Sealed Tube	$\text{Si}_3\text{N}_4$	$\geq 500$	1200	30	Yes	—	25	Film conversion
B	Sealed Tube	$\text{Si}_3\text{N}_4$	1000	1250	10	Yes	—	30	
B	Sealed Tube	$\text{Si}_3\text{N}_4$	$\leq 600$	1250	10	No	Spikes	30	Spiking failure
B	Sealed Tube	$\text{Si}_x\text{O}_y\text{N}_z$	500	1100	4	No	6	6	
B	Sealed Tube	$\text{Si}_x\text{O}_y\text{N}_z$	1000	1100	4	Yes	—	6	
B	Box	$\text{Si}_3\text{N}_4$	500-1500	1100	5	Yes	—	4	
B	Box	$\text{Si}_3\text{N}_4$	1500	1200	5	No	—	—	Film conversion
P	Sealed Tube	$\text{Si}_3\text{N}_4$	$\geq 1500$	1100	3	Yes	—	—	
P	Sealed Tube	$\text{Si}_3\text{N}_4$	$\geq 1000$	1100	3	No	—	—	
P	Sealed Tube	$\text{Si}_3\text{N}_4$	$\geq 1500$	1100	5	Yes	—	5	
P	Sealed Tube	$\text{Si}_3\text{N}_4$	$\geq 1500$	1100	10	Yes	—	9	
P	Sealed Tube	$\text{Si}_3\text{N}_4$	$\geq 1100$	1100	10	No	—	9	
P	Sealed Tube	$\text{Si}_3\text{N}_4$	1500	1200	4	No	3	12	
P	Sealed Tube	$\text{Si}_x\text{O}_y\text{N}_z$	$\geq 1500$	1100	4	Yes	—	5	
P	Box	$\text{Si}_3\text{N}_4$	1000	1100	1	No	—	6	Film conversion
Ga	Sealed Tube	$\text{SiO}_2$	2000	1100	4	No	6+	6	Oxide control
Ga	Sealed Tube	$\text{Si}_3\text{N}_4$	1000	1100	4	Yes	—	6	
Ga	Sealed Tube	$\text{Si}_x\text{O}_y\text{N}_z$	$\leq 1000$	1100	4	No	3.4	6	
Ga	Sealed Tube	$\text{Si}_x\text{O}_y\text{N}_z$	1500	1100	4	Yes	—	6	
Ga	Sealed Tube	$\text{Si}_3\text{N}_4$	300	1185	15	No	10	18	
Ga	Sealed Tube	$\text{Si}_3\text{N}_4$	1200	1185	15	Yes	Spikes	—	Localized spiking
Ga	Sealed Tube	$\text{Si}_3\text{N}_4$	1500	1200	4	Yes	Spikes	14	Localized spiking
As	Sealed Tube	$\text{Si}_3\text{N}_4$	1500	1100	4	Yes	—	0.6	
As	Sealed Tube	$\text{Si}_x\text{O}_y\text{N}_z$	1500	1100	4	Yes	—	0.6	
As	Sealed Tube	$\text{Si}_3\text{N}_4$	1000	1150	6	Yes	—	1.8	
As	Sealed Tube	$\text{Si}_3\text{N}_4$	1500	1150	6	Yes	Spikes	1.8	Films cracked
As	Sealed Tube	$\text{Si}_x\text{O}_y\text{N}_z$	$\geq 1000$	1150	6	Yes	Spikes	1.8	Films cracked
As	Sealed Tube	$\text{Si}_3\text{N}_4$	1500	1200	20	No	6	11	

\* Where mask failure is noted but no masked junction depth is given, masking failure was determined by using a thermoelectric probe.

evidenced by the very rapid etch rate in concentrated HF. The results of a number of box diffusions indicate that  $P_2O_5$  or  $P_2O_3$  glass cannot be used as a diffusion source when thin  $Si_3N_4$  films are used because of the formation of a glass which promotes mask failure. Similar results have been observed by Chu *et al.* (5) using a phosphorus oxytrichloride source.

**Gallium.**—2000Å of thermally grown  $SiO_2$  does not mask Ga. However, 1000Å of  $Si_3N_4$  completely masks Ga at 1100°C for 4 hr. This is also true of the silicon oxynitride film if it is 1500Å thick. The masking ability of the nitride is questionable above 1100°C. For instance, 300Å is not a satisfactory barrier at 1185°C for 15 hr; and as the thickness of the film is increased, cracking of the film occurs at these times and temperatures. Evidence for this problem are the diffusion spikes which occur at localized spots under the film. In one case, the film did not completely etch off in concentrated HF even after many hours. In this instance, a number of rod-shaped purple crystals were observed and identified as  $\alpha-Si_3N_4$ . Apparently the amorphous nitride was partially converted to the more dense crystalline form by the high temperature. This conversion may be catalyzed by gallium. Thus, we see that  $Si_3N_4$  and silicon oxynitride can mask against Ga if the diffusion temperatures are not too high. However, at high temperatures, diffusion spikes appear which are probably caused by the cracking that occurs when the nitride films transform into the crystalline phase; thinner films do not crack, but do not mask either.

**Arsenic.**—As shown in Table I, 1500Å of silicon nitride and oxynitride mask at 1100°C for 4 hr; however, the diffusion depth into the unmasked Si is only 0.6 $\mu$ . On the other hand, sealed tube diffusions at 1200°C for 20 hr showed that 1500Å of  $Si_3N_4$  is not thick enough. Experiments at 1150°C showed that 1000Å masks for 6 hr; however, thicker films or oxynitride films cracked and allowed the As to penetrate these imperfections. When cracking occurred, it also crazed the Si surface.

### Summary

A range of diffusion conditions using thin silicon nitride and silicon oxynitride films as a diffusion barrier against B, P, Ga, and As indicates that thin layers of nitrides are suitable diffusion masks for B if sealed tube diffusions are performed. For example, 1000Å of pure nitride will mask for at least 10 hr at 1250°C. In fact, no masking failure was ever found for these sealed tube diffusions if the film thickness

was at least 1000Å. However, high temperatures and borosilicate glass sources can result in masking failure which may be caused by a film conversion to a borosilicate-nitride glass phase. This behavior is also generally true for phosphorus diffusions; however, in addition, masking failures at high temperatures in the elemental phosphorus sealed tube diffusions did occur. High temperature masking failure for thin films also occurs for sealed tube As diffusions. In the case of Ga, nitrides are much better diffusion masks than oxides, which do not deter this diffusant species at all. However, here again the nitride has a limited application. Although it masks at low diffusion temperatures, high temperature Ga diffusion experiments seem to indicate that the films of thicknesses required for complete masking crack as they change from an amorphous to crystalline phase.

Generally speaking, thin nitride and oxynitride films (thicknesses  $\leq 1500$ Å) can be used as diffusion masks for the times and temperatures suitable for shallow ( $\leq 9\mu$ ) junctions if the proper diffusant sources are used. In these instances, our results generally agree with those of Hu and Doo. Thin film nitride masking and much deeper Si junction depths (30 $\mu$ ) can be attained by using higher temperatures if boron is the diffusant and a sealed tube system is used. Masking of P, As, and Ga and deeper junctions might be obtained by using much thicker films and longer diffusion times, provided of course that the diffusion conditions are such that no catastrophic masking failure (film conversion, cracking) occurs.

### Acknowledgments

We wish to thank Gerry Gidley for the many sample preparations required for this study.

Manuscript received July 21, 1967; revised manuscript received Sept. 8, 1967.

Any discussion of this paper will appear in a Discussion Section to be published in the December 1968 JOURNAL.

### REFERENCES

1. S. M. Hu, *This Journal*, **113**, 693 (1966).
2. V. Y. Doo, *IEEE Trans. on Electron Devices*, **13**, 561 (1966).
3. D. M. Brown, P. V. Gray, F. K. Heumann, H. R. Philipp, and E. A. Taft, *This Journal*, To be published.
4. R. C. Thomas, J. W. Sprague, and E. L. Marcy, Paper presented at the Dallas Meeting of the Society, May 7-12, 1967, Abstract 93.
5. T. L. Chu, C. H. Lee, and G. A. Gruber, *This Journal*, **114**, 717 (1967).

## Technical Notes



### Silicon Oxide As An Etching Mask for Silicon Nitride

N. C. Tombs<sup>1</sup> and F. A. Sewell, Jr.

Sperry Rand Research Center, Sudbury, Massachusetts

The use of silicon nitride (1, 2) as a diffusion mask and passivation layer in semiconductor devices involves the etching of defined areas in the nitride. The relatively low etch rate of silicon nitride, compared with silicon oxide, can lead to problems in the securing of

adequate definitions and steep etching angles when using conventional photoresist techniques with hydrofluoric acid etches. Van Gelder and Hauser (3, 4) have described the use of hot phosphoric acid ( $H_3PO_4$ ) as an etch for silicon nitride, in conjunction with a pyrolytically deposited layer of silicon oxide as a mask against the phosphoric acid. Patterns were etched in

<sup>1</sup> Present address: NASA, Electronics Research Center, Cambridge, Massachusetts.

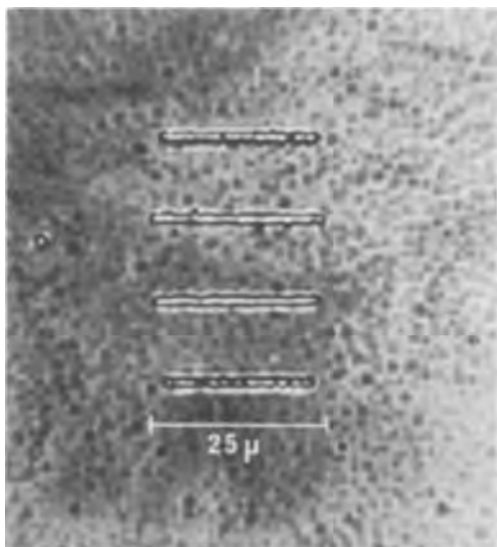


Fig. 1. Test pattern etched through 1500Å thick silicon nitride film using phosphoric acid with silicon oxide mask.

the silicon oxide overlayer using photoresist and hydrofluoric acid etch.

We have successfully utilized an analogous technique, in which the layer of silicon oxide was formed by thermal oxidation of the surface of the silicon nitride. The silicon nitride layer was pyrolytically deposited on a 10-mil silicon substrate to a thickness of 2500Å. The sample was then heated for 8 hr at 1200°C in oxygen. A surface layer of silicon oxide was thereby formed. Infrared absorption measurements revealed the presence of this oxide by an absorption maximum at  $9.2\mu$ . The height of the nitride absorption maximum at  $\sim 11\mu$  was correspondingly decreased, although its wavelength remained unchanged. A test pattern was etched in the oxide layer using the photoresist-buffered HF method. The phosphoric acid etch was prepared by heating 85%  $H_3PO_4$  to 190°C in an open beaker for 2 hr and cooling to 180°-185°C. The sample was immersed in the etch for 10-min periods. After each period it was removed, washed in water, and observed

under the microscope. The interference colors given by the window (nitride) and mask (nitride plus oxide) regions at the different stages are shown below, together with the approximate thickness indicated by the colors. The nitride:oxide etch rate ratio was  $\sim 5:1$ .

Etch time min	Nitride color	(Nitride + Oxide) Å	color	Å
0	gold	2000	violet	2500
10	dark blue	1000	orange-red	2300
20	colorless	<400	orange	2100
30	colorless	0	blue	1500

A test pattern including lines of width  $1\mu$  was used to determine the possibility of etching windows of this width in the nitride. Figure 1 is a photomicrograph of the result obtained in a final nitride thickness of  $\sim 1500\text{Å}$ . Measurements of the width of the windows were made using a filar eyepiece with movable cross-hair, calibrated against a stage micrometer. The results confirmed that the width was close to  $1\mu$ , although the resolution limits make it difficult to give a precise figure. The ultimate limitation in the technique would appear to be the photoresist stage for defining and etching the pattern in the oxide. Advantage can be taken of the fact that the oxide layer ( $\sim 500\text{Å}$ ) is much thinner than the layers normally required for diffusion masking and surface passivation. The photoresist layer likewise can be made thinner, and the pattern definition is thereby improved.

Practical advantages of the technique described include the excellent adherence between the oxide and nitride layers, and the avoidance of porosity or other imperfections in the oxide which might interfere with its effectiveness as an etching mask.

Manuscript received Sept. 25, 1967.

Any discussion of this paper will appear in a Discussion Section to be published in the December 1968 JOURNAL.

#### REFERENCES

1. V. Y. Doo, D. R. Nichols, and C. A. Silvey, *This Journal*, **113**, 1279 (1966).
2. J. J. Comer and N. C. Tombs, Paper presented at the Philadelphia Meeting of the Society, Oct. 9-14, 1966, as Abstract 153.
3. W. Van Gelder and V. E. Hauser, *This Journal*, **113**, 315C (1966).
4. W. Van Gelder and V. E. Hauser, *ibid.*, **114**, 869 (1967).

## Defect Structure Model for Wustite

Per Kofstad and A. Zeev Hed

*Metal Science Group, Columbus Laboratories, Battelle Memorial Institute, Columbus, Ohio*

Wustite is a metal-deficient oxide ( $Fe_{1-y}O$ ) (1-9). Its defect structure is commonly interpreted in terms of doubly charged iron ion vacancies (5-9). However, as discussed below such a defect structure model does not give a satisfactory interpretation of the observed behavior, and the purpose of this note is to propose a defect structure model which gives a more consistent interpretation of the experimental results.

The nonstoichiometry as a function of temperature and oxygen pressure has been studied by several investigators (1-4), and the results of the various studies are in good agreement. The results of Vallet and Raccah (3) at 800°-1200°C are shown in Fig. 1.

When assuming small defect concentrations, a defect structure model involving doubly charged iron ion vacancies predicts an oxygen pressure dependence of  $y \propto p_{O_2}^{1/n}$  with  $n = 6$ . As seen in Fig. 1 such a relationship only accounts for the oxygen pressure dependence in the middle of the field, but does not explain the observed behavior over the whole homo-

geneity range. In view of the high defect concentrations in wustite, it would be highly surprising if such a model were applicable; one would rather expect that the activities of all atoms and sites involved in the defect reaction would have to be taken into account.

The assumption of divalent vacancies in wustite also seems doubtful in terms of charge carrier concentrations and their distribution on the iron lattice sites. A neutral iron vacancy consists of a vacant iron site associated with two nearest-neighbor atoms with trapped electron holes (trivalent iron atoms). The ionization of the vacancy essentially represents the transfer of the electron holes away from the neighborhood of the vacant site. When considering that each iron atom on a normal (octahedral) lattice site in  $Fe_{1-y}O$  is surrounded by 12 nearest neighbor iron atoms, it follows that the structure can only contain about 4% of doubly ionized iron vacancies (8%  $Fe^{3+}$  ions on octahedral sites). At higher defect concentrations ( $y > 0.04$ ), the divalent vacancies will have



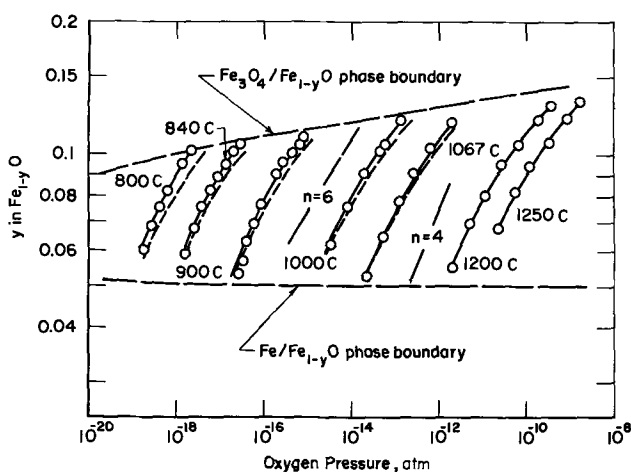


Fig. 1. Nonstoichiometry in wustite,  $y$  in  $\text{Fe}_{1-y}\text{O}$ , as a function of temperature and partial pressure of oxygen ( $y \propto p_{\text{O}_2}^{1/n}$ ). Experimental results after Vallet and Raccach (3). Broken lines show calculated values for  $y$  if only singly charged complex defects are considered, while solid lines show calculated values when taking into account both singly charged and neutral defects.

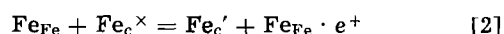
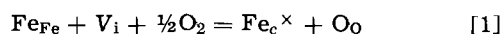
$\text{Fe}^{3+}$  ions on neighboring sites, and as such they really represent singly charged vacancies.

Neutron diffraction studies have suggested that for each vacancy which is formed in  $\text{Fe}_{1-y}\text{O}$ , an equal number of iron Frenkel defect pairs are formed in the metal lattice (9). Each defect may on this basis be considered as a complex defect consisting of two iron vacancies associated with an interstitial atom (9). Such a complex defect also results in the same local structure configuration as found in  $\text{Fe}_3\text{O}_4$ .

It is also noteworthy that the heat of formation of the defects in  $\text{Fe}_{1-y}\text{O}$  is negative, *i.e.*, the deviation from stoichiometry at a given oxygen pressure increases with decreasing temperature. In oxides with single, unassociated vacancies the heat of formation is commonly positive (10), and the negative value found for  $\text{Fe}_{1-y}\text{O}$  thus serves as a further indication that defects in this oxide are complex. In  $\text{UO}_{2+x}$ , which also contains complex oxygen defects, the heat of formation of the defects is also negative (11).

From these considerations we conclude that it is highly unlikely that the defects are doubly charged iron ion vacancies. From the available data it seems reasonable to assume that the predominating defects consist of the complex species, *i.e.*, two iron ion vacancies associated with an interstitial iron ion ( $\text{V}_{\text{Fe}}\text{Fe}_i\text{V}_{\text{Fe}}$ ). Proceeding on this basis, we have considered several possible defect structure models, *e.g.*, simultaneous presence of simple vacancies and complex defects, ordering and association of defects, complex defects only, etc., in order to explain the data. In all these alternative models activities or concentrations of all atoms and sites were considered. The model which to us was the most consistent and simple in principle and which gave the best description of the observed behavior is given in the following.

It is assumed that the complex defects, ( $\text{V}_{\text{Fe}}\text{Fe}_i\text{V}_{\text{Fe}}$ ) =  $\text{Fe}_c$ , may be neutral or singly charged. In writing the equations for the formation of these defects, one may write the equations for the formation of a single vacancy and a Frenkel defect pair followed by strong association between these defects. If the association is strong, as is assumed in this case, it is in terms of the law of mass action simpler to consider the complex defect as a unit, and the formation of these complex defects may then be written (13)



$\text{Fe}_c^\times$  and  $\text{Fe}_c'$  are neutral and singly ionized complex

defects, respectively;  $\text{V}_i$  represents an interstitial (tetrahedral) site available for occupancy by the complex defect,  $\text{Fe}_{\text{Fe}}$  is a divalent Fe atom on a normal (octahedral) site,  $\text{Fe}_{\text{Fe}} \cdot e^+$  atom is a Fe atom on an octahedral site with one trapped electron hole (a trivalent iron ion), and  $\text{O}_o$  is an oxygen atom on an oxygen lattice site.

In terms of the law of mass action Eq. [1] and [2] may be written

$$[\text{Fe}_c^\times][\text{O}_o] = K_1[\text{V}_i][\text{Fe}_{\text{Fe}}]p_{\text{O}_2}^{1/2} \quad [3]$$

$$[\text{Fe}_c'][\text{Fe}_{\text{Fe}} \cdot e^+] = K_i[\text{Fe}_c^\times][\text{Fe}_{\text{Fe}}] \\ = K_iK_1[\text{V}_i][\text{Fe}_{\text{Fe}}]^2[\text{O}_o]^{-1}p_{\text{O}_2}^{1/2} \quad [4]$$

where  $K_1$  is the equilibrium constant for the formation of neutral complex species, and  $K_i$  is the equilibrium constant for the first ionization. In terms of single defects,  $K_1$  is a combined value for the formation of the single defects and their association. The electroneutrality conditions require that

$$[\text{Fe}_{\text{Fe}} \cdot e^+] = [\text{Fe}_c'] \quad [5]$$

Expressing the concentrations of the defects in molar fractions,  $y$  is given by

$$y = [\text{Fe}_c^\times] + [\text{Fe}_c'] \quad [6]$$

As oxygen defects are considered to be negligible,  $[\text{O}_o] = 1$ . However, at the high defect concentrations in  $\text{Fe}_{1-y}\text{O}$  activities (or corrections for nonstoichiometry and interactions of defects) for  $[\text{Fe}_{\text{Fe}}]$  and  $[\text{V}_i]$  have to be considered. In this respect,  $[\text{Fe}_{\text{Fe}}]$  is not equal to unity, but part of  $\text{Fe}_{\text{Fe}}$  sites are occupied by electron holes ( $\text{Fe}^{+3}$ -ions on octahedral sites) and part of the  $\text{Fe}_{\text{Fe}}$ -sites are unoccupied due to the formation of the complex defects. When making these corrections, the concentration or activity of  $\text{Fe}_{\text{Fe}}$ -atoms available for the defect formation is given by

$$[\text{Fe}_{\text{Fe}}] = 1 - [\text{Fe}_{\text{Fe}} \cdot e^+] - 2([\text{Fe}_c^\times] + [\text{Fe}_c']) \quad [7]$$

In considering the activity of  $[\text{V}_i]$  a correction must be made for the fact that part of the sites are occupied by the complex defects. In addition, we also propose a correction for defect interaction and suggest that once a tetrahedral site is occupied by a defect, some neighboring sites are blocked for occupancy by additional defects (9). Specifically we propose that each occupied tetrahedral site blocks the six nearest-neighbor tetrahedral sites. The number of tetrahedral interstitial sites is twice that of the octahedral (normal  $\text{Fe}_{\text{Fe}}$ ) sites, and on this basis  $[\text{V}_i]$  is given by

$$[\text{V}_i] = 2 - ([\text{Fe}_c^\times] + [\text{Fe}_c']) \\ - 6([\text{Fe}_c^\times] + [\text{Fe}_c']) = 2 - 7y \quad [8]$$

This proposed blocking mechanism accounts for the marked decrease in the oxygen pressure dependence of  $y$  as the  $\text{FeO}/\text{Fe}_3\text{O}_4$  phase boundary is approached.

By combining Eq. [3]-[8], the value of  $y$  may be expressed as a function of  $p_{\text{O}_2}$  but for the sake of brevity the complicated relationship is not given. The internal consistency of the model is illustrated in Fig. 1, where the solid lines represent calculated values of  $y$  by simultaneous solution of Eq. [3]-[8] for values of the equilibrium constants

$$K_iK_1 = 1.45 \times 10^{-6} \exp(+64,000/RT) \quad [9]$$

$$K_1 = 1.9 \times 10^{-10} \exp(+81,500/RT) \quad [10]$$

$$K_i = 7.65 \times 10^{-4} \exp(-17,500/RT) \quad [11]$$

The stippled lines represent values when only singly charged defects are considered, and the model thus suggests that the neutral defects become increasingly important the lower the temperature. The model suggests an ionization energy of 17.5 kcal/mole or 0.75 eV for the neutral complex defect.

Additional ordering or association of the complex defects is not considered in the model. This may take place, particularly as one approaches the temperature (570°C) at which  $\text{Fe}_{1-y}\text{O}$  becomes unstable or in specimens which are quenched below the decomposi-

tion temperature. However, in terms of the model such additional association is suggested to be of secondary importance in considerations of over-all defect concentrations above 800°C. Only two different states (neutral and singly charged) of the defect are considered, and this does not seem unlikely in view of the fact that the defect concentration only changes by a factor of 3 (from 5 to 15%) when going from the Fe/FeO to the FeO/Fe<sub>3</sub>O<sub>4</sub> phase boundaries.

The electrical conductivity of Fe<sub>1-y</sub>O exhibits the same general oxygen pressure dependence as that for *y* at high temperatures (7, 8). This is also to be expected in terms of the proposed model at temperatures where the singly charged defects predominate. However, under conditions where the neutral vacancies affect the values of *y*, the oxygen pressure dependence of the electrical conductivity ( $\sigma \propto p_{O_2}^{1/n}$ ), should yield somewhat larger values of *n* than that for the deviation from stoichiometry. At the high defect concentrations in Fe<sub>1-y</sub>O the mobility of the charge carriers may also be a function of the defect concentration. In addition, there is evidence that grain boundaries affect the semiconducting properties, as polycrystalline Fe<sub>1-y</sub>O exhibits n-conductivity at the highest defect concentrations, while single crystal oxide remains p-conducting under the same conditions (8).

Kleman (14) has interpreted the results of Vallet and Raccach (Fig. 1) in terms of three separate "phases" within the Fe<sub>1-y</sub>O domain, but no interpretation is given in terms of the defect structure. Carel *et al.*, have later briefly described dilatometric (15) and x-ray diffraction (16) studies on Fe<sub>1-y</sub>O, the results of which are interpreted as a confirmation of the existence of these three phases. The transformations from one phase to another are proposed to reflect second order transitions (15), but no attempt is made to give physical interpretations of the transitions. The possible existence of these three phases reflecting minor changes in the properties is not necessarily at variance with the proposed model. If the transitions are of the second order, this implies that there is no latent heat involved and this, in turn, means that the transitions do not significantly affect thermodynamic properties such as the partial molar heat of dissocia-

tion of oxygen (7) or the heat of formation of the defects. As such the proposed phases are of but minor importance in consideration of the over-all equilibrium defect concentrations and have not at this stage been considered in the above model.

#### Acknowledgment

One of the authors (P. Kofstad) is indebted to the Battelle Memorial Institute for a Battelle Institute Fellowship in the Metal Science Group, Columbus Laboratories, where this work was carried out.

Manuscript received May 17, 1967; revised manuscript received Oct. 8, 1967.

Any discussion of this paper will appear in a Discussion Section to be published in the December 1968 JOURNAL.

#### REFERENCES

1. L. S. Darken and R. W. Gurry, *J. Am. Chem. Soc.*, **68**, 798 (1946).
2. L. Himmel, R. F. Mehl, and C. E. Birchenall, *Trans. AIME*, **197**, 822 (1953).
3. P. Vallet and P. Raccach, *Mem. Sci. Rev. Met.*, **62**, 1 (1965).
4. N. A. Hovgard and P. N. Jensfelt, *Jernkontorets Ann.*, **140**, 467 (1956).
5. K. Hauffe and H. Pfeiffer, *Z. Metallk.*, **44**, 27 (1953).
6. D. M. Smyth, *J. Phys. Chem. Solids*, **19**, 167 (1961).
7. G. H. Geiger, R. L. Levin, and J. B. Wagner, Jr., *J. Phys. Chem. Solids*, **27**, 947 (1966).
8. I. Bransky and D. S. Tannhauser, *Trans. AIME*, **239**, 75 (1967).
9. W. L. Roth, *Acta Cryst.*, **13**, 140 (1960).
10. P. Kofstad, *J. Phys. Chem. Solids*, **28**, 1842 (1967).
11. For a review of studies on UO<sub>2+x</sub>, see F. A. Kröger, *Z. Physik, Chem.*, **49**, 178 (1966).
12. B. T. M. Willis, *Nature* (London), **167**, 755 (1963); *J. Phys.*, **25**, 431 (1964).
13. F. A. Kröger, "The Chemistry of Imperfect Crystals," North Holland, Amsterdam, John Wiley and Sons, Inc., New York (1964).
14. M. Kleman, *Mem. Scient. Rev. Met.*, **62**, 457 (1965).
15. C. Carel and P. Vallet, *Compt. rend.*, **258** 3281 (1964).
16. C. Carel, D. Weigel, and P. Vallet, *ibid.*, **260**, 4325 (1965).

## Luminescence of Dy<sup>3+</sup>-Activated $\beta$ -Ga<sub>2</sub>O<sub>3</sub>

William C. Herbert,<sup>1</sup> Henry B. Minnier, and Jesse J. Brown<sup>2</sup>

Chemical and Metallurgical Division, Sylvania Electric Products, Inc., Towanda, Pennsylvania

Although trivalent dysprosium is a known coactivator or sensitizer in luminescent systems (1), few phosphors of significance are known in which Dy<sup>3+</sup> is the sole activator ion. Jenkins, McKeag, and Ranby (2) have activated various alkaline earth phosphate compounds, most notably Ca<sub>2</sub>P<sub>2</sub>O<sub>7</sub>, with Dy<sup>3+</sup> and made special note of their x-ray and cathode-ray-excited luminescent decay characteristics.

In the present note we describe the photoluminescence of Dy<sup>3+</sup>-activated  $\beta$ -Ga<sub>2</sub>O<sub>3</sub>. Although this material is not as efficient as the general class of commercial phosphors, it is one of the brightest Dy<sup>3+</sup>-activated oxide phosphors thus far reported. In addition, the emission of  $\beta$ -Ga<sub>2</sub>O<sub>3</sub> : Dy is remarkably similar to that of the standard commercial warm white phosphor, Ca<sub>5</sub>F(PO<sub>4</sub>)<sub>3</sub> : Sb : Mn.

Dy<sup>3+</sup>-activated  $\beta$ -Ga<sub>2</sub>O<sub>3</sub> is prepared by intimately blending the constituent oxides and heat-treating the

mixture in air at 1400°C, for several hours. Dy<sub>2</sub>O<sub>3</sub> additions from 0.5 to 20.0 m/o (mole per cent) were investigated. Maximum photoluminescent brightness was observed in the range 5-10 m/o activator concentration.

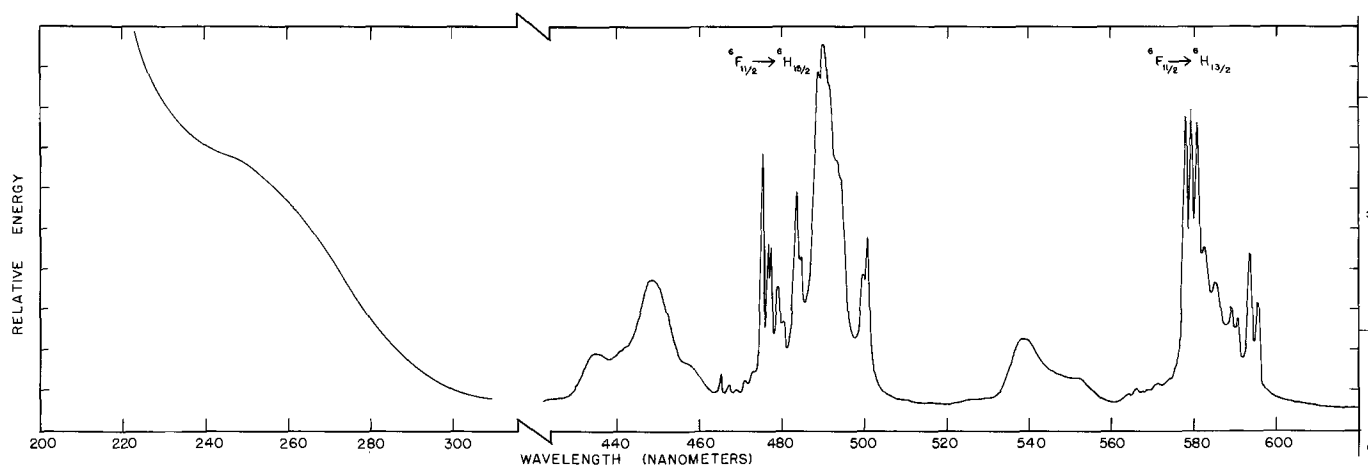
Luminescence spectral measurements were obtained using a Perkin-Elmer Model 236 Spectrophotofluorimeter. Emission spectra were recorded in terms of relative energy. Identification of the intense line emissions is accurate to  $\pm 3\text{\AA}$ . C.I.E. chromaticity coordinates were obtained using a Librascope integrator.

The excitation and emission spectra of  $\beta$ -Ga<sub>2</sub>O<sub>3</sub> : Dy are shown in Fig. 1. Since no direct absorptions by dysprosium are observed in the excitation spectrum, it must be assumed that the major portion of the energy involved in luminescence arises from the broad host lattice absorptions. These peak at 250 nm and below.

The emission spectrum is dominated by two main groups of lines in the ranges 460-505 and 570-600 nm. A third group of weak lines, not shown in Fig. 1, was

<sup>1</sup> Present address: Drexel Institute of Technology, Philadelphia, Pennsylvania.

<sup>2</sup> Present address: Department of Metals and Ceramic Engineering, Virginia Polytechnic Institute, Blacksburg, Virginia. Electrochemical Society Active Member.

Fig. 1. Excitation and emission spectra of  $\beta$ -Ga<sub>2</sub>O<sub>3</sub>:Dy

observed between 660 and 690 nm. Several diffuse bands occurring near 435, 450, 540, and 550 nm are believed to be caused by either impurities or host lattice emissions and are not characteristic of Dy<sup>3+</sup> fluorescence.

Table I lists the observed emission lines, their intensities, and most probable ground state for the  $\beta$ -Ga<sub>2</sub>O<sub>3</sub>:Dy fluorescence. In Table II the fluores-

Table I. Visible fluorescence spectrum of  $\beta$ -(Ga<sub>0.95</sub>, Dy<sub>0.05</sub>)<sub>2</sub>O<sub>3</sub>

$\lambda$ , Å	I/I <sub>0</sub>	Lowest state
4650*	9	<sup>6</sup> H <sub>15/2</sub>
4675*	7	
4690*	5	
4710*	8	
4730*	10	
4752	72	
4765	49	
4772	47	
4790	35	
4802	25	
4835	61	
4845	42	
4887	95	
4900	100	
4915	91	
4930	69	
4940	65	
4995	38	
5005	48	
5780	82	<sup>6</sup> H <sub>13/2</sub>
5795	83	
5805	80	
5825	46	
5850	35	
5890	28	
5905	25	
5935	43	
5955	25	
6678	4	<sup>6</sup> H <sub>11/2</sub>
6775	8	
6840	11	
6865	7	

\* These lines may be due to impurities.

Table II. Comparison of fluorescence of  $\beta$ -(Ga<sub>0.95</sub>, Dy<sub>0.05</sub>)<sub>2</sub>O<sub>3</sub> with a standard warm white halophosphate phosphor

Phosphor	Relative peak height	Chromaticity coordinates x	Chromaticity coordinates y	% Total light output
Ca <sub>2</sub> F(PO <sub>4</sub> ) <sub>3</sub> :Sb:Mn (Sylvania No. 4356)	100	0.445	0.420	100
$\beta$ -(Ga <sub>0.95</sub> , Dy <sub>0.05</sub> ) <sub>2</sub> O <sub>3</sub>	495 nm emission	173	0.036	0.422
	588 nm emission	167	0.585	0.415
	Sum of both	—	0.439	0.416

cence of this new phosphor is compared with that of a standard "warm white" halophosphate phosphor, Sylvania Type 4356.

Hund's rule for a 4f<sup>9</sup> electronic configuration predicts that the ground state of Dy<sup>3+</sup> is an inverted <sup>6</sup>H state. The lowest-lying level in this multiplet would be the <sup>6</sup>H<sub>15/2</sub> with 8 doubly degenerate Stark components, the next <sup>6</sup>H<sub>13/2</sub> with 7 components, etc. Dicke and Singh (3) have successfully identified the experimental absorption and fluorescence transitions of DyCl<sub>3</sub> · 6H<sub>2</sub>O in this framework.

An equally successful term assignment of the Dy<sup>3+</sup> transitions in  $\beta$ -Ga<sub>2</sub>O<sub>3</sub> (Table I) is not immediately possible. The three observed groups of emission lines at 460-505, 570-600, and 660-690 nm apparently arise from <sup>6</sup>F<sub>11/2</sub> → <sup>6</sup>H<sub>15/2</sub>, <sup>6</sup>H<sub>13/2</sub>, and <sup>6</sup>H<sub>11/2</sub> transitions, respectively. However, in the first group at least 14 lines are observed when one would not expect more than 8 Stark components for a <sup>6</sup>H<sub>15/2</sub> transition; likewise 9 lines are observed for the <sup>6</sup>H<sub>13/2</sub> transition when not more than 7 are predicted. (The lines corresponding to the <sup>6</sup>F<sub>11/2</sub> → <sup>6</sup>H<sub>11/2</sub> transition are too weak and diffuse to be accurately resolved.)

Assuming that all observed fluorescence lines in  $\beta$ -Ga<sub>2</sub>O<sub>3</sub>:Dy arise from the <sup>6</sup>F<sub>11/2</sub> level and not higher-lying excited levels, and that Hund's rules are valid for this case, one possible explanation of the extra emission lines is that Dy<sup>3+</sup> occupies two non-equivalent sites in the  $\beta$ -Ga<sub>2</sub>O<sub>3</sub> lattice. This would effectively double the number of fluorescence transitions expected experimentally and be much more in line with the observed spectrum. In fact, Geller (4) has established the existence of two different cation sites in the  $\beta$ -Ga<sub>2</sub>O<sub>3</sub> crystal structure, one tetrahedrally and one octahedrally coordinated by oxygen.

#### Acknowledgment

The authors are indebted to Mr. D. T. Palumbo for several helpful discussions and for assisting with the fluorescence measurements.

Manuscript received Sept. 28, 1967.

Any discussion of this paper will appear in a Discussion Section to be published in the December 1968 JOURNAL.

#### REFERENCES

- M. J. Taylor, *Proc. Phys. Soc.*, **87**, 281 (1966).
- H. G. Jenkins, A. H. McKeag, and P. W. Ranby, U.S. Pat. 2427728, Sept. 23, 1947.
- G. H. Dieke and S. Singh, *J. Opt. Soc. Am.*, **46**, 495 (1956).
- S. Geller, *J. Chem. Phys.*, **33**, 676 (1960).

# Optical Properties by Far Infrared Ellipsometry

Charlie E. Jones and A. Ray Hilton

Texas Instruments Incorporated, Dallas, Texas

The authors recently described (1), an infrared ellipsometer used to measure the thickness of thin silicon and germanium epitaxial layers. The measurement of thin film thickness by ellipsometry requires an accurate knowledge of the optical constants,  $n$  and  $k$ , of the film and substrate at the wavelength of measurement ( $54.6\mu$  in this case). The optical constants  $n$  and  $k$  (real and imaginary parts of the refractive index, respectively) were calculated from an expression given by Lyden (2) for free carrier and lattice absorption in semiconductors. The method was used by the authors in earlier studies (3). The experimental data required for the calculations was supplied from electrical measurements of the semiconductor films and substrates (1). Optical constants can also be calculated directly from ellipsometric measurement of the substrate surface and is the technique commonly used in the visible spectrum range (4). This note presents a comparison of the optical constants obtained on highly doped silicon using ellipsometric measurements to those obtained using the above mentioned techniques. The ellipsometric curves generated for epitaxial layers of undoped silicon on substrates having the different optical constants are presented and compared. Comments are made regarding the fit of experimental data to the various curves.

Four methods have been used to determine  $n$  and  $k$ :

A. Measure the resistivity (probe), determine the number of carriers from a literature curve relating resistivity to carriers (5), and the mobility from a literature curve relating resistivity to mobility (6). Calculate  $n$  and  $k$  from Lyden's expression.

B. Same as A except mobility is calculated from:

$$\text{Mobility} = \frac{6.25 \times 10^{18}}{(\text{number of carriers})(\text{resistivity})}$$

C. Measure the number of carriers and mobility by Hall techniques then proceed with Lyden's expression.

D. Measure, with the infrared ellipsometer, the  $\Delta$  and  $\psi$  value for the substrate and calculate the optical constants from the exact equation given by Winterbottom (7).

Methods A and B depend on resistivity values obtained by the simple probe technique and are therefore not expected to yield as accurate values for optical constants as will method C which utilizes the reliable Hall technique.

The optical constants obtained from each method for a substrate of 0.016 ohm-cm n-type silicon were:

Method	$n$	$k$
A	2.18	2.44
B	2.48	2.18
C	2.21	1.49
D	2.59	1.38

Four curves relating to the ellipsometer parameters  $\Delta$  and  $\psi$  were plotted assuming each of the above optical constants for the substrate and undoped silicon (optical constants  $3.38 - 0.i$ ), as the epitaxial layer. The other parameters of interest are  $\lambda = 54.6\mu$ ; angle of incidence =  $50^\circ$ . These curves are shown in Fig. 1. The arrows on each curve indicate the thickness of the epitaxial layer in microns. The data points (solid dots) are  $\Delta$  and  $\psi$  measurements made on 16 samples of undoped silicon layers deposited on 0.016 ohm-cm n-type silicon. The data points fit best the curve plotted

using the ellipsometrically measured substrate optical constants. The measuring accuracy of the ellipsometer in present form is about  $\pm 3^\circ$  for  $\psi$  and  $\Delta$ . Since in method C the electrical properties were measured to a high degree of reliability, curve C represents the best of the calculated optical constants. Curves A and B can be considered deviations from curve C due to a lack of accuracy in the electrical values obtained by methods A and B. The difference between the optical constants obtained by methods C and D are not due to inaccuracies in the equations relating resistivity and mobility to the optical constants. We have previously shown (1) good agreement between measured and calculated absorption coefficients of 0.01 to 1.0 ohm-cm n-type silicon using these same relationships. The difference probably results from the fact that in method C the resistivity and mobility, used to calculate the optical constants, are values of bulk material while the ellipsometer measures the optical constants of the materials surface.

If ellipsometry is used in the far infrared to measure layer thicknesses ellipsometry should be used for determining the optical constants of the materials in question. It should be noted that by using the  $n$  and  $k$  calculated from the ellipsometric readings and back calculation some insight may be gained as to the accurate electrical characteristics of the surface of the material. This will of course depend on the exactness of the theory relating the electrical and optical properties.

Manuscript received Aug. 17, 1967; revised manuscript received Oct. 15, 1967.

Any discussion of this paper will appear in a Discussion Section to be published in the December 1968 JOURNAL.

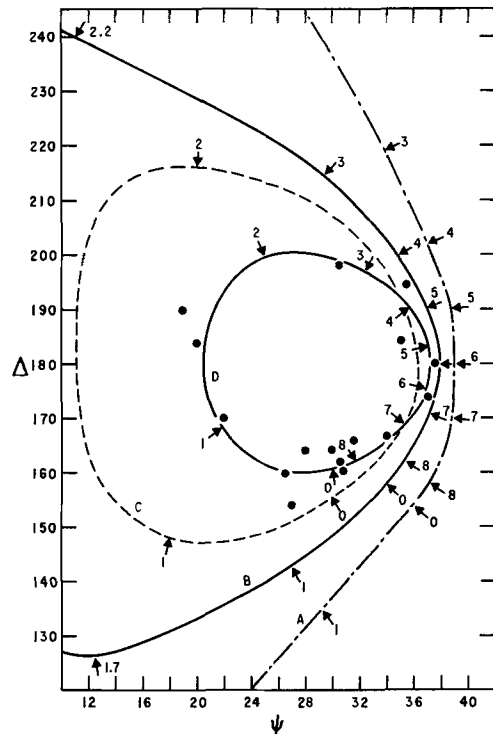


Fig. 1. Ellipsometer curves

## REFERENCES

1. A. Ray Hilton and Charlie E. Jones, *This Journal*, **113**, 472 (1966).
2. Henry A. Lyden, *Phys. Rev.*, **134**, A1106 (1964).
3. Charlie E. Jones and A. Ray Hilton, *This Journal*, **112**, 908 (1965).
4. R. J. Archer, *Phys. Rev.*, **110**, 354 (1958).
5. R. C. Wackwitz, TI Memo ICRL-M 103 63621-02.
6. M. Bullis, Private communication.
7. A. B. Winterbottom, "Optical Studies of Metal Surfaces," Publisher F. Burns, Trondheim Norway.

## The Preparation and Examination of PbTe by Transmission Electron Microscopy

E. Levine

*Department of Mechanics, Rutgers—The State University, New Brunswick, New Jersey*

and R. N. Tauber

*Department of Metallurgy and Materials Science and The Materials Research Center, Lehigh University, Bethlehem, Pennsylvania*

The preparation of thin foils of the compound semiconductor PbTe for transmission electron microscopy has not been reported previously. Electron microscopy can be employed in this compound for the study of defects and precipitation effects. The following note describes the preparation technique and some preliminary observations made on thin foils of PbTe.

It has been suggested by various investigators (1-3) that the change of carrier concentration of PbTe on annealing is due to precipitation of Pb or Te from the supersaturated crystal. This is further evidenced by the fact that both the Pb and Te concentration are retrograde in nature (1,2). In this investigation a single crystal of PbTe grown by the Bridgman technique was heat-treated so as to produce precipitation of Pb from the lattice. The procedure was as follows: (a) diffusing the specimens in a Pb-rich atmosphere at 775°C for 28 hr and brine quenching; this produces a maximum Pb-rich PbTe (1, 2). (b) Aging the specimens at 504°C for 25 hr and brine quenching; this should produce precipitates of Pb in the lattice, particularly on dislocation sites (3).

Thin foils of the specimen were prepared for electron microscopy using a combination of mechanical and electropolishing. The specimen was mechanically polished to approximately 200 $\mu$  on various grades of paper with a final polishing on both sides using Linde Gamma AB alumina powder. It was then electropolished using a solution described by Norr (4) which consisted of 20g KOH in 45 ml H<sub>2</sub>O, 35 ml glycerol, 20 ml of ethyl alcohol. The polishing was performed at 4-6v and 0.2 amp/cm<sup>2</sup>. The sample was suspended without any edge masking in the electropolishing solution. Small black dots of apezion wax were placed on opposite sides in the center of the specimen. Accelerated attack occurred in the vicinity of these dots and also around the periphery of the specimen. Polishing was continued until the hole formed under the dots joined up with the peripheral region. Extremely rapid stirring was necessary in order to prevent the build up of a contamination layer.

The PbTe was found to be very brittle before polishing, and considerable care was necessary to avoid shattering. The electropolished thin specimen, however, was found to be very ductile in certain thin regions and could be bent plastically at the edges by 180° and then straightened out again without fracture occurring. This behavior is similar to that found with alkali halide crystals when deformed in a solvent environment (5), i.e., the specimens are notch brittle. The removal of notches or cracks renders the crystal somewhat ductile although even in the thinned specimen cutting with a knife results in brittle fracture along the cleavage planes.

The thinned specimen was examined in a Hitachi Electron Microscope operated at 100 kv. The density of dislocations was found to be quite high and accurate estimates were not possible due to their inhomogeneity. A typical area is shown in Fig. 1. Precipitation was not observed at dislocations as has been previously suggested (3). Arrays of dislocations on their inclined slip planes were observed throughout the foil. Some of these dislocations appeared to be either dipoles or dissociated dislocations (Fig. 2). Stacking fault contrast was not observed between these dislocation pairs. Further contrast experiments on their exact nature are planned for the future. The presence of dissociated dislocations in PbTe has been proposed previously by Rachinger (6).

In the background of Fig. 2 in the neighborhood of the extinction contour many elongated images may be seen which are not visible in the area on the right side of the figure. These images were only visible in the vicinity of an extinction contour and may correspond to an early stage in a precipitation process. The associated diffraction pattern did not show any evidence of such precipitates indicating their volume fraction is small or we are observing a preprecipitation stage of clustering similar to that found in Al-4% Cu alloys (7). Figure 3 is a diffraction pattern of a {100} orientation from a bent portion of the specimen. (The major portion of the thinned specimen was of {112} orientation.) Weak streaking in the <100> directions may be observed which usually

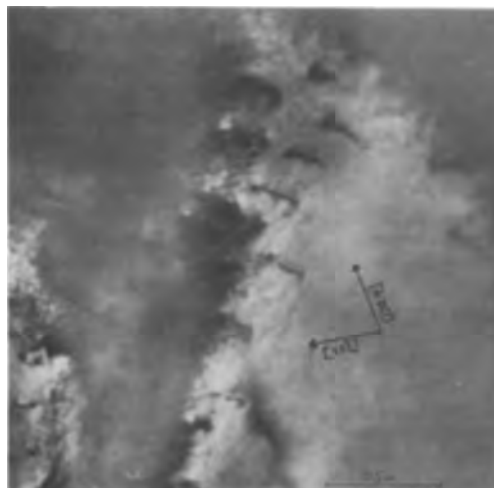


Fig. 1. Dislocation arrays in PbTe

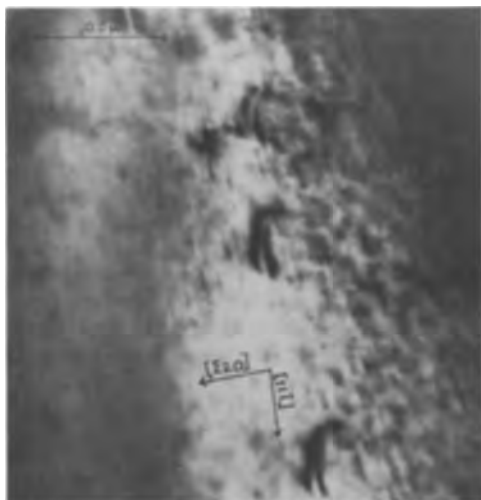


Fig. 2. Possible dipole or dissociated dislocations in PbTe. In the background anomalous images, possibly precipitates, are observed.

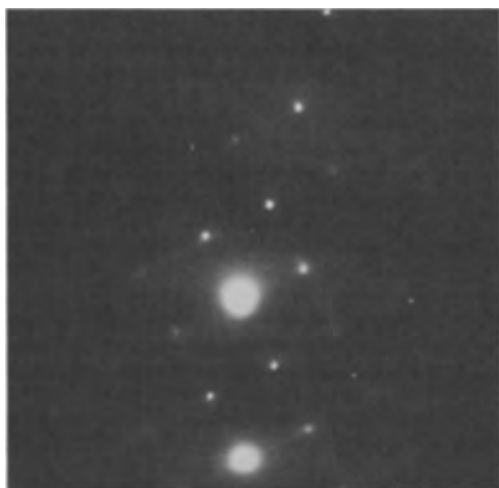


Fig. 3.  $\{100\}$  Diffraction pattern of PbTe. Streaks are observed in  $\langle 100 \rangle$  directions indicating either anisotropic expansion coefficient or a strain displacement in this direction.

characterizes the preprecipitation stage in metal systems (7). However, one cannot unambiguously assign these "streamers" to precipitation. Similar streaking has been observed in Ge crystals in the  $\langle 110 \rangle$  directions and their origin is speculative. They may arise from thermal vibrations or anisotropic strain displacements (8). The latter may be created by clustering of atoms. Further work on aging experiments is now in progress to clarify this point.

The dislocations were observed to be quite mobile during observation in the electron microscope. Dislocations in thin foils may move as a result of the stresses set up by the electron beam. That such movement readily occurred is another indication of the possible room temperature ductility of suitably prepared specimens. The movement of dislocations produced a variety of slip trace contrasts as may be seen in Fig. 4 at A and B. The slip trace contrast in some cases rapidly disappeared after a few seconds while other slip traces were of indefinite duration.

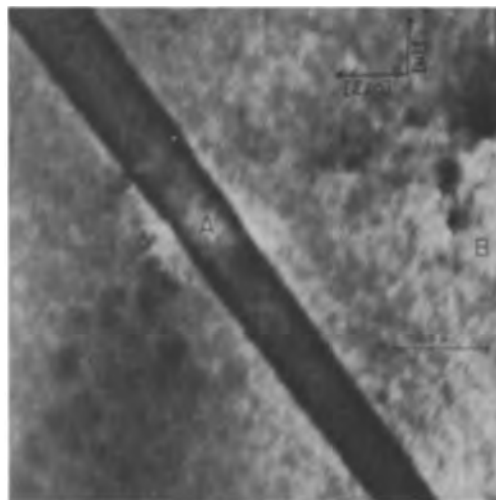


Fig. 4. Persistent slip traces due to movement of dislocations while under observation in electron microscope. Slip trace at A clearly visible while that at B is weakly visible.

Slip trace contrast is thought to be due to a surface layer of oxide or other contamination layer on the foil which prevents the slip from penetrating the surface. The observation of the variability of duration and contrasts produced in the same area of the foil suggests that the phenomenon is strongly dependent on the slip vector of the dislocations involved.

Slip trace analysis assuming either  $\{110\}$  or  $\{100\}$  glide planes indicated that dislocations on both planes were capable of movement. Rachinger (6) using trace analysis in bulk specimens observed both glide planes to be operative in PbTe although Buerger (9) had found only evidence of  $\{100\}$  glide plane activity. Evidence of both  $\{110\}$  and  $\{100\}$  glide plane activity had been observed by Seltzer (10) and Matthews *et al.* (11) in PbS. Our observation suggests that PbTe behaves similarly to PbS in that slip (at least in thin films) occurs on both glide planes.

#### Acknowledgment

This work was supported in part by the National Science Foundation under Grant No. GK-1607.

Manuscript received July 17, 1967; revised manuscript received Sept. 19, 1967.

Any discussion of this paper will appear in a Discussion Section to be published in the December 1968 JOURNAL.

#### REFERENCES

1. R. F. Brebrick and R. S. Allgaier, *J. Chem. Phys.*, **32**, 1826 (1960).
2. R. F. Brebrick and E. Gubner, *ibid.*, **36**, 1283 (1962).
3. W. W. Scanlon, *Phys. Rev.*, **126**, 509 (1962).
4. M. K. Norr, DDC Document AD 423 367, Naval Ordnance Laboratory, White Oak, Maryland (1963).
5. A. R. C. Westwood, *Ind. Eng. Chem.*, **56**, 15 (1964).
6. W. A. Rachinger, *Acta Met.*, **4**, 647 (1956).
7. R. B. Nicholson and J. Nutting, *Phil. Mag.*, **3**, 531 (1958).
8. R. D. Heidenreich, "Fundamentals of Transmission Electron Microscopy," p. 260, Interscience Publishers, (Wiley), New York (1964).
9. M. J. Buerger, *Am. Mineralogist*, **13**, 1 (1928).
10. M. S. Seltzer, *J. Appl. Phys.* **37**, 4780 (1966).
11. J. W. Matthews and K. Isebeck, *Phil. Mag.*, **8**, 469 (1963).

# Formation of Crystalline Films by Laser Evaporation

P. D. Zavitsanos and W. E. Sauer

Space Sciences Laboratory, Missile and Space Division,  
General Electric Company, King of Prussia, Pennsylvania

Vacuum evaporation techniques have been used for the preparation of films of elements and some compounds. When these techniques are applied to compounds or alloys which contain elements of widely different vapor pressures, vapor fractionation takes place to produce films containing an excess of the most volatile component.

A definite improvement was brought about by the "flash" evaporation technique as outlined first by Siegel and Harris (1) and applied in the preparation of compound semiconductor films (2). The "co-evaporation" technique (3-5) also served as an improvement.

Both techniques, however, sometimes suffer from contamination effects due to impurity vapors present in high-temperature furnaces and vacuum atmospheres. Another disadvantage present in the above techniques, as well as in the "sputtering" technique, is the fact that for many materials of interest, amorphous films are produced unless the substrate is independently heated (6, 7).

The evaporation of solids with a pulsed laser beam for the purpose of producing good optical films has been investigated by Smith and Turner (8), and Schwartz (9) with some degree of success. In the present work, the use of a laser beam appears to produce (a) congruent vaporization and films of the same composition as the parent material, and (b) crystalline films without heating the substrate (independently).

## Experimental

The laser used in this investigation was a Lear-Siegler Model H-140Q. It had a maximum output of 10 joules, and a pulse duration of  $5-6 \times 10^{-4}$  sec, and was operated in the burst mode.

The vapor generated by laser evaporation formed a jet, the center of which was always normal to the surface of the source material, independent of the incident angle of the laser beam. For this work, the laser beam entered a glass vacuum system through a glass window and was focused by a 75 mm focal length lens on the surface of the source material at a 45° angle. The source material was mounted (inside the vacuum system) on a holder which could be moved up and down or rotated for focusing or exposure of a new segment of the surface to the beam. Films of Ge and GaAs were prepared by condensing the vapor on various substrates, at room temperature, placed parallel to the specimen 2.5 cm away. Prior to vaporization, the substrates were washed first with acetone and then with ethyl alcohol and air dried at 120°C. Satisfactory films were produced at chamber pressures as high as  $1\mu$ .

For lasers operating in the burst mode, it can be assumed that there is sufficient power density in the beam to raise the surface temperature of the target to its boiling point at a relatively short time compared to the length of the pulse, and the rate of surface recession reaches a steady state rapidly (10). (Time resolved microwave attenuation measurements (11) indicate that this assumption is correct.) If energy losses due to reflection, radiation, conduction through the solid, superheating of solid and gas are negligible, the mass of the generated vapor,  $m$  is given by

$$m = E / [(C\Delta T_1)_{\text{solid}} + \Delta H_f + (C\Delta T_2)_{\text{liquid}} + \Delta H_v]$$

where  $E$  = energy output of laser,  $C$  = specific heat capacity,  $(C\Delta T_1)_{\text{solid}}$  = energy required to heat the solid to its melting point,  $\Delta H_f$  = heat of fusion and or heat of decomposition,  $(C\Delta T_2)_{\text{liquid}}$  = energy required to heat the liquid to its boiling point, and  $\Delta H_v$  = heat of vaporization of liquid at the boiling point. The energy output,  $E$ , used in these experiments was 3 joules per pulse. In the case of Ge and GaAs, the amounts of vapor generated (per pulse) are calculated to be 0.48 and 0.9 mg, respectively.<sup>1</sup>

The deposited area was usually about 3-4 cm<sup>2</sup>, and if the condensation coefficient was unity, the resulting films would have a thickness in the order of 1600-3500Å. Our present estimates, however, (based on optical opacity) indicate that the film thickness (per pulse) was considerably less and of the order of 500-1000Å. In view of the high reflectance of the Ge and GaAs source materials, it is felt that reflection was not negligible and probably was the dominant mechanism of energy loss. The extent of laser energy absorption by the vapor is usually considered to be small at this power level (10) although not proven for our experimental conditions. The resulting deposition rate is extremely high compared to conventional techniques and in the range of  $10^6$  Å/sec. As far as the source temperature is concerned, although it was not measured, by analogy to graphite (13) targets it is felt that it did not exceed the boiling point of the less volatile component by a significant amount. The temperature of the substrates could not have been significantly raised by the laser energy in view of the fact that the substrates were transparent and rather massive (10-15g); even if all the available energy went into heating the substrate, its temperature could not be raised by more than 2°-3°.

## Results

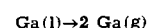
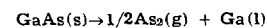
The results which follow were typical of those obtained from measurements on several films (2-3 of each case). Films prepared by laser evaporation were studied by reflection and transmission optical microscopy. Figure 1 shows optical photomicrographs of Ge and GaAs films deposited on glass and sodium chloride substrates. It can be seen that the films are smooth, continuous, and free of "chunks" of materials.

The films were removed from their substrates, and high resolution transmission electron diffraction patterns were obtained using an Hitachi HU-11 electron microscope. Figure 2A is an electron diffraction pattern from a germanium film which had been laser deposited on a glass substrate. Figure 2B is from another germanium film which had been produced by evaporation of the same source material from a resistance heated molybdenum boat. In neither case was the substrate heated by external means. The conventionally

<sup>1</sup> For germanium, the following steps were assumed to lead to vaporization



with  $T_{\text{melting}} = 1210^\circ\text{K}$ ,  $T_{\text{boiling}} = 3100^\circ\text{K}$ ,  $C = 6 \text{ cal} \cdot \text{deg}^{-1} \cdot \text{mole}^{-1}$ ,  $\Delta H_f = 8.83 \text{ kcal} \cdot \text{mole}^{-1}$ , and  $\Delta H_v = 79.1 \text{ kcal} \cdot \text{mole}^{-1}$ . For gallium arsenide, the corresponding gasification processes (12) are



with  $T_{\text{decomposition}} = 1000^\circ\text{K}$ ,  $T_{\text{boiling}}(\text{Ga}) = 2520^\circ\text{K}$ ,  $\Delta H_{\text{decomposition}} = 45 \text{ kcal/mole}(\text{GaAs})$ , and  $\Delta H_v = 61.5 \text{ kcal/mole}(\text{Ga})$ .





Fig. 1A. Reflection optical photomicrograph of laser evaporated film: germanium film on glass substrate. Magnification 350X.

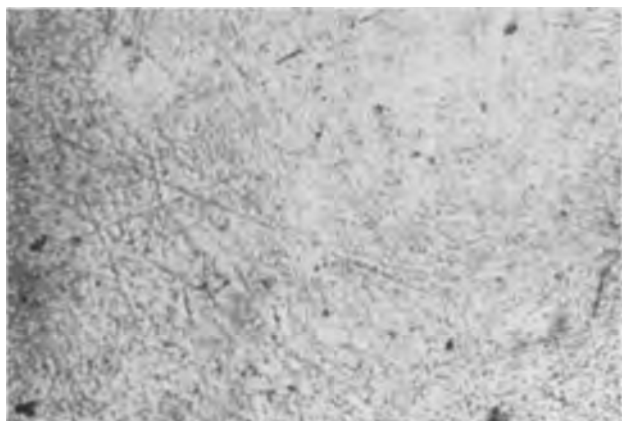


Fig. 1B. Reflection optical photomicrograph of laser evaporated film: gallium arsenide film on sodium chloride substrate. Magnification 350X.

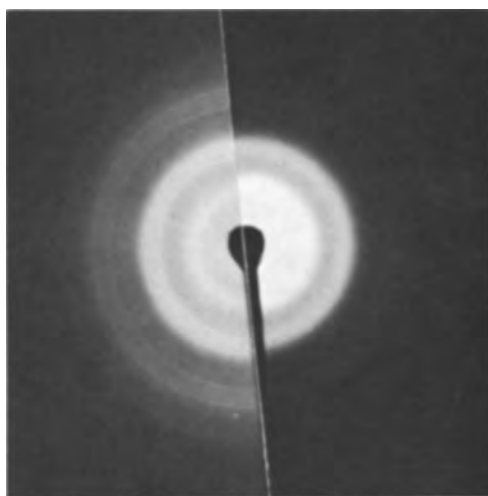


Fig. 2. Transmission electron diffraction patterns produced by evaporated germanium films. A(left), laser evaporation; B(right), conventional evaporation.

evaporated film exhibits an amorphous structure which is typical of germanium films condensed on unheated substrates. However, the laser evaporated film exhibits a degree of crystallinity which is typical of films deposited by conventional evaporation onto substrates heated to 300°C or more (7).

In addition to the elemental films, films of GaAs were prepared. The laser evaporation of GaAs was found to proceed congruently. Figure 3A is an electron diffraction pattern produced from a film which had been prepared on a calcium fluoride substrate by

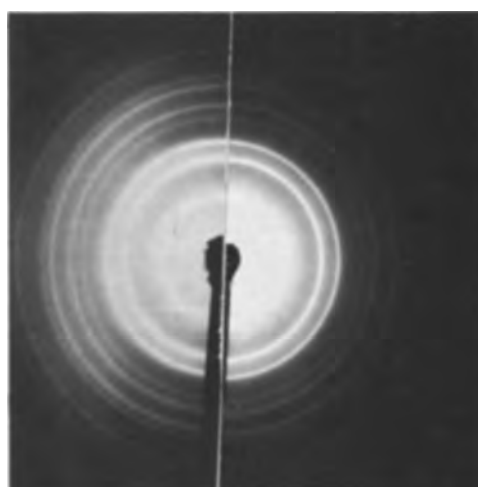


Fig. 3. Transmission electron diffraction patterns produced by evaporated gallium arsenide films. A(left), calcium fluoride substrate; B(right), sodium chloride substrate.

the laser evaporation of gallium arsenide. Figure 3B is from a gallium arsenide film similarly deposited on sodium chloride. The diffraction lines in these two patterns are listed in Table I. Both sets of data are in good agreement with the literature interplanar spacing values for gallium arsenide (14). If the constituents of the deposited film had condensed noncongruently, a second phase would have been present, because of the very limited solubility of gallium and arsenic in gallium arsenide (15). Thus, since all of the diffraction lines could be assigned to gallium arsenide, it was concluded that laser evaporation did produce congruent deposition and crystalline films of gallium arsenide on calcium fluoride and sodium chloride substrates. In the case of laser evaporation (16), coevaporation (4, 16) and sputtering (17) techniques, substrate temperatures of the order of 220°-400°C were required to produce crystalline films of GaAs.

### Discussion

The two most evident features of films prepared by the laser evaporation technique are the congruent deposition of compounds and the degree of film crystallinity achieved on unheated substrates. The reason for congruent evaporation is that conduction of heat away from the focal point and through the solid (target) is a slow process compared to local heating and evaporation. A small volume of material (at the focal point) is raised to a high temperature which is apparently sufficient to produce vapor having the stoichiometry of the target. In a way, this heating process is similar to flash evaporation but more efficient.

Table I. Analysis of electron diffraction patterns from gallium arsenide films

GaAs* on CaF <sub>2</sub>	d(A)	GaAs* on NaCl	d(A)	ASTM value for GaAs <sup>14</sup>	d(A)	I/I <sub>0</sub>	GaAs <sup>14</sup>
I		I					hkl
S	3.25	S	3.25	3.26	100		111
				2.83		1	200
S	2.00	S	2.00	2.00	35		220
S	1.71	S	1.70	1.70	35		311
W	1.38	W	1.39	1.41	6		400
MS	1.29	MS	1.29	1.30	8		331
MS	1.51	MS	1.16	1.15	6		422
M	1.08	M	1.08	1.09	4		333
W	1.00	W	0.99	0.999	2		440
M	0.953	M	0.953	0.956	2		531
VVW	0.910	VVW	0.890	0.894	4		620
WW	0.870	VVW	0.857	0.862	2		533
VVW	0.817	VVW	0.811	0.816	4		444
VW	0.794	VW	0.788	0.792	2		711
W	0.753	W	0.753	0.755			642**
W	0.728	W	0.733	0.736			731**

\* S = Strong; M = Medium; W = Weak; V = Very.  
\*\* Calculated from ASTM value for  $a_0$ .

The crystallization of the films is probably affected by several factors. The high deposition rates and temperatures would tend to increase the mobility of atoms in the depositing films by providing a high energy environment. Heating of the films (during formation) by reflected laser light (which is preferentially absorbed in the film as compared to the substrate) could also take place and, thus, increase the mobility of the condensing vapor.

#### Acknowledgments

The authors are grateful to Dr. J. R. Richardson and Dr. C. A. Neugebauer (of the R&D Center, General Electric Company) and to Dr. E. Feingold (of the Space Sciences Laboratory, General Electric Company) for helpful discussions and comments. The technical assistance of B. Migliorino is also gratefully acknowledged.

Manuscript received June 9, 1967; revised manuscript received Sept. 14, 1967.

Any discussion of this paper will appear in a Discussion Section to be published in the December 1968 JOURNAL.

#### REFERENCES

1. L. Harris and B. M. Siegel, *J. Appl. Phys.*, **19**, 739 (1948).

2. J. L. Richards, P. B. Hart, and L. M. Gallone, *ibid.*, **34**, 3418 (1963).
3. K. G. Gunther, *Z. Naturforsch.*, **13**, 1081 (1958).
4. J. E. Davey and T. Pankey, *J. Appl. Phys.*, **35**, 2203 (1964).
5. R. F. Bis, A. S. Rodolakis, and J. N. Zemel, *Rev. Sci. Instr.*, **36**, 1626 (1965).
6. E. Krikorian, "Single Crystal Films," M. H. Francombe and H. Sato, Editors, Macmillan Co., New York (1964).
7. R. E. Thun, "Physics of Thin Films," Vol. 1, G. Hass, Editor, Academic Press, New York (1963).
8. H. M. Smith and A. F. Turner, *Appl. Optics*, **4**, 147 (1965).
9. H. Schwartz, 1966 Natl. Vac. Symp. Abstracts, p. 87.
10. J. F. Ready, *J. Appl. Phys.*, **36**, 462 (1964).
11. P. D. Zavitsanos and L. E. Brewer, *J. Chem. Phys.*, **35**, 3093 (1967).
12. H. B. Guthrie, *Z. Naturforsch.*, **16a**, 268 (1961).
- 13a. Hugo Weichel and P. V. Avizonis, *Appl. Phys. Lett.* **9**, 334 (1966); b. J. Berkowitz and W. A. Chupka, *J. Chem. Phys.*, **40**, 2735 (1964); c. P. Zavitsanos, *J. Carbon*, to be published.
14. ASTM, Card #14-450.
15. Max Hansen, "Constitution of Binary Alloys," p. 165, McGraw-Hill Book Co., New York (1958).
16. J. Richardson, Private communication.
17. B. Molnar, J. J. Flood, and M. H. Francombe, *J. Appl. Phys.*, **35**, 3554 (1964).

## Brief Communications



### Reply to Comments on the Paper "Transport Processes in the Thermal Oxidation of Silicon"

Douglas O. Raleigh

Science Center, North American Rockwell Corporation, Thousand Oaks, California

A recent communication (1) has raised a number of questions concerning my paper "Transport Processes in the Thermal Oxidation of Silicon" (2). Since it is felt that the comments made represent a misunderstanding of the assertions in this paper, a reply was felt necessary.

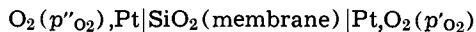
In a paper in 1962, Jorgenson (3) reported experiments on the effect of an electric field on the thermal oxidation of silicon at elevated temperatures. From the results, he asserted that the normal thermal oxidation process occurred by the diffusion of oxygen ions through the  $\text{SiO}_2$  reaction layer. My own paper was an attempt to clarify the matter of what can be meant by the "effect of an electric field" on a thermal oxidation process. I asserted that an electric field *per se* cannot provide a steady-state driving force for diffusion-controlled thermal oxidation, since the net process involved in normal oxidation is the transport of an electroneutral species (elemental oxygen in the case of  $\text{SiO}_2$ ) through the reaction layer. Accordingly, in examining electric field effects, one must consider the role of the experimental arrangement in altering the nature of the oxidizing system. Specifically, the application of an electric field via ohmic leads provides an external path for electron flow and results in an electrolysis experiment rather than an electric field experiment. Since thermal oxidation by an ionic mechanism involves the transport of both ions and electrons through the oxide layer and electrolysis involves only

ion transport, it is not possible to say *a priori* that an electrolysis experiment proves normal oxidation occurs by an ionic mechanism. It may well be that the electronic conductivity in the oxide is too low to permit more than a minor contribution by an ionic mechanism.

In the recent communication (1), it was said that I asserted the so-called halt voltage is, as a general matter, unrelated to the free energy of formation of the oxide. Reference to an unpublished memo by Wagner was made to show that this is not the case in cells of the type  $\text{Me}|\text{MeO}|\text{O}_2$  with an externally applied voltage. In fact, while I might have made myself clearer, I did not assert this as a general matter, but merely for the cell arrangement Jorgenson (3) employed. In the latter case, a constant current was passed through two conjoined cells  $\text{O}_2|\text{Pt}|\text{SiO}_2|\text{Si}$  and the voltage monitored across each oxide layer. The  $\text{SiO}_2$  in these cells was a growing oxide layer on the surface of an initially clean silicon sample with sputtered platinum electrodes on the two ends. An oxygen atmosphere served for both the normal oxidation and the oxygen electrodes. If the voltage leads across the cells were properly contacted, the cell voltages should have been given by  $V = E \pm iR$ , where  $E$  is the galvanic emf and the sign of the  $iR$  drop depends on the direction of the current.  $E$  is ideally given by  $t_{\text{ions}}\Delta F^\circ_f(\text{SiO}_2)/4F$ , equal to  $t_{\text{ions}}(1.69\text{v})$  at  $850^\circ$ , where  $t_{\text{ions}}$  is the effective ionic transport number in the ox-

ide film. Since the  $iR$  drop would be proportional to the  $\text{SiO}_2$  film thickness, extrapolation of  $V$  vs.  $t$  back to  $t = 0$  should give  $E$ . Instead, all  $V$  vs.  $t$  plots extrapolated back to zero volts, indicating no galvanic emf contribution. As explained in my paper, this would have been the case if the voltage lead to the Si were unprotected from oxidation, since one would then have had an  $\text{O}_2/\text{SiO}_2$  electrode at this site, identical to the main oxide electrode. In this case, one would have been measuring purely  $iR$  drop in the oxide film, which would be unrelated to the free energy of formation of  $\text{SiO}_2$ .<sup>1</sup>

Jorgenson's report of recent galvanic emf data on the cell



is very interesting and may, indeed, indicate both sufficient ionic and electronic conduction in  $\text{SiO}_2$  to support an ionic oxidation mechanism. Caution, however, is required in interpreting the experimental results. It was said that  $p''_{\text{O}_2}$  was 323 Torr and that  $p'_{\text{O}_2}$  was maintained at an ambient value of  $10^{-7}$  Torr by vacuum pumping on the right-hand side of the cell. Ionic transport numbers of 0.40-0.53 were obtained, which were presumably calculated from the galvanic emf via the expression

$$E = t_{\text{ions}} \frac{RT}{4F} \ln \frac{p''_{\text{O}_2}}{p'_{\text{O}_2}}$$

In this, of course, it is important that the ambient value of  $10^{-7}$  Torr for  $p'_{\text{O}_2}$  be also the pressure value inside the sputtered Pt film at the Pt|oxide interface, since it is the latter pressure that determines  $E$ . This is a matter of concern, since oxygen was continually permeating the silica membrane and, indeed, the permeation rate was measured in the same experiment. Jorgenson implied that there was no pressure differential across the Pt, since his measured permeation rates agreed to 10% with those of Norton (4). This, however, is not very convincing, since the permeation rate only depends on  $\Delta p$  and would be essentially the same for any  $p'_{\text{O}_2}$  value small compared that of  $p''_{\text{O}_2}$ . Thus, any of a wide range of  $p'_{\text{O}_2}$  values  $> 10^{-7}$  Torr could have been present at the Pt| $\text{SiO}_2$  interface and would have the effect of lowering the calculated values of the ionic transport number. Experiments with

<sup>1</sup>Note added in proof: Dr. Jorgenson has communicated to the author that he has re-examined his original voltage-time data and finds that it is best fitted to a zero-time intercept not of zero volts, but of 0.61v. If so, this would indicate that there was a galvanic contribution, which should be added to my estimate of the  $iR$  drop. This would yield 1.86v for the predicted halt voltage, in somewhat better agreement with the observed value than my previous estimate.

silica membranes thick enough to retard permeation greatly would be very helpful. Likewise helpful would be the use of a "buffered" oxygen atmosphere, such as a  $\text{CO-CO}_2$  gas mixture, which establishes a low oxygen pressure chemically instead of by evacuation.

Regarding the many small points in my paper which were allegedly incorrect, I can only comment on the two that were actually brought up. Regarding Jorgenson's experiments on the effect of an electric field on the oxidation of zinc (5), I stand corrected in that the author did not assert the results showed diffusion control by oxygen ions, but merely by ions. I must still maintain, however, that the results did not prove diffusion control by ions, but merely showed the presence of some ionic conductivity in the oxide, for the reasons mentioned above and in my original paper. Regarding my model for the stopping voltage, its calculation did not require an assumed value for the ionic transport number, but a value for the ionic conductivity. The latter was obtained from Jorgenson's own data and a value in good agreement with it was obtained from oxygen diffusion data in  $\text{SiO}_2$ . Thus, the original prediction for the stopping voltage remains.

In conclusion, it is felt that the distinction between experiments on the effect of an electric field on thermal oxidation and electrolysis experiments is still an important one. Wagner, in fact, has independently employed the concept of superposed electrolysis to explain oxidation effects in the presence of an external electric field in what I believe is the same unpublished memo to which Jorgenson referred (6). It is felt that this concept provides a rational electrochemical basis for such field effects and clearly indicates their limited relevance in deducing the predominant oxidation mechanism.

Manuscript received Sept. 11, 1967.

Any discussion of this paper will appear in a Discussion Section to be published in the December 1968 JOURNAL.

#### REFERENCES

1. P. J. Jorgenson, *This Journal*, **114**, 820 (1967).
2. D. O. Raleigh, *ibid.*, **113**, 782 (1966).
3. P. J. Jorgenson, *J. Chem. Phys.*, **37**, 874 (1962).
4. F. J. Norton, *Nature*, **191**, 701 (1961); "Transactions of the 8th Vacuum Symposium and 2nd International Congress," pp. 8-16, Pergamon Press, New York (1962).
5. P. J. Jorgenson, *This Journal*, **110**, 461 (1963).
6. C. Wagner, Unpublished memo, "Considerations on the Effect of an External Electrical Field Applied to an Oxide Layer Growing on a Metal in Oxygen," Feb. 13, 1966.

## Application of the Peltier Effect for the Determination of Crystal Growth Rates

Ranjit Singh, August F. Witt,\* and Harry C. Gatos\*

Department of Metallurgy and Center for Materials Science and Engineering,  
Massachusetts Institute of Technology, Cambridge, Massachusetts

A method for the determination of microscopic rates of solidification during crystal growth has been reported recently (1). The method is based on the introduction of relatively high-frequency impurity striations in the growing crystal. Such striations referred to from here on as "rate striations" were induced by establishing controlled low amplitude vibrations of known frequency in the melt during crystal growth. While the exact mechanism responsible for the for-

mation of these striations is as yet not unambiguously determined, it is most likely that they are caused by instantaneous growth rate fluctuations associated with thermal and fluid-dynamic perturbations. It was found that they do not interfere to any detectable extent with the over-all solidification process (2).

The present communication reports on the successful formation of rate striations by employing the Peltier effect. Current pulses of short duration and of the appropriate frequency applied across the crystal-

\* Electrochemical Society Active Member.

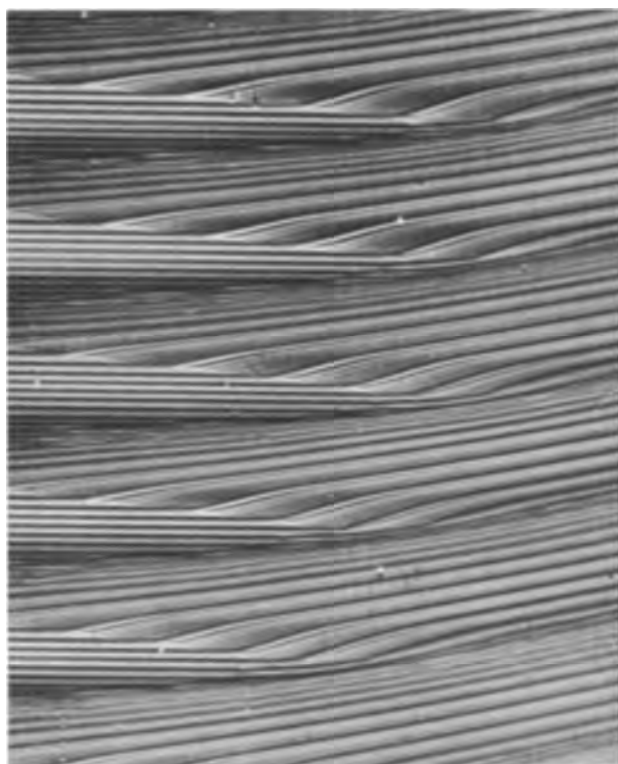


Fig. 1. Off-core on-core transition region in a Czochralski grown single crystal of InSb. Rate striations (introduced by employing the Peltier effect) reveal major variations of the microscopic crystal growth rate. Magnification 380X.

melt interface during crystal growth cause corresponding fluctuations in the instantaneous growth rate due to Peltier heating (or cooling). These fluctuations are incorporated in the growing crystal as impurity striations [revealed by polishing and etching (1)] which exhibit the same characteristics as the previously discussed rate striations introduced by vibrations. Like the vibrational striations, the presently reported striations do not effect the over-all crystal growth process and can thus be utilized for the investigation of localized microscopic growth rates and interface morphologies. Instantaneous growth rate changes resulting from Peltier heating (or cooling) have been previously studied extensively in connection with the formation of p-n junctions (3, 4).

In the present study a standard Czochralski pulling system was modified to permit the passage of current pulses across the crystal-melt interface during rotational and nonrotational pulling. A pulse generator in conjunction with a low-frequency current amplifier provided pulses of the desired frequency (5 to 40 cps). With this arrangement it was possible to control the current density and the duration of the current pulses which in turn determine the intensity and width of the induced striations respectively.

Some typical results obtained with Te-doped InSb single crystals are shown in Fig. 1 and 2. Local variations in growth rate within a given single crystal are readily seen in Fig. 1. It is apparent that these variations can be quantitatively evaluated. The constancy of the microscopic growth rate in the "core" of the

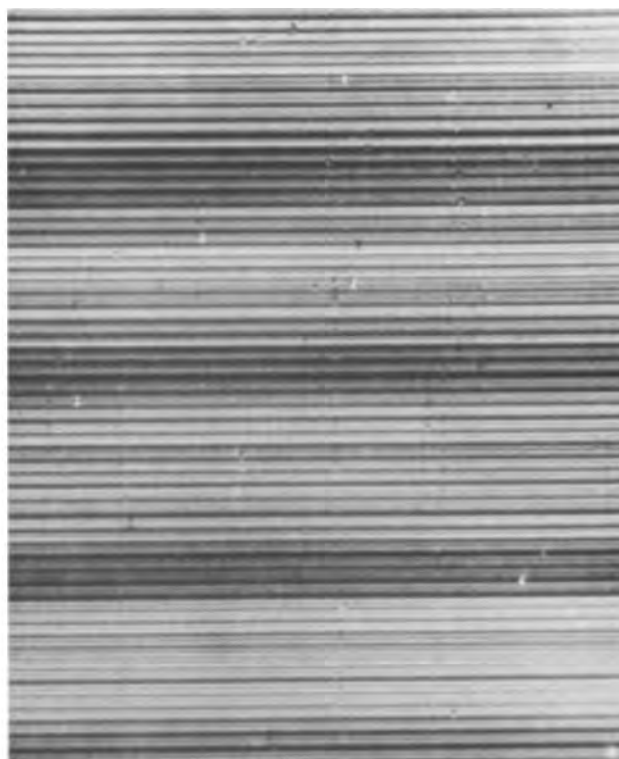


Fig. 2. Core region (facet growth) in an InSb single crystal. The microscopic rate of growth as revealed by the rate striations is constant. The alternating light and dark areas indicate impurity concentration changes which are unrelated to the microscopic rate of growth. Magnification 410X.

crystal (2) is seen in Fig. 2. This figure shows also impurity concentration changes (dark and light areas) which obviously do not result from microscopic growth rate changes.

The Peltier effect permits excellent control of the intensity and the width of the induced rate striations. Possible side effects associated with the current transport across the growth interface (mass transport) may limit its usefulness particularly in multicomponent systems.

The detailed nature of the rate striations and their application to the study of solidification processes is being studied in our laboratory.

#### Acknowledgment

This work was supported by the National Science Foundation under contract GK-1653.

Manuscript received Oct. 17, 1967.

Any discussion of this paper will appear in a Discussion Section to be published in the December 1968 JOURNAL.

#### REFERENCES

1. A. F. Witt and H. C. Gatos, *This Journal*, **114**, 413 (1967).
2. A. F. Witt and H. C. Gatos, *ibid.*, **115**, 70 (1968).
3. W. G. Pfann, K. E. Benson, and J. H. Wernick, *J. Electronics*, **2**, 597 (1957).
4. C. A. Domenicali, *J. Appl. Phys.*, **28**, 749 (1957).

# Discharge Characteristics of Some Copper Oxide-Magnesium Thermal Cells

Lawrence H. Thaller\*

Lewis Research Center, National Aeronautics and Space Administration, Cleveland, Ohio

## ABSTRACT

Previously single cells of the system Mg/LiCl-KCl/Cu<sub>2</sub>O were built that had service lives of several days at 425°C. Further studies are conducted to investigate the effect on discharge characteristics, both chemical and electrochemical, of different cell designs. The average rate of self-discharge taking place concurrently with electrochemical discharge at constant load varies from less than one to more than 200 ma. As cell designs are changed to decrease the rates of self-discharge (greater electrode spacings, higher current densities in the electrolyte, and different electrolytes), the over-all cell polarizations increased. The equivalent internal resistance of these cells varies from about 0.2 to about 2 ohms.

Thermal cells are a class of primary electrochemical devices which at room temperatures are inactive. The electrolytes used in these cells are usually mixtures of solid inorganic salts which require the application of heat to melt the electrolyte and thus to activate the cells. For certain applications, these cells have advantages over the more common aqueous or nonaqueous cells (1-3). While in the active state, these cells are not subject to internal chemical reactions of the active materials which lower the output of the cells. A less obvious advantage of a thermal battery is simply the ability of being able to operate at temperatures hundreds of degrees above the operating temperatures of aqueous batteries. It is this latter advantage that this research program is concerned with.

Earlier studies (4) on this system employed magnesium anodes, mixed copper oxide cathodes, and electrolytes of the eutectic mixture of lithium chloride (LiCl) and potassium chloride (KCl). This material when melted (mp, +352°C) has a high specific conductivity ( $K = 1.6 \text{ ohm}^{-1} \text{ cm}^{-1}$  at 450°C) and possesses a high decomposition potential of about 3v. The anode material (Mg) and the cathode material (CuO-Cu<sub>2</sub>O) both have rather high half-cell potentials, low equivalent weights, and were thought to have low solubilities in the electrolyte. The cells discharged in these earlier studies were opened and the contents analyzed quantitatively for products of reaction and unused reactants. Results of a typical analysis are shown in Table I.

The results of Table I show that during the cell discharge magnesium is oxidized to the +2 state and that both the cupric and cuprous oxide are reduced finally to metallic copper. As shown in these earlier studies the open-circuit voltage of these cells at the early stages of discharge are due to magnesium being oxidized to magnesium plus two ion and cuprous ion being reduced to metallic copper.

It was evident from the results of the material balances made on the discharged cells and from the continuous recordings of the cell voltage and cell current taken during the testing of the cells, that self-discharge was a major cause of poor performance. The losses of electrochemical efficiency by internal chemical reactions were of two types. The first type was caused simply by the diffusion of copper ions from the vicinity of the cathode to the magnesium anode. At the anode, the copper ions reacted chemically with the magnesium to form submicron particles of copper. The second type occurred when these small particles of copper suspended in the electrolyte actually formed an electrical short circuit between the anode and either the cell case or the cathode. The former type

affected the cell performance by lowering the yield of current from the cell. The latter type of self-discharge was characterized by erratic voltage and current fluctuations. The object of this research program was to understand and to control the diffusional type of self-discharge and to try to prevent the internal short circuits.

## Experiment

**Electrolytes.**—Mixtures of lithium chloride (LiCl), potassium chloride (KCl), and cesium chloride (CsCl) were used as the electrolytes for these cells. The reagent grade alkali halides were predried at 200°C for several weeks in a drying oven. Three different compositions of electrolyte were used in these studies. They were:

1. 59 m/o (mole per cent) LiCl — 41 m/o KCl
2. 59 m/o LiCl — 20.5 m/o KCl — 20.5 m/o CsCl
3. 59 m/o LiCl — 41 m/o CsCl

The proper proportions of these materials were weighed out in a porcelain crucible. After slowly bringing the ingredients to the melting point, magnesium chips were added in an effort to remove the last traces of water. When all evidence of reaction had ceased, the electrolyte was poured into a waiting cell.

**Sealed cells.**—The cells used in these studies are shown in Fig. 1 and 2. One type had the electrodes arranged in a vertical fashion and will be referred to as the vertical type; the other configuration will be referred to as the horizontal type. Both types of cells had the same nominal inside dimensions of 2.9 cm in diameter by 5.1 cm in height. The material used for the cell case was either commercially pure copper or

Table I. Chemical analysis of discharged cell

Material		Weight		
In fresh cell	In spent cell	g	Milli-equivalents	amp-hr
Mg <sup>0</sup>		5.66	466	12.48
	Mg <sup>0</sup>	4.16	343	9.20
	Mg <sup>+2</sup> (MgO)	1.55	131	3.41
	Mg total	5.71	474	12.69
Cu <sup>+2</sup> (CuO)		1.49	46.8	1.25
Cu <sup>+1</sup> (Cu <sub>2</sub> O)		13.36	210.0	5.63
Cu total		14.85	256.8	6.88
	Cu <sup>+2</sup> (CuO)	0.48	15.2	0.41
	Cu <sup>+1</sup> (Cu <sub>2</sub> O)	8.50	133.7	3.57
	Cu <sup>0</sup> (from CuO)	1.00	30.4	.84
	Cu <sup>0</sup> (from Cu <sub>2</sub> O)	4.79	75.4	2.10
	Cu total	14.76	254.7	6.92

\* Electrochemical Society Active Member.

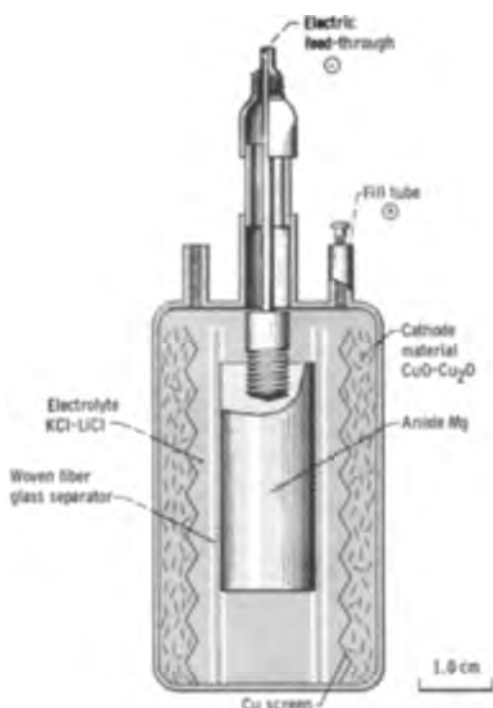


Fig. 1. Vertical-type cell

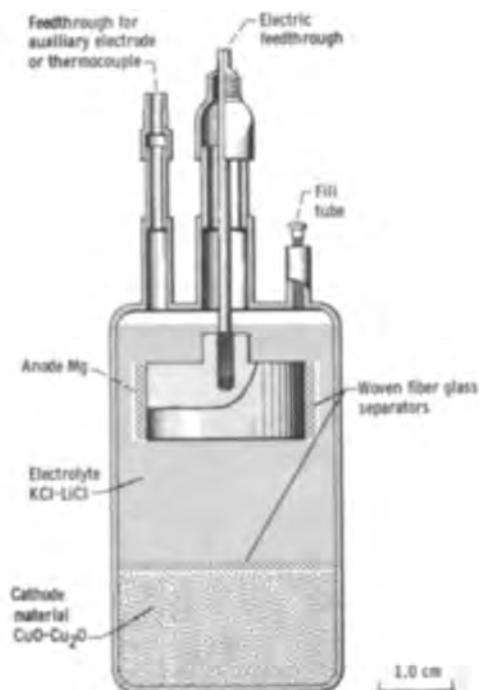


Fig. 2. Horizontal-type cell

nickel. The top assembly of the cell included the lid with the threaded fill tubes and either one or two electrical feedthroughs. The centrally located feedthrough served to insulate the anode from the cell case which was the current collector for the cathode. The other feedthrough was used for the insertion of a thermocouple or a reference electrode.

In all instances, an anode of the desired shape was screwed onto a shaft which extended up through the central feedthrough and was silver soldered onto the top of it. The grade of magnesium used for the anodes is called primary (99.8% Mg). The wire form of cupric oxide was used as the cathode material. The composition of this material varies from batch to batch and with supplier. In general its composition was between 65 and 85 m/o CuO, and the remainder was

Table II. Makeup of a typical open cell

Component	Weight or size
Cell case (20-ml beaker)	29-mm ID by 41 mm tall
Cathode current collector	25-mm ID by 45 mm tall
Cathode weight (CuO wires)	29.1g (85 m/o CuO)
Electrolyte weight (LiCl-KCl)	22.0g
Separators	2 thicknesses at anode
Anode size	12.7-mm diam by 38 mm tall
Anode weight	7.95g (17.5 amp-hr)

cuprous oxide ( $\text{Cu}_2\text{O}$ ). This cathode material was placed either in the bottom of the cell case for horizontal type cells or behind a cylindrical copper screen for the vertical-type cells. Woven glass cloth was used as a separator material in these cells. This tightly woven fabric was manufactured in the form of a continuous cylinder. After being coated with a resin, this material is sold as a flexible electrical insulation. The fabric thickness was about 1 mm. After oxidizing away the resin in a  $500^\circ\text{C}$  furnace, this fiberglass material was suitable for use as a separator in these cells. Its main function was to act as a mechanical barrier through which particles of copper could not form a continuous electronically conducting path. Usually one layer of separator material was placed against the cathode and one layer was placed against the anode.

With all the cell components in the cell, except for the electrolyte, the top assembly was welded onto the cell case. The electrolyte was added to these cells in a furnace which had been preheated to about  $450^\circ\text{C}$ . The final step in the construction was to screw stainless steel screws into the threaded fill tubes and to seal the two together with silver solder.

**Open cells.**—Open cells were used from time to time to perform certain preliminary experiments. These cells employed 20 ml beakers as cell cases and close fitting copper tubes as the cathode current-collectors. These cells used the same anodes, separators, and cathode material as the sealed cells, but were open at the top and thus were exposed to the atmosphere inside the furnace. The spacing between the anode and cathode was provided by the thickness of two layers of glass separator material (approximately 2 mm). A typical makeup of an open cell is shown in Table II.

#### Experimental Setup and Procedure

An unsealed furnace was used for the electrolyte addition step and also for the discharge of the open cells. Figure 3 shows a block diagram of the equipment used for the discharge of the sealed test cells. A fresh cell was wired to the proper leads of the disassembled furnace. The furnace used for heating the sealed cells was pressurized with nitrogen to retard oxidation of the lead wires and cell components during the prolonged exposure to the elevated temperatures. After making the proper exterior electrical

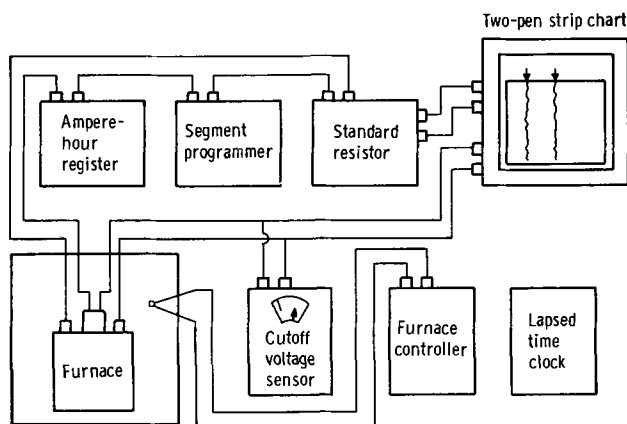


Fig. 3. Block diagram of experimental setup

connections, the furnace as well as the strip chart recorder, were turned on. These test cells had four leads. One positive and one negative wire from the cell went to one pen of a two-pen strip chart recorder. This pen thus recorded the load voltage of the cell while it was under load or the open-circuit voltage of the cell when it was in the no load condition. This same set of wires also went to the cutoff voltage sensor. When the voltage of the cell dropped below a preselected value (cutoff voltage), the sensor would shut off all power to all the equipment.

The other set of wires from the test cell was used to discharge the cell at the proper rate and also to measure the output of the cell in ampere-hours (A-h). One of the wires of this pair went to an electronic counting device. The rate at which this device counted was proportional to the current that passed through the device. The sum of all the counts was thus related to the integral of Idt. This device was in essence an electronic coulometer. From this device, the wire went next to the segment programmer. A complete discharge segment was divided as follows:

- 100-min cell under load  $R_1$
- 10-min cell under load  $R_1 + R_2$
- 10-min cell under no load

This discharge segment was repeated until the cell voltage fell below the cutoff voltage. From the segment programmer, the wire went to a standard resistor. The voltage drop across this resistor was a measure of the current that was flowing through the cell. The current was continuously recorded on the other pen of the strip chart recorder. A lapsed time meter was also used to record the time between the startup of a fresh cell and the termination of the experiment.

After a test had been terminated, the discharged cells were opened, and the unused anode was washed and weighed. The weight loss represented the sum of two different types of reaction. Part of the weight loss was due to electrochemical dissolution and the other was due to chemical dissolution caused by the self-discharge reaction of copper ions with the magnesium. Using the proper conversion factor ( $1\text{g Mg} \equiv 2.20\text{ amp-hr}$ ) these weight losses may be expressed in terms of ampere hours. The total weight loss  $A-h_T$  is then the sum of the weight loss due to electrochemical action  $A-h_{ec}$  and that due to self-discharge  $A-h_{sd}$ . Since the electrochemical output of the cell is measured for each of the cell discharges, all three of these quantities may be determined. By dividing these weight losses by the total lapsed time of the discharge, three average currents were calculated. They were  $I_T$  the total current,  $I_{ec}$  the electrochemical current, and  $I_{sd}$  the self-discharge current. The anode efficiency (AE) is defined as the ratio of the loss of anode weight due to useful electrochemical processes to the total loss of anode weight. For each experiment, the information appearing in Table III was recorded or calculated.

### Results and Discussion

*Determination of optimum amount of electrolyte.*— Since the object of these experiments was the investigation of the discharge characteristics of some com-

pleted cells, preliminary work was necessary to find a suitable group of design parameters from which the cells could be constructed. One of most important parameters was the selection of the amount of electrolyte to be used in the cells. With this particular combination of anode, electrolyte, and cathode, there was no *a priori* reason to believe that the electrolyte would be consumed during the discharge of these cells. Since the earlier studies (4) had shown that the major products of reaction were sparingly soluble MgO and insoluble  $\text{Cu}^0$ , there was no reason to believe the melting point of the electrolyte would be altered during the discharge of the cell. The particles of MgO, however, were held in suspension in the electrolyte and did change its consistency from a free flowing liquid to a semisolid paste.

The role played by the electrolyte in an electrochemical device varies from one system to another. Recent publications indicate that with certain cathode materials the discharge mechanism involves a solid-state electron transfer coupled with the increase of the hydrogen ion content of the solid. This is called the electron-proton mechanism (5), and the electrolyte supplies the protons. When a solid-state electron transfer cannot take place, the solid cathode material must first go into solution. This step is then followed by an electrochemical reduction involving these dissolved species. Although mixed copper oxides are good electronic conductors, lithium ion would not be expected to be able to migrate through the oxide lattice and thus complete an electron-proton type of reaction. Indeed, x-ray analysis of discharged cells showed no evidence of a mixed oxide between copper and lithium. For these reasons, it is felt that in the magnesium-copper oxide cell being studied, copper oxide must first go into solution. The function of the electrolyte, therefore, would be to act as a solvent for the cathode material and also as an accumulator for the products of reaction. The extent to which the cathode material is soluble, therefore, will affect the amount of copper species available both for electrochemical discharge and for transport to the anode.

An open cell was constructed and discharged to find how the over-all polarization was effected by the products of discharge. Using the equivalent circuit concept (6) which assigns an equivalent resistance to the concentration polarization as well as the ohmic resistance of the electrolyte; equivalent cell resistances were plotted as a function of products of reaction in the electrolyte. Figure 5 shows how this over-all equivalent resistance varied as a function of W, the grams of MgO per gram of total electrolyte (Fig. 4). In

Table III. Representative information recorded for each cell

Cell configuration	Horizontal
Anode weight (fresh cell)	5.9g (12.98 amp-hr)
Case material	Nickel
Anode weight (spent cell)	0.52g (1.15 amp-hr)
Electrolyte weight	25g
Separators	1 anode, 1 cathode
Anode to cathode spacing	14 mm
Duration of test	290.8 hr
Anode weight loss	5.38g
Ampere hours delivered	10.90 (amp-hr)
Ampere hours of self-discharge	0.92 (amp-hr)
Electrochemical discharge rate	37.4 ma
Self-discharge rate	3.10 ma
Anode efficiency	92.2%

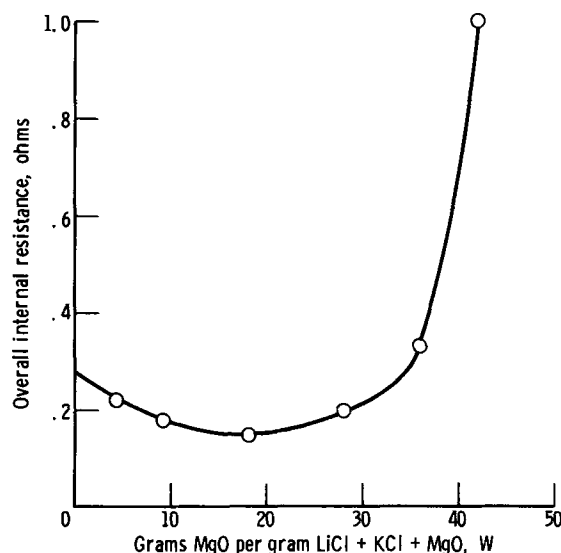


Fig. 4. Effect of ratio of magnesium oxide to electrolyte on over-all internal resistance.



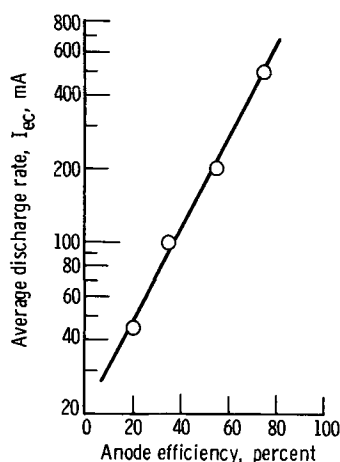


Fig. 5. Plot of average discharge rate and anode efficiency

this plot, it is seen that the equivalent resistance remains about the same to a  $W$  value of about 28. From information like this, it was decided that about 2g of the LiCl-KCl eutectic were required for every ampere-hour of reaction products. The cells shown in Fig. 1 and 2 use this electrolyte loading factor along with the woven glass fabric separators discussed in the section, Experiment.

**Controlling the self-discharge process.**—The first group of cells to be tested were all alike (class 1-Table IV). They were the vertical type and had copper cases, lids, screens, and shafts. The use of copper throughout was an attempt to eliminate any possible side reactions between the cupric ion and any less noble material of construction to form reducible ions other than copper. Four of these cells were discharged at different average currents. Figure 5 shows the results of this series; the anode efficiencies are plotted against the average current. Here it is seen that although the average electrochemical currents vary over a wide range (43-487 ma), the rate of self-discharge,  $I_{sd}$ , for all these cells is about the same (160-230 ma). From this plot it is seen that at an average electrochemical drain of about 190 ma, the anode efficiency is 50%, or, in other words, the average rate of nonelectrochemical discharge is also 190 ma. This rate is high considering the total capacity of these cells is only about 15 amp-hr.

In all probability, this self-discharge process is caused by the diffusion of copper ions from the vicinity of the cathode to the anode where chemical reaction takes place. This over-all process may be divided into three stages or steps: (i) the solution of the copper ions at the cathode; (ii) the diffusion of the copper ions from the vicinity of the cathode to the anode; and (iii) the reaction of the copper ions with the magnesium anode.

In principle, any one of these three processes could have the slowest rate and thus could control the over-all process. Considering the high temperatures and the large change in free energy (about 40 kcal) for the reaction of copper ions with magnesium metal, the rate of this reaction would be very fast and therefore not rate controlling. Either the rate of solution or the rate of diffusion would control the over-all process.

Table IV. Parameters studied

Cell Class	Type	Distance from anode to cathode, mm	Electrolyte	Separators
1	Vertical	2.0	LiCl-KCl	1 anode, 1 cathode
2	Vertical	5.0	LiCl-KCl	1 anode, 1 cathode
3	Vertical	5.0	LiCl-KCl-CsCl	1 anode, 1 cathode
4	Vertical	5.0	LiCl-CsCl	1 anode, 1 cathode
5	Horizontal	14	LiCl-KCl	1 anode, 2 cathode
6	Horizontal	14	LiCl-CsCl	1 anode, 2 cathode

The basic diffusion equation was used to differentiate between these two processes (solution and diffusion).

$$\text{Rate of diffusion } \frac{dN}{dt} = -DA \frac{dc}{dx}$$

Although the exact applicability of this simple equation to this particular system is not implied, it is instructive to investigate the implications of such an assumption. Fick's first law of diffusion simply states that rate of diffusion  $dN/dt$  is equal to the diffusion coefficient  $D$  of the species that diffuse times the area  $A$  available for diffusion times the concentration gradient  $dc/dx$  of the diffusing species. Several short wide cells were made that contained the same weights of electrode material (same area for dissolution of CuO-Cu<sub>2</sub>O wires) and electrolyte but only had one-half the area available for diffusion between the anode and the cathode. There also was a greater distance between the anode and the cathode. If the rate of self-discharge was controlled by the rate of solution of the copper oxides, these alterations would not be expected to alter the rate of self discharge. Table V shows the results of altering the area for diffusion by a factor of two and decreasing the concentration gradient by a factor of about two.

The fact that the rate of self-discharge was reduced by about a factor of three (although the equation predicted four) makes plausible the conclusion that the factor controlling the self-discharge process was the rate of diffusion of copper ions from the vicinity of the cathode to the anode. Therefore, it should be possible to alter the diffusional characteristics of these cells by any one of the following means:

1. Decrease the area available for diffusion; this can be done, for example, by constructing a short wide cell.
2. Decrease the concentration gradient of the species that diffuse; this may be accomplished by increasing the separation between the two electrodes.
3. Decrease the diffusion coefficient of the species involved in the self-discharge process. Alterations in the ion size and character of the electrolyte might bring this about.
4. Reduce the activity of the ions causing the self-discharge. The formation of complex ions would perform this task.
5. Introduce a separator between the electrodes which would preferentially hinder the passage of the particular ion of interest.

**Studies on alterations of diffusional characteristics.**—The method of data presentation is somewhat different than for other battery studies so it will be explained prior to the discussion of the results of these studies. The anode efficiency as stated earlier may be defined as

$$AE = \frac{I_{ec}}{I_{ec} + I_{sd}}$$

If the assumption is made that the rate of self-discharge,  $I_{sd}$ , of a particular cell configuration and electrolyte is a constant for all rates of electrochemical discharge,  $I_{ec}$ , then a curve may be generated as shown in Fig. 6. Here, it was arbitrarily assumed that  $I_{sd}$

Table V. Self-discharge rates for tall and short cells

Cell	Anode area (for diffusion), cm <sup>2</sup>	Rate of self-discharge, $I_{sd}$ , ma	Average rate of self-discharge, $I_{sd}$ , ma	Self-discharge current per unit area per concentration gradient, $\frac{I_{sd}}{A dc/dx}$
Tall	14.1	160, 160, 205, 235	181	12.8
Short	6.2	40, 51, 63	51	16.7

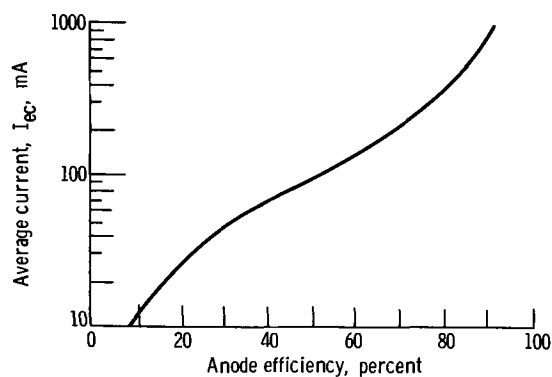


Fig. 6. Plot of average electrochemical current and anode efficiency. Self-discharge rate, 100 ma.

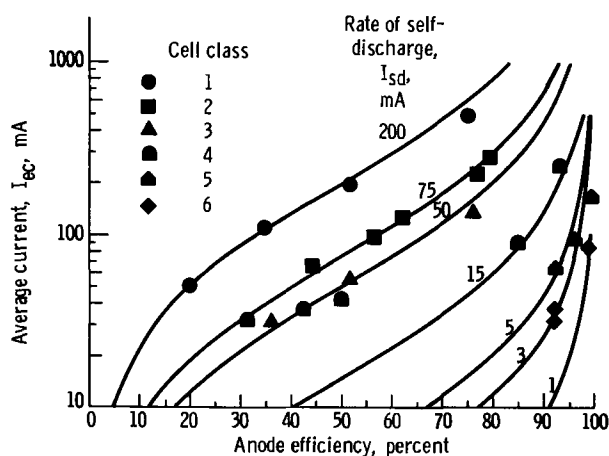


Fig. 7. Plot of average electrochemical current and anode efficiency.

would be 100 ma. For any assumed  $I_{ec}$ , the anode efficiency can be calculated. For a different assumed  $I_{sd}$ , the curve would be moved up or down, but would maintain the same general shape being asymptotic at zero and 100% anode efficiency. Figure 7 shows a whole family of these curves along with data points for some of the cells run in these studies. It is to be noted that in general the data points for a particular class of cell fall near a line of constant self-discharge, and thus the assumption of constant rates of self-discharge is valid over a wide range of operating conditions. A class of cell is defined as a group of cells having the same electrode spacing, electrolyte, and separator configuration as shown in Table IV. The points near the 200-ma line (class 1) are those seen earlier in Fig. 5. The electrolyte was the eutectic mixture of LiCl-KCl. The points near the 75-ma line are again for vertical type cells but with a greater separation between the anode and the cathode (class 2) (i.e., smaller concentration gradient of the copper ions). With this latter configuration and replacing 50 m/o of the KCl with CsCl, the points fall near the 50-ma line (class 3). The effect of the larger ion size of cesium on the diffusional characteristics is more dramatically shown where all the KCl is replaced with CsCl. The points for these cells of class 4 now fall near the 15-ma line. The eutectic of LiCl-CsCl has about the same composition and melting point as the LiCl-KCl eutectic (mp, 333°C ~ 42.5 m/o LiCl).

For cells of the horizontal type, the same general trend was noticed. When the electrolyte was LiCl-KCl, the rate of self-discharge was about 5 ma for class 5 cells, and when the electrolyte was LiCl-CsCl, the rate was about 3 ma (class 6).

With all these cells, it was found that erratic performance and intermittent short circuits occurred when cells were discharged at average currents less than

about 30 or 40 ma. Figure 7 has a number of points of several classes of cells that are off their respective lines of constant self-discharge. The exact reason for this is not known. At higher values of  $I_{ec}$ , on the other hand, it appears that the cells display a lower value of  $I_{sd}$  than predicted from the curves. This behavior is reasonable since, at the higher rate of electrochemical discharge, the higher concentration polarizations will act to hinder the diffusion of the copper ions from the cathode.

Although it is not obvious from the material presented in Fig. 7, the cells with the lowest rates of self-discharge have the highest over-all equivalent internal resistance. For these cells, a hundredfold decrease in the rate of self-discharge was accompanied by only a tenfold increase in the equivalent internal resistance. In general, the values of the equivalent internal resistance for the horizontal cells was of the order of 2-4 ohms while for the vertical cells it was in the range of 0.2-0.4 ohm. The value of the internal resistance limits the upper value of the current that may be withdrawn from a cell.

Discharge curves of three representative cell classes are shown in Fig. 8 to 10. Figure 8 is the discharge curve of a class 2 cell illustrating the performance over a short discharge time (34 hr) of a cell that used a LiCl-KCl electrolyte. Figure 9 illustrates the performance of a cell (class 3) at a moderate duration discharge (77 hr) using an electrolyte of LiCl-KCl-CsCl. Figure 10 shows the long term (290 hr) operating characteristics of a class 5 cell with a LiCl-CsCl electrolyte. In addition to the open-circuit voltage, the load voltage, and the current, Fig. 10 also has plotted equivalent cell resistance ( $\Delta E/\Delta I$ ) as a function of time to illustrate how this value varies as the cell is discharged. The main point to be noted on these three figures is that abrupt changes in the open-circuit voltage curves occur accompanied with only small and gradual changes in the current and in the voltage under load.

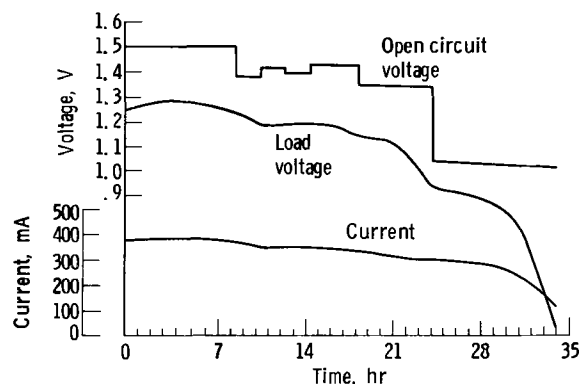


Fig. 8. Discharge curve of vertical cell. Electrolyte, 59 m/o LiCl, 41 m/o KCl; rate of self-discharge, 72 ma; rate of electrochemical discharge, 280 ma.

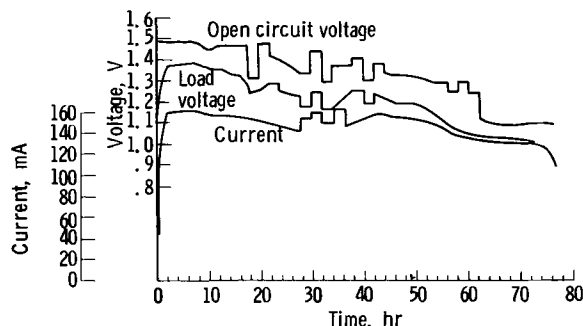


Fig. 9. Discharge curve of vertical cell. Electrolyte, 59 m/o LiCl, 20.5 m/o KCl, 20.5 m/o CsCl; rate of self-discharge, 41 ma; rate of electrochemical discharge, 132 ma.

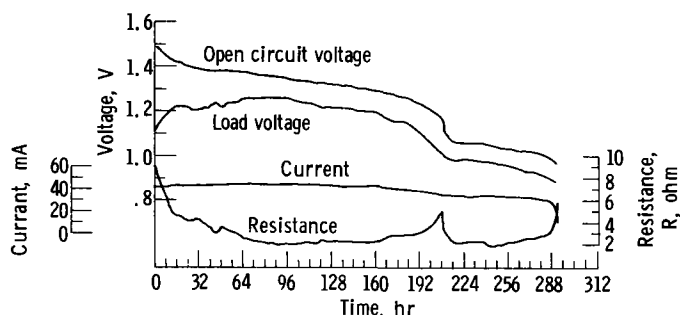


Fig. 10. Discharge curve of horizontal cell. Electrolyte, 59 m/o LiCl, 41 m/o CsCl; rate of self-discharge, 3.1 ma; rate of electrochemical discharge, 37.4 ma.

**Explanation of steps in the open-circuit voltage.**—These steps or abrupt changes in the open-circuit voltage may be explained in terms of the following electrochemical model. Assume there are two over-all electrochemical reactions possible (reaction I and II). Over-all reaction I will have an open-circuit voltage  $E_I$  which is greater than  $E_{II}$  by say 100 mv or more. During the initial stages of discharge, the observed open-circuit voltage and the load voltage will be due predominately to the presence of the reactants and the products of reaction I. As the discharge proceeds, there will be fewer type I species, and this reaction may become polarized to the extent that reactants of type II will be discharged concurrently with those of type I. Gradually the proportion of type II species reacting during discharge will become greater until the load voltage will be due predominately to reaction II. However, until almost all the type I reactants have been consumed, the open-circuit voltage will be a consequence of the type I species. Later, of course, the open-circuit voltage will be due predominately to the over-all reaction II. With cells of all classes discharged in these studies, there was at least one abrupt change in the open-circuit voltage during the discharge. The magnitude of these changes ranged from about 50-250 mv.

Figure 11 will illustrate what two successive discharge segment traces look like as the transition (from reaction I to II) is made complete. Figure 11 is based on data from a class 2 cell, and this transition occurred between discharge segments 18 and 19. During the 18th segment, there is an electroactive specie present (type I) that is responsible for the open-circuit voltage, but it is not present in large enough amounts to be able to maintain the higher currents (I drops quickly from 142 to 112 ma). That is, they are subject to extreme concentration polarization. At the 19th segment, this more active specie (type I) has disappeared, and the less active (type II) but more abundant specie is now responsible for both the open-circuit voltage and the load voltage of the cell.

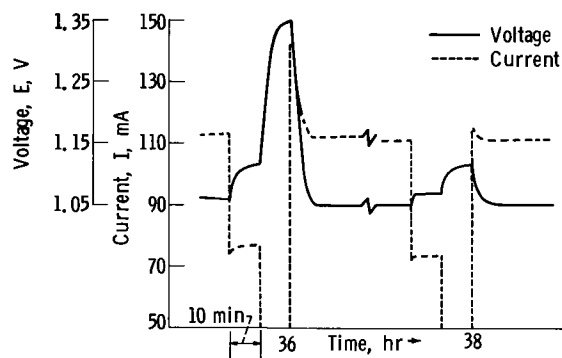
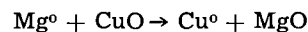


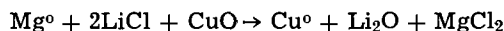
Fig. 11. Variance of current and voltage with time. Sequence of events: starting with constant-load discharge, load is increased for 10 min, then circuit is open for 10 min, after which original load is applied for 100 min and then changes are repeated.

At this time it is not known exactly what this latter over-all electrochemical reaction is. However, x-ray analyses on some cells that had undergone these abrupt changes in open-circuit voltage tended to confirm the contention that a change in over-all reaction had occurred.

**X-ray analysis of the electrolyte after cell discharge.**—The method of analysis was as follows. A discharged horizontal-type cell was opened, and the unused anode was washed and weighed as before. Next, the cell was split down the middle, one-half being placed in a desiccator and the other left out in contact with the moist air. As the materials in the cell picked up hydration water, characteristic colors began to form in horizontal bands in the cathode area. From each of the areas which were made evident by the "wet" half of the cell, x-ray samples were taken from the cell half that had been kept as dry as possible. Figure 12 shows a typical set of results. The existence of the associated compound  $KCl \cdot MgCl_2$  in the anolyte and the presence of  $Li_2O$  in the lower layers of the cathode area are to be noted. The upper area of the cathode area contained  $Cu^0$  and  $MgO$ . The lack of any  $MgO$  in the anolyte is also to be noted. From this set of information, it may be concluded that cations from the anolyte migrate to the catholyte to maintain over-all charge neutrality in these cells. Since the upper portion of the cathodes react first, it may further be deduced that during the latter stages of discharge the lithium ion moves instead of the magnesium ion. The over-all reaction I, therefore, is associated with a reaction that would have  $MgO$  as a product of reaction, such as



whereas reaction II would be associated with a reaction that would have  $Li_2O$  as a product of reaction. One possibility might be



### Conclusions

Long-life high-temperature primary cells can be built that have predictable discharge characteristics. The woven-glass separator material was found to prevent internal short circuits for certain cell configurations. For the cell configurations employed in these studies, the rate-controlling step in the self-discharge process was found to be the rate of diffusion of copper ions from the vicinity of the cathode to the anode. The rate of self-discharge could be considerably reduced by increasing the electrode spacing and by adding CsCl to the electrolyte to reduce ion diffusion rates. The open-circuit voltage of these cells decreased in a stepwise fashion during discharge, with at least two steps observable.

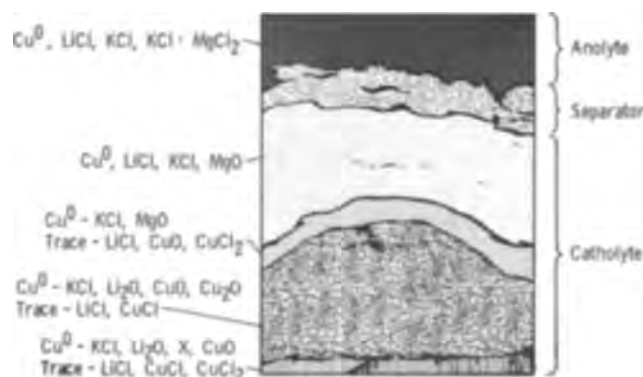


Fig. 12. X-ray analysis of spent cell

Manuscript received July 26, 1967; revised manuscript received Oct. 14, 1967. This paper was presented at the Philadelphia Meeting, Oct. 9-14, 1966, as Abstract 50.

Any discussion of this paper will appear in a Discussion Section to be published in the December 1968 JOURNAL.

## REFERENCES

1. G. W. Vinal, "Primary Batteries," pp. 324-329, John Wiley & Sons, Inc., New York (1950).
2. R. B. Goodrich and R. C. Evans, *This Journal*, **99**, 207 (1952).
3. E. McKee, "Thermal Cells," Proc. Tenth Annual Battery Res. and Dev. Conf., Power Sources Div., Signal Corps Eng. Labs., Fort Monmouth, N. J., pp. 26-28 (1956).
4. L. H. Thaller, *This Journal*, **113**, 309 (1966).
5. A. Kozawa and R. A. Powers, *ibid.*, **113**, 870 (1966).
6. J. Randles, *Proc. Faraday Soc.*, **1**, 11 (1947).

## Cathodic Polarization of the Manganese Dioxide Electrode in Alkaline Electrolytes

A. Kozawa\* and R. A. Powers\*

Consumer Products Division, Research Laboratory, Union Carbide Corporation, Cleveland, Ohio

## ABSTRACT

Polarization of  $\beta$ - and  $\gamma$ - $MnO_2$  is measured at various constant currents in 9M KOH and KOD electrolytes in reduction from  $MnO_2$  to  $Mn(OH)_2$ . Two limiting currents are observed in high-current discharges of  $\gamma$ - $MnO_2$ , one around  $MnO_{1.75}$  and the other after  $MnO_{1.5}$ . The former is attributed to formation of a lower oxide structure on the surface of  $\gamma$ - $MnO_2$  structure. Around  $MnO_{1.9}$ , a Tafel relation is observed for  $\gamma$ - $MnO_2$  and  $i_0$  values are obtained. The polarization is always greater in 9M KOD than in 9M KOH under the same discharge conditions.

In previous work, Kozawa and Yeager (1) found two steps in the cathodic reduction process of  $\gamma$ - $MnO_2$  in alkaline electrolyte; the first step from  $MnO_2$  to  $MnO_{1.5}$  and the second step from  $MnO_{1.5}$  to  $MnO_{1.0}$ . The first step was a homogeneous-phase discharge and the open-circuit potential *vs.*  $x$  value in  $MnO_x$  has been established and its significance was discussed by Kozawa and Powers (2). The second step was a heterogeneous phase discharge, for which a new mechanism was proposed (1) based on the presence of dissolved Mn(III) and Mn(II) ions (3).

The purpose of this work is to investigate the general pattern and magnitude of polarization in the course of cathodic reduction of  $\gamma$ - and  $\beta$ - $MnO_2$  in an alkaline electrolyte in the entire range of the two steps mentioned above. Another purpose is to establish the magnitude of polarization of  $\gamma$ - $MnO_2$  in KOD solutions and compare it to that in KOH solutions.

The nature of the polarization of the first step was studied by Scott (4), and by Kornfeil (5) in ammonium chloride electrolyte, and by Era *et al.* (6) in alkaline electrolyte. These previous studies were mainly based on the analysis of build-up and decay curves in order to test the proton diffusion theory in the solid. No attempt, however, has been made to investigate the steady-state polarization in relation to the stages of the discharge (or  $x$  value in  $MnO_x$ ).

In this investigation, polarization at various constant currents in the course of reduction from  $MnO_{2.0}$  to  $MnO_{1.0}$  was measured in KOH and KOD electrolytes.

## Experimental

**Samples.**—The manganese dioxide powder samples used in this work were electrolytic  $\gamma$ - $MnO_2$ , and  $\beta$ - $MnO_2$  which was prepared from the  $\gamma$ - $MnO_2$  by heating at 400°C for 10 days in air and subsequent washing with 2M  $H_2SO_4$  solution. Details of the physical and chemical properties of these samples are reported in the previous paper (9). The  $\beta$ - $MnO_2$  (III) in this paper was the same as the  $\beta$ - $MnO_2$  (III) in the previous paper (9).

**Discharge cell.**—The discharge cell (Fig. 1) which was used in this work is similar to the previous one

- (9), but modified in order to achieve more homogeneous current-distribution in the cathode mix. One gram of coke, 0.5g of graphite powder, and 50 mg of  $MnO_2$  powder were ground together in a glass mortar for 1 min and transferred into the cell. The mixture was then stirred with 0.35 ml of 9M KOH solution. Two layers of separator paper and a perforated Teflon disk were then placed in the cell and pressed tightly. Electrolyte was added drop by drop at one edge in order to let it soak homogeneously through the mix. Finally the Lucite plug was tightly screwed down and more electrolyte was added from the top.

**Polarization measurements.**—A constant current (1-60 ma) was passed continuously between the  $MnO_2$

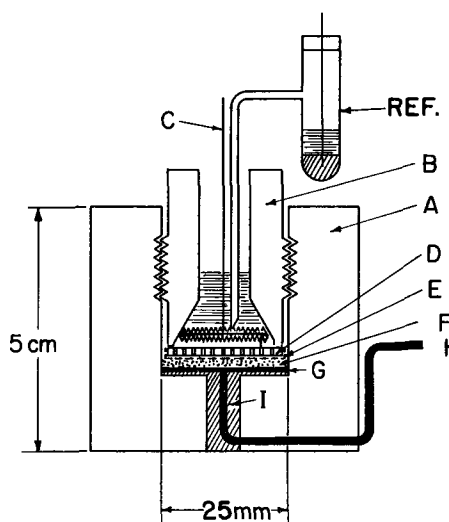


Fig. 1. Discharge cell: A, Lucite cell; B, Lucite plug; C, gold wire (0.85 mm diameter) spiraled at the bottom with expanded zinc metal pressed on the spiral part; D, perforated Teflon disk; E, two layers of separator paper made of synthetic fiber; F, a mixture of 1.0g coke + 0.5g graphite + 50 mg  $MnO_2$  sample; G, gold plate fixed at the bottom of the cell by epoxy resin; H, gold wire welded to the gold plate (G); I, epoxy filling.

\* Electrochemical Society Active Member.

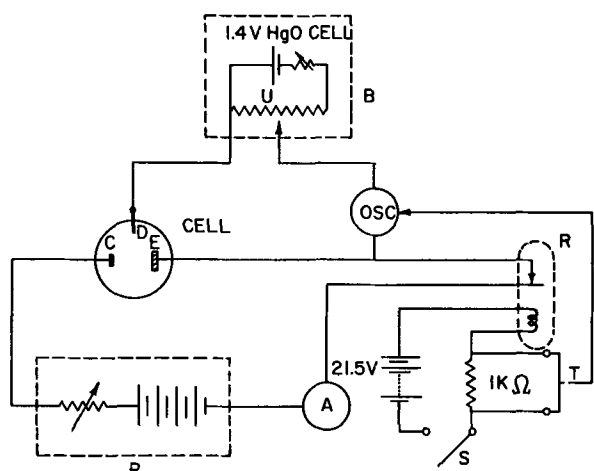


Fig. 2. Schematic diagram for the oscilloscopic polarization measurement: A, milliammeter; B, potential biasing box; C, counter electrode (expanded Zn on gold wire); D, reference electrode [Hg/HgO (9M KOH)]; E,  $\text{MnO}_2$  mixed with coke and graphite; OSC, Tektronix-type 564 storage oscilloscope; P, d-c power source; R, mercury wetted contact relay (HGS-1005); S, switch to operate the relay to interrupt the polarizing current; T, to trigger of OSC; U, Heliopot (1000 ohms) adjusted to 1.000v.

cathode and the zinc electrode in the entire course of reduction from  $\text{MnO}_2$  to  $\text{Mn}(\text{OH})_2$ . The IR-free closed circuit voltage (CCV) of the  $\text{MnO}_2$  cathode was measured against a Hg/HgO (9M KOH) reference electrode every 1 ma-hr using a Sargent Model MR recorder or an oscilloscopic method (Fig. 2). A curve of open-circuit voltage (OCV) vs. depth of discharge (ma-hr or  $x$  in  $\text{MnO}_2$ ) has been established for both  $\text{MnO}_2$  samples as reported in a previous paper (9). The potential difference between the IR-free CCV and the OCV was taken as polarization at each stage during the constant-current discharge.

**Electrolytes.**—9M KOH was prepared from reagent grade KOH pellets, and 9M KOD was prepared from 40% KOD in  $\text{D}_2\text{O}$  solution and 99.7%  $\text{D}_2\text{O}$ .

**Errors in the polarization measurements.**—The IR-free CCV shown in Fig. 4, 5, 6, and 8 were obtained by the recorder method in which the circuit was opened for a few seconds while the potential was recorded at a chart speed of 20 ipm. The polarization data in Fig. 7 were measured by the oscilloscopic method (Fig. 2) in which an accurate IR drop was determined from a trace on the screen. A few examples of such a trace are shown in Fig. 3, which also shows typical examples of decay of polarization.

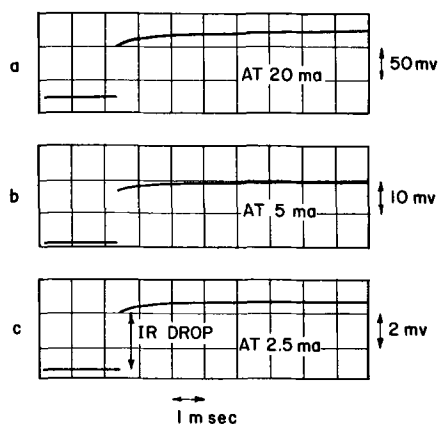


Fig. 3. Oscillographic traces of the current interruption with the circuit shown in Fig. 2. Current is for a single cell containing 50 mg of  $\gamma\text{-MnO}_2$  sample. These traces were obtained at a discharge stage of 1 ma-hr in 9M KOH.

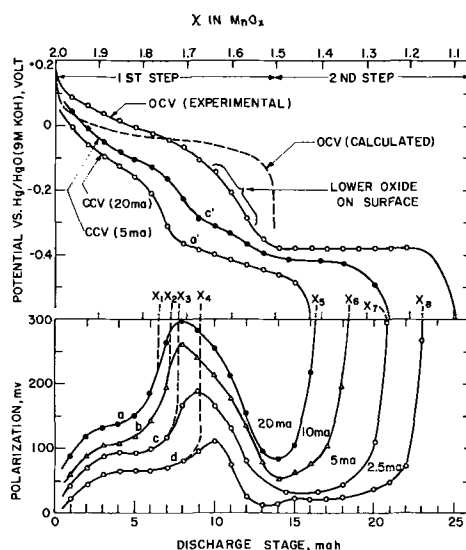


Fig. 4. Constant current polarization of  $\gamma\text{-MnO}_2$ . The currents shown on the curves are for a single cell containing 50 mg  $\gamma\text{-MnO}_2$  sample. The OCV (calc.) was calculated as described previously (2). Curves a and a' are polarization and CCV respectively at 20 ma discharge. Curves c and c' are those at 5 ma discharges.

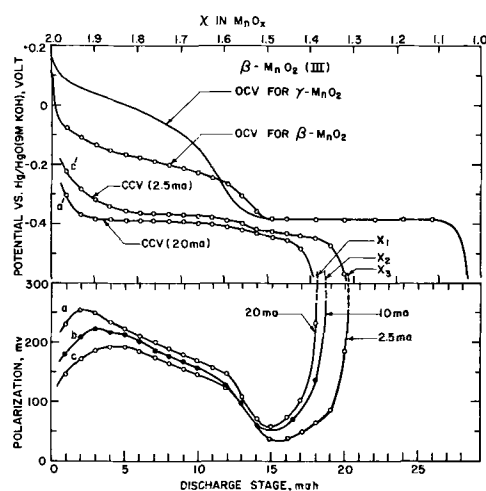


Fig. 5. Constant current polarization of  $\beta\text{-MnO}_2$  (III). The currents on the curves are for a single cell containing 50 mg  $\beta\text{-MnO}_2$  (III) sample. Curves a and a' are polarization and CCV respectively at 20 ma discharge. Curves c and c' are those at 2.5 ma discharge.

A large portion of the polarization decay may be attributed to the potential change of the R-C network of the carbon materials. The IR drops measured by the oscilloscopic method at various currents for a single cell were proportional to the current. The cell resistance varied from one cell to another in a range of 1.1-3.6 ohms. Table I shows the comparison of the polarization data measured by the two methods. We can see that, at 10 ma or lower currents, the error is less than 10%, but at 20 ma or higher currents, the error is greater than 20%.

Another error which may enter into the polarization measurement, particularly at high current, is due to nonhomogeneous current distribution in the cathode mix caused by the IR drop. In the present mix composition, the volume of the  $\text{MnO}_2$  sample constitutes only 0.5% of the total volume (50 mg  $\text{MnO}_2$  sample in 1.5g of coke and graphite). Error in the polarization value due to the nonhomogeneous current distribution must increase with increasing total current. A qualitative examination was made on this point as follows. Three different amounts of the  $\gamma\text{-MnO}_2$  sample (25, 50,

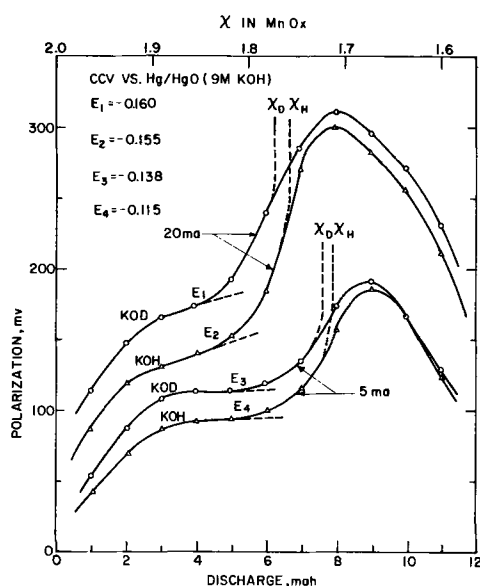


Fig. 6. Constant current polarization in 9M KOH and 9M KOD. The current is for a single cell containing 50 mg of  $\gamma$ -MnO<sub>2</sub> sample.

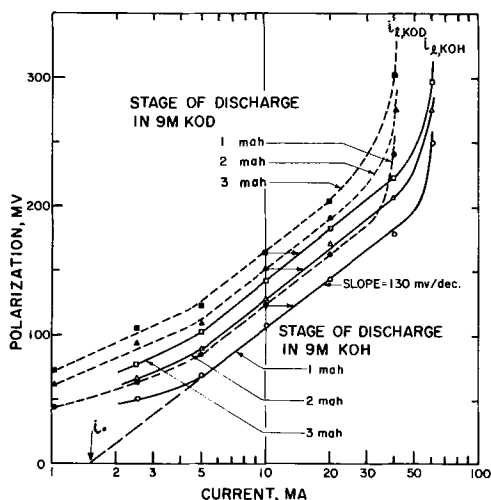


Fig. 7. Polarization of  $\gamma$ -MnO<sub>2</sub> vs.  $\log i$  at high current densities at early stages of the discharge. The current is for a single cell containing 50 mg of  $\gamma$ -MnO<sub>2</sub> sample.

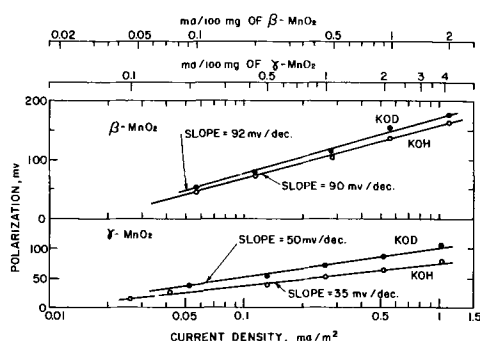


Fig. 8. Polarization vs.  $\log i$  at low current densities. The current density (ma/m<sup>2</sup>) is based on the BET surface area.

and 100 mg) were mixed with 1.0g of coke and 0.5g of graphite in the manner described earlier and discharged at the same current density of 0.2 ma/mg of sample (i.e., 5, 10, and 20 ma in total current per cell, respectively). The polarization values for these three cells agreed with each other within the experimental error. This indicated the error due to nonhomogeneous

Table I. Error of polarization\* measured by Sargent MR recorder

Polarizing current, ** ma	Electrolyte	Polarization† by oscilloscope, mv	Polarization† by recorder, mv	Error mv	Error %
1.0	9M KOD	70	68.5	1.5	2.2
2.5	9M KOH	78	76	2	2.6
2.5	9M KOD	117	115	2	1.7
5.0	9M KOH	102	95	7	6.9
10.0	9M KOH	142	130	12	8.5
10.0	9M KOD	176	165	11	6.3
20.0	9M KOH	188	146	42	22.4
40	9M KOH	220	170	50	22.7
40	9M KOD	312	255	57	18.2
60	9M KOH	299	194	105	35.2

\* Measured at 3 ma-hr-discharge stage of  $\gamma$ -MnO<sub>2</sub>.

\*\* For a single cell containing 50 mg sample.

† See Fig. 3 for the circuit.

‡ Sargent MR Recorder with pen speed of 1 sec for full scale, measured at 1v range.

current distribution may be small except at very high current densities.

When the polarization was measured immediately after packing the cell, the polarization was considerably smaller (about 15-20% smaller than several hours later. This was found to be due to a chemical reduction of MnO<sub>2</sub> by a small amount of reducing substance present in the coke and graphite. The chemical reduction proceeds slowly. We can see this by the decrease in the initial open-circuit potential; it was initially +0.165v vs. Hg/HgO (9M KOH), +0.145 after a few hours, +0.130 after 8-10 hr, and changed very little thereafter. When accurate data are needed, the polarization measurements should be started at least several hours after packing the cell, because the OCV vs.  $x$  value relation was obtained under such a condition. The data of Fig. 4, 5, and 6 were measured 3-4 hr after the packing, and those of Fig. 7 and 8 were measured 8-10 hr after the packing.

## Results

Figures 4 and 5 show polarization (lower part of the figure) and CCV and OCV (upper part) in the entire range of the discharge at various constant currents for  $\gamma$ -MnO<sub>2</sub> and  $\beta$ -MnO<sub>2</sub>(III), respectively. The polarization of  $\gamma$ -MnO<sub>2</sub> initially increases with the depth of discharge to around 2-3 ma-hr (around  $x = 1.9$ ) depending on the current, then remains approximately the same value. The polarization then increases rapidly indicating the presence of limiting  $x$  value around MnO<sub>1.7</sub> depending on the current density. After passing a maximum, the polarization decreases rapidly and reaches a minimum around MnO<sub>1.5</sub> which is the end of the first step. In the second step, from MnO<sub>1.5</sub> to MnO<sub>1.0</sub>, the polarization is at first low and for a while at low currents (below 5 ma) remains approximately constant, then reaches a limiting  $x$  value. These limiting  $x$  values ( $x_1, x_2, \dots, x_8$ ) are summarized in Table II.

The polarization curves of  $\beta$ -MnO<sub>2</sub>(III) looks much different from that of  $\gamma$ -MnO<sub>2</sub> for the first step (MnO<sub>2</sub> to MnO<sub>1.5</sub>), but the polarization curves for the second step are similar in general shape to those for  $\gamma$ -MnO<sub>2</sub>. It was reported in our previous paper (9) that magnitude of polarization of  $\beta$ -MnO<sub>2</sub>(III) is not much different from that of  $\gamma$ -MnO<sub>2</sub> at low current densities (0.05 ~ 0.5 ma/m<sup>2</sup> or below 2 ma/100 mg MnO<sub>2</sub> sam-

Table II. Limiting  $x$  values

Current, ma	$\gamma$ -MnO <sub>2</sub>		$\beta$ -MnO <sub>2</sub> (III)
	$x_1$ for the 1st step	$x_1$ for the 2nd step	$x_1$ for the 2nd step
20	$x_1 = 1.77 \pm 0.01$	$x_5 = 1.41 \pm 0.02$	$x_1 = 1.39 \pm 0.02$
10	$x_2 = 1.74 \pm 0.01$	$x_6 = 1.34 \pm 0.02$	$x_2 = 1.37 \pm 0.02$
5	$x_3 = 1.71 \pm 0.02$	$x_7 = 1.25 \pm 0.02$	—
2.5	$x_4 = 1.68 \pm 0.03$	$x_8 = 1.17 \pm 0.02$	$x_3 = 1.31 \pm 0.02$

ple) in Leclanché electrolytes (5M NH<sub>4</sub>Cl + 2M ZnCl<sub>2</sub> + NH<sub>3</sub>) of pH 5.0 ~ 8.8. However, we can see in Fig. 4 and 5 that the magnitude of polarization of  $\beta$ -MnO<sub>2</sub>(IV) is much greater than that of  $\gamma$ -MnO<sub>2</sub> in 9M KOH particularly at high current densities (2.5 ~ 20 ma per 50 mg MnO<sub>2</sub> sample) in a range of from MnO<sub>2.0</sub> to MnO<sub>1.8</sub> which is important for practical batteries.

Figure 6 shows the comparison of polarization in 9M KOH and 9M KOD at two discharge currents (5 and 20 ma). Polarizations in KOD are greater by about 10-30% than those in KOH, and the limiting  $x$  values (indicated as  $x_D$  and  $x_H$ ) come at an earlier stage in KOD than in KOH. Figure 7 shows polarization ( $\eta_c$ ) vs. logarithm of current at early discharge stages (1, 2, and 3 ma-hr stages) in 9M KOH and 9M KOD. The curves have a straight line portion (at least one decade) and also show a limiting current. The slope of the straight line portion is approximately 130 mv per decade for all the lines. Figure 8 shows polarization vs. logarithm of current in a low current range at the 5 ma-hr discharge stage. These data were obtained in the old cell (containing 100 mg of MnO<sub>2</sub> sample) which was described in a previous paper (9). Even at a low current range, polarization in 9M KOD is greater (by about 10-25%) than in 9M KOH. The slopes of the Tafel lines were 90-92 mv and 35-50 mv per decade for  $\beta$ -MnO<sub>2</sub>(III) and  $\gamma$ -MnO<sub>2</sub>, respectively, and were much smaller than those in Fig. 7.

### Discussion

Among the results obtained in this work, three main points for the first step will be discussed here: the first is the limiting  $x$  value around MnO<sub>1.75</sub>, the second is a sudden decrease of the overpotential after the maximum, and the third is the Tafel relation (Fig. 7) at the early stage of the discharge. Details of the second step (after MnO<sub>1.5</sub>) will be reported in a separate paper.

*Limiting  $x$  value around MnO<sub>1.75</sub>.*—The authors would like to attribute the limiting  $x$  values to the formation of a new lower oxide structure on the surface of the original oxide. It has been pointed out in our previous paper (2) that around the region marked as "lower oxide on the surface" in the upper part of Fig. 4, the OCV deviates considerably from the calculated OCV curve, because the lower oxide structure is formed on the surface of  $\gamma$ -MnO<sub>2</sub> structure and at this stage the whole system cannot be considered as a homogeneous phase (Mn<sup>4+</sup> — Mn<sup>3+</sup> — O = — OH<sup>-</sup> system). We can see in Fig. 4 that as soon as the CCV curves (a' and c') reach the potential of the lower oxide region (-0.12 to -0.16v), the overpotential begins to increase suddenly. This can be seen more clearly in Fig. 6 by the potentials marked as  $E_1$ ,  $E_2$ ,  $E_3$ , and  $E_4$  where the overpotential curve begins to deviate, and the beginnings of the deviation are between -0.115 and -0.160v. This suggests that the determining factor in the formation of the lower oxide structure is not the  $x$  value (or depth of the discharge), but the electrode potential; namely, concentration of [Mn<sup>3+</sup>] on the oxide surface. This lower oxide structure on the surface appears to have extremely high overpotential for the following discharge reaction.



From this discussion we can tentatively conclude that the limiting  $x$  value around MnO<sub>1.75</sub> is probably attributable to the kinetically limited charge transfer process (reaction [1]) on the lower oxide covered surface.

*Overpotential decrease after the maximum.*—The polarization decreases rapidly after the maximum as is seen in Fig. 4. This seems to be due to the beginning of the second step reaction; reduction of dissolved trivalent Mn(III) complex ion (3) to the divalent

state and also reduction of Mn(III) to Mn(II) on the oxide surface. At this stage the potential (CCV) is approaching that of the second step reaction, of which the OCV is -0.385v vs. Hg/HgO (9M KOH); therefore, reaction of the second step reduction is taking place to some extent in addition to the main reaction [1].

This situation can be seen more clearly for  $\beta$ -MnO<sub>2</sub>(III) in Fig. 5. The polarization of  $\beta$ -MnO<sub>2</sub>(III) is much greater than that of  $\gamma$ -MnO<sub>2</sub> in addition to the much lower OCV than that of  $\gamma$ -MnO<sub>2</sub>. Therefore the CCV of  $\beta$ -MnO<sub>2</sub>(III) reaches the second step potential [-0.385v vs. Hg/HgO (9M KOH)] at a very early stage in the discharge and the CCV remains around -0.38v during most of the first step.

The approximate standard potential of the Mn(III)-Mn(II) system in 9M KOH was found to be approximately -0.40v vs. Hg/HgO (9M KOH), as reported previously, based on the polarographic (1) and voltammetric (3) current potential curves in a 9M KOH solution containing Mn(III) and Mn(II) ions.

*Tafel relation at early stages of the discharge.*—The accurate polarization of the reaction [1] at various currents (Fig. 7) was measured only at very early stages of the discharge in order to escape the complications due to both the presence of the lower oxide on the MnO<sub>2</sub> surface and the trivalent manganese reduction. The limiting currents (marked in Fig. 7 as  $i_{L,KOD} = 43$  ma and  $i_{L,KOH} = 62$  ma) cannot be discussed on the basis of pure proton diffusion process, because at the current the polarization (200-250 mv) is high and the CCV is very close to, or already entering into, the potential region of the lower oxide on the MnO<sub>2</sub> surface.

The slopes of these Tafel lines are not far from 120 mv per decade. This can be interpreted that the rate determining step is reaction [1] having  $\alpha$  value of approximately  $\frac{1}{2}$  in the following equation.

$$\eta = \frac{RT}{\alpha nF} \left( \ln \frac{i_0}{i} \right) = a - b \log i \quad [2]$$

The  $i_0$  values were obtained by extrapolation as shown in Fig. 7 for one case. The exchange currents are shown in Table III.

The Tafel slopes in a low current range (Fig. 8) are much smaller than those for the high current ranges (Fig. 7).

When the current values are compared at a constant overpotential for KOH and KOD solutions (in Fig. 7, as indicated by small horizontal arrows), the current ratio  $i_{KOH}:i_{KOD}$  is 1.35-1.55 for the data in Fig. 7. It is interesting to note that the ratio is close to the ratio derived from a simple diffusion rate ratio of deuterium and proton; namely,  $1/\sqrt{H} : 1/\sqrt{D} = 1.41$ .

### Acknowledgment

The authors wish to thank Mr. W. L. Adams, Mrs. H. M. Joseph, and Dr. R. L. Brubaker for their experimental assistance or aid in the preparation of the manuscript, and also thank Professor E. B. Yeager of Western Reserve University and Professor H. A. Laitinen of the University of Illinois for their comments and suggests on this paper.

Table III. Exchange currents obtained from the lines in Fig. 7

Electrolyte	Stages of the discharge					
	1 ma-hr		2 ma-hr		3 ma-hr	
	ma/g	ma/m <sup>2</sup> *	ma/g	ma/m <sup>2</sup> *	ma/g	ma/m <sup>2</sup> *
In 9M KOH	30.0	0.71	20.4	0.51	17.6	0.45
In 9M KOD	22.0	0.59	14.8	0.38	10.6	0.27

\* Based on the BET surface area 39.7 m<sup>2</sup>/g (9).



Manuscript received March 20, 1967; revised manuscript received Oct. 26, 1967. This paper was presented at the Dallas Meeting, May 7-12, 1967, as Abstract 196.

Any discussion of this paper will appear in a Discussion Section to be published in the December 1968 JOURNAL.

## REFERENCES

1. A. Kozawa and J. F. Yeager, *This Journal*, **112**, 959 (1965).
2. A. Kozawa and R. A. Powers, *ibid.*, **113**, 870 (1966).
3. A. Kozawa, T. Kalnoki-Kis, and J. F. Yeager, *ibid.*, **113**, 405 (1966).
4. A. B. Scott, *ibid.*, **106**, 839 (1959).
5. F. Kornfeil, *ibid.*, **109**, 349 (1962).
6. A. Era, Z. Takehara, and S. Yoshizawa, *J. Electrochem. Soc., Japan (Denki Kagaku.)* **34**, 483 (1966).
7. D. T. Ferrel and W. C. Vosburgh, *This Journal*, **98**, 334 (1951).
8. W. C. Vosburgh, *ibid.*, **106**, 839 (1959).
9. A. Kozawa and R. A. Powers, *Electrochem. Technol.*, **5**, 535 (1967).

# Chromium Oxide Scale Growth on Iron-Chromium Alloys

## I. The Influence of Variables on the Oxidation of Fe-28% Cr

G. C. Wood and D. P. Whittle

*Corrosion Science Division, Department of Chemical Engineering,  
University of Manchester Institute of Science and Technology, Manchester, England*

## ABSTRACT

The oxidation of Fe-28% Cr in oxygen at 800°-1200°C has been studied in detail by thermogravimetric methods, metallography, and electron probe microanalysis. The oxidation rate is critically related to the surface finish and alloy purity but not significantly to variations in specimen size or geometry. Uniform single-layered scales, consisting of Cr<sub>2</sub>O<sub>3</sub> containing a low concentration of dissolved iron, are produced. The oxidation rate shows minor negative deviations from a parabolic law, with an activation energy of  $36 \pm 6$  kcal mole<sup>-1</sup> for the over-all diffusion-controlled process. The deviations from a parabolic law are discussed in light of general oxidation theory and the self-diffusion coefficients of Cr<sup>3+</sup> ions in the scales are derived.

There is considerable general evidence (1-4) that the nature of Cr<sub>2</sub>O<sub>3</sub>-rich scales produced on chromium and iron-chromium alloys depends critically on the alloy purity, heat-treatment, surface finish, and specimen geometry, and on the oxidizing environment and temperature. The present paper presents a study of certain of these features of scale growth on Fe-28% Cr alloys in oxygen, making detailed use of thermogravimetric measurements, metallography, and electron probe microanalysis. In a sequel (5) the influence of the underlying alloy composition on the oxidation behavior is considered more fully.

## Experimental

The compositions of nominally Fe-28% Cr alloys from three different sources, designated A, B, and C, respectively, are given in Table I. All the alloys were produced by vacuum melting and, after appropriate heat-treatments, described in detail elsewhere (6), were cold-rolled to strip 0.04-0.05 cm thick. Alloys A and B were made from the same special Swedish iron base, but purer electrolytic chromium was used for alloy A. The ultrapure alloy C was prepared from zone-refined iron (C 33, N 0.9, H 0.3, Mg 1 ppm) and electrolytic chromium (C 10, H 0.5, Mg 0.5, Al 0.5, Ca 1, Cu 1, O 8, and Se 2 ppm).

Batches of specimens, generally 2.5 x 0.5 x 0.040 cm, were annealed for 5 hr at 1000°C at  $5 \times 10^{-5}$  Torr to remove residual stresses and to give an approximately constant grain size. The latter aim was not fully realized because samples of different purity and chromium content experienced grain growth to varying extents.

The abraded surface used previously (3) was not entirely satisfactory because of residual stresses developed in the surface, incorporated abrasive, and an undefined roughness factor. Consequently, after annealing, each specimen was electropolished (1, 4) immediately prior to use. The electropolishing was per-

formed in a glacial acetic acid/perchloric acid (S.G. 1.72) mixture (20:1 by volume) for 3 min at 0.4-0.8 amp cm<sup>-2</sup>, 10 $\mu$  thus being removed from each alloy surface. Generally, this was followed by a cathodic etch at 10  $\mu$ a cm<sup>-2</sup> in 4N HCl, lasting for 90 sec after the onset of activity (1, 4). The specimen, from which the film left after electropolishing had now been removed (1, 4), was then washed, degreased, dried, and located in the conventional silica spring thermobalance (accuracy of measurement  $\pm 0.05$  mg cm<sup>-2</sup>) for kinetic runs. The whole specimen assembly was sealed into the cold top section of the balance and oxygen was passed for a further hour. At this stage the specimen was rapidly lowered by a winch into a position directly above a Cr<sub>2</sub>O<sub>3</sub>-coated crucible, the furnace already being set at the required temperature. This method was adopted to avoid problems involving pre-oxidation if specimens are brought slowly to temperature *in vacuo*. The first weight gain measurement was made within 2-3 min. At the end of the run the specimen was slowly winched out of the hot zone over a 15-min period and cooled in oxygen.

The oxygen gas had the following analysis: O<sub>2</sub> 99.5%, CO<sub>2</sub> 5 ppm, CO nil, hydrocarbons 10 ppm, H<sub>2</sub> 50 ppm, Ar 0.5%, N<sub>2</sub> trace, H<sub>2</sub>O less than 0.15 g m<sup>-3</sup>. It was further purified by passage at 5 l/hr through a Deoxo cartridge, magnesium perchlorate, and phosphorus pentoxide drying tubes and a concentrated sulfuric acid bubbler. On the exit side a magnesium perchlorate tower and a bubbler minimized back-diffusion. The object of the Cr<sub>2</sub>O<sub>3</sub>-covered crucible was to saturate the atmosphere with the volatile species from Cr<sub>2</sub>O<sub>3</sub>, possibly CrO<sub>3</sub>, so avoiding weight losses from the specimen caused by this process. The furnace temperature was controlled at  $\pm 5^\circ$ C once equilibrium was established.

Conventional metallographic techniques were used to examine the oxidized specimens in plan, or in section after they had been vacuum mounted. A Cam-

Table I. Chemical analysis of the iron-chromium alloys, weight per cent

Alloy	Cr	Fe	C	N	S	P	O	B	Al	Ni	Mn	Si	W	Ti	Cu	Mo	V	Sn	Nb
A	27.4	bal.	0.006	0.0065	0.010	0.001	0.027	<0.0015	<0.008	0.02	0.02	0.003	<0.05	<0.03	<0.009	<0.005	<0.004	<0.002	<0.006
B	28.0	bal.	0.023	0.023	0.014	0.002	0.023	<0.0015	0.04	0.01	0.02	0.08	<0.05	<0.04	<0.01	<0.005	<0.004	<0.002	<0.006
C	28.5	bal.	0.004	—	—	—	—	—	—	—	—	—	—	—	—	—	—	—	—

bridge MK II "Microscan" instrument operating at 29 kv was used for the electron probe microanalysis. This means that the x-ray source size, producing 95% of the total x-rays generated, was approximately  $1.7\mu$  in the alloy and  $2.5\mu$  in the oxide. The concentration profiles presented represent line scans. Individual points on these profiles indicate where corrections for absorption and fluorescence effects were made, using a computer program, the entire profiles then being adjusted accordingly. Certain compositions were checked by static probe measurements, pure metals being used as standards.

### Results and Interpretation

**Reproducibility and method of presentation.**—The weight gain/time curves for six Fe-27.4% Cr alloy specimens (alloy A) at  $1000^\circ\text{C}$  show the reproducibility of typical runs (Fig. 1). It was difficult to decide whether irregularities in kinetic curves were due to inaccuracies in operating the quartz spring/cathetometer arrangement of the thermobalance or to cracking of the protective oxide at temperature. However, subsequent examination of all specimens in plan and section indicated single-layer scales, so justifying the smooth kinetic curves drawn in Fig. 1.

Reproducibility is seen to be quite good. The largest deviations occurred at low temperatures and short times due to the bigger thermobalance error in measuring small weight gains and to difficulty in fixing zero time for the oxidation run. Substantial deviations were also sometimes seen at  $1200^\circ\text{C}$  [particularly with higher chromium alloys referred to elsewhere (5)] due to irregular scale growth.

**Influence of surface preparation.**—Figure 2 shows that etching after electropolishing considerably reduced the oxidation rate of Fe-27.4% Cr (alloy A) at  $1000^\circ\text{C}$ , there being little significant difference for etching times of 45 and 90 sec, respectively. This effect was also observed at other temperatures.

The oxide grew on all three types of surface at a declining rate, consistent with a small negative deviation from a parabolic growth law, (i.e., in the relationship  $w^n = Kt$ ,  $n$  is slight greater than 2). Etching significantly improved the reproducibility of results. Approximate parabolic rate constants from the first few hours of oxidation were  $3.3$ ,  $1.1$ , and  $1.4 \times 10^{-10} \text{ g}^2 \text{ cm}^{-4} \text{ sec}^{-1}$  for electropolished, 45-sec etched and 90-sec etched batches, respectively. However, all

the rates of oxidation became comparable in the later stages of the runs.

Before oxidation, the electropolished specimens had a specular surface, marred only by a few pits produced during electropolishing by inclusions in the alloy, whereas with the etched alloys the alloy grain boundary structure was delineated but not significantly grooved. Morphologies of scales formed at  $1000^\circ$  and  $1200^\circ\text{C}$  were similar and are described below. However, those formed at  $800^\circ\text{C}$ , and on alloys B and C (which oxidized slower at  $800^\circ$  and  $1000^\circ\text{C}$  as indicated later) showed that the grain boundary pattern persisted in the oxide layer [Fig. 3(a), in the region where scale has not spalled off on cooling]. The alloy grain boundaries appear as ridges in the oxide which, together with Fig. 3(b) which shows the same effect for the under side of the scale, tends to indicate that the scale is thicker at grain boundaries. However, this was never observed in section, perhaps suggesting that the features on one side of the scale are depressions. The individual oxide grains are barely visible at this magnification. Figure 3(c) is typical of all the scale surfaces at  $1000^\circ$  irrespective of the method of surface preparation. The scale is very wrinkled, consistent with substantial scale lifting (shown later to occur on cooling), and the surface has a slightly faceted appearance. Scales formed at  $1200^\circ\text{C}$  were similar except that the emerging scale promontories were not as angular. When the scale was removed mechanically the alloy grain boundaries were still evident but not grooved, Fig. 3(d), and the entire surface was covered by a thin temper-color film. With electropolished surfaces the latter was nonuniform and in places had spalled, revealing specular alloy surface.

Metallographic examination in section always indicated the presence of a single-layer, single-phase oxide, shown later to be  $\text{Cr}_2\text{O}_3$ , containing small quantities of dissolved iron. Scales of this type will subsequently be referred to as ' $\text{Cr}_2\text{O}_3$ ' for convenience. These scales were similar in appearance but different in thickness on the differently finished surfaces at all temperatures. The oxide was relatively uniform in thickness [see Fig. 8(a)-(c)]. In many

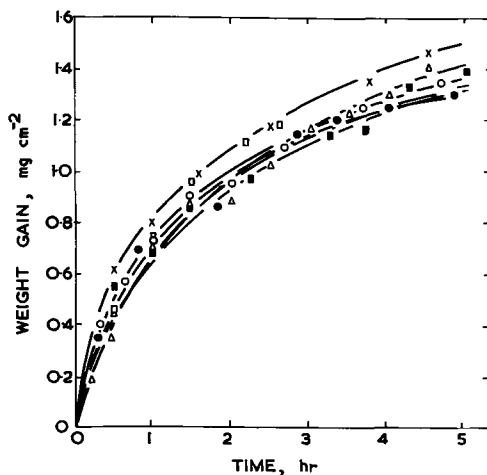


Fig. 1. Reproducibility of weight gain/time curves for the oxidation of Fe-27.4% Cr at  $1000^\circ\text{C}$ .

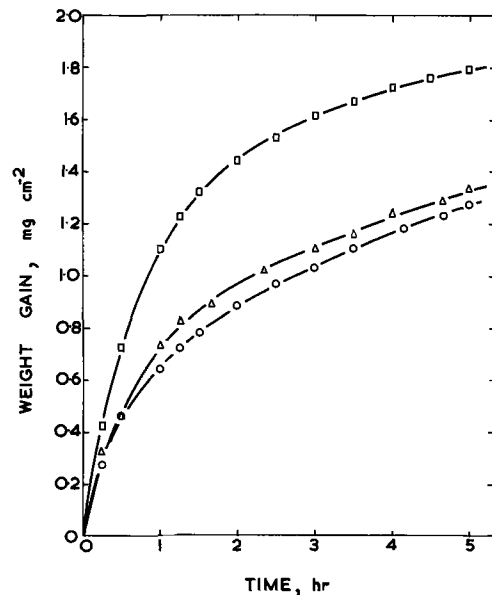


Fig. 2. Influence of surface preparation on the oxidation of Fe-27.4% Cr at  $1000^\circ\text{C}$ .  $\square$  Electropolished;  $\circ$  electropolished and etched 45 sec;  $\triangle$  electropolished and etched 90 sec.

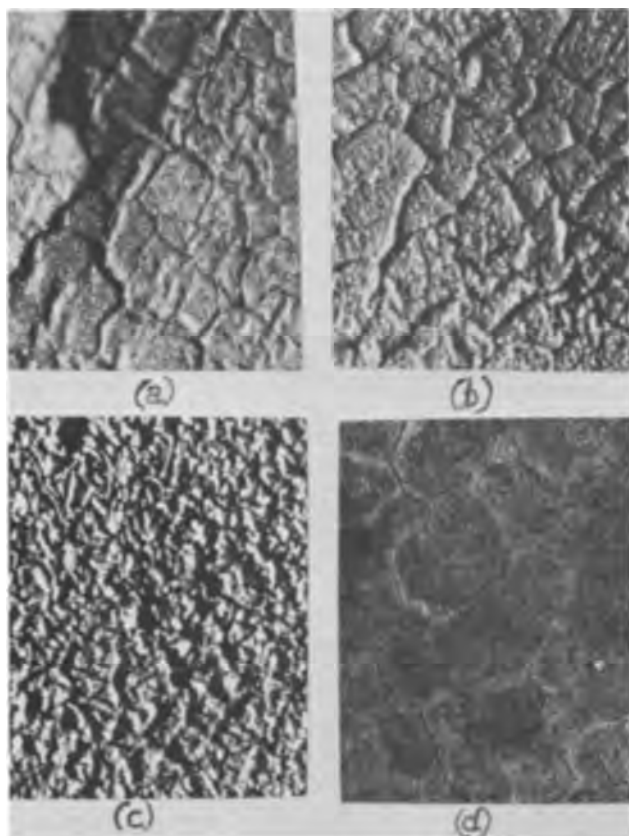


Fig. 3. Surface topography of scales formed on electropolished and etched Fe-27.4% Cr. (a) 2.5 hr at 800°C; (b) under side of scale produced in 2.5 hr at 800°C; (c) 5 hr at 1000°C; (d) surface of specimen oxidized for 10 hr at 800°C after removal of the main scale. Magnification 75X; oblique illumination.

cases, the scales had become detached from the substrate and had taken up a wrinkled form at some distance from the alloy. This scale detachment, for both etched and electropolished specimens, occurred on cooling the samples at the end of the runs, because

(A) The oxide could be seen to crack and sometimes fly off the alloy on cooling, generally when the temperature had fallen to 200°-300°C.

(B) There was no gross variation of scale thickness around any cross sections, even at 800°C where possible vapor phase transfer of chromium across closed voids would have been negligible.

(C) The alloy-oxide interface did not contain any massive irregularities, which would have occurred if certain areas had oxidized faster than others.

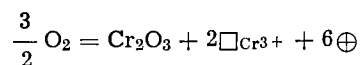
(D) Scarcely any multilayer 'Cr<sub>2</sub>O<sub>3</sub>' scales were observed. Admittedly the scales could still have detached from the alloy but remained intact around the specimen. This is considered unlikely because specimens where the scale was still fully attached on cooling gave similar growth kinetics.

(E) It is shown later by electron probe microanalysis that the chromium concentration at the edge of the alloy did not vary between regions where the scale was still attached to the alloy and regions where it had separated.

It is thus reasonable to state that an adherent scale similar in appearance to Fig. 8(c) was produced on all specimens at temperature.

The most probable explanation of the enhanced scaling rate on electropolished surfaces is that, under the strongly oxidizing conditions of electropolishing, the initial oxide film formed on the fresh surface contains more Cr<sup>6+</sup> or Cr<sup>4+</sup> ions than usual (7). Each Cr<sup>6+</sup> ion is associated with an extra cation vacancy in the p-type semiconducting oxide postulated, thus permitting a faster cation diffusion rate and con-

sequently a faster scaling rate. After continued scaling, the vacancy concentration diminishes to a level more normal in 'Cr<sub>2</sub>O<sub>3</sub>,' since vacancies are destroyed at the alloy-oxide interface and their rate of production at the oxide-gas interface, by the reaction



(where  $\Box_{\text{Cr}^{3+}}$  is a chromium ion vacancy and  $\oplus$  is an electron hole) is no greater than for any other 'Cr<sub>2</sub>O<sub>3</sub>' scale. Thus the oxidation rate should also decrease and approach that of the etched specimens, as is indeed found (Fig. 2). It is surprising that the effect can persist for so long, considering the thinness of the initial film. There was no evidence of the enhanced scale blistering and layering observed by other workers (1, 4, 7) on pure chromium.

An alternative cause of the increased oxidation rate of electropolished specimens could be that oxide grain boundaries act as short-circuit diffusion pipes (1). One possibility is that on etched specimens the oxide microcrystallites are highly oriented on any particular alloy grain, with negligible mismatch at the microcrystallite boundaries, whereas on electropolished specimens the oxide is randomly oriented, the more highly mismatched boundaries acting as low resistance diffusion paths for ions. Alternatively the initial oxide grain size may simply be greater on etched surfaces than on electropolished surfaces. However, this is the reverse of what would be expected, unless the argument refers merely to the contaminated, air-formed film left after electropolishing or etching, because nucleation is potentially harder on a specular surface. In either explanation the increased oxidation rate may persist because plastic strain of the rapidly formed oxide increases the ionic mobility.

*Influence of specimen geometry.*—Experiments on finely abraded (600 grit) prisms of triangular, rectangular, hexagonal and octagonal section and on cylinders respectively 0.5, 1, and 1.5 cm in diameter, made from Fe-27.4% Cr, (alloy A), displayed few exceptional topographical features after oxidation at 1200°C for 5 or 50 hr. The scale was apparently adherent at temperature, but always tended to flake off on cooling. It was particularly adherent on the cylindrical surfaces and spalled most readily at the ends of prisms where three faces meet. The scale had a slightly more 'sintered' appearance after 50 hr at 1200°C than after 5 hr. It was uniform in section, except for a possible slight thickening at corners accompanied by a rounding of the alloy surface. There was no evidence of even localized scale lifting at temperature.

*Influence of alloy purity.*—Figure 4, depicting the weight gain/time curves at 1000°C for the three purities of nominally 28.0% Cr alloy, shows that the ultrapure alloy C oxidized at a rate similar to the least pure alloy B after about 1.5 hr, but its behavior was nearer that of alloy A in the early stages. The effects persisted for times up to 50 hr. The parabolic rate constants for the first few hours of oxidation are  $1.4 \times 10^{-10}$ ,  $4.7 \times 10^{-11}$ , and  $5.2 \times 10^{-11}$  g<sup>2</sup> cm<sup>-2</sup> sec<sup>-1</sup> for the alloys A, B, and C, respectively. Alloy C obeyed the parabolic law for the entire 5 hr, but the other alloys showed negative deviations.

The alloy grain size decreased in the order C, A, and B because of impurity effects on grain growth, and the number of pits developed during electropolishing increased in this order, but their number was never really significant. The scales on alloys B and C were of comparable thickness and always lifted from the alloy on cooling. However, scales on alloy C tended to crack and fly off the alloy substrate, those on alloy A cracked open but remained on the substrate, and those on alloy B did not appear to alter during this period. Examination in section again revealed a wrinkled single-layer of 'Cr<sub>2</sub>O<sub>3</sub>' of almost uniform

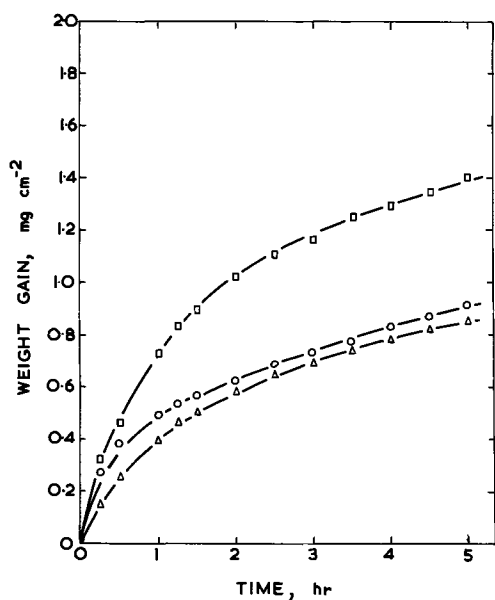


Fig. 4. Influence of purity on the oxidation of Fe-28% Cr at 1000°C

□ Alloy A  
 △ Alloy B  
 ○ Alloy C

thickness, detached from the alloy; the alloy/oxide interface generally remained virtually straight.

In discussing the kinetic measurements, those on alloy C, which is at least 99.997% pure, may be taken as the standard. Possibly with alloy A, which is still quite pure by usual Fe-Cr alloy standards, impurities may enter the scale and increase the cation vacancy concentration. If  $\text{Cr}_2\text{O}_3$  is a metal-deficit p-type semiconductor these would have to be at least quadrivalent (e.g., tungsten and titanium, see Table I). It is doubtful whether carbon is responsible, by producing CO and subsequent scale disruption, particularly as it has been shown (2) that carburization of chromium does not affect its oxidation rate. Presumably the additional impurities present in alloy B cause it to oxidize slower than alloy A (Table I) by a similar mechanism. It is noteworthy that the silicon content (0.08% in B, 0.003% in A) and aluminum content (0.04% in B, 0.008% in A) are significantly higher in B than A, which might affect matters by preferential oxide formation at the alloy/oxide interface or in the internal oxide zone, so reducing the rate of entry of ions into the scale.

Thus there is no simple explanation of the purity effect, and some subtler differences may be involved such as the degree of stress or strain-enhanced ionic lattice diffusion, grain boundary or dislocation pipe diffusion, or the variation in the number of sites for vacancy coalescence both in the alloy and at the alloy/oxide interface. There is no evidence of cracking being relevant in causing the differences in oxidation rate.

*Influence of temperature.*—Most work was carried out on electropolished and etched (90 sec) samples of the relatively pure alloy A, with confirmatory runs on the ultrapure alloy C. Figure 5 shows the temperature-dependence of the oxidation of Fe-27.4% Cr. The absence of discontinuities in the individual growth curves (not shown here), of variations in general or localized scale thickness (nodules), and of multilayering of the ' $\text{Cr}_2\text{O}_3$ ' scales (such layers occupied less than 1% of the specimen sections and then only occurred at 1100° and 1200°C), and information given elsewhere favoring scale attachment at temperature, justify the calculation of parabolic rate constants in all cases. Larger specimens, 3.0 x 1.5 x 0.040 cm, pro-

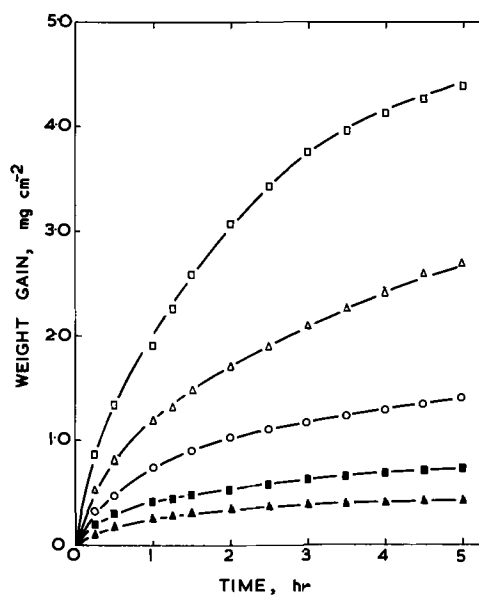


Fig. 5. Oxidation of Fe-27.4% Cr at 800°-1200°C

□ 1200°C  
 △ 1100°C  
 ○ 1000°C  
 ■ 900°C  
 ▲ 800°C

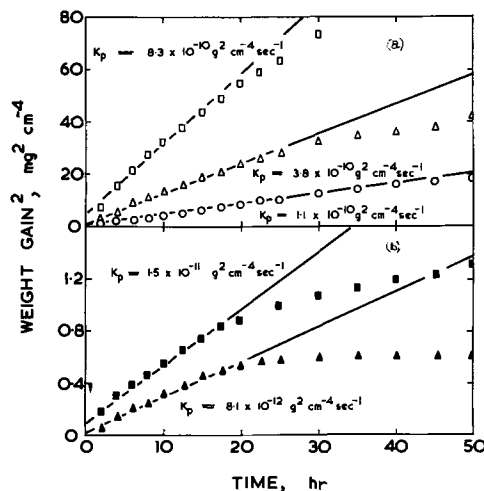


Fig. 6. Plot of (weight gain)<sup>2</sup>/time for the oxidation of Fe-27.4% Cr

(a) □ 1200°C  
 △ 1100°C  
 ○ 1000°C  
 (b) ■ 900°C  
 ▲ 800°C

duced identical kinetic curves and metallographic scale features, but much more of the oxide spalled off completely on cooling. Figure 6(a) and (b) display the (weight gain)<sup>2</sup>/time plots for 50-hr oxidation. At each temperature a curve, slightly concave to the time axis, is evident but generally the deviation from linearity is not sufficient to invalidate the assumption of the parabolic rate law. The deviation is admittedly sometimes more significant after longer times. However, it is important when comparing parabolic rate constants for various sets of oxidizing conditions to use values calculated over corresponding time ranges because the value of each rate constant depends on the 'degree of fit' of the straight line drawn through the experimental points.

The effect of temperature on the scale growth rate is governed by an Arrhenius relationship as shown in Fig. 7, thus,

$$K_p = A \exp(-Q/RT)$$

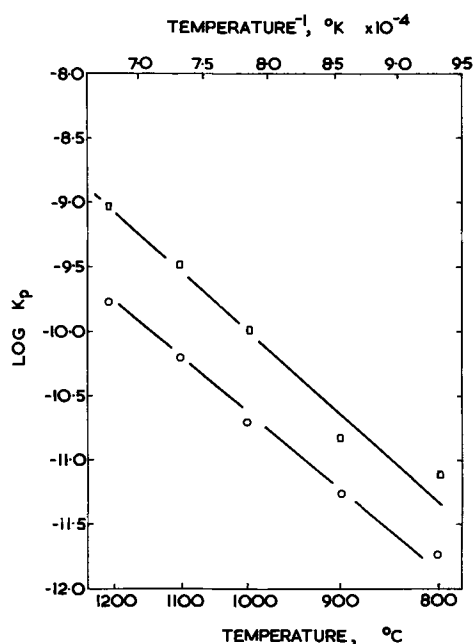


Fig. 7. Arrhenius plot for the oxidation of Fe-27.4% Cr: □ alloy A; ○ alloy C.

where  $K_p$  is the parabolic rate constant,  $T$  the absolute temperature,  $R$  the gas constant, and  $Q$  the activation energy of the rate-controlling process. The activation energy for the oxidation mechanism, as calculated from the method of least mean squares using a 95% confidence level, was  $36 \pm 6$  kcal mole<sup>-1</sup>. A similar plot for the ultrapure alloy C gave a similar activation energy of  $35 \pm 6$  kcal mole<sup>-1</sup>. Thus, despite the slower scaling rate of the purer alloy C, the same rate-controlling process was apparently involved.

**Metallography of scales in section and electron probe microanalysis.**—All the scales examined were single-layer, single-phase 'Cr<sub>2</sub>O<sub>3</sub>' and, particularly for low temperatures and short times, detached from the alloy on cooling and were left with an undulating profile [Fig. 8(a) and 8(b)]. The oxide formed after 0.5 hr at 1000°C [Fig. 8(a)] is only about 1μ thick and could curl up easily, but after 5 hr it is 4–5μ thick and appears to have cracked in one place. The inner edge of the scale is far longer than the outer edge of the alloy because there is a differential contraction on cooling between oxide and alloy, and it is impossible to match corresponding places along the alloy-oxide interface. There are no gross variations in the oxide thickness around a cross-section, a typical scatter being  $\pm 30\%$ . Also the average scale thickness always corresponds to the thickness computed from the thermogravimetric data within  $\pm 10\%$ , even at 1200°C where any error in fixing zero weight gain for the specimen would be a maximum. Similar behavior persisted for times up to 50 hr.

Figure 8(c) illustrates the somewhat rarer occasions where the oxide remained attached to the alloy on cooling. The oxide is uniformly thick around the whole cross section. Scales such as this support the legitimacy of applying oxidation rate theory to scale growth, particularly since this specimen received the most severe treatment of all specimens, namely, 50 hr at 1200°C. Presumably it did not spall on cooling because of some stress relaxation by scale (or alloy) plastic deformation during the long period at 1200°C, and additionally it would be difficult for such a thick scale to balloon. The pores visible in the oxide, and in Fig. 8(b), are not necessarily genuine and may have been accentuated during metallographic preparation. Similar attached scales were also sometimes observed after shorter oxidation times and at lower oxidation temperatures.

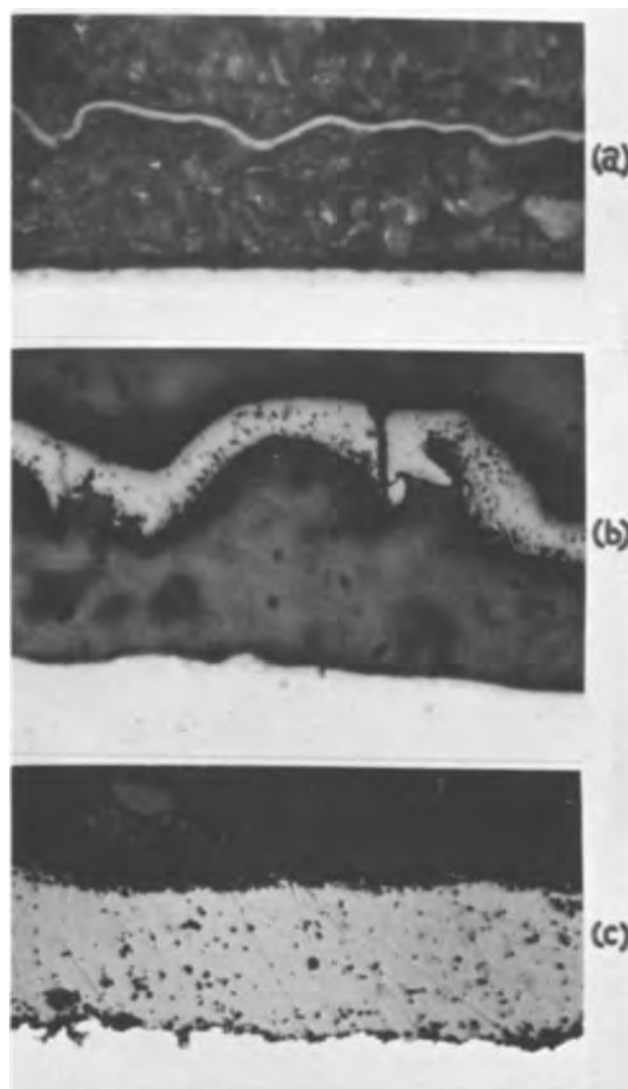


Fig. 8. Cross sections of scales on electropolished and etched Fe-27.4% Cr: (a) 30 min at 1000°C (x830); (b) 5 hr at 1000°C (x830); (c) 50 hr at 1200°C (x415).

When the scale thickness was only of the order of the x-ray source size, a region where the oxide had separated from the alloy was selected for microanalysis, thus avoiding any possibility of iron radiation apparently from the oxide really originating the alloy. Scales generally contained 0.4–5% Fe, but no gradient through them could be measured because the layers were either too thin or contained too low an iron concentration, although more recent evidence suggests it really existed (14).

Figure 9(a), presenting the concentration profiles through scale and adjoining alloy for the Fe-27.4% Cr alloy oxidized at 1200°C for 50 hr, gives an apparently uniform chromium content (63.6%) and iron content (0.4%) across the entire scale section. Repeated determinations on this and similar thick scales always gave low total metal contents (compared with 68.4% Cr for stoichiometric Cr<sub>2</sub>O<sub>3</sub>). The actual interface positions are located at the mid-points of the "inter-faces" measured due to the finite size of the x-ray source. Figure 9(b) gives two traces across sections of a scale formed after 5 hr at 1000°C on Fe-27.4% Cr; the full lines show the concentration profiles across a region where the scale is separated from the alloy by a large void and the broken line where the scale is still attached to the alloy. That the chromium concentration at the alloy/oxide interface is the same in both cases adds support to the idea that scale lifting occurred on cooling because, even if chromium vapor

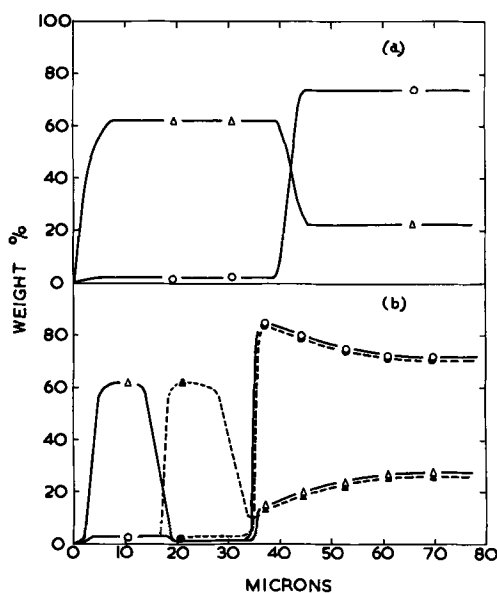


Fig. 9. Concentration profiles across alloy and scale: (a) Fe-27.4% Cr oxidized for 50 hr at 1200°C, ○ Fe, △ Cr; (b) Fe-27.4% Cr oxidized for 5 hr at 1000°C ○● Fe, △▲ Cr. ——— Scale detached; - - - scale attached.

transport across voids is possible (8), it will not be very significant at this temperature.

### Discussion

*Qualitative considerations of the kinetics and oxide growth mechanism.*—After its rapid establishment,  $\text{Cr}_2\text{O}_3$  containing a low concentration of iron, probably in solid solution, is the only oxide formed, and there are no large compositional changes with time or temperature. It is likely in view of the almost parabolic growth curves that a diffusional mechanism is the rate-controlling factor. At present there are conflicting theories regarding whether  $\text{Cr}^{3+}$  or  $\text{O}^{2-}$  ions have the dominant mobility, but here the more widely accepted cationic mode of transport will be assumed. It is possible that some  $\text{O}^{2-}$  movement occurs, perhaps down grain boundaries or dislocations, but in the absence of evidence this suggestion will be neglected.

There are at least three possible reasons for the small negative deviations from a parabolic growth relationship in the later stages:

(i) Grain growth during oxidation could reduce the number of paths of easy diffusion down grain boundaries, if such ionic transport is significant at this temperature.

(ii) The scales are highly stressed and some plastic flow could occur, possibly enhancing diffusion in the scale. The effect might decrease as the reaction slows and possibly as the iron content of the ' $\text{Cr}_2\text{O}_3$ ' declines.

(iii) The most likely explanation is that the cation vacancies migrating inward through the scale can (a) condense and form pores within the bulk oxide, (b) diffuse to the alloy-oxide interface and condense to form invisible vacancy clusters or visible voids, or (c) diffuse to the alloy/oxide interface and enter the alloy becoming attached to dislocations or inclusions. If voids or pores are formed as in (a) or (b) above, they will tend to obstruct the continued transfer of cations from the alloy to the scale-atmosphere interface. The scale growth is still diffusion-controlled, the effective specimen area simply being decreased. Presumably ionic diffusion around the small voids can occur, thus avoiding uneven scale growth. There is some evidence of pores both in the scales and at the alloy/scale interface, but it cannot definitely be concluded that these are the pores involved.

In the following derivation all the voids are assumed to form and stay at the alloy-oxide interface, although

a similar but not identical result is expected if they are formed within the scale. If  $\phi$  is the effective area of the oxidizing specimen, as indicated above it can be shown that

$$\phi = C \exp(-kt) \quad [1]$$

where  $k$  and  $C$  are constants and depend on the initial conditions. In the early stages of oxidation there are no voids and growth obeys the parabolic law. After a time, the effective area of the oxidizing specimen is reduced to  $\phi$  times its original value; then, the ratio of the experimental weight gain to that calculated from a parabolic relationship (using the  $K_p$  value calculated from the data at early times of oxidation) is equal to  $\phi$ .

The degree of linearity of  $\log \phi$  against  $t$  plots enables the validity of Eq. [1] to be assessed. Most of the kinetic data showed reasonable agreement with the derived equation. Figure 10 shows results for the three metal purities. Alloy C follows the parabolic law over the entire 5 hr of the run; thus  $\phi$  is always equal to 1. Possibly the lack of impurities in the alloy reduces the number of sites available for the condensation of vacancies at the alloy/oxide interface. Also the relatively slow, over-all oxidation rate minimizes the formation of micropores in the bulk oxide. For the impure alloy B there is slight divergence from the parabolic law but this is greater for alloy A. However even here  $\phi$  is still 0.85 after 5 hr (and 0.75 after 50 hr) so the deviation is not great.  $\phi$  and  $\log \phi$  are greater for electropolished than for etched specimens, as expected.

*Quantitative discussion of the oxidation mechanism.*—If reproducible self-diffusion coefficients for  $\text{Cr}^{3+}$  diffusion in  $\text{Cr}_2\text{O}_3$  (preferably scales rather than bulk oxide) were available, it would be most suitable to use them to calculate parabolic rate constants for oxidation to be compared with the present measured values. Figure 11 shows that this is not the case so it appeared more pertinent to adopt the reverse procedure and obtain values of apparent self-diffusion coefficient of  $\text{Cr}^{3+}$  ions in a growing ' $\text{Cr}_2\text{O}_3$ ' scale.

Adaptation of the derivation of Wagner (9) to the case of a single-phase oxide on an iron-chromium alloy (6), in which thermodynamically ideal behavior may be assumed (15), yields

$$K_r = (1 + z) C_{\text{eqCr}^{3+}} \cdot (D^*_{\text{Cr}})_g \left( 1 - \frac{(\pi_{\text{Cr}_2\text{O}_3})^{1/n} \cdot (N_{\text{Cr}})^{3/4n}}{(p_{\text{O}_2})_g^{1/n}} \right) \quad [2]$$

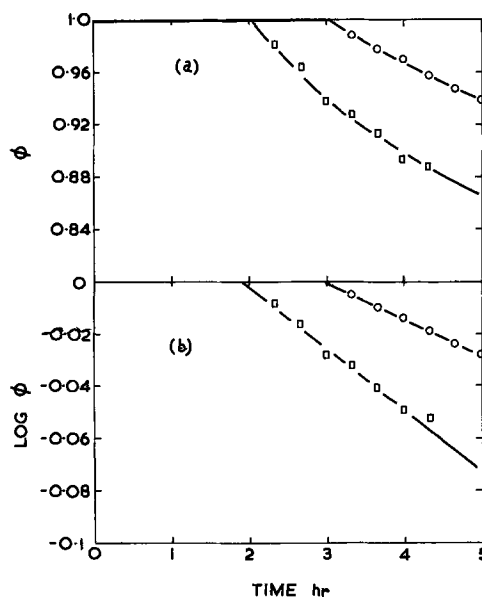


Fig. 10. Influence of alloy purity on  $\phi$  and  $\log \phi$  for the oxidation of Fe-28% Cr alloys at 1000°C: (a)  $\phi/t$  curve; (b)  $\log \phi/t$  curve. □ Alloy A; ○ alloy B.

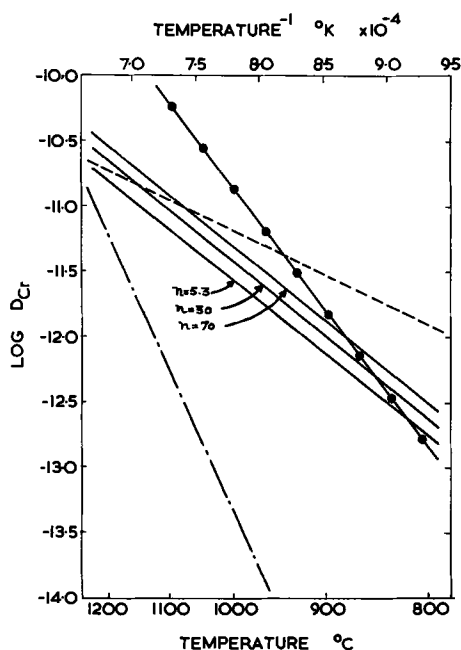


Fig. 11. Derived values of the self-diffusion coefficient of  $\text{Cr}^{3+}$  ions in  $\text{Cr}_2\text{O}_3$ . — Present work for various values of  $n$ ; ---- ref. (18); - · - · - ref. (17); —●— ref. (11).

where  $K_r$  = the rational rate constant for oxidation, defined as the reaction rate in equivalents per  $\text{cm}^2$  per sec for a scale 1 cm thick;  $z$  = cation valency;  $C_{\text{eqCr}^{3+}}$  = the concentration of  $\text{Cr}^{3+}$  ions in the scale in equivalents per  $\text{cm}^3$ ;  $(D^*_{\text{Cr}})_g$  = the self-diffusion coefficient of  $\text{Cr}^{3+}$  ions in a  $\text{Cr}_2\text{O}_3$  scale in equilibrium with the atmosphere;  $\pi_{\text{Cr}_2\text{O}_3}$  = the dissociation pressure of  $\text{Cr}_2\text{O}_3$ ;  $(N_{\text{Cr}})_m$  = the mole fraction of chromium at the alloy/oxide interface;  $(p_{\text{O}_2})_g$  = the oxygen partial pressure at the atmosphere/oxide interface;  $n$  = an exponent giving the oxygen pressure dependence of the concentrations of cation vacancies  $C_{\square_{\text{Cr}^{3+}}}$  and positive holes  $C_{\oplus}$  thus

$$C_{\square_{\text{Cr}^{3+}}} = 1/3 C_{\oplus} = K(p_{\text{O}_2})^{1/n} \quad [3]$$

where  $K$  is a constant. Theoretically  $n = 5.3$ .

Experimental determinations of the exponent  $n$ , by electrical conductivity measurements on hot sintered  $\text{Cr}_2\text{O}_3$  powder compacts at pressures of  $10^{-2}$  Torr at temperatures up to  $1400^\circ\text{C}$ , gave values varying between 30 (10) and 70 (2,11). Single crystal measurements (12) also predicted virtual independence of oxygen partial pressure, but it was found (13) that the oxidation rate, and also the cationic diffusion rate, varied at pressures of the order of the dissociation pressure of  $\text{Cr}_2\text{O}_3$ , with the  $3/5$ th power of the  $p_{\text{H}_2\text{O}}/p_{\text{H}_2}$  ratio [equivalent to  $(p_{\text{O}_2})^{1/5.3}$ ]. Pressure dependence of defect transport was not observed at higher oxygen pressures, probably due to the saturation of sites available for oxygen adsorption at the growing oxide surface.

Now, the chromium weight fraction never falls below 0.1 after the very early oxidation stages (5), and consequently the mole fraction, which is approximately equal to the weight fraction in this system, always exceeds 0.1.  $K_p$  is not very critically dependent on  $(N_{\text{Cr}})_m$ , so a constant value of 0.1 can be safely employed.

The dissociation pressure of  $\text{Cr}_2\text{O}_3$  has been calculated as a function of temperature (16), and  $K_r$  may be calculated from the  $K_p$  values given earlier. Consequently if assumptions are made about the value of  $n$ , an assessment of  $D^*_{\text{Cr}}$  may be made. Thus, for the formation of  $\text{Cr}_2\text{O}_3$

$$K_r = \frac{1}{2} (K_p/\rho_{\text{Cr}_2\text{O}_3}) (1/g \text{ eqO}_2) \quad [4]$$

where  $\rho_{\text{Cr}_2\text{O}_3}$  = the density of  $\text{Cr}_2\text{O}_3$  (taken as  $5.3 \text{ g cm}^{-3}$ ) and  $g \text{ eqO}_2$  = the gram equivalent of oxygen. Various values of  $n$ , namely 5.3, 30, and 70, were tried.  $C_{\text{eqCr}^{3+}}$  is given by

$$C_{\text{eqCr}^{3+}} = \rho_{\text{Cr}_2\text{O}_3} \cdot 2 z_{\text{Cr}}/M_{\text{Cr}_2\text{O}_3} \quad [5]$$

where  $z_{\text{Cr}}$  is the valency of chromium,  $\rho_{\text{Cr}_2\text{O}_3}$  the density of  $\text{Cr}_2\text{O}_3$  and  $M_{\text{Cr}_2\text{O}_3}$  the g molecular weight of  $\text{Cr}_2\text{O}_3$ . Values of  $K_r$  calculated from Eq. [4] and of  $D^*_{\text{Cr}^{3+}}$  from Eq. [2] are given in Table II. Figure 11 shows a plot of  $\log D^*_{\text{Cr}}$  against  $1/T$  for derived values for Fe-27.4% Cr and also for the measured values for bulk nominally pure  $\text{Cr}_2\text{O}_3$  derived from the literature (11, 17, 18). The pressure dependence of the vacancy concentration, parameter  $n$ , has no effect on the activation energy for self-diffusion at the oxygen pressure employed, nor has it any great influence on the absolute values of  $D^*_{\text{Cr}}$ . Despite the numerous assumptions there is moderate correlation between calculated and observed values. In particular, the results agree well with one set of work at  $1100^\circ\text{C}$ - $1200^\circ\text{C}$  (18) and with another set at  $800^\circ\text{C}$ - $900^\circ\text{C}$  (11). This tends to support the concept of cationic transport as being predominant in ' $\text{Cr}_2\text{O}_3$ ' scales at high temperature. The differences observed could well be related to variations in sample purity which were shown earlier to affect scaling rates substantially and would probably similarly influence behavior in bulk oxides. Also it should be emphasized that the derived values refer to diffusion in a growing scale containing some dissolved iron.

The rational rate constants and values of  $D^*_{\text{Cr}}$  in ' $\text{Cr}_2\text{O}_3$ ' are also given in Table II for scales produced on various other alloys (5), assuming  $n = 5.3$ , and show similar trends.

Any similarity between the activation energy for the oxidation mechanism and for the self-diffusion of  $\text{Cr}^{3+}$  ions in  $\text{Cr}_2\text{O}_3$  would be further evidence of solely  $\text{Cr}^{3+}$  ion motion. Unfortunately the values for bulk  $\text{Cr}_2\text{O}_3$  vary tremendously (11, 17, 18) (Table III). The situation for oxidation activation energies is better, values lying either around  $35 \text{ kcal mole}^{-1}$  or around  $60 \text{ kcal mole}^{-1}$ . In particular, all the low-temperature values approximate to the lower figure. Furthermore, it is shown elsewhere (5) that if temperature ranges where scale cracking are extensive are ignored, all alloys in the range 14-68% Cr gave values which were remarkably close to it too. It is suggested, therefore, that where higher values of activation en-

Table II. Values of rational rate constants and of  $D^*_{\text{Cr}^{3+}}$  for ' $\text{Cr}_2\text{O}_3$ ' on Fe-28% Cr and other alloys

Alloy % Cr	800°C		900°C		1000°C		1100°C		1200°C			
	$K_r$ eq·cm <sup>-2</sup> sec <sup>-1</sup>	$D^*_{\text{Cr}}$ cm <sup>2</sup> sec <sup>-1</sup>	$K_r$ eq·cm <sup>-2</sup> sec <sup>-1</sup>	$D^*_{\text{Cr}}$ cm <sup>2</sup> sec <sup>-1</sup>	$K_r$ eq·cm <sup>-2</sup> sec <sup>-1</sup>	$D^*_{\text{Cr}}$ cm <sup>2</sup> sec <sup>-1</sup>	$K_r$ eq·cm <sup>-2</sup> sec <sup>-1</sup>	$D^*_{\text{Cr}}$ cm <sup>2</sup> sec <sup>-1</sup>	$K_r$ eq·cm <sup>-2</sup> sec <sup>-1</sup>	$D^*_{\text{Cr}}$ cm <sup>2</sup> sec <sup>-1</sup>		
27.4 (A)	$1.6 \times 10^{-18}$		$4.6 \times 10^{-13}$		$1.6 \times 10^{-12}$		$4.8 \times 10^{-12}$		$1.4 \times 10^{-11}$			
27.4 (A)												
$n = 5.3$		$1.9 \times 10^{-18}$				$2.0 \times 10^{-12}$				$1.7 \times 10^{-11}$		
$n = 30$		$2.2 \times 10^{-18}$				$2.4 \times 10^{-12}$				$2.3 \times 10^{-11}$		
$n = 70$		$3.3 \times 10^{-18}$		$3.9 \times 10^{-12}$		$4.0 \times 10^{-11}$						
28.0 (B)					$5.6 \times 10^{-13}$	$6.8 \times 10^{-13}$						
22.9					$5.6 \times 10^{-13}$	$6.8 \times 10^{-13}$						
37.4					$5.6 \times 10^{-13}$	$6.8 \times 10^{-13}$						
59.5	$2.3 \times 10^{-14}$	$2.5 \times 10^{-14}$	$1.3 \times 10^{-13}$		$6.3 \times 10^{-13}$	$6.8 \times 10^{-13}$	$8.3 \times 10^{-12}$		$1.7 \times 10^{-11}$	$2.1 \times 10^{-11}$		
68.0					$2.7 \times 10^{-12}$	$3.3 \times 10^{-12}$						



Table III. Values of the activation energy for the oxidation of chromium and iron-chromium materials and for self-diffusion in  $\text{Cr}_2\text{O}_3$

Materials and references	Temperature range, °C	Activation energy, kcal mole <sup>-1</sup>
Fe-27.4% Cr (A) (present work)	800-1200	36.0
Fe-28.5% Cr (C) (present work)	800-1200	35.7
Fe-59.5% Cr (present work)	800-1200	50.4
	800-1000	37.0
Iodide chromium (1)	980-1200	37.0
Iodide chromium (2)	700-1300	59.4
Iodide chromium (8)	700-900	66.3
Iodide chromium (8)	700-953	37.5
	1000-1100	59.4
Fe-25% Cr (19)	700-1200	70.0
Fe-37.5% Cr (19)	700-1200	70.0
Self-diffusion in $\text{Cr}_2\text{O}_3$ (17)	1000-1350	100.0
Self-diffusion in $\text{Cr}_2\text{O}_3$ (18)	1000-1500	22.3
Self-diffusion in $\text{Cr}_2\text{O}_3$ (11)	1050-1500	61.1

ergy are detected scale cracking has not been properly considered. An alternative mechanism (8) involving the participation of chromium vapor to transport at higher temperatures seems less likely in the present work where compact adherent scales existed at temperature. While noting that activation energy values for oxidation are notoriously inaccurate, it is concluded that the most likely value is about 35 kcal mole<sup>-1</sup>.

Manuscript received June 26, 1967; revised manuscript received Oct. 27, 1967.

Any discussion of this paper will appear in a Discussion Section to be published in the December 1968 JOURNAL.

#### REFERENCES

1. D. Caplan, A. Harvey, and M. Cohen, *Corr. Sci.*, **3**, 161 (1963).

2. W. C. Hagel, *Trans. Am. Soc. Metals*, **56**, 583 (1963).
3. G. C. Wood and D. P. Whittle, *J. Iron Steel Inst., London*, **202**, 979 (1964).
4. D. Caplan and M. Cohen, *This Journal*, **112**, 471 (1965).
5. D. P. Whittle and G. C. Wood, *ibid.*, **115**, 133 (1968).
6. D. P. Whittle, Ph.D. Thesis, University of Manchester (1965).
7. D. Caplan, A. Harvey, and M. Cohen, *This Journal*, **108**, 134, 1005 (1961).
8. E. A. Gulbransen and K. F. Andrew, *ibid.*, **104**, 334 (1957); **99**, 402 (1952).
9. C. Wagner, "Atom Movements," 153, ASM Symposium, Cleveland, Ohio (1950).
10. K. Hauffe and J. Block, *Z. Phys. Chem.*, **198**, 232 (1951).
11. W. C. Hagel and A. U. Seybolt, *This Journal*, **108**, 1146 (1962).
12. J. A. Crawford and W. A. Vest, *J. Appl. Phys.*, **35**, 2413 (1964).
13. T. F. Kassner, L. C. Walters, and R. E. Grace, Paper presented to I.A.E.A. Symposium, Vienna, 1965.
14. G. C. Wood and J. Boustead, To be published.
15. Y. Jeannin, C. Mannerskantz, and F. D. Richardson, *AIME Trans. Met. Soc.*, **227**, 300 (1963).
16. E. A. Gulbransen and K. F. Andrew, *J. Phys. Colloid Chem.*, **53**, 690 (1949).
17. R. Lindner and A. Akerstrom, *Z. Phys. Chem.*, **6**, 162 (1956).
18. D. V. Ignatov, I. N. Belokuvova, and I. A. Belyanin, *Trudy, Vsesoyuz. Nauch-Tekh. Konf. i Nauk, Met. i Metalloved.*, **1957**, 304 (1958).
19. E. J. Felten, *This Journal*, **108**, 490 (1961).

## Chromium Oxide Scale Growth on Iron-Chromium Alloys

### II. Influence of Alloy Composition

D. P. Whittle and G. C. Wood

Corrosion Science Division, Department of Chemical Engineering,  
University of Manchester Institute of Science and Technology, Manchester, England

#### ABSTRACT

$\text{Cr}_2\text{O}_3$ , containing small quantities of dissolved iron, is the only oxide formed in the oxidation of iron-chromium alloys in the range 22-68% Cr in oxygen at 800°-1200°C; it is also formed, at least initially, on alloys containing 14 and 18% Cr. The oxide growth is diffusion-controlled, with an apparent activation energy of 36 kcal mole<sup>-1</sup>. The increase in oxidation rate with alloy chromium content is slight up to 37% Cr, but becomes more marked with the chromium-rich alloys. Iron only enters the scale during the very early stages of oxidation, so the weight fraction of iron in the oxide decreases with time. Alloy interdiffusion coefficients have been determined from chromium concentration profiles in the underlying alloy. The activation energies for interdiffusion are 51 and 59 kcal mole<sup>-1</sup> for Fe-27% Cr and Fe-59% Cr, respectively, but interdiffusion is much slower for the chromium-rich alloy. The chromium concentration at the alloy/oxide interface, which is determined largely by the ratio of oxidation rate to alloy interdiffusion rate, governs the type of oxide formed if lifting and cracking of the stressed scale occurs. Factors affecting the tendency for scale failure in this way are discussed.

In an earlier paper (1), it was shown that the scales produced on iron-chromium alloys, containing 28-68% Cr, in air at 1100°C were composed of  $\text{Cr}_2\text{O}_3$  containing very small amounts of iron (' $\text{Cr}_2\text{O}_3$ '). There was some evidence that the oxidation rate increased slightly as the alloy chromium content was raised, and it was demonstrated that chromium from the alloy was less readily replenished at the alloy/oxide interface in the chromium-rich alloys.

Detailed data obtained under much more carefully controlled conditions are reported here. Special em-

phasis is placed on the quantitative determination of the variation of scale and alloy composition with time. The study is particularly related to alloys containing 22-68% Cr but formation of ' $\text{Cr}_2\text{O}_3$ ' scales on more dilute alloys is also referred to briefly.

#### Experimental

The chromium and carbon contents of the alloys are listed in Table I. Full details of the compositions of alloys A and B and of the methods of alloy preparation were given previously (1-3). The 59.5 and 68.0% Cr

Table I. Chemical analyses of the iron-chromium alloys (w/o)

Chromium	14.0	18.0	22.9	27.4	28.0	37.4	59.5	68.0
				(A)	(B)			
Carbon	0.006	0.017	0.048	0.006	0.023	0.029	—	—

alloys were prepared from vacuum-melted electrolytic iron and hydrogen-treated electrolytic chromium by arc melting, homogenization, and hot rolling to strip 0.0375 cm thick (4). All the other alloys were produced (1) by vacuum melting, heat-treatment, and cold rolling to 0.04 cm thick strip, using a Swedish iron base and electrolytic chromium, a slightly purer sample of the latter being employed for the 14.0 and 27.4% Cr alloys. The various alloys had impurity levels comparable to those of alloy A (14.0% Cr alloy) and alloy B (18.0, 22.9, and 37.4% Cr alloys) (2).

The specimen preparation, consisting of electropolishing followed by a cathodic etch, was performed exactly as described previously (2). With dilute chromium alloys the specimens were etched immediately on entering the solution, but at intermediate levels the passive state persisted for several seconds before etching commenced. When etching the 59.5 and 68.0% Cr alloys, the HCl had to be carefully deaerated by bubbling nitrogen through the solution, otherwise the specimen remained passive indefinitely.

The oxidation procedure, metallographic methods, and electron probe techniques were conventional (2).

### Results and Interpretation

**Kinetics and metallography.**—Detailed data for Fe-28% Cr of various purities have been given elsewhere (2).

**Oxidation of Fe-59.5% Cr.**—Reasonably blemish-free surfaces were obtained on electropolishing, although there was a greater tendency to pitting than for Fe-27.4% Cr, due either to more critical conditions or to more inclusions in the alloy. On etching, a smaller alloy grain size was revealed.

Figure 1(a) shows the mean short-term weight gain/time plots, whereas for the long-term runs in Fig. 1(b) individual curves are presented because of irregularities observed at 1100° and 1200°C. The sudden increases in weight after 6-hr oxidation were caused by extensive lifting of the protective oxide from the underlying alloy and subsequent scale cracking, allowing rapid oxidation of the bare alloy. Three breaks are observed in the curves at 1200°C but only two at 1100°C. Reproducibility was naturally some-

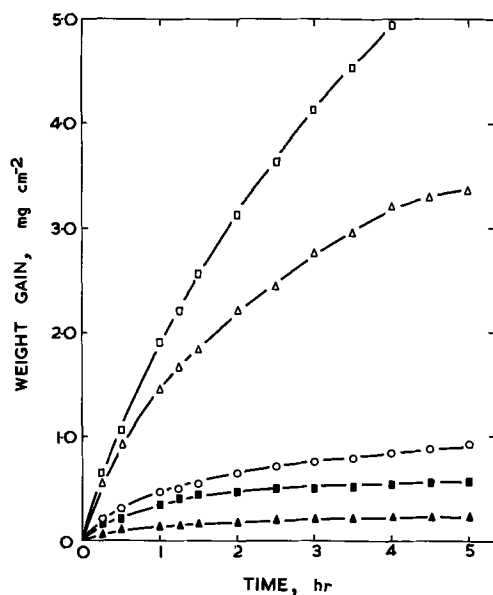


Fig. 1. Oxidation of Fe-59.5% Cr at 800-1200°C. (a) Mean weight gain/time curves for 5-hr runs.

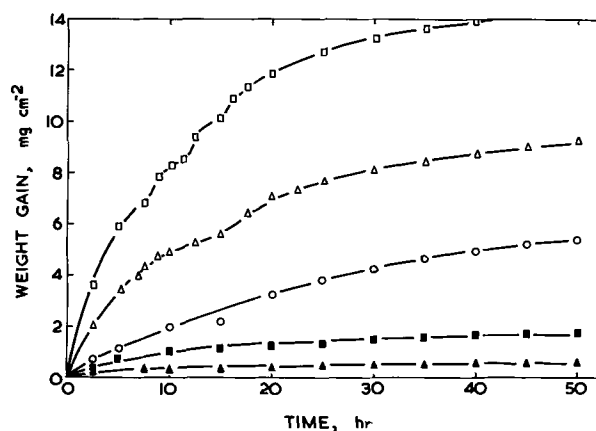


Fig. 1 (b). Individual weight gain/time curves for 50-hr runs. □ 1200°C; △ 1100°C; ○ 1000°C; ■ 900°C; ▲ 800°C. Symbols refer to Fig. 1(a) and 1(b).

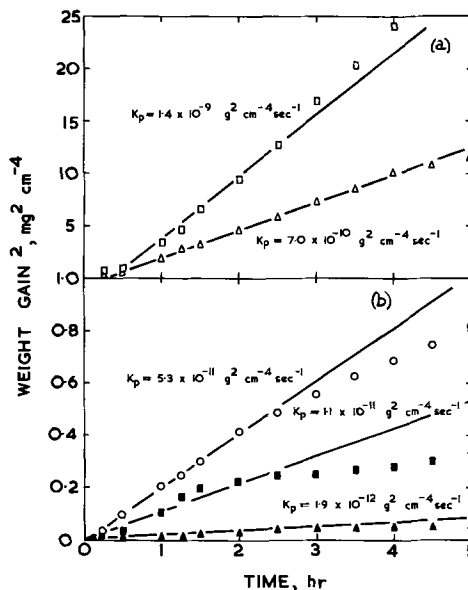


Fig. 2. Plot of (weight gain)<sup>2</sup>/time for the oxidation of Fe-59.5% Cr. (a) □ 1200°C; △ 1100°C. (b) ○ 1000°C; ■ 900°C; ▲ 800°C.

what poorer than for Fe-27.4% Cr (2) due to this scale cracking.

The (weight gain)<sup>2</sup>/time curves for the first 5 hr of oxidation [Fig. 2(a) and 2(b)] show the usual negative deviation from parabolic behavior [as defined previously (2)] at the lower temperatures. At 1200°C, the increased oxidation produced by scale lifting and cracking causes positive deviations from parabolic behavior, even after 1-hr oxidation. Consequently, there is little merit in extending the parabolic plots to 50 hr. The Arrhenius plot for the data Fe-59.5% Cr in Table II is given in Fig. 3 and yields an apparent activation energy for the oxidation process of  $50 \pm 7$  kcal mole<sup>-1</sup>, using the method of least mean squares and a test for a 95% confidence level. The value is higher than the  $36 \pm 6$  kcal mole<sup>-1</sup> de-

Table II. Comparison of short-term parabolic rate constants for Fe-59.5% Cr and Fe-27.4% Cr at 800°-1200°C (5-hr values)

Temp, °C	Parabolic rate constant, g <sup>2</sup> cm <sup>-4</sup> sec <sup>-1</sup>	
	Fe-59.5% Cr	Fe-27.4% Cr
800	$1.9 \times 10^{-12}$	$1.4 \times 10^{-13}$
900	$1.1 \times 10^{-11}$	$3.7 \times 10^{-13}$
1000	$5.3 \times 10^{-11}$	$1.4 \times 10^{-10}$
1100	$7.0 \times 10^{-10}$	$4.1 \times 10^{-10}$
1200	$1.4 \times 10^{-9}$	$1.2 \times 10^{-9}$

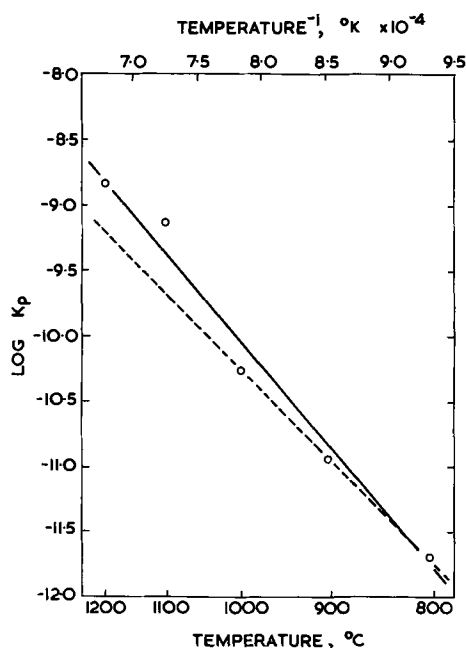


Fig. 3. Arrhenius plot for the oxidation of Fe-59.5% Cr.

duced from similar data (rate constants for 5-hr oxidation) for Fe-27.4% Cr and its accuracy is also reduced, doubtless due to the mild ballooning at the higher temperatures. If the  $K_p$  values for Fe-59.5% Cr at 1100° and 1200°C are ignored because single-layer scales are not formed, the activation energy for oxidation is 35 kcal mole<sup>-1</sup> (dotted curve in Fig. 3), which is much closer to the Fe-27.4% Cr value. Presumably the same rate-controlling mechanism holds in both cases and the difference in the rate constants at 800°-1000°C (Table II) is simply a purity effect (2), which is not understood.

The surface topography of scales was similar to that on Fe-27.4% Cr (2) except that, where the alloy grain structure was replicated, the grain size was smaller. There was no evidence of the oxide wrinkling apparent in section, probably because this was on a fine scale and would not be evident in the oblique illumination of the microscope. At 1000°C the single-layer scale tended to be more flaky than for Fe-27.4% Cr.

At and below 1000°C, the single-layer, single-phase, and approximately uniform scales detached from the alloy on cooling [Fig. 4(a)] and were similar to those on Fe-27.4% Cr. In contrast, Fig. 4(b) displays a multilayered scale after 5 hr at 1200°C. Two major scale layers are visible, but each individual layer appears to contain several minor blisters. Some of the porosity in the layers is probably related to the metallographic preparation. There is the same number of major scale layers around the entire specimen cross section, and the alloy appears to have been attacked relatively uniformly. Probably the scale lifted from the entire alloy surface simultaneously or nearly so, otherwise the breaks would not have been obvious in the kinetic curves. All the specimens oxidized at 1200°C showed scale multilayering, even after only 1-hr oxidation. After 1-, 5-, 10-, and 50-hr oxidation there were, respectively, 2, 2, 3, and 4 major scale layers. These do not exactly correlate with the number of breaks in the kinetic curves. This is not surprising because localized layering would not show up in the kinetics in the early rapid stages of oxidation.

*Influence of alloy chromium content on oxidation rate mainly at 1000°C.*—Figure 5, showing the short-term and long-term kinetic curves for five of the alloys of most comparable purity, indicates that the increase in oxidation rate with alloy chromium content was slight up to 37.4% Cr but became more marked



Fig. 4. Cross sections of scales on Fe-59.5% Cr: (a) 5 hr at 1000°C, magnification ca. 500X; (b) 5 hr at 1200°C, magnification ca. 250X.

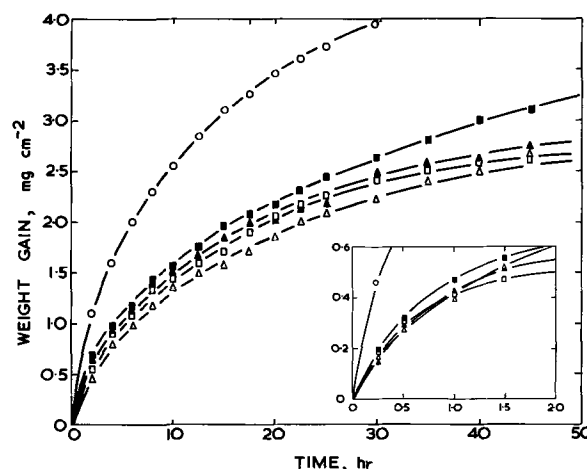


Fig. 5. Influence of chromium content on the oxidation of iron-chromium alloys at 1000°C. Inset shows short-term curves.  $\Delta$  Fe-22.9% Cr;  $\square$  Fe-28.0% Cr (alloy B);  $\blacktriangle$  Fe-37.4% Cr;  $\blacksquare$  Fe-59.5% Cr;  $\circ$  Fe-68.0% Cr.

with Fe-59.5% Cr. Fe-68.0% Cr, on the other hand, oxidized much faster during the first 5 hr, but after 50 hr the slopes of the weight gain/time curves are similar for all the alloys. This is not thought to be simply a purity effect because the alloy came from the same source as the Fe-59.5% Cr alloy. The reproducibility of the kinetic curves was roughly comparable for all alloy compositions. Figure 6 indicates a negative deviation from the parabolic oxidation rate law, referred to previously (2).

The parabolic rate constants derived (2) from Fig. 6 are given in Table III and confirm the above trends. Fe-18.0% Cr, which was from the same stock as the 22.9, 28.0, and 37.4% Cr alloys, had only a slightly lower parabolic rate constant. Fe-14.0% Cr and Fe-27.4% Cr, which were made from purer chromium showed comparable rate constants to each other but the values were higher than for the other alloys. All the kinetic curves for all the alloys were smooth at 1000°C, consistent with single-layer scales. Crude estimates of the activation energy of oxidation for Fe-14.0 and Fe-18.0% Cr, where 'Cr<sub>2</sub>O<sub>3</sub>' only was de-

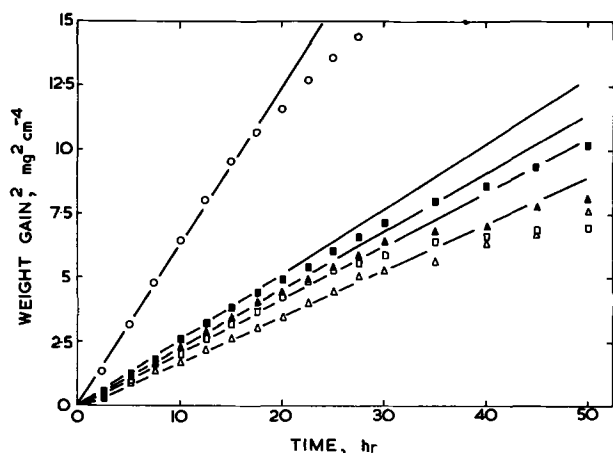


Fig. 6. Plot of  $(\text{weight gain})^2/\text{time}$  for the oxidation of various iron-chromium alloys at  $1000^\circ\text{C}$ .  $\triangle$  Fe-22.9% Cr;  $\square$  Fe-28.0% Cr (alloy B);  $\blacktriangle$  Fe-37.4% Cr;  $\blacksquare$  Fe-59.5% Cr;  $\circ$  Fe-68.0% Cr.

tected, gave  $37 \text{ kcal mole}^{-1}$ , which is close to the values for more chromium-rich alloys.

The external surfaces of scales of comparable thickness appeared the same at 100X magnification on all the alloys, except Fe-68.0% Cr. For thinner scales, there was a difference in grain size of the original alloy, replicated by the scale. Figure 7(a) shows the typical scale structure on Fe-22.9% Cr oxidized for 1 hr at  $1000^\circ\text{C}$ , but after 10-hr oxidation the scale ballooning on cooling is more apparent than usual [Fig. 7(b)]. The tendency of the scale to crack and lift on cooling decreased as the chromium content of the alloy decreased. Thus, it tended to fly off Fe-59.5% Cr and Fe-68.0% Cr, whereas with Fe-37.4% Cr only scale cracking occurred. With the other alloys only scale lifting occurred. Figure 7(c) shows the unusual surface scale morphology for Fe-68.0% Cr after oxidation for 5 hr at  $1000^\circ\text{C}$ . The oxide has a more 'sintered' appearance, and oxide promontories adopt a spheroidal form rather than the angular structure of other scales.

Figure 8(a) and 8(b) are respectively typical examples of nonadherent and adherent single-phase, single-layer ' $\text{Cr}_2\text{O}_3$ ' scales formed on these alloys. The nonadherent scale is very wrinkled, but multilayered scales were never observed. No porosity is apparent even at the alloy-oxide interface. For Fe-22.9% Cr at  $1200^\circ\text{C}$  the scale adhered on cooling [Fig. 8(c)], but the alloy-oxide interface was far more irregular than after oxidation at  $1000^\circ\text{C}$ , or for the more chromium-rich alloys at any temperature. This behavior was even more pronounced for Fe-14.0% Cr and Fe-18.0% Cr and is probably related to plastic deformation of the alloy due to stresses developed in the alloy/scale combination at this elevated temperature, as mentioned later. Over about 1% of the surface of Fe-22.9% Cr at  $1200^\circ\text{C}$ , ballooning occurred in the early stages, there being three layers of scale in places, the two outer layers being extremely thin [Fig. 8(d)]. The pores in these oxides are probably artifacts. Comparable behavior with 14.0 and 18.0% Cr alloys (2), and with abraded Fe-22.9% Cr in air

Table III. Variation of long-term parabolic rate constant with alloy chromium content at  $1000^\circ\text{C}$  (50-hr values)

Alloy, % Cr	Parabolic rate constant, $\text{g}^2 \text{ cm}^{-4} \text{ sec}^{-1}$
14.0	$7.6 \times 10^{-11}$
18.0	$4.3 \times 10^{-11}$
22.9	$5.1 \times 10^{-11}$
27.4 (A)	$1.1 \times 10^{-10}$
28.0 (B)	$5.8 \times 10^{-11}$
37.4	$5.9 \times 10^{-11}$
59.5	$6.8 \times 10^{-11}$
68.0	$1.7 \times 10^{-10}$

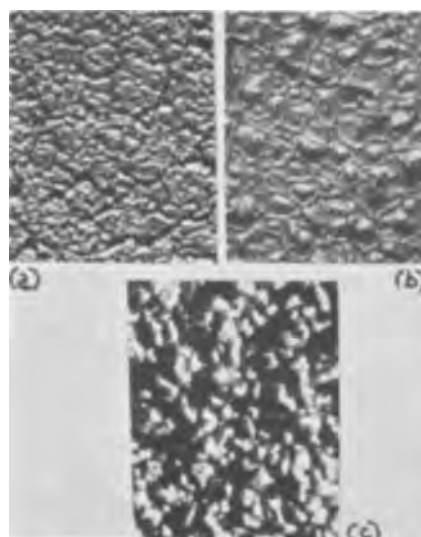


Fig. 7. Surface topography of scales under oblique illumination: (a) Fe-22.9% Cr oxidized for 1 hr at  $1000^\circ\text{C}$ , magnification 50X; (b) Fe-22.9% Cr oxidized for 10 hr at  $1000^\circ\text{C}$ , magnification 50X; (c) Fe-68.0% Cr oxidized for 5 hr at  $1000^\circ\text{C}$ , magnification 15X.

at  $1100^\circ\text{C}$  (1), led to breakthrough and stratified iron-rich scale development because, at the time of scale cracking, chromium had not been replenished enough at the alloy/oxide interface to permit fresh ' $\text{Cr}_2\text{O}_3$ ' development.

*Electron probe microanalysis of the oxides.*—Electron probe microanalyses of all the oxide scales are presented in Tables IV-VI. The inaccuracies inherent in this method of analysis, particularly scale thinness and possibly its porosity and difficulties in applying accurate corrections, have resulted in the analyses being low in apparent metal content. Thus, to facilitate comparisons, the analyses have been normalized to a total metal content of 67.6%, this being the figure quoted for slightly nonstoichiometric  $\text{Cr}_2\text{O}_3$  scales (5).

Perusal of Tables IV-VI produces the following general conclusions:

(i) For all the alloys, the percentage of iron in the scale at any given temperature decreases with time. This may be because either the  $\text{Fe}^{2+}$  or  $\text{Fe}^{3+}$  ions are reduced by the chromium to metallic iron or, much more likely, the iron content stays constant and its weight fraction is decreased by the growth of the ' $\text{Cr}_2\text{O}_3$ ' by the addition of chromium only. It is also conceivable that iron ions in the ' $\text{Cr}_2\text{O}_3$ ' can diffuse to the outside of the scale and form a complete thin but undetectable layer there, consistent with the high dissociation pressure of  $\text{Fe}_2\text{O}_3$ . No iron gradients could be detected through the scales. Recent work (22) has detected the outer layer, although this is mainly residual initially nucleated oxide.

(ii) The percentage of iron in the scale decreases as temperature increases for any given oxidation time for Fe-27.4% Cr and Fe-59.5% Cr. This cannot be taken immediately as a genuine trend because the scale thicknesses are vastly different. Thus, dilution of iron in the ' $\text{Cr}_2\text{O}_3$ ' scale occurs to varying extents.

(iii) The percentage of iron in scales of corresponding thickness decreases as the alloy chromium content increases.

*Compositional changes in the underlying alloy during oxidation.*—Only certain of the chromium concentration profiles are presented in the interests of brevity, iron contents obviously following a reverse trend. The abscissas' scales have been selected so that results for various oxidation times are measured from a common interface, namely, the original alloy surface. The position of the actual alloy-oxide interface after a given oxidation time, marked by the start of each

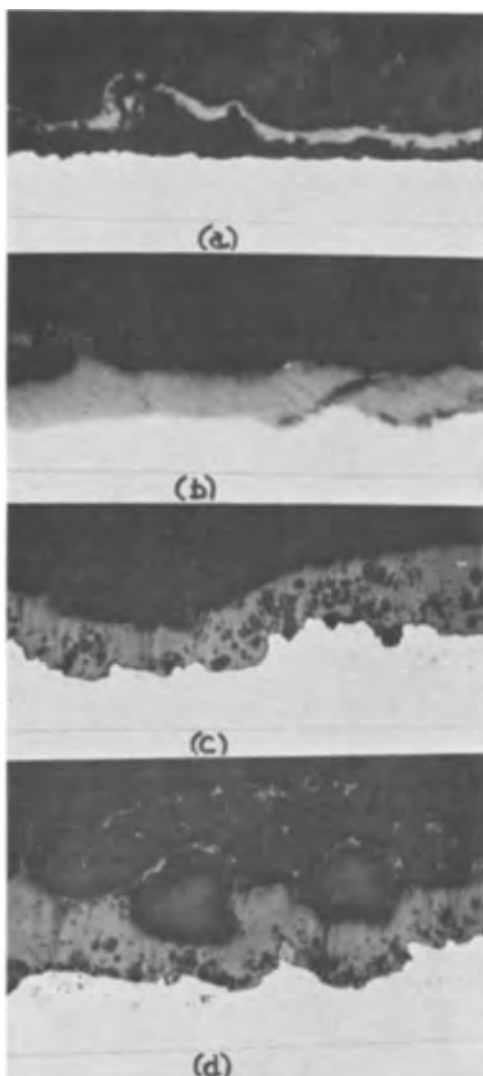


Fig. 8. Cross sections of scales on Fe-22.9% Cr: (a) 1 hr at 1000°C, magnification 1050X; (b) 5 hr at 1000°C, magnification 1400X; (c) 50 hr at 1200°C, magnification 350X; (d) 50 hr at 1200°C, magnification 350X.

profile, is easily computed from a modified form of the parabolic rate law of oxidation written thus

$$d/dt (\Delta x) = \frac{K_c}{\Delta x} \quad [1]$$

where  $\Delta x$  is the location of the alloy-oxide interface measured from the original surface of the alloy after time  $t$ , and  $K_c$  is a modified parabolic rate constant. It may readily be shown that if stoichiometric  $\text{Cr}_2\text{O}_3$  is assumed to form on the alloy surface then

$$K_c = 1/2 K_p \cdot (2A_{\text{Cr}})^2 / (3/2 M_{\text{O}_2} \rho)^2 \quad [2]$$

where  $A_{\text{Cr}}$  is the g atomic weight of chromium,  $M_{\text{O}_2}$  is the g molecular weight of oxygen, and  $\rho$  is the density of the alloy. Thus,  $\Delta x$  can be obtained on integration of Eq. [1].

Detailed profiles were obtained for most of the oxidation specimens previously described, typical results for Fe-27.4% Cr and Fe-59.5% Cr at 800, 1000 and 1200°C being shown in Fig. 9 and 10, respectively. The ends of the profiles mark the position of the inwardly moving alloy/oxide interface with time. Although there are several minor anomalies the following conclusions are possible:

(i) The depth of the chromium-depleted zone (where the alloy chromium content is less than 99% of its original value) increases with time at all temper-

Table IV. Analyses of ' $\text{Cr}_2\text{O}_3$ ' scales formed on Fe-27.4% Cr at 800°-1200°C

Temp, °C	Oxidation time, hr	Actual analysis		Normalized analysis	
		% Cr	% Fe	% Cr	% Fe
800	0.5	27.3	22.6	—	—
	1.0	23.3	3.4	59.0	8.6
	2.5	33.1	2.0	63.7	3.9
	5.0	45.6	3.6	62.6	5.0
	10.0	38.0	2.8	63.1	4.5
	20.0	48.8	0.9	66.5	1.1
900	50.0	58.9	2.2	65.3	2.3
	1.0	35.2	7.4	57.2	10.0
	2.5	29.1	1.2	64.9	2.7
	5.0	58.0	2.1	65.2	2.4
	10.0	52.8	2.6	64.8	2.8
1000	20.0	64.1	0.4	67.2	0.4
	0.5	43.8	0.9	66.2	1.4
	1.0	57.5	0.5	67.0	0.6
	2.5	56.4	0.5	67.0	0.6
	5.0	64.1	0.6	67.0	0.6
1100	10.0	59.7	1.6	66.8	0.8
	50.0	62.6	1.0	66.6	1.0
	5.0	61.9	0.4	67.1	0.5
1200	20.0	64.2	0.3	67.3	0.3
	0.5	58.9	2.6	64.8	2.8
1200	1.0	59.7	1.2	66.3	1.3
	2.5	50.1	0.8	66.7	0.9
	5.0	59.7	0.6	66.9	0.7
	12.0	61.9	0.3	67.2	0.4
	25.0	61.1	0.3	67.2	0.4
	50.0	63.6	0.4	67.2	0.4

Table V. Analyses of ' $\text{Cr}_2\text{O}_3$ ' scales formed on Fe-59.5% Cr at 800°-1200°C

Temp, °C	Oxidation time, hr	Actual analysis		Normalized analysis	
		% Cr	% Fe	% Cr	% Fe
800	1.0	28.0	2.0	63.0	4.6
	50.0	59.9	1.1	66.3	1.0
1000	1.0	54.0	0.3	67.2	0.4
	5.0	58.3	0.2	67.3	0.3
	10.0	63.5	1.0	66.5	1.1
	50.0	58.9	0.5	67.0	0.6
1200	1.0	65.7	0.8	66.8	0.8
	5.0	66.9	0.6	67.0	0.6
	10.0	58.7	0.9	66.9	0.7

Table VI. Analyses of ' $\text{Cr}_2\text{O}_3$ ' scales formed on various alloys at 1000°C

Alloy, % Cr	Oxidation time, hr	Actual analysis		Normalized analysis	
		% Cr	% Fe	% Cr	% Fe
22.9	1.0	49.1	5.7	60.6	7.0
	5.0	57.8	3.0	64.3	3.3
	50.0	44.1	0.38	67.1	0.57
37.4	1.0	54.1	1.9	65.3	2.3
	5.0	64.1	1.3	66.2	1.4
	10.0	62.4	0.4	67.2	0.4
68.0	50.0	60.2	0.4	67.1	0.5
	1.0	52.9	0.4	67.1	0.5
	5.0	65.1	0.7	66.8	0.8
	10.0	65.6	0.2	67.4	0.2
	50.0	59.2	3.0	64.4	3.2

atures and is deeper the higher the temperature and the lower the bulk alloy concentration.

(ii) The chromium content at the alloy-oxide interface rises with oxidation time, although this is not always apparent from short-term runs. Unfortunately this trend cannot be followed experimentally with any great accuracy as both siting and analysis at the interface are difficult. Nevertheless, as is shown elsewhere (6) by theoretical considerations, the measured values are approximately correct.

(iii) The percentage change at any time in chromium concentration at the alloy-oxide interface is greater for Fe-59.5% Cr than for Fe-27.4% Cr. This, together with the smaller depth of depletion, is mainly due to the smaller interdiffusion coefficient in this alloy. The relatively flat chromium profiles immedi-

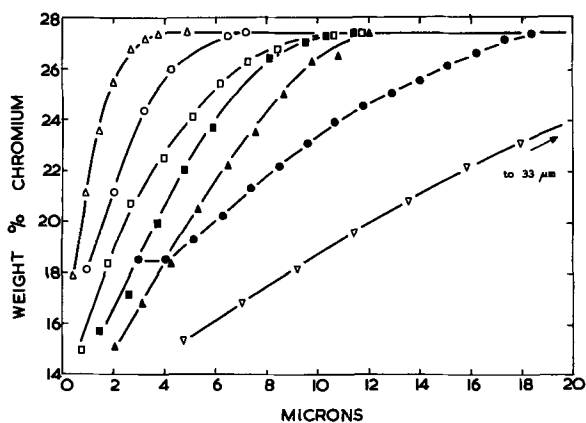


Fig. 9(a). Chromium concentration profiles in the underlying alloy, measured by electron probe microanalysis, after oxidation of Fe-27.4% Cr, at 800°C.

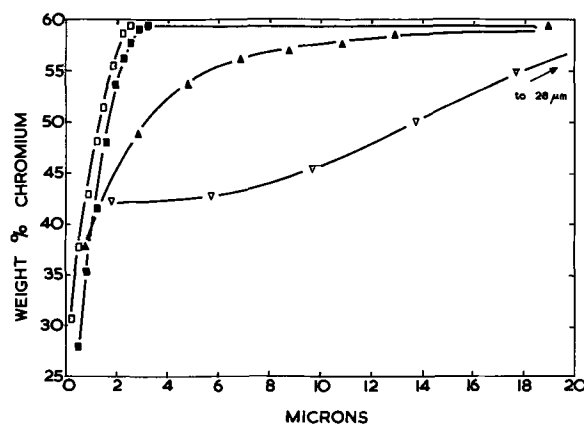


Fig. 10(a). Chromium concentration profiles in the underlying alloy, measured by electron probe microanalysis, after oxidation of Fe-59.5% Cr at 800°C.

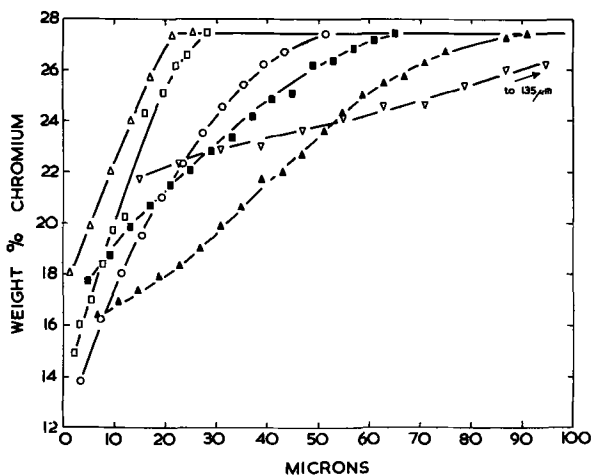


Fig. 9(b). Same as Fig. 9(a) at 1000°C

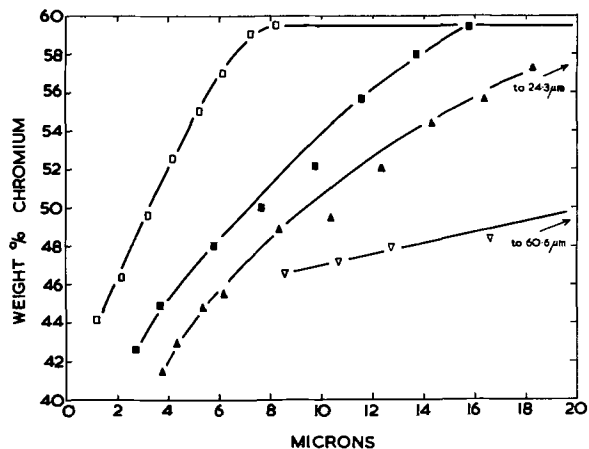


Fig. 10(b). Same as Fig. 10(a) at 1000°C

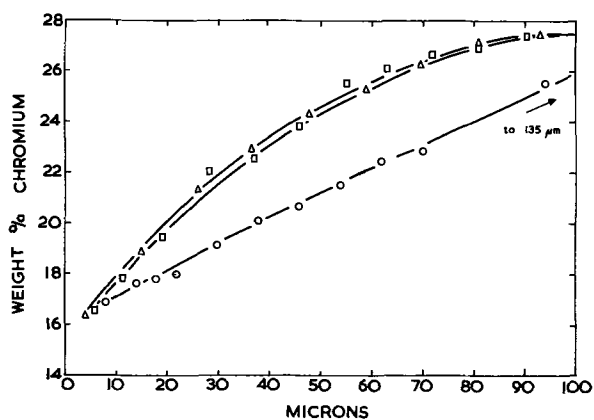


Fig. 9(c). Same as Fig. 9(a) at 1200°C.  $\Delta$  0.5 hr;  $\square$  1 hr;  $\circ$  2.5 hr;  $\blacksquare$  5 hr;  $\blacktriangle$  10 hr;  $\bullet$  20 hr;  $\nabla$  50 hr. Symbols refer to Fig. 9(a) and 9(b) also.

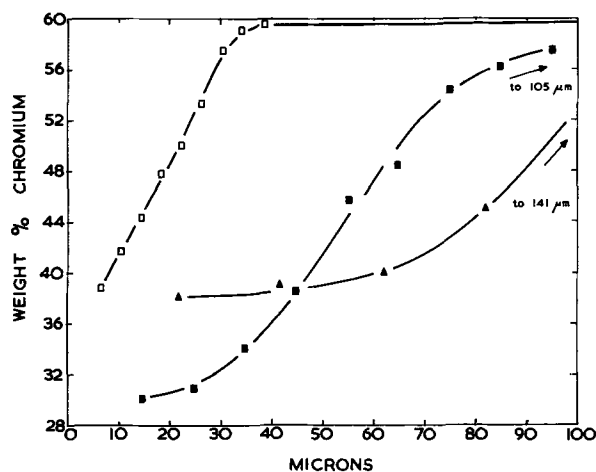


Fig. 10(c). Same as Fig. 10(a) at 1200°C.  $\square$  1 hr;  $\blacksquare$  5 hr;  $\blacktriangle$  10 hr;  $\nabla$  50 hr. Symbols refer to Fig. 10(a) and 10(b) also.

ately next to the oxide after longer times, again particularly prevalent for Fe-59.5% Cr, are also due to more rapid interdiffusion in the chromium-depleted alloy there.

(iv) The chromium concentrations at the alloy-oxide interface are all in the range 12-18% for Fe-27.4% because the ratio of parabolic rate constant to alloy interdiffusion coefficient is approximately constant in the range 800°-1200°C. The value is more variable for Fe-59.5% Cr at 1200°C, possibly because multilayering is encountered.

(v) For Fe-27.4% Cr and other dilute alloys, where  $D$  is large enough (generally only at 1200°C), zones from the two sides of the oxidizing specimens meet in

the specimen center. This appreciably affects the profiles, so all such results have been omitted.<sup>1</sup>

Fe-28% Cr alloys of different purities (2) showed higher chromium values at the alloy/oxide interface than the Fe-27.4% Cr alloy (A) after oxidation for 5 hr at 1000°C. However, this smaller depletion was simply related to the oxidation rates because the alloy interdiffusion coefficients, as calculated in the Discussion section, showed no significant variation.

Comparison of corresponding profiles is not a simple matter because concentrations at equivalent points along traverses are functions of the alloy interdiffusion coefficient and the oxidation rate as well as other factors. However, the depths of the chromium-depleted

<sup>1</sup> Such behavior essentially produces an alloy more dilute in chromium which could eventually display breakdown.

zones (as defined earlier) at fixed oxidation times are independent of the oxidation rate and are simply related to the alloy interdiffusion coefficient by

$$x_d / (Dt)^{1/2} \approx 2 \quad [3]$$

where  $x_d$  is the depth of the chromium-depleted zone measured (as accurately as microanalysis will permit) from the original alloy surface,  $t$  is the time, and  $D$  is the alloy interdiffusion coefficient, assumed independent of composition in the relevant range. After 1 hr at 1000°C, the depths of the chromium-depleted zones were 33, 28, 27, 13, and 8  $\mu$  for the 22.9, 27.4, 37.4, 68.0, and 59.5% Cr alloys, respectively. The same general order was maintained after longer oxidation times, although there were slight discrepancies with Fe-22.9% Cr. Thus, on a semiquantitative basis there is a minimum interdiffusion rate at about 60% Cr. A further significant feature is that for all the alloys, Fe-14.0% Cr and Fe-18.0% Cr excepted, the chromium concentration at the alloy/oxide interface is never sufficiently low for stratified scale to develop at any stage when cracking is likely to occur.

### Discussion

**Scale compositions.**—The most important conclusion from the scale analyses is that little, if any, iron enters the scale during the later stages of oxidation. If the reduction of the percentage of iron in the scale is simply due to the dilution effect, then the actual amount of iron in the scale will be constant throughout growth. This amount may be calculated as follows.

Let  $M$  be the mass of iron per square centimeter in the thermodynamically unstable film formed on the alloy in the first few minutes (subsequently termed "the initial film") and assume that no further iron enters the scale at longer times.  $M$  g. cm<sup>-2</sup> will then be the actual mass of iron in the scale during the entire oxidation. If  $W$  is the weight fraction of iron in the scale at time  $t$ , then

$$W = M / (\text{Total weight of oxide/cm}^2) \quad [4]$$

The total mass of oxide at time  $t$  follows from the parabolic law and thus

$$W = M (3 M_{O_2}/2) / (K_p \cdot t)^{1/2} \cdot M_{Cr_2O_3} \quad [5]$$

where  $M_{O_2}$  and  $M_{Cr_2O_3}$  are the g. molecular weights of oxygen and Cr<sub>2</sub>O<sub>3</sub>, respectively, and  $K_p$  is the parabolic rate constant measured in terms of mass increase. The weight fraction of iron in the scale is, then, inversely proportional to the square root of the oxidation time.

Unfortunately, the experimental data are not sufficiently accurate to assess the validity of such a law, but it is instructive to calculate and compare the values of  $W$  for the various alloys. Table VII gives the average values for all the data for any set of conditions of temperature and alloy composition.

Before commenting on the trends of  $W$ , some idea of the significance of the term initial film must be presented. The first film produced on iron-chromium alloys entering the hot zone contains mixtures or solid solutions of the component oxides, with iron and chromium present in their alloy proportions or even at this stage with some chromium enrichment (7). In this system, where Fe<sub>2</sub>O<sub>3</sub> and Cr<sub>2</sub>O<sub>3</sub> are isomorphous,

the initial oxide is probably a solid solution, (Fe, Cr)<sub>2</sub>O<sub>3</sub>, although some spinel, Fe Fe<sub>(2-x)</sub>Cr<sub>x</sub>O<sub>4</sub> ( $0 \leq x \leq 2$ ) is also possible. The effective thickness of this initial film depends on the temperature and the oxygen partial pressure, these factors also controlling the extent, if any, of chromium enrichment in the oxide. As soon as the superior affinity of chromium for oxygen becomes predominant, the layers at the base of the film become chromium-rich by the direct formation of 'Cr<sub>2</sub>O<sub>3</sub>' from the oxygen effectively available at the alloy/oxide interface (22). Chromium then continues to enter the scale and the iron present in the initial film is able to distribute itself apparently uniformly through the scale.

For the rapid establishment of a 'Cr<sub>2</sub>O<sub>3</sub>' layer, the 'Cr<sub>2</sub>O<sub>3</sub>' must be formed near the alloy-oxide interface not within the alloy. This implies rapid chromium diffusion to the surface and slow entry of oxygen into the alloy, a condition met by Fe-Cr alloys. For other systems, e.g., Ni-Cr, because chromium diffusion is slower and oxygen solubility apparently greater in the alloy, relatively thick (up to 5  $\mu$  or more) NiO scales are formed on the surface of the comparable alloy before selective chromium oxidation asserts itself (7, 8). Further, since NiO and Cr<sub>2</sub>O<sub>3</sub> are heteromorphous and unable to form solid solutions, and NiCr<sub>2</sub>O<sub>4</sub> formation in this situation is slow, the NiO remains on the surface of the growing Cr<sub>2</sub>O<sub>3</sub>.

By reference to the 1000°C values of  $W$  (Table VII), it is seen, as expected, that there is generally a slight increase in the amount of iron in the initial film as the alloy chromium content is decreased. If it is assumed that the initial film is a mixture of the component oxides in the proportions of iron and chromium in the alloy, then its thickness can be calculated as  $1.2 \times 10^{-2}$  mg cm<sup>-2</sup> (about 250Å) for an oxide of density and metal content corresponding to Cr<sub>2</sub>O<sub>3</sub>.

**Influence of alloy composition on the oxidation rate and scale characteristics.**—Some detailed discussion of the mechanism of 'Cr<sub>2</sub>O<sub>3</sub>' scale formation on iron-chromium alloys has already been given (2). It has been shown here that, neglecting effects due to impurity variations in the starting materials, the rate of oxidation at 1000°C, and probably at other temperatures, only rises slightly (barely within experimental error) with alloy chromium content in the range 18.0-37.4%. Fe-59.5% Cr oxidizes significantly, and Fe-68.0% Cr substantially, faster but these results could again be due to impurities. It was postulated earlier (1) that the observed slight increase in oxidation rate with alloy chromium content is due to iron as Fe<sup>2+</sup> ions decreasing the concentration of cation vacancies and hence the diffusion rate of Cr<sup>3+</sup> ions through the scale. However, it is equally possible for Fe<sup>3+</sup> ions merely to replace Cr<sup>3+</sup> ions in the normal lattice with no resultant effect on oxidation rate according to Wagner-Hauffe valency rules. Nevertheless, the stoichiometry of the resulting Cr<sub>2</sub>O<sub>3</sub>-Fe<sub>2</sub>O<sub>3</sub> solid solution may depend on its exact composition and could vary between metal-deficient p-type for pure Cr<sub>2</sub>O<sub>3</sub> and oxygen-deficient n-type for pure Fe<sub>2</sub>O<sub>3</sub> (23). Thus, in view of the general trend of the higher the alloy chromium content the lower the iron content of the Cr<sub>2</sub>O<sub>3</sub>, the tendency for the oxidation rate to increase with alloy chromium content may be explained because the oxide

Table VII. Calculated values of the weight of iron in the initial film on iron-chromium alloys at 800°-1200°C

		Weight of iron, mg cm <sup>-2</sup>				
% Cr		800°C	900°C	1000°C	1100°C	1200°C
27.4		$5.5 \times 10^{-3}$	$4.6 \times 10^{-3}$	$4.4 \times 10^{-3}$	$4.7 \times 10^{-3}$	$9.5 \times 10^{-3}$
59.5		$1.8 \times 10^{-3}$		$3.4 \times 10^{-3}$		$1.1 \times 10^{-3}$
% Cr	14.0	18.0	22.9	27.4	37.4	59.5
1000°C		$4.8 \times 10^{-3}$	$12.0 \times 10^{-3}$	$4.4 \times 10^{-3}$	$3.8 \times 10^{-3}$	$3.4 \times 10^{-3}$
						$2.4 \times 10^{-3}$

The value for Fe-14.0% Cr at 1200°C is  $8.8 \times 10^{-3}$  (10-min run only).



with least lattice defects will be 'Cr<sub>2</sub>O<sub>3</sub>' containing a certain relatively low iron concentration. As the variation of the iron content of the 'Cr<sub>2</sub>O<sub>3</sub>' with alloy composition is actually rather small after the initial oxidation stages, little variation of oxidation rate is expected or indeed found.

A similar slight trend would also be expected because, as the bulk alloy chromium concentration is increased, so is the chromium concentration at the alloy/oxide interface. The cation vacancy concentration in the oxide at this interface is thereby decreased, so increasing the vacancy gradient across the scale and therefore the oxidation rate. This effect would only be expected to be small. Previous reports (1) of larger effects of alloy composition on the oxidation rate may have been due to inadequate correlation between kinetic and metallographic data, particularly if scale multilayering occurred.

That the 'Cr<sub>2</sub>O<sub>3</sub>' scales are undoubtedly heavily stressed during formation is deduced from the following observations: (a) the occasional scale ballooning and multilayering at temperature, (b) the formation of a wavy alloy/oxide interface, at least for very pure alloys and lower-chromium alloys at 1200°C. On cooling, additional stressing occurs, as witnessed by: (c) the spalling, sometimes explosive, of parts of the scales on cooling, (d) the tendency of the oxide to wrinkle when released from the constraining influence of the alloy.

The actual oxidation behavior of any specimen depends on the way the stress is developed and relieved by slip, creep, or fracture of the alloy or scale and the extent to which they maintain contact during oxidation or cooling. Such matters are related in a complex way to the specimen geometry, the alloy composition (including phase changes), heat-treatment (degree of cold work and impurity segregation), and surface finish, grain growth, and recrystallization of the alloy and scale, void formation by vacancy coalescence at the alloy/oxide interface, and the oxidation atmosphere and temperature.

It is often stated that stress development due to epitaxial effects and volume changes only occurs when scales grew by the inward movement of O<sup>2-</sup> ions, but this is an oversimplification because stresses undoubtedly develop in all types of oxides. The compressive stress is concentrated in a thin layer immediately adjacent to the alloy and, unless it is relieved by plastic flow of the alloy/film combination, theoretically increases progressively with film thickness until spalling occurs by fracture of the scale from the alloy or of the scale itself. In practice, the stress developed is often not so severe because misfit dislocations are introduced into the oxide at the interface and further stress relief is obtained by slip and climb of dislocations moving away from the surface. Thus, although most of the stress is located near the alloy/oxide interface the entire scale must try to deform to maintain continuity with the core. Therefore, stress of a similar or different sign may be developed in outer parts of the scale and may determine local (*e.g.*, at corners) and to some extent general, scale behavior.

Interface and other stresses are at least partly relieved by slip and creep of the alloy and/or oxide in the appropriate direction. For at least some alloys in the present system, both alloy and scale appear to be deformed, partly explaining the generally maintained adhesion at temperature. Such plastic deformation is most important in the adherent compact oxide supporting the ionic flux building the film, but it should not be neglected elsewhere because specimen continuity depends on deformation of the entire scale.

Behavior on cooling is determined more by thermal contraction characteristics and adhesion, but the former is not very important at temperature, except in the presence of overheating, which should be small here. The stressed oxide may adhere to an alloy in-

definitely, if its cohesion and its adhesion to the alloy are excellent. Adhesion is partly determined by interlocking effects between the alloy and scale, related to surface roughness. However, vacancy coalescence and the nucleation of Kirkendall voids at the alloy/oxide interface weaken adhesion. These phenomena are determined partly by the ability of the alloy (often related to purity) to accept the vacancies diffusing in through the scale. Crack propagation between the alloy and scale, or through the inner barrier layer of oxide, parallel to the alloy/oxide interface, leaving a thin layer of oxide still adherent to the alloy, can also occur.

It is not possible to state exactly which of the above factors is vital in causing failure of 'Cr<sub>2</sub>O<sub>3</sub>' on Fe-Cr alloys. Nevertheless, some pertinent observations may be made.

1. The optimum alloy chromium content for the maintenance of scale adhesion at temperature and the consequent production of uniform single-layer scales was in the range 23-40%, in agreement with indications from previous work (3, 9, 10). With higher chromium concentrations multilayered scales could be obtained, and with low-chromium alloys scale failure was followed by stratified scale development. The influence of alloy chromium content or impurities on the degree of stoichiometry of the scale, the ratio of Cr<sup>3+</sup>/O<sup>2-</sup> ion movement in the oxide, the ability of the alloy to absorb vacancies and the nature of the alloy/oxide interface, and the influence of these factors and the iron content of the scale on the stress development plasticity, and adhesion is unknown.

The plasticity of iron-chromium alloys decreases progressively as alloy chromium content increases at high temperatures. Thus, the optimum chromium content for scale retention at temperature may occur at a composition where the scale and alloy plasticities are just sufficient to relieve the stresses built up in the oxide. At higher chromium levels scale cracking occurs because the alloy cannot yield sufficiently, although it is also possible that the scale (with a lower iron content) is less plastic. There is definite evidence that the alloy can deform with the scale with very pure alloys at high temperature, and with alloys containing 14-23% Cr, producing a highly irregular alloy/oxide interface. It is possible that local scale failure occurs because the alloy can yield easily, but the scale is not sufficiently plastic to bend in the way required. Additionally a greater contribution from O<sup>2-</sup> migration during scale growth might increase the stresses developed here. Experiments with variable specimen geometry also indicated that corners led to scale failure much more readily on Fe-14.0% Cr than with Fe-27.4% Cr. It is not clear how important vacancy coalescence at the alloy/oxide interface was here, but void formation is apparently more likely with the dilute alloy. Scale adhered more readily on abraded Fe-14.0% Cr than annealed alloy at 1200°C, either because scale and alloy interlocking was more complete or because vacancies could more readily enter the alloy.

2. Evidence exists (3) that 'Cr<sub>2</sub>O<sub>3</sub>' grown at 10<sup>-3</sup>-10<sup>-4</sup> Torr was much more uniform, compact, and adherent at temperature, and to a lesser extent on cooling, than scale produced at 1 atm pressure, even though the alloy/oxide interface was much smoother. This tends to indicate that less stress was developed, or even conceivably that the oxide was more plastic, although this is perhaps unlikely because the oxide would be more stoichiometric and contain less iron. However, fewer vacancies would be arriving at the alloy/oxide interface so adhesion could be more readily maintained. Indeed the oxide could still be reasonably heavily stressed, but this would not be evident as long as adherence was maintained.

Adhesion was much more readily lost on cooling, presumably because of the extra stresses induced by

differential thermal contraction between alloy and oxide, lower alloy and oxide plasticity, and thermal shock effects. Adhesion was retained most readily the thicker the scale, presumably because it could not balloon so easily, because more stress had been relieved in the longer oxidation periods when the scale was not growing rapidly, and because it was often formed at higher temperatures, permitting maximum stress relief by plastic deformation. Adhesion on cooling was also better the lower the alloy chromium content, partly due to the superior keying effects of the irregular interface and the other factors mentioned earlier such as the greater alloy plasticity. However, adhesion was also sometimes observed on quite smooth surfaces.

The spalling on cooling was not continuous over the entire surface, but its irregularity did not appear related to any special features such as alloy grain boundaries. Presumably the irregularity does mean that the stresses are not uniformly distributed through the scale or that plastic flow or adhesion is uneven, perhaps due to irregular growth from grain to grain or area to area. There was a greater tendency for spalling on large plane surfaces of specimen than elsewhere, because this approximated more closely to a semi-infinite specimen where cracking by shear failure is more necessary. Scales adhered better at temperature to alloys made from zone-refined metals but spalled off more completely on cooling, indicating that some of the parameters determining the mechanical behavior are purity-dependent.

*Calculation of the interdiffusion coefficient.*—It is possible to calculate interdiffusion coefficients in the underlying alloy from concentration profiles like Fig. 9 and 10. The analysis was not applied to specimens where depleted zones from both sides impinged. Such interdiffusion coefficients, although not fundamental parameters, are important in oxidation problems where concentration changes in the underlying alloy potentially affect the oxidation behavior. Interdiffusion coefficients are composition-dependent, but as derived below can only refer to a small range of chromium concentrations. Thus, the interdiffusion coefficient,  $D$ , is assumed to be independent of alloy composition.

Making the reasonable assumption that only chromium enters the oxide scale, Fick's second law of diffusion may be solved (3) to give the interdiffusion coefficients in the alloy. In order to obtain a complete solution, finite difference techniques have to be employed (6) because the mole fraction of chromium at the alloy/oxide interface  $(N_{Cr})_i$  is an unknown function of time. However, for the present oxidation system, the assumption that  $(N_{Cr})_i$  is independent of time does not produce errors in the interdiffusion coefficients greater than their reproducibility. Thus, the analytical solution (11)

$$\frac{(N_{Cr})_x - (N_{Cr})_i}{(N_{Cr})_b - (N_{Cr})_i} = \frac{\text{erf}[\frac{1}{2}x/(Dt)^{1/2}] - \text{erf}[(\frac{1}{2}K_c/D)^{1/2}]}{\text{erfc}[(\frac{1}{2}K_c/D)^{1/2}]} \quad [6]$$

was used, where  $(N_{Cr})_x$  and  $(N_{Cr})_b$  are the chromium mole fractions at a distance  $x$  from the original alloy surface and in the bulk alloy, respectively, erf denotes the Gaussian error function, erfc, its complement.

Equation [6] enables  $D$  to be computed from the measured values of the other quantities. Initially a crude value of  $D$  is obtained from the depth of the chromium-depleted layer,  $x_d$ . At this depth, Eq. [6] gives

$$\text{erf}[\frac{1}{2}x_d/(Dt)^{1/2}] = 1 \quad [7]$$

from which  $D$  can be obtained by simply plotting  $x_d$  against  $t^{1/2}$  and calculating the gradient of the line.

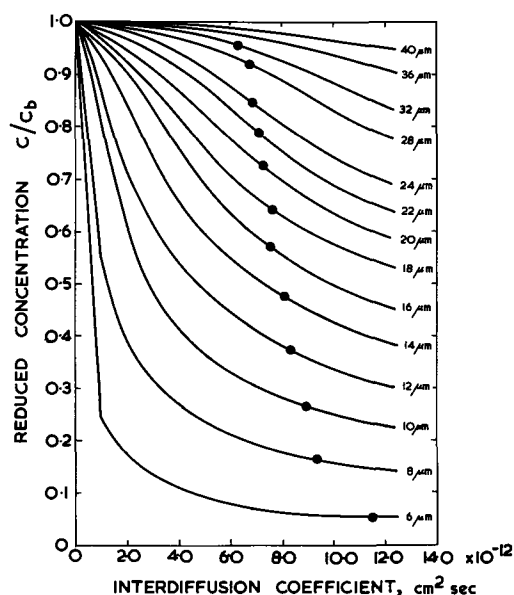


Fig. 11. Reduced concentration/interdiffusion coefficient plot for specimen of Fe-27.4% Cr oxidized for 50 hr at 800°C. The distances marked on the curves refer to distances from the alloy-oxide interface.

Precise values of  $D$  are then calculated by computing the reduced concentration

$$\frac{(N_{Cr})_x - (N_{Cr})_i}{(N_{Cr})_b - (N_{Cr})_i}$$

as a function of  $x$  and  $t$  for a range of  $D$  values of approximately the same magnitude as the crude  $D$  values. Thus, for each set of oxidizing conditions of alloy chromium content and temperature, a series of curves of reduced concentration against  $D$  at each oxidation time was constructed, e.g., Fig. 11. Values of reduced concentration were also obtained from the experimental concentration profiles, e.g., Fig. 9 and 10, and marked as heavy circles on the constructed curves, Fig. 11. In this way, over a hundred values of  $D$  were obtained for each alloy at each temperature. The arithmetic means of these data are presented in Table VIII, and the coefficients of variation of  $D$ , about 20%, indicate that the assumptions described earlier are not unreasonable.

Close agreement at 1000°C between the present values and values obtained from diffusion data in the literature [calculated (12) from partial chemical diffusivities and self-diffusion coefficients for various alloys assuming ideality in the Fe-Cr system] is indicated in Fig. 12. Thus there is a steady decrease in  $D$  until the value for pure chromium (about  $10^{-13}$  cm<sup>2</sup> sec<sup>-1</sup>) is achieved. It must, of course, be remembered that the  $D$  values refer to a range of chromium concentrations. Arrhenius plots for interdiffusion in Fe-27.4% Cr and Fe-59.5% Cr gave approximate activation energies of 51 and 59 kcal mole<sup>-1</sup>.

Table VIII. Calculated values of the interdiffusion coefficient for iron and chromium,  $D$ , in various alloys at 800°-1200°C

Alloy, % Cr	Temp, °C	Mean interdiffusion coefficient, $D$ , cm <sup>2</sup> sec <sup>-1</sup>
22.9	1000	$7.5 \times 10^{-10}$
27.4	800	$6.5 \times 10^{-12}$
27.4	900	$9.4 \times 10^{-11}$
27.4	1000	$4.1 \times 10^{-10}$
27.4	1100	$1.5 \times 10^{-9}$
27.4	1200	$3.9 \times 10^{-9}$
37.4	1000	$2.0 \times 10^{-10}$
59.5	800	$5.8 \times 10^{-13}$
59.5	1000	$2.9 \times 10^{-11}$
59.5	1200	$8.3 \times 10^{-10}$
68.0	1000	$4.7 \times 10^{-11}$

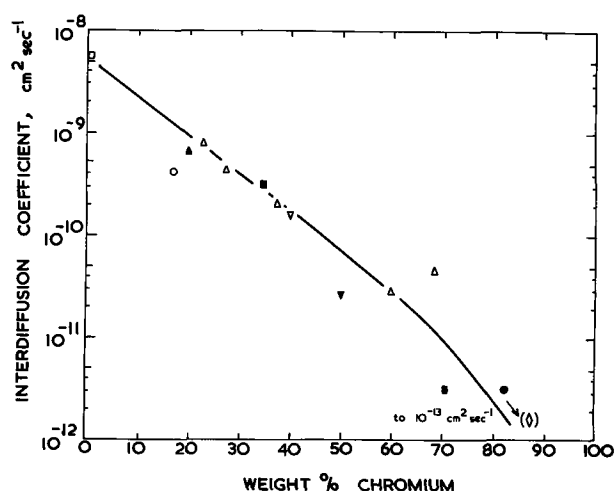


Fig. 12. Influence of chromium content on the interdiffusion coefficient of iron-chromium alloys at 1000°C. ○ 13; ▲ 14; △ present work; ■ (15); ▽ (16, 17); ▼ (17-19); ● (20-21); ◇ (18).

The interdiffusion coefficients derived here, although fundamentally less significant, are more meaningful in oxidation studies than the normal diffusion parameters referring to self-diffusion. Concentration gradients always exist in the alloy underlying the scale so what is required is an average over-all value of diffusion rate.

**Significance of the interdiffusion rate in the underlying alloy.**—It has been demonstrated (3) that if the chromium-depleted alloy under a 'Cr<sub>2</sub>O<sub>3</sub>' scale is suddenly exposed to oxygen by scale cracking, it will oxidize in a manner appropriate to its surface chromium content. When this value is below about 13%, 'Cr<sub>2</sub>O<sub>3</sub>' scale is unlikely to re-form and local catastrophic scaling is probable. With the chromium-rich alloys considered here such chromium levels are only likely in the very early stages, making breakthrough improbable (6). Nevertheless, bearing in mind the possible destruction of Cr<sub>2</sub>O<sub>3</sub> scales by complex vanadium-ash-containing environments and subsequent reaction with the alloy, factors affecting the compositional changes in the underlying alloy are worth considering.

The chromium concentration at the alloy-oxide interface depends on: (a) the rate of loss of chromium from the alloy to the scale (measured by  $K_c$ , the modified parabolic rate constant for oxidation); (b) the rate of chromium diffusion to the alloy surface (measured by  $D$ , the interdiffusion coefficient); and (c) the amount of chromium the alloy contained originally (measured by the bulk alloy chromium content).

It has been shown (6) that for this latter factor the percentage of chromium depletion is inversely proportional to the bulk weight fraction of chromium in the alloy. Dependence on the other two factors,  $K_c$  and  $D$ , cannot be given exactly (6), but obviously the greater the value of the ratio ( $K_c/D$ ) the greater will be the percentage of chromium depletion.

Table IX gives the appropriate values of ( $K_c/D$ ) and the reciprocal bulk weight fraction of chromium for the various alloys discussed in the present paper. Thus, the extent of chromium depletion at the alloy/oxide interface is greater for Fe-59.5% Cr than Fe-27.4% Cr, but fortunately the chromium level is still higher so iron-rich scale could not form if the scale cracked.

The situation is complicated in the dilute alloys by  $\alpha/\gamma$  phase changes in the underlying alloy, but the same general principles hold. In all cases the chromium concentration at the alloy/oxide interface drops

Table IX. Values of ratio of modified parabolic rate constant for oxidation and alloy interdiffusion coefficient for various alloys at 800°-1200°C

Alloy, % Cr	Temp, °C	$K_c/D$	$1/W_{Cr}$
22.9	1000	$4.0 \times 10^{-3}$	4.36
27.4	800	$8.5 \times 10^{-2}$	3.65
27.4	900	$1.6 \times 10^{-2}$	3.65
27.4	1000	$1.4 \times 10^{-2}$	3.65
27.4	1100	$1.1 \times 10^{-2}$	3.65
27.4	1200	$1.2 \times 10^{-2}$	3.65
37.4	1000	$9.5 \times 10^{-3}$	2.68
59.5	800	$1.4 \times 10^{-1}$	1.68
59.5	1000	$7.8 \times 10^{-2}$	1.68
59.5	1200	$7.2 \times 10^{-2}$	1.68
68.0	1000	$2.1 \times 10^{-1}$	1.47

very rapidly to a low level initially and then rises progressively with time to a limiting value (6).

### Acknowledgments

The authors' thanks are due to Professor T. K. Ross for encouraging this study and for providing facilities. They also thank the Science Research Council (formerly D.S.I.R.) for providing the electron probe microanalyzer and for the award of a Research Studentship to one of the authors (D.P.W.) from October 1963-September 1965 when this work was conducted.

Manuscript received June 26, 1967; revised manuscript received Oct. 27, 1967.

Any discussion of this paper will appear in a Discussion Section to be published in the December 1968 JOURNAL.

### REFERENCES

- G. C. Wood and D. P. Whittle, *J. Iron Steel Inst. (London)*, **202**, 979 (1964).
- G. C. Wood and D. P. Whittle, *This Journal*, **115**, 126 (1968).
- D. P. Whittle, Ph.D. Thesis, Univ. Manchester (1965).
- A. U. Seybolt, *This Journal*, **107**, 147 (1960).
- A. Michel and J. Benard, *Bull. Soc. Chim.*, **10**, 315 (1946).
- D. P. Whittle, G. C. Wood, D. J. Evans, and D. B. Scully, *Acta Met.*, **15**, 1747 (1967).
- G. C. Wood, T. Hodgkiess, and D. P. Whittle, *Corrosion Sci.*, **6**, 129 (1966).
- G. C. Wood and T. Hodgkiess, *This Journal*, **113**, 319 (1966).
- D. Caplan, A. Harvey, and M. Cohen, *Corrosion Sci.*, **3**, 161 (1963).
- D. Caplan, A. Harvey, and M. Cohen, *This Journal*, **112**, 471 (1965).
- C. Wagner, *ibid.*, **99**, 369 (1952).
- L. S. Darken, *AIME Trans. Met. Soc.*, **175**, 184 (1948).
- T. Heumann and H. Bohmer, *Arch. Eisenhuttentw.*, **30**, 15 (1959).
- T. Kunitake, *Nippon Kinzoku Gakkaishi*, **25**, 698 (1961).
- N. Radwan and P. Zmija, *Biul-Wojskowej Akad. Tech.*, **11**, 73 (1962).
- A. YA. Shinyayev, "Metallurgy and Metallography," All-Union Conf. Use of Isotopes and Nuclear Radiations, Moscow, 1958, 299.
- H. W. Paxton and E. G. Goudolf, *Arch. Eisenhuttentw.*, **30**, 55, (1959).
- N. A. Bognadov, *Russ. Met. Fuels (English Transl.)*, **3**, 95 (1960).
- N. A. Bognadov, *Izvest. Akad. Nauk. SSSR, Otdel Tekh. Nauk. Metii Toplivo*, **3**, 99 (1960).
- W. C. Hagel, *AIME Trans. Met. Soc.*, **224**, 430 (1962).
- J. Askill and D. H. Tomlin, *Phil. Mag.*, **11**, 467 (1965).
- G. C. Wood, J. Boustead, and D. P. Whittle, To be published.
- G. C. Wood, *Corrosion Sci.*, **2**, 173 (1962).

# Volume Diffusion During Anodic Dissolution of a Binary Alloy

Howard W. Pickering

*Edgar C. Bain Laboratory for Fundamental Research,  
United States Steel Corporation Research Center, Monroeville, Pennsylvania*

## ABSTRACT

The occurrence of volume diffusion during anodic dissolution of Cu-Au alloys at room temperature is shown again by x-ray and electron diffraction, confirming the result of a previous study. After dissolution the intensity of the diffracted x-rays is increased at Bragg angles,  $\theta$ , corresponding to intermediate Cu-Au compositions. Electron diffraction patterns exhibit new broad diffraction rings corresponding to the formation of intermediate compositions after very early stages of anodic dissolution of about 100 atomic layers of Cu dissolved.

X-ray results of a previous study (1) show that enrichment of Au in Cu-Au alloy occurs during anodic dissolution at room temperature. Accordingly Cu diffuses from the bulk of the alloy toward the surface, and Au diffuses in the opposite direction. Volume diffusion was indicated to be operative via excess divacancies; calculations using the known diffusivity of mono- and divacancies in Cu and Au at room temperature showed that di but not monovacancies have sufficient mobility to enhance interdiffusion of the atoms. Vacancies were concluded to be formed at the surface during anodic dissolution, a consequence of the accumulation of Au on the surface. Furthermore measurements with a rotating disk-ring electrode indicate that ionization of Au does not take place; thus it was concluded that transport of Au does not occur by an ionization and redeposition mechanism. Prior to these results, Graf (2) in 1932 obtained similar, although less conclusive, x-ray diffraction patterns from Cu-Au alloys chemically etched in various aqueous solutions.

It is the purpose of this paper to demonstrate the occurrence of volume diffusion in several Cu-Au alloys during anodic dissolution at room temperature. This is accomplished by x-ray diffraction as previously done for a Cu 10 a/o (atomic per cent) Au (Cu10Au) alloy (1) and by electron diffraction which permits examination at much earlier stages of anodic dissolution. The large difference in atomic sizes makes diffraction techniques particularly useful in this investigation. The occurrence of volume diffusion in a region next to the surface leads to a gradual variation in lattice parameter as a function of distance from the surface, i.e., there results a gradient of the mole fraction of Au between unity and that of the original alloy and of Cu between zero and that of the original alloy. On account of this gradient the diffraction pattern consists of very broad diffraction rings, i.e.,  $\Delta\theta$  of about  $2^\circ$ , with a maximum of the intensity at a certain angle.

The intensity of the x-rays diffracted from regions of variable composition is low in the early stages of dissolution (initially) when the alloy has an essentially plane surface. This is a consequence of the fact that the depth of x-ray penetration is very much greater than the diffusion distance, a few thousand as compared to a few hundred angstroms, respectively (1). At later stages of anodic dissolution, however, the occurrence of severe surface roughening leads to the formation of a porous layer [as much as a 100-fold and more increase in surface area has been found by measurement of the polarization capacity during anodic dissolution of Cu-Au alloys (3)]. Consequently, the thickness of the layer in which compositional differences result is very much greater than the actual

solid-state diffusion distance. Accordingly these regions now can make a significant contribution to the x-ray diffraction pattern. Porous layers have been reported previously for etched Cu-Au alloys on the basis of optical (4-6) and electron (7) metallography. The occurrence of severe surface roughening during anodic dissolution of Cu-Au alloy is in agreement with theory [Harrison and Wagner (8)]: a plane surface is unstable, i.e., perturbations in the surface tend to grow, when preferential dissolution of one component of a binary alloy occurs via interdiffusion of the metals. Conditions are more favorable for obtaining information at an early stage of anodic dissolution with the help of electrons since the depth of penetration of the electrons is of the same order of magnitude as the diffusion distance.

## Experimental

Foils of homogenized (700°C for four days in evacuated quartz capsules, then quenched) Cu1Au, Cu3Au, Cu10Au, and Cu22Au alloys made from metals of 99.999% Cu and 99.995% Au, were prepared by rolling, annealing at 700°C for 1 hr in evacuated quartz capsules and quenching. The foil surfaces were prepared with fine emery and partially lacquered to limit a geometrical area to 5 and 2 cm<sup>2</sup> for x-ray and electron diffraction, respectively. The foil was then inserted vertically in a closed Pyrex cell with a platinum wire counter electrode centered around it. The electrolyte was mainly 1M H<sub>2</sub>SO<sub>4</sub> prepared from reagent-grade acid and doubly distilled water of conductivity  $3 \times 10^{-7}$  ohm<sup>-1</sup> cm<sup>-1</sup>. Before and during the experiment the electrolyte was flushed with He in order to remove oxygen. Current densities of 1 and 5 ma/cm<sup>2</sup> were applied. For these current densities, the potential is in the range where only the anodic dissolution reaction may occur at the Cu-Au electrode. (1, 5, 9).

X-ray diffraction examination of foils mounted in a diffractometer stage was made with nickel-filtered Cu radiation using a Siemens diffraction apparatus. Electron diffraction examination was made in a 50 kv RCA electron microscope modified by removal of the lens between the specimen and the film. For the electron diffraction experiment, prior to anodic dissolution a surgical knife was used for scoring so that a lip was raised on the surface of the foil; this step improved the diffraction patterns.

*X-ray diffraction investigations.*—Broad regions of diffracted intensity, extending approximately from the Bragg angle  $\theta$  characteristic of pure gold to that of the original alloy, were observed after anodic dissolution of the Cu1Au, Cu3Au, Cu5Au, Cu10Au, and Cu22Au alloys in 1M H<sub>2</sub>SO<sub>4</sub>. This agrees with results

previously obtained for Cu<sub>10</sub>Au (1). For example, patterns b of Fig. 1 and 2, corresponding to a relatively early stage of dissolution, contain a broad region of diffracted intensity between the  $2\theta$  positions corresponding to Cu<sub>3</sub>Au and Cu<sub>5</sub>Au, respectively, and pure Au for diffraction of CuK $\alpha$  radiation by {111} planes. Similar results were observed for the first four diffraction planes investigated. The small peak at  $2\theta \approx 38.8^\circ$  in Fig. 1 (most easily seen in pattern a) is due to diffraction of CuK $\beta$  radiation by {111} planes. In Fig. 2 superimposed traces of the x-ray patterns for the different stages of dissolution are substituted for the actual patterns. Broad regions of diffracted intensity are also seen in the x-ray pattern of Fig. 3 which was not obtained directly from the foil itself but rather from particles which had become detached from the Cu<sub>1</sub>Au alloy during anodic dissolution and fell to the bottom of the cell.

At a later stage of dissolution a maximum develops at a  $2\theta$  position corresponding to a Au-rich composition. With further dissolution the maximum shifts toward a certain (higher) gold composition. This is shown for the various alloys in Fig. 4 where the  $2\theta$  position of the maximum is plotted as a function of the dissolution time. Eventually when the specimen is nearly consumed resulting in partial disintegration,

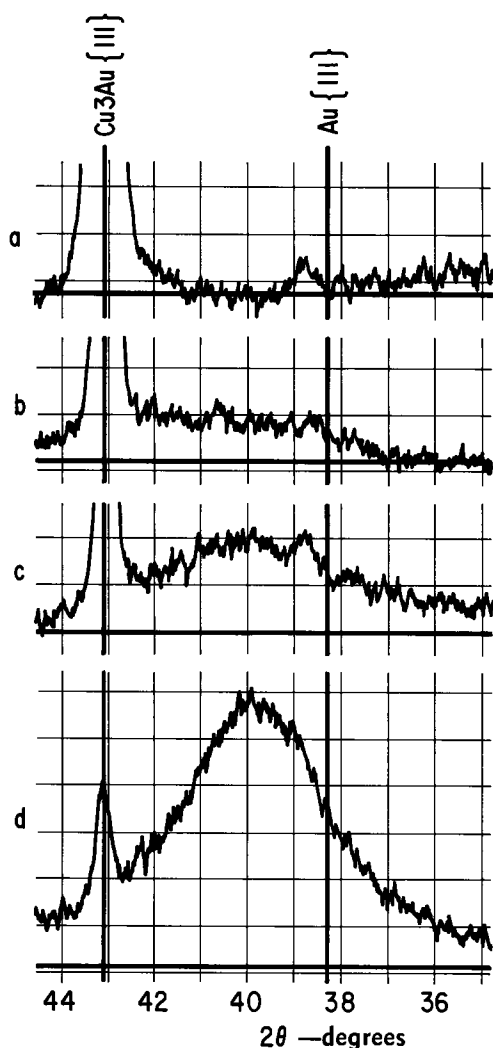


Fig. 1. X-ray diffraction patterns for a Cu<sub>3</sub>Au sheet specimen after various amounts of dissolution at 5 ma/cm<sup>2</sup> in 1M H<sub>2</sub>SO<sub>4</sub>, illustrating a broad region of increased diffracted intensity corresponding to the presence of a composition gradient to the gold-rich side of the original alloy composition. The  $2\theta$  position of pure Au is indicated by the vertical line at  $2\theta = 38.2^\circ$ . (a) prior to anodic dissolution; (b) 3.0 C/cm<sup>2</sup> passed; (c) 6.0 C/cm<sup>2</sup> passed; (d) 24.0 C/cm<sup>2</sup> passed.

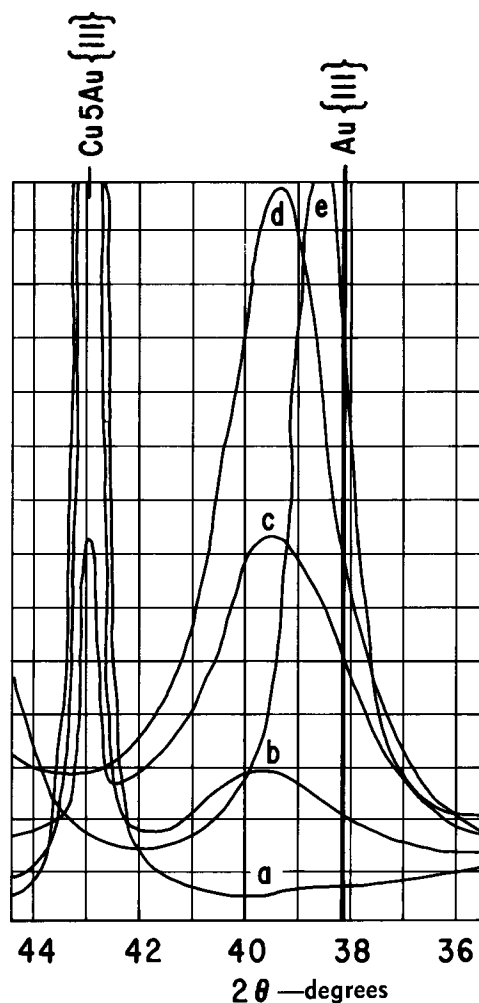


Fig. 2. Same as Fig. 1 but for Cu<sub>5</sub>Au. Superimposed traces of the x-ray patterns are substituted for the actual patterns. (a) prior to anodic dissolution; (b) 3.0 C/cm<sup>2</sup> passed; (c) 12.0 C/cm<sup>2</sup> passed; (d) 48.0 C/cm<sup>2</sup> passed; (e) 96.0 C/cm<sup>2</sup> passed.

an appreciable shift of the maxima toward the pure Au composition occurs as seen for the Cu<sub>5</sub>Au alloy in Fig. 2 and 4. Prior to the onset of this final shift in composition the original alloy peaks are already decreased to background intensity.

Figure 4 shows too that for a given current density and time of electrolysis, the position of the maximum is at a lower  $2\theta$  value (corresponding to a greater gold concentration) the higher the gold content of the original alloy. For the most gold-rich alloy, viz., Cu<sub>22</sub>Au, the predominate composition of the reacted region is virtually pure Au after the first several minutes of dissolution. Table I gives the estimated Cu-Au composition corresponding to the position of each maximum after 80 min of dissolution at 5 ma/cm<sup>2</sup>. The composition admittedly has wide error limits. The assignment of a definite composition to the maximum implies only a preponderance of material of this composition with other compositions still present. For this reason the term maximum is used, peak being reserved for profiles corresponding to a single composition. The position of the maximum depends also on the composition of the electrolyte as shown in a previous paper (1); it occurs at a composition less rich in Au for buffered 1N NaCl (pH 5) than for the H<sub>2</sub>SO<sub>4</sub> electrolyte. The influence of current density appears to be slight and within the experimental error (Table I).

As one increases the gold content of the original alloy from 3 to 22 a/o, (a) the intensity of the gold-rich maxima for a given current density and time of electrolysis increases, and (b) the appearance of broad

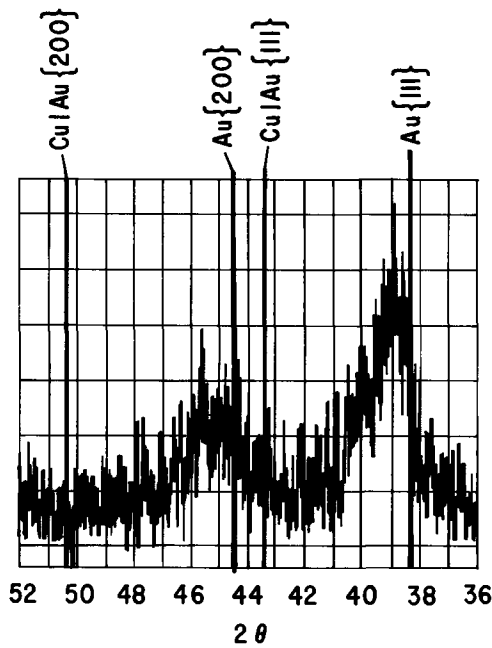


Fig. 3. X-ray diffraction pattern of particles which became dislodged from a Cu1Au foil specimen during dissolution at 1 ma/cm<sup>2</sup> in oxygen saturated 1.0N CuSO<sub>4</sub> + 0.1N H<sub>2</sub>SO<sub>4</sub> and which fell to the bottom of the cell, illustrating broad regions of increased diffracted intensity at 43 > 2θ > 38.2° and 51 > 2θ > 44.4°, corresponding to diffraction of CuK<sub>α</sub> radiation by {111} and {200} planes, respectively.

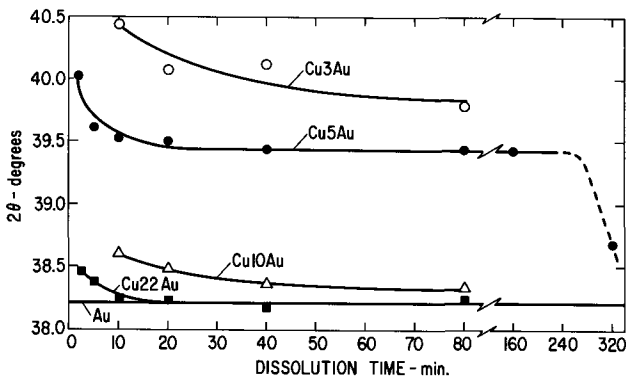


Fig. 4. Plot of the 2θ position of the maximum as a function of the dissolution time of the various alloys in 1M H<sub>2</sub>SO<sub>4</sub> at 5 ma/cm<sup>2</sup>.

regions of increased diffracted intensity is detected at an earlier stage of dissolution. These observations might have been predicted on the basis of theoretical considerations (1); for a given current density and time of electrolysis the depth of the interdiffusion zone and the extent of surface roughening may be expected to be greater as the gold content increases.

Optical metallography showed that the final shift of the maximum (e.g., pattern e of Fig. 2) occurs in the absence of original, unreacted alloy. This is seen in Fig. 5, taken of the Cu5Au specimen after 320 min of dissolution at 5 ma/cm<sup>2</sup>. Prior to this final shift of the maximum, unreacted alloy was always observed to be present, e.g., as seen in Fig. 6 for the Cu3Au and Cu22Au specimens after dissolution at 5 ma/cm<sup>2</sup> for 80 min.

In the case of alloys low in Au the reacted layer adheres rather poorly. For Cu1Au alloy, particles are dislodged and may be collected from the bottom of the cell for subsequent diffraction analysis (Fig. 3); the observed dislodging of particles is in accord with industrial experience especially during electrolytic refining of copper containing a small amount of Au.

Table I. Compositions corresponding to the newly formed maxima in the x-ray patterns. These results are for various Cu-Au alloys dissolved mainly in 1M H<sub>2</sub>SO<sub>4</sub> at 5 ma/cm<sup>2</sup> for 80 min

Starting alloy	Position (2θ) of the half-maximum width, in degrees	Estimated compositions†
Cu3Au	39.8	Cu60Au
Cu5Au	39.4	Cu69Au
Cu10Au	38.5	Cu96Au
Cu22Au	38.2	Nearly pure Au
Cu5Au*	39.5	Cu68Au
Cu10Au**	39.5	Cu68Au

\* Anodically dissolved at 1 ma/cm<sup>2</sup> for 400 min.  
 \*\* Anodically dissolved in buffered 1N NaCl of pH 5 at 20 ma/cm<sup>2</sup> for 16 min (1).  
 † Approximate average composition estimated from these data and lattice parameter as a function of composition (10).

Partial disintegration of the reacted layer is seen for Cu3Au in Fig. 6a.

Electron diffraction investigations.—Electron diffraction examination of Cu-Au foils was made in order to confirm the occurrence of volume diffusion dur-

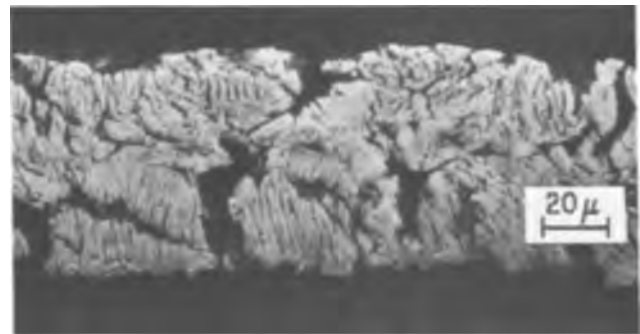


Fig. 5. Cross section of Cu5Au foil specimen after anodic dissolution at 5 ma/cm<sup>2</sup> in 1M H<sub>2</sub>SO<sub>4</sub> for 320 min (96 C/cm<sup>2</sup> passed) illustrating complete penetration of the alloy with a meeting of the reacted layers at about the midplane of the foil specimen.

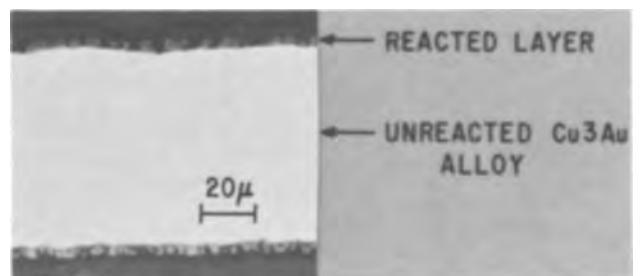


Fig. 6a. Cross section of a Cu3Au foil specimen after anodic dissolution at 5 ma/cm<sup>2</sup> in 1M H<sub>2</sub>SO<sub>4</sub> for 80 min (24 C/cm<sup>2</sup> passed).

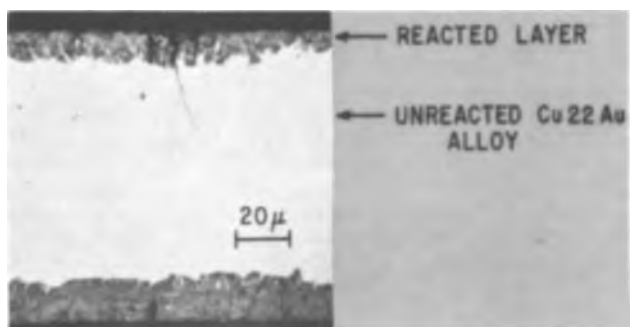


Fig. 6b. Same as Fig. 6a, but for a Cu22Au foil specimen

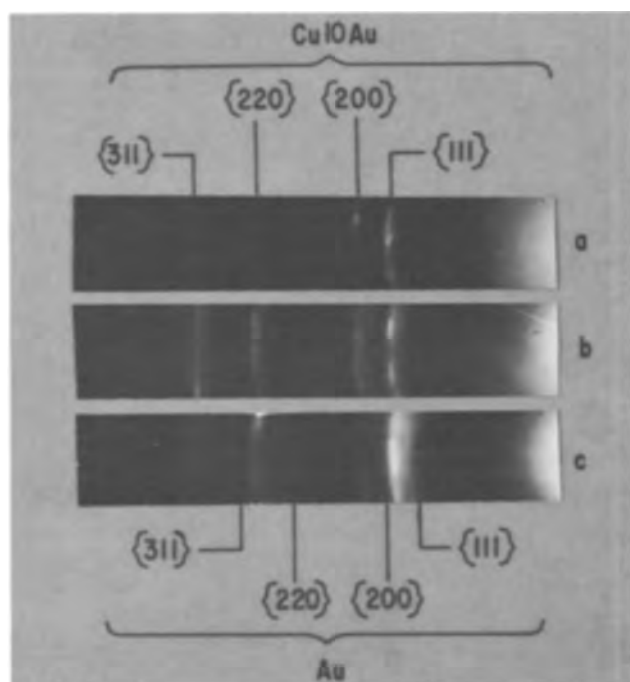


Fig. 7. Reflection electron diffraction patterns of Cu<sub>10</sub>Au after anodic dissolution in 1M H<sub>2</sub>SO<sub>4</sub>, illustrating broad lines at gold-rich compositions, in addition to Cu<sub>10</sub>Au alloy lines, in accord with enrichment of Au in the alloy layer immediately next to the alloy-electrolyte interface: (a) prior to anodic dissolution; (b) after 0.10 C/cm<sup>2</sup> passed (1 ma/cm<sup>2</sup> for 100 sec); (c) after 0.14 C/cm<sup>2</sup> passed (20 ma/cm<sup>2</sup> for 7 sec).

ing the very early stages of anodic dissolution. After passage of as little as 0.1 C/cm<sup>2</sup> broad rings corresponding to intermediate Cu-Au compositions appear in the electron diffraction patterns. This is seen in Fig. 7 for Cu<sub>10</sub>Au anodically dissolved in 1M H<sub>2</sub>SO<sub>4</sub>. Similar results were obtained for the other Cu-Au alloys. Passage of 0.1 C/cm<sup>2</sup> corresponds to about 100 atomic layers of dissolved Cu, calculated on the basis of a uniform current density. Actually the current density may be rather nonuniform especially as a result of geometrical and defect inhomogeneities introduced by the surface preparation. Consequently the electron diffraction data at 0.1 C/cm<sup>2</sup> may correspond to somewhat more than 100 atomic layers of Cu dissolved. The data of Fig. 7 and the estimated compositions corresponding to them are tabulated for the first four diffraction planes in Table II. Differences in the 2θ positions of the maxima for different diffraction planes may be due to different depths of penetration, as well as to limited sensitivity in the pattern.

**Electron microprobe investigations.**—Electron microprobe analysis through the cross section of an anodically dissolved Cu<sub>10</sub>Au foil specimen was made in order to determine the gradient of Au and Cu throughout the reacted layer. An over-all increase in

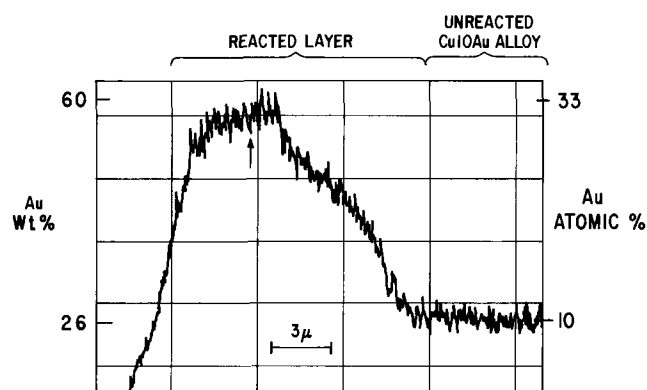


Fig. 8a. Electron microprobe patterns taken through the cross-section of a Cu<sub>10</sub>Au foil specimen after anodic dissolution, illustrating increasing Au contents in the reacted layer as one proceeds outward from the alloy-reacted layer interface. Arrows point out plateaus and maxima presumably resulting from reflection of the beam mainly from particles of remaining, virtually unreacted alloy. As the beam approaches the outer surface of the reacted layer only part of the beam intersects it; consequently the intensity falls off even though the element content may actually increase as in the case of Au in this pattern.

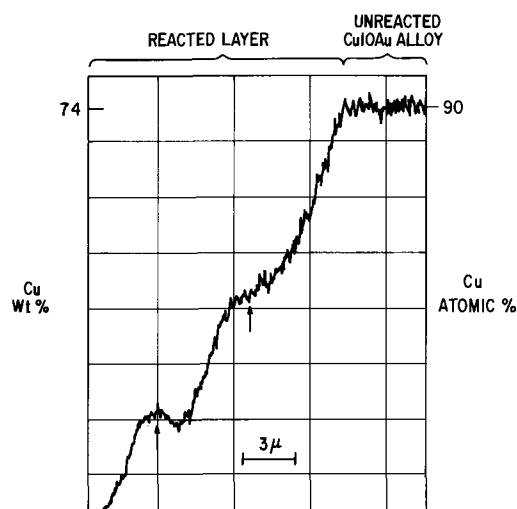


Fig. 8b. Same as Fig. 8a, illustrating decreasing Cu

Au content and decrease in Cu content proceeding outward from the interface between the alloy and the reacted layer were indicated, as shown in Fig. 8. The intensity curves are not smooth but contain plateaus and maxima. These are thought to be due to the presence in the reacted layer of particles of virtually unreacted Cu<sub>10</sub>Au alloy as determined by optical metallography (see for example Fig. 6b); although the effects of porosity in the layer are not known. Porosity may also produce errors in the microprobe determination of concentration.

Table II. Radii of the electron diffraction rings shown in Fig. 7. The value for pure Au is also shown

Diffraction plane	Radius (cm) of			Pure Au
	Original Cu <sub>10</sub> Au alloy ring	Gold-rich ring, 1 ma/cm <sup>2</sup> for 100 sec (0.10 C/cm <sup>2</sup> )	Gold-rich ring, 20 ma/cm <sup>2</sup> for 7 sec (0.14 C/cm <sup>2</sup> )	
{111}	3.47	3.30	3.15	3.09
{200}	3.96	3.80	3.61	3.56
{220}	5.56	5.43	5.16	5.04
{311}	6.48	—	5.97	5.92
		Cu <sub>40</sub> Au*	Cu <sub>85</sub> Au*	

\* Approximate average composition estimated from above data and lattice parameter as a function of composition (10).



### Conclusion

The present investigation confirms the result of a previous study (1) that the preferential anodic dissolution of Cu from Cu-Au alloys involves transport of Cu to the surface *via* solid-state diffusion of Cu and Au in the alloy. The use of the diffraction method was definitive in this regard since a spectrum of Cu-Au composition to the gold-rich side of the original Cu-Au composition (as would result during dissolution of Cu *via* volume diffusion) leads to increased diffracted intensity over a broad range of  $2\theta$  between the  $2\theta$  values corresponding to the original alloy composition and pure Au; whereas the formation only of crystals relatively pure in Au [as would result if either of the alternative mechanisms, *viz.*, surface diffusion or ionization-redeposition (1), operates] yields diffracted intensity only at the  $2\theta$  position for pure Au.

### Acknowledgment

The author makes grateful acknowledgment to Dr. Carl Wagner of the Max Planck Institut für Physikalische Chemie who made many suggestions leading to confirmation of the conclusion of a previous joint study (1). Appreciation is also expressed to P. J. Byrne, in particular for his skillful operation of the electron diffraction apparatus, to Messrs. H. Hughes, L. Zwell, and J. Gula, all of this laboratory, for their help with the metallographic, x-ray and electron microprobe investigations, and to Dr. H. Birch of the

Applied Research Laboratory for use of his specially designed electron diffraction apparatus. Helpful comments on the electron microprobe investigation were given by Dr. Th. Hehenkamp of the Institut für Metallforschung, Münster.

Manuscript received Aug. 29, 1967; revised manuscript received Oct. 26, 1967.

Any discussion of this paper will appear in a Discussion Section to be published in the December 1968 JOURNAL.

### REFERENCES

1. H. W. Pickering and C. Wagner, *This Journal*, **114**, 698 (1967).
2. L. Graf, *Metallwirtschaft*, **11**, 77 (1932).
3. H. W. Pickering, To be published.
4. L. Graf, *Metallforschung*, **2**, 193, 207 (1947); *Z. Metallkunde*, **40**, 275 (1949).
5. H. Gerischer and H. Rickert, *Z. Metallkunde*, **46**, 861 (1955).
6. R. Bakish and W. D. Robertson, *Trans. AIME*, **206**, 1278 (1956).
7. H. W. Pickering and P. R. Swann, *Corrosion*, **19**, 369t (1963).
8. J. D. Harrison and C. Wagner, *Acta Met.*, **7**, 722 (1959).
9. H. W. Pickering, Unpublished data.
10. W. B. Pearson, "Handbook of Lattice Spacings and Structures of Metals and Alloys," p. 441, Pergamon Press, N.Y. (1958).

## The Oxidation of Lithided Chromium

C. S. Tedmon, Jr.

*General Electric Research and Development Center, Schenectady, New York*

and W. C. Hagel\*

*University of Denver, Denver, Colorado*

### ABSTRACT

Chromium samples have been electrochemically coated with thin layers of Cr-Li alloy and subsequently oxidized in the temperature range of 1100°-1350°C. Parabolic kinetics were observed in the range of 1100°-1300°C, in both air and dry oxygen. Parabolic rate constants for the Li-coated samples were reduced by nearly one order of magnitude compared with pure chromium samples. Increased spalling resistance and enhanced resistance to nitrification attack were also observed for the Li-coated samples.

In another paper (1), a technique was described for the electrochemical formation of lithium-alloy coatings on a variety of substrate materials. Briefly, the technique involved electrodepositing lithium on cathodic samples, using a molten LiF electrolyte with a carbon anode. Since the process was carried out at temperatures much above the melting point of lithium, the only lithium retained in the sample was that which was present in solid solution or combined as an intermetallic compound with the substrate metal.

Extensive testing was done with chromium samples, and the effects of electrodeposition temperature and time were investigated. Metallographic evidence indicated that the lithium combined with chromium to form what were tentatively identified as a series of intermetallic compounds. Typical microstructures of coated samples are presented in Fig. 1 to 5. It is apparent that the structure of the coating is dependent on both time and temperature of the electrodeposition. In general, the coatings were thin, on the order of 10 $\mu$  in thickness.

It is well known that the presence of lithium in

thermally produced scales on metals which form p-type, semiconducting oxides can be beneficial, producing markedly reduced oxidation rates. This effect, which has been discussed in detail by Haufler (2), has been demonstrated with nickel (3-5), iron (6), chromium (7), and an iron-25% chromium alloy (8). Presumably the Li<sup>+</sup> ions enter the oxide crystal lattice to reduce the cation vacancy concentration and hence decrease cation diffusion. This results in decreased oxidation rates, since the rate-limiting step in the oxidation process for these metals normally depends on cation diffusion.

A principal difficulty in adding lithium to the metals cited above resides in the fact that the melting point of these metals exceeds the boiling point of lithium (1330°C at 1 atm). Consequently, attempts to make direct additions of lithium to the melt frequently result in explosive reactions, and the quantity and distribution of any retained lithium is difficult to control. In order to obtain improved oxidation resistance, it is not necessary that lithium be present uniformly throughout the entire sample; rather, it need only be present near the surface where it can interact with the oxide. Therefore a method of electrochemically pro-

\* Electrochemical Society Active Member.



Fig. 1. Photomicrograph of a transverse cross section of a chromium sample run at 900°C in LiF for 10 min. Tapered section,  $\sim 8:1$ . Magnification ca. 100X.

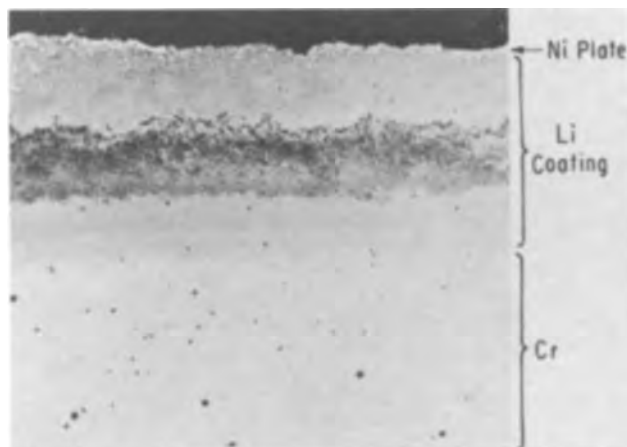


Fig. 2. Photomicrograph of a transverse cross section of a chromium sample run at 900°C in LiF for 360 min. Tapered section,  $\sim 8:1$ . Magnification ca. 160X.



Fig. 3. Photomicrograph of a transverse cross section of a chromium sample run at 1000°C in LiF for 30 min. Tapered section,  $\sim 10:1$ . Magnification ca. 50X.

ducing a layer or coating of lithium-containing metal near the sample surface appeared to be a promising means of effecting composition and possibly structure control, and of obtaining improved oxidation resistance.

In the previous paper (1), details of the electrodeposition process and the structural characteristics of the resulting lithium-alloy coated chromium samples were discussed. In this paper, the oxidation behavior of such samples in air and pure oxygen at elevated temperatures is described.

#### Experimental

The samples used in these experiments were made from high-purity, iodide-grade chromium. Prior to the electrodeposition operation, they were ground through No. 4/0 paper, and degreased in toluene and acetone. After electrodeposition, the samples were



Fig. 4. Photomicrograph of a transverse cross section of a chromium sample run at 1000°C in LiF for 120 min. Tapered section,  $\sim 10:1$ . Magnification ca. 50X.

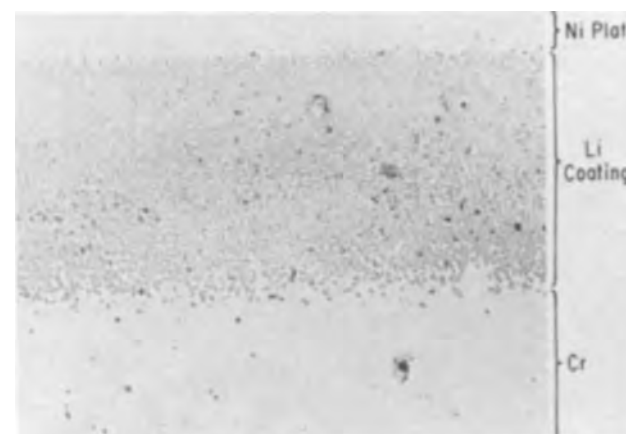


Fig. 5. Photomicrograph of a transverse cross section of a chromium sample run at 1100°C in LiF for 120 min. Tapered section,  $\sim 8:1$ . Magnification ca. 130X.

washed to remove any residual adhering LiF, and then again washed with toluene and acetone immediately before insertion in the spring-balance furnace.

Isothermal weight-gain data were obtained using a helical quartz spring. For the size samples used (3-5 cm<sup>2</sup>) the sensitivity was about  $\pm 100$   $\mu$ g. The procedure was to place the sample in the furnace, evacuate the system, and bring the furnace to temperature. The desired atmosphere (either dry O<sub>2</sub> at 100 Torr or dry air at 760 Torr) was introduced and the run was started. Sample temperature was measured with a Pt/Pt-10Rh thermocouple located in an Alundum tube about 0.3 cm from the sample. Temperature control was about  $\pm 5$ C°. When a run was completed, the furnace was shut off and the system evacuated.

Metallographic and x-ray diffraction data were obtained using standard procedures.

#### Results

The structures of samples after electrodeposition, shown in Fig. 1 to 5, are representative of the samples used in the oxidation runs. There was considerable variation in the coating structure, depending on the time and temperature of the electrodeposition process, and consequently a dependence of scaling behavior on the original structure might be expected. All of the samples shown here and used in the oxidation experiments were prepared under conditions of constant current density (0.03 amp/cm<sup>2</sup>).

Kinetic data for oxidation at 1100°, 1200°, and 1300°C are presented in Fig. 6 to 8. The electrodeposition treatment (time and temperature) are indicated for each sample. Note the correspondence between the

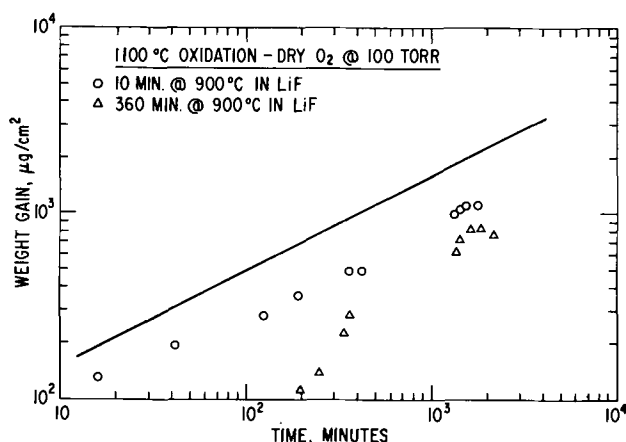


Fig. 6. Kinetic weight-gain data for samples oxidized at 1100°C

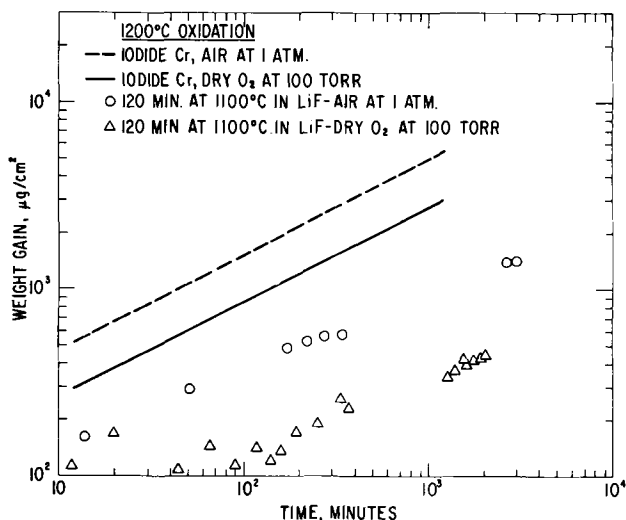


Fig. 7. Kinetic weight-gain data for samples oxidized at 1200°C

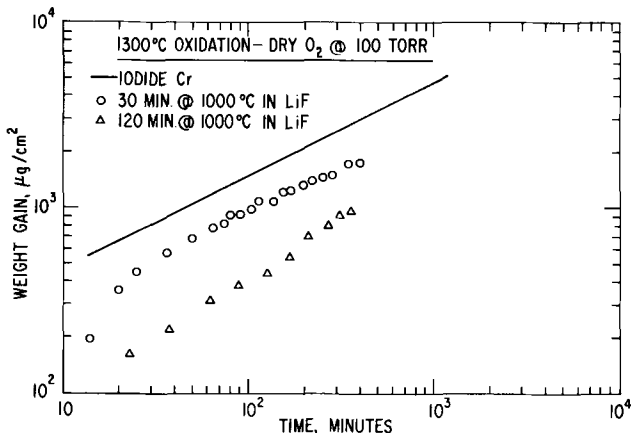


Fig. 8. Kinetic weight-gain data for samples oxidized at 1300°C

samples used in the oxidation runs and the samples shown in Fig. 1 to 5.

An attempt was made to oxidize a sample at 1350°C; however, when the sample was nearly at temperature, it was observed to suddenly start gyrating rapidly in the furnace. The run was terminated, and subsequent examination of the sample showed that the coating had erupted from the surface, causing considerable weight loss. This was apparently caused by rapid and catastrophic volatilization of the lithium from the coating.

The weight-gain data shown in Fig. 6 are from oxidation at 1100°C in dry oxygen of two samples prepared at 900°C for different times. Comparison

with Fig. 1 and 2 indicates that the 360-min sample had a thicker coating than the 10-min sample; furthermore, the coating on the 360-min sample is multi-layered. Oxidation kinetics for the 10-min sample were parabolic throughout the run, whereas the 360-min sample exhibited a region of linear kinetics before conversion to parabolic behavior. Comparison may be made to the oxidation kinetics for high-purity, iodide-grade chromium, shown by the solid line (7). Although the oxidation behavior of chromium is dependent on impurity content, it has been demonstrated (7) that iodide-grade chromium oxidizes at generally slower rates than other commercial grades of chromium.

From the 1200°C data presented in Fig. 7, the beneficial effects of the lithium treatment are obvious. The oxidation rate in dry oxygen is markedly reduced. Similar improvement is seen for oxidation in air. When pure chromium is oxidized in air, in addition to  $\text{Cr}_2\text{O}_3$  formation, there is an additional weight-gain due to the production of  $\text{Cr}_3\text{N}$ . This latter compound forms at the oxide-metal interface and frequently penetrates grain boundaries in the metal. Although the nitride is considered to be unstable with respect to the oxide (9), it is invariably present when pure chromium is oxidized in air. The general phenomena of nitrification of chromium and chromium-based alloys is not well understood and is a problem of current research interest. One aspect of it which does seem clear, however, is that the extent of nitrification is highly sensitive to the structural integrity of the oxide scale. Nitrification appears to be most severe when the scale contains gross defects such as blisters, cracks, and porosity which apparently permit access of air to the metal/oxide interface. This point will be discussed in greater detail in a subsequent section.

Figure 8 presents weight-gain data for samples oxidized in dry oxygen at 1300°C. Again, parabolic kinetics were observed; the improvement brought about by the lithium treatment is apparent. Best results were obtained with the sample which had been run the longest in the LiF, which was also the case with the samples which had been oxidized at 1100°C (Fig. 6). It should also be noted that the 30-min. LiF treated sample oxidized with linear kinetics for about the first 30 min before the transition to parabolic behavior occurred. The scales which formed on the lithium-treated chromium samples were very adherent and nonspalling. This is in marked contrast to the behavior encountered with pure chromium, which spalls very severely when oxidized above about 1000°C.

Parabolic rate constant data for coated samples oxidized at 1100°, 1200°, and 1300°C are presented in Table I; corresponding data for iodide chromium are included for comparison in Table II.

It is readily seen that the coated samples oxidized at considerably slower rates than the iodide chromium. Since lithium is volatile, it is possible that the observed weight-gains may not be representative of only the chromium oxidation reaction, but, rather, might indicate the difference between weight-gain from chromium oxidation and weight-loss from lithium volatilization. There are several reasons why the latter

Table I. Parabolic rate constant data for lithiated chromium

Electrodeposition time, min	Electrodeposition temperature, °C	Oxidation temperature, °C	Parabolic rate constant, $\text{g}^2 \text{cm}^{-4} \text{sec}^{-1}$
10	900	1100	$1.1 \times 10^{-11}$
360	900	1100	$\sim 6.0 \times 10^{-12}$
120	1100	1200*	$2.7 \times 10^{-11}$
120	1100	1200	$1.8 \times 10^{-12}$
30	1000	1300	$1.6 \times 10^{-10}$
30	1000	1300	$2.7 \times 10^{-11}$

\* Oxidized in air, 1 atm pressure.

Table II. Parabolic rate constant data for pure chromium (7)

Oxidation temperature, °C	Parabolic rate constant, $g^2 \text{ cm}^{-4} \text{ sec}^{-1}$
1100	$4.5 \times 10^{-11}$
1200	$1.9 \times 10^{-10}$
1200*	$4.0 \times 10^{-10}$
1300	$6.9 \times 10^{-10}$

\* Oxidized in air, 1 atm pressure.

is probably not the case. First, during the kinetic runs in the range 1100°-1300°C, there was no indication in the furnace tube of the presence of lithium oxide. Second, metallographic observations show that the observed weight-gains are consistent with scale thickness and with the total weight change of the sample. Also, if significant lithium volatilization were occurring, the kinetics would not be parabolic. The effect of volatilization reactions on oxidation kinetics of chromium-based alloys has been previously discussed (10).

Metallographic analysis of oxidized samples disclosed several important features. One of the most interesting is the observation that the metal/oxide interface was very irregular, with the oxide essentially interlocked with the metal. An example of this is shown in Fig. 9, which is a micrograph of a sample which had been given a lithium treatment at 1100°C for 120 min prior to oxidation at 1200°C for 30 hr. In addition to the irregular appearance of the interface, there is metal entrapped in the scale. The general appearance of the latter is characteristic of subscale formation. The scale is quite dense.

Specimens oxidized at 1100° and 1300°C resulted in structures quite similar to that shown in Fig. 9. X-ray diffraction results indicated the scales were  $\text{Cr}_2\text{O}_3$ , with lattice parameters essentially equivalent to those of pure  $\text{Cr}_2\text{O}_3$ .

Figure 10 presents a micrograph from a sample oxidized for about 130 hr in air at 1100°C. This sample had been treated for 120 min at 1100°C in LiF prior to oxidation. The oxide/metal interface is again rather irregular. In addition to the  $\text{Cr}_2\text{O}_3$ , there is a small amount of  $\text{Cr}_2\text{N}$  present. The extent of nitrification, however, is greatly reduced compared with that forming on pure chromium (11).

### Discussion

The presence of lithium in the chromium samples has three beneficial effects, *viz.*, it promotes slow oxidation rates, increases spalling resistance, and enhances resistance to nitrification attack during air oxidation.

The decreased oxidation rates arising from the presence of the lithium can be accounted for by the Verwey-Hauffe mechanism, wherein  $\text{Li}^+$  ions sub-

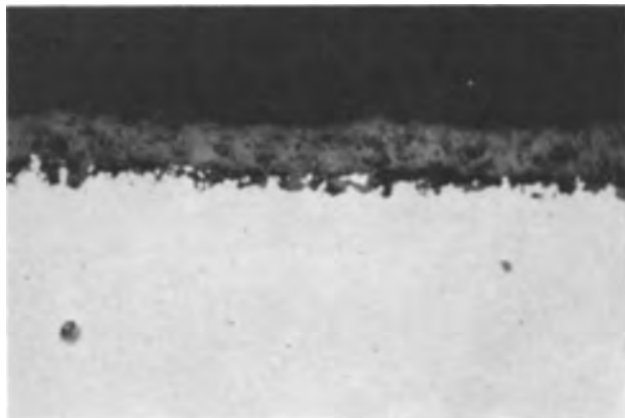


Fig. 9. Photomicrograph of a transverse cross section of a sample treated in LiF at 1100°C for 120 min, followed by oxidation at 1200°C. Magnification ca. 550X.

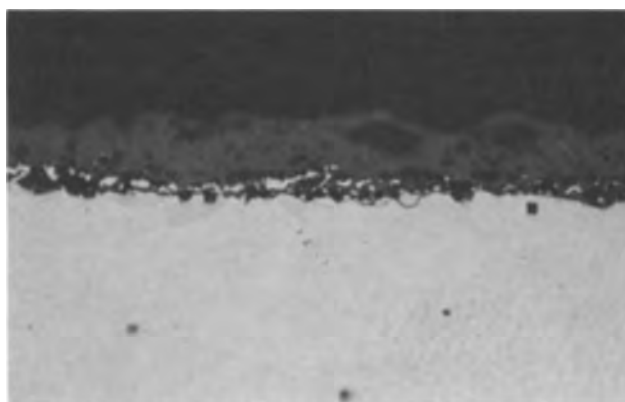


Fig. 10. Photomicrograph of a transverse cross section of a sample treated in LiF for 120 min at 1100°C, followed by oxidation at 1100°C in air. Magnification ca. 550X.

stitute in the cation sublattice of the  $\text{Cr}_2\text{O}_3$ , thereby reducing the  $\text{Cr}^{+3}$  vacancy concentration. It is reasonably well established that the oxidation rates of alloys which form  $\text{Cr}_2\text{O}_3$  protective scales is primarily controlled by cation diffusion (7, 11-13), and thus a decrease in the cation vacancy concentration results in slower diffusion rates and hence decreased oxidation rates. Supporting this model are the results of Hagel (14), who found that the electronic conductivity of  $\text{Cr}_2\text{O}_3$  is increased by doping with  $\text{Li}_2\text{O}$ .

The increased spalling resistance probably arises from the irregular boundary at the metal/oxide interface, such as shown in Fig. 9 and 10. The irregular boundary would tend to "key" the oxide in place. The irregular interface is a consequence of what appears to be subscale formation, probably caused by composition inhomogeneities in the lithium alloy layer. Although x-ray diffraction studies identified only  $\text{Cr}_2\text{O}_3$ , there is the possibility that more than one oxide may be involved in this scale and sub-scale, such as  $\text{LiCrO}_2$ ,  $\text{Li}_2\text{CrO}_4$ , or  $\text{Li}_2\text{Cr}_2\text{O}_7$ . Of these,  $\text{LiCrO}_2$  is the most stable (15, 16). That the latter was not found by x-ray diffraction implies that if it exists in the scale, it probably is there in concentrations of less than about 5%.

The origin of this enhanced resistance to nitrification of these alloys on exposure to air is not completely understood. It has been suggested that the mechanisms of nitride formation in Cr-rich alloys requires the presence of gross structural defects in the oxide scale, such as cracks and blisters, which permit access of air to the metal. Presumably if these defects were absent, then the nitride would not form. Therefore it might be expected that since the oxide scales formed on samples in these experiments were adherent and well-bonded to the metal, air was denied access to the metal/oxide interface and only the oxide was formed. Tentative support for this argument is presented in Fig. 11, which is a micrograph of a sample that was treated in the LiF for 120 min at 1100°C, and subsequently oxidized at 1200°C in air. Although the sample was generally free from nitride, there were several regions where it did form, which combined with blisters in the scale, as shown. It is evident from the data presented in Fig. 7 that some amount of nitride formed. The presence of the lithium, although beneficial, does not completely prevent nitrification.

### Conclusions

1. Samples of iodide chromium have been alloyed with lithium by electrochemical reaction in molten LiF.
2. The oxidation behavior of these samples was investigated in the range of 1100°-1350°C; parabolic kinetics were observed in both air and dry oxygen.
3. The lithium alloying had three significant beneficial effects: (a) it resulted in markedly reduced

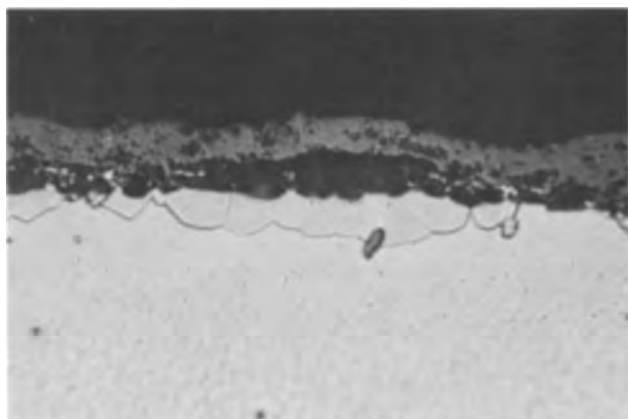


Fig. 11. Photomicrograph of a sample treated in LiF at 1100°C for 100 min, followed by oxidation at 1200°C in air. Magnification ca. 550X.

oxidation rates, (b) improved resistance to spalling, and (c) increased resistance to nitride formation during air oxidation.

#### Acknowledgments

The authors wish to extend their appreciation to the Metallography Unit of the General Electric Research and Development Center for their excellent services. The advice and counsel of Dr. N. C. Cook throughout this project is appreciated.

Manuscript received Sept. 18, 1967; revised manuscript received Nov. 1, 1967.

Any discussion of this paper will appear in a Discussion Section to be published in the December 1968 JOURNAL.

#### REFERENCES

1. C. S. Tedmon, Jr. and W. C. Hagel, *This Journal*, **115**, 151 (1968).
2. K. Hauffe, "Progress in Metal Physics," 4, p. 89, Pergamon Press, London (1963).
3. K. Hauffe and H. Pfeiffer, *Z. Elektrochem.*, **56**, 390 (1952).
4. H. Pfeiffer and K. Hauffe, *Z. Metallk.*, **43**, 364 (1952).
5. W. C. Hagel, *Trans. Met. Soc. AIME*, **233**, 1184 (1965).
6. E. Brauns and A. Rahmel, *Werkstoffe u. Korrosion*, **7**, 448 (1956).
7. W. C. Hagel, *Trans. ASM*, **56**, 583 (1963).
8. C. S. Tedmon, Jr., *Corr. Sci.*, **7**, 525 (1967).
9. A. U. Seybolt and R. A. Oriani, *Trans. AIME*, **206**, 556 (1956).
10. C. S. Tedmon, Jr., *This Journal*, **113**, 766 (1966).
11. A. U. Seybolt, *ibid.*, **107**, 147 (1960).
12. E. J. Felten, Unpublished research quoted in ref. (7).
13. W. C. Hagel and A. U. Seybolt, *This Journal*, **108**, 1146 (1961).
14. W. C. Hagel, *J. Appl. Phys.*, **36**, 2586 (1965).
15. R. Scholder and H. Schwarz, *Z. anorg. u. allgem. Chem.*, **326**, 1 (1963).
16. J. Aubrey and C. Gleitzer, Cong. intern. chim. pure et appl. *16e*, Paris (1957).

## Electrochemical Formation of Lithium Alloys from Molten Lithium Fluoride

C. S. Tedmon, Jr.

General Electric Research and Development Center, Schenectady, New York

and W. C. Hagel\*

University of Denver, Denver, Colorado

#### ABSTRACT

Lithium-rich coatings have been successfully produced on platinum, silver, copper, and chromium samples by electrode position from molten LiF, using a graphite anode. Coatings may also have been made on nickel samples, although the data are less definitive. The coatings produced on copper and silver appear to be solid solutions of lithium with the sample metal, whereas the coatings on platinum and chromium are probably intermetallic compounds. Extensive testing at constant current density was carried out with chromium samples at temperatures between 900° and 1100°C, for deposition times varying from 10 to 360 min. Coating thickness and morphology was found to be time and temperature dependent. Generally low coulombic efficiencies were observed, and it is postulated that diffusion of lithium into the sample is rate-controlling. Possible electrode reactions are discussed.

Electrochemical methods for the deposition of various metals from molten halide salts have been known for many years. Some of the more important procedures have been discussed in a review on molten salt electrochemistry by Reddy (1). The deposition of metals from molten fluoride salts has been an especially active area in recent years. Senderoff *et al.* (2-6) have described methods for the electrodeposition of coherent, dense, and pure deposits of refractory metals, including niobium, tantalum, zirconium, chromium, molybdenum, tungsten, hafnium, and vanadium.

In their experiments, the electrolytes were usually eutectic mixtures of alkali fluoride salts, containing small amounts [e.g., ~10 w/o (weight percent)] of refractory metal fluoride salts, such as NbF<sub>5</sub> and K<sub>2</sub>TaF<sub>7</sub>, in the cases of deposition of niobium and tantalum, respectively. In general, soluble anodes were used, and they were able to produce electrodeposits on a variety of substrates.

In contrast to the methods of Senderoff and Mellors are the techniques developed by Cook (7-10) for the electrodeposition of silicon, boron, chromium, and beryllium from molten fluoride electrolytes. Whereas Senderoff and Mellors essentially produced electro-

\* Electrochemical Society Active Member.

plates of pure metal on the substrate, the metals Cook deposited reacted with the substrate to produce compounds or alloys. This mode of deposit was probably due to several factors, particularly the low current densities and relatively high temperatures at which Cook carried out his processes. Both effects would encourage interdiffusion between the substrate and the deposited metal, leading to the formation of alloy coatings. In fact, Cook has implied (7-10) that the rate of deposition in his processes was controlled essentially by solid-state diffusion rates in the substrate or reaction layer. Thus, for example, when electrodepositing silicon on molybdenum,  $\text{MoSi}_2$  was the principal product, with lesser amounts of  $\text{Mo}_3\text{Si}$  and  $\text{Mo}_5\text{Si}_3$  being present (9). When depositing chromium on mild steel, solid solution single-phase Fe-Cr alloys were formed (10). The electrolytes used by Cook were alkali-fluoride salt mixtures, usually of eutectic composition; consumable anodes were employed. Unlike the methods of Senderoff and Mellors, the techniques developed by Cook were highly sensitive to the nature of the substrate. Electrodeposits could be made on a wide variety of metals, but since compounds or alloys were always formed between the substrate and the element being deposited, plating characteristics varied with each kind of substrate.

Molten alkali fluorides possess several unique properties that make them advantageous for use as electrolytes in electroplating in preference to other halide salts. One of the more significant characteristics is the ability of molten fluorides to flux and dissolve oxides. Consequently, when a substrate metal is introduced into the molten salt bath, any residual oxide scale or film is quickly dissolved, leaving a clean metal surface exposed to the electrolyte. This will help promote mass transport across the surface. In addition, alkali fluorides are in general stable to higher temperatures and less hygroscopic than other alkali-halide electrolytes.

Because of the success in electrodeposition of various metals from molten alkali-fluoride salt baths as described above, it was decided that the feasibility of electrodepositing on certain structural metal substrates using a molten lithium-fluoride electrolyte should be investigated. Since the melting point of lithium fluoride ( $845^\circ\text{C}$ ) is much higher than that of lithium ( $183^\circ\text{C}$ ), appreciable deposits of pure metallic lithium would not be expected on the sample surface. Rather, it would be expected that the lithium retained in the sample would be present as an alloying species, either in solid solution, or as a compound. Excess lithium which might be deposited would either dissolve into the molten salt or migrate away as a second phase in the salt mixture.

There are a number of incentives for developing a process for the electrodeposition of lithium on base metals at elevated temperatures. High-temperature electrodeposition is a possible technique for producing alloys, or at least lithium-alloy coatings on certain metals that cannot be prepared by more conventional methods.

One particular application is in the area of oxidation-resistant materials. It is well-known that the oxidation resistance of certain metals can be improved by either alloying with lithium or by oxidizing the metal surface in an atmosphere containing lithium (11-15). Consequently, the notion of electrochemically producing a layer of lithium-containing metal near the surface of the sample appeared promising.

It was decided to study the electrodeposition of lithium on a number of metals, including some whose solubility for lithium was known to be relatively high, such as copper and silver (16). In addition, it was desired to attempt electrodeposition on metals for which the solubility of lithium is either unknown, such as in platinum, or else believed to be quite small, such as in the case of nickel or chromium (17).

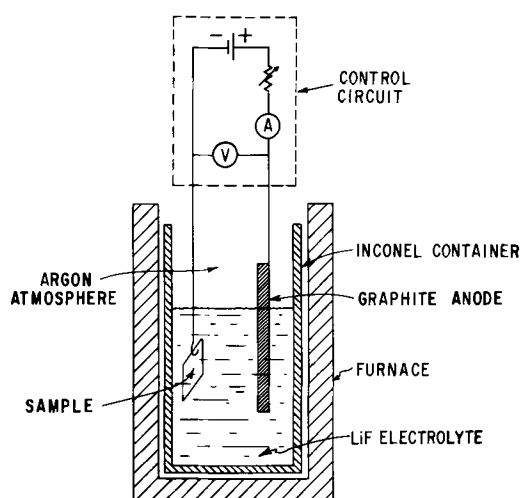


Fig. 1. Schematic diagram of molten fluoride electrodeposition apparatus.

### Experimental

**Sample preparation.**—High-purity sample metals were used throughout the investigation, *viz.*, “thermocouple”-grade platinum, iodide-chromium, carbonyl-nickel, OFHC copper, and 99.99% pure silver. The samples were usually in the form of thin plates, about  $1 \times 2 \times 0.05$  cm, although in the case of platinum, wire of 0.15 cm diameter was used. All samples were abraded through No. 4/O metallographic paper and were rinsed in toluene and acetone prior to the electrodeposition treatment.

**Electrodeposition cell.**—The lithium-fluoride electrolyte was contained in an Inconel vessel which was about 12.7 cm in diameter and 46 cm long. The Inconel vessel was situated inside a multiple-winding furnace which could heat the electrolyte to  $1200^\circ\text{C}$  (Fig. 1). Suitable covers for the vessel were made so that an inert atmosphere could be maintained over the salt. Initially, argon was used; later, forming gas (90%  $\text{N}_2 + 10\% \text{H}_2$ ) was found to be more convenient.

The anode was spectroscopic-grade graphite, which was further purified by a bake-out treatment at  $2300^\circ\text{C}$  for about 15 min.

The lithium fluoride was obtained from the American Potash and Chemical Corporation and was claimed to be about 99.9 w/o pure. As has been reported (2-10), the purity of the electrolyte salt is an extremely important factor in determining the quality and success of the electrodeposition method. In an effort to purify the salt further, two procedures were carried out. First, the salt was vacuum-melted and held above its melting point in vacuum for several hours to drive out volatile impurities. Subsequently, cleanup runs were carried out, in which sheet samples of iron and nickel, having large surface areas, were placed in the cells as cathodes. Current was applied through the cell in an effort to plate out metallic impurities. The composition of the salt after these runs is presented in Table I.

**Mass-spectrometric analyses.**—Standard analytical procedures proved to be unreliable and inadequate for the determination of the small amounts of lithium

Table I. Analysis of LiF electrolyte  
(All figures in weight per cent)

Be	0.0003	B	0.0095
Mn	0.0020	Mg	0.0004
Si	0.0040	Cr	0.0060
Fe	0.0035	Al	0.0025
Cu	0.00003	Nb	0.0020

Bal—LiF. All other metallic elements not detected.

present in most of the samples, and a mass-spectrometric method was found to be the most satisfactory. Samples were sent to the Technology Division of the GCA Corporation, Bedford, Massachusetts, for the analysis. The lithium concentration in the sample as a function of distance from the surface was determined in the following manner. A sharply focussed beam of ionized argon was directed onto the sample surface, which locally vaporized a small volume of material from the sample. Because of the fine focussing of the ion beam, the volume of vaporized material was on the order of a few cubic microns. The vaporized species were then analyzed with a mass-spectrometer. By repeated bombardment of the ion beam, composition as a function of distance from the specimen surface could be determined. With the use of suitable standards, the sputter-ion yield for the various elements of interest can be determined, and conversion of intensity data to composition may be made.

*Auxiliary measurement.*—Standard metallographic and x-ray diffraction procedures were employed to study the structures of the electrodeposited coatings. Because these coatings were usually very thin, tapered sections were used in metallography. Microhardness measurements were also made on certain selected samples.

### Results and Discussion

*General observations.*—Electrochemically deposited lithium-alloy coatings were successfully produced on silver, copper, platinum, chromium, and perhaps nickel. The solubility of lithium in silver and copper is probably much larger than for the others, and it is not unexpected that the lithium-alloy coatings in the former were found to be thicker than in the last two. In general, however, coulombic efficiencies were low. For the conditions employed, this suggests that the rate-limiting step is the diffusion of lithium into the sample, rather than the transport of lithium through the electrolyte to the sample. Presumably excess lithium arriving at the sample faster than it can be assimilated would dissolve into the molten LiF, in which it has a solubility of about 2 m/o (mole per cent) metal at 1000°C (18).

Table II presents a summary of operating data and results for a number of different samples. It is interesting to note that the highest coulombic efficiency was obtained on the platinum sample. Silver samples (not listed in Table II) also had high efficiencies; however, since the liquidus temperature at the silver-rich side of the Ag-Li phase diagram decreases rapidly with increasing lithium content, melting of the sample usually occurred for deposition at temperatures as low as 900°C. Consequently, quantitative deposition data for the silver samples could not be obtained.

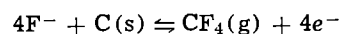
Table II. Operating data and results for various samples

Sample	Electrolyte temperature, °C	Current density, amp/cm <sup>2</sup>	Potential difference, volts	Time, min	Sample wt gain, mg/cm <sup>2</sup>	Coulombic efficiency, %
Cu	900	0.010	1.1	360	1.5	10.0
Cu	925	0.010	1.2	15	0.1	17.0
Pt	1000	0.028	1.7	20	2.6	100
Ni	950	0.166	3.6	35	0.5	1.9
Ni	900	0.030	2.3	360	N.D.*	—
Ni	1000	0.017	2.25	30	0.12	4.6
Ni	1000	0.155	2.7	35	0.31	1.4
Cr	900	0.031	2.52	10	0.16	12.2
Cr	900	0.031	2.53	30	0.1	2.5
Cr	900	0.031	2.50	120	0.68	4.3
Cr	900	0.031	2.45	360	0.5	1.1
Cr	1000	0.031	2.05	10	0.07	5.4
Cr	1000	0.031	1.90	30	0.3	7.7
Cr	1000	0.031	1.88	120	0.5	3.2
Cr	1000	0.031	1.80	360	1.1	4.3
Cr	1100	0.031	0.92	10	0.11	9.2
Cr	1100	0.030	1.05	30	0.3	7.7
Cr	1100	0.031	1.25	120	0.3	1.9
Cr	1100	0.030	1.02	360	0.5	1.1

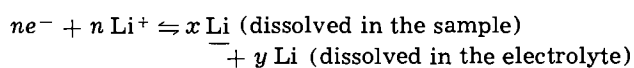
\* Not determined.

The potential difference between anode and cathode was usually observed to decrease with increasing temperature, which is the expected trend. Since part of the voltage drop between the anode and cathode includes IR losses in the leads, care must be taken in interpreting the potential data. However, since the electrical leads were of essentially constant geometry in all of the runs, variation of the IR losses from run to run, and with temperature, will be small, so that most of the temperature variation in the electrical potential can be attributed to either the electrolyte and/or interface reactions such as solution of lithium into the sample.

Loss of carbon from the anode was observed below the saltline. It was not possible to relate quantitatively the loss of carbon to operating conditions, since adherence of the LiF to the anode, after removal from the bath, precluded accurate weight-loss measurements. The solubility of carbon in molten LiF is believed to be very small (19). The anode reaction is probably



and the cathode reaction would be of the form



where  $n = x + y$ . Because free energies for solution of lithium in either the sample or the electrolyte are not known, open-circuit potentials for the net reaction were not calculated.

*Platinum sample.*—Figure 2 is a micrograph of the platinum sample which is listed in Table II. There is a very clear and well-defined interface between the lithium diffusion zone and the interior of the platinum. Irregularities along this interface are magnified by the 8:1 taper on the sample. The true thickness of the coating is estimated to be about 40-50 $\mu$ . Microhardness data for the platinum sample are presented in Fig. 3. Although there is some scatter in the data obtained on the coating, it is apparent that there is a very pronounced hardening effect due to the presence of the lithium. Also, the hardening effect is clearly limited to the coating, with a sharp discontinuity in hardness occurring at the boundary. The hardness of



Fig. 2. Photomicrograph (8:1 taper section) of a platinum sample held at 1000°C for 20 min. Magnification 60X.



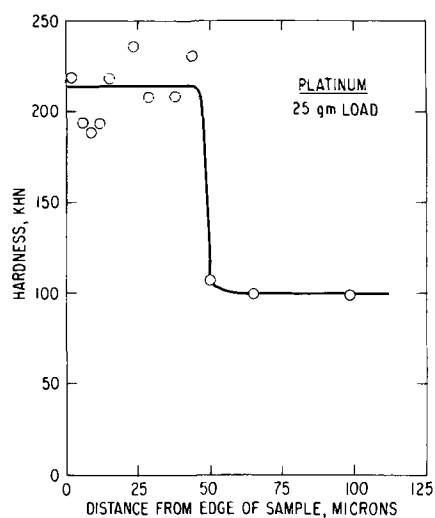


Fig. 3. Microhardness traverse across same platinum sample shown in Fig. 2.

the interior of the sample decreases to a value of 100 KHN at a distance of about  $50\mu$  from the surface. The hardness of the coating appears to be essentially constant. This fact, together with the metallographic observation of the sharp boundary, suggests that coating has a constant composition as would be found for a single intermetallic compound. If the coating were a solid solution of lithium in platinum, a composition gradient in the coating would be expected, which would result in a corresponding hardness gradient. Also, there would not be a sharp interface between the coating and the interior of the sample. The region of the sample extending inward from the coating may be a solid solution of lithium and platinum, since the hardness decreases from about 100 KHN at  $50\mu$  from the surface to 84 KHN at a 0.4 mm depth. The identity of the surface compound is unknown, although the compound  $\text{LiPt}_2$  has been reported in the literature (20). X-ray diffraction patterns were obtained, but could not be indexed. Spectrographic analysis of the sample showed lithium to be present; quantitative analysis was not possible.

**Copper sample.**—Figure 4 is a photomicrograph of a copper sample which had been run for 6 hr at  $900^\circ\text{C}$ . The thickness of the outer zone is about  $200\text{--}250\mu$ . The structure of that zone suggests that the material was molten at some point during treatment. Spectrographic analyses of copper samples showed lithium present, but the concentration was not determined. According to the work of Klemm and Volavsek (21), there is a substantial solid solubility of lithium in copper, which increases with decreasing temperature. At  $900^\circ\text{C}$ , the

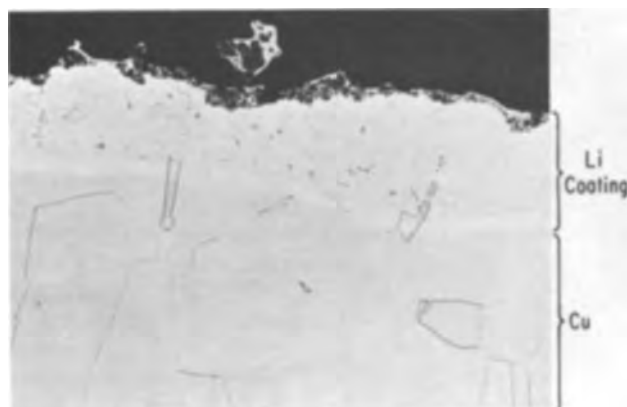


Fig. 4. Photomicrograph (10:1 taper section) of a copper sample which had been run for 6 hr at  $900^\circ\text{C}$ . Sample appearance suggests that partial melting had occurred. Magnification ca. 40X.

solidus composition is about 7 a/o lithium. If melting occurred, then presumably the composition of the solidified material must be at least the solidus composition, i.e., about 20 a/o Li.

Microhardness tests on copper samples disclosed a hardness maximum near the edge, with hardness decreasing towards the sample interior, indicating solid-solution hardening of the copper by lithium. Hardness values near the sample surface were about KHN 68-70 (10g load); in the center of the sample, KHN 45-50.

**Nickel samples.**—The solubility of lithium in nickel is not known, but our results indicate it is quite low. Figure 5 is a photomicrograph of a sample of nickel run at  $900^\circ\text{C}$  for 6 hr. The diffusion zone is thin; the sample is mounted with a 10:1 taper in the picture, so the actual thickness is about  $1.0\text{--}1.5\mu$ . Spectrographic analysis did not show lithium to be present; however, with the thin coating on the sample, the negative result is not necessarily conclusive. It is quite possible, however, that lithium is not present in the sample, and the coating is due to deposition of some impurity from the salt. In any case, the morphology of the structure is suggestive of a compound rather than a solid solution.

**Chromium samples.**—The most extensive testing program was carried out with chromium samples. In addition to studying the electrochemical deposition process, the oxidation behavior of coated samples was investigated in detail. The results of that study are discussed elsewhere (22). Operating data for one set of experiments are presented in Table II, in which the effects of deposition time and electrolyte temperature were studied. Several points should be noted. It is apparent that coulombic efficiencies were the greatest for the shortest deposition times, and in general decreased with increasing time, as shown in Fig. 6. Since lithium is being supplied to the sample at a constant rate isothermally, this indicates that it is being taken into the sample at a continually decreasing rate. If the rate of solution of lithium into the sample is controlled by solid-state diffusion, and if the activity of lithium at the electrolyte/sample interface remains constant throughout the operation, then the rate of solution of lithium into the sample would decrease parabolically with time.

There was no strong correlation between coulombic efficiency and electrolyte temperature. The effects of deposition time and electrolyte temperature on the resultant lithium-containing coatings on chromium samples are summarized in Table III. In additional experiments, samples were immersed in the electrolyte for various times and at different temperatures, with no applied potential. None of these samples showed any weight change, and they did not have any surface coating, but remained bright, thus demonstrating that lithium was introduced into the specimen only under the influence of an applied external potential.



Fig. 5. Photomicrograph of a (10:1 taper section) nickel sample which was run at  $900^\circ\text{C}$  for 6 hr. Magnification ca. 200X.

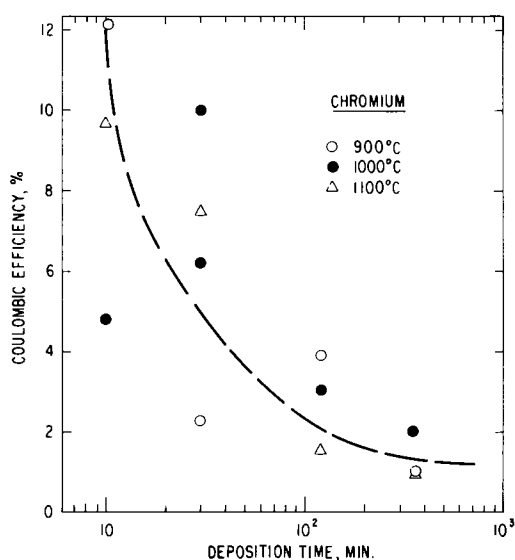


Fig. 6. Coulombic efficiency vs. time for chromium samples run at 900°, 1000°, and 1100°C.

It would be expected that the thickness of a coating ought to increase with increasing time at constant temperature. For samples run for 360 min at 900° and 1000°C, that was not the case, as indicated in Table III. There is, of course, some uncertainty in determining coating thickness metallographically from taper sections, but the data are estimated to be accurate to within  $\pm 4\mu$ . Consequently it may be that the growth rate after 120 min is negligible.

Photomicrographs of some of the more interesting coating structures are shown in Fig. 7-9. Figure 7 presents a sequence of structures that were developed on chromium samples which had been treated at 900°C for varying lengths of time. Some of the samples were electroplated with nickel prior to metallographic preparation, in order to preserve edge detail. It appears that the number of layers in the coatings increases with increasing time at temperature. As is seen from the data in Table III, this was a general trend, although it was more pronounced with samples run at 900°C than with the 1000° and 1100°C samples. The morphology of the outer layer in both the 120-min sample (Fig. 7c) and the 360-min sample (Fig. 7d) shows a coring effect, suggesting possibly the presence of a molten phase during deposition.

Figure 8a shows the structure of a sample coated at 1000°C for 30 min. Only one layer is present. Samples run for 10 min at 1000°C were quite similar in appearance to this 30-min sample. Figure 8b is a micrograph of a chromium sample run for 120 min at 1000°C. This coating is somewhat thicker than the coating shown in Fig. 8a and consists of two layers. The inner layer in Fig. 8b is similar in appearance to the coat-

Table III. Effect of deposition time and electrolyte temperature on the morphology of lithium-containing coatings on chromium

Deposition time, min	Electrolyte temp, °C	Number of layer in coating	Total thickness of coating, $\mu$
10	900	2	10
30	900	2	10
120	900	2 or 3	22
360	900	4	15-18
10	1000	1	13-15
30	1000	1	18
120	1000	2	22
360	1000	2	18
10	1100	1	13
30	1100	1	18
120	1100	1	22
360	1100	2	26

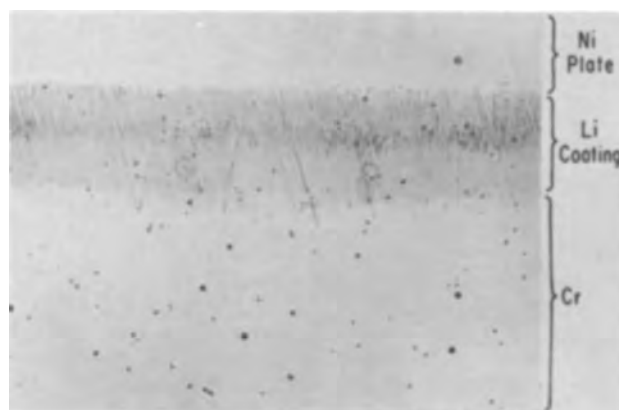


Fig. 7a

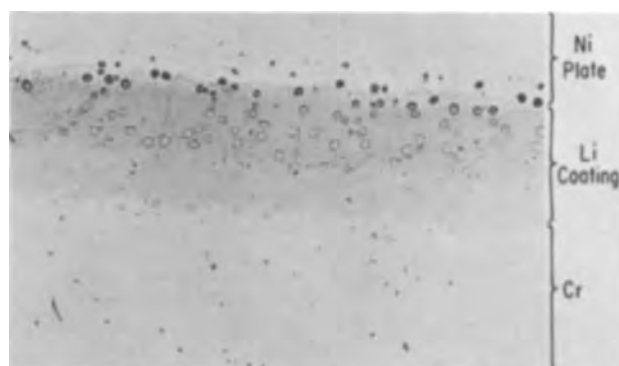


Fig. 7b

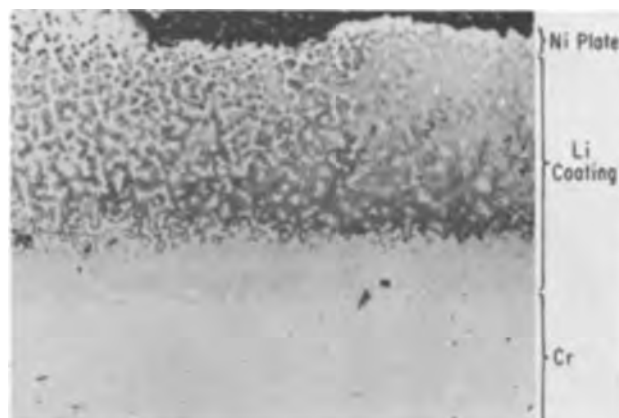


Fig. 7c

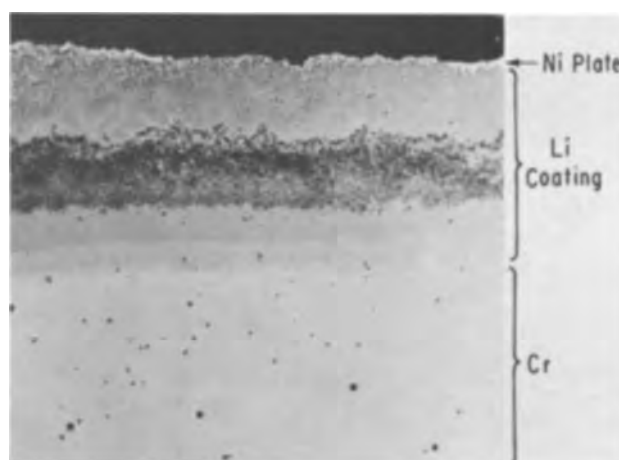


Fig. 7. Photomicrographs (8:1 taper sections) of chromium samples run at 700°C for various times: a, 10 min; b, 30 min; c, 120 min; d, 360 min. Magnification ca. 100X.

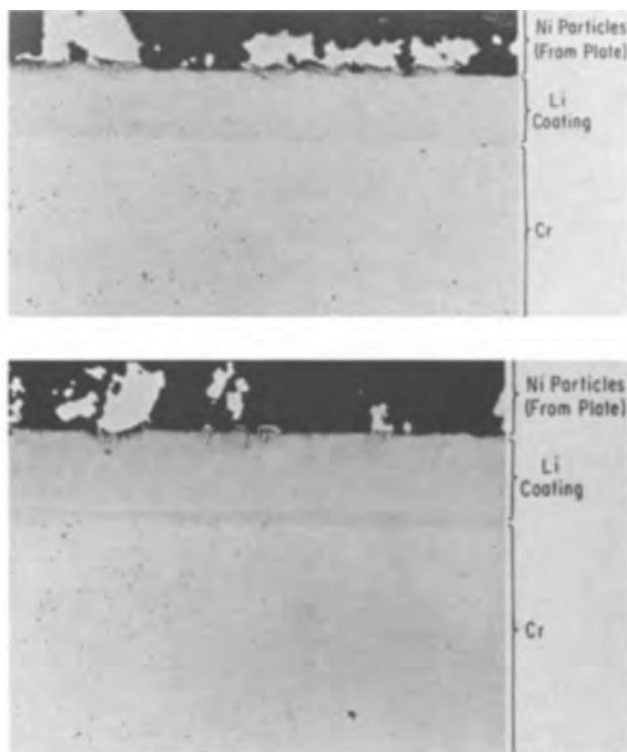


Fig. 8. Photomicrographs (8:1 taper sections) of chromium samples run at 1000°C: a (top) for 30 min; b (bottom) for 120 min. Magnification ca. 40X.

ing shown in Fig. 8a, suggesting that it might be the same phase. If that were the case, then the thicker outer layer shown in Fig. 8b would be a more Li-rich phase. Samples run for 360 min at 1000°C had coatings with structures closely resembling those run for 120 min.

The micrographs shown in Fig. 9 present representative structures for samples run at 1100°C for various times. Samples run for 10, 30, and 120 min all had similar coating structures, of which that shown in Fig. 9a for a 120-min sample is typical. When samples were run for 360 min at 1100°C, a different structure resulted, consisting of two layers (Fig. 9b). At higher magnification, there is some resemblance in appearance between the inner layer (Fig. 9c), and the coating produced on samples run for shorter times (Fig. 9a). In Fig. 9c, reaction at the grain-boundaries is evident. The grain-boundary structure shown here is quite similar in appearance to that which was found in Fe-25% Cr-0.5% Li alloys that had been produced by induction melting under argon pressur-

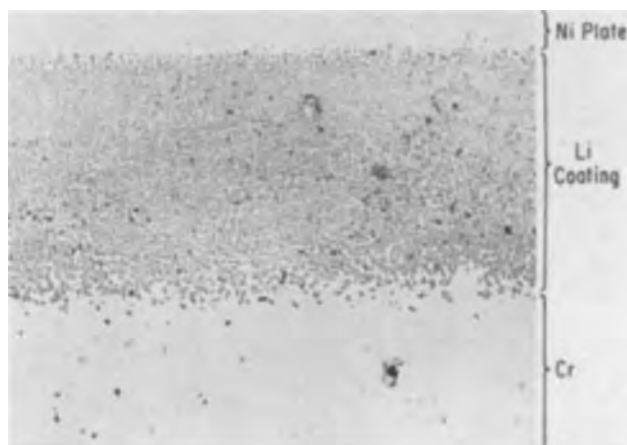


Fig. 9a



Fig. 9b

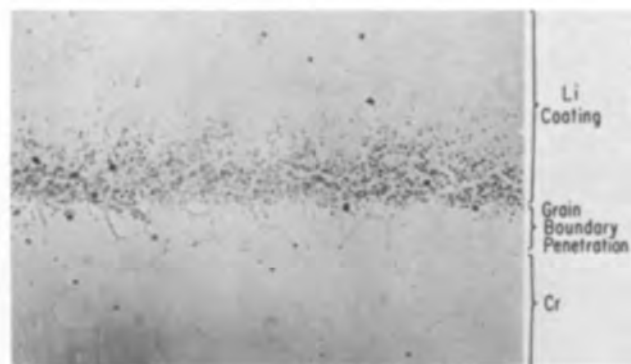


Fig. 9. Photomicrographs (8:1 taper sections) of chromium samples run at 1100°C for various times: a, for 120 min, magnification ca. 100X; b, for 360 min, magnification ca. 50X; c, for 360 min, magnification ca. 190X. Note grain boundary penetration.

ized to several atmospheres to minimize lithium loss by volatilization (15).

Figure 10 presents some results obtained with the ion bombardment technique for a sample which had been run for 360 min at 1000°C. Standards for determining exactly the sputter-ion yields for lithium and chromium were not available, so exact conversion of the intensity data to compositions is not possible. However, it is estimated the sputter-ion yield for lithium may be as much as 100 times that of chromium (23). If that were the case, then the peak in the curve in Fig. 10. would correspond to a lithium concentration of about 0.5 a/o. The presence of the maximum at a position of about  $2\mu$  below the specimen surface, rather than at the surface, is not understood. It may be artificial, arising from the difficulties inherent in trying to resolve distances less than about  $1-2\mu$  by this technique.

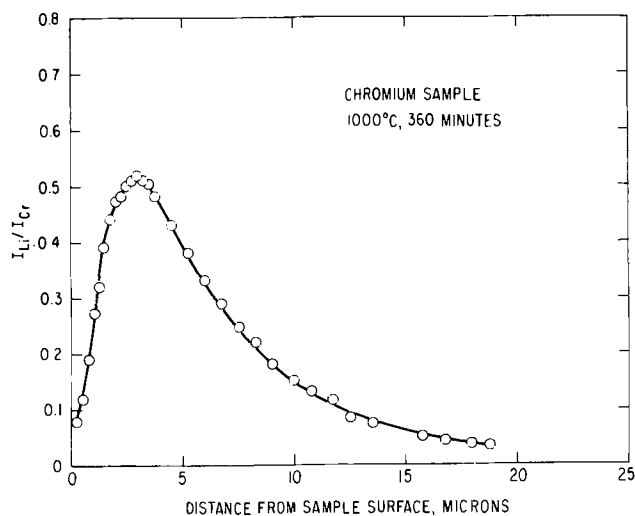


Fig. 10. Relative intensity vs. distance into chromium sample, which had been run for 360 min at 1000°C.

A comparison of the data in Fig. 10 with those listed in Table III shows very good agreement between the depth of reaction observed metallographically and that observed by the mass-spectrometric method. It was stated previously that the existence of well-defined boundaries between the coatings and the substrate, as observed metallographically, implied that the coating was an intermetallic compound, rather than a solid solution of lithium in chromium. The data presented in Fig. 10 do not seem to support that argument. Unfortunately, the coatings on chromium samples were too thin to permit definitive micro-hardness data to be obtained, so the question remains unresolved. What is definitely established by the data shown in Fig. 10 is that lithium is clearly present in the sample to a depth of at least  $18\mu$ .

If it is assumed that the data presented in Fig. 10 are a valid representation of the lithium profile in the sample, then an estimate of a diffusion coefficient for lithium in chromium may be made. Assuming that the diffusion coefficient is independent of composition, and also that the effective surface composition is constant and equal in relative magnitude to the value given by the maximum in Fig. 10, then the following solution to Fick's second law applies

$$c(x, t) = c_0 \left[ 1 - \operatorname{erf} \left( \frac{x}{2\sqrt{Dt}} \right) \right]$$

where  $c(x, t)$  is the relative lithium concentration at any time  $t$  and position  $x$ ,  $c_0$  is the surface composition, and  $D$  is the diffusion coefficient. The term  $\operatorname{erf}$  denotes the error function. Note that it is not necessary to know the absolute concentration; only the composition profile is required. That the above solution to Fick's second law applies to the concentration data presented in Fig. 10 is demonstrated in Fig. 11, which is a probability plot of relative composition vs. the distance-time parameter,  $x/\sqrt{t}$ . If the equation given above is a valid solution to the diffusion equation, a straight line should result. It is clear that a good fit obtains. A value of  $c_0 = 0.52$  was used. For the interdiffusion coefficient of lithium in chromium at  $1000^\circ\text{C}$ , a value of  $D \cong 5 \times 10^{-12} \text{ cm}^2 \text{ sec}^{-1}$  is obtained, which is essentially independent of composition, as indicated by the good linear fit of the data in Fig. 11. Although there are no other data available with which to make a comparison, this value seems reasonable.

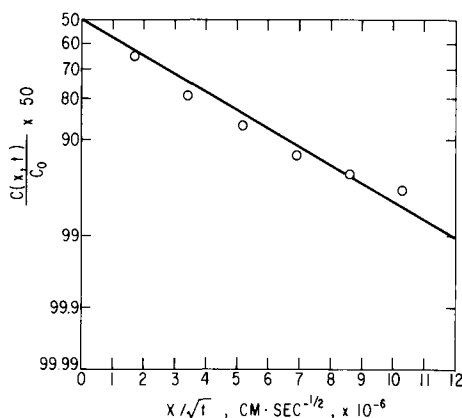


Fig. 11. Probability plot of relative lithium concentration vs. the distance time parameter,  $x/\sqrt{t}$ , for a chromium sample which had been run 360 min at  $1000^\circ\text{C}$ .

## Conclusions

1. Lithium-rich coatings have been successfully electrodeposited on Ag, Cu, Pt, Ni, and Cr using a molten LiF electrolyte and a graphite anode. The electrodeposition was carried out in the temperature range of  $900^\circ\text{--}1100^\circ\text{C}$ , for times varying from 10 to 360 min.

2. The coulombic efficiency obtained was dependent on the metal being coated, varying from 100% in the case of Pt to about 1% for Cr and Ni, under certain conditions.

3. The coatings produced on Cu and Ag samples appeared to be solid solutions of Li with the substrate metal.

4. The coatings produced on Pt appeared to be an intermetallic compound, possibly  $\text{LiPt}_2$ .

5. Metallographic data suggested that the coatings produced on chromium samples were intermetallic compounds; however, mass-spectrometric data obtained as a function of distance from the sample surface did not confirm that, showing instead a smooth lithium concentration gradient. The extent of Li penetration in Cr samples, as determined metallographically, was in good agreement with the mass-spectrometric data.

## Acknowledgments

The authors wish to extend their appreciation to W. A. Roman, R. R. Russell, and Mrs. E. M. Raviola for metallographic services, and to N. C. Cook, D. A. Vermilyea, and D. W. White of the General Electric Research and Development Center, and C. J. Rosa of the University of Denver, for critical reviews of the manuscript. The continuing assistance, counsel, and interest of N. C. Cook is gratefully acknowledged.

Manuscript received Sept. 18, 1967; revised manuscript received Nov. 1, 1967.

Any discussion of this paper will appear in a Discussion Section to be published in the December 1968 JOURNAL.

## REFERENCES

1. T. B. Reddy, *Electrochem. Technol.*, **1**, 325 (1963).
2. G. W. Mellors and S. Senderoff, *This Journal*, **112**, 266 (1965).
3. S. Senderoff, G. W. Mellors, and W. J. Reinhart, *ibid.*, **112**, 840 (1965).
4. G. W. Mellors and S. Senderoff, *ibid.*, **113**, 60 (1966).
5. G. W. Mellors and S. Senderoff, *ibid.*, **113**, 66 (1966).
6. G. W. Mellors and S. Senderoff, Canadian Pat. 688,546, June 9, 1964.
7. N. C. Cook, U.S. Pat. 3,024,175, March 6, 1962.
8. N. C. Cook, U.S. Pat. 3,024,176, March 6, 1962.
9. N. C. Cook, U.S. Pat. 3,024,177, March 6, 1962.
10. N. C. Cook, U.S. Pat. 3,232,853, Feb. 1, 1966.
11. H. Pfeiffer and K. Hauffe, *Z. Metallk.*, **43**, 364 (1952).
12. H. Pfeiffer and K. Hauffe, *Werkstoffe u. Korrosion*, **7**, 448 (1956).
13. K. Hauffe, "Progress in Metal Physics 4," p. 89, Pergamon Press, London (1963).
14. W. C. Hagel, *Trans. ASM*, **56**, 583 (1963).
15. C. S. Tedmon, Jr., *Corr. Sci.*, **7**, 525 (1967).
16. R. Elliott, "Constitution of Binary Alloys, First Supplement," McGraw-Hill Book Co., New York (1965).
17. N. C. Cook, Private communication.
18. M. A. Bredig, J. E. Sutherland, and A. S. Dworkin, *Chem. Ann. Prog. Rep.*, June 20, 1958, ORNL-2584, p. 73.
19. J. F. Elliott, Private communication.
20. C. P. Nash, F. M. Boyden, and L. D. Whittig, *J. Am. Chem. Soc.*, **88**, 6203 (1960).
21. W. Klemm and B. Volavsek, *Z. anorg. u. allgem. Chem.*, **296**, 184 (1958).
22. C. S. Tedmon, Jr., and W. C. Hagel, *This Journal*, **115**, 147 (1968).
23. F. J. Satkiewicz, Private communication.

## Two Remarks on the Resistive Contribution to Overpotential

Benson R. Sundheim

Department of Chemistry, New York University, Washington Square, New York, New York

### Placement of Reference Electrodes

In order to minimize the contribution of the  $iR$  drop to the apparent overpotential, it is generally thought that it is desirable to place the reference electrode on an isopotential surface near the electrode being studied. That is, the potential drop along the current streamlines traversed in passing from one electrode to the other should be small. It is not always possible to do this efficiently. For example, if the indicator electrode is small, the major part of the  $iR$  drop will occur near the surface end. A reference electrode or Luggin capillary cannot reach closely enough to obviate most of the  $iR$  drop. In other cases, the pressing of the Luggin capillary close to the surface of the indicator electrode gets rid of most of the  $iR$  drop, but because of its geometrical blocking of the electrode reduces the current density in the immediate vicinity of the capillary tip. It is sometimes thought that if the Luggin capillary is close enough to the surface it will correctly represent the overpotential contribution characteristic of the instantaneous state of the electrode with little or no effect from the ohmic potential. That this view is incorrect when activation overpotential is significant can be seen as follows.<sup>1</sup>

We select first an extreme case which displays clearly the essential features of the argument. Referring to Fig. 1, we note that B and C have the same potential (with respect to any reference point). We assume that E and D are the locations of two identical reference electrodes placed so as to measure the potentials of B and C, respectively, with essentially no direct contribution from  $iR$ . We further assume that the electrode in question (B and C) has a characteristic current voltage relation; e.g.,  $E = a - b \ln i$ , so that the overpotential  $\eta$  is some specific function of the current  $i$ . Following the two current loops and applying Kirchoff's law to the circuit we obtain

$$\begin{aligned} i_1 R_1 + \delta E_1 &= i_2 R_2 + \delta E_2 \\ i_1 R_1 - i_2 R_2 &= \eta(i_1) - \eta(i_2) \end{aligned}$$

We assume that the reference electrode measures the potential difference between the electrode and the solution immediately adjacent to this indicator electrode. This quantity will be different because of the different current densities of the two electrodes. Let us assume that  $a = 0.1$ ,  $E = E_0 - b \ln i$ ,  $i_t = i_1 + i_2 = 1$  ma,  $R_1 = 10$  ohms, and  $R_2 = 1000$  ohms. By using these values in the above equations it is found that  $i_1 = 0.894$  ma,  $i_2 = 0.106$  ma, and  $\eta_1 - \eta_2 = 0.0927$  v. Thus the two reference electrodes will differ in their readings by approximately 93 mv. If the total current is reduced to  $1 \mu$ a, then  $\eta_1 - \eta_2 = 0.5$  mv and  $i_1 = 0.502 \mu$ a,  $i_2 = 0.497 \mu$ a.

We note that the relative partition of the current varies with the total current and that the two reference electrodes, both placed so as to obviate  $iR$  drop, give different readings with respect to what is in a sense the same electrode (parts connected by an ideal conductor).

<sup>1</sup> This discussion is not meant to be novel, since the "ohmic drop" is well understood by experienced electrochemists, but rather is intended to correct an all too frequently occurring misunderstanding.

Now let us extend this idea to a more common experimental arrangement. In Fig. 2 the indicator electrode B faces the counter electrode A and the rear surface of B is close to a reference electrode C. It may be (falsely) reasoned that C measures the appropriate potential of B at the current density equal to the net current divided by the total area of both sides. In fact, the situation is analogous to the one previously considered. The two surfaces of B are not equally accessible to current streamlines so that differing current densities combine with differing overpotentials to make the electrode an isopotential surface. (For simplicity, we consider that all parts of the rear are equally accessible and all parts of the front of a uniform but different accessibility.) For example, the resistance along a path from the counter electrode to the indicator electrode may be taken to be 10 ohms and that to the rear as 1000 ohms. Then the argument given above applies. We note that the current density as calculated by dividing the net current by the total area (or by one-half of the total area) does not correspond to the apparent measured overpotential. The extent of the discrepancy depends on the net current and on the details of the correct current-overpotential relationship. For other geometries and resistance distributions the error may be greater or lesser.

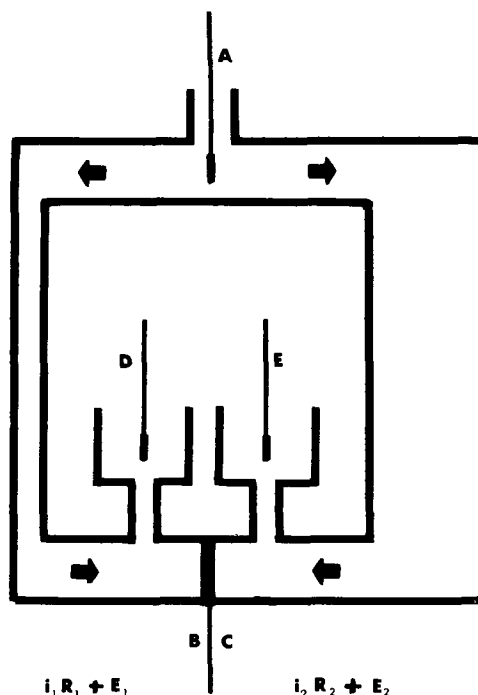


Fig. 1. Current paths to two parts of an electrode: A, counter electrode; B, C, opposite sides of indicator electrode; D, E, reference electrodes;  $i_1$ ,  $i_2$ ,  $R_1$ ,  $R_2$ , currents and resistances of the respective paths;  $E_1$ ,  $E_2$ , the activation overpotentials appropriate to the two current densities.

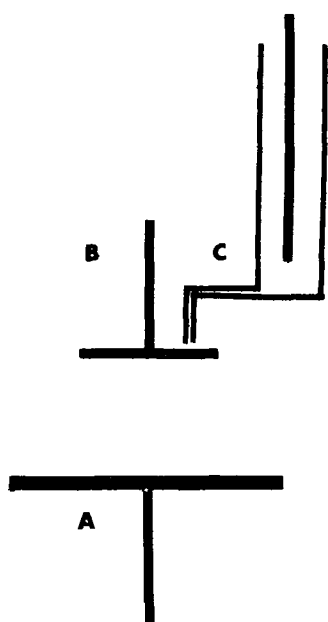


Fig. 2. One method of placing a reference electrode: A, counter electrode; B, indicator electrode; C, reference electrode.

In the case of a plane electrode, against which a Luggin capillary is pressed (Fig. 3), the situation is similar. The presence of the capillary raises the  $iR$  drop on the path to the surface immediately adjacent to the tip so that the current density at that point falls correspondingly. The capillary will then give a true reading of the potential difference between reference electrode and working electrode but at a current density which may be far less than that calculated.

The current distribution in a system without overpotential may be calculated by obtaining the potential from Laplace's equation,  $\nabla^2\phi = 0$ , in the interior of

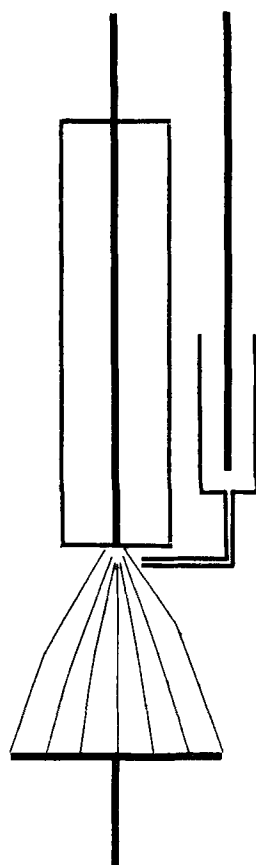


Fig. 3. Current streamlines near a microelectrode

the solution together with the boundary conditions (electrodes at preassigned potentials), the current being determined by Ohm's law from the potential distribution. In the presence of activation overpotential, the boundary conditions should assign potential drops at the electrode/solution interface which are a given function of the local current density. For an activation controlled reaction in general this leads to a transcendental equation (which, however, is readily solved by computer methods). When concentration overpotential is present the situation is further complicated by the fact that the current distribution changes with time until the steady state is reached.

One means of dealing with the situation experimentally is to make the electrode surface as uniformly accessible as possible and to tolerate an  $iR$  drop which is known. This can be done by the device of placing the reference electrode at a point where it does not interfere significantly with the current streamlines and determining the  $iR$  contribution as outlined below.

#### *Determination of the Resistive Contribution to the Overpotential*

In the study of electrode reactions, substantial currents are sometimes experienced in the course of the study so that contributions to the observed potential from  $iR$  drop are not negligible. The electrode being studied is usually small, may be shielded, or embedded in a cylinder which is being rotated. Thus the placement of the reference electrode can rarely be optimum, that is, the current streamlines proceeding from the counter electrodes to the indicating electrode will lead to a potential distribution and the reference electrode is placed along this potential distribution in such a way that the potential difference between it and the indicator electrode may be considerable.

It is desired to identify this contribution in order that the maximum accuracy may be obtained. Let us assume that a placement of the reference electrode with respect to the indicating electrode has been devised and that the cell is constructed in such a way that the relative positions of the three electrodes are precisely maintained. We now face the problem of evaluating accurately the numerical value of the resistive contribution. It is important to notice that this is not the resistance measured between the reference electrode and the indicating electrode, since this resistance corresponds to the potential difference between the two electrodes for a current distribution which is different from that occurring when the current flows between the indicating and the counter electrode. We proceed as follows: the cell is filled with a solution which is known to behave quite reversibly at the electrodes. We then arrange to apply a signal between the counter electrode and the indicating electrode, the signal being a sinusoidal alternating voltage applied from the signal generator whose peak to peak value is measured as accurately as possible. The potential between the reference electrode and the indicating electrode is now measured as well and compared to that applied between the indicating and counter electrodes. This ratio may be taken at a series of applied frequencies. In the absence of large contributions from shunt capacitance and double layer effects it is expected that the ratio will not be strongly dependent on the frequency. If necessary, it is possible to obtain the ratio at a series of audio frequencies so that, by extrapolating towards zero frequency, the effective d-c resistance can be obtained.

When the cell is now filled with the electrolyte which is to be used in the experiment, the resistance between the working electrode and the indicating electrode is now carefully measured with an alternating current bridge (as a function of frequency if necessary). When the d-c resistance for unpolarized electrodes has been calculated by extrapolation of the a-c value, the effective resistance between the ref-

erence electrode and the indicating electrode is obtained by multiplying this d-c resistance by the limiting value of the ratio obtained above.

This effective resistance can be determined readily with care to four significant figures. (Naturally, double layer corrections, where applicable, would then have to be made.)

When a relationship between the applied potential and the observed current has been obtained, the con-

tribution to the potential arising from  $iR$  drop can be evaluated by simply subtracting from the quantity  $i \times \tau_{\text{eff}}$ , either manually or by appropriate instrumentation.

Manuscript received Oct. 5, 1967; revised manuscript received Nov. 6, 1967.

Any discussion of this paper will appear in a Discussion Section to be published in the December 1968 JOURNAL.

## Brief Communications



### Ion Exchange Membrane Separators for Organic Electrolyte Batteries

A. N. Dey\*

*P. R. Mallory & Co., Inc., Laboratory for Physical Science, Burlington, Massachusetts*

The self-discharge of the nonaqueous Li/CuCl<sub>2</sub> cell has been attributed to the dissolution of the cathode salt in the organic electrolyte (1, 2). The dissolution was caused by the formation of highly soluble chlorocuprate complexes, CuCl<sub>3</sub><sup>-</sup> and CuCl<sub>2</sub><sup>-</sup> (2) which were reduced at the anode. The self-discharge process may be suppressed by a thermodynamic control of the complexation equilibria (1) or by a kinetic control of the rate of reduction or rate of transfer of the oxidant to the anode. We report here on the feasibility of using ion-specific membranes to retard the diffusion of chlorocuprate complexes in organic electrolyte systems.

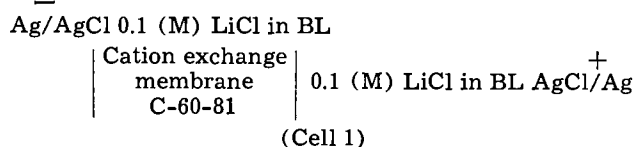
Data on the behavior of ion exchange membranes or resins in organic solvents like propylene carbonate (PC) and  $\gamma$ -butyrolactone (BL) are scarce. The extent of permselectivity of conventional ion exchange membranes in the above solvents has not yet been established. It has been attempted here to demonstrate the existence of permselectivity of a conventional ion-exchange membrane in BL by studying the transference and self-diffusion properties of the counter ion and co-ions of the membranes.

#### Experimental

**Membrane.**—The ion exchange membrane used was a cation exchange membrane (C-60-81) supplied by American Machine and Foundry Corporation. The membrane was converted into the lithium form by equilibrating with aqueous LiCl solutions for three days with occasional change of solution. The end of conversion was determined by testing aliquots of the LiCl solution for acid. The membrane was superficially dried before use.

**Solutes.**—Anhydrous LiCl, CuCl<sub>2</sub> (Fisher Scientific certified), LiClO<sub>4</sub>, and AgClO<sub>4</sub> (G. Frederick Smith Chemical Company) salts were used as received.

**Transference number.**—The transference number of Li<sup>+</sup> through the cation-exchange membrane (C-60-81) was determined using a cell of the following composition (3).



\* Electrochemical Society Active Member.

The construction of the cell is shown in Fig. 1. The reversible Ag/AgCl electrodes (A) were prepared by pressing thin foils of AgCl on both sides of a silver screen. The electrodes did not show significant polarization at current densities as high as 5 ma/cm<sup>2</sup>. The total capacity of the Ag/AgCl electrode was approximately 100 ma hr. The membrane (B) and the 'O' ring (C) were placed between the two halves of the cell which were clamped together. The 'O' ring provided an adequate seal.

The transference number of Li<sup>+</sup> ion was established by determining the total amount of Cl<sup>-</sup> ion in the anode chamber before and after the passage of the current. The amount of Cl<sup>-</sup> ions in the BL solution was determined by potentiometrically titrating the solutions with standard (0.1(M)) AgClO<sub>4</sub> solutions in BL. The inflexions at the end point were extremely sharp, thus enabling accurate determination of very small concentration changes of the Cl<sup>-</sup> ion.

The procedure was as follows. First, 10 cc of 0.1 (M) LiCl in BL (stock solution) was titrated with standard AgClO<sub>4</sub> solutions in BL. Both anode and cathode compartments of the cell were then filled with 10 cc each of the 0.1(M) LiCl in BL. A current of 0.5 ma (0.25 ma/cm<sup>2</sup>) was passed through the cell for 2 hr.

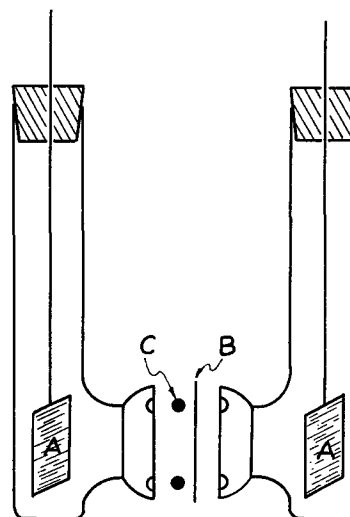
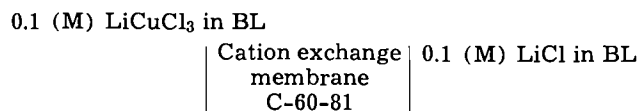


Fig. 1. The cell for transference number measurement. (A) Ag/AgCl electrode, (B) Cation exchange membrane, (C) 'O' ring.



The solution in the anode compartment was then removed, the compartment rinsed with BL, and the combined solution and rinsings titrated with standard  $\text{AgClO}_4$  solution. The change in  $\text{Cl}^-$  ion in the compartment due to the passage of current was determined from the difference in titration values.

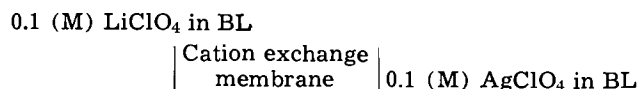
*Diffusion flux.*—The cell used for diffusion flux measurements was identical with that of Fig. 1, except that there were no  $\text{Ag}/\text{AgCl}$  electrodes. The arrangement used to determine the diffusion flux of copper species, e.g.,  $\text{CuCl}_3^-$  through the membrane, was



The diffusion flux of the copper species from the left compartment to the right compartment was determined by following the concentration of copper (polarographically) or  $\text{CuCl}_3^-$  by visual color matching (the solutions of  $\text{CuCl}_3^-$  were highly colored) in the right compartment as a function of time.

The 0.1 (M)  $\text{LiCuCl}_3$  was prepared by taking excess  $\text{CuCl}_2$  in 0.1 (M)  $\text{LiCl}$  in BL. It was shown (2) before that the moles of  $\text{CuCl}_2$  dissolved in BL were roughly equivalent to the moles of  $\text{LiCl}$  present in BL. This was presumed to be due to the formation of highly soluble chlorocuprate complex, e.g.,  $\text{LiCuCl}_3$ .

The arrangement used for determining the diffusion flux of the counter ion,  $\text{Li}^+$ , through the membrane was



The flux of  $\text{Li}^+$  from the left to the right compartment was determined by monitoring the concentrations of lithium in the right compartment by flame photometry (Beckman Du Flame Spectro photometer Model 2400) as a function of time. The  $\text{Ag}^+$  ion was chosen as the cation in the right compartment to avoid interference in flame photometric determination of lithium.

*Sorption measurement.*—Sorption of the copper species by the ion exchange materials was studied by equilibrating known weights of the ion exchange materials with solutions of known concentration of copper in BL and analyzing the solution for the copper after the equilibration. The ion exchange materials used were cation exchange resin, Rexyn (101) and anion exchange resin, Rexyn RG (1) (from Fisher Scientific Co.) and cation exchange membrane C-60-81 and anion exchange membrane A-103-FF (from American Machine & Foundry Corporation). These materials were converted to the  $\text{Li}^+$  and  $\text{Cl}^-$  forms from the  $\text{H}^+$  and  $\text{OH}^-$  forms, respectively, by equilibration with aqueous  $\text{LiCl}$  for one week with occasional change of solution.

The ion exchange materials were weighed after superficial drying. The actual weight of the materials was determined by taking into consideration the amount of water retained according to the manufacturer's specifications. The quantity of the materials used for equilibration with the copper species was such that the total capacity if the ion exchange materials was in excess (approximately ten times) compared to the copper species available in solution. Thus, the presence of small amounts of sorbable copper species could be detected.

The equilibration was carried out by stirring the ion exchange material and the BL solutions of the copper species in a conical flask for three days. No attempt was made to determine the completion of the exchange. The solutions were analyzed for copper polarographically at the beginning and end of the equilibration.

## Results and Discussion

A truly permselective membrane should exclude the co-ions and permit only the counter ions to pass. For a univalent counter ion the transference number through an ideally permselective membrane should be unity. Thus, the determination of the transference number of the counter ion ( $t_+$ ) of an ion exchange membrane gives direct indication of the degree of permselectivity of the membrane.

Considering the cell reaction, it will appear that with electrolysis there will be a decrease in the  $\text{Cl}^-$  ion concentration in the anode compartment. If only the  $\text{Li}^+$  ion is transferred (i.e.,  $t_{\text{Li}^+} = 1$ ), the decrease in  $\text{Cl}^-$  ion will be 1 mole for each faraday. Thus, the transference number for  $\text{Li}^+$  can be determined by using the following relationship

$$t_{\text{Li}^+} = \frac{M_{\text{Cl}^-}^0 - M_{\text{Cl}^-}}{Q} \quad [1]$$

where,  $M_{\text{Cl}^-}^0$  = initial number of moles of  $\text{Cl}^-$  ion in the anode compartment,  $M_{\text{Cl}^-}$  = number of moles of  $\text{Cl}^-$  ion in the anode compartment after passage of  $Q$  faradays of charge. In the above experiments, the total amount of  $\text{Cl}^-$  ion was determined instead of the concentration in order to avoid the errors due to the volume change as a result of electroosmotic solvent transport. The average value of  $t_{\text{Li}^+}$  determined from three experiments was  $0.98 \pm 0.01$ .

The degree of permselectivity  $P$  for an ion exchange membrane can be expressed (4) as

$$P = \frac{t_M - t_S}{1 - t_S} \quad [2]$$

where  $t_M$  = transference number of the univalent counter ion through the membrane and  $t_S$  = transference number of the same ion through the solution. For an ideally permselective membrane  $P \approx 1$ . Using the value of  $t_S$  for  $\text{Li}^+$  as 0.23 [experimental (5) value in  $PC$  is 0.20 and in  $DMF$  is 0.25] and  $t_M$  as 0.98, the degree of permselectivity  $P$  was calculated using Eq. [2]

$$P = 0.97$$

This indicates that a reasonably high degree of permselectivity exists in the nonaqueous system with respect to  $\text{Li}^+$  ion for the cation exchange membrane under consideration.

The results of the sorption measurements are expressed in terms of per cent of initial copper (present in solution) sorbed by the ion-exchange material at the end of the equilibration and are shown in Table I. The results in Table I show that the copper species in solution are preferentially sorbed by the anion exchange materials, thus qualitatively confirming that the copper species in solution are mainly in the anionic ( $\text{CuCl}_3^-$ ) form. The fact that the copper species are preferentially excluded by the cation exchange materials also indicates that the cation exchange mem-

Table I. Sorption of copper species from BL solutions of  $\text{LiCl}$  and  $\text{CuCl}_2$

Ion exchange materials	Concentration of copper species in BL in moles/liter in 100 cc of total solution		Per cent of initial copper species sorbed by the ion exchange materials
	Initial	Final	
Anion exchange resin	$2 \cdot 28 \times 10^{-3}$	$2 \cdot 35 \times 10^{-4}$	90
Anion exchange membrane	$2 \cdot 28 \times 10^{-3}$	$5 \cdot 10 \times 10^{-4}$	80
Cation exchange resin	$2 \cdot 28 \times 10^{-3}$	$1 \cdot 99 \times 10^{-3}$	12
Cation exchange membrane	$2 \cdot 28 \times 10^{-3}$	$2 \cdot 12 \times 10^{-3}$	7

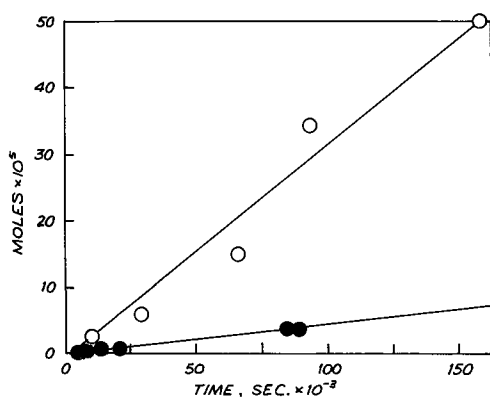


Fig. 2. Diffusion flux of  $\circ$  lithium and  $\bullet$  chlorocuprate complex through the cation exchange membrane.

branes could be permselective with respect to the copper species.

Another indication of permselectivity was obtained from the self-diffusion measurements of the  $\text{Li}^+$  ion (counter-ion) and the copper species (co-ion) through a cation exchange membrane (e.g., C-60-81). It can be shown (3) that for a permselective membrane at moderate concentrations of the electrolyte (e.g., less than 1M), the self-diffusion flux of the counter-ions should be considerably greater than the self-diffusion flux of the co-ion. The results of the diffusion flux measurements for the counter ion and the co-ion of the cation exchange membrane C-60-81 in BL are shown in Fig. 2. The diffusion flux of the copper species obtained from the slope of the linear plot was  $2 \cdot 40 \times 10^{-10}$  moles/sec  $\text{cm}^2$ . This flux could be either the diffusion flux of the  $\text{Cl}^-$  ion from the right to the left compartment or the flux of the  $\text{CuCl}_3^-$  ion from the left to the right compartment of a cell, whichever is lower (controlling). It is reasonable to assume from the ion sizes that the self-diffusion flux of the  $\text{CuCl}_3^-$  ion will be lower than that of the  $\text{Cl}^-$  ion as the self-diffusion is mainly dependent on the mobility (3) of the species through the membrane.

The diffusion flux of the counter ion,  $\text{Li}^+$ , obtained from the linear plot was  $3 \cdot 0 \times 10^{-9}$  moles/sec  $\text{cm}^2$ . Again this value represents the diffusion flux of either the  $\text{Ag}^+$  ion or the  $\text{Li}^+$  whichever is controlling. Thus, the comparison between the two values will still be valid. The diffusion of the counter ion is one order of magnitude higher than that of the co-ion. Thus, it is established that ion exchange membranes C-60-81 can be permselective with respect to the dissolved chlorocuprate complex in organic solvents like BL.

The feasibility of retarding the self-discharge of  $\text{CuCl}_2$  cathodes in  $\text{Li}/\text{CuCl}_2$  organic rechargeable systems by using ion exchange membranes is indicated from the above work. Further work in this direction is therefore warranted.

#### Acknowledgment

The author wishes to thank Dr. Per Bro and Dr. J. R. Huff for helpful discussions and Mr. R. W. Holmes for some experimental assistance. Some of this work was carried out under USAMERDC Contract No. DA-44-009-AMC-1537 (T).

Manuscript received Oct. 30, 1967.

Any discussion of this paper will appear in a Discussion Section to be published in the December 1968 JOURNAL.

#### REFERENCES

1. M. L. B. Rao and K. R. Hill, "Evaluation of Rechargeable Lithium-Copper Chloride Organic Electrolyte Battery System." Technical Report No. 2, March, 1967, U.S. Army Mobility Equipment Research and Development Center, Contract No. DA-44-009-AMC-1537 (T), P. R. Mallory & Co. Inc.
2. M. L. Bhaskara Rao, *This Journal*, **114**, 13 (1967).
3. F. Helfferich, "Ion Exchange," McGraw-Hill Book Co., Inc., New York (1962).
4. A. G. Winger, G. W. Bodamer, and R. Kunin, *This Journal*, **100**, 178 (1953).
5. R. Keller, J. N. Foster, J. F. Hon, O. F. Kalman, and J. M. Sullivan, "Properties of Nonaqueous Electrolytes." Fourth Quart. Rept. No. NASA CR-72277, R-6754-4. Rocketdyne Corp., July 1967.

## On the Role of Lattice Vacancies in Metal Dissolution

D. A. Vermilyea\*

General Electric Research and Development Center, Schenectady, New York

It is usually considered that the dissolution of a clean metal in aqueous solutions takes place by removal of atoms from kink sites in surface steps. The edges of the crystal, as well as screw dislocations, normally provide an abundance of step sources, and under such conditions the driving force at the interface is not great enough to remove atoms from sites other than kink sites.

During corrosion, and especially during stress corrosion, however, a situation which differs in two important respects may be encountered. First, because of the passivity phenomenon the potential may be far more positive than that for the reversible metal-metal ion system. Second, the clean area available for reaction may be minute, especially if this clean area is generated by deformation of the substrate. It is the purpose of this note to consider dissolution when the driving force is high and when no dislocations intersect the bare surface.

Imagine a clean metal surface of arbitrary shape produced, for example, by the emergence of a slip

step on the metal surface and concomitant rupture or drastic thinning of the passive film. The metal will dissolve rapidly because the driving force is high and the surface has high index faces which are stepped. Very shortly, however, the pit will be bounded by low index faces without steps, and rapid dissolution will cease. The surface is now clean but, because there are no kinks, it is unreactive as shown by the following nearest-neighbor calculation.

The activation energy,  $\epsilon$ , for dissolution from a kink site is typically 0.5 ev. An equation valid for high overvoltage is of the type

$$i = zen\nu \exp - (\epsilon - \alpha zF\eta)/kT \quad [1]$$

where  $n$  is the kink density,  $\nu$  the vibration frequency,  $e$  the electronic charge,  $\eta$  the overvoltage, and where the other symbols have the customary meanings. If  $n = 10^{11} \text{ cm}^{-2}$ ,  $\nu = 10^{13} \text{ sec}^{-1}$ ,  $\alpha = 0.5$ , and  $\eta = 0.15\text{v}$ , the current density calculated from this equation for a divalent metal is about 0.3 amp/cm<sup>2</sup> at room temperature, which is plausible. An atom at a kink site on the close packed plane of a face centered cubic metal has

\* Electrochemical Society Active Member.

six nearest neighbor bonds, the strength of each of which is thus  $H_v/6$  where  $H_v$  is the enthalpy of vaporization of the metal. At a site within the close packed plane the atom has nine nearest neighbor bonds, and thus has an additional binding energy of  $H_v/2$ . The activation energy for dissolution would be expected to increase by at least  $H_v/2$ . Using Eq. [1] with  $n = 10^{15} \text{ cm}^{-2}$  then gives for  $H_v = 3.0 \text{ eV}$  a current density of  $10^{-22} \text{ amp/cm}^2$  at  $\eta = 0.15v$ . While this calculation assumes direct transfer at kink sites the same conclusion would be reached if a mechanism involving adsorbed atoms was considered.

The atoms adjacent to a surface vacancy have 8 nearest neighbor bonds, while those near a divacancy have only 7 bonds. The average time required to remove an atom from a vacancy is smaller than from the close packed plane by the factor  $\exp(H_v/6kT)$ , or about  $10^9$  for  $H_v = 3 \text{ eV}$ . At a divacancy the time is  $10^{18}$  times smaller. Suppose the surface has some vacant lattice sites and that the overvoltage is increased until the average time to remove an atom near a vacancy is  $10^2 \text{ sec}$ ; the required overvoltage is about  $0.6v$  for our example. Such an overvoltage would give the negligible current of  $10^{-14} \text{ amp/cm}^2$  from the close packed plane. If there are  $10^{12}$  vacancies per  $\text{cm}^2$ , however, then  $10^{10}$  atoms per  $\text{cm}^2$  would be removed per second near vacancies. Each divacancy created by this process becomes a step nucleus, for the time to remove succeeding atoms from such sites is only  $10^{-7} \text{ sec}$ . A rough estimate of the dissolution current density can be made by noting that  $10^7$  nuclei/ $\text{cm}^2$  would be created in  $10^{-3} \text{ sec}$  and that the steps generated from these nuclei would impinge in about  $10^{-3} \text{ sec}$ . Hence the time to remove an atomic layer would be of the order of  $10^{-3} \text{ sec}$ ; the corresponding current density is  $0.3 \text{ amp/cm}^2$ .

The absolute values obtained in these calculations should not be taken very seriously, and the only point

to be made is that at high overvoltages lattice vacancies may serve as step nuclei. It is also worth noting that divacancies are even more efficient nuclei than are vacancies. If impurities associate with vacancies, then the dissolution of the impurity, which might be more rapid than removal of a solvent atom, can create a divacancy. Conversely, impurities which are more noble could retard step nucleation at a vacancy.

There are two interesting consequences of this possible role of lattice vacancies. The first is that it provides a mechanism for very restricted dissolution during stress corrosion cracking. A slip band may contain many lattice vacancies and be rapidly corroded, while the lattice on each side may be relatively perfect and corrode more slowly. Corrosion tunnels could be formed if the debris was suitably distributed on the slip band. For such a mechanism to be effective it is necessary that steps from dislocation sources be absent or blocked. Steps from sources back along the crack may be blocked by the passive film, but eventually the sides of an advancing crack will encounter other screw dislocations, and it seems that they should be effective step sources. It is not obvious why the crack should not then be rapidly widened; the answer may lie in the mechanism of repassivation, the details of which are poorly understood.

The second consequence is that the injection of vacancies during dissolution of solid solutions appears unlikely. If the overvoltage is raised sufficiently to create vacancies, the vacancies are automatically step sources and have a negligible lifetime.

Manuscript received Oct. 30, 1967.

Any discussion of this paper will appear in a Discussion Section to be published in the December 1968 JOURNAL.

### Correction

To the paper by T. B. Warner, S. Schuldiner, and B. J. Piersma, "On the Activity of Platinum Catalysts in Solution I. Effects of Thermal Treatment and Chemical Etching on the Pt-O/hydrogen Specific Reaction Rate," *This Journal*, **114**, 1120 (1967).

The photograph given in Fig. 2 came out poorly in reproduction and the flat regions discussed in the section entitled *Thermal Annealing* could not be seen. The photograph should have appeared as reprinted here.

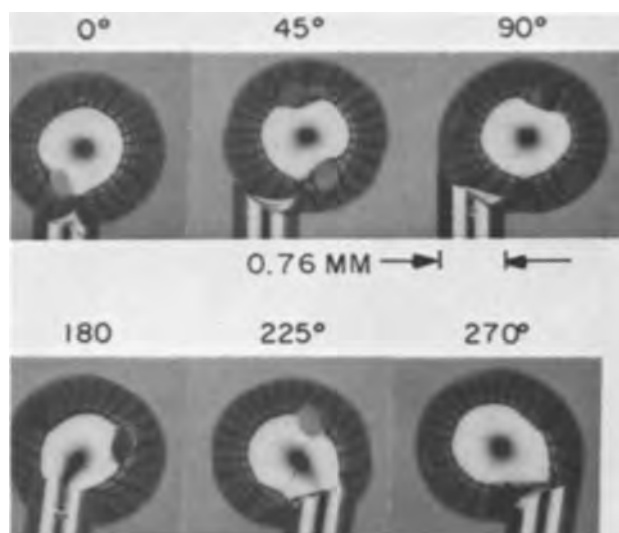


Fig. 2. Views of flame-formed platinum bead at various approximate amounts of clockwise rotation. Magnification  $\approx 12X$ . Photos by A. C. Simon.

# "Electrolytic Rectification and Conduction Mechanisms in Anodic Oxide Films"

A Symposium on the "Electrolytic Rectification and Conduction Mechanisms in Anodic Oxide Films" was held at the 131st National Meeting of The Electrochemical Society in Dallas, Texas, May 7-12, 1967. This symposium was sponsored by the Dielectrics and Insulation Division and organized by P. F. Schmidt to bring together the many workers in the field to discuss the current status in this area. Anodic oxides have been used for over fifty years in wet and dry capacitor and rectifier structures, yet concrete mechanisms for asymmetric conduction in these thin dielectric layers have not been completely elucidated. This complexity can be attributed to both the very thin nature (100-5000Å thick) and amorphous state of the oxide which probably lead to the existence of several mechanisms of conduction. These mechanisms have sufficient similar observable conduction characteristics to require extremely careful experimental techniques and diagnostic tests which have not been pursued in all investigations. Moreover, the amorphous state of the oxides, their high impurity content, and the low mobilities of the charge carriers have provided conceptual difficulties since the conventional energy band picture for single crystal or polycrystalline solids may be inadequate for describing transport properties.

Most of the papers presented in this Symposium appear in this issue of the Journal, but for completeness the actual symposium consisted of the following papers:

- \*1. "On the Mechanisms of Electrolytic Rectification," by P. F. Schmidt, Bell Telephone Laboratories, Allentown, Pa.
- \*2. "Anodic Films, Protons, and Electrolytic Rectification," by D. A. Vermilyea, General Electric R&D Center, Schenectady, New York.
- \*3. "Ionic Transport and Membrane Potentials in Amorphous Oxides," by R. H. Doremus, General Electric R&D Center, Schenectady, New York.
- \*4. "Electroluminescence and Conduction in Anodic Films," by T. W. Hickmott, IBM, East Fishkill Facility, Hopewell Junction, New York.
- \*5. "Asymmetric Conduction in Thin Film Tantalum/Tantalum Oxide/Metal Structure," by N. Schwartz and N. N. Axelrod, Bell Telephone Laboratories, Murray Hill, N. J.
- \*6. "Conduction Mechanism in Tantalum Thin Film Capacitors," by I. F. M. Walker, Northern Electric Co. R&D Laboratories, Ottawa, Ont., Canada.
- \*7. "Conduction and Stoichiometry in Heat-Treated Anodic Oxide Films," by D. M. Smyth and G. A. Shirn, Sprague Electric Co., North Adams, Mass.
- \*8. "Conduction Mechanisms in Annealed Ta/Ta<sub>2</sub>O<sub>5</sub> Structures," K. Lehovc, Sprague Electric Co., North Adams, Mass.
- \*9. "Oxygen Evolution of Semiconducting TiO<sub>2</sub>," by P. J. Boddy, Bell Telephone Laboratories, Murray Hill, N. J.
- \*10. "On the Rectification of Anodic Oxide Films of Titanium," by F. Huber, Radio Corporation of America, Somerville, N. J.
- \*11. "Equilibrium Properties of the Space Charge Injected into an Insulator by an Electrolyte," J. M. Hale, Cyanamid European Research Institute, Cologny, Geneva, Switzerland.
- \*12. "The Dynamic Current-Voltage Characteristics of Porous Anodic Oxides in Aluminum," C. E. Michelson, Metals Research Laboratories, Olin Mathieson, New Haven, Conn.

Both the metal/oxide/electrolyte and the metal/oxide/metal systems were treated. Three papers (Boddy, Hale, and Doremus) tried to approach the subject from a comparative point of view by correlating electrode effects of "bulk" materials with the electrical properties of thin insulating films (by "bulk" is meant  $\gg 1000\text{\AA}$ ). P. J. Boddy presented evidence that the primary step in the mechanism of electronic current flow through semiconducting TiO<sub>2</sub> electrodes, biased anodically in contact with an electrolyte, is electron tunneling from lattice oxide ions at the oxide/electrolyte interface. An interesting and apparently hitherto unexplored effect is the insensitivity of the semiconducting TiO<sub>2</sub> electrode to the kind of ions in the electrolyte, whereas the anodic current density of insulating oxide films appears to be sensitive to the redox potential of the electrolyte.

J. M. Hale treated the insulator/electrolyte system from the theoretical point of view assuming that the oxide is ideally perfect. The predictions of the theory can be checked by means of anthracene electrodes, single crystals of this material being available in good quality. Recent work (Hale, Gerischer) seems to indicate that injection of protons can assist the potential bending inside the solid to the extent that hole injection by the electrolyte becomes possible under conditions where the redox potential of the solution would not suffice by itself.

A group of papers (Doremus, Schmidt, Vermilyea, Michelson) was concerned with the injection and motion of protons in oxide films. R. H. Doremus reviewed the ionic transport and membrane potentials at the interface amorphous oxide/aqueous electrolyte, with emphasis on fused silica for which system the theory is well advanced. The surface hydration and injection of protons into thin anodic oxide films is obviously a closely related subject.

P. F. Schmidt presented evidence that hydration of anodic SiO<sub>2</sub> films is a prerequisite for proton injection, the latter in turn being required to cause appreciable current flow, due either to enhanced field emission or to space charge neutralization of trapped electrons. He also provided a literature review from 1960-1966 of papers dealing directly or indirectly with electronic and/or protonic current flow through oxide films. The paper by D. A. Vermilyea consisted of an analysis of the discrepancies between results obtained from current-voltage and from capacitance-voltage curves on tantalum and niobium pentoxide films. While the evidence for proton injection is very strong, especially when comparing results obtained with H<sub>2</sub>O to those obtained with D<sub>2</sub>O, it appears quite likely that electronic currents are responsible for some of the observed discrepancies.

C. E. Michelson analyzed the current-voltage characteristics of porous Al<sub>2</sub>O<sub>3</sub> films; his model is based on proton transfer in a hydrogen-bonded network assumed to exist in the partially hydrated oxide film.

The substrate metal/oxide interface was the subject of two papers. Ta/Ta<sub>2</sub>O<sub>5</sub> or Nb/Nb<sub>2</sub>O<sub>5</sub> structures show an enhanced conductivity after annealing in air at 300°-500°C, which is apparently due to the gettering of some oxygen from the oxide by the substrate metal. D. M. Smyth and G. A. Shirn treated an exponential conductivity profile in the oxide after annealing, whereas K. Lehovc fitted the data to a model of tunneling from and to states in the oxide. Detailed studies of the interface substrate metal/oxide are clearly very important in understanding the electrical properties of thin oxide films. Studies on double injection and recombination luminescence, in which the injecting properties of the substrate are varied in controlled fashion, would be of considerable interest.

Control of the current flow not by barriers at the interface but by electronic processes in the bulk of the thin film was the topic of papers by T. W. Hickmott and by F. Huber. The paper by Hickmott, who was able to present a fairly detailed energy band picture for anodic Nb<sub>2</sub>O<sub>5</sub>, including an impurity band located 1.2 eV below the oxide conduction band, served to highlight the danger in carrying generalization about any mechanism of electrolytic rectification too far. Clearly the density and location in energy of impurity states will vary from one metal oxide to the next. Hickmott also presented conclusive evidence for double injection in Nb<sub>2</sub>O<sub>5</sub> film, the hole injection being dependent on the work function of the outer metal contact. Hickmott's work raises the interesting question whether the p-i-n junction observed by Huber in anodic oxide films on titanium is due to hole injection

\* These papers appear in this Journal issue.

† This material can be found in *J. Appl. Phys.*, 37, 4380 (1966); *J. Electrochem. Soc.*, 113, 1223 (1966).

‡ These papers will be submitted to the Journal.

from the high work function metal contact [as also observed for CdS by Boer and Ward, *Phys. Rev.*, **154**, 757 (1967)], or whether the p-region indeed exists in the outer oxide surface as a consequence of the anodic growth mechanism in the electrolyte used by Huber; the high work function contact metal would then be required only to make ohmic contact to the p-region. The field effect transistor action reported by Huber is certainly of considerable interest.

Evidence for the existence of electrical flaws in thin Ta/Ta<sub>2</sub>O<sub>5</sub> metal structures and the effect of impurity additions to the tantalum substrate on the number and perhaps kind of flaws was presented by N. Schwartz and N. N. Axelrod. Such additions can decrease the number of flaws and thereby also the degree of asymmetry of the electrical properties of the oxide. It is rather surprising that while additions of 10-30 a/o (atom per cent) of such elements as N, O, or C are

required to affect the number of flaws appreciably, as little as 1 a/o of Mo is sufficient for this purpose. Here is clearly a vast and as yet hardly touched field for further material research.

Space charge limited current flow and trap distribution in anodic oxide films on tantalum, as well as drift phenomena on aging which may permit predictions concerning the reliability of devices, was studied by I. M. Walker.

The symposium raised many interesting questions and final answers are still to be sought in many areas. This collection of papers will serve as a current review of the field and hopefully will stimulate further detailed experimental and theoretical work on this subject.

Paul F. Schmidt  
Newton Schwartz

## On the Mechanisms of Electrolytic Rectification

P. F. Schmidt\*

*Bell Telephone Laboratories, Incorporated, Allentown, Pennsylvania*

### ABSTRACT

A literature survey of papers dealing with electrolytic rectification and related topics is given for the period 1959-1966. Experiments on current flow in the system n-type Si/SiO<sub>2</sub>/electrolyte are then presented, which indicate the importance of adsorbed water for the electrical properties of this system. The initial increase in conductivity after exposure of the anodic SiO<sub>2</sub> film to water is likely to be of electronic origin. However, protons can be injected at low voltages into the hydrated SiO<sub>2</sub> but not into dry SiO<sub>2</sub>. The injected protons cause a gradual increase of current with time at constant voltage due to enhanced field emission from traps and/or from the cathode. Hydration of the oxide, and its electrical properties, can be reversed by a bake at 150°C in air. Either alkali ions or protons, or both, incorporated into an anodic oxide film by anodization in an incompletely "dry" organic solvent, have a strong effect on lowering the cathodic breakdown voltage at which the current begins to increase with time at constant voltage.

When we first started to concern ourselves with the mechanism of electrolytic rectification, some ten years ago, we approached the problem from the point of view that there ought to be a common cause to the seemingly common phenomenon of oxide covered valve metals passing large currents when biased cathodically in an aqueous electrolyte. The common cause, we presumed, was the penetration of protons into anodic oxide films under cathodic bias in aqueous solution. We, therefore, set forth to prove that no appreciable current would flow in an aprotic solvent like liquid sulfur dioxide in the presence only of large cations like rubidium. This prediction certainly proved correct, but we also came across some unexpected phenomena which we could not explain at the time. We should like to summarize here briefly the main points of that work, published in 1960 with Huber and Schwarz (1), because the results will be of interest in connection with more recent work.

Large alkali ions like K<sup>+</sup> and Rb<sup>+</sup> were found to block the cathodic current very effectively in liquid SO<sub>2</sub>, and up to quite large voltages, whereas small alkali ions like Na<sup>+</sup> and Li<sup>+</sup> pass currents as much as a factor of 10<sup>5</sup> larger at the same applied voltage. Addition of water to the solutions of Rb<sup>+</sup> or K<sup>+</sup> in liquid SO<sub>2</sub> is unimportant, the water apparently freezes out or is complexed without affecting the electrode reaction. At low cathodic voltages, however, the picture was inverted and the larger cations gave somewhat larger currents. Apparently, the large cations are adsorbed to the oxide surface, whereas the small cations are not and must first displace other adsorbed

species under cathodic bias before they can become effective. It was definitely not possible to account for the effect by assuming that Na<sup>+</sup> or Li<sup>+</sup> is able to penetrate into the oxide films, especially in view of the observation that the current in solutions containing a mixture of Rb<sup>+</sup> and Na<sup>+</sup> iodide fluctuated between small and large values. It is difficult to see how the current could decay again once sodium ions have penetrated into the oxide, whereas an explanation is readily available if competing adsorption to the surface of the oxide is held responsible. Vermilyea (2) has since shown for Ta<sub>2</sub>O<sub>5</sub>, one of the oxides studied by Schmidt *et al.* (1), that penetration of sodium ions is not possible even at room temperature. He also showed that Li<sup>+</sup> ions can penetrate from certain non-aqueous solvents but not from aqueous solution where they are apparently too strongly bonded. The same apparently applies to Li<sup>+</sup> in liquid SO<sub>2</sub>, where it is known to be very strongly complexed.

Another remarkable effect was the large activation energy for cathodic current flow in Ta<sub>2</sub>O<sub>5</sub> in the presence of Na<sup>+</sup> and Li<sup>+</sup> ions, *i.e.*, much larger rates coupled with much higher activation energies. Figures 1 and 2 illustrate these points.

The most plausible explanation at the time was that the high local field in the vicinity of a small cation is able to extract electrons from traps in the forbidden gap of the insulator. The inefficiency of the large cations to promote cathodic current flow was attributed to the lower local field strength in their vicinity. A possible alternate explanation arises from the higher deposition potential of the larger alkali ions: an electron arriving at the oxide/electrolyte interface would

\* Electrochemical Society Active Member.

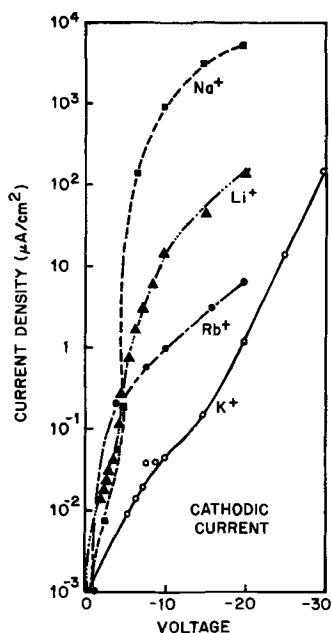


Fig. 1. Cathodic current in the system Ta/Ta<sub>2</sub>O<sub>5</sub>/liquid SO<sub>2</sub> as a function of cation size. Ta/Ta<sub>2</sub>O<sub>5</sub> formed to +50v, temperature of measurement -60°C. [Fig. 2 of ref. (1)].

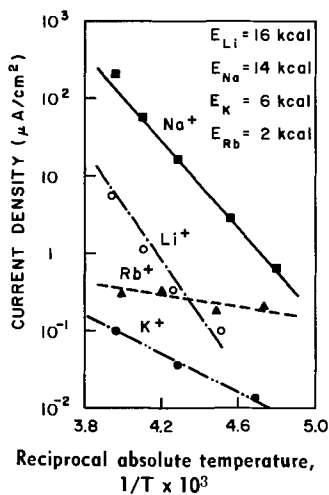


Fig. 2. Apparent activation energies for cathodic current flow in the system Ta/Ta<sub>2</sub>O<sub>5</sub>/liquid SO<sub>2</sub> as a function of cation size. Ta/Ta<sub>2</sub>O<sub>5</sub> formed to +50v, cathodic field strength  $9.0 \times 10^5$  v/cm. [Fig. 7(a) of ref. (1)].

see a higher barrier. Expressing this in another manner: the empty levels of the K<sup>+</sup> and Rb<sup>+</sup> ions in solution may be located above the conduction levels for electrons in the oxide. It is worth noting, however, that the explanation offered for Na<sup>+</sup> and Li<sup>+</sup> ions should still apply because the cathodic current in the case of these ions is many orders of magnitude larger than with high work function metal contacts.

Two other, and apparently contradictory findings concerned the conductivity of thin anodic Al<sub>2</sub>O<sub>3</sub> windows sandwiched between two aqueous electrolyte contacts and the increased conductivity of tantalum pentoxide films with platinum contacts when inserted in a hydrogen atmosphere. It was found that the Al<sub>2</sub>O<sub>3</sub> window passed negligible currents when a bias was applied between the two electrolyte contacts; this observation seemed to negate the penetration of protons into the alumina. The tantalum pentoxide with Pt contacts, on the other hand, showed increased conductivity in a hydrogen atmosphere under cathodic bias, which was largely removed under anodic bias. This experiment clearly pointed toward protonic con-

ductivity. Faced with this discrepancy, we chose not to say much about protons or aqueous contacts in our 1960 paper and limited ourselves mostly to the liquid SO<sub>2</sub> system.

We know now that the two results just quoted are not really as contradictory as they appeared to us at the time, and that it is a gross oversimplification to apply the same criteria to all anodic oxide films irrespective of their chemical composition. We shall hear more about these differences between individual metal oxides during the course of this meeting. It is also worth noting that our 1960 work was carried out exclusively on films 500Å or thicker; we thus missed the pronounced differences in the behavior of films in the 100-300Å range, since then discovered by Vermilyea (2).

In our 1960 paper we included a literature survey in addition to presenting our own work. We shall follow the same course here, taking 1959 as the starting point and in this manner trying to provide continuity of literature coverage.<sup>1</sup>

In this survey we shall include not only studies directly concerned with electrolytic rectification, but also other work which we feel is related to this problem. In doing so a certain arbitrariness of judgment has, of course, been unavoidable. I shall mention only very briefly the fascinating work by Vermilyea, Hickmott, Smyth, and Huber, since we shall have the pleasure of personal presentation by these researchers later in the symposium.

#### New Work since 1959

**Nonuniformity of anodic oxide films.**—The cathodic resistivity of sputtered and then anodized Ta films was shown by Schwartz and Gresh (5) to increase with decreasing size of the metal counter electrode, indicating the existence of "weak spots." The resistivity of the weak spots was shown to be very dependent on the relative humidity under anodic bias, whereas there was little effect of humidity under cathodic bias. The existence of weak spots is also known from the Al/Al<sub>2</sub>O<sub>3</sub>/Al thin film capacitor field, where weak spots can be destructively eliminated by biasing the sandwich into breakdown; the Al top electrode at the breakdown spots is either evaporated or converted to oxide. The emission of lights from "hot spots," as observed, for instance, by Hickmott (68) in his work on negative resistance in metal/oxide/metal sandwiches, is also indicative of "weak spots." One may presume that the occurrence of "weak spots" is related to the intrinsic purity of the substrate and to the perfection of surface treatment prior to anodization. Working with epitaxially deposited silicon films anodized immediately after epitaxy, the author has indeed found it quite difficult to detect weak spots; essentially the whole surface has uniform properties.

**Porosity of anodic oxide films.**—Politycki and Fuchs (6) showed by transmission electron microscopy (TEM) that SiO<sub>2</sub> films grown in N-methylacetamide/KNO<sub>3</sub> solution were free from pores, whereas SiO<sub>2</sub> films grown in aqueous borate solution are quite porous. In fact, the anodization of silicon in aqueous electrolytes bears distinct similarity to the anodization of aluminum in acidic solutions. Claussen and Flower (7) found some pores in SiO<sub>2</sub> grown in N-methylacetamide by means of TEM, but attributed the porosity to insufficient surface preparation. Schmidt *et al.* (8) showed by TEM that SiO<sub>2</sub> films grown in KNO<sub>2</sub>/tetrahydrofurfuryl alcohol (THFA) solution were completely free from pores. Duffek *et al.* (9) compared the "pin-hole" density of thermal and of anodic SiO<sub>2</sub>

<sup>1</sup> In the 1960 survey, reference was inadvertently omitted to the old but probably significant observations by Van Geel (3) that Cu<sub>2</sub>S or CuI pressure contacts to anodic Al<sub>2</sub>O<sub>3</sub> films give cathodic currents of the same magnitude as aqueous electrolytes. The p-i-n junction theory by Sasaki (4) appeared too late for inclusion in the survey, but a reference to a talk by Kobayashi on the same topic was included.

films, grown in a solution of  $\text{KNO}_3$  in ethylene glycol,<sup>2</sup> and found by means of the chlorine etching test that anodic films contained an order of magnitude fewer pin-holes than did the thermal  $\text{SiO}_2$  films.

*Adsorption on and penetration of protons into oxide films.*—The accepted picture of a solid oxide in contact with water is that of a hydration of the outermost or the outer oxide layers, with a certain mobility of protons in this structure. Wei and Bernstein (10) and Feitknecht *et al.* (11) measured the proton diffusivities in  $\text{AlO}(\text{OH})$ ,  $\text{Ni}(\text{OH})_2$ , and  $\text{FeOOH}$ , and found values between  $10^{-19}$  and  $2 \times 10^{-23}$   $\text{cm}^2 \text{sec}^{-1}$ . Onoda and De Bruyn (12) studied the system  $\text{Fe}_2\text{O}_3/\text{H}_2\text{O}$  and showed that a very fast surface reaction was followed by a slow diffusion of protons into a goethite-like interphase separating the bulk oxide from the solution. Proton conductivity in borax was studied by Maricic *et al.* (13) who observed that protonic conduction ceases below  $21^\circ\text{C}$ .

Schwabe (14) measured the release of tritium from alumina films, grown in tritiated solution, when an anodic bias was applied after transfer of the specimen to a nontracer solution. Krembs (15) published similar work on  $\text{Ta}_2\text{O}_5$ . Vermilyea (16) studied in detail the adsorption or desorption of protons on  $\text{Nb}_2\text{O}_5$  and  $\text{Ta}_2\text{O}_5$  films. In a later paper (17) he measured a potential dependent protonic space charge in thin anodic oxide films on Ta, Nb, Ti, W, and Sb, but could not detect the same effect on metals like Al, Zr, or Si; this may be attributable to a much lower mobility of protons in these latter oxides. The proton mobility in  $\text{Ta}_2\text{O}_5$  above  $25^\circ\text{C}$  seems to be indeed unusually large,  $10^{-7}$   $\text{cm}^2/\text{volt sec}$ ; below  $25^\circ\text{C}$  it drops sharply. The room temperature mobility of protons, introduced by electrolysis into vitreous silica, is only  $2.1 \times 10^{-23}$   $\text{cm}^2/\text{volt sec}$ , extrapolating the data by Hetherington *et al.* (18) and using their activation energy of 1.1 ev. [The activation energy for sodium migration in vitreous silica is 1.34 ev according to Owen and Douglas (19).] Hofstein (20) recently observed an extremely fast relaxation process in sodium contaminated thermal  $\text{SiO}_2$  films on silicon, which he attributes to protons. Even the mobility of this very fast species in  $\text{SiO}_2$  films is only  $1.7 \times 10^{-12}$   $\text{cm}^2/\text{volt sec}$  at room temperature, using the activation energy reported by Hofstein (0.68 ev) for the extrapolation. The higher mobility of protons in thermal  $\text{SiO}_2$  films as compared to vitreous silica is perhaps not unreasonable in view of the higher hydroxyl content and possible structural differences of the thermal film. Hofstein's measurements were taken at temperatures above  $27^\circ\text{C}$ . In view of the findings of Maricic *et al.* (13) and of Vermilyea (17) it would be of interest to determine the temperature at which protonic conduction in  $\text{SiO}_2$  ceases. The drift of sodium in thermal  $\text{SiO}_2$  films has, of course, been studied intensively in connection with silicon device work. Snow *et al.* (21) found the activation energy for sodium migration to be approximately the same as in vitreous silica (19). Hofstein (20), however, suggests that the activation energy measured by Snow *et al.* (21) actually applies to the release of the migrating species from a potential well at the outer oxide surface, and not to migration through the bulk of the oxide; the numerical agreement of the activation energy with that measured for sodium in vitreous silica (19) would thus be fortuitous. Yon *et al.* (22) used tracer counting techniques and stepwise dissolution of the oxide to measure the sodium distribution before and after drift. He showed on rather heavily sodium contaminated oxide films that the bulk of the sodium does not redistribute itself significantly during the fast relaxation process reported by Hofstein (20). Kerr (23), on the other hand, using lower levels of contamination and radioautographs in con-

junction with stepwise dissolution of the oxide, finds that all of the sodium reverts to the outer oxide surface.<sup>3</sup> Garino-Canina and Priqueler (24) and Hetherington *et al.* (18) studied the introduction of protons in vitreous silica by high-temperature electrolysis; protonic conductivity of the  $\text{SiO}_2$  is promoted by an aluminum content (or presumably other equivalent defects). Fowkes *et al.* (25) showed that the bulk of tritium incorporated into  $\text{SiO}_2$  by growing  $\text{SiO}_2$  at high temperatures in tritiated water is quite immobile under an applied bias. However, these tritium tracer experiments did not have the same sensitivity as electrical measurements on silicon, and a small fraction of highly mobile protons may have escaped detection. Mitchel and Salomon (26) investigated the permeation of aqueous  $\text{KNO}_3$  solution through anodic  $\text{ZrO}_2$  films, isolated from the substrate by etching in dry chlorine. Significant permeation rates, with an activation energy of 0.74 ev, were observed. The high activation energy, together with the reproducibility of the phenomenon, were considered as evidence that permeation occurs through a network of interstices, rather than through random gross flaws. Free diffusion in water requires activation energies of 0.17–0.22 ev. Dreiner (27) studied the increase in capacitance of anodic  $\text{SiO}_2$  films when in contact with water or a solvent containing water. The rate of capacitance increase obeys a square root of time relationship, with an activation energy 0.66 ev, and could be accelerated by application of a moderate anodic bias. Water is assumed to diffuse into the surface layers of the oxide film where it dissociates to form OH groups which can be acted on by the electric field. Schmidt and Rand (28) investigated the mutual transformation of thermal and anodic  $\text{SiO}_2$  films by anodic or heat-treatment, respectively. The thermal and anodic  $\text{SiO}_2$  films are structurally different, the volume of the anodic  $\text{SiO}_2$  being about 3.8% larger, depending on the electrolyte used. Anodization of thermal  $\text{SiO}_2$  films introduces a hydroxyl band in the IR spectrum of the bulk oxide and increases drastically the insulation resistance of the thermal film. This increase in resistance is probably due only in part to plugging of pin-holes by anodization; generation of deep traps appears to be involved. Ehrenberg *et al.* (29) suggest that OH groups in fused silica provide very deep electron traps. Isaacs and Llewelyn Leach (30) studied the capacitance of a large number of anodized metals by means of a square current pulse technique. They attributed the very large capacitance changes observed under cathodic bias on a number of the transition group metal oxides to reversible chemical reactions occurring within the film.

*Enhanced conductivity in the presence of water.*—The donor action of adsorbed water vapor is well known (31). Thus adsorption of water onto the surface of an insulator or a high resistivity n-type semiconductor can increase the conductivity of the substrate due to the electrons transferred from the adsorbate. This transfer of electrons, of course, causes the appearance of empty levels on the water molecules, and Stutz and De Mars (32) have indeed suggested that hole-type electronic conductivity can occur in layers of water adsorbed onto  $\text{SiO}_2$ . It is, of course, difficult to distinguish between hole conduction in the adsorbed water layer, and electron conduction in the dielectric directly underneath.

A protonic conductivity can arise at adsorbate concentrations such that hydrogen bonded networks exist on the surface of the adsorbent. The elegant work by Eigen and De Maeyer (33) and by Riehl *et al.* (34) on the conductivity of ice leaves no doubt about the reality and importance of this mechanism. It was

<sup>3</sup>Note added in proof: The existence of a fast and of a slow moving Na species, as well as of electrically active and inactive Na in thermal  $\text{SiO}_2$  films seems by now well established, largely due to further work by Hofstein; the same applies to protons in thermal  $\text{SiO}_2$  films (20a).

<sup>2</sup>In the experience of the author, ethylene glycol is not one of the best solvents for the anodization of silicon.



found possible to inject protons into ice by suitable electrodes, to measure space charge limited proton currents, and to observe the trapping of protons at lattice defects, *i.e.*, to establish a full analogy to electronic semiconductors. Gosar (35) actually attributed the proton mobility in ice not to a "hopping process" but to a proton conduction band. It is worth noting that a 1000Å thick film of pure ice with injecting electrodes would pass currents in the milliamperes/square centimeter range under application of a few volts bias. Klotz (36) suggested a mechanism by which hydrogen in a bonded network can transport electrons.

Shockley *et al.* (37) studied quantitatively the charge separation in humid atmosphere on SiO<sub>2</sub> in the fringing field of a p-n junction underneath a SiO<sub>2</sub> film. He was able to show that the electric effects in the silicon observed under these conditions were due to lateral charge motion on the silica surface, as suggested by Atalla *et al.* (38) and not due to charge motion in the oxide perpendicular to the surface. He did not specify the nature of the charge carriers. A phenomenological model of enhanced conductivity due to adsorbed water vapor is due to Rosenberg (39) who showed that there exists an inverse logarithmic relationship between the ratio of the conductivities before and after adsorption and the dielectric constant of the adsorbate/adsorbent complex. The relationship has been shown to hold for a large number of adsorbents and adsorbates. The additional conductivity is ohmic up to the highest field strengths tested (10<sup>5</sup> v/cm). Rosenberg was also able to prove that the conductivity is strictly electronic at low levels of water adsorption, and that protonic conductivity appears only at large percentages of adsorbed water. The increase of conductivity is a d-c or low-frequency phenomenon and disappears at about 10<sup>4</sup> Hz.

Anderson (40) combined infrared measurements with measurements of the conductivity of silica exposed to water vapor at various pressures, and observed enhanced conductivity which he attributed to proton migration on the basis of the conductivities in H<sub>2</sub>O and in D<sub>2</sub>O vapor. He also observed that, while the conductivity of his samples increased with increasing water content, it decreased at constant water content with increasing hydroxyl content (IR evidence). Because of this latter observation he prefers to explain the enhanced conductivity as due to an increase in dielectric constant, as suggested by Rosenberg, rather than on the structural model for protonic conduction in a hydrogen bonded network suggested by E. J. Murphy (41). Anderson's work was done mostly under conditions of high water vapor pressure, so that there exists no discrepancy between his postulate of protonic conductivity and Rosenberg's results.

J. F. Murphy (42) applied the concepts of proton transfer in a hydrogen bonded network to explain the formation and conduction properties of porous Al<sub>2</sub>O<sub>3</sub> films in acidic anodizing media. His model avoids some of the difficulties of earlier theories of porous oxide formation on aluminum (43).

*Injecting contacts and space charge limited currents in solids.*—A great many papers have been published on this subject during the past decade, especially by the group at RCA (44), by Wright in England (45) and by Stöckmann in Germany (46). Double injection of holes and electrons has received particular attention more recently (47), and this work is being extended to electrolyte contacts (48). Mehl *et al.* (49) observed double injection and space charge limited currents for both holes and electrons in anthracene crystals, Van Ruyven and Williams (50) hole injection into n-type ZnS. These findings, as well as the work of Gerischer (51) and of Brattain and Boddy (52) on germanium are of particular interest here because they permit unambiguous determination of the energy

levels in the electrolyte relative to those in the solid and enable prediction whether hole injection by the electrolyte may be expected for a given system. Keating (53) studied hole injection into CdS films by Cu<sub>2</sub>S contacts. This work immediately brings to mind the old experiments by Van Geel on Cu<sub>2</sub>S pressure contacts to anodic Al<sub>2</sub>O<sub>3</sub> films. Lindmayer (54) considered discharge transients from a dielectric sandwiched between metal electrodes. He also observed an inverse time relationship, as did Dreiner (84). In view of what has just been said it is clear that double injection is also a definite possibility if protons can be injected into an oxide film. One would then want to know the efficiencies of the two contacts, potential distribution in the film, mobilities of the species in the film, the capture cross section and trapping probabilities, etc.

*Barrier heights at the metal/oxide interface.*—Barrier heights at the Al<sub>2</sub>O<sub>3</sub> interface have been measured by a number of authors (55) in connection with work on tunnel diode or triode structures. The barrier heights have kept increasing with time, apparently as the purity of the materials and the experimental techniques improved.

Very precise data on the barrier height at the Al/Al<sub>2</sub>O<sub>3</sub> interface have been obtained by Pollack and co-workers (56) who showed that at room temperature both tunnel emission and Schottky emission occurs from the Al substrate of sufficiently thin Al<sub>2</sub>O<sub>3</sub> films, whereas at low temperatures Schottky emission ceases. Williams (57) determined the barrier height for photoemission of electrons from Si into SiO<sub>2</sub>. The work was extended to the Au/SiO<sub>2</sub> barrier by Goodman (58), and very recently to five other metal/SiO<sub>2</sub> barriers (Ag, Al, Cu, Mg, and Ni) by Deal *et al.* (59). Deal *et al.* used both the photoemission threshold and MOS capacitance-voltage measurements for determination of the barrier heights. For the Si/SiO<sub>2</sub> barrier energy, as measured from the silicon valence band, they find 4.35 eV, independent of silicon orientation or type. A barrier of 4.35V is obviously much too high for thermionic emission at room temperature. If appreciable electron emission is nevertheless observed under conditions where the externally applied field is too low to cause a significant tilting of the energy bands, then one must look for mechanisms that could reduce the barrier height. Impurity bands in impure oxides, or migration of small cations like H<sup>+</sup> or Na<sup>+</sup> to the SiO<sub>2</sub>/Si interface are distinct possibilities for lowering of the effective barrier height. Mead (60) drew attention to the fact that a relationship: log current density prop. V<sup>1/2</sup>, may be interpreted as field enhanced thermal excitation of trapped electrons into the conduction band (Poole-Frenkel effect), and that careful measurements are required to distinguish this mechanism of current flow from Schottky emission. Mead's argument, however, that the current through quite thin Ta<sub>2</sub>O<sub>5</sub> films is completely bulk controlled appears somewhat vulnerable in view of his use of the static dielectric constant of Ta<sub>2</sub>O<sub>5</sub> as pointed out also by Goruk, Young, and Zobel (78).<sup>4</sup> Williams (61) investigated the prebreakdown current in CdS, NaCl, and CdF<sub>2</sub>, and found that in all cases the steep rise in current just prior to breakdown must be ascribed to field emission from the electrodes but not to impact ionization. Exclusive control of the current by bulk processes rather than by the electrodes is thus not likely to be the rule in thin metal/oxide/metal sandwiches.

Standley and Maissel (62) published a paper on barriers of various counter electrodes on Ta<sub>2</sub>O<sub>5</sub> thin films (100-200Å). They also observed an effect of a nitrogen content of the Ta substrate on the electrical

<sup>4</sup>Note added in proof: This question has since been clarified by work by Mead *et al.* [J. Appl. Phys., 38, 2384 (1967)], and by J. G. Simmons [Phys. Rev., 155, 657 (1967)]. The papers by J. J. O'Dwyer [J. Appl. Phys., 37, 599 (1966)] and by S. M. Sze [J. Appl. Phys., 38, 2951 (1967)] and by A. K. Jonscher [Thin Solid Films, 1, 213 (1967)] should also be consulted in this context.

properties of the oxide, as studied in more detail by Schwartz *et al.* (63).

*Heat-treatment of anodic oxide films.*—Smyth *et al.* (64) studied the effect of heat-treatment on anodic oxide films on Ta and Nb. They found a permanent conductivity increase at temperatures exceeding 200°C, which they attributed to the gettering of oxygen from the film by the substrate. It would be quite interesting to see the results of photoelectric measurements on such films before and after heat-treatment. Somewhat similar trends, but of course not nearly so pronounced, were observed by Heine and Sperry (65) for oxide films on aluminum. Anodic oxide films (not heat-treated) show a region of uniform resistivity extending through most of their thickness, deviations occurring only directly at the two interfaces. Thermally grown  $\text{Al}_2\text{O}_3$  films on the other hand show a resistivity increasing monotonically from the metal to the outer surface, reflecting the ionic gradients during oxidation.

*Semiconducting anodic oxide films on titanium.*—Huber reported a series of measurements (66) on thin (200–300Å) anodic oxide films on Ti formed in certain electrolytes under conditions of very high current densities. The evaporated Ti films, serving as the anode, may also have been Ta doped, due to the use of a Ta boat during evaporation. The oxide films showed I-V characteristics, capacitances, and photovoltages which are much more suggestive of semiconductor diodes than of insulator films. This appears to be an outstanding example of how much properties can vary from one metal oxide to the other, especially with the transition group metals, and how important impurities and forming conditions can be. Chopra and Bobb (67) also reported on semiconductor-type photovoltages in Nb/Nb<sub>2</sub>O<sub>5</sub> semitransparent metal sandwiches.

*Negative resistances in anodic oxide films.*—Voltage controlled negative resistance (VCNR) in anodic oxide films on a variety of metals, and also in evaporated SiO films, has been studied extensively by Hickmott (68). Very high current densities, up to 34 amp/cm<sup>2</sup>, can be drawn nondestructively through 350Å  $\text{Al}_2\text{O}_3$  films. The true current densities are presumably higher still if one allows for the "bright spots" observed by Hickmott in the light emission from his diodes.

The current controlled negative resistance in Nb/Nb<sub>2</sub>O<sub>5</sub>/metal sandwiches studied by Chopra, (69), Geppert (70), Beam and Armstrong (71), and by Hiatt and Hickmott (72) can be developed also in air. The insulating oxide is "deformed" by forcing a critical current density through it; thermally grown oxides are more easily deformed than anodic oxides. Chopra (69) interprets the phenomenon as avalanche multiplication of carriers in a thin, high field region of the oxide attended by space charge limited flow conditions. The relationship  $I \propto V^n/d^3$  was observed by him both at 77° and at 298°K. Current controlled negative resistance in  $\text{Al}_2\text{O}_3$  was reported recently by Argall (73).

*Conductivity type of anodic oxide films.*—One often finds in the older literature the statement that anodic oxide films are n-type due to an excess of metal at the oxide/metal interface. P-type conductivity at the oxide/electrolyte interface has also been postulated (4). Harrop and Wanklyn (74) measured the conductivity type of anodic oxide films on zirconium produced by anodization in a dilute solution of potassium hydroxide in water, and found p-type conductivity from the sign of the thermoelectric power. Extension of the thermoelectric measurements to other oxide films, and produced in a variety of anodizing solutions, appears desirable.

*Mechanism of anodic oxide growth.*—Implantation of radioactive noble gas ions was used by Davies *et al.* (75) and by Amsel and Samuels (76) to study the

mechanism of anodic oxide growth, whether by cation or anion migration. The general conclusion is that both species are mobile, and that the fraction of current transported by cations or anions is a function of the applied field strength, and probably also of the forming electrolyte. Silicon appears to present a special case, since here only the cation was found to be mobile for the electrolytes and current density ranges investigated (77). The conclusion is based on the use of radioactive phosphorus as a marker, and since the measurements were made at phosphorus concentrations as low as  $10^{18}$  cm<sup>-3</sup>, it does not appear likely that the result is falsified by the phosphorus content of the oxide.

An extensive review of ionic and electronic currents at high fields in anodic oxide film by Goruk, Young, and Zobel (78) has just appeared in Volume 4 of "Modern Aspects of Electrochemistry."

*Stresses in anodic oxide films.*—Strongly stressed films may be expected to crack easily, for instance, when exposed to a strong current pulse; the mechanical condition of the film may therefore be a relevant factor. Stress measurements as a function of polarity of bias, current density during formation, and anodizing medium were reported by Vermilyea (79) and by Bradhurst and Llewelyn Leach (80). Schmidt and Rand (28) showed that no or only weak stresses were present in anodic SiO<sub>2</sub> films grown in relatively concentrated KNO<sub>2</sub>/THFA solution to a thickness of 1400Å. Increased tensile stresses, however, are observed in thicker SiO<sub>2</sub> films (unpublished results), grown in more dilute solution of KNO<sub>2</sub>/THFA.

*Photoeffects in anodic oxide films.*—Lewowski (81) investigated the cathodic light flashes of Al/Al<sub>2</sub>O<sub>3</sub> electrodes under a-c bias. He reported that the cathodic light flash observable in a 1% aqueous solution of oxalic acid is suppressed by the addition of borax to the oxalic acid solution. Ganley (82) repeated these experiments under better controlled conditions (measurement of the potential rather than the cell voltage) and noticed that the oxide became conductive at a small negative potential in the solution containing borax, but showed a high resistance up to large cathodic voltages in the pure oxalic acid solution. The reason for the absence of cathodic electroluminescence in the solution containing oxalic acid plus borax is thus simply the absence of a high electric field across the oxide layer. More interesting than this somewhat trivial explanation is the observation that the addition of borax, which affects the over-all pH of the solution only very little, produces such a pronounced difference in the conductivity of the oxide, at least under a-c bias. Apparently we are here again dealing with a specific sodium ion effect.

Ikonopisov and Nankov (83), who also investigated the cathodic light flashes in oxalic acid, were able to show that the light emission actually continues for tens of minutes under cathodic bias, although at a greatly reduced intensity compared to the first few milliseconds.

Electroluminescence and electron emission from thin metal/oxide/metal sandwiches was studied by Hickmott for a number of systems (68/1965 + 1966/). The threshold for photoconductivity in Nb/Nb<sub>2</sub>O<sub>5</sub>/Au diodes is about 1.2 eV and is attributed to excitation of electrons from an impurity band. The effect of illumination on stored charge from Ta/Ta<sub>2</sub>O<sub>5</sub>/ electrolyte was studied by Dreiner (84). To explain the inverse time law for the residual discharge current, a model is proposed in which a positive space charge in the film, generated during the forming process, gives rise to two opposing electric fields in the oxide.

Chopra (85) described interesting polarity reversals of the integral photovoltage generated by weakly rectifying metal/oxide/metal sandwiches under steady illumination. Chopra assumes the photocurrents to be

generated in the transition regions between the metal contacts and the bulk of the oxide, and explains the polarity reversal as due to the superposition of a fast growing, fast decaying photocurrent with a slow growing, slowly decaying component.

Schuermeyer and Crawford (55) analyze a simple method of separating the opposing photocurrents generated by emission from the metal electrodes into the oxide sandwich. Polack and Morris (86) were able to measure the built-in voltage across a thermally grown  $\text{Al}_2\text{O}_3$  film, predicted by the Mott-Cabrera theory of thin film growth (87), by analyzing the currents through an  $\text{Al}/\text{Al}_2\text{O}_3/\text{Al}$  tunneling structure.

Grove and Snow (88) were able to measure a trap density of  $10^{18} \text{ cm}^{-3}$  at the  $\text{Si}/\text{SiO}_2$  (thermal) interface just inside the  $\text{SiO}_2$  by analysis of the MOS characteristics after irradiation with 35 keV x-rays. Significant differences in the response to ionizing radiation between thermal  $\text{SiO}_2$  films grown in dry oxygen and in steam were noted by Kooi (89).

*Current-time relationship of the cathodic current.*—Van Geel and Pistorius (90) noted that the cathodic current was both a function of the time under forward bias, and of the value of the anodic bias to which the system  $\text{Al}/\text{Al}_2\text{O}_3$  had been last exposed. These experiments were carried out with alternating rectangular voltage pulses of about equal amplitude.

### The $\text{Si}/\text{SiO}_2$ System<sup>5</sup>

I should like to turn now to a description and interpretation of my own experiments on electrolytic rectification, using low resistivity n-type silicon as the substrate. In my 1957 paper with Michel (91) we showed cathodic I-V characteristics as a function of oxide thickness on n-type Si formed in a solution of potassium nitrate in N-methyl acetamide (NMA), the best anodizing medium for silicon known at that time. The purity and crystal perfection of the silicon available in 1957 was quite inferior to the material now available, but even so it was considerably better than the purity of any other valve metal like Ta or Nb available at that time. The curves of cathodic current vs. oxide thickness showed next to no slope, and we concluded at the time that the ability to pass cathodic current in contact with an electrolyte containing protons must be an intrinsic property of the anodic oxide film on silicon. In retrospect, however, the fact that these old experiments were carried out in open beakers becomes of importance since N-methylacetamide is hygroscopic. As we shall see, the presence of water vapor absorbed into the solution must have affected those results.

More recently we have been using a solution of potassium nitrite in tetrahydrofurfuryl alcohol (THFA), which in our experience is a considerably better anodizing medium for silicon than is the  $\text{KNO}_3/\text{NMA}$  solution; we have also taken the necessary precautions to prevent uptake of moisture from the air. Our initial concern was with the phenomenological differences between anodic and thermally grown  $\text{SiO}_2$  films, and we intended to show that the two kinds of films can be mutually transformed into each other by heat-treatment or by anodization, respectively. This work, including the infrared absorption spectra, is reported in the paper with Rand (28). We noticed that anodization of a thermal film caused the appearance of a hydroxyl band in the bulk of the film, but the intensity of this band seemed to vary.

We shall report here on the cathodic current of purely anodic oxide films on Si as a function of forming conditions and of exposure of the  $\text{SiO}_2$  film to liquid water. Concerning thermally grown  $\text{SiO}_2$  films we shall merely state at this time that they block the cathodic current quite well, but that the blocking ability can be increased further by anodization, as one would expect to happen if anodization results in the

plugging of a few pin-holes which the thermal oxide is known to contain. Introduction of trapping centers may also be involved.

### Experimental Techniques

Epitaxial n-type Si of resistivity 0.07 ohm-cm was deposited in a layer  $9\mu$  thick on very low resistivity n-type substrates. The slices were anodized immediately after epitaxial deposition, and great care was taken not to touch the epitaxial surface mechanically before or after anodization. Anodization was to 250v in a solution of  $\text{KNO}_2$  in tetrahydrofurfuryl alcohol (10.8 g/liter) at a current density of  $6 \text{ ma/cm}^2$ ; on reaching 250v, the sample was kept at constant voltage for 24 hr. The leakage current at the end of the anodization was typically  $5 \mu\text{a/cm}^2$  at 250v.

Some oxide was removed in HF from the back surface of the wafer at one edge, and the wafer was clamped in a horizontal position by means of a metal clip. Due to the low resistivity of the substrate, the voltage drop at the contact is negligible for the low currents tested.

The electrolyte contact was established by moving the orifice of a capillary directly in front of the anodized epitaxial surface and pressing a droplet of the liquid out of the capillary until it touched the oxide surface and established electrical contact. It was found of utmost importance not to touch the surface of the oxide with the orifice of the capillary, even though it had been fire-polished. Low cathodic breakdown voltages resulted almost invariably if the tip of the capillary accidentally was made to touch the oxide surface. It is believed that the effect is related to a greater degree of hydration of a mechanically damaged oxide surface. This is in sharp contrast to the behavior of "dry" contacts; even stainless steel points can be used without destroying the blocking ability of the oxide underneath the point.

To investigate this phenomenon somewhat further, an anodized epitaxial surface was subjected to indentations by a Tukon Microhardness Tester, the metal point having been replaced by a Pyrex glass point with a radius of curvature of  $6 \times 10^{-2} \text{ cm}$ . The indentations were carried out with increasing loads in steps of 1, 2, 5, 10, and 50g. A platinum-preshadowed-direct-carbon replica was then taken of the test area, but no structure could be detected below 10g loads. It must be concluded that the aqueous contact is sensitive to mechanical damage to the surface which does not affect dry contacts, and which cannot be detected electronically.

The electrolyte used for testing the cathodic current behavior was concentrated nitric acid, which satisfied the dual requirement of being an ample reservoir of protons, and of not attacking the  $\text{SiO}_2$  film chemically.

### Results

It was found that an oxide grown in a fresh solution of  $\text{KNO}_2$  in THFA blocks the cathodic current very well, and that the current is independent of time up to about 10v applied to  $1500\text{\AA}$  films, i.e., a field strength of about  $7 \times 10^5 \text{ v/cm}$ . The test voltage can often be raised as high as 30v, but in this range of field strengths the current usually begins to become unstable with time, and eventually increases to large values. A typical current density at 10v is  $2 \times 10^{-7} \text{ amp/cm}^2$ . The blocking ability of the oxide and its cathodic breakdown strength are very uniform across the whole epitaxial surface. Most of the current flows through an area only slightly larger than the diameter of the liquid contact. This was established by use of a conductive silver paste guard ring circuit, painted around the periphery of the epitaxial layer. Only when the electrolyte contact was moved very close to the guard ring (approximately a contact diameter, 1 mm, away), did the guard ring circuit begin to draw current comparable in magnitude to the current through

<sup>5</sup> See note added in proof, at end of paper.

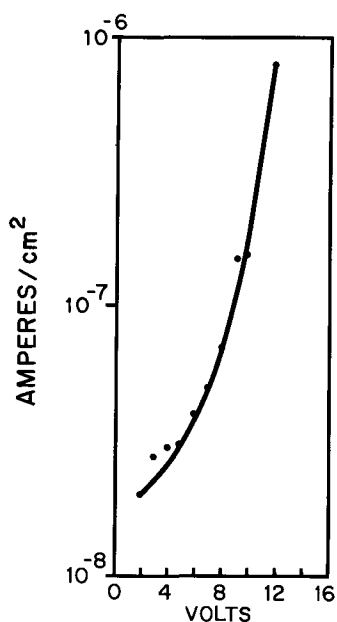


Fig. 3. Cathodic current in the system n-type Si/dry anodic SiO<sub>2</sub>/concentrated nitric acid. Si/SiO<sub>2</sub> formed to + 250v in a solution of KNO<sub>2</sub> in tetrahydrofurfuryl alcohol.

the oxide. Figure 3 shows a typical cathodic I-V characteristic.

On the basis of these results we can now assert that there exists no appreciable cathodic conductivity in dry anodic SiO<sub>2</sub> films even when in contact with a protonic electrolyte, but the emphasis is on the word dry.

The infrared spectra of anodic or of anodized thermal SiO<sub>2</sub> films suggested that water can be introduced into the oxide film by anodization under certain conditions, and that this water might have an effect on the electrical properties of the oxide. It has indeed recently been shown by Dreiner (27) that water diffuses into anodic SiO<sub>2</sub> when the film is left in contact with liquid water, or with a solvent containing water. The slow hydration of oxide films on aluminum when in contact with atmospheric moisture has, of course, been known for a long time.

To investigate the effect of water absorption, epitaxial n-type Si wafers which had been anodized and then tested with HNO<sub>3</sub> contacts without driving the test spots into breakdown, were immersed in deionized water at room temperature for 48 hr or more, and were then again tested with the HNO<sub>3</sub> droplet method. Wafers bearing the conductive silver paste guard ring were not immersed in water, but were kept in a container saturated with water vapor at room temperature and with a large droplet of H<sub>2</sub>O placed on the anodized surface inside the guard ring area.

The exposure to liquid water rendered the oxide surface hydrophilic to an extent that the nitric acid from the capillary would spread out over a large and irregularly defined area, so that no measurements could be taken immediately after the exposure to liquid water. It was, however, noticed that large cathodic currents would flow on application of only 1.5v bias. Placing the wafer in the vacuum of a vac-ion pump at  $3 \times 10^{-8}$  Torr at room temperature for 6 hr, however, restored hydrophobicity to the extent that the droplet of HNO<sub>3</sub> from the capillary did not spread much beyond its normal size, and measurements could be taken conveniently. Figure 4 shows that the current compared to the dry condition has increased about a hundredfold, and that the current is now time dependent at much lower voltages than before. Actually, the current in the time independent region is never completely steady but fluctuates about an average value, characteristics of a high field process. The surface after

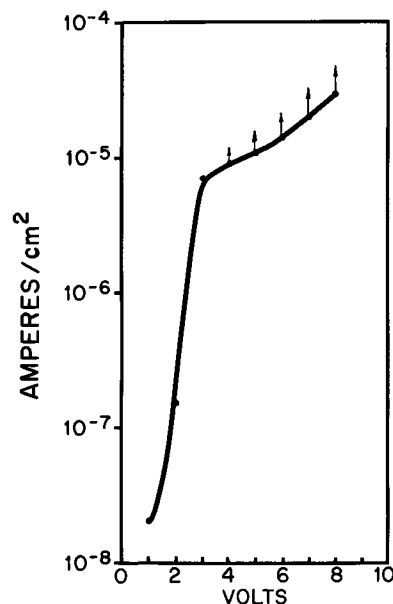


Fig. 4. Cathodic current in the system n-type Si/hydrated anodic SiO<sub>2</sub>/concentrated nitric acid. Si/SiO<sub>2</sub> formed to + 250v as in Fig. 3, then exposed to liquid H<sub>2</sub>O at room temperature for 48 hr, thereafter dehydrated by keeping in hard vacuum for 6 hr.

hydration was not completely uniform, some spots still showing rather high resistance. Evidently the hydration (and dehydration) process does not occur in uniform fashion, but rather starts at preferred sites.

It should be noted that only the current flowing through the oxide was being measured since the guard ring arrangement was used to obtain the data. It was also noticed during these experiments that the acid on a slightly hydrophilic surface would initially spread out to a larger spot size than usual, but that on application of a cathodic bias the liquid withdrew into the capillary without, of course, losing contact with the oxide. This is the behavior expected for a negatively charged liquid and thus constitutes direct evidence for the transfer of protons to the oxide by adsorption.<sup>6</sup> From the measurements of Parks and De Bruyn (92) it is known that the zero point of charge of SiO<sub>2</sub> in contact with water occurs at a pH of somewhat less than 2. In contact with concentrated nitric acid it is therefore to be expected that the acid will be charged negative with respect to the oxide due to transfer of protons. Protons and hydroxyls are the potential-determining ions for a nonporous SiO<sub>2</sub> film on Si. This observation also rules out the penetration of solution into pores of the oxide film as the mechanism of conduction, at least as far as the Si/SiO<sub>2</sub>/ conc. HNO<sub>3</sub> system is concerned.

Subsequent to testing the water-exposed anodic SiO<sub>2</sub> films with HNO<sub>3</sub> contacts, the wafers were baked in air at 150°C, and were then again tested by the same method. All traces of increased conductivity had disappeared, and the cathodic blocking ability of the oxide was as good or better than before. It was then tried to repeat the cycle, but apparently the heating

<sup>6</sup> It should be noted that the volume of nitric acid displaced on the SiO<sub>2</sub> surface under application of a cathodic bias ( $10^{-3}$ - $10^{-2}$  cm<sup>3</sup>), is several orders of magnitude too large to be explained by electroosmosis through the capillary at the very small currents involved ( $10^{-6}$ - $10^{-5}$  amp), according to the equation  $V = \frac{\epsilon \cdot \zeta \cdot i}{4\pi\eta\lambda}$ , where  $\epsilon$  =

dielectric constant,  $\zeta$  = zeta potential glass/acid,  $i$  = current,  $\eta$  = dynamic viscosity,  $\lambda$  = conductivity of the concentrated acid. It was also noticed that the effect was related to the magnitude of the applied bias (which is dropped almost exclusively across the oxide film) rather than to the magnitude of the current. The system is also different from a simple electroosmotic set-up in that here the area of oxide wetted by the acid changes under application of the bias. The physical parameters involved are the surface areas and surface energies in the system SiO<sub>2</sub>/HNO<sub>3</sub>/air, the ionization of the surface hydroxyl groups, the electrostatic forces, and the hydrostatic pressure of the liquid. The shape of the capillary appears to be critical; with some capillaries the effect could not be observed.

at 150°C had been sufficient to slow down the uptake of water markedly. Warming to 35°C in contact with liquid water for 48 hr was required to restore the "wet" condition of the oxide.

In another experiment an anodized Si wafer, part of which had been exposed to liquid water for 48 hr, was immersed in an acidic gold plating bath and was kept under a cathodic bias of 6v for ½ hr. Gold plating took place only in the area previously exposed to liquid water. While the gold deposit was nonuniform and of low density in the hydrated area, a well-defined continuous gold plate marked the previous periphery of the water droplet used to hydrate the oxide. We do not understand the reason for this latter effect; it may perhaps be related to a different pH at the surface of the water droplet in contact with air, or could be an effect of surface tension at the three phase boundary SiO<sub>2</sub>/H<sub>2</sub>O/air.

In the case of a contact between SiO<sub>2</sub> and concentrated HNO<sub>3</sub>, protons are transferred from the acid to the oxide, setting up a surface dipole which opposes the further entry of protons. When applying a negative bias to the silicon, most of the voltage is dropped across the bulk of the insulator and only a small fraction across the Helmholtz double layer. Penetration of protons is thus reduced until the fraction of voltage dropped across the Helmholtz layer equals the surface dipole due to charge transfer from the liquid to the SiO<sub>2</sub>. Part of the blocking ability of the oxide is thus due to this dipole. If a less acidic electrolyte were used as the contact, the surface dipole would be smaller or, in the case of an electrolyte with pH higher than 2.0 (the isoelectric point of SiO<sub>2</sub>) would even point in the other direction and would favor the injection of protons.

The corresponding experiment was carried out with a solution of potassium nitrate in deionized water, and on a wafer on which the anodic oxide had previously been tested with concentrated HNO<sub>3</sub>, and current blocking to at least 10v applied bias had been observed for every spot tested. In contact with the KNO<sub>3</sub>/H<sub>2</sub>O solution the cathodic breakdown voltage was only 4v initially, but rose slightly from each test spot to the next, apparently reflecting decrease in pH of the liquid at the very tip of the capillary, perhaps due to uptake of CO<sub>2</sub> from the air. It was also noticed that breakdown occurred in a very abrupt fashion; i.e., the current was very small below, and quite large above the breakdown voltage. Breakdown in contact with the concentrated HNO<sub>3</sub> solution is much more gradual, so that a forward I-V characteristic can be plotted in this voltage region, as shown in Fig. 4.

The experiment described is not completely unambiguous because a certain degree of chemical attack on the SiO<sub>2</sub> can occur at higher pH values; in view of the experiments with water soaked anodic SiO<sub>2</sub> films, which regained their blocking ability completely upon heating to 150°C in air, it is felt that the observed phenomena are probably correctly ascribed to charge transfer reactions.

It was stressed before that good blocking ability of anodic SiO<sub>2</sub> films is observed if the oxide is formed in a fresh solution of KNO<sub>2</sub> in THFA. An oxide formed in an "aged" KNO<sub>2</sub>/THFA solution; i.e., one in which several consecutive anodizations have been carried out before, shows a much reduced breakdown voltage. In a particular case tested, the cathodic breakdown voltage in contact with concentrated HNO<sub>3</sub> was only 5v, but extremely uniform across the whole epitaxial surface. From previous anodization with K<sup>42</sup>NO<sub>2</sub> in THFA (72/1965/) it is known that the amount of potassium incorporated into the oxide film increases with each successive anodization and reaches values larger by a factor of 100 compared to a fresh solution. Another possibility is, of course, an increased incorporation of protons with aging of the solution. This would not be unreasonable in view of the measure-

ments by Duffek *et al.* (93) who showed that electrolysis of KNO<sub>3</sub>/NMA solutions produces water by oxidation of the NMA at the Si anode. A similar mechanism may well occur in KNO<sub>2</sub>/THFA solutions. Tracer measurements with T and K<sup>42</sup> are now in preparation to clarify these points. The role of potassium ions or protons in lowering the cathodic breakdown voltage could be related to an enhancement of proton mobility in the oxide, or to enhanced field emission from traps or from the cathode.

#### Discussion

We know now that the ability of SiO<sub>2</sub> to pass cathodic current is strongly dependent on the water content of the oxide, and we must inquire about the role which the water plays in the conduction mechanism. Here we are faced by a dilemma, but it seems that the gradual increase with time of cathodic current in the system n-type Si/SiO<sub>2</sub>(H<sub>2</sub>O)/protonic electrolyte, may well provide a clue to the correct answer. The dilemma we are referring to is the question whether the current is carried by protons, by electrons, or by both.

Actually, a one-carrier proton mechanism in dry SiO<sub>2</sub> can be ruled out just on the basis of the very low mobility of protons in SiO<sub>2</sub>. Even if the room temperature mobilities extrapolated from Hofstein's work (20) are used, by far the highest values reported for protons in SiO<sub>2</sub>, unrealistically large carrier concentrations result in order to satisfy the relationship  $\sigma = n \cdot e \cdot \mu$  at current densities in the ma/cm<sup>2</sup> range. Similarly, a one-carrier electron mechanism is ruled out in view of the blocking behavior of SiO<sub>2</sub> films of the given thickness with metal counter electrodes. Equally impossible is a double-injection mechanism with both types of carriers present in approximately equal concentrations and able to reach the collecting electrode; in this case a very strong dependence on oxide thickness, proportional to 1/d<sup>5</sup>, would be expected, which is clearly not being observed in the case of high forward conductivity. What one has to choose from are therefore two-carrier mechanisms, but with one type of carrier in excess and more mobile than the other.

From the work of Rosenberg (39) it is known that a water content of a dielectric can increase its conductivity by many orders of magnitude. It is also unreasonable to assume that the electronic conductivity of the SiO<sub>2</sub> film has not increased in the presence of the absorbed water. Thus one would not have to postulate a protonic contribution to explain the initial increase in conductivity after exposure to water. The slow increase of current with time of hydrated SiO<sub>2</sub>, however, is difficult to understand if purely electronic conduction were involved. It is known that the conductivity of insulating CdS can be changed in irreversible fashion by application of a critical field strength (94), but the initial increase in conductivity on application of a cathodic bias to hydrated SiO<sub>2</sub> is reversed by simply heating the oxide to 150°C; induced conductivity has been observed in anodic oxide films by Hickmott (68) and by Chopra (69) when a critical current density was forced through the oxide, but the current densities involved were far in excess of the very small currents initially flowing through the hydrated SiO<sub>2</sub> film upon application of a few volts cathodic bias.

Injection of protons accompanying electronic current flow must of necessity result in an increase of current with time. The injected protons will compensate part of the negative space charge in the oxide and increase the current in much the same way as trapped holes increase the gain of secondary photocurrents. In addition, the injected protons can cause enhanced field emission both from traps in the film (Frenkel-Poole mechanism) or from the cathode.

If field emission from the n-type Si into the SiO<sub>2</sub> is the rate-limiting step, as indeed postulated for very

thin (175Å) dry SiO<sub>2</sub> films by Forlani and Minnaja (95), then the bands must be tilted by the same extent to produce the same amount of electron emission for oxide films of different thickness, i.e., the field strength at the contact must be the same. This is not too different from what is actually observed in practice. Essentially the same consideration applies if field emission from traps is the rate-limiting step. Continuous injection of a small proton current would lead to a gradual reduction of the effective barrier height, regardless of whether the barrier at the N-Si/SiO<sub>2</sub> interface or the trap depth is involved, thus causing the slow increase of current with time experimentally observed. When the current density becomes very large, there may, of course, result mechanical damage to the oxide from the evolution of hydrogen gas by recombination of protons and electrons. Proton injection into a completely dry SiO<sub>2</sub> is not readily possible, as we have seen; permeation of water must first generate some kind of hydrogen bonded network along which the protons can migrate. The water thus serves a dual function in SiO<sub>2</sub> films: it increases the electronic conductivity, and it enhances the proton mobility in the oxide. It should perhaps be noted that the electronic conductivity of SiO<sub>2</sub> films, relative to their ionic conductivity, is much better than that of Ta<sub>2</sub>O<sub>5</sub> films, as can be deduced from the fact that the current during formation of Ta<sub>2</sub>O<sub>5</sub> films is nearly 100% ionic, whereas the current during formation of SiO<sub>2</sub> is 96% or more electronic. On the other hand, the mobility of protons in SiO<sub>2</sub> is much lower than in Ta<sub>2</sub>O<sub>5</sub>. Thus the ratios of proton to electron injection under cathodic bias may be considerably different for Ta<sub>2</sub>O<sub>5</sub> and SiO<sub>2</sub> films.

It is possible to substantiate further that the positive carriers injected into the SiO<sub>2</sub> are indeed protons and not holes (an unlikely process anyhow for a material with the forbidden bandwidth of SiO<sub>2</sub>). When biasing the anodized n-side of a p-n junction in silicon cathodically (i.e., in the forward direction) vs. an aqueous electrolyte, while maintaining a reverse bias across the p-n junction, no increase in the reverse current of the junction could be detected, up to the highest current densities tested in the emitter/base circuit. Electron injection by the electrolyte through an anodic oxide on the other hand is readily observed when biasing the anodized p-side of a p-n junction positive vs. the electrolyte. The former experiment is not fully conclusive because the surface recombination velocity at the Si/SiO<sub>2</sub> interface under cathodic current flow should really be known but was not measured in this experiment. In general, however, the surface recombination velocity of silicon is not excessive under a large forward bias, when the Fermi level at the surface is in the vicinity of one of the band edges.

### Conclusions

A literature survey has been given for the period 1959-1966, of papers dealing with electrolytic rectification or related subjects.

It has been shown that the conductivity of anodic SiO<sub>2</sub> increases after exposure to water. This initial increase in conductivity is likely to be electronic rather than protonic in origin. However, protons can be injected into a hydrated SiO<sub>2</sub> film causing an increase of current with time at constant voltage due to space charge neutralization and field emission from traps or from the cathode. Hydration of the oxide can be reversed by a bake at 150°C in air. This bake actually renders the oxide more resistant to hydration than it is immediately after anodization.

Either alkali ions or protons, incorporated into the oxide film by anodization in an incompletely dry organic solvent, have a strong effect on lowering the cathodic breakdown voltage, at which the current begins to increase with time under constant voltage.

### Acknowledgments

The author is indebted to J. D. Ashner for help with many of the experiments. B. F. Howells made the indentation tests and J. Drobek the electron microscopic surface replicas. Stimulating discussions with K. Lehovec and T. W. Hickmott are gratefully acknowledged.

Manuscript received June 15, 1967; revised manuscript received Sept. 15, 1967. This paper was presented at the Anodic Oxides Symposium at the Dallas Meeting, May 7-12, 1967, as Abstract 21.

Any discussion of this paper will appear in a Discussion Section to be published in the December 1968 JOURNAL.

### REFERENCES

1. P. F. Schmidt, F. Huber, and R. F. Schwarz, *J. Phys. Chem. Solids*, **15**, 270 (1960).
2. D. A. Vermilyea, *J. Appl. Phys.*, **36**, 3663 (1965).
3. W. Ch. Van Geel, "Halbleiterprobleme I," p. 299, W. Schottky, Editor, Vieweg & Sohn (1954); *Physica*, **17**, 761 (1951).
4. Y. Sasaki, *J. Phys. Chem. Solids*, **13**, 177 (1960); *J. Appl. Phys.*, **34**, 867 (1963).
5. N. Schwartz and M. Gresh, *This Journal*, **110**, 938 (1963).
6. A. Politycki and E. Fuchs, *Z. Naturforschung*, **14a**, 271 (1959).
7. B. H. Claussen and M. Flower, *This Journal*, **110**, 983 (1963).
8. P. F. Schmidt, R. Stickler, G. D. Rose, and A. N. Knopp, *Electrochem. Technol.*, **3**, 49 (1965).
9. E. F. Duffek, E. A. Benjamini, and C. Mylroie, *ibid.*, **3**, 75 (1965).
10. Y-K. Wei and R. B. Bernstein, *J. Phys. Chem.*, **63**, 738 (1959).
11. W. Feitknecht, A. Wyttenbach, and W. Buser, "Reactivity of Solids," p. 234, J. H. De Boer, Editor, Elsevier Publishing Co., New York (1961).
12. G. Y. Onoda, Jr., and P. L. De Bruyn, *Surface Sci.*, **4**, 48 (1966).
13. S. Maricic, V. Pravdic, and Z. Veksli, *J. Phys. Chem. Solids*, **23**, 1651 (1962).
14. K. Schwabe, *This Journal*, **110**, Sect. II, 663 (1963).
15. G. M. Krembs, *ibid.*, **110**, 938 (1963).
16. D. A. Vermilyea, *Surface Sci.*, **2**, 444 (1964).
17. D. A. Vermilyea, *J. Phys. Chem. Solids*, **26**, 133 (1965).
18. G. Hetherington, K. H. Jack, and M. W. Ramsay, *Phys. Chem. Glasses*, **6**, 6 (1965).
19. A. E. Owen and R. W. Douglas, *J. Soc. Glass Tech.*, **43**, 159 (1959).
20. S. R. Hofstein, *IEEE Trans. Electron Devices*, **ED-13**, 222 (1966); (20a), *ibid.*, **ED-14**, 749 (1967).
21. E. H. Snow, A. S. Grove, B. E. Deal, and C. T. Sah, *J. Appl. Phys.*, **36**, 1664 (1965).
22. E. Yon, W. H. Ko, and A. B. Kuper, *IEEE Trans. Electron Devices*, **ED-13**, 276 (1966); A. B. Kuper, IEEE Silicon Interface Specialist Conference, Las Vegas, March 1967.
23. D. R. Kerr, IEEE Silicon Interface Specialist Conference, Las Vegas, March 1967.
24. V. Garino-Canina and M. Priqueler, *Phys. Chem. Glasses*, **3**, 43 (1962).
25. M. Fowkes, T. Burgess, and G. Hutchins, Paper presented at the Philadelphia Meeting of the Society, Oct. 9-14, 1966, Electron. Div. Extended Abstract No. 175.
26. A. H. Mitchell and R. E. Salomon, *This Journal*, **112**, 361 (1965); *ibid.*, **114**, 599 (1967).
27. R. Dreiner, *ibid.*, **113**, 1210 (1966).
28. P. F. Schmidt and M. J. Rand, *Solid State Communications*, **4**, 169 (1966).
29. W. Ehrenberg, V. B. Gutan, and L. K. Vodopyanov, *Brit. J. Appl. Phys.*, **17**, 63 (1966).
30. H. S. Isaacs and J. S. Llewelyn Leach, *This Journal*, **110**, 680 (1963).
31. H. J. Engell, "Halbleiterprobleme I," p. 249, W. Schottky, Editor, Vieweg & Sohn (1954).
32. H. Statz and G. A. De Mars, *Phys. Rev.*, **111**, 169 (1958).
33. M. Eigen and L. De Maeyer, *Proc. Royal Soc. (London)*, **247A**, 505 (1958); *Ber. der Bunsenges. Phys. Chem.*, **68**, 19 (1964).
34. H. Blinks, O. Dengel, and N. Riehl, *Phys. Kondens. Materie*, **4**, 375 (1966); H. Engelhardt and N. Riehl, *ibid.*, **5**, 73 (1966).



35. P. Gosar, *Nuovo Cimento*, **30**, 931 (1963); *Phys. Stat. Sol.*, **4**, 675 (1963).
36. I. M. Klotz, "Horizons in Biochemistry," p. 523-550, Kasha and Pullman, Editors, Academic Press, New York (1962).
37. W. Shockley, W. W. Hooper, H. J. Queisser, and W. Schroen, *Surface Sci.*, **2**, 277 (1964).
38. M. M. Atalla, A. R. Bray, and R. Lindner, *Suppl. Proc. Inst. Elect. Engrs. (London) Pt. B.*, **106**, 1130 (1959).
39. B. Rosenberg, "Physical Processes in Radiation Biology," p. 111-123, Academic Press, New York (1964).
40. J. H. Anderson, Dissertation, University Microfilms 65-12, 737, Ann Arbor, Michigan.
41. E. J. Murphy, *Phys. Chem. Solids*, **15**, 66, 115 (1960).
42. J. F. Murphy, Proc. Conf. on Anodizing of Aluminum, Univ. of Nottingham, 1961; Publ.: Aluminum Development Ass., London (1962).
43. F. Keller, M. S. Hunter, and D. L. Robinson, *This Journal*, **100**, 411 (1953); M. S. Hunter and P. E. Fowle, *ibid.*, **101**, 514 (1954).
44. A. Rose, *Phys. Rev.*, **97**, 1538 (1955); M. A. Lampert, *ibid.*, **103**, 1648 (1956); A. Rose, *Helv. Phys. Acta*, **29**, 199 (1956); M. A. Lampert, A. Rose, and R. W. Smith, *J. Phys. Chem. Solids*, **8**, 464 (1959); R. H. Bube, *J. Appl. Phys.*, **33**, 1733 (1962); M. A. Lampert, *Repts. Progr. Phys.*, **27**, 329 (1964).
45. G. T. Wright, *J. Brit. I.R.E.*, **20**, 337 (1960); *Solid State Electronics*, **2**, 165 (1961); *Proc. IEEE*, **51**, 1642 (1963), and further references there.
46. F. Stöckmann, "Halbleiterprobleme VI," pp. 279-320, W. Schottky, Editor, Vieweg & Sohn (1960); *Acta Physica Austriaca*, **20**, 71 (1965).
47. M. A. Lampert, *RCA Rev.*, **20**, 682 (1959); R. H. Parmenter and W. Ruppel, *J. Appl. Phys.*, **30**, 1548 (1959); M. A. Lampert and A. Rose, *Phys. Rev.*, **121**, 26 (1961); N. Holonyak, S. W. Ing, Jr., R. C. Thomas, and S. F. Bevaqua, *Phys. Rev. Letters*, **8**, 1 (1962); R. A. Logan, H. G. White, P. F. Foy, and C. S. Frosch, *Solid State Electronics*, **7**, 473 (1964); R. Baron, J. W. Mayer, and O. J. Marsh, *Appl. Phys. Letters*, **4**, 65 (1964); M. A. Lampert, *Repts. Progr. Phys.*, **27**, 329 (1960).
48. H. Kallmann and M. Pope, *Nature (London)*, **186**, 31 (1960); *J. Chem. Phys.*, **32**, 300 (1960).
49. W. Mehl, J. Hale, and F. Lohmann, *This Journal*, **113**, 1166 (1966), and further references there.
50. L. J. Van Ruyven and F. E. Williams, *Phys. Rev. Letters*, **16**, 889 (1966).
51. H. Gerischer, *Z. Physik. Chem., N.F.*, **26**, 223 (1960).
52. P. J. Boddy, *J. Electroanal. Chem.*, **10**, 199 (1965), and further references there.
53. P. N. Keating, *J. Phys. Chem. Solids*, **24**, 1101 (1963).
54. J. Lindmayer, *J. Appl. Phys.*, **36**, 196 (1965).
55. J. C. Fisher and I. Giaever, *ibid.*, **32**, 172 (1961); G. T. Advani, J. G. Gottling, and M. S. Osman, *Proc. IRE*, **50**, 1530 (1962); F. L. Schuermeyer and J. A. Crawford, *Appl. Phys. Letters*, **9**, 317 (1966), and further references there.
56. S. R. Pollack and C. E. Morris, *J. Appl. Phys.*, **35**, 1503 (1964); W. E. Flannery and S. R. Pollack, *ibid.*, **37**, 4417 (1966).
57. R. Williams, *Phys. Rev.*, **140**, A569 (1965).
58. A. M. Goodman, *ibid.*, **144**, 588 (1966).
59. B. E. Deal, E. H. Snow, and C. A. Mead, *J. Phys. Chem. Solids*, **27**, 1873 (1966).
60. C. A. Mead, *Phys. Rev.*, **128**, 2088 (1962).
61. R. Williams, *ibid.*, **125**, 850 (1962); *J. Phys. Chem. Solids*, **25**, 853 (1964).
62. C. L. Standley and L. I. Maissel, *J. Appl. Phys.*, **35**, 1530 (1964).
63. N. Schwartz, M. Gresh, and J. Deaderick, *This Journal*, **109**, 64C (1962); D. A. McLean, N. Schwartz, and E. D. Tidd, *Proc. IEEE*, **52**, 1450 (1964).
64. D. M. Smyth, G. A. Shirn, and T. B. Tripp, *This Journal*, **110**, 1264 (1963); **111**, 1331 (1964); **113**, 1048 (1966).
65. M. A. Heine and P. R. Sperry, *ibid.*, **112**, 359 (1965).
66. F. Huber, *Solid State Electronics*, **5**, 410 (1962); *J. Appl. Phys.*, **33**, 3385 (1962); *This Journal*, **110**, 846 (1963); *Microelectronics & Reliability*, **4**, 283 (1965).
67. K. L. Chopra and L. C. Bobb, *Proc. IEEE*, **51**, 1784 (1963).
68. T. W. Hickmott, *J. Appl. Phys.*, **33**, 2669 (1962); **34**, 1569 (1963); **35**, 2118, 2679 (1964); **36**, 1885 (1965); *This Journal*, **113**, 1223 (1966).
69. K. L. Chopra, *J. Appl. Phys.*, **36**, 184 (1965).
70. D. V. Geppert, *Proc. IRE*, **51**, 223 (1963).
71. W. R. Beam and A. L. Armstrong, *ibid.*, **52**, 300 (1964).
72. W. R. Hiatt and T. W. Hickmott, *Appl. Phys. Letters*, **6**, 106 (1965).
73. F. Argall, *Electronics Letters*, **2**, 282 (1966).
74. P. J. Harrop and J. N. Wanklyn, *Brit. J. Appl. Phys.*, **16**, 155 (1965).
75. J. A. Davies, J. P. S. Pringle, R. L. Graham, and F. Brown, *This Journal*, **109**, 999 (1962); **110**, 849 (1963); **112**, 675 (1965).
76. G. Amsel and D. Samuels, *J. Phys. Chem. Solids*, **23**, 1707 (1962).
77. P. F. Schmidt and A. E. Owen, *This Journal*, **111**, 682 (1964); P. F. Schmidt, T. W. O'Keeffe, and A. E. Owen, *ibid.*, **112**, 800 (1965).
78. W. S. Goruk, L. Young, and F. R. G. Zobel, "Modern Aspects of Electrochemistry," J. O'M. Bockris, Editor, **4**, pp. 176-250 (1966).
79. D. A. Vermilyea, *This Journal*, **110**, 345 (1963).
80. D. H. Bradhurst and J. S. Llewellyn Leach, *ibid.*, **110**, 1289 (1963).
81. T. Lewowski, *Acta Phys. Polon.*, **20**, 161 (1961); **23**, 215 (1963).
82. W. P. Ganley, *J. Opt. Soc. Am.*, **56**, 470 (1966).
83. S. Ikonopisov and N. Nankov, *Phys. stat. sol.*, **11**, K9 (1965).
84. R. Dreiner, *This Journal*, **111**, 27 (1964).
85. K. L. Chopra, *Solid State Electronics*, **8**, 715 (1965).
86. S. R. Pollack and C. E. Morris, *Solid State Communications*, **2**, 21 (1964).
87. N. F. Mott and N. Cabrera, *Rep. Progr. Phys.*, **12**, 163 (1948-9).
88. A. S. Grove and E. H. Snow, *Proc. IEEE*, **53**, 894 (1966).
89. E. Kooi, *Philips Res. Repts.*, **20**, 595 (1965).
90. W. Ch. Van Geel and C. A. Pistorius, *ibid.*, **14**, 123 (1959).
91. P. F. Schmidt and W. Michel, *This Journal*, **104**, 230 (1957).
92. G. A. Parks and P. L. De Bruyn, *J. Phys. Chem.*, **66**, 967 (1962); G. A. Parks, *Chem. Rev.*, **65**, 967 (1965).
93. E. F. Duffeck, C. Mylroie, and E. A. Benjamini, *This Journal*, **111**, 1042 (1964).
94. J. Woods, *Proc. Phys. Soc.*, **B69**, 975 (1956).
95. F. Forlani and N. Minnaja, *Phys. stat. sol.*, **5**, 407 (1964).

Note Added In Proof: Brander, Lamb, and Rundle [*Brit. J. Appl. Phys.*, **18**, 23 (1967)] report on anomalously large space-charge-limited one-carrier electronic flow through SiO<sub>2</sub> thermally grown on Si in low moisture content O<sub>2</sub> and under conditions of high purity of ambient and quartz tube. Provided that the current indeed flows through the conduction band of the oxide, as suggested by the authors, the alignment of the bands in the silicon and in the oxide must be drastically different from the situation investigated in ref. (57) and (58).

Lamb and Rundle [*Brit. J. Appl. Phys.*, **18**, 29 (1967)] describe the reversible switching between a high- and a low-resistance state of Si/SiO<sub>2</sub>/Al structures. The oxide in this case was contaminated with sodium during thermal growth, and the switching action was observed only if the system was subsequently heated in an hydrogen containing atmosphere. This work bears resemblance to the current controlled negative resistance effects observed in Al<sub>2</sub>O<sub>3</sub> and in Nb<sub>2</sub>O<sub>5</sub> (69-73), and also appears to have some bearing on the fast diffusing hydrogen species reported by Hofstein (20).



# Anodic Films, Protons, and Electrolytic Rectification

D. A. Vermilyea\*

General Electric Research and Development Center, Schenectady, New York

## ABSTRACT

Anodic films contain many flaws which for thick films are the sites of electrolytic rectification. For  $Ta_2O_5$  and  $Nb_2O_5$  films below 1000Å in thickness, however, bulk conduction also occurs. For such films the capacitance also increases markedly on polarization in the forward direction (base metal negative). One interpretation of the capacitance changes involves a proton space charge in the film. The relationship between capacitance change and current flow is examined in some detail, and it is shown that there is not a good correlation between the two effects; it therefore appears that two separate phenomena are involved. Possible interpretations are discussed.

During the past several years, the author conducted a number of investigations of various phenomena pertinent to electrolytic rectification. This paper presents a brief summary, some previously unpublished results, and a discussion of problems of interpretation.

### Summary of Previous Studies

**Flaw conduction.**—Anodic barrier films have macroscopic structures ranging from extremely heterogeneous to fairly homogeneous. The substrates on which they are grown are generally neither chemically pure nor geometrically ideal, and film growth on such surfaces results in imperfect films. A study of  $Ta_2O_5$  films revealed the presence of characteristic flaws (1), a schematic drawing of which is shown in Fig. 1. Such flaws resulted from film growth on surfaces which were geometrically irregular or which contained oxides or carbides. There is probably a gap of some kind between the metal surface and the central portion of the flaw. Electronic conduction through thick (>1000Å)  $Ta_2O_5$  films occurs almost exclusively at such flaws (2). The mechanism of such conduction and the entire chemical and physical nature of such flaws are mostly unknown, although some flaws are known to open physically in aqueous solutions. Marked hysteresis of current as a function of voltage has been observed for heavily flawed films, and with gold electrodes the conductivity sometimes increased with decreasing temperature. Such behavior suggests a degenerate semiconductor, but the phenomena are very complicated; probably some electrolysis is also involved. It should be noted that such flaw conduction may involve current densities of many thousands of amperes per square centimeter.

**Bulk conduction.**—Of more interest because potentially some attempts at understanding may be made are results obtained for  $Ta_2O_5$  and  $Nb_2O_5$  films in the thickness range below 1000Å. For such films on reasonably pure smooth substrates bulk conduction predominates. It is believed that  $WO_3$  films also exhibit bulk conduction, while  $ZrO_2$  and  $Al_2O_3$  films conduct only at flaws.

Bulk conduction is not uniform at low fields, some areas conducting much more readily than others. At very high fields, probably approaching  $10^6$  v/cm, the entire surface participates in the conduction process, and the current seems to be more uniform. The potentials

at which the easiest and most difficult paths become active differ by about 1v. There is a strong temperature dependence of conduction, corresponding to activation energies of 0.5-1.0 ev. The current voltage relationships for such films are the same with either aqueous solution contacts or with metal electrodes provided a correction is made for the contact potential. Rectification appears to be determined by the contacts to the film. If a high work function contact is used, the film conducts easily when the base metal is negative. High work function contacts include gold, mercury, and most aqueous solutions. If a low work function electrode is used, conduction may be about equal in both directions or may be slightly higher when the base metal is positive. Low work function electrodes include aluminum, alkali metals dissolved in mercury, and an aqueous solution containing  $Cr(CN)_6^{-3}$  ions. The results of changing the work functions of aqueous solutions indicate that electrons are the predominant charge carriers. Bulk conduction can be increased many orders of magnitude by diffusion of lithium into the film and by a much smaller amount on application of large fields in the forward direction. The presence of liquid water is essential for the latter conductivity increase. Bulk conduction is also sensitive to the forming solution, especially as the film thickness increases. Hydrogen peroxide has a remarkable effect in reducing forward conduction (3); this effect is unstable on continued application of large forward bias. Bulk conduction in thicker films is also a function of the formation rate, temperature, and film history.

The results described for bulk conduction are all consistent with a mechanism in which electrons enter the film at the electrode and move through some kind of states in the film to exit at the other electrode. The substrate-film barriers are low for  $Nb_2O_5$  and  $Ta_2O_5$ , and many contacts give high barriers, so that rectification occurs. If the second contact has a low work function, rectification either does not occur or has a reversed easy flow direction. The effects of forming solution and large forward bias could probably be explained with a suitable distribution of traps. Lithium evidently supplies more electron states in the film and increases the conduction.

**Space charges.**—Prior to the studies of electronic conduction a study was made (4) of capacitance increases accompanying forward bias in aqueous solutions not containing any ready electron acceptors, so that the current flow through the films was small. Under such conditions the electrical capacitance of the film increases markedly, and for  $Nb_2O_5$ , may reach values of the order of  $10^2 \mu F/cm^2$ . The form of the capacitance-voltage relationship is in rough quantitative agreement with a theory involving a space charge within the film. The space charge was thought to be the result of protons evaporating from the surface into the film as the potential was made more nega-

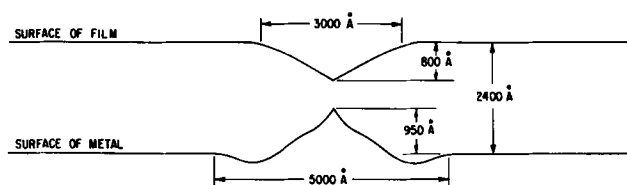


Fig. 1. Flaws in  $Ta_2O_5$

\* Electrochemical Society Active Member.

tive. For thin films, for which equilibrium of the carriers may be assumed, there is no dependence on frequency within the range of 100 cycles to 10 kc, or on temperature between 24° and 75°C. At lower temperature, and for thicker films the capacitance change becomes frequency and temperature dependent as though the mobility of charge carriers was not great enough to allow the equilibrium space charge to develop. Charge carrier mobilities of  $10^{-6}$  to  $10^{-8}$  are consistent with the results. Various experiments were performed in an effort to demonstrate that protons were in fact present in the film, and while all the results are consistent with the proton hypothesis they do not constitute a proof that protons form the space charge.

The evidence adduced in support of proton entry is that slightly different results are obtained with  $D_2O$ , as might be expected from the lower mobility of the deuteron; and that much smaller capacitance changes are observed when mercury, evaporation metal, or nonaqueous solution contacts were used.

One of the reasons for postulating that protons could enter the film was that a study of the double layer at the  $Ta_2O_5$ -solution interface showed convincingly that protons were strongly adsorbed on the interface and that they exchanged rapidly with the solution (5). Presumably they might also be expected to enter the film readily. At that time it was thought that electrolytic rectification occurred only at flaws, so that presumably electrons could only enter the film at scattered sites, while the large values of capacitance attained on negative polarization made it necessary to conclude that the entire surface area was affected. Since the later studies showed that bulk conduction also occurred it is now conceivable that electronic phenomena are responsible for both the conduction and the capacitance change. It is also conceivable, on the other hand, that protons form the space charge and also create the electronic states which allow conduction. The results obtained with lithium add some credence to this suggestion; since lithium enters the film and greatly increases its conductivity could not protons act in the same fashion?

In view of the uncertainty in the interpretations of the observed phenomena it seems worthwhile to compare results for capacitance change and bulk conduction on the same films under similar conditions to see whether any clarification can be achieved.

### Experimental Results

All of the techniques used have already been described (2-4). An important feature of the conduction measurements with aqueous solution contacts is the use of  $Ce^{+4}$  ions as an electron acceptor to preclude control by some slow electrochemical reaction in the solution.

Figures 2 and 3 show data for 350Å  $Nb_2O_5$  films formed at two rates in 0.1M  $HClO_4$  at room temperature. It may be seen that while both slowly formed specimens give higher currents and larger capacitance changes than do the rapidly formed films, the correlation of capacitance change and current is not perfect. Thus samples 1 and 2 give nearly the same C-V curve but very different currents at a given potential, while sample 3 gives a larger current but a smaller capacitance change than does number 4.

Figures 4 and 5 further demonstrate the lack of a detailed correlation between capacitance change and current. In these figures 105Å  $Ta_2O_5$  films formed in dilute and concentrated  $H_2SO_4$  give current-voltage curves which differ relatively little considering the great difference in the nature of the films formed in the two solutions. On the other hand the film formed in dilute  $H_2SO_4$  shows very little capacitance change, while for the other, the capacitance increases by more than an order of magnitude at  $-0.9v$ . The current for the film formed in dilute  $H_2SO_4$  was higher, in contrast to the capacitance change.

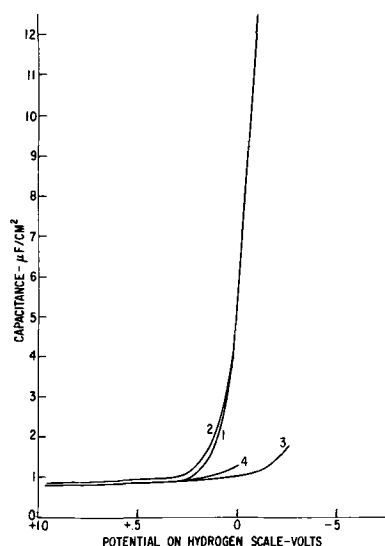


Fig. 2. Effect of formation rate on capacitance change. 350Å  $Nb_2O_5$  film formed at 25°C in 0.1M  $HClO_4$ . Specimens 1 and 2 formed in 2 min; samples 3 and 4 in 5 sec.

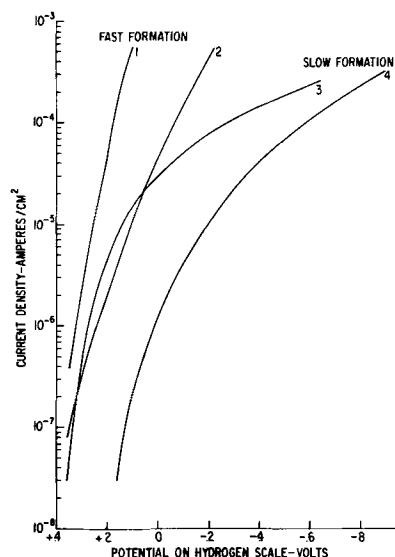


Fig. 3. Effect of formation rate on current; specimens of Fig. 2

Figures 6 and 7 show that the hysteresis effects associated with electronic current flow and capacitance change also differ. The capacitance is always higher on returning to positive potentials after negative polarization, and stays large to at least  $+1.5$  to  $+2v$ . The current, on the other hand, shows much less hysteresis which is usually of the opposite sign, and the hysteresis loop always closes by about  $+0.5v$ .

For films formed in concentrated solutions irreversible changes occur after negative polarization. Figures 8 and 9 show that sometimes the result of negative polarization may be to change the current-voltage curve and capacitance-voltage curve in opposite directions.

Figures 10 and 11 show data for the same 210Å  $Nb_2O_5$  film tested in mercury (solid lines) and in  $Ce^{+4}$  (circles), the potential scale having been adjusted so that the current-voltage curves coincide. There is a much smaller capacitance increase in the mercury. Note that in the aqueous solutions the presence of  $Ce^{+4}$  does not alter the capacitance-voltage behavior since the same results are obtained in  $HClO_4$  solutions.

### Discussion

It seems clear from the data presented that there is no detailed correlation between current flow and ca-

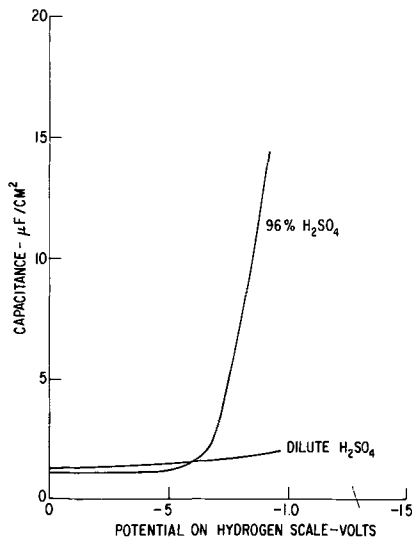


Fig. 4. Effect of solution composition on capacitance change.  $105\text{\AA}$   $\text{Ta}_2\text{O}_5$  films formed at  $25^\circ\text{C}$ .

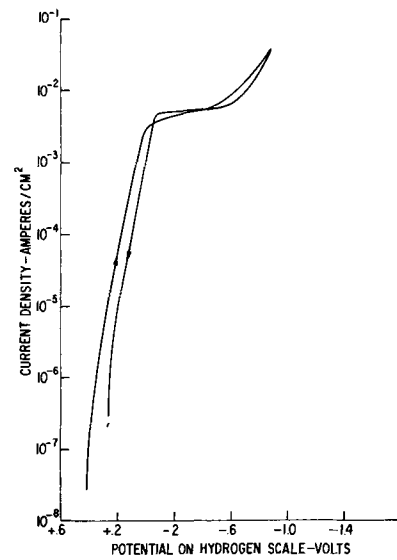


Fig. 7. Hysteresis of current; specimen of Fig. 6

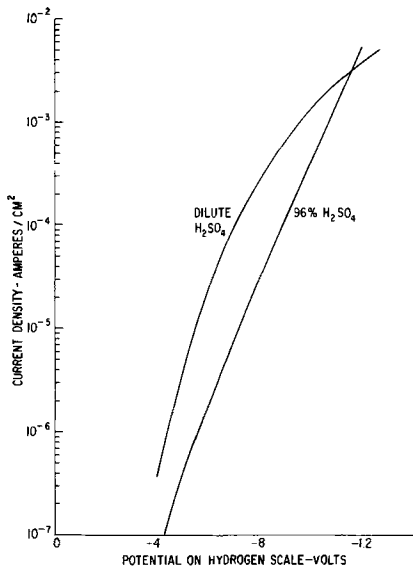


Fig. 5. Effect of solution composition on current; specimens of Fig. 4.

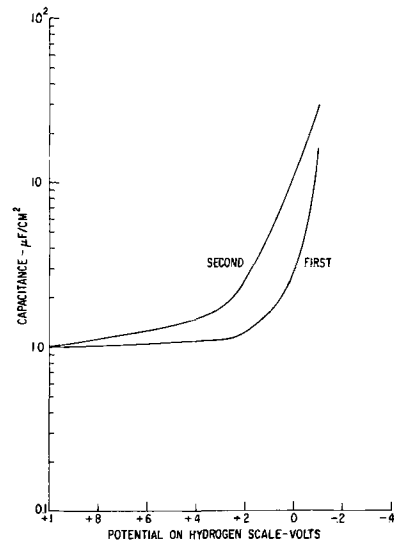


Fig. 8. Successive capacitance-potential curves for  $210\text{\AA}$   $\text{Nb}_2\text{O}_5$  film formed at  $25^\circ\text{C}$  in 96%  $\text{H}_2\text{SO}_4$ .

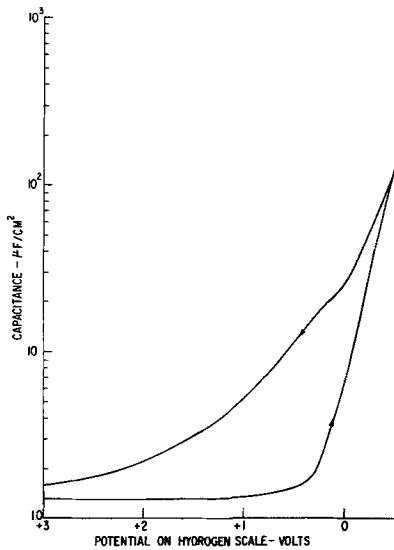


Fig. 6. Hysteresis of capacitance change.  $210\text{\AA}$   $\text{Nb}_2\text{O}_5$  film formed at  $25^\circ\text{C}$  in 0.1M  $\text{HClO}_4$ .

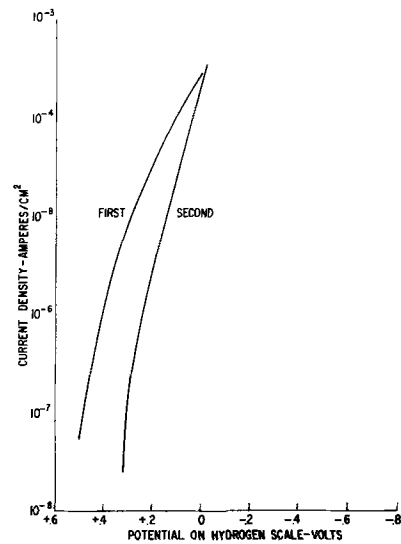


Fig. 9. Successive current-potential curves for specimen of Fig. 8.

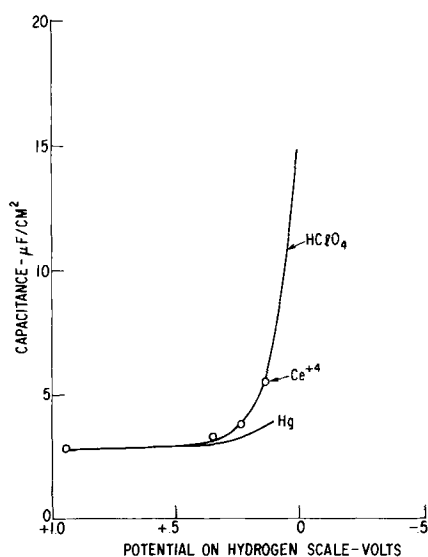


Fig. 10. Effect of contact on capacitance change. 210Å  $\text{Nb}_2\text{O}_5$  formed at 25°C in 0.1M  $\text{HClO}_4$ .

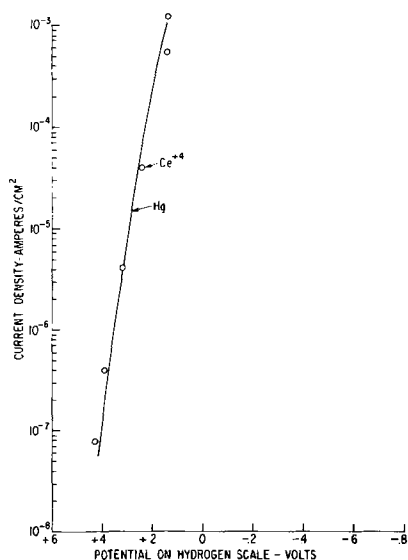


Fig. 11. Effect of contact on current; specimen of Fig. 10

capacitance change. Perhaps the outstanding example of lack of correlation was published in ref. (2). After alternating current formation, the easy conduction paths are blocked by deposits from the solution, and the current-voltage curve is shifted to more negative potentials. Such films may show very large capacitance changes with negligible current flow even in solutions containing ceric ions. Finally, the current is strongly influenced by temperature over the range  $-73^\circ$  to

$+100^\circ\text{C}$ , while the capacitance change is independent of temperature above some critical temperature.

There are at least two possible interpretations of these results. It could be assumed that electronic phenomena are responsible for both conduction and capacitance change, the conduction occurring through easy paths at somewhat less negative potentials than are required for the capacitance change. At high negative potentials the entire area becomes available for electron conduction, and the capacitance increases because of space charge formation. In order to explain the absence of large electronic currents when metal counter electrodes are used and still allow ready entry of electrons for space charge formation it seems necessary to postulate a large barrier to electron egress at the oxide-solution interface. The absence of large capacitance changes with mercury and nonaqueous contacts is not explained, but there are complications because of contact potential differences and double layer phenomena which may account for such discrepancies.

The alternative explanation is that electrons flow out to carry current and protons flow in to create the space charge. This explanation fits most of the facts, but is somewhat less appealing because of its greater complexity. It might also be argued that more hydrogen than was measured (4) should appear in the metal after prolonged negative polarization. However, it is perhaps easier to imagine a barrier to keep protons from entering the metal than one to keep electrons from tunneling into the mercury, as required by the alternative hypothesis. The question whether protons supply electron states in the oxide appears to be impossible to answer without further information. Suppose that the low capacitance change observed with mercury and with nonaqueous solutions results from a scarcity of protons. It would then be expected that if the current flow depends on protons it would also diminish with dry contacts, but that does not seem to be true. On the other hand, protons may be available at the easy sites even in dry conditions but not generally on the surface.

A final decision between the various possibilities requires more study. The most crucial need is for experiments which would settle conclusively the question of proton motion in the oxide films.

Manuscript received June 15, 1967; revised manuscript received ca. Oct. 3, 1967. This paper was presented at the Dallas Meeting, May 7-12, 1967, as Abstract 22.

Any discussion of this paper will appear in a Discussion Section to be published in the December 1968 JOURNAL.

#### REFERENCES

1. D. A. Vermilyea, *This Journal*, **110**, 250 (1963).
2. D. A. Vermilyea, *J. Appl. Phys.*, **36**, 3663 (1965).
3. D. A. Vermilyea, *This Journal*, **112**, 1232 (1965).
4. D. A. Vermilyea, *J. Phys. Chem. Solids*, **26**, 133 (1965).
5. D. A. Vermilyea, *Surface Science*, **2**, 444 (1964).

# Ionic Transport in Amorphous Oxides

R. H. Doremus

*General Electric Research and Development Center, Schenectady, New York*

## ABSTRACT

To aid in understanding the electrical conductance of amorphous oxide films, some experimental and theoretical results on ionic transport in bulk oxide glasses are reviewed. Results on alkali and hydroxyl ion movement in fused silica are perhaps the most pertinent; results on other glasses help to test theories and to show the effects of additives and hydration of the glass.

The electrical conductivity of amorphous anodic films often involves foreign ions in the films. When the film is formed in aqueous solution these ions are most likely to be hydrogen or hydroxyl. The electrical conductivity of bulk silicate glasses, except for a few special compositions, is controlled by diffusion of ions that are not part of the silicon-oxygen network of the glass. In this paper ionic transport in silicate glasses is reviewed to aid in understanding of ionic motion in amorphous oxide films.

This paper contains sections on the following subjects: structures of silicate glasses and their possible relation to structures of anodic films of other metals; factors that influence the selectivity or binding of small cations in an oxide network, and experiments and theories of transport measurements in silicate glasses that seem to be closest to the situation in anodic films.

### Structure of Amorphous Oxides

The basic building block of silicates is the silicon-oxygen tetrahedron. Each silicon atom is surrounded by four oxygen atoms; the bond distances and angles in this basic unit are very similar within a particular silicate and even from one silicate to another. In fused silica glass ( $\text{SiO}_2$ ) these tetrahedra are attached at their corners. Small displacements from one tetrahedron to another give rise to an amorphous structure that shows no long-range order, but retains the basic silicon oxygen tetrahedron with its usual bond angles and distances.

Zachariasen emphasized that it is this sharing of corners of a tetrahedral or triangular unit that makes an amorphous structure possible (1). As Young (2) has pointed out, Zachariasen included tantalum and niobium pentoxides in his list of probable glass formers, although they had not been made as glasses at that time. One might therefore expect the basic structural unit of amorphous tantalum and niobium oxide films to be oxygen-metal ion tetrahedra that are similar to the phosphorus-oxygen tetrahedra found in amorphous and polymeric phosphates (3). However, there seems to be no direct evidence to support this tetrahedral configuration. In  $\beta\text{-Ta}_2\text{O}_5$  the tantalum seems to be either in the center of a square surrounded by four oxygens, or an octahedron (4). In amorphous aluminum oxide films the aluminum atom may be in a mixture of four and six coordinated states with oxygen; amorphous aluminum oxide is often mixed with crystalline oxide [ref. (2), p. 212ff]. Therefore even the basic structure of various oxide films may be quite different, and it is difficult to know how far one can transpose results on silica to other oxides. Since extensive studies of ionic transport have been made only in silicates, this review is limited to them.

When alkali oxides are melted with silica the viscosity of the melt is greatly reduced, because the silicon-oxygen network is broken up by the formation of, for example,  $\text{SiO-Na}^+$  groups. These alkali ions are much more loosely held in the glass structure so they can easily migrate through it. Therefore when even a

small amount of alkali ion is present in a silicate glass, the electrical conductivity of the glass results entirely from the transport of this ion. This assertion is confirmed by many experiments which show that the alkali ions transport all the electrical current in silicate glasses (5, 6), and that their diffusion is much more rapid than that of other ions in silicate glasses (7). The alkali ions are called "network modifiers"; many other monovalent, divalent, and trivalent ions can act as network breakers or modifiers, but the monovalent are by far the most mobile.

A complication in the structure of silicate glasses is the formation of a second amorphous phase. Most borosilicates, as well as binary sodium and lithium silicate glasses, separate into two phases (8). Most commercial glasses other than borosilicates probably do not separate into two phases, since the presence of many components, especially aluminum, seems to inhibit phase separation. However, this possibility must always be kept in mind when interpreting properties of these glasses.

Hydrated oxides are of particular interest in the study of anodic oxide films, since the latter are usually formed from aqueous solution. However, there seems to be little information on the effect of hydration on the structure of anodic oxide films. When fused silica is treated with water vapor the silicate network is broken and two  $\text{SiOH}$  groups are formed (9, 10). At low water concentrations these groups are isolated from one another, and no molecular water is detectable in the silica (9). There is little known of the structure of silicate glasses extensively hydrated by contact with liquid water. Water slowly dissolves silicates, the rate increasing with increasing temperature (11). There is a gradient of "water" (hydroxyl group) concentration from the surface into the glass interior. With high degrees of hydration the silica becomes like a gel; the equilibrium solubility of liquid water in silica at room temperature apparently has not been measured. In fact it seems likely that the hydrated surface layers of oxides in contact with water are metastable, and given sufficient time the entire sample would dissolve. The rate of dissolution is, of course, a strong function of the composition of the solutions with which it is in contact, and may be very low, so that for practical purposes the hydrated oxides are often stable, although their composition may be slowly changing.

### Ion Selectivity of Oxides

Often it is found that alkali ions do not penetrate into an anodic oxide film from solutions (12), or that certain ions "block" the current in such a film (13). It seems possible that at least some of these phenomena are related to the ion exchange selectivity of the oxides. This selectivity also influences ionic transport in the oxide. Therefore a brief review of factors that determine this selectivity is presented in this section.

The selectivity of hydrated silicate glasses for monovalent ions was studied in detail by Eisenman (14). He found that the selectivity of glass between alkali ions of different sizes was determined by the composition of the glass. For example, glasses containing

silicon as the only network-forming ion showed a strong preference for small ions, particularly hydrogen ions. On the other hand certain sodium aluminosilicate or borosilicate glasses showed a preference for the larger cations, such as potassium, rubidium, and cesium, over sodium or lithium ions. These glasses still preferred hydrogen ions, but much less than the silicates without aluminum or boron. Eisenman related these differences to the structure of the anionic group in the glass. In Fig. 1 are shown his simplified models for the  $\text{SiO}^-$  and  $\text{AlOSi}^-$  groups. In the silicate group the negative charge is concentrated on a single oxygen ion, while in the aluminosilicate group this charge is spread over several oxygen ions. Thus the silicate is more "compact"; it has a higher "field strength" or smaller effective anionic radius. Conversely the aluminosilicate group has a larger effective anionic radius. Therefore the latter group tends to select larger ions from solution, while the silicate group selects smaller ions. Detailed calculations of binding energies relative to the hydration energies in solution illustrate these points (14). Eisenman calculated effective anionic radii of about 0.9 and 2.0 Å for the silicate and aluminosilicate group; these numbers are not exact, but give a rough guide of the relative binding or selecting power of the groups.

The detailed structure of the anionic groups in many hydrated anodic films, such as on tantalum and niobium, is not known, as mentioned earlier, so it does not seem possible to make a direct calculation of their effective anionic radii. However, it is possible to get some idea of these radii from the dissociation behavior of acids containing these anionic groups. For example, Eisenman observed that silicic acid is very weak, while the aluminosilicate group gives a strong acid. He calculated anionic radii close to those of the last paragraph by comparing the dissociation constants of these groups with those of halide acids (14). It is known that niobic and tantalum acids are very weak (15). Also, the first acid dissociation constant of  $\text{Al}(\text{O}-\text{H})_3$  is  $6(10)^{-12}$  (16). Therefore these groups in a hydrated oxide should have small anionic radii and be very selective for small monovalent ions, particularly hydrogen ions. Thus Vermilyea's finding that sodium or lithium ions do not penetrate into tantalum oxide films from aqueous solution (12) is understandable. Vermilyea also found that lithium ions could be introduced into the film from certain nonaqueous solvents (12); in this case the hydrogen ion concentration was apparently so low that some lithium ions were bound to the tantalate groups. It seems possible that other effects of ions on anodic oxide films can be understood in these terms.

Glass-forming ions are sometimes used in the electrolyte in the growth of anodic films, for example, borate ions for films on aluminum. It seems likely that small amounts of these ions are incorporated into the films. They could have a considerable influence on the properties of the films because of their different binding energies with cations, leading to faster diffusion of ions.

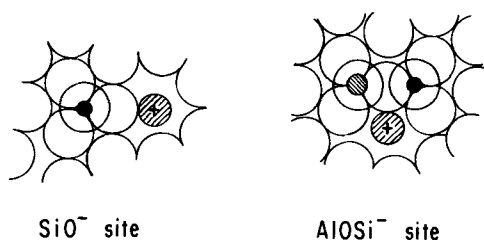


Fig. 1. Schematic drawings of  $\text{SiO}$  and  $\text{AlOSi}$  sites using crystal-line ionic radii. Open circles are oxygen ions, solid dot is silicon, finely shaded circle is aluminum ion, shaded cation is sodium, from ref. (14).

### Transport of Ions in Amorphous Oxides

Information about transport of ions is available from both diffusion and electrical conductivity measurements, so it is important to consider the relation between them. In a material in which only one ion is involved in transport, and there is no electronic conduction, the Einstein equation relates the tracer diffusion coefficient  $D$  of this ion to the specific electric conductivity  $\sigma$  of the substance:

$$D = \frac{\sigma RT}{cZ^2F^2} \quad [1]$$

In this equation  $c$  is the concentration of ions,  $Z$  the number of elementary charges on the ion,  $F$  the faraday,  $R$  the gas constant, and  $T$  the absolute temperature. The equation can be derived from strictly kinetic considerations with the assumption that the ionic mobility in the two experiments is the same (7, 17). When this assumption is not valid deviations from Eq. [1] occur, which can often be ascribed to effects of structure or mechanism of transport.

Diffusion coefficients and electrical conductivities in rigid glasses vary exponentially with temperature, so that

$$D = D_0 \exp(-Q_D/RT); \quad \sigma = \sigma_0 \exp(-Q_\sigma/RT) \quad [2]$$

where the pre-exponentials  $D_0$  and  $\sigma_0$  and the activation energies  $Q_D$  and  $Q_\sigma$  are constant with temperature. These quantities are related by Eq. [1]. This equation would indicate a temperature factor  $T$  in one pre-exponential term, but the experiments are not accurate enough to show this dependence. Therefore the activation energies are somewhat different; in the temperature range of interest here  $Q_D$  is about 1 to 2 kcal/mole greater than  $Q_\sigma$ .

As mentioned before, results of transport measurements on amorphous oxides are limited almost entirely to silicates. Extensive measurements for sodium ions in silicates have been made and these are considered first; then results on hydrogen ion transport in silicates are discussed.

*Sodium ions in silicates.*—Tracer diffusion coefficients measured for sodium ions in binary sodium silicate glasses are shown in Fig. 2, taken from Johnson's measurements (7, 18). At lower and higher temperatures Eq. [2] is satisfied, with a region between resulting from the glass transition, in which the structure of the glass is changed by progressive rupturing of the silicon-oxygen network. Attention is here focussed on the lower temperature region where the glass is rigid and has an unchanging structure. The activation energies  $Q_\sigma$  for conductivity in binary sodium silicate

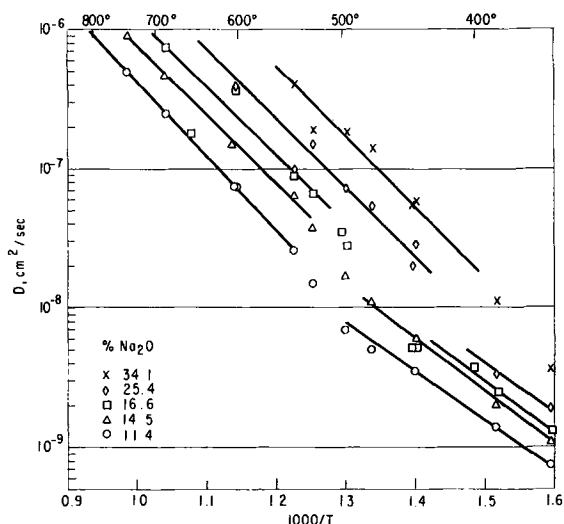


Fig. 2. Tracer diffusion coefficients of sodium in various binary sodium silicate glasses, as measured by Johnson (18).

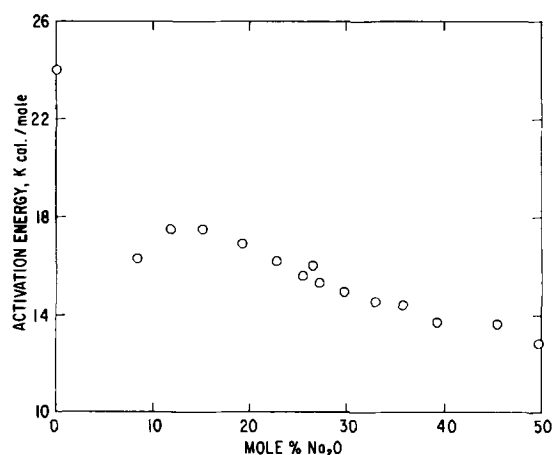


Fig. 3. Activation energy for electrical conduction in various binary sodium silicate glasses, from ref. (19).

glasses, are shown in Fig. 3 taken from the work of Seddon, Tippett, and Turner (19). Also shown in the figure are results for Vycor (20) and fused silica (21), which contain low concentrations of sodium. These results may not be directly comparable with the others, as mentioned below. The activation energies  $Q_D$  calculated from the tracer diffusion coefficients for sodium silicates in Fig. 1 are not very accurate, but seem to be nearly constant with composition at about 14 kcal/mole. The values of  $D$  calculated from the conductivity and Eq. [1] and those measured directly are different, as shown in Table I. Therefore, Eq. [1] is apparently not valid for these systems. It can be corrected with a factor  $f$

$$D = \frac{f \sigma FT}{cZ^2F^2}$$

Calculated values of  $f$  for binary sodium silicate glasses of different composition are shown in Table I also. These differences between conductivity and tracer diffusion in binary sodium silicates possibly result from phase separation, which is known to occur in these glasses (8).  $f$  Factors in glass have been attributed to a special mechanism of "interstitialcy" diffusion (22, 23), but it seems unlikely that this mechanism can explain the wide variations in  $f$  shown in Table I. Furthermore, an  $f$  of one (Eq. [1] is obeyed) was found for a soda lime glass that was very likely not phase separated (17); there is no reason to expect a different diffusion mechanism for this glass than for the binary sodium silicates. In Vycor glass  $f$  is about one also, while in Pyrex, which contains two phases,  $f$  is about 0.6 (20).

In a hydrated sodium aluminosilicate glass Eisenman (24) found sodium ion mobilities about 1000 times higher than in the dry glass. Apparently hydration changes the mechanism of diffusion.

*Theories and mechanisms.*—The diffusion coefficients of sodium in sodium silicate glasses cannot be described by considering the glass as a viscous liquid. The values calculated from the Stokes-Einstein equation, which describes diffusion in many molecular liquids, are much lower than the measured ones; furthermore, the latter are unrelated to the viscosity of the glass (7). The transport of sodium in these glasses is much more rapid than for the lattice elements

Table I. Diffusion coefficients of sodium in binary sodium silicate glasses at 350°C

Mole % Na <sub>2</sub> O	Diffusion coefficients $\times 10^{10}$		$f$
	Measured (18)	Calc. (Eq. [1])	
12	7.5	10	0.74
15	11	15	0.74
25	19	33	0.57
36	37	150	0.25

silicon and oxygen (7), so the glass can be treated as a rigid solid in describing diffusion.

A reasonable model for ionic diffusion in silicate glass should therefore be an alkali halide in which the cation diffuses much more rapidly than the anion. In these materials, transport occurs by motion of a structural defect, since direct exchange of two ions is energetically much harder than the motion of defects such as interstitials or vacancies. The same reasoning should apply to ionic diffusion in a glass, except that vacancy diffusion is also unfavorable in them (7), leaving interstitial diffusion as the most likely mechanism. At any temperature there are a certain number of sodium ions that are not in the normal site, but in an "interstitial" site somewhat removed from the normal one. In this formal description a detailed knowledge of the structure of this site is not necessary; in any event it is not known. The fraction  $N$  of the sodium ions that are in these interstitial sites is given by the statistical equation (7, 25, 26)

$$N = \sqrt{p} \exp(-\Delta G_f/RT)$$

where  $\Delta G_f$  is the free energy of formation of the interstitial defect and  $p$  is the number of interstitial sites available to each normal sodium ion.

The diffusion coefficient  $D$  can be described in terms of a random walk of molecules in discrete steps. From the probability of finding a molecule at a certain place after a fixed number of steps

$$D = g \bar{\lambda}^2 \Gamma \quad [3]$$

where  $g$  is a geometrical constant,  $\bar{\lambda}^2$  is the average of the squares of the step lengths, and  $\Gamma$  is the average number of steps made in unit time. The jump rate  $\Gamma_m$  for ionic motion can be calculated from various models; its usual form is (7)

$$\Gamma_m = \nu \exp(\Delta S_m/R - \Delta H_m/RT) \quad [4]$$

where  $\nu$  is the vibration frequency of the diffusing atom, and  $\Delta S_m$  and  $\Delta H_m$  are the entropy and enthalpy of activation for the motion of an atom from one site to another.

In a defect model the jump rate  $\Gamma$  is the product of the number of defects and the probability of jumping given by Eq. [4]. Then from the above equations

$$D = g \bar{\lambda}^2 \sqrt{p} \nu \exp\left[\frac{\Delta S_f/2 + \Delta S_m}{R} - \frac{\Delta H_f/2 + \Delta H_m}{RT}\right] \quad [5]$$

Equation [5] has the form of Eq. [2], with  $Q_D = \Delta H_f/2 + \Delta H_m$  and  $D_0$  a constant. It is difficult to estimate quantitatively the various quantities in Eq. [5]; one can only say that it is consistent with the experimental data.

Some results on the conductivity of sodium silicate glasses in high fields are consistent with some of the assumptions needed to derive Eq. [4] for the jump probability. One assumption is that the ions sit in an energy "well," and to move to a neighboring site the ion must possess the energy to surmount the barrier between sites. If a Boltzmann distribution of energy exists amongst the ions, their jump rate is given by Eq. [4]. When an electric field  $E$  is imposed on them, jumps in one direction become more probable than in the other, giving rise to the following equation for the conductivity (27)

$$\sigma = \frac{cF\lambda\Gamma}{E} \sinh \frac{FE\lambda}{RTg} \quad [6]$$

For low fields  $\sinh X = X$  and Eq [6] becomes

$$\sigma = \frac{cF^2\lambda^2\Gamma}{gRT}$$

which is Eq. [1] and [3] combined. When the fields



are very high, Eq. [6] becomes

$$\sigma = \frac{cF\lambda_1}{E} \exp\left(\frac{FE\lambda_1}{gRT}\right) \quad [7]$$

so that the conductivity depends exponentially upon the field  $E$ . This exponential dependence at high fields has been confirmed for sodium silicate glasses by several authors (28-31); Maurer (29) also found the hyperbolic sine law for intermediate fields. Maurer and Vermeer (31) found the temperature dependence of the pre-exponential and exponential factors of Eq. [7] expected from their low-field results on the same glasses. Maurer calculated jump distances from Eq. [7]; they were high and increased with increasing temperature. However, when these  $\lambda$  values were corrected by using the effective local field  $E_L$  calculated from the Lorentz-Lorenz relation

$$E_L = \left(\frac{\epsilon + 2}{3}\right) E$$

where  $\epsilon$  is the d-c dielectric constant, instead of the external field  $E_0$ , reasonable values of  $\lambda$  (about 5Å) independent of temperature were found. This correction has been questioned (32), but it probably is valid. This distance of 5Å is close to the separation of interstices expected in fused silica (7).

The most important factor in the energy of formation of the interstitial ion is probably the electrostatic energy needed to tear away the cation from its anion. This energy is therefore directly related to the anionic field strength or effective radius discussed in the section on Ionic Selectivity of Oxides. For a particular glass structure this energy should increase as the monovalent cation becomes smaller. The energy for motion of the ion, on the other hand, depends mainly on the energy needed to squeeze through the "doorways" between interstitial sites; this energy should increase with increasing cationic radius. Therefore one might expect a minimum in activation energy and a maximum in diffusion coefficient for ions in glass as their size is increased. Such a maximum is found for ionic diffusion in soda glasses; sodium and lithium ions diffuse most rapidly in these glasses, while hydrogen and potassium ions diffuse more slowly (33).

The effect of the changing structure of the anionic group is shown by Isard's results on the electric conductivity of sodium aluminosilicate glasses (34). The activation energy for conduction, as shown in Fig. 4, decreases as aluminum replaces silicon in the glass

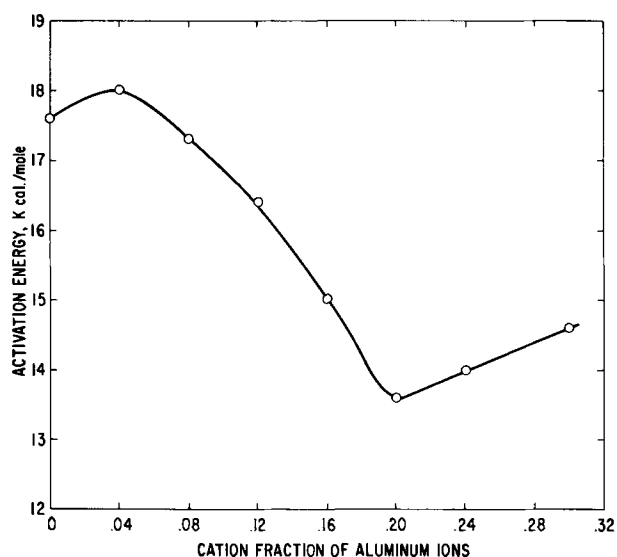


Fig. 4. Activation energy for electrical conduction in various sodium aluminosilicate glasses. Sodium cation fraction held at 0.2, silicon 0.8-X, and aluminum X. From ref. (34).

network, as would be expected from the considerations of the previous paragraph and the section on Ionic Selectivity of Oxides.

The glasses with low sodium ion concentration, Vycor, and fused silica contain some aluminum. It seems likely that the sodium in these glasses is associated with the aluminum, giving aluminosilicate groups, as is the case in quartz (35). Therefore the activation energies for conduction and diffusion of sodium in these glasses may not be directly comparable to those in the binary sodium silicates, because of the probable difference in the anionic group.

*Hydrogen ions in silicates.*—Water diffuses readily into fused silica over a wide range of temperatures. As mentioned before it reacts with the silicon-oxygen network, giving two SiOH groups for each water molecule. The solubility of water in fused silica is proportional to the square root of the water vapor pressure and is little affected by temperature and impurities above about 900°C (10, 36). Below this temperature the solubility is apparently influenced by the thermal history of the silica (10). Roberts and his colleagues studied the diffusion of water into silica over a range of temperatures, and with a variety of techniques (10, 37-39). The diffusion coefficient varied with water concentration; its temperature dependence from 600° to 1200°C was

$$D = 10^{-6} \exp(-18.3/RT)$$

the activation energy being in kilocalories per mole. This equation may be used as a guide for the rate of hydration of fused silica. At 25°C the extrapolated value of  $D$  is  $3.7(10)^{-20}$  cm<sup>2</sup>/sec. This diffusion coefficient implies a very slow rate of hydration of silica at room temperature. For example, the concentration of water is one-tenth that of the surface concentration at distance of 2.7Å in 1 hr and at 72Å in a month.

The reaction of water with alkali silicates involves at least two processes, interdiffusion of hydrogen and alkali ions and dissolution of the silicon-oxygen network (11). The rate of reaction with the network is speeded at higher pH, but the extraction of alkali is slowed because not all the surface sites are occupied by hydrogen ions (see section on Ionic Selectivity of Oxides).

Owen and Douglas concluded that the conductivities of various fused silica samples they examined resulted from sodium ion conduction (21). However, their data, shown in Table II and Fig. 5, show a relation between sodium ion concentration and conductivity only for higher sodium ion concentrations; for lower sodium concentrations no such relation exists. As described below, sodium ions are about 10<sup>4</sup> times as mobile as hydrogen ions in fused silica. Therefore in types OG, OS, and 7940, where the hydrogen ion concentration is about 10<sup>4</sup> times that of sodium, it seems likely that both hydrogen and sodium ions contribute to the conductivity. Furthermore the differences between samples probably reflect the type of site at which these ions are bound. The analyses of the various types of fused silica in Table II are taken from ref. (36), since these should be more accurate than the values given by Owen and Douglas. The higher conductivity of sample OG results from the higher aluminum content of this material, since the monovalent ions are bound less tightly to the aluminosilicate sites (see section on

Table II. Electrical resistivity of fused silicas

Type	Analysis, ppm			Log <sub>10</sub> resistivity log <sub>10</sub> at 350°C	Ref.
	Sodium	OH-	Aluminum		
Vycor	240	240	1300	8.3	(20)
Taylor's	20	low	60	8.8	(21)
Thermal syndicate	IR	4	60	9.7	(21)
	OG	0.06	400	9.2	(21)
	OS	0.04	400	0.02	12.1
Corning 7940	low	1200	low	10.6	(21)

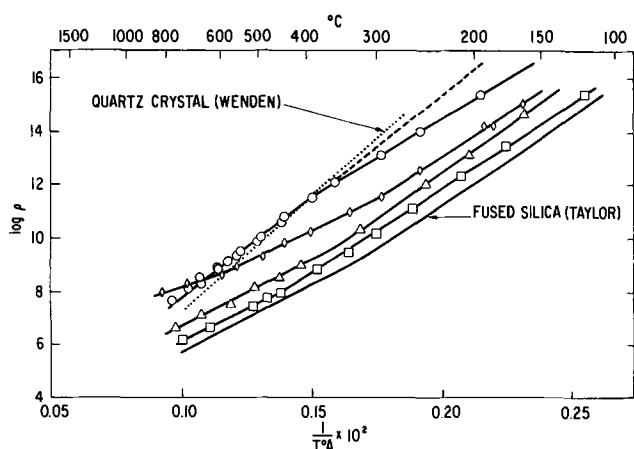


Fig. 5. Temperature dependence of electrical conductivity of various fused silicas (see Table II). ○ OS; △ 1R; □ OG; ◇ 7940; line without points, Taylor's. From ref. (21).

Ionic Selectivity of Oxides). The very low conductivity of sample OS results from the low aluminum content of this sample; the diffusing cations are bound more tightly by the silicate groups. This view is further substantiated by some results of Jorgensen and Norton (40) who found a resistivity of  $4.5(10)^8$  ohm-cm at  $1000^\circ$  for Corning 7940 fused silica that had been baked out to remove most of the  $\text{OH}^-$  groups. This is about an order of magnitude higher than the resistivity of the same material before baking out, as shown in Fig. 5.

The temperature dependence of the conductivity of the silicas shown in Fig. 5 cannot be simply explained. The change in activation energy with temperature may result from transport by different species (hydrogen and alkali ions), the presence of different anionic sites (silicate and aluminate), perhaps other impurities, and possibly some electronic conduction. Because of these possibilities the mobility of hydrogen ions in silica at room temperature, which is of interest in the study of anodic films, is uncertain. If all the conductivity of sample OG could be attributed to hydrogen ions at low temperature, their diffusion coefficient would be about  $2(10)^{-24}$   $\text{cm}^2/\text{sec}$  from the data in Fig. 5. This result should probably be considered a maximum.

The motion of hydrogen ions in fused silica in an electrical field was investigated by Garino-Canina and Priquelier (41). They found no appreciable change in a sample of pure fused silica containing  $10^{20}$  hydroxyl groups per  $\text{cm}^3$  after holding at  $1050^\circ\text{C}$  and  $1500$  v/cm up to 300 hr. However, when a similar material containing about  $10^{20}$  aluminum atoms per  $\text{cm}^3$  was electrolyzed, the hydrogen ions moved to the cathode, judging from changes in the infrared absorption of the sample. After 400 hr at  $1050^\circ\text{C}$  and  $1500$  v/cm a sample 2 cm thick showed no more infrared absorption characteristic of hydroxyl groups. These experiments show conclusively that hydrogen ions associated with  $\text{SiOH}$  groups are much less mobile than those with  $\text{SiOAlOH}$  groups. This result is expected from the tighter binding of cations to the  $\text{SiO}^-$  group, as described earlier.

Hetherington, Jack, and Ramsay electrolyzed fused silica in which the current was carried by sodium ions (42). They showed that hydroxyl ions were introduced at the anode from water vapor in the air, and that after a short time the rate of electrolysis was controlled by the mobility of the hydrogen ions, which was about  $10^4$  smaller than for the sodium ions. Their fused silica contained more than enough aluminum to accommodate the monovalent cations. From their data at different temperatures ( $800^\circ$ - $1300^\circ\text{C}$ ) they calculated a resistivity  $\rho$  for the hydroxyl-containing material to be  $\log_{10} \rho = 5.4 + 5400/T$ . This equation gives an activation energy for hydrogen ion conduction of 24.6 kcal/mole, which is almost identical to the

Table III. Diffusion of various species in fused silica

Species	Diffusion coefficient at $1050^\circ\text{C}$ , $\text{cm}^2/\text{sec}$	Activation energy, kcal/mole	Ref.
Sodium ion	$10^{-6}$	24	(42)
Hydrogen ion	$10^{-10}$	24	(42)
Water	$10^{-9}$	18	(10)
Dissolved oxygen	$10^{-8}$	27	(43)
Lattice oxygen	$2(10)^{-11}$	30-80	(44-46)

activation energy for sodium conduction in fused silica and Vycor, mentioned above. This result is not in accord with the description of the paragraphs on Theories and Mechanisms above, where the difference between the mobilities of hydrogen and sodium ions is explained on the effect of binding on the activation energy, so that a higher activation energy for hydrogen ion conduction would be expected. Experiments on the transport of other ions in fused silica are needed to clarify this discrepancy. The value of  $D$  for hydrogen ions in fused silica, extrapolated to room temperature from the data of Hetherington *et al.*, is about  $8.4(10)^{-24}$ , which is not too far from the value calculated above from the conductivity of type OG silica.

The diffusion coefficients of various species in fused silica at  $1050^\circ\text{C}$  are compared in Table III. The diffusion coefficient of sodium was calculated from conductivities in Vycor (20) and fused silica (21) with Eq. [1]. These materials all contained aluminum; without it a lower diffusion coefficient of sodium might be expected. The diffusion of dissolved molecular oxygen was measured by a permeation technique (43), while the diffusion of lattice oxygen was measured by exchange with isotopically enriched oxygen (44-46).

Hydrogen ions apparently occur at several different sites in fused silica. From measurements of hydrogen permeability, Lee concluded that there were a loosely and tightly bound species (47-49). The "loosely bound" hydrogen ions were introduced by reaction with gaseous hydrogen and were easily removed by pumping out. The hydrogen ions introduced during manufacture of the fused silica, and those introduced with water vapor, were more "tightly bound" and could be removed only by long pumping out at high temperature. Hetherington *et al.* found that the hydroxyl groups introduced by electrolysis of fused silica (described above) could not be removed by pumping for long times at high temperatures and so concluded that they were even more stable (42). The results of Lee (49) and Hetherington *et al.* (42, 50) can be combined to describe three types of sites for hydrogen ions in fused silica as follows.

1. Lee's loosely bound hydrogen ions are at reduced  $\text{SiOAlOR}$  groups, where R is some monovalent cation. In the neighborhood of an aluminosilicate group the network links are weaker and, therefore, may be more easily reduced with hydrogen. The resulting hydrogen ion is loosely bound, however, because of the other monovalent cation already present, and is readily removed. Introduction and removal of these sites takes place by diffusion of hydrogen molecules through the glass, and is therefore rapid.

2. Hydrogen ions introduced in manufacture or with water vapor, if the aluminums are already satisfied, form  $\text{SiOH}$  groups. Their introduction and removal takes place by diffusion of water through the silica, which is slow compared to hydrogen diffusion.

3. Hydrogen ions introduced by electrolysis are fixed at aluminosilicate sites. They cannot be removed by pumping out the silica, because they are required for electroneutrality.

In the results described above it was shown from conductivities that hydrogen ions in type 3 sites are much more mobile than those in type 2 sites, even though the latter can be pumped out as water. Thus the terms loosely and tightly bound are misleading. Hydrogen ions in type 1 sites may be more mobile than the others; however, there are no measurements to substantiate this possibility.

The interdiffusion of hydrogen and sodium ions has been studied in a sodium calcium silicate glass (51). The sodium mobility was found to be about 1800 times greater than the hydrogen, supporting the idea of tighter binding and lower mobility for the small hydrogen ion.

Manuscript received May 19, 1967; revised manuscript received Sept. 5, 1967. This paper was presented at the Dallas Meeting, May 7-12, 1967, as Abstract 23.

Any discussion of this paper will appear in a Discussion Section to be published in the December 1968 JOURNAL.

#### REFERENCES

- W. H. Zachariasen, *J. Am. Chem. Soc.*, **54**, 3841 (1932).
- L. Young, "Anodic Oxide Films," p. 171, Academic Press, New York (1961).
- J. R. Van Wazer, "Phosphorous and its Compounds," p. 272, 719ff, Interscience Publishers, Inc., New York (1958).
- K. Lehovec, *J. Less Common Metals*, **7**, 397 (1964).
- G. W. Morey, "The Properties of Glass," 2nd ed., p. 465ff, Reinhold Publishing Corp., New York (1954).
- J. M. Stevels in "Handbuch der Physik," Vol. 20, "Electrical Conduction, II," p. 350ff, Springer-Verlag, Berlin (1957).
- R. H. Doremus in "Modern Aspects of the Vitreous State," Vol. 2, p. 1, J. D. Mackenzie, Editor, Butterworths, London (1962).
- R. J. Charles, *J. Am. Ceram. Soc.*, **46**, 235 (1963); *ibid.*, **47**, 559 (1964).
- R. V. Adams and R. W. Douglas, *J. Soc. Glass Tech.*, **43**, 147 (1959).
- A. J. Moulson and J. P. Roberts, *Trans. Faraday Soc.*, **57**, 1208 (1961).
- R. W. Douglas and T. M. M. El-Shamy, *J. Am. Ceram. Soc.*, **50**, 1 (1967).
- D. A. Vermilyea, *J. Appl. Phys.*, **36**, 3663 (1965).
- P. F. Schmidt, F. Huber, and R. F. Schwarz, *J. Phys. Chem. Solids*, **15**, 270 (1960).
- G. Eisenman, *Biophys. J.*, **2**, 259 (1962).
- N. V. Sidgwick, "The Chemical Elements and Their Compounds," pp. 837, 846, Oxford (1951).
- Ref (15), p. 420.
- R. H. Doremus, *J. Phys. Chem.*, **68**, 2212 (1964).
- J. R. Johnson, R. H. Bristow, and H. H. Blan, *J. Am. Ceram. Soc.*, **34**, 165 (1951); see also J. R. Johnson, Thesis, Ohio State University (1950).
- E. Seddon, E. J. Tippet, and W. E. S. Turner, *J. Soc. Glass Tech.*, **16**, 450 (1932).
- R. H. Doremus, Unpublished data.
- A. E. Owen and R. W. Douglas, *J. Soc. Glass Tech.*, **43**, 159 (1959).
- Y. Haven and J. M. Stevels, in *Travaux du IV Congress Inter. du Verre*, Imprimerie Chaix 20, p. 343, rue Bergere, Paris (1957).
- Y. Haven and B. Verkerk, *Phys. Chem. Glasses*, **6**, 38 (1965).
- G. Eisenman in "Glass Electrodes for Hydrogen and Other Cations," p. 133, G. Eisenman, Editor, Marcel Dekker, New York (1967).
- A. B. Lidiard in "Handbuch der Physik," Vol. 20, Electrical Conduction, II, Springer-Verlag, Berlin (1957).
- R. J. Charles, *J. Appl. Phys.*, **32**, 1115 (1961).
- A. E. Owen in "Progress in Ceramic Science," Vol. 3, p. 84, J. E. Burke, Editor, Pergamon, London (1963).
- H. Schiller, *Ann. Physik*, **83**, 137 (1927).
- R. J. Maurer, *J. Chem. Phys.*, **9**, 579 (1941).
- A. M. Venderovitch and V. J. Chenykh, *J. Tech. Phys. U.S.S.R.*, **18**, 317 (1948).
- J. Vermeer, *Physica*, **22**, 1257 (1956).
- Ref. (26), p. 129 (footnote).
- R. H. Doremus in "Glass Electrodes for Hydrogen and other Cations," p. 101, G. Eisenman, Editor, Marcel Dekker, New York (1967).
- J. O. Isard, *J. Soc. Glass Tech.*, **43**, 113T (1959).
- A. Kats, "Hydrogen in Alpha-Quartz," Thesis, Delft, (1961).
- G. Hetherington and K. H. Jack, *Phys. Chem. Glasses*, **3**, 129 (1962).
- G. J. Roberts and J. P. Roberts, *ibid.*, **5**, 26 (1964).
- T. Drury and J. P. Roberts, *ibid.*, **4**, 79 (1963).
- G. J. Roberts and J. P. Roberts, *ibid.*, **7**, 82 (1966).
- P. J. Jorgensen and F. J. Norton, VII International Congress on Glass, Paper 310, Gordon and Breach, New York (1966).
- V. Garino-Canina and M. Priqueler, *Phys. Chem. Glasses*, **3**, 43 (1962).
- G. Hetherington, K. H. Jack, and M. W. Ramsay, *ibid.*, **6**, 6 (1965).
- F. J. Norton, *Nature*, **191**, 701 (1961).
- R. Haul and G. Dumbgen, *Z. Elektrochem.*, **66**, 636 (1962).
- E. W. Sucov, *J. Am. Ceram. Soc.*, **46**, 14 (1963).
- E. L. Williams, *ibid.*, **48**, 190 (1965).
- R. W. Lee, R. C. Frank, and D. E. Swets, *J. Chem. Phys.*, **36**, 1062 (1962).
- R. W. Lee, *ibid.*, **38**, 448 (1963).
- R. W. Lee, *Phys. Chem. Glasses*, **7**, 19 (1966).
- T. Bell, G. Hetherington, and K. H. Jack, *ibid.*, **3**, 141 (1962).
- P. Ehrmann, M. de Billy, and J. Zarzycki, *Verres et Ref.*, **18**, 169 (1964).

## Conduction and Stoichiometry in Heat-Treated, Anodic Oxide Films

D. M. Smyth<sup>†</sup> and G. A. Shirn<sup>\*</sup>

Research and Development Laboratories, Sprague Electric Company, North Adams, Massachusetts

#### ABSTRACT

The dielectric properties of heat-treated, anodic oxide films on certain valve metals can be explained by an exponential gradient of conductivity which decreases monotonically from the metal-metal oxide interface. Evidence is presented that the activation energy of this conduction process is a function of the conductivity. An analysis of the bias dependence of capacitance is presented which indicates that the donor distribution across the heat-treated oxide also depends exponentially on position. These observations are discussed in terms of specific conduction models.

The dielectric properties of anodic oxide films on tantalum are drastically affected by heat-treatment in air at 300°-500°C. It has been shown that the prop-

erties subsequent to heat-treatment are consistent with there being an exponential gradient of conductivity which decreases monotonically across the oxide from the Ta-Ta<sub>2</sub>O<sub>5</sub> interface (1-4). It has been assumed that the conductivity is related to local deviations from

<sup>†</sup> Electrochemical Society Life Member.

<sup>\*</sup> Electrochemical Society Active Member.

the stoichiometric composition. The conduction is thermally activated, and an activation energy of 0.6 eV has been reported (3). Systematic deviations from this value have been noted, however, and a more detailed analysis of the activation energy of conduction is given in this report.

In addition, analysis of the bias dependence of capacitance according to the Schottky depletion-layer theory (5) sheds some light on the spatial distribution of donors in the oxide (oxygen vacancies).

#### The Activation Energy

It has been shown that the equivalent series capacitance of the heat-treated oxide can be considered to be related to an effective dielectric thickness which is defined as the oxide thickness between the  $Ta_2O_5$ -counterelectrode interface and the intersection of the conductivity profile with a conductivity level designated as  $\sigma_0$  and defined, to a good approximation, as  $\sigma_0 = \omega\epsilon\epsilon_0$  ( $\omega$  is the angular frequency of the bridge signal,  $\epsilon$  is the dielectric constant of the oxide, and  $\epsilon_0$  is the permittivity of free space,  $8.85 \times 10^{-14}$  F/cm). In other words, the effective dielectric thickness is that part of the oxide where  $\sigma < \sigma_0$ . The capacitance is then obtained from this effective dielectric thickness and the parallel plate equation (see Fig. 1). Thus the conductivity profile is obtained from the frequency dependence of capacitance; the reciprocal capacitance defines the position at which the conductivity,  $\sigma$ , equals  $\sigma_0$ , whose value can be calculated from  $\sigma_0 = \omega\epsilon\epsilon_0$ . Plots of log frequency vs.  $1/C_s$  at several temperatures give a family of straight lines which represent the conductivity profiles at those temperatures (see Fig. 2). The activation energy of conduction is obtained from plots of log frequency vs.  $1/T$  taken at constant  $1/C$ , in other words from the temperature dependence of conductivity at a given position in the oxide.

It is possible to create a conductivity profile that has a very distinct demarcation between conducting and insulating oxide. One way in which this can be accomplished is by partial reanodization of a sample previously heat-treated in air or vacuum (heat-treatment in vacuum causes the film to become conducting throughout its entire thickness). During reanodization at or near the original anodization voltage, the conductivity is removed stepwise from the  $Ta_2O_5$ -counterelectrode interface, and a sharp interface between conducting and nonconducting oxide moves gradually through the film toward the underlying tantalum. As shown in Fig. 1, when the reanodization is halted at some intermediate state, the conductivity profile is made up of the original gradient, decreasing into the oxide from the Ta- $Ta_2O_5$  interface to some point

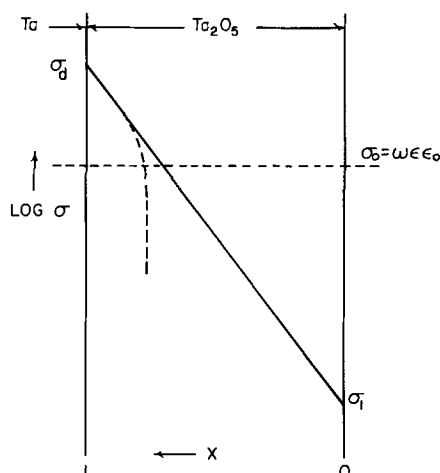


Fig. 1. Schematic representation of the conductivity gradients across heat-treated (solid line) and heat-treated and partially reanodized (dashed line) Ta- $Ta_2O_5$ .

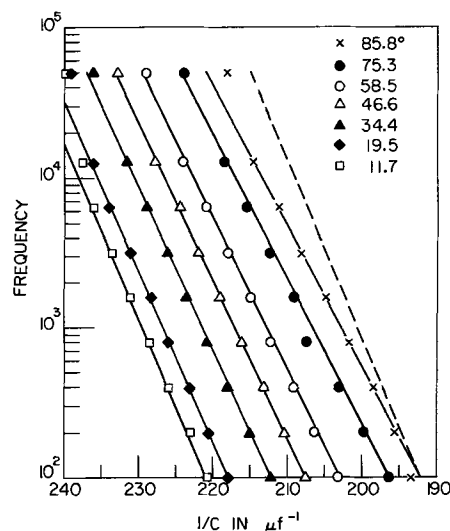


Fig. 2. Conductivity gradients across heat-treated, anodized tantalum. 75v anodization, heat-treated 400°, 30 min in air, Ni dot counterelectrode. Points are from experiment; lines calculated from Eq. [4].

whose location lies closer to the tantalum the more complete the reanodization, where the conductivity abruptly drops to undetectable levels (2). A similar configuration is obtained when samples anodized in concentrated solutions of  $H_3PO_4$  are heat-treated in air. In this case the conductivity profile consists of an inner, shallow gradient near the Ta- $Ta_2O_5$  interface and an outer, very steep gradient. These two gradients correspond to the phosphorus-free and the phosphorus-containing portions of the oxide, respectively (6, 7). When the conductivity distribution lies in a discrete layer, as in the two cases just described, there is a distinct maximum in  $\tan \delta$  as a function of either frequency or temperature (Maxwell-Wagner effect). The temperature dependence of the frequency at which  $\tan \delta$  has its maximum value is another measure of the activation energy of conduction (3).

The experimentally determined activation energies for a variety of samples are listed in Table I. The values 1a and 1b are those described previously (3), and are typical of a large number of samples, all anodized in dilute  $H_2SO_4$  and heated in air. The other values are distinctly smaller, ranging down to 0.44 eV. It is also seen that there is good agreement between the two methods on the same sample (the value of 0.63 eV obtained by the  $\tan \delta$  method for sample 4 is very uncertain because the  $\tan \delta$  maxima were very flat and broad). The different values cannot be correlated with sample preparation since the low values are found for two widely different types.

There is one common aspect of those samples which exhibit anomalously low activation energies; the activation energy was measured for a region of high conductivity compared with the value obtained from

Table I. Activation energy of conduction by two different methods for various sample types

Anodization voltage = 75v and heat-treatment in air at 400° for all samples unless specified otherwise.

Sample type	$E$ by $C = f(\omega)T$ ev	$E$ by $\tan \delta = f(\omega)T$ ev
1. a. Anodized in 0.01M $H_2SO_4$ Heated in air	0.61	
b. Partially reanodized		0.57
2. Heated in vacuum and reanodized at 40v		0.46
3. Heated in vacuum and reanodized at 50v	0.44	0.46
4. Anodized in 1M $H_3PO_4$	0.51	0.63 (?)
5. Anodized in 10M $H_3PO_4$	0.52	0.49
6. Anodized in 14.6M $H_3PO_4$	0.53	0.51

the conventional samples. For a normal sample, heat-treated in air,  $E$  is usually measured by taking a cross-section across the  $\log f$  vs.  $1/C$  plots at about  $x = 0.9$  (see Fig. 1 for definition of  $x$ ). At this point the conductivity is two orders of magnitude below that at the Ta-Ta<sub>2</sub>O<sub>5</sub> interface. For all those samples in Table I giving low values of  $E$ , the conductivity gradient is very shallow near the metal so that the experimentally determined  $E$  is characteristic of the conductivity value near the Ta-Ta<sub>2</sub>O<sub>5</sub> interface. This suggests that the activation energy may decrease with increasing conductivity. Such behavior has indeed been observed for a variety of bulk semiconductors, including Ta<sub>2</sub>O<sub>5</sub> and Nb<sub>2</sub>O<sub>5</sub> (8, 9).

As a further check on this behavior, a sample anodized in 8M H<sub>3</sub>PO<sub>4</sub> and heat-treated in air was analyzed in detail. The activation energy measured in the middle of the shallow, inner gradient was 0.52 eV by the  $\log f$  vs.  $1/C$  method (at  $x = 0.775$ ) and 0.49 eV by the  $\tan \delta$  method, whereas the former method gave a value of 0.7-0.8 eV at  $x = 0.63$  which was on the steep outer gradient. The conductivities at these two positions differed by a factor of 70. A careful examination of families of conductivity profiles for several samples has revealed a tendency for the profiles at different temperatures to converge very slightly toward the Ta-Ta<sub>2</sub>O<sub>5</sub> interface. This would represent a decrease in  $E$  with increasing conductivity. The convergence is very small and is not readily apparent since only that portion of the conductivity profile in the range  $0.85 < x < 1.00$  is experimentally accessible.

In the case of a family of simple, exponential conductivity gradients which converge toward the Ta-Ta<sub>2</sub>O<sub>5</sub> interface, and where the temperature dependence of conductivity at each position fits an Arrhenius-type expression

$$E_x = -k \frac{d \ln \sigma_x}{d 1/T} \quad [1]$$

the appropriate analytical expression is

$$\sigma = A e^{-(E_0 - ax)/kT} \quad [2]$$

i.e., there is an apparent linear dependence of activation energy on position in the oxide. It had previously been proposed that

$$\sigma = A_1 e^{a_1 x} e^{-E/kT} \quad [3]$$

where the first exponential term signifies the position dependence of conductivity and the second exponential the temperature dependence (6). The new form is the same except that the slope of the position dependence is now temperature dependent. Figure 2 shows a set of data taken on a sample with a small, electrolessly deposited, nickel electrode (anodization voltage = 75v, heated 30 min at 400°C in air). The symbols represent the experimental points and the lines are calculated from

$$f = A_2 e^{-(E_0 - a_2 1/C)/kT} \quad [4]$$

with  $a_2 = 0.06638$  eV —  $\mu f$ ,  $E_0 = 2.205$  eV, and  $\log A_2 = 15.036$ . The agreement, particularly with respect to the slope which changes by 26% over this temperature range, is excellent. The dashed line is drawn with the same slope as that of the 11.7° data to demonstrate more dramatically the extent of the change in slope.

In Eq. [2] the activation energy is taken as a function of position in the oxide film. Such a direct relationship is, of course, unlikely, and the variation must be in terms of some other parameter which is a function of position. As stated earlier, it is probable that the activation energy is a function of the local conductivity.

#### The Gradient of Stoichiometry

As previously described, the application of an anodic bias (Ta +) to a heat-treated sample results in a

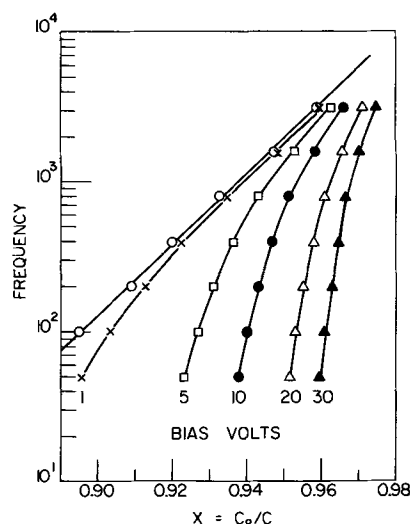


Fig. 3. Effect of d-c bias on the conductivity profile. 100v anodization; standard heat-treatment; measured in 40% H<sub>2</sub>SO<sub>4</sub>. Each bias held 15 min.

temporary reduction of the capacitance (1, 2). The effect is completely reversible up to about one third of the anodization voltage. The effect on the conductivity profile, as determined by the frequency dependence of capacitance, is shown in Fig. 3. The effect of bias is seen to result from the addition of a depletion layer in series with the original dielectric thickness. The depletion layer becomes wider with increasing bias. If this interpretation of the observations is correct, such data can be analyzed by a method derived by Schottky to give the spatial distribution of donors (5). The following section is a description of such an analysis.

According to the Schottky analysis, an increase in bias will result in the depletion of mobile charges (electrons) until a certain total charge has been removed. The thickness of the depletion layer will thus depend on the local density of mobile charges. The depletion layer then contains an equal amount of fixed charges (ionized oxygen vacancies). As long as the applied field is insufficient to move these fixed charges, the effect of bias is reversible.

When a d-c bias is applied to a heat-treated anodic oxide, the capacitance does not adjust quickly to a new stationary value. There is a very rapid change which is immediately followed by a drift whose rate decreases with time. This drift can begin in either direction but will eventually be such as to reduce the effect of bias. An example of such behavior is shown in Fig. 4. The magnitude of the drift can be comparable to the magnitude of the instantaneous change. This drift results in a subsequent history-dependence of the sample which may require several hours to dissipate. As a result, there is a continuous drift of sample prop-

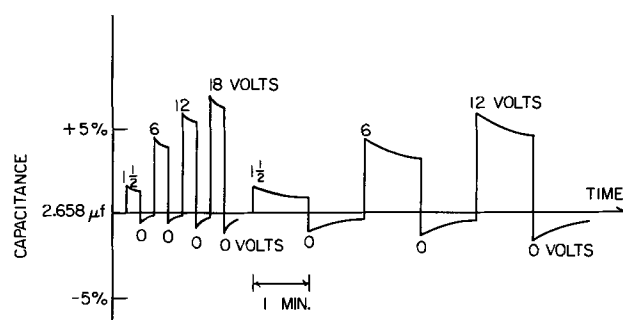


Fig. 4. Time dependence of the effect of bias on capacitance. Same conditions as in Fig. 3.

erties throughout a bias analysis unless several hours of recovery are allowed between each measurement.

In the analysis that follows we have taken the following position. The instantaneous change of capacitance with change of bias represents an immediate electronic response by the system. The subsequent drift is assumed to be a polarization process, perhaps ionic in nature, which is related to the effect of heat-treatment, but is of no consequence to the Schottky analysis. This position is supported by the observation that the instantaneous response is essentially independent of the sample history. A given bias change will result in a given instantaneous change in capacitance,  $C_1 - C_2 = \Delta C$ , even though the actual values of  $C_1$  and  $C_2$  may differ widely, depending on the recent bias history of the sample. The drift with bias must be related to the effects of heat-treatment since its magnitude is far greater than that observed for unheated samples.

In order to obtain the instantaneous capacitance response, the measurements were made with a General Radio Impedance Comparator Type 1605-A in the circuit shown in Fig. 5.  $C_x$  represents the heat-treated sample which could be connected to either of two bias voltages by the switch  $S$ . The bias voltages were supplied by large dry cells and, in each case, the two voltages were shunted by identical, large capacitances ( $C_A = C_B = 686 \mu f$ ) so that the only change in impedance between switch positions was due to  $C_x$ .  $C_d$  and  $R_s$  were respectively a General Radio 1419-A Decade Capacitor plus a Solar Model DK-1 Decade Capacitor, and a ten-turn 500 ohm potentiometer with read-out dial. The former was used to balance the unknown capacitor so that the  $\pm 1\%$  or  $\pm 3\%$  impedance scales could be used. The phase angle was always closely balanced out with  $R_s$ . All measurements were made with a 100 Hz signal.

The procedure was to allow the sample to set for a few minutes at the lower bias to reduce the drift. The impedance difference between  $C_x$  and  $C_d$  was read;  $R_s$  was reduced to the value necessary to balance the phase angle at the higher bias; the bias was switched to the higher value; and the impedance change was read. This procedure was repeated several times between the two biases and the resulting values of  $\Delta(1/C^2)$  were averaged. The scatter was generally within 5%. The setting of  $R_s$  was only a guess for the first cycle, but for subsequent cycles it could be preset to within a phase angle difference of  $\pm 0.0005$  radians. Changes within this range had no significant effect on the impedance. The cycle time had very little effect; a time of 2 min at each bias was used. When the bias was changed there was a flurry of rapid meter fluctuation on the comparator due to charging currents, etc. There was a distinct halt, however, before the slower drift began, and the value at this pause was read visually.

In order to obtain the true, corresponding values of capacitance without drift effects, values of  $C_d$  and  $R_s$

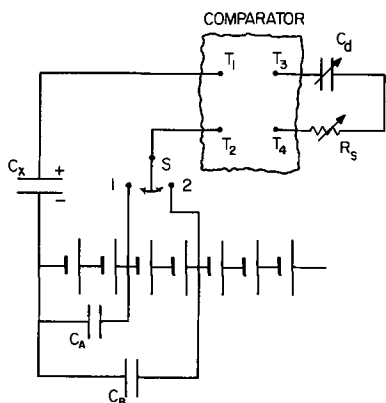


Fig. 5. Diagram of impedance comparator circuit

necessary to give an on-scale impedance reading and a close balance of phase angle were found for the well-rested sample by switching quickly from zero bias to each bias in turn. The sample was rested again and the readings repeated, once at each bias with preset  $C_d$  and  $R_s$ . Each bias was connected for only the 1-2 sec required to obtain the initial response. This technique gave reproducible results, and these values were used to locate the depletion layers in the film.

Reproducible sets of data were obtained for both increasing and decreasing bias, but the two sets differed somewhat since there was more drift after increasing the bias than after decreasing it. The values taken with decreasing bias gave about 20% greater donor concentrations, although the spatial dependence was the same for both sets.

The samples were prepared as described previously (1). The sample area was 18.4 cm<sup>2</sup>, and the measurements were made in an electrolyte of 40% H<sub>2</sub>SO<sub>4</sub>.

The basic expression for the Schottky analysis is

$$\frac{d(1/C^2)}{dV} = \frac{1}{\epsilon\epsilon_0 e N_x} \quad [5]$$

where  $N_x$  is the donor concentration at  $x \propto 1/C$ , and  $e$  is the electronic charge. In the actual evaluation the differential increments were replaced by finite differences.  $N_x$  was plotted as a function of the reciprocal of the capacitance measured for the well-rested sample at the higher bias of each pair.

Figure 6 shows the results obtained from a sample anodized to 150v and then heat-treated at 400° for 30 min in air. The results are plotted as  $\log [\Delta V / \Delta(1/C^2)]$ , which is proportional to  $\log N$ , against the reciprocal capacitance, which is proportional to position in the film. Data obtained for both increasing and decreasing bias are shown. Results are in good agreement with an exponential gradient of donors.

Results from several samples of different thicknesses are shown in Fig. 7. In this case the calculated value of  $N$  is plotted against the normalized distance coordinate,  $x = C_0/C$ , where  $C_0$  represents the capacitance of the entire film without conduction.  $C_0$  has been approximated by the usual parallel plate expression with the thickness taken as  $19.5 \times 10^{-8}$  cm times the anodization voltage, and the dielectric constant as 29 [27.6  $\times$  1.05, which takes into account an irreversible 5% increase in dielectric constant probably caused by slight structural changes in the oxide (1, 2)].  $x = C_0/C = 1.00$  represents the Ta-Ta<sub>2</sub>O<sub>5</sub> interface. The donor distributions shown in Fig. 7 can be approximated by

$$N = 2 \times 10^6 e^{32x}$$

which corresponds to  $\log N_d/N_1 = 14$ , where the sub-

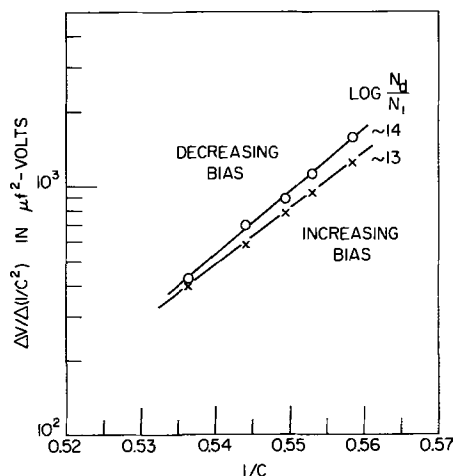


Fig. 6. Schottky plot for 150v anodization, standard heat-treatment.

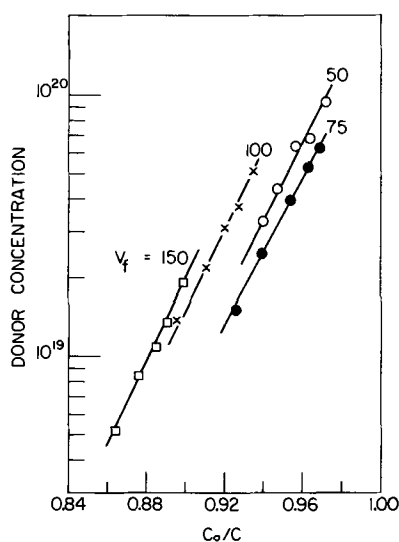


Fig. 7. Donor distributions for samples of different thickness

scripts  $d$  and  $l$  refer, as usual, to the Ta-Ta<sub>2</sub>O<sub>5</sub> and Ta<sub>2</sub>O<sub>5</sub> electrolyte interfaces, respectively.

For a donor distribution determined solely by interface equilibria during heat-treatment, one would expect the data for the various samples in Fig. 7 to be superimposable. The agreement in slope is very good; the agreement in the  $N$  values is good except for the 150v sample; but there seems to be a slight lateral displacement among the samples. The latter may be largely due to the approximation used to calculate  $C_o$ . The 5% increase in dielectric constant is a typical value which may vary some among different samples. The  $N$  values for the 150v sample are significantly lower than the others. This is partly due to the use of lower bias fields for this sample, 2 – 24% of the anodization voltage as compared with 6 – 33% for the 50v sample. The effect seems too large to be entirely accounted for in this way, however.

The results shown in Fig. 7 extrapolate to about  $2 \times 10^{20}$  donors/cm<sup>3</sup> at the Ta-Ta<sub>2</sub>O<sub>5</sub> interface ( $C_o/C = x = 1$ ). This corresponds to an oxygen vacancy content of about 0.3%, or a composition of Ta<sub>2</sub>O<sub>4.984</sub>. This is a reasonable value for an oxygen deficient transition metal oxide.

### Discussion

A dependence of the activation energy of conduction on the conductivity or on the defect concentration of semiconductors is a well-known phenomenon. As early as 1937, Meyer and Neldel noted that for Fe<sub>2</sub>O<sub>3</sub>, ZnO, UO<sub>2</sub>, and TiO<sub>2</sub>, an expression of the form

$$E \propto -\log \sigma_T \quad [6]$$

is obeyed in the region  $\sigma_{20^\circ} \geq 10^{-2} \text{ ohm}^{-1} \text{ cm}^{-1}$  (10). Such a relation may be expected when a semiconductor obeys an expression of the form

$$\sigma_D = A_D e^{-E_D/kT} \quad [7]$$

where the subscript  $D$  denotes a particular defect concentration, and where the conductivity changes much more rapidly with defect concentration than can be accounted for by the change in the pre-exponential term. It should be noted that this does not represent a direct dependence of the activation energy on the donor or acceptor concentration. Pearson and Bardeen found that for doped silicon

$$E = E_o - cN_A^{1/3} \quad [8]$$

where  $N_A$  is the acceptor concentration (11). More recent work on SnO<sub>2</sub> (12), UO<sub>2</sub> (13), Nb<sub>2</sub>O<sub>5</sub> (9), and Ta<sub>2</sub>O<sub>5</sub> (8) gives indications of activation energies which depend on the conductivity level. Marley and

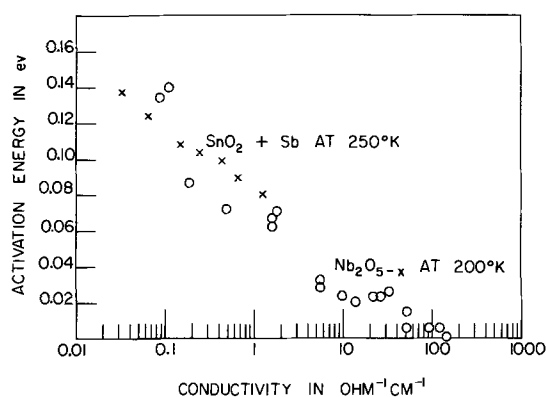


Fig. 8. Meyer-Neldel relationship between activation energy and conductivity for Nb<sub>2</sub>O<sub>5</sub> (9) and SnO<sub>2</sub> (12).

Dockerty present their results on SnO<sub>2</sub> in terms of the Pearson and Bardeen equation (Eq. [8]); actually their data are in better agreement with the Meyer-Neldel rule (Eq. [6]) as shown in Fig. 8. Janninck and Whitmore have made an extensive study of the conductivity of nonstoichiometric Nb<sub>2</sub>O<sub>5</sub> and find activation energies decreasing from 0.486 to 0.0014 eV with increasing reduction (9). Except for the two samples having the highest activation energies (21 samples in all), where the determination of composition was least certain, their results are in good accord with Meyer-Neldel rule, Fig. 8. [The activation energy for sample 59-39 is listed as 0.0580 eV in the paper by Janninck and Whitmore. It is clearly placed at a much lower value in their plot of  $E$  vs. weight per cent reduction and is listed as 0.00580 eV in Janninck's thesis (14). The latter value is in much better accord with samples of similar composition and is the value used in Fig. 8.] Moreover, the slope of the Meyer-Neldel plot for the data of Janninck and Whitmore and the extrapolated value of the activation energy for the conductivity levels with which we are concerned are similar to the values required to fit the experimental data for heat-treated, anodized tantalum and niobium.

There are several possible interpretations, based on a conductivity-dependent activation energy, for the observed exponential conductivity profile across the heat-treated oxide. First of all, for a system which obeys [6] and [7], we can write

$$-E_D = kT(\ln \sigma_D - \ln A) \quad [9]$$

where  $A$  is taken as constant since strict adherence to [6] requires that  $\sigma_D$  be a function only of  $E$ . Then for the case of an exponential conductivity gradient

$$\sigma = \sigma_1 e^{bx} \quad [10]$$

[9] becomes

$$-E_D = kT(\ln \sigma_1 + bx + \ln A) \quad [11]$$

For  $E_D \equiv E_o$  at  $x = 0$

$$-E_D = -E_o + kTbx = -E_o + ax \quad [12]$$

This gives the observed form of the activation energy, as shown in Eq. [2], and  $kTb$  gives the correct value for  $a$ . Note that the result is independent of the temperature at which the basic observation [10] is made.  $E_o$  can then be calculated if the activation energy is known at any one value of  $x$ . Thus the slope of the profile at one temperature and the activation energy at one position leads to an expression which is in quantitative agreement with the observations at all positions and temperatures. Although this is an interesting arithmetical exercise, it unfortunately tells us very little about the physical nature of the conduction process, and, in fact, assumes a negligible contribution to the slope of the conductivity gradient by the slope of the donor gradient.

The problem can be approached differently with the acceptance of the Schottky analysis which yields an



exponential gradient of donors with  $\log N_d/N_1 \approx 14$ . If these donors are oxygen vacancies and if the conduction results from their partial ionization,

$$V_o^x \rightleftharpoons V_o \cdot + n \quad [13]$$

[Kröger notation (15)], the mass-action expression and the condition for charge neutrality lead to

$$n \propto [V_o^x]^{1/2} K e^{-E_i/2kT} \quad [14]$$

$E_i$  is the ionization energy of the first electron from a neutral oxygen vacancy at a given  $[V_o^x]$ . For constant mobility and introducing the spatial dependence of  $[V_o^x]$  and a position dependent activation energy we can write

$$\sigma = K_1 e^{\beta x} e^{-(E_o - \alpha x)/kT} \quad [15a]$$

$$= K_1 e^{-[E_o/kT - (\alpha/kT + \beta)x]} \quad [15b]$$

This expression differs from [2] in that part of the spatial dependence in the exponent is independent of temperature. In view of the excellent agreement of [2] with experimental results, as shown in Fig. 2, it is clear that not very much of the spacial coefficient can be extracted into a temperature independent term. Table II indicates the relative temperature dependence of  $d \ln \sigma/dx$  [which is proportional to  $d \log f/d(1/C)$ ] for four cases: (i) the experimental results from Fig. 2; (ii) from Eq. [2] in which the slope term is inversely proportional to temperature,  $\beta = 0$ ; (iii) from Eq. [15] with  $\beta$  taken as half of  $d \ln [V_o^x]/dx$  ( $\beta = 16.1$ ) as indicated by [14]; and (iv) from [15] with  $\beta = d \ln [V_o^x]/dx = 32.2$ . The agreement with  $\beta = 16.1$  is not as good as for  $\beta = 0$ , although it would take more extensive data to distinguish decisively between the two cases (moreover, the experimental results are the "raw data" and have not been corrected for the temperature and frequency dependence of the dielectric constant). The calculated results with  $\beta = 32.2$  are more clearly in disagreement with the experimental results.

Two questions may be raised about a model which involves the donor gradient determined by the Schottky analysis. The first question involves the stability of such an extremely steep gradient. Since the heat-treated samples remain unchanged in properties over long periods, the diffusion constant for donors at room temperature must be small enough to support this donor gradient without appreciable diffusion. If one takes an upper limit of a 1Å diffusion length over a time of one year, the diffusion constant must be less than  $10^{-24}$  cm<sup>2</sup>/sec. Multiplying this times the donor concentration gradient for the worst case, i.e., at the Ta-Ta<sub>2</sub>O<sub>5</sub> interface for the thinnest films (about  $10^{27}$  donors/cm<sup>4</sup> for an anodization voltage of 25v), a donor flux of  $10^3$  donors/cm<sup>2</sup> sec is obtained which means that about 10 years would be required to change the donor concentration by 1%. Using the activation energy of 1.95 ev found by Pawel and Campbell for the thermal transport of oxygen through anodic Ta<sub>2</sub>O<sub>5</sub> (16), the diffusion constant at 400° should be greater

than that at 25° by a factor of  $10^{18}$ . Thus if  $10^{-24}$  cm<sup>2</sup>/sec is suitable for a room temperature value, then a value of  $10^{-6}$  cm<sup>2</sup>/sec would be anticipated at 400°. This would correspond to a flux which is far larger than necessary to account for the very short equilibration times observed at 400°. It can be concluded that the donor gradients indicated by the Schottky analysis could be stable at room temperature and still lead to the rapid transport of oxygen observed at moderately elevated temperatures.

The second question concerns the time-constant of the donor levels. Since the bias dependence measurements were taken for the instantaneous response ( $\tau \leq 1$  sec), we must consider whether or not such a response is compatible with the depth of the electronic states in question. The time constant for the emptying of traps of depth  $E_i$  can be written

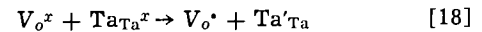
$$\frac{1}{\tau} \simeq \nu e^{-E_i/kT} \quad [16]$$

where  $\nu$  is generally taken to be the lattice vibration frequency of about  $10^{13}$  sec<sup>-1</sup>. For the conduction model just described,  $E_i$  corresponds to twice the observed activation energy of conduction (Eq. [14]) and thus lies in the range 0.9-1.4 ev for the pertinent region in the film. This would appear to lead to incompatible time constants, but one should consider that the effective trap depth will be reduced by the field according to the Poole-Frenkel effect (17). Equation [16] should be modified to

$$\frac{1}{\tau} = \nu e^{-(E_i/kT - \gamma F^{1/2})} \quad [17]$$

where  $F$  is the applied field and  $\gamma = (q^3/\pi\epsilon\epsilon_0)^{1/2} \cdot 1/kT = 1 - 3 \times 10^{-2}$  (cm/v)<sup>1/2</sup> depending on whether the optical dielectric constant for Ta<sub>2</sub>O<sub>5</sub> ( $\epsilon_r = 4.8$ ) or the dielectric constant for free space ( $\epsilon = 1$ ) is used (18). Since the applied fields lie in the range  $2 \times 10^5$  to  $2 \times 10^6$  v/cm, the Poole-Frenkel correction reduces the calculated time constants to the region of a few seconds for the worst case (highest  $E_i$  and lowest field). This is in accord with the observed response. Some of the observed polarization effects, such as shown in Fig. 4, may arise from the time dependence of the deeper vacancy levels which lie further from the Ta-Ta<sub>2</sub>O<sub>5</sub> interface. As these levels slowly empty, the depletion layer should both widen and move away from the Ta-Ta<sub>2</sub>O<sub>5</sub> interface. This is in the direction of the observed long-term drift.

Three other conduction models might be mentioned which should have very rapid bias-responses. The first two are based on the electron transfer.



going essentially to completion. Conduction could then occur either by a hopping mechanism for cation to cation or by direct ionization to the conduction band from Ta'\_{Ta} (Ta<sup>4+</sup>). For the first case the number of charge carriers would be temperature independent and the observed activation energy would be an activation energy of mobility for the hopping process. This leads to very low mobilities ( $\sim 10^{-8}$  cm<sup>2</sup>/v sec), but these are adequate to give very fast response to a d-c bias because of the short distances and high fields involved. A third possibility would involve partial compensation such that the acceptor concentration is less than  $[V_o]$  but much greater than the concentration of ionized electrons. For the last two possibilities (partial compensation and direct ionization from Ta'\_{Ta}) the ionization energy would correspond to the observed activation energy. For all three models the temperature independent part of the conductivity gradient would correspond to the full Schottky slope ( $\beta = 32.2$ ). These mechanisms are considered unlikely because of the poor agreement for this case shown in Table II.

Table II. Absolute and relative values of the conductivity gradient,

$$d \ln \sigma/dx = \frac{\alpha}{kT} + \beta, \text{ calculated from Eq. [15] for}$$

$$d \ln \sigma/dx = 56.3 \text{ at } 34^\circ \text{ and } E = 0.45 \text{ ev at } x = 1$$

T, °K	$d \ln \sigma/dx$			$(d \ln \sigma/dx)_{284.9^\circ K}$			Observed
	$\beta = 0$	$\beta = 16.1$	$\beta = 32.2$	$\beta = 0$	$\beta = 16.1$	$\beta = 32.2$	
359.0	48.10	50.51	52.83	1.260	1.197	1.101	1.25
348.5	49.53	51.54	53.44	1.223	1.173	1.089	1.21
331.7	52.04	53.33	54.52	1.164	1.134	1.067	1.15
319.8	53.99	54.72	55.35	1.122	1.105	1.051	1.11
307.6	56.12	56.25	56.27	1.080	1.075	1.034	1.10
292.7	58.99	58.30	57.50	1.027	1.037	1.012	1.05
284.9	60.59	60.45	58.19	1.000	1.000	1.000	1.00

In summary, we can propose a detailed model based on acceptance of the donor profile as determined by the Schottky depletion layer analysis. This accounts for slightly more than half of the observed  $\log \sigma_d/\sigma_1 \approx 24$ . Conduction then arises from partial ionization of an electron from the donors (the more weakly bound electron in the case of oxygen vacancies), and the ionization energy corresponds to twice the observed activation energy of conduction. The ionization energy decreases with donor concentration according to the empirical Meyer-Neldel relationship, giving an apparent linear dependence of activation energy on position in the film. The remainder of the slope of the conductivity profile is accounted for by the resulting increased degree of ionization of donors as the Ta-Ta<sub>2</sub>O<sub>5</sub> is approached. This model leads to a space-independent electron mobility of the order of 0.2 cm<sup>2</sup>/v sec.

Manuscript received June 15, 1967; revised manuscript received Aug. 28, 1967. This paper was presented at the Dallas Meeting, May 7-12, 1967, as Abstract 27.

Any discussion of this paper will appear in a Discussion Section to be published in the December 1968 JOURNAL.

#### REFERENCES

1. D. M. Smyth, G. A. Shirn, and T. B. Tripp, *This Journal*, **110**, 1271 (1963).

2. D. M. Smyth and T. B. Tripp, *ibid.*, **110**, 1277 (1963).
3. D. M. Smyth, G. A. Shirn, and T. B. Tripp, *ibid.*, **111**, 1331 (1964).
4. D. M. Smyth, *ibid.*, **114**, 723 (1967).
5. W. Schottky, *Z. Phys.*, **118**, 539 (1942).
6. D. M. Smyth, T. B. Tripp, and G. A. Shirn, *This Journal*, **113**, 100 (1966).
7. D. M. Smyth, *ibid.*, **113**, 1271 (1966).
8. P. Kofstad, *ibid.*, **109**, 776 (1962).
9. R. F. Janninck and D. H. Whitmore, *J. Chem. Phys.*, **37**, 2750 (1962).
10. W. Meyer and H. Neldel, *Z. Tech. Phys.*, **18**, 588 (1937).
11. G. L. Pearson and J. Bardeen, *Phys. Rev.*, **75**, 865 (1949).
12. J. A. Marley and R. C. Dockerty, *ibid.*, **140**, A304 (1965).
13. P. Nagels, J. Devreese, and M. Denayer, *J. Appl. Phys.*, **35**, 1175 (1964).
14. R. F. Janninck, Thesis, Northwestern University (1962).
15. F. A. Kröger, "Chemistry of Imperfect Crystals," North-Holland Publishing Co., Amsterdam (1964).
16. R. E. Pawel and J. J. Campbell, *This Journal*, **113**, 1204 (1966).
17. C. A. Mead, *Phys. Rev.*, **128**, 2088 (1962).
18. W. Goruk, Private communication.

## Impedance for Tunnel Exchange of Electrons Across the Annealed Ta/Ta<sub>2</sub>O<sub>5</sub> Interface

K. Lehovc\*

Research and Development Laboratories, Sprague Electric Company, North Adams, Massachusetts

#### ABSTRACT

Tunneling of electrons from the tantalum metal into the adjacent oxide is an alternative explanation to a conductivity profile for the observed impedance of annealed Ta/Ta<sub>2</sub>O<sub>5</sub> capacitors as function of frequency, bias voltage, and temperature. The transformation of the Schottky-distribution [ $\partial E/\partial(1/C)^2$  vs.  $(1/C)$ ] into the distribution of recipient sites for tunneling electrons is derived. An explanation for the observed dependence of the activation energy of "conductivity" on position is given. A method is suggested for studying polarization by means of the tunnel impedance.

Smyth and co-workers have analyzed capacitance and loss angle measurements of annealed Ta/Ta<sub>2</sub>O<sub>5</sub> structures in terms of an exponential conductivity profile (1-4). This paper shows that a different model, namely, tunneling of electrons from the tantalum metal into the adjacent oxide, may generate an impedance whose frequency dependence is formally identical with that of an exponential conductivity profile. The observed "Schottky profile" (4), while not providing the actual vacancy distribution, can be accounted for by the tunnel model also.

#### Description of the Tunnel Model

The model to be analyzed in what follows considers tunneling of electrons between the tantalum and recipient sites in the adjacent oxide under the stimulus of an applied a-c voltage. The recipient sites are believed to be oxygen vacancies. While no specific distribution for these vacancies needs to be postulated, at least initially, it is reasonable to expect some sort

of decrease of the recipient concentration with distance,  $\delta$ , from the tantalum. To be specific, we shall assume that the recipient sites are electrically neutral if "empty" and become negatively charged, when "occupied" by an electron. Similar arguments could be advanced, however, for recipients which are neutral when occupied and positively charged when empty, and, for the simultaneous presence of two types of recipients, one positively and the other negatively charged.

The fundamental steps of the tunnel exchange of electrons across the Ta/Ta<sub>2</sub>O<sub>5</sub> interface will be discussed using the schematic energy level diagram of Fig. 1. The Fermi level  $\epsilon_F$  in the metal and a recipient state for an electron at the distance  $\delta$  in the oxide have been indicated. At equilibrium, the occupation of this state corresponds to that of a state of the same energy,  $\epsilon^o_T$ , in the metal. When an a-c voltage  $\tilde{E}$  is applied to the oxide, the a-c voltage drop across the distance  $\delta$  is

$$\tilde{V} = \tilde{E}\delta/d \quad [1]$$

\* Electrochemical Society Active Member.

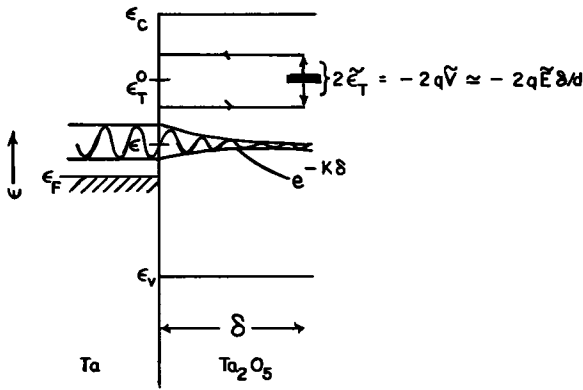


Fig. 1. Schematic energy level diagram for the Ta/Ta<sub>2</sub>O<sub>5</sub> interface to explain electron tunnel exchange with a trap of energy  $\epsilon_T$ . Horizontal arrows indicate electron flow; vertical arrows mark modulation of trap energy due to the applied voltage  $\tilde{E}$ . An attenuated wave function for a tunneling electron of energy  $\epsilon$  is shown schematically.

neglecting polarization effects. Accordingly, the receptor state is lifted or lowered with respect to the energy state  $\epsilon_T^0$  in the metal as indicated in Fig. 1. In each instant the electron population tends to equilibrate with that of an equal state in the metal. This causes an outflow of electrons when the energy state is lifted and an inflow of electrons when it is lowered, as indicated by the arrows in the figure. If the electron exchange between the receptor state and the metal is characterized by the time constant  $\tau$ , a phase shift arises between applied voltage  $\tilde{E}$  and the induced current resulting in a lossy capacitive impedance.

The wave function for a conduction electron of the tantalum metal tunneling into the forbidden band of the oxide is exponentially attenuated as shown schematically in Fig. 1. The rate of transition of such an electron to the receptor state is in proportion to the electron density at the position of the receptor state and depends on distance  $\delta$  as  $e^{-2K\delta}$  therefore. Thus, the time constant for the electron exchange between the tantalum metal and the receptor state is of the form

$$\tau = \tau_0 e^{+2K\delta} \quad [2]$$

where  $\tau_0$  is a suitable average over all energies of tunneling electrons and their respective capture cross sections by the recipient state.

In general,  $K$  and  $\tau_0$  will depend (i) on the recipient state, in particular its energy  $\epsilon_T$ , and (ii) on the applied potential  $E$ , which modifies the shape of the barrier through which the electrons tunnel. However, it will be shown later that the expression for the impedance contains the Fermi-factor product  $f(1-f)$ . In the case of a quasicontinuous energy spectrum of traps, the attenuation of this term with energy is much stronger than that arising from the dependence of  $K$  and  $\tau_0$  on  $\epsilon_T$ , so that we may take  $K$  and  $\tau_0$  as the values at the maximum of  $f(1-f)$  over the range  $\epsilon_T$ .

Since tunnel distances are typically only of the order of  $10^{-7}$  cm, and the applied fields are fractions of the formation field, i.e., several  $10^5$  v/cm only, it is unlikely that the deformation of the barrier by the field has an effect of magnitude comparable to that of the field on the Fermi factor.<sup>1</sup> We shall, therefore, consider  $K$  and  $\tau_0$  as empirical constants in this paper, which are the same for all recipient states.

The exponential dependence on distance of the time constant  $\tau$  for tunnel exchange has been pointed out already by Heiman and Warfield (5) who considered tunnel exchange of electrons from the conduction band

<sup>1</sup> Comparing  $\exp(-2K\delta)$  to  $\exp(-qE\delta/kTd)$  and using  $K \approx [2m^*/\hbar^2 (\epsilon_c - \epsilon_T + qE\delta/d)]^{1/2}$ , one realizes that  $\partial K/\partial E \approx q\delta K/2(\epsilon_c - \epsilon_T)d$  is small vs.  $q\delta/kTd$ , for  $K\delta \approx 1$ ,  $(\epsilon_c - \epsilon_T)/q \approx 1$  V and  $qE\delta/d \ll \epsilon_c - \epsilon_T$ .

of a semiconductor into trap levels in an adjacent insulator. The driving force, in their case, was the modulation of the electron density at the surface of the semiconductor by the applied field. In the present case, there is no modulation of the electron concentration in the tantalum metal; rather the "driving force" is the shift of the energy level in the receptor state relative to the Fermi level in the tantalum metal by the applied a-c voltage. The differences between the case of a MOS structure discussed in ref. (5) and the present case of a MOM structure will be discussed in more detail in Appendix I.

For a system of time constant  $\tau$  under the influence of a stimulus of angular frequency  $\omega$ , the case of resonance

$$\omega\tau \approx 1 \quad [3]$$

plays a significant role. Since  $\tau$  varies exponentially with position, according to Eq. [2], we obtain a linear dependence on  $\ln\omega$  for the position  $\delta_0$  where resonance occurs

$$\delta_0 = [2K]^{-1} \cdot [\ln 1/\tau_0 - \ln\omega] \quad [4]$$

It will be shown later that this is the reason for the exponential conductivity profile  $\sigma(\delta^*)$  of Smyth *et al.* (1-4) obtained by plotting a conductivity defined by

$$\sigma = \epsilon\epsilon_0\omega \quad [5]$$

vs. a "distance" defined by

$$\delta^* = d(1 - C_x/C^s) = A\epsilon\epsilon_0(1/C_x - 1/C^s) \quad [6]$$

where  $C_x$  is the ideal oxide capacitance which is related to the oxide thickness  $d$  by

$$C_x = A\epsilon\epsilon_0/d \quad [7]$$

and  $C^s$  is the measured equivalent series capacitance at the frequency  $\omega$ . We have introduced a new symbol  $\delta^*$  rather than the tunnel distance  $\delta$ , since we consider  $\delta^*$  defined by Eq. [6] as an empirical quantity which need not necessarily be equal to the tunnel distance  $\delta_0$  of Eq. [4].

Figure 2 serves to illustrate the origin of the "Schottky profile" according to the tunnel model. The energy levels of recipient states located at different distances  $\delta$  from the tantalum metal are shown: (i) at zero applied bias  $E = 0$ , and (ii) at the anodic bias voltages  $E_1$  and  $E_2$  ( $> E_1$ ). At a frequency  $\omega$  the states communicate with the tantalum metal up to about the distance  $\delta$  for which  $\omega\tau(\delta) \approx 1$ , resulting in the dependence of  $\delta$  on  $\omega$  indicated in the figure.

The energy level of the receptor states is tilted by the angle  $qE/d$  by an applied anodic bias voltage  $E$ .

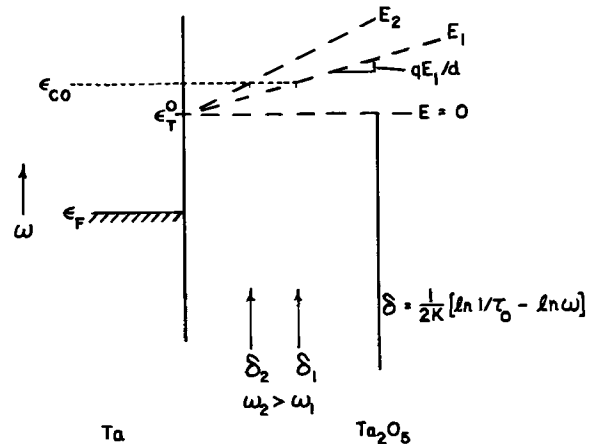


Fig. 2. Concerning the bias dependence of the tunnel impedance. The tunnel distance at resonance  $\omega\tau \approx 1$  is related to the frequency as noted in the figure on the lower right. Lack of electrons in the metal of energies greater than  $\epsilon_{C0}$  leads to a cut-off distance which depends on bias [ $\delta_1(E_1)$  and  $\delta_2(E_2)$ ].

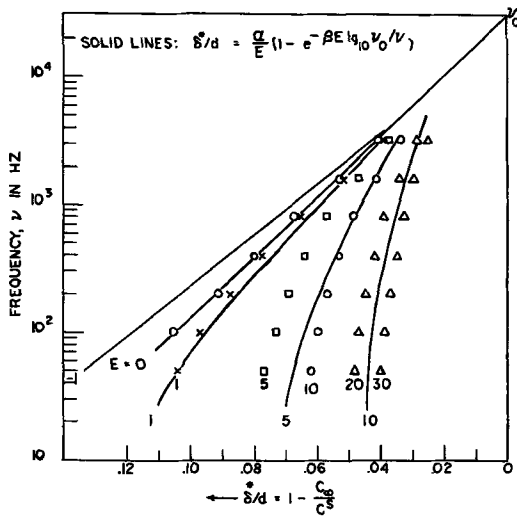


Fig. 3. Points are experimental conductivity profiles by [5] and [6] according to Smyth and Shirn (4). Theoretical curves by Eq. [43] with parameters of Table I, second column.

In order to understand the origin of the vertical drop of the conductivity profile under bias from which the Schottky plots are derived (4) and which is shown in Fig. 3, let us assume that there are no electrons above a cut-off energy  $\epsilon_{c0}$  in the tantalum metal. This is, of course, a gross oversimplification, introduced here only for the purpose of a simplified explanation of the bias effect. The exact relations will be derived later based on a Fermi distribution. Because of the energy cut-off for electrons, recipient states above the dotted line  $\epsilon_{c0}$  in Fig. 2 cannot exchange electrons with the tantalum metal under an a-c stimulus. The intersects of the energy levels of the recipient states with the cut-off energy correspond to the distances  $\delta_1$  and  $\delta_2$  at the applied d-c bias voltages  $E_1$  and  $E_2$ , respectively. These distances in turn correspond to the cut-off frequencies  $\omega_1$  and  $\omega_2$ , respectively, defined by the relation [4]. At frequencies lower than the cut-off frequency  $\omega_1$ , the tunnel capacitance is independent of frequency since tunneling to the states  $\epsilon > \epsilon_{c0}$  at  $\delta > \delta_1$  is not possible. This leads to the vertical drop-off of the conductivity profile for frequencies  $\omega < \omega_1$  when the bias  $E_1$  is applied. The vertical drop-off of the conductivity profile under bias is illustrated in Fig. 3 using experimental points obtained by Smyth and Shirn (4). The solid lines are theoretical curves according to the tunnel theory, which will be derived later on.

#### Detailed Expressions for the Tunnel Impedance

Designating the density of traps of energy  $\epsilon_T$  by  $n_T$ , i.e., number of traps per unit volume per unit trap energy range, a space charge density

$$\rho = -q \int_{\epsilon_0}^{\epsilon_c} n_T f_T^* \partial \epsilon_T \quad [8]$$

results where  $f_T^*$  is the occupation factor, i.e., the fraction of traps of energy  $\epsilon_T$  which are occupied, and the integration extends over the forbidden band of the oxide. In the case of thermal equilibrium the occupation factor becomes equal to the Fermi factor

$$f_T = [1 + \exp(\epsilon_T - \epsilon_F/kT)]^{-1} \quad [9]$$

However, during nonequilibrium conditions such as the "drift" of the impedance after applying or removing a bias voltage,  $f_T^*$  need not equal  $f_T$ . When applying a small a-c voltage  $\tilde{E}$  to the oxide, the potential  $V(\delta)$  at the position  $\delta$  in the oxide is modulated. This changes the energy of a trap relative to the

Fermi-level  $\epsilon_F$  in the tantalum metal by

$$\epsilon_T - \epsilon_F = \epsilon_T^0 - \epsilon_F - qV(\delta) \quad [10]$$

where  $V(\delta=0) = 0$  has been chosen. The a-c component of [10] (indicated by a wave symbol above the notation) is

$$\tilde{\epsilon}_T = -q\tilde{V} \quad [11]$$

Since the electrons in the traps tend to equilibrate by tunneling with the electrons of the corresponding energy level in the tantalum metal, the modulated trap energy  $\tilde{\epsilon}_T$  induces an alternating charge flow between the trap and the tantalum metal. Thus, the occupation factor  $f_T^*$  contains an a-c component,  $\tilde{f}_T^*$ , generated by the applied a-c voltage  $\tilde{E}$ .

Poisson's equation integrated twice over the oxide provides

$$\tilde{E} = \tilde{V}_{d'} \cdot d + \int_0^d \frac{\tilde{\rho}}{\epsilon \epsilon_0} \delta \partial \delta \quad [12]$$

where  $\tilde{V}_{d'}$  is the field modulation at the electrode at  $\delta = d$ . The second term on the right-hand side is the contribution to the potential from dipoles consisting of the space charge  $\tilde{\rho}$  at  $\delta$  and the opposite charge at the tantalum metal. The field at  $\delta = d$  is related to the charge  $\tilde{Q}_M$  by Gauss' law

$$\tilde{Q}_M = -A\tilde{V}_{d'} \cdot \epsilon \epsilon_0 \quad [13]$$

Inserting the component of [8] which arises from the small a-c modulation into [12] and substituting [13] for  $\tilde{V}_{d'}$ , one obtains the admittance

$$\Sigma = i\omega \tilde{Q}_M / \tilde{E} = i\omega C_x + \Sigma_T \quad [14]$$

where

$$\Sigma_T = i\omega A q^2 \int_0^d \left[ (\delta/d) \cdot (\tilde{V}/\tilde{E}) \cdot \int_{\epsilon_0}^{\epsilon_c} n_T (\tilde{f}_T^* / \epsilon_T) \partial \epsilon_T \right] \partial \delta \quad [15]$$

Evaluation of this integral requires expressions for  $\tilde{V}/\tilde{E}$ ,  $\tilde{f}_T^*/\epsilon_T$  and  $n_T = n_T(\epsilon_T, \delta)$ . To simplify the analysis we shall assume that the a-c space charge  $\int_0^d \tilde{\rho} \partial \delta$  is small compared to  $\epsilon \epsilon_0 \tilde{E}/d$ , so that

$$\tilde{V}/\tilde{E} \approx \delta/d \quad [16]$$

If this assumption is not justified, Poisson's equation must be used to relate  $\tilde{V}/\tilde{E}$  to  $\tilde{\rho}$  and  $\delta$ .

The analysis (to be presented elsewhere) of the tunnel process for electrons between the metal and a single trap level of energy  $\epsilon_T$  in the oxide at the distance  $\delta$  provides

$$\tilde{f}_T^* / \epsilon_T = f_T (1 - f_T) (1 + i\omega \tau_T)^{-1} / kT \quad [17]$$

where  $\tau_T$  is the time constant given by Eq. [2].

The factor  $f_T(1 - f_T)$  in Eq. [17] arises from the fact that a-c exchange of electrons with traps is only possible if the traps are neither completely empty nor completely occupied: In the first case,  $f_T \approx 0$ , emission of electrons is impossible and in the second case,  $f_T \approx 1$ , absorption of electrons is impossible. The occurrence of the factor  $f_T(1 - f_T)$  is well known for other electron transition processes to traps, e.g., transitions between electrons in surface states and those in the conduction band of a semiconductor lead

(6) to a surface state capacitance in proportion to  $f_T(1 - f_T)$ .

In deriving Eq. [17] it was assumed that the traps which participate in the a-c electron exchange with the tantalum metal at the angular frequency  $\omega$  have reached d-c equilibrium with the metal, i.e.,  $f_T^* = f_T$ . During the transient conditions following a switch of d-c bias voltage, when  $f_T^* \neq f_T$ , another contribution to  $\tilde{f}_T^*/\epsilon_T$  may arise in addition to that of Eq. [17] due to the modulation of the attenuation constant  $K$  by the applied field. However, the analysis of transient conditions by means of the tunnel model will not be considered further in this paper.

Inserting [16] and [17] into Eq. [15] and defining

$$\frac{N_T}{1 + i\omega\tau} \equiv \int_{\epsilon_v}^{\epsilon_c} \frac{n_T f_T (1 - f_T)}{1 + i\omega\tau_T} \partial\epsilon_T \quad [18]$$

one obtains

$$\Sigma_T = i\omega A q^2 / kT \cdot \int_0^d (\delta/d)^2 N_T (1 + i\omega\tau)^{-1} \partial\delta \quad [19]$$

Since the experimental data are expressed in terms of a series arrangement  $C^s, R^s$ , we shall transform the parallel conductance  $\Sigma_T$  which shunts the ideal capacitance [7] into a series arrangement (Fig. 4)

$$R^s + [i\omega C^s]^{-1} = [i\omega C_\infty + \Sigma_T]^{-1} \simeq [i\omega C_x]^{-1} + \Sigma_T / (\omega^2 C_x^2) \quad [20]$$

where  $\Sigma_T \ll \omega C_\infty$  has been assumed.

Furthermore, letting

$$\Sigma_T \equiv \omega(\Gamma_T + iC_T) \quad [21]$$

one has

$$\delta^*/d = 1 - C_\infty/C^s \simeq C_T/C_x \quad [22]$$

and

$$\tan \theta \simeq \Gamma_T/C_x \quad [23]$$

#### Comparison of Tunnel Impedance with that of a Conductivity Profile

The impedance resulting from a conductivity profile  $\sigma(\delta^*)$  is

$$R^s + [i\omega C^s]^{-1} = \frac{1}{A} \int_0^d (\sigma + i\omega\epsilon_0)^{-1} \partial d^* \\ = [i\omega C_x]^{-1} - [iA\omega\epsilon_0]^{-1} \cdot \int_0^d (1 + i\omega\epsilon_0/\sigma)^{-1} \partial\delta^* \quad [24]$$

Equation [24] becomes identical to [20] with [19] by the substitutions

$$\delta = \lambda\delta^* \quad [25]$$

with

$$\lambda = \left[ \frac{q^2}{kT\epsilon_0} \frac{N_T}{N_T\delta^2} \right]^{-1} \quad [26]$$

and

$$\epsilon_0/\sigma = \tau \quad [27]$$

The upper limit  $d$  of the integrals in [24] and [19] can safely be replaced by infinity since practically no contributions arise in either integral from the outer oxide region  $\delta \simeq d$ . Equation [27] is satisfied for an

exponential conductivity profile

$$\sigma = \sigma_0 e^{-K\delta^*/d} \quad [28]$$

if we identify

$$\epsilon_0/\sigma_0 = \tau_0 \quad [29]$$

and

$$K\sigma = 2Kd\lambda \quad [30]$$

where  $\tau_0$  and  $K$  are the values in [2].

On the other hand, inserting the tunnel time constant [2] into [19] and using [20] and [6], one obtains [25] as follows: Assume that  $\omega\tau \ll 1$ . Since  $\tau$  varies extremely rapidly with position we may substitute in [19]  $1 + i\omega\tau \simeq 1$  for  $\delta < \delta_0$  and  $1 + i\omega\tau \simeq 0$  for  $\delta > \delta_0$  where  $\delta_0$  is the value defined by [4]. We thus obtain for the capacitive part  $C_T$  of the conductance  $\Sigma_T$

$$C_T \simeq \frac{Aq^2}{kT} \int_0^{\delta_0} (\delta/d)^2 N_T \partial\delta \simeq \frac{Aq^2}{kT} (\delta/d)^2 \bar{N}_T \cdot \delta_0 \quad [31]$$

Equation [25] results from [22] with [26] and [31].

The temperature dependence of the zero bias conductivity profile can be obtained from [22] with [31] and [4]. Smyth *et al.* (4) define the activation energy as

$$U_\sigma = -k \partial \ln \omega / \partial (1/T)_{\delta^* = \text{constant}} \quad [32]$$

Since  $\delta^* = \text{constant}$  implies  $C_T = \text{constant}$ , one has from [31]<sup>2</sup>  $\partial[N_T\delta_0/T]/\partial T^{-1} = 0$ , i.e.,

$$U_\sigma = U_{\tau_0} + 2K\delta[U_{\bar{N}_T} - kT] = U_{\tau_0} + \lambda 2K\delta^*[U_{\bar{N}_T} - kT] \quad [33]$$

where

$$U_{\tau_0} = -k \frac{\partial \ln 1/\tau_0}{\partial 1/T} \quad [34]$$

and

$$U_{\bar{N}_T} = -k \frac{\partial \ln \bar{N}_T}{\partial 1/T} \quad [35]$$

Thus the activation energy of the zero bias "conductivity profile" depends on position as is indeed observed (4).

A dependence of the "conductivity profile" on the bias voltage may arise from the Fermi factor  $f_T$  which enters the definition [18] of  $N_T$ . There is also an influence of the bias voltage on the attenuation "constant"  $K$ , but this effect will be ignored in what follows.

For an energy level sufficiently above the Fermi level that  $\epsilon_T - \epsilon_F \gg kT$  one has  $1 - f_T \simeq 1$ , and

$$f_T \simeq \exp[-(\epsilon_T - \epsilon_F)/kT] = f_T^0 e^{-qpE/kTd} \quad [36]$$

where  $f_T^0 = [f_T]_{E=0}$ . The exponential term containing  $E$  results from the shift of the energy level of the recipient state *vs.* the Fermi level in the metal (see Eq. [10]) and assuming that

$$V = pE\delta/d \quad [37]$$

where  $p \leq 1$  is a factor accounting for the possible presence of polarization.

At this point, detailed assumptions on the energy distribution of the recipient states are required. In the case of a broad energy spectrum of traps overlapping the Fermi energy one has

$$N_T/(1 + i\omega\tau) = n_F \cdot kT/(1 + i\omega\tau_F) \quad [38]$$

with  $\tau_F, n_F$  being the values of  $\tau_T, n_T$  taken at the energy  $\epsilon_T = \epsilon_F$ . Equation [38] results from the sharp attenuation of  $f_T(1 - f_T)$  with energy difference  $\epsilon_T - \epsilon_F$ . This bias dependence of  $\Sigma_T$  is thus expected to be small, resulting only from the dependence of  $n(\epsilon)$  on  $\epsilon$ .

<sup>2</sup> The factor  $(\delta/d)^2$  does not change with temperature if the variation of  $N_T$  with temperature does not depend on position.

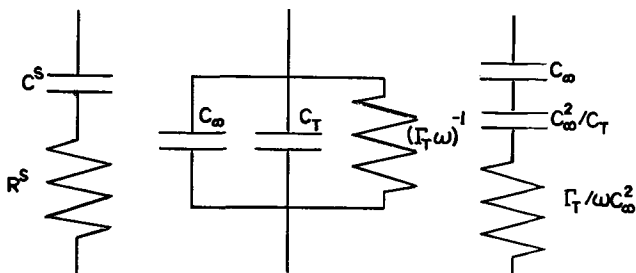


Fig. 4. Equivalent series and parallel networks. The network at the right assumes that  $C_T, \Gamma_T \ll C_x$ .

On the other hand, in the case of a single trap level one has

$$N_T \cdot (1 + i\omega\tau)^{-1} = \int n_T \delta \epsilon_T \cdot f_T (1 - f_T) (1 + i\omega\tau)^{-1} \\ \simeq N_T^0 \cdot f_T^0 \exp(-qpE\delta/kTd) (1 + i\omega\tau)^{-1} \quad [39]$$

where [36] has been used and  $N_T^0 = \int n_T \delta \epsilon_T$  is the total recipient concentration.

Inserting [39] into [19] and using [22], one obtains

$$\delta^*/d \equiv 1 - \frac{C_\infty}{C^s} \simeq \frac{C_T}{C_\infty} \\ = \frac{q^2 d}{kT\epsilon\epsilon_0} \int_0^d \frac{(\delta/d)^2 N_T^0 \cdot f_T^0 e^{-qpE\delta/kTd}}{1 + (\omega\tau)^2} \delta \quad [40]$$

This integral becomes nearly independent of  $\omega$  for sufficiently low frequencies that  $qpE\delta_0/kTd \gg 1$ , causing the vertical drop-off of the conductivity profile in Fig. 3 at low frequencies when an anodic bias voltage is applied.

Applying the same considerations which led to [40] to the loss angle, one obtains

$$\tan \theta \simeq \Gamma_T/C \\ = \frac{q^2 d}{kT\epsilon\epsilon_0} \int_0^d \frac{(\delta/d)^2 N_T^0 f_T^0 e^{-qpE\delta/kTd} \omega\tau}{1 + (\omega\tau)^2} \delta \quad [41]$$

which differs from [40] only by the factor  $\omega\tau$  in the integrand.

#### Detailed Analysis for a Special Distribution of Monoenergetic Recipient States

We shall evaluate [40] and [41] for the special case that

$$N_T^0 f_T^0 = N_0/(\delta/d)^2 \quad [42]$$

where  $N_0$  is a constant (independent of position). The inverse  $\delta^2$ -distribution has been chosen since it provides exactly an exponential conductivity profile, as seen readily from the definition of the conductivity profile, [5] with [6], and [22], [31], and [4]. The factor  $d^2$  in [42] has been added for convenience, giving  $N_0$  the dimension of a concentration and is not supposed to indicate explicitly a dependence of the recipient profile on the oxide thickness. Such a dependence need not be specified in what follows; the mathematical analysis applies for  $N_0$  being any arbitrary function of  $d$ . If the recipient distribution  $N_T^0$  were independent of oxide thickness,  $N_0$  would be inversely proportional to  $d^2$ .

With the assumption [42] the product  $N_T^0 f_T^0 (\delta/d)^2$  in the integrand of [40] and [41] becomes equal to the constant  $N_0$ . The expression [40] has been evaluated in approximate form by (i) replacing the upper limit  $d$  by  $\delta_0$  of [4] and (ii) replacing  $1 + (\omega\tau)^2$  by unity. These are the same approximations as have been introduced when deriving [31]. We thus obtain

$$\delta^*/d \simeq \alpha(pE)^{-1} \cdot [1 - e^{-\beta p E \delta_{10} \nu_0 / \nu}] \quad [43]$$

with  $\alpha$ ,  $\beta$ , and  $\nu_0$  the constants listed in Table I. The theoretical curves in Fig. 3 were calculated by [43] for zero polarization, that is,  $p = 1$ , with the values for  $\alpha$ ,  $\beta$ , and  $\nu_0$  of the second column of Table I. These values were chosen to match the intersect ( $\nu_0$ ), and slope ( $\alpha \cdot \beta$ ) of the zero-bias conductivity profile and to fit the 50 Hz point on the curve  $E = 1$  v. The last column of Table I lists numerical values for the constants  $\tau_0$ ,  $N_0$ , and  $K$  obtained from the nu-

merical values for  $\nu_0$ ,  $\alpha$ , and  $\beta$  by the equations listed in column 1. Using these values the parameter  $\lambda = \delta/\delta^* = kT/q\alpha$  becomes 0.054.

The theoretical curves fit the shape of the experimental curves well; however, there is a discrepancy between the bias voltages of the coinciding experimental and theoretical curves for  $E > 1$  v. A possible explanation for this discrepancy is polarization, i.e.,  $p < 1$ , as will be discussed later.

The "Schottky profile" is defined (7) by

$$N_s(\delta^*) = \frac{\partial E}{\partial(1/C^s)^2} [qA^2 \epsilon\epsilon_0]^{-1} = -\frac{\epsilon\epsilon_0}{q} \frac{\partial E}{\partial(\delta^*)^2} \quad [44]$$

Inserting the "cut-off distance"  $\delta^* = d\alpha/(pE)$  of [43] for  $\nu \rightarrow 0$  one obtains

$$N_s(\delta^*) = N_0/[2p(\delta^*/d)^3] \quad [45]$$

where the value for  $\alpha$  listed in Table I has been used. Considering [42] and [45], the charged recipient profile  $N_T f_T^0$  vs.  $\delta/d$  is obtained from the Schottky profile  $N_s$  vs.  $\delta^*/d$  as follows: (i) contract the abscissa by the factor  $\lambda = \delta/\delta^*$ ; (ii) multiply the ordinate  $N_s$  by  $2p(\delta^*/d)^3$  and divide by  $(\delta/d)^2$ , i.e.,

$$N_T^0 f_T^0 \equiv 2N_s \cdot p \cdot (\delta^*/d)\lambda^2 \quad [46]$$

Figure 5 shows an example for such a transformation. The experimental points of  $N_s$  vs.  $\delta^*/d$  are for the sample formed to 100v shown in Fig. 7 of ref. (4). The points  $N_T^0 f_T^0$  vs.  $\delta/d$  were obtained with  $p = 1$  and  $\lambda = 0.05$  and 0.1, respectively. The value  $\lambda = 0.05$  arises from the  $\alpha$ -value of Table I. The origin of the value  $\lambda = 0.1$  will be explained later. The straight line plotted through the  $N_T^0 f_T^0$ -points corresponds to a  $(\delta/d)^{-2}$  dependence which was postulated by us previously to obtain the exponential conductivity profile at zero bias. The line drawn through the  $N_s$  vs.  $\delta^*/d$  points has a slope of  $-3$  as expected from [45].

It should be emphasized that the  $\delta^{-2}$ -dependence of the recipient state concentration was postulated to obtain the observed frequency dependence of the capacitance at zero bias. This space dependence enabled us to predict a  $\delta^{-3}$ -dependence of the Schottky slope which is derived from the bias dependence of the capacitance. The fact that the tunnel theory predicts an observed interrelation between two independent sets of measurements ( $C^s$  vs.  $\omega$  at  $E = 0$ , and  $C^s$  vs.  $E$  at a constant  $\omega$ ) supports our interpretation.

The value

$$N_0 \equiv N_T^0 f_T^0 \cdot (\delta/d)^2 = 2N_s p (\delta^*/d)^3 \quad [47]$$

is independent of the assumptions on  $\lambda$ . From the straight lines plotted in Fig. 5, one obtains  $N_0 = 3 \times$

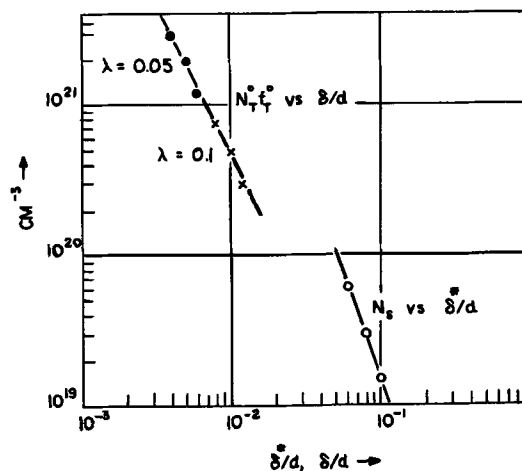


Fig. 5. Transformation of a Schottky profile  $N_s$  vs.  $\delta^*/d$  taken from Fig. 7, of ref. (4) with a distribution of recipient states,  $N_T^0 f_T^0$  vs.  $\delta/d$ . The straight lines have the slopes  $-2$  and  $-3$ , respectively, expected from [42] and [45]

Table I. Empirical parameters for the theoretical curves of Fig. 3, and corresponding basic quantities

Empirical parameter	Numerical value	Basic quantity
$\nu_0 = (2\pi\tau_0)^{-1}$	$3.10^4 \text{ sec}^{-1}$	$\tau_0 = 5 \times 10^{-6} \text{ sec}$
$\alpha = qd^2 N_0 / \epsilon\epsilon_0$	0.475v	$N_0 = 1.5 \times 10^{18} \text{ cm}^{-3}$
$\beta = 2.3(kT/q \cdot 2Kd)^{-1}$	$0.09\text{v}^{-1}$	$K = 2.5 \times 10^7 \text{ cm}^{-1}$

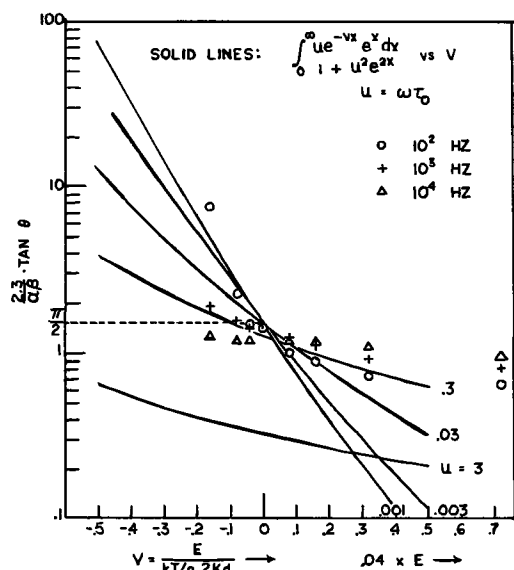


Fig. 6. Loss angle at different frequencies vs. bias voltage. Experimental points assuming  $\alpha\beta = 50$  and  $K = 2.5 \times 10^7 \text{ cm}^{-1}$ . Theoretical curves by Eq. [41] with [42]. For  $\tau_0 = 5 \times 10^{-6} \text{ sec}$  (Table I),  $u = 0.003$  at 100 Hz, and  $u = 0.3$  at  $10^4 \text{ Hz}$ .

$10^{16} \text{ cm}^{-3}$ . This is twice the value listed in Table I, which was derived from Fig. 4 by [43] with  $p = 1$ .

Figure 6 shows theoretical curves for  $\tan \theta$  calculated by [41] with [42] as a function of bias voltage for the frequencies indicated as parameters and using  $p = 1$ . The pertinent integral listed in the right upper corner of the figure was evaluated numerically using a computer. Experimental points are plotted using the value of  $K$  from Table I, and the slope  $\alpha\beta$  of the semilogarithmic zero bias conductivity profile.

At 100 Hz, one has  $u = \omega\tau_0 = 3 \times 10^{-3}$  using the value for  $\tau_0$  of Table I. In spite of the fact that the sample used for Fig. 6 was not the same as that for Fig. 3 and Table I, the experimental points fit reasonably well except for a discrepancy of the abscissa ( $E$ ) scale similar to that of Fig. 3 and to be discussed later.

### Discussion

It has been shown that a tunneling model based on the relation [2] is capable of accounting for the principal features of impedance measurements (1-4) on annealed Ta/Ta<sub>2</sub>O<sub>5</sub> structures without invoking an actual conductivity profile. These features are: (i) the exponential "conductivity profile" defined by [5] and [6] at zero bias (Fig. 3); (ii) the temperature dependence of the zero-bias conductivity profile, showing an activation energy which depends on position (4); (iii) the conductivity profiles under bias voltage showing a cut-off distance at low frequencies (Fig. 3); (iv) the Schottky profile derived from the conductivity profiles under bias voltage (4).

The fact that two physically completely different models, (a) a conductivity distribution extending over several hundreds of angstroms and (b) a tunnel effect through, at most, a few tens of angstroms is capable of explaining the experimental data is not surprising because both models lead to a distribution of time constants, which depend exponentially on distance. The frequency dependence of any system having a distributed time constant spectrum exhibits certain features which are independent of the physical origin of the time constant spectrum.

In order to distinguish between the two models, we need to explore (a) which model accounts more naturally, i.e., with fewer assumptions, for the observed phenomena; (b) which model utilizes numerical values for empirical parameters which are more reasonable, and (c) which model explains experimental features which cannot be explained by the other model.

The conductivity profile involves five empirical parameters: (i) magnitude of conductivity at the metal interface; (ii) slope of the semilogarithmic conductivity profile; (iii) the position independent part of the activation energy of  $\sigma$ ; (iv) the position-dependent part of this activation energy; (v) mobility factor.

The tunnel model also involves five parameters: (i) pre-exponential factor,  $\tau_0$ , of the time constant [2]; (ii) attenuation factor  $K$  of [2]; (iii) activation energy of  $\tau_0$ ; (iv) activation energy of  $\bar{N}_T$ ; (v) constant  $N_0$ .

The conductivity model postulates an exponential distribution of vacancies acting as donors of conduction electrons. The tunnel model postulates an inverse-distance-square profile of recipient sites. The conductivity model postulates a linear dependence of the activation energy defined by [32] for the impurities on position. In contrast, the linear dependence on distance of this activation energy is automatically obtained by the tunnel model [33].

Concerning the numerical values of  $K$ ,  $\bar{U}_{NT}$  and  $N_0$  used for matching the tunnel model to the experimental data:

Simple wave mechanical theory provides  $K \approx 10^8 \text{ cm}^{-1}$  for a barrier 1 eV high, and an electron of free electron mass. The experimental value given in Table I is about four times smaller. This could be attributed formally to a small effective electron mass,  $m^*$ , and/or a low energy barrier,  $\epsilon_c - \epsilon$  in Fig. 1. Indeed, measurements by Mead (8) suggest a low barrier at the Ta/Ta<sub>2</sub>O<sub>5</sub> interface. However, it seems to us more likely that the concept of the potential energy barrier and of the conduction band as shown in Fig. 1 and 2 is not strictly valid for the following reasons:

1. Anodic tantalum oxide is amorphous.
2. The distances involved in tunneling are so small that the discrete atomic structure and image charge potentials should become important.
3. The wave function of a tunneling electron may not be evenly attenuated as shown in Fig. 1, but the attenuation could be arrested in the vicinity of a recipient site, although the tunneling electron may not be trapped at that site. Considering the large concentration of recipient sites, the penetration of a tunneling electron into the oxide could be considerably extended by such an effect.

Comparing [33] with the empirical values of Smyth *et al.* (4), one obtains  $\bar{U}_{NT} \approx 0.055 \text{ eV}$ , i.e., the energy level of the traps lies about  $2kT$  above the Fermi level and  $f_T^0 \approx 0.1$ , accordingly. This is in agreement with  $f_T^0 \ll 1$ , as was postulated to explain the Schottky profile by means of a discrete energy level for traps lying above the Fermi level. With this value for  $f_T^0$  and the  $N_T^0 f_T^0$ -values of Fig. 5 we obtain recipient concentrations in the range of  $10^{21}$  to  $10^{22} \text{ cm}^{-3}$ . Such high concentrations would indicate the presence of a suboxide where a significant fraction of all the atoms can act as recipients. Indeed, suboxides have been observed under more extreme annealing conditions (9). However, at such high concentrations the presence of a single well-defined energy level is unlikely. This aspect of the tunnel model is still unsatisfactory. It is conceivable that [2] with  $\tau_0$  and  $K$  independent of bias needs revision, or else that the profile [39] with [42] on which the detailed comparison is based is not fully adequate.

The tunnel model is capable of describing the bias dependence of the impedance for both anodic and cathodic biases. While no systematic experiments have been made with cathodic bias voltages, the few experimental points in Fig. 6 are in general agreement with the trend of the theoretical curves. Furthermore, Fig. 4 of ref. (4) shows that after returning from an anodic bias to zero bias, the capacitance "overshoots," i.e., the stationary capacitance value at zero bias lies between the value at the anodic bias and that at zero



bias immediately following an anodic bias. In the framework of the tunnel model, this suggests that temporarily a cathodic bias transient is effective, resulting from a positive space charge which has formed in the oxide adjacent to the tantalum during application of the anodic bias voltage. A possible space charge located close to the tantalum decreases the anodic field at the tantalum during the anodic bias by an amount equal to the cathodic field induced by that space charge immediately after switching to zero bias. Thus, in a range of sufficiently small polarization, so that a linear dependence of capacitance on field applies, the capacitance change during the switch of bias should be independent of the amount of polarization, i.e., of the time of application of anodic bias. This has been observed (4). According to this interpretation, we could expect a polarization factor  $p < 1$  in [37], [39], [40], [41], [43], [45], and [46]. This may account for the discrepancy between the applied bias  $E$  of the experimental points in Fig. 3 and 6, and the  $E$  values of the theoretical curves through these points; the actual bias voltages of the experimental points should be replaced by the effective bias voltages  $pE$  which are smaller than  $E$ . For instance, the theoretical bias voltage  $E = 10\text{v}$  in Fig. 3 corresponds to the applied bias  $E \simeq 25\text{v}$ , so that  $p \simeq 0.4$  in this case, provided that  $p = 1$  for the curve  $E = 1\text{v}$  as assumed in deriving  $\beta$ . The experimental points on Fig. 3 have been taken after applying the bias voltage for 15 min (4). Figure 4 of ref. (4) shows that the capacitance change after applying 12v for 1 min is only about  $\frac{3}{4}$  of the instantaneous capacitance change. The suggested polarization factor of about 0.4 for 15 min application of the bias does not seem unreasonable, therefore. Figure 4 of ref. (4) shows that there is already some significant polarization at 1.5v. It may be suspected, therefore, that even at 1v one has  $p < 1$  contrary to the assumptions made in evaluating  $\alpha$  and  $\beta$  from Fig. 3. In this case, the numerical values in the second column of Table I are not  $\alpha$  and  $\beta$ , but  $\alpha/p$  and  $\beta p$ , respectively, where  $p$  is the polarization factor pertaining to 1v. Accordingly,  $\alpha$  would be smaller, and  $\beta$  larger than in the previously assumed case  $p = 1$ . As a consequence,  $\lambda = kT/q\alpha$  would become larger. The value  $\lambda = 0.1$  used in Fig. 5 is based on the assumption that  $p = 0.5$  at 1v.

It is interesting to note that this interpretation, if correct, provides a tool to determine polarization fields at the tantalum interface by means of measuring tunnel impedance. This opens a prospect for the study of residual charge phenomena in metal-insulator structures, comparable to the common use of the depletion capacitance in semiconductor-insulator structures to assess the field at the semiconductor-insulator interface.

The tunneling model discussed here has important implications for the design of capacitors in microcircuits. A prime parameter for comparing the capacitor performance of different materials is the maximum stored energy  $CV^2/2$  per unit volume, which is  $\epsilon\epsilon_0 F_b^2/2$  with  $F_b$  the breakdown field. Since voltages in microcircuits are frequently only of the order of volts, and breakdown fields are of the order of  $10^7$  v/cm, dielectric layers only several tens angstroms wide become of potential interest. Loss mechanisms arising from electrons tunneling several angstroms into the dielectric may thus become quite important.

Pronounced effects such as in annealed Ta/Ta<sub>2</sub>O<sub>5</sub> are unusual. Nevertheless, a significant density of recipient sites may be present in ordinary dielectrics close to a metal electrode, perhaps due to mobile ions in the dielectric which drift toward the boundaries (e.g., Na in SiO<sub>2</sub>)<sup>10</sup> or else due to inherent structural perturbances near the interface of two different materials. Thus, the tunnel model may provide useful information for a much wider range of capacitors and materials than annealed Ta/Ta<sub>2</sub>O<sub>5</sub>.

While the proposed tunnel model may apply to ordinary annealed Ta/Ta<sub>2</sub>O<sub>5</sub> structures and perhaps

even to unannealed Ta/Ta<sub>2</sub>O<sub>5</sub> samples, it is unlikely to apply to vacuum annealed Ta/Ta<sub>2</sub>O<sub>5</sub> combinations and certain phosphorus anodized samples where extremely shallow conductivity profiles through a large portion of the oxide have been observed (11, 12). In these cases, the interpretation of the impedance measurements by an ordinary conduction mechanism (1-4, 11, 12) appears to be valid.

### Summary

1. Formulas are derived for the tunneling of electrons from a metal into sites in an adjacent insulator.
2. These equations account qualitatively and quantitatively for the frequency and bias dependencies of annealed Ta/Ta<sub>2</sub>O<sub>5</sub> structures. Thus tunneling is an alternative explanation to that based on a conductivity profile.
3. The distances  $\delta^*$  obtained for the conductivity profile have to be contracted by a factor  $\lambda$  to give the tunnel distances.
4. The vacancy concentration obtained by the Schottky method has to be multiplied by  $2p(\delta^*/d)/i^2$  in order to provide the concentration of recipient sites.
5. In order to arrive at a strictly exponential conductivity profile, an inverse-square-distance distribution of the recipient sites is postulated.
6. The observed dependence of the activation energy of the conductivity profile on position has a natural explanation by the tunnel model.
7. There are indications of space charge polarization affecting the field at the Ta/Ta<sub>2</sub>O<sub>5</sub> interface and thus the tunnel impedance.

### Acknowledgment

The author would like to express his appreciation to D. M. Smyth for making recent experimental results available to him prior to publication and for many stimulating discussions. He would also like to thank R. Linzey for the measurements shown in Fig. 5.

Manuscript received June 15, 1967; revised manuscript received Sept. 6, 1967. This paper was presented at the Dallas Meeting, May 7-12, 1967, as Abstract 28.

Any discussion of this paper will appear in a Discussion Section to be published in the December 1968 JOURNAL.

### REFERENCES

1. D. M. Smyth, G. A. Shirn, and T. B. Tripp, *This Journal*, **110**, 1264 (1963).
2. D. M. Smyth and T. B. Tripp, *ibid.*, **110**, 1271 (1963).
3. D. M. Smyth, G. A. Shirn, and T. B. Tripp, *ibid.*, **111**, 1331 (1964).
4. D. M. Smyth and G. A. Shirn, *ibid.*, **115**, 186 (1968).
5. F. P. Heiman and G. Warfield, *IEEE Trans. Electron Devices*, **ED-12**, 167 (1965).
6. K. Lehovc and A. Slobodskoy, *Solid State Electronics*, **7**, 59 (1964).
7. W. Schottky, *Z. Phys.*, **118**, 539 (1942).
8. C. A. Mead, *Phys. Rev.*, **128**, 2088 (1962).
9. R. E. Pawel and J. J. Campbell, *This Journal*, **113**, 1204 (1966).
10. E. Yon, W. H. Ko, and A. B. Kuper, *IEEE Trans. Electron Devices*, **ED-13**, 276 (1966).
11. D. M. Smyth, T. B. Tripp, and G. A. Shirn, *This Journal*, **113**, 100 (1966).
12. D. M. Smyth, *ibid.*, **113**, 1271 (1966).
13. H. Preier, *Appl. Phys. Letters*, **10**, 361 (1967).

### APPENDIX I

#### Comparison of MOS Tunneling (5) with the MOM Tunneling of This Paper

In the case of a MOS structure, considered in ref. (5), one has

$$\tilde{V}(\delta) = \tilde{\psi}_s + V'd \cdot \delta = \tilde{\psi}_s + (\tilde{E} - \tilde{\psi}_s) \delta/d$$

where  $\psi_s$  is the surface potential of the semiconductor with respect to its bulk. The dominant term on the

right-hand side is  $\tilde{\psi}_s$  so that the variation of charge in the oxide can be treated (5) as a function of the surface potential  $\psi_s$  [viz., Eq. [46], etc., of (5)] or, expressed differently, of the free carrier density at the surface of the semiconductor, which is a well-defined function of  $\psi_s$ . Thus, in a good approximation,  $\tilde{V}(\delta) \simeq \tilde{\psi}_s$ , independent of the tunnel distance  $\delta$ . In other words, the variation of an energy level at the distance  $\delta$  vs. an energy level at  $\delta = 0$ , induced by an a-c field applied at the oxide, can be neglected as a second order effect. On the other hand, this second order effect is the principal effect in our case of a metal-insulator structure, where  $\psi_s = \tilde{\psi}_s = 0$  and  $\tilde{V}$  is in proportion to  $\delta$  [1]. Unlike the case of a semiconductor, the surface potential and the free carrier density at the metal surface are not noticeably varied by the applied field.

The mathematical consequences of this difference between the MOS structure of (5) and the MOM structure are as follows: Our equivalent parallel conductance Eq. [15] with [16] and [17] corresponds to  $i\omega C_{ox} dV_{SS}/d\psi_s$  in (5) with  $dV_{SS}/d\psi_s$  given by their Eq. [64] (see also ref. (13), Eq. [1] and [2]). Several factors in the integrands of Eq. [15] of this paper and of Eq. [64] of (5) can easily be identified with each other, e.g.,  $n_T$  with  $K \cdot g$ ;  $f_T(1 - f_T)/kT$  with  $\partial f/\partial \epsilon_T$ ; and  $(1 + i\omega\tau_T)^{-1}$  with  $[1 + j\omega\tau_C]^{-1}$ . However, our [15] with [16] contains the factor  $(\delta/d)^2$ , which is missing in [64] of (5). This has the following

reason: In our case the "driving force" for the tunneling is the a-c potential variation between surface and recipient state, which accounts for one factor  $\delta/d$  in [16]. The second factor  $\delta/d$  results from the "dipole distance" between the trapped electron and the positive charge left behind on the metal, and the

corresponding change in  $\tilde{V}'_d$  at a given  $\tilde{E}$  as expressed by [12]. The first factor  $\delta/d$  is absent in [64] of (5), since their driving force  $\tilde{\psi}_s$  is independent of  $\delta$ : In the

MOS structures, the tunneling charge  $\tilde{Q}_{SS}$  changes the voltage distribution between depletion layer voltage  $\psi_s$  and oxide voltage by the shift to the bulk side of the depletion layer of the positive charge left behind by a tunneling electron at the semiconductor surface. Since the charge shift across the depletion layer (which, in general, does not occur by tunneling, but by diffusion and field drift) occurs over a larger distance than the tunnel distance, the charge displacement (dipole distance) is much larger in the case of the MOS structure and rather independent of  $\delta$ . As a consequence, much larger charges must tunnel in the case of MOM structures than in MOS structures to obtain impedance effects of comparable magnitude.

In summary, the case of metal-insulator tunneling differs from that of semiconductor-insulator tunneling physically as to the dominant effect, and mathematically by a factor  $(\delta/d)^2 \ll 1$ , occurring in the integrand of the expression for the equivalent parallel conductance.

## Oxygen Evolution on Semiconducting TiO<sub>2</sub>

P. J. Boddy

*Bell Telephone Laboratories, Incorporated, Murray Hill, New Jersey*

### ABSTRACT

Semiconducting n-type TiO<sub>2</sub> evolves oxygen under anodic polarization despite the presence of an exhaustion layer. Addition to the solution of species more oxidizable than water causes no increase in current at a given potential, hence electron emission over the surface barrier is unimportant. The data may be interpreted in terms of electron tunneling from oxide ions in the crystal surface as the rate-determining step followed by faster electrochemical processes. Implications for electrolytic rectification are discussed.

The underlying reasons for the phenomenon of electrolytic rectification on anodically formed valve-metal oxide films are still imperfectly understood. Indeed it may well be that no one single cause explains the rectifying behavior in general. Several theories have been suggested in specific cases. Principally, electrolytic rectification has been ascribed to penetration of protons into the films (1), the existence of localized conducting defects in otherwise essentially insulating films (2), and to semiconducting properties (3) including the possible existence of junctions within the films (4).

Many of the pertinent properties of semiconducting films can be more conveniently investigated on massive semiconducting electrodes. By this means processes at the various interfaces (electrolyte/oxide, oxide/metal) may be separately observed. In addition, under appropriate conditions high fields may be applied across a relatively narrow region just within the surface of the oxide, producing a layer devoid of carriers of either sign. In this way fields of quite high magnitude may be conveniently applied across an essentially insulating oxide film of the order of a few thousand angstroms in thickness. Since the field in the bulk of the electrode is negligible, the occurrence of ionic currents through the bulk may be ruled out. The proper choice of an ohmic contact eliminates complicating effects at the oxide/metal interface, hence

the electrolyte/oxide interface, including the high field region just inside the oxide surface, may be investigated directly.

In the course of a series of studies of the electrochemical behavior of semiconducting oxides and mixed oxides [e.g., KTaO<sub>3</sub> (5)] we have had occasion to investigate the rutile form of TiO<sub>2</sub>. The film forming properties of titanium and the high dielectric constant of rutile ( $\epsilon = 89$  along the a-axis, 173 along the c-axis) have led to a good deal of interest in its possible use in electrolytic capacitors. However, some unfavorable features of its electrochemical behavior have prevented its use in this direction.

We believe that our measurements of semiconducting single crystal rutile are relevant to the behavior of anodic TiO<sub>2</sub> films. In addition, our experience with a number of materials leads us to believe that generalizations may be made about the behavior of semiconducting oxides, with appropriate modifications for individual properties, e.g., band gap, carrier densities, crystal structure, etc.

Although, as we will show, n-type semiconducting oxides show rectification behavior when in contact with electrolytes which is in the same sense (anodic direction blocking) as that observed with valve-metal oxides, we most definitely are not implying that electrolytic rectification in general is necessarily due to n-type semiconduction in the oxide films. This, of

course, does not eliminate semiconduction as either a major, or one of several minor contributing factors in specific cases. The object of this paper is to discuss, through the particular example of  $\text{TiO}_2$ , some electrochemical properties of semiconducting oxides, and thus help to clarify ideas which have been proposed relating semiconduction to electrolytic rectification.

### Experimental

Large pieces of single crystal rutile were reduced in hydrogen atmosphere at temperatures in the range  $600^\circ\text{--}700^\circ\text{C}$  for varying times. From these reduced samples electrodes were cut with dimensions about  $6 \times 6 \times 1 \text{ mm}$  with the larger faces perpendicular either to the a- or c-axis. One face was polished through successive grits to  $0.05\mu$  after an ohmic contact (chromium overlaid with gold) had been applied to the opposing face. The electrodes were finally mounted in silicone rubber cement applied so that only the polished face contacted the solution.

The interfacial capacitance was measured, as a function of potential, by means of short duration current pulses (6). Provided the higher values of polarization were not prolonged there was no difference in the capacitance values for increasing and decreasing values of polarization except as mentioned below.

Current-voltage data were measured potentiostatically. Some transient phenomena were observed, the exact nature depending on the donor density and crystal face.

The solutions were not purified in any special way in view of the use of silicone material to mount the electrodes. Most data were taken in neutral buffered phosphate solutions although a few measurements were made at the extremes of the pH range.

The photocurrents due to chopped uv illumination were measured by focussing the light from a mercury arc on to an electrode placed very close to a sapphire window cemented to the side of an electrolytic cell. The a-c voltage across a 10-ohm resistor placed between the electrode and ground was displayed on an oscilloscope and measured as a function of applied voltage.

The transient currents flowing in response to a rectangular anodic voltage pulse were observed with an oscilloscope in a similar manner.

### Results

*Face perpendicular to a-axis.*—Capacitance vs. electrode potential data for two differently doped samples are shown in Fig. 1. Anodic polarization of a wide band-gap n-type semiconductor produces an exhaustion layer devoid of either holes or electrons, this being a direct consequence of the low rates of thermal generation of electron-hole pairs in wide band-gap materials. The exhaustion layer capacitance is generally much smaller than typical values for the Helmholtz layer ( $>20 \mu\text{f cm}^{-2}$ ), hence the measured interfacial capacitance is essentially that of the semicon-

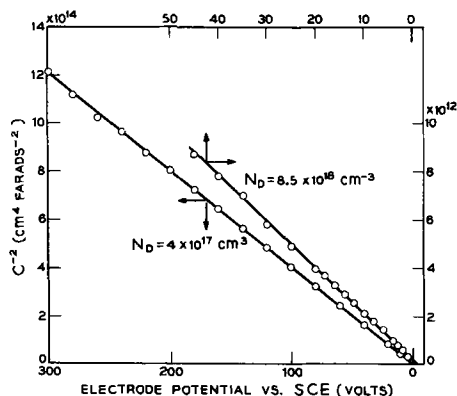


Fig. 1.  $1/C^2$  vs.  $V$  for two samples oriented perpendicular to a-axis.

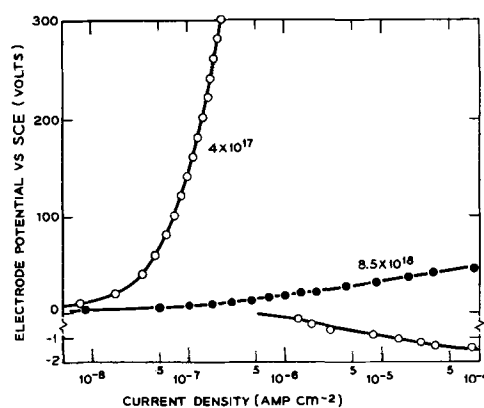


Fig. 2. Current-voltage behavior of samples from Fig. 1. Note different voltage scale for anodic and cathodic processes.

ductor space charge layer and the applied potential occurs almost entirely within this region. The theory relating capacitance, per unit area,  $C$ , and potential,  $V$ , across an exhaustion layer (7) yields

$$\frac{d(1/C^2)}{dV} = \frac{2}{q\epsilon\epsilon_0 N_D} \quad [1]$$

where  $q$  is the electronic charge,  $\epsilon$  the relative dielectric permittivity, and  $N_D$  the donor density.

Donor densities for the various samples may be easily obtained from the slopes of the plots in Fig. 1 by application of Eq. [1]. The surface field immediately inside the semiconductor,  $F_s$ , is then given by

$$F_s = qN_D/C \quad [2]$$

Anodic current-voltage curves for two differently doped samples are shown in Fig. 2. The large electrode potentials necessary to produce small currents, particularly in the lower doped sample, are very evident. The cathodic i-v curve which is similar for both samples is shown here for comparison although it will not be discussed in detail in this paper. The system shows a considerable degree of rectification (note the different voltage scales for anodic and cathodic processes).

The passage of anodic current requires either injection of electrons or consumption of holes. If electron injection is occurring directly from species in the solution, the current at a given voltage should be increased by the addition of easily oxidizable species to the solution. In fact, the addition of sodium borohydride to the solutions resulted in no increase in current. This result is very similar to that already observed for n-type potassium tantalate electrodes (5). Hence, electron injection from solution species is ruled out. Also the rates of hole generation by thermal processes are too low to be the source of the observed current.

When the data from Fig. 2 are replotted vs. surface field in Fig. 3 a better correlation between the differ-

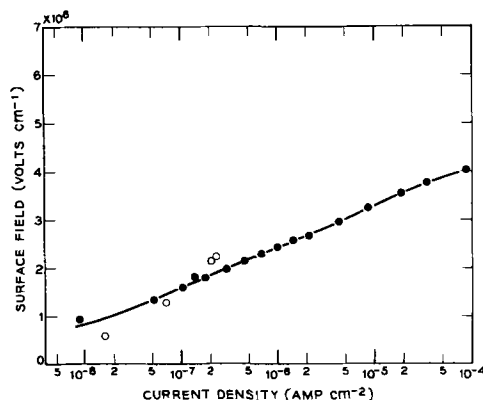


Fig. 3. Data from Fig. 2 replotted vs. surface field

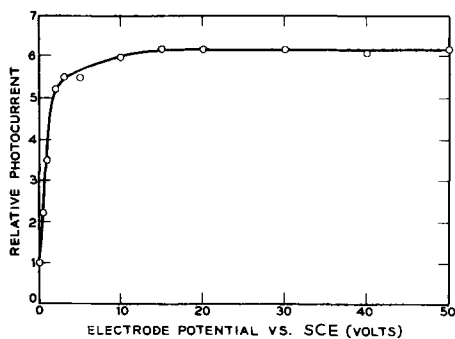


Fig. 4. Relative photocurrent due to chopped uv light as a function of bias. ( $N_D = 8.5 \times 10^{18} \text{ cm}^{-3}$ ).

ently doped samples is obtained. The charge transport mechanisms which would show such a dependence on surface field are either avalanche multiplication or tunneling.

The occurrence of avalanche multiplication may be checked by observing the current due to injected carriers as a function of bias. The sample of highest doping ( $8.5 \times 10^{18} \text{ cm}^{-3}$ ) was illuminated by chopped uv radiation with energy greater than that of the optical band gap ( $\sim 3.05 \text{ eV}$ ) and the resulting a-c photocurrent observed on an oscilloscope. The relative value as a function of anodic bias is shown in Fig. 4. The range of bias was that covered by the i-V curves in Fig. 2. The lack of increase in the current at high fields ( $50 \text{ V} \approx 5 \times 10^6 \text{ v cm}^{-1}$  for this sample) indicates that avalanche multiplication does not make a major contribution to the anodic current.

When the surface field is sufficiently high, tunneling of electrons may occur from occupied levels at the surface directly into the empty conduction band. The field configuration is shown schematically in Fig. 5. The occupied levels from which tunneling occurs may be either surface states within the forbidden gap or levels at the top of the valence band.

Some further evidence for tunneling from surface levels comes from transient experiments. When a voltage step is applied to the interface it is expected that a transient current will be observed flowing through the external circuit due to the charge stored in the space charge region according to

$$q = \int_{V_0}^V C \cdot dV \quad [3]$$

where  $C$  is a function of  $V$ . On returning the voltage to the original value, an equal and opposite charge would be expected. In practice the transient observed when turning on an anodic voltage exceeds that at turn-off. The magnitude of the difference increases with increase in the voltage step and is plotted in Fig. 6. This result is interpreted in terms of field induced tunneling from surface levels. Since the experiment was carried out at constant pulse width ( $10^{-3} \text{ sec}$ ) the

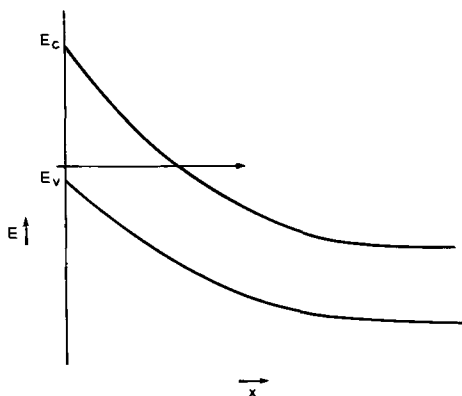


Fig. 5. Field configuration in an exhaustion layer

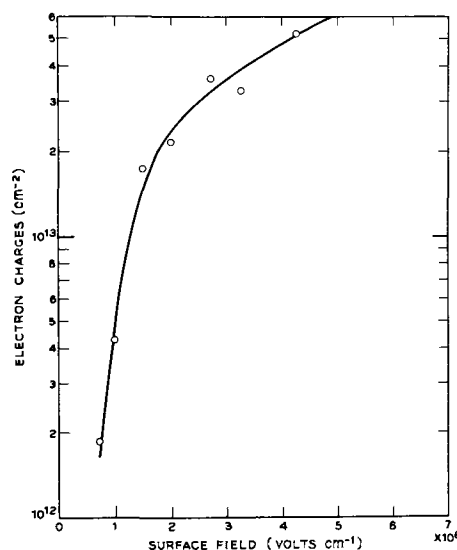


Fig. 6. Excess transient at turn-on as a function of surface field. ( $N_D = 8.5 \times 10^{18} \text{ cm}^{-3}$ ).

amount of excess charge is a function of field. At low fields where the barrier to tunneling is wide and thus the tunneling rate is small, very little charge is transported during the time the pulse is on. At higher fields greater amounts of charge should be observed due to the higher tunneling probability. For sufficiently high fields all of the surface levels will be emptied during the pulse and the charge difference should become constant with increasing field. The data in Fig. 6 seem to be approaching a saturation value of  $\approx 10^{14}$  electron charges at high fields.

*Face perpendicular to c-axis.*—The results for this orientation are much more qualitative. The plots of  $(1/C^2)$  vs.  $V$  are strongly nonlinear and are sensitive to bias. Some data for the lower doped of the two samples, which shows this effect to the greatest extent, are shown in Fig. 7. Anodic bias has the effect of increasing the slope of the plots, which indicates a probable decrease in the donor density near the surface. The effect can be reversed by cathodic polarization. The drift of ionized impurities and defects along the c-axis of TiO<sub>2</sub> is known to be very rapid (8). We feel that the donor densities are nonuniform near the surface of samples of this orientation, and are influenced strongly by the surface field. Under these circumstances the surface fields cannot be deduced without determining the distribution profile of the donors.

Current-voltage curves for two samples are shown in Fig. 8. A considerable degree of rectification is still evident although not so marked as with the samples oriented perpendicular to the a-axis which were nominally of approximately the same donor densities. The

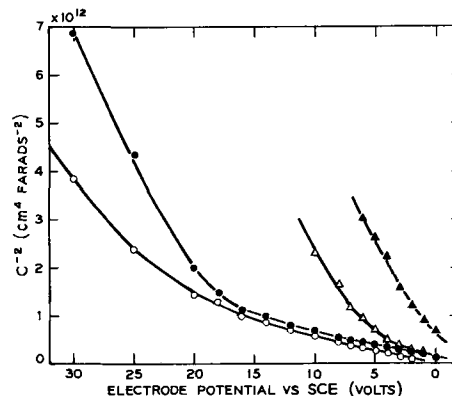


Fig. 7.  $1/C^2$  vs.  $V$  for relatively low doped TiO<sub>2</sub> oriented perpendicular to c-axis.  $\circ$ , original condition of electrode;  $\bullet$ , 500  $\mu\text{A}$  for 30 min;  $\triangle$ , 500  $\mu\text{A}$  for 60 min;  $\blacktriangle$ , 500  $\mu\text{A}$  for 150 min.

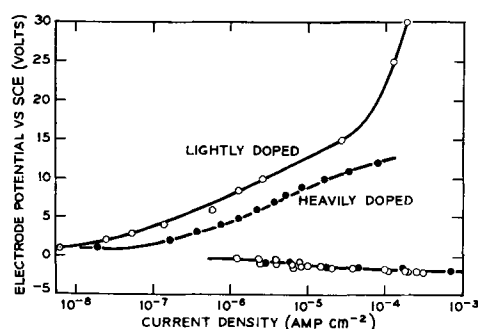


Fig. 8. Current-voltage behavior of samples oriented perpendicular to *c*-axis.

fact that the bulk dopings were widely different in the two samples was indicated by conductivity measurements made by the four-point probe technique and also by the coloration, the lightly doped being quite clear and the highly doped being strongly blue and almost opaque to visual inspection. However, the similarity in surface doping in the two cases was indicated both by the  $1/C^2$  vs.  $V$  plots at low fields and the  $i$ - $V$  curves which were much more similar for these two samples, than for those oriented perpendicular to the *a*-axis.

### Discussion

**Oxygen evolution.**—At higher current densities the evolution of gas may be observed, and this can only be oxygen for an anodic process in aqueous solutions. It is presumed that oxygen evolution is the only process at all current densities.

The rate-determining step is interpreted as tunneling by electrons from surface levels within the gap or at the valence band edge into the empty conduction band.

The valence band of  $\text{TiO}_2$  consists of overlapping oxygen 2p states. The simplest interpretation of the oxygen evolution reaction is that electrons tunnel from oxygen 2p states at the crystal surface under the influence of the high surface field. This concept is discussed in more detail in our paper on potassium tantalate anodes (5) and will be dealt with only in brief in the present case.

At high values of surface field, where the space charge depth is great, the surface field may be considered constant for some distance into the electrode. In this simplified case the trapezoidal barrier model of Franz (9) may be applied, where the tunneling probability,  $D$ , is given by

$$D = \exp\left(-\frac{4\sqrt{2}(m^*)^{1/2}E^{3/2}}{3\hbar F}\right) \quad (4)$$

$m^*$  being the tunneling effective mass,  $E$  the energy difference between the tunneling level and the top of the barrier, and  $F$  the field.

Calculations based on this model indicate that in order to fit the data it is necessary to postulate a set of states extending into the forbidden gap, distributed exponentially in energy according to

$$N \approx N_0 \exp(-10E) \quad (5)$$

The currents are given by

$$i = \nu \cdot q \cdot \int (N.D.) dE \quad (6)$$

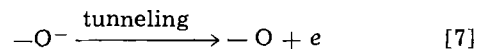
where  $\nu$ , the frequency factor, is taken as  $\sim 10^{13} \text{ sec}^{-1}$ .

The product  $N.D.$  was evaluated as a function of energy for a number of fields and integrated manually. Current densities were then derived from Eq. [6]. A quantitative analysis is made difficult by lack of knowledge of the magnitude of  $m^*$ , but if it is assumed that  $m^* = m_0$ , then a reasonable fit as shown in Fig. 3 may be obtained by assuming a total density of states of  $\sim 10^{14}$  distributed as a delta function at 3.2

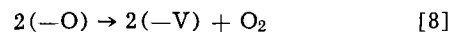
ev below the conduction band edge, with an exponential tail on the high energy side as indicated by Eq. [5]. This distribution is consistent with complete emptying of the states in  $10^{-3} \text{ sec}$  at fields  $\geq 5 \times 10^6 \text{ volts cm}^{-1}$  as indicated in the pulse experiments.

We propose that the states in question are oxygen 2p states of surface oxide ions perturbed out of the valence band by termination of the lattice. The assignment of the delta function to 3.2 ev below  $E_C$  is consistent with this since  $E_C - E_V \approx 3.05 \text{ ev}$ .

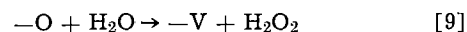
Electrochemically, the sequence of events is as follows



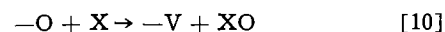
Subsequent to this rate-determining step, one of several processes may occur



where  $-\text{V}$  is a surface vacancy. Alternatively



or



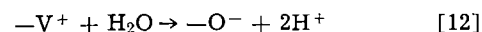
where  $\text{X}$  is some solution species. Subsequently  $\text{H}_2\text{O}_2$  or  $\text{XO}$  may react to yield  $\text{O}_2$ .

Oxide ion vacancies in  $\text{TiO}_2$  are donors, therefore

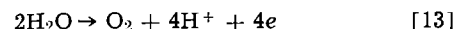


will occur rapidly.

Since continuous current may be passed it is necessary to have some means of replenishing the surface states. A likely process is



The net result of Eq. [7], [8], [11], and [12] is the familiar oxygen evolution reaction



The excess transient charge in the voltage pulse experiment is identified with electrons tunneling from surface oxide ions. These electrons are transferred to the conduction band of the oxide and hence are observed in the external circuit.

The process of recharging the states during the off time involves reaction with water molecules in the solution. This process is localized at the oxide/solution interface and hence does not cause current to flow in the external circuit.

The essential novelty of this system is that the barrier to charge transfer lies within the electrode and may be directly perceived through measurements of the dielectric properties of the space charge region, rather than in the Helmholtz region as for metal electrodes. The surface oxide ions correspond to reactive intermediate species in the over-all process of Eq. [13].

**Comments on electrolytic rectification.**—It is clear that rectifying behavior somewhat similar to that exhibited by anodic oxides is observed also on *n*-type semiconducting oxides. We point out in passing that current work on semiconducting tantalum pentoxide shows behavior somewhat similar to that reported here for rutile, although we have not eliminated avalanche breakdown as a possibility in this case.

It might be questioned what comparison there could be between an anodic oxide film a few hundred angstroms in thickness and an electrode  $\sim 1 \text{ mm}$  thick. However, in the semiconductor case we have to be concerned only with the width of the barrier imposed by the space charge region. This, of course, may be much less than the width of the space charge itself. For instance at a field of  $4 \times 10^6 \text{ volts cm}^{-1}$ , the barrier at 3 ev below the conduction band edge is only  $75 \text{ \AA}$ , whereas the total space charge depth is many thousands of angstroms.

It is a natural consequence of the properties of an exhaustion layer that a sample of smaller donor den-

sity requires higher potentials to attain the same surface field. This indicates greater blocking ability for anodic current as the donor density decreases, until, in the limit, the field becomes uniform across the whole width of the electrode (or film, as the case may be).

We find that cathodic current flow occurs very readily in our experiments even for semiconductors of low doping. The flat band potential is approximately  $-0.6\text{v}$  vs. SCE in neutral solutions. At this point no further space charge barrier exists at the oxide/electrolyte interface to cathodic current flow. Provided an ohmic (electron injecting) contact exists at the metal/oxide interface the current is limited only by the conductivity of the film and the barrier in the Helmholtz region, analogous with a metal electrode. Thus, for a hypothetical film with a resistivity of  $10^{10}\text{ ohm-cm}$  and a thickness of  $1000\text{\AA}$ , a cathodic current of  $10^{-6}\text{ amp cm}^{-2}$  involves an ohmic potential drop in the film of only  $0.1\text{v}$ . For rutile, this resistivity corresponds to  $10^9\text{-}10^{10}\text{ donors cm}^{-3}$ , a very low value and pronounced rectification should ensue, extrapolating from the present data.

Some lack of stoichiometry in anodic oxide films would seem to be inevitable, and it is usually very much easier to achieve n-type semiconduction than p-type. It is tempting to consider a slight degree of n-type semiconduction as being an important factor in some cases. There are however some aspects of the experimental observations of electrolytic rectification which are not consistent with a homogeneous n-type film.

Vermilyea (2) has shown that "weak spots" are responsible for much of the cathodic current and has suggested that the film is modified by inclusions originating from the metal. Young (10) is of the opinion that such spots are also responsible for the anodic leakage current. Possibly such spots could be n-type regions in an otherwise insulating, or very slightly n-type, film.

Another problem, less easily disposed of, is the influence of species in solution on the anodic leakage current. Our work on semiconducting oxides has re-

vealed no effect of solution species on anodic current flow in the several cases investigated (KTaO<sub>3</sub>, TiO<sub>2</sub>, Ta<sub>2</sub>O<sub>5</sub>, ZnO). This is presumably a consequence of the relative alignment of energy levels in solution with the band structures of these various oxides. It might be argued that the anodic films are glassy and hence the same band structure picture does not apply. However we find that, at least as far as optical properties are concerned, anodic films of TiO<sub>2</sub> behave similarly to rutile (11). It seems unlikely, although perhaps not impossible, that electron injection could occur into the glassy form but not the single crystal. We rather tend to the view that such direct influence of solution species indicates either fissures through the oxide or some degree of porosity.

#### Acknowledgments

The authors wish to thank W. J. Sundberg, R. Hephewwhite, and A. Timko for technical assistance.

Manuscript received June 15, 1967; revised manuscript received Aug. 30, 1967. This paper was presented at the Dallas Meeting, May 7-12, 1967, as Abstract 29.

Any discussion of this paper will appear in a Discussion Section to be published in the December 1968 JOURNAL.

#### REFERENCES

1. P. F. Schmidt, *J. Appl. Phys.*, **28**, 278 (1957).
2. D. A. Vermilyea, *ibid.*, **27**, 963 (1956).
3. W. Ch. van Geel, *Physica*, **17**, 761 (1961).
4. W. Ch. van Geel and B. C. Bouma, *Philips Research Repts.*, **5**, 461 (1950).
5. P. J. Boddy, D. Kahng, and Y. S. Chen, *Electrochim. Acta*, To be published.
6. W. H. Brattain and P. J. Boddy, *This Journal*, **109**, 574 (1962).
7. W. Schottky, *Z. Physik*, **113**, 367 (1939); N. F. Mott, *Proc. Roy. Soc. (London)*, **A171**, 27 (1939).
8. D. C. Cronemeyer, *Phys. Rev.*, **113**, 1222 (1959).
9. W. Franz, *Handbuch der Physik*, Vol. 17, "Dielectric Breakdown," Springer, Berlin (1956).
10. L. Young in "Anodic Oxide Films," p. 144, Academic Press, New York (1961).
11. A. Frova, P. J. Boddy, and Y. S. Chen, *Phys. Rev.*, **157**, 700 (1967).

## On the Rectification of Anodic Oxide Films of Titanium

Franz Huber\*

Radio Corporation of America, Somerville, New Jersey

#### ABSTRACT

The phenomenon of electrolytic rectification in anodic oxide films has been studied extensively for the valve metal-valve metal oxide-electrolyte system for many years. This paper describes experimental results on the rectification of the electric current in anodic oxide films, especially TiO<sub>2</sub> enclosed between two metallic electrodes. The rectification of the electric current is interpreted on the basis of a p-n junction within these oxide films. In addition, these junctions can exhibit photovoltaic effects and can be used for the fabrication of field effect devices. In these field effect transistors the electrical current flowing between two narrowly spaced electrodes deposited on the oxide surface can be modulated by the application of voltage to the titanium bottom electrode. This experiment shows that a conductive surface layer is adjacent to an insulating layer underneath.

It is a well-known fact that anodically formed oxide films of valve metals (metals such as Ti, Ta, Zr, Al, and Hf) or semiconductors rectify the electric current in a valve metal-valve metal oxide-electrolyte system to a high degree; a number of theories have

been developed to explain this electrolytic rectification (1-3). However, when the electrolyte is replaced by a metallic electrode (preferably applied by vacuum evaporation), the rectification of the electric current disappears in many cases; a large variety of experimental current-voltage characteristics has been observed and reported in the literature. Extremely thin

\* Electrochemical Society Active Member.

oxide films, usually below a thickness of 100Å, exhibit current-voltage characteristics which can be explained by quantum-mechanical tunneling (4, 5).

The rectification of the electric current in thick anodic oxide films (100 to about 5000Å thick) has been interpreted by some investigators to be due to the existence of microfissures in the oxide film (6-9). Undoubtedly, microfissures can exist in anodic oxide films and can be responsible for an increase of conduction or an asymmetry of electric conduction, but many other phenomena of anodic oxide films, such as photo-effects, are explained in a more natural way by the p-n junction theory. For example, increased conduction at localized areas has been observed in Ta<sub>2</sub>O<sub>5</sub> films during plating of silver or copper as counter electrodes. When silver or copper is electrolytically plated at the surface of a thick film of Ta<sub>2</sub>O<sub>5</sub>, the metals are precipitated as fine needles at individual spots on the surface of the oxide, indicating high current flow through small localized areas. This observation is in agreement with experimental results of mercury contacts applied to anodically formed tantalum. Vermilyea (7) found that with tantalum large area mercury contacts rectified, but point contacts did not rectify the electric current. It was concluded that weak spots were responsible for the low cathodic resistance of the large area mercury contacts (8). Anodic oxide films of titanium, however, can be prepared so that electroplating of silver results in a homogeneous and coherent metallic counterelectrode.

On the other hand, anodic oxide films enclosed between two metallic conductors can also be highly insulating. These oxide films can have resistive values of 10<sup>16</sup> ohm-cm and greater (10-12), particularly when the oxide film has been grown at high forming voltages. In these anodic oxide films, the material of the counter electrode can significantly influence the insulation resistance of the oxide layer (13), specifically in the cathodic direction.

A number of investigators believe that the rectification of the electric current in anodic oxide films is basically attributed to the existence of an p-n junction or p-i-n junction within the oxide film (14-23). This interpretation does not exclude the superposition of an electric current flow caused by microfissures that may be present in the oxide film and is independent of whether the counter electrode consists of a metal or of an electrolyte. This interpretation allows a large number of experimental results to be explained by one model. The experiments described in this paper were performed on TiO<sub>2</sub> films, predominantly with metallic electrodes applied to the oxide layer. The experiments support the theory of p-n junction rectification in anodic oxide films.

### Experimental Work

Titanium films have been prepared by evaporation of the metal from a tantalum boat in a vacuum system usually at a pressure of 10<sup>-5</sup> mm Hg. Fast evaporation of the titanium is accomplished by placing the titanium sheet parallel to a flat tantalum boat of about the same ohmic resistance. This arrangement minimizes the amount of gettered gases. A passing electric current simultaneously heats the supporting tantalum boat and the evaporating titanium strip; overheating of the tantalum boat is not necessary. As soon as the titanium ribbon melts due to the direct resistive heating, the liquid metal strip is supported by the flat tantalum boat. A fast evaporation rate can be achieved because the evaporation takes place from a relatively large area (4 cm<sup>2</sup>). Titanium films of several thousand angstroms thickness can be deposited in about 15 sec. At the end of the deposition, the tantalum boat usually breaks after alloying with the liquid titanium. It is suspected that a small amount of tantalum also evaporates and is incorporated into the titanium film. This doping of the anodized TiO<sub>2</sub> film with Ta<sup>5+</sup> ions would lead to increased conduction (analogous to crystalline rutile) (24).

Glass slides have been used as the substrate in most cases during these investigations. However, for the investigation of the piezoelectric effects of these TiO<sub>2</sub> junctions, a flexible substrate consisting of mica or polyethylene has been used. Mechanical stress can then be easily applied by bending the substrate.

In the beginning of the investigations, the titanium films peeled frequently during the anodization process. It was found that excellent adhesion of the titanium film can be accomplished by applying the negative potential to the substrate not only during the glow discharge period in the beginning of the evaporation, but also during evaporation at high vacuum.

The pattern of the titanium films and that of the evaporated counter electrodes is determined by means of mechanical masks. Figure 1 shows 20 test diodes of thin-film TiO<sub>2</sub>.

*Anodic oxidation of titanium.*—The titanium metal was made the anode in an electrolytic cell, and a platinum gauze was used as the cathode. The electrolyte consisted of ethylene glycol, water, and oxalic acid. TiO<sub>2</sub> films with most pronounced rectification of the electric current were formed with an electrolyte consisting of about equal parts per volume of saturated aqueous solution of oxalic acid and ethylene glycol. The influence and importance of the composition of the electrolyte was not investigated further, because satisfactory results were obtained with the electrolyte used. The anodization of the titanium films was performed with the instantaneous application of the full forming voltage from a power source with low impedance, thus allowing the flow of a high initial forming current through the cell. The forming voltage was usually 12v. The thickness of these oxide films was about 1000Å. It is assumed that the high anodization rate is attributable to the large forming current at the beginning of the anodization process and to the electrolyte employed. Higher forming voltages as well as lower current densities for the anodization produce TiO<sub>2</sub> films with less pronounced rectification of the electric current after applying a metallic counter electrode. The reduced rectification ratio is principally created by the increased leakage current in the reverse or anodic direction (titanium positive).

*P-N junction characteristics.*—A number of different materials have been applied as counter electrodes to the TiO<sub>2</sub> layer after anodization. The work function for TiO<sub>2</sub> is reported to be 4.2 ev (25) and, therefore, one group of materials with larger work functions and one group with smaller work functions were selected. Platinum with a work function of 5.3 ev (26), palladium with a work function of 4.99 ev (26), and nickel with a work function of 5.01 ev (26) produce junctions with pronounced rectification of the elec-

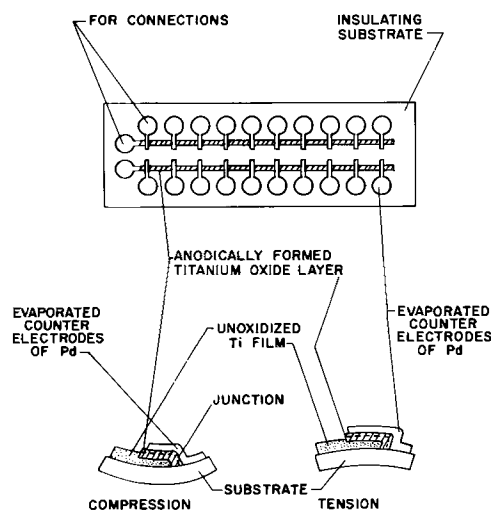


Fig. 1. Schematic drawing of thin-film TiO<sub>2</sub> diodes



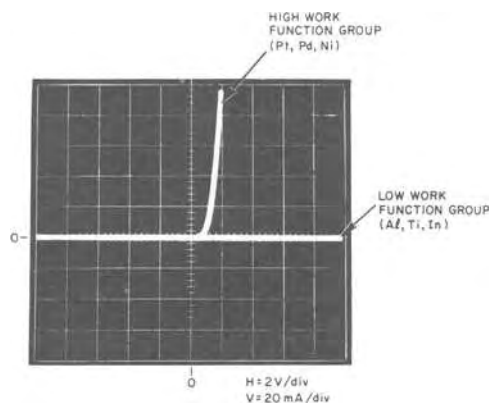


Fig. 2. Current-voltage characteristics of thin-film  $\text{TiO}_2$  diodes with various counterelectrodes.

tric current, as shown in Fig. 2. Counterelectrodes consisting of low work function materials, such as aluminum, titanium, and indium, block the electric current in anodic and cathodic (reverse and forward) directions. Gold electrodes seem to allow some current flow in cathodic direction. These experimental results imply the existence of a p-n junction within the oxide; therefore a number of additional experiments were performed to prove this assumption. Rectification of the electric current based on a difference of work functions can be excluded because the surface of the semiconducting  $\text{TiO}_2$  would have to be of n-type conduction in order to establish rectification with a platinum or palladium electrode. (The growth mechanism of anodically formed oxide layers opposes the assumption of n-type conductivity of the surface.) Anodic oxidation is a diffusion process in which metal as well as oxygen ions diffuse under the electric field applied across the oxide layer. This diffusion process leads automatically to an excess of metal ions and/or a deficiency of oxygen ions at the valve metal-valve metal oxide interface. On the other hand, an excess of oxygen ions and/or a deficiency of metal ions prevails at the surface of the anodic oxide film. This deviation from stoichiometry of the oxide results in layers of n-type and p-type conductivity, respectively. These findings are in agreement with earlier observations made on anodically-formed  $\text{Al}_2\text{O}_3$  (16-18). The center region of the oxide, according to this model, consists of stoichiometric semiconducting oxide, and the thickness of this i-layer increases with increasing forming voltage. The thicknesses of the surface p-type layer and the inner n-type layer are practically independent of forming voltage and are each about 20-50Å (18).  $\text{TiO}_2$  films anodized to forming voltages higher than 12v show a decrease of conduction in the forward direction. Figure 3 shows the current-voltage characteristics of titanium-titanium dioxide-metal structures of various forming voltages ( $V_f$ ) and various counter electrodes. A diode with a forming voltage of 12v and a counter electrode of palladium has a rectification ratio of  $10^6$ . The series resistance of an enlarged i-layer reduces the forward conduction of the diodes and leads finally to a nonpolar, thin-film capacitor.

For  $\text{Ta}_2\text{O}_5$  films, Sasaki (18) calculated a thickness of 50Å for the surface p-layer. These calculations were based on measurements of the capacitance variation of the  $\text{Ta}_2\text{O}_5$  films (with a forming voltage less than 20v) as a function of bias. For larger forming voltages, the voltage dependence of capacitance becomes less pronounced (19). Schmidt *et al.* (3) claim that the surface barrier can be as thick as 250Å. This claim is based on the fact that the photoeffect in  $\text{Ta}_2\text{O}_5$  and  $\text{Nb}_2\text{O}_5$  films (3000Å thick) disappears after a surface barrier of about 250Å has been removed by chemical etching. Rectification in the  $\text{TiO}_2$  film is eliminated by removing approximately 200Å of the anodically

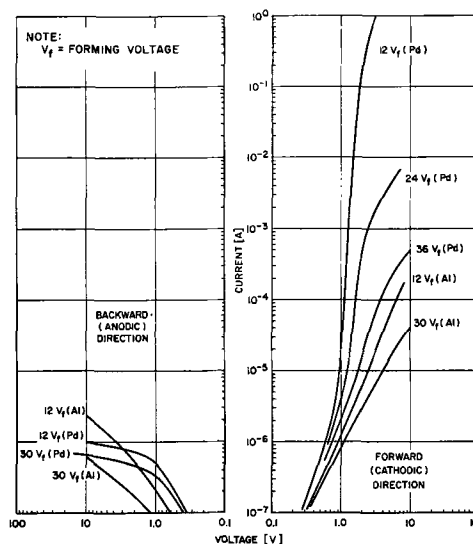


Fig. 3. Current voltage characteristics of  $\text{TiO}_2$  films as a function of forming voltage and counterelectrodes.

formed  $\text{TiO}_2$  film by chemical etching prior to applying the palladium counterelectrode; a nonohmic symmetrical current-voltage characteristic is obtained. In Fig. 4, the I-V characteristic of a Ti- $\text{TiO}_2$ -Pd diode with the complete oxide film is shown. The nonohmic, but symmetrical characteristic obtained after etching 200Å of the oxide film, prior to the application of the palladium counterelectrode, is also shown in the figure. The application of a large current then destroys the unit completely. The chemical etching does not destroy the oxide film but removes only the top p-layer of the anodic oxide film, as indicated by the resulting I-V characteristic and by the uniformity of the interference color of the remaining oxide film as observed with and without optical magnification. This experiment suggests further that the anodic oxide film consists of layers of different types of conductivities and that the total oxide film does not consist of one type of semiconductor only. Otherwise, if the rectification were due to a work function difference, rectification of the electric current would always be observed with one type of counter electrode material, regardless of the chemical etching of the oxide layer.

In as much as the forming voltage and initial forming current significantly affect the I-V characteristic of a thin-film Ti- $\text{TiO}_2$ -Pd diode, the forming time influences the rectification as well. Figure 5 shows the I-V characteristic of a  $\text{TiO}_2$  layer which has been anodized for 1 and 15 min, respectively. The second characteristic exhibits a very high forward conduction. The interference color of the 1-min anodized film was yellow, while that of the 15-min anodized film was dark blue. Similar I-V characteristics with pronounced rectification of the electric current can be obtained

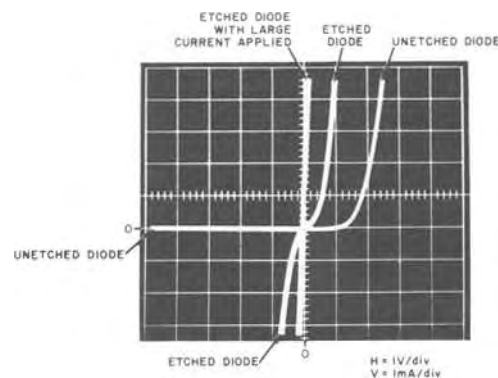


Fig. 4. Current-voltage characteristics of etched and unetched Ti- $\text{TiO}_2$ -Pd diodes.

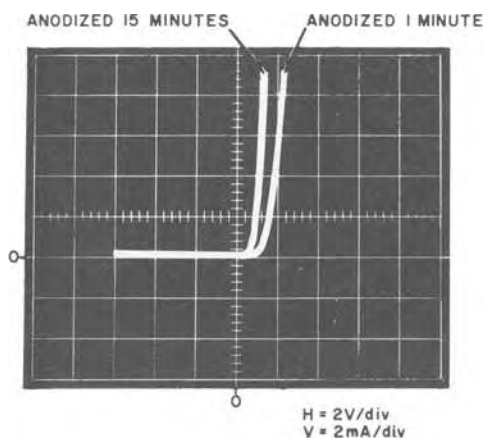


Fig. 5. Influence of forming time on forward characteristics of  $\text{TiO}_2$  diodes.

with other valve metal oxides, such as  $\text{Ta}_2\text{O}_5$  or  $\text{HfO}_2$ , as shown in Fig. 6(a) and (b). In this case, the oxide films have been formed in the same way as the  $\text{TiO}_2$  at 12v with high initial forming current, and the electrodes consist of palladium or platinum. It is again true that if larger forming voltages and/or smaller current densities are employed during the anodization process, the rectification becomes less pronounced and nonpolar, thin-film capacitors of tantalum (10) and hafnium (27, 28) with high-performance characteristics are obtained.

Current-voltage characteristics which are similar to those of Zener diodes have also been observed (see Fig. 7) for thin-film  $\text{Ti-TiO}_2\text{-Pd}$  diodes.  $\text{TiO}_2$  layers frequently exhibit this type of conduction. It is assumed that this conduction results from excessive amounts of tantalum incorporated into the titanium films, resulting in the doping of the semiconducting  $\text{TiO}_2$  layer to a higher degree than by the excess of Ti (n-type semiconductor) only.

Plasmionic anodization of titanium has also been studied to some degree. In this process, the oxygen

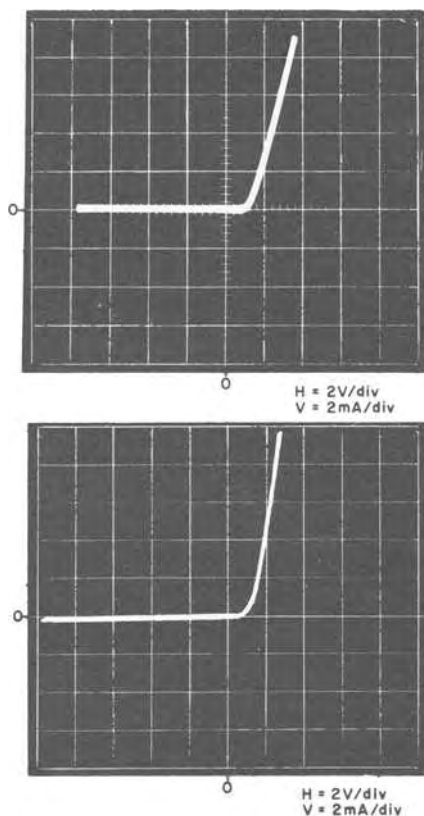


Fig. 6. Current-voltage characteristics of (a) (top) thin-film  $\text{Ta-Ta}_2\text{O}_5\text{-Pd}$  and (b) (bottom) thin-film  $\text{Hf-HfO}_2\text{-Pd}$  diodes.

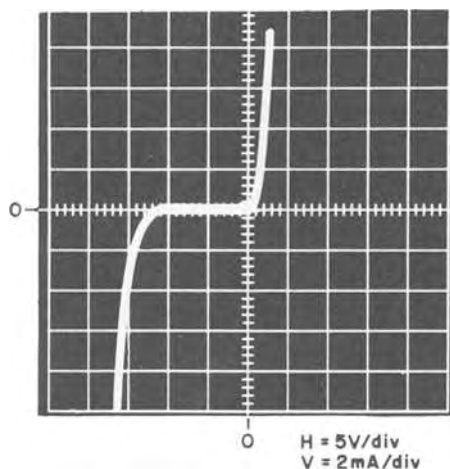


Fig. 7. Current-voltage characteristics of thin-film  $\text{Ti-TiO}_2\text{-Pd}$  diode with Zener breakdown.

ions are supplied for the oxide formation by the glow discharge of a partial oxygen atmosphere maintained in the vacuum system. These  $\text{TiO}_2$  films, anodized to 12v, exhibit rectification of the electric current with a smaller ratio of forward to backward current than the "wet" anodized  $\text{TiO}_2$  films. The increased conductivity in the anodic direction is mainly responsible for this observation due to incomplete anodization. The anodization cannot be performed with a high initial forming current; the leakage current at the end of anodization, even after several hours, is several hundred microamperes. Qualitative agreement between wet and plasma anodization can be established and rectification of the electric current can be observed if a large work function material (Pt, Pd) is again employed as a counter electrode. The process, however, is not very useful for quantitative experiments.

The thin-film structure of  $\text{TiO}_2$  diodes is extremely suitable for investigations of piezoelectric effects (29) in p-n junctions of semiconductors. Stress can easily be applied to the junction by bending the diode which is deposited on a flexible substrate (Fig. 8). The p-n junctions are elastically deformed by bending the substrate, either by compression (diode on concave side of substrate) or by tension (diode on convex side of substrate) as shown in Fig. 1. Increasing elastic compression causes a decrease of the junction resistance in forward and backward direction (Fig. 9). These results are in good agreement with similar investigations on shallow p-n junctions in germanium as reported by Rindner (30). In Rindner's experiment, a diamond stylus was pressed onto the semiconductor surface to elastically deform the junctions and decrease the junction resistance. Figure 9 shows the piezoresistive effect for various compression and ten-

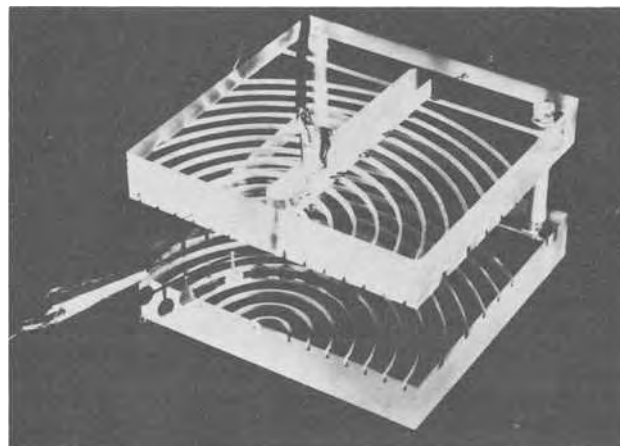


Fig. 8. Application of mechanical stress by elastic deformation

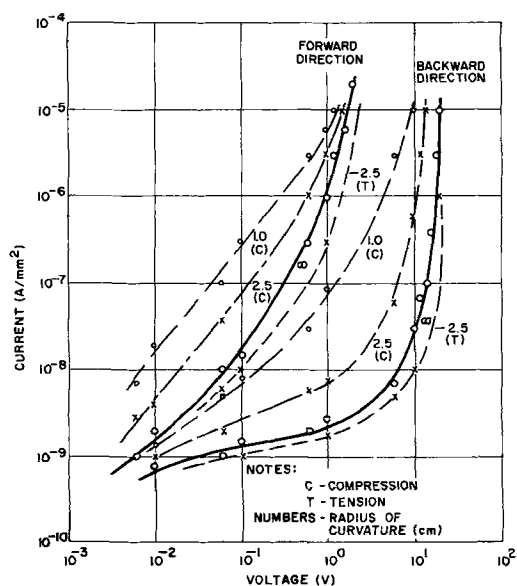


Fig. 9. Piezoresistive effect in thin-film p-n junction diodes of semiconducting  $\text{TiO}_2$ .

sion radii of curvature in centimeters. If tension were applied to the thin-film diodes, an effect opposite to that caused by compression takes place on the junction resistance, and the junction resistance increases. At the same time the capacitance of the junction changes by a few per cent with elastic deformation.

Crystallinity of the semiconducting oxide, contact resistance between the crystallites, and piezoresistance of the oxide contribute certainly to the change of the junction resistance of these diodes, but do not explain fully the large changes of junction resistance or the presence of the piezoelectric effect (29).

The voltage dependence of the capacitance has been used previously (18) to determine the thickness of the p-layer and n-layer in anodically formed  $\text{Ta}_2\text{O}_5$  and to calculate the influence of the increase of the space-charge region with increasing forming voltage. Measurements on the voltage dependence of the capacitance in thin-film Ti-TiO<sub>2</sub>-Pd diodes (31) show a decrease of the capacitance with increasing voltage (reverse direction), leading to a linear relationship between voltage and  $1/C^3$  as expected for a linear graded p-n junction (Fig. 10). The slope of the  $1/C^3$ -vs.-voltage curve changes with thickness and with impurity concentration.

In another experiment, two narrowly spaced counter electrodes were applied to the surface of the anodically formed  $\text{TiO}_2$ . The oxide film was again formed by anodization at 12v, and the counter electrodes consist of palladium. The two electrodes, separated by a

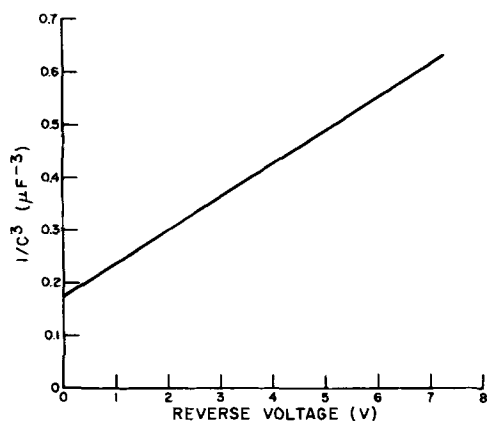


Fig. 10. Voltage dependence of capacitance ( $1/C^3$ ) of thin-film Ti-TiO<sub>2</sub>-Pd diodes as a function of reverse bias.

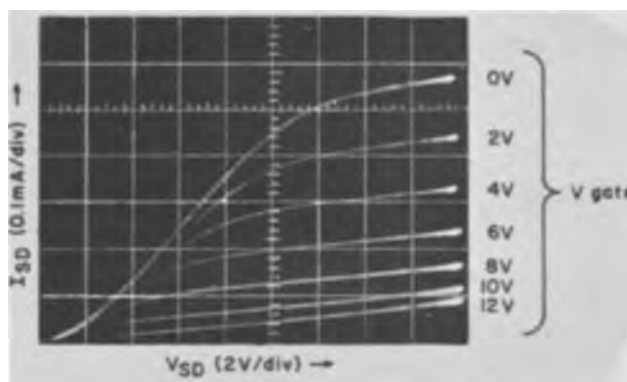


Fig. 11. Transfer characteristics of  $\text{TiO}_2$  unipolar field effect transistor.

gap of 0.001 in., formed the source and drain electrodes of a unipolar field-effect transistor (32). The titanium film acted as the gate electrode. The current flowed in the p-layer from source to drain. Under operating conditions, a reverse bias was applied to the p-n junction by applying the voltage to the titanium film to vary the width of the space-charge region. Figure 11 shows the transfer characteristics of such a device with gate voltages applied in 2-v steps. Transconductance values in the range of 100 microsiemens were obtained. This experiment demonstrates that a conductive surface layer, the conductivity of which can be measured, exists, and this surface layer is adjacent to an insulating layer located underneath.

It is obvious that the performance characteristics of this device have to be improved for practical purposes, but these experiments further support the postulation of the existence of a p-n junction within anodic oxide films of titanium (which were formed in the described way). The effect of current modulation decreases with increasing thickness of the oxide film (higher forming voltages), which is understandable from the point of view of a p-i-n junction model for thicker oxide films.

### Conclusion

The rectification of the electric current in anodic oxide films of titanium has been studied and the experimental results are interpreted on the basis of a p-n junction within the oxide layer. Evaporated electrodes of large work function materials establish ohmic contact to the surface of the anodic oxide layer (p-layer) leading to  $\text{TiO}_2$  diodes. These oxide films are prepared by anodization at 10-15v with high initial forming currents. With increasing forming voltage and thickness of the oxide film, the rectification of the electric current decreases.

The voltage dependence of capacitance, as measured on these junctions, requires a graded p-n junction which is to be expected due to the diffusion process of the oxide formation. Results on piezoresistive and photovoltaic effects of the  $\text{TiO}_2$  films are in agreement with p-n junction theory.

The electric current between two narrowly spaced electrodes deposited on the surface of the oxide film can be modulated by the application of a reverse bias to the junction through the titanium film which acts as the gate electrode. This experiment shows clearly that a conductive surface layer is adjacent to an insulating layer underneath.

If a thin surface layer of about 200Å is removed from the anodic oxide film prior to the application of the electrodes, the rectification of the electric current, as well as the other effects described in this paper, disappear. Preliminary results show that other valve metal oxide films such as  $\text{Ta}_2\text{O}_5$  and  $\text{HfO}_2$  can also exhibit high rectification of the electrical current similar to the  $\text{TiO}_2$  layers.

### Acknowledgment

The author wishes to thank Dr. S. Hofstein of RCA Laboratories for many helpful discussions and for the presentation of the paper at the Dallas Meeting.

Manuscript received June 15, 1967; revised manuscript received Sept. 29, 1967. This paper was presented at the Dallas Meeting, May 7-12, 1967, as Abstract 30.

Any discussion of this paper will appear in a Discussion Section to be published in the December 1968 JOURNAL.

### REFERENCES

1. A. Guenterschulze and H. Betz, "Elektrolytkondensatoren," 2nd ed., Herbert Cram, Berlin (1952).
2. L. Young, "Anodic Oxide Films," Academic Press New York (1961).
3. P. F. Schmidt, F. Huber, and R. F. Schwarz, *J. Phys. Chem. Solids*, **15**, 270 (1960).
4. C. A. Mead, *J. Appl. Phys.*, **32**, 646 (1961).
5. D. Meyerhofer and S. A. Ochs, *ibid.*, **34**, 2535 (1963).
6. A. Dobias, L. Kramp, and O. Lebedinskaya, *Z. Physik*, **61**, 852 (1930).
7. D. Vermilyea, *J. Appl. Phys.*, **27**, 963 (1956); *J. Appl. Phys.*, **36**, 3663 (1965).
8. L. Young, *Trans. Faraday Soc.*, **55**, 437, 842 (1959).
9. N. W. Silcox and L. I. Maissel, *This Journal*, **109**, 1151 (1962).
10. D. A. McLean, N. Schwartz, and E. D. Tidd, *Proc. IEEE*, **52**, 1450 (1964).
11. F. Huber, Proc. Electronic Components Conf., Washington, D. C., May 1967.
12. P. F. Schmidt and M. J. Rand, *Solid State Communications*, **4**, 169 (1966).
13. F. Huber, Paper presented at the New York Meeting of the Society, Sept. 29-Oct. 3, 1963, as Abstract 18.
14. W. Ch. van Geel, *Physica*, **17**, 761 (1951).
15. W. Ch. van Geel and J. W. A. Scholte, *Philips Research Rept.*, **6**, 54 (1951).
16. J. W. A. Scholte and W. Ch. van Geel, *ibid.*, **8**, 47 (1953).
17. B. M. Tareev and M. M. Lerner, *Fiz. Tverdogo Tela*, **2**, 2487 (1960).
18. Y. Sasaki, *J. Phys. Chem. Solids*, **13**, 177 (1960).
19. A. P. Belova, L. G. Gorskaya, and L. N. Zakgeim, *Fiz. Tverdogo Tela*, **3**, 1851 (1961).
20. T. I. Komolova and D. N. Nasledov, *ibid.*, **3**, 3400 (1961).
21. F. Huber, *Solid State Electronics*, **5**, 410 (1962).
22. F. Huber, *This Journal*, **110**, 846 (1963).
23. Y. Ishikawa, Y. Sasaki, Y. Seki, and S. Inowaki, *J. Appl. Phys.*, **34**, 867 (1963).
24. A. von Hippel, J. Kalnajs, and W. B. Westphal, *J. Phys. Chem. Solids*, **23**, 779 (1962).
25. International Critical Tables, Vol. 6, p. 54, McGraw-Hill, New York (1929).
26. Handbook of Chemistry and Physics, 41st ed., p. 2560, Chem. Rubber Publishing Co., Cleveland (1959).
27. F. Huber, W. Witt, and W. Y. Pan, 3rd Intern. Vacuum Congress, Stuttgart (1965).
28. F. Huber, W. Witt, W. Y. Pan, and I. Pratt, Electronic Components Conf., Washington, D. C., May 1966. F. Huber, *RCA Engineer*, **13**, 57 (1967).
29. F. Huber, *Appl. Phys. Letters*, **2**, 76 (1963).
30. W. Rindner, *J. Appl. Phys.*, **33**, 2479 (1962).
31. F. Huber and M. Rottersman, *ibid.*, **33**, 3385 (1962).
32. W. Shockley, *Proc. IEEE*, **40**, 1365 (1952).

## The Insulator-Electrolyte Interface

J. M. Hale

Cyanamid European Research Institute, Cologne, Geneva, Switzerland

### ABSTRACT

The mechanism of electrolytic rectification would depend on the properties of the insulator-electrolyte interface, if anodic oxide films were sufficiently perfect. These properties are reviewed and a quantitative theoretical interpretation given. Correlations between different experimental measurements and a predictable dependence of observables on controllable parameters should be achieved through use of the equations presented if the metal-insulator-electrolyte structure is responsible for a particular case of electrolytic rectification. Formulas derived after making the assumption that all of the equilibrium potential difference in the insulator-electrolyte interface is located within the solid, seem to be in agreement with experiment. Justification of this approximation is not found in the classical description of the interface, however, since point charged particles are able to approach the hypothetical "surface" without restriction. These formulas would suggest that the layer becomes unrealistically thin at high injection levels. It appears from the solution of a simplified quantum mechanical problem, that electrostatic compression of the real space charge layer might be avoided by "squeezing" of the particles out of the bottom of the potential well.

In order to ascertain the mechanism of conduction and rectification by anodic films, it is useful to know what behavior to expect from the system metal-perfect oxide film-electrolyte. A range of easily applied tests which would detect this structure, if it existed in a particular case, is also useful. The role of flaws might then be clarified.

The oxides of interest are usually insulating, although occasionally semiconducting (1, 2). Several theoretical papers, and a considerable body of experimental works, have been devoted to the study of the semiconductor-electrolyte system (3-13). This paper is concerned with the less well investigated insulator-electrolyte case (14-17). The metal contact will not be considered, though some of the formulas

presented have been derived assuming it to be "blocking."

In support of some of the theoretical findings experimental evidence will be cited gained from an anthracene electrode. This model system differs from an anodic film in its ease of fabrication and reproducibility. Anthracene can be highly purified and is easily shown to be nonporous, a degree of perfection which is difficult, if not impossible, to attain with an anodic film. Once a principle has been verified with a single crystal of anthracene, however, it may be applied with confidence to the anodic film case.

The original proposal that anodic films should show characteristics of a metal-insulator-electrolyte system (18) was at a later date retracted by its author

(19). It has since, however, received some experimental support in studies by Vermilyea (20) and Makrides (21) concerning the variation of forward current with character of a redox system included in the electrolyte. Also the reports of photocurrents, photovoltages, and luminescence can be accommodated into this scheme without the need of introduction of a new mechanism for each phenomenon. At the same time it cannot be claimed that any single picture can fit all of the data recorded in the literature.

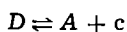
The first part of this paper presents a survey of the main tenets of insulator-electrode reactions, together with their current physical interpretations. Then the theory behind one of the familiar approximations made in insulator-electrode theory is submitted to critical examination, namely, that which asserts all of the equilibrium potential difference in the interface to be located inside the solid.

### Properties of the Insulator-Electrolyte Interface

It is well known that a "space charge limited current" can be made to flow through an insulator, provided that one of the contacts to the solid is "ohmic" (22-24). As originally formulated, the theory (22, 26) of this phenomenon required an infinite reservoir of carriers to exist just inside the surface of the solid which could be "drained" by an applied electric field, the magnitude of the current at any particular field being determined only by the rate of penetration of these carriers into the charged solid.

The current in such a model system increases with the applied voltage without limit. Real systems differ from this model, however, partly because of effects originating at the contact. In the insulator-electrolyte system, these differences provide information of importance to electrochemistry (15). We do not discuss the voltage dependence of the current, since this is found to vary strongly with the sample due to "traps" for the carriers inside the solid.

Since there are no intrinsic carriers present in an insulator, the reservoir at the surface must be generated by injection from the ohmic contact; indeed the term ohmic merely describes the type of contact through which charge transfer is possible. Kinetically a dynamic exchange of carriers takes place through the interface, the current in each direction being identical at equilibrium. When the exchange is with a solution of a redox system this current may be called "the exchange current for the redox system at the insulator electrode" without any consequent confusion of terms, since the implication here is quite analogous to its implication at a metal electrode. We shall write the redox reaction in the form



The donor species  $D$  in solution transfers the carrier  $e$  to the solid with formation of the acceptor species  $A$ .

In order that an electrolyte forms an ohmic contact to a solid, there must be a large concentration of carriers in the surface of the solid at equilibrium. The carrier band must therefore be bent at the surface so that it approaches the Fermi level. This is not the only requirement for an injecting contact, however. Application of a potential across the solid removes carriers from the surface layer and hence slows down the capture of carriers by the acceptor species. In the first approximation it does not affect the rate of the donation reaction. Hence the reservoir of carriers will be emptied very quickly by the field unless the rate of replenishment is high so that large rates of drainage can be maintained, that is, the exchange current must be large. The current can become saturated when the voltage becomes high enough to reduce to zero the density of carriers at the surface, so "switching off" the capture reaction. Then the maximum injection current is numerically equal to the exchange current. A limiting diffusion rate of the donor species also leads to current limitation, however. Here, therefore, is a major influence of the interface

upon a current voltage measurement; it leads to current saturation.

These points have been confirmed experimentally, using an anthracene membrane sandwiched between two electrolytes as a model system (16). The passage of continuous hole currents is possible if one of the solutions contains a redox system having a high redox potential, and which has a large exchange current at a metal electrode. This is taken to mean that the very oxidizing electrolytes inject positive holes into the valence band of the insulator until the electrostatic work of injection balances the chemical energy gained in the donation reaction. Evidently the potential in the interface in this condition must be proportional to the standard potential of the redox system,  $D/A$ . The analogous requirements for electron currents, very reducing systems having large exchange currents have also been demonstrated. Recent experiments have indicated the possibility that injection might also be possible from weaker oxidizing agents in the presence of strong acids. This has been interpreted to mean that proton injection into the solid can assist the potential bending due to the oxidant alone, the combined effect being sufficient to create an ohmic contact.

*Theoretical interpretation.*—A quantitative interpretation of these requirements has also been made. For this purpose the donation reaction was assumed to be a member of the simplest class of electron transfer reactions, the so-called "outer sphere" type, having very weak interaction of the orbitals of the solution phase species and the electrode. Extensive theoretical work on such systems has been performed by Marcus (27), who used a quasithermodynamic description of the transition state of the reaction, and by Dogonadze, Chizmadzhev, Chernenko, and Kuznetsov (28) who calculated the quantum mechanical probability of electronic transition under perturbation by a phonon arriving from the solution. These treatments agree that in the first approximation the cross section through the potential energy surface made by the reaction coordinate is parabolic. The reaction coordinate itself may be imagined to be the effective charge on the solution phase species changing gradually from its value in the initial state to its value in the final state. The energy of activation is required to change the configuration of the solvent from equilibrium with the reactants to a compromise configuration in the transition state.

Using these theories and the approximation that all of the potential difference in the interface is located within the solid it is possible to show that the exchange current  $i_0$  for the redox system at the insulator electrode is (15)

$$i_0 = Z F N_c [D] \exp \left\{ - \frac{\lambda}{4RT} [1 + (\Delta - FV)/\lambda]^2 \right\}$$

A formula for  $Z$  was given in the papers by Dogonadze and Chizmadzhev (4); it has the approximate magnitude  $10^7 \text{ cm}^4 \text{ mole}^{-1} \text{ sec}^{-1}$ .  $F$  is the faraday,  $N_c$  the molar density of vacant states in the electrode ( $\sim 10^{-2} \text{ cm}^{-3}$ ),  $[D]$  the concentration (moles  $\text{cm}^{-3}$ ) of the donor species,  $\lambda$  ( $\sim 2 \text{ eV}$ ) the energy scaling parameter for the potential energy parabolas assumed to describe the reaction path (27),  $\Delta$  the gap between the carrier band and the Fermi level in the bulk of the solid, and  $V$  the magnitude of the potential difference at equilibrium between the surface and the bulk of the solid when the activities of  $D$  and  $A$  are equal.  $R$  is the gas constant and  $T$  the absolute temperature. This formula embodies the requirements for an ohmic contact in the following way: In order that  $i_0$  be large, the argument of the exponential factor must be as small as possible, which in turn requires that  $\lambda$  and  $(\Delta - FV)/\lambda$  be small. The first restraint is one which also applies if the redox couple is to have a large  $i_0$  at a metal electrode (29), while the second is true only if  $V$  is made large by the creation of a space charge layer. If only electronic charge separation through the interface is possible, then  $V$  is linearly

related to the redox potential  $E_o$  of D/A as argued above

$$V \simeq E_o - E_{FB}$$

where  $E_{FB}$  is the "flat band potential" of the solid. Then a large magnitude for  $V$  requires that  $E_o$  is well separated from  $E_{FB}$ , which implies a very oxidizing or reducing couple.

If ionic charge separation across the interface is also possible, then a further calculation becomes necessary to deduce the magnitude of  $V$ .

*Simultaneous electronic and ionic charge separation through an interface.*—We retain the model of electron or hole conduction through the insulating layer, but assume that an ion L of the same charge type having a very small mobility in comparison with that of the "carrier," so that the ionic current is much less than electron or hole current, can penetrate the solid to some extent. This increases the charge density in the double layer and hence deepens the potential well for carriers. It is a curiosity that addition of ions, which themselves repel the electronic species, actually leads to an increase in the concentration of the latter. This phenomenon is due to the fact that the partition coefficient for an ion between the two phases fixes the concentration of the ion just inside the solid, in a plane which has the same potential as the solution, while the concentration of carriers is fixed at the other side of the space charge layer, in the bulk of the solid. The concentration of the ion, and that of the carrier, however, have the same functional dependence on the potential at any point in the layer. Hence the increase in potential which accompanies penetration of ions into the solid leads to additional injection of carriers from the solution.

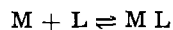
The calculation of  $V$  is made by collecting together equations describing the partition of ions between the phases, the equilibrium between the ions and the molecules of the solid within the solid phase (if one exists), the concentration of carriers, and Poisson's equation describing the space charge layer (30). The first three of these provide an expression for the total charge density at the solid-electrolyte interface in terms of  $V$ , which is precisely the boundary condition needed for solution of Poisson's equation. If  $V \gg 2RT/F$  an approximation can be made which permits the potential to be expressed explicitly in terms of the parameters of interest. This equation is

$$V = V_1 + (2RT/F) \ln \{ \frac{1}{2} [1 + (1 + \beta a_L)^{1/2}] \}$$

where  $a_L$  is the activity in solution of the ions able to penetrate the solid,  $V_1$  is the potential due to the redox system alone (see previous section) at  $a_L = 0$ , and  $\beta$  is a constant specified by

$$\beta = 4z K_p (1 + K) / (\pi N_c v^o) \arccos \{ \exp(-FV_1/2RT) \} \exp [(\Delta - FV_1/2)/RT]$$

$z$  is the valency of the ion,  $K_p$  is the chemical partition coefficient for the ion between the two phases,  $K$  is the equilibrium constant for the "complexing" reaction



where  $M$  is a molecule of the solid,  $v^o$  is the molar volume of the solid, and other symbols have been introduced previously. The complexing equilibrium was included in order that the results might apply to the case of anthracene in contact with strong acids, since it is known that the aromatic hydrocarbons are weakly basic. The magnitude of ionic effects caused by incorporation of ions into the space charge layer depends upon the size of the constant  $\beta$ . If  $a_L \sim \beta^{-1}$  is an attainable activity, then a potential shift, with consequent enhancement of injection current, must accompany increase of ionic activity in solution beyond this point. For  $a_L \ll \beta^{-1}$  the equilibrium potential at the insulating film must be identical to that at a metal (measured against the same reference elec-

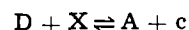
trode). For  $a_L \gg \beta^{-1}$ , however, the potential varies with  $a_L$  according to the equation

$$V \propto (RT/F) \ln a_L$$

Experiments designed to check this theory, through measurement of the potential and of the injection current as a function of acidity, are at present in progress in our laboratory. It is certain that effects of acid on injection into anthracene do arise, but as yet we are unable to separate conclusively the effects outlined above from those introduced by varying thicknesses of the anthraquinone film which covers the anthracene surface. Another complicating factor is the variation of the standard potential of many redox systems, which otherwise would be quite suitable, because of complexing effects. Ionic space charges in anodic films have previously been proposed by Vermilyea (31), and by Schmidt (32).

*Photoinjection at the insulator-electrolyte interface.*—Particularly revealing, as a tool for investigation of the properties of the insulator-electrolyte interface is the photocurrent which flows when the insulator is irradiated through the electrolytic contact by strongly absorbed light. There are two principal mechanisms of generation of photoconduction, distinguishable by the relation between the energy of the radiation involved and the energy gap between the valence and conduction bands of the photoconductor. Intrinsic photoconduction can occur when the light is sufficiently energetic to cause direct band to band transitions. This is independent of the nature and polarity of the illuminated contact. Extrinsic photoconduction can occur when the radiation is absorbed to produce electrically neutral, nonconducting states of the crystal ("excitons") which, however, interact with electronic states in the electrolyte. This is likely to happen in a wide variety of materials, including anodic films, yet researches have concentrated on the aromatic hydrocarbons. Naturally these currents are sensitive to the nature and polarity of the electrolyte.

A photocurrent is generated at the anthracene/water ( $O_2$ ) interface, for example, when the solid is irradiated with visible light of energy 3.1 eV (less than the energy of the lowest conducting state at 3.65 eV). Singlet excitons formed in the solid at this wavelength, being electrically neutral, are transported only by diffusion (33, 34). Following a suggestion by Kallmann and Pope (33) we formulate their interaction with a donor species in the electrolyte in the following manner



where  $X$  stands for the exciton.

If  $D$  is an oxidized species, for example, the reaction with the exciton involves an electron transfer from the solid to the solution with release of a hole into the valence band. Thus the process is similar to "dark" injection by an oxidizing medium, but differs in that the electron comes from a state with energy comparable with that of the conduction band, while in the dark case the electron originates from the valence band. A nonradiative mechanism for this reaction does exist, and the process can be very much faster than the dark injection (36).

An interesting point about this system is that at open circuit, when no net current flows through the interface, a steady state exists. The exciton annihilation reaction proceeds with a net formation of carriers, but at the same time the carriers are captured by the acceptor species to fall down to the ground state. One might say, quite correctly, that the photo- and dark-injection reactions are proceeding at the same rate, though in opposite directions (37).

A calculation of the photocurrent requires solutions of the diffusion problem for excitons and the migration problem for carriers, with the kinetic equation for the current through the interface as a common boundary condition. As is the case with dark injection currents, the interface has very little influence on the current-



voltage behavior over most of the range of variation of the current, but it can be responsible for the appearance of saturation at high voltages. This limiting current can be expressed (36)

$$i_{\text{lim}} = i_0 + \mathbf{F} I_0 \left[ (1 + 1/\epsilon_s \sqrt{D_x \tau_x}) (1 + 1/k_f [D] \sqrt{\tau_x/D_x}) \right]^{-1}$$

$i_0$  is the exchange current for the "dark" reaction discussed above.  $I_0$  is the intensity of illumination,  $\epsilon_s$  the extinction coefficient of the solid,  $D_x$  and  $\tau_x$  the diffusion coefficient and lifetime, respectively, of the exciton.  $k_f$ , the heterogeneous rate constant of the photoinjection reaction, is given by

$$k_f = Z \exp \{ -(\lambda/4RT) [1 + (\Delta - \mathbf{F}V - E_x)/\lambda]^2 \}$$

$E_x$  is the energy of the exciton, and  $V$  the potential difference in the interface at equal activities of D and A and in the absence of illumination.

That the photocurrent shows an identical spectral dependence to the light absorption by the solid, because of the influence of  $\epsilon_s$ , has been pointed out previously (34, 38) and is experimentally verifiable for a number of insulators (39). More interesting from the point of view of electrochemistry is the prediction about the variation of the incremental photocurrent,  $i_{\text{lim}} - i_0$ , with the redox potential of the D/A couple, under otherwise identical conditions.

$E_x$  is often so large ( $\sim 3.1$  eV for the first singlet exciton in anthracene) that  $(\Delta - \mathbf{F}V - E_x)/\lambda$  can take the value  $-1$  for a possible choice of  $V$  and  $\lambda$ .  $k_f$ , and therefore the photocurrent, is a maximum under these conditions since the exponential factor becomes unity (40).

This behavior has been checked experimentally at the anthracene membrane. As expected, the photocurrent plotted against redox potential for a series of hole injecting D/A couples (in acid solution) shows a maximum in the region of 1.2V NHE. Knowledge of the positions of the bands, the energy of the exciton, and the value of  $\lambda$  enables the flat band potential of the solid to be calculated from these measurements.

According to this model of the photoinjection process, an increase of the concentration of carriers in the surface must accompany increase of illumination intensity at open circuit. Hence there must be a photopotential developed in the interface. Using the formula

$$V_I = V + (RT/\mathbf{F}) \ln (c_I/c)$$

the subscript I indicating the magnitude of a quantity in the presence of illumination and  $c$  connoting the density of carriers of the surface, together with the formula for  $c_I$  resulting from the earlier calculation, we find an equation which relates the open-circuit photopotential to the total limiting current at the same light intensity:

$$V_I = V + (RT/\mathbf{F}) \ln (i_{\text{lim}}/i_0)$$

This result may be used to estimate the exchange currents,  $i_0$ , of those dark reactions which yield immeasurably small currents in the absence of illumination.

*Double injection and luminescence.*—If the opposite faces of a platelike crystal of an insulator are furnished with contacts ohmic to oppositely charged carriers, then double injection occurs (41). The cancellation of space charge accompanying the superposition of the distributions of electrons and holes within the solid leads to an enhancement of the current over that observed at the same voltage in the single injection case (42-44). The system rectifies, however, Recombination of the oppositely charged carriers in the center of the solid leads to the formation of excitons, some of which decay radiatively giving rise to luminescence.

Electrochemically interesting effects are observed when the injection of one of the carriers becomes interface limited, for the over-all current can increase beyond that level although light output saturates (14).

We have not yet determined the mechanism of transfer of the additional current through the "saturated" contact; this might either be due to the excess carriers of the opposite sign reacting directly with the donors in the electrolyte, or there may be "photoinjection" due to a reaction between excitons and donors at the surface.

#### Distribution of the Space Charge at Equilibrium

In the theoretical description of the properties of the insulator-electrolyte interface, it is often convenient to make the assumption that all of the potential difference generated in the interface by injection is located within the solid. This approximation is known to be reasonable in semiconductors having low carrier densities, and has been justified in that case by means of the formula (4, 13)

$$\frac{V_{S_n}}{V} \approx \left[ \frac{c_{S_d} \epsilon_{S_d}}{c_{S_n} \epsilon_{S_n}} \right]^{1/2}$$

where  $V$  is the total potential difference in the interface and  $V_{S_n}$  the part of that potential across the outer Helmholtz layer;  $c_{S_d}$  and  $\epsilon_{S_d}$  are the concentration of carriers and the dielectric constant of the solid;  $c_{S_n}$  and  $\epsilon_{S_n}$  are the corresponding quantities for the solutions. If  $c_{S_d} \ll c_{S_n}$  for a semiconductor in contact with a reasonably concentrated solution, and  $\epsilon_{S_d} \sim \epsilon_{S_n}$ , then  $V_{S_n} \ll V$ .

In an insulator the carrier density is even smaller than it is in a semiconductor, and hence, at first sight the same approximation appears to be justified. A reexamination of the whole question reveals, however, that the appropriate carrier density to be inserted into the foregoing formula should not be the density in the uncharged solid, but an average density in the space charge layer. This, of course, can be quite different from the bulk value when injection is allowed, so that further consideration becomes necessary. The approximation seems to be satisfactory in practice since it gives formulas in quantitative accord with experiment, but the theoretical explanation for its validity might be different from that applicable to the depletion layer.

*The classical theory.*—The description of the space charge layer provided by classical physics becomes quite untenable at high injection levels. We recall that this theory deals with point charges which experience no net force at equilibrium because an electrical attraction to the layer of counter ions on the outer Helmholtz plane just balances the diffusion force driving the particles down the concentration gradient into the bulk of the solid. Two simultaneous relationships between the particle density  $n$  and the electrostatic potential  $V$  are available, namely the Boltzmann equation

$$n = n(0) \exp [-\mathbf{F}(V - V(0))/RT]$$

and Poisson's equation

$$\frac{d^2V}{dx^2} = -\frac{4\pi n \mathbf{F}}{\epsilon \epsilon_0}$$

which when combined provide an explicit functional dependence for  $n$  or  $V$  on  $x$  the distance into the solid from the interface.  $\epsilon$  is the dielectric constant of the solid, and  $\epsilon_0$  the permittivity of vacuum. For definiteness we choose  $dV/dx = 0$  at  $x = d$ , the "rear" contact to the crystal, which describes a contact establishing the flat band potential at equilibrium. Then charge transfer through that contact is not permitted.

The solution to this problem (26, 45, 46) contains a characteristic length,  $l_c$ , within which significant changes of  $V$  and  $n$  occur. It may be expressed in the form:

$$l_c = \frac{B d}{\sqrt{2} \arccos B} \rightarrow \frac{\sqrt{2} B d}{\pi} \text{ for } V_s \gg \frac{2RT}{\mathbf{F}}$$

Here

$$B = \exp [-\mathbf{F}V_s/2RT]$$



and  $V_s$  is used for the total potential drop within the solid. The startling prediction is made, that if  $V_s = 2v$  so that  $B \sim 4 \cdot 10^{-18}$  at room temperature, then  $l_c < 10^{-18}$  cm. This is a physically unrealistic value. Another manifestation of the same phenomenon becomes evident if the potential difference across the inner Helmholtz layer is calculated. This is

$$V_H = \sqrt{2} \frac{d_H}{l_c} \frac{RT}{F} \frac{\epsilon_s}{\epsilon_H} \sqrt{1 - B^2}$$

Taking  $d_H$ , the thickness of the inner Helmholtz layer, to be 5Å as at a metal, and assuming approximate equality of the dielectric constants of the solid  $\epsilon_s$  and the inner layer  $\epsilon_H$ , we find  $V_H \sim 10^{10}v$  at  $V_s = 2v$ . At first sight the failure of classical physics would not be ascribed to "degeneracy" (the breakdown of Boltzmann statistics), since the usual criterion that the bands should not approach within several  $kT$  of the Fermi level need not be violated, with only  $2v$  of band bending, in the arbitrary wide gap material. It is illuminating to study the simplest theory of a space charge of totally degenerate particles, however, since this does not predict compression of the layer by a field in the same way.

*The totally degenerate space charge layer.*—If the one-electron states for "the particle in a box" are filled up to an energy  $E$ , the density of particles at any point in the box is

$$n = (8\pi/3) (2Em/h^2)^{3/2}$$

$m$  is the mass of the particle and  $h$  Planck's constant. This is called the Thomas-Fermi equation (47, 48). The total energy of any particle in a space charge layer at a point at which the electrostatic potential is  $V$  (consisting of a sum of potential and kinetic energies) is  $ev$ , where  $e$  is the magnitude of the electronic charge. Thus in a "flat bottomed box" the density of particles at the point would be

$$n = (8\pi/3) (2eVm/h^2)^{3/2}$$

Regarding this as a relation between the particle density and the potential at each point in the layer, and assuming Poisson's equation to be valid, a soluble equation in the potential alone may be constructed having the solution

$$V = V_s [1 - (1 + x/l_c)^{-4}]$$

where  $l_c$  is the Thomas-Fermi characteristic length in the layer

$$l_c = (15\epsilon\epsilon_0/8\pi^2 e^2)^{1/2} (h^2/2m)^{3/4} (eV_s)^{-1/4}$$

Evidently  $l_c$  is only weakly dependent on  $V_s$  in this case. At  $V_s = 2v$ , for example,  $l_c \sim 1.2\text{Å}$  if the free electron mass is used for  $m$ .<sup>1</sup> The potential difference across the inner Helmholtz layer is given by

$$V_H = 4 \frac{d_H}{l_c} \cdot V_s \sim 33v \text{ at } V_s = 2v$$

Thus the particles in a degenerate space charge layer, whose density is of the same order of magnitude as the density of allowed eigen states, are unable to approach the surface as closely as do the unrestricted "classical" particles. We are prompted to examine the quantum mechanical problem for the space charge layer, therefore, to enquire whether the densities of states and particles can become comparable.

*The quantum mechanical problem.*—Regarding the layer of ions on the outer Helmholtz plane as the creators of a potential well within which the car-

riers move, we anticipate that the one-electron eigen states will consist of discrete levels with the upper states penetrating deeper into the solid than the lower ones. The separation between these levels, and therefore the density of states will be determined by the width of the well (50). The solid electrolyte interface will represent a nearly vertical potential energy barrier which will reflect the particles incident on the surface, while particles moving in the opposite direction will be confined to the region of the phase boundary by the screened attraction to the ions outside the solid. The well must get narrower as the number of particles in it increases, or synonymously as the total potential difference inside the solid rises.

There is no method of calculating the potential distribution explicitly with this approach. Only a self-consistent procedure would seem to be possible, consisting of alternately solving Schrödinger's equation for the eigen functions using a guessed effective potential well, squaring and adding these to yield the density as a function of position, then solving Poisson's equation for the potential using this estimated density.

We have not carried out this computation. Instead we have sought to gain insight into the behavior to be expected by recalling a much simplified problem originally studied by Dewald (51). This approximates the effective one-electron potential by

$$eV \simeq e\mathcal{E}x \quad x > 0 \\ = \infty \quad x = 0$$

where  $\mathcal{E}$  is a constant field and  $x$  is measured from the interface. Schrödinger's equation is equivalent to Bessel's equation in this case (52). In order to satisfy the condition that the wave function should vanish at  $x = 0$ , the eigen values  $E_n$  must obey the equations

$$-E_n = (3S_n/2)^{2/3} (h^2 e^2 \mathcal{E}^2/8\pi^2 m)^{1/3}$$

where  $S_n$  is a root of the equation

$$J_{1/3}(S) + J_{-1/3}(S) = 0$$

$J_{1/3}$  is the cylinder function of the first kind (52).

Dewald pointed out that, if  $\mathcal{E}$  is given the value  $10^6v \text{ cm}^{-1}$ , then the lowest lying eigen value ( $n = 1$ ) is already 0.17 eV above the bottom of the well, and that the spacing of the first few levels<sup>2</sup> is of the same order of magnitude. At  $\mathcal{E} = 10^7v \text{ cm}^{-1}$  this figure becomes 0.79v. In comparison the zero point energy, and spacing of the lowest energy levels in the free electron band is  $\sim 10^{-15}$  eV. Instead of being distributed over energy as  $E^{1/2}$ , the density of states function within the space charge layer becomes proportional to  $E^{3/2}$ .

Thus, as the potential energy well becomes deeper, tending to confine the particles into a narrower region adjacent to the interface, so the eigen states get squeezed out of the bottom of the well. This is merely an effect of the uncertainty principle, of course, and is a consequence of the wavelike character of the carriers.

We are led, therefore, to distrust any method of calculation of density of particles or of electrostatic potential in a space charge layer, which does not take account of the discreteness of the states occupied by the particles. Both the classical method based upon Boltzmann's equation, and the Thomas-Fermi equation for a degenerate gas, assume a continuous distribution of states over potential energy, and therefore must fail when the potential gradient becomes large. At the same time we can assert that a space charge layer cannot become compressed into a region less than a few angstroms thick. In the absence of quantitative proof we will assume that this is the explanation for the observed sharing of potential between the Helmholtz double layer and the solid in the insulator-electrolyte interface.

<sup>1</sup> In practice the potential varies rapidly within the wavelength of the carrier, inside the space charge layer, so that the use of formulas derived from the flat bottomed box problem is suspect. Swiatecki (49) suggested an improvement to the method which corrects the density for a potential gradient. The numerical integration he recommends shows that this improvement leads to a further expansion of the layer. At  $V_s = 2v$   $V_H$  becomes  $\sim 18v$ .

<sup>2</sup> The levels referred to are for motion in the direction normal to the surface. The spacing of levels for motion in the plane parallel to the surface are unaltered by the field.

Manuscript received June 15, 1967; revised manuscript received Oct. 2, 1967. This paper was presented at the Dallas Meeting, May 7-12, 1967 as Abstract 31.

Any discussion of this paper will appear in a Discussion Section to be published in the December 1968 JOURNAL.

## REFERENCES

- L. Young, "Anodic Oxide Films," Academic Press, London and New York (1961).
- P. F. Schmidt, F. Huber, and R. F. Schwarz, *J. Phys. Chem. Solids*, **15**, 270 (1960).
- H. Gerischer, "Advances in Electrochemistry and Electrochemical Engineering," Vol. 1, P. Delahay, Editor, Chap. 4, Interscience, New York.
- R. R. Dogonadze and Yu. A. Chizmadzhev, *Proc. Acad. Sci. USSR, Phys. Chem. Sect.* (Engl. Trans.), **150**, 402 (1963).
- R. R. Dogonadze, A. M. Kuznetsov, and Yu. A. Chizmadzhev, *Russ. J. Phys. Chem.*, (Engl. Trans.) **38**, 652 (1964).
- A. M. Kuznetsov and R. R. Dogonadze, *Izvestiya Akad. Nauk SSSR, Seriya Khimicheskaya*, (Engl. Trans.), **1964**, 2042.
- A. M. Kuznetsov and R. R. Dogonadze, *ibid.*, **1964**, 1787.
- R. R. Dogonadze and A. M. Kuznetsov, *Electrokhimiya* (Engl. Trans.), **1**, 898 (1965).
- H. Gerischer, *This Journal*, **113**, 1174 (1966).
- Yu. A. Vdovin, V. G. Levich, and V. A. Myamlin, *Proc. Acad. Sci. USSR, Phys. Chem. Sec.*, (Engl. Trans.), **124**, 53 (1959).
- J. F. Dewald, in "Semiconductors," p. 727, N. B. Hannay, Editor, Reinhold Publishing Co., New York (1959).
- M. Green, in "Modern Aspects of Electrochemistry," J. O'M. Bockris, Editor, Vol. 2, p. 343, Butterworth, London (1959).
- V. A. Myamlin and Yu. V. Pleskov, *Usp. Khim.*, **32**, 470 (1963).
- W. Mehl and J. M. Hale, in "Advances in Electrochemistry and Electrochemical Engineering," P. Delahay, Editor, Vol. 6, Interscience, New York, To be published.
- J. M. Hale and W. Mehl, *Surface Sci.*, **4**, 221 (1966).
- W. Mehl, *Ber.*, **69**, 583 (1965).
- W. Mehl, J. M. Hale, and F. Lohmann, *This Journal*, **113**, 1166 (1966).
- A. W. Smith, *Can. J. Phys.*, **35**, 1151 (1957).
- A. W. Smith, *ibid.*, **37**, 591 (1959).
- D. A. Vermilyea, *J. Appl. Phys.*, **36**, 3663 (1965).
- A. C. Makrides, *This Journal*, **111**, 392 (1964).
- N. F. Mott and R. W. Gurney, "Electronic Processes in Ionic Crystals," Oxford University Press, London (1940).
- M. A. Lampert, *Rept. Prog. Phys.*, **27**, 329 (1964).
- R. H. Tredgold, "Space Charge Conduction in Solids," Elsevier, Amsterdam (1966).
- M. A. Lampert, *Phys. Rev.*, **103**, 1648 (1956).
- G. T. Wright, *Solid State Electronics*, **2**, 165 (1961).
- R. A. Marcus, *Ann. Rev. Phys. Chem.*, **15**, 155 (1964).
- R. R. Dogonadze, A. M. Kuznetsov, and A. A. Chernenko, *Russ. Chem. Rev.*, (Engl. Trans.) **34**, 759 (1965).
- R. R. Dogonadze and Yu. A. Chizmadzhev, *Proc. Acad. Sci. USSR, Phys. Chem. Sect.*, (Engl. Trans.), **145**, 563 (1962).
- J. M. Hale, Submitted for publication.
- D. A. Vermilyea, *J. Phys. Chem. Solids*, **26**, 133 (1965).
- P. F. Schmidt, *J. Appl. Phys.*, **28**, 278 (1957).
- H. Kallmann and M. Pope, *Nature*, **186**, 31 (1960).
- V. V. Eremanko and V. S. Medvedev, *Soviet Physics, Solid State*, (Engl. Trans.), **2**, 1426 (1960).
- L. E. Lyons, *J. Chem. Phys.*, **23**, 220 (1955).
- J. M. Hale and W. Mehl, *Electrochim. Acta*, to be published.
- W. Van Geel, C. Pistorius, and P. Winkel, *Philips Research Rept.*, **13**, 265 (1958).
- J. W. Steketeer and J. de Jonge, *ibid.*, **17**, 363 (1962).
- B. J. Mulder and J. de Jonge, *ibid.*, **21**, 188 (1966).
- R. A. Marcus, *J. Chem. Phys.*, **43**, 2654 (1965).
- W. Mehl and W. Büchner, *Z. Physik. Chem. N.F.*, **47**, 76 (1965).
- M. A. Lampert and A. Rose, *Phys. Rev.*, **121**, 26 (1961).
- R. H. Parmenter and W. Ruppel, *J. Appl. Phys.*, **30**, 1548 (1959).
- R. Baron, *Phys. Rev.*, **137A**, 272 (1965).
- K. Klier, *Coll. Czech. Chemical Communications*, **27**, 920 (1962).
- S. M. Skinner, *J. Appl. Phys.*, **26**, 498, 509 (1955).
- L. H. Thomas, *Proc. Camb. Phil. Soc.*, **23**, 542 (1927).
- E. Fermi, *Z. Physik*, **48**, 73 (1928).
- W. J. Swiatecki, *Proc. Phys. Soc. (London)*, **A68**, 285 (1955).
- P. M. Morse and H. Feshbach, "Methods of Theoretical Physics," 1st ed., p. 1650, McGraw-Hill, New York, Toronto, London.
- J. F. Dewald, *Ann. New York Acad. Sci.*, **101**, 872 (1963).
- G. N. Watson, "Theory of Bessel Functions," 2nd ed., p. 97 Eq. (11), Cambridge University Press, (1966).

## The Current-Voltage Characteristics of Porous Anodic Oxides on Aluminum

C. E. Michelson\*

*Finishing and Joining Section, Metals Research Laboratories,  
Olin Mathieson Chemical Corporation, New Haven, Connecticut*

### ABSTRACT

Rapid voltage reduction across porous anodic coatings results in zero current, and a relatively long time is required for recovery to the new equilibrium current. The recovery time is dependent on the voltage change, rate of change, and electrolyte temperature. Capacity measurements show that physical thinning occurs only when current begins to increase late in the recovery period. This behavior appears inconsistent with the conventional pore base dissolution mechanism of porous oxide growth.

Anodic treatment in certain electrolytes, such as sulfuric acid, causes porous coatings to form on aluminum. Other electrolytes, typically boric acid, form nonporous film. Anodizing electrolytes are frequently

classified as dissolving or nondissolving according to their supposed chemical action on the aluminum oxide. This dissolution has been accepted as the direct cause of the pore development and the reason why anodizing does not stop in spite of the films of oxide built up on the metal surface.

\* Electrochemical Society Active Member.

The purpose of this paper is to present some qualitative observations on the dynamic current-voltage characteristics exhibited by porous anodic oxides in the electrolytic cell. These will be discussed in the light of the classical model conceived by Keller, Hunter, and Robinson (1) and the more recent alternative proposed by Murphy and Michelson (2).

## Two Concepts of Structure and Growth of Anodic Films on Aluminum

Before describing the experimental work, two models and mechanisms of oxide growth are reviewed briefly.

### Geometric Pore Model

Keller, Hunter, and Robinson (1) have hypothesized that electrolytic oxidation of aluminum proceeds simultaneously with dissolution of the oxide at selected points. As a result of the dissolution at regularly spaced points a cellular structure arises. Figure 1 illustrates the concept of a hexagonal cell of aluminum oxide containing a star-shaped pore extending from the surface to a point near the metal.

Keller *et al.* call this separation of the pore base from the metal the barrier layer. They have proposed that the barrier layer, cell wall, and pore diameter are related to the anodizing parameters.

On the basis of this model, Hunter and Fowle (3) have concluded that dissolution at the pore base must proceed at a much faster rate than is possible under the usual electrolyte temperature and concentration. The authors hypothesize that the temperature of the pore base must be about 125°C and the acid concentration almost 50% while the bulk electrolyte is operating at 21°C and 15% concentration.

Hunter and Fowle (4) have found that the unit barrier thickness of films formed in sulfuric acid is about constant and close to 10 Å/v. They conclude that voltage and current density affect only the over-all thickness of the coating, not the unit barrier thickness.

### Colloidal Gel Model

The model (Fig. 2) proposed by Murphy and Michelson (2) explicitly considers such important factors as the type of electrolyte, chemical nature of the anodic oxide, and the role of voltage in the growth process. In this model the anodic film is considered to be a duplex in structure. The innermost layer, the barrier, is believed to be largely anhydrous aluminum oxide containing some anions of the electrolyte. Under the influence of the field, aluminum ions move outward from the metal to a region near the outer edge of this layer where the aluminum ions react with the oxygen carrier, probably hydroxyl ions, to form alumi-

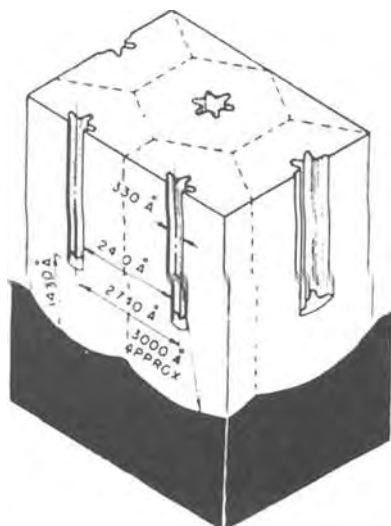


Fig. 1. Geometric model of aluminum anodic oxide structure

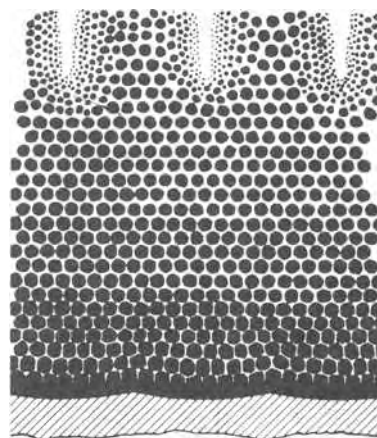


Fig. 2. Colloidal gel model of aluminum anodic oxide structure

num oxide. The thickness of this barrier layer is determined by the anodizing voltage and it is approximately 10 Å/v applied during anodizing.

The process of converting the newly formed anhydrous oxide proceeds immediately at selected points. The electrolyte and hydroxyl ions moving under the influence of the applied field probably plays an important role in this process of breaking up the continuous anhydrous layer to form discrete particles. These particles finally become the porous layer. The process of conversion from relatively continuous anhydrous layer to an agglomeration of hydrated particles of aluminum oxide is field sensitive. Therefore the field determines the amount of unconverted or barrier layer present at a given time.

The next layer, the outermost layer, is considered to be an agglomeration of submicrocrystalline particles of anhydrous aluminum oxide surrounded by, and held one to another by, submicroscopic regions containing electrolyte anions, water molecules, hydroxyl ions, and hydrogen ions in a relatively complex hydrogen bonded system. The internal surfaces surrounding the submicrocrystallites are considered to be essentially structural features of the outer portion of the anodic films formed in highly acid electrolytes. The pores normal to the metal surface observed by electron microscopy are recognized, but the importance of such pores in the mechanism of film formation is held to be considerably less than in previous models.

The anion of electrolyte plays an important and different role in the colloidal gel model. These anions are oxyanions which can stabilize the surface of the particles of oxide converted from the barrier layer. They adsorb to the surface of the particles as the particles are separated from the barrier layer, and these anions are further capable of forming hydrogen bonded complex containing water, protons, and anions of the electrolyte. It is through this hydrogen-bonded complex surface that ionic conduction occurs. Hydrogen bond shifts between adjacent atoms result in the net transfer of proton and hydroxyl ions in opposing directions at relatively high rates.

The proposed mechanism of anodic coating formation is as follows. Under the influence of the anodizing field, aluminum ions migrate from the metal surface through the barrier layer to the oxygen-rich upper portions of the barrier layer where they react with oxide or hydroxide ion to form essentially anhydrous aluminum oxide. Oxygen containing species (hydroxide ions or water) are brought to the barrier layer by a kind of electrolytic conduction through or along the internal surfaces of the porous layer above the barrier layer. The anodizing field is such that it assists migration of hydroxide and water in the direction of the barrier layer. The hydroxide ion, water, and electrolyte anion which migrate into the barrier layer/porous layer interphase, cause a modification of previously formed barrier layer oxide into a more proton-

ated and hydrous oxide in localized regions, thereby tending to decrease the effective electrical thickness of the layer.

#### Important Differences in the Models

The two models differ in important respects. According to the physical-geometric model, dissolution accounts for the propagation of the pore base. This means that the composition of the porous layer is identical to that of the barrier layer, and it is porous only because it is penetrated by many holes. The colloidal gel model pictures the porous oxide as a "converted" barrier layer consisting of many crystallites, the surfaces of which are highly hydrated and contain anions of the electrolyte. The anion is considered to be important in promoting the formation of the hydrated and hydrogen-bonded surface rather than by promoting the complete dissolution of the oxide at the pore base.

In the case of the geometric model, conduction is assumed to occur by mass transport of electrolyte in and out of the 100Å pores. In the alternative model, it is proposed that site-to-site migration of ions occur in the region near the porous layer interphase.

In the conventional pore model, the applied voltage serves only to move the aluminum ions across the barrier, and the barrier thickness is controlled by the dissolution rate at the pore base. The colloidal gel model assumes that the voltage not only serves to control movement of the aluminum ions across the barrier but, in addition, it plays a role in the conversion of the barrier to the porous layer thereby controlling its thickness. The voltage is also important in the movement of negative ions inward and positive ions outward.

The two models also differ with respect to the events that can be predicted when the voltage is reduced and a new equilibrium attained. In either case, one predicts a drop in current followed by recovery to the new equilibrium value. In the case of the geometric model, dissolution of the barrier would have to occur whereas in the colloidal gel model a conversion of barrier to porous layer would be required to attain the new barrier thickness characteristic of the lower applied voltage.

#### The Recovery Phenomenon

A change in the voltage applied to a sample undergoing anodizing results in a characteristic curve shown in Fig. 3. In this paper we are concerned primarily with the interval between the time voltage is changed and the current attains its new equilibrium value. This is the recovery period. It is convenient to attach symbols to some of the variables in the recovery phenomenon.

- $E_1$ , Higher value of anodic potential applied  
 $E_2$ , Lower value of anodic potential applied

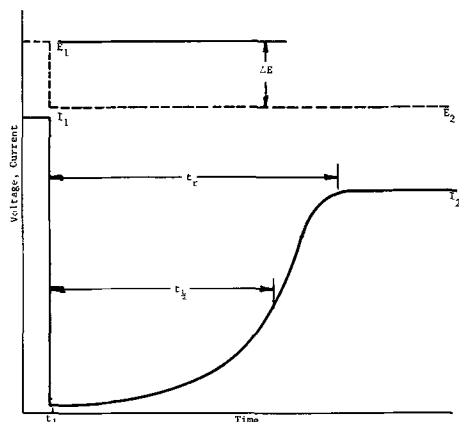


Fig. 3. Characteristic current-voltage relation during recovery period.

$$E_1 - E_2 = \Delta E$$

$I_1$ , Equilibrium current with  $E_1$  applied

$I_2$ , Equilibrium current with  $E_2$  applied

$t_1$ , Time of application of  $E_1$

$t_r$ , Time required for transition from  $I_1$  to  $I_2$

$t_{1/2}$ , Time required for current to recover to  $\frac{1}{2}I_2$

$dE/dt$ , Rate of change between  $E_1$  and  $E_2$

The current recovery phenomenon was examined by the several experimental methods described below.

Anodizing was done in an electrolytic cell and a recorder was used to follow the current transients as the voltage was changed.

#### Experimental

The equipment arrangement used to produce the anodic coatings under controlled conditions is shown in Fig. 4. Power was supplied from a regulated d-c source (Lambda Electronics) of 500 ma capacity and test coupons 2 in. square were used in all tests. By using relatively low currents an excellent control of temperature during anodizing could be achieved. Temperature rise of the electrolyte was held to less than 0.5°C by immersion of the cell in a water bath maintained at 22°C. The electrolyte was stirred during the experiments.

In all experiments the cell current was recorded on a Sargent recorder which placed a resistance of 1 ohm in series with the cell. Voltage changes were made by opening the circuit, readjusting the supply to the new value, then closing the circuit again. Slow changes were made with the "fine" voltage control on the supply.

All aluminum samples (alloys and high-purity metal) were degreased with solvent, chemically brightened, rinsed, and dried with methanol. Electrolytes were made up from chemically pure reagents and demineralized water of less than 1 ppm impurities. Bright platinum cathodes were used in all experiments.

Capacity measurements were made with a General Radio impedance bridge. Measurements were carried out in 15% sulfuric acid using a bright platinum cathode of approximately five times the area of the anode.

#### Results

*Forming and recovery in the same electrolyte.*—Samples of aluminum alloy 1100 were anodized for various times at voltage  $E_1$  to produce coatings of various thicknesses. At the end of each anodizing period the current was suddenly interrupted. With the circuit open the power supply was adjusted to a new value of voltage,  $E_2$ , and the circuit again closed. This voltage change,  $\Delta E = E_1 - E_2$ , always produced a curve of the general shape shown in Fig. 3.

The time of anodizing,  $t_1$ , at voltage  $E_1$  did not produce significant changes in the recovery time,  $t_r$ , provided  $t_1$  was greater than 5 sec. The maximum recovery time was required when  $E_1$  was applied for approximately 1 sec. At times less than 1 sec recovery

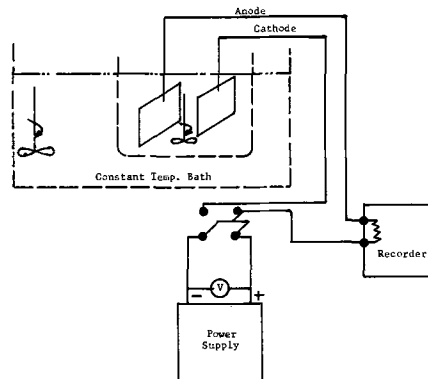


Fig. 4. Basic circuit required for anodizing

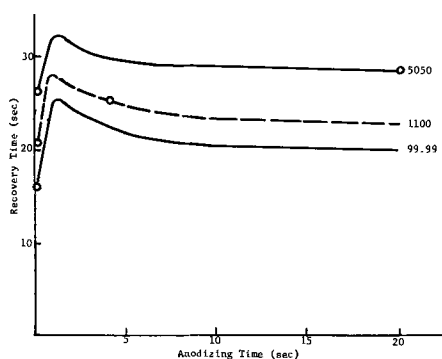


Fig. 5. Effect of anodizing time on recovery time (voltage changed from 11 to 8v).

was more rapid. This relation is shown for several alloys in Fig. 5.

Samples anodized for periods as long as 20 min did not exhibit appreciably different recovery characteristics than those anodized at least 5 sec.

Figure 6 shows that recovery time,  $t_r$ , depends on the concentration of the bath. Coatings formed in 30 v/o (volume per cent) sulfuric acid showed recovery in about one fourth the time required at 5% concentration. The displacement of the two curves shows that the recovery time also depends on the magnitude of  $\Delta E$ . An increase in  $\Delta E$  of 1v increased the recovery time approximately tenfold. Figure 7 shows in more detail how the recovery time varies with  $\Delta E$  and  $E_1$ .

As  $E_1$  is increased, with  $\Delta E$  constant, the recovery time is decreased. That is, as the increment of change is moved to higher voltage levels, the recovery period becomes shorter. For example, a change of 4v from 10 to 6 requires about 3 min to recovery whereas a change of 4v from 11 to 7 requires less than 1 min for recovery.

If the experiment is taken to the limiting conditions where  $\Delta E = E_1$ , then  $E_2 = 0$ , the recovery time is measured without voltage applied. The results of such experiments show that the recovery is extremely slow compared with recovery with voltage applied. For example, if a  $\Delta E$  is chosen to give a 2-min recovery time with voltage applied, recovery is found to be incomplete even after standing 20 min without voltage applied. The degree of agitation or thickness of the porous oxide does not affect this result.

Figure 8 is a current recording obtained under conditions where short (1-min) recovery times are involved. The voltage during the recovery period was applied intermittently, and it is proposed that any local heating effects due to current flow would thereby be eliminated and that the oxide-metal-bath temperature should remain fairly close to equilibrium. It is evident that the total time to recover is almost 3 times as long as when voltage is continuously applied.

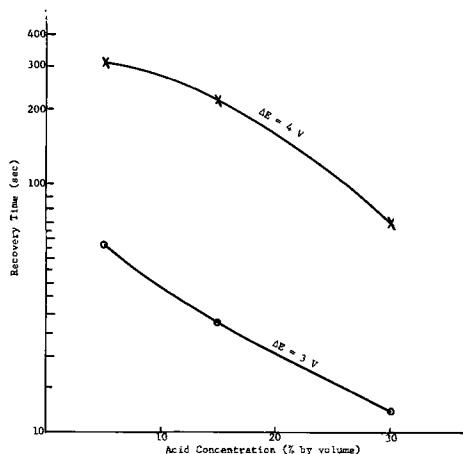


Fig. 6. Effect of sulfuric acid concentration on recovery time

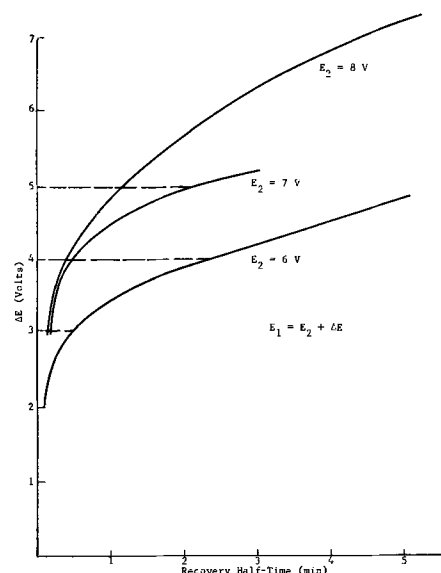


Fig. 7. Recovery at various levels of applied voltage,  $E_2$  (24°C, 1100 alloy). (Half time, time to one half the equilibrium current, is used because the steep slope of the curve at this point facilitates time measurement.)

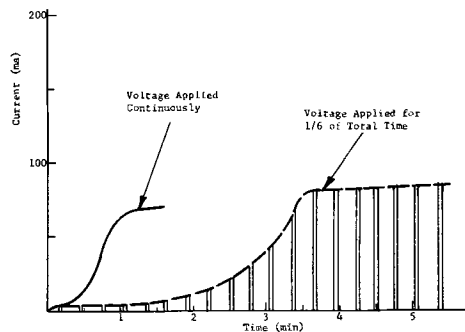


Fig. 8. Recovery characteristics using continuous and intermittent voltage application.

*Effect of continuity of voltage change.*—The results reported above were obtained with a discontinuous change from  $E_1$  to  $E_2$ . Completely different characteristics are exhibited if this change is made to occur in a continuous manner. If at the end of time,  $t_1$ , the voltage is slowly and continuously reduced to  $E_2$  by means of the power supply fine voltage control, the recovery time for the current to reach equilibrium is greatly reduced. Figure 9 illustrates this behavior.

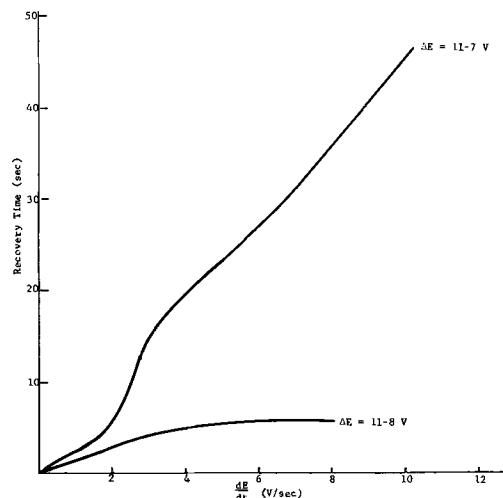


Fig. 9. Effect of rate of change of voltage on recovery

*Additional observations of the behavior in the cell.*—A number of experiments were made wherein samples were anodized under one condition and allowed to recover under other conditions. The results showed that, if formation is carried out in an electrolyte of different concentration than the recovery electrolyte, the recovery time is characteristic of the electrolyte used in the formation. That is, samples anodized in 15% sulfuric acid which are then transferred to 30% sulfuric, recover as though they had been allowed to recover in the 15% acid. The same behavior was observed for the reverse order of concentration used in formation and recovery.

Samples anodized at one temperature and allowed to recover at another showed recovery characterized by the temperature of the recovery electrolyte, not the formation electrolyte.

A number of experiments were carried out to determine if recovery could be at least partially induced in a nondissolving system. Samples were anodized in sulfuric acid, transferred to boric acid and held at a potential somewhat less than the potential  $E_2$ . They were then transferred back to the sulfuric acid system for recovery at  $E_2$ . Holding these samples at a potential of about  $E_2$  for periods of 10 min or more in the boric acid reduced the time required for recovery in the sulfuric acid significantly. For example, the time required for recovery at 10v was decreased from 2 min to 1.25 min by holding the sample for 10 min in boric acid at 7v. (The boric acid voltage, 7v, was chosen so as to produce a barrier of about 100Å which is roughly that obtained in sulfuric acid at 10v.)

Finally, capacity measurements were made at various times during the recovery process. The shape of the capacity time curve was nearly identical to that of the current recovery which indicates no appreciable thinning occurs while the current is very low. No doubt capacity changes would occur on prolonged standing with no applied voltage, but during the relatively short times required for recovery with voltage applied this change was not evident.

### Discussion

*Barrier layer adjustments.*—The porous outer layer of anodized aluminum does not contribute significantly to the resistance of the anodizing cell since the resistance does not change significantly as the porous layer thickness increases nearly two orders of magnitude. The electrical behavior of anodized aluminum in the cell must therefore be explained on the basis of changes occurring in the barrier region.

The physical-geometric model postulates dissolution of the barrier layer, thereby permitting continuous growth. The result is the formation of aluminum oxide penetrated by many pores, hence the porous layer. In proposing this simple dissolution theory it was necessary to postulate high temperature and high acid concentration to obtain the high observed rates under normal anodizing voltages.

The experimental evidence given here indicates that dissolution in this simple sense (solution kinetics determined by temperature and concentration) is an unlikely or, at least, incomplete explanation of the changes occurring during current recovery.

When the applied voltage is changed, certain readjustments in the barrier layer are necessary. The barrier layer must satisfy a fixed relation (4) to the anodizing voltage

$$\text{thickness} = (10.5) (\text{anodizing voltage}) \quad [1]$$

The amount by which the barrier thickness must be adjusted, therefore, depends only on the voltage change. If the voltage change is from 14 to 10, then  $\Delta E$  is 4v requiring a thinning of approximately 40Å. Likewise, in going from 10 to 6v, the change is 4v, again equivalent to a change of 40Å in the barrier thickness.

If the process of recovery is one involving a simple temperature dependent dissolution, one would expect that about the same amount of time would be required to dissolve the 40Å in the above example. This follows from the observation that the current drops to 0 in both cases and, accordingly, the temperature at the pore base must drop to that of the body of the solution surrounding the test sample. Since the temperature would be the same in the two cases, the dissolution rate and the time to recovery would be the same in the two examples.

It is an experimental fact, however, that the time required to thin the barrier is dependent on the voltage applied during recovery. For example, Fig. 7 shows that with 8v applied during recovery, it takes about 1½ min to make a 50Å adjustment in the barrier ( $\Delta E = 13-8$ ). On the other hand, when recovery occurs at 6v, it takes nearly 10 min to make a 50Å adjustment ( $\Delta E = 11-6$ ). The times required to thin the barrier 50Å are obviously quite different in the two examples. If no voltage is applied, it was shown that more than 20 min is required to effect recovery.

*Reactions influenced by applied voltage.*—The strong dependence of current recovery on the applied voltage suggests a further look at the voltage dependent reactions in the system. These include the transport of aluminum ions across the barrier, movement of charge species to and away from the barrier-porous interphase, and movement of the barrier into the metal.

It is assumed that the aluminum moves as a charged entity through the barrier under the influence of the applied field. It is unlikely that the barrier contains aluminum and oxygen in stoichiometric amounts, but it is more likely rich in aluminum near the metal. The oxygen-rich portion would be expected near the porous-barrier interphase. The oxygen and aluminum concentration profile probably changes according to the rate at which anodizing proceeds and appears likely to be further from stoichiometric  $Al_2O_3$  at higher anodizing currents.

As aluminum moves from the metal lattice into the barrier, oxygen atoms must move counter to this direction in order to advance the barrier into the metal. Whether or not this movement occurs by individual atom jumps or by movement of the entire lattice is not known. It does seem reasonable, however, to postulate that the lattice at the metal-oxide interface contains many vacancies. It also seems reasonable that the number of such vacancies will depend on the rate of aluminum ion removal from the lattice and the availability of oxygen atoms to fill the vacancies. Again, the vacancies would be expected to increase as the anodizing current is increased. Little is known about the phenomenon of barrier movement, but movement of charged entities into the vacancies would be expected to be dependent on the field.

The third voltage-sensitive reaction involves the movement of charges in the barrier-porous interphase region. It is in this region that reaction occurs between the aluminum ion and the oxygen-containing species and, as a result, protons will accumulate. This accumulation constitutes a space charge which is counter to the applied field, and its magnitude would be expected to depend on the number of atoms entering the reaction. This in turn depends on the anodizing current and the rate at which protons can migrate under the influence of the field.

Therefore, we have a somewhat complex equilibrium condition at any constant current which involves: (i) aluminum ions in transit across the barrier; (ii) oxygen movement into the metal; (iii) a proton space charge density near the outer region of the barrier; and (iv) barrier thickness.

If the voltage is suddenly decreased to a lower value, the system must go through a transition to a new set of equilibrium conditions. This transition would involve thinning of the barrier layer to satisfy the 10Å/v condition, a reduction in the number of aluminum ions

in transit across the barrier, and a lower proton space charge. So little is known about the barrier movement into the metal that no further comment on the rate of this movement can be made.

When the voltage is suddenly interrupted and a lower one reapplied, the accelerating field which appears across the barrier is reduced and the rate at which ions can be moved will also be reduced. In addition, the space charge characteristic of the higher current is present, and it is counter to the field moving the aluminum ions, thereby reducing the net field even more. As a consequence, the migration stops completely, and the current goes essentially to zero leaving the barrier with a space charge, thickness, and stoichiometry characteristic of the current and voltage which was applied just before interruption.

If the oxide is allowed to stand without voltage applied, the space charge and excess aluminum ions in transit must move purely by diffusional processes. Protons can migrate outward or negatively charged ions inward to dissipate the space charge. This could be a relatively slow process since the region of the space charge does not have a highly developed surface area. Rapid site-to-site migration of charge particles is proposed to occur only in the highly porous region which has been converted from the barrier layer.

The redistribution of excess aluminum ions in transit across the barrier could also occur without the influence of an applied field. This process would be expected to be slower under the reduced field, but certainly more rapid than if no voltage whatever is applied.

*Agreement between observations and proposed reactions.*—There is no question that under the influence of an applied field the migration of charged particles is facilitated. The movement of these charged particles would not affect the electrical thickness of the barrier layer as measured by its capacity. The experimental observations indicate that this capacity remains constant during most of the recovery time and only increases when the current begins to increase toward its new equilibrium. The gradual dissipation of the protonic space charge and the redistribution of aluminum ions are two field-sensitive reactions which could account for these experimental observations. One would expect no change in thickness (constant capacity) during this redistribution process and the process should be temperature dependent. This part of the recovery should be attainable in electrolytes such as boric acid, again in agreement with observation. One would not expect the concentration of the recovery electrolyte to exert any marked influence on the redistribution part of the recovery, again in agreement with the experimental observation.

The fact that recovery occurs more rapidly as the recovery voltage is increased is simply a manifestation of the higher fields present. The field during recovery is given by

$$\text{Field (volts/\AA)} = \frac{E_2 \text{ (recovery voltage)}}{E_1 \times 10.5 \text{ (barrier thickness in \AA)}} \quad [2]$$

The recovery voltage,  $E_2$ , can also be expressed in terms of the initial voltage and the voltage change,  $\Delta E$

$$E_2 = E_1 - \Delta E \quad [3]$$

As  $E_2$  is increased,  $E_1$  must increase a like amount to hold  $\Delta E$  constant and the ratio

$$\frac{E_1 - \Delta E}{E_1 \times 10.5} = \text{Field} \quad [4]$$

must also increase.

If the recovery voltage is made sufficiently high, the current can be made to recover very rapidly. Figure 10 illustrates a circuit in which a large series resistance is introduced. The voltage is switched between

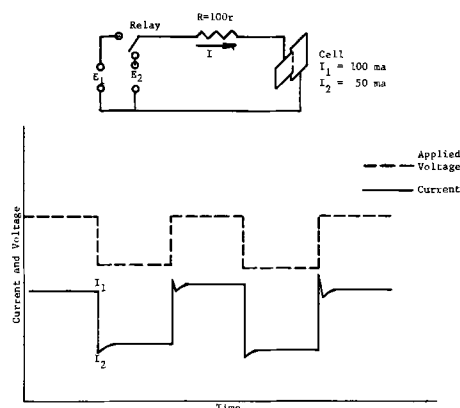


Fig. 10. Characteristic recovery with large series cell resistance (square wave voltage cycle is 10 sec).

supplies  $E_1$  and  $E_2$  which are of very high voltage compared to that appearing across the cell. In other words, most of the supply voltage is dropped across the series resistance.

When the circuit is interrupted by a relay and reconnected to the other supply, the cell momentarily sees a very high voltage because the current is low and hence the voltage drop in the series resistance is low. As the current builds up, the drop across the series resistance increases, and consequently the voltage across the cell rapidly and continuously decreases. In effect, this means that the recovery is occurring at a relatively high voltage until the equilibrium current is reached.

If the process is now reversed, that is, the voltage is raised to a higher value, the current will immediately increase. The current transient shows an overshoot before attaining its final equilibrium. This overshoot is understandable because the space charge is not as high as at equilibrium. The barrier oxide is thinner, and the concentration of aluminum ions in transit across the barrier is also lower than at equilibrium for the higher voltage. The net result is a much higher than equilibrium field across the barrier layer which accounts for the momentary high current before equilibrium can be attained.

The dependence of recovery on the rate of voltage change, as illustrated in Fig. 9, also shows that the charge redistribution is a slow process especially at low voltage. It can be seen that reducing the voltage from 11 to 7v in about  $\frac{1}{2}$  sec requires a recovery time of about 40 sec before equilibrium is re-attained. When the same voltage change is made in 2 sec, the recovery is very rapid. If the voltage is changed discontinuously ( $dE/dt$  extremely large), recovery now requires a matter of minutes. This latter observation also indicates the possibility that the discontinuity of the change is an important factor.

### Summary

The current flow during anodizing of aluminum drops to near zero when the voltage applied to the cell is reduced below a critical value. The time required to attain equilibrium current at the reduced voltage is dependent on the voltage change, rate of change, level of reduced voltage, and temperature and concentration of the forming electrolyte.

It is not possible to explain the current recovery on the basis of the simple geometric pore model, but the experimental observations are consistent with the colloidal gel model proposed by Murphy and Michelson.

It is believed that the recovery must be preceded by dissipation of a protonic space charge arising from the reaction between aluminum ions and the ionic oxygen carrier. In addition, it is believed that the stoichiometry of the barrier must be adjusted before the new equilibrium current can be attained. The final



step involved is that of barrier conversion to porous layer to effect the thinning that is observed at the end of the recovery period.

Manuscript received June 15, 1967; revised manuscript received Aug. 30, 1967. This paper was presented at the Dallas Meeting, May 7-12, 1967, as Abstract 32.

Any discussion of this paper will appear in a Discussion Section to be published in the December 1968 JOURNAL.

## REFERENCES

1. F. Keller, M. S. Hunter, D. L. Robinson, *This Journal*, **100**, 411 (1953).
2. J. F. Murphy and C. E. Michelson, Proceedings of the Symposium on Anodizing Aluminum, Nottingham University, September 1961. Published by the Aluminium Development Association, London (1962) p. 83 ff.
3. M. S. Hunter and P. Fowle, *This Journal*, **101**, 514 (1954).
4. M. S. Hunter and P. Fowle, *ibid.*, 487.

## Information on Anodic Oxides on Valve Metals: Oxide Growth at Constant Rate of Voltage Increase

C. G. Dunn\*

General Electric Research and Development Center, Schenectady, New York

### ABSTRACT

The formation of nonporous anodic oxide films is treated mathematically for the constant rate of voltage increase method to provide a basis for interpreting reanodization current-voltage curves. Illustrative reanodization I-V curves are considered for such initial anodic oxide films as nonporous oxide, porous  $\text{Al}_2\text{O}_3$ , plastically deformed  $\text{Al}_2\text{O}_3$  and  $\text{Ta}_2\text{O}_5$ , and annealed nonporous  $\text{Al}_2\text{O}_3$ . Evidence obtained for pore filling in and the conversion of a porous film into a nonporous film is supported by electron microscopy and thickness measurements. Confirmation of low ductility in  $\text{Al}_2\text{O}_3$  and high ductility in  $\text{Ta}_2\text{O}_5$  is obtained. Information is provided on the restoration of ionic conductivity in  $\text{Al}_2\text{O}_3$ , which is lost by annealing.

Dekker and van Geel (1) obtained information on the porosity and the total thickness of porous anodic oxide films on aluminum from reanodization data. Thus, employing the constant-current method of adding nonporous anodic oxide, they observed an initial rapid rise in voltage, which was ascribed to a filling in of the pores in the initial film and a later slower rise in voltage, which was identified with uniform oxide formation at a rate expected from Faraday's law. In this instance, and in other situations described later, the current density associated with oxide formation is not constant under constant-current reanodization. Some improvement in this respect arises, however, if rate of voltage rise is held constant by a controlled rate of voltage increase. Moreover, the method of holding the rate of voltage increase constant provides more uniform conditions of anodic film formation if many specimens of different (or unknown) surface areas are being compared. Dignam (2) found the "constant rate of voltage increase" or CRVI method both convenient and useful in a study of ionic currents in oxide films on aluminum.

If the anodic film or an outer layer of the film on a valve metal is quite different from the film being formed during reanodization [e.g., the porous layer obtained on tantalum using ultraviolet irradiation and low electric fields (3, 4) is probably in this category (5), and the hydrated oxide produced by a boiling water treatment of aluminum covered with anodic oxide is certainly such a film (6)], certain complications arise making analysis of the reanodization data difficult. In such circumstances more supplementary data than usual are needed for a correct interpretation of CRVI current-voltage data.

In the present paper the illustrations are limited to the oxides; other anodic films including hydrated oxides are beyond the scope of the paper. Equations are given for oxide film formation by the CRVI

method. These include initial steady-state anodization as well as transitions to steady-state conditions on reanodization. Illustrations of current transitions together with interpretations have been selected from such studies as "the nature of porous oxide films," "ductility of nonporous films," and "effect of heat treatment on ionic conduction."

### Theory and Illustrative Results

*Nonporous film formation.*—Consider a flat valve-metal specimen of surface area  $A$  on which a nonporous anodic oxide is growing. At time  $t$  the potential drop across the oxide of thickness  $x$  is  $V_{ox}$ , and across the cell an external electrical circuit is  $V_a$ , with  $V_a$  increasing at a constant rate  $\eta \equiv dV_a/dt$ , where  $\eta$  is a controllable parameter. When the current  $I$  is constant  $dV_a/dt$  and  $dV_{ox}/dt$  are equal. If the Maxwell field strength  $E$  is independent of  $t$  for a given value of  $\eta$ , then

$$dx/dt = (1/E\eta)\eta \quad [1]$$

describes a constant rate of film growth and a steady-state condition. Replacing  $\eta$  by  $dV_a/dt$  gives

$$dx = (1/E\eta) dV_a \quad [2]$$

For a voltage increase of  $\Delta V_a$ , the thickness increase  $\Delta x$  may be measured, and a Maxwell field strength  $E_\eta$  determined since  $\Delta V_{ox} = \Delta V_a$ .

Another equation for  $dx/dt$  is given by Faraday's law as follows

$$dx/dt = \Omega J_{ox} \quad [3]$$

where the constant  $\Omega$  depends on units and is proportional to  $e/\rho$ ,  $e$  is the electrochemical equivalent of the oxide,  $\rho$  is the density of the oxide, and  $J_{ox}$  is the ionic current density associated with oxide formation (at 100% current efficiency  $I/A = J_{ox}$ ). This equation is independent of both  $\eta$  and the steady-state condition. Combining [1] and [3] and solving for  $J_{ox}$  under

\* Electrochemical Society Active Member.

steady-state conditions gives

$$J_{ox} = \eta/\Omega E_{\eta} \quad [4]$$

Now a simple and useful relation between film thickness and capacity holds for the parallel-plate configuration and is

$$A/C_{ox} = \lambda x/\epsilon \quad [5]$$

where  $C_{ox}$  is the capacity,  $\epsilon$  is the dielectric constant, and  $\lambda$  is a numerical factor depending on units. A change in  $x$  equal to  $\Delta x$  produces a change in  $A/C_{ox}$  of  $\Delta(A/C_{ox})$ , which is equal to  $\Delta(A/C)$ , where  $C$  is the measured capacity. In terms of rate of film growth Eq. [5] becomes

$$d(A/C)/dt = (\lambda/\epsilon) dx/dt \quad [6]$$

with  $C$  replacing  $C_{ox}$ . Combining [6] and [1] gives

$$d(A/C)/dt = (\lambda/\epsilon E_{\eta}) \eta \quad [7]$$

If  $\eta$  is replaced by  $dV_a/dt$ , then [7] reduces to

$$d(A/C) = (\lambda/\epsilon E_{\eta}) dV_a \quad [8]$$

which describes how reciprocal capacity varies with voltage at constant  $\eta$ . When  $\epsilon$  is constant, Eq. [8] and [2] are equivalent. (On the other hand, a linear relation between  $A/C$  and  $V_a$ , obtained for example in a sequence involving changes in electrolyte, could also involve discontinuous changes in both  $\epsilon$  and  $E_{\eta}$  with  $\epsilon E_{\eta}$  constant. In such circumstances measured values of  $dx/dt$  would change as  $E_{\eta}$  changed according to Eq. [1], and  $J_{ox}$  would also change unless the ratio  $(dx/dt)/\Omega$  remained constant in Eq. [3].)

The slope  $\lambda/\epsilon E_{\eta}$  in Eq. [8] determines  $\epsilon E_{\eta}$  and depends of course on the rate parameter  $\eta$ . If  $\epsilon$  is known,  $E_{\eta}$  can be calculated from the measured slope.

Considering anodic film growth at 100% coulombic efficiency and constant temperature for simplicity a first approximation between ionic current density and electric field strength (7) may be expressed by

$$J_{ox} = \alpha \exp \beta E \quad [9]$$

where  $\alpha$  and  $\beta$  are constants and  $E \gg 0$  ( $\alpha$  depends strongly on temperature,  $\beta$  depends little on it). If only nonporous film forms along with little or no cation dissolution, these two constants and Eq. [9] summarize the rate effects expected (Eq. [9] applies also to more general situations, including  $E$  varying continuously with time; later considerations will require limited time intervals when  $dE/dt \neq 0$ ). The appropriate parametric expression for calculating  $E$  for given values of  $\eta$  is obtained by combining [9] and [4] and is

$$\Omega E_{\eta} \alpha \exp \beta E_{\eta} = \eta \quad [10]$$

Depending on anode material and electrolyte there are lower limits to the rate of film formation that results only in nonporous oxide. The following application of the above equations to oxide formation on tantalum and on aluminum in terms of specific values of  $\Omega$ ,  $\alpha$ , and  $\beta$  therefore outlines the sort of results expected if nonporous films form at 100% coulombic efficiency and  $Ta^{5+}$  and  $Al^{3+}$  are involved. Table I assembles values of  $\Omega$ ,  $\rho$ ,  $\alpha$ , and  $\beta$  that are used to obtain  $E_{\eta}$  as a function of  $\eta$  from Eq. [10] when  $dx/dt$

Table I. Illustrative values of  $\Omega$  ( $\text{\AA} \text{ sec}^{-1} \text{ ma}^{-1} \text{ cm}^2$ ),  $\rho$  ( $\text{g cm}^{-3}$ ),  $\alpha$  ( $\text{ma cm}^{-2}$ ), and  $\beta$  ( $\text{\AA v}^{-1}$ ) for use with Eq. [3] and [10]. References indicated in parenthesis.

Valve metal	$\rho\Omega$	$\rho$	$\Omega$	$\beta$	$\alpha$
Tantalum	45.8	8.00 (8, 9)	5.72	550 (11)*	$\exp(-35.05)**$
Aluminum	17.6	3.17 (10)	5.55	430 (10, 12)	$\exp(-37.79)**$

\* 505 A/v corrected for density; \*\* see text.

and  $J_{ox}$  are in  $\text{\AA}/\text{sec}$  and  $\text{ma}/\text{cm}^2$ , respectively, in Eq. [3]. Values of  $\alpha$  are taken from current work with  $\eta = \frac{1}{6}$  v/sec and an electrolyte temperature controlled at 27°C; the values are equivalent to selecting 16.0 A/v ( $Ta_2O_5$ ) and 11.7 A/v ( $Al_2O_3$ ) for  $E_{\eta}^{-1}$  in Eq. [1] when  $\eta = \frac{1}{6}$  v/sec.

Results of the calculation of electric field strength as a function of rate of voltage increase are shown in Fig. 1. The variation of  $E_{\eta}$  with  $\log \eta$  is nearly linear (with  $\log J_{ox}$  it is linear according to Eq. [9]); and  $E_{\eta}$  of course changes slowly with  $\eta$ , resulting in  $J_{ox}$  being nearly proportional to  $\eta$  in Eq. [4], or current being roughly proportional to  $dV/dt$  for constant current formation (7). Estimates of  $1/E_{\eta}$  in A/v vs.  $\eta$  are also indicated in the figure.

If cations go into solution during steady-state nonporous film formation, the result is an ionic current density  $J$  which is greater than the current density  $J_{ox}$  for residue oxide

$$J = g J_{ox} \quad [11]$$

where  $g$  is a numerical factor greater than unity. Under this condition it turns out that  $\eta$  in Eq. [10] is multiplied by  $g$ . The actual electric field therefore is the same as the field at 100% efficiency and a rate of  $g\eta$ .

Electronic currents which arise at isolated points or flaws in the oxide have in principle no effect on the electric field in flaw-free areas. Elements of surface area act like parallel electrical circuits in the CRVI method, so isolated electronic currents only produce a higher average current.

Either Eq. [9] or [4] may be used to determine the current density expected for a given value of  $\eta$ . Equation [4] implies that current density depends on both  $\eta$  and  $E_{\eta}$ ; actually  $\eta$  is the only independent parameter. The dependence of  $J_{ox}$  on  $E$  in Eq. [9] is a dependence on  $\eta$  through Eq. [10].

*Reanodization after initial formation to voltage  $V_i$  or to thickness  $x_i$ —"The Current Transition".*—An illustration of anodic oxidation of 99.99% aluminum followed by reanodization is given by the current-voltage curves in Fig. 2. During initial anodization with  $\eta = \frac{1}{6}$  v/sec, the current remained constant.

At 170v the voltage switch was opened, the voltage setting was reduced, and reanodization started at  $\eta = \frac{1}{6}$  v/sec. Essentially no current appeared until the potential drop across the cell was about 150v. The

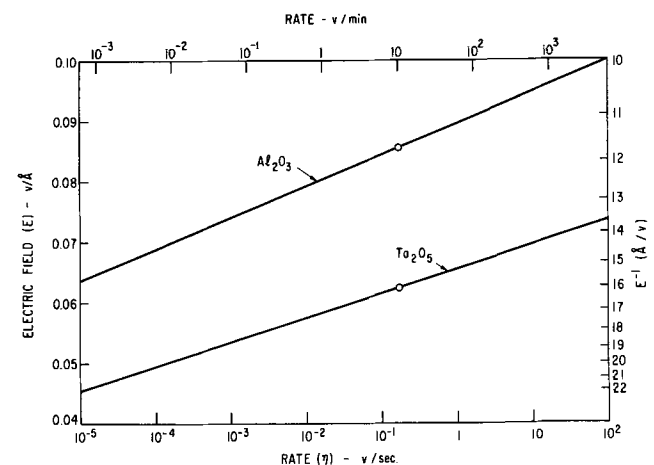


Fig. 1. Dependence of electric field strength  $E$  or reciprocal field  $E^{-1}$  (at right) on rate of voltage increase  $\eta$  (lower scale v/sec, upper scale v/min) for steady-state oxide formation.

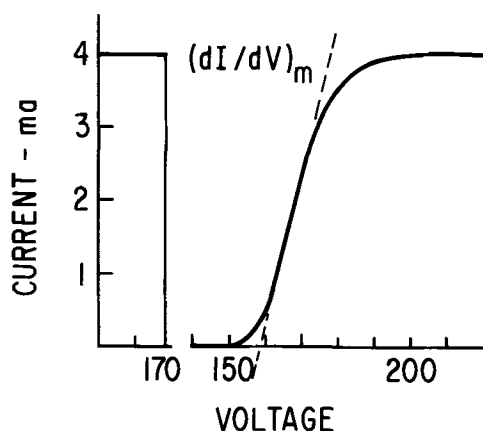


Fig. 2. Steady-state oxide formation at 10 v/min to 170v (at left) followed by reanodization (at right) which produced a sharp current transition with maximum slope at 170v.

current then rose rapidly and leveled off beyond about 195v at the value formerly observed, producing a curve of sigmoidal shape. We call it a current transition.

In the current transition, both oxide thickness and Maxwell field strength vary, *i.e.*,

$$dV_{ox}/dt = E dx/dt + x dE/dt \quad [12]$$

where  $x \cong x_i$ .

Since both the IR drop across "the electrolyte and external electrical circuit" and the cathodic overpotential  $V_c$  increase with increasing current, the rate of voltage increase across the oxide differs from the rate of voltage increase  $dV_a/dt$  (the emf of the oxide reaction  $\xi$  will be taken as a constant). During the current transition, therefore

$$dV_a/dt = dV_{ox}/dt + R dI/dt + dV_c/dt \quad [13]$$

Prior to oxide growth, *i.e.*,  $dx/dt = 0$ , Eq. [12] reduces to  $dE/dt = \eta/x_i$ . A capacitor charging current is involved (see Appendix), but it never increases. In fact, it decreases in the current transition and becomes zero. It also is negligible compared with the oxide forming currents (see Appendix).

Two aspects of the current transition are of principal interest. These are (i) the increase of  $x$  to  $x_i + \delta x$  on reanodization to  $V_i$  and (ii) the slope  $dI/dV$  of the I-V curve at  $V = V_i$ . The current transition occurs over a small voltage range if  $\delta x$  is relatively small or if the slope  $dI/dV$  is large. Both quantities depend explicitly on  $\beta$  in Eq. [9]. They also depend on the so-called constant  $\alpha$  if  $\alpha$  fails to remain constant in the transition. The end of the transition is characterized as steady state with  $I = I_s$ ,  $E = E_s$ ,  $\alpha = \alpha_s$ , etc. Since  $V_{ox}/x$  determines  $E$  at all points of the current transition, both  $V_{ox}$  and  $x$  need to be determined. If the IR drop and the cathode overpotential are negligible, then  $V_{ox} = V_a + \xi$ . The thickness increase may be determined using Faraday's law. Application of Eq. [9] gives

$$(I/I_s) = (\alpha/\alpha_s) \exp \beta E_s [-\delta x/(x_i + \delta x)] \quad [14]$$

for  $x = x_i + \delta x$  and  $V_{ox} = (V_{ox})_i$ . Experimentally, it is found that  $(I/I_s)$  at  $V = V_i$  is close to  $1/2$ . Thus if  $\alpha/\alpha_s$  is constant for a given value of  $E_s$ , then  $\delta x/(x_i + \delta x)$  must be constant for various values of  $x_i$ . This means that  $\delta x$  depends on  $x_i$ . Similarly, the voltage range of the current transition depends on  $x_i$ .

For the current transition in Fig. 2, a calculation gave 0.020 for  $\delta x/(x_i + \delta x)$ ; *i.e.*, the thickness increased 2% on reanodization to  $V_i$ ; it should have increased 1.89% for  $\beta = 430$  A/v and  $\alpha = \alpha_s$ .

The maximum slope  $(dI/dV)_m$  of the current transition occurs near  $V = V_i$  and to a first approximation is

given by

$$(dI/dV)_m \cong I_s \beta / 4x_i \quad [15]$$

if  $d\alpha/dt = 0$ , and if the last two terms in Eq. [12] are negligible. The result expressed in Eq. [15] is essentially independent of  $\eta$ , the rate of reanodization, if  $d\alpha/dt = 0$  (note later comments on  $\alpha$ , however). The maximum slope varies inversely with  $x_i$  as does the maximum slope per unit steady-state current,  $I_s^{-1}(dI/dV)_m$ . A value of this latter term for the curve in Fig. 2 is  $5.1 \times 10^{-2} \text{ v}^{-1}$ . This may be compared with  $5.4 \times 10^{-2}$  for  $\beta/4x_i$  with 430 A/v for  $\beta$  and 1990 Å for  $x_i$ , the 170v film formed at  $\frac{1}{6}$  v/sec.

Transitions of the kind shown in Fig. 2 also occur when reanodization is carried out at a different rate  $\eta'$ . The voltage  $V_i$  for the rate  $\eta$  now becomes  $V_i'$  for the rate  $\eta'$ . From Eq. [2] one obtains  $V_i' = V_i(E\eta'/E\eta)$ . Since the electric field is increased when  $\eta$  is increased (Eq. [9] or Fig. 1), it follows that  $V_i' > V_i$  when  $\eta' > \eta$ .

Application of Faraday's law after reanodization also determines  $V_i'$ . Thus the actual area under the I-V curve to some point  $V$  beyond the current transition is set equal to the area that would be produced at constant current beginning at  $V_i'$  and ending at the same point  $V$ .

Good agreement was obtained experimentally between known values of  $x_i$  or  $V_i$  and values of  $x_i$  determined either by the maximum slope method or by the area under the curve method. Consequently, the reanodization method may be used to determine the thickness of an oxide film. Experimental agreement has also been obtained between reciprocal capacity and voltage for a given value of  $\eta$ , as expressed in Eq. [8], for a sequence of voltage increments involving current transitions when the end of each increment is taken beyond any current transition and anodization is terminated sharply. Smaller transitions occur, however, if voltage is reapplied at the prior terminal voltage during open-circuit advance of voltage.

On the other hand, if the prior voltage is exceeded on open-circuit advance, say by a per cent or two, and this situation is easily obtained during anodization by opening the circuit at voltage  $V_i$  and closing it later at  $V_i + \Delta V$ , one obtains a rapid rise in current and a slow decay to the final steady-state value (an illustration appears later in connection with annealing effects). Such a current transition involves a decreasing electric field during the approach to the steady-state whereas the sigmoidal curve already discussed (Fig. 2) involves only an increasing field.

*Idealized case of two current transitions.*—Consider that a single specimen is covered with oxide, part to a thickness  $x_1$  and the remainder to a thickness  $x_2$ , with  $x_1 < x_2$ . The area of the thinner part is taken as the sum of many separate areas, each having linear dimensions  $l$  such that  $l \gg x_1$  and ionic transport therefore is negligible across boundaries between thin and thick areas. Under these conditions the specimen is equivalent to two flat specimens connected in parallel, one having an area  $A_1$  and oxide thickness  $x_1$  and the other an area  $A_2$  and oxide thickness  $x_2$ . As may be verified experimentally, the I-V curve of such a parallel pair equals the sum of two I-V curves obtained separately; it has a final steady-state current for an area equal to  $A_1 + A_2$  and two current transitions with a constant current between them if  $x_2 - x_1$  is sufficiently large. On the other hand, if  $l \sim x_1$  or  $l \ll x_1$ , as is the case for porous  $\text{Al}_2\text{O}_3$  films for example, the equivalence of two areas in parallel should not be assumed except for determining the total area, the average oxide thickness, and the thickness of the thinner layer.

*Initial porous anodic oxide films.*—Porous films of amorphous  $\text{Al}_2\text{O}_3$  are easily produced anodically on aluminum (7). They consist of a nonporous (barrier)

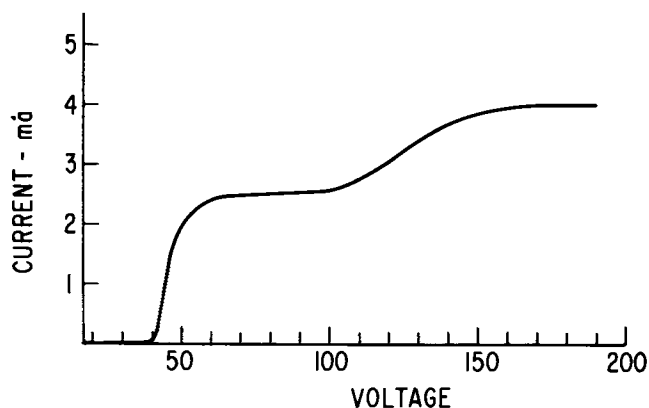


Fig. 3. Reanodization at 10 v/min of initial porous  $\text{Al}_2\text{O}_3$  film showing two current transitions, the first due to the barrier-layer thickness and the second due to the total thickness of the initial porous film.

layer next to the metal and an outer porous layer adjacent to the electrolyte (13). Porous films of  $\text{Ta}_2\text{O}_5$  may be produced anodically on tantalum using a strong alkaline electrolyte (14). Reanodization under conditions of nonporous film formation often results in an I-V record with two current transitions and an intermediate current plateau as shown in Fig. 3. In other cases, the curve is more complicated.

Regarding the initial oxide for Fig. 3, a porous film was produced on 99.99% Al (with clean surfaces) during anodization to 40v at (5/36) v/min in an aqueous solution of 1% ammonium pentaborate (APB). The average (and nearly constant) current density was  $17.8 \mu\text{a}/\text{cm}^2$ , about a factor of 3.24 higher than the current calculated from Eq. [4] and Fig. 1 for nonporous film formation (similar results were observed for high-purity Al films on glass slides obtained by vacuum vapor deposition). The same electrolyte, 1% APB, however, could be used for reanodization at 10 v/min because only nonporous film forms at this rate and the coulombic efficiency is relatively high.

Analysis of the I-V curve in Fig. 3, along with anodization data, gives the following information: (a) 77v or 900A for the average initial oxide thickness (from the area under the curve); (b) a possible 1710Å average thickness if  $17.8 \mu\text{a}/\text{cm}^2$  for 288 min produced only  $\text{Al}_2\text{O}_3$  film at 100% current efficiency; (c) a current efficiency for forming adherent  $\text{Al}_2\text{O}_3$  of about 53%; (d) 46v or 540A for the barrier-layer thickness from the first current transition (i.e.,  $x_1 \approx 540\text{Å}$ ); (e) a possible outer layer porosity of about 62% if the first current plateau is not high due to  $l \ll x_1$ ; and (f) a possible total film thickness of about 126v or about 1480Å according to the second current transition (however, 1480Å would necessarily be high if 62% porosity is high).

Supplementary data were obtained from appropriate equivalent specimens. Thus, transmission electron micrographs of initial 40v films lifted by the bromine-methanol method (15) revealed a porous structure with a pore density of about  $7 \times 10^{11} \text{cm}^{-2}$ , with pore diameters near 100Å, (i.e.,  $l \sim 100\text{Å}$ ), and with roughly 50% porosity in the outer layer. From 50% porosity, a 540Å barrier-layer thickness, and 900A average thickness one obtains 1260Å as a rough estimate of the initial oxide thickness. Also, a value of 1500Å for the initial oxide thickness was obtained using a Taylor Hobson Talysurf (16) on lifted films (transferred onto glass slides). This number agrees well with 1480Å obtained from Fig. 3, indicating that departure from the  $l \gg x_1$  condition may not involve a large effect. (More data involving thicker porous layers appear to be needed on this point.) Finally, transmission electron micrographs of lifted films after reanodization to the steady-state condition revealed only a nonporous structure and no evidence of the initial porous struc-

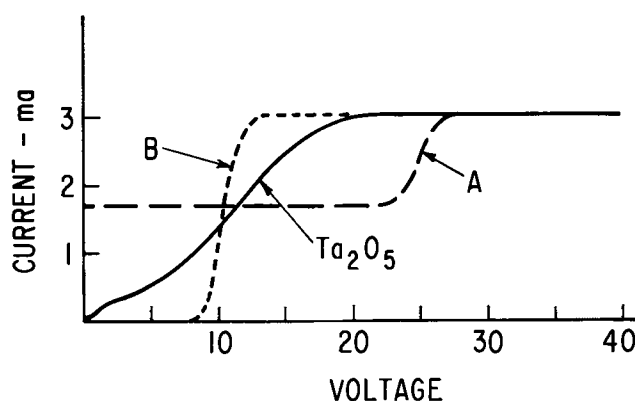


Fig. 4. Reanodization of a  $\text{Ta}/\text{Ta}_2\text{O}_5$  specimen with 25v anodic film after a cold-rolling reduction of 56% (solid curve), I-V curve expected for zero ductility (curve A), and I-V curve for uniform oxide thinning (B).

ture. This means that reanodization at the faster rate filled in the pores.

*Plastic deformation of nonporous  $\text{Al}_2\text{O}_3$  and  $\text{Ta}_2\text{O}_5$  films.*—The idealized case of two current transitions discussed previously is well represented by  $\text{Al}_2\text{O}_3$  films, which deform little or not at all during deformation of the substrate aluminum (17,18), because there is a new area with near zero thickness of oxide and a retained old area covered with oxide of the initial thickness. The reanodization method of analysis was applied to cold rolled specimens with either 15 or 100v anodic films. The position of the second current transition was not changed, within experimental error, for reductions in specimen thickness of 20 and 35%. This indicates that the oxide thickness was not changed during substrate deformation.

Anodic  $\text{Ta}_2\text{O}_5$  films on the other hand have relatively high ductility when adherence<sup>1</sup> to the substrate tantalum is strong (7, 18, 19). High ductility is also shown in the present illustration involving a 0.07 mm-thick tantalum strip which was annealed at 2200°C *in vacuo*, anodized to 25v at 10 v/min in 1%  $\text{H}_3\text{PO}_4$ , cold rolled slowly in 12 passes to keep the temperature from rising excessively during a reduction in cross-section area of 56%, cleaned of rolling lubricant, and then reanodized in 1%  $\text{H}_3\text{PO}_4$  at 10 v/min. Figure 4 shows the I-V curve obtained and two fictitious curves marked A and B that were added for comparison. Curve A, with a 25v current transition, is for zero ductility but excellent adherence, i.e.,  $\text{Al}_2\text{O}_3$ -like behavior. Curve B, with a 10.2v transition, is for uniform oxide thinning to an average thickness of the final film (determined from the area under the curve). Within experimental error this average thickness is 56% less than the initial oxide thickness. The large spread in final thickness is due to nonuniform deformation of the relatively large-grained tantalum specimen. This nonuniformity of substrate deformation is passed on to the oxide leading to striking color variations not only among the substrate grains but also within the surface area of individual grains. Such color differences disappear during reanodization.

*Heat-treated nonporous anodic oxide prior to reanodization.*—Dignam (2) found that annealing thin (5v or less) anodic films on aluminum, under conditions producing no crystallization of the amorphous films, completely changed the character of the current transition (or polarization curve) obtained by reanodization. Instead of a sigmoidal curve there were now current peaks.

The present illustrations of this effect of annealing involve thicker films. Thus, in Fig. 5 and 6 are shown reanodization I-V curves for 30 and 120v nonporous

<sup>1</sup> Poor adherence during cold rolling may be overcome, however, using a large reduction (~40%) in the first pass (19).

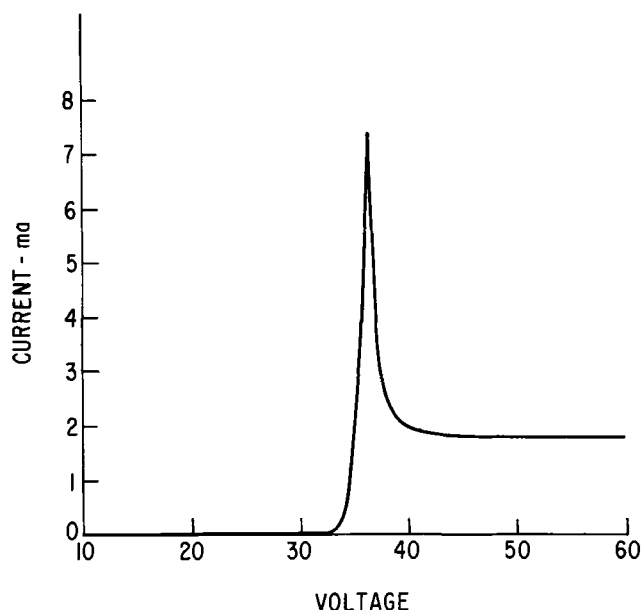


Fig. 5. Reanodization at 10 v/min of 30v (10 v/min) nonporous  $\text{Al}_2\text{O}_3$  film after a 1-hr anneal at  $300^\circ\text{C}$  in argon.

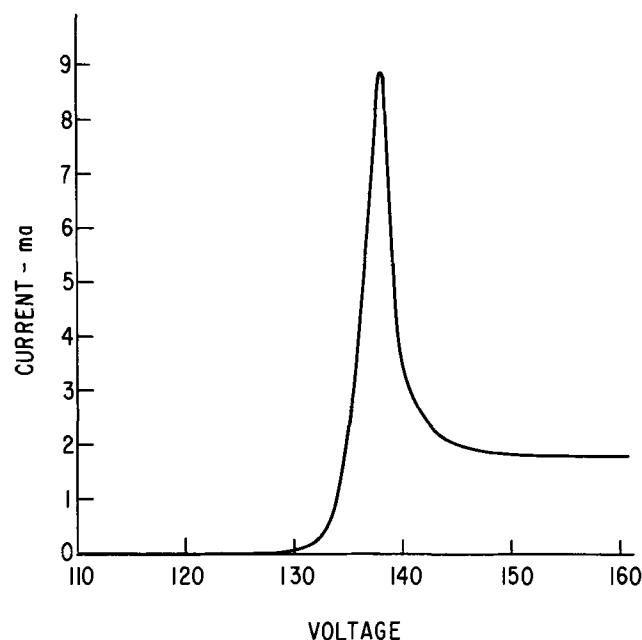


Fig. 6. Reanodization at 10 v/min of 120v (10 v/min)  $\text{Al}_2\text{O}_3$  film after same 1-hr anneal at  $300^\circ\text{C}$  as in Fig. 5.

$\text{Al}_2\text{O}_3$  films; these were formed at 10 v/min, dried, and annealed at  $300^\circ\text{C}$  for 1 hr in argon. Some 40 and 90v films prepared and annealed in the same manner produced similar current peaks and I-V curves on reanodization at 10 v/min. Unlike unannealed films with a current rise beginning at voltages below  $V_i$  (Fig. 2), all films annealed at  $300^\circ\text{C}$  had the current rise begin at voltage above  $V_i$  (Fig. 5 and 6). These transitions in  $300^\circ\text{C}$  annealed films therefore involve a decreasing electric field. For comparison purposes an example of a decreasing field transition in an unannealed film was obtained as follows. During anodization at 10 v/min, the voltage circuit was opened at 70v and closed 12 sec later at 72v (Fig. 7). The current rose rapidly to a peak value in less than 1 sec, then decayed slowly as the voltage advanced. The steady state was obtained near 83v.

The areas under the curves to steady-state conditions, i.e.,  $I = I_s$  and  $E = E_s$ , were found to be equal within experimental error to those expected for steady-state

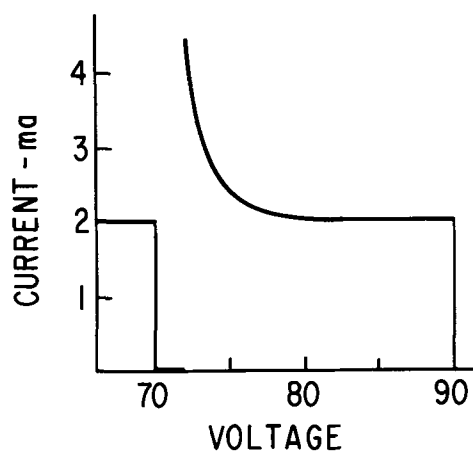


Fig. 7. Anodization at 10 v/min except for voltage removal between 70 and 72v to produce a current transition with decreasing electric field.

anodization beyond  $V_i$  to the same termination voltage. This indicates no change in the mass of oxide due to annealing 1 hr at  $300^\circ\text{C}$ . It agrees with the results found by Dignam (2).

A second reanodization of the annealed specimens after completion of the current transition resulted in normal behavior, i.e., sigmoidal curve transitions. The effect produced by annealing on reanodization behavior was therefore removed during reanodization through the transition region. This confirms Dignam's belief that the effect of annealing was reversed by reanodization (see also Discussion comments). The effect of reanodization through part of the transition will be considered later.

For further analysis of the I-V curves of the five films described previously, use is made of five voltage points; these are assembled in Table II in the order of increasing voltage. They are (i)  $V_i$ , the anodization voltage prior to annealing, (ii) 1%  $I_s$ , estimated voltage for a current of 1% of steady-state value, (iii)  $E_m$ , voltage for maximum electric field (a calculated point), (iv)  $I_m$ , maximum current, and (v)  $I_s$ , or the end of the transition. The voltage for maximum field may be obtained from a calculated curve showing  $E$  vs.  $V$ . Since the change in oxide thickness is proportional to the area under the curve, such areas may be used to calculate  $E/E_s$  as a function of voltage when both the IR drop and the cathode overpotential are negligible. Results of such calculations for the 30v and 120v films appear in Fig. 8. The straight lines passing through the point where  $E/E_s = 1$  determine the maximum values of  $d(E/E_s)/dV$  set by the initial oxide thicknesses. The plot of  $E/E_s$  follows these lines as long as the ionic current (and oxide growth) is negligible. Other calculations appear in Table III.

The time intervals given in Table III are determined from increases in voltage at  $\frac{1}{6}$  v/sec between the points listed in Table II. Since  $dE/dt$  varies inversely with initial oxide thickness when the oxide is not growing, an increasing time sequence with increasing  $V_i$ , like column one, is perhaps not unexpected.

Table II. Five voltage points for the transition current curves of four annealed specimens and one (70v) unannealed specimen.  $V_i$  also identifies each specimen

$V_i$	1% $I_s$	Voltage points		$I_s$
		$E_m$	$I_m$	
30	32.4	34.8	36.4	~45
40	42.8	46.8	48.7	~58
90	96.7	101.2	103.6	~117
120	128.6	134.6	138.0	~153
70	—	72 +	72 +	~83

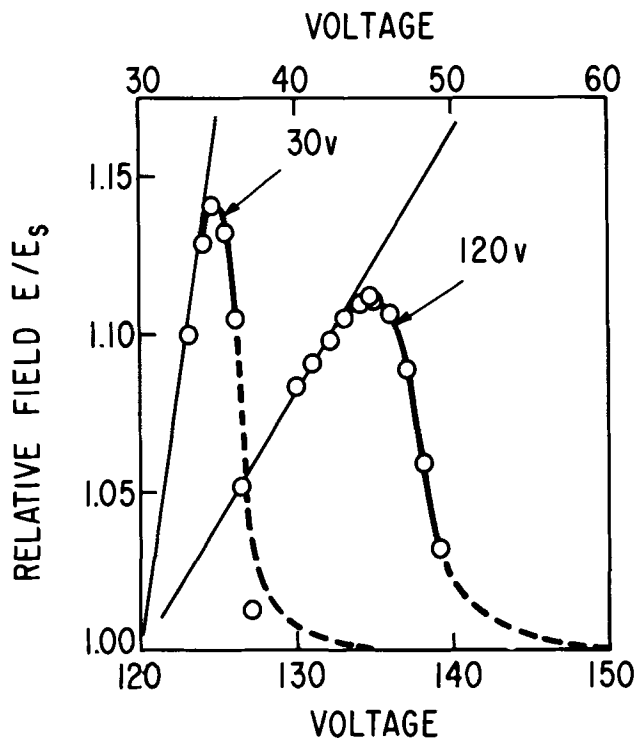


Fig. 8. Calculated curves showing variation of electric field with voltage (or time) in the transition region for 30v (top scale) and 120v (bottom scale) annealed  $\text{Al}_2\text{O}_3$  films; straight lines give curves for no oxide growth.

The time to reach maximum field after the oxide starts to grow should also depend on the rate of increase of the electric field, and it does (column two). The time-voltage sequence in column three involves increasing current but decreasing field (on the average  $E/E_s$  decreases from about 1.13 to 1.07). Column four lists the current rise and for the entire transition are given in columns five and six, respectively. Inspection of the table or a plot of each time sequence against initial anodization voltage shows consistent trends of increasing time with increasing oxide thickness (*i.e.*,  $V_i$ ) except for included points from the unannealed specimen. The long current decay time for the unannealed film does, however, fit into the trend set by the annealed films. A few experiments were therefore made to determine whether the initial part of the reanodization transition played a more significant role in reversing the annealing effect.

Two specimens with 40v films and a 300°C 1-hr anneal in argon were used in the study of reanodization through part of the transition. One involved opening the voltage circuit when the current reached its maximum value during reanodization and the other involved terminating the reanodization when a current about 12% above  $I_s$  was reached during the current rise. Each specimen was reanodized a second time beginning near zero voltage. A sigmoidal curve was obtained for the specimen reanodized to the current peak, thus indicating essentially no residue of the change produced by the anneal. There was a small current peak, however, for the second specimen, indicating incomplete removal of the change produced by the anneal on reanodizing to a point definitely beyond  $E_m$ . Reversal of the annealing changes evidently begins with the ionic current. It probably continues throughout the current rise period since the phenomenon of "rising current with decreasing electric field" occurs here.

Although relatively long periods of time are involved when the current is rising and the electric field is decreasing in the annealed specimens (Table III), much longer periods arise when the reanodization is

Table III. Time intervals in the transition region (in seconds)

Specimen	$V_i$ to $1\%I_s$	$1\%I_s$ to $E_m$	$E_m$ to $I_m$	fall $I_m$ to $I_s$	rise $1\%I_s$ to $I_m$	rise and fall $1\%I_s$ to $I_s$
30	14.4	14.4	9.6	~52	23.4	~76
40	16.8	24.0	11.4	~56	35.4	~91
90	40.2	27.0	14.4	~79	41.4	~122
120	51.6	36.0	20.4	~90	56.4	~146
70	0	<1	—	~66	~1	~66

done at rates far below 10 v/min in an electrolyte that produces only nonporous film. Thus, reanodization in 0.1% APB at (5/36) v/min of another 40v film annealed 1 hr at 300°C gave a period of 250 sec. In this run the current was greater than the steady-state current for a period of 30 min.

### Discussion

The CRVI and constant current methods of anodization are entirely equivalent at 100% current efficiency of forming adherent oxide, and at less than 100% efficiency they differ only in a minor way unless the efficiency is very low. Equations [1] and [3], therefore, give current density for a given rate of voltage increase and conversely give the rate of voltage increase for a given current density. The results of Fig. 1 also apply for the constant current method if electronic currents are low and the factor  $g$  in Eq. [11] is taken into account for less than 100% ionic current efficiency.

The constant current and CRVI methods appear to be far more different for reanodization experiments. In the constant current method, the current transition shown in Fig. 2 appears as a starting voltage, and the two current transitions shown in Fig. 3 appear as a starting voltage and a break in the rate of voltage rise (1).

The property constant  $\beta$  in Eq. [9] appears explicitly in the maximum slope of the current transition obtained with CRVI reanodization in the presence of an initial anodic oxide film (Eq. [15]). Since  $\beta$  is relatively large,  $(dI/dV)_m$  is also relatively large. This feature provides a simple method of determining the initial oxide thickness. Reanodization studies indicate that this method may also be used in the study of porous oxide films to determine the average oxide thickness, the barrier-layer thickness, and either (a) the total film thickness (and porosity of the outer layer) or (b) an apparent total thickness, which is too large if growth in total thickness occurs prior to the second current transition because of anion transport and favorable geometrical conditions (*i.e.*, pore dimensions near the barrier-layer thickness and considerable porosity in the outer layer). Theoretically an increase in total thickness may arise if anion transport is not small relative to cation transport.<sup>2</sup> The constant current in Fig. 3 following the first current transition, may be interpreted as evidence for cylindrical pores in the outer layer; this interpretation is in agreement with the model of Keller, Hunter, and Robinson (13). The final steady-state current (and particularly the nonporous structure revealed by transmission electron microscopy) confirms the pore filling process described by Dekker and van Geel (1).

A discussion of the significance of "pore formation during slow anodization in 1% ammonium pentaborate" and "pore filling during more rapid reanodization in the same electrolyte" to mechanisms involving ionic current carriers is outside the scope of the present paper.

As in the work of Dignam (2), annealing anodic  $\text{Al}_2\text{O}_3$  films moves the position of maximum slope in the I-V

<sup>2</sup> When the condition  $l \gg x_1$  (which was introduced for the idealized case of two current transitions) is satisfied, no increase in thickness of the thicker areas is expected regardless of the nature of the transport mechanism.

curves to higher voltages. The shape of the I-V curves are of course no longer sigmoidal, and the maximum slope method of determining the initial oxide thickness is no longer valid. The method based on Faraday's law or areas under the curve, however, still applies. No porous films were included in the study of annealing effects. However, it seems reasonable that a shift in position of either "the start of current rise" or "the maximum slope" would occur. Therefore, if annealing has occurred and the annealing effect is present but not allowed for, then an error is expected in the barrier-layer determination by the present CRVI method or the limiting thickness method (20), based on 14 Å/v for Al<sub>2</sub>O<sub>3</sub>.

The lack of a current peak in Fig. 4 may be taken as evidence of no appreciable annealing change due to film heating during the plastic deformation of Ta<sub>2</sub>O<sub>5</sub>. Many light reductions per pass were of course employed and this may have kept the temperature from rising excessively. The contrary experiment of possibly increasing the ionic conductivity of an annealed Ta<sub>2</sub>O<sub>5</sub> film through plastic deformation is suggested on the assumption that annealing removes structure defects (21, 22) and that plastic deformation probably introduces defects.<sup>3</sup>

Vermilyea has shown that annealing is a temperature accelerated process, involving an activation energy (21, 22). Regarding effects of long time at room temperature, limited data for Ta<sub>2</sub>O<sub>5</sub> with three years at room temperature and Al<sub>2</sub>O<sub>3</sub> with several months at room temperature revealed no current peaks for reanodization at 10 v/min. This is not to say that nothing happened but rather that the extent of change must have been small compared with the change produced during 1 hr at 300°C. No attempt was made to enhance low temperature annealing by means of an electric field below the level for ionic conduction, i.e., the field assisted annealing effect reported by Vermilyea (22).

Regarding the effects of annealing on ionic conductivity, free use is made of the ideas advanced by Vermilyea (21, 22), Young (7), and Dignam (2) that the structure of the oxide is altered to some degree by the annealing, which results in a drastic reduction in the number of potential current carriers, and that reanodization reverses this annealing change [in this connection, Vermilyea (23) found that passing constant current until the voltage transient vanished increased the dissolution rate of Ta<sub>2</sub>O<sub>5</sub> in an HF solution from a low "annealed" rate back to the high "as anodized" rate; the reversal by reanodization of x-ray line sharpening produced by annealing (22) was not studied]. Accordingly, it turns out that  $\alpha$  in Eq. [9] for isothermal but not steady-state conditions is a variable parameter and that the value of  $\beta$  determined experimentally depends on how  $\alpha$  varies. However, for a sequence of steady-state measurements, involving currents  $I_1, I_2, I_3, \text{ etc.}$ , or rates  $\eta_1, \eta_2, \eta_3, \text{ etc.}$ , for one temperature the dependence of  $\beta$  on  $\alpha$  tends to be lost. Despite this feature, relationships of the sort given in Fig. 1 for  $\alpha$  and  $\beta$  both constant have value experimentally for steady-state or quasisteady-state conditions.

The Al<sub>2</sub>O<sub>3</sub> films that were annealed for 1 hr at 300°C are apparently unable to attain a quasisteady-state condition even for very low rates of field increase. Perhaps the simplest way to allow for this is to assume that  $\alpha$  in Eq. [9] is now a parameter capable of increasing by several orders of magnitude and  $\beta$  is essentially constant. Thus, under constant voltage and  $E$  nearly constant initially (22, 7) or, as in present experiments with decreasing  $E$ , one may observe a rising current, only because  $\alpha$  is increasing at a rapid rate. In a sense the current depends on both  $\alpha$  and  $E$ , and conversely  $\alpha$  depends on an initial value  $\alpha = \alpha_0$  at  $t = 0$ , with the changes in  $\alpha$  occurring over some time

<sup>3</sup> Along similar lines Bubar and Vermilyea (25) find evidence of enhanced ionic conductivity when plastic deformation and anodization are simultaneous processes.

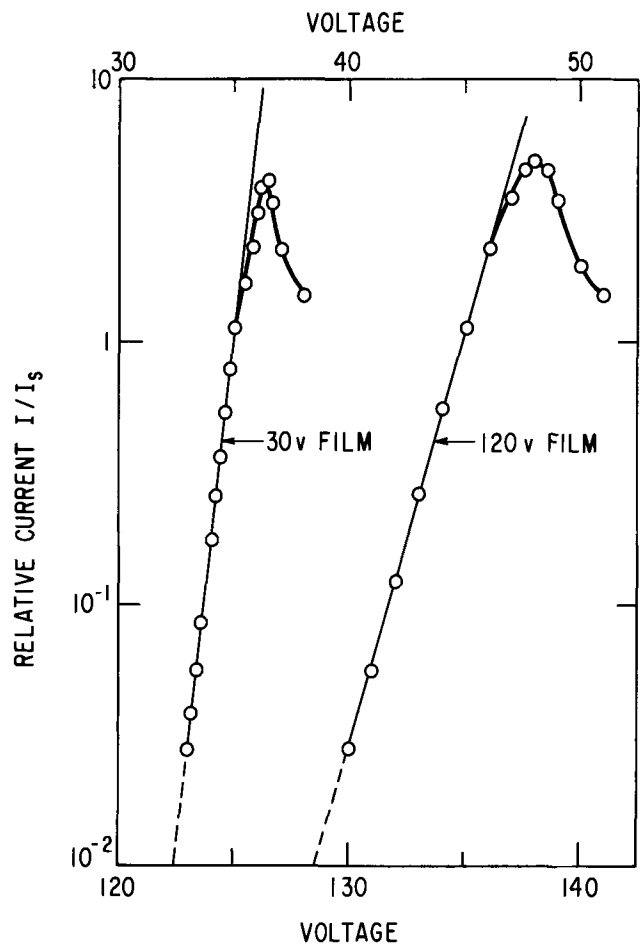


Fig. 9. Initial portions of I-V curves of Fig. 5 and 6 replotted in terms of  $\log I/I_s$  against reanodization voltage (30v film: top scale; 120v film: bottom scale).

interval  $t$ . Assuming that Eq. [9] gives the amount  $\alpha$  has varied during part of the reversal of the annealed state one writes

$$\alpha/\alpha_0 = (I/I_0) \exp[-8(E - E_0)] \quad [16]$$

with  $\alpha = \alpha_0$  near the beginning of the transition, where  $I = I_0 \neq 0$  and  $E = E_0$ , and  $\alpha = \alpha_s$  at the end of the transition. If  $E_0$  is taken at 1.07  $E_s$  for the present examples of annealing and  $E_m$  at 1.12  $E_s$ , then Eq. [16] gives  $\alpha/\alpha_0 \approx 500$  at the point of maximum field when  $\beta = 430$  Å/v and  $E_s^{-1} = 11.7$  Å/v. At the current peak  $\alpha/\alpha_0 \approx 700$  and at the end of the transition, where  $E_s < E_0$ ,  $\alpha/\alpha_0 = \alpha_s/\alpha_0 \approx 1300$ . These values of  $\alpha/\alpha_0$  suggest that a relatively large change in  $\alpha$  occurs early in the period of rising current.

A plot of  $\log(I/I_s)$  against voltage for the 30v and 120v Al<sub>2</sub>O<sub>3</sub> films is given in Fig. 9 mainly to point out that the curves are nearly linear to points just beyond maximum  $E$ , but the slopes are different. The latter feature is not surprising since the electric field rises more rapidly for the 30v film than for the 120v film. The linear relationship suggests that  $dI/dt$  is proportional to the current. On the other hand, Young (23) reported  $dI/dt$  being proportional to the second power of the current for  $E$  essentially constant. Either relation, however, is consistent with ionic current being responsible for the change in  $\alpha$ .

Reanodization data show that the change in  $\alpha$  produced by annealing may be reversed by a large current in a short time or by a small current in a long time. This suggests that the change in the oxide on reanodization is related to the amount of electric charge passed, a feature noted also by Dignam (24). It is not clear, however, if the amount of charge or extent of oxide growth needed for a given anneal is



independent of oxide thickness or if it increases with oxide thickness (the area under the curve to peak current is considerably larger for the 120v film than for the 30v film, but the ratio is less than the ratio of oxide thickness). This is important if the annealed films are in the same physical state. However, depending on the nature of the annealing change such films may or may not have exactly the same state after a single anneal, which kept annealing variables at a minimum. Thickness might be a factor in the kinetics of the annealing changes. More information on this point would of course be valuable for the purpose of comparing models of ionic conduction, including physical changes produced by annealing and by additional oxide growth after annealing.

### Summary

Holding the rate of voltage increase,  $\eta$ , constant in the formation of an anodic oxide film on a valve metal determines a Maxwell electric field strength  $E_\eta$ . The value of  $E_\eta$  depends on two property parameters  $\alpha$  and  $\beta$ , which appear in the equation  $J = \alpha \exp \beta E$  for isothermal variation of ionic current density with electric field strength. Calculated curves showing the variation of  $E_\eta$  with  $\eta$  are given for  $\text{Al}_2\text{O}_3$  and  $\text{Ta}_2\text{O}_5$  films.

When nonporous  $\text{Al}_2\text{O}_3$  and  $\text{Ta}_2\text{O}_5$  films are reanodized at constant  $\eta$ , relatively sharp current transitions are obtained in the I-V curves due to the relatively large values of  $\beta$ . For initial porous oxide films there are two current transitions; the first transition determines a value for the barrier-layer thickness and the second transition a value for either the total initial oxide thickness or the total thickness attained through growth prior to the second current transition. An example of pore "filling in" by reanodization is given together with supporting electron microscopy and thickness measurements that confirms earlier work by Dekker and van Geel.

Reanodization I-V curves provide a simple method for studying the ductility of nonporous oxide films. Evidence is given for essentially zero ductility in  $\text{Al}_2\text{O}_3$  films and high ductility in  $\text{Ta}_2\text{O}_5$  films, in agreement with published data.

The effect of annealing nonporous  $\text{Al}_2\text{O}_3$  films on the reanodization I-V curves for  $\eta$  constant is studied and discussed in terms of the property parameter  $\alpha$ . Thus, anodic  $\text{Al}_2\text{O}_3$  films formed in the range 30-120v suffer a drastic decrease in  $\alpha$  during a 1-hr anneal at 300°C in argon. Reanodization reverses the annealing effect when a certain amount of new oxide is formed. At fields above steady-state fields, the reversal of  $\alpha$  from a small to a large value is accomplished by a large ionic current in a short time or a small current in a long time.

### Acknowledgments

The author wishes to thank D. A. Vermilyea for discussions on the work and the preparation of the manuscript. Aid was provided by R. R. Russell in the electron microscope studies, and W. R. Reed, Jr. made the Talysurf oxide thickness measurements.

Manuscript received June 14, 1967; revised manuscript received Sept. 6, 1967. This paper was presented at the Dallas Meeting, May 7-12, 1967, as Abstract 45.

Any discussion of this paper will appear in a Discussion Section to be published in the December 1968 JOURNAL.

### REFERENCES

1. A. J. Dekker and W. Ch. van Geel, *Philips Research Rept.*, **2**, 313 (1947).
2. Michael J. Dignam, *This Journal*, **109**, 184 (1962).
3. D. A. Vermilyea, *ibid.*, **104**, 212 (1957).
4. D. A. Vermilyea, *J. Appl. Phys.*, **26**, 489 (1955).
5. A. R. Bray, P. W. M. Jacobs, and L. Young, *J. Nuclear Materials*, **1**, 356 (1959).
6. M. S. Hunter, P. F. Towner, and D. L. Robinson, *Proc. Amer. Electroplaters Soc.*, 220 (1959).
7. L. Young, "Anodic Oxide Films," Academic Press, London and New York (1961).
8. Julius Klerer, *This Journal*, **112**, 896 (1965).
9. A. J. Schrijner and A. Middlehoek, *ibid.*, **111**, 1167 (1964).
10. W. J. Bernard and J. W. Cook, *ibid.*, **106**, 643 (1959).
11. D. A. Vermilyea, *Acta Met.*, **1**, 283 (1953).
12. K. Nagase, *Mem. Inst. Sci. Ind. Research, Osaka Univ.*, **12**, 67 (1955).
13. F. Keller, M. S. Hunter, and D. L. Robinson, *This Journal*, **100**, 411 (1953).
14. K. Huber, *ibid.*, **110**, 1286 (1963).
15. T. J. Nurse and F. Wormwell, *J. Appl. Chem. (London)*, **2**, 550 (1952).
16. R. E. Reason, M. R. Hopkins, and R. I. Garrod, "Measurement of Surface Finish by Stylus Methods," Taylor and Hobson Ltd., Leicester, England.
17. C. Edeleanu and T. J. Law, *Phil. Mag.*, **7**, 573 (1962).
18. S. F. Bubar and D. A. Vermilyea, *This Journal*, **113**, 892 (1966).
19. C. G. Dunn, Unpublished work. Also, U.S. Pat. 3,335,073 issued to the General Electric Co., Aug. 8, 1967.
20. M. S. Hunter and P. Fowle, *This Journal*, **101**, 481 (1954).
21. D. A. Vermilyea, *ibid.*, **104**, 427 (1957).
22. D. A. Vermilyea, in "Non-Crystalline Solids," p. 323, John Wiley & Sons, Inc., New York, London (1958).
23. L. Young, *Proc. Roy. Soc. Series A*, **263**, 395 (1961).
24. M. J. Dignam, Private communication.
25. S. F. Bubar and D. A. Vermilyea, Private communication.

### APPENDIX

*Capacitor charging current.*—Assuming no space charge in the dielectric, Gauss's law gives  $(\lambda 10^3/\epsilon)\sigma$  for the electric field in v/Å, where  $\lambda$  is  $36\pi \times 10^{-3}$  and  $C_{ox}$  in Eq. [5] is in  $\mu\text{F}/\text{cm}^2$  and  $\sigma$  is the charge density ( $\text{mc}/\text{cm}^2$ ) at the metal/oxide interface. Therefore  $dE/dt = (36\pi/\epsilon) d\sigma/dt$ , and  $d\sigma/dt$  is the capacitor charging current density in  $\text{ma}/\text{cm}^2$ . The latter has its maximum value initially when  $dE/dt = \eta/x_i$ . After the current transition,  $J_{ox}$  is constant at its maximum value of  $\eta/\Omega E_\eta$  according to Eq. [4]. Substituting and solving for  $(d\sigma/dt)_m/J_{ox}$  gives  $\Omega \epsilon E_\eta/36\pi x_i$ . For  $\text{Al}_2\text{O}_3$  with  $\epsilon = 8.4$ ,  $E_\eta < 0.1$  v/Å, and  $x_i > 10\text{Å}$  the maximum possible charging current is less than 0.4% of the steady-state current and therefore is usually negligible. Similarly the charge density required for the steady-state field  $E_\eta$  is less than the charge needed to form an angstrom of oxide; it is negligible in the application of Faraday's law.



## Determination of the Etch Rate and the Refractive Index of Silicon Nitride Films with an Ellipsometer

A. N. Saxena\* and O. Tkal

Research and Development Laboratories, Sprague Electric Company, North Adams, Massachusetts

The etch rates in concentrated HF (49%) at room temperature and the refractive indices of silicon nitride films prepared by two different methods were determined with an ellipsometer<sup>1</sup> using light of wavelength  $\lambda = 5461\text{\AA}$ . In the first method (1), the silicon nitride film, 5300Å thick, was deposited on 10 ohms-cm, (111), p-type Si using reactive sputtering in N<sub>2</sub>. In the second method (2), the silicon nitride film, 4000Å thick, was deposited on 10 ohms-cm (111), p-type Si using chemical vapor deposition (NH<sub>3</sub> + SiH<sub>4</sub>) in a glow discharge at 400°C. The samples were mounted on the ellipsometer and aligned carefully (3).  $\Delta$  and  $\psi$  were measured at an angle of incidence  $\phi_0 = 70^\circ$ .  $\Delta$  is the change in the difference between the phases of the parallel (p) and the perpendicular (s) components of light on reflection, and  $\tan \psi$  is the factor by which the ratio of the amplitudes of the p and s components changes on reflection. After the initial measurements of ( $\Delta$ ,  $\psi$ ) on the samples, they were etched in concentrated HF at room temperature for 30 sec, rinsed in deionized (D. I.) water and blown dry with N<sub>2</sub> immediately prior to making the next measurement of ( $\Delta$ ,  $\psi$ ). Successive etching in concentrated HF for 30 sec and the measurement of ( $\Delta$ ,  $\psi$ ) were repeated until bare Si surface was reached in the sputtered silicon nitride sample. In the sample in which the silicon nitride film was deposited by chemical vapor deposition in a glow discharge, the etching of the film was stopped around 1700Å due to excessive pinholes appearing in the film.

Figure 1 shows theoretical curves for the variation of  $\Delta$  and  $\psi$  with the film thickness  $d$  as given by the exact equation of ellipsometry (4, 5)

$$\tan \psi e^{i\Delta} = \frac{r_{1p} + r_{2p} e^{-2i\delta}}{1 + r_{1p} r_{2p} e^{-2i\delta}} \cdot \frac{1 + r_{1s} r_{2s} e^{-2i\delta}}{r_{1s} + r_{2s} e^{-2i\delta}} \quad [1]$$

where  $r_1$  and  $r_2$  are the Fresnel reflection coefficients at the ambient-film and the film-substrate interfaces, respectively. Subscripts p and s denote the parallel and the perpendicular (to the plane of incidence) components. Film thickness  $d$  is related to the phase difference  $\delta$  as

$$d = C_{n_1} \delta \quad [2]$$

where

$$C_{n_1} = (\lambda/2\pi) (n_1^2 - n_0^2 \sin^2 \phi_0)^{-1/2} \quad [3]$$

In the derivation of Eq. [1], a discrete interface is assumed between the film of refractive index  $n_1$  and the substrate having the optical constants  $n_2 - ik_2$ . An IBM 360 computer was used to solve Eq. [1] and relate  $\Delta$  and  $\psi$  with ( $n_2 - ik_2$ ),  $n_1$  and  $\delta$ . Figure 2 shows  $C_{n_1}$  vs.  $n_1$  from which the film thicknesses  $d$  can be calculated knowing  $\delta$ . In Fig. 1, theoretical curves are plotted for films having refractive indices  $n_1 = 1.9, 2.0, 2.1, 2.2,$  and  $2.3$  on silicon substrate having  $n_2 = 4.051$  and  $k_2 = 0.027$ . The point 0 in Fig. 1 corresponds to ( $\Delta$ ,  $\psi$ ) for a film-free silicon substrate where  $\Delta = 179.05^\circ$  and  $\psi = 11.77^\circ$ . As the film thickness increases,

the ( $\Delta$ ,  $\psi$ ) point moves counterclockwise on the curve. When  $\delta = \pi$ , the point coincides again with 0 corresponding to  $\delta = 0$ . This is defined as the completion of the zeroth order of film thickness. When the film thickness increases further, the curve is retraced counterclockwise provided, of course,  $n_1$  remains constant. Thus for each "order"  $m$  of thickness, the point 0 is crossed  $m$  times. For a film in the  $m^{\text{th}}$  order, if the measured ( $\Delta$ ,  $\psi$ ) gives  $\delta = x$ , as read from the curve in Fig. 1, then the total film thickness is given by

$$d = (m\pi + x) C_{n_1} \quad [4]$$

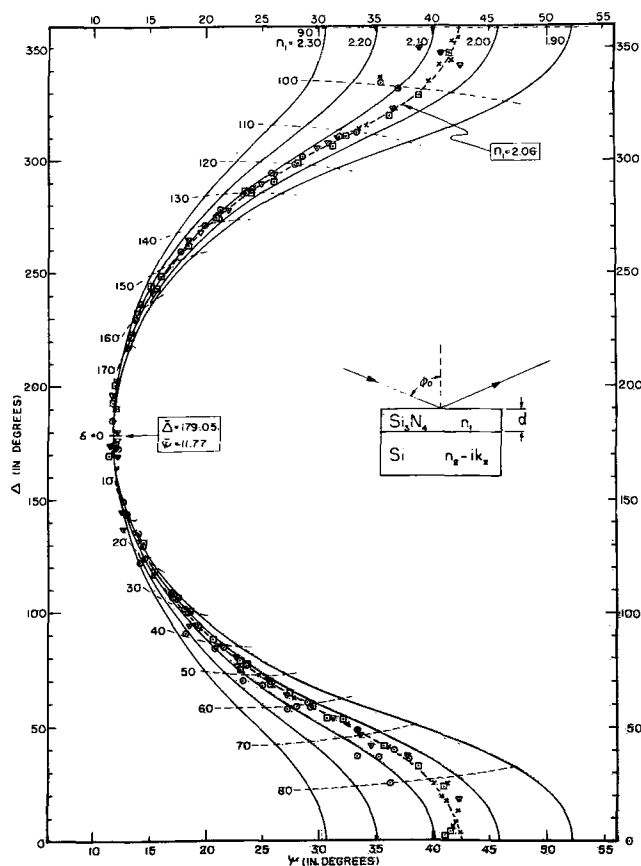


Fig. 1. Solid curves show the variation of  $\Delta$  and  $\psi$  with the film thickness  $d$  as given by the exact equation of ellipsometry. Film thickness  $d$  is related to the phase difference  $\delta$  by Eq. [2]. Dashed lines are for constant  $\delta$  indicating its locus when the refractive index of the film  $n_1$  varies. Optical constants of the Si substrate used in the calculation were  $n_2 = 4.051$  and  $k_2 = 0.027$ ; wavelength of light  $\lambda$  was 5461Å, and the angle of incidence  $\phi_0$  was 70°. The experimentally measured ( $\Delta$ ,  $\psi$ ) points as the sputtered silicon nitride film was etched down are plotted in this figure. A heavier dashed line is drawn through the experimental points corresponding approximately to an average value of  $n_1 = 2.06$ .

<sup>1</sup> Gaertner Ellipsometer, Model No. L 119.  
\* Electrochemical Society Active Member.

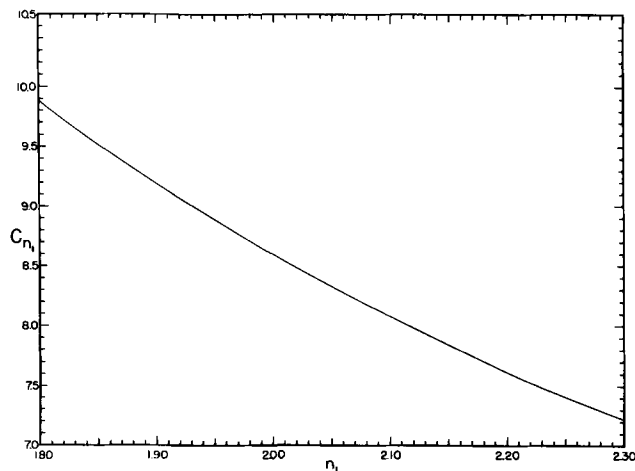


Fig. 2. Plot of the constant  $C_{n_1}$  vs. refractive index of the film  $n_1$ , as given by Eq. [3].

In Fig. 1, the  $(\Delta, \psi)$  points are plotted, which were measured on the sputtered silicon nitride sample after each successive 30 sec etch in concentrated HF at room temperature. The initial thickness of the film was in the third order, and it was about 5250Å. The data points fit a  $(\Delta, \psi)$  curve for  $n_1 = 2.06$  approximately. Accurate determination of  $n_1$  throughout the film as it is etched down is not possible for the thickness ranges for which  $\delta$  lies approximately between 0 and 20 and between 160 and 180 because the  $(\Delta, \psi)$  curves merge at 0 for various values of  $n_1$ . For each point, the values of  $n_1$  and  $\delta$  were read off from Fig. 1. Using Fig. 2,  $C_{n_1}$  were determined for different values of  $n_1$  and, using Eq. [2], the film thicknesses were calculated.

From these data, the average etch rate for the sputtered silicon nitride film in concentrated HF at room temperature was calculated to be  $291 \pm 16$  Å/min. This is about 50 times the etch rate reported recently by Bean *et al.* (6) who had used Bell No. 2 etch (300 cc  $H_2O + 200g NH_4F + 45$  cc HF).

The average value of the refractive index  $n_1$  of the sputtered silicon nitride film from the above data was found to be  $2.06 \pm 0.03$ . This agrees quite well with the value 2.05 reported by Bean *et al.* (6) It can be concluded from Fig. 1 that the interface between the silicon substrate and the sputtered silicon nitride film is discrete, as expected, because the experimental data points lie on a curve for  $n_1 = 2.06$  as the  $(\Delta, \psi)$  values change when the film is etched down through three orders of film thickness. The refractive index of the sputtered silicon nitride film was also measured with oil immersion technique (7) which gave  $2.1 > n_1 > 2.0$ . This checks fairly well with the average value  $n_1 = 2.06$  determined by the ellipsometric measurements.

Measurements of  $(\Delta, \psi)$  on silicon nitride films deposited by chemical vapor deposition ( $NH_3 + SiH_4$ ) in a glow discharge were also made after successive etching for 30 sec in concentrated HF similar to the procedure described above for the sputtered silicon nitride. Figure 3 shows the data plotted on the theoretical  $(\Delta, \psi)$  curve as in Fig. 1. The film was initially 4000Å thick, and its etching was stopped at a thickness of about 1700Å; no further measurements of  $(\Delta, \psi)$  were made. This was due to the appearance of excessive pinholes in this silicon nitride film. The film thickness  $d$  and the refractive index  $n_1$  for each of the data points were calculated as described above for the sputtered silicon nitride case. The etch rate in concentrated HF for the silicon nitride film deposited by chemical vapor deposition was calculated to be 340 Å/min, however, after a removal of about 1000Å from the top layer, the etch rate increased to 489 Å/min. This increase in the etch rate could be due to the

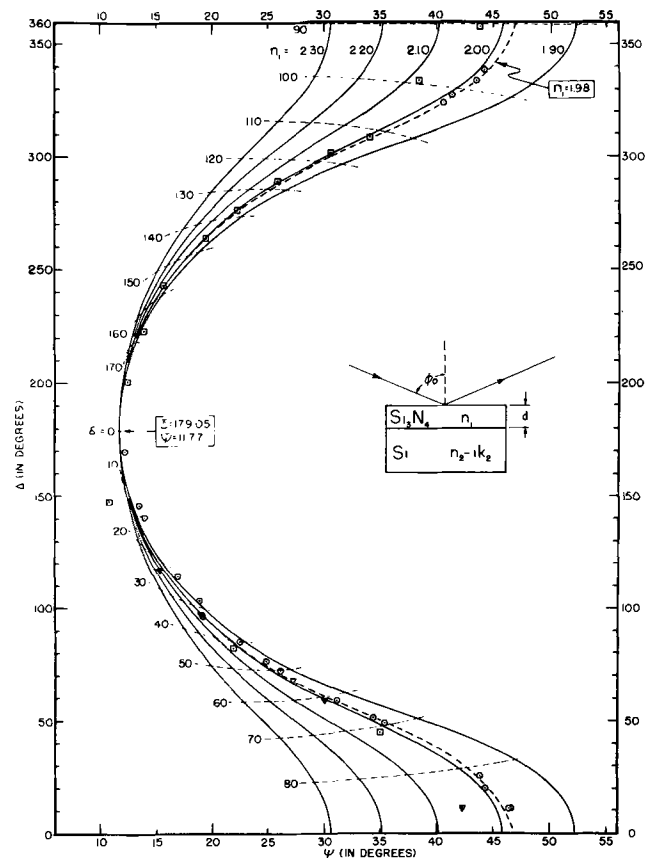


Fig. 3. This plot is similar to that shown in Fig. 1 except that the experimental  $(\Delta, \psi)$  points are for the silicon nitride film deposited by chemical vapor deposition in a glow discharge. Average refractive index for this film is found to be  $n_1 = 1.98$ .

pinholes in the film. The refractive index of this film remained fairly constant, even after removal of 1000Å from the top layer, and its average value was found to be  $1.98 \pm 0.03$ . Except for a few cases, the data points in Fig. 3 lie fairly well on a curve for  $n_1 = 1.98$  as the  $(\Delta, \psi)$  values change when the film is etched through two orders of film thickness. It can be concluded that the interface between this silicon nitride film and the silicon substrate is also discrete.

#### Acknowledgments

The authors wish to thank G. A. Shirn, A. Janus, and W. Patterson for depositing the silicon nitride films used in this investigation. Helpful discussions with K. M. Busen and M. Ghezzi are appreciated.

Manuscript received July 12, 1967; revised manuscript received Nov. 3, 1967.

Any discussion of this paper will appear in a Discussion Section to be published in the December 1968 JOURNAL.

#### REFERENCES

1. A. Janus and G. Shirn, *J. Vac. Sc. Tech.*, **4**, 37 (1967).
2. G. Shirn and W. Patterson, To be published; H. F. Sterling and R. C. G. Swann, *Solid State Electronics*, **8**, 653 (1965); R. C. G. Swann, R. R. Mehta, and T. P. Cauge, *This Journal*, **114**, 713 (1967).
3. F. L. McCrackin *et al.*, *J. Research Natl. Bur. Standards*, **67A**, 363 (1963); R. J. Archer, *J. Opt. Soc. Am.*, **52**, 970 (1962).
4. A. N. Saxena, *J. Opt. Soc. Am.*, **55**, 1061 (1965).
5. P. Drude, *Ann. Phys. Chem.*, **36**, 865 (1889); A. B. Winterbottom, *Kgl. Norske Videnskab. Selskabs Skrifter*, **1**, 38 (1955).
6. K. E. Bean, P. S. Gleim, R. L. Yeakley, and W. R. Runyan, *This Journal*, **114**, 733 (1967).
7. A. E. Lewis, *ibid.*, **111**, 1007 (1964).

# Zirconium Phosphate Membranes for Intermediate Temperature Fuel Cells

C. Berger\*<sup>1</sup> and M. P. Strier\*

Astropower Laboratory, Advance Systems and Technology, Missile and Space Systems Division,  
Douglas Aircraft Company, Inc., Newport Beach, California

## ABSTRACT

A new type of solid inorganic membrane for intermediate temperature hydrogen-oxygen fuel cell application is described. This is based on zirconium phosphate sintered with the zeolite material "Zeolon-H." The zeolite material contributes to maintenance of water balance in the membrane which is required especially at temperatures above 25°C. Under fuel cell operational conditions, the resistivities of this membrane are at the 20-25 ohm-cm level. Stable fuel cell performance over the temperature range of 25°-151°C was obtained. A maximum performance of 0.790v (64% of the theoretical) at 30 ma/cm<sup>2</sup> was obtained at 130°C.

The principal advantages to be gained from the use of solid membrane electrolytes in fuel cells are compactness, simplicity of design, and minimization of zero gravity limitations. The impetus behind the selection of inorganic membranes in this application is that they are insensitive to oxidation both from a chemical as well as from an electrochemical standpoint, and their dimensional, thermal, and radiation stabilities are high.

Since 1962 this laboratory has been conducting a systematic investigation on cationic inorganic ion exchange membrane materials for fuel cell application. Exploratory work with zeolites demonstrated that they were lacking in both ionic conductivity and mechanical strength (1). Utilization of metallic oxide-phosphoric acid systems, particularly zirconium dioxide, has yielded unique membranes manifesting transverse strength levels of 5000-9000 psi (2a) and resistivities at the 20-25 ohm-cm level (2b).

The original pioneering effort on the use of zirconium phosphate as cation exchange material was performed by Kraus (3), Amphlett (4), and Larsen and Vissers (5). Hamlen (6) studied the conductivity of zirconium phosphate under various conditions of hydration and found that at the highest level of hydration, the mechanism of conductance corresponds to that of an aqueous phase. Hamlen (6) and Dravnieks and Bregman in 1961 and 1962 (7,8) were the first to employ zirconium phosphate membranes in hydrogen-oxygen fuel cells; this was done at ambient temperature. The performances were marginal, and the membranes were weak. More recently, Hamlen and Szymalak (9) have used a specially prepared zirconium phosphate-Teflon matrix with hydrogen and propane fuel cell studies with oxygen over the temperature range 125°-175°C.

Significantly, it has been found in our laboratory that the use of the zeolite material Zeolon-H<sup>2</sup> in these membranes has permitted the maintenance of the water balance at elevated temperatures with resulting stable fuel cell performance. It appears that the water retention action of the zeolite water balancing agent minimizes dehydration at elevated temperatures.

As described by Amphlett (10), zirconium phosphate is ordinarily prepared by two techniques. A salt, such as zirconyl nitrate, is precipitated from acidic solution either by the addition of phosphoric acid or by a soluble phosphate. In the second method, zirconium dioxide is treated directly with phosphoric acid. The nature of the products obtained as far as crystallinity, hydrolytic stability, and ion exchange character is critically dependent on the mode of preparation,

as demonstrated by Amphlett (10) and Clearfield and Stynes (11).

The form of zirconium phosphate obtained by our preparative procedure was found to be amorphous in nature by x-ray analysis (12). The x-ray analysis indicated that the Zeolon-H phase remained intact, indicating no deleterious action by phosphoric acid or the heat imposed during the preparation steps. As pointed out by Clearfield (11), the amorphous form of zirconium phosphate [Zr(HPO<sub>4</sub>)<sub>2</sub> · H<sub>2</sub>O] undergoes hydrolysis in the presence of water, liberating phosphoric acid; however, complete removal of phosphoric acid is not possible without refluxing in alkaline solutions (13). In the type of membranes used in the fuel cell studies described herein, the amount of phosphoric acid lost during fuel cell operation by the end of 300 hr appears to be that which is weakly bonded and in excess of that which reacts with zirconia to form ZrP<sub>2</sub>O<sub>7</sub>.

Herein are presented procedures for preparing inorganic membranes for fuel cell application, together with results of fuel cell behavior over the temperature range of 25°-151°C.

## Experimental

**Membrane preparation.**—The membrane was prepared as a 5.1 cm diameter disk in the following manner: 1000g of cp zirconia and 1000g of 85% phosphoric acid to which were added 200 cc of water were mixed for 20 min in a Waring Blender to a creamy consistency. The blend was poured into a Teflon beaker and dried at 160°C for 18 hr. Then, the dried material was granulated to -16 mesh and calcined at 200°C for 2 hr. A mixture comprised of 1000g of the calcined material, 1000g of 85% phosphoric acid, 600 cc of water, 1000g of Zeolon-H and 60g of Carbowax was ball-milled for 18 hr. Next, the mixture was granulated to -32 + 80 mesh. Then it was pressed at 6.9 x 10<sup>2</sup> kg/cm<sup>2</sup> pressure into a 5.1 cm diameter membrane having a thickness of about 0.7 mm. Finally, the membrane was sintered for 2 hr at 500°C. This comprised the type A membrane.

When it was desired to incorporate platinum black catalyst into the surface of the membrane in efforts to improve fuel cell performance, the following procedure was used. A 20% mixture of platinum black (-350 mesh) with the -32 + 80 mesh zirconium phosphate-Zeolon-H mixture described above was prepared. Then a composite three-layer compression molded membrane was prepared by filling the bottom of the die with this mixture to the extent of 10% by volume, followed by 80% of the original (type A) mixture and, finally, the 10% platinum-containing mixture. The three-layer composite was pressed at 6.9 x 10<sup>2</sup> kg/cm<sup>2</sup> pressure. After pressing, the composite was placed on

\* Electrochemical Society Active Member.

<sup>1</sup> Present address: 13401 Kootenay Drive, Santa Ana, Calif. 92705

<sup>2</sup> Product of the Norton Company, Worcester, Massachusetts.

flat, smooth refractory plates and sintered in air for 2 hr at 500°C. On cooling to room temperature the composite membrane-catalyst wafer was impregnated by being dipped in 85% phosphoric acid for 5 min. The membrane was oven-dried at 120°C for ½ hr and finally sintered at 500°C for 2 hr. This treatment was repeated twice. The platinum impregnated membrane constitutes the type B membrane. Herein, the total weight of platinum black per membrane was of the order of 0.07g, consisting of 2% of the total membrane weight.

**Apparatus and procedure.**—The fuel cell shown in Fig. 1 was used. It was comprised of two covers or outer plates fabricated from "Multimet" metal. An "O" ring was used to maintain electrical insulation between the plates, while an epoxy resin was applied around the pressure annulus to prevent leaks. The electrodes were supported by backup plates as shown in Fig. 2. The design accommodates a 5.1-cm diameter membrane. Free volume space on both the hydrogen and oxygen sides was 9.8 cm<sup>3</sup>. American Cyanamid Type AA-1 gas diffusion electrodes were used throughout this study.

The procedure for assembling the fuel cell fixture was as follows. First, the membrane-catalyst-electrode backup plate wafer was prepared. Before the gas diffusion electrode was placed over the membrane, 0.3g of platinum black powder ( $\leq 325$  mesh) was sprinkled over the membrane surface. Constant pressure was applied within the backup plate, electrode, and membrane arrangement by the use of "C" clamps tightened by means of a torque wrench kept at a constant setting. Then a gas-tight seal was effected between both backup plates by the application of a heat-cured epoxy resin over the periphery of the membrane. The assembled wafer was inserted between the chamber covers and held in place by means of six plastic screws.

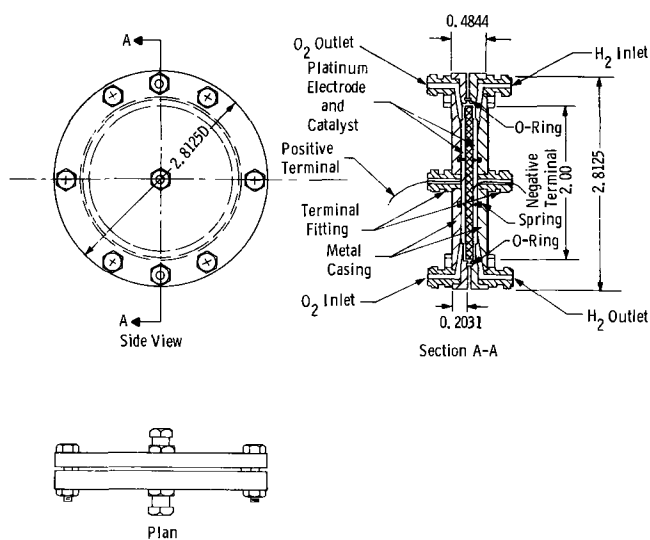


Fig. 1. Astropower fuel cell

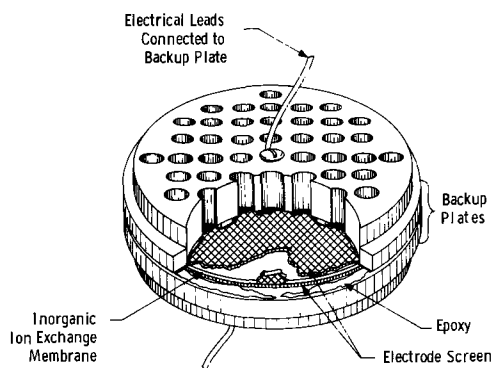


Fig. 2. Inorganic ion exchange membrane backup plate sandwich

The fuel cell runs were performed at a flow rate of hydrogen of 1-2 cc/min and a flow rate of oxygen of 3-4 cc/min, which afforded optimum performance under these experimental parameters. As all determinations were performed under open-ended conditions, the pressures of the reactant gases could be considered as being at atmospheric. The product water was collected. Calibrated electrical instruments were used for the monitoring of current and voltage characteristics for each test. Most tests were performed with membranes having a thickness in the range of 0.5-1.0 mm.

A-C resistance measurements were performed during the course of fuel cell tests to determine the contribution of ohmic resistance of the membrane to the over-all resistance obtained from the slope of the polarization curve. An a-c signal of 10<sup>4</sup> Hz was superimposed as polarization data were taken so that the d-c polarization and a-c resistance at different external loads could be obtained simultaneously. The a-c resistance was calculated from a-c potentials superimposed across the cell. Potential readings were obtained with a high impedance vacuum tube voltmeter (HP-400 H) having an estimated accuracy to within  $\pm 2\%$ .

### Results and Discussion

**Fuel cell studies.**—Fuel cell test results obtained over the temperature range of 25°-151°C inclusive are summarized in Tables I through III inclusive. In Table I, the results at 25°C indicate that stable continuous operation for 340 hr is possible. Test 7 was performed at a current density of 30 ma/cm<sup>2</sup> during which the voltage output was in the range of 0.450-0.494v. Results of tests performed at 65°C are given in Table II. At

Table I. Inorganic membrane fuel cell test results at 25°C (type A membrane)

Test No.	Type of measurement from start of run, hr	Open circuit voltage, v	Current density at 0.5v, ma/cm <sup>2</sup>	Voltage at 30 ma/cm <sup>2</sup> , v	Fuel cell resistance, <sup>(a)</sup> ohms
7	98	0.953	29.4	0.494	0.61
	140	0.962	28.7	0.483	0.61
	166	0.967	28.6	0.474	0.64
	231	0.983	28.0	0.474	0.64
	255	0.982	27.5	0.465	0.68
	279	0.975	25.7	0.450	0.70
	340	0.982	27.5	0.465	0.68

<sup>(a)</sup> Obtained from the slope of the polarization curve.

Table II. Inorganic membrane fuel cell test results at 65°C

Test No.	Time of measurement from start of run, hr	Open circuit voltage, v	Current density 0.5v, ma/cm <sup>2</sup>	Voltage at 30 ma/cm <sup>2</sup> , v	Fuel cell resistance, ohms
Type A membrane					
3	72	0.905	90.4	0.721	0.18
	90	0.900	88.6	0.714	0.18
	118	0.908	90.4	0.721	0.18
	114	0.905	90.4	0.721	0.18
	230	0.900	88.6	0.714	0.18
	254	0.900	90.4	0.721	0.18
	279	0.892	90.4	0.714	0.18
302	0.892	88.6	0.704	0.18	
Type B membrane					
42	26	0.987	81.0	0.717	0.21
	48	0.995	92.0	0.739	0.19
	95	1.000	98.4	0.750	0.18
	119	1.010	98.4	0.750	0.18
	145	1.015	92.0	0.739	0.19
	168	0.992	84.0	0.739	0.22
	192	1.010	84.0	0.739	0.22
267	1.005	73.0	0.725	0.26	
311	1.015	51.7	0.710	0.48	
Type B membrane					
6	21	0.965	102.2	0.764	0.18
	43	0.975	109.1	0.774	0.17
	67	0.970	111.0	0.764	0.16
	98	0.965	109.1	0.774	0.17
	140	0.962	102.2	0.764	0.18
	164	0.960	102.2	0.764	0.18

the operational current density of 30 ma/cm<sup>2</sup>, the voltage output is as high as 0.774v (63% of the theoretical value) for the type B membrane. Although both tests 6 and 42 were performed with the same type of membrane, the somewhat higher performance achieved for the former could be attributed to the use of a more porous backup plate offering less resistance for the passage of gases to the gas diffusion electrodes. It is to be noted that there is significantly improved performance at 65° over that at 25°C.

Membrane resistivities determined by the superimposed a-c resistance method are included for tests 81, 83, and 85 in Table III. The highest performance obtained during this study was in test 85. From polarization data for this test, the output voltage at 50 ma/cm<sup>2</sup> was 0.73v (59% efficiency). It appears that fuel cell performance does not change very much over the temperature range of 65°-151°C. From Table III, it is evident that membrane resistivity is unaffected by increasing temperature from 25° to 130°C. A similar situation exists for the zirconium phosphate-Teflon membranes studied by Hamlin and Szymalak (9) over the temperature range of 125°-175°C. Somewhat lower resistivities were attained in the present study. An attempt was made to improve fuel cell performance by the use of moist hydrogen gas. The gas was maintained at relative humidities ranging from 11 to 55% over the temperature range of 98°-126°C. It was found that membrane resistivity and fuel cell performance did not change appreciably during these tests. It appears that the use of zeolite material in the membrane structure is conducive to maintenance of "water balance," as excessive loss of water at elevated temperature would have caused an increase in resistivity. Since in this investigation membrane resistivity has been found to be independent of temperature, it must be concluded that the diminished fuel cell performance observed consistently at ambient temperature is due to inadequate removal of product water from the gas diffusion electrode.

**Hydrolysis studies.**—According to Clearfield (11) there would be justification for considering that the pyrophosphate structure, i.e., ZrP<sub>2</sub>O<sub>7</sub> is obtained by the preparative method described above. On that basis, as well as on the basis of the relative amounts of starting materials employed in the preparation of type A membrane, the following is the assumed composition of the membrane in the dry state: ZrP<sub>2</sub>O<sub>7</sub> 48.8%; H<sub>3</sub>PO<sub>4</sub> 14.5%; Zeolon-H 36.7%. This means that 14.5% of the total dry membrane weight is unreacted phosphoric acid which could be assumed to be weakly bonded in the matrix.

In order to establish the hydrolytic stability of the membrane, the following procedure was used. Type A membrane was exhaustively treated with 0.1N sodium hydroxide solution at 74°C. Treatment was continued until there was no further liberation of phosphoric acid as manifested by potentiometric titration of residual sodium hydroxide with 0.1N hydrochloric acid. This determination indicated an amount of H<sub>3</sub>PO<sub>4</sub> equivalent to 21.9% of the total original dry membrane weight. Assuming that complete hydrolysis of the

ZrP<sub>2</sub>O<sub>7</sub> would have taken place, then an amount of H<sub>3</sub>PO<sub>4</sub> equivalent to 50.6% of the original dry membrane weight would be obtained. Therefore, based on the assumed starting membrane composition indicated above, the exhaustive caustic treatment used herein causes liberation of the unreacted H<sub>3</sub>PO<sub>4</sub> and partial hydrolysis of the ZrP<sub>2</sub>O<sub>7</sub> constituent. Evidence for hydrolyzability of the latter constituent has been presented by Clearfield (11).

The hydrolytic stability of type A and type B membranes under fuel cell operational conditions was determined by analyzing dry membranes which had previously been employed in fuel cell tests by the hot caustic treatment described above. This would yield the total amount of free H<sub>3</sub>PO<sub>4</sub> remaining in the membrane, as well as the H<sub>3</sub>PO<sub>4</sub> derived from the hydrolysis of the ZrP<sub>2</sub>O<sub>7</sub> component remaining in the membrane at the conclusion of the fuel cell test. The results obtained are summarized in Table IV wherein this amount (column 6) is expressed in terms of the percentage of phosphoric acid recovered from the membrane based on the weight of the dry membrane remaining after the fuel cell run. In column 6, the differences in values from that of 21.9% as indicated above for the starting type A membrane show that there is no direct correlation between extent of hydrolysis during fuel cell operation and decrease in performance. Enough acidic component remains in the membrane matrix after 300 hr to permit continuation of significant fuel cell performance.

The results of this investigation show that there must be a sufficiently high concentration of phosphate groups present which are at most only partially leachable as well as an adequate degree of hydration through incorporated zeolite to achieve worthwhile fuel cell performance for as long as 300 hr at temperatures above 25°C.

### Summary and Conclusions

By the reaction of zirconia, phosphoric acid, and the zeolite material, Zeolon-H, under sintering conditions, it was possible to obtain a fuel cell membrane manifesting the following characteristics. These membranes have resistivities of 20-25 ohm-cm under fuel cell operational conditions over the temperature range of 25°-130°C. An optimum performance level of 0.79v at 30 ma/cm<sup>2</sup> was obtained at 130°C. At temperatures below 65°C, the significantly lower performances obtained must be due to inadequate water removal from the cathode, as membrane resistivity is essentially unaffected. The presence of incorporated zeolite material is conducive to maintaining an adequate water balance in the membrane permitting continuous stable operation above 65°C for at least 300 hr.

A gradual loss of that amount of the phosphoric acid which is weakly bonded occurs during the first 300 hr of operation. This does not appear to have a critical controlling effect on fuel cell operation. Fuel cell operation

Table III. Inorganic membrane fuel cell test results over the temperature range of 25°-151°C after 40 hr of continuous operation with type B membrane

Test No.	Temp. °C	Open circuit voltage v	Voltage at 30 ma/cm <sup>2</sup> v	Fuel cell resistance at 30 ma/cm <sup>2</sup> , ohms	A-C. resistance at 3 kc, ohms	Membrane resistivity, ohm-cm
81	25	0.995	0.512	0.57	0.106	24
83	99	0.980	0.706	0.25	0.078	25
85	130	0.950	0.790	0.20	0.071	21
52 <sup>(a)</sup>	151	0.917	0.698	0.24	(b)	(b)

<sup>(a)</sup> Determined with less optimum designed back-up plates.

<sup>(b)</sup> Not measured.

Table IV. Summary of analysis for phosphoric acid content remaining after various fuel cell life tests with inorganic membrane

Test No.	Temp. °C	Current density range at 0.5v, ma/cm <sup>2</sup>	Voltage range at 30 ma/cm <sup>2</sup>	Duration of test, hr	% H <sub>3</sub> PO <sub>4</sub> recovered after fuel cell run <sup>(a)</sup>
Type A membrane					
7	25	29.4-27.5	0.494-0.465	340	6.3
8	25	31.2-21.0	0.512-0.370	624	19.6
16	64	61.4-21.9	0.665-0.385	1174	7.6
3	65	99.6-90.4	0.721-0.714	307	10.8
Type B membrane					
33	65	61.9-56.7	0.673-0.662	305	6.3
42	66	81.0-51.7	0.750-0.710	311	7.2
43	69	64.2-61.8	0.657-0.639	310	6.9
37	100	80.7-54.7	0.696-0.530	312	10.4

<sup>(a)</sup> Hydrolyzable phosphoric acid recovered from membrane based on dry membrane weight.

for as long as 1200 hr and probably longer are possible. In addition these membranes appear to be sufficiently thermally stable to permit fuel cell operation at still higher temperatures, if required.

#### Acknowledgment

The authors wish to acknowledge the support of NASA under Contract NAS 3-6000. They also wish to thank Mr. Georges Belfort, Rubert Hubata, and Albert Rosa for their contributions to the measurements and analytical procedures.

Manuscript received Aug. 25, 1966; revised manuscript received ca. Oct. 27, 1967.

Any discussion of this paper will appear in a Discussion Section to be published in the December 1968 JOURNAL.

#### REFERENCES

1. "Investigation of Zeolite Membrane Electrolytes for Fuel Cells," NASA-Lewis Research Center, Contract NAS 7-150, Astropower Laboratory Report SM-108-F, March 1964.
2. "Inorganic Ion Exchange Membrane Fuel Cell," NASA-Lewis Research Center, Contract NAS 3-6000, Astropower Laboratory Report SM-46221-F, October 1965, a, pp.23-28; b, pp. 119-122.
3. K. A. Kraus, *Chem. and Eng. News*, **34**, 4760 (1956); *J. Am. Chem. Soc.*, **78** 694 (1956); "Proceedings of the International Conference on Peaceful Uses of Atomic Energy," Vol. 7, pp. 113, 131, United Nations (1956); *Nature*, **177**, 1128 (1956), Abstracts Boston Meeting, American Chemical Society, 1958.
4. C. B. Amphlett, L. A. McDonald, and M. J. Redman, *Chem. and Industry*, 1314 (1956); *J. Inorg. Nucl. Chem.*, **6**, 220 (1958); C. B. Amphlett, L. A. McDonald, J. S. Burgess, and J. C. Maynard, *ibid.*, **10**, 69 (1959).
5. E. M. Larsen and D. R. Vessers, *J. Phys. Chem.*, **64**, 1732 (1964).
6. R. P. Hamlen, *This Journal*, **109**, 746 (1962).
7. A. Dravnieks and J. I. Bregman, Paper presented at the Detroit Meeting of the Society, Oct. 1-5, 1961, as Abstract 27.
8. A. Dravnieks, D. B. Bois, and J. I. Bregman, 16th Annual Power Sources Conference, Session of Fuel Cell Materials and Mechanisms, pp. 4-6, May 22-24, 1962.
9. R. P. Hamlen and E. J. Szymalak, *Electrochem. Technol.*, **4**, 172, (1966).
10. C. B. Amphlett, "Inorganic Ion Exchangers," Chap. 5, p. 93, Elsevier Publishing Co., New York (1964).
11. A. Clearfield and J. A. Stynes, *J. Inorg. Nucl. Chem.*, **26**, 177 (1964).
12. C. Berger, M. J. Plizga, and F. C. Arrance, "Inorganic Ion Exchange Membranes I. Methods of Formulation, Structure, Conductivity and Strength of Inorganic Ion Exchange Membranes, Douglas Paper No. 4071.
13. "Evaluation of Life Support Chemical Techniques, Vol. I, Part I: Development of Inorganic Ion-Exchange Membranes," NASA Manned Spacecraft Center Contract NAS 9-0143, Air Research Manufacturing Co., Aug. 1, 1965.

## The Use of Electrochemical Sectioning in the Study of Diffusion in Tungsten

R. E. Pawel and T. S. Lundy

*Metals and Ceramics Division, Oak Ridge National Laboratory, Oak Ridge, Tennessee*

#### ABSTRACT

A microsectioning technique based on metal anodization and subsequent removal of the anodic oxide film was developed and tested by using it to determine the concentration profiles of  $^{95}\text{Nb}$  in tungsten single crystals after diffusion at 1800°C. The anodization characteristics of tungsten pertinent to quantitative serial sectioning were studied and several techniques for increasing the efficiency of isotope removal during chemical dissolution of the anodic film were tried. The resulting data were highly self-consistent and demonstrate the value of the method in investigating diffusion behavior in tungsten, particularly at low temperatures.

The need for experimental techniques which permit a sensitive and critical examination of extremely steep concentration gradients in solids has increased due to growing interest in the characterization of several aspects of low-temperature diffusion phenomena. When dealing with diffusion at low temperatures, an experiment generally involves not only small diffusion distances, but concentration gradients which may be influenced by the presence of short-circuit paths of various kinds and efficiencies. In addition, diffusion from a free surface has sometimes been observed to result in unusual concentration profiles in the near-surface regions. Since the extraction of the conventional diffusion parameters from experimental data requires fitting the data to a simple, sometimes over-idealized mathematical model, it becomes particularly important that the experimental technique be sufficiently sophisticated to be consistent with the mathematical description. As has been indicated previously (1-3), this problem is magnified for the study of diffusion at low temperatures, and a sectioning method having high resolution is one essential requirement.

The development of microsectioning techniques for the study of concentration gradients has progressed utilizing physical, chemical, and electrochemical means. The electrochemical methods have demonstrated a very high resolution in the few cases where they have been used. Davies and his associates (4, 5) used anodization and chemical stripping techniques to obtain range measurements for heavy ions in aluminum and tungsten. Mortlock (6) recently applied a similar technique, suggested by Whitton and Davies (7), to a tracer diffusion study of near-surface effects in gold single crystals. The present authors have used mechanical stripping of anodic films to study diffusion in tantalum and niobium (1, 8-10). In these investigations, the small section thicknesses of the order of 100Å permitted a quantitative description of the concentration gradients to be made in the region near the surface of the specimen. Diffusion coefficients as small as  $10^{-19}$  cm<sup>2</sup>/sec were determined.

Electrochemically formed films on the "valve" metals generally are of uniform thickness and follow the specimen contours almost exactly. This characteris-



tic offers a potential advantage for diffusion studies which is not always shared by chemical and physical methods of metal removal. The tendency for etching or nonuniform metal removal during chemical dissolution of most metals limits the applicability of this procedure for microsectioning. Similarly, mechanical grinding produces a contour which is generally different on a fine scale from that of the original surface. The size and machining behavior of the abrasive particles must also be considered in determining the limiting sensitivity of this method of sectioning. Particularly in the study of diffusion, the preservation of surface contours during sectioning may be of importance. Although there can be exceptions, the general result of a low resolving power caused by nonuniform metal removal is to flatten the concentration gradient resulting in higher apparent diffusion coefficients.

From the impressive results of range measurements described by McCargo, Davies, and Brown (5) and by Uhler, Domeij, and Borg (11), it appeared that the anodic film-sectioning technique might be applied to the study of diffusion in tungsten much in the same manner as it was applied to tantalum and niobium. In principle, diffusion behavior could then be studied at much lower temperatures than previously possible and short-circuit phenomena (more pronounced at lower temperatures) could be accurately characterized. This paper describes the technique developed for such a study and presents some preliminary measurements on the diffusion of  $^{95}\text{Nb}$  in tungsten in support of its applicability.

### Results and Discussion

**Calibration.**—While tungsten anodizes in a number of electrolytes to form uniform anodic oxide films exhibiting sharp interference colors, it is clear that the characteristics of the process important to a sectioning technique are influenced dramatically by the particular electrolyte and other experimental variables. Pitman and Hamby (12) described many of these characteristics for dilute sulfuric acid electrolytes; McCargo, Davies, and Brown (5) used an electrolyte consisting of 0.4M  $\text{KNO}_3$  and 0.04M  $\text{HNO}_3$ . In the latter work, a film-thickness calibration was obtained by a radiochemical technique and checked by weight-loss measurements after dissolving the films from the anodized specimens.

The experimental procedure and film-thickness calibration utilized in this investigation were established after a series of "screening" tests were performed in various electrolytes. Anodizing characteristics were observed and weight-gain measurements (after anodization) and weight-loss measurements (after film dissolution) were made on tungsten specimens each consisting of electropolished sheets having total surface areas of about 500  $\text{cm}^2$ . By making such a calibration on the basis of both weight-gain and weight-loss values, it was possible to establish the efficiency<sup>1</sup> of film formation for each electrolyte and anodization procedure. For example, while the thickness of anodic oxide formed on tungsten in 0.5%  $\text{Na}_2\text{SO}_4$  to a given voltage was equivalent to that formed in other electrolytes, the efficiency of film formation was much less and more highly dependent on the current density during anodization. At the lowest efficiencies, about 55% at low currents, sufficient tungsten was actually lost to the electrolyte so as to result in a weight loss, rather than a weight gain, during anodization of the specimen. Several dilute acids and solutions of sulfate and nitrate salts were tested at room temperature as possible anodizing electrolytes; solutions exhibiting poor efficiency were characterized by comparatively high decay or leakage currents after full voltage had been applied across the cell.

<sup>1</sup> The efficiency of film formation is defined here as the ratio of the amount of tungsten in the anodic oxide film to the amount actually lost by the specimen during anodization. This value is independent of the "current efficiency" values sometimes used to characterize anodic processes.

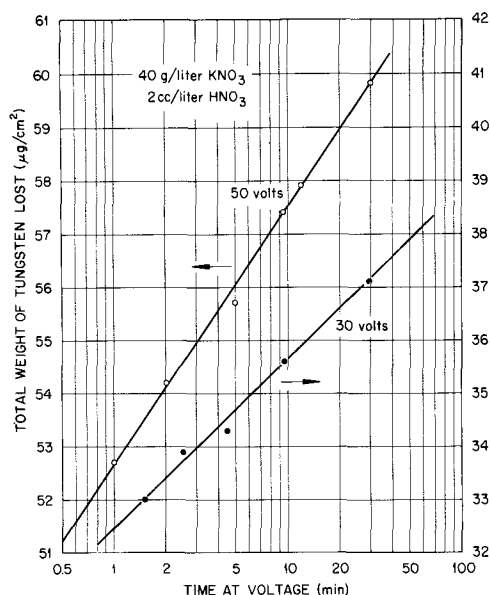


Fig. 1. Total amount of tungsten lost by metal specimen during anodization in  $\text{KNO}_3$ - $\text{HNO}_3$  electrolyte.  $\circ$  specimen held at 50v;  $\bullet$  specimen held at 30v.

The electrolyte combination recommended by McCargo, Davies, and Brown (5) was confirmed as a "high-efficiency" electrolyte which was insensitive to minor variations in composition, and this solution (40 g/liter of  $\text{KNO}_3$  plus 2 cc/l of concentrated  $\text{HNO}_3$ ) was used in all work reported in this paper. Efficiencies of film formation of about 99% were observed for this electrolyte when currents during the initial period of anodization were varied from about 0.2-5  $\text{ma}/\text{cm}^2$ . In comparison, the formation efficiency for an anodic film formed in 0.5%  $\text{Na}_2\text{SO}_4$  at 0.5  $\text{ma}/\text{cm}^2$  to 50v was about 88%.

When tungsten specimens were anodized to a given voltage, the films continued to grow after full voltage had been applied across the cell as a function of time as illustrated in Fig. 1. The increase in film thickness, in this case measured as the decrease in weight of the specimen after forming and dissolving the anodic film, is shown to vary linearly with the logarithm of the time. In order to utilize a calibration based on a constant-voltage anodization, a "standard" time of 2 min was arbitrarily chosen so as to limit errors arising from slight differences in the anodization time and procedure. The specimen for calibration was weighed, anodized in the prescribed manner at a given voltage and weighed again. The anodic film was then dissolved in dilute  $\text{NaOH}$  and the specimen reweighed. All weight measurements were made after the specimen had been carefully washed and dried. These measurements appear in columns 2 and 5 of Table I along with the calculated quantities necessary to compare the total amount of tungsten lost by the specimen with the amount that appeared in the anodic oxide film.<sup>2</sup> As these values are nearly identical, all the tungsten is satisfactorily accounted for and thickness-voltage calibrations may be constructed and converted to any basis by simple mass balances.

Figure 2 shows the amount of tungsten removed from the surface of the metal by anodizing to a given voltage. The time dependence taken from Fig. 1 is included in the figure to indicate the extent of the influence of anodization time on such a calibration curve. The corresponding oxide thickness-voltage calibration is presented in Fig. 3. The thickness of the tungsten layer removed may be obtained by multiplying the ordinate values of Fig. 3 by the factor 0.2787A

<sup>2</sup> The anodic oxide formed on tungsten under these conditions was assumed to be  $\text{WO}_3$  with a density of 6.8  $\text{g}/\text{cm}^3$  (12); this value is slightly less than the accepted value for bulk crystalline  $\text{WO}_3$  (7.16  $\text{g}/\text{cm}^3$ ) which is probably due chiefly to structural differences.

Table I. Anodization of tungsten<sup>a</sup>

Voltage <sup>b</sup> v	Weight of WO <sub>3</sub> in film <sup>c</sup> , μg/cm <sup>2</sup>	Thick- ness of WO <sub>3</sub> <sup>d</sup> , Å	Weight of W in film <sup>e</sup> , μg/cm <sup>2</sup>	Total weight of W re- moved <sup>f</sup> , μg/cm <sup>2</sup>	Thickness of W removed <sup>g</sup> , Å	Film for- mation effi- ciency <sup>h</sup> , %
2.40	4.53	66.6	3.59	3.89	20.1	92.3
4.80	8.42	123	6.68	6.69	34.6	99.9
7.45	11.9	175	9.44	9.93	51.3	95.1
9.95	15.5	228	12.3	12.3	63.6	100
12.40	19.0	279	15.1	15.3	71.9	98.7
14.95	22.4	329	17.8	17.9	92.5	99.4
19.85	28.7	422	22.8	23.1	119	98.7
24.9	34.8	512	27.6	28.1	145	98.2
29.9	42.1	619	33.4	33.7	174	99.1
35.2	48.8	718	38.7	38.6	199	100
39.8	54.8	806	43.5	43.6	225	99.8
45.1	62.0	912	49.2	49.4	255	99.6
49.8	67.6	994	53.6	54.0	279	99.3
54.8	74.3	1093	58.9	58.9	304	100
60.0	80.7	1187	64.0	63.9	330	100
65.0	87.4	1285	69.3	69.5	359	99.7
70.1	93.0	1368	73.8	73.8	381	100

<sup>a</sup> Electrolyte: 40 g/l KNO<sub>3</sub> plus 2 cc/l HNO<sub>3</sub>; time: 2.0 min at set voltage; area of specimen: 463.3 cm<sup>2</sup>.

<sup>b</sup> Final voltage across cell.

<sup>c</sup> Measured quantity: Weight of anodized specimen less weight of specimen after film dissolution.

<sup>d</sup> On the basis that the film density is 6.8 g/cm<sup>3</sup> (12).

<sup>e</sup> Calculated via (c).

<sup>f</sup> Measured quantity: Original weight of specimen less weight after anodizing and film dissolution.

<sup>g</sup> Calculated via (f).

<sup>h</sup> Comparison of columns 4 and 5.

of tungsten per angstrom of oxide. The data could be adequately described by two straight lines. Up to 12v, a least-squares analysis yielded

$$T_{\text{WO}_3, \text{Å}} = 23.28 + 20.972v$$

or

$$T_{\text{W, Å}} = 6.49 + 5.845v$$

where  $T_{\text{WO}_3, \text{Å}}$  is the thickness in angstroms of anodic oxide formed,  $T_{\text{W, Å}}$  is the thickness of the tungsten layer consumed by anodizing, and  $v$  is the voltage. Similarly, from 12-70v

$$T_{\text{WO}_3, \text{Å}} = 51.93 + 18.933v$$

or

$$T_{\text{W, Å}} = 14.47 + 5.277v$$

These values are in quite satisfactory agreement with those reported by McCargo *et al.* (5).

While a mechanical stripping technique for anodic films on tungsten [such as that which was used for films on tantalum and niobium (8)] has not yet been found, quantitative separations were achieved simply by dipping the anodized specimen into a dilute (3 g/l)

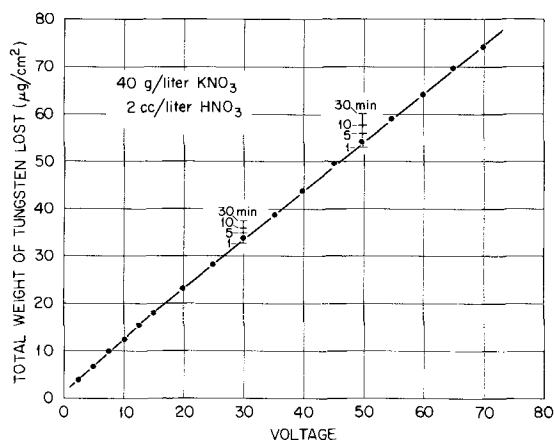


Fig. 2. Total weight of tungsten lost during constant voltage anodization for 2.0 min in KNO<sub>3</sub>-HNO<sub>3</sub>. Superimposed time scale indicates expected shift for other anodization times.

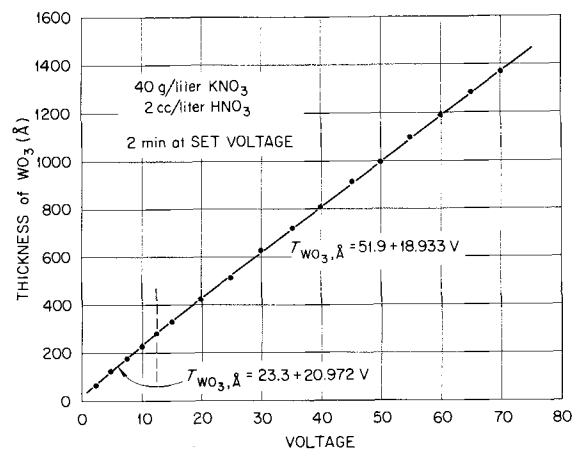


Fig. 3. Oxide thickness-voltage calibration for tungsten anodized for 2 min at full voltage in KNO<sub>3</sub>-HNO<sub>3</sub> solution. The thickness of the tungsten layer removed by forming this oxide is 0.2787 Å metal per Å oxide (see text).

sodium hydroxide solution for about 1 min. While negligible amounts of the tungsten metal not associated with the oxide were dissolved along with the film, it should be mentioned that the actual dissolution rates of tungsten metal in such environments were observed to be strongly dependent upon the oxygen content of the solution. In a typical solution of NaOH in distilled water at room temperature, tungsten dissolution rates equivalent to about 3 Å/hr were observed after the initial anodic or air-formed film was dissolved. However, if this solution were aerated by bubbling oxygen gas through it for a few minutes, the dissolution rates were observed to increase by more than an order of magnitude. Maximum rates were observed when the bubbler was left in operation while the specimen was immersed, but this additional increase may have been due to stirring or other mechanical effects. The thickness of the air-formed film on tungsten (actually the film formed during our washing and drying procedure, which included a period in a drying oven at 50°C) was determined from these experiments to be approximately 12 Å.

*Diffusion specimens.*—Specimens for the diffusion measurements were prepared as 0.25-in.-diameter cylinders from single-crystal rods of tungsten obtained from Materials Research Corporation. One face of each specimen was prepared metallographically and electropolished in a 130 g/l sodium phosphate solution. The resulting mirrorlike surfaces appeared smooth in the microscope and back-reflection x-ray patterns showed that most surface disturbances were removed during the electropolishing. The axes of the specimens were about 10° from <100>. A thin uniform layer of <sup>95</sup>Nb was deposited on the face by vacuum evaporation of a small quantity of isotope-containing oxalate solution from a hot tungsten filament. The specimens were diffusion-annealed in a tantalum resistance furnace under about 1 atm of high-purity argon. After the annealing treatment, a length of 0.020-in.-Ta wire was securely spot-welded to the back part of the specimen to facilitate handling and to serve as an inert electrical contact during anodization.

The first exploratory experiments on sectioning the diffusion specimens indicated that the minute amount of niobium tracer and accompanying impurities in the diffusion zone had no measureable effect on the characteristics of anodization or subsequent dissolution of the film. In addition, consistent with the high efficiency of film formation, a negligible amount of tracer was observed to be lost to the electrolyte during anodizing. Thus, it appeared that the anodizing technique and calibration presented earlier is applicable to the precision sectioning of tungsten into which small amounts of tracer elements had been diffused.

Shell vials (small test tubes) 15 mm in diameter were used to hold the liquid solution containing the "stripped" metal section. The isotope concentration in each section was then determined in a well-type counter using a NaI(Tl) crystal in conjunction with a single-channel analyzer. Initially, the anodic films were stripped by dipping the specimen into the test tube partially filled with dilute sodium hydroxide. After 1 min, the specimen was raised above the liquid level in the tube and washed with additional solution from a squeeze bottle until the tube was filled to the desired final level. While this procedure seemed to remove the anodic film completely, as was our experience with the films formed on plain tungsten, the erratic behavior of the resulting tracer activity data obtained in this way indicated that the  $^{95}\text{Nb}$  isotope tended to remain on the metal surface as the host oxide dissolved. It appeared that this "left-behind" isotope neither interfered with the anodizing of the tungsten nor was removed into the anodizing electrolyte during the subsequent formation of the film. However, the sporadic removal of portions of this residue into the stripping solution was a serious experimental problem which had to be dealt with in order to utilize the technique efficiently. Until the exact nature of the surface holdup of the tracer is known, this type of experimental difficulty will probably be faced and solved on an individual basis for each isotope.

In order to bring as much as possible of the  $^{95}\text{Nb}$  associated with the anodic oxide layer into the sodium hydroxide stripping solution, we tried several schemes including cathodic stirring,<sup>3</sup> ultrasonic vibration, and gentle swabbing with wet cotton. Each of these procedures by itself improved the consistency of the data; however, it was found that a combination of the last two methods produced results that were most satisfactory. Thus, virtually complete stripping of the  $^{95}\text{Nb}$ -containing tungsten oxide films from the specimens was accomplished in the following manner: a test-tube containing a small wad of cotton packed into its bottom was partially filled with dilute NaOH to which a small amount of detergent had been added. The tube was placed in the tank of an ultrasonic cleaner and the specimen immersed. During the ultrasonic treatment (about 1 min) the specimen was agitated and rubbed gently against the cotton in the bottom of the tube. The specimen was then washed with plain dilute NaOH to fill the tube to the desired level in the manner previously described. The tube was capped and stored for future counting while the anodizing-stripping sequence was repeated until the desired number of "sections" had been obtained.

**Diffusion data.**—As a means to establish the accuracy and the reliability of this method of determining diffusion profiles, the diffusivity of  $^{95}\text{Nb}$  in tungsten at 1800°C was measured several times with the annealing time and section thickness being the principal variables. The experimental procedures were chosen so that the "thin-film" solution to Fick's law for unidirectional diffusion would be applicable to the data. Thus,

$$A_{(x,t)} = \frac{M}{\sqrt{\pi Dt}} \exp\left(-\frac{x^2}{4Dt}\right)$$

where  $A_{(x,t)}$  = the activity (concentration of the isotope) at a distance  $x$  into the specimen at time  $t$ ,  $M$  = the total activity per unit area in the infinitesimally thin isotope layer at  $x = 0$ ,  $t = 0$ , and  $D$  = the diffusion coefficient. Therefore, barring excessive contributions from spurious or secondary mass transport mechanisms, the logarithm of the activity should be a linear function of the square of the penetration distance with the slope of the line being equal to  $-(4Dt)^{-1}$ . The conditions pertinent to this work under which this equation applies have been discussed previously.<sup>1</sup>

<sup>3</sup> Stirring and surface agitation which occurs by gas evolution when a negative potential is applied to the specimen (cathode) in the stripping solution.

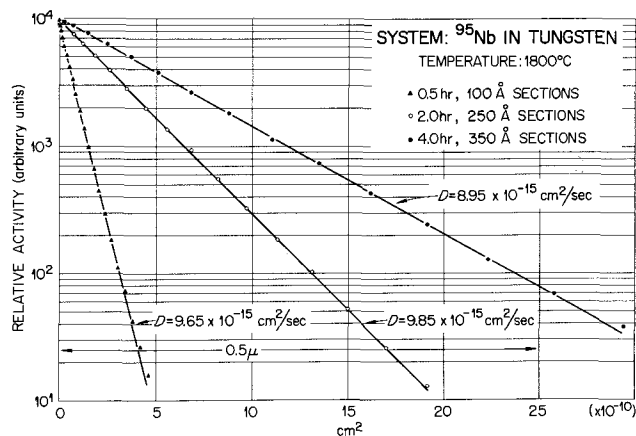


Fig. 4. Activity profiles for diffusion of  $^{95}\text{Nb}$  into tungsten single crystals after diffusion for 0.5, 2, and 4 hr at 1800°C.

The concentration profiles of  $^{95}\text{Nb}$  in tungsten single crystals after diffusion for 1/2, 2, and 4 hr at 1800°C are shown in Fig. 4. The specimens were all sectioned by the anodizing-stripping technique utilizing section thicknesses of 100, 250, and 350 Å, respectively. In all three cases the profiles were virtually ideal straight lines from which the diffusion coefficients could be found unambiguously.  $D$  values of 9.65, 9.85, and  $8.95 \times 10^{-15} \text{ cm}^2/\text{sec}$  were determined from the three sets of data indicating a high degree of reproducibility as well as self-consistency for the data. In addition, since different section thicknesses were employed, the data serve as a check on the section thickness calibration and other aspects of the technique as a whole.

These diffusion coefficients agreed well with that determined by a single experiment in which a tungsten specimen was diffusion-annealed for 8 hr at 1800°C and sectioned by the more conventional grinding method. Although in the latter experiment, the penetration profile was obviously not as accurately determined, the agreement provided an additional bit of confidence in the anodizing-stripping procedures. While the data presented in Fig. 4 show substantially ideal penetration behavior, it should also be pointed out that significant deviations from the ideal were observed in these specimens for penetration depths greater than about  $4$  to  $6 \sqrt{Dt}$ . Similar characteristics in the case of low-temperature diffusion in tantalum (1, 9) and niobium (10) single crystals were associated with the contribution made by the relatively low density of various short-circuit diffusion paths to the final mass distribution. Again, this behavior emphasizes the need for high resolution techniques in order to study diffusion phenomena at low temperatures as well as the need to interpret such data with care, even in the case of single-crystal specimens.

### Summary and Conclusions

The applicability of anodic film sectioning techniques to the study of diffusion phenomena in tungsten has been demonstrated. Characteristics of the anodization of tungsten pertinent to sectioning were studied, and a quantitative calibration was determined for a high efficiency electrolyte. Methods for stripping the isotope-containing oxide film from the surface of the specimen were also examined. The propensity of the isotope to remain on the specimen surface during chemical dissolution of the anodic film was counteracted, at least in the case of the  $^{95}\text{Nb}$  isotope, by physical and ultrasonic agitation during the dissolution step.

Concentration profiles for  $^{95}\text{Nb}$  into tungsten single crystals after diffusion for various times at 1800°C were determined by this sectioning technique. The high degree of self-consistency and reproducibility of the data, even when utilizing sectioning thicknesses as small as 100 Å, was encouraging evidence that the method will prove invaluable to low-temperature diffusion investigations in tungsten.

### Acknowledgments

The authors wish to thank R. A. Padgett and J. J. Campbell for their contributions to the experimental work. The assistance of J. V. Cathcart during the course of the investigation is also appreciated. Research was sponsored by the USAEC under contract with the Union Carbide Corporation.

Manuscript received Aug. 31, 1967; revised manuscript received Oct. 25, 1967.

Any discussion of this paper will appear in a Discussion Section to be published in the December 1968 JOURNAL.

### REFERENCES

1. R. E. Pawel and T. S. Lundy, *Acta Met.*, **13**, 345 (1965).
2. A. J. Mortlock, *ibid.*, **12**, 675 (1964).
3. A. F. Brown and D. A. Blackburn, *ibid.*, **11**, 1017 (1963).
4. J. A. Davies, J. Friesen, and J. D. McIntyre, *Can. J. Chem.*, **38**, 1526 (1960).
5. M. McCargo, J. A. Davies, and F. Brown, *Can. J. Phys.*, **41**, 1231 (1963).
6. A. J. Mortlock, "The Near-Surface Diffusion Anomaly in Gold," ORNL-4141 (July 1967).
7. J. L. Whitton and J. A. Davies, *This Journal*, **111**, 1347 (1964).
8. R. E. Pawel and T. S. Lundy, *J. Appl. Phys.*, **35**, 435 (1964).
9. R. E. Pawel and T. S. Lundy, *J. Phys. Chem. Solids*, **26**, 937 (1965).
10. T. S. Lundy, F. R. Winslow, R. E. Pawel, and C. J. McHargue, *Trans. Met. Soc. AIME*, **233**, 1533 (1965).
11. J. Uhler, B. Domeij, and S. Borg, *Arkiv Fysik*, **24**, 413 (1963).
12. H. W. Pitman and D. C. Hamby, Linfield Research Institute Report, DA Proj. No. 3-99-15-104, McMinnville, Oreg. (1959).

## Some Aspects of the Parallel Differential Conductance Measured at an Electrode-Electrolyte Interface

H. S. Isaacs\*<sup>1</sup> and J. S. Li. Leach

*Department of Metallurgy, University of Nottingham, Nottingham, England*

### ABSTRACT

Impedance measurements using a square current wave on electrodes of tin, zinc, titanium, chromium, and a uranium alloy show that the measured conductance is related to the measured capacitance and to the Faradaic current through the electrode.

In a previous paper (1) the measured voltage response of oxide-covered metal electrodes to a square current wave was described in terms of an analogue circuit consisting of a resistor and a capacitor in parallel. Particular attention was given to interpreting the values of capacitance observed; in this paper, the other analogue component is considered in detail. The general discussion given here is applicable both to the oxide-covered and oxide-free metals. Although the differential capacitance of electrodes has previously been extensively considered, little attention has been given to the differential conductance. This attitude perhaps stems from investigations of the mercury-electrolyte interface, which is almost ideally polarizable (2), with no resistive component and with a capacitance independent of frequency. The analogue of the solid metal-electrolyte interface (4-6) on the other hand, includes both capacitive and resistive components which are frequency dependent. The frequency dependence has been attributed to the effects of surface roughness (2), but it may also be a characteristic of nonideally polarizable electrodes.

When a potential determining ion is present, the capacity is large and has a maximum at the reversible half wave potential (3, 7). The components of the analogue of the reaction occurring at a mercury-electrolyte interface can be derived from the diffusion characteristics of the potential determining ions and the rate constant for the reaction (3, 8, 9). The analogue of the impedance for the diffusion effects alone is known as the "Warburg impedance" and is frequency dependent. With solid metal-electrolyte systems (6) or when the potential determining ion is specifically adsorbed on mercury (10), the variation with frequency of the analogue is complicated by the

contribution of secondary processes to the Warburg impedance.

Although the effect of reversible adsorption has been considered by a number of authors (9, 11, 12), little attention has been given to the contribution of adsorption processes to the resistive component of the analogue, this often being taken to depend only on the current-voltage characteristics [i.e.,  $(dV/di)$  (9, 13)].

A number of investigators have noted that the impedance of an electrode falls markedly at negative potentials (4, 14, 15) or high current densities (4, 15). A square current wave makes it possible to measure small impedances, and attention is given here to the low impedance measured at negative potentials corresponding to high cathodic current densities.

### Experimental Method

The measuring apparatus has been described previously (1, 14). Basically, the method consists of comparing the voltage change at a point in the solution close to the surface of the test electrode with that of an analogue consisting of a capacitor and a resistor in parallel when a square current wave is applied to each. It is important to note that it is the response of the test electrode and not that of the test cell which is measured. This method has the advantage of eliminating from the measured impedance most of the series resistance associated with the electrolyte (which at times may cause a voltage change of the order of ten times that of the electrode) and all of the impedance of the counter electrode. The residue of the electrolyte resistance can be separated from the electrode impedance as the former gives rise to a voltage change in phase with the applied current wave while the voltage response of the latter shows a phase shift. The use of a square current wave permits the separation of these two components without studying the

\* Electrochemical Society Active Member.

<sup>1</sup> Present address: Metallurgy Department, Brookhaven National Laboratory, Upton, New York.

frequency response. Processes occurring at the electrode having effective time constants (relaxation times) less than one tenth of the period of the square pulse do not influence the results as they also behave effectively as series resistances. By varying the repeat frequency of the square wave these rapid processes may be examined separately.

Many of the difficulties encountered with more conventional measuring methods do not arise with this method, but difficulties occur when the parallel resistive component is very large or very small. In the former case, an almost linear voltage response results and in the latter case, difficulty arises both from the design of the apparatus being sensitive to calibration, and from the very small, highly nonlinear voltage response. Later developments, in particular the mathematical analysis of the voltage response (1) instead of comparison with an analogue have reduced many of the difficulties associated with small resistances.

The square wave of current with a repeat frequency of 400 Hz was passed through an auxiliary electrode and the test electrode to earth. This frequency was chosen as it gave a satisfactory compromise between the conflicting requirements of a large impedance (to get an adequate voltage response) and a parallel resistance which was not too large for the range of the bridge. The a-c voltage response of the test electrode to the square current wave was measured with reference to a silver wire electrode connected to a high impedance amplifier. The d-c potential of the test electrode was controlled with reference to a saturated calomel electrode, by a potentiostat, which included a choke (100 henry) and a variable high resistance ( $5 \times 10^4$  ohm). The choke prevented leakage of the a.c. through the potentiostat, while the resistance damped the response of the potentiostat and prevented the oscillation frequently encountered when using potentiostats with high impedance circuits. The d.c. supplied by the potentiostat was measured with a galvanometer; no d.c. was produced by the bridge. The mean potential of the electrode was measured by a high impedance valve voltmeter ( $10^{13}$  ohm) with reference to a saturated calomel electrode. All the results have been corrected to refer to a standard hydrogen electrode.

Each measurement was made at a fixed potential after which the potential was changed. The measurements required about 10 sec each and were made at varying intervals of potential as shown in the figures. In this way potentiodynamic conditions were approached, but due to the need to balance the bridge at each potential these conditions could not be fully attained.

The purity of the metals used was: tin 99.99%; zinc 99.9%; chromium 99%; titanium 99.99%; uranium 12%; molybdenum 99.95%. The final preparation of the electrodes, with the exception of titanium, was abrasion on 600 grade emery paper. This technique was used, in spite of its disadvantages, because it could be applied to all the metals studied. The reagents for etching and polishing the metals investigated all differ resulting in different undefined surface conditions. The titanium electrode was chemically polished in a solution of 90 cc hydrogen peroxide (10 vols.) and 10 cc 40% hydrofluoric acid.

The solutions were prepared from "Analar" reagents and distilled water and had the oxygen content reduced to a low level by bubbling oxygen-free nitrogen through them. The carbonate solution was 0.1M in sodium carbonate and sodium bicarbonate and had a pH of 9.7. The pH of the 0.5M sodium sulphate solution was increased by the addition of sodium hydroxide.

### Results and Discussion

The variation with potential of the parallel differential conductance of metal electrodes, measured at a square wave repeat frequency of 400 Hz shows a rela-

tion between the conductance and the capacitance usually observed at low current densities and a relation between the conductance and the applied current which is particularly apparent at high currents during the evolution of hydrogen.

Under conditions of concentration polarization the properties of the interface are described by the Warburg impedance which expressed as a parallel network is given by (3)

$$C_p = \frac{1}{2\eta W^{1/2}} \frac{1}{R_p} = \frac{W^{1/2}}{2\eta}$$

where  $\eta$  is a function of the concentration at the electrode-solution interface of the reacting ions in solution and its variation with potential and  $W$  is the angular frequency of the applied sine wave, which, during measurements, is considered constant as a function of potential. These equations depend only on concentration polarization, and it would be expected that the capacitance and conductance would vary with potential in a similar manner. When activation polarization becomes significant, the measured capacitance and conductance would no longer be simply related by the equations given above.

Maxima in both the capacitance and conductance are observed at  $-0.67v E_H$  as the potential of a tin electrode (Fig. 1 and 2) is decreased from a point where an anodic current of about  $2.5 \times 10^{-4}$  amp/cm<sup>2</sup> flows. The potential for zero current is  $-0.64v E_H$ . Similar maxima have been observed for zinc both on decreasing and on increasing the potential (Fig. 3) at potentials close to that for zero current (Fig. 4). The high values of capacitance were observed over a range of 0.15v, which corresponds to that expected on the

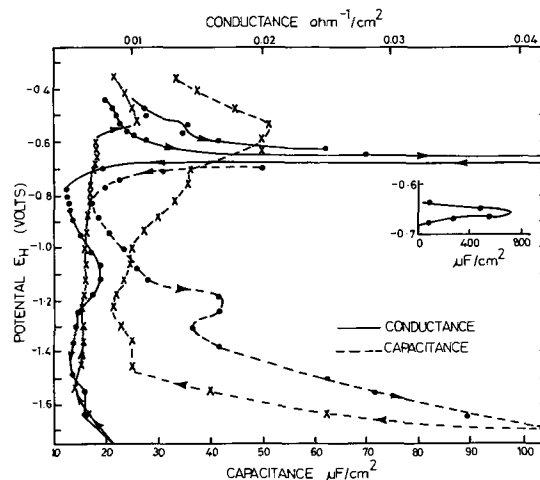


Fig. 1. Potential dependence of the parallel capacitance and conductance at 400 Hz for tin in a carbonate solution of pH 9.7.

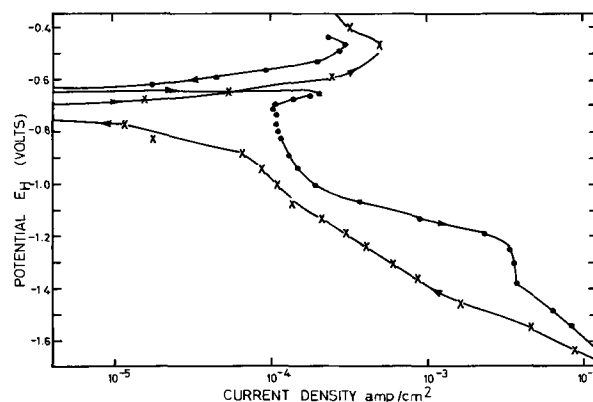


Fig. 2. Potential dependence of the current for tin in a carbonate solution of pH 9.7.

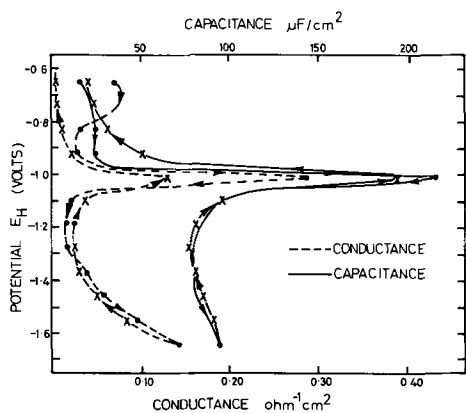


Fig. 3. Potential dependence of the parallel capacitance and conductance at 400 Hz for zinc in a carbonate solution of pH 9.7.

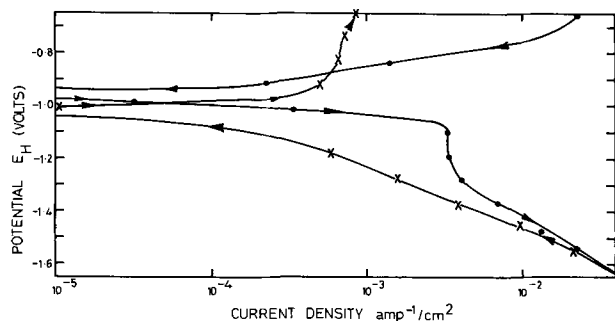


Fig. 4. Potential dependence of the current for zinc in a carbonate solution of pH 9.7.

basis of Faradaic admittance. Low values would be expected for the series resistance of the Warburg impedance for a reversible reaction over a range of about 3 units of  $RT/\alpha nF \ln 10$  (3). Taking  $\alpha$ , the distribution coefficient as  $1/2$ ,  $n$ , the number of electrons involved in the reaction as 2, and  $RT/F \ln 10$  as 0.06v at 298°K, the calculated potential range of low resistance is about 0.18v, in good agreement with the observed value.

The conditions for the measurements on tin differ in many respects from those used by Grahame, but the basic phenomenon of concentration polarization is the same, and approximately the same ranges of potential would therefore be expected. The soluble species taking part in the reversible reaction in the experiment on tin were produced during the flow of anodic current. With cathodic currents the concentration of the soluble tin ion falls due to diffusion into the bulk of the solution and deposition on the electrode; on increasing the potential the capacitance maximum and zero polarization current do not occur, as would be expected for a reversible reaction, at exactly the same potential. This difference of 0.03v could also arise from an additional cathodic reaction (*e.g.*, oxygen depolarization) which would shift the zero current to more a positive potential in which case the capacitance maximum would indicate the reversible potential for the reaction of the tin ions, under the conditions of measurement.

The similarity in the potential variation of the conductance and of the capacitance is always marked when the value of the capacitance is high ( $>100 \mu\text{F}/\text{cm}^2$ ) and shows a maximum as a function of potential. This can clearly be seen for tin, zinc and titanium in Fig. 1, 3, and 5. With titanium the high values of capacitance result from a valency change reaction occurring in the surface oxide (1). In this case the variations of the concentration of the reacting species occur in the solid oxide and the potential range over which the high capacitances and conductances are ob-

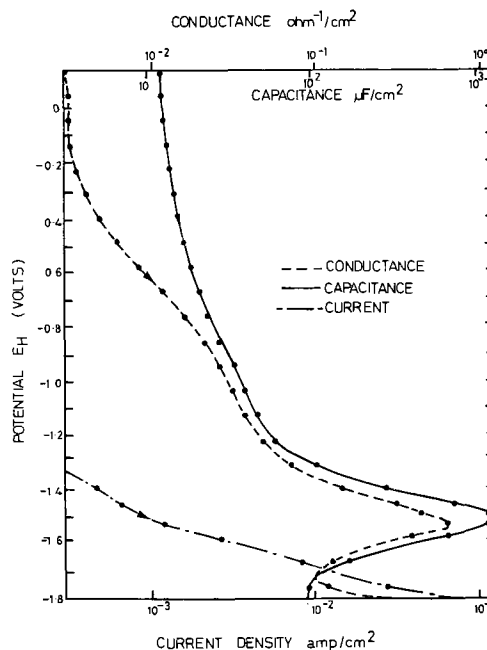


Fig. 5. Potential dependence of the current and the parallel capacitance and conductance at 400 Hz for titanium in a sulphate solution of pH 14.

served is greater than for reactants dissolved in the liquid phases.

The relation between the capacitance and the conductance is less marked when the value of the capacitance does not vary rapidly with potential, but usually can be discerned. On decreasing the potential below that for the capacitance maximum for tin (Fig. 1) the variation of the conductance and capacitance are similar down to a potential of  $-1.05\text{v } E_H$ . On increasing the potential again the conductance increases more rapidly than the capacitance, but both values decrease again after reaching maxima at a potential of  $-0.55\text{v } E_H$ . The cause of this increase in the conductance on increasing the potential for tin and to a lesser extent for zinc (Fig. 3) after hydrogen has been evolved is not known. The difference between the hysteresis<sup>2</sup> in the conductance and in the capacitance for zinc in the range  $-1.3$  to  $-1.1\text{v } E_H$  is unusual and is an exception to the general observation that the hysteresis for both conductance and capacitance are in the same direction at low current densities. However, the hysteresis is not marked and the differences might arise from instrumental causes. With chromium (Fig. 6) at potentials more positive than  $-1.1\text{v } E_H$  the measured conductance (curve A) and capacitance behave in a similar manner with potential.

The parallel differential conductance of all the metal electrodes tested shows a continuous increase at the more negative potentials, independent of the changes in capacitance. This marked increase in the conductance begins in most cases at a potential close to that at which the current curve shows a change of slope associated with a change in the predominant electrolytic reaction occurring at the electrode-solution interface (16). At potentials more positive than that of the change in slope, the reaction is apparently diffusion controlled; at potentials more negative than the change, the current increases almost exponentially with decreasing potential indicating that an activation controlled reaction, probably hydrogen evolution, predominates.

The similarity between the behavior of the current and conductance as a function of potential change during the evolution of hydrogen may be seen on considering the hysteresis observed in the polarization of

<sup>2</sup> Hysteresis: The difference at a given potential in the values observed on decreasing and increasing the potential.

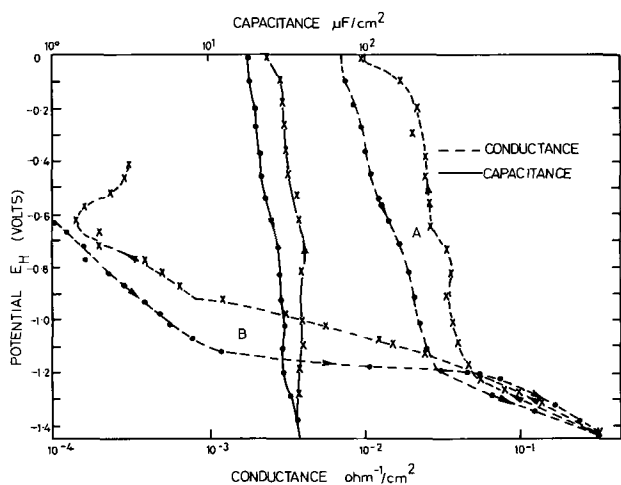


Fig. 6. Potential dependence of the parallel capacitance and conductance (curve A) at 400 Hz for chromium in a carbonate solution of pH 9.7. The d-c conductance, curve B, is derived from Fig. 7.

metal electrodes. During the evolution of hydrogen, it has been observed that the oxide-covered metals show a larger current on increasing the potential (14, 17, 18) whereas metals which may not be expected to have an oxide film usually show a larger current on decreasing the potential (17, 19).

The current observed on decreasing the potential of a tin electrode (Fig. 2) is larger than that on increasing the potential. This hysteresis is also observed in the conductance (Fig. 1) at potentials below  $-1.1v E_H$ , where the hydrogen evolution reaction occurs. With zinc, the hysteresis in the current (Fig. 4) is again the same as that of the conductance (Fig. 3). Both zinc and tin behave in respect of the hysteresis, as oxide-free metals. Chromium (Fig. 6 and 7), behaves as an oxide-covered metal, judging from the hysteresis in the current and conductance. The type of hysteresis found for a uranium-molybdenum alloy (14), (Fig. 8 and 9) for both current and conductance is also that characteristic of oxide-covered metals.

The results for the conductance of a tin electrode (Fig. 1) give a further indication of a relation between the differential conductance and current. At about  $-1.2v E_H$  on decreasing the potential, the conductance shows a maximum followed by a minimum at  $-1.3v E_H$  which are not reflected in the capacitances at these potentials. The current, however, (Fig. 2) shows a rapid increase at about  $-1.2v E_H$  followed by a concentration controlled reaction at about  $-1.3v E_H$ . If the conductance is given by

$$\frac{1}{R_{dc}} = \frac{1}{\theta} = \frac{di_{dc}}{dE_H} \quad [1]$$

these results would be explained.

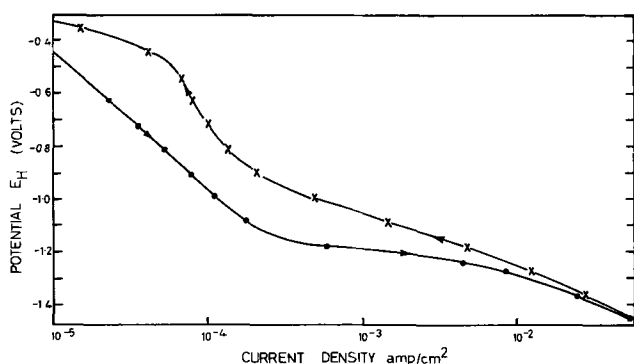


Fig. 7. Potential dependence of the current for chromium in a carbonate solution of pH 9.7.

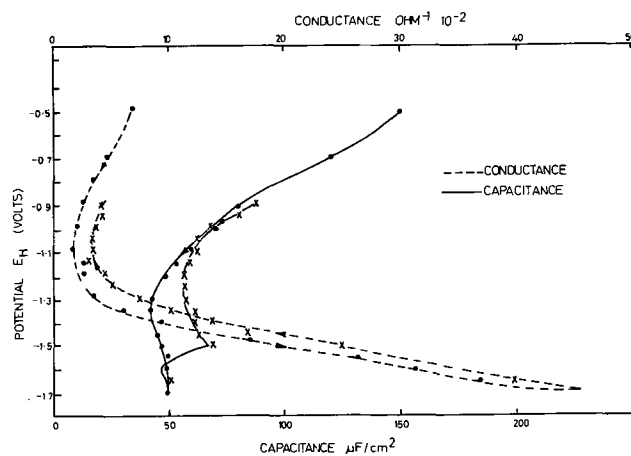


Fig. 8. Potential dependence of the parallel capacitance and conductance at 400 Hz for a uranium-12% molybdenum alloy in a carbonate solution of pH 9.7.

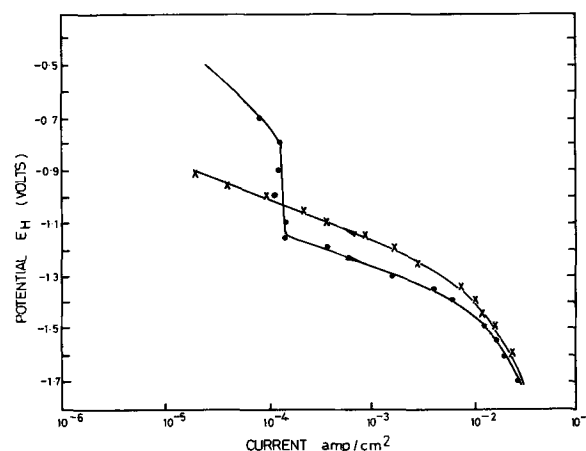


Fig. 9. Potential dependence of the current for a uranium-12% molybdenum alloy in a carbonate solution of pH 9.7.

Assuming that the hydrogen evolution reaction can be described by the Tafel equation

$$E_H = a + b \log i$$

the d-c conductance should be given by

$$\frac{1}{\theta} = \frac{di_{dc}}{dE_H} = \frac{i \cdot \ln 10}{b} \quad [2]$$

The above equation indicates that the d-c conductance is directly proportional to the current when the reaction occurs only under activation control. As the d-c conductance must represent a resistive component of the analogue impedance of the electrode-solution interface, this component should be measurable by a-c impedance measurements, unless relaxation processes occurring at the interface have analogue conductance components comparable to that arising from the direct current.

In Fig. 10 the values of the a-c conductance (Fig. 8) are plotted against the values of the direct polarization current (Fig. 9), both measured at given potentials for a uranium-molybdenum alloy electrode. A straight line is observed at the higher current densities which from the slope ( $b/\ln 10$ ) gives a Tafel slope ( $b$ ) of 0.157. This is close to the value of the Tafel slope calculated for the relevant portion of the curves shown in Fig. 9. The curvature in current plots (Fig. 9) as a function of potential may result from resistance polarization, but this would not be expected to influence the derived value of  $b$ , the Tafel slope, as the resistance affecting the potential measurements appears in the impedance measurements as a series resistance



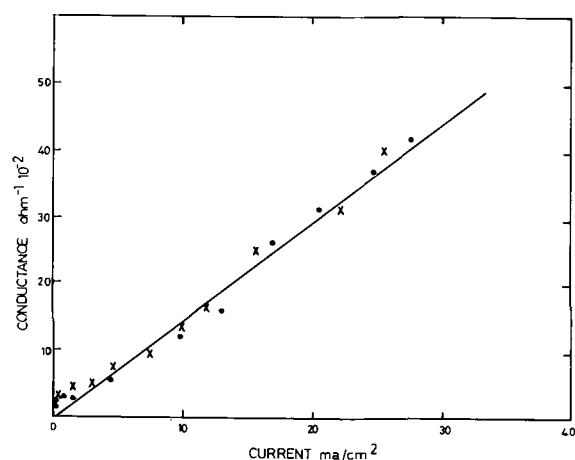


Fig. 10. Variation of the current and conductance measured at 400 Hz for a uranium-12% molybdenum alloy. The values have been taken from Fig. 8 and 9.

and would not be measured by the techniques employed here.

This method appears attractive for obtaining the Tafel slope, but it is not generally applicable, as the conductance usually includes a component, related to the capacitance, which varies with potential. As the value of  $1/R_p$  usually decreases with decreasing frequency of the applied signal, this method may be applicable at low measuring frequencies.

Figure 6 shows a comparison of a-c (curve A) and d-c (curve B) conductances for chromium. The d-c conductance ( $1/\theta$ ) was determined from the current curve shown in Fig. 7. At low current densities, the d-c resistance is high and orders of magnitude greater than that observed by the a-c measurements, while at the higher current densities (at potentials more negative than  $-1.2v E_H$ ) the a-c and d-c values are similar. No explanation has been found to account for the measured d-c conductances being slightly larger than the measured a-c values, and it is therefore believed that the a-c measurements were slightly in error. The d-c conductance ( $1/\theta$ ) is low at low current densities (Fig. 6) and other processes are taking place at the electrode-solution interface which do not contribute to the direct polarization current. As the current increases,  $1/\theta$  increases, and at high current densities becomes large and contributes significantly to the measured a-c conductance. The contribution to the total conductance of that associated with the polarization current can also be seen for titanium (Fig. 5) at high current densities. At potentials above about  $-1.7v E_H$  the conductance is related to the capacitance while below  $-1.72v E_H$  the conductance increases markedly, independent of the capacitance. This increase is attributed to the contribution of the d-c conductance ( $1/\theta$ ) to the interfacial admittance.

The contribution of  $1/\theta$  is also apparent with applied anodic currents. At potentials more positive than  $-0.8v E_H$  for zinc (Fig. 4) the hysteresis in the anodic current is large. On decreasing the potential the anodic current is larger and a similar behavior is observed with the conductance (Fig. 3). On increasing the potential the conductance is more closely related to the capacity as the contribution associated with the direct polarization current is small due to the high value of  $b$  in the range  $-0.9v E_H$  to  $-0.7v E_H$ . On decreasing the potential the conductance varies in a manner similar to that of the current as the value of  $b$  in this range is now low and the d-c contribution predominates. These measurements indicate that, under anodic currents, the behavior of the measured conductance of an electrode is related to the capacitance at low current densities and/or high values of the Tafel slope while at higher current densities and/or small Tafel slopes, the conductance varies in a manner depending on the polarization current.

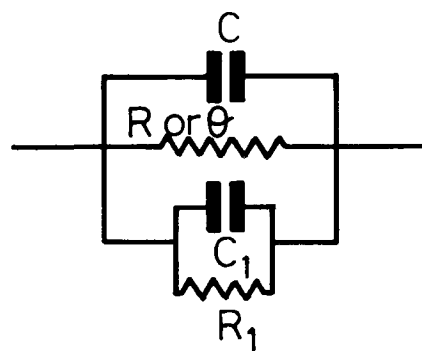


Fig. 11. An electrical analogue of the electrode-electrolyte interface.

The impedance of an electrode-electrolyte interface can be represented by the analogue shown in Fig. 11. Here  $C$  represents the capacitance of the electrical double layer which may be assumed to be independent of frequency (3);  $C_1$  represents a capacitance resulting from one or more reversible processes or effective relaxation processes (e.g., adsorption, reversible redox reaction, or a valency change in an oxide), and  $R_1$  a resistance inversely related to the capacitance  $C_1$ ; the resistance  $\theta$  is given by Eq. [1] and results from the polarization current-potential characteristics. This approach has been found to be applicable to all of a wide range of metals measured at a square wave repeat frequency of 400 Hz (20).

The derivation of the frequency dependence of the effective relaxation processes (3) indicates that the capacitance ( $C_1$ ) increases, while the conductance ( $1/R_1$ ) decreases with decreasing frequency. Hence with decreasing frequencies the currents at which  $\theta$  contributes significantly to the impedance decrease, and at low frequencies of measurement it should be possible to obtain information about the polarization characteristics with only very small changes in the electrode potential.

### Summary

The parallel differential conductance measured at 400 Hz at the electrode-electrolyte interface contains two dominant components which are associated with the reactions taking place at the interface. Reversible processes result in a variation in the conductance with potential which is similar to that of the capacitance, while with irreversible reactions controlled only by an activation process, the magnitude of this conductance will be directly proportional to the polarizing current and inversely proportional to the Tafel slope (b) of the activating polarizing process.

### Acknowledgments

The financial support for this research provided by the U.K.A.E.A. is gratefully acknowledged. One of us (H.S.I.) was seconded from the South African Atomic Energy Board. The work was carried out in laboratory space kindly provided by Professor J. G. Ball, in the Department of Metallurgy at Imperial College, London.

Manuscript received July 18, 1966; revised manuscript received Nov. 6, 1967.

Any discussion of this paper will appear in a Discussion Section to be published in the December 1968 JOURNAL.

### REFERENCES

1. H. S. Isaacs and J. S. Ll. Leach, *This Journal*, **110**, 680 (1963).
2. R. Parsons, "Modern Aspects of Electrochemistry," p. 103, Butterworths, London (1954).
3. D. C. Grahame, *This Journal*, **99**, 370C (1952).
4. K. Franke, C. A. Knorr, and M. Breiter, *Z. Elektrochem.*, **63**, 226 (1959).

5. J. Oresova and B. V. Erchler, *Zhur. Fiz. Khim.*, **24**, 337 (1950).
6. J. O'M. Bockris and B. E. Conway, *J. Chem. Phys.*, **28**, 707 (1958).
7. D. C. Grahame, *J. Am. Chem. Soc.*, **63**, 1204 (1941).
8. J. E. B. Randles, *Discussion Faraday Soc.*, **1**, 119 (1947).
9. B. V. Erchler, *ibid.*, **1**, 269 (1947).
10. H. Laiten and J. E. B. Randles, *Trans. Faraday Soc.*, **51**, 54 (1955).
11. M. Breiter, "Transactions of Symposium on Electrode Processes," E. Yeager, Editor, John Wiley & Sons, Inc., New York (1961).
12. B. E. Conway and E. Gileadi, *Trans. Faraday Soc.*, **58**, 12 (1962).
13. J. O'M. Bockris and H. Kita, *This Journal*, **108**, 676 (1961).
14. J. S. Ll. Leach, *J. Inst. Metals*, **88**, 24 (1959).
15. G. M. Schmid and N. Hackerman, *This Journal*, **107**, 142 (1960).
16. M. Stern, *ibid.*, **104**, 645 (1957).
17. G. D. Fawkes, M.Sc. Thesis, London 1962.
18. J. W. A. Scholte and W. G. L. van Geel, *Philips Research Repts.*, **8**, 47 (1953).
19. A. C. Makrides, *This Journal*, **109**, 977 (1962).
20. H. S. Isaacs, Ph.D. Thesis, London 1964.

## Anodic Processes of Acetate Ion in Methanol and in Glacial Acetic Acid at Various Anode Materials

Norio Sato, Taro Sekine, and Kiichiro Sugino\*

*Department of Applied Electrochemistry, Tokyo Institute of Technology, Ookayama, Meguro-ku, Tokyo, Japan*

### ABSTRACT

The anodes used in this study were platinum, gold, palladium, lead dioxide, and graphite. The normal Kolbe process, the formation of ethane (and methane) and carbon dioxide, can be realized at a potential higher than 2.0v (vs. SCE) in both methanol and glacial acetic acid. In methanol, only platinum and gold seem to be suitable for realizing the process. In glacial acetic acid, however, all of the anodes except graphite can be used successfully for the same process. Another process, the formation of methyl acetate, occurs in both solvents at graphite in the potential range 1.4-2.0v. A side reaction observed in methanol at palladium, graphite, and lead dioxide was the formation of formaldehyde (and methyl formate in case of lead dioxide) which occurs at potentials as low as 1.2v.

In previous work (1, 2) anodic processes of acetic acid-acetate mixture in aqueous solution were studied first at platinum and then at gold, palladium, lead dioxide,<sup>1</sup> and graphite anodes by carrying out the electrolysis at definite potentials, followed by the accurate determination of the products mainly by gas chromatography.

As shown in the above work, at a platinum anode the stoichiometric formation of ethane and carbon dioxide, the normal Kolbe process, was observed with almost quantitative current efficiency. On the other hand, at gold and palladium anodes, no Kolbe process occurred, and oxygen was evolved with 100% current efficiency. At a lead dioxide anode, the current efficiency for oxygen evolution was reduced to 50%, and no ethane, but carbon dioxide was mainly obtained with a small amount of methanol,<sup>2</sup> formaldehyde etc. At graphite, the current efficiency for the formation of carbon dioxide, methanol,<sup>2</sup> and methyl acetate was 97%. There were also remarkable differences among the potentials at which the reactions occur at these different electrodes. These results suggested that different types of electrode processes were proceeding. In aqueous solution, the existence of OH<sup>-</sup> complicates the mechanism of the "true" Kolbe process which is characterized by the discharge of CH<sub>3</sub>COO<sup>-</sup>.

In the present work, therefore, the same anodic process has been studied in methanol and in glacial acetic acid at various anodes (platinum, gold, palladium, lead dioxide, and graphite), employing similar procedures as those of previous work. In these cases, the influence of OH<sup>-</sup> was eliminated, and the dis-

charge of acetate ion at the anode was more accurately observed.

There are a few papers concerning the electrolysis of acetate in methanol and acetic acid with suggestions about the mechanism of the process involved (4). However most of them have been carried out at a platinum anode. It seems that no systematic investigation of the behavior of various anode materials has yet been made.

### Experimental

*Apparatus.*—The H-type cell (2) shown in Fig. 1 was used. To prevent contamination by water, a salt bridge

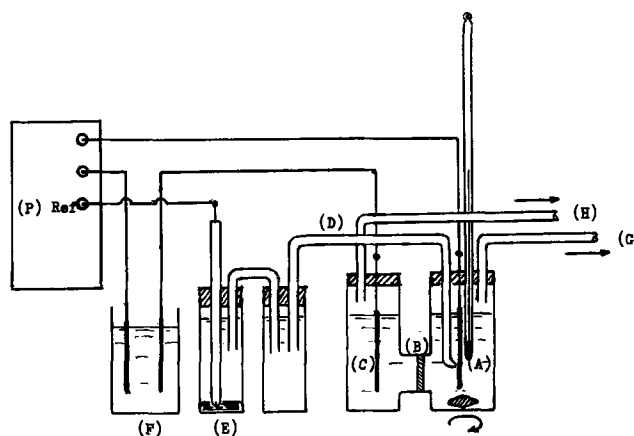


Fig. 1. Electrolysis cell: (A) anode, (B) diaphragm, (C) cathode, (D) salt bridge, (E) SCE, (F) copper coulometer, (G) to gas buret, (H) gas outlet through pressure regulator, (P) controlled potential d-c power supply.

\* Electrochemical Society Active Member.

<sup>1</sup> An anode consisting entirely of lead dioxide (3). This is manufactured by Sanwa Pure Chemicals Ltd.

<sup>2</sup> The formation of methanol is an example of Hofer-Moest reaction in acidic medium.

Table I. Conditions of gas chromatograph analysis of products

	CO <sub>2</sub>	C <sub>2</sub> H <sub>6</sub>	CH <sub>4</sub>	O <sub>2</sub>	CO	CH <sub>3</sub> COOCH <sub>3</sub>	HCOOCH <sub>3</sub>
Stationary phase, 2m	SG	SG	SG	MS	MS	PEG	PEG
Carrier gas*	H <sub>2</sub>	H <sub>2</sub>	H <sub>2</sub>	Ar	Ar	H <sub>2</sub>	H <sub>2</sub>
Temp. °C	60	60	60	20	20	120	120
Retention time, min	7.5	5.5	1.4	1.2	4.0	2.0	1.8

SG: Silica gel  
MS: Molecular Sieve 5 A  
PEG: Polyethyleneglycol 1500  
\* Flow rate: 40 cc/min

filled with methanol or glacial acetic acid saturated with potassium acetate was connected with the cell.

**Electrolyte.**—Mixtures of 1N potassium acetate and 1N glacial acetic acid in methanol or glacial acetic acid saturated with potassium acetate were used for the anolyte and the catholyte. The amount of water in the electrolyte was reduced to 0.1-0.2% except in those experiments to check the influence of water.

**Analysis of the products.**—The main method utilized for the determination of products (Table I) was a gas chromatographic technique previously described (1).

At the same time ordinary analytical procedures were used for the determination and identification of formaldehyde and methyl formate. Formaldehyde was determined as the dimedon derivative gravimetrically. The identification of methyl formate was carried out by hydrolyzing it to formic acid which was obtained as sodium formate, mp 255°C.

### Results and Discussion

**Current density-anode potential curve in methanol.**—In Fig. 2, current density-anode potential curves in methanol at various anode materials are plotted. As shown in Fig. 2, at platinum and gold anodes the curves showed a steep increase of current at around 2.0v (vs. SCE). On the other hand, at lead dioxide anodes a similar steep increase of current was observed at a potential of about 1.2v. At palladium and graphite, although the increase of current first started at 1.2v, the curves tended to approach those obtained at platinum or gold within the range of high current density. It seems that the obvious differences in current-potential curves suggest the particular anodic process in each case.

**Macroelectrolysis in methanol.**—It was confirmed that even at constant anode potential the change of

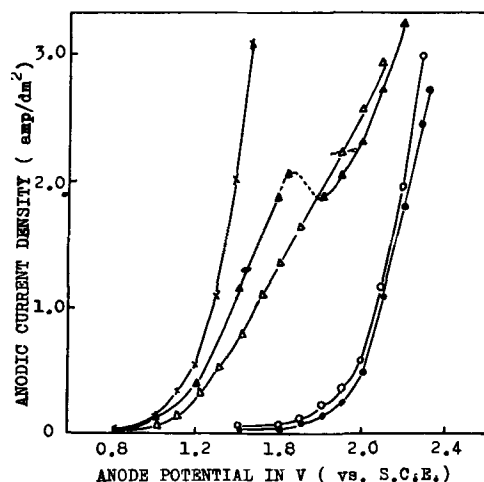


Fig. 2. Current density vs. anode potential curves in methanol at 20°C. Electrolyte, 1M CH<sub>3</sub>COOH + 1M CH<sub>3</sub>COOK; ● Pt, ○ Au, ▲ Pd, × PbO<sub>2</sub>, and △ graphite.

current density could scarcely be observed during the electrolysis. Therefore, the following experiments were carried out at constant current for the sake of convenience. The results are shown in Table II.

At a platinum electrode (Table II) almost quantitative formation of ethane and carbon dioxide was observed at higher current density (2.8 amp/dm<sup>2</sup>). The amount of methane produced increased with decreasing current density as would be the case for aqueous solutions.

The main process at gold was quite similar to that at platinum. The products were ethane and carbon dioxide although the current efficiency was a little less. That is, even at gold, in the absence of OH<sup>-</sup> ion, the probable process is the discharge of acetate ion at potentials above 2.0v where the normal Kolbe process can occur.

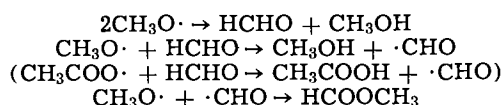
However, in both cases, it should be pointed out that some formaldehyde was found in the product, especially at gold anodes at the lower potentials. Assuming the formation of CH<sub>3</sub>O· at the anode,<sup>3</sup> the formation of formaldehyde may be represented as follows



This side reaction was clearly observed at palladium and at lead dioxide at lower potentials than those at a platinum or gold anode.

At palladium, the products corresponded to the result of a current density-anode potential curve. At the lower potentials (as low as 1.2-1.6v) and the lower current densities, formaldehyde was the main product; whereas, at about 2.0v and at the higher current density (2.8 amp/dm<sup>2</sup>), ethane and carbon dioxide were obtained with 45% current efficiency.

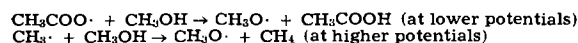
At lead dioxide, it is interesting to note that no carbon dioxide, ethane, or methane were obtained. The main product was found to be methyl formate accompanied by formaldehyde after twice the amount of current in other runs was passed. The process might be as follows, assuming the same CH<sub>3</sub>O· formation as described above



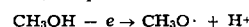
This reaction is characteristic of the lead dioxide anode. The difference in behavior between platinum or gold and lead dioxide led us to suppose that the acetoxy radical was adsorbed by the surface of platinum<sup>4</sup> or gold, but that it was not adsorbed so tightly by the surface of lead dioxide.

To confirm the methoxy radical formation directly, another electrolysis was conducted by adding furane to the electrolyte and using a current density of 2.8

<sup>3</sup>A possible route for the formation of CH<sub>3</sub>O· is the reaction of anodically formed acetoxy radical (and methyl radical) with solvent.



Another possible route for CH<sub>3</sub>O· is as follows



The difficulty in interpreting the latter route is the fact that at platinum or gold there is no increase of current at 1.2v, a potential at which the formation of CH<sub>3</sub>O· may occur at the other three anodes. This led us to support the former route.

Although breaking the O-H bond in methanol by a radical is less favorable than breaking the C-H bond, it becomes conceivable if we consider the fact that, in anodic processes, methanol is attracted to the anode surface (5) and polarized so as to facilitate the fission of its O-H bond.

In contrast, the theory of acetoxy radical stability has gained support from the work of other investigators both in radical reaction (6) and in anodic process of acetate at platinum (7). Additionally, it should be pointed out that the acetoxy radical is formed at a potential far lower than that of the Kolbe reaction at lead dioxide, palladium, and graphite.

<sup>4</sup>According to Conway et al. (8), the acetoxy radical is adsorbed on a platinum anode with its COO group facing the surface; this orientation facilitates the ethane formation on the anode surface. At lead dioxide the same adsorption orientation is difficult due to the nature of the surface which consists entirely of higher oxide; consequently, the acetoxy radical formed can undergo reaction with solvent.

Table II. Macroelectrolysis of HAc-KAc mixture in methanol at various anodes

Anode	Current density, amp/dm <sup>2</sup>	Amount of current, amp-hr	Current efficiency for decarboxylation, ** %	Products					
				CO <sub>2</sub> cc	C <sub>2</sub> H <sub>6</sub> cc	CH <sub>4</sub> cc	CH <sub>3</sub> COOCH <sub>3</sub> g	HCHO g	HCOOCH <sub>3</sub> g
Pt	2.8	2.02 (2.02) *	98	1402	819	16	—	0.022	—
	1.4	2.00 (1.92)	91	1263	747	31	—	0.052	—
	0.7	2.01 (1.94)	88	1200	668	132	—	0.100	—
Au	2.8	2.13 (2.13)	88	1336	777	17	—	0.142	—
	1.4	1.98 (1.90)	81	1268	661	14	—	0.170	—
	0.7	2.00 (1.74)	53	767	436	15	—	0.350	—
Pd	2.8	2.03 (1.92)	45	642	380	—	—	0.565	—
	2.0	2.04 (1.97)	5	75	45	—	—	1.007	—
	0.7	2.01 (1.67)	0	—	—	—	—	0.935	—
Graphite	2.8	2.03 (2.04)	64	448	45	34	1.6	0.410	—
	1.4	2.02 (1.78)	54	373	12	26	1.4	0.400	—
	0.7	2.15 (1.98)	30	198	5	17	0.8	0.750	—
PbO <sub>2</sub>	2.8	4.35 (4.74)	0	—	—	—	—	0.847	1.8
	1.4	3.91 (3.81)	0	—	—	—	—	0.760	1.4
	0.7	3.82 (3.51)	0	—	—	—	—	0.585	1.4

\* Figures in parentheses were calculated from the products obtained.

\*\* Theoretical value, 1 Fr (Pt, Au, Pd); 2 Frs (graphite) for methyl acetate, 1 Fr (graphite) for hydrocarbons.

Table III. Possible anodic process at various anodes in methanol

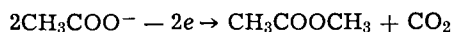
	Pt	Au	Pd	C	PbO <sub>2</sub>
1. CH <sub>3</sub> COO <sup>-</sup> - e → CH <sub>3</sub> COO·	+	+	+	+	+
2. CH <sub>3</sub> COO· → CH <sub>3</sub> · + CO <sub>2</sub>					
3. CH <sub>3</sub> · + CH <sub>3</sub> · → C <sub>2</sub> H <sub>6</sub>	+	+	+	(+)	-
4. 2CH <sub>3</sub> COO· → CH <sub>3</sub> COOCH <sub>3</sub> + CO <sub>2</sub>	-	-	-	+	-
5. CH <sub>3</sub> · + CH <sub>3</sub> COO· → CH <sub>3</sub> COOCH <sub>3</sub>					
6. CH <sub>3</sub> COO· + CH <sub>3</sub> OH → CH <sub>3</sub> COOH + CH <sub>3</sub> O·					
or					
CH <sub>3</sub> OH - e → CH <sub>3</sub> O· + H <sup>+</sup>	(+)	(+)	+	+	+
7. 2CH <sub>3</sub> O· → HCHO + CH <sub>3</sub> OH					
8. CH <sub>3</sub> O· + HCHO → CH <sub>3</sub> OH + ·CHO					
CH <sub>3</sub> COO· + HCHO → CH <sub>3</sub> COOH + ·CHO	-	-	-	-	+
9. CH <sub>3</sub> O· + ·CHO → HCOOCH <sub>3</sub>					

\* occurred; (+) occurred a little; - did not occur.

\* { + (at the higher potential and the higher current density).  
- (at the lower potential and the lower current density).

amp/dm<sup>2</sup>. After 4 amp-hr of current were passed, a fraction of bp 150°-157°C was isolated from the anolyte by fractional distillation. This fraction was identified by gas chromatography as 2,5-dimethoxydihydrofuran.

At graphite, the main product was methyl acetate accompanied by formaldehyde and a small amount of hydrocarbons. The formation of methyl acetate may be represented as follows, regardless of the reaction path which will be described later.



No evidence for the formation of ethyleneglycol, succinic acid, or glyoxal could be obtained. This indicated no formation of ·CH<sub>2</sub>OH or ·CH<sub>2</sub>COOH radicals.

The anodic process of acetate in methanol at various anode materials are summarized in Table III.

Since methanol complicates the processes some further experiments were carried out in glacial acetic acid.

*Current density-anode potential curves in glacial acetic acid.*—In Fig. 3, current density-anode potential curves in glacial acetic acid at various anode materials are plotted.

As shown in Fig. 3, with the exception of the case at graphite, the curves showed a steep increase of current at around 2.1v (vs. SCE) at any kind of anode, even at lead dioxide. From these curves similar electrode processes were expected at platinum, gold, palladium, and lead dioxide anodes at potentials more positive than 2.1v.

*Macroelectrolysis in glacial acetic acid.*—According to the information from current density-anode poten-

tial curves the controlled potential electrolyses were carried out at a certain potential with various anode materials. Results are condensed in Table IV.

As shown in Table IV and expected from Fig. 3, very high current efficiencies, more than 90%, were evident at platinum, gold, palladium, and even at lead dioxide anodes for the formation of ethane and carbon dioxide. In these cases there was no distinctive differ-

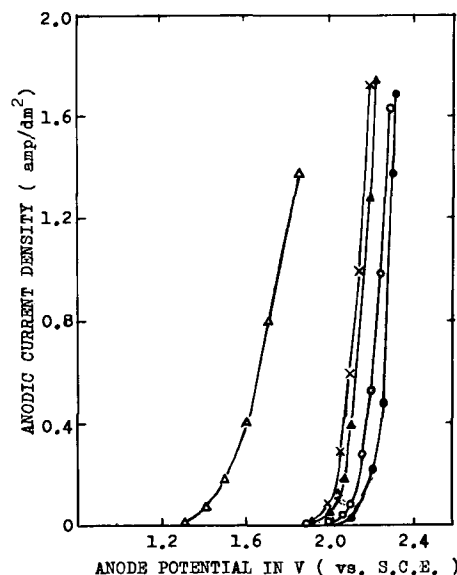


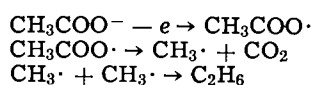
Fig. 3. Current density vs. anode potential curves in glacial acetic acid at 20°C. Electrolyte, 1M CH<sub>3</sub>COOK; ● Pt, ○ Au, ▲ Pd, × PbO<sub>2</sub>, and △ graphite.

Table IV. Macroelectrolysis of potassium acetate in glacial acetic acid at various anodes

Anode	Anode potential (vs. SCE) v	Current density, amp/dm <sup>2</sup>	Amount of current, amp-hr	Current* efficiency, %	Products			
					CO <sub>2</sub> cc	C <sub>2</sub> H <sub>6</sub> cc	CH <sub>4</sub> cc	CH <sub>3</sub> COOCH <sub>3</sub> g
Pt	2.30	1.3	2.01	98	1628	780	49	—
	2.20	0.5	1.99	95	1578	745	38	—
Au	2.30	1.2	1.99	95	1580	748	26	—
	2.20	0.4	2.02	92	1552	772	28	—
Pd	2.20	1.4	2.01	95	1596	735	44	—
	2.10	0.4	2.00	91	1520	710	37	—
PbO <sub>2</sub>	2.20	1.3	2.00	94	1570	763	32	—
	2.10	0.5	1.98	91	1505	720	27	—
Graphite	1.80	0.8	2.02	95	720	15	25	2.7
	1.60	0.4	1.98	93	670	—	—	2.5

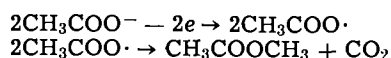
\* For total products.

ence in the product and its proportion. From the stoichiometric relation between the products in each case, available reaction was supposed to be the normal Kolbe process and simply represented as follows.

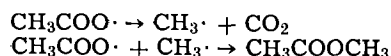


That is, even at the surface of lead dioxide, if the radical formed is not removed from the surface, the potential rises above 2.0v and Kolbe products can be obtained just as at other metallic anodes.

In the case at a graphite anode, the amount of hydrocarbon was quite small, and the main product was methyl acetate just as with aqueous or methanolic medium. The current efficiency for methyl acetate reached 95%. Since the formation of ethane or methane was very much lower, it seemed to be better to assume the formation of methyl acetate mainly as the result of decarboxylation from two acetoxy radicals.<sup>5</sup>



At the higher potentials, the following reaction may also be possible.



*Influence of water in glacial acetic acid.*—Further experiments were carried out in glacial acetic acid containing a small amount of water at platinum, gold, and lead dioxide anodes. Current density-anode potential curves for each anode in acetic acid solutions containing 2 and 5% water are shown in Fig. 4.

At platinum and gold a steep current increase was observed at around 2.0v, and no remarkable change could be found from that obtained in glacial acetic acid, except for a little shift of potential to the negative side at gold. On the other hand at lead dioxide, a remarkable difference was seen between the curves in Fig. 3 and those in Fig. 4 on the potentials at which the current flows. Controlled potential electrolyses were then carried out, the results are shown in Table V.

At platinum and gold anodes a high current efficiency was noted except for a small amount of methanol formation at gold even when 5% of water was added in the electrolyte. On the other hand, at lead dioxide the current efficiency for normal Kolbe process was reduced to 6% without agitation and to 0% with agitation even with addition of 2% water. In the last case, the formation of methanol was observed the same as in aqueous solution. It is indeed an anomalous phe-

<sup>5</sup> An alternative route involves the formation of carbonium ion intermediates which can react with acetate ion or acetic acid to give methyl acetate (9). Since normal Kolbe reaction occurs at the other four anodes in glacial acetic acid, this route should be taken into consideration in the case of graphite not only in glacial acetic acid, but also in aqueous or methanolic medium. However, it seems to us that it is indeed platinum rather than graphite at which the formation of CH<sub>3</sub><sup>+</sup> would be possible at the higher potentials.

nomenon and should be clarified by further experiments.<sup>6</sup>

Anyway, the behavior of lead dioxide anode is very interesting as well as that of graphite and further research on these problems will become a key to clarify the Kolbe process.

### Summary and Conclusion

1. In methanol, Kolbe products, ethane (and methane), and carbon dioxide, could be obtained at platinum, gold, and palladium anodes at a potential higher than 2.0v (vs. SCE). A high current efficiency was noted at platinum and even at gold anodes. The formation of formaldehyde due to side reactions was observed in all cases, especially at palladium at lower potentials. At lead dioxide, the whole reaction occurred within the range of 1.2-1.4v, resulting in the formation of methyl formate accompanied by formaldehyde.

2. In glacial acetic acid, Kolbe products formed at platinum, gold, palladium, and lead dioxide anodes at almost the same potentials (above 2.1v) with more than 90% current efficiency. However, when acetic acid containing 2-5% water was used as solvent, a big

<sup>6</sup> The reason is assumed to be that at platinum and even at gold the acetoxy radical, if it is once formed, is adsorbed on the anode surface and undergoes Kolbe reaction; while at lead dioxide, the radical, which is not so tightly adsorbed on the anode as compared with the above cases, can react with water attracted to the lead dioxide surface, resulting in the formation of carbon dioxide and methanol. The possibility of simultaneous electron release from acetate and water cannot be eliminated as a possible mechanism leading to the same products.

Assuming the carbonium ion instead of the radical seems to be more likely to interpret its reaction with water. However, the difficulty in the assumption lies on the fact that, in glacial acetic acid, there is no formation of methyl acetate at lead dioxide.

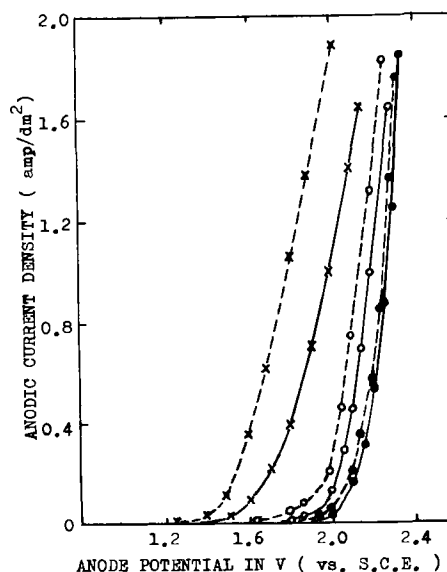


Fig. 4. Current density vs. anode potential curves in acetic acid containing 2 and 5% water. Electrolyte, 1M CH<sub>3</sub>COOK, ——— 2% water, - - - 5% water, ● Pt, ○ Au, and × PbO<sub>2</sub>.

Table V. Macroelectrolysis of potassium acetate in acetic acid containing small amount of water

Anode	Anode potential (vs. SCE)	Current density, amp/dm <sup>2</sup>	Amount of current, amp-hr	Current* efficiency, %	Amount of water, %	Agitation	Products					
							CO <sub>2</sub> , cc	C <sub>2</sub> H <sub>6</sub> , cc	CH <sub>4</sub> , cc	O <sub>2</sub> , cc	CH <sub>3</sub> OH, g	HCHO, g
Pt	2.30	1.2	2.00	96	2	—	1598	745	32	—	—	—
	2.30	1.3	2.00	95	2	+	1559	760	56	—	—	—
	2.30	1.3	2.02	92	5	—	1550	738	40	trace	—	—
	2.30	1.2	2.01	89	5	+	1452	750	38	—	—	—
Au	2.30	1.2	2.01	93	2	—	1562	715	27	25	trace	trace
	2.30	1.2	2.02	91	2	+	1527	642	19	40	trace	—
	2.20	1.3	1.98	88	5	—	1456	596	23	48	0.04	trace
	2.20	1.3	2.00	84	5	+	1415	570	18	45	0.06	trace
PbO <sub>2</sub>	2.10	1.4	2.00	6	2	—	508	45	20	—	0.70	0.07
	2.10	1.5	1.99	0	2	+	490	—	trace	17	0.65	0.08
	2.00	1.7	2.01	0	5	—	496	—	—	27	0.75	0.09

\* For ethane (and methane) formation.

difference was noticed between lead dioxide and the metallic anodes.

3. At graphite, the main product was methyl acetate in both solvents. The potential for this process was somewhat lower than that of the normal Kolbe process and laid in the range of 1.4–2.0v.

By combining the results obtained herein with those in aqueous solution, the following conclusions are obtained. In water, the formation of Kolbe products occurs only at platinum; in methanol, however, platinum, gold, and even palladium may be used. In glacial acetic acid any insoluble anode seems to serve, but in all cases and in all solvents Kolbe reaction only occurs at a potential higher than 2.0v. The behavior of a graphite anode is the only exception from the above as it is characterized by the formation of methyl acetate in all solvents. In addition, the formation of methanol at graphite and at lead dioxide in aqueous acidic medium is also significant.

#### Acknowledgment

This investigation was supported in part by a grant for fundamental scientific research from the Ministry of Education of Japan, for which the authors wish to express their deep appreciation.

Manuscript received Feb. 15, 1967; revised manuscript received Nov. 3, 1967. This paper was presented at the San Francisco Meeting of the Society, May 9–13, 1965 as Abstract 167. Part of the paper (Results in methanol) had been presented at the Annual Meeting of the Electrochemical Society of Japan, Fukuoka, April 25–26, 1964 and at the Fifth Seminar on Electro-

chemistry held at Central Electrochemical Research Institute, Karaikudi, India, Jan. 27–30, 1965. A summarized paper entitled "Anodic process of Acetate" including the results of this paper, was also presented at the 17th CITCE Meeting, Tokyo, Japan, Sept. 5–9, 1966.

Any discussion of this paper will appear in a Discussion Section to be published in the December 1968 JOURNAL.

#### REFERENCES

1. K. Sugino, T. Sekine, and N. Sato, *Electrochem. Technol.*, **1**, 112 (1963).
2. N. Sato, T. Sekine, and K. Sugino, *J. Electrochem. Soc. Japan (Denki Kagaku)*, **34**, 119 (1966); this paper was presented at the Fourth Seminar of Electrochemistry held at Central Electrochemical Research Institute, Karaikudi, India, Dec. 28–31, 1963.
3. T. Osuga and K. Sugino, *This Journal*, **104**, 448 (1957).
4. (a) J. Salauze, *Bull. soc. chim.*, **37**, 522 (1925); (b) Fr. Fichter and R. E. Meyer, *Helv. Chim. Acta*, **16**, 1408 (1933); (c) C. L. Wilson and W. T. Lippincott, *J. Am. Chem. Soc.*, **78**, 4209 (1956); (d) S. D. Ross, M. Finkelstein, and R. C. Petersen, *ibid.*, **86**, 4139 (1964).
5. For example, M. W. Breiter, *This Journal*, **110**, 449 (1963).
6. For example, J. J. Shine and J. R. Slagle, *J. Am. Chem. Soc.*, **81**, 6309 (1959).
7. Ref. (4) (d).
8. B. E. Conway and M. Dzieciuch, *Can. J. Chem.*, **41**, 38 (1963).
9. W. J. Koehl, Jr., *J. Am. Chem. Soc.*, **86**, 4686 (1964).

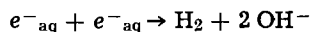
# The Reaction of Solvated Electrons at Metal Electrolyte Interfaces

T. Pyle and C. Roberts<sup>1</sup>

Department of Chemistry and Metallurgy, Lanchester College of Technology, Coventry, England

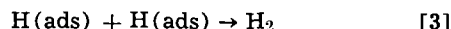
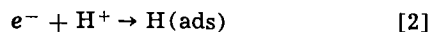
## ABSTRACT

The formation of solvated electrons at metal electrolyte interfaces is discussed. It is suggested that hydrogen molecules may be formed at an interface, without the prior formation of hydrogen atoms, by the reaction

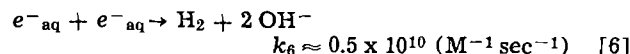
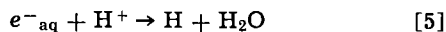
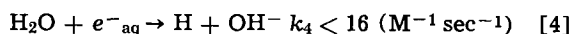


The evolution of hydrogen by this reaction, both electrolytically and spontaneously during the dissolution of a metal, is discussed. For metals which form hydroxides of low solubility, it is proposed that the hydroxyl ions produced by this reaction form a film across the metal surface and that it is the dissolution of this film which determines the characteristics of the hydrogen evolution process. Calculations of the rates of dissolution of iron in reducing acids made on the basis of this model show good agreement with experimentally observed rates. In addition the activation energies for the dissolution of the hydroxide film on iron and mercury, estimated from the dissociation constants of the hydroxides, are 11.4 and 19 kcal/mole, respectively. These values compare favorably with the observed activation energies for the dissolution of iron, 11.5 kcal/mole, and for hydrogen evolution at a mercury surface, 22 kcal/mole.

Conventionally the reaction by which metals evolve hydrogen from aqueous electrolytes is written in several steps which may vary depending on the pH of the electrolyte. For acids the steps most frequently referred to are given below.



For many metals it is reaction [2] that is thought to determine the over-all rate of hydrogen evolution. Indeed Bass (1) has suggested a criterion for the stability of metals in aqueous electrolytes based on the conservation of energy when an electron tunnels from the metal to a hydrogen ion adjacent to the metal. Recently however Walker (2) observed the formation of solvated electrons during the electrolysis of aqueous electrolytes with a silver cathode. The solvated electron is not stable in water and can react to form either hydrogen atoms or molecules by the reactions



While the latter reaction between two negative entities appears unusual, it is well documented and provides an interesting possibility for the formation of hydrogen molecules directly from electrons and water molecules without the prior formation of hydrogen atoms.

The object of this paper is to examine the possible contribution to hydrogen evolution that may be expected from [6] when hydrogen is evolved, either spontaneously or electrolytically, at a metal surface. A model is developed in which the hydroxyl ions that are formed by the reaction are considered to produce a film across the metal surface; it is the dissolution of this film by hydrogen ions that determines the rate of dissolution of the metal and provides the dependence on pH of the stability of metals, and the pH dependence of the current at a mercury electrode in acid/salt mixtures.

<sup>1</sup> Present address: Unilever Research Laboratory, The Fryth, Welwyn, Herts., England.

## Spontaneous Dissolution of Metals in Aqueous Electrolytes

*Formation of solvated electrons.*—The simplest way in which a metal can dissolve in an electrolyte is for the metal to dissociate into positively charged ions and electrons. The alkali metals are known to dissolve in liquid ammonia (3) in this way, the solvated electrons that are formed are stable, and no further reaction occurs over a period of several days. Walker (4) has suggested that the alkali metals could dissolve in water in a similar manner; the solvated electrons that are formed will dissociate to form hydrogen atoms and hydroxyl ions, reaction [4], or hydrogen molecules and hydroxyl ions, reaction [6]. Because the ratio of the rate constants  $k_6/k_4$  for the reaction is  $> 10^7$ , reaction [6] will be dominant if the concentration of  $e^-_{aq}$  close to the metal surface exceeds  $10^{-7}$  moles/l. Indeed the evolution of nitrogen, rather than hydrogen, when sodium is added to water in which  $N_2O$  is dissolved (5) indicates that it is reaction [6] by which hydrogen is evolved from water rather than reactions [1] to [3].

In order to decide whether or not a metal will dissociate into its ions and electrons when immersed in an electrolyte we shall use a modified form of the criterion proposed by Bass. On this model when the metal is dipped in an electrolyte containing none of the metal ions, ions dissolve from the metal leaving electrons behind and thus charge up the double layer at the interface between the metal and the electrolyte. The field of the double layer will continue to grow until it reaches a value which is sufficient either (a) to permit energy to be conserved in electron transitions to sites in the electrolyte or, (b) to saturate the orientational polarizability of the dielectric, the field strength necessary to accomplish this is  $E \approx 3kT/\mu$  approximately, where  $\mu$  is the dipole moment of the solvent molecule,  $k$  is Boltzmann's constant, and  $T$  the absolute temperature.

Bass showed that metals, which could form hydrogen atoms spontaneously, obeyed the relationship for the work function  $\phi$

$$\phi < (I - W) + 6aekT/\mu \quad [7]$$

where  $I$  is the ionization potential,  $W$  the solvation energy of the hydrogen ion,  $e$  is the charge on the electron, and  $2a$  is the diameter of a water molecule. Inserting values for the constants into [7] Bass showed that there is an upper limit to the work function



$\phi \approx 2.3$  ev above which the metal will apparently be stable in aqueous electrolytes. While this describes satisfactorily the behavior of the alkali metals in water it does not lead to a ready understanding of the pH dependence of the stability of metals such as magnesium and zinc in aqueous electrolytes. However it is possible that the metal could dissociate into metal ions and solvated electrons providing that energy was conserved in the transition of electrons from the metal to the solvent. Because the work done to remove an electron from a metal depends strongly on the distance to which it is removed, a metal will be considered to be unstable if the work done to remove an electron through the double layer to infinity is smaller than the energy gained in solvating the electron at an infinite distance from the metal. This corresponds to the metal dissociating into ions and electrons separated by an infinite distance and on this criterion a metal is unstable if

$$\phi < W_e + 3kTd/\mu \quad [8]$$

where  $d$  the thickness of the double layer is  $\sim(2r_s + r_m)$ ,  $2r_s$  is the diameter of a solvent molecule,  $r_m$  is the radius of a metal ion, and  $W_e$  is the solvation energy of the electron. In liquid ammonia at  $-70^\circ\text{C}$ , where  $d \sim 5\text{\AA}$ ,  $W_e \sim 1.7 \pm 0.4$  ev (3), and  $\mu \sim 1.48 \times 10^{-18}$  esu,  $\phi \leq 2.5 \pm 0.4$  ev, the inequality therefore predicts closely the known behavior of metals in liquid ammonia (3). In water, where  $d \sim 3.8\text{\AA}$ ,  $W_e \sim 1.75$  ev (6), and  $\mu \sim 1.84 \times 10^{-18}$  esu,  $\phi \leq 2.5$  ev which gives essentially the same division of metals into stable and unstable elements as [7] from Bass. However metals with work functions greater than that given by [8] can form solvated electrons close to the metal surface, although these electrons will be effectively locked in the solution unable to diffuse away from the interface into the bulk of the solution. Such metals will be stable and will not react with the solution unless the solvated electrons can be removed continuously. In ammonia, where the decomposition of the solvated electron does not readily occur, further reaction of metals with  $\phi > 2.5$  ev is unlikely to happen under normal conditions. However, in aqueous electrolytes the solvated electron is unstable and consequently the reaction of the metal with the electrolyte can continue. Thus hydrogen molecules may be formed at the interface, by reaction [6], even though it may be energetically unfavorable to form hydrogen atoms on the criterion proposed by Bass. The rate of hydrogen evolution,  $R$ , in moles  $\text{cm}^{-2} \text{sec}^{-1}$  from the reaction of solvated electrons will be given by

$$R = \left[ \sum_{x=0}^{x=\infty} c_x^2 k_6 dx \right] \cdot 10^{-3} \quad [9]$$

where  $c_x$  is the concentration of solvated electrons,  $e_{aq}$ , in moles/l at a distance  $x$  cm from the surface of the metal,  $dx$  is the increment over which  $c_x$  is constant, approximately the diameter of a water molecule, and  $k_6$  is the rate constant for reaction [6]  $\sim 0.5 \times 10^{10}$  ( $\text{M}^{-1} \text{sec}^{-1}$ ) (7). To determine the rate of hydrogen evolution, from the reaction of solvated electrons during dissolution, it is necessary therefore to know the distribution of electrons in the interface.

*Distribution of solvated electrons in the metal-electrolyte interface.*—To become solvated at the interface the electron must be separated from the metal sufficiently to permit it to interact with the water molecules lying adjacent to the surface. We have previously suggested, in a discussion of the activation energy for the solvation of an electron at a metal surface (8), that this position is approximately the radius of a water molecule distant from the surface and is electrically indistinguishable from the metal surface. The concentration of electrons at this point can be obtained therefore by equating the chemical potentials of the electrons in the metal and the solution and is given by

$$c_a = c \exp (\mu_m - \mu_s^0)/kT \quad [10]$$

where  $c_a$  is the concentration of solvated electrons at the inner Helmholtz plane,  $c$  is the concentration of sites,  $\mu_m$  the chemical potential of the electrons in the metal,  $\mu_s^0$  is the standard chemical potential of the electrons at sites in the solution,  $k$  is Boltzmann's constant, and  $T$  the absolute temperature.  $\mu_m - \mu_s^0$  may be calculated as the work done to take a mole of electrons from the metal and solvate them in the solution. Loeb (9) has remarked that close to the metal an electron can be considered to move against a constant field  $e/4x^2_0$  where  $x_0 = e^2/2\phi$ ; it is only at distances larger than  $x_0$  that the electron moves against a mirror image force. For metals such as zinc, magnesium, and iron  $x_0 > a$  the radius of a water molecule and the work done in removing an electron from the metal to a distance  $a$  is  $ae^2/4x^2_0$  ergs. The electron is solvated at this point and the solvation energy regained. Because the dielectric constant of the electrolyte in the double layer is saturated, the solvation energy will be reduced by an amount  $\Delta W$  compared to that in the bulk solution (10).  $\Delta W$  may be calculated by summing the change in the energy stored in a series of concentric shells, of radius  $r$  and thickness  $dr$ , when the dielectric constant is changed from  $\epsilon_1 = 80$  to  $\epsilon_2 = 3$ . The effect will only occur at points in the double layer where the field due to the double layer is greater than that due to the electron, that is for a radius  $r$ , from the electron, greater than  $b$  where  $b$  is given by  $3kT/\mu = e/\epsilon_2 b^2$ . The change in energy stored in a shell of radius  $r$ , thickness  $dr$ , and width  $d$  is  $e^2 d/4r^3 (1/\epsilon_1 - 1/\epsilon_2) dr$ . The total change in energy,  $\Delta W$ , is obtained by summing between  $r = b$  and  $r = \infty$  and is given by

$$\Delta W = \frac{e^2 d}{8b^2} (1/\epsilon_1 - 1/\epsilon_2) \approx -0.11 \text{ ev} \quad [11]$$

The concentration of solvated electrons at the inner Helmholtz plane is given by

$$c_a = c \exp [-ae^2/4x_0^2 - (W_e - \Delta W)]/kT \quad [12]$$

Values of  $c_a/c$  are given in Table I for iron, magnesium, and zinc.

The work required to remove an electron from the surface of magnesium is so small that all the sites adjacent to the surface are occupied. However, because the energy to remove an electron increases rapidly with the distance to which it is taken, the concentration falls by a factor of  $10^{12}$  in the second layer of water molecules for magnesium and  $10^{20}$  for iron and zinc. The very low concentration of solvated electrons, formed in the second layer of water molecules, is in agreement with the criteria we suggested earlier for the stability of metals and indicates that only those electrons formed in the electrolyte directly adjacent to the metal surface can make a significant contribution to hydrogen evolution through reaction [6]. Equation [9] therefore can be written as

$$R = 2ac_a^2 k_6 10^{-3} \quad [13]$$

*Formation and removal of hydroxyl ions at the interface.*—When the solvated electrons react to form hydrogen, the hydroxyl ions that are produced will reduce the number of sites available for the formation of solvated electrons. If the metal forms a soluble hydroxide, the ions will be able to diffuse into the bulk of the solution. However if the metal hydroxide has a limited solubility, the hydroxyl ions will form a film over the metal surface displacing water molecules and reducing the rate of hydrogen evolution. Dissolution

Table I. Values of  $c_a/c$

Metal	$x_0$ (Å)	$\phi$ (ev)	$c_a/c$
Fe	1.4	4.4	$6.15 \times 10^{-6}$
Zn	1.67	4.3	$1.62 \times 10^{-4}$
Mg	2.00	3.6	1

of this film can only occur by the reaction of the hydroxyl ions with hydrogen ions. If the activation energy for the combination of a hydrogen ion with a hydroxyl ion in the film is  $\Delta H$  and the concentration of hydrogen ions in gram ions/liter is  $[H^+]$ , the number of collisions on unit area in unit time which result in the combination of a hydrogen ion and a hydroxyl ion is given by  $N_H$  ( $\text{sec}^{-1} \text{cm}^{-2}$ )

$$N_H = N_{Av}[H^+](kT/2\pi m)^{1/2} 10^{-3} \exp - \Delta H/kT \quad [14]$$

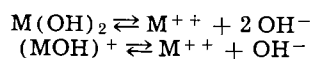
where  $N_{Av}$  is Avogadro's number,  $m$  is the mass of the hydroxonium ion,  $k$  is Boltzmann's constant, and  $T$  is the absolute temperature. If the concentration of water molecules in the surface film is  $c_2$  moles/l, the fraction of the surface covered by the hydroxide film is  $(1 - 0.018c_2)$  and the rate of dissolution of the film,  $R_f$ , in moles  $\text{sec}^{-1} \text{cm}^{-2}$  is

$$R_f = (1 - 0.018c_2)[H^+](kT/2\pi m)^{1/2} 10^{-3} \exp - \Delta H/kT \quad [15]$$

For most reactions, between ions in solution, the rate is controlled by the activation energy required to unsolvate the reacting species. This is not so for the proton, and it will be able to combine with the hydroxyl ion if it is able to provide the energy to cause the dissociation



For magnesium, iron, and zinc we are concerned with the  $II^+$  oxidation state, consequently  $n = 2$ . While the enthalpy of this dissociation is not available, an estimate of the free energy for the dissociation can be obtained from the difference in the free energies of the reactions



the free energies of these reactions can be estimated using the relationship  $\Delta G^\circ = -RT \ln K$ . Because of the spread of the values quoted in Bjerrum, Schwarzenbach, and Sillen (11) an average for both  $K_{s0}$  and  $K_1$  has been taken where

$$\begin{aligned} K_{s0} &= [M^{++}][OH^-]^2 \\ K_1 &= [MOH^+]/[M^{++}][OH^-] \end{aligned}$$

Values for the free energy of dissociation  $\Delta G^\circ$  are given below for magnesium, iron, and zinc in kcal/mole.

The combination of the hydroxyl ions with the hydrogen ions will occur randomly across the surface of the metal, leaving water molecules as defects in the film. Because hydroxides are insoluble, the defects will not remain randomly distributed in the film, but will segregate so that some areas of the metal surface will be covered by the hydroxide while the remaining areas are covered by water molecules. Thus a steady state will be reached between the formation and dissolution of the film. Hydroxyl ions will be formed by the reaction of solvated electrons in the areas covered by the water molecules and will diffuse through the water molecules by proton transfer until they reach the water-hydroxide phase boundary, while water molecules formed in the hydroxide will diffuse in a similar manner, through the hydroxide, parallel to the surface until they also cross the hydroxide-water boundary.

If, in the areas covered by the water, the molecules are considered to be spheres in contact, sites for the solvated electrons will exist at the tricuspoid formed

Table II. Values for free energy of dissociation

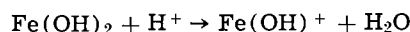
Metal	$\log_{10}K_{s0}$	$\log_{10}K_1$	$\Delta G^\circ_{s0}$	$\Delta G^\circ_{K_1}$	$\Delta G^\circ$
Mg	-10.68	2.335	14.61	-3.19	11.4
Fe	-14.15	5.819	19.36	-7.96	11.4
Zn	-16.20	4.757	22.16	-6.51	15.6

Table III. Rates of dissolution of pure metals in reducing acids ( $\text{amp/cm}^2$ ). Calculated from [13] and [15]

Metal	$[H^+]$ (g ions/l)			
	10	1	$10^{-1}$	$10^{-2}$
Mg	$6.3 \times 10^{-2}$	$6.3 \times 10^{-3}$	$6.3 \times 10^{-4}$	$6.3 \times 10^{-5}$
Fe	$3.7 \times 10^{-1}$	$3.3 \times 10^{-1}$	$1.9 \times 10^{-1}$	$4.2 \times 10^{-2}$
Zn	$5.0 \times 10^{-5}$	$5.0 \times 10^{-6}$	$5.0 \times 10^{-7}$	$5.0 \times 10^{-8}$

by three molecules lying in contact with each other and the plane of the surface. The electron will also associate with other molecules lying in the next layer of water molecules, but the concentration of sites,  $c$ , in the layer immediately adjacent to the metal surface will be  $\sim c_2/3$ . Thus for a given pH the value of  $c_2$  can be obtained by equating  $R_f$  to  $2R$  and solving for  $c_2$ . The rate of dissolution can then be obtained from [15] or [13]. Examples of the rates of dissolution of the metals magnesium, iron and zinc are given in Table III for different values of the hydrogen ion concentration.

The predicted rates of dissolution given in Table III indicate the correct order of the reactivities of the metals with reducing acids as it is well known that zinc, in the pure state, dissolves less readily in hydrochloric acids than pure iron. In Fig. 1 experimental rates of the dissolution of pure iron in reducing acids, taken from Bond (12) and Podesta and Arvia (13), are compared to the calculated values over a range of pH. In the pH range 0-3 the agreement between the calculated and observed results is good. From their work Podesta and Arvia also obtained a value of  $11.5 \pm 0.5$  kcal/mole for the activation energy of dissolution of iron in HCl/NaCl mixtures. On the basis of the model that we suggest the removal of the hydroxide film by the reaction



determines the rate of the reaction at values of the  $pH > 1$ . The estimate of the free energy of activation for this reaction, from the dissociation constants of the hydroxide Table II, is 11.4 kcal/mole, a value which is, considering the simplicity of the model, remarkably close to that found by Podesta and Arvia.

It appears therefore that for  $pH > 0$  the model is able to account for the differing reactivities of metals such as sodium, magnesium, iron, and zinc and is able also to predict values of the absolute rates and activation energies for the dissolution of iron in hydrochloric acid that are in close agreement with the experimental results. Because the stability of metals which are capable of displacing hydrogen from aqueous electrolytes appears, on this model, to depend on the formation of an adherent hydroxide film across the metal surface, it is to be expected that any condition which prevents the formation of the film will

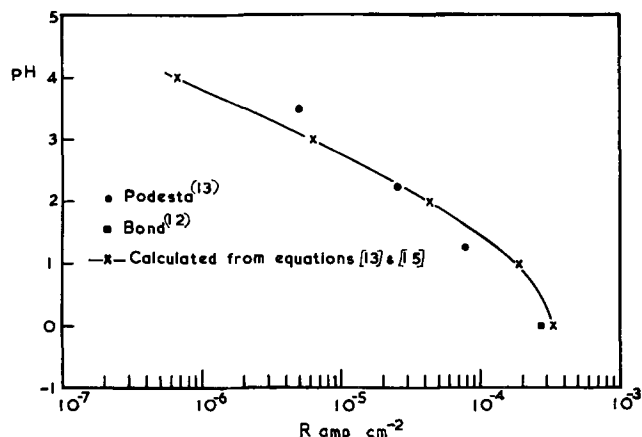
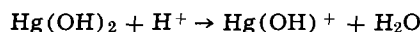


Fig. 1. Comparison of calculated and experimental rates of dissolution of iron (300°K).

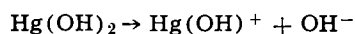
result in the metal dissolving at a rate independent of pH. It is of interest to note that commercially pure zinc is found to dissolve at similar rates in acids of  $\text{pH} \sim 3$  and alkalies of  $\text{pH} \sim 12$ .

### Electrolytic Evolution of Hydrogen from Aqueous Electrolytes

*Evolution of hydrogen at a mercury surface.*—While experiments of the type performed by Walker (2) have not yet been carried out on a mercury cathode, measurements of the volume of activation for the evolution of hydrogen at a mercury surface led Hills and Kinnibrugh (14) to suggest that the negative volume of activation that was observed must be due to the formation of a solvated electron as the slow step in hydrogen evolution on this metal. This is not the only process which would lead to a negative volume of activation, Hills and Payne (15) have shown that the inclusion of an ion in the double layer leads to an increase in volume. Conversely it is to be expected that for a process in which the removal of an ion from the double layer is rate determining a negative volume of activation would result. If hydrogen is evolved as we suggest, at low current densities the surface will be covered by hydroxide and the reaction



will be the rate-determining step. The combination of a hydroxyl ion and a hydrogen ion in this way will give rise to a negative volume of activation. From the dissociation constants for  $\text{Hg}(\text{OH})_2$  (11),  $\log_{10} K_{s0} = -25.5$  and  $\log_{10} K_1 = 11.5$ , a value for the free energy of dissociation for the reaction



of 19 kcal/mole is obtained. While this is only an approximation to the activation energy for the dissolution of the hydroxide, it is very close to the experimentally observed value of 22 kcal/mole for the activation energy for hydrogen evolution on mercury (16). The observed pH dependence of the current flowing at a mercury electrode (17) would also follow if the dissolution of the hydroxide was the rate-determining step as we suggest.

While the mechanism that we propose appears to be consistent with the behavior of a mercury electrode, it is known that atomic hydrogen is formed on certain electrodes during the cathodic discharge of hydrogen. In particular electrolytically formed hydrogen is found to dissolve in iron and palladium cathodes. It is usually assumed that this must indicate a step of type [2], the combination of an electron and a hydrogen ion, taking place. However it does not preclude the formation of a solvated electron as both reactions [4] and [5] could lead to the formation of atomic hydrogen which, on metals with a high heat of adsorption of hydrogen, will be stabilized despite the criterion proposed by Bass. Thus reactions [2], [4], [5], and [6] can be considered as competing processes, the one which is dominant at a particular time being dependent on the rate constants for the reactions, the concentration of solvated electrons and hydrogen ions in the interface and the heat of adsorption of hydrogen on the metal surface. Any change in any of these factors for a particular metal-electrolyte system would upset the balance between the reactions. In this context it is of interest to note that the adsorption of  $\text{AsH}_3$  and  $\text{H}_2\text{S}$  on an iron surface greatly increases the proportion of electrolytically formed hydrogen that

diffuses into the metal. Presumably the adsorption of these molecules on the surface reduces the mobility of the solvated electrons across the interface and thus reduces the rate of reaction [6].

### Conclusion

The fact that solvated electrons are formed at metal electrolyte interfaces permits the formation of hydrogen molecules, without the prior formation of atomic hydrogen, to be considered. Such a reaction could play a significant role in the hydrogen evolution process at surfaces which do not adsorb hydrogen strongly, and we have shown that a mechanism of hydrogen evolution based on the reaction of solvated electrons is consistent with the known behavior of a mercury cathode. In addition the mechanism permits quantitative predictions to be made concerning the reactivities of metals such as sodium, magnesium, iron, and zinc with liquid ammonia and aqueous electrolytes.

The formation of atomic hydrogen is not entirely prevented, however, even when solvated electrons are formed, but the balance between competing reactions will depend on the concentration of solvated electrons, hydrogen ions, and the heat of adsorption of hydrogen on the metal cathode.

### Acknowledgments

The authors wish to thank Dr. M. E. Foss and Dr. A. J. Richmond for the provision of facilities for this work.

Manuscript received July 24, 1967; revised manuscript received Oct. 26, 1967.

Any discussion of this paper will appear in a Discussion Section to be published in the December 1968 JOURNAL.

### REFERENCES

1. L. Bass, *Proc. Roy. Soc.*, **A277**, 129 (1964).
2. D. C. Walker, *Can. J. Chem.*, **45**, 807 (1967).
3. W. D. Jolly, "Progress in Inorganic Chemistry," Vol. 1, p. 235, Interscience Publishers Inc., New York (1959).
4. D. C. Walker, *Quart. Revs.*, **21**, 79 (1967).
5. E. A. Shaede and D. C. Walker, *Chem Soc. Special Publ. No. 22*, 277 (1967).
6. E. J. Hart, *Science*, **146**, 19 (1964).
7. N. Anbar and P. Nata, *Intern. J. Appl. Radiation*, **16**, 227 (1965).
8. T. Pyle and C. Roberts, *This Journal*, **114**, 651 (1967).
9. L. B. Loeb, "Static Electrification," Springer Verlag, Berlin (1958).
10. L. Bass and T. Pyle, *Nature*, **202**, 1003 (1964).
11. T. Bjerrum, G. Schwarzenbach, and L. G. Sillen, *Stability Constants, Part 11, Inorganic Ligands*, Chem. Soc. Special Publ. No 7 (1958).
12. A. P. Bond, Sc.D. Thesis, Department of Metallurgy, MIT. (1958).
13. J. J. Podesta and A. J. Arvia, *Electrochim. Acta*, **10**, 159 (1965).
14. G. J. Hills and D. R. Kinnibrugh, *This Journal*, **113**, 1111 (1966).
15. G. J. Hills and R. Payne, *Trans Faraday Soc.*, **61**, 326 (1965).
16. J. O'M Bockris, "Modern Aspects of Electrochemistry," Vol. 1, p. 180, Butterworths, London (1954).
17. A. N. Frumkin, "Advances in Electrochemistry and Electrochemical Engineering," Vol. 1, p. 65, Interscience Publishers Inc., New York (1961).

# Ring-Disk Amperometry: A Study of Indium Dissolution

B. Miller\* and R. E. Visco\*

Bell Telephone Laboratories, Incorporated, Murray Hill, New Jersey

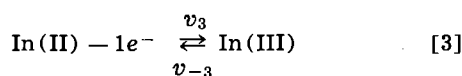
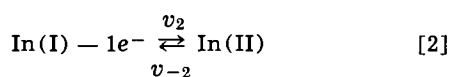
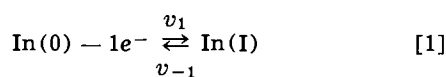
## ABSTRACT

By means of the rotating disk-ring electrode technique, the mechanism of the anodic dissolution of indium at a disk in 0.7M HClO<sub>4</sub> at current densities to above 10 ma/cm<sup>2</sup> has been determined to be a rapid one-electron reaction to an In(I) species sufficiently stable to be detected in theoretical amount at the ring. The Tafel behavior of the disk reaction and the anodic and cathodic ring collection efficiencies are in accord with the above; the ring current-potential curves further show that the slowness of the In(I)-In(III) reaction permits the thermodynamically less-favored state to be formed in quantity. Anodic dissolution of indium from amalgams is placed on a consistent basis by a quantitative treatment which takes into account the variable metal activity.

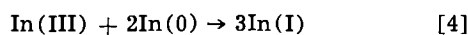
The mechanism of the electrochemical oxidation in acid solution of indium metal and its amalgams has been investigated by several groups of workers using a variety of experimental techniques. Recent studies on indium metal have been reported by Losev (1), Visco (2), Straumanis (3), and Kiss (4). The recent work on amalgams has ranged from studies on very concentrated amalgams by Kozin (5-7) to studies on more dilute amalgams by Losev (8-11), Markovac (12-14), Visco (2,15), and Straumanis (3). In most studies, current-voltage curves, usually under steady-state conditions, were recorded and analyzed. Coulometric studies with subsequent analysis and radiochemical measurements with tagged indium have also been reported (2, 3, 5-7, 9, 10).

A controversy has arisen concerning the existence and role of oxidation states of indium intermediate between zero and three. The evidence that In(I) does exist under most experimental conditions seems overwhelming (1, 2, 4-7, 15-17). The role it plays in the mechanism is yet to be unambiguously established. The species In(II) has not been characterized with certainty. Only one report of its detection exists (17); this, however, rests on an interpretation of the non-ideal behavior of an In(I) disproportionation reaction to give In(0) and In(III). In a similar set of experiments Biedermann and Wallin (16) found no evidence for In(II).

The role played by In(I) in the oxidation of the metal or the amalgam is, as yet, not clear. Losev (1) and Visco (2) have suggested that, as a consequence of successive one-electron unit steps, a finite concentration of In(I) can be built up during anodization both in a reaction layer about the electrode and in the bulk of the solution, reactions [1]-[3]

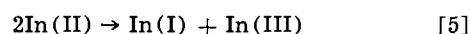


Straumanis (3), on the other hand, has taken the position that In(0) is quantitatively oxidized to In(III) and any In(I) seen is a consequence of reaction [4]



Alternate schemes have been proposed by Markovac (12-14), based on studies of dilute amalgams, where it is proposed that disproportionation of In(II) could

occur *via* reaction [5]



or that reaction [1] could be slow and rate-controlling.

Based on his studies of concentrated amalgams, Kozin (5-7) has concluded that for current densities up to 100 ma/cm<sup>2</sup> on a 20 a/o (atom per cent) amalgam, indium atoms are oxidized to In(I) via reaction [1], and that In(I) disproportionation is the dominant path to In(III).

To suppose that all of these mechanisms are operative in the redox chemistry of indium, even under the diverse experimental conditions studied, leads to untenable contradictions. We therefore chose to reinvestigate this system using a ring-disk electrode system. This multielectrode configuration operates under well-defined mass transport conditions, and it is also a configuration which allows the simultaneous detection and identification of intermediates (18-20). By monitoring intermediates at the ring for varying disk potentials and/or current densities and by comparing the observed behavior with calculations for the various models, some further understanding of the mechanism can be achieved. Investigations using two working electrodes have been used in previous studies on this system. Losev (1) used a rotating indium disk and a stationary solid indium electrode. Visco (2) used a stationary solid or amalgam electrode and a dropping mercury electrode. Although the results of these experiments are valid, some ambiguity remains because of the lack of controlled mass transport conditions. Kiss (4) has reported the use of an indium disk-indifferent metal ring in a solution containing In(III) in which the ring is employed for the potentiometric detection of disk dissolution products. A negative shift of potential at the indicating ring was qualitatively viewed as evidence for intermediate formation of a lower valent indium state, by comparison to the similar behavior of an iron disk-indifferent ring in ferric solution.

We describe experimental observations of the oxidation of solid and amalgam disk electrodes of indium and compare these results with the several reasonable models already proposed. The results of such a comparison clearly eliminate several schemes and impose certain restrictions on others. Based on these conclusions, a mechanism is proposed which is consistent with results on both solid and liquid electrodes. Further, when due consideration of the activity of indium is made, no difference is seen between the behavior of a solid and an amalgam indium electrode.

## Experimental

Indium electrodes were prepared by plating the metal onto a graphite or an amalgamated gold disk electrode from the indium solution to be studied (5-20 mM

\* Electrochemical Society Active Member.

In(III) in 0.7M HClO<sub>4</sub>) as required during the course of the experiment. For a pure gold surface the hydrogen overvoltage was too low to plate indium *in situ*, and the initial indium coat was deposited from a 20 mM indium perchlorate bath adjusted to approximately pH 2. Three types of disk-ring electrodes were employed: a graphite disk-graphite ring electrode fabricated from General Electric type EC-2 graphite rod, a mercury-coated gold disk-gold ring, and an all-gold split-ring-disk design (21). The gold surfaces were polished using Linde A (0.3 $\mu$ ), and the graphite surface, which contains microvoids due to its finite porosity, was polished on wet twill cloth. On the amalgamated surfaces the mercury layer was reduced in thickness as much as possible by polishing with twill cloth. The graphite and solid gold electrodes had nominally the same dimensions with disk, internal ring, and external ring diameters of 0.187, 0.206, and 0.253 in., respectively. For such geometry the theoretical collection efficiency,  $N_A$ , is 0.34 (22). Experimentally  $N_A$  equals  $(i_r n_d)/i_d n_r$  where  $i_r$  and  $i_d$  are ring current and disk current, respectively, and  $n_d$  and  $n_r$  are the number of electrons transferred in disk and ring reactions.

The range of collection efficiencies observed in our experiments was 0.29 to 0.34. The corresponding diameters for the gold electrode system which was later amalgamated were 0.168, 0.190, and 0.250 in. The calculated collection efficiency for this configuration was 0.40.

The electrode materials were bonded to stainless steel rod and tubing using either conductive-silver epoxy cement or conventional brazing and then machined to match the steel. Assembly of the rod and tube with inner and outer epoxy insulating rings was basically similar to that of Alberty and Bruckenstein (22) except that all contacts were designed for operation with silver-graphite brushes. In the split ring design the completed ring electrode was sawed through at about the 180° points with a 4-mil blade and electrical isolation completed with a 10-mil cut of one section further up the tube. A wire from the separated half-ring was carried up in an outside axial slot machined in the steel tube to a section of the tube which had been isolated from the lower end. Vacuum impregnation with epoxy backfilled the saw cut assuring electrical insulation. Three separate pairs of silver-graphite brushes were used for the split ring electrode.

The tubular electrode passed through a spindle (H. P. Smith Associates, Cheshire, Connecticut) with two nylon collets providing insulation from the metal assembly. The mounted electrode was belt driven from the side through a tachometer and servo-regulated motor system obtained from Electro Devices, Inc., Paterson, New Jersey. Speed regulation over the range employed was  $\pm 0.5\%$ . Exact speed was measured with a photoelectric pick-off and frequency counter (General Radio Company, West Concord, Massachusetts).

Solutions were prepared by anodization of 99.999% indium rod (American Smelting and Refining Company, South Plainfield, New Jersey) to reach the desired concentration. Other chemicals were of reagent grade.

The cylindrically jacketed cell was of approximately 100 ml working volume. Into a standard taper joint in the base of the cell was inserted a Teflon gland through which was mounted a vertical glass bridge ending in a capillary tip under the disk electrode. A fiber-tipped saturated calomel electrode (SCE) completed the reference circuit. Negative tests with silver ion for chloride ion were always obtained after experiments were completed. Potentials are reported vs. SCE. The SCE electrode was determined to be +0.253v vs. a hydrogen electrode in the same solution. A gold wire counter electrode was wrapped around the bridge just above the standard tapered joint, exiting through the gland. Nitrogen was passed

continuously into and over the solution. Experiments were carried out at 23°C.

Measurements were made by means of a locally fabricated three electrode operational amplifier galvanostat-potentiostat to which was added circuitry (21) employing differential amplifiers to operate the ring electrode(s) potentiostatically. Such a configuration required only a single reference electrode and a single counter electrode, as in other designs (23, 24). A controlled potential sweep capability for the ring electrode with an independent choice of disk operating mode (potentiostatic or galvanostatic) was available with the apparatus. The disk current could be linearly scanned while maintaining constant ring potential, for example, to measure collection efficiencies; to examine the current-potential behavior of disk products, the ring potential could be scanned at constant disk current.

According to the display desired, outputs were fed into a Tektronix 564 Storage Oscilloscope equipped with a 3A3 dual differential amplifier (Y<sub>1</sub> and Y<sub>2</sub> axis) and a 2A63 differential amplifier or 3B4 time base (X axis). To regain the higher accuracy inherent in the operational amplifier signals lost in the  $\pm 3\%$  scope display, a Varian F-80 X-Y recorder with a 11  $\times$  17 in. chart was employed. For Tafel measurements a Rubicon 2730 potentiometer served as precision offset to make the 20 mv/in scale of the F-80 accessible. A mercury relay interrupter was used to measure the resistive correction for Tafel data.

## Results

**Indium disk electrode.**—When an indium plate on a graphite or gold disk is made to dissolve anodically in 0.7M HClO<sub>4</sub> under either controlled potential or controlled current conditions, limiting anodic and cathodic currents are found over appropriate potential regions on the ring electrode. The Tafel plot, Fig. 1, of the disk reaction, as obtained from controlled linear current scan experiments, indicates a single 59 mv/decade process (experimental slopes for various runs were 57-62 mv/decade) over the current density range up to at least 50 ma/cm<sup>2</sup>. At this current density a  $\pm 3$  mv variation in disk potential results from a  $\pm 10\%$  uncertainty in the interrupter-determined resistance between reference capillary tip and the disk electrode. In the next current decade, the uncertainty in this resistance precludes a certain assessment of any incipient curvature in the Tafel plot.

A previous potentiometric measurement (2, 15) of the formal potential of the In(0)-In(I) couple in 0.7M HClO<sub>4</sub> with the In(I) concentration estimated polarographically gave a value of -0.388v vs. SCE. Assuming the process yielding the Tafel behavior of Fig. 1 is simply an equilibrium between In(0) and In(I) with subsequent diffusive loss of the In(I) and utilizing the same diffusion coefficient for In(I) as in the

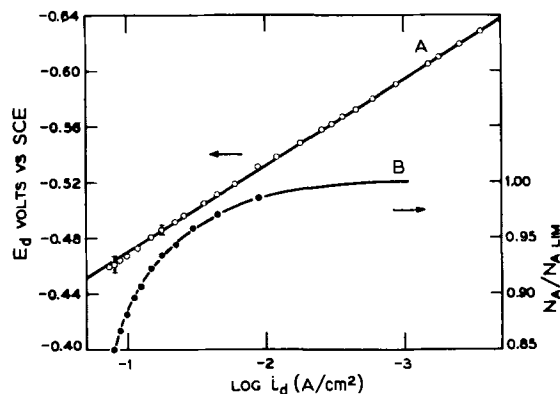


Fig. 1. Curve A, Tafel plot for indium disk at 3000 rpm in 20 mM In(III)-0.7M HClO<sub>4</sub>, corrected for 3.4 ohm resistance; curve B, anodic ring collection efficiency,  $N_A$ , plotted as the ratio to the limiting value, as  $i_d \rightarrow 0 N_A \text{ lim}$ .

polarography with interpolated handbook values for the kinematic viscosity of the solution, a value for the surface concentration of In(I) may be obtained for all currents by means of the Levich equation (25). The calculated value of the conversion factor at 3000 rpm is  $1.36 \text{ (ma/cm}^2\text{) / (millimole/liter)}$ . For the points corresponding to the Tafel line in Fig. 1, insertion in the Nernst equation gives a formal potential of  $-0.40\text{v vs. SCE}$ , in satisfactory agreement with the previous determination. For consistency in subsequent calculations, the value of the formal potential determined in this study with the disk electrode is used.

Substantiating the above assumption that the potential-determining reaction is  $\text{In(0)/In(I)}$  is the rotational speed dependence of the disk potential at constant disk current. On substitution of the surface concentration of In(I) given by the Levich equation, the Nernst equation for the  $\text{In(I)/In(0)}$  couple transforms to

$$E_d = E^{\circ'}_{1/0} + 0.059 \log \frac{i_d}{0.62 D^{2/3} \nu^{-1/6} F A} + 0.059 \log \omega^{-1/2} \quad [6]$$

where  $D$  is the diffusion coefficient of In(I),  $\nu$  the kinematic viscosity,  $F$  Faraday's constant,  $A$  the electrode area, and  $\omega$  the rotational speed. Thus for constant disk current, the disk potential should vary  $59/2 \text{ mv/decade}$  in  $\omega$ . The data for two disk current densities, 1.12 and  $5.62 \text{ ma/cm}^2$ , are shown in Fig. 2. The observed slopes are 27 and  $29 \text{ mv/decade}$   $\omega$ , respectively, in good agreement with the predicted 29.5.

The current-potential behavior of the potentiostatically scanned ring electrode for a fixed anodic current at the disk is shown in Fig. 3. The anodic process exhibits a particularly well-defined limiting-current plateau extending to electrolyte oxidation. The limiting cathodic current region is close to hydrogen evolution on indium and is accordingly less well-defined. The residual current line in Fig. 3 is for a carbon surface. Hydrogen evolution on indium is a slower process than on carbon, and therefore for indium the residual current under the reduction wave can be approximated by a linear extrapolation of the  $+0.3$  to  $-0.5\text{v}$  region on carbon. With proper compensation for residual currents, the anodic to cathodic limiting current ratio is 2 to 1. For the potential sweep in the anodic direction shown in Fig. 3, dissolution of indium from the ring appears to correspond reversibly to the ring reduction process and occurs at potentials consonant with the Tafel behavior seen in Fig. 1. Moreover, indium dissolution at the ring takes place several tenths of a volt lower than the anodic

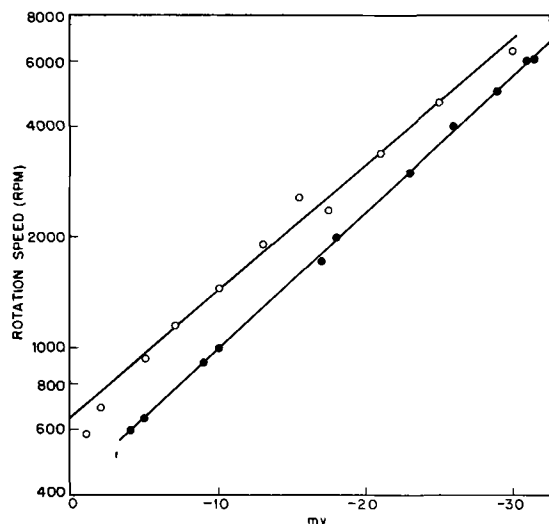


Fig. 2. Rotation speed vs. disk potential for ● ● ● 1.12  $\text{ma/cm}^2$  and ○ ○ ○ 5.6  $\text{ma/cm}^2$ . Zero volts are  $-570$  and  $-525 \text{ mv vs. SCE}$ , respectively.

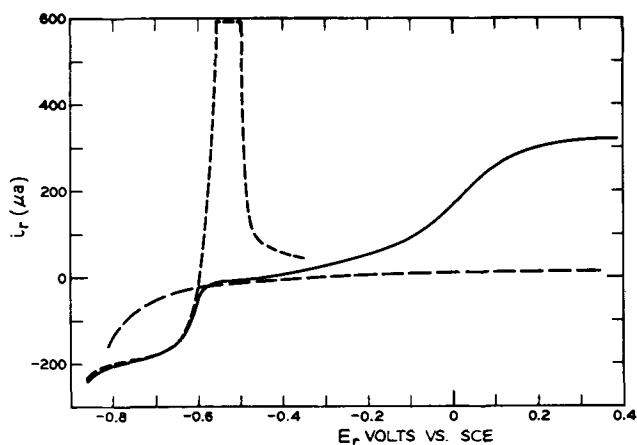


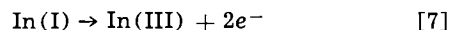
Fig. 3. Graphite ring scanned at  $20 \text{ mv/sec}$  from  $+0.4$  to  $-0.85\text{v}$  (solid line) then  $-0.85$  to  $-0.3\text{v}$  (short dashes);  $i_d$   $2.8 \text{ ma/cm}^2$ , rotation speed  $3000 \text{ rpm}$ . Residual current (scan at  $i_d=0$ ) is long-dashed line.

reaction of the disk dissolution product, which at this disk current density for either carbon or gold surfaces does not commence until  $0.0\text{v vs. SCE}$ . It is also to be noted that reduction at the disk of  $20 \text{ mM In(III)}$  in  $0.7\text{M HClO}_4$  does not yield detectable intermediates at the ring in any potential region.

The above behavior implies indium dissolution to be a one-electron reversible process giving In(I), which at the ring can be either reduced by one electron to In(0) or oxidized by two electrons to In(III). To establish this important point definitively, ring current-disk current relationships were examined in two independent ways.

First, the number of electrons involved in the ring reaction was determined by comparing the collection efficiency to that of the known ferro-ferricyanide system. Second, by using a split ring-disk to compare simultaneously the ratio of the anodic ring current to the cathodic ring current as a function of disk current density in a single run, a ratio of electrons was determined.

Results of the first method are collected in Fig. 4. For current densities in the range of curve 1 there is no detectable deviation from linearity of the anodic  $i_{r+}$  vs.  $i_d$ , and the slope obtained is 2.0 times that for the one-electron ferro-ferricyanide couple and the cathodic  $i_{r-}$  (curve 4). The over-all anodic reaction at the ring when indium is being anodized is therefore sensibly only



At current densities higher than about  $3 \text{ ma/cm}^2$  the collection efficiency begins to fall off gradually, but the

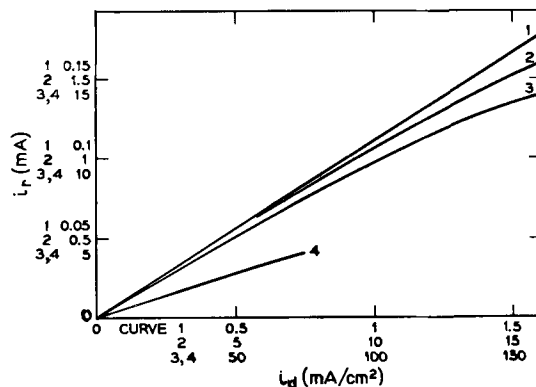


Fig. 4. Curves 1-3: ring current-disk current density relation for the conditions  $E_r + 0.8\text{v}$ ,  $20 \text{ mM In(III)}$ ,  $0.7\text{M HClO}_4$ ,  $3000 \text{ rpm}$ ; curve 4: corresponding results for  $E_r -0.6\text{v}$  and  $0.10\text{M Fe(CN)}_6^{4-}$  —  $1\text{M NaOH}$  (disk oxidation, ring reduction).

majority of the indium species detected by the ring appears to be In(I) even up to the 200 ma/cm<sup>2</sup> region. In neither ring-disk current nor Tafel behavior was there any noticeable dependence on current scan direction in the anodic region or on the current sweep rates employed. These curves showed no hysteresis and could be exactly retraced for decreasing current. The  $N_A$  data are also shown on Fig. 1 to relate  $N_A$  to  $E_d$  in the form of the reduced variable  $N_A/N_{A \text{ lim}}$ , where  $N_{A \text{ lim}}$  is the value of  $N_A$  when  $i_d \rightarrow 0$ . For the data plotted  $N_{A \text{ lim}}$  is 0.583/2.

Experimental results for the second method of determining the number of electrons transferred in both ring reactions required the simultaneous measurement of cathodic current on one half-ring,  $i_{r-}$ , and anodic current on the other half ring,  $i_{r+}$ . Oscilloscope traces are shown in Fig. 5. In the  $i_d$  range to 0.5 ma/cm<sup>2</sup> both  $i_{r+}$  and  $i_{r-}$  traces are close to linear and the ratio of the anodic to cathodic slopes as  $i_d \rightarrow 0$  is 2. Even more exact measurements with the higher accuracy of the X-Y recorder, in which  $i_{r+}$  was plotted against  $i_{r-}$ , show that the limiting slopes are in quantitative agreement with a two-electron oxidation and a one-electron reduction, respectively, for the product swept from the disk during dissolution. With half-ring "A" anodic and "B" cathodic, the conditions prevailing in Fig. 5, the slope was 2.30; with connections reversed the slope was 1.64, an average of 1.97. The averaging of the two values eliminates the small geometric differences due to construction which make the collection efficiency of A about 15% larger than that of B. The results of the second method have the considerable advantage of being independent of calibration against a known electrode reaction. The conclusion that the ring reactions involve either one or two electrons assumes only the absence of dimeric (or higher) species such as  $\text{In}_2^{+2}$  as products of the initial disk reaction or their failure to form in transit to the ring. Such an assumption is supported by the Tafel behavior and the essential lack of dependence of ring current on rotational speed for potentials in the linear region of Fig. 4 ( $N_A$  constant  $\pm 3\%$ , 750-6000 rpm at  $i_d = 2.8 \text{ ma/cm}^2$ , see Table I).

To examine the possible origins of a decrease in collection efficiency at high  $i_d$ , the aforementioned rotational speed dependence of  $i_{r+}$  was examined over the current range of interest. The data of Table I, showing the collection efficiencies normalized to the values at 2000 rpm, indicate only a small rotational speed dependence with somewhat lower values at the low speed end at  $>100 \text{ ma/cm}^2$ . The fraction of In(I) lost by a homogeneous reaction in the transit from the disk to the ring must therefore be small. The data

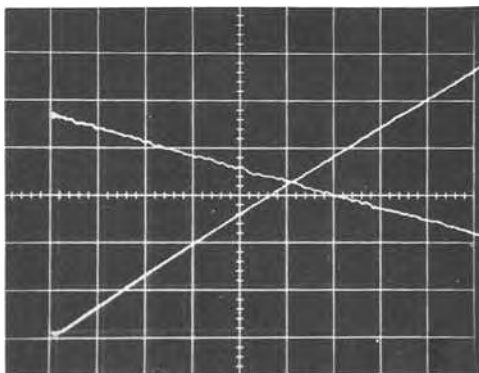


Fig. 5. Oscilloscope trace of split-ring currents vs. disk current for split-ring electrode where  $E_{r+} = 0.8\text{v}$ ,  $E_{r-} = -0.8\text{v}$ ; rotation speed 2000 rpm. Current sensitivity;  $i_{r-}$  and  $i_{r+}$  50  $\mu\text{a}$ /major division. Trace  $i_{r-}$  upper left to lower right (increasing cathodic current), trace  $i_{r+}$  lower left to upper right (increasing anodic current). Left-hand initial points at  $i_d = 0$ . Disk current may be converted to current density by multiplication by  $5.6 \text{ cm}^{-2}$ .

Table I. Collection efficiencies

Rotation speed, rpm	Anodic disk current density, ma/cm <sup>2</sup>		
	2.8	56	112
500	0.94		
750	0.97	0.94	0.85
1000	0.98		0.92
1500		1.02	
2000	1.00	1.00	1.00
3000		1.03	1.03
4000	0.99	1.00	1.00
5000			1.00
6000	0.98	1.01	0.98

Tabulated values are normalized to the collection efficiency at 2000 rpm for a graphite ring in 20 mM In(III) - 0.7M HClO<sub>4</sub>.

quoted in Fig. 1, 3, and 4, however, are at rotational speeds of 3000 rpm for which minimal homogeneous effects appear to occur. The appreciable drop-off in  $N_A$  occurs in the current density region where the surface concentration of In(I) approaches 0.1M as calculated from the Levich equation (25). The deviation from collection efficiency constancy for the  $\text{Fe}(\text{CN})_6^{-4}$  results is less than 0.5% at 56 ma/cm<sup>2</sup> for 3000 rpm and less than 1% at 80 ma/cm<sup>2</sup> for 5000 rpm.

Another approach to assessing changes in the disk reaction or possible homogeneous reactions at higher currents is to compare the  $i_{r+}$  and  $i_{r-}$  values in this region by the split-ring technique or by measuring the quantities on successive scans at the same ring. The latter tends to cancel changes in transport factors such as eccentricity. A set of successive scans for a single ring is given in Fig. 6. In contrast to the roll-off in  $i_{r+}$ ,  $i_{r-}$  tends to increase; their sum, accounting for three electrons, remains constant. The simplest explanation is that at high anodic currents, disk oxidation to In(II) becomes important. Such a process would account for the increase in  $i_{r-}$  and a compensating decrease in  $i_{r+}$ . Calculated on this basis, the data in Fig. 6 represent a conversion of only about 30% of In(I) to In(II) at the disk even at the highest current densities studied. The corresponding change in the slope of the Tafel plot would therefore be small and within the probable error indicated by the vertical bar drawn on the  $iR$ -free Tafel line near the highest current density in Fig. 1. However, at such high surface concentrations of In(I), the assumption of the absence of migration in the transport from disk to ring may fail. Thus,  $i_{r-}$  should be enhanced by electrical migration of In(I) and  $i_{r+}$  decreased, as is found. In addition, the surface concentrations are proportional to (rotation speed)<sup>-1/2</sup> at a given current, so these postulated field effects are in agreement with the direction of the rotational speed dependence trend ( $N_A$  drops

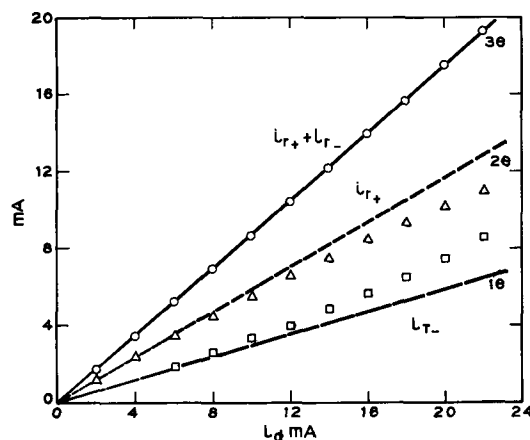


Fig. 6. Successive runs with graphite electrode at 3000 rpm of  $i_{r+}$  at  $E_r 1.0\text{v}$  and  $i_{r-}$  at  $E_r -0.65\text{v}$  vs.  $i_d$  in 20 mM In(III) - 0.7M HClO<sub>4</sub>. Absolute sum of the ring currents also plotted. Solid lines are calculated for 1, 2, and 3 electron reactions using the experimental collection efficiency of the electrode,  $N_{A \text{ lim}}$ .



faster at lower speeds, Table I). Hence, interpretation in terms of In(II) formation at the disk remains speculative.

**Indium amalgam disk electrodes.**—A comparison between the electrochemical behavior of a solid indium electrode and an indium amalgam electrode is desirable. Relationships between potentials, indium activities, and the products generated are necessary to determine if a single mechanism is operative for both types of electrodes. These quantities can be determined by using a mercury-coated gold ring disk electrode and then comparing these results to the ones described above for the solid indium electrodes.

Deposition of indium on the disk portion of the electrode allows the *in situ* preparation of amalgams of varying activity. Short deposition time gives a dilute amalgam; continued deposition will eventually give a saturated amalgam [70 m/o (mole per cent)] with an activity of indium equal to that of the solid metal (26). Further deposition will give only solid indium.

The behavior of dilute amalgams, concentrated amalgams, and saturated amalgams with excess solid indium were examined using anodic galvanostatic polarization of the disk. The collection efficiency for In(I), as determined by its oxidation at the ring electrode, was studied as a function of disk currents for several rotational speeds. The potential of the disk electrode,  $E_d$ , was simultaneously monitored. A plot of both disk potential,  $E_d$ , and ring current,  $i_{r+}$ , vs. increasing disk current starting with a saturated amalgam is shown in Fig. 7. Up to a certain level of disk current density, the disk potential and collection efficiency are consistent with the behavior of a solid indium electrode (*vide supra*). However, when the solid phase is exhausted and concentration polarization of the amalgam becomes important, it is observed that the collection efficiency falls quickly to zero. Other experiments of this type have been carried to the point where mercury dissolution commences, and below that potential range, no further electroactive species could be detected at the ring electrode.

The region where indium concentration polarization in the disk becomes significant is one of rapidly changing potential. A more detailed study of this potential region is shown in Fig. 8 where the variation of  $E_d$  and  $i_{r+}$  with time is plotted for a constant  $i_d$ . The data are for a dilute amalgam and show clearly that the quantity of In(I) formed is critically potential-dependent. In Fig. 9  $i_{r+}$  is plotted as a function of  $E_d$  for a constant  $i_d$ . (This run and others at different  $i_d$ 's and rotational speeds are subsequently analyzed in a quantitative kinetic treatment.)

It is possible to calculate what the surface indium activity is at the potential,  $E_{r.o.}$ , where the collection efficiency begins to roll off. Putting both the value of the standard potential for the In(I)/In(0) couple de-

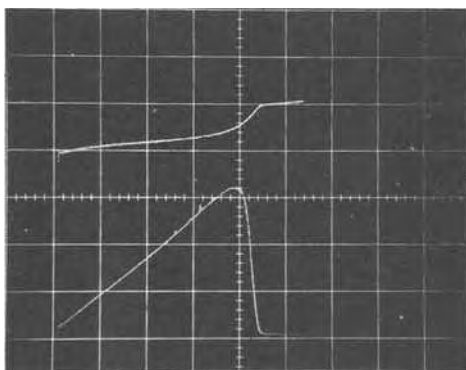


Fig. 7. Upper trace is  $E_d$  and lower trace  $i_{r+}$ , both vs. linearly increasing  $i_d$ . Amalgam disk, 2000 rpm in 20 mM In(III) —0.7M HClO<sub>4</sub>. Current sensitivity 50  $\mu$ A/major division for both  $i_{r+}$  and  $i_d$ .  $E_r = -0.1$  v vs. SCE. Top line 0.0v vs. SCE, sensitivity 0.2v/major division.

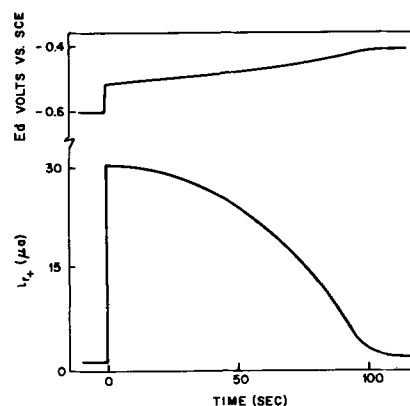


Fig. 8. Upper trace is  $E_d$  and lower trace  $i_{r+}$ , both vs. time at 50  $\mu$ A  $i_d$ . Amalgam disk as in Fig. 7.

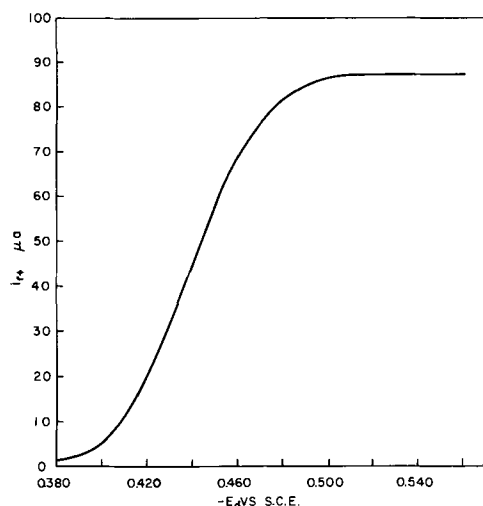


Fig. 9. Anodic ring current ( $E_r = 0.0$  v vs. SCE) vs.  $E_d$  for amalgam disk. Conditions correspond to entry 4 in Table II.

termined above for this medium and the surface concentration of In(I) obtained from the Levich equation for the disk current into the Nernst equation, the log of the indium activity, based on a Henry's law mole fraction scale (26), may be obtained (Table II).<sup>1</sup> The observation by Kozin (7) that In(I) is the sole product formed in amalgam dissolution for amalgams more concentrated than 20 m/o, for which Butler's data (26) show a log activity of  $-0.08$ , is in accord with our experimental observations and the calculation just described, especially considering that the equivalent potential difference between the values is approximately 4 mv.

**Kinetic analysis of amalgam dissolution.**—In order to treat the drop-off in collection efficiency with in-

<sup>1</sup> Activities based on Henry's law (mole fraction scale) may be obtained from activities on a solid indium equals one basis by multiplying them by 21.6.

Table II. Log of indium activity

$E_{r.o.}$ vs. SCE	$i_d$ , ma/cm <sup>2</sup>	$\omega$ , rpm	In(I), mM	$E_{r.o.} + 0.059$ log In(I)	log { $a_{In(I)}$ }
-0.480	1.40	500	2.34	-0.325	0.08
-0.490	1.40	2000	1.17	-0.317	-0.06
-0.495	0.70	500	1.17	-0.322	0.04
-0.507	0.70	2000	0.585	-0.316	-0.08
-0.515	0.35	500	0.585	-0.324	0.07
-0.523	0.35	2000	0.293	-0.315	-0.10
Average				-0.320 $\pm 0.004$	-0.10

$$\log \{a_{In(I)}\} = \log 21.6 + \frac{E_0'}{0.059} - \frac{1}{0.059} (E_{r.o.} + 0.059 \log \{In(I)\})$$

creasing anodic polarization quantitatively, a kinetic model is necessary. The model chosen has already been given as Eq. [1]-[3], where the rates for the forward and reverse reactions are indicated by the respective  $v$ 's. It is clear from the data of Visco (15) that the homogeneous reaction of In(I) with  $H^+$  is slow. At 20°C in 0.7M  $H^+$ , the half life for the reaction



is 2.2 min. The data presented above on solid disk electrodes for current densities below 2 ma/cm<sup>2</sup> show that In(I) is stable with respect to any homogeneous disproportionation reaction on the time scale of disk-ring transit, as expected from the half-life. Therefore, at low current densities, once In(I) is formed at the interface of a rotating amalgam disk or, for that matter, at any indium anode, it can only be further oxidized heterogeneously to In(II) and/or In(III), or, swept away from the electrode and detected at the ring. Those ions not detected at the ring are then swept to the bulk. Once in the bulk, In(I) ions are slowly oxidized to In(III) by the homogeneous reaction with hydrogen ions, Eq. [8]. If some of the In(I) were oxidized at the amalgam disk, these oxidized species too must either be swept away from the disk, possibly to be detected at the ring or effectively to be lost to the bulk.

In the following derivation certain assumptions are made about the relative rates of the several charge-transfer reactions. It is assumed that the rates  $v_1$  and  $v_{-1}$  are always sufficiently great that reaction [1] is never significantly displaced from equilibrium and therefore the Nernst equation relates the surface activities of In(I) and indium in the amalgam. Kozin (7) has shown this relationship to be true over a wide current density range for the 20 m/o amalgam he studied. The same behavior is seen here in the Tafel plot for a solid indium electrode, Fig. 1.

Of the two charge-transfer reactions remaining, either can be the rate-controlling step. Let us assume, however, that reaction [3] is rate-determining and reaction [2], like [1], is always effectively at equilibrium, although the absence of detectable In(II) indicates that it lies far to the left, making the interfacial concentration of In(II) vanishingly small, at least for the low current density conditions later used to test this model.

Based on the above, the usual steady-state assumption of an equal division of current between successive steps in a sequence of one-electron steps cannot be made for this model. One intermediate, In(I), has a significant interfacial concentration under all conditions, and therefore, as a consequence of the motion of the solution near the interface, some of this species will be swept away from the electrode. The current is still given by

$$i_d/AF = (v_1 - v_{-1}) + (v_2 - v_{-2}) + (v_3 - v_{-3}) \quad [9]$$

The quantity  $(v_1 - v_{-1})$  is greater than  $(v_2 - v_{-2})$  since some of the In(I) is lost from the interface by means of the solution laminar flow. It is possible, however, to relate the rates of the three unit steps by

$$(v_1 - v_{-1}) - m\{\text{In(I)} - \text{In(I)}_{\text{Bulk}}\} = (v_2 - v_{-2}) = (v_3 - v_{-3}) \quad [10]$$

where  $m$  is the mass transport coefficient for a given rotational speed. (Concentrations are to be understood as surface values unless otherwise labeled.) The quantity  $(v_3 - v_{-3})$  may be written as

$$(v_3 - v_{-3}) = k_3 \text{In(II)} \exp(\beta_3 F \Delta\phi/RT) - k_{-3} \text{In(III)} \exp(-\alpha_3 F \Delta\phi/RT) \quad [11]$$

where  $\Delta\phi$  is the potential measured against a standard hydrogen electrode. Substituting [10] and [11] appropriately into [9] gives

$$i_d/FA = 3\{k_3 \text{In(II)} \exp(\beta_3 F \Delta\phi/RT) - k_{-3} \text{In(III)} \exp(-\alpha_3 F \Delta\phi/RT)\} + m\{\text{In(I)} - \text{In(I)}_{\text{Bulk}}\} \quad [12]$$

The reduction of In(III) in strong acids in the absence of any complexing anions such as halide is known to be a highly irreversible process (27-30), and therefore the back reaction (the term involving  $k_{-3}$ ) can be neglected. The bulk concentration of In(I) is always much smaller than the interfacial concentration of this species and the last term in the above equation can be accordingly simplified. Through the Nernst equation a substitution for the In(II) surface concentration in terms of the corresponding quantity for In(I) is possible; the standard potential for this redox couple is then defined as  $E_{O_2/1}$  vs. the standard hydrogen electrode. With this simplification and substitution, Eq. [12] reduces to

$$i_d/FA = 3k_3 \text{In(I)} \exp\left\{(1 + \beta_3) \frac{F \Delta\phi}{RT}\right\} \exp\left\{\frac{-FE_{O_2/1}}{RT}\right\} + m \text{In(I)} \quad [13]$$

In the absence of significant  $iR$  losses for the low disk current densities studied using amalgams, the concentration of In(I) is uniform over the surface of the disk, and  $m$  is therefore given by the Levich equation. The ring current for oxidation of In(I) to In(III) is related to  $m \text{In(I)}$  through the collection efficiency

$$m \text{In(I)} = \frac{i_{r+}}{2FA N_A \text{lim}} = 0.62D^{2/3} \nu^{-1/6} \omega^{1/2} \text{In(I)} \quad [14]$$

Substitution of [14] into [13] gives

$$\frac{i_d - i_{r+}/2N_A \text{lim}}{i_{r+}} = \frac{2.42 k_3 \exp\left\{(1 + \beta_3) \frac{F \Delta\phi}{RT}\right\} \exp\left\{-\frac{FE_{O_2/1}}{RT}\right\}}{N_A \text{lim} D^{2/3} \nu^{-1/6} \omega^{1/2}} \quad [15]$$

A plot of the quantity  $\log\{(i_d - i_{r+}/2N_A \text{lim})/i_{r+}\}$  vs.  $\Delta\phi$  should therefore be linear with a slope of  $(1 + \beta_3)F/2.3RT$ . Such a plot for runs at two rotational speeds and three different disk currents is shown in Fig. 10. The quantity  $2.3RT/(1 + \beta_3)F$  is, for all 6 runs,  $35 \pm 1$  mv, so that  $(1 + \beta_3) = 1.7$ . The potential separation between pairs of lines in Fig. 10 is expected to be  $35 \log(i_{d1}/i_{d2})$  mv. The calculated separation of 10.5 mv may be compared with the observed 11 and 13 mv differences. Losev (11) has measured the

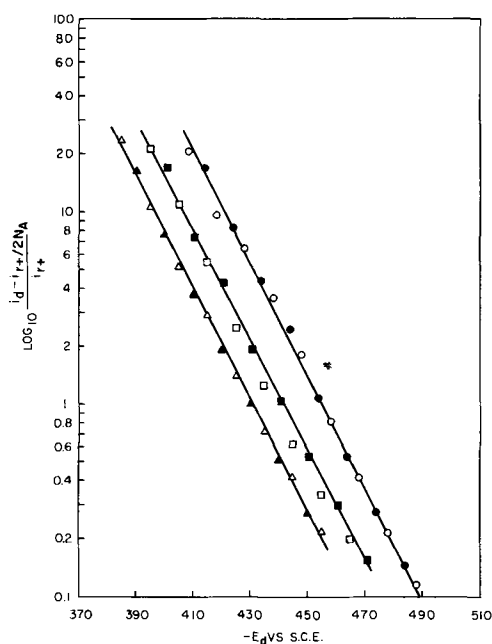


Fig. 10. Experimental test of Eq. [15]; conditions correspond to Table II entries;  $\Delta$  to 1,  $\blacktriangle$  to 2,  $\square$  to 3,  $\blacksquare$  to 4,  $\circ$  to 5 and  $\bullet$  to 6.

Tafel slope for the dissolution of dilute amalgams and obtained a value of 27 mv/decade. Assuming the third electron transfer to be slow, Losev finds  $(2 + \beta_3)$  equal to 59/27 or 2.2. The unit difference between the theoretical quantities results from the fact that Losev measured the oxidation of  $\text{In}(0) \rightarrow \text{In}(\text{III})$  at amalgams of assumed constant surface composition, while Eq. [15] was derived for amalgams of variable composition, where oxidation of  $\text{In}(0)$  to  $\text{In}(\text{I})$  was not accounted for in the exponential but rather in a changing interfacial concentration of  $\text{In}(\text{I})$  as determined by an experimental measurement of the ring current. The latter method appears more likely to represent the actual situation accurately.

### Discussion

The experimental conclusions summarized below warrant the interpretation that, in acidic noncomplexing media as represented by 0.7M  $\text{HClO}_4$ , indium metal at current densities up to at least 10  $\text{ma}/\text{cm}^2$  quantitatively goes into solution in the  $\text{In}(\text{I})$  state. Further,  $\text{In}(\text{I})$  is the major product to above 100  $\text{ma}/\text{cm}^2$ .

(A) The Tafel slope at a rotating disk is 59 mv/decade, in keeping with a reversible one-electron oxidation and diffusive transport of  $\text{In}(\text{I})$  away from the surface.

(B) The product of dissolution may be oxidized in a two-electron step or reduced in a one-electron step, as determined by ring current behavior.

(C) The separation between the dissolution potential of indium metal and the oxidation wave of the dissolution product is compatible with a  $0 \rightarrow 1$  reversible reaction and a slow  $1 \rightarrow 3$  reaction, overcoming the fact that the  $0 \rightarrow 3$  reaction is thermodynamically most favorable.

(D) Neither disproportionation nor homogeneous hydrogen ion reduction of  $\text{In}(\text{I})$  is fast enough to cause measurable loss of this species in transit from ring to disk, as evidenced by the linearity of  $i_r$  vs.  $i_d$  plots and the exact numerical relation of the slope of this plot to that for the known one-electron ferro-ferricyanide couple.

Views of indium dissolution involving one-electron steps have already been mentioned: Visco (2, 15), Losev (1), and Kozin (5, 6, 7). The formation of finite concentrations of  $\text{In}(\text{I})$  is suggested in all these mechanisms; major differences exist on the fate of the species. Losev (1) claims  $\text{ClO}_4^-$  reduction to  $\text{Cl}^-$  provides a path to  $\text{In}(\text{III})$ . However, in this work and in previous results from this laboratory (2, 15), no sign of  $\text{Cl}^-$  formation (silver ion and anodic polarography tests) has been detected. Furthermore, recent ring-disk experiments with added  $\text{Cl}^-$  (31) indicate very significant effects of this ion on the dissolution process itself, effects which were not observed in the present study. The Kozin (7) proposal of disproportionation of  $\text{In}(\text{I})$  as the route to  $\text{In}(\text{III})$  reflects the appearance of indium particles in solution in his experiments. Measurements of the first order  $\text{In}(\text{I}) + \text{H}^+$  reaction rate (15) show no influence of disproportionation up to millimolar initial  $\text{In}(\text{I})$  levels. Since disproportionation must be of higher order in  $\text{In}(\text{I})$ , it is reasonable that this route may become faster than  $\text{H}^+$  reduction at high  $\text{In}(\text{I})$  concentrations. It is to be noted, however, that disproportionation would cause  $i_{r-}$  to fall off at higher anodic disk dissolution currents since neither  $\text{In}(\text{III})$  nor  $\text{In}(0)$  is reduced at the cathodic ring potential of the experiment; this prediction is opposite to the direction found. In the bulk solution, disproportionation may be competitive with  $\text{H}^+$  reduction since they depend on the  $\text{In}(\text{I})$  to  $\text{H}^+$  concentration ratio. Neither reaction is rapid enough, however, to be detected within the transit time of the ring-disk experiments.

The position of Straumanis (3) that  $\text{In}(\text{I})$  is a product only of reaction [4] is clearly contradicted by the present results. The further insistence of Strau-

manis (32) that conclusions of coulometric experiments which indicate lower oxidation states of indium, whether from solid or amalgam dissolution, are due to anode disintegration is sharply disputed, particularly by the fact that  $\text{In}(\text{I})$  is formed most nearly quantitatively at the lowest current densities, an effect exactly opposite to all arguments based on physical disintegration processes. In addition, the ring-disk experiments are not in disagreement with the Straumanis coulometric studies on indium dissolution in acid (3). In those experiments the indium was shorted to a large platinum electrode, effectively potentiostatically controlling the anode at about  $-0.25\text{v}$  on the scale of Fig. 1, or at a sufficiently anodic potential for oxidation to  $\text{In}(\text{III})$  to occur at a dilute amalgam. The appearance of metal particles in solution is also, as noted by Kozin, reasonably a product of  $\text{In}(\text{I})$  formation, not necessarily electrode disintegration.

The process of indium dissolution from an amalgam has been shown to be the same as that at a solid if one takes proper cognizance of the indium activity in the amalgam. With the fixed activity of the solid metal, only increasing the current density can move the anode more positive. With an amalgam, the lowered indium concentration (activity) at the surface in a dilute amalgam or in the concentration polarization of a more concentrated amalgam on anodization has the same effect of a positive shift of potential, but at much lower current densities. The rate of the  $\text{In}(\text{I}) \rightarrow \text{In}(\text{III})$  reaction will then effectively catch up at some moderate current density, and  $\text{In}(\text{I})$  will cease to be detected. Negative results in coulometric tests for the existence of lower valent intermediates, as by Straumanis (3), which are based on dissolution from very dilute amalgams at relatively high anodic overpotentials (33), are thus always to be suspect. When such intermediates can be formed because of kinetic reasons (e.g., a slow further electron transfer step to a higher valence state), these two conditions (dilute amalgams, i.e., a low activity of metal, and high anodic overvoltage) are very unfavorable for their detection. The latter applies to the case at hand; needless to add, the conditions are likewise unfavorable on a direct thermodynamic basis.

The quantitative confirmation of the kinetic model for amalgams has been described above. These ideas also reconcile various literature data about indium dissolution from amalgams. Thus, Straumanis' experiments (3) were with extremely dilute amalgams at high polarizations from which  $n = 3$  is expected. Those of Kozin (7), with 20 m/o and higher amalgams gave  $n = 1$ . Values quoted by Visco (2) of  $1 < n < 3$  were for concentrations yielding a spectrum of indium activities corresponding to the  $i_{r+}$  roll-off region in Fig. 9 and thus an intermediate number.

The views of Markovac (12-14) on the dissolution mechanism of indium have been obtained from experiments on dilute amalgams and fail particularly to take into account the indium activity factors discussed in the above treatment of amalgams. The reversibility of the  $\text{In}(0)$ - $\text{In}(\text{I})$  reaction at both solid and amalgam electrodes and the lack of needing to invoke an  $\text{In}(\text{II})$  disproportionation contradict his various interpretations.

The predictions of the kinetic model for amalgam electrodes are experimentally verified in a region of current densities ( $< 1.5 \text{ ma}/\text{cm}^2$ ) corresponding to the unequivocally clear  $\text{In}(\text{I})$  formation in the Tafel and ring current behavior of the solid, Fig. 1. Experimentally, it is not feasible to carry out the described experiment with amalgam disks at much higher current densities, since the resulting roll-off in potential is too rapid to assure  $i_{r+}$  and  $E_d$  measurements corresponding to the same time scale even at high rotation speeds. The requirement in the model for an amalgam electrode with vanishingly low  $\text{In}(\text{II})$  concentration is satisfied since the  $E_d$  potentials never approach the values that may be suspect with regard

to this assumption at the 100 ma/cm<sup>2</sup> end of the Tafel data on the solid electrodes. Whether an appreciable surface concentration of In(II) can be formed over a narrow potential range at the high current limit of the present Tafel measurements is, as previously discussed, not excluded from the ring current data. This leaves open the question of whether, over some limited potential region, it is possible to remove the second electron (reaction [2]) before the In(I) → In(III) process is sufficiently accelerated to prevent the In(II) concentration from ever becoming significant. Experimentally a nonindium ring must be employed to detect In(I) by its oxidation. Ring current-potential behavior at carbon, mercury, and gold surfaces of this oxidation process does not necessarily characterize quantitatively the behavior of the same reaction at an indium or amalgam disk.

Manuscript received Oct. 6, 1967.

Any discussion of this paper will appear in a Discussion Section to be published in the December 1968 JOURNAL.

#### REFERENCES

1. A. P. Pchel'nikov and V. V. Losev, *Protection of Metals*, **1**, 432 (1965); *Zashchita Metallov*, **1**, 482 (1965).
2. R. E. Visco, *This Journal*, **112**, 932 (1965).
3. M. E. Straumanis and R. L. Martin, *Z. anorg. u. allgem. Chem.*, **334**, 321 (1965).
4. L. Kiss, *Magy. Kem. Folyoirat*, **72**, 191 (1966).
5. L. F. Kozin and E. E. Kobrand, *Zhur. Prikl. Khim.*, **38**, 579 (1965).
6. L. F. Kozin and I. A. Sheka, *Ukrain. Khim. Zhur.*, **32**, 154 (1966).
7. L. F. Kozin and I. A. Sheka, *ibid.*, **32**, 951 (1966).
8. V. V. Losev and A. I. Molodov, *Electrochim. Acta*, **6**, 81 (1962).
9. A. I. Molodov and V. V. Losev, *Elektrokhimiya*, **1**, 1253 (1965).
10. G. M. Budov and V. V. Losev, *Doklady Akad. Nauk. SSR*, **129**, 1321 (1959).
11. V. V. Losev and A. I. Molodov, *ibid.*, **135**, 1432 (1960).
12. B. Lovrecek and V. Markovac, *This Journal*, **109**, 727, (1962).
13. V. Markovac and B. Lovrecek, *ibid.*, **112**, 520 (1965).
14. V. Markovac and B. Lovrecek, *ibid.*, **113**, 838 (1966).
15. R. E. Visco, *J. Phys. Chem.*, **69**, 202 (1965).
16. G. Biedermann and T. Wallin, *Acta Chem. Scand.*, **14**, 594 (1960).
17. L. Hepler, Z. Z. Hugus, Jr., and W. M. Latimer, *J. Am. Chem. Soc.*, **75**, 5652 (1953).
18. A. N. Frumkin and L. N. Nekrasov, *Doklady Akad. Nauk. SSSR*, **126**, 115 (1959).
19. A. N. Frumkin, L. N. Nekrasov, V. Levich, and Yu. Ivanov *J. Electroanal. Chem.*, **1**, 84 (1959).
20. L. N. Nekrasov and N. P. Berezina, *Doklady Akad. Nauk. SSSR*, **142**, 855 (1962).
21. B. Miller, Paper Presented at the Chicago Meeting of the Society, October 1967, Abstract 53.
22. W. J. Albery and S. Bruckenstein, *Trans. Faraday Soc.*, **62**, 1920 (1966).
23. L. B. Anderson and C. N. Reilley, *J. Electroanal. Chem.*, **10**, 295 (1965).
24. D. T. Napp, D. C. Johnson, and S. Bruckenstein, *Anal. Chem.*, **39**, 481 (1967).
25. V. G. Levich, "Physicochemical Hydrodynamics," chap. VI, Prentice-Hall, Englewood Cliffs, N. J. (1962).
26. J. N. Butler, *J. Phys. Chem.*, **68**, 1828 (1964).
27. D. Cozzi and S. Vivarelli, *Z. Elektrochem.*, **57**, 408 (1953).
28. E. D. Moorhead and W. M. MacNevin, *Anal. Chem.*, **34**, 269 (1962).
29. A. J. Engel, J. Lawson, and D. A. Aikens, *ibid.*, **37**, 203 (1965).
30. R. E. Visco, *J. Electroanal. Chem.*, **10**, 82 (1965).
31. B. Miller and R. E. Visco, Unpublished observations.
32. M. E. Straumanis, *This Journal*, **113**, 636 (1966).
33. M. E. Straumanis and M. Dutta, *Inorg. Chem.*, **5**, 992 (1966).

## Determination of the Composition of Complexes and Their Instability Constants by Calorimetry

### III. The Complex in Fused Sodium Molybdate and Molybdenum Trioxide

Abner Brenner\* and William H. Metzger, Jr.

National Bureau of Standards, Washington, D. C.

#### ABSTRACT

A method of determining the composition of complexes in solution and their instability constants, which is based on the measurement of the partial molal heat effect developed when a small increment of each salt is added in turn to a series of mixtures covering the range of composition from 0 to 100%, has been applied to the molten Na<sub>2</sub>MoO<sub>4</sub>-MoO<sub>3</sub> system at 800°C. The data show that one complex is formed consisting of one molecule of Na<sub>2</sub>MoO<sub>4</sub> and two molecules of MoO<sub>3</sub>. The instability constant is approximately unity, and the complex is between 50% and 75% dissociated.

A general method for determining the composition of complex ions and their instability constants by calorimetry was developed and described in two previous publications. In the first publication (1) the mathematical aspect of the subject was developed, and the method was applied to an aqueous system containing copper cyanide complexes. In the second paper (2) the method was applied to a fused salt system consisting of potassium and cadmium chlorides. This is the

Key words: Complex salts; calorimetry; fused salts; sodium molybdate-molybdenum trioxide system; partial molal heat effect; composition of complex salts.

\* Electrochemical Society Active Member.

third and final paper of the series. It deals with a complex present in the molten sodium molybdate-molybdenum trioxide system.

The laboratory procedure is as follows. Let the two components of the complex be designated by A and B. A series of perhaps 8 or 10 different mixtures of A and B is prepared covering the whole range of composition from pure A to pure B. To a given mixture of approximately 500g is added a small increment of A (a few grams) and the temperature effect measured. Then a small increment of B is added and the temperature effect again measured. The increments should be so

small that they do not change the composition of the mixture by more than 1%. The experimental results are converted into heat changes per mole of A or B added, i.e., into partial molal heat effects (designated as  $\Delta H$ ). These are the amounts of heat that would be evolved if one mole of A or B were added to an infinite amount of mixture. These  $\Delta H$  values are plotted against the composition of the mixtures.

The mathematical derivations in the first paper showed that, if only one complex is present, the curves cross at the stoichiometric composition. This unambiguously determines the composition of the complex even if it is largely dissociated, for example, if the instability constant is unity. The law regarding the heat effects at the stoichiometric composition can be most simply stated in the form:

At the stoichiometric composition, equimolar additions of each component produce equal heat effects.

If the two components form more than one complex, the composition of each can be determined by solving simultaneous equations or by graphical methods.

The instability constant of the complex can be calculated from either the value of the partial molal heat effect or the slope of either curve at the stoichiometric point.

The addition of increments of both A and B is required only when the instability constant is large. If it is of the order of  $10^{-3}$  or smaller, the curves have sharp changes of slopes in the vicinity of the stoichiometric point, and this break in the curve is sufficient to indicate the stoichiometric composition. In this case only one of the constituents needs to be added to the mixture, as was done in the investigation of the copper cyanide complexes (1).

The investigation herein reported was made simply for the purpose of further testing the applicability of the incremental method, and sodium molybdate and molybdenum trioxide were chosen, because they both melt at a high temperature but still within the range of the calorimetric equipment (sodium molybdate,  $687^\circ\text{C}$  and molybdenum trioxide,  $795^\circ\text{C}$ ).

### Experimental

The equipment and technique used were the same as those described in the previous publication (2). The experiments were run at about  $800^\circ\text{C}$ . The increment of sodium molybdate or molybdenum trioxide was contained in a fused silica ampoule which was held in a platinum stirring device immersed in the molten mixture. The ampoule was broken by a tungsten rod while the stirrer was in motion, and the reaction was complete in about 15 sec. The temperature rise was measured with three chromel-alumel thermocouples in series attached to a recorder having a  $100\ \mu\text{v}$  range. The heat capacity of the calorimeter was determined electrically. The tungsten rod used for breaking the silica ampoule was slightly attacked by the mixture. The mixture had a dark color in the molten condition.

### Results

The partial molal heat effects are shown in Fig. 1 by curves 1 and 2. They cross at a point corresponding to a melt containing 66 m/o (mole per cent) of  $\text{MoO}_3$ , which indicates that only one complex is present at  $800^\circ\text{C}$  and that its composition is:  $\text{Na}_2\text{MoO}_4 \cdot 2\text{MoO}_3$ , or  $\text{Na}_2\text{O} \cdot 3\text{MoO}_3$ .

The phase diagram for  $\text{MoO}_3$  and  $\text{Na}_2\text{MoO}_4$  (3) shows very definitely the phase  $\text{Na}_2\text{O} \cdot 2\text{MoO}_3$  melting at  $612^\circ\text{C}$  and the scarcely discernible, incongruently melting compounds  $\text{Na}_2\text{O} \cdot 3\text{MoO}_3$  (melting point  $528^\circ\text{C}$ ) and  $\text{Na}_2\text{O} \cdot 4\text{MoO}_3$  (melting point  $515^\circ\text{C}$ ). The composition of the melt at  $800^\circ\text{C}$ , as shown by the calorimetric method, thus differs from that at  $600^\circ\text{C}$ . Morris, Cook, Sykes, and Templeman (4) measured the densities, molal volumes, and electrical conductivities of the molten mixtures at temperatures above

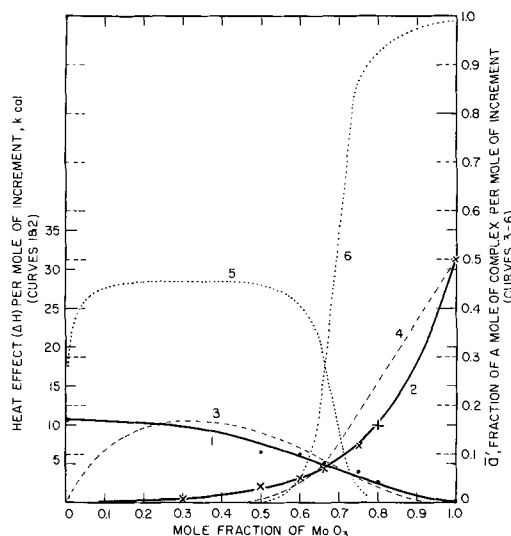
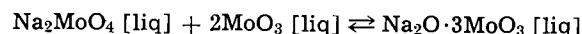


Fig. 1. Partial molal heat effects produced by the addition of increments of  $\text{Na}_2\text{MoO}_4$  and of  $\text{MoO}_3$  to fused mixtures of the compounds at approximately  $800^\circ\text{C}$ . Curves 1 and 2 are based on experimental results; curves 3 and 4 are calculated on the basis that  $K = 1.0$ , and curves 5 and 6 are calculated on the basis that  $K = 0.01$  for the reaction:  $\text{Na}_2\text{MoO}_4 + 2\text{MoO}_3 \rightleftharpoons \text{Na}_2\text{O} \cdot 3\text{MoO}_3$ . Curves 1, 3, and 5 represent increments of  $\text{MoO}_3$ , and curves 2, 4, and 6 represent increments of  $\text{Na}_2\text{MoO}_4$ .

$800^\circ\text{C}$ . Their data, however, do not indicate the existence of a complex.

### Calculations of the Instability Constant

The instability constant is readily calculated from the value of the partial molal heat effect ( $\Delta H = 4.8$  kcal/mole) at the point of intersection of the curves at the stoichiometric point. The largest value of  $\Delta H$ , at the right-hand end of curve 2, for increments of sodium molybdate is 31.3 kcal/mole, and it will be designated as  $\theta$ . If we assume that the increment of sodium molybdate completely reacts when added to pure  $\text{MoO}_3$ , then  $\theta$  is approximately the heat of reaction for the formation of 1 mole of complex, according to the equation



The ratio,  $\Delta H/\theta$ , represents the fraction of a mole of complex that would be formed if a mole of either  $\text{MoO}_3$  or  $\text{Na}_2\text{MoO}_4$  were to be added to an infinite amount of a mixture. This ratio can also be represented by a partial differential. If  $x$  and  $y$  represent, respectively, the moles of  $\text{MoO}_3$  and  $\text{Na}_2\text{MoO}_4$  used in preparing a given mixture and  $\bar{a}$  represents the moles of complex present in this mixture at equilibrium, then

$$\frac{\Delta H_x}{\theta} = \frac{\partial \bar{a}}{\partial x} = \bar{a}'_x \quad \text{and} \quad \frac{\Delta H_y}{\theta} = \frac{\partial \bar{a}}{\partial y} = \bar{a}'_y$$

At the point of intersection,  $\bar{a}'_x = \bar{a}'_y = \bar{a}'$ .

The equation for calculating  $K$  from  $\bar{a}'$  is

$$K = \frac{4(1 - 3\bar{a}')^3}{3\bar{a}'[3(1 - 2\bar{a}')]^2} \quad \bar{a}' = \frac{4,800}{31,300} = 0.15 \quad [1]$$

This equation is obtained from Eq. 33 of (1), and it gives  $K = 0.33$ . If the calculation were based on the value of  $\Delta H$  at the left side of the curve, then  $\theta = 2 \times 10,600$  kcal and  $\bar{a}' = 4,800/21,200 = 0.23$ . This gives a value of  $K = 0.07$ .

The instability constant can also be obtained from the slope of the curves at the stoichiometric point. A sample calculation is made for curve 1 for  $\text{MoO}_3$ . The quantity required for calculation is  $\bar{a}''_x$ , the second

derivative of the moles of complex,  $\bar{a}$ , formed with respect to  $x$ , moles of  $\text{MoO}_3$

$$\bar{a}''_x = \frac{\partial \bar{a}'_x}{\partial x} = \frac{\frac{\partial}{\partial \theta} \frac{\Delta H_x}{\theta}}{\frac{\partial x}{\partial \theta}} = \frac{1}{\theta} \cdot \frac{\partial \Delta H_x}{\partial x} \quad [2]$$

Since the abscissa represent mole fraction,  $f$ , the slope of the curve is  $(\partial \Delta H_x)/(\partial f)$ , and it must be multiplied by

$$\frac{\partial f}{\partial x} = \frac{y}{(x+y)^2}$$

to give  $(\partial \Delta H_x)/(\partial x)$  (1).

The equation for calculation is

$$K = \frac{2\bar{a}' - 1}{2\bar{a}'} \cdot \left( \frac{\bar{a}'}{3\bar{a}''_x} \right)^3 \quad [3]$$

This equation is derived from Eq. 37 of ref. (1). The slope of the curve,  $(\partial \Delta H_x)/(\partial f)$ , at the stoichiometric point is  $-14.7$  kcal/mole, and  $(\partial \Delta H_x)/(\partial x) = -14.7 \cdot y/(x+y)^2 = -14.7/9 = -1.63$ , if for ease of calculation we let  $y = 1$  and  $x = 2$  at the stoichiometric point. From Eq. [2],  $\bar{a}''_x = \frac{1}{\theta} \cdot \frac{\partial \Delta H_x}{\partial x} = \frac{-1.63}{31.3} = -0.052$

Substitution of  $-0.052$  for  $\bar{a}''_x$  and  $0.15$  for  $\bar{a}'_x$  in Eq. [3], gives

$$K = 2.0$$

A similar calculation can be made for curve 2, which requires finding  $\bar{a}''_y$ . The slope of the curve,  $\partial H/\partial f = 24.7$  kcal/mole.

$$\frac{\partial \Delta H}{\partial y} = \frac{\partial \Delta H}{\partial f} \cdot \frac{\partial f}{\partial y} = \frac{\partial \Delta H}{\partial f} \cdot \frac{-x}{(x+y)^2} = (24.7) \cdot \frac{-2}{9} = -5.5, \text{ if } x = 2 \text{ and } y = 1$$

$$\bar{a}''_y = \frac{1}{\theta} \cdot \frac{\partial \Delta H}{\partial y} = \frac{-5.5}{31.3} = -0.176$$

The formula for computing  $K$  is obtained from Eq. 37 of ref. (1) by interchanging the coefficients for  $x$  and  $y$  in the chemical equation

$$K = \frac{32 \cdot (2\bar{a}' - 1)}{\bar{a}'} \left( \frac{\bar{a}'}{3\bar{a}''_y} \right)^3 = 3.4$$

The values of  $K$  calculated from the slope of the curves do not agree closely with the values of 0.33 and 0.07 calculated from the ordinate of the intersection of the curves. An approximate value of  $K = 1.0$  will be used in the following discussions.

An estimate of the degree of dissociation can be obtained by calculating the heat effect produced by the addition of sufficient components to an infinite amount of mixture of the stoichiometric composition to form one mole of complex. One mole of  $\text{Na}_2\text{MoO}_4$  and two moles of  $\text{MoO}_3$  would have to be added. Since each mole forms 0.15 moles of complex in the stoichiometric mixture the total amount of complex formed would be 0.45 mole. Hence, the complex is 55% dissociated at the stoichiometric point.

According to the derivation given in (1), the values of  $\bar{a}''_x$  and  $\bar{a}''_y$  derived from the slopes of the curves at the stoichiometric point should be inversely proportional to the square of the coefficients of A and B in the balanced equation of their reaction

$$\frac{\bar{a}''_y}{\bar{a}''_x} = \frac{2^2}{1^2} = 4$$

The value of  $\bar{a}''_x$  for the  $\text{MoO}_3$  curve, 1, was  $-0.052$ . The value of  $\bar{a}''_y$  for the  $\text{Na}_2\text{MoO}_4$  curve, 2, was  $-0.176$ . The ratio is 3.4 instead of the theoretical value of 4.

## Discussion

Part of the difficulty in calculating the instability constant comes from the uncertainty in the value of  $\bar{a}'$ , which is determined from the ratio of  $\Delta H$  at the stoichiometric point to the largest value,  $\theta$ . The latter value is not known very exactly when the instability constant is large, for example, near unity. For systems having an instability constant smaller than  $10^{-3}$ , the  $\Delta H$  produced by adding an increment of A to pure B and *vice versa*, should be close to the heat of complete reaction (or a simple fraction of it). In the present example, the  $\Delta H$  for adding an increment of pure  $\text{Na}_2\text{MoO}_4$  to molten  $\text{MoO}_3$  would be the heat of reaction for the formation of a mole of complex (if  $K$  were small), and the  $\Delta H$  obtained by adding  $\text{MoO}_3$  to pure  $\text{Na}_2\text{MoO}_4$  would be exactly half, since only  $1/2$  mole of the complex would be formed per mole of  $\text{MoO}_3$ . However, the ratio between the two partial molal heat effects is very nearly 3 instead of 2. The application of the law of mass action teaches that a reaction is driven toward completion by the presence of an excess of one of the reactants. *A priori*, it might be supposed that a small increment of one reactant added to an infinite quantity of the other would react completely to form the complex. However, that is not generally true, and it was shown in the previous publication (2) that the fraction of conversion of a reactant, A, approaches the limit of  $1/K + 1$ , if one molecule of A is involved in the chemical equation. If  $K = 1$ , as in the  $\text{MoO}_3 - \text{Na}_2\text{MoO}_4$  system, then the largest fraction of conversion of an increment of  $\text{Na}_2\text{MoO}_4$  would be only one-half.

The limit,  $1/K + 1$ , can be derived directly from the expression for the mass action law in terms of mole fraction

$$K = \frac{\left( \frac{y-\bar{a}}{x+y-n\bar{a}} \right) \cdot \left( \frac{x-n\bar{a}}{x+y-n\bar{a}} \right)^n}{\left( \frac{\bar{a}}{x+y-n\bar{a}} \right)} \quad [4]$$

where  $x$  and  $y$  are the moles of reactants initially used to form the mixture and  $\bar{a}$  is the moles of product formed. We seek the value of the ratio  $\bar{a}/y$  as  $y$  and  $\bar{a}$  approach zero, but  $x$  remains appreciable, for example, 1 mole.

$$\frac{(y-\bar{a})}{\bar{a}} = \frac{K(x+y-n\bar{a})^n}{(x-n\bar{a})^n} \quad [5]$$

The limit of this, as  $\bar{a}$  and  $y$  approach zero is

$$\frac{y-\bar{a}}{\bar{a}} = K, \text{ and } \frac{\bar{a}}{y} = \frac{1}{K+1} \quad [6]$$

On the other hand, the limit is different for the reactant, B, which is raised to a power in the mass action equation. In this case, we seek the limit of  $\bar{a}/x$  as  $x$  and  $\bar{a}$  approach zero while  $y$  is held at an appreciable value, such as 1 mole.

Equation [4] may be put in the form

$$\left( \frac{x-n\bar{a}}{x+y-n\bar{a}} \right)^n = \frac{K\bar{a}}{y-\bar{a}}$$

If  $\bar{a}$  and  $x$  are small compared to  $y$ , this reduces to

$$\left( \frac{x-n\bar{a}}{y} \right)^n = \frac{\bar{a}K}{y}$$

$$x = \sqrt[n]{\bar{a}Ky^{n-1} + n\bar{a}}$$

$$\frac{\bar{a}}{x} = \frac{\bar{a}}{\sqrt[n]{\bar{a}Ky^{n-1} + n\bar{a}}}$$

where  $Z$  represents the other multipliers.

$$\frac{\bar{a}}{x} = \frac{1}{Za^{(1-n)/n} + n}$$

As  $\bar{a}$  becomes smaller,  $\bar{a}^{(1-n)/n}$  becomes larger. This is because  $n = 2$  or more and the exponent is negative. Thus, the right side of the equation approaches zero as  $\bar{a}$  becomes smaller and  $\bar{a}/x$  approaches zero.

In Fig. 1, curves 3 and 4 were computed from the law of mass action for the reaction:  $A + 2B \rightarrow C$ , with  $K = 1$  and curves 5 and 6 were computed for  $K = 0.01$ . The ordinates are  $\bar{a}'_x$  and  $\bar{a}'_y x$ . It will be noted that the ordinate of curve 4 approaches the value of  $0.5 = 1/1+1$  whereas, the ordinate of curve 6 approaches the limit of  $0.99 = 1/0.01+1$ . On the basis of curves 3 and 4, the complex would be 75% dissociated at the stoichiometric point.

The limits of curves 3 and 5 approach zero. This prediction of the law of mass action was not verified by the data (curve 1) which we obtained. The authors have no explanation for this discrepancy, but suggest the following two possibilities: that the mass action expression does not hold in an environment consisting of essentially only one of the components, or that a simpler complex, for example,  $\text{Na}_2\text{MoO}_4 \cdot \text{MoO}_3$ , may be formed.

The scale of the ordinate for curves 3 and 4 was chosen so that the curves would intersect at about the same point as the experimental curves. The agreement between the two sets of curves is satisfactory. It may be noted that the ratio of the maximum ordinates for the calculated curves 3 and 4 is about 3, and this matches the ratio obtained experimentally.

### Summary

The calorimetric method of determining the composition of complexes and their instability constants is simple. If only one complex is present, the determination of its composition involves only finding that composition of the mixture of the two constituents, A and B, which gives the same heat effect with small, equimolar additions of A and B. For determining the instability constant, the only other measurement required is the maximum heat effect resulting from the addition of a small sample of A to pure B, or *vice versa*. The ratio of the heat effect at the stoichiometric composition to the maximum heat effect is essentially all that needs to be used in the calculation of the instability constant.

In this and the preceding two papers, we have shown that the calorimetric method gives results even for

systems that are considerably dissociated. This method is of general application, and we are of the opinion that it will yield useful results where other methods are inapplicable or fail. Therefore, we believe that the method warrants further investigation and use.

### Acknowledgment

The authors wish to thank the Atomic Energy Commission, Division of Research, Chemistry Branch, for the financial support of this project.

Manuscript received Aug. 1, 1967; revised manuscript received Nov. 3, 1967.

Any discussion of this paper will appear in a Discussion Section to be published in the December 1968 JOURNAL.

### REFERENCES

1. A. Brenner, *This Journal*, **112**, 611 (1965).
2. W. H. Metzger, Jr., Abner Brenner, and H. I. Salmon, *ibid.*, **114**, 131 (1967).
3. Gmelins Handbuch der Anorganischen Chemie, 8th ed., System-number 53, 219 (1935).
4. K. B. Morris, M. I. Cook, C. Z. Sykes, and M. B. Templeman, *J. Am. Chem. Soc.* **77**, 851 (1955).

### APPENDIX

The formulas used for computing curves 3 to 6 are as follows: (They are obtained from Eq. 30 or 31 of reference 1.) Equation 4 is the basic equation.

$$\bar{a}'_x = \frac{\beta}{1+2\beta} \quad [7]$$

$$\bar{a}'_y = \frac{\bar{a}(2\beta+1) - \beta x}{y(2\beta+1)} \quad [8]$$

and

$$\beta = \frac{2\bar{a}^2 K(x+y-2\bar{a})}{(x-2\bar{a})^3} = \frac{2a(y-\bar{a})}{(x-2\bar{a})(x+y-2\bar{a})} \quad [9]$$

The computations are simplified if  $y$  is allowed to have the constant value of unity,  $\bar{a}$  is given various values, and  $x$  is calculated from the equation:

$$x = 2\bar{a} - \frac{y}{1 - \sqrt{\frac{y}{ak} - \frac{1}{k}}} \quad [10]$$

The abscissa is the mole fraction:  $\frac{x}{x+y} = \frac{x}{x+1}$ .

## Digital Computer Treatment of Electrocapillary Data

David M. Mohilner\* and Patricia R. Mohilner

Department of Chemistry, Colorado State University, Fort Collins, Colorado

### ABSTRACT

A digital computer method for the thermodynamic analysis of electrocapillary data has been developed based on least-squares parabolic smoothing and exact cubic fitting of a segment moving along a curve. The accuracy of integration is comparable to that of graphical methods while the accuracy of differentiation is increased to approach that of integration. The speed provided by computer analysis permits continuous monitoring of experimental data without the time-lag associated with graphical techniques.

In the past the thermodynamic analysis of double layer data has involved a tedious, graphical procedure requiring substantially more time than the measurements themselves. Although graphical integration,

used in some parts of the analysis of differential capacitance measurements, can be performed with reasonable accuracy, graphical differentiation, required in any analysis of data from a capillary electrometer as well as in determining surface excesses from dif-

\* Electrochemical Society Active Member.



ferential capacitance measurements, is inherently inaccurate and leads to serious questions in the interpretation of experimental results. In order to provide rapid and accurate assessments of data obtained in electrocapillary and differential capacitance experiments, a series of computer programs have been developed to carry out the thermodynamic analysis digitally without recourse to any graphical techniques.

The resulting computational procedures provide, in addition to vastly increased speed and significant gains in accuracy, a new concept in double layer studies, namely, the ability to operate a meaningful monitor of the electrocapillary data as it is being collected.

In this paper we report on the basic ideas involved in the computer analysis of electrocapillary data with especial reference to the differentiation technique.

Related computational techniques have been reported by Parsons and Zobel (1) and Butler (2) for the integration of differential capacitance curves and by Staicopoulos (3) and Butler (4) for the calculation of interfacial tension from sessile drop measurements. Savitsky and Golay (5) have considered the problems of computer differentiation and smoothing with particular reference to chromatographic data. Recently Parsons (6) and Barradas (7) investigated the problems of differentiation of double layer data by computer techniques.

#### Computational Procedure

All programs have been written in the FORTRAN language. The basic developmental work was done on an IBM 1620 computer while additional work employed IBM 7094 and Control Data Corporation 6400 computers. Graphs were prepared using a Calcomp plotter on-line with an IBM 1620. To prevent serious cumulation of errors, 16 digit precision was used on the 1620 and double precision on the 7094, while normal (14-15 digit) precision was sufficient on the CDC 6400 computer.

#### Sequence of Data Processing

The series of steps required for the thermodynamic analysis of measurements made by capillary electrometer have been applied to the particular case of the adsorption of neutral organic compounds at the mercury-solution interface. The input data include calibration constants and manometer reading—electrode potential pairs for a set of solutions of constant chemical potential (or concentration) of supporting electrolyte and varying chemical potential of organic solute. Digital computation is then utilized to calculate the interfacial tension for each electrode potential at each chemical potential of organic solute, smooth the experimental interfacial tension as a function of both electrode potential and chemical potential of the organic solute, calculate the surface pressure at constant electrode potential,  $\pi$ , and generate the desired partial derivatives of the double layer parameters. The first derivatives of the interfacial tension,  $\gamma$ , give rise to the charge density on the metal,  $q^M$ , and the relative surface excess of the organic solute in the double layer,  $\Gamma_o$ .

$$q^M = - \left( \frac{\partial \gamma}{\partial E^\pm} \right)_{T,p,\mu} \quad [1]$$

$$\Gamma_o = - \left( \frac{\partial \gamma}{\partial \mu_o} \right)_{T,p,\mu',E^\pm} \quad [2]$$

where  $E^\pm$  is the potential of the ideal polarized electrode with respect to an indicator electrode reversible to one of the ions in solution (8),  $\mu_o$  is the chemical potential of the organic solute, the subscripts  $T$ ,  $p$ , and  $\mu$  imply that the temperature, pressure, and composition are held constant while the subscripts  $T$ ,  $p$ ,  $\mu'$ , and  $E^\pm$  imply that temperature, pressure, composition except for the organic solute, and electrode potential are held constant.

A second stage of differentiation, which necessarily includes cumulated errors, may be applied to deter-

mine various cross partial differential coefficients such as the Esin and Markov coefficient,  $(\partial E / \partial \mu_o)_{T,p,q^M,\mu'}$ , or the coefficient which is thermodynamically equal, but opposite in sign,  $(\partial \Gamma / \partial q^M)_{T,p,\mu}$ . These coefficients require that the potential and relative surface excess values be known on the basis of constant charge density on the metal rather than the electrode potential basis provided in the experimental data. Programs have been written to carry out this change in independent electrical variable by digital computation. As a part of the change-of-variable programs, the values of Parsons' auxiliary variable  $\xi$  (9) and of the surface pressure at constant charge density,  $\Phi$ , are also calculated.

#### Differentiation Technique

The method of digital differentiation developed here differs from other systems (5-7) in two significant ways: (a) no attempt is made to fit the entire electrocapillary curve with a higher order polynomial, and (b) there is no restriction on the spacing of potentials or concentrations. Although the exact analytical equation of an electrocapillary curve is not known, it is possible to fit a sufficiently small interval of the curve by a quadratic or cubic equation to a very good approximation. The differentiation technique, then, is based on fitting a moving four-point interval of any curve with an exact cubic equation, as illustrated in Fig. 1 for an enlarged portion of a hypothetical electrocapillary curve. Since the slope of this cubic will best represent the actual data in the central part of the interval, the derivative is calculated from the coefficients  $a$ ,  $b$ ,  $c$ , and  $d$  of this one cubic equation only for the second point of the interval according to

$$q^M = -0.1 (3aE^2 + 2bE + c) \quad [3]$$

where the factor 0.1 arises to give  $q^M$  in microcoulombs/cm<sup>2</sup> when  $\gamma$  is in dynes/cm and  $E$  in volts. To obtain the charge density at the next point, the interval is moved one point along the curve by dropping the first point and adding the next, and the coefficients  $a$ ,  $b$ ,  $c$ , and  $d$  of this new cubic equation are calculated. Thus, with the exception of the leftmost and two rightmost points on any curve, all derivatives are calculated from different cubic fittings of the experimental data. The key subroutines for cubic fitting and calculation of charge density are included in the Appendix.

#### Smoothing and Plotting

The technique of differentiation used here is quite sensitive to experimental errors in the values of interfacial tension. Successful smoothing has been obtained by applying least squares parabolic fitting to moving segments of the electrocapillary curve and calculating the smoothed point only at an internal point in the interval. A discussion of several ways in which moving segments may be selected from a curve is included in the Appendix.

Since the normal tabulated output of digital computation fails to convey a picture of the data as clearly as graphical representation, programs have been developed to utilize a high-speed plotter in conjunction

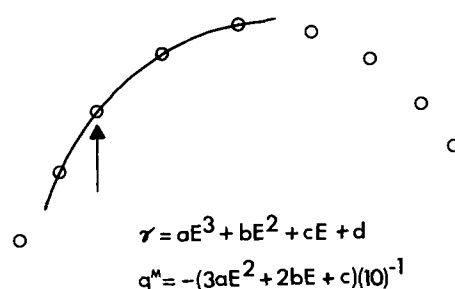


Fig. 1. Schematic drawing of hypothetical electrocapillary curve showing segment used for fitting and the internal point in that segment at which actual calculation is performed.

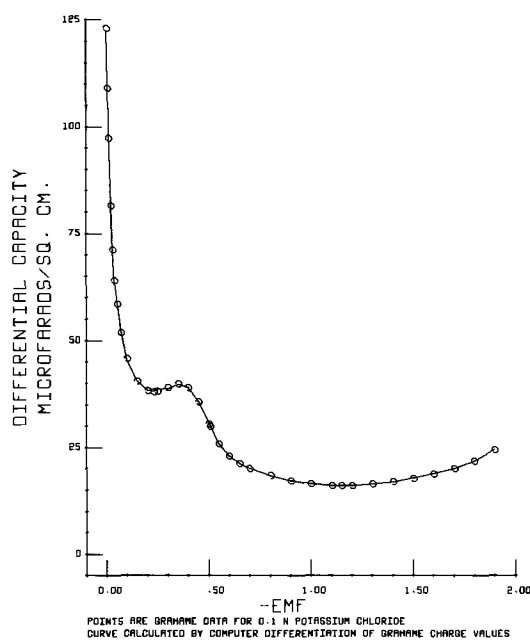


Fig. 2

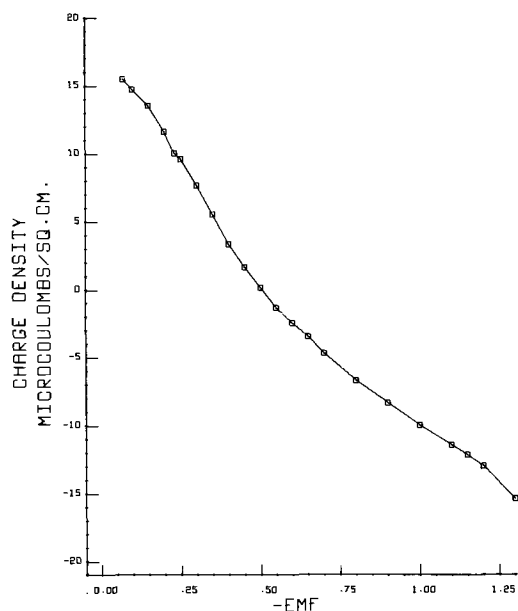


Fig. 3. Charge density calculated from the data of Devanathan and Peries (11).

with the computer to provide a more readily grasped presentation of the results of computations.<sup>1</sup>

### Results and Discussion

As a critical test of the validity of the differentiation technique, differential capacitance data were regenerated from Grahame's charge density calculations for 0.1N KCl (10). The points in Fig. 2 are the original differential capacitance measurements and the curve is the computer-calculated differential capacitance using Grahame's integrated data as input to a computer differentiation program. The median error for the computer calculations was 4 parts per thousand. From this example, it can be seen that accurate differentiation of electrocapillary data can be accomplished provided the input data are good.

The computer calculation of charge density from interfacial tension is illustrated in Fig. 3. The small

<sup>1</sup> The Calcomp plotter used in this work actually plots by connecting points by straight line segments. To produce reasonable rounded curves, interpolated points are calculated by moving cubic fittings to provide additional points which the plotter connects by shorter straight line segments.

inflection in the region,  $-0.23$  to  $-0.25$ v, might be ascribed to a property of the electrochemical system, but it is more likely an artifact due to experimental error. When these data were collected (1954), high-speed digital analysis of electrocapillary curves was unavailable, and graphical analyses could not usually be completed in time to permit ready experimental verification of suspect points. The computer techniques described in this paper make it possible for the experimenter to obtain such a charge density curve from raw electrocapillary data within minutes after the measurements are completed.<sup>2</sup> Thus, it is now feasible to use a computer as a continuous monitor of the experimental measurements. Suspect points can thus be located in time to be checked experimentally on the same solution with the same apparatus.

### Computation Time

The speed of digital computation, coupled with the accuracy indicated by Fig. 2, will not only make the experimental work itself the time-limiting factor in electrical double layer studies, but will also, and more significantly, permit much more complete analysis of electrocapillary data. For example, both the Esin and Markov coefficient and its negative, which may be calculated from the relative surface excess and charge density data, may be computed independently to test the internal consistency of the data. Additional cross-partial differential coefficients inherent in the electrocapillary equation may also be calculated as the quality and quantity of experimental data warrant.

As a result of the increased speed and accuracy of thermodynamic analysis it is reasonable to expect fuller exploitation of electrocapillary data, including critical tests of nonthermodynamic relationships such as the Gouy-Chapman-Stern (GCS) theory of the diffuse layer. A program (GCS1) based on the moving cubic fit principle has been written to calculate surface excesses and charge densities for mixed electrolyte solutions of arbitrary composition.

### Experimental Implications

The most striking result of this computer study of electrocapillarity is illustrated in Fig. 4-7. (The straight line segments are apparent in these computer

<sup>2</sup> Naturally the "turn-around" time of the particular computation facility determines the time lag between recording data and obtaining results. The ideal situation would be to have available in the laboratory a remote terminal of a time-sharing computer. Typical turn-around time on the Colorado State University CDC 6400 time-sharing computer without remote terminal is 30 min.

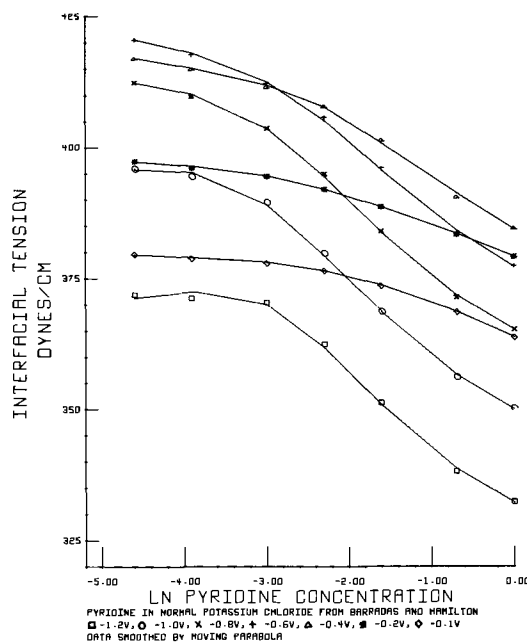


Fig. 4

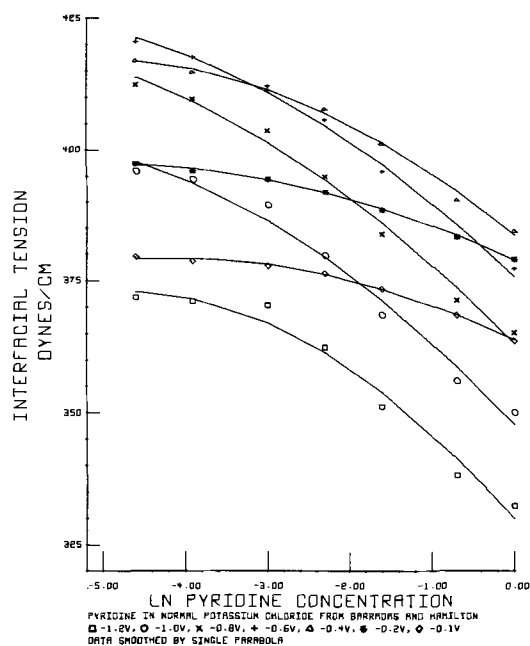


Fig. 5

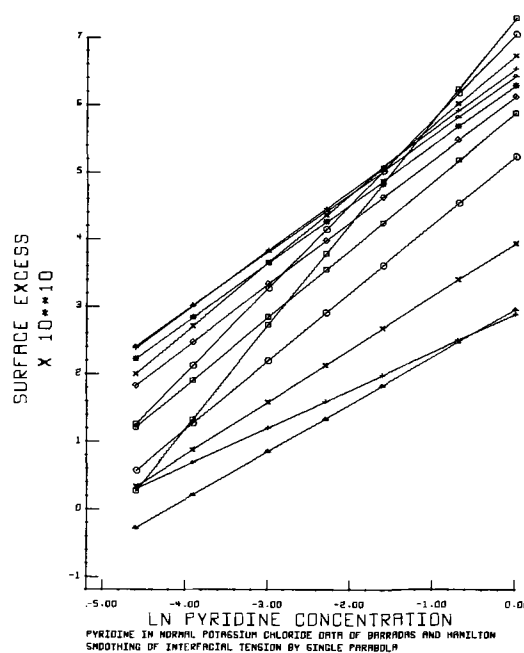


Fig. 7

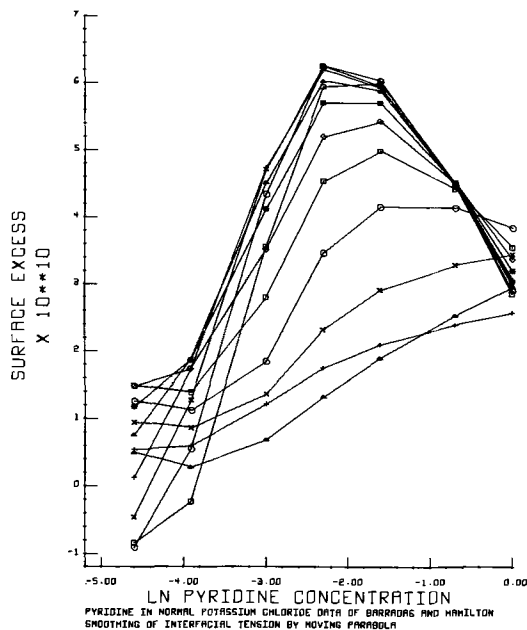


Fig. 6

produced graphs because interpolated data were not used).

These data pertain to the adsorption of pyridine on mercury (12, 13) from 1N KCl. The points in Fig. 4 and 5 are derived from the original interfacial tension measurements by smoothing as a function of electrode potential. The curves connect the corresponding points obtained by two different techniques of smoothing the interfacial tension as a function of the logarithm of the pyridine concentration. In Fig. 4 a moving least-squares parabola was applied to four-point intervals, while in Fig. 5 a single least-squares parabola was used for each complete curve. The curves of Fig. 5 are probably closer to those which would be drawn by the conventional "eyeball" technique. The data smoothed by each procedure were differentiated to produce the relative surface excesses shown in Fig. 6 and 7, respectively. The maximum shown in Fig. 6 would imply a most peculiar behavior of the system, if it were real. The straight lines of Fig. 7 would fit more comfortably into the usual concepts of adsorptive behavior at the metal-solution interface. In fact, these straight lines

have no theoretical significance because they are a necessary mathematical consequence of fitting the entire interfacial tension curve with a parabola and then differentiating it.

The hitherto unnoticed consequence of this analysis of reputable data is that the method of smoothing exerts profound influence on the appearance of the adsorption isotherms. In graphical smoothing, no attempt is usually made to assess the effect of a curve drawn in a slightly different manner so that this effect passed unobserved.

Computer analysis makes it apparent that a decision about the best method of smoothing required more points to be available for the analysis. For meaningful consideration of adsorption in the electrical double layer it is essential to examine data for a large number of concentrations closely spaced along the axis of the logarithm of activity. The number of concentrations to be used should be comparable to the number of potentials now measured for an individual electrocapillary curve.

Until experimental data for systems obtained at closely spaced concentration intervals are available, little can be said about the validity of present reports of relative surface excess data. The reported 10% differences in such values obtained by independent workers in the same laboratory (14), however, can be readily understood in terms of the inaccuracy of graphical differentiation.

#### Differential Capacitance

Computer integration of differential capacitance to obtain charge density by means of the moving cubic fit has been tested using Grahame's differential capacitance data (10) as computer input, and the results are shown in Fig. 8 where the points are the values reported by Grahame and the curve connects the output points from the computer integration. The median error for the computer calculations was less than one part per thousand. In this phase of data analysis the contribution of the computer is speed since graphical integration is recognized as accurate. Applications for the computer in treating differential capacitance measurements in conjunction with the coordinates of the electrocapillary maximum are being developed, since the calculation of relative surface excesses from such data amounts to the analysis of an electrocapillary curve which has been obtained by double integration of the differential capacitance curve. Digital computation can make a significant contribution to the inter-

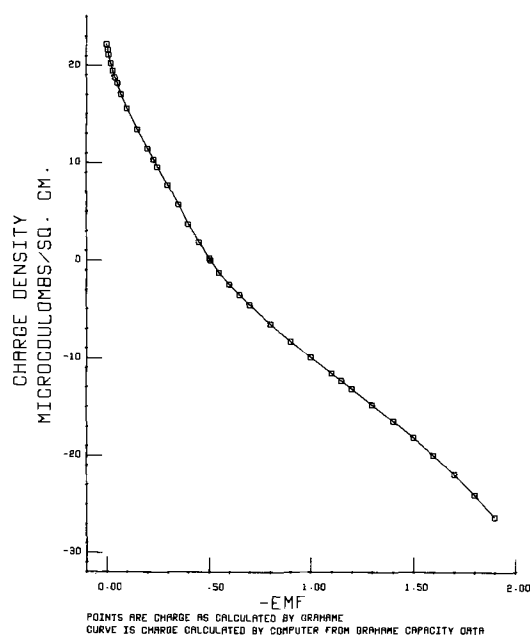


Fig. 8

comparison of capillary electrometer and differential capacitance measurements, an area of current concern (15).

#### Acknowledgment

The authors wish to express their appreciation to Professor R. G. Barradas of the University of Toronto for making available original experimental electrocapillary data to use in "debugging" the programs. The authors thank the Computer Center of Colorado State University and the Western Data Processing Center for making facilities available. This work was supported by Faculty Research Grants Nos. 311 and 524, Colorado State University.

Manuscript received April 19, 1967; revised manuscript received Oct. 16, 1967. This paper was presented at the Cleveland Meeting, May 1-6, 1966, as Abstract 169.

Any discussion of this paper will appear in a Discussion Section to be published in the December 1968 JOURNAL.

#### APPENDIX

The key subroutine, CUBFIT, for calculating the coefficients for each individual cubic equation is presented in Table I. Programs available on request to the authors are described in Table II. Illustrative of differentiation procedures is the subroutine QCAL, to calculate the charge density on the metal, presented in Table III.

Several versions of smoothing programs have been prepared, and work is in progress to determine rational criteria for the concept of "best" smoothing. The routines which have been developed to date are all based on applying a least-squares parabola to segments of the data. The differences in these routines arise in the selection of the segments to be used for any one parabola. The techniques are: (a) calculating one internal point from each least squares parabola obtained for a moving four-point segment, (b) calculating internal points from least squares parabolas based on segments selected by the experimenter who supplies coded designations of the starting point of each interval as input to the program, (c) performing the fitting in (a), testing the curvature of the parabola, and either computing an internal point or extending the interval to five or more points until the curvature is correct, (d) performing the fitting in (a), extending the interval one point at a time until, for each successive fitting, the sum of the squares of the differences between experimental and fitted points fails to decrease.

Preliminary comparisons of differing smoothing techniques did not reveal striking differences in charge density data as a result of the choice of smoothing

Table I. FORTRAN subroutine for cubic fit process

```

Subroutine cubfit
Dimension Y(4), DEN(4)
Common/cube/X(4),S(4), A,B,C,D
Y(1) = S(1)
Y(2) = -S(2)
Y(3) = S(3)
Y(4) = -S(4)
BA = X(2) - X(1)
CA = X(3) - X(1)
DA = X(4) - X(1)
CB = X(3) - X(2)
DB = X(4) - X(2)
DC = X(4) - X(3)
DEN(1) = BA*CA*DA
DEN(2) = BA*CB*DB
DEN(3) = DC*CA*CB
DEN(4) = DC*DA*DB
GB = X(2)
GC = X(3)
GD = X(4)
J = 1
A = 0.
B = 0.
C = 0.
D = 0.
8001 WA = GB + GC + GD
WE = GB*GC + GB*GD + GC*GD
WI = -Y(J)/DEN(J)
A = A + WI
WI = Y(J)*WA/DEN(J)
B = B + WI
WI = -Y(J)*WE/DEN(J)
C = C + WI
WI = Y(J)*GB*GC*GD/DEN(J)
D = D + WI
GO TO (8002,8003,8004,8005),J
8002 GB = X(1)
J = 2
GO TO 8001
8003 GC = X(2)
J = 3
GO TO 8001
8004 GD = X(3)
J = 4
GO TO 8001
8005 RETURN
END

```

Table II. FORTRAN programs now available for electrocapillary data analysis

Program Name	Function of the Program
SURF	Calculate interfacial tension from data obtained from a capillary electrometer. Smooth interfacial tension as a function of electrode potential with provision for interpolation of smooth interfacial tension data. Calculate charge density on the metal and, optionally, surface pressure at constant potential, $\sigma$ .
XCESS	Smooth interfacial tension as a function of the logarithm of activity. Calculate relative surface excess.
QSHIFT	Place interfacial tension, electrode potential, and relative surface excess on the basis of a preselected set of charge densities. Calculate Parsons' auxiliary variable, $\xi$ , the surface pressure at constant charge density, the Esin and Markov coefficient and $\left(\frac{\partial \Gamma}{\partial q^M}\right)_{T,p,\mu}$ .
CAPCAL	Calculate the differential capacitance from charge density-electrode potential curves.
QGRAL	Calculate charge density by integration of differential capacitance.
GCS1	Calculate charge density and surface excesses at preselected values of $\phi_2$ for arbitrary mixed electrolyte solutions using formulas from Gouy-Chapman-Stern theory.

Table III. FORTRAN subroutine for calculating charge density

```

Subroutine QCAL
Common DUMMY(30),EMF(30),SURF(30),Q(30),SCRAP(32),
NEMF
Common/cube/X(4),Y(4),A,B,C,D
DO 5312 M = 1,4
X(M) = EMF(M)
5312 Y(M) = SURF(M)
Call CUBFIT
Q(1) = (-3.*A*EMF(1)*EMF(1) - 2.*B*EMF(1) - C)/10.
Q(2) = (-3.*A*EMF(2)*EMF(2) - 2.*B*EMF(2) - C)/10.
L = NEMF - 3
DO 5314 I = 2,L
J = I + 1
DO 5313 M = 1,4
MM = M + I - 1
X(M) = EMF(MM)
5313 Y(M) = SURF(MM)
Call CUBFIT
5314 Q(J) = (-3.*A*EMF(J)*EMF(J) - 2.*B*EMF(J) - C)/10.
J = NEMF - 1
Q(J) = (-3.*A*EMF(J)*EMF(J) - 2.*B*EMF(J) - C)/10.
J = NEMF
Q(J) = (-3.*A*EMF(J)*EMF(J) - 2.*B*EMF(J) - C)/10.
Return
End

```

method. This result supports the contention that the effects shown by a comparison of Fig. 6 and 7 are due to an insufficient quantity of experimental data.

## REFERENCES

1. R. Parsons and F. G. R. Zobel, *J. Electroanal. Chem.*, **9**, 333 (1965).
2. J. N. Butler, ONR Report, May 1964, Tech. Memo #12, Contract #Nonr-3765(00), ARPA Order #302-62, Proj. Code 9800.
3. D. N. Staicopolus, *J. Colloid Sci.*, **17**, 493 (1962).
4. J. N. Butler, *Surf. Sci.*, **4**, 1 (1966).
5. A. Savitsky and M. J. E. Golay, *Anal. Chem.*, **36**, 1627 (1964).
6. R. Parsons, Private communication.
7. R. G. Barradas and F. M. Kimmerle, *Can. J. Chem.*, **45**, 109 (1967).
8. D. M. Mohilner, "The Electrical Double Layer, Part I. Elements of Double Layer Theory" in A. J. Bard, Editor, "Electroanalytical Chemistry," pp. 241-409, Vol. 1, Dekker, New York (1966).
9. R. Parsons, *Trans. Faraday Soc.*, **51**, 1518 (1955).
10. D. C. Grahame, *J. Am. Chem. Soc.*, **71**, 2975 (1949).
11. M. A. V. Devanathan and P. Peries, *Trans. Faraday Soc.*, **50**, 1236 (1954).
12. R. G. Barradas and P. G. Hamilton, Private communication.
13. R. G. Barradas and P. G. Hamilton, *Can. J. Chem.*, **43**, 2468 (1965).
14. E. Blomgren, J. O'M. Bockris, and C. Jesch, *J. Phys. Chem.*, **65**, 2000 (1961).
15. J. Lawrence, R. Parsons, and R. Payne, Abstracts of Papers, 153rd meeting, American Chemical Society, April 1967.

# Brief Communication



## Selective Electroreduction of the Benzene Nucleus

Akira Misono, Tetsuo Osa, Takamichi Yamagishi, and Teruyuki Kodama

Department of Industrial Chemistry, Faculty of Engineering, University of Tokyo, Hongo, Tokyo, Japan

During recent years many studies concerning the electroreduction of aromatic hydrocarbons have been reported (1), but the substrates examined were those with a more anodic reduction potential than benzene. The reduction potential of benzene has been estimated to be about 1v more negative than that of naphthalene from the difference between the electron affinities of the two compounds (2). The polarographic study of electroreduction of benzene has not yet been achieved because solvents, such as acetonitrile, N,N-dimethylformamide or dioxane-water, suitable for the reduction of naphthalene, are decomposed or reduced prior to the reduction of benzene at the potential where the benzene ring may be reduced.

It is well known that alkali metals in liquid ammonia or in low molecular weight amines reduce the benzene nucleus giving dihydro- or tetrahydroproducts (3). Sternberg (4, 5) and Benkeser (6) have reported the reduction of the benzene nucleus by the electrolytic reduction in a solution of ethylenediamine or ethylamine saturated with lithium chloride. Sternberg has also reported the electroreduction of the benzene nucleus in ethanol-hexamethylphosphoramide mixture containing 0.3M lithium chloride (7).

We have been interested in the electroreduction of the benzene nucleus under controlled potential conditions. We have examined the possibility of the above

reaction using many solvents and supporting electrolytes which are supposed to be fairly stable at the potential required to reduce the benzene nucleus, and have obtained unconjugated dienes in good yields in a system of diglyme-water-tetra-n-butylammonium bromide. The cell used was a cylindrical one with a glass filter to separate the catholyte and anolyte. Mercury and platinum were used as cathode and anode, respectively. To a 80 ml solution of diglyme and water was added 12g of tetra-n-butylammonium bromide. The catholyte was prepared by dissolving the substrate (benzene or toluene) in this solution. The anolyte was the solution prepared above. The cathode potential during electrolysis was  $-3.3v$  vs. SCE as indicated in Table I. The cell was constantly cooled by a water bath to keep the temperature at about  $25^{\circ}$ - $30^{\circ}C$ . In the reduction of benzene, the main reduction product was 1,4-dihydrobenzene, and in the case of toluene 2,5-dihydrotoluene was formed predominantly. 1,4-Dihydrobenzene and 2,5-dihydrotoluene were isolated by preparative gas chromatography and identified by IR and NMR absorption spectra (in the NMR spectra, 1,4-dihydrobenzene has absorptions at  $\tau = 7.45$  and  $4.40$  whereas 2,5-dihydrotoluene at  $\tau = 8.35, 7.46, 4.54,$  and  $4.25$ ). The quantitative analyses of the products were performed by the gas chromatographic method. The yield of cyclohexene was small, and 1,2-dihydro-

Table I. Electroreduction of benzene and toluene in diglyme-H<sub>2</sub>O-(C<sub>4</sub>H<sub>9</sub>)<sub>4</sub>NBr

Substrate	Temp, °C	Applied potential, v	Current passage, Faraday	Time, min	Current efficiency			$\eta_{1,4DH} + \eta_{1,2DH} + \frac{1}{2}\eta_{TH}$
					$\eta_{1,4DH}$	$\eta_{1,2DH}$	$\eta_{TH}$	
Benzene <sup>a</sup>	24-27	39	0.0350	450	66.1	....	5.1	96.3
Benzene <sup>b</sup>	26-30	39	0.0497	420	62.4	....	4.3	96.6
Toluene <sup>a</sup>	24-27	39	0.0352	450	55.2	....	5.8	95.0
Toluene <sup>b</sup>	24-25	38	0.0396	420	53.7	....	10.2	91.3

<sup>a</sup> Mole of the substrate 0.05 moles, water concentration 8.75 v/o.

<sup>b</sup> Mole of the substrate 0.025 moles, water concentration 15 v/o. Cathode potential is  $-3.3v$  vs. SCE in every case.

<sup>c</sup> The value at the end of the reaction.

The last column means the molar percentage of the unconjugated dienes in the monomeric reduction products, and these values nearly represent the selectivity for the formation of the unconjugated dienes.

benzene was either absent or present only in trace amounts. In the case of toluene, three types of tetrahydrotoluene were formed in small amounts, but neither 1,4-dihydrotoluene nor conjugated dienes was observed. Results are summarized in Table I.  $\eta_{1,4DH}$  represents the current efficiency for the formation of unconjugated dienes and  $\eta_{TH}$ , for tetrahydroproducts. In the cases examined, the selectivity for the formation of 1,4-dihydrobenzene or 2,5-dihydrotoluene was higher than that reported by Sternberg who performed the reduction by using lithium chloride in the ethylenediamine solution (4). During electrolysis, bromine formed at the anode diffused through the glass filter to the catholyte thus lowering the current efficiencies. In order to raise the current efficiency, an ion exchange membrane may be used in place of the glass filter so as to prevent the diffusion of bromine to the catholyte.

The electroreduction of the benzene nucleus in our system does not cause the isomerization of unconjugated dienes to conjugated dienes in contrast to the reduction by alkali metal in liquid ammonia or in amine. In the presence of substrate, the cathode potential was nearly the same as that in the absence of substrate at the same current density, and naphthalene was reduced at about 0.5v more anodic potential than that at which the benzene ring was reduced. Based on these results and previously published works (5, 7), we believe that the benzene ring may be reduced by solvated electrons. Detailed results and discussion of

the electroreduction of the benzene ring in this system will be reported in the near future.

Manuscript received June 12, 1967; revised manuscript received Nov. 8, 1967.

Any discussion of this paper will appear in a Discussion Section to be published in the December 1968 JOURNAL.

#### REFERENCES

1. S. Wawzonek and H. A. Laitinen, *J. Am. Chem. Soc.*, **64**, 2365 (1942); S. Wawzonek and D. Wearing, *ibid.*, **81**, 2067 (1959); P. H. Given, *J. Chem. Soc.*, **1958**, 2684; P. H. Given and M. E. Peover, *ibid.*, **1960**, 385; L. H. Klemm and A. J. Kohlik, *J. Org. Chem.*, **28**, 2044 (1963); A. Misono, T. Osa, and T. Yamagishi, *Bull. Chem. Soc. Japan*, **40**, 427 (1967).
2. L. E. Lyons, *Nature*, **166**, 193 (1950).
3. W. Hückel and H. Bretschneider, *Ann.*, **540**, 157 (1937); A. J. Birch, *Quart. Rev.*, **4**, 69 (1950); A. J. Birch and D. Naspuri, *Tetrahedron*, **6**, 148 (1959); A. P. Krapcho and A. A. Bothner-By, *J. Am. Chem. Soc.*, **81**, 3658 (1963).
4. H. W. Sternberg, R. Markby and I. Wender, *This Journal*, **110**, 425 (1963).
5. H. W. Sternberg, R. Markby, I. Wender, and D. M. Mohilner, *ibid.*, **113**, 1060 (1966).
6. R. A. Benkeser, E. M. Kaiser, and R. F. Lambert, *J. Am. Chem. Soc.*, **86**, 5272 (1964).
7. H. W. Sternberg, R. E. Markby, I. Wender, and D. M. Mohilner, *ibid.*, **89**, 186 (1967).

# Contact Electrification of Insulators and Its Relevance to Electrets

D. K. Donald

Research Laboratories, Xerox Corporation, Rochester, New York

## ABSTRACT

Surface charge densities on electrets are frequently measured by means of electrodes which can be lifted from the insulator surface; however, electrification of the surface can occur as a result of this contact between electrode and insulator, and this can be a source of difficulty in interpreting the results. In these experiments, measurements have been made on the contact electrification of paraffin, polystyrene, and polyethylene, among other materials, using mercury as the electrode. In these cases it is found that the contact charge exchange decreases with decreasing contamination of the insulator. Under controlled conditions, equilibrium surface charge densities as low as  $0.003 \text{ nC/cm}^2$  have been observed for paraffin. When the contact event produces both high electric fields and also high local surface potentials, the surface charge causes electrical breakdown during the separation of insulator and electrode. We find that it is useful to "develop" the resulting electrostatic charge distribution by xerographic means. The resultant charge distribution frequently shows the gross patchy structure of Lichtenberg figures previously reported for high voltage discharges to insulators in air.

Studies of contact electrification and of electrets have proceeded separately for some time. It is not clear, however, why they should be handled as two distinct areas of investigation because there are in fact strong similarities in the two areas. Both electret and contact electrification studies usually use very high resistivity materials with long dielectric relaxation times. Therefore it is easy for one in the electret field to see that samples used for contact electrification can be strongly disturbed by frozen-in impurities like those sometimes found in electrets. What can equally well occur in lifted electrode, electret experiments is spontaneous contact-electrification charge on the surface of samples. The discussion that follows centers around these "cross terms" between the two areas.

Lifted electrode experiments (1) are a common tool in observing electrets, but they are also a particular case of contact electrification. Usually the contact is highly patchy between the electrode and the electret. In order to study a better defined contact we have done lifted electrode experiments using liquid mercury as a highly compliant metallic contact. These contacts are without any applied field (in Fig. 1,  $V_B = 0$ ). Nevertheless, surface charge densities above  $16 \text{ nC/cm}^2$  have been recorded on samples of Carnauba wax and  $50 \text{ nC/cm}^2$  recorded on Mylar. The initial charge density may have been higher but in both cases electrical breakdown frequently occurred during contact separation and made the charge non-uniform. At the other extreme we have seen contact charge densities  $< 0.01 \text{ nC/cm}^2$  for other materials.

## Experimental Apparatus

The experimental arrangement uses a mercury bead (2) on a nickel or stainless steel pedestal and a flat insulator sample as a pair forming a triboelectric couple or a contact-electrification couple. The polymer sample is brought near to or contacted with the mercury using a micromanipulator. When the sample and mercury are contacted charge exchange occurs between the sample surface and the mercury. Thus later when the electrode is lifted this charge is observed by the electrometer. Still later the portion of charge which has not leaked away over the insulator is again observed in the electrometer's deflection when the electrode is returned into contact with the sample. For good insulators the charge on lifting and the charge on reconnecting the electrode is the same.

Key words: Contact electricity, Triboelectricity, Electrets, Dielectric phenomena gas breakdown.

For good insulators where the charge decays slowly the surface potential is used as a check on the surface charge density. When the sample and mercury are near one another a bias battery  $V_B$  (Fig. 1) can be used to null the electric field produced between the surface potential  $V_s$  on the polymer sample and the contact potential of the mercury. This method is commonly used in observing work-function differences between metals (3).

For surface potential measurements, the Model 31-V Cary electrometer was used without shunt capacitance ( $C_m$ ) at high sensitivity. A large shunt capacitance ( $C_m = 10^{-9} \text{ F}$ ) was added to the instrument when contact charge was measured.

Both the surface of the mercury and that of the insulator were important in these experiments. The mercury was reagent grade material and either freshly dispensed or aged for several hours in the ambient. By aging the mercury in the ambient the mercury's work-function is shifted, and thereby the character of contact events could be studied in two situations. While we could not control or predict the work-function of the mercury, we could look for differences in contact potential for the mercury in one case *vs.* the other. Polymer samples were also subjected to different surface treatments. The polymer samples were melted in air, "cleaved" with a razor blade or microtome, and were rinsed with solvents. The gas ambients used were laboratory air, dried or moisture-saturated air, argon, and  $\text{CO}_2$  from dry ice. Rough pump vacuum conditions have also been used in the experiments.

The second experimental tool was a special xerographic developer akin to Villarsy's mixture (1788)

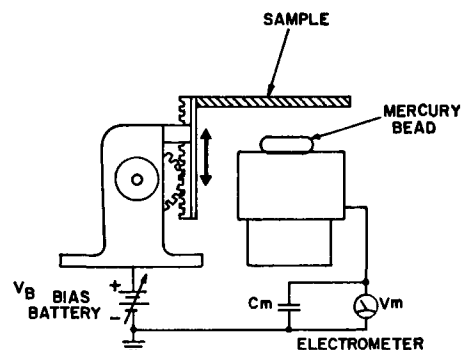


Fig. 1. Contact electrification scheme



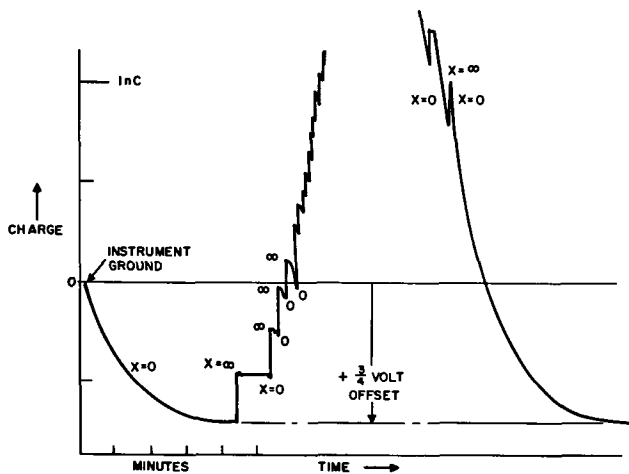


Fig. 2. Charge separated by mercury from tetradecanal where the degree of mechanical separation is denoted by "X".

(4) used previously by Woodland and Ziegler (5) as a diagnostic scheme. The developer was dispensed from a "squeeze bottle" as a mixed-powder aerosol. Two Day Glo pigments<sup>1</sup> were used; one color portrays the positively charged areas and the other the negative areas. In this way patchiness could be clearly discerned in the charge patterns resulting from the contact events.

This patchiness indicates that a simple electrometer measurement of charge can be misleading. Indeed, only if the developer shows a uniformly charged spot can the electrometer's reading be taken at face value. On the other hand, highly structured contacts frequently occur. Lichtenberg figures are produced in the events at high levels of surface charge density, and these figures in themselves are a useful guide to the events which occur during contact separation.

### Observations

Figure 2 demonstrates the raw electrometer data for charge exchange in a particular run. The tetradecanol in this run shows contact or separation charging of about  $1/3$  nano-Coloumbs per event, but several other phenomena are evident from the figure as well. The figure shows a residual d-c potential of  $3/4$ v which remained on the tetradecanol after casting. This may be an electret effect produced in casting the film, but it exists on in spite of a conductivity. This conductivity is large enough to produce a dielectric relaxation time of about a minute and a half. With multiple contacts the electrometer shows a large cumulative offset, but as soon as the sample and mercury are left in contact the charge is dissipated in the conductivity of the sample.

With most of the experimental materials the resistivity was very high and a charge once established on a sample did not disappear. However, the charge was hidden from the electrometer when sample and mercury were reconnected, and this formed a convenient base line for the observations. In Fig. 3 the heavy line represents this in-contact state. The electrometer offset produced by separation is indicated schematically by the dots. Incidentally, when the bias battery was changed a corresponding offset occurred in the base line. Such offsets occur for Samples A and E of Fig. 3. Figure 3 also demonstrates how the treatment of the paraffin while it was liquid influenced the charge exchange of the dip-coated paraffin samples. For example, samples B and C in Fig. 3 were made while the liquid was aerated by stirring. These two samples exchanged more charge than the others in the figure, yet they came from the same container of paraffin. The container, incidentally, was of stainless steel, and deep enough to exclude random air from

<sup>1</sup> Every combination of pairs of the Switzer Brothers (Cleveland, Ohio) Day Glo® gave proper two-color images. A 1:1 mixture of lead chromate and xerox toner also worked well.

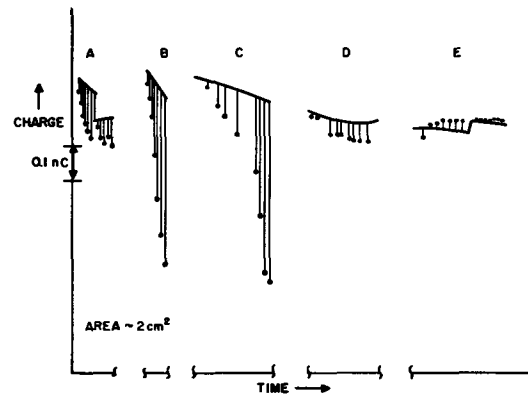


Fig. 3. Charge separated by mercury from cast paraffins: A, cast from initial melt; B, paddle aerated 5 min following A; C, paddle aerated  $1\frac{1}{2}$  hr following B; D, liquid quiescent in paraffin vapor 2 hr after C; E, liquid quiescent in paraffin vapor 16 hr after D.

the liquid's surface. When glass containers were used the contact charge was always at or above  $0.1$  nC/cm<sup>2</sup>. We blame sodium from the glass for this difference. Paraffin heated for long periods in open air or over-heated for short periods exchanged appreciable charge ( $\sim 1$  nC/cm<sup>2</sup>) with the mercury, but for these samples we also saw evidence of degradation in infrared spectra.

We examined numerous commercial products and films. Our polystyrene Petri dishes, for example, showed no overt charge of the kind reported by Woodland and Ziegler (5) for polystyrene wall tiles, but we could not exclude the possibility of heterocharge covered with counter charge, forming a double layer. Our surface treatments could have left a conducting film on the samples. This may have occurred, but it probably did not. First two-terminal conductivity measurements showed treated surfaces had surface resistivities at or above  $10^{14}$  ohms/square. Second, liquid gallium was contacted to freshly air-dried polystyrene. Charging occurred at many patchy spots on the oxidized gallium's surface and then this structured event was recorded xerographically. Any surface conductivity on the polystyrene must have been small, otherwise the structured charge from the gallium would have been washed out.

We attempted to avoid electret-like histories by preparing our own samples from a conducting state. We relied on the mobility in the liquid to remove gross charged impurities. Dissociated ion pairs were not extracted. In particular, paraffin, octacosane, tetradecanol, polystyrene, polyethylene and Carnauba wax were prepared as solid layers from the melt or extracted from solution and then observed. The range of surface charge densities encountered for several materials is listed in Table I. The lowest charge densities for the top four entries in Table I were associated with improved sample handling and, by inference, greater purity in the samples.

At very low levels of charge ( $< 0.01$  nC/cm<sup>2</sup>) the xerographic developer fails to show any image. As the charge density increases, first circular patches, then structured circular patches can be seen. At moderate charge densities Lichtenberg figures of two colors emerge indicating clearly that there are regions of both positive and negative surface charge density

Table I. Mercury contact charge on samples

Material	Sign	Range of charge density
Paraffin	-	0.003 to 1 nC.cm <sup>2</sup>
Octacosane	-	0.025 to 0.7
Polystyrene	-	0.005 to 10
Polyethylene	-	0.5 to 10
Tetradecanol	±	-1 to +1
Carnauba wax	-	1 to 16
Mylar	-	5 to 50

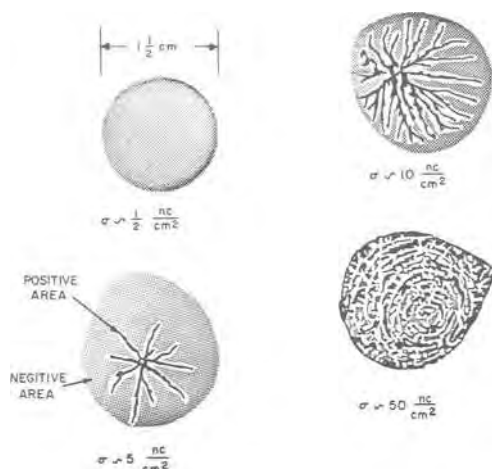


Fig. 4. Developed xerographic images at different surface charge densities.

on the polymer. At still higher surface charge densities, multiple Lichtenberg figures superimpose on each other forming a welter of radial line segments broken by the wave-like lines of charge deposited in circles. Figure 4 shows sketches of low, moderate, and high levels of surface charge density developed xerographically.

Thus the xerographic developer permits a plan view of the history of a contact separation. The simplicity or complexity of this history occasionally tell the observer about local splotches of impurity, but more frequently indicate that air breakdown must have occurred during separation. In the absence of air breakdown the electrometer observations can be considered reliable. With reference to air breakdown, two parameters are important: Any ground plane influences the nature of the electric fields and therefore the threshold of breakdown. In addition, the absolute pressure influences the nature of the gas discharge through its influence on the mean free path. We have seen both these parameters strongly influence the threshold for formation of Lichtenberg figures. For example, Fig. 4 depicts the behavior of 1-mm thick polystyrene. At this thickness a ground plane behind the polystyrene raised the threshold for Lichtenberg figures from below 5 to 10 nC/cm<sup>2</sup>.

#### Discussion

Our electrometer observations and the xerographic pictures complement each other in this work. Frequently the electrometer observations could be used alone, but at and near the threshold of air breakdown

the xerographic pictures were far more useful than the electrometer's readings. Differential effects due to surface handling were graphically distinguished through the pictures. From our observations we concur with Miller and Murphy (6) that, if ionized impurities can be removed, probably both the electret effects which they saw and the contact electrification reported here will all but disappear, for simple materials such as polystyrene.

It is worth noting that in certain particular cases surface charges produced by simple contact alone can be as large as the electret charge densities observed in the literature. For this to occur both intimate contact and also a strong triboelectric relationship between sample and electrode must obtain. But when an electret is first made and the top electrode is stripped off or when an electret is cut with a knife intimate contact is established.

This work shows again how important careful electrometry (7) and/or high resolution two-dimensional charge patterns are in properly judging air breakdown on electrets. In the author's opinion the xerographic method described here is both simpler and less ambiguous than electrometry in judging the onset of air breakdown in experiments where a worker wishes particularly to exclude air breakdown.

#### Acknowledgment

The author acknowledges the numerous discussions with and the helpful suggestions of P. Keith Watson both during the progress of the work and in the manuscript stage.

Manuscript received Aug. 31, 1967; revised manuscript received Nov. 13, 1967. This paper was presented at the Chicago Meeting, Oct. 15-19, 1967, as Abstract 134.

Any discussion of this paper will appear in a Discussion Section to be published in the December 1968 JOURNAL.

#### REFERENCES

1. B. Gross, *Phys. Rev.*, **66**, 26 (1944); H. H. Wieder and S. Kaufman, *J. Appl. Phys.*, **24**, 156 (1953).
2. J. A. Medley, *Br. J. Appl. Phys. Supplement #2*, 28 (1953).
3. W. A. Zisman, *Rev. Sci. Instr.*, **3**, 367 (1932).
4. C. F. Carlson in "Xerography and Related Processes," Dessauer and Clark, p. 16 The Focal Press (1965).
5. P. C. Woodland and E. E. Ziegler, *Modern Plastics*, **28**, 95 (1951); V. J. Webers, *J. Appl. Polymer Sci.*, **7**, 1317 (1963).
6. M. L. Miller, *J. Polymer Sci., Part 2A*, **4**, 685 (1966); M. L. Miller and J. R. Murphy, *ibid.*, 697.
7. B. Gross, *Brit. J. Appl. Phys.*, **1**, 259 (1950).

# Conduction Properties of Pyrolytic Silicon Nitride Films

J. R. Yeagan<sup>1\*</sup> and H. L. Taylor<sup>†</sup>

Department of Electrical Engineering, The University of Texas, Austin, Texas

## ABSTRACT

Thin film silicon nitride deposited from the reaction of silane and ammonia exhibits reproducible current characteristics at high fields less than breakdown. Conduction behavior with thickness is similar for films from 60 to 1600Å on quartz and silicon substrates. A large temperature dependence, a linear variation of  $\ln I$  with  $V^{1/2}$ , and no electrode dependence indicate thermal emission from the bulk as the dominant injection mechanism at room temperature.

Insulating films conduct a small current before destructive breakdown occurs. The characteristics of this current indicate the reproducibility of the films and help design devices with regard to leakage and breakdown. This paper reports results of a study of the conduction properties of silicon nitride films deposited from the reaction of silane and ammonia.

### Film Deposition

Figure 1 shows the system used for depositing the films. Table I describes the deposition cycle.

The Matheson Company furnishes the semiconductor-grade silane and ammonia. The hydrogen is commercial grade. The quartz reaction chamber with vertical flow uses a resistive-heated graphite substrate holder. After flowing over the heated substrate, the excess gases are burned and vented via a hood. A chromel-alumel thermocouple measures the temperature of the top of the substrate.

Substrates are metal-coated quartz and polished silicon. Metals used for the base contact are Mo, Ni, and Pt. The silicon is 0.01 ohm-cm p-type mechanically polished with a 10-sec etch in 48% HF just before placing in the reaction chamber. Vapor degreasing in trichloroethylene cleans the metals. An electron gun at a pressure of  $10^{-9}$  Torr evaporates the molybdenum. All other metals are evaporated from tungsten filaments at a pressure of  $10^{-6}$  Torr. After film deposition the top electrode of Al or Au is evaporated through a metal mask at  $10^{-6}$  Torr.

A break in the film growth-rate curve shown in Fig. 2 occurs at an ammonia to silane ratio of 7:1. Bean (1) and others attribute this break to the film becoming silicon rich. Deposition temperature is approximately 700°C for all films. An x-ray diffractometer reveals no structure of the films which are transparent and apparently amorphous.

### Thickness Determination

The thickness determination used capacitance measurements and the color of the interference fringes. A value of 2.0 for the index of refraction (1, 2) in the color determination seemed appropriate. The dielectric constant was determined as 5.5 from a series of devices as shown in Fig. 3. The error in thickness from color determination averages out with the several thicknesses and devices used. This value of dielectric constant was used to determine thickness of the very thin films. The capacitance readings are stable to 5 significant figures on metal-nitride-metal devices with zero bias.

### Conduction Properties

Figures 4 and 5 show the conducting properties for a series of MIM and MIS devices with thicknesses ranging from 1600 to 60Å. Curve (a) is from a film on a molybdenum-coated quartz substrate. The rest are from films on 0.01 ohm-cm p-type silicon. The top

electrodes are Al and Au with an area of 1.0 mm<sup>2</sup>. The metal is biased negative for the MIS devices. No difference is observed for the MIM devices when the polarity is reversed; however, on some MIS devices a behavior similar to Fig. 6 is seen. Since the silicon is p-type the difference might be due either to a penetration of the electric field into a surface layer or to hole injection from the semiconductor.

Figures 7 and 8 show the current variation with temperature. Figure 7 is more typical of behavior usually seen. Figure 8 shows two activation energies of 0.72 and 0.11 ev.

The nitride forms uniform pinhole-free films below 100Å as shown by the curves of Fig. 5. The devices usually exhibit "good" electrical characteristics if no defects are observed with a x30 microscope. Contacts to these films are made by lowering a drop of mercury or an indium-gallium paste onto the electrode. This reduces the danger of punching a hole in the very thin films. If pits occur in the silicon substrate the MIS device is usually shorted.

Although no difference in current behavior occurs for the different substrates at the thicker films, several attempts to grow films below 100Å on quartz coated with nickel strips resulted in ohmic characteristics for the nitride. These Ni-nitride-Al devices were not shorted, but exhibited steady capacitance readings which corresponded to film thickness from 49 to 115Å and resistivities of  $10^8$ - $10^{10}$  ohm-cm. The breakdown field on these devices was low ( $\approx 2 \times 10^6$  v/cm) compared to that on the thicker devices ( $1 \times 10^7$  v/cm).

Fig. 10 is a Schottky plot ( $\ln I$  vs.  $V^{1/2}$ ) for curve A of Fig. 4. A straight line curve for this type of plot is characteristic of Schottky emission from the metal electrode into the insulator governed by the equation

$$J = AT^2 e^{-q\phi/kT} e^{[(q^3E/4\pi\kappa\epsilon_0)^{1/2}/kT]} \quad [1]$$

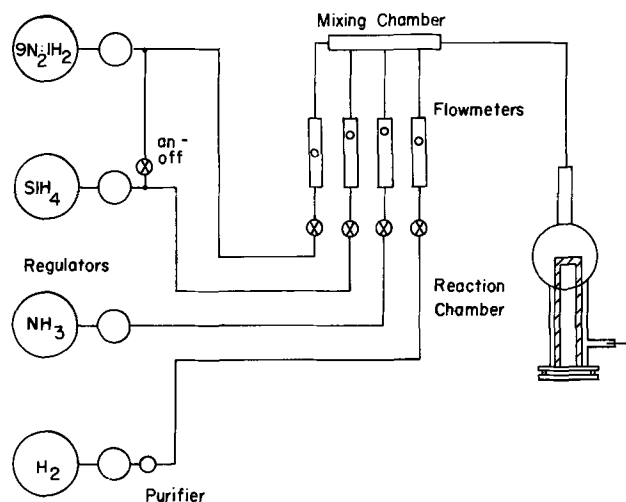


Fig. 1. Deposition system

<sup>1</sup> Present address: Department of Electrical Engineering, The University of Arkansas, Fayetteville, Arkansas.

\* Electrochemical Society Student Member.

† Electrochemical Society Active Member.

Table I. Deposition cycle

1. System flush with forming gas (9N <sub>2</sub> :1H <sub>2</sub> )	5 min	10 l/min
2. H <sub>2</sub> purge and warmup	5-10 min	2 l/min
3. Reactants added	—	2 l/min-H <sub>2</sub> 0.200 l/min-NH <sub>3</sub> 0.01 l/min-SiH <sub>4</sub>
4. H <sub>2</sub> purge and cool down	7-20 min	2 l/min
5. System flush with forming gas	5 min	10 l/min

where  $A = 120 \text{ amp}/(^{\circ}\text{K})^2$ ,  $T = \text{temperature in } ^{\circ}\text{K}$ ,  $q = \text{the electronic charge}$ ,  $K = \text{Boltzmann's constant}$ ,  $\epsilon_0 = \text{the permittivity of free space}$ ,  $\kappa = \text{the relative dielectric constant}$ ,  $E = \text{the electric field}$ , and  $\phi = \text{the barrier the electron sees at the metal-insulator interface}$ .

Closer examination shows that the slope of Fig. 10 is approximately a factor of 2 greater than that predicted from Eq. [1] ( $\kappa = 4.0 - \eta^2$ ). If indeed the electrodes control the current, the barrier ( $\phi$ ) should vary with different metals. From Eq. [1], a variation of only 0.06 eV at room temperature results in a decade difference in current density at equal fields; however, forward and reverse polarity current measurements on MIM devices with the different metal electrodes show little difference.

A bulk or internal Schottky emission (the Poole-Frenkel effect) has been proposed for the mechanism of current injection (3-5).<sup>2</sup> This model assumes that the electrons are thermally emitted from traps leaving a charged site after emission. Frenkel (6) calculates the current expression as

$$\sigma = \sigma_0 e^{q(qE/\pi\kappa\epsilon_0)^{1/2}}/kT \quad [2]$$

At the fields involved in these measurements a straight line results whether current or conductivity is plotted because the exponential term dominates. The main difference between Eq. [1] and [2] is a factor of 2 in the exponent. This difference arises because the barrier lowering is greater for an electron leaving a trap than for emission from a metal surface.

Equation [2] describes the observed behavior of the devices of Fig. 4 and 5 well; however, Fig. 9 shows a

<sup>2</sup>Sze (5) identifies three components of current. He finds that (i) Poole-Frenkel or internal Schottky emission dominates at high temperatures and high fields, (ii) field ionization dominates at high fields and low temperatures, and (iii) at low fields and moderate temperatures the current is dominated by thermal hopping of carriers from one isolated state to another. In general, our data are very similar to Sze's. In fact, the activation energies and barrier heights of Fig. 8 are approximately the same as he reports. However, we do not observe the ohmic current behavior characteristics of the thermal hopping.

Field ionization is characterized by a very small temperature dependence and a linear variation of  $\ln I$  with  $1/V$ . As seen in Fig. 8, the temperature dependence is still quite large for our devices even at lower temperatures. At very high fields ( $> 8 \times 10^6 \text{ v/cm}$ ) the current characteristics do become linear on a Fowler-Nordheim plot ( $\ln I$  vs.  $1/E$ ), however, more work is needed to establish that this is indeed field ionization.

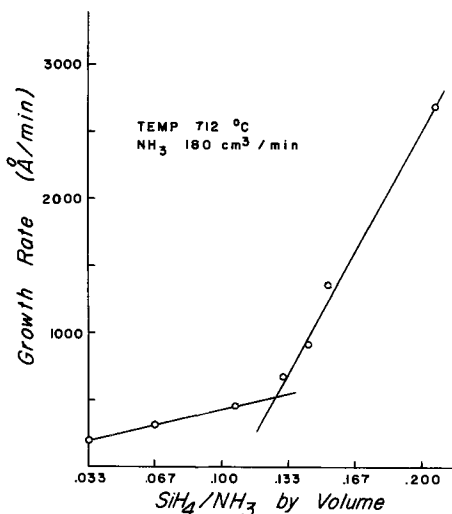


Fig. 2. Deposition rate vs. silane concentration

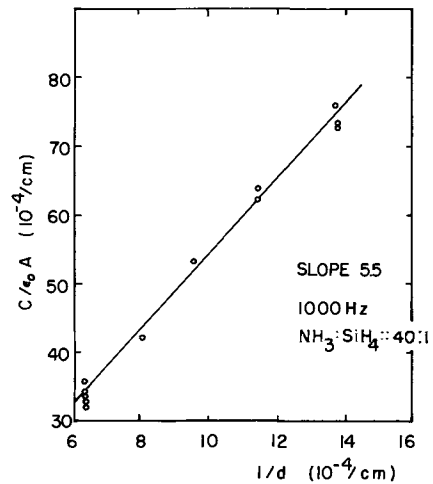


Fig. 3. Determination of dielectric constant

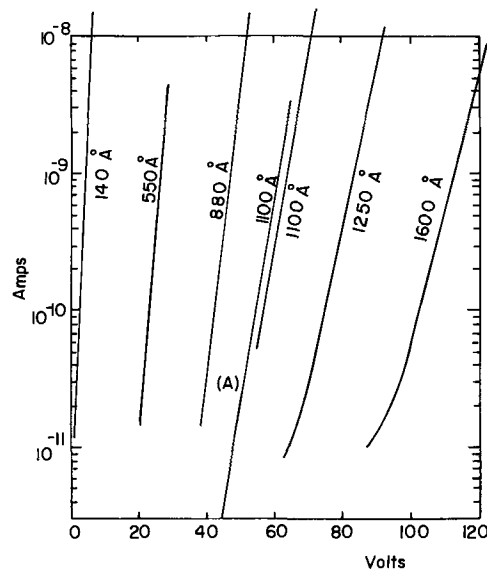


Fig. 4. Current variation with thickness: 1600-140Å

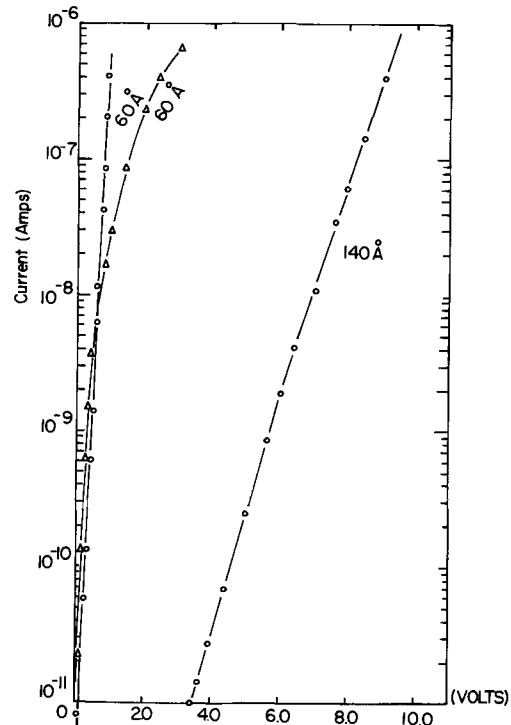


Fig. 5. Current variation with thickness: 140-60Å

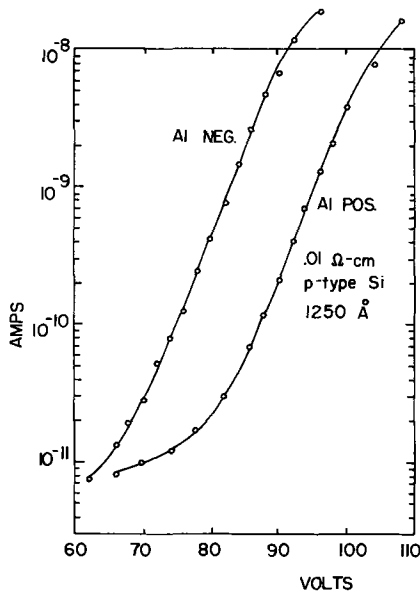


Fig. 6. Electrode effect on Al-nitride-Si device

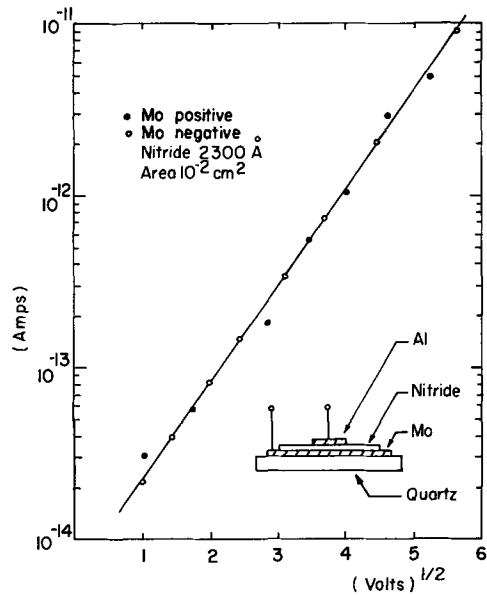


Fig. 9. Schottky plot of MIM device: low resistivity

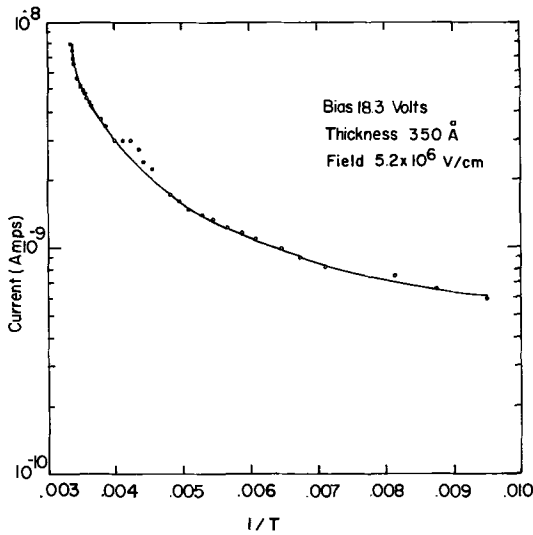


Fig. 7. Current variation with temperature

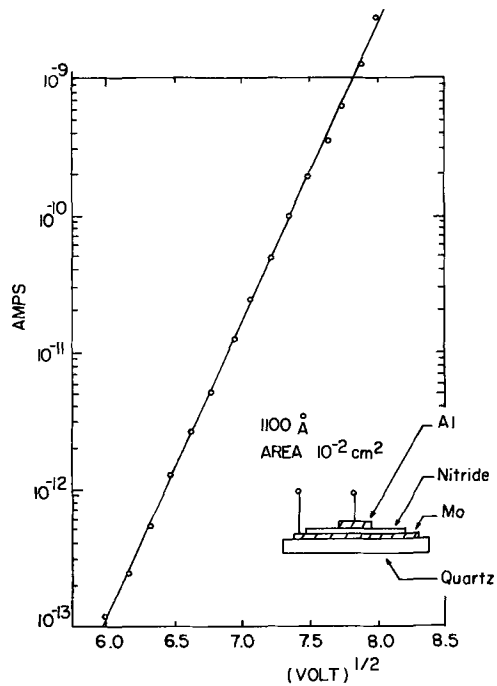


Fig. 10. Schottky plot of MIM device: high resistivity

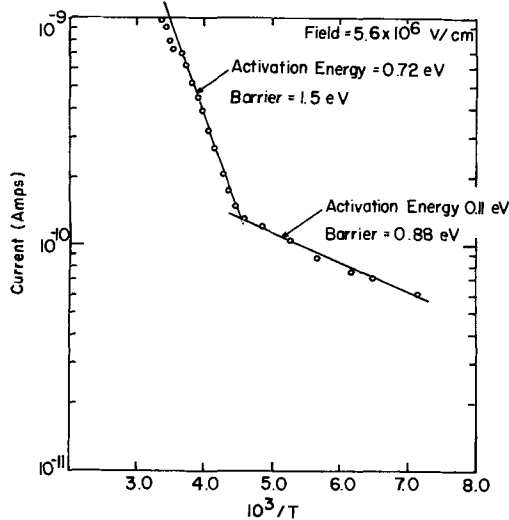


Fig. 8. Current variation with temperature showing 2 activation energies.

behavior seen on some devices in which the slope is that expected for Schottky emission. The behavior of these devices are quite different from those described above. These devices exhibit slow transient currents

when the bias is increased similar to those observed on SiO<sub>2</sub> (7), and several minutes are sometimes required before the steady-state value is attained. The ammonia to silane ratio for the device of Fig. 10 was 10:1 and quite probably the film was nonstoichiometric with silicon-rich areas in the films. Johansen (8) proposes a model for SiO<sub>x</sub> in which the electrons are emitted from small islands of silicon embedded in the oxide. The behavior is similar to emission from a metal if the islands are larger than the distance from the interface to the position of maximum barrier. This model could explain the data of Fig. 10.

Figure 11 shows the slopes of plots of  $\ln I$  vs.  $V^{1/2}$  as a function of the film thickness. The data divide into two groups. The upper group corresponds to devices with current characteristics similar to Fig 9 and the lower group corresponds to devices similar to Fig. 10. Figure 11 implies that the lower group tends to occur at thicker films and the upper group occurs with thinner films. While this may be true in part, we believe that the film composition is probably the determining factor.

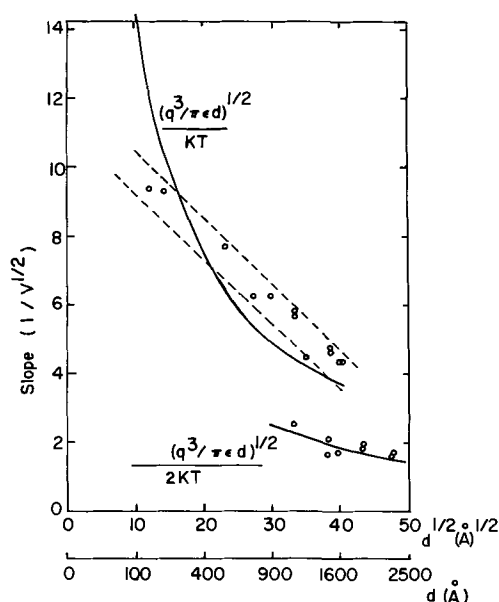


Fig. 11. Variation of slope of  $\ln I$  vs.  $V^{1/2}$  with film thickness

### Discussion

Two types of current behavior have been observed in thin films of silicon nitride. One type tends to occur at fields of  $2 - 9 \times 10^6$  v/cm with steady behavior that follows the Poole-Frenkel model for internal field-assisted thermal emission. Another type seen on some samples exhibits a lower slope on a plot of  $\ln I$  vs.  $V^{1/2}$  and transient effects similar to those observed on  $\text{SiO}_2$ . Different substrates and electrode materials have no observable effects on the current, suggesting that bulk effects control the current. A strong temperature dependence is characteristic of both types.

The nitride forms films below 100Å thickness that exhibit similar current behavior to thicker films indicating that the nitride has fewer pinholes than films of

thermally grown  $\text{SiO}_2$ . This suggests its possible use in tunneling devices.

### Conclusions

Thin films of silicon nitride deposited on substrates of quartz and silicon exhibit a reproducible d-c current component that occurs at high fields but before breakdown. A strong temperature dependence, a linear dependence of  $\ln I$  on  $V^{1/2}$ , and an absence of electrode control indicate that the dominant mechanism at room temperature is thermal emission from the bulk of the nitride.

### Acknowledgment

The authors received generous support from the Bureau of Engineering Research, University of Texas at Austin, Joint Services Electronics Program Grant AF-AFOSR-766-67, NASA Grant NGR 44-012-043 and NSF Grant GK-1395. Many colleagues working on related problems assisted considerably in developing the experiment and analysis.

Manuscript received Aug. 2, 1967; revised manuscript received Oct. 16, 1967. This paper was presented at the Dallas Meeting, May 7-12, 1967, as Abstract 51.

Any discussion of this paper will appear in a Discussion Section to be published in the December 1968 JOURNAL.

### REFERENCES

1. K. E. Bean, P. S. Gleim, R. L. Yeakley, and W. R. Runyan, *This Journal*, **114**, 773 (1967).
2. V. Y. Doo and D. R. Nichols, Paper presented at the Philadelphia Meeting of the Society, Oct. 9-14, 1966, as Abstract 146.
3. G. A. Brown, W. C. Robinette, and H. G. Carlson, A Recent News Paper, presented at the Philadelphia Meeting of the Society, Oct. 9-14, 1966, as Recent News Abstract 1.
4. S. M. Hu, D. R. Kerr, and L. V. Gregor, *Appl. Phys. Lett.*, **10**, 97 (1967).
5. S. M. Sze, *J. Appl. Phys.*, **38**, 2951 (1967).
6. J. Frenkel, *Phys. Rev.*, **54**, 647 (1938)
7. T. E. Hartman, J. C. Blair, and R. Bauer, *J. Appl. Phys.*, **37**, 2468 (1966).
8. J. T. Johansen, *ibid.*, **37**, 499 (1966).

## Electropolymer Studies, I

### Dielectric Properties of Ionic Membranes

Zeljko Urban

Sea Water Conversion Laboratory, College of Engineering, University of California, Berkeley, California

and Richard A. Wallace

Department of Chemical Engineering, Polytechnic Institute of Brooklyn, New York

### ABSTRACT

The dielectric properties of polystyrenesulfonic acid membranes in their hydrogen form have been studied over the frequency range of  $10^2$ - $10^5$  Hz, with water content and temperature as parameters. Dielectric dispersion is observed for slightly wet sulfonate membranes and is considered to be water-induced. Two distinct membrane hydration stages have been noted at low water contents. Dielectric dispersion processes of the wet ionic membrane in its sodium and potassium forms are also discussed.

Little is known about the influence of absorbed water on dielectric properties of ionic polymer materials. Dickel and Bunzl (1) measured dielectric constants of a variety of sulfonate resins as a function of their water content. They showed that the sorption

process of water in these ionic polymers is not continuous but stepwise. They also found that the hydrogen ion in the hydrated  $-\text{SO}_3^{(-)}\text{H}_3\text{O}^{(+)}$  complex of the sulfonic acid group favors a position closer to the sorbed water rather than to the  $-\text{SO}_3^{(-)}$  group. This

finding supports earlier work of Zundel, Noller, and Schwab (2) who studied hydration stages in sulfonic acid films by means of IR-spectrography.

Kurosaki (3) evaluated the dielectric behavior of sorbed water on silica gel and experimentally showed that three distinct regions of water absorption existed. Invoking Fuoss-Kirkwood theory (4), Kurosaki derived an expression for the differential specific polarization of sorbed water. This expression can be useful in analyzing effect of water on dielectric constant. It should be noted, however, that the values of polarization calculated by Kurosaki's formula are approximate. They are useful when comparing differential specific polarizations of various water-absorption stages.

In this paper we present the dependence of dielectric properties of cationic membranes on their sorbed water content and temperature in the low frequency range. Membrane electrical response characteristics are interpreted in terms of specific polarization and by Cole-Cole analysis.

### Experimental

Polystyrenesulfonic acid membranes were manufactured by Asahi Chemical Company under brand name DK-1. They were converted into the hydrogen form, leached several times with distilled water, and cut into disks. Samples were 2.54 cm in diameter and, on the average, 0.23 mm thick.

Dielectric measurements were made with frequency as a variable and membrane water content and temperature as parameters. Apparatus for the measurements is shown schematically in Fig. 1. G.R. 716-C bridge was used in conjunction with G.R. oscillator, type 1210-C and G.R. 1232-A tuned amplifier as a null-detector. A stainless steel electrode assembly was connected in series with a 1000 pF standard capacitor to the bridge.

Each membrane disk was vacuum dried at 55°C prior to testing. Dielectric tests were carried out in a vacuum oven maintaining temperature within 0.5°C. Membrane weight was measured before and after tests and then averaged. Membrane water content, expressed as molecules of water per equivalent of exchange group  $n$ , is given by

$$n = \frac{(m_w/m_d - 1) 55.5}{Q} \quad [1]$$

where  $Q$  is exchange capacity of the membrane, and  $m_w$  and  $m_d$  are the wet and dried membrane weight, respectively.  $m_d$  was measured after vacuum drying at 70°C for 24 hr. The membrane in this virtually dry condition is referred to as dried. The thickness of membrane disks was measured with Gaertner cathetometer M930 to within 0.001 mm.

Membrane capacitance,  $C$ , and dissipation factor,  $D$ , were measured in the frequency range  $10^2$  through  $10^5$  Hz. Since both  $C$  and  $D$  averaged relatively high, the 1000 pF standard capacitor,  $C_{ST}$ ,  $D_{ST}$ , was added in series with the sample to bring the measured capacitance,  $C_M$ , and dissipation factor,  $D_M$ , to within the measuring range of the bridge. Then the unknown membrane capacitance and dissipation factor were calculated from the values of  $C_M$ ,  $D_M$ ,  $C_{ST}$ , and  $D_{ST}$ .

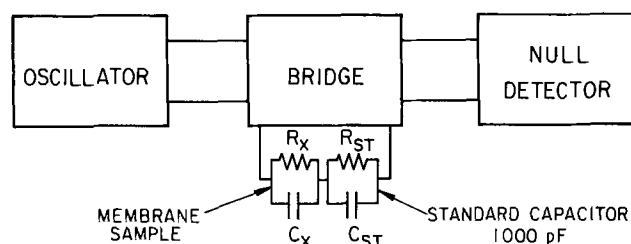


Fig. 1. Schematic diagram of apparatus to measure the dielectric properties of ion-permeable membranes.

Dielectric constant,  $\epsilon'$ , and loss,  $\epsilon''$ , are computed from membrane capacitance and dissipation factor

$$\epsilon' = \frac{Cd}{\epsilon_r A}; \quad \epsilon'' = D \cdot \epsilon' \quad [2]$$

where:  $\epsilon_r = 8.85 \times 10^{-14}$  F/cm, absolute dielectric constant of vacuum or dry air;  $d$  = distance between electrodes, cm; and  $A$  = electrode area, cm<sup>2</sup>.

Electrode polarization represents a serious error in dielectric measurements especially at low frequencies. In order to record meaningful results, electrode polarization effects must be minimized.

In Fig. 5 is shown the frequency dependence of dielectric loss  $\epsilon''$  for slightly wet ( $n = 1.1$ ) membrane at various temperatures. All four curves display a deviation from a standard bell-shaped  $\epsilon''$  vs. frequency curve. This deviation, due to electrode polarization, seems to occur only at frequencies lower than 2000 Hz. Therefore, it was felt justified to neglect the electrode polarization effect at frequencies higher than 2000 Hz.

Measured values of dielectric constant at frequencies below 2000 Hz were corrected for electrode polarization effects. Cole-Cole circular plots (5) were constructed using the values at frequencies higher than 2000 Hz. Then the values of the static dielectric constant  $\epsilon'_0$  were determined from these plots. Based on this information, membrane dielectric constant values were plotted for frequencies below 2000 Hz, such as shown in Fig. 4.

### Results and Discussion

The sulfonic acid membrane dielectric constant,  $\epsilon'$ , is given in Fig. 2 as a function of water content at 100,000 Hz. This curve illustrates the sorption process of water in the cationic membrane. Similar results were reported by Rosen on effect of water on protein systems (6). Two distinct water-sorption regions are evident. A transition occurs at a water content of  $n \approx 1$ .

Using Kurosaki's Eq. [3] for specific polarization

$$\bar{P}_n = \frac{2\epsilon'^2 + 1}{9\epsilon'^2 \rho} \frac{\partial \epsilon'}{\partial n} \quad [3]$$

where  $\epsilon'$  = measured dielectric constant,  $\rho$  = membrane specific gravity, and  $(\partial \epsilon' / \partial n)$  = variation of dielectric constant with the change of water content, membrane polarizations were calculated. At low water content ( $0 < n < 1$ )  $\bar{P}_n$  is about 0.35. For the higher water content ( $n > 1$ ),  $\bar{P}_n \approx 42$ . This big difference

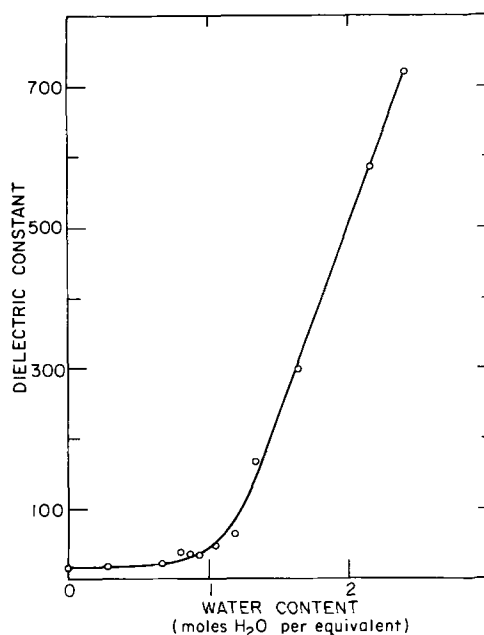


Fig. 2. Effect of water content on dielectric constant  $\epsilon'$  for sulfonic acid membrane at 100,000 Hz and 20°C.



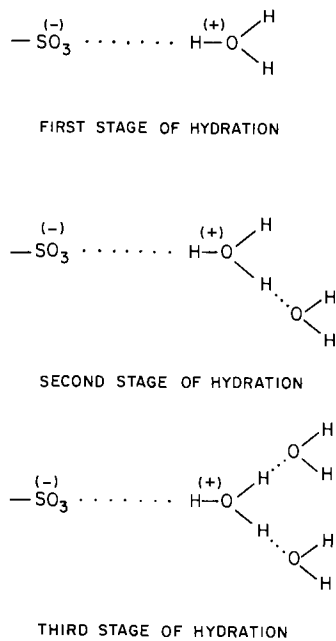


Fig. 3. Initial hydrations in sulfonic acid membrane

suggests that the sorbed water could cause the membrane to change drastically in its degree of polarizability. Once the water content exceeds the value of  $n \approx 1$  the membrane seems to become highly polarizable.

There is a possible explanation for this abrupt change of specific polarization. In the dried membrane the hydrogen ions are associated with  $-\text{SO}_3^{(-)}$  groups by strong ionic bonds. The whole group  $-\text{SO}_3^{(-)}\text{H}^{(+)}$  is stiff and difficult to polarize. Therefore, the differential specific polarization  $\bar{P}_n$  is rather low.

As the water is sorbed by the membrane the  $-\text{SO}_3^{(-)}\text{H}^{(+)}$  groups hydrate into  $-\text{SO}_3^{(-)}\text{H}_3\text{O}^{(+)}$  ( $n = 1$ ) then  $-\text{SO}_3^{(-)}\text{H}_5\text{O}_2^{(+)}$  ( $n = 2$ ),  $-\text{SO}_3^{(-)}\text{H}_7\text{O}_3^{(+)}$  ( $n = 3$ ), etc. The hydrogen ions begin to dissociate from the  $-\text{SO}_3^{(-)}$  groups and associate with water molecules (1). Now  $-\text{SO}_3^{(-)}$  groups will be coordinated with hydrated hydrogen ions by hydrogen bonding. These bonds confer on hydronium ions a flexibility to move in applied electrical field, enabling them to polarize. Thus the  $\bar{P}_n$  number is high.

Figure 3 illustrates the hydration process in a sulfonic acid membrane. The hydrogen ion is depicted in its preferred position adjacent to the hydrated water (1, 2).

A family of curves representing the relationship of dielectric constant on frequency for slightly wet membrane at various temperatures is shown in Fig. 4. The membrane water content is 4.9% by weight or  $n = 1.1$ . The dashed portions of the curves are corrected for electrode polarization effects as described in experimental section. All four curves display a similar shape. The dielectric constant decreases with increasing frequency passing through a point of inflection. The point of inflection determines the position of characteristic frequency,  $f_c$ . The locations of characteristic frequencies were found by means of Cole-Cole plots. The position of  $f_c$  moves toward higher values as the temperature increases. This shift is probably due to the decrease of membrane microviscosity at higher temperatures.

In Fig. 5 are shown the dielectric loss-frequency curves for the same slightly wet membrane.

Dependence of maximum loss,  $\epsilon''_{\text{max}}$ , on water content at room temperature is shown in Fig. 6. The general trend follows the linear rise of  $\epsilon''_{\text{max}}$  with increasing water content. This seems to suggest that the dielectric absorption in the wet membrane is water-induced. Water-induced dielectric absorption was also

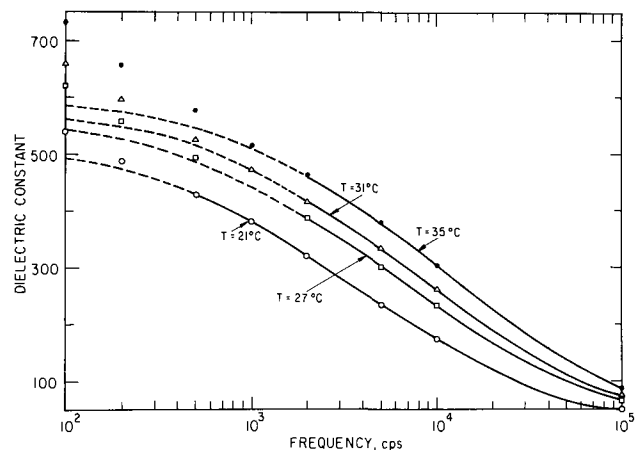


Fig. 4. Frequency dependence of dielectric constant  $\epsilon'$  of slightly wet ( $n=1.1$ ) sulfonic acid membrane at various temperatures. Dashed portions are corrected for electrode polarization effects.

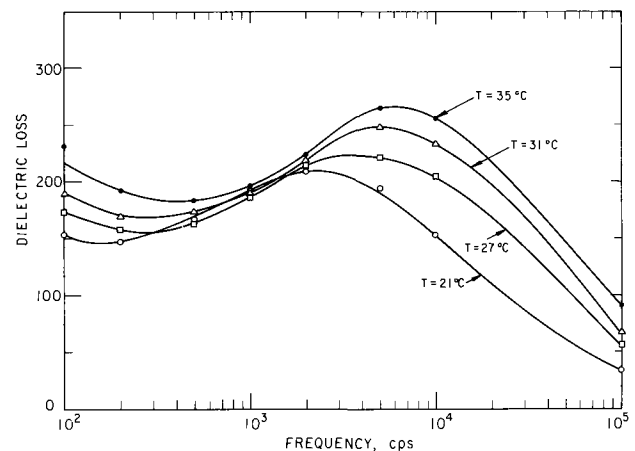


Fig. 5. Frequency dependence of dielectric loss  $\epsilon''$  of slightly wet ( $n=1.1$ ) sulfonic acid membrane at various temperatures.

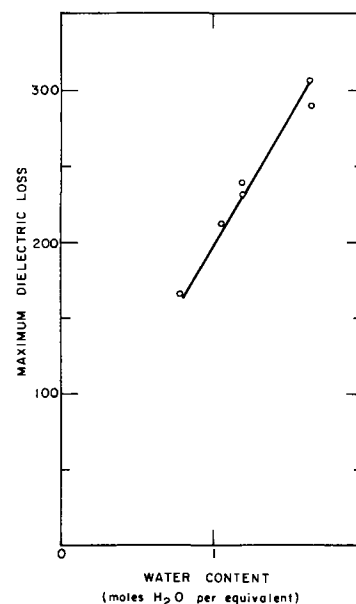


Fig. 6. Effect of water content on maximum loss for sulfonic acid membrane at room temperature.

found by other investigators for a series of various polymeric materials (7, 8).

The change of membrane dielectric properties caused by sorbed amounts of water is represented by Cole-Cole plots in Fig. 7. Relatively small amounts of

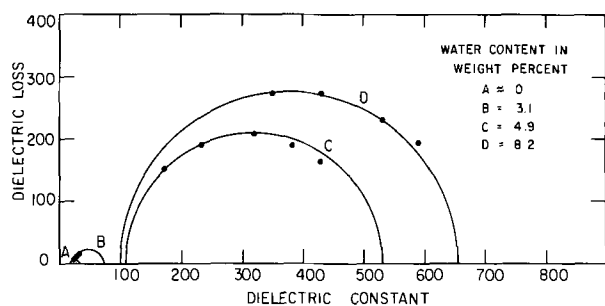


Fig. 7. Cole-Cole plots for sulfonic acid membrane at 20°C for various water contents.

sorbed water appreciably influence the shape and position of Cole-Cole plots.

Results suggest that the presence of water in sulfonic acid membrane gives rise to a specific, water-induced relaxation process. This process is characterized by high dielectric constant, loss, and dielectric increment,  $\Delta\epsilon'$ . Its characteristic frequency occurs between  $10^3$  and  $10^4$  Hz.

Measurements have also been carried out for the slightly wet sulfonic acid membrane in sodium and potassium forms. From  $\log f_c$ , vs. reciprocal absolute temperature plots, experimental activation energies have been calculated. Typical results are summarized in Table I. For comparison our experimental value for the activation energy of slightly wet membrane in hydrogen form is given.

Table I points out that the activation energy for the membrane in its hydrogen form is about three times smaller than in its sodium or potassium form even though its water content is three times lower. The presence of water within the membrane lowers the

Table I. Activation energies of dielectric dispersion within sulfonic acid membrane in three ionic forms

Ionic form	Water content, moles H <sub>2</sub> O per equivalent	Experimental activation energy, kcal/mole
Hydrogen	1.1	10.8 ± 10%
Sodium	3.8	28.6 ± 10%
Potassium	3.1	31.5 ± 10%

energy barrier of the ionic polarization process. In response to an applied electric field, hydrogen ions seemingly polarize an order of magnitude easier than either sodium or potassium ions.

Manuscript received June 21, 1967; revised manuscript received Nov. 3, 1967. Research on this paper was sponsored jointly by the Office of Saline Water, U. S. Department of the Interior, and Water Resources Center, University of California, Berkeley, California.

Any discussion of this paper will appear in a Discussion Section to be published in the December 1968 JOURNAL.

#### REFERENCES

1. G. Dickel and K. Bunzl, *Macromol. Chem.*, **79**, 54 (1964).
2. G. Zundel, H. Noller, and G. M. Schwab, *Z. Elektrochem.*, **66**, 129 (1962).
3. S. Kurosaki, *J. Phys. Chem.*, **58**, 320 (1954).
4. R. M. Fuoss and J. G. Kirkwood, *J. Am. Chem. Soc.*, **63**, 385 (1941).
5. K. S. Cole and R. H. Cole, *J. Chem. Phys.*, **9**, 341 (1941).
6. D. Rosen, *Trans. Faraday Soc.*, **59**, 2178 (1963).
7. D. J. Scheiber and D. J. Mead, *J. Chem. Phys.*, **37**, 81 (1962).
8. L. V. Krasner, G. P. Mikhailov, and D. I. Mendeleeva, *Vysokomol. Soedin. Vsesoyuz. Khim. Obschestvoim.*, **1**, 558 (1959).

## Direct Observation of Precipitate Phenomena and Dislocations in Annealed CdS:Cu and CdS:Au Single Crystals

Arthur Dreeben\*

RCA Laboratories, Radio Corporation of America, Princeton, New Jersey

#### ABSTRACT

The procedure of high-temperature annealing followed by quenching was used to produce significant changes in the microstructures of as-grown CdS:Cu and CdS:Au single crystals. The use of optical microscopy enabled these changes to be directly observed with high resolution. The solubility of copper is retrograde, the maximum being about 0.2 w/o between 475° and 650°C; the maximum solubility of gold is less than 0.03 w/o. Annealing CdS:Cu between 700° and 1100°C causes temperature dependent microchanges that include the formation and growth of precipitates and the generation of dislocations by prismatic punching. In the case of gold, initial precipitates change only when crystals are annealed at or above 900°C. High-temperature precursors of room temperature precipitates are identified from reversible changes in morphology, and unique, high-temperature dislocation structures are observed. Gold also diffuses to the crystal surface where it forms characteristic epitaxial deposits.

This study of the effects of annealing on impurity structures in CdS crystals has a dual purpose. First, treatment of CdS luminescent materials frequently involves heating samples to temperatures of 800°C and higher for various time intervals, after which the material is either slowly cooled or rapidly quenched.

\* Electrochemical Society Active Member.

Although variations in these treatments can produce profound effects in the electrical or luminescent properties of the solids, the accompanying changes in the internal state of the impurities is not always understood.

Second, the detailed behavior of impurities in semiconductors and insulators is a subject of continuing

interest. In semiconductors such as germanium and silicon, donor and acceptor impurities exhibit a retrograde solubility (1) and tend to precipitate out if annealed at temperatures where their solubility is low. Nevertheless, because of their relatively small diffusion constants in these materials, the impurities can be preserved in a metastable state by quenching to room temperature. However, these semiconductors are not transparent to visible light, so that the detailed nature of the precipitate states are often inferred from relatively indirect procedures with only poor definition.

In the case of CdS, direct optical microscopy with high resolution has recently been used to observe decorated dislocations and the morphology and crystallography of precipitate phases in slowly cooled, as-grown crystals (2-5). This highly successful technique has now been employed to view the temperature dependent, transient changes in microstructures that occur when CdS:Cu and CdS:Au single crystals are annealed.

It is found that copper exhibits a retrograde solubility, and that the maximum solubility of copper is greater than gold, 0.2 w/o compared to less than 0.03 w/o. Classical precipitate behavior and morphologies, including formation and dissolution at grain boundaries, conversion of one species into another, and the appearance of new species are clearly observed. Evidence is presented for the generation of dislocations by precipitate particles, and by the mechanism of prismatic punching.

### Experimental

Crystallographically oriented and polished (0001) slices from large vapor grown boules of CdS:Cu and CdS:Au (2-4) were examined for internal microstructures, and photographed under the optical microscope. These crystals were placed in quartz vials that were subsequently evacuated to about  $10^{-6}$  Torr and then filled with purified argon to provide approximately 1 atm pressure at the annealing temperature. The sealed vial was placed in a vertical furnace for the desired length of time after which it was quenched in liquid nitrogen. Some crystals were lightly repolished to remove effects of thermal etching before microscopic examination.

### CdS:Cu Crystals

**Results.**—The internal appearance of the as-grown crystals, as viewed with the optical microscope using transmitted light, was characterized by a polygonal structure as shown in Fig. 1. Chemical analyses of representative crystals showed that they contained 0.05-0.06 w/o Cu, and subsequent analyses after an-

nealing established that no copper was lost during annealing.

The initial microstructure appeared invariant in samples quenched from annealing temperatures lower than 450°C. Treatment at 450°C, however, caused perceptible changes including the elimination of some sub-boundary decoration and a general decrease in precipitate density. Raising the annealing temperature to 475°C appeared to effect complete solution of the precipitate after 45 min. No microstructures, precipitates, boundaries, or other decorations, could be observed even under high power (1050X) magnification. This condition prevailed with no other detectable changes for annealing temperatures up to 650°C, and for prolonged firing times. Above 650°C, however, new precipitate formations occurred in several temperature dependent stages.

The first change, observed in samples annealed at 700°C, was the formation of submicron sized particles distributed almost exclusively along sub-boundaries. The next modification occurred between 700°-800°C in crystals annealed for about 1 hr. It was observed that the particles had grown appreciably to form discrete clusters with an average size of about  $15\mu$ . The clusters were randomly distributed and also arranged linearly along dislocation lines. As seen in Fig. 2, the clusters consist of a dark, circular precipitate with several short radiating arms. The arms themselves are diffusely decorated and often terminate with circular precipitates similar to the central one. Slight additional growth of the system occurred, particularly in the clusters along dislocation lines, when samples were annealed at 850°C for 1 hr, but the configurations were then unaffected by further annealing at the same temperature for up to 5 hr.

A third stage which occurs in some samples after annealing at 900°C for 45 min is marked by a considerable growth of the clusters into asterisk-shaped aggregates up to  $70\mu$  across as shown in Fig. 3. These aggregates are also characterized by a central precipitate with decorated arms. The particular decoration along arm a in Fig. 3B, is characteristic of helical dislocations. Some crystals also had circular loops composed of small precipitates.

The shape itself of the asterisk-like structures, suggests that a particular process may be responsible for their formation in the following manner. After the crystals are annealed at 700°C, the first visible particles appear at boundaries which are well-known preferred sites for precipitation. At higher temperatures, these precipitate particles grow into clusters which then also appear at other sites where nucleation occurs less readily than at boundaries. It is reasonable to assume that these enlarged precipitates cause local strains in the host lattice; generation of dislocations by the process of prismatic punching is one way by which these

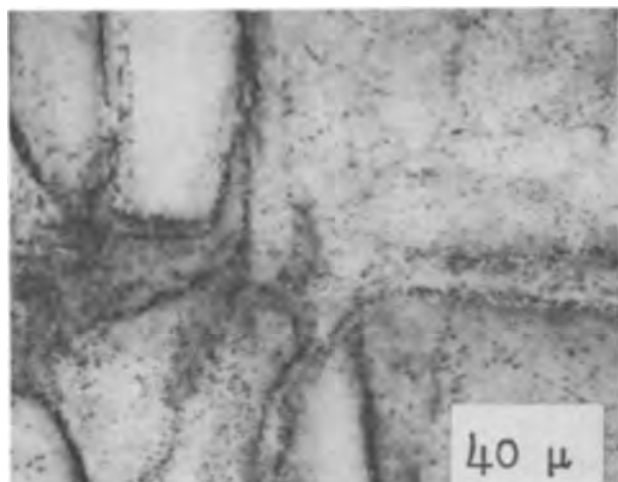


Fig. 1. Microstructure in as-grown CdS:Cu crystal. Plane of observation: (0001).

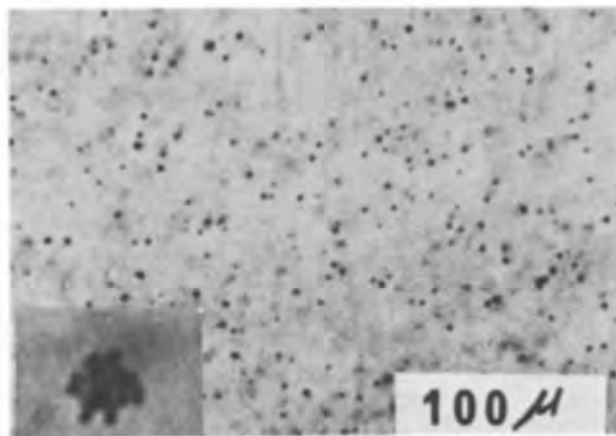


Fig. 2. Aggregates formed after anneal at 800°C. High magnification insert (4X larger) shows typical formation.

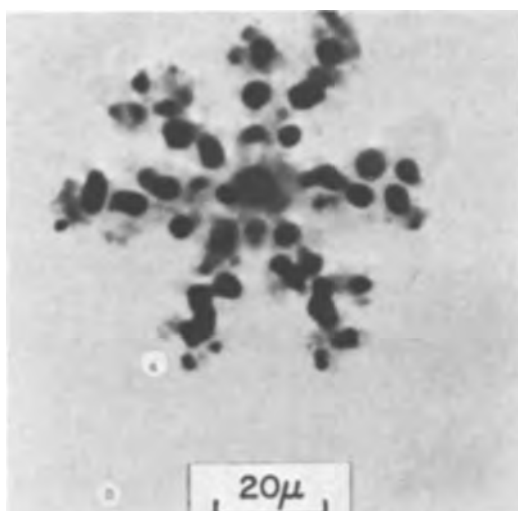
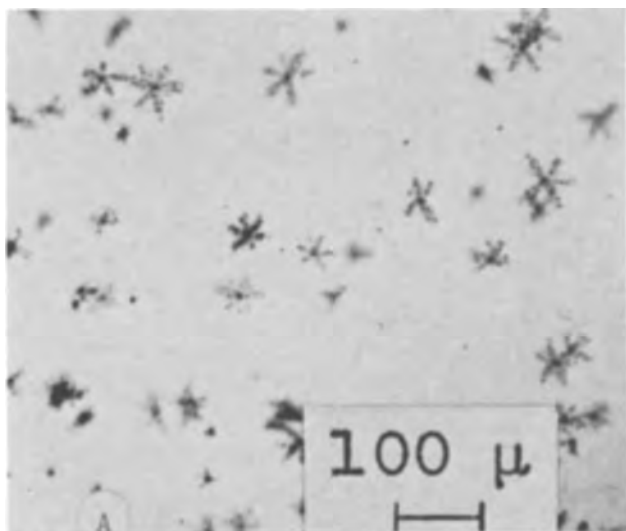


Fig. 3. (A) Asterisk decorations after anneal at 900°C; (B) high magnification detail of asterisk. Note helix at arm a.

strains can be relieved (6). The asterisk shapes, and the appearance of helical dislocations in their arms (as in Fig. 3B) are strong characteristics of this process. It has been recognized in many other crystals (7) containing precipitates that are insoluble at high temperatures, including (Zn,Cd)S:Er (5).

The progressive growth of the asterisk configurations apparently terminates between 900° to 1100°C. After 30 min at the higher temperature, the larger aggregates reformed into discrete precipitates often having a hexagonal morphology and arranged in hexagonal arrays as in Fig. 4. Regions were also observed in which the precipitates were arranged in parallel lines suggestive of slip bands. All of these decorations were further changed by longer annealing at 1100°C. After 5 hr for example, columnar subgrains and low angle boundaries, as shown in Fig. 5, were predominant features; low energy configurations, such as these boundaries, are known to arise during annealing at elevated temperatures (8).

Reheating these crystals to 900°C and then slowly cooling instead of quenching them caused a reversible change in the precipitation to a pattern similar to the original in Fig. 1. In previous work (4), cardioids, dipoles, and other dislocation configurations were observed in slowly cooled as-grown CdS:Cu crystals. It is noteworthy that none of these types were found in any of the quenched crystals. These observations provide evidence that the dislocations seen in the as-grown crystals are probably generated by the second

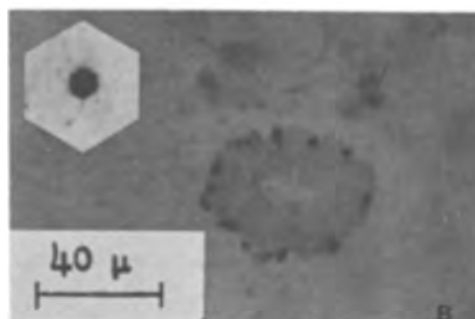
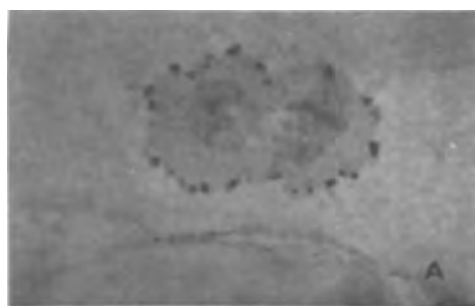


Fig. 4. (A) and (B) Discrete precipitates, randomly distributed and arrayed in hexagonal formations. Insert in B (1.7X larger) shows hexagonal shape of precipitate itself. All results after 30-min anneal at 1100°C.



Fig. 5. Columnar subgrains in crystal annealed for 5 hr at 1100°C

phase particles as they precipitate from solution when the crystal cools below 475°C.

To establish some limit for the high-temperature solubility, selected crystals with 0.2 and 0.8 w/o Cu were annealed at 650°C and then quenched. In the sample with 0.2 w/o, a very slight precipitate remained visible, whereas a heavy precipitate persisted in the 0.8 w/o sample. At an annealing temperature of 800°C, precipitates remained in both samples. Therefore, copper exhibits a retrograde solubility with a maximum of slightly less than 0.2 w/o occurring in the temperature interval between 475° to 650°C. This is about an order of magnitude greater than the value of 0.02 w/o found in slowly cooled, as-grown crystals (2).

In addition to reduced solubility of the added impurity, two other mechanisms that can account for precipitation in crystals have been pointed out by Black and Jungbluth (9). The first is the formation of

a stable, insoluble compound between the impurity and host. In relation to the present results, it may be pointed out that the existence of a (Cu,Cd)S complex or compound was postulated in connection with experiments on some electroluminescent phosphors (10). However, in the present case, attempts to distinguish different chemical species among the precipitates by microprobe analyses were inconclusive. The second mechanism involves exsolution of residual impurities analogous to the common ion effect that occurs in aqueous chemistry. The low concentration of other impurities in these crystals, however, makes this alternative much less likely.

Another experiment demonstrates that the quenched-in high-temperature solid solutions can be metastable. In the as-grown, polygonized sample shown in Fig. 6A, it has been estimated that the copper concentration at the boundaries is about 0.8 to 1.0 w/o, but that it is only about 0.2 w/o within the grains (4). This sample was annealed at 900°C in a high-pressure bomb under an Ar pressure of 600 psi and then quenched. At that time, microscopic observation showed that all of the precipitates had been eliminated, but that the boundaries were still visible as shown in Fig. 6B. Subsequent reexamination of the sample, which had been aging at room temperature for about one year, revealed that discrete precipitates were again beginning to form at the boundaries as shown in Fig. 6C. During a still later examination, precipitates were also found within grains. It may be pointed out that some influence of pressure on solubility is indicated by the absence of detectable precipitates after the high-pressure anneal, contrasted with only partial solubility in the previously described similar samples, also annealed at 900°C, but under 1 atm pressure.

The CdS:Cu crystals used in these experiments had a very high initial resistivity that did not change detectably in the samples quenched between 475° and 650°C, i.e., those with a maximum amount of copper in solution. This result is consistent with recent conclusions that due to self-compensation (11), p-type conductivity cannot be induced in CdS merely by incorporating acceptor atoms such as copper (2, 12). In experiments on low resistivity CdS:Cu,Cl crystals, Woods (13) reported that copper decorations disappeared, and the resistivity greatly increased when the crystals were rapidly quenched from 700°C. From

this he concluded that a supersaturated concentration of copper acceptors had been quenched in. In that case, however, the copper acted to partially compensate the chloride donors, thereby accounting for the increased resistivity.

### CdS:Au Crystals

In the as-grown samples, the important microfeatures are best observed by viewing the basal (0001) plane. These initial features consist of two types of individual and arrayed precipitate platelets having an extremely regular, hexagonal morphology, together with associated dislocations (3), all of which may be seen later in Fig. 9A. Type I platelets are 2.5-7 $\mu$  across, and are found in clusters or as randomly distributed individuals. They also appear in the highly symmetrical decorations that mark dislocations around type II platelets. The type II are much larger, 160 $\mu$  across, and have a different composition and crystallographic orientation with respect to CdS (3). It is also noteworthy that the hexagonal precipitates are the only ones present in as-grown crystals, and the symmetrical dislocation arrays are observed only in strained regions around the type II hexagons (3). The microscopic changes that occur when the crystals are annealed involve both types of precipitates, and each will be considered separately.

*Results.—Type I precipitates.*—At annealing temperatures below 900°C, no changes could be found in quenched samples. The first change, occurring in crystals heated at 900°C, was an appreciable growth in the size of the platelets from an initial average of 5 $\mu$  to about 9 $\mu$ . A group of three clusters in a crystal are compared before-and-after being heated and quenched, in Fig. 7. It is interesting that neither the general make-up of clusters nor their positions in crystals were appreciably changed. Simultaneously, micron sized particles appeared, often decorating dislocation lines and sub-boundaries not originally present in the as-grown specimens. In addition the particles were found in radially arrayed decorations above (or below) the clusters of enlarged hexagons and individual platelets.

In crystals annealed at 1000°C, further development of the particle network was noted; some hexagons assumed a spherical shape, and large radial decora-

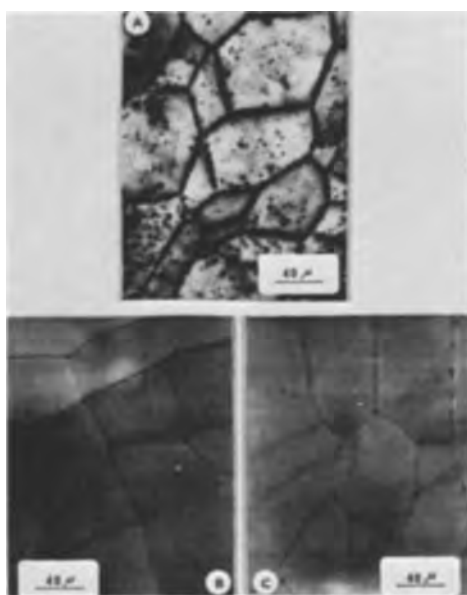


Fig. 6. Metastable, quenched-in solid solution in CdS:Cu crystal. (A) Structure in as-grown CdS:Cu crystal; (B) same crystal after being annealed under pressure; note absence of precipitates; (C) same crystal after long aging at room temperature, showing re-precipitation at boundaries.

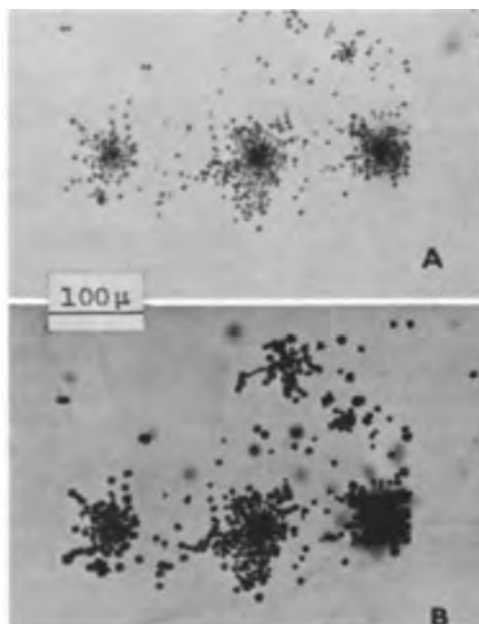


Fig. 7. Clusters of type I hexagonal precipitates in basal plane of CdS:Au crystal: (A) as-grown, (B) after being annealed for 2 hr at 900°C and rapidly quenched. Note identical arrangement of precipitates, but with increased size. Note also new decoration of sub-boundaries in (B).

tions, more clearly defined as asterisk formations, continued to develop locally around cluster and single hexagons. In addition to acting as sources for these localized dislocations, some hexagons also acted as pinning points for line dislocations.

At 1100°C, several additional observations were made. In the midst of the changing microfeatures, original low angle boundaries remained relatively unchanged even after 30 min at temperature. Many hexagon clusters along the boundaries survived the annealing, but many of those within the grains did not. Individual precipitates were still present, but most of these formerly hexagonal species were now spherical. There was an additional and final development of the previously noted dislocations around the remaining clusters, and these features are illustrated in Fig. 8. It can be seen that the asterisk has now been enclosed by a loop with distorted hexagonal symmetry, and that the particles decorating both configurations have become rod-like. Note particularly that these typical arrays are not in the plane of the cluster (3).

The experimental results suggest a possible connection between the rod-like and type I precipitates. It has been shown that the type I hexagons persist and even grow in size when crystals are quenched from 900°C, but that they are replaced by a rod-like species when quenched from 1100°C. On the other hand, however, it was found that upon being slowly cooled from this temperature, many hexagons reform, sometimes with an increase in size, at the same crystal sites they formerly occupied. The before-and-after appearances are very much like those in Fig. 7. Enlarged hexagons are more often found in the interior of crystals while smaller ones are observed nearer the surface.

From these observations together with the well known finding that a rod-like morphology is often adopted by precipitates in an early stage of growth (14), it is reasonable to assume that the rods are early precursors of the type I precipitates. The observed increase in the size of type I hexagons may occur at the expense of smaller ones, perhaps by the process of Ostwald ripening (15) which involves the mobility of precipitate atoms in the "solvent" (CdS) phase, and of the matrix atoms themselves.

The processes that occur during annealing at 1100°C are also affected by time, about 1 hr being required

to establish an apparent steady-state condition with respect to microfeatures. (No additional changes were observed after a 2-hr period.) The notable final characteristics included the destruction of clusters and their dislocation systems, and the development of asterisks quite similar to the CdS:Cu formation shown in Fig. 3. These are believed to arise from the same prismatic punching process previously discussed. Circular loops and spirals were also observed.

The lowest grown-in amount of gold was 0.03 w/o in boules containing only type I precipitates. Even in these samples, however, some kind of precipitate was observed at intermediate annealing temperatures up to 1100°C, showing that the high-temperature solubility of Au in CdS is significantly less than that of Cu. This may be related to the formation of stable high temperature compounds (9) between Au and CdS, and to the larger radius of gold. Evidence for the possible retrograde solubility of gold could not be established in these experiments since the continued presence of precipitates after each annealing step implies that the maximum solubility of gold was always exceeded.

*Type II precipitates.*—Typical localized type II hexagons in as-grown crystals are shown in Fig. 9A, together with their associated dislocation networks decorated with type I precipitates. Figure 9B of the same field but between crossed polarizers, shows the strain birefringence around the giant precipitates, while Fig. 9C illustrates the ultimate situation after annealing at 1050°C for 1 hr destroyed the large hexagons. New dislocation lines, or possibly low angle boundaries can now be seen together with configurations remaining at their original sites. The rate at which this situation is attained depends on time and temperature, but 1050°C was found to be convenient for determining intermediate annealing effects in reasonable time intervals.

It was found that an extensive erosion begins at the centers of the hexagons as shown in Fig. 10, simultaneously with a less rapid over-all reduction in their size. The faster disintegration of the broad face may result from a difference in surface energy between it and the prism planes. Enlarged details of the situation after type II sources are completely removed are shown in Fig. 11.

In this final state, it was observed that the strain birefringence (see Fig. 9B) was still present around the former type II sites, and it is not surprising, therefore, that the decorations seen in Fig. 11 also remain. It will be noted, however, that these decorations are now comprised of particles and rods instead of the

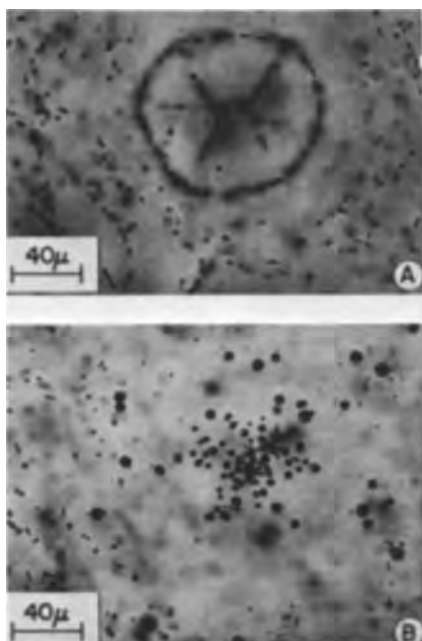


Fig. 8. Decorated dislocation arrays in CdS:Au crystal annealed for 1 hr at 1100°C. Depth of observation in A is 0.24 mm above cluster of type I precipitates in B. Note rod-like decorating species.

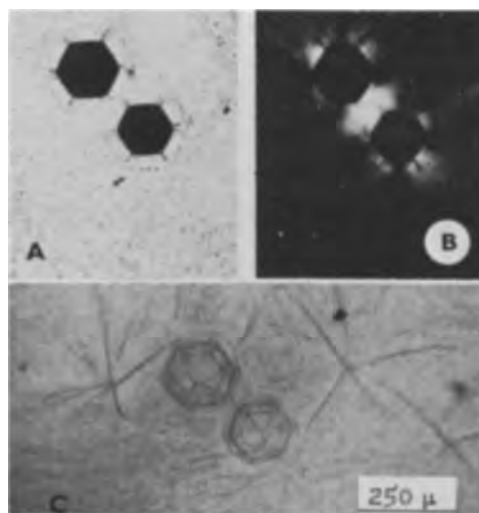


Fig. 9. (A) Type II precipitates in (0001) plane of CdS:Au crystal; (B) same field between crossed polarizers showing strain birefringence; (C) same field after quenching crystal from 1-hr anneal at 1050°C.

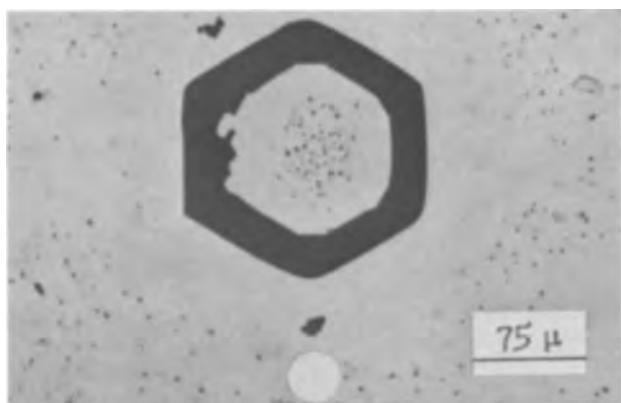


Fig. 10. CdS:Au crystal annealed at 1050°C for 30 min showing central erosion of type II hexagon.

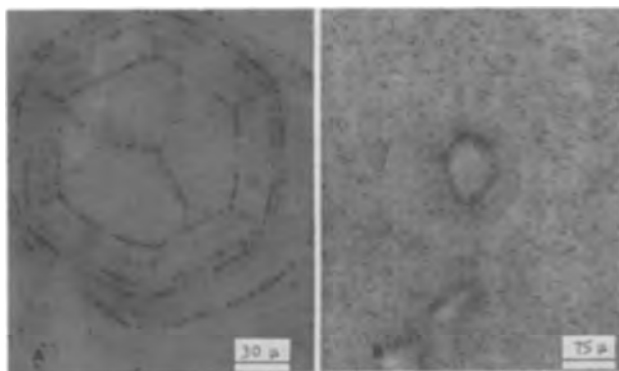


Fig. 11. (A) Detail of decoration remaining at type II site after 1-hr anneal at 1050°C; (B) another type II site after similar treatment, showing loop formation.

original type I hexagons. The possible relationship between these two configurations was discussed earlier. Many dislocation loops, as seen in Fig. 11B were found near the former locations of type II hexagons, but no further study was made of these or other loops pointed out previously.

The difference in size between type I and type II hexagons as effective dislocation sources is noteworthy. In as-grown crystals, no decorations at all were found associated with type I hexagons (3). It will be remembered, however, that in annealed crystals, decorated arrays were observed around individual type I hexagons as small as 9 to 12 $\mu$ , and also around type I clusters 80 $\mu$  in diameter as seen in Fig. 8B. Here, however, the diameter of the generated loop (Fig. 8A) is less than one-half the size typically found with type II hexagons in as-grown crystals (Fig. 9). This kind of decoration was associated with type II precipitates 140-160 $\mu$  across, but was absent when the size was less than 100 $\mu$  (3).

The explanation is believed to be related to the misfit between precipitate and host, and the fact that the two types of hexagons have different compositions and orientations in CdS (3). Apparently the generation of dislocations to relieve the limited strain resulting from the small type I precipitates, can occur only in the more mobile lattice environment at the annealing temperature. In rapidly quenched samples, these dislocations are frozen-in, but the effects are annealed out when the crystals are slowly cooled to room temperature. The greater size of the effective type II hexagons, however, creates a relatively large strain that persists at room temperature not only in as-grown crystals (3), but also in quenched samples, even when the hexagon itself is thermally degraded (Fig. 9C and 11).

The effects of annealing on the type II hexagons were much more rapid when their original locations

were on grown-in dislocation lines. This result is attributed to the well known faster solute diffusion along such dislocation "pipes." Slow cooling of previously annealed specimens in which the hexagons had been destroyed, did not cause them to reprecipitate, in contrast with the type I hexagons. However, there was some preferential particle precipitation around remnants at the type II sites.

In addition to the internal microfeatures described so far, some surface deposits were found on the crystals after annealing steps. The most significant of these was observed after the final annealing treatment at 1050°C for 1 hr and consisted of clusters of individual, truncated hexagonal pyramids. Figure 12 shows a typical example in which the top (in focus) is 54 $\mu$  above the base on the crystal surface.

Chemical analyses for gold showed that as-grown crystals contained about 0.06 w/o, whereas samples annealed and quenched after 1 hr at 1050°C contained only 0.04 w/o. Crystal slices, sectioned to remove any type II precipitates, thus leaving only the small species, also lost some gold, but the surface deposits were not extensive or geometrically defined. The hexagonal morphology of the deposits also reflects the orientation symmetry of type II hexagons which are believed to be gold precipitates (3). It is concluded, therefore, that the pyramids are epitaxial growth forms that result primarily from out-diffusion of the type II precipitates. The diffusion and loss of gold is to be contrasted with the stable behavior of copper in CdS.

#### Summary and Conclusions

The grown-in microstructures in CdS:Cu and CdS:Au single crystals undergo appreciable changes when samples are quenched from elevated annealing temperatures. Copper has a retrograde solubility, and the maximum is estimated to be about 0.2 w/o in the temperature range between 475° and 650°C. Quenching preserves this increased solubility in the solid, but even this greater concentration of acceptor atoms did not cause formation of p-type CdS. The quenched-in solid solution is metastable and reprecipitates when aged at room temperature. Pressure may have an influence on solubility. Evidence has been presented to account for the generation of dislocations by second phase particles and by prismatic punching, to relieve strains at high temperatures.

In contrast to the CdS:Cu crystals, the CdS:Au samples remain unchanged when heated below 900°C. At higher temperatures, however, they undergo remarkable changes involving the growth and eventual reversible deformation of the small (type I) hexagons, and the development of new dislocations and rod-like

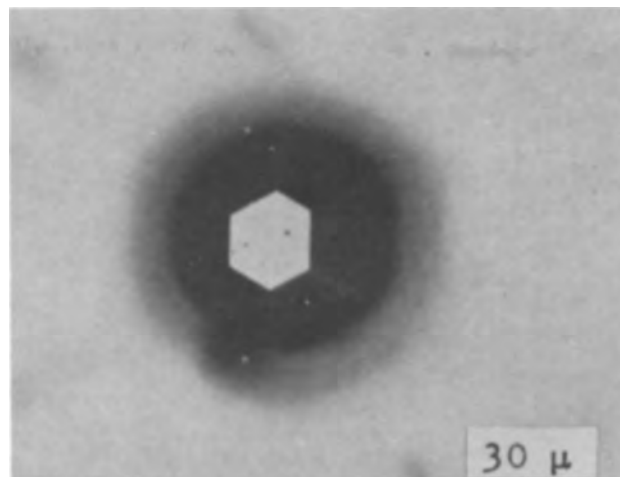


Fig. 12. Detail of truncated hexagonal pyramid surface deposits from out-diffusion of gold after annealing a CdS:Au crystal with type II hexagons.



microstructures. The rods are believed to be precursors of the type I precipitates. Giant (type II) hexagons undergo irreversible thermal destruction accompanied by diffusion of Au to the crystal surface where it forms characteristic epitaxial deposits. This loss of Au from CdS is an important difference from the stable behavior of copper. Finally the solubility of Au at high temperatures is apparently less than 0.03 w/o, a much lower value than the estimate for copper.

The results described in this paper demonstrate significant changes in microstructures that occur when slowly cooled, as-grown crystals are subsequently annealed and quenched. It has been seen that the high-temperature precipitate morphology, clusters, asterisks, etc., in crystals quenched from above 650°C, is distinctly different from that in the starting, as-grown crystals. This suggests that the processes for generating these dislocations can operate only at the higher temperatures. It is also possible that the frozen-in structures occur at sites that are available for nucleation only at higher temperatures, and which anneal out on slow cooling.

The appearance and disappearance of directly observable microstructures can serve as guides to the selection of crystal growth conditions that tend to minimize certain imperfections. In addition, the various temperature dependent forms adopted by impurity precipitates, visually demonstrate one of the difficulties in determining solubility and diffusion data in semiconductors, as recently discussed by Woodbury (16). Changes in the solubility of copper, and in dislocation structures are also the kinds of variations that are known to influence some properties of many materials.

It is interesting to speculate, for example, that some recently reported effects of heat-treatments on the conductivity and luminescence of CdS, some of which occur in samples quenched from 500° to 600°C (17-19) may have been influenced by undetected formation of dislocations or changes in solubilities of active impurities. The present finding that copper forms metastable, supersaturated solutions suggests that well-known temporal changes in the photoconductivity of doped CdS could, among other reasons, be connected with gradual reprecipitation of impurities. This work provides new insights into impurity behavior in semiconductors and emphasizes the importance of knowing the thermal history of materials.

#### Acknowledgment

The assistance of W. M. Anderson in the synthesis and preparation of the crystals for examination is

greatly appreciated. M. Fornoff supplied the electron microprobe data, and B. L. Goydich and Mrs. M. Ippolito performed the chemical analyses. The author also wishes to thank M. S. Abrahams for helpful discussions, and L. R. Weisberg and J. Tietjen for critically reviewing the manuscript. The research reported in this paper was sponsored by the Department of Defense, Advanced Research Projects Agency, Materials Science Office, under Contract No. SD-182.

Manuscript received Sept. 29, 1967.

Any discussion of this paper will appear in a Discussion Section to be published in the December 1968 JOURNAL.

#### REFERENCES

1. B. I. Boltaks, "Diffusion in Semiconductors," Academic Press, New York (1963).
2. A. Dreeben, *This Journal*, **111**, 174 (1964).
3. A. Dreeben, *ibid.*, **112**, 493 (1965).
4. A. Dreeben, *ibid.*, **113**, 1275 (1966).
5. M. S. Abrahams and A. Dreeben, *J. Appl. Phys.*, **36**, 1688 (1965).
6. A. S. Parasnis and J. W. Mitchell, *Phil. Mag.*, **4**, 171 (1959).
7. K. Matsuura and S. Koda, *J. Phys. Soc. Japan*, **20**, 251 (1965).
8. A. S. Argon in "Molecular Designing of Materials and Devices," p. 84, A. R. von Hippel, Editor, The MIT Press, Cambridge, Mass. (1966).
9. J. F. Black and E. D. Jungbluth, *This Journal*, **114**, 181 (1967).
10. A. Dreeben, *ibid.*, **110**, 1045 (1963).
11. G. Mandel, *Phys. Rev.*, **134**, A1073 (1964).
12. H. H. Woodbury, *J. Appl. Phys.*, **36**, 2287 (1965); W. Szeto and G. A. Somorjai, *J. Chem. Phys.*, **44**, 3490 (1966).
13. J. Woods, *Br. J. Appl. Phys.*, **11**, 296 (1960).
14. W. Rostoker and J. R. Dvorak, "Interpretation of Metallographic Structures," Academic Press, New York (1965).
15. M. Kahlweit in "Progress in Solid State Chemistry," Vol. 2, H. Reiss, Editor, Pergamon Press, New York (1965).
16. H. H. Woodbury in "Physics and Chemistry of II-VI Compounds," M. Aven and J. S. Prener, Editors, John Wiley & Sons, Inc., New York (1967).
17. F. J. Bryant and F. J. Cox, *Br. J. Appl. Phys.*, **16**, 1065 (1965).
18. E. T. Handelman and D. G. Thomas, *J. Phys. Chem. Solids*, **26**, 1261 (1965).
19. S. Ibuki and A. Ohsu, *ibid.*, **27**, 1753 (1966).

## Wide Range Measurements of Cathodoluminescence

J. J. Donoghue

*Tektronix, Inc., Beaverton, Oregon*

and K. E. Davis

*Reed College, Portland, Oregon*

#### ABSTRACT

Instrumentation is described for determination of the persistence characteristic of a phosphor screen after cathode-ray excitation. Excitation times shorter than 50 nsec are possible. Measurements are made to 0.01% of initial light intensity. Evidence of a "limiting" decay curve for short intense excitations is obtained and possible theoretical implications discussed.

With very few exceptions (1) most studies of phosphor light output under cathode-ray excitation have been confined to a range of two or three decades of intensity or excitation times of the order of microseconds or longer (2-7). Such excitation times are long compared to those of a moving electron beam in a regularly operated cathode-ray tube. The "dwell time,"

i.e., the time for the electron beam to move its own diameter, is frequently less than 20 nsec.

For such short excitation times, it is found that the luminescence decay is more rapid the shorter the excitation time and the higher the beam current density. However, a limiting decay curve is approached at excitation times of 0.2-0.5  $\mu$ sec and current densities of 5-10 ma/cm<sup>2</sup>. For phosphors with power-law decays,

\* Electrochemical Society Active Member.



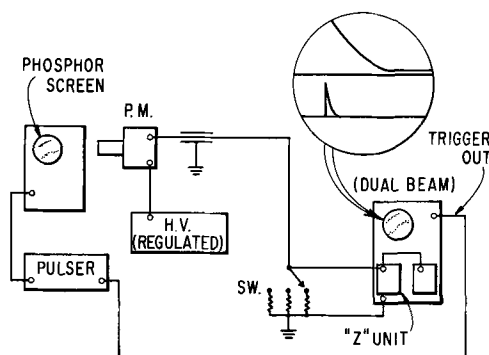


Fig. 1. Instrumentation for observing rise and decay of light from phosphor screen.

it is well known (8) that the decay time<sup>1</sup> after extended excitation (compared to 1  $\mu$ sec) increases, but it has not been as clearly recognized that under these conditions the shape of the decay curve is altered in its very early stages.

To measure less than 0.1% of initial intensity after very short excitation has usually meant construction of highly specialized equipment. With commercially available instruments one can now extend the range of such studies to more than four decades in intensity (from time zero) and to excitation times shorter than 50 nsec.

### Instrumentation, General

The arrangement used is illustrated in the block diagram of Fig. 1. The phosphors studied were incorporated in standard high-speed cathode-ray tubes (CRT's).<sup>2</sup> The CRT was then installed in an appropriate model oscilloscope (which will be called the "exciter" oscilloscope) to take advantage of the input circuitry for producing the necessary beam deflection and hence, phosphor excitation time.

The face of the CRT was covered with an opaque mask near the center of which was a 5 mm diameter hole. The electron beam was focused at a point vertically above the hole (about 2 cm above center in the 3-in. tubes and 3 cm in the 5-in. tubes), but short of the position where beam reflection from the deflecting plates would cause a bright background fluorescence on the screen. A single square pulse was then fed to the vertical deflection plates to pull the beam down to the 5 mm window for the duration of the excitation and then return it to the quiescent position at the top of the screen.<sup>3</sup>

Although a method using beam unblanking and reblanking was experimented with to provide excitation times, it was found to have several disadvantages and to be unable to provide the shortest excitation times required. One advantage of such a method would be elimination of the low level background light present when the deflected beam is not at the center of the screen. Careful study of this problem, however, showed that it can be minimized. Nearly all of what remains is a small constant background at the window contributed by the quiescent off-screen spot. The resulting constant photomultiplier (PM) output provides the reference trace ("zero line") on the output (or "viewing") oscilloscope.

Light output from the screen was picked up by a DuMont 6291 photomultiplier (PM). In the wide range of output current measurements made, regula-

tion and stability of the dynode voltages is extremely important with any PM. After some difficulty with random corona-like noise in various power supplies tried at very low signal levels, the P.D.P.14 model 1565 was found to be most satisfactory.

Dynode biases were provided from a voltage-dividing resistor string. To reduce voltage shifts at the higher multiplier output currents, resistors of higher power and lower resistance ratings than usual were used (20 kohms for cathode to first dynode and 10 kohms for all others). The divider current was nominally 10 ma. With a final dynode (output) current of 1 ma this meant a maximum bias shift on the last stage of 10%. The resultant measured shift in output current linearity was always less than 2%. Since this difficulty arises only in the last one or two stages, the error can be further reduced by providing those biases from separate batteries or well-regulated supplies (9). We found less sensitivity of output pulse voltage to variations in bias current of the last multiplier stage than is predicted by Lush (9).

The sharp rise and fall of the excitation pulses impose minimum bandwidth requirements on the output circuitry. In addition, in order to measure the very lowest light levels, maximum gain of the viewing oscilloscope must be used as well as large load resistors in the PM output. The larger load resistances produce an impedance mismatch with the 170-ohm cable. This, with the input capacitance of the two paralleled plug-in amplifiers (approximately 20 pf each) produces an integrating effect on the signal, resulting in a lowering and rounding of the peak of the output signal when the excitation time is very short. When the user is aware of this it can be allowed for and a proper calibration produced by extrapolation from the case of proper impedance matching.

A diffuser<sup>5</sup> was placed between the screen and the PM to eliminate trouble from variations in sensitivity across the photocathode and to avoid localized overloading of the photocathode. To extend the observed intensities to larger values without overloading the PM, an additional gray filter was used from time to time in front of the photocathode.<sup>6</sup> This filter gave no observable fluorescence to visible light in the region used as was checked by noting no change in shape of persistence curves when the filter was inserted. When employed at all it was used throughout the determination of a complete persistence curve.

### Amplifiers and Viewing Oscilloscopes

The primary reasons for the ability to cover the wide range of intensities were the nonoverloading amplifiers used in the viewing oscilloscope.<sup>7</sup> With such amplifiers and the Dual Beam CRT, it is possible to examine the full persistence signal on one trace and a magnified segment of that signal on the other (Fig. 2). This has the equivalent effect of increasing the available screen height from  $\pm 2$  to  $\pm 2000$  cm, with a smallest measurable signal of 1-2 mm. One thus has an immediate reference check on the initial intensity and a precise determination of the persistence down to less than 0.01% of initial amplitude.

To measure the lowest of these intensities involves very high sensitivities and a need to eliminate all source of noise. Stray daylight (white noise) and light from fluorescent fixtures (white noise plus 120 cycle) are strong sources but easily eliminated. However, 120-cycle noise from pilot lights, cathode heaters, etc., is more troublesome and sometimes cannot be completely eliminated at such low signal levels. As a final step in such elimination the signal trace and the sweep zero line can be triggered successively at the same phase of the residual 120-cycle noise and the difference between the two traces easily measured.

<sup>1</sup> Although susceptible to misinterpretation or mistaken extrapolation, "decay time" as used here will be the time necessary for  $I$  to decrease to  $I_0 e^{-1}$ , conforming to the usage of Leverenz and many others. Various definitions are used by some others, i.e.,  $I/I_0 = e^{-1}$ , 1/2, 1/3, 10%, 1%, etc. A danger in using  $(I/I_0) = e^{-1}$  is that it is not a constant time for any  $(I_2/I_1) = e^{-1}$  (as it is in the case of a pure exponential).

<sup>2</sup> CRT's: Tektronix T310 or T547 or equivalent. CRO's: Tektronix model 310 or 547 or equivalent.

<sup>3</sup> The necessary square pulses can be obtained from Tektronix Pulse Generators No. 114 (10 nsec rise time and pulse lengths of 100 nsec to 10 msec) and No. 293 (1 nsec risetime and pulse lengths of 2 nsec to 250 nsec) or their equivalent.

<sup>4</sup> Power Design Pacific, Inc. Model H.V. 1565, 1-2000 V, 15 ma max.

<sup>5</sup> Made of "Duratrace" Mylar drafting sheet; transmissivity, 60%.

<sup>6</sup> Kodak Wratten Filter No. 96, N.D. 1.0.

<sup>7</sup> Tektronix Z and 1A1 Plug-in Amplifiers or equivalent.

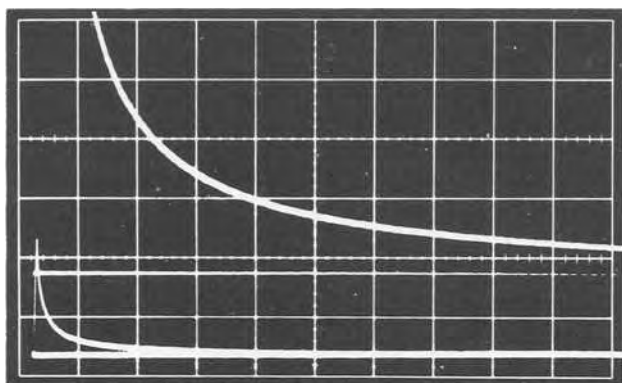


Fig. 2. Sample dual trace CRT display of initial light intensity (lower trace) and expanded view of phosphorescence (upper trace).

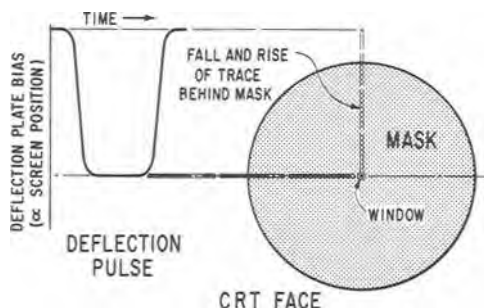


Fig. 3. Mask, aperture arrangement, and their relation to the deflected exciting beam.

**Time Resolution**

In all cases the response time of the exciter oscilloscope circuitry was much longer than the rise and fall time of the pulser; hence the fall time of the pulse delivered to the deflecting plates was indistinguishable from that of the exciter oscilloscope (Fig. 3). This pulse was in turn clipped optically through use of the mask and aperture. In studying the persistence characteristic of a phosphor one is concerned with the fall time of the exciting pulse, especially when investigating the early stages of the decay.

At the shorter excitation times used it was observed that the buildup and decay of the output light were unchanged whether the beam was constantly on the same crystals or was moved rapidly around on crystals in the window area. Therefore, the fall time of the excitation was governed by the transit time of the spot across the mask edge (0.5 mm maximum diameter for a high current, focused spot). The resulting fall times for the light pulse seen by the multiplier, independent of the buildup and decay of the phosphor output itself, are given in Table I. In cases when the early stages of the persistence characteristic are under careful study and one does not need the dual beam display, System C (Table I) provides greater time

Table I. Time resolution

System	A	B	C*
Pulser	114 (10 nsec)	293 (1 nsec)	293 (1 nsec)
Exciter 'Scope	310	547 with 1A1 Plug-in (7 nsec)	585 with 82 Plug-in (4 nsec)
Exciter Pulse Rise time	<5 nsec	<1 nsec	~0.1 nsec
Length	{ 100 nsec to 10 msec }	{ 2 nsec to 250 nsec }	{ 2 nsec to 250 nsec }
Viewing Unit	Z	1A1	82
Amplifier	551	551 or 547*	585
'Scope	(27 nsec)	(13 nsec) (7 nsec)	(4 nsec)

\* Single trace. Used only for observing closely the initial part of the decay.

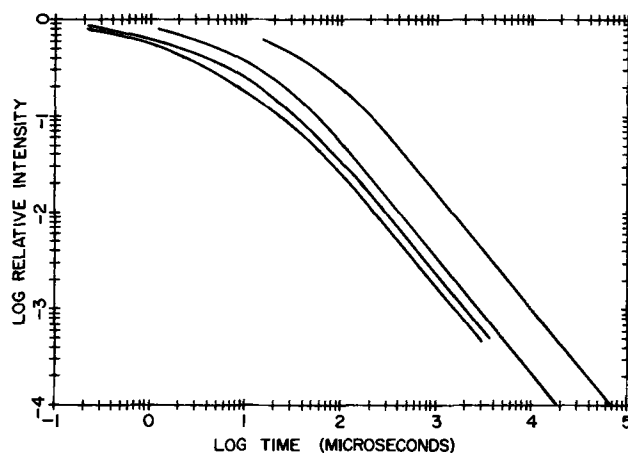


Fig. 4. Dependence of phosphorescence on duration of excitation for a P31 phosphor sample (0.25, 1, 10, and 100 μsec, respectively, left to right).

resolution with a circuitry fall time of 4 nsec. The possible variation of persistence time with beam current density is easily studied by using conditions ranging from high current focused beams to lower current defocused ones. A factor of 3000 in current density is readily available.

**Survey of Experimental Results**

It is well known (8) that the phosphorescent decays of most ZnS phosphors are hyperbolic or power law in form and that the decay characteristic varies with duration of excitation.<sup>8</sup> It is equally well known that the characteristics of some other phosphors are almost completely fitted by exponentials (e.g., CaWO<sub>4</sub>) and are independent of the manner of excitation. A primary reason for the present study of short excitations of power law phosphors was to determine whether there was a fundamental decay (characteristic of the phosphor) which was independent of the duration and intensity of excitation at very short excitations.

In this study a decay curve was found which is characteristic in that it is not affected by decreasing the excitation time to a value below approximately 0.5 μsec. Although, as expected, the latter part of the curve implies a power law ("hyperbolic") decay, the upper part is not fitted by continuation of the same dependence to shorter times, nor does the upper part of the curve appear to be fitted solely by an exponential.

Principal phosphors studied were P 11 (ZnS:Ag,Cl) —(two suppliers), P 22B (ZnS:Ag,Cl), and P 31 (ZnS:Cu,Cl). Experimental results for the P 31 are plotted in Fig. 4. It can be seen that with increasing *t* the curve approaches a straight line on a log *I* vs. log *t* plot and the slope implies an exponent of approximately 1.20 in the relation

$$I(t) \propto t^{-n} \quad \text{for large } t$$

As the duration of excitation is decreased the curve is shifted to shorter and shorter times, approaching a limiting location for excitations of ≤0.5 μsec (checked to excitations of less than 50 nsec) with the slope of the straight portion essentially unchanged.<sup>9</sup> It was found that a similar shift to shorter times was produced with increase in excitation (increase in beam current density) though this effect is less marked for the shorter excitations. This dependence is illustrated in Fig. 5.

In summary, the straight line portion of the decay curve is translated (with apparently unchanged slope)

<sup>8</sup>One exception is ZnS:Mn (no coactivator) where the decay is exponential and independent of the mode of excitation (6,8 p. 256,10).

<sup>9</sup>There may be some indication of a small (possibly within experimental error) systematic change of slope in some cases. If real, it is in the direction of slightly steeper slope for greater duration of excitation.

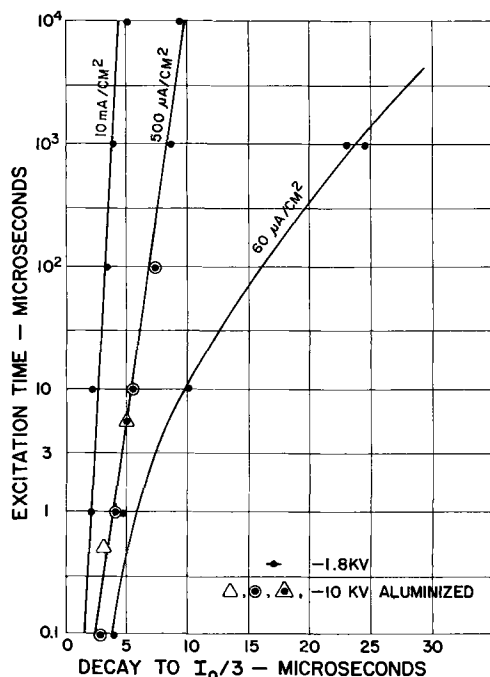


Fig. 5. Relation between phosphorescence decay and excitation parameters (current density and duration) for a P 31 [ZnS: Cu, (Cl?)] phosphor.

to shorter times by shortened excitation pulses and by increased intensity of excitation, toward a limiting value. This tends to support the concept of a characteristic decay, i.e., traps are occupied in such a short time that no appreciable number have emptied during the exciting period. The "limiting" curves for P 22 and P 11 are shown in Fig. 6.

### Theoretical

If an electron falls into a trap it will escape after a mean lifetime,  $\tau$ . It can then combine with an empty center giving phosphorescence of characteristic lifetime  $\tau$  after the original excitation, provided the probability for the transition to the empty center is large compared to that for escape from the trap. Considering a single level (11 p 150):

$$(dn/n) = -(dt/\tau) \quad \text{and} \quad n = n_0 \exp(-t/\tau)$$

where  $n_0$  is the number of electrons in the level at time zero. If one assumes levels in the band gap and near the conduction band, the lifetime depends on the location,  $E$ , of the level below the conduction band (12, 13)

$$\tau = 1/s \exp(-E/kT) = (1/p)$$

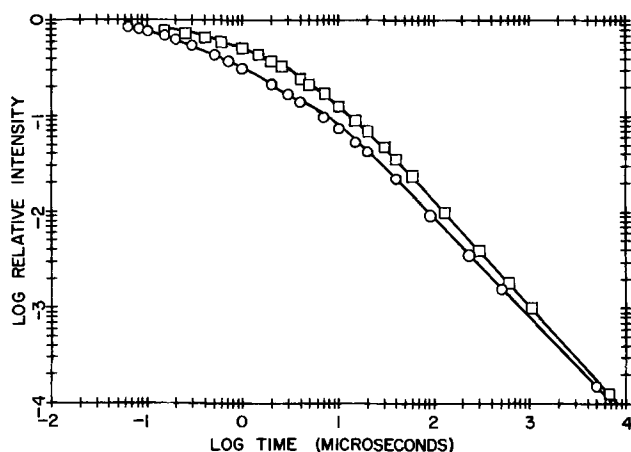


Fig. 6. "Limiting" phosphorescence curves (i.e. for excitations of short duration and high intensity). Samples are P 22B and P 11, left to right, respectively.

where  $p$  is the probability of escape of the trapped electron per second and  $s$ , the absolute rate constant (15), is sometimes called the "attempt-to-escape-frequency" at a given temperature.<sup>10</sup> Since the luminous intensity is proportional to the rate at which the electrons escape, we may write for the single (ith) level

$$I_i = C(dn/dt) = Cn_0s \exp(-E/kT) \exp[-st \exp(-E/kT)]$$

where  $C$  is the light energy produced per electron released.

Let us now consider a distribution density ( $dN/dE$ ) of occupied trapping levels between  $E$  and  $E + dE$ . The number of occupied traps in the interval will be  $dN$ . The total light intensity,  $I$ , from all the levels in a band extending from  $E_s$  (shallow) to  $E_d$  (deep) will be the sum of the  $I_i$ 's for the levels in the band, or

$$I = \int_{E_s}^{E_d} (dN/dE) \{C s \exp(-E/kT) \exp[-st \exp(-E/kT)]\} dE$$

Let us assume a trap density of the form ( $dN/dE$ ) =  $(dN/dE)_s \exp[-\alpha(E - E_s)]$ , i.e., a distribution which at the top of the band of traps is  $(dN/dE)_s$  and diminishes as  $\exp[-\alpha(E - E_s)]$ ...  $E \geq E_s$ . Randall and Wilkins (16) have shown that a distribution of this form for  $E_s = 0$  and  $E_d \rightarrow \infty$  leads to a power law decay of the form:  $I \propto t^{-(\alpha kT + 1)}$ ... for large  $t$ .

To evaluate  $I$  for any  $t$ ,  $E_s$ , and  $E_d$ , we make the substitution:  $\eta = \exp(-E/kT)$ ,  $dE = -kT d\eta/\eta$ ,  $\exp[-\alpha(E - E_s)] = \eta^{+\alpha kT}$

Then:

$$I = C(dN/dE)_s \int_{\eta_s}^{\eta_d} \eta^{+\alpha kT} (-skT) \exp(-st\eta) d\eta$$

Case I: A uniform density of traps, i.e.,  $\alpha = 0$

$$I = (dN/dE)_s (kT/t) [\exp(-st\eta_d) - \exp(-st\eta_s)]$$

$$I(t=0) = I_0 = (dN/dE)_s (skT) (\eta_s - \eta_d) \dots (17)$$

Hence the normalized intensity  $I/I_0$ , or  $I(t)$ , for an initially uniform density of occupied traps is

$$I(t) = [\exp(-st\eta_d) - \exp(-st\eta_s)] / (\eta_s - \eta_d) st$$

When  $E_d \gg E_s$

$$I(t) = [1 - \exp(-st\eta_s)] / st\eta_s$$

and at large  $t$ :  $I(t) \rightarrow 1/(st\eta_s)$

Case II:  $\alpha = (kt)^{-1}$ <sup>11</sup>

$$I(t) = 2 \{ [1 + st \exp(-E_d/kT)] \exp[-st \exp(-E_d/kT)] - [1 + st \exp(-E_s/kT)] \exp[-st \exp(-E_s/kT)] \}$$

$$X \{ [\exp(-2E_s/kT) - \exp(-2E_d/kT)] (st)^2 \}^{-1}$$

For  $E_s = 0$ , and  $E_d \rightarrow \infty$ :  $I(t) = 2 [1 - (1 + st) \exp(-st)] / (st)^2$ . In addition, for  $t \rightarrow \infty$ :  $I(t) \rightarrow 2/(st)^2$ . Note that this shows, as also pointed out by others (18), a  $t^{-2}$  dependence does not necessarily imply a bimolecular process.

In second order kinetics, if the number of excited electrons  $\mathcal{N}$ , is comparable with the number of available centers, the probability for recombination is proportional to  $\mathcal{N}$  and hence  $\mathcal{N}$  decreases hyperbolically with time. The luminescence decay can be written:

$$I/I_0 = 1 / [1 + (I_0 p)^{1/2} t]^2$$

that is, at large  $t$ ,  $I \propto t^{-2}$ . However, the decay is independent of the duration of excitation and also becomes more rapid as the intensity is increased (11, 19). In the present study we do observe a dependence

<sup>10</sup>  $E$  = the minimum energy required to liberate a trapped electron and hence is called the activation energy.

<sup>11</sup> This value of  $\alpha$  is chosen because it is the only other one in the range  $1 \leq n \leq 2$  (or  $0 \leq \alpha \leq 1$ ) for which we have found it possible to perform the integration in closed form and, to our knowledge, the result has not previously been published.

Table II.  $n$  values

Phosphor	Value of $n$
P 22B (ZnS:Ag,Cl)	$1.035 \pm 0.01$
P 11 (ZnS:Ag,Cl)	$1.10 \pm 0.01$
P 31 (ZnS:Cu,Cl)	$1.20 \pm 0.01$

of the decay on duration of excitation. Hence we must conclude either that (a) first order kinetics are dominantly involved or (b) if second order, the two processes involved must have widely different characteristic times since, in that case, the slower process would be the controlling one.

The Modified Bimolecular Decay model (20) (with unequal numbers of electrons and available centers) would not be a possibility since it leads to the prediction of an exponential decay at large  $t$ . If retrapping were involved and considered as a replenishment of the shallower empty traps, the effect on the decay curve after a period greater than a few average lifetimes would be negligible.<sup>12</sup>

Case III:  $0 < \alpha < 1$

Although it was not found possible to secure a closed form for the  $I(t)$  integral in these cases, a numerical integration was performed by computer. Curves were obtained for values of  $n$  ranging from 1.00 to 2.00. It was established that the limiting form at large  $t$  was

$$I(t) = n(st)^{-n} \quad (13)$$

The values of  $n$  found are given in Table II.

The numerical integration curves most nearly matching these experimental results at large  $t$  were plotted and compared with the data. In all cases the calculated curves rose above the experimental points for the smaller values of  $t$  (Fig. 7). It was found that if one added to the calculated  $I(t)$  a pair of appropriately chosen exponential contributions (with lifetimes much shorter than  $\tau$ ) a very much closer fit was obtained (Fig. 7). Such exponential contributions to the emission would be just those produced by pairs of (a) a single short life time originating in the conduction band, (b) one or two very shallow traps, or (c) excited centers. There are five possible pair combinations. The results are consistent with the observed importance of very shallow levels (22-26) and the fast exponential decay observed by others (27). The work of Belikova (22), ZnS:Cu,Cl, and Shionoya (27), self-activated ZnS, show that short excitation times by uv give decay times comparable with those observed in this work.

### Conclusions

One hypothesis can be proposed: in a given material, when shallow traps are more abundant one gets greater relative efficiency and shorter decay<sup>14</sup> (e.g., the P 22B and P 11's studied here are ZnS:Ag, Cl phosphors quite possibly involving different preparation and processing<sup>15</sup>). The P 22B had a higher efficiency and a faster decay (10% point: 7  $\mu$ sec vs. 12.5  $\mu$ sec). The difference is consistent with the supposition that there is a greater density of shallow traps in this P 22B sample than in the P 11's. Such marked effects of preparation and processing on phosphor characteristics strongly underscore the recommendation of Bube (28) and several others that as many different types of measurement as possible should be made on the same sample in order that correlations

<sup>12</sup> Although Garlick and Gibson (21) concluded that retrapping was negligible in the time range 0.01-10 sec, its importance would increase with shorter times as studied here, hence the reason for discussing its possible effect.

<sup>13</sup> Note that in Cases I and II we already had a hint of the factor  $n$  when we obtained  $1/X(st)^{-1}$  and  $2/X(st)^{-2}$ .

<sup>14</sup> By relative efficiency in this context is meant the light output from the phosphor screens of cathode-ray tubes (under the same beam current density and accelerating potential) as recorded photographically.

<sup>15</sup> The effect of preparation and processing on the density and location of shallow traps has been pointed out by others such as Riehl (29) and Bundel (26).

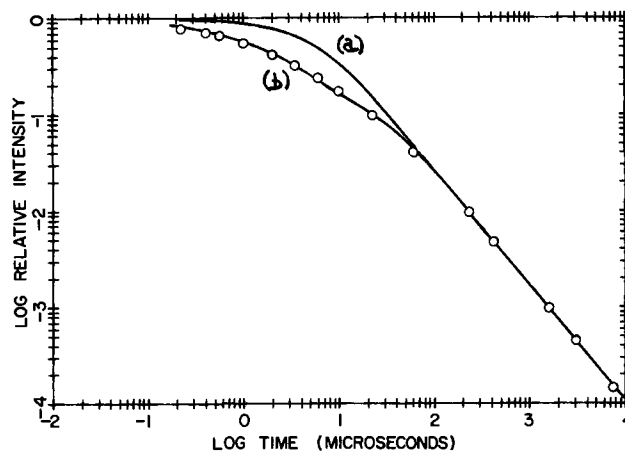


Fig. 7. Comparison of experimental "limiting" phosphorescence data for a P 31 phosphor with (a) calculated curve on basis of assumed trap band density:  $\exp(-0.2E)$ ,  $0 \leq E \leq 15kT$  and (b) calculated curve assuming (a) plus two appropriately weighted, short life time (shallow?) levels.

of such measurements may be made with maximum assurance and reliability.

A summary of the best match to the experimental results is given in Table III. The final equation for total (normalized) intensity is

$$\text{Total } (I/I_0) = XI(t) + Y \exp(-t/\tau_2) + Z \exp(-t/\tau_3)$$

Although, for the P 22B, a weighting of  $X = 0.25$  was tried with resultant values of  $\tau = 3.75$ ,  $Y = 0.30$ ,  $\tau_2 = 0.16$ ,  $Z = 0.45$ , and  $\tau_3 = 0.68$  it was found that the fit was only about half as good as that finally obtained.

From the present work two general conclusions may be drawn for these particular commercial phosphor samples. (a) the luminescence decay at  $t \gg \tau$  is hyperbolic (power law), but (b) in the measurements made (i.e., short duration of cathode-ray excitation) the light sum was primarily from centers of short lifetime and the major part of the light (i.e., that which in our analysis was ascribed to the power law decay) must be due to the emptying of levels shallow compared to those determined by glow curve measurements made above liquid nitrogen temperatures. That the shallow traps yield a light sum comparable to that observed from the more commonly studied peak at about 175°K is indicated in the results of several authors (14, 29-31). Specific shallow traps observed by Riehl (29) were in a ZnS: 0.01% Cu, Cl phosphor. For each of his low-temperature peaks (25° and 50°K) he found concentrations of filled traps comparable with those of the deeper traps usually observed via glow peaks above 100°K. The results of Thoma (32) indicate that the concentration of the additional filled traps at 4.2°K is even larger than that observed for the same phosphors at 80°K.

In the analysis of the data a value of  $\tau$  is obtained and hence a  $p$  in the power law expression. Since  $p = s \exp(-E/kt)$  (the  $E$  being for a single trap or for the top of our assumed band), one must choose a value of  $E$  and then compute the implied  $s$ , or *vice versa*. It is commonly assumed that  $s$  is a constant of the host crystal. If this assumption is made the different values of  $\tau$  (Table III) can be attributed to different locations of the top of the continuous band of filled traps in the

Table III. Constants for best match to experiment (times in  $\mu$ sec)

Phosphor	Trap Band		1st Add'l. Level		2nd Add'l. Level	
	X	$\tau$	Y	$\tau_2$	Z	$\tau_3$
P 22B	0.20	4.7	0.45	0.17	0.35	1.10
P 11	0.20	8.0	0.35	0.27	0.45	2.90
P 31	0.20	16.9	0.35	0.48	0.45	3.30

proposed model. If one chooses three values for  $E$  in the range shown possible by Riehl, an implied value for  $s$  of approximately  $10^6/\text{sec}$  is found. For example,  $E_s = 0.02$  eV for the P 22B yields an  $s$  of  $0.5 \times 10^6/\text{sec}$ . Using this value for  $s$  one gets  $E_s = 0.035$  eV for the P 11 and an  $E_s$  of 0.046 eV for the P 31. If, instead, one takes  $E_s = 0.05$  eV for the P 22B this yields an  $s$  of  $1.6 \times 10^6/\text{sec}$ , in turn implying an  $E_s$  of 0.063 eV for the P 11 and an  $E_s$  of 0.075 eV for the P 31. Because of the difficulty of determining  $s$  with precision, a wide range of possible values may be found in the literature (11, 13, 14, 21, 33). Because of the complexities involved, the possibility that  $s$  may be different for different traps (and hence not a constant of the host crystal) will not be considered here. One of the most recent determinations, by Kröger (33), gives  $s \approx 10^5$  (converted to room temperature) for a ZnS:Cl ("self-activated") phosphor.

In addition to the evidence for the existence of significant shallow traps, it does not seem that the decay times observed can be ascribed to the emptying of those deeper traps indicated by the glow peaks near 175°K. As can be seen in the work of Bube (14), the phosphor was heated slowly (30 sec/°K) for good resolution of peaks, yet there was no substantial shift in the location of the peak. The phosphor was held many minutes in the temperature range 125°-150°K. Thus, one must ascribe a decay time of the order of several minutes to the traps whose thermal emptying contributed to that glow peak. If the 175°K traps were responsible for the phosphorescence seen at room temperature, it can easily be shown that (because of the exponential temperature dependence of trap emptying) the computed  $\tau$  would be more than two orders of magnitude greater than that which is observed.

It appears unlikely that many of the conventionally obtained glow curves indicate the true concentration of shallow traps. Those curves which begin near liquid nitrogen temperature show a significant level of light intensity at their beginning (14, 34, 35). In addition, some authors state that they wait as long as minutes for the initial luminescence to decay before beginning the warming process (36, 37).

#### Acknowledgments

Grateful acknowledgment is made for the original circuit work and associated luminescence measurements made by Mr. Craig J. W. Gunsul. The authors are similarly indebted to Mr. Frank Christiansen and Mr. James Richardson for help in making the persistence measurements and the advice of Dr. Richard Coover in refining programming procedures.

Manuscript received Aug. 24, 1967; revised manuscript received ca. Oct. 5, 1967. This paper was presented at the Cleveland Meeting, May 1-6, 1966, as Abstract 21.

Any discussion of this paper will appear in a Discussion Section to be published in the December 1968 JOURNAL.

#### REFERENCES

1. R. W. Tyler and C. Straub, *Photog. Sci. and Eng.*, **7**, 289 (1963).
2. J. W. Strange and S. T. Henderson, *Proc. Phys. Soc.*, **58**, 369 (1946).
3. P. A. Einstein, *Brit. J. Appl. Phys.*, **8**, 190 (1957).
4. R. Feinberg, *Nature*, **183**, 1546 (1957).
5. JEDEC, Publication No. 16 (1960).
6. A. I. Blazhevich and V. A. Chikhacheva, *Trans. Lebedev Phys. Inst.*, **23**, 98 (1963).
7. A. Pfahnl, *Bell System Tech. J.*, **42**, 181 (1963).
8. H. W. Leverenz, "An Introduction to the Luminescence of Solids," Chap. V, John Wiley & Sons, Inc., New York 1950.
9. H. J. Lush, *J. Sci. Instr.* (GB), **42**, 597 (1965).
10. C. J. W. Gunsul, Unpublished thesis, Reed College, 1963.
11. D. Curie, "Luminescence in Crystals," John Wiley & Sons, Inc., New York (1963).
12. F. Urbach, *Wien. Ber. (IIA)*, **139**, 363 (1930).
13. J. T. Randall and M. H. F. Wilkins, *Proc. Roy. Soc.*, **A184**, 365 (1945).
14. R. H. Bube, *Phys. Rev.*, **80**, 655 (1950).
15. F. Urbach, N. R. Nail, and D. Perlman, *J. Opt. Soc. Am.*, **39**, 675 (1949).
16. J. T. Randall and M. H. F. Wilkins, *Proc. Roy. Soc.*, **A184**, 390 (1945).
17. T. Kikuchi, *J. Phys. Soc. Japan*, **12**, 204 (1957).
18. A. J. Dekker, "Solid State Physics," Prentice Hall, Englewood Cliffs, N. J. (1963).
19. G. F. J. Garlick and M. H. F. Wilkins, *Proc. Roy. Soc.*, **A184**, 408 (1945).
20. N. F. Mott and R. W. Gurney, "Electronic Processes in Ionic Crystals," Oxford University Press (1948).
21. G. F. J. Garlick and A. F. Gibson, *Proc. Phys. Soc.*, **A60**, 574 (1948).
22. T. P. Belikova and M. D. Galanin, Luminescence Suppl. No. 1 to *Optika i Spektroskopiya*, 149 (1966).
23. D. E. Brodie, H. E. Petch, and R. R. Haering, *Can. J. Phys.*, **40**, 665 (1962).
24. R. R. Haering, *ibid.*, **37**, 1374 (1959).
25. V. F. Tunitskaya, *Optika i Spektroskopiya*, **14**, 236 (1963).
26. A. A. Bundel and V. Zhukov., *ibid.*, **18**, 270 (1965).
27. S. Shionoya, K. Era, and H. Katayama, *J. Phys. Chem. Solids*, **26**, 697 (1956).
28. R. H. Bube, *Solid State Physics*, **2**, [2], 825 (1960).
29. N. Riehl and P. Thoma, *Z. Ang. Phys.*, **14**, 751 (1962).
30. H. A. Klasens, *This Journal*, **100**, 72 (1953).
31. N. Riehl and H. Ortman, *Z. Naturf.*, **10a**, 896 (1955).
32. P. Thoma, *Zeits Ang. Phys.*, **16**, 106 (1963).
33. F. A. Kröger, *Physica*, **22**, 637 (1956).
34. W. Hoogenstraaten, *Philips Research Repts.*, **13**, 515 (1958).
35. H. Gobrecht and D. Hofmann, *J. Phys. Chem. Solids.*, **27**, 509 (1965).
36. G. F. Neumark, *Phys. Rev.*, **103**, 41 (1956).
37. F. F. Morehead and R. S. Title, *J. Phys. Chem. Solids*, **24**, 719 (1963).

# Ellipsometric Investigations of Boron-Rich Layers on Silicon

K. M. Busen,\* W. A. FitzGibbons, and  
W. K. Tsang

Research & Development Laboratories, Sprague Electric Company, North Adams, Massachusetts

## ABSTRACT

It is shown that exposure of a silicon substrate to sufficiently high concentrations of diborane results in a surface layer which most likely consists of a silicon-boron phase. This phase, which is controlled by the diborane concentration and the temperature, gives rise to a prediffused layer of boron in the adjacent substrate. Good control of the phase layer affords good control of the prediffused layer. When the phase layer is removed prior to drive-in, optimal control is achieved with respect to the final diffused structure.

The diffusion of impurities in silicon for the processing of electrical components and circuits is determined by the well-known parameters: composition of the gas phase which contains the impurity, time of diffusion, and temperature of the silicon sample. At very high impurity concentrations, a new influential parameter may be introduced by formation of a surface layer whose phase differs from that of the bulk of the sample. Such a layer has been observed by Schmidt and Owen (1). The authors report "the occurrence of a steep spike in the phosphorus concentration at the Si/SiO<sub>2</sub> interface" for samples which were diffused from oxide films on silicon as the impurity carrying source. The nature of the phosphorus layer has been discussed by Kooi (2) who suggests that it may consist of a "Si-P" phase. The investigations described in this article are concerned with samples which were exposed to very high concentrations of diborane gas, and it was concluded that similar to the findings above the formation of a Si-B phase constituting a layer is very likely. It will be shown in this article that under proper conditions such a layer acts as a source for boron diffusion into the adjacent silicon bulk and that control of this layer offers precise control of the diffusion itself.

## Preparation of Samples and Measurements

Silicon slices (1 ohm-cm n-type) were annealed in an ambient of N<sub>2</sub> + O<sub>2</sub> and then were exposed for 5 min at temperatures ranging from 930° to 1100°C to an ambient of N<sub>2</sub> + O<sub>2</sub> + B<sub>2</sub>H<sub>6</sub> (300-1000 ppm) with a total flow of 2 l/min. The O<sub>2</sub> concentration was kept constant at 1% at all times. After diborane exposure, the ambient was changed to an N<sub>2</sub> + O<sub>2</sub> atmosphere again, and heating was continued for 15 min. Glass layers form on the slices during this procedure. The samples thus obtained were subdivided into three groups and, after the samples had been subjected to specific treatments, ellipsometric measurements of the change in the amplitude ratio  $\psi$  and of the relative phase change  $\Delta$  as described by Archer (3) were performed:

(a) The glass layer of samples in this group was removed in small steps by a glass etch. Ellipsometric measurements were taken after each step until  $\psi$  and  $\Delta$  remained constant. The etch consisted of 16 ml conc. HF and 40g NH<sub>4</sub>F dissolved in 100 ml of water (buffered HF).

(b) The glass layer of samples in this group was removed in large steps by another glass etch, which consisted of 1 ml conc. HF diluted in 10 ml H<sub>2</sub>O. Application of the glass etch was terminated when  $\psi$  and  $\Delta$  no longer changed. Then a new etch was applied repeatedly. This etch, which dissolves silicon, consisted of a mixture of HF:HNO<sub>3</sub>:CH<sub>3</sub>COOH =

1:2:6. Subsequent measurements by the ellipsometer showed new changes in  $\psi$  and  $\Delta$ . The etching was terminated when  $\psi$  and  $\Delta$  remained constant again.

(c) This last group was formed by samples which had been reoxidized successively in dry, wet and dry oxygen at 1130°C. The resulting silicon oxide layer was removed in small steps by buffered HF. Ellipsometric measurements were taken after each step until  $\psi$  and  $\Delta$  remained constant.

The results of the ellipsometric measurements are summarized in Fig. 1, where curves I, II, and III are plots of  $\Delta$  vs.  $\psi$  for surfaces as treated according to (a), (b), and (c), respectively.

For reasons to be discussed later, two special samples, A and B, were prepared by exposing silicon slices to an ambient of low and of high B<sub>2</sub>H<sub>6</sub> content, respectively. After removal of the glass,  $\psi$  and  $\Delta$  were determined for each sample. The values were  $\psi_A = 13.27^\circ$ ,  $\Delta_A = 145.65^\circ$  and  $\psi_B = 18.17^\circ$ ,  $\Delta_B = 108.60^\circ$  for sample A and B, respectively. Measurements of the r<sub>p</sub>-component (light vibrating in the plane of incidence after reflection) showed that the intensity of r<sub>p</sub> changed with the angle of incidence and went through a minimum at 76° for sample A, whereas, the intensity of r<sub>p</sub> decreased monotonically with the angle of incidence for sample B.

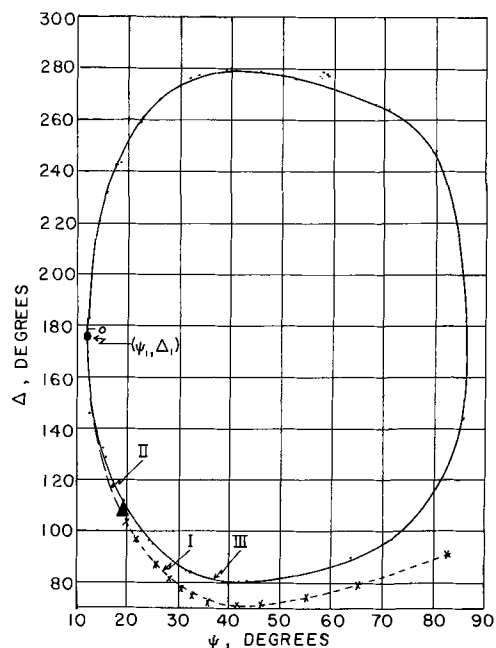


Fig. 1. Experimental results for samples subjected to specific treatments. Curves I, II, and III refer to measurements on a glass layer, on a phase layer, and on a silicon oxide layer, respectively.

\* Electrochemical Society Active Member.

It will be shown later that silicon slices which are exposed to  $B_2H_6$  concentrations between 300 and 1000 ppm acquire a layer consisting of a silicon-boron phase. This phase is sandwiched between glass and silicon bulk and is insoluble in any glass etch. If one wants to remove the phase layer, one either can use the silicon etch mentioned above or one can apply a two-step process consisting of a 10 min boil in conc.  $HNO_3$  followed by a 30-sec dip in diluted HF. Very thin phase layers dissolve completely after application of the two etching steps, but thicker layers may require repetitions. Since neither step affects the silicon bulk, a selective "phase removal" is possible.

The thickness of the phase layer on sample B was measured by multiple beam interferometry (4) and was found to be  $245 \pm 20 \text{ \AA}$ . This value is representative for the majority of the samples in groups (a) and (b) because these samples and sample B differ only slightly in their measured  $\psi$  and  $\Delta$ . The phase layer on sample A is about  $120 \text{ \AA}$  thick according to investigations by the ellipsometer.

### The Si-B Phase

The ellipsometric measurements are summarized by the curves shown in Fig. 1. In this figure, curve III fits points which refer to some samples in group (c). The curve, when traced in clockwise direction, signifies a sequence of oxide layers whose thickness is decreasing. For a vanishing layer, one theoretically should arrive at  $\psi$  and  $\Delta$  values which are marked by O in Fig. 1. This hardly ever occurs because the silicon surface is always covered by small amounts of residues from etching or other treatments. Archer measured values of  $\psi = 11.80^\circ$  and  $\Delta = 175^\circ$  for a cleanest etched silicon surface. In the present investigation, the end of curve III was found to be at  $\psi_1 = 12.2^\circ$  and  $\Delta_1 = 176.5^\circ$ . The values are close to Archer's values and indicate, therefore, that after removal of the oxide a bare silicon surface was left. According to Fig. 1 of ref. (3), curve III corresponds to an index of refraction of about 1.46.

Curve I goes through points which originate from measurements on samples of the first group. The curve is terminated by the black triangle shown in Fig. 1. The fact that curve I does not end at  $\psi_1$  and  $\Delta_1$  characterizes a surface which is different from a silicon surface. This particular surface seems to be formed by a Si-B phase because: (i) glass etches did not move the end of curve I to  $\psi_1$  and  $\Delta_1$ , and, thus, it is not a glass layer which causes the deviation; (ii)  $V/I$  values measured by the four-probe on phase surfaces were typically around 10 for samples whose phase layers were about  $250 \text{ \AA}$  thick. If the surface belonged to a glass or to an oxide of the same thickness, a  $V/I$  value could not be measured by the four-probe because of the very high resistivity; (iii) phase surfaces of many samples could be converted to silicon surfaces by application of the silicon etch mentioned in (b). This is demonstrated by curve II, which starts at the triangle in Fig. 1 and moves to the black circle in the neighborhood of  $\psi_1$  and  $\Delta_1$ . The triangle represents the average of ellipsometric values which were measured for many phase surfaces and similarly the circle represents the average of values obtained after treatment by the silicon etch.

For sample A, which had a  $120 \text{ \AA}$  thick phase layer, the intensity of the  $r_p$ -component went through a minimum at  $76^\circ$ . Because this angle is identical to the principal angle of  $76^\circ$  for silicon [see, e.g., Ditchburn (5)], it was thought first that this would be indicative of a "silicon-rich" nature of the phase (6). Measurements on anodically oxidized samples (7) having about the same oxide thickness showed, however, that these samples had minima which were close to the  $76^\circ$  angle too. A special method to compute the minima for the oxidized samples as a function of layer thickness (8) led to values which were in good agreement with the measurements. This shows that the observation of

the  $76^\circ$  angle for sample A does not offer enough evidence for the assumption in ref. (6) "... that the reflection comes from a silicon-like surface." The missing minima for sample B and for a sample with a  $250 \text{ \AA}$  thick oxide layer demonstrate, in addition, that no relevant distinction can be made between a phase and an oxide. Sample B was used to determine the refractive index of the phase layer. It was assumed that the layer was sufficiently thin so that no substantial attenuation of the light could take place. Together with the measured thickness of the phase layer the  $\psi$  and  $\Delta$  values give a refractive index of 1.7. Measurements on other phase layers resulted in indices of refraction between 1.6 and 1.7.

### Effect of the Phase Layer on Diffusion

For the following discussion, it is useful to establish some terminology: The term "deposition" refers to a thermal process which results in the formation of two adjacent layers, one being a boron-containing layer intimately associated with the silicon substrate and the other one being a glass layer. A "diffused layer" is the layer which is confined by the silicon surface and the junction which forms by diffusion. "Drive-in" is a process where the boron originating from deposition penetrates further into the silicon bulk by diffusion. A "profile" is the concentration distribution of boron after diffusion. The expression, "control in  $V/I$ ", is related to the differences in  $V/I$  measurements from run to run.

$V/I$  measurements by the four-point probe in combination with the junction depth,  $x_j$ , offer a convenient way to examine the control of diffused layers. For the samples in this investigation it is assumed that the diffused layer is small in comparison with the probe distance, that the surface concentration,  $C_0$ , is much greater than the background concentration of the silicon and that  $x_j$  stays practically constant. Then the average resistivity,  $\bar{\rho}$ , of the layer can be expressed by  $\bar{\rho} = (V/I) 4.53 x_j \rho$  on the other hand, is determined by the diffusion profile as has been shown, e.g., by Busen and Shirn (9). Thus  $V/I$  values can be used as a criterion for diffusion control. During the investigations, junction delineations were performed on various samples. All of these delineations resulted in junction depths which differed by less than  $0.05 \mu$ .

In a number of extra experiments, two sets of samples were subjected to a deposition process. The samples of the first set had a Si-B phase. The second set, which was prepared with a lower  $B_2H_6$  concentration, was free of a phase layer. The samples of each set were then divided into two parts. One part was subjected to phase removal. The other part was left unetched. Finally, all samples were subjected to a drive-in process. The processing steps for this investigation are summarized in Fig. 2. An examination of the samples by  $V/I$  measurements after drive-in led to results which are listed in Table I.

Table I demonstrates that the formation of a phase layer affords a good control of  $V/I$  and that phase removal before drive-in improves the control. When no phase layer is formed, the control becomes poor. Thinner layers, which are not removed prior to drive-in, do not change the control substantially, whereas, thicker layers do. The temperature at which the phase layer is formed during deposition is high enough to cause a diffusion of boron into silicon with the layer acting as a source. In order to distinguish this process from the diffusion which takes place during drive-in, the diffusion into silicon during deposition is called "prediffusion." When the phase layer has been removed, the only remaining boron source for drive-in is the layer which was formed by prediffusion and, consequently, a good control for drive-in is based on a good control of the prediffused layer. Since the prediffused layer originates from the phase layer, the formation and control of the latter layer is an important factor in the control of the "total" diffusion.



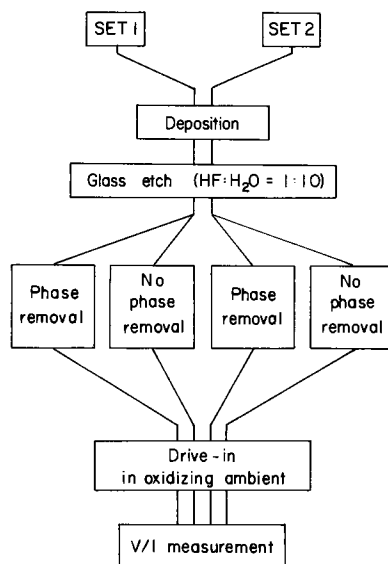


Fig. 2. Processing steps for the investigation of diffusion control. The deposition was for 5 min at 1000°C in an ambient of  $B_2H_6 + N_2 + O_2$ . Set 1,  $B_2H_6$  concentration > 300 ppm; set 2,  $B_2H_6$  concentration < 200 ppm.

The term "total" expresses here the combined action of prediffusion and drive-in diffusion. Experimental evidence shows that the phase layer is controlled by two parameters. The first one is the critical range for the diborane and oxygen concentration and the second one is the temperature control during deposition. In the experiments described here, this control was better than  $\pm 0.5^\circ C$ .

The experimental results, showing good control in the presence of a phase layer, are easily interpreted by the assumption that the amount of boron in the prediffused layer is well controlled by the surface concentration,  $C_0$ , which, in turn, depends on the composition of the Si-B phase according to  $C_0 = k_s C_s$ . In the last equation,  $C_s$  is the concentration of boron in the phase, and  $k_s$  is the distribution coefficient of boron between silicon and the phase. Since  $C_s$  is a function of the temperature only, control of the temperature is synonymous with control of the total diffusion. One of the authors (10) observed in former investigations that a phosphorus-rich layer formed on the surface of silicon slices which had been exposed to sufficiently high  $POCl_3$  concentrations. The necessity to remove this phase for better diffusion control pointed to a model which is very similar to the one described for Si-B in this article.

The foregoing discussion offers an insight into the mechanism of the prediffusion, and Fig. 3 illustrates the relations existing for this kind of diffusion. The figure shows the  $SiO_2-B_2O_3$  glass, which forms during deposition, the phase layer which forms underneath the glass and the silicon substrate with boron prediffused from the phase layer. Boron concentrations are indicated by heavy lines. The concentration distribution of boron after drive-in diffusion is not shown here. For optimal control of the concentration dis-

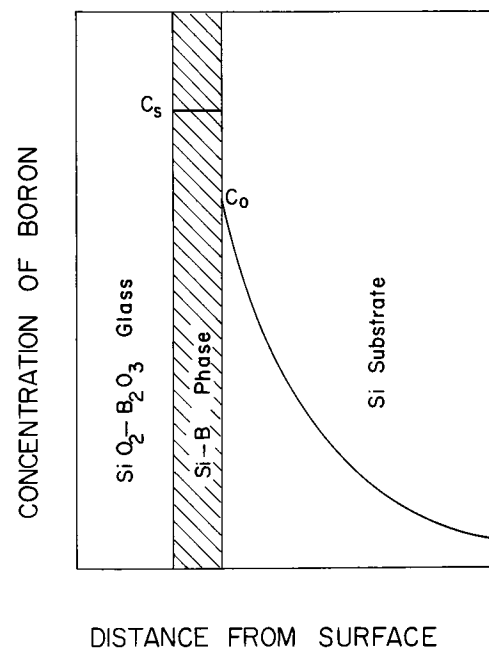


Fig. 3. Model for prediffusion

tribution in the substrate after drive-in diffusion, the deposition has to be carried out in such a way that the composition of the phase is solely a function of the temperature. The phase layer must be removed after deposition so that a well-controlled prediffusion layer can act as a finite source for subsequent drive-in diffusion. It is of interest to compare the above diffusion mechanism with the mechanism observed by Duffy *et al.* (11). The authors report that their diffusion experiments were carried out "in the concentration region where no insoluble phases form." Therefore, their  $C_0$  was directly "dependent . . . on the  $B_2O_3$  concentration in the glass at the silicon surface," whereas, the  $C_0$  here in Fig. 3 depends on the boron concentration in the phase layer.

Some simple experiments confirmed the expectation that the phase layer grows when the time of deposition increases. Thicker layers normally looked brownish or golden and changed their color on etching. If no action is taken to remove the phase layer after deposition, the supply of boron is unlimited during subsequent drive-in diffusion as long as the layer is only negligibly depleted and consequently a erf-distribution is formed. A severe depletion of the phase during drive-in diffusion, however, would cause a deviation from the erf-distribution. A profile resulting from such a deviation would pose some problems for a mathematical treatment and, therefore, would be unsuitable for device design.

Another problem arises from the observation that the phase layer may not be uniform because of a temperature gradient or of an inhomogeneous gas flow pattern in the furnace tube. This nonuniformity can be observed either on a single sample or among two samples which, for themselves, are uniform. In this case, it is not practical to rely on the phase layer as an additional source during the drive-in process, but it is preferable to remove the layer because then only the very precisely controlled prediffused layer acts as a boron source. For very thin phases (less than 50Å), the drive-in diffusion is not affected very much because the amount of boron is substantially higher in the prediffused layer than in the phase layer.

#### Acknowledgment

The authors are grateful to M. Ghezzi for ellipsometric calculations.

Manuscript received June 16, 1967; revised manuscript received Oct. 9, 1967.

Any discussion of this paper will appear in a Dis-

Table I. Control of V/I by the Si-B phase after drive-in

Si-B phase	Thickness, Å	Phase etching	V/I from run to run
Yes	<100	Yes	< $\pm 3\%$ for 100% of all samples
Yes	<100	No	< $\pm 5\%$ for 75% of all samples
Yes	>300	Yes	< $\pm 3\%$ for 100% of all samples
Yes	>300	No	$\sim \pm 10\%$ for 75% of all samples
No		Yes	$\sim \pm 50\%$ for all samples
No		No	$\sim \pm 50\%$ for all samples



Discussion Section to be published in the December 1968 JOURNAL.

## REFERENCES

1. P. F. Schmidt and A. E. Owen, Paper presented at the Pittsburgh Meeting of the Society, April 15-18, 1963, as Abstract 42.
2. E. Kooi, *This Journal*, **111**, 1383 (1964).
3. R. J. Archer, *J. Opt. Soc. Am.*, **52**, 970 (1962).
4. S. Tolanski, "Surface Microtopography," Interscience Publishers, Inc., New York (1960).
5. R. W. Ditchburn, *J. Opt. Soc. Am.*, **45**, 743 (1955).
6. K. M. Busen, W. A. FitzGibbons, and W. K. Tsang, Paper presented at the Philadelphia Meeting of the Society, Oct. 9-14, 1966, as Abstract 195.
7. K. M. Busen and R. Linzey, *Trans. AIME*, **236**, 306 (1966).
8. "The Generalized Fresnel Formulae as a Linear Fractional Transformation and Its Graphical Treatment by the Smith Chart," M. Ghezzi and K. M. Busen, paper presented at the Meeting of the Optical Society of America, Columbus, Ohio (1967).
9. K. M. Busen and G. A. Shirn, *Solid State Electronics*, **7**, 49 (1964).
10. W. K. Tsang, Unpublished work.
11. M. C. Duffy, D. W. Foy, and W. J. Armstrong, *Electrochem. Tech.*, **5**, 29 (1967).

## The Hydrothermal Growth of Beryllium Oxide Single Crystals

V. G. Hill and R. I. Harker

*Tem-Pres Research, Inc., A Subsidiary of The Carborundum Company, State College, Pennsylvania*

## ABSTRACT

Beryllium oxide crystals weighing up to 1.3g have been grown hydrothermally with the nutrient temperature at  $530^{\circ} \pm 5^{\circ}\text{C}$  and the growth temperature at  $500^{\circ} \pm 5^{\circ}\text{C}$ . An alkali hydroxide solution of 4N KOH and 0.06N LiOH was used as the hydrothermal solvent. Growth occurred in the vapor phase above the solution. The quality of the seeds used has a major effect on the quality of the crystals grown. The mean growth rate parallel to the c-axis was 0.0026 in./day, but rates of over 0.0056 in. have been measured. The relative growth rates in the various crystallographic directions are

$$[11.0] > [00.1] \sim [00.\bar{1}] > [11.1] > [10.1] > [10.0]$$

The effects of the seed orientation on the quality of the crystals produced are

$$[10.1] \sim [11.1] > [11.0] \sim [10.0] > [00.1] \sim [00.\bar{1}]$$

It is the positive pyramidal termination which is nucleated and grown on the seed.

Beryllium oxide has recently attracted special attention as a ceramic material because, in comparison to alumina which is currently being used, it has a very high melting point, comparable mechanical strength, lower specific gravity, higher electrical resistance particularly at elevated temperatures, and a much greater thermal conductivity. These properties, particularly the latter two, make it unique for heat sink applications in microelectronics, specifically in the area of silicon monolithic integrated circuits. The deposition of a thin semiconductor film on BeO substrates has been achieved (1, 2). The single crystal silicon films were grown from both  $\text{SiCl}_4$  and silane on most of the natural faces of BeO at a substrate temperature of  $1150^{\circ}\text{C}$ . Because of the high deposition temperature, it is necessary that the crystals be of high quality, or they will decrepitate.

Although BeO single crystals have been successfully grown from lithium molybdate fluxes (3-5), the hydrothermal method of crystal growth, which has been successfully applied to the growth of large crystals of quartz, corundum, and other crystals, is potentially capable of growing single crystals of a very refractory oxide at moderate temperatures (6). This enables the growth of more perfect, and strain free crystals than are generally obtained using high temperature methods.

*Previous work.*—Many previous attempts to grow BeO crystals involved either crystallization from molten salts or vapor phase techniques (3-5). In addition, Newkirk and Smith (5) investigated the application of hydrothermal methods to the growth of BeO crystals in both neutral and alkaline environments. In other work, Newkirk (7) has also determined the stability relations for the systems  $\text{BeO-H}_2\text{O}$  and in NaOH solutions with concentrations to 8.02M, as a function of temperature and pressure up to  $600^{\circ}\text{C}$ , and 4100 bars. No noticeable difference was found between the phase diagram for the neutral solutions and that

for NaOH solutions. Newkirk found that the univariant reaction curve passes through the points  $200^{\circ}\text{C}$  at 4100 bars, and  $170^{\circ}\text{C}$  at 300 bars. He also observed that BeO formed in the range  $175^{\circ}$ - $250^{\circ}\text{C}$  was not well developed and possessed a larger unit cell than that normally attributed to BeO. Newkirk and Smith (5) demonstrated that small BeO crystals could be grown hydrothermally in 2.03M NaOH solutions at  $400^{\circ}$ - $425^{\circ}\text{C}$  and 2000 bars. They obtained prismatic crystals 0.125 in. long, which grew in the positive polar direction at a rate of 0.005 in./day.

### Equipment and Materials

*Hydrothermal equipment.*—The hydrothermal equipment used in this work for solubility determinations and preliminary crystal growing runs was two Tem-Pres hydrothermal research units Model HR-1B, fitted with "test tube" type autoclaves fabricated of René or Stellite super alloys. The vessels operating at lower pressures were fitted with cone seals. For the higher pressure range, modified Bridgman-type seals were used. The maximum inside diameter of the test tube-type reactors was 0.5 in.

Three hydrothermal crystal growing systems were used. These were designed to take the Tem-Pres LRA-150 series of autoclaves. The furnaces were Kanthal wound and had two independently controlled temperature zones. Two of these systems had variacs between the control system and the furnace so that the furnace power could be varied to give better control of the temperature gradient in the furnace. The third system incorporated saturable core reactors between the controllers and the furnace. This was particularly useful when small thermal gradients were required. The Tem-Pres LRA-150 autoclaves used were of René and Stellite. The interiors of the vessels were lined with closely fitting silver thimbles. The internal dimensions of the vessels were 1.25 in. diameter and 7.0 in. deep. The seal was of the modified Bridgman type, with one

Table I. Semiquantitative spectrographic analysis of BeO starting materials

Element*	Powder, ppm	Pellets, ppm
Ca	2	1000—40
Al	20	1000—300
Si	100	1000
Ag	<2	<2 not detected
Mg	<5	1000—300
Ti	10	20—10
Na	<10	<10
K	<10	<10

\* Sought but not detected: Sr, Ba, Cr, B, Mn, Sb, Zn, Pb, Ge, Co, Zr, Bi, V, Ni, Li, and Cd (Mr. N. H. Suhr, analyst).

silver and one brass washer. The inclusion of the brass washer produced a good seal with little distortion of the silver washer. This was particularly important at temperatures above 500°C, because of the plastic flow of silver at the pressures involved.

**Starting materials.**—The manufacturer's batch analysis of the BeO powder used was 99.9%, and the KOH 99.9+%. These were both supplied by the Gallard-Schlesinger Chemical Manufacturing Corporation, Carle Place, New York. Demineralized water from a mixed bed unit was used to prepare solutions. The BeO powder was formed into pellets and fired to about 1400°C by Coors Porcelain Company, Golden, Colorado. The spectrographic analysis of the BeO powder and the pellets made from it are given in Table I. The semiquantitative spectrochemical analyses show that the pellets were contaminated at some stage in the fabrication process. The contamination was, however, not homogeneous. It will be shown later that of the contaminants only SiO<sub>2</sub> is significant in growing crystals of BeO.

### Procedures

The solubility determinations were made on pelletized polycrystalline BeO and on selected single crystals. The solvents used were usually made up as standard solutions from which aliquots were pipetted into noble metal capsules. Where the solubility of the particular compound in water at room temperatures was too low for solutions of the desired strengths to be made up, weighed amounts of the compounds and water were placed in the tube, and the strength of the solutions used at elevated pressures and temperatures calculated from this data. In either case, weighed amounts of BeO and the solvent were sealed in the capsule, which was then placed in the test tube type autoclave and rapidly brought to the required temperature and pressure. The run was usually maintained under these conditions for two days. However, at the higher temperatures and pressures some runs were for a shorter time. In the cases where single crystals of BeO were used in the low temperature range, the period was sometimes extended to five days as a check on equilibrium. The autoclave was quenched and the pressure lowered at the end of the run.<sup>1</sup> The loss in weight of the thoroughly washed and dried pellet was used to calculate the solubility of BeO in the particular solvent in grams of BeO per 100g solvent. When polycrystalline aggregates were used, it was sometimes noticed, particularly in the alkaline solvents, that the pellet recrystallized during the run, and there was nucleation and growth of new BeO crystals. Since it was not practical to collect all the primary crystals quantitatively and at the same time exclude secondary crystals produced during the quench, the run was repeated for a shorter time until the only crystals found were very fine-grained crystals which were presumed to be formed by supersaturation of the solvent with respect to BeO during quenching. In spite of this, it was difficult to prevent recrystallization of BeO in some of the higher temperature runs because of spontaneous nucleation.

<sup>1</sup> Temperatures were lowered to below 100°C in less than 30 sec.

It was, therefore, necessary to use single crystals for these determinations.

The solvents evaluated were 0.1 to 10 normal solutions of H<sub>2</sub>SO<sub>4</sub>, HNO<sub>3</sub>, HCl, HF; 2-8 normal solutions of LiOH, NaOH, KOH, and K<sub>2</sub>CO<sub>3</sub>; 100% Ca(OH)<sub>2</sub>, and the eutectic mixtures in the system Ca(OH)<sub>2</sub>-CaF<sub>2</sub>-CaCO<sub>3</sub>. The lime flux was specifically included in this study because BeO (bromellite) occurs as 1 mm long prismatic crystals in calcite rich rocks from Langban-shyttan, Vermland, Sweden (8), and it was desirable to investigate the use of a solvent which is related to the known geological occurrence of the mineral.

**Culture and preparation of seeds.**—Large high-quality crystals of bromellite (BeO) are not known to occur in nature and so were grown as part of the project. Small seeds 0.1 and 0.2 in. were obtained from runs in sealed 10 mm gold tubes and also from the walls of the LRA-150 vessels in most crystal growth runs. However, because of the mutual interference of the crystals the layer self-nucleated crystals were often of poor quality. This was particularly evident at high temperatures. A 0.0013 in. diameter hole was drilled through the better crystals and a 0.01 in. diameter platinum wire threaded through. These crystals were then suspended in 5 or 10 mm diameter gold tubes. A 4N KOH solution was used as solvent and pelletized BeO as nutrient. These overgrown crystals were further examined and the best ones selected for growth studies. When large enough seed plates of the required orientations were cut from them, the surfaces of these plates were cleaned by boiling in nitric acid.

It was necessary in all cases to determine the quality of the seeds to be used in each run. To do this the opposite faces of the seeds were polished. They were then examined under the binocular and petrographic microscopes. Particular attention was paid to the presence of twinning, inclusions, cracks and strain. A defect which was present in most of the seeds was the ghost boundary of each overgrowth cycle. These boundaries were not well defined when the overgrowth occurred in the lower temperature region of the solubility curve. However, when rapid growth occurred a well-defined junction was observed. Often these contained a small amount of fluid.

**Crystal growth technique.**—The seeds were suspended by platinum wires strung through the holes drilled in them as illustrated in Fig. 1. The autoclaves were divided into two "isothermal" regions by a baffle with a 10% opening. The baffle was held in position by two silver rods joining it to a silver basket at the bottom of the vessel. This basket contained the nutrient material. The thimble lining the autoclave, baffle and basket assembly, and closure plate were all made from silver of the same composition (99.99% pure, supplier's specification).

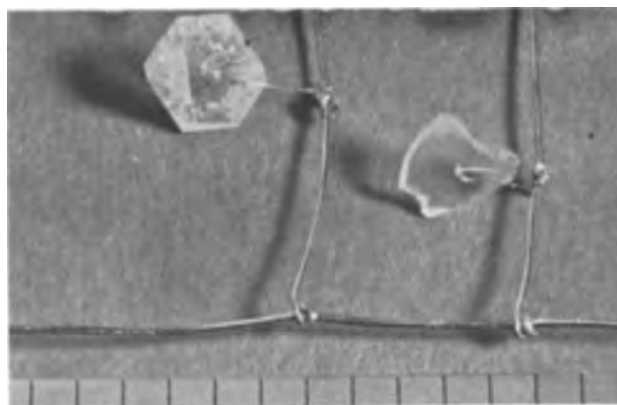


Fig. 1. BeO seed suspended on platinum ladder assembly (small divisions are 0.1 in.).

## Results

**Solubility studies.**—The solubility of BeO in acid solvents ( $\text{H}_2\text{SO}_4$ ,  $\text{HNO}_3$ ,  $\text{HCl}$ , and  $\text{HF}$ ) is dependent on the concentration of the acid used. A syrup was formed in 10N  $\text{H}_2\text{SO}_4$  runs below  $600^\circ \pm 25^\circ\text{C}$ , while in some runs at a somewhat higher temperature both crystals and syrup were obtained. Runs at temperatures of  $1000^\circ\text{C}$  and above gave a most interesting sulfate "glass" of a faint purple to gray color. This "glass" was deliquescent, and on exposure to air it changed to a thick plastic mass. Both the glass and syrup were soluble in water. The glass devitrified on standing at room temperature. Spherulites were present in some of the glasses.

It was established that in acid solutions there was an initial reaction between BeO and the dissolved ions, followed by the decomposition of the product of this reaction to provide BeO nutrient material. The decomposition temperature of these intermediate products varied over wide limits, and in runs with  $\text{HNO}_3$  the nitrate was sometimes found intergrown with BeO. BeO was found to have appreciable solubility in 10N  $\text{H}_2\text{SO}_4$ , but preliminary attempts at crystal growing with this solvent showed that there was a strong tendency for spontaneous nucleation of crystals above the decomposition temperature of beryllium sulfate. This resulted in a mass of fine-grained crystals which did not show any marked tendency to grow as the duration of the runs was increased.

The solubility of BeO in fluxes such as  $\text{Ca}(\text{OH})_2$ , the eutectic mixtures in the system  $\text{Ca}(\text{OH})_2\text{-CaF}_2\text{-CaCO}_2$  and  $\text{CaF}_2$  was very low and only very fine grained BeO was produced. Studies of the solubility of BeO in the alkali solvents  $\text{LiOH}$ ,  $\text{NaOH}$ ,  $\text{KOH}$ , and  $\text{Na}_2\text{CO}_3$  showed that the alkalis had slightly lower solvent power than the acid solvents and (but for  $\text{LiOH}$  and  $\text{Na}_2\text{CO}_3$ ) the crystals grown increased in size with the duration of the run. Figure 2 shows the change in solubility with respect to temperature for some of these solvents at several pressures.

**Growth measurements.**—On the basis of the solubility studies and the quality of the BeO crystals nucleated during these runs, 4N KOH was selected for the growth rate measurements. These data also suggested that the optimum temperature for growth is in the range  $500^\circ\text{-}700^\circ\text{C}$ . The results of these studies are summarized in Table II.

**Some factors influencing crystal quality.**—The determination of the growth rate of the crystals at different temperature conditions using seeds of various orientations served to define closely the best temperature conditions for growth. However, although it

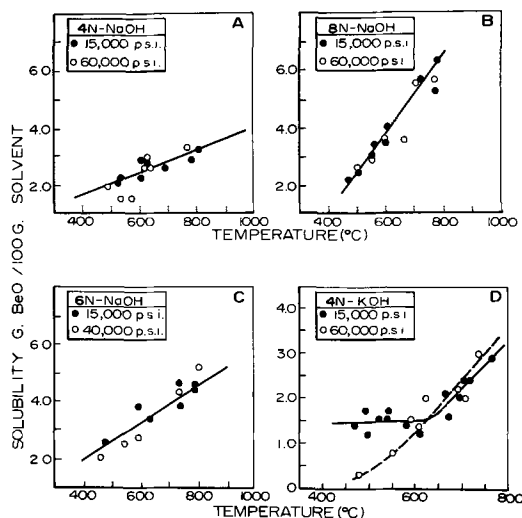


Fig. 2. Solubility curves of BeO in NaOH and KOH solutions as a function of temperature and pressure.

Table II. Growth rate measurements of BeO crystals in 4N KOH

Run No.	Temperature, °C		Orientation	Run, duration in days	No. of meas. <sup>1</sup>	Growth rate in./day	
	Nutri-ent	Seed				Parall. to C-axis	Perp. to c-axis
700	728	700	Prism. cryst. <sup>2</sup>	8	1	0.014	—
810	590	580	Prism. cryst.	11	3	0.009	0.002
829	580	570	Pyrd. term. <sup>3</sup>	31	3	0.006	0.003
			{00.1} plate <sup>4</sup>		2	0.008	0.003
			{00.1} term. <sup>5</sup>		1	0.012	—
921	581	575	{10.1} plate	23	1	0.003	0.002
			{00.1} plate		1	0.003	0.0004
			Prism. cryst.		1	0.003	0.001
919	575	554	{10.1} plate	20	1	(0.002)	0.001
			{00.1} plate		1	0.005	0.001
			Prism. cryst.		1	0.007	0.001
880	571	551	{00.1} plate	37	2	0.006	0.002
657	561	550	{00.1} plate	14	5	0.005	0.001
656	548	532	{00.1} plate	14	5	0.004	0.001
833	543	523	Pyrd. term.	62	4	0.002	0.0006
938	535	502	{10.1} plate	90	1	0.0026	0.0015
			{11.1} plate		1	0.0031	0.0010
			{00.1} plate		1	0.0032	0.0002
			Pyrd. term.		1	0.0023	0.0004
			Prism. cryst.		1	0.0011	0.0033
			{11.0} plate		1	0.0037	0.0014
1160	536	501	{11.0} plate	68	1	0.0034	0.0020
			{00.1}		1	0.0016	0.0035
1136	531	502	Pyrd. cryst.	31	1	0.0058	0.0010
1172	530	497	{11.0}	32	1	0.0031	0.0031
920	527	504	{10.1} plate	68	1	0.0007	0.0021
			{00.1} plate			(0.0001)	(0.0001)
			Prism. cryst.			0.001	0.0001

<sup>1</sup> Measurements.

<sup>2</sup> Prismatic crystal with positive pyramidal termination.

<sup>3</sup> Positive pyramidal termination of crystal.

<sup>4</sup> Plate of the orientation indicated sawn from the crystal.

<sup>5</sup> Seed cut to expose {00.1} and with the positive pyramid on small hexagonal prism.

was possible to readily grow BeO crystals weighing over 1g, these were sometimes of poor quality. Evaluations of the various factors involved in these runs served to demonstrate that the major factors affecting the quality of the crystals are (a) quality of the seeds, (b) orientation of the seed used, (c) presence of impurities in the autoclave, (d) too rapid growth rate, and (e) level of the meniscus in the vessel.

Figure 3 illustrates both the effects of seed quality and orientation on the quality of the crystal grown. Defects present in the seed were continued out into the new growth. The effects of seed orientation were also marked. Examination of several overgrown seeds including whole crystals under the microscope showed that the growing area was the positive pyramidal termination. It was this pyramid that was nucleated and subsequently generated the other crystal faces. The (00.1) plane acted as a twin plane. The result was that where the (00.1) was exposed for growth positive pyramids were nucleated there initially and resulted in an area of poor growth. However, since all of these were in the same crystallographic orientation,



Fig. 3. BeO crystals grown from seeds shown in Fig. 1

it was possible for them to heal by lateral growth. Unfortunately, this only occurred when the growth perpendicular to the c-axis was sufficiently fast to keep pace with the growth along the c-axis. Usually the lateral growth was much slower than that along the c-axis and a zone of inclusions occurred parallel to the c-axis. This means that the orientation of the seed must be such that the nucleation on this plane will not cause the crown-type growth which occurs when the (00.1) orientation is exposed for growth. To minimize this, the rate of growth of the seed must be such that few of these positive pyramids are nucleated and these spread out rather than form spires. The use of the [11.0], [11.1], and [10.1] seed plates would seem to encourage this type of growth. The first is not a naturally occurring face, the second occurs very rarely, and the third is a prism face. These seed plates along with others were tested to determine the effects of seed orientation of growth rate and crystal quality. The relative growth rates in the various directions are:

$$[11.0] > [00.1] \sim [00.\bar{1}] > [11.1] > [10.1] \sim [10.0]$$

The effects of the seed orientation on the quality of the crystals produced are:

$$[10.1] \sim [11.1] > [11.0] \sim [10.0] > [00.1] \sim [00.\bar{1}]$$

Impurities like cobalt and lithium affect the morphology of the crystals causing rounding of faces, etc. The effects of silica are not known, but it possibly increases the ease of nucleation of the crystal face. The incorporation of a trace of lithium in the structure minimizes this.

The growth rate of the crystal, particularly in the early stages has a marked effect on crystal quality. Part of the reason for this may be that cutting the crystal creates imperfections, and these become larger and more significant as growth takes place. The surface imperfections on the seed must be removed *in situ* etching followed by an initial period of very slow growth.

The presence of a poor junction between the seed and the overgrowth material has been a major factor in the growth of poor quality crystals because of the concentration of imperfections trapped at the interface. This problem was successfully solved by programming the heating cycle of the vessel. Three heating cycles were studied: (a) rapid heating to temperature, (b) slow heating to temperature, (c) rapid heating to a fixed temperature followed by slow heating. The first procedure gave the poorest junction of overgrowth to the seed and often caused seed dissolution. The second did not improve the quality over the first, but the seed usually remained undissolved. In the third cycle, satisfactory results were obtained by heating the autoclave to  $400^\circ \pm 20^\circ\text{C}$  and maintaining this temperature for 24 hr. The temperature of the autoclave was then raised to the desired value over a 24-hr period, while at the same time a temperature gradient of  $10^\circ\text{C}$  was maintained between the nutrient and growth zones. The autoclave was finally adjusted to the desired operating temperature when the temperature of the nutrient zone was within  $20^\circ\text{C}$  of that desired for the seed zone. This method permitted the dissolving of sufficient material from the seed for it to present a "clean" surface for growth, and so a good junction is possible. The BeO crystals in Fig. 3 were grown using this technique. The nutrient temperature was  $527^\circ\text{C}$  and the seed temperature  $504^\circ\text{C}$ . The stepwise heating cycle outlined above was used. The crystal grown on the [00.1] seed plate was of slightly lower quality, containing a significantly higher dislocation density than the other which was grown on a [10.1] plate. It was observed that the optimum amount of liquid required was such that it was initially below the level of the seeds, and when the vessel was operating, it should be just below the baffle. The level of the liquid inside the vessel during

Table III. Spectrochemical analyses of BeO crystals

Element	Run 880 <sup>1</sup> ppm	Hydro- thermal <sup>2</sup> ppm	Hy- droly- sis of BeF <sub>2</sub> <sup>3</sup> ppm	PbF <sub>2</sub> :PbO Flux <sup>2,4</sup> ppm
Ca	10	—	20	—
Al	20	—	60	—
Si	100	100	30	20
Ag	n.d.	—	—	—
Mg	10	—	30	—
Ti	n.d.	—	40	—
Na	n.d.	—	—	—
Fe	10	10	100	50
Pb	n.d.	—	—	100
F	—	—	1000	—
B	n.d.	7	—	10

<sup>1</sup> BeO crystal from T.P.R. Run 880. Sought, but not detected: Ni, Ag, Co, V, Ti, Sr, Zr, Cu, Ba, Ba, Nm, Sb, Sn, Ge (Norman Shur, Analyst).

<sup>2</sup> Newkirk and Smith (5).

<sup>3</sup> Newkirk and Smith (5).

<sup>4</sup> Newkirk and Smith (5).

n.d., = not detected.

a run was indicated by the location of the silver dendrites in runs which contained a small amount of oxygen.

**Growth conditions.**—Our experience with growing BeO crystals hydrothermally has established that the best conditions for growth under laboratory conditions are:

Vessel	150 ml autoclave fitted with a silver liner <sup>2</sup>
Solvent	Solution 4N with respect to KOH and 0.06N with respect to LiOH, 65 ml
Wt. nutrient	7g fired BeO pellets
Seeds	High quality BeO seed plates of [10.1] or [11.0] orientation
Baffle opening	10%
Nutrient temperature	$530^\circ\text{C}$
Seed temperature	$500^\circ\text{C}$

To avoid recrystallization of the silver by the KOH solution, the system must be purged of all traces of oxygen. This is easily accomplished by reacting a small piece of pure beryllium metal in the nutrient zone during the run (9).

Figure 3 illustrates the best BeO crystals grown to date, and Table III the purity of some of these crystals. The largest BeO crystal grown to date weighs 1.3g.

### Discussion of Results

One advantage of the hydrothermal method is the fact that the growing crystal is able to reject most of the impurities in the nutrient. Table I shows that the BeO pellets used as nutrient were contaminated with Ca, Mg, Al, and Si during the fabrication process. It is, however, significant that of these only  $\text{Si}^{4+}$  was incorporated in the growing crystal to any extent, and even here it was significantly reduced as compared to the level present in the nutrient. This is important because we have demonstrated that in the production growth of BeO it may not be necessary to use ultra-pure BeO. Experiments with the addition of small amounts of  $\text{Li}^+$  to the growth solution have shown that it is possible to offset the effects of the  $\text{Si}^{4+}$  entering the structure by  $\text{Si}^{4+}$  and  $2\text{Li}^+$  substitute for  $3\text{Be}^{2+}$ . This mechanism permits the filling of all metal ion sites in the structure. However, the amount of LiOH in the solution has to be carefully controlled, otherwise it causes the crystals to grow with curved faces.

One of the unique features of this work is the fact that the crystals are grown in a dense vapor phase above the liquid phase containing the nutrient. A baffle is, however, necessary to separate the vessel into two isothermal zones. The lower nutrient zone contains a

<sup>2</sup> Our experience shows that the design of the pressure vessel and liner affect the convection pattern and temperature profile inside the autoclave.

liquid phase and a vapor phase above it. The upper growth zone contains a vapor phase. The recrystallization process substantially improves the purity and quality of the crystals grown, particularly as the nutrient material has to go from the liquid layer to the vapor layer. It is also important that the meniscus of the liquid not be in contact with the growing crystals, otherwise poor quality crystals result. This may be due to the phase changes in the solution near the growing crystal.

#### Acknowledgments

This work was done as part of a research project on hydrothermal crystal growth sponsored by the U.S. Air Force Materials Laboratory, Wright-Patterson Air Force Base, Ohio. Mr. Paul W. Dimiduk was Project Engineer.

Manuscript received Sept. 6, 1967; revised manuscript received Oct. 16, 1967.

Any discussion of this paper will appear in a Discussion Section to be published in the December 1968 JOURNAL.

#### REFERENCES

1. H. M. Manasevit, D. H. Forbes, and I. B. Cadoff, Tech. Conf. Mater. Sci. Technol. Integrated Electron. (AIME), San Francisco (1965).
2. A. Miller and H. M. Manasevit, *J. Vacuum Sci. Technol.*, **3**, 68 (1966).
3. S. B. Austerman, *J. Am. Ceram. Soc.*, **46**, 6 (1963).
4. H. W. Newkirk, and D. K. Smith, *Am. Min.*, **50**, 22 (1965).
5. H. W. Newkirk, and D. K. Smith, *ibid.*, **50**, 44, (1965).
6. A. A. Ballman, and R. A. Laudise, "Hydrothermal Growth; The Art and Science of Growing Crystals," p. 44, pp. 231-351, J. J. Gilman, Editor, John Wiley & Sons, Inc., New York (1963).
7. H. W. Newkirk, *J. Inorg. Chem.*, **3**, 1041 (1964).
8. G. Aminoff, *Z. Kristallograph.*, **42**, 113 (1962).
9. V. G. Hill, In manuscript (1967).

## Growth of Large Single Crystals of Gallium Phosphide from a Stoichiometric Melt

S. E. Blum\* and R. J. Chicotka

IBM Watson Research Center, Yorktown Heights, New York

#### ABSTRACT

A procedure is described for the growth of large single crystals of gallium phosphide. A vertical Bridgman apparatus is employed with a controlled phosphorus pressure source to maintain stoichiometric conditions during freez- ing. The high phosphorus pressure is contained by the use of heavy-walled quartz in the low temperature zone, and by permitting the thin-walled quartz in the hot zone to soften and expand out against a graphite support tube. Crystals doped with both zinc and tellurium have been prepared. The electrical properties of these and "undoped" crystals are presented.

The growth of single crystals of gallium phosphide from a stoichiometric melt is difficult because of the compound's high melting temperature and high dissociation pressure, which are about 1500°C and 35 atm (1), respectively. These extreme conditions impose severe requirements on the usual materials of construction of crystal growing equipment.

The problems that beset crystal growth of GaP from stoichiometric melts have been reviewed by Miller (2) and Shmartsev (3). Generally, such crystal growing operations as pulling, Bridgman growth, or float zoning must be performed in high pressure autoclaves. These are complicated and expensive to construct and only a limited amount of work has been done on such systems. [Frosch (4) described the preparation and floating zone processing of GaP, and Weisberg (5) reported growth in an autoclave crystal puller.]

An appreciably simpler method for high melting high dissociation pressure compounds was developed and described by Fischer (6) for the growth of II-VI compounds. In this method the ingot to be melted and regrown is sealed within a quartz ampoule. The ampoule is in turn held within a close fitting graphite container. On heating the system to the melting point of the compound (ca. 1500°C) the quartz softens and expands against the back-up graphite container which has sufficient strength to contain the pressure. Throughout the remainder of the crystal growth the quartz serves as a semiliquid seal to prevent loss of vapor.

#### Experimental Procedure and Apparatus

A few experiments were sufficient to demonstrate that large grained GaP ingots could not be grown in

the apparatus just described for the following reasons: (i) When GaP alone was loaded into the ampoule it dissociated at the high temperature to an extent determined by the volume of free space that must be filled with vapor, and the gallium-rich liquid that resulted would not crystallize readily as large grains. (ii) When the amount of phosphorus necessary to fill the free space was added to the ampoule to overcome this difficulty, the ampoule frequently ruptured because softening of the quartz ampoule could not be achieved before the phosphorus pressure became too large. This problem was aggravated by the uncertainty in the amount of phosphorus required because of inability to estimate the free volume accurately.

The procedure that we developed consisted of a "two-zone bomb" technique that incorporated both the liquid seal feature employed by Fischer and the controlled condensed phosphorus source of a conventional two-zone Bridgman apparatus.

A general description of the experiment will be given first, followed by details of the apparatus.

*General description.*—A schematic diagram of the apparatus is shown in Fig. 1. Previously synthesized GaP (7) is placed in a cylindrical crucible and sealed with an excess of phosphorus and 100 Torr pressure of argon in the quartz ampoule. The ampoule is placed within the close-fitting graphite tube and held firmly with a graphite screw cap. The tube is now positioned vertically within a resistance furnace-graphite susceptor ensemble. The entire furnace apparatus is housed within a quartz envelope which is capped at both ends. The caps are provided with appropriate feed-throughs to bring power to the resistance furnace and for the control thermocouples. The quartz envelope is evacuated and the system is slowly heated until the

\* Electrochemical Society Active Member.

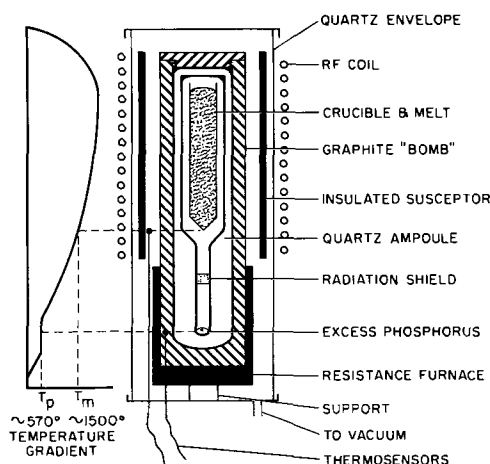


Fig. 1. Schematic diagram of the apparatus and temperature profile used to grow GaP single crystals.

indicated temperature profile (see Fig. 1) is achieved. The phosphorus overpressure ( $\sim 35$  atm) is maintained during the entire run. Solidification of the ingot is achieved by slowly lowering the temperature of the RF-heated upper zone. Generally, the temperature is lowered to provide a rate of freezing estimated to be between 0.5–1.0 cm/hr.

#### Experimental Details

**Crucible material.**—Boron nitride crucibles were generally used. These are cylindrical in shape with a 45° conical bottom, and are 1.5 cm ID  $\times$  7–15 cm long. They are available as "Boralloy" from High Temperature Materials, Inc. Lowell, Massachusetts. The crucible is cleaned prior to use by white etch ( $3\text{HNO}_3\text{-1HF}$ ). The crucible is supported within the growth ampoule by "Boralloy" tubing not shown in the diagram.

**Quartz ampoule.**—The ampoule is constructed from two sizes of quartz tubing. The upper portion, containing the charge and crucible, is 25 mm OD  $\times$  18 mm ID  $\times$  200 mm long. It is this portion of the ampoule that will be heated to temperatures above the softening point of quartz and must then be supported by the graphite back-up tube. The lower portion of the ampoule is 25 mm OD  $\times$  5 mm ID  $\times$  300 mm. At the temperature of the experiment, this portion of the ampoule remains solid and has sufficient strength to withstand the high internal pressure without the support of the graphite. The greater part of this tube is well below the softening temperature (nominally it is kept below 1100°–1150°C), whereas no portion of the thinner walled section of the ampoule is below 1250°C when the pressure in the system is appreciably elevated, i.e.,  $> 10$  atm.

A quartz wool plug is placed in the lower portion of the ampoule to prevent direct radiation from the crucible onto the condensed phosphorus.

**Graphite bomb.**—The graphite tube is bored so that the quartz ampoule fits snugly. The tube is closed by a graphite screwcap. The lower portion of the tube in the region of the condensed phosphorus is fitted with four thermocouple wells. The tube is 56 cm long over-all.

**Resistance furnace.**—The resistance furnace is tubular and closed at the lower end and serves, in addition to providing heat, to support the graphite tube. It is constructed of solid copper, plated with nickel and gold to lessen oxidation. Inconel-sheathed resistance wire (a product of the Ampere Electronic Corporation) is used as the heating element and it is wound in a spiral groove on the furnace's outer surface. This design was found to be effective in maintaining a shallow temperature gradient in the region of the condensed phosphorus.

**RF heater.**—The crucible portion of the graphite tube is positioned within an insulated susceptor ensemble. This ensemble is a vertical array of tubing (80 mm OD  $\times$  70 mm ID) comprising from top to bottom a 28-cm long graphite susceptor, a 4-cm long alumina spacer (not indicated on the diagram), and a 12.5-cm long lower susceptor. The ensemble is sheathed with graphite wool insulation and held snugly within the quartz envelope. The vertical temperature gradient in the hot zone is achieved by appropriately spacing the turns of the RF work coil. The horizontal temperature gradient in the region of the melt is essentially zero, thereby resulting in a planar liquid-solid interface; the shape of the interface could be delineated from partially solidified ingots whose slow freezing was interrupted by rapid termination.

**Temperature control.**—The temperature of the hot zone is sensed by a commercial thermopile device, using as a light pipe a sapphire rod in a ceramic well within the hot zone (8). The d-c output voltage of the thermopile is used to control the temperature in the conventional way. The temperature of the hot zone is slowly reduced to provide solidification of the melt by the gradient freeze technique.

The temperature of the condensed phosphorus, and hence its pressure, is controlled by thermocouples. Four are used: one for the actual control of the temperature at the condensed phosphorus interface, a second to measure this temperature, and two thermocouples to monitor the ampoule temperature both above and below this point. The temperature of the graphite tube at the phosphorus control point is held to  $\pm 0.1^\circ\text{C}$ . The temperature gradient in this region is about  $1^\circ\text{C}/\text{cm}$ . L&N speedomax H-AZARs with a series 60 CAT unit are used to control the resistance furnace and the Lepel 30 kva generator.

**Argon backfill.**—The ampoule is back-filled with argon at about 100 Torr before sealing. This backfill provides an inert gas pressure of about 1/2 atm during solidification of the GaP. Its purpose is to prevent internal "boiling" of the phosphorus in the melt. Without it, minor fluctuations in temperature can result in phosphorus gas nucleation at the solid-liquid interface and at the crucible-melt interface. These gas pockets remain during solidification and voids are observed in the solid ingot.

#### Experimental Results

Photographs of the starting GaP material and of two different recrystallized ingots are shown in Fig. 2. These photographs are of 1.5 cm diameter wafers cut transverse to the growth direction. The starting material (2a) exhibits the typical polycrystalline growth of synthesized GaP (7). Wafer 2(b) is from a regrown crystal and shows large grain growth; approximately one-half of the wafer is a single grain. This grain pattern remained essentially the same from the 2-cm position to the last-to-freeze portion of the crystal at about 10 cm. Figure 2(c) is of a wafer of our best regrowth. With the exception of a few small grains at the first-to-freeze portion of this ingot, the crystal was entirely single, and weighed 76g. The crystal was

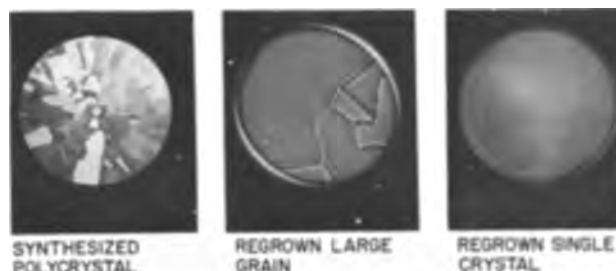


Fig. 2. Transverse slices of polycrystalline synthesized GaP and of regrown ingots (diameter 1.5 cm).

Table I. Hall measurements of recrystallized GaP

No.	Dopant	Type	300°K		77°K	
			R <sub>H</sub> , cm <sup>2</sup> /C	ρ, ohm-cm	R <sub>H</sub> , cm <sup>2</sup> /C	ρ, ohm-cm
1	—	n	-45	0.45	-76, 100	850
2	—	n	-28	0.22	-48, 500	152
3	Te	n	-57	0.46	-17 × 10 <sup>4</sup>	728
4	Te	n	-15	0.14	-1190	11
5	Zn*	p	+0.79	0.03	+0.46	0.05

\* The zinc doped sample appears to be nearly degenerate.

tellurium doped at about the 10<sup>18</sup> cm<sup>-3</sup> level. This crystal grew 9° off the <111>.

The electrical properties of several regrown crystals are given in Table I. The starting GaP material used in these regrowths was p-type with net carrier concentrations of about 1 × 10<sup>17</sup> cm<sup>-3</sup>. Regrown crystals, if undoped, are n-type with net carrier concentrations of about 10<sup>17</sup> cm<sup>-3</sup>. The reason for this change in type is, as yet, unproven. Doped crystals have been prepared by adding the dopant, generally zinc or tellurium, directly to the melt.

### Discussion

The procedure described above has consistently produced gallium phosphide ingots that contain single crystal portions that are larger than one quarter of the ingot in cross section and longer than 5 cm. These results, as well as the growth of one completely single crystal ingot, are promising and we believe that the method can be improved to consistently yield ingots that are wholly single. In particular, two modifications are being instituted; these are the substitution of a well shunted resistance furnace for the RF-susceptor unit and provision for seeding the melt. The use of a shunted furnace will provide a better means for tailor-

ing the temperature profile in the melt as well as a better reproducibility of the profile from run to run. The temperature profile is difficult to maintain with the graphite susceptors because they suffer some oxidation at the high operating temperatures. This oxidation alters the temperature profile in an unpredictable way. Seeding of the melt is desirable because it will (i) aid in the control of the growth direction and (ii) prevent supercooling and hence improve control of the rate of solidification of the melt.

### Acknowledgments

The authors are pleased to acknowledge Johannes Grandia and William A. Kahn for aid in the design and construction of the apparatus and Stephen Baliozian for the electrical measurements. Part of this work was supported by the United States Army, Fort Belvoir, Virginia, Contract No. DA-44-009-AMC-1674(X).

Manuscript received Oct. 5, 1967; revised manuscript received Dec. 4, 1967.

Any discussion of this paper will appear in a Discussion Section to be published in the December 1968 JOURNAL.

### REFERENCES

1. D. Richman, *J. Phys. Chem. Solids*, **24**, 1131 (1963).
2. J. F. Miller, "Preparation of Gallium Phosphide" in "Compound Semiconductors," R. K. Willardson and H. L. Goering, Editors, Chap. 23, Reinhold Publishing Corp., New York (1962).
3. Yu. V. Shmartsev, Yu. A. Valov, and A. S. Borshchevskii, "Refractory Semiconductor Materials," New York, Consultants Bureau, 1966.
4. C. J. Frosch and L. Derick, *This Journal*, **108**, 251 (1961).
5. L. R. Weisberg and E. A. Miller, RCA Tech. Report #2, ARPA 446, Contract SD-182 (1964).
6. A. G. Fischer, *Electrochem. Soc., Extended Abstracts*, **12**, 142 (1963).
7. S. E. Blum and R. J. Chicotka, and B. K. Bischoff, *This Journal*, **115**, 324 (1968).
8. S. E. Blum and R. J. Chicotka, To be published.

## Electrical Properties of Vapor-Deposited Silicon Nitride and Silicon Oxide Films on Silicon

B. E. Deal,\* P. J. Fleming, and P. L. Castro\*

Research and Development Laboratories, Fairchild Semiconductor, Palo Alto, California

### ABSTRACT

The electrical properties of vapor-deposited silicon nitride and silicon oxide films on silicon have been investigated. The silicon nitride films were produced by the SiCl<sub>4</sub>-NH<sub>3</sub> reaction at 950°C, while the oxides were prepared at 400°C using the SiH<sub>4</sub>-O<sub>2</sub> reaction. The properties were compared with those of thermal oxides prepared in dry O<sub>2</sub> at 1200°C. As contrasted to the thermal oxides, the silicon nitride films are characterized by polarization and room temperature trapping instabilities, relatively high conductance, and high surface state charge densities. The vapor-deposited oxides tend to resemble the nitrides in those properties which are associated with the silicon-dielectric interface, but the bulk properties are more like those of thermal oxides.

For several years, silicon dioxide has been used as a masking and passivating layer over semiconductor devices. For silicon, these films have generally been prepared by the thermal oxidation of the silicon in oxygen or water ambients at temperatures ranging from 900°-1200°C. Other methods of producing passivating layers of silicon dioxide, both on silicon and other semiconductor materials, include pyrolytic decomposition of

\* Electrochemical Society Active Member.

oxysilanes, vapor phase reactions of silicon and oxygen-containing compounds, sputtering, plasma oxidation, and anodization (1, 2). In addition, other dielectrics and glasses have been deposited by sedimentation techniques, either directly on the semiconductor or over a previously formed oxide (3).

In 1965, Sterling and Swann (4) reported a method for depositing films involving chemical reactions in an r.f. discharge. These films included silicon, silicon di-



oxide, and silicon nitride. Shortly after this, Hu (5) and also Doo, Nichols, and Silvey (6) reported the use of vapor-deposited silicon nitride films for passivating silicon devices. Other investigators, such as Tombs *et al.* (7) reported several possible advantages of silicon nitride films as compared to the conventional silicon oxides. One of the most important advantages appeared to be the ability of silicon nitride to mask against diffusing impurities, especially sodium ions. The latter have been a source of considerable difficulty in the fabrication of stable surface-controlled devices (8).

The interest in the use of silicon nitride films as passivating layers over semiconductor devices was considerable.<sup>1</sup> Various deposition methods were reported which included both high-temperature (800°–1200°C) vapor reactions of SiH<sub>4</sub> or SiCl<sub>4</sub> with NH<sub>3</sub> as well as lower temperature sputtering techniques. Two important characteristics of silicon nitride films were emphasized by the various papers. First, it was demonstrated that the structure of amorphous silicon nitride leads to higher density than fused silica, resulting in a lower etch rate, higher refractive index and dielectric constant, and greater masking ability mentioned above. These properties are dependent on the temperature and method of deposition. Second, the silicon nitride-silicon structure gives rise to considerable room temperature electrical instability, other than ion migration, as well as exhibiting a relatively high surface charge, *i.e.*,  $>10^{12}$  cm<sup>-2</sup>.

Because silicon nitride films might offer certain advantages in semiconductor technology, such as enhanced masking of impurities, its electrical properties were studied in further detail. The deposition method used in this investigation was the silicon tetrachloride-ammonia reaction process. Preliminary results concerning etch rates and electrical properties indicated lower temperature depositions would be more satisfactory;<sup>2</sup> therefore, most of the subsequent depositions were carried out at 950°C.

Vapor-deposited silicon oxides were also included in these studies when it was discovered that their interface properties were very similar to those of silicon nitride. They were deposited using the technique involving the oxidation of silane (9). The low temperature required for deposition (~400°C) makes this method attractive for additional passivation of metallized device structures. This type of dielectric might be considered a hybrid between the vapor-deposited nitride and the thermal oxide, since the method of deposition resembles the former while the chemical composition is similar to the thermal SiO<sub>2</sub>. Properties of the two vapor-deposited dielectrics were compared to those of thermal oxide films. Also, properties of silicon nitride and vapor-deposited oxide layers over thermal oxides were determined.

Electrical properties of the above dielectric films on silicon which are reported include dielectric constant, breakdown field, surface charge, surface recombination velocity, work function difference, conductance, polarization, and trapping. The characteristics of these films are compared with one another with particular emphasis being placed on the room temperature instability phenomena.

### Experimental

Silicon used for these studies was in the form of circular slices, 2 cm in diameter, prepared by the Czochralski method. Dislocation count was specified to be less than 100 cm<sup>-2</sup>. Both (111) and (100) surface orientations were used as well as p- and n-type (boron and phosphorus) doping impurities in concentrations of approximately  $1.5 \times 10^{18}$  cm<sup>-3</sup>. After lapping, the

silicon slices were cleaned in organic and inorganic solvents and chemically polished in a 4:10 HF:HNO<sub>3</sub> solution. Final thickness was 150μ.

For those samples involving a thermal oxide, the silicon was oxidized at 1200°C in dry oxygen under conditions described previously (10). The silicon nitride deposition was carried out in a horizontal, r.f. heated quartz reactor. The reactor tube was rectangular in shape, with inside dimensions of 5.0 by 7.5 cm. Hydrogen and ammonia were passed into the reactor along with silicon tetrachloride, the latter titrated at room temperature into the hydrogen stream. The relative flow rates were as follows: H<sub>2</sub> 4 l/min; NH<sub>3</sub> 4 ml/min; SiCl<sub>4</sub> (liquid) 0.2 ml/min (~40 ml/min vapor). As mentioned earlier, all depositions were carried out at 950°C, the deposition rate being approximately 0.12 μ/min.

The vapor-deposited oxide was prepared by the reaction of SiH<sub>4</sub> (diluted in argon) with O<sub>2</sub> at 400°C. The reactants, together with nitrogen as a carrier gas, were directed through a nozzle to the silicon substrates positioned on a hot stage. Flow conditions were as follows: SiH<sub>4</sub> (15%) in argon 0.080 l/min; O<sub>2</sub> 0.085 l/min; N<sub>2</sub> 2.7 l/min. Deposition rate of the oxide was approximately 0.6 μ/min. While this is a relatively rapid deposition, film thickness uniformity was ±2.5% over a major portion of the slice. The nitride uniformity was not quite as good, being about ±7%. Thickness reproducibility from run to run was about ±10% for both types of films.

A number of the electrical evaluations involved MIS (metal-insulator-semiconductor) structures. These were prepared by evaporating aluminum field plates, 375μ diameter, over the dielectric through a mask. Aluminum was also evaporated on the bare, back side of the silicon for contact.

Gate-controlled diodes, used for the surface recombination velocity measurements, were prepared as described in ref. (11). Essentially this structure is a planar diode with an aluminum gate or field plate over the oxidized junction and extending over the substrate region about 125μ. An outside gate is also available for electrically isolating the device from the rest of the semiconductor slice. After preparation of the diffused diodes, the original oxide was stripped in HF and the dielectric to be evaluated (silicon dioxide, silicon nitride over oxide, or silicon nitride) was deposited by the appropriate method. Aluminum contacts and gates were then prepared by conventional metallization and photoresist techniques.

Where low temperature thermal treatments were required, these were accomplished by treatment in nitrogen at 550°C for 2 to 5 min. Various electrical measurements were then carried out as described later in this paper. Thickness measurements were made for all oxidations and nitride depositions using the Tolanski method described earlier (10).

### Results: Physical Properties

It was reported in a number of papers at the Fall 1966 Meeting of the Society in Philadelphia that physical, chemical, and electrical properties of deposited dielectric films depend considerably on deposition conditions, *i.e.*, temperature, composition of reactants, *etc.* For this reason, certain physical properties of the three types of films studied here are listed in Table I. These values will help to characterize the particular films prepared by the process conditions described above. For purposes of this discussion, the formula of the nitride is specified as Si<sub>3</sub>N<sub>4</sub> and that of the vapor deposited oxide as SiO<sub>2</sub>.

Examination of infrared spectra (transmission) of the nitride films indicated a broad absorption peak at 12.0μ; in agreement with the value reported by Hu (5) for films prepared by the SiH<sub>4</sub>-NH<sub>3</sub> reaction deposition. No peaks or shoulders were observed in the 9.2μ range, thus indicating that no Si-O was present. For the vapor deposited oxide, the absorption peak of 9.2μ associated with thermally produced oxides was shifted

<sup>1</sup> It resulted in a special symposium at the Philadelphia Meeting of The Electrochemical Society, Oct. 9-14, 1966, where 24 papers were presented on the subject.

<sup>2</sup> In general, etch rates were slightly higher at lower temperatures. Also, the higher temperature nitrides exhibited very unstable electrical characteristics, *i.e.*, C-V plots could not be made at room temperature as they shifted during the plotting itself.



Table I. Properties of dielectric films on silicon

	Vapor deposited Si <sub>3</sub> N <sub>4</sub>	Thermal SiO <sub>2</sub>	Vapor deposited SiO <sub>2</sub>
Density, 25°C	~3.2 g/cc	2.25 g/cc	2.1 g/cc
Refractive index, 5460 Å	1.95	1.46	1.45
Etch rate: HF, 49% Oxide etch*	30 Å/sec 1 Å/sec	300 Å/sec 23 Å/sec	1065 Å/sec 85 Å/sec

\* Oxide etch composition: 1360g NH<sub>4</sub>F; 500 ml HF (49%); 2000 ml H<sub>2</sub>O.

to a higher wavelength (9.7 $\mu$ ), characteristic of less dense, deposited oxides (12).

### Results: Electrical Properties

**Dielectric constant.**—The dielectric constants of silicon nitride films, prepared under the conditions described above, were obtained by measuring the capacitance at 100 kHz of an MIS structure under bias conditions corresponding to strong accumulation of the silicon surface. These values were found to be in the range 4.8–5.8, as compared with 3.85 for thermal oxides. The dielectric constant of the vapor-deposited oxide was 4.5. Goldsmith and Kern (9) report a value of 4.3 for an as-deposited oxide film prepared at 475°C.

**Breakdown field.**—The breakdown field or dielectric strength of silicon nitride films is somewhat difficult to determine due to the high conductance that exists at higher voltages (see later section). However, values were found to be approximately 10<sup>7</sup> v/cm (d.c.). This agrees with findings of Hu (5) and Doo *et al.* (6) and is slightly higher than values found for thermal oxides (9 x 10<sup>6</sup> v/cm) (13). The dielectric strength of vapor-deposited oxides (8.5 x 10<sup>6</sup> v/cm) was found to be very close to that of thermal oxides. These values for vapor-deposited oxides agree with those reported by Goldsmith and Kern (9).

**Surface charge.**—The total charge per unit area  $Q_s'$  induced in the silicon by charges in the dielectric layers was determined from the capacitance-voltage characteristics of MIS structures. This method of charge analysis is described in detail elsewhere (14). Essentially one determines the flatband voltage  $V_{FB}$  of the experimentally measured capacitance-voltage curve. The induced charge  $Q_s'$  is related to  $V_{FB}$  by the expression:

$$Q_s' = (-V_{FB} + \phi_{MS})C_o$$

where  $\phi_{MS}$  is the metal-semiconductor work function difference, and  $C_o$  is the capacitance per unit area of the dielectric layer. For example, for a 0.2 $\mu$  thermal oxide, a flatband voltage of 1v will correspond to 1 x 10<sup>11</sup> electronic charges/cm<sup>2</sup> induced in the silicon if the  $\phi_{MS}$  term is neglected.

Typical C-V plots are shown in Fig. 1 for a silicon nitride film, a vapor-deposited silicon oxide film and a

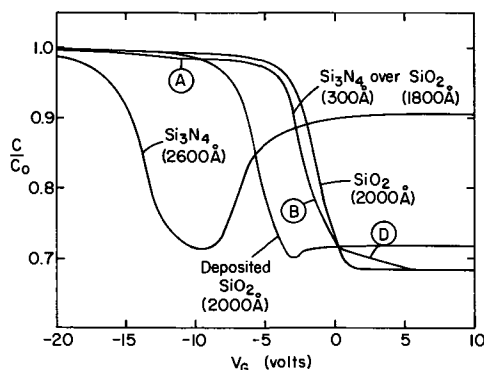


Fig. 1. Typical capacitance-voltage plots for MIS structures

thermal oxide film on silicon, as well as a double layer of silicon nitride over thermal oxide. Measurements were made at 100 kHz. All structures were prepared using (111), 1.4 x 10<sup>16</sup> cm<sup>-3</sup> p-type silicon substrates and circular (375 $\mu$  diameter) aluminum field plates. After metallization they were annealed at 550°C for 2 min in dry nitrogen. It can be observed from Fig. 1 that the nitride film results in a relatively high surface charge,  $Q_s'/q > 10^{12}$  cm<sup>-2</sup>, compared to 6 x 10<sup>11</sup> cm<sup>-2</sup> for the vapor-deposited oxide and 2 x 10<sup>11</sup> cm<sup>-2</sup> for the thermal oxide. The nitride-over-oxide structure has a charge just slightly higher than that of the plain thermal oxide.

The high charge associated with the nitride-silicon interface appears to be typical (5). It was also found that the vapor-deposited nitride and oxide charges did not vary with silicon orientation. On the other hand, double layers of both nitride over thermal oxide and vapor-deposited oxide over thermal oxide showed the same orientation-dependence of surface charge previously reported by Balk, Burkhardt, and Gregor (15) for thermal oxides on silicon, i.e.,  $Q_s'$  (111) = 2 to 3 times  $Q_s'$  (100). The origin of the charges found in the vapor-deposited oxides and nitrides is not known. While the data reported above indicate they are associated with the dielectric-silicon interface, the lack of orientation dependence would indicate they are not the same as  $Q_{ss}$ , the fixed surface state charge associated with thermally oxidized silicon.  $Q_{ss}$  has been proposed to be due to an excess silicon species from the substrate taking part in the oxidation reaction (16). That no substrate silicon takes part in the reactions involving vapor deposition of silicon nitride and oxide films on silicon has been verified by special weight experiments.

One other observation that may be made regarding the C-V plots of Fig. 1 is the difference in shape between the thermal oxide and the nitride-over-oxide curves. The distortions of the double layer curve, labeled (A), (B), and (D), are probably related to fast surface states, and their significance will be discussed in the next section.

**Surface states and surface recombination velocity.**—The C-V curves of Fig. 1 for the thermal and vapor-deposited oxides are nearly identical in shape to theoretical curves of the same silicon doping and oxide thickness. This implies that over the surface potential range corresponding to the capacitance variation, the fast surface state density is less than 5 x 10<sup>10</sup> cm<sup>-2</sup> (14) for these annealed structures. On the other hand, both the nitride layer and the nitride-over-oxide layer curves show considerable distortion as compared to the theoretical case. This would imply higher densities of fast surface states, especially for the plain nitride film. It should be noted that the curve for the nitride-over-oxide structure after the 550°C annealing treatment is practically identical to that obtained for the thermal oxide alone before annealing. The nitride film evidently prevents the reduction of fast surface states normally occurring during the low-temperature annealing process when aluminum is present over the dielectric (17). Measurements of the surface recombination velocity  $s_o$  were made for these structures. It was found that, while values before annealing varied depending on processing conditions, the values of the thermal oxide, vapor-deposited oxide, and the nitride-over-thermal oxide all were in the range  $s_o = 5$ –10 cm/sec after the annealing treatment. On the other hand, surface recombination velocity values of the nitride film remained high at  $s_o = 200$  cm/sec.

**Work-function effects.**—As mentioned above, the charge induced in the semiconductor of an MIS structure includes a contribution from the metal-semiconductor work function difference,  $\phi_{MS}$ . For most metals in conjunction with thermally oxidized silicon, the value of  $\phi_{MS}$  ranges from +1 to -1v, depending on the metal and silicon doping impurity concentration and type (18). It was found from C-V plots of MIS

structures incorporating either p- or n-type silicon and/or different metal field plates that the  $\phi_{MS}$  values of either silicon nitride or vapor-deposited oxide MIS structures appear to be equal to those previously reported for MOS structures using thermal oxides. It should be noted that while  $\phi_{MS}$  values may be the same, the individual barrier heights at either the Si-dielectric or metal-dielectric interfaces are probably different than the corresponding thermal  $\text{SiO}_2$  values.

**Conductance.**—The current flow through silicon nitride, vapor-deposited oxide, and thermal oxide films was measured using a Keithley Instruments Model 416 Picoammeter. Current was measured as a function of d-c positive and negative bias. The results are shown in Fig. 2, where log current is plotted vs. the square root of voltage of  $0.2\mu$  silicon nitride, vapor-deposited oxide, and thermal oxide films. In addition to the standard nitride used for most of these studies, data are also included in Fig. 2 for a nitride prepared by bubbling  $\text{H}_2$  through  $\text{SiCl}_4$  just to show the effect of processing variables. This film, while exhibiting a higher conductance, etched at the rate of only  $2 \text{ \AA}/\text{sec}$  in concentrated HF.

It can be observed from Fig. 2 that for the same film thickness, the nitride films are the most conductive while the thermal oxide is several orders of magnitude lower in current at a given voltage. The vapor-deposited oxide has a current level near the less-conductive nitride film at lower voltages, but as the voltage increases the current saturates and the characteristic crosses the thermal oxide curve. This observation was quite reproducible for a number of samples of vapor-deposited oxides and occurred for both positive and negative bias.

It can be observed in Fig. 2 that the slopes for the nitride and thermal oxide films, as well as the vapor-deposited oxide at lower voltages, are similar. The data for the nitrides are very similar to those reported by Sze (19). According to Sze, the straight line portion of the plots in Fig. 2 (at least for the nitrides) indicates a bulk-controlled conduction process and is due to field-enhanced emission of trapped electrons into the conduction band of the insulator. This process is called the "internal Schottky" or the Poole-Frenkel effect, and predicts the square root of field-log current density relationship indicated in Fig. 2. This model also predicts a temperature dependence and this was demonstrated by a decrease in conductance at  $-196^\circ\text{C}$  for the silicon nitride films.

It is much less likely that the conductance of thermal oxides would depend on emission of trapped elec-

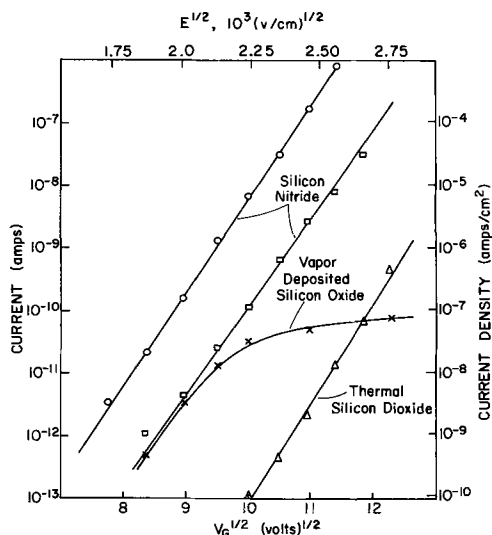


Fig. 2. Current-voltage relationships for three types of dielectric films on silicon. Data are for negative voltages,  $0.20\mu$  films on  $1.5 \text{ ohm-cm}$  p-type silicon.

trons. This conduction would probably be due to a tunneling mechanism. The latter should be temperature independent and this was found to be the case over the range from  $-196^\circ$  to  $25^\circ\text{C}$ . The results for the vapor deposited oxides are not clear, although it was observed that the current tended to saturate at that voltage where trapping commenced (see later section).

The data shown in Fig. 2 are for negative bias, although the positive values are very similar in all cases. It was found that the measurements could not be switched back and forth between positive and negative bias in the case of nitrides and vapor-deposited oxides without extraneous results being obtained. This was undoubtedly related to the trapping instabilities discussed in a later section. For the same bias, however, measurements could be made from low to high or high to low values of voltage with reproducible results.

**Polarization.**—Preliminary capacitance-voltage measurements of vapor-deposited dielectrics demonstrated certain instabilities that are not typical of MIS structures incorporating clean, thermal oxides. These instabilities are prevalent, even at room temperature, to such a degree that accurate C-V measurements themselves are difficult to obtain. Two distinct types of instability have been distinguished (20-22). They are indicated in Fig. 3 and are denoted as polarization and trapping. The polarization effect characterized in Fig. 3(a) will be discussed first.

The polarization of insulators in MIS devices has been observed in phosphosilicate layers ( $\text{P}_2\text{O}_5$  polarization) (13) and certain vapor-deposited oxides (23). It is characterized by a shift of the C-V plot in the same direction as that caused by ion migration. The amount of displacement will depend on the applied field and its rate increases with temperature. This field effect is demonstrated in Fig. 4 for a  $0.4\mu$  silicon nitride layer over n-type silicon. After subjecting the silicon nitride layer to  $\pm 15$  and  $\pm 30\text{v}$  for 2 min each at  $300^\circ\text{C}$  and then cooling rapidly to room temperature, considerable shifting of the characteristics is observed. The magnitude of the voltage displacement appears to be roughly proportional to the field applied at the elevated temperature. As shown in Fig. 3(a), this polarization may be due to the orientation of dipoles in the silicon nitride layer, similar to that proposed for phosphosilicate layers (13). The field due to these dipoles induces a charge in the silicon which is reflected by a shift in the C-V plot. The effect is thus related to the bulk of the dielectric, not to the interface between the silicon and the silicon nitride. The instability should therefore be present whether or not a thin thermal oxide (which itself does not exhibit

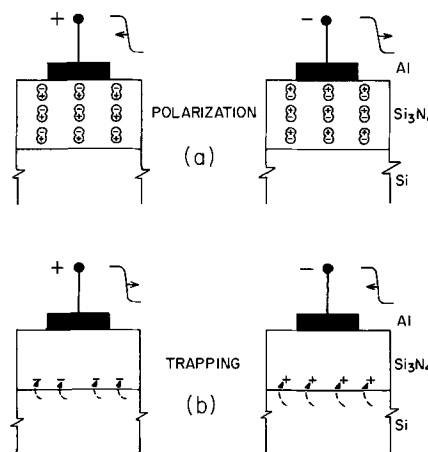


Fig. 3. Two types of proposed mechanisms for charge instabilities of MIS structures incorporating deposited dielectric films on silicon. Also shown in each case is the direction in which the corresponding C-V curve is displaced.

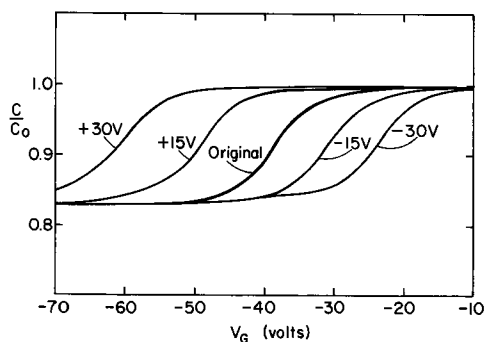


Fig. 4. Example of polarization of silicon nitride layer on silicon due to bias-temperature stress test. Test conditions:  $\pm 15$  and  $30\text{v}$  at  $300^\circ\text{C}$  for 2 min each. [(111)  $1.4 \times 10^{16} \text{ cm}^{-3}$  n-type silicon;  $x_N = 0.40\mu$ .]

polarization) is between the silicon and the nitride layer. This indeed has been found to be the case.

Only a small amount of such polarization (less than  $1\text{v}$  for a  $0.2\mu$  layer) has been observed in the vapor deposited oxides studied in this program and then only at high fields; none in the thermal oxides.

**Trapping.**—A different instability related to silicon nitride films on silicon was first reported by Hu (5). He noted that a displacement along the voltage axis of MIS capacitance-voltage plots occurred at room temperature after application of a negative or positive bias to the field plate. The direction of this displacement was opposite to that caused by ion migration or polarization. Further, this phenomenon occurred only after the applied voltage exceeded some critical threshold voltage or field. Various investigators at the Fall 1966 Meeting of the Society confirmed this effect with values of threshold field ranging over a considerable range. It is generally held that the phenomenon is due to trapping of carriers in the insulator much as described by Heiman and Warfield (24). Accordingly, we shall refer to this effect as the trapping phenomenon. This mechanism is illustrated in Fig. 3b. The application of positive or negative bias to the field plate of an MIS structure would according to this picture bring about trapping of carriers of the opposite polarity in the dielectric near the silicon surface, thus causing the C-V curve to shift in a direction opposite to that in the case of polarization. The trapping effect is thus associated with the silicon-dielectric interface.

Experiments with a typical  $0.2\mu$  silicon nitride layer deposited directly over silicon at  $950^\circ\text{C}$  resulted in room-temperature instabilities as shown in Fig. 5. The original C-V plot of the MIS structure is shown, along with plots obtained after various applied biases. For small applied bias values, either negative or positive, no appreciable displacement of the C-V characteristic is observed. However, at about  $-30\text{v}$  the curve starts to shift in the negative direction and at  $+40\text{v}$  (on a

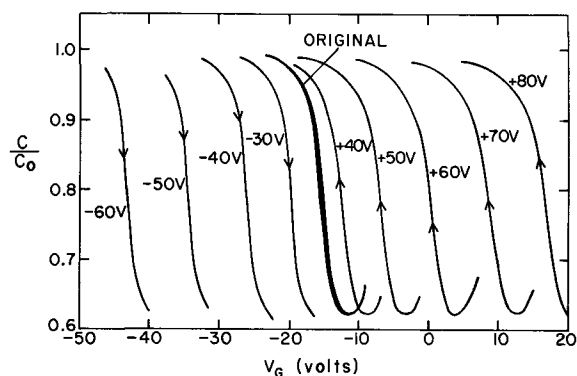


Fig. 5. Capacitance-voltage plots showing example of room temperature trapping in silicon nitride layer on silicon. [(100)  $1.4 \times 10^{16} \text{ cm}^{-3}$  p-type silicon;  $x_N = 0.21\mu$ .]

separate device from the same run) it shifts in the positive direction. Subsequently, the curves shift about  $8\text{--}10\text{v}$  for each additional  $10\text{v}$  applied, up to  $130\text{v}$  applied bias. Above  $130\text{v}$ , no further displacement in the curves due to trapping is observed. However, at this point, the displacement reverses direction and further small changes in the C-V characteristics are believed to be due to the polarization phenomenon described earlier.

Times of 10 sec were allowed for each bias application. These times appeared to provide a total displacement of at least 90% of that obtained in times up to 30 min for that particular bias.

It was found that exactly the same trapping effect occurs with vapor-deposited oxides on silicon. This phenomenon is similar for various silicon substrates, p-type or n-type, and (111) and (100) orientations. The critical or threshold field is about the same for positive and negative polarities, although that for the negative polarity is generally slightly less. If the displacement  $\Delta V$  of the C-V characteristic is plotted against applied bias, curves of the type shown in Fig. 6 can be obtained. These data are for various silicon nitride and vapor-deposited silicon oxide MIS structures. The dielectric thicknesses are approximately  $0.2\mu$ . It is observed that the positive threshold field for the nitrides is about  $2 \times 10^6 \text{ v/cm}$ , while the vapor-deposited oxide values are about  $4 \times 10^6 \text{ v/cm}$ . Corresponding negative threshold fields are slightly less. The slope of the plots approaches a value of 1.0. Additional experiments for dielectric thicknesses varying from  $0.09$  to  $0.90\mu$  resulted in approximately the same threshold field and slope as in Fig. 6. No such trapping effects could be noted for thermal oxides up to destructive breakdown.

Once the C-V curve has been displaced by a particular amount due to trapping (see Fig. 5), the direction of displacement can be reversed by application of lower voltages of the same polarity or of voltages of the opposite polarity. This process does not appear to be completely reversible but rather is dependent on previous bias history. An example is shown in Fig. 7 for a silicon nitride MIS structure, where voltage displacement  $\Delta V$  is plotted vs. applied bias. It can be seen that the curve obtained by first applying negative bias (dots) can eventually be reached even after first applying positive bias and then negative bias (circles), or vice versa. However, considerable hysteresis is obtained, depending on the magnitude of the initial bias. This hysteresis effect associated with the trapping phenomenon of silicon nitride layers on silicon was previously reported by Hu (5, 20) and by Chu, Szedon and Lee (22). It is also observed for vapor-deposited oxide structures.

Special experiments involving thin thermal oxides under silicon nitride layers resulted in asymmetric trapping characteristics. Nitride layers,  $0.25\mu$  thick,

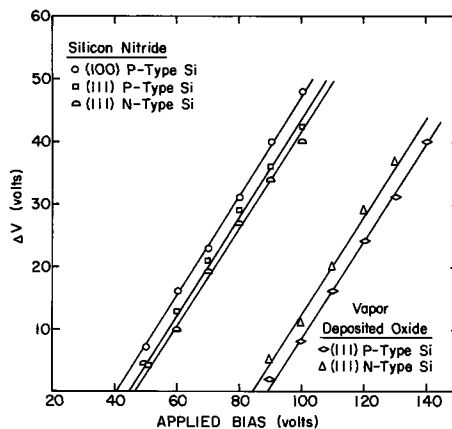


Fig. 6. Relationship between voltage shift  $\Delta V$  (due to room temperature trapping) and positive applied bias for several MIS structures. Thickness of dielectric films is  $0.20\mu$ .

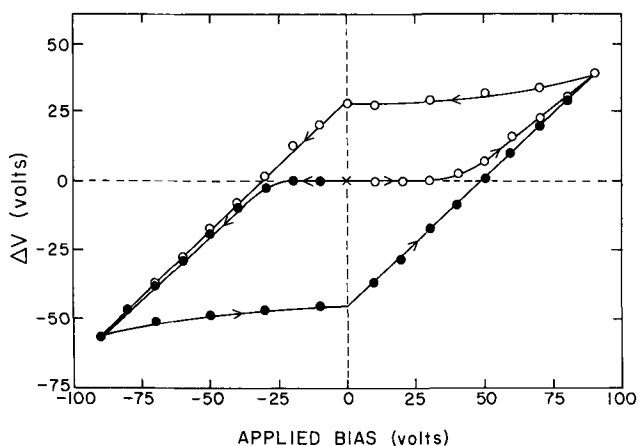


Fig. 7. Dependence of voltage shift  $\Delta V$  vs. applied bias on previous bias treatment of silicon nitride MIS structure. [(100)  $1.4 \times 10^{16} \text{ cm}^{-3}$  p-type silicon;  $x_N = 0.21\mu$ .]

were deposited over silicon dioxide layers of 60, 290, and 500Å thickness. With increasing oxide thickness the original high charge density induced in the silicon decreased by about an order of magnitude to that of the oxide  $Q_{ss}$  value. Further, the critical or threshold voltage required to initiate trapping increased with thermal oxide thickness. The increase was greater for the negative polarity, in fact trapping under negative bias could no longer be observed for the 500Å oxide samples up to breakdown of the dielectric. These results are indicated in Fig. 8 where the displacement  $\Delta V$  of the C-V curve is plotted vs. applied bias for the series of nitride-over-thermal oxide structures described above. The increase of positive threshold field with thermal oxide thickness is readily apparent. Similar effects are noted for the negative bias curves for 0, 60, and 290Å thermal oxide samples, where trapping occurs. The negative threshold voltages are considerably higher than the corresponding positive bias values, however. Szedon and Chu have reported similar findings for the positive bias polarity case (25). They propose that the increased field required for trapping when a thin oxide is present is due to the fact that the carriers must first tunnel into the conduction band of the oxide and then drift into the nitride before being trapped. The asymmetry found to exist between the positive and negative polarities may simply be due to differences between tunneling probabilities of electrons and holes through the thermal oxide.

Again, results very similar to those obtained for nitride over thermal oxides were obtained for vapor-deposited oxides over thin thermal oxides. The trap-

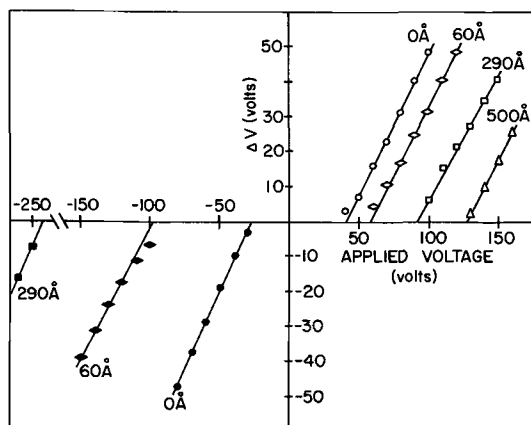


Fig. 8. Plot of MIS voltage shift  $\Delta V$  (room temperature trapping) vs. applied bias for various thicknesses of thermal oxide under  $0.25\mu$  silicon nitride films. [(111)  $1.4 \times 10^{16} \text{ cm}^{-3}$  p-type silicon.]

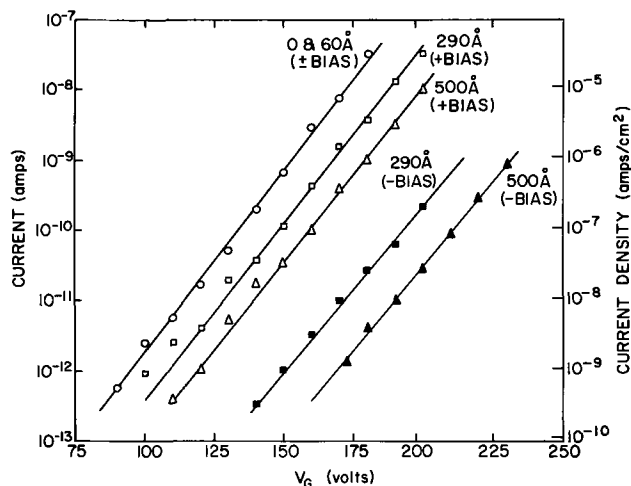


Fig. 9. Plot of current vs. voltage in MIS structures for various thicknesses of thermal oxide under silicon nitride layers. Structures are same as in Fig. 8.

ping threshold field increases with thermal oxide thickness, with the increase for negative bias being much greater than for the positive case.

If a thin thermal oxide beneath a vapor-deposited nitride or oxide layer causes an increased threshold field for trapping, then it might be expected that conductance through the double layer structure should be reduced. I-V relationships were determined for the same nitride-thermal oxide samples used for the data given in Fig. 8. The results are shown in Fig. 9. As predicted, the conductance decreases with increasing thermal oxide thickness. Further, the same asymmetry between negative and positive bias is noted, the negative bias conductance being considerably lower at a given voltage.

An over-all comparison between trapping and conduction in the various dielectric structures is shown in Fig. 10. Here the critical field required for trapping is plotted against the field at an arbitrary conduction current density, i.e.,  $\sim 10^{-8} \text{ amp/cm}^2$ . Data are included for various silicon nitride, vapor-deposited oxide, thermal oxide, and double layer structures. The thermal oxides break down before any trapping occurs. The relationship obtained in Fig. 10 indicates that there is a reasonable correlation between the trapping and conduction processes. This probably means that conduction, obeying a bulk-limited process relationship, may be initially limited by the transfer of carriers across the silicon-dielectric interface or

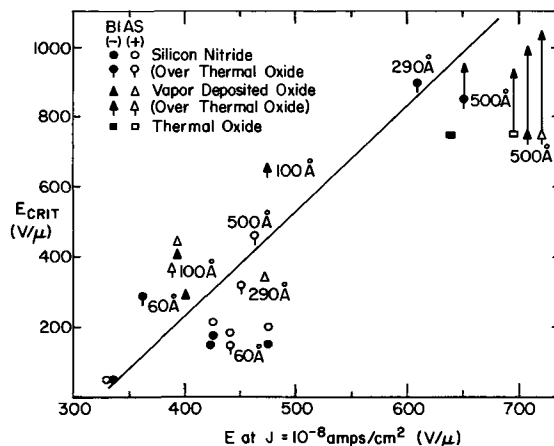


Fig. 10. Relationship between critical field required for room temperature trapping and field at arbitrary conduction current for various dielectrics in MIS structures. Dielectric thicknesses range from 0.2 to  $0.3\mu$ , on p- or n-type, (111) or (100) silicon ( $1.4 \times 10^{16} \text{ cm}^{-3}$ ).

Table II. Electrical properties of dielectric films on silicon

	Thermal SiO <sub>2</sub> (1200°C dry O <sub>2</sub> )	Deposited SiO <sub>2</sub> (400°C, SiH <sub>4</sub> + O <sub>2</sub> )	Deposited Si <sub>3</sub> N <sub>4</sub> (950°C, SiCl <sub>4</sub> + NH <sub>3</sub> )	Deposited Si <sub>3</sub> N <sub>4</sub> /thermal SiO <sub>2</sub>
Dielectric constant (100 kHz)	3.85	4.52	4.8 - 5.8	—
Breakdown field (d-c)	9.0 × 10 <sup>6</sup> v/cm	8.5 × 10 <sup>6</sup> v/cm	1 × 10 <sup>7</sup> v/cm	—
Surface charge (Q <sub>s</sub> )	2 × 10 <sup>11</sup> cm <sup>-2</sup>	6 × 10 <sup>11</sup> cm <sup>-2</sup>	> 10 <sup>12</sup> cm <sup>-2</sup>	3 × 10 <sup>11</sup> cm <sup>-2</sup>
Q <sub>s</sub> ' orientation dependence	(111) > (100)	None	None	(111) > (100)
Surface recombina- tion velocity (s <sub>0</sub> )	5-10 cm/sec	5-10 cm/sec	200 cm/sec	5-10 cm/sec
Work function differ- ence (Al-10 <sup>18</sup> cm <sup>-3</sup> p-type Si)	-1.0v	-1.0v	-1.0v	-1.0v
Conduction current density at 5 × 10 <sup>6</sup> v/cm (100 v/0.2μ)	8.8 × 10 <sup>-11</sup> amp/cm <sup>2</sup>	2.65 × 10 <sup>-9</sup> amp/cm <sup>2</sup>	1.05 × 10 <sup>-7</sup> amp/cm <sup>2</sup>	—
Polarization	None	Very little	Occurs at 25°C. Increases with temperature and field.	$\propto \frac{x_N}{x_{total}}$
Trapping	None	Occurs at 25°C above critical field.	Occurs at 25°C above critical field.	None if x <sub>0</sub> > 0.1μ.

across a thin thermal oxide between the silicon and dielectric layer.

### Summary

The electrical properties of vapor-deposited oxides and nitrides studied in this investigation are tabulated in Table II. Data are also included for thermal SiO<sub>2</sub> as well as a nitride-over-thermal oxide double layer. Electrical properties of vapor-deposited oxide-thermal oxide double layers are quite similar to those of thermal oxides, and, therefore, are not included in the table. The important characteristics of the vapor-deposited nitrides and oxides are summarized as follows.

**Silicon nitride.**—Silicon nitride films have a relatively high surface charge as well as a large density of fast surface states which are both associated with the interface region between the dielectric and the silicon. The fast states are not annealed out by low-temperature annealing processes (with or without the presence of aluminum field plates). The nitride films exhibit two types of electrical instabilities. The first is a temperature dependent bulk polarization, possibly due to the orientation of dipoles under the influence of applied electric fields. The second is a temperature independent interface trapping effect in which carriers from the silicon are trapped in the nitride near the silicon-silicon nitride interface. This trapping requires a certain critical field which is also related to a relatively high, room temperature conductance through the silicon nitride structure.

If a thermal oxide is present between the silicon and the nitride film, then those properties characterized by the silicon-dielectric interface become those normally associated with thermal oxides, i.e., low surface charge densities, no interface trapping, etc. If, however, the thermal oxide is reasonably thin (50-500Å) room temperature trapping and high conductance can occur once a critical field is reached, whereby carriers can tunnel into the conduction band of the oxide and into the nitride. This field is higher for negative gate voltages than for positive voltages.

Silicon nitride films are rather dense, which leads to fairly high dielectric strengths, low etch rates, and excellent masking ability against impurity ion migration.

**Vapor-deposited silicon oxide.**—Many of the electrical properties of vapor-deposited silicon oxide films on silicon, especially those associated with the silicon-dielectric interface, tend to resemble those found for silicon nitride films. This could well be expected since the method of chemical deposition is quite similar. Thus, these low-temperature vapor-deposited oxides exhibit room temperature trapping, higher surface charge densities, and at lower fields tend to have higher conductance than thermal oxides. Further, the introduction of a thermal oxide beneath the vapor-deposited oxide film either eliminates the trapping

instability or causes the threshold field to increase as with the nitrides. The same polarity asymmetry associated with trapping threshold field is also found as with nitride-thermal oxide double layers. The thin thermal oxide beneath the vapor-deposited oxide also reduces the surface charge density and makes it orientation dependent which is not the case for either of the vapor-deposited dielectrics.

Bulk properties of the vapor-deposited oxides tend to resemble thermal oxides. Little polarization has been noted and the conductance is lower than for nitride films at higher fields. However, there is still a relationship between the conductance and the threshold field required for trapping. The vapor-deposited oxides permit fast surface states to be annealed out during low-temperature annealing in the presence of aluminum field plates as is the case for thermal oxides.

Other physical and chemical properties of vapor-deposited oxides, such as density, refractive index, dielectric strength, etch rates, and lack of masking against impurity ion migration are much more related to those of thermal oxides.

### Acknowledgments

The authors wish to thank Maija Sklar, J. Goodell, and M. Barry who provided assistance and advice with certain experimental portions of this investigation. They also greatly appreciate the helpful discussions and suggestions concerning this work which were provided by A. S. Grove, C. A. Mead, and E. H. Snow.

Manuscript received Sept. 11, 1967; revised manuscript received Oct. 17, 1967.

Any discussion of this paper will appear in a Discussion Section to be published in the December 1968 JOURNAL.

### REFERENCES

1. "Integrated Silicon Device Technology, Volume VII, Oxidation," Technical Report No. ASD-TDR-63-316, Research Triangle Institute, June (1965).
2. T. L. Chu, SCP and *Solid State Tech.*, p. 36, May (1967).
3. W. A. Pliskin and E. E. Conrad, *Electrochem. Technol.*, **2**, 196 (1964).
4. H. F. Sterling and R. C. G. Swann, *Solid-State Electronics*, **8**, 653 (1965).
5. S. M. Hu, Recent News paper presented at the Buffalo Meeting of the Society, Oct. 10-14, 1965; *This Journal*, **113**, 693 (1966).
6. V. Y. Doo, D. R. Nichols, and G. A. Silvey, Recent News paper presented at the Buffalo Meeting of the Society, Oct. 10-14, 1965; *This Journal*, **113**, 1279 (1966).
7. N. C. Tombs, H. A. Wegener, R. Newman, B. T. Kenney, and A. J. Coppola, *Proc. IEEE*, **54**, 87 (1966).
8. E. H. Snow, A. S. Grove, B. E. Deal, and C. T. Sah, *J. Appl. Phys.*, **36**, 1664 (1965).

9. N. Goldsmith and W. Kern, *RCA Rev.*, **28**, 153 (1967).
10. B. E. Deal and A. S. Grove, *J. Appl. Phys.*, **36**, 3770 (1965).
11. A. S. Grove and D. J. Fitzgerald, *Solid-State Electronics*, **9**, 783 (1966).
12. W. A. Pliskin and H. S. Lehman, *This Journal*, **112**, 1013 (1965).
13. E. H. Snow and B. E. Deal, *ibid.*, **113**, 263 (1966).
14. A. S. Grove, B. E. Deal, E. H. Snow, and C. T. Sah, *Solid-State Electronics*, **8**, 145 (1965).
15. P. Balk, P. J. Burkhardt, and L. V. Gregor, *Proc. IEEE*, **53**, 2133 (1965).
16. B. E. Deal, M. Sklar, A. S. Grove, and E. H. Snow, *This Journal*, **114**, 266 (1967).
17. P. Balk, Paper presented at the Buffalo Meeting of the Society, Oct. 10-14, 1965, as Abstract 111.
18. B. E. Deal, E. H. Snow, and C. A. Mead, *J. Phys. Chem. Solids*, **27**, 1873 (1966).
19. S. M. Sze, *J. Appl. Phys.*, **38**, 2951 (1967).
20. S. M. Hu, Paper presented at the Philadelphia Meeting of the Society, Oct. 9-14, 1966, as Abstract 156.
21. S. M. Hu, D. R. Kerr, and L. V. Gregor, *Appl. Phys. Letters*, **10**, 97 (1967).
22. T. L. Chu, J. R. Szidon, and C. H. Lee, Paper presented at the Philadelphia Meeting of the Society, Oct. 9-14, 1966, as Abstract 158.
23. Y. Haneta and S. Nakanuma, Recent News paper presented at the Dallas Meeting of the Society, May 7-12, 1967.
24. F. P. Heiman and G. Warfield, *IEEE Trans. Electron Devices*, **ED12**, 167 (1965).
25. J. R. Szidon and T. L. Chu, "Tunnel Injection and Trapping of Electrons in Aluminum-Silicon Nitride-Silicon Dioxide-Silicon (MNOS) Capacitors," Paper presented at the IEEE Solid-State Device Research Conference, Santa Barbara, Calif., June 19-21, 1967.

## Semiconductor Doping by High Energy 1-2.5 Mev Ion Implantation

S. Roosild, R. Dolan, and B. Buchanan

*Air Force Cambridge Research Laboratories, Office of Aerospace Research, Bedford, Massachusetts*

### ABSTRACT

The formation of junctions in silicon through the use of mono-energetic ions in the energy range from 1 to 2.5 Mev has been studied. Boron, nitrogen, and phosphorous ions were used. Results are presented on the annealing temperatures required to place these ions in substitutional states and on the distribution of these ions in the host material. A way for localized masking against the ion beam, to obtain planar structures, is also discussed.

The use of ion implantation for doping semiconductors, and especially silicon, has been studied by various workers during recent years. This work can be divided into two broad categories: channeling and nonchanneling (1-4). In the channeling experiments one uses the open channeling directions in the crystalline lattice, as for instance the  $\langle 110 \rangle$  direction for Si, in order to obtain significant penetration of the ions. Most channeling experiments have been carried out with implantation energies in the 10-100 kev range. The channeling mechanism suffers from two disadvantages: the crystal must be very carefully oriented, to within a 1/10 of a degree (5, 6) to obtain repeatable results, and the channels tend to become clogged when deep layers of significant ion concentration are attempted (7). In the nonchanneling work one hopes to minimize channeling and regards the lattice as an amorphous substance for first order theoretical predictions. Although some ions can be expected to be scattered into the channeling directions, their number is small in comparison to the total number of implanted ions (8). The reported work in the nonchanneling area has been done below 500 kev, in which case the peak of the implanted ion distribution is well below  $1\mu$ . Since semiconductor device applications often necessitate deeper junctions, we have undertaken the investigation of ion implantation doping for the energy interval of 1-2.5 Mev. The experiments were conducted with singly charged boron, nitrogen, and phosphorous ions. Initially, some annealing studies to determine necessary annealing temperatures were performed. The emphasis in the study was placed on obtaining distribution profiles for the implanted ions, since these profiles are of prime importance to device design. Other workers in the area have assumed that the ions have a gaussian distribu-

tion about the peak (4). Preliminary experiments indicated that this was not the case in the 1-2.5 Mev range.

To obtain the doping ions, a gas containing the desired ion specie is passed through a thermomechanical leak into a radio frequency activated ion source. A variable voltage probe is used at the top of the source to drive the positive ions into the Van de Graaff accelerator. On emerging from the accelerator tube the ions are allowed to drift into a magnetic analyzing system. Only the desired ion specie, with the desired energy and charge is bent  $90^\circ$  into the exit port. On emerging from the analyzer they are defocused and allowed to drift down a 4-ft tube before hitting the target.  $\text{BF}_3$ ,  $\text{PF}_5$ , and  $\text{N}_2$  have been used as source gases for the boron, phosphorous, and nitrogen ions, respectively. In all cases the implantation target was silicon held at room temperature and oriented within a few degrees to the  $\langle 111 \rangle$  crystalline direction.

When the samples were tested right after the implantation they exhibited a very low conductivity surface layer with no evidence of any type change having occurred. In all cases, evidence of doping by the implanted ions was observed only after annealing at a temperature above  $200^\circ\text{C}$ . The observation of type change after annealing is evidence of the implanted ions having attained substitutional lattice positions (9). Figure 1 shows the annealing data obtained for 2 Mev  $\text{B}^+$  ions that were implanted into 40-50 ohm-cm n-type material in concentrations from  $2 \times 10^{13}$  ions/cm<sup>2</sup> to  $2 \times 10^{16}$  ions/cm<sup>2</sup>. Under these conditions the material is converted to p-type from the surface to a depth of about  $4\mu$ . The samples were implanted over a large area to facilitate sheet resistivity measurements with a resistivity probe having 45-mil probe spacings. The ion beam was not uniform

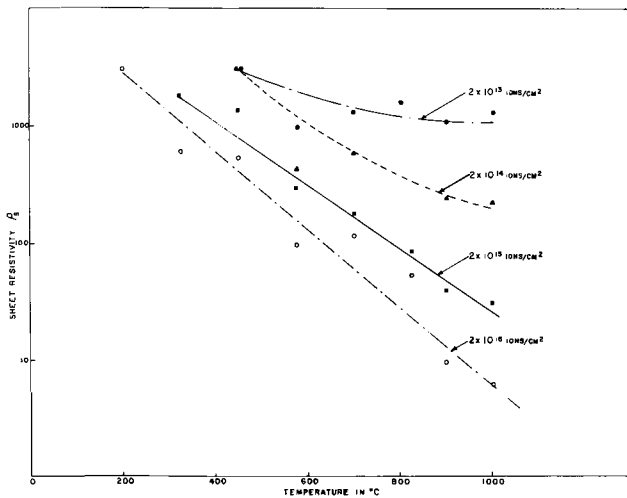


Fig. 1. Annealing curves for 2 Mev B<sup>+</sup> ion implantations

over this large an area. This is evidenced by the considerable fluctuation in the data points. The samples were annealed for 1 hr at the temperatures corresponding to each data point on the curves. The resistivity is seen to be continually decreasing for all except the lowest concentration implantations. Yet angle lapped and stained bevels taken on higher doped target materials, in which the implanted junctions appear buried, show no measurable increase in the width of the boron implanted p-layers when observed after a 575°C anneal and then viewed again after a 900°C anneal. Figure 2 shows such a comparison. This observation seems to indicate that no additional boron ions have found substitutional sites in the annealing temperature interval from 575° to 900°C. This leads us to speculate that it is the recovery in the mobility with higher anneal temperatures that is responsible for the decreased resistivity.

Table I shows a first order comparison between the total number of implanted ions and the number expected to be in active sites as inferred from the sheet resistivity measurements taken after the 1000°C anneal. Rows 3 and 6 are well within experimental error and thus we conclude that for 2 Mev boron ion implantations as heavy as  $2 \times 10^{16}$  ions/cm<sup>2</sup> there exists approximately a one to one correspondence between the number of implanted ions and the number of impurities that contribute to electrical conductivity.

Profiling of the implantations was accomplished by preparing 100 by 100 mil dice of different resistivities and mounting these into the sample holder as seen in Fig. 3. The samples were then subjected to different total ion doses. Later they were annealed for 1 hr at 700°, angle lapped and stained to allow interferometric measurement of the junctions that resulted from the implanted ions. It should be noted that the dark area on the sample holder is the imprint left by the ion beam, indicating that all four samples were in the center of the beam. Uniformity was further checked by interchanging the sample positions and repeating

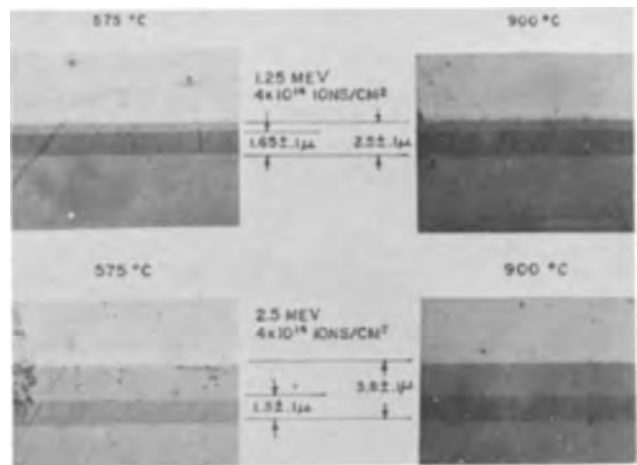


Fig. 2. Annealed B<sup>+</sup> implantations into 0.1 ohm-cm n-type targets

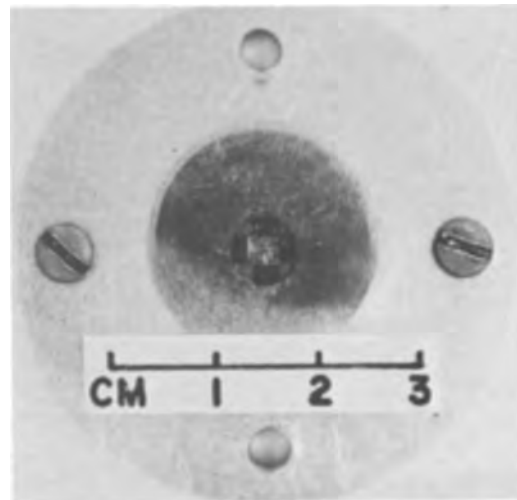


Fig. 3. Sample holder

the experiments, in all such cases the results agreed within measurement accuracy.

Figure 4 shows the resulting p-type layers formed by  $4 \times 10^{14}$  ions/cm<sup>2</sup> boron ion implantations at 1¼ Mev and 2½ Mev into n-type silicon varying in resistivity from 18 ohm-cm to 0.01 ohm-cm. Actual depths were measured by a Zeiss interferometer. The measuring accuracy was at least  $\pm \frac{1}{2}$  fringe or approximately  $\pm 0.15 \mu$ . It should be emphasized that the npn structures (buried layers) are formed by just a single processing step, a unique feature of the high energy implantations. When these junction positions are plotted vs. the concentration level of the target materials the implantation profile is obtained. Figure 5 shows these results plotted for a  $10^{13}$  and a  $4 \times 10^{14}$  ions/cm<sup>2</sup> boron implantation at 1¼ and 2 Mev. The

Table I. Implanted impurity concentrations of 2 Mev B<sup>+</sup> ions

Implantation dose in ions/cm <sup>2</sup>	$2 \times 10^{13}$	$2 \times 10^{14}$	$2 \times 10^{15}$	$2 \times 10^{16}$
Depth of junction after 1000°C anneal, $\mu$	4.1	4.2	4.4	4.7
Average concentration of ions in the layer	$4.9 \times 10^{16}$	$4.8 \times 10^{17}$	$4.6 \times 10^{18}$	$4.3 \times 10^{19}$
Measured sheet resistivity after 1000°C anneal in ohms per square	1300	230	30	6
Average resistivity of implanted layer in ohm-cm	0.53	0.097	0.013	0.0028
Corresponding average concentration of electrically active ions	$3.2 \times 10^{16}$	$3.0 \times 10^{17}$	$4.8 \times 10^{18}$	$3.4 \times 10^{19}$

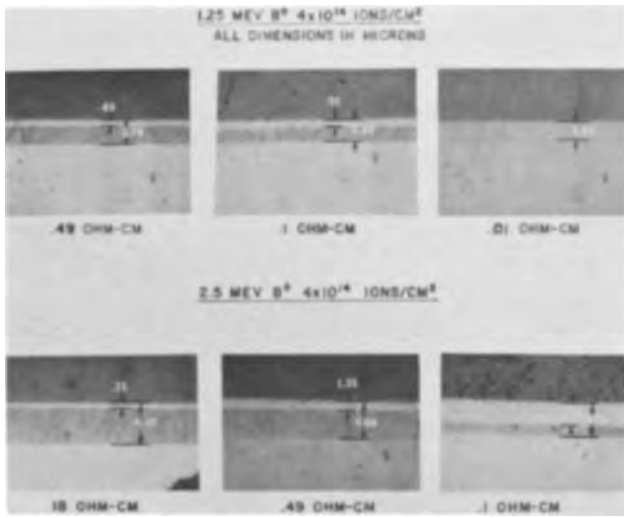


Fig. 4. Profiling samples for B<sup>+</sup> ion implantations

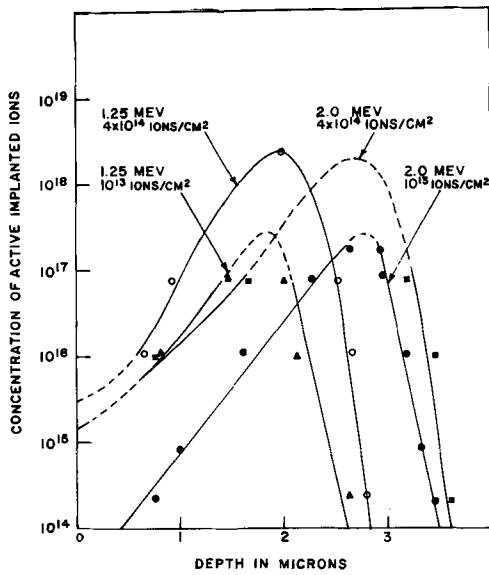


Fig. 5. Distribution curves for B<sup>+</sup> ion implantations annealed at 700°C.

data indicate a tendency for the ions to pile up toward the implantation surface. Only in the case of the 1¼ Mev implantation was a p-region observed in the 0.01 ohm-cm target. It appeared as a very narrow line and thus gave the value of the peak concentration of the implanted ions for that case. In all other cases the peaks are but estimates, and thus are dashed lines on the curves, but the general features of the ion distributions are evident.

Nitrogen was investigated as a possible n-type dopant over the 1 to 2½ Mev range because other n-type dopant ions required higher magnetic field strengths than was available in our analyzing magnet. Nitrogen implanted p-type samples showed n-type layer formation by hot probe conductivity checking as well as by junction staining (10). Low leakage p-n diodes have also been fabricated by nitrogen implantation. Figure 6 shows stains taken after 1-hr anneals at both 700° and 900°C. For nitrogen implantations one observes large junction movement to have occurred between the two annealing conditions. All this movement is toward the implantation direction, so one must postulate that additional impurities have moved into active sites. If some form of enhanced diffusion were responsible for the widening one would expect this to occur equally in both directions. Figure 7 shows a doping profile plot similar to those shown for boron. Although the total number of ions, as found by integrating under the curve, is close

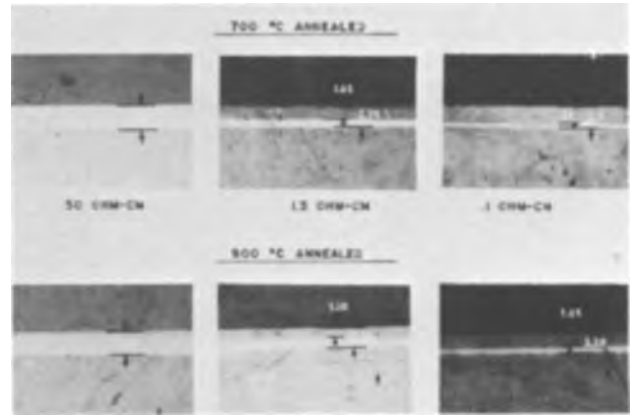


Fig. 6. Profiling samples for n<sup>+</sup> ion implantations, 4 × 10<sup>14</sup> ions/cm<sup>2</sup>.

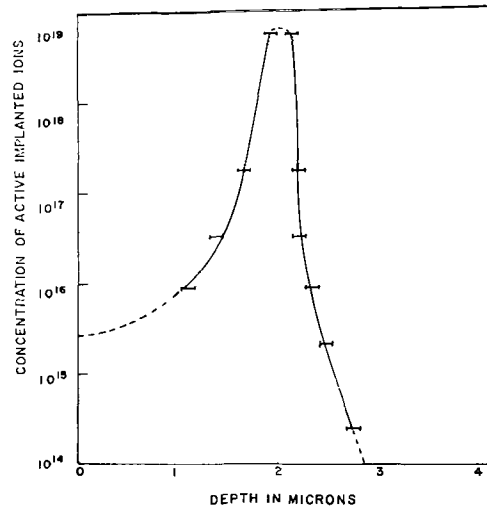


Fig. 7. Distribution curve for n<sup>+</sup> ion implantation, 2 meV, 4 × 10<sup>14</sup> ions/cm<sup>2</sup>, annealed at 900°C.

to the number of ions implanted, sheet resistivity measurements on low doped background samples show the implanted layer conductivity to be an order of magnitude lower than would be the case for this number of commonly used active donors. Higher temperature anneals begin to increase the resistivity and long anneals at 1200°C can cause the n-layer to disappear, indicating compound formation, such as possibly silicon nitride. Nitrogen doping of silicon by ion implantation provides a first example wherein ion implantation has been used to achieve doping with an element previously considered not feasible for doping. The low conductivity of the nitrogen implanted layer however leaves some doubt to the practicality of using it as a dopant in silicon.

Phosphorous implantations, performed to obtain n-type implanted layers, could only be performed at 1 Mev. Figure 8 shows a plot of the distribution of phosphorous donors as a function of depth after a 1-hr, 700°C anneal; also plotted is a theoretical curve derived from Lindhard's "simple unified range theory" (11). The curves show that close agreement between theory and experiment exists. Yet, again one notes that there is still a tendency for the ions to pile up toward the implantation direction, although markedly less than that observed in the case of boron.

Figure 9 shows the estimates of the depth at which the ion distribution peaks as a function of energy. Since our experimental method actually determines only the limits between which the peaks must be, the error here is larger than the measurement error. The depth of the peaks as calculated from the "simple unified range theory" is also plotted. Good agreement can only be found for phosphorous; the disagreement



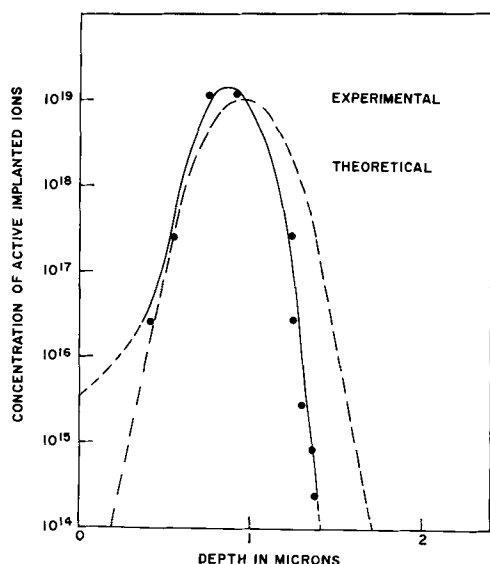


Fig. 8. Distribution curve for  $p^+$  ion implantation, 1.0 Mev  $p^+$ ,  $4 \times 10^{14}$  ions/cm<sup>2</sup>, annealed at 700°C.

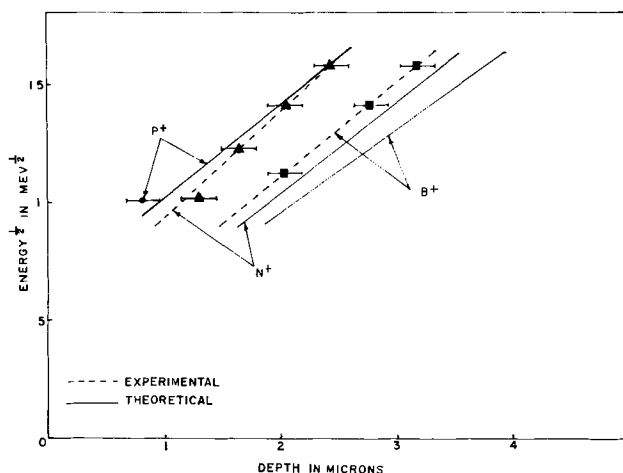


Fig. 9. Distribution peaks of implanted impurities

for boron and nitrogen however is not surprising, since discrepancies in the predictions of the theory for collisions where one of the elements has atomic number less than 11 were found by Lindhard when he compared his theoretical predictions to data available to him (11).

In order for the ion implantation method to be practical for electronic applications a convenient masking technique must be available.  $\text{SiO}_2$  has been used by those workers who have been using 500 keV or lower energies. 3 or  $4\mu$  of  $\text{SiO}_2$ , that would be needed for the 2 and 2½ MeV implantations, is rather impractical to work with. Evaporated Au was found to serve well as a mask for the ions. The ions penetrate only 1/3 as deep into Au as they do into silicon. The top of Fig. 10 shows an implantation that was terminated by an evaporated Au mask. Planar passivated junctions can still be obtained by growing a sufficient layer of  $\text{SiO}_2$  over the silicon before the gold evaporation. The implanted ions are attenuated by the  $\text{SiO}_2$  by approximately the same amount as by Si, so that the implantation profile can be determined by just shifting the profile curve to the left a distance corresponding to the thickness of the oxide. An advantage of using such a metal mask is that no ions will be in the passivating  $\text{SiO}_2$  layer as is the case with oxide masked, implanted or diffused structures. The I-V characteristics of a planar diode fabricated by Au masking are shown on the bottom of the figure.

We have shown that 1-2.5 MeV ions of boron, nitrogen, and phosphorous can be used to form p-n junc-

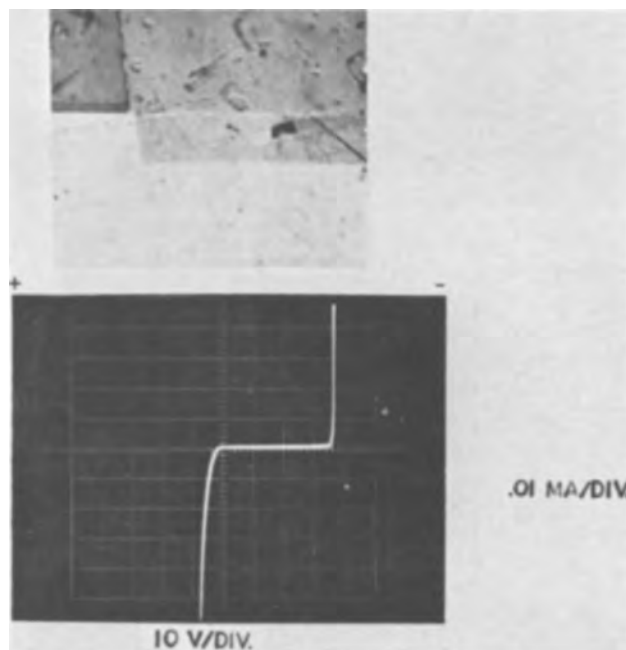


Fig. 10. Au masking for implanted diodes. Top, 2 MeV  $B^+$   $4 \times 10^{14}$  ions/cm<sup>2</sup>, 0.5 ohm-cm n-type target. Bottom,  $B^+$  implanted diode, 2 MeV,  $4 \times 10^{14}$  ions/cm<sup>2</sup>, 0.5 ohm-cm, n-type target.

tions as well as n-p-n or p-n-p buried layers in silicon. Only phosphorous seems to behave according to the predictions of Lindhard's theory; boron and nitrogen differ both in range and variance from the theory. In all cases the distribution of implanted ions was not gaussian about the peak.

### Acknowledgment

The authors would like to acknowledge the invaluable support of W. McLaughlin and J. Lorenzo in performing the laboratory experiments. They also wish to thank L. Lowe and M. Deane for operating the Van de Graaff used for these implantations.

Manuscript received June 19, 1967, revised manuscript received Oct. 20, 1967. This paper was presented at the Dallas Meeting, May 7-12, 1967, as Abstract 97.

Any discussion of this paper will appear in a Discussion Section to be published in the December 1968 JOURNAL.

### REFERENCES

1. D. B. Medved, "Research of Ion Implantation Doping Techniques," AFAL-TR-65-214, Contract AF33(615)-1989 (August 1965).
2. K. E. Manchester and C. B. Sibley, *Trans. AIME*, **236**, March 1966.
3. O. J. March, *et al.*, "Ion Implantation Doping Techniques," Interim Technical Reports No. 1 and No. 2, Contract AF33(615)-3821, September 1966 and November 1966.
4. C. M. Kellett, *et al.*, "High Energy Ion Implantation of Materials," Scientific Report No. 1, Contract AF19(628)-4970, May 1966.
5. J. A. Davies, *et al.*, *Nuclear Instruments and Methods*, **38** (1965).
6. F. Martin, *et al.*, Paper presented at International Conference on Applications of Ion Beams to Semiconductor Technology, Grenoble, France (May 1967).
7. P. Glotin and J. Grapa, Paper presented at International Conference on Application of Ion Beams to Semiconductor Technology, Grenoble, France (May 1967).
8. K. E. Manchester, *SCP and Solid State Technology*, September 1966.

9. J. O. McCaldin, "The Doping of Semiconductors by the Injection of Energetic Ions," "Progress in Solid State Chemistry," Vol. 2, Pergamon Press, New York (1965).

10. R. P. Dolan, *et al.*, Paper presented at the Cleveland Meeting of Society, May 1-6, 1966, as Recent News Paper 26.

11. J. Lindhard, M. Scharff, and H. Schiott, *Mat. Fys. Medd. Dan. Vid. Selsk.*, **33** [14] (1963).

## Properties of $\text{Si}_x\text{O}_y\text{N}_z$ Films on Si

D. M. Brown,\* P. V. Gray, F. K. Heumann, H. R. Philipp, and E. A. Taft

General Electric Research and Development Center, Schenectady, New York

### ABSTRACT

The properties of silicon nitride, oxynitride, and oxide films formed by the pyrolysis of various mixtures of  $\text{SiH}_4$ ,  $\text{NH}_3$ , and  $\text{NO}$  are presented. The variation in physical, optical, and electrical properties of this oxynitride ( $\text{Si}_x\text{O}_y\text{N}_z$ ) series is examined. The electrical and passivation properties of these films on Si are examined and compared with oxides. These electrical data describe the general characteristics of nitride and oxynitride on top of Si and over thin ( $\sim 300\text{\AA}$ ) and thick ( $\sim 1000\text{\AA}$ ) thermal oxide films.

The subject of passivating dielectric films on Si has had a varied history. The early work of Attalla *et al.* (1) showed that Si surfaces could be stabilized by using thermally grown  $\text{SiO}_2$  films. It was found, however, that ionic conduction can occur in  $\text{SiO}_2$  at very low temperatures ( $\sim 150^\circ\text{C}$ ), and these and other experiments subsequently suggested that planar transistor degradation is caused by the accumulation of positive space charge within the oxide (2). Kerr *et al.* (3) showed that this degradation phenomenon could be retarded by formation of phosphosilicate glass before metalization. Subsequently, Snow *et al.* (4) showed that most, if not all, of the positive space charge degradation and low-temperature ionic conduction within the  $\text{SiO}_2$  films was due to alkali ion contamination. Many other workers have subsequently studied the drift effects and stabilization properties of silicate glass films on Si. For example, phosphosilicate glass coatings do not appear to be a stabilization "cure all" judging from the variability of the published results. In fact, the experiments of Snow and Deal (5) suggest that double layer polarization effects will always make this stabilization method less stable than clean oxides covered with high purity metals. Nor does the alkali ion model appear to explain all the various kinds of drift observed by temperature bias experiments. For instance, some types of instability appear to be associated with electrochemical changes of the  $\text{SiO}_2$  at the insulator-Si interface. A recent example of this is the increase in stored positive charge in the oxide that occurs when negative bias is applied to clean MOS samples at elevated temperatures (6).

It is within this historical context that the passivation properties of silicon nitride ( $\text{Si}_3\text{N}_4$ ) and silicon oxynitride ( $\text{Si}_x\text{O}_y\text{N}_z$ ) films must be considered. The early observations about the high chemical stability of this material and the low diffusivity of ions through silicon nitride films has endured. In fact, the low reactivity of silicon nitride to etches has posed a difficulty in pattern forming, which has been successfully overcome by the use of special masking techniques (7-8). The low permeability of nitride to alkali ions (9), oxygen, water vapor (10, 11), and even hydrogen (12) remains one of its most attractive features. On the other hand, the reported electrical qualities of so-called silicon nitride films have been highly variable; and in fact, pyrolytic, glow discharge, and reactively sputtered nitride films appear to be generally inferior to silicon dioxide as insulators.

This work is subdivided into two major sections: the first covers the basic physical properties of pyro-

lytic nitride and oxynitride films; the second section covers their electrical properties on Si and their passivation properties when used to "seal" thermal oxides. The films studied in this investigation were pyrolytically formed; however, comparisons with other types of "nitride" films were made and will be described.

### Experimental Techniques

**Chemistry.**—The reaction kinetics taking place during the pyrolytic formation of  $\text{Si}_3\text{N}_4$  films from gaseous mixtures of  $\text{SiH}_4$  (undiluted) and  $\text{NH}_3$  are obviously quite complicated. Some of the possible reactions that can occur are shown in the free energy of reaction vs. temperature plot of Fig. 1. The direct reaction of silane with ammonia (A) may not be the only primary reaction for the formation of silicon nitride. One must also consider an initial pyrolysis of silane (B) and the reaction of freed Si with ammonia

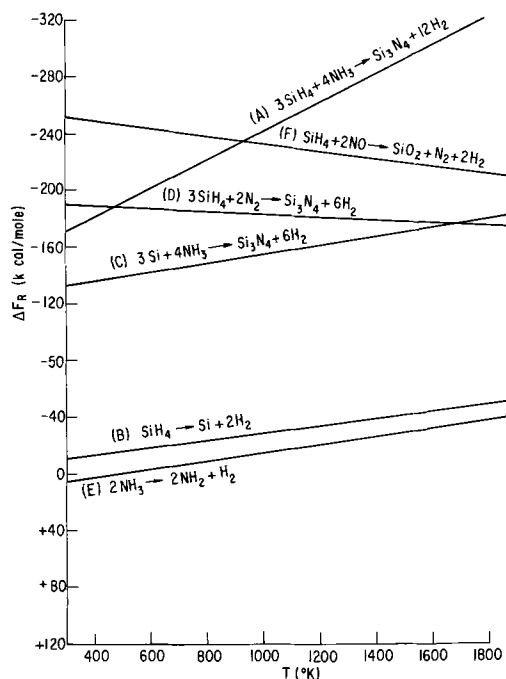


Fig. 1. Free energy of reaction vs. temperature plot for the possible reactions taking place during the pyrolysis of mixtures of  $\text{SiH}_4$ ,  $\text{NH}_3$ , and  $\text{NO}$ . From JANAF Thermochemical Tables (Dow Chemical Company).

\* Electrochemical Society Active Member.

(C) and the reaction of silane with nitrogen (D) formed by the pyrolysis of ammonia (E). It is quite likely that all the Si released from the rapid pyrolysis of silane is not converted to  $\text{Si}_3\text{N}_4$ , and, as a result, films formed in this manner may contain detectable amounts of excess Si. Inclusion of excess and chemically bonded H is also quite likely, particularly with the use of  $\text{H}_2$  as a carrier gas. In order to minimize these problems, no  $\text{H}_2$  was used, and the  $\text{NH}_3$  to  $\text{SiH}_4$  ratio used was about 40,000:1.

Silicon oxynitride films were formed by introducing NO. In this case, the pyrolytic nitride-forming and oxide-forming reactions (F) are taking place simultaneously.

Figure 2 shows the film growth rates vs.  $1/T$ . Nitride growth rate curves A and B are for a  $\text{SiH}_4$  injection rate of 0.1 ( $\text{NH}_3/\text{SiH}_4 = 40,000$ ) and 0.27 cc/min, respectively. Curve C shows the rate of pyrolytic  $\text{SiO}_2$  growth using  $\text{SiH}_4$  and NO at a NO to  $\text{SiH}_4$  ratio of 800:1 in a  $\text{N}_2$  carrier gas. Notice that in this instance the growth rate saturates with increasing temperature. This is probably due to a premature reaction between  $\text{SiH}_4$  and NO in the gas stream some distance above the heated substrate.

Process control is so important to the interpretation of the results that an extensive coverage of experimental procedure at this point is not thought to be worthwhile. Details of this aspect of the work will therefore be included during the presentation of the results and in the summary where its importance is seen much better in retrospect. Suffice for now that the films used for electrical measurements were all formed on 1 ohm-cm n- and p-type Si and were all about 1500Å thick. The depositions were made on wafers set on a pedestal heated by RF induction. The film thickness variation over the surface of each 2.5 cm diameter wafer was about  $\pm 5\%$  and only  $\pm 3\%$  over a center section, covering about  $3/4$  of the wafer diameter. For the electrical measurements, Al dots 2 mm in diameter were placed on the insulating film by evaporating Al from a W filament through a metal mask. The wafer was not heated during this deposition step. It must be emphasized at this point that the purity of the gases used throughout the process is extremely important. As we will see, many of the previously reported results on silicon nitride films have been anomalous because the experimental system was not "clean."

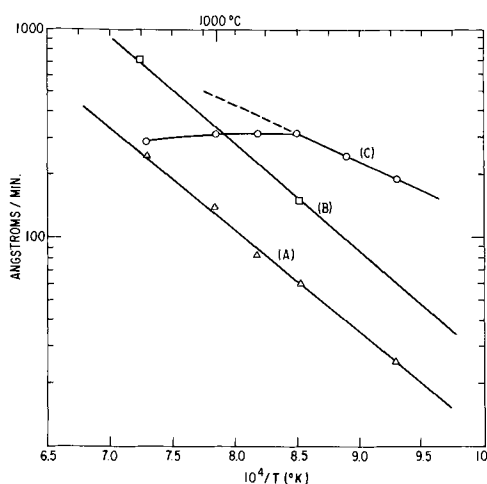


Fig. 2. Film growth rate curves vs. reciprocal substrate surface temperature. Curves A and B respectively are for a  $\text{SiH}_4$  injection rate of 0.1 cc and 0.27 cc/min into a 4000 cc/min  $\text{NH}_3$  gas flow (activation energy of 23 kcal/mole). Curve C is the rate of  $\text{SiO}_2$  deposition using  $\text{SiH}_4$  and NO for an NO/ $\text{SiH}_4$  ratio of 800 (activation energy of 11 kcal/mole) in an  $\text{N}_2$  carrier gas (50 cc/min NO + 0.06 cc/min.  $\text{SiH}_4$  in 4000 cc/min  $\text{N}_2$ ). Temperatures are uncorrected optical pyrometer readings.

## Results

**Basic physical properties.**—Table I lists the fundamental constants for  $\text{Si}_3\text{N}_4$  and for the series of films formed by varying the amount of injected NO from 0 to 10% (substrate temperature  $\cong 1000^\circ\text{C}$ ). The parameters are as follows: (i) the low-frequency dielectric constant K as determined by measuring MOS accumulation capacity and physical thickness; (ii) the optical index of refraction as found by measuring reflective interference minima at two angles of incidence at an energy of about 2 eV (this method also gives physical thickness); (iii) the density of pyrolytic nitride and oxide films; (iv) the bandgap as defined by the photon energy at which the absorption coefficient is  $100 \text{ cm}^{-1}$ ; (v) the peak of the broad IR absorption band occurring at 8–14 $\mu$  which is produced by some of the Si-N absorption modes; and (vi) the electron affinity of nitride and oxide as determined by the energy difference between the threshold for optical absorption and photoelectric emission.<sup>2</sup> The numbers in the last column labeled est. equivalent %  $\text{SiO}_2$  were found by assuming that each parameter varies linearly between pure nitride and oxide. The range covers the variation in %  $\text{SiO}_2$  as found by using K, n, IR peak, and  $E_G$  as listed in Table I. Plots of any of these parameters vs. injected % NO saturate as the % NO increases. This may also be due to a premature reaction between  $\text{SiH}_4$  and NO in the gas stream above the substrate. The dielectric constant of pure nitride films appears to be about 7.4 while that of the oxynitride decreases continuously from this to about 5.8 for an equivalent  $\text{SiO}_2/\text{Si}_3\text{N}_4$  ratio of 1.0.

X-ray diffraction analysis indicates that the films are completely amorphous in nature. This and the fact that all the parameters in Table I vary smoothly as the NO% varies indicates that these substances are essentially glassy atomic mixtures of Si, N, and O.<sup>3</sup> Furthermore, when oxynitride films are made, the shift in the 11.7 $\mu$  band is quite apparent; however, there is no indication of any oxide absorption at 9.2 $\mu$  that one ordinarily sees when discrete layers of oxide and nitride are deposited on the same wafer. Because of these facts, the equivalent percentage of  $\text{SiO}_2$  quoted in Table I indicates the percentage of bound oxygen. A very small amount of absorption at 3 $\mu$  due to N-H bonds indicates the presence of some excess hydrogen; however, it is not known as yet how this impurity alters the physical properties of these films. No absorption appears at 4.7 $\mu$  unless the ammonia/silane ratio is reduced to about 100. This band has been shown to be due to Si-H bonds (13), and when observable, probably indicates that the films contain excess Si.<sup>4</sup> Of course, the absence of any detectable amounts of absorption at 4.7 $\mu$  does not necessarily indicate that there is no excess Si. Even films prepared using an ammonia/silane ratio of 40,000/1 probably contain small but optically undetectable amounts of Si.

The bandgap and electron affinity measurements make it possible to formulate a basic model for MIS structures using silicon nitride or silicon oxynitride as the dielectric insulating material. Figure 3 com-

<sup>1</sup> A complete absorption curve for silicon nitride was constructed using transmission measurements determined on films of various thicknesses between  $10^2$  and  $2 \times 10^6$  Å. Transmission data were obtained on oxynitride films of 1 $\mu$  thickness. The energy separation of these curves at an absorption coefficient of  $\sim 4 \times 10^4 \text{ cm}^{-1}$  was assumed to be the same as for  $100 \text{ cm}^{-1}$ .

<sup>2</sup> These optical refraction, absorption and photoelectric emission techniques are described by: F. A. Jenkins and H. E. White, "Fundamentals of Optics," p. 255, McGraw Hill Co., N. Y. (1950); E. A. Taft and H. R. Philipp, *J. Phys. Chem. Solids*, 3, 1 (1957).

<sup>3</sup> Therefore, terms like " $\text{Si}_3\text{N}_4$ " and "silicon nitride" mean glassy amorphous substances.

<sup>4</sup> In the case of d-c reactively sputtered films, the effects of excess Si are observable. No 4.7 $\mu$  band is observed if the sputtering is carried out at low voltages (<3 kv) in pure  $\text{N}_2$ . Annealing these films at  $1000^\circ\text{C}$  lowers their conductivity by about 2.5 orders of magnitude and moves the fundamental absorption edge toward shorter wavelengths. This is thought to be caused by the chemical bonding of some of the excess Si with incorporated N. Furthermore, if the sputtering is carried out in a mixture of  $\text{N}_2$  and  $\text{H}_2$ , the 4.7 $\mu$  absorption band occurs and the conductivity is also lowered (13). Other discussions of the 4.7 $\mu$  band can be found in ref. (10) and (14).

Table I. Physical properties of pyroelectric films

	Injected % NO	K	n	$\rho$ (g/cc)	$E_g$ (ev)	IR ( $\mu$ )	X (ev)	Estimated equivalent % $\text{SiO}_2$
Nitride	0.00	$7.4 \pm 0.2$	$2.03 \pm 0.01$	$3.11 \pm 0.07$	4.5	11.7	2.0	0
Oxynitride	0.25	$7.3 \pm 0.1$	$1.98 \pm 0.02$	—	4.7	11.5	—	$7 \pm 2$
Oxynitride	1.25	$7.0 \pm 0.4$	$1.92 \pm 0.01$	—	5.1	11.2	—	$17 \pm 5$
Oxynitride	2.25	$6.7 \pm 0.2$	$1.89 \pm 0.01$	—	5.3	10.9	—	$25 \pm 7$
Oxynitride	5.00	$6.5 \pm 0.1$	$1.79 \pm 0.03$	—	5.6	10.7	—	$34 \pm 8$
Oxynitride	10.00	$5.8 \pm 0.1$	$1.71 \pm 0.03$	—	5.8	10.1	—	$50 \pm 12$
Oxide	—	3.9	1.44	$2.14 \pm 0.07$	8.0	9.2	1.0	100

compares the MNS structure with that of the well-known MOS varactor. This energy model shows that the considerably smaller bandgap of  $\text{Si}_3\text{N}_4$  coupled with a larger electron affinity produces much lower potential barriers at each electrode for the MNS structure; furthermore, this model shows that hole injection from the Si into the nitride is more probable than electron injection.

**Etch rates.**—Table II shows how the  $\text{Si}_3\text{N}_4$  etch rate in concentrated HF acid increases as the deposition temperature is decreased below  $1000^\circ\text{C}$ . For temperatures of a  $1000^\circ\text{C}$  and higher, the etch rate is a constant 140  $\text{\AA}/\text{min}$ . The reason for the rapid increase in etch rate for temperatures of preparation below  $1000^\circ\text{C}$  is not known. However, Chu *et al.* (15) have suggested that the increase in etch rate for low deposition temperatures is caused by the decrease in film density. Another point to consider is the increase in H content, as indicated by the increase in absorption at  $3\mu$ , that occurs when the deposition temperature is lowered. Also shown in Table II are the comparative etch rates for the silicon oxynitride series ( $\text{Si}_x\text{O}_y\text{N}_z$ ) formed by varying the amounts of NO injected into the ammonia stream. Here we see a continuous variation starting at 350  $\text{\AA}/\text{min}$  at the 0.25% NO level and increasing to 5000  $\text{\AA}/\text{min}$  at the 10% NO injection level.

Pattern forming is an important aspect of the application of these materials to device making, and Table III shows how one can form patterns in multiple layers of Mo,  $\text{Si}_3\text{N}_4$ , and  $\text{SiO}_2$  in almost any layer order by using the selective etches<sup>5</sup> listed in Table III.

**Electrical properties.**—The reported electrical properties of silicon nitride films deposited on Si show great variance even in their qualitative character. One of the difficulties with this type of investigation is that the so-called nitride films contain undefined and

<sup>5</sup> Holes in  $\text{Si}_3\text{N}_4$  films on Si can also be formed by selective anodization to  $\text{SiO}_2$  followed by etching in "buffered" HF [see ref. (16)].

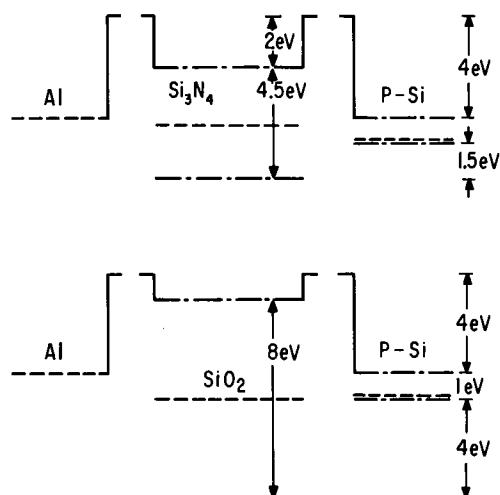


Fig. 3. Basic band models for the formation of rectifying barriers between materials Al,  $\text{Si}_3\text{N}_4$  or  $\text{SiO}_2$  and p-type Si (before contact). - - - represents Fermi levels; - - - represents band edges.

variable quantities of Si, N, H, O and their compounds. Another major difficulty is that these films are generally deposited on top of an undefined Si surface or  $\text{SiO}_2$  boundary layer. For instance, Hu (10) and Doo, Nichols, and Silvey (17) initially reported very high electrical resistivity. More recently, however, Doo and Nichols (18) and Hu, Kerr, and Gregor (19) have investigated the possible causes for the excessive d-c conduction seen in MNS varactors. And indeed, the results of Doo *et al.* (17) appear to have been determined more by the properties of an  $\text{SiO}_2$  film between the Si and nitride film than by the nitride itself.<sup>6</sup> Confusion on whether there is or is not a very thin oxide film underneath the nitride and what the electrical properties of nitride on Si should be still exists.

Such difficulties, among others, led to the early application of nitride films as a final oxide sealant since in this way one can combine the excellent dielectric and controllable interface qualities of  $\text{SiO}_2$  on Si with the chemical inertness and low permeability of nitride. This approach called MNOS will be investigated in a later section. Another approach is to try to combine these properties in a single film by the formation of oxynitride films on Si (20). Because of this subject diversification, three separate subsections are used to

<sup>6</sup> The data in ref. (17) Fig. 8 appear to support this view, since it shows that the dielectric constant for films of 2000 $\text{\AA}$  or less was surprisingly only about 4, and for thicknesses greater than 2000 $\text{\AA}$ , it was only 6.3.

Table II. Etch rates of  $\text{Si}_3\text{N}_4$  and  $\text{Si}_x\text{O}_y\text{N}_z$  in conc. HF (48%)

$\text{Si}_3\text{N}_4$	
Temp. Made*	Etch rate in $\text{\AA}/\text{min}$
800°C	1000
900°C	750
950°C	330
1000°C	140
1100°C	140

$\text{Si}_x\text{O}_y\text{N}_z$ (All made at $1000^\circ\text{C}$ ) *	
Vol. % NO	Etch rate ( $\pm 15\%$ ) in $\text{\AA}/\text{min}$
0.25	350
0.75	670
1.25	1500
1.75	2800
2.25	3000
10.00	5000

\* Uncorrected optical pyrometer readings.

Table III. Comparative etch rates of various films, ( $\text{\AA}/\text{min}$ )

Etchant	Si	$\text{SiO}_2$	$\text{Si}_3\text{N}_4$	$\text{Si}_x\text{O}_y\text{N}_z$	Mo
Mo etch*	0	0	0	0	9000
HF (48%)	0	30-50,000	130-150	300-5000	0
Buffered HF**	0	1000	5	10-50	0
$\text{H}_3\text{PO}_4$ (85%)	5	8-10	60-100	10-100	0
( $180^\circ\text{C}$ )					
Dim etch***	25,000	1000	16	20-200	$\sim 2 \times 10^3$

\* 92g  $\text{K}_2\text{Fe}(\text{CN})_6$ , 20g KOH, 300g  $\text{H}_2\text{O}$ .

\*\* 1 HF (48%) : 10  $\text{NH}_4\text{F}$  (40%)

\*\*\* 125 ml  $\text{HNO}_3$ , 25 ml HF, 110 ml  $\text{CH}_3\text{COOH}$

discuss the electrical and passivation properties of these films. The first will deal with nitride and oxynitride films placed directly on Si immediately after reactor etching the Si to insure that all the last vestiges of  $\text{SiO}_2$  are removed from the surface of the Si wafer; the second subsection will show what happens when very thin films ( $\sim 300\text{\AA}$ ) of  $\text{SiO}_2$  are between the nitride film and silicon substrate; and the third will present the results of temperature-bias passivation experiments on composite films composed of about 1200Å of thermally grown oxide covered with thin layers ( $\sim 300\text{\AA}$ ) of nitride or oxynitride (MNOS).

*Silicon nitride and oxynitride films directly on Si.*—

Each of these samples was prepared by the following procedure: (i) the wafer was etched in white etch ( $3\text{HNO}_3:1\text{HF}$ ) and rinsed with distilled  $\text{H}_2\text{O}$ ; (ii) the wafer was placed in the pyrolytic reactor and the reactor was purged with  $\text{N}_2$  and evacuated; (iii) the wafer was heated to  $\sim 1225^\circ\text{C}$  in a flow of purified  $\text{H}_2$  and  $\text{HCl}$  gas was introduced ( $\sim 1\%$   $\text{HCl}$  in  $\text{H}_2$ ) with wafer etching continuing for 3 min; (iv) the system was purged with  $\text{H}_2$  and cooled to  $1000^\circ\text{C}$  at which point the  $\text{NH}_3$  flow was turned on, the  $\text{H}_2$  off, and film deposition was initiated by turning on the  $\text{SiH}_4$  flow.

Before describing the results of the various electrical measurements, let us point out the extreme difficulties in characterizing the exact electrical nature of these films. This is because these pyrolytic nitride films belong to a class of materials which can perhaps be generally described as "leaky insulators with traps." Generally, their characteristics are as follows: Electronic current is strongly time dependent because of space charge and trapping effects. The charge and discharge currents decrease with time in a manner like that of  $\text{SiO}_2$  (21). The electronic currents, besides being strongly time dependent, are also strongly dependent on the polarity of the applied voltage which must be caused by the differences in the potential barriers for hole and electron injection at the Si and Al interfaces. These characteristics together with the poor insulating (especially pure nitride) and trapping effects cause hysteresis in the differential a-c capacitance vs. voltage curves [ $C(V)$ ] as electronic charge is alternately driven in and out of the film by the voltage sweep. The amount of hysteresis of course similarly depends on the magnitude of the voltage excursions and sweep speed. Because of these difficulties, the over-all electrical behavior of these films will be examined and trends in their characteristics will be determined as their chemical nature is changed from pyrolytic nitride to oxynitride and oxide.

Because of the current-time dependence, d-c current vs. field data were taken by waiting one minute after each increase in bias. Log  $i$  vs.  $E$  data for a nitride, oxynitride (10% NO injection), and pyrolytic oxide are compared in Fig. 4. Also shown in Fig. 4 for comparative purposes is the curve given by Hu *et al.* (19) for a RF reactively sputtered nitride which has no polarity dependence and no time dependence, but orders of magnitude higher leakage currents than those of all the pyrolytic films.<sup>8</sup> Notice also that the polarity dependence of nitrides and oxynitrides is the opposite of that of oxide and that the oxynitride has a stronger polarity dependence than the nitride. The polarity dependence shown in Fig. 4 agrees with that predicted by the models of Fig. 3 but does not necessarily prove the correctness of these models. Such a proof is made difficult by the space charge and trapping effects that occur. The initial surge of charge into the film is probably largely controlled by the poten-

<sup>7</sup> The high-purity tank  $\text{H}_2$  was further purified by passing it through a deoxyo unit and two  $\text{LN}_2$  traps in series. Without this precaution, oxide formation would occur in the interval between etching and pyrolytic deposition. The purity of the  $\text{NH}_3$  and  $\text{H}_2$  gases were checked by heating Si wafers for extended times in these gases at  $1000^\circ\text{C}$  and checking for oxide formation.

<sup>8</sup> Current-time dependence of d-c reactively sputtered nitrides increases with annealing and inclusion of  $\text{H}_2$  in the sputtering gas (L. F. Cordes, Private communications).

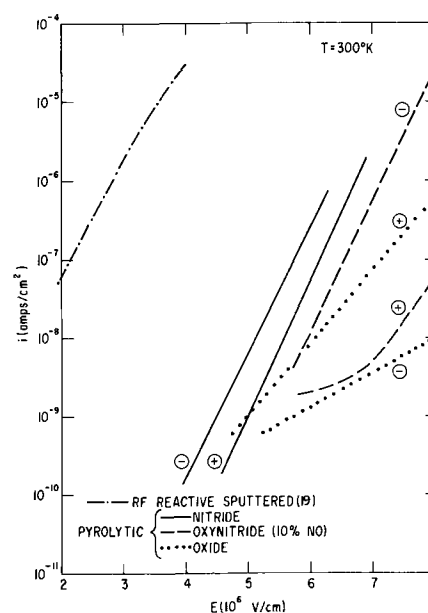


Fig. 4. Current density vs. field curves of reactively sputtered (19) nitride, and pyrolytic nitride, oxynitride and oxide films on 1 ohm-cm n-type Si. Pyrolytic film data taken after waiting 1 min after each increase in field. (Plus bias means that positive voltage is applied to Al electrode.)

tial barrier heights at the electrodes; however, as the dielectric charging due to trapping continues, the field within the dielectric relaxes near the interface barrier; and hence, the charging currents decrease with time.

The amounts of hysteresis appearing in a  $C(V)$  curve is apparently controlled by the amount of current passing into and through the film and by the amount of charge that is trapped. Measurements of the shifts in flat band voltage are a good measure of this phenomenon and a summary of this behavior for a series of samples is given in Table IV and Fig. 5. Figure 5 shows a typical  $C(V)$  hysteresis loop together with a swept  $I(V)$  curve all taken for the same sweep speed (20 v/sec). Curve 1 is that which occurs if one sweeps negatively from zero, curve 2 returning from negative bias, and curve 3 sweeping negatively but returning from positive bias. If one limits the bias sweep to low but equal and opposite fields, the size of the hysteresis loop, called  $\Delta V_{FB}$  in Fig. 5B, decreases as the oxygen content in the oxynitride series increases. This is shown in Table IV where the third and fourth columns give  $\Delta V_{FB}$  voltages for field sweep limits of  $\pm 4 \times 10^6$  v/cm. Column 3 is for rapid reversal of the sweep direction, and column 4 is for 1-min stops at each end of the sweep limits before reversal. In the fifth column of Table IV,  $\Delta V_{FB}$  voltages are presented for the case when the samples are driven to equal and opposite current levels ( $\pm 2\mu$  amp/cm<sup>2</sup>). In this instance, one uses data such as those shown in Fig. 5A. Very large voltages are required to reach these current levels for the oxynitride films.

Table IV. Hysteresis in pyrolytic films on Si;  $\Delta V_{FB}$  (300°K) in volts\*

	1 Injected % NO	2 Si	3 $\Delta V_{FB}$	4 $\Delta V_{FB}$	5 $\Delta V_{FB}$
Nitride	0.0	n	16	30	30
Nitride	0.0	p	23	39	46
Oxynitride	2.5	n	13	24	44
Oxynitride	2.5	p	11	24	27
Oxynitride	10.0	n	7	18	22
Oxynitride	10.0	p	8	15	19
Oxide	—	n	2	2	11

\* 20 v/sec sweep. Sweep limits are:  $\pm 4 \times 10^6$  v/cm;  $\pm 4 \times 10^6$  v/cm (1-min stops);  $\pm 2 \times 10^{-6}$  amp/cm<sup>2</sup> for the data in columns 3, 4, and 5, respectively.

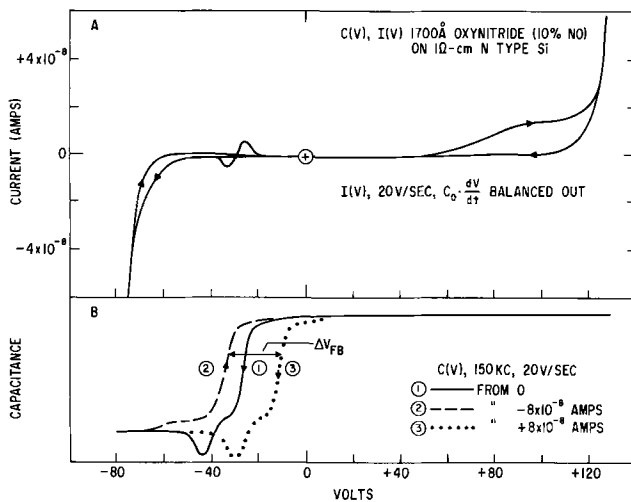


Fig. 5.  $I(V)$  and  $C(V)$  curves using a 20 v/sec sweep rate. In Fig. 5A the  $C_0 \frac{dv}{dt}$  signal is nulled out by using a bridge circuit. The data shown are for an oxynitride film ( $\text{SiO}_2/\text{Si}_3\text{N}_4 \sim 1$ ) on 1 ohm-cm n-type Si.

Nevertheless, the films with high oxygen content still produce smaller hysteresis loops.

It is interesting to surmise that the pattern shown by the data in Fig. 4 and 5 and Table IV are controlled by two factors. The increase in band gap with oxygen content which increases the barrier heights at the Si insulator interface and the decrease in the amount of excess Si contained within these films as the NO injection level is increased. Many models have been proposed to explain the various current-voltage characteristics of nitride films. Most of these models are based on mechanisms of carrier excitation from traps within the silicon nitride (19, 22). These models have been tested on samples which exhibit current densities several orders of magnitude higher than those described here [see, e.g., Fig. 4 and ref. (22)]. And indeed, excess Si may be the cause of the carrier traps discussed by Sze (22) and Hu *et al.* (19). Furthermore, Haneta and Nakanuma (23) have shown that hysteresis loops in pyrolytic oxide films are caused by excess Si in the films which occurs when the concentration of the oxidizing gas ( $\text{H}_2\text{O}$ ) is too low.

**Nitride on top of thin thermal oxides.**—An initial layer of thermal oxide makes the electrical situation much more controllable. If the layer is thick enough ( $\sim 200$ – $300\text{\AA}$ ), all traces of the "soft hysteresis" described in the previous section are eliminated because the oxide's insulating properties effectively block the passage of charge into the nitride if the fields are kept low enough. If, however, the field and/or temperature are high enough, charge can be forced through the thin oxide layer into the nitride where some of it becomes trapped. This results in a polarization effect which persists at  $300^\circ\text{K}$ . This effect may have been originally observed by Hu (10) and was ascribed as being a fundamental bulk property of nitride. In our studies, this effect occurs only when a very thin layer of oxide is between the Si and the nitride film. A typical result is described below. The chemically etched Si wafer was placed in the reactor and heated to  $1050^\circ\text{C}$  in  $\text{N}_2$  at which point very dry  $\text{O}_2$  was introduced and the  $\text{N}_2$  flow shut off. After 5 min, the  $\text{N}_2$  flow was reinitiated and the  $\text{O}_2$  shut off.<sup>9</sup> After purging with  $\text{N}_2$ ,  $\text{NH}_3$  was introduced and subsequently followed by  $\text{SiH}_4$  injection and nitride film deposition. A resultant  $C(V)$  curve is shown by curve A of Fig. 6. Originally, the sample has a negative flatband voltage and with equal and opposite voltage sweeps the  $C(V)$

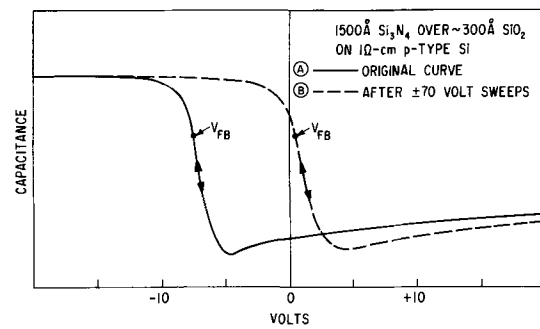


Fig. 6.  $C(V)$  curve showing the lack of hysteresis and room temperature polarization effect (curve B) which occurs when high fields are applied to MIS varactors composed of nitride films ( $\sim 1500\text{\AA}$ ) over a thin ( $\sim 300\text{\AA}$ ) film of thermal oxide.

curve at first looks perfectly normal with no detectable hysteresis for  $\pm 50\text{v}$  sweeps; however, after applying  $+60\text{v}$ , the flatband voltage suddenly moves in the positive direction. With alternate  $\pm 70\text{v}$  sweeps this effect is even more pronounced and ultimately results in a positive flatband voltage as shown by curve B of Fig. 6. This behavior also correlates with the  $I$  vs.  $V$  data for these particular samples. For instance, the high field polarity dependence is that of oxide (plus  $V$  gives larger  $I$  than neg.  $V$ ). At higher temperatures, the oxide can be made to conduct at lower voltages, and if the sample is then cooled with the stress bias still applied, similar polarization effects will occur. The voltages at which this polarization effect occurs are, of course, dependent on the thickness of the underlying oxide.<sup>10</sup> Preliminary stability experiments indicate that the internal field caused by the excess number of electrons trapped within the nitride is not stable; positive flatband voltages produced by high field stressing decrease when the MIS varactor is short circuited at elevated temperatures.

**Thin nitrides on top of thick oxides, MNOS.**—In this final section, the passivation properties of thin nitrides ( $\sim 300\text{\AA}$ ) on top of thick ( $\sim 1200\text{\AA}$ ) thermal oxides (MNOS) will be examined. This section has a very practical orientation since (i) thermal oxides on Si which have excellent dielectric and insulating properties can also be controllably formed with low oxide positive space charge ( $Q_{so}$ ) and negligible fast interface state densities ( $N_{FS}$ ) and (ii) the low permeability of nitride films to alkali ions, water vapor, and hydrogen can be used to passivate and thus preserve the excellent qualities of the underlying oxide. The specialized thermal oxidation and/or annealing methods for attaining the first set of oxide conditions are well known (6, 24–27). The low permeability of silicon nitride to alkali ions and water vapor have also been reported (9–11). It was therefore the purpose of this set of experiments to see what could be attained in terms of stability by this combination, and especially to see what differences might occur if oxynitride films were substituted for nitrides. It was not our purpose to attain low  $Q_{so}$  but only to determine the drift in  $Q_{so}$  during temperature-bias stress conditions. In this instance, the oxide must be thick enough to prevent any of the double layer polarization effects described in the previous section.

All the Al evaporations were made using a W wire filament that contains between 100 and 1000 ppm K. This potassium is ordinarily present in all drawn W wire. The oxides were made by first etching the wafers in white etch and thermally oxidizing them in very dry oxygen ( $< 80$  ppm  $\text{H}_2\text{O}$ ) using an extremely clean RF heated furnace. The oxidation was followed by slow cooling from the oxidation temperature ( $1000^\circ\text{C}$ ). A thin layer (200–400 $\text{\AA}$ ) nitride or oxynitride was

<sup>9</sup> Results in  $300 \pm 20\text{\AA}$  of  $\text{SiO}_2$  as determined by weight using a microbalance (Cahn Instrument Company).

<sup>10</sup> This type of polarization effect has also been investigated by T. L. Chu, J. R. Szecson, and C. H. Lee, *Solid-State Electronics*, 10, 897 (1967).

Table V. Stability of silicon nitride and oxynitride covered oxides (MNOS)

Sample	Thicknesses (Å)	Temp (°C)	Time (hr)	Set	Bias (v)	$(\Delta Q_{so}/q) \times 10^{-11}/\text{cm}^2$	Comments		
MOS	2800 Oxide	200	2	A B	+24	+83.0	$Q_{so}/q = 1.6 \times 10^{12}/\text{cm}^2$ $N_{FS} \approx 2.4 \times 10^{12}/\text{cm}^2$ Rapid drift Interface annealing		
					-24	-2.8			
MNOS 1	1200 Oxide 350 Nitride	200	21	A	+24	-0.8	$Q_{so}/q = 6.4 \times 10^{11}/\text{cm}^2$ $N_{FS} \leq 2 \times 10^{11}/\text{cm}^2$ Excellent stability Increase in stored positive charge with $-3 \times 10^6$ v/cm at 250°C		
				B	-24	-0.2			
		A	+46	+0.5					
		B	-47	+3.0					
		250	18	A	+46	-0.4			
				B	-47	+2.3			
MNOS 2	1500 Oxide 240 Oxynitride (2.5% NO)	200	68	A	+24	+0.5	$Q_{so}/q = 6.5 \times 10^{11}/\text{cm}^2$ $N_{FS} \approx 1 \times 10^{11}/\text{cm}^2$ Excellent stability at 200°C and $\pm 1.4 \times 10^6$ v/cm, also at $+3 \times 10^6$ v/cm, and 250°C Drift at $-3 \times 10^6$ v/cm At 250° and 300°C		
				B	-24	+0.1			
		B	+24	+0.4					
		A	-24	-0.1					
		A	+45	+0.2					
		B	-45	+1.4					
		300	8	A+B	-45	+2.0			
MNOS 3	1350 Oxide 460 Oxynitride (10% NO)	200	21	A	+23	+2.2	+ Ion permeation Interface annealing		
				B	-24	-0.8			
				C	Open	-0.6			
				D	Short	-0.8			
				200	72	C	+23	+3.0	+ Ion permeation Interface annealing
						D	-23	-0.2	
						A	Short	-0.5	
						B	Open	+0.1	

then pyrolytically deposited at 1000°C on top of this 1200-1500Å oxide film, and temperature-bias experiments were performed using a 25-point probe and an automatically recording  $C(V)$  bridge. A summary of the results of these experiments is shown by a set of representative results in Table V. It must be emphasized at this point that Table V presents a representative "best" set of results. Poorer results occur if the sample's oxide becomes contaminated by improper techniques. The limit of detectable drift in these experiments was  $\Delta Q_{so}/q \approx 10^{10}/\text{cm}^2$ . Each contact of any set deviated only slightly from the average values given in Table V.

Table V presents the following: layer thicknesses in Å, stress temperature in °C, stress time in hours, contact set (5-10 contacts), set bias in volts, and average change in oxide space charge ( $\Delta Q_{so}/q$ ) in units of  $10^{11}/\text{cm}^2$  as determined by the subsequent shift in the room temperature flatband voltage after each stress experiment. (Positive  $\Delta Q_{so}$  corresponds to negative  $C(V)$  shift.) The initial values of  $Q_{so}$  and  $N_{FS}$  (as determined by the shift in the flatband voltage caused by cooling the sample to 78°K) (27) are given in the comment column. Briefly, the results are as follows: (i) as expected, the oxide control sample shows very rapid increases in  $Q_{so}$  with positive bias at 200°C caused by K or Na ion permeation into the oxide; (ii) interface annealing of the type which reduces  $Q_{so}$  can apparently occur even at 200°C as evidenced by the decrease in  $Q_{so}$  with applied negative bias on the MOS control sample. Some further evidence for this is seen in MNOS sample 3 where almost identical decreases in  $Q_{so}$  occurred under negative bias, open, and shorted conditions. (iii) All three MNOS samples have much lower initial  $Q_{so}$  and  $N_{FS}$  values than the dry thermal oxide because of the interface annealing that takes place during the 1000°C pyrolytic deposition of the nitride film and very much better stability for all sets of stress conditions. (iv) No appreciable instability occurs in the MNOS samples for large positive bias even at 250°C except in

MNOS sample 3 which utilizes an oxynitride passivation film of high equivalent  $\text{SiO}_2$  content (see Table I). However, appreciable instability does occur for large negative bias at 250°C. This type of instability, which has already been observed by others using clean MOS structures, is apparently a fundamental and intrinsic property of the  $\text{SiO}_2$ -Si interface.<sup>11</sup> It is thought to be due either to the electrochemical reduction of the  $\text{SiO}_2$  at the  $\text{SiO}_2$ -Si interface or field diffusion of excess Si into the oxide or both. In any case, it is the only type of surface instability that cannot be overcome by any of the presently known oxide passivation schemes.

### Summary

In retrospect, the difficulties of attaining a correct description of the properties of nitride films have been caused by the difficulties encountered in reaching a point at which the processes were clean enough to attain reproducible results. This particular investigation required the fabrication of hundreds of samples before the difficulties could be identified. One example of this occurred when reactor etching was introduced. Previous to reactor etching the dielectric strength of pure nitrides on Si appeared to be exceedingly low ( $\ll 10^6$  v/cm). This was probably caused by pinholes in the nitride under the Al electrode. After reactor etching, all pure nitride films on Si suddenly exhibited high dielectric strength ( $\approx 10^7$  v/cm) and the  $C(V)$  curves had no hysteresis. However, the lack of hysteresis was caused by the fact that thin ( $\sim 100\text{Å}$ ) thermal oxide layers were being formed after reactor etching because the  $\text{H}_2$  used as a carrier gas for the HCl contained some water vapor. The pure nitrides still had as high dielectric strength after the water vapor in the  $\text{H}_2$  was eliminated but now gave the  $C(V)$  curve hysteresis described in the text. A general summary of the results now follows.

The physical properties of glassy-amorphous oxynitride films on Si are strongly dependent on the oxynitride concentration. The details of this variation in going from  $\text{Si}_3\text{N}_4$  to  $\text{SiO}_2$  are shown in the text. These variations in the properties of oxynitride films have also aided the definition of the properties of pure nitride films on Si. For instance, the measurements of band gap and electron affinity have led to a basic model for the nitride-Si contact, which explains, tentatively at least, the polarity dependent leakage and polarization currents. This survey also suggests that

<sup>11</sup> This increase in stored positive charge with negative bias heat treatments was initially reported by Y. Miura and Y. Matukura, *Jap. J. Appl. Phys.*, 5, 180 (1966). The same effect was subsequently reported by A. Goetzberger, Recent News Paper presented at the Cleveland Meeting of the Society, May 1-6 (1966); A. Goetzberger and N. E. Nigh, *Proc. IEEE*, 54, 1454 (1966); and also by Deal *et al.*, ref. (6). For additional details also see Y. Miura and Y. Matukura, *Jap. J. Appl. Phys.*, 6, 582 (1967).

the  $\text{Si}_3\text{N}_4$  trapping centers, which cause the various hysteresis and polarization effects in MNS and MNOS structures, are produced by excess Si in the nitride films.

All the pyrolytic films prepared in the manner described in the text had very high dielectric strength ( $\cong 10^7$  v/cm) as determined by d-c point probe measurements. The variations in leakage and polarization currents for nitrides and oxynitrides had the following general characteristics: (i) for fields between 4 and  $8 \times 10^6$  v/cm, the current varied exponentially with applied voltage; (ii) negative bias (Al negative) currents are higher than those for positive bias; and (iii) the amount of hysteresis in the  $C(V)$  curves decreases as the oxygen content in the film is increased; however, it was never found to be as low as that of oxide. Furthermore, the amount of stored positive charge ( $Q_{so}$ ) in these nitride and oxynitride films on Si as estimated by a flatband voltage for the middle of the hysteresis loop is high ( $1-5 \times 10^{12}/\text{cm}^2$ ).

When thin oxide films ( $\sim 100\text{\AA}$ ) are under nitride films, polarization effects occur when the field is sufficiently high to force electrons through the oxide into the nitride film where it is trapped. Control of Si surface potential and attainment of low stored positive charge and negligible fast interface state densities together with excellent passivation properties can be obtained by covering thicker ( $\sim 1000\text{\AA}$ ) thermal oxide films with thin films ( $\sim 300\text{\AA}$ ) of oxynitride or pure nitride.

#### Acknowledgments

The authors acknowledge with thanks the contributions of G. Gidley for the preparation of samples and to G. Charney in making measurements.

Manuscript received Aug. 23, 1967; revised manuscript received ca. Oct. 2, 1967.

Any discussion of this paper will appear in a Discussion Section to be published in the December 1968 JOURNAL

#### REFERENCES

- M. M. Atalla, E. Tannenbaum, and E. J. Scheibner, *Bell System Tech. J.*, **38**, 749 (1959).
- IBM Journal*, **8**, No. 4 (1964).
- D. R. Kerr, J. S. Logan, P. J. Burkhardt, and W. A. Pliskin, *ibid.*, p. 376.
- E. H. Snow, A. S. Grove, B. E. Deal, and C. T. Sah, *J. Appl. Phys.*, **36** (1965).
- E. H. Snow and B. E. Deal, *This Journal*, **113**, 263 (1966).
- B. E. Deal, M. Sklar, A. S. Grove, and E. H. Snow, *ibid.*, **114**, 266 (1967).
- D. M. Brown, W. E. Engeler, M. Garfinkel, and F. K. Heumann, *ibid.*, **114**, 730 (1967).
- W. van Gelder and V. E. Hauser, *This Journal*, **114**, 869 (1967).
- J. V. Dalton, Paper presented at the Cleveland Meeting of the Society, May 1-6, 1966; Electronics Division Abstract 23.
- S. M. Hu, *This Journal*, **113**, 693 (1966).
- F. M. Fowkes, J. E. Burgess, and G. Hutching, Paper presented at the Philadelphia Meeting of the Society, Oct. 9-14, 1966, Electronics Division Abstract 175.
- D. M. Brown and P. V. Gray, Unpublished data.
- L. F. Cordes, To be published in *Appl. Phys. Letters*, **11**, 383 (1967).
- S. M. Hu and L. V. Gregor, *This Journal*, **114**, 826 (1967).
- T. L. Chu, C. H. Lee, and G. A. Gruber, *ibid.*, **114**, 603 (1967).
- P. F. Schmidt and D. R. Wonsidler, *ibid.*, **114**, 603 (1967).
- V. Y. Doo, D. R. Nichols, and G. A. Silvey, *ibid.*, **113**, 1279 (1966).
- V. Y. Doo and D. R. Nichols, Paper presented at the Philadelphia Meeting of the Society, Oct. 9-14, 1966, Electronics Division Abstract 146.
- S. M. Hu, D. R. Kerr, and L. V. Gregor, *Appl. Phys. Letters*, **10**, 97 (1967).
- See also T. L. Chu, C. H. Lee, and J. R. Szeldon, Paper presented at the Dallas Meeting of the Society, May 8-11, 1967, Electronics Division Abstract 83.
- J. Lindmayer, *J. Appl. Phys.*, **36**, 196 (1965).
- S. M. Sze, *ibid.*, **38**, 2951 (1967).
- Y. Haneta and S. Nakanuma, Recent News Paper presented at the Dallas Meeting of the Society May 8-11, 1967; Electronics Division Subsession I (surfaces and thin films) Abstract No. 9.
- J. F. DeLord, D. G. Hoffman, and G. Stringer, *Bull. Am. Phys. Soc.*, **10**, 546 (1965).
- P. Balk, P. J. Burkhardt, and L. V. Gregor, *Proc. IEEE*, **53**, 2133 (1965).
- K. H. Zaininger and A. G. Revesz, *Appl. Phys. Letters*, **7**, 108 (1965).
- P. V. Gray and D. M. Brown, *ibid.*, **8**, 31 (1966); D. M. Brown and P. V. Gray, Recent News Paper presented at the Philadelphia Meeting of the Society, Oct. 9-14, 1966, Electronics Division Abstract 13.



# Films of Silicon Nitride-Silicon Dioxide Mixtures

T. L. Chu,<sup>1\*</sup> J. R. Szedon, and C. H. Lee

Westinghouse Research Laboratories, Pittsburgh, Pennsylvania

## ABSTRACT

Amorphous films of silicon nitride-silicon dioxide mixtures have been deposited on silicon substrates by the pyrolysis of silane in ammonia-oxygen mixtures in a gas flow system. The properties of these films such as composition, density, dissolution rate, dielectric constant, refractive index, infrared absorption, etc., were determined as a function of the reactant composition. MIS (metal-insulator-silicon) and MIOS (metal-insulator-oxide-silicon) structures were prepared by using silicon nitride-silicon dioxide mixtures as the insulator, and their capacitance-voltage behavior compared with that of MNS (metal-nitride-silicon) and MNOS (metal-nitride-oxide-silicon) structures. Similar to MNS structures, the MIS structures under study are characterized by high charge densities in the silicon-insulator interface region and by the ease of charge transfer across the interface. These effects are considerably reduced in MIOS structures; however, MIOS structures are less stable than MNOS structures under electrical and thermal stresses.

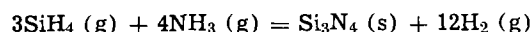
Dielectric films are used for many purposes in semiconductor devices. For most applications, these films should be amorphous in structure to provide uniform properties, impervious to contaminants to minimize instability effects, and compatible with the substrate to yield satisfactory mechanical and electrical characteristics. Films of amorphous silicon dioxide (silica) are the most commonly used dielectric in silicon devices because of the ease of preparation. However, silica is structurally porous; the high permeability of silica films toward impurities and the migration of impurity ions in silica films are undesirable in device applications. On the other hand, amorphous silicon nitride is more dense and therefore more impervious than silica. The density of amorphous silicon nitride is 2.8-3.0 g cm<sup>-3</sup> (1) compared to 2.2 g cm<sup>-3</sup> for thermally grown silica. The ion-migration effect has been shown to be negligible in silicon nitride films even at high temperatures (2). Nevertheless, silicon nitride is not compatible with silicon in properties, and Al-Si<sub>3</sub>N<sub>4</sub>-Si (MNS) structures have been shown to possess inherently unstable charge distribution under the application of large insulator fields ( $\pm 6 \times 10^6$  v/cm) at room temperature (3). Although this instability can be suppressed by using a thin silica interlayer between the silicon and the silicon nitride, the low dissolution rate of silicon nitride films by hydrofluoric acid requires additional masking steps in the photolithographic processes. One may thus deduce that the use of Si<sub>3</sub>N<sub>4</sub> + SiO<sub>2</sub> mixtures optimized with respect to dissolution rate and imperviousness could be a compromise for some applications.

In the present work, a series of films of Si<sub>3</sub>N<sub>4</sub> + SiO<sub>2</sub> mixtures with composition over a wide range were deposited on silicon substrates by the simultaneous nitridation and oxidation of silane in a gas flow system. The properties of these films, such as composition, density, dissolution rate, dielectric constant, refractive index, and infrared absorption, were studied as a function of the reactant composition. A number of capacitor structures Al-(SiO<sub>2</sub> + Si<sub>3</sub>N<sub>4</sub>)-Si and Al-(SiO<sub>2</sub> + Si<sub>3</sub>N<sub>4</sub>) - SiO<sub>2</sub> - Si were prepared, and their electrical characteristics were compared with those of Al-Si<sub>3</sub>N<sub>4</sub>-Si and Al-Si<sub>3</sub>N<sub>4</sub>-SiO<sub>2</sub>-Si structures. The experimental approaches and results are discussed in this paper.

## Films of Si<sub>3</sub>N<sub>4</sub> + SiO<sub>2</sub> Mixtures

Mixtures of silicon nitride and silicon dioxide can be prepared by the reaction of silane with an ammonia-oxygen mixture. These reactions presumably

involve the decomposition of silane and the subsequent nitridation and oxidation of silicon. The over-all reactions are



The equilibrium constants of these reactions in the temperature range 800°-1500°K, calculated from the JANAF thermochemical data (4), are shown in Fig. 1. In the temperature range of interest, 1000°-1200°K, the oxidation of silane is thermochemically more favorable than the nitridation of silane. Furthermore, the rate of the oxidation reaction is also higher than that of the nitridation reaction. Thus, the partial pressure of oxygen in the reactant mixture must be carefully controlled in the preparation of Si<sub>3</sub>N<sub>4</sub> + SiO<sub>2</sub> mixtures.

## Experimental

The deposition of films of Si<sub>3</sub>N<sub>4</sub> + SiO<sub>2</sub> mixtures was carried out in a gas flow system using an apparatus shown schematically in Fig. 2. Appropriate flowmeters and valves were used to control the flow of various reactants, i.e., ammonia, silane, oxygen, and hydrogen chloride. Semiconductor grade silane, anhydrous ammonia of better than 99.99% purity, and oxygen of 99.95% min. purity, all purchased from the Matheson Company, were used without further purification. The reactant mixture of the desired composition was passed through a filter into a fused silica reaction tube of 55 mm ID. Single crystal silicon substrates with main faces of {111} orientation were sup-

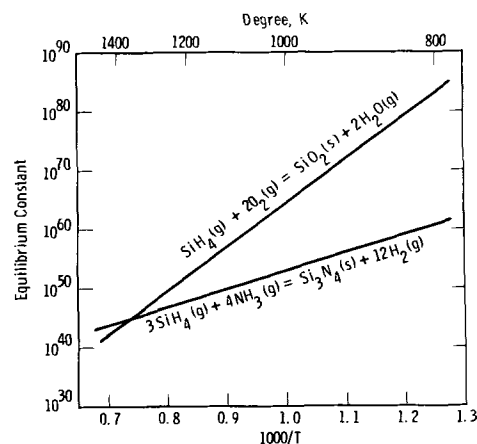


Fig. 1. Equilibrium constants of the nitridation and oxidation of silane as a function of temperature.

<sup>1</sup> Present address: Electronic Sciences Center, Southern Methodist University, Dallas, Texas 75222.

\* Electrochemical Society Active Member.

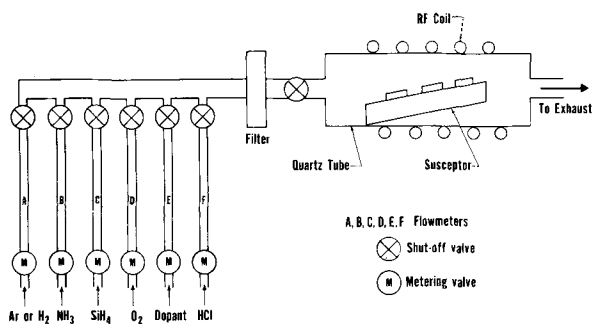


Fig. 2. Schematic diagram of the apparatus for the deposition of silicon nitride—silicon dioxide mixtures.

ported on a silicon-coated susceptor in the reaction tube, and the susceptor was heated externally by an rf generator. The silicon substrates were n-type, 20-50 ohm-cm resistivity and were mechanically lapped and chemically polished in a nitric acid-hydrofluoric acid mixture. In several experiments, the substrate surfaces were etched *in situ* prior to the deposition process by using a hydrogen-hydrogen chloride mixture (5), and approximately  $5\mu$  of silicon was removed from the substrate surface.

The most important variables affecting the deposition rate of  $\text{Si}_3\text{N}_4 + \text{SiO}_2$  mixtures and their properties are the substrate temperature and the composition and flow rate of the reactant mixture. All deposition experiments in this work were carried out at a substrate temperature of  $900^\circ\text{C}$  using ammonia as the major component in the reactant mixture. The flow rate of ammonia was 40 l/min, the flow rate of silane was 2-10 ml/min, and the  $\text{O}_2/\text{SiH}_4$  molar ratio in the reactant mixture was 0.5-50. In many cases, a thin silicon dioxide film was deposited on the substrate by the oxidation of silane in an argon atmosphere prior to the deposition of  $\text{Si}_3\text{N}_4 + \text{SiO}_2$  mixtures.

The thickness, nitrogen and silicon content, density, refractive index, dissolution rate, and infrared absorption of films of  $\text{Si}_3\text{N}_4 + \text{SiO}_2$  mixtures were determined by techniques used previously in the study of silicon nitride films (1). The analysis of the nitrogen and silicon content was believed to be accurate within  $\pm 0.3\%$ .

#### Results and Discussion

The films of  $\text{Si}_3\text{N}_4 + \text{SiO}_2$  mixtures deposited on silicon substrates under conditions used in this work were uniform, transparent, and adherent to the substrate. They exhibited no structural features when examined with an optical microscope and were found to be amorphous by electron diffraction examinations. In contrast to silicon nitride films (1), these films were not readily crystallized by electron beam bombardment in an electron microscope.

Since ammonia is present in large excess in all reactant mixtures studied [molar ratio  $\text{NH}_3/(\text{SiH}_4 + \text{O}_2) > 10^3$ ], the properties of  $\text{Si}_3\text{N}_4 + \text{SiO}_2$  mixtures can be conveniently compared in terms of the  $\text{O}_2/\text{SiH}_4$  molar ratio in the reactant mixture. In the range of the silane flow rate used in this work, the deposition rate of  $\text{Si}_3\text{N}_4 + \text{SiO}_2$  mixtures is approximately a linear function of the flow rate of silane. Using silane at a flow rate of 2 ml/min, the deposition rate is about  $0.02 \mu/\text{min}$ , essentially independent of the  $\text{O}_2/\text{SiH}_4$  molar ratio in the reactant mixture. However, the composition of the deposited film depends strongly on the  $\text{O}_2/\text{SiH}_4$  molar ratio when the reactant mixture is of low  $\text{O}_2/\text{SiH}_4$  molar ratio. Figure 3 shows the mole per cent of silicon nitride in the  $\text{Si}_3\text{N}_4 + \text{SiO}_2$  mixture as a function of the  $\text{O}_2/\text{SiH}_4$  molar ratio in the reactant mixture. These mixtures were prepared by using ammonia and silane at flow rates of 40 l/min and 10 ml/min, respectively. As expected, the addition of a small amount of oxygen into the silane-ammonia mixture results in a drastic decrease in the silicon nitride content of the deposit, in spite of the large  $\text{NH}_3/\text{O}_2$  molar

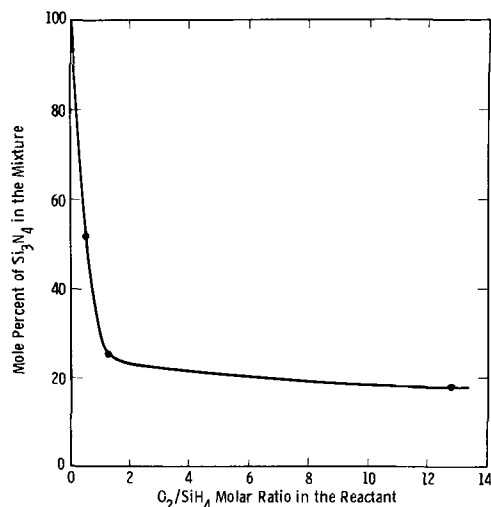


Fig. 3. Composition of  $\text{Si}_3\text{N}_4 + \text{SiO}_2$  mixtures deposited at  $900^\circ\text{C}$  as a function of  $\text{O}_2/\text{SiH}_4$  molar ratio in the reactant mixture. Flow rate of  $\text{NH}_3 = 40$  l/min, flow rate of  $\text{SiH}_4 = 10$  ml/min.

ratio in the reactant mixture. For example, using reactants of molar ratios  $\text{O}_2 : \text{SiH}_4 : \text{NH}_3 = 1 : 2 : 8000$  and  $\text{O}_2 : \text{SiH}_4 : \text{NH}_3 = 2.7 : 2 : 8000$ , the deposit contained 53 and 25% of silicon nitride, respectively. The composition of the deposit levels off as the  $\text{O}_2/\text{SiH}_4$  molar ratio in the reactant is further increased. Thus, under the conditions used in this work, the control of the composition of  $\text{Si}_3\text{N}_4 + \text{SiO}_2$  mixtures is more difficult for nitride-rich mixtures than for oxide-rich mixtures.

Similar to the dependence of the composition of the deposited mixtures on the  $\text{O}_2/\text{SiH}_4$  molar ratio in the reactant other properties of the deposit behave in a similar manner. The density, refractive index, and dissolution rate of the deposit are shown as a function of the  $\text{O}_2/\text{SiH}_4$  molar ratio in the reactant in Fig. 4, 5, and 6, respectively. A buffer solution consisting of 1:6 49% HF : Saturated  $\text{NH}_4\text{F}$  solution was used as an etchant in the dissolution rate measurements. The samples used for the refractive index and dissolution rate measurements were prepared by using silane at a flow rate of 2 ml/min as compared to 10 ml/min used in the preparation of samples for composition and density determinations. The effect of using lower flow rate of silane on the composition —  $\text{O}_2/\text{SiH}_4$  molar ratio relation shown in Fig.

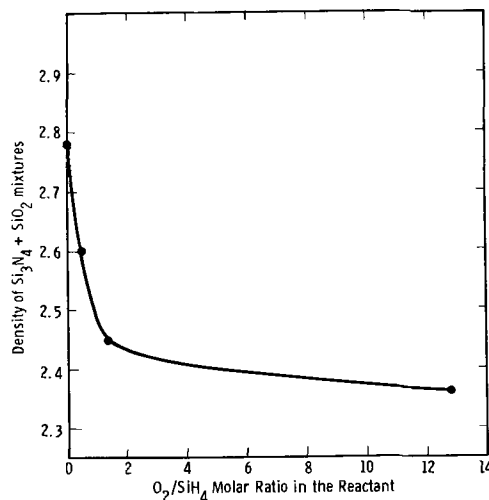


Fig. 4. Density of  $\text{Si}_3\text{N}_4 + \text{SiO}_2$  mixtures deposited at  $900^\circ\text{C}$  as a function of  $\text{O}_2/\text{SiH}_4$  molar ratio in the reactant mixture. Flow rate of  $\text{NH}_3 = 40$  l/min, flow rate of  $\text{SiH}_4 = 10$  ml/min.

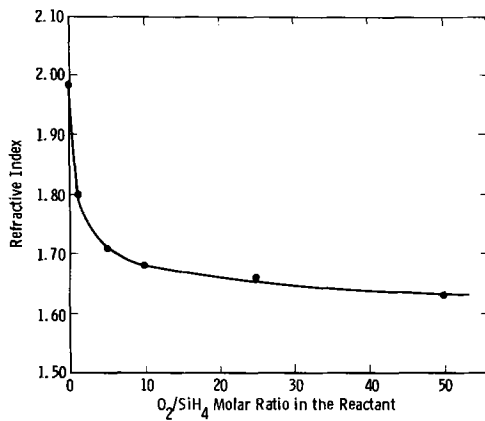


Fig. 5. Refractive index of  $Si_3N_4 + SiO_2$  mixtures deposited at  $900^\circ C$  as a function of  $O_2/SiH_4$  molar ratio in the reactant mixture. Flow rate of  $NH_3 = 40$  l/min, flow rate of  $SiH_4 = 2$  ml/min.

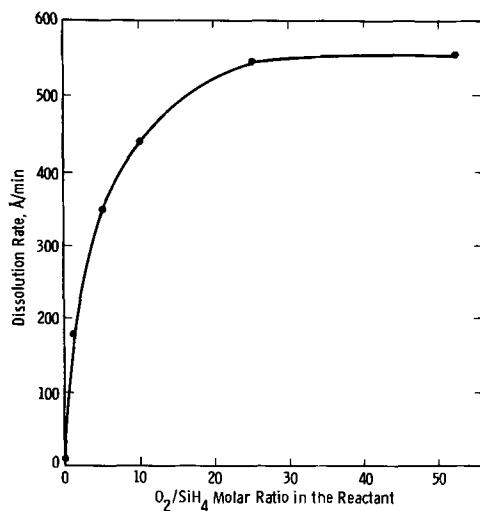


Fig. 6. Dissolution rate of  $Si_3N_4 + SiO_2$  mixtures in buffered hydrofluoric acid as a function of  $O_2/SiH_4$  molar ratio in the reactant mixture. Deposition temperature =  $900^\circ C$ . Flow rate of  $NH_3 = 40$  l/min, flow rate of  $SiH_4 = 2$  ml/min.

3 is presumably small because of the large excess of ammonia in the reactant.

The infrared absorption spectra of three  $Si_3N_4 + SiO_2$  mixtures prepared by using a silane flow rate of 2 ml/min and  $O_2/SiH_4$  molar ratios of 1, 5, and 50, are shown in Fig. 7. Amorphous silicon nitride shows a broad absorption band at  $830-860\text{ cm}^{-1}$ , characteristic of the stretching of the Si-N bond. This absorption band is shifted toward higher frequencies in  $Si_3N_4 + SiO_2$  mixtures (one of the Si-O stretching bands is at  $1090\text{ cm}^{-1}$ ), and the shift is pronounced even when the  $O_2/SiH_4$  molar ratio is 1. The magnitude of the shift increased with increasing  $O_2/SiH_4$  molar ratio in the reactant.

#### Al-( $Si_3N_4 + SiO_2$ )-Si Capacitors

A number of Al-( $Si_3N_4 + SiO_2$ )-Si, or MIS, capacitors were prepared by depositing  $0.1-0.15\mu$  of the films of  $Si_3N_4 + SiO_2$  mixtures on n-type silicon substrates of 20-40 ohm-cm resistivity, followed by the evaporation of aluminum electrodes of  $3.3 \times 10^{-4}\text{ cm}^2$  area on the insulating films. The capacitors were mounted on TO-5 headers for capacitance measurements at 100 kHz and 1 MHz.

The capacitance of the MIS capacitors measured at 1 MHz was used to determine the relative dielectric constant of the films of  $Si_3N_4 + SiO_2$  mixtures. The results are shown in Fig. 8 as a function of the  $O_2/SiH_4$  molar ratio in the reactant mixture. The film

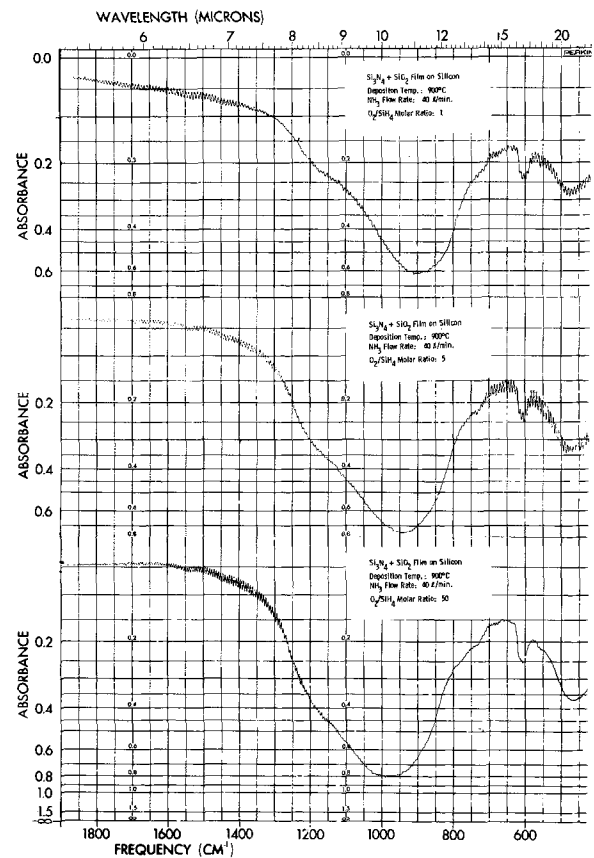


Fig. 7. Infrared spectral absorbance of films of  $Si_3N_4 + SiO_2$  mixtures deposited on silicon substrates at  $900^\circ C$ .

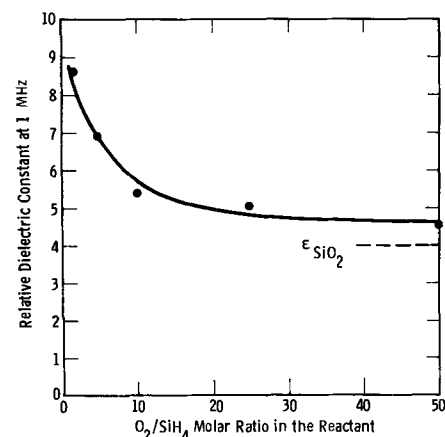


Fig. 8. Relative dielectric constant (1 MHz) of  $Si_3N_4 + SiO_2$  mixtures deposited at  $900^\circ C$  as a function of  $O_2/SiH_4$  molar ratio in the reactant mixture. Flow rate of  $NH_3 = 40$  l/min, flow rate of  $SiH_4 = 2$  ml/min.

thickness was determined by ellipsometric measurements. As the  $O_2/SiH_4$  molar ratio in the reactant was increased, the dielectric constant of the resulting mixture decreased monotonically from a value of about 9, characteristic of deposited silicon nitride films, toward one of about 4, characteristic of deposited silicon dioxide films. No measurement of dissipation in the insulating films was made, since the dominant loss mechanism in the capacitors was due to the resistance of the silicon substrate.

The capacitance-voltage behavior of MIS capacitors using  $Si_3N_4 + SiO_2$  mixtures as the dielectric is very similar to that of Al- $Si_3N_4$ -Si (MNS) capacitors. The charge density in the Si- $Si_3N_4$  interface region has been deduced from the flat-band voltage of MNS capacitors to be of the order of  $10^{12}$  charges/cm<sup>2</sup>. Fur-

thermore, the interface charge density has been found to vary under large voltage bias ( $\pm 6 \times 10^6$  v/cm of insulator field) at room temperature. This charge instability has been attributed to the charge transfer across the Si- $\text{Si}_3\text{N}_4$  interface with subsequent trapping at sites in the nitride and has been concluded to be a basic property of the MNS capacitors prepared by the chemical deposition technique (3). The effective charge density in Si-( $\text{Si}_3\text{N}_4 + \text{SiO}_2$ ) interface region was also found to be quite high for all the mixtures studied (up to about 80%  $\text{SiO}_2$ ), irrespective of the *in situ* etching of the substrate or other process parameters of the deposition process. Typical values were 1 to  $3 \times 10^{12}$  charges/cm<sup>2</sup>, compared to  $6 \times 10^{11}$  and 1 to  $4 \times 10^{12}$  charges/cm<sup>2</sup>, respectively, in chemically deposited Si- $\text{SiO}_2$  and Si- $\text{Si}_3\text{N}_4$  structures. Since the interface state density in Si-( $\text{Si}_3\text{N}_4 + \text{SiO}_2$ ) structures is independent of the composition of the mixture, these states cannot be directly associated with bulk properties of the dielectrics. The interface charge behavior must be characteristic of silicon-nitrogen bonding at the interface.

Similar to MNS structures, all MIS structures under study exhibited charge instability under large voltage bias at room temperature. This charge instability can be best represented by the flat-band voltage vs. stress voltage loops used for the characterization of MNS structures (3). A polarizing voltage was applied to a MIS at room temperature for about 30 sec, and the flat-band voltage obtained by capacitance-voltage measurements. Results for several MIS structures and an MNS structure are shown in Fig. 9. In all cases, the maximum polarizing voltage used was approximately  $\pm 50$ v. The total flat-band shift for the MNS structure is about 25v. The charge instability in MIS structures is less pronounced. The total flat-band shift for the MIS structures decreases rapidly with increasing  $\text{O}_2/\text{SiH}_4$  molar ratio in the reactant. This shift is only 3v or less when the  $\text{O}_2/\text{SiH}_4$  molar ratio in the reactant exceeds 10.

#### Al-( $\text{Si}_3\text{N}_4 + \text{SiO}_2$ )- $\text{SiO}_2$ -Si Capacitors

The charge instability in MNS structures under large voltage bias at room temperature can be suppressed by using a thin silicon dioxide interlayer between the silicon and the silicon nitride. The same approach was used for MIS capacitors in this study. Approximately 100Å of silicon dioxide was deposited prior to the deposition of the  $\text{Si}_3\text{N}_4 + \text{SiO}_2$  mixture. The interface charge density in these capacitors was found to be considerably reduced, usually to about  $10^{12}$  charges/cm<sup>2</sup>. When stressed at room temperature under  $\pm 30$ v, the MIOS capacitors (total insulator thickness = 1000-1500Å) also exhibited no measurable instability due to charge transfer or rearrangement (the flat-band voltage changes were less than 0.2v).

To determine the imperviousness of the  $\text{Si}_3\text{N}_4 + \text{SiO}_2$  mixtures toward ion migration, the MIOS capacitors were subjected to +20v stress at 200°C for 2 min. The C-V curve was found to shift in voltage in the direction expected from ion migration or

Table I. Effect of  $\pm 20$ v, 200°C stress on interface charge of Si- $\text{SiO}_2$ -( $\text{Si}_3\text{N}_4 + \text{SiO}_2$ ) structures

$\text{O}_2/\text{SiH}_4$ ratio	Total insulator thickness, Å	$E_s$ , v/cm	$\Delta N_i$ charges/cm <sup>2</sup>	$\frac{\Delta N_i}{E_s} \times 10^{-5}$ volt <sup>-1</sup> cm <sup>-1</sup>
0.5:1	1025	$1.95 \times 10^6$	$1.28 \times 10^{11}$	0.65
1:1	1070	$1.87 \times 10^6$	$1.89 \times 10^{11}$	0.99
10:1	1400	$1.43 \times 10^6$	$2.0 \times 10^{11}$	1.06
25:1	1450	$1.38 \times 10^6$	$7.2 \times 10^{11}$	5.22
50:1	1440	$1.39 \times 10^6$	$1.5 \times 10^{12}$	10.8

other charge rearrangement in the insulator. Voltage shifts of the C-V curves resulting from the stresses were interpreted, using the insulator capacitance in each case, in terms of the total change in interface charge,  $\Delta N_i$ , at room temperature resulting from positive and negative stresses. Results are shown in Table I. Since differences in film thickness exist among the samples, the ratio of  $\Delta N_i$  to the average stress field,  $E_s$ , was chosen for comparison. The  $\Delta N_i/E_s$  value of the capacitors also increases rapidly with increasing  $\text{O}_2/\text{SiH}_4$  molar ratio in the reactant.

#### Summary and Conclusions

Amorphous films of silicon nitride-silicon dioxide mixtures have been deposited on silicon substrates by the pyrolysis of silane in ammonia-oxygen mixtures, using ammonia as the major component in the reactant mixture. Because of the greater reactivity of silane toward oxygen, the partial pressure of oxygen in the reactant must be carefully controlled, particularly at low  $\text{O}_2/\text{SiH}_4$  molar ratios. The  $\text{O}_2/\text{SiH}_4$  molar ratio in the reactant must be maintained at  $\frac{1}{2}$  or smaller to obtain  $\text{Si}_3\text{N}_4 + \text{SiO}_2$  mixtures containing 50% or more  $\text{Si}_3\text{N}_4$ . When the  $\text{O}_2/\text{SiH}_4$  molar ratio exceeds two, the deposited mixture contains less than 20%  $\text{Si}_3\text{N}_4$  and its composition becomes less sensitive to variations in the reactant composition. Parallel to the change in the composition of the deposit with the  $\text{O}_2/\text{SiH}_4$  molar ratio in the reactant, other properties of the deposit, such as density, dissolution rate, refractive index, infrared absorption, etc., change in a similar manner.

The C-V behavior of MIS capacitors using  $\text{Si}_3\text{N}_4 + \text{SiO}_2$  mixtures as the dielectric is very similar to that of MNS capacitors. They are characterized by high interface charge densities, 1 to  $3 \times 10^{12}$  charges/cm<sup>2</sup>, independent of the composition of the  $\text{Si}_3\text{N}_4 + \text{SiO}_2$  mixtures, or the preparative conditions. They also exhibit charge instability under large voltage bias at room temperature; the instability becoming less pronounced as the silicon dioxide content in the mixture is increased. The high interface charge density and the charge instability in MIS structures can also be reduced by the use of a silicon dioxide interlayer between the silicon and the insulator. However, MIOS capacitors are less stable than MNOS capacitors under electrical and thermal stresses because of the permeability of the  $\text{Si}_3\text{N}_4 + \text{SiO}_2$  mixture toward ion migration.

#### Acknowledgments

The authors wish to thank Dr. A. J. Noreika for electron diffraction examinations, Dr. T. W. O'Keefe for ellipsometric measurements, and Mrs. M. Theodore for chemical analysis. This work was supported in part by the U.S. Naval Air Development Center, Johnsville, Pennsylvania, under Contract N 62269-67-C-0189.

Manuscript received July 14, 1967; revised manuscript received Oct. 26, 1967. This paper was presented at the Dallas Meeting, May 7-12, 1967.

Any discussion of this paper will appear in a Discussion Section to be published in the December 1968 JOURNAL.

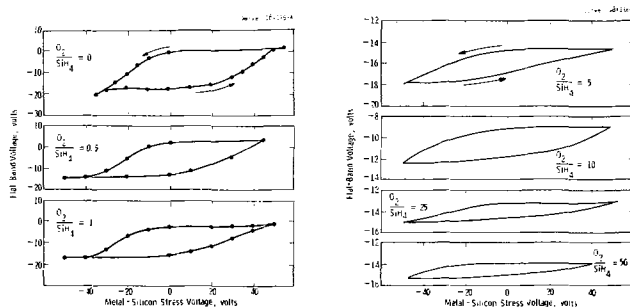


Fig. 9. Room temperature polarization effects on the flat-band voltage behavior of MIS capacitors prepared from  $\text{Si}_3\text{N}_4 + \text{SiO}_2$  mixtures of different composition.

## REFERENCES

1. T. L. Chu, C. H. Lee, and G. A. Gruber, *This Journal*, **114**, 717 (1967).
2. S. M. Hu, *ibid.*, **113**, 697 (1966).
3. (a) T. L. Chu, J. R. Szedon, and C. H. Lee, *Solid State Electronics*, **10**, 897 (1967). (b) S. M. Hu, D. R. Kerr, and L. V. Gregor, *Appl. Phys. Ltrs.*, **10**, 97 (1967).
4. JANAF Interim Thermochemical Tables, The Dow Chemical Co., Midland, Mich.
5. G. A. Lang and T. Stavish, *RCA Rev.*, **24**, 488 (1963).

## Uranium-Uranium Monoarsenide Phase Diagram

Robert Benz and M. C. Tinkle

*Los Alamos Scientific Laboratory of the University of California, Los Alamos, New Mexico*

### ABSTRACT

Uranium-uranium monoarsenide phase boundaries are deduced from thermal analyses and from x-ray diffraction and microscopic analyses of quenched products. The uranium-uranium monoarsenide eutectic occurs at  $1125^\circ \pm 5^\circ\text{C}$  with a composition near pure uranium. Uranium solubility in the UAs phase does not exceed 0.15%. The highest melting point observed with the UAs (+U) phase is  $2705^\circ\text{C}$ .

The phases in the uranium-arsenic system have been reported by Iandelli (1) to be face-centered cubic UAs, body-centered cubic  $\text{U}_3\text{As}_4$ , and tetragonal  $\text{UAs}_2$ . Iandelli found no evidence of formation of solid solutions in preparations that had been heated to temperatures as high as  $900^\circ\text{C}$ . Information on the uranium and UAs phase boundaries at more elevated temperatures is reported below.

### Preparations and Procedure

Preparations with different As/U ratios up to 2 were made by reaction of uranium powder (2) obtained from calcium-reduced metal ( $99.9 \pm 0.1\%$  pure) and arsenic (Johnson, Matthey and Company, Ltd., London, "99.9995%" pure lump arsenic) in a heated ( $400^\circ\text{--}800^\circ\text{C}$ ) silica tube. Phase transitions that occur below  $1000^\circ$  in uranium saturated with arsenic were determined with a resistance furnace and a platinum-rhodium thermocouple for temperature measurement. Higher temperatures were obtained with an induction heater and temperature measurements were made with a calibrated optical pyrometer. The experimental procedures were essentially the same as previously described (3). Lattice parameters were determined from high-angle lines in powder x-ray diffraction pattern photographs obtained with nickel-filtered copper- $\text{K}_\alpha$  radiation. The compositions of the cooled products were determined micrographically by cutting out different phases seen in photomicrographs and weighing. Results are summarized in Fig. 1.

### Results and Discussion

**Uranium phase transitions and the liquidus.**—The solid-solid transitions in arsenic-saturated uranium were obtained by thermal analysis of a single cylinder with the As/U ratio of 0.05. The  $\alpha \rightarrow \beta$  transition initiated at  $665^\circ\text{C}$  and the  $\beta \rightarrow \alpha$  transition initiated at  $642^\circ\text{C}$  at the rate of temperature change of  $5^\circ\text{C}/\text{min}$  indicating an appreciably greater hysteresis than that previously reported (2) for nitrogen-saturated uranium. The  $\beta\text{--}\gamma$  transition occurred at  $775^\circ \pm 3^\circ\text{C}$  on heating and cooling.

The eutectic thermal arrest was determined with an apparatus for measurement of changes in optical emission (4). The arrest occurred  $7^\circ\text{C}$  lower in a specimen with the As/U ratio of 0.5 than in a pure uranium specimen. The melting point of pure uranium has been reported to be  $1132.3^\circ\text{C}$  (5), from which the eutectic temperature of  $1125^\circ \pm 5^\circ\text{C}$  is deduced.

Liquidus compositions as deduced from specimens that had been equilibrated at different temperatures and cooled are plotted in Fig. 1. As shown in Fig. 1,

extrapolation of these data to the uranium melting point and the above described small effect of arsenic on the uranium melting point suggests that the U-UAs eutectic composition is very near pure uranium. X-ray diffraction patterns of powder samples taken from the cooled products in each case contained lines corresponding to the uranium and the UAs phase. Figure 2 is a photomicrograph of a uranium specimen that had been saturated with arsenic at  $1880^\circ\text{C}$  and cooled.

**UAs phase boundaries.**—In order to investigate the uranium-rich UAs phase boundary at approximately 100-degree intervals between  $1600^\circ$  and  $2200^\circ\text{C}$ , reacted powders with an As/U ratio in excess of 1.0 were compacted and heated in a tungsten Knudsen-type crucible *in vacuo*. The period of heating ranged from 30 days at  $1600^\circ\text{C}$  to 7 days at  $1700^\circ\text{C}$  and to successively shorter periods of time at higher temperatures. At first, specimens with the initial As/U ratio of 1.1 were investigated. The phases UAs and  $\text{U}_3\text{As}_4$  were identified in the starting specimens from x-ray diffraction pattern photographs. When heated at selected temperatures between  $1600^\circ\text{C}$  and above, the specimens suffered weight loss by vaporization with preferential loss of arsenic. The cooled products were found to consist of U + UAs phases. Virtually

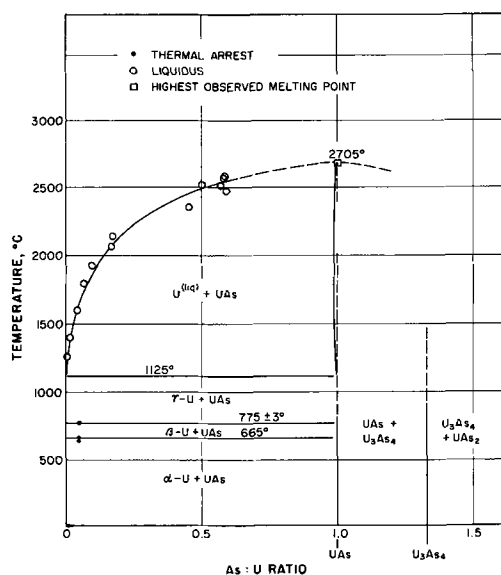


Fig. 1. Uranium-UAs phase diagram

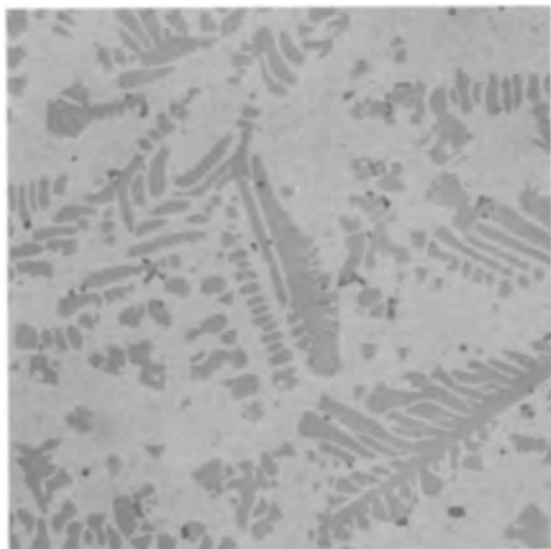


Fig. 2. Photomicrograph of uranium specimen



Fig. 3. Photomicrograph of a typical product

all the uranium was present at UAs grain boundaries and as irregularly distributed 2- $\mu\text{m}$  inclusions within the UAs grains. The bulk of the uranium in the inclusions was probably present as free uranium in the starting specimen; however, the quantity was too small to be identified from the x-ray diffraction pattern photographs. Samples of the cooled products were subsequently annealed for 1 day at 1100° and at 900°C, cooled, and examined with a microscope for uranium precipitate as evidence for solubility of uranium in the UAs phase. No uranium precipitate could be positively identified and, therefore, the solubility is probably small.

The presence of the uranium particles described as inclusions above made difficult the identification of any small quantities of uranium that might have formed by precipitation as the specimens were cooled. Therefore, the above described experiments were repeated by starting with specimens with which greater care was taken to eliminate free uranium. These specimens were prepared as follows: reacted powder with the As/U ratio of 2.0 was cold pressed, and the excess arsenic was distilled off at 1400°C in an atmosphere of helium until the specimen consisted of a mixture of UAs + U<sub>3</sub>As<sub>4</sub> phases as determined from x-ray diffraction pattern photographs. The previous experiments were then repeated by heating 1.5g cylinders of this material for periods necessary to produce 10-20% weight loss by vaporization. The products that had been heated at temperatures of 1830°C (2 days) or below were found to be porous but single phase UAs with the lattice parameters of  $5.7789 \pm 0.0004\text{\AA}$ . No uranium was detectable with a microscope. Products that had been heated at temperatures of 1900°C (16 hr) and above were found to consist of dense 50- $\mu\text{m}$  UAs grains and of uranium present at the grain boundaries. Some uranium particles, similar to the inclusions described above, were also found in some of the UAs grains located near the surface of the products. The occurrence was, however, appreciably less frequent, supporting the interpretation of their being inclusions. These inclusions may have been formed by decomposition at the surfaces of open pores that subsequently disappeared. The UAs grains in products that had been heated at temperatures near 2200°C contained, in addition, 0.05  $\pm$  0.03 v/o (volume per cent) of uranium as smaller 0.5- $\mu\text{m}$  particles. Figure 3 is a photomicrograph of a typical product. These particles may have formed by precipitation from uranium-rich UAs, but the possibility that they were inclusions at temperature cannot be excluded. From this result and the assumption that the UAs phase as

seen in the microscope is stoichiometric, the solubility of uranium is inferred not to exceed 0.15% below 2200°C corresponding to a solidus with an As/U ratio of not less than 0.998. Based on this result and the results obtained with melting point products described in the next section, the composition range of the uranium-saturated UAs phase is shown in Fig. 1 to be very narrow. In Fig. 1, the solidus is suggested to be weakly retrograde in agreement with the rules for the occurrence of a retrograde solidus as stated by Meijering (6).

In the course of the latter set of experiments, single phase UAs was observed to decompose under steady-state vaporization conditions in a tungsten crucible to liquid uranium at temperatures of  $1865^\circ \pm 60^\circ\text{C}$  and above, but did not decompose at lower temperatures. The analogous UN phase has been reported (2) to decompose to liquid uranium at 1820°C and above. The uncertainties of the two temperatures overlap.

The arsenic-rich UAs phase boundary was investigated by examination of UAs + U<sub>3</sub>As<sub>4</sub> phase mixtures that were heated for different periods of time at selected temperatures ranging from ½ hr at 1400°C to 0.1 min at 1800°C. The mixtures were heated under an atmosphere of helium to reduce the rate of arsenic vaporization. The UAs and U<sub>3</sub>As<sub>4</sub> phases were identified from x-ray diffraction powder patterns as obtained with samples of the porous products. The lattice parameters of the UAs phase were found to be  $5.7783 \pm 0.001\text{\AA}$ , the values of which do not differ significantly from those obtained with uranium-saturated UAs that had been heated to comparable temperatures. These results suggest that any solubility of arsenic in the UAs phase is small. No U<sub>3</sub>As<sub>4</sub> precipitate in the UAs phase was perceptible with a microscope. Corresponding to these results, the arsenic-rich UAs boundary is shown in Fig. 1 to be a vertical line, but the line is broken to indicate (i) an uncertainty due to the rapid rates of vaporization that limited the anneal periods and (ii) an uncertainty in the microscopic examination of the porous products.

**UAs melting points.**—Because arsenic vaporized rapidly and preferentially from UAs at elevated temperatures, melting point compositions could not be controlled at will and the melted products generally consisted of uranium + UAs phases. The melting points were determined by heating cylinders with an initial arsenic:uranium ratio of 1.1 either *in vacuo* or in a helium atmosphere. Those heated *in vacuo* melted at different temperatures between 2200° and 2450°C. The arsenic:uranium ratios in the corresponding products ranged from 0.72 to 0.90. Those heated in a helium

Table I. Analyses of UAs incongruent melting points

Melting point, °C	Atmosphere	Bulk As:U, ±0.05	UAs lattice parameter, ±0.002Å
2705	1 atm. He	0.98	5.774
2695	1 atm. He	0.98	5.777
2640	1 atm. He	0.97	5.775
2560	1 atm. He	0.96	5.776
2500	1 atm. He	0.96	5.777
2486	½ atm. He	0.89	5.775
2412	½ atm. He	0.88	5.776
2370	<i>in vacuo</i>	0.85	5.777

atmosphere melted at temperatures between 2420° and 2705°C and the values of the arsenic:uranium ratios in these products were found to range from 0.89 to 0.98. The highest melting points and the highest arsenic:uranium ratios were obtained with the specimens that were heated in a helium atmosphere. An analogous behavior has been reported for UP when it was melted under similar conditions (7).

Typical melting points are listed in column 1 of Table I. The arsenic:uranium ratios of the products are listed in column 3. As shown in Table I, the temperature at which liquid was observed increases from 2370° to 2705°C as the uranium:arsenic ratio increases from 0.85 to 0.98. Microscopically, the melted products consisted of the phases uranium and UAs with small amounts of UO<sub>2</sub> as impurity. The uranium phase appeared mostly at the UAs grain boundaries indicating that the specimens melted incongruently with an arsenic:uranium ratio of less than 1.0. The specimens that melted at temperatures between 2370° and 2560°C contained a trace of uranium present as small spheroidal particles of uranium within the grains of UAs. These particles were virtually absent in the products

melted above 2600°. Lattice parameters obtained with samples of the cooled products are listed in column 4 of Table I. As seen in Table I, the lattice parameters range in value from 5.774 to 5.777Å with no systematic dependence on thermal history. Differences between these values and the above mentioned values of 5.7783 ± 0.001Å as obtained with UAs heated at lower temperatures may be due to impurities such as carbon, tungsten, and oxygen. From the results obtained with the specimen having the highest melting point, the congruent melting point is estimated to be 2705°C at the arsenic:uranium ratio of 1.00.

#### Acknowledgments

The author thanks M. G. Bowman for discussions. Figure 1 was made by C. G. Delano.

Manuscript received Dec. 16, 1966; revised manuscript received Oct. 10, 1967. This work was done under the auspices of the United States Atomic Energy Commission.

Any discussion of this paper will appear in a Discussion Section to be published in the December 1968 JOURNAL.

#### REFERENCES

1. A. Iandelli, *Atti. Accad. nazl. Lincei, Rend., Classe sci. fis., mat. e nat.*, **13**, 138 (1952).
2. R. Benz and M. G. Bowman, *J. Am. Chem. Soc.*, **88**, 264 (1966).
3. C. A. Javorsky and R. Benz, *J. Nucl. Materials*, **23**, 192 (1967).
4. G. N. Rupert, *Rev. Sci. Instr.*, **34**, 1184 (1963).
5. B. Blumenthal, *J. Nucl. Mater.*, **2**, 23 (1960).
6. J. L. Meijering, *Philips Research Repts.*, **3**, 281 (1948).
7. Robert Benz and C. H. Ward, *J. Inorg. Nucl. Chem.*, To be published.

## Technical Notes



### Gallium Phosphide: Its Preparation in Bulk Ingot Form

S. E. Blum,\* R. J. Chicotka, and B. K. Bischoff

IBM Watson Research Center, Yorktown Heights, New York

Recent interest in gallium phosphide has made it desirable to obtain relatively large bulk ingots as a material source for both crystal growth and device studies. Reviews of the various methods that have been used are given in the literature by Miller (1) and Shmartsev *et al.* (2). In general, the preparation is complicated by the high melting temperature (~1500°C) and high dissociation pressure (~35 atm) of the compound (3). However, GaP can be prepared from its elements in polycrystalline form quite readily at pressures appreciably below the dissociation pressure. Of the methods described in the above reviews, the vertical Bridgman is the most adaptable to the routine synthesis of GaP.

#### Method of Preparation

Gallium phosphide was prepared from commercially available materials. Both the gallium and red phosphorus were nominally 6-9's quality and were obtained from both domestic and foreign suppliers.<sup>1</sup> The boron nitride ("Boralloy") crucibles (1.5 cm OD x 7 cm long) were produced by High Temperature Mate-

rials, Inc., Lowell, Massachusetts, and were cleaned prior to use with white etch (3 HNO<sub>3</sub>-1 HF).

The apparatus used to synthesize GaP is shown schematically in Fig. 1. It consists of a heavy wall quartz ampoule<sup>2</sup> (18 mm ID x 24 mm OD) within which the gallium charge (30g) and crucible and an excess of phosphorus is sealed *in vacuo*. The ampoule is positioned within a vertical tubular furnace as shown. Synthesis is achieved by heating the gallium inductively while slowly elevating the temperature of the phosphorus, and hence its pressure, until the phosphorus pressure is controlled at ten atmospheres. At this pressure the melt is at about 1500°C and has a composition of about 0.45 atom fraction of phosphorus (4). Solidification can be obtained either by lowering the ampoule and phosphorus temperature control thermocouple simultaneously or by raising the RF coil. Clear, transparent, single phase GaP is obtained at freezing rates of about 1 cm/hr.

Boron nitride was chosen as the crucible material because it has a low emissivity, and therefore overheating and softening of the quartz ampoule is mini-

\* Electrochemical Society Active Member.

<sup>1</sup> 6-9's phosphorus can be obtained from Leico Industries, Inc., New York, N. Y.

<sup>2</sup> Heavy walled quartz ware is available from General Electric, Cleveland, Ohio and from Thermal American Fused Quartz Company, Dover, New Jersey.

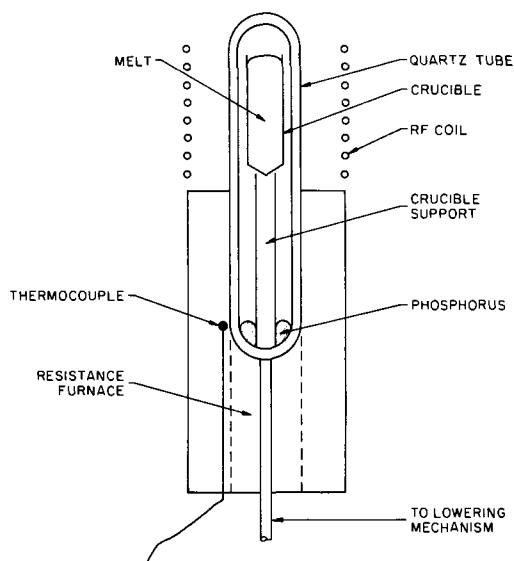


Fig. 1. Schematic diagram showing the vertical Bridgman apparatus.

mized. In addition, the GaP does not wet BN appreciably and this facilitates the removal of the ingot. By maintaining sufficient clearance between the crucible and the ampoule (several millimeters) we have been able to synthesize GaP in other crucible materials, e.g., graphite and quartz.

### Results

Gallium phosphide ingots produced by this method are generally completely sound (i.e., free of voids and inclusions) and, if undoped, golden in color. Occasionally, the ingots will have a small region at the first-to-freeze portion of the ingot that is dark and gallium rich. This is sometimes observed at the tail portion as well. In both cases, this is caused by rapid freezing at the front end because of supercooling and, at the tail end of the crystal, because of rapid loss of RF coupling to the melt. However, in most cases when this occurs, no more than about 10% of the crystal is so affected and at least 40g of sound material is obtained in each run.

The gallium phosphide ingots produced are quite polycrystalline. In general, the crystallites are columnar and arrayed with the long axis parallel to the direction of growth. Usually, individual grains are sufficiently large for Hall spiders ( $6 \times 3 \times 1$  mm).

The freezing interface during solidification of the melt is concave toward the solid phase. Such an interface permits growth of crystallites nucleated at the crucible-melt-solid interface. Some attempts were made to alter the shape of this interface by the use of radiation reflectors external to the ampoule. Although the growing interface could be flattened appreciably, it was impossible to do this completely without risking a softening, and hence rupturing, of the quartz ampoule.

Gallium phosphide ingots have been produced in this apparatus over a phosphorus pressure range of 5-25 atm. At pressures below 10 atm, gallium rich material invariably is produced. At the higher pressures, the risk of explosion, due to flaws in the quartz ware, is of course greater. For the purpose of producing GaP at reasonable rates, a phosphorus pressure of ten atmospheres was quite satisfactory. Of about 170 charges prepared at 10 atm, no explosions resulted.

### Electrical Properties and Purity

Gallium phosphide prepared as described above has always yielded p-type material and invariably contains some boron (<10 ppm). Although some variation from ingot to ingot is observed, net carrier concentrations in the low  $10^{17}$  range with room temperature mobilities of about  $115 \text{ cm}^2/\text{v sec}$  are generally

Table I. Electrical properties of synthesized GaP

Crystal	300°K			77°K		
	$\mu, \text{cm}^2/\text{v sec}$	$p, \text{cm}^{-3}$	$\rho, \text{ohm-cm}$	$\mu, \text{cm}^2/\text{v sec}$	$p, \text{cm}^{-3}$	$\rho, \text{ohm-cm}$
143	123	$1.4 \times 10^{17}$	0.35	1110	$4.5 \times 10^{15}$	1.3
145	127	$6.2 \times 10^{16}$	0.79	970	$1.2 \times 10^{15}$	5.5
147	130	$1.2 \times 10^{17}$	0.42	1780	$5.0 \times 10^{15}$	0.75

obtained. Net carrier concentrations of about  $10^{15} \text{ cm}^{-3}$  with mobilities of about  $300 \text{ cm}^2/\text{v sec}$  are typical at 77°K. Gallium phosphide prepared in a graphite crucible yielded semi-insulating material of about  $10^4 \text{ ohm-cm}$ . Material prepared in a quartz crucible was dark and opaque and extremely brittle. Electrical measurements of this ingot could not be made. However, emission spectrographic analysis showed extremely high contamination from the quartz with a silicon content greater than 300 ppm.

Since the impurity content of the GaP is appreciably greater than that of its constituent elements, it is assumed that the major sources of contamination are the quartz ampoule and/or the boron nitride crucible (possibly carbon). Woods and Ainslie (5) have shown in the case of GaAs that the presence of oxygen during synthesis reduces silicon contamination. Cochran and Foster (6) suggested the theoretical possibility of suppressing silicon contamination by using  $\text{Ga}_2\text{O}$  generated by the reaction of gallium and water vapor. Frosch *et al.* (7) demonstrated that the presence of water vapor in GaP vapor transport system effectively reduced the silicon donor concentration. To determine whether or not the same effect could be observed in gallium phosphide, crystals were synthesized in the presence of water vapor (a backfill of 20 mm at room temperature). The electrical properties of three ingots so prepared are shown in Table I.

The most noticeable effect produced by the presence of water vapor during synthesis is the marked increase in the 77°K mobility. This difference is attributed to a decrease in compensation as a result of the decrease in concentration of the minority donor silicon; i.e., the effect of the water is to suppress reaction with either the quartz ampoule or silica in the boron nitride crucible (ca. 50 ppm). The possibility of other reasons for the effect of water cannot be precluded. For example, the reaction of BN with water might form  $\text{B}_2\text{O}_3$  which then acts as a barrier between the crucible and melt.

### Summary

The vertical Bridgman method of synthesis can be easily applied to materials with high melting temperatures and high dissociating pressures. The method described can produce sound gallium phosphide ingots. The presence of water vapor during synthesis and growth produced a marked effect on the 77°K mobility of the crystal. This effect is attributed to a lowering of the silicon concentration.

Manuscript received Oct. 5, 1967; revised manuscript received Nov. 24, 1967.

Any discussion of this paper will appear in a Discussion Section to be published in the December 1968 JOURNAL.

### REFERENCES

1. J. F. Miller, "Preparation of Gallium Phosphide" in "Compound Semiconductors," R. K. Willardson and H. L. Goering, Editors, Chap. 23, Reinhold Publishing Corp., New York (1962).
2. YU. V. Shmartsev, YU. A. Valov, and A. S. Borshchevskii, "Refractory Semiconductor Materials," New York, Consultants Bureau (1966).
3. D. Richman, *J. Phys. Chem. Solids*, **24**, 1131 (1963).
4. C. D. Thurmond, *ibid.*, **26**, 785 (1965).
5. J. F. Woods and N. G. Ainslie, *J. Appl. Phys.*, **34**, 1469 (1963).
6. C. N. Cochran and L. M. Foster, *This Journal*, **109**, 149 (1962).
7. C. J. Frosch *et al.*, *Trans. Met. Soc. AIME*, **239**, 365 (1967).



# Thickness Measurements of Silicon Dioxide Films on Silicon by Infrared Absorption Techniques

J. E. Dial, R. E. Gong, and J. N. Fordemwalt

Microelectronics Division, Philco-Ford Corporation, Santa Clara, California

Infrared techniques have been used previously in the study of silicon dioxide films (1-4). It is well known that silicon dioxide has strong absorption peaks at 9.2 and 21.9 $\mu$  with a weaker peak at 12.1 $\mu$  (5). If radiation of intensity  $I_0$  impinges on a layer of substance of thickness  $d$ , the intensity of the emerging radiation is given by the equation,  $I = I_0 e^{-\epsilon d}$ , known as the Lambert-Bouguer law (6). Lambert-Bouguer's law plots have been made by plotting the optical density of SiO<sub>2</sub> films on Si at 9.2 and 12.1 $\mu$  as a function of thickness. These plots have been found to be linear within experimental error. Thus, infrared absorption may be used as a nondestructive technique for the thickness determination of unknown SiO<sub>2</sub> layers on silicon samples. The 9.2 $\mu$  peak was used for thin films (<10,000Å), whereas the 12.1 $\mu$  micron peak was used for thicker films.

## Experimental

The measurements were made using a Beckman IR-10 spectrophotometer. A simple fixture was fabricated to hold the oxidized silicon wafer. Double beam transmission was used in all cases. The reference beam attenuator was adjusted so that the initial transmission for all samples was the same (nearly 100%) at a wavelength of 5 $\mu$ . This adjustment was necessary to insure adequate response and sensitivity during a scan. The cross-sectional area of the incident beam was 2 cm<sup>2</sup>.

The silicon substrates used were chemically polished Czochralski grown, n-type wafers with 10<sup>15</sup> atoms/cc phosphorus. The wafers were oxidized either in dry oxygen drawn from a liquid oxygen source, or in steam. After the infrared absorption had been measured, the wafers were prepared for interferometer measurement by first etching a step in the oxide down to the silicon and then evaporating 2000Å of aluminum over the step. A Watson multiple-beam interferometer was used to measure the SiO<sub>2</sub> film thickness (7). The thickness measurements made by using the Watson interferometer were calibrated against a Gaertner ellipsometer. The error was found to be less than 2% for measurements between these two methods.

Figure 1 shows a typical IR scan of a wafer with 1470Å of dry oxide on both sides of the wafer. The optical density of the peak was taken as the maximum reading at 9.2 $\mu$  less the reading of the base line at the same wavelength. It was assumed that the thickness of the oxide was the same on both sides of the wafer (since both had received identical treatment), hence,

the thickness value used for the Lambert-Bouguer's law plot for the wafer in Fig. 1 was 2940Å (i.e., 2 x 1470Å). After the thickness had been measured with the Watson interferometer, the aluminum and the SiO<sub>2</sub> were completely stripped from one side, being careful not to damage the oxide on the other side, and the spectrum of the wafer run again. These data were used to construct the Lambert-Bouguer's law plot in Fig. 2 for the 9.2 $\mu$  infrared absorption peak of SiO<sub>2</sub>. The data for oxide on both sides of the wafer are shown as circles whereas triangles represent the data for oxide on one side only.

Figure 3 shows the spectrum of an oxide 16,400Å thick grown in steam. Figure 4 is the Lambert-Bouguer's law plot for thicker oxides based on the 12.1 $\mu$  peak. With thinner steam-grown oxide films, where the 9.2 $\mu$  peak was not totally absorbing, the thicknesses determined using this peak were found to give excellent correlation with the Lambert-Bouguer's law plot generated for dry oxides at 9.2 $\mu$ .

Extrapolation of Fig. 2 and 4 to zero thickness gives zero optical density as anticipated by the method of establishing the base line. The tangent method used compensates for scattering and reflection caused by the surfaces; thus, failure to obtain an optical density of zero for zero thickness would indicate serious problems with the technique.

## Conclusion

From these Lambert-Bouguer's law plots, it appears that infrared absorption may be successfully

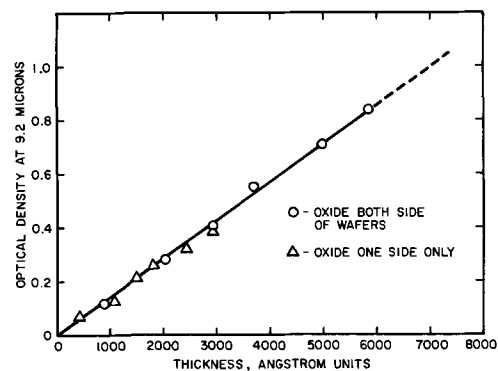


Fig. 2. Optical density of dry silicon dioxide vs. film thickness

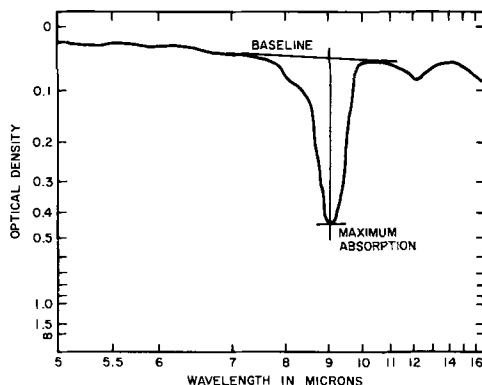


Fig. 1. Typical infrared absorption spectrum of a 2940Å thick film of SiO<sub>2</sub> on silicon.

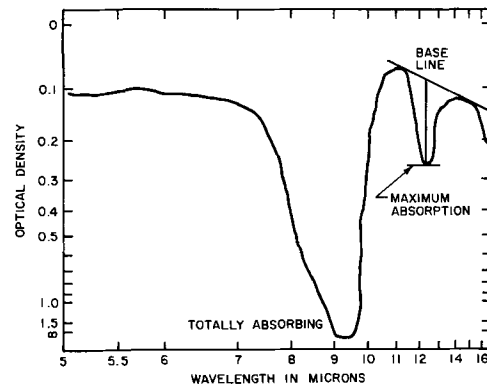


Fig. 3. Infrared spectrum of a 16,400Å thick steam-grown SiO<sub>2</sub> film on silicon.

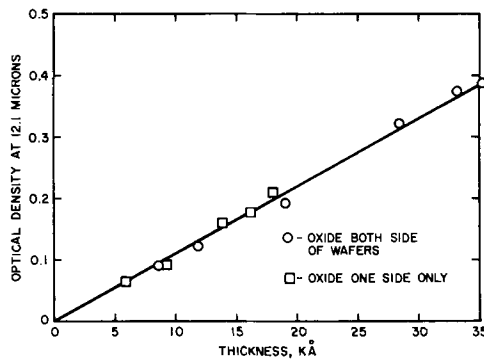


Fig. 4. Optical density of steam-grown silicon dioxide vs. film thickness.

employed as a nondestructive technique for determining the thicknesses of silicon dioxide films. It is felt that the accuracy of these data is limited as much by the Watson interferometer used for the thickness measurements as by the basic infrared equipment and techniques. Limits of error within  $\pm 3\%$  are possible for films from 1000Å to  $3\mu$  thick with this technique. Films as thin as 400Å have been measured with errors of less than 50Å.

## Silver-Manganese Evaporated Ohmic Contacts to p-type Gallium Arsenide

C. J. Nuese and J. J. Gannon

RCA Laboratories, Princeton, New Jersey

As GaAs devices become more sophisticated, the technology of forming low-resistance ohmic contacts to them becomes increasingly important. These contacts can be formed by alloy (1-3), plating (4) liquid regrowth (5), or evaporation (6,7) procedures, each of which has its particular advantages (and disadvantages). However, for many present-day GaAs devices requiring the precise and reproducible location of various geometrical contact patterns, the evaporation of metal through a mask (either an oxide or a metal mask) is particularly desirable. Such an evaporation procedure is even more useful if it is applicable over a wide range of conditions. For n-type GaAs an evaporation procedure using a Au-Ge-Ni alloy (7) has recently been reported.<sup>1</sup>

We report here a Ag-Mn alloy evaporation procedure for p-type single-crystal GaAs which forms low-resistance ohmic contacts over a wide range of temperature and resistivity. The Ag-Mn evaporation provides ohmic contacts to lapped, chemically-polished, or epitaxial as-grown surfaces, and readily supports ultrasonic or thermocompression wire bonding. The contact has a very small penetration depth (no more than a fraction of a micron), and is therefore useful for contacting surfaces adjoining a reasonably shallow junction. The Ag-Mn evaporation procedure is also applicable to p-type GaAs<sub>1-x</sub>P<sub>x</sub> alloys with moderate-to-heavy doping concentrations.

### Procedure

The technique described here is a modification of that used by Schmidt (6) for the evaporation of Ag ohmic contacts on heavily doped GaAs. We have found that Ag evaporated on chemically-polished or as-grown surfaces of lightly doped p-type GaAs ( $p < 10^{18}$  cm<sup>-3</sup>) frequently leads to nonohmic contacts, whereas

<sup>1</sup> In addition, R. H. Cox and H. Strack [*Solid-State Electronics*, **10**, 1213 (1967)] have just reported the evaporation of low-resistance ohmic contacts to GaAs using Ag-In alloys.

### Acknowledgments

The authors are indebted to Mr. D. M. Brettner for his contributions to this paper and to Dr. M. L. Hammond and Mr. M. J. Selser for their assistance in the interpretation of the spectral measurements.

Manuscript received Oct. 6, 1967; revision received ca. Nov. 20, 1967.

Any discussion of this paper will appear in a Discussion Section to be published in the December 1968 JOURNAL.

### REFERENCES

1. W. A. Pliskin and H. S. Lehman, *This Journal*, **112**, 1013 (1965).
2. R. M. Valleta, J. A. Perri, and J. Riseman, *Electrochem. Technol.*, **4**, 402 (1966).
3. D. B. York, *This Journal*, **110**, 271 (1963).
4. L. A. Murry and N. Goldsmith, *ibid.*, **113**, 1297 (1966).
5. M. M. Atalla, Paper presented at Boston Meeting of Metallurgical Society of AIME, Sept. 1959.
6. M. L. Hair, "Infrared Spectroscopy In Surface Chemistry," Marcel Dekker, Inc., New York (1967).
7. S. Tolansky, "Multiple Beam Interferometry of Surfaces and Films," Clarendon Press, Oxford (1948).

the addition of manganese, an acceptor in GaAs, to the Ag remedies this problem. Because Ag and Mn have vapor pressures of roughly the same magnitude, the Ag-Mn alloy is readily evaporated; however, the replacement of Mn by other frequently used acceptors such as Zn or Cd leads to erratic and irreproducible evaporations because of their high vapor pressures as compared to that of Ag.

Ohmic contacts are formed by evaporating a metal alloy composed of 96 parts by weight of Ag and 4 parts of Mn, both metals having a manufacturer's reported purity of 99.999%. For our particular device applications, the GaAs surface is usually chemically polished on pellow cloth with a dilute sodium hypochlorite solution, or is used in the as-grown condition on vapor-grown epitaxial layers; however, mechanically lapped or polished surfaces have also been contacted with equal success. Following a clean-up bath in dilute HCl and a rinse in distilled water and ethyl alcohol, the wafer is placed on a ceramic heater in a vacuum chamber, and is gradually heated under vacuum ( $10^{-5}$  Torr) to 300°C. The Ag-Mn alloy is then evaporated onto the hot GaAs surface to a thickness of approximately 5000Å. For evaporating a particular array of contacts, a molybdenum mask is placed directly against the GaAs wafer. Finally, the wafer is removed from vacuum and heated to 550°C for 2 min in a hydrogen atmosphere in order to sinter the contacts more thoroughly to the GaAs. It should be noted that the 550°C sintering process is usually not necessary to obtain ohmic contacts; however it does improve the contact adhesion, thereby facilitating ultrasonic wire bonding to the contacts.

### Results

The current-voltage characteristics between a pair of Ag-Mn dots (5 mils in diameter) evaporated on a large variety of single-crystal GaAs wafers with Zn

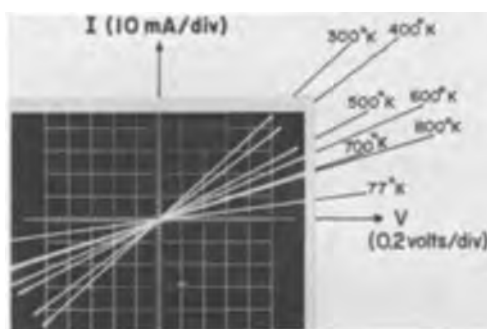


Fig. 1. I-V characteristics at various ambient temperatures of Ag-Mn contacts evaporated onto a lightly doped ( $1.5 \times 10^{17} \text{ cm}^{-3}$ , Cd) GaAs wafer. The increase in resistivity at  $77^\circ\text{K}$  is due to carrier freeze-out.

or Cd acceptor concentrations between  $1 \times 10^{16} \text{ cm}^{-3}$  and  $1 \times 10^{20} \text{ cm}^{-3}$  have always been linear. Similar ohmic behavior was also found between contacts to a high resistivity (650 ohm-cm, p-type) Mn-doped sample. Ohmic behavior has been obtained for evaporations on {100} and {111} oriented surfaces with no observable distinction between them.

The linearity of these contacts over an extended temperature range is shown in Fig. 1. Here, a pair of the small dots was evaporated onto a Cd-doped GaAs wafer ( $p = 1.5 \times 10^{17} \text{ cm}^{-3}$  at  $300^\circ\text{K}$ ), and the I-V characteristics between the dots were photographed on a curve tracer at several temperatures between  $77^\circ$  and  $800^\circ\text{K}$ . The characteristics of the contacts are clearly linear at each temperature within this range. The increase in the resistance between the dots from a value of 22 ohms at  $300^\circ\text{K}$  to 142 ohms at  $77^\circ\text{K}$  is due primarily to the large increase in the sample resistivity with cooling. Hall measurements on this sample using conventional In-Zn alloyed contacts (8) showed a freeze-out of carriers from  $1.5 \times 10^{17} \text{ cm}^{-3}$  at  $300^\circ\text{K}$  to  $1.6 \times 10^{16} \text{ cm}^{-3}$  at  $77^\circ\text{K}$ , and a corresponding increase in resistivity by a factor of 4 at  $77^\circ\text{K}$ . The gradual increase in total resistance with increasing temperature is probably due mainly to increased sample resistivity.

It is difficult to separate bulk and spreading resistances accurately from the contact resistance, particularly on lightly doped samples. However, with a low-resistivity sample, an upper limit for the contact resistance is conveniently obtained by measuring the total resistance between two contacts to the sample. A total resistance of 0.16 ohms was so obtained between two 5 mil diameter Ag-Mn dots evaporated on a heavily Zn-doped ( $p = 8.5 \times 10^{19} \text{ cm}^{-3}$ ,  $\rho = 1.2 \times 10^{-3} \text{ ohm-cm}$ ) GaAs wafer, thus placing an upper limit of approximately 0.08 ohms on the contact resistance of each Ag-Mn contact. A "specific contact resistance" (contact resistance  $\times$  contact area) of  $1 \times 10^{-5} \text{ ohm-cm}^2$

is thus calculated for these contacts, which is comparable with Schmidt's measurements for Ag contacts to GaAs (6). We should note that these values of contact resistance and specific contact resistance apply only to the particular low-resistivity sample measured here.

The Ag-Mn contacting procedure has been used extensively in the fabrication of GaAs diodes with reasonably shallow p-n junctions (typically  $5\mu$ , but as small as  $1.5\mu$ ) without noticeably degrading device performance. In an attempt to determine the contact penetration depth, an n-type GaAs sample with Ag-Mn contacts was mounted in epoxy and beveled at an angle of  $2^\circ$  to the crystal surface. A variety of chemical etchants were used to delineate any p-n junction bordering a regrown or diffused layer, however to the accuracy of this technique (approximately  $0.2\mu$ ), none was evident. As long as the sintering temperature does not exceed the GaAs-Ag eutectic temperature of approximately  $650^\circ\text{C}$ , no appreciable alloying occurs.

Last, these contacts have also been used extensively to provide ohmic contacts to moderately-doped ( $p > 10^{17} \text{ cm}^{-3}$ ) single-crystal  $\text{GaAs}_{1-x}\text{P}_x$  with  $0 \leq x \leq 0.6$ , and have been used to a lesser extent (but always with success) to heavily doped ( $10^{18} < p < 10^{19} \text{ cm}^{-3}$ )  $\text{GaAs}_{1-x}\text{P}_x$  with  $0.6 \leq x \leq 1.0$ .

### Acknowledgments

The authors wish to thank H. F. Gossenberger for preparing several wafers used in evaluating the contacts. Furthermore they gratefully acknowledge the assistance of H. P. Maruska for performing the Hall measurements, C. W. Benyon for evaluating the wire bonding capabilities, and J. J. Tietjen and L. R. Weisberg for critically reviewing this paper. This research was supported by the Advanced Research Projects Agency, Materials Sciences Office under Contract No. SD-182.

Manuscript received Sept. 27, 1967; revised manuscript received Dec. 6, 1967.

Any discussion of this paper will appear in a Discussion Section to be published in the December 1968 JOURNAL.

### REFERENCES

1. J. R. Dale and R. G. Turner, *Solid-State Electronics*, **6**, 388 (1963).
2. J. R. Dale and M. J. Josh, *ibid.*, **7**, 177 (1964).
3. D. K. Jadas, H. E. Reedy, and D. L. Feucht, *This Journal*, **114**, 408 (1967).
4. R. Proebsting, *SCP and Solid State Technology*, pp. 33-37, Nov. 1964.
5. K. L. Lawley, *Electrochem. Technol.*, **5**, 374 (1967).
6. W. A. Schmidt, *This Journal*, **113**, 860 (1966).
7. N. Braslau, J. B. Gunn, and J. L. Staples, *Solid-State Electronics*, **10**, 381 (1967).
8. L. D. Libov *et al.*, *Instruments and Experimental Techniques*, pp. 746-753, Feb. 1966.

# Measurement of Electrolyte Gradient in an Operating Fuel Cell

M. L. Miller and H. J. Fornasar

Central Research Division, American Cyanamid Company, Stamford, Connecticut

## ABSTRACT

Reference mercury, mercuric oxide electrodes have been developed for monitoring the concentration of potassium hydroxide in hydrogen-oxygen fuel cells operating at 27° and 70°C.

The distribution of electrolyte in the matrix of an operating fuel cell can be measured by imbedding appropriate reference electrodes in various parts of the fuel cell matrix. Knowledge of the concentration distribution in a fuel cell is important for understanding the operation of a cell and for designing fuel cells. Mercury, mercuric oxide electrodes have been shown to be reversible to hydroxyl ions (1, 2) at concentrations less than 0.85M. These electrodes will be useful for measuring the distribution of potassium hydroxide in fuel cells provided the electrodes can be shown to respond to hydroxyl ions at the higher concentrations encountered in an operating fuel cell.

## Experimental

**Fuel cells.**—Two types of hydrogen-oxygen fuel cells were used in the development of reference electrodes. One was a small poly(methylmethacrylate) cell similar to the cell described by Bone (3). A circular area of matrix 2.5 cm in diameter was exposed to gases. This cell was run at room temperature without temperature control, and at 70°C in an air bath. A second cell, which is described in ref. (4), was made from stainless steel plates separated by polytetrafluoroethylene gaskets. The surface of the matrix exposed to gases in this cell was 5.0 x 5.0 cm. The larger cell was heated externally by two electric heaters, and its temperature was regulated by a temperature-control unit connected to a thermocouple within the cell. The pattern of gas flow in each cell was determined by the position of the ports through which gases entered and left the cell. These positions are shown in Fig. 1. The catalytic electrodes were Cyanamid AB1 electrodes (5). The gel membrane was made from crosslinked poly(vinyl alcohol) and contained filler (6). The matrix asbestos was Fuel Cell Asbestos supplied by Johns-Manville.

**Calibration electrodes.**—The ability of mercury, mercuric oxide electrodes to respond to changes in hydroxyl ion concentration at high concentrations of potassium hydroxide was determined in a series of experiments which made use of relatively large electrodes, referred to as "calibration electrodes." The calibration electrodes were made from 2.4 mm diameter glass tubes, one end of which was covered with a poly(vinyl alcohol) membrane (unfilled) which allowed transport of water and ions, but retained solid materials within the tube. A slurry of mercury and mercuric oxide (prepared by triturating with a solution of potassium hydroxide having the concentration of the standard solution in which the electrode was to be used) was placed in the electrode tube together with a platinum wire that had been gold plated and then amalgamated.

Electrodes were made with potassium hydroxide solutions containing 3.25, 4.67, 6.00, 6.56, 7.40, 8.85, and 10.58 moles of potassium hydroxide per kg of water. These electrodes were compared in the cell



at 27° or 70°C. The potential of cell 1 was measured with a Minneapolis Honeywell Potentiometer—Model

2700. The concentration of the reference solution,  $C_1$ , was arbitrarily chosen as 6.56M (6N at 27°). The concentration  $C_2$  ranged from 3.25 to 10.58M. The potentials (in millivolts) of cell 1 at 27° and at 70°C are plotted against  $C_2$  (in molality) in Fig. 2.

**Microelectrodes and matrix assembly.**—The electrodes used to determine the relationship between potential and concentration were not suited for use in an operating fuel cell. Electrodes had to be small enough to insert into a cell without disrupting the gas-tight seal of the gaskets. Gold-plated platinum wires (0.075 mm diameter), amalgamated with mercury to hold the mercury immobile during operation, were used to make these small electrodes. The tip of each amalgamated platinum wire was painted with a slurry of mercuric oxide in a potassium hydroxide solution having the concentration of the solution to be used in the fuel cell (~8M). Laminated matrices (maximum thickness one millimeter) incorporating microelectrodes and gel membranes were assembled as shown in the inserts in Fig. 3. A new set of microelectrodes was used whenever a cell was reassembled. When cells were run at room temperature, polytetrafluoroethylene-coated glass filter sheets (Bel-Art Company, Pequannock, New Jersey) separated the outer reference electrodes from the catalytic electrodes. When cells were run at 70°C with gel membranes, the filter sheets (which decomposed in alkali at high temperatures) were replaced by thin gel membranes. When cells were run at 70°C with Fuel Cell Asbestos the outer reference electrodes were placed in a pocket in the outer layer of asbestos. During assembly, a wick of etched polytetrafluoroethylene felt was inserted in the matrix laminate to serve as a salt bridge. The polytetrafluoroethylene felt (American Felt Company) was etched by treatment with a 10% solution of potassium in liquid ammonia at -50°C. Between measurements the wick was kept dry and covered to prevent carbonate formation. Prior to making a potential

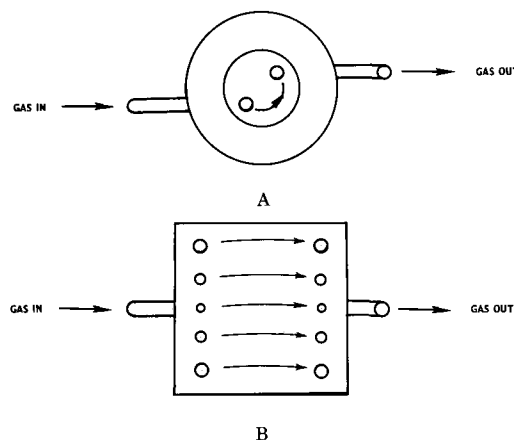


Fig. 1. Location of gas ports in (A) 2.5 cm diameter cell and (B) 5 x 5 cm cell.

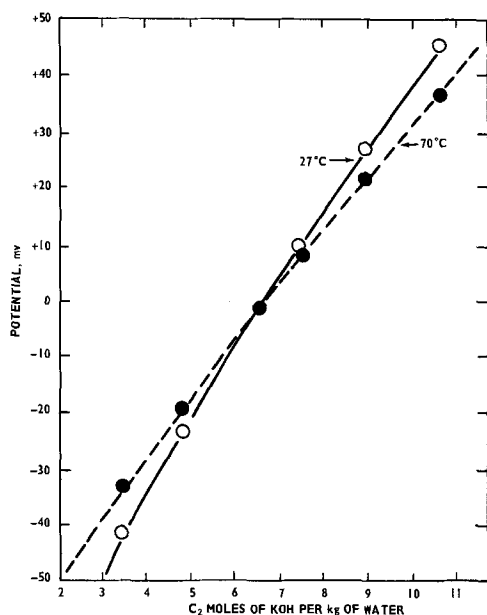


Fig. 2. Relationship between the potential of cell 1 and  $C_2$  when  $C_1$  is 6.56M.

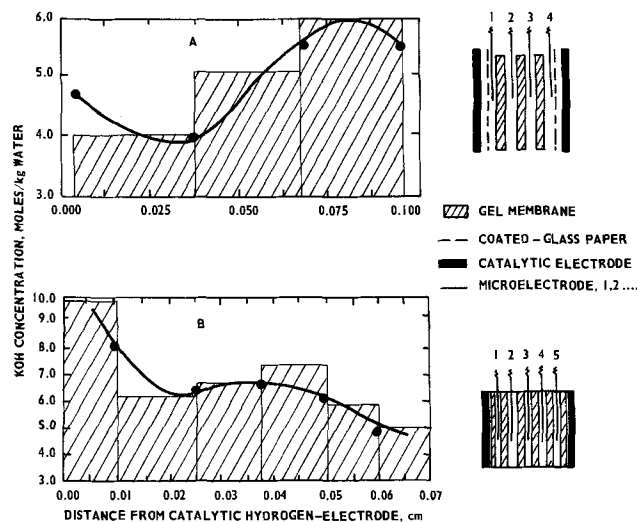


Fig. 3. Electrolyte profiles in cells with gel-type matrices. Cross-hatched areas obtained by titration, —●— by reference electrode. (A) 2.5 cm cell 27°C, 65 ma/cm<sup>2</sup>, 0.623v. Gas flows: O<sub>2</sub>—21.5 ml/min, H<sub>2</sub>—41.0 ml/min. (B) 5 x 5 cm, 70°C, 100 ma/cm<sup>2</sup>, 0.816v. Gas flows: O<sub>2</sub>—350 ml/min, H<sub>2</sub>—350 ml/min.

measurement the wick was wetted thoroughly with 6.56M potassium hydroxide solution.

The arrangement of a fuel cell containing reference electrodes is shown in Fig. 4. Cells at room temperature, approximately 27°C, were run without temperature control. At 70°C the external reference electrode was held at 27°C and the cell temperature was thermostatically controlled at 70°C. The fuel-cell current was interrupted for approximately 30 sec when the potential was measured. After each potential reading the fuel-cell current was restored and the fuel cell was allowed to re-equilibrate (2-3 min) before proceeding with the next reading. Electrolyte concentrations in the matrix were estimated from measured potentials by the plots in Fig. 2.

**Reliability of the microelectrodes.**—Comparison with calibrating electrodes.—Microelectrodes were placed between asbestos sheets soaked in various concentrations of potassium hydroxide. These sheets were placed in a fuel cell in which no gas was flowing and the potential difference between the microelectrodes in the cell and the large calibrating electrodes outside of the cell was measured. The potential differences

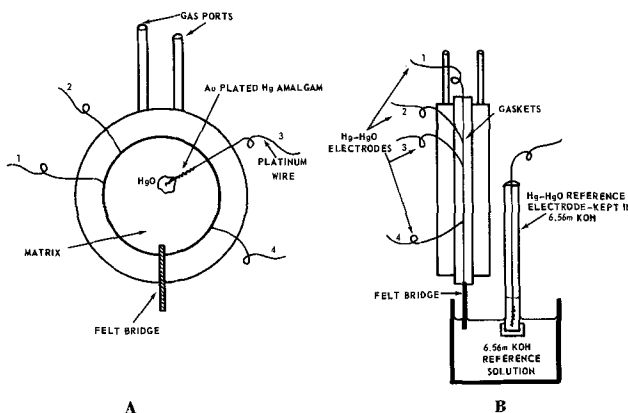


Fig. 4. Assembly for observing potassium hydroxide concentrations in an operating fuel-cell matrix. (A) Section of matrix laminate containing microelectrodes; (B) fuel cell and reference electrodes.

observed in this test at 26° and at 70°C were identical with the potential difference between the large calibrating electrodes shown in Fig. 2.

**Reliability of microelectrodes in an operating fuel cell.**—To determine the reliability of the microelectrodes in an operating fuel cell, it was necessary to find a technique for determining the concentration of potassium hydroxide in the individual layers of the matrix by another method. One method for doing this was to freeze the fuel cell rapidly while running and to separate and titrate individual layers of the frozen matrix. Fuel Cell Asbestos could not be used for this test because the asbestos lacks wet strength. Gel membranes are, however, much stronger than asbestos when saturated with potassium hydroxide solution. Laminates consisting of gel membranes can be frozen, separated and titrated without tearing. In previous work at 27° and 70°C we operated fuel cells containing gel membranes, and fuel cells containing Fuel Cell Asbestos, continuously under constant loads of 55 to 150 ma/cm<sup>2</sup> for periods of 150-200 hr. In these tests the cells containing gel membranes performed exactly the same as the cells containing Fuel Cell Asbestos.

A fuel cell was assembled using a gel matrix which consisted of three layers of gel membrane each approximately 0.4 mm thick. A microelectrode was placed at each interface. The cell was run at constant current for 24 to 48 hr after the microelectrodes indicated that a stable distribution of electrolyte had been established in the cell. Then the cell (while running) was placed in a polyethylene bag and quickly frozen in a dry ice-alcohol mixture. The rapid freezing slowed diffusion of hydroxyl ions and enabled the cell to be disassembled without changing the electrolyte distribution. The laminated gel matrix was separated into layers, the thickness of each layer was measured and the hydroxyl content of each layer was determined by titration. The concentration of potassium hydroxide in each layer was computed by assuming that a section of gel membrane, 5 x 5 x 0.025 cm, after compression and use in a fuel cell, contained 0.03 ml of electrolyte solution. This figure was obtained by titrating a membrane (saturated with 6.56M potassium hydroxide solution) that had been compressed in a fuel cell. Since cells used at 70°C were assembled at room temperature the same figure was used for calculating the volume of electrolyte in membranes used at 70°C. The concentration of electrolyte in the fluid contained in the catalytic electrodes in contact with the membranes was not measured. Figure 3A is a plot of the concentration gradient that was observed after 48 hr in a 2.5 cm diameter cell operated at ambient temperature (~27°C). Figure 3B is a similar plot of the concentration gradient in a 5 x 5 cm cell operated at 70°C. Filled circles represent concentrations mea-

sured with microelectrodes, and crosshatched areas represent concentrations measured by titration. The good agreement between the two types of data attests to the reliability of the microelectrodes at both temperatures.

**Effect of continuous operation in a fuel cell on microelectrodes.**—Two other questions remain to be answered before we can use microelectrodes with confidence to monitor fuel-cell concentrations. These questions are: Does the presence of microelectrodes effect the operation of a fuel cell, and can the microelectrodes withstand continuous exposure to a fuel cell environment? In order to answer these questions a fuel cell containing microelectrodes was run at ambient temperature for 215 hr. During this time the output averaged 0.537v at 100 ma/cm<sup>2</sup>. This is the same performance that we observed with similar fuel cells operating under the same conditions but without microelectrodes. At the end of this test neither the fuel cell nor the microelectrodes showed visible deterioration. Microelectrodes removed from a fuel cell after 200 hr of continuous operation gave correct readings in standard potassium hydroxide solutions.

## Results

**Effect of gas-flow ratios.**—The foregoing experiments establish the reliability of microelectrodes in an operating fuel cell. These electrodes can now be used to measure the effect of operational variables on electrolyte distribution. In the work reported in this paper the electrodes were placed in the center of the matrix. Thus the profile of electrolyte concentrations which we observed is the electrolyte profile in the center of the cell between the catalytic hydrogen and the catalytic oxygen electrodes. The fraction of water removed by the hydrogen (or oxygen) gas streams in an operating fuel cell can be varied by varying the ratio of hydrogen to oxygen in the total gas flow. The data in Fig. 5 show that in a 2.5 cm cell operating at 0.70v with gel matrix, the fraction of water removed by the hydrogen (or oxygen) gas stream is proportional to the percentage of hydrogen (or oxygen) in the total gas flow. The data in Fig. 5 were obtained by passing the emergent gas streams through gas-absorption bottles filled with anhydrous calcium sulfate and weighing the bottles. Before the cell was used for this test it was allowed to operate at a steady rate of 0.70v and 70 ma/cm<sup>2</sup> for 24 hr at a 1:1 (v:v) gas-flow ratio. Then the water collection was started and the gas-flow ratio varied from 3:1 to 1:1 to 1:3 keeping the total gas flow (hydrogen plus

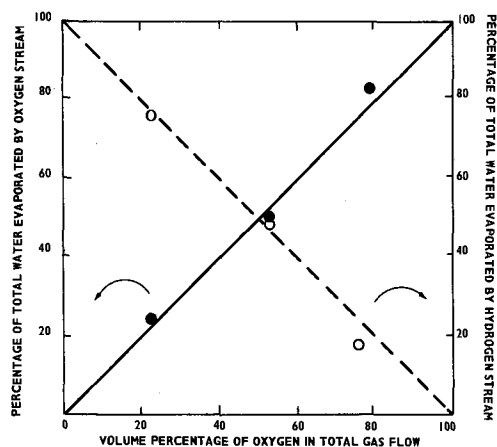


Fig. 5. Percentage of water evaporated by oxygen and hydrogen gas-streams for a 2.5 cm diameter cell at 27°C. Total gas flow 74-83 ml/min, current 70 ma/cm<sup>2</sup>, 0.70v, gel matrix. Arrows indicate scale to be used in reading a particular plot.

oxygen) constant at 74-83 ml/min. In all these tests the amount of water recovered was within 5% of the total water formed.

Figure 6 shows the electrolyte profiles observed under similar conditions in a 2.5 cm diameter cell using Fuel Cell Asbestos at room temperature. Notice that the general character of the profile is the same at the various gas ratios indicating that the transfer of water through the matrix is rapid compared to the changes in other variables that influence the shape of the electrolyte profile.

**Effect of current density.**—The effect of current density on electrolyte was observed in a 5 x 5 cm cell (asbestos matrix) that was run continuously for 348 hr at 70°C. During this time the cell was operated

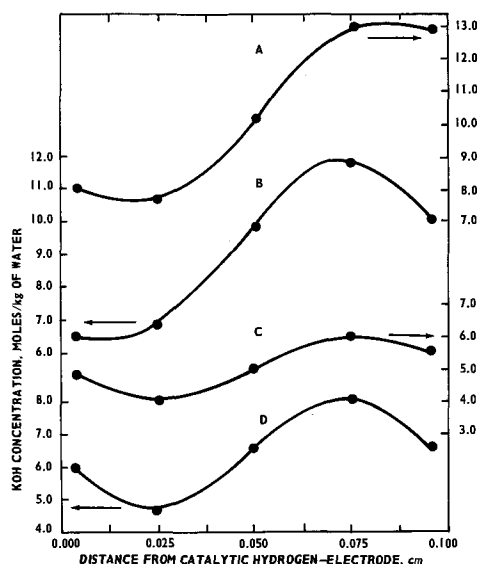


Fig. 6. Electrolyte profiles in a 2.5 cm cell, with Fuel Cell Asbestos matrix at 27°C. (A) Gas flows: O<sub>2</sub>—10.5 ml/min, H<sub>2</sub>—73.5 ml/min, 55 ma/cm<sup>2</sup>, 0.550v; (B) gas flows: O<sub>2</sub>—22.5 ml/min, H<sub>2</sub>—67.5 ml/min, 57 ma/cm<sup>2</sup>, 0.568v; (C) gas flows: O<sub>2</sub>—43 ml/min, H<sub>2</sub>—43 ml/min, 64 ma/cm<sup>2</sup>, 0.641v; (D) gas flows: O<sub>2</sub>—60 ml/min, H<sub>2</sub>—30 ml/min, 60 ma/cm<sup>2</sup>, 0.594v. Arrows indicate scale to be used in reading a particular plot.

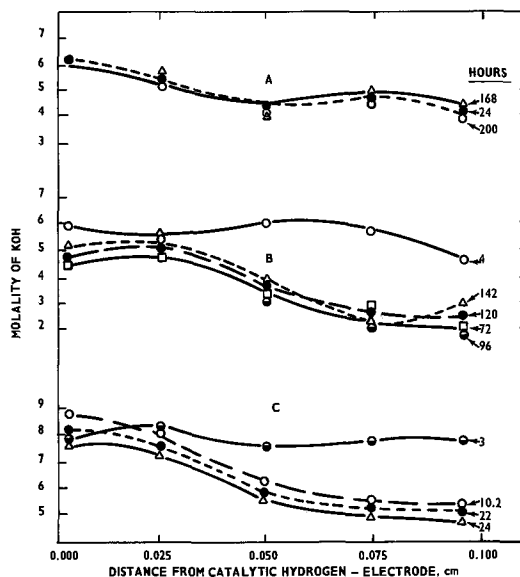


Fig. 7. Electrolyte profiles in 5 x 5 cm cell after various times of operation at a steady performance. (A) ~27°C, 100 ma/cm<sup>2</sup>, 0.710v; (B) 70°C, 100 ma/cm<sup>2</sup>, 0.810v; (C) 70°C, 100 ma/cm<sup>2</sup>, 0.831v.

for periods of 3 to 4 days at loads ranging from 50 to 150 ma ( $\pm 1$  ma) per  $\text{cm}^2$ . These tests showed that current densities between 50 and 150 ma/ $\text{cm}^2$  have little effect on the shape of the electrolyte profile in the center of this cell.

*Time required to establish a steady-state electrolyte distribution.*—Experiments showed that although a stable operation with respect to current and voltage was established in minutes after start-up of operation, the attainment of a steady state in the electrolyte distribution required between 3 and 6 hr in the 2.5 cm diameter cell at room temperature and approximately the same length of time in the 5 x 5 cm cell at 70°C. However, some other cells which had less uniform gas flow-patterns required as long as 48 hr to reach a steady electrolyte distribution. The time required to attain a steady electrolyte profile and the constancy of the shape of this profile, once attained, is shown by the curves in Fig. 7.

It is evident that the general shape of the concentration profiles in Fig. 3A and 3B is characteristic of the particular cell used and is not radically altered by changes in temperature (Fig. 7), flow rate (Fig. 6), or current density (Fig. 7). The difference in shape of the profiles in Fig. 3A and 3B appears to be related to the difference in gas-flow patterns in the two types of cells. Apparently it will be necessary to measure concentration profiles over the whole face of the exposed matrix, not just through the center, in order to understand the operation of the cell.

### Acknowledgment

The authors wish to thank Dr. R. G. Haldeman and Professor B. E. Conway for advice and encouragement during the course of this work, Mr. J. Skogman for carrying out the water-balance experiments, Dr. K. E. Olsen, Mr. D. Gershberg, and Mrs. D. Bernstein for valuable suggestions in connection with the preparation of the manuscript. They are also indebted to Professor Conway for suggesting the mercury, mercuric oxide electrodes to them.

Manuscript received Sept. 19, 1967; revised manuscript received Nov. 3, 1967.

Any discussion of this paper will appear in a Discussion Section to be published in the December 1968 JOURNAL.

### REFERENCES

1. Ming Chow, *J. Am. Chem. Soc.*, **42**, 488 (1920).
2. G. J. Samuelson and D. J. Brown, *ibid.*, **57**, 2711 (1935).
3. J. S. Bone, *Proc. Ann. Power Sources Conf.*, **14**, 62 (1960).
4. R. G. Haldeman, W. A. Barber, W. P. Coleman, J. DiPalma, D. Gershberg, and J. P. Ward, NASA Report #CR 54436.
5. R. G. Haldeman, W. P. Colman, S. H. Langer, and W. A. Barber, *Advan. Chem. Ser. No. 49*, Am. Chem. Soc., Washington, D. C. (1965).
6. M. L. Miller, J. Skogman, and J. E. Sutherland, U.S. Pat. 3,265,536 (1966).

## The Alkaline Manganese Dioxide Electrode

### II. The Charge Process

David Boden,\* C. J. Venuto,\* D. Wisler, and R. B. Wylie

ESB Incorporated, Research Center, Yardley, Pennsylvania

### ABSTRACT

The reactions occurring during the discharge and charge of manganese dioxide electrodes in 7M KOH are studied by x-ray diffraction and charge and discharge curves. The discharge at first results in the formation of an amorphous oxide by incorporation of protons and electrons into the  $\text{MnO}_2$  lattice. Then the amorphous compound is electroreduced to give  $\text{Mn}_3\text{O}_4$  and finally  $\text{Mn}(\text{OH})_2$  depending on the electrode potential. When electrodes are recharged, the amorphous phase is converted to  $\text{MnO}_2$  whereas the  $\text{Mn}_3\text{O}_4$  remains unchanged in the electrode. It is proposed that on recharge  $\text{Mn}(\text{OH})_2$  is oxidized to  $\text{Mn}_3\text{O}_4$ . The cause of failure of electrodes during cycling seems to be the formation of a film of  $\text{Mn}_3\text{O}_4$  around the electrical contact wire.

The reactions occurring during the discharge of a manganese dioxide electrode in alkaline electrolyte have been investigated by several workers (1-7). However, the charge process, after the electrodes have been discharged, appears not to have been studied. This is of practical importance in understanding the reactions which limit the performance of the rechargeable alkaline manganese dioxide battery.

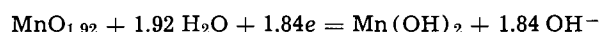
It is observed in these cells, that if the discharge is limited to a relatively small fraction of the total manganese dioxide capacity, a considerable number of discharge/charge cycles can be obtained, whereas if the cells are deeply discharged, very few cycles are obtainable. At the present time, the source of this restriction is unknown. It was thought desirable, therefore, to investigate the reactions occurring at the manganese dioxide electrode when it is charged after varying degrees of partial discharge.

This paper presents the results of a study whereby x-ray crystallography, chemical analysis, and the analysis of potential-time transients are used to characterize the reactions.

\* Electrochemical Society Active Member.

### Experimental

The method of preparation, the size and weight of the electrodes, and the electrolytic cell were identical to those described previously (7). Available oxygen analyses conducted by the arsenious acid method (8) showed the sample of  $\text{MnO}_2$  had an empirical formula of  $\text{MnO}_{1.92}$ , giving the electrodes a calculated capacity of 0.45 amp-hr based on the following reaction



All the discharge and charge operations were carried out at 25°C in 7M KOH solution and the electrode potentials were recorded against a Hg/HgO reference electrode in the same electrolyte using a Texas Instruments Servoriter in conjunction with a Hewlett Packard vacuum tube voltmeter Model 412A.

### X-ray Crystallographic Analyses

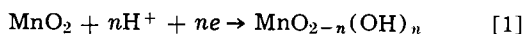
Groups of electrodes were discharged at 5 ma  $\cdot$   $\text{cm}^{-2}$  (12.5 ma total) in 7M KOH at 25°C in 0.1C increments of the theoretical capacity (0.1C, 0.2C, 0.3C, etc.). Representative samples were removed from the

Table I.  $d$  Values of  $MnO_2$  electrodes during discharge and charge

Dis. to	Chg. to											
1.00 C		3.35	3.11								2.40	
0.90 C		3.35	3.11							2.43	2.40	
	1.00 C	3.35	3.11				2.44				2.40	
0.80 C		3.35	3.11					2.47			2.40	2.19
	0.90 C	3.34	3.11					2.44			2.40	
	1.00 C	3.34	3.11							2.41	2.40	
0.70 C		3.34	3.11			2.51					2.40	2.19
	0.80 C	3.34	3.11				2.49			2.44		2.18
	0.90 C	3.34	3.11					2.44				
	1.00 C	3.34	3.11									
0.60 C		3.35				2.53					2.41	
	0.70 C	3.34					2.51				2.40	
	0.80 C	3.34		2.98				2.48			2.40	2.18
	0.90 C	3.34	3.11		2.75						2.40	
	1.00 C	3.34	3.11						2.43			
0.50 C		3.35								2.42		
	0.60 C	4.92	3.07	2.87	2.75			2.48			2.41	
	0.70 C	4.90	3.34	3.07	2.87	2.74		2.48				2.19
	0.80 C		3.34	3.07	2.74			2.48				
	0.90 C		3.34	3.07	2.74			2.48				
	1.00 C		3.35	3.07	2.74			2.48		2.42		
0.40 C		4.90	4.71	3.35	3.07	2.87	2.76	2.48			2.41	2.36
	0.50 C	4.90	4.70	3.35	3.07	2.87	2.76	2.48			2.41	2.35
	0.70 C	4.90		3.35	3.08	2.87	2.75	2.48	2.45			2.35
	0.80 C	4.90		3.35	3.08	2.88	2.75	2.48	2.46			2.36
	1.00 C	4.90		3.35	3.08	2.88	2.75	2.48				2.36
0.30 C		4.90	4.71	3.35	3.07	2.87	2.76	2.48			2.41	2.36
	0.40 C	4.90	4.72	3.35	3.08	2.88	2.76	2.48	2.45			2.36
	0.60 C	4.90		3.35	3.08	2.88	2.75	2.48	2.45			2.36
	0.80 C	4.90		3.35	3.08	2.88	2.75	2.48				2.36
	1.00 C	4.89		3.35	3.08	2.88	2.75	2.48			2.41	2.35
0.20 C		4.92	4.71	3.35	3.08	2.87	2.76	2.48	2.45			2.36
	0.40 C	4.90	4.73	3.35	3.08	2.88	2.76	2.48	2.46			2.36
	0.60 C	4.90		3.35	3.08	2.89	2.76	2.48	2.45		2.41	2.35
	0.80 C	4.90		3.35	3.08	2.87	2.76	2.48	2.45			2.35
	1.00 C	4.90		3.35	3.08	2.88	2.76	2.48	2.45			2.35
Dis. to	Chg. to											
0.1 C		4.90	4.71	3.35	3.08	2.87	2.76	2.48	2.45			2.36
	0.20 C	4.90	4.71	3.35	3.08	2.87	2.76	2.48	2.45			2.36
	0.40 C	4.90	4.72	3.34	3.08	2.88	2.76	2.48	2.45			2.36
	0.60 C	4.90		3.35	3.08	2.88	2.76	2.48	2.45			2.36
	0.80 C	4.90		3.35	3.08	2.88	2.75	2.48				2.35
	1.00 C	4.90		3.34	3.07	2.87	2.75	2.48	2.45			2.35
0.0 C		4.90	4.71	3.34	3.08	2.86	2.76	2.47	2.45			2.36
	0.20 C	4.90	4.71	3.35	3.08	2.87	2.76	2.48	2.45			2.36
	0.40 C	4.90		3.34	3.07	2.87	2.76	2.48	2.45			2.35
	0.60 C	4.90		3.35	3.08	2.88	2.75	2.48				2.36
	0.80 C	4.90		3.35	3.08	2.87	2.76	2.48				2.36
	0.90 C	4.90		3.35	3.08	2.87	2.76	2.48	2.45			2.35
	1.00 C	4.89		3.35	3.08	2.88	2.75	2.48				2.35

cells at each 0.1C increment, crushed, and analyzed with a G. E. XRD-5 x-ray diffractometer using vanadium filtered  $K\alpha$  radiation. Groups of electrodes which had been partially discharged were then charged at 2.5 ma · cm<sup>-2</sup> and samples were analyzed as before at 0.1C charge intervals. For example, a group of electrodes would be discharged to 0.5C with samples being analyzed at 0.9, 0.8, 0.7, 0.6, and 0.5C. The remaining electrodes would then be charged with samples being withdrawn for x-ray analysis at 0.6, 0.7, 0.8, 0.9C, and C. No washing or drying procedures were carried out and all the samples were immediately x-rayed after being covered with a thin film prepared from Duco cement and acetone to prevent possible atmospheric oxidation during the analysis. The  $d$ -values calculated from the x-ray patterns are shown in Table I. For comparison, the ASTM values for the  $d$  values and the relative intensities of the peaks for various manganese oxides are shown in Table II.

The starting material is essentially  $\gamma$ - $MnO_2$  but there appears to be a small amount of  $\beta$ - $MnO_2$  present as indicated by the line at  $d = 3.11\text{\AA}$ . As discharge proceeds the lattice expansion noted previously (7) is again observed and is most clearly seen in the peaks at 2.43 and 2.14 $\text{\AA}$  in the electrode discharged to 0.90 of its calculated capacity ( $MnO_{1.82}$ ). The peak originally appearing at 2.43 $\text{\AA}$  shifts through 2.47, 2.51, and 2.53 $\text{\AA}$  before any new phase is observed, while the peak originally appearing at 2.11 $\text{\AA}$  shifts through 2.14, 2.17, and 2.19 $\text{\AA}$  in the same discharge period. No new compounds are identified in the x-ray pattern until the electrodes have been discharged to 0.5C ( $MnO_{1.46}$ ) at which point  $Mn_3O_4$  is produced. By referring to the x-ray diffraction patterns of Fig. 1, it can be seen that as the discharge proceeds, the x-ray peaks become increasingly less well defined which is characteristic of the take up of protons by the lattice to form an amorphous, strained phase according to



or



At a discharge depth equivalent to 0.50C peaks characteristic of  $Mn_3O_4$  can be seen.

If electrodes which have been reduced in the range of 1.0 to 0.60C are recharged, the original  $\gamma$ - $MnO_2$  structure is regained although there is still evidence of some residual lattice expansion. This is evident from examination of Table I and also from Fig. 2 which shows the x-ray diffraction patterns of an electrode being charged after an initial discharge to 0.6C. Since chemical analyses were not performed on the charged electrodes, the data are given in terms of the fraction

Table II.  $d$  Values and relative intensities of manganese oxides

$\gamma$ - $MnO_2$		$\gamma$ - $Mn_2O_3$		$Mn_3O_4$		$Mn(OH)_2$	
ASTM 14-644	$d(\text{\AA})$	ASTM 6-0540	$d(\text{\AA})$	ASTM 1-1127	$d(\text{\AA})$	ASTM 12-696	$d(\text{\AA})$
	$I/I_1$		$I/I_1$		$I/I_1$		$I/I_1$
3.96	100	4.93	40	4.92	20	4.726	100
2.60	60	3.08	60	3.08	31	2.870	18
				2.87	8		
2.42	100	2.74	70	2.75	63	2.453	40
2.32	80	2.48	100	2.48	100	2.361	6
				2.36	13		
				2.03	15		
2.12	80	2.39	40	1.79	18	1.825	25
				1.70	5		
				1.64	5		
2.05	40	2.03	20	1.57	50	1.658	6
				1.54	50	1.567	4
1.637	80	1.83	30	1.47	3	1.381	8
				1.44	18	1.346	4
1.605	60	1.79	20	1.38	4	1.180	4
1.486	10			1.34	8		
				1.30	3		
1.422	60	1.59	30	1.28	13		
1.362	40	1.55	60	1.24	4B		
1.306	10						
1.250	10			1.19	5B		
1.211	Tr			1.12	4		
1.169	Tr						
1.104	Tr						
1.066	40						





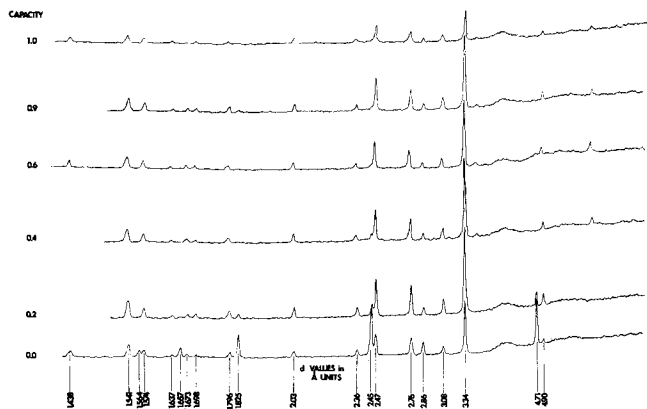


Fig. 3. X-ray diffraction patterns of  $\gamma\text{MnO}_2$  electrodes charging in increments after discharge to 0.0C.

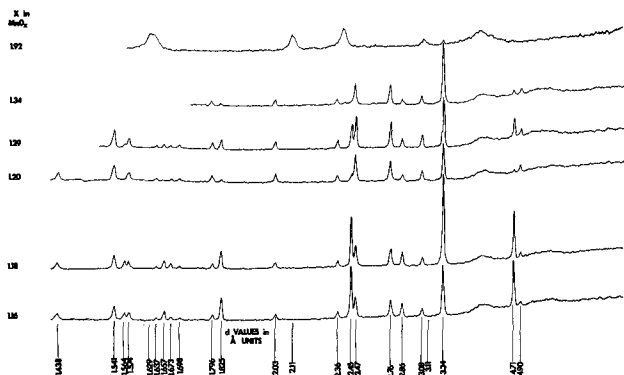
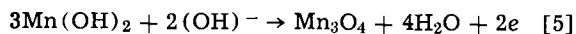


Fig. 4. X-ray diffraction patterns of  $\gamma\text{MnO}_2$  electrodes discharged in increments to  $\text{MnO}_{1.16}$ .

When the fully discharged electrode is charged the  $\text{Mn}(\text{OH})_2$  peaks disappear as shown in Fig. 3 and no new peaks are observed in the x-ray patterns. This indicates that  $\text{Mn}(\text{OH})_2$  is oxidized to either  $\text{Mn}_3\text{O}_4$  or to the amorphous phase noted previously. We think it unlikely that  $\text{Mn}(\text{OH})_2$  can be oxidized to the amorphous phase directly without passing through the lower oxide  $\text{Mn}_3\text{O}_4$ . It is thus probable that  $\text{Mn}(\text{OH})_2$  is oxidized to  $\text{Mn}_3\text{O}_4$  which then remains unchanged. The reaction can probably be written as



#### Discharge and Charge Curves

Four groups of electrodes were discharged and charged as follows: the first group was discharged at  $5 \text{ ma} \cdot \text{cm}^{-2}$  to 0.9C ( $\text{MnO}_{1.82}$ ) and then recharged to 1.0C ( $\text{MnO}_{1.92}$ ) at  $2.5 \text{ ma} \cdot \text{cm}^{-2}$ , the second was discharged to 0.6C ( $\text{MnO}_{1.55}$ ) and recharged, the third to 0.3C ( $\text{MnO}_{1.29}$ ) and recharged, and the fourth to 0.0C ( $\text{MnO}_{1.16}$ ) and recharged. The empirical formulas in parentheses are the experimentally determined values obtained by chemical analysis of the discharged electrodes. The lack of agreement between the calculated and experimental values is due to the low current efficiency towards the end of discharge because of concurrent hydrogen evolution.

These electrodes thus encompassed a range of composition where in the first series only the amorphous phase was present, in the second, amorphous phase plus  $\text{Mn}_3\text{O}_4$ , in the third, amorphous phase plus  $\text{Mn}_3\text{O}_4$  and  $\text{Mn}(\text{OH})_2$ , and in the fourth,  $\text{Mn}_3\text{O}_4$  and  $\text{Mn}(\text{OH})_2$ .

The discharge/charge curves obtained from group one are shown in Fig. 5. The discharge curve proceeds smoothly and the charge curve shows two fairly well defined steps. The first step is attributed to the oxidation of the amorphous compound to  $\text{MnO}_2$ , the quantity of electricity consumed in this reaction almost being equal to that withdrawn during the discharge. The oxidation of the amorphous phase prob-

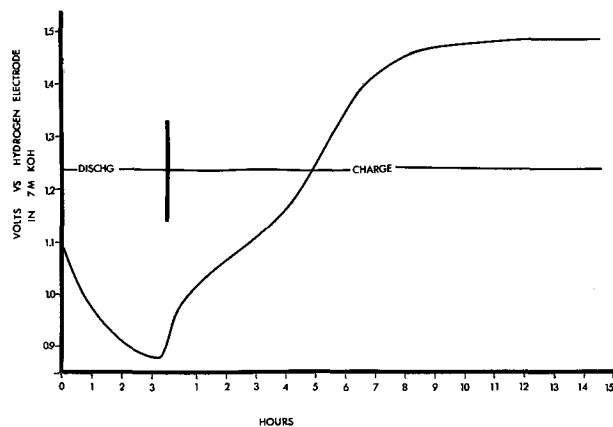


Fig. 5. Alkaline  $\text{MnO}_2$  electrode discharge-charge potentials at 0.9C.

ably occurs according to the reverse of Eq. [1]. After completion of the first oxidation step, the potential increases rapidly to a well defined plateau at 1.45v. This is probably a mixed potential due to the evolution of oxygen and the oxidation of  $\text{MnO}_2$  to  $\text{K}_2\text{MnO}_4$ . This is supported by the appearance in the electrolyte of a green color due presumably to  $\text{MnO}_4^-$  ions. The charging curves of electrodes in groups 2, 3, and 4 are shown in Fig. 6. The curve of the electrodes discharged to 0.6C again shows two steps and as before, the quantity of electricity consumed in the first step is almost equal to that withdrawn on discharge indicating that, at this point, the electrodes are still chemically reversible. In the electrodes discharged to 0.3C, the existence of highly irreversible  $\text{Mn}_3\text{O}_4$  is evidenced by the rapid increase in polarization at the start of charge. A plateau occurs at 0.65v which most probably corresponds to the oxidation of  $\text{Mn}(\text{OH})_2$  to  $\text{Mn}_3\text{O}_4$ . An inflection is observed after about 8 hr which corresponds to the passage of  $0.050 \text{ amp} \cdot \text{hr}$ . If the reaction is assumed to be identical to Eq. [5], this amount of electricity corresponds to 0.248g of  $\text{Mn}(\text{OH})_2$  or approximately 25% of the electrode weight. A fairly rapid rise in potential then occurs followed by a poorly defined plateau which probably corresponds to the oxidation of the residual amorphous compound to  $\text{MnO}_2$ .

The electrodes of the fourth group contain the same discharge products as those of group three except that

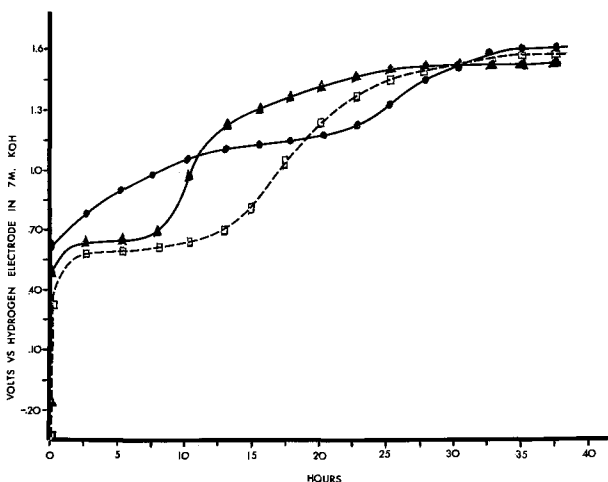


Fig. 6.  $\text{MnO}_2$  potentials during charge

	Discharge to	Charge to
Group 2 ●—●	0.6C	1.0C
Group 3 ▲—▲	0.3C	1.0C
Group 4 □- - -□	0.0	1.0C

Charge current density  $2.5 \text{ ma/cm}^2$ .

the amount of  $Mn(OH)_2$  is now larger and little or no  $MnO_2$  or amorphous phase exists in the electrode. Thus the plateau at 0.65v due to oxidation of  $Mn(OH)_2$  is longer and is followed again by an increase in the potential to the final plateau.

#### Cycling Experiments

A group of electrodes was cycled by discharging at  $5 \text{ ma} \cdot \text{cm}^{-2}$  for 8 hr and charging at  $2.5 \text{ ma} \cdot \text{cm}^{-2}$  for 16 hr. This was equivalent to a cycling between a depth of 1.0C and 0.89C. The potential/time curves of Fig. 7 show that up to 45 cycles, the electrodes cycle with only slight loss in performance. At cycle 63, a large polarization was observed after which the potential was erratic. This was also observed on the charge curve.

The behavior of the electrode suggested that a rapid increase in resistance had occurred at this point. This was thought to be perhaps due to the formation of a film of  $Mn_3O_4$  around the electrical contact wire or the electrode/electrolyte interface. To investigate this, electrodes were prepared containing two electrical contacts; one embedded in the center of the mix and the other tightly wound around the outside. It was thought that if failure was caused by the formation of a layer of  $Mn_3O_4$  around the contact wire, then switching from one contact to the other after failure should restore the performance. These electrodes were cycled between 1.0 and 0.75C using the same conditions as before. The IR drop was determined by use of an interruptor technique employing a Tektronix oscilloscope Model No. 535. The potential time curves are shown in Fig. 8 and the IR measurements in Fig. 9. The electrodes were seen to fail at cycle 9 at which point a high polarization was observed together with an increase in the IR drop. At this point, the current was switched to pass through the other contact. Immediately, the high polarization disappeared and the IR drop fell to that of a fresh electrode. Several additional cycles were obtained before the electrodes failed again.

It is clearly seen that the source of electrode failure is at the  $MnO_2$ /contact wire interface. From the potential of the electrodes, when they fail, it can be concluded that this film is  $Mn_3O_4$ . The magnitude of the IR drop at failure was insufficient to account for the high total polarization observed at this point. Since previous experiments (7) have shown the extremely high irreversibility of  $Mn_3O_4$ , it is not surprising that its precipitation is accompanied by a very large increase in polarization.

A second experiment was conducted using an electrode which, after failure, had a thin concentric layer cut away from the electrode/electrolyte interface and

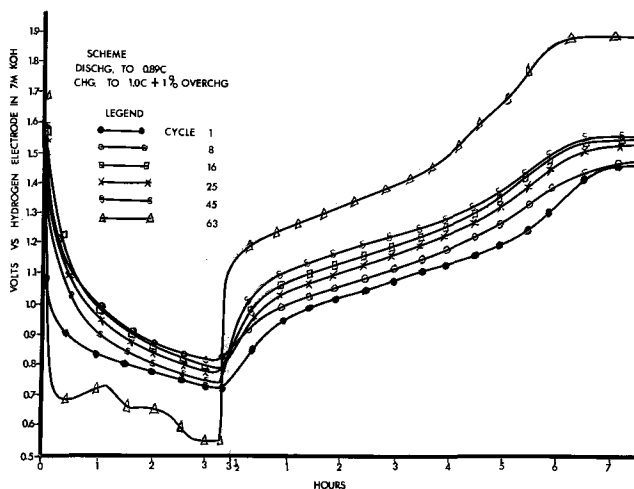


Fig. 7. Alkaline  $MnO_2$  electrode cycle test. Discharge to 0.89C, C.D.  $5 \text{ ma} \cdot \text{cm}^{-2}$ ; charge to 1.0C + 1% overchg., C.D.  $2.5 \text{ ma} \cdot \text{cm}^{-2}$ .

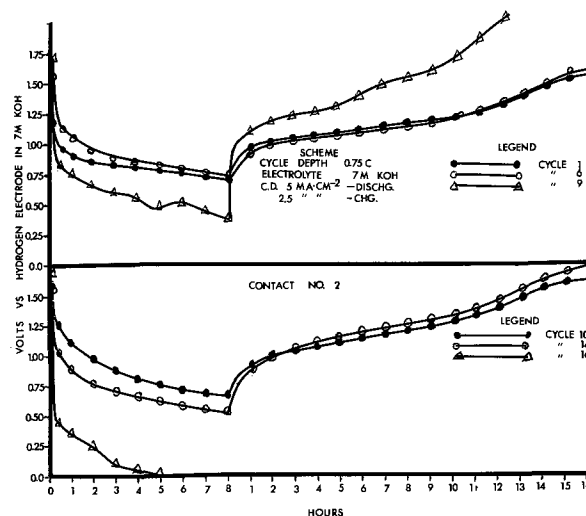


Fig. 8. Double contact alkaline  $MnO_2$  electrode potential vs. time. Discharge to 0.75C, C.D.  $5 \text{ ma} \cdot \text{cm}^{-2}$ ; charge to 1.0C, C.D.  $2.5 \text{ ma} \cdot \text{cm}^{-2}$ .

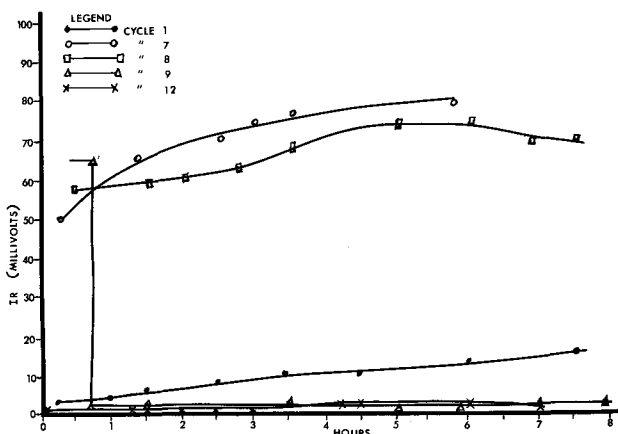


Fig. 9. Alkaline  $MnO_2$  electrode IR measurements of a double contact electrode, cycling at 0.76C.

then was recycled. This treatment did not reduce the polarization thus indicating once again that the film is formed at the contact/ $MnO_2$  interface.

#### Discussion

The x-ray diffraction data show, as observed before, that in the initial stages of discharge, a lattice expansion occurs with the formation of an amorphous product which cannot be ascribed to any of the well known manganese oxides. This is in agreement with results obtained by Brenet (9) and co-workers in LeClanche cells and appears to be general feature of the discharge of  $MnO_2$  electrodes. No evidence of  $MnO(OH)$  was obtained in contradiction to the results of some other investigations. In the early stages of the discharge, the electrodes are rechargeable as evidenced by the x-ray data and the discharge and charge curves. The charge/discharge reaction can be written as Eq. [2]. At greater depth of discharge, the amorphous phase is reduced to  $Mn_3O_4$  which is evidently not rechargeable and thereafter remains unchanged in the electrode. As the electrode approaches full discharge,  $Mn(OH)_2$  is formed and this is the final product. On recharge,  $Mn(OH)_2$  is observed to disappear from the electrodes as indicated by the disappearance of the  $Mn(OH)_2$  peaks in the x-ray diffraction patterns and the plateau in the charge curves at 0.6v. It is proposed that on recharge,  $Mn(OH)_2$  is oxidized to  $Mn_3O_4$  according to Eq. [5].

On the basis of the x-ray and discharge/charge curve data, one would expect a manganese dioxide electrode in 7M KOH to be rechargeable provided that

the depth of discharge is restricted so that  $Mn_3O_4$  is not formed. This is in fact so, as shown by the data in Fig. 7. However, a gradual deterioration in the performance occurs which allows the electrode potential to fall to the level at which  $Mn_3O_4$  is produced. The IR curves and the data from electrodes containing two contacts show that failure is caused by the precipitation of a film of  $Mn_3O_4$  around the current collector wire.

Manuscript received Aug. 28, 1967; revised manuscript received Nov. 25, 1967.

Any discussion of this paper will appear in a Discussion Section to be published in the December 1968 JOURNAL.

## REFERENCES

1. W. S. Herbert, *This Journal*, **99**, 190C (1952).
2. N. C. Cahoon and M. P. Korver, *ibid.*, **106**, 745 (1959).
3. G. S. Bell and R. Huber, *Electrochim. Acta.*, **10**, 509 (1965).
4. G. S. Bell and R. Huber, *This Journal*, **111**, 1 (1964).
5. A. Kozawa and J. F. Yeager, *ibid.*, **112**, 959 (1965).
6. A. Kozawa and R. A. Powers, *ibid.*, **113**, 870 (1966).
7. D. P. Boden, C. J. Venuto, D. Wisler, and R. B. Wylie, *ibid.*, **114**, 415 (1967).
8. I. M. Kolthoff and E. B. Sandell, "Textbook of Quantitative Inorganic Analysis," Macmillan Co., New York (1946).
9. J. P. Brenet and S. Ghosh, *Electrochim. Acta.*, **7**, 449 (1962).

## The Diffusional Properties of Oxygen in Niobium Pentoxide Crystals and Scales Formed on Niobium

J. S. Sheasby<sup>1</sup> and W. W. Smeltzer\*

Department of Metallurgy and Materials Science, McMaster University, Hamilton, Ontario, Canada

and A. E. Jenkins

School of Metallurgy, University of New South Wales, Kensington, N.S.W., Australia

## ABSTRACT

Single crystals of  $\alpha$ - $Nb_2O_5$  were grown by the Verneuil technique and machined into cylinders. Measurements of electrical conductivity of these specimens as a function of temperature and oxygen pressure were made and compared with similar work by previous investigators. By following the resistance change as a function of time on changing the environmental pressure, determinations of the diffusion coefficient of oxygen were made at varying degrees of nonstoichiometry. Oxygen diffusion coefficients were several hundredfold lower in oxide of large nonstoichiometry. Similar work was performed on  $\gamma$ - $Nb_2O_5$  scales stripped from niobium specimens after oxidation. Although absolute measurements could not be undertaken on these extensively cracked specimens,  $\gamma$ - $Nb_2O_5$  showed similar properties to  $\alpha$ - $Nb_2O_5$ . The relationship is considered of these conclusions to be oxidation behavior of niobium.

In an analysis of the effect of oxygen pressure on the parabolic oxidation rate constants of niobium, Sheasby *et al.* (1) suggested that oxygen diffusion was most rapid in near stoichiometric  $\gamma$ - $Nb_2O_5$ . Other investigators (2-4) have reported in their studies on both  $\alpha$ - and  $\gamma$ - $Nb_2O_5$  that equilibrium was attained far more rapidly in nearly stoichiometric oxide than at larger departures from stoichiometry. As such behavior is not predicted by proposed models of the defect structure of these oxides, the purpose of this investigation was to determine oxygen diffusion constants in  $\alpha$ - and  $\gamma$ - $Nb_2O_5$  at various oxide compositions.

Terao (5) has suggested that the structures of  $\alpha$ - and  $\gamma$ - $Nb_2O_5$  are closely related. The structure of  $\alpha$ - $Nb_2O_5$ , particularly when nonstoichiometric, is not known with certainty (6) but can be indexed by a monoclinic cell (5). Brauer (7) reports a composition range for this phase expressed as  $NbO_x$  where  $2.4 < x < 2.5$ , but Norin and Magneli (8) have identified two compounds  $NbO_{2.46}$  and  $NbO_{2.48}$  in this region. Isopiestic experiments of Blumenthal *et al.* (2) did not indicate the presence of these phases; a value of  $-164$  kcal/mole was determined for the relative partial molar enthalpy of oxygen for the pentoxide phase, its lower stoichiometric limits being  $x = 2.42$  and  $2.44$  at  $1090^\circ$  and  $889^\circ C$ , respectively.

Although the defect structure of  $\gamma$ - $Nb_2O_5$  has not been extensively studied (3), the defect equilibria

describing oxygen deficiency in  $\alpha$ - $Nb_2O_5$  has been studied by several investigators using electrical conductivity and gravimetric techniques (4, 9-14). The majority of investigators agree that in the temperature range  $600^\circ$ - $1400^\circ C$  and pressure range  $1$ - $10^{-6}$  atm the isothermal conductivity is proportional to  $P_{O_2}^{-1/4}$ , and that the conductivity exhibits an exponential temperature dependence with an activation energy of 1.4-1.7 eV (electron volt). These results are interpreted by a defect model involving oxygen vacancies with one trapped electron. At larger departures from stoichiometry at lower oxygen pressures, the picture is less clear. The work of Blumenthal *et al.* (2) suggests no change in defect type, whereas Kofstad and Anderson (14) find that both the isothermal weight change and conductivity of  $\alpha$ - $Nb_2O_5$  are proportional to  $P_{O_2}^{-1/6}$ . These results are interpreted in terms of oxygen ion vacancies without trapped electrons due to a decrease in the ionization energy of electrons from these defects as their concentration increased, in agreement with the work of Jannick and Whitmore (12).

## Experimental

Two sources of reagent grade  $\alpha$ - $Nb_2O_5$  powder and high purity niobium sheet, both 99.5 w/o (weight per cent) pure, were utilized as materials.

Coarse-grained boules of  $\alpha$ - $Nb_2O_5$  were grown by the Verneuil technique using a hydrogen-oxygen flame. The boules were split into individual crystals and these were machined, using an air-abrasive unit, into cylinders approximately 1 mm diameter and 6

<sup>1</sup> Present address: Faculty of Engineering Science, University of Western Ontario, London, Ontario, Canada.  
\* Electrochemical Society Active Member.

mm long, Fig. 1. The [010] monoclinic direction was approximately parallel to the cylinder axis. Polycrystalline plates of  $\gamma\text{-Nb}_2\text{O}_5$  approximately  $1\text{ cm}^2$  and 190 or  $270\mu$  thick, Fig. 2, were obtained by anodically dissolving the metal from specimens oxidized at  $770^\circ\text{C}$ . The oxide was composed of columnar crystals oriented with the [100] tetragonal axis perpendicular to the plane. The oxide plates were extensively cracked and could not be heated above  $750^\circ\text{C}$  without transforming to the alpha modification.

Resistances were measured by two and four point probe direct current techniques. Platinum current and potential leads were wrapped directly on the specimen and contact improved with platinum paint. Four point probe measurements were initially taken; however, the contact resistances were found to be negligible, so many of the experiments were performed using two point contacts. A Keithley 610A electrometer was used as a source of constant current and the potential drop across a specimen was measured either with this instrument, or a Leeds and Northrup Type K3 potentiometer or a Honeywell recorder. Resistances measured in the forward and reverse directions were ohmic within experimental errors of  $\pm 1\%$ .

The diffusion assembly was of a conventional glass design for attaining vacuo of  $10^{-4}$  Torr. Medical grade oxygen, high purity argon, carbon dioxide of 99.95 v/o (volume per cent) purity, and carbon monoxide of 96.6 v/o purity were dried by passage through columns containing phosphorous pentoxide. A specimen was suspended by the electrical leads into the hot zone of a vertically mounted mullite tube heated by an electrical resistance tubular furnace. The temperature was measured with a Pt-Pt 10% Rh thermocouple sited adjacent to the specimen. Pressures in the range  $10^{-3}$ -1 atm were effected statically. To achieve environmental purity in the range  $10^{-3}$ - $10^{-5}$  atm, oxygen was

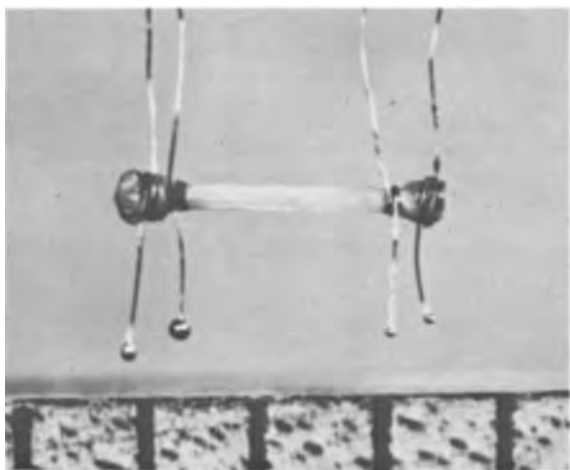


Fig. 1. Cylindrical crystal of  $\alpha\text{-Nb}_2\text{O}_5$ . Magnification 5X



Fig. 2. Specimen of  $\gamma\text{-Nb}_2\text{O}_5$  stripped from a niobium specimen oxidized at  $760^\circ$  in 1 atm oxygen for 120 min.

continually admitted through a needle valve, the pressure being automatically controlled by magnetic valves in the vacuum line. At oxygen pressures below  $10^{-5}$  atm, flowing atmospheres of either  $\text{CO}/\text{CO}_2$  or  $\text{Ar}/\text{O}_2$  were passed through the reaction tube. The oxygen potentials of these latter atmospheres were measured with a stabilized zirconia galvanic cell placed adjacent to the specimen and controlled by manipulation of needle valves in the gas lines.

To measure the oxygen diffusion constant for  $\alpha\text{-Nb}_2\text{O}_5$ , the specimens were held at a fixed temperature and pressure until the resistance was constant. The pressure was then changed and the variation in the resistance was recorded with time. Specimens were considered as infinite cylinders of radius  $r$  and analyzed using the diffusion equation (15)

$$\frac{C_t - C_f}{C_i - C_f} = \sum_1^{\infty} \frac{4}{\xi_v^2} \exp \left[ -\frac{\xi_v^2 D t}{r^2} \right] \quad [1]$$

$\xi_v$  are the roots of the equation  $J(x) = 0$  where  $J(x)$  is the Bessel function of zero order,  $C_i$ ,  $C_f$ , and  $C_t$  are the initial, final, and value at time  $t$  of the oxide oxygen concentration. These concentrations, in turn, are directly related to the corresponding electrical conductivities. Consequently, this equation was solved for  $Dt/r^2$  for each experimental point on a computer and these values plotted vs. time to obtain the best value of  $D/r^2$ . The oxygen diffusion constant for  $\gamma\text{-Nb}_2\text{O}_5$  was determined under the same experimental conditions and the results analyzed by the diffusion equation for a plate (16).

X-ray diffractometer patterns of powdered oxide were obtained using copper radiation with a nickel filter.

## Results

*Alpha-niobium pentoxide.*—Values of the resistivity at various temperatures of specimens equilibrated with oxygen over the range  $10^{-5}$ -1 atm are shown in Fig. 3. The resistance was proportional to the  $1/4$  power of the pressure. Specimens were also equilibrated with atmospheres of much lower oxygen potentials to  $10^{-16}$  atm. Because of the excessively long equilibration periods of several days, the resistance measurements were not as precise as those at higher pressures. However, the oxygen pressure dependence of the resistance remained within experimental error to the  $1/4$  power, Fig. 4. This relationship was valid for crystals prepared from both stocks of  $\alpha\text{-Nb}_2\text{O}_5$ .

The specific resistances of several specimens prepared from the oxide materials obtained from two sources agreed well and gave a good fit to an Arrhenius plot, Fig. 5. The activation energy was 1.61 eV

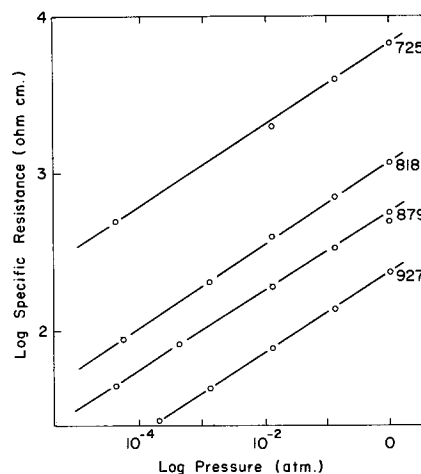


Fig. 3. The dependence of the electrical resistivity of  $\alpha\text{-Nb}_2\text{O}_5$  on oxygen pressure over the range  $10^{-5}$  to 1 atm at temperatures of  $927^\circ$ ,  $879^\circ$ ,  $818^\circ$ , and  $725^\circ\text{C}$ .

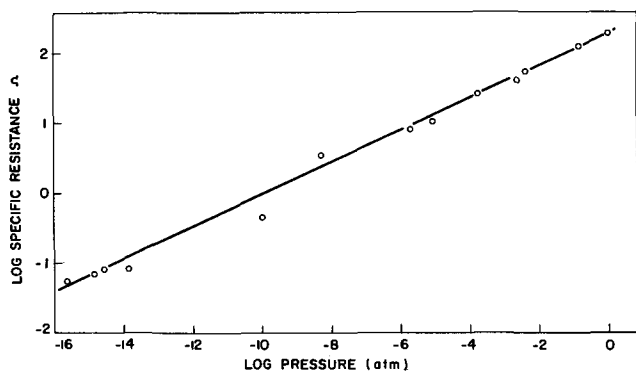


Fig. 4. The dependence of the electrical resistivity of  $\alpha\text{-Nb}_2\text{O}_5$  on oxygen pressure over the range  $10^{-16}$  to 1 atm at  $909^\circ\text{C}$ .

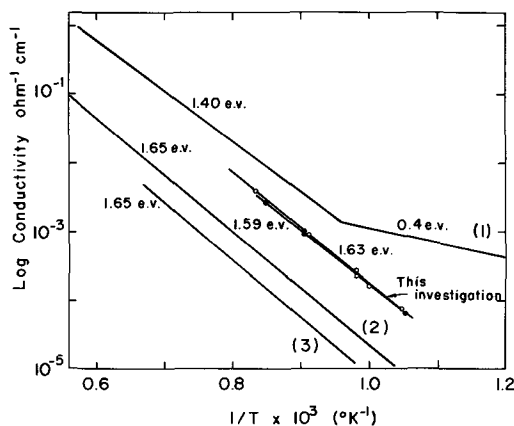


Fig. 5. Arrhenius plots with determinations for the activation energy for the electrical conductivity of  $\alpha\text{-Nb}_2\text{O}_5$  at 1 atm. The plots 1, 2, and 3 are from references (4), (10), and (3), respectively.

which is to be compared to the value of 1.4-1.65 ev from previous investigators (3,4,10).

The diffusion constant was evaluated from data obtained by changing the pressure over a narrow range and recording the resistance change with time. On plotting  $Dt/r^2$  vs. time as described in the last section to obtain the best value of  $D/r^2$  the linear plots intersected the co-ordinates close to the origin, Fig. 6. However the values of  $D/r^2$  obtained from different determinations under the same experimental conditions varied by as much as a factor of 3. Further difficulty was encountered on raising the pressure to close to atmospheric, e.g., 100-760 Torr, at low temperatures,

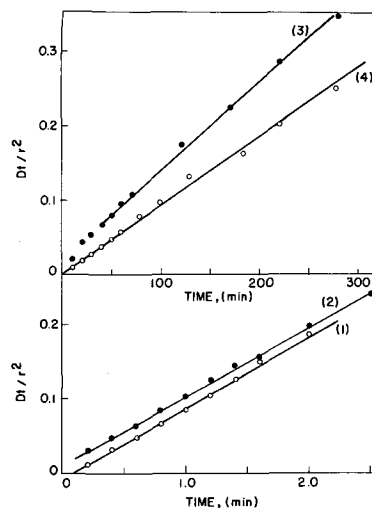


Fig. 6. Plots of  $Dt/r^2$  vs. time at  $909^\circ\text{C}$  for  $\alpha\text{-Nb}_2\text{O}_5$  for oxygen pressure changes of 104 to 7.38 Torr, curve 1; 6.28 to 127 Torr, curve 2;  $5.0 \times 10^{-9}$  atm to  $2.5 \times 10^{-15}$  atm, curve 3; and  $2.3 \times 10^{-16}$  to  $1.2 \times 10^{-14}$  atm, curve 4.

when the equilibrium specimen resistance was attained in an unexpectedly short time.

Values for the oxygen diffusion constant at various pressures and temperatures are recorded in Table I. An Arrhenius plot is shown in Fig. 7 of diffusion constant determinations from four specimens. The data points form two bands with the determinations relating to pressure changes in the range  $10^{-5}$ -1 atm being approximately 300 times larger than those made at pressures lower than  $10^{-13}$  atm. The activation energies of 2.2 and 2.3 ev demonstrate that the temperature dependence for diffusion did not change significantly over the investigated pressure range.

A comparison of the powder x-ray diffraction patterns of black nonstoichiometric with white stoichiometric oxide gave an extra line corresponding to  $d = 3.85\text{\AA}$  and  $1.693\text{\AA}$  while the lines at  $d = 2.684\text{\AA}$  and  $1.219\text{\AA}$  were absent, and the line at  $d = 2.070\text{\AA}$  was greatly reduced in intensity.

*Gamma-niobium pentoxide.*—The instability of this oxide imposed restrictions on the system that could be studied. Since the specimens were cracked, no attempt was made to obtain specific resistances. As illustrated in Fig. 8, the resistances of the specimens studied were proportional to the  $0.25 \pm 0.04$  power of the oxygen pressure.

Oxygen diffusion in the oxide as a function of oxygen pressure was determined in the range  $10^{-6}$ -1 atm

Table I. Oxygen diffusion constants in  $\alpha\text{-Nb}_2\text{O}_5$

Temperature, $^\circ\text{C}$	Initial pressure, atm	Final pressure, atm	$D$ , $\text{cm}^2/\text{sec}$	Temperature, $^\circ\text{C}$	Initial pressure, atm	Final pressure, atm	$D$ , $\text{cm}^2/\text{sec}$
Specimen 435 $\mu$ diameter							
965	$8.5 \times 10^{-5}$	$6.8 \times 10^{-9}$	$1.47 \times 10^{-8}$	965	$1.52 \times 10^{-6}$	$3.6 \times 10^{-11}$	$3.16 \times 10^{-8}$
965	$2.0 \times 10^{-12}$	$2.1 \times 10^{-11}$	$5.5 \times 10^{-8}$	965	$9.8 \times 10^{-14}$	$2.2 \times 10^{-12}$	$6.75 \times 10^{-8}$
909	1.0	$1.32 \times 10^{-1}$	$1.10 \times 10^{-6}$	909	$1.32 \times 10^{-1}$	$7.15 \times 10^{-8}$	$1.22 \times 10^{-6}$
909	$7.15 \times 10^{-3}$	$6.05 \times 10^{-4}$	$2.53 \times 10^{-6}$	909	$2.08 \times 10^{-4}$	$6.45 \times 10^{-6}$	$1.51 \times 10^{-6}$
909	$9.01 \times 10^{-6}$	$8.16 \times 10^{-5}$	$1.17 \times 10^{-6}$	909	$8.25 \times 10^{-5}$	$1.07 \times 10^{-5}$	$8.64 \times 10^{-7}$
909	$1.04 \times 10^{-4}$	$1.16 \times 10^{-5}$	$1.00 \times 10^{-6}$	909	$1.16 \times 10^{-5}$	$1.84 \times 10^{-4}$	$1.80 \times 10^{-6}$
909	$1.37 \times 10^{-4}$	$1.15 \times 10^{-5}$	$1.17 \times 10^{-7}$	909	$1.15 \times 10^{-5}$	$1.84 \times 10^{-4}$	$1.44 \times 10^{-6}$
909	$1.37 \times 10^{-4}$	$9.72 \times 10^{-6}$	$7.55 \times 10^{-7}$	909	$8.27 \times 10^{-6}$	$1.67 \times 10^{-4}$	$7.03 \times 10^{-7}$
909	$3.95 \times 10^{-3}$	$1.32 \times 10^{-1}$	$1.41 \times 10^{-6}$	909	$1.32 \times 10^{-1}$	1.0	$1.82 \times 10^{-6}$
909	$1.26 \times 10^{-15}$	$2.09 \times 10^{-10}$	$7.45 \times 10^{-9}$	909	$2.3 \times 10^{-16}$	$1.18 \times 10^{-14}$	$7.48 \times 10^{-9}$
909	$5.02 \times 10^{-9}$	$2.52 \times 10^{-16}$	$8.93 \times 10^{-9}$	909	$7.1 \times 10^{-5}$	$5.1 \times 10^{-14}$	$8.24 \times 10^{-9}$
819	1.0	$1.30 \times 10^{-1}$	$9.49 \times 10^{-7}$	819	1.0	$8.10 \times 10^{-1}$	$7.00 \times 10^{-7}$
819	$1.34 \times 10^{-1}$	1.0	$2.04 \times 10^{-6}$	819	$8.10 \times 10^{-1}$	1.0	$1.34 \times 10^{-6}$
819	1.0	$1.32 \times 10^{-1}$	$2.51 \times 10^{-6}$	737	1.0	$1.32 \times 10^{-1}$	$1.15 \times 10^{-7}$
737	$1.04 \times 10^{-2}$	$1.32 \times 10^{-1}$	$3.96 \times 10^{-7}$	737	$1.32 \times 10^{-1}$	$1.04 \times 10^{-2}$	$1.52 \times 10^{-7}$
737	$8.62 \times 10^{-3}$	$1.32 \times 10^{-1}$	$4.60 \times 10^{-7}$	737	$1.32 \times 10^{-1}$	$8.62 \times 10^{-3}$	$1.71 \times 10^{-7}$
680	$2.03 \times 10^{-4}$	$4.14 \times 10^{-5}$	$2.04 \times 10^{-8}$	680	$4.14 \times 10^{-5}$	$1.85 \times 10^{-4}$	$2.51 \times 10^{-8}$
680	$1.03 \times 10^{-5}$	$3.86 \times 10^{-5}$	$2.36 \times 10^{-8}$	680	$3.86 \times 10^{-5}$	$1.57 \times 10^{-4}$	$1.62 \times 10^{-8}$
680	$1.40 \times 10^{-4}$	$3.83 \times 10^{-5}$	$1.25 \times 10^{-8}$	680	$3.83 \times 10^{-5}$	$1.76 \times 10^{-4}$	$2.28 \times 10^{-8}$
680	$1.71 \times 10^{-4}$	$3.68 \times 10^{-5}$	$8.25 \times 10^{-9}$	661	1.01	$1.45 \times 10^{-1}$	$8.48 \times 10^{-9}$
Specimen 330 $\mu$ diameter							
809	1.47	8.48	$1.23 \times 10^{-6}$	809	8.48	1.32	$2.82 \times 10^{-6}$
809	$6.31 \times 10^{-15}$	$1.26 \times 10^{-10}$	$2.18 \times 10^{-9}$	809	$1.59 \times 10^{-13}$	$5.1 \times 10^{-20}$	$1.08 \times 10^{-9}$
809	$5.1 \times 10^{-20}$	$5.1 \times 10^{-17}$	$2.32 \times 10^{-9}$	809	$5.1 \times 10^{-17}$	$1.0 \times 10^{-14}$	$2.98 \times 10^{-9}$

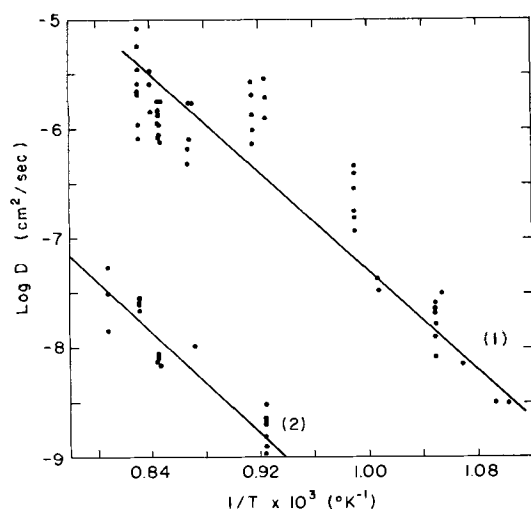


Fig. 7. Oxygen diffusion constants from four  $\alpha$ - $\text{Nb}_2\text{O}_5$  specimens as a function of temperature at different pressures. Values in pressure range  $10^{-5}$ -1 atm, curve 1; values in pressure range  $10^{-13}$ - $10^{-16}$  atm, curve 2.

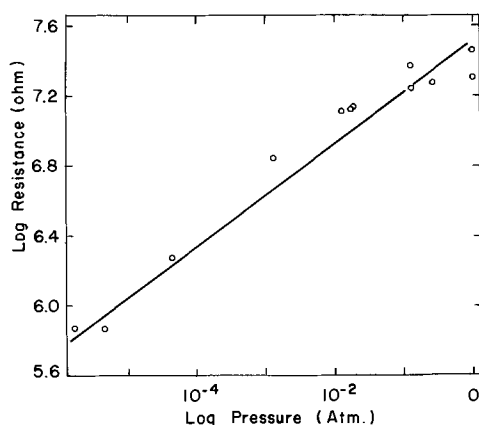


Fig. 8. The dependence of the electrical resistance of a  $\gamma$ - $\text{Nb}_2\text{O}_5$  specimen on oxygen pressure over the range  $10^{-8}$  to 1 atm at  $658^\circ\text{C}$ .

and typical data for plates of thickness,  $a$ , are shown in Fig. 9. Although absolute values of diffusion constants for the cracked specimens could not be obtained, the relative values at different pressures are recorded in Table II. It can be seen that the oxygen diffusivity was insensitive to pressure from  $0.5$ - $10^{-4}$  atm, but decreased rapidly at pressures below this value.

White stoichiometric oxide transformed readily to black nonstoichiometric oxide in an oxygen atmosphere of  $10^{-5}$  atm pressure at  $750^\circ\text{C}$ . The powder x-ray diffraction pattern of the black compared with the white oxide gave extra lines corresponding to  $d =$

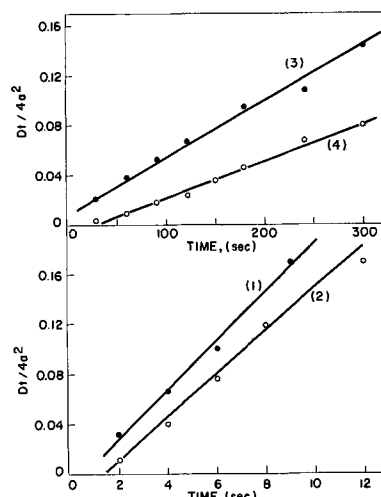


Fig. 9. Plots of  $Dt/4a^2$  vs. time at  $628^\circ\text{C}$  for  $\gamma$ - $\text{Nb}_2\text{O}_5$  for oxygen pressure changes of 43 to 96 Torr, curve 1; 160 to 73, curve 2; 1.4 to 2.0, curve 3; and 2.5 to 0.14 Torr, curve 4.

$3.643\text{\AA}$ ,  $3.311\text{\AA}$ , and  $2.971\text{\AA}$  and the lines at  $d = 5.18\text{\AA}$  and  $1.54\text{\AA}$  were absent.

### Discussion

The conductivity of  $\alpha$ - $\text{Nb}_2\text{O}_5$  at pressures in the range  $10^{-5}$ -1 atm was proportional to  $P_{\text{O}_2}^{-1/4}$  in agreement with previous results on polycrystalline specimens (14) but only in partial agreement with those for single crystals. The decreased pressure dependence below  $800^\circ\text{C}$  reported by Chen and Swalin (4) was not observed. Moreover, the conductivity at  $907^\circ\text{C}$  obeyed this pressure relation to  $10^{-16}$  atm whereas a  $P_{\text{O}_2}^{-1/6}$  relation was found for polycrystalline specimens in the pressure range  $10^{-13}$ - $10^{-18}$  atm by Kofstad and Anderson (14).

Arrhenius plots of the specific conductivities from four investigations were illustrated in Fig. 5. The conductivities of polycrystalline material were smaller by an order of magnitude than those for single crystals but the activation energies, irrespective of the type of material, were of the same magnitude 1.4-1.65 ev. Although Chen and Swalin (4) accounted for the high conductivity of their single crystal specimens at temperatures below  $800^\circ\text{C}$  by ionization of impurities, the present results demonstrate that the conductivity is determined entirely by oxide stoichiometry at pressures close to atmospheric over the temperature range  $600^\circ$ - $1400^\circ\text{C}$ . Also, the conductivity experiments demonstrated that the rapidity with which a specimen changed its conductivity was itself a function of the conductivity (stoichiometry). In relating these relaxation periods to the oxygen diffusion constant it was assumed that in the pressure increment under analysis the electron concentration was directly proportional to the oxygen concentration. As it has been shown that the conductivity of  $\text{Nb}_2\text{O}_5$  is proportional to  $\log(P_{\text{O}_2})$  in this study, and that the weight loss of  $\text{Nb}_2\text{O}_5$  is a

Table II. Relative oxygen diffusivities in  $\gamma$ - $\text{Nb}_2\text{O}_5$  at  $628^\circ\text{C}$

Initial pressure, atm	Final pressure, atm	D	Initial pressure, atm	Final pressure, atm	D
Oxide nominally $190\mu$ thick					
$5.26 \times 10^{-1}$	$2.58 \times 10^{-1}$	$7.65 \times 10^{-5}$	$9.08 \times 10^{-5}$	$2.90 \times 10^{-5}$	$3.83 \times 10^{-6}$
$2.38 \times 10^{-1}$	$5.26 \times 10^{-1}$	$1.07 \times 10^{-4}$	$6.58 \times 10^{-5}$	$3.42 \times 10^{-5}$	$3.02 \times 10^{-6}$
$2.58 \times 10^{-1}$	$1.16 \times 10^{-1}$	$6.13 \times 10^{-5}$	$3.01 \times 10^{-5}$	$2.38 \times 10^{-6}$	$1.09 \times 10^{-5}$
$1.26 \times 10^{-1}$	$2.38 \times 10^{-1}$	$3.95 \times 10^{-5}$	$2.50 \times 10^{-5}$	$1.80 \times 10^{-6}$	$1.26 \times 10^{-6}$
$5.86 \times 10^{-2}$	$1.26 \times 10^{-1}$	$7.20 \times 10^{-5}$	$1.80 \times 10^{-6}$	$2.63 \times 10^{-6}$	$1.59 \times 10^{-6}$
$5.92 \times 10^{-4}$	$2.24 \times 10^{-4}$	$4.17 \times 10^{-5}$	$1.97 \times 10^{-6}$	$3.29 \times 10^{-6}$	$2.45 \times 10^{-6}$
$4.87 \times 10^{-4}$	$2.10 \times 10^{-4}$	$7.25 \times 10^{-5}$	$3.29 \times 10^{-6}$	$1.84 \times 10^{-7}$	$1.12 \times 10^{-6}$
$2.10 \times 10^{-4}$	$9.60 \times 10^{-5}$	$5.75 \times 10^{-5}$			
Oxide nominally $270\mu$ thick					
$1.63 \times 10^{-1}$	$5.92 \times 10^{-2}$	$3.50 \times 10^{-4}$	$5.92 \times 10^{-2}$	$2.04 \times 10^{-2}$	$3.25 \times 10^{-4}$
$5.80 \times 10^{-2}$	$1.63 \times 10^{-1}$	$4.25 \times 10^{-4}$	$2.04 \times 10^{-2}$	$1.97 \times 10^{-2}$	$3.50 \times 10^{-4}$
$2.76 \times 10^{-2}$	$1.05 \times 10^{-2}$	$3.75 \times 10^{-4}$	$2.63 \times 10^{-7}$	$7.50 \times 10^{-7}$	$9.64 \times 10^{-6}$
$1.05 \times 10^{-2}$	$5.80 \times 10^{-2}$	$6.00 \times 10^{-4}$	$7.50 \times 10^{-7}$	$2.24 \times 10^{-7}$	$1.02 \times 10^{-5}$

function of  $\log(P_{O_2})$ , (2), this assumption is reasonable. The oxygen diffusion constant,  $D$ , so measured is equivalent to the phenomenological diffusion constant defined by Fick's first law.

It will now be demonstrated that the diffusional properties of oxygen in niobium pentoxide cannot be inferred from theory based on ideal solution of point defects exhibiting constant mobility. A  $(P_{O_2})^{-1/4}$  pressure dependence of the electrical conductivity was found over four orders of resistance change, and in agreement with other workers (4, 9, 13) this is interpreted in terms of a vacancy model involving only singly ionized oxygen vacancies. Wagner (17) has shown that for an ionic solid

$$D = \frac{V_m RT}{8F^2 \delta} \frac{K_{ion} K_e}{K_{ion} + K_e} \frac{d \ln(P_{O_2})}{d \ln \delta} \quad [2]$$

where, in this instance,  $K_{ion}$  and  $K_e$  would be the specific conductivities of the singly ionized oxygen vacancies ( $\square\cdot$ ) and electrons (e),  $\delta$  is the oxygen deficit represented by the formula  $Nb_2O_{5-\delta}$ , and  $V_m$  is the molar volume. These conductivities are related to the mobility,  $\mu$ , of charged species by:

$$K_{ion} = \frac{F}{V_m} x_{\square\cdot} \mu_{\square\cdot}$$

and

$$K_e = \frac{F}{V_m} x_e \mu_e \quad [3]$$

where  $x$  represents the atom fraction of the respective point defect.

From the pressure dependence of the resistivity

$$\frac{d \ln P_{O_2}}{d \ln \delta} = -4 \quad [4]$$

If the Nernst-Einstein relation is invoked

$$D_{\square\cdot} = \mu_{\square\cdot} \frac{RT}{F} \quad [5]$$

Substituting Eq. [3], [4], [5] in Eq. [2] and in view of  $K_{ion} \ll K_e$

$$D = \frac{D_{\square\cdot}}{2} \quad [6]$$

According to Eq. [4-6], the magnitude of the oxygen diffusion constant is not dependent on oxygen pressure or oxide stoichiometry providing that the activity coefficient and mobility of vacancies remains constant. In the case of  $\alpha$ - $Nb_2O_5$ , this behavior is valid over the pressure range  $10^{-5}$ -1 atm. It is definitely invalid over the entire investigated pressure range because the values are much smaller at pressures less than  $10^{-14}$  atm (Table I and Fig. 7). A similar behavior was exhibited by  $\gamma$ - $Nb_2O_5$  with the transition to lower values of the diffusion constant occurring at higher pressures. For this oxide modification, the diffusion constant is constant only over the pressure range  $10^{-3}$ -1 atm (Table II).

Knowledge of diffusion in ionic solids is not sufficiently advanced for interpretation of this similar but complex oxygen diffusion behavior for both oxides. With increasing nonstoichiometry the point defects interact giving varying activity coefficients and mobilities. Furthermore, according to Wadsley (6) and Gatehouse and Wadsley (18), removal of oxygen from niobium pentoxide leads to compression of the structure by shear along certain planes, the unit  $ReO_3$  type polyhedra being condensed upon each other. When these shear planes are ordered, a series of related oxides can be recognized as identified by Norin and Magneli (8), and when they are not they are retained in a disordered form difficult to recognize except as a berthollide. Since different x-ray diffraction lines occur and line intensities change when both oxides are changed from small to large nonstoichiometry, it is therefore more reasonable to consider the limiting

rates of oxygen diffusion as the mobilities in particular structures.

Different rates of oxygen diffusion in particular berthollidic structures can account for the unusual oxygen pressure dependence of the parabolic oxidation rates for niobium. When only one ionic species such as oxygen diffuses in an oxide scale over a relatively narrow homogeneity range, the general expression given by Wagner (19) for the parabolic oxidation rate constant may be placed in the form

$$k_r = C_{eq} \int_{a_{O_2}^1}^{a_{O_2}^{11}} \frac{|Z_2|}{Z_1} D_o^* d \ln a_{O_2} \quad [7]$$

Here,  $C_{eq}$  is the oxygen concentration in equivalents per  $cm^3$ ,  $Z_1$  and  $Z_2$  are the valencies of metal and oxygen,  $D_o^*$  is the self-diffusion constant for oxygen, and  $a_o$  is the oxygen activity. The integration would be carried out for the oxygen activity range to the oxide-gas interface from an inner surface of the oxide. Converting  $k_r$  to  $k_p$  ( $cm$  oxide) $^2$ /sec and placing Eq. [7] in differential form

$$D_o^* = \frac{1}{9.21} \frac{d k_p}{d \log P_{O_2}} \quad [8]$$

Figure 1 of ref. (1) shows plots of the parabolic constants for niobium oxidation vs. the logarithm of oxygen pressure over the range  $10^{-3}$ -1 atm at temperatures in the range  $720^\circ$ - $825^\circ C$ . If growth of the oxide scale is governed by volume diffusion, these linear plots demonstrate that the oxygen self-diffusion constant is essentially constant only over a small pressure range wherein the oxide composition remains close to stoichiometry, and that below approximately  $10^{-3}$  atm the oxygen self-diffusion constant has a much smaller value. These and all other available oxidation data (20) for the temperature range  $540^\circ$ - $840^\circ C$  were analyzed according to Eq. [8] and an Arrhenius plot of the diffusion constant is shown in Fig. 10. The self-diffusion constant for oxygen in the  $\gamma$ - $Nb_2O_5$  scale is

$$D_o^* \text{ (cm}^2\text{/sec)} = 1.0 \exp - 42600/RT \quad [9]$$

The self-diffusion constant for oxygen in the essentially stoichiometric oxide is related to the diffusion constant for vacancies by the relation

$$x_o D_o^* \simeq D_o^* \simeq x_{\square} D_{\square} \quad [10]$$

where  $x_o$  and  $x_{\square}$  represent the mole fractions of occupied and vacant oxygen lattice sites. Substituting [6] into [10] gives

$$D_o^* = 2x_{\square} D \quad [11]$$

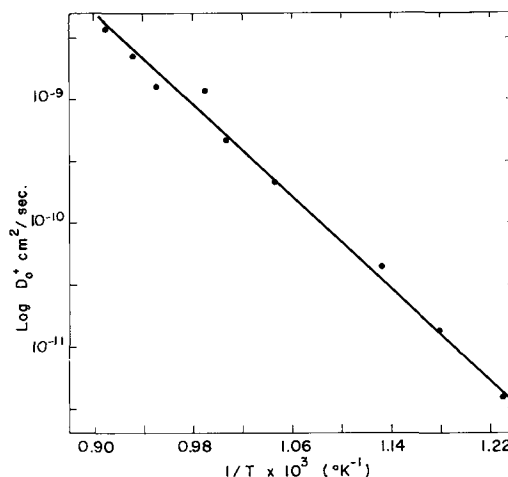


Fig. 10. Arrhenius plot of the oxygen self-diffusion coefficient for  $\gamma$ - $Nb_2O_5$  calculated from oxidation data for the pressure range  $10^{-3}$  to 1 atm, references (1), (20).



According to Eq. [11] a large decrease in the magnitude of  $D_0^*$  for  $\gamma$ - $\text{Nb}_2\text{O}_5$  at oxygen pressures less than  $10^{-3}$  atm would be primarily caused by the variation in  $D$ . The existence of this variation has been confirmed by the present measurements. Hence, the unusual pressure dependence of the parabolic oxidation kinetics is associated with the formation of a  $\gamma$ - $\text{Nb}_2\text{O}_5$  scale consisting of a series of structures changing with the oxygen potential. These structures would be distinct Magneli phases or blocks of a basic structure joined by regular discontinuities (18). If, as it has been suggested (6), the vacancy concentration in such berthollides is largely independent of composition, the observed decrease in oxygen diffusion rate in  $\gamma$ - $\text{Nb}_2\text{O}_5$  with stoichiometry would be sufficient to account for the decrease in oxidation rate of niobium with oxygen pressure. To determine the validity of these considerations, the self-diffusion coefficient of oxygen in  $\gamma$ - $\text{Nb}_2\text{O}_5$  must be determined as a function of both stoichiometry and structure.

#### Acknowledgments

This investigation was completed under the auspices of the U.S. Air Force Office of Scientific Research, Office of Aerospace Research, and the National Research Council of Canada.

Manuscript received March 3, 1967; revised manuscript received ca. Nov. 6, 1967.

Any discussion of this paper will appear in a Discussion Section to be published in the December 1968 JOURNAL.

#### REFERENCES

1. J. S. Sheasby, W. W. Smeltzer, and G. R. Wall-work, *This Journal*, **113**, 1255 (1966).
2. R. N. Blumenthal, J. B. Moser, and D. H. Whitmore, *J. Am. Ceramic Soc.*, **48**, 617 (1965).
3. P. Kofstad, *J. Phys. Chem. Solids*, **23**, 1571 (1962).
4. W. K. Chen and R. A. Swalin, *ibid.*, **27**, 57 (1966).
5. N. Terao, *Japanese J. Appl. Physics*, **2**, 156 (1963).
6. A. D. Wadsley, "Non-stoichiometric Compounds," p. 98, Academic Press, New York (1964).
7. G. Brauer, *Z. anorg. allgem. Chem.*, **248**, 1 (1941).
8. R. Norin and A. Magneli, *Naturwissenschaften*, **47**, 354 (1960).
9. E. H. Greener, D. H. Whitmore, and M. E. Fine, *J. Chem. Phys.*, **34**, 1017 (1961).
10. E. H. Greener and W. H. Hirthe, *This Journal*, **109**, 600 (1962).
11. E. H. Greener, F. J. Barone, and W. M. Hirthe, *J. Am. Ceramic Soc.*, **48**, 623 (1965).
12. R. F. Jannick and D. H. Whitmore, *J. Chem. Phys.*, **37**, 2750 (1962).
13. E. H. Greener, G. A. Fehr, and W. M. Hirthe, *J. Chem. Phys.*, **38**, 133 (1963).
14. P. Kofstad and P. B. Anderson, *J. Phys. Chem. Solids*, **21**, 280 (1961).
15. W. Jost, "Diffusion," p. 45, Academic Press, New York (1960).
16. *Ibid.*, p. 37.
17. C. Wagner, *Z. Physik Chem.*, (B) **21**, 25 (1933).
18. B. M. Gatehouse and A. D. Wadsley, *Acta Cryst.*, **17**, 1545 (1964).
19. C. Wagner, "Atom Movements," p. 153, American Society for Metals (1941).
20. J. S. Sheasby, Ph.D. Thesis, University of New South Wales, Australia (1963).

## The Electrochemical Behavior of 4,4'-Azopyridine-1,1'-Dioxide

Joe L. Sadler and Allen J. Bard\*

Department of Chemistry, The University of Texas at Austin, Austin, Texas

#### ABSTRACT

The electroreduction of 4,4'-azobispyridine-1,1'-dioxide (APDO) in dimethylformamide solutions was studied by polarography, cyclic voltammetry, controlled potential coulometry, and electron spin resonance. Voltammetric reduction showed two well-defined, reversible one-electron transfers. Coulometric reduction at a potential corresponding to the plateau of the first wave gave evidence of chemical reactions following the initial electron transfer producing intermediates which were also electroactive at the same potentials. Coulometry at the second wave gave an over-all value of six Faradays per mole for the complete reduction of APDO to the dianion of azopyridine (AP), identified by electrochemical and electron spin resonance techniques. A mechanism for the reduction process consistent with the experimental evidence is presented.

The polarographic behavior of a number of tertiary amine oxides in aqueous systems has been reported (1-9). Kubota and Miyazaki (6a) performed a polarographic study of pyridine N-oxide and its alkyl derivatives followed by a study (6b) of the effect of substituents on the polarographic reduction of pyridine N-oxide derivatives. Recently, Date (7a) reported a thorough polarographic investigation of dimethylaniline N-oxide, followed by an investigation of the relationship between the  $E_{1/2}$  values of a series of similar compounds and the  $\text{pK}_a$ 's of their parent amines (7b). Chambers (8) studied the polarographic and adsorption behavior of dimethyldodecylamine N-oxide and Elving and Warner (9) have reported a study of the polarographic behavior of adenine 1-N-oxide.

In all of the above work, the amine oxide group gives a well-defined, irreversible polarographic wave

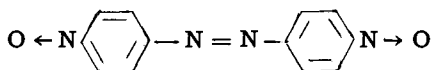
between pH values of 1 to 6. Date proposed that the amine oxide group is reduced to the corresponding parent amine in a reaction involving two electrons, the first electron addition being rate controlling. This mechanism agrees quite well with his experimental data and is further supported by Chambers' work on N,N-dimethyldodecylamine N-oxide.

Recently Nasielski and co-workers (10) studied the polarographic reduction of pyridine N-oxide and other heterocyclic N-oxides in DMF solution. They proposed that the reduction involves a single, two-electron wave (composed of reduction to the anion radical, fast protonation, and further reduction, protonation, and dehydration), leading to the free base. We report here a study of the amine oxide 4,4'-azobispyridine-1,1'-dioxide (APDO) in DMF, in which a clear separation of the step leading to formation of the anion radical and to formation of the dianion is obtained.

\* Electrochemical Society Active Member.

### Results

Voltammetric methods. The polarographic reduction of APDO,



in a *N,N*-dimethylformamide (DMF) solution containing 0.1 *M* tetra-*n*-butyl-ammonium perchlorate (TBAP) showed two well-defined waves (Fig. 1) with half-wave potentials ( $E_{1/2}$ ) of  $-0.73$  and  $-1.35$  v. vs. an aqueous saturated calomel electrode (SCE). The values of  $E_{3/4} - E_{1/4}$  for the two waves (Tômes criterion for reversibility) 0.06 and 0.07 v, respectively, suggested that the first wave involved a reversible, one-electron reduction and that the second wave may be complicated by a following chemical reaction. The diffusion currents of both waves were directly proportional to the square root of the height of the head of the dropping mercury electrode (dme). The diffusion current constants for the first and second waves were 2.97 and 5.45  $\mu\text{a}\text{-sec}^{1/2}\text{-mM}^{-1}\text{-mg}^{-2/3}$ , respectively.

A cyclic voltammogram of APDO in DMF containing 0.1M TBAP at a hanging mercury drop electrode (hmde) is shown in Fig. 2. At all scan rates employed, the reverse scan clearly shows two anodic peaks, corresponding to the oxidation of APDO monoanion and dianion. The cyclic voltammogram obtained on a planar platinum electrode is illustrated in Fig. 3. The behavior of the first wave is essentially the same as that observed on a hmde; however, the second wave shows a much larger cathodic-to-anodic peak current ratio. Typical results of cyclic voltammetric (linear potential sweep chronoamperometry with reversal) experiments for both a hmde and platinum disk electrode are given in Table I. At both a platinum disk electrode and a hmde, the ratio of the peak current ( $i_{pa}$ ) of the first anodic wave to the peak current of the corresponding cathodic wave ( $i_{pc}$ ) is about 1, as would be expected for the formation of a radical species which is stable during the duration of the measurement. The value of  $E_{pc} - E_{pa}$  for this couple is very

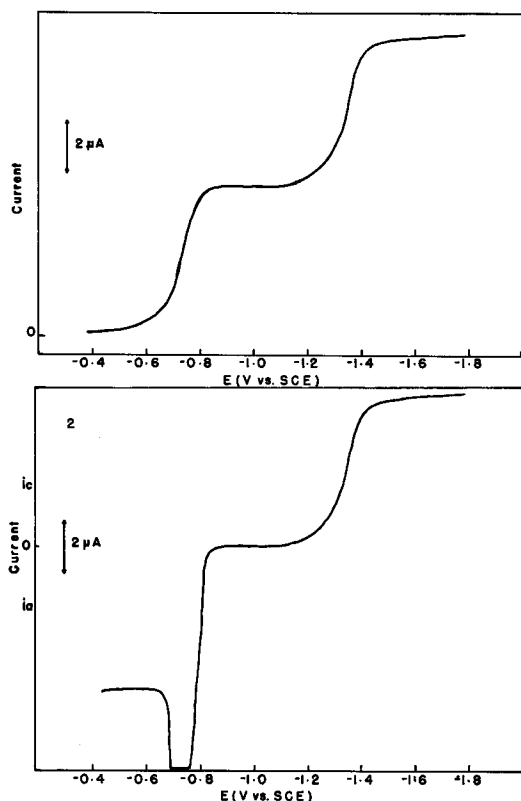


Fig. 1. Polarograms before and after reduction of a 1.32 mM APDO solution in DMF containing 0.1M TBAP at a mercury pool electrode: 1, before reduction; 2, after reduction at  $-1.0$  v vs. SCE.

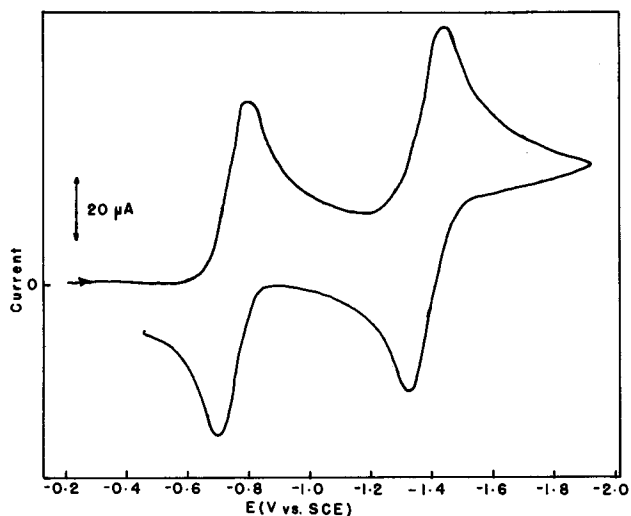


Fig. 2. Cyclic voltammetry of APDO at a HMDE. The solution contained 0.1M TBAP in DMF and was 1.32 mM in APDO.

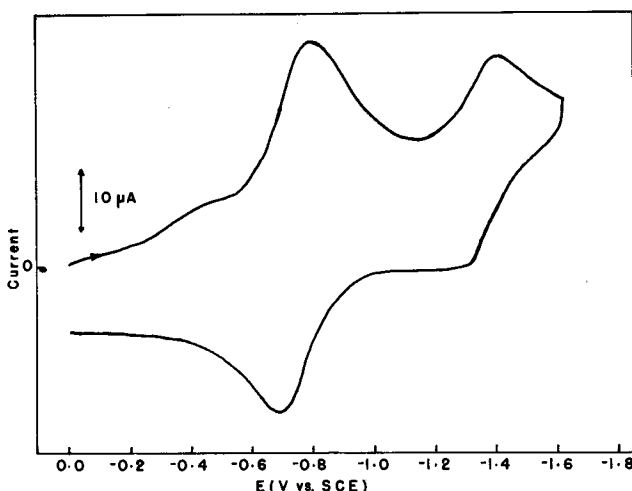


Fig. 3. Cyclic voltammetry of APDO at a planar platinum disk electrode. The solution contained 0.1M TBAP in DMF and was 1.32 mM in APDO.

close to the value (0.057v) for a reversible, one-electron reaction.  $E_{pc}$  and  $E_{pa}$  for this couple are independent of scan rate  $v$ , and plots of the current function ( $i_p/v^{1/2}$ ) and  $i_{pa}/i_{pc}$  vs. scan rate [diagnostic criteria given in the work of Nicholson and Shain (11) show this wave to be reversible].

The second reduction wave in cyclic voltammetric experiments utilizing a hmde shows some evidence of a chemical reaction following the reduction to give another electroactive species. The current function decreases about 20% for a 10-fold increase in scan rate, which indicates an ECE-type process (i.e., an electron transfer reaction followed by a chemical reaction generating a species reducible at these potentials). A simple EC process is eliminated, because it is characterized by a change of only 10% in the current function for a 10-fold change in scan rate (11). The anodic-to-cathodic peak current ratios increase with increasing scan rate, as expected for an ECE process.

The results obtained in cyclic voltammetric experiments using a platinum disk electrode also give evidence for the presence of an irreversible chemical reaction following the second charge transfer step. At scan rates up to 657 mv/sec, however, essentially no corresponding anodic wave is seen for the second reduction wave. This suggests that either the following reaction is catalyzed at platinum or perhaps adsorption of the product at mercury occurs. This difference

Table I. Cyclic voltammetric data for the two-step reduction of 4,4'-azobispyridine-1,1'-dioxide<sup>a</sup>

Scan rate, mv/sec	First wave						Second wave					
	$i_{pc}$ , $\mu A$	$i_{pa}^b$ , $\mu A$	$i_{pa}/i_{pc}$	$-E_{pc}$ v vs. SCE	$-E_{pa}$ v vs. SCE	$i_{pc}/v^{1/2}$	$i_{pc}^c$ , $\mu A$	$i_{pa}^b$ , $\mu A$	$i_{pa}/i_{pc}$	$-E_{pc}$ v vs. SCE	$-E_{pa}$ v vs. SCE	$i_{pc}/v^{1/2}$
Hanging mercury drop electrode; <sup>d</sup> conc. = 1.03 mM												
73	5.4	5.0	0.93	0.76	0.71	0.63	5.8	3.9	0.67	1.40	1.33	0.68
91	6.0	5.8	0.97	0.76	0.70	0.63	5.9	4.8	0.81	1.40	1.33	0.62
203	8.1	7.9	0.98	0.76	0.70	0.67	8.5	6.1	0.72	1.40	1.33	0.60
298	11.0	10.4	0.96	0.76	0.70	0.64	10.1	7.5	0.74	1.40	1.33	0.59
430	14.0	13.2	0.95	0.76	0.70	0.68	12.2	8.7	0.71	1.40	1.33	0.59
657	17.9	17.0	0.95	0.80	0.69	0.70	15.6	12.0	0.77	1.41	1.30	0.61
Concentration = 1.29 mM												
73	6.5	6.0	0.93	0.76	0.70	0.77	6.1	4.4	0.72	1.42	1.35	0.72
91	7.7	6.5	0.85	0.76	0.70	0.80	6.5	4.4	0.68	1.42	1.35	0.68
203	11.0	10.0	0.91	0.76	0.70	0.77	8.5	6.3	0.74	1.42	1.35	0.60
298	13.3	12.5	0.94	0.76	0.70	0.77	10.4	7.9	0.76	1.42	1.34	0.60
430	15.8	15.0	0.95	0.76	0.70	0.76	11.7	8.9	0.76	1.42	1.34	0.57
657	19.5	18.5	0.95	0.80	0.67	0.76	14.4	9.3	0.65	1.42	1.32	0.56
Concentration = 3.25 mM												
73	20.1	16.1	0.80	0.76	0.70	2.4	23.6	19.7	0.84	1.39	1.31	2.8
91	22.8	18.5	0.81	0.76	0.70	2.4	26.4	22.1	0.84	1.39	1.31	2.8
203	33.0	26.8	0.81	0.76	0.70	2.3	37.0	30.7	0.83	1.39	1.31	2.6
298	40.2	33.1	0.82	0.76	0.70	2.3	44.1	37.0	0.84	1.40	1.31	2.5
430	48.0	41.7	0.87	0.76	0.70	2.3	50.0	43.4	0.87	1.40	1.30	2.4
657	60.0	50.0	0.83	0.77	0.67	2.3	60.0	55.0	0.92	1.41	1.30	2.3
Platinum disk electrode; <sup>e</sup> concentration = 1.74 mM												
73	8.0	6.5	0.81	0.77	0.71	0.94						
91	9.0	7.5	0.83	0.77	0.71	0.94						
203	13.0	13.0	1.00	0.77	0.71	0.91						
298	16.5	16.0	0.97	0.77	0.71	0.95						
430	18.0	17.5	0.97	0.78	0.70	0.97						
657	24.5	23.5	0.96	0.78	0.69	0.96						

<sup>a</sup> The solution was 0.1M TBAP in DMF.

<sup>b</sup> For scan reversed at a potential 100mv more negative than  $E_{pc}$ . Potentials given may also include some uncompensated iR drop.

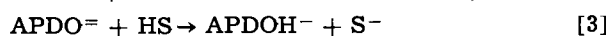
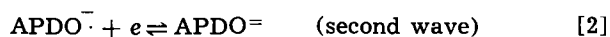
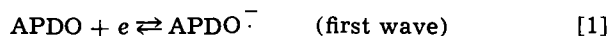
<sup>c</sup> Measured using extrapolation of decreasing current of first peak as base-line.

<sup>d</sup> Electrode area = 0.088 cm<sup>2</sup>.

<sup>e</sup> Apparent electrode area = 0.031 cm<sup>2</sup>.

in behavior at platinum and mercury electrodes was not investigated further.

These results suggest that the following reactions occur during voltammetry



where HS represents any source of protons and APDOH<sup>-</sup> is reducible at the potential of the second wave.

Coulometric experiments at a mercury pool electrode controlled at a potential on the diffusion plateau of both the first (-1.0v) and second (-1.8v) reduction waves were undertaken to study the electrochemical behavior of APDO<sup>-</sup> and APDO<sup>=</sup> and to obtain, via electron spin resonance (esr) techniques, further evidence for the above-postulated mechanism. Reduction of APDO at -1.0v gave values of  $n_{app}$  ranging from 1.40 to 1.92 faradays per mole (Table II). In all experiments the electrolysis current decayed to a value significantly higher than the corresponding background currents. For example, in the case of  $n_{app} = 1.70$ , the current decreased from an initial value of 38 ma to a steady value of 1.4 ma after 30 min, indicating that continued electrolysis does not bring about complete cessation of all reduction reactions. This behavior is indicative of a slow secondary process which produces a product that is electroactive at the same potential. Reversal coulometry at -0.20v vs. SCE gave  $n_{app}$  values for oxidation significantly lower than the corresponding initial reduction  $n_{app}$  values (Table II).

The solution resulting from reduction of APDO at -1.0v vs. SCE was a deep reddish-brown in color and gave an intense esr spectrum of about 75 lines. The spectrum was significantly nonsymmetrical about the center, indicating that the signal obtained was due to a mixture of two or more radical species. The presence of two radical species is also consistent with an ECE mechanism.

### Voltammetry after Reduction

Polarograms for a APDO solution before and after

reduction at -1.0v vs. SCE are shown in Fig. 1. The polarogram for a reduced APDO solution (Fig. 1, curve 2), shows an anodic wave with a large maximum which abruptly drops to near the expected diffusion current value at a potential (-0.68v) near the potential of the electrocapillary maximum for this medium, -0.70v. This behavior is similar to that observed by Santhanam and Bard (12) in their study of 9,10-diphenylanthracene and can probably be attributed to the anodic streaming mechanism proposed by

them. The reduction of APDO<sup>-</sup> to APDO<sup>=</sup> occurs at the same potential as the second polarographic wave in the reduction of APDO (Fig. 1, curve 2). The diffusion current of the second wave is about the same before and after electrolysis at -1.0v. Cyclic voltammetry, utilizing a hmde, on a reduced solution of APDO is shown in Fig. 4, curve 2. The very large anodic current for the oxidation is attributed to the same stirring effect mentioned above. Cyclic voltammetry on a platinum disk electrode does not exhibit this stirring phenomena (Fig. 4, curve 4). The value of  $i_{pc}$  for the first wave at a platinum electrode decreases by about 20% after reduction of APDO at -1.0v (24.5  $\mu A$  before vs. 19.4  $\mu A$  after). Peak potentials ( $E_{pc}$  and  $E_{pa}$ ) for the first reduction step are unchanged.

Further controlled potential reduction of the reduced solution at -1.80v, corresponding to the plateau of the second wave gave an additional 4.1 faradays

Table II. Controlled potential coulometric results<sup>a</sup>

Conc., mM	$n_{app}$		
	Reduction at -1.0v	Oxidation at -0.20v	Reduction at -1.80v
0.90	1.63	—	5.92
1.05	1.92	—	—
1.32	1.92	—	—
1.73	1.40	0.47	—
3.25	1.70	0.70	—
1.05	—	—	5.84

<sup>a</sup> The solution was DMF containing 0.1M TBAP. The cathode was a mercury pool with an approximate area of 12 cm<sup>2</sup> and the anode was platinum wire, isolated by a fine-porosity, sintered glass disk. Potentials given above are vs. SCE. Electrolysis times were 0.5 to 1.5 hr.

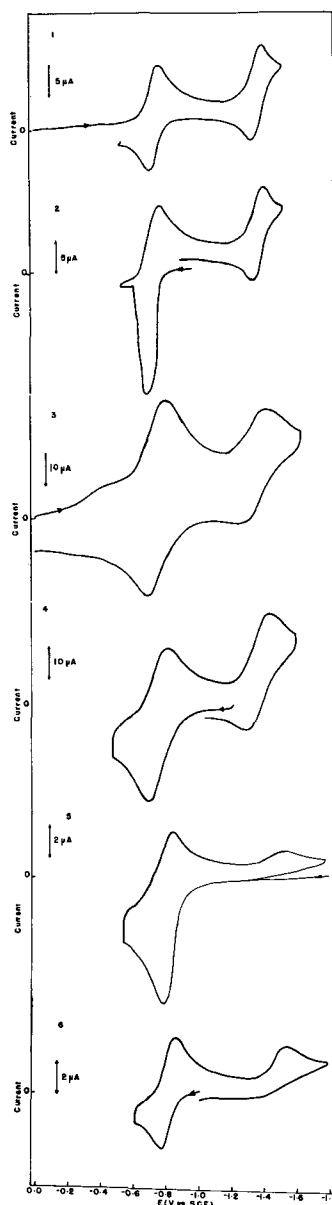


Fig. 4. Cyclic voltammetry of APDO on a hmde and platinum disk electrodes at various stages of reduction at a mercury pool working electrode. The solution was 1.73 mM in APDO in DMF containing 0.1M TBAP: 1, C.V. at hmde of original solution; 2, C.V. at hmde after reduction at  $-1.0$  v; 3, C.V. at platinum disk electrode of original solution; 4, C.V. at platinum disk electrode after reduction at  $-1.0$  v; 5, C.V. at a platinum disk electrode after reduction at  $-1.80$  v; 6, C.V. at a platinum disk electrode of an authentic sample of azopyridine in the same medium as described above.

per mole for an over-all value of  $n_{app} = 5.84$ . Cyclic voltammetry, employing a platinum disk electrode, of an APDO solution after complete reduction at  $-1.80$ v, is shown in Fig. 4, curve 5. With the scan initiated in a positive direction from  $-1.80$ v, an oxidation wave occurs at  $-0.76$ v followed, on reversal, by two reduction steps at  $-0.84$  and  $-1.53$ v. These peak potentials are significantly different from those observed for APDO itself.

Reversal coulometry (oxidation) at  $-1.0$ v resulted in no anodic current flow, indicating that the reduced species was not oxidizable at this potential. On changing the potential to  $-0.20$ v, however, this species was oxidized, giving a value of  $n_{app} = 1.44$ . Cyclic voltammetric reduction and oxidation of the species resulting from this oxidation showed waves at the same potentials as those observed for the completely reduced species as noted above; the first charge transfer was apparently reversible with a reduction wave at  $-0.84$ v and was followed by an irreversible reduction with a peak potential of  $-1.53$ v.

Controlled potential electrolysis of this product at a potential corresponding to the first reduction step ( $-1.0$ v) gave a value of  $n_{app} = 1.30$ . The solution was sampled at this stage for esr analysis. The resulting esr spectrum, containing approximately 40 lines, was significantly different from the spectrum of APDO mentioned above.

The most logical product of the complete reduction of APDO, based on the behavior of other amine oxide systems, would involve the 4,4'-azobispyridine (AP) system; hence, the electrochemical behavior of AP was examined. Cyclic voltammetry, employing a platinum disk electrode, of AP is shown in Fig. 4, curve 6. The voltammetric behavior of AP is the same as that of the reduction product of APDO obtained by complete reduction at  $-1.8$ v. Controlled potential electrolysis of AP, using conditions identical to those employed for APDO, was performed at a potential of  $-1.0$ v, which corresponds to the plateau of the first reduction wave. An  $n_{app}$  value of 1.09 electrons per molecule was observed for this reduction. A sample was taken at this stage for esr analysis. The resulting esr spectrum was identical to that obtained from reversal coulometry reported in the previous paragraph.

#### Effect of Proton Donor

To gain some insight into the intermediate steps involved in the reduction of APDO, its electrochemical behavior in the presence of varying amounts of a proton-donating agent was studied. Hydroquinone (HQ), previously employed in a study of 9,10-diphenylanthracene (12) was used as the proton donor. The effect of varying amounts of HQ on the polarographic behavior of APDO is shown in Fig. 5. The first wave is unaffected by increasing concentrations of HQ; however, the second wave is shifted in an anodic direction and the diffusion current is increased as the HQ concentration is increased. The second reduction step changes from near reversible behavior, at zero concentration of HQ ( $E_{3/4} - E_{1/4} = 65$  mv), to completely irreversible character ( $E_{3/4} - E_{1/4} = 150$  mv) in the presence of excess HQ (HQ/APDO ratio = 8.0). The cyclic voltammetric behavior of APDO at a hmde in the presence of HQ is illustrated in Fig. 6. The first reduction step is unaffected by addition of excess HQ with the second reduction showing behavior analogous to that seen in polarography ( $i_{pc}$  increasing and  $E_{pc}$  shifting anodically with increasing HQ concentration). These results suggest that if the chemical reaction following the first reduction step involves protonation, its rate is still negligible during the duration of the voltammetric experiment. However, the rate of the reaction following the second reduction step is increased considerably. Controlled potential electrolysis at  $-0.80$ v was performed on the above-mentioned solution with a resulting  $n_{app}$  of 5.92 electrons, which is the same as the  $n_{app}$  found for the over-all reduction in the absence of proton donor.

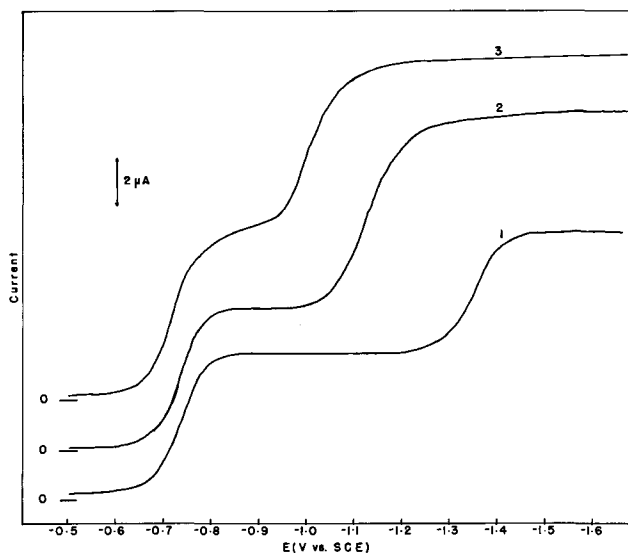


Fig. 5. Polarograms for reduction of 1.05 mM APDO in 0.1M TBAP in DMF in the presence of varying amounts of hydroquinone (HQ): 1, no HQ added; 2, HQ concentration is 1.77 mM; 3, HQ concentration is 8.10 mM.

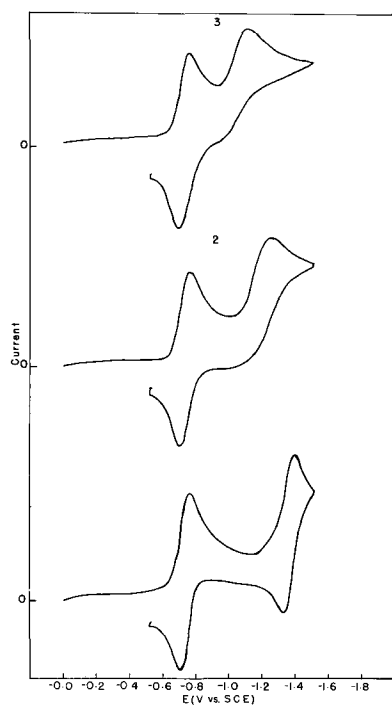


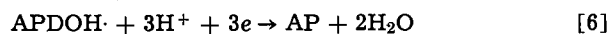
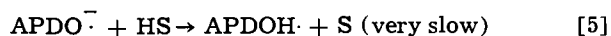
Fig. 6. Cyclic voltammograms for the reduction of 1.05 mM APDO at a hmde in 0.1M TBAP in DMF in the presence of varying amounts of hydroquinone (HQ): 1, no HQ present; 2, 1.77 mM HQ; 3, 8.10 mM HQ.

### Discussion

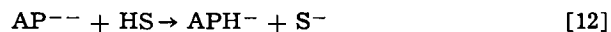
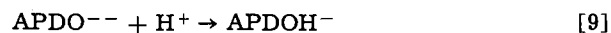
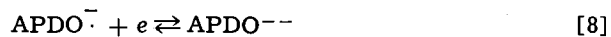
The mechanism of the electrochemical reduction of APDO is shown in the schematic diagram in Fig. 7. In this diagram electron transfer processes at the electrode are indicated by straight lines (reductions downward and oxidations upward) and chemical reactions are shown as wavy lines. Compounds which are reduction products of APDO are shown as lines below the APDO line; these lines are spaced in increasing numbers of electrons added to the parent molecule. Where the appropriate electrode potentials are known, they are indicated next to the couple. Downward arrows show reduction and upward ones oxidations.

We proposed to explain the experimental results with the following mechanism:

At potentials corresponding to the first wave:



At potentials corresponding to the second wave:



The polarographic and cyclic voltammetric results show that during the small duration of these experiments (3-20 sec), the results can be explained by reactions [1] to [3]. Only a small contribution of the following reactions [9] through [11] is found, resulting in the ECE-type behavior of the second voltammetric wave.

Controlled potential coulometric reduction at a potential corresponding to the plateau of the first wave gives  $n_{\text{app}}$  values significantly greater than one and evidence of production of an electroactive species (current not decaying to the background value). Reversal coulometry (oxidation at the foot of the first wave)

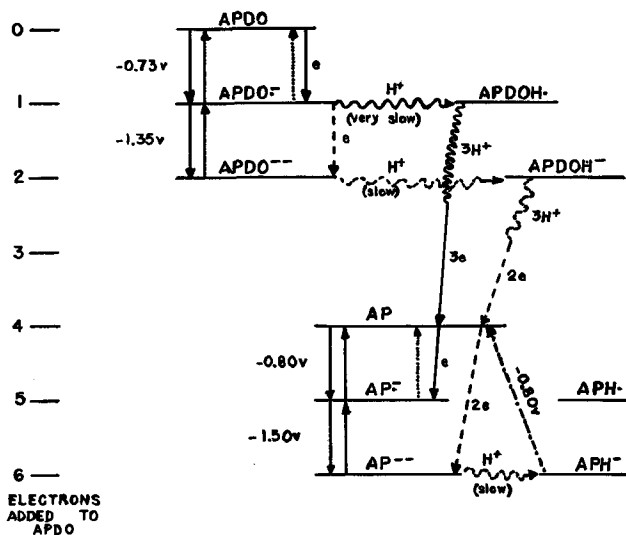


Fig. 7. Schematic diagram of mechanism of the electroreduction of APDO. Electron transfer processes at the electrode are indicated by straight lines (reductions downward and oxidations upward) and chemical reactions by wavy lines. The extent of reduction, in terms of electrons added to APDO, is indicated by the distance down from the APDO line. The potentials at which reactions occur ( $E_{1/2}$ , vs. SCE) are indicated near the appropriate couple, when known. Some qualitative measure of the rates of chemical reactions has been given ("slow" denotes a reaction which does not proceed to an appreciable extent during a time characteristic of voltammetric experiments but is appreciable on the coulometric time scale; "very slow" denotes a reaction which proceeds only partially even in coulometric experiments). — Reduction at  $-1.0\text{v}$ ; ..... oxidation at  $-0.20\text{v}$  following this reduction; - - - - - reduction at  $-1.8\text{v}$ ; -●-●-● oxidation at  $-0.2\text{v}$  following this reduction.

gives a smaller value of  $n_{\text{app}}$ , for example ( $n_{\text{app}}$  reduction = 0.70, Table II). This behavior is ascribed to a

very slow reaction of the anion radical  $\text{APDO}^-$  to form an electroactive species; a protonation reaction to  $\text{APDOH} \cdot$  seems reasonable. Since the first reduction wave of APDO is unaffected by addition of a proton donor, this reaction must be slow, even in the presence of excess hydroquinone. Further reduction and protonation eventually leads to azopyridine (AP), which is reduced at these potentials to the stable anion

radical  $\text{AP}^-$ . Since  $\text{APDOH} \cdot$  is reduced at these potentials in a series of steps involving 4 electrons, only a small amount of reaction of  $\text{APDO}^-$  will give an appreciable contribution to  $n_{\text{app}}$ . For example, the decompo-

sition of about 20% of the  $\text{APDO}^-$  would account for these results. The fact that voltammetry of the reduced solution shows a cathodic peak current, on reversal, of about 80% of the original cathodic peak current, is also in agreement with this mechanism and suggests that some of the intermediates involved in [6] are not oxidizable. Since the second reduction wave is about the same after reduction as in the original solution, reduction of both products and intermediates is suggested. The esr spectra obtained following reduction at potentials of the first wave are probably those of

$\text{APDO}^-$ ,  $\text{AP}^-$  and perhaps some intermediates.

Reduction at a potential on the plateau of the second wave leads in a series of protonation and reduction reactions to  $\text{APH}^-$ , with  $n_{\text{app}} = 6$  (within experimental error). The electrochemical behavior of the solution resulting from this reduction is identical with that obtained from reduction of AP itself.<sup>1</sup> After complete

<sup>1</sup> A complete study of the electrochemistry of azopyridine and other aromatic azocompounds in DMF has been completed (J. Sadler, Ph.D. Dissertation, The University of Texas at Austin, 1967) and has been submitted for publication elsewhere. The behavior of azopyridine shown in the lower part of Fig. 7 has been established in this study.

reduction, oxidation at  $-0.2\text{v}$ , and re-reduction, an esr signal which can unequivocally be ascribed to  $\text{AP}^-$  is obtained, giving further support to this mechanism.

### Experimental

The cell and vacuum line used were essentially the same as reported by Santhanam and Bard (12). DMF purification and storage also followed the procedure outlined there. The filling of the electrochemical cell was accomplished by first evacuating the cell containing the supporting electrolyte and mercury pool, cooling with liquid nitrogen, then distilling DMF under vacuum into the cell. After the distillation had been completed, the cell and contents were allowed to warm to room temperature with continuous evacuation. The cell was then brought to atmospheric pressure by introducing helium through the vacuum line. The helium was obtained from the Matheson Company, LaPorte, Texas. It was passed successively through anhydrous magnesium perchlorate, copper turnings (heated to  $350^\circ\text{C}$ ), activated charcoal cooled to liquid nitrogen temperature, and finally to the cell. A helium blanket over the solution was maintained throughout the experiment. The auxiliary electrode was a platinum wire. The reference electrode was an aqueous SCE connected via an agar plug and sintered glass disk to the test solution. Stirring was by a magnetic stirrer.

The voltammetric experiments were carried out using a multipurpose instrument employing operational amplifier circuitry with three-electrode configuration, similar to those discussed in the literature (13). Controlled potential coulometry was carried out using a previously described apparatus (14).

The APDO was from Aldrich Chemical Company. It was recrystallized twice from absolute ethanol and twice from benzene. The melting point of the resulting product was very sharp at  $236.5^\circ\text{C}$  (decomp.). AP was synthesized by reduction of APDO in ethanol with zinc dust and ammonia. The melting point of the product after recrystallization from petroleum ether, was  $106.5^\circ\text{C}$  as compared to a literature value of  $107^\circ\text{C}$  (15). The TBAP was obtained from Southwestern Analytical Chemicals, Austin, Texas. It was dried in a vacuum oven for 8 hr at  $70^\circ\text{--}80^\circ\text{C}$  and stored in a desiccator until use.

A Varian Associates V-4502 spectrometer employing 100-kc field modulation was used for esr spectroscopy.

### Acknowledgment

The support of this research by the Robert A. Welch Foundation and the National Science Foundation (GP 6688X) is gratefully acknowledged. The authors are indebted to Tom V. Atkinson and Larry O. Wheeler for aid in the esr spectroscopy and to K. S. V. Santhanam for helpful discussions during the work.

Manuscript received July 17, 1967; revised manuscript received ca. Nov. 23, 1967.

Any discussion of this paper will appear in a Discussion Section to be published in the December 1968 JOURNAL.

### REFERENCES

1. A. Foffani and E. Fornasari, *Gazz. Chim. Ital.*, **83**, 1051, 1059 (1953).
2. A. Foffani and E. Fornasari, *Atti. Acad. Naz. Lincei*, Ser. 8, **23**, 62 (1957).
3. G. Horn, *Acta Chimica Acad. Hung.*, **27**, 123 (1961); **33**, 287 (1962).
4. L. V. Varyukhina and Z. V. Pushkareva, *J. Gen. Chem. USSR*, **26**, 1953 (1956).
5. O. N. Nechaeva and Z. V. Pushkareva, *ibid.*, **28**, 2721 (1958).
6. T. Kubota and H. Miyazaki, (a) *Bull. Chem. Soc. Japan*, **35**, 1549 (1962); (b) *ibid.*, **39**, 2057 (1966).
7. Y. Date, (a) *J. Chem. Soc. Japan (Nippon Kagaku Zasshi)*, **84**, 875 (1963); (b) *ibid.*, **84**, 964 (1963).
8. L. M. Chambers, *Anal. Chem.*, **36**, 2431 (1964).
9. P. J. Elving and C. R. Warner, *Coll. Czechoslov. Chem. Commun.*, **30**, 4210 (1965).
10. G. Anthoine, J. Nasielski, E. Vander Donckt, and N. Vanlaudem, *Bull. Soc. Chim. Belges*, **76**, 230 (1967).
11. R. S. Nicholson and I. Shain, *Anal. Chem.*, **36**, 706 (1964).
12. K. S. V. Santhanam and A. J. Bard, *J. Am. Chem. Soc.*, **88**, 2669 (1966).
13. (a) W. M. Schwarz and I. Shain, *Anal. Chem.*, **35**, 1770 (1963); (b) W. L. Underkofler and I. Shain, *ibid.*, **35**, 1778 (1963).
14. A. J. Bard, *Anal. Chem.*, **35**, 1121 (1963).
15. H. I. den Hertog, C. H. Henkens, and J. H. Van Roon, *Rec. Trav. Chim.*, **71**, 1145 (1962).

## The Cu/CuF<sub>2</sub> Couple in Anhydrous Hydrogen Fluoride

Brian Burrows\* and Raymond Jasinski\*

Tyco Laboratories, Inc., Waltham, Massachusetts

### ABSTRACT

The electrochemical behavior of a Cu electrode was investigated in basic, anhydrous HF. Anodization of Cu established the Cu/CuF<sub>2</sub>(s) couple. Micro-polarization and bias tests indicated that this couple was reversible, and its potential vs. an H<sub>2</sub> electrode in the same solution agreed well with that predicted from thermodynamic data. Thus the couple is suitable for use as a reference electrode in basic HF. The formation of a relatively thick, insoluble anodic film at a copper electrode was demonstrated by cyclic voltammetry and chronopotentiometry. Anodic-cathodic cycling of an electrode gave rise to significant roughening of the electrode surface as shown by *i*-E curves, E-t curves, and differential capacitance measurements on cycled electrodes. X-ray analysis of the anodic film confirmed the presence of crystalline copper fluoride. The formation of CuF<sub>2</sub> appears to proceed via dissolution of Cu to form Cu<sup>2+</sup> ions, followed by precipitation of the CuF<sub>2</sub> on the electrode surface. The polarization behavior of Cu electrodes in anhydrous HF solution containing added KF showed that anodic film formation can be approximated by Tafel lines with an apparent exchange current density of about  $3 \times 10^{-6}$  amp/cm<sup>2</sup>. Properties of the anodic film of CuF<sub>2</sub> are quite similar to those observed for noncontinuous anodic films formed in aqueous solutions.

Very little work on the characterization of electrode reactions in anhydrous or aqueous HF has been reported. A small number of potentiometric investiga-

tions have been made (1-3); a brief report on the construction of a rotating nickel electrode for use in anhydrous HF is available (6), and a dropping mercury electrode using a Teflon capillary in aqueous HF

\* Electrochemical Society Active Member.

has also been described (4, 5). The process of electrochemical fluorination of organic compounds has been known for some time (7, 8) and is a commercial operation. Recently, the anodic behavior of metals in HF has been examined, and an attempt was made to find an inert or passive anode at which the mechanisms of electrochemical fluorination could be studied (8). Monel, platinum, and nickel were least reactive; the anodic passivity of nickel in HF was studied in some detail (9).

The Cu/CuF<sub>2</sub>(s) couple has been used as a reference electrode of the second kind in anhydrous HF solutions (2, 3). The electrode was formed by anodizing a Cu plate in HF at +1.0v against a Pt electrode. No direct evidence on the reversibility or composition of the electrode was given. A Hg/Hg<sub>2</sub>F<sub>2</sub>(s) couple has also been used as a reference electrode of the second kind (1, 8, 9). Mention has been made (11) of a direct measurement of the potential of the cell H<sub>2</sub>/HF(KF)/F<sub>2</sub> ( $E = 2.768\text{v}$  at 0°C). It was noted that the fluorine electrode was irreversible.

Cupric fluoride is of interest as a cathode in battery systems using aprotic organic solvents. One method for its preparation is by anodization of copper in anhydrous HF. This paper describes studies of the Cu/CuF<sub>2</sub> electrode and the mechanism of formation of CuF<sub>2</sub> at a copper electrode in basic, anhydrous HF.

### Experimental

Experiments were carried out in a 1M solution of KF in anhydrous HF at 0°C and 25°C. The water content of the HF was nominally 0.04 m/o (mole per cent) corresponding to approximately 0.02M (19).

**Apparatus and procedure.**—A schematic diagram of the apparatus for handling anhydrous HF (Matheson Company, 99.9 m/o) is shown in Fig. 1. B<sub>1</sub>, B<sub>2</sub>, B<sub>3</sub>, and B<sub>4</sub> are Teflon FEP bottles (4 oz capacity). The connecting tubing was of flexible Teflon (0.25 in. ID) and the stopcocks were of polyethylene. Kel-F wax (3M Company) was used to seal all the joints and inlets.

Since the ambient temperature was 25°C, HF was delivered from the cylinder in the gaseous state. Nitrogen was first flushed through the apparatus followed by HF vapor. An ice-bath was then placed around B<sub>1</sub> to condense HF. After about 40 cc of liquid HF had been collected, the ice-bath was removed and placed in position around B<sub>2</sub> (the electrochemical cell with counter, working, and reference electrodes already in position). An incandescent lamp was held under B<sub>1</sub> to warm the HF gently and distill it over to B<sub>2</sub>. A small residual amount of liquid was left in B<sub>1</sub>. An amount of KF (B & A, reagent grade) had previously been added to B<sub>2</sub> so that an ionically conducting solution, approximately ( $\pm 10\%$ ) 1M in KF, would result. It was observed that KF dissolved quite readily in HF with-

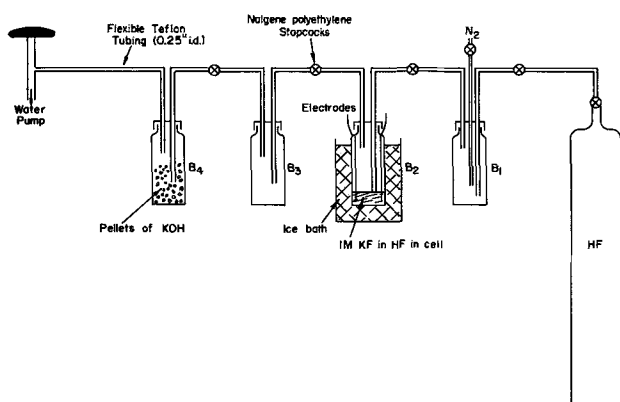


Fig. 1. Schematic representation of the apparatus used for handling anhydrous HF. B<sub>1</sub>, B<sub>2</sub>, B<sub>3</sub>, B<sub>4</sub> were Teflon FEP bottles (4 oz capacity). The connecting tubing was flexible Teflon; the stopcocks were polyethylene.

out mechanical stirring. Dry nitrogen was then bubbled through the cell for up to 2 hr until a current-voltage scan at a Cu electrode indicated the absence of impurities (see below).

At the end of an experiment the HF was transferred from B<sub>2</sub> by removing the ice bath, allowing the HF solution to warm up, and applying a gentle vacuum with a water pump. This vaporized the HF into B<sub>4</sub> which contained pellets of KOH. It was possible to remove a working electrode from B<sub>2</sub> during an experiment and replace it with a new one without overly contaminating the HF.

HF vapor could vent through the caustic trap (B<sub>4</sub>) during cell measurements. However, the apparatus did provide a sufficient back pressure to make this leak rate negligible, even at 25°C where the vapor pressure of HF is slightly above 1 atm.

**Electrodes.**—Working electrodes were prepared from sections of electrolytic copper wire 1 mm diameter, covered with shrinkable Teflon (Rayclad Tubes, Inc.) which gave a tight, insulating layer. Sufficient Teflon was removed at the working end of the electrode to expose 1 cm of Cu. The working area (0.33 cm<sup>2</sup>) was cleaned in dilute HNO<sub>3</sub> and washed in distilled water and acetone. The electrodes were placed in the cell (B<sub>2</sub>) through small holes drilled around the lip of the bottle so that a close fit was obtained. The inlet holes were sealed with Kel-F wax. Electrodes of Ag (0.16 cm<sup>2</sup> in area), Pt (0.16 cm<sup>2</sup> in area), and Ni (0.20 cm<sup>2</sup> in area) were prepared similarly. The counter electrode was a coil of Ni wire; a 1 cm square piece of porous copper plaque (Clevite Corporation) was used to form the reference electrode.

The H<sub>2</sub> electrode was of the fuel cell type (15), consisting of Pt black (Engelhard Industries, Inc.) bonded with Teflon and supported on a Pt mesh screen of 2 cm<sup>2</sup> area. This electrode was placed in a Teflon tube (1 cm in diameter) with a hydrophilic porous Teflon frit (Chemplast, Inc.) at one end and held in place with Kel-F wax (3M Company).

**Electrochemical measurements.**—Potentiostatic current-potential curves (cyclic voltammograms) were obtained in the usual manner using a motor-driven, slow-function generator (maximum scan rate 800 mv/min). The output of the function generator was applied to a Wenking potentiostat (Model 61 RS). The i-v curve was recorded on an X-Y recorder (Houston Omnigraphic, Model HR-98T). Since the input impedance of the X-Y recorder was low (0.2 Mohm), a cathode follower was used in the potential-measuring circuit to avoid undue loading of the reference electrode-working electrode cell. The unity-gain follower was constructed from an operational amplifier (Philbrick Researches, Inc., Type P65AU); the input impedance of this device was 33 Mohm. Unless stated otherwise, all i-v curves were obtained using a scan rate of 800 mv/min.

Potential-time curves (chronopotentiograms) were recorded on the same X-Y recorder using the time base. A constant-current power source (Electronic Measurements, Model C623) was used to supply the current at voltages up to 400v.

Steady-state, constant current polarization curves were obtained by recording the change of potential with time on the X-Y recorder with a full scale deflection of 20 sec. The potential assumed a constant value within several seconds and steady-state potential values were read off the plateau. By using relatively short times to measure the activation polarization, convective and concentration polarization effects were minimized.

Micropolarization tests on the Cu plaque were carried out by passing a small constant current and measuring the potential with a differential d-c voltmeter (John Fluke, Model 825A).

The capacity measurements were based on a method in which a triangular wave of 100 cps and an amplitude of 25 mv (i.e., a sweep rate of 5v/sec), biased by

a convenient d-c voltage, was fed into the signal input of the potentiostat (20). The d-c voltage was selected so that Faradaic currents were avoided. The small triangular potential wave (Exact Electronics, Inc., fast function generator, Type 255) was fed via a differential amplifier (Tektronix, Type 2A63 plug-in) into one axis of an oscilloscope (Tektronix, Type 561A). Via another differential amplifier of the same type, the voltage drop across a suitable precision resistor was fed into the other axis of the oscilloscope. The resulting trace on the oscilloscope screen was a rectangular box from which the peak-to-peak current was measured. The differential double layer capacity  $C_{dl}$  was then equal to  $i/2(dE/dt)$ .

**X-ray analysis.**—Qualitative identification of anodic films was obtained from analyses of Debye-Scherrer powder patterns using  $\text{CuK}\alpha$  radiation with a Ni filter at 50 kv and 20 ma. The films were formed on 0.5 mm Cu wire in HF and then exposed to radiation up to 6 hr. The lines arising from Cu were determined during the analysis and eliminated.

### Results and Discussions

The initial studies of the Cu/CuF<sub>2</sub> couple were complicated by the presence of an electroactive impurity. This impurity also reacted at Ag electrodes but not at Pt and Ni. An i-E curve taken at a Cu electrode in impure HF is shown in Fig. 2. The anodic wave beginning at 0 mv (vs. Cu/CuF<sub>2</sub>) was diffusion controlled. After anodization, a black film was present on the Cu electrode; the same film was found on Cu electrodes left in contact with HF for some time. An x-ray analysis of this film showed the pattern of Cu<sub>2</sub>S and possibly CuOH; CuF<sub>2</sub> was not detected.

The impurity was removed by bubbling dry nitrogen (or argon) through the cell for periods of up to several hours. The absence of the impurity was indicated by the disappearance of the diffusion controlled anodic wave and the anodic peak current, as well as the absence of a black film after Cu had been standing in contact with HF. All electrochemical experiments described here were carried out in HF purified by N<sub>2</sub> bubbling.

In an attempt to identify the nature of the impurity, i-E curves were run at Cu electrodes in pure HF after bubbling SO<sub>2</sub> and H<sub>2</sub>S through the solution for about 15 min in separate experiments. Neither of these impurities showed any anodic activity. Bubbling O<sub>2</sub> through the solution also decreased the impurity wave. The presence of dissolved O<sub>2</sub> was detected on a Pt

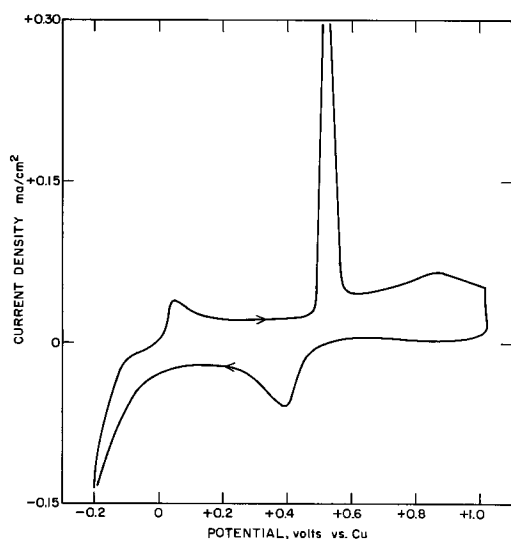
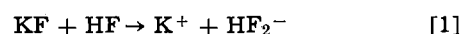


Fig. 2. Cyclic voltammogram at Cu electrode in impure HF (1M KF) at 0°C. Scan rate was 800 mv/min, and scan was started at 0 mv.

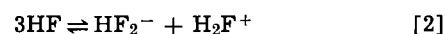
electrode by a reduction wave at +0.5 to +0.6v vs. Cu/CuF<sub>2</sub>. N<sub>2</sub> bubbling removed this reduction wave.

Ag was observed to dissolve anodically in the purified HF and no anodic film was formed. Figure 3 shows a background scan on a platinum electrode in anhydrous HF. The diffusion controlled anodic wave at +1.2 to +1.3v was presumably due to oxidation of traces of water. The limiting cathodic process was H<sub>2</sub> evolution. An order of magnitude calculation can be made of the concentration of water present. Using the equation given by Delahay (24) for the current as a function of potential scan rate with  $\nu = 0.078 \text{ v-sec}^{-1}$ ,  $n = 2$ , and taking  $D = 10^{-6} \text{ cm}^2 \text{ sec}^{-1}$  for the diffusion coefficient of H<sub>2</sub>O in HF, then  $C_{\text{H}_2\text{O}}$  calculates to 0.01M. This is close to the nominal impurity concentration of 0.02M.

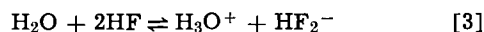
As mentioned above, KF was added to HF in order to produce a solution with reasonable conductivity (10). In liquid HF, solutions of the alkali metal fluorides act as bases (10), so that the dissolution of KF may be formally represented as follows



Thus, the solvated fluoride ion acts as a base and its concentration is related to that of solvated protons through



with an equilibrium constant of approximately  $2 \times 10^{-12}$  (10). H<sub>2</sub>O also acts as a base in liquid HF and the following equilibrium is established



with an equilibrium constant of 0.55 (3) at 0°C. Thus all HF<sub>2</sub><sup>-</sup> ion concentrations should include the contribution from the solvolysis of impurity H<sub>2</sub>O according to Eq. [3]. The concentration of H<sub>2</sub>O in HF as taken from the cylinder is nominally 0.02M. Using the approach of Clifford *et al.* (3), the concentration of HF<sub>2</sub><sup>-</sup> contributed from equilibrium [3] was calculated to be 0.01M.

Thus this additional concentration had an insignificant effect on the potential of the Cu/CuF<sub>2</sub> electrode potential in a solution already 1M in HF<sub>2</sub><sup>-</sup> and, for the same reason, a negligible effect on the observed transition times for CuF<sub>2</sub> formation (see below). There may be, however, a specific chemical interaction between CuF<sub>2</sub> and undissociated H<sub>2</sub>O, resulting in a slightly increased solubility of CuF<sub>2</sub>, which would affect transition times. The magnitude of this effect would appear to be negligible since the solubility of CuF<sub>2</sub> in HF (containing about 0.01M H<sub>2</sub>O) at 0°C was found to be less than  $2 \times 10^{-5}\text{M}$  (2). In the presence of 1M KF the solubility of CuF<sub>2</sub> may be even lower.

**Reference electrode.**—Copper electrodes immersed in a 1M solution of KF in HF at 0°C always had low differences (<5 mv) in rest potentials, which differences remained constant. The potential of a fresh Cu

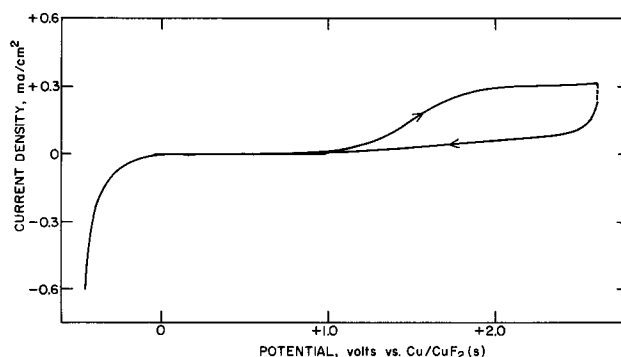
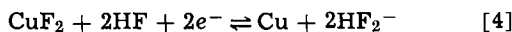


Fig. 3. Cyclic voltammogram at Pt electrode in purified HF (1M KF) at 0°C. Scan rate was 800 mv/min, and scan was started at 0 mv.



electrode placed in solution was less than 5 mv with respect to an electrode which had been immersed for several days. Furthermore, the potentials of fresh or aged electrodes were little different from those of electrodes previously anodized at +200 mv. This behavior suggested that a reversible couple was associated with the Cu electrode in a basic HF solution, namely



To check the reversibility, a polarization test was carried out on a porous Cu electrode (geometric area 2 cm<sup>2</sup>). Small constant currents were passed between the Cu electrode and a Ni counter electrode. The resulting polarization was measured with respect to an unpolarized Cu electrode as shown in Fig. 4. It can be seen that there was no significant hysteresis and only a small displacement of potential when several microamperes were flowing.

It is probable that some CuF<sub>2</sub> was formed at open circuit by corrosion involving trace amounts of reducible impurities in the solvent (12). As will be shown below, the quantity of CuF<sub>2</sub> formed in this manner is small compared with anodically formed CuF<sub>2</sub> at more positive potentials.

The composition of the film formed on copper after repetitive anodization was shown, by x-ray analysis, to be crystalline CuF<sub>2</sub> · 2H<sub>2</sub>O (23). It is probable that CuF<sub>2</sub> formed in the cell hydrolyzed (23) upon exposure to the atmosphere during the x-ray measurements.

The potential of the Cu/CuF<sub>2</sub> couple at 25°C was measured with respect to a hydrogen electrode immersed in the same solution. A Teflon-bonded, high surface area platinum black electrode was introduced into the cell and was separated from the copper electrode and the bulk of the electrolyte by a junction of porous Teflon. The hydrogen electrode was only half immersed in the electrolyte so that a three phase contact could be maintained between the electrode, HF, and hydrogen gas. A flow of H<sub>2</sub> was sustained over the electrode rather than bubbling gas through the electrolyte during the measurements to keep the pressure of hydrogen close to one atmosphere and still avoid significant changes in HF content. The results of three such experiments are shown in Table I; the

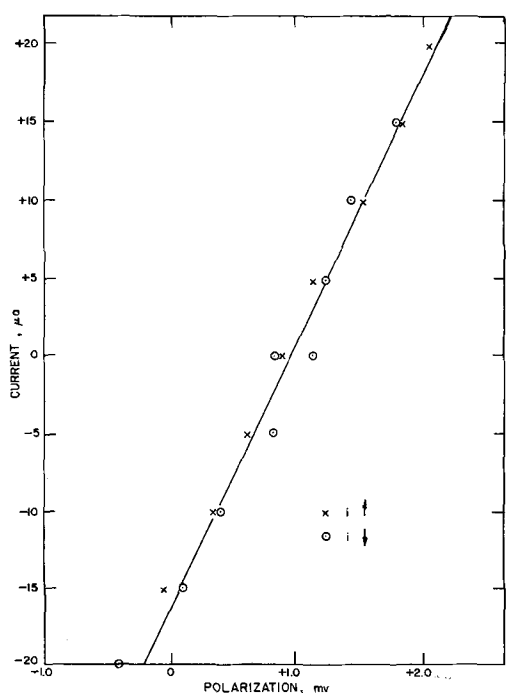


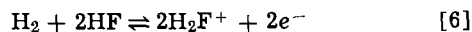
Fig. 4. Polarization (mv) as a function of current density ( $\mu\text{A}$ ) for a porous Cu electrode (2 cm<sup>2</sup>) in purified HF (1M KF) at 0°C.

Table I. Potential of the Cu/CuF<sub>2</sub> couple vs. the hydrogen electrode at 25°C

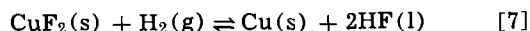
Run	Potential, mv
1	+0.274
2	+0.278
3	+0.277
Avg. +0.276 $\pm$ 5	

potentials were stable within  $\pm 3$  mv for the duration of the experiments (approximately 30 min).

In terms of the self ionization equilibria for HF described above, the half cell reactions are probably as follows

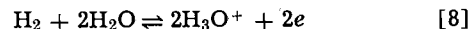


The total cell reaction is thus



with all components in their standard states. Equation [7] assumes that the activity of HF (approximately 50M) in 1M KF equals that of liquid HF. The data of ref. (25) implies that this assumption is valid within the limits quoted in Table I. Although the potentials for each half cell reaction (Eq. [5] and [6]) are dependent on the activity of the HF<sub>2</sub><sup>-</sup>, the total cell potential (Eq. [7]) is independent of this factor because of equilibrium [2].

The theoretical cell potential is also independent of the activity of H<sub>3</sub>O<sup>+</sup> arising from the presence of H<sub>2</sub>O. Thus the two half-cell reactions in a solution containing H<sub>3</sub>O<sup>+</sup> ions are probably [5] and



Adding [5] and [8] together results in the theoretical over-all cell reaction [7], which is independent of the HF<sub>2</sub><sup>-</sup> activity as well as the H<sub>3</sub>O<sup>+</sup> activity because of equilibrium [3]. The standard cell potential at 25°C can be computed from thermodynamic data and a value of +0.27v was obtained in this manner (13, 14) in reasonable agreement with the observed potential. This value at 25°C is in disagreement, however, with that of +0.52v given by Clifford and co-workers (3) for Cu/CuF<sub>2</sub> in HF at 0°C.

**Polarization measurements.**—A cyclic voltammogram for Cu in purified 1M KF-HF is shown in Fig. 5. The scan rate was 800 mv/min, scanning first from 0 to +200 mv vs. a Cu/CuF<sub>2</sub> reference electrode. The current scale in this figure is in terms of ma/cm<sup>2</sup> so that the small currents noted in Fig. 4 are not observable. The form of the curve is substantially different than that of the impure solutions. Apparently only one major process, presumably formation of CuF<sub>2</sub>, is involved.

The i-E curve (Fig. 5) has two principal features: an anodic current peak and a less pronounced cathodic current peak. The anodic peak height was dependent on stirring, scan rate, and number of anodic-cathodic cycles to which the electrode had been subjected. In a quiescent solution the area under the anodic peak (between 0 to 200 mv) and the area under the corresponding cathodic peak (between 0 and -400 mv) was found to be equal at a scan rate of 800 mv/min. In cases when the anodic scan was taken to potentials more positive than +200 mv, the subsequent cathodic area was smaller. This may be attributed to partial dissolution of the film. Such behavior has been observed for anodic films in aqueous solutions (16).

When scan rates much slower than 800 mv/min (160 and 80 mv/min) were used, it was observed that the anodic peak areas were significantly larger than those at 800 mv/min, although the cathodic areas were unchanged. This indicates a loss by convection and diffusion of a soluble intermediate from the vicinity

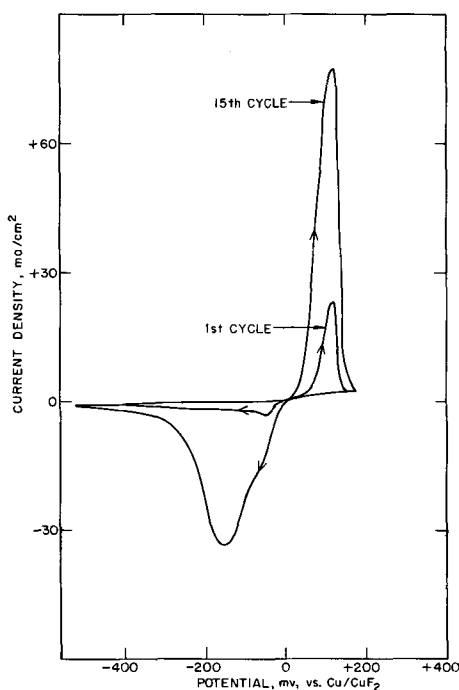


Fig. 5. Cyclic voltammograms at a Cu electrode in purified HF (1M KF) at 0°C. Scan rate was 800 mv/min, and scans were started at the open-circuit potential, i.e., 0 mv.

of the electrode surface during the formation of the film of  $\text{CuF}_2$ . Similar behavior was observed in the chronopotentiometric experiments (see below).

With each subsequent anodic-cathodic scan, the anodic and cathodic peak heights (and areas) increased, suggesting that the electrode was progressively roughened (Fig. 5). The same behavior was observed with respect to transition times during repetitive constant-current cycling. In 2M KF, the anodic and cathodic peaks were considerably greater, indicating a proportionality between the basicity of the HF solution and the extent of  $\text{CuF}_2$  formation.

A summary of the initial peak areas on fresh Cu electrodes and peak areas after 15 anodic-cathodic cycles in 1M and 2M KF solutions is given in Table II.

From the data in Table II, the initial average film thickness was estimated as  $4 \times 10^{-6}$  cm in 1M KF solution and  $1 \times 10^{-5}$  cm in 2M KF. Alternatively, using the data of Table II, one can estimate an apparent number of molecular layers of  $\text{CuF}_2$  after the method of Hickling and Taylor (18). Thus the initial film thickness in 1M and 2M KF solution was calculated to correspond to 47 and 125 molecular units, respectively. These estimates of molecular units would, in the case of a compact film, correspond to the number of molecular layers. However, the fact that the initial film is as thick as it is suggests that the film has relatively poor protective powers; i.e., the film is noncontinuous or porous. Hackerman, Snavely, and Fiel (8) concluded that Cu was intermediate in its corrosion resistance in HF. They placed Cu between metals such as Ta and Ag which corroded rapidly, and Pt and Ni which were quite stable.

**Differential capacitance measurements.**—Double layer capacitance measurements were made at  $-200$

Table II. Anodic peak areas from i-E curves (scan rate 800 mv/min) recorded at Cu electrodes in HF at 0°C

	Basicity of HF	
	1M KF, mc/cm <sup>2</sup>	2M KF, mc/cm <sup>2</sup>
Initial scan	58	155
15th Cycle	421	531

Table III. Differential double layer capacitance of Cu electrode and charge associated with anodic film formation in HF (1M KF) at 0°C

	C at $-200$ mv ( $\mu\text{f}/\text{cm}^2$ )	Q anodic (mc/cm <sup>2</sup> )	Q <sub>a</sub> /C <sub>dl</sub> (mc/ $\mu\text{f}$ )
1st Cycle	20	58	2.9
2nd Cycle	36	120	3.3
3rd Cycle	105	139	1.3
4th Cycle	138	176	1.3
5th Cycle	167	194	1.2

mv vs.  $\text{Cu}/\text{CuF}_2$  before each anodic potential scan. The results are shown for the first five cycles in Table III, together with the total anodic charge passed to  $+200$  mv (Q anodic) and with the ratio Q anodic/C<sub>dl</sub>. It can be seen that the increase in anodic charge with cycling is primarily due to surface roughening. There is not, however, a direct proportionality between the increase of surface area and the anodic charge.

**Chronopotentiometry.**—A potential-time curve obtained for the formation and discharge of  $\text{CuF}_2$  in 1M KF-HF is shown in Fig. 6 at a current density of 6.7 ma/cm<sup>2</sup> in an unstirred solution. The main feature is the equality of the anodic and cathodic transition times. This implies that an insoluble film is formed on anodization, in agreement with the observations from cyclic voltammetric scans (Fig. 5). These observations also imply that the effect of small amounts of water present (ca. 0.01M) on the anodic formation and cathodic reduction of  $\text{CuF}_2$  was negligible. At lower current densities, it was observed that two poorly defined transition times actually were present on the reduction step. At current densities much higher than 20 ma/cm<sup>2</sup>, the cathodic transition time became too distorted to measure.

The question of diffusion control was checked by observing the effect of stirring ( $\text{N}_2$  bubbling) on the transition times. It was found that stirring increased the transition time for the oxidation step ( $\tau_{\text{ox}}$ ) by about 100% at 15 ma/cm<sup>2</sup>, indicating some form of diffusion control, but  $\tau_{\text{red}}$  was independent of stirring and approximately equal to the  $\tau_{\text{ox}}$  at the same current density in an unstirred solution. This effect of stirring at short transition times is equivalent in terms of convection and diffusion to the effect of using slow scan rates (see below). These effects can be discussed

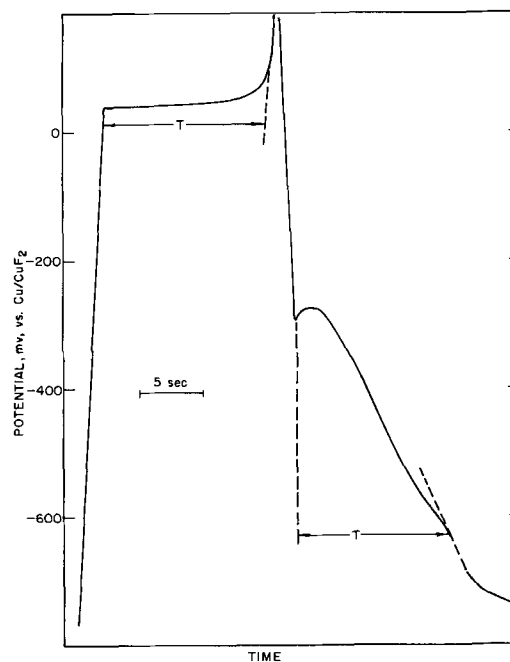
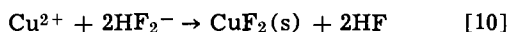
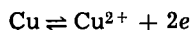


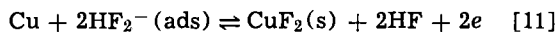
Fig. 6. Potential-time curve at a Cu electrode in purified HF (1M KF) at 0°C. Current density was 6.7 ma/cm<sup>2</sup>.

in terms of the two possible general mechanisms of CuF<sub>2</sub> film formation.

One mechanism involves the dissolution of Cu to Cu<sup>2+</sup> followed by precipitation of CuF<sub>2</sub> at the electrode surface, *i.e.*



The other mechanism involves the direct formation on the electrode surface of CuF<sub>2</sub>, *via* an adsorbed film of HF<sub>2</sub><sup>-</sup>, *i.e.*



If [11] were the operative process, then stirring would enable the passive film to be formed more rapidly, shortening (or in any case not increasing)  $\tau_{\text{ox}}$ . On the other hand with [10] as the process, stirring would have the effect of removing some of the Cu<sup>2+</sup> ions from the vicinity of the electrode surface or of removing some of the CuF<sub>2</sub> before it had precipitated on the surface. In either event the effect would be to increase  $\tau_{\text{ox}}$ , as was observed. Thus the film of CuF<sub>2</sub> was most likely formed *via* the dissolution of Cu to Cu<sup>2+</sup> ions. The same argument can be applied to explain the observed increase of anodic charge with decreasing scan rates.

The results of the galvanostatic charging experiments on individual electrodes are summarized in Table IV. The interesting points to note are that  $i\tau$  decreases with increasing  $i$ , while  $i\tau^{1/2}$  increases with increasing  $i$ . This indicates that processes controlled by diffusion become increasingly important at higher current densities. This is at variance with the usual observation that either  $i\tau$  or  $i\tau^{1/2}$  is constant with increasing  $i$  during the formation of porous (or non-continuous) anodic films (16). Generally, at low  $i$  (large  $\tau$ ) diffusion is more important and  $i\tau^{1/2}$  is constant. At large  $i$  (small  $\tau$ ) it is usually found that  $i\tau$  is constant.

The explanation for the observed behavior in the present case probably involves the influence of a rate-limiting step associated with the crystallization of the precipitated CuF<sub>2</sub> (21).

**Tafel parameters.**—As shown in Fig. 6, the CuF<sub>2</sub> electrode comes to a steady potential within approximately 1 sec after the application of a constant current. At low current densities, *e.g.*, 2  $\mu\text{amp}/\text{cm}^2$ , this potential was constant for over 1 hr. It was therefore possible to characterize the initial surface in terms of the Tafel parameters by exposing the surface to a series of constant current pulses of sufficient duration (*e.g.*, 2 sec) to establish a steady potential, but not so long as to consume a substantial portion of the surface. The anodic polarization behavior was determined first, followed by the cathodic behavior.

These Tafel parameters represent a complex combination of overpotentials involving the dissolution of copper metal, the potential dependence of nucleation and growth of the anodic CuF<sub>2</sub> film, and possibly other processes. Nevertheless, this representation is convenient for summarizing experimental data.

A Tafel plot is given in Fig. 7. Tafel behavior was obtained for both anodic and cathodic processes. It can be seen that the anodic and cathodic processes have

Table IV. Analysis of E-t curves recorded at Cu electrodes in unstirred 1M KF solution in HF at 0°C

$i$ , ma/cm <sup>2</sup>	$\tau$ , sec	$i\tau^{1/2}$ , sec <sup>1/2</sup>	$i\tau$ , mc/cm <sup>2</sup>	$i\tau^{1/2}$ , mc sec <sup>1/2</sup> cm <sup>-2</sup>
9.1	9.25	3.0	85	27.6
15.5	5.25	2.3	79	34.9
21.2	3.63	1.9	76	40.3
30.4	1.90	1.4	58	42.0
33.4	2.00	1.4	67	47.0
39.5	1.60	1.3	63	50.0
45.5	0.88	0.9	39	42.7
51.5	0.94	1.0	49	50.0

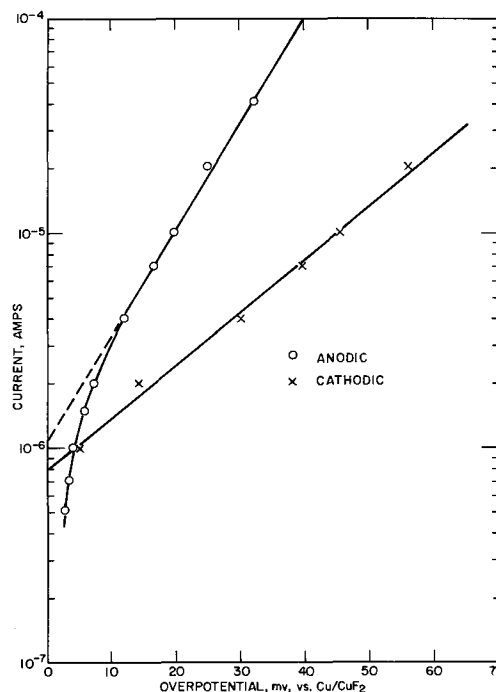


Fig. 7. Tafel plots for Cu electrode in purified HF (1M KF) at 0°C. Electrode area was 0.33 cm<sup>2</sup>.

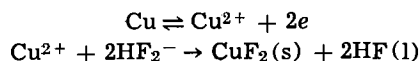
different intercepts on the current axis and hence different apparent exchange current densities. This is indicative of two different processes which may or may not be multistep processes (22). The apparent exchange current density for the anodic process is  $3.0 \times 10^{-6}$  amp/cm<sup>2</sup> and for the cathodic process,  $2.4 \times 10^{-6}$  amp/cm<sup>2</sup>. The anodic Tafel slope is 20 mv and the cathodic Tafel slope 42 mv. The apparent exchange current density for the formation of NiF<sub>2</sub> at a nickel electrode in anhydrous HF containing 0.01M NaF is of the same order of magnitude (9), namely  $3.7 \times 10^{-6}$  amp/cm<sup>2</sup>.

### Conclusions

The Cu/CuF<sub>2</sub>(s) couple is a reliable reference electrode in basic, anhydrous HF. The electrode meets the requirements of satisfactory polarization and has a meaningful thermodynamic potential *vs.* an H<sub>2</sub> electrode in the same solution. The value measured, +276  $\pm$  5 mv agrees well with that calculated from thermodynamic data at 25°C.

The formation of an insoluble anodic film at a Cu electrode in a 1M KF solution in HF at 0°C was demonstrated by cyclic voltammetry and chronopotentiometry. A film thickness of  $4 \times 10^{-6}$  cm (400Å) was estimated for the initial anodic formation of CuF<sub>2</sub>. Anodic-cathodic cycling of Cu electrodes gave rise to a significant roughening of the electrode surface as shown by *i*-E curves, E-t curves, and differential capacitance measurements on cycled electrodes. X-ray analyses of these films confirmed the presence of crystalline copper fluoride.

Evidence from the chronopotentiometric and cyclic voltammetric experiments indicates that the anodic formation of CuF<sub>2</sub> proceeds *via* a soluble intermediate according to the following mechanism



rather than through the surface reaction of Cu with adsorbed HF<sub>2</sub><sup>-</sup>. During the formation of CuF<sub>2</sub>,  $i\tau$  decreased and  $i\tau^{1/2}$  increased with increasing  $i$  over the range 10 to 50 ma/cm<sup>2</sup>.

The polarization behavior of Cu electrodes in basic HF solution showed that film formation can be approximated by Tafel lines with an apparent exchange

current density for the anodic process of about  $3.0 \times 10^{-6}$  amp/cm<sup>2</sup> and a Tafel slope of 20 mv.

The properties of the anodic film of CuF<sub>2</sub> formed in basic HF solutions are similar to the properties observed for noncontinuous, anodic films formed in aqueous solutions (21). Thus such films tend to be thick ( $>10^{-6}$  cm) and crystalline, have low resistance to current flow during film formation, and their formation leads to surface roughening.

#### Acknowledgment

The authors wish to acknowledge the support of the U. S. Navy Air Systems Command (NOW 66-0621-C).

Manuscript received Aug. 1, 1967; revised manuscript received Dec. 2, 1967.

Any discussion of this paper will appear in a Discussion Section to be published in the December 1968 JOURNAL.

#### REFERENCES

- G. C. Koerber and T. De Vries, *J. Am. Chem. Soc.*, **74**, 5008 (1952).
- A. F. Clifford and E. E. Zamora, *Trans. Faraday Soc.*, **57**, 1963 (1961).
- A. F. Clifford, W. D. Pardieck, and M. W. Wadley, *J. Phys. Chem.*, **70**, 3241 (1966).
- H. P. Raaen, *Anal. Chem.*, **34**, 1714 (1962).
- H. P. Raaen, *ibid.*, **37**, 1355 (1965).
- J. W. Sargent, A. F. Clifford, and W. R. Lemmon, *ibid.*, **25**, 1727 (1953).
- J. H. Simons *et al.*, *This Journal*, **95**, 47 (1949).
- N. Hackerman, E. S. Snavely, and L. D. Fiel, *Corrosion Science*, **7**, 39 (1967).
- N. Hackerman, E. S. Snavely, and L. D. Fiel, *Electrochim. Acta*, **12**, 535 (1967).
- H. H. Hyman and J. J. Katz, in T. C. Waddington, "Non-Aqueous Solvent Systems," Academic Press, London and New York (1965).
- H. K. Fredenhagen and O. Kreft, *Z. Electrochem.*, **35**, 670 (1929).
- J. H. Simons, in J. H. Simons, "Fluorine Chemistry," vol. 5, Academic Press, London and New York (1964).
- O. Kubaschewski and E. L. Evans, "Metallurgical Thermochemistry," 2nd edition, John Wiley & Sons, New York (1956).
- D. D. Wagman *et al.*, "Selected Values of Chemical Thermodynamic Properties," NBS Technical Note 270-1.
- L. W. Niedrach and H. R. Alford, *This Journal*, **112**, 117 (1965).
- T. P. Hoar, in J. O'M. Bockris, "Modern Aspects of Electrochemistry," No. 2, Butterworths, London (1959).
- R. C. Weast, Editor, "Handbook of Chemistry and Physics," 45th Edition, Chemical Rubber Co., Cleveland, Ohio (1964).
- A. Hickling and D. Taylor, *Trans. Faraday Soc.*, **44**, 262 (1948).
- K. Fredenhagen and G. Cadenbach, *Z. physik. Chem.*, **A146**, 245 (1930).
- F. Will and C. A. Knorr, *Z. Electrochem.*, **64**, 258 (1960).
- D. A. Vermilyea, in P. Delahay, "Advances in Electrochemistry and Electrochemical Engineering," vol. 3, Interscience, New York, London (1963).
- K. Vetter, "Electrochemical Kinetics," English ed., Academic Press, New York, London (1967).
- J. M. Crabtree, C. S. Lees, and K. Little, *J. Inorg. and Nucl. Chem.*, **1**, 213 (1955).
- P. Delahay, "New Instrumental Methods in Electrochemistry," p. 119, Academic Press, New York (1955).
- G. Cady, *J. Am. Chem. Soc.*, **56**, 1431 (1934).

## LEED Studies, Adsorption of Carbon Monoxide on the Tungsten (112) Face

Chuan C. Chang

Bell Telephone Laboratories, Murray Hill, New Jersey

#### ABSTRACT

Carbon monoxide adsorbs on the clean tungsten (112) face with an initial sticking probability of  $>0.9$  at room temperature and desorbs with heat in three stages, the W(112)- $\alpha$ ,  $-\beta_1$ , and  $-\beta_2$  at 400°, 1000°, and 1200°K with about  $5 \times 10^{14}$  molecules/cm<sup>2</sup> in each state at maximum coverage. Room temperature adsorption is nondissociative and almost random. Heating a CO covered surface produces well defined C(6x4), P(2x1), C(2x4) and "Complex" structures. The  $\alpha$ -CO does not contribute directly to any diffraction pattern. The  $\beta_1$  is associated with the P(2x1) and C(2x4) structures, and an irreversible temperature activated conversion at about 1000°K produces  $\beta_2$  molecules; these are responsible for the C(6x4) and Complex structures. Experiments with (112) substrates containing adsorbed oxygen show that CO does not react to produce CO<sub>2</sub>, that CO does not adsorb onto an adsorbed oxygen atom and that in the presence of oxygen not all exposed tungsten atoms adsorb CO. The (112) surface is composed of two exposed (112) planes, and by covering only the second layer tungsten atoms with oxygen, it was found that CO adsorbs on the topmost layer as well as on the second layer. Molecules adsorbed on the top layer desorb as  $\beta_1$  and the maximum number of  $\beta_2$  molecules on the surface was proportional to the number of second layer tungsten atoms not covered by oxygen.

Low Energy Electron Diffraction (LEED) studies of carbon monoxide adsorption on the tungsten (112) face are of interest because of the possibilities of obtaining reliable values for sticking probabilities and coverages and of studying the atomistics of the adsorption process. Adsorption of CO on the (110) (1, 2) and (100) (3) faces of this bcc metal has been studied with LEED. The CO-W system has also been investi-

gated by other methods, notably flash desorption (4-14), field microscopy (15-19), and calorimetry (20).

The present investigation is an extension of the work on the oxidation of the tungsten (112) face (21) and is part of a wider program in which the interaction of oxygen, carbon monoxide, and nitrogen with this face was studied (22). We are concerned here with adsorption of CO on the clean tungsten

surface, and also on surfaces previously exposed to oxygen.

### Experimental Procedure

A tungsten crystal was cut to expose a (112) face to a precision of about  $0.1^\circ$ . The thickness was 0.15 mm and the surface area  $4 \times 14$  mm. The ends of the crystal were welded to tungsten supports. The crystal was heated with a.c. and the temperature could be found from tungsten-rhenium thermocouple wires welded to the side not studied by electron diffraction. The studies were made in a Varian LEED chamber equipped with a gas handling system, a quadrupole gas analyzer, and an ion gauge. During exposure of the crystal to CO, the total amount of active residual gases could be maintained (22a) at below 1% for CO pressures above  $2 \times 10^{-8}$  Torr. The crystal was cleaned by repeated oxidation followed by flashing above  $2200^\circ\text{K}$ . Electron micrographs of the cleaned surface showed no discernible features down to a resolution of  $70\text{\AA}$ . Since large numbers of steps and other imperfections smaller than  $70\text{\AA}$  would have been detected with LEED, it is concluded that the surface was effectively atomically smooth.

### Adsorption on the Clean Surface

The clean surface was found to have the ideal bcc (112) configuration (22b). A marble model of this surface is shown in Fig. 1. This surface consists of two exposed (112) planes; each plane is made up of parallel rows of close-packed atoms and the inter-row distance is a relatively large  $4.46\text{\AA}$ . Thus the  $[\bar{1}\bar{1}\bar{1}]$  close-packing direction (vertical in the photograph) and the  $[1\bar{1}0]$  direction (horizontal) are "non-degenerate;" this, together with the fact that the unit cell vectors are orthogonal, make this a most appropriate surface for LEED work.

*Flash desorption.*—Much information not obtainable from LEED can be obtained from flash off experiments; these are presented first [for descriptions of flash off methods, see ref. (23, 24)].

Three pressure bursts were found in flash desorption, as shown in Fig. 2. These are the  $W(112)\text{-CO-}\alpha$ ,  $-\beta_1$ , and  $-\beta_2$  with desorption temperatures of  $400^\circ$ ,  $1000^\circ$ , and  $1200^\circ\text{K}$ . These temperatures correspond closely to those for the  $\alpha$ ,  $\beta_1$ , and  $\beta_2$  peaks from polycrystalline tungsten (4, 9). Known desorption temperatures of various peaks from single crystal faces and from polycrystalline tungsten are shown in Table I.

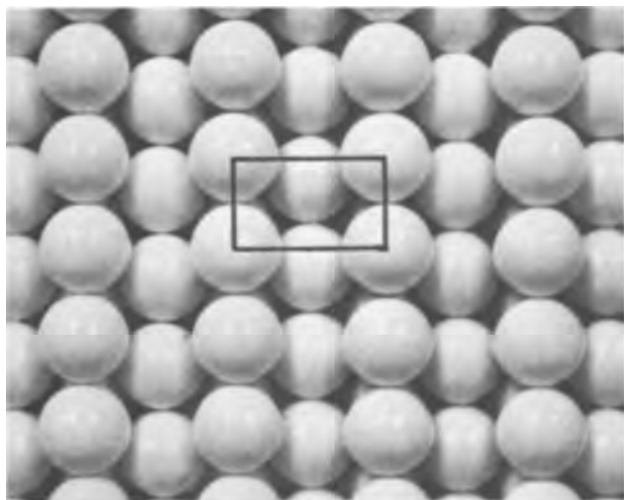


Fig. 1. Marble model of the bcc (112) face. The central rectangle outlines a surface unit mesh. The close packed rows of top layer atoms are separated by open channels or troughs. The asymmetric positioning of the second layer with respect to the topmost layer introduces an asymmetric intensity distribution in diffraction patterns observed at normal incidence.

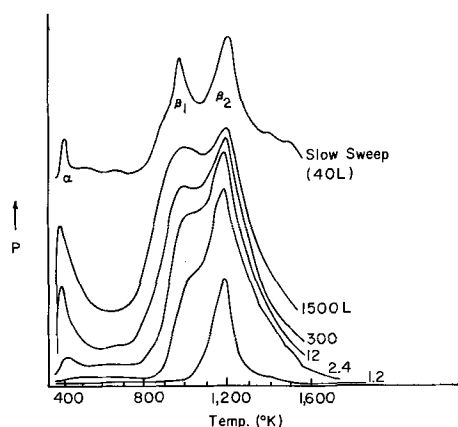


Fig. 2. Flash desorption from the (112) face after different exposures to CO (the exposure unit 1L =  $10^{-6}$  Torr-sec). Heating rate  $300^\circ\text{K/sec}$ , except for the top trace. The zero of pressure has been changed for each curve to avoid overlapping.

It was found in the present experiments that most of the  $\alpha$ -CO on the surface can be "pumped off" in good vacuum even after a heavy exposure. Also, the  $\alpha$  desorption temperature falls from about  $500^\circ\text{K}$  to below  $400^\circ\text{K}$  with increasing coverage. These observations indicate that for this physisorbed component, there is a dynamic balance between adsorption and desorption. In contrast,  $\beta$ -CO molecules do not spontaneously desorb at room temperature. We can therefore conclude that a firmly bound state already exists after room temperature adsorption.

Others have also found that the  $\alpha$  peak height and desorption temperatures are pressure and exposure dependent (8, 10), and in addition, that the  $\beta$ -CO adsorbs as an immobile layer (15, 16) and that CO does not dissociate upon adsorption (4, 15, 16, 26). For the (112), the  $\beta$  desorption temperatures are independent of coverage. At maximum coverage  $\beta_1$  and  $\beta_2$  contain equal amounts as measured by comparing areas under flash off curves.

*Sticking probability and coverage.*—Sticking probabilities and coverages were measured in three ways; flash desorption, gas uptake (22c), and analyses of changes in diffraction patterns. Results from the first two methods for the initial sticking probability  $S(O)$  and saturation coverage  $\sigma_0$  are presented in Group A of Table II; this group lists results obtained from measurements of changes in CO pressure. The data for the present results are summarized in Fig. 3. Results from diffraction pattern studies (next section) are given in Group B of the table with results of several other workers; this group did not depend primarily on measurements of changes in CO pressure. In addition, they are concerned only with the  $\beta$  component.

Entries in Group B show remarkable agreement; in contrast, values in Group A show scatter and are consistently low, especially for  $S(O)$ . The source of error for Group A is the well known wall desorption (and adsorption) of CO. This is why  $S(O)$  is affected more and workers who reduced these effects obtained the highest values for  $S(O)$ , ref. (6, 7) of Table II. In the present experiments, wall desorption is known to be appreciable from the slow response of the pressure to

Table I. Temperatures ( $^\circ\text{K}$ ) of CO desorption peaks from tungsten

Surface	$\alpha$	$\beta_1$	$\beta_2$	$\beta_3$	Reference
(110)	450	1100	None	None	1
(100)	—	None	1150	1380	3
(112)	400	1000	1200	None	This work
(114)	500	None	None	1300	25
(113)	—	—	—	—	7, 14
Polycryst.	500	1000	1200	1300	8
Polycryst.	400	1000	1300	1500	10

Table II. Initial sticking probability and final coverage, carbon monoxide on tungsten, 300°K

Surface <sup>a</sup>	Method <sup>a</sup>	S(O)	$\sigma_0(\theta_0)^b$	Reference
<b>Group A</b>				
(112)	U, F	0.25	6	This work
(114)	U	0.36	6.5	25
(113)	U	0.62	5.8	7
(113)	U, F	0.2	7.5	14
P	U, F	0.62	6	6
P	U, F	0.5	9.5	8
P	U, F	—	10	13
P	U	0.27	10.1	27
P	F	0.5	4.8	4
P	F	0.3	—	5
P	F	—	5	10
<b>Group B</b>				
(110)	LEED	~0.9*	10 (0.71)*	1
(100)	LEED	~1	10 (1.00)	3
(112)	LEED	>0.9	10 (1.25)	This work
P	FEM	0.97	—	11

<sup>a</sup> P = polycrystalline (except for the single crystal Field Microscopy tip labeled FEM), U = uptake, F = flash desorption.

<sup>b</sup> Saturation coverage,  $\sigma_0$ , in units of  $10^{14}/\text{cm}^2$  and  $(\theta_0)$ , in monolayers, where a monolayer equals the density of atoms in one (hkl) plane.

\* Not values given in ref. (1), as those were "normalized" to agree with some of the results of Group A above; values presented here were obtained by comparing areas under flash off curves from the (110) and (112) faces, since LEED observations on the (110) do not readily give coverages as for the (100) and (112).

sudden changes in CO leak rate, as compared to the rapid response for oxygen.

**LEED observations.**—CO adsorbed at room temperature produces a diffuse diffraction pattern with no well defined extra spots and with high background intensity. The bright background is indicative of disorder. This is very different from the sharp patterns with high contrast seen after oxygen adsorption (21). Sharp diffraction patterns are, however, seen after heating.

In experiments involving heating, the crystal was given various exposures to CO at room temperature and then heated to progressively higher temperatures in good vacuum. Well defined C(6x4), P(2x1) and C(2x4) patterns were found with this treatment; in addition, a "Complex" pattern was found which has no well defined symmetry. These are displayed in Fig. 4. Much of the data can be summarized in a temperature-exposure diagram showing the conditions under which each pattern is observed; this diagram is shown in Fig. 5. Significant findings about the surface structures are presented in Table III.

The two most important results are that each structure can be associated with a particular gas burst observed in flash desorption and that for three of the structures, their coverages have been found.

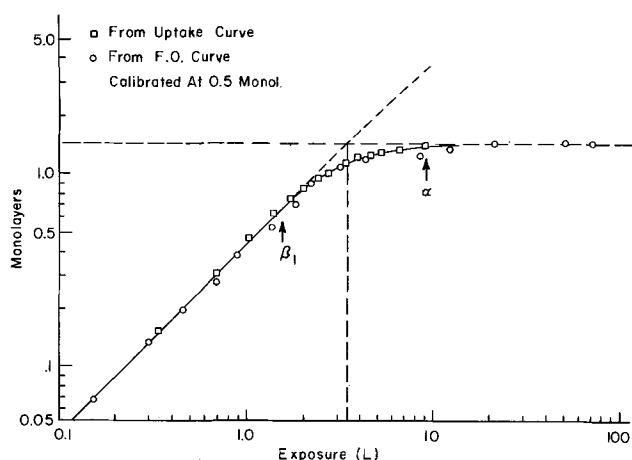


Fig. 3. Amounts of adsorbed CO against exposure, obtained from uptake and flash off curves. Arrows show the minimum exposures at which the  $\beta_1$  and  $\alpha$  peaks appear on the flash off curves. Calibrated using LEED results by assigning the value of  $\frac{1}{2}$  monolayer to the amount absorbed after 1.2L.

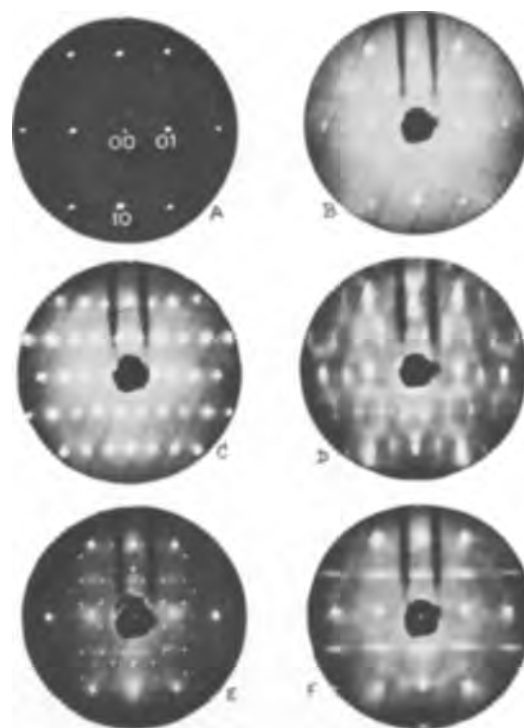


Fig. 4. Diffraction patterns from CO adsorption. (A) clean surface, Miller indices shown on some of the spots. (B) after saturation exposure at room temperature. (C) to (F), the C(2x4), Complex, C(6x4) and P(2x1) patterns. All taken at 80v except (E) and (F), at 81v, normal incidence.

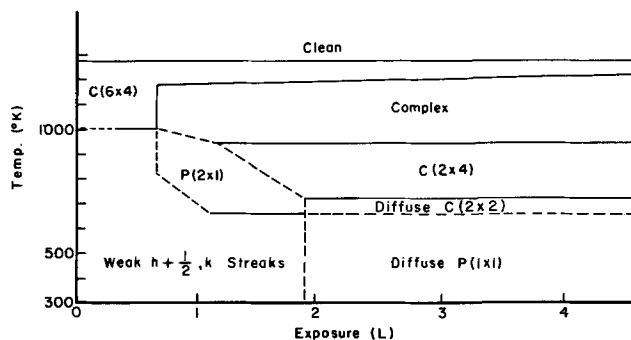


Fig. 5. Temperature-exposure ranges in which various CO patterns appear for initial room temperature exposures shown on the abscissa followed by heating to progressively higher temperatures in good vacuum.

As an example of how the entries in the table were obtained, consider the P(2x1). This pattern will develop to its best if the crystal is heated to about 750°K after an exposure of 1.2L (1L =  $10^{-6}$  Torr-sec), see Fig. 5. Since a P(2x1) symmetry represents multiples of  $\frac{1}{2}$  monolayer of scatterers (1 monolayer =  $8 \times 10^{14}/\text{cm}^2$  on this face) and 1.2L represents 0.57 monolayer of molecular collisions with the crystal, the coverage must be  $\frac{1}{2}$  monolayer. The average sticking probability up to  $\frac{1}{2}$  monolayer is then about 0.9. The P(2x1) is stable up to about 1000°K (Fig. 5) when it changes to a weak Complex pattern with no detectable gas evo-

Table III. CO structures on the (112) face

Pattern	Exposure, L	Coverage, monolayer	Destruction temperature, °K	Associated F. O. peak
C(6 × 4)	0.6	1/4	1200	$\beta_2$
P(2 × 1)	1.2	1/2	1000	$\beta_1$
C(2 × 4)	>1.4	5/8 to 10/8	1000	$\beta_1$
Complex	>1.5	5/8	1200	$\beta_2$

lution and then to a C(6x4) at about 1200°K with loss of some CO. Because the destruction temperature of the P(2x1) coincides with the  $\beta_1$  desorption temperature, we are led to associate the P(2x1) with the  $\beta_1$ -CO.

It is unmistakable that  $\beta_2$  molecules are responsible for the C(6x4) and Complex structures since all the  $\beta_1$  molecules have been desorbed when either of these patterns is seen. However, the  $\beta_1$  can only be loosely associated with its structures. Strong supporting evidence that  $\beta_1$  molecules produce the P(2x1) and C(2x4) comes from the fact that the  $\beta_1$  desorption temperature is the same as the destruction temperature for these structures. Further evidence will be presented in the section on LEED observations and surface structures.

The C(2x4) pattern first appears at a coverage of about  $\frac{5}{8}$  monolayers. Additional molecules, up to full coverage, do not substantially affect the diffraction pattern. This is one example of the many possible pitfalls wherein coverage estimates based on diffraction patterns alone can go wrong. Fortunately, for the P(2x1), a unique value could be found so that the flash off data could be calibrated at  $\frac{1}{2}$  monolayer. This calibration is, therefore, all important and a separate check of its correctness will be provided in the section on LEED observations and surface coverage.

The Complex pattern was so named because it has no well defined symmetry. It is nevertheless interesting, as adsorbed nitrogen produces a practically identical pattern (22d). Note that this unusual pattern (Fig. 4D) consists of streaky features quite unlike the spot patterns normally observed in LEED. It is therefore surprising that two gases give this same strange pattern. A little investigation shows, however, that these gases have much in common. First, CO and N<sub>2</sub> are iso-electronic. Second, they have been associated with the concept of surface complexes which arose out of attempts to account for the kinetics of the nitrogen-tungsten system (28,29) and the results from isotopic mixing experiments with CO (13) and N<sub>2</sub> (30,31).

Conditions under which isotopic mixing becomes appreciable correspond to conditions for the formation of the Complex structures for both CO and N<sub>2</sub>. Under these same conditions it is generally believed that both atoms of the nitrogen molecule are in contact with the metal. Since the CO-Complex pattern indicates that CO has the same configuration, it is concluded that both atoms of this molecule also contact the substrate in the  $\beta_2$  state.

Diffraction pattern studies do not give direct information on the coverage for the Complex structure as it has no well defined symmetry. The coverage was estimated to be about  $\frac{5}{8}$  monolayer by comparing the flash desorption amount with that from  $\frac{1}{2}$  monolayer coverage.

**Surface structures.**—Of the four CO structures on the clean surface, the P(2x1) is simplest. It is like the oxygen P(2x1)  $\frac{1}{2}$  monolayer structure so that every trough site h,k with h even is occupied by a CO molecule. Accordingly, the intensity-voltage curves from these two P(2x1) patterns are quite similar. Although the tungsten surface is undisturbed in the P(2x1) structure, the possibility of reconstruction (32, 33) has not been ruled out for the other three structures. Note, however, that because of the simplicity of the P(2x1) structure and the large minimum distance of 4.46Å between scatterers, the conclusion that this structure requires  $\frac{1}{2}$  monolayer of adsorbates is expected to remain valid whether the surface is reconstructed or not.

The C(2x4), C(6x4), and Complex patterns show a diversity of behavior which indicates that not enough is as yet known about them for a meaningful structure analysis.

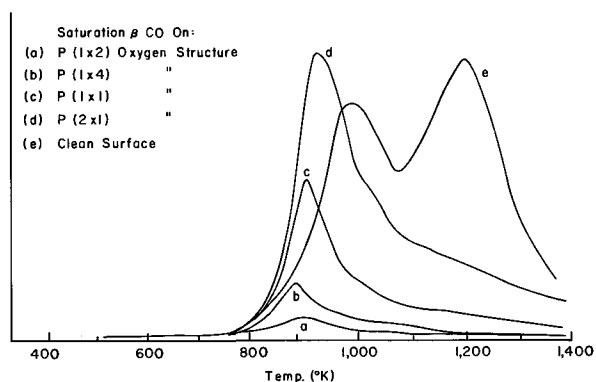


Fig. 6. CO flash off from oxygen structures after saturation exposure at room temperature. Heating rate 300°K/sec. (a) to (e) in order of decreasing oxygen content.

A simple model that can account for all of the present results is the one in which  $\beta_1$  molecules adsorb at room temperature undissociated, with only the carbon contacting the metal. A temperature activated transformation to the  $\beta_2$  occurs after heating to about 1000°K and in this state both carbon and oxygen contact the metal. In the Complex structure,  $\beta_2$  "molecules" agglomerate into surface stabilized complexes that can be studied at room temperature.

### Adsorption onto Oxygen Structures

Experiments in which CO is adsorbed on a surface previously covered by oxygen might seem to have special interest because of this bearing on the catalytic formation (2) of CO<sub>2</sub>. These experiments could also provide a check for the CO coverage estimates because the oxygen coverages are quite reliably known. In carrying out such experiments, the oxygen surface structures (21, 22e) were used as substrates. These are the facet structures produced by exposing a hot crystal to oxygen and five nonfacet structures.

**Flash desorption.**—No CO<sub>2</sub> was observed to flash off from any of the oxygen structures and repeated adsorption and desorption of CO left the surface oxygen content undiminished. In most cases, the original oxygen structure remained apparently undisturbed, as reported earlier (2). Thus no oxygen could be removed by CO from these structures.

The flash off data of Fig. 6 shows that only one  $\beta$  peak desorbs from the oxygen structures. These structures, together with their oxygen coverages and their per cent of tungsten atoms still uncovered, are listed in Table IV. The amounts of  $\beta$ -CO that adsorb are shown in row 4 as a per cent of the maximum that adsorbs on the clean surface.

Figure 6 shows that the  $\beta_2$  peak is suppressed by pre-adsorption of oxygen and that the observed  $\beta$  desorption occurs essentially at the  $\beta_1$  temperature [actually, almost 100°K lower, as also happens in the case of CO on W(110)-O[ $\frac{1}{2}$ ] structure; compare Fig. 5 of ref. (1) with Fig. 3B of ref. (2)]. Accordingly, we shall see below that the  $\beta_2$  structures are never seen.

Table IV shows that the per cent of adsorbed CO decreases faster than the per cent of exposed tungsten atoms as more of the surface is covered with oxygen.

Table IV.  $\beta$ -CO flash off from the oxygen structures

1. Clean	P(2 x 1)	P(1 x 1)	P(1 x 4)	P(1 x 2)	P(1 x 3)	Facet
0	$\frac{1}{2}$	1	$1\frac{1}{4}$	$1\frac{1}{2}$	1-2/3	~2
100	75	50	38	25	17	0
100	80	40	15	3	0	0
100	75	50	13	0	0	0

1. Oxygen structures; 2. oxygen coverage in monolayers; 3. per cent of exposed tungsten atoms; 4. per cent of  $\beta$ -CO observed to flash off; and 5. amounts of adsorbed  $\beta$ -CO as predicted from diffraction pattern observations (section on LEED observations and surface structures).



**LEED observations and surface structures.**—The above flash off experiments show that adsorbed oxygen inhibits CO adsorption. We now examine this in more detail as the (112) face is gradually covered with more and more oxygen atoms.

We start by covering half of the second layer tungsten atoms with oxygen. This is accomplished by using the oxygen P(2x1) structure which is constructed by placing an oxygen atom into every other trough site, thus exposing 75% of the original 2 monolayers of surface tungsten atoms.

Adsorption of CO on the P(2x1) results in a P(1x1) pattern so that the spaces between oxygen atoms have become filled with CO. Heating this P(1x1) produces a C(2x4) as with adsorption on the clean surface. This C(2x4) is destroyed near 900°K with desorption of about  $\frac{3}{8}$  monolayer of CO, leaving a second, much sharper, P(1x1). If we hypothesize that CO does not stick to an adsorbed oxygen, then all the CO desorbed during the formation of this P(1x1) was initially adsorbed on the top layer tungsten atoms. Here is a second evidence that molecules adsorbed on the top layer desorb essentially as  $\beta_1$  and that these molecules produce the C(2x4) pattern. We are now ready to perform a very important experiment, since all the excess CO has now been removed so that the remaining P(1x1) must be a monolayer structure.

When all the CO is flashed off from this second P(1x1), the area under the flash off curve is equal to that from the P(2x1)-CO structure. This serves as a check for the  $\frac{1}{2}$  monolayer calibration of the CO flash off, as the only other calibration used the extremely streaky P(2x1)-CO pattern (Fig. 4F) which could not be made as sharp and bright as the oxygen P(2x1). Unlike the case with CO, the  $\frac{1}{2}$  monolayer estimate for the P(2x1) oxygen structure could be checked with the uptake method, and most important, it was shown that the P(2x1) oxygen structure covered the entire surface. Moreover, a deviation from  $\frac{1}{2}$  monolayer of only 5% would be easily detectable for the P(2x1) oxygen pattern (22f).

In the above P(1x1)-O[ $\frac{1}{2}$ ] + CO [ $\frac{1}{2}$ ] structure, the CO is lodged into the spaces between adsorbed oxygen atoms so that the CO molecule has an effective diameter of less than about 2.8Å, much smaller than the 3.2-4.1Å obtained from several other methods.

Next we use the P(1x1)-O[1] structure in which the troughs are completely filled with a monolayer of oxygen atoms so that only the close packed rows of top layer tungsten atoms are exposed. With this substrate, the C(2x4) is observed, but not the P(2x1). This again shows that the  $\beta_1$  and C(2x4) are associated with the top layer tungsten atoms and that molecules responsible for the P(2x1) are located above the second layer tungsten atoms. All these conclusions, however, depend on the hypothesis that CO does not adsorb onto the oxygen atoms. This is quite clearly shown in the following experiment in which an oxygen structure with the next higher coverage, the P(1x4)-O[ $\frac{1}{4}$ ], is used.

The P(1x4) is constructed by covering every fourth top tungsten row on the P(1x1)-O[1], say rows 0, 4, 8, . . . , with oxygen. Upon adsorption of CO, this pattern changes to a P(1x2) so that rows 2, 6, 10, . . . become covered with CO, leaving 1, 3, 5, . . . still bare. Thus about 13% of the original surface tungsten atoms adsorb CO.

Adding more oxygen, we use the P(1x2)-O[ $\frac{1}{2}$ ] structure in which only every second top row is bare, and the P(1x3)-O[ $\frac{1}{3}$ ] structure in which only every third row is bare. Since CO does not adsorb on these surfaces, not all exposed tungsten atoms can accept CO although these actively adsorb oxygen.

Finally, the oxygen faceted surface exposes to the CO only (110)-type planes covered with a monolayer of oxygen atoms. Failure to find any CO adsorption on

faceted surfaces again confirms the hypothesis that CO does not stick to an adsorbed oxygen.

Enough was described above so that entries in row 5 of Table IV can be found from a knowledge of the oxygen structures and the diffraction pattern changes accompanying CO adsorption. A tacit assumption was made throughout that adsorbates scatter slow electrons sufficiently to produce the observed patterns. That this assumption is valid is most dramatically illustrated by the close match in Table IV between the observed flash off amounts in row 4 and the predicted values in row 5, since the predictions were based on models arrived at from diffraction pattern analyses.

#### Acknowledgment

The author would like to thank Dr. L. H. Germer for his support and encouragement and for reading the manuscript.

This work was performed at Cornell University, Ithaca, New York, supported by the Advanced Research Projects Agency through the Cornell Material Science Center.

Manuscript received Sept. 22, 1967; revised manuscript received ca. Nov. 13, 1967. This paper was presented at the Dallas Meeting, May 7-12, 1967, as Abstract 177.

Any discussion of this paper will appear in a Discussion Section to be published in the December 1968 JOURNAL.

#### REFERENCES

1. J. W. May and L. H. Germer, *J. Chem. Phys.*, **44**, 2895 (1966).
2. J. W. May, L. H. Germer, and C. C. Chang, *ibid.*, **45**, 2383 (1966).
3. J. Anderson and P. J. Estrup, *ibid.*, **46**, 563 (1967).
4. G. Ehrlich, *ibid.*, **34**, 39 (1961).
5. G. Ehrlich, *ibid.*, **36**, 1171 (1962).
6. R. E. Schlier, *J. Appl. Phys.*, **29**, 1162 (1958).
7. V. M. Gavrilyuk and V. K. Medvedev, *Sov. Phys., Solid State*, **4**, 1737 (1963).
8. P. A. Redhead, *Trans. Faraday Soc.*, **57**, 641 (1961).
9. P. A. Redhead, Proc. Symp. on Electron and Vac. Phys., Hungary (1962).
10. L. J. Rigby, *Can. J. Phys.*, **42**, 1256 (1964).
11. A. A. Bell and R. Gomer, *J. Chem. Phys.*, **44**, 1065 (1966).
12. T. W. Hickmott and G. Ehrlich, *ibid.*, **24**, 1263 (1956).
13. T. E. Madey, J. T. Yates, and R. C. Stern, *ibid.*, **42**, 1372 (1965).
14. J. Eisinger, *ibid.*, **27**, 1206 (1957).
15. R. Gomer, *ibid.*, **28**, 168 (1958).
16. R. Klein, *ibid.*, **31**, 1306 (1959).
17. L. W. Swanson and R. Gomer, *ibid.*, **39**, 2813 (1963).
18. E. Menzel and R. Gomer, *ibid.*, **41**, 3329 (1964).
19. A. A. Holscher, Doctoral Thesis, Univ. of Leiden, Netherlands, (1967).
20. D. Brennan and F. J. Hayes, *Phil. Trans. Roy. Soc., London*, No. 1089, **258**, 325 (1965).
21. C. C. Chang and L. H. Germer, *Surface Sci.*, **8**, 115 (1967).
22. C. C. Chang, Doctoral Thesis, Cornell Univ., Ithaca, N. Y., (1967).
- 22a *Ibid.*, chap. II. 1.
- 22b *Ibid.*, chap. III.
- 22c *Ibid.*, Appendix III.
- 22d *Ibid.*, chap. VI.
- 22e *Ibid.*, for descriptions of the oxygen structures, see chap. IV. 2d.
- 22f *Ibid.*, chap. IV. 2b.
23. P. A. Redhead, *Vacuum*, **12**, 203 (1962).
24. G. Ehrlich, *J. Chem. Phys.*, **32**, 4 (1961).
25. J. A. Becker, *Solid State Phys.*, **7**, 379 (1958).
26. W. J. M. Rootsaert, L. L. von Reijen, and W. H. M. Sachtler, *J. of Catalysis*, **1**, 416 (1962).
27. F. Ricca, A. G. Nasini, and G. Saini, *ibid.*, **1**, 458 (1962).
28. W. K. Warburton, M. S. Thesis, Cornell Univ., Dept. Engineering Physics, Ithaca, N. Y. (Sept. 1965).
29. J. L. Robins, W. K. Warburton, and T. N. Rhodin, *J. Chem. Phys.*, **46**, 665 (1967).
30. J. T. Yates and T. E. Madey, *ibid.*, **43**, 1055 (1965).
31. T. E. Madey and J. T. Yates, *ibid.*, **44**, 1675 (1966).
32. L. H. Germer, *Surface Sci.*, **5**, 147 (1966).
33. E. Bauer, *ibid.*, **5**, 152 (1966).



# Environmental and Reaction Studies on Electrochemical Cells Based on Solid Charge-Transfer Complexes

F. Gutmann,<sup>1</sup> A. M. Hermann,<sup>2</sup> and A. Rembaum

Jet Propulsion Laboratory, California Institute of Technology, Pasadena, California

## ABSTRACT

Solid state electrochemical cells using metal anodes with charge transfer complexes as cathodes which were previously reported have been further studied. The presence of the  $I^-$  ion has been verified in cells with iodine as the acceptor. Quantitative recovery of the reaction product in amounts proportional to the total charge delivered, substantiates the originally proposed reaction mechanism. Long time decay data under a steady load as well as under a pulsed load, extending over periods of up to nine months, are presented. It is shown that the performance of the cells is considerably improved by the admission of vapors of high permittivity liquids into the anode-electrolyte interface. Evidence is presented that the effect is primarily due to improved availability of reactant at the electrode surface.

We have previously reported (1) data on solid state electrochemical cells using metal anodes and a charge transfer complex as cathode. In the present communication, we wish to present further results on cells of the type Mg/Phenothiazine- $I_2$ /Pt. The well-known phenothiazine-iodine charge transfer complex (2) has the advantage of high electronic conductivity; however, donors other than phenothiazine have also been employed yielding similar results.

## Experimental

The cells were assembled in the holders previously described (1); the complex was produced by intimately mixing reagent grade phenothiazine and iodine as received in the stoichiometries indicated below.

The currents and voltages were measured by means of a Hewlett Packard 412A-VTVM unless stated otherwise.

## Reaction Mechanism

We have proposed a reaction mechanism (1) involving the  $I^-$  ion. In order to support this contention,  $MgI_2$  was recovered thus:

A cell was prepared using a 1:2 phenothiazine:iodine complex and then continuously discharged in ambient atmosphere and at room temperature over a period of nine months into a constant 31.6 ohm load; i.e., for this cell, virtually a short circuit load. The integration of the area under the current vs. time curve showed that a total of 216 coulombs had been delivered by this cell. The cell was then dismantled and analyzed for  $MgI_2$  (the electrolyte) by extracting the contents with distilled water. This solution was stirred, filtered, and the filtrate was treated with aqueous ammonia and an excess of  $(NH_4)_2HPO_4$  was then added. The precipitate formed was filtered, dried, and analyzed for Mg and for phosphate. The recovery was 190 mg of  $MgNH_4PO_4$  corresponding to the passage of 282 coulombs. Thus, the difference of 66 coulombs must have been consumed in a side reaction. This reaction is most likely an internal corrosion process at the Mg anode, probably associated with traces of water present in the ambient atmosphere.

The above data, therefore, support the reaction mechanism which was based on the formation of  $MgI_2$  (1).

## Long Time Decay Curves. Effect of Solvent Vapors

The above test commenced with the rather low short circuit current density of  $560 \mu A/cm^2$ ; after two days, the short circuit density was of the order of  $30 \mu A/cm^2$ ;

after nine months, the current density had dropped to about  $4 \mu A/cm^2$ . The initial open circuit voltage was 1.7v; after one week, it recovered to a value of 1.5v after removal of the load for a few seconds. This recovery voltage was maintained to  $\pm 0.1v$  for seven months of the total test period. After nine months, the recovery open circuit voltage had dropped to 1.2v. The results of a further decay test are shown in Fig. 1. These data refer to another cell of the type Mg/phenothiazine:iodine 1:2/Pt, but in an atmosphere saturated with acetonitrile vapor. The cell had an initial open circuit voltage of 1.7v. Its voltage under a continuous load of 5000 ohm was recorded over a period of 415 hr. The voltage is seen to keep substantially constant over about 10 hr whence it commences to decay approximately linearly at a rate of about 7 mv/hr. This rate is then maintained over about 70 hr.

A further series of discharge tests was performed using an electromechanical oscillator (3) as the load. A typical oscillogram is reported in Fig. 2. This oscillator draws a current pulse of 200-300  $\mu A$  of 6-8 msec duration at a repetition frequency of 6  $sec^{-1}$ ; its impedance is partly inductive, causing the transient waveshape of the sharp spikes. The discharge test was carried out at room temperature in (uncontrolled) laboratory atmosphere. The cell, with initial open circuit voltage 1.62v and short circuit current 3.4 ma, operated in a room atmosphere with the oscillator load for 480 hr. At this point, the open circuit voltage

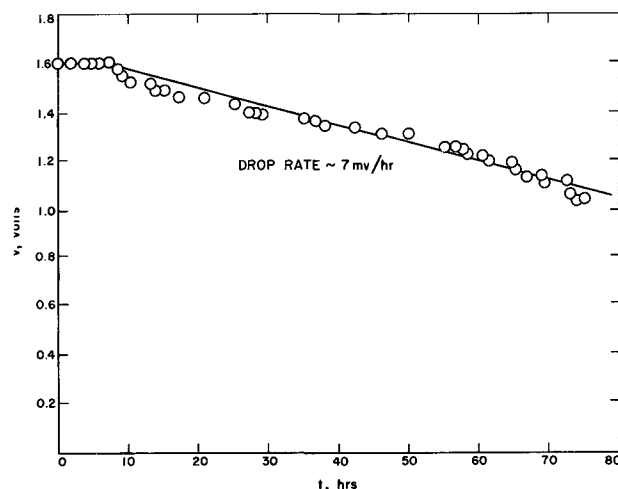


Fig. 1. Decay of the terminal voltage for the system Mg/phenothiazine;  $I_2$  1:2/Pt. The test was conducted in saturated vapors of acetonitrile under a constant load of 5000 ohm.

<sup>1</sup>Present address: Institute for Direct Energy Conversion, University of Pennsylvania, Philadelphia, Pennsylvania 19104.

<sup>2</sup>Present address: Physics Dept., Tulane University, New Orleans, Louisiana 70118.

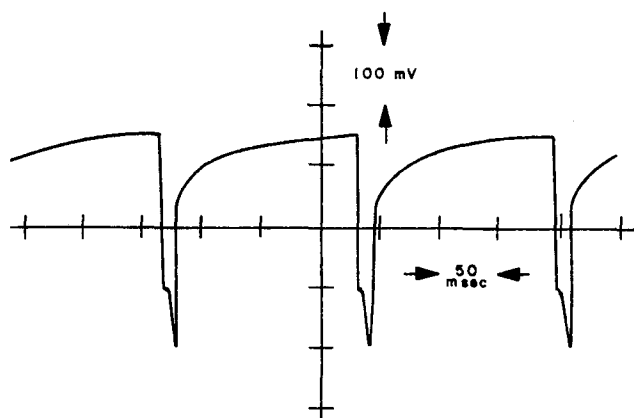


Fig. 2. Pulsed oscillogram depicting the time dependence of the terminal voltage for the cell Mg/phenothiazine;  $I_2$  1:2/Pt. Current was drawn for 6-8 msec at a repetition frequency of  $6 \text{ sec}^{-1}$  causing the terminal voltage drop shown.

had dropped to 0.5v. Upon exposure without load to a high humidity atmosphere for 24 hr, the open circuit voltage recovered completely. Continuing the test under load in the high humidity environment, 550 hr were required for the voltage to drop to 0.5v. The difference  $\Delta V$  between open circuit and loaded voltage remained fairly constant, even though the open circuit voltage itself dropped. Total operating time was 1032 hr (43 days) of which 552 hr occurred in a humid atmosphere. Another cell was tested with a purely resistive load of 4700 ohm, which was periodically connected to the battery by a switching circuit (8 msec "on", 172 msec "off"). The open circuit voltage was 1.59v, and the current through a 10 ohm load was 4.2 ma. In room temperature, an open circuit voltage of 0.5v was reached after 192 hr. The cell was then subjected for 24 hr to the humidity treatment described above. Only an additional 48 hr of operation in room atmosphere were obtained before the open circuit voltage again dropped to 0.5v. Recharging with  $500 \mu\text{a}$  for 72 hr did not restore the cell. Total accumulated operating time was 250 hr, all in laboratory atmosphere.

In this experiment, carried out in uncontrolled laboratory atmosphere,  $\Delta V$  increased significantly with time.

In the experiment carried out in a controlled, humid atmosphere, the wave forms obtained remained constant and showed no variation with time, *i.e.*, there was no difference in the shape nor in the amplitude of the voltage pulses as measured by connecting an oscilloscope across the cell throughout the duration of the test.

The difference  $\Delta V$  between the terminal voltage under a load  $R_L$  and the voltage  $V'$  to which the cell recovers just before the start of the following pulse thus remains constant though the recovery voltage itself decreases approximately linearly during the test. We shall now investigate the conditions under which one could expect  $\Delta V$  to be constant with time.  $\Delta V$  represents the voltage drop across the internal resistance due to the current pulse

$$\Delta V = \frac{V'}{\frac{\partial V}{\partial I} + R_L} \frac{\partial V}{\partial I} \quad [1]$$

Since the decay of  $V'$  is approximately linear<sup>3</sup> with time  $t$ , we may write an explicit decay function in

<sup>3</sup> Prima facie one would expect the decay to be exponential; the linear decay characteristic observed during a limited time interval thus might well be the equivalent to taking only the first, linear, term in an exponential series. Since Fig. 1 indicates that such a linear approximation does hold for the time interval considered, the following analysis will apply to the same degree of approximation.

terms of an open circuit voltage  $V$

$$V' = V(1 - \alpha t) \quad [2]$$

where  $\alpha$  is a decay constant. Since  $\Delta V$  is independent of time

$$\left. \frac{\partial \Delta V}{\partial t} \right|_I = 0 \quad [3]$$

Hence

$$(1 - \alpha t) \left( \frac{\partial V}{\partial I} + R_L \right) \frac{\partial^2 V}{\partial I \partial t} - \alpha \frac{\partial V}{\partial I} \left( \frac{\partial V}{\partial I} + R_L \right) - \frac{\partial V}{\partial I} (1 - \alpha t) \frac{\partial^2 V}{\partial I \partial t} = 0 \quad [4]$$

Since this must hold for all values of  $t$ , the terms containing  $t$  explicitly must vanish

$$(1 - \alpha t) R_L \frac{\partial^2 V}{\partial I \partial t} = 0 \quad [5]$$

$$\therefore \frac{\partial}{\partial t} \frac{\partial V}{\partial I} = 0 \quad [6]$$

Thus the dynamic internal resistance must remain constant with time. This leaves only one term remaining in Eq. [4]

$$\alpha \frac{\partial V}{\partial I} \left( \frac{\partial V}{\partial I} + R_L \right) = 0 \quad [7]$$

so that

$$\frac{\partial V}{\partial I} = -R_L \quad [8]$$

The second condition for the time independence of  $\Delta V$  (Eq. [8]) therefore is the requirement that the load resistance matches the internal dynamic resistance of the cell. The latter quantity is, of course, negative since the cell is an active circuit element; an increase in current is accompanied by a drop in cell voltage. To the extent that this very simplified analysis holds—see footnote—the constancy of the voltage drop  $\Delta V$  during the tests in a humid atmosphere is thus seen to be associated with the dynamic internal resistance of the cell remaining constant, plus the rather fortuitous approximate equality between the values of the load resistance and the dynamic internal cell resistance. We note that the latter quantity remains constant in the humid environment though not in the uncontrolled laboratory atmosphere. Since the dynamic internal resistance ( $\partial V/\partial I$ ) is the sum of a constant ohmic series resistance plus a polarization or diffusion resistance term, it follows that the diffusion resistance is held constant in the presence of a vapor of high permittivity liquid, but not in its absence. Hence the admission of solvent, although not necessarily water, vapor tends to assist the diffusion processes, causing a substantially constant and improved rate of diffusion of  $I^-$  ions into the reaction site. The decay involves the shift of the entire polarization curve to lower voltage values, parallel to itself, without a change in its slopes.

Further experiments aimed at determining the influence of gases and vapors on the performance of these cells showed that the complete removal of all solvent and water vapors reduces the short circuit current by 2 to 3 orders of magnitude below the value recorded in ambient laboratory atmosphere (1) (see Fig. 3). Likewise, the introduction of benzene or  $\text{CCl}_4$  vapor into the otherwise dry and solvent free system causes no increase in the short circuit current density. However, dry vapors of acetone, methylalcohol, or acetonitrile cause the current density to rise to values of up to several 100 ma/cm<sup>2</sup>, higher by about an order of magnitude than the best current densities obtainable in an uncontrolled room atmosphere. Water vapor has a similar effect. In brief, it appears that the presence of vapors of liquids of high permittivity improves

the performance of these cells while vapors of low permittivity liquids do not affect the short circuit current densities available as compared to those under vacuum or dry conditions.

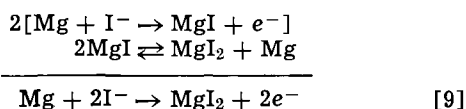
Thus, e.g., a cell prepared and tested in air gave a short circuit current of 4.0 ma which, upon drying out with  $\text{CaCl}_2$  dropped to 50  $\mu\text{a}$ . Introduction of methanol vapor raised the current to 70 ma. Likewise, admission of acetonitrile vapor into a dried and solvent-free cell raised the current from 50  $\mu\text{a}$  to 50 ma.

Moreover, the open circuit voltages of cells kept in a solvent-free environment produced by either evacuating or exposure to a drying agent such as  $\text{CaCl}_2$ , drop from the thermodynamical value of 1.85v to values in the vicinity of 1.2v. There is no increase in open circuit voltage nor short circuit current on admission of vapors of benzene or  $\text{CCl}_4$ .

Figure 3 illustrates the effect of admission of acetonitrile vapor on the short-time decay of the current into a constant 5000 ohm load, with vapor pressure as the parameter: the cells were kept in an evacuated glass vessel and acetonitrile vapor at controlled pressures was then admitted.

The beneficial effect of a high permittivity solvent vapor atmosphere must be due to the permeation of the vapors into the anode-electrolyte interface. This contention is supported by the following observations: (i) corrosion of the electrode surface starts at the edges and thence penetrates inwards; (ii) assembly of a complete cell under high pressure in a hydraulic press yields cells with characteristics essentially those of cells maintained in a completely solvent free environment; (iii) insertion of a semipermeable membrane, say a thin sheet of cellulose or of polypropylene-acrylic acid graft copolymer, between the Mg anode and the solid, tends to raise the value of the short circuit current considerably; the open circuit voltage likewise is brought even closer to its thermodynamical value of 1.87v. Insertion of such a separator anywhere else but directly into the anode-solid interface causes both open circuit voltage and short circuit current to decrease. It appears that the separator acts as a wick assisting the penetration of solvent vapor into the interface. Cells assembled with the separator extruding beyond the electrode and then wetted with acetonitrile produced current densities of the order of hundreds of  $\text{ma}/\text{cm}^2$ , significantly in excess of the performance of untreated cells; (iv) the constancy of the polarization resistance in the presence of vapors, discussed above, indicates that such vapors are effective in assisting processes within the reaction zone near the anode.

The introduction of vapor of a high permittivity solvent may either increase the reaction rate in the energy producing reaction (1)



or it may retard poisoning of the electrode surface by assisting in the removal of the reaction product, *viz.*,  $\text{MgI}_2$ . However, the voltage pulse waveforms obtained are considerably different from those expected in a regime in which poisoning of the electrode surface is the main effect. Such waveforms have been reported, e.g., by Schuldner and Hoare (4). The time constants involved here (see Fig. 2) are too long, by at least a factor of a hundred, to be entirely caused by electrode poisoning. Moreover, the admission of such vapors into a solvent-free cell causes an immediate and sudden rise in the current density, far too fast for an effect associated with the dissolution of the  $\text{MgI}_2$ .

Thus, it appears that this effect involves an increase in the rate of the first step of the above reaction sequence, which is the rate-determining step. More specifically, the energy of the activated complex  $\text{MgI}^-$

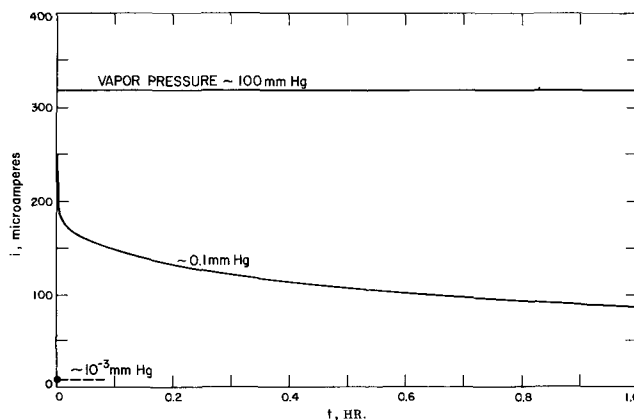


Fig. 3. Current decay curve for the system Mg/phenothiazine;  $\text{I}_2$  1:2/Pt. The cell was operated into a constant load of 5000 ohm at various vapor pressures of acetonitrile.

must be substantially lowered: this may occur by solvation or, perhaps more likely, by an increase in the polarization energy of the activated complex, since only highly polarizable molecules enhance the current.

This suggestion is supported by the work of Hale and Mehl (5) who ascribe current limitation in a Redox organic electrolyte system to either diffusion limitation or to a reorientation of the solvation shell of the reactant. Thus, the vapor in the present case might well form an adsorbed liquid thin film yielding sufficient surface solvation energy (6) to facilitate the reaction: the solvated ion then becomes isoenergetic with an appropriate energy band of the solid (5).

Another contributing factor to such a "flat-band condition" would be changes in the work function and electron affinity of both the metal anode and of the charge transfer complex: high permittivity media are known (7) to be active in this respect; thus an adsorbed water layer changes the work function of a solid polymer by several hundred millivolts (8).

During each current pulse of the pulse experiment,  $1.3 \times 10^{13}$  electrons were consumed. At the anode surface, even assuming complete coverage, about  $6 \times 10^{11}$   $\text{I}^-$  ions are available. Thus, these data refer to a regime of diffusion control. Furthermore, consider a cell discharged continuously into a matched load, corresponding to a reaction rate (1) of  $1.5 \times 10^{15}$  ions  $\text{cm}^{-2} \text{sec}^{-1}$ , and a calculated diffusion layer (1) of 0.05 cm thick containing  $2.7 \times 10^{16}$  ions. At these current densities, diffusion would be rate determining.

In the solid system, it is to be expected that diffusion limitation sets in at lower overvoltages already than in a corresponding liquid system: indeed, the exchange current density  $i_0$  obtained (1) for the present, solid, system is of the order of  $10^{-5}$  amp- $\text{cm}^{-2}$ , while Vetter (9) reports values of the order of  $10^{-2}$  to  $10^{-3}$  amp- $\text{cm}^{-2}$  for a liquid iodine/iodide Redox system. Since (9)

$$\left( \frac{\partial \log i_0}{\partial \log [\text{I}^-]} \right)_{E=\text{const}} \cong 1 \quad [10]$$

it appears that it is the exhaustion of the  $\text{I}^-$  supply at the anode surface which causes the current to become diffusion limited.

Thus, at the higher current densities, where the current tends to become diffusion controlled, the introduction of vapor also involves an improved diffusion rate. At least in part, this is due to the increased diffusion gradient caused by the increase in reaction rate discussed above. However, it may well be that a liquid layer at the interface as such substantially assists in the diffusion processes.

#### Acknowledgment

The continued interest and constructive criticism of Professor Pierre van Rysselberghe, Stanford University, are gratefully acknowledged.

This paper represents one phase of research performed by the Jet Propulsion Laboratory, California Institute of Technology, sponsored by the National Aeronautics and Space Administration, Contract NAS7-100.

Manuscript received July 12, 1967; revised manuscript received Nov. 24, 1967.

Any discussion of this paper will appear in a Discussion Section to be published in the December 1968 JOURNAL.

#### REFERENCES

1. F. Gutmann, A. M. Hermann, and A. Rembaum, *This Journal*, **114**, 323 (1967).

2. Y. Matsunaga, *Helv. Phys. Acta*, **36**, 800 (1963); F. Gutmann and L. E. Lyons, "Organic Semiconductors," p. 726, John Wiley & Sons, Inc., New York (1967).
3. See, for example, R. J. Brodd, *This Journal*, **106**, 471 (1953).
4. S. Schuldner and J. P. Hoare, *J. Chem. Phys.*, **26**, 1771 (1957).
5. J. M. Hale and W. Mehl, *Surface Science*, **4**, 221 (1966).
6. D. O. Raleigh, *J. Phys. Chem.*, **71**, 1785 (1967).
7. F. Gutmann and L. E. Lyons, *op. cit.*, p. 197.
8. V. B. Margulis, L. I. Boguslavskii, and N. A. Bakh, *Elektrokhimiya*, **3**, 329 (1967).
9. K. Vetter, *Z. Physik. Chem.*, **195**, 337 (1950); **199**, 285 (1952); *Z. Elektrochem.*, **55**, 123 (1951).

## Oxidation of Hydrogen on a Passive Platinum Electrode

Sigmund Schuldiner\*

Naval Research Laboratory, Washington, D. C.

#### ABSTRACT

Under potentiostatic, steady-state conditions and at anodic potentials above 0.7v (NHE), the rate of oxidation of molecular hydrogen decreases at a high activity Pt electrode in 1M H<sub>2</sub>SO<sub>4</sub>. It is shown that this decrease is not owing to the formation of oxygen species on the electrode surface. It is believed that this passive behavior of Pt is due to anion adsorption, at least between 0.7 and 1.2v. Depending on potential and previous potential sequence, passivity in this region is evidently sensitive to the amount of sulfate ion adsorbed, its heat of adsorption, and the presence of dermasorbed oxygen. At higher potentials both sorbed oxygen species and sulfate ion may be present and may contribute to the passivity. In the 0.7-1.2v passive region, hydrogen oxidation is electrochemical. There is no significant chemical oxidation via an oxygen intermediate.

A steady-state electrochemical investigation (1) in a high-purity closed system (2) showed very slow oxidation of water on Pt in helium-saturated 1M H<sub>2</sub>SO<sub>4</sub> in the potential region from 0.46 to 1.6v (*vs.* NHE). That work (1) established the solvent (water) reaction rates in this potential region. Since the oxidation of water occurs at such slow rates, it appears that on the addition of an easily oxidizable species to the system, the oxidation of this added species would predominate.

Several papers (3,4) by Wroblowa *et al.* demonstrated that even though the rate of hydrocarbon oxidation is increased as the potential is increased to about 0.9v, the rate of oxidation decreases at higher potentials. They postulated that this decrease in reaction rate was caused by the formation of a Pt oxide which passivated the surface. Even though the work was done at 80°C, compared to the previously mentioned study (1) on water oxidation, which was at 26°C, there is a question as to why an oxide should be formed in the presence of an oxidizable species in the potential region of interest.

The answer to this question is, of course, a matter of mechanisms. If water oxidation is rate-controlling, then in the presence of a species which is electrochemically inert but which is chemically oxidized rapidly by the oxidation product of water on Pt, the rate of water oxidation may be increased. However, in such a case the accumulation of the oxidation product of water would not occur and could not cause passivation of the surface. If the oxidizable species is electrochemically oxidized faster than water and a significant accumulation of an oxygen species from water occurs the reaction may be retarded. However, it is difficult to conceive of an oxidation product of water on a Pt surface which would not be very easily re-

duced, so that chemical reaction of water oxidation products with added oxidizable species is very likely. In any case, if the current density is much greater at a given potential in the presence of an added oxidizable species, the very slow oxidation of water plus the high reactivity of resulting oxygen species makes the passivation of the surface by an oxide or oxidation product of water hardly feasible.

Anodic passivation of a surface has been explained in another possible way by Frumkin (5). He believes that passivation could be caused by the saturation of the free valencies of the electrode surface by chemisorbed anions. Anodic passivation of Pt for the hydrogen reaction has been repeatedly observed by many investigators [see review by Frumkin (6)]. Aikazyan and Fedorova (7) and Wicke and Weblus (8) attributed this passivation to either adsorption of anions or the appearance of surface oxides. Frumkin (6) claims that at high disk-electrode rotation rates the drop in the current maxima can occur at potentials of about 0.05v, which is much too low for an oxide formation and he believes must be due to anion adsorption. Frumkin and co-workers believe that passivation by oxygen occurs at potentials of about 0.8v.

Kazarinov and Balashova (9) showed that as the potential of platinumized Pt became more positive, the concentration of adsorbed sulfate ion increased linearly until a potential of 0.8v was reached. At higher potentials the sulfate ion concentration decreased. They interpreted this decrease as due to the formation of an oxygen species on the surface (their work was done in N<sub>2</sub>-saturated solutions of H<sub>2</sub>SO<sub>4</sub>) which caused a partial displacement of SO<sub>4</sub><sup>=</sup>. On smooth Pt they found that at potentials above 1.5v that there was a sharp increase in adsorbed SO<sub>4</sub><sup>=</sup> which they attributed to the incorporation of these anions in the oxides on the surface. Here one can ask

\* Electrochemical Society Active Member.

the question: "If an oxidizable species (other than water) is present will it, under steady potentiostatic conditions, interfere with the formation of oxygen species on the surface and influence the adsorption of the sulfate ion?"

To try to answer the question of water oxidation in the presence of other oxidizable species and to try to gain some further insight into the passivation of Pt, it was decided to study further the oxidation of hydrogen in the passive Pt region. Hydrogen was selected because it is easily oxidized on active Pt and its maximum rate of oxidation of  $2 \times 10^{-3}$  amp/cm<sup>2</sup> (true area basis) in H<sub>2</sub>SO<sub>4</sub> is from 2 to 7 orders of magnitude greater than water oxidation (1) in the same potential region. Use of the high-purity closed system (1, 2) developed at this Laboratory would permit long-time steady-state measurements where relatively slow sorption phenomena could affect electrode behavior. This system also allowed a determination of the hysteresis, when high potentials are decreased, noted by Frumkin and Aikazyan (10).

### Experimental and Results

The experimental setup and conditions were the same as described in ref. (1), except that a constant flow of hydrogen, purified by flowing through heated Pd-Ag tubes and saturated with pure water, replaced helium. It was found that an N<sub>2</sub> atmosphere in the environment box was unnecessary and part of the data was taken with the front panel removed. The hydrogen flow into the cell remained at about 40 ml/min until a constant current was reached under potentiostatic control. The time required ranged from a quarter of an hour to many hours, depending both on the set potential and the previous sequence of potentials. The hydrogen flow rate was then increased to well over 1000 ml/min and the constant current recorded. Potentiostatic control was by a Pt/H<sub>2</sub> wire electrode in the cell. The sulfuric acid solution was one molar, the temperature  $25^\circ \pm 2^\circ\text{C}$ , and the true (11) area of the three Pt bead working electrodes used were each close to 0.2 cm<sup>2</sup>.

The experimental results, which are steady-state values, are shown in Fig 1. Figure 1 is for the case of very rapid stirring with H<sub>2</sub> and gives potentiostatic current density vs. potential relations under conditions where diffusion effects in solution are minimized. For the slopes shown,  $b = \Delta E / \Delta \log i$ . The  $b = -0.025$  and  $0.025$  values shown are the well-known Tafel slopes (12) in the cathodic and anodic polarization regions, respectively. At anodic potentials above 40 mv, a limiting current density of  $2 \times 10^{-3}$  amp/cm<sup>2</sup> is observed up to a potential of about 0.7v. At potentials above this value, the current density decreases, at first slowly up to 1.0v, then rapidly along the slope designated as  $b = -0.11$  down to a second limiting current density of about  $1.5 \times 10^{-5}$  amp/cm<sup>2</sup>. At potentials above 1.6v ( $b = 0.13$  slope) the normal oxygen evolution reaction is observed. The diamond-shaped symbols show that potential reversal within a given region gave the same current densities.

After the oxygen evolution region was reached, a subsequent decrease in potentials gave the hysteresis shown. The time required to obtain steady-state for each point in this region ranged from a few hours to a day. The scatter of points and especially the two paths shown in the potential range from 1.16 to 0.88v appeared to be real. Using the same electrode a consistent set of points on either path was followed for a particular run. The path shown by the solid line, however, was favored over the dotted line. The broken line shown in Fig. 1 comes from Fig. 1 of ref. (1) and represents the potential vs. current density relation found in a pure helium-saturated solution.

### Discussion

A comparison of Fig. 1 with the data shown by Frumkin and Aikazyan (6, 10) for hydrogen ionization

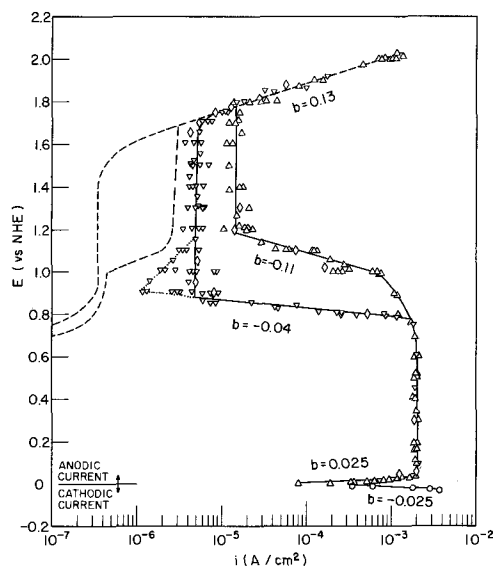


Fig. 1. Steady-state potentiostated current density vs. potential relation on Pt in hydrogen-saturated 1M. H<sub>2</sub>SO<sub>4</sub>·H<sub>2</sub> flow rate > 1000 ml/min: ○ cathodic current, △ anodic current, increasing applied potentials; ▽ anodic current, decreasing applied potentials; ◇ anodic current, intermediary reversal of applied potential values. Broken line is relation in helium-saturated solution (1), where hysteresis line to the right is for increasing applied potentials, to the left for decreasing applied potentials. See text for meaning of dotted line.

on a smooth Pt disk electrode in 1N H<sub>2</sub>SO<sub>4</sub> at a rotation speed of 20,000 rpm shows some important differences. Figure 1 shows a maximum current density from 0.04 to 0.7v of 2 ma/cm<sup>2</sup> (since this current density is on a true area basis it is equivalent to about 4 ma on a geometric area basis). This limiting current density is essentially the same as the Frumkin and Aikazyan value of 3.8 ma/cm<sup>2</sup> (geometric area). In the Frumkin and Aikazyan case, however, the current density maximum is at 0.05v and there is a continuous dropping off of current density with increasing potential up to 1.2v. Figure 1 shows a constant current density at 2 ma/cm<sup>2</sup> up to 0.7v (for both the increasing and decreasing sequence of potentials) followed by a slow decrease and then a linear log decrease in current density up to 1.2v.

The essentially equivalent maximum current densities found by Frumkin and Aikazyan and this work show that the Pt electrodes were of equal activity. The important difference is that Frumkin and Aikazyan anodically and cathodically pre-electrolyzed their electrode just before taking measurements, which were then taken in a matter of minutes at each potential setting. With the high purity system, long time steady-state measurements were possible because poisoning of the electrode did not occur (as, for example, evidenced by the constancy of the maximum current density for long periods of time). Whether the Frumkin and Aikazyan decrease in current density (from 0.05 to 0.7v) was due to impurity adsorption or a lack of true steady-state conditions at the electrode is uncertain.

Considering Pt passivation above 0.7v, the possibility of a stable oxygen species remaining on the surface is remote. In the first place, the oxidation of water, which appears to be limited by slow discharge (1), occurs at rates from about five to one order of magnitude slower. In addition, Schuldiner and Warner (13) have shown that oxygen chemisorbed on Pt reacts rapidly with molecular hydrogen. Warner and Schuldiner (14) have shown also that the reaction rate is potential independent and zero order in both hydrogen and chemisorbed oxygen when the initial fractional coverage with chemisorbed oxygen is less than 0.8. Reaction rates of chemisorbed oxygen with hy-

drogen in this particular system for the three different working electrodes used were 0.4, 1.2, and 8 ma/cm<sup>2</sup>. All three electrodes gave virtually the same potential vs. current density results.

The chemical rate of reaction of any oxygen which may be formed on the surface with hydrogen would with a few exceptions always be faster than the rate of anodic hydrogen oxidation. Hence, there is little possibility that chemisorbed oxygen or an oxygen species exists on the surface at least up to a potential of 1.2v. This analysis does not, of course, prove that an oxygen species may not be formed which rapidly oxidizes the hydrogen and that the rate-controlling process depends either on the rate of formation of this oxygen species or its reaction rate with hydrogen. However, it is very unlikely that the anodic hydrogen reaction under these conditions would be slower than the oxidation of water. (It will subsequently be shown that in this region a chemical oxidation of H<sub>2</sub> with an oxygen intermediate does not occur.) These results show that the oxidation of Pt or the formation and adsorption of oxygen species are not the cause of the Pt passivation and retardation of the anodic hydrogen oxidation reaction at least up to 1.2v.

The cause of passivation is much more likely the anion adsorption explanation as given by Frumkin (5); specifically, the adsorption of sulfate ion as was demonstrated by Kazarinov and Balashova (9). In the Kazarinov and Balashova paper a dropping off of the amount of sulfate ion adsorbed above 0.8v was observed. However, this was done in a nitrogen-saturated solution where formation and adsorption of an oxygen species and the partial replacement of sulfate are possible. In a hydrogen-saturated solution, a residue of oxygen would not remain on the surface so that as the potential increased beyond 0.8v, an increase in the amount of sulfate would be expected. And, in fact, as was shown by Kazarinov and Balashova, at higher potentials the coverage with sulfate ion can increase even in the presence of oxygen. With the elimination of a chemisorbed oxygen species, or Pt oxide, the bonding and coverage of the surface with sulfate ion should increase and is a reasonable explanation of the increased passivity shown in Fig. 1. The limiting current density from 1.2 to  $\approx$  1.8v can be due to a saturation of the surface with sulfate ion.

It should be noted that the  $b = -0.11$  and  $-0.04$  slopes in Fig. 1 are not Tafel slopes. The fact that the rate of hydrogen oxidation decreases with increasing potential demonstrates that the rates are not controlled by the exponential overvoltage term in the kinetic equation. The controlling term is obviously in the free energy of activation for the oxidation of hydrogen. As the potential increases, the free energy of activation can increase because of the increased coverage with sulfate ion and because of the increase in bonding of the sulfate ion with the surface.

In the oxygen generating region ( $b = 0.13$ ) the presence of hydrogen has no apparent effect on the rate of oxidation of water. There is no "so-called" depolarization effect. This must be because the combined sulfate and oxygen sorption in this region is so extensive that significant anodic oxidation of hydrogen is virtually completely blocked. The data also show that the oxidation of water is primarily under charge transfer control. Otherwise, the chemical reaction of hydrogen with oxygen on the surface could influence the rate. In this region current densities were independent of stirring rate which also indicates virtually complete kinetic control.

The effects of dermasorbed oxygen (15) can be seen in the Fig. 1 data. Once the potential exceeds 1.8v, extensive dermasorption occurs and hysteresis results. In the potential range from 1.7 to 1.2v, the rate of hydrogen oxidation is reduced by about one-half. From about 1.16 down to 0.88v either the solid or dotted line was followed. Evidently the amount or distribution of

dermasorbed oxygen may vary from run to run and may markedly influence the passivity behavior of the electrode. This influence of dermasorbed oxygen is evinced also by the scatter of points, which were, however, consistent for a particular run, in the entire region from 1.7 to 0.88v.

Something remarkable occurs in the  $b = -0.04$  region. At current density values greater than  $1.5 \times 10^{-5}$  amp/cm<sup>2</sup>, the potential required for the oxidation of hydrogen at a given current density can be as much as 0.3v less than in the  $b = -0.11$  region. In the  $b = -0.04$  region most of the dermasorbed oxygen would be removed, but a trace must remain because one can go up and down in potential in this region and remain on the  $b = -0.04$  line. Once the intersection at about 0.8v is reached, increasing potentials will follow the path leading to the  $b = -0.11$  slope. This eliminates the possibility of an impurity in the region of decreasing potential. However, at the same potentials on the increasing potential arm of the curve, the current densities are considerably higher. The lower current densities in the  $b = -0.11$  region are evidently due to increased sulfate ion adsorption. Hence in the  $b = -0.04$  region, the presence of dermasorbed oxygen plus the lower sulfate ion adsorption reduces the activation energy (potential) required to oxidize hydrogen at a given rate. However, at a given amount of sulfate ion adsorption the rate of hydrogen oxidation would always be lower in the presence of dermasorbed oxygen.

Another interesting consequence of this region is that the previous work (1) in helium-saturated solution showed that in the presence of dermasorbed oxygen a given rate of oxidation of water to an oxygen species (which was not retarded by increased sulfate ion adsorption) always occurred at a higher potential. If the oxidation of hydrogen took place via an intermediate oxygen species, then in the presence of dermasorbed oxygen a given rate of hydrogen oxidation should never occur at a lower potential. Since in the  $b = -0.04$  region oxidation of hydrogen at a given rate can occur at a lower potential than in the  $b = -0.11$  region [which is free of dermasorbed oxygen (1)] the oxidation cannot be through an oxygen intermediate, but must involve a direct electrochemical oxidation of hydrogen. Another conclusion is that pulsing or other electrochemical activation procedures of electrodes may do more than just clean the surface.

The catalytic properties of platinum are strongly affected by adsorbed sulfate ions and by dermasorbed oxygen. The relationships are very complex, but it appears that a narrowing down of possibilities is resulting. Since information is available concerning very slow solvent oxidation and relatively fast oxidation of the ideal fuel, hydrogen, similar studies made with organic fuels of intermediate oxidizability should be revealing.

Manuscript received Sept. 28, 1967; revised manuscript received Nov. 20, 1967. This paper will be presented at the Boston Meeting, May 5-9, 1968, as Abstract No. 185.

Any discussion of this paper will appear in a Discussion Section to be published in the December 1968 JOURNAL.

#### REFERENCES

1. S. Schuldiner, T. B. Warner, and B. J. Piersma, *This Journal*, **114**, 343 (1967).
2. S. Schuldiner, B. J. Piersma, and T. B. Warner, *ibid.*, **113**, 573 (1966).
3. H. Wroblowa, B. J. Piersma, and J. O'M. Bockris, *J. Electroanal. Chem.*, **6**, 401 (1963).
4. J. O'M. Bockris, H. Wroblowa, E. Gileadi, and B. J. Piersma, *Trans. Faraday Soc.*, **61**, 2531 (1965).
5. A. N. Frumkin, *This Journal*, **107**, 461 (1960).
6. A. N. Frumkin, in "Advances in Electrochemistry and Electrochemical Engineering," vol. 3, pp. 340-358, Paul Delahay, Editor, Interscience Publishing Co., New York (1963).

7. E. A. Aikazyan and A. I. Fedorova, *Dokl. Ak. Nauk, SSSR*, **86**, 1137 (1952).
8. E. Wicke and B. Weblus, *Z. Elektrochem.*, **56**, 169 (1952).
9. V. E. Kazarinov and N. A. Balashova, *Dokl. Ak. Nauk, SSSR*, **157**, 1174 (1964); *Dokl. Phys. Chem.*, **157**, 795 (1964).
10. A. N. Frumkin and E. A. Aikazyan, *Dokl. Ak. Nauk, SSSR*, **100**, 315 (1955).
11. S. Schuldiner and R. M. Roe, *This Journal*, **110**, 332 (1963).
12. S. Schuldiner, *ibid.*, **107**, 452 (1960).
13. S. Schuldiner and T. B. Warner, *ibid.*, **112**, 212 (1965); T. B. Warner, S. Schuldiner, and B. J. Piersma, *ibid.*, **114**, 1120 (1967).
14. T. B. Warner and S. Schuldiner, *ibid.*, **115**, 28 (1968).
15. T. B. Warner and S. Schuldiner, *ibid.*, **112**, 853 (1965).

## Technical Notes

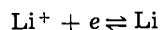


### The Li/Li<sup>+</sup> Reference Electrode in Propylene Carbonate

Brian Burrows\* and Raymond Jasinski\*

Tyco Laboratories, Inc., Waltham, Massachusetts

Recent investigations of the Li(Hg)/Li<sup>+</sup> electrode couple in LiCl-DMSO solutions (1) indicate that the electrochemical reaction



has a relatively high exchange current density, thereby making the system suitable for use as a reference electrode. It is reasonable to expect that the exchange current density of the same electrode couple in LiClO<sub>4</sub>-PC solutions would also be high enough to allow its use as a reference electrode. However, for simplicity in use, a solid electrode would be preferred.

The evaluation of a reference electrode of the metal-metal ion type (in absence of a liquid junction) involves showing that (i) potential differences between pairs of the same electrodes in the same electrolyte solution are reproducibly small and constant over long periods; (ii) the electrode potential responds to varying cation concentrations in accordance with the Nernst equation; (iii) the passage of small amounts of current (microamperes) through the electrode does not permanently polarize it.

#### Experimental

All electrochemical measurements and associated materials handling were carried out in a water and oxygen free (<1 ppm) argon-atmosphere dry box at 28°C (Vacuum Atmospheres Corporation).

Both "anhydrous" LiClO<sub>4</sub> (K&K Laboratories 99.9%) and dried LiClO<sub>4</sub> (Anderson Physics Laboratories) were used to make up solutions. The purified LiClO<sub>4</sub> was prepared from 99.9% LiClO<sub>4</sub>, recrystallized three times from water, and heated to just below the melting point in a vacuum over a period of several days to remove water. Finally, the sample was fused in vacuum and sealed in an argon atmosphere. This crystalline LiClO<sub>4</sub>, obtained from Anderson Physics Laboratories, contained approximately 0.0015% water (15 ppm) and less than 0.0005% chloride. Both "as-received" PC (Matheson, Coleman and Bell) and distilled PC were used to make up 1M solutions with the dried LiClO<sub>4</sub>.

A conventional three-compartment Pyrex glass cell was used, except where stated otherwise. The test lithium electrode was placed in the middle compartment, the reference compartment contacted the middle

compartment through a Luggin capillary, and the counter electrode was in the third compartment. A cathode follower was employed to avoid undue loading of the reference electrode-working electrode cell. The unity-gain follower was constructed from an operational amplifier (Philbrick Researches, Inc., Type P65AU); the input impedance of this device was 33 Mohm.

#### Results

An electrodeposited Li (on a Pt-metal substrate)-Li<sup>+</sup> ion couple was first investigated for use as a reference electrode. Initially, experiments were carried out in 1M solutions of LiClO<sub>4</sub> in distilled PC, in a beaker using Pt foil counter and pseudoreference electrodes. Under these conditions, it was found that the residual current was <60 μa cm<sup>-2</sup> up to -3.0v vs. Pt foil electrode. At -3.6 to -3.8v vs. Pt, a deposit of lithium became visible with the concurrent evolution of gas. Gas evolution during the electrodeposition of lithium was also reported by Selim *et al.* (2). The bias potentials between four of the electroplated lithium electrodes were ± 80 mv for periods of time up to 2 hr.

The next set of experiments was carried out in a 1M solution of LiClO<sub>4</sub> in distilled PC, which had been passed over lithium powder. Currents of 60 μa cm<sup>-2</sup> were observed up to -2.4v vs. Pt and a Li deposit became visible at about -3.2v. No gassing was observed during the deposition of lithium; however, no significant improvement in the potential difference between electroplated lithium electrodes was observed.

Up to this point no effort had been made to separate the counter electrode and the reaction products arising at this electrode from reaching the working electrode. When this was done by the use of a fritted glass plug in a three-compartment cell, lithium was deposited on Pt wire electrodes (area 0.2 cm<sup>2</sup>) from the same solution. For example, when a current of >1 ma cm<sup>-2</sup> was used to form a relatively thick and coherent deposit of Li without gassing, a stable potential difference of ±15 mv was obtained.

Lithium was then deposited onto two platinum foils (area = 1 cm<sup>2</sup>) from a 1M solution of LiClO<sub>4</sub> in PC at current densities of 1 ma/cm<sup>2</sup>, and the potential difference was monitored in a fresh solution. After about 3 hr a stable difference of 23 mv developed and remained steady for a period of 10 hr before the experi-

\* Electrochemical Society Active Member.



ment was discontinued. Polarization tests indicated that the electrodes had a very poor response; considerable hysteresis was observed.

Electrodes were then prepared from Li powder with a copper wire forming the contact to the external circuit. The electrode consisted of a glass tube 0.5 cm in diameter and drawn to a tip of 0.1 cm at one end. A plug of glass wool was placed in the contracted end, and powdered lithium was poured over the plug to a depth of about 0.5 cm. A copper wire spiral contact was inserted and another plug of glass wool pressed over the top of the lithium. Two electrodes of this type, when immersed in a 1M solution of  $\text{LiClO}_4$  in PC, had a potential difference of 1 mv, which remained steady for 10 hr.

Polarization tests were carried out on the lithium powder electrodes by applying a small constant current from a constant current power supply (Electronic Measurement Model C623). The polarization was measured on a differential d-c voltmeter (John Fluke Model 825A). The results are shown in Fig. 1.

The linear relation between overpotential and current as well as the absence of significant hysteresis indicate that the electrodes were behaving reversibly. It will be noticed, however, that the inverse slope has a value of  $2.4 \times 10^6$  ohms. This large value of resistance is probably due in large part to a poor contact between the lithium powder and the copper.

Finally, reference electrodes based on bulk lithium ribbon as a substrate were investigated. The Li ribbon (K&K Laboratories, Inc., 99.9%, approximately 3 mm diameter) was cleaned with acetone before being passed into the dry box. Inside the box the surface was scraped with a spatula until it was bright and metallic in appearance. Three electrodes were then placed in a cell containing distilled PC (1M  $\text{LiClO}_4$ ). The potential differences between these three electrodes were then monitored over a period of several days. It was found that the potential difference between any pair was always  $<1$  mv. Furthermore, it was found that when a fresh electrode was added to the solution after those already present had been submerged for several days, the potential differences were still  $<1$  mv.

A Li electrode in "wet"  $\text{LiClO}_4$  solution rapidly developed a dark gray film on its surface, accompanied by visible gassing. After the gassing subsided, the potential difference with respect to a fresh Li electrode was always  $<1$  mv. The gray film dried to a white

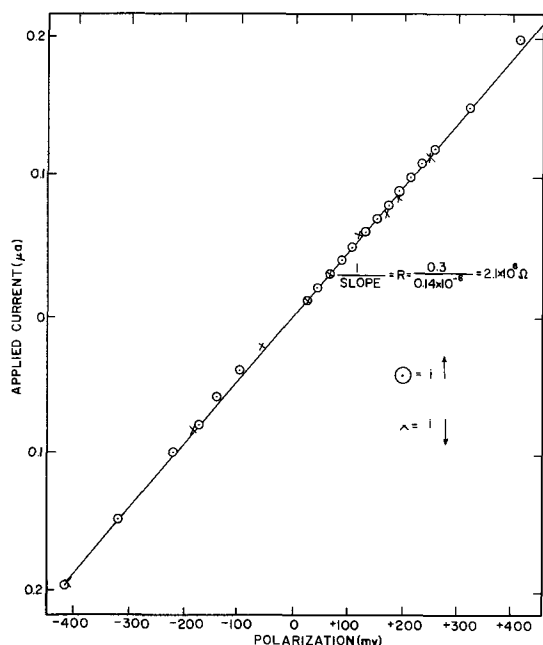


Fig. 1. Micropolarization test on a lithium powder reference electrode in  $\text{LiClO}_4/\text{PC}$  solution at  $28^\circ\text{C}$ .

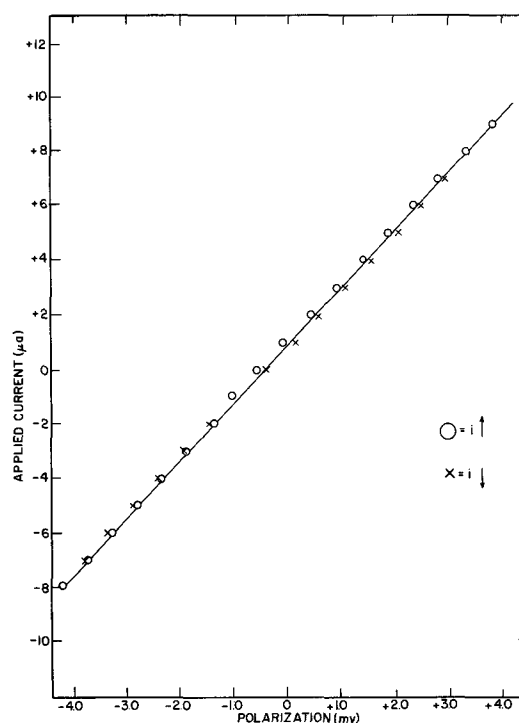


Fig. 2. Micropolarization test on a Li wire electrode (area approx.  $2 \text{ cm}^2$ ) in  $\text{LiClO}_4/\text{PC}$  solution at  $28^\circ\text{C}$ .

color after the electrode was removed from the solution.

Having established that the bias potentials were small and reproducible, we next carried out polarization tests on the solid Li electrodes. It can be seen (Fig. 2) that there is a linear relation between overpotential and current, indicating that the electrodes were behaving reversibly; there was no significant hysteresis. The fact that the line does not go through the origin is due to the slight bias in potential between two lithium rods. A comparison of Fig. 1 and 2 shows that the Li ribbon electrode structure is a considerable improvement over the Li powder structure and is also much simpler to set up.

### Summary

Three forms of  $\text{Li}/\text{Li}^+$  electrodes were evaluated as reference electrodes in 1M lithium perchlorate-propylene carbonate solutions. Electrodeposited lithium proved to be very susceptible to poisoning by impurities in the electrolyte and by those generated at the counter electrode. An electrode constructed from lithium powder in a glass tube was stable over prolonged periods of time and showed little hysteresis in the micropolarization tests. However, the ohmic resistance was high, due presumably to poor contact with the copper lead wire.

A lithium ribbon electrode, scraped clean before immersion in solution, was satisfactory for most work and was quite simple to prepare. Hysteresis in the micropolarization tests was negligible ( $<1$  mv). Replicate electrodes gave potential differences less than 1 mv for extended periods of time (days). The electrode potential was also quite stable in the presence of sufficient water impurity to give visible gassing. The Nernst behavior of the  $\text{Li}/\text{Li}^+$  couple in PC has been established by others (3).

### Acknowledgments

The authors wish to acknowledge the support of the U.S. Naval Air Systems Command (Contract Now 66-06212).

Manuscript received Oct. 23, 1967.



Any discussion of this paper will appear in a Discussion Section to be published in the December 1968 JOURNAL.

## REFERENCES

1. D. Cogley and J. N. Butler, *This Journal*, **113**, 1074 (1966).
2. R. Selim, K. Hill, and M. Rao, Final Rept. Contract No. NAS 3-6017 (Dec. 1965).
3. D. Boden, H. Buhner, and V. Spera, First Quart. Rept. Contract DA-28-043-AMC-01394(E), (Oct. 1965).

## A New Technique for Studying the Rate of Gas Evolution Reactions

N. Marincic\*

P. R. Mallory & Co., Inc., Laboratory for Physical Science, Burlington, Massachusetts

Low rate gassing processes were found difficult to study, whenever the amount of gas, consumed or liberated by chemical reaction, was used as an indicator of the reaction rate. The proper choice of the gas measuring technique is of particular importance in the case when the control of the gaseous reaction participant stands as the only practical alternative. A typical example of this kind is the corrosion reaction of a zinc electrode in battery systems, in an alkaline electrolyte containing an appreciable concentration of dissolved zinc (1). A significant quantity of gas is evolved in this corrosion reaction before the change of the zinc concentration in solution becomes measurable. The reaction rate measurement through the depletion of the metallic zinc, as one of the possibilities, is of no practical value in this case due to an undefined distribution of the corrosion products between the liquid and the solid phase.

Gassing also occurs in rechargeable battery systems during charging processes. The quantity of gas produced in the latest phase of charging (or overcharging) is of crucial importance for the battery performance, particularly when a sealed structure is employed. The participation of the gassing processes in the overall energy consumption during the charging could easily be estimated, provided an accurate method was available for measuring the amount of gas evolved. A more convenient and eventually more accurate method is needed for this type of study than the usual gas coulometry with direct volume reading of the quantity of gas collected (2).

The two examples mentioned above dictated the design of the technique for the gas measurement described in this paper.

A very detailed study of the gas coulometer has been done in the past (3) as a part of general effort to establish the true value of the Faraday. The weight of mercury displaced by the hydrogen-oxygen mixture evolved in an electrolysis reaction was measured. A balance of a remarkable high capacity-accuracy relation was used in this method among other precautions undertaken to maximize the accuracy of the measurement. A limitation of the method, however, rested on the fact that the displaced mercury was being collected in drops coming out of a capillary with the single drop weight being anywhere between 1 and 20 mg.

Several other basic studies have been done on coulometric technique dealing either with the problem of the impurities incorporated in silver deposits in the silver coulometer (4, 5) or with the other experimental conditions concerning the accuracy of the measurement (6, 9). The hydrogen-oxygen coulometer was thoroughly re-examined (10, 11) long after the basic study of the instrument has been done (3). It was found to be a sensitive instrument, if all the influencing factors were under control. No major change in

the *modus operandi* was suggested, apart from the very careful evaluation of the performance determining factors.

The method employed in this work was designed for the determination of small amounts of gas produced either in a corrosion reaction in solution or as a by-product of an electrochemical reaction. It is based on the measurement of the change of buoyancy due to the gas collected under a glass bell, immersed in the solution. The method can be applied in any reaction rate study, whenever gas is involved, either as a reaction product or one of its participants.

### Theoretical

A schematic representation of the technique employed is shown in Fig. 1. An increase of the volume of gas, generated under the bell ( $V - V_0$ ) will result in a buoyancy change ( $\Delta G$ ) under constant pressure and temperature.

$$\Delta G = (V - V_0)u_0 \quad [1]$$

if  $u_0$  is the density of the liquid in which the bell is immersed. The total quantity of gas under the bell at the beginning of the experiment can be expressed as

$$n_0 = (P_{b0} + \Delta H u_0) V_0 / RT \quad [2]$$

where  $n_0$  is the number of moles,  $P_{b0}$  is the initial barometric pressure  $\Delta H u_0$  is the hydrostatic component of the total pressure of the gas. With the number of moles of  $n_g$  of the gas generated during the experiment,  $n_v$  moles of vapor will be formed over the liquid in order that constant vapor pressure be preserved. These two quantities are related to each other as follows

$$n_v = n_g P_v / (P_b + \Delta H u_0 - P_v) \quad [3]$$

where  $P_v$  is the vapor pressure of the liquid and  $P_b$

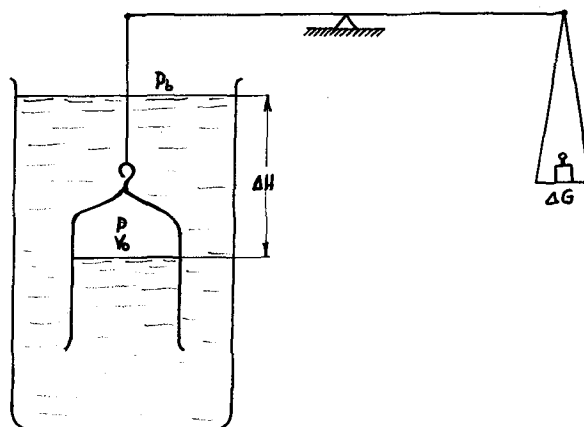


Fig. 1. Schematic representation of the gas measuring technique.

\* Electrochemical Society Active Member.

is the actual barometric pressure at the moment of the measurement. Since the total quantity of gas under the bell is related to the volume of the gas in the manner

$$V = (n_o + n_g + n_v)RT / (P_b + \Delta H u_o) \quad [4]$$

Eq. [2] and [3] with Eq. [4] lead to the expression

$$V = V_o (P_{b_o} + \Delta H u_o) / (P_b + \Delta H u_o) + n_g RT / (P_b + \Delta H u_o - P_v) \quad [5]$$

Equation [5] gives with Eq. [1] after rearranging a final expression relating the moles of the gas generated at the measured buoyancy change

$$n_g = \Delta G (P_b + \Delta H u_o - P_v) / u_o RT + V_o (P_b + \Delta H u_o - P_v) (P_b - P_{b_o}) / (P_b + \Delta H u_o) RT + V_1 C \quad [6]$$

The  $V_1 C$ —member of the right-hand side of Eq. [6] is added to the expression afterward in order to provide the correction for gas solubility ( $C$ ) in a given volume of liquid ( $V_1$ ).

Certain correction factors can be eliminated from the general expression (6) depending on the conditions of the experiment and the accuracy requirements.

(a) The barometric pressure change during the course of the experiment ( $P_b - P_{b_o}$ ) becomes irrelevant in high reaction rate measurements, when the experiment is completed in a short period of time, or when the barometric pressure is otherwise stable during the experiment. In such a case no calibration of the initial volume is necessary.

(b) The initial volume of the gas ( $V_o$ ) can be eliminated from the expression if the bell is completely filled with the solution at the beginning of the experiment. This also eliminates the need for barometric pressure change correction, ( $P_{b_o}$ ) and *vice versa*.

(c) The hydrostatic pressure ( $\Delta H u_o$ ) depends on the design of the bell and can be made negligibly small for the majority of the experimental requirements particularly when low density solutions are used. A 100 mm difference between the inside and the outside liquid level means 1% difference in pressure reading under standard pressure and temperature conditions.

(d) The correction for the gas solubility is of some importance depending on the nature of the gas. Since hydrogen evolution occurs in a majority of metallic corrosion processes, its low solubility in a variety of the electrolytes (12) has no significant influence on the results of the measurement.

(e) The vapor pressure of the solution has to be known in order to estimate its influence on the results of the measurement. It is well-defined for a large number of solutions and can also be calculated for dilute solutions.

The general expression (6) is reduced to

$$n_g = \Delta G P_b / u_o RT \quad [7]$$

when a high degree of accuracy of the measurement is not required, *i.e.*, under the conditions described above. Reduced Eq. [7] shows the direct transfer of each ml of the gas generated into 1g difference in the buoyancy recorded on the balance.

### Experiments and Results

The validity of the experimental technique was tested in a cell similar to the one represented in Fig. 2.

Two platinum electrodes were used to generate hydrogen electrolytically with the anode situated outside the bell. The central tube with the stopcock at the end was used for bleeding the bell in order to flood the electrode. It also provided the means for removal of the gas collected under the bell without dismounting the cell. The testing was done with 3M KOH and the results are shown in Fig. 3.

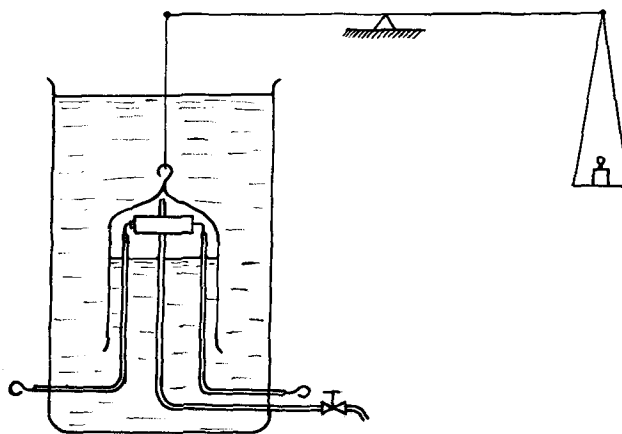


Fig. 2. Experimental set-up for the cell gassing measurement

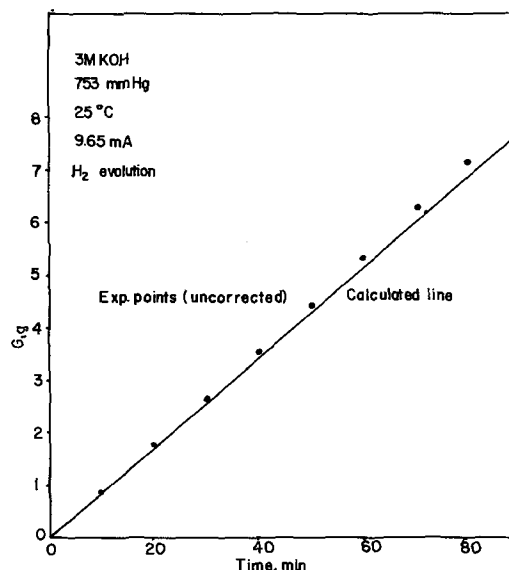


Fig. 3. Comparison of the results with the theoretical hydrogen evolution rate.

The discrepancy between the experimental points and the theoretical line illustrates the effect of the correction factors, summarized in general Eq. [6]. The accuracy of the measurement is proved to be higher than required for the experimental conditions given.

The set-up shown in Fig. 2 was used for the evaluation of experimental galvanic cells, *i.e.*, for gas evolution measurement in the course of charging of rechargeable cells. The platinum electrodes were used only as leads to the cell electrodes in this type of measurement. They were, obviously, not flooded in this case. The initial free volume in the bell had to be calibrated ( $V_o$ ) for an accurate gas quantity calculation. A typical charging curve for an alkaline  $MnO_2$ -zinc cell is represented in Fig. 4 accompanied with the corresponding gas generation curve. The charging process was continued beyond the practical voltage cut-off point in order to follow the gas evolution curve all the way to water electrolysis. The ultimate slope of the gassing curve represents a gas evolution rate of 1.07 ml/min and is in good agreement with the theoretical gas evolution rate of 1.05 ml/min for the given set of the experimental conditions.

### Conclusion

The measurement method described above is found to be reliable for gas evolution studies. In fact, an accuracy of the measurement can be achieved beyond that required for the majority of practical problems. It offers a means of registering the gas bubbles as they are generated with no need to collect the gas at

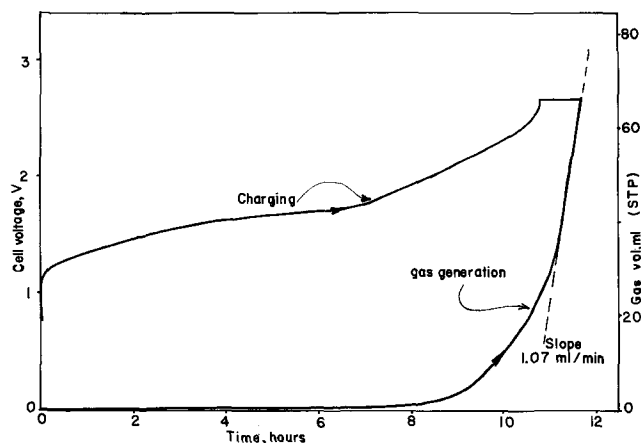


Fig. 4. Typical charging curve for an alkaline  $\text{MnO}_2$ -zinc system with the corresponding gas generation curve.

certain particular section of the measuring device. This seems to be very convenient in the study of porous electrodes where the collection of the gas generated represents the major obstacle to reliable quantity measurements.

A recently published paper (13) describes the technique for the study of the rechargeable electrodes by measuring the buoyancy change of the electrode material during the metal-metal oxide transformation. That technique combined with the gas measuring technique described in this work could be utilized for a simultaneous recording of the solid-state transformation rate and the accompanying gas evolution rate in more detailed studies of electrode and/or the corrosion processes. The schematic representation of the set-up proposed is illustrated in Fig. 5.

Two analytical balances (or recording balances) could be used; one for the gas measurement, and one for the solid electrode transformation measurement. The corrosion of the electrodes in practical galvanic cells could be studied by this combined method in order to establish the corrosion product distribution between the liquid and the solid phase. The simultaneous gas evolution measurement could be an additional means of a net corrosion rate measurement in a system metal/electrolyte in the absence of oxygen.

The usefulness of the method in coulometric measurements can be illustrated by comparison with the electrogravimetry with copper as an example. A 1 amp-sec equivalent of copper amounts to 0.33 mg weighed directly on the balance. When the equivalent quantity of hydrogen is measured as in the present

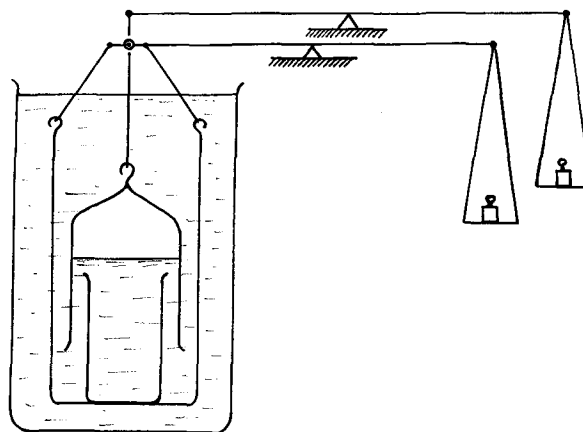


Fig. 5. Proposed set-up for the simultaneous recording of the gas evolution rate and the solid-state transformation rate.

method, 1 amp-sec results in a change of buoyancy of 116 mg. This represents the increase in the sensitivity of the measurement by factor of 350.

#### Acknowledgment

The author is indebted to Dr. P. Bro for stimulating discussions and to P. R. Mallory & Co. Inc. for permission to publish this work.

Manuscript received Aug. 17, 1967. This paper was presented at the Chicago Meeting, Oct. 15-19, 1967, as Abstract 44.

Any discussion of this paper will appear in a Discussion Section to be published in the December 1968 JOURNAL.

#### REFERENCES

1. N. Marincic and P. Bro, To be published.
2. P. Ruetschi, *This Journal* **114**, 301 (1966).
3. R. A. Lehfeldt, *Phil. Mag.*, (6) **15**, 614 (1908).
4. F. E. Smith, Report of Nat. Phys. Lab. 1910, p. 32.
5. T. W. Richards, *J. Am. Chem. Soc.*, **37**, 20 (1915).
6. G. W. Vinal and S. J. Bales, *U. S. Bur. Standards, Bull.* **10**, 425 (1914).
7. E. B. Rosa, G. W. Vinal, and A. S. McDaniel, *ibid.*, 475 (1914).
8. E. B. Rosa and G. W. Vinal, *U. S. Bur. Standards, Bull.* **9**, 151 (1913).
9. E. B. Rosa, G. W. Vinal, and A. S. McDaniel, *ibid.*, 493 (1913).
10. J. J. Lingane, *J. Am. Chem. Soc.*, **67**, 1916 (1945).
11. J. J. Lingane, Discussion Faraday Soc., **1**, 203 (1947).
12. R. D. Walker, Report to NASA on Grant 10-005-022, March 1966.
13. A. Langer and J. T. Patton, *This Journal*, **114**, 113 (1967).

## Influence of Thin Noble Metal Films on Zirconium Oxidation

A. Fiegna<sup>1</sup> and P. Weisgerber

EURATOM-CCR, Ispra, Italy

Attempts were made for several years to measure electrical properties of oxides on metal surfaces during the oxide forming reaction between metal and gas phase (1-5). In those cases where the current density or the dielectric capacitance were investigated, the area of current flow was limited by a suitable con-

tact. Some investigators (4,5) used noble metal films deposited by evaporation techniques on the metal surfaces. Joergensen (4) observed that thin films of platinum, deposited by cathodic sputtering, did not alter the reaction rate of zinc single crystal faces in oxygen.

In order to find suitable contacts for the measurements of electrical properties of zirconium oxide on zirconium metal during the oxide forming reactions,

Key words: Reaction kinetics, oxidation, zirconium, metal films, gold, silver, platinum, cathode sputtering, markers.  
<sup>1</sup> Present address: Centro di Studi sulla Corrosione—Istituto Chimico dell'Università di Ferrara—Ferrara—Italy.

the influence of the metallic deposits on the reaction rate had to be investigated. At first sight a possible decrease of the reaction rate was expected, assuming that the noble metals blocked the access of the oxidant to the zirconium.

### Experimental Procedure

Sheets 0.1 x 15 x 50 mm were made from crystal bar zirconium by repeated rolling, cleaning of the surface by electropolishing, and annealing at 750°C in vacuum ( $p < 10^{-5}$  Torr).

Different series of samples were coated on both sides with uniform films of platinum, gold, silver, palladium, iridium, or rhodium by cathodic sputtering in high-purity argon. The thickness of the noble metal film deposits could be roughly estimated between 100 and 300 Å from the transparency of the underlying glass plates, which served as target supports during the sputtering process. This was confirmed by later measurements carried out with a quartz crystal monitor.

Thickness control during the sputtering process was achieved by resistance monitoring between silver paint contacts of 1 cm length and 1 cm distance. All Pt and Au deposits were stopped at a resistance of 100 ohm and those of Ag at 30 ohm.

Thermogravimetric experiments were carried out in a continuously recording thermobalance. The oxygen atmosphere in the balance was established by filling the preevacuated system with high-purity oxygen to a pressure of 10 Torr. The water vapor atmosphere was made from distilled water, degassed by boiling in vacuum in a glass flask. The latter was then held at 11.2°C by a cryostat and connected to the preevacuated system. The temperature regulation of the cryostat maintained the pressure in the system automatically at 10 Torr.

For every experiment a series of 6 specimens, corresponding to a total surface area of 90 cm<sup>2</sup>, was inserted on a platinum specimen holder into the thermobalance. The reaction temperature was in all cases 450°C and the duration of the experiments between 100 and 120 hr.

### Experimental Results

Weight gains for the experiments in oxygen atmosphere are plotted in Fig. 1 on double logarithmic scale. Values for noncoated zirconium were in reasonable agreement with the literature (6). The reproducibility between series of specimens from the same preparation lot was within the precision of the thermobalance. After the oxidation process the specimens were covered with the usual black oxide.

The weight gain of the platinum coated specimens was about two times higher than that of the uncoated zirconium while the order of the reaction did not change considerably. After the oxidation the surface of the specimens were metallic, brilliantly reflecting, and only slightly darker than platinum coated, but nonoxidized specimens. It can therefore be concluded that at least the greater part of the deposited platinum remained unaltered at the oxide-gas interface.

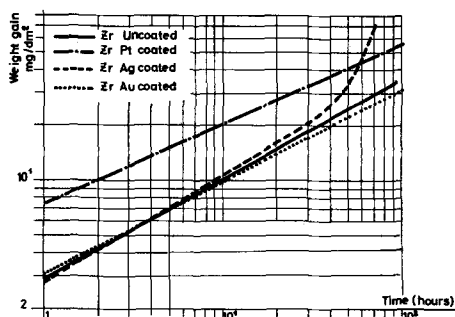


Fig. 1. Oxidation in dry oxygen at  $P_{O_2} = 10$  Torr and  $T = 450^\circ\text{C}$ .

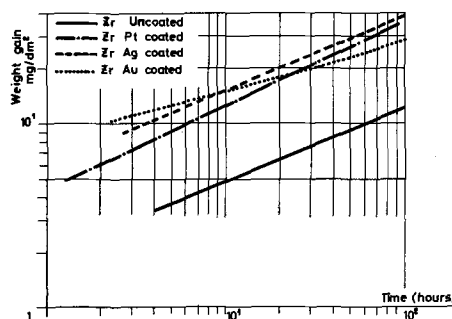


Fig. 2. Oxidation in water vapor at  $P_{H_2O} = 10$  Torr and  $T = 450^\circ\text{C}$ .

The weight gain of the gold coated specimens differed only slightly from that of uncoated specimens. The surface after oxidation was that of the normal black oxide with a few isolated small areas of a slight gold tint. Here the original metal deposit had almost completely disappeared, probably by diffusion into the zirconium oxide.

The weight gain of the silver coated specimens agreed with that of the uncoated specimens for the first 24 hr of the oxidation process. Afterward a rapid increase in the reaction rate took place, approaching linearity with time. The oxidized specimens looked brilliantly metallic, but at several places aggregates of white powdery material were found. This is similar to the "post transition corrosion" observed during the aqueous corrosion of zirconium. Obviously the same phenomenon occurred here as an effect of the silver film.

The results of the oxidation experiments in water vapor are plotted in Fig. 2. Recently experiments in water vapor of 10 mm Hg were carried out (8). Results are not comparable because that work concerned the early stages of the oxidation process, and observation times and temperatures differ too much from our conditions. Despite the lack of literature values for the oxidation of zirconium in water vapor at pressures lower than 1 atm, the weight gains found seem to be reasonable. Compared with weight gains at 100 and 1 atm at 450°C which differ by a factor of about 40 (6), these values at 0.001 atm differ by a factor of 38 from those at 1 atm.

In water vapor all noble metal coated specimens had an increased reaction rate.

The surface of the platinum and silver covered specimens were brilliantly metallic and only slightly darker than before oxidation. "Break-away" phenomena were not found. The gold again disappeared leaving only a few gold tinted spots at some places.

The reaction constants followed Eq. [1]

$$m^n = (k t) \quad [1]$$

where  $m$  = mass of oxide formed in g/cm<sup>2</sup>,  $t$  = time in sec, and  $n$  and  $k$  are reaction constants given in Tables I and II. The time during which these constants are valid is also indicated.

The hydrogen uptake of the specimens oxidized in water vapor was analyzed, and the data are given in Table III. The yield was calculated from the total weight gain, assuming 100% uptake for the case that all hydrogen formed from the water would be absorbed. The relatively low yield in the case of platinum may be due to the fact that, during this experiment,

Table I. Reaction constants for the oxidation at 450°C in dry oxygen ( $P_{O_2} = 10$  Torr) following equation  $m^n = k t$

	$n$	$k[(\text{g cm}^{-2})^n \text{sec}^{-1}]$	Validity (hr)
Uncoated	2.18	$1.4 \cdot 10^{-12}$	1-100
Silver coated	2.03	$5.2 \cdot 10^{-12}$	1-30
Gold coated	2.31	$0.51 \cdot 10^{-12}$	1-100
Platinum coated	2.42	$0.81 \cdot 10^{-12}$	3-100

Table II. Reaction constants for the oxidation at 450°C in water vapor ( $P_{H_2O} = 10$  Torr) following equation  $m^n = k t$

	$n$	$k[(g\text{ cm}^{-2})^n\text{sec}^{-1}]$	Validity (hr)
Uncoated	2.51	$12 \cdot 10^{-13}$	3-100
Silver coated	2.46	$3.4 \cdot 10^{-13}$	3-100
Gold coated	2.62	$0.51 \cdot 10^{-13}$	32-100
Platinum coated	2.15	$19 \cdot 10^{-13}$	3-100

Table III. Hydrogen uptake from oxidation in water vapor at  $P_{H_2O} = 10$  Torr and 450°C

Specimen	$H_2$ (ppm)	Yield Mol %
Uncoated	80	13
Platinum coated	69	4.5
Gold coated	73	10.2
Silver coated	251	15.5

a vacuum pump was connected to the system with a needle valve. The water vapor was drawn off continuously at a constant pressure of 10 Torr in the system, but had the effect of keeping the partial pressure of hydrogen involved from the reaction at a lower value. Because of the failure of the pump the other experiments were carried out in the static system, i.e., with increasing partial pressure of hydrogen during reaction.

Oxidation of specimens coated with palladium, rhodium, and iridium were expected to form the stable noble metal oxides (7).

### Conclusions

Thin noble metal film deposits of 100-300Å thickness on zirconium did not block the surface from reaction with oxygen and water vapor at 450°C. This is not surprising if one takes into account that film deposits in that thickness range are not uniform, but consist of isolated nuclei. Instead of blocking oxygen, a catalytic effect was observed which resulted in an increase of the reaction rate for platinum and silver coated samples in water vapor, and for platinum coated samples in oxygen. Silver coating did not influence the rate in oxygen in the initial phase, but later on transition to "breakaway corrosion" began.

The catalyzing effect could be explained by different assumptions:

1. The metal deposits increase the adsorption of oxygen or water at the oxide-gas interface.
2. The metal deposits catalyze the ionization of adsorbed oxygen or water at the oxide-gas interface.
3. The metal deposits produce stresses in the underlying oxide influencing the number and mobility of dislocations.
4. Small fractions of noble metal ions diffusing into the oxide increase the number of oxygen ion vacancies and thereby the mobility of oxygen.
5. The metal deposits emit electrons into the oxide increasing the oxygen vacancy concentration and the mobility of oxygen.

Whichever of these explanations is right, the influence of the deposits on the oxide has to be taken into account when measuring electrical properties. Because there is little hope of eliminating these effects, and their magnitude in the case of zirconium is within the limits known to result from different surface treatments or specimen preparations, platinum seems to be the most suitable contact material.

The behavior of the gold deposits excludes application at reaction temperatures on zirconium.

On the other hand, care has to be taken in the choice of noble metals for inert marker experiments to determine the mobile ion species during oxide forming reactions. It is shown here, that different noble metals could lead to contradictory conclusions.

Manuscript received Oct. 4, 1967; revised manuscript received Dec. 18, 1967.

Any discussion of this paper will appear in a Discussion Section to be published in the December 1968 JOURNAL.

### REFERENCES

1. L. D. Kirkbride and D. E. Thomas, WAPD-T-308, Feb. 1956.
2. R. D. Misch and F. H. Gunzel, Jr., *This Journal*, **106** 15 (1959).
3. D. W. Shannon, *Corrosion*, **19**, 414 (1963).
4. P. J. Joergensen, *This Journal*, **110**, 461 (1963).
5. D. K. Dawson and R. H. Creamer, *Brit. J. Appl. Phys.*, **16**, 1643 (1965).
6. Lustman and Kerze, "The Metallurgy of Zirconium," p. 623, McGraw-Hill Publishing Co., New York (1953).
7. J. C. Chaston, *Platinum Metals Rev.*, **9**, [2], pp. 51-6, [4], pp. 126-8.
8. J. K. Dawson, U. C. Baugh, and F. T. White, *Electrochem. Technol.*, **4**, 137 (1966).

## Multiple Twin Structures in Electrodeposited Silver Dendrites

J. Smit, F. Ogburn,\* and C. J. Bechtoldt

National Bureau of Standards, Washington, D. C.

The structure of electrodeposited dendrites of FCC metals, particularly of silver, has been the subject of several communications (1-7). These investigations have been conducted on dendrites produced from both fused salt and aqueous systems. The dendrites are described as being usually in one of two forms, i.e., acicular and growing in the  $\langle 110 \rangle$  direction or planar and growing in the  $\langle 112 \rangle$  direction. Twinning in these dendrites has not been uniformly reported. With respect to silver dendrites formed in fused salt systems, Bockris (2), on the basis of x-ray diffraction and metallographic evidence, reports twinning in the planar form dendrites. Reddy (7) also reports twinning, but on the basis of metallographic evidence alone, as does Faust and John (8) in their examination of dendrites supplied by Hudson (3). In aqueous systems Kikuchi (6) has observed twinning in planar

form dendrites growing in the  $\langle 112 \rangle$  direction. Wranglen, however, does not report twinning (1,4). Faust *et al.* (9) report observing twinning in the form of crossed lamella within the matrix of a single orientation. In the last case the lamella are each in twin relation to the matrix but not in twin relation to each other. In no case has multiple twinning, i.e., more than three orientations about a common zone axis, been reported in silver.

Faust and John (10) describe multiple twinning configurations in semiconductor FCC materials deposited from the melt. They classify twinning modes or configurations as follows: (i) Class I twinning, in which  $\{111\}$  composition planes appear to radiate from a central point and are  $70^\circ 32'$  apart. The orientations are pie shaped and mutually exclusive. (ii) Class II twinning, in which  $\{111\}$  composition planes are parallel. In this case one orientation is minor to another

\* Electrochemical Society Active Member.

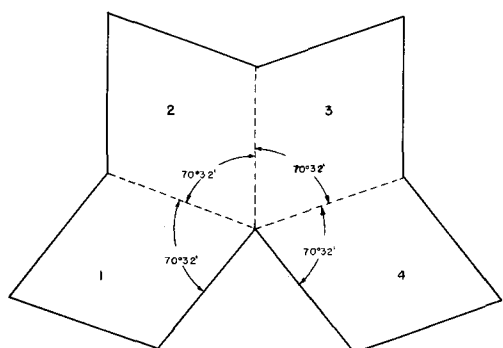


Fig. 1. Class I twinning. Four orientations. Dashed lines indicate  $\{111\}$  composition planes.  $\langle 110 \rangle$  direction normal to paper.

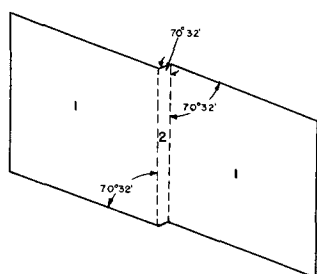


Fig. 2. Class II twinning. Two orientations. Dashed lines indicate  $\{111\}$  composition planes.  $\langle 110 \rangle$  direction normal to paper.

and contained within it in the form of a band or lamella.

Figures 1 and 2 are sketches of idealized cases of both classes of twinning.

It is the purpose of this communication to report experimental observations of the structure of silver dendrites electrocrystallized from aqueous solutions with reference to the classes of Faust and John. This investigation was undertaken to supplement our fragmentary knowledge of the roll of growth twins in the formation of electrodeposited dendrites.

#### Description of Apparatus and Techniques

Electrocrystallization was conducted in Pyrex vessels 44 mm in diameter and 80 mm high. The dendrites were produced on silver wire cathodes in 70 ml of 0.5M  $\text{AgNO}_3$ . The solution was prepared from reagent grade  $\text{AgNO}_3$  and distilled water. A silver wire in a Luggin capillary was used as a reference electrode. The tip of this electrode was positioned approximately halfway between the two active electrodes and was used to maintain potentiostatic control of the system during deposition. The potential values reported here include the IR drop between the reference electrode and cathode, which varies substantially as the dendrite grows toward the anode. Dendritic growth was induced at cathode potentials of at least 300 mv and then maintained potentiostatically at approximately 160 mv. Growth was permitted to proceed until the dendrites attained a length of at least 1 cm. Dendritic growth often proceeded at a rapid pace and has been observed here at rates up to 1.2 mm/min. After growth termination the dendrites were removed carefully from the electrolytic solution, washed in distilled water, air dried, and mounted with the base end secured in clay plugs fixed to the inner surface of polyethylene bottle caps. These caps were then secured to 4 or 6 dram vials. The dendrites were now fully enclosed and protected against mechanical shocks and corrosion. The dendrites remained thus secured until such time as detailed optical goniometric, x-ray diffraction, and metallographic examinations were undertaken.

#### Observations

In the course of this investigation 38 dendrites were examined. The dendrites ranged from one-fourth to one millimeter thick and were at least one centimeter long. All specimens contained bright shiny well-defined facets. Preliminary two circle optical goniometric surveys and x-ray diffraction examinations (precession alignment and rotating crystal patterns) indicated the dendrites to be fundamentally twin crystals with composition planes and growth axis parallel to the  $\langle 110 \rangle$  direction. Although the full extent of multiple twinning is not necessarily revealed by the use of optical equipment alone, the optical data did indicate in all cases the existence of twinning. All dendrites examined were of acicular form and were clearly faceted, mainly on the  $\langle 110 \rangle$  zone. The most frequently observed facets on this zone were the  $\{111\}$  facets, then the  $\{100\}$  and  $\{112\}$  facets;  $\{110\}$  facets were seen also, but only rarely. As many as six orientations in twin relation were identified in this manner. Low orders of twinning, that is, two and three orientations in twin relation, are exhibited generally in those crystals having relatively large smooth bright surfaces. These crystals frequently appeared x shaped in cross section with crevasses extending down the entire crystal length. High orders of twinning, that is, four and more orientations in twin relation, are characteristic of crystals having jagged appearing surfaces containing many nodes or knobby protuberances.

Zero level  $\langle 110 \rangle$  Weissenberg patterns of the dendrites confirmed and, in some cases, expanded on the preliminary findings. The extent of twinning was determined from the number and position of the  $\{111\}$  spots. The  $\langle 110 \rangle$  zone of a single orientation (FCC) contains in a  $180^\circ$  interval two  $\{111\}$  spots, providing the interval does not start on a spot. Each additional orientation in twin relation generates one new  $\{111\}$  spot. The  $\{111\}$  spot common to two orientations represents the composition plane. Up to eight orientations in twin relation were revealed in this way. Figures 3, 4, 5, and 6 are zero level  $\langle 110 \rangle$  Weissenberg patterns showing 2, 4, 6, and 7 orientations, respectively. The film translation is approximately 100 mm (200 degrees).  $K_\alpha$  molybdenum radiation was used to produce the patterns. This radiation was selected principally because of the atomic number and irregular thickness of the dendritic material. In photographs 5 and 6 some streaking is observable between  $\{111\}$  spots 3.6 mm (7.4 degrees) apart. It is slight and has been enhanced by both over exposure of the original photo-

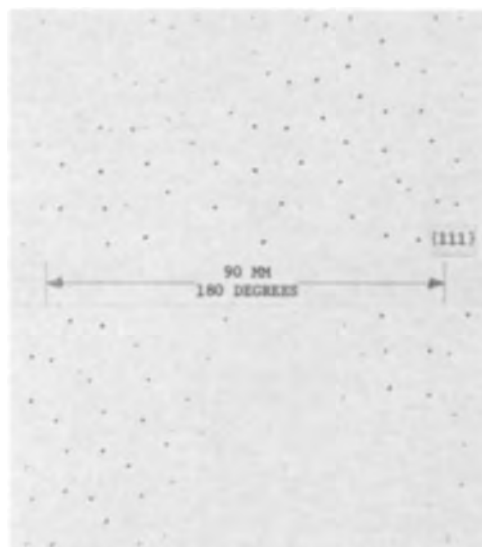


Fig. 3. Zero level.  $\{111\}$  Weissenberg diffraction pattern showing two orientations in twin relation.

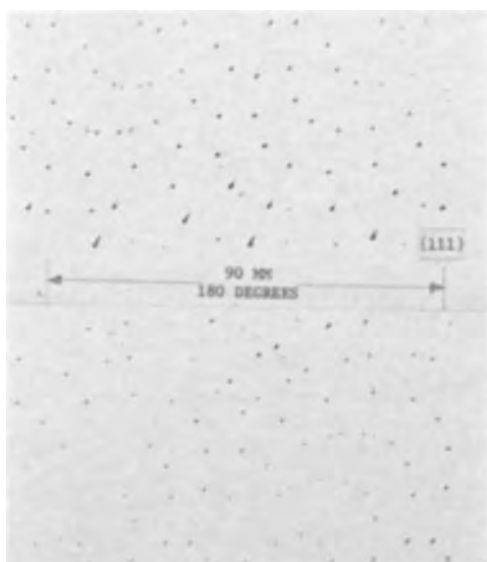


Fig. 4. Zero level.  $\{110\}$  Weissenberg diffraction pattern showing four orientations in twin relation.

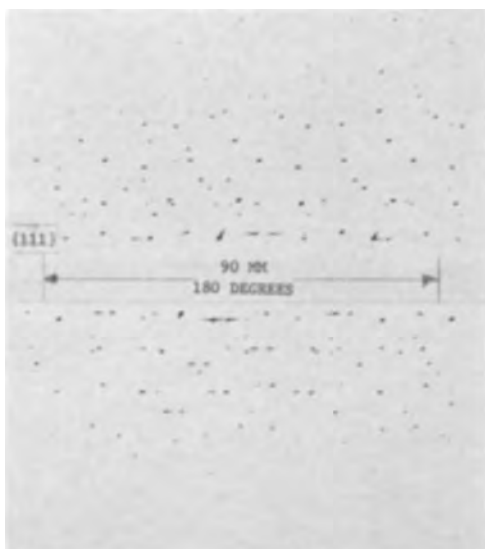


Fig. 5. Zero level.  $\{110\}$  Weissenberg diffraction pattern showing six orientations in twin relation.

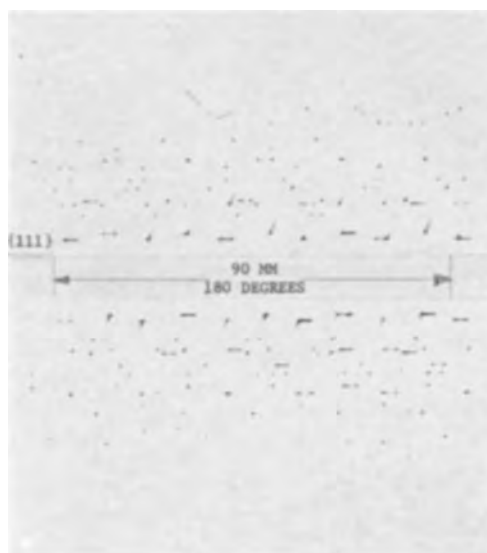


Fig. 6. Zero level.  $\{110\}$  Weissenberg diffraction pattern showing seven orientations in twin relation.

graphs and by reproduction. Nonetheless it may be indicative of strains in the orientations involved.

In the majority of cases the number of orientations discerned optically was the same as the number of orientations as determined from the Weissenberg patterns. This was particularly so for the low orders of twinning. The majority rule held for the higher orders of twinning as well except that in several cases more orientations were revealed on the Weissenberg patterns than were displayed optically.

A determination of the consistency of twinning through a dendrite was made by examining some dendrites at two positions along the growth axis. Weissenberg  $\{110\}$  zero level patterns were obtained of these dendrites near the growth tip and in the base region. In each case the number and position of the orientations at the tip agreed with the number and position at the base.

The classes of twins as described by Faust and John (10) and detailed here in the introduction were observed in metallographic sections taken normal to the growth axis of dendrites electrodeposited during this investigation.

Figure 7 is an example of Class I twinning showing five orientations about an axis. The observations here reported were made on specimens mounted, ground, and polished according to standard metallographic practices. The details of the structure were most often, though not consistently, brought out using an etchant prepared by combining, just prior to use, at a ratio of 1:1 a 5% solution of KCN in distilled water with a 5% solution of  $(\text{NH}_4)_2\text{S}_2\text{O}_8$  in distilled water. However, no etching system and schedule used produced good results consistently. It appeared that simple twin boundaries could not be clearly developed consistently. The maximum number of related orientations observed in Class I type specimens was six. This was in agreement with both the optical and x-ray data for that specimen. The maximum number of orientations observed in Class II type specimens was three. This also was in agreement with optical and x-ray data. In the latter specimen two orientations appeared as  $10\mu$  wide crossed lamella in a third predominant orientation. This same specimen showed only one orientation on a 27-hr exposure Weissenberg pattern taken using a Mo target tube at 50 kv and 15 ma. An increase of exposure time to 90 hr at the same conditions brought out faintly the two orientations of the lamella forms.

Dendrites containing both classes of twins simultaneously were also observed. This is illustrated in Fig. 8 and 9.

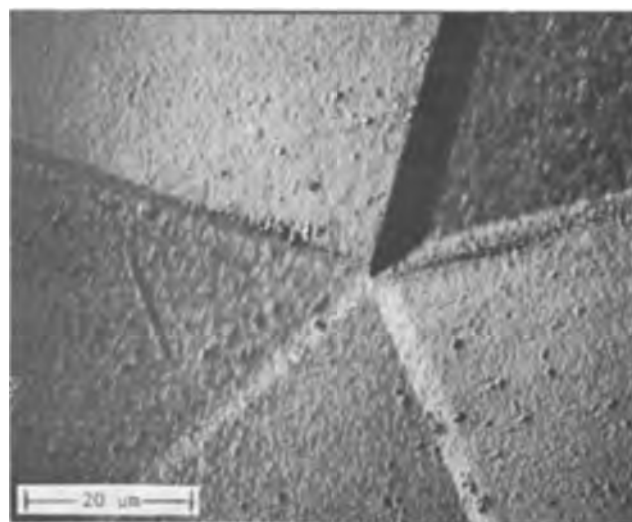


Fig. 7. Class I twinning showing five orientations about a central axis. X1500 before reduction.

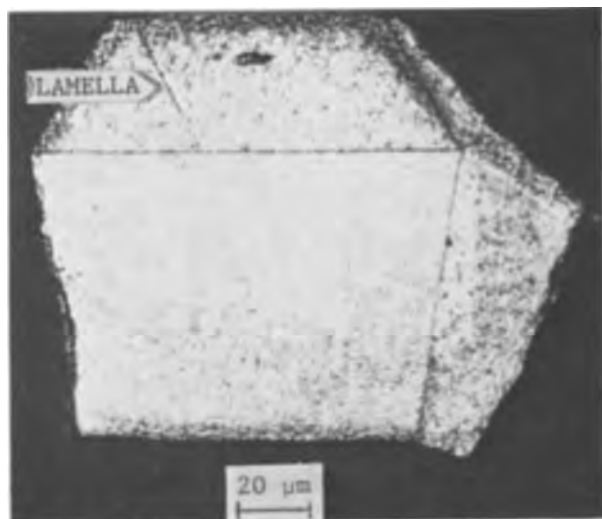


Fig. 8. Combination of Class I and II twinning. X500 before reduction.

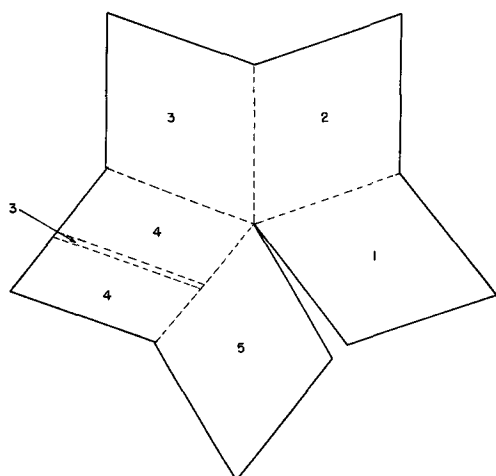


Fig. 9. Combination of Class I and II twinning. Five orientations. Dashed lines indicate  $\{111\}$  composition planes.  $\langle 110 \rangle$  direction normal to paper.

### Discussion

This note has brought to attention modes of multiple twinning as encountered in the electrocrystallization of silver from aqueous solution. Multiple twinning involving up to eight orientations is reported. No exception to twinning was uncovered among the 38 silver dendrites examined during this study. Every one was made up of two or more crystals in twin relation with all the composition planes parallel to the growth axis. Our observations were, of course, limited to a specific set of conditions and to rapidly growing dendrites. Hence, we cannot make any generalized statement concerning all dendritic growth. The inference here, however, is that the twinned structure is involved in the growth mechanism. We are also impressed by the fact that in the literature, wherever dendritic growth by electrodeposition has been rapid, *i.e.* mm/hr, a twinned structure has been present. This has been reported by Barton and Bockris (2) (silver), Reddy (7) (silver), Ogburn *et al.* (5) (lead), and Bechtoldt *et al.* (11) (molybdenum). From these and other experimental observations it is evident that twinning plays an important role in the growth process. It exerts a profound influence on the shapes of dendrites, on their directions of growth, and on the

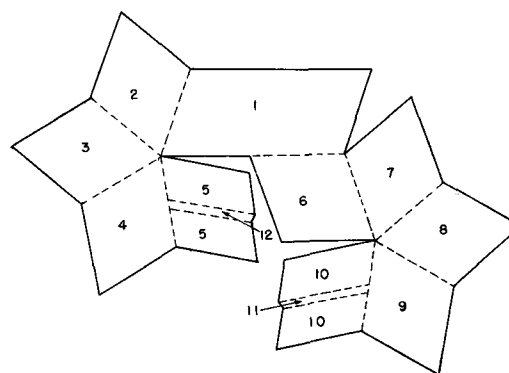


Fig. 10. Composite Class I twinning. Twelve orientations. Two axes of twinning. Dashed lines indicate  $\{111\}$  composition planes.  $\langle 110 \rangle$  direction normal to paper.

cathodic polarization. Where twin lamella occur, the twin plane re-entrant-edge mechanism of Faust and John seems adequate. The same mechanism may also be applicable to the radiating twin structure, although it remains to be shown that faceting suitable for re-entrant edges occurs.  $\{111\}$  faceting is suitable for twin lamella, but not for radiating twin structures. However, electrodeposited silver develops other facets, such as  $\{571\}$  observed by von Dauber (12) and by us.

One may ask how many twin related orientations are possible in a dendrite. We have detected eight and no more, but there is no reason to think that more than eight could not occur. At this time the only rules that we can apply to this twinning are (i) the composition planes are  $\{111\}$  and (ii) they are parallel to the growth axis. Faust *et al.* (9) show that in the case of radial twinning, a mismatch boundary or void must occur. With no more restrictions, it is very easy to conceive of a variety of twin configurations, many of which include more than eight orientations. For example, Fig. 10 shows twelve orientations associated with two centers for radial twinning and lamella.

### Acknowledgment

This research was supported by the Advanced Research Projects Agency of the Department of Defense under Project DEFENDER.

Manuscript received Oct. 5, 1967; revised manuscript received Dec. 14, 1967.

Any discussion of this paper will appear in a Discussion Section to be published in the December 1968 JOURNAL.

### REFERENCES

1. G. Wranglen, *Trans. Roy. Inst. Technol. Stockholm*, **94**, 13-15 (1955).
2. J. L. Barton and J. O'M Bockris, *Proc. Royal Soc.*, **268**, 494 (1962).
3. L. Yang, C. Chien, and R. G. Hudson, *This Journal*, **106**, 632 (1959).
4. A. M. Shams El Din and G. Wranglen, *Electrochim. Acta*, **7**, 79 (1962).
5. F. Ogburn, C. Bechtoldt, J. B. Morris, and A. de Koranyi, *This Journal*, **112**, 574 (1965).
6. M. Kikuchi and R. Yamazaki, *Denki Kagaku*, **33**, 283 (1965).
7. T. B. J. Reddy, *This Journal*, **113**, 117 (1966).
8. J. W. Faust, Jr., and H. F. John, *ibid.*, **108**, 109 (1961).
9. J. W. Faust, Jr., Daniel Kahan, Fielding Ogburn, and A. W. Ruff, Jr., *ibid.*, **114**, 1311 (1967).
10. J. W. Faust, Jr., and H. F. John, *J. Phys. Chem. Solids*, **25**, 1409 (1964).
11. C. J. Bechtoldt, F. Ogburn, and J. Smit, To be published.
12. H. von Dauber, *Ann. Chem. & Pharm.*, **78**, 68 (1851).



# Time-Temperature Superposition Theory for Electrets

Bernhard Gross

National Nuclear Energy Commission of Brazil, Rio de Janeiro, Brazil

## ABSTRACT

The previous theory applies to isothermal behavior of dielectrics. It correlates current transients and dielectric loss curves obtained at different, but constant temperatures. A theory of nonisothermal effects is, however, needed to describe the conductivity glow curves during heating or the current transient during the thermal release of a "frozen-in" charge. The outline of such a theory is developed in the present paper. It is based on the principles of linearity and of charge invariance. Charge invariance means that the amount of charge which can be released by reheating a dielectric containing a frozen-in charge is a state variable depending only on the state of the system at the time when the reheating begins. The relaxation time can then be expressed in terms of a time- and temperature-independent distribution parameter. The generalized distribution function, which corresponds to the distribution of relaxation times of the isothermal system, is a function only of the distribution parameter and therefore independent of temperature. The formalism of rate theory is used to obtain an explicit expression for the relaxation time in terms of temperature and of activation energy. A simple mathematical model is obtained using an empirical expression for the distribution function. To account for the extremely strong temperature dependence of the current one must assume that states with high activation energies are much more frequent than states with low energies.

The isothermal behavior of dielectrics under different types of stress, in the time and frequency domains, has been investigated extensively. At an early stage of the theory, Wagner (1) formulated his "Law of Corresponding States" by which he was able to correlate discharge current and dielectric loss curves at different, but constant temperatures. In the analogous case of linear viscoelasticity a similar method has yielded "master" curves which correctly describe the behavior of systems over wide ranges of time, frequency, and temperature (2). The method is now called time-temperature superposition theory. The behavior of electrets is, however, characterized by nonisothermal transitions to which the theory in its present form does not apply (3). The lack of an adequate analytic theory of nonisothermal effects makes it difficult to obtain a systematic presentation of experimental results. In the present paper an attempt is made to formulate such a theory. For numerical applications an explicit expression for the distribution of relaxation times must be given. It is shown how such an expression can be obtained under rather general conditions and how it leads to a simple mathematical model.

### Charge Invariance

The theory is based on the postulate of charge invariance: The amount of charge which can be released by reheating an electret containing a "frozen-in" charge is a constant which depends only on the state of the system at the time when the reheating begins, not on subsequent heating rate and temperature. This assumption is by no means trivial although it seems to have been made implicitly by most authors on the subject. Thus it seems worth while to present here the experimental evidence (4) in some detail and subsequently to give a mathematical formulation.

*Experimental.*—Experiments were made with samples of filtered yellow prime carnauba wax with painted-on silver electrodes, of 1 mm thickness and 20 cm<sup>2</sup> area, under a voltage of 118v.

Figure 1 gives heating transients for different heating rates. Samples were first polarized at room temperature for 24 hr; subsequently the temperature was raised as shown in the bottom part of Fig. 1. The voltage was applied during the heating period. Currents increased strongly with increasing heating rate

and reached peak values when the temperature became constant. The final constant value of the current represents the ohmic conductance. Thus when the heating rate was very low, the transient became obliterated by the ohmic current. The current transients indicated that the polarization of the system increased due to the increase in temperature although the applied voltage remained constant.

Figure 2 gives current as a function of temperature, during heating and during cooling. The heating curves are derived from the corresponding curves of Fig. 1. During all measurements, i.e., during heating and during cooling, the same constant voltage was applied. For the cooling curves, samples were charged at 60.5°C during 13 hr before the temperature was reduced. All cooling curves are identical although cooling rates varied within a wide range of values. This absence of any current transient during cooling, contrasting strongly to what happens during heating, proves that the polarization of the sample remains constant if the temperature is reduced while the voltage remains applied. Obviously if there was any change in polarization this would have to manifest

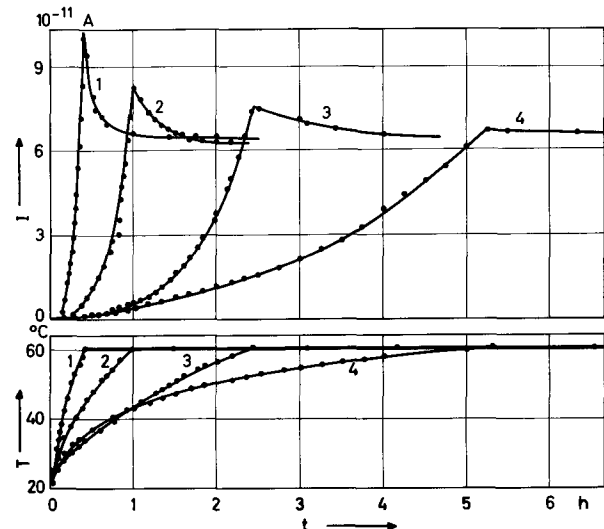


Fig. 1. Polarization currents as a function of time for different heating rates. Top: currents as a function of time; bottom: corresponding temperatures.

**Key words:** Electrets; dielectric theory (nonisothermal); linear superposition theory; electrical relaxation systems.

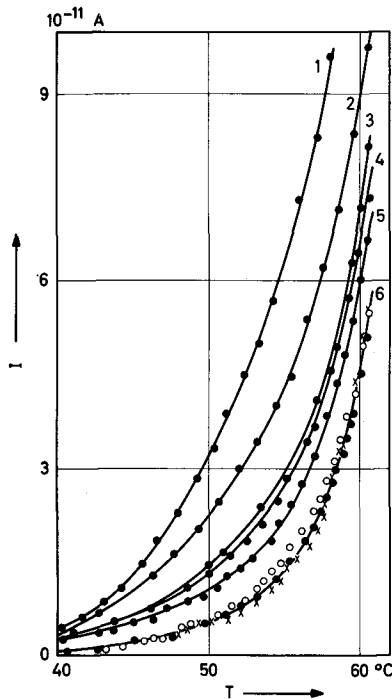


Fig. 2. Current as a function of temperature. Curves 1 to 5: heating curves. (Curves 2 to 5 of this figure correspond to curves 1 to 4 of Fig. 1). Average heating rates were: curve 1, 1.35°C/min; curve 2, 1.25°C/min; curve 3, 0.5°C/min; curve 4, 0.21°C/min; curve 5, 0.095°C/min. Curve 6: Cooling curves. Average cooling rates were: open circles 0.6°C/min; solid circles, 0.23°C/min; crosses 0.05°C/min.

itself by a depolarization or discharge transient in the same way as the polarization of the sample gives a charging transient.

Figure 3 gives depolarization curves in short-circuit following polarization experiments during which charge was "frozen-in" under different cooling conditions. Samples were charged at 60.5°C during 3 hr, cooled to room temperature with different cooling rates, and shorted. They were kept in short-circuit and subsequently reheated under identical conditions. Depolarization curves, as shown in Fig. 3, are approximately identical and indicate no systematic dependence on cooling rate.

These experiments show that the storage capacitance is independent of temperature during cooling. Further direct evidence has been obtained by Murphy (5). He found that the time integral over the depolarization current of a series of identically polarized samples was

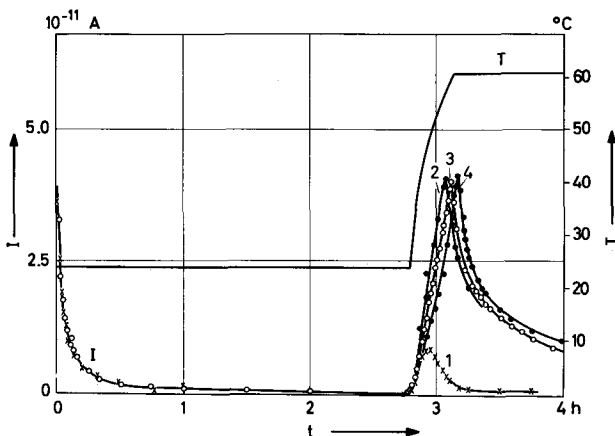


Fig. 3. Depolarization curves. Polarization time: 3 hr at 60.5°C. Average cooling rates (with voltage applied): for curve 2, 0.22°C/min; for curve 3, 0.55°C/min; for curve 4, 0.48°C/min. For curve 1 the sample was charged at room temperature.

independent of the rate of reheating in short-circuit between 0.19 and 0.75°C/min.

**Theoretical.**—An absorptive dielectric which has been polarized at a given (high) temperature and subsequently cooled and shorted, contains at the moment of the short-circuit (taken as  $t = 0$ ) a frozen-in or stored charge  $q(0)$ . This charge is defined as the time-integral over the transient component of the charging current. Thus it depends on the electrical and thermal treatment for  $t < 0$ , but is always the same for a given polarization process. The system is discharged by reheating in short-circuit. The temperature during this period is an arbitrary function of time  $T(t)$ . The discharge current  $J(t, T)$  is a function of time and temperature, different temperature functions giving different discharge currents. The released charge is defined as the time integral over the discharge transient, i.e., as  $\int_0^\infty J ds$ . There is no *a priori* reason to assume that the released charge is always the same, independently of the temperature function  $T(t)$  and that a unique value can be assigned to it. But in the case of charge invariance, the released charge is a constant which depends only on the initial state of the system at the moment of the short-circuit, not on subsequent heating rate and temperature. Under these conditions the released charge is equal to the stored charge and one has

$$\int_0^\infty J[s, T(s)] ds = q(0) \quad [1a]$$

where  $q(0)$  is a constant which depends only on the values of the system parameters at  $t = 0$ . If  $t_0$  is an arbitrary time  $0 < t_0 < \infty$  one has also

$$\int_{t_0}^\infty J[s, T(s)] ds = q(0) - \int_0^{t_0} J[s, T(s)] ds = q(t_0) \quad [1b]$$

$q(t_0)$  is the charge released between the arbitrary time  $t_0$  and infinity; according to Eq. [1b] this depends only on the thermal treatment prior to  $t_0$ , not on what might happen afterward. Therefore if charge invariance applies at the time  $t = 0$ , it applies also for any later time  $t_0$ . Since  $t_0$  is arbitrary we shall write briefly

$$\int_t^\infty J(s) ds = q(t) \quad [2a]$$

$$J = -dq/dt \quad [2b]$$

$q$  is a state variable which depends on the state of the system at time  $t$ ,  $Jdt$  is a total differential.

We shall exclude the case of resonance absorption. Thus we consider systems containing only two types of parameters, a dissipative (ohmic) one and a charge-storing (capacitive) one, i.e., pure relaxation systems. Transformation of electrostatic into electromagnetic energy is excluded. Under these conditions the released charge has always the same polarity, is uniformly decreasing, bounded, and disappears for  $t \rightarrow \infty$ . This gives the relations, for  $t > 0$ ,

$$M \cong q(t) \cong 0; dq/dt \leq 0; q(\infty) = 0; J \cong 0 \quad [2c]$$

where  $M$  is finite.

### Superposition Theory

**Linearity.**—In this paper the electret is treated as a linear electrical system, in line with the author's theory which considers the nonisothermal charging and discharging transients of solid dielectrics in the context of the general theory of dielectric anomalies (6). The application of the principle of linearity has already been successful in the treatment of dielectric absorption, open-circuit behavior of absorptive dielectrics (7) and electret polarization (8) at different, but constant temperatures. It appears also as a convenient basis for the discussion of the nonisothermal transient currents characteristics of electret behavior.

Linear systems are defined as systems which can be described by means of linear differential equations. Systems with a finite or infinite number of lumped parameters correspond, respectively, to a finite or an infinite set of total differential equations; systems with continuously distributed parameters correspond to partial differential equations. The knowledge of the linearity of these equations provides one with important information without a knowledge of the detailed structure of the physical system. Linear systems are conveniently discussed in terms of electrical network analogues. The network analogue of an electret is a two-terminal, passive, pure relaxation system. The current transient produced by a unit voltage step is called indicial admittance. The purpose of this paper is, therefore, to give an expression for the nonisothermal indicial admittance.

*Isothermal.*—System parameters change with temperature, but are constant, *i.e.*, time-independent, for all measurements performed with constant temperature throughout. Thus under isothermal conditions a linear system theory applies in its conventional form. Consider a system composed of a finite number of lumped parameters. This is described by a set of total differential equations, of the first order, containing mesh currents and applied voltage. The relation between the applied voltage  $V(t)$  and the external current  $J(t)$  is obtained by the elimination of all other currents. This gives (9) the linear differential equation with constant coefficients

$$\sum_{m=0}^n a_m d^m J/dt^m = \sum_{m=0}^{n'} b_m d^m V/dt^m \quad [3a]$$

The short-circuit current, for  $V \equiv 0$ , is the solution of the homogeneous equation

$$\sum_{m=0}^n a_m d^m J/dt^m = 0 \quad [3b]$$

the solution of which is

$$J = \sum_{i=1}^n (q_i/\tau_i) \exp(-t/\tau_i) \quad [4]$$

The  $\tau_i$  are the relaxation times, the  $q_i$  are the integration constants giving the initial charges of the individual systems, and  $\tau_i > 0$ ,  $q_i \geq 0$ . The open-circuit voltage, from which the potential of the unshielded electret could be obtained, is given by the differential equation in  $V(t)$  obtained by putting  $J \equiv 0$ .

A system with continuously distributed parameters has a continuous distribution of relaxation times. The short-circuit current is obtained by a generalization of Eq. [4], replacing the sum by an integral and  $q_i$  by  $dq(\tau)$ , where  $\tau$  now is a continuous variable. This gives the integral transform

$$J = \int_0^\infty \phi(t, \tau) \frac{dq}{d\tau} d\tau \quad [5]$$

where  $dq/d\tau$  is the distribution function of relaxation times  $\tau$ . The kernel

$$\phi(t, \tau) = (1/\tau) \exp(-t/\tau) \quad [6a]$$

is the solution of the differential equation

$$d\phi/dt + \phi/\tau = 0 \quad [6b]$$

that satisfies the normalization condition

$$\int_0^\infty \phi(t, \tau) d\tau = 1 \quad [6c]$$

*Nonisothermal lumped parameter system.*—The electret effect is typically nonisothermal. During the course of the experiment the temperature is a func-

tion of time; therefore the system parameters are time-dependent. This obliges one to generalize the theory and to reformulate the expressions for the distribution function and the kernel of the integral-transform representation for the current.

The time-dependence of the system parameters does not affect the linearity of the system. Therefore the relation between  $J$  and  $V$  has the same form as before, but the coefficients of the differential equation are now functions of time. The same applies to the differential equation for the short-circuit current. Thus it is sufficient to replace the constant coefficients  $a_m$  by time-dependent coefficients  $k_m(t)$ . This gives for the current the equation

$$\sum_{m=0}^n k_m(t) d^m J/dt^m = 0, \quad t > 0 \quad [7]$$

The time  $t = 0$  is taken as the moment when the applied voltage is removed and the system is short-circuited. The solution has the form

$$J = \sum_{i=1}^n A_i \phi_i(t) \quad [8]$$

where the  $\phi_i$  are linearly independent particular solutions of Eq. [7].  $A_i$  are the integration constants which define the state of the system for  $t = 0$ . This is supposed to be always the same, *i.e.*, the system shall have been completely polarized with a given constant voltage before the stored charge is released. Now we consider two depolarization experiments, corresponding to two temperature-time functions  $T^{(1)}(t)$  and  $T^{(2)}(t)$  which shall be identical for  $0 \leq t \leq t_0$ , but different for  $t_0 < t < \infty$ .

Thus

$$T^{(1)}(t) = T^{(2)}(t) \quad 0 \leq t \leq t_0 \quad [9a]$$

$$T^{(1)}(t) \neq T^{(2)}(t) \quad t_0 < t < \infty \quad [9b]$$

The coefficients  $k_m$  will therefore also be identical for  $0 \leq t \leq t_0$  and different for  $t > t_0$ . Under these conditions one has two solutions

$$J^{(1)} = \sum_{i=1}^n A_i \phi_i^{(1)}(t) \quad \left. \begin{array}{l} \\ \\ \end{array} \right\} t_0 < t < \infty \quad [10a]$$

$$J^{(2)} = \sum_{i=1}^n A_i \phi_i^{(2)}(t) \quad [10b]$$

$$J^{(1)}(t) = J^{(2)}(t) \quad 0 \leq t \leq t_0 \quad [10c]$$

The functions  $\phi_i^{(1)}$  and  $\phi_i^{(2)}$  in the interval  $t_0 < t < \infty$  are different because they correspond to different temperature-time functions, but the integration constants  $A_i$  are the same in both cases because the initial state of the system is the same (Fig. 4). The released charge as a function of time is given by

$$q^{(1)}(t) = \sum_{i=1}^n \int_t^\infty A_i \phi_i^{(1)}(t) dt \quad [11a]$$

$$q^{(2)}(t) = \sum_{i=1}^n \int_t^\infty A_i \phi_i^{(2)}(t) dt \quad [11b]$$

Charge invariance requires that

$$q^{(1)}(t) = q^{(2)}(t) = q(t), \quad 0 \leq t \leq t_0 \quad [12]$$

or

$$\sum_{i=1}^n A_i \int_t^\infty \phi_i^{(1)}(t) dt - \sum_{i=1}^n A_i \int_t^\infty \phi_i^{(2)}(t) dt = 0, \quad 0 \leq t \leq t_0 \quad [13]$$

Since the  $A_i$  are arbitrary constants, it follows that

$$\int_t^\infty A_i \phi_i^{(1)}(t) dt = \int_t^\infty A_i \phi_i^{(2)}(t) dt = q_i(t), \quad 0 \leq t \leq t_0, \quad i = 1, 2, \dots, n \quad [14]$$

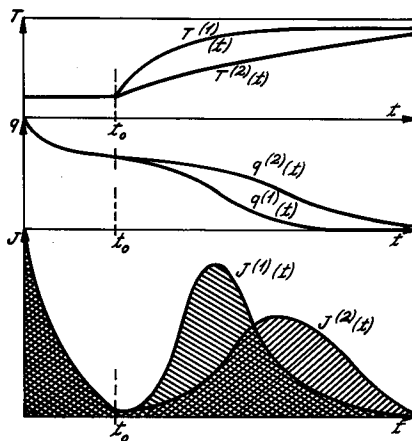


Fig. 4. Temperature, charge, and current for different heating rates.

independent of the particular temperature-time function  $T(t)$ , and

$$A_i \phi_i(t) = -dq_i/dt \tag{15a}$$

$$q(t) = \sum_1^n q_i(t) \tag{15b}$$

So far the two "test" functions  $T^{(1)}$  and  $T^{(2)}$  were arbitrary for  $t \geq t_0$ . Now consider a function  $T^{(2)}$  which is constant for  $t_0 < t < \infty$ . The corresponding isothermal relaxation current is given by a series of real exponentials with positive amplitudes. The integral over each term is also positive and equals  $q_i(t)$  since relation [14] is valid for any function  $T(t)$ , in particular the function  $T = \text{const}$ . It follows that

$$M_i > q_i(t) \geq 0; \quad q_i(\infty) = 0 \tag{16}$$

Since  $t_0$  was arbitrary, charge invariance applies to each particular solution  $A_i \phi_i(t)$  in the whole discharge interval.

Any function subject to these conditions can be written as

$$q_i(t) = q_i(0) \exp[-F_i(t)] \tag{17}$$

where  $F_i$  is a continuous function and  $q_i(0)$  is positive. Writing  $dF_i/dt = 1/\tau_i$  this gives

$$J(t) = \sum_1^n [q_i(0)/\tau_i(t)] \exp[-\int_0^t ds/\tau_i(s)] \tag{18}$$

The integration constants  $A_i$  have been replaced by the initial charges  $q_i(0)$ .

The case of an infinite number of lumped parameters does not present any difficulty, the series in Eq. [18] then extending from 1 to infinity.

*Relaxation times as state variables.*—If the temperature is constant, equal to  $T_0$ , the isothermal current is

$$J = \sum_1^n [q_i(0)/\tau_i(T_0)] \exp[-t/\tau_i(T_0)] \tag{19}$$

in accordance with Eq. [3] and [5], the  $\tau_i$  being the relaxation times for the temperature  $T_0$ .

If the temperature is not constant, the functions  $\tau_i$  might depend on the temperature and its derivatives and, in addition, explicitly on time. If  $\tau_i$  depends explicitly on time, an instantaneous variation of  $T$  is followed by a delayed variation of  $\tau_i$ . If  $\tau_i$  depends on the heating and cooling rates, the same value of  $T$  gives different values of  $\tau_i$ . Here we shall exclude these effects and assume that the  $\tau_i$  depend only on the value of  $T$  itself. The functions  $\tau_i$  of the nonisothermal system at any given temperature are then identical with the relaxation times of the isothermal system at the same temperature; since the latter are always positive,

the  $\tau_i$  are always positive and  $dq_i/dt \leq 0$ . With this assumption we postulate the existence of relaxation times as state variables. This is justified within the context of rate theory, as discussed below. It is, however, not a necessary consequence of the assumption that the system parameters, or network elements in the case of the electrical network analogue, are state parameters, because the coefficients  $k_m(t)$  of the differential Eq. [7] in general contain the values of the system parameters at a given temperature and their temperature derivatives.

*Network representation.*—It is easy to find an electrical network model which represents Eq. [18] when all  $\tau_i$  are positive. Consider the parallel arrangement of independent "relaxators" of Fig. 5. The differential equation for the short-circuit current in branch  $i$  is

$$dJ_i/dt + J_i [1/R_i C_i] + d \ln(R_i C_i)/dt = 0 \tag{20}$$

which gives

$$J_i(t) = [q_i(0)/R_i C_i] \exp \left[ -\int_0^t ds/R_i C_i \right] \tag{21}$$

where  $q_i(0)$  is the charge of the capacitor  $C_i$  at  $t = 0$ . Equation [21] becomes identical with Eq. [19] if one takes

$$\tau_i = R_i C_i \tag{22}$$

The network elements  $R_i$  and  $C_i$  are always positive. Equation [22] can, therefore, be satisfied only if  $\tau_i$  is positive. This condition is fulfilled according to the previous discussion. Therefore any system whose current is given by expression [19] with  $\tau_i > 0$  can be represented by the network of Fig. 5. A more detailed discussion of network representations will be given in a subsequent paper. Here it might be mentioned in passing that any "impulsive" network (10) is charge-invariant. A charge-invariant system, whose polarization current contains a steady-state component, can therefore always be represented by an impulsive network connected in parallel with a pure resistance.

The two types of parameters appear in the equations only in the form of the product  $R_i C_i$ . Therefore short-circuit measurements do not allow one to discover whether both are temperature-dependent or only one of them, i.e.,  $R_i$ . The situation is different when an external voltage is applied. Consider a sample which has been polarized at temperature  $T_2$  with the constant voltage  $U_0$ . At the end of the polarization period the total charge is  $q_2 = U_0 C_0(T_2) + U_0 \sum_1^n C_i(T_2)$ . Subsequently the temperature shall be reduced to  $T_1$ . The corresponding final charge is  $q_1 = U_0 C_0(T_1) + U_0 \sum_1^n C_i(T_1)$ . If the  $C$ 's depend on temperature,  $q_2 \neq q_1$ , the charge difference  $\Delta q = q_2 - q_1$  flows through the external circuit and a current results. A distinction must be made between the effects of a temperature dependence of  $C_0$  and of the  $C_i$ ,  $i \geq 1$ .  $C_0$ , which rep-

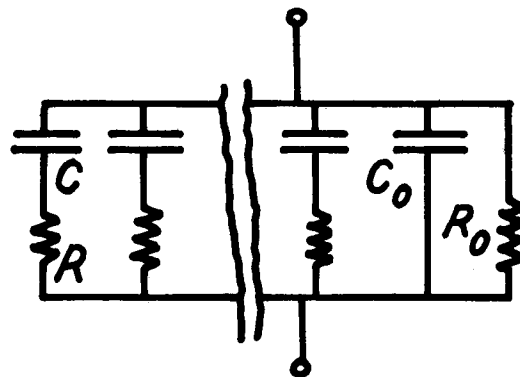


Fig. 5. Network representation

resents the high-frequency dielectric constant, is not connected in series with a resistive element. If it is a function of temperature, the corresponding current  $U_o(dC_o/dT)dT/dt$  is proportional to the rate of temperature change, but it is an "in-phase" current. Like the "ohmic" current  $U_o R_o(T)$  it becomes constant when the temperature becomes constant. The  $C_i$ ,  $i \geq 1$ , are in series with resistive elements. Their temperature dependence is associated with an "out-of-phase" current which extends beyond the period during which the temperature changes with time, i.e., a transient current. In our experiments the current was found to be independent of the rate of temperature change during cooling and became constant at the same time as temperature. Therefore within the precision of these experiments all capacitive elements remained constant and the temperature effect was due entirely to the dissipative elements.

### Continuous Systems

*Distribution function.*—The transition to continuous systems is made by considering a dense distribution of infinitesimal elements each characterized by a relaxation time and an amplitude factor  $dq$ , the latter being the contribution of that system to the polarization charge. In the isothermal case one could associate  $dq$  directly with  $\tau$ , writing  $dq = (dq/d\tau)d\tau$ , and thus obtain an integral of type [3]. When  $\tau$  is a function of temperature, and thus implicitly of time, this procedure makes the spectrum time-dependent and would lead to a violation of charge invariance unless limiting conditions are introduced subsequently. The difficulty is avoided by introducing a time- and temperature-independent parameter  $U$ . The relaxation time is a function of both  $U$  and  $T(t)$ , while the amplitude factor is a function of  $U$  alone, i.e.

$$\tau = \tau[U, T(t)] \quad [23a]$$

$$dq = (dq/dU)dU \quad [23b]$$

Replacing in Eq. [18]  $q_i(0)$  by  $dq(U)$ ,  $\tau_i$  by  $\tau(U, T)$ , and the series by an integral one obtains the integral transform

$$J(t) = \int_0^\infty \phi(t, U) \frac{dq}{dU} dU \quad [24a]$$

$$\phi(t, U) = \frac{1}{\tau[U, T(t)]} \exp \left[ - \int_0^t \frac{ds}{\tau[U, T(s)]} \right] \quad [24b]$$

The condition of charge invariance is fulfilled because the amplitude factor  $dq/dU$  is independent of time and

$$\int_t^\infty \phi(t, U) dt = \exp \left[ - \int_0^t \frac{ds}{\tau[U, T(s)]} \right] \quad [25]$$

Equation [25] expresses the integral over the interval  $t$  to  $\infty$  on the left side in terms of an integral over the interval 0 to  $t$  on the right side. The kernel itself is the integral of the differential equation

$$d\phi/dt + \phi/f(t) = 0 \quad [26a]$$

$$1/f(t) = (1/\tau) + d \ln \tau \quad [26b]$$

These relations generalize the corresponding relations [3]–[6]. A heuristic method of derivation could, therefore, start with Eq. [23], [24a], and [26a], with the additional conditions (a) that the differential Eq. [26a] for the kernel  $\phi$  transforms into the isothermal Eq. [5] and (b) that  $\phi$  is charge-invariant. These conditions give for  $f(t)$  the relation [26b] and for  $\phi$  the expression [24b].

*Distribution parameter.*—To get an explicit expression for  $\phi$  one can use the formalism of rate theory (11) writing

$$\tau = (h/kT) \exp [F/RT] \quad [27]$$

where  $F$  is the molar free energy increase for the ac-

tivated system,  $R$  the gas constant,  $k$  the Boltzmann constant,  $h$  Planck's constant, and  $T$  the absolute temperature. Since  $F = U - TS$ , where  $U$  is the molar activation energy and  $S$  the entropy increase one has

$$\tau = \tau_o \exp U/RT \quad [28]$$

with

$$\tau_o = (h/kT) \exp (-S/R) \quad [29]$$

A distribution of relaxation times corresponds to a system of energy states with different activation energies and entropy increases. In the general case (12) one would have to introduce distributions for both  $U$  and  $S$ . The usual treatment considers, however, only a single distribution of energy levels. Paralleling this treatment we consider only a distribution of activation energies, identifying activation energy with the parameter  $U$  in Eq. [23] and taking a single value  $S$ , an average value.

One might object that Eq. [28] does not lead to a law of corresponding states as has been found by many authors. Such a law is obtained if the temperature dependence is the same for all values of  $\tau$ , i.e.,  $\tau = \tau_o U$ . Here  $U$  is a dimensionless parameter, the temperature function  $\tau_o(T)$  is usually assumed to be exponential. This alternative will, however, not be discussed in this paper.

It is worth noting that for a single relaxation time and uniform heating rate the system of Eq. [24] and [28] becomes identical with the function that has been used to describe current glow curves and thermoluminescence with monomolecular kinetics (13).

### Model Distribution Function

Froehlich (14) has considered a model assuming a dilute solution of dipolar molecules in an amorphous solid, each molecule having two equilibrium positions with opposite dipole directions and equal energy in the ground level. He assumed the potential barrier between the two positions to have different heights equally distributed between two extreme values, or what is equivalent an equal distribution of the number of molecules over the energy interval. This gives a continuous distribution of energy levels with activation energies between a minimum value  $U_1$  and a maximum value  $U_2$  and a population of dipolar molecules  $N(U)$  independent of  $U$ . Then  $dq = eN_o dU / (U_2 - U_1)$  where  $N_o$  is the total number of molecules and  $e$  the electron charge. This expression can be generalized by abandoning the restriction  $N(U) = \text{const}$  and writing

$$dq = neN_o U^{n-1} dU / (U_2^n - U_1^n) \quad [30]$$

where  $n \geq 1$  is a constant coefficient. This Eq. [30] is more general than the above model. It also applies for instance to the case where one has a number of charge carriers with equilibrium positions in potential wells separated by barriers of different heights. For  $n = 1$  one has Froehlich's expression. Equation [30] satisfies the normalization condition  $q = \int_{U_1}^{U_2} dq = eN_o$ . Since from Eq. [28],  $U = RT \ln \tau/\tau_o$ , one has also

$$dq = \frac{neN_o (RT)^n}{U_2^n - U_1^n} \ln^{n-1} (\tau/\tau_o) d \ln (\tau/\tau_o) \quad [31]$$

Substitution into Eq. [24] gives for  $T = \text{constant}$

$$J = \frac{neN_o (RT)^n}{U_2^n - U_1^n} \int_{\tau_1}^{\tau_2} \frac{\exp [-t/\tau]}{\tau \ln^{n-1} (\tau/\tau_o)} d \ln (\tau/\tau_o) \quad [32]$$

where

$$\tau_i = \tau_o \exp [U_i/RT] \quad i = 1, 2 \quad [33]$$

The logarithmic term in Eq. [32] is slowly varying compared with the rest of the integrand. For an approximate evaluation of the integral this term will

be taken out of the integral, with that value of  $\tau$  for which  $\exp(-t/\tau) = 1/e$ , i.e., for  $\tau = t$ . This gives

$$J = \frac{neN_0(RT)^n}{U_2^n - U_1^n} \ln^{n-1}(t/\tau_0) \int_{\tau_1}^{\tau_2} \frac{\exp(-t/\tau)}{\tau} d \ln \tau/\tau_0 \quad [34]$$

and after integration

$$J = \frac{neN_0(RT)^n}{U_2^n - U_1^n} \frac{\ln^{n-1}(t/\tau_0)}{t} [\exp(-t/\tau_2) - \exp(-t/\tau_1)] \quad [35]$$

This expression satisfies the condition of charge invariance. The factor in square brackets is approximately a "unit box" function, i.e., it equals unity for  $\tau_2 \cong t \cong \tau_1$  and 0 for  $t$  outside the interval. Therefore one has

$$q = \int_0^\infty J dt = \frac{neN_0(RT)^n}{U_2^n - U_1^n} \int_{\tau_1}^{\tau_2} \ln^{n-1}(t/\tau_0) d \ln(t/\tau_0) = eN_0 \quad [36]$$

For  $n = 1$  one obtains correctly Froehlich's formula

$$J = \frac{eN_0RT}{U_2 - U_1} \frac{[\exp(-t/\tau_2) - \exp(-t/\tau_1)]}{t} \quad [37]$$

To discuss Eq. [35] consider first the time dependence. According to what has been said about the square bracket term, the current at any temperature is given by

$$J = \begin{cases} 0 & t > \tau_2 \\ c(1/t) \ln^{n-1}(t/\tau_0) & \tau_2 > t > \tau_1 \\ 0 & \tau_2 > t \end{cases} \quad [38]$$

Within a limited interval of time  $J$  decreases approximately like  $1/t$ , while over a wider range the influence of the logarithmic factor makes  $J$  decrease with time somewhat slower than  $1/t$ . This behavior is in agreement with most experiments which give  $J \sim (1/t^m)$  with  $m$  slightly less than 1.

Currents at different temperatures differ by a constant factor  $(RT)^n$ . To assure charge conservation, the increase in current amplitude must be compensated by a decrease in width of the interval  $\tau_1 - \tau_2$ , as is shown by Eq. [38]. This is again in qualitative agreement with experiment.

The temperature dependence of the current is certainly much stronger than would be given by a linear term, as in Eq. [37]. Therefore the exponent  $n$  must be considerably greater than unity, and the generalization  $dq \sim U^{n-1}dU$  with  $n > 1$  is in the right direction, although possibly an exponential increase would fit better the observed data. Since  $dq = edN(U)$ , one has also  $N(U) \sim U^n$  and, instead of an equipartition of energy, one has a much higher occupation of states with high activation energy than with low activation energy. The power law, however, does not give the right increase; a function  $N \sim \exp(cU)$  should give a better representation of the experimental situation.

### Conclusions

The discussion has been in terms of electrets. Electret behavior is a general property of solid dielectrics, like dielectric absorption and dielectric loss, and caused by the same mechanism as these effects. Froehlich's

theory and its generalization, as presented here, are charge-invariant and refer to dielectrics in general. The principle of charge invariance might not be rigorously valid in all cases, but in most is a good approximation. The conclusions of the present paper are, therefore, of interest to dielectric theory in general. Some consequences will be examined in following papers.

### SYMBOLS

$T$	= absolute temperature, °K
$t$	= time, sec
$J$	= current, amp
$q$	= charge, coul
$\tau$	= relaxation time, sec.
$\phi$	= kernel of integral transform
$R_i$	= resistance, ohms
$C_i$	= capacitance, F
$h$	= Plank's constant, J sec
$R$	= gas constant, J °K <sup>-1</sup> mol <sup>-1</sup>
$k$	= Boltzmann constant, J °K <sup>-1</sup>
$F$	= molar free energy, J mol <sup>-1</sup>
$S$	= entropy, J °K <sup>-1</sup> mol <sup>-1</sup>
$U$	= molar activation energy, J mol <sup>-1</sup>

Manuscript received Sept. 22, 1967; revised manuscript received Jan. 3, 1968. This paper was presented at the Electrets Symposium at the Chicago Meeting, Oct. 15-19, 1967, as Abstract 121.

Any discussion of this paper will appear in a Discussion Section to be published in the December 1968 JOURNAL.

### REFERENCES

1. K. W. Wagner, *Elektrotechn. Z.*, **36**, 135, 163 (1915).
2. J. Ferry, "Viscoelastic Properties of Polymers," p. 201, John Wiley & Sons, Inc., New York (1961).
3. Cf. B. Gross, "Charge Storage in Solid Dielectrics," p. 86, Elsevier Publishing Co., Amsterdam (1964).
4. B. Gross and L. F. Denard *An. Brasil. Acad. Cienc.*, **14**, 349 (1942).
5. P. V. Murphy, Information Storage by Persistent Electric Polarization Systems, Report No. 1, June 1, 1963-Dec. 15, 1963, Panoramic Research Inc., Palo Alto, Calif. presented at the Symposium on Electrets, Chicago Meeting, Oct. 15-19, 1967; The Electrochem. Soc., Dielectrics and Insulation Division, Extended Abstracts J-2, Vol. 4, No. 2, p. 90.
6. B. Gross, Universidad Nacional de Tucuman (Argentina), *Revista A1*, 35 (1940); *An. Acad. Brasil Cienc.*, **17**, 219 (1945); *J. Chem. Phys.*, **17**, 866 (1949).
7. B. Gross, *Z. Phys.*, **107**, 217 (1937); *Phys. Rev.*, **57**, 57 (1940); **62**, 683 (1942).
8. B. Gross *An. Acad. Brasil. Cienc.*, **17**, 219 (1945); G. Wiseman and G. R. Feaster, *J. Chem. Phys.*, **3**, 521 (1957); M. M. Perlman and J. L. Meunier, *J. Appl. Phys.*, **36**, 420 (1965); D. E. Tilley, *ibid.*, **38**, 2543 (1967).
9. B. Gross and W. Guttinger, *J. Appl. Sci. Res.*, **B16**, 189 (1956).
10. For physical representation of relaxation systems see for instance H. W. Bode, "Network Analysis and Feedback Amplifier Design," p. 177, D. Van Nostrand Co., New York (1945); B. Gross, *J. Polymer Sci.*, **20**, 371 (1956); *Nuovo Cimento*, Vol. 3, Serie X, Supplemento No. 2, p. 235 (1956).
11. W. Kauzman, *Rev. Mod. Phys.*, **14**, 1 (1942).
12. J. R. MacDonald, *J. Appl. Phys.*, **34**, 538 (1963).
13. C. Bucci and R. Fieschi, *Phys. Rev.*, **148**, 148 (1966).
14. H. Froehlich, "Theory of Dielectrics," p. 90, Oxford Clarendon Press (1949).

# Electret Behavior and Ionic Thermal Currents in Alkali Halides

N. Januzzi

Physics Department, Faculdade de Ciencias, Rio Claro, Sao Paulo, Brazil

and S. Mascarenhas

Physics Department, Escola Engenharia, Sao Carlos, Sao Paulo, Brazil

## ABSTRACT

The behavior of alkali-halide electrets of KCl/Sr and double doped KCl/Ca, OH is investigated by the glow peak discharge method of Fieschi, Bucci *et al.* (1) (ionic thermal conductivity method or ITC). In this case a complete analysis of the trapped polarization is possible quantitatively. The electret polarization is due to impurity vacancy dipoles. It is shown that the electret behavior in this case can be used as a very powerful tool to investigate the motion of defects in the solid matrix. As an application, the dipole diffusion to form higher aggregates is studied by a thermal annealing technique. By studying the variation of the electret released charge for various temperatures it is shown that trimers (3 dipole aggregates) are formed. The reaction is found to be of third order, and the activation energy for defect motion is (0.71 eV). The dipole relaxation frequency at 0°K is  $10^{-13}$  sec $^{-1}$ . All data agree very well with that obtained by other techniques and confirms the results of Dryden and Cook (2). In the case of double-doped systems, it is shown that the ITC method allows a quantitative determination of the solid-state reaction between OH and Ca. A correlation between F center formation by x-irradiation and electret behavior is also found, showing that the reaction is probably the precipitation of Ca(OH) $_2$  in the matrix leading to dipole destruction and quenching of the color center production. This is perhaps the only case in which the electret behavior is completely understood in a quantitative way, and, used as a tool, to obtain important solid-state parameters such as relaxation times, number of defects in the matrix, activation energies, and to investigate defect production and reactions in the solid state.

In a series of very complete and fundamental papers Fieschi Bucci *et al.* (1) established the foundations of the ITC (ionic thermal conductivity) method. The present paper is an application of their method using electret behavior and ITC as a tool to investigate solid-state problems. The electret trapped polarization arises in this case from the well-established presence of dipoles in the solid matrix. These dipoles are associated with impurity-vacancy complexes. In Fig. 1 this is indicated for the case of a fcc lattice such as that of KCl. It is seen that the addition of the divalent impurity (indicated by a double-charge in Fig. 1) such as Ca, Sr, Mg, Cd is associated with the presence of an additional positive ion vacancy to satisfy charge conservation in the matrix. This impurity may be added to the melt when the crystal is grown by techniques such as the Kyropoulos technique, or can be diffused into the material at temperatures near the melting point (3). Depending on the temperature and association energy the vacancy may be in a nearest neighbor position to the divalent impurity. In the case of the fcc lattice this will correspond to a dipole oriented in a general 110 position. Because of ionic diffusion this dipole can change its orientation. It is found that the reorientation is due mainly to positive ion mobility, or if we want, to vacancy jumps around the more or less fixed divalent impurity. To this process we can associate of course a thermal activation energy (related to the potential function seen by the vacancy in its neighborhood), a relaxation time, and eventually even an activation energy connected with the motion of the entire entity. In the physics of defects in solids this is a classical problem which has been extensively investigated (4). Other configurations of the IV (impurity vacancy complex) are also possible, in which the vacancy is at a next-neighbor distance ( $n^2$  complex), or next-next-neighbor distance ( $n^3$  complex), and these also have associated dipole moments, relaxation times and other corresponding parameters, and in some phenomena may play a prominent role. The presence

of the IV complex has also been detected by lattice expansion effects (5), by the use of the photoelastic technique of color center investigation (6), by dielectric relaxation measurements (7), by magnetic resonance (8), by dielectric absorption measurements (9) as well as by internal friction measurements (10). The ITC technique is however the most powerful one in our opinion. It is also very straightforward experimentally. The detection limit for dipoles is surprisingly small, in some cases concentrations as low as  $10^{15}$  dipoles/cm $^3$  can be detected.

The essential points related to the theoretical interpretation of the peaks have been discussed by Fieschi, Bucci *et al.* (1), and we will only summarize here the main results that are needed for the objectives of the present paper.

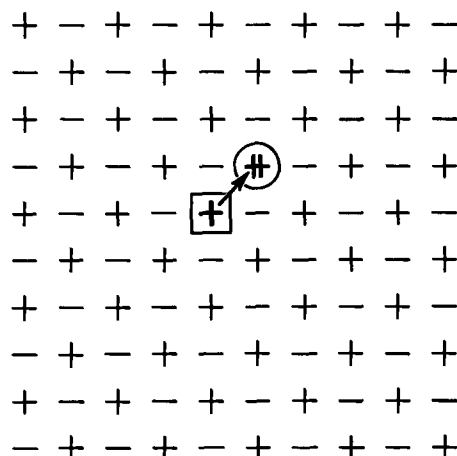


Fig. 1. Divalent impurity and associated positive ion-vacancy in a fcc alkali halide. The dipole moment (arrow) is along a (100) direction.

The electret polarization and depolarization by the glow peak obtained while heating the sample is conducted in the same way as first introduced by Gross in his now classical papers (11). In the case of the alkali-halides doped with divalent impurities, we know however that (a) by applying the polarization field we are orienting at the polarization temperature,  $T_p$ , a certain fraction of the IV dipoles in total number per unit volume  $N_d$ . If the temperature is high enough, we can suppose these dipoles to be rotating freely in the matrix. If the concentration is not too high, we can safely assume that these dipoles do not interact with each other. The relaxation time for dipole reorientation will be given by

$$\tau = \tau_0 \exp E/kT \quad [1]$$

(b) When we cool the electret under the applied field to a lower temperature  $T_1$  the relaxation time may change drastically (see Eq. [1]), and the oriented dipole configuration and its associated polarization will be frozen in the matrix.

If we now switch off the external field, we shall be left with the frozen polarization due to the orientation of the IV dipoles. If we then warm the electret, the relaxation time of the dipoles will gradually decrease and a displacement current will be observed in the external circuit because of the polarization change. This current  $i(t)$  is a function of temperature  $T$  and time  $t$  (we assume a constant heating rate) and is given by [see ref. (1)]

$$i(t) = N_d \frac{p^2 E_p}{3kT_p} \left[ \tau_0 \exp \left\{ \frac{E}{kT} \right\} \right]^{-1} \times \exp \left( - \int_0^t \left[ b \tau_0 \exp \left\{ \frac{E}{kT'} \right\} \right]^{-1} dT' \right) \quad [2]$$

This follows directly from the unimolecular nature of the dipole orientation process. The factor 1/3 is due to the hypothesis of freely rotating dipoles of moment. As expected intuitively this  $i(t)$  will present a maximum at a certain temperature  $T_m$ , the glow peak function being asymmetric in time (or temperature). The maximum peak position in temperature is related to the activation energy,  $E$ , heating rate,  $b$ , and relaxation time in the following way

$$T_m = \left\{ \frac{bE\tau(T_m)}{k} \right\}^{1/2} \quad [3]$$

It is very interesting to observe that the maximum peak position temperature is independent of the polarization temperature  $T_p$  and of the polarization field  $E_p$ . The activation energy can be obtained from the glow-peak in two independent ways. The easiest and most direct way is to calculate it from the initial rise in current. The low temperature tail of the band, at temperatures away from  $T_m$ , is given by

$$i(T) = i_0 \exp (-E/kT) \quad [4]$$

The other way to obtain  $E$  is by a global analysis of the whole band, which is much more difficult and requires a pure band form. That is, no overlapping bands may be present, so that Eq. [1] is valid during all of the charge release process.

When these conditions are satisfied we can apply the following relation

$$\ln \left[ \int_t^\infty i(t') dt' \right] - \ln i(T) = \ln \tau_0 + E/kT \quad [5]$$

The equation above expresses the  $\ln$  of the relaxation time  $\tau(T)$  as a function of the observed glow in an integral form. By plotting the latter as a function of  $1/T$  a straight line is obtained that furnishes directly the activation energy and  $\tau_0$ . This process is more cumbersome because several graphical integrations of the

band have to be performed. It is, however, independent of the heating rate. Bucci and Fieschi (1) have shown in the case of overlapping bands that the bands can be properly "cleaned" by a proper choice of the polarization temperature  $T_p$ , and by letting the lower temperature bands discharge and subsequently recooling to obtain the next band.

Finally, the total number of dipoles in the electret can also be found with good precision from the area of the band. At saturation the total polarization  $P_0$  is given by the following relation

$$P_0 = N_d (1/3 p^2 E_p)/kT_p \quad [6]$$

Thus by measuring  $P_0$  from the underlying area of the band  $N_d$  the total number of dipoles per unit volume can be obtained, if their dipole moment is known. In the case of the IV complex this is known.  $E_p$  and  $T_p$  as above are the polarizing field and temperature.

Equation [6] above is important if we wish to investigate the variation of the number of dipoles associated with some particular phenomenon like a solid-state reaction or defect production that may be dependent on the dipole sources.

### Experimental

The samples used were grown in our Laboratory at S. Carlos by the pulling or Kyropoulos technique from the melt. In the case of doped samples the impurity was added to the melt in the desired concentration. In some cases where necessary the direct analysis of the impurity in the solid was made by spectrophotometric or activation analysis techniques and will be described when appropriate. The samples were cleaved in thin plates of thickness approximately 1 mm and area of circa 1 cm<sup>2</sup> along a (100) plane. Aquadag or alcohol-dag electrodes were painted to obtain good electrical contact with the electrodes. The field was applied to the sample in vacuum or in a controlled atmosphere of dry N<sub>2</sub>, and the electrodes were held together by magnetic attraction so that no dielectric was present at the site where the temperature would be cycling. The current was measured with a Keithley 603 electrometer. The warming rate was kept constant and of the order of 0.1°K/sec, which was found to be the ideal rate for the quantitative and reproducible measurements obtained. Reproducibility for the currents and peaks was of the order of 5% or better. The activation energies could be measured to within 0.05 eV.

For the radiation damage of the samples to produce color centers, a 100 kv tungsten tube was used with proper filtration to ensure uniformity of defect production. The experimental sequence was the following. The sample was polarized at a desired temperature  $T_p$  for a certain time  $t_p$  (usually a few minutes) under a certain polarizing field  $E_p$ . The temperature was then lowered by pouring liquid nitrogen into the Dewar which contained the whole experimental assembly. After the crystal attained the lower temperature  $T_1$  the field was switched off, and the crystal warmed at a constant rate. The current due to the dipole relaxation which appeared in the form of glow peaks was then continuously recorded as well as the temperature. For convenience two recorders were used. One a X-Y recorder for  $i(T)$  and the other a recorder for the temperature as a function of time, so that the warming rate was directly observed during the experiments. The temperature was measured with an iron-constantan thermocouple situated in one of the electrodes. It is important in this work that the samples receive the proper thermal treatment. As shown in this paper the dipoles can aggregate to form dimers, trimers, or the divalent metal may precipitate in various sites like grain boundaries, dislocations, and other favorable places. It is then essential with an old sample, or a sample that is cleaved from a certain block which received no special thermal treatment, to



warm it to a temperature where the dipoles and the impurities will be dissolved properly in the matrix. This was done in an oven under controlled temperature and atmosphere conditions. The crystal was then quenched to room temperature or slowly cooled, depending on the type of experiment to be performed as will be described below. The optical measurements were made using a Beckman DK-2 double-beam automatic recording spectrophotometer in the range of 200 nm to  $3\mu$ .

### Results

**Dipole aggregation in KCl/Sr.**—It was shown by Cook and Dryden using a dielectric loss method that the IV dipoles in KCl/Sr aggregated to form trimers. Because of this aggregation process the resulting trimer has a negligible dipole moment, and thus the total polarization in our samples should decrease with their formation. This should be a temperature dependent process because of the thermal activation energy involved in the diffusion mechanism. In our ITC measurements the total area under the glow corresponding to isolated dipoles should then diminish with the aggregation process. We thus measured the polarization  $P_0$  as a function of time  $t$ . We kept the samples at different temperatures  $T$ . This polarization aging diminished, as expected, with time, as is shown in the results of Fig. 2. The particular way in which we plotted our results is related to the equations of the association process that will be discussed below. The results of Fig. 2 were obtained by polarizing the crystal always at the same temperature  $T_p$  for the same polarization time  $t_p$ . After the desired thermal treatment the polarization  $P$  was measured under the same field for all experiments. The crystal was then taken to a constant-temperature oven for the required length of time (days, hours, or minutes, depending on the temperature). After this time a new ITC measurement was made and the sample returned to the oven to continue with the aging process at a constant temperature.

**Ca Precipitation with OH in KCl.**—The OH impurity is now one of the more important defects in the physics of alkali halides. Luty *et al.* (12), Feher *et al.* (13), and Kanzig *et al.* (14) studied important paraelectric, paraelastic, and cooling effects of the OH dipole in alkali halides. Kuhn and Luty were the first to explain the apparent paradoxical behavior of the electrical conductivity of some of these solids as a function of temperature, by assuming a solid state reaction between Ca and OH ions. The same argument was used by Ikeya to explain the absence of F center sensitization in Cd containing samples. In the present work we give direct experimental evidence for this reaction

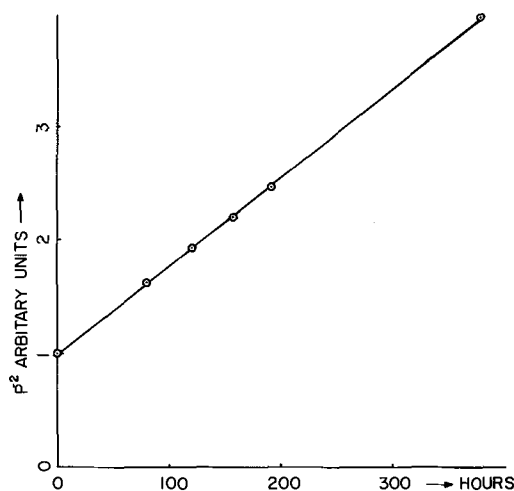


Fig. 2. Decay of polarization for a fixed temperature (293°K) as a function of time (KCl:Sr).

Table I. Results

Sample	CaCl <sub>2</sub> (10 <sup>-3</sup> M)	KOH(10 <sup>-3</sup> M)	Polarization (arbitrary units)
A	1.0	2.0	0.2
B	1.0	1.0	20.0
C	1.0	0.5	40.0

using the electret behavior. For this, we doubly doped KCl with Ca and OH in different proportions. We then measured the ITC band corresponding to the Ca IV complexes as a function of their different concentrations. Results are shown in Table I.

It is seen that we used concentrations corresponding to partial (OH)<sub>2</sub>Ca formation and complete reaction stoichiometry. While it was possible to detect directly the total amount of Ca in the solid by chemical analysis, the presence of free Ca was inferred in the following indirect way: The OH ion has an electronic absorption band in the uv region of the spectrum when substitutionally dissolved in the alkali halide. This OH absorption was extensively studied by many workers (15), and its oscillator strength is well known. The OH ion also has a vibrational absorption band in the near infrared portion of the spectrum. The precipitation of OH by Ca destroys the electronic absorption, but the vibrational band is still present. By measuring in both regions of the spectrum, we were able thus to distinguish between "free" OH and the precipitated OH.

### Discussion and Conclusions

**Dipole aggregation in KCl/Sr.**—The reaction for trimer formation is that of a third order reaction

$$\frac{dc}{dt} = -Kc^3 \quad [7]$$

where  $c$  is the dipole concentration,  $t$  is the time, and  $K$  a proportionality rate parameter. The polarization  $P$  that is proportional to dipole concentration is then obtained as a function of time by integration of Eq. [7] above as

$$P^{-2} = P_0^{-2} + 2\alpha^2 Kt \quad [8]$$

where  $\alpha$  is a proportionality factor between  $P$  and the number of dipoles per unit volume, and  $P_0$  is the polarization immediately after thermal quenching. Following Cook and Dryden we assume the reaction is diffusion controlled and set

$$K = A_d \exp(-E_d/kT)$$

Using Eq. [7] with this value for  $K$ , we get

$$C^{-2} - C_0^{-2} = 2A_d t \exp(-E_d/kT)$$

We can now define a half-life  $t_{1/2}$ , for the reaction at the time where  $C = C_0/2$ . This is given by

$$t_{1/2} = \frac{3}{2C_0^2 A_d} \exp(E_d/kT) \quad [9]$$

We can thus determine  $t_{1/2}$  from Eq. [8]. That Eq. [8] is followed is shown by the results of Fig. 2. If we get  $t_{1/2}$  as a function of temperature from Eq. [9], we can obtain the relevant quantities  $A_d$  and  $E_d$ . At the same time a new check of the whole model is provided. In Fig. 3 we show the results for several temperatures.

Our values for  $A_d$  and  $E_d$  and those determined by Cook and Dryden are in excellent agreement with each other.

The reaction is thus of third order, the process is diffusion controlled, and the electret polarization  $P$  and its quantitative analysis provided all the relevant conclusions in excellent agreement with other techniques.

**Ca precipitation with OH in KCl.**—It is clearly seen that polarization  $P$  increased from sample A to C, that

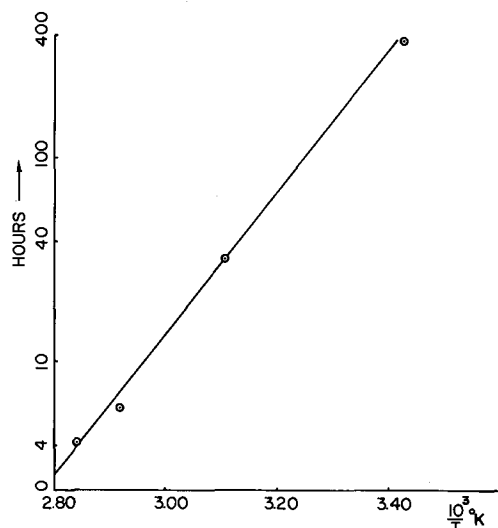


Fig. 3. Polarization half-life in hours as a function of the inverse of the absolute annealing temperature. Activation energy is 0.71 eV (KCl:Sr).

is, in the expected direction, if the  $(\text{OH})_2 \text{Ca}$  compound stoichiometry is considered. In order to understand further and discuss this result we decided to make another experiment: It is known that the "free" Ca ion sensitizes F-center production. In a recent paper Ikeya (16) has shown in part that the presence of OH in Cd crystals hindered the F-center sensitization by precipitation. We thus make an experimental analysis of the F-center growth curves and 100 kv x-ray irradiation for the different doubly doped samples. Ikeya showed that the square of the extrapolated optical density at zero time was proportional to the free Ca content in the samples. In order to discuss our results further we plotted this magnitude as a function of the electret polarization  $P$  as measured by the glow-peak technique

If the precipitation reaction was really being followed by the electret polarization, there should be a direct proportionality between the free Ca as measured by the F-center growth curves and  $P$ .

The results of the experiments are shown in Fig. 4. These results taken together with those of Table I

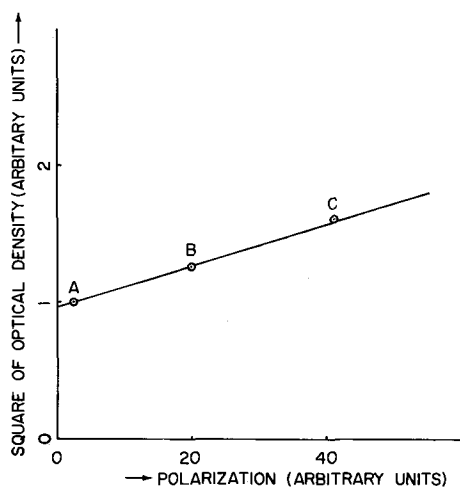


Fig. 4. Square of extrapolated optical density for the F band as a function of polarization for sample A ( $\text{KCl} + 1 \times 10^{-3} \text{M CaCl}_2 + 2 \times 10^{-3} \text{M KOH}$ ); B ( $1 \times 10^{-3} \text{M CaCl}_2 + 1 \times 10^{-3} \text{M KOH}$ ); and C ( $1 \times 10^{-3} \text{M CaCl}_2 + 0.5 \times 10^{-3} \text{M KOH}$ ).

show that we have detected the defect reaction directly from the electret behavior.

We think this paper exemplifies that in the case of the alkali-halides the electret behavior is not only very well understood quantitatively but can even be used as a powerful tool to investigate solid-state physics and solid-state chemistry phenomena. We are now in the process of investigating new phenomena using alkali-halide electrets, such as: (a) action of an electric field to break dipole aggregates; (b), action of the internal electric field of the electret on defects like the F center; (c) presence of negative ion vacancy divalent negative-ion dipoles in alkali halides; and (d) investigation of electret behavior due to impurity-vacancy dipoles in other inorganic materials like ZnO and MgO.

We hope that this paper will encourage other investigators in the field of electrets to join efforts in this very promising area.

#### Acknowledgments

The authors are deeply grateful to Dr. C. Bucci and Dr. M. Ferreira de Souza for helpful and valuable discussions and experimental suggestions; to all our colleagues at S. Carlos and especially to Dr. G. Leal Ferreira for several discussions; to C. Bicegli, Sebastiao Pereira, Carlos Trombella, and Salvador Sanchez Vera for technical help, and to Bartyra de Oliveira for secretarial help during the preparation of this paper.

This work was done under ONR contract and partial support of C. N. Pq. and Fapesp.

Manuscript received Sept. 7, 1967; revised manuscript Dec. 6, 1967. This paper was presented at the Electrets Symposium at the Chicago Meeting, Oct. 15-19, 1967, as Abstract 123. Part of this work was done to fulfill the requirements for the Ph.D. degree of one of the Authors (N. J.) at the University, S. Paulo, S. Carlos.

Any discussion of this paper will appear in a Discussion Section to be published in the December 1968 JOURNAL.

#### REFERENCES

1. C. Bucci and R. Fieschi, *Phys. Rev. Letters*, **12**, 16 (1964); M. Beltrami, R. Capelletti, and R. Fieschi, *Phys. Letters*, **10**, 3 (1964); C. Bucci, R. Fieschi, and G. Guidi, *Phys. Rev.*, **148**, 816 (1966).
2. Dryden and Cook, *Proc. Phys. Soc.*, **80**, 479 (1962).
3. Milton Ferreira de Souza, Ph.D. Thesis, University Sao Paulo, Brazil (1966).
4. A. Lidiard, in *Handbuch der Physik*, Vol. XX, p. 246.
5. See for instance J. Schulman and D. Compton, *Color Centers in Solids*, Pergamon Press, New York.
6. Milton Ferreira de Souza and G. Leal Ferreira, *Bull. Am. Phys. Soc.*, **12**, 3,351 (1967).
7. R. W. Dreyfus, *Phys. Rev.*, **121**, 1675 (1961).
8. G. Watkins, *ibid.*, **113**, 91 (1958).
9. Y. Haven, *J. Chem. Phys.*, **21**, 171 (1953).
10. R. Dreyfus and R. Leibowitz, *Phys. Rev.*, **135**, A1413 (1964).
11. See for instance B. Gross and S. Denard, *Phys. Rev.*, **67**, 253 (1945).
12. H. Hartel and F. Luty, *Phys. Stat. Solidi.*, **12**, 347 (1965); U. Kuhn and F. Luty, *Solid State Comm.*, **2**, 281 (1964); B. Fritz, F. Luty, and J. Anger, *Z. Phys.*, **174**, 240 (1963).
13. G. Feher, I. Shepherd, and H. Shore, *Phys. Rev. Letters*, **16**, 500 (1966).
14. W. Kanzig, *J. Phys. Chem. Solids*, **23**, 479 (1962).
15. H. Etzel and D. Patterson, *Phys. Rev.*, **112**, 1113 (1958).
16. H. I. Keya and N. Itoh, *J. Phys. Soc. Japan*, **20**, 1284 (1965).

# Studies on HF-Doped Ice Thermoelectrets

S. Mascarenhas

Physics Department, Escola Engenharia, Sao Carlos, Sao Paulo, Brazil

and C. Arguello<sup>1</sup>

Faculdade de Ciencias, Rio Claro, Sao Paulo, Brazil

## ABSTRACT

Pure and doped ice thermoelectrets were prepared at different polarization temperatures ( $-10^{\circ}$  to  $-135^{\circ}\text{C}$ ). Stored charge was then investigated by the glow peak method. A main band was observed at  $-50^{\circ}\text{C}$ , with a total charge of  $10^{-6}$  to  $10^{-8}$  coulombs/cc depending on doping. The total charge released by the glow varied with the square root of HF concentration indicating that the  $\text{OH}^{-}$  and  $\text{H}_3\text{O}^{+}$  ions are responsible for the effect. Space charge formation was also shown to be associated with the electret behavior by investigating the influence of sample thickness on the polarization and of the temperature of the glow peak maximum on polarization temperature.

In recent papers (1) Gellin and the present authors reported observations on the ice thermoelectret. Riehl and co-workers (2) also reported recently on the behavior of ice subjected to thermal changes under electric fields and claimed to have observed ferroelectric behavior in ice. Pinatti and Mascarenhas (3) described the behavior of ice crystals during growth from the melt and reported strong electrical effects. In the present work we report on the ice thermoelectret, using the glow peak discharge method, and demonstrate that the effect is strongly dependent on or related to the HF doping of the samples. The nature of the trapped polarization that is released during the thermal glow was investigated by the analysis of the variation of the charge with concentration of the dopant as well as by changing the thickness of the sample and the polarization temperature. In view of the claim for ferroelectric behavior of ice made by Riehl and collaborators this is a very important question to be decided. Our investigations on the Costa Ribeiro effect in ice and its possible importance for the explanation of atmospheric electricity also stimulated the present investigations.

## Experimental

We have designed and constructed a special Dewar in which the ice single crystals were grown and the electret was prepared and measured. This is shown in Fig. 1. Initially, the bottom electrode E was positioned with the desired separation from the top electrode M by means of a ring stopper R, movable through the vacuum seal S. Both the bottom electrode E and the top one contained small Alnico magnets M so that the bottom one was maintained in position by magnetic attraction. This was a very convenient way of obtaining variable interelectrode distance and of avoiding any insulator in this part of the Dewar where the temperature would be cycling. The top electrode was the ground connection for the electrometer and the lower one was the high insulation electrode. The lead from E came out of the Dewar through a Teflon insulator I. V are vacuum connections. LS are levelling screws and W are windows through which the ice single crystal could be observed under polarized light with an optical system. Liquid nitrogen or any proper coolant was introduced inside the stainless steel tube T. The whole system was enclosed in a metal cylinder C. The liquid to be solidified (either pure water or HF solution) was initially placed between the two electrodes. At this time the ring-stopper would still be maintaining the proper electrode separation. A coolant was then introduced inside T causing solidification of the liquid. After com-

plete solidification the ring R was raised. The quality of the single crystal was then ascertained with the polarized light system. In this way we were able to grow very good single crystals of thicknesses ranging from 0.5 to 2 mm. The current was measured with a Keithley 603 electrometer and a  $10^9$  ohm grid resistor. The electrodes were platinum or palladium covered and their area approximately  $3\text{ cm}^2$ . What we call pure water in this paper is doubly distilled water from a quartz still of conductivity circa  $10^{-6}$  mhos/cm. Nitrogen gas was introduced in the Dewar in order to maintain good thermal contact to the sample during the warm up and cooling.

## Results

A typical experimental sequence would be as follows: The electric field  $E$  was applied to the sample

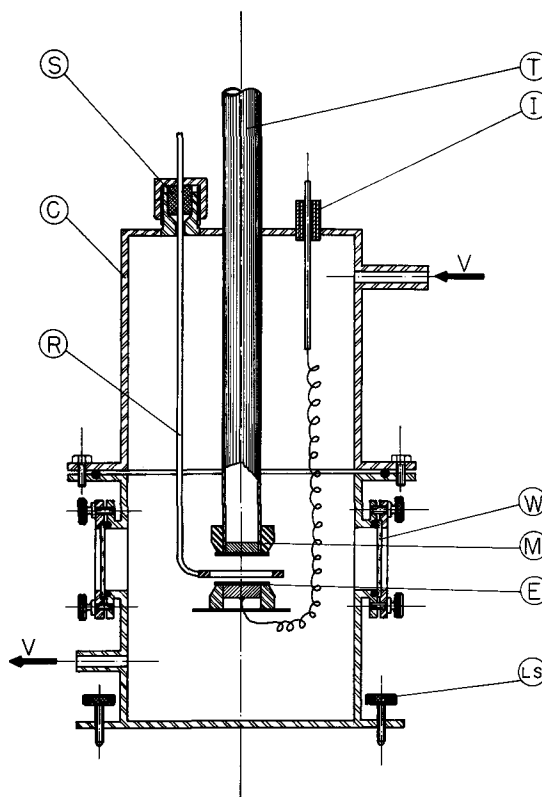


Fig. 1. Apparatus for single-crystal growth and electret preparation and measurement. T, stainless steel tube; I, Teflon insulator; S vacuum seal; C, external metal cylinder; R, ring-stopper; W, optical window; M, magnet; E, electrode (platinum or palladium); LS, levelling screws; V, vacuum outlets.

<sup>1</sup> Present address: University of Southern California, Los Angeles, California.

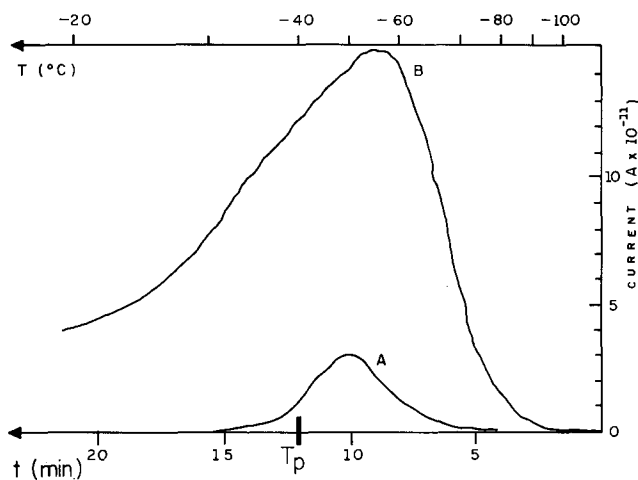


Fig. 2. Electrical glow-peaks due to charge release in the ice thermoelectret. A, pure ice; B, HF-doped ice.

for a specified time at the chosen polarization temperature  $T_p$ . The crystal was then cooled under the electric field to *circa*  $-100^\circ\text{C}$ . The electric field was then switched off and the crystal warmed up to  $-10^\circ\text{C}$  again. During the warm up the current was constantly monitored and both the temperature and the current were recorded on a X-Y recorder so that the glow peaks could be directly observed.

Immediately after formation the ice single crystal would present some charge, probably due to the Costa Ribeiro effect. When this charge had dissipated the external field was applied. The discharge of the electret under its own field to produce the glow peaks was first used by Gross (4). A very well-defined and reproducible discharge was observed here peaking at around  $-50^\circ\text{C}$ , as is shown in Fig. 2. In the same figure the larger peak is connected with HF doping. After observing the discharge with pure water, we decided to investigate the possible influence of defects on the electret behavior, and also to look for possible ferroelectric behavior. We decided to dope the samples with HF. Much larger peaks were then observed with HF doped ice in concentrations ranging from  $2.5 \times 10^{-6}$  to  $10^{-4}\text{M}$ . The total integrated charge under the glow peak is shown as a function of concentration in Table I.

One can see that the effect of doping is rather large and that the integrated charge may change by two orders of magnitude in the range of concentrations used. The polarization time  $t_p$ , the polarization temperature  $T_p$ , the thickness and the applied voltage  $V_p$ , were kept constant in these experiments.

We have also investigated, due to reasons mentioned in the discussion section of this paper, the influence of the thickness of the sample on the total measured charge  $Q$  of the glow. The results shown in Fig. 5 were obtained for a constant field of  $335\text{ v/cm}$  for all samples. The linear behavior of  $Q$  with thickness will help us to clarify the nature of the trapped charge.

### Discussion

As is discussed below, in order to decide on the nature of the phenomenon, or more specifically on the nature of the trapped polarization of the ice thermoelectret the HF doping proved to be very important. It is known from previous theories on the physics of

ice (5) that HF doping will change the concentration of d and l defects (Bjerrum defects) as well as the concentration of ionic states ( $\text{OH}^-$  and  $\text{H}_3\text{O}^+$ ). From thermodynamic arguments it is expected that the d and l defects will change their concentration in a linear way with HF doping, while the ionic states will change with the square root of HF concentration. If we were dealing with orientation of dipoles which would be directly related to d and l defects our effect might be expected to depend on a linear way on HF doping.

The results of Table I are plotted on a double logarithmic scale in Fig. 3. From it we clearly see a square root dependence was found. This indicates that probably we are dealing with an effect related to  $\text{OH}^-$  and  $\text{H}_3\text{O}^+$  ionic carriers. This would tend to indicate that we are not dealing with a dipole orientation effect, or in fact, with any collective dipole effect that might even lead us to think of ferroelectric behavior. On the other hand, we are led to conclude that space-charge effects due to the motion of ionic carriers (specially the more mobile  $\text{OH}_3^+$ ) may be the main cause of the electret behavior.

In order to investigate this point further we did one more experiment. It is known that space-charge glow-peaks do not present a constant peak-position temperature, but rather this is strongly dependent on the polarization temperature (6). Keeping the warming rate cycle reproducible, because this is known to affect slightly the peak-position, we obtained several electret glows by varying the polarization temperature from  $-88^\circ$  to  $-26^\circ\text{C}$ . We found large changes in the corresponding peak position as shown in Fig. 4. Again this indicates space-charge behavior.

Finally, the experiment described by Fig. 5, in which we found a linear dependence of the charge  $Q$  on thickness seems to us to rule out any possibility of uniform polarization and thus reinforces very strongly the case for space charge as the main cause for the electret behavior.

When we tried to apply the Fieschi and Bucci dipole model (6) to our results, applying their expression for the total charge, we calculated an absurd concentration of  $10^{25}$  dipoles/cm<sup>3</sup>, assuming a dipole moment of one Debye. The peaks also do not allow the determination of any single activation energy  $E$ .

We thus conclude that: the electret effect in ice is greatly enhanced by HF doping; the electret charge can be released by glow peaks around  $-50^\circ\text{C}$  depending on the polarization temperature; the nature of the electret charge is related to space-charge effects; the nature of the space charge is connected to  $\text{H}_3\text{O}^+$

Table I. Integrated charge under the glow peak

HF concentration	Q coul.
$10^{-7}$	$6.0 \times 10^{-8}$
$2.5 \times 10^{-6}$	$3.5 \times 10^{-7}$
$5.0 \times 10^{-6}$	$7.2 \times 10^{-7}$
$1.0 \times 10^{-5}$	$8.5 \times 10^{-7}$
$5.0 \times 10^{-5}$	$10.5 \times 10^{-7}$
$10^{-4}$	$1.75 \times 10^{-6}$

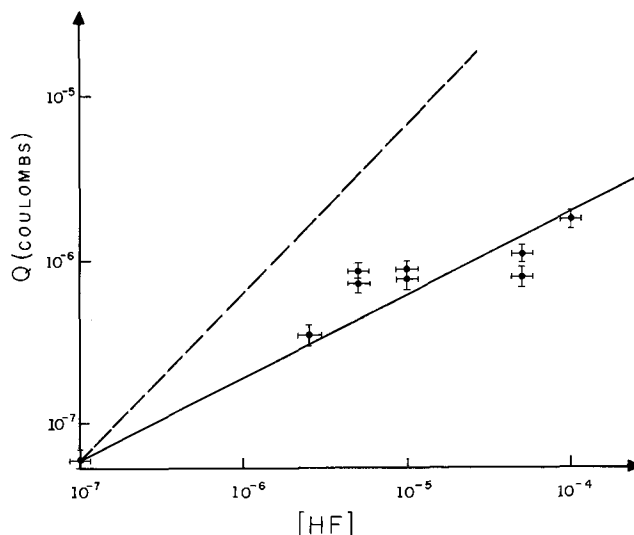


Fig. 3. Dependence of released charge  $Q$  on HF doping. A square root-dependence is found. The dashed line indicates a linear function (see text for discussion).

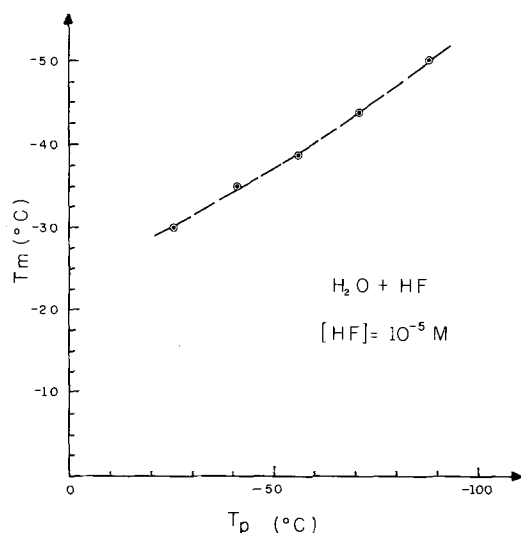


Fig. 4. Dependence of temperature of maximum peak position  $T_m$  on polarization temperature  $T_p$  for a HF doped sample ( $10^{-5}M$ ).

and  $OH^-$  ionic states. We also found that a claim for ferroelectric behavior of ice (2) cannot be substantiated. Explanation of the present effects using dipoles would require an enormous number, indicating the absence of a collective effect.

It is our opinion that any claim for ferroelectricity would have to include a very careful study of the influence of sample thickness and possibly doping to check for possible space-charge effects.

Finally, we think that the present results may be important for the understanding of the Costa Ribeiro effect in ice (3), in which large currents and voltages appear during phase changes. The fields at the solid-liquid interface may be effective in producing space-charge effects similar to those described here. In this respect it is interesting to point out that a large change in the freezing potentials due to the Costa Ribeiro effect has in fact been reported in the literature (7). We are proceeding with our investigations, trying to detect directly the presence of the space charge by doping the ice with chemical dye indicators.

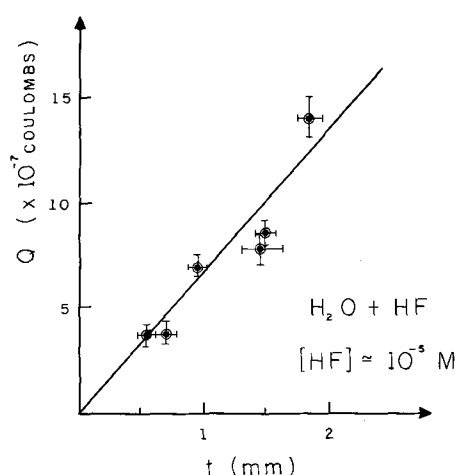


Fig. 5. Dependence of the released charge  $Q$  on the sample thickness  $t$ , indicating a space-charge effect.

Manuscript received Sept. 7, 1967; revised manuscript received ca. Dec. 6, 1967. This paper was presented at the Electrets Symposium at the Chicago Meeting, Oct. 15-19, as Abstract 126. The work was done under ONR contract and partial support of C.N. Pq. and Fapesp.

Any discussion of this paper will appear in a Discussion Section to be published in the December 1968 JOURNAL

#### REFERENCES

1. H. Gellin and R. Stubbs, *J. Chem. Phys.*, **42**, 967 (1965); see also C. Arguello and S. Mascarenhas, *Bull. Am. Phys. Soc.*, **12**, 4, 558 (1967).
2. H. Engelhardt and N. Riel, *Phys. Letters*, **14**, 20 (1965); O. Dengel, U. Eckener, H. Plitz and N. Riel, **9**, 291 (1964).
3. D. Pinatti and S. Mascarenhas, *J. Appl. Phys.*, **38**, 2648 (1967).
4. B. Gross and S. Denard, *Phys. Rev.*, **67**, 253 (1945).
5. Granicher, Jaccard, Scherrer, and Steineman, *Discussions Faraday Soc.*, **23**, 50 (1957).
6. C. Bucci, R. Fieschi, and G. Guidi, *Phys. Rev.*, **148**, 816 (1966).
7. E. Workman and S. Reynolds, *ibid.*, **78**, 254 (1950).

## Glow Peak Analysis of Pure and Doped Naphthalene Thermoelectret

M. Campos, G. Leal Ferreira, and S. Mascarenhas

Physics Department, Escola Engenharia, Sao Carlos, Sao Paulo, Brazil

#### ABSTRACT

Polarization current for pure and doped naphthalene thermoelectrets is investigated. The thermal depolarization of the electret is used as a technique to investigate trapped polarization. Doped crystals with alpha and beta naphthol present new independent peaks in addition to the pure matrix peaks. The peaks are analyzed quantitatively for total integrated charge and activation energy by the initial rise method. The OH vibrational band of the impurities was used as an optical probe to detect their presence in the solid. Charges trapped in the dielectric absorption process corrected for the released charge at the low-temperature depolarization, compare satisfactorily with the total integrated glow peak charge for both pure and doped samples. It was possible to differentiate between alpha and beta naphthol through the electret behavior using the glow peak position and activation energy of the peaks. The electret state is shown to be due to electronic carriers, trapped in a set or sets of exponentially distributed traps, as indicated by the  $at^n$  dependence of the polarization current on time.

Naphthalene is a very important example of a pure substance, an organic molecular semiconductor, exhibiting electret behavior. Naphthalene was first reported to present natural electret behavior by Costa

Ribeiro (1) and Tavares (2). Baldus (3), and, later, Mascarenhas (4) also reported on its electret properties. Extensive photoconductivity studies on this substance were carried out by Tavares in a very in-

teresting series of papers (5). Its general semiconductor properties were investigated by Pick (6) and Riehl (7). Mascarenhas and Freitas reported (8) anisotropic electrical properties of the material during phase changes. In many ways naphthalene is an excellent system for electret studies. It forms very good single crystals from the melt (9), it is easily orientable (10); it can be purified by several techniques such as zone melting, chromatography and sublimation (11); it has a very well-known electronic and molecular structure (12); and is a known electronic organic semiconductor (13). The conduction mechanism in the dark is still somewhat obscure, but this is a general question still to be solved for most molecular solids, where it is very difficult to distinguish among tunneling, hopping, or a trap-controlled mechanism (14). In this work we make an analysis of the electret state in oriented naphthalene crystals by the glow peak technique. For the first time, to our knowledge, controlled doping is introduced in an organic semiconductor electret system and independent glows obtained due to the specific dopant. Furthermore, the presence of the dopant can be monitored by optical analysis. For this purpose we availed ourselves of the presence of a very well-defined and prominent vibrational absorption band of OH radicals in the dopant, in our case alpha and beta naphthol.

### Experimental

Single crystal plates were grown by the Tavares (2) technique from double sublimed C. P. naphthalene. From a large plate, analyzed by polarized light, good single crystal areas were chosen and cut. The samples all had the same orientation, that of the cleavage plane in the plane of the plate. The samples were polished to an optical finish with alcohol. We used crystals of approximately 0.5 mm thickness and areas varying from 4 to 9 cm<sup>2</sup>. In the case of the doped samples, alpha or beta naphthol were added to the melt, and the presence of the dopant was ascertained from optical analysis in a Beckman DK 2 automatic spectrophotometer. These substances present an absorption band in the near infrared due to the presence of an OH radical, as shown in Fig. 1. The spectrum of pure naphthalene is also shown for comparison.

The crystals were painted with conducting silver on both faces. One one of the faces a guard ring was used. This is essential because of the high specific bulk resistance of naphthalene. Spurious or undesirable surface effects are thus avoided.

A special system was built for preparing the electret and for the measurement of the release of charge. This permitted the measurement of conductivity, electret preparation, glow peak investigations, and dielectric absorption measurements at variable or constant

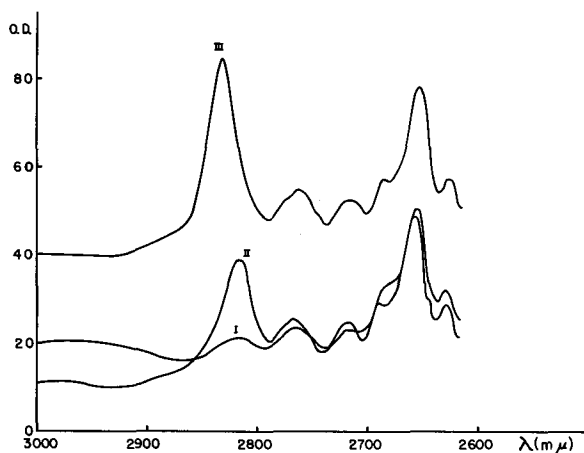


Fig. 1. Optical absorption of pure naphthalene, (curve I); doped with alpha naphthol, (curve II); and doped with beta naphthol (curve III).

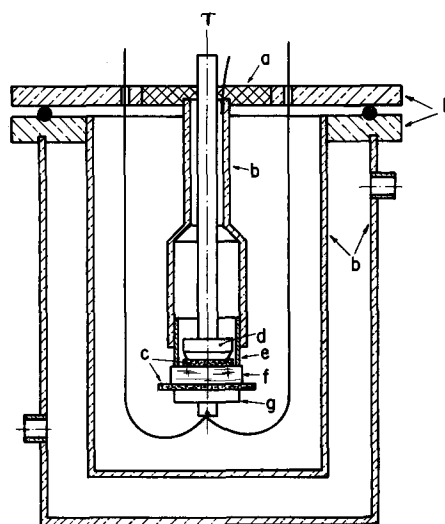


Fig. 2. System for electret production and measurements: a, Teflon insulation; b, brass walls; c, graphite electrodes; d, magnets for electrode assembly; e, guard ring; f, crystal (see text).

temperature in a vacuum or in a controlled atmosphere (Fig. 2).

The crystal (f) was placed between two graphite electrodes and the guard ring. The electrodes and the crystal were held together by the attraction of two small magnets (d) and (g). The guard ring was connected to an outer metal tube insulated by Teflon on the top plate of the system (see Fig. 2). The top central electrode was grounded, and the guard ring and the lower measuring electrode were insulated practically at the same potential, so that surface currents were negligible. The whole assembly was shielded by a metal case. An outer jacket (b) allowed water circulation from a precision Haake thermostat. The temperature of the sample was maintained constant to within 0.2°C during polarization. A liquid coolant could be introduced into tube T and the crystal brought to a low temperature. The temperature was measured by a properly insulated thermocouple placed in the lower electrode which also served as a lead for the electrometer. Electrical measurements were made using a Cary 31 vibrating reed electrometer with a 10<sup>11</sup> ohm resistor. The current was recorded with a Brown potentiometer. Dry nitrogen gas was used inside the inner container to avoid sublimation of the samples and insure good thermal conductivity.

The measurements comprised the following three steps: (a) During polarization, the exponential current decay was recorded as a function of time at a chosen temperature,  $T_p$ , until it approached a constant value. (b) While maintaining the field, the sample was cooled to a lower temperature,  $T_1$ . Then the field was removed, and the depolarization current recorded as a function of time. (c) Finally, the crystal was heated at a constant rate, and this depolarization current recorded. The whole sequence was very reproducible, and it was found that the proper stabilization of the polarization temperature to 0.2° was essential for this purpose.

### Results

We usually performed the whole sequence described above after previous warming of fresh samples to 60°C to empty all traps and release all accumulated charges due to growth, polishing, and handling. Results for the polarization current for pure naphthalene are shown in Fig. 3. Typical depolarization behavior for two different temperatures is also shown. The polarization current approached a constant current asymptotically under the applied field, and in the case of depolarization the current decayed to zero under no field. Similar results were found for the doped samples and are discussed below in more detail. Samples were then warmed under a constant rate. Very prominent

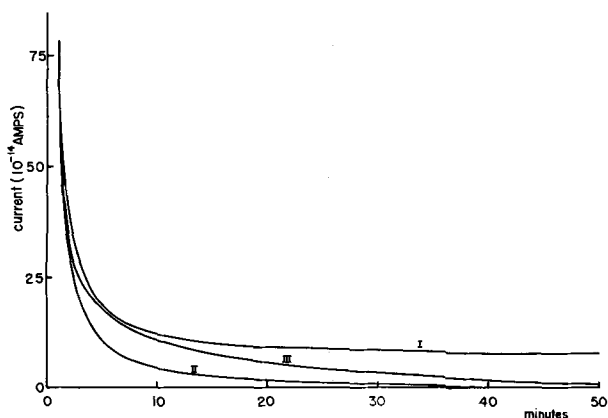


Fig. 3. Polarization current for pure naphthalene (curve I: 305°K); depolarization current at 305°K (curve II), and 280°K (curve III).

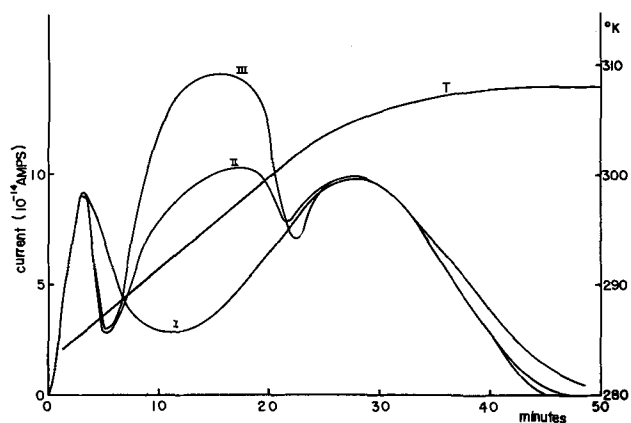


Fig. 4. Glow peaks obtained with pure naphthalene (I), doped with alpha-naphthol (II), and doped with beta-naphthol (III). Also shown is temperature  $T$  as a function of time during warm-up.

peaks were found for all samples. Figure 4 shows glow peaks obtained for both pure and doped samples. It is seen that the pure matrix peaks are present in the doped samples and that a new peak appears at an intermediate temperature. This peak was found to depend on the presence of the dopant.

### Discussion

With the quantitative results of the polarization, depolarization, and glow peaks in our possession, we can now proceed to a quantitative analysis of the electret behavior. As a first step we should try to understand, at least partially, the polarization mechanism. To do this the data were analyzed in a log plot of the total current minus the constant final direct current *vs.* time *j* to investigate the dielectric absorption current. From this figure two straight lines are obtained. The total charge  $Q_p$  trapped in the dielectric via the dielectric absorption mechanism can also be determined.

From the lower temperature depolarization current as a function of time (Fig. 3) a value for the charge  $Q_d$  released from the dielectric at this temperature can be found. Finally, from the glow peak curves the total integrated charge  $Q_g$  that was released from the dielectric during warm up is calculated. Table I shows the values of  $Q_p$ ,  $Q_d$  and  $Q_g$  for pure naphthalene. Within the experimental errors common for this type of experiment (order of 5-10%) the relation

$$Q_g = Q_p - Q_d$$

is satisfied. A similar analysis was done for the doped samples. The polarization behavior of these samples showed the same general behavior as that of the pure

Table I. Charges due to impurities

Kv/cm	Type	$Q_p$ $10^{-10}$ coul.	$Q_d$ $10^{-10}$ coul.	$Q_g$ $10^{-10}$ coul.	$Q_i$ $10^{-10}$ coul.
1.08	doped with $\alpha$ naphthol	1.24	0.96	0.23	1.19
0.54	doped with $\beta$ naphthol	1.08	0.81	0.31	1.12
1.08	pure	6.24	5.07	1.06	6.13

samples. Again depolarization currents at the low temperature and the glow peak allowed us to obtain  $Q_p$ ,  $Q_d$ , and  $Q_g$ . These magnitudes are shown in Table I. The glow peaks were also analyzed to determine the activation energy in the following way: If the internal field is approximately constant for temperatures well away from the maximum peak position, the initial rise method may be applied to determine a trap depth. In this case the current, at the initial rise of the peak, is given by

$$i = i_0 \exp -E/kT$$

This analysis was applied to the main pure naphthalene band (peaking at 308°K) and consistent and reproducible values of the activation energy obtained. Good results were also obtained for the impurity peaks of alpha and beta naphthol. Experimental difficulties prevented a proper analysis of the lower temperature pure naphthalene peak. We hope to do this in the near future. The activation energies found were reproducible to within 0.05 eV. Since the field is not constant during the glow, especially near the maximum, other methods will have to be used to analyze the peak for trapping cross section, activation energy, and other parameters. The complete analysis of the functional form of the peak depends on a model for the trapped polarization of the electret and the way in which the internal field varies with time.

It is interesting to observe that the alpha and beta naphthol maximum temperatures are slightly different, and that the activation energies for the corresponding glow peaks are also different. This shows the sensitivity of the glow discharge method of analysis of the electret. The results above can be summarized in the following way:

1. The naphthalene thermoelectret can be analyzed very conveniently by the glow peak technique. Two bands are present for the range of temperatures studied, the main band being situated at 308°K.

2. Activation energies can be obtained consistently from the glow by an initial rise method of analysis. The total charge associated with the glows is of the order of  $10^{-10}$  coulombs for fields of the order of 1 kv/cm. The activation energy for the main band is 0.75 eV, the same as that found for the thermal activation energy of the conductivity itself.

3. Controlled doping of the naphthalene thermoelectret with alpha and beta naphthol resulted in the appearance of independent peaks for each impurity. The total charge under the new glow was found to add to the dielectric absorption and to be of the same order of magnitude as that of the pure naphthalene main band for concentrations of  $10^{-2}$  molecules of impurity per molecules of naphthalene in the melt. The presence of the impurity in the matrix was monitored by the vibrational absorption band of the OH radical of the naphthol. No oscillator strength is available for this band so the concentration cannot be quoted. The activation energies for both peaks were measured and found to be noticeably different (Table II). This indicates that the method may constitute in the future a very sensitive technique for the investigation of impurities in solids.

We would like now to present some possible inferences from the above results. It seems that in the present case the electret behavior cannot be ascribed to dipoles or ions, but rather to electron or hole carriers trapped in defects or impurity levels in the solid. Considering a charge per unit volume of  $10^{-11}$

Table II. Activation energies (in eV)

Pure	Doped with $\alpha$ naphthol	Doped with $\beta$ naphthol
0.75	0.65	0.47

coulombs/cm in our electret samples about  $10^8$  to  $10^9$  carriers/cm<sup>3</sup> are associated with the effect. This exceedingly small number points out the following: (a) the enormous sensitivity of the glow peak analysis of the electret to detect defects or impurities, compared to other methods used in physics like E.P.R., optical analysis or electrical conductivity; only luminescence effects can probably be compared with the present technique; (b) that practically any way of purifying the matrix will be useless, because no purification method is available for this range of concentration. Besides, the number of structural or thermodynamical defects in the solid is probably much larger than the above number. Thus an essential and perhaps unique way to proceed with investigations of this type is to dope the solid in a controlled manner, as we have done.

From the results presented here one cannot decide whether electrons or holes are the predominant mechanism. Nothing can be said concerning the nature of the trapping levels introduced by alpha or beta naphthol. New experiments, in which selective filling of electron and hole trap is possible, are now being carried out (15). With this new technique we hope to clear up the latter questions. To measure the concentration of the dopants in the solid a determination of the oscillator strength of the optical absorption of the OH ion is necessary.

Finally, using Tavares' data on natural naphthalene electrets, it was shown that these samples also followed the same polarization behavior as the thermoelectret. It is perhaps appropriate to point out that similar (at<sup>n</sup>) behavior was found for ice electrets (16), carnauba wax electrets (17), our pure and doped naphthalene thermoelectrets and, as mentioned above, for natural electrets (10) obtained from the Costa Ribeiro effect. In the case of naphthalene, this tends to show that the same traps or sets of traps are involved in both phenomena. The anisotropy of the thermoelectret could then be expected, in view of the anisotropy of the Costa Ribeiro effect as found by Mascarenhas and Freitas (8). This is also being investigated in our laboratory.

This problem brings into discussion the question of the mobility of the carriers in naphthalene. Our samples showed the same activation energy for conductivity as that found by Riehl. Since we found the

definite presence of trapping centers as revealed by the polarization and glow peak behavior of the electret, it would seem that the mobility is also trap-controlled. The fact that the thermal activation energy for the conductivity coincided with the glow peak activation energy for the case of pure naphthalene (0.75 eV) is in agreement with the above observation. Finally the possible space-charge nature of the phenomenon is being investigated

#### Acknowledgments

The authors would like to thank Carlos Biscegli, S. Bastos Pereira, Carlos Trombella, and S. Sanchez Vera of the technical staff of our Laboratory. Special thanks are due to Professor Milton Ferreira de Souza for extensive discussions and experimental suggestions. Thanks are also due to Bartyra de Oliveira for secretarial help on the present paper.

This work was done under ONR contract and partial support of C.N. Pq. and Fapesp.

Manuscript received Sept. 7, 1967; revised manuscript received Dec. 7, 1967. This paper was presented at the Electrets Symposium at the Chicago Meeting, Oct. 15-19, 1967, as Abstract 127.

Any discussion of this paper will appear in a Discussion Section to be published in the December 1968 JOURNAL

#### REFERENCES

1. J. C. Ribeiro, Thesis, University of Brazil (1945); see also *An. Brazil. Acad. Ci.*, **22**, 325 (1950).
2. A. D. Tavares, *An. Acad. Brasil. Ci.*, **25**, 53 (1953); **25**, 357 (1953); see also A. D. Tavares and H. Marques da Fonseca, **37**, 201 (1965).
3. W. Baldus, *Z. Angew. Phys.*, **6**, 481 (1954).
4. S. Mascarenhas, *An. Acad. Brazil. Ci.*, **31**, 395 (1959).
5. A. D. Tavares, Thesis, University of Rio de Janeiro (1960); see also *Boletim de Física*, August 1953.
6. H. Pick and W. Wissman, *Z. Physik*, **138**, 436 (1954).
7. N. Riehl, *Ann. Phys.*, **20**, 93 (1957).
8. S. Mascarenhas and L. G. Freitas, *J. Appl. Phys.*, **31**, 1685 (1960).
9. A. D. Tavares and H. Marques da Fonseca, *An. Acad. Braz. Ci.*, **37**, 201 (1965).
10. F. Lipsett, *Can. J. Phys.*, **35**, 284 (1957).
11. H. Inokuchi and H. Akamatu, "Solid State Physics," Vol. 12, Seitz and Turnbull, Editors, Academic Press, New York.
12. S. Abrams, J. Robertson, and J. White, *Acta Cryst.*, **2**, 233 (1949).
13. S. Glarum, *J. Phys. Chem. Solids*, **24**, 1577 (1963).
14. D. Gibbons and Spear, *ibid.*, **27**, 1917 (1966).
15. F. S. Sinencio, S. Mascarenhas, and B. Royce, *Bull. Am. Phys. Soc.*, **12**, 1048, (1967).
16. H. Gellin, *J. Chem. Phys.*, **42**, 967 (1965).
17. R. Gerson and J. Rhorbaugh, *ibid.*, **23**, 2381 (1955).

## Effect of Low Pressure on Surface Charge of Electrets

Robert A. Draughn and Avery Catlin

Department of Materials Science, School of Engineering and Applied Science,  
University of Virginia, Charlottesville, Virginia

#### ABSTRACT

Electrets prepared from Mylar and a polystyrene material were exposed to low pressure. The effective surface charge of the electrets decreased as the pressure was lowered. It is proposed that the charge decrease is due to either desorption of charge sources from the electret surfaces or spark breakdown on the electret surface.

When electrets are exposed to pressures less than atmospheric, the magnitude of the effective surface charge is reduced. Previous investigators (1-3) have suggested that this effect is due to neutralization of a portion of the surface charge by ions formed by spark

breakdown in the air gap between the electret surface and adjacent electrodes. This paper presents experimental evidence which shows that this is not a suitable explanation for the observed charge decrease. The data show that the charge decrease is due to either



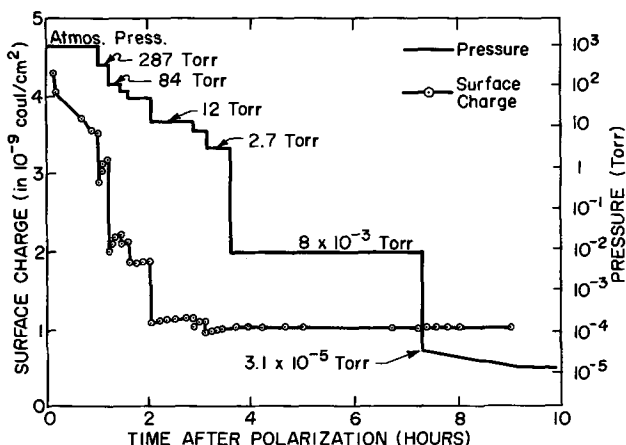


Fig. 1. Relationship of effective surface charge and pressure of surrounding air. Forming field: 140 kv/cm for 30 sec at 23°C.

desorption of ions from the electret surface or spark breakdown on the electret surface.

### Experimental

The electret materials used in this study were a commercially obtained polystyrene material<sup>1</sup> and Mylar.<sup>2</sup> Infrared, x-ray, and chemical analysis of the polystyrene material showed it to be polystyrene containing 10% by weight TiO<sub>2</sub>. The polystyrene sheet was 5 × 10<sup>-2</sup> cm thick and the Mylar thickness either 2.6 × 10<sup>-2</sup> cm or 1.3 × 10<sup>-2</sup> cm. The dielectric constants, measured at 1 kc were: polystyrene, 3.2; Mylar, 3.3.

The electrets were formed by positioning the specimens between guarded machined brass electrodes of 20 cm<sup>2</sup> area and applying a voltage of 5-7 kv across the electrodes. Most of the electrets were prepared by applying the high field for 30 sec at room temperature (23°, ±1°C) and room relative humidity (25%, ±3%).

The movable electrode of the dissectible capacitor used to measure the effective surface charge was of machined brass with a surface area of 5 cm<sup>2</sup>. Surface charge measurements were made both at reduced pressures and at atmospheric pressure following exposure of the electret to reduced pressure.

All specimens were stored with their surfaces exposed to the environment, i.e., in the unshielded condition.

### Results and Discussion

Figure 1 shows the behavior of the effective surface charge when a polystyrene electret was formed at atmospheric pressure, then exposed to low pressure. The charge measurements were made at the pressures indicated. The dissectible capacitor arrangement employed allowed the specimen to be stored between measurements with both of its surfaces freely exposed to the vacuum. During storage, the measuring electrode was positioned 5 cm above the electret surface. All specimens formed at atmospheric pressure exhibited a homocharge which was maintained throughout the period of observation. The data shown are taken from the negatively charged side of the electret. For graphic clarity, all data are shown as positive numbers. All effects reported in this paper were observed for both surfaces of the electrets.

As is shown in Fig. 1, the effective surface charge ( $Q$ ) of the electret decreased as the pressure was lowered. Below 2.7 Torr, no further changes of  $Q$  occurred as the pressure was lowered to a minimum of 2 × 10<sup>-5</sup> Torr.

Following each sudden drop in the magnitude of  $Q$ , the charge partially recovers. The recovery results from the response of the internal polarization to a de-

crease in the internal field of the electret. The removal of a portion of the surface charge at low pressures causes a reduction in the internal field of the electret thereby allowing a partial decay of the internal polarization. Since the contribution of internal polarization to effective surface charge is opposite in sign to the real charge on the electret surface, the decay of internal polarization appears as a growth of effective surface charge. The response of internal polarization to changes in internal field has been treated phenomenologically by other authors (4-6). A theory of dielectric aftereffect (7, 8) has been applied to the polarization decrease by one of the present authors (9).

There are two apparent explanations for the drop in  $Q$  as a function of pressure. The drops could be due to neutralization of surface charge by ions produced by spark breakdown of the air in the vicinity of the electret. This breakdown could occur in the gap between the measuring electrode and the electret surface or it could possibly occur on the electret surface between regions having different charge intensity. Also, desorption of ions from the electret surface could produce the observed effects.

For experiments in which the dissectible capacitor is used to measure  $Q$  at reduced pressure (as in Fig. 1), the occurrence of spark breakdown between the electret surface and the measuring electrode seems quite feasible. However, the following analysis of the experimental conditions shows that such sparking probably does not occur.

Figure 2 compares a plot of the voltage between the measuring electrode and the electret surface with the voltage required to initiate spark breakdown. The external voltage of the electret was calculated using the expression (3, 10)

$$E_1 = \frac{-Q_1}{\epsilon_1 \left[ \frac{\epsilon(d_1\epsilon_2 + d_2\epsilon_1)}{\epsilon_1\epsilon_2 L} + 1 \right]}$$

where:  $E_1$  = field between the electret surface and the movable induction electrode of the dissectible capacitor (in volts/m);  $Q_1$  = effective surface charge of the electret (in coul/m<sup>2</sup>);  $d_1$  = distance between the electret surface and the induction electrode (in m);  $d_2$  = distance between the electret surface and the stationary electrode (in m).  $d_2$  is taken as 0.01 cm in this calculation;  $L$  = thickness of electret (in m);  $\epsilon$  = permittivity of the electret material (in coul<sup>2</sup>/Newton-m),  $\epsilon_1, \epsilon_2$  = permittivities of the media adjacent to the electret surfaces. In these experiments,  $\epsilon_1 = \epsilon_2 = \epsilon_0$ , where  $\epsilon_0$  is the permittivity of free space.

The voltage ( $V_1$ ) between the electret surface and the induction electrode is given by

$$V_1 = E_1 d_1$$

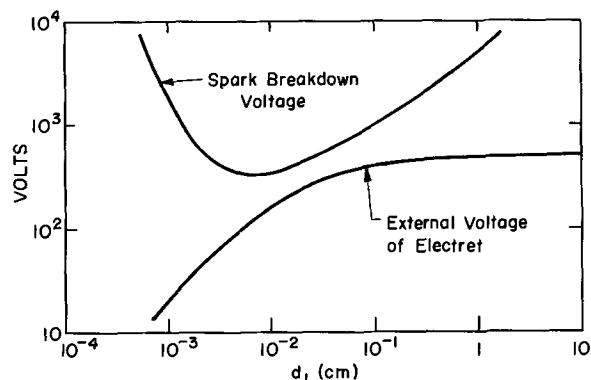


Fig. 2. Comparison of external voltage of electret and voltage required to initiate spark breakdown. Closest approach of the curves occurs at  $d_1 = 2 \times 10^{-2}$  cm where the difference between voltage required to initiate spark breakdown and electret voltage is 200v.

<sup>1</sup> Cadillac Plastics and Chemical Company, Detroit, Michigan.

<sup>2</sup> Mylar is a registered trademark of E. I. du Pont de Nemours & Company.

The value of  $Q$  is taken from the large charge drop ( $Q$  decreasing from  $3.2 \times 10^{-9}$  coul/cm<sup>2</sup> to  $2.0 \times 10^{-9}$  coul/cm<sup>2</sup>) of Fig. 1. The spark voltage curve is taken from the literature (11) with the assumption that the observed drop in  $Q$  occurred at the minimum pressure of 84 Torr. As Fig. 2 shows, the spark breakdown voltage curve and the electret voltage curve do not intersect for any value of  $d_1$ . Thus no breakdown could occur to produce the observed charge drop. This same analysis was applied to many charge-pressure conditions at which  $Q$  drops were observed, and it was found that the spark voltage curve and the electret voltage curve never intersected.

Another series of experiments showed that the effective surface charge of Mylar and polystyrene electrets decreased with decreasing pressure when the electrets were positioned in the vacuum bell jar in such a way that the distance between the electret surfaces and any conductor ranged from 4.5 to 40 cm. With these separation distances, the external electret field which could act to produce spark breakdown was quite small. The electrets were evacuated to a given pressure, then returned to atmospheric pressure, where the effective surface charge was measured. The charge measurements were made at atmospheric pressure in order to insure that breakdown could not occur during the measurement. Even though the possibility of spark breakdown between the electret surface and a nearby conductor was eliminated in these experiments, the effective surface charge still decreased as a function of pressure. The charge decreased slightly as the pressure was lowered from atmospheric and underwent a large decrease in the pressure range of 1-10 Torr.

The occurrence of spark breakdown between an electret surface and nearby metal depends on the pressure of the surrounding air, the length of the available discharge path, and the magnitude of the external electric field of the electret. The external field in turn depends on the magnitude of the effective surface charge, according to expression [1]. The data shown in Fig. 3 show that the occurrence of the charge drops do not depend on the magnitude of the external field of the electret. These data were obtained from a polystyrene electret formed by application of 140 kv/cm for 4 hr at 105°C. These forming conditions produce a large internal polarization of the electret. On removal of the forming field, the effective surface charge ( $Q$ ) of the unshielded electret initially increased due to relaxation of the internal polarization. When  $Q$  equalled  $4.6 \times 10^{-9}$  coul/cm<sup>2</sup>, the electret was evacuated to 43 Torr and then returned to atmospheric pressure. Measurement of  $Q$  at atmospheric pressure showed that the evacuation had caused a charge drop.  $Q$  resumed its slow increase in magnitude as the electret was held in room atmosphere with its surfaces ex-

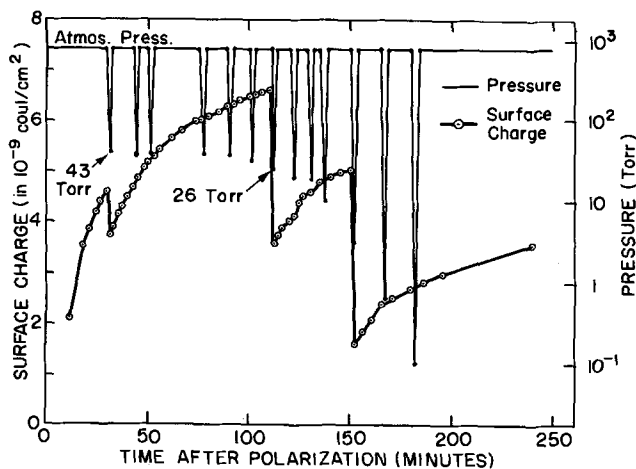


Fig. 3. Effect of reduced pressure on effective surface charge of polystyrene electret.

posed. When  $Q$  had grown to  $4.7 \times 10^{-9}$  coul/cm<sup>2</sup>, the bell jar containing the electret was evacuated to 41 Torr, again returned to atmospheric pressure and  $Q$  measured. It was found that the charge had not been affected by the second evacuation. The process was repeated as  $Q$  continued to increase, and no further reduction of the charge was observed until the electret was evacuated to 26 Torr. Evacuation to 26 Torr produced the second charge drop shown in Fig. 3. The process was then continued to lower pressures. If the charge drop on the initial evacuation was due to spark breakdown between the electret surface and nearby conductors, then another charge drop should have occurred on the second evacuation where the external field of the electret was slightly higher and the pressure slightly lower. The fact that no further charge drop was observed until the pressure was lowered to 26 Torr, even though the external field of the electret was continuously increasing, appears to support an ion desorption mechanism for the charge drops. If a desorption mechanism is active, then  $Q$  should not drop on the second evacuation because the initial evacuation would desorb all ions which could be desorbed in that pressure range. According to this theory, further ion desorption did not occur until the pressure was reduced to 26 Torr.

It would be expected that the forming conditions employed for electrets of this paper would produce an uneven distribution of surface charge, thus the charge decreases might be due to spark breakdown between regions of different charge intensity on the electret surface. However, an uneven distribution of surface charge would provide a continuous distribution of possible spark distances, thus for the electret of Fig. 3, for pressures between 43 and 26 Torr, there should exist some distance for which the potential would be sufficient to initiate spark breakdown and thereby cause charge drops. The absence of any indication of charge decrease between the pressures where large charge drops are observed apparently opposes spark breakdown along the electret surface as the source of the charge drops.

Figure 4 depicts the behavior of the effective surface charge when electrets are exposed to gases other than air. Both Mylar and polystyrene electrets were formed in room atmosphere and placed in oxygen, nitrogen, and helium at atmospheric pressure. The results for polystyrene electrets are shown in Fig. 4. The surface charge of Mylar electrets behaved similarly. Exposure of the electrets to oxygen and nitrogen caused small drops in  $Q$ , and exposure to helium caused a more drastic charge decrease. When the electrets were rapidly evacuated to  $10^{-2}$  Torr, the charge dropped further. The potential required to initiate spark breakdown in these gases is less than that required in air. The sparking potential is significantly lower in helium, where for a distance of  $10^{-2}$  cm sparking will occur at a potential of 170v, while in air at atmospheric pressure, 900v are required (11). In view of this, spark

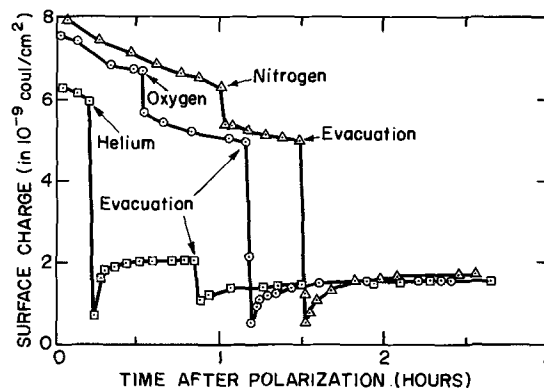


Fig. 4. Effect of oxygen, nitrogen, and helium on effective surface charge of polystyrene electrets.

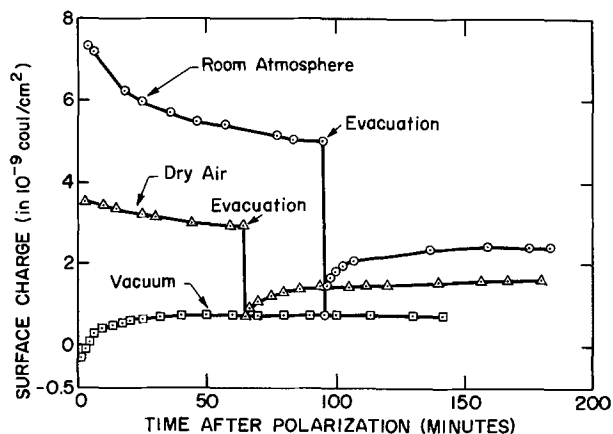


Fig. 5. Effective surface charge of polystyrene electrets formed in various environments. Forming field: 140 kv/cm for 30 sec at 23°C.

breakdown on the electret surface might account for the initial charge drops of Fig. 4. However, spark breakdown by itself does not adequately explain the later drops in surface charge. One of the authors has proposed a theory of ion desorption to account for the drops in surface charge when electrets are exposed to reduced pressure (9). According to this theory, it appears that ion desorption is a significant contributor to the second charge drops of Fig. 4.

That oxygen, nitrogen, and water are primary sources of electret surface charge is shown by the data of Fig. 5. Here is shown the effective surface charge of polystyrene electrets formed in room atmosphere, dry air, and a vacuum of  $2 \times 10^{-5}$  Torr. Since the charge is less for the electret formed and stored in dry air than for the electret formed and stored at 23% relative humidity, water vapor must be a significant source of the surface charge. Similarly, the low (in fact initially negative) value of charge for the vacuum formed electret shows that the components of air are major sources of surface charge.

### Summary

Experiments reported in this paper yielded the following results:

1. The magnitudes of external fields of the electrets studied are not sufficient to initiate spark breakdown.
2. The occurrence of charge drops does not depend on the distance between the electret surface and nearby conductors.

3. The charge drops are not controlled by the magnitude of the effective surface charge (and hence the external field) of the electret.

4. Charge decreases occur at atmospheric pressure in environments other than air.

5. Oxygen, nitrogen, and water are primary sources of electret surface charge.

The results lead to the conclusion that the decrease in effective surface charge observed when electrets are exposed to low pressure is not the result of spark breakdown between the electret surface and nearby conductors. The data indicate that the charge drops are due to ion desorption. However, the experiments do not definitely distinguish between the mechanisms of ion desorption and spark breakdown on the electret surface as sources of the charge drops. There are apparently no previously reported studies of conditions present in the experiments of this paper, i.e., the room temperature exposure to reduced pressure of a polymer having a significant concentration of gaseous ions on its surfaces. In view of this lack of available information, further investigations are required in order to show the relative importance of the surface breakdown and desorption processes in causing the observed charge decrease.

### Acknowledgment

This work was supported by the National Institute of Dental Research, Grant DE-2111-02.

Manuscript received Sept. 8, 1967; revised manuscript received Dec. 18, 1967. This paper was presented at the Electrets Symposium at the Chicago Meeting; Oct. 15-19, 1967, as Abstract 135.

Any discussion of this paper will appear in a Discussion Section to be published in the December 1968 JOURNAL.

### REFERENCES

1. G. E. Shepherd and J. D. Stranathan, *Phys. Rev.* **60**, 360 (1941).
2. J. W. Wild and J. D. Stranathan, *J. Chem. Phys.*, **27**, 1055 (1957).
3. A. N. Gubkin and G. I. Skanavi, *Sov. Phys.—Solid State*, **3**, 215 (1961).
4. G. G. Wiseman and G. R. Feaster, *J. Chem. Phys.*, **26**, 521 (1957).
5. M. M. Perlman, *J. Appl. Phys.*, **31**, 356 (1960).
6. M. M. Perlman and J. L. Meunier, *ibid.*, **36**, 420 (1965).
7. D. Kuhlmann, *Z. Physik.*, **124**, 468 (1947).
8. D. Kuhlmann, G. Masing, and J. Raffelsieper, *Z. Metallkde.*, **40**, 241 (1948).
9. R. A. Draughn, Doctoral thesis, University of Virginia (1968).
10. A. N. Gubkin, *Sov. Phys.—Tech. Phys.*, **2**, 1813 (1957).
11. "Tabellen der Elektronenphysik, Ionenphysik, and Übermikroskopie," M. von Ardenne, Berlin: VEB Deutscher Verlag der Wissenschaften (1956).

# Measurement of Quantum Efficiencies of $\text{Eu}^{3+}$ -Activated Phosphors Using Excitation to Selected $\text{Eu}^{3+}$ -Levels

A. Bril, G. Blasse, and J. A. A. Bertens

Philips Research Laboratories, N. V. Philips' Gloeilampenfabrieken, Eindhoven-Netherlands

## ABSTRACT

A method to determine the efficiency of the red  $\text{Eu}^{3+}$ -fluorescence of phosphor powders using excitation of the  $^5D_1$ -,  $^5D_2$ -, and  $^5L_7$ -levels is described. These efficiencies were compared with those found with short-wave ultraviolet excitation, in order to study the transfer of the absorbed energy to the europium ion.

The quantum efficiency of a fluorescent substance is generally defined as the ratio of the number of emitted quanta to the number of absorbed exciting quanta, while the radiant efficiency (energy-conversion efficiency) is defined as the ratio of the corresponding radiant powers. The measurement of quantum efficiency is simple in principle but sometimes rather difficult in practice (1, 2)! One of the difficulties in measurement of efficiencies of powders is the determination of the absorption of the exciting radiation. Phosphors such as are used in fluorescent lamps gives the least difficulties because they have both a high light output and a high absorption in the host lattice or in the activators (2). This means that small spurious absorptions (e.g., absorptions in contaminations which do not give rise to fluorescence) play only a minor role. Problems arise when activator absorptions are low in comparison with absorptions of the host or of contaminations. This is the case in the rare earth activated phosphors when they are excited in the narrow energy levels of the rare earth ions themselves.

In this paper a method is described for the measurement of efficiencies of  $\text{Eu}^{3+}$ -activated phosphor powders when excited in the  $^5D_1$ -,  $^5D_2$ -, and  $^5L_7$ -levels (see Fig. 1) which are very narrow (about  $10 \text{ cm}^{-1}$ ) and for which the absorption is only some per cent. (The absorption at the  $^5D_3$ -level is generally too weak, in accordance with the selection rules, for the determination of the efficiency.) It is of interest to determine these efficiencies for phosphors which have a low efficiency under short-wave u.v.- and cathode-ray excitation to see where the exciting energy is lost. Excitation at the  $^5D_0$ -level has not been considered because fluorescence and absorption cannot be easily separated in the case of powders. Moreover, the absorption at the  $^5D_0$ -level is very weak. Measurements of this type with selective excitation at  $\text{Eu}^{3+}$ -levels have been performed for liquids (Eu-chelates) by Dawson, Kropp, and Windsor (3).

## Apparatus and Method

The experiments are carried out by use of a Perkin-Elmer grating spectrophotometer model 13G, which we modified slightly and used in single beam mode. The Nernst filament with mirror was replaced by a tungsten-iodine lamp in combination with a quartz lens, so that more energy was obtained in the short wavelength region. A Bausch and Lomb grating, blazed at 500 nm and with 600 grooves/mm, was used.

The phosphor was placed behind the exit slit (see Fig. 2), so that it was irradiated monochromatically. To reduce stray light to a still lower level a Schott VG 12 filter was placed in the exciting beam, to absorb energy in the longer wavelength region.

Two measurements were carried out for each  $\text{Eu}^{3+}$ -absorption region of every phosphor:

1. The excitation spectrum. The fluorescent radiation emitted by the phosphor was collected and measured

as a function of the exciting wavelength with a photomultiplier tube (EMI, Type 9558 Q), in front of which a filter was placed (4 mm Schott OG 5) which transmitted only the orange and red fluorescent energy while absorbing the exciting energy. A curve of the type given in Fig. 3a was then obtained.

2. The diffuse reflection spectrum. In this measurement only one thing was different from the previous measurement: The OG 5 filter is replaced by a VG 12 filter, which transmitted only the exciting energy and absorbed the fluorescence. Everything else remained the same (lamp current, photomultiplier voltage, etc.). Then the absorption curve as a function of wavelength was obtained, as shown in Fig. 3b.

The width of the peaks in the excitation spectrum are found to be equal to the corresponding peaks in the reflection spectrum. We have described earlier (2) that for powder phosphors the angular distribution of the reflected radiation is the same as that of the fluorescence (nearly Lambertian distribution).

As has been said in the introduction, the radiant efficiency is the ratio of the emitted power and the power absorbed from the exciting radiation. The emitted power is determined by the maximum ordinate  $U_{em}$  of the peak in the excitation spectrum with two corrections: (i) The transmission  $\tau_{OG5}$  of the filter used is not unity and moreover it varies as a function of the wavelength of the emission. (ii) The response  $G(\lambda)$  of the photomultiplier, given in  $\mu\text{a}/\mu\text{w}$ , varies as a function of wavelength. Therefore the total emitted power is

$$E = U_{em} \frac{\int_{em} \rho(\lambda) d\lambda}{\int_{em} \rho(\lambda) G(\lambda) \tau_{OG5}(\lambda) d\lambda}$$

where  $\rho(\lambda) d\lambda$  is the relative emitted power in a region  $d\lambda$  at wavelength  $\lambda$ , derived from the spectral energy distribution curve. The integration has to be extended over the total spectral region of the emission.

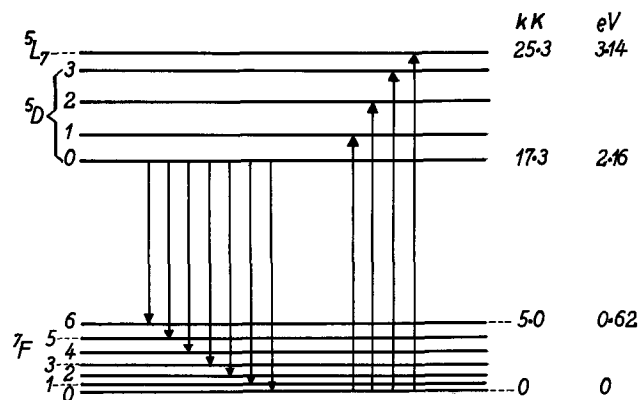


Fig. 1. Part of the energy level scheme of the  $\text{Eu}^{3+}$ -ion

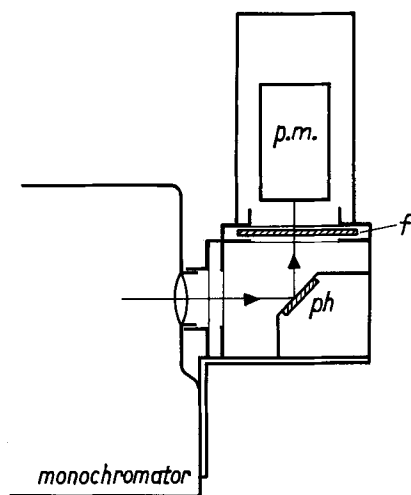


Fig. 2. Schematic diagram of experimental arrangement: p.m., photomultiplier; ph, phosphor; and f, filters.

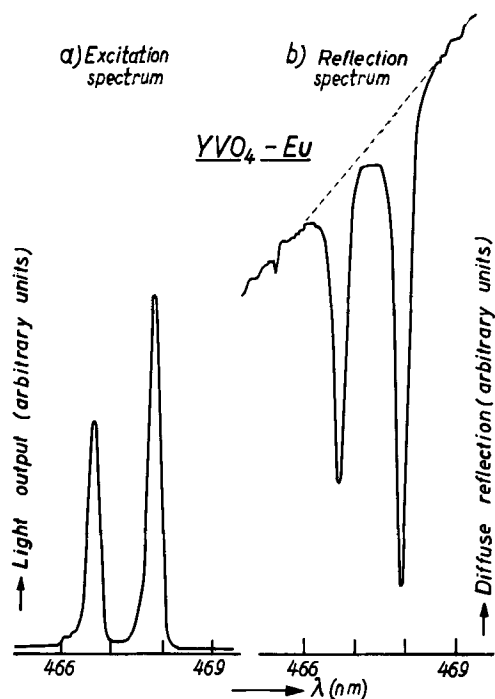


Fig. 3. Relative light output of  $\text{Eu}^{3+}$ -emission (curve a) and diffuse reflection (curve b) as a function of wavelength for  $\text{YVO}_4\text{-Eu}$ . For curve b the zero line is suppressed (the absorption peak has a depth of about 13%).

The radiant energy absorbed from the excited beam is determined by the peak height  $U_{\text{abs}}$  of the diffuse reflection spectrum, corrected in a similar way for (i) the transmission  $\tau_{\text{VG}12}$  of the filter used, and (ii) for the response  $G$  of the photomultiplier in the excitation region. Because the width of the excitation peak is only a few angstrom units, we can take here the transmission and response at the peak wavelength  $\lambda_{\text{exc}}$ . Thus the absorbed power is proportional to

$$A = U_{\text{abs}}/G(\lambda_{\text{exc}}) \cdot \tau_{\text{VG}12}$$

The radiant efficiency  $\eta$  is then determined by

$$\eta = \frac{E}{A} = \frac{U_{\text{em}} \cdot \tau_{\text{VG}12} \cdot G(\lambda_{\text{exc}}) \cdot \int_{\text{em}} \rho(\lambda) d\lambda}{U_{\text{abs}} \cdot \int_{\text{em}} \rho(\lambda) G(\lambda) \tau_{\text{OG}5}(\lambda) d\lambda}$$

The quantum efficiency  $q$  is found by multiplying the radiant efficiency with

$$q/\eta = \frac{\int_{\text{em}} \lambda \rho(\lambda) d\lambda}{\lambda_{\text{exc}} \int_{\text{em}} \rho(\lambda) d\lambda}$$

being the ratio of the energy of the exciting and the emitted quanta. The response of the photomultiplier was determined by comparing its output with that of a photocell calibrated by the National Physical Laboratory in Teddington (England). The spectral energy distributions for most phosphors were measured up to  $\lambda \approx 720$  nm. Those of  $\text{Gd}_2\text{O}_3\text{-Eu}$  and  $\text{YVO}_4\text{-Eu}$  were measured up to 900 nm. We found that the intensities of the  ${}^5D_0 \rightarrow {}^7F_5$  and  ${}^5D_0 \rightarrow {}^7F_6$  lines located in this region were negligible, in accordance with theoretical considerations of Ofelt (4). Therefore we ignored these lines in the case of the other phosphors, too.

The error in this type of measurement will be of the order of 25%. This large error is caused by the very low value of the absorption, as has been already mentioned in the introduction.

## Results and Discussion

When exciting in the  ${}^5D_2$  ( $\lambda = 465$  nm) and  ${}^5D_1$  ( $\lambda = 535$  nm)  $\text{Eu}^{3+}$ -levels quantum efficiencies of about 100% were measured for  $\text{Gd}_2\text{O}_3\text{-Eu}$ ,  $\text{Y}_2\text{O}_3\text{-Eu}$ , and  $\text{YVO}_4\text{-Eu}$  with the method described in the previous section. This is in agreement with the high efficiency figures found for these phosphors when excited with cathode rays or short wave u.v. radiation (quantum efficiency  $q = 70\%$ ) (5). For  $\text{YVO}_4\text{-Eu}$  the spectral energy distributions were measured for excitation with  $\lambda = 525$  nm,  $\lambda = 465$  nm,  $\lambda = 395$  nm and for short wave u.v. radiation ( $\lambda = 254$  nm). No differences between these distributions were found, within the limits of experimental accuracy.

It is assumed that this is valid for all phosphors. The same correction (see previous section) is applied in determining the radiant efficiencies for different excitations. The emission peaks in the regions near 595, 610-620, and 700 nm are all taken into account.

There are other phosphors which have a lower quantum efficiency for short wave u.v. excitation, e.g.  $\text{Y}_{0.8}\text{Eu}_{0.2}\text{Al}_3\text{B}_4\text{O}_{12}$  with  $q = 35\%$ . When excited in the selected  $\text{Eu}^{3+}$ -levels, however,  $\text{Y}_{0.8}\text{Eu}_{0.2}\text{Al}_3\text{B}_4\text{O}_{12}$  and even  $\text{EuAl}_3\text{B}_4\text{O}_{12}$  have a quantum efficiency near 100%.

In the phosphors mentioned above and many others evidently practically no radiationless processes occur from the  ${}^5D_1$  and  ${}^5D_2$  levels.

Excitation in the  ${}^5L_7$ -level ( $\lambda = 395$  nm) gives also quantum efficiencies near 100% in many cases:  $\text{YAl}_3\text{B}_4\text{O}_{12}\text{-Eu}$ ,  $\text{Gd}_2\text{O}_3\text{-Eu}$ ,  $\text{YPO}_4\text{-Eu}$ ,  $\text{YNbO}_4\text{-Eu}$ . However, difficulties arise when the  ${}^5L_7$ -absorption is superimposed on the host lattice absorption or a tail of this absorption, as is the case in substances like  $\text{YVO}_4\text{-Eu}$ ,  $\text{Y}_2\text{WO}_6\text{-Eu}$ , and  $\text{Gd}_2\text{WO}_6\text{-Eu}$  (see the survey spectrum of  $\text{Y}_2\text{WO}_6\text{-Eu}$  in Fig. 4). This curve has not been used for the calculation of the efficiency; for that purpose higher resolved spectra with suppressed zero line are determined as given in Fig. 3). If we take as absorption the area of the narrow absorption peak as is done for the  ${}^5D_2$  and  ${}^5D_1$  absorption (see Fig. 3, the area under the dashed line), apparent efficiencies of about 200% are obtained. Since there is no reason to expect quantum efficiencies higher than 100%, our method seems not to work, if the rare earth absorption coincides with the host lattice absorption. This can be explained at least partly by the fact that the procedure used is not valid in cases where there is considerable absorption in the host lattice: To determine  $U_{\text{abs}}$  of the narrow peak the dashed line, connecting the host lattice reflection at both sides of this peak, is considered as a separation between activator absorption (narrow band) and host lattice absorption. However, following common absorption rules, in the presence of additional absorption, the host lattice cannot absorb as many photons as would be the case without it. Hence the activator absorption, as has been determined in this way, is underestimated leading to quantum efficiency figures which are too high.

An interesting case is the comparison of the efficiencies of  $\text{Gd}_2\text{WO}_6\text{-Eu}$  and  $\text{Y}_2\text{WO}_6\text{-Eu}$ . We found for

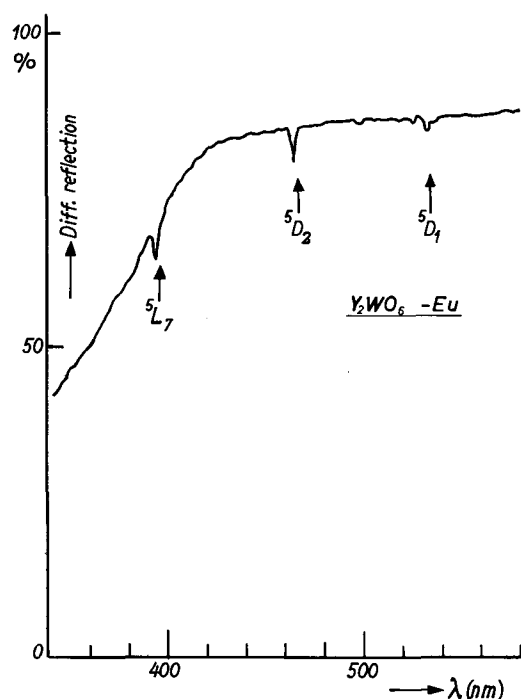


Fig. 4. Reflection spectrum of  $Y_2WO_6$ -Eu (survey spectrum with low resolving power).

both phosphors quantum efficiency values near 100%, when they are excited in the selected  $^5D_2$  and  $^5D_1$ -levels. When excited in the broad u.v. excitation band  $Y_2WO_6$ -Eu is a reasonably efficient phosphor ( $q = 55\%$ ), while  $Gd_2WO_6$ -Eu is not ( $q = 10\%$ ). These results are in agreement with our earlier given explanation concerning the different energy transfer efficiency from the host lattice to the  $Eu^{3+}$  centers (7). The transfer from the tungstate group to the  $Eu^{3+}$ -ion is efficient, if the angle Eu-O-W is about  $180^\circ$  as is the

case in  $Y_2WO_6$ -Eu, whereas it is not efficient when this angle is  $90^\circ$  as in  $Gd_2WO_6$ -Eu. Our measurements confirm this difference in energy transfer efficiency, since both phosphors show efficiencies near 100%, when the  $Eu^{3+}$  ions are directly excited in the selected  $^5D_2$  and  $^5D_1$  levels.

The difference between the results of Dawson, Kropp, and Windsor (2) for Eu-chelates and ours for oxides is that we generally find no increase of efficiency from the  $^5L_7$ - to lower excitation levels, whereas they do find such an increase. Apparently the population of the  $^5D_0$ -level from the higher levels is not much different in our phosphors.

#### Acknowledgments

The authors wish to express their thanks to the Reviewer of this Journal for suggesting an explanation for the apparent efficiencies higher than 100%. Further they are greatly indebted to Dr. W. L. Wanmaker and Mr. J. Broos for the preparation of some of the phosphors and to Dr. W. C. Nieuwpoort for stimulating discussions.

Manuscript received Aug. 3, 1967; revised manuscript received Oct. 16, 1967.

Any discussion of this paper will appear in a Discussion Section to be published in the December 1968 JOURNAL.

#### REFERENCES

1. M. H. Bhaumik and C. L. Telk, *J. Opt. Soc. Am.*, **54**, 1211 (1964).
2. A. Bril and W. Hoekstra, *Philips Research Reports*, **16**, 356, (1961).
3. W. R. Dawson and J. L. Kropp, *J. Opt. Soc. Am.*, **55**, 822 (1965); W. R. Dawson, J. L. Kropp, and M. W. Windsor, *ibid.*, **45**, 2410 (1966).
4. G. S. Ofelt, *J. Chem. Phys.*, **37**, 511 (1962).
5. A. Bril and W. L. Wanmaker, *This Journal*, **111**, 1363 (1964), **112**, 111 (1965); A. K. Levine and F. C. Palilla, *Appl. Phys. Letters*, **5**, 118 (1964); F. C. Palilla, A. K. Levine, and M. Rinkevics, *This Journal*, **112**, 776 (1965).
6. G. Blasse, *J. Chem. Phys.*, **46**, 2583 (1967).
7. G. Blasse and A. Bril, *ibid.*, **45**, 2350 (1966); G. Blasse, *ibid.*, **45**, 2356 (1966).

## Kinetics of Hydrolysis of Single Crystal $CaF_2$ from $1000^\circ$ to $1120^\circ C$

D. R. Messier<sup>1</sup>

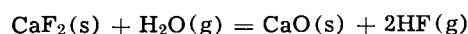
Argonne National Laboratory, Argonne, Illinois

#### ABSTRACT

The kinetics of the reaction  $CaF_2(s) + H_2O(g) = CaO(s) + 2HF(g)$  were determined on single crystal  $CaF_2$  specimens by a gravimetric technique in the temperature range from  $1000^\circ$  to  $1120^\circ C$  at water vapor partial pressures from 1 to 20 Torr. Parabolic rate behavior was observed; i.e., the reaction rate, which is initially parabolic, eventually becomes linear. The parabolic and linear rates were both found to be dependent on the partial pressure of water vapor. Activation energy values of 63.6 and 38.4 kcal/mole, respectively, were obtained for the parabolic and linear reaction periods. The complexity of the reaction mechanism prohibits assigning the activation energy values to specific processes.

A literature survey reveals considerable interest in the role of oxygen and hydroxyl ion impurities in producing optical effects in calcium fluoride (1-6). Bontinck (1) reported the only measurements which have been made on the kinetics of the hydrolysis of  $CaF_2$ .

He showed that the net reaction responsible for the rapid oxidation of  $CaF_2$  in air at high temperatures is



Bontinck's measurements were made on powder specimens in air containing a low but unspecified partial pressure of water vapor. The present measurements were undertaken to provide kinetic data on single crystal specimens in atmospheres containing known partial pressures of water vapor.

<sup>1</sup>At the time the experimental work was done, the writer was Graduate Research Assistant in the Inorganic Materials Research Division, Lawrence Radiation Laboratory and in the Department of Mineral Technology, University of California at Berkeley. He is now Assistant Ceramic Engineer, Metallurgy Division, Argonne National Laboratory, Argonne, Illinois.

### Experimental Procedure

Specimens were fabricated from single crystal  $\text{CaF}_2$  (Harshaw Chemical Company). Specimen blanks in the form of thin plates were made by cleaving the crystals along parallel [111] planes. The blanks were then diamond-sawed parallel to [110] and [112] planes to form square plates. The plates were ground to their final dimensions in a slurry of 600 mesh silicon carbide and water. Although  $\text{CaF}_2$  reacts readily with water vapor at elevated temperatures, it is unreactive with water at room temperature. The approximate dimensions of the specimens were  $9 \times 9 \times 2$  mm. The dimensions of each specimen were determined to within 0.01 mm with a micrometer.

The kinetics of the hydrolysis reaction were determined by following the weight loss of a specimen as a function of time. The quartz spring weight-loss apparatus that was used is described elsewhere (7).

A run was initiated by heating a specimen to the desired reaction temperature in flowing, dry argon. The reaction was started by introducing water vapor at the desired partial pressure. A gas flow rate of 400 cc/min was used for all of the runs. At the end of a run the atmosphere was again changed to dry argon and the furnace power was shut off.

### Results

Figure 1 is a schematic representation of a typical section from a quenched, reacted specimen. The outer region, labeled zone 1, contained precipitate particles of uniform size and concentration in a transparent matrix. Zone 2 represents the fluorescent region shown by Adler and Kveta (2) to contain dissolved oxygen. Zone 3 contains unreacted  $\text{CaF}_2$ . Under no circumstances was a single phase product layer observed.

X-ray diffraction patterns showed that the precipitate was  $\text{CaO}$ . Although  $\text{Ca}(\text{OH})_2$  is another possible reaction product (4), none was observed.

Figure 2 shows the results of all but two of the reaction runs. The latter duplicate two of the runs shown, and were omitted for the sake of clarity. Figure 2 illustrates the typical parabolic rate behavior that obtained in every run.

Figure 3 shows plots of weight-loss vs. the square root of time for the initial period assuming that a parabolic rate law applies. Although data from four runs at high water vapor pressures were arbitrarily selected for Fig. 3, the fit was equally good for all of the data.

Table I contains the rate data for runs made at various water vapor partial pressures in the temperature range from  $1000^\circ$  to  $1120^\circ\text{C}$ . The parabolic rates,  $R_p$ , were obtained from the slopes of plots of weight loss vs. the square root of time. The linear rates,  $R_l$ , were calculated from the slopes of the linear portions of the weight-loss plots. Both sets of rates were normalized for surface area. The surface area, which was assumed to be equal to the initial surface area, was calculated from measured dimensions.

### Discussion

The results of this and earlier studies (2, 3, 8) indicate that oxygen is highly soluble in  $\text{CaF}_2$  at elevated temperatures. Existing evidence also indicates that oxygen can be substituted for  $\text{F}^-$  as  $\text{O}^{--}$  (with the formation of anion vacancies) (2, 3, 5, 6) and as  $\text{OH}^-$  (3, 4, 6). It is therefore evident that the mechanism of the hydrolysis process is more complex than

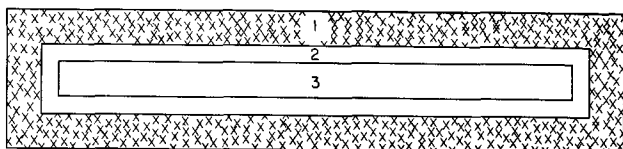


Fig. 1. Appearance of the cross section of a typical  $\text{CaF}_2$  specimen after hydrolysis.

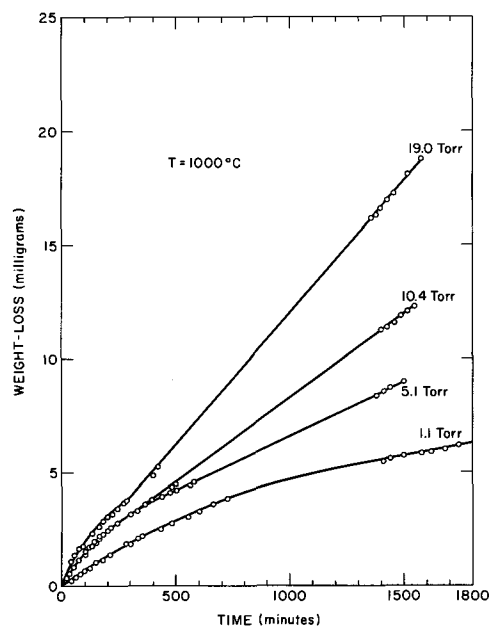


Fig. 2A. Weight-loss vs. time curves for the hydrolysis of single crystal  $\text{CaF}_2$  specimens at  $1000^\circ\text{C}$ .

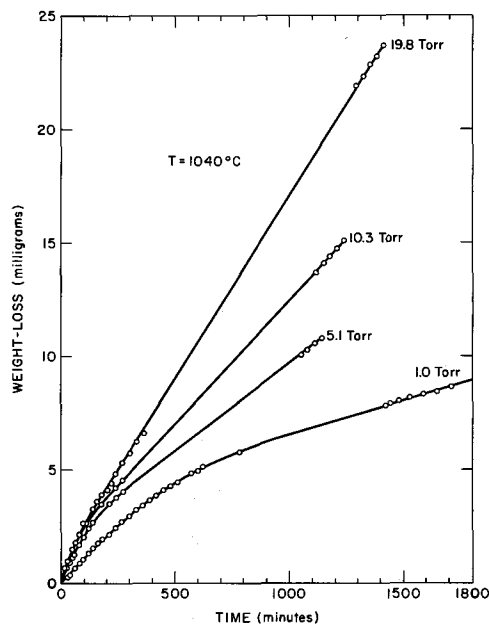


Fig. 2B. Weight-loss vs. time curves for the hydrolysis of single crystal  $\text{CaF}_2$  specimens at  $1040^\circ\text{C}$ .

was previously thought (1) and that a detailed description of the process requires more experimental data than are presently available. The following discussion attempts to point out some of the complexities involved in the interpretation of the results, and to suggest the existence of possible reaction mechanisms not heretofore considered.

The qualitative observation that the precipitate particles found in quenched specimens in this and a previous investigation (8) were uniform in size and distribution suggests that the precipitate formed only on quenching. If the precipitate had existed at the temperature of reaction, one would expect the precipitate particles to be larger in the region of higher oxygen concentration near the surface of the specimen. One might also expect such a size gradient to result from slower cooling which would allow more time for growth of the precipitate. Indeed, Bruch et al., (5) observed just such a gradient in specimens that were cooled slowly.

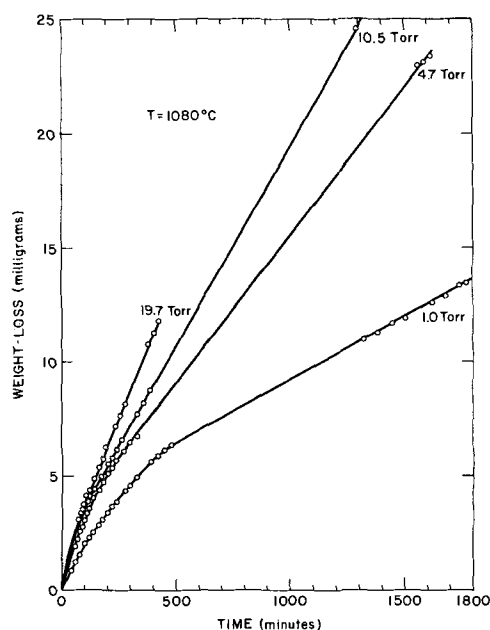


Fig. 2C. Weight-loss vs. time curves for the hydrolysis of single crystal CaF<sub>2</sub> specimens at 1080°C.

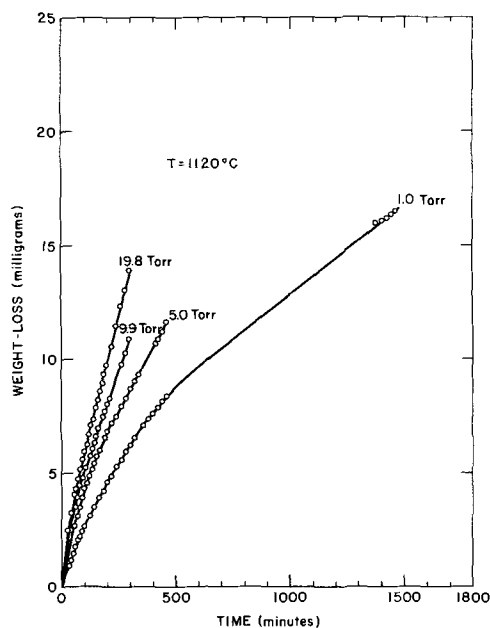


Fig. 2D. Weight-loss vs. time curves for the hydrolysis of single crystal CaF<sub>2</sub> specimens at 1120°C.

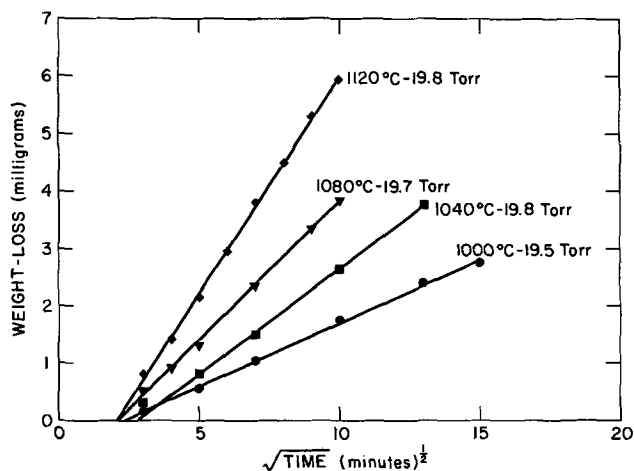


Fig. 3. Plots of weight-loss vs.  $t^{1/2}$  for the initial portion of the hydrolysis reaction.

Table 1. Collected rate data

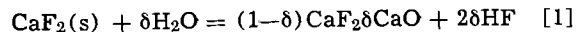
Temp, °C	P <sub>H<sub>2</sub>O</sub> , Torr	R <sub>1</sub> × 10 <sup>4</sup> , g cm <sup>-1</sup> min <sup>-1</sup>	R <sub>2</sub> × 10 <sup>4</sup> , g cm <sup>-2</sup> min <sup>-1/2</sup>
1000	1.1	0.750	0.440
1000	5.1	1.94	0.898
1000	10.4	3.04	0.978
1000	19.0	4.45	1.05
1000	19.5	4.69	0.913
1040	1.0	1.25	1.14
1040	1.0	1.47	0.988
1040	5.1	3.26	1.32
1040	10.3	4.60	1.43
1040	19.8	6.78	1.46
1080	1.0	2.26	1.48
1080	4.7	5.25	1.92
1080	10.5	7.36	2.02
1080	19.7	9.70	1.99
1120	1.0	3.34	1.78
1120	5.0	7.78	2.55
1120	9.9	11.5	2.93
1120	19.8	15.7	3.03

If, for the purpose of calculation, it is assumed that all of the oxygen was dissolved as O<sup>2-</sup>, minimum values for the solubility of oxygen in CaF<sub>2</sub> can be estimated from the maximum observed weight losses. These values are in the range from 5 to 20 m/o (mole per cent).

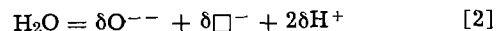
The parabolic rate behavior demonstrated by the curves in Fig. 2 was also observed by Bontinck (1) in experiments on the hydrolysis of CaF<sub>2</sub> powder specimens over a similar temperature range. Bontinck ascribed the parabolic to linear rate transition to saturation of the specimen with oxygen and formation of a precipitate. The present results, however, are inconsistent with this interpretation because they indicate that the transition is dependent on the partial pressure of water vapor, while the solubility limit should be independent of pressure. Furthermore, one would expect the growth of precipitate particles to exhibit nonlinear kinetics (9) instead of the linear kinetics actually observed.

It is evident from Fig. 2 that the extent of reaction at the transition point is dependent on both temperature and water vapor pressure. Unfortunately, the breaks in the curves cannot be established with sufficient precision to deduce quantitative relationships. One can see qualitatively, however, that the transition point weight-loss is inversely proportional to pressure under isothermal conditions, and directly proportional to temperature under isobaric conditions.

Bontinck (1) suggested that the initial stage of the hydrolysis process involved the substitution of OH<sup>-</sup> for F<sup>-</sup> at the crystal surface with the formation of one molecule of HF gas. He also interpreted his measurements as indicating that the OH<sup>-</sup> disappeared after several hours of heating and that the final net reaction was



or



However, Wickersheim and Hanking (4) presented clear evidence that OH<sup>-</sup> exists in the CaF<sub>2</sub> even after prolonged heating. They reported that the OH<sup>-</sup> absorption band at 3650 cm<sup>-1</sup> was at least as strong after 6 hr of heating as it was after 4 hr of heating at 1020°C, and that the disappearance of the peak observed by Bontinck was actually a result of an increase in background. The ESR and EPR measurements of Sierró (3, 6) on gadolinium doped CaF<sub>2</sub> also indicate the presence of OH<sup>-</sup> within CaF<sub>2</sub> crystals after hydrolysis. Sierró's measurements further indicate that OH<sup>-</sup> decomposes within the crystal to form O<sup>2-</sup>. Presumably, the decomposition process results in the formation of anion vacancies and HF along with O<sup>2-</sup>.

The magnitudes of the weight losses obtained in this study indicate that decomposition of OH<sup>-</sup> must be



occurring throughout the course of the reaction. The mere substitution of a hydroxyl ion (M.W. = 17) for a fluoride ion (A.W. = 19) could not account for the large weight changes which were observed.

On the basis of existing data, one can list a number of rate processes that may be involved in the over-all hydrolysis reaction. Some of these are: (i) chemisorption of water vapor and desorption of HF; (ii) surface reaction to form  $\text{OH}^-$  and HF; (iii) surface reaction to form  $\text{O}^{--}$ , anion vacancies and HF; (iv) diffusion of  $\text{O}^{--}$ ,  $\text{OH}^-$ , and anion vacancies into the crystal; (v) diffusion of  $\text{F}^-$  toward the surface by the interstitial mechanism proposed by Ure (10); (vi) internal decomposition of  $\text{OH}^-$  to yield  $\text{O}^{--}$ , anion vacancies, and HF; and (vii) diffusion of HF out of the crystal.

The following discussion deals with the parabolic and linear portions of the reaction with respect to the possible rate-controlling mechanisms listed above.

The parabolic character of the initial reaction period suggests that a diffusion process is rate controlling; if a surface-reaction process were rate controlling, a linear rate law would be observed (11). Interpretation of the parabolic weight-loss rates therefore requires relating the weight loss data to a diffusion coefficient and identifying the diffusing species.

The parabolic rate exhibited a strong dependence on the partial pressure of water vapor with a tendency toward a limiting value at the higher pressures. Similar pressure dependencies have been observed for reactions in which a chemisorption equilibrium step precedes the rate-controlling one. (7, 12). If the rate is assumed to be proportional to the extent of surface coverage by the reacting gas, and if the surface concentration is expressed by the Langmuir adsorption isotherm, the applicable rate expression is (7)

$$-\frac{P}{R_p} = \frac{kT}{k_p K_c \sigma_0} + \frac{P}{k_p \sigma_0} \quad [3]$$

where  $P$  is the partial pressure of water vapor,  $R_p$  is the parabolic reaction rate,  $k$  is Boltzmann's constant,  $T$  is the absolute temperature,  $k_p$  is the parabolic rate constant,  $K_c$  is the chemisorption equilibrium constant, and  $\sigma_0$  is the concentration of reactive surface sites. Equation [3] predicts that a plot of  $P/R_p$  vs.  $P$  should yield a straight line of slope equal to  $1/k_p \sigma_0$ . Figure 4 shows that the parabolic rate data fit Eq. [3].

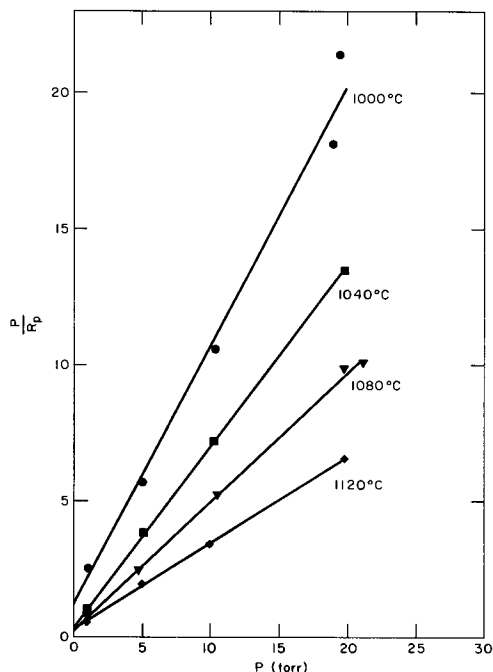


Fig. 4. Plots of  $P/R_p$  vs.  $P$  according to Eq. [1]

If it is assumed that the parabolic period corresponds to steady-state diffusion in a semi-infinite medium, the applicable rate expression is (13)

$$R_p = \left( \frac{D_i}{\pi t} \right)^{1/2} C_i \quad [4]$$

where  $D_i$  is the diffusion coefficient,  $C_i$  is the concentration per unit volume of the diffusing species adjacent to the surface, and  $t$  is the time. As Eq. [3] was derived from the expression  $R_p = k_p (\sigma/t^{1/2})$ ,  $D_i$  can be related to  $k_p$  by

$$k_p \sigma = (D_i/\pi)^{1/2} C_i \quad [5]$$

When the surface is saturated with chemisorbed water vapor,  $\sigma = \sigma_0$ , and  $C_i$  is the concentration of the diffusing species present at saturation.

Values of  $k_p \sigma_0$  (arbitrary units) were obtained from the reciprocal slopes of the lines given in Fig. 4. It was assumed that  $\sigma_0$  was constant. Figure 5 shows a semilog plot of  $(k_p \sigma_0)^2$  vs.  $1/T$ . According to Eq. [3],  $(k_p \sigma_0)^2$  should be proportional to  $D_i C_i^2$ . If it is assumed that  $D_i = D_0 \exp(\Delta H_D/RT)$ , and  $C_i = C_0 \exp(\Delta H_c/RT)$ , the activation energy obtained from Fig. 5 is the sum of terms for diffusion and carrier concentration. It was calculated that  $(\Delta H_D + 2\Delta H_c) = 63.6$  kcal.

Although, in principle, values for  $K_c$  are obtainable from Fig. 4, the intercepts could not be established with sufficient precision to do so.

An unambiguous identification of the diffusing species is not possible by evaluation of the parabolic rate data. If one assumes that the surface concentration of carriers is independent of temperature, the activation energy of 63.6 kcal/mole obtained here is close to the value of 67 kcal/mole for interstitial diffusion of argon in  $\text{CaF}_2$  obtained by other investigators (14, 15). This correlation would suggest that the interstitial diffusion of HF out of the crystal is rate-controlling. On the other hand, if the diffusion of  $\text{OH}^-$  or  $\text{O}^{--}$  and anion vacancies were rate controlling, one would expect an activation energy close to that for self diffusion of  $\text{F}^-$  in  $\text{CaF}_2$ , i.e., 46 kcal/mole (10, 15, 16). Because the value obtained is a composite one, the latter possibility is not ruled out.

The dependence of the linear reaction rate on the partial pressure of water vapor is clearly different than

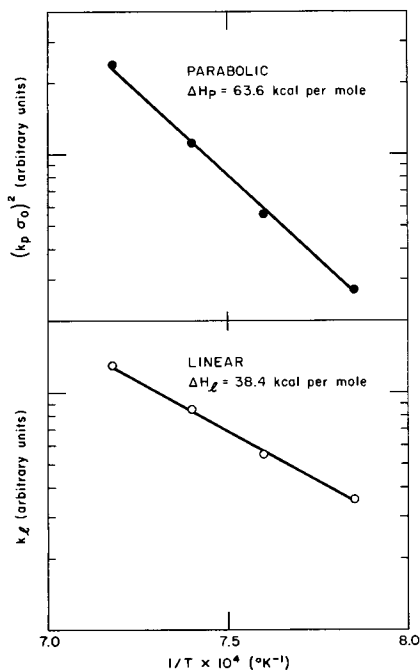


Fig. 5. Arrhenius plots of the rate data for the parabolic and linear reaction stages.

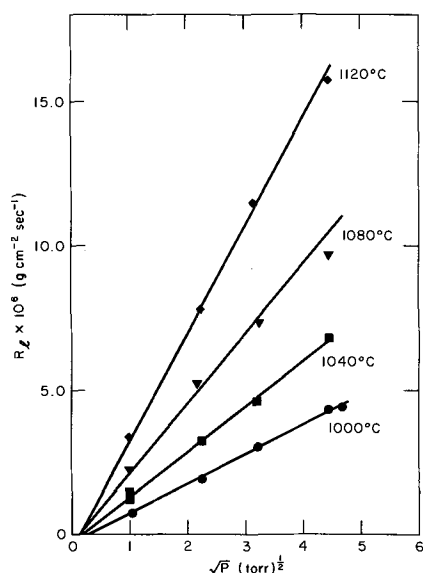


Fig. 6.  $R_1$  vs.  $P^{1/2}$  according to Eq. [5]

the dependence of the parabolic rate. As shown in Fig. 6, the linear reaction rate is proportional to the square root of the partial pressure of water vapor. Assuming a rate expression of the form

$$R_1 = k_1 P^{1/2} \quad [6]$$

rate constants were calculated from the lines in Fig. 6. The Arrhenius plot shown in Fig. 5 yielded a value of 38.4 kcal/mole for the apparent activation energy.

The interpretation of the linear reaction period is uncertain. It could correspond to rate control by a surface reaction process of the type given in Eq. [1] and [2], i.e., reaction at the surface to form substituted oxygen and anion vacancies. If such were the case, Eq. [2] indicates that the concentration of dissolved oxygen would be proportional to the square root of

the partial pressure of water vapor. An enthalpy of 38 kcal/mole that was obtained by Mollwo for the formation of F centers in  $\text{CaF}_2$  was quoted by Bontinck (1). It appears, however, that detailed speculation about the mechanism that gives linear kinetics is unwarranted at the present time.

#### Acknowledgments

The author is deeply indebted to Joseph A. Pask for his generous support in this work. He also thanks Marcus P. Borom for many helpful criticisms and Barry R. Rossing for useful comments. This work was done under the auspices of the United States Atomic Energy Commission.

Manuscript received Sept. 28, 1967; revised manuscript received Nov. 22, 1967.

Any discussion of this paper will appear in a Discussion Section to be published in the December 1968 JOURNAL.

#### REFERENCES

1. W. Bontinck, *Physica*, **24**, 650 (1958).
2. H. Adler and J. Kveta, *Osterr. Akad. Wiss., Math. naturw. Kl., Sitzer. Abt. II*, **166**, 199 (1957).
3. J. Sierro, *J. Chem. Phys.*, **44**, 2183 (1961).
4. K. A. Wickersheim and B. M. Hanking, *Physica*, **25**, 569 (1959).
5. H. Bruch, P. Gorlich, H. Karras, and R. Lehmann, *Phys. Stat. Sol.*, **4**, 685 (1964).
6. J. Sierro, *Helv. Phys. Acta.*, **36**, 505 (1963).
7. D. R. Messier, *J. Am. Ceram. Soc.*, **48**, 452 (1965).
8. W. L. Phillips, Jr., and J. E. Hanlon, *ibid.*, **46**, 447 (1963).
9. W. E. Garner, "Chemistry of the Solid State," Butterworths, London (1955).
10. R. W. Ure, Jr., *J. Chem. Phys.*, **26**, 1363 (1957).
11. W. Jost, "Diffusion in Solids, Liquids, Gases," Academic Press, New York (1960).
12. J. N. Ong, Jr., M. E. Wadsworth, W. M. Fassell, Jr., *Trans. AIME*, **206**, 257 (1956).
13. J. Crank, "The Mathematics of Diffusion," Clarendon Press, Oxford (1956).
14. T. Lagerwall, *Nukleonik*, **6**, 179 (1964).
15. H. J. Matzke, *J. Nucl. Mat.*, **11**, 344 (1964).
16. H. J. Matzke and R. Lindner, *Z. für Naturforsch.*, **19a**, 1178 (1964).

## Low-Temperature Silicon Epitaxy

R. G. Frieser\*

Research and Development Laboratories, Sprague Electric Company, North Adams, Massachusetts

#### ABSTRACT

Highly oriented large-area silicon films have been deposited onto single crystal Si,  $\langle 111 \rangle$  substrates. Illumination of the substrates with a mercury vapor lamp during deposition appeared to be essential for obtaining oriented films. The deposition was accomplished by an  $\text{H}_2$  reduction of  $\text{Si}_2\text{Cl}_6$ . The energy of activation for this reaction was found to be 35.7 kcal/mole  $\pm 5\%$ . Utmost chemical cleanliness of the substrate surface is essential and more critical than for high temperature deposition.

The objective of this work was to explore the possibility of growing single crystal films of silicon by a simple chemical vapor phase deposition at temperatures considerably below those presently employed ( $< 900^\circ\text{C}$ ). Such a technique would supplement and extend existing semiconductor technology and would permit the manufacture of devices with properties presently not feasible with existing techniques. The following examples will illustrate these points. Low temperature silicon films would permit formation of abrupt, almost perfect step junctions on silicon, by reducing migration of impurities from the

substrate into the epitaxial layer during formation of the film. Another possibility would be the prevention of junction movements, if such are already present in the substrate, while depositing new semiconductor material. The same technology would permit formation of metal base- or metal gate-transistor structures in one apparatus in a continuous operation. This is not possible at present, because temperatures needed to obtain single crystal silicon are high enough to form silicides, thus destroying the thin ( $\sim 400\text{\AA}$ ) metal layer (base).

*Prior technology.*—Reports of low temperature silicon (Lot Si) deposition in the literature usually

\* Electrochemical Society Active Member.

deal with temperatures of about 850°C (1). These results have been achieved by sputtering, evaporation, or sublimation. A few investigators, however, reported deposition temperatures below 850°C (1-4).

All these techniques involve cumbersome, expensive, and especially sophisticated equipment. For these reasons, such techniques limit the depositions usually to small area films. Deposition rates are quoted as correspondingly slow if mentioned at all.

Therefore, chemical vapor deposition (CVD) seemed to be a more promising technique to achieve the goal of a simple, flexible, open tube, flow process of depositing single crystal silicon at low temperatures. However, no oriented, much less single crystal, silicon films are reported in the literature below 900°-1000°C by CVD (6). The one exception is Nakanuma (7), who deposited silicon epitaxially at 850°C after having deposited a 0.2 $\mu$  layer of silicon at 1200°C. This makes Nakanuma's technique less generally applicable than one wherein the total deposition occurs at the lower temperature.

### Experimental

**Substrate**—Silicon substrates used were <111> oriented, 0.007 ohm-cm, p-type, ~ 3 cm diameter. Conductivity and type were chosen in order to easily measure thickness by infrared spectroscopy and more readily see the junction after angle lapping and staining. Because the source material (Si<sub>2</sub>Cl<sub>6</sub>) was not doped, deposited silicon layers were expected to be n-type, as is usually the case with SiCl<sub>4</sub> or SiHCl<sub>3</sub>.

**Reagents**—Pure line nitrogen was used for flushing the apparatus. Bottled hydrogen was passed through a palladium hydrogen purifier (Surfass Model L-15-D) prior to use. Anhydrous HCl as well as SiHCl<sub>3</sub> (electronic grade purity) were supplied by Pittsburgh Materials and Chemical Company. SiCl<sub>4</sub> used, was obtained from Sylvania and (1%) SiH<sub>4</sub> in H<sub>2</sub> from Matheson Company. Disiliconhexachloride (Si<sub>2</sub>Cl<sub>6</sub>) was supplied by K and K Chemicals.

Si<sub>2</sub>Cl<sub>6</sub> was chosen as the source material for several reasons. This compound has an extended liquid range (-1° to 144°C). Control of the vapor pressure, and, therefore, of the concentration of Si<sub>2</sub>Cl<sub>6</sub> in H<sub>2</sub> carrier gas, becomes simply a matter of controlling the source temperature. If the Si-Si bond remains intact, and there are indications it may (8, 9), and if film growth is by way of a two-dimensional nucleation process (10), then Si<sub>2</sub>Cl<sub>6</sub> may have an advantage over monosilicon compounds as a source material. Furthermore, Si<sub>2</sub>Cl<sub>6</sub> has been reported to be readily decomposed at 450°C to Si, SiCl<sub>4</sub>, and Cl<sub>2</sub> (12). This reaction is presumed to be surface catalyzed.

**Light source**.—To supply other than thermal energy to the substrate, ultraviolet light was a reasonable choice. While it would not increase the deposition temperature, it would aid in the decomposition of the Si<sub>2</sub>Cl<sub>6</sub> molecule. This expectation seemed justified, because u.v. light of 3160Å corresponding to 92 kcal should strip the chlorines from the molecule. The bond energy of the Si-Cl bond is 91 kcal/mole for SiCl<sub>4</sub>. Furthermore, the u.v. illumination may be expected to have an effect on the surface nucleation as well since the energy of 3160Å radiation corresponds to about the work function of Si (4.1 eV = 95 kcal).

A Hanovia Utility Model Lamp (100w) was used as a light source. This lamp employs a U shaped quartz mercury-arc tube. To achieve selectivity of wavelength, a set of 8 monopass u.v. interference filters from Optics Technology were used. These filters covered the range of 230-370 m $\mu$ . Their half width was rated at 6-10% of peak wavelength, transmission at peak was 10-22%. Two additional blocking filters were employed, one blocking u.v., the other visible light.

**System**.—The deposition apparatus was of the conventional upright, one-slice quartz reactor. A silicon pedestal with a molybdenum insert was used in-

stead of graphite to eliminate possible carbon contamination, which could cause spurious nucleation during deposition. Evidence of this has been reported in the literature (10). Deposition temperatures were measured with an Iron IR pyrometer directly on the surface during deposition.

**Substrate preparation**.—Lustro-polished silicon substrates were further subjected to the following routine: The substrates were first degreased in hot organic solvents. To remove any polishing compound embedded in the surface (*i. e.*, alumina, zirconia) the substrates were subjected to a copper displacement plating step and the copper was subsequently removed (11). Since this left a pitted surface, the substrates were chemically polished (5-20 min in 5% HF in HNO<sub>3</sub>) to a smooth mirror finish by removing a total of 3-10 mils from both surfaces. The final thickness of substrates was ~ 8 mils. Immediately after chemical polishing, these substrates were quenched in a solution of anhydrous methanol saturated with iodine (12). The substrates were placed wet in the reactor and iodine was sublimed off at temperatures below 600°C in a stream of H<sub>2</sub>.

HCl etching was performed *in situ* at 1175°C using a 6% (vol.) mixture of anhydrous HCl and H<sub>2</sub>, about 3 mils of material were removed.

All substrates were handled with Teflon tweezers to minimize mechanical damage.

**Characterization**.—Deposited silicon films were characterized visually, electrically and crystallographically. Surface structure and roughness were examined on the Leitz metallograph, or under the Reichert microscope, using a Nomarski polarization interferometer. Occasionally, the surface smoothness was studied using the "Talysurf." Thickness measurements of deposited films were determined either by angle lapping on a 3° block, staining, and using an interference fringe technique (13), or directly by IR spectrophotometry (Beckman, IR 10).

The electrical properties were observed in the customary manner with a four-point and hot-point probe.

Low angle reflection electron diffraction techniques were used to study the degree of orientation of the films.

### Results

Films having a high degree of orientation were achieved when Si<sub>2</sub>Cl<sub>6</sub> was used as a source at a deposition temperature of 700°C in the presence of u.v. illumination. This conclusion was based on reflection electron diffraction studies as shown in Fig. 1a. The films were also evaluated by angle lapping and staining as shown in Fig. 1b. This 3.4 $\mu$  thick film is seen to be well defined and uniform in depth.

Possible evidence that the interface is abrupt is shown in Fig. 2. This picture shows two IR interference fringe curves of Si films of comparable thickness on similar substrates. Their only difference is that one was deposited at 700°C from a Si<sub>2</sub>Cl<sub>6</sub> source in the presence of u.v., the other at 1100°C from SiCl<sub>4</sub> with no illumination. The fact that the Lot Si film shows many more distinct absorption peaks can be interpreted to mean an abrupt "interface" between film and substrate. In the absence of u.v. illumination, the deposition rate is about 1/2 of that with u. v. light (1  $\mu$ /hr) and the resulting films were polycrystalline in nature (Fig. 1c).

**Preferred conditions**.—The above experiments are taken as evidence that highly oriented Si films can be deposited at 700°-800°C under the following conditions: source Si<sub>2</sub>Cl<sub>6</sub>, source temperature 10°C (2 Torr), H<sub>2</sub> flow rate 1.5 l/min, and u. v. illumination of substrate during deposition. All subsequent information will refer to these conditions unless otherwise specified.

Table I summarizes the observations made when using various silicon halides as source materials, such as doped (n- and p-) as well as undoped SiCl<sub>4</sub>,

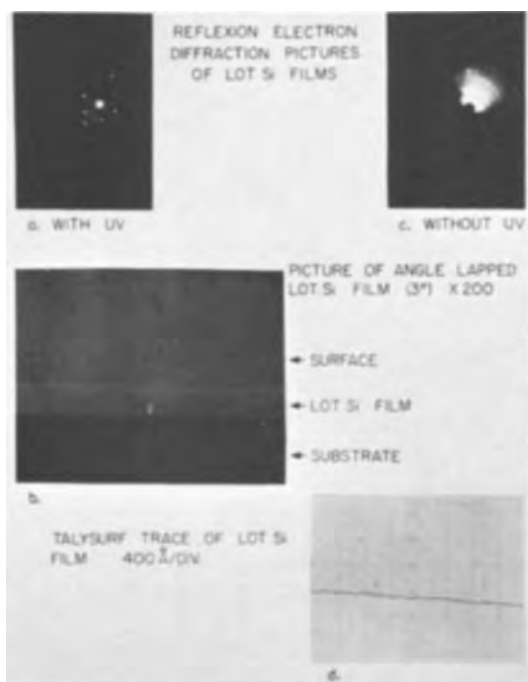


Fig. 1a. Reflection electron diffraction picture of Lot Si film (with u.v.). Fig. 1b. Picture of angle lapped ( $3^\circ$ ) Lot Si film. Fig. 1c. Reflection electron diffraction picture of Lot Si film (without u.v.). Fig. 1d. Talysurf trace of a representative Lot Si film.

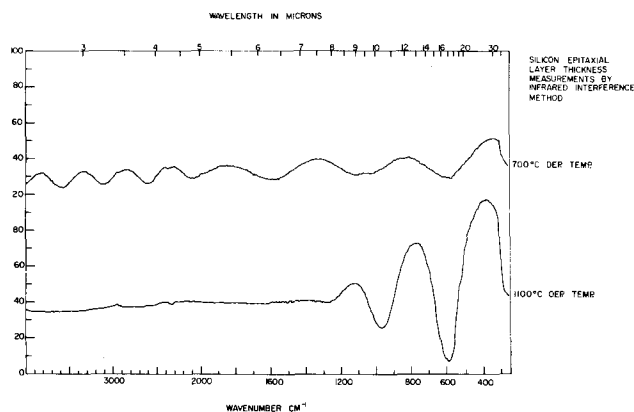


Fig. 2. Comparison of IR interference fringe measurement of Lot Si film and high temperature deposited silicon film.

$\text{SiHCl}_3$ , and  $\text{SiH}_4$ .  $\text{H}_2$  flow rates and source temperatures were varied to result in a gas stream composition that would correspond (assuming the Si-Si bond breaks) to the preferred concentration of  $\text{Si}_2\text{Cl}_6$ .

A recent report (14) describes single crystal films of Si on Si at temperatures as low as  $740^\circ\text{C}$  using  $\text{SiCl}_4$  as a source (0.6% in  $\text{H}_2$ ) and u.v. illumination. No flow rates were indicated. This experiment was repeated at two flow rates (0.5 and 1.5 l/min), but continuous films were not observed, only occasional isolated crystallites.

Either no deposits at all or polycrystalline films were obtained at deposition temperatures of  $700^\circ\text{C}$  when source material was used containing one Si atom only. At higher temperatures, oriented and single crystal films were obtained as was expected from previous published accounts.

**General appearance of lot Si films.**—The quality of the surface varied greatly; the higher the deposition temperature the greater was the aggregation, and the rougher the final surface. At  $700^\circ\text{C}$ , the surfaces were consistently smooth with a surface roughness of about  $100\text{\AA}$  according to Talysurf measurements (Fig. 1d). The surfaces were metallic and highly reflective,

Table I. Effect of source material on structure of epitaxial films

Source	Dep. temp.	Film Structure	
		With u.v.	No u.v.
$\text{SiCl}_4$	700 900 1000	No dep. No dep. Oriented	
$\text{SiCl}_4$ (n-type)	(5 ppm $\text{AsBr}_3$ ) 700 900 1000 1100	No dep. Polycrystalline Oriented Oriented	Polycrystalline Polycrystalline Single crystal
$\text{SiCl}_4$ (p-type)	(30 ppm $\text{BBr}_3$ ) 1100	Isolated crystals on surface	Single crystal
$\text{SiHCl}_3$	700 1000	No dep. Polycrystalline	No dep. Polycrystalline with some orientation
$\text{SiH}_4$	700	Polycrystalline	Polycrystalline
$\text{Si}_2\text{Cl}_6$	700	Oriented	Polycrystalline

although they showed a milky white, but still specular appearance.

**General information.**—The resistivity of the deposited films varied greatly (from 0.04 to 0.8 ohm-cm). All deposits were found to be n-type. The only exceptions were those which were HCl etched (*in situ*) as a final surface preparation step. These surfaces were all p-type.

Deposition rates, also, varied greatly ( $0.4$ – $2.5 \mu/\text{hr}$ ), but were reasonably constant for each batch of  $\text{Si}_2\text{Cl}_6$  and varied linearly with the deposition temperature (Fig. 3) in the range of  $600^\circ$ – $1000^\circ\text{C}$ . From this data, a tentative activation energy of  $35.7 \text{ kcal/mole} \pm 5\%$  was calculated.

**Substrate predeposition treatment.**—Various substrate treatments prior to deposition under preferred conditions were evaluated by reflection electron diffraction techniques of deposited films. Unbroken diffraction rings were considered evidence of polycrystallinity, segmented rings indicated orientation; the closer the "arc pattern" was to a "spot pattern" the higher the orientation assigned to the film in question. Using these criteria, the following observations were made:

Omission of the copper displacement plating step would invariably result in unequivocal polycrystalline

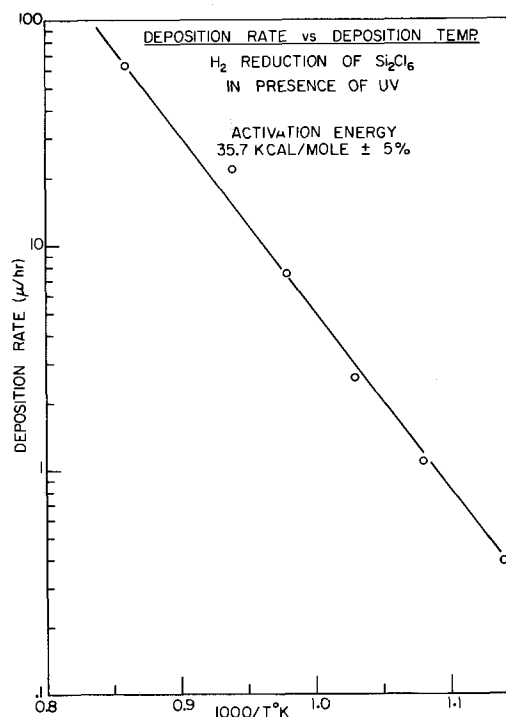


Fig. 3. Deposition rate vs. deposition temperature of Lot Si films

films, regardless of other surface preparation. Even a final HCl etching step did not prevent the formation of polycrystalline films. This may indicate that particles of polishing compound left behind after chemical or HCl etching still contaminated the surface and were apparently only removed by copper displacement plating. Finishing the substrate preparation with an alcohol quench (without  $I_2$ ) gave ambiguous results; resulting films might be completely polycrystalline or a mixture of oriented and polycrystalline materials. However, when the alcohol was permitted to dry prior to insertion in the reactor, only polycrystalline films were noted. These observations were not changed if the alcohol step (dry or wet) were followed by HCl etching in situ. On the other hand, it appears that a consistently high degree of orientation was obtained free from any polycrystalline material when the substrate was treated in the following manner: copper displacement plating, chemical polishing, quenching in  $I_2$ -saturated methanol, insertion wet in the reactor in an argon atmosphere, and removal of  $I_2$  by heating the substrate to below 600°C ( $\sim 550^\circ\text{C}$ ) in  $H_2$ .

**Effect of Wavelength.**—Using the above surface preparation and the preferred deposition conditions, the best oriented films with no evidence of polycrystallinity were observed when a 230  $m\mu$  narrow band pass filter was employed. Judging by the electron diffraction pictures, the orientation decreased and polycrystallinity increased with an increase in the passing wavelength of the optical filter. Figure 4 shows two representations of reflection electron diffraction pictures of films deposited with the aid of a 230  $m\mu$  filter in one case and, in the other, with the aid of a 360  $m\mu$  filter. The inference from these pictures is that wavelengths below 230  $m\mu$  may even be more advantageous.

### Summary and Conclusions

It is obviously too early to draw any firm conclusions concerning the mechanisms of this reaction. However, certain inferences can be made on the basis of the above work and the following facts emerged:

a. Highly oriented silicon films can be deposited on single crystal silicon substrates at deposition temperatures of  $\sim 650^\circ\text{--}800^\circ\text{C}$  provided u.v. illumination is employed during the deposition and the silicon source is  $Si_2Cl_6$ .

b. Surface treatment of substrates appears to be more critical when depositing at  $700^\circ\text{C}$  than at  $1000^\circ\text{C}$ . Therefore, lapping debris must be removed. Marked improvement in crystalline perfections was obtained by copper displacement plating that was not observed with wet chemical etching or in situ HCl high temperature etching. Elimination of a polishing step using oxides other than  $SiO_2$  should eliminate this problem.

To prevent formation of an oxide layer prior to deposition, quenching the chemically polished substrate in an alcohol solution saturated with  $I_2$  was found to be necessary.

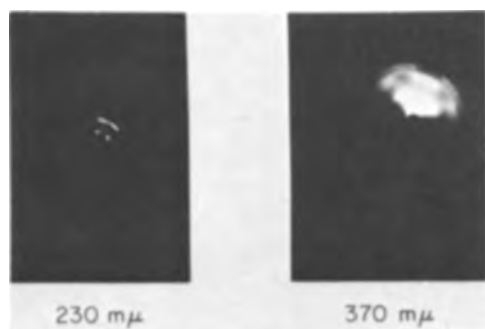


Fig. 4. Reflection electron diffraction pictures of Lot Si films deposited under 230 and 370  $m\mu$  illumination.

c. The relatively large variations in electrical and physical properties expressed in the variation of resistivities and deposition rates indicate that the source material was not sufficiently pure and varied from batch to batch. For this reason, inferences about the kinetics are very tentative.

d. Oriented epitaxial films were obtained only when: (i) the substrate was illuminated (with u. v. light) during the deposition, and (ii) Lot Si oriented films were obtained only when  $Si_2Cl_6$  was used as the source. No deposit was obtained at  $700^\circ\text{C}$  using  $SiCl_4$  or  $SiHCl_3$  sources and only polycrystalline films were obtained using  $SiH_4$  at  $700^\circ\text{C}$ . One might expect that the Si-Si bond (42 kcal/mole) would break easily when illuminated with u. v. light. Yet the dissociation energy for  $Si_2Cl_6$  is reported to be 85 kcal/mole (9). Indications from organic reactions with  $Si_2Cl_6$  are that the Si-Si bond is not as easily broken as one might expect from thermodynamic considerations alone. A large activation energy could account for the observed stability of the Si-Si bond. Steric hindrance of the Cl atoms as well as electronic effect from this ( $p \rightarrow d$ ) $\pi$  bond could account for this high activation energy. It appears then that the Si-Si bond may survive and thus play an important part in the oriented growth of the nuclei.

Furthermore, the effect of the light indicates that the reaction is surface catalyzed. In view of the fact that the energy is almost the same as that of the work function (4.1 eV or 95 kcal/mole) of Si, it appears that this could be further evidence for the surface model for Si proposed by Chung and Haneman (15). The light quanta may indeed draw electrons to the surface and produce a surface which may, for all intents and purposes, appear to the oncoming atoms like a plane through the crystal. In other words, on a statistical basis the effect of the light may be that each surface atom has now a "dangling bond" most of the time as compared to one for every five surface atoms (15). Thus, the oncoming Si atoms do not have to search about for a favorable site, but could stay where they land. If all sites are equivalent, growth is then oriented at all nucleation sites in the same manner.

### Acknowledgments

The author would like to express his appreciation to J. J. Casey, R. P. Auty, and F. W. Anderson for stimulating discussions and for their interpretations of the electron diffraction data. The assistance of T. Horner and C. Sweeney must be acknowledged for their help in the preparation of the epitaxial layers, and the electron diffraction data, respectively. And, finally, thanks are due to W. Bracht for his advice on the substrate preparation.

Manuscript received Sept. 6, 1967; revised manuscript received ca. Nov. 7, 1967. This paper was presented at the Philadelphia Meeting, Oct. 9-14, 1966, as Abstract 191.

Any discussion of this paper will appear in a Discussion Section to be published in the December 1968 JOURNAL.

### REFERENCES

1. a. A. J. Mountvala and G. Abowitz, *Vacuum*, **15**, 359 (1965); b. H. Widmer, *Appl. Phys. Letters*, **5**, 108 (1964); c. K. L. Chopra, *J. Appl. Phys.*, **37**, 3405 (1966).
2. J. D. Filby and S. Nielsen, *Microelectron. Rel.*, **5**, 11 (1966).
3. R. Kikuchi a.o., Technical Report AFML-TR-66-326, p. 48, Wright-Patterson Air Force Base, Ohio.
4. F. Jona, a. Abstract BD10; *Bull. Am. Phys. Soc.*, 1966 (Annual Meeting at New York City, 1966); b. *Appl. Phys. Letters*, **9**, 235 (1966).
5. E. T. Handelman and E. I. Povilonis, *This Journal*, **109**, 201C (1962).
6. a. J. Bloem and J. W. Scholte, *ibid.*, **112**, 1211 (1965); b. Hewlett-Packard, Annual Summary

- Report, 1965 Contract No. AF 33 (615)-2035, Air Force Avionics Laboratory.
7. S. Nakanuma, *IEEE Trans., Electron Devices* ED 13(7), 578-589 (1966).
  8. W. C. Steele and F. G. A. Stone, *J. Am. Chem. Soc.*, 84, 3599 (1962).
  9. E. A. V. Ebsworth, *Volatile Silicon Compounds*, Int. Series of Monographs on Inorg. Chem., pp. 91-92 (1963).
  10. S. Nielsen and G. J. Rich, *Microelectron. Rel.*, 3 165 (1964).
  11. D. L. Klein, U. S. Patent 3,224,902 (1965).
  12. D. L. Klein, Personal communication.
  13. W. L. Bond and F. M. Smits, *Bell Syst. Tech. J.*, 35, 1209 (1956).
  14. M. Kumagana, H. Sunami, and J. Nishizawa, RIEC. Tech. Rep., TR-23 (1967) Tohoku Univ., Japan.
  15. M. F. Chung and D. H. Haneman, *J. Appl. Phys.*, 37, 1879 (1966).

## Influence of Substrate Temperature on GaAs Epitaxial Deposition Rates

Don W. Shaw

Texas Instruments Incorporated, Dallas, Texas

### ABSTRACT

The effects of substrate temperature on the GaAs deposition rates were studied for {111}A, {112}A, {113}A, {115}, {100}, {113}B, {112}B, and {111}B substrate orientations. An open tube chloride transport system with elemental gallium and arsenic sources was employed. This apparatus allowed independent control over the gallium monochloride, arsenic, and hydrogen chloride partial pressures. The sensitivity of the deposition rate to substrate orientation is observed to be strongly temperature dependent. Experimental evidence is provided which indicates that the deposition rate is kinetically limited in the temperature range from 725° to 800°C.

Recent stress has been placed on improved material quality in order to realize the numerous potential applications for gallium arsenide. At present, vapor phase epitaxial deposition is the most successful method for production of such high quality material. However, continued material improvements have become increasingly difficult due to the need for fundamental information concerning the deposition process itself. In order to partially satisfy this need, a fundamental study concerning the influence of substrate temperature on the GaAs deposition rate was carried out. An investigation of this nature is a logical initial step toward understanding the basic nature of an epitaxial process.

Numerous investigators have studied GaAs epitaxial deposition processes. However, detailed studies concerning the effects of a single variable are rare. Magomedov and Sheftal (1) studied the effect of substrate temperature on the GaAs deposition rate using an open tube iodide process. The deposition rate was found to pass through a maximum as the substrate temperature was raised from 570° up to 690°C. Taylor (2) observed a similar effect with a chloride transport system. In the present study, an effort was made to isolate the substrate temperature as a single variable and study its effect on the deposition rate. The effects of substrate orientation and flow rate on the deposition rate were then related to the rate-temperature data.

### Experimental

The apparatus shown in Fig. 1 was employed throughout the study. It was designed to allow independent control of the partial pressures of the gallium and arsenic species. The arsenic partial pressure was controlled by the flow rate of hydrogen over the elemental arsenic source and the temperature of the source. Transport experiments were carried out to establish empirically the arsenic transport rate as a function of the source temperature and hydrogen flow rate. The results indicated complete saturation of the hydrogen stream with arsenic up to the maximum flow rate studied (300 ml/min). The HCl used for gallium transport was obtained by reduction of AsCl<sub>3</sub>

with hydrogen at a temperature > 900°C. Transport experiments established that one gram atom of gallium was transported for each mole of HCl entering the gallium source chamber. This indicated complete formation of GaCl at the temperature of the gallium source (900°C). Additional experiments established that complete reduction of AsCl<sub>3</sub> occurred in the reduction tube. The arsenic obtained from AsCl<sub>3</sub> reduction was condensed on the reduction tube walls and did not enter the main reaction tube with the HCl. These transport experiments enabled calculation of the initial gallium monochloride partial pressure from the vapor pressure of AsCl<sub>3</sub> at the bubbler temperature and the hydrogen flow rate through the bubbler. The purity of the elemental source materials was rated at 99.9999%. Redistilled arsenic trichloride was utilized. In all of the experiments to be described the initial vapor composition was  $P_{\text{GaCl}}^0 = 7.9 \times 10^{-3}$  atm and  $P_{\text{As}_4}^0 = 3.7 \times 10^{-3}$  atm. Unless otherwise specified, the total flow rate was constant at 0.383 l/min.

Care was taken to prevent extraneous deposition of GaAs on the tube walls between the substrate holder and the source material as well as on the substrate holder itself. Prevention of this deposition was essential because such wall deposits would deplete the gas

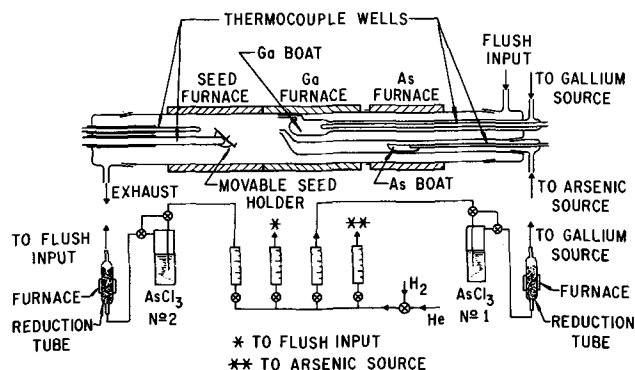


Fig. 1. Experimental apparatus for epitaxial deposition

stream of reactants before reaching the substrate region. The wall deposition was prevented by adding HCl to the gas stream. This HCl, which was also obtained by reduction of  $\text{AsCl}_3$ , entered the flush input of the reaction tube and did not react with the gallium source. In all of the experiments the HCl initial partial pressure was  $3.0 \times 10^{-3}$  atm. Since growth occurred only on the GaAs substrate, the deposition process may be treated as a special case of heterogeneous catalysis. However, unlike ordinary heterogeneous catalysis a considerable amount of information concerning the nature of the single crystal catalyst surface is available.

Usually four substrate orientations were simultaneously subjected to deposition in each run. Preliminary experiments established that the deposition rates were independent of the relative positions of the substrates on the holder. The substrates were vapor etched prior to deposition by raising the substrate temperature to  $850^\circ\text{C}$ . All temperatures were controlled to  $\pm 1^\circ\text{C}$ . Initial experiments established that the deposit thicknesses were linear functions of time up to 90 min. Thus 1 hr runs were employed and the rate was computed from the deposit thickness. Thickness measurements for the thicker deposits were obtained from measurement of cleaved cross-sections after the interface was revealed by anodic oxidation. For the thinner specimens angle-lapping and anodic oxidation were employed. The thickness was checked on the angle-lapped samples by interferometry. The reproducibility of the deposition rates for a given set of conditions was approximately 10%.

Chromium doped and tin doped substrates, oriented to within  $0.5^\circ$  of the desired direction, were used in all runs. Generally, with large area substrates growth in the direction perpendicular to the substrate surface is actually the result of the lateral propagation of steps across the surface. These steps may be inherent in the substrate prior to deposition (because of small errors in orientation), or they may result from a two-dimensional nucleation process. Accordingly, in an investigation of chemical transport epitaxial growth, the concept of surface steps must be considered. This may be accomplished by intentionally introducing steps whose nature and number could be resolved theoretically. For example, a  $\{112\}$  GaAs surface may be considered to be composed of  $\{100\}$  unit steps together with twice as many  $\{111\}$  steps (3). Likewise, the  $\{113\}$  surface consists of equal numbers of  $\{100\}$  and  $\{111\}$  steps and the  $\{115\}$  has a  $\{100\}:\{111\}$  ratio of 2:1. Accordingly, a self-consistent series was chosen for study which consisted of  $\{100\}$ ,  $\{115\}$ ,  $\{113\}$ ,  $\{112\}$ , and  $\{111\}$  orientations. However, the polarity of the  $\{111\}$  planes must be considered. Polarity effects should decrease in the order:  $\{111\}$ ,  $\{112\}$ ,  $\{113\}$ , and  $\{115\}$ ; with the  $\{100\}$  surface being essentially nonpolar. Indeed, the  $\{115\}$  was sufficiently nonpolar that no differences were observed in deposition rate between the front and back surfaces of a  $\{115\}$  substrate when both surfaces were polished. The following eight substrate orientations were employed:  $\{111\}$ A,  $\{112\}$ A,  $\{113\}$ A,  $\{115\}$ ,  $\{100\}$ ,  $\{113\}$ B,  $\{112\}$ B,  $\{111\}$ B. The "A" designation indicates the gallium face or the surface terminating in more gallium than arsenic atoms. Arsenic rich surfaces are designated as "B" orientations.

All substrates were polished with sodium hypochlorite on a rotating Pellon cloth in the manner described by Reisman and Rohr (4). After final polishing, the substrate orientation was again checked to determine if any failed to meet the  $0.5^\circ$  misorientation limitation.

### Results and Discussion

Figure 2 shows the results obtained as the temperature is varied at constant vapor composition for  $\{100\}$ ,  $\{115\}$ ,  $\{113\}$ A, and  $\{112\}$ A substrates. The rates for all four orientations increase with increasing temperature up to a maximum at approximately  $800^\circ\text{C}$ . Further in-

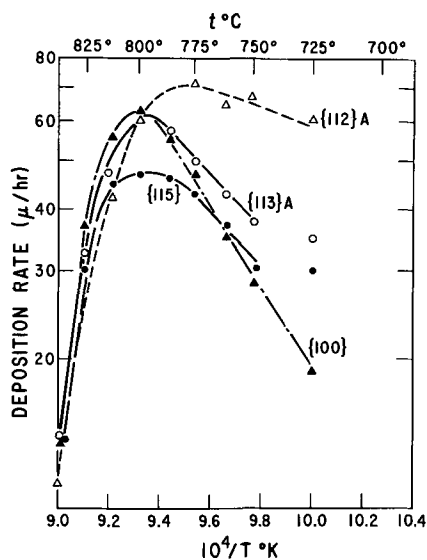


Fig. 2. Effect of substrate temperature on the  $\{112\}$ A,  $\{113\}$ A,  $\{115\}$ , and  $\{100\}$  deposition rates.

creases in temperature resulted in sharply reduced deposition rates until etching occurred near  $850^\circ\text{C}$ . The  $\{111\}$ A deposition rate exhibited a similar temperature dependence with the exception that, in general, the rate was much greater than for the other orientations. This dependence is shown in Fig. 3. Finally, the deposition rate variations as a function of temperature for  $\{100\}$ ,  $\{112\}$ B, and  $\{113\}$ B substrates are shown in Fig. 4. The  $\{100\}$  was studied together with the  $\{111\}$ B orientations as well as with the  $\{111\}$ A in order to provide a reference. In addition, this permitted a check on reproducibility of the data, since the B orientations were studied several weeks after completion of the A series. Comparison of Fig. 2 and 4 reveals that similar results were obtained for both experiments. However, good quantitative agreement was obtained only in the low temperature regions before the peaks on the  $\{100\}$  rate-temperature curves. For this reason quantitative comparison of deposition rates between the  $\{111\}$ B and  $\{111\}$ A orientations was limited to the low temperature region ( $725^\circ\text{C}$ ). In general, the B orientations exhibited the same temperature dependence as the A series. The  $\{111\}$ B orientation behaved anomalously in comparison with the others. Its rate never exceeded  $6 \mu/\text{hr}$  over the entire temperature range.

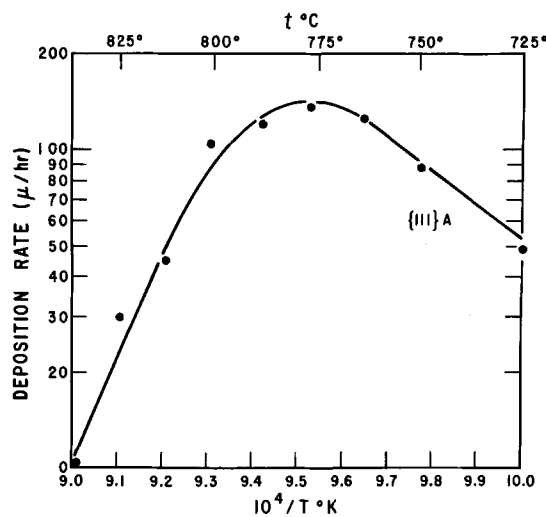


Fig. 3. Effect of substrate temperature on the  $\{111\}$ A deposition rate.

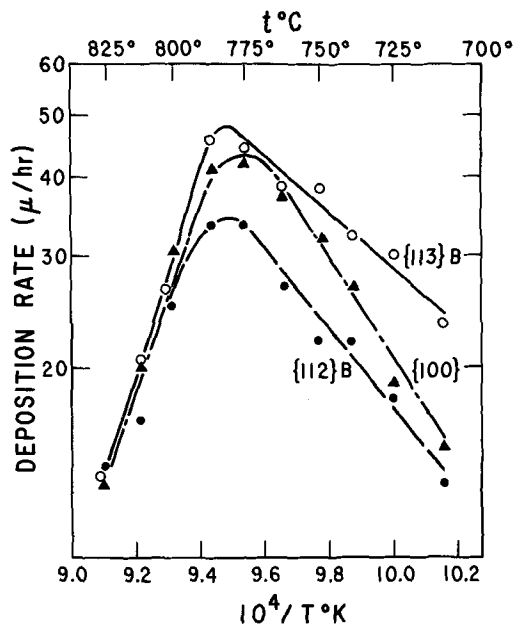


Fig. 4. Effect of substrate temperature on the {113}B, {112}B, and {100} deposition rates.

In the low temperature region before the maximum, the GaAs deposition rate shows a strong orientation dependence. The extent of this effect may be judged from the deposition rates at 750°C as shown in Fig. 5. However, beyond the maxima in the temperature curves, the orientation effects diminish and the curves for all orientations tend to converge. At temperatures below 700°C poor crystal perfection was obvious. However, the higher index orientations had much better surface appearances at these low temperatures. In general, over the entire temperature range from 700° up to 800°C the brightest, most defect-free surfaces were obtained on the {113}A substrates.

The steps involved in nonequilibrium vapor growth processes are generally divided into diffusion and surface reaction steps. Diffusion steps include diffusion of the reactants through the gas up to the substrate surface and diffusion of the products away from the surface. The surface reaction steps consist of adsorption, surface reactions, and desorption. All steps occur in series and if any step is significantly slower than the other steps, it will define the over-all deposition rate. Thus, depending on which is the slow step, deposition processes are often said to be diffusion controlled or surface reaction (kinetically) controlled. In addition to these two divisions, one should also consider a process where the rate is not limited by either a diffusion step or a surface reaction step, but which goes to equilibrium. In this case, the extent of deposition is limited by input rates of the reactants.

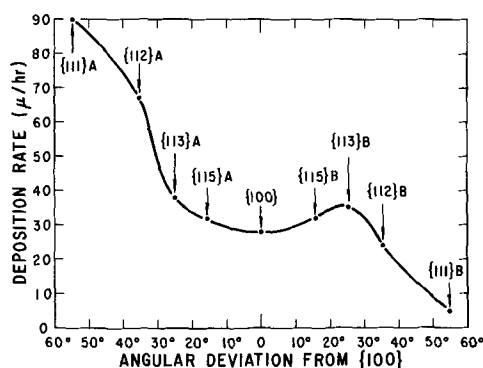


Fig. 5. Effect of substrate orientation on the GaAs deposition rate at 750°C.

Diffusion controlled processes are generally encountered where flow conditions are unfavorable or where adsorption-desorption processes and surface reactions are rapid. Such processes ideally exhibit rates relatively insensitive to temperature and thus have low activation energies. In addition, the reaction rates for diffusion-controlled mechanisms are independent of the substrate orientation (5). Kinetically controlled processes have relatively high activation energies. Since the slow steps either involve the substrate surface or take place on it, the over-all rates for kinetically controlled processes should vary with the crystallographic orientation of the surface. Unfortunately, deposition processes are sometimes so complicated that it is difficult to describe a given process in terms of a single rate limiting step.

The wide differences in deposition rates for various orientations indicate that the rates measured in low temperature regions before the maxima in the curves shown in Fig. 2-4 may represent kinetically controlled processes. This conclusion is further supported by the relatively high activation energies deduced from the slopes of the curves in the low temperature regions. These activation energies range from 15-40 kcal/mole which is in the range expected for surface limited kinetics.

Certainly the system is far from equilibrium in the low temperature region. Computer calculations were carried out to determine the extent of deposition as a function of temperature assuming an equilibrium system. The calculations were based on the actual input rates used in the experiments and the following species were considered: GaCl(g), GaCl<sub>3</sub>(g), H<sub>2</sub>(g), As<sub>4</sub>(g), As<sub>2</sub>(g), HCl(g), Cl<sub>2</sub>(g), and GaAs(s). The thermodynamic values were taken from Day's compilation (6). The results are shown in Fig. 6. Over the entire temperature range the equilibrium extent of deposition decreases with increasing temperature. Experimentally, such a rate-temperature dependence is observed only at higher temperatures (Fig. 2-4).

In order to distinguish further diffusion and surface limited kinetics, a series of experiments was carried out to determine the influence of flow rate on the deposition rate. These experiments were carried out at 750°C, i.e., well within the region where the deposition rate increases with increasing substrate temperature. The total flow rate was increased from 210 up to 840 ml/min while the partial pressures of all reactant species were held constant. Since the reaction tube was unchanged, the linear gas stream velocities and the reactant input rates were varied in this experiment. If the deposition rates were limited by a diffusion process, the rates should increase as the gas stream velocity is increased due to a reduction in the thickness of the diffusion boundary. The results are shown

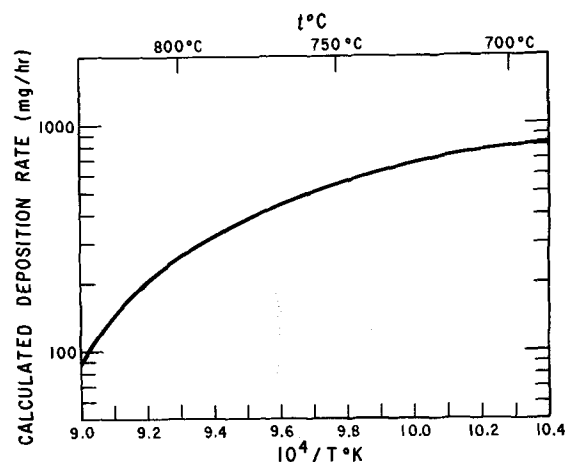


Fig. 6. Calculated extent of deposition as a function of temperature assuming equilibrium.



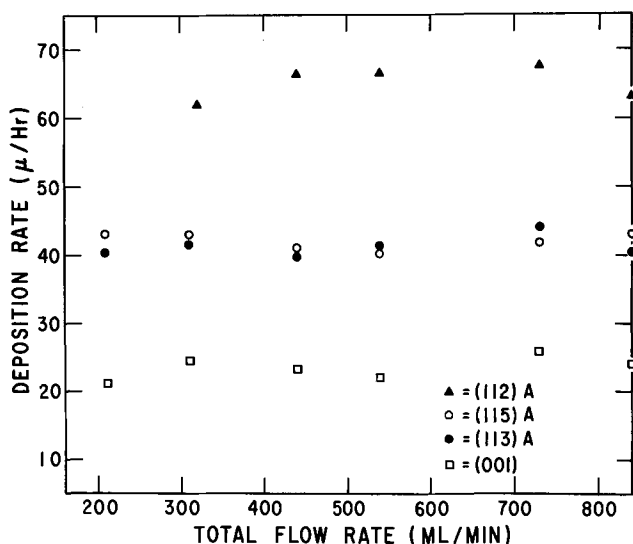


Fig. 7. Effect of total flow rate on the GaAs deposition rates at 750°C.

in Fig. 7. As is evident, the deposition rate is practically independent of the total flow rate. This is also indicative of a kinetically controlled process. This experiment was repeated for the B type orientations with similar results.

Flow rate independence is a necessary but insufficient condition for elimination of diffusion controlled processes since it could be due to peculiar flow conditions such as poor mixing at high flows (7). However, all available evidence is consistent with the concept of a kinetically controlled deposition process in the region where the deposition rate increases with increasing substrate temperature. This evidence may be summarized as (i) a strong dependence of the deposition rate on the substrate orientation, (ii) rapidly increasing deposition rate with increasing substrate temperature, and (iii) insensitivity of the deposition rate to the total gas flow rate.

The rate behavior in high temperature region beyond the maximum may indicate a close approach to equilibrium. Within experimental error the high temperature regions of the curves approximate the shape of the equilibrium curve (Fig. 6) in this region. However, the decreasing rate at high temperatures could also be due to an activated etching process whose rate increases with increasing temperature and becomes the dominant process at temperatures above 800°C. The fact that the {111}B rate was found to be low and relatively constant over the entire temperature range remains unexplained. One possibility is that an impurity is selectively adsorbed at the critical growth sites on the {111}B surface. Perhaps the answer may be found by a study of the effects of gas composition on epitaxial growth. This study is now in progress.

The variation of the deposition rates as a function of the substrate orientation is interesting. The high {111}A deposition rates attest to the ease of arsenic addition to the growing surface. For an ideal {111}A surface, an incoming arsenic makes fewer surface bonds than with any other orientation. However, this same {111}A surface has the greatest deposition rate for the reactant gas composition used in this study. The decrease in polarity effects is also obvious in this series as the surface deviates by greater amounts from a {111} toward the nearest {100}. Thus the differences between the A and B surfaces at 750°C were {111} = 85  $\mu$ /hr, {112} = 43  $\mu$ /hr, and {113} = 3  $\mu$ /hr. This trend confirms the earlier results which indicated no significant polarity effects for the {115} orientation. The increase in deposition rate in the vicinity of the {113}B orientation on the curve shown in Fig. 5 offers support for Sangster's theoretical predictions (3). Thus {113} is a favorable orientation for crystal growth since it tends to combine the good nucleation characteristics of a {100} with the favorable surface packing and stoichiometry of the {111}. Further clarification of the effects of orientation and surface polarity must await completion of the study concerning the effects of vapor composition on the deposition rate.

#### Acknowledgments

The author wishes to thank Mr. N. Tetlow for supplying the chemical equilibrium computer program used to construct Fig. 6. In addition, the assistance of Mr. D. G. Vieaux with the experimental work is acknowledged. Appreciation is extended to Drs. L. G. Bailey, R. C. Bracken, and G. O. Krause for their helpful suggestions and discussions.

Manuscript received Oct. 9, 1967; revised manuscript received ca. Nov. 20, 1967. This paper was presented in part at the Dallas Meeting, May 7-12, 1967, as Electronics Division Recent News Abstract 30.

Any discussion of this paper will appear in a Discussion Section to be published in the December 1968 JOURNAL.

#### REFERENCES

1. Kh. A. Magomedov and N. N. Sheftal, *Kristallografiya*, **9**, 902 (1964); [*Soviet Physics-Crystallography*, **9**, 756 (1965)].
2. R. A. Taylor, *This Journal*, **114**, 410 (1967).
3. R. C. Sangster in "Compound Semiconductors," pp. 241-253, R. K. Willardson and H. L. Goring, Editors, Reinhold Publishing Corp., New York (1962).
4. A. Reisman and R. Rohr, *This Journal*, **111**, 1425 (1964).
5. E. G. Bylander, *ibid.*, **109**, 1171 (1962).
6. G. F. Day, "Heterojunction Device Concepts," prepared for Air Force Avionics Laboratory, Contract AF 33(615)-1988, Varian Associates, September 1966.
7. D. E. Rosner and H. D. Allendorf, *This Journal*, **114**, 305 (1967).

#### Correction

In the paper by D. M. Brown, P. V. Gray, F. K. Heumann, H. R. Philipp, and E. A. Taft "Properties of Si<sub>3</sub>O<sub>2</sub>N<sub>2</sub> Films on Si," which was published in the

March 1968 JOURNAL, pages 311-317, the head for Table I should read:

Table I. Physical properties of pyrolytic films

# Effects of Phosphorus Diffusions in Epitaxial Silicon Layers

E. D. Wolley,<sup>\*1</sup> R. Stickler, and T. L. Chu<sup>\*2</sup>

Westinghouse Research Laboratories, Pittsburgh, Pennsylvania

## ABSTRACT

The diffusion of phosphorus into epitaxial silicon has been investigated by evaluating the electrical and structural characteristics of the epitaxial diffused guard-ring junctions. The effects of stacking faults in epitaxial silicon on the junction characteristics were found to depend on the surface condition of the epitaxial layer before diffusion. Localized breakdown, as evidenced by light emission, was observed at the stacking fault grooves only when the epitaxial layer was etched before diffusion. Stacking faults were also found to be transformed into other defects after diffusion; chemical etching of the epitaxial layer also had a great influence on this transformation. Dislocations were observed in the phosphorus-diffused regions. The dislocations occur in hexagonal networks parallel to the diffusion front and come to the surface at the intersection of the junction and the surface in planar devices. Guarded junctions formed by these phosphorus diffusions exhibit localized breakdown with microplasma phenomena. The dislocation density was determined and correlated reasonably well with Prussin's model.

The diffusion technique is used in the further processing of epitaxial silicon for the fabrication of many devices. The diffusion of dopants into silicon crystals to yield high surface concentrations is known to generate dislocations in the crystal (1-8), and a model relating the distribution of dislocations to the diffusion profile has been proposed by Prussin (1). Since other structural defects, such as stacking faults, are frequently present in epitaxial silicon, these defects may undergo transformation during the diffusion process and affect the device performance. In this work, the effects of the diffusion of phosphorus into epitaxial silicon have been studied by evaluating the electrical and structural characteristics of epitaxial diffused planar junctions. The experimental approaches and results are discussed below.

## Experimental

A guard-ring test junction shown in Fig. 1 was used for the study of the effects of phosphorus diffusion into epitaxial silicon. This junction design was first used by Goetzberger *et al.* (9) to evaluate resistivity variations in silicon crystals by observing light patterns associated with the reverse breakdown of fabricated devices. In the guarded junction device the outer or guard junction is diffused more deeply than the main central junction and thus has a higher breakdown voltage. The breakdown voltage of the central junction is not limited by surface breakdown or the cylindrical edge (10-13) of a planar junction. Because of the guard junction, the shallow junction would break down uniformly except for imperfections or localized resistivity variations. For visual observation it is necessary to have the shallow junction near enough to the surface (less than 1  $\mu\text{m}$ ) so that the light generated in the junction is not totally absorbed in the silicon.

Six groups of epitaxial silicon wafers were prepared for the fabrication of planar epitaxial diffused devices by depositing 15  $\mu\text{m}$  of 0.1 ohm-cm p-type epitaxial layers on p-type substrates, as shown in Table I. Dislocation and stacking fault densities were determined by microscopic counts from one Sirtl etched wafer from each epitaxial group. Groups 1, 3, and 5 specimens were prepared under carefully controlled conditions, and the epitaxial layers were essentially free from stacking faults and had a dislocation density similar to that of the substrate. (Groups 1 and 3,

however, were deposited on float-zone substrates and had relatively high dislocation densities.) In the other groups, the mechanical damage generated during the lapping of substrates was intentionally not completely removed, and the epitaxial layers had high concentrations of stacking faults,  $3-6 \times 10^4 \text{ cm}^{-2}$ , and also high dislocation densities. The epitaxial material was diffused without any etching of the silicon, except for Groups 5 and 6 wafers which were etched, prior to diffusion, with the Sirtl etch (14). The Sirtl etch reveals dislocations and stacking faults in epitaxial silicon in the form of pits and grooves, respectively.

The epitaxial wafers were oxidized for 2 hr in wet argon at 1200°C. The oxide thickness was 12,000 Å. A window with an I.D. of 50  $\mu\text{m}$  and an O.D. of 640  $\mu\text{m}$  was opened for the guard-ring diffusion, as shown in Fig. 1. A phosphorus predeposition was done for 30 min at 1000°C in an open-tube system using  $\text{P}_2\text{O}_5$  as a source and nitrogen as a carrier gas. The  $\text{P}_2\text{O}_5$  was removed by boiling in  $\text{H}_2\text{O}$ , leaving the original oxide. A redistribution diffusion of 4 hr at 1200°C was done with the first hour in a wet ambient. This gave guard junctions of 12-13  $\mu\text{m}$  depth.

A window for the main junction was etched with a diameter of 410  $\mu\text{m}$  centered over the guard-ring. A two-step phosphorus diffusion was carried out with the predeposition at 900°C for 30 min and the redistribution in a wet ambient for 20 min at 1000°C. The depth of the main junctions diffused in this way was less than 1  $\mu\text{m}$ . A window for contact to the guarded structure, 130  $\mu\text{m}$  I.D. and 380  $\mu\text{m}$  O.D., was etched, and an aluminum layer was vapor deposited. Aluminum was removed from all areas except in the window and then alloyed at 605°C.

For most examinations a pressure contact was made to the devices with a fine tip probe. Reverse voltage was applied to the junction and the breakdown light observed through a light microscope. In order to obtain smaller working distances and to allow observations at greater magnification, some devices were mounted

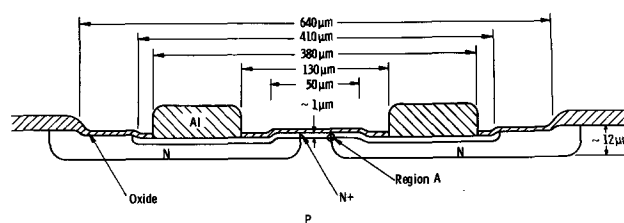


Fig. 1. Cross section of guarded junction structure

\* Electrochemical Society Active Member.

<sup>1</sup> Present address: Semiconductor Division, Westinghouse Electric Corporation, Youngwood, Pennsylvania 15697.

<sup>2</sup> Present address: Electronic Sciences Center, Southern Methodist University, Dallas, Texas 75222.

Table I. Epitaxial layers for guarded junction devices

Group	Surface type and resistivity	Substrate treatment	Resistivity of epitaxial layer, ohm-cm	Defects in epitaxial layer
1	Float zone 200 ohm-cm, p	Chemical polish to remove 50 $\mu\text{m}$	0.1	$1.6 \times 10^4$ disloc./cm <sup>2</sup> 1 stacking fault/cm <sup>2</sup>
2	Float zone 200 ohm-cm, p	Chemical polish to remove only 10 $\mu\text{m}$	0.1	$1.6 \times 10^4$ disloc./cm <sup>2</sup> $3.6 \times 10^4$ stacking faults/cm <sup>2</sup>
3	Float zone 25 ohm-cm, p	Chemical polish to remove 50 $\mu\text{m}$	0.1	$1.6 \times 10^6$ disloc./cm <sup>2</sup> 4 stacking faults/cm <sup>2</sup>
4	Float zone 25 ohm-cm, p	Chemical polish to remove only 10 $\mu\text{m}$	0.1	$2.2 \times 10^6$ disloc./cm <sup>2</sup> $5.8 \times 10^4$ stacking faults/cm <sup>2</sup>
5	Czochralski 1 ohm-cm, p	Chemical polish to remove 50 $\mu\text{m}$	0.1	160 disloc./cm <sup>2</sup> 3 stacking faults/cm <sup>2</sup>
6	Czochralski 1 ohm-cm, p	Chemical polish to remove only 10 $\mu\text{m}$	0.1	$6 \times 10^6$ disloc./cm <sup>2</sup> $6 \times 10^4$ stacking faults/cm <sup>2</sup>

on TO-18 headers with gold leads bonded to the aluminum alloyed ring contact.

Replica and thinning techniques of sample preparation for the examination of stacking faults and dislocations by the transmission electron microscope (TEM) method have been described elsewhere (15, 16). Transmission electron micrographs will be referred to as TEM. Specimens for light microscope observation were prepared by dissolving the oxide in HF and etching very lightly (5-10 sec) in Sirtl etch (14). Light micrographs will be designated as LM.

### Results

**Generation of light in reverse breakdown.**—In nearly all of the phosphorus-diffused guarded junctions under reverse breakdown, microplasmas (9, 17) were observed at the periphery of the junction, *i.e.*, the intersection of the shallow  $n^+$  diffusion and the guard junction. This region corresponds to the region labeled A in Fig. 1, and as seen from the figure, occurs inside the step in the surface caused by the oxidation during the redistribution diffusion of the guard junction. These microplasmas can be seen in Fig. 2. In some phosphorus-diffused junctions, the concentration of microplasmas at the periphery was more prevalent than in others. Most junctions had at least a few

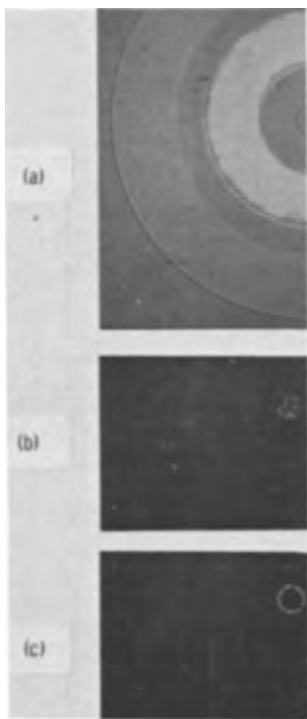


Fig. 2. Microplasma from epitaxial, phosphorus-diffused guarded junctions, epitaxial layer not etched before diffusion: (a, top) guarded  $N^+P$  junction with aluminum contact, (b, center) randomly distributed microplasma from a Group 2 wafer, and (c, bottom) microplasma concentrated at the periphery of a junction (region A in Fig. 1) on a Group 1 wafer.

microplasmas in this region. In other devices of Group 1 through 3, microplasmas appeared randomly distributed as shown in Fig. 2(b). The wafers of Groups 1 through 3 all showed microplasmas distributed either randomly or at the periphery as shown in Fig. 2. No pattern characteristic of stacking faults was observed on Group 2 wafers. Again, note that the extent of the breakdown region in Fig. 3(c) is smaller than the step in the silicon surface visible in Fig. 3(a).

Groups 5 and 6 were etched prior to diffusion of the guarded junctions with the Sirtl etch in order to reveal the stacking faults and dislocations. The light emission from the junctions of Group 6 which contained a large number of stacking faults are shown in Fig. 3. Note that the light appears to come from the bottom of the etch groove of the stacking fault and the bottom of the dislocation etch pits. Thus light comes from only part of the stacking fault on the left center and none from the one on the right center. As the reverse voltage was increased, light first appeared in one of the dislocation pits (at B in Fig. 3(b)). Figure 3(c) shows that as the voltage was further increased, light appeared in the other dis-

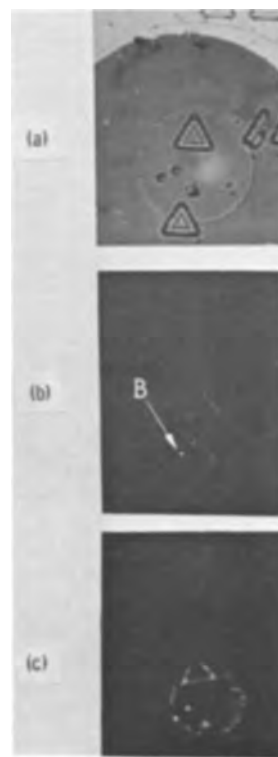


Fig. 3. Microplasmas from epitaxial, phosphorus-diffused, guarded junctions, epitaxial layer etched before diffusion, a Group 6 wafer: (a, top) etch figures by using bright field illumination with no applied bias, (b, center) light generated in one dislocation pit just above the breakdown voltage and (c, bottom) light generated in dislocation pits, stacking fault grooves, and the device periphery at voltages considerably above the breakdown.

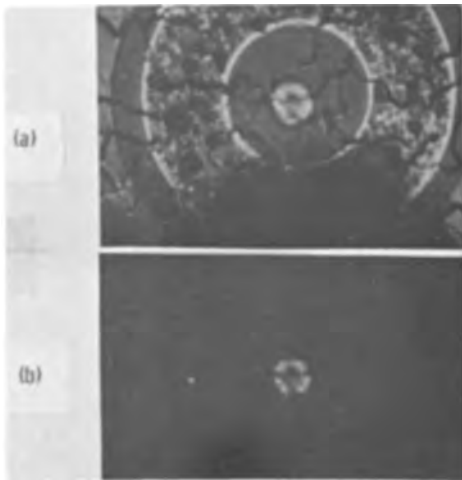


Fig. 4. Light emission from a device on a Group 4 wafer: (a, top) breakdown generated light with bright field illumination, and (b, bottom) breakdown generated light only. No patterns characteristic of stacking faults were observed.

location pits and the stacking fault groove and finally the microplasma at the periphery appeared.

Figure 3 shows that the light associated with the stacking fault appears to be continuous lines not made up of individual points and is more intense at the apices of the fault. Observations as a function of applied reverse voltage showed that the light appeared at the apices before it appeared in the grooves.

Group 4 wafers which also had a large number of stacking faults and dislocations, but were not etched prior to diffusion, did not show any of the well-defined triangular patterns observed in the Group 6 wafers, but yielded diffusion patterns of light modified by the rough surface structure evident in Fig. 4. The lack of well-defined triangular patterns is also evident in Fig. 2 which shows a device from a Group 2 wafer. Group 2 wafers were not etched prior to diffusion.

*Dislocation generation in the diffusion process.*—Figure 5 shows an alignment cross after diffusion treatment, oxide mask removal in HF, and a short Sirtl etch. Many small pits can be observed in the cross areas as well as in a region approximately 20  $\mu\text{m}$  outside the cross area. In Fig. 6 a network of fine lines can be seen running from the cross area into the surrounding regions protected during diffusion by the oxide mask. These lines always end at a small pit. The cross section and the phosphorus con-

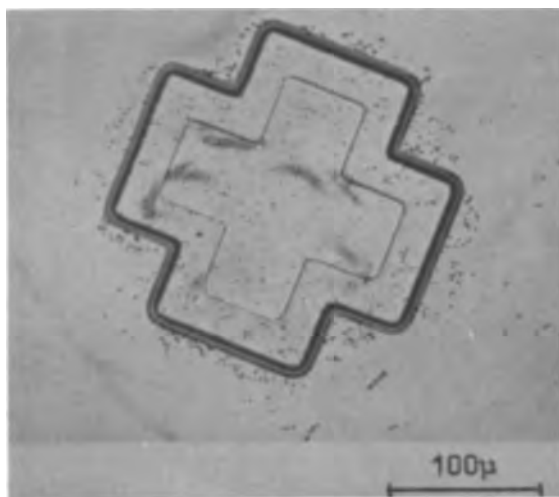


Fig. 5. Alignment cross on a Group 3 wafer after the oxide removal and a 1 min Sirtl etch. Note that the etch figures are concentrated only in and near the phosphorus-diffused areas.

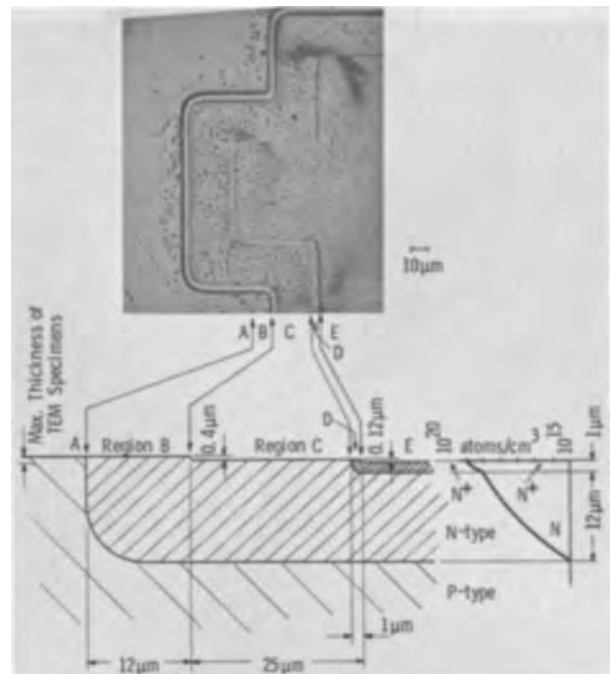


Fig. 6. Schematic cross-section through phosphorus-diffused epitaxial layer shown in Fig. 5. Schematic phosphorus concentration profile is on the right.

centration profile in the double-diffused region is also given schematically in Fig. 6. Region A indicates the undiffused area, region B the area under the oxide mask of the first diffusion treatment which was phosphorus-diffused by the lateral double-diffused area underneath the second oxide mask, and region E the double-diffused area. The surface steps resulted from the oxidation treatment to form the various oxide masks.

After light microscope examination, similar areas on the same wafer were thinned from the substrate side for TEM examination. The maximum thickness of a TEM specimen is indicated in Fig. 6, from which the layers examined by TEM can be deduced. Figure 7 is a TEM from an area close to the outer edge of the alignment cross. Dislocation lines and networks are revealed in the region B, see Fig. 7(a). In the single-diffused region C, see Fig. 7(b), several dislocation networks of varying mesh size appear to be arranged on top of each other, Fig. 7(b). In the TEM of Fig. 7(c), the regions C, D, and E are visible. Clearly, a decrease in the network mesh size in region D can be seen, while remnants of coarse and fine networks are present in the double-diffused region E. The smaller mesh size in region D can be explained by a phosphorus concentration gradient parallel to the layer surface due to lateral diffusion underneath the oxide mask.

*Modification of stacking faults.*—The appearance of a test diode area in the epitaxial layers containing high numbers of stacking faults (Group 4 wafers) after oxide removal and a short Sirtl etch is shown in Fig. 8. Stacking fault triangles can be seen in the undiffused regions. However, in the diffused regions the stacking fault triangles are completely absent. Only a few traces of stacking fault lines in the single-diffused region can be seen, while in the double-diffused regions numerous faint lines oriented along  $\langle 211 \rangle$  directions ending in small etch pits can be seen. The star-like configuration of the lines seen in Fig. 8 are almost exactly the same size as the stacking fault triangles. This suggests a correlation of the stars to the former sites of the stacking fault tetrahedrons. The faint lines may represent the remaining crystallographic defects after a rearrangement in the fault area during the diffusion treatment.

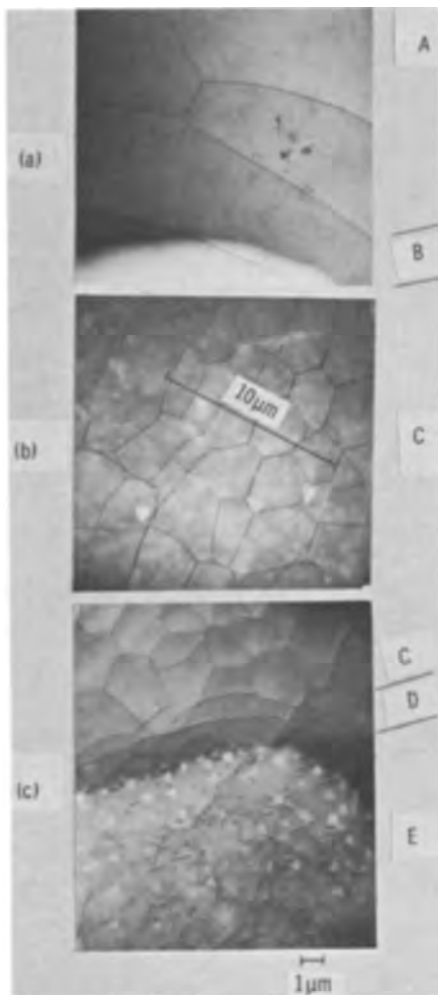


Fig. 7. TEM of various regions shown in Fig. 5 and 6. The letter designations at the right identify the regions labeled in Fig. 6: (a, top) low dislocation density region A, (b, center) note the superposition of networks of different mesh sizes, (c bottom) note the smaller mesh density in region D.

Further evidence of the modification of stacking faults after diffusion is shown in Fig. 9. A phosphorus-diffused epitaxial layer that had been etched prior to diffusion to reveal the stacking fault defects was etched a second time after the diffusion. The initially sharply grooved etch lines became flat-bottomed. In addition, many faint lines were revealed, oriented along  $\langle 211 \rangle$  directions and ending in small pits.

Figure 10(a) is a TEM typical of stacking faults in epitaxial wafers which were not phosphorus-diffused. Figure 10(b) is a TEM of the remnant of a stacking fault in a phosphorus-diffused wafer of Group 4. The banded contrast of Fig. 10(a) and the absence of it in Fig. 10(b) is typical of all the observations. Note that in Fig. 10(b) one of the dislocations of the network generated by phosphorus diffusion is parallel to the stacking fault remnant indicating the possibility of some sort of interaction of the fault and dislocation. A TEM of the bottom of a stacking fault groove of a phosphorus-diffused region of a Group 6 wafer is shown in Fig. 11. The dislocations tend to lie in  $\langle 211 \rangle$  directions which is the same as shown in the LM of Fig. 9.

#### Discussion

In the groups of wafers which were not Sirtl etched before diffusion, microplasmas were observed predominately near the periphery of the guarded diode (at A in Fig. 1). A plausible explanation for these microplasmas is that they occur at dislocations generated during the phosphorus-diffusion of the guard

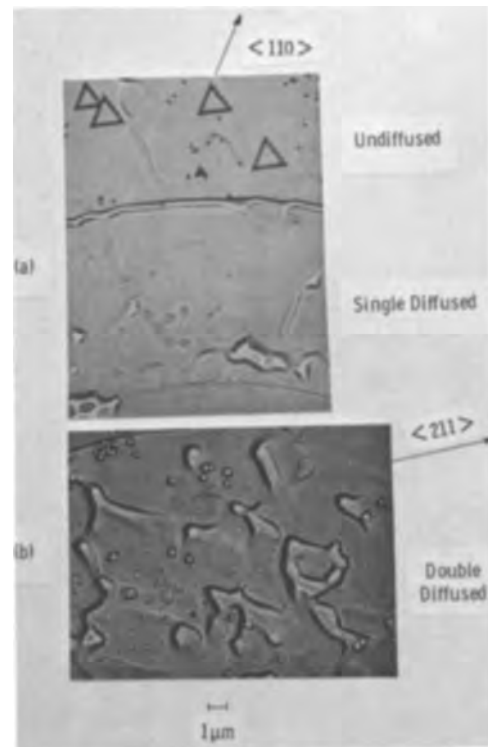


Fig. 8. LM showing the etch figures of a Group 4 wafer Sirtl etched after the phosphorus diffusion. The stacking fault grooves in the undiffused region and the remnant of a stacking fault (single straight line) in the single-diffused area (region C in Fig. 6) are shown in (a, top); (b, bottom) shows details of a double-diffused area, note fault lines ending in small etch pits often pointing in three  $\langle 211 \rangle$  directions.

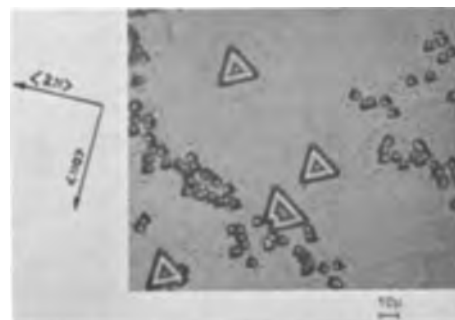


Fig. 9. Etch figures in a phosphorus-diffused epitaxial layer, Sirtl etched prior to diffusion. Note the flat-bottomed triangle etch grooves and faint lines in  $\langle 211 \rangle$  directions ending in small etch pits.

junction. The generation of these dislocations could result from the phosphorus diffusion itself, as discussed later in this section, and/or from strain resulting from the difference of coefficient of expansion of Si and  $\text{SiO}_2$  (18). Region A of Fig. 1 corresponds to the boundary between the regions A and B of Fig. 6 where the dislocations are inclined to the surface because the phosphorus gradient of the guard junction diffusion is perpendicular to the surface. Thus these dislocations would intersect the shallow junction and possibly serve as sites for localized breakdown.

Regarding the light associated with the stacking faults and dislocation etch pits of wafers etched before diffusion, one explanation is that breakdown occurs because of the curvature of the junction (10-13) resulting from the surface contouring. Evidence of the effect of etching on surface topography can be seen in Fig. 12. The groove profile was deduced from the contrast effects produced by shadow casting the Si surface with Pd (at an angle of  $45^\circ$ ) prior to the

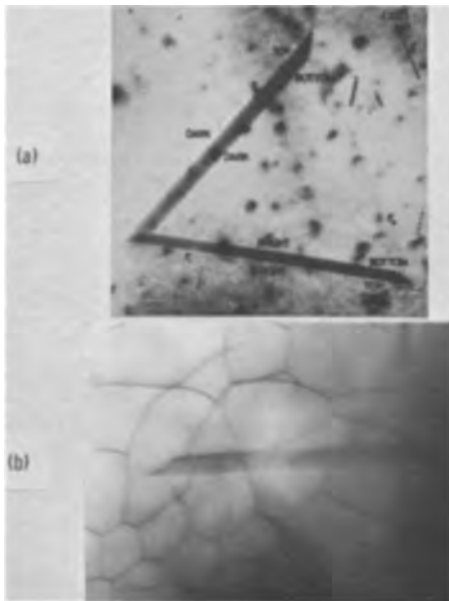


Fig. 10. (a, top) TEM of stacking faults showing banded contrast typical of undiffused material, (b, bottom) TEM of a remnant of a stacking fault in phosphorus-diffused area of a Group 6 wafer (same as diffraction condition).

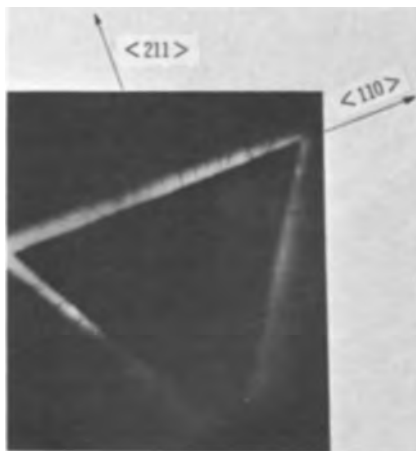


Fig. 11. TEM of the bottom of an etch groove of a Group 6 wafer. Note that dislocations tend to be in  $\langle 211 \rangle$  directions. Only the bottom of the groove can be seen because other areas are too thick for electron transmission.

carbon deposition for a replica. This contrast was interpreted as shown in Fig. 13(a) which allowed a determination of the depth of the etch groove. As can be seen from the schematic in Fig. 13(b), the outer slope of the etch groove deviates only slightly from the (111) stacking fault plane, while the inner, heavily faceted slope seems not to correspond to any low-index crystal plane. Sharp lines at the bottom of the grooves are clearly visible, revealing the V-shaped form of the groove.

Since the main junction of the guarded junction is  $1 \mu\text{m}$  or less deep, it can be seen from Fig. 13(b) that the junction will have a small radius of curvature at the bottom of the groove and will consequently have a lower breakdown voltage. It is also apparent from Fig. 12(a) that the curvature of the diffused junction at the intersection of the grooves will be greater than along the grooves themselves. Thus the light from reverse breakdown would appear first and be more intense at these points as was observed in Fig. 3. Queisser and Goetzberger (19) observed light only from the apices of stacking faults. Since in their samples they did not observe light from all apices they conjectured that the breakdown might be due to

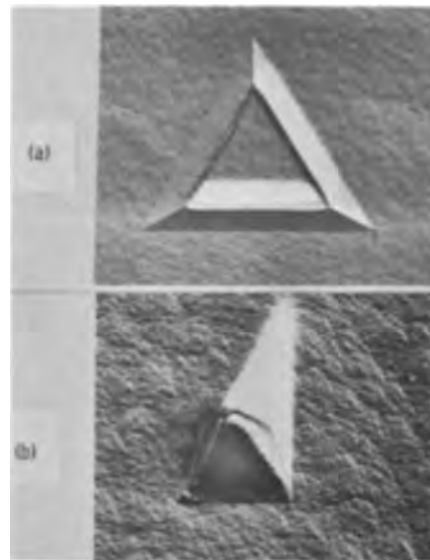


Fig. 12. Electron micrograph of a direct carbon replica of a Group 6 wafer showing (a, top) a stacking fault etch groove, and (b, bottom) a dislocation etch pit.

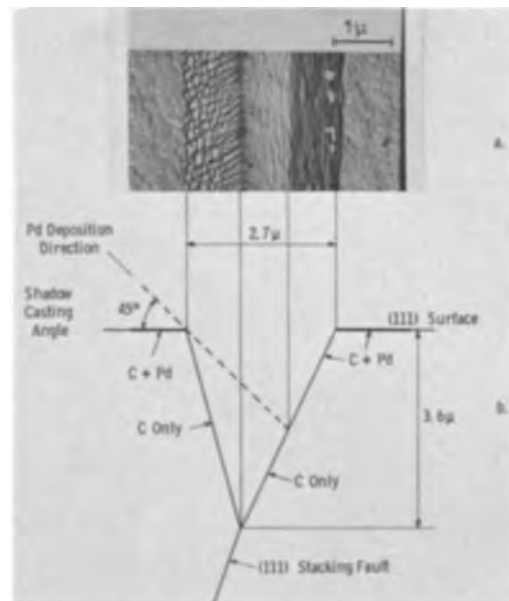


Fig. 13. Profile of a stacking fault etch groove resulting from the Sirtl etch of an epitaxial silicon layer. (a, top) Electron micrograph of direct carbon replica of etch groove along stacking fault, (b, bottom) schematic cross-section of epitaxial layer showing contrast features in etch groove due to shadow casting.

precipitates such as heavy metals or  $\text{SiO}_2$  at the stair-rod dislocation bundles that exist there. Since the stacking faults were visible in the micrographs of their diodes, the wafers were undoubtedly subject to some etching during the processing and thus breakdown at the apices might occur for the same reasons (i.e., curvature of the junctions) postulated above. On the other hand, in our junctions dislocations were present in the grooves as well as at the apices, and thus precipitation at the dislocations or the dislocations themselves might also be responsible for the preferential breakdown.

The uniformity of the light from the grooves favors the curved junction hypothesis. Further support for this hypothesis comes from the fact that no light emission corresponding to stacking faults was evident in those wafers which were etched prior to diffusion. However, this argument may be partially negated by the difference in the configuration of dislocations gen-

erated in the two types of wafers during the diffusion process (compare Fig. 10 and 11).

We also feel that the curved junction hypothesis is the explanation for the intense light observed at the dislocation pits such as seen in Fig. 3. The curvature of the junction at the bottom of such a pit should be large as is apparent from the replica of a dislocation pit shown in Fig. 12(b).

We do not intend to argue that breakdown cannot occur at dislocations. In fact, it appears likely that the breakdown at the edge of the guarded junctions occurs as a direct or indirect result of the dislocations generated ahead of the phosphorus-diffusion front during the diffusion of the deeper guard junction or at the edge of the oxide window (18). The fact that dislocations occur beyond the extent of the phosphorus diffusion under the oxide can be determined from Fig. 6. In Fig. 3(c) it will be noted that the microplasma which might be associated with these dislocations is less intense and occurs at a higher reverse voltage than the light associated with the dislocation etch pits in the central part of the junction.

The total number of dislocations generated by the two-step phosphorus diffusion shown in Fig. 7 agrees quite well with the model proposed by Prussin (1). Prussin derives a formula for the total number of dislocations  $N$  per unit length in a diffused layer which is given by

$$N = \beta/\alpha [C_s - C(b)] \quad [1]$$

where  $\beta$  is the linear lattice contraction coefficient,  $\alpha$  is the component in  $z$  direction (any arbitrary direction in the plane of the diffusion),  $C$  is the surface concentration of the solute, and  $C(b)$  is the concentration at the point  $b$ , which is a point in the direction of the diffusion at which the strain from the point to the surface is relieved by the generation of dislocations. If as in a TEM examination of a relatively deeply diffused layer we look at a region of thickness  $t$  which is less than  $b$ , then [1] becomes

$$N = \beta/\alpha [C_s - C(t)] \quad [2]$$

The thickness of the specimen examined by TEM lies between 0.5 and 1.0  $\mu$ . We assume that the maximum value of  $t$  in [1] which would influence the generation of dislocations in this layer would be about 1.5  $\mu$ . The diffusion profile calculated from the sheet resistivity junction depth and background resistivity using Irving's (20) curves and assuming a Gaussian distribution is

$$C = 2 \times 10^{20} \exp \left[ \frac{-x^2}{13.8 \mu^2} \right]$$

from which  $C_s - C(1.5\mu) = 3 \times 10^{19}$ . The linear contraction is given by

$$\beta = \left[ 1 - \frac{r_{\text{sol}}}{r_{\text{Si}}} \right] N^{-1} \quad [3]$$

where  $r_{\text{sol}}$  is the radius of the solute,  $r_{\text{Si}}$  is the radius of the silicon, and  $N$  is the atom concentration of silicon ( $5 \times 10^{22}$  atom/cm<sup>3</sup>). Lawrence (7) calculates  $\beta$  using a volumetric contraction or  $\beta = [1 - (r_{\text{sol}}/r_{\text{Si}})^3] N^{-1}$  which appears inconsistent with the model of Prussin. Using Queisser's (2) proposed value of 1.07Å for the radius of the ionized phosphorus donor and 1.17Å for the radius of silicon and [3],  $\beta$  equals  $1.7 \times 10^{-24}$  cm<sup>3</sup>/atom.

Joshi and Wilhelm (5) determined that the dislocations forming regular hexagonal arrays in phosphorus-diffused wafers were almost pure edge type. If we assume the dislocations in Fig. 7 are almost pure edge type and measure the number of dislocations per centimeter ( $N$ ) in a plane perpendicular to the dislocations, then  $\alpha$  is equal to the magnitude of the Burgers vector, or approximately  $4 \times 10^{-8}$  cm.

Substituting the above values of  $\alpha$ ,  $\beta$ , and  $C_s - C(1.5\mu)$  into [2] gives  $N \sim 1 \times 10^3$  dislocations/cm.

In Fig. 7(b) there are 7 lines crossing the line perpendicular to the dislocations which is 10  $\mu$  in length yielding a value of  $7 \times 10^3$  dislocations/cm for  $N$ . The agreement between the measured and calculated values of  $N$  is relatively good considering the approximations involved. Joshi and Wilhelm (5) also found reasonably good correlation between the density of dislocations near the surface and that calculated from Prussin's model.

The fact that there is some sort of transformation of stacking faults in epitaxial layers, both as-grown and Sirtl-etched before diffusion, is evident from the LM and TEM results. The fact that etch grooves were not developed by the Sirtl etch in the as-grown wafers and became flat-bottomed in the previously Sirtl-etched wafers indicates a change in the lattice energy associated with the stacking faults. Further evidence of some rearrangement of the lattice structure is evident from the change in contrast patterns of the stacking fault after phosphorus diffusion as shown in Fig. 10. Further evidence of a relationship between stacking faults and dislocations are the star-like patterns observed in Fig. 8 and the lines perpendicular to the fault sides in Fig. 9.

It has been shown that this transformation takes place only in the phosphorus-diffused regions. Thus it is probable that the transformation is a result of interaction of the stacking faults with the dislocations generated by the phosphorus diffusion. There is some evidence for such a hypothesis in that a dislocation line is parallel to the stacking fault remnant in Fig. 10(b).

We propose the interaction of dislocations and stacking faults and dislocations generated by the phosphorus diffusion as a possibility for the transformation and not as a model. The exact mechanism of the transformation cannot be deduced from this work.

### Summary and Conclusions

1. Microplasmas were observed most frequently near the periphery of the phosphorus-diffused guarded junctions. These microplasmas may have resulted from dislocations generated by the phosphorus diffusion of the guard junction intersecting the shallow-diffused junction.

2. No light from preferential breakdown characteristic of the pattern of stacking faults was observed in wafers which were not etched prior to diffusion. Figure 2(b) is typical of devices on such unetched wafers and shows no triangular patterns.

3. In wafers Sirtl-etched before diffusion, light was observed at the bottom of stacking fault grooves and dislocation etch pits. The preferential breakdown was attributed to the curvature of the shallow junction resulting from the junction following the surface contour.

4. The density of dislocations generated as a result of the mismatch of the atomic radii of phosphorus and silicon and the gradient present from the diffusion process was determined and compared with the model of Prussin. Experimental and calculated values compared favorably.

5. A change in the nature of stacking faults resulting from phosphorus diffusion was observed. From etching results it was concluded that the lattice energy as associated with the fault was decreased or redistributed.

### Acknowledgments

The authors wish to thank H. F. John for suggesting and encouraging this work. We also acknowledge the assistance of S. Hillbeck in the diode fabrication and analysis, and of W. Hughes in the preparation of TEM and LM specimens. Figure 10(a) was provided by Dr. G. R. Booker, University of Oxford. This work was supported in part by NASA, George C. Marshall Space Flight Center, under Contract NAS8-11432.

Manuscript received Aug. 11, 1967; revised manuscript received Oct. 26, 1967. This paper was pre-



sented at the Buffalo Meeting, Oct. 10-14, 1965, as an Electronics Division Recent News Paper.

Any discussion of this paper will appear in a Discussion Section to be published in the December 1968 JOURNAL.

## REFERENCES

1. S. Prussin, *J. Appl. Phys.*, **32**, 1876 (1961).
2. H. J. Queisser, *ibid.*, **32**, 1776 (1961).
3. G. H. Schwuttke and H. J. Queisser, *ibid.*, **33**, 1540 (1962).
4. J. Washburn, G. Thomas, and H. J. Queisser, *ibid.*, **35**, 1909 (1964).
5. M. L. Joshi and F. Wilhelm, *This Journal*, **112**, 185 (1965).
6. W. Czaja, *J. Appl. Phys.*, **37**, 3441 (1966).
7. J. E. Lawrence, *This Journal*, **113**, 819 (1966).
8. E. Levine, J. Washburn, and G. Thomas, *J. Appl. Phys.*, **38**, 81 (1967); **38**, 87 (1967).
9. A. Goetzberger, B. McDonald, R. Haitz, and R. M. Scarlett, *ibid.*, **34**, 1591 (1963).
10. Von K. H. Zschauer, *Z. Naturforsch.*, **19A**, 653 (1964).
11. S. R. Hofstein and G. Warfield, *IEEE Trans. on Electron Devices*, **ED-12**, 66 (1965).
12. G. Gibbons and J. Kocsis, *ibid.*, 193 (1965).
13. S. M. Sze and G. Gibbons, *Solid State Electronics*, **9**, 831 (1966).
14. E. Sirtl and A. Adler, *Z. Metallkunde*, **52**, 529 (1961).
15. G. R. Booker and R. Stickler, *Brit. J. Appl. Phys.*, **13**, 446 (1962).
16. R. Stickler, *J. Sci. Instruments*, **41**, 523 (1964).
17. J. M. Fairfield and G. H. Schwuttke, *J. Appl. Phys.*, **37**, 1536 (1966).
18. R. J. Jaccodine and W. A. Schlegel, *ibid.*, **37**, 2429 (1966).
19. H. J. Queisser and A. Goetzberger, *Phil. Mag.*, **8**, 1063 (1963).
20. J. C. Irving, *Bell System Tech. J.*, **41**, 387 (1962).

## Strain Effects Around Planar Diffused Structures

J. M. Fairfield\* and G. H. Schwuttke

Components Division, International Business Machines Corporation, East Fishkill Laboratories, Hopewell Junction, New York

## ABSTRACT

Dislocations have been found to extend for considerable distances outside of planar diffused structures in silicon and to affect the electrical properties of the diffused junctions. The mechanism of dislocation propagation outside of phosphorus-diffused structures has been studied by x-ray diffraction microscopy and other techniques. It is shown that these dislocations are propagated through an anomalously large compressive stress that results from large strains in some high-concentration phosphorus-diffused structures. These strains cannot be attributed to the residual effects of substitutional phosphorus atomic mismatch with the silicon lattice. The anomalous stress and dislocations usually appear after an oxidizing diffusion or drive-in cycle at temperatures less than 1150°C. Also, the dislocations are much less likely to occur in (100) or (110) oriented surfaces as opposed to (111) surfaces.

In the semiconductor industry, impurity diffusion is a very common fabrication process for transistors and diodes. Typical diffusions result in localized lattice strain, which often is relieved through the formation of dislocations and other lattice disorder. Principally, the strain is believed to result from the mismatch between the ionic radius of an impurity atom that is occupying a substitutional site and the covalent radius of the silicon (1, 2). The dislocations usually appear as dislocation networks confined within the diffused structure and often are accompanied by precipitation effects, which may also relieve the crystallographic strain. This type of crystal disorder has been widely studied, particularly for phosphorus and boron as the diffusants, by employing a variety of techniques (3-11). In addition, other investigators have reported that dislocations may propagate outside the diffused areas: both below the diffusion front and, for planar structures, laterally under the oxide diffusion mask (12-16). This latter phenomenon is important in semiconductor device fabrication since these dislocations would extend through the electrical junctions of the devices and have potential deleterious effects on the electrical characteristics of the devices.

There has been some confusion about these "outside" dislocations (*i.e.*, outside the diffusion structure) with respect to (i) their nature, (ii) the mechanism by which they form and propagate, and (iii) the conditions under which they occur. However, recently

these questions have been at least partially clarified and resolved. In an earlier report (16) we presented evidence that the dislocations outside the diffused structure are distinct from and often in addition to the diffusion-induced dislocation networks within the structure and that they nucleate at the boundaries of the planar structures and propagate outward. Also, Schwuttke and Wilhelm (17) have recently confirmed by electron microscopy that the dislocations of the networks within the diffused area bend up to the surface at the planar boundaries and do not extend significantly into the undiffused regions.

The outward propagation of the outside dislocations is by means of macroscopic stress transmitted from the diffused structure. Lawrence (18) has suggested that this stress results from relatively small residual strains not fully relieved by crystal disorder within the diffused area. He further states that, in otherwise unstrained material, the residual strain necessary to nucleate outside dislocations is only realized when the total concentration of diffusant is greater than about  $5 \times 10^{16} \text{ cm}^{-2}$  for both boron and phosphorus. However, Duffy *et al.* (19) have observed these outside dislocations for total concentrations less than  $3 \times 10^{16} \text{ cm}^{-2}$  of phosphorus. Furthermore, recent measurements of lattice contraction by Cohen (20) tend to indicate that the maximum stress in diffused areas, similar to those investigated by both Lawrence and Duffy, is in itself not excessively greater than the yield stress of silicon at elevated temperatures, which is about  $2 \times 10^9 \text{ dynes/cm}^2$ , as estimated from an extrapolation

Key words: semiconductor, silicon, diffusion, dislocations, stress, strain.

\* Electrochemical Society Active Member.



of data of Pearson *et al.* (21) or from the investigations of Patel and Chaudhuri (22).

It would seem improbable that smaller residual strains would generate sufficient stress to nucleate and propagate dislocations to significant distances outside the diffused areas. Joshi *et al.* (23) have reported residual strains in phosphorus-diffused areas of  $\sim 4 \times 10^{-4}$  which would result in stresses that are marginally sufficient for dislocation formation; however, these authors have apparently used total concentrations well above  $5 \times 10^{16} \text{ cm}^{-2}$ . Thus, the conditions and the mechanism by which the dislocations form outside the diffused structure are still unclear, and further study is required.

These outside dislocations, around the periphery of diffused emitters (emitter edge dislocations) have been directly correlated with a reduction in transistor gain ( $\beta$  or  $h_{fe}$ ) (19, 24). In addition, since they extend through the base of a transistor, they may encourage emitter-to-collector shorts, i.e., pipes, through a possible localized dislocation-enhanced diffusion mechanism (25). Also, they may influence the characteristics of the collector junction. Indeed, Loro (26) has reported a collector junction degradation that can be attributed to dislocations extending through the collector junction caused by the emitter diffusion. Finally, for the case of modern integrated circuitry, this type of dislocation may extend from one device or isolation diffusion into another and create potential coupling problems. Therefore, we have further investigated these outside dislocations, principally for boron and phosphorus as diffusants, with emphasis on understanding both the mechanism and the control of their formation. We have studied the nucleation and propagation of these dislocations and their relationship to diffusion conditions, crystal disorder inside the diffused structure, and the macroscopic strains as independently determined. This report describes our investigation.

### Experimental Procedure

Silicon slices were cut from dislocation-free Czochralski or Lopex single crystals, lapped, and chemically polished to remove surface damage and strain. Wafer orientations were mainly (111), but (110) and (100) orientations were used in a few specific experiments; thicknesses were between 0.5 and 1.0 mm.

Both blanket diffusions over entire wafers and planar diffusions using standard oxide masking techniques were performed; masking oxides were grown in steam at  $1000^\circ\text{C}$ . Most diffusions were accomplished by a two-step process consisting of a deposition and a drive-in cycle similar to that reported previously (19, 27). The deposition cycle was  $970^\circ\text{C}$  for phosphorus and  $1100^\circ\text{C}$  for boron; impurity sources were phosphorus oxychloride, phosphorus pentoxide, or diborane; and the ambient was nitrogen with a small amount ( $\sim 1\%$ ) of oxygen. The drive-in cycle was usually  $970^\circ\text{C}$  for  $1\frac{1}{4}$  hr in an oxidizing ambient; however, some experiments were conducted using temperatures of up to  $1200^\circ\text{C}$  with decreasing times. Also, inert ambients were used for a few special experiments. Finally, some diffusions were made using the evacuated capsule technique (28) with a powdered silicon alloy as the source and, generally, with similar times and temperatures as above, though a few such diffusions were made for very long times.

Junction depths were measured by beveling and copper staining, and sheet resistances were measured by a four-point probe. In all cases, the surface concentrations were at, or very near, saturation. An example of a phosphorus profile is shown in Fig. 1. The total concentrations were determined by activation analysis [see ref (19)]; and the electrically active concentrations were determined by incremental sheet resistance measurements (29) and an extrapolation of Irwin's curve to these high concentrations. The electrically active curve is an approximation, since the ac-

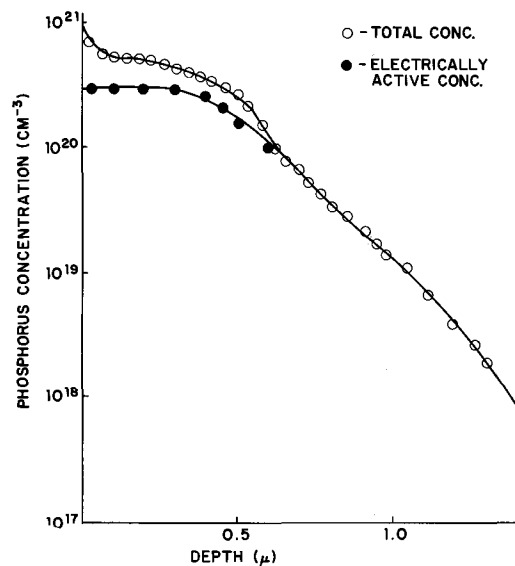


Fig. 1. Diffused phosphorus concentration profiles after a drive-in cycle of  $1\frac{1}{4}$  hr at  $970^\circ\text{C}$  in an oxidizing ambient. Total concentrations were determined by activation analysis, and electrically active concentrations were determined by incremental sheet resistance measurements.

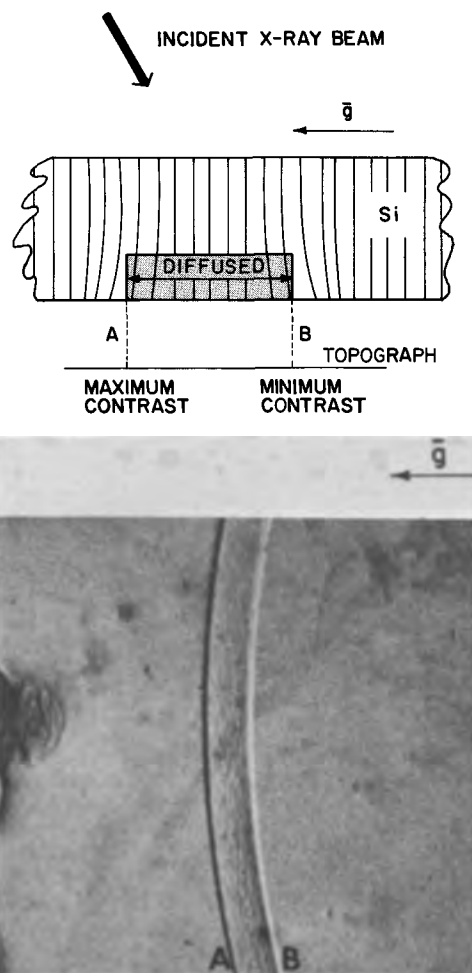


Fig. 2. Transmission diffraction contrast around planar diffused structures: a (top), schematic diagram of diffused structure exerting a compressive strain on surrounding crystal; b (bottom), x-ray topograph of similar structure.

curacy of this extrapolation is uncertain; however, it would be safe to say that a significant amount of phosphorus is not electrically active and thus exists in a state other than substitutional, in agreement with pre-

vious investigations (29, 30). It is not possible to discuss strain contribution of a single representative atom because the state of a significant portion of them is unknown.

The crystallographic damage in and around the diffused areas was investigated by x-ray transmission diffraction microscopy, using scanning oscillator technique (SOT) (9) to record topographs of entire wafers, and by transmission electron microscopy (4, 8). SOT topographs were used extensively to study dislocation and precipitation structure in a manner described previously (9, 31) and to analyze strain effects as described in the next paragraph. Electron microscopy was used to examine the crystal structure of the surface layers of some representative samples. Specimens for electron microscopy were chemically thinned from the reverse side to about 2000Å.

Strain effects were determined by the sign of anomalous x-ray diffraction contrast around the boundary discontinuity of planar structures and by the degree of bowing induced in a wafer by a blanket-diffused layer on one side. For the first technique, Howard and Schwuttke (32, 33) have shown that the apparent sign of anomalous transmitted x-ray diffraction contrast (i.e., either dark or light contrast for an anomalously strong or weak diffracted x-ray beam) can be used to determine the direction of lattice plane curvature, which is due to strains. Hence, the nature of anomalous x-ray contrast on SOT topographs can be used to determine the sense of lattice strain. An example is illustrated in Fig. 2a and b in which a diffused structure exerts a compressive strain on the surrounding lattice, bending the lattice planes in the indicated direction. Following Howard and Schwuttke, the diffracted contrast will be high when the diffraction vector  $\bar{g}$  (or a significant component of  $\bar{g}$ ) has the same direction as the radius of curvature of the strained lattice planes, as at point "A," and will result in a black line on the topograph, Fig. 2b. When the direction of  $\bar{g}$  is opposite to the radius of lattice plane curvature, as at point "B," the contrast is low and results in a white line. Therefore, the white-black contrast across the diffused boundaries in the direction of  $\bar{g}$  (Fig. 2b) is indicative of compressive strain around the diffused structure. Similarly a black-white contrast, in the same direction, indicates tensile strain. For the present study, this technique was used to determine the sense of the strain only although, in principle, it could be used for quantitative strain measurements as well.

In addition, the magnitude of the stress in a diffused layer was studied by measuring the degree to which a blanket-diffused layer macroscopically strains a wafer. The bowing of a wafer owing to a very thin diffused layer was determined by measuring wafer curvature before and after the layer was removed, employing a light section microscope and a technique developed by Glang *et al.* (34). The data were interpreted by regarding this diffused layer as a thin film of some other material deposited on the silicon wafer as the substrate and using elastic plate theory to analyze the stress-strain relationships of this system in a manner first used by Stoney (35) for thin deposited metal films, and subsequently improved and used by others for a variety of materials (36). Accordingly, the deflection  $\delta$  of a circular wafer under strain from a thin film is given by

$$\delta = 3 \left( \frac{1 - \nu}{E} \right) \frac{t_f}{t_s^2} \rho^2 \sigma_f \quad [1]$$

where  $E$  and  $\nu$  are Young's modulus and Poisson's ratio of silicon;  $t_f$  and  $t_s$  are the thicknesses of the film and substrate;  $\rho$  is the distance from the center; and  $\sigma_f$  is the stress in the film. Assuming  $t_f \ll t_s$  and following Stoney's analysis, one can relate the maxi-

mum stress in the wafer to the film stress by

$$\sigma_s(\max) = -4 \sigma_f \left( \frac{t_f}{t_s} \right) \quad [2]$$

Equations [1] and [2] can be used to relate deflection to stress in the diffused layer and the wafer. For our application, very thin layers (0.1-0.3 $\mu$ ) were removed by anodic sectioning in order to determine the distribution of stress in the diffused layer. The effective ratio  $t_f/t_s$  was less than  $10^{-3}$ ; and the substrate can be considered as unchanged by the removal of the thin layers. Deflection measurements were taken every 25 mils along a  $\langle 110 \rangle$  and a  $\langle 11\bar{2} \rangle$  diameter of (111) wafers to about 50 mils from an edge. The experimental uncertainty of each deflection measurement is  $\pm 0.5\mu$  (34); and the final uncertainties can be judged accordingly.

## Results

Generally, phosphorus diffusions, in which maximum or near maximum surface concentrations and oxidizing ambients were used, resulted in dislocations outside the planar diffused structure (i.e., outside dislocations) even when the total electrically active phosphorus concentration was  $2 \times 10^{16} \text{ cm}^{-2}$  or a little lower. Their formation was not significantly affected by the presence or absence of the original mask during drive-in. These dislocations have been described in ref. (16); and a detailed analysis of their physical structure will be published elsewhere. They are illustrated by the contrast pattern in Fig. 3a around the boundaries of the planar structures, which are the triangles and the circular area, and also by the relatively straight lines in the electron micrographs, Fig. 3b and c. The abnormal contrast within the planar areas in Fig. 3a and the network pattern at the extreme right of Fig. 3c are due to the normal, interior diffusion-induced dislocations. The occurrence of the outside dislocations can be directly related to the conditions of the process steps, as will be described in more detail later in this section.

The dislocations themselves appear as dislocation loops in the primary slip planes  $\{111\}$ . They extend laterally out into the undiffused regions for distances of  $\sim 300\mu$  and perpendicularly down into the silicon for distances up to  $20\mu$  from the surface as shown in Fig. 4, in which the indicated amounts have been removed by controlling etching. (Note that the diffusion-induced dislocations within the diffused regions are confined to within  $0.5\mu$  of the surface or about 1/3 of the junction depth, in agreement with other investigators.) Therefore, the outside dislocations would extend well through the active regions of a transistor with this type of phosphorus diffusion as the emitter, and they should logically cause potential problems for transistor electrical properties through either a degradation of gain through carrier recombination in the base, poor collector junction quality, or pipes owing to an enhanced diffusion in the dislocation areas. The mode of dislocation propagation was primarily through slip in the plane of diffusion. It is interesting to note that the presence of metallic impurities tended to restrict the outward propagation of the dislocations. Figure 5 shows a topograph and an electron micrograph of outside dislocation loops where an excessive amount of gold was present. The loops appear to be pinned at specific points, presumably by small metallic precipitates that are smaller than the resolution of this micrograph, i.e.,  $< 50\text{Å}$ . A similar phenomenon has been reported by Batavin (37), who found evidence that  $\text{SiO}_2$  particles inhibited the propagation of dislocations outside of boron diffused areas.

Empirically, the presence of the outside dislocations was accompanied by an anomalous macroscopic strain effect associated with the planar diffused structure: in Fig. 3a, the white-black strain pattern across the windows in the direction of  $\bar{g}$  is indicative of a com-

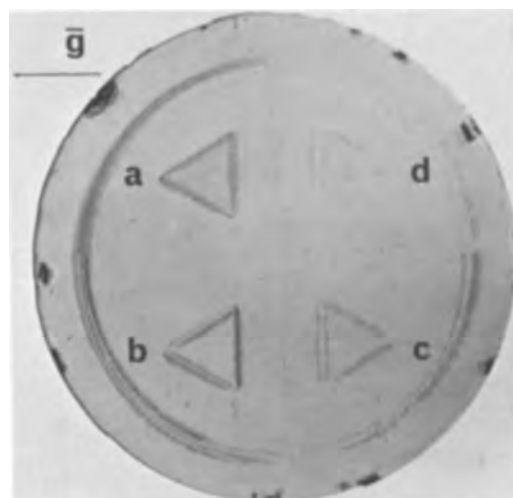
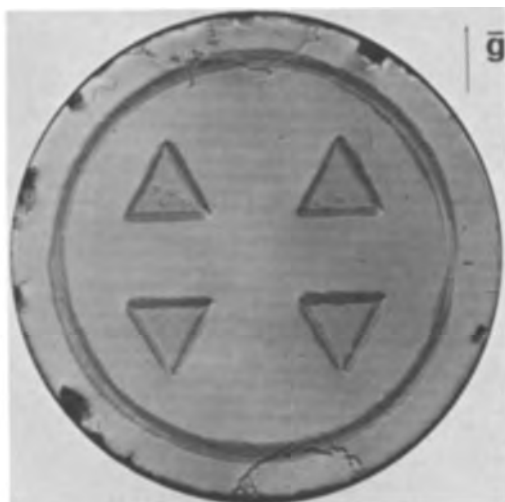


Fig. 4. SOT x-ray topograph of diffused structures similar to Fig. 3 with the following thicknesses of surface removed: a, nothing removed; b,  $0.5\mu$ ; c,  $10.0\mu$ ; d,  $19.0\mu$ .

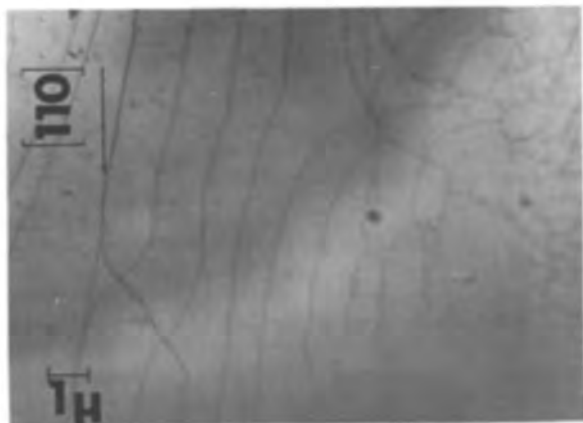


Fig. 3. High-concentration phosphorus structures; impurity profile and diffusion procedure are similar to that of the example in Fig. 1; triangle side =  $0.5\text{ cm}$ : a (top), SOT x-ray topograph (220) reflection; b (center), electron micrograph of undiffused area about  $60\mu$  from diffusion boundary; c (bottom), electron micrograph of a small section at the planar boundary.

pressive strain surrounding the diffused structure. However, as seen in Fig. 4, areas a and b, the stress switches to tensile when  $0.5\mu$  is removed from the surface. The compressive nature is unexpected since a substitutional phosphorus atom in the silicon lattice has a smaller ionic radius than the silicon covalent radius and should stretch the neighboring covalent bonds, resulting in a tensile strain effect around the periphery.

The actual compressive effect can be seen more clearly in Fig. 6b, which is the topograph of a two-cycle planar diffusion with only a very small amount of oxygen in the ambient of the drive-in cycle

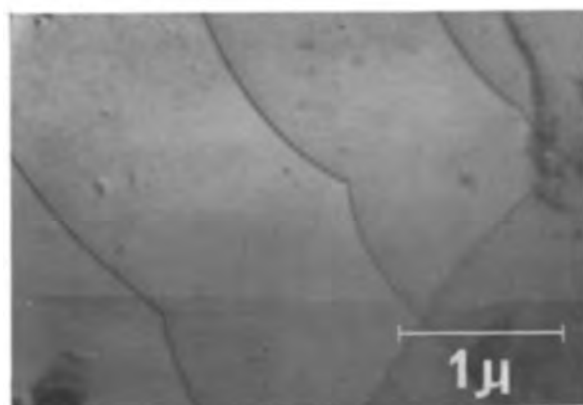
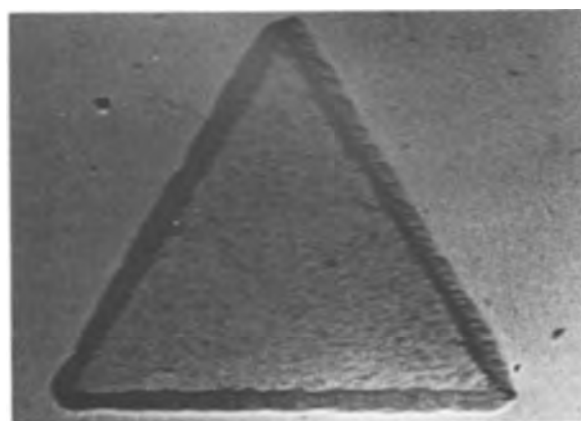


Fig. 5. Phosphorus diffused structures with large amounts of gold added: a (top), x-ray topograph; b (bottom), electron micrograph outside of diffused area.

( $970^\circ\text{C}$ ). Here is a case of stress that is anomalous in sense but not of sufficient degree to cause outside dislocations. Figure 6a is an x-ray topograph of the same structure with the oxide diffusion mask still on the wafer surface, indicating that the oxide mask opposes and, in this case, reverses the resultant strain. This is logical since the strain in a thermally grown oxide mask is compressive (38) and would tend to bend the lattice planes toward the center of a window (opposite to the case illustrated in Fig. 6b). In practice, when the anomalous strain, i.e., compressive, approaches a value sufficient to cause outside dislocations, it dominates over the influence from the mask.

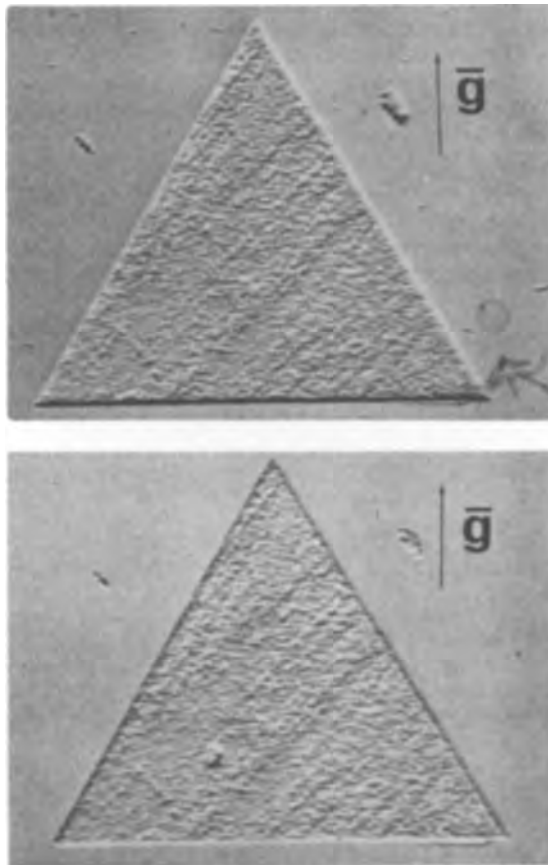


Fig. 6. SOT x-ray topograph of high-concentration phosphorus-diffused structures illustrating anomalous strain effects: a (top), oxide mask on wafer; b (bottom), oxide mask removed.

However, the formation of dislocations reduces its magnitude and may return the strain to a case dominated by the oxide mask; thus, the apparent strain, or stress, may switch sign according to the formation of dislocations or the removal of the mask, giving the effect of "stress jumping" (33).

Conversely, dislocations around boron diffused structures appear only for deep diffusions performed at the higher temperatures ( $1200^{\circ}\text{C}$ ) from maximum surface concentrations regardless of the diffusion technique used. Figure 7a is the SOT topograph of a section of planar boron diffused wafer whose profile is shown in Fig. 7b. The degree of dislocation around the outside is variable. Lesser junction depths, e.g.,  $< 8\mu$  for a similar profile, yield much fewer or no dislocations. The dislocations extend for about the same distances as phosphorus but appear in a variety of forms.

Irrespective of dislocation formation, the strain around boron diffused structures was always tensile, as would be expected, since boron also has a small ionic radius relative to silicon. These dislocations around boron diffused structures were not studied as extensively, but they appear to be caused by tensile stress which may well result from residual strain effects of the substitutional boron atoms when total concentrations greater than  $10^{17}\text{ cm}^{-2}$  are involved.

Finally, the specific relationship of the phosphorus process steps to the anomalous strain will be described in the final paragraphs of this section. First in (111) oriented wafers, after an open-tube deposition cycle only, the macroscopic strain is anomalous in sign, i.e., compressive, but not of sufficient magnitude to cause dislocations, a case similar to that shown in Fig. 6. After an oxidizing drive-in at lower temperatures, at about  $1000^{\circ}\text{C}$ , both dislocation and anomalous strain effects almost always appeared. The degree of stress in these phosphorus diffused layers was determined by measurements of bowing of blanket-diffused wafers,

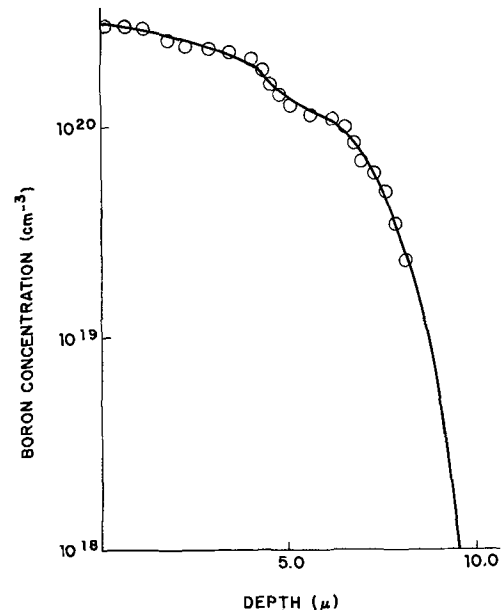
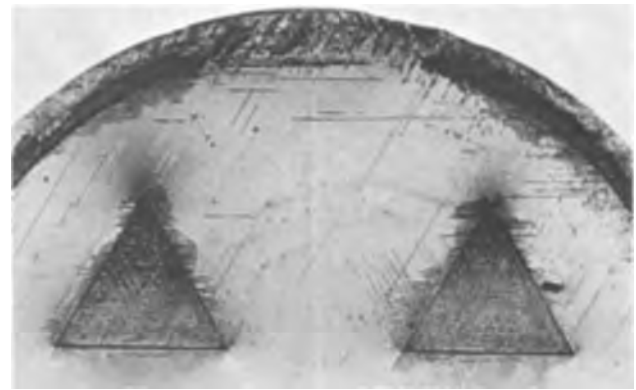


Fig. 7. a (top), SOT x-ray topograph of high concentration, deep boron diffused planar structure; b (bottom), electrically active impurity profile, total concentration is  $\sim 1.3 \times 10^{17}\text{ cm}^{-2}$ .

whose diffusion utilized this two-cycle process with an oxidizing drive-in at  $970^{\circ}\text{C}$ . The stress was compressive, bowing the wafer down away from the diffused side, in agreement with that indicated by the sign of the x-ray contrast, and the values ranged from  $3\text{--}8 \times 10^9$  dynes/cm $^2$ . This high stress was confined to within about  $0.5\mu$  of the surface, confirming the apparent stress switching in Fig. 4 by the removal of  $0.5\mu$  of surface. Figure 8a shows the actual deflection of one wafer; each deflection value represents the average of two values taken at opposite points, i.e.,  $+\rho$  and  $-\rho$ , in the manner of Glang *et al.* (34). Also shown are "deflection" values taken on an undiffused wafer to illustrate qualitatively the sensitivity for this application. The crystallographic direction, along which the deflection was measured, had no measurable influence. Figure 8b shows stress values on a few wafers as a function of distance from the surface. There is considerable scatter, sometimes even on the same wafer, but the values are generally equal to or greater than  $3 \times 10^9$  dynes/cm $^2$ , above the yield stress of silicon. By way of comparison, stress values in boron diffused layers were around  $1.5 \times 10^9$  dynes/cm $^2$  and were tensile, as expected.

If inhomogeneous precipitation occurred within the phosphorus planar structure, the anomalous strain was less, and the peripheral dislocation loops were much less likely to occur. In particular, if many points of large precipitates appeared within the diffusion, shown

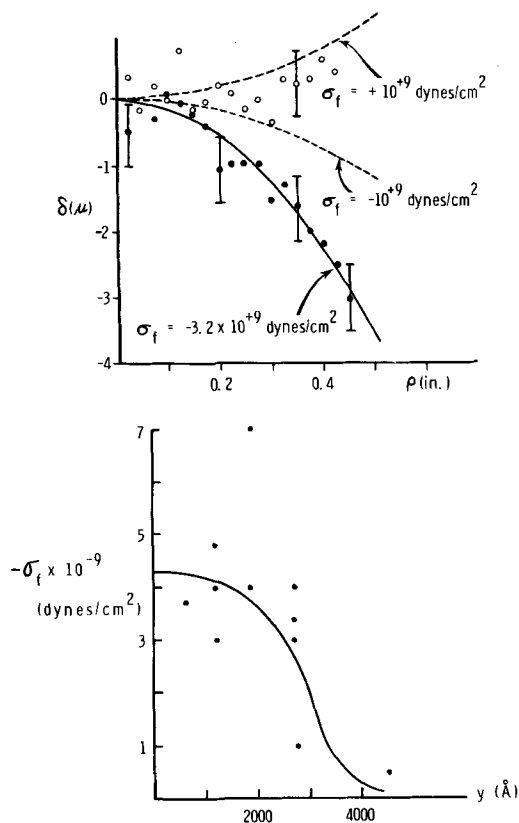


Fig. 8. Data from wafer bowing experiments: a (top), closed circles are deflection values of blanket phosphorus diffused wafer and open circles are similar measurements of an undiffused wafer; b (bottom), stress values as a function of depth in phosphorus diffused wafers.

in Fig. 9 by the points of abnormally high contrast in two of the planar triangles, the peripheral dislocations did not occur; and the macroscopic stress was tensile, in contrast to the normal case without large precipitates. These precipitates normally did not occur if the diffusion system was clean and reasonably careful procedures were employed. They appeared to be nucleated at or near the surface through contaminants or cool areas on the wafer during the deposition cycle. Sheet resistance and junction depth measurements showed that the electrically active phosphorus concentration was not significantly affected by the formation of the large precipitates. Figure 9b is a transmission electron micrograph of a section of one such large precipitate, which is amorphous in structure except for a small portion just outside the main precipitate which appears as platelets oriented parallel to  $\{111\}$  planes. Conversely, electron micrographs of interior areas of the more common planar structures, those that caused compressive strain and outside dislocations, revealed very few visible precipitates of any size. Since all of these high-concentration diffusions contain significant amounts of phosphorus in excess of that which is electrically active, as indicated by Fig. 1 and by the investigations of others (29,30), excess phosphorus in the more common diffused structures must exist either interstitially as single atoms or in small clusters ( $<20\text{\AA}$ ).

In addition, certain modifications in the diffusion procedure could reduce or eliminate the peripheral outside dislocations. These conditions are, in themselves, significant; they are specified here and discussed in the next section. First, the dislocations usually did not occur on wafers oriented in the (100) or (110) plane though the strain was still compressive. Second, if the drive-in cycle utilized a nonoxidizing ambient, strain decreased significantly, sometimes switching to tensile; and the outside dislocations again did not form. Total concentrations were comparable

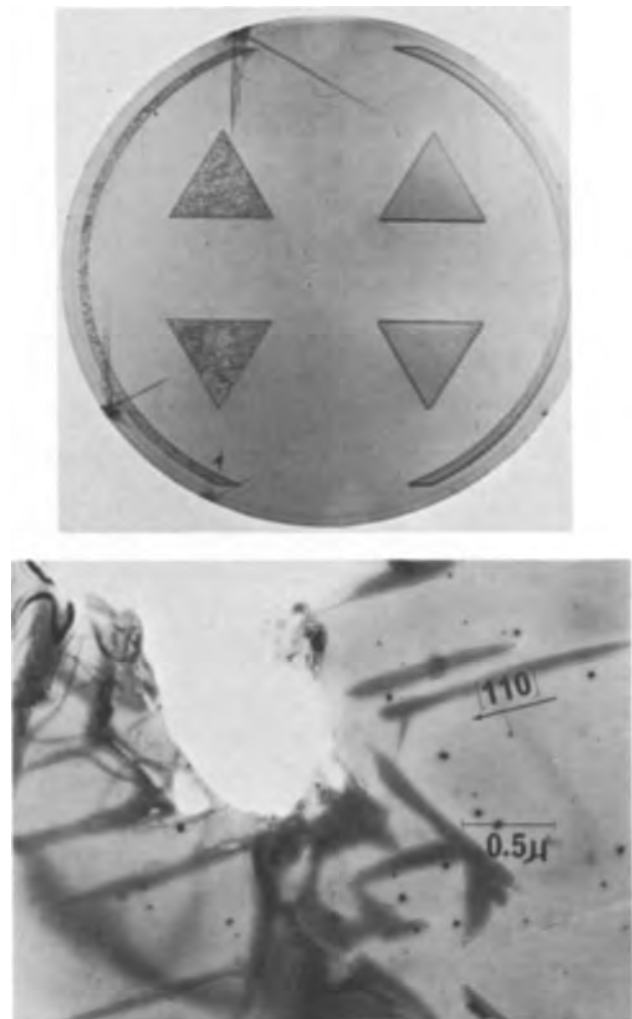


Fig. 9. Phosphorus planar diffused structures, two of which have large precipitates: a (top), x-ray topograph; b (bottom), electron micrograph of a section of one large precipitate, precipitate is indicated by white area since it dissolved during thinning operation.

to the case of an oxidizing ambient illustrated in Fig. 1 or for the wafer in Fig. 3. Third, if the drive-in cycle was done at higher temperatures ( $1150^{\circ}\text{--}1200^{\circ}\text{C}$ ), regardless of the ambient the dislocations did not form; and the stress was tensile ( $<10^9$  dynes/cm $^2$ ) even for concentrations greater than  $5 \times 10^{16}$  cm $^{-2}$ . Finally the evacuated sealed capsule diffusion process did not produce the outside dislocation loops, except in a few cases where excessively long diffusion times were employed, which yielded junction depths of greater than  $10\mu$ . The strain around all these structures was tensile, similar to the case of boron. However, if a wafer was phosphorus diffused by a capsule technique with high surface concentration and subsequently oxidized at  $1000^{\circ}\text{C}$ , the outside dislocations appeared; and the strain switched to compressive. This did not happen for boron capsule diffused wafers.

### Discussion

First, in order to relate the macroscopic stress measured experimentally in blanket-diffused layers to the stress in undiffused material around planar structures, the stress-strain conditions of the problem, which are illustrated in Fig. 10a, must be considered in some detail. In this way, the stress available for dislocation formation can be estimated and compared with the results.

The surface loading at the sides required to confine the planar structure is represented by  $F'$  in Fig. 10b, and a reactive force  $F$  is exerted on the undiffused material, also at the planar boundaries. The shearing

interaction in the  $x$ - $z$  plane is of lesser degree owing to both the lower value of shearing modulus in silicon and the reduction of coherency across the  $x$ - $z$  plane through the formation of the interior diffusion induced dislocation networks. Thus, the forces at the side boundaries of the planar structure are related to the stress in the film by

$$F' = -F \approx - \int_0^a \sigma_f dy \quad [3]$$

where  $F$  is in units of force per unit length and  $a$  is the effective depth of anomalous stress. In order to find the stresses at a given distance  $r$  from the diffusion boundary, certain limitations of the dimensions can be made in order to simplify the problem. The dimensions of interest are greater than the electrical junction depth and roughly limited by the maximum dislocation propagation. Therefore, the problem can be restricted by

$$\begin{aligned} y_{(\max)} &\approx 20\mu \ll t \\ x_{(\max)} = z_{(\max)} &\approx 200\mu \ll D \\ x_{(\min)} = y_{(\min)} = z_{(\min)} &> 2a \end{aligned} \quad [4]$$

where  $D$  represents the wafer diameter ( $\sim 2$  cm) and  $t$  represents the wafer thickness ( $> 0.5$  mm). Based on these limitations, we can regard the substrate as a semi-infinite body. Now the two-dimensional problem is treated by considering a thin (with respect to  $l$ ) slab at  $z = 0$  and analyzing the stress distribution around the origin, see Fig. 10b. It would be reasonable from inequalities [4] that the shear force can be considered as concentrated at the surface, i.e.,  $a \rightarrow 0$ . With this assumption, the problem is similar to that first solved by Flamant (39), following whom the stress distributions are

$$\begin{aligned} \sigma_x &= - \frac{2F}{\pi} \frac{x^3}{(x^2 + y^2)^2} \\ \sigma_y &= - \frac{2F}{\pi} \frac{xy^2}{(x^2 + y^2)^2} \\ \tau_{xy} &= - \frac{2F}{\pi} \frac{x^2y}{(x^2 + y^2)^2} \end{aligned} \quad [5a]$$

and the maximum shear stress would be given by

$$\tau_{(\max)} = \frac{-F}{\pi} \frac{x}{(x^2 + y^2)} \quad [5b]$$

The applicability of assuming that the force is concentrated at the surface can best be shown by actually considering a distributed stress. This is shown in the Appendix (see Eq. [6]), and it is seen that Eq. [5] can be used to estimate the stresses in the undiffused areas of the silicon when only one edge of the planar structure is near the point of interest, a case that includes the greater portion of the problem. The effects of surface loading at other boundaries can be calculated by superposition of two-dimensional-type solutions. For example, the effect of the planar boundary at the opposite side,  $x = -w$ , is not significant until  $r$  becomes comparable to  $w$ . For  $r > w$ , the stresses fall off more rapidly with distance; and, for  $r \gg w$ , the stresses fall off as  $x^{-2}$  instead of  $x^{-1}$  as would be dictated by Eq. [5]. The effects of surface loading at perpendicular surfaces,  $z = \pm (\frac{1}{2})l$ , are of similar magnitude.

If the reasonable assumption is made that the stresses in the planar structures are similar in magnitude to the stresses in the blanket diffused layers, it is seen that stresses can be above the yield stress of silicon in the neighborhood of the planar boundary and can remain greater than the flow stress (22) for considerable distances into the undiffused areas. It is important to note that precise quantitative comparison is inappropriate in this application, since these dis-

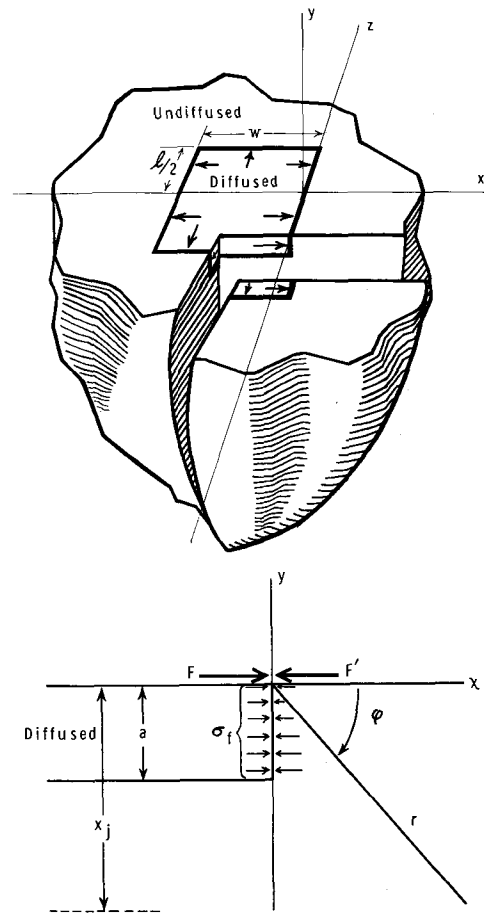


Fig. 10. a (top), Schematic diagram of stress effects from a planar structure; b (bottom), cross section at  $z = 0$ .

locations propagated at elevated temperatures and the stress measurements were made at room temperature. However, it is logical that these anomalous compressive stresses directly cause the deeply penetrating dislocations at the edges of the appropriate phosphorus diffused planar structures. The stresses decrease as the inverse of the distance in the direction of applied force

$$\sigma_x \sim \tau_{(\max)} \sim x^{-1} \quad (x > y = \text{const.})$$

and as the inverse of the distance squared perpendicular to the applied force

$$\sigma_y \sim \tau_{(\max)} \sim y^{-2} \quad (y > x = \text{const.} \neq 0)$$

The distribution of dislocations qualitatively conforms with these relations; dislocations extend considerable distances in both directions but considerably further parallel to the surface, i.e., in the direction of applied force. For smaller diffused structures, the stresses and dislocation distribution fall off more rapidly, as has been confirmed experimentally; but the dislocations still extend well through the base of a transistor with the resulting deleterious effects. The fact that dislocation formation is most favored for (111) oriented wafers as opposed to (100) and (110) is most likely because, for the case of (111) wafers, the applied force is in the plane of the primary slip system.

It is apparent from this investigation that the high stress, which causes dislocations outside of relatively shallow phosphorus emitter type diffusions, cannot result from residual strains from substitutional atomic phosphorus atoms but must result through some other mechanism that is dependent upon procedure. This conclusion might appear to be contradictory to Lawrence's investigation (18); however, it is not: Lawrence studied high temperature ( $1200^\circ\text{C}$ ) diffusions exclusively and, thus, did not consider the dislocations

that are of primary interest in this investigation. It is possible that dislocations outside of deep boron structures are related to residual mismatch strains of substitutional atoms. The measured stress values in boron diffused silicon ( $\sim 1.5 \times 10^9$  dynes/cm<sup>2</sup>) would indicate that sufficient stress might be available.

At this time, the source of the anomalous compressive strain is uncertain; however, it might be speculated that it is related to the phosphorus atoms in excess of the substitutional (see Fig. 1) as is suggested by the requirements of maximum concentrations and an oxidizing ambient. The oxidation of the phosphorus diffused surfaces would even result in a supersaturation of excess phosphorus since the advancing oxide front rejects phosphorus (40). Assuming that the excess phosphorus in this supersaturated state exists interstitially or as very small ( $< 20\text{\AA}$ ) interstitial type clusters, it could dilate the lattice and cause compressive strain around the planar structures. If larger areas of incoherent precipitation exist, these could act as sinks for the excess phosphorus that would otherwise dilate the lattice structure to induce compressive strain and, therefore, result in the expected lower tensile strains and no outside dislocations.

### Summary

An anomalous, compressive macroscopic strain appeared around high concentration (though relatively shallow) phosphorus emitter-type diffused structures when an oxidizing diffusion or drive-in cycle was employed at temperatures less than 1150°C. This compressive stress cannot be due to residual strains from substitutional phosphorus atoms. It was often found to be of sufficient magnitude to cause dislocation nucleation and propagation for significant distances into the undiffused silicon; such dislocations commonly occurred in (111) oriented silicon wafers but were much less likely to occur in (100) and (110). The probability of dislocation formation outside of the diffused areas is significantly reduced if the diffusion or drive-in cycles are performed in an inert ambient or at higher temperatures, i.e., in the neighborhood of 1200°C.

### Acknowledgment

The authors wish to thank Karl Brack for providing the electron micrographs used in this study and C. Hoogendoorn for the x-ray topography. Part of this work was sponsored under Government Contract AF19(628)-5059.

Manuscript received Aug. 3, 1967; revised manuscript received Oct. 30, 1967.

Any discussion of this paper will appear in a Discussion Section to be published in the December 1968 JOURNAL.

### APPENDIX

We now establish the applicability of regarding the force as concentrated at the surface, and, thereby, the stress distributions [5]. If the magnitude of the stress is assumed constant down to  $a$  where it abruptly drops to zero,  $a$  is still considered small compared to  $r$ ; and the origin is adjusted slightly to

$$(0, -a/2, 0)$$

Then, Flamant's solution becomes

$$\sigma_x = \frac{-2\sigma_f}{\pi} \int_{-a/2}^{+a/2} \frac{x^3}{[x^2 + (y - \zeta)^2]^2} d\zeta \quad [6]$$

with similar expressions for  $\sigma_y$  and  $\tau_{xy}$ .

It is readily seen that Eq. [6] goes quickly to Eq. [5] as  $a$  is allowed to go to zero. For the application of this investigation, the force can be regarded as concentrated at the surface.

We also wish to point out that, with respect to the three-dimensional problem, a more rigorous approach would involve considering a distribution of concentrated point forces acting at the surface of the semi-

infinite substrate and using the principle of superposition, see Timoshenko and Goodier (41). Such solutions are not difficult; but they are long, appear burdensome, and tend to distract from the physical significance of the problem. The requirements of this investigation do not require this degree of rigor.

### REFERENCES

- H. J. Queisser, *J. Appl. Phys.*, **32**, 1776 (1961).
- S. Prussin, *ibid.*, **32**, 1876 (1961).
- G. H. Schwuttke and H. J. Queisser, *ibid.*, **33**, 1540 (1962).
- J. Washburn, G. Thomas, and H. J. Queisser, *ibid.*, **35**, 1906 (1964).
- P. F. Schmidt and R. Stickler, *This Journal*, **111**, 1188 (1964).
- W. Czaja and G. H. Wheatly, *J. Appl. Phys.*, **35**, 2782 (1964).
- R. J. Jaccodine, *Appl. Phys. Letters*, **4**, 114 (1964).
- M. L. Joshi and F. Wilhelm, *This Journal*, **112**, 185 (1965).
- G. H. Schwuttke, *J. Appl. Phys.*, **36**, 2712 (1965).
- H. Rupprecht and G. H. Schwuttke, *ibid.*, **37**, 2862 (1966).
- E. Levine, J. Washburn, and G. Thomas, *ibid.*, **38**, 81 and 87 (1967).
- J. M. Sukhodreva, *Soviet Phys.-Solid State*, **6**, 311 (1964).
- Y. Sato and H. Arata, *J. Appl. Phys. (Japan)*, **3**, 511 (1964).
- M. Ino, T. Kawamura, and M. Yasufuku, *ibid.*, **3**, 492 (1964).
- I. A. Blech, E. S. Meieran, and H. Sello, *Appl. Phys. Letters*, **7**, 176 (1965).
- G. H. Schwuttke and J. M. Fairfield, *J. Appl. Phys.*, **37**, 4394 (1966).
- G. H. Schwuttke and F. Wilhelm, *Bull. Am. Phys. Soc.*, **12**, 120 (1967).
- J. E. Lawrence, *This Journal*, **113**, 819 (1966).
- M. C. Duffy, F. Barson, J. M. Fairfield, and G. H. Schwuttke, *This Journal*, **115**, 84 (1968).
- B. C. Cohen, *Solid-State Electron.*, **10**, 33 (1967).
- G. L. Pearson, W. T. Read, and W. L. Feldmann, *Acta Met.*, **5**, 181 (1957).
- J. R. Patel and A. R. Chaudhuri, *J. Appl. Phys.*, **34**, 2788 (1963).
- M. L. Joshi, C. H. Ma, and J. Makris, *ibid.*, **38**, 715 (1967).
- J. M. Fairfield, G. H. Schwuttke, M. C. Duffy, and F. Barson, Recent News paper presented at the Philadelphia Meeting of the Society, Oct. 9-14, 1966 as RN Abstract 25.
- F. Barson, Private communication.
- A. Loro, *Solid-State Electron.*, **9**, 904 (1966).
- M. C. Duffy, D. W. Foy, and W. J. Armstrong, *Electrochem. Technol.*, **5**, 29 (1967).
- W. J. Armstrong and M. C. Duffy, *ibid.*, **4**, 475 (1966).
- E. Tannenbaum, *Solid-State Electron.*, **2**, 123 (1961).
- R. A. McDonald, G. G. Ehlenberger, and T. R. Huffman, *ibid.*, **9**, 807 (1966).
- G. H. Schwuttke, AFCRL-64-542 (1964).
- J. K. Howard and G. H. Schwuttke, "Advances in X-ray Analysis," 11, G. R. Mallet and J. B. Newkirk, Editors, Plenum Press, New York (1967); Also 1966 Pittsburgh Diffraction Conference, Pittsburgh, November 1966.
- G. H. Schwuttke and J. K. Howard, *J. Appl. Phys.*, **39**, March 1968.
- R. Glang, R. A. Holmwood, and R. L. Rosenfeld, *Rev. Sci. Instr.*, **36**, 7 (1965).
- G. G. Stoney, *Proc. Roy. Soc.*, **A82**, 172 (1909).
- A. A. Brenner and F. Senderoff, *J. Research Natl. Bur. Standards*, **42**, 105 (1949).
- V. V. Batavin, *Soviet-Physics Solid State*, **8**, 2478 (1967).
- R. J. Jaccodine and W. A. Schlegel, *J. Appl. Phys.*, **37**, 2429 (1966).
- M. J. Flamant, *Compt. Rend.*, **114**, 1465 (1892); see also M. J. Boussinesq, *ibid.*, **114**, 1510 (1892).
- M. M. Atalla and E. Tannenbaum, *Bell System Tech. J.*, **39**, 933 (1960).
- Timoshenko and Goodier, "Theory of Elasticity," McGraw Hill Publishing Co., New York (1951).



# Preparation and Properties of Thin Film Boron Nitride

Myron J. Rand\* and James F. Roberts

Bell Telephone Laboratories, Inc., Allentown, Pennsylvania

## ABSTRACT

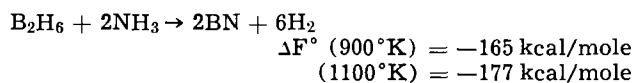
Clear, vitreous films of boron nitride up to 6000Å thick have been deposited on a variety of substrates at 600°-1000°C by a reaction between diborane and ammonia in hydrogen or inert carrier gas. Deposition rate may be readily adjusted to 50-1000 Å/min. Most samples were made at either 600° or 800°, with some attendant variation in film properties. The 600° material contains some residual B-H bonding. The film is essentially amorphous to electron diffraction. The refractive index is 1.7-1.8, the 1 MHz dielectric constant  $\sim 3\frac{1}{2}$ , the dielectric strength  $\sim 5 \times 10^6$  v/cm, and the 25°C resistivity  $\geq 10^{14}$  ohm-cm. The band gap is 3.8 eV and the phonon temperature in the neighborhood of 2000°K. For semiconductor junction protection boron nitride has no advantage over silicon nitride. 600° deposition directly on Si has produced surface charges as low as  $4 \times 10^{11}$ /cm<sup>2</sup>, but there are room-temperature drifts, and high-field conduction also. BN deposited at 800° on Si is electrically similar to silicon nitride. Etching of BN film also presents the same problems as does silicon nitride. BN is not as good a barrier against sodium ion permeation. Attack by atmospheric moisture over a long period has varied from insignificant to extensive conversion to orthoboric acid.

BN film on Si dopes the substrate with boron at temperatures above 900°C in inert ambient. Uniform junction depths are produced. D-C conductivity in 500-4000Å films has been studied from room temperature to 270°C. With fields  $\geq 10^6$  v/cm BN film shows stable, nonohmic conductivity which is independent of polarity. The 25°C d-c conduction is describable over at least seven decades of current by  $J \propto E^n$ ,  $n = 13-15$ , where  $J$  = current density,  $E$  = field strength. The 600°-deposited BN is the more conductive and can carry 0.1 amp/cm<sup>2</sup> indefinitely.  $\log J$  vs.  $E^{1/2}$  at 25° is linear, and the slope of the curve is in good agreement with the theoretical value for a Frenkel-Poole conduction mechanism. Possible use of BN as a thin film varistor is discussed.

The preparation and properties of pyrolytic boron nitride have been reviewed in ref. (1). BN, ordinarily regarded as an insulator, may also be considered a wide band-gap III-V semiconductor, and it displays multiband electro-, photo-, and cathode-ray luminescence (2). The crystal structure is very similar to that of graphite. Data on the pure compound are thus of intrinsic interest for potential electronics uses, but much of the literature on conventional commercial BN is valid only for the particular sample studied because of the oxide impurity and the strong anisotropy resulting from hot-pressing.

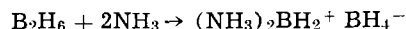
There is very little formally published work on thin film boron nitride. Films less than 1 $\mu$  thick have been prepared by Haberecht *et al.* (3) and characterized as capacitor dielectrics. The method used was a low-pressure, static pyrolysis of B-trichloroborazine vapor on a substrate heated to 700°-1400°C. The films were microcrystalline, with a minimal degree of short-range order (so-called "turbostratic") to x-rays. They probably contained residual chlorine. Crystalline films have also been made at Raytheon Company (4) from  $\text{BCl}_3 + \text{NH}_3$  at 1100°-1300°C.

We report here the first results of a study of thin film boron nitride made by vapor deposition from a reaction between diborane and ammonia. This system was chosen because high-purity reactants are available, and because the product should not be contaminated by anything except, possibly, residual bonded hydrogen. Also, a favorable free energy change offers the hope that the reaction will be complete at relatively low temperatures. The over-all reaction is



The reaction occurs in separable steps (5). At room

temperature there is immediate formation of a stable white solid borohydride, the diammoniate of diborane



which at  $\geq 200^\circ$  rearranges to the ring compound  $\text{B}_3\text{N}_3\text{H}_6$  (borazine), and some polymeric material  $(\text{BNH}_2)_n$ . Stronger heating drives off the hydrogen progressively, forming polymeric  $(\text{BNH})_n$  and finally BN.

The results reported here summarize some eighty runs in a single-slice deposition apparatus. The many variables of operation have not been investigated exhaustively, but it is evident that a smooth, transparent, and adherent thin film is obtained reliably over a considerable range of conditions. The potential applications for which the material has been examined include semiconductor surface protection and sodium diffusion barrier, boron diffusion source, and thin film dielectric or varistor. Most films were 1000-6000Å thick.

## Deposition of Thin Film BN

*Apparatus.*—Figure 1 is a simplified schematic diagram of the apparatus. The substrate rests on a molybdenum pedestal which is inductively heated at 3 Mc. The reaction vessel is fused silica; all tubing is stainless steel. An important feature is the mixing of the reactants only after they enter the reactor and the heating of the reactor wall to at least 200°C. This prevents the deposition of the solid borohydride compound and is essential in obtaining a vitreous film. The substrate is heated after establishing the ammonia flow, with the diborane introduced last and turned off first. Without adequate ammonia a smooth film of amorphous boron is deposited. A green color in the burnoff flame is a sensitive indicator of the presence of gaseous boron compounds.

*Deposition conditions.*—The reaction was carried out at 600° to 1080°C, with most of the work at 600°

Key words: Boron nitride, thin films, vapor deposition, conduction, varistors.

\* Electrochemical Society Active Member.



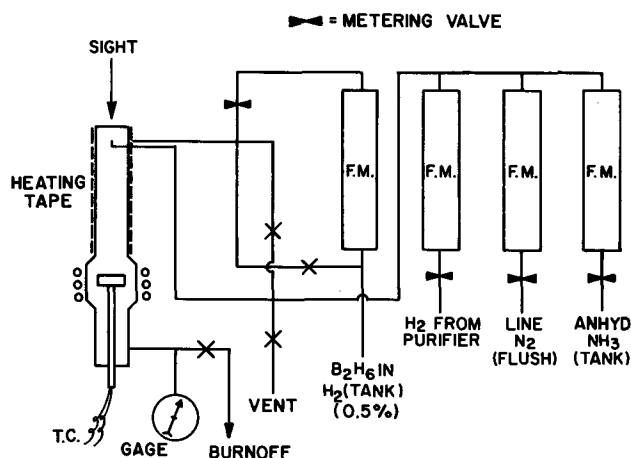


Fig. 1. Schematic diagram of deposition equipment

and 800°. The substrate was usually silicon, but Ta, Mo, Ge, and fused silica were also coated. Film thicknesses were monitored continuously during growth: at 600° simply by color, and at  $\geq 800^\circ$  by measuring emitted light intensity fluctuations at 6000Å caused by interference in the growing film (6). Hydrogen ambient was used most commonly and is preferred at present on the basis of film properties, but the reaction was also successful in nitrogen or helium. For these latter the tank diborane diluent was nitrogen, so that the only hydrogen present was the reaction by-product. Other conditions of operation are given in Table I.

**Rates.**—Observed deposition rates are not true kinetic rates since they vary with transport rate of reactants. Furthermore, there is considerable evidence that there is a reaction at the heated tube wall. Deposition rate is sensitive to the proximity of the wall: in a straight-walled tube the rate is 2-4 times faster than in the slightly bulged tube (see Fig. 1). BN films are more nonuniform than SiO<sub>2</sub> or silicon nitride films made in the same equipment at the same temperature. Furthermore, a freshly cleaned reaction tube depresses the deposition rate. All these observations suggest a reactant, probably borazine, being supplied by a local wall reaction.

The 800° deposition rate is only about 1.5 times faster than the 600° rate, and the 1000° rate is slower than the 800° (probably because of premature reaction at some distance from the substrate). The rate is proportional to the diborane concentration, but the influence of ammonia is anomalous. The ammonia concentration used was at least ten times that of B<sub>2</sub>H<sub>6</sub>, yet in the NH<sub>3</sub>/B<sub>2</sub>H<sub>6</sub> = 10-20 range the rate was sensitive to NH<sub>3</sub> concentration. Furthermore, the proportionality is inverse (more NH<sub>3</sub> decreased the rate, and to a power greater than one). Probably ammonia, or one of its pyrolysis products, acts as a chain terminator for some free-radical mechanism. At any rate, it is evident that the reaction sequence is complicated and that the conditions used are unsuitable for a study of kinetics.

Boron nitride deposition, like silicon nitride deposition from SiH<sub>4</sub> and NH<sub>3</sub>, is much slower in the presence of traces of water vapor. One tank of so-called anhydrous ammonia gave persistent low deposition

Table I. Operating conditions

	Range	Most common
Total flow rate, l/min	0.5-4.5	3.0
Linear velocity, cm/sec	1-10	6.8
$\% \text{ B}_2\text{H}_6$	0.01-0.2	0.04
$\% \text{ NH}_3$	0.4-5	0.7
NH <sub>3</sub> /B <sub>2</sub> H <sub>6</sub>	10-80	17
Deposition rate, Å/min	50-700 (in H <sub>2</sub> or He)	125-600
	200-1900 (in N <sub>2</sub> )	~1000

rates; when it was transferred to another apparatus used for Si<sub>3</sub>N<sub>4</sub> deposition, rates were one-third normal, and tests indicated that the film was actually mostly SiO<sub>2</sub>. This result is typical of the presence of moisture, of the order of 200 ppm.

### Physical Properties of the Film

**Spectra.**—The identification of the deposited film as boron nitride rests primarily on examination by infrared spectra and electron diffraction. Spectra of commercial boron nitrides may be found in ref. (7-9). Our thin-film spectra are shown in Fig. 2. The chief features are a strong asymmetric band near 1380 cm<sup>-1</sup>, undoubtedly the B-N stretch, and a weaker, sharper band near 790 cm<sup>-1</sup>. Both are considerably broader in the film deposited at 600° and shifted to slightly lower frequencies, indicating a more disordered structure on the atomic level. The weak absorption at 3430 cm<sup>-1</sup> is most probably hydroxyl impurity, strongly H-bonded, for example adsorbed molecular water. In addition, the 600° film shows a band at 2500 cm<sup>-1</sup>, the B-H stretching region, and thus contains some residual hydrogen-containing polymeric material.

**Crystallinity.**—Grazing-angle electron diffraction shows broad, diffuse rings whose positions are in agreement with the established pattern for hexagonal boron nitride. From line widths the crystallite sizes (near the surface) are estimated as follows:

Deposition temp, °C	600	800	900	950
Size, Å ( $\pm 15\%$ )	10	20	30	65

The 600° BN film thus has about as much crystalline order as steam-grown silica. The figures above are for hydrogen ambient; films made in nitrogen have a larger crystallite size, but no value more than 80Å has been found for any deposition conditions.

**Band gap.**—No published measurement of the band gap of hexagonal boron nitride could be found. A BN film 0.6μ thick was deposited at 800° on fused silica to study transmission in the 185-750 mμ range. There are no bands in the visible. Absorption commences at about 340 mμ, but the absorption edge is not as sharply defined as for crystalline materials. Figure 3 is a plot of the square root of the absorption coefficient vs. the photon energy. There is a discontinuity in slope similar to those shown by Si and Ge (10). From the two intercepts on the zero absorption axis (11) an energy gap of 3.8 eV is calculated. The phonon temperature is about 2000°K, but the absorption data are not of the precision required for good accuracy in this figure.

**Refractive index.**—Film refractive index, as determined by ellipsometer, varies considerably. Hexagonal BN, with its graphite-like structure, is highly anisotropic; furthermore, the degree of crystallinity varies with deposition temperature. Results below are

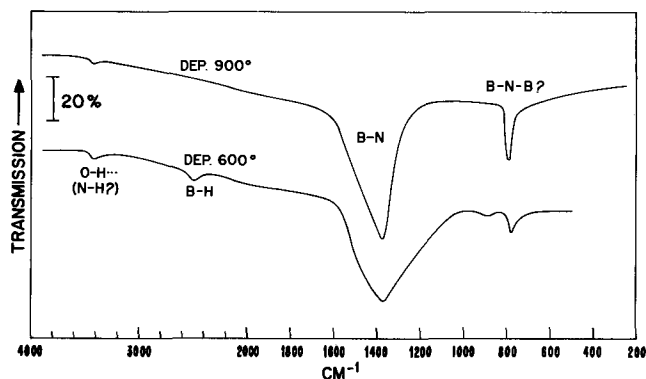


Fig. 2. Infrared spectra of boron nitride films deposited at 900°C (upper curve) and 600°C. The curves have been displaced for clarity.

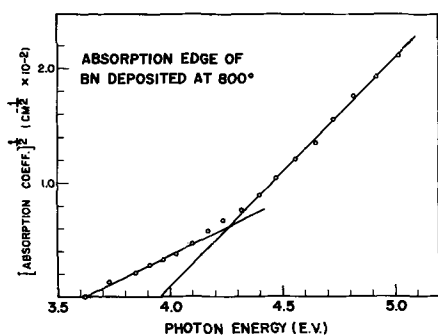


Fig. 3. Macfarlane-Roberts plot of absorption edge of BN deposited at 800°C.

reliable to  $\pm 0.03$ :

Deposition temp. °C	950	900	800	600
Refractive index, 541 $\mu\text{m}$	1.70	1.73	1.75	1.80

These values are for films deposited in hydrogen. Films made in nitrogen at 800° have crystallite sizes like those made in hydrogen at 950°, and correspondingly show  $n \sim 1.70$ .

**Adherence.**—Generally, BN film adherence to the substrate has been entirely satisfactory. An occasional occurrence of peeling during etching indicates that it is not so adherent as deposited silica or silicon nitride. Adherence to Ge substrates, however, was unsatisfactory, possibly because of nitriding. Although film appearance was normal immediately after deposition, if the film was disturbed, *e.g.*, by tweezers, local puckering and reticulation appeared instantly. In the course of a few days this effect spread entirely across the Ge slice.

**Surface properties.**—BN films are quite hydrophobic. Water contact angles from 42° to as high as 80° have been measured, even after many days' exposure to atmospheric moisture.

Film surfaces are quite smooth. Relatively few surface features were visible to 8000X electron microscopy, and even these few were low hillocks rather than fissures or other kinds of film discontinuities.

**Sodium drift and diffusion experiments.**—Tests of the film as a diffusion barrier were carried out with  $^{22}\text{NaCl}$ . Unlike silica films, however, diffusion of sodium in a voltage field and straight thermal diffusion gave very different pictures of the permeability. At 400°C, with the surface bias plate at +4 to +10v (field about  $10^5$  v/cm) for 1 hr, no sodium ion drift was detected in any boron nitride film. No charge storage was detected.

Thermal diffusion profiles are shown in Fig. 4. The data show considerable scatter, but it is immediately evident that deposition temperature influences the result. In the film deposited at 850° the steep drop in Na ion concentration with depth is like that shown by an oxygen-free pyrolytic silicon nitride. Note, however, the single datum point, at 2100Å, which is a decade higher than the previous one and which seems to indicate a pileup of sodium at some sort of barrier, since beyond this point none could be detected. The film structure was examined by step-etching and electron diffraction, and it was found that the crystallite size was  $\sim 30\text{Å}$  at the original surface but decreased with depth; at 2100Å and beyond the film was essentially amorphous, *i.e.*, size  $< 10\text{Å}$ . This correlation between crystallinity and permeability has also been reported recently for silicon nitride films. (12)

Boron nitride deposited at 600° is not a barrier to sodium ion diffusion. All the profiles are relatively flat, even the one for diffusion conditions of 1 hr at 400° instead of 22 hr at 600°.

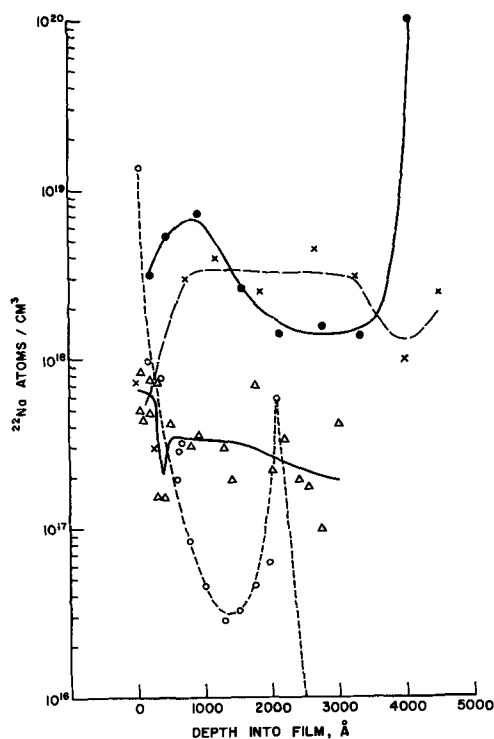


Fig. 4. Sodium diffusion profiles in boron nitride films: ---○--- 5000Å film deposited at 850°, diffused 22 hr at 600°C in forming gas; —●— 4100Å film deposited at 600°, diffused as before; —△— two samples of a 3100Å film deposited at 600°, diffused as before; —X— 4500Å film deposited at 600°, diffused 1 hr at 400°C in room air.

### Chemical Properties

**Etching.**—Bulk boron nitride is considered highly resistant to all aqueous acids and bases and is slowly attacked by high concentrations of water vapor. Thin film BN behaves similarly. Buffered HF etches at  $< 10$  Å/min. Some samples could be etched at  $\sim 35$  Å/min by 3% hydrogen peroxide at 80°C, but this solution is destructive to conventional etch-resist films. A deposited silica film might be used for masking, but if this method is chosen, one might as well etch with hot phosphoric acid, as is done with silicon nitride (13). Boiling  $\text{H}_3\text{PO}_4$  at 180° etches boron nitride at about 150 Å/min.

A BN film on silicon was exposed to boiling methanol vapor for 1½ hr with no change in appearance, thickness, or film weight ( $\pm 1\%$  sensitivity). This treatment would have dissolved any boric oxide. With a 2-hr exposure to 100° steam or boiling water there was little thickness change, but the film became hazy. Microscopic examination revealed numerous shallow blisters or craters, with film fragments curled back at the edges, as if lateral attack (or separation of laminae) were the chief effect.

**Anodization.**—Since BN film is difficult to etch, several attempts to convert it to the oxide by anodization (14) were made. All failed because the film peeled from the substrate. This is further evidence that boron nitride adherence is not so tight as that of silicon nitride.

**Silicon doping.**—From free energy data one would predict that silicon may reduce boron nitride to boron and form  $\text{Si}_3\text{N}_4$ . In other words, if BN is deposited on Si at temperatures at which diffusion rates of boron in Si are significant, the substrate may be doped. This does indeed occur: with deposition at 900° and above, the rather flat capacitance-voltage traces invariably obtained in MIS measurements indicated plainly that the substrate surface was low-resistivity p-type.

Figure 5 shows results of two experiments on deliberate doping of 4 ohm-cm n-type silicon from a BN

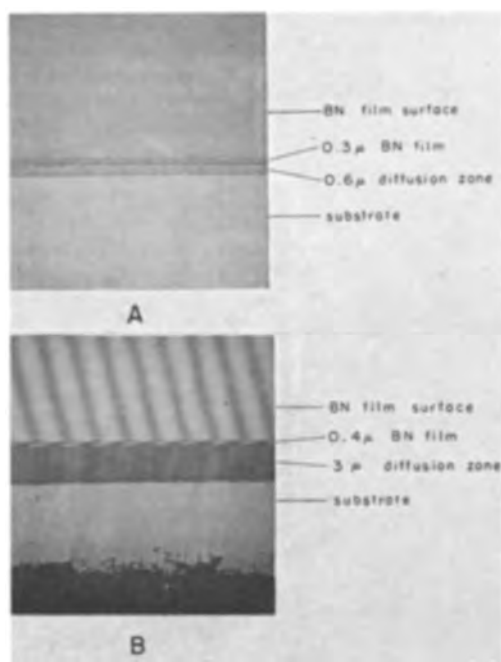


Fig. 5. Angle-lapped and stained sections showing use of boron nitride film as a diffusion source. (A) 1½ hr in nitrogen, 1100°, (B) 2 hr, 1150° helium.

film source. The upper picture is the angle-lapped and stained interface after 1½ hr in nitrogen at 1100°C; for the lower, 2 hr at 1150° in helium. Junction depths are quite uniform. There was little change in the appearance of the deposited film.

Boron nitride film should thus be useful as a restricted area boron diffusion source. The diffusion should be carried out in inert ambient; any water or oxygen present would convert the nitride to the oxide, and the high vapor pressure of the oxide would result in some doping outside the desired area. As a solid diffusion source BN has the advantages of thermal stability, constant composition, and simplicity of deposition compared to B<sub>2</sub>O<sub>3</sub>-SiO<sub>2</sub> codeposits.

**Weathering phenomena.**—It has already been mentioned that boron nitride, in both massive and thin film form, is slowly attacked by water vapor. Thus there are grounds for concern about BN film stability with prolonged exposure to the atmosphere. Indeed, changes with time are observed; these appear to depend on the conditions of deposition, and probably on other factors as well. They range from the trivial to the catastrophic.

A freshly deposited BN film is not as hard as SiO<sub>2</sub> or Si<sub>3</sub>N<sub>4</sub>, but it is not readily scratched by stainless steel tweezer tips. It will remain this way indefinitely if stored in a desiccator. If stored in room ambient, it will become soft enough to scratch in a few weeks. A broad, shallow absorption band develops near 3300 cm<sup>-1</sup> in the spectrum; this is hydrogen-bonded hydroxyl, and indicates adsorption or absorption of molecular water. There are no other significant spectrum changes.

Some specimens have shown a much more serious form of attack, whose manifestation is the appearance of single-crystal boric acid (identified by electron diffraction) growing out of the film surface. A particularly severe example is shown in Fig. 6. B<sub>2</sub>O<sub>3</sub> and HBO<sub>2</sub> are probably intermediates, judging by the behavior during heating and cooling cycles. Such extensive hydrolytic attack is seldom seen in films deposited in hydrogen at 600°. Perhaps one in four of the 800° films eventually showed a few crystals. But almost all the films made in inert ambient, nitrogen or helium, developed serious cases of the boric acid pox, some in only one or two weeks. For this reason the deposition

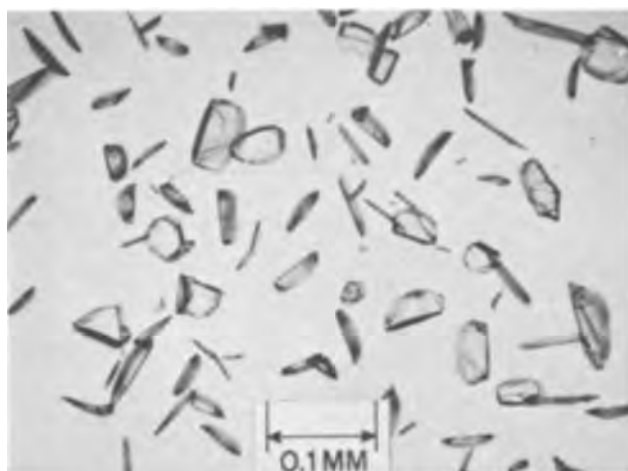


Fig. 6. Boric acid crystals growing from a boron nitride film made in nitrogen at 670°, after 5 months exposure to room atmosphere. Magnification ca. 150X.

of films in inert ambient was not pursued, even though it should produce a purer product. The presence of residual bonded hydrogen seems to be associated with BN film resistance to water attack.

### Electrical Properties

**Surface charge.**—Most of the BN films were deposited on silicon, and a number of samples of MIS capacitor structures were made by evaporating 10 mil diameter Al field plates onto the film. Adherence of the Al was normal. In some cases the substrate was oxidized in steam at 1000° to provide a 1000Å SiO<sub>2</sub> layer under the nitride deposited afterwards. A summary of the MIS results appears in Table II.

Films deposited on bare Si in hydrogen at or above 800°C behave electrically like those of silica or silicon nitride in showing the so-called anomalous shift as the bias range is increased in the negative direction, and also in showing hysteresis loops as the scan is retraced. The interfacial surface charge was high, in the 2-5x10<sup>12</sup> range.

BN deposited over SiO<sub>2</sub> gave C-V traces which shifted with time as though some sort of slow polarization or structural alteration were occurring at room temperature. A similar effect has been observed with thick phosphorus-glass layers on SiO<sub>2</sub> (15), and also on lead glass (16), but only at elevated temperatures. On one sample measurements of the flat-band voltage shift as a function of field-plate voltage and time were made. The extent of shift was the same when the sample was held at +25 or -25v, although of course the directions were opposite. At a given voltage the shift was linear with log time, at least up to 2 hr.

Table II. Summary of MIS measurements (measuring frequency = 1 MHz)

Dep'n temp, °C	Ambient	Substrate	Capacitors	Surface charge density (× 10 <sup>-11</sup> cm <sup>-2</sup> )	Comments
900	H <sub>2</sub>	SiO <sub>2</sub> /Si	3	5.3-6.9	Shifts with time
850	H <sub>2</sub>	Si	4	23-25	Normal curve
800	H <sub>2</sub>	Si	20	32-52	Normal curve
800	H <sub>2</sub>	SiO <sub>2</sub> /Si	12	28-34	Shifts with time
800	N <sub>2</sub>	Si	5	7.5-8	Anomalous behavior, see text
800	He	Si	3	4	Conduction; capacity drift
600	H <sub>2</sub>	Si	16	4-8	
600	H <sub>2</sub>	SiO <sub>2</sub> /Si	6	6.4-6.9	Shifts with time
	H <sub>2</sub>	fast states*	2	1.0-1.1	

\* By the technique of ref. (25).

The sample deposited on bare Si in nitrogen exhibited a different sort of anomaly. Scans from 0 to  $-15\text{v}$  looked normal, but at higher negative voltages the insulator capacitance decreased. After stress at  $30\text{v}$  or more a pronounced knee appeared in the step of the C-V trace, and the capacitance had decreased by 20%. These effects may be due to film conductivity. The same sample measured two months later, after boric acid crystals had appeared, was highly conducting at  $1\text{v}$ . The inert-ambient deposits did have low surface charges, as Table II indicates, but because of susceptibility to hydrolysis they were not further investigated.

BN deposited in hydrogen on bare Si at  $600^\circ$  was also in the  $4\text{-}8 \times 10^{11}$  surface charge range, but here the evidence of high conductivity was pronounced; the samples could not be measured on a capacitance bridge, and required a capacitance meter such as the Boonton Model 71A. A typical C-V curve for these samples is shown in Fig. 7. The usual limiting insulator capacitance does not seem to be reached. (The curves finally do level off at about  $-40\text{v}$ , however.) Some upward drift of capacitance is seen at constant large negative bias.

**Dielectric constant.**—On conducting samples like those just described no accurate dielectric constant can be determined. For  $800\text{-}1800\text{\AA}$  BN deposited at  $800^\circ\text{C}$  on Si some twenty measurements on three different samples at  $1\text{ MHz}$  gave  $K = 3.7 \pm 0.3$  (range).

**Dielectric strength.**—The "room temperature" breakdown strength of BN deposited at  $800^\circ$  is  $6 \times 10^6\text{ v/cm}$ , and of the film deposited at  $600^\circ$ ,  $4 \times 10^6\text{ v/cm}$ . These values are probably low because of resistive heating of the film by high-field conduction. This property, which is shown to a surprising degree for a material ordinarily considered an insulator, is perhaps the most interesting feature of these films, and is discussed in detail in the next section.

### Nonohmic Conductivity

Recently there have been reports of high-field nonohmic d-c conductivity in thin films of silicon nitride made by the  $\text{SiH}_4\text{-NH}_3$  process (17), the  $\text{SiCl}_4\text{-NH}_3$  process (18, 19), and by reactive sputtering (20, 21). Evaporated  $\text{SiO}_x$  insulating films also show the phenomenon (22). Conductivity depends strongly on conditions of film deposition, and there are conflicting results on whether it is polarity-dependent. Various conduction mechanisms have been proposed, particularly the Frenkel-Poole and Schottky types. Obviously, present knowledge is fragmentary, but at any rate it seems to be widely known that silicon nitride films can pass considerable current (by semiconductor standards) without destruction, and thus have a built-in protection against occasional overload.

Thin film boron nitride, as described here, also shows stable, strongly nonohmic high-field conductivity, to such an extent that films of  $1000\text{\AA}$  or thinner may be useful in integrated circuits as thin varistors or voltage-limiters. As with the other films, the conduc-

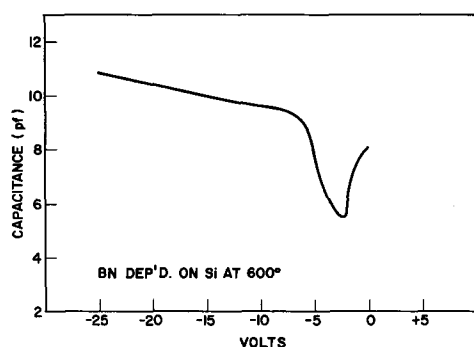


Fig. 7. Typical MIS curve for BN deposited at  $600^\circ\text{C}$  on Si

tivity depends on deposition conditions, particularly the deposition temperature, and thus must be governed largely by the structure of the film. The effects of thickness, electrode material and area, polarity, and temperature were also examined and are summarized below.

**Method of measurement.**—The voltage source was a bank of dry cells discharging through a  $20\text{K}$  potentiometer which allowed selection of any appropriate applied potential over the range  $0\text{-}500\text{v}$ . This potential was read on a Keithley 610B electrometer. The current in the sample circuit was read on a Keithley 414 micromicroammeter. A 1-megohm resistor in the measuring circuit protected the instruments against surges caused by sample breakdown. For conductivity work the film samples were deposited on  $0.001\text{ ohm-cm}$  n-type silicon and an array of 10 and 20-mil aluminum or gold electrodes applied by evaporation through a mask. The back of the Si slice was coated with evaporated gold. The sample was mounted in a micrometer-drive positioner and the electrode dots contacted with a 7-mil brass probe.

For measurements at elevated temperatures the Si slice was scribed and broken into chips containing two dots each. After a brief ultrasonic cleaning to remove scribing debris the chips were mounted on TO-18 headers and gold wire bonded to the electrode. Conventional mounting and bonding techniques and temperatures had no adverse effect on the BN films. The assembly was mounted in a small copper oven and measurements taken at various temperatures between  $75^\circ$  and  $270^\circ\text{C}$ .

Measurements were always made by scanning the current-voltage curve several times with both increasing and decreasing voltages, and frequently points were taken out of sequence. The first application of high field caused a permanent decrease in resistance; thereafter the samples were quite stable. For this reason each sample was aged ("formed," in the language of some authors) at  $10^{-1}\text{-}10^{-2}\text{ amp/cm}^2$  for a few minutes before the measurements were begun.

At no time was any emission of light observed.

**Effect of certain parameters.**—Film deposition temperature has a strong effect on conductivity. Most of the samples measured had been prepared at either  $800^\circ$  or  $600^\circ$ ; the latter has about  $10^4$  times greater high-field conductivity at a given field strength. However, the ohmic component, i.e., the conductivity at  $\leq 10^5\text{ v/cm}$ , is about the same. Conductivity increases with temperature, with an activation energy of  $1.0\text{-}1.1\text{ ev}$  in the ohmic region. In the nonohmic regions this quantity decreases with increasing field strength.

Changing from Al to Au electrodes had no effect on the conductivity. Increasing the area fourfold also had no effect on the current density vs. field strength curves. Reversing polarity had little or no effect: with some samples a few per cent difference was observed, but the curves were of the same form. Varying film thicknesses from  $500\text{ to }4000\text{\AA}$  was also without effect, as long as field strength was considered.

**Results and discussion.**—Figures 8 and 9 summarize the results of many measurements on films deposited at  $800^\circ$  and  $600^\circ\text{C}$ , respectively. It is evident that up to  $\sim 10^5\text{ v/cm}$  BN film shows only minute and ohmic electronic conductivity. Resistivities are  $\geq 10^{14}\text{ ohm-cm}$  at room temperature and  $\sim 10^{12}\text{ ohm-cm}$  at  $200^\circ\text{C}$ . At higher fields this behavior is gradually overwhelmed by a conductivity describable by  $J \propto E^n$ , where  $n = 13\text{-}15$ . The transition is more gradual for the film deposited at  $600^\circ$ , and occurs at lower fields. The negative resistance in the breakdown region is not stable.

For a varistor the  $600^\circ$  film would be preferred, since it is both more conductive and more stable. A  $1000\text{\AA}$ -thick film should be capable of dissipating up to  $\sim 15\text{ w/cm}^2$  continuously. As an aid in visualizing the possible use of the BN film, Fig. 10 presents its charac-

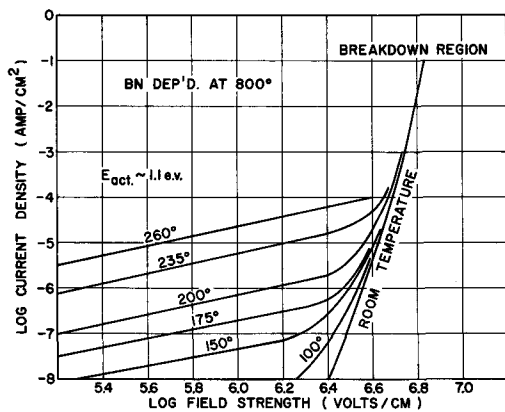


Fig. 8. D-C conductivity of 500-4000Å BN films deposited at 800°C on 0.001 ohm-cm n-Si.

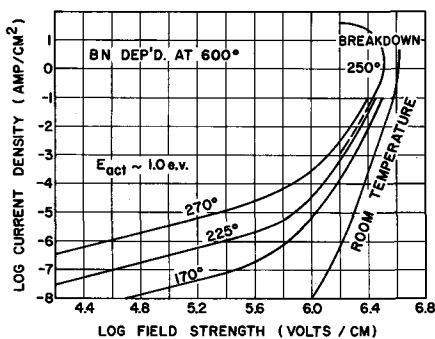


Fig. 9. D-C conductivity of 2000Å BN film deposited at 600°C on 0.001 ohm-cm n-Si.

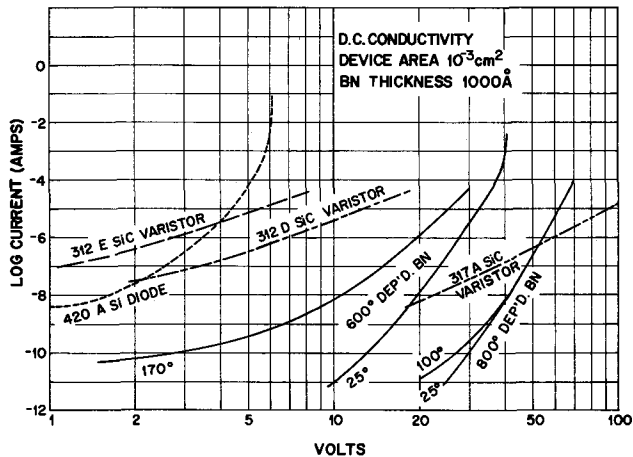


Fig. 10. Characteristics of 1000Å BN film as a varistor. Silicon carbide and regulator diode devices, reduced to the same area, are included for comparison. (Identifications are Western Electric Co. codes.)

teristics on the same scale with those of commercially available silicon carbide varistors and a regulator diode reverse characteristic. For comparability all of the devices have been reduced to the same active-element area,  $10^{-3}$  cm<sup>2</sup>. It is evident that the BN film, particularly the 600° film, occupies a potentially useful intermediate position between the others; furthermore, the SiC varistor and the Zener diode are not currently manufactured in thin film form. Note that for the SiC device the current varies as about the fourth power of the voltage; for 600° BN the exponent at room temperature is about 13; and for the diode it varies from near unity to 50 or more.

Many of the experimental observations given above have implications for the mechanism of conduction. For example, the fact that the current does not de-

crease with time, coupled with its nonohmic behavior, rules out any large contribution from ionic conduction. Models of space-charge limited flow (23) predict current density dependence varying between  $V^2/l^3$  and  $V^3/l^5$ , depending on region and on whether a single or double-injection model is assumed ( $l$  is the thickness). This seems rather far removed from the  $J \propto (V/l)^{13}$  dependence observed. An impurity-band conduction mechanism would have a low activation energy and would give an ohmic characteristic.

In Fig. 11 the room temperature conductivity data are replotted as log current density vs. the square root of field strength. Very good straight lines are obtained over seven decades of current for both the 600° and 800°-deposited films. Two possible mechanisms have this characteristic: conductivity limited by electron emission into the insulator from the electrode (Schottky emission), or by the field-assisted thermal excitation of electrons from traps into the conduction band of the insulator (Frenkel-Poole effect).

The Schottky emission equation may be written

$$J = AT^2 \exp \left\{ -\frac{e}{kT} \left[ \phi - \left( \frac{eE}{4\pi\epsilon_i} \right)^{1/2} \right] \right\}$$

where  $J$  = current density,  $A$  = the Richardson-Dushman constant, theoretically 120 amp cm<sup>-2</sup> deg<sup>-2</sup> for emission into a vacuum,  $T$  = absolute temperature,  $e$  = electronic charge,  $k$  = Boltzmann constant,  $\phi$  = barrier height,  $E$  = field strength,  $\epsilon_i$  = permittivity of the insulator =  $K\epsilon_0$ ,  $K$  = dielectric constant of the insulator,  $\epsilon_0$  = permittivity of free space =  $8.85 \times 10^{-12}$  farad/meter. At a given temperature the Schottky equation yields

$$\ln J = \text{constant} + \frac{e^{3/2}}{2kT(\pi\epsilon_i)^{1/2}} \cdot E^{1/2} \quad [1]$$

For the Frenkel-Poole effect the barrier lowering in the presence of a field (24) is  $2(e^3E/4\pi\epsilon_i)^{1/2}$ , that is, twice that for Schottky emission. The difference is a consequence of considering the positively charged trap fixed in position as the electron is removed from it, instead of considering the electron moving away from an image charge in the conductor. As a result, the Frenkel-Poole equation corresponding to Eq. [1] lacks the 2 in the denominator. Thus in principle the two kinds of conduction could be distinguished by the value of the slope of the  $\ln J$  vs. (field strength)<sup>1/2</sup> plot. Some authors argue that there are so many assumptions involved both in equations and the method of measurement that a mere factor of 2 does not offer safe grounds for decision.

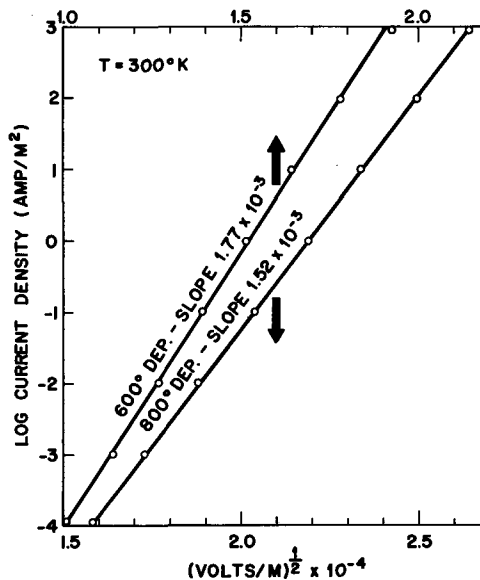


Fig. 11. Schottky plot of room-temperature d-c conductivity of BN film.

When the high-frequency (optical) dielectric constants of the BN film are used, the theoretical slope of Eq. [1] is calculated to be  $0.82 \times 10^{-3}$  (v/meter) $^{-1/2}$  for the 600° BN and  $0.84 \times 10^{-3}$  for the 800° BN. These values would of course be  $1.66 \times 10^{-3}$  if the factor of 2 is removed. The experimental slopes (Fig. 11) are  $1.77 \times 10^{-3}$  for 600° BN and  $1.52 \times 10^{-3}$  for 800° BN. The results are thus in better agreement with a Frenkel-Poole than with a Schottky-type conduction mechanism.

#### Acknowledgments

The authors are indebted to H. E. Nigh for MIS measurements, to J. Drobek for electron microscopy and electron diffraction, to J. V. Dalton for radiosodium drift and diffusion work, and to P. F. Schmidt for film anodization experiments. In addition, much helpful discussion and advice were provided by L. P. Adda, M. C. Waltz, and P. F. Schmidt. Dr. R. Haberecht of Texas Instruments kindly supplied copies of the talks cited in ref. (3).

Manuscript received Aug. 18, 1967; revised manuscript received Nov. 9, 1967. This paper was presented at the Dallas Meeting, May 8-12, 1967, as Abstract 87.

Any discussion of this paper will appear in a Discussion Section to be published in the December 1968 JOURNAL.

#### REFERENCES

1. For a summary of the preparation and properties of pyrolytic BN, see "Vapor Deposition," C. F. Powell, J. H. Oxley, and J. M. Blocher, Jr., Editors, pp. 663-7, John Wiley & Sons, Inc., New York (1966).
2. S. Larach and R. E. Shrader, *Phys. Rev.*, **104**, 68 (1956).
3. R. J. Patterson, R. D. Humphries, and R. R. Haberecht, Papers presented at the Pittsburgh Meeting of the Society, April 15-18, 1963, Abstract 103, and the New York Meeting, Sept. 29-Oct. 3, 1963 as Abstract 197; R. R. Haberecht, R. J. Patterson, and R. D. Humphries, Paper presented at the Annual Meeting of the Conference on Electrical Insulation, National Research Council, Washington, D. C., 1964. Abstracts of these papers were published by The Electrochemical Society and in National Academy of Sciences—National Research Council Pub. No. 1238 (1965).
4. "Research on Thin Film Tunnel Cathodes, Recombination Cathodes, and Similar Cold Cathodes," Report No. 10, Contract No. DA28-043-AMC-00035(E), March-June, 1965, et seq.; Raytheon Co. See also the reports under Contract No. DA28-043-AMC-01343(E).
5. "Boron, Metallo-boron Compounds, and Boranes," R. M. Adams, Editor, p. 590, Interscience, New York (1964).
6. J. F. Roberts, To be published.
7. E. G. Brame, Jr., J. L. Margrave, and V. W. Meloche, *J. Inorg. Nucl. Chem.*, **5**, 48 (1957).
8. P.-C. Li and M. P. Lepie, *J. Amer. Ceram. Soc.*, **48**, 277 (1965).
9. R. Geick, C. H. Perry, and G. Rupprecht, *Phys. Rev.*, **146**, 543 (1966).
10. G. C. Macfarlane and V. Roberts, *ibid.*, **97**, 1714 (1955); **98**, 1865 (1955).
11. T. S. Moss, "Optical Properties of Semiconductors," p. 37, Academic Press, Inc., New York (1959).
12. J. Drobek and J. V. Dalton, Recent News paper presented at the Philadelphia Meeting of the Society, Oct. 9-14, 1966.
13. W. van Gelder and V. E. Hauser, *This Journal*, **114**, 869 (1967).
14. P. F. Schmidt and D. R. Wonsidler, *ibid.*, **114**, 603 (1967).
15. E. H. Snow and B. E. Deal, *ibid.*, **113**, 263 (1966).
16. E. H. Snow and M. E. Dumesnil, *J. Appl. Phys.*, **37**, 2123 (1966).
17. V. Y. Doo and D. R. Nichols, Paper presented at Philadelphia Meeting of the Society, Oct. 9-14, 1966 as Abstract 146; H. Lawrence and C. Simpson, *ibid.*, as Abstract 159.
18. S. M. Sze, *J. Appl. Phys.*, **38**, 2951 (1967).
19. M. J. Grieco, F. L. Worthing, and B. Schwartz, *This Journal*, in press.
20. S. M. Hu and L. V. Gregor, *ibid.*, **114**, 826 (1967).
21. S. M. Hu, Paper presented at the Philadelphia Meeting of the Society, Oct. 9-14, 1966, as Abstract 150.
22. L. E. Terry, U. S. Atomic Energy Commission SC-TM 315-63 (14).
23. M. A. Lampert, *RCA Rev.*, **20**, 682 (1959); M. A. Lampert and A. Rose, *Phys. Rev.*, **121**, 26 (1961); M. A. Lampert, *Phys. Rev.*, **125**, 1 (1962), *inter alios*.
24. J. Frenkel, *Phys. Rev.*, **54**, 647 (1938).
25. E. H. Nicollian and A. Goetzberger, *Appl. Phys. Letters*, **7**, 216 (1965).

## Intense Interjunction Strain in Phosphorus-Diffused Silicon

E. D. Jungbluth\* and H. C. Chiao\*

The Bayside Laboratory, Research Center of General Telephone and Electronics Laboratories Incorporated, Bayside, New York

#### ABSTRACT

Extensive strain effects are revealed by x-ray topography in the areas between shallow junctions formed by selective-area phosphorus diffusion in silicon. Diffusion-induced strains extend at least  $500\mu$  laterally into the non-diffused portion of the substrate and penetrate to  $1/4$  of the junction depth. Unusual x-ray contrast effects are observed in that both extinction contrast and Borrmann effects simultaneously operate to reveal strain gradients when the lattice adjusts to compensate for stresses introduced by impurity diffusion. These residual unrelieved stresses can be minimized by stress-relief mechanisms involving the generation of dislocations.

Previous investigators have demonstrated that planar impurity diffusion techniques can introduce imperfections into semiconductor substrates (1-3). Dislocation arrays and precipitates can result from the diffusion of impurity atoms of boron and phosphorus into silicon. These defects are generally at-

tributed to stresses arising from solute concentration gradients and total impurity content. Similar effects may also occur when zinc is diffused into GaAs (4). Diffusions are normally accomplished by selectively diffusing through windows opened up in oxide masks by photolithographic techniques. Strain effects at the boundaries of Si-SiO<sub>2</sub> interfaces have been analyzed

\* Electrochemical Society Active Member.

by x-ray topography (5). One would normally expect that subsequent diffusions through the oxide windows would result in lattice defects which would be confined to the diffused area. Recently, Lawrence has shown that impurity diffusions cause dislocation formation not only within the diffused region but also outside or in the nondiffused portion of the matrix (6). He observed that impurity-induced lattice strain contributes to dislocation formation in nondiffused zones wherein the dislocations appear as parallel or intersecting lines. Joshi *et al.* (7) have measured residual strain levels in phosphorus diffused silicon by means of x-ray line-broadening. The observed broadening results from residual strains only and is attributed to insufficient penetration of the diffusion-induced dislocations from inside the diffused layers.

In this paper, direct evidence of the effects of residual strain in phosphorus diffused silicon is presented by means of x-ray transmission topography (8). The residual strain is distributed into the nondiffused zones but is not as well defined as the deformed regions reported by Lawrence (6). Indeed, deformations large enough to create dislocations do not occur in the present case. Residual strains, hereafter referred to as interjunction strains, are shown to arise as a consequence of the diffusion process and are intimately related to the creation of diffusion-induced dislocations.

### Experimental

The silicon wafers used in this study were Czochralski grown and solution doped with boron to an average concentration ranging from  $10^{19}$  to  $2 \times 10^{15}$  atoms/cm<sup>3</sup>. The wafers were oriented for the (111) plane and polished either electrochemically or mechanically. The results reported are independent of surface preparation and substrate doping concentration. The diffusion masks were formed by thermal oxidation at 1100°C in a wet oxygen ambient. The resulting oxide thickness was 5000Å.

The diffusion windows were opened in the oxide by KTR photoresist and etching techniques. The photomask pattern consisted of large square or triangular windows 0.200 in. on a side or circles of 0.200 in. diameter. The diagonal corners of the square windows are oriented approximately in the  $[\bar{1}10]$  and  $[11\bar{2}]$  directions.

Standard diffusion techniques using a P<sub>2</sub>O<sub>5</sub> vapor source and N<sub>2</sub> carrier gas were employed. Temperature and time of diffusions were 1100°C and 1 hr, respectively, resulting in measured junction depths in the order of 2μ. The electrically measured surface concentrations were about  $5 \times 10^{20}$  atoms/cm<sup>3</sup>, although the actual impurity content is probably higher (9).

Crystal defects were analyzed using an x-ray transmission topographical method similar to the Lang method (10). Molybdenum K<sub>α1</sub> radiation was employed under the condition that  $\mu t \approx 1$  ( $\mu$  is the linear absorption coefficient and  $t$  the thickness of the wafer) so that the normal expected mode of diffraction would be by extinction contrast. In practice, this means that structurally imperfect regions should diffract x-rays more intensely than perfect regions. Frequently a reversal of x-ray contrast or a reduction of x-ray intensity accompanying strained regions is simultaneously observed with intensity enhancement. This reduction of x-ray intensity is known as the Borrmann effect. Similar simultaneous displays have been observed to sharply delineate window patterns cut into SiO<sub>2</sub> masks on silicon substrates (5).

### Results

Several investigators have demonstrated that silicon exists in a state of compression due to a mismatch in thermal expansion coefficients when SiO<sub>2</sub> is thermally grown on Si substrates. Blech and Meieran (11) critically analyzed x-ray topographical displays of

strains at oxide steps on Si, and x-ray contrast effects at edges of thin films grown or deposited on single crystal substrates have been attributed by Haruta (12) to strain gradients. Substrates which are in a uniform state of compression due to thin films covering the entire substrate appear in x-ray topographs similar to topographs recorded prior to thin film deposition. Strain gradients, at oxide edges for instance, give rise to x-ray intensities which sharply define the window patterns cut into the oxide. This is clearly demonstrated in Fig. 1 where the contrast is relatively uniform between windows formed in an SiO<sub>2</sub> diffusion mask on silicon. The diffraction vectors are indicated in each figure. Frequently, even after a high concentration emitter type diffusion, the observed contrast appears similar to Fig. 1 except within the diffused areas where diffusion-induced dislocations are observed. That is, the contrast between diffused junctions remains unchanged which implies an unaltered substrate perfection.

In the course of this study, a characteristic type of interjunction strain associated with the diffusion process was observed. The remaining portions of this paper characterize the strain gradient responsible for the observed contrast effects and describes the conditions necessary to control the occurrence of these effects. Finally, a mechanism is suggested to explain these interjunction strain effects.

The x-ray topograph of Fig. 2 was recorded after diffusion. There are obviously two distinct differences in the defect display when compared to Fig. 1: (i) diffusion-induced dislocation arrays are confined to each diode area, and (ii) pronounced dark regions, at each corner of the diffusion mask, extend into the nondiffused portion of the matrix. These dark regions or strain lobes are the so-called interjunction strains. The visibility of such effects in x-ray topographs is a consequence of the strain gradients which result from the lattice adjustment to stresses introduced by the impurity diffusant.

The visibility of strain gradients is also strongly dependent on the reflection chosen. In Fig. 3 the characteristic pattern is completely dissimilar in both its geometrical shape and recorded contrast. Between the four corners of four different junctions the contrast not only reverses (*i.e.*, Borrmann effect is operative) but also the strain gradient appears as a four cornered re-entrant curve which extends over 2500μ to the adjacent junction areas. However, between parallel sides of adjacent junctions the x-ray contrast is dark, indicating diffraction by extinction contrast.

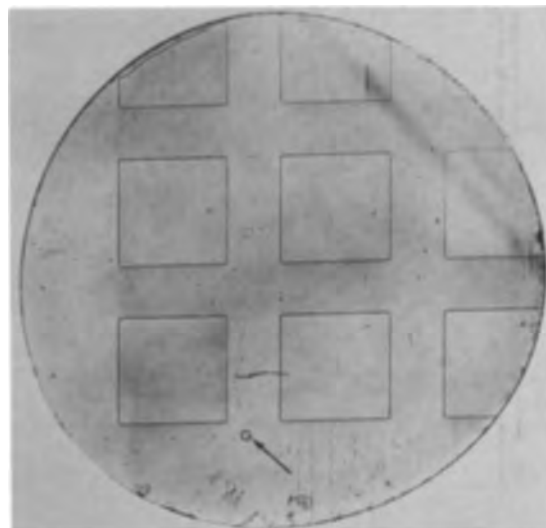


Fig. 1. X-ray topographical displays of strain gradients at oxide edges cut into an SiO<sub>2</sub> diffusion mask on Si;  $\bar{g} = [\bar{1}10]$ .



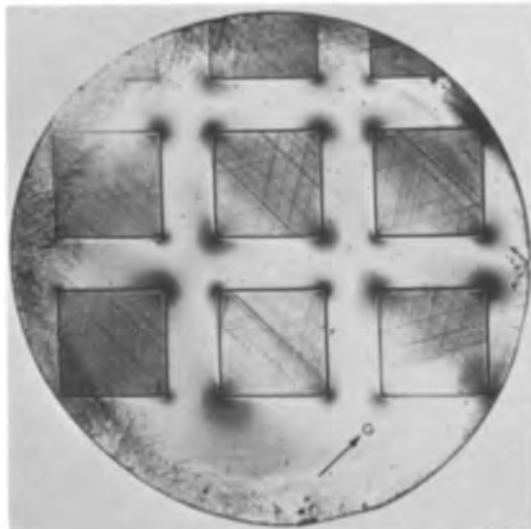


Fig. 2. Pronounced interjunction strain gradients (strain lobes) which extend laterally  $500\mu$  into the nondiffused matrix at the four corners of the diffusion mask;  $\bar{g} = [11\bar{2}]$ .

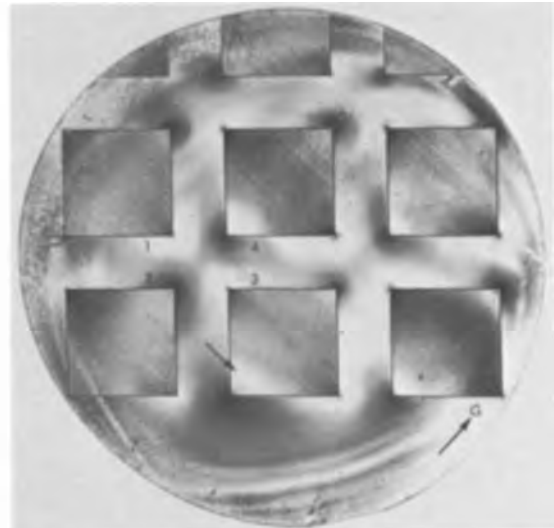


Fig. 4. Interjunction strain lobes visible by extinction contrast in a direction paralleling  $\bar{g}$  and by Borrmann effects in a direction perpendicular to  $\bar{g}$ ; arrow indicates reverse contrast within the diffused area;  $\bar{g} = [11\bar{1}]$ .

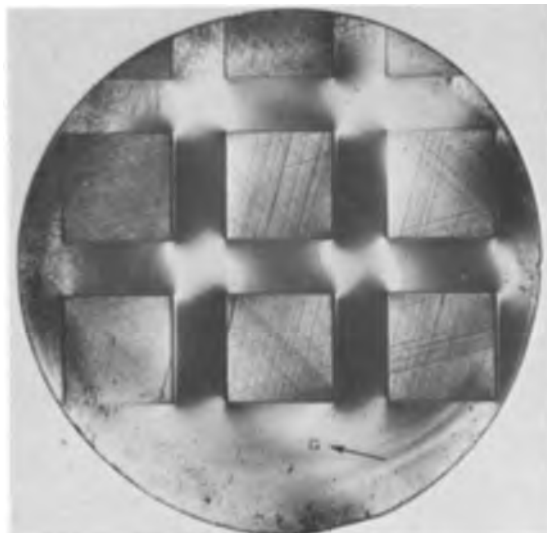


Fig. 3. Contrast variation of interjunction strain gradients for  $\bar{g} = [21\bar{1}]$ ; visibility by extinction contrast between parallel sides of adjacent junctions and by Borrmann effects between four corners of four adjacent junctions.

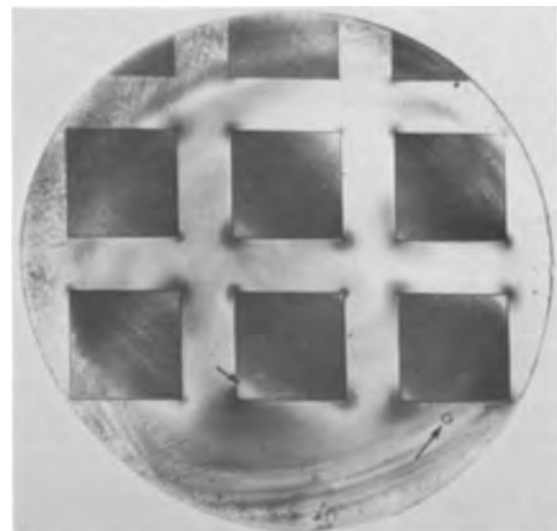


Fig. 5. Corresponds to Fig. 4 except that the oxide has been chemically removed; all four interjunction strain lobes are visible by extinction contrast only;  $\bar{g} = [11\bar{1}]$ .

The four strain lobes again appear in Fig. 4 when the operating diffraction vector  $\bar{g}$  is  $[11\bar{1}]$ . Now however, the two lobes parallel to  $\bar{g}$  (at areas 2 and 4) are visible by extinction contrast (dark regions) while the two lobes perpendicular to  $\bar{g}$  (at areas 1 and 3) are visible over large areas by Borrmann effects (white regions) and by extinction contrast at the tips of the sharp corners. An indication of inelasticity is observed in Fig. 5 where all four strain lobes are visible after chemically removing the oxide. Apparently a portion of the strain is built into the oxide as indicated by the visibility of all four strain lobes by extinction contrast ( $\bar{g} = [11\bar{1}]$ ) in contradistinction to the observation made in Fig. 4. Note also that the strain gradient defining the  $\text{SiO}_2$  window pattern is still visible even though the  $\text{SiO}_2$  has been removed. The intense interjunction strain concentration lies on  $\{111\}$  planes and arises as a consequence of the diffusion cycle. The strain is inelastic inasmuch as it is equally well observed after removing the oxide mask, although the character of the strain pattern does depend on whether

the diffusion mask is intact or removed from the substrate (compare Fig. 4 and 5).

Generally, each highly faulted diffused area contributes to an enhanced x-ray intensity (Fig. 5) which may not be directly related to the diffusion-induced line defects. However, the intensity within the junction areas at the sharp corners appears to reverse contrast or appear white (see arrow in Fig. 4 and 5) while outside the junction the strain contrast is dark. Apparently the fault vector corresponding to the strain lobes is directional. That is, the fault vector is tilting the lattice planes in different directions at the corner boundary separating the diffused/nondiffused matrix.

So far, three distinct strain effects, other than dislocation formation, have been observed: (i) strain gradients which sharply delineate oxide boundaries (Fig. 1); (ii) extensive residual strain effects at oxide boundaries which extend outside and into the diffused areas (Fig. 4 and 5), and (iii) an additional strain built into the oxide due to the diffusion cycle (Fig. 4 and 5).



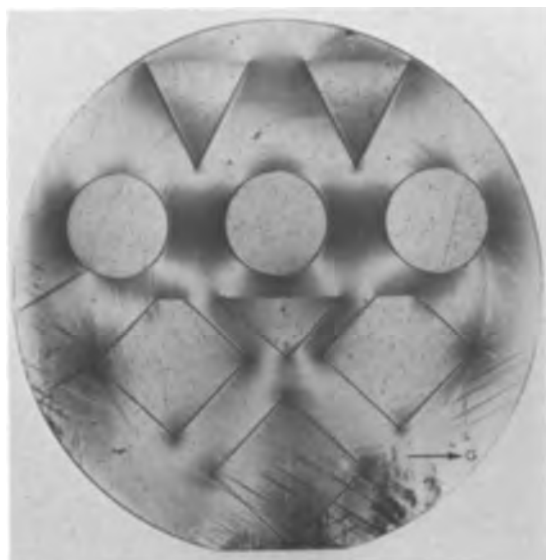


Fig. 6. Low vapor pressure phosphorus diffusion revealing pronounced interjunction strain gradients and no diffusion-induced dislocations;  $\bar{g} = [111]$ .

Using similar diffusion conditions, the occurrence of interjunction strains was found to be independent of the cooling rate. Also under simulated diffusion conditions (without the vapor source), these strain effects were not observed. However, by changing only the vapor pressure of the source it was possible not only to control the occurrence of interjunction strains but it was also possible to control the generation of diffusion-induced dislocations (13). Under low vapor pressure (Fig. 6) no diffusion-induced dislocation arrays are detected by x-ray topography. However the interjunction strain effects are quite pronounced and their occurrence is independent of the particular shape of the window openings. Only the character of the strain pattern is altered by window geometry. The dark spots throughout the wafer are defect markings introduced during the surface polishing. Under high vapor pressure (Fig. 7) each diode is highly dislocated or faulted as evidenced by the excessive intensity within each junction area. However no interjunction strain is evident. Juleff and LaPierre (14) have observed the extension of strain, originating at locally diffused regions in the Si substrate, into epitaxial Si layers

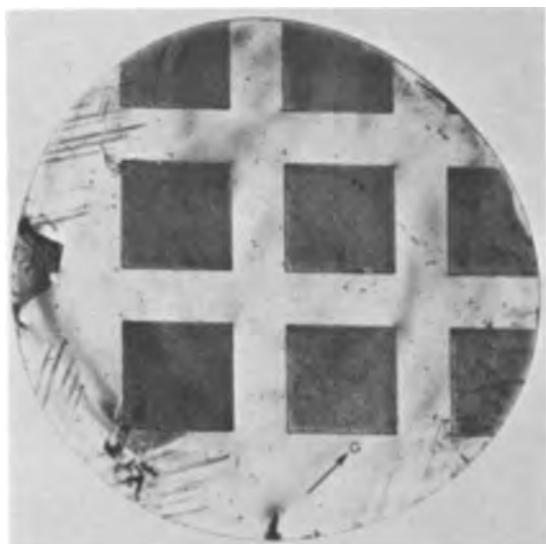


Fig. 7. High vapor pressure phosphorus diffusion revealing no interjunction strain gradients and highly faulted junction areas;  $\bar{g} = [111]$ .

grown over the diffused Si substrate. Even in this case the observed strain effects clearly define the diffused junction geometry, although in some cases diffusion-induced dislocations do propagate laterally from the junction into the non-diffused areas of Si.

### Discussion

The deformed regions between diffused junction areas are clearly related to the generation of dislocations within the junction area. These dislocations are caused by the contraction of the silicon lattice due to the diffusion of smaller phosphorus atoms. The difference in the tetrahedral covalent radii between Si and P is 0.07Å. Joshi et al. (7) have reported that the lattice parameter of Si decreases with increased amounts of phosphorus when solution doping techniques are employed in growing Si crystals. Furthermore, the lattice parameter,  $a_0$ , in phosphorus diffused Si (very high concentrations) more nearly corresponds to the value of  $a_0$  in lightly solution doped Si, probably as a consequence of strain relief and lattice relaxation when diffusion-induced dislocations are

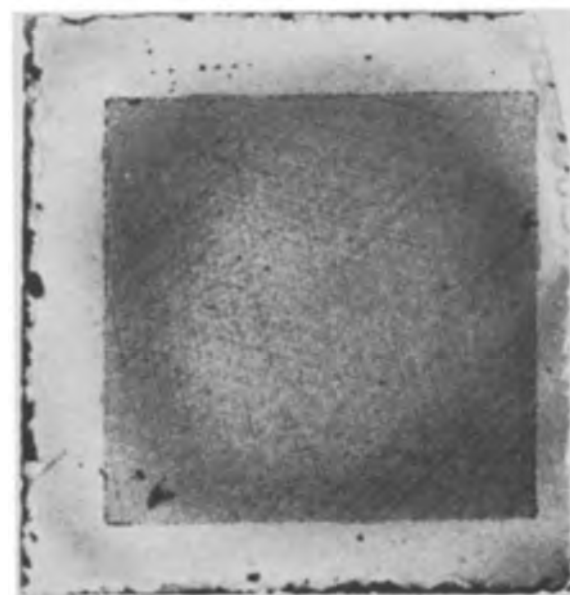


Fig. 8. X-ray topographs recorded after removal of  $1.3\mu$  of Si; (a) junction area sectioned from sample shown in Fig. 2; (b) junction area sectioned from sample shown.

formed. Joshi *et al.* (7) have measured by x-ray line broadening techniques the average strain levels associated with diffusion-induced dislocations and an additional residual strain in diffused silicon layers. The interjunction strain effects observed in our x-ray topographs confirm the existence of these residual strains. Such residual strains are distributed laterally into the nondiffused matrix. The dependence of these strains on the absence of misfit-type dislocations agrees with their observations of lattice parameter variations *vs.* dopant level. Joshi interprets the presence of residual strains in thin surface layers as being due to an insufficient penetration of the diffusion-induced dislocations (7). The distribution of dislocations in samples which showed interjunction strain (*i.e.*, Fig. 2) and samples without interjunction strain (*i.e.*, Fig. 7) was measured by x-ray topography after shallow Si layers were removed by anodic oxidation techniques. A series of topographs were recorded after each incremental removal of 1000Å of Si. In Fig. 8, 1.3 $\mu$  of Si have been removed from the diffused side (junction depth  $x_j = 2\mu$ ) of each specimen shown in Fig. 2 and 7. Most of the dislocations have been removed in Fig. 8a while a high density still remains in Fig. 8b indicating a movement of dislocations deeper into the substrate toward the junction. The interjunction strains seen in Fig. 2 are no longer visible after 0.5 $\mu$  of Si has been removed.

A final observation should be made. The interjunction strains observed in this report do not appear similar to the deformations, observed by Lawrence (6), which result in dislocations formed within highly restricted zones of the nondiffused matrix. He has observed that total impurity stress relief is affected by the type of dislocation formed. Our observations imply that total stress relief, resulting in minimum impurity-induced strain in the nondiffused lattice, occurs when the junction is heavily faulted. This seems to be a consequence of the total number of dislocations formed and their movement into the substrate. Relaxation of solute lattice contraction stresses is affected by the generation of dislocations which, under the conditions stated, balance the impurity-induced strain due to solute indiffusion.

### Summary

Extensive interjunction strain gradients are manifestly observed by x-ray topography. The visibility of such strains is dependent on both the strain gradients due to high concentration impurity diffusions and on the operating reflection employed. Their occurrence is dependent on the magnitude of the unrelieved residual stress which can be compensated by stress-relief generation of dislocations. The depth of penetration of such strains is about  $\frac{1}{4}$  of the junction depth and extends at least 500 $\mu$  laterally from the junction-area boundary.

### Acknowledgments

The authors gratefully acknowledge the assistance of R. J. Modena and Virgil Ragusin in some of the experimental work.

Manuscript received May 2, 1967; revised manuscript received ca. Oct. 30, 1967.

Any discussion of this paper will appear in a Discussion Section to be published in the December 1968 JOURNAL.

### REFERENCES

1. H. J. Queisser, *J. Appl. Phys.*, **32**, 1176 (1961).
2. G. H. Schwuttke and H. J. Queisser, *ibid.*, **33**, 1540 (1962).
3. M. L. Joshi and F. Wilhelm, *This Journal*, **112**, 185 (1965).
4. J. F. Black and E. D. Jungbluth, *ibid.*, **114**, 188 (1967).
5. E. S. Meieran and I. A. Blech, *J. Appl. Phys.*, **36**, 3162 (1965).
6. J. E. Lawrence, *This Journal*, **113**, 819 (1966).
7. M. L. Joshi, C. H. Ma, and J. Makris, *J. Appl. Phys.*, **38**, 725 (1967).
8. E. D. Jungbluth and H. Chiao, *Bull. Am. Phys. Soc.*, **12**, 672 (1967).
9. E. Kooi, *This Journal*, **111**, 1383 (1964).
10. A. R. Lang, *J. Appl. Phys.*, **30**, 1748 (1959).
11. I. A. Blech and E. S. Meieran, *ibid.*, **38**, 2913 (1967).
12. K. Haruta and W. J. Spencer, *ibid.*, **37**, 2232 (1966).
13. R. A. McDonald, G. G. Ehlenberger, and T. R. Huffman, *Solid St. Electron.*, **9**, 807 (1966).
14. E. M. Juleff and A. G. LaPierre, *Int. J. Electronics*, **20**, 273 (1966).

## Technical Notes



### Phase Transformations in the System $\text{Cu}_2\text{S}-\text{Ag}_2\text{S}$

R. B. Graf

United Aircraft Corporation, Research Laboratories, East Hartford, Connecticut

Both end members of the system  $\text{Cu}_2\text{S}-\text{Ag}_2\text{S}$  have been of interest for many years as naturally occurring minerals as well as for their electrical properties.  $\text{Cu}_2\text{S}$  has been of importance as a rectifier material and  $\text{Ag}_2\text{S}$  is a semiconductor that has a polymorphic transformation at 177°C. This phase transformation is accompanied by an abrupt electrical resistivity change of about 3 orders of magnitude and has been mentioned as being suitable for a-c switching applications (1). In addition to this phase transformation, it was considered that the equilibrium diagram (2) (Fig. 1) might contain other invariant points which would exhibit interesting electrical properties. The points selected for this investigation were: the eutectoid reaction between acanthite ( $\text{Ag}_2\text{S}$ ) and jalpaite ( $\text{Cu}_{0.45}\text{Ag}_{1.55}\text{S}$ ) to form argentite at 106°; the phase transformation in jalpaite to form argentite at 117°; and the eutectoid reaction between orthorhombic chal-

cocite ( $\text{Cu}_2\text{S}$ ) and stromeyerite ( $\text{CuAgS}$ ) (not shown in Fig. 1) at 67°. The transformation of acanthite ( $\text{Ag}_2\text{S}$ ) to argentite was investigated using thin films as well as bulk pieces to determine if the large change in resistivity could be obtained easily in thin film samples.

The compounds were formed by reacting the elements (99.999% purity) in evacuated and sealed glass tubes. The reactants were sintered at 400°C until none of the free elements remained visible, and the formation of the compounds was verified by powder x-ray diffraction. The samples for resistivity measurements were fabricated by compressing powders which had been filed from the sintered ingots. The powder compacts, which were 0.250 in. in diameter and 0.125 in. long, were pressed in a split die so constructed as to make it possible to press a chromel-alumel thermocouple into the center of the pellet. At this same time

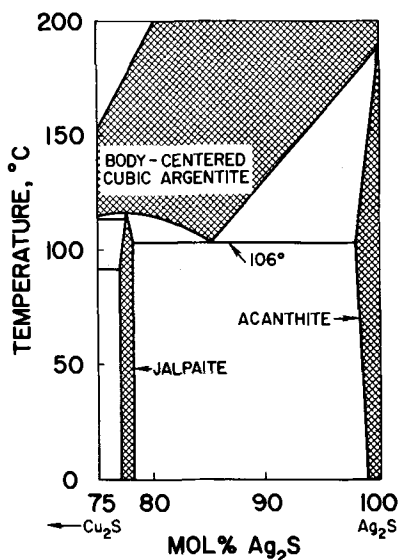


Fig. 1. The system  $\text{Cu}_{0.45}\text{Ag}_{1.55}\text{S}-\text{Ag}_2\text{S}$

gold powder was pressed onto either side of the pellet to form electrodes. The thin films of  $\text{Ag}_2\text{S}$  were formed by evaporating silver onto glass substrates which were then heated with sulfur at  $200^\circ\text{C}$  in sealed glass tubes. Electrodes of silver paste were spaced on the film so as to make the sample resistance about 10,000 ohms at approximately  $170^\circ$ . Because of the known ionic conductivity in  $\text{Ag}_2\text{S}$ , the electrical resistivity measurements were made by passing a constant, 60 cycle current of 100 ma through the samples and measuring the voltage change as a function of temperature. The voltage was measured with a Moseley log converter and the output of the log converter was plotted against the output of the thermocouple on a Moseley x-y plotter. Such an arrangement makes it possible to obtain the transformation time for a sample of a given size. A heating rate of  $5^\circ\text{C}/\text{min}$  was used for all samples.

The resistance changes on heating the samples vs. temperature are shown in Fig. 2. The eutectoid reaction between acanthite and jalpaite (curve A) begins at  $106^\circ$  and is essentially over at  $110^\circ$ . On cooling the sample, the reverse reaction exhibits about  $12^\circ$  hysteresis, measured at the mid-point of the highest slope. Heating and cooling the sample through 12 cycles does not change the characteristics of the plot; the heating curve is almost exactly reproduced and the cooling curve is reproduced to within  $\pm 1.5^\circ$ . Jalpaite, which also transforms to argentite on heating, has a resistance change as shown by curve B. The transformation begins at  $117^\circ$  and is over at  $120^\circ$ . There is about  $7^\circ$  hysteresis on cooling. Curve C in Fig. 2 depicts the resistance change in a thin film of  $\text{Ag}_2\text{S}$  on a  $\frac{1}{4}$  in. square glass substrate as it was heated through the transition temperature of  $177^\circ$ . This reaction occurs

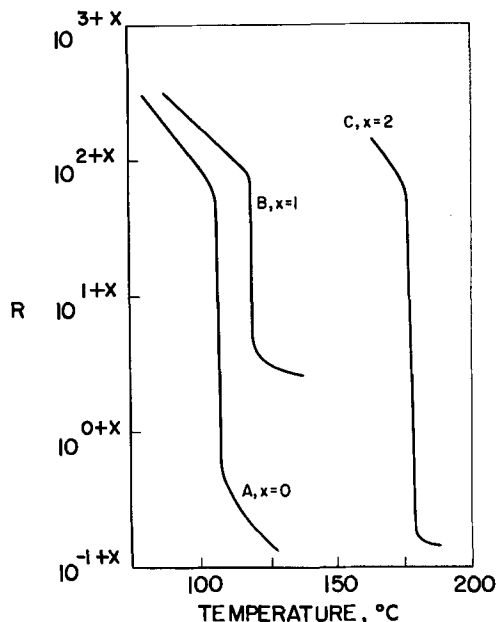


Fig. 2. Resistance vs. temperature for: A, acanthite-jalpaite eutectoid reaction; B, transformation of jalpaite to argentite; C, transformation of acanthite to argentite in thin film form.

over a temperature span of  $3^\circ$  and the reverse reaction had about  $6^\circ$  hysteresis. The transformation in a sample of  $\text{Ag}_2\text{S}$  0.125 in. thick and 0.250 in. in diameter occurred over a temperature span of  $2^\circ$  or  $3^\circ\text{C}$ . The eutectoid reaction between orthorhombic chalcocite ( $\text{Cu}_2\text{S}$ ) and stromeyerite ( $\text{CuAgS}$ ) at  $67^\circ$  to form hexagonal high-chalcocite (not shown in Fig. 2) is accompanied by an increase in resistance of less than one order of magnitude and does not occur as quickly as the others, being spread over a temperature range of  $20^\circ$ .

These results indicate that by using invariant points on a phase diagram, it may be possible to obtain solid-solid reactions which would be suitable for a-c switching in those cases where switching time is not so important. The transformation times may be varied by using thin films of the materials on the proper substrates.

#### Acknowledgment

The author would like to acknowledge the valuable assistance of Jane Pinto in various phases of the experimental work.

Manuscript received Oct. 26, 1967.

Any discussion of this paper will appear in a Discussion Section to be published in the December 1968 JOURNAL.

#### REFERENCES

1. R. G. Cope and H. J. Goldsmid, *Brit. J. Appl. Phys.*, **16**, 1501 (1965).
2. B. J. Skinner, *Econ. Geol.*, **61**, 1-26 (1966).

## Gas Phase Etching of Sapphire

### II. Fluorinated Hydrocarbons

H. M. Manasevit

*Autonetics, A Division of North American Rockwell Corporation, Anaheim, California*

Of various processes and techniques that have been used to etch and/or polish inorganic oxide systems, the least used but probably the most desirable approach is a gas phase process. Until quite recently, no gas phase etchant was reported in the literature that would etch-polish sapphire at what might be con-

sidered a reasonable rate (about  $1 \mu\text{m}/\text{min}$ ). However, studies in our laboratories have indicated that a host of different gas-phase etchants will etch-polish sapphire. The successful etch-polishing of sapphire with sulfur tetrafluoride ( $\text{SF}_4$ ) and sulfur hexafluoride ( $\text{SF}_6$ ) has already been reported (1). Only two ori-

entations were studied,  $(11\bar{2}3)$  and  $(1\bar{1}02)$  of sapphire, with the former showing preferential polish while the latter etched under comparable conditions.

Since the probable aluminum product of etching with the sulfur fluorides is  $AlF_3$  (indications of  $AlF_3$  epitaxy on  $Al_2O_3$  were obtained at temperatures of  $1150^\circ C$ ) (1), it was anticipated that other fluorine containing compounds were possible sapphire etchants. From a fundamental point of view, knowledge of the etching capability of hydrogen fluoride and fluorine would be interesting, but their reactivity with Pyrex and quartz deterred study with these materials in our epitaxial system. Therefore, we chose to consider the etching potential afforded by a most readily available group of fluorine containing compounds, the fluorinated hydrocarbons. These compounds are relatively inexpensive, have low toxicity levels, are easily handled, seem to be stable at room temperature, and are commercially available in a reasonably good purity.

To date, seventeen fluorocarbon gases have been examined as possible etch-polish agents for sapphire. As will be shown, some of these have a potential as dislocation etchants for different sapphire orientations.

### Experimental

Studies were performed in a vertical reactor system similar to that previously described (2). It includes a tank of inert carrier gas, such as helium, upstream from a tank of the "etchant" to be studied. These are connected via Matheson No. 607 and No. 600 flowmeters, respectively, to a stainless steel manifold joined to the quartz reactor by a Teflon connector. For liquid fluorinated hydrocarbons, a portion of the carrier gas is bubbled through the liquid stored in a stainless steel container, passed into the flowing ambient kept at approximately one atmosphere total pressure, and directed into the reactor. Carrier gas flow rates were arbitrarily set at 2.5 liters/min. The gases are passed over a substrate resting on an  $Al_2O_3$  spacer covering a carbon pedestal inductively heated to the etching temperature. The spacer seems to help provide a more even heat distribution and to reduce reaction between the etching gases and the carbon pedestal. Pedestal temperatures were measured with an optical pyrometer, and uncorrected values are reported. The actual substrate temperature is estimated to be  $50^\circ$ – $100^\circ$  lower than the observed  $1450^\circ C$  etching temperature used to compare the etch-polishing ability of the fluorinated hydrocarbons.

To facilitate the experiments, the studies included mostly those fluorinated hydrocarbons that have relatively low boiling points. The effect of etching-gas concentrations up to about 1 m/o (mole per cent) was investigated and compared with all of the fluorinated hydrocarbons noted in Table I.

### Results and Discussion

Carbon tetrafluoride ( $CF_4$ ) was the only fluorinated hydrocarbon in Table I that did not attack sapphire

Table I. Fluorinated hydrocarbons studied as etchants for sapphire at  $1450^\circ C$

Chemical formula	Common name
$CHF_3$	Fluoroform
$CHClF_2$	Chlorodifluoromethane
$CHCl_2F$	Dichlorofluoromethane
$CH_2F_2$	Methylene fluoride
$CClF_3$	Chlorotrifluoromethane
$CCl_2F_2$	Dichlorodifluoromethane
$CBF_3$	Bromotrifluoromethane
$CF_4$	Carbon tetrafluoride
$C_2F_6$	Hexafluoroethane
$C_2ClF_5$	Chlorotrifluoroethylene
$C_2ClF_4$	Monochloropentafluoroethane
$C_2Cl_2F_4$	1, 1, 2-Trichlorotrifluoroethane
$C_2Cl_2F_4$	1, 2-Dichlorotetrafluoroethane
$C_3F_8$	Perfluoropropane
$C_4F_{10}$	Hexafluoroacetone
$C_4F_8$	Octafluorocyclobutane
$C_4F_8$	Perfluorobutene-2

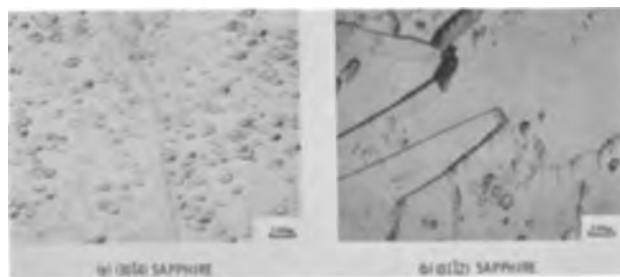


Fig. 1. Dislocation structure revealed by etching with hexafluoroacetone ( $C_3F_8O$ ) for (a)  $(10\bar{1}4)$  sapphire; (b)  $(01\bar{1}2)$  sapphire.

at  $1450^\circ C$  during a 30-min period at 0.5 m/o concentration with either He or  $H_2$  as the carrier gas. The other compounds were found to etch and/or polish sapphire to different degrees in helium. Some of the etchants revealed major defects in the sapphire, others left carbonaceous residues, and some revealed dislocation arrays.

As with the sulfur fluorides, selectivity for sapphire orientation was also demonstrated by the fluorocarbon etchants. For example, hexafluoroacetone polished  $(11\bar{2}3)$  sapphire but roughened both  $(10\bar{1}4)$  and  $(01\bar{1}2)$  Verneuil sapphire at the same gas concentration. The effect of this etching is indicated in Fig. 1, both a and b.

By bubbling He through the liquid fluorocarbon 1, 1, 2-trichlorotrifluoroethane ( $C_2Cl_3F_3$ ) equilibrated at  $0^\circ C$  and passing the gases over the heated substrate, considerable etching was found for the  $(10\bar{1}4)$  and  $(11\bar{2}0)$  sapphire (Fig. 2).  $C_2Cl_2F_4$ , 1, 2-dichlorotetrafluoroethane, revealed structure in basal plane ( $0^\circ$ ) sapphire (Fig. 3a) and an unusual oval-type defect structure in  $(01\bar{1}2)$  sapphire (Fig. 3b).

Except for Fig. 3b, the figures referred to heretofore have been found to be typical surface etch characteristics for the different sapphire orientations noted and, in general, are produced by almost all of the fluorocarbon etchants, especially when concentrations exceeding 1 m/o are used. Reasonable polishing of most orientations studied, however, has been achieved with many of the fluorocarbons when etchant concentrations are kept below about 0.5 m/o. As might be expected, less etch-pitting and surface character were

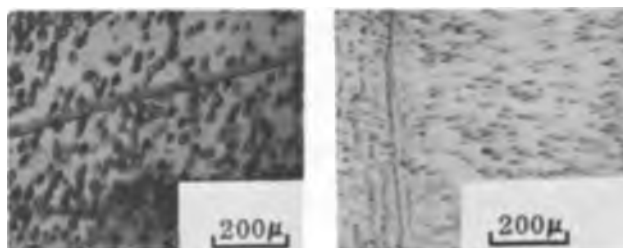


Fig. 2. Dislocation structure revealed by etching with trichlorofluoroethane ( $C_2Cl_3F_3$ ) for (a)  $(10\bar{1}4)$  sapphire; (b)  $(11\bar{2}0)$  sapphire.

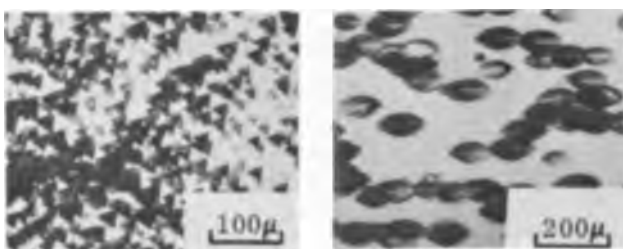


Fig. 3. Dislocation structure as revealed by etching with 1, 2-dichlorotetrafluoroethane ( $C_2Cl_2F_4$ ) for (a)  $(0001)$  sapphire; (b)  $(01\bar{1}2)$  sapphire.

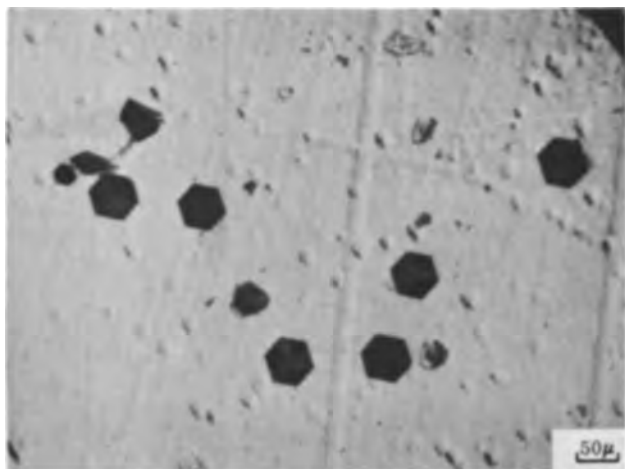


Fig. 4. Defect structure revealed in basal plane Czochralski ruby by etching with chlorotrifluoromethane ( $\text{CClF}_3$ ).

obtained when good quality Czochralski sapphire was exposed to the etchants. This is demonstrated in Fig. 4 for basal plane Czochralski ruby etched by monochlorotrifluoromethane ( $\text{CClF}_3$ ). The origin of the defect that caused the large hexagonal pits, which are prominent in a field of comparatively few pyramidal etch pits, is not known. Figure 5 was produced by etching (0112) sapphire with octafluorocyclobutane ( $\text{C}_4\text{F}_8$ ). The tombstone-like etch pits were usually found to be characteristic of this orientation. The oval pits produced in (0112) sapphire by 1, 2-dichlorotetrafluoroethane ( $\text{C}_2\text{Cl}_2\text{F}_4$ ) (Fig. 3b) may have been caused by a different type of etching species and reaction.

The reactivity of chlorotrifluoromethane ( $\text{CClF}_3$ ) as compared to  $\text{CF}_4$  is undoubtedly due to the weakening of the C-F bond by the presence of the less electronegative Cl ion in the molecule. Although hexafluoroethane ( $\text{C}_2\text{F}_6$ ) is completely saturated like  $\text{CF}_4$ , the C-C bond is susceptible to rupture, thereby providing the reactive species.

It was observed that when linear C-C double bonds or C-H bonds are present in the structure of the fluorinated hydrocarbon, etching also produced sooty surfaces, especially at the higher gas concentrations. Some of the minor carbon contamination may be attributed to impurities in the gas, but major carbon deposits are more likely due to the cleavage of these bonds in the bulk material. Therefore, complete saturation of the C atoms by halogens, at least one of which is fluorine, seems to be required in choosing

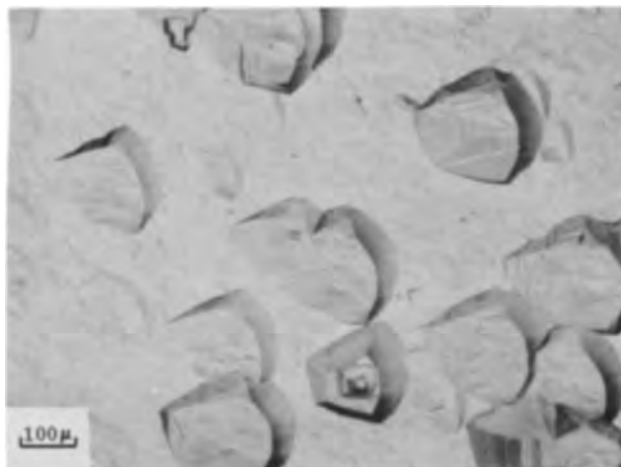
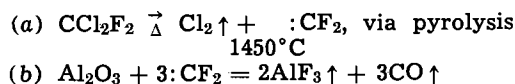


Fig. 5. Effect of etching (0112) sapphire with octafluorocyclobutane ( $\text{C}_4\text{F}_8$ ).

a fluorocarbon etchant: for example, hexafluoroethane ( $\text{C}_2\text{F}_6$ ), perfluoropropane ( $\text{C}_3\text{F}_8$ ), dichlorodifluoromethane ( $\text{CCl}_2\text{F}_2$ ), and/or monochloropentafluoroethane ( $\text{C}_2\text{ClF}_5$ ). Octafluorocyclobutane ( $\text{C}_4\text{F}_8$ ), a fluorocarbon with a ring structure, produced some dark product at  $1450^\circ\text{C}$  but etched sapphire at a rather rapid rate at relatively low concentrations compared to the linear chained materials studied. This suggests a weaker C-C bond in the ring structure, with bond breakage making more fluoride per molecule per unit time available for etching. It was also observed that 1, 2-dichlorotetrafluoroethane ( $\text{C}_2\text{Cl}_2\text{F}_4$ ) possessed the capability of etching sapphire at about  $0.1 \mu\text{m}/\text{min}$  at temperatures as low as  $950^\circ\text{C}$  (observed uncorrected optical pyrometer reading). (Other highly fluorinated hydrocarbons in the group have not been evaluated at this relatively low temperature.) It is not known if a change in the etching mechanism occurred at  $950^\circ\text{C}$ , producing aluminum products other than  $\text{AlF}_3$ . This might be the case if different carbon-fluorine radicals are produced, e.g.,  $\cdot\text{CF}_2$  (difluorocarbene) or  $\cdot\text{CF}_3$  (trifluoromethyl radical), at different temperatures.

It is indeed difficult to write reasonable equations to explain the etching of sapphire without knowing the products of the reaction with the fluorinated hydrocarbons. Some of the products that collected on the cool reactor wall could be vacuum distilled at room temperature; some seemed water soluble; others had to be scraped off the walls or undercut with  $\text{HF-HNO}_3$  solutions for removal. It is probable that many of the reactions involve, as previously suggested, the formation of free radicals containing at least one carbon-fluorine bond that might react with  $\text{Al}_2\text{O}_3$  to produce  $\text{AlF}_3$  (volatile at  $1450^\circ\text{C}$ ) and other products. For dichlorodifluoromethane, a plausible reaction scheme is proposed by the following equations



If more complex fluorinating agents are used as etchants, a study of the reaction products could disclose new materials, perhaps polymers containing aluminum-carbon bonds as well as other fluorinated carbon by-products.

#### Addendum

Under the etching conditions previously described, a number of inorganic fluorides other than  $\text{SF}_4$  and  $\text{SF}_6$  were also found to etch sapphire. These include the chlorine fluorides ( $\text{ClF}_3$  and  $\text{ClF}_5$ ), nitrogen trifluoride ( $\text{NF}_3$ ), and phosphorus pentafluoride ( $\text{PF}_5$ ). These, of course, produce no organic by-products but introduce in some cases a problem in handling because of their room temperature chemical reactivity with glass flowmeters and other materials.

#### Conclusions

The etching capabilities of a number of fluorinated hydrocarbons have been demonstrated. These materials show promise of being new reagents for evaluating the quality and improving the surfaces of sapphire prior to its use as a substrate for epitaxy.

#### Acknowledgment

The author wishes to express his thanks to W. I. Simpson, J. E. Coker, and F. Erdmann for their assistance in the etching studies, to T. J. LaChapelle for suggesting the study, and to James Beeman and the Linde Company for supplying the Czochralski wafers.

This study was supported in part by the Naval Electronics Systems Command under Contract NObsr 93145.

Manuscript received Nov. 16, 1967; revised manuscript received ca. Jan. 10, 1968. This paper was

presented at the Chicago Meeting, Oct. 15-19, 1967, as Abstract 183.

Any discussion of this paper will appear in a Discussion Section to be published in the December 1968 JOURNAL.

## Thermally Activated Diffusion of Electronic Carriers in Iron Phosphate Glasses

Gary S. Snow\*<sup>1</sup>

Department of Ceramic Engineering and Materials Research Laboratory,  
University of Illinois, Urbana, Illinois

Hansen (1) recently measured conductivity and Seebeck coefficient on phosphate glasses containing 45 m/o (mole per cent) P<sub>2</sub>O<sub>5</sub>. The remaining 55 m/o consisted of FeO and MgO in various proportions. In the 45% P<sub>2</sub>O<sub>5</sub>-55% FeO composition the ratio of [Fe<sup>3+</sup>] to [Fe<sup>2+</sup>] was varied over a wide range. This data offers an excellent opportunity to check the agreement between the experimentally observed dependence of resistivity on valence state distribution and that predicted by the hopping model. Hansen discussed his data qualitatively in terms of the hopping mechanism; however, there are inconsistencies in his discussion which should be clarified.

If the electronic carriers move by a thermally activated diffusion process, the conductivity can be written

$$\sigma = \frac{nq^2d^2zP\nu e^{-\Delta E/kT}}{6kT} \quad [1]$$

where  $n$  is the carrier concentration,  $q$  is the charge on the carrier,  $d$  is the jump distance,  $z$  is the number of nearest neighbor sites,  $P$  is the probability that a particular nearest neighbor site will be available to receive a carrier,  $k$  is Boltzmann's constant,  $T$  is the absolute temperature,  $\nu$  is a frequency factor characteristic of the lattice vibrations, and  $\Delta E$  is the energy necessary to remove the lattice distortion around the trapped carrier. In this equation Hansen omitted the factor  $P$  which is extremely dependent on the valence state distribution. Evaluation of this factor allows one to obtain a quantitative fit between Eq. [1] and Hansen's experimental data.

In the iron phosphate glasses studied by Hansen let  $x$  be the fraction of the iron ions which are in the Fe<sup>3+</sup> state, let  $y$  be the fraction of the cations which are iron, and let  $c_0$  be the total concentration of cations. Then if one assumes that conduction occurs by hopping of electrons from Fe<sup>2+</sup> sites to Fe<sup>3+</sup> sites, the carrier concentration will be equal to the concentration of Fe<sup>2+</sup> ions; thus  $n = (1-x)y c_0$ . Assuming that phosphorous ions and iron ions of either valence have equal probability of being on any given cation site, the probability that a particular nearest neighbor site will be available to receive a carrier is just equal to the fraction of the cation sites which are occupied by Fe<sup>3+</sup> ions; thus  $P = xy$ . Using these relations, Eq. [1] then becomes

$$\sigma = K e^{-\Delta E/kT} y^2 (1-x) x \quad [2]$$

where

$$K = \frac{c_0 q^2 d^2 z \nu}{6kT} \quad [3]$$

It should be noted that the same equation results if the carriers are assumed to be holes moving from Fe<sup>3+</sup>

### REFERENCES

1. H. M. Manasevit and F. L. Morritz, *This Journal*, **114**, 204 (1967).
2. H. M. Manasevit, D. H. Forbes, and I. B. Cadoff, *Trans. AIME*, **236**, 275 (1966).

sites to Fe<sup>2+</sup> sites, in which case  $n = xyc_0$  and  $P = (1-x)y$ .

In Fig. 1 and 2 the data of Hansen is compared with this theory. In plotting Eq. [2],  $\Delta E$  was obtained as a function of  $x$  and  $y$  from Hansen's data, and  $K$  was chosen as 563 (ohm-cm)<sup>-1</sup>. There is excellent agreement between the experimental data and the calculated points. From Fig. 1 it is apparent that another transport mechanism becomes dominant below  $y = 0.05$ .

Taking  $K = 563$  (ohm-cm)<sup>-1</sup> an order-of-magnitude value for  $\nu$  can easily be calculated from Eq. [3]. Assuming a simple cubic distribution of cation sites and taking  $c_0$  as approximately 10<sup>22</sup> cm<sup>-3</sup>, then  $z = 6$  and  $d = 4.7 \times 10^{-8}$  cm. The other parameters are known constants. The resulting value for  $\nu$  is  $6.5 \times 10^{12}$  sec<sup>-1</sup> which is in good agreement with the expected value of the vibrational frequency of the lattice.

Since  $d$  can be treated as independent of  $x$  and  $y$ , it appears likely that electronic transfer always occurs between nearest neighbor iron sites, at least for  $y > 0.05$  (10 m/o FeO).

Allersma and Mackenzie (2) have shown that the Seebeck coefficient data which Hansen obtained for iron phosphate glasses qualitatively fits the following equation developed by Heikes (3) for the hopping

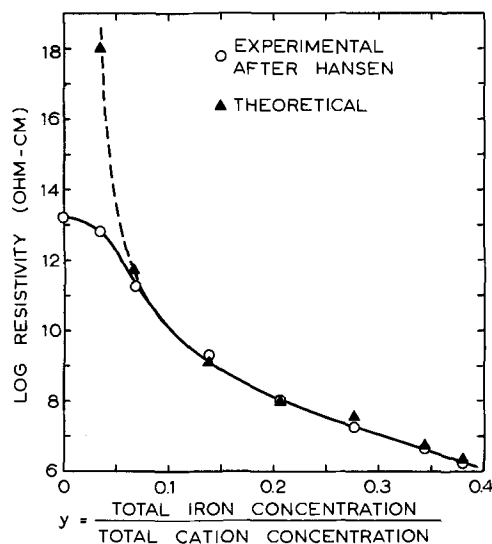


Fig. 1. Logarithm of resistivity at 200°C as a function of the fraction of the total cations which are iron. Experimental data was taken from Fig. 1 of ref. (1). Theoretical points were calculated from Eq. [2] using the  $\Delta E$  values from Fig. 1 of ref. (1) and taking  $K = 563$  (ohm-cm)<sup>-1</sup>.

\* Electrochemical Society Active Member.

<sup>1</sup> Present address: Inorganic Materials Science Division, 1123, Sandia Corporation, Albuquerque, New Mexico.

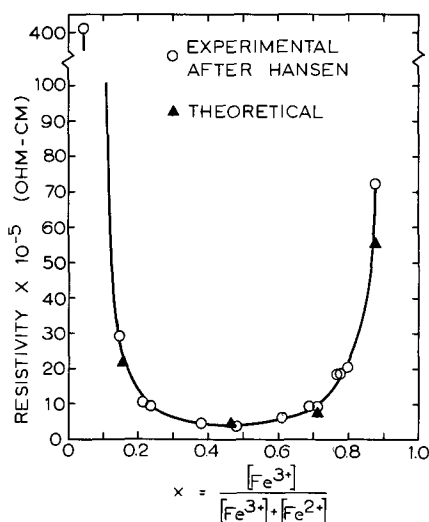


Fig. 2. Variation of resistivity with  $x = [\text{Fe}^{3+}]/[\text{Fe}_{\text{total}}]$  at  $200^\circ\text{C}$  for glasses containing 55% FeO-45%  $\text{P}_2\text{O}_5$ . Experimental data was taken from Fig. 4 of ref. (1). Theoretical points were calculated from Eq. [2] using  $\Delta E$  values from Fig. 3 of ref. (1) and taking  $K = 563 (\text{ohm-cm})^{-1}$ .

mechanism

$$\alpha = \frac{k}{q} \ln \frac{n_0 - n}{n} \quad [4]$$

In Eq. [4]  $\alpha$  is the Seebeck coefficient,  $n$  is the concentration of carriers (equal to  $[1-x]yc_0$  if the carriers are electrons and equal to  $xyz_0$  if they are holes),  $n_0$  is the concentration of accessible sites (equal to  $yc_0$  in either case), and  $q$  has the sign of the charge carrier. It is worth noting that Eq. [4] becomes

$$\alpha = \frac{-k}{|q|} \ln \frac{x}{1-x} \quad [5]$$

and fits the data over the entire range of  $x$  whether the carriers are holes or electrons; thus, it is not neces-

sary that the sign of the carriers change when the Seebeck coefficient goes from positive to negative as was concluded by previous investigators (1, 2). From the currently available data no conclusions can be drawn concerning the sign of the charge carrier.

In order to calculate the carrier mobility, Hansen obtained the carrier concentration from the equation  $n = n_0 \exp(-q\alpha/k)$ . He took  $n_0$  as the absolute difference between the ferric and ferrous concentrations. This assumption contradicts the data since it would result in an infinite resistivity at  $x = 0.5$  rather than a minimum as shown in Fig. 2. Hansen obtained values for the frequency factor  $\nu$  which were extremely dependent on  $\Delta E$  and on his choice of valence state distribution. In the present analysis  $\nu$  is independent of these parameters as one would expect.

This treatment yields a carrier mobility which (at  $200^\circ\text{C}$  in the 55% FeO glass) varies from  $1.3 \times 10^{-8} \text{ cm}^2/\text{v-sec}$  to zero as the concentration of carriers goes from zero to  $yc_0$ .

The correlation between Hansen's data and Eq. [2] and [5] strongly supports the treatment of electronic conduction in the iron phosphate glasses as a thermally activated diffusion process. It appears doubtful that conduction in a partially filled  $3d$  band would have this dependence on valence state distribution.

#### Acknowledgment

This work was supported in part by the U.S. Atomic Energy Commission, Contract No. AT(11-1)-1198.

Manuscript received July 24, 1967; revised manuscript received Dec. 18, 1967.

Any discussion of this paper will appear in a Discussion Section to be published in the December 1968 JOURNAL.

#### REFERENCES

1. K. W. Hansen, *This Journal*, **112**, 994 (1965).
2. T. Allersma and J. D. Mackenzie, Technical Report No. 4, Contract No. Nonr-591(21), December 1966.
3. R. R. Heikes, A. A. Maradudin, and R. C. Miller, *Ann. Phys.*, **8**, 733 (1963).

## Brief Communications



### Impurity Heterogeneities and Multiple-Beam Interferometry

D. C. Johnston, A. F. Witt,\* and H. C. Gatos\*

Department of Metallurgy and Center for Materials Science and Engineering,  
Massachusetts Institute of Technology, Cambridge, Massachusetts

Multiple-beam interferometry (1) combined with high resolution etching techniques has been successfully employed for revealing relative microscopic concentration changes of impurities in InSb. In view of the fact that "rate striations" intentionally introduced into single crystals allow the precise determination of microscopic rates of crystal growth (2), it was possible to demonstrate further in the present study that multiple-beam interferometry can directly reveal relationships between microscopic rates of growth and impurity concentration. The impurity present in the crystals was tellurium (about  $10^{17}/\text{cm}^3$ ).

\* Electrochemical Society Active Member.

Figure 1 depicts the "off-core" region of a single crystal of InSb pulled in the  $\langle 111 \rangle$  direction with seed rotation and subjected to controlled vibrations (frequency 12 per sec). The interference fringes were aligned in a vertical direction (1). In this way a uniform impurity distribution or complete absence of impurities would be reflected by the appearance of straight and parallel interference fringes aligned from top to bottom (a perfectly flat semiconductor surface after etching). Under the present experimental conditions a relative decrease or increase in impurity concentration (depressions or elevations on the etched semiconductor surface, respectively) will appear as



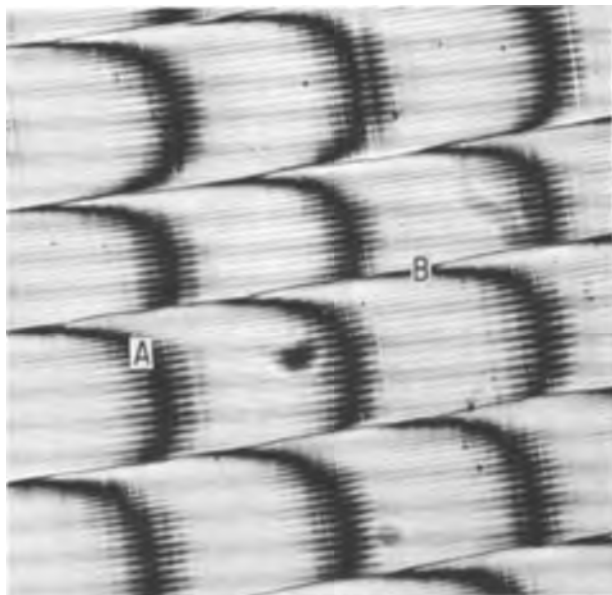


Fig. 1. Interferogram of an "off-core" region of InSb grown in the  $\langle 111 \rangle$  direction (top to bottom) exhibiting pronounced "remelt" rotational striations, B. The abrupt interference fringe deflections to the left, A, associated with the rotational striations reflect a sharp decrease in impurity concentration. The "rate striations" are also clearly seen (see text). Magnification 700X.

deflections of the fringes to the left and right, respectively. Tellurium impurities decrease the etching rate of InSb under the present experimental conditions. Figure 1 shows abrupt fringe deflections to the left, A, which are associated with slightly curved rotational striations, B, traversing from left to right. The rate striations are readily visible as small spikes emanating from the fringes. Thus the fringe pattern permits the simultaneous determination of microscopic growth rates and the associated impurity concentration changes.

The information contained in the interferogram of Fig. 1 can best be extracted by analyzing the pattern of the individual fringes running from top to bottom (along the growth axis). The separation of the rate striations reflects the growth rate changes associated with rotational striations as discussed in detail elsewhere (2). It can readily be seen that immediately below each remelt striation the growth rate assumes very small values which gradually increase (increasing spacing of subsequent spikes proceeding from top to bottom) before they become very small again at the next striation. The abrupt fringe deflections to the left associated with rotational striations indicate a sharp drop in impurity concentration in the area of decreased growth rate. With increasing growth rate (below the remelt striations) the fringes move to the right indicating a relative increase in impurity concentration. The observed concentration changes on either side of each striation is consistent with the corresponding growth rate changes discussed in detail elsewhere (2).

Figure 2 depicts the "off-core" to "on-core" transition region in a single crystal (InSb) pulled in the  $\langle 111 \rangle$  direction with seed rotation (no rate striations were introduced). On the left-hand side, A, (off-core region) the impurity concentration decrease associated with the rotational striation is clearly vis-

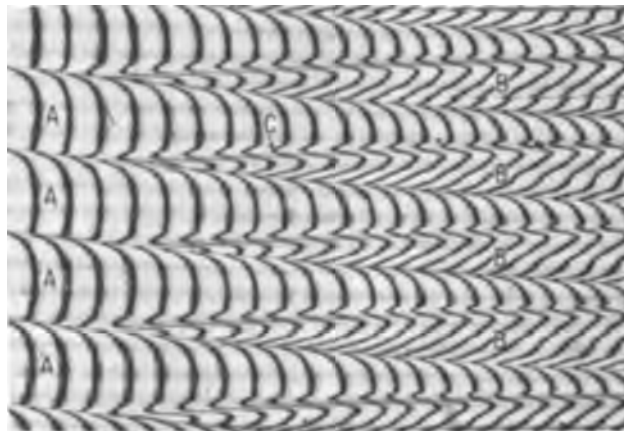


Fig. 2. Interferogram of an etched "off-core" to "on-core" transition region of InSb grown in the  $\langle 111 \rangle$  direction (top to bottom). Note impurity concentration changes in the off-core region (on the left side, A) associated with rotational striations (same as in Fig. 1). The on-core regions, B, exhibit strong fringe deflections to the right corresponding to increased impurity concentration. Within the core regions very pronounced impurity concentration variations are visible (changes in slopes of the deflected interference fringes). A small but readily visible impurity concentration decrease is present in the off-core region adjacent to the "core" region, C. See text. Magnification ca. 470X.

ible. The on-core regions, B, (increasing in area from left to right) are characterized by the strong fringe deflections to the right which correspond to a marked increase in impurity concentration. This region which grows under a relatively constant vertical microscopic growth rate (2) exhibits impurity concentration fluctuations which clearly are not related to vertical growth rate changes and thus indicate the operation of a growth mechanism different from that in the off-core region. Unexplained is also the small impurity concentration decrease in the off-core, C, region just preceding the transition to the "core" region.

The ultimate value of the present-type interferogram depends on the availability of quantitative relationships between etching rates and impurity concentration for varying etching times. Actually in our experiments it was found that the ratio of the interference fringe deflections remained constant for a given impurity concentration change over a wide range of etching times (30 sec to 3 min) and etchant compositions. Consequently it appears that the relative dependence of the etching rate on impurity concentration is invariant. Thus it is expected that etching rate calibrations with known impurity concentrations will permit the determination of absolute impurity concentrations and concentration changes on a micro-scale.

#### Acknowledgment

This work was supported by the National Science Foundation under contract GK-1653.

Manuscript received Jan. 4, 1968.

Any discussion of this paper will appear in a Discussion Section to be published in the December 1968 JOURNAL.

#### REFERENCES

1. S. Tolansky, "An Introduction to Interferometry," John Wiley & Sons, Inc., New York (1962).
2. A. F. Witt and H. C. Gatos, *This Journal*, **115**, 90 (1968).



# On the Trapping Level Disposition in Cadmium Sulfide

Paul A. Faeth<sup>1</sup>

Lewis Research Center, National Aeronautics and Space Administration, Cleveland, Ohio

The tendency has been to consider trapping states in CdS as being in different classes depending on their position within the energy gap (1) and the particular phenomena being observed. It appears, however, that there is a regularity in their values and that these states might be considered as part of a single energy scheme. Such an idea has been proposed by Klasens (2) among others for luminescent and trapping centers in ZnS.

The electron trapping level disposition within the band gap of CdS has been found to include the values of 0.05, 0.14, 0.25, 0.41, 0.63, and 0.83 eV (3). These values are the averages obtained using various experimental techniques and several methods of calculation, and are given as energy displacements,  $E_i$ , from the conduction band. Deeper states have been established which are thought to act as hole traps (1). Studies involving the deeper states indicate these levels occur at  $E_i = 1.2$  eV (1, 4) and 1.56 eV (1, 5). A self-activated luminescent level at 1.98 eV has been reported by Lehmann (6). Usually all levels do not appear simultaneously in one crystal although that could happen. When levels do appear, however, they occur very near the values mentioned above and are listed in Table I.

A study of trapping states in cadmium sulfide (7) revealed that the experimentally determined trap energies can be related to one another and to the band gap energy  $E_g$  of 2.4 eV. The disposition of energy levels can be represented by the equation

$$E_i = a - (bi - ci^2) \quad [1]$$

where  $a$ ,  $b$ , and  $c$  are constants and  $i$  is a whole number which numbers successive energy levels  $E_i$ . A similar formulation is used for preliminary evaluations of molecular spectra (8). The constants of Eq. [1] can be determined from the values of  $E_i$  in Table I. The choice of a starting point for the energy level progression is arbitrary. As an example, a case for  $i = 0$  is given at line 11 in Table I for which situation  $a = 2.406$ ,  $b = 0.475$ , and  $c = 0.0238$  eV. A level at 0.031 eV (1) is generated which might be related to the exciton level observed by Reynolds *et al.* (9) at about 0.028 eV or the optical absorption reported at  $\sim 40\mu$  by Manabe *et al.* (10). The wavelengths in microns corresponding to  $E_i$  and  $E_g - E_i$  are listed in Table I and represent regions where photoactivity is observed in CdS.

The energy scheme suggested above may represent part of a band system, in a spectroscopic sense, extending across the energy gap of CdS. A plot of Eq. [1] is parabolic and is suggestive of similar parabolas observed for molecular species such as CN and CuH, for example (8). As the conduction band is approached from the valence band, a "band head" appears to be formed by the trap levels near the conduction band. The system could be tied to the conduction band or the valence band or both. The system limit at the valence band is not as well defined. Fine structure associated with these levels seems likely in view of the recent work of Bryant and Cox (11) involving luminescent emission from CdS. Such structure associated with all levels might give the appearance of a continuous trapping spectrum. Assignments due to

<sup>1</sup>Present address: ITT Industrial Laboratories, Fort Wayne, Indiana.

Table I. Experimental and calculated values of the trapping spectrum of CdS

	$E_i$	$i$	$E_i$	$\lambda_i$	$E_g - E_i$	$\lambda_{g,i}$
1	—	10	0.031	40.0	2.378	0.521
2	0.05	9	0.055	22.5	2.351	0.527
3	0.14	8	0.130	9.531	2.276	0.543
4	0.25	7	0.245	5.057	2.161	0.573
5	0.41	6	0.411	3.015	1.995	0.621
6	0.63	5	0.625	1.982	1.781	0.696
7	0.83*	4	0.886	1.398	1.520	0.816
8	1.2	3	1.195	1.037	1.211	1.024
9	1.56	2	1.551	0.799	0.855	1.451
10	1.98	1	1.955	0.634	0.451	2.747
11	2.4	0	2.406	0.515	0.0	—

\* More recent studies concerning this level indicate this value may be larger; 0.86 eV (14).

specific transitions, however, are not available at this time.

The exact identity of the species involving the energy scheme suggested above is unknown. The levels have been postulated as states of complex impurity-vacancy systems in the bulk. The addition of impurities to crystals stimulates the development of these levels. They seem to occur even in the absence of deliberate doping. The incorporation of impurities might cause slight shifting (Franck-Condon) of potential minima associated with the trapping centers, thus causing some transitions to be unlikely while others are more likely to occur. Previous studies of electrical properties of CdS as affected by sorbed gases have indicated a possible correlation between the amounts of sorbed gases and the appearance of trapped electron populations (7, 12, 13). Such studies suggest the traps may be related to surface states.

Manuscript received Dec. 16, 1967; revised manuscript received Jan. 17, 1968.

Any discussion of this paper will appear in a Discussion Section to be published in the December 1968 JOURNAL.

## REFERENCES

1. R. H. Bube, "Photoconductivity of Solids," John Wiley & Sons, Inc., New York (1960).
2. H. A. Klasens, *This Journal* **100**, 72 (1953).
3. K. H. Nicholas and J. Woods, *Brit. J. Appl. Phys.*, **15**, 783 (1964).
4. E. Grillot, *J. Phys. Radium*, **17**, 624 (1956).
5. E. A. Taft and M. H. Hebb, *J. Opt. Soc. Am.*, **42**, 249 (1952).
6. W. Lehmann, *This Journal*, **113**, 788 (1966); *ibid.*, **113**, 449 (1966).
7. P. A. Faeth, *ibid.*, **114**, 511 (1967).
8. G. Herzberg, "Molecular Spectra and Molecular Structure I. Spectra of Diatomic Molecules," D. Van Nostrand and Co., New York (1957).
9. D. C. Reynolds and R. G. Wheeler, Extract des Comptes rendus du 7<sup>e</sup> Congres International; Physique des Semiconductors, Paris (1964).
10. A. Manabe, A. Mitsuishi, and H. Yoshinaga, *Japan. J. Appl. Phys.*, **6**, 593 (1967).
11. F. J. Bryant, and A. F. Cox, *J. Phys. Stat. Sol.*, **14**, 427 (1966).
12. C. E. Reed and C. G. Scott, *Brit. J. Appl. Phys.*, **15**, 1045 (1964); **16**, 471 (1965).
13. P. Mark, *J. Phys. Chem. Solids*, **26**, 959 (1965).
14. F. J. Bryant and A. F. L. Cox, *Brit. J. Appl. Phys.*, **16**, 1065 (1965).



### Remarks on the Theory of Electrophoretic Deposition

William F. Pickard

*Department of Electrical Engineering, Washington University, Saint Louis, Missouri*

#### ABSTRACT

Following a definition of "electrophoretic," electrophoretic deposition is discussed as a three-step process: (i) the charging phase in which the particles to be deposited are given a net electrostatic charge; (ii) the transporting phase in which the now charged particles are moved in some specified fashion; and (iii) the collecting phase in which the transported particles reach their destinations and are discharged. The characteristics of each of these phases are discussed, and various illustrative examples are given.

The term "electrophoretic" is commonly used to designate those motion phenomena which arise from the direct coulombic action of an electric field on unneutralized charge contained in matter. Thus, either

$$\vec{F} = Q\vec{E} \quad \text{or} \quad \vec{F} = \int_V \rho\vec{E}dV + \int_S \eta\vec{E}dS \quad [1]$$

(particle)                      (extended region)

will provide a fundamental description of the causative process; in this equation,  $\vec{F}$  is the force produced by the electric field  $\vec{E}$  acting either on the total charge  $Q$  of a particle or on the volume ( $\rho$ ) and surface ( $\eta$ ) densities of free charge which characterize an extended region. However, the utilization of electrophoretic force for particle deposition depends not so much on elegant solutions of this equation coupled with the laws of mechanics as it does on careful practical engineering within which the nature of electrophoretic motion is but one of several important factors. For this reason, and also because of the great diversity of possible applications, electrophoretic deposition as a field has resisted formalization. Even so, it is useful to analyze an electrophoretic process by splitting it somewhat arbitrarily into three phases: (i) a "charging" phase within which the particles (objects, entities, things, etc.) to be deposited are charged and started on their trajectories; (ii) a "transporting" phase within which the particles are moved near to some specified destination (it is within this phase that Eq. [1] finds its chief utility); and (iii) a "collecting" phase within which the particle trajectories terminate and the particles are discharged.

These three phases are discussed sequentially in the next three sections of this paper. To make the discussion exhaustive will not, however, be possible since books could be devoted to any one of the phases. Neither will it be possible to erect an elegant mathematical framework within which to cast the discussions since much of the underlying electrochemical theory is but inadequately developed; and, in any event, the associated mathematics is decidedly nonlinear. Rather, the author will attempt to characterize

the types of problems encountered and to outline some of the methods of solution developed to date.

Finally, before proceeding to descriptions of the several phases of deposition, it is informative to consider a simple example of an electrophoretic process. In the 1740's G. M. Bose (1) discovered the capillary siphon effect illustrated in Fig. 1. Here the efflux of water from a nozzle fastened to a metal container is much increased by applying a high voltage to the container; in addition, the formerly thin stream breaks up into a cone of spray. (That this phenomenon is electrophoretic can also be inferred from the fact that the region adjacent to the orifice often appears luminous when viewed under low light intensities.) The splitting then can be made as follows: (a) the metal container, functioning as an "emitter," injects charge into the liquid which is then coulombically pushed outward away from the nozzle; the container is thus the precursor of the gun used in modern electrocoating; (b) the charged liquid droplets then move away toward the basin under the influence of gravity and of the applied electric field. Since particle trajectory, not particle deformation, is important here and since the electric field will be essentially constant over the particle, the particle form of Eq. [1] is the more appropriate; and (c) the basin, functioning as a "collector," receives the droplets and bleeds off their charge.

#### *The Charging Phase*

A feature common to most electrophoretic systems is a metallic electrode called an emitter which injects free charge into the system. This charge is transferred, either by conduction or by an electrochemical reac-

REVIEW  
SECTION

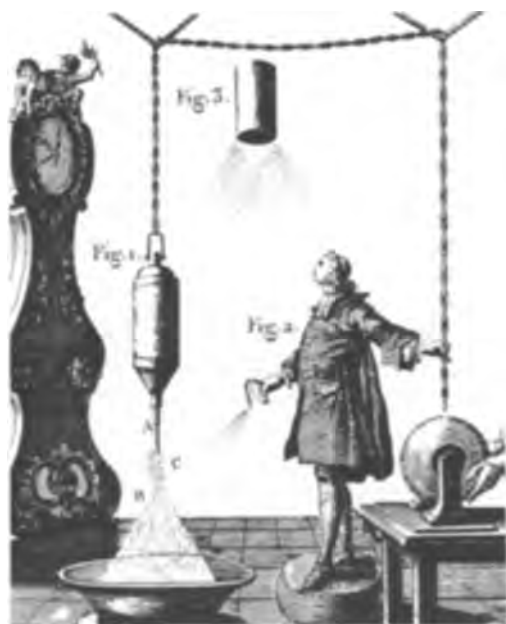


Fig. 1. The capillary siphon as illustrated in an old print (2). *Vide text.*

tion, to matter coming into fairly intimate contact with the emitter. In the former case the electrode design is most often dictated by mechanical considerations, although it is necessary that the surface be kept clean of any nonconducting films which would inhibit charge transfer; in the latter it is commonly controlled by the need for a high surface field and suitably reactive electrode material to enhance the reaction, and for this reason electrodes with small curvature radii are preferred.

If the particles charged at the emitter surface are the ones on which the charge was desired, the charging process can be termed "direct"; otherwise it can be termed "indirect" since one or more charge transfers will be needed to effect the desired charging. As stated above, the three criteria for designing a direct charging process are (i) that there be no insulating barrier at the emitter surface, (ii) that the surface field be high enough to effect the transfer, and (iii) that, in the case of an electrochemical reaction, the emitter surface be compatible with the particles to be charged. In the case of an indirect process the charge is acquired by capturing directly charged particles dielectrophoretically. Thus, a directly charged particle, moving into the neighborhood of a particle to be indirectly charged, induces a dipolar charge distribution on it and in consequence is attracted; if the trajectories of the two particles were appropriate initially, this interaction will lead to trajectory modifications terminating in collision and capture. Obviously, emitter design for an indirect process will emphasize the production of high densities of directly charged particles since this will promote indirect charging.

Two examples will serve to make these considerations more concrete. First, a classic example of a direct charging process is given by the static field, conductance separator (3) used in a variety of mineral purification processes; this is illustrated in Fig. 2. A mixture of conducting (solid dots) and insulating (hollow dots) particles is dumped onto a revolving charged cylinder. The conducting particles are directly charged at once and are drawn off toward the other electrode, falling eventually into hopper C; the insulating particles are weakly held to the revolving electrode by a dielectrophoretic interaction with its modest surface field until they have been rotated far enough for gravity to draw them off into hopper I. Second, the electrostatic precipitation of flue dust (4, 5) provides an excellent example of an indirect

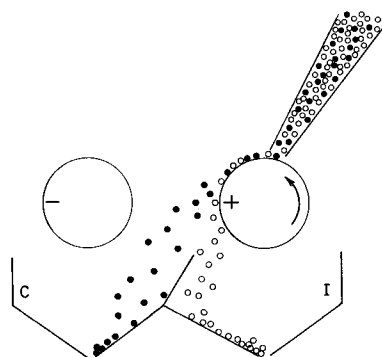


Fig. 2. Schematic illustration of a conductance separator. *Vide text.*

charging process; this is illustrated schematically in Fig. 3. Here a high voltage corona wire is run up the center of a grounded pipe. Gas, flowing axially in the pipe, is ionized by the wire and the resultant ions repelled into the gas stream where, electrodiffusing, they collide with and/or are attracted to particles of dust. The dust particles so charged are then attracted to the pipe where they are collected.

#### The Transporting Phase

In the transporting phase the trajectories of individual charged particles are considered. Each trajectory is specified by a set of initial conditions and the equation

$$\mu \frac{d^2 \vec{r}}{dt^2} = QV\vec{E}_o(\vec{r};t) + \vec{M}(\vec{r};t) - \lambda \left( \frac{d\vec{r}}{dt} - \vec{v} \right) \quad [2]$$

where  $\vec{r}$  is a vector describing the particle's position,  $\mu$  is the particle's mass,  $V$  is a scaling factor to describe the magnitude of the electric field,  $\vec{E}_o$  is the value of the applied field when  $V = 1$ ,  $\vec{M}$  is the mechanical (gravitational, convective, etc.) force, and  $\lambda$  is the coefficient of viscous drag and  $\vec{v}$  the velocity of the medium surrounding the particle. In addition, of course, it is also necessary to set up and solve equations for  $\vec{v}$ ,  $\vec{E}_o$ , and  $\vec{M}$ ; these equations are coupled to Eq. [2] since (i)  $\vec{E}_o$  is influenced by space charge which is in turn influenced by the density of charged particles, and since (ii) by Newton's third law the viscous retardation which the particle experiences produces an acceleration of the fluid surrounding it. Obviously Eq. [2] and its subsidiary equations form a system too complicated to admit of a useful closed form solution in any significant number of cases, and one is reduced to analyzing it to extract rules of thumb.

First, although  $\vec{M}$  and  $\vec{v}$  can be thought of as being in some sense mechanical perturbations on the basic electrophoretic process, they are of considerable significance.  $\vec{M}$  includes, for example, the force of gravity, constraints introduced by various surfaces, and buoyancy. Of these, gravity and buoyancy are the more important, mechanical constraints normally being significant only in the charging and collecting phases. As an illustration, gravity is of prime importance in electrostatic ore beneficiation, the separation normally being effected using crossed electrical and gravitational fields. Conversely, gravitation is much less important in the electrodeposition of paint from aqueous media since its effects on the paint particles tend to be annulled by the buoyancy of the water.  $\vec{v}$  is often one of the parameters of the system as, for example, in the case of electroprecipitation of flue dust. However, it

may be due largely, or in significant part, to motions set up in the fluid by the electrophoretic process itself, and in this case it could impair process efficiency. It has, for instance, been found (6) that conduction currents as small as 1 pA/cm<sup>2</sup> can produce in insulating liquids motions so large as to render uninterpretable the usual carrier mobility measurements; and there is no reason to suppose that similarly significant effects will not exist at the much higher currents used in electrodeposition.

Second, if one neglects  $\vec{M}$  and  $\vec{v}$ , Eq. [2] becomes

$$\mu \frac{d^2 \vec{r}}{dt^2} + \lambda \frac{d \vec{r}}{dt} = QV \vec{E}_o(\vec{r}) P(\omega t) \quad [3]$$

if the physically realistic assumption of periodic  $E_o$  is made. The inertia and viscous drag terms on the left of Eq. [3] can sometimes be manipulated by changing the size of the objects transported, but size is often dictated by other factors. The relative importance of these terms depends on the exact application, but, in

processes where  $\vec{M}$  is neglected, drag normally predominates.

The term on the right of Eq. [3] is the one over which the engineer has greatest control, it being possible (i) to manipulate  $Q$  and  $V$  to some extent, (ii) to specify arbitrarily the periodic function  $P(\omega t)$ , and (iii) to vary  $\vec{E}_o(\vec{r})$  over a wide range by designing so-called "field electrodes" which may or may not include prominently the emitter and collector. The optimal settings of these quantities vary greatly from application to application. Normally, however, the a-c components of  $P(\omega t)$  produces a primarily oscillatory motion of the charged particle, the amplitude of the oscillation decreasing as  $1/\omega$ ; the d-c component produces the desired translation. To increase efficiency, then,  $P(\omega t)$  should possess a moderately low ripple factor unless transient peaks are useful in promoting better particle charging as in electroprecipitation. Also,  $|\vec{E}_o(\vec{r})|$  is commonly adjusted to be monotonically decreasing along a particle trajectory so that the particle will tend not to acquire a new charge at or near the collector and subsequently move off on a new trajectory.

Finally, if the device has been capably engineered, then the charged particles will arrive in the neighborhood of the collector with some suitable spatial distribution. This may be relatively loosely specified as, for instance, in the case of the separator shown in Fig. 2 where it is necessary merely to get the conducting particles into hopper C. Or it may be relatively stringent as, for instance, in the case of electrically depositing a uniform coating of paint in metal parts moving along an assembly line.

An example of these considerations is provided by the electrostatic precipitator (cf. Fig. 3). Here the principal velocity is axial, and mechanical forces are not of primary importance if the gas velocity is sufficiently high and if turbulence is suppressed; in practice these conditions are not always easy to fulfill (5). Inertial effects are normally outweighed by viscous drag, but reentrainment of precipitated particles in the gas stream is a real problem, and hence the collector field should be kept low. On the other hand, it is desirable to have as large a  $Q$  as possible, and this is facilitated by emitter fields strong enough to produce ionization. Thus, the coaxial geometry shown produces

a most suitable  $\vec{E}_o$ .  $VP(\omega t)$  is commonly adjusted to give a d-c level near sparkover and an a-c level producing, near the emitter, copious ionization at waveform crests and quenching of any sparkover at minima. Finally, the criteria on the distribution of transported particles at the collector are very loose, it being re-

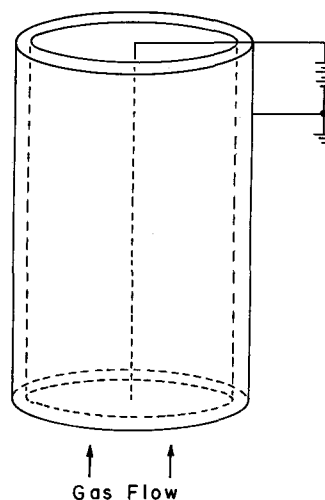


Fig. 3. Schematic illustration of an electrostatic precipitator. *Vide text.*

quired merely that there be no radical nonuniformities over the collector surface.

#### The Collecting Phase

In the collecting phase the transported particles settle on a surface which normally bleeds off their net charge. Thus, in some limited time after touchdown, the electrical force holding the particle has shifted from electrophoretic toward dielectrophoretic and the particles are held by (i) adhesive, (ii) dielectrophoretic, and (iii) other mechanical forces. Cases in which adhesion predominates represent electrocoating processes, while those in which dielectrophoresis predominates usually represent electroseparation processes. "Other mechanical forces" could include, for example, the vertical component of gravity holding the particle in a surface depression or small surface hairs which tend to trap the particles; an illustration of the latter would be an electrostatically dusted plant leaf [cf. 7, 8]. The problems of collection arising in these several cases are radically different.

In electrocoating applications [cf. (9)] there is no question of designing the collector since this has normally been set by the requirements of the product into which it is to be assembled or by other forces beyond the engineer's control: all one can try to do is work with the existing constraints. It is normally required (i) that the coating be of some specified thickness, (ii) that it be of some specified uniformity, and (iii) that the process be as efficient as possible. Thickness is commonly controlled by adjusting the coating time, that is, either the collector or the emitter is moved or the unit is turned off when the coating is thick enough. Uniformity is often provided by the insulating properties of the coating which reduce the surface electric field as the coating thickens thus promoting deposition elsewhere; that is, the asperities on the collector's front surface will be coated first, followed by smooth areas on the front and ultimately by the rear surface and various recesses. In addition, coating uniformity can obviously be aided by rotating the collector or by causing the emitter to revolve around it. In many processes, electrostatic crop dusting, for example, the increase of efficiency compared to the no field case is so great that one is not strongly motivated toward optimization. But, if it is necessary to optimize one should use suitable carriers for the coating material, properly prepare the collector's surface as, for example, by degreasing, and have a good charging phase.

In electroseparation adhesion is not commonly a problem, and the requirements on particle distribution are typically much simpler, being "not too nonuniform" for electroprecipitation and "into the correct

hopper" for ore beneficiation. Moreover, one is able to control to a large extent the collector shape. There are two problems of note. First, lightweight conducting particles tend to acquire the collector's charge and be repelled toward the emitter. And second, the particles collected may be held to the collector's surface by slow charge loss or other electrical processes, and build up a thick and undesirable coating. The designer's job is then to produce a collector which disposes of the particles in an acceptable manner, and, to this end, three expedients have been adopted. First, the collector is so arranged that gravity will tend to pull the particle off in a suitable direction; thus, the precipitator shown in Fig. 3 should be arranged vertically rather than horizontally. Second, the surface electric field of the bare collector is made as small as possible since recharging of the collected particles commonly increases with this quantity; thus, where recharging is a problem, it is designed with large curvature radii. Third, where necessary, the collected particles can be dislodged mechanically and allowed to drop under the influence of gravity; thus, the collectors in flue dust precipitators are commonly subjected to a mechanical rapping.

#### Conclusion

Rather than boldly assaying the *tour de force* of knotting together this diversity of loose ends, I would like to conclude with a description of yet another class of experiments which will serve to explain why in defining "electrophoretic" at the start of this paper I chose to stipulate that the action of the electric field on the entity transported be "direct" and "Coulombic."

Specifically, many organisms exhibit galvanotactic behavior; that is to say, they tend to move in predictable directions in an applied electric field. This phenomenon has long been known (10), and appears, like the phenomena discussed above, to have commercial application (11). An interesting example of galvanotaxis is provided (12) by the motile colonial alga *Volvox* which, when subjected to an electric field, swim toward and accumulate at the cathode, unless surprisingly, they have been conditioned by several days of suitable light deprivation, in which case they move toward the anode.

From this one might conclude that the galvanotactic response could be described as "behavioral" or "voltage-

tional." But, recent researches (13) have indicated that galvanotaxis in ciliates is often the result of a reversal of ciliary beat related to cytoplasmic depolarization. In either case, it would seem that the phenomenon is electrophysiological or electropsychological in nature rather than electrophysical.

And hence the restrictions imposed in defining "electrophoretic" served to rule out those depositional phenomena which, though incontestably electrical in origin, are not readily explained by the direct action of the applied electric field on the net free charge of the transported object.

Manuscript received November 28, 1967. This paper was presented at the Dielectro- and Electrophoretic Deposition Symposium at the Chicago Meeting, October 15-19, 1967, as Abstract 144.

Any discussion of this paper will appear in the Discussion Section to be published in the December 1968 JOURNAL.

#### References

1. G. M. Bose, *Phil. Trans. Roy. Soc.*, **43**, 419 (1745).
2. J. A. Nollet, "Recherches sur les Causes Particulières des Phénomènes Electriques," Les Frères Guerin, Paris (1749).
3. O. C. Ralston, "Electrostatic Separation of Mixed Granular Solids," Elsevier, Amsterdam (1961).
4. H. E. Rose and A. J. Wood, "An Introduction to Electrostatic Precipitation in Theory and Practice," 2nd Ed., Constable, London (1966).
5. H. J. White, "Industrial Electrostatic Precipitation," Addison-Wesley, Reading (1963).
6. T. J. Lewis, Annual Report Conference on Electrical Insulation and Dielectric Phenomena (1967). To be published.
7. S. E. Law and H. D. Bowen, *Trans Amer. Soc. Agric. Engr.*, **9**, 501 (1966).
8. S. E. Law, "Bibliography of Electrostatic Dusting and Spraying," Department of Biological and Agricultural Engineering, North Carolina State University, Raleigh, North Carolina (1967).
9. R. L. Yeates, "Electropainting," Draper, Teddington (1966).
10. W. Biedermann, "Electrophysiology," Macmillan, London (1896).
11. R. B. Northrup, *IEEE Trans. Biomed. Engr.*, **BME-14**, 191 (1967).
12. O. P. Terry, *American J. Physiol.*, **15**, 235 (1906).
13. S. Dryl and A. Grebecki, *Protoplasma*, **62**, 255 (1966).

## Unsolved Problems Concerning Metal Surfaces and Corrosion<sup>1</sup>

Herbert H. Uhlig\*

Department of Metallurgy and Materials Science,  
Massachusetts Institute of Technology, Cambridge, Massachusetts

Almost any worthwhile discipline, whether in the humanities or in the sciences, has its unsolved problems. And it is often true that an inventory of the contributions made by any viable discipline reveals many additional contributions that would be welcome were they available. The study of metal surface properties and of metal reaction rates (corrosion) fits this description. On a practical level, a quick survey shows

that research on metal surfaces has already contributed appreciably to the development of catalysts for chemical processing, to the reduction of friction and wear of metals, and to prolonging the life and safety of metal equipment exposed to aggressive environments. On a scientific level, the relation between adsorption on transition metal alloys and unfilled d electron levels has contributed better insight into both the mechanism of catalysis (1) and the nature of passive films (2-4) accounting for the excellent corrosion resistance of chromium, titanium,

<sup>1</sup> Presented at Dedication of Graduate Center for Materials Research, University of Missouri, Rolla, Mo., October 31, 1967.

\* Electrochemical Society Active Member.

stainless steels, Monels, and related metals.<sup>2</sup> Furthermore, current knowledge of heterogeneous reaction rates has been appreciably advanced by the well-established electrochemical theory of corrosion and by the Wagner theory of metal oxidation at elevated temperatures. Increased meaning has been given to potential and polarization measurements beyond anything available during the early development of classical electrochemistry. As a result, it is now possible to calculate instantaneous reaction rates from rapid polarization data, a technique that proves especially valuable in assessing metals for use in the human body. Advances in electrode kinetics have contributed a clearer insight into factors which add efficiency to corrosion inhibitors. On the other hand, they also identify with devices such as the fuel cell which has captured public attention because of its high theoretical efficiency and its possible alleviation of air pollution. But the advances which are necessary to move the fuel cell out of the laboratory into large-scale commercial use, still remain undiscovered among the properties of metal surfaces.

### Advances in Corrosion Science and Engineering

To list all of the many technological advances that have benefitted from corrosion research is not my present purpose. In a brief outline such as this, one should however at least mention the advent of the rust-resistant stainless steels which first appeared on the scene about 50 years ago as a result of empirical probing. They made an initial major impact on the synthetic nitric acid industry, on design of cutlery and hospital equipment, and on architectural and automotive trim. Similarly the technique of cathodic protection, a long-established development resulting from basic studies of electrochemistry by Sir Humphrey Davy, has made it feasible to transport gas and oil, as is now done, over thousands of miles through buried steel piping securely guaranteed against corrosion. Any unpredictable deterioration of such piping is not tolerable because of catastrophic consequences, particularly with internal gas pressures reaching 1000 psi. Furthermore the classical galvanized corrosion-resistant coatings on steel, first patented in France as early as 1836, still find increasing use today for marine and atmospheric exposures. Some recent applications extend the life and safety of steel automobile frames and accessory equipment exposed to corrosive salt applied to snow-laden streets of northern climates. Mention can also be made of corrosion control methods applied to steam boilers such as deaeration of feed water and the addition of various chemical inhibitors in order to increase the efficiency and safety of boiler operation and at the same time to materially reduce the cost of generated power. It is not always realized that use of commercial corrosion inhibitors in a variety of industries, including the utilities, plays an important part in supporting our industrial economy.

<sup>2</sup> For illustration, the good catalytic properties of Pd for the ortho-para hydrogen conversion are retained, more or less, by Pd-Au alloys so long as the d band of electronic energy levels in Pd remain unfilled. At 60 A/o (atom per cent) Au, the d band becomes filled by donor electrons of alloyed Au, resulting in poorer catalytic properties for alloys of this or higher Au compositions, paralleling the properties of pure Au (1).

Similarly, in the Cu-Ni alloy system, the alloys are passive so long as the d band of energy levels remain unfilled (2, 3). Passivity in this case is measured by an observed passive current density lower in value than a critical current density needed to achieve passivity in polarization curves for the alloys in 1N H<sub>2</sub>SO<sub>4</sub> (Fig. 1). As Cu is added to Ni, the single 4s electron of the Cu atom fills the 1.6 vacancies per surface atom of Ni, increasing the critical current density and also the passive current density (Fig. 2). At the composition at which the d band is 100% filled, or any composition above this value, the passive current densities disappear (or critical and passive current densities intersect) and the alloys up to and including pure Cu are therefore not passive. Other elements alloyed with Cu-Ni alloys may also be a source of donor electrons. In single-phase solid solution alloys, it is observed that alloyed Zn contributes 2 electrons per atom (4), (and hence one Zn is equivalent to two Cu atoms in the Ni alloy), Al contributes 3 electrons (5), Ga contributes 3 electrons, and Ge contributes 4 electrons (6) per atom as is expected from the number of electrons in the outermost orbits of these elements. In each case, the alloy loses its passive characteristics very near to the composition corresponding to 100% filled d band. These results support the view that the passive film on such alloys has an adsorbed structure rather than a structure consisting of a single or mixed stoichiometric metal oxide.

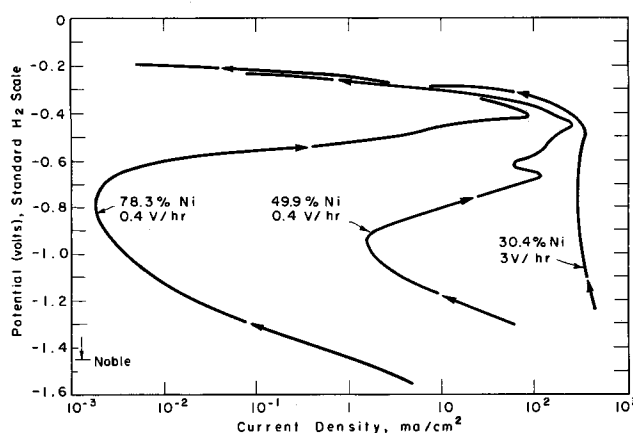


Fig. 1. Potentiostatic anodic polarization curves for 78.3% Ni-Cu, 49.9% Ni-Cu (unfilled d bands) and 30.4% Ni-Cu (filled d band) in 1N H<sub>2</sub>SO<sub>4</sub>, 25°C. Rates of potential change as shown.

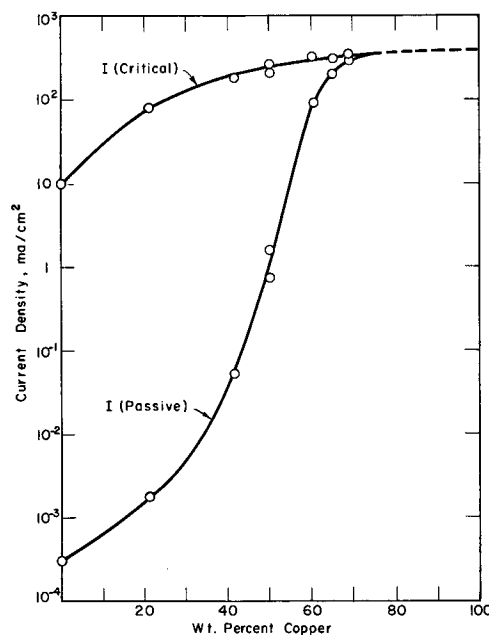


Fig. 2. Critical current densities and passive current densities for Cu-Ni alloys in 1N H<sub>2</sub>SO<sub>4</sub>, 25°C. The d band of electronic energy levels is filled by electrons from Cu at about 60% Cu.

They are employed, for example, to increase the life of automotive engines (as added to lubricating oils), heat exchangers, storage tanks, distribution piping, air conditioning equipment, pickling tanks, and steam lines.

Recent corrosion research has produced titanium alloys containing a few tenths per cent palladium with greatly improved resistance to aggressive acids. Alloyed steels are available, much less expensive than stainless steels, which do not need painting or other types of maintenance. They make use of an adherent natural rust film which essentially protects the underlying metal from further attack. Their promise derives from the present high labor costs of painting which, over the life of a steel structure, may exceed the original cost of construction. Mention might also be made of anodic protection, a new technique for corrosion control in the chemical industry which resulted from fundamental studies of passivity. Using a moderate electric current at controlled potential, it is possible to employ ordinary steels in contact with hot corrosive acids avoiding the extremely high reaction rates which otherwise occur. Cathodic protection in similar applications require uneconomically high current densities attended by undesirable gas evolution.

### Unsolved Problems

The number of unsolved problems relating to metal surfaces is limited only by human imagination. Potentially important advances could obviously be made through improved catalysts, better lubricants, and more efficient corrosion inhibitors, to name but a few. And it should also be recognized perhaps that any scientific breakthrough on knowledge of surfaces has an immediate impact on several fields rather than on one field alone. Hence fundamental research in corrosion, about which the writer is most familiar, is in position to benefit present knowledge of catalysis (e.g., effect of d electron vacancies, mentioned earlier, or the structure and composition of initially formed films on metals) or of our present understanding of lubrication and wear (through studies of mechanically activated chemical reactions such as occur in fretting corrosion or in cavitation-erosion) or of devices which depend on electron emission (through studies of surface films).

The unsolved problems of today which exert pressure for some satisfactory practical solution are usually approached either empirically or more effectively through some depth of scientific understanding. Basically, the most important unsolved problem of metal surfaces is the achievement of an adequate scientific understanding. Is the passive film on stainless steels a metal oxide or is it instead an adsorbed complex of oxygen and water? It makes a great difference if one plans to expend development funds for improving protective surface films by the particular approaches of anodizing or of low-temperature oxidation. Or what is the optimum chemical structure of a nontoxic corrosion inhibitor suited to avoid rusty water in steel distribution mains? Polyphosphates, the action of which is little understood, are used by many communities, but how should one best go about finding a better inhibitor? Or to cite a more spectacular example, by what basic mechanism do high-strength metals fail unexpectedly by cracking when exposed to natural environments? Does an electrochemical mechanism apply, or does a brittle surface film continuously rupture, or does the surface instead undergo reduction in energy (hence favoring the crack process) because of environmental adsorption? All three mechanisms have been suggested. The practical problem presents a serious bottleneck to engineering designs making use of high-strength materials whether for the aircraft, hydrospace or aerospace programs. If one includes threatened stress corrosion cracking of high-nickel alloys used for atomic energy installations, it is obvious that this unsolved surface problem alone affects progress in practically every important outpost of modern technology. Again, the best approach to overcoming environmental cracking depends very much on which mechanism is finally shown to apply. Otherwise, the approach remains a shotgun effort with scattered results.

At least three scientific areas must be expanded if a more satisfactory background on surface problems is to become available. These are: (a) studies of electrode kinetics, (b) studies on the nature of initially formed surface films on metals, (c) studies of how metals subject to a tensile stress interact with their environments.

Under the subject of electrode kinetics, more general quantitative information is needed, including that related to adsorption and desorption of ions and of organic complexes on metals as a function of applied potential. Additional information is required, for example, on factors both within the metal and within the environment which influence the Tafel constants expressing anodic dissolution rates of metals.

Regarding surface films, more information is needed on the composition and structure of passive films common to the stainless steels, and which are also germane to the phenomenally passive metals like tantalum and hafnium. For thicker oxide films which form at elevated temperatures, the question arises as to the role of space charges, reaching a distance of

10,000Å into the oxide, on both surface properties and on the oxidation mechanism. How do small additions of rare earth metals improve the spalling characteristics of oxide films, thereby improving high temperature oxidation resistance? What is the nature of the chemical reaction between metals and their environment during fretting corrosion (caused by sliding surfaces)? It is known that in air at room temperature, iron frets to form particles of metallic iron and of  $\alpha$   $\text{Fe}_2\text{O}_3$ , but in  $\text{H}_2\text{S}$  it is  $\text{FeS}$  that forms and in  $\text{CO}_2$  the reaction product is  $\text{FeCO}_3$ .

In problems of environmental cracking, called stress corrosion cracking, what is the role of complex ions and what part does the corrosion potential play in determining initiation or rate of cracking? What are detailed factors in the metal which determine whether dislocations emerge and which determine their half life at a metal surface during which adsorption presumably occurs? What are the effects of impurities, lattice structure and alloying components on densities of emergent dislocations? What are the chemical properties of surface dislocations which account for  $\text{NO}_3^-$  adsorbing, or otherwise interacting with iron, causing subsequent cracking, and which also account for the ineffectiveness of  $\text{Cl}^-$  to cause the same damage? Or in austenitic stainless steels, which are essentially iron-base alloys, what are the properties of surface imperfections which make  $\text{Cl}^-$  damaging and  $\text{NO}_3^-$  nondamaging?

### Conclusions

Fundamental knowledge necessary to solve various surface problems of the kind described have traditionally been supported on a hit-or-miss basis fluctuating with the number of military or industrial crises at any given moment. The modest accumulated science of metal surfaces presently at hand has been helpful, but unfortunately not adequate to contribute what is needed for continuing technological progress. The establishment of materials science centers, of which the present center at the University of Missouri is a welcome example, promises to supply more of the science which is now missing. Contributions of such research centers to surface properties, and to corrosion problems in particular, are patiently awaited by many of those who hope to use materials to optimum advantage when exposed, as they most always are, to some environment which affects their ultimate properties and useful life. In the long run, increased attention to chemical and surface properties of materials, on par with mechanical or physical properties, will lead to a better evaluation of the environmental effects which are becoming increasingly important to modern engineering design. This kind of information must be available, of course, for both metallic and nonmetallic materials, because all materials are subject to some degree of environmental damage, the extent of which sensitively bears on their satisfactory incorporation into some machine or structure.

At one time I recommended (7) that corrosion research would greatly benefit through the continuous support provided by a National Institute of Corrosion Control established on a smaller scale but similar to our well-known National Institutes of Health. Perhaps the need for such an Institute is made less urgent by the several materials science centers which have since been established. Yet the variety of problems which are inherent to advanced materials and which fully occupy present research facilities all over the nation, suggest that a special coordinated research effort at such a national center with specific emphasis on chemical and surface properties deserves further consideration. The added functions which such an Institute could provide, for example, are (A) detailed expert attention to corrosion engineering problems of broad public concern affecting the many small businesses and communities unlikely to undertake a broad range research program on their own initiative. (B) The effective dissemination of general corrosion control know-how to all those able to make use of it. (C) The



support and prosecution of fundamental research on properties of surfaces supplying new knowledge not only on metal reaction rates but also on other properties of value to related scientific disciplines similarly concerned with surface behavior.

In whatever way it is finally accomplished, we stand as a nation to benefit from research programs, considered in depth, which bring the many disciplines of the physical sciences to bear on solutions of surface problems. Only a relatively short time ago these problems, including corrosion phenomena, were considered, like the weather, to be unpredictable and hardly amenable to scientific insight. The dedication of this Graduate Center of Materials Research at Rolla symbolizes our entry into a more enlightened era of materials research.

Manuscript received December 17, 1967.

#### References

1. A. Couper and D. Eley, *Discussions Faraday Soc.*, **8**, 172 (1950).
2. H. Uhlig, *Z. Elektrochem.*, **62**, 700 (1958).
3. J. Osterwald and H. Uhlig, *This Journal*, **108**, 515 (1961).
4. D. Stolica and H. Uhlig, *ibid.*, **110**, 1215 (1963).
5. F. Mansfeld and H. Uhlig, Paper Presented at the Chicago Meeting of the Society, Oct. 15-19, 1967, as Abstract 54.
6. F. Mansfeld and H. Uhlig, Unpublished observations.
7. H. Uhlig, *Corrosion*, **18**, 311t (1962).

## DIVISION NEWS

### Dielectrics and Insulation Division

The Annual Luncheon and Business Meeting of the Dielectrics and Insulation Division will be held during the Spring Meeting of the Society in Boston, Mass., May 5-9, 1968. As a continuation of the policy of offering an outstanding speaker for the occasion, Jerome B. Wiesner, Provost of the Massachusetts Institute of Technology and former Scientific Advisor to Presidents Kennedy and Johnson, will speak on a topic of current interest. Dr. Wiesner is internationally known for his interest in the relationships between scientific and governmental affairs.

During the Business Meeting the presentation of the first T. D. Callinan Award will be made. Details on the award are given below.

The Luncheon and Business Meeting will be held in the Bay State Room of the Statler Hilton Hotel from 12:15 to 2:00 P.M. on Monday, May 6. Tickets may be purchased in the Registration area at the Statler Hilton.

Donald M. Smyth,  
Secretary

### T. D. Callinan Award Of the Dielectrics and Insulation Division

In recognition of their contributions to the study of anodic oxide growth mechanisms, J. A. Davies and J. P. S. Pringle, Atomic Energy of Canada, Ltd., Chalk River Nuclear Laboratory, Chalk River, Ont., Canada, have been selected as joint recipients of the T. D. Callinan Award. Their work, which was reported in a group of separate and joint publications, extended over the period 1962 through 1967. Within this period Dr. Davies and Dr. Pringle developed and used Beta-ray spectroscopy and radio-tracer techniques as an experimental tool for the study of anodic oxide growth mechanisms. The reliability of the results obtained with this technique

is perhaps its most outstanding feature and has substantially contributed to an understanding of the mechanism involved.

Dr. Pringle's recent participation at the 1967 Dallas Meeting was based on a continuation and extension of these techniques and dealt with the concentration profiles of atomic species within anodic oxide tantalum film. His presentation was well received and represented one of the outstanding contributions at the Divisional level.

With the presentation of this award, the Dielectrics and Insulation Division inaugurates a new program which originated during Dr. B. Eichbaum's Chairmanship. The Division through this award seeks recognition of recent meaningful contributions. Consistent with these objectives the award bears the name Thomas D. Callinan who during his life generously contributed both his time and energy to the growth and development of the Division in addition to being its Divisional Editor on the JOURNAL and member of the Board of Directors of the Society.

Presentation of the T. D. Callinan Award will take place at the Division Luncheon and Business Meeting being held in the Spring of 1968.

Edward M. DeSilva,  
Vice-Chairman

### Industrial Electrolytic Division

The Nominating Committee of the Industrial Electrolytic Division, comprised of E. F. Kiefer, V. J. Cable and R. M. Hunter, Chairman, presents the following slate of nominees for the two-year terms for each of the offices listed:

Chairman—T. R. Beck, Boeing Scientific Research Laboratories, Seattle, Wash.

Vice-Chairman—J. H. Nichols, Monsanto Co., St. Louis, Mo.

Secretary-Treasurer—R. N. Hyer, Vulcan Materials, Co., P. O. Box 545, Wichita, Ka., J. H. Sullivan, Dow Chemical Co., Midland, Mich., and L. E. Vaaler, Union Carbide Corp., P.O. Box 6116, Cleveland, Ohio.

The election of officers will be held at the Division's annual luncheon and

business meeting May 8, 1968 during the Boston Meeting of the Society.

Clifford A. Hampel,  
Chairman

## SECTION NEWS

### Chicago Section

On January 11, 1968 the Chicago Section met at the Chicago Engineers Club to hear Z. Andrew Foroulis, Esso Research and Engineering Co., Florham Park, N. J., present a paper "On the Kinetics of Iron Dissolution in Acid Chloride Solutions."

The following is a summary:

The mechanism of the corrosion of iron in acid chloride solutions is examined in detail. Galvanostatic transients are used to investigate dissolution kinetics. Influences of potential, pH and ferrous iron concentration on steady-state dissolution and deposition reactions are illustrated. Dependency of the hydrogen evolution reaction on pH and potential are also considered for this system.

On February 15, 1968 the Chicago Section met at the Chicago Engineers Club, to hear Dr. James H. Greenwald, St. Catherine Hospital, Heart

Review Section .....	105C
Division News .....	111C
Section News .....	111C
Officers Take Office .....	112C
People .....	112C
Boston Meeting Committee .....	114C
Obituary .....	115C
Book Reviews .....	115C
New Books .....	116C
Membership Statistics .....	116C
News Items .....	117C
Out-of-Print Extended Abstract Volumes .....	118C
Positions Available .....	120C
Call For Papers Montreal Meeting .....	121C
Montreal Symposia .....	122C
75-word Abstract Form .....	124C



# The Anodic Behavior of Zinc in KOH Solutions

T. P. Dirkse,\* David De Wit, and R. Shoemaker

Calvin College, Grand Rapids, Michigan

## ABSTRACT

The anodic behavior of zinc in strongly alkaline solutions was studied making special note of the limiting current density and of the overvoltage for the zinc/zincate reaction. The effect of temperature, KOH concentration, presence of zincate, and amalgamation on these values was measured. Under the conditions studied, zincate ion diffusion away from the electrode controls the limiting current density. The overvoltage at amalgamated electrodes is that for the charge transfer reaction, while at nonamalgamated electrodes it is due to adatom diffusion.

In developing and designing alkaline batteries using zinc anodes, there are several modifications that can be made to improve the performance of the system. One such modification is the amalgamation of the zinc electrode. This is done in practically all zinc-alkaline batteries. The purpose is to raise the hydrogen overvoltage and thus reduce the corrosion or open-circuit reaction. This amalgamation, however, may also affect the other zinc electrode processes.

A review of the published literature revealed that few factual data are available to show what effect electrolyte concentration, amalgamation, zincate concentration, and temperature have on the anodic processes of the zinc/zincate electrode. For this reason a program of work was undertaken to obtain such information, and the results are reported here.

It is generally agreed that the anodic zinc processes in an alkaline solution consist of at least: (a) the formation of the charge transfer product, probably zinc hydroxide; (b) the dissolution of this product in the electrolyte; and (c) the formation finally of a passivating layer, either by precipitation from the electrolyte or because of inability of the electrolyte to dissolve the charge transfer product as fast as it is formed. While this model serves to account satisfactorily and qualitatively for most observations made on the zinc electrode, still there is little agreement as to the details of these various steps. Furthermore, it has been difficult to get sufficient experimental information to describe some of these processes in detail.

## Experimental

Two methods were used to study the zinc electrode processes.

**Interrupter.**—An interrupted d.c. was used to study the overvoltage of the zinc electrode processes. The circuit has been described (1). A standard resistor was placed in the circuit, and the voltage drop across this was measured on an oscilloscope to determine the current rate. All traces on the oscilloscope were photographed, and in calculating the overvoltage, correction was made for the internal IR drop. The cell, Fig. 1, held about 20 ml of electrolyte. The working zinc electrode area was the cross-sectional area of a 0.063-in. diameter zinc wire encased in a Teflon tube. This was polished smooth on an emery cloth (3/0) before use in the cell. The reference electrode was a 1-in. length of similar wire which had previously been amalgamated. It was held in a polyethylene tube. The auxiliary electrode was a circular zinc sheet, about 0.75 in. diameter, embedded in the bottom of the Plexiglas cell case. In making a series of measurements the current was first increased in several steps then decreased, and finally increased again. In the anodic direction measurements were discontinued when the electrode became passive or a limiting current density was reached.

**Sine wave.**—In the second approach to the study of the zinc electrode reactions, the method of Kordes and Marko (2) was used. A zinc wire served as the reference electrode in some instances, while in others a HgO/Hg reference was used. The latter was connected to the cell by a capillary and contained the same KOH concentration as the cell. The cell case was 8.8 x 5.4 x 2.3 cm. The counter electrodes were two commercial zinc electrodes, 4 x 5 cm, and these were encased in fibrous sausage casing separator. The working electrode, amalgamated where required by dipping it for 30 sec in a solution containing 50 g/l of HgCl<sub>2</sub>, was inserted between these electrodes. The current was increased manually at prescribed time intervals and the polarization (IR free) of the working zinc electrode was measured. A typical anodic curve is shown on Fig. 2.

## Results

In making measurements on the anodic processes, two values were used for comparisons: (a) the limiting current density (*a* in Fig. 2); and (b) the overvoltage associated with the formation of zincate. For convenience this latter was taken as the overvoltage at a current density of 50 ma/in<sup>2</sup> (*b* in Fig. 2). These values were all obtained by use of the sine wave pulse tester method.

Four variables were considered: (i) KOH concentration; (ii) zincate concentration; (iii) effect of amalgamation; and (iv) temperature. A summary of the results at room temperature is given on Fig. 3 and 4.

**Limiting current density.**—The limiting current density (lcd), Fig. 3, shows a general tendency to decrease markedly with increasing KOH concentration in the range of 30-45%. Below 30% KOH the lcd varies somewhat erratically with KOH concentration. For KOH solutions saturated with ZnO there is no apparent effect of KOH concentration on lcd in solutions of 20-30% KOH. Furthermore, the presence of appre-

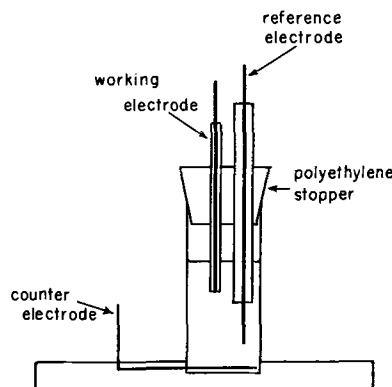


Fig. 1. Cell case used for studying anodic zinc electrode processes.

\* Electrochemical Society Life Member.

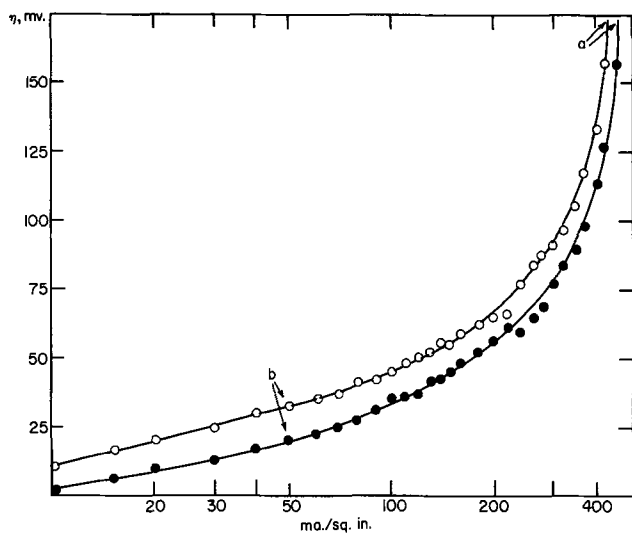


Fig. 2. Anodic overvoltage current curve for a zinc electrode in 35% KOH saturated with ZnO. Open circles, zinc; closed circles, amalgamated zinc.

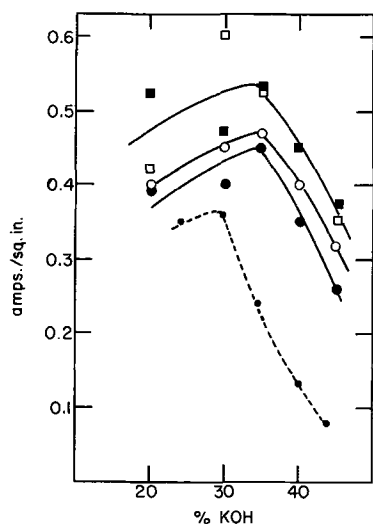


Fig. 3. Limiting anodic current density for zinc electrodes at room temperature. Circles, zinc; squares, amalgamated zinc; open symbols, KOH solutions; closed symbols, KOH saturated with ZnO; dashed line, diffusion coefficients (relative scale) for zincate ions, from ref. (7).

ciable amounts of zincate in the solution results in a slightly lower lcd for plain zinc electrodes but has no significant effect on the lcd of amalgamated zinc electrodes.

**Zincate overvoltage.**—The overvoltage for the zincate reaction, Fig. 4, shows irregularities with KOH concentration. But in all cases it is lower at the amalgamated electrodes. This is true in the presence as well as in the absence of zincate ions. The overvoltages in KOH solutions containing no zincate originally (open symbols, Fig. 4) are subject to some uncertainty because of the uncertainty in the open circuit voltage in plain KOH solutions. Since no zincate is present, it is possible that no equilibrium potential for the zinc/zincate reaction is obtained. However, a fairly constant potential was obtained at the beginning of each run, and this value was within the experimental uncertainty of that which was obtained by extrapolation of the potentials obtained in solutions containing varying amounts of zincate.

**Temperature effect.**—These anodic processes were also studied over the temperature range of 0–50°C. The lcd did increase with temperature for both types of

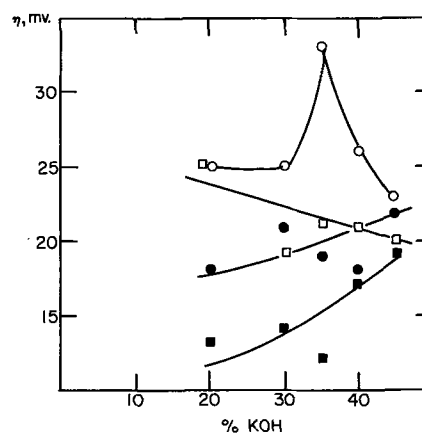


Fig. 4. Overvoltage for zincate formation at zinc electrodes in KOH solutions. Symbols same as for Fig. 3.

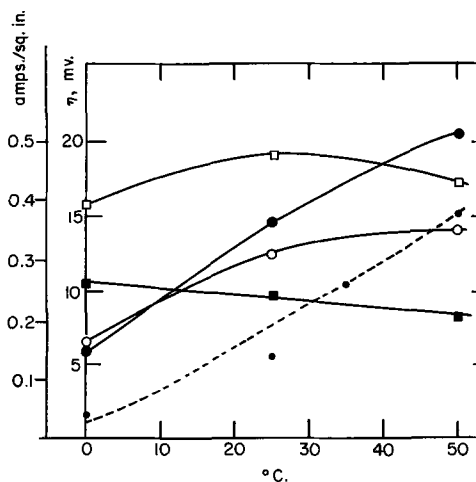


Fig. 5. Variation of lcd and overvoltage at a zinc/zincate electrode with temperature. Circles, lcd; squares, overvoltage; open symbols, zinc; closed symbols, amalgamated zinc. All solutions were 40% KOH + 0.5M ZnO. Dashed line, diffusion coefficients (relative scale) for zincate ion, from ref. (7).

electrodes but the difference between amalgamated and nonamalgamated zinc became less as the temperature was lowered, Fig. 5. The effect of temperature on the overvoltage of the zinc/zincate reaction is very slight.

### Discussion

The results obtained in this study for nonamalgamated electrodes can readily be accounted for and explained in terms of the generally accepted outline of the mechanism for the anodic zinc reactions as outlined in the introductory paragraphs. However, the effects of amalgamation on the zinc electrode performance cannot be so readily explained in terms of this scheme. The effects are two:

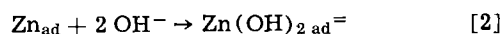
1. Amalgamation raises the lcd, except at temperatures near 0°C.

2. Amalgamation lowers the overvoltage for the zinc/zincate reaction.

The extensive work of Hampson *et al.* (5) suggests a possible explanation for these phenomena. This explanation assumes that the oxidation of nonamalgamated zinc begins with the movement of zinc atoms from the kink sites (lattice dissolution points, *e.g.*, screw dislocations) to become mobile surface atoms with a low coordination number (adatoms).



These adatoms readily adsorb  $\text{OH}^-$  ions and this may stabilize them.



Metallic zinc electrodes have a high double layer capacity (5a). This results from the charge transfer reaction, Eq. [3], which may proceed in two one-electron stages.

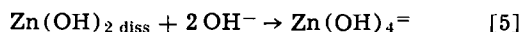


$i_0$  for reaction [3] is of the order of 200 ma/cm<sup>2</sup> (5b).

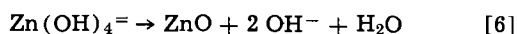
Reaction [3], which is in agreement with the work of Gerischer (6), is followed by



and

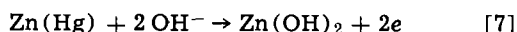


As the zincate concentration increases, a further reaction occurs (3).

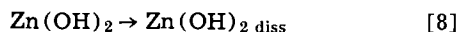


The rate-controlling processes may be [1], [4], or [5]. Reaction [3] is likely not rate controlling because of the high value for  $i_0$ . Reaction [2] probably is also a fast reaction.

The anodic oxidation of amalgamated zinc electrodes proceeds by a somewhat different mechanism because the surface is different. Amalgamation "smooths out" the surface or makes it approach a liquid. Consequently atoms can dissolve at any point on the surface. There are no kink sites and no adatoms. Furthermore, there is no evidence for OH<sup>-</sup> adsorption at a zinc amalgam electrode, in contrast to a nonamalgamated electrode (5d). Therefore the first step likely is



The Zn(OH)<sub>2</sub> is not necessarily adsorbed and goes into solution



This is then followed by reactions [5] and [6].

The fact that the variation of lcd with KOH concentration, Fig. 3, is the same for both types of electrodes suggests that the same process is rate-limiting in each case. This could be reaction [4] or [8]. Reaction [5] is a fast reaction and reaction [6] is too slow to take any part in the results we obtained.

Reactions [4] and [8] are step (b) in the anodic process outlined in the introductory paragraphs. The rate of dissolution of the charge transfer product is an important factor especially because of the apparent high solubility of this substance and the slow decomposition of the resulting solute species (3). It is reasonable to expect that this rate of dissolution will decrease with decreasing temperature. This qualitatively accounts for the temperature effect on the lcd. Unfortunately, no quantitative data are available to evaluate this suggestion.

However, the rate of dissolution of the charge transfer product will also depend on the zincate concentration in the layer of electrolyte in contact with the electrode surface. In order for the charge transfer product to continue to dissolve, it is necessary that the zincate ions diffuse away from the electrode. The diffusion of zincate ions from the electrode thus controls the lcd because it affects the rate of dissolution of the charge transfer product. The shape of the curves on Fig. 2 does suggest such a diffusion controlled process.

The diffusion currents and the diffusion coefficients for zincate ions have been measured by a polarographic method over a range of temperatures and KOH concentrations (7). These values for the diffusion coefficients at 25°C are included on Fig. 3 and 5.

There is a marked similarity between the variation of lcd and of diffusion coefficient with KOH concen-

tration at the higher concentrations. There is likewise a similarity between these values as a function of temperature, Fig. 5. Thus it is reasonable to conclude that the lcd's observed in our work can be explained by the diffusion control of the zincate ion (4). In our work, convection as well as diffusion undoubtedly played a role and so the processes cannot be expected to be strictly or only diffusion controlled.

It was noted also that the lcd was higher at the amalgamated electrodes. This is likely a surface area effect. Amalgamation produces more reaction sites on the surface. This larger available area serves to reduce the actual current density at which the electrode is being oxidized. The current densities used in Fig. 2, for example, are calculated on the basis of the gross geometrical area. A lower current density would give rise to a lower overvoltage, Fig. 2. In either event, the result would be to give a higher lcd at the amalgamated electrodes.

It may be argued that if the above explanation is correct, then the presence of zincate ions in the solution should result in a lower lcd. A solution already containing zincate ions can dissolve fewer additional zincate ions (from the electrode reaction) than can a solution which originally contained no zincate ions. There is some evidence for this at the plain zinc electrodes, Fig. 3. The fact that this effect is so slight is explained by the high solubility of the charge transfer product. This substance gives zincate concentrations considerably higher than those obtained by saturating aqueous KOH with ZnO (3).

The difference in overvoltage for the zinc/zincate reaction at the two types of electrodes can be explained by the difference in the mechanism of the reaction at the two electrodes. The overvoltage, or energy barrier, for nonamalgamated zinc electrodes is associated with reaction [1] while for amalgamated electrodes it is associated with reaction [7], the charge transfer reaction.

### Acknowledgment

This work was sponsored and supported by the U.S. Air Force Aero Propulsion Laboratories. The authors also wish to thank Dr. N. A. Hampson for his many helpful discussions and suggestions.

Manuscript received Aug. 9, 1967; revised manuscript received Nov. 13, 1967. This paper was presented at the Chicago Meeting, Oct. 15-19, 1967, as Abstract 27.

Any discussion of this paper will appear in a Discussion Section to be published in the December 1968 JOURNAL.

### REFERENCES

1. T. P. Dirkse and G. Werkema, *This Journal*, **106**, 88 (1959).
2. K. Kordesch and A. Marko, *ibid.*, **107**, 480 (1960).
3. T. P. Dirkse, *ibid.*, **102**, 497 (1955).
4. R. Landsberg, H. Furtig, and L. Muller, *Wiss. Z. Techn. Hochschule fur Chemie Leuna-Merseburg*, **2**, 453 (1959/60).
5. (a) J. P. G. Farr and N. A. Hampson, *Trans. Faraday Soc.*, **62**, 3493 (1966); (b) J. P. G. Farr and N. A. Hampson, *J. Electroanalytical Chem.*, **13**, 433 (1967); (c) J. P. G. Farr, N. A. Hampson, and M. E. Williamson, *ibid.*, **13**, 462 (1967); (d) N. A. Hampson, Ph.D. Thesis, University of London, 1966.
6. H. Gerischer, *Z. physik. Chem.*, **202**, 302 (1953).
7. J. McBreen, "Study to Improve the Zinc Electrode for Spacecraft Electrochemical Cells," 2nd Quarterly Report on Contract NAS 5-10231, June 1967, Yardney Electric Corp, New York, N.Y.

# Solubility and Complex Formation of AgCl in Propylene Carbonate-Water Mixtures

James N. Butler,\* David R. Cogley,\*\* and Walter Zurosky

Corporate Research Division, Tyco Laboratories, Inc. Waltham, Massachusetts

## ABSTRACT

The solubility and complex formation equilibria of silver chloride in propylene carbonate-water mixtures (0.004 to 3.57M H<sub>2</sub>O) have been studied potentiometrically in a constant ionic medium of 0.1M tetraethylammonium perchlorate, at 25°C. The complexes are predominately mononuclear, and the principal species in solution is AgCl<sub>2</sub><sup>-</sup>. The over-all complex formation constants β<sub>n</sub> (n = 1,2,3) decrease and the solubility product K<sub>so</sub> increases with increasing water concentration. Approximate empirical expressions describing these changes are: log K<sub>so</sub> = -20.0 + 3.25 √C<sub>H<sub>2</sub>O</sub> and log β<sub>2</sub> = +21.2 - 4.87 √C<sub>H<sub>2</sub>O</sub>. The intrinsic solubility of AgCl (K<sub>s1</sub>) is 10<sup>-4.7</sup>, essentially independent of the water content of the solvent.

Although the dielectric constant of propylene carbonate [ε = 64.4 (1)] is nearly as large as that of water (ε = 78.54), the solubility and complex formation equilibria of silver chloride are vastly different in the two solvents. Our studies (2) have established that mononuclear complexes predominate in solutions containing excess chloride and have provided accurate values of the equilibrium constants in anhydrous propylene carbonate. These constants are summarized in Table I and are compared with the corresponding constants for aqueous solutions (3, 4). Although the solubility product (K<sub>so</sub>) is more than ten orders of magnitude smaller in propylene carbonate than in water, the complex AgCl<sub>2</sub><sup>-</sup> is so stable that the solubility equilibrium of AgCl in excess chloride, represented by the reaction



(equilibrium constant K<sub>s2</sub>) is six orders of magnitude greater in propylene carbonate.

These dramatic differences in equilibrium constants reflect large differences in solvation of ions in the two solvents, and their detailed variation is of interest in the general context of solvation theory. In addition, the current interest in silver chloride both as a reference electrode and as a battery cathode material in aprotic electrolytes (5-9), has prompted us to study these equilibria in mixtures of propylene carbonate with water.

## Experimental

Propylene carbonate was obtained from Matheson, Coleman, and Bell, and purified by distillation, as described in detail elsewhere (10). Gas chromatographic analysis indicated that the purified solvent contained less than 10 ppm organic impurities and water. Silver perchlorate (Chemical Procurement), tetraethyl ammonium chloride (Eastman), and tetraethyl ammonium perchlorate (Eastman) were dried over anhydrous CaSO<sub>4</sub> in a desiccator before solutions were prepared. Solutions were analyzed (± 0.1%) for chloride ion by potentiometric titration with aqueous silver nitrate, and for silver ion (± 0.2%) by potentiometric titration with the propylene carbonate-chloride solutions of known concentration. Mixtures of propylene carbonate with triple-distilled water were prepared by weight, and their density measured with a pycnometer. The density values (Table II) were used in converting to molar concentrations.

The cell consisted of two electrode compartments connected by a salt bridge with coarse glass frits at each end. One of the electrode compartments con-

tained a Teflon-coated magnetic stirrer, and the entire cell was jacketed and maintained at 25.0° ± 0.1°C by means of a Haake circulating thermostat. Solution preparation, storage, and all experiments were carried out in a dry nitrogen atmosphere in a glovebox. Etched silver wires were used for electrodes in both compartments, and a uniform ionic strength of 0.100M was maintained in all three compartments with Et<sub>4</sub>NClO<sub>4</sub>. The reference compartment contained either Ag<sup>+</sup> at approximately 0.004M concentration or Cl<sup>-</sup> saturated with AgCl at the same concentration. The compartment with the stirrer contained various concentrations of Ag<sup>+</sup> and Cl<sup>-</sup> which were added from 2 ml RGI micrometer burettes containing 0.1M AgClO<sub>4</sub> or 0.1M Et<sub>4</sub>NCl in the same solvent mixture as was used for the supporting electrolyte. Potentials were measured with a Fluke high-impedance differential voltmeter, and were usually steady to within 0.1 mv.

## Results

The results of nine experiments in different solvent mixtures are summarized in Table III. The values given in the table were selected to give a representative shape of both the saturated and unsaturated portions of the titration curve. Sufficient data have been given to permit future workers to make different statistical curve-fitting calculations, but when measurements were so closely spaced that they provided no additional information, the extra points were elim-

Table I. Solubility and complex formation equilibria for AgCl in water and propylene carbonate (0.1M ionic strength, 25°C)

Solvent	Water (3, 4)	Propylene carbonate (2)
Dielectric constant	78.54	64.4 (1)
log K <sub>so</sub> (AgCl (s) = Ag <sup>+</sup> + Cl <sup>-</sup> )	-9.42	-19.86 ± 0.02
log β <sub>1</sub> (Ag <sup>+</sup> + Cl <sup>-</sup> = AgCl (soln))	+2.85	+15.15 ± 0.15
log β <sub>2</sub> (Ag <sup>+</sup> + 2 Cl <sup>-</sup> = AgCl <sub>2</sub> <sup>-</sup> )	+4.72	+20.86 ± 0.02
log β <sub>3</sub> (Ag <sup>+</sup> + 3 Cl <sup>-</sup> = AgCl <sub>3</sub> <sup>2-</sup> )	+5.04	+23.39 ± 0.06
log K <sub>s2</sub> (AgCl (s) + Cl <sup>-</sup> = AgCl <sub>2</sub> <sup>-</sup> )	-4.70	+1.00 ± 0.03

Table II. Density of propylene carbonate-water mixtures at 25°C

Weight % H <sub>2</sub> O	C <sub>H<sub>2</sub>O</sub> , mole/liter	Density, g/ml
0	0	1.206
1.27	0.845	1.199
3.17	2.09	1.192
5.43	3.57	1.187

\* Electrochemical Society Active Member.  
\*\* Electrochemical Society Associate Member.



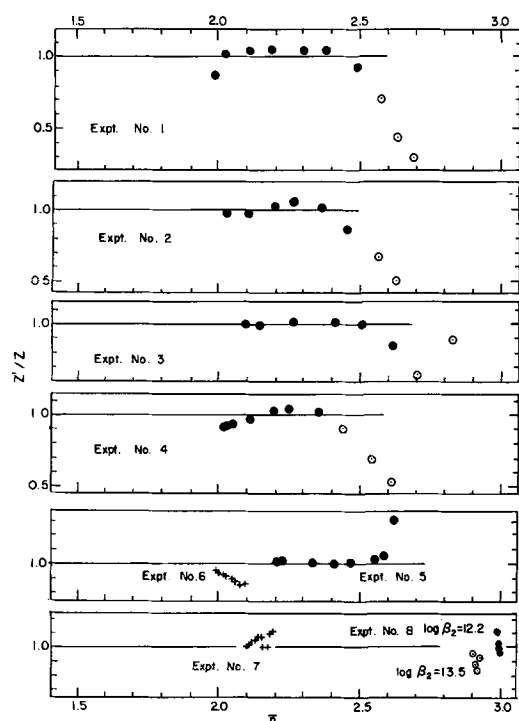


Fig. 1. Variation of experimental measurements from theoretical Eq. [2-4]. The detailed data are given in Table III and the constants used for the theoretical curves are given in Table IV.

rides bound to a silver ion, defined by the equation

$$\bar{n} = \frac{C_{Cl^-} [Cl^-]}{C_{Ag}} \quad [5]$$

i.e.,  $\bar{n} = 2$  corresponds to the predominance of  $AgCl_2^-$  and  $\bar{n} = 3$  to the predominance of  $AgCl_3^-$ . For a good fit, the values of  $Z'/Z$  should be normally distributed about unity. The constants were obtained with the set of crosses or solid points, the open points being discarded.

Systematic deviations from the theoretical equations were observed at high values of  $\bar{n}$  (high  $C_{Cl^-}/C_{Ag}$  ratios). Similar deviations were observed previously (2) and were attributed to the failure of the constant ionic medium assumption. However, the deviations are smaller for experiment 5, even though the total concentrations are nearly ten times larger than in experiment 4. One possible explanation is that complexes of higher  $\bar{n}$ , possibly polynuclear, may exist in solutions of high chloride-to-silver ratio, but these are of less importance as the water content is increased.

The predominance of mononuclear complexes has been confirmed in experiments 5 and 6. The to-

tal concentrations in 5 were approximately ten times those in 6, and the combined sets of data were fitted with the same three constants. The values of  $Z'/Z$  agreed (Fig. 1) to within 10%, although a slightly different set of constants would have produced a better fit to experiment 6. The slight difference, which appears to be outside the precision of the individual experiments, may reflect small amounts of polynuclear complexes, but is small enough to be accounted for by systematic errors in the measurements.

The value of  $\beta_1$  calculated from experiment 7 is uncertain, but is probably less than  $10^{14}$ . Saturation of the solution at low  $C_{Ag}/C_{Cl^-}$  ratios made it difficult to cover a wide range of  $\bar{n}$  without doing experiments in very dilute solutions; and since these would be subject to systematic errors from impurities in the solvent and supporting electrolyte, they were not attempted. The constants  $\beta_n$  calculated from experiments 8 and 9 are uncertain for the same reason. The best fit to experiment 3 was obtained with  $\log \beta_2 = 12.2$ , but an almost equally good fit was obtained with  $\log \beta_2 = 13.5$  (see Fig. 1). Thus we have indicated in Table IV that  $\log \beta_2$  is between 12 and 14. Since a large excess of chloride is present and  $\bar{n}$  is nearly 3,  $\log \beta_3$  is more certain. For this set of data  $\beta_1$  could not be determined, but it is almost certainly less than  $\beta_2$ .

In experiment 9, the shape of the curve was not even close to the theoretical, and no amount of parameter adjustment (within reasonable values) could make  $Z'/Z$  close to unity for all three points. Therefore we assumed that  $\bar{n} = 3$  and hence that the complex  $AgCl_3^-$  predominates. This gave  $\log \beta_3 = 14.2 \pm 0.5$ , which we have listed in Table IV.  $\beta_2$  and  $\beta_1$  are probably less than  $10^{12}$ , but more detailed studies of these solutions with high water concentrations are required before accurate estimates of the constants are possible.

From each point obtained in the saturated region, a value of the solubility product  $K_{s0}$  can be obtained by solving the equation (2)

$$(C_{Cl^-} - C_{Ag} + [Ag^+])[Ag^+]^2 = K_{s0}(1 + \beta_2 K_{s0})[Ag^+] + 2\beta_3 K_{s0}^3 \quad [6]$$

using Newton's approximation method. These values are shown in Fig. 2 and 3. Systematic variations of  $-\log K_{s0}$  to smaller values as  $C_{Ag}/C_{Cl^-}$  increases are observed in all the experiments, but were greatest for the lowest and highest water content. Similar deviations were observed before (2) but no simple explanation is apparent. The values of the solubility product listed in Table IV were obtained from the region close to the saturation point.

Values of the constant  $K_{s2}$  were obtained by combining the experimental values of  $\beta_2$  and  $K_{s0}$  according to the relation

Table IV. Equilibrium constants for AgCl in propylene carbonate-water mixtures

Expt. No. (see Table III)	$C_{H_2O}$ mole/liter	Log of equilibrium constant <sup>a</sup>				
		$\beta_1$	$\beta_2$	$\beta_3$	$K_{s0}$	$K_{s2}^b$
1	0.004	$15.0 \pm 0.5$	$20.95 \pm 0.04$	$23.65 \pm 0.13$	$-19.90 \pm 0.05$	$+1.05 \pm 0.07$
2	0.0094	$14.5 \pm 1.0$	$20.58 \pm 0.03$	$23.07 \pm 0.06$	$-19.72 \pm 0.03$	$+0.86 \pm 0.04$
3	0.0147	$<15$	$20.04 \pm 0.05$	$23.0 \pm 0.1$	$-19.46 \pm 0.02$	$+0.58 \pm 0.06$
4	0.0308	$13.3 \pm 1.7$	$20.48 \pm 0.03$	$22.89 \pm 0.03$	$-19.64 \pm 0.02$	$+0.84 \pm 0.04$
5	0.25	$14.1 \pm 0.3$	$18.51 \pm 0.03$	$20.10 \pm 0.06$	$-18.17 \pm 0.04$	$+0.34 \pm 0.05$
6	0.25				$-18.15 \pm 0.01$	$+0.36 \pm 0.03$
7	0.845	$<14$	$16.52 \pm 0.02$	$17.28 \pm 0.04$	$-16.91 \pm 0.01$	$-0.39 \pm 0.03$
8	2.09	$<12$	$12-14$	$16.0 \pm 0.05$	$-15.36 \pm 0.02$	$-1 ?$
9	3.57	$<12$	$<12$	$14.2 \pm 0.5$	$-13.79 \pm 0.02$	$<-2$

<sup>a</sup> Errors are standard deviations except for  $\beta_2$  and  $\beta_3$  in 8 and 9, where the data sets were too small for statistical treatment.

<sup>b</sup> Calculated using the relation  $K_{s2} = K_{s0}\beta_2$ .

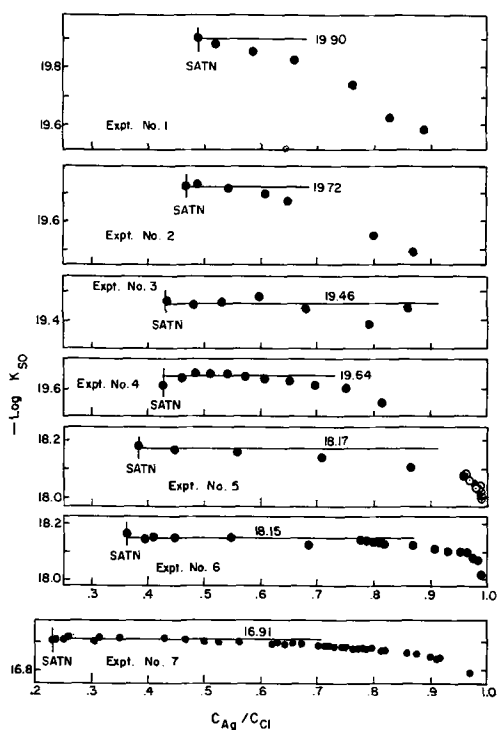


Fig. 2. Variation of experimental solubility product throughout the saturated region of the titration curve. Best values are listed in Table IV.

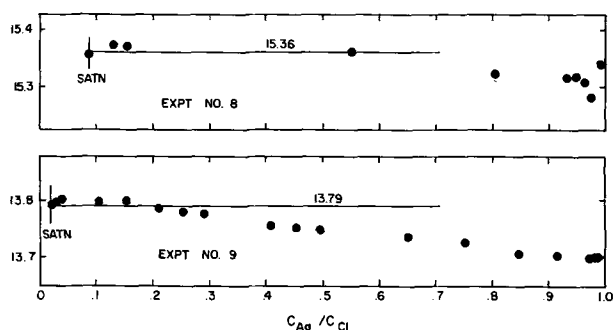


Fig. 3. Variation of experimental solubility product throughout the saturated region of the titration curve. Best values are listed in Table IV.

$$K_{s2} = \beta_2 K_{s0}$$

and assuming that the variances were additive.

### Discussion

The results of our experiments have shown a smooth variation in all the equilibrium constants as the concentration of water increases. The constants obtained in this study with the lowest water concentration are in agreement with those obtained previously (2); and for water contents below  $10^{-2}M$ , the constants vary by an amount approximately equal to the experimental error.

Although no simple equilibrium or structural model predicts the form of the equations, a convenient empirical expression of the dependence on water concentration is a linear function of the square root of  $C_{H_2O}$ . A similar dependence has been observed for the standard potential of the Ag/AgCl electrode in ethanol-water mixtures (12). Approximate expressions for the constants obtained in this work are

$$\log \beta_1 = +15.3 - 3.25 \sqrt{C_{H_2O}}$$

$$\log \beta_2 = 21.1 - 4.87 \sqrt{C_{H_2O}}$$

$$\log \beta_3 = 23.75 - 7.55 \sqrt{C_{H_2O}} \text{ for } C_{H_2O} < 0.5M$$

$$\log K_{s0} = -20.0 + 3.25 \sqrt{C_{H_2O}}$$

$$\log K_{s1} = -4.7$$

$$\log K_{s2} = +1.1 - 1.62 \sqrt{C_{H_2O}}$$

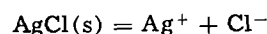
$$\log K_{s3} = +3.75 - 4.3 \sqrt{C_{H_2O}} \text{ for } C_{H_2O} < 0.5M$$

These equations give the experimental values of the constants within approximately  $\pm 0.5$  logarithmic units and are convenient for rough interpolation or extrapolation.

Figure 4 is a graphical representation of the results of this study, calculated using the above empirical expressions. Curves showing the solubility  $S$  of AgCl as a function of the concentration of added chloride  $C$  are drawn for solvents of various composition. In solutions of moderate chloride concentration ( $10^{-2}M$ ), the solubility of AgCl decreases by about a factor of 20 as the solvent is changed from pure propylene carbonate to propylene carbonate containing 3M  $H_2O$ , and by an additional factor of 1000 as the solvent is changed to pure  $H_2O$ . It is curious coincidence, however, that the solubility of AgCl in the absence of added chloride (left of diagram) is almost exactly the same ( $2 \times 10^{-5}M$ ), independent of the composition of the solvent. This coincidence is all the more remarkable because in propylene carbonate the predominant species are undissociated AgCl molecules, and in water the predominant species are  $Ag^+$  and  $Cl^-$  ions.

Although large changes are observed as the water concentration is increased from zero to the two-phase boundary (approximately 3.6M), the equilibrium constants for solubility and complex formation of silver chloride in this water-saturated propylene carbonate solution are still very different from those in pure water. Since the solutions on opposite sides of the miscibility gap are in equilibrium, this implies that similar dramatic changes in equilibrium constants would be found if small amounts of propylene carbonate were added to water.

A qualitative explanation of these large changes may be found in a discussion of the factors influencing the free energy of solvation of ions in the mixed solvents. The solubility product  $K_{s0}$  reflects the free energy change for the reaction



and is larger (less negative  $\log K_{s0}$ ) the more strongly the ions are solvated. Thus a medium of higher dielectric constant, or stronger specific interactions be-

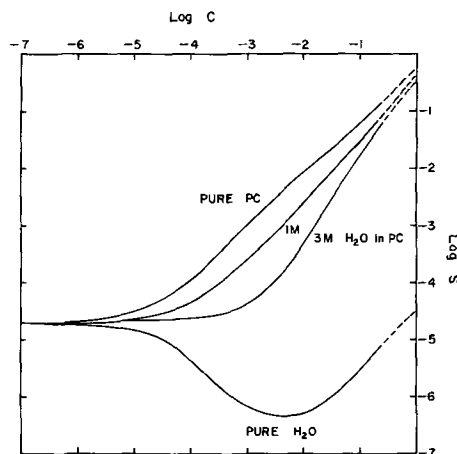
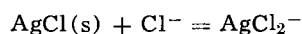


Fig. 4. Solubility ( $S$ ) of silver chloride in propylene carbonate water mixtures containing excess chloride of concentration  $C$ . These curves were calculated using the equilibrium constants in Table IV.

tween the ions and solvent, would tend to increase  $K_{s0}$ . As the medium is changed from propylene carbonate to water, the dielectric constant changes very little, but the hydrogen bonding of the solvent to chloride ions is very much less in propylene carbonate than in water. Thus we may attribute the changes in  $K_{s0}$  which we observe largely to the differences in hydrogen bonding between chloride ion and solvent. Since propylene carbonate is probably a relatively weakly coordinating ligand, the free energy of solvation of the cation probably does not change very much as the composition of the solvent changes. Of course, the separation of the observed variation in  $K_{s0}$  into contributions from solvation of cation or anion is a non-thermodynamic procedure, and we can discuss rigorously only the variation of the sum of the two free energies of solvation.

The other constant for which simple qualitative arguments may be clearly made is  $K_{s2}$ , which reflects the free energy change for the reaction



Here we observe directly the difference in free energy of solvation for two anions. If there were no specific interactions with the solvent, we would expect  $K_{s2}$  to be somewhat greater than unity, simply because  $\text{AgCl}_2^-$  is a larger ion than  $\text{Cl}^-$ . As the dielectric constant of the medium increases, we would expect the effect of size to be less, and thus expect  $K_{s2}$  to approach closer to unity. As is clear from Table IV, the observed values of  $K_{s2}$  decrease below unity at water concentrations around 0.5M, and are nearly five orders of magnitude smaller than unity in pure water (Table I). Hydrogen bonding of the solvent to  $\text{Cl}^-$  would tend to decrease  $K_{s2}$ , and this apparently causes the overwhelming change as the solvent is changed from propylene carbonate to water. Coordination of the solvent to silver would be expected to increase  $K_{s2}$ , and this may be a partial contribution to observed value  $K_{s2} = 10$  in the anhydrous solvent, but is certainly a much smaller effect than hydrogen bonding. This observation tends to confirm our previous statement that most of the increase in  $K_{s0}$  with increasing water content was attributable to increased solvation of  $\text{Cl}^-$  and not  $\text{Ag}^+$ .

The intrinsic solubility of AgCl ( $K_{s1} = \beta_1 K_{s0}$ ) reflects the free energy of solvation of the neutral complex AgCl, and this varies only slightly over the range from anhydrous propylene carbonate ( $K_{s1} = 10^{-5}$ ) to water ( $K_{s1} = 10^{-6.5}$ ). If anything, this variation implies that the coordinate bonding of propylene carbonate to silver is greater than water, but the effect is much smaller than the variations involving the solvation of the chloride ion.

Since these experiments were carried out in a constant ionic medium of 0.1M  $\text{Et}_4\text{NClO}_4$ , it is of interest to estimate the effect of the tetraethylammonium and perchlorate ions on the observed concentration equilibrium constants. The effect of ionic strength can be

estimated from the Debye-Hückel theory and is essentially the same for all the solvent mixtures. At zero ionic strength,  $\log \beta_1$  and  $\log \beta_2$  would be approximately 0.35 units greater and  $\log K_{s0}$  would be approximately 0.35 units more negative. The effect of ionic strength on the constants  $\beta_3$ ,  $K_{s1}$ , and  $K_{s2}$  is negligible in the range where the Debye-Hückel theory is applicable. Ion pairing with the supporting electrolyte would tend to increase  $\beta_1$ ,  $\beta_2$ , and  $\beta_3$ , and decrease  $K_{s0}$ , but have little effect on  $K_{s1}$ ,  $K_{s2}$ , and  $K_{s3}$ . However, since the dielectric constant of these solvent mixtures is high, and since little evidence for ion pairing between alkali metal, tetraalkyl ammonium, halide, or perchlorate ions, has been observed in water, the effects of ion pairing on the measurements described here is probably very small.

As is well-known (5-8), the solubility of AgCl can be suppressed by using electrolytes such as  $\text{LiAlCl}_4$  which have a low concentration of free chloride ion. Studies are now in progress which are intended to elucidate the equilibria in such systems.

### Acknowledgments

The authors thank Dr. Raymond Jasinski and Mrs. Susan Kirkland for providing us with samples of purified propylene carbonate, and Mr. Marcel Fajnzylber for assistance with preliminary experiments. This work was supported by but does not necessarily constitute the opinion of the Air Force Cambridge Research Laboratories, Office of Aerospace Research, under Contract No. AF 19(628)-6131.

Manuscript received Nov. 1, 1967; revised manuscript received Jan. 19, 1968. This paper was presented at the Chicago Meeting, Oct. 15-19, 1967, as Abstract 4.

Any discussion of this paper will appear in a Discussion Section to be published in the December 1968 JOURNAL

### REFERENCES

1. W. S. Harris, Thesis, University of California, 1958. U.S. Atomic Energy Commission Report UCRL-8381.
2. J. N. Butler, *Anal. Chem.*, **39**, 1799 (1967).
3. I. Leden, *Svensk Kem. Tidskr.*, **64**, 249 (1952).
4. E. Berne and I. Leden, *ibid.*, **65**, 88 (1953).
5. R. J. Jasinski, "High Energy Batteries," Plenum Press, New York (1967).
6. J. E. Chilton, Jr., Report ASD-TDR-62-1, April 1962. AD 277 171.
7. H. F. Bauman, J. E. Chilton, W. J. Conner, and G. M. Cook, Report RTD-TDR-63-4083, Oct. 1963. AD 425 876.
8. J. E. Chilton, W. J. Conner, G. M. Cook, and R. W. Holsinger, Report AFAPL-TR-64-147, Feb. 1965. AD 612 189.
9. R. J. Jasinski, *J. Electroanal. Chem.*, **15**, 89 (1967).
10. R. J. Jasinski and S. Kirkland, *Anal. Chem.*, **39**, 1663 (1967).
11. N. Ingri and L. G. Sillen, *Acta Chem. Scand.*, **16**, 159 (1962).
12. C. L. LeBas and M. C. Day, *J. Phys. Chem.*, **64**, 465 (1960).



# The Nickel Positive Electrode

## II. Semiconduction and Electrode Performance

Donald Tuomi

Roy C. Ingersoll Research Center, Borg-Warner Corporation, Des Plaines, Illinois

and G. J. B. Crawford

Schlumberger Technology Corporation, Ridgefield, Connecticut

### ABSTRACT

The anodic oxidation of nickel hydroxide in pure lithium hydroxide electrolytes produces an n-type semiconductor. The anodic oxidation involves lithium migration into the active material. The beta phase is characterized at room temperature by Seebeck coefficients near  $-100 \mu\text{V}/^\circ\text{K}$  and electrical conductivities of 1 mho/cm. This is in contrast to the positive Seebeck coefficient for lithium nickelate.

The nickel hydroxide positive electrode is considered to involve a divalent  $\text{Ni}(\text{OH})_2$  and a trivalent nickelate discharge and charge state. The designation beta phase was used by Tuomi (1) to describe the oxidized state without giving an explicit chemical composition formulation. Variations in the electrochemical processing conditions can modify the beta phase structural characteristics. The beta phase, however, appeared to be consistently an n-type semiconductor through hot point probe tests. On the other hand, the beneficial effects of LiOH additions to the battery electrolyte frequently are attributed to "p" type semiconduction enhancement in the charged phase as noted in Li doped NiO.

The following brief electrical property study was performed to clarify the experimental problem.

### Experimental

The oxidized product formed from crystalline  $\text{Ni}(\text{OH})_2$  during charge in pure LiOH electrolytes is structurally related to lithium nickelate (1). An Edison tubular positive electrode set was charged at 25° and 85°C in 5M LiOH using a 300 ma rate for 216 hr (69.8 amp-hr) to give complete oxidation to trivalent beta phase. After charging, the active material was removed, pulverized, and fractionated to beta plus nickel flake using magnetic separation. The beta powder was processed further to give the four samples: (a) C:uw, a 25°C charge unwashed; (b) C:w, a 25°C charge washed with distilled water; (c) H:uw, a 85°C charge unwashed; and (d) H:w, a 85°C charge washed with distilled water. The chemical analyses and x-ray diffraction examinations were performed on portions using earlier procedures (1). One sample set was fired in oxygen at 850°C for 16 hr.

Samples compressed into the annulus between two contact rings were used to measure the electrical properties. The Seebeck coefficient was calculated from the temperature and voltage differences measured when the center ring was heated. The electrical conductivity measurement involved a four point probe using very low frequency a-c current to minimize contact resistance effects.

The chemical analysis results are summarized in Table I, while the electrical and structural observations appear in Table II. The sample titled  $\text{Li}_x\text{Ni}_{1-x}\text{O}$  was formed by repeated grinding and refiring of a NiO-LiC<sub>2</sub>H<sub>3</sub>O<sub>2</sub> mixture at 850°C in oxygen for a 12 hr total time.

### Discussion

The material structure depended on the processing. The initial product was identified as small particle size beta phase with the hexagonal lithium nickelate structure. Firing in oxygen converted three samples to the cubic NiO phase with  $x < 0.3$  in  $\text{Li}_x\text{Ni}_{1-x}\text{O}$ , and

one to a hexagonal lithium nickelate at  $x = 0.41$ . The reaction product of NiO and LiC<sub>2</sub>H<sub>3</sub>O<sub>2</sub> was hexagonal nickelate at  $x = 0.45$ . The general observations are consistent with the prior investigators (2). However, the hexagonal unit cell volumes were 6% greater than anticipated.

The electrochemical oxidation in LiOH converted the  $\text{Ni}(\text{OH})_2$  to a trivalent oxide with a 2.86 to 3.07 valence as shown in Table I. This was accompanied by a nickel content decrease from 63.4% to 56-59%. This is higher than 53.9% for  $\text{HNiO}_2 \cdot \text{H}_2\text{O}$  and less than 74% for  $\text{HNiO}_2$  or 60.1 for  $\text{LiNiO}_2$ . Since no attempt was made to remove sorbed water the solid phase is more consistently viewed as an anhydrous oxide than a simple hydrate such as  $\text{Ni}_2\text{O}_3 \cdot x\text{H}_2\text{O}$ .

The C:uw and C:w 25°C product has a lower lithium content than the 85°C material. The difference in Li content for the washed and unwashed materials could not readily be explained by extraneous Li<sub>2</sub>CO<sub>3</sub> formation. The comparable product valence states suggest protons effectively exchange for Li. The data clearly indicate Li sorption during charge. A loaded tube impregnated with electrolyte and dried as above contained only 0.16% Li.

The lithium to nickel molar ratio varied from 0.2 to 0.7 for dried materials and did not change during 850°C firing. This ratio is not consistent with viewing the reaction product as  $\text{LiNiO}_2$ . On the other hand, the charged phase lithium content implies oxidation in LiOH electrolyte is best not simply viewed as proton migration out of  $\text{Ni}(\text{OH})_2$  to form an  $\text{HNiO}_2$  phase. Rather hydroxyl at the double layer reacts with protons forming water while lithium ions make transitions into the active phase interior. Process details depend on the charge distribution through solid-electrolyte interphase.

The 850°C oxygen atmosphere firing process increased the nickel content to the 70% range with corresponding lithium percentage increases. By contrast, the nickel valence dropped to 2.2-2.5 from 3. The cubic fired products  $\text{Li}_x\text{Ni}_{1-x}\text{O}$  with  $x < 0.3$  showed calculated  $x$  values based on both Li and Ni were consistent with the nickel valence determination. The fired H:uw sample with the highest Li content corresponded to hexagonal  $\text{Li}_{0.41}\text{Ni}_{0.59}\text{O}$ . After firing the measured and calculated (% Li in  $\text{Li}_x\text{Ni}_{1-x}\text{O}$ ) valence states are related as shown in Table III. The valence change and structural modifications are consistent with a  $(\text{H,Li})_x\text{Ni}_{1-x}\text{O}$  containing sorbed H<sub>2</sub>O transformation to  $\text{Li}_x\text{Ni}_{1-x}\text{O}$  accompanied by water and oxygen evolution.

The electrical measurements, Table II, provide more detailed insight into the problem complexity. Conventionally, the addition of lithium to NiO is viewed as introducing holes into the band structure (i.e.,  $\text{Ni}^{+3}$

Table I. Chemical analyses and structural form for dried and fired anodic oxides as described in text

Sample		C:uw	C:w	H:uw	H:w	Li <sub>x</sub> Ni <sub>1-x</sub> O
Ni Valence	Dried	3.07	2.97	2.97	2.86	—
	Fired	2.31	2.19	2.53	2.30	2.88
	$\delta$	-0.76	-0.78	-0.44	-0.56	—
Ni	Dried	55.86	59.28	55.62	56.84	—
	Fired	69.44	72.85	64.54	70.47	61.7
	$\delta$	+13.58	+13.57	+8.92	+13.63	—
Li	Dried	2.63	1.58	4.73	2.32	—
	Fired	3.25	1.82	5.35	2.99	5.70
	$\delta$	+0.62	+0.24	+0.62	+0.67	—
Li <sub>x</sub> Ni <sub>1-x</sub> O	Dried	0.398	0.225	0.719	0.343	—
	Fired	0.40	0.22	0.69	0.81	0.81
Crystal Symm.	Dried	—	—	—	—	—
	Fired	0.29	0.18	0.41	0.26	0.45
Crystal Symm.	Dried	Hex	Hex	Hex	Hex	—
	Fired	Cubic NiO	Cubic NiO	Hex	Cubic NiO	Hex

Table II. Electrical data from dried and fired anodic oxide samples as described in text

Sample		C:uw	C:w	H:uw	H:w	Li <sub>x</sub> Ni <sub>1-x</sub> O
S $\mu\text{V}/^\circ\text{C}$	Dried	-107	-58	-92	-85	—
	Fired	+97	+137	+113	+99	+70
$\sigma$ Mho/cm	Dried	3.3	4.5	0.68	0.92	—
	Fired	0.7	0.77	0.70	0.51	0.16

Table III. % Li in Li<sub>x</sub>Ni<sub>1-x</sub>O valence states after firing

	Calc	Anal
C:uw	2.41	2.31
C:w	2.22	2.19
H:uw	2.69	2.53
H:w	2.36	2.30

local sites) and forming a p-type semiconductor (3). The anodic oxidation, however, converted the Ni(OH)<sub>2</sub> insulator to a high electrical conductivity n-type semiconductor. The reaction product has a negative Seebeck coefficient varying from -58 to -107  $\mu\text{V}/^\circ\text{C}$  at 0.7-5.0 mho/cm. The firing process produces the expected p-type conduction with S between +97 to +137  $\mu\text{V}/^\circ\text{C}$  and  $\sigma$  near 0.7 mho/cm. This compares to +70  $\mu\text{V}/^\circ\text{C}$  at 0.16 mho/cm for the direct reaction product Li<sub>0.45</sub>Ni<sub>0.55</sub>O. Lower nickel valence state fired products are also p-type. Thus, the LiOH electrolyte modification of the charged phase does not involve the anticipated semiconductor doping effect (4). It should be noted that Richardson (5) observed that the higher valence state precipitated nickelic oxides are also n-type semiconductors as has been previously noted for the KOH anodic oxidation product (6).

Even for a pure LiOH electrolyte the electrochemically oxidized Ni(OH)<sub>2</sub> is an n-type semiconductor beta phase. The semiconductor gross features are not under drastic control by alkali cation content. The n-to p-type transformation on heat treatment suggests the lattice or local electronic coordination imperfection depends on the hydrogen ion distribution effect on local band structure.

The characteristic Li<sub>x</sub>Ni<sub>1-x</sub>O composition formed by firing at 850°C is consistent with a trivalent nickel stabilization by local site symmetry conditions. The p-type conductivity for 0 < x < 0.5 is not simply interpretable as trivalent ion promotion through the local band electrostatic neutrality condition as in slightly Li doped NiO.

The recent results of Bosman and Crevecoeur (7) indicate a band model rather than the thermally activated carrier hopping model applies to nickel oxide. The detailed study of anodic oxidation products as well as the simple Li<sub>x</sub>Ni<sub>1-x</sub>O system could provide considerable insight into electronic processes in electrochemical systems. The local site symmetry constraints in high density, well-ordered, lithium nickel-

ates are markedly stronger than in the less crystalline anodic product which frequently can approach an amorphous structure having only first and second nearest neighbor symmetry. The dilemma is accentuated when it is noted that the case of trivalent nickel oxidation to tetravalent alpha phase depends on electrolyte composition and electrode processing. Clearly interpreting chemical additive effects as altering semiconductor processes is questionable without detailed study.

The high electrical conductivity of the oxidized phase does not necessarily inhibit mass transport in the relevant electrochemical processes. A high electronically active site density is implied by the high conductivity with the probable low carrier mobility along with contact resistance in the fine grain material. Under such conditions, a variety of unusual behaviors related to imperfection densities would not be surprising. The space charge distributions within the compounds during cycling will depend partially on the electronic transport properties interactions with the mass transport as well as the interphase phenomena including Peltier effects, and the electronic-ionic exchange processes.

Detailed studies on the importance of impurity banding, metallic conduction, etc. to electrode behavior may be undertaken through a systems approach to the problem. The interpretation of n-type high conductivity in the anodic oxidation product with p-type in the cubic and hexagonal divalent-trivalent nickel solid solution of Li<sub>x</sub>Ni<sub>1-x</sub>O compounds requires a detailed knowledge of imperfection structure relationships to band structure. It should be emphasized that the semiconductor under consideration is an extremely complex chemical and structural system reflecting the formation conditions. A priori the system is not conceptually related to ceramic or single crystal cubic NiO. Rather the material represents a solid solution with nonstoichiometric characteristics and considerable disorder in the system Ni-O-Li-H. Mott's review (8) on electrons in disordered structures brings attention on to one class of problems to be solved. The mass and charge transport in the electrochemical oxidation-reduction process provides a general phase transformation kinetics problem.

### Acknowledgments

The assistance of J. Bronson and L. Middlecamp in the experimental work is gratefully acknowledged. The analytical services were provided through the cooperation of B. D. Brummet. The research benefited from discussions with Drs. G. T. Croft, J. B. Johnson, and P. F. Grieger at the T. A. Edison Research Laboratory. The continued support of Dr. D. W. Collier is appreciated. Special acknowledgments are due to W. W. Smith and associates of the Electric Storage Battery Company for their encouragement and support during the preparation of this paper for publication.

Manuscript received June 19, 1967; revised manuscript received Dec. 11, 1967.

Any discussion of this paper will appear in a Discussion Section to be published in the December 1968 JOURNAL.

### REFERENCES

1. D. Tuomi, *This Journal*, **112**, 1 (1965).
2. J. B. Goodenough, P. G. Wickham, and W. J. Croft, *J. Phys. Chem. Solids*, **5**, 107 (1958).
3. E. J. W. Verwey, "Semiconducting Materials," pp 151-161, Butterworths Scientific Pub. Ltd., London (1951).
4. R. L. Tichenor, *Ind. Eng. Chem.*, **44**, 973 (1952).
5. J. T. Richardson, *J. Phys. Chem.*, **67**, 1377 (1963).
6. D. Tuomi, *ibid.*
7. A. J. Bosman and C. Crevecoeur, *Phys. Rev.*, **144**, 763 (1966).
8. N. F. Mott, *Adv. in Physics*, **16**, 49 (1967).

# The Electrolysis of Ammonium Bifluoride in Anhydrous Hydrogen Fluoride

Larry G. Spears\*<sup>1</sup>

TRACOR, Inc., Austin, Texas

and Norman Hackerman\*

The University of Texas, Austin, Texas

## ABSTRACT

The electrolysis of ammonium bifluoride in anhydrous hydrogen fluoride (AHF) was investigated. Polarization curves of Monel in solutions of  $\text{NH}_4\text{HF}_2$  in AHF did not show any diffusion-limited regions indicative of a potential-dependent stepwise reaction. The results of this study indicate that the fluorination of  $\text{NH}_4\text{HF}_2$  in AHF occurs by a radical mechanism involving anodically generated fluorine. Chronopotentiometric data, current-potential curves, and product yields *vs.* time curves, indicate that the fluorinating agent, during electrolysis, is a "loose" complex between  $\cdot\text{F}$  and  $\text{NiF}_2$  and/or  $\text{CuF}_2$ . *Trans-N}\_2\text{F}\_2* was the only N-F product formed from the electrolysis of  $\text{NH}_4\text{HF}_2$  in AHF.

The use of anhydrous hydrogen fluoride (AHF) as a solvent for the electrolysis of ammonium salts has not been investigated in much detail. Several investigators have reported using AHF as a solvent for the electrolysis of  $\text{NH}_4\text{HF}_2$  (1, 2) but their results indicated that the solvent was not anhydrous. Several electrolyses (3, 4) have been performed using molten  $\text{NH}_4\text{HF}_2$ ; however, they were not reported in much detail either.

Anhydrous HF has many properties which make it a valuable solvent system for studying the chemistry of both organic and inorganic fluorine-containing species. Among these are its ability to dissolve a variety of ionic and covalent compounds in significant amounts and its ionizing powers toward dissolved ionic species. In both of these aspects, it is very similar to water. Also, like water, its self-dissociation constant is small, so that the activity of ionic species contributed directly by AHF to a system under study will be low. Such properties are particularly valuable to an electrochemical approach for studying reaction kinetics in AHF, since the more "waterlike" the solvent system, the more applicable will be past electrochemical experience.

In this investigation an attempt was made to determine the electrochemical mechanism involved in the anodic fluorination of  $\text{NH}_4\text{HF}_2$  dissolved in AHF. A free radical mechanism involving fluorine atoms has long been recognized by many workers as the mechanism involved in the electrochemical fluorination of organic materials in HF (5). Some workers claim the fluorinating agent is a higher valent metal fluoride or metal fluoride compound. Cotton (6) suggests that a nickel anode in HF and KF might form  $\text{K}_2\text{NiF}_6$  and  $\text{K}_3\text{NiF}_6$  which could act as fluorinating agents at the electrode surface. However, none of these higher valent fluorides have ever been identified. Of course, it is possible that these fluorides might be next to the metal and covered with the normal valency metal fluoride such that electron diffraction studies or other analytical devices would not detect them.

## Experimental

The system developed for handling and storing the HF and the electrolytic cells used in this work has been previously described (7, 8). The electrolytic cells were constructed of Kel-F and Teflon with Teflon fit-

tings and valves. All tubing in contact with the cells was either Teflon or Kel-F.

Anhydrous HF was prepared, using commercial HF, by a distillation and electrolysis procedure similar to that of Rogers, Johnson, and Evans (9). Conductivity of AHF prepared in this manner was usually around  $10^{-5}$  ohm<sup>-1</sup> cm<sup>-1</sup>. Water concentration was estimated from an empirical relation given by Ukaji and Kageyama (10).

Monel (alloy No. 400), in the form of 0.125 in. rod, was used as the working electrode. Previously reported data (8, 11) indicates that Monel is probably the most desirable anode material for use in AHF. The Monel electrodes were prepared by mechanical sanding and buffing to a smooth surface. Then they were degreased in hot benzene, washed with distilled water, and vacuum dried. Nickel screen was used for the auxiliary electrode.

The reference electrode used was the Hg/Hg<sub>2</sub>F<sub>2</sub> electrode. Initial work on this electrode was reported by Koerber and DeVries (12); details of construction and performance have been discussed previously (8, 13).

Volatile electrolysis products were analyzed using a Beckman IR 5-A infrared spectrometer, an F & M gas chromatograph (Model 720 with a nickel block), and a modified Electrochemical Corporation mass spectrometer (Model 21-620). A description of the techniques involved in these analyses has been reported (7, 8). Cryogenic programming (using 2 coiled, 7 ft, ¼ in. OD Monel tubes) from -196°C to room temperature was used to separate the volatile products for identification by IR and mass spectral methods. A 70 ft column packed with 50% Halocarbon Oil 13-21 on 30-50 mesh Kel-F molding powder at 0°C, was used for quantitative GC analysis of the volatile products (14). Irtran-2 (Eastman Kodak Company) was used as the liquid and gas IR cell window material.

A unique IR liquid cell was developed in this laboratory to analyze the soluble products (15).

All ammonia used for the  $\text{NH}_4\text{HF}_2$ -AHF solutions was double-distilled and all potentials were *vs.* Hg/Hg<sub>2</sub>F<sub>2</sub> at -20°C.

## Results

A typical steady-state polarization curve for Monel in AHF is shown in Fig. 1. The current increase past ~2.8v is due mainly to F<sub>2</sub> evolution. A hysteresis is noted when reverse polarization is done rapidly, indicating existence of a film on the electrode surface. The passive-type region between open circuit and

\* Electrochemical Society Active Member.

<sup>1</sup> Present address: Gulf South Research Institute, New Iberia, Louisiana.

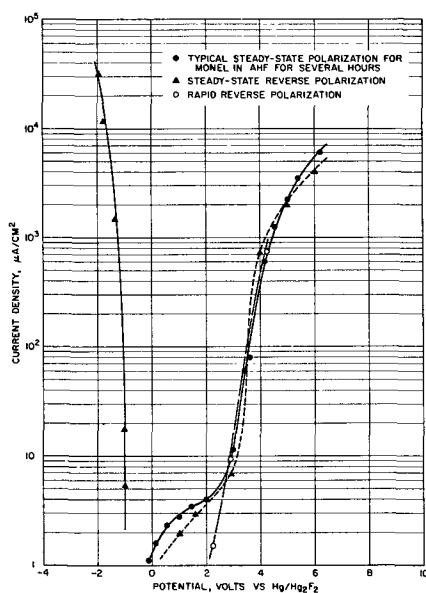


Fig. 1. Polarization curves for Monel in AHF

$\sim 2.8$ v is due mainly to formation of a metal fluoride film. Weight losses for Monel between open circuit and 2.8v were similar to those at open circuit. A typical anodic polarization curve for a Monel electrode in AHF for only 30 min is shown in Fig. 2. The current density peak at  $\sim 1.4$ v indicates an initial film formation. Curves run after an electrode had been in AHF for at least 2 hr did not exhibit this peak.

Anodic polarization curves were made in solutions of  $\text{NH}_3$  dissolved in AHF to determine if the fluorination of  $\text{NH}_4^+$  proceeded in a stepwise fashion as a function of potential. Liquid IR spectra showed that  $\text{NH}_3$  dissolved in AHF formed  $\text{NH}_4\text{HF}_2$  and possibly some  $\text{NH}_4\text{H}_2\text{F}_3$  (7, 8). Two typical steady-state polarization curves made in a 1M solution of  $\text{NH}_4\text{HF}_2$  in AHF are shown in Fig. 3. A plateau-like region can be seen between 3.4 and 3.8v. This current limited region was noted in all polarization curves run in AHF- $\text{NH}_4\text{HF}_2$  solutions; however, its magnitude was not dependent on the  $\text{NH}_4\text{HF}_2$  concentration. Fast polarization curves were also made with a voltage increase of 0.9 v/min. Figure 4 shows two fast anodic polarization curves made in 0.1M  $\text{NH}_4\text{HF}_2$  in AHF.

Galvanostatic cathodic reduction curves were made in an attempt to clarify the diffusion-limited region described above. Reduction curves for Monel, polarized anodically at 2, 4, 5, and 6v in 0.021M  $\text{NH}_4\text{HF}_2$  in AHF, are shown in Fig. 5. The potential arrest at  $\sim 2.7$ v

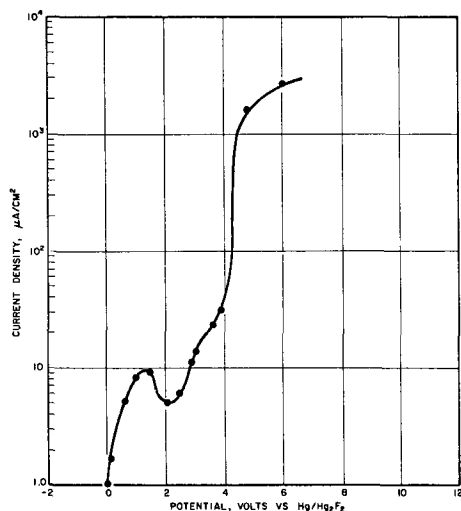
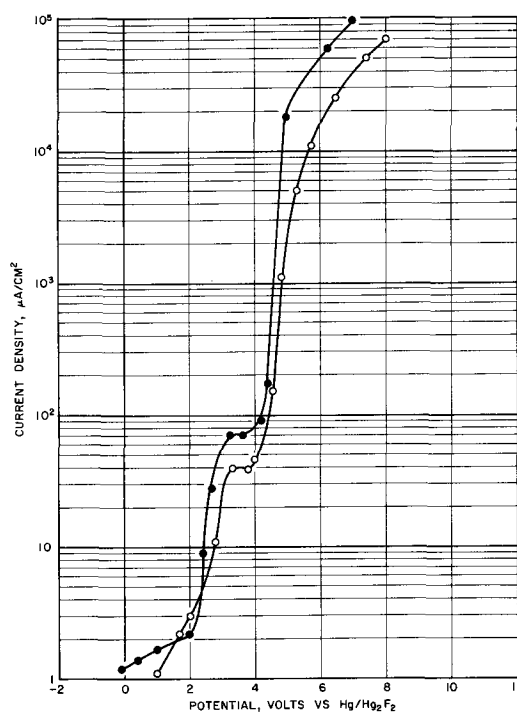
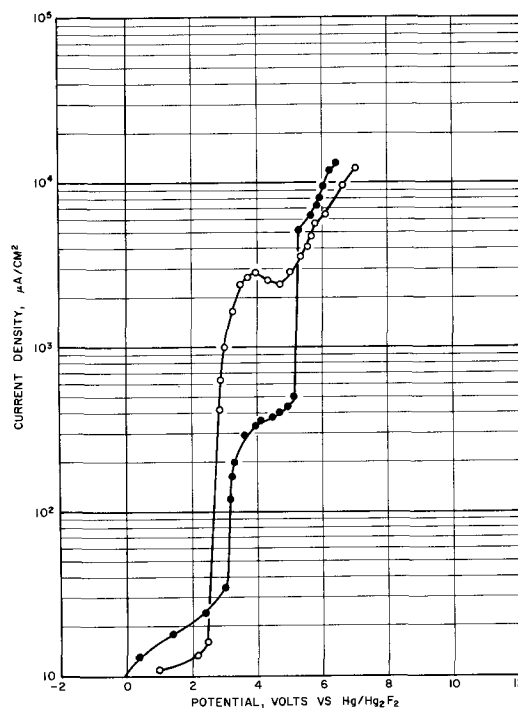


Fig. 2. Polarization curve for Monel (in AHF for 30 min)

Fig. 3. Anodic polarization curves of Monel in 1M  $\text{NH}_4\text{HF}_2$  in AHFFig. 4. Fast anodic polarization curves of Monel in 0.1M  $\text{NH}_4\text{HF}_2$  in AHF.

is close to the reduction potential for fluorine according to Fig. 1. As shown in Fig. 6, the cathodic charge required for reduction appears to depend on the total charge passed at 6v rather than the increment of charge passed between reductions. These results indicated that a species other than the metal fluoride was being reduced during these reduction experiments.

If the potential arrest at  $\sim 2.7$ v was due to the reduction of fluorine, it should be possible to reach a state where the metal fluoride film would be saturated with fluorine. This effect is shown in Fig. 7. It should be noted that 154 coulombs were passed at 6.0v and a cathodic current applied until the potential returned to approximately the initial open circuit potential before the runs in Fig. 7 were made. Once the metal

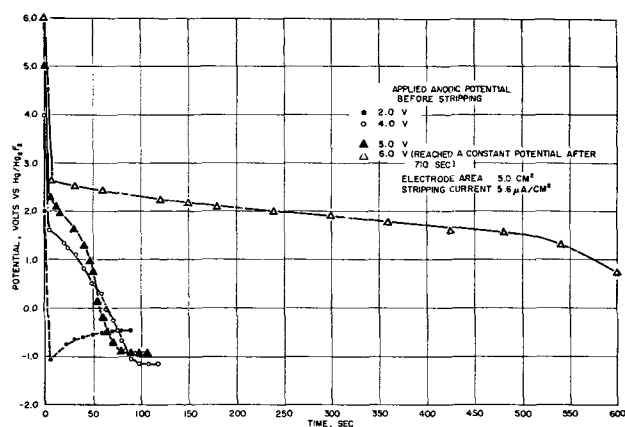


Fig. 5. Stripping curves for Monel electrodes polarized anodically in 0.021M NH<sub>4</sub>HF<sub>2</sub> in AHF.

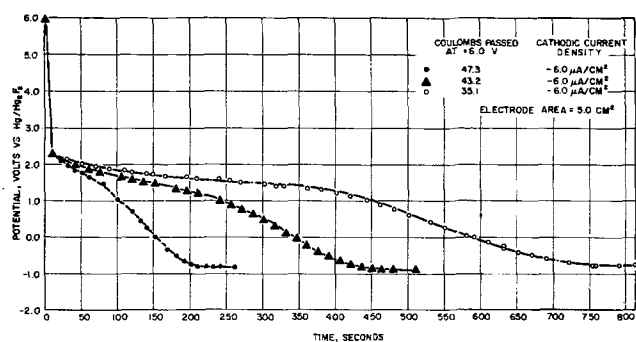


Fig. 6. Cathodic stripping of Monel electrodes from +6.0v in 2.13 X 10<sup>-2</sup>M NH<sub>4</sub>HF<sub>2</sub> in AHF.

fluoride film is saturated, it should be possible to decrease the applied anodic charge and thus have a decrease in the cathodic charge required to reduce the sorbed fluorine. This is shown in runs 3 to 8 of Fig. 7. In Table I, values obtained from reduction measurements in 0.01M NH<sub>4</sub>HF<sub>2</sub> in AHF are given. It can be seen from the table that as the anodic charge and anodic charge begins to approach unity. Also, it should be noted that the anodic and cathodic charges for 6.0 v/2 sec and 4.0 v/30 sec were almost identical.

Constant potential electrolyses were performed using various concentrations of NH<sub>4</sub><sup>+</sup> and anodic potentials. Initially these electrolyses were made in order to identify the products formed. As described above, a cryogenic GC column was utilized for this work. After the volatile products were identified, the coulombic yields of the products were determined as a function of time using a 70 ft Halocarbon Oil Kel-F powder GC column.

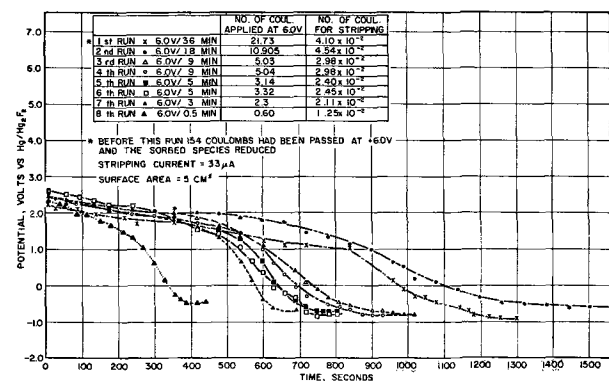


Fig. 7. Cathodic reduction curves for Monel in 2.16 X 10<sup>-3</sup>M NH<sub>4</sub>HF<sub>2</sub> in AHF.

Table I. Values obtained from the cathodic reduction measurements made on Monel in a solution of 0.01M NH<sub>4</sub>HF<sub>2</sub> in AHF

Anodic potential/sec applied	No. of reduction coul. required × 10 <sup>3</sup> (C <sub>1</sub> )	No. of coul. applied anodically (C <sub>2</sub> )	C <sub>1</sub> /C <sub>2</sub> × 100
6.0 v/30 sec	5.95	2.55	0.233
6.0 v/15 sec	4.25	1.22	0.348
6.0 v/5 sec	2.96	0.35	0.845
6.0 v/2 sec	1.84	0.136	1.35
4.0 v/30 sec	1.87	0.135	1.36
4.0 v/15 sec	1.12	0.063	1.75
4.0 v/11 sec	0.918	0.044	2.09
4.0 v/5 sec	0.740	0.015	4.93
4.0 v/3 sec	0.442	0.008	5.46

None of the liquid IR spectra indicated the presence of any soluble electrolysis products (7, 8). Liquid spectra taken before and after extended electrolysis were identical except for the relative size of the NH<sub>4</sub><sup>+</sup> absorption bands.

Figures 8, 9, and 10 show the yields of the anodic products formed from the electrolysis of 0.1M and

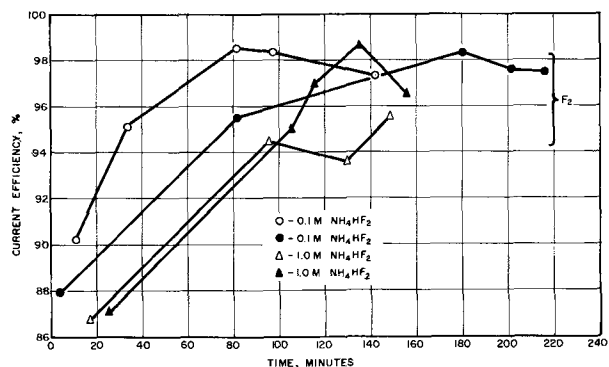


Fig. 8. Yield of 5.0v electrolysis products as a function of time

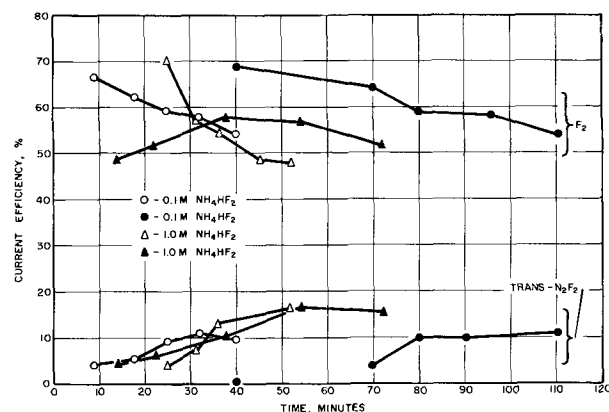


Fig. 9. Yield of 7.0v electrolysis products as a function of time

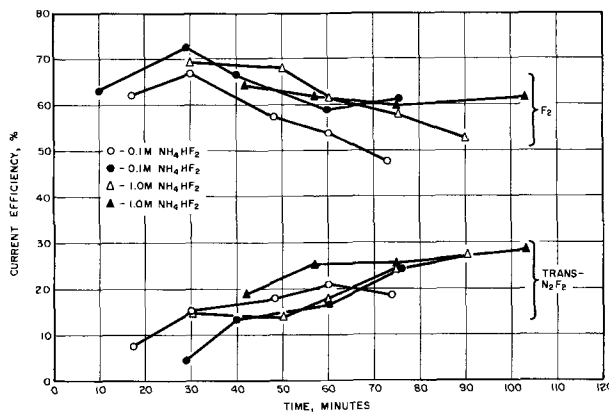


Fig. 10. Yield of 9.0v electrolysis products as a function of time

1.0M solutions of  $\text{NH}_4\text{HF}_2$  in AHF at potentials of 5.0, 7.0, and 9.0v. Table II summarizes these results giving the net current efficiency for each of the electrolysis products. The equivalent weight of the metal fluoride was calculated assuming formation of  $\text{NiF}_2$  and  $\text{CuF}_2$ . The current density range given in Table II is the variation of the observed current densities during electrolysis. Most of these runs had a lower current initially. During electrolysis, the current usually increased with time until a relatively constant current region was reached.

### Discussion

Polarization curves of Monel in solutions of  $\text{NH}_4\text{HF}_2$  in AHF were made in an attempt to detect a potential-dependent stepwise reaction (see Fig. 3 and 4). A plateau-like region was noted around 4.0v; however, it did not appear to be dependent on the  $\text{NH}_4\text{HF}_2$  concentration. Polarization curves of metals or alloys in solutions of ammonium salts in HF could not be found in the literature for comparison. Constant potential electrolyses at 5.0v, in 0.1M and 1.0M solutions of  $\text{NH}_4\text{HF}_2$  in AHF, produced no volatile or soluble N-F or nitrogen containing species. Thus, it was concluded that the constant current region was probably due to a phenomena not directly related to the presence of  $\text{NH}_4\text{HF}_2$ .

Fast polarization curves were made to see if the lack of a thick fluoride film (the type formed during steady-state polarization) would result in different anodic polarization characteristics. The only differences noted were a broader plateau region around 4v and erratic behavior in the slope of the curve past the plateau region. Both of these changes are probably due to the inability of the system to reach equilibrium conditions during the fast scan (0.9 v/min.) Points taken for the steady-state curves were recorded after approximately 20 min at each potential.

The galvanostatic reduction curves presented above indicate that both metal fluoride and fluorine were formed on the electrode surface during anodic charging. When cathodic current was applied, only the trapped or sorbed fluorine was reduced. Continuous anodic charging resulted in more sorbed or trapped fluorine, this being due to the increasing film thickness. Experiments performed on nickel anodes in HF indicated similar phenomena (8, 16).

Constant potential electrolyses showed that *trans*- $\text{N}_2\text{F}_2$  was the only N-F species formed during the electrolysis of  $\text{NH}_4\text{HF}_2$  in AHF. Previously reported data (7, 8) indicated that the formation of  $\text{N}_2\text{F}_2$  decreased rapidly with the addition of increasing concentrations of water. Also, as the water concentration increased, increasing amounts of  $\text{OF}_2$  and  $\text{NF}_3$  were formed. The "induction period" (the time required for the yields to reach a constant value) noted in Fig. 10 and 11, are typical of electrolytic fluorination studies reported by other workers (1, 17, 18) including two studies on the electrolysis of molten  $\text{NH}_4\text{HF}_2$  (3, 4).

The effect of increasing current density on the yield of  $\text{N}_2\text{F}_2$  should be noted (see Table II). A previously

reported study of the electrolysis of molten  $\text{NH}_4\text{HF}_2$  (3) stated that a minimum current density of 30 ma/cm<sup>2</sup> was required in order to obtain N-F species.

From the data presented above, it is concluded that the electrolytic fluorination of  $\text{NH}_4^+$  in AHF occurs by chemical reaction with anodically formed fluorine. A free radical mechanism is thought to occur in the electrochemical fluorination of organic materials in HF (5). Some workers claim that the fluorinating agent is a higher valent metal fluoride or metal fluoride compound (6). Another possibility for the identity of the fluorinating agent for this study is a loose complex between  $\text{NiF}_2$ ,  $\text{CuF}_2$ , and  $\cdot\text{F}$  or  $\text{F}_2$  (5).

If the agent was a loose complex, fluorination would occur between the complex and the substrate adsorbed on the anodic film. This type process would thus require an induction period for buildup of the film containing the complexed  $\text{NiF}_2$  and/or  $\text{CuF}_2$ . Initially, low yields of fluorinated species would occur due to the small amount of film on the anode. As the film increased, so would the concentration of fluorinating agent in the film, thus increasing the yield of fluorinated species.

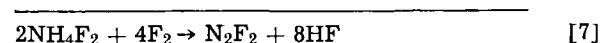
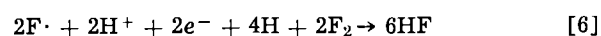
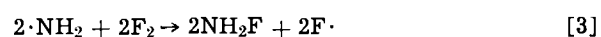
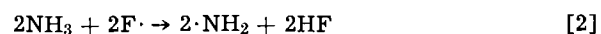
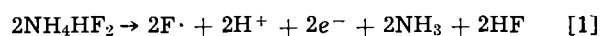
If the fluorination process were due only to  $\text{F}_2$  formed at the anode, there would be no need for the relatively long induction periods noted in Fig. 9 and 10. If fluorination occurred due to formation of higher metal fluorides, it is still difficult to explain the long induction periods. Of course, it is possible that the loose complex involved  $\text{F}_2$  instead of  $\cdot\text{F}$ . However, if a complex is formed, the more active fluorine radical would be preferred to the molecule. This would also help to explain previously reported data (8, 16) where an anodically charged (in KF-AHF solution) Ni electrode was put under vacuum and then returned to the electrolytic cell and cathodically reduced. Very little of the sorbed fluorine had been removed from the film as a result of the vacuum.

Morrow and co-workers studied reactions between  $\text{F}_2$  and  $\text{NH}_3$  in a copper T-shaped reactor (19). They were able to form  $\text{NF}_3$ ,  $\text{N}_2\text{F}_4$ ,  $\text{N}_2\text{F}_2$ , and  $\text{HNF}_2$  along with small amounts of  $\text{N}_2$  and HF. With an excess of  $\text{NH}_3$  only  $\text{N}_2\text{F}_4$ ,  $\text{N}_2\text{F}_2$  and  $\text{HNF}_2$  were formed. When an excess of fluorine was used only  $\text{NF}_3$  and  $\text{NH}_4\text{F}$  were formed. They concluded that the initial step in these reactions was the formation of  $\cdot\text{F}$  from  $\text{F}_2$ . The copper reactor could have acted as a catalyst for the dissociation.

A reason for excess fluorine, in the above reactions, to hinder  $\text{N}_2\text{F}_2$  formation might be that large amounts of fluorine result in relatively fewer fluorine radicals to react with  $\text{NH}_3$ . This might also explain the effect of water on the yields of  $\text{NF}_3$  and *trans*- $\text{N}_2\text{F}_2$  in liquid HF. In aqueous HF, there should be fewer fluorine atoms in the film, thus decreasing the yield of any species dependent on  $\cdot\text{F}$  for its formation.

### Conclusions

In view of the above data, the following mechanism is proposed for the formation of  $\text{N}_2\text{F}_2$  in these studies. This mechanism is similar to that proposed by Morrow (19) and Colburn (4).



The first step in the mechanism above occurs at the electrode surface as a result of an anodic bias equal to or greater than the fluorine evolution poten-

Table II. Current efficiency of products formed from the electrolysis of  $\text{NH}_4\text{HF}_2$  in AHF

NH <sub>4</sub> HF <sub>2</sub> concentration	Potential, v	Current density range, ma/cm <sup>2</sup>	Total charge passed, coulombs	% Yield of current passed		Anode corrosion
				F <sub>2</sub>	Trans-N <sub>2</sub> F <sub>2</sub>	
0.1M	5	0.68-1.25	42.83	97.5	—	4.10
0.1M	5	0.32-0.44	7.58	97.3	—	7.44
1.0M	5	0.14-0.54	10.20	95.8	—	0.76
1.0M	5	0.81-2.10	39.77	96.5	—	2.24
0.1M	7	4.9-79.0	1082	54.0	11.20	27.36
0.1M	7	54.5-81.8	1086	56.8	10.01	30.10
1.0M	7	4.0-96.0	716	48.4	16.47	27.05
1.0M	7	48.8-97.6	1638	51.5	15.15	31.10
0.1M	9	113-191	818	47.7	19.0	27.30
0.1M	9	50-175	382	60.8	24.6	25.70
1.0M	9	26.7-233	1440	53.7	27.5	25.42
1.0M	9	63.8-264	1564	61.2	28.5	21.30

tial. As a result of our experiments, it is felt that the fluorine radicals utilized in step [2] are associated in a loose complex with  $\text{NiF}_2$  and/or  $\text{CuF}_2$  in the anodic film. By use of bond dissociation energies given by Wilson (2), the following values were calculated (in units of kcal/mole) for the heats of formation of steps [2] to [6]: [2]  $-78$ , [3]  $-62.4$ , [4]  $347.8$ , [5]  $-107.9$ , and [6]  $-662$ . Upon addition of these values,  $-562.5$  kcal/mole is obtained for  $\Delta H_f$  of the net equation given in step [7]. Another factor which makes this mechanism more probable is that  $\text{NH}_2\text{F}$  formation has never been observed. If fluorine gas were the fluorinating agent in step [2], the heat of formation would be reduced to  $-31$  kcal/mole, making the initial step of this mechanism less favorable.

Why *trans*- $\text{N}_2\text{F}_2$  is formed instead of *cis*- $\text{N}_2\text{F}_2$  is difficult to explain. One answer might be that either the metals (Ni, Cu, Hg, or Pt) or metal fluorides present in the electrolytic cells catalyzed the formation of *trans*- $\text{N}_2\text{F}_2$  from any *cis*- $\text{N}_2\text{F}_2$  that was formed. It is also possible that under the experimental conditions used, the *trans* isomer required the least energy. *Cis*- $\text{N}_2\text{F}_2$  is reported to be the more active form of  $\text{N}_2\text{F}_2$  (20).

#### Acknowledgments

This work was supported in part by the United States Navy, Office of Naval Research, under Contract Nonr-4054(00) with TRACOR, Inc., Austin, Texas. The authors also wish to express appreciation to E. S. Snavely, Jr., L. D. Fiel, W. E. Harrell, Jr., and J. O. Spears, for contributions to this project. One of the authors (N.H.) takes this opportunity to express his thanks to The Robert A. Welch Foundation, Houston, Texas, and to the Office of Naval Research, under Contract Nonr-375(15), for their support of the work in his laboratory which led in part to this work.

Manuscript received Nov. 16, 1967.

Any discussion of this paper will appear in a Discussion Section to be published in the December 1968 JOURNAL.

#### REFERENCES

1. H. H. Rogers, S. H. Evans, and J. H. Johnson, Contract Nonr-1818(00), Report No. R-5077, Rocketdyne (1963).
2. A. R. Young and S. I. Morrow, Contract Nonr-4364(00), ARPA Order No. 417, Report RMD 5043-Q2-64, Thiokol Chemical Corp. (1964).
3. M. Schmeisser and P. Satovi, *Angew. Chem.*, **71**, 523 (1959).
4. Colburn *et al.*, *J. Am. Chem. Soc.*, **81**, 6397 (1959).
5. M. Stacy, J. C. Tatlow, and A. Sharpe, "Advances in Fluorine Chemistry," Vol. I, p. 162, Butterworth, London (1960).
6. F. A. Cotton, "Progress in Inorganic Chemistry," Vol. II, p. 200, Interscience Publishers, Inc., New York (1960).
7. L. G. Spears, Ph.D. Dissertation, The University of Texas (1967).
8. E. S. Snavely, Jr., L. G. Spears, L. D. Fiel, J. L. Lindgren, and W. E. Harrell, Jr., Summary Report, Contract No. Nonr-4054(00), ARPA Order No. 399, TRACOR, Inc., (1966).
9. H. H. Rogers, S. H. Evans, and J. H. Johnson, *This Journal*, **111**, 701 (1964).
10. R. Ukaji and I. Kageyoma, *Bunseki Kagaku*, **9**, 604 (1960).
11. N. Hackerman, E. S. Snavely, Jr., and L. D. Fiel, *Corrosion Science*, **7**, 39 (1967).
12. G. G. Koerber and T. J. DeVries, *J. Am. Chem. Soc.*, **74**, 5008 (1952).
13. R. M. Hurd and E. S. Snavely, Jr., Metal and metal/metal fluoride electrode systems in anhydrous hydrogen fluoride, ARPA Propellant Contractors Synthesis Conf. IIT Research Institute, Chicago, Illinois, 13-15 (April 1964).
14. L. G. Spears and N. Hackerman, To be published.
15. L. G. Spears and N. Hackerman, To be published.
16. L. D. Fiel, Ph.D. Dissertation, The University of Texas (1966).
17. O. Ruff and L. Staub, *Z. Anorg. Allgem. Chem.*, **198**, 32 (1938).
18. R. N. Hazeldine and F. Nyman, *J. Chem. Soc.*, 2684 (1956).
19. S. I. Morrow *et al.*, *J. Am. Chem. Soc.*, **82**, 5301 (1960).
20. J. N. Wilson, *et al.*, Contract DA-31-124-ARO(D)-54, ARPA No. 3910 ARO (D), Report No. 1, Shell Development Co. (1963).
21. A. Zletz, *et al.* Contract No. DA-31-224 ARO (D)-78, ARPA Order No. 402, Task 3, American Oil Co. (1965).

## On the Mechanism of Formation of Thin Oxide Layers on Nickel

K. Hauffe,\* L. Pethe,<sup>1</sup> and R. Schmidt

*Institut für physikalische Chemie der Universität in Göttingen, Germany*

and S. Roy Morrison

*Stanford Research Institute, Menlo Park, California*

#### ABSTRACT

It could be demonstrated that the initial period of oxidation of nickel at  $400^\circ$  and  $500^\circ\text{C}$  is governed by a logarithmic rate law. However, after approximately 5 hr at  $400^\circ\text{C}$  and 1 hr at  $500^\circ\text{C}$  the rate of oxidation changes into a fourth power rate law ruling in a special oxide-thickness region. This rate law can be understood if a negative space charge, caused by nickel-ion vacancies, in the growing  $\text{NiO}$  layer is assumed and if the current of nickel-ion vacancies from the surface of the oxide layer to the metal-oxide interface is caused predominantly by an electric field established over the layer. The experimental results of the oxidation of nickel are in fair agreement with the proposed mechanism.

During the oxidation of nickel, generally, the metal is covered with a practically pore-free coherent oxide layer of  $\text{NiO}$  in which the reacting components, nickel and oxygen, are spatially separated from one another

\* Electrochemical Society Active Member.

<sup>1</sup> Present address: Chemistry Department, Marathwada University, Aurangabad, India.

so that one of the reactants, nickel or oxygen, or both, must diffuse through the oxide layer. The oxidation rate of nickel is slower than that of most other metals. Since nickel oxide is a p-type semiconductor, the assumption of the existence of electron holes  $|e|^\ominus$  and nickel-ion vacancies  $|\text{Ni}|^\ominus$  in nickel oxide is

justified (1). Accordingly, a preferred diffusion of nickel ions and electrons via vacancies and holes, respectively, should occur during the oxide growth causing a parabolic rate law if the oxide layer is thick enough so that this diffusion process is rate-determining. Such a rate law was found at high temperatures when a rather thick oxide layer was formed (2).

As could be demonstrated, however, the oxidation of nickel between 400° and 500°C in the thin oxide film region cannot be evaluated by a parabolic rate law. By a log-log representation of the oxide layer thickness *vs.* the time, a rate law was found to lie between  $t^{1/3}$  and  $t^{1/4}$  indicating that under these experimental conditions additional phenomena become predominant. Oxidation experiments with nickel at 400°C in oxygen at various gas pressures performed by Engell, Hauffe, and Ilschner (3) showed a rate law of the form

$$\xi \sim t^{1/3.7}$$

where  $\xi$  is the thickness of the oxide layer formed in time *t*. This rate law was found up to 1000Å thickness of the oxide. The kinetics of oxidation obtained at 475°C by Gulbransen and Andrew (4) also obeys this time law up to an oxide layer thickness corresponding to 13  $\mu\text{g}/\text{cm}^2$ . For thicknesses larger than this value, a transition to the parabolic rate law has been found by us (3). In this investigation, however, such a transition could not be detected because the oxidation time was not long enough. Below 400°C, several authors could evaluate their experimental results by a logarithmic rate law, especially when the thickness of the oxide layer was very small (< 50Å) (5) or also larger than 200Å (6).

The nickel oxidation at 400°C was repeated and enlarged by 500°C experiments. As shall be demonstrated from the theoretical viewpoint below, the nickel oxidation in the thin oxide layer region can be described by a fourth power rate law ( $\Delta\xi^4 \sim t + \text{const}$ ). This was, indeed, the case for the oxidation experiments performed at 400° and 500°C at various oxygen pressures.

### Experimental

A Sartorius vacuum microbalance was used which operated automatically and recorded the changes in the weight of the sample with time. The sensitivity of the balance could be varied between 1 and 100  $\mu\text{g}$  for a maximum load of 1g. The balance was connected with a flexible red brass tube to enable a horizontal movement of the balance in order to center the sample, suspended by a glass fiber, in the glass reaction tube. The temperature of the latter was controlled to  $\pm 0.5^\circ\text{C}$  by means of a regulated furnace. A grounded steel block was used near the constant temperature zone to minimize the temperature gradient in the reaction vessel. All experiments have been performed in oxygen with  $\text{N}_2 < 1\%$ , in a static system, where  $\text{H}_2\text{O}$  and  $\text{CO}_2$  have been removed by a cooling trap. Because of the large gas reservoir, the uptake of oxygen by the sample during oxidation did not cause a change of pressure in the reaction vessel. The vacuum system consisted of a mechanical pump and an oil diffusion pump with a cooling trap containing solid  $\text{CO}_2$  in acetone.

Pressures higher than 1 Torr were read on a mercury manometer, separated from the rest of the system by another cooling trap while those between 1 and  $10^{-3}$  Torr were measured with a thermotron valve supplied by Leyboldt. For pressures below  $10^{-3}$  Torr an ionization gauge of Heraeus was used. In order to decrease the gas turbulence and convection currents in the system, the portion of the reaction vessel passing through the zone of the temperature gradient was made narrower than the rest by connecting a 20 cm long piece of 7 mm diameter glass tube above the reaction vessel of 32 mm diameter. In addition,

such an arrangement prevents a significant flux of hot gas from the reaction chamber to the balance.

Pure nickel sheets (99.9% Ni), 0.2 mm thick, were supplied by the courtesy of Vacuumschmelze AG, Hanau, who provided the following analysis in weight per cent: 0.061 Fe, 0.001 Mn, 0.0045 Si, 0.001 Cu, 0.007 Co, 0.029 C, and 0.044 Mg. Specimens  $2 \times 2.7 \text{ cm}^2$ , weighing nearly 950 mg were degreased and abraded under pure benzene with emery paper of 6/0. Subsequently, the grinding dust was wiped off by a piece of filter paper. They were then dried at room temperature in vacuum. Since before suspension, the sample had to pass through the hot zone of the reaction vessel, oxygen free pure nitrogen was continuously passed through the system during hanging in order to avoid any uncontrolled preoxidation.

After suspending the nickel sample, the reaction vessel was closed, evacuated, and the furnace moved into the required position. The sample was then reduced in hydrogen at 1 atm for 15 to 20 min and later annealed for 1 hr at a pressure of  $10^{-3}$  Torr. Oxygen was then introduced into the reaction chamber to start the reaction. Experiments have been carried out at 400° and 500°C at various oxygen pressures between 50 and 700 Torr.

Since the attainment of pressure equilibrium in the system, after introducing oxygen, took nearly 2-3 min, the initial weight was found by extrapolation for the experiments at 400°C. The rate of oxidation at 500°C was fast enough to make the extrapolation inaccurate. Therefore, the initial readings were taken in an inert nitrogen atmosphere at the same pressure employed for oxidation.

### Results

For illustration of our results, the rate of oxide growth is plotted both as weight increase per square centimeter,  $\Delta m/A$ , and as thickness,  $\xi$ , of the oxide layer *vs.* time. While  $\Delta m/A$  is represented in  $\mu\text{g}/\text{cm}^2$ , the thickness  $\xi$  is in angström (Å) units. For the calculation of  $\xi$ , a roughness factor *r* of 2 has been assumed as an empirical average surface increase. Therefore, in all graphical representations, 1  $\mu\text{g}/\text{cm}^2$  of weight increase corresponds to 31.4Å.

Unfortunately, the oxidation experiments at 400°C had poor reproducibility of the order of  $\pm 25\%$ . The reason for the lack of reproducibility is not yet known. No oxygen-pressure dependence of the oxidation rate could be derived at 400°C since the expected change of the rate lies within the limits of reproducibility. At 500°C, however, a significant dependence of the oxidation rate on the oxygen pressure has been observed.

For the evaluation of the measurements, different rate laws have to be considered. The first period of oxidation is found best represented by a logarithmic rate law

$$\Delta m/A = k_1 \ln(t + t_0) + \text{const} \quad [1]$$

$k_1$  is a constant and  $t_0$  must be evaluated by trial and error. In Fig. 1 and 2, the measuring data at 400° and 500°C are plotted in a semilogarithmic diagram. The constants  $k_1$  and  $t_0$  are summarized in Table I. As can be seen from Fig. 3 and 4, the following larger periods of oxidation can be evaluated by a fourth power rate law

$$(\Delta m/A)^4 = k_0(t + t_0) \quad [2]$$

According to Eq. [2], the measuring points are plotted as  $(\Delta m/A)^4$  *vs.* the time *t*. The values of  $k_0$  in Table I have been calculated from the slopes of the straight lines in Fig. 3 and 4. Furthermore, the time *t* and the oxide-layer thickness  $\xi$  for the transfer from the logarithmic to the fourth power rate law are summarized.

As can be seen from Fig. 4, the kinetics of the oxidation obtained both by Gulbransen and Andrew and by us (4, 3), can be represented by the same rate law. While the absolute values of the rate of oxidation



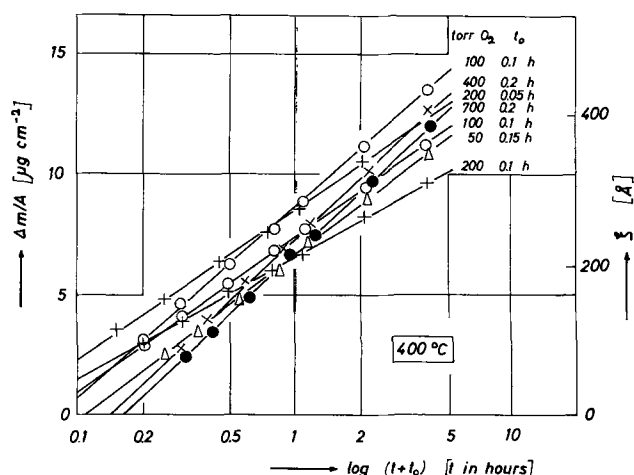


Fig. 1. Semi-logarithmic plot of the rate of oxidation of nickel at 400°C and various oxygen pressures. Only the first 5 hr of oxidation have been plotted since later on deviations from the straight lines occur.  $t_0$  was determined by trial and error.

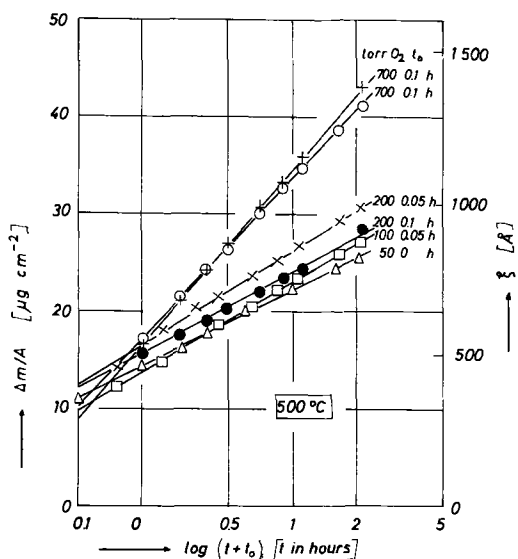


Fig. 2. Semi-logarithmic plot of the rate of oxidation of nickel at 500°C and various oxygen pressures. Only the first 2 hr of oxidation have been plotted since later on deviations from the straight lines occur.  $t_0$  was determined by trial and error.

quoted in (3) are in fair agreement with the present data, those of Gulbransen and Andrew are smaller in spite of the higher temperature (475°C). Obviously, this discrepancy is caused by the higher iron content of our nickel samples. A high impurity of a trivalent metal causes an increase in the rate of oxidation but has no influence on the time law.

Finally, in Fig. 5 there is represented the oxygen-pressure dependence of the rate constant of the fourth power rate law. The reproducibility is not good. But the increase of the rate with increasing oxygen pressure can be clearly demonstrated.

### Discussion

According to other oxidation experiments with nickel, the oxide layer growth was expected to follow a logarithmic rate law at the very beginning of oxidation. The period of this rate law becomes smaller with increasing temperature. At 500°C this period lasted only approximately 1 hr while at 400°C the period was about 4 hr. The isothermal logarithmic rate constants are nearly independent of the oxygen pressure (see Table I). The understanding of the logarithmic rate law is at present not satisfying in spite of the large effort in theoretical treatment (7-9, 11, 12). This

Table I. Oxidation of nickel with thin oxide layers at 400° and 500°C

Temperature of oxidation °C	Constants of the logarithmic rate law		Transition from the logarithmic to the fourth rate law at about Hour	Rate constant $k_0$ of the fourth power rate law.		
	$P_{O_2}$ Torr	$t_0$ hr		$k_1$ $\mu\text{g}/\text{cm}^2$	A*	$\mu\text{g}^4 \text{cm}^{-3} \text{h}^{-1}$
400	50	0.15	3.0	6	380	$2.9 \cdot 10^3$
	100	0.1	2.8	5-9	390	$3.5 \cdot 10^3$
	100	0.1	3.4	7-10	490	$3.4 \cdot 10^3$
	200	0.1	2.2	5-6	330	$4.7 \cdot 10^2$
	200	0.05	2.7	5-10	420	$7.4 \cdot 10^2$
	400	0.2	3.6	5-6	440	$1.0 \cdot 10^3$
	700	0.2	3.7	6	430	$5.3 \cdot 10^2$
500	50	0	4.8	2	820	$1.0 \cdot 10^6$
	100	0.05	5.8	3-4	970	$1.7 \cdot 10^6$
	200	0.1	5.3	2-4	990	$2.1 \cdot 10^6$
	200	0.05	6.1	2-4	1050	$3.2 \cdot 10^6$
	700	0.1	9.8	3-4	1460	$9.9 \cdot 10^6$
	700	0.1	10.8	3	1510	$1.5 \cdot 10^6$

\* Calculated with the estimated value for the surface roughness  $r = 2$ .

unsatisfying situation was discussed by Hauffe and Schottky (10).

After the logarithmic period of oxidation, the experimental data obtained at longer exposure time both at 400° and 500°C fit very well the relation of the fourth power rate law derived below. Furthermore, it is predicted by our theory that the validity of the fourth power rate law is limited. At a certain thickness of the oxide layer, it starts to obey the rate law and approximately after doubling the thickness of the oxide layer, the rate law is no longer valid. At 400°C, the validity of the fourth power rate law could

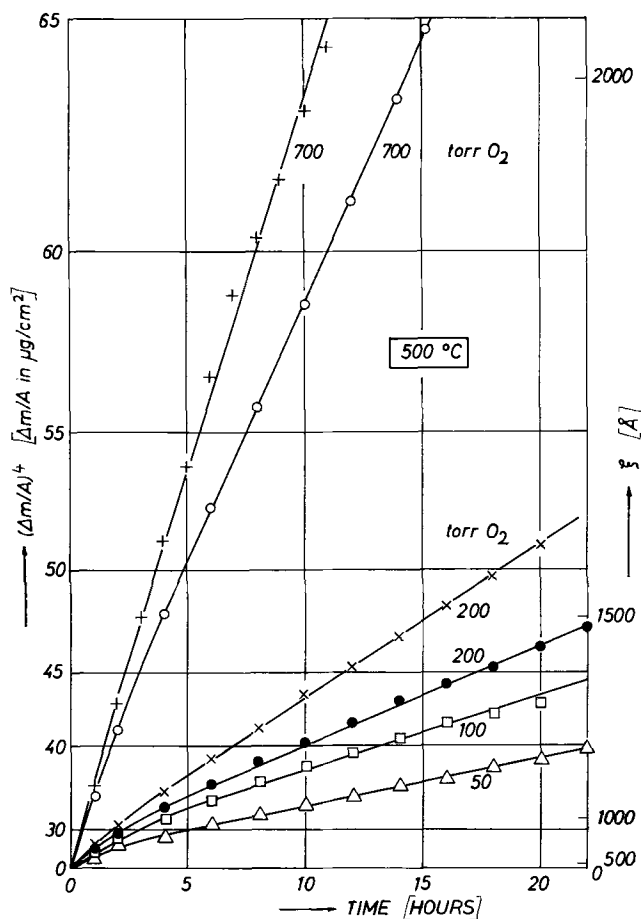


Fig. 3. Oxidation of nickel at 500°C and different oxygen pressures. In order to demonstrate the validity of the fourth power rate law,  $(\Delta m/A)^4$  is plotted vs. time.

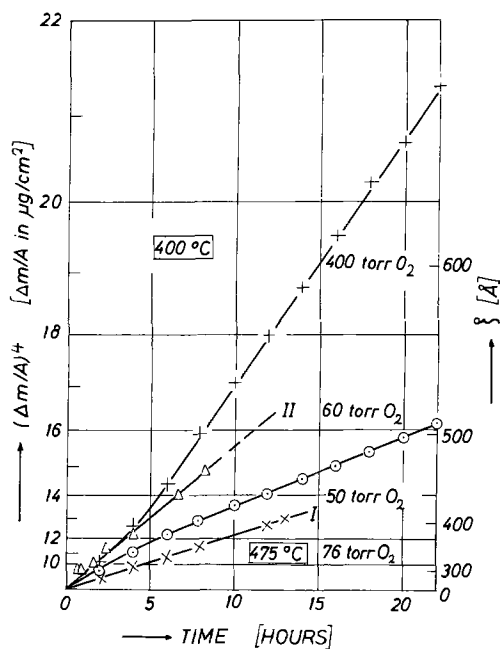


Fig. 4. Oxidation of nickel at 400°C.  $(\Delta m/A)^4$  vs. time is plotted. The reproducibility of these experiments was unsatisfactory ( $\pm 25\%$ ), but nevertheless, each experiment followed the fourth power rate law. Only two curves are represented as examples. As comparison to other measurements, the lines I and II are plotted from experimental data obtained by Gulbransen and Andrew and by Engell *et al.*, respectively.

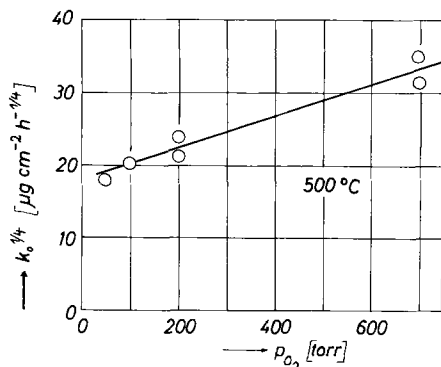


Fig. 5. Oxygen-pressure dependence of the rate of oxidation at 500°C.  $k_0^{1/4}$  is plotted vs.  $p_{O_2}$ .

be observed after the thickness had reached about 500Å and at 500°C, about 1000Å. That is in rather good agreement with the theoretically predicted value given below. Since the oxidation rate became rather slow with increasing thickness of the oxide layer, we did not wait for the doubling of the initial thickness. The change into the parabolic rate law at longer oxidation time has been found.

In the present paper, the mechanism of the dependence of the rate of oxidation on the oxygen pressure is not discussed because more experimental data are necessary. In spite of the scattering of the values around the straight line in Fig. 5, the oxygen pressure dependence of  $k_0$  is demonstrated.

**The fourth power rate law.**—Under the assumption that the corresponding chemical equilibrium is established at the phase boundaries  $O_2/NiO$  and  $NiO/Ni$ , the ambipolar diffusion and/or the electric field transport of nickel ions via nickel-ion vacancies  $[Ni]''$  and electron holes  $|e|^\circ$  must be the rate-determining step of the oxidation. The rate of oxidation is proportional to the flux of nickel ions,  $j_{[Ni]''}$ , via nickel-ion vacancies. In the following derived equations,  $x$  shall de-

note the local coordinate perpendicular to the surface ( $NiO/O_2$ ) of the sample with  $x = 0$  at the surface and  $x = \xi$  at the interface  $NiO/Ni$ . As already discussed (10, 15),  $j_{[Ni]''}$  can be written as a function of  $x$

$$j_{[Ni]''}(x) = -D_{[Ni]''} \frac{dc_{[Ni]''}(x)}{dx} - c_{[Ni]''} u_{[Ni]''} \frac{dV(x)}{dx} \quad [3a]$$

$D_{[Ni]''}$ ,  $c_{[Ni]''}$ , and  $u_{[Ni]''}$  are the diffusion coefficient, the concentration, and the mobility of the nickel-ion vacancies, respectively, and  $V$  is the electrical potential. A similar equation can be employed for the description of the flux of holes. Both relations have to be combined with the Poisson equation

$$\frac{d^2V}{dx^2} = -\frac{1}{\epsilon\epsilon_0} (z_{[Ni]''} c_{[Ni]''} + c_+)e \quad [3b]$$

which results in rather complex integro-differential equations (15, 10, 11).  $z_{[Ni]''}$  ( $= -2$ ) is the valence of the nickel-ion vacancy,  $e$  the elementary charge,  $c_+$  the concentration of electron holes,  $\epsilon_0$  the permittivity of free space, and  $\epsilon$  the dielectric constant.

Since the mathematical evaluation yields in equations which cannot be tested directly by available experimental data, we have decided to introduce physically reasonable simplifications supplying time laws which can be employed for the evaluation of oxidation experiments.<sup>2</sup> Therefore, the following two cases have been introduced

$$c_+ \gg z_{[Ni]''} c_{[Ni]''} \quad [4a]$$

and

$$c_+ \ll z_{[Ni]''} c_{[Ni]''} \quad [4b]$$

The first case is characterized by a strong chemisorption of oxygen and by a positive space charge in the  $NiO$  layer. This results in a cubic rate law (3). As can be seen from the experimental data, both in the former (3) and in the present paper, the obtained data fit better the  $(\Delta m/A)^4 \sim t$  rate law which is derived below under the validity of condition [4b]. This condition is characterized by a negative space charge in the  $NiO$  layer usually involved in an ambipolar diffusion of ionic and electronic species. Under our experimental conditions, such space-charge layers can have a thickness of several hundreds or thousands of angstroms depending on the disorder of the oxide lattice (16).

It is assumed, as in the metal semiconductor-rectifier theory, that the position of the valence band in  $NiO$  with respect to the Fermi level in the metal is independent of the thickness of the oxide, and, to our approximation, the doping of the oxide. It is, furthermore, similarly assumed that the surface state due to the oxygen ion pins the Fermi potential at the oxide-gas interface, independent of oxide thickness. Furthermore, it is speculated that the energy levels of electrons on the adsorbed oxygen are deep, so the Fermi potential is pinned near the valence band at the oxide-gas interface, closer than the pinning of the Fermi potential at the oxide-metal interface. It is also assumed that the acceptors in  $NiO$  are reasonably shallow.

In the mathematical analysis below, the p-type situation is specified, as the system to be analyzed, although of course the n-type case will be similar. In

<sup>2</sup>With this approximation we digress from the approach of Fromhold, who considered in detail the influence of space charge effects in oxide growth (11). In the cited work, no approximation was made and numerical methods of solution were therefore required. The present approximation, limiting the range of validity of the expression is not a drawback as the range of validity is where space charge effects show the strongest influence. Because of the approximation analytical methods become possible. The characterization of oxide growth is then separated into three parts, first the region of very thin oxide (parabolic), second an intermediate region dominated by space charge effects (present work), and third, the region of thick oxides dominated by diffusion (parabolic). Analysis of the laws for the transition between these regions requires numerical methods.

the following, we substituted  $j_{\text{Ni}^{2+}} = c_{\text{Ni}^{2+}}$ , etc. by  $j$ ,  $c$ , etc. We assume the current of nickel-ion vacancies from the surface to the metal is predominantly driven by the electric field. Therefore, we write

$$\left| D \frac{dc}{dx} \right| \ll \left| c u \frac{dV}{dx} \right| \quad [4c]$$

Thus with Eq. [3a] we obtain

$$j(x) = -c u dV/dx \quad [5]$$

With the relation, fulfilled in the first approximation (10)

$$dj(x)/dx = 0$$

we obtain

$$\frac{dc}{dx} \frac{dV}{dx} + c \frac{d^2V}{dx^2} = 0$$

Inserting  $dV/dx$  from Eq. [5] and  $d^2V/dx^2$  from the Poisson relation

$$\frac{d^2V}{dx^2} = -\frac{zce}{\epsilon\epsilon_0} \quad [6]$$

yields

$$\frac{dc}{dx} = -\frac{\alpha}{2} c^3 \quad \text{with} \quad \alpha = \frac{2zeu}{j\epsilon\epsilon_0} \quad [7]$$

Integration with the limiting condition that the density of nickel-ion vacancies is constant at the surface, i.e.

$$c = c_0 \text{ for } x = 0 \text{ at the interface gas/oxide}$$

supplies

$$c = 1/(\alpha x + 1/c_0^2)^{1/2} \quad [8]$$

By insertion of Eq. [5],  $dV/dx$  and  $V$  itself become calculable

$$\frac{dV}{dx} = -\frac{j}{u} (\alpha x + 1/c_0^2)^{1/2} \quad [9]$$

Integration with the boundary condition

$$V = 0 \text{ for } x = 0$$

supplies

$$\beta V = (\alpha x + 1/c_0^2)^{3/2} - 1/c_0^3 \quad [10a]$$

with

$$\beta = -\frac{3}{2j} \alpha u = -3zeu^2/(\epsilon\epsilon_0 j^2) > 0 \quad [10b]$$

From our model we conclude that the difference of the valence band in NiO at both the interfaces, NiO/O<sub>2</sub> and NiO/Ni, is constant, which leads to a boundary condition of the form

$$V = V_0 \quad \text{at } x = \xi$$

where  $V_0$  is a constant potential (with respect to the potential at the surface) at the metal-oxide interface, and  $\xi$  represents the locus of the oxide-metal interface, i.e.  $\xi$  is the width of the NiO layer. Therefore, Eq. [10] can be reformulated

$$\beta V_0 = (\alpha\xi + 1/c_0^2)^{3/2} - 1/c_0^3 \quad [11]$$

This equation is a fundamental one because it brings the interrelation between the cation flux  $j$  and the other entities  $c_0$ ,  $V_0$ , and  $u$  as the dominant variables.

In order to avoid an equation of the 3rd order during the evaluation of  $j$ , the following reasonable assumption is allowed

$$c_0 \gg (\alpha\xi)^{-1/2} \approx c(\xi)$$

which is equivalent to the relation

$$\alpha\xi \gg 1/c_0^2 \quad [12]$$

Therefore, Eq. [11] will be modified to

$$\beta V_0 = (\alpha\xi)^{3/2} \quad [13]$$

By raising to second power and inserting  $\alpha$  and  $\beta$

from Eq. [7] and [10], we obtain

$$j = \frac{9\epsilon\epsilon_0 u V_0^2}{8ze} \cdot \frac{1}{\xi^3} \quad [14]$$

and with the relation

$$j = c_{\text{Ni}} d\xi/dt \quad [15]$$

where  $c_{\text{Ni}}$  is the concentration of nickel ions in the oxide, finally, the fourth power rate law reads

$$\frac{d\xi}{dt} = \frac{k_0}{4} \cdot \frac{1}{\xi^3} \quad [16]$$

with

$$k_0 = \frac{9\epsilon\epsilon_0 u V_0^2}{2z e c_{\text{Ni}}} \quad [17]$$

or integrated

$$\xi^4 = k_0(t + t_0) \quad [18a]$$

or

$$\xi = k_0^{1/4}(t + t_0)^{1/4} \quad [18b]$$

with  $t_0$  as integration constant.

For further considerations, it is necessary to investigate the limits of the applicability of Eq. [18]. By inserting Eq. [5] into the dissimilar terms [4c] and substituting  $dc/dx$  by Eq. [7], then we obtain with the Nernst-Einstein relation

$$j^2 \gg \frac{u^2 kT c^3}{\epsilon\epsilon_0} \quad [19]$$

Since in the interior of the oxide layer  $c_0 \cong c(x)$ , the applicability of this relation is permitted only if condition [19] is fulfilled. With Eq. [14], it follows

$$\xi^6 \ll \left(\frac{9}{8}\right)^2 \frac{(\epsilon\epsilon_0)^3 V_0^4}{(ze)^2 kT c_0^3}$$

and we obtain for the upper limit of  $\xi$

$$\xi < \gamma \left| \frac{3zeV_0}{kT} \right|^{1/6} \quad [20]$$

with

$$\gamma = \left\{ \frac{3}{4} \left| \frac{\epsilon\epsilon_0 V_0}{z e c_0} \right| \right\}^{1/2} \quad [20a]$$

Correspondingly, we obtain under consideration of Eq. [14] with the relation [12] if  $\alpha$  from Eq. [7] is inserted

$$\xi^4 \gg \left( \frac{3}{4} \frac{\epsilon\epsilon_0 V_0}{z e c_0} \right)^2$$

or with Eq. [20a]

$$\xi^4 \gg \gamma^4$$

and finally, we obtain for the lower limit of  $\xi$

$$\xi > \gamma \quad [21]$$

Therefore, the validity of Eq. [18] is given by

$$|3zeV_0/kT|^{1/6} > \xi/\gamma > 1 \quad [22]$$

From the relation [22], it can be concluded that the  $\xi^4$  rate law is applicable only in a small region of oxide thickness. With the data  $V_0 = 1\text{v}$ ,  $c_0 = 10^{17} \text{ cm}^{-3}$ ,  $\epsilon = 3$ ,  $T = 800^\circ\text{K}$ , and  $z = -2$ , we obtain for

$$\gamma \approx 3 \cdot 10^{-6} \text{ cm}$$

and for

$$|3zeV_0/kT|^{1/6} = 2$$

By means of these values and Eq. [22], it can be seen that the law should be obeyed after an oxide thickness of 300Å has been built up. Furthermore, the thickness of the oxide layer where the validity of the  $\xi^4$  rate law ceases, should be double the thickness at which it starts, i.e., when the oxide layer has grown approximately by a factor of 2.

According to our experiments at 400°C, the kinetics of oxidation fit the relation  $\xi^4$  vs.  $t$  rather well when

the thickness of the oxide layer has attained nearly 400Å. For higher temperatures, the validity region of this time law is shifted to lower thicknesses of the oxide layer. Engell, Hauffe, and Ilschner (3) have also found for the oxidation of nickel at 400°C a fourth power rate law ( $\Delta m \sim t^{1/3.7} - t^{1/3.9}$ ) which changed later on to a parabolic one.

Another parabolic rate law should govern if the following relation is valid

$$\alpha \xi \ll 1/c_0^2 \quad [12a]$$

instead of Eq. [12] which is a presupposition of the fourth power rate law. Such a parabolic rate law was first formulated by Cabrera and Mott (13). Relation [12a] is equivalent with

$$c = c_0 \quad [8a]$$

and

$$dV(x)/dx = -j/(uc_0) \quad [9a]$$

Such a field-aided parabolic rate law could be found for the oxidation of zinc (14). Recently, Fromhold (18) has generalized the discussion on the validity of the parabolic rate law.

In order to compare our rate constant  $k_0$  to the data available in the literature, we tried to calculate  $k_0$  with the aid of the Nernst-Einstein equation and the relation between the tracer-diffusion coefficient and the component-diffusion coefficient  $D_{Ni}^3$

$$k_0 = \frac{9 \epsilon \epsilon_0 D_{Ni} V_0^2}{2ckT}$$

$D_{Ni}$  can be estimated from tracer-diffusion measurements carried out by Lindner and Akerström (19) between 740° and 1400°C, by Choy and Moore (20) between 1000° and 1400°C, and by Klotsman, Timofeef, and Trakhtenberg (21) between 1200° and 1400°C if the diffusion data are extrapolated to 500° and 400°C, a procedure in many respects doubtful. From the extrapolation of the data of the last mentioned authors, the following values for  $D_{Ni}$  have been obtained:  $10^{-19}$  (400°C) and  $10^{-17}$  (500°C)  $\text{cm}^2/\text{sec}$ . The corresponding values of Choy and Moore are an order of magnitude higher and those of Lindner and Akerström an order of magnitude lower.

If we employ the data of  $c_{Ni} \equiv c$  published by Schlosser (22) ( $c = 4 \cdot 10^{14}$  at 400°C and  $c = 1 \cdot 10^{15}$   $\text{cm}^{-3}$  at 500°C) and take  $\epsilon = 3$  and  $V_0 = 1v$ , then the following values for  $k_0$  are obtained

$$\left. \begin{aligned} k_0 &= 1.2 \cdot 10^4 \mu\text{g}^4 \text{cm}^{-8} \text{h}^{-1} \text{ at } 400^\circ\text{C} \\ k_0 &= 4 \cdot 10^5 \mu\text{g}^4 \text{cm}^{-8} \text{h}^{-1} \text{ at } 500^\circ\text{C} \end{aligned} \right\} \text{and 1 atm air}$$

As can be seen by comparison of these data with those in Table I, in spite of the rough extrapolation, the agreement is rather good.

Summarizing we may conclude that the oxidation of nickel should start in analogy to the oxidation of zinc (14) with a field-aided parabolic rate law and changes into a fourth power rate law. After this period, a parabolic rate law again rules, but now under the condition of a diffusion-controlled mechanism.

<sup>3</sup> This relation has been derived explicitly by Schottky (10).

Unfortunately, the kinetics of the nickel oxidation at the very beginning with oxide thicknesses below 300Å does not obey the parabolic plot as expected in analogy for the oxidation of zinc. But this result is not confusing since in the first period of oxidation, nucleation, and oxide needle formation can become predominant causing a logarithmic rate law (12). For the oxidation of bismuth (17), however, the rate of oxide layer growth between 175° and 250°C at 30 Torr oxygen can be represented from the very beginning up to 10-13  $\mu\text{g}/\text{cm}^2$  by a parabolic rate law and later on by a fourth power rate law.

### Acknowledgment

We are greatly indebted to the Deutsche Forschungsgemeinschaft for supplying the experimental equipment and the Max-Buchner-Forschungstiftung for the financial support to one of us (R.S.) Furthermore, we wish to thank Hüttenwerk Oberhausen AG for the salary of Dr. L. Pethe during his stay at the Institute.

Manuscript received Oct. 19, 1967; revised manuscript received ca. Jan. 16, 1968.

Any discussion of this paper will appear in a Discussion Section to be published in the December 1968 JOURNAL.

### REFERENCES

1. See for instance K. Hauffe, "Oxidation of Metals," p. 171 ff, Plenum Press, New York (1965).
2. C. Wagner and K. Grunewald, *Z. phys. Chem. (B)*, **40**, 455 (1938).
3. H. J. Engell, K. Hauffe, and B. Ilschner, *Z. Elektrochem.*, **58**, 478 (1954).
4. E. A. Gulbransen and K. F. Andrew, *This Journal*, **101**, 128 (1954).
5. W. Campbell and U. Thomas, *Trans. Electrochem. Soc.*, **91**, 623 (1947); K. Hauffe and B. Ilschner, *Z. Elektrochem.*, **58**, 382 (1954).
6. H. H. Uhlig, J. Pickett, and J. MacNairn, *Acta Met.*, **7**, 111 (1959).
7. N. F. Mott, *Trans. Faraday Soc.*, **43**, 429 (1947).
8. P. T. Landsberg, *J. Chem. Phys.*, **23**, 1079 (1955).
9. H. H. Uhlig, *Acta Met.*, **4**, 541 (1956).
10. K. Hauffe and W. Schottky, *Deckschichtbildung auf Metallen, in Halbleiterprobleme*, Vol. 5, pp. 316-319, Braunschweig (1960).
11. A. T. Fromhold, Jr., *J. Chem. Phys.*, **38**, 282, 2041 (1963), **39**, 2278 (1963), **40**, 3335 (1964).
12. U. R. Evans, "The Corrosion and Oxidation of Metals," London (1960).
13. N. Cabrera and N. F. Mott, *Rept. Progress Physics*, **12**, 163 (1949).
14. H. J. Engell and K. Hauffe, *Metall.*, **6**, 285 (1952).
15. K. Hauffe and B. Ilschner, *Z. Elektrochem.*, **58**, 467 (1954).
16. B. Ilschner, *Z. Elektrochem.*, **59**, 542 (1955).
17. M. G. Hapase, V. B. Tare, and A. B. Biswas, *Acta Met.*, **15**, 131 (1967).
18. A. T. Fromhold, Jr., *J. Chem. Phys.*, **41**, 509 (1964).
19. R. Lindner and A. Akerström, *Disc. Faraday Soc.*, **23**, 133 (1957).
20. J. S. Choy and W. J. Moore, *J. phys. Chem.*, **66**, 1308 (1962).
21. S. M. Klotsman, A. N. Timofeef, and I. Sh. Trakhtenberg, *Fiz. Metal. i Metalloved.*, **14**, 428 (1962).
22. E. G. Schlosser, *Z. Elektrochem.*, **65**, 453 (1961).

# Ignition Behavior of Plutonium Metal and Certain Binary Alloys

J. G. Schnizlein and D. F. Fischer

Argonne National Laboratory, Argonne, Illinois

## ABSTRACT

The ignition behavior of plutonium and binary alloys containing nominally 2 a/o additives was studied by two methods in air and oxygen. Ignition temperatures in both air and oxygen lie in two regimes. Cubes, 5 mm on an edge, ignite near 500°C while thin foils, less than 0.2 mm thick, ignite near 300°C. The transition from one regime to the other occurs sharply at a specific area that depends on whether ignition takes place in air or in oxygen. The existence of two regimes is consistent with a change of oxidation kinetics between 300° and 400°C which is characterized by a minimum in oxidation rate near 400°C. The effects of additives are sometimes significant and must be considered in each regime and on the position of the transition between them. In the high temperature regime: (i) Increased resistance to ignition and oxidation is found on addition of aluminum, copper, gallium, or silicon; (ii) The same ignition and oxidation behavior as plutonium occurs with addition of nickel, chromium, uranium, cerium, or iron; and (iii) Decreased resistance to ignition and oxidation results from addition of carbon, cobalt or manganese. In the low temperature regime: (i) Increased resistance to ignition and oxidation is produced by additions of aluminum, cerium, carbon, cobalt, gallium, manganese or possibly chromium; (ii) The same ignition and oxidation behavior as plutonium is obtained with addition of nickel or silicon; and (iii) Decreased resistance to ignition and oxidation follows from addition of iron or uranium.

The transition from the high temperature regime to the low temperature regime does not occur in air for alloys of aluminum, cerium, carbon, or cobalt for specimens with specific areas of up to about 1 cm<sup>2</sup>/g. Addition of silicon, nickel, manganese, or uranium have little influence on the transition in air which occurs at a specific area of 1.5 cm<sup>2</sup>/g for pure plutonium. The presence of moisture had a negligible effect on the ignition temperatures of pure plutonium and the aluminum alloy.

The increasing use of plutonium in the nuclear energy program and the concomitant handling makes the development of safe handling procedures imperative. Accidental ignition of the metal is a hazard (1) per se and the possibility of dispersing extremely toxic fine particulate plutonium oxide extends the danger. Moreover, inordinately large expenses of time, money, and manpower in the past have been incurred in the decontamination procedures which must follow accidental ignition of the metal.

The literature on ignition of plutonium is largely restricted to reports of the USAEC and UKAEA. The first direct study of the ignition of plutonium was reported by Dempsey (2). Earlier, Dempsey and Kay (3) observed ignition during an experiment intended to be isothermal at 487°C. Ignition occurred after oxidation had proceeded for about 300 min. During a study of the particulate material produced during the burning of plutonium, Carter, Foy, and Stewart (4) observed ignition temperatures of turnings and small billets.

Thompson (5) observed ignitions to occur between 230° and 420°C in oxygen and between 310° and 505°C in air at 35% relative humidity. No positive correlations between temperature and weight, area, or rate of heating were observed. In atmospheres containing less than 6.5% oxygen in argon, no ignition occurred below 900°C. Above about 10% oxygen the ignition temperatures were between 400° and 500°C. Rhude (6) found that in a glovebox with only 5% oxygen in nitrogen the metal will burn readily. At the 1% level combustion will not continue unless heat is supplied. Cope (7) has developed a ternary eutectic salt mixture which shows promise (8) as a dry powder extinguisher for some plutonium fires. The problems of airborne particulate plutonium have recently been reviewed by Mishima (9) in the United States and Stewart (10) in Great Britain.

Although oxidation studies of plutonium alloys have been reported (11-14) at somewhat elevated temperatures, the only ignition studies of binary alloys are those by Dempsey (2) and Carter *et al.* (4) in which an aluminum additive was used to stabilize the delta phase of plutonium.

The present study of the ignition characteristics of plutonium and certain alloys was undertaken in conjunction with a study of the kinetics of isothermal oxidation (15) to aid in evaluating hazards in handling plutonium. Two experimental methods were developed for determining ignition temperatures. In addition to the study of pure plutonium, the influence of potential impurities and possible additives was appraised by the study of a series of binary alloys containing nominally 2 a/o (atom per cent) of various elements. Some elements were chosen because they are typical impurities in plutonium; other elements were chosen to study the effects of a given series in the periodic chart. Additives of aluminum, carbon, cerium, chromium, cobalt, copper, iron, gallium, manganese, manganese, nickel, silicon, uranium, and zinc were used.

## Materials and Procedures

Because of the extreme toxicity of plutonium, all experiments were performed in gloveboxes. To avoid accidental ignitions or oxidation of metal surfaces, a dry nitrogen atmosphere was used. Oxygen or air and helium were used directly from gas cylinders except in experiments where the moisture content was controlled. The contents of each cylinder used were analyzed by mass spectrometry to avoid accidental contaminants.

The plutonium and alloy cubes and foil specimens were prepared at Hanford.<sup>1</sup> Specially selected reactor

<sup>1</sup> Preparations were under the supervision of R. R. King, P. G. Pallmer, T. Nelson, R. W. Stewart, and O. J. Wick, General Electric Company, Hanford Atomic Products Division, Richland, Washington.

Table I. Plutonium analyses  
Parts per million

Impurity element	Typical reactor grade plutonium	Alloys <sup>a</sup>	Unalloyed pure plutonium
C	50-400	200-500	90
O	100-600	50-200	50
Fe	50-1000	20-300	120
Ni	30-500	10-30	16
Mn	50-200	5-75	5
Cr	20-250	2-20	10
Mg	10-500	2-500	50
Al	20-100	<10	<10
Cu	10-80	5-70	20
Ca	5-250	5-50	10
Total metallic impurities	200-2900	50-1050	250

<sup>a</sup> Excluding intentional additive.

grade plutonium was used to minimize impurity content of both pure plutonium samples and binary alloy samples. Analyses of plutonium used for preparation of samples and of alloys are compared with typical reactor grade plutonium in Table I. Pure plutonium specimens were in the form of 5 mm cubes and 3 x 20 mm sections of foils having thicknesses ranging from 1 to 0.1 mm.

The binary alloys of plutonium contained nominally 2 a/o of various chosen elements. Additives of aluminum, carbon, cerium, chromium, cobalt, copper, iron, gallium, magnesium, manganese, nickel, silicon, uranium, and zinc were of the highest purity available. The additive element content was determined at Hanford by the most accurate method then known. The binary alloys were used in this study in the form of 5 mm cubes and such foils as it was possible to fabricate. For the manganese alloy it was possible to prepare samples with thickness down to 0.07 mm (17.2 cm<sup>2</sup>/g specific area), whereas for the uranium alloy, the thinnest foil that could be produced was 0.89 mm thick (1.9 cm<sup>2</sup>/g specific area).

The ignition experiments are a kind of thermal analysis originally used by Fassel (16) for magnesium alloys. Two methods were used: The first, in which the oxidizing gas was present during the heating, is called a burning-curve experiment; the second method is called a shielded ignition experiment because the oxidizing gas was excluded by helium until the test temperature was reached. These methods have previously been used for the study of ignition of uranium and its alloys (17-19) and were found to provide reproducible results. Burning-curve and shielded-ignition experiments were performed with air or oxygen.

In the burning-curve experiment, the specimen was supported on a thermocouple in a vertical tube furnace and was heated at a programmed rate in a flowing oxidizing gas until ignition occurred. The programming was such that the temperature of an inert sample increased at a uniform rate (usually 10 deg/min). The heat of oxidation of a reactive sample caused an increase of temperature (self-heating) above the control temperature. An increase of oxidation rate caused an increase of the slope of the temperature-time trace. When ignition occurred, the slope rapidly approached an infinite value and the sample usually self-heated to its maximum burning temperature. The ignition temperature was determined graphically from the temperature-time trace as the intersection of the pre-ignition heating curve with the post-ignition self-heating curve. Some thermogravimetric experiments were performed in this manner on a thermobalance equipped with a transducer to permit simultaneous weight and temperature measurement (20). A platinum crucible was hung under the sample to avoid loss of weight due to dropping oxide.

In a shielded-ignition experiment the sample was heated to the test temperature in a protective atmosphere of helium. The protective gas was then rapidly

replaced by the oxidant to determine whether ignition occurred at the test temperature. For these experiments the ignition temperature is reported as the range between the highest temperature at which ignition did not occur and the lowest temperature at which ignition did occur.

## Experimental Results

Comparison of the temperature-time curves of various samples in an oxidizing atmosphere provides a measure of the relative oxidation rate and ignition behavior. The relative oxidation rate can be assessed by the extent of self-heating or temperature increase above the control temperature at a particular time. The ignition behavior of various samples can be compared by consideration of the temperature or time of sudden temperature increase. Burning curves in air for 5 mm cubes of plutonium and a plutonium-silicon alloy are illustrated in Fig. 1. The ignition temperature for pure plutonium was found to be 508°C and for the silicon alloy, 544°C.

After ignition in air the resulting oxide was considerably larger than the original metal sample and had numerous protuberances. Figure 2 illustrates the appearance of a 5 mm cube in the platinum crucible before and after ignition at 508°C in air.

*Pure plutonium.*—Burning-curve and shielded-ignition experiments were performed with pure plutonium specimens in both air and oxygen. The specimens were 5 mm cubes and 3 x 20 mm sections of foils having thickness of 1, 0.5, 0.22, 0.17, and 0.13 mm. Ignition temperatures determined by both methods in air and oxygen are listed in Table II. In most cases ignition temperatures determined by the shielded method are somewhat lower than those obtained by the burning-curve method. Ignition temperatures obtained by the burning-curve method are plotted as a function of specific area of the sample in Fig. 3. Ignition data from Dempsey and Kay (3) and from Carter, Foy, and Stewart (4) are also included for comparison. The variation of ignition temperature with specific area yields a step function instead of a gradual change over the range studied. Ignition occurs in one of two regimes, one at about 300°C (282°-322°) and the other at about 500°C (468°-535°). The transition from one regime to the other occurs at a specific area of

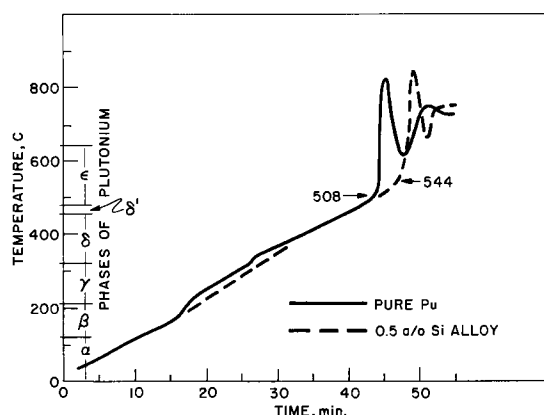


Fig. 1. Burning curves in air



Fig. 2. Plutonium cube before and after ignition at 508°C in air.

Table II. Ignition temperatures of plutonium in air and oxygen

Foil thickness, mm	Specific area, cm <sup>2</sup> /g	Burning curve ignition temperatures, °C		Shielded-ignition temperatures, °C	
		Air	O <sub>2</sub>	Air	O <sub>2</sub>
~5 (cube)	0.65	520	512	442-492	—
1.0	1.5	508	494	378-408	327-374
		492	490		
		322			
0.52	2.5	310	468	303-337	353-398
		314	505		
0.22	5.3	518	524	375-403	322-350
		520	527		
		535			
		519 <sup>b</sup>			
0.17	6.7	521 <sup>b</sup>		299	
		282	299		
0.13	11.0	282	305	266-280	273-284

<sup>a</sup> Indicated as the highest temperature at which ignition did not occur and the lowest temperature at which ignition did occur.

<sup>b</sup> Samples were polished with 600 grit SiC paper; all others as received.

1.5 cm<sup>2</sup>/g in air and at 6.0 cm<sup>2</sup>/g in oxygen. The sharpness of the change is illustrated in Fig. 4 where two burning curves for 1.0 mm thick (1.5 cm<sup>2</sup>/g) foil specimens heated in air are shown. At this specific area the ignition might occur in either regime although the difference of specific area of the two samples was indistinguishable. It will be noted that the thermal effects of plutonium phase transitions can be detected on the curves. These were observed in most experiments and provide assurance of good contact between the thermocouple and the sample.

The 0.22 mm thick foil gave anomalous results in air. Its ignition temperature in air was consistently in

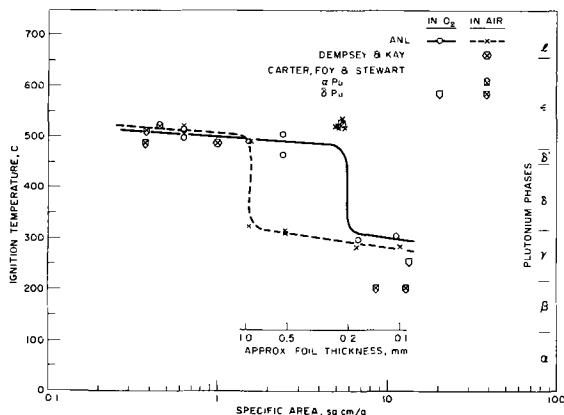


Fig. 3. Ignition temperatures of plutonium by the burning-curve method.

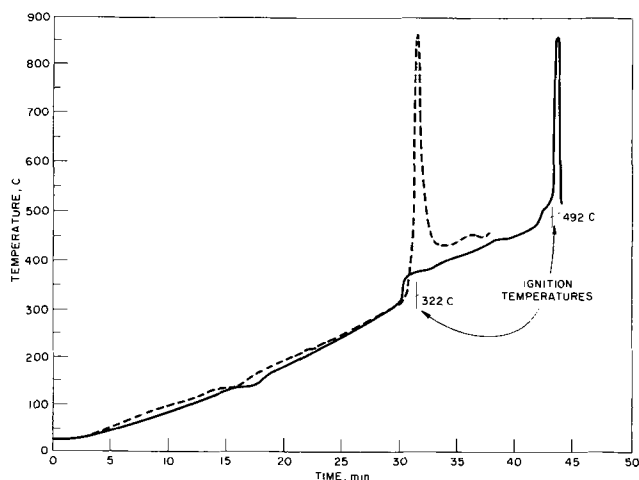


Fig. 4. Burning-curve ignitions in air of 1 mm thick pure plutonium foil specimens, specific area 1.5 cm<sup>2</sup>/g.

the high temperature regime even though its specific area, 5.3 cm<sup>2</sup>/g, was considerably greater than the 1.5 cm<sup>2</sup>/g point of transition for other foil samples. No explanation for this anomalous behavior was found.

In air the ignition temperatures in the low temperature regime are somewhat lower than in oxygen. However, in the high temperature regime no difference is observed. Ignition results reported by Dempsey and Kay (3) and by Carter, Foy, and Stewart (4) were generally consistent with the other results plotted in Fig. 3.

Shielded-ignition temperatures (Table II) are appreciably lower than burning-curve ignition temperatures in the high temperature regime but are only slightly lower in the low temperature regime.

**Plutonium binary alloys.**—All chosen alloys were available in the form of 5 mm cubes. However, it was impossible to fabricate some of the alloys into foils as thin as was desired. Burning-curve experiments were performed in both air and oxygen for all cubes and foils. Shielded-ignition experiments were performed in both air and oxygen for most foils. Because of the large number of samples required to define a narrow temperature range between ignition and nonignition, only a few cubes were studied in this manner; the range of shielded-ignition temperature for a few of the foils is also larger than desirable.

Results of ignition temperature determinations for the alloys are presented in Table III. The additive elements were intended to be 2 a/o but in some cases segregation, evaporation, or reaction with crucible material altered the final concentration. The analyzed (or estimated if no satisfactory analytical procedure was available) content of the additive and the specific area of the samples are included.

For samples in the form of 5 mm cubes ignition temperatures lie in the high temperature regime, and additives have only small effects on the ignition temperature; the greatest effects were found for aluminum, nickel, and cobalt. The ignition temperature of the 3.4 a/o aluminum-plutonium alloy was 60° higher than that of the plutonium base metal. The 2 a/o gallium-plutonium, 2.4 a/o copper-plutonium, and the 1.2 a/o silicon-plutonium alloys ignited at temperatures about 30° higher than did the base metal. In contrast, the 1.8 a/o cobalt and 1.8 a/o nickel alloy ignition temperatures were 30°-40° lower than that of the plutonium base metal. Additives of cerium, carbon, chromium, iron, magnesium, manganese, uranium, and zinc had little effect.

Appraisal of the effect of variation of specific area on ignition temperature for most of the alloys is possible by considering the data on foils. Ignition temperatures were plotted as a function of the logarithm of specific area and a composite trace of the behavior in air for the various additives is presented in Fig. 5. The shapes of the curves are similar to those for pure plutonium except for alloys of aluminum, cerium, carbon, cobalt, and gallium. The transition from the high temperature regime to the low temperature regime does not occur for samples of these alloys with specific areas up to about 10 cm<sup>2</sup>/g. The addition of silicon to plutonium causes a shift of the transition in air from a specific area of 1.5 cm<sup>2</sup>/g for pure plutonium to 4 cm<sup>2</sup>/g for the alloy. Additions of nickel, manganese, and uranium to plutonium cause no change in the transition region in air.

In oxygen the transition to the low temperature regime for the alloys occurs at lower specific areas than it does for pure plutonium.

**Effect of moisture on ignition behavior of plutonium and plutonium 3.4 a/o aluminum alloy.**—To appraise the effect of moisture on the ignition of plutonium and its alloys, burning curves have been obtained in air saturated with moisture at room temperature (20,000 ppm water). Isothermal studies (15) have shown

Table III. Ignition data for plutonium alloys  
Nominally 2 a/o additives

Additive	Analyzed content, a/o	Foil thickness, mm	Specific area, cm <sup>2</sup> /g	Burning-curve ignition temperature, °C		Shielded-ignition <sup>a</sup> temperature, °C	
				Air	O <sub>2</sub>	Air	O <sub>2</sub>
Al	3.4	5 (cube)	0.79	588, 590	576		
	1.8		4.4	544	555		
	3.4		0.26	557	546	250-388	350-388
	8		0.24	620	590, 604		382-455
	11		0.82	425	390		400-432
	11		0.13	10	412	440	
Ce	0.5 <sup>b</sup>	5 (cube)	0.64	510	485		
	0.5 <sup>b</sup>		1.6	488	478	398-436	406-442
	0.5 <sup>b</sup>	0.11	11.0	478	481	325-351	299-342
C	2 <sup>b</sup>	5 (cube)	0.65	498	486		
	1.55	5 × 5.6 diam rod	0.63	295, 459	208, 447, 455		
	2 <sup>b</sup>		1.6	474	478	401-440	287-328
	0.9		0.28	370	330		270-300
Co	2 <sup>b</sup>	0.16	7.8	469	466	386-428	275-309
	1.8	5 (cube)	0.67	474	462		
	1.8	0.93	1.7	456	465	410-477	380-413
Cr	1.8	0.23	5.2	465	462	346-389	340-390
	2 <sup>b</sup>	5 (cube)	0.65	512, 514	498, 507		
	2 <sup>b</sup>	1.01	1.70	513	503	325-375	
	2 <sup>b</sup>	0.15	7.5	575	527	380-421	268-380
	2 <sup>b</sup>	0.08	14.5	No ign.	517	243-292	
Cu	0.2	0.21	5.8	380	No ign., 320		275-307
	2.4	5 (cube)	0.65	555	533, 546		
Fe	1.8	5 (cube)	0.65	548	515		
	1.8	0.85	1.71	596	266		
	1.8	0.39	3.33	589	567	327-377	
	1.8	0.21	5.7	602	289	271-315	243-287
				No ign.			
	1.8	0.11	11.5	352	253	246-288	
	2.0	5 × 5.7 diam rod	0.60	476, 485	520		
				490, 516			
	2.5	0.26	4.88	372	330		307-348
	2.0	0.25	5.16	358	310		
Ga	2.0	0.19	6.60	550	532, 537, 539		
	2	5 (cube)	0.78	550	534		
		0.25	5.1	546, 539	523, 598	381, 405	350-375
		0.25	5.1	546	528		391-416
Mg	0.2	(cold rolled)					
Mn	2.7	5 (cube)	0.7	520	512		
	2.7	5 (cube)	0.66	499	477		
	2.7	1.0	1.6	496	482	362-406	249-294
	2.7	0.53	2.7	293	320	221-258	240-288
	2.7	0.24	5.3	365, 598	293	257-288	276-300
	2.3	0.21	5.6	330	247		214-230
	2.7	0.10	12.1	No ign. <sup>c</sup>	289	282-317	242-278
	2.7	0.07	17.2	No ign. <sup>c</sup>	279	251-258	251-282
Ni	1.8	5 (cube)	0.66	490, 529	468		
	1.3	5 (cube)	0.64		489, 509		
	1.8	1.05	1.55	486	470	420-263	367-422
	3.2	0.24	5.1	325	316		297-317
	1.8	0.24	5.4	No ign. <sup>d</sup>	288		
	1.8	0.25	5.4	302			
Si	1.8	0.15	7.6	No ign.	467	282-335	238-282
	0.3	5 (cube)	0.65	544, 548, 548	525, 537, 537	462-511	412-467
	1.2 <sup>b</sup>	5 (cube)	0.72	553	540		
	1.2	0.95	1.67	528	515		
	1.2	0.28	4.29	202, 286, 295	318		
U	1.2	0.20	5.85	537	310	281-325	265-297
	2 <sup>b</sup>	5 (cube)	0.65	510, 513	490		
	2 <sup>b</sup>	0.89	1.9	252, 550	242	(e)-443	(e)-233
Zn	1.03	5 (cube)	0.7	528	523		
	0.40	5 (cube)	0.7	528	503		

<sup>a</sup> Indicated as the highest temperature at which ignition did not occur and the lowest temperature at which ignition did occur.

<sup>b</sup> Estimated content, no satisfactory analysis performed.

<sup>c</sup> Sample completely oxidized or disintegrated before ignition occurred.

<sup>d</sup> There was a thermal spike of 150° at 309°C with no visual ignition. Another spike of 80° was observed at 610°C with no visual ignition.

<sup>e</sup> Insufficient samples were available to determine lower limit of shielded ignition range.

that the presence of moisture increases the linear rate of oxidation at temperatures below 200°C, but has negligible effects at higher temperatures.

Although burning curves indicate that ignition occurs in slightly shorter periods of time in moist air, the graphic method of defining ignition temperatures yields values for experiments carried out in dry air which are essentially identical with those for experiments carried out in moist air. These temperatures, determined by the burning-curve method, are given in Table IV.

### Discussion and Summary

Two experimental procedures were used to define the temperatures at which the ignition of plutonium occurs. The first, which is a thermal analysis of the sample heated in an oxidizing atmosphere, is called a burning-curve experiment. In the second, the temperature at which ignition occurs if suddenly exposed to an oxidizing gas, is called shielded-ignition temperature.

*Pure plutonium.*—The ignition temperatures determined by the burning-curve method for pure pluto-

nium in air or oxygen lie in two regimes: about 500°C for large samples with low specific area, and at about 300°C for thin foils with high specific areas. The existence of these two ignition temperature regimes is consistent with the isothermal oxidation behavior of plutonium (15). A change in the oxidation kinetics occurs just above 300°C. The oxidation rate decreases sharply between 350° and 450°C and the oxide is more protective above 400°C. Evidently, the rate of heat generation by oxidation in the region of 300°C is just sufficient to cause ignition of specimens having large specific areas. Specimens having smaller specific areas have greater thermal inertia, and the temperature increase caused by self-heating occurs more slowly. This allows the formation of a more protective oxide at temperatures near 400°C, where there is a minimum in the oxidation rate. The decreased oxidation rate prevents ignition from occurring until the sample temperature is increased by external heating beyond 450°C whereupon the oxidation rate again rapidly increases with increasing temperature.

For samples igniting in the high temperature regime with the burning-curve method, shielded-ignition tem-



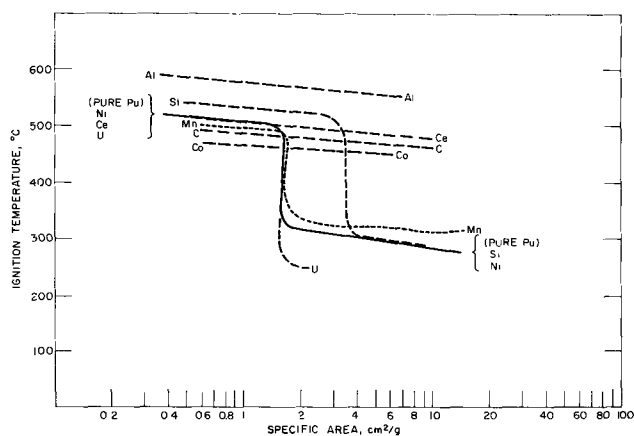


Fig. 5. Effect of additives on ignition behavior in air of plutonium. Each curve labeled with additive element present nominally at 2 a/o conc.

peratures are noticeably lower. In the low temperature regime shielded- and burning-curve experiments provide similar ignition temperatures.

**Binary alloys.**—Because the ignition temperatures fall in two regimes (consistent with the two regimes observed in the isothermal oxidation), it is necessary to consider the influence of an additive on each regime and on the transition region.

In the high temperature regime the influence of the additives (using the behavior of pure plutonium as the standard for comparison) were as follows:

(i) Increased resistance to ignition and oxidation; aluminum, copper, gallium, and silicon.

(ii) The same ignition and oxidation behavior as plutonium; nickel, chromium, uranium, cerium, and iron.

(iii) Decreased resistance to ignition and oxidation; cobalt, carbon, and manganese.

In the low temperature regime, the influence of the additives was as follows:

(i) Increased resistance to ignition and oxidation; aluminum, cerium, carbon, cobalt, gallium, manganese, and possibly chromium.

(ii) The same ignition and oxidation behavior as plutonium; nickel and silicon.

(iii) Decreased resistance to ignition and oxidation; iron and uranium.

The transition from the high temperature regime to the low temperature regime does not occur in air for alloys of aluminum, cerium, carbon, and cobalt for specimens with specific areas of up to approximately 10 cm<sup>2</sup>/g. The addition of silicon to plutonium causes a shift of the transition in air from the specific area of 2 cm<sup>2</sup>/g for pure plutonium to 4 cm<sup>2</sup>/g for the alloy. Additions of nickel, manganese, and uranium to plutonium caused no change in the transition point from that of pure plutonium.

**Moisture.**—The presence of moisture in air has negligible effect on ignition temperatures of plutonium and of a plutonium-3.4 a/o aluminum alloy as determined by burning-curve experiments. Because isothermal studies (15) have shown that the presence

Table IV. Temperature determined by burning-curve method

		Burning-curve ignition temperature, °C	
		In dry air	In wet air
Pu	5 mm cube	524	522
Pu	0.11 mm foil	283	282
Pu-3.4 a/o Al	5 mm cube	585, 590	569

of moisture has negligible effects on the oxidation kinetics above 220°C, ignition temperatures of samples above 220°C in dry air will not be affected by moisture. It must be pointed out that it does not follow that long term corrosion by moist air or water vapor will not influence the ignition of plutonium.

### Acknowledgments

The encouragement of R. C. Vogel, the advice of L. Baker, Jr., and the assistance of J. D. Bingle are gratefully acknowledged. In addition, the authors appreciate the services of the many persons who maintained the glovebox facility, obtained materials, and performed analyses.

Manuscript received March 20, 1967; revised manuscript received ca. Nov. 16, 1967.

Any discussion of this paper will appear in a Discussion Section to be published in the June 1968 JOURNAL.

### REFERENCES

- R. B. Smith, *Nucleonics*, **14**, 28 (1956).
- E. Dempsey, British Report No. 0-49/58, December 1958.
- E. Dempsey and A. E. Kay, *J. Inst. Metals*, **86**, 379 (1958).
- R. F. Carter, B. Foy, and K. Stewart, British Report AERO Conf/8 (1960).
- M. A. Thompson, USAEC Report RFP 491, March 12, 1966.
- H. V. Rhude, USAEC Report TID 16826, July 1962.
- L. H. Cope, UKAEA Report DEG 29 (also British Patent 884,946, December 20, 1961).
- R. F. Powell, E. Demsey, and J. Holliday, UKAEA-AWRE Report No. 0-45/60.
- J. Mishima, USAEC Report HW 83668 (1964).
- K. Stewart, in "Progress in Nuclear Energy," Series IV, Vol. 5, p. 535, Pergamon Press, New York (1963).
- J. T. Waber, W. M. Olson, and R. B. Roff, *J. Nucl. Mat.*, **3**, 201 (1961).
- M. J. F. Notley, E. N. Hodkin, and J. A. C. Davidson, UKAEA Report AERE-R-4070, June 1962.
- D. M. Poole, J. K. Critchley, J. A. C. Davidson, P. M. French, E. N. Hodkin, and M. J. F. Notley, "Plutonium 1960," p. 627, Cleaver-Hume Press, London (1961).
- G. Picton and J. F. Sackman, *J. Nucl. Mat.*, **18**, 292 (1966).
- J. G. Schnizlein and D. F. Fischer, *J. Electrochem. Soc.*, **114**, 23 (1967).
- W. M. Fassel *et al.*, *J. Metals*, **3**, 522 (1951).
- J. G. Schnizlein *et al.*, USAEC Report ANL-5974, 1959.
- L. Baker, Jr., J. G. Schnizlein, and J. D. Bingle, *J. Nucl. Mat.*, **20**, 22 (1966).
- J. G. Schnizlein, L. Baker, Jr., and J. D. Bingle, *ibid.*, **20**, 39 (1966).
- J. G. Schnizlein, John Brewer, and D. F. Fischer, *Rev. Scientific Instruments*, **36**, 591 (1965).

# A Film-Thickness Determination of Nitrogen Diffusion in Zirconium Nitride

C. J. Rosa\* and W. C. Hagel\*

Metallurgy Division, University of Denver Research Institute, Denver, Colorado

## ABSTRACT

Calculations of the diffusion coefficient for nitrogen in zirconium nitride are given in terms of a unidirectional, two-phase, volume-diffusion model. These calculations require the knowledge of both the thicknesses of nitride films and of nitrogen diffusion coefficients in the underlying zirconium metal. The values obtained can be represented by  $D_{N \rightarrow ZrN} = 7.87 \times 10^{-5} \exp(-35,900/RT)$  cm<sup>2</sup>/sec for the temperature range of 650°-850°C. Zirconium nitriding kinetics for extended exposures up to 900 hr are also reported. The portion of nitrogen confined to the  $\alpha$ -zirconium phase amounts to about 80 w/o of the total nitrogen consumed during the over-all nitriding process.

The zirconium-nitrogen reaction has not attracted the interest of many investigators. Gulbransen and Andrew (1) described this metal-gas reaction in the temperature range of 400°-825°C and Dravnieks (2) studied the kinetics at 862°-1043°C. Mallett *et al.* (3) measured the rate of surface reaction of zirconium with nitrogen in the range of 975°-1640°C at 1 atm pressure. All these investigators report that the reaction conformed strictly to a parabolic relationship and that the reaction rate was much slower than with oxygen. These experiments were carried out for short time exposures, up to 7 hr.

More recently, Rosa and Smeltzer (4) investigated nitriding kinetics in terms of models based on the growth of the reaction product layer and simultaneous dissolution of the reactant in the metal substrate. They found that over the temperature range 750°-1000°C, and for exposures up to 170 hr, the reaction obeys the parabolic rate law. Using microhardness measurements, they determined the diffusion coefficient of nitrogen in  $\alpha$ -zirconium as  $D_{N^{\alpha-Zr}} = 0.15 \exp(-54,100/RT)$  cm<sup>2</sup>/sec, which to the best knowledge of the present authors is the only relationship available at this time.

The purpose of this investigation is to evaluate the diffusion coefficients of nitrogen in hypostoichiometric zirconium nitride for the temperature range of 650°-850°C in terms of data from nitriding kinetics and from the growth rates of the nitride layer. A comprehensive model relevant to the forthcoming calculations is presented.

## Experimental

The commonly used gravimetric method has been employed for measuring nitriding kinetics of  $2 \times 1 \times 0.2$  cm, 99.93 w/o (weight per cent) pure, zirconium samples. High-purity, better than 99.9 v/o (volume per cent) pure, nitrogen was passed through a cold trap and glass columns containing silica gel and phosphorous pentoxide to remove residual water vapor. Before exposing to nitrogen at a pressure of 400 Torr, specimens were treated by wet abrasion on 200 through 600-grit silicon carbide papers followed by final polishing on 8 and  $1\mu$  diamond-dust impregnated laps, acetone washing, and careful drying to avoid water stains.

To prevent formation of a gap between the metal and mounting material, whenever microscopic measurements of nitride thicknesses had to be taken, all samples are cold mounted in "Hysol" self-setting epoxy resin and prepared for metallography by using methods advised by Cprek (5) and Evans (6). Final polishing, for scale thickness measurements, was per-

formed by  $1\mu$  diamond-dust and vibrator polishing with  $0.05\mu$  gamma-alumina solution.

To accentuate the mount/specimen interface, the nitrided surfaces were coated with dyed "Eastman 910" adhesive diluted in "GA-1A" accelerator and allowed to harden for a few hours. Dark blue recorder ink was used as a dye. Measurements of nitride thicknesses were made by projection on a metallographic glass screen or by using a filar micrometer eyepiece on sections cut at an angle of 6° with respect to the normal surface.

The zirconium nitride, although quite thin, covered the metal substrate uniformly, and no appreciable edge or corner effects could be observed. X-ray analyses, using Ni-filtered Cu radiation, showed that the yellow film formed on heating zirconium in nitrogen was ZrN having  $a_0 = 4.56\text{\AA}$  for the fcc structure. This evidence then eliminated the possibility of formation of ZrO(NO<sub>3</sub>)<sub>2</sub>·2H<sub>2</sub>O, Zr<sub>2</sub>O<sub>3</sub>(NO<sub>3</sub>)<sub>2</sub>·5H<sub>2</sub>O, and Zr(NO<sub>3</sub>)<sub>4</sub>·5H<sub>2</sub>O nitrates reported by Elinson and Petrov (7).

## Theoretical

Figure 1 shows schematically the zirconium-nitrogen equilibrium phase diagram and the associated semi-infinite diffusion couple formed during nitriding of zirconium at temperature  $T$ . Assuming that the nitrogen diffusion coefficients  $D_{II}$  and  $D_I$  are independent of nitrogen concentration,  $c$ , the equations for the two concentration curves in the nitride and in the metal can be obtained from solution of Fick's second law. These are given by

$$c_I = k_1 - B_I \operatorname{erf}(x/2\sqrt{D_I t}) \text{ at } 0 < x < \infty \quad [1]$$

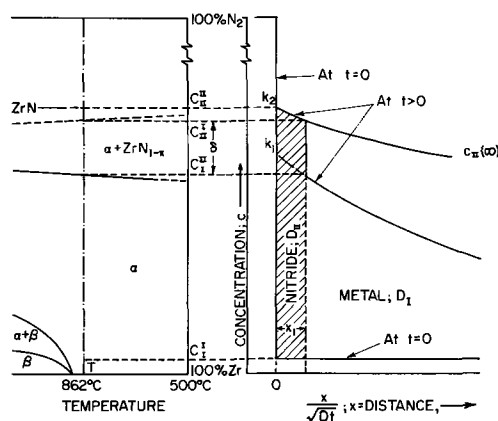


Fig. 1. Schematic presentation of zirconium-nitrogen equilibrium phase diagram and associated diffusion couple formed during nitriding of zirconium at temperature  $T$  and for time  $\infty > t > 0$ .

\* Electrochemical Society Active Member.

for the metal phase (I) and

$$c_{II} = k_2 - B_{II} \operatorname{erf} (x/2\sqrt{D_{II}t}) \text{ at } 0 < x < x_1 \quad [2]$$

for the zirconium nitride phase (II).

In terms of the nomenclature used in these equations,  $k_1$  and  $k_2$  represent the values of  $c$ 's at the surface, i.e., where  $x = 0$ .  $D_{II}$  and  $D_I$  are diffusion coefficients of nitrogen in phases II and I, respectively, and  $B_{II} = k_2 - c_{II}(\infty)$  and  $B_I = k_1 - C_I^I$ . All remaining symbols used follow directly from inspection of Fig. 1.

Diffusion analysis applicable to this type of a system has been advanced by Wagner (8) and applied by many investigators (4, 9, 10). At time  $0 < t < \infty$ , subject to boundary conditions, Eq. [1] and [2] must satisfy

$$c_I = k_1 \text{ and } c_{II} = k_2 \cong C_{II}^{II} \quad [3]$$

for  $x = 0$ , and similarly at  $x > 0$

$$c_I = C_I^I \text{ and } c_{II} = c_{II}(\infty) \quad [4]$$

for  $t = 0$ .

Considering the flux at the  $\alpha$ -zirconium/zirconium nitride interface  $x_1$ , one can write for the mass balance that

$$D_I \frac{\partial c_I}{\partial x} \Big|_{x=x_1+0} - D_{II} \frac{\partial c_{II}}{\partial x} \Big|_{x=x_1-0} = \delta \dot{x}_1 \quad [5]$$

where  $\delta = C_{II}^I - C_I^{II}$  and  $\dot{x}_1$  is the rate of movement of  $x_1$ .

In a previous investigation (4) describing the partition of nitrogen between metal and the nitride phase, it has been shown that the portion of nitrogen confined to the  $\alpha$ -zirconium phase can be expressed as

$$(k_p)_{\alpha-Zr} = 2 B_I \sqrt{D_I/\pi} \exp(-\gamma^2 D_{II}/D_I) \quad [6]$$

In this equation,  $(k_p)_{\alpha-Zr} = \Delta m/A\sqrt{t}$  represents the parabolic rate constant for nitrogen weight gain ( $\Delta m$ ) per unit area ( $A$ ) within time ( $t$ ).  $\gamma$  is a proportionality constant as in Eq. [8] and

$$B_I = k_1 - C_I^I = \frac{C_{II}^{II} - C_I^I}{\operatorname{erfc}(x_1/\sqrt{D_I t})} \quad [7]$$

which can be evaluated if the movement of interface  $x_1$  and  $D_I$  are known.

Should one neglect the small volume change associated with conversion of zirconium metal to zirconium nitride (calculated Pilling-Bedworth ratio:  $V_{ZrN}/V_{\alpha-Zr} = 1.05$ ), then the two values of  $x$  in Eq. [1] and [2] become equal at the nitride/metal interface. Consequently, it follows directly from Eq. [6] that

$$\gamma' \sqrt{D_I} = \gamma \sqrt{D_{II}} = \gamma_{\text{expt}'}/2 \quad [8]$$

where  $\gamma_{\text{expt}'}$  is the experimentally measured slope of  $x_1$  vs.  $\sqrt{t}$ , and

$$\gamma' = [\ln(2 B_I \sqrt{D_I/\pi}) - \ln(k_p)_{\alpha-Zr}]^{1/2} \quad [9]$$

In terms of conditions implied by Eq. [3] and [8] we can express the difference of nitrogen concentration as a function of distance  $x$  from the surface. Thus at  $x = x_1$  we have

$$C_{II}^{II} - C_I^I = (k_1 - C_I^I) (1 - \operatorname{erf} \gamma') \quad [10]$$

for the metal phase, and similarly for the nitride phase

$$C_{II}^{II} - C_{II}^I = B_{II} \operatorname{erf} \gamma \quad [11]$$

Differentiating Eq. [1] and [2] with respect to  $x$  and making use of the mass balance Eq. [5], one obtains in terms of relationship [8] that

$$\frac{(C_{II}^{II} - C_{II}^I) (\operatorname{erf} \gamma)'}{\gamma \operatorname{erf} \gamma} - \frac{(C_I^{II} - C_I^I) (\operatorname{erf} \gamma)'}{\gamma' \operatorname{erfc} \gamma'} = 2\delta \quad [12]$$

where the index "prime" behind parentheses is being used to designate the derivative of the respective error functions, e.g.  $(\operatorname{erf} \gamma)' = 2(\pi)^{-1/2} \exp -\gamma^2$ .

Equation [12] may be simplified by introducing the following arbitrary definitions

$$\xi(\gamma) = (\operatorname{erf} \gamma)'/2 \gamma \operatorname{erf} \gamma \quad [13]$$

and

$$\xi(\gamma') = (\operatorname{erf} \gamma')'/2 \gamma' \operatorname{erf} \gamma' \quad [14]$$

and therefore

$$(C_{II}^{II} - C_{II}^I) \xi(\gamma) - (C_I^{II} - C_I^I) \xi(\gamma') = \delta \quad [15]$$

Knowledge of  $D_I$  and  $\gamma_{\text{expt}'}$  allows one to evaluate the proportionality constant  $\gamma'$  from Eq. [8], and consequently calculation of  $\xi(\gamma')$  becomes possible. For a given value of  $\xi(\gamma')$ , one obtains a corresponding value of  $\xi(\gamma)$  by virtue of Eq. [15] because the nitrogen concentration differences are known. The unique value of  $\gamma$  satisfying relationship [13] may be obtained by means of a graphical solution, e.g., by plotting  $\exp(-\gamma^2)/\sqrt{\pi} \gamma \xi(\gamma)$  and  $\operatorname{erf} \gamma$  vs.  $\gamma$ . Consequently, we can determine the diffusion coefficient,  $D_{II}$ , of nitrogen in zirconium nitride from relationship [8].

### Evaluation of Nitrogen Diffusivity in ZrN

Nitriding kinetics for  $\alpha$ -zirconium in the temperature range 650°-850°C are shown in Fig. 2 together with the evaluated portion of nitrogen confined to the metal phase. Zirconium exhibits an exceptionally large solubility for nitrogen, above 20 a/o (atomic per cent), and accordingly the amount of nitrogen taken up by the metal is about 80 w/o of the total nitrogen consumed during the nitriding process.

Figure 3 is a plot of ZrN thicknesses formed at different temperatures as a function of nitriding time. Visual inspection of these figures indicates that, to a good approximation, parabolic relationships are obeyed for both the nitride growth and nitrogen dissolution in the metal. This then implies that volume diffusion of nitrogen may be the controlling factor in the nitriding mechanism of zirconium.

Densities of  $\alpha$ -zirconium and ZrN are 6.5 (11) and 7.09 (12) g/cm<sup>3</sup>, respectively. The boundary concentrations of nitrogen in zirconium nitride and in the metal saturated with nitrogen are summarized in Table I and were obtained from the Zr-N<sub>2</sub> equilibrium phase diagram (13). The initial concentration of nitrogen in the zirconium samples used was  $C_I^I = 0.65 \times 10^{-5}$  gN/cm<sup>3</sup>. Values for nitrogen diffusion coefficients in  $\alpha$ -zirconium were taken from ref. (4) and those for  $\gamma_{\text{expt}'}$  from Fig. 3.

Knowledge of these experimental data makes possible the evaluation of the remaining parameters:  $\gamma'$ ;

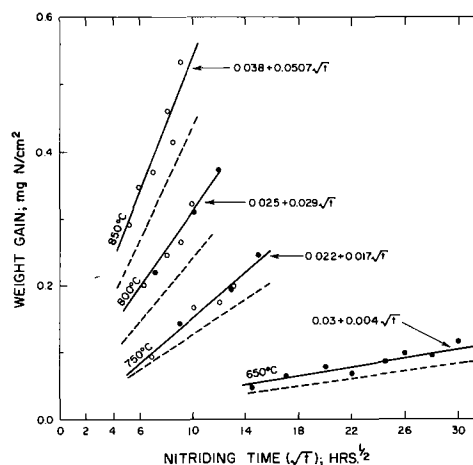


Fig. 2. Nitriding rates of zirconium at different temperatures. Solid lines, total nitrogen uptake; dashed lines, nitrogen dissolved in  $\alpha$ -zirconium; open circles, from ref. (4); closed circles, from this study.

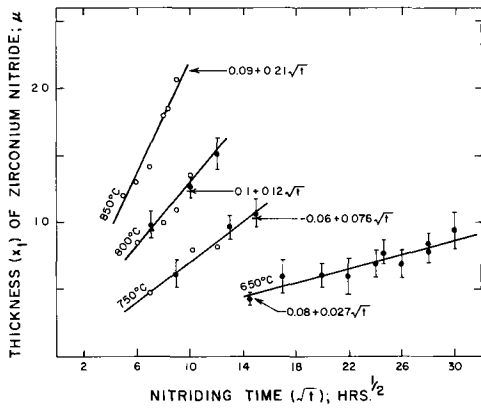


Fig. 3. Zirconium-nitride thicknesses for various nitriding times and temperatures. Open circles, from ref. (4); closed circles, from this study.

$\xi(\gamma)$ ;  $\xi(\gamma)$ ;  $B_I(x=0)$  and hence  $(k_p)_{\alpha-Zr}$ . The numerical values thus obtained are summarized in Table II.

Figure 4 shows the graphical solution of Eq. [13] for arbitrary values of  $\gamma$ . The unique results for  $\gamma$ , at various temperatures, which satisfy this equation are obtained from intersections of the exponential functions and are also recorded in Table II.

The values for diffusion coefficients of nitrogen in hypostoichiometric ZrN, obtained under conditions of nitriding polycrystalline  $\alpha$ -zirconium for exposures up to 900 hr, are represented in Fig. 5 in Arrhenius form. The method of least squares has been employed to obtain an expression for the diffusion coefficient, this is

$$D_{II} = 7.87 \times 10^{-5} \exp(-35,900/RT) \text{ cm}^2/\text{sec} \quad [16]$$

for the temperature range of 650°-850°C

While deriving the mathematical expressions it was tacitly assumed that the treatment of semi-infinite plate is applicable to the 2 mm-thick zirconium samples. Figure 6 which is a plot of concentration of nitrogen within the metal phase, at limiting temperatures of 850° and 650°C, provides satisfactory justification for this premise.

**Discussion of Results**

In the absence of other measurements of nitrogen diffusion in zirconium nitride it is difficult to assess how closely the calculated values of  $D_{II}$  approximate those from experimental evidence. The knowledge of

Table I. Summary of experimental data used for evaluation of nitrogen diffusivities in zirconium nitride

	Temperature, °C			
	650	750	800	850
$C_I^I$ ; gN/cm <sup>3</sup>	$0.65 \times 10^{-5}$	$0.65 \times 10^{-5}$	$0.65 \times 10^{-5}$	$0.65 \times 10^{-5}$
$C_I^{II}$	0.239	0.260	0.268	0.274
$C_{II}^I$	0.938	0.933	0.929	0.925
$C_{II}^{II}$	0.945	0.945	0.945	0.945
$\delta$	0.699	0.673	0.661	0.651
$D_I$ ; cm <sup>2</sup> /sec	$2.32 \times 10^{-11}$	$4.20 \times 10^{-13}$	$1.39 \times 10^{-12}$	$4.60 \times 10^{-12}$
$\gamma_{\text{expt. I}}$ ; cm <sup>2</sup> /sec	$0.45 \times 10^{-7}$	$0.13 \times 10^{-6}$	$0.21 \times 10^{-6}$	$0.35 \times 10^{-6}$

Table II. Compilation of values obtained from theoretical evaluations

Parameter	Temperature, °C			
	650	750	800	850
$\gamma$ ; Eq. [8]	$14.8 \times 10^{-2}$	$9.80 \times 10^{-2}$	$9.47 \times 10^{-2}$	$8.14 \times 10^{-2}$
$\xi(\gamma)$ ; Eq. [14]	4.48	6.42	6.62	7.61
$\xi(\gamma)$ ; Eq. [15]	$2.53 \times 10^3$	$1.95 \times 10^2$	$1.52 \times 10^2$	$1.37 \times 10^2$
$\gamma$ ; Fig. 4	$4.50 \times 10^{-2}$	$5.00 \times 10^{-2}$	$5.75 \times 10^{-2}$	$6.05 \times 10^{-2}$
$D_{II}$ ; Eq. [8]	$2.5 \times 10^{-13}$	$1.6 \times 10^{-12}$	$3.6 \times 10^{-12}$	$8.4 \times 10^{-12}$
$B_I$ ; Eq. [7]	0.287	0.293	0.300	0.302
$(k_p)_{\alpha-Zr}$ ; Eq. [9], gN/cm <sup>2</sup> sec <sup>1/2</sup>	$4.81 \times 10^{-3}$	$2.12 \times 10^{-7}$	$3.96 \times 10^{-7}$	$7.28 \times 10^{-7}$

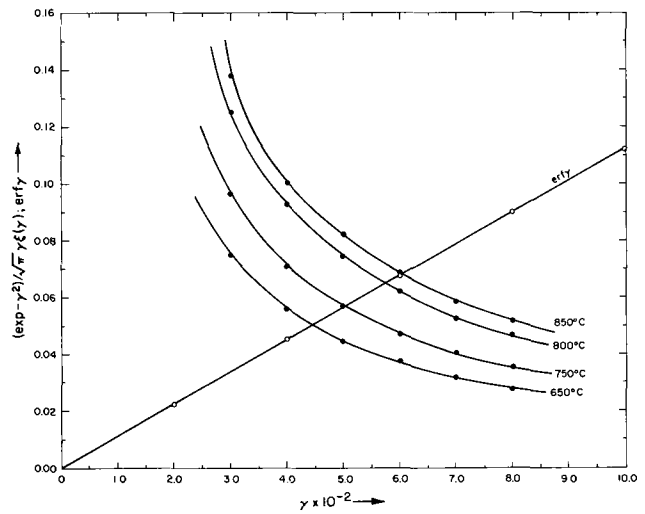


Fig. 4. Plots of  $\exp(-\gamma^2)/\sqrt{\pi} \gamma \xi(\gamma)$  and  $\text{erf } \gamma$  vs.  $\gamma$  for different temperatures.

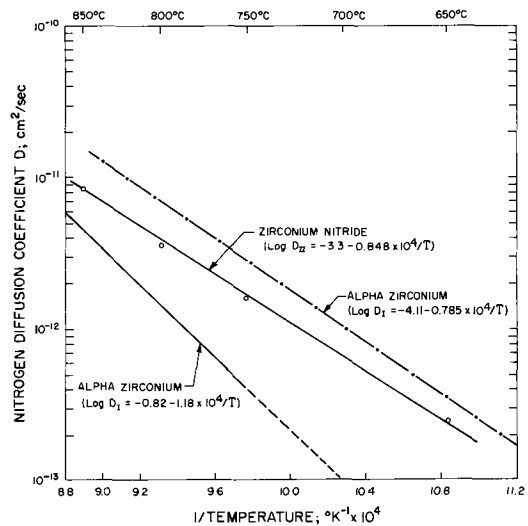


Fig. 5. Arrhenius plots for nitrogen diffusion in zirconium nitride and  $\alpha$ -zirconium (4). Dot-dash line is for values obtained from kinetic studies; see Appendix.

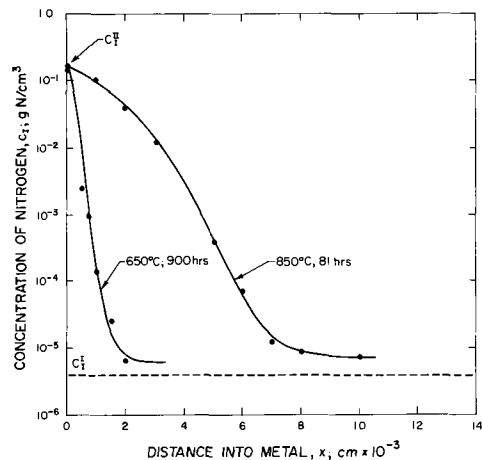


Fig. 6. Theoretical distribution curves for nitrogen in  $\alpha$ -zirconium as functions of nitriding time and distance into the metal. Points shown were calculated from Eq. [1] with  $k_1 = C_I^{II}$ .

error arising by considering the diffusion coefficient  $D_{II}$  as a concentration independent factor would be of particular interest.

The accuracy of evaluation of  $D_{II}$  depends on the precision with which the value of  $D_I$  is known. Com-

parison of the latter value from microhardness measurements with that from kinetic data shows appreciable discrepancy as depicted by Fig. 5. The  $D_I$  value from microhardness determinations is lower by a factor of 4 to 22 for the temperature range of interest. A question then arises which of these two values should be employed in evaluating  $D_{II}$ .

Results from Fig. 2 indicate that as much as 80% of the total amount of nitrogen consumed is confined to the metal phase. Consequently, when evaluating  $D_I$  (see appendix), omission of the thin ZrN film formed in the initial stages of nitriding seems to be plausible. However, inspection of Eq. [4A] in the appendix reveals that  $D_I$  is strongly dependent on the accuracy with which the total nitrogen uptake,  $M_I$ , can be measured, and unfortunately this is not very high. The following example will accentuate this point. Reference (2) gives for the total nitrogen uptake  $M_I = 3.91 \times 10^{-5}$  for 2-hr exposure at 862°C, or  $M_I \approx 3.0 \times 10^{-5}$  gN/cm<sup>2</sup> if extrapolated to 825°C. This value is to be compared with  $M_I = 8.32 \times 10^{-5}$  gN/cm<sup>2</sup> at 825°C for 2 hr exposure from ref. (1). It means that at the temperature considered  $D_I$  can vary from  $1.04 \times 10^{-11}$  to about  $1.5 \times 10^{-12}$  cm<sup>2</sup>/sec. The latter value is in close agreement with that from microhardness determinations. Due to the paucity of precise and consistent kinetic studies, the value of  $D_I$  resulting from microhardness measurements has been employed for evaluating  $D_{II}$ .

Some mention should be made about the accuracy of  $D_{II}$  in terms of errors in  $C_{II}^I$ . The  $\alpha + \text{ZrN}_{1-x}/\text{ZrN}_{1-x}$  phase boundary is drawn as a dashed line indicating poor accuracy. This phase boundary has been determined from the limited x-ray investigations by Domagala et al. (14), who believe that its position is accurate within  $\pm 0.5$  w/o N for the temperature range of 1600°-1850°C and that it reaches nearly stoichiometric ZrN at temperatures below 600°C. Unfortunately, for the temperatures of this study, it is impossible to evaluate the errors attached to  $D_{II}$  by considering the positive deviation from  $C_{II}^I$ , because this would mean the presence of hyperstoichiometric ZrN and the existence of such a compound has never been reported. It is, however, possible to account for the negative value of  $-0.5$  w/o N, and thus, e.g., at 850°C the value of  $D_{II} = 3.1 \times 10^{-12}$  cm<sup>2</sup>/sec as compared with  $D_{II} = 8.4 \times 10^{-12}$  for the average value of  $C_{II}^I$ .

The value of 35.9 kcal/mole for the diffusion activation energy could indicate an interstitial type of diffusion. This, however, seems to be highly improbable if we consider the relatively closely packed ZrN fcc lattice. The formation of hypostoichiometric zirconium nitride during the nitriding process provides a vacancy-type structure, and accordingly diffusion of nitrogen via nitrogen vacancies appears to be a more plausible mechanism for diffusion. In this case, the activation energy will consist of two terms: the energy of formation of vacancies and the energy required to move the diffusing species across these vacancies.

Diffusion across the  $\alpha$ -zirconium structure is seen to be very sensitive to temperature change, in accord with what one would expect from the rate of diffusion through hcp lattice of the metal.

#### Acknowledgments

The authors wish to express their gratitude to Dr. C. B. Magee for valuable comments and suggestions during the course of this work. The technical assistance and financial support by the University of Denver Research Institute are greatly appreciated.

Manuscript received Nov. 13, 1967; revised manuscript received ca. Jan. 15, 1968. This paper was presented at the Dallas Meeting, May 7-12, 1967, as Abstract 212.

Table III. Diffusion coefficients obtained from kinetic measurements

Temperature, °C	Exposure time, hr	ZrN thickness, $\mu$	$C_{II}^I$ , gN/cm <sup>3</sup>	$D_I$ , cm <sup>2</sup> /sec
825	2	0.17-0.30	0.270	$1.1 \times 10^{-11}$
800	2	0.17	0.268	$5.5 \times 10^{-12}$
700	2	0.038-0.11	0.252	$8.4 \times 10^{-13}$
600	2	—	0.230	$1.1 \times 10^{-13}$

Any discussion of this paper will appear in a Discussion Section to be published in the December 1968 JOURNAL.

#### APPENDIX

According to Fick's first law the quantity of nitrogen  $M_I$ , which penetrated metal per unit area at the end of time  $t$  can be expressed as

$$M_I = -D_I \int_0^t \left( \frac{\partial c_I}{\partial x} \right)_{x=x_1} dt \quad [1A]$$

If we assume that the concentration of nitrogen  $C_I^I = 0$  (about 1 ppm in our samples), then we can write in terms of Eq. [1] that

$$\frac{\partial c_I}{\partial x_1} = -\frac{k_1}{\sqrt{\pi D_I t}} \exp - (\gamma')^2 \quad [2A]$$

for  $x_1 = 2 \gamma' \sqrt{D_I t}$ .

Substituting [2A] into [1A] yields

$$M_I = \frac{2k_1 \sqrt{D_I t}}{\sqrt{\pi}} \exp - (\gamma')^2 + C \quad [3A]$$

where  $C = 0$  if  $t = 0$ .

Expressing  $k_1 = C_I^{II}$  when  $x_1 = 0$  (i.e., no nitride film) we have

$$D_I = \pi M_I^2 / 4t (C_I^{II})_{x_1=0}^2 \quad [4A]$$

This relationship is of the form sometimes used for evaluation of diffusivity in the metal assuming that the film thickness is negligible. We shall utilize this equation in determining  $D_I$  for nitrogen diffusion in  $\alpha$ -zirconium for short exposure times.

As already mentioned in the text, Gulbransen and Andrew obtained a strictly parabolic relationship for nitriding kinetics up to 2-hr exposures. In view of the present investigation, the estimated thicknesses of nitride films formed on their samples are given in Table III. Included also are values for  $D_I$  resulting from solution of Eq. [4A]. Utilizing the principle of least squares, the diffusion coefficient for nitrogen diffusion in  $\alpha$ -zirconium may be represented as  $D_I = 5 \times 10^{-4} \exp (-38,000/RT)$  cm<sup>2</sup>/sec.

#### REFERENCES

1. E. A. Gulbransen and K. F. Andrew, *Metals Trans.*, **185**, 515 (1949).
2. A. Dravnieks, *J. Am. Chem. Soc.*, **72**, 3568 (1950).
3. W. M. Mallett, J. Belle, and B. B. Cleveland, *This Journal*, **101**, 1 (1954).
4. C. J. Rosa and W. W. Smeltzer, *Electrochem. Technol.*, **4**, 149 (1966).
5. E. R. Cprek, *Trans. ASM*, **55**, 369 (1962).
6. W. Evans, *Can. Mining and Met. Bull.*, **53**, 897 (1960).
7. S. V. Elinson and K. I. Petrov, *Zirconium-Chemical and Physical Methods of Analysis*, AECTr-5373, 22 (1960).
8. C. Wagner, "Diffusion in Solids, Liquids, Gases," p. 72, W. Jost, Editor, Academic Press, New York (1960).
9. G. Beranger and P. Lacombe, *J. Nucl. Materials*, **16**, 190 (1965).
10. T. Smith, *This Journal*, **112**, 39 (1965).
11. C. J. Smithells, "Metals Reference Book," London, Vol. 2, p. 696 (1962).
12. C. D. Hodgman, R. C. Weast and S. M. Selby, "Handbook of Chemistry and Physics," p. 687, Cleveland (1960).
13. M. Hansen and K. Anderko, "Constitution of Binary Alloys," p. 996, McGraw-Hill, New York (1958).
14. R. F. Domagala, D. J. McPherson, and M. Hansen, *Trans. AIME*, **206**, 98 (1956).

# The Properties of Oxide Films Formed on a Zirconium-2.7 w/o Niobium Alloy in the Temperature Range 300°-500°C

M. G. Cowgill<sup>1</sup> and W. W. Smeltzer\*

Department of Metallurgy and Materials Science, McMaster University, Hamilton, Ontario, Canada

## ABSTRACT

Electron microscopy techniques were employed to determine the morphologies and structures of oxide films formed on martensitic and Widmanstätten alloys in an oxygen atmosphere. Morphological development of a film in the very early stages of its formation was dependent on surface preparation, the substructure of an alloy being replicated by the film formed on a pickled specimen. Pustules occurred in the oxide films with their growth being confined to the  $\alpha'$ -Zr phase of Widmanstätten alloys. Also, films on this alloy phase in comparison to those on a martensitic specimen commenced cracking at smaller thicknesses. The films consisted of monoclinic zirconia and, in addition, a second phase which was either tetragonal zirconia or an intramolecular oxide of zirconia and niobium pentoxide. This latter oxide occurred as small crystallites 50-150Å in diameter.

The reaction kinetics were previously reported for martensitic and several Widmanstätten alloys oxidized at temperatures in the range 300°-500°C (1). Little difference was found between the oxidation rates of these alloys in the early stages of the reaction, but prolonged exposures demonstrated that the martensitic alloys consisting of  $\alpha'$ -Zr oxidized much more rapidly in the range of linear kinetics, the linear kinetics of the Widmanstätten alloys decreasing with increasing amounts of proeutectoid  $\alpha$ -Zr. This latter phase oxidized at much slower rates than  $\alpha'$ -Zr. The oxide layer consisted essentially of monoclinic zirconia, and the formation of oxide pustules on martensitic specimens was the only distinct feature indicating a difference in the mode of oxide formation on differently structured alloys. The purpose of this investigation was to gain more detailed information by the techniques of electron microscopy on the structural properties of the oxide films and on their role as barriers to oxidation processes.

## Experimental

The electron microscopy studies were of two types: replication studies of oxide film surfaces and transmission microscopy of oxide films stripped from the alloys. For the former, two-stage replication was used, the parlodion film being shadowed at 20° to the surface with gold-palladium, before carbon evaporation at right angles to the surface. Transmission studies necessitated first coating the oxidized surface of the specimen with carbon in order to strengthen the thin film. The stripping of the oxide from the metal was then performed with a solution of 10% bromine in ethyl acetate held at 75°C.

Microscopy was carried out on a Siemens Elmiskop I operating with voltages of 80 kv for replicas and 100 kv for thin oxide films. In order to facilitate accurate measurement of lattice spacings by selected area diffraction, gold was evaporated on the oxide to provide a standard diffraction pattern. Distance measurements on the patterns were made with a Joyce recording densitometer.

The alloy material, the procedures for preparing alloys in martensitic and Widmanstätten structures, surface preparation, and oxidation of specimens in oxygen at 1 atm pressure have been described in a previous paper (1). The aqueous pickling solution, 30 v/o H<sub>2</sub>SO<sub>4</sub>, 30 v/o HNO<sub>3</sub>, and 10 v/o HF, was held at a temperature in the range 68°-75°C. Weight gains of specimens by oxidation were converted to approximate average film thicknesses based upon the factor  $1\mu\text{g O/cm}^2 = 62\text{Å}$ .

\* Electrochemical Society Active Member.

<sup>1</sup> Present address: Atomic Power Division, Westinghouse Electric Corporation, Madison, Pennsylvania.

## Results

*Oxide film morphologies.*—The changes in the topographies of specimens oxidized at 400°C were studied from the initial protective stage of film formation, through the transition region, and into the final stage where oxidation approximated to linear kinetics (1).

Representative surfaces of martensitic specimens and the film at various stages of oxidation are shown in Fig. 1-3. Although the surfaces of mechanically polished specimens were featureless, surfaces of pickled specimens showed areas of selective etching at the boundaries of the martensite plates. Irrespective of

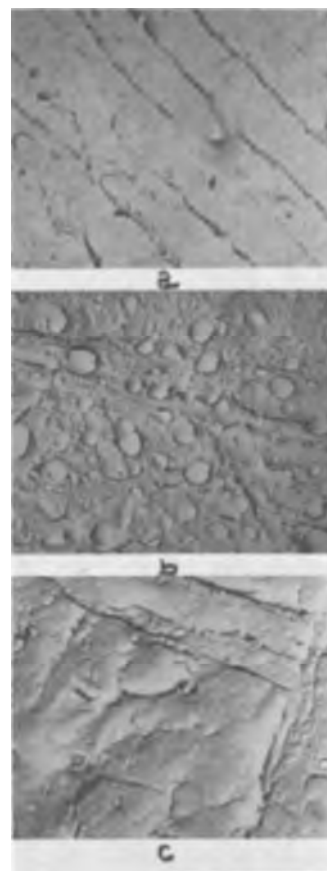


Fig. 1. Surface replicas of pickled martensitic alloy surfaces after oxidation at 400°C. Oxygen uptake: top, unoxidized, 26,665X; middle, 0.10 mgO/cm<sup>2</sup>, 14,665X; bottom, 0.20 mgO/cm<sup>2</sup>, 14,665X.

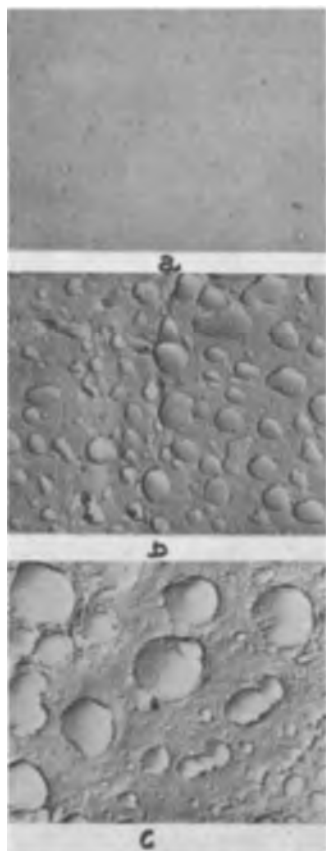


Fig. 2. Surface replicas of mechanically polished martensitic alloy surfaces after oxidation at 400°C. Oxygen uptake: top, unoxidized; middle, 0.09 mgO/cm<sup>2</sup>; bottom, 0.15 mgO/cm<sup>2</sup>. 14,665X.

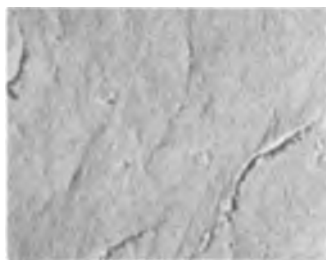


Fig. 3. Typical surface replica of martensitic specimen oxidized to the range of linear kinetics. Oxygen uptake: 1.56 mgO/cm<sup>2</sup>. 14,665X.

surface treatment, the films were uneven in the initial stages of the reaction, Fig. 1b and 2b, exhibiting pustular growths with sizes varying from grain to grain. In addition to pustules, fine cracks were to be observed in the films as the specimens were progressively oxidized into the period for transition to linear kinetics, Fig. 1c and 2c. At long times, a film exhibited an uneven surface populated with cracks, Fig. 3.

A similar series of micrographs for the Widmanstatten alloys is illustrated in Fig. 4. There was not a noticeable difference between the pickled and unpickled surfaces, other than that, with the former type of specimen, the alloy structure could be more easily distinguished. Micrographs of films formed on both alloy phases, Fig. 4b, demonstrated that the films were considerably thicker on the  $\alpha'$ -Zr phase even at small oxygen uptakes. Moreover, the films formed on this phase were characterized by pustules as previously shown for the martensitic specimens. Cracking of this oxide became very extensive before any evidence was found for cracking of the oxide formed on the  $\alpha$ -Zr phase, Fig. 4c, and even occurred in films thinner than those formed on martensitic specimens. For example,

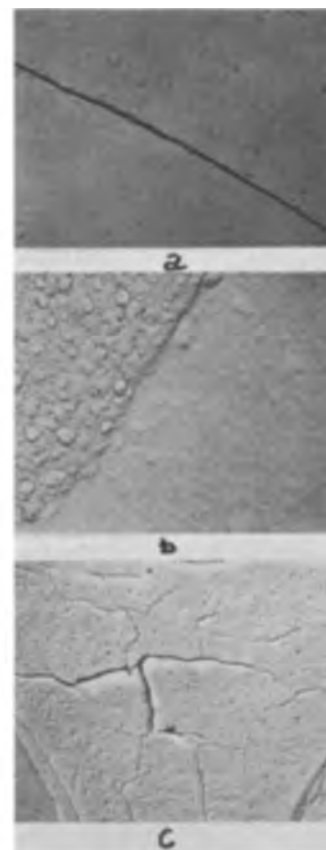


Fig. 4. Surface replicas of mechanically polished Widmanstatten alloy surfaces after oxidation at 400°C. Oxygen uptake: top, unoxidized, 25,330X; middle, 0.01 mgO/cm<sup>2</sup>, 14,665X; bottom, 0.2 mgO/cm<sup>2</sup>, 2,665X. The pustular oxide and extensively cracked oxide occur on the  $\alpha'$ -Zr alloy phase.

cracks were readily observable in a 1500Å film on an alloy containing 30 v/o  $\alpha$ -Zr, whereas evidence was only found for the initiation of cracking in films corresponding to approximately 2500Å on martensitic specimens.

*Oxide film structures.*—Films formed at 300°C and with thicknesses varying from 100 to 800Å were examined by the transmission technique. Their appearance was dependent on the surface preparation of the specimens. A film stripped from a specimen whose surface was mechanically polished was relatively featureless. On the other hand, the films stripped from pickled specimens exhibited structures related to the alloy microstructures. The microstructures of the martensitic and Widmanstatten alloys replicated by their oxide films are illustrated in Fig. 5. Absence of electron transmission through the films at alloy transformation boundaries indicated enhanced oxide growth in these regions.

Selected area diffraction spot patterns obtained from films formed on alloy pickled surfaces could often be indexed as monoclinic zirconia (2-4). It was also possible to index some patterns as a mixture of monoclinic zirconia and another phase. Most of the spots could be accounted as coming from the monoclinic oxide, but one pair of spots arose from planes with d-spacing of 2.95Å. Such a lattice spacing would be compatible with the (111) spacing of tetragonal zirconia (5), or, possibly, of the mixed oxide 6ZrO<sub>2</sub>·Nb<sub>2</sub>O<sub>5</sub> (6). A typical diffraction pattern from a film containing both oxides is illustrated in Fig. 6. In the case of a mechanically polished surface, the diffraction patterns were those of a polycrystalline oxide and they could be indexed generally as monoclinic zirconia.

In the earlier reported paper (1), examination by a recording x-ray diffractometer of the surfaces of

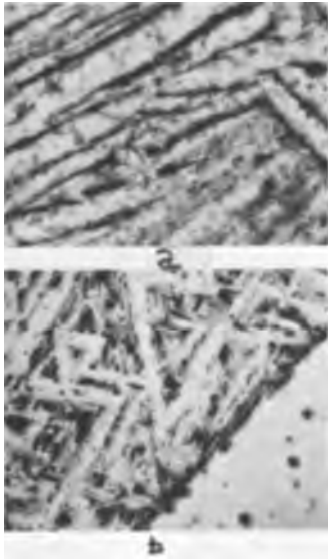


Fig. 5. Electron transmission micrographs of oxide films stripped from pickled alloys oxidized at 300°C: top, martensite, 0.001 mgO/cm<sup>2</sup>; bottom, Widmanstätten structure, 0.002 mgO/cm<sup>2</sup>. 13,330X.

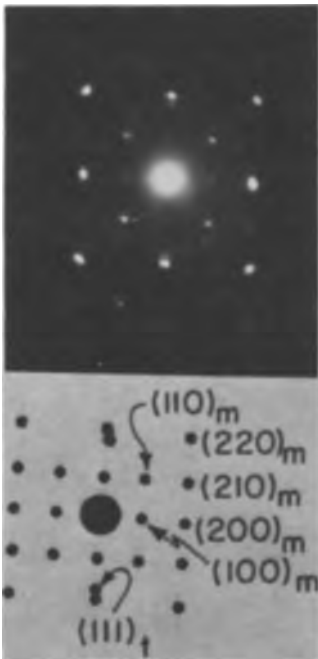


Fig. 6. Selected area diffraction pattern from film formed on pickled martensitic alloy oxidized at 300°C. Oxygen uptake: 0.004 mgO/cm<sup>2</sup>. Symbols m and t refer to monoclinic and tetragonal oxide, respectively.

specimens oxidized for extended exposures to form scales demonstrated that monoclinic zirconia was the major reaction product, little evidence being found for the existence of another oxide phase. To gain more detailed information, powder x-ray diffraction experiments were carried out on scales formed at the temperatures of 300°, 400° and 500°C on both martensitic and Widmanstätten specimens. The patterns from oxide formed under all these conditions were similar and reflections were consistently obtained from a plane with lattice spacing 2.94-2.95Å in addition to those of monoclinic zirconia. This is the same value as that found by electron diffraction from thin films and the existence of a tetragonal oxide in both monoclinic zirconia films and scales is considered definite.

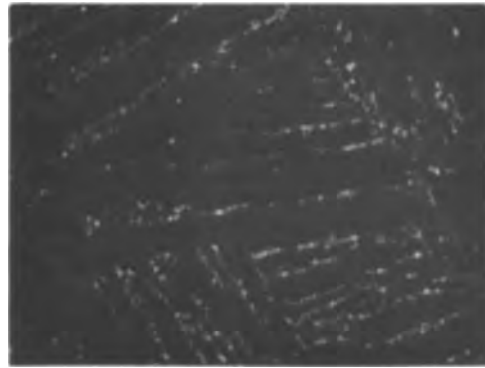


Fig. 7. Dark field transmission micrograph from oxide film formed on pickled martensitic alloy oxidized at 300°C showing crystallites of tetragonal oxide at alloy transformation boundaries. 20,000X.

Attempts were made to locate the tetragonal crystallites in the films formed on pickled specimens by dark field electron microscopy. This was done using the diffraction spots from the (111) plane of this phase as all other planes gave rise to spots coincident, or nearly coincident, with spots from monoclinic zirconia. Examination of many films demonstrated that this oxide was distributed as small crystallites in a size range between 50 and 150Å at areas bounding transformation boundaries in a martensitic alloy, Fig. 7, and over the main surface, the distribution appearing to be dependent on the orientation of the alloy matrix surface. Although several films stripped from specimens with Widmanstätten structures were composed of both monoclinic and tetragonal oxide, it was impossible to form conclusions regarding the distribution of crystallites.

### Discussion

Oxide pustules in the films on martensitic specimens were found previously by light microscopy to be the only distinct feature indicating a difference in the mode of oxide formation on different structured alloys (1). The current observations at the high magnifications of an electron microscope show that pustules also occur in films on Widmanstätten alloys, albeit not on such a large scale and then only on  $\alpha'$ -Zr. The size of these pustules was restricted to about 0.1-0.2 $\mu$ , whereas those on martensitic specimens ranged upwards to 0.5 $\mu$  by electron microscopy and 500 $\mu$  by light microscopy. Apparently both the mode of oxide formation and the properties of the films differ. Film growth on martensitic alloys was characterized by the lateral growth of pustules. On the other hand, pustules in the  $\alpha'$ -Zr phase of the Widmanstätten specimens attained smaller ultimate size before cracking of the film occurred at a relatively small thickness.

Film growth was uneven on all alloy structures with enhanced oxide growth occurring about the transformation boundaries in the alloy microstructures. These latter regions would exhibit niobium enrichment brought about during quenching and/or tempering at reaction temperatures. This enrichment would eventually lead to the segregation of  $\beta$ -Nb (92 w/o Nb) which may play a role in oxide formation in these regions. Since the crystallites of the tetragonal oxide phase, an allotropic modification of zirconia or the double oxide, 6ZrO<sub>2</sub>·Nb<sub>2</sub>O<sub>5</sub> were distributed both around transformation boundaries and on the martensitic plates, niobium may only dissolve in the tetragonal zirconia, without leading to the formation of the double oxide.

The crystallite size of the tetragonal oxide was small lying in the range 50 to 150Å. This observation stimulates comparison with other work despite the limitation of not being able to distinguish whether this phase



was an allotropic modification of zirconia or an intramolecular oxide. A tetragonal oxide was reported by Schwartz *et al.* (7) to occur on zirconium oxidized in water at 400°C and by Korobkov *et al.* (8) on zirconium and alloys containing titanium, aluminum and tin oxidized in air at temperatures between 300°-1100°C. Its transformation to a monoclinic structure was suggested by these investigators as the cause for film breakdown. This supposition would not appear to be valid for the alloy of the present investigation because the films formed before the breakaway region in a reaction curve consisted largely of monoclinic zirconia with only small amounts of tetragonal oxide.

To account for the diverse features of film formation, account must be given to the alloy phases upon which oxide is forming. The films on the  $\alpha$ -Zr phase of Widmanstätten alloys, which would be most homogeneous with respect to niobium concentration, were more uniform than those on the  $\alpha'$ -Zr phase or the fully martensitic alloy. The niobium content of  $\alpha'$ -Zr depends upon the annealing treatment for the alloy and was approximately 4 w/o compared with 2.7 w/o for martensite. Thus a higher degree of niobium enrichment in the zirconia film on  $\alpha'$ -Zr is to be expected. The oxide in this film may exhibit the same properties as shown by Douglass (9) for zirconia where metal additives decreased its plasticity. A similar decrease in oxide plasticity possibly played a role in determining the most extensive cracking of the film on the  $\alpha'$ -Zr phase at the earliest stage of reaction. It would appear, however, that the cracks observable by electron microscopy did not play a dominant role in determining the protective properties of the total film because the linear oxidation kinetics of a marten-

sitic alloy were much larger than those for the Widmanstätten alloys (1).

### Acknowledgments

The authors were indebted to D. J. Embury for many helpful discussions on electron microscopy techniques. This research was completed under the auspices of the Atomic Energy of Canada Limited and the Defence Research Board of Canada.

Manuscript received Nov. 20, 1967; revised manuscript received ca. Jan. 10, 1968. This paper was presented at the Chicago Meeting, Oct. 15-19, 1967, as Abstract 88.

Any discussion of this paper will appear in a Discussion Section to be published in the December 1968 JOURNAL.

### REFERENCES

1. M. G. Cowgill and W. W. Smeltzer, *This Journal*, **114**, 1089 (1967).
2. J. D. McCullough and K. N. Trueblood, *Acta Cryst.*, **12**, 507 (1959).
3. J. Adam and M. D. Rogers, *ibid.*, **12**, 951 (1959).
4. W. B. Pearson, "A Handbook of Lattice Spacing and Structures of Metals and Alloy," p. 246, Pergamon Press (1964).
5. L. N. Komissarova, Yu. P. Simanov, and Z. A. Vladimirova, *Russ. J. Inorg. Chem.*, **5**, 687 (1960).
6. R. S. Roth and L. W. Coughanour, *J. Research Natl. Bur. Standards*, **55**, 209 (1955).
7. C. M. Schwartz, D. A. Vaughan, and G. C. Cocks, *BMI-793* (Dec. 1952).
8. I. I. Korobkov, D. V. Ignatov, A. E. Evstyukhin, and V. S. Emelyanov, *Proc. 2nd. U. N. Conf. on Peaceful Uses of Atomic Energy*, **5**, 60 (1958).
9. D. L. Douglass, *Corrosion Sci.*, **5**, 255 (1965).

## The Attraction of Liquids by Electric Fields

E. P. Damm, Jr.

*Systems Development Division, International Business Machines Corporation, Poughkeepsie, New York*

### ABSTRACT

The attraction of liquids by electric fields is studied. The time between application of electric field and liquid contact with electrode (response time) serves as the basis for determining the effects of various system parameters. Variation of response time with electrode voltage and with air gap is plotted for a high-dielectric-constant liquid. It is shown that response time is largely independent of the liquid's conductivity, solids concentration, particle size and particle polarity of dissolved or dispersed solids in water. Response time does vary significantly with viscosity, and, up to certain field strengths, with the surface tension of the liquid. Also, for the liquids used in these experiments, response times were lowest for liquids having highest dielectric constants and highest for those with lowest dielectric constants, if viscosity effects are taken into consideration. The evaporation rate or the presence of vapor molecules of a volatile nonpolar or only slightly polar liquid also appears to increase the response time. However, the presence of polarizable materials dispersed in a liquid of low polarity such as toluene produces a decrease in the response time of the liquid.

It has long been known that liquids can be influenced by electric fields. The phenomenon of "ink flying" in the printing industry (1) and the rise of the level of the liquid with oil-insulated high-tension equipment are examples. Swan (2), Schott and Kaghan (3) have also reported some interesting experiments with this phenomenon.

Pohl (4-8) and Kok (9) have experimented with and tried to develop a theoretical mechanism for the motion of particles in dielectric liquids by high-intensity divergent fields. The motion of these particles was, at least initially, the result of a phenomenon which Pohl called dielectrophoresis. The term dielec-

trophoresis was defined as the motion of electrically polarized matter in a nonuniform field, in contrast to electrophoresis, which is defined as the phenomenon of the migration of charged particles through a fluid under the influence of an electric field. While both phenomena were known, the experiments of Pohl served to emphasize that polarization effects, while somewhat neglected in the area of particle motion in an electric field, were of practical use and could account for certain occurrences which otherwise might be loosely accounted for only by electrophoresis. There is little record (10) of work on the attraction of highly conducting liquids by divergent electric fields and

especially on the quantitative comparison of their characteristics with those of dielectric liquids under an applied electric field.

This paper describes several experiments with liquids of varying dielectric constant and conductivity. The system variables of electrode voltage and gap are discussed, as well as the liquid variables of conductivity, surface tension, viscosity, particle polarity, solids concentration, and particle size of the dissolved or dispersed phase. The importance of the dielectric constant of the liquid and the evaporation rate of liquids with extremely low dielectric constant are also shown. The response time of the liquid is used as the dependent variable to quantitatively define the system behavior. Response time in this paper refers to the time interval between the initiation of the attraction voltage and the contact of the attraction electrode by liquid.

#### A Simple Model

In attempting to understand how response time is related to the properties of dielectric liquids and the electric fields that attract them, the equation for the force between a point charge and an unbounded, planar dielectric medium provides useful clues. This equation is given by (11)

$$F = \frac{1}{4\pi K_0 K_1} \frac{K_1 - K_2}{K_1 + K_2} \frac{q^2}{a^2}$$

where  $K_0$  = the permittivity of free space;  $K_1$  = the dielectric constant of the material between the point charge and the plane;  $K_2$  = the dielectric constant of the planar dielectric medium;  $q$  = the charge at the point; and  $a$  = the distance between the point charge and the plane of the dielectric.

While more rigorous equations can be developed to explain the phenomenon whereby, for example, the geometry of one of the equipotential surfaces of the point charge is assumed to be the geometry of the attraction electrode, the simple model does illustrate that, for a given  $q$  and  $a$ , the attractive force decreases significantly only when  $K_2$  approaches  $K_1$ . For example, if the medium between the point charge and the planar surface is air ( $K_1 = 1$ ) and the dielectric is water ( $K_2 = 80$ ), the attractive force is  $79/81 = 97.5\%$  of the force available if  $K_2$  were infinite. For the case of glycerine (98%) ( $K_2 = 43$ ), the force is  $42/44 = 95.5\%$  of that available if  $K_2$  were infinite. Hence, it could be expected that response time, which is inversely related to the attracting force, will not vary significantly for different liquids of low viscosity and high dielectric constant. Also, from this simple model one would expect that changes in conductivity, liquid depth, and solids concentration in a high-dielectric-constant liquid will not radically affect response time. On the other hand, it may be expected that surface tension and viscosity, which are not shown in this equation, might be important factors affecting the response time.

In the case of low-dielectric-constant liquids such as toluene ( $K_2 = 2.4$ ), any factors which significantly alter the dielectric constant of either the liquid or the air gap would be expected to seriously affect response time. For example, condensation in the air could alter  $K_1$  enough to cause a significant change in response time.

#### High-Dielectric-Constant Liquids

**Characteristic curves.**—In our initial experiments, we studied the response time of a high-dielectric-constant liquid as a function of air gap and applied voltage. A 1% aqueous solution of the colloidal electrolyte, crystal violet, extra pure,<sup>1</sup> was chosen as representative of this class of liquids. In order to minimize the effect of surface tension, we added a surfactant to the

<sup>1</sup> A product of du Pont de Nemours & Co., Wilmington, Delaware.

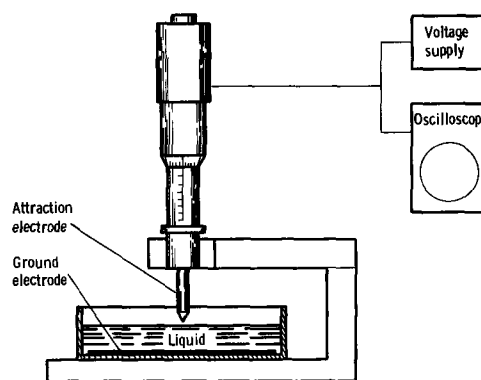


Fig. 1. Responsometer

solution. With 1% Fluorochemical L-1006<sup>2</sup> (nonionic) it was possible to bring the surface tension as low as 23.4 dynes/cm (measured with a DuNuoy-type tensiometer).

To measure response times, an instrument called a responsometer was devised (Fig. 1). A petri dish contains the liquid to be tested and a brass, flat-disk electrode. The upper, attracting electrode is a micrometer head ground to a conical tip (0.021 in. radius, 45° taper) to provide a divergent electrical field. The accuracy of the vertical adjustment is to the nearest 0.0001 in. A 5000v d-c power supply with a 10-Mohm current-limiting resistor is used to supply the voltage, which is controlled with a standard powerstat. An oscilloscope connected to the attracting electrode is used to monitor the voltage.

When voltage is applied to the micrometer head, the oscilloscope trace rises accordingly and remains at the upper level until the attracted liquid makes contact with the electrode. At this time the circuit is electrically shorted, and the trace drops back to zero. Response times can be measured directly from photographs of the oscilloscope trace (Fig. 2). We found that the response times of reasonably polar liquids having specific conductivities as low as  $2 \times 10^{-8}$  mho/cm could be directly measured with this instrument.

The characteristic curves of the water and crystal violet solution are given in Fig. 3 and 4, which show response time as a function of air gap and applied voltage, respectively.

**Effect of solution properties.**—Since surface tension and viscosity resist the attracting force of the electric field, they were expected to have an important effect on response time. The response time *vs.* surface tension characteristic was determined for the aqueous crystal violet solution. Different amounts of surfactant were added to vary the surface tension over the range from 76 to 23.4 dynes/cm. Figure 5 shows that the variation in surface tension has a significant effect on response time only for low values of applied voltage. Above 500v, the slopes of the response time *vs.* surface tension curves are close to zero. The limiting effect of the restraining forces at low surface tension is observed in Fig. 6, which shows the maximum gap through which the aqueous crystal violet solution with minimum surface tension can be attracted for various voltages.

The effect of viscosity on response time was measured in an experiment which used different concentrations of glycerine in water to provide a range of viscous solutions. Figure 7 shows that response time increased linearly by a factor of about 3 as the viscosity was increased from 1.7 to 360 centipoise.

Other solution properties that were checked included conductivity, concentration of colloidal particles, and size of dissolved or dispersed particles. Response time was virtually independent of these properties. To test the effect of conductivity, potas-

<sup>2</sup> A product of the 3M Corporation, St. Paul, Minnesota.

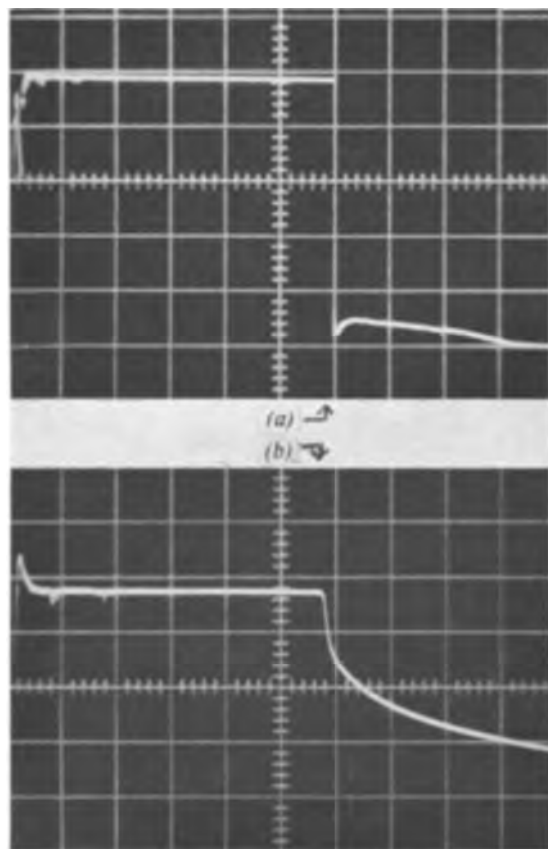


Fig. 2. Typical curves: (a) response curve displayed by a conductive liquid. Vertical axis = applied potential, horizontal axis = time; (b) capacitance-type decay curve displayed by demineralized water and polar liquids of high resistivity.

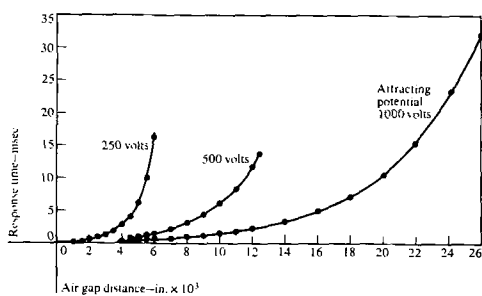


Fig. 3. As air gap distance increases, the response time increases.

sium chloride was titrated into demineralized water. As the conductivity of the solution was varied from 6 to 3000  $\mu$ mhos (monitored during titration by a conductance bridge with dip-type cells), response time remained relatively constant (Fig. 8).

The concentration of crystal violet in water was varied from 0 to 1% to test the possibility that the concentration of colloidal electrolyte in a liquid could significantly affect response time. It did not (Fig. 9).

In none of the experiments with solution properties of high-dielectric-constant liquids was there a difference in response time which could be attributed to the size of the particles in solution. The solutions studied had particles that ranged from ions to colloidal electrolytes to colloids to coarse particles.

*Effect of electric field properties.*—The simple model of the attraction process assumes a point electrode.

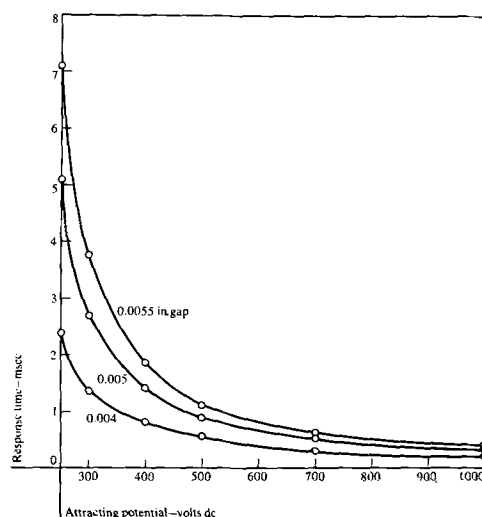


Fig. 4. At small gaps, the response time decreases rapidly as attracting potential increases in the range from 250 to 500v (aqueous solution).

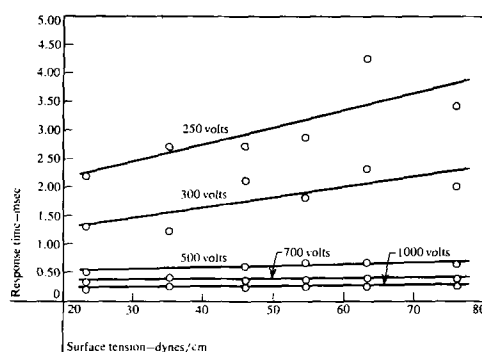


Fig. 5. Effect of surface tension on response time decreases with increasing voltage (0.004 in. gap, aqueous solution).

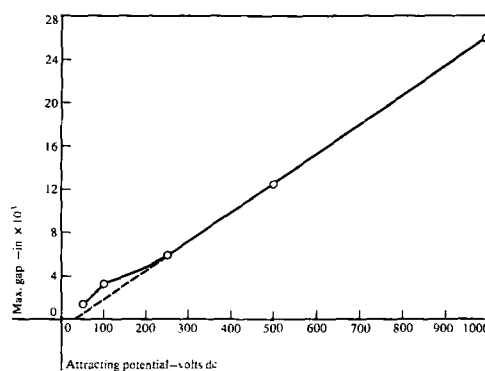


Fig. 6. As attracting potential increases, the maximum gap at which liquid will jump increases (aqueous solution).

Electrode geometry, however, is important in a real system. Therefore, variations in the electrode geometry and their effect on response time were studied. When the electrode was altered from a conical tip with 0.021 in. radius to a hemisphere with 0.115 in. radius to a flat surface, the response time increased accordingly. The effect of these gross changes is to make the attracting force weaker by reducing the divergence of the field and the results in Table I are not unexpected based on a model using a dielectric-constant relationship. However, a much subtler change in electrode geometry produced an interesting result. When the radius of the tip of the conical micrometer head was reduced from 0.021 to 0.008 in., the response time was significantly higher for the smaller tip (Table II). This seems to indicate the

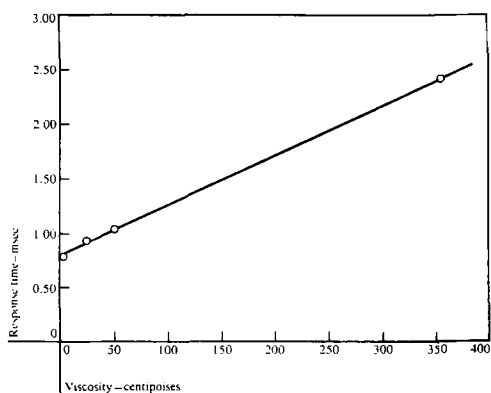


Fig. 7. Response time increases with increasing viscosity (surface tension corrected to 39.1 dynes/cm, 0.004 in. gap, aqueous solution).

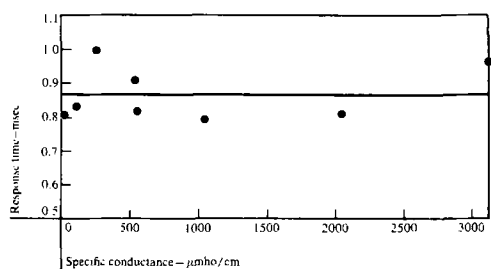


Fig. 8. Specific conductance has no effect on response time in the range from 6 μmhos/cm to 3000 μmhos/cm (0.004 in. gap, surface tension corrected to 75.0 dynes/cm).

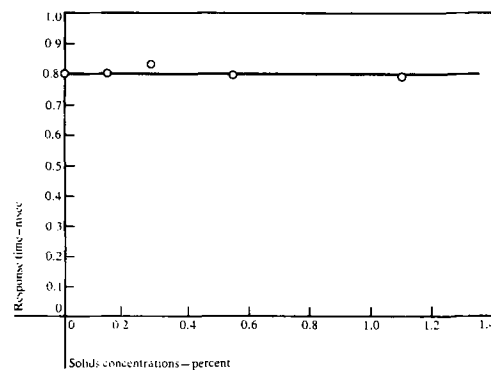


Fig. 9. Solid concentration of crystal violet dye has no effect on response time (0.004 in. gap, aqueous solution).

existence of an inflection point in the variation of response time with electrode diameter. Perhaps the divergence of the electric field with the smaller-radius electrode is great enough to result in such a substantial decrease in the field near the surface of the liquid that the high acceleration caused by the field near the tip is not enough to compensate.

Also, to find out whether variation in liquid depth would change the shape of the field, we measured response time at several liquid depths from 0.2509 to 0.0076 in. No change was noted. It was concluded that for relatively conductive liquids, the liquid surface itself could be assumed to act as the ground electrode. In fact, removing the brass-disk electrode from the

Table I. Effect of gross changes in electrode geometry

Electrode shape	Response time in msec	
	applied voltage + 500v	- 500v
Point	0.52	0.29
Hemisphere	0.63	0.57
Flat	0.77	0.73

Table II. Effect of small change in electrode geometry

Radius of conical tip in inches	Response time in msec			
	air gap in inches			
	0.004	0.006	0.008	0.010
0.021	0.56	1.16	2.42	4.85
0.008	0.70	2.40	5.90	14.31

petri dish has almost no effect on response time as long as the liquid makes contact with an electrical ground.

Finally, an experiment was run to test the possibility that a negatively charged attraction electrode would produce different response times than did the positively charged ones. Different behavior would not be unexpected since it has been observed in the breakdown voltages of point-plane surfaces in air (12) and in some work with liquids (13, 14) where large changes in the refractive index of the liquids occurred with a negatively charged point but not with a positively charged point. Figure 10 shows that, in general, response times obtained with negative potential on the attraction electrode were lower than those with positive potential. However, response times were much more erratic for the negative potentials. In addition, in our experiments, response time results already obtained for the aqueous crystal violet solution at an attracting voltage of +500v were compared with those response times obtained for the negatively charged colloidal electrolyte, Amaranth Red U.S.P. in a 1% aqueous solution at +500v. For equivalent surface tensions they were identical.

Low-Dielectric-Constant Liquids

If the simple model suggested earlier for the liquid attraction process is at all realistic, a large increase in response time should be noticed as the dielectric constant of liquids closely approaches that of air. Our experiments with low-dielectric-constant liquids bore out this suggestion. However, it was necessary to use a different means of measuring response time for these liquids. Since low-dielectric-constant liquids have low conductivity, no change in voltage could be observed on the oscilloscope when the liquid made contact with the attracting electrode. So, a detection system utilizing a high-speed movie camera was used. In this system a timer on the camera triggered the electrode voltage after the film had accelerated to a reasonably constant speed. Timing lights were used to determine the speed of the film at the time of attraction. An oscilloscope trace identifying the time at which voltage was applied to the electrode was superimposed on the

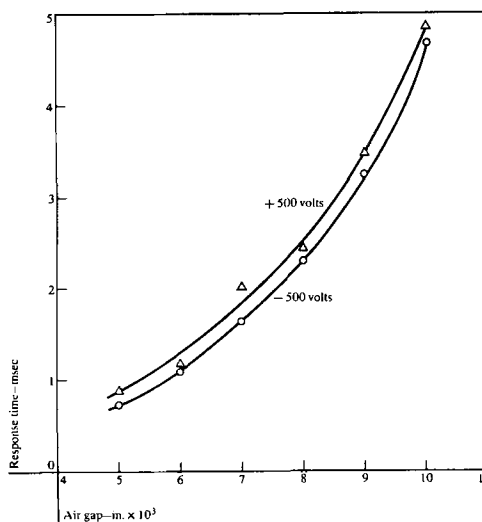


Fig. 10. Negative potentials give lower (but more erratic) response times than do positive potentials (aqueous solution).

film by means of a side-viewing port of the camera (Fig. 11).

*Effect of liquid properties.*—Viscosity is a measure of the internal friction of the liquid. Therefore, if the attraction phenomenon is dependent on dipole forces, the relaxation time of the dipoles can become very important in viscous liquids having low dielectric constants. The polarization forces in an electric field can

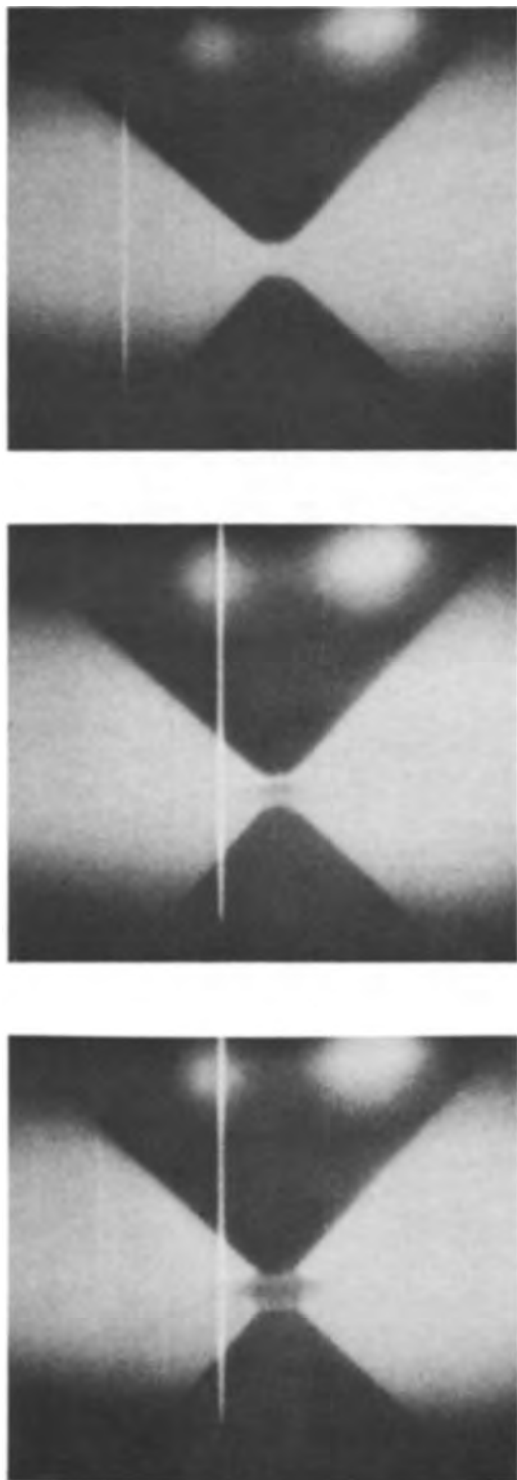


Fig. 11. Photographs of high-speed movies taken with a Fastax Model WF-17 camera. Film speed was 8000 frames per second. The dark area in the upper portion of the photo is the attraction electrode. The lower dark area is the reflection of the attraction electrode in the liquid. The white line in the left of center is the oscilloscope trace which was superimposed on the film. The shift in the position of this line took place at the time of the application of the pulse. Top, 0 sec; center, 3.0 msec; bottom, 4.5 msec.

be separated into two components: one slow-acting and the other fast. The fast polarization consists largely of electronic distortion because of the displacement of electrons relative to the positive nucleus. The slow polarization consists of dipole orientation in the electric field and in some respect depends on the frictional resistance of the medium to changes in molecular orientation.

With small-chain polar molecules, the dipole forces are usually strong enough to overcome viscosity forces in a short period of time, e.g.,  $10^{-11}$  to  $10^{-6}$  sec. With nonpolar or only slightly polar liquids, however, dipole forces are quite small. Thus the dipoles of very viscous nonpolar and slightly polar liquids can remain in a semi-oriented state minutes after the external field is removed. This is especially true of long chain molecules. Further complications arise because trace polarizing materials, including air bubbles, can change the effective dipole moment and thus the relaxation time of the molecules (15).

We ran into trouble in experimenting with the effect of viscosity on response time for low-dielectric-constant liquids. We had thought that the dimethyl silicones would be useful liquids for this type of study because their viscosity can be varied over a wide range without changing the dielectric constant by much. However, the results obtained were very unreliable, apparently because of the hysteresis effects mentioned above. Toluene ( $K_2 = 2.4$ ), the liquid we used for several subsequent experiments, could not be used to study viscosity. Also, it was not possible to vary surface tension and conductivity significantly, so the effects of these properties were not studied either.

The significance that various additives have on the response time of toluene is shown in Table III. Materials having different particle sizes and solubilities were dissolved or dispersed in toluene. It appears that response time decreases accordingly as the particles have greater polarizing power. The most marked effect on response time was produced by the presence of colloid particles.

Table IV shows that ambient conditions also have a great effect on the response time of toluene. It is possible that the variation is caused by water condensed from the atmosphere by evaporating molecules of the liquid. This condensation could change the dielectric constant of the air gap enough to significantly alter the attracting force on the liquid. Another explanation is that air-vapor electrophoresis-dielectrophoresis occurring at high relative humidity and/or high vapor pressure of solvent produces a down pressure [the "electric wind" described by Pohl (5)]. The importance of evaporation rate was noted when hexane ( $K_2 = 1.9$ ), which has a high evaporation rate, was

Table III. Effect of additives in toluene on response time

Additive	Response time in msec
1% Amaranth dye (large particle)	53.0
1% Foron blue (partial solution plus flocculated particles)	46.2
1% Acetate red (partial solution plus large particles)	17.9
1% Oil red (solution)	11.7
1% Crystal violet, extra pure (colloidal plus medium-sized particles)	4.36

Table IV. Effect of temperature and humidity on response time of toluene

Temperature in °F	Relative humidity, %	Response time in msec
78	30	10.7
72.5	42	14.2
70.3	52	30.2

Table V. Effect of gross changes in electrode geometry

Electrode shape	Maximum gap in inches	
	applied voltage + 500v	- 500v
Point	0.0130	0.0130
Hemisphere	0.0187	0.0180
Flat	0.0283	0.0273

compared with toluene. The maximum gap across which the hexane could jump at 500v was only 0.0025 in. as compared with 0.0123 in. for toluene. Furthermore, when the level of the toluene was raised to the top of the container, response time increased sharply, no matter where the ground electrode was placed. Hence, it appears that for low-dielectric-constant liquids an increase in evaporation rate, whether it is inherent or caused by greater exposure of the liquid to air currents, increases response time.

**Electric field effects.**—The effect of electrode geometry on the maximum gap of toluene was also studied (Table V). The electrodes were the same as those used in the electrode geometry study for liquids with high-dielectric constants. The results showed that the maximum gap through which the liquid could be attracted increased in this order: pointed, rounded, and flat attraction electrode. This seemed to indicate that for these three electrodes, the more uniform the field, the longer the response time, but the higher the maximum gap through which the liquid can be attracted. One possible reason is that while more-divergent fields produce a higher acceleration, less force is available at the surface of the liquid to overcome surface tension. It should be kept in mind that the mass of the liquid attracted may be varying with the radius of the attraction electrode.

As another consideration, if electrode-to-electrode distance is very critical, a difference in maximum gap should be noticed as the depth of toluene is varied. While the surface of a conductive liquid can be expected to act as a ground electrode, this is certainly not true for the low-conductivity liquids. No great difference in maximum gap was noticed when the depth of toluene was varied from 0.250 to 0.019 in. at 500v. Furthermore, when the ground disk was removed from the petri dish the liquid continued to jump under the applied potential. This indicates that for the depths of liquid studied, as long as some reference ground is present, the electrode-to-liquid distance is more important than electrode-to-electrode distance.

A study of some liquids having dielectric constants in the range between what have been called high- and low-dielectric-constant liquids was performed. Response times of these liquids are given in Table VI.

### Conclusion

It has been shown that response time is largely independent of the conductivity, solids concentration, and particle size of dissolved or dispersed materials in a highly polar liquid such as water, although response time does vary with the surface tension and viscosity of the liquid. However, above a certain field strength, surface tension plays a minor role in determining the rate of attraction. In addition, studies with high-, intermediate-, and low-dielectric constant liquids, have shown that response time appears to be lowest for liquids with high-dielectric constants and *vice versa*. Also, the evaporation rate or the presence of vapor molecules of a volatile nonpolar or only slightly polar liquid appears to increase the response

Table VI. Response times for liquids with intermediate dielectric constants

Liquid	Surface tension in dynes/cm	Viscosity in centipoise	Dielectric constant	Response time in msec
Methyl alcohol	22.6	0.59	33.0	4.1
Acetone	23.7	0.33	21.3	4.7
G. E. nitrile silicone XF-1150	36.7	800-1300	19.6	18.5
G. E. nitrile silicone XF-1112	23.6	100 ± 20	7.2	4.1
G. E. nitrile silicone XF-1112 plus crystal violet extra pure	—	—	—	3.0
G. E. nitrile silicone XF-1105	21.9	100 ± 20	4.7	10.6
G. E. nitrile silicone XF-1105 plus dispersed dye Foron blue	—	—	—	10.4

time. However, the presence of particles capable of producing polarization effects in a low-polarity liquid reduces this effect and produces a decrease in the response time of the liquid.

Based on the above data and the fact that the effects of electrical polarity within the liquid appear to be negligible or at least quite obscure, a stand can be taken that the phenomenon studied was largely dielectrophoresis. An analogy can be drawn to the work of Pohl (4-8) if the air between the attraction electrode and the liquid is considered as the fluid of low-dielectric constant and the liquid attracted is considered as a large, easily deformable particle.

### Acknowledgment

The author acknowledges the contribution of E. R. Mondou, who performed most of the measurements reported here.

Manuscript received Nov. 28, 1967. This paper was presented at the Chicago Meeting, Oct. 15-19, 1967, as Abstract 151.

Any discussion of this paper will appear in a Discussion Section to be published in the December 1968 JOURNAL.

### REFERENCES

1. A. Voet, "Ink and Paper in the Printing Process," p. 81, Interscience Publishers, New York (1952).
2. J. W. Swan, *Proc. Royal Soc.*, **62**, 38 (1897).
3. H. Schott and W. S. Kaghan, *Appl. Phys.*, **36**, 3399 (1965).
4. H. A. Pohl, *ibid.*, **22**, 869 (1951).
5. H. A. Pohl, *ibid.*, **29**, 1182 (1958).
6. H. A. Pohl and J. P. Schwar, *ibid.*, **30**, 69 (1956).
7. H. A. Pohl and C. E. Plymale, *This Journal*, **107**, 386 (1960).
8. H. A. Pohl, *Scientific American*, p. 107 (December 1960).
9. J. A. Kok, "Electrical Breakdown of Insulating Liquids," p. 40, Philips Technical Library, Netherlands (1961).
10. W. F. Pickard, "Electrical Force Effects in Dielectric Liquids," in "Progress in Dielectric," p. 24, J. B. Birkes and J. Hart, Editors, Academic Press, New York (1965).
11. G. P. Harnwell, "Principles of Electricity and Magnetism," p. 74, McGraw-Hill Book Co. Inc., New York (1949).
12. J. M. Meek and J. D. Craggs, "Electrical Breakdown of Gases," Clarendon Press, Oxford, (1953).
13. B. Farazmand, *Brit. Appl. Phys.*, **12**, 251 (1961).
14. S. S. Hakim and J. B. Higham, *Nature*, **189**, 996 (1961).
15. C. P. Smyth, "Dielectric Behavior and Structure," p. 52, McGraw-Hill Book Co., Inc., New York (1955).

# Evidence of Nickel Phosphide $\text{Ni}_2\text{P}$ in As-plated Electroless Nickel

J.-P. Randin and H. E. Hintermann\*

Laboratoire Suisse de Recherches Horlogères, Neuchâtel, Switzerland

## ABSTRACT

The dissolution rate of as-plated electroless nickel containing between 3.2 and 12.5 w/o phosphorus is studied in hydrochloric acid. Two reaction rates can be distinguished: first the dissolution of the nickel phase (fast), second that of a phase containing 21 w/o phosphorus whose stoichiometry corresponds to the composition of the nickel phosphide  $\text{Ni}_2\text{P}$  (slow). The  $\text{Ni}_2\text{P}$  content of the as-plated electroless nickel corresponds to the entirety of phosphorus bonded to nickel.

In a previous publication (1) the study of electroless nickel by differential thermal analysis revealed that the heat evolution during the heating corresponds to 11-17% of the heat of formation of  $\text{Ni}_3\text{P}$ , which is the final reaction product. According to this data and the findings of Graham, Lindsay, and Read (2) we proposed that as-plated electroless nickel might be a supersaturated solid solution of phosphorus in nickel. This state could be considered as a metastable intermediate state between that of a mixture of nickel plus phosphorus and that of the equilibrium system of nickel plus  $\text{Ni}_3\text{P}$ . We suggested (1) that the intermediate state could include phosphorus atoms chemically bonded to nickel atoms as a phosphide since 83-89% of the heat of formation of the stable state of nickel plus  $\text{Ni}_3\text{P}$  is released.

In this study it is shown how the dissolution rate of electroless nickel in hydrochloric acid allows to establish the nature of the chemical state of phosphorus in the as-plated alloy.

## Experimental Procedure

**Preparation of deposits.**—An acid bath of the following composition was used:  $\text{NiCl}_2 \cdot 6\text{H}_2\text{O}$ : 30 g/l;  $\text{CH}_2(\text{OH})\text{COOH}$ : 30 g/l;  $\text{COOH}(\text{CH}_2)_2\text{COOH}$ : 10 g/l;  $\text{NaF}$ : 3 g/l;  $\text{NaOH}$  to adjust the desired pH. The reducing agent was sodium hypophosphite, added to the bath as a concentrated solution of 500 g/l at constant rate. The temperature of the bath was 94°C. If the pH and the nickel concentration are kept constant during the entire deposition time, coatings of uniform phosphorus distribution are obtained (3). By adjusting the pH of the bath between 5.0 and 4.0, deposits with phosphorus contents between 3.5 and 11.4 w/o (weight per cent) are produced for an introduction rate of the hypophosphite of 0.05 M/hr. For the deposition at pH 5.0, the concentration of the glycolic acid has to be increased in regard to the concentration at lower pH to prevent the precipitation of the orthophosphite. At pH 5.0 the bath of the aforementioned composition was used and the nickel concentration was kept constant during the entire reaction time by addition of a solution containing: 500 g/l  $\text{NiCl}_2 \cdot 6\text{H}_2\text{O}$ , 500 cm<sup>3</sup> of a 56 w/o aqueous solution of glycolic acid completed to 1000 cm<sup>3</sup> with demineralized water. For lower pH, an aqueous solution of  $\text{NiCl}_2 \cdot 6\text{H}_2\text{O}$  at a concentration of 800 g/l was used. If the orthophosphite which precipitates during the deposition from the bath with normal concentration is dissolved in the bath at pH  $\approx$  4, the residue of dissolution in 7.8N hydrochloric acid at room temperature contains about 23 w/o phosphorus whereas it contains only 21 w/o if the solvent is at boiling temperature. As will be seen further on, the phosphorus content of the residue represents 21 w/o for both solution temperatures, providing that the orthophosphite precipitation in the bath is prevented.

Powdery samples were prepared by seeding the bath with palladium chloride. The powders used were previously ground and screened to obtain particles smaller than 37  $\mu\text{m}$  (400 mesh ASTM).

**Dissolutions and analyses.**—The dissolutions of electroless nickel are made in hydrochloric acid either at room temperature and slightly agitated, or at boiling temperature. The amount of hydrochloric acid used is twice as high as that required assuming that electroless nickel contains only nickel. The acid concentrations reported in this work always are the initial values. During the dissolution these concentrations may decrease by one half if all the powder is dissolved. For each run, the amount of electroless nickel used is 5 or 10 mM depending on the acid concentration.

After the test, the residue is filtered on Millipore,<sup>1</sup> then oxidized with the filter in nitric acid. The Millipore filters have been used because the as-plated deposit of electroless nickel consists of very small crystals. Moreover the oxidation of the residue with the filter is more practical and safer (avoiding any loss of substance) than the use of ordinary filters. By the Tyndall effect, we made sure that the filtration was efficacious, i.e., that no solid particles of colloidal size of the residue had passed the filter.

The nickel and the phosphorus are spectrophotometrically determined by the dimethylglyoxime oxidizing agent method (4) and the molybdenum blue method using the ascorbic acid as a reducing agent (5), respectively. The relative error is of  $\pm 1\%$  for each element.

We verified that, under our experimental conditions, no phosphine  $\text{PH}_3$  was produced, or in negligible amounts only.

The nickel and the phosphorus of both the residue and the filtrate of one particular test were determined in order to check the material balance. In further experiments the nickel and the phosphorus were determined only from the residue.

Moreover, we verified that the sum of the phosphorus plus the nickel corresponds to the weight of the residue. At this point, difficulties have arisen with the residues from electroless nickel with initial phosphorus contents of about 4 w/o. These residues, washed with demineralized water then dried in air at 70°C, present a difference from 10 to 17% between their weight and the sum nickel plus phosphorus analytically determined. The reason for this discrepancy is the oxidation of the residue during its drying. It could be shown that the oxidized precipitate can be reduced at 600°C in hydrogen. The undesired oxidation can be avoided by maintaining the residue during and after the filtration continuously under a film of water. The wet slurry is then transferred into an oven and

<sup>1</sup> Millipore Filter Corporation, Bedford, Massachusetts, (Type GS WP 04700, Mean Pore Size 0.22  $\mu\text{m}$ .)

\* Electrochemical Society Active Member.

dried at 700°C during 1 hr under vacuum, and cooled when still under reduced pressure. By the heat treatment the powder is recrystallized and its activity and ease to oxidize are decreased. For powders thus treated the analytical results for nickel and phosphorus add up to 100% of the weighed sample. The reactivity of the residue is unique for electroless nickel deposits containing about 4 w/o phosphorus. This phenomenon certainly comes from the following fact. After a certain time of deposition at pH 5.0, a spontaneous seeding of the bath occurs and leads to a deposition of much finer particles than those issuing from the palladium nucleates.

### Results

*As-plated electroless nickel.*—The dissolution of electroless nickel in hydrochloric acid is studied as a time dependent function with the acid concentration, the initial phosphorus contents of the deposited alloys, and the solvent temperature as parameters.

*Influence of the HCl concentration at room temperature.*—Figure 1 shows that for an initial phosphorus content of 3.26 w/o, the rate of dissolution at the beginning of the reaction is the faster the higher the concentration of the acid. After a certain time, a maximum of the rate of dissolution occurs for a concentration of 2.0N. For a concentration of 7.8N (azeotropic mixture,  $d = 1.12 \text{ g/cm}^3$ ), the curve is composed of two linear sections of different slope. Figure 2 shows the phosphorus content in the residue which increases rapidly with the dissolution time to approach a limiting value. After a certain time, the residue has the same composition as what is analyzed in the solution. Therefore the dissolution curve showing two intersecting straight lines (Fig. 1) can be explained by the successive dissolutions of two phases: first the nickel one and second a phase containing about 21 w/o phosphorus, that is to say a compound with the stoichiometry of the nickel phosphide Ni<sub>2</sub>P (20.87 w/o P). The linear extrapolation at time zero of the second section of the straight line (Fig. 1) yields the initial content of the phosphide phase present in the alloy. The calculated value obtained by supposing that all phosphorus initially present in the alloy is bonded to the nickel as the nickel phosphide Ni<sub>2</sub>P, indicated down at right of Fig. 1, agrees well with the extrapolated value.

*Influence of the initial phosphorus content of electroless nickel at room temperature.*—The results obtained with a sample containing 3.26 w/o phosphorus are reported on Fig. 1 and 2; Fig. 3 shows the same types of curves combined in a single figure for a sample containing 6.85 w/o phosphorus dissolved in 7.8N hy-

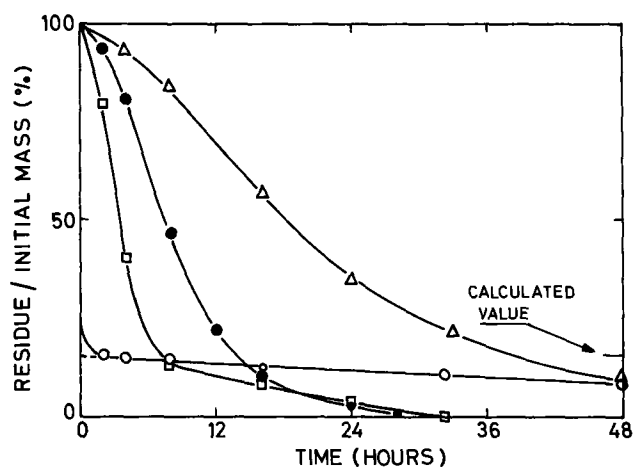


Fig. 1. Dissolution rate at room temperature (21°C) of as-plated electroless nickel with an initial phosphorus content of 3.26 w/o. ○ HCl 7.8N, □ HCl 2.0N, ● HCl 0.78N, △ HCl 0.20N.

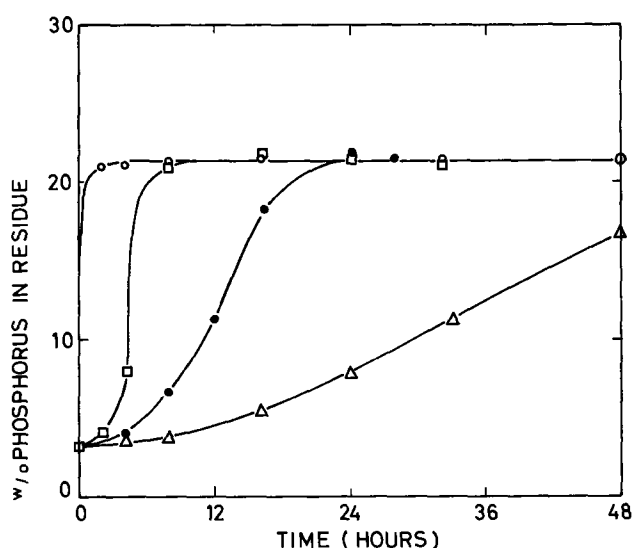


Fig. 2. Phosphorus content of the residue as a function of the time of dissolution at room temperature (21°C) for as-plated electroless nickel with an initial phosphorus content of 3.26 w/o. Legend same as Fig. 1.

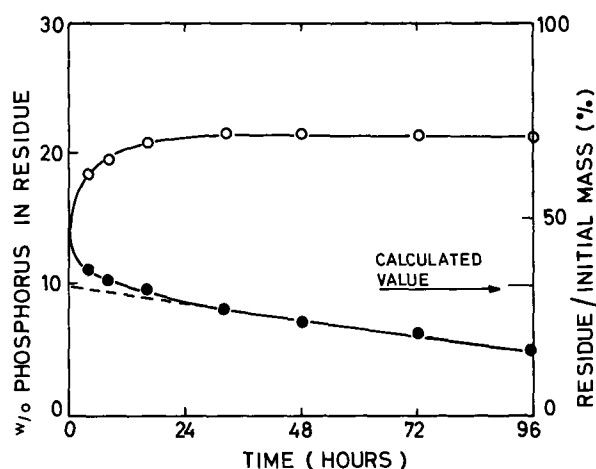


Fig. 3. Phosphorus content of the residue as a function of the time and dissolution rate of as-plated electroless nickel with an initial phosphorus content of 6.85 w/o at room temperature (21°C) in 7.8N HCl. ○ w/o P in residue, ● residue/initial mass in per cent.

drochloric acid. Again the limiting value for the phosphorus content in the residue reaches about 21 w/o corresponding to the nickel phosphide Ni<sub>2</sub>P. The extrapolated value pertinent to the initial Ni<sub>2</sub>P content present in the electroless nickel and drawn from the time when the phosphorus content of the residue varies no more, corresponds well to the calculated value for 6.85 w/o phosphorus, supposing the totality of the initial phosphorus is bonded to nickel at Ni<sub>2</sub>P.

For phosphorus contents higher than 8 w/o, the dissolution time is very long and the separation less efficacious than for alloys with lower phosphorus contents.

*Influence of the HCl concentration at boiling temperature.*—As an example the dissolution of electroless nickel of 12.5 w/o initial phosphorus content in boiling acid is reported. For acid concentration  $\leq 2N$  it is found that the higher the acid concentration, the more rapid the dissolution rate (Fig. 4). For a concentration of 7.8N, the dissolution rate is more rapid initially than for an acid concentration of 2.0N. The most efficacious separation of the two phases initially present in the as-plated alloy is realized at boiling temperature with an acid concentration of 7.8N. The



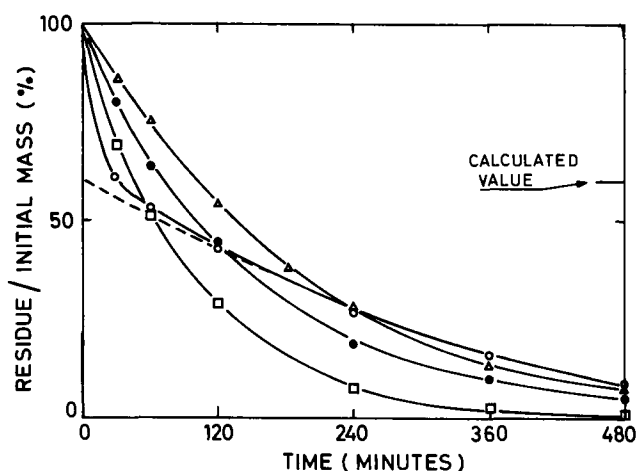


Fig. 4. Dissolution rate at boiling temperature of as-plated electroless nickel with an initial phosphorus content of 12.5 w/o. Legend same as Fig. 1.

same phenomenon was already observed with samples dissolved at room temperature (Fig. 1). The phosphorus content of the residue as a function of the time of dissolution shows that the limiting value reaches 20.9 w/o phosphorus which exactly corresponds to the stoichiometric composition of the nickel phosphide  $\text{Ni}_2\text{P}$  (Fig. 5). Again, the extrapolated value of the initial content of the  $\text{Ni}_2\text{P}$  phase corresponds to the calculated one, assuming that all the phosphorus is present as  $\text{Ni}_2\text{P}$ . In the case under discussion, the curve is not a segment of a straight line any longer hence the extrapolation has to be made from the time when the phosphorus content of the residue varies no more (upper curve of Fig. 6).

*Influence of the initial phosphorus content of electroless nickel at boiling temperature.*—Samples containing 8.78, 6.85, and 3.26 w/o phosphorus are studied in an acid concentration of 7.8N (Fig. 6, 7, and 8). For all these contents, the dissolution leads to the isolation of a  $\text{Ni}_2\text{P}$  phase. The extrapolated values of the initial contents of  $\text{Ni}_2\text{P}$  phase in the as-plated alloys agree well with the calculated values, assuming that all phosphorus is present as  $\text{Ni}_2\text{P}$ .

*Heat-treated electroless nickel.*—The method of dissolution in hydrochloric acid is applied to heat-treated electroless nickel, whose structure and chem-

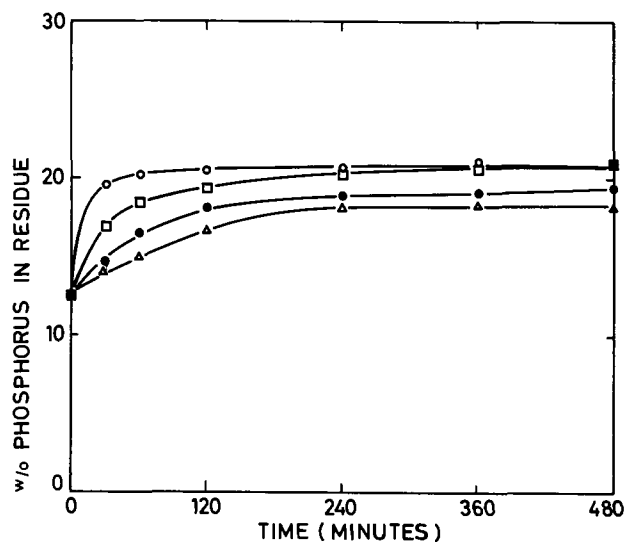


Fig. 5. Phosphorus content of the residue as a function of the time of dissolution at boiling temperature for as-plated electroless nickel with an initial phosphorus content of 12.5 w/o. Legend same as Fig. 1.

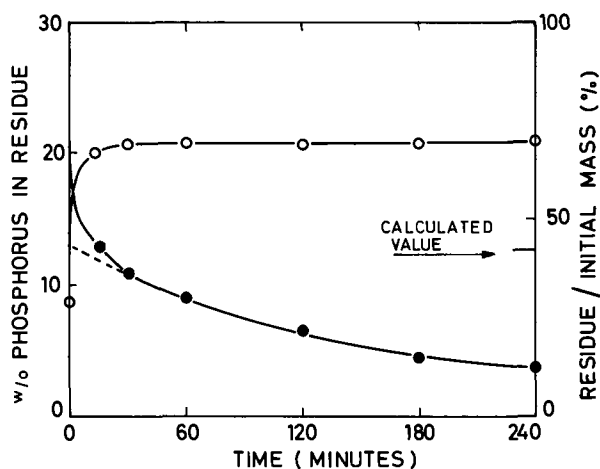


Fig. 6. Phosphorus content of the residue as a function of the time and dissolution rate of as-plated electroless nickel with an initial phosphorus content of 8.78 w/o at boiling temperature in 7.8N HCl. Legend same as Fig. 3.

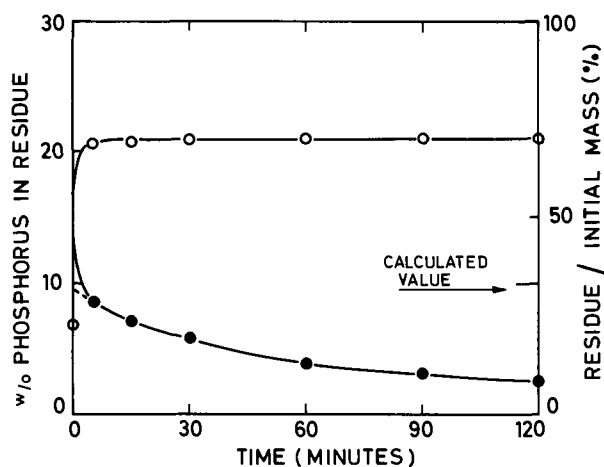


Fig. 7. Phosphorus content of the residue as a function of the time and dissolution rate of as-plated electroless nickel with an initial phosphorus content of 6.85 w/o at boiling temperature in 7.8N HCl. Legend same as Fig. 3.

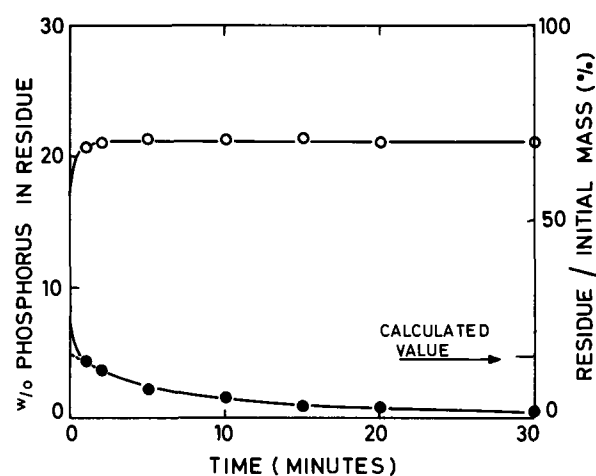


Fig. 8. Phosphorus content of the residue as a function of the time and dissolution rate of as-plated electroless nickel with an initial phosphorus content of 3.26 w/o at boiling temperature in 7.8N HCl. Legend same as Fig. 3.

ical composition are well established. The heat treatment was conducted under a vacuum better than  $10^{-3}$  Torr for 5 hr, at  $800^\circ\text{C}$ .

Samples containing 3.71, 8.78, and 12.5 w/o phosphorus are dissolved in 7.8N hydrochloric acid (Fig. 9, 10, and 11). For each of these phosphorus contents,

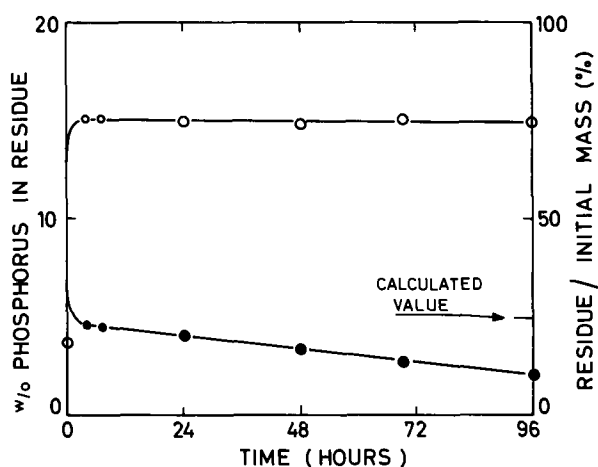


Fig. 9. Phosphorus content of the residue as a function of the time and dissolution rate of heat-treated electroless nickel with an initial phosphorus content of 3.71 w/o at room temperature (24°C) in 7.8N HCl. Legend same as Fig. 3.

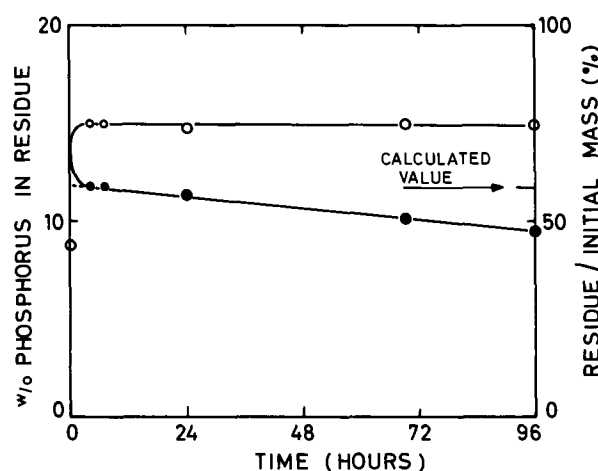


Fig. 10. Phosphorus content of the residue as a function of the time and dissolution rate of heat-treated electroless nickel with an initial phosphorus content of 8.78 w/o at room temperature (24°C) in 7.8N HCl. Legend same as Fig. 3.

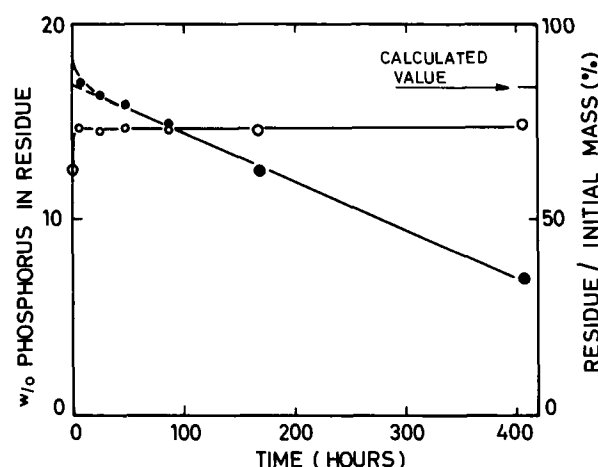


Fig. 11. Phosphorus content of the residue as a function of the time and dissolution rate of heat-treated electroless nickel with an initial phosphorus content of 12.5 w/o at room temperature (24°C) in 7.8N HCl. Legend same as Fig. 3.

the dissolution leads to the isolation of a phase containing about 15 w/o phosphorus in good agreement with the stoichiometry of the nickel phosphide Ni<sub>3</sub>P (14.96 w/o P). The extrapolated values of the initial contents of the Ni<sub>3</sub>P phase in the heat-treated electroless nickel correspond well to the calculated values,

supposing all the phosphorus is present as Ni<sub>3</sub>P. These results confirm those obtained by the x-ray method (1).

### Discussion and Conclusions

For all the phosphorus contents of the electroless nickel studied, and independently of the temperature of dissolution, a nickel phosphide phase whose stoichiometry corresponds to Ni<sub>2</sub>P could be isolated. In as-plated electroless nickel, nickel phosphide Ni<sub>2</sub>P is best separated from nickel by using 7.8N hydrochloric acid as a solvent, for low phosphorus alloys at room temperature, and for high phosphorus alloys at boiling temperature. The Ni<sub>2</sub>P content of the as-plated electroless nickel accounts for all the phosphorus present in the samples.

The identification of the nickel phosphide Ni<sub>2</sub>P as such is the residue of dissolution of as-plated electroless nickel was also attempted by x-ray diffraction analysis and DTA.

The x-ray diffraction study of the residue of dissolution leads to the results of Table I. The small number of lines observed and the accuracy of their position for the nonheat-treated residue do not allow one to assert the presence of Ni<sub>2</sub>P only. The x-ray diagram obtained from a sample annealed for 24 hr at 800°C in hydrogen confirms the previously found line positions for the nonheat-treated residue. It reveals however an additional number of diffraction lines of Ni<sub>2</sub>P as well as some of Ni<sub>12</sub>P<sub>5</sub> which is formed during the heat treatment. The positions of the lines measured on the residue of dissolution and the calculated values of Ni<sub>2</sub>P agree within 1%. The relative intensities of the observed values on the residue compare reasonably well with those tabulated. Thus, the residue of dissolution of as-plated electroless nickel consists of Ni<sub>2</sub>P; it contains no nickel and no other nickel phosphide.

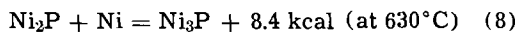
A DTA curve of the residue of dissolution does not show any deviation. An as-plated electroless nickel alloy containing about 8 w/o phosphorus was reconstituted by mechanically mixing a residue of dissolution and a carbonyl-nickel powder, then studied by DTA. The exothermic energy evolved between 520° and 640°C corresponds to about 5.7 kcal/mole Ni<sub>3</sub>P, the reaction product being identified as Ni<sub>3</sub>P. In a previous work (1) a DTA study of electroless nickel revealed two reaction areas in the energy vs. temperature diagram: one below 300°C, the other above 300°C. The reaction heat of the former was called Q<sub>1</sub>, that of the latter Q<sub>2</sub>. The heat Q<sub>2</sub> = 5.9 kcal/mole Ni<sub>3</sub>P is proportional to the phosphorus content of the electroless nickel. Q<sub>1</sub> passes through a maximum at about 8 w/o phosphorus and vanishes thereafter at a concentration higher than 10 w/o. The total heat of reaction Q<sub>1</sub> + Q<sub>2</sub> for alloys with less than 8 w/o phosphorus is 8.9 kcal/mole Ni<sub>3</sub>P.

Table I. Comparison of observed line spacings and intensities of residue against calculated values of Ni<sub>2</sub>P

d (Å) measured on residue	d (Å) measured on residue heat-treated 24 hr, 800°C	d (Å) Ni <sub>2</sub> P Pearson (6)	I/I <sub>0</sub> measured on residue	I/I <sub>0</sub> measured on residue heat-treated 24 hr, 800°C	I/I <sub>0</sub> Ni <sub>2</sub> P ASTM (7)	Reflection hkl
2.214	2.217	2.216	100	100	100	111
2.028	2.031	2.031	85	50	80	201
1.914	1.918	1.919	69	40	80	120
—	1.692	1.693	—	28	70	300/002
—	1.670	1.670	—	15	40	121
1.39*	1.408	1.409	24	20	40	310
—	1.300	1.300	—	40	40	311
1.26*	1.271	1.270	48	67	60	212
1.18*	1.197	1.199	30	55	60	302
—	1.188	1.189	—	24	—	401
—	1.101	1.102	—	100	88	231
—	1.083	1.083	—	20	40	132

\* Less accurate measurement.

The heats  $Q_1$  and  $Q_2$  obtained below 400°C are difficult to compare with the value reported in the present work which was measured between 520° and 640°C, since specific heat data of nickel phosphides are not available. However, the energy of 5.7 kcal/mole  $Ni_3P$  evolved during heating of a mixture of  $Ni_2P$  plus nickel corresponds to the heat previously called  $Q_2$ , i.e., 5.9 kcal/mole  $Ni_3P$ . The energy of the reaction



more or less corresponds to the heat previously called  $Q_1 + Q_2$ , i.e., 8.9 kcal/mole  $Ni_3P$ .

The comparison of results of the dissolution rates with those obtained by DTA (1) leads to the following comments. The DTA study (1) revealed two reaction areas for phosphorus contents below 10 w/o while only one such area was observed above this concentration. According to the results of the present study showing that the as-plated electroless nickel has the same qualitative composition for any phosphorus content, the two reaction areas previously observed for phosphorus contents below 10 w/o could eventually correspond to the formation of  $Ni_5P_2$  from  $Ni_2P$  and of  $Ni_3P$  from  $Ni_5P_2$ . This hypothesis would not explain the case of phosphorus contents higher than 10 w/o. In order to verify this supposition, samples containing 3.26, 7.32, and 12.5 w/o phosphorus, respectively, were analyzed after heating up to 285°C under the same conditions as those used in the DTA study, i.e., a heating rate of 2°/min. This temperature delimits the two reaction areas. After dissolution in 7.8N hydrochloric acid at boiling temperature, the three samples lead to a residue with the stoichiometry of  $Ni_2P$ . These very samples further investigated under the same experimental conditions after heating up to a temperature high enough to allow a complete reaction, i.e., 500°C, leave a dissolution residue whose stoichiometry corresponds to that of  $Ni_3P$ . The intermediate state of the  $Ni_5P_2$  does not represent any one of the two reaction areas and, therefore, cannot be isolated by controlling merely the temperature of the heat treatment.

As a consequence, the heat previously called  $Q_2$  which is proportional to the phosphorus content of the electroless nickel may correspond to the reaction:  $Ni_2P + Ni = Ni_3P$ , though the measured energy is only 5.9 kcal/mole  $Ni_3P$ , i.e., about 70% of that indicated by Weibke and Schrag (8). This hypothesis is supported by the fact that the energy evolved during the rise of temperature of a reconstituted electroless nickel alloy from  $Ni_2P$  plus nickel leads to a value close to the heat  $Q_2$ . The discrepancy between our energy result and that of Weibke and Schrag can possibly be explained by the fact that the heats of formation cannot be compared at the same temperature (see above). The heat previously called  $Q_1$  could be explained by the reaction of a little amount of phosphorus as a solid solution in the nickel producing a nickel phosphide  $Ni_2P$  or/and  $Ni_3P$ . The maximum

energy of the heat  $Q_1$  which occurs for phosphorus contents of about 8 w/o, could correspond to a free phosphorus content <0.5 w/o.

The accuracy of the analytical results concerning the  $Ni_2P$  phase content in the as-plated alloys would allow the presence of a little amount of phosphorus not bonded to nickel. The presence of elementary phosphorus in the freshly prepared residue of dissolution, in amounts more important than only traces, cannot be measured either by reaction with sodium hydroxide, or by solubility in absolute alcohol. In carbon disulfide, the maximum solubility observed in a dissolution residue of electroless nickel with an initial phosphorus content of 4.41 w/o in 7.8N hydrochloric acid at room temperature is <0.02 w/o phosphorus in regard to the initial mass of electroless nickel. Therefore it might be concluded that the as-plated electroless nickel contains only very little phosphorus in the elementary state, the rest being bonded to nickel as nickel phosphide  $Ni_2P$ .

The temperature at which the electroless nickel is deposited, in this study at 94°C, has perhaps an influence on the nature of the chemical bond between phosphorus and nickel in the as-plated state. This parameter has not been investigated.

#### Acknowledgment

The authors wish to thank Professor P. Dinichert, Director of the L.S.R.H. for his advice and interest in this work and permission to publish this paper. They also thank Mr. J.-P. Renaud and Dr. M. Delaloye for helpful discussions and for providing facilities. They acknowledge the valuable assistance of Mr. J. C. Jaquet in the x-ray analysis and of Mr. A. Verbay in differential thermal analysis.

Manuscript received Nov. 8, 1967; revised manuscript received Jan. 22, 1968.

Any discussion of this paper will appear in a Discussion Section to be published in the December 1968 JOURNAL.

#### REFERENCES

1. J.-P. Randin, P. A. Maire, E. Saurer, and H. E. Hintermann, *This Journal*, **114**, 442 (1967).
2. A. H. Graham, R. W. Lindsay, and H. J. Read, *ibid.*, **112**, 401 (1965).
3. J.-P. Randin and H. E. Hintermann, *Plating*, **54**, 523 (1967).
4. E. B. Sandell, "Colorimetric Determination of Traces of Metals," p. 671, Interscience Publishers, New York (1959).
5. L. Duval, *Chim. Anal.*, **45**, 237 (1963).
6. W. B. Pearson, "A Handbook of Lattice Spacings and Structures of Metals and Alloys," Vol. 2, p. 1132, Pergamon Press, New York (1967).
7. ASTM X-Ray Powder Data File, ASTM Special Technical Publication 48-J, 3-0953 (1960).
8. F. Weibke and G. Schrag, *Z. Elektrochem.*, **47**, 222 (1941).

# Electroless Nickel Plating on Silicon

Hitoo Iwasa, Masami Yokozawa, and Iwao Teramoto

Research Laboratory, Matsushita Electronics Corporation, Takatsuki, Osaka, Japan

## ABSTRACT

In the study of electroless Ni plating of Si wafers with p-n junctions using conventional solutions, a pronounced difference in plating rate between p- and n-type surfaces is observed. Further experiments show that rate difference probably should not only be attributed to the photovoltaic effect generated at the p-n junctions but also to the electronegativity difference between p- and n-type Si. The latter effect can be changed by addition of such material as  $\text{NH}_4\text{SCN}$  or  $2\text{NH}_4\text{-EDTA}$  to the plating solution. Whereas  $\text{SCN}^-$  addition increases the rate difference, EDTA addition decreases it. This fact which can be put to practical use gives an extra support for the explanation given above.

Electrical connections to Si transistors up to now are often made by Au-Al thermocompression bonds. Another technique uses a simple method: electroless Ni plating followed by soldering. Advantages are the excellent chemical and mechanical properties of the connections. Also the cost of the processing is much lower than of the thermocompression bonding technique. However, this latter technique is not now widely used.

Since Sullivan and Eigler (1) first applied the electroless Ni plating to Si, one of the difficulties often found for actual Si devices has been the difference in plating rate between adjacent p- and n-type surfaces. Silverman (2) reported that, during Au plating by autocatalytic reduction, the difference in plating rate between adjacent p- and n-type Si surfaces was changed by strong illumination owing to the created photovoltaic effect at the p-n junction. We observed a similar effect in the electroless Ni plating as have other observers.

The theory of electroless plating has not been well defined yet, although many explanations have been proposed. For example, Gutzeit's explanation (3), based on the autocatalytic reduction of Ni ions, may be clear for the acidic solution, but in an alkaline solution hypophosphite is spontaneously oxidized at an elevated temperature. Moreover, the effect of photovoltage on plating rate can hardly be explained by the argument that a nickel ion is reduced only by an atomic hydrogen.

One of the most promising models for the process in an alkaline bath (4) may be that in which the reactions involved are divided into anodic and cathodic reactions, forming many local cells at the interface between substrate and solution, as indicated in Fig. 1. The different reaction occurring can be summed up as follows:

1. Diffusion of reactants to the interface

2. Oxidation of  $\text{H}_2\text{PO}_2^-$  (anodic)



3. Migration of the electrons in the substrate

4. Reduction of  $\text{Ni}^{++}$  and  $\text{H}^+$  (cathodic)



5. Diffusion of reaction products from the interface into the solution. Similar oxidation and reduction processes may occur if instead of electrons, holes move in the opposite direction in the substrate. The electron (or hole) migration in the substrate and the transfer through the interface will be determined by: (a) electron concentration within the substrate; (b) thin oxide layers on the substrate; (c) photovoltage at the

p-n junctions; (d) electronegativity of the substrate. If electron (or hole) migration determines the deposition rate, one can easily imagine that this rate will be different for adjacent p- and n-type substrate materials. For this reason we studied the possibility of diminishing the difference in plating rate by transferring the rate-determining step from the migration in the substrate to one of the other steps of the reaction occurring inside the solution.

Results of experiments carried out to analyze the effect of each of these factors are reported below.

## Experimental Procedures

The composition of the plating bath used in the present experiment is substantially the same as that of the Brenner solution (5), that is

$\text{NiCl}_2 \cdot 6\text{H}_2\text{O}$	30 g/l
$\text{NH}_4\text{Cl}$	50 g/l
$(\text{NH}_4)_2\text{HC}_6\text{H}_5\text{O}_7$	65 g/l
$\text{NaH}_2\text{PO}_2 \cdot \text{H}_2\text{O}$	10 g/l

The bath is heated to a temperature of  $90^\circ\text{C}$ , at which temperature about 200 cc of  $\text{NH}_4\text{OH}$  is added to 1000 cc of the plating solution; the bath temperature is then elevated to  $95^\circ\text{C}$ , at which temperature the Si sample is immersed in the bath for 30 sec. Ni films plated in this way were 1000-2000Å thick.

Si wafers with polished surfaces were used as samples; they were cleaned by etching slightly and rinsing with distilled water and methyl alcohol. Then the wafers were stored in isopropyl alcohol. Prior to plating, the wafer was dipped in  $\text{NH}_4\text{F}$  solution (50%) for 30 sec and again rinsed thoroughly with methyl alcohol. The whole process was carried out without drying the wafer surfaces until the plating was completed to protect the Si surfaces from oxidation and staining.

The Ni film thickness for thick films was measured by the conventional interference method. For thin films the autoradiographic method was applied by making use of radioactive  $\text{Ni}^{63}$  in the plating bath.

Electrode potentials were measured using a saturated calomel electrode as the standard electrode. The

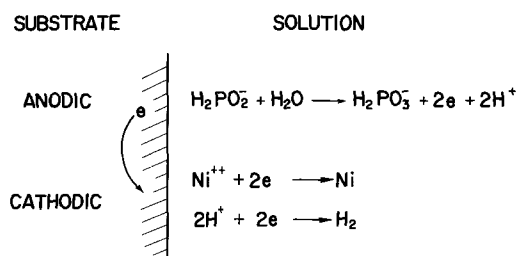


Fig. 1. Schematic representation of the "local cell" model

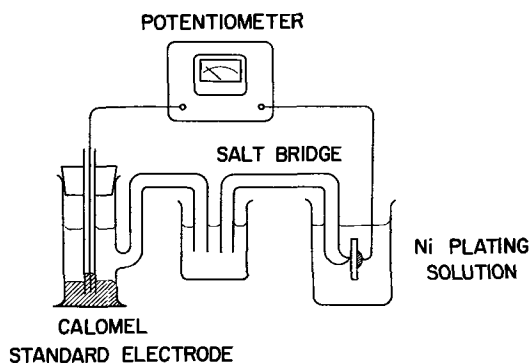


Fig. 2. Experimental arrangement for measuring electrode potentials.

schematic arrangement for this measurement is shown in Fig. 2; the electrical connection on the back side of the Si wafer was made by means of Ni plating and soldering.

The reduction potential of  $\text{Ni}^{++}$  in the plating solution was estimated by measuring the current-voltage characteristics of the solutions without the hypophosphite. The current through two Pt plates with an area of  $1 \text{ cm}^2$ , placed  $1 \text{ cm}$  apart from each other, as a function of applied voltage was traced on an X-Y recorder.

### Results

**Migration of charge carriers in the Si substrate.—Thin oxide films on silicon.**—A p-type surface is more likely covered with an oxide film than an n-type surface. Plating on a p-type surface was hardly possible without a cleaning treatment to remove the oxide. Cleaning the surface with HF or  $\text{NH}_4\text{F}$  solution or adding  $0.1$  to  $0.2 \text{ mol/l}$  of  $\text{F}^-$  to the plating bath made the plating reproducible (6), and Ni film was easily plated even on p-type surface. However, any cleaning treatment could not eliminate the difference in plating rate between p- and n-type surfaces.

**Electron concentration in silicon.**—If electrons would act as charge carriers in the substrate, the plating rate on p-type should be much smaller than that on n-type Si. However, a rather small difference in plating rate was found between separated p- and n-type surfaces.

Strong illumination on semiconductors generates electron and hole pairs and makes the conduction type intrinsic. The plating rate on p-type silicon was not affected by illumination, showing that the electron concentration above a certain value has only small effect on the plating rate.

**Photovoltage at the p-n junction.**—With illumination on a p-n junction the plating rate on adjacent p- and n-type materials proved to be different. The difference increases with an increase of illumination density, suggesting a contribution of the photovoltaic effect. The plating rate on the n-type material was found to be higher than on the adjacent p-type material. However, an appreciable small difference was still found under weak room light.

**Electronegativity of silicon.**—The electronegativity of p-type Si is greater than that of n-type Si. It seems feasible that the electronegativity difference between p- and n-type Si causes a difference in rate of electron transfer from Si to  $\text{Ni}^{++}$  and consequently gives rise to a difference in plating rate.

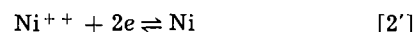
Summarizing we may say that the difference in plating rate observed between adjacent p- and n-type surfaces as far as the substrate is concerned is due to the photovoltage generated at the p-n junction, and possibly to the difference in electronegativity between p- and n-type Si.

**Rate limitations imposed by the solution.—Effect of Ni concentration.**—The concentration of  $\text{NiCl}_2$  in the

plating solutions was reduced. It was found that the ratio of the plating rates on adjacent p- and n-type materials changed only slightly with  $\text{Ni}^{++}$  concentration.

**Effect of additives in the plating solution.**—The ammonium salt of EDTA was added to the plating solution. The observed plating rate and its ratio on adjacent p- and n-type materials are shown in Fig. 3 and Fig. 6, respectively. The ratio increased to unity with increasing concentration of EDTA. The plating rate on p-type showed a maximum at an EDTA concentration of  $5 \text{ g/l}$ , whereas on n-type material it was constant. Further addition of EDTA resulted in a remarkable decrease in plating rate, and no films were grown at an EDTA concentration above  $10 \text{ g/l}$ , corresponding to one third of  $\text{Ni}^{++}$  concentration; film growth stopped completely. Figure 4 represents autoradiographs of plated Ni: (a) without EDTA and (b) with EDTA ( $6 \text{ g/l}$ ). Figure 5 shows the thickness of films on both types of the p-n junction (a) without EDTA, (b) with EDTA ( $6 \text{ g/l}$ ) and (c) with EDTA ( $10 \text{ g/l}$ ).

The electrode potential of the half-cell of the system



was measured. Addition of EDTA to this system made the potential more negative, as shown in Fig. 7.

The relative deposition voltages of Ni were obtained from the I-E characteristics of different  $\text{H}_2\text{PO}_2^-$ -free solution. The results shown in Fig. 8 indicate a tendency similar to those based on the half-cells in solutions with  $\text{H}_2\text{PO}_2^-$ .

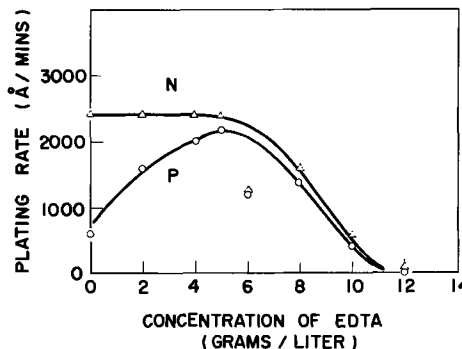


Fig. 3. Plating rate on p- and n-type Si as a function of concentration of EDTA added to the solution.

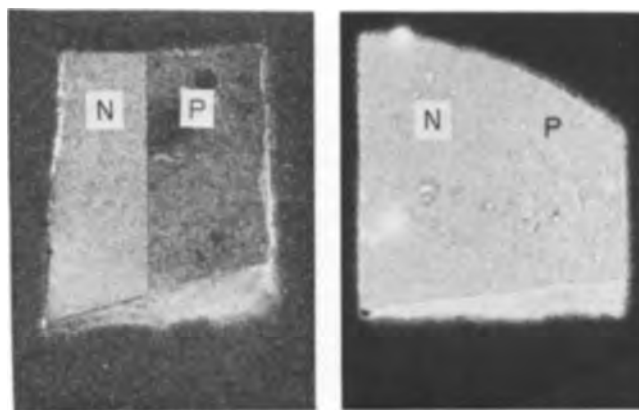


Fig. 4. Autoradiographs of plated Ni on Si: (a) with the EDTA-free solution, (b) with the EDTA-added solution ( $6 \text{ g/l}$ ).

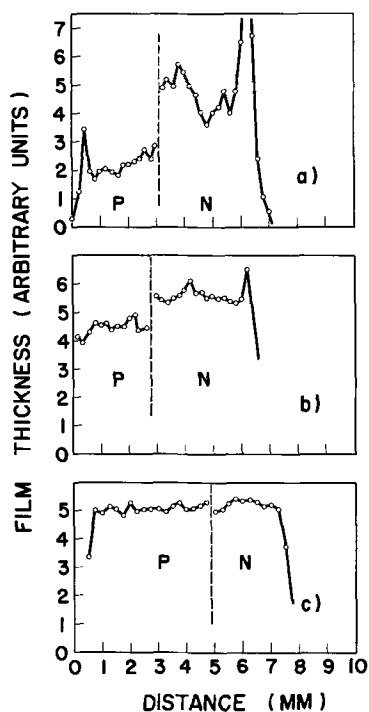


Fig. 5. Relative thickness of Ni films plated on p- and n-type Si: (a) with the EDTA-free solution, (b) with the EDTA-added solution (6 g/l), (c) with the EDTA-added solution (10 g/l).

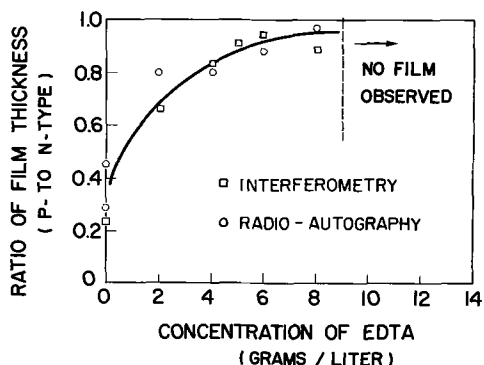


Fig. 6. Thickness ratio of Ni films plated p- and n-type Si as a function of concentration of EDTA added to the solution.

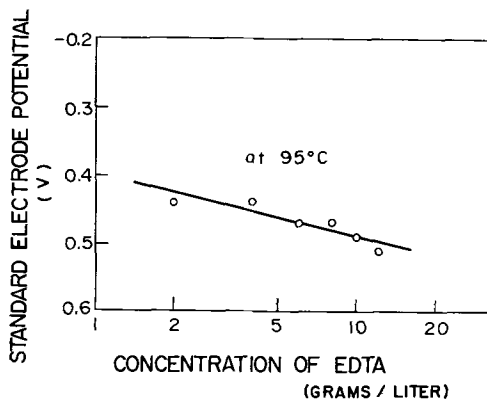


Fig. 7. Electrode potential as a function of concentration of EDTA added to the solution.

Ni-EDTA<sup>++</sup> gives a larger negative value to the electrode potential than Ni(NH<sub>3</sub>)<sub>4</sub><sup>++</sup>. One may expect that the addition of SCN<sup>-</sup> to the plating solution will cause an opposite effect to EDTA, and that the difference in plating rate will increase with increasing SCN<sup>-</sup> concentration. Figure 9 shows a photograph

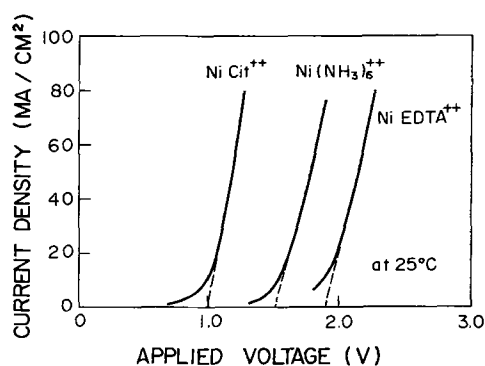


Fig. 8. Dependence of the electrode potential on complex formers, citrate, NH<sub>3</sub>, and EDTA, added to the solution.

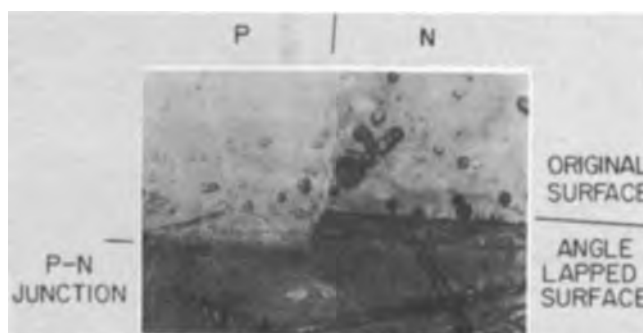


Fig. 9. Photograph of the plated Ni with the SCN<sup>-</sup>-added solution.

of an SCN<sup>-</sup> solution; the difference was remarkably enhanced and the p-n junction was plainly revealed.

### Discussion

The difference in plating rate of electroless nickel between p- and n-type surfaces under strong illumination can be attributed substantially to the photovoltage generated at p-n junctions. However, this may not be the only cause for the rate difference, because the appreciable difference was observed in plating rate even under weak room light, where the photovoltage is negligibly small. Two different causes, as previously described, would be considered. One concerns the surface condition of substrate silicon. The surface of silicon is usually covered with thin oxide layers, which impede the plating reaction. However, it was found that careful cleaning can prevent the effect of oxide. The alternative cause is due to redox potential of the substrate. With some exceptions, electroless nickel plating is more easily applied to less electronegative materials, being consistent with the result observed on p- and n-Si. Thus, both the photovoltage generated at p-n junctions and the electronegativity difference between p- and n-substrates may affect the plating rate in a similar way. The effect of potential difference between p- and n-types, however, will appear relatively to the potential of nickel ions. When the potential required for reduction of nickel ions is larger than the potential difference between the substrates, the plating rates on both surfaces are small and consequently the rate difference becomes negligible in comparison with the plating rates.

From this view point, the effect of addition of EDTA can be explained as follows. By addition of EDTA salt to the plating solution, the nickel complex ion changes its form from Ni(NH<sub>3</sub>)<sub>4</sub><sup>++</sup> to Ni-EDTA<sup>++</sup> making the potential more negative (or less noble). The potential difference between p- and n-type surfaces relative to the reduction potential of the complex ions apparently decreases, resulting in diminished difference in plating rate.

On the contrary, Ni(SCN)<sub>2</sub> formed by addition of SCN salt makes the potential more positive. This gives rise to faster plating and enhanced rate difference between p- and n-substrates.

### Conclusion

It is probable that the difference in plating rate between adjacent p- and n-type surfaces may be attributed to the electronegativity difference between p- and n-type Si as well as to the photovoltage generated at p-n junctions. This difference can be suppressed by addition of EDTA to the plating solution. The stable Ni-EDTA<sup>++</sup> complex then formed in the solution elevates the redox potential to such a high value that the electronegativity difference and the photovoltage will have a negligible effect.

Manuscript received Feb. 23, 1967; revised manuscript received Nov. 13, 1967.

Any discussion of this paper will appear in a Discussion Section to be published in the December 1968 JOURNAL.

### REFERENCES

1. M. V. Sullivan and J. H. Eigler, *This Journal*, **104**, 226 (1957).
2. S. J. Silverman and D. R. Benn, *ibid.*, **105**, 170 (1958).
3. G. Gutzeit and G. Goldstein, *ibid.*, **104**, 104 (1957).
4. S. Ishibashi, *J. Metal Finishing Soc. Japan*, **12**, 447 (1961).
5. A. Brenner, *Metal Finishing*, **52**, [11] 68 (1954).
6. S. L. Matlow and E. L. Ralph, *Solid State Electronics*, **2**, 202 (1961).

## The Measurement of Diffusion Coefficients in Binary Liquid Metals with a Concentration Cell

John B. Edwards,<sup>†</sup> Edward E. Huccke\*  
and Joseph J. Martin

Department of Chemical and Metallurgical Engineering, The University of Michigan, Ann Arbor, Michigan

### ABSTRACT

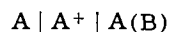
An experimental technique has been developed for measurement of diffusion coefficients in liquid metals. A liquid metal concentration cell was designed to measure cell potential and discharge current while insuring that diffusion in the cathode was the over-all rate limiting process. The technique was used to obtain diffusion coefficients in three binary liquid metal systems; potassium-mercury, sodium-lead, and sodium-tin.

Unlike the study of diffusion in aqueous and in organic systems, it is not possible to use optical methods to study diffusion in liquid metals. The principal advantage of optical methods is that it is possible to determine the rate at which material enters the diffusion path. From this rate, anomalies such as disturbances during the initial stages of the experiment can be detected. A number of methods have been developed to measure diffusion coefficients for liquid metals in which only the over-all concentration change and/or the total quantity of diffusate is accessible. One of the authors has presented an extensive review and critique of these methods (1).

In this paper the development of a new technique for measuring diffusion coefficients of binary liquid metal systems is described. A liquid metal concentration cell with a capillary cathode is discharged at constant potential. The diffusion coefficients are calculated from the cell potential and discharge current. The unique contribution of this technique is that it allows measurement of the rate at which diffusate enters the diffusion path, and thus, detection of anomalies in the diffusion process. The technique has been utilized for measurement of coefficients in three binary systems; potassium-mercury, sodium-lead, and sodium-tin.

### Experimental

**Technique.**—A liquid metal concentration cell may be constructed with a pure alkali metal anode, A, a fused salt electrolyte containing cations of A<sup>+</sup> only, and an alloy of A with a heavier metal B. The cell is written as



For a given metal couple, the reversible (open circuit) potential of such a cell, theoretically depends

<sup>†</sup> Electrochemical Society Student Member.  
\* Electrochemical Society Active Member.

only on its temperature and the atomic fraction of A in the cathode alloy at the cathode-electrolyte interface. When current flows, reversible conditions no longer exist and the cell potential differs from its equilibrium value due to resistance, concentration and activation polarization.

A concentration cell of this type, together with the appropriate solution of Fick's second law, may be utilized to determine the diffusion coefficient of A through the alloy A(B) if the following conditions are met. First, the cell design must insure that diffusion of A through A(B) in the cathode is rate controlling. Second, the relationship between discharge current and quantity of alkali metal transferred from anode to cathode must be known. Third, the relationship between reversible cell potential and cathode composition must be known.

Table I summarizes the liquid metal systems investigated, the fused salt electrolytes used, and the temperature ranges studied.

Thermodynamic data are available for each of the metal couples (2) from which the equilibrium cell potential may be calculated as a function of cathode composition. Concentration units of gram atoms alkali metal per cubic centimeter of alloy were used. Alloy densities were obtained from (3, 4) for potassium amalgams. For the sodium-lead and sodium-tin al-

Table I. Summary of the liquid metal systems

Diffusion couple	Anode	Electrolyte	Cathode	Temp. °K
K in K (Hg)	K	KOH-KI-KBr	K (Hg)	500, 550, 600
Na in Na (Pb)	Na	NaOH NaI-NaCl	Na (Pb)	625, 903
Na in Na (Sn)	Na	NaOH NaI-NaCl	Na (Sn)	625, 903

loys, experimental data were not available, and densities were estimated by linear interpolation of the pure component densities on a mole fraction basis.

High current efficiencies with respect to  $A^+$  were obtained by the use of discharge potentials well below the decomposition potentials of the fused salts, and by selection of salts with cations of  $A^+$  only. The ionization potentials of sodium and potassium reveal that oxidation states greater than +1 did not occur. The solubility of alkali metals in the fused salts over the temperature ranges investigated was not large enough to affect the current efficiencies appreciably. The current densities obtained in this investigation were less than 1 amp/cm<sup>2</sup>, while exchange currents in metal-metal ion systems are often 1-4 amp/cm<sup>2</sup>. Therefore, activation polarization was assumed not to be rate limiting. The high specific conductivities of the molten salts gave low values of resistance polarization. Finally, the capillary cathode geometry was used to insure that concentration polarization of A diffusing through A(B) was the over-all limiting step during cell discharge.

**Apparatus.**—A typical diffusion cell is shown in Fig. 1. To preclude phase inversions the most dense phase must be located on the bottom and the least dense on the top. The cathode compartment was constructed from quartz tubes. These were examined under a binocular microscope, only sections with uniform bore were selected. The activity of the alkali metal in the cathode was lowered by the heavy metal addition, and the alloy did not attack the quartz. The anode compartment which was exposed to pure alkali metal was constructed of alumina. A new cell was constructed for each experiment.

The lead or tin was heated in a graphite crucible to remove surface oxides and dissolved gases. The sodium was weighed under dry box conditions and transferred under n-pentane with the lead or tin to the furnace. The heated charge was stirred to assure uniform composition after which the cathode compartments were filled by submerging them in the alloy and applying a positive pressure. The potassium amalgams were pre-

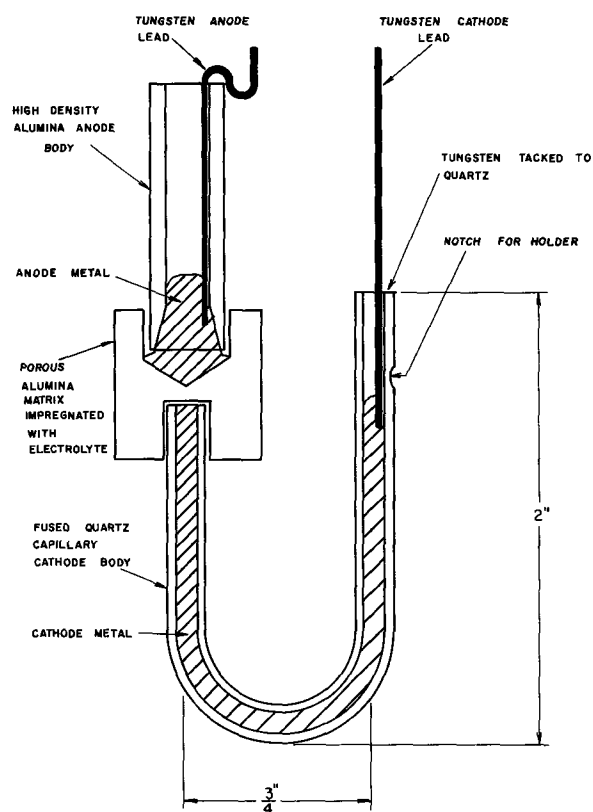


Fig. 1. Diffusion cell

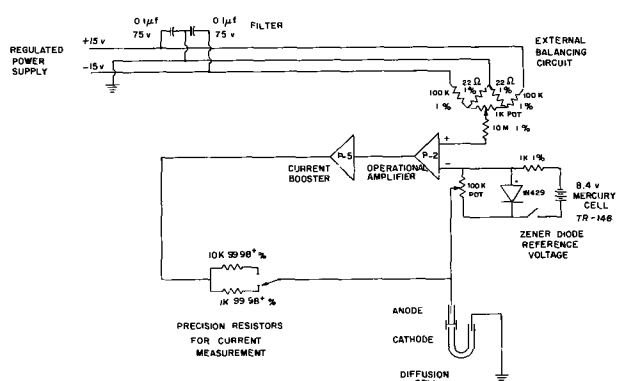


Fig. 2. Potentiostat circuit

pared in quartz rather than graphite crucibles since potassium readily forms lamellar compounds with graphite (6). The fused salts were prepared from reagents weighed in the dry box and heated in graphite crucibles. The matrices were impregnated by immersing them in the melt and pressurizing with argon. Each cell was assembled under dry box conditions.

Constant discharge potentials were obtained with a voltage follower circuit as shown in Fig. 2. This was constructed from a differential input operational amplifier and a current booster amplifier. This negative feedback circuit was capable of handling discharge currents to 20 ma. A Zener reference source was used to select the discharge potential. The discharge current was determined by measuring the potential drop across a precision resistor in the feedback circuit.

The 3-in. diameter furnace had three independently controlled windings. Power to the furnace was regulated with a proportional controller such that it was possible to maintain a stable gradient of 0.5°C/in. in the central portion of the furnace. The Vycor sleeve used to contain the cell was evacuated to less than a micron before pressurizing with high-purity argon.

**Mathematical formulation.**—For the case where concentration polarization of the cathode is rate limiting, the capillary may be treated as a one-dimensional semi-infinite diffusion path. Fick's second law applies.

$$\frac{\partial C}{\partial t} = D \frac{\partial^2 C}{\partial x^2} \quad [1]$$

If the cathode-electrolyte interface is the origin and the cell is discharged at constant potential, the concentration profile in the cathode at any point  $x$  and time  $t$  is (7)

$$C(x,t) = \left[ C_0 + (C_s - C_0) \operatorname{erfc} \frac{x}{2\sqrt{Dt}} \right] \quad [2]$$

where  $C_0$  and  $C_s$  are, respectively, the initial cathode alloy concentration and the concentration at the cathode-electrolyte interface for time greater than zero. The flux  $J(0,t)$  at the interface is obtained by differentiating Eq. [2]

$$J(0,t) = (C_s - C_0) \left( \frac{D}{\pi t} \right)^{1/2} \quad [3]$$

In this solution it is assumed that the diffusion coefficient is independent of concentration and that no volume changes occur during diffusion. Experimentally the error due to these assumptions is minimized by using small concentration intervals ( $C_s - C_0$ ).

At small times Eq. [3] predicts  $J(0,t) \rightarrow \infty$  as  $t \rightarrow 0$ . However, for small times the resistance polarization in the electrolyte becomes small compared to the over-all cell potential. This occurs as the concentration gradient in the cathode becomes progressively smaller.

The one-dimensional treatment above implies the cathode-electrolyte interface is planar and perpendicular



ular to the axis of the capillary. Surface energy will lead to a nonplanar interface. A contact angle of  $127^\circ$  has been reported for a lead drop on a quartz surface covered with KCl-NaCl (8). Few data on other systems are available. Based on the single result for the lead-salt couple, the cathode-electrolyte interface would tend to be convex with respect to the cathode alloy. The perturbations introduced by a nonplanar interface were investigated by considering the diffusion path to be a semi-infinite cylinder terminating in a hemispherical surface at the bounded end. An analytical solution of Fick's law for this geometry is greatly complicated by the boundary conditions at the bounded end. A computer solution, however, was obtained using the implicit alternating direction technique (9). Figure 3 compares the flux obtained for the case of the hemispherical nonlinear interface to that for the one-dimensional case. A diffusivity of  $1 \times 10^{-5}$  cm<sup>2</sup>/sec was used. For a hemispherical interface, initially the flux is larger than Eq. [3] predicts due to the contribution of radial diffusion. However, for times in excess of a few hundred seconds the two become indistinguishable as diffusion in the cylindrical capillary becomes rate limiting.

### Results and Discussion

A typical current-time discharge curve is shown in Fig. 4. The general shape conforms to that predicted by mathematical analysis. For small times,  $t < 10$  sec, the flux (current/diffusion path area) is smaller than Eq. [3] predicts due to ohmic polarization in the electrolyte. For the time interval  $10 < t < 100$  sec, the flux is greater than Eq. [3] predicts due to the contribution of the larger area of a nonplanar interface. For  $t > 100$  sec, the discharge current behaves as is expected for one-dimensional diffusion. Equation [3] was solved to obtain the diffusion coefficient,  $D$ , explicitly. Calculation of the coefficients was based on

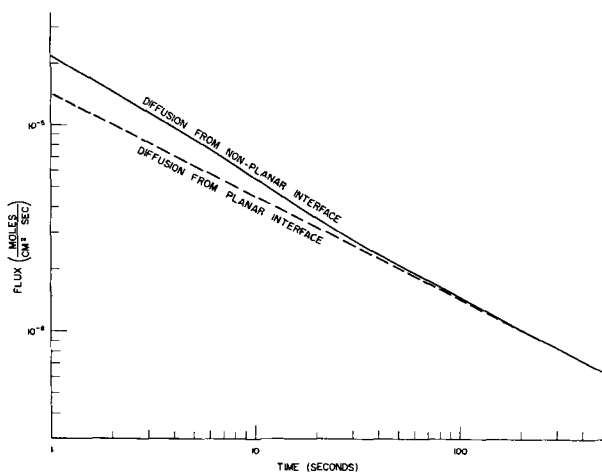


Fig. 3. Flux for coupled diffusion problem

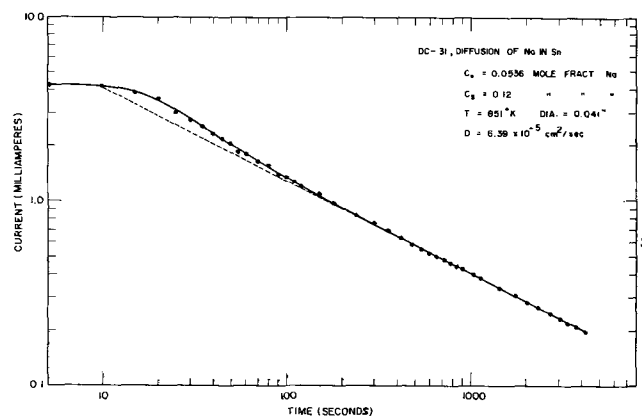


Fig. 4. Typical discharge curve

that portion of the curve which is a straight line on a plot of  $\log i$  vs.  $\log t$ . The open-circuit potential of the cell was not stable. Presumably this was due to the small but finite solubility of the alkali metal anode in the fused salt electrolyte.

Activation polarization was assumed to be negligible and the current efficiency was taken as 100%. Both these assumptions seem reasonable in view of available data in the literature for liquid metal concentration cells. Concentration intervals ( $C_s - C_0$ ) of from 4 to 8 m/o (mole per cent) alkali metal were used. This lower limit was determined by the smallest concentration interval which gave stable cell discharge characteristics. In each of the systems investigated two or more cells were run at a common point to insure reproducibility and to compare results from cells with 1.0 and 1.6 mm diameter diffusion paths. In no case was the path diameter found to affect the results significantly.

Coefficients for the diffusion of potassium in potassium-amalgams are shown in Fig. 5. The values of the diffusion coefficient at infinite dilution were calculated from the Stokes-Einstein equation using the viscosity reported in (10) and the Pauling ionic radius of potassium (11). The results are compared with the smoothed data of Bonilla *et al.* (3). Both investigations report a maximum in the diffusion coefficient close to  $N_K = 0.30$ . The phase diagram (2) shows a congruently melting compound  $Hg_2K$  at  $N_K = 0.33$ . Thermodynamic data (2) reveal that negative deviations from Raoult's law exist for this system. Diffusion coefficients have been measured as a function of composition for two other systems which show negative deviations from Raoult's law, Hg-Tl (12) and Bi-Pb (13). In both cases a maximum exists.

For the range  $0.25 < N_K < 0.35$ , Bonilla *et al.* report much higher values than were found in the present investigation. Diffusion coefficients over a wide range of compositions have been reported for the following binary liquid metal systems; Hg-Tl (12), Bi-Sn (13), In-Sn (14, 15, 16), Bi-Pb (13, 17, 18), Zn-Hg (19), Pb-Sn (13), and Na-Pb (20). With the exception of one investigation, Pb-Bi (13), in no case did the diffusion coefficients vary by more than a factor of 2.2 over the composition range. In this exception the variation was more than an order of magnitude. However, the investigators noted that large concentration gradients inherent in the experimental method probably gave rise to convection currents. Large variations in the value of the diffusion coefficient with composition are common in solids where marked structure changes can occur. In liquids where the atoms are less rigidly bound the variations are not expected to be as pronounced. Variations of an order of magnitude are not expected. Several investigators (21-24) have observed convection effects with liquid metals in diffusion paths of greater than 2-mm diam-

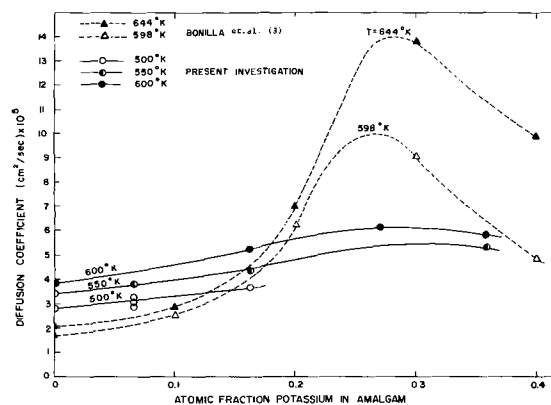


Fig. 5. Diffusion coefficients for potassium in potassium amalgams.

Table II. Activation energy and pre-exponential,  $D_0$ 

System	N	$D_0$ , cm <sup>2</sup> /sec	E, cal/g atom
K-Hg	0.165	$3.7 \times 10^{-4}$	2100
Na-Pb	0.120	$2.0 \times 10^{-4}$	2500
Na-Sn	0.160	$1.9 \times 10^{-4}$	1900

eter. Convection may result from the presence of vibrations or from negative temperature gradients (top end cooler) as small as 0.1°C/cm (25). The data of Bonilla *et al.* were obtained in paths of 1/2 and 1/4-in. diameter which greatly increases the possibility of convection. They maintained a small positive temperature gradient to reduce the possibility of convection as was done in the present investigation. However, the potassium-mercury system is strongly exothermic and liberation of heat occurs during diffusion of the components. This heat liberation is most likely to be pronounced where compounds exist in the solid state, such as Hg<sub>2</sub>K, and may persist into the liquid state. Analogous thermal generation conditions exist in the electromobility experiments where internal heat liberation results from ohmic heating by the high current densities. Several investigators have noted the existence of convection in liquid metals under these conditions (26-29). On the basis of these considerations, the explanation for the inordinately high coefficients reported by Bonilla *et al.* in the range  $0.25 < N_K < 0.35$  may be convection resulting from a combination of a large diameter diffusion path and exothermic heat liberation causing local temperature disturbances. The discrepancy between the coefficient of diffusion at infinite dilution reported in the two investigations is explained by the choice of different sources for the viscosity data used in the calculation.

The coefficients obtained for diffusion of sodium in sodium-lead are shown in Fig. 6. The values at infinite dilution were calculated from the Stokes-Einstein equation using viscosity data from (30) and the Pauling ionic radius of sodium (11). Results are compared with values reported by Morachevsky (20) who used the capillary reservoir technique and sectioned the path after diffusion for chemical analysis. His concentration gradients were as large as 40 a/o (atom per cent) sodium. The sodium-lead system exhibits large negative deviations from Raoult's law. The minimum in Morachevsky's data is not consistent with this as explained earlier. Rather, a maximum as was obtained in the present investigation is expected.

The coefficients obtained for the diffusion of sodium in sodium-tin are shown in Fig. 7. No other investigators have reported diffusion coefficients for this system.

The data for each of the three systems can be represented by the Arrhenius equation

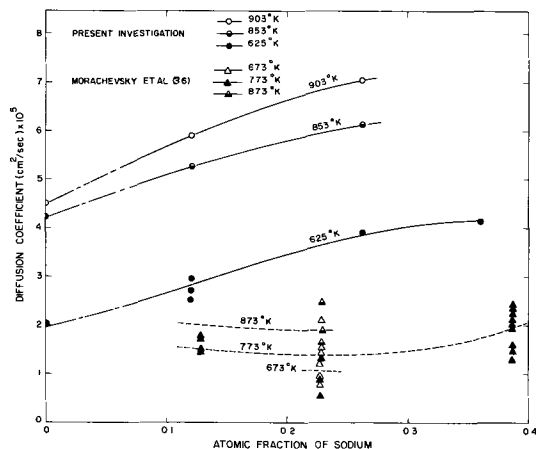


Fig. 6. Diffusion coefficients for sodium in sodium-lead alloys

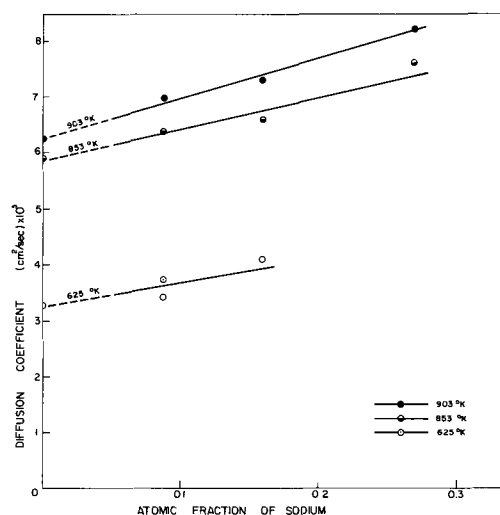


Fig. 7. Diffusion coefficients for sodium in sodium-tin alloys

$$D = D_0 e^{-E/RT} \quad [4]$$

The activation energy,  $E$ , and the pre-exponential,  $D_0$ , are given in Table II for each of the systems at the indicated mole fraction of alkali metal,  $N$ .

### Summary

A method has been developed of measuring diffusion coefficients in binary liquid metals. This method, unlike others available, allows observation of the rate at which diffusate enters the diffusion path and detection of anomalous effects which may occur particularly in the early stages of the experiment. The electrical measurements of current and potential are substituted for the traditional chemical or radiochemical analyses. Since very small quantities of diffusate enter the diffusion path during an experiment, typically  $10^{-4}$ g, the advantage of measuring electrical quantities over chemical analysis for this small a composition change is apparent. The method has been tested on three liquid metal systems, potassium-mercury, sodium-lead, and sodium-tin. It was found to give results consistent with available thermodynamic data and theoretical models. The concentration cells were discharged at constant potential in this investigation. They could, however, be discharged at constant current providing the appropriate solution of Fick's law is used in analysis of the data.

### Acknowledgments

The authors are grateful to the United States Atomic Energy Commission who supplied the support for this project under contract AT (11-1)-1352.

Manuscript received Sept. 14, 1967; revised manuscript received Dec. 8, 1967.

Any discussion of this paper will appear in a Discussion Section to be published in the December 1968 JOURNAL.

### REFERENCES

1. J. B. Edwards Ph.D. Thesis, The University of Michigan, Ann Arbor, December 1961.
2. R. Hultgren, R. L. Orr, P. D. Anderson, and K. K. Kelly, "Selected Values of Thermodynamic Properties of Metals and Alloys," John Wiley, & Sons, Inc., New York (1963).
3. C. F. Bonilla, Do-ik Lee, and P. J. Foley, Advances in Thermophysical Properties at Extreme Pressures and Temperatures, 3rd Symposium, March 22-25, 1965, pp. 207-15.
4. J. Degenkolbe and F. Sauerwald, *Z. anorg. und allgem. Chem.*, **270**, 317 (1952).
5. "Handbook of Chemistry and Physics," 40th ed., C. D. Hodgeman, Editor, Chemical Rubber Publishing Co., Cleveland (1958).
6. M. L. Dzurus and G. R. Henning, "Carbon—Proceedings of the Fifth Conference," **1**, 139, Pergamon Press (1962).

7. J. Crank "Mathematics of Diffusion," Oxford University Press, Fair Lawn, N.J. (1956).
8. L. T. Gul'din and A. V. Buzhinskaya, Surface Phenomena in Metallurgical Processes, Proceedings of an Inter-institute Conference, Edited by A. I. Belgaev, Consultants Bureau, New York, 1965, pp. 177.
9. B. Carnahan, H. A. Luther, and J. O. Wilkes, "Applied Numerical Methods," Preliminary Edition, Vol. II, Chap. 7, John Wiley & Sons, Inc., New York (1964).
10. A. V. Grosse, *J. Phys. Chem.*, **68**, 3419 (1964).
11. L. Pauling, *J. Am. Chem. Soc.*, **49**, 765 (1927).
12. W. T. Foley and L. E. Reid, *Can. J. Chem.*, **41**, 1782 (1963).
13. K. Niwa, M. Shimoji, S. Kado, Y. Watanabe, and T. Yokokawa, *J. Metals*, **9**, 96 (1957).
14. G. Careri, A. Paoletti, and M. Vincentini, *IL Nuovo Cimento*, **X**, 1088 (1958).
15. A. Paoletti and M. Vincentini, *J. Appl. Phys.*, **32**, 22 (1961).
16. M. Vincentini and A. Paoletti, *IL Nuovo Cimento*, **XIV**, 1373 (1959).
17. R. E. Grace and G. Derge, *J. Metals*, **6**, 839 (1955).
18. S. J. Rothman and L. D. Hall, *ibid.*, **8**, 1580 (1956).
19. H. W. Schadler and R. E. Grace, *Trans AIME*, **215**, 559 (1959).
20. A. C. Morachevsky, E. A. Cherespanova, and A. F. Alabyshev, *Isvestiia. VUZ-Tsvetnaya Metallurgiya*, **70**, (1960).
21. D. W. Morgan and J. A. Kitchner, *Trans. Faraday Soc.* **51**, 51 (1954).
22. S. J. Rothman and L. D. Hall, *J. Metals*, **8**, 199 (1956).
23. J. W. Gorman and G. W. Preckshot, *Trans. Met. Soc. AIME*, **212**, 367 (1958).
24. G. W. Preckshot and R. E. Hudrlik, *ibid.*, **212**, 516 (1960).
25. G. Careri, A. Paoletti and F. L. Salvetti, *IL Nuovo Cimento*, **X**, 399 (1954).
26. J. C. Angus, Ph.D. Thesis, The University of Michigan, 112, (1960).
27. A. R. E. Lodding, "Isotope Transport Phenomena in Liquid Metals, Gothenburg Studies in Physics," Nils Ryde, Editor. Acta Universitatis Gothoburgensis (1961).
28. J. Rohlin and A. Lodding, *Z. Naturforsch.*, **17a**, 1081 (1962).
29. J. D. Verhoeven, *Metals*, **1**, 26 (1966).
30. E. Rothwell, *J. Inst. Metals*, **90**, 389 (1961-62).

## The Mechanism of Oscillatory Behavior During the Anodic Oxidation of Formaldehyde

Herbert F. Hunger\*

*U. S. Army Electronics Command, Fort Monmouth, New Jersey*

### ABSTRACT

Galvanostatic studies of formaldehyde half-elements in sulfuric acid at room temperature were made. In addition to kinetic measurements with constant bulk concentration of formaldehyde, adsorption and desorption experiments were performed. The oscillatory behavior is described in terms of current-potential characteristics and potential transients. Two reaction sequences are postulated to explain the oscillations. In path I a catalytic decomposition step and in path II a diffusion-readsorption step are suggested as the coupling steps which are required to continue the oscillations. At potentials of or above +0.8v vs. SHE, the participation of the oxidized platinum surface in the oxidation of formaldehyde becomes noticeable. From adsorption and desorption experiments it can be concluded that readsorption from a liquid film on top of the ad-layer is essential for the occurrence of the first oscillation. This excludes the coupling mechanism of path I.

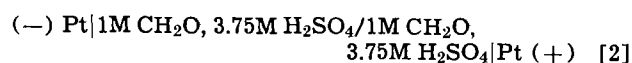
In previous papers we have reported on oscillation phenomena occurring during the anodic oxidation of formaldehyde in sulfuric acid at platinum electrodes and room temperature (1, 2). The objective of this paper is to report on further work concerning the reaction mechanism.

### Experimental

The half element investigated can be presented by the scheme



and the cell used to study the oscillation phenomena by



It contained either a smooth or platinized platinum electrode in an anolyte consisting of 1M formaldehyde in 3.75M sulfuric acid. The anolyte was separated by a cation exchange membrane (Nepton CR-61 from Ionics Incorporated) or a sintered glass disk from a catholyte of the same composition. A smooth platinum cathode was placed into the catholyte. Both

smooth and platinized platinum electrodes were made from platinum-foil (0.076 cm thickness with a geometrical cross section area of 1 cm<sup>2</sup>, except otherwise noted). A hydrogen reference electrode of the type described by Giner was arranged in a separate electrolyte compartment (3.75M H<sub>2</sub>SO<sub>4</sub>) and connected with a properly arranged Luggin capillary to the anode (3). The Giner hydrogen electrode was 26 mv negative to SHE. One type of experimental cell was constructed from Lucite except the gasketing material (Teflon or rubber) (4). The adsorption and desorption experiments were performed in glass-H-cells (E. H. Sargent & Company) with standard glass joints and controlled atmosphere (CO<sub>2</sub> or argon). The electrodes were platinized in a controlled manner (5). Nominal amounts up to 30 mg platinum black per square centimeter of geometrical area were electrolytically deposited. These nominal amounts correspond to the electrical charge passed during platinization. Corrections for the Faradaic efficiency showed that 10 mg platinum/cm<sup>2</sup> nominal correspond to 3.05 mg/cm<sup>2</sup> and 30 mg/cm<sup>2</sup> nominal to 7.5 mg/cm<sup>2</sup>. The experiments were conducted at controlled temperature conditions (21° and 25°C). The chemicals used to prepare the electrodes and the electrolytes were of highest purity grade commercially available.

\* Electrochemical Society Active Member.

A precision current source (Model CS-12, North Hills, Electronics, Inc.) was used to control the current ( $1 \mu\text{a}$ -999 ma) between the working anode and the counter electrode. A potentiometric recorder (Model FW 5A-3332 from Texas Instruments, Inc.) was used for measuring the stationary anode potentials and the potential transients *vs.* the reference electrode.

In addition to the kinetic measurements with constant bulk concentration of formaldehyde, adsorption experiments, similar to those performed by Pavela and Breiter for methanol were made (6, 7). Adsorption of formaldehyde at platinized platinum took place from the electrolyte (1M  $\text{CH}_2\text{O}$  in 3.75M  $\text{H}_2\text{SO}_4$ ) under open circuit conditions. Adsorption times were in the range of 1 to 900 sec. After adsorption the electrodes were dipped shortly in 3.75M  $\text{H}_2\text{SO}_4$  in order to remove the adherent liquid and transferred immediately into the anode chamber of the cell which contained in this case only 3.75M sulfuric acid as the electrolyte. A preset circuit permitted to oxidize the adsorbed organic species immediately at constant current just above the threshold current for the oscillations (50 ma). The voltage maxima of the pulsations under these conditions were about 0.78v *vs.* SHE. Thus, as shown later, strong participation of an oxidized surface state in the mechanism was avoided.

The dipping procedure described above did not completely eliminate the adherent liquid film as desorption experiments showed; however, this technique proved to be useful to obtain a defined amount of organic species at the electrode.

Desorption experiments in order to determine the amount of adherent liquid film in addition to the ad-layer after rinsing were also made. For this purpose the adsorption time was held at 300 sec, a time which was required to obtain constant amounts (saturation coverage plus liquid film) of organic species at the electrodes. After adsorption the electrode was dipped for time periods of 1-10,980 sec in  $\text{H}_2\text{SO}_4$  to obtain removal of the adherent film and desorption of the ad-layer. The remaining organic amount was stripped off as described before. It was noticed from a plot of  $\log \mu\text{C}/\text{cm}^2$  of anodically oxidized organic species *vs.* time that up to 15 sec of desorption a significant amount of liquid film was still present. A rapid decrease in the amount of organic species was observed up to 300 sec. After that the curve followed the desorption relationship

$$\log(\mu\text{C}/\text{cm}^2)_t = \log(\mu\text{C}/\text{cm}^2)_{t=0} - k_{DT} \quad [3]$$

Extrapolation of the straight line to  $t=0$ , permitted to measure the  $(\mu\text{C}/\text{cm}^2)_{t=0} = 182 \mu\text{C}/\text{cm}^2$ . We shall refer to this value in the following as the ad-layer in contrast to the amount of organic species at the electrode which can consist of the ad-layer plus a liquid film. Rinsing for one second reduced the original liquid film ( $t=0$ , no rinsing) from about  $1443 \mu\text{C}/\text{cm}^2$  to  $976$ - $1020 \mu\text{C}/\text{cm}^2$  corresponding to about 5.5 ad-layers.

Before each adsorption or desorption experiment, the electrochemical surface area of the electrode was estimated. The following procedure was used. The electrode was submitted to cathodic charging at 50 ma for 1 min, followed immediately by an anodic current of 50 ma. The voltage trace was recorded. The transients permitted to determine the electrical charges corresponding to the anodic oxidation of hydrogen (0-0.3v *vs.* SHE) and that of the anodic oxidation of the platinum surface, noticeable at about +0.8v and ending at about +1.6v with the evolution of oxygen. All these events are clearly marked by a change in the slopes of the transient. The length of the latter region corresponds to the build up of a monolayer of oxygen. Using the value of  $420 \mu\text{C}/\text{cm}^2$  corresponding to one oxygen monolayer, the absolute electrochemical surface area could be estimated. This theoretical value of  $420 \mu\text{C}/\text{cm}^2$  was found to be in excellent agreement with our experimental data. When cathodic hydrogen

transients were compared with anodic oxygen transients, it was found that an oxygen coverage corresponding to one monolayer was reached at about 1.6v *vs.* SHE. In this comparison a hydrogen monolayer corresponded to  $210 \mu\text{C}/\text{cm}^2$  of real platinum surface (8).

It was further checked to what degree the charge in the oxygen transient depended on the current density used. The current was varied between 5 and 500 ma, corresponding to a current density range of 2-200  $\mu\text{a}/\text{cm}^2$  (the average real surface area of the electrode being  $2.5 \cdot 10^3 \text{ cm}^2$ ). Between 5 and 200 ma the mean error was 2.87%. Negative deviations up to -23.3% were observed at 500 ma. The current of 50 ma normally used in the surface area determination corresponds to 13.8 - 50  $\mu\text{a}/\text{cm}^2$  for the range of surface areas observed for platinum black in our experimentation ( $10^3$  -  $3.2 \cdot 10^3 \text{ cm}^2$ ) per electrode.

## Results and Discussion

*Kinetic measurements with constant bulk concentration of formaldehyde.*—The current-potential curves, both for smooth and platinized platinum are shown in Fig. 1 and 2. The open circuit potentials of the formaldehyde anodes are varying from +0.07 to +0.49v, specifically for smooth platinum, and from +0.175 to +0.33v for platinized platinum. Analogy

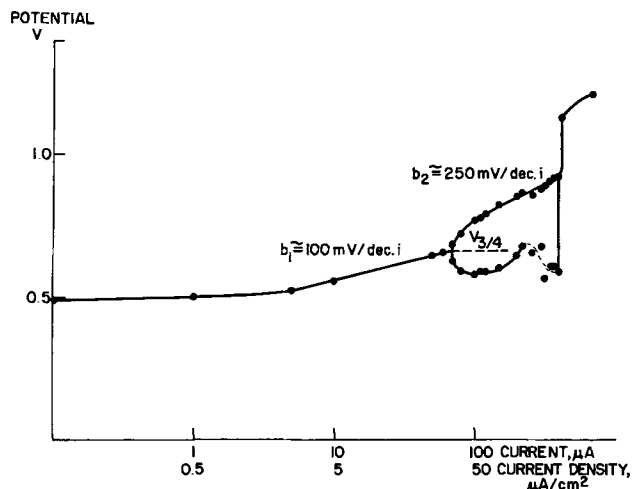


Fig. 1. Galvanostatic current-potential curve for smooth platinum electrode (1  $\text{cm}^2$  cross section) in 1M  $\text{CH}_2\text{O}$ , 3.75M  $\text{H}_2\text{SO}_4$  at 21°C. Potential measured *vs.* hydrogen reference electrode (-0.026v).

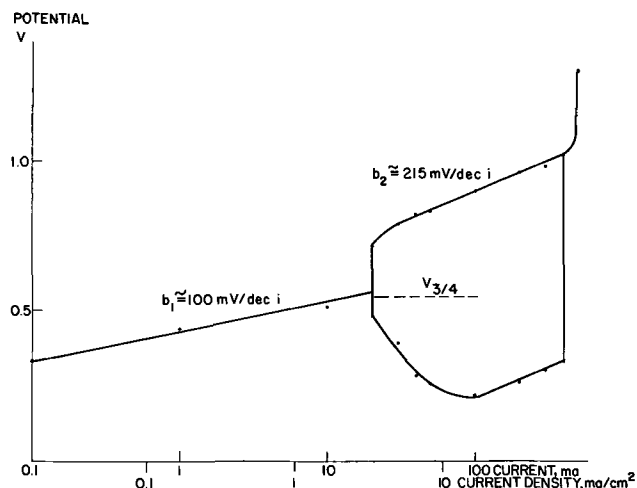


Fig. 2. Galvanostatic current-potential curve for platinized platinum electrode (3  $\text{cm}^2$  cross section) in 1M  $\text{CH}_2\text{O}$ , 3.75M  $\text{H}_2\text{SO}_4$  at 21°C. Potential measured *vs.* hydrogen reference electrode (-0.026v).

with formic acid supports the hypothesis that these potentials are mixed potentials caused perhaps by the simultaneous low-potential anodic oxidation of the organic specie with cathodic deposition of hydrogen (9, 10).

The current-potential curves, both for smooth and platinized platinum, showed a stationary region up to a threshold current of  $70 \mu\text{a}$  and  $20 \text{ ma}$ , respectively. The slope  $b$ , in the stationary region is  $100 \pm 5 \text{ mv}$  per decade of current for all three types of electrodes, corresponding approximately to a  $2.3 (2RT/F)$  value. Since the slopes for smooth platinum and platinized platinum are identical, no effects of electrode porosity on the value of the slope were observed (11). Thus the platinized platinum electrodes can be considered essentially as nonporous. The estimated exchange current density values, obtained by extrapolation of the stationary Tafel slopes to the reversible potential for formaldehyde oxidation were  $10^{-11} \text{ a/cm}^2$  for smooth platinum and  $7.5 \cdot 10^{-9} \text{ a/cm}^2$  as an average value for platinized platinum. Similar data are reported for the anodic oxidation of formic acid at platinum electrodes. (9, 12).

Oscillatory behavior expressed in periodic voltage transients was observed at higher current densities. For platinized platinum these potential transients range from  $+0.22$  to  $+1.02 \text{ v}$  vs. the hydrogen reference electrode. An upper and a lower curve limit the oscillation region. These two curves represent stable states according to the theory of stability of electrode states (13).

The slope of the upper curve,  $b_2$ , is about  $215 \text{ mv}$  per decade of current for platinized platinum and approximately  $250 \text{ mv}$  for smooth platinum. Such slopes obtained under nonsteady-state conditions, however, can not be used as a diagnostic tool for the reaction mechanism.

The lower boundaries of the oscillation planes approach at first more negative potentials when the current is increased. Above  $100 \text{ ma}$  the potentials become again more positive in the case of platinized platinum. The new slope corresponds approximately to that of the upper boundary. In the case of smooth platinum, a similar behavior is observed up to  $220 \mu\text{a}$ . Then the lower boundary becomes ill-defined.

A second transition region is observed at higher currents, at about  $400 \mu\text{a}$  for smooth platinum and between  $400$  and  $500 \text{ ma}$  for platinized platinum, indicating electrode surface oxidation and leading finally to oxygen evolution.

It was noticed that the intersection between the stationary part of the  $V - \log i$  curve and the threshold current gave another interesting characteristic which we termed  $V_{3/4}$  potential.

In analyzing the potential transients in the oscillation region (Fig. 3 and 4), the following approach was used. Besides measuring the coulombs per oscillation cycle, the coulombs corresponding to  $\frac{3}{4}\tau$  ( $\tau =$  time for one cycle) were determined for various currents and the corresponding potential values were registered. They were found to be identical with the  $V_{3/4}$  potentials. The  $V_{3/4}$  potential levels shown in Fig. 1 and 2 divide the initial oscillation planes in two parts. The upper part corresponding to  $\frac{3}{4}\tau$  and the lower one to  $\frac{1}{4}\tau$ , a  $3e^-/1e^-$  ratio.

For smooth platinum the results are recorded in Table I. In the last column, the process frequency is noted. The  $V_{3/4}$  level, average value calculated from Table I:  $\bar{V}_{3/4} = +0.654$ .

Results for platinized platinum are given in Table II. The voltage transients are larger than in the case of smooth platinum and  $\bar{V}_{3/4} = +0.542 \text{ v}$ .

Figure 5 relates the upper oxidation potential (last figure in column 3, Table I and II) to the millicoulombs per cycle. A strong increase in the amount of species oxidized occurs above  $+0.8 \text{ v}$  in the case of smooth platinum and above  $+0.9 \text{ v}$  in the case of

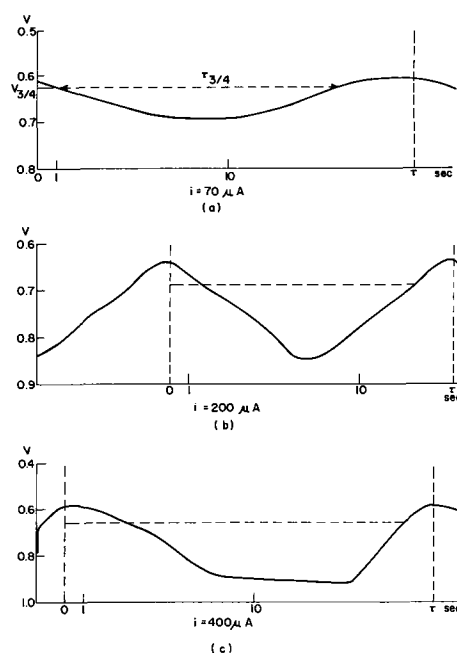


Fig. 3. Potential transients. Smooth platinum electrode potential  $V$  measured vs. hydrogen reference electrode ( $-0.026 \text{ v}$ ), recorder speed  $24 \text{ in./min}$ : (a)  $i = 70 \mu\text{a}$ , (b)  $i = 200 \mu\text{a}$ , and (c)  $i = 400 \mu\text{a}$ .

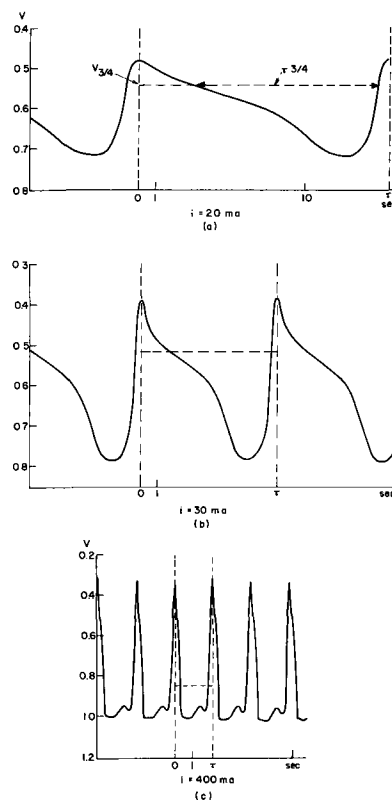


Fig. 4. Potential transients. Platinized platinum electrode potential measured vs. hydrogen reference electrode ( $-0.026 \text{ v}$ ), recorder speed  $24 \text{ in./min}$ : (a)  $i = 20 \text{ ma}$ , (b)  $i = 30 \text{ ma}$ , and (c)  $i = 400 \text{ ma}$ .

platinized platinum. This increase in millicoulombs per cycle is related to the onset of increasing oxygen coverage and participation of the oxidized electrode surface in the oxidation of organic species. Breiter and Becker report that anodic oxidation of platinum in acid electrolytes becomes noticeable at  $+0.7$  and the surface coverage becomes a monolayer at about  $+1.5 \text{ v}$  (14).

Table I. Coulombic analysis of galvanostatic potential transients

1M CH<sub>2</sub>O, 3.5M H<sub>2</sub>SO<sub>4</sub>; smooth platinum; 1 cm<sup>2</sup> cross section; 21°C

<i>i</i> , μA	m Cbs/cycle	V	V <sub>3/4</sub>	<i>ν</i> , Hz
0		0.49		
1		0.5		
5		0.522		
10		0.55		
50		0.642		
60		0.651		
70	1.4	0.62-0.68	0.65	0.05
80	1.59	0.585-0.715	0.61	0.051
100	1.8	0.575-0.76		0.056
110	1.96	0.585-0.77	0.62	0.056
120	2.13	0.585-0.785	0.615	0.056
150	2.47	0.595-0.815	0.63	0.061
200	3.0	0.64-0.845	0.685	0.067
220	3.27	0.67-0.855	0.705	0.067
260	3.6	0.65-0.85	0.692	0.072
300	4.12	0.67-0.87	0.71	0.073
320	4.71	0.56-0.885	0.64	0.068
350	6.82	0.6-0.9	0.67	0.051
370	7.05	0.6-0.91	0.67	0.053
400	7.76	0.58-0.915	0.66	0.052
420		1.12		
500		1.16		
700		1.2		

Table II. Coulombic analysis of galvanostatic potential transients

1M CH<sub>2</sub>O, 3.5M H<sub>2</sub>SO<sub>4</sub>, platinized platinum;  
10 mg platinum/cm<sup>2</sup>, 3 cm<sup>2</sup> cross section; 21°C

<i>i</i> , ma	m Cbs/cycle	V	V <sub>3/4</sub>	<i>ν</i> , Hz
0		0.212		
10 <sup>-3</sup>		0.221		
10 <sup>-2</sup>		0.235		
10 <sup>-1</sup>		0.331		
1		0.44		
10		0.51		
20	303	0.48-0.715	0.54	0.049
30	246	0.39-0.79	0.52	0.091
40	407	0.28-0.82	0.53	0.099
50	257	0.255-0.83	0.545	0.194
100	383	0.22-0.9	0.576	0.262
200	813	0.26-0.96	0.66	0.246
300	1028	0.3-0.98	0.82	0.292
400	1082	0.33-1.02	0.84	0.37
500		1.3		

With the increase in millicoulombs per cycle a change in the shape of the voltage transients is observed (Fig. 3 and 4): For smooth platinum at 70 μA, a symmetrical transient and at 400 μA, a flat, extended potential maximum. For platinized platinum a relatively slow attainment of a potential maximum is observed at low current densities and the return to less positive potentials is rapid (Fig. 4a, b). At higher current densities this return is delayed by an additional small pulsation next to the potential maximum (Fig. 4c).

Certain conclusions with respect to the mechanism of the oscillations can be made from the kinetic behavior: The oscillatory behavior of formaldehyde at

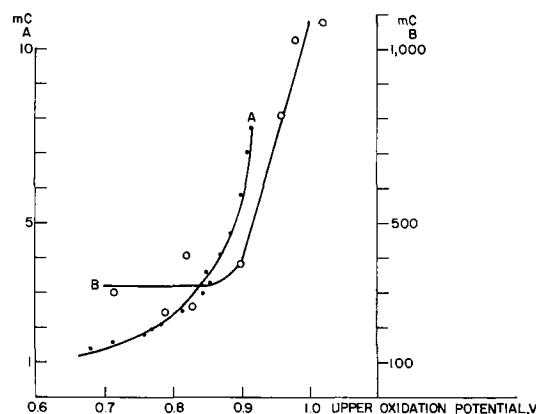
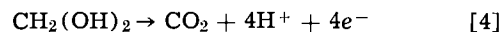


Fig. 5. mCb/cycle vs. upper oxidation potential: (a) smooth Pt, (b) platinized Pt.

platinum electrodes is a special case of a general phenomenon, the periodic electrode process. At least two electrode processes have to occur simultaneously to result in a periodic process (15). Periodic behavior can also be observed by coupling more than two parallel reactions. Coupling means that the reaction rates depend mutually on the condition of the parallel reactions, following a periodic function of time. The rate determining step of the periodic process has therefore also to be time dependent.

The complete anodic oxidation of formaldehyde is a 4e<sup>-</sup> process

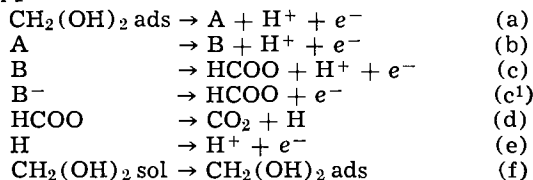


The occurrences within the low current region of the oscillation plane can be formulated by two postulated reaction sequences:

The postulated reaction path I considers a chemical step as the coupling step, path II a diffusion-adsorption step. The coupling step is required to continue the periodic electrode process and is the reason for the reverse of the potential during oscillations.

Path I is an extension to the mechanisms proposed by Mueller and Conway for the anodic oxidation of formic acid (12, 16-18)

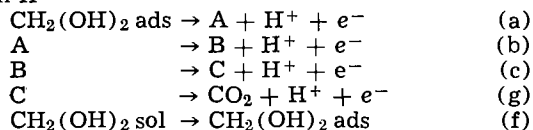
## Path I



The anodic oxidation of formaldehyde occurs through the electron transfer steps (a), (b), (c), or (c<sup>1</sup>) and results in formation of adsorbed formate radicals, sometimes identified with the so-called "blocking intermediate." Build up of the blocking intermediate occurs up to a critical surface concentration (17). After this is reached, rapid catalytical decomposition of this specie to carbon dioxide and hydrogen occurs. This leads to a rapid change in surface coverage from partially oxygenated organic species to hydrogen in step (d), the coupling step. The anodic oxidation of hydrogen occurs at a less positive potential. Anodic oxidation of hydrogen has been observed in that potential region during periodic phenomena (19). Partially oxygenated hydrocarbons as methanol and formic acid adsorb at platinum from acid solutions in the potential region of +0.1 to +0.6v vs. SHE (7, 20). The surface coverage is high at the less positive potentials, but decreases with increasing positive potential. Thus reabsorption of organic species (f) can occur in this potential region simultaneously with step (e) and the oscillations are continued.

Path II postulates the stepwise anodic oxidation of formaldehyde with participation of the anodically oxidized platinum surface at the more positive potentials.

## Path II



Steps (a), (b), (c), and (g) are charge transfer steps. Step (f) is a diffusion-adsorption step. Coupling occurs here as a consequence of step (g) through step (f).

From experiments in which the anode was driven by an external emf, the behavior during simultaneous current and voltage oscillations was studied (1, 2). It was observed that the anodic current decreases with increasing anodic polarization during one oscillation cycle. This indicates inhibition of the oxidation of

the organic species by a small, but increasing coverage of the electrode with oxygen species. Since adsorption of organic species is known to occur at the less positive potentials, adsorption will decrease with increasing positive potential during a cycle and finally become zero. Then only the previously adsorbed amount of organic species becomes completely oxidized in step (g) and depletion of the surface of organic species leads finally to re-adsorption at less positive potentials through step (f). The original maximum current is observed and a new cycle starts. These occurrences are also reflected in the potential transients (Fig. 3) and marked in Fig. 4.

Above +0.8v noticeable surface oxidation was observed probably by discharge of water. Such reactions shift the three to one electron ratio observed previously to a higher value. An analysis of the potential transients above +0.9v showed ratios up to  $13e^-/1e^-$  for the original  $V_{3/4}$  level. These occurrences explain the change in the shape of the potential transients with increasing positive potential (Fig. 3c, Fig. 4c). Correspondingly the apparent increase of the  $V_{3/4}$  potential above an upper oxidation potential of 0.9v (Table II) is due to these reactions.

Adsorption and desorption experiments, discussed in the following, permitted to distinguish between the coupling steps of the mechanisms.

**Adsorption and desorption experiments.**—Two general types of potential transients were noted after adsorption of formaldehyde. In case of short adsorption times (1 to 5 sec in case of electrode A), no oscillations were observed, but after longer periods one to four pulses, depending on the length of the adsorption time, were obtained (Fig. 6a, b). In the first case (a), the potential rose fast from open circuit potential to about +0.7v, followed by a plateau region and above +0.8v by platinum surface oxidation. The latter was marked by a change in the slope of the transient. Above +1.62v visible oxygen evolution occurred. In the second case (b), potential oscillations between +0.47 and +0.78v replaced the plateau region. The

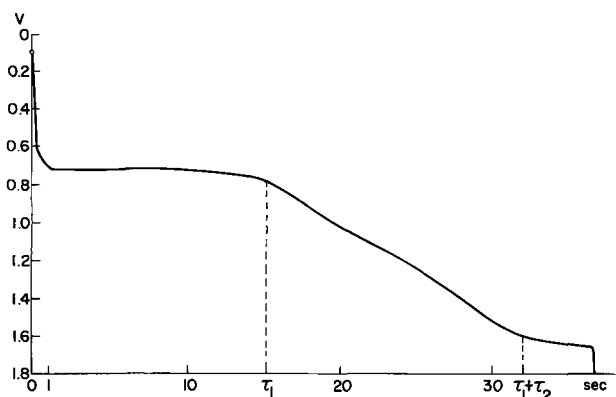


Fig. 6a. Potential transient. Platinumized platinum electrode adsorption time: 5 sec,  $i = 50$  ma. Potential measured vs. hydrogen reference electrode ( $-0.026v$ ), recorder speed 24 in./min.

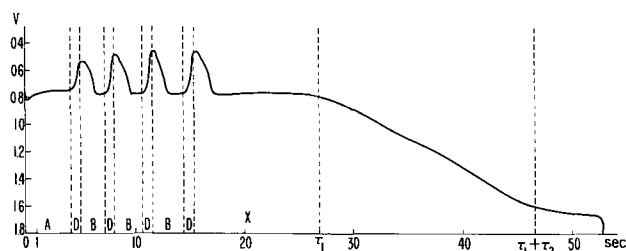


Fig. 6b. Potential transient. Platinumized platinum electrode adsorption time: 420 sec,  $i = 50$  ma. Potential measured vs. hydrogen reference electrode ( $-0.026v$ ), recorder speed 24 in./min.

average potential for start of visible carbon dioxide evolution was +0.757v for the given current density. At about +1.05v, this gas evolution ceased. In the case of electrode B, which had a larger surface area than A, up to ten pulses were observed. The frequency of the oscillations decreased somewhat with the order of the pulses.

The millicoulombs of organic species oxidized between open circuit potential and onset of surface oxidation (time  $\tau_1$ ) are a function of the adsorption time.

The amounts of organic species oxidized during various phases of the oscillations were estimated by dividing the potential transients in certain segments (Fig. 6b). Segment A was termed the preoscillation period, D the (potential) decrease period, B the (potential) build up period, and X the after oscillation period. B plus D form one oscillation cycle. A and B were found to be identical. Coulometric analysis of the segments was done in two ways. For electrode A only the averaged values of D, B, and X over all oscillations were computed. For electrode B this was done also, but in addition a range of values for D, B, and X considering the frequency dampening effect observed for the pulses with higher order was calculated. The results are given in Table III.

Desorption experiments with electrode C were also evaluated coulometrically as in the case of electrode B. The results are compared with those of the adsorption experiments in Table III. In detail the pulse analysis of the desorption experiments gave the results shown in Table IV.

Analysis of the data yielded the following conclusions concerning the mechanism of the oscillations.

The after oscillation period ranges from 174 to about  $400 \mu C/cm^2$ . The first oscillation occurred when a total organic amount of about  $400 \mu C/cm^2$  had adsorbed or was still adsorbed at the electrode. Thus the critical amount required at the electrode to make one oscillation lies around  $400 \mu C/cm^2$ . Any amount in surplus of the critical one led to additional oscillations and/or an after oscillation period in accordance with Table III.

Relating these data to specific coverage estimates leads to the following. Assuming complete oxidation of formaldehyde to carbon dioxide (4), one coulomb corresponds to  $7.78 \cdot 10^{-5}g$   $CH_2O$ . One  $CH_2O$  molecule weighs  $5.10 \cdot 10^{-23}g$ . The area requirement for one formaldehyde molecule adsorbed on the platinum surface,

Table III. Coulometric analysis of the segments of the voltage transients

Surface area, $cm^2$	Electrode A $1.94 \cdot 10^3$	Electrode B $3.05 \cdot 10^3$	Electrode C $2.46 \cdot 10^4$
Oscillation period $\mu C/cm^2$	76	84*	94*
Decrease period $\mu C/cm^2$	20	27.9	—
Build up period $\mu C/cm^2$	56	56.1	—
After oscillation period $\mu C/cm^2$	200	278-400	174-346

\* Considering the frequency dampening effect, the value observed for the first oscillation was at  $46 \mu C/cm^2$  for B and  $59 \mu C/cm^2$  for C, respectively.

Table IV. Coulometric analysis of desorption experiments

Desorption time, sec	Number of pulses	Total pulse-charge ( $\tau_1 - X$ ), $\mu C/cm^2$	After oscillation period (X), $\mu C/cm^2$	Average $\mu C/cm^2$ /pulse
0	14	1451	174	104
0	10	934	346	93
1	8	645	322	81
3	4	337	313	85
7	3	353	244	118
15	1	84	322	84
30	0		258	

attached to two surface atoms, is about  $15\text{\AA}^2$ . On one square centimeter of absolute surface area we can accommodate  $6.66 \cdot 10^{14}$  molecules of formaldehyde. This corresponds to  $3.33 \cdot 10^{-8}\text{g CH}_2\text{O}$  or  $4.28 \cdot 10^{-4}\text{Cb}$ . Thus the electrical charge connected with the anodic oxidation of formaldehyde if a 2 site adsorption would occur is  $428\ \mu\text{C}/\text{cm}^2$ . If one site attachment occurred, the formaldehyde monolayer would give  $856\ \mu\text{C}/\text{cm}^2$ .

According to these data, the value of the ad-layer ( $182\ \mu\text{C}/\text{cm}^2$ ) indicates that the platinum surface is only partially covered with the adsorbed organic species (to about 21%). During one pulse about one half of the ad-layer is oxidized. The critical amount about doubles the value of the ad-layer.

This means that readsorption from a liquid film on top of the ad-layer is essential for the occurrence of the first oscillation. This excludes the coupling mechanism of path I where the first oscillation would occur by self-decomposition of the "blocking" intermediate formed by partial oxidation of the ad-layer. The coupling mechanism suggested in path II is therefore probable.

#### Acknowledgment

The author gratefully acknowledges the continued interest and support of Dr. E. A. Gerber, Director, Electronic Components Laboratory, U.S. Army Electronics Command, Fort Monmouth, New Jersey. The author wishes also to thank Miss R. Rinaldi for her technical assistance.

Manuscript received March 1, 1967; revised manuscript received Nov. 4, 1967. This paper was presented at the Dallas Meeting, May 7-12, 1967, as Abstract No. 110.

Any discussion of this paper will appear in a Discussion Section to be published in the December 1968 JOURNAL.

#### REFERENCES

1. H. F. Hunger, J. E. Wynn, and N. J. Sanfilippo, *Proc. 19th Ann. Power Sources Conf.*, Atlantic City (1965).
2. H. F. Hunger, *Proc. Journees Int. D'Etude des Piles Combustible*, Bruxelles (1965).
3. J. J. Giner, *This Journal*, **111**, 3, 376 (1964).
4. H. F. Hunger, J. E. Wynn, and N. J. Sanfilippo, Technical Report ECOM-2670, March 1966.
5. H. F. Hunger, J. E. Wynn, and N. J. Sanfilippo, Technical Report ECOM-2520, Oct. 1964.
6. T. O. Pavela, *Ann. Acad. Sci. Fennicae*, Series A, II *Chimica* 59 (1954).
7. W. M. Breiter and S. Gilman, *This Journal*, **109**, 622 (1962).
8. F. G. Will and C. A. Knorr, *Z. Elektrochem.*, **64**, 258 (1960).
9. M. H. Gottlieb, *This Journal*, **111**, 465 (1964).
10. M. W. Breiter, *ibid.*, **111**, 1298 (1964).
11. L. G. Austin, "Fuel Cells" V II, p. 100, C. J. Young, Editor (1963).
12. B. E. Conway and M. Dzienciuch, *Can. J. Chem.*, **41**, 21, 38, 55 (1963).
13. U. F. Franck, *Z. f. Phys. Chem., N.F.*, **3**, 183 (1955).
14. M. Breiter and M. Becker, *Z. Elektrochem.*, **60**, 1080 (1950).
15. K. F. Bonhoeffer, *ibid.*, **51**, 24 (1948).
16. E. Mueller, *ibid.*, **29**, 264 (1923).
17. E. Mueller and G. Hindemith, *ibid.*, **33**, 561 (1927).
18. E. Mueller and S. Tanaka, *ibid.*, **34**, 256 (1928).
19. J. A. V. Butler and G. Armstrong, *Disc., Faraday Soc.*, **1**, 122 (1947).
20. S. B. Brummer and A. C. Makrides, *J. Phys. Chem.*, **68**, 1448 (1964).

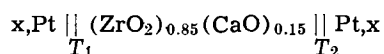
## Seebeck Coefficient of a $(\text{ZrO}_2)_{0.85}(\text{CaO})_{0.15}$ Electrolyte Thermocell\*

R. J. Ruka, J. E. Bauerle, and L. Dykstra

Westinghouse Research Laboratories, Pittsburgh, Pennsylvania

#### ABSTRACT

The Seebeck coefficients of thermocells of the type



were measured at temperatures near  $1000^\circ\text{C}$ . In these cells x represents any of several oxygen-inert gas or hydrogen-water-inert gas mixtures. It was found that the change in Seebeck coefficient corresponding to a change in the partial molar entropy of oxygen in the gas at the electrodes agreed closely with the values predicted from irreversible thermodynamic theory. Two principal assumptions were made in applying the theory to these cells: (i) that the transported entropy of the oxygen ions in the electrolyte was constant for the different gas mixtures used, and (ii) that gas-solid reactions were at equilibrium at each electrode. The temperature dependence of the Seebeck voltage was found to be small.

An electrochemical cell with identical electrodes develops an emf when the electrodes are at different temperatures. The thermal emf per degree temperature difference is termed the Seebeck coefficient. Holtan (1) and others (2, 3) have derived equations based on irreversible thermodynamics for the Seebeck coefficient in such thermocells.

Measurement of the Seebeck coefficient gives information on the simultaneous transfer of charge and

heat in the oxide electrolyte, allowing us, e.g., to calculate the Peltier-type heat transfer during isothermal operation of a related galvanic cell.

The purpose of this paper is a comparison of the experimentally with theoretically determined difference in Seebeck coefficient which results from a change in the partial molar entropy of oxygen in the gas phase at the electrodes of a thermocell with  $(\text{ZrO}_2)_{0.85}(\text{CaO})_{0.15}$  electrolyte and gas-platinum electrodes. The temperature dependence of the Seebeck voltage is also examined briefly.  $(\text{ZrO}_2)_{0.85}(\text{CaO})_{0.15}$  is

Key words: Seebeck coefficient; zirconia; thermocell.

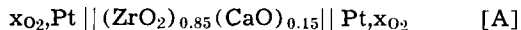
\* Supported by ARPA through the Office of Naval Research.



an attractive oxide for this study since necessary experimental information on transference numbers of ions and electrons in the oxide and on electrode reactions of corresponding galvanic cells is already available. Several studies of this electrolyte are of particular significance for the interpretation of the present paper. These include contributions by Wagner and co-workers (4) on cell emf, Rhodes and Carter (8) on cation diffusion, Kingery and co-workers (5) on oxygen ion diffusion, Weissbart and Ruka (6) on oxygen concentration cells, and Schmalzried (7) on electrolyte stability to oxidizing and reducing atmospheres. Essential information from these papers for consideration of our current experiments is that conduction in the oxide is due almost 100% to oxygen vacancy or ion migration (4, 8, 5) over the temperature range of interest to the present experiments, i.e., 700°-1280°C, that electrode reactions with oxygen or hydrogen-water using this oxide as electrolyte of a galvanic cell with platinum electrodes can be made essentially reversible (6) and that the oxide is stable to oxidizing or reducing atmospheres at oxygen partial pressures between 1 atm and the order or 10<sup>-22</sup> atm (7).

Reinhold and co-workers (9) and Holtan (1) have experimentally measured the thermal emf of several halogen-containing solid electrolytes. Holtan concludes from this data that transported entropy terms are either small or absent in these cells. On the other hand, Patrick and Lawson (10), and Christy and co-workers (11) present Seebeck coefficient data for pure and doped AgBr and AgCl thermocells with Ag electrodes which apparently contain sizable entropy of transport terms at some temperatures. Significant data on oxide thermocells for comparison has not been available.

Consider the following thermocell



where  $x_{O_2}$  is an oxygen containing atmosphere at the electrodes such as pure O<sub>2</sub>, air, an H<sub>2</sub>-H<sub>2</sub>O mixture, etc., Pt represents the platinum electrodes and leads, and (ZrO<sub>2</sub>)<sub>0.85</sub>(CaO)<sub>0.15</sub> is the oxide electrolyte with conductivity resulting almost exclusively from diffusion of O<sup>=</sup> ions.

The measured value of the thermal emf  $\Delta\phi$  in this thermocell is a function of three individual potentials as given by the relationship

$$\Delta\phi = \Delta\phi_{(O^=,E)} - \Delta\phi_{(e^-,Pt)} + \Delta\phi_c \quad [B]$$

where  $\Delta\phi_{(O^=,E)}$  is an emf across the electrolyte resulting from the thermally induced flow of O<sup>=</sup> ions,  $\Delta\phi_{(e^-,Pt)}$  is an emf across the platinum metal electrodes and leads, due to thermally induced flow of electrons, and  $\Delta\phi_c$  is the difference between contact potentials of the two electrolyte-electrode interfaces at the two temperatures.

Holtan (1), Lidiard and co-workers (2, 3) have derived general equations for thermal emf in thermocells, and we list below pertinent equations for the above thermocell as adapted from their considerations.<sup>1</sup> The equations are simplified by assuming that electronic conductivity is nil, that chemical diffusion gradients do not occur, and that O<sup>=</sup> is the only diffusing ionic species. The treatment assumes that the reference frame for diffusion is a plane in the lattice. This is also consistent with a choice of the positive ions as reference since these remain essentially immobile. For a small difference in electrode temperatures

$$\Delta\phi_{(O^=,E)} = \frac{\Delta T}{F} \left[ \frac{1}{2} \bar{S}_{O^=} - \frac{1}{2} s_{O^=} \right]$$

Thermal emf across electrolyte [1]

<sup>1</sup> It is of interest to note that the derivations of Eq. [1-4] involve electrochemical potentials, and there is a term  $e\phi'$  in each electrochemical potential for the usually accidentally occurring electrical state of the system. However, these terms all cancel in the final results and the partial molar entropies of the ions or electrons in Eq. [1-5] do not contain the extra term  $e\phi'$  which would otherwise give an indeterminate character to the entropy terms.

$$\Delta\phi_{(e^-,Pt)} = \frac{\Delta T}{F} \left[ \bar{S}_{(e^-,Pt)} - s_{(e^-,Pt)} \right]$$

Reverse thermal emf across platinum electrodes and leads [2]

$$\Delta\phi_c = \frac{\Delta T}{F} \left[ -\frac{1}{4} \bar{S}_{O_2} + \frac{1}{2} s_{O^=} - s_{(e^-,Pt)} \right]$$

Difference between contact potentials at the two electrodes [3]

By combining expressions [1], [2], and [3] into Eq. [B], we obtain

$$\frac{\Delta\phi}{\Delta T} = \frac{1}{F} \left[ \frac{1}{2} \bar{S}_{O^=} - \bar{S}_{(e^-,Pt)} - \frac{1}{4} \bar{S}_{O_2} \right]$$

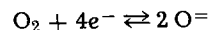
Seebeck coefficient<sup>2</sup> of thermocell [4]

where  $\Delta T$  is the temperature of the hot electrode minus that of the cold electrode,  $F$  is the Faraday,  $\bar{S}_{O^=}$  and  $\bar{S}_{(e^-,Pt)}$  are the transported entropies of O<sup>=</sup> ions and electrons, respectively, in the electrolyte, and  $\bar{S}_{O_2}$  is the partial molar entropy of O<sub>2</sub> in the gaseous atmosphere at the electrodes. With the restrictions listed,  $\bar{S}_{O_2}$  represents the partial molar entropy of oxygen in a pure oxygen atmosphere or in a gas mixture such as H<sub>2</sub>-H<sub>2</sub>O-N<sub>2</sub>. In the latter mixture the calculation of  $\bar{S}_{O_2}$  involves the reacting species, namely O<sub>2</sub>, H<sub>2</sub>O, and H<sub>2</sub> of the gas mixture, but is independent of the "inert" component N<sub>2</sub>. For the purpose of calculation,  $\bar{S}_{O_2}$  is defined in a conventional way as the change in entropy of the oxygen-containing gas mixture at the electrode per mole of oxygen added, with the addition being made at constant temperature and pressure and in such small quantity that the composition of the gas mixture remains essentially the same.

While the absolute Seebeck coefficient cannot as yet be calculated, the Seebeck coefficient difference for two gas mixtures  $(d\phi/dT)_{gas 1} - (d\phi/dT)_{gas 2}$  can in principle be calculated for a range of oxygen partial pressures over which the electrolyte and electrode material remain invariant. Under these conditions  $\bar{S}_{O^=}$  is constant, and applying Eq. [4] to two different gas atmospheres at the same temperature, we obtain by subtraction

$$\left( \frac{d\phi}{dT} \right)_{gas 1} - \left( \frac{d\phi}{dT} \right)_{gas 2 (ref.)} = \left( \frac{\bar{S}_{O_2}}{4F} \right)_{gas 2 (ref.)} - \left( \frac{\bar{S}_{O_2}}{4F} \right)_{gas 1} \quad [5]$$

where in our present experiments gas 2 is a convenient reference gas, pure O<sub>2</sub> at atmospheric pressure, and where the electrode reaction is written to involve a reversible 4-electron step



Relation [5] contains no entropy of transport terms and  $\bar{S}_{O_2}$  values can be calculated from data available in standard thermodynamic tabulations.

$\bar{S}_{O^=}$ , the transported entropy of the oxygen ion, cannot be directly calculated from present theory. However, the quantities measured in the current experiments enable us to obtain from Eq. [4] experimental values for  $\bar{S}_{O^=}$ , since  $\bar{S}_{O_2}$  is a known value and

<sup>2</sup>  $\Delta\phi/\Delta T$ , the Seebeck coefficient is considered positive if the hot terminal is positive.

$\bar{S}_{(e^-, Pt)}$  is known from experimental and theoretical considerations of others based on comparison with a lead superconductor which serves as a reference having a Seebeck coefficient of zero (13).  $\bar{S}_{O=}$  is composed of both kinetic and thermodynamic terms which are related to the heat of transport  $Q^*$  by

$$\begin{aligned} \bar{S}_{O=} &= + \frac{Q^*_{O=}}{T} + \bar{s}_{O=} \\ &\cong \frac{Q^*_{O=}}{T} + s_{O=}^{-vib.} + \bar{s}_{O=}^{config.} \quad [6] \end{aligned}$$

where  $\bar{s}_{O=}$  is the partial molar entropy of the oxygen ion,  $s_{O=}^{-vib.}$  and  $\bar{s}_{O=}^{config.}$  are the partial molar entropies of vibration and configurational entropy respectively of the  $O=$  ion, and  $Q^*_{O=}$ , the heat of transport, is a kinetic term depending on details of the heat transfer by the  $O=$  ion diffusing along the temperature gradient.

No satisfactory theoretical treatment has yet been proposed to evaluate quantitatively the heat of transport term in any systems of this nature. Haga (12) proposed a "thermodynamic" treatment which appears to give semiquantitative agreement between experimental and theoretical results for some silver halide systems. However, Haga's use of the Zener-Wert analysis has been criticized both from the standpoint of mathematics (15) and applicability to the framework of the derivation (16). Agreement found by Haga thus would appear to be fortuitous or at best of an empirical nature. To account properly for the continuous interactions of the diffusing ionic species with the lattice, a theory based on lattice dynamics rather than purely thermochemical reasoning appears to be necessary.

Wirtz (14) proposed a physical model of the transport process, but gave no quantitative treatment.

Gonzalez and Oriani (18) criticize the Wirtz model and discuss  $Q^*$  in terms of the mechanism by which activation energy is dissipated back into the lattice. They conclude that the ratio of the heat of transport to the activation energy for migration is a function of the ratios of the mean free paths of phonons and electrons to the jump distance of the diffusing atom.  $Q^*$  may be positive or negative according to this concept.

### Experimental

**Specimens.**—Three specimens of  $(ZrO_2)_{0.85}(CaO)_{0.15}$  were used in the measurements. Specimen 1 was prepared by fusing  $(ZrO_2)_{0.85}(CaO)_{0.15}$  powder in an arc image furnace to give a dense polycrystalline sample. The powder used for this was prepared by sintering and grinding a properly proportioned mixture of  $ZrO_2$  (major impurity, 0.1% Si) and  $CaCO_3$  (major impurity, 0.1% Sr). Specimen 2 was prepared by sintering the appropriate mixture of  $ZrO_2$  (major impurity, < 0.09% Fe) and  $CaCO_3$  (major impurity, 0.1% Sr). The sintering treatment consisted of 2 hr at 1400°C, 12 hr at 2000°C, and an annealing of 2 days at 1400°C, all in  $O_2$  atmosphere. Specimen 3 was purer, containing about 50 ppm combined impurities of Fe, Si, Mg, Al, and Cu, and was sintered in the arc image furnace to eliminate contamination by furnace wall materials. Specimens were ground to a disk form of 1 mm thickness and 9 mm diameter.

**Atmospheres.**—In the course of the measurements a variety of atmospheres were used, each flowed through the system at a rate of approximately 250 cc per minute. The volume of the system was about 500 cc.

For the  $O_2$ -inert gas atmospheres, tank gas mixtures, made to specification by the Matheson Company were employed.

For the  $H_2$ - $H_2O$  inert gas atmospheres, tank gas mixtures of  $H_2$ -inert gas were passed through a cooled

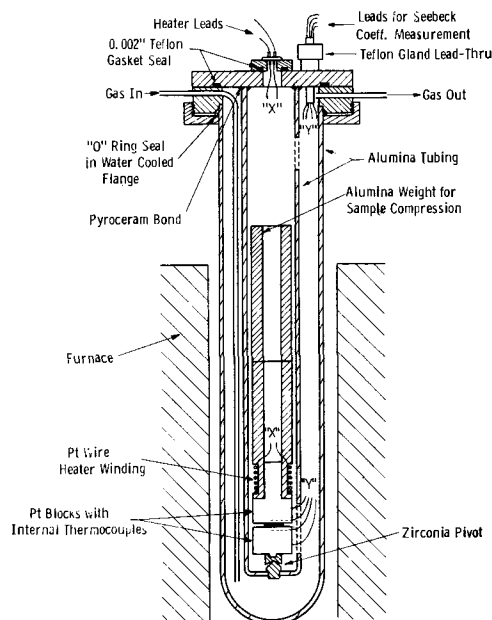


Fig. 1. Apparatus for high temperature Seebeck coefficient measurements.

water bubbler which introduced the  $H_2O$  component but avoided saturation.

The constitution of each atmosphere was checked by mass spectrometric analysis of a sample. Water content of the atmospheres was determined by standard adsorption and weighing methods on the effluent gases from the system.

**Apparatus and technique.**—Seebeck coefficient measurements were carried out with the apparatus shown schematically in Fig. 1. The specimen was situated between the polished faces of two platinum blocks. On the upper block a close-fitting alumina cylinder acted as a compression weight and in addition carried a heater winding for controlling the temperature gradient of the specimen. The lower block was supported by a calcia stabilized zirconia cone pivot which insured that the specimen and blocks were aligned for uniform contact pressure at all times.

The specimen thermal emf was measured by means of 0.020 in. Pt wires attached to the Pt blocks. To measure the temperature of each block at a point as near to the specimen as possible, a 0.020 in. Pt-10% Rh wire was led into the block through alumina-insulating tubing. The end of this wire was then bonded to the block by means of two small Pt plugs. This produced an internal junction near the interface, whose lead wires were the Pt-10% Rh wire and the previously mentioned Pt wire. These details are shown in Fig. 1.

Each measurement was taken at two or more specimen temperature gradients which corrects for thermocouple mismatch and eliminates other stray thermal or galvanic emf's (17). With this procedure a change of one microvolt in the specimen Seebeck coefficient was easily detectable.

### Results and Discussion

Equation [5] has been experimentally verified over a wide range of gas compositions as shown by the data in Fig. 2. In Fig. 2 the Seebeck coefficient difference  $(d\phi/dT)_{(mixture)} - (d\phi/dT)_{(pure O_2)}$  at open circuit, atmosphere pressures of  $730 \pm 2$  Torr and about 1005°C, is plotted vs.  $[\bar{S}_{O_2(mix.)} - \bar{S}_{O_2(pure O_2)}]$  for several mixtures of oxygen and inert gas, and for water-hydrogen-nitrogen mixtures. The solid line in this figure is a theoretical line calculated from Eq. [5] assuming the following over-all reversible electrode reactions for the  $O_2$ -inert gas and  $H_2$ - $H_2O$ - $N_2$  mixtures respectively

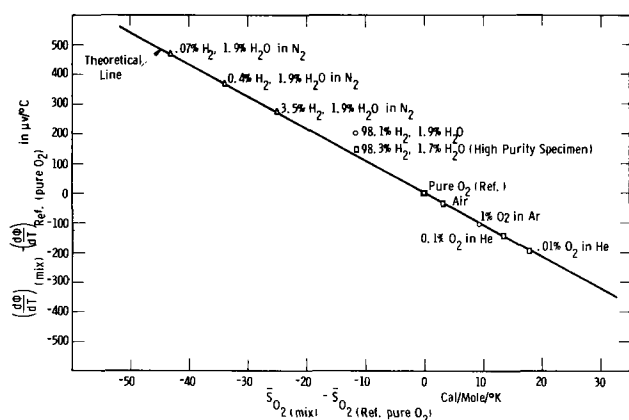
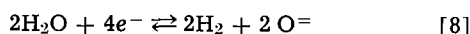
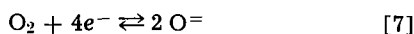


Fig. 2. Difference in Seebeck coefficient vs. difference in partial molar entropy of oxygen for various gas mixtures for thermocell  $X(\bar{S}_{\text{O}_2})$ , Pt ||  $(\text{ZrO}_2)_{0.85}(\text{CaO})_{0.15}$  || Pt,  $X(\bar{S}_{\text{O}_2})$ . Temperature range 1000°-1005°C,  $\sim 730$  Torr—Total pressure for all atmospheres. Experimental points:  $\circ$  specimen 1,  $\triangle$  specimen 2,  $\square$  specimen 3 (high purity).  $\bar{S}_{\text{O}_2}$  in calories per mol per degree K.



All experimental points in Fig. 2 fit the calculated line within the probable error of measurement and gas analysis except for the points at 1.9% H<sub>2</sub>O-98.1% H<sub>2</sub> and 1.7% H<sub>2</sub>O-98.3% H<sub>2</sub>. These mixtures are the most reducing atmospheres used (equivalent equilibrium oxygen partial pressure is  $\sim 10^{-18.1}$  atm at 1000°C), and it is possible that the electrolyte is being slightly altered chemically. Since data of Schmalzried (7) indicate that appreciable reduction does not occur until about  $10^{-22}$  atm O<sub>2</sub> partial pressure for this electrolyte, it is possible that impurities are at least in part responsible for the deviation. The highest purity specimen used, No. 3, gave a much smaller deviation from the theoretical value which is consistent with this viewpoint.

The information obtained in these measurements indicates that our assumption of a constant transported entropy,  $\bar{S}_{\text{O}^\ominus}$ , for a wide range of partial pressures of oxygen is valid. This allows us to determine an "experimental" value of  $\bar{S}_{\text{O}^\ominus}$  directly from Eq. [4] since the other terms of the equation can be measured or calculated.

While the difference values  $(\frac{d\phi}{dT})_{\text{mixture}} - (\frac{d\phi}{dT})_{\text{pure O}_2}$  were, except for the point noted, consistent for all specimens, the experimental value of  $\bar{S}_{\text{O}^\ominus}$  in cal deg<sup>-1</sup> mole<sup>-1</sup>, varied from 10.3 to 10.9 for specimens from batches 1 and 3 to 11.7 for specimen 3, the highest purity specimen. Part of these differences may be linked to subtle temperature-dependent structural changes which are suggested by neutron diffraction and conductivity studies of others (22, 23). To check this point, specimen 1 was cycled between 1250° and 800°C and held for periods up to 14 days. Slow changes

of 3 to 5% in  $\bar{S}_{\text{O}^\ominus}$  were measured. These changes and effects arising from impurities, inhomogeneities (21), differences in crystalline character of the oxides and other sources may contribute to the spread in the values.

An unusual feature of the data is the relatively small temperature dependence of the Seebeck coefficient. As shown in Fig. 3 curve 1,  $\Delta\phi/\Delta T$  changes only a few per cent between temperatures of 700° and 1280°C.

Referring to Eq. [4] and [6], it appears that the term most likely to introduce a large temperature dependence is  $Q^*/T$ . To illustrate this more clearly, Fig. 3 curve 2 gives values of  $\Delta\phi/\Delta T$  as a function of

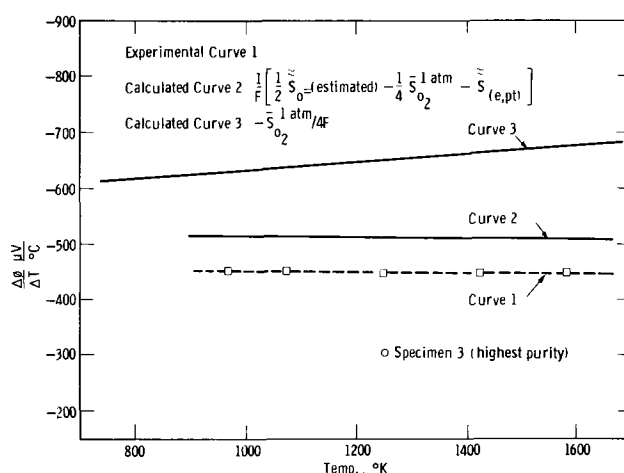


Fig. 3. Effect of temperature on the Seebeck coefficient

temperature based on the values of  $\bar{S}_{\text{O}_2}$  calculated from JANAF thermochemical tables (19),  $\bar{S}_{\text{e,Pt}}$  for the platinum electrode from the data of Cusack and Kendall (13) and a "calculated" value of  $\bar{S}_{\text{O}^\ominus}$  based on Eq. [6], except that  $Q^*/T$  is neglected,  $\bar{S}_{\text{O}^\ominus}^{\text{config}}$  is assumed to be given by the ideal relation of the form  $R \ln 1-C/C$  where  $C$  is the fraction of filled O<sup>⊖</sup> sites based on the perfect fluorite lattice, and  $\bar{S}_{\text{O}^\ominus}^{\text{vib}}$  is estimated on the basis of equipartition of entropy between ions of the oxide. For lack of specific data on the mixed oxide the entropy is assumed to be about that of a simple mixture of 85 m/o (mole per cent) ZrO<sub>2</sub> (tetragonal) and 15% CaO using thermochemical data assembled by Kelly and King (20) for ZrO<sub>2</sub> and CaO. This simple procedure does not take into account such problems as electronic contribution to the entropy at high temperatures, entropy differences of ions next to vacancies, effect of specimen inhomogeneities (21), possible preferred conduction paths due to the high vacancy concentration and other effects. As a consequence we may expect large errors in the absolute value of  $\bar{S}_{\text{O}^\ominus}$  calculated in this way. However, it would seem that the error due to variation of  $\Delta\phi/\Delta T$  with temperature may be small which would suggest the relative importance of the  $Q_{\text{O}^\ominus}^*/T$  term which might be expected to have a large temperature dependence. It is seen that the temperature dependence of curve 2 is small, similar to the actual experimental data indicating either that  $Q^*/T$  is small or not appreciably temperature dependent. This is clearly speculation, however, since, as indicated, curve 2 can at best give only a poor estimate of the absolute value of this collection of terms due to uncertainties in the procedure for estimating  $\bar{S}_{\text{O}^\ominus}$ . Figure 3 curve 3 shows the relative contribution of the term  $\bar{S}_{\text{O}_2(1 \text{ atm})}/4F$  calculated from thermodynamic data (19) for reference.

This analysis suggests that further information on the problem might come from experimental measurements at lower temperatures where a temperature dependence of  $Q^*/T$  could result in a larger contribution to the Seebeck coefficient and from measurements of contact potentials for the cell and the work function of electrons in platinum as a function of temperature which would give experimental information for evaluating  $\bar{S}_{\text{O}^\ominus}$ .

#### Acknowledgment

The authors wish to thank D. Watt for help with part of the measurements, J. Hrizo and T. Y. Tien for part of the sample preparations, and R. Ure, P. Klemens, and A. Panson for helpful discussions.

Manuscript received Sept. 11, 1967; revision received Jan. 19, 1968.

Any discussion of this paper will appear in a Discussion Section to be published in the December 1968 JOURNAL.

## REFERENCES

- Hans Holtan, Jr., *Koninkl. Ned. Akad. Wetenschap. Proc.*, **56B**, 498 (1953); H. Holtan Jr., P. Mazur, and S. R. DeGroot, *Physica*, **19**, 1109 (1953).
- A. B. Lidiard, "Reports on Progress in Physics" (1964).
- R. E. Howard and A. B. Lidiard, *Disc. Faraday Soc.*, **23**, 113 (1957).
- Kalevi Kiukkola and Carl Wagner, *This Journal*, **104**, 379 (1957).
- W. D. Kingery, J. Pappis, M. E. Doty, and D. C. Hill, *J. Am. Chem. Soc.*, **42**, 394 (1959).
- J. Weissbart and R. Ruka, *Rev. Sci. Instr.*, **32**, 593 (1961).
- H. Schmalzried, *Z. Elektrochem.*, **66**, 572 (1962).
- W. H. Rhodes and R. E. Carter, "Ionic Self-Diffusion in Calcia Stabilized Zirconia," Abstract in *Bull. Am. Ceram. Soc.*, April 1962.
- H. Reinhold, *Z. Physik Chem. (Leipzig)*, **B11**, 321 (1930); H. Reinhold and A. Blachny, *Z. Electrochem.*, **39**, 290 (1933).
- L. Patrick and A. W. Lawson, *J. Chem. Phys.*, **22**, 1492 (1954).
- R. W. Christy, E. Fukushima, and H. T. Li, *ibid.*, **30**, 136 (1959); R. W. Christy, *ibid.*, **34**, 1148 (1961).
- Eijiro Haga, *J. Phys. Soc. Japan*, **15**, 1949 (1960).
- N. Cusack and P. Kendall, *Proc. Phys. Soc. (London)*, **72**, 898 (1958).
- K. Wirtz, *Phys. Z.*, **44**, 221 (1943).
- A. B. Lidiard, Personal communication.
- C. Zener, Personal communication.
- R. W. Ure, Jr., in "Thermoelectricity," p. 321, Interscience Publishers, New York (1961).
- O. D. Gonzalez and R. A. Oriani, *Trans. Met. Soc. AIME*, **233**, 1878 (1965).
- JANAF Thermochemical Tables PB 168370-1, U.S. Dept. of Commerce Oxygen (Diatomic), Sept. 30, 1965.
- K. K. Kelly and E. G. King, Bureau of Mines Bulletins 584 and 592.
- Conyers Herring, *J. Appl. Phys.*, **31**, 1939-1953 (1960).
- T. Y. Tien and E. C. Subbarao, *J. Chem. Phys.*, **39**, 1041-1047 (1963).
- W. L. Roth, "Structure and Vacancy Ordering in Calcia-Stabilized Zirconia," Abstract presented at Am. Cryst. Assoc. Meeting, July 1964; R. E. Carter and W. L. Roth, "The Decomposition of Calcia-Stabilized Zirconia," Abstract presented at 31st Annual Chemical Engineering Symposium, A.C.S., at University of Michigan, November 1964.

## Poisson's Equation as a Condition of Equilibrium in Electrochemical Systems

H. A. Christopher\* and C. W. Shipman

Worcester Polytechnic Institute, Worcester, Massachusetts

## ABSTRACT

The available analyses of the conditions for equilibrium in electrochemical systems do not consider the electrostatic field as a possible variable. Since there is a voltage difference between the electrodes in an electrochemical system, an electrostatic field must be present, and this field must be considered in the treatment of equilibrium because it affects the internal energy of the system. This paper presents an analysis in which the electric displacement vector is included as a possible variable. The results show that Poisson's equation is a condition of equilibrium in addition to the usual conditions of uniformity of the electrochemical potential, the pressure, and the temperature.

The conditions of equilibrium in electrochemical systems (systems which contain charged species and in which there may be electrostatic fields) have been discussed by several authors. In each case the proof is incomplete. Gibbs (1) uses a variational treatment but does not consider the electrostatic field as a possible variation. Guggenheim (2) states that uniformity of the electrochemical potential is a requirement for equilibrium but does not give a detailed proof. He also does not consider the electrostatic field as a possible variable in the system although he later shows that variation of the electric displacement vector can alter the internal (intrinsic) energy. Kirkwood and Oppenheim (3) use a variational analysis but assume as a starting point that the electrochemical potential is the intensive factor for variations in energy with mass addition. Here again, consideration of the electric displacement vector as a possible variable is omitted.

The fact that in an electrochemical cell there is a voltage difference between the electrodes means that there is an electrostatic field present in the system, and this electrostatic field is not always applied but can arise spontaneously. This means that the consequences

of variations in the electric displacement vector must be considered when the equilibrium is considered.

Both ref. (2) and (3) discuss at some length the fact that separate measurement of the electrostatic and chemical potentials cannot be made and that separation of these potentials is, therefore, "nonoperational." Gibbs (1), on the other hand, considers these two potentials separately in his analysis, but in a later note (4) points out that separate measurement is impossible. The present authors take the position that the question of separate measurement is a consequence of rather than a basis for the equilibrium analysis. Further, the use of separate terms for the chemical and electrostatic potentials facilitates the treatment of mass transfer in electrochemical systems (5).

Finally, it is noted that the usual criteria for equilibrium involve terms of the form  $(dE)_{S,V}$ ,  $(dS)_{E,V}$ , or  $(dG)_{p,T}$ , and, therefore, require that some purely thermodynamic property of the system be fixed at the outset. This is restrictive because these restraints cannot be imposed experimentally by direct control.

The present analysis considers the electric displacement vector as a possible variable, and does not require, at the outset, the fixing of any purely thermo-

\* Electrochemical Society Active Member.

dynamic property except as a controlled boundary condition. Separate terms for the chemical and electrostatic potentials are retained for the reasons cited earlier.

### The Conditions for Equilibrium

A general criterion of equilibrium is:

If a system be in such state that any possible variation from that state, within the restrictions that the first law of thermodynamics and any physical constraints be satisfied, requires a violation of the second law of thermodynamics, then such variation cannot occur, and the system is at equilibrium.

The most convenient form of the second law for the present purpose is the inequality of Clausius which, for a real process, is

$$dS - (\delta Q/\tau) > 0 \quad [1]$$

(A table of nomenclature is included at the end of the paper.) In a derivation of this statement by Phillips as quoted by Keenan (6), it is shown that  $\tau$  is the temperature of that part of the system to which heat is transmitted. This does not imply uniformity of temperature in the system or constancy of  $\tau$ , only that there are not multiple sources of heat for the system at different temperatures simultaneously. The entropy term is for the entire system. Equation [1] is, of course, restricted to systems of fixed total mass.

To apply the criterion of equilibrium, we consider a system of constant total mass confined by a piston at an applied pressure,  $P$ . The system will consist of several phases,  $\Phi$  in number (e.g., as a minimum two electrode phases and an electrolyte phase; or for a fuel cell, a fuel phase, an anode phase, an electrolyte phase, a cathode phase, and an oxidant phase). For simplicity, magnetic and gravitational fields are excluded, surface phenomena are neglected, and any variations are in one dimension only. No current passes to an external circuit from the system (i.e., attention is restricted to open-circuit conditions). The system contains several chemical species,  $J$  in number, each of which has a charge per unit mass,  $z_j$ . (The possibility that  $z_j=0$  is not excluded.) Such a system is shown schematically in Fig. 1. In this figure  $X$  is the total length of the system from the fixed boundary at the left to the piston on the right and may vary as the piston moves to maintain the applied pressure,  $P$ ;  $x_{1,\phi}$  and  $x_{2,\phi}$  are the boundaries of one of the phases;  $\delta x$  is an incremental length of the system within one of the phases; and  $x$  is the distance from the fixed boundary to the plane considered. The locations of  $x_{1,\phi}$  and  $x_{2,\phi}$  may, of course, be altered as the system varies. The heat source (or sink) is at the left where the temperature of the system is  $\tau$ . (This heat source may be viewed as a constant temperature bath, but this is unnecessarily restrictive.)

In the system as described several variables are not controlled directly, and changes in these are, therefore,

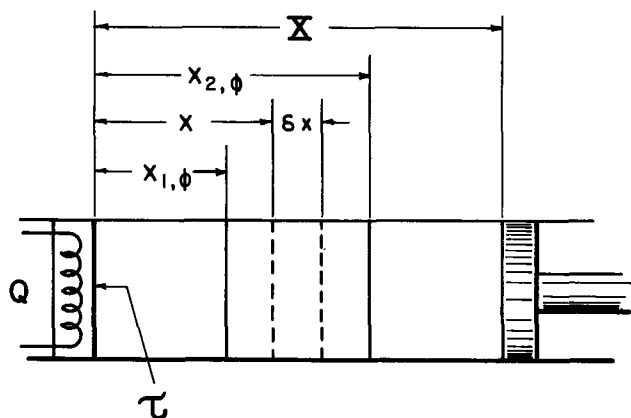


Fig. 1. Schematic showing system of constant total mass

“possible.” (The term possible variation is used in the sense indicated, i.e., not specified by a fixed parameter. This means that some variations considered possible herein are restricted by the laws of thermodynamics and the material balances.) These possible variations are:

1. The electrostatic field vector,  $\vec{\mathcal{E}}$  and the corresponding electrostatic potentials.
2. Chemical composition. (Changes may be a consequence of migration of a species from one part of the system to another or of chemical reaction.)
3. Thermodynamic properties: entropy, internal (intrinsic) energy, specific volume, pressure, etc.
4. The total volume of the system.

We now seek the state of the system such that for any of the possible variations, there results

$$(\delta Q/\tau) - dS \geq 0 \quad [2]$$

i.e., violation of the second law of thermodynamics.

The possible variations in the system are subject to restraint by: (a) the first law of thermodynamics, (b) the material balances, and (c) the functional relations among the thermodynamic properties. These will be discussed in turn.

(a) The first law of thermodynamics, for the fixed mass system considered herein, may be written

$$\begin{aligned} \delta Q = d \sum_{\phi=1}^{\Phi} \int_{x_{1,\phi}}^{x_{2,\phi}} E_{\phi} \rho_{\phi} A \delta x \\ + d \sum_{\phi=1}^{\Phi} \int_{x_{1,\phi}}^{x_{2,\phi}} (\Psi_{\phi} \rho_{\phi} \sum_{j=1}^J z_j \chi_{j,\phi}) A \delta x \\ + P d \int_0^X A \delta x \quad [3] \\ j = 1, 2, \dots, J \\ \phi = 1, 2, \dots, \Phi \end{aligned}$$

The integral forms have been used to allow for the point-to-point variations in the integrands within a phase, as in electrolyte composition and electrostatic potential. The summations over the various phases are considered because properties may not be continuous at phase boundaries, e.g., electrodes. The only work term is that resulting from expansion of the movable boundary against the fixed, applied pressure,  $P$ . (Note:  $P$  is the pressure applied to the system by the piston, not the pressure of the system at some point inside.) Changes in the internal energy have been distinguished from changes in the potential energy of charged masses in the electrostatic field which may be computed from Coulomb's law. It is important that these latter variations be distinguished from those due to the electrostatic field alone because variations in the electrostatic field will affect the internal energy. While the two effects are not always physically independent (changing the position of a charged particle can alter the electrostatic field vector), they are described by different physical laws.

(b) Any variations in composition must be consistent with the appropriate material balance expressions. A quantitative statement of the material balance is

$$d \sum_{\phi=1}^{\Phi} \int_{x_{1,\phi}}^{x_{2,\phi}} \rho_{\phi} \chi_{j,\phi} A \delta x - \sum_{\phi=1}^{\Phi} \sum_{r=1}^R \nu_{j,r} d\xi_{r,\phi} = 0 \quad [4]$$

( $J$  equations)

The possibility that some of the species,  $j$ , do not react chemically ( $\nu_{j,r}=0$ ) is not excluded. The quantities  $\nu_{j,r}$  are the stoichiometric coefficients of the  $j^{\text{th}}$  chemical species in the  $r^{\text{th}}$  independent stoichiometric relation of the form

$$\sum_{j=1}^J \nu_{j,r} M_j = 0 \quad (r = 1, 2, \dots, R) \quad [5]$$

The quantities  $\xi_{r,\phi}$  are the parameters representing variations due to chemical reaction as indicated by the  $r^{\text{th}}$  stoichiometric relation (extent of reaction parameters). These are, in Eq. [4], integral averages over a phase.

It should be noted that either mole or mass units may be used in these equations so long as one is consistent. That is,  $\rho$  is either a mole or mass density,  $\chi_j$  is mole or mass fraction, and  $z_j$  is the charge per mole or per unit of mass of  $j$ . The stoichiometric coefficients,  $\nu_{j,r}$ , must, of course, be changed accordingly.

(c) In order to relate the specific internal energy,  $\bar{E}$ , to the other properties of the system, the necessary relationships among the thermodynamic properties must be given. Further, because these relations are to be applied to individual volumes of the entire system, and because the total mass of the individual volumes may vary, the applicable relationships must apply to variable mass systems. Since these relations are not available elsewhere, the derivations will be given in some detail.

In general the internal energy,  $E$ , is related to the other properties of the system in the usual way, *viz.*

$$E = E(S, V, m_j, \vec{D}) \quad [6]$$

(It should not be inferred that  $S$ ,  $V$ ,  $m_j$ , and  $\vec{D}$  are the independent variables of the electrochemical system

considered; only that fixing  $S$ ,  $V$ ,  $m_j$ , and  $\vec{D}$  fixes the value of  $E$ .) The relevant form for variations of the internal energy is

$$dE = TdS - pdV + \sum_{j=1}^J \mu_j dm_j + \vec{V}\vec{G} \cdot d(\vec{D}) \quad [7]$$

where the last term on the right represents variations in the internal energy due to variations in the electrostatic field (7). Recognizing that the electric displacement vector,  $\vec{D}$ , is related to the electric intensity,  $\vec{G}$ , by

$$\vec{D} = \epsilon \vec{G} \quad [8]$$

one may write Eq. [7] in the alternative forms

$$dE = TdS - pdV + \sum_{j=1}^J \mu_j dm_j + (\vec{V}\vec{D}/\epsilon) \cdot d\vec{D} = TdS - pdV + \sum_{j=1}^J \mu_j dm_j + d(\vec{V}\vec{D}^2/2\epsilon) - (\vec{D}^2/2)d(V/\epsilon) \quad [9]$$

It is important to recognize that Eq. [7] and, therefore, Eq. [9] can be applied only to regions in which the coefficients are single-valued.

Equations [9] may be integrated over a region for which the intensive factors ( $T$ ,  $p$ ,  $\mu_j$ ,  $\vec{D}$ ) are constant to give

$$E = TS - pV + \sum_{j=1}^J \mu_j m_j + \vec{V}\vec{D}^2/2\epsilon - (\vec{D}^2/2)(V/\epsilon) \\ = TS - pV + \sum_{j=1}^J \mu_j m_j \quad [10]$$

(It is striking that in this integration the terms involving the electrostatic field drop out. This is a consequence of the fact that the expression is being applied to a region in which the intensive factors are uniform. While it is clear that the internal energy is altered by the presence of the electrostatic field, the other thermodynamic properties are also altered. Note also that in the integration we are not computing the work required to establish the electrostatic field; it is already present.)

We consider next variations in the properties of the system generally by differentiating [10], *viz.*

$$dE = TdS - pdV + \sum_{j=1}^J \mu_j dm_j \\ + SdT - Vdp + \sum_{j=1}^J m_j d\mu_j$$

Comparison of this equation with [9] requires that

$$0 = SdT - Vdp + \sum_{j=1}^J m_j d\mu_j - (\vec{V}\vec{D}/\epsilon) \cdot d\vec{D} \quad [11]$$

For purposes of utilization in the energy balance (Eq. [3]), the relationships among the specific properties for variable mass systems are required. Such relationships may be obtained by dividing Eq. [10] and [11] by the total mass to obtain

$$\bar{E} = T\bar{S} - p\bar{V} + \sum_{j=1}^J \mu_j \chi_j \quad [12a]$$

$$0 = \bar{S}dT - \bar{V}dp + \sum_{j=1}^J \chi_j d\mu_j - (\vec{V}\vec{D}/\epsilon) \cdot d\vec{D} \quad [12b]$$

Differentiation of Eq. [12a] and subtraction of [12b] from the result gives the desired expression.

$$d\bar{E} = Td\bar{S} - p d\bar{V} + \sum_{j=1}^J \mu_j d\chi_j + (\vec{V}\vec{D}/\epsilon) \cdot d\vec{D} \quad [13]$$

(The reader will note that obtaining Eq. [13] by division of Eq. [9] by the total mass restricts the result to a system of fixed mass. The seemingly circuitous route herein used avoids that problem and makes the result more general.) Equations [12] and [13] constitute the necessary relations among the specific properties. It is emphasized that the chemical potentials,  $\mu_j$ , are functions of the electric displacement,  $\vec{D}$ , and represent the change of internal energy with mass of  $j$  with all of the other variables held constant.

$$\mu_j = (\partial E / \partial m_j)_{S, V, D, m_{k \neq j}}$$

It is important to recognize that an electrostatic field can be imposed on the system without changing its composition.

Returning, now, to the conditions for equilibrium, the nonproperty term,  $\delta Q$ , may be eliminated from the criterion expression [2] by substitution from the energy balance [3]. After multiplication by  $\tau$  the result is

$$d \sum_{\phi=1}^{\Phi} \int_{x_{1,\phi}}^{x_{2,\phi}} \bar{E}_{\phi\rho\phi} A \delta x \\ + d \sum_{\phi=1}^{\Phi} \int_{x_{1,\phi}}^{x_{2,\phi}} \Psi_{\phi\rho\phi} \left( \sum_{j=1}^J \chi_{j,\phi} z_j \right) A \delta x \\ + P d \int_0^X A \delta x - \tau d \sum_{\phi=1}^{\Phi} \int_{x_{1,\phi}}^{x_{2,\phi}} \bar{S}_{\phi\rho\phi} A \delta x \geq 0 \quad [14]$$

By carrying out the indicated differentiations of Eq. [14] one obtains

$$\begin{aligned}
& \sum_{\phi=1}^{\Phi} \int_{x_{1,\phi}}^{x_{2,\phi}} \left( d\bar{E}_{\phi} + \Psi_{\phi} \sum_{j=1}^J z_j d\chi_{j,\phi} \right. \\
& \quad \left. + d\Psi_{\phi} \sum_{j=1}^J z_j \chi_{j,\phi} - \tau d\bar{S}_{\phi} \right) \rho_{\phi} A dx \\
& + \sum_{\phi=1}^{\Phi} \int_{x_{1,\phi}}^{x_{2,\phi}} \left( \bar{E}_{\phi} + \Psi_{\phi} \sum_{j=1}^J z_j \chi_{j,\phi} - \tau \bar{S}_{\phi} \right) d\rho_{\phi} A dx \\
& + \sum_{\phi=1}^{\Phi} \left( \bar{E}_{\phi} \rho_{\phi} + \Psi_{\phi} \rho_{\phi} \sum_{j=1}^J z_j \chi_{j,\phi} - \tau \rho_{\phi} \bar{S}_{\phi} \right)_{x_{2,\phi}} A dx_{2,\phi} \\
& \quad - \sum_{\phi=1}^{\Phi} \left( \bar{E}_{\phi} \rho_{\phi} + \Psi_{\phi} \rho_{\phi} \sum_{j=1}^J z_j \chi_{j,\phi} \right. \\
& \quad \left. - \tau \rho_{\phi} \bar{S}_{\phi} \right)_{x_{1,\phi}} A dx_{1,\phi} + P A dX \geq 0 \quad [15]
\end{aligned}$$

The internal energy may be eliminated from [15] by means of Eq. [12a] and [13] to give

$$\begin{aligned}
& \sum_{\phi=1}^{\Phi} \int_{x_{1,\phi}}^{x_{2,\phi}} \left( (T_{\phi} - \tau) d\bar{S}_{\phi} + \sum_{j=1}^J (\mu_{j,\phi} + z_j \Psi_{\phi}) d\chi_{j,\phi} \right. \\
& \quad \left. + \vec{V}_{\phi} \vec{\mathcal{E}}_{\phi} \cdot d\vec{D}_{\phi} + \left( \sum_{j=1}^J z_j \chi_{j,\phi} \right) d\Psi_{\phi} \right) \rho_{\phi} dx \\
& + \sum_{\phi=1}^{\Phi} \int_{x_{1,\phi}}^{x_{2,\phi}} \left( -p_{\phi} \rho_{\phi} d(1/\rho_{\phi}) - (p_{\phi}/\rho_{\phi}) d\rho_{\phi} \right) dx \\
& \quad + \sum_{\phi=1}^{\Phi} \int_{x_{1,\phi}}^{x_{2,\phi}} \left( (T_{\phi} - \tau) \bar{S}_{\phi} \right. \\
& + \sum_{j=1}^J (\mu_{j,\phi} + z_j \Psi_{\phi}) \chi_{j,\phi} \left. \right) d\rho_{\phi} dx + \sum_{\phi=1}^{\Phi} \left( (T_{\phi} - \tau) \bar{S}_{\phi} \rho_{\phi} \right. \\
& \quad \left. + \sum_{j=1}^J (\mu_{j,\phi} + z_j \Psi_{\phi}) \chi_{j,\phi} \rho_{\phi} \right)_{x_{2,\phi}} dx_{2,\phi} \\
& - \sum_{\phi=1}^{\Phi} \left( (T_{\phi} - \tau) \bar{S}_{\phi} \rho_{\phi} + \sum_{j=1}^J (\mu_{j,\phi} + z_j \Psi_{\phi}) \chi_{j,\phi} \rho_{\phi} \right)_{x_{1,\phi}} dx_{1,\phi} \\
& \quad - \sum_{\phi=1}^{\Phi} \left( [p_{\phi} (1/\rho_{\phi}) \rho_{\phi}]_{x_{2,\phi}} dx_{2,\phi} \right. \\
& \quad \left. - [p_{\phi} (1/\rho_{\phi}) \rho_{\phi}]_{x_{1,\phi}} dx_{1,\phi} + P dX \right) \geq 0 \quad [16]
\end{aligned}$$

The area term,  $A$ , has been divided out. Note that the second integral on the left of [16] is identically zero. Note also that the sum of the changes in the volumes of the separate phases must be the change in volume of the system.

$$dX = \sum_{\phi=1}^{\Phi} (dx_{2,\phi} - dx_{1,\phi})$$

By means of this expression the last three terms on the left of [16] may be combined, viz.

$$- \sum_{\phi=1}^{\Phi} \left( (p_{\phi} - P)_{x_{2,\phi}} dx_{2,\phi} - (p_{\phi} - P)_{x_{1,\phi}} dx_{1,\phi} \right)$$

The variations ( $d\bar{S}_{\phi}$ ,  $d\chi_{j,\phi}$ ,  $d\vec{D}_{\phi}$ ,  $d\Psi_{\phi}$ , etc.) in Eq. [16] are not all independent. The variations in  $\chi_{j,\phi}$  and  $\rho_{\phi}$  are restricted by Eq. [4] and by the requirement that at any point

$$\sum_{j=1}^J \chi_{j,\phi} = 1 \quad \text{or} \quad \sum_{j=1}^J d\chi_{j,\phi} = 0 \quad [17]$$

Equation [16] as modified, [17], and [4] then indicate an extremum with two conditions of restraint. The inequality [16] indicates that the equilibrium condition is at the minimum value of the function whose variation is given by the left side of [16] with restraints represented by Eq. [4] and [17]. Lagrange's method of multipliers may be used. After carrying out the indicated differentiations in Eq. [4] (there are  $J$  equations) and multiplying each by the arbitrary functions  $\lambda_j$  and after multiplying the differential form of [17] by  $\lambda_{17}$ , the results are subtracted from [16] to yield

$$\begin{aligned}
& \sum_{\phi=1}^{\Phi} \int_{x_{1,\phi}}^{x_{2,\phi}} \left[ (T_{\phi} - \tau) d\bar{S}_{\phi} \right. \\
& \quad \left. + \sum_{j=1}^J (\mu_{j,\phi} + z_j \Psi_{\phi} - \lambda_j - \lambda_{17}) d\chi_{j,\phi} \right. \\
& \quad \left. + \vec{V}_{\phi} \vec{\mathcal{E}}_{\phi} \cdot d\vec{D}_{\phi} + \left( \sum_{j=1}^J z_j \chi_{j,\phi} \right) d\Psi_{\phi} \right] \rho_{\phi} dx \\
& \quad + \sum_{j=1}^J \sum_{\phi=1}^{\Phi} \sum_{r=1}^R \lambda_j \nu_{j,r} d\xi_{r,\phi} \\
& \quad + \sum_{\phi=1}^{\Phi} \int_{x_{1,\phi}}^{x_{2,\phi}} \left( (T_{\phi} - \tau) \bar{S}_{\phi} \right. \\
& \quad \left. + \sum_{j=1}^J (\mu_{j,\phi} + z_j \Psi_{\phi} - \lambda_j) \chi_{j,\phi} \right) d\rho_{\phi} dx \\
& \quad + \sum_{\phi=1}^{\Phi} \left( (T_{\phi} - \tau) \bar{S}_{\phi} + \sum_{j=1}^J (\mu_{j,\phi} \right. \\
& \quad \left. + z_j \Psi_{\phi} - \lambda_j) \chi_{j,\phi} \right)_{x_{2,\phi}} \rho_{x_{2,\phi}} dx_{2,\phi} \\
& \quad - \sum_{\phi=1}^{\Phi} \left( (T_{\phi} - \tau) \bar{S}_{\phi} + \sum_{j=1}^J (\mu_{j,\phi} \right. \\
& \quad \left. + z_j \Psi_{\phi} - \lambda_j) \chi_{j,\phi} \right)_{x_{1,\phi}} \rho_{x_{1,\phi}} dx_{1,\phi} \\
& \quad - \sum_{\phi=1}^{\Phi} \left( (p_{\phi} - P)_{x_{2,\phi}} dx_{2,\phi} - (p_{\phi} - P)_{x_{1,\phi}} dx_{1,\phi} \right) \geq 0 \quad [18]
\end{aligned}$$

The values of the functions  $\lambda_{17}$  and  $\lambda_j$  will be chosen so that the variables in Eq. [18] which are not independent will be eliminated. The function  $\lambda_{17}$  is chosen such that for some particular species, say  $k$ , it is identically equal to the function  $(\mu_{k,\phi} + z_k \Psi_{\phi} - \lambda_k)$  at all points in the system. The values of the functions  $\lambda_j$  are chosen so that the functions  $(\mu_{j,\phi} + z_j \Psi_{\phi} - \lambda_j)$  are identically zero at some point in the system. This procedure effectively eliminates the dependent variables from Eq. [18]; either the variables  $d\bar{S}_{\phi}$ ,  $d\chi_{j,\phi}$ ,  $d\rho_{\phi}$ ,  $d\Psi_{\phi}$ , etc., are independent or their coefficients are identically zero. Satisfaction of Eq. [18] for regions wherein "j" is an actual component ( $d\chi_{j,\phi}$  can take any sign) requires that

- I.  $T_{\phi} = \tau$
- II.  $p_{x_{1,\phi}} = P \quad p_{x_{2,\phi}} = P$
- III.  $\mu_{j,\phi} + z_j \Psi_{\phi} = \lambda_j \quad (j = 1, 2, \dots, J)$
- IV.  $\sum_{j=1}^J \nu_{j,r} \lambda_j = 0 \quad (j = 1, 2, \dots, J)$   
 $(r = 1, 2, \dots, R)$
- V.  $\vec{V}_{\phi} \vec{\mathcal{E}}_{\phi} \cdot d\vec{D}_{\phi} + \left( \sum_{j=1}^J z_j \chi_{j,\phi} \right) d\Psi_{\phi} = 0$

These five conditions must obtain at equilibrium. Con-

dition I requires that the temperature be uniform; condition II requires that the pressure at each phase boundary be the pressure applied to the system; condition III is the familiar requirement of uniformity of the electrochemical potential; condition IV (combined with condition III) is the familiar form for chemical equilibrium except that the electrochemical potential  $(\mu_j + z_j\psi)$  appears instead of the chemical potential alone.

Condition V is new and is a consequence of considering the effect of the electrostatic field. Actually condition V reduces to Poisson's equation for a medium of constant permittivity. This may be easily demonstrated by considering adjacent parts of the system and applying condition V in one-dimensional form. Using Eq. [8] and the definition

$$\vec{G}_\phi = -\text{grad}(\psi_\phi)$$

one finds

$$\bar{V}_\phi (-d\psi_\phi/dx) \frac{d}{dx} \left( -\epsilon_\phi \frac{d\psi_\phi}{dx} \right) + \left( \sum_{j=1}^J z_j \chi_{j,\phi} \right) (d\psi_\phi/dx) = 0 \quad [19]$$

For constant permittivity this becomes

$$d^2\psi_\phi/dx^2 = - \left( \sum_{j=1}^J z_j \chi_{j,\phi} \right) / (\epsilon_\phi \bar{V}_\phi) \quad [20]$$

which is Poisson's equation. Thus, Poisson's equation is a consequence of the equilibrium analysis if the permittivity of the medium is constant. Since permittivity is, in general, dependent on composition, use of [20] implies uniform composition.

The expression deduced directly from [19] without assumption is

$$\frac{d}{dx} (\vec{D}_\phi) = \left( \sum_{j=1}^J z_j \chi_{j,\phi} \right) / \bar{V}_\phi \quad [20a]$$

which may be obtained directly from Maxwell's equations (8). Since the electrostatic field term in Eq. [7] was also obtained by use of Maxwell's equations (5) such a result is not surprising.

Condition V may also be used to develop relations between the electrochemical potential and the other thermodynamic properties. For example, substitution of condition V into Eq. [12b] yields

$$0 = \bar{S}dT - \bar{V}dp + \sum_{j=1}^J \chi_j d(\mu_j + z_j\psi) \quad [21]$$

which is the analog of the Gibbs equation for electrochemical systems. Note that according to Eq. [21] the equilibrium requirements of uniformity of the electrochemical potentials and of the temperature mean that the pressure must also be uniform.

Use of condition V in Eq. [7] gives the relation

$$dE = TdS - pdV + \sum_{j=1}^J \mu_j dm_j - \left( \sum_{j=1}^J z_j m_j \right) d\psi \quad [22]$$

or in Eq. [13]

$$d\bar{E} = Td\bar{S} - p d\bar{V} + \sum_{j=1}^J \mu_j d\chi_j - \left( \sum_{j=1}^J z_j \chi_j \right) d\psi \quad [23]$$

By adding the quantity

$$d \left( \psi \sum_{j=1}^J (z_j m_j) \right)$$

to both sides of [22] one obtains

$$d \left( E + \psi \sum_{j=1}^J z_j m_j \right) = TdS - pdV + \sum_{j=1}^J (\mu_j + z_j\psi) dm_j \quad [24]$$

Equations [21] and [23] may be used to obtain interrelationships among the various properties by relations of the Maxwell type in the usual way.

Equation [24] is effectively the fundamental expression used by Kirkwood and Oppenheim (3) except that their symbol  $E$  represents the group in parenthesis on the left of [24]. The present treatment makes this a consequence of the equilibrium analysis. Kirkwood and Oppenheim state in developing [24] that they make the assumption that the quantity denoted by the symbol  $E$  as used herein depends only on the pressure, temperature, and composition and not on the charge, and point out that verification of the assumption has been obtained from experiment. The present analysis shows that such an assumption is unnecessary. It is emphasized that  $E$  is, in virtue of Eq. [17], dependent on  $\vec{D}$  (5).

Finally, in obtaining conditions I through V it was assumed that all chemical species,  $j$ , are present in all phases. For species which are not actually present in some particular phase,  $\phi_1$ , the sign of  $d\chi_{j,\phi_1}$  can only be positive, and therefore, Eq. [18] will be satisfied if

$$\mu_{j,\phi_1} + z_j\psi_{\phi_1} \geq \lambda_j \quad [25]$$

### Conclusions

The results of an equilibrium analysis in which the electric displacement vector is considered as a possible variable show that the usual conditions of equilibrium involving uniformity of temperature, pressure, and electrochemical potential are unaffected. The treatment also shows that the usual conditions of equilibrium will apply across regions where the electric displacement vector is varying. Furthermore, the analysis yields Poisson's equation (or rather its more general equivalent) as a condition of equilibrium.

### Acknowledgment

The authors gratefully acknowledge the financial support of the Research and Advanced Development Division of the AVCO Corporation. Dr. Christopher was supported by an NDEA (Title IV) Fellowship. The helpful comments of Professors J. P. van Alstyne, B. A. Wooten, and M. V. Evans of the Worcester Polytechnic Institute, and Jeong-long Lin of Boston College are also appreciated.

Manuscript received May 3, 1967; revised manuscript received Jan. 19, 1968.

Any discussion of this paper will appear in a Discussion Section to be published in the December 1968 JOURNAL.

### REFERENCES

1. J. W. Gibbs, "Collected Works," Vol. I, p. 331 *et seq.*, Yale University Press, New Haven (1948).
2. E. A. Guggenheim, "Thermodynamics," 2nd ed., p. 330 *et seq.*, Interscience, New York (1950).
3. J. G. Kirkwood and I. Oppenheim, "Chemical Thermodynamics," p. 205, McGraw-Hill, New York (1961).
4. J. W. Gibbs, *op. cit.*, p. 429.
5. P. L. T. Brian, *et al.*, *A.I.Ch.E. Journal*, **10**, 727 (1964).
6. J. H. Keenan, "Thermodynamics," p. 79, John Wiley & Sons, Inc., New York (1941).
7. E. A. Guggenheim, *op. cit.*, p. 361.
8. J. A. Stratton, "Electromagnetic Theory," p. 5, McGraw-Hill, New York (1941).

### NOMENCLATURE

- $A$  Cross-sectional area (see Fig. 1)  
 $\vec{D}$  Electric displacement vector



$d$	Differential operator (small change in operated quantity)	$\lambda$	Lagrangian multiplier (a function)
$E$	Internal (intrinsic) energy	$\mu$	Chemical potential of subscript species
$\vec{E}$	Electric intensity vector	$\nu_{j,r}$	Stoichiometric coefficient of $j^{\text{th}}$ species in $r^{\text{th}}$ reaction
$J$	Total number of chemical species	$\xi$	Reaction parameter
$m$	Mass of subscript species	$\rho$	Density
$P$	Pressure applied to the system	$\tau$	Temperature of that part of the system in contact with heat source
$p$	Pressure in the system	$\Phi$	Total number of phases present
$Q$	Heat added to the system	$\chi$	Mass (or mole) fraction of subscript species
$R$	Number of independent stoichiometric relations	$\Psi$	Electrostatic potential
$S$	Entropy		
$T$	Temperature	Subscripts	
$V$	Volume	$j$	Species index
$X$	Length of the system (see Fig. 1)	$k$	Species index
$x$	Dummy variable, length in the system (see Fig. 1)	$r$	Reaction index
$z$	Charge per unit mass of subscript species	$\phi$	Phase index
		1	Lower limit of phase boundary
		2	Upper limit of phase boundary
Greek		Superscripts	
$\delta$	Differential operator (small amount of operated quantity)	—	(overscore) Denotes quantity per unit mass or per mole
$\epsilon$	Permittivity		

# Brief Communications



## The Standard Potential of the Silver-Silver Chloride Electrode in N-N Dimethylacetamide at 25°C

Bruno Scrosati, Gianfranco Pecci, and Gianfranco Pistoia

Istituto di Chimica Fisica ed Elettrochimica, Università di Roma, Roma, Italy

Although interest in nonaqueous electrolytes has been greatly increased in the last few years because of their use in high energy battery systems, relatively few determinations of standard potentials of suitable reference electrodes have been carried out in nonaqueous solvents (1-10).

In this work we extend the series to report the behavior of the silver-silver chloride electrode in N-N-Dimethylacetamide (DMA) at 25°C, with respect to the normal hydrogen electrode using the following cell



From the emf data of cell [1] activity coefficients of HCl solutions in DMA at 25°C have been calculated.

DMA (C. Erba reagent grade) was purified by fractional distillation under reduced pressure (2 mm Hg). The final product had a specific conductance of  $4 \times 10^{-7} \text{ ohm}^{-1}$  in good agreement with the value given in the literature (11).

The HCl gas was obtained by dropping concentrated  $\text{H}_2\text{SO}_4$  on reagent grade NaCl and passing the evolved gas first through concentrated  $\text{H}_2\text{SO}_4$  and finally through two traps at dry ice temperature. The solutions used in cell [1] were prepared by passing HCl gas into DMA. The concentration of HCl was determined by Mohr titrations, after neutralizing with sodium bicarbonate. The reliability of volumetric titrations in DMA has been shown by Pistoia and Scrosati (12).

The cell was an all glass type of the design recommended by Ives and Janz (13). The silver-silver chloride electrodes were of the thermal type and were prepared according to the method described by Ives

and Janz (13). Hydrogen electrodes were prepared in the usual manner (13).

Hydrogen gas was purified by Engelhard Hydrogen Purifier Mod. 0-50 and passed through the cell at a rate of 1-2 bubbles/sec. The emf measurements were made at  $25.00^\circ \pm 0.05^\circ\text{C}$  by a differential voltmeter Keithley 662. The emf readings were taken 30 min after starting the hydrogen flow.

The emf values of cell [1], corrected to 760 mm of pressure, are given in Table I as a function of HCl molality.

The standard potential of the silver-silver chloride electrode was determined by the use of the function  $E'$ , defined by the equation

$$E' = E + \frac{2(2.3026)RT}{F} \log m - \frac{2(2.3026)RT}{F} \alpha \sqrt{m} \\ = E^\circ - \frac{2(2.3026)RT}{F} \beta m \quad [2]$$

Table I. Emf data and activity coefficients for HCl solutions in N-N-dimethylacetamide at 25°C

mHCl	E (volt)	E' (volt)	$\gamma_{\pm}$
0.0052	0.4305	0.1475	0.818
0.0064	0.4183	0.1444	0.843
0.0145	0.3814	0.1422	0.763
0.0204	0.3617	0.1359	0.796
0.0260	0.3500	0.1334	0.784
0.0319	0.3389	0.1297	0.793
0.0348	0.3336	0.1275	0.806
0.0425	0.3224	0.1229	0.821
0.0500	0.3120	0.1178	0.854
0.0584	0.3022	0.1127	0.885

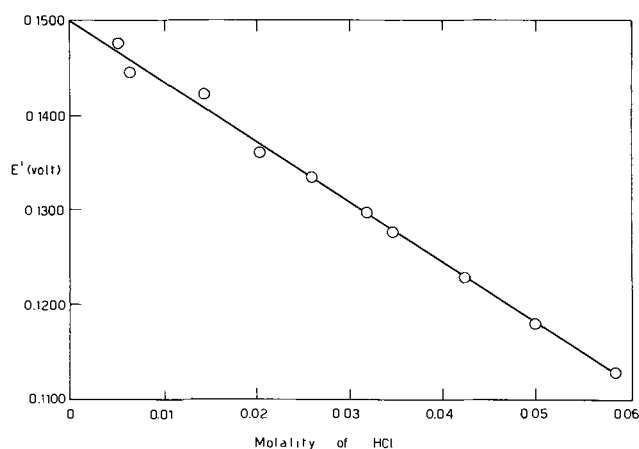


Fig. 1.  $E'$  as a function of HCl molality

where the Debye-Hückel constant  $\alpha$  for DMA at 25°C is 1.526. Figure 1 shows the values of  $E'$  vs. the corresponding values of  $m$ . Extrapolation to zero molality by the method of least squares gives the standard potential of the Ag, AgCl electrode in DMA at 25°C,  $E^\circ$ , as  $0.1500 \pm 0.0006$ v. The best fit of the data corresponds to a straight line with a slope of  $-0.640$  and, consequently, the value of  $\beta$  in Eq. [2] is 5.410. The mean molal activity coefficient,  $\gamma_{\pm}$ , of HCl in DMA at 25°C may be calculated by the equation

$$\log \gamma_{\pm} = \frac{E^\circ - E}{0.1183} - \log m \quad [3]$$

The values of  $\gamma_{\pm}$  obtained by Eq. [3] are listed in Table I. Studies on the properties of the silver-silver chloride and other reference electrodes are being extended in this laboratory to other nonaqueous solvents.

Manuscript received Jan. 18, 1968.

Any discussion of this paper will appear in a Discussion Section to be published in the December 1968 JOURNAL.

#### REFERENCES

1. H. S. Harned and T. R. Paxton, *J. Phys. Chem.*, **57**, 531 (1953).
2. L. M. Mukherjee, *J. Am. Chem. Soc.*, **79**, 4040 (1957).
3. D. H. Everett and S. E. Rasmussen, *J. Chem. Soc.*, **1954**, 2812.
4. H. Taniguchi and G. J. Janz, *J. Phys. Chem.*, **61**, 688 (1957).
5. I. T. Ojima, *ibid.*, **60**, 754 (1956).
6. R. K. Agawarl and B. Nayak, *ibid.*, **70**, 2568 (1966).
7. M. Mandel and P. Delcroly, *Nature*, **182**, 794 (1958).
8. M. De Rossi, G. Pecci, and B. Scrosati, *Ric. Sci.*, **37**, 342 (1967).
9. W. Sen, K. K. Kundu, and M. N. Das, *J. Phys. Chem.*, **71**, 3665 (1967).
10. L. R. Dawson, R. C. Sheridan, and H. C. Eckstrom, *ibid.*, **65**, 1829 (1961).
11. G. Lester, T. Grover, and P. Sears, *J. Phys. Chem.*, **60**, 1076 (1956).
12. G. Pistoia and B. Scrosati, *Ric. Sci.*, in press.
13. D. J. G. Ives and G. J. Janz, "Reference Electrodes," Academic Press, New York (1961).

## Mechanism of the Formation of Zinc Dendrites

A. R. Despic,<sup>1</sup> J. Diggle, and J. O'M. Bockris\*

*Electrochemistry Laboratory, University of Pennsylvania, Philadelphia, Pennsylvania*

During Zn dendrite formation at constant overpotential, the current grows exponentially with time, the time constant decreasing with increasing overpotential, concentration of zincate, and temperature.

This is consistent with a model of dendrite initiation according to which the rate of deposition onto any part of a microrough surface entering deeper than the average surface into the diffusion layer, relative to the rate of growth of the average surface, increases exponentially with time. The relative height of a protrusion can be shown to be

$$y = y_0 \exp\left(\frac{t}{\tau}\right) \quad [1]$$

where the time constant  $\tau$ , given by

$$\tau = \frac{\left[\frac{(i_L)_0}{i_0 f_c(\eta)} + \delta_0\right]^2}{\frac{M}{\rho n F} \left[1 - \frac{f_a(\eta)}{f_c(\eta)}\right] (i_L)_0} \quad [2]$$

and where  $y_0$  is the original protrusion height at  $t = 0$ ,  $f_a(\eta) = \exp\left(\frac{(2-\beta)F}{RT}\eta\right)$ ,  $f_c(\eta) = \exp\left(-\frac{\beta F}{RT}\eta\right)$ ,  $(i_L)_0 = nFD_0C_0$ , and  $\delta_0$  is the diffusion layer thickness. Thus the height of the protrusion in-

creases exponentially with time (Fig. 1) until it becomes comparable to the diffusion layer thickness. After this initial process, the protrusion forms its own diffusion layer, the conditions of spherical diffusion to the tip are established, and growth becomes governed by a law of the type derived by Barton and

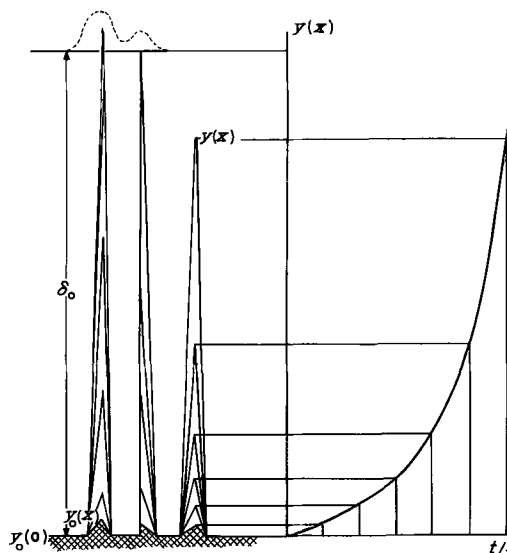


Fig. 1. Height of protrusions at equal time intervals exhibiting exponential dependence.

\* Electrochemical Society Active Member.

<sup>1</sup> On leave of absence from the University of Beograd (Yugoslavia).

Bockris (1). Such a model avoids the concept of dendrite nucleation.

To test the model, its consequences on the current flowing through the interface, at a given overpotential, were evaluated. It was shown that the current should follow a relationship similar to Eq. [1], i.e.,

$$i = i_{\text{init.}} \left\{ 1 + \left[ \frac{y_0}{\frac{(i_L)_0}{i_0 f_c(\eta)} + \delta_0} \right] \exp\left(\frac{t}{\tau}\right) \right\} \quad [3]$$

where

$$i_{\text{init.}} = \frac{(i_L)_0}{\frac{(i_L)_0}{i_0 f_c(\eta)} + \delta_0} \left( 1 - \frac{f_a(\eta)}{f_c(\eta)} \right) \quad [4]$$

The time constants,  $\tau$ , were extracted from experimental plots, by plotting  $\log(i - i_{\text{init.}})$  vs.  $t$  with  $i_{\text{init.}}$  being taken as equal to the initial current density for that overpotential ( $t = 0$ ). Good straight lines were obtained with slope  $2.3\tau$ .

The dependence of  $\tau$  on overpotential, concentration, and temperature was found to follow quantitatively the dependence predicted from analyzing Eq. [2] in those directions. The diffusion layer thickness was found to be  $\sim 10^{-3}$  cm, which is in the expected range.

To interpret the growth rate data, the Barton-Bockris theory was extended to encompass mixed activation and diffusion control of the current density in the nonlinear regions ( $\eta > 10$  mv) and this for two cases of deposition mechanisms: (a) the single electron discharge of univalent ions (pertinent to silver) and (b) a two-step single electron discharge (pertinent to zinc and other divalent metal depositions). The current density at the dendrite tip, i.e., the rate of propagation of the dendrite, is for (a)

$$i_n = \frac{f_c(\eta) \exp(-1/r_n) - f_a(\eta) \exp(1/r_n)}{K/i_0 + f_c(\eta) r_n \exp(-1/r_n)} \quad [5]$$

and for (b)

$$i_n = \frac{f_c(\eta) - f_a(\eta) \exp(1/r_n)}{K/i_0 + f_c(\eta) r_n} \quad [6]$$

where  $i_n = i/K$ ,  $\tau_n = \frac{RT}{2\gamma V} \cdot r$  and  $K = RTnFDC_0/2\gamma V$ ,

$\gamma$  being the surface tension at the metal-solution interface.

The observed rates of growth for Zn were found to follow relation [6] as far as the dependence on potential concentration and temperature implicit in [6] is concerned.

Important conclusions can be made from an analysis of Eq. [5] and [6], which can be understood from analyzing the graphs in Fig. 2.

(a) The curves showing the relation between tip c.d. (i.e., growth rate) and the tip radius for different overpotentials are found to cross a line indicating the value of the limiting current density  $(i_{L,l})_n$  in Fig. 2 for linear diffusion onto a flat surface at overpotentials coinciding remarkably well with the experimentally observed critical overpotentials (e.g., from Fig. 2b, dendritic growth for Zn would start at 60 mv as ex-

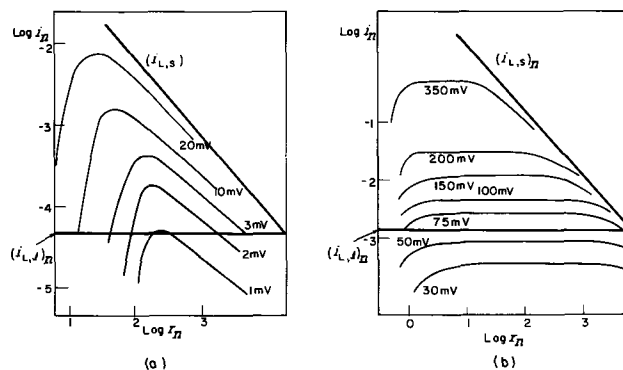


Fig. 2. Dependence of the tip current density on tip radius at different constant overpotentials (a) in the case of silver; (b) in the case of zinc.  $i_{L,l}$  is the limiting current density for diffusion onto a flat surface;  $i_{L,s}$  the limiting current density of spherical diffusion.

perimentally observed). Hence, the criterion for a critical current density of the dendrite tip which grows under activation control, past which the conditions for dendritic growth are established, as well as the criterion for critical overpotential are defined as

$$i_c = i_0[f_c(\eta) - f_a(\eta)] \geq i_{L,l} \quad [7]$$

and

$$-\eta_c \geq \frac{RT}{\beta F} \ln\left(\frac{i_{L,l}}{i_0}\right) \quad [8]$$

The critical current density depends solely on the conditions of diffusion to the flat surface, while the critical overpotential depends also on  $i_0$  for the deposition process.

(b) The difference in mechanism, and even more so the difference in  $i_0$ , results in a significant difference in the range of tip radii in which dendrite formation can occur for the two systems: those for silver show sharp peaks of growth rate in a narrow range of tip radii, while those for zinc show broad plateaus over a wide range of tip radii. This explains the observed difference in the character of the deposit for the two metals: the dendrites of silver are propagating fast at low overpotentials but are scarce, since the probability of the protrusions falling into the right range of radii is small; zinc dendrites are propagating slowly, but they are more abundant because of the high probability of the appearance of a protrusion with radii in the required range.

#### Acknowledgments

The authors thank the National Science Foundation for their support under Grant No. GK-1724.

Manuscript received Jan. 8, 1968.

Any discussion of this paper will appear in a Discussion Section to be published in the December 1968 JOURNAL.

#### REFERENCE

1. J. L. Barton and J. O'M. Bockris, *Proc. Royal Soc. London*, **A268**, 485 (1962).

# Field Ion Microscopical Studies of Exchange Current Density on Iridium

Leonard Nanis

School of Chemical Engineering, University of Pennsylvania, Philadelphia, Pennsylvania

and Philippe Javet

Institute for Direct Energy Conversion, University of Pennsylvania, Philadelphia, Pennsylvania

The recently developed technique of field ion microscopy (FIM) is a powerful tool for the investigation of metal surfaces. In many instances, resolution of individual atoms in the metallic lattice has been possible (1). Recent progress in electrode kinetics has shown the need for models on a true atomic scale for the interpretation of phenomena occurring at the electrified interface.

The use of FIM for electrochemistry provides an opportunity to observe surface effects on a scale in which the elementary electrochemical steps occur. Experiments have been performed based on the sequence:

1. image iridium tip (after shaping to almost perfect hemispherical form and atomic smoothness by field induced evaporation);
2. bring to atmospheric pressure and remove tip from FIM;
3. immerse for specified time in electrolyte with iridium ions;
4. rinse electrolyte from tip;
5. return to FIM and image again.

Changes on the surface have been photographically recorded and compared with those occurring in a "blank" experiment during which the tip is treated in a similar electrolyte, but free of iridium ions.

The rate of exchange of charge at the equilibrium potential between a metal and its ions is the exchange current density, a central concept of electrode kinetics (2). Thus, rearrangement of a previously smooth surface should be expected as atoms from the metal become involved in the exchange of charge. The extent of this perturbation is expected to be an increasing function of the time of contact of the metal with the electrolyte and of the magnitude of the exchange current. FIM prepared iridium tips have been immersed for various times in acid solution (2N H<sub>2</sub>SO<sub>4</sub>) containing 10<sup>-6</sup>M iridium ion. A blank experiment using the same acid without iridium ions has shown that the surface perturbation following a treatment of up to 10 min in electrolyte and 10 min in air extends to a depth of only 3 ± 1 atom layers. An example of a blank experiment is shown by comparing Fig. 1 and 2. The field evaporated (111) region of an iridium tip is shown in Fig. 1. After the tip was brought to atmospheric pressure, it was removed from the FIM, dipped for 3 min in 1N H<sub>2</sub>SO<sub>4</sub> and then returned to the FIM. After reestablishment of the vacuum, one atomic layer was removed by field evaporation, leading to the structure shown in Fig. 2.

The numerous bright spots superimposed on the previous features are most probably displaced iridium atoms. After evaporation of two more atomic layers, bright spots no longer appear and the original image, as in Fig. 1, is obtained. When a field evaporated tip is exposed to air only, bright spots similar to those shown in Fig. 2 appear, but the original image is generally restored after the field evaporation of only two layers.

For the solution containing iridium ions, however, the perturbation extends very much deeper than for blank experiments. The relationship between the time

of contact with solution and the depth of penetration (corrected for blank) is shown in Fig. 3. Correlation of the observed atom redistribution with time of immersion, exchange current density, and, e.g., crystallographic factors is now under study. However, two important features are readily obtained from the immersion experiments:

(A) For brief times of contact (less than 5 min), comparison of the damage which occurs in various crystallographic directions permits ordering of relative exchange current density on different crystal faces as

$$J_o(111) < J_o(100) < J_o(210)$$

A similar order

$$J_o(111) < J_o(100) < J_o(110)$$

has been determined for copper (fcc, as is iridium) by Damjanovic *et al.* (3) in a study of electrodeposition kinetics.

(B) With prolonged contact (greater than 5 min) between the metal and its ions, the formation of "spikes" on the surface has been observed.

Figure 4 shows a field-evaporated clean iridium tip with a central (100) region. The fourfold symmetry decoration is caused by field-stabilized protruding atoms in the [110] directions. The nearly hemispherical tip has an average radius of curvature of about 800Å.

Following imaging, this tip was immersed for 10 min in iridium ion solution as mentioned above. Figure 5 shows the image of the treated tip after the removal of 10 atom layers by field evaporation.

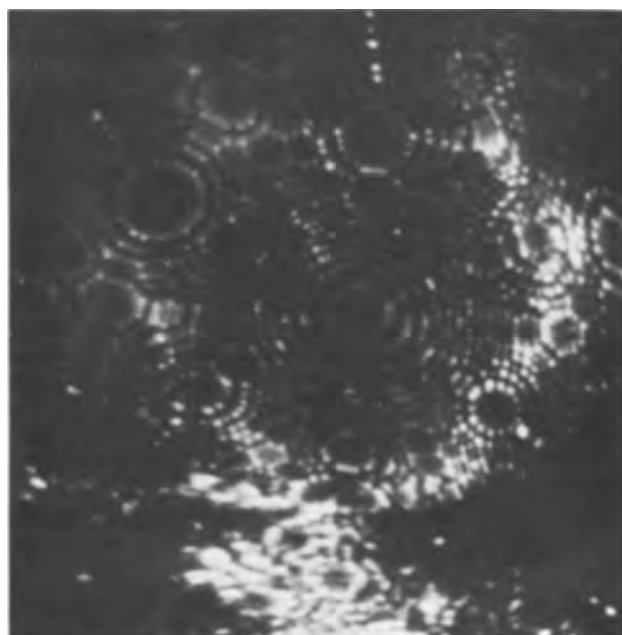


Fig. 1. Field evaporated iridium tip with central (111) region before blank treatment.

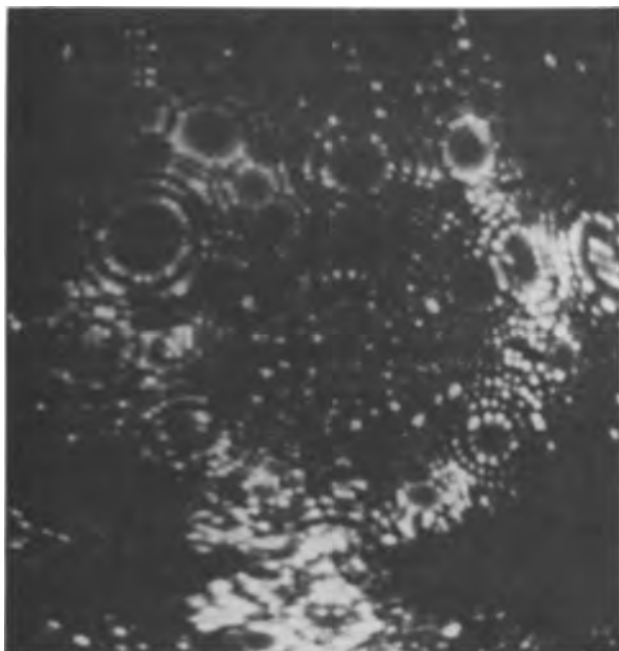


Fig. 2. Same as Fig. 1 following 3-min immersion in 1N  $\text{H}_2\text{SO}_4$

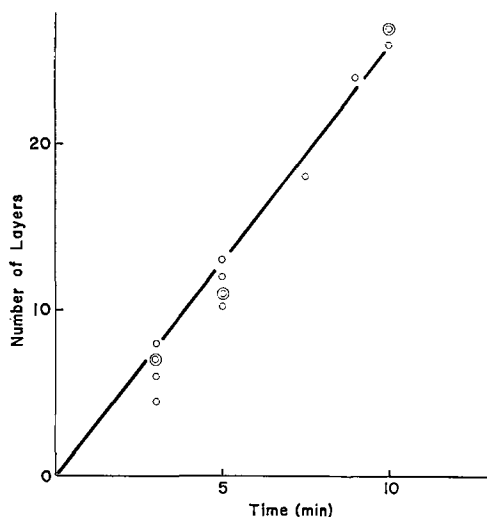


Fig. 3. Number of perturbed layers on iridium tip as a function of time of contact with iridium ions.

The two spike regions centered around the [310] direction have smaller radius of curvature than the original tip, i.e., the radius in the upper region of Fig. 5 is 450 to 500 Å with an even smaller radius for the lower region.

The field enhancement associated with the decreased local radius produces an effective increase in image magnification and resolution and permits imaging at much lower potential than for Fig. 4. At the reduced potential, imaging does not occur for the remainder of the tip because of the reduced field. Further field evaporation restores the original image as in Fig. 4. Figure 6 shows the tip after the removal of twenty atom layers from the protruding (310) plane. Features of the original structure (Fig. 4) are increasingly evident. The last traces of over-all irregularities disappear completely after evaporation of the 29th layer.

By postulating a simple model for the transfer of material on the surface, an estimate for the magnitude of the exchange current density may be obtained. It has been observed that a general roughening of the entire surface occurs during the first 5 min of immersion, followed by a growth pattern which favors

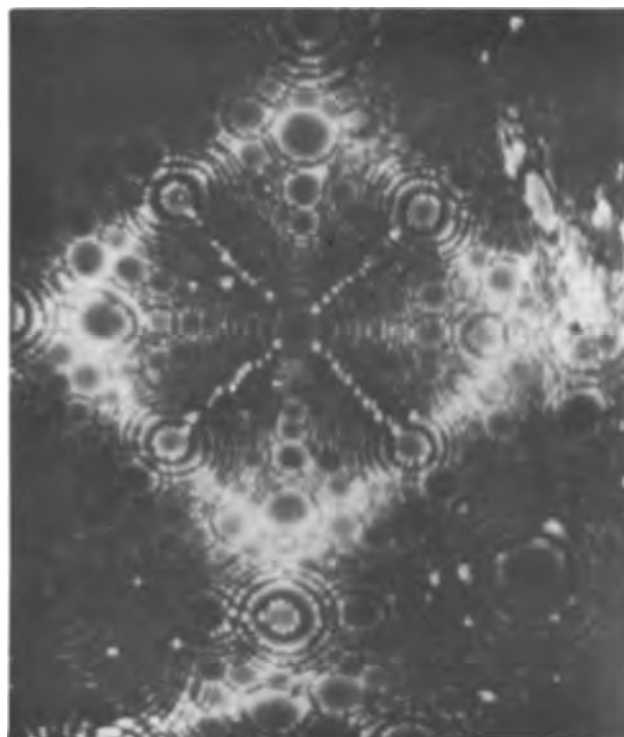


Fig. 4. Field ion image of smooth, field evaporated iridium tip before electrochemical treatment; (100) plane in center, (111) planes in picture corners. Image potential 17.3 kv; imaging gas helium 2  $\mu\text{m}$  Hg.

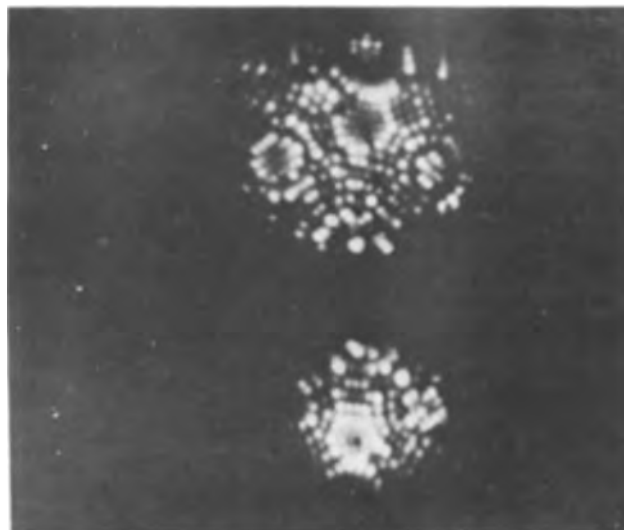


Fig. 5. Iridium tip, same as Fig. 4, after 10 min contact with solution,  $10^{-6}\text{M}$  Ir, followed by return to FIM and field evaporation of 10 atomic layers. The two "spike" growth features are each centered on [310] directions. Imaging potential 11.5 kv.

specific directions (Fig. 5). Accordingly, suppose that all discharge of ions after five minutes takes place at the favored position, causing this region to grow, i.e., a hypothetical separation of the cathodic and anodic components of the exchange current density.

The approximate volume of the spike region may be readily computed from direct measurements of the area at different levels as layers are removed by field evaporation. Using Fig. 4, 5, 6 and images at other levels, assuming a tetravalent iridium ion, an upper limit of  $10^{-4}$   $\text{Acm}^{-2}$  for the exchange current density is obtained.

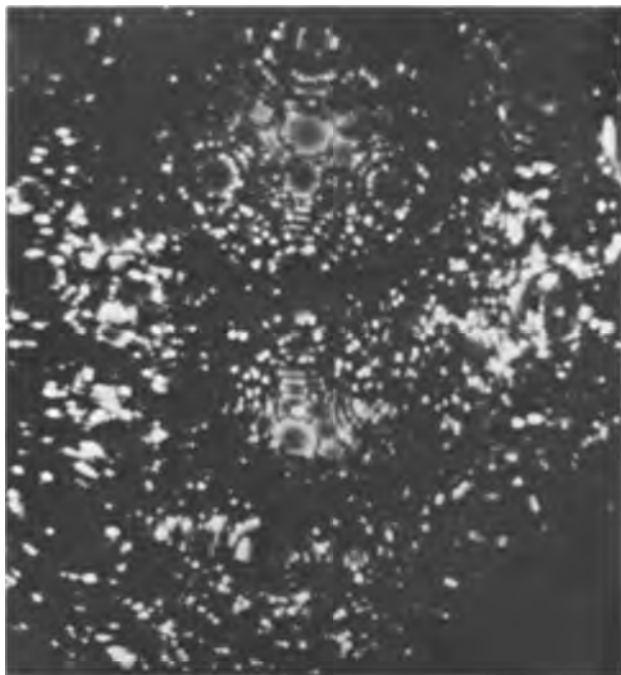


Fig. 6. Iridium tip, same as Fig. 5 after field evaporation of 20 layers. The structure of Fig. 4 has partially reappeared. Imaging potential 15.5 kv.

It is expected that direct FIM observation of treated electrode surfaces will be helpful in devising models for electrochemical reactions, not only by the observation of the changes induced on the surface by electro-

chemical treatment, but also through consideration of the analogy between the field used for image formation and the field at the electrode-electrolyte interface.

Although there is evidence for the existence of vacancies in Fig. 5, spiral dislocations are apparently absent. Provided the imaging field following electrochemical treatment does not interact to remove dislocations, the mechanism presently accepted for the initiation and continuation of electrolytic growth, requiring spiral dislocations intersecting the growth surface, bears re-examination.

Some of the well-known features of the FIM method such as field-stabilized protruding atoms (fourfold decoration in Fig. 4) and field-induced mechanical stresses require incorporation in models of the electrochemical interface.

#### Acknowledgment

This work was supported by NASA Grant NSG-316.

Manuscript received Jan. 23, 1968; revised manuscript received Feb. 19, 1968.

Any discussion of this paper will appear in a Discussion Section to be published in the December 1968 JOURNAL.

#### REFERENCES

1. E. Müller, *Advances in Electronics*, **13**, 89 (1960).
2. H. Gerischer, *Z. Elektrochem.*, **54**, 362 (1950); **55**, 98 (1951); **59**, 604 (1955).
3. A. Damjanovic, T. H. V. Setty, and J. O'M. Bockris, *This Journal*, **113**, 429 (1966).

# Effect of Ionic Additives on the Heterocharge in Carnauba Wax Thermoelectrets

Preston V. Murphy

Thermo Electron Corporation, Waltham, Massachusetts

## ABSTRACT

Thermopolarization and depolarization studies have been carried out on Carnauba wax electrets with controlled impurity content. While the initial impurity content was found to have little influence on the density of heterocharge, the addition of certain inorganic salts, in 10-50 ppm concentration, increased the heterocharge by factors of 2-5. The temperature dependence of electrical conductivity varied considerably with ion doping, but the heterocharge density in all samples showed the same thermal activation energy for polarization.

Carnauba wax, being a mixture of compounds, is not as ideal a choice as pure compounds. However, its dielectric properties have been studied for many years, and the electret effect has been studied more extensively in Carnauba wax than in any other material. Among the many studies on this material are the early papers of Eguchi (1) which described the main features of the electret effect including charge reversal, existence of a volume polarization, and long polarization lifetime for electrets in short-circuit. Adams (2), who proposed one of the early phenomenological theories, used Carnauba. Gross (3) likewise used the material while developing the currently accepted theories on heterocharge and homocharge (3). Wiseman *et al.* (4) carried out experiments which substantiated the two charge theory of Gross. Gubkin (5), at the same period, studied the effects of short circuiting on charge stability in Carnauba and other materials. In more recent studies, Gross (6) showed that the heterocharge is distributed uniformly throughout the volume of Carnauba electrets. Murphy *et al.* (7) have reported on Carnauba radio-electrets, and Perlman *et al.* (8) extended earlier phenomenological theories on the electret effect in Carnauba.

## Carnauba Wax

Carnauba wax is a natural product obtained from the palm *Copernicia Cerifera* Martins (9). It consists primarily of long-chain esters (10). About two-thirds of these are n-alkanoic acid esters composed predominantly of the n-alcohols, C<sub>32</sub>, C<sub>34</sub>, and C<sub>27</sub>, (listed in decreasing abundance) and the n-acids C<sub>24</sub>, C<sub>28</sub>, C<sub>26</sub>, and C<sub>20</sub>. The remaining third are esters of the  $\omega$ -hydroxy n-alkanoic acids, C<sub>28</sub>, C<sub>24</sub>, and C<sub>26</sub>.

The dielectric constant of Carnauba wax measured at 1 kHz increases from 2.5 at room temperature to a maximum of 3.0 at the melting point (79°-80°C). Dielectric measurements (11) have shown that the  $\omega$ -hydroxy acid esters are oriented in a trans-trans configuration, and that rotation about the chain axis occurs in the solid state.

The highest grade of Carnauba, #1 yellow, has been used in this investigation as well as in earlier work including that of Gross (3). It is common practice to filter the wax to remove dark, particulate matter. However, there have been no reports on the nature of the contaminants, neither the portion removed by filtration nor the portion that inevitably remains in the filtrate. The inorganic contaminant might be expected to contribute significantly to the internal polarization of the wax by providing mobile ions or polarizable, colloidal aggregates.

Samples of Carnauba have been purified by simple filtration, by filtration with diatomaceous silica, and by zone refining. The resultant levels of inorganic im-

purities are shown in Table I. After purification, the wax was cast in the shape of small disks and machined to a size of 1.75 in. diameter by 0.079 in. thickness. Electrodes of Aquadag were applied to the flat surfaces.

## Heterocharge Measurement

The heterocharge was measured by the thermodepolarization technique which was developed by Frei and Groetzinger (12) and used extensively by Gross (3). A rather sophisticated, automatic measuring system shown in Fig. 1 was employed.

Four disks of Carnauba wax were mounted in the chrome-plated copper block, C, (Fig. 1), and measurements of both conductivity and polarization were made. The upper and lower electrodes, of chrome-plated copper, were both mounted symmetrically on 1/8 in.-diameter sapphire spheres which maintained a leakage resistance in excess of 10<sup>14</sup> ohm at 250°C. The symmetrical mounting provided for uniform heat transfer between the electrodes and the surrounding block, and minimized thermal gradients in the samples. The four equivalent sample mounting positions enabled measurements to be made under identical

Table I. Spectrographic analysis of inorganic impurities in Carnauba wax after purification by different techniques

Spectrographically determined element	Crude wax, <sup>2</sup> ppm	Filtered wax, <sup>3</sup> ppm	Zone refined top, <sup>1</sup> ppm	Zone refined bottom, <sup>5</sup> ppm	Activated silica, <sup>6</sup> ppm
Mg	7.0	0.4	0.5	0.7	0.2
Al	25	4.0	2.0	3.0	0.25
Na	15	2.0	3.0	4.0	0.2
Si	80	8.0	3.5	5.5	0.75
Ca	3.5	4.0	3.0	3.0	1.25
Ti	2.8	0.2	0.15	0.15	0.03
V	0.1	0.02	0.21	0.01	—
Cr	0.1	0.01	0.01	0.01	0.02
Mn	1.0	0.15	0.06	0.07	0.01
Fe	50	5.0	3.0	4.0	0.4
Ni	0.1	0.04	0.01	—	—
Cu	0.7	0.4	0.15	0.2	0.12
Sr	0.06	0.02	0.02	0.02	—
Sn	0.25	0.1	—	—	—
Ba	0.35	0.08	0.02	0.02	0.01
Pb	0.25	0.1	—	—	—
K	20	—	—	—	—
Zr	0.1	—	—	—	—
Ag	0.05	—	—	—	—
Li	0.75	—	—	—	—
Total impurities	212.1	24.5	15.4	20.7	3.2

<sup>1</sup> Reported by American Spectrographic Laboratories, San Francisco, California.

<sup>2</sup> No. 1 yellow grade Carnauba wax as received from the S. L. Abbot Company, San Francisco, California.

<sup>3</sup> Crude wax<sup>2</sup> filtered twice through Eaton Dikeman No. 617 filter paper at 100°C.

<sup>4</sup> Filtered wax<sup>3</sup> refined by zone melting; 50 passes at 3 in./hr; top portion (mp = 82.5°-83.5°C).

<sup>5</sup> Same as<sup>4</sup>, bottom portion (mp = 84°-85°C).

<sup>6</sup> Filtered wax<sup>3</sup> mixed with "Celite" diatomaceous silica and refiltered through Whatman No. 3 paper (mp = 83° ± 0.5°C).

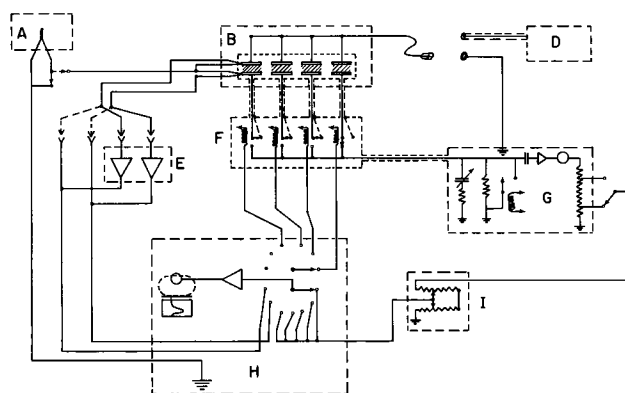


Fig. 1. Schematic diagram of polarization and measurement system. A, constant-temperature bath; B, Blue-M cam-programmed, proportionally controlled oven with sample holder; D, Baird-Atomic Model 319A, 0-5 kv power supply; E, microvolt thermocouple amplifier; F, coaxial relays; G, Cary Model 31 electrometer; H, Honeywell Elektronik 10 mv 6-point recorder; I, F & M Model 50 Automatic Attenuator.

thermal conditions on samples with different composition.

The temperature could be controlled between the limits of 25° and 250°C by means of the cam-programmed, proportionally-controlled oven, B (Fig. 1). The temperature usually was increased at a rate of either 0.19° or 0.75°C/min during depolarization.

Samples were polarized and depolarized in the same apparatus. In the case of polarization, the upper electrodes were connected in parallel to the output of a Baird Atomic Model 319A, 0-5 kv power supply, D. The lower electrodes were grounded through a high resistance so that conductivity could be measured with the electrometer, G; guard rings were used on the lower electrodes. The standard polarizing voltage for samples 2 mm in thickness was 1 kv.

The temperature of the block and of one of the upper electrodes usually was measured by a thermocouple circuit during depolarization. (The positions indicated by the dotted lines at locations "a", "b", and "c" in Fig. 1 were used.) The reference temperature of 15°C was provided by a constant temperature bath, A. The thermocouple output without additional amplification drove the recorder, H.

The coaxial relay system, F, connected one sample at a time to the input of the Cary model 31 electrometer, G. Each time a relay was energized, the input was shorted for 2 sec by the Cary 3098150 automatic shorting switch in order to suppress transients. Rigid coaxial line with air insulation was used on all of the input circuits.

The usual measurement procedure involved increasing the temperature to some specific value above ambient and applying 1000v bias for a period of 1-65 hr. The value of conductivity measured at either 14 or 36 hr was recorded. The temperature was reduced to the ambient during a 16-hr period. The samples were shorted through the electrometer for 1 hr and decay currents recorded. Finally, the samples were reheated at a linear rate to a maximum of 76°C and depolarization currents recorded. Typical recorder traces showing the depolarization "glow curves" are shown in Fig. 2. The heterocharge was obtained from the time integral of the depolarization current.

#### Dependence of Heterocharge on Initial Impurity Content

The heterocharge was determined for Carnauba wax purified by simple filtration, by filtration with activated silica, and by zone refining. Results are shown in Table II.

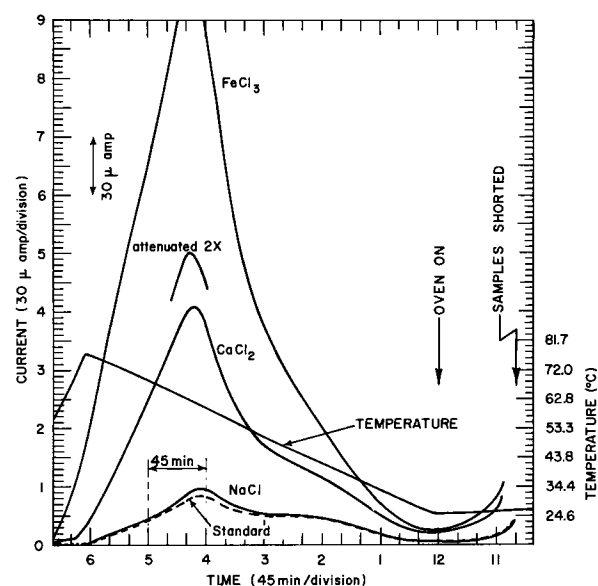


Fig. 2. Typical recorder trace showing the temperature of one electrode and the depolarization current for four samples vs. time. The samples were polarized at 50°C for 5 hr, cooled to 25°C, and shorted as indicated. Original curves are color coded.

It will be noted that although the impurity content was reduced by nearly an order of magnitude, there was no significant change in the heterocharge density.

#### Modification of Heterocharge by Added Impurities

A different lot of wax was purified with activated silica and reserved for studies on specific added impurities. Solutions of inorganic halides in methanol were sprayed into molten wax to give additive concentrations of about 50 ppm. Sodium and potassium salts formed precipitates in the wax and were removed by the filtration step. Electrets were prepared by polarization for hours at 5 kv/cm and 72°C.

The measured values of heterocharge density are shown in Table III. It will be noted that the heterocharge was doubled by  $\text{Ca}^{+2}$  and  $\text{Ce}^{+3}$  additive and was increased fivefold by  $\text{Fe}^{+2}$  and  $\text{Fe}^{+3}$  additive. NaCl produced no effect while NaBr increased the heterocharge slightly although analysis for Na showed only 1 ppm.

#### Dependence of Heterocharge on Polarization Temperature

The effect of the polarization temperature on the ultimate polarization charge was determined for a standard, purified sample of wax and for a selected

Table II. Heterocharge density in purified Carnauba wax

	Charge density, $\text{m}\mu\text{ coul}\cdot\text{cm}^{-2}$	Total impurities, ppm
Filtered—E. D. 617 paper	60-70	24.5
Filtered—activated silica	60	3.2
Zone refined—top	65	15.4
Zone refined—bottom	70	20.7

Table III. Polarization density for Carnauba wax doped with inorganic ions

Compound added	Cation content, ppm	Polarization charge density, $\text{m}\mu\text{ coul}\cdot\text{cm}^{-2}$
None	—	140
NaCl	1	130
NaBr	1	160
$\text{CaCl}_2$	50	300
$\text{CeCl}_3$	50 (est.)	300 (est. from 50°C data)
$\text{FeCl}_2$	50	700
$\text{FeCl}_3$	65	700



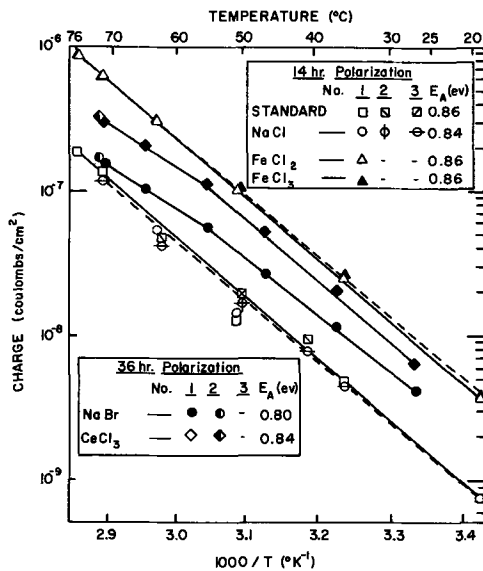


Fig. 3. Specific depolarization charge vs. reciprocal polarization temperatures for Carnauba samples doped with inorganic salts. The symbols in column 1 represent values obtained for 2-in. diameter disks banded with 3/32 in. guard rings; in column 2, the values were obtained for 1 3/4 in. disks; in column 3, the values were interpolated from the data of Fig. 7.

number of doped samples. It was shown by Van Calker and Frohlich (13) that a plot of polarization charge versus reciprocal polarization temperature gave a straight line for mixtures of Carnauba wax and resin. Plots of heterocharge density vs. reciprocal temperature are shown in Fig. 3 for doped samples. It will be noted that the lines are all nearly parallel (with the exception of the NaBr sample and the CeCl<sub>3</sub> sample above 60°C). Activation energies for polarization were calculated to be 0.86 ev for undoped and Fe-doped samples, and 0.84 ev for NaCl- and CeCl<sub>3</sub>-doped samples. If the heterocharge were caused by space charge due to the migration of the ionic contaminants, one would expect a wider variation in energies of activation.

In Fig. 4, a similar plot is shown for wax samples treated with ZnCl<sub>2</sub>-docosanol, and with ZnCl<sub>2</sub>-docosanol-FeCl<sub>3</sub>. The docosanol treatment was intended to esterify residual acids and thus increase the probability of precipitating colloidal iron oxide. However, the apparent result was an increase in polarizability in

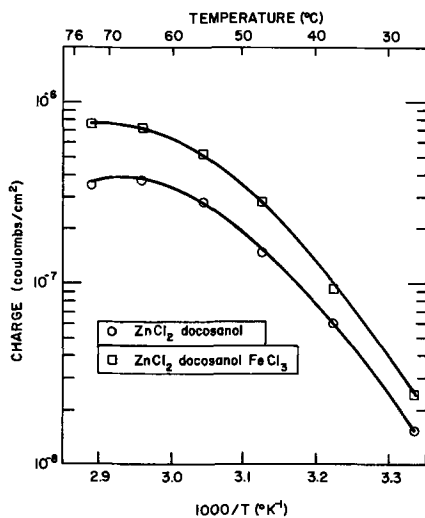


Fig. 4. Specific depolarization charge vs. reciprocal temperature for Carnauba samples doped with ZnCl<sub>2</sub>-docosanol and ZnCl<sub>2</sub>-docosanol-FeCl<sub>3</sub>.

the 40°-60°C temperature region, presumably due to excess free alcohol.

Decay Current

At the end of each polarization, the samples were held in short-circuit at 25.3°C for a 1-hr period. During this time the decay current was read on the electrometer and recorded in the usual manner. The time variation of the decay current is shown in Fig. 5. The integral of the decay current taken over the 1-hr period is plotted against the reciprocal of the polarization temperature in Fig. 6. The decay current and its time integral reached maximum values at about 40°C and decreased at higher temperatures. This behavior is rather unusual in view of the steadily increasing value of heterocharge. The decrease in decay current might result either from an increasing surface homocharge or from an increase in the stability of heterocharge.

Polarization Time

It is usually assumed that the polarization charge reaches a saturation value at elevated temperatures

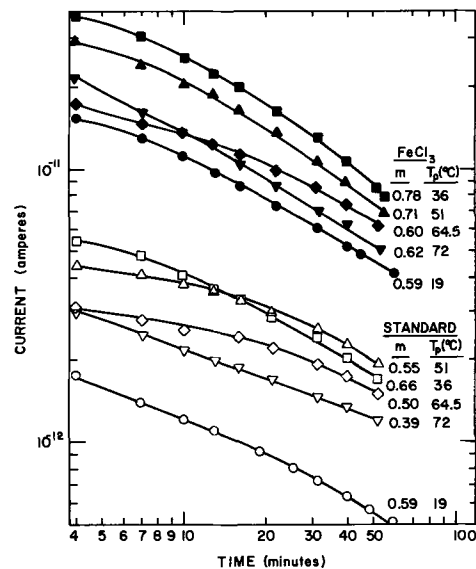


Fig. 5. Decay current vs. time for polarized samples of standard and iron-doped wax at 25°C. Polarizing bias was removed at zero time.  $T_p$  is the polarizing temperature and  $m$  the slope of the final portion of the curve.

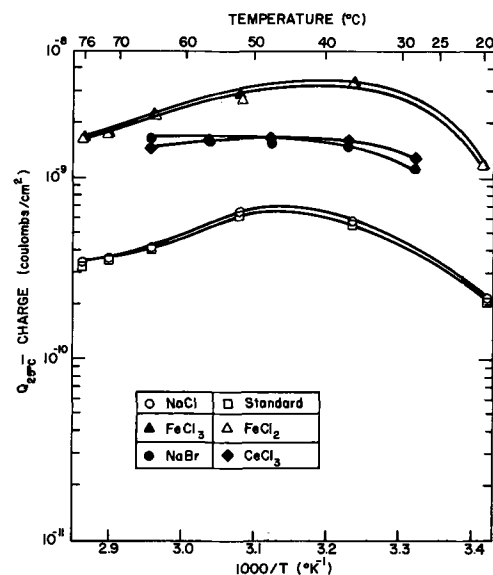


Fig. 6. Decay charge at 25°C,  $Q_{25^\circ C}$  (given by the decay current at 25°C integrated for 60 min) vs. reciprocal polarizing temperature.

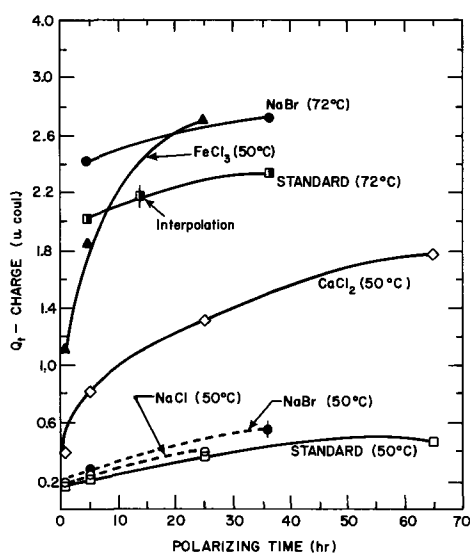


Fig. 7. Depolarization charge,  $Q_t$  vs. polarizing time for samples polarized at 50° and 72°C.

after voltage has been maintained for a few hours. In order to verify this assumption and to explore the lower-temperature region, several samples were polarized repeatedly at 50° and at 72°C for different periods of time. The results (Fig. 7) indicate that the polarizing voltage must be maintained for a very long time at 50°C or below in order to attain saturation. However, a temperature-dependent saturation limit appears to exist, and this limit is approached exponentially in time.

#### Sample Compaction

Carnauba wax is subject to considerable shrinkage when cooled from the melt. It has been postulated that the presence of microscopic voids might lead to interfacial polarization as a result of localized surface conduction. Therefore, we have attempted to alter the degree of compaction by solidifying samples under conditions of both high pressure and vacuum. The heterocharge density for some of these samples is shown in Table IV. It will be noted from the table that the effect of compaction is small; we believe the differences in charge noted in Table IV are within the limits of error for these measurements. The data on vacuum-formed samples are not included because a different batch of wax was involved; indirect evidence, however, has shown no appreciable change in polarization as a result of vacuum-forming.

#### Depolarization Rate

It is well known that the maximum value of depolarization current increases with the rate of heating; however, it has not been established that the time integral of depolarization current is independent of heating rate. Therefore, depolarization measurements were carried out on several identical samples at two different heating rates. The results (shown in Table V) indicate that the measured charge is independent of heating rate within the limits of 0.19° and 0.75°C/min.

#### Sample Conductivity

The dependence of electric conductivity on temperature was determined for purified and impurity-doped

Table IV. Polarization density of compacted Carnauba wax

Forming pressure, psi	Charge density, $\mu\text{coul}\cdot\text{cm}^{-2}$	Sample thickness	
		Before measurement, mm	After measurement, mm
None	0.117	1.83	1.84
10,000	0.093	1.88	1.94
20,000	0.100	1.83	1.89

Table V. Effect of depolarization rate of measured charge

Sample	Measured charge	
	Heating rate 0.19°C·min <sup>-1</sup> , $\mu\text{coul}$	Heating rate 0.75°C·min <sup>-1</sup> , $\mu\text{coul}$
Standard	0.20	0.20
NaCl (doped)	0.21	0.20
CaCl <sub>2</sub> (doped)	0.82	0.82
FeCl <sub>3</sub> (doped)	1.82	1.92

samples of wax. Guard rings were used to prevent surface leakage. The conductivity as a function of reciprocal temperature is shown in Fig. 8 and 9. Values of conductivity were taken after application of bias for periods of 11-36 hr as noted in the figures. The conductivity increased with temperature much more rapidly than did polarization charge (Fig. 3 and 4). The data of Fig. 8 and 9 fail to give straight lines from which activation energies for conduction can be calculated.

#### Discussion

The studies involving purified samples of wax demonstrated that the original inorganic contaminants have little effect on the internal polarization; the in-

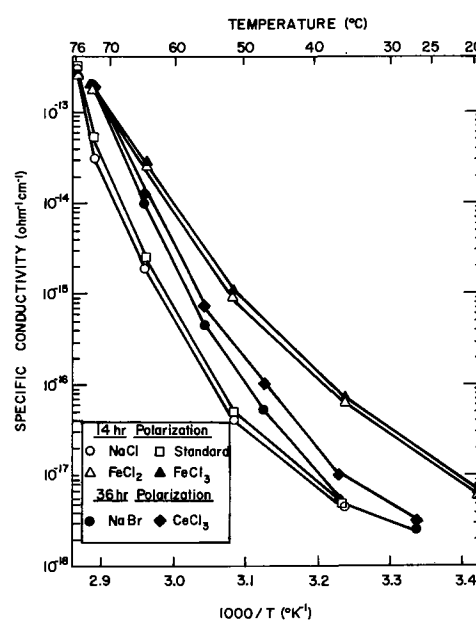


Fig. 8. Specific conductivity vs. reciprocal temperature for standard and doped Carnauba samples.

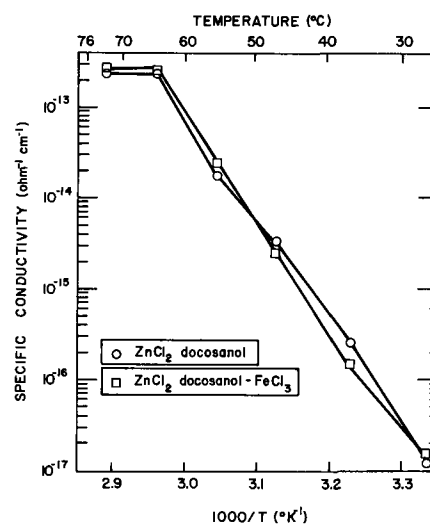


Fig. 9. Specific conductivity vs. reciprocal polarizing temperature for  $\text{ZnCl}_2$ -docosanol and  $\text{ZnCl}_2$ -docosanol- $\text{FeCl}_3$  doped Carnauba samples.

ternal polarization or, heterocharge, is a property of the wax itself.

The heterocharge was changed substantially by inorganic additives, but the mechanism of heterocharge formation remains somewhat elusive. The data suggest that free ions are not contributing to the heterocharge since there was no correlation of charge density with valency. For example,  $\text{Fe}^{+2}$  and  $\text{Fe}^{+3}$  behave identically and cause a larger increase in polarization than do  $\text{Ca}^{+2}$  and  $\text{Ce}^{+3}$ . Also, the conductivities of all samples converge to the same value at high temperature, suggesting a common conduction mechanism characteristic of the wax itself.

The quantity of polarization charge appears to increase exponentially with polarization temperature. It is significant that inorganic additives cause the polarization curves to be displaced to higher values of charge but do not affect the slopes. On the other hand the slopes of the conductivity-temperature curves are much steeper than the slope of the polarization-temperature curves. Also, there is no convergence of the polarization curves at high temperature as there is for the conductivity curves.

In view of the observed exponential dependence of heterocharge density on polarizing temperature, the isothermal decay curves and thermodepolarization "glow" curves were examined for similar exponential dependences. The applicability of luminescence and conductivity glow curve analysis to thermodepolarization curves has been pointed out by the writer (7) and expanded by Bucci *et al.* (14). If depolarization is characterized by a single energy of activation the initial increase of current with temperature should follow a simple exponential law. Also the isothermal, short-circuit, decay current should decrease exponentially with time. The current variations found for Carnauba wax were not exponential in either of these cases. Therefore, although the energy of activation for the thermopolarization process appears to be single

valued, no such discrete energy level is associated with depolarization. While a unique physical mechanism for the heterocharge cannot be established as yet, the data are compatible with a distortable double-well model of the type proposed by Fuchs and Von Hippel (15) in connection with dielectric absorption.

Manuscript received Sept. 5, 1967; revised manuscript received Feb. 6, 1968. This paper was presented at the Electrets Symposium at the Chicago Meeting, Oct. 15-19, as Abstract 128.

Any discussion of this paper will appear in a Discussion Section to be published in the December 1968 JOURNAL.

#### REFERENCES

1. M. Eguchi, *Phil. Mag.*, **49**, 178 (1925).
2. E. Adams, *J. Franklin Inst.*, **204**, 469 (1927).
3. B. Gross and L. Denard, *Phys. Rev.*, **67**, 253 (1945); B. Gross, *An. Acad. Bras. Cien.*, **20**, 247 (1948); B. Gross, *J. Chem. Phys.*, **17**, 866 (1949).
4. C. Wiseman and G. Feaster, *J. Chem. Phys.*, **26**, 521 (1957).
5. A. Gubkin, *Zhur. Tekh. Fiz.*, **27**, 1954 (1957).
6. B. Gross and R. deMoraes, *J. Chem. Phys.*, **37**, 710 (1962).
7. P. Murphy, S. Costa-Ribeiro, F. Milanez, and R. deMoraes, *J. Chem. Phys.*, **38**, 2400 (1963).
8. M. Perlman and J. L. Meunier, *J. Appl. Phys.*, **36**, 420 (1965).
9. A. Warth, "The Chemistry and Technology of Waxes," Reinhold Publishing Co., New York (1960).
10. K. Murray and R. Schoenfeld, *Australian J. Chem.*, **8**, 424 (1955).
11. T. Callinan and A. Parks, Private communication.
12. H. Frei and G. Groetzinger, *Physits. Z.*, **37**, 720 (1936).
13. J. Van Calker and W. Frohlich, *Ann. der Physik*, **7**, 216 (1959).
14. C. Bucci, R. Fieschi, and G. Guidi, *Phys. Rev.*, **148**, 816 (1966).
15. R. Fuchs and A. von Hippel, *J. Chem. Phys.*, **34**, 2165 (1961).

## Ionic Membrane Electrets

Richard A. Wallace\*

*Polytechnic Institute of Brooklyn, Brooklyn, New York*

and Zeljko Urban

*University of California, Berkeley, Berkeley, California*

#### ABSTRACT

Heterocharges in the polystyrenesulfonate membrane in its hydrogen, sodium, and silver forms have been measured by means of thermal depolarization. We found that the membrane in sodium form stored the largest amount of electric charges and made for the best ionic membrane electret. Membrane electrets were formed at 60°C in electrical fields of 1.25, 2.5, and 5 kv/cm. In this range the total accumulated charge within the membrane does not depend on the strength of the forming field.

The high dielectric constant of polystyrenesulfonate membranes (1) suggests the possibility that these ionic membranes might be capable of storing large amounts of electric charge. To what extent these electrostatic or internal electric charges can be preserved has not yet been determined. Provided that the charges remain orientated within the membrane after electroformation, then ionic membrane electrets could be prepared. Experiments are now being performed at the Polytechnic to determine the role of the electret

effect in water desalination by electro dialysis and in nonthrombogenic bipolymer materials.

In this paper results are presented of measurements of electric charges, formed on the application of d-c fields ranging from 1.25 to 5.0 kv/cm, in sulfonated polymeric membranes. The method of thermal depolarization was used to measure the stored heterocharges released by the membrane electret (2, 3).

#### Experimental

Sulfonated polymer membranes (AMF, C-60) consisted of approximately 25% by weight of polystyrenesulfonic acid (PSA) supported in a matrix of poly-

\* Electrochemical Society Active Member.

This research was sponsored by the Office of Saline Water, United States Department of the Interior.

ethylene. Fixed negative charges within the membrane are carried by sulfonic ( $\text{SO}_3^-$ ) sites along the PSA molecules. These charges are each balanced by positive counter ions, such as H or Na. Each membrane was purified by five batchwise washings with deionized water. Circular strips of membrane, 1.5 in. in diameter and 0.01 in. thick, were cut, silver-coated on both faces, and then vacuum-dried for 24 hr.

Each membrane was clamped between stainless steel electrodes and a d-c electric field applied to the membrane sample, maintained at  $60^\circ\text{C}$ . After an arbitrary cut-off time of 4 hr, membrane sample was allowed to cool down to  $28^\circ\text{C}$  in the presence of the electroforming field. Membrane charging current and temperature were recorded during electroformation.

Immediately after the forming field was removed, the charged membrane was short-circuited and its discharge current measured at  $28^\circ\text{C}$ . This measurement was continued until the current gradually approached zero. After a 24-hr period, the short-circuited membrane was reheated up to  $60^\circ\text{C}$  and its discharge current measured again. The variations of this current with time were then recorded.

### Results and Discussion

Electroforming of a typical membrane eletret by means of a  $1.25\text{ kv/cm}$  electric field is illustrated in Fig. 1. In the beginning, the charging current decays as it normally would at room temperature. Later, the trend reverses and the current starts to increase in response to rising temperature. It experiences a peak approximately at the same time as the temperature reaches its maximum value. After that, the current gradually decays, forming a small knee close to the point where the cooling starts. After 350 min, the applied electric field is turned off, the specimen shorted, and its discharge current measured.

Figure 2 shows the discharge current as a function of time at  $28^\circ\text{C}$  for various forming field strengths. From this data the stored charge in the cation-exchange membrane is calculated, using the relationship

$$Q = \int_t^\infty J(t) dt \quad [1]$$

where  $Q$  = charge, coulombs,  $J(t)$  = discharge current, amp, and  $t$  = time, sec.

According to classical circuit theory, the discharge current of a short-circuited capacitor follows the equation

$$J(t) = I_0 e^{-t/RC} \quad [2]$$

where  $I_0$  = discharge current at  $t = 0$  and  $RC$  = time constant of capacitor (product of resistance and capacitance).

This current, which decays very fast, is present in the case of eletret discharge. However, an additional anomalous current appears, slowly decreasing with time. To allow for decay of the classical discharge

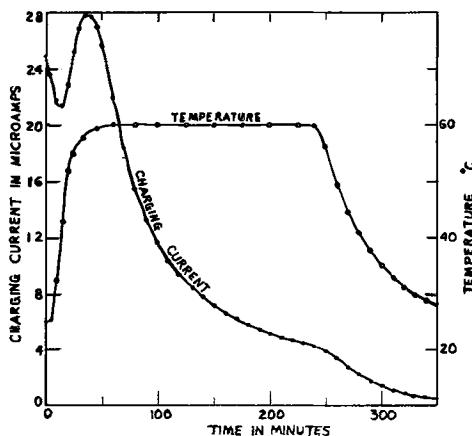


Fig. 1. Electroformation of a PSA membrane eletret at  $1.25\text{ kv/cm}$ .

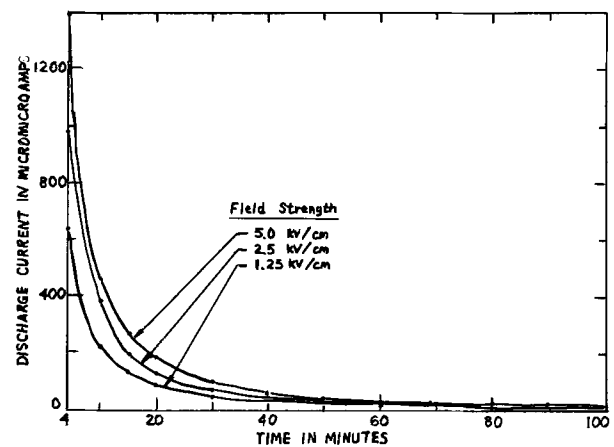


Fig. 2. First discharge at  $28^\circ\text{C}$  for PSA membrane eletrets formed at various electrical fields.

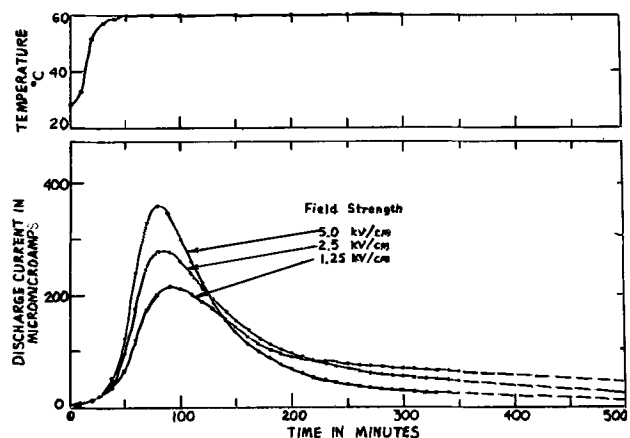


Fig. 3. Second discharge at  $60^\circ\text{C}$  of PSA membrane eletrets formed at various electrical fields.

current, a 4-min period of discharge time was allowed to pass before the data were recorded. The charges released during the 96-min period, corresponding to the area under the curve, are given in the second column of Table I. Higher forming field yields the higher quantity of released charge during the first discharge period. Similar results were also reported on Carnauba wax eletrets (4).

The second discharge was started 24 hr later. Temperature was raised to  $60^\circ\text{C}$ , and the discharge current was measured as shown in Fig. 3. The measurements were conducted for 350 min. For the purpose of charge calculations, all the curves are extrapolated to the point where the discharge current reaches zero. The values of released charges were obtained by graphical integration of the curves in Fig. 3, and are listed in the third column of Table I. These charges are up to 9 times larger than the charges released during the first discharge at room temperature.

The total charge is obtained by addition of released charges listed in the second and third columns of Table I and is tabulated in the fourth column of Table I. It can be seen that the total charge essentially does

Table I. Eletret properties of the sulfonate membrane in sodium form

Forming field strength, kv/cm	Charge (coulombs $\times 10^{-4}$ )			Position of discharge peak, min	Internal field, v/cm $\times 10^4$
	First discharge at $28^\circ\text{C}$	Second discharge at $60^\circ\text{C}$	Total charge		
1.25	0.32	2.98	3.30	90	3.27
2.5	0.54	2.86	3.40	85	3.37
5.0	0.70	2.54	3.24	80	3.21

not vary with the change of forming field strength. The lack of dependence of total charge storage on the strength of the forming field indicates that the membrane probably polarized at the lowest forming field used and reached its saturation level at 1.25 kv/cm. However, the position of the peak of current-time curve seems to be dependent on the strength of forming electric field. This dependence, in minutes, is given in the fifth column of Table I.

Reheating shows dramatically how large quantities of residual charge have been left in the membrane after the first discharge. Apparently, charges were locked in and could not be liberated at room temperature during one day of discharge time. As soon as the temperature was raised, they were released. Therefore, the current surge shown in Fig. 3 indicates the liberation of frozen-in charges during the reheating period.

The corresponding internal electric fields produced by these charges have been calculated using the expression

$$E = 1.13 \times 10^{13} \frac{Q}{A} \quad [3]$$

where  $E$  = internal electric field, v/cm,  $Q$  = charge, coulombs, and  $A$  = area, cm<sup>2</sup>.

The calculated values of internal electric fields are given in the last column of Table I. Charge  $Q$  in Eq. [3] is the total charge listed in the fourth column of Table I.

In Fig. 4 is shown the 350-min reheating period at 53°C for membrane electrets in three ionic forms: Na, Ag, and H. Charging time was 1.5 hr at a forming field strength 1.25 kv/cm. The membrane electret in sodium form stored the largest amount of charge.

We have recently demonstrated excellent blood compatibility with PSA-incorporated elastomeric and thermoplastic membranes. PSA was also grafted to surfaces of common elastomers; these polysulfonated materials have high electrical resistance ( $> 10^7$  ohm-cm) and make ionic electret materials in solution. Their bulk equilibrium water absorption contents are low and, as a result, are relatively impermeable to

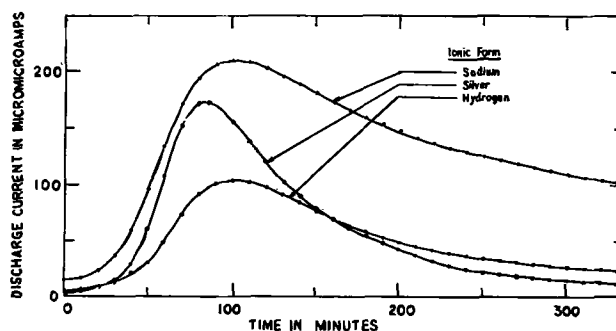


Fig. 4. Discharge at 53°C of PSA membrane electrets in three ionic states.

salt and water in 0.1M NaCl, and in human whole blood.

We deduce that the effects of the matrix on ionic electret phenomena are indirect. The plastic matrix separates the adjacent PSA molecules, reduces the effective dielectric constant and imparts mechanical strength and support to the material. It is suggested that the electret effect and good blood compatibility results are primarily related to the electrochemical properties of the PSA molecule. More detailed data and techniques will be reported in a subsequent article.

Manuscript received Aug. 17, 1967; revised manuscript received Feb. 23, 1968. This paper was presented at the Electrets Symposium at the Chicago Meeting, Oct. 15-19, 1967, as Abstract 129.

Any discussion of this paper will appear in a Discussion Section to be published in the December 1968 JOURNAL.

#### REFERENCES

1. Z. Urban and R. A. Wallace, *This Journal*, **115**, 276 (1968).
2. S. Wikström, *Arkiv för Fysik*, **7**, 213 (1954).
3. A. I. Froiman and V. M. Fridkin, *Kristallograf.*, **1**, 342 (1956).
4. R. Gerson and J. H. Rohrbaugh, *J. Chem. Phys.*, **23**, 2381 (1955).

## On the Origin of an Exponential Vacancy Distribution in Annealed Ta/Ta<sub>2</sub>O<sub>5</sub>-Structures

K. Lehovc\*

Research & Development Laboratories, Sprague Electric Company, North Adams, Massachusetts

#### ABSTRACT

An attempt is described to explain the exponential vacancy profile in annealed Ta/Ta<sub>2</sub>O<sub>5</sub> structures postulated by Smyth *et al.* by a Boltzmann distribution in a constant electric field arising from the emf of the reaction between tantalum and oxygen during the anneal. Implications of this model for the oxygen uptake during the anneal are discussed and compared to experimental data. While the model is able to account for the origin and the attenuation constant of the observed exponential vacancy profile, it involves still unproven assumptions on space charge compensation and electron conduction mechanism.

Smyth and co-workers (1-4) have analyzed capacitance and loss angle measurements of annealed Ta/Ta<sub>2</sub>O<sub>5</sub>-structures in terms of an exponential conductivity profile at zero d-c bias voltage. The bias voltage dependence of the capacitance was interpreted by means of an exponential oxygen vacancy profile. However, the origin of such a profile has not been clarified.

\* Electrochemical Society Active Member.

Defining an attenuation constant  $K_\sigma$  of the conductivity

$$K_\sigma = -\partial \ln \sigma / \partial (x/d) \quad [1]$$

where  $x$  is the distance of a point in the oxide of conductivity  $\sigma$  from the metal, and  $d$  is the oxide thickness one obtains (1-4)  $K_\sigma$ -values of the order 50. We noted sometime ago (5) that an exponential conductivity profile could arise from a Boltzmann distribution of

carriers of charge  $zq$  in a constant field  $F$ , and that the attenuation constant of this Boltzmann factor,  $zqFd/kT$ , has indeed the same order of magnitude as  $K_S \simeq 50$ , if  $Fd = E$  is taken as the emf of the chemical reaction between tantalum and oxygen. More recent results of Smyth and Shirn (4) suggest that the ionization energy of the oxygen vacancies (which act as donors of electrons) depends on their concentration, and that the attenuation constant of the oxygen vacancy distribution

$$K_s = -\partial \ln N_s / \partial [(x/d)] \quad [2]$$

is only about 30. The subscript  $s$  has been chosen since the vacancy concentration  $N_s$  has been obtained (4) by a Schottky plot (6), i.e., from the bias voltage dependence of capacitance at a constant frequency.

The measurements of Smyth and co-workers (1-4) were made on tantalum anodized at various formation voltages and then annealed at elevated temperatures in the range 300°-400°C for periods ranging from 10 min to several hours. During the anneal, no oxide growth occurred. However, there was a weight increase attributed to oxygen uptake of the tantalum metal (1). Anneal time in the investigated range did not have much influence on the room temperature impedance indicating that a quasistationary state was reached within minutes. Most of the measurements were made on anodic films of the thickness range  $d = 1500$ -3000 Å.

The present paper explores in detail the concept of an exponential vacancy distribution arising from a Boltzmann distribution in a constant field. Its implication on the oxygen uptake during the anneal investigated by Pawel and Campbell (7) and recently by Steidel (8) will also be discussed.

It will be shown that justification of the exponential vacancy profile by a Boltzmann distribution, although enticing at first sight, nevertheless requires a number of ad hoc assumptions, and thus raises problems of its own. However, publication of the present paper, while not leading to a fully convincing model, can be justified by the extensive pertinent experimental work and by the need to investigate critically all consequences of an explanation which appears plausible at first sight.

#### Origin of an Exponential Distribution of Oxygen Vacancies

During the anneal, oxygen is dissolved in the tantalum metal. This creates oxygen vacancies in the adjacent tantalum oxide. These vacancies move toward the outer oxide surface and generate an oxygen flow from the ambient into the tantalum metal. It is well known that tantalum can dissolve large quantities of oxygen (1, 7, 8). Changes of tantalum resistivity and of its temperature coefficient by oxygen uptake have been demonstrated (8). During anneal an emf of a few tenths of a volt (8, 9) appears across the oxide, the tantalum substrate becoming negative. The fact that the electric properties of annealed Ta/Ta<sub>2</sub>O<sub>5</sub>-samples, after cooling to room temperature, do not return to the preannealed state indicates a lack of oxygen uptake of the reduced tantalum oxide from the ambient atmosphere at room temperature.

An exponential vacancy distribution would arise under quasiequilibrium conditions from the Boltzmann factor at a constant field,  $F$

$$[V_0^z] = [V_0^z]_{x=0} \exp(-zqFx/kT) \quad [3]$$

where  $zq$  is the charge of the mobile vacancies of concentration  $[V_0^z]$ .<sup>1</sup> Comparison of [3] with the empirical relation [2] shows that

$$K_S = zqFd/kT \quad [4]$$

By inserting the values  $K_S = 30$  and  $kT/q \simeq 60$  mv at the anneal temperature, we obtain  $zFd \simeq 1.8$ v. Since

the oxide thickness  $d$  is of the order of  $2 \cdot 10^{-5}$  cm for most of the samples investigated by Smyth *et al.* (1-4), we are here concerned with an electric field  $F$  of the order of  $10^5$  v/cm. A space independent field implies absence of a significant space charge density, i.e.,

$$\int \rho \delta x \ll \epsilon \epsilon_0 F \quad [5]$$

the integral extending over the region of constant field. For  $F \simeq 10^5$  v/cm, the right side is about  $2 \cdot 10^{-7}$  C/cm<sup>2</sup> or  $10^{12}$  electron charges per cm<sup>2</sup>. This is much smaller than the number of charges derived from the Schottky profile [2]

$$\int_0^d N_s \delta x = N_s^0 d/K_S \simeq 2 \times 10^{14} \text{ cm}^{-2} \quad [6]$$

where  $N_s^0 = 3 \cdot 10^{20}$  cm<sup>-3</sup>,  $K_S = 30$ , and  $d \simeq 2 \times 10^{-5}$  cm have been used (4). This leaves us with two possibilities:

- The concentration of charged vacancies at the anneal temperature is much smaller than  $N_s$ , derived from the Schottky profile, perhaps due to partial ionization, or else
- There exists a mechanism for compensation of the charge of the mobile vacancies at the anneal temperature. The compensating charge must be immobile or else it would assume a Boltzmann distribution of the opposite slope of that of the mobile oxygen vacancies. Such a charge compensation may indeed arise by means of oxygen vacancies occurring in different charged states as will be pointed out in the Appendix.

#### Implications for the Oxygen Uptake during Anneal

During a quasistationary uptake of oxygen ions *via* a vacancy mechanism, an electron current of equal magnitude flowing from the tantalum outward is necessary for charge compensation. This equality is assured by the establishment of an electric potential of suitable polarity and magnitude. The emf (= difference of the electrochemical potential of electrons at the two boundaries of the oxide divided by charge  $q$ ) becomes identical to the electrostatic potential if the electron concentration is constant with position, the chemical potential (or "diffusion potential") being then zero. This is the situation we visualize in the Ta<sub>2</sub>O<sub>5</sub> during the anneal (or, at least, in the region from which most contributions to the emf arise), for reasons to become clear later. The polarity of the observed emf is such as to generate a field in the oxide driving electrons from the tantalum to the outer oxide, indicating that the electric current is the rate-determining step, at least in a portion of the oxide film. This is in agreement with our previous postulation of a Boltzmann-distribution of oxygen vacancies, which implies quasithermal equilibrium, i.e., the vacancy transport rate is not rate determining. We conclude from the constancy of the electron current  $i_e$  through the oxide and from the constancy of the electric field, postulated to explain the exponential vacancy profile, that the electron concentration

$$n = i_e / q \mu_e F \quad [7]$$

is also a constant, when  $\mu_e$  is the electron mobility. This justifies the relation

$$F = E/l \quad [8]$$

between the electric field, the emf  $E$  and the width  $l$  of the region from which the emf arises and in which the conditions discussed above are realized.

In distinguishing between the oxide thickness  $d$  and the region  $l$  across which the emf arises, we have taken into account the fact that the exponential vacancy profile has not been established experimentally throughout the entire oxide, and that a Boltzmann distribution of vacancy need not exist across the entire oxide.

<sup>1</sup> A different notation has been used for the vacancy concentration in Eq. [3] at the anneal temperature and the concentration of the Schottky profile, since both are not necessarily identical as will be discussed later.

Within the region of width  $l$ , we expect the following inequality between electric ( $\sigma_e$ ) and ionic ( $\sigma_I$ ) conductivities

$$\sigma_e = nq\mu_e \ll \sigma_I = [V_0^z] \cdot zq\mu_I \quad [9]$$

expressing the fact that the electron transport is rate determining. Outside of this region we may well have  $\sigma_e > \sigma_I$ , and  $l$  may then be defined as the position at which

$$\sigma_e = \sigma_I \text{ at } x=l \quad [10]$$

Since  $\mu_e \ll \mu_I$ , one has there  $n \ll [V_0^z]$ . It follows from the Boltzmann distribution [3] that

$$\begin{aligned} E &= kT/zq \ln [V_0^z]_{x=0}/[V_0^z]_{x=l} \\ &= kT/zq \ln \sigma_I(x=0)/\sigma_e(x=l) \end{aligned} \quad [11]$$

where [10] has been used and the ionic mobility  $\mu_I$  was assumed to be independent of the vacancy concentration.

#### Comparison with Experimental Data

The importance of electron conduction for the oxygen transfer rate is in agreement with observations by Pawel and Campbell (7) on oxygen uptake of tantalum protected by an anodic oxide film at elevated temperatures. They found that "anodic films exhibiting low leakage currents were more efficient in protecting the metal from oxidation. Local breakdown at a point of weakness may, instead of being self healing, lead to an accelerated deterioration of the remainder of the film." The latter observation is in accordance with our model if lateral electron conduction along the outer oxide surface may occur.

Additional evidence for the electron transfer being the rate-determining step for oxygen flow through part of the oxide is the electromotive force at the anneal temperature (7, 8, 9).

The emf corresponding to the free energy of the reaction  $2\text{Ta} + 5/2 \text{O}_2 \rightarrow \text{Ta}_2\text{O}_5$  at  $400^\circ\text{C}$  is 1.83v for oxygen-free tantalum and an ambient of 0.2 atm oxygen pressure. The fact that the observed emf (8, 9) is only a fraction of this value can be attributed partially to the outer portion of the oxide film having dominant electronic conduction and partially to oxygen dissolved in tantalum. The end product of the reaction between tantalum and the oxygen ambient at moderate anneal conditions is not tantalum oxide, but oxygen dissolved in tantalum.

Comparing the value  $zFd = 1.8\text{v}$  obtained by [4] from the slope  $K_S$  of the observed (4) Schottky profile at room temperature, with the observed (8, 9) emf during the anneal  $E = F \cdot l \simeq 0.3\text{v}$ , we conclude that for  $z = 1$ :  $l/d \simeq 1/6$ , and  $F \simeq 10^5 \text{ v/cm}$ , while for  $z = 2$ :  $l/d \simeq 1/3$  and  $F \simeq 5 \times 10^4 \text{ v/cm}$ .

The Boltzmann factor for  $E = 0.3\text{v}$  and  $kT/q = 0.06\text{v}$  ( $T \simeq 400^\circ\text{C}$ ) is  $e^{-qE/kT} = 6.7 \times 10^{-3}$  in case that  $z = 1$  and  $e^{-2qE/kT} = 4.6 \times 10^{-5}$  in case that  $z = 2$ . Using  $N_s^0 = 3.10^{20} \text{ cm}^{-3}$ , we arrive at vacancy concentrations at  $x = l$  of  $2.10^{18} \text{ cm}^{-3}$  and  $1.4 \times 10^{16} \text{ cm}^{-3}$  for the cases  $z = 1$  and  $z = 2$ , respectively. Since experimental Schottky profiles have been measured which extend to  $10^{17} \text{ cm}^{-3}$ , we conclude that  $z = 2$ .

The magnitude of  $\sigma_e$  in that part of the oxide where the Boltzmann distribution of vacancies exists can be estimated by extrapolation to  $400^\circ\text{C}$  of data from Fig. 5 or ref. (7). For the film of 1000Å thickness, an oxygen flow of  $10^{-11} \text{ g-moles/cm}^2 \text{ min}$  is obtained, which corresponds to  $1.2 \times 10^{-7} \text{ amp/cm}^2$  (assuming that  $z = 2$ ). Using a field of  $5 \times 10^4 \text{ v/cm}$  for the region where [7] is valid, one arrives at  $\sigma_e \simeq 2.4 \times 10^{-12} \text{ ohm}^{-1} \text{ cm}^{-1}$ .

At room temperature Smyth and Shirn (4) obtain  $\mu_e \simeq 1 \text{ cm}^2/\text{v sec}$ . Using this value as a rough estimate of the mobility at the anneal temperature, one has  $n \simeq 1.5 \times 10^7 \text{ cm}^{-3}$ .

By means of [11], we are able to estimate the vacancy mobility

$$\mu_I \simeq [\sigma_e]_{x=l}/zq[V_0^z]_{x=l} \quad [12]$$

Using the previously estimated value  $[V_0^z]_{x=l} \simeq 1.4 \times 10^{16} \text{ cm}^{-3}$ , one obtains  $\mu_I \simeq 5 \times 10^{-10} \text{ cm}^2/\text{v sec}$  for  $z = 2$ , which is not unreasonable.

For a nondegenerate electronic semiconductor, the band model provides

$$n = N_c \exp[-(\epsilon_c - \epsilon_F)/kT] \quad [13]$$

where  $N_c$  is the density of states (partition sum) for the conduction band and  $\epsilon_c - \epsilon_F$  is the energy difference between the bottom of the conduction band  $\epsilon_c$  and the Fermi level (electrochemical potential per electron)  $\epsilon_F$ . Provided that  $\epsilon_F$  does not depend on temperature and neglecting the small temperature dependence of  $N_c$  vs. that of the exponential term, we obtain an activation energy of  $\epsilon_c - \epsilon_F$ .

Pawel and Campbell (7) find an activation energy for oxygen uptake of 1.96 eV, while Steidel (8) observed 1.5-1.6 eV. Inserting  $n = 1.5 \times 10^7 \text{ cm}^{-3}$ ,  $\epsilon_c - \epsilon_F = 2.0$  and 1.5 eV, respectively, and  $kT/q = 0.06\text{v}$  into [9], one obtains  $N_c = 3.10^{20} \text{ cm}^{-3}$  and  $10^{18} \text{ cm}^{-3}$ , respectively; neither value is objectionable.

The magnitude of the ionic conductivity in the outer oxide film can be estimated if we assume that it is of the same order as that of unannealed anodic oxide films. The anodic oxidation rate depends on field as (10-13)

$$i_I = A'(e^{B'F} - e^{-B'F}) \quad [14]$$

For  $B'F \ll 1$ , one obtains

$$\sigma_I = i_I/F = 2 A'B' \quad [15]$$

Extrapolating the room temperature values (10-13) of  $A' \simeq 5.10^{-19}$  to  $6.10^{-21} \text{ amp/cm}^2$  and  $B' \simeq 5.10^{-6} \text{ cm/v}$  to the anneal temperature of  $400^\circ\text{C}$  by using the activation energy  $U_{A'} = 1.2 \text{ eV}$  (12) for  $A'$  and the inverse absolute temperature dependence (12) for  $B'$ , we obtain  $\sigma_I = 10^{-15}$  to  $10^{-17} \text{ ohm}^{-1} \text{ cm}^{-1}$ . These values are indeed small compared to  $\sigma_e = 2.4 \times 10^{-12} \text{ ohm}^{-1} \text{ cm}^{-1}$ . Thus, it is reasonable to expect that oxygen flow in the outer film region, which is in equilibrium with the oxygen ambient, is limited by ionic flow while in the reduced inner film region it is limited by electron transport.

It should be noted that the electron current  $i_e = nqF$  as the rate-determining step for oxygen flow could lead to a parabolic growth since  $F = E/l$ , provided that  $E$  and  $l$  do not vary with the oxide thickness. Thus, the anneal mechanism here described is not necessarily in disagreement with parabolic growth, which is usually taken as an indication (7) for a growth rate limited by ion diffusion.

#### Difficulties Encountered by the Present Model

A complete clarification of the anneal mechanism requires knowledge of the oxygen flow mechanism in the outer oxide film region, i.e.,  $l < x < d$ , and of the nature and location of the positive charges which generate the constant electric field in the oxide region  $0 < x < l$ .

In the case of a simple diffusion current of vacancies through the outer oxide region

$$\begin{aligned} i_I &\simeq \frac{kT}{zq} \mu_I zq [V_0^z]_{x=l}/(d-l) \\ &= \sigma_e \frac{kT}{zq}/(d-l) \end{aligned} \quad [16]$$

Since  $kT/zq/(d-l) \ll F$  for  $d-l$  of the order of  $d$ , it follows that  $i_I \ll i_e = \sigma_e F$ , while for quasi-stationary oxygen uptake  $i_I = i_e$  is necessary.

It would thus appear that either the field in the outer oxide region is of opposite polarity than that in the inner oxide region, or else the vacancy mobility in the outer oxide region is significantly larger than in the inner region. Arguments for each of these suggestions can be found. Field reversal is not unlikely considering that the rate determining step is electron transport for  $0 < x < l$  and vacancy transport for  $l <$

$x < d$ . A two-layer structure for anodically grown oxide films has been established experimentally by means of tracer studies (14). Some discontinuity in the structure at  $x = l$  is thus quite possible if this position marks the interface between the two-layer structure. It is even conceivable that a positive charge layer might form there. However, these assumptions, while possibly correct, have not yet been proven to be so.

Another difficulty of the present model involves the discrepancy between the rather low electron conductivity at the anneal temperature  $\sigma_e \simeq 2.4 \times 10^{-12}$  ohm $^{-1}$  cm $^{-1}$  in contrast to the fairly high electron conductivity  $\sigma_e \simeq 10^{-7}$  ohm $^{-1}$  cm $^{-1}$  at room temperature in the region adjacent to the tantalum, postulated by ref. (1) to (4). Clearly, this calls for two different conduction mechanisms. Yet both mechanisms must originate from the oxygen vacancies or we lose the relation between vacancy profile established at the anneal and the experimental Schottky profile at room temperature, which formed the starting point of our considerations. It will be shown in the Appendix that space charge neutrality may arise by equal concentrations of  $[V'_0]$  and  $[V''_0]$  vacancies at the anneal, one of them,  $[V''_0]$ , being highly mobile. It is reasonable to expect, therefore, that upon cooling, clustering to  $V^{x_{20}}$  complexes takes place.

To provide space charge neutralization, the Fermi level at the anneal temperature is located halfway between the energy levels of the  $V'_0$  and  $V''_0$  vacancies. On the other hand, at room temperature, the Fermi level would be determined by the ionization equilibrium of the  $V^{x_{20}}$  complexes and thus might be considerably closer to the conduction band, resulting in a large increase in the electron conductivity.

Perhaps the observed (8, 9) decrease of the emf with decreasing temperature in the lower temperature range can be attributed to the increasing dominance of electronic conduction due to clustering. It might arise also, of course, by the decreased ionic mobility, which shifts the position  $x = l$  to smaller values and thus reduces the emf across the region  $0 < x < l$ .

According to the present hypothesis, the Schottky concentration  $N_S$  would be the concentration of ionized clusters  $[V'_{20}]$ . It is believed that at an applied anodic bias voltage a space charge layer forms adjacent to the tantalum metal by depletion of electrons and complete ionization of the  $V_{20}$  clusters. Thus  $N_S = [V'_{20}]$ . If, at the anneal temperature, all clusters are dissociated, then  $[V_0] = 2[V'_{20}] = 2N_S$ . The concentration of mobile doubly charged vacancies,  $[V''_0]$  at the metal boundary would be less, and possibly significantly less, than  $[V_0] = 2N_S$ . The use of  $N_S^0 = 3.10^{20}$  cm $^{-3}$  for  $[V''_0]_{x=0}$  in Eq. [11] is thus not justified and the distinction between  $z = 2$  and  $z = 1$  based thereon becomes questionable. Also, the ionic mobility calculated by [13] might be considerably higher than the numerical estimate based on  $[V''_0] \simeq 1.4 \times 10^{16}$  cm $^{-3}$ .

### Conclusions

The possible origin of an exponential vacancy distribution in annealed Ta/Ta $_2$ O $_5$  samples by means of a Boltzmann distribution of vacancies during the anneal was investigated. If this interpretation is correct, oxygen uptake during the anneal is limited by electron transfer rather than ion diffusion, at least in a portion of the oxide film. This view is consistent with the observed appearance of an emf during the anneal and with the rate of oxygen uptake. However, the electron conductivities at the anneal temperature appear much smaller than those at room temperature. The difficulty could be removed by the unproven hypothesis of clustering of vacancies. It is shown in the Appendix that space charge compensation could occur even at large concentrations of vacancies and is consistent with a Boltzmann distribution of mobile vacancies in a constant field.

In summary, a model has been found which leads to a strictly exponential vacancy profile as postulated

by Smyth *et al.* The model accounts for the order of magnitude of the attenuation distance. It permits significant conclusions in the mechanism of the anneal process. The model includes, however, several speculative features, which cannot be tested by existing experimental data, thus suggesting further experimental work.

Other models, such as tunneling (15), can also account for the electrical measurements of Smyth *et al.* on annealed Ta/Ta $_2$ O $_5$ . Thus it is conceivable that the Schottky distribution and conductivity profile need not necessarily have the straightforward interpretation (1-4) which was accepted in this paper.

### Acknowledgment

The author would like to express his appreciation to D. M. Smyth for making recent experimental results available to him prior to publication and for many stimulating discussions.

Manuscript received Aug. 14, 1967; revised manuscript received ca. Dec. 11, 1967.

Any discussion of this paper will appear in a Discussion Section to be published in the December 1968 JOURNAL.

### APPENDIX

#### Space Charge Compensation by Means of Oxygen Vacancies of Different Valency States

Consider the oxygen vacancy species  $V'_0$ ,  $V''_0$ ,  $V'_0$ , and  $V^{x_0}$  in the notation of Kröger (16). The existence of a single vacancy as either donor or else trap for an electron is well known for the case of F and F $^1$  centers in alkali-halides. A single vacancy can change its charge by "reaction" with electrons, e.g.



Several reactions between vacancies and electrons and the corresponding mass action laws are listed in Table I. Also included, are values for the mass action constants in terms of the energy levels involved using customary (16) notation.

Since the concentrations of the various charged vacancy states are in proportion to each other, and, therefore, to the total vacancy concentration, the zero space charge condition for the case of negligible contributions by electrons provides a value for the electron concentration, which does not depend on the vacancy concentration, but only on the mass action constants, which are space independent. A space independent electron concentration was indeed a key feature of our model. For instance, in the case

$$[V''_0] \simeq [V'_0] \quad [A-2]$$

one has

$$n = \sqrt{K_2 K_3} = N_c e^{-\epsilon_c/kT} e^{+(\epsilon^x + \epsilon'/2kT)} \quad [A-3]$$

Comparison to Eq. [13] shows

$$\epsilon_F = (\epsilon' + \epsilon^x)/2 \quad [A-4]$$

i.e., the Fermi level lies half-way between the  $\epsilon'$  and  $\epsilon^x$  levels, independent of position and vacancy concentration (Fig. 1).

Since the levels  $\epsilon_c$ ,  $\epsilon'$ , and  $\epsilon^x$  at the oxide-tantalum interface and the Fermi level in the tantalum metal are well defined and independent of each other, the assumption that the levels  $\epsilon'$  and  $\epsilon^x$  are an equal distance above and below, respectively, of the Fermi level in the tantalum metal may appear quite arbitrary.

Table I. Electron reactions involving oxygen vacancies and corresponding mass action laws and mass action constants (the energy of electrons in the conduction band and on the  $V'_0$ ,  $V^{x_0}$ ,  $V''_0$  levels are designated by  $\epsilon_c$ ,  $\epsilon'$ ,  $\epsilon^x$  and  $\epsilon^*$ , respectively).

Reaction	Mass action law	$K_i$ ( $i = 1, 2, \text{ or } 3$ )
$V''_0 \rightarrow V'_0 + e$	$[V''_0] \cdot n = K_1 [V'_0]$	$N_c e^{-(\epsilon_c - \epsilon'/kT)}$
$V'_0 \rightarrow V''_0 + e$	$[V'_0] \cdot n = K_2 [V''_0]$	$N_c e^{-(\epsilon_c - \epsilon^x/kT)}$
$V'_0 \rightarrow V^{x_0} + e$	$[V'_0] \cdot n = K_3 [V^{x_0}]$	$N_c e^{-(\epsilon_c - \epsilon^*/kT)}$



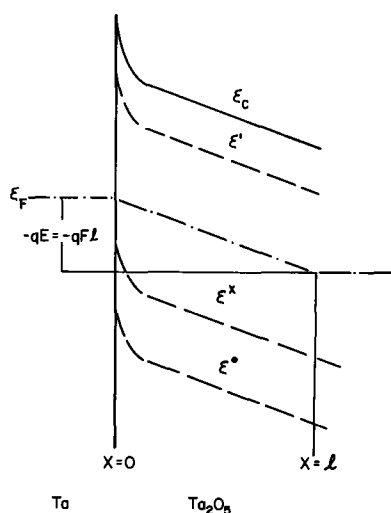


Fig. 1. Hypothetical energy level diagram for the Ta/Ta<sub>2</sub>O<sub>5</sub> interface during anneal.  $\epsilon_c$  is the bottom of the electron conduction band,  $\epsilon'$  is the energy level for negatively charged oxygen vacancies, i.e., for the third electron at the vacancy;  $\epsilon^x$  is the level for the second electron at a neutral oxygen vacancy and  $\epsilon^o$  is the energy for the electron at a positively charged vacancy. Doubly positive charged oxygen vacancies are believed to be mobile and assume a Boltzmann distribution in the region  $0 < x < l$ , causing the electromotive force  $E \simeq Fl$ . The emf in the region  $x > l$  is just about shorted by dominant electronic conduction. Electron concentration in the region  $0 < x < l$  is constant, viz., constancy of  $\epsilon_c - \epsilon_F$ . A thin space charge layer in the oxide at the metal boundary (indicated schematically by the upward bending of energy levels) adjusts the Fermi level in the metal to the value of  $(\epsilon' - \epsilon^x)/2$  in the adjacent portion of the neutral oxide.

However, considering the large concentration of vacancies at the interface, a very thin space charge region should suffice to adjust the levels  $\epsilon'$  and  $\epsilon^x$  to positions of equal distance above and below, respectively, of the Fermi level in the adjacent metal. This has been indicated by the upwards bending of the levels in Fig. 1 near the metal interface (assuming a positive space charge).

In order to obtain a Boltzmann distribution of vacancies, we must postulate that only the vacancy species of one sign is mobile. If both positive and negative vacancies were mobile, they would establish two Boltzmann distributions, one decreasing with position and the other increasing with position, while [A-2] requires both species to vary in unison with each other.

A high mobility of positively charged vacancies in contrast to a comparable immobility of negatively charged vacancies can be rationalized as follows: Oxygen vacancies move by jumps of adjacent oxygen ions. A negatively charged vacancy  $V'_o$  repels the adjacent oxygen ions and this suppresses their mobility. The opposite is true for positively charged vacancies and, in particular, of the doubly charged state  $V''_o$ . While the  $V'_o$ -centers are immobile as an entity, their concentration can still change in proportion to that of the mobile  $V''_o$ -centers by the electron transfer reaction



Thus, at a space-independent electron concentration  $n_e$ , the ratios of the concentrations  $[V'_o]$ ,  $[V''_o]$  and  $[V''_o]$  are independent of position irrespective of the total concentration  $[V''_o] + [V'_o] + [V''_o] + [V''_o]$ , which assumes a Boltzmann distribution if only the  $V''_o$  species is mobile. In this manner, the mass action relations (Table I), the zero space charge condition<sup>2</sup> [A-2], the Boltzmann distribution of mobile vacancies [3] and the condition of a space independent electron concentration [7] can all be satisfied.

<sup>2</sup> Equation [A-2] assumes that  $[V''_o] \ll [V'_o]$ . Similar arguments can be advanced in the case that  $[V''_o]$  contributes measurably to the zero space charge condition.

#### REFERENCES

1. D. M. Smyth, G. A. Shirn, and T. B. Tripp, *This Journal*, **110**, 1264 (1963).
2. D. M. Smyth and T. B. Tripp, *ibid.*, **110**, 1271 (1963).
3. D. M. Smyth, G. A. Shirn, and T. B. Tripp, *ibid.*, **111**, 1331 (1964).
4. D. M. Smyth and G. A. Shirn, Paper presented at the Dallas Meeting of the Society, May 7-12, 1967, as Abstract 27.
5. K. Lehovc, Paper presented at the Cleveland Meeting of the Society, May 1-5, 1966, as Abstract 28.
6. W. Schottky, *Z. Phys.*, **118**, 539 (1942).
7. R. E. Pawel and J. J. Campbell, *This Journal*, **113**, 1204 (1966).
8. C. A. Steidel, Paper presented at Dallas Meeting of the Society, May 7-12, 1967, as Abstract 39.
9. Yoshioki Ishikawa, Yozo Sasaki, Yasuo Seki, and Shuichi Inowaki, *J. Appl. Phys.*, **34**, 867 (1963).
10. L. Young, *Trans. Faraday Soc.*, **50**, 153 (1954).
11. D. A. Vermilyea, *Acta Met.*, **1**, 282 (1953).
12. R. Dreiner, *This Journal*, **111**, 1350 (1964).
13. P. H. G. Draper and P. W. M. Jacobs, *Trans. Faraday Soc.*, **59**, 2895 (1963).
14. J. J. Randall, Jr., W. J. Bernard, and R. R. Wilkinson, *Electrochim. Acta*, **10**, 183 (1965).
15. K. Lehovc, *This Journal*, **115**, 192 (1968).
16. F. A. Kröger, "Chemistry of Imperfect Crystals," North-Holland Publishing Company, Amsterdam (1964).

# Silicon Nitride Thin Films from SiCl<sub>4</sub> Plus NH<sub>3</sub>: Preparation and Properties

M. J. Grieco,<sup>1</sup> F. L. Worthing, and B. Schwartz\*

Bell Telephone Laboratories, Incorporated, Murray Hill, New Jersey

## ABSTRACT

Silicon nitride thin films have been deposited on silicon substrates by reacting SiCl<sub>4</sub> and NH<sub>3</sub> at 550°-1250°C. The effects of deposition temperature and of SiCl<sub>4</sub> and NH<sub>3</sub> concentrations on the deposition rate have been studied. The etch rate of the deposited films is shown to be a function of the deposition temperature. Electrical evaluation has shown the dielectric strength to be independent of contact area and film thickness and the dielectric constant to be in the range seven to eight. Surface charge plus surface state density values range from 7 to 18 x 10<sup>11</sup>/cm<sup>2</sup>. Nonlinear I-V characteristics of the films have been observed. The deposited films are extremely effective diffusion masks for sodium.

Thin layers of silicon dioxide have found extensive use in the fabrication of semiconductor devices for surface passivation (1), as diffusion masks (2), and as dielectric layers (3). Technological advances and more demanding requirements (4) have led to the need for insulating films with properties superior to those of the oxide. One of the materials currently receiving a great deal of attention as a possible substitute for SiO<sub>2</sub> is silicon nitride. This material has been evaluated for its passivation properties on p-n junctions (5), for its use as a dielectric in a field-effect structure (6), and for its usefulness as a diffusion mask (7, 8), and it has been found to be satisfactory.

From the data in Table I, it is apparent that there are many reactions for forming the nitride that are thermodynamically feasible. However, passing nitrogen or ammonia over solid silicon substrates heated to 1300°C results in extremely thin nitride layers (9), owing to the high efficiency of the material as a diffusion mask. When ammonia is passed over molten silicon, crystals of nitride result, as reported by Kaiser and Thurmond (10), Doo and his co-workers (11) have reported on the deposition of silicon nitride films by the high-temperature reaction of SiH<sub>4</sub> plus NH<sub>3</sub>. A number of investigators (12, 13) have made use of various high-field discharge techniques in order to obtain nitride deposition at low temperatures.

This paper will report on deposited nitride thin films obtained by reacting SiCl<sub>4</sub> and NH<sub>3</sub> in the presence of silicon substrates heated in the temperature range 550°-1225°C. The kinetics of the deposition process will be discussed and the properties of the deposited films will be described.

## Experimental Procedure

Figure 1 is a schematic of the apparatus used for this study; the system was similar to that normally used for silicon epitaxy by the hydrogen reduction of silicon tetrachloride (14). The reaction chamber is shown in Fig. 2; it was an air-cooled, single-walled, 50 mm ID quartz chamber containing a susceptor heated with an externally placed r.f. coil. The susceptor was a high-purity graphite pedestal covered with a quartz sleeve; without the quartz sleeve, NH<sub>3</sub> was adsorbed by the graphite, causing the carbon pedestal to powder and crumble. When a silicon susceptor was used, thick deposits of the nitride formed on the pedestal (the susceptor temperature was normally almost 200°C higher than the substrate temperature), making it necessary to relap the top surface of the susceptor after each run.

Three separate feed lines were used to introduce the reagents into the reaction chamber. In the very early phases of this study, the reagents were mixed together well upstream of the reactor, but it was found that no deposit was formed on the substrate. It was quickly realized that the NH<sub>3</sub> and SiCl<sub>4</sub> were reacting immediately on contact, and most of the reaction products were precipitating out of the gas phase. By converting to the system of individually feeding the reagents into the reaction chamber, nitride deposition on the substrate was achieved.

The outlets of the two feed lines inside the reaction chamber were varied from ½ to 4 in. above the silicon substrate. With the outlets of the feed lines close (~1 in.) to the substrate, films of nonuniform thickness were produced. However, with the substrate approximately 3-4 in. below the feed-line outlets, the layer thickness (~3000Å) varied by only about 200Å across a ½ in. square substrate. These last dimensions for the reactor geometry were maintained throughout these experiments.

The silicon substrates were 10 mils thick, p-type, 2-70 ohm-cm, (111) oriented, and chemically polished with an iodine etch (15). Just before the substrates were loaded into the reactor, they were chemically etched for 2 min in 10:1:HNO<sub>3</sub>:HF, nitric acid quenched, immersed in concentrated HF for 2 min, and finally rinsed in deionized water. After the substrate was loaded, the entire system was purged with nitrogen, then heat-treated in H<sub>2</sub> at the deposition temperature for 30 min. Deposition was initiated after a second purge with nitrogen. The deposition reaction was carried out using nitrogen as the inert carrier of the silicon tetrachloride vapor. A total flow of 2600 cc/min of gas, composed of approximately 150 cc/min of N<sub>2</sub> + SiCl<sub>4</sub> vapor, 50 cc/min of NH<sub>3</sub>, and 2400 cc/min of N<sub>2</sub> bypass, was passed through the reactor. The SiCl<sub>4</sub> bubbler was maintained at -30°C. The maximum deposition temperature of 1000°C was chosen

Table I. Free energy of over-all reactions\*

Reaction	ΔG° kcal/mol	
	298°K	1300°K
3Si + 2N <sub>2</sub> → Si <sub>3</sub> N <sub>4</sub>	-154.8	-71.4
3Si + 4NH <sub>3</sub> → Si <sub>3</sub> N <sub>4</sub> + 6H <sub>2</sub>	-138.8	-165.4
3Si + 2N <sub>2</sub> H <sub>4</sub> → Si <sub>3</sub> N <sub>4</sub> + 4H <sub>2</sub>	-230.8	-257.8
3SiCl <sub>4</sub> + 2N <sub>2</sub> + 6H <sub>2</sub> → Si <sub>3</sub> N <sub>4</sub> + 12HCl	+15.3	-15.0
3SiCl <sub>4</sub> + 4NH <sub>3</sub> → Si <sub>3</sub> N <sub>4</sub> + 12HCl	+31.3	-109.0
3SiCl <sub>4</sub> + 2N <sub>2</sub> H <sub>4</sub> + 2H <sub>2</sub> → Si <sub>3</sub> N <sub>4</sub> + 12HCl	-61.9	-202.6
3SiH <sub>4</sub> + 2N <sub>2</sub> → Si <sub>3</sub> N <sub>4</sub> + 6H <sub>2</sub>	-194.4	-179.1
3SiH <sub>4</sub> + 4NH <sub>3</sub> → Si <sub>3</sub> N <sub>4</sub> + 12H <sub>2</sub>	-178.4	-283.1
3SiH <sub>4</sub> + 2N <sub>2</sub> H <sub>4</sub> → Si <sub>3</sub> N <sub>4</sub> + 10H <sub>2</sub>	-270.4	-365.5

\* Electrochemical Society Active Member.

<sup>1</sup> Present address: IBM Components Division, East Fishkill Facility, Hopewell Junction, New York.

\* JANAF Thermochemical Tables, Dow Chemical Company.

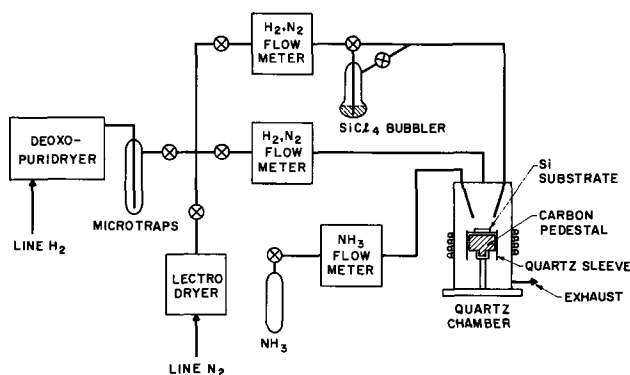


Fig. 1. Schematic diagram of apparatus

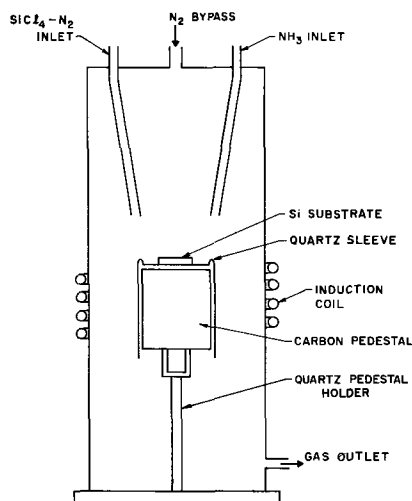


Fig. 2. Quartz reaction chamber

to avoid any substrate conversion; unless it is otherwise stated, this was the deposition temperature used.

The  $N_2$  and  $H_2$  gases were purified by use of a McGraw-Edison Lectrodryer and an Englehard Industries Deoxo Puridryer, respectively. The  $NH_3$  gas (99.99%), obtained from Matheson Company, Inc., was used as received and did not undergo any subsequent purification.

Films in the thickness range 1000-6000Å were generally used for all the measurements made. Film thickness and refractive index of the nitride films were determined by use of variable angle monochromatic fringe observation (VAMFO) (16). In order to use the VAMFO instrument it was necessary to mask a portion of the substrate during deposition or etch a portion of the film down to the substrate to produce a step in the nitride film. Refractive indices measured by VAMFO were in the range of  $2.00 \pm 0.02$ .

A Carey spectrophotometer (Model 14) was adapted to measure the thickness of the nitride film (17, 18). The visible and ultraviolet regions were used for the measurement of thickness down to about 1500Å. Measurements of thickness by the spectrophotometer and the VAMFO were in agreement to within 200-300Å, with the spectrophotometer always giving the higher value.

In order to make the necessary electrical measurements, gold dots 5000Å thick and 0.004-0.025 in. in diameter were filament evaporated onto the layers. Back contact to the samples was made by gold plating the silicon substrate.<sup>2</sup>

Dielectric strength tests were made using dc potential applied as a voltage ramp, increasing at a constant rate of 100 v/min. The voltage ramp was generated

<sup>2</sup> The plating was accomplished by use of an HF + E55 acid-gold solution (Englehard Industries), followed by 25 msl of alkaline cyanide electroplate gold.

by use of a motor-driven potentiometer, supplied by a regulated high-voltage power supply. The measurements were made using a Keithley Model 610A electrometer and a Hewlett-Packard Model 425A microammeter; the raw data were displayed on a strip chart recorder fed directly from the microammeter. For most tests, the polarity of the gold dot was negative (silicon positive). For the tests described, dielectric breakdown is defined as occurring at that voltage which is sufficient to produce sudden and irreversible damage to the film, resulting in the permanent loss of its normal insulating properties under the contact being tested.

MIS capacitance measurements were made using a Boonton capacitance bridge, Model 74C-S8, operating at a frequency of 100 kc, with a peak-to-peak signal of approximately 10 mv. The technique used was to start at zero and then apply an increasing negative bias to the gold dot until the maximum desired voltage was reached. The bias was then decreased back to zero and on to the maximum positive bias before it was returned finally to zero. From the capacitance-voltage curves the sum of surface charge plus surface state densities was determined from the flat-band condition, as described by Grove *et al.* (19). Dielectric constant values were also computed from the maximum capacitance values of these curves. In some instances, surface state densities were also obtained from conductance curves, as described by Nicollian and Goetzberger (20).

Tests for charge storage were made as previously described by Yamin and Worthing in their study of silicon dioxide (21, 22).

Sodium drift and diffusion experiments were conducted as previously described by Dalton (7).

### Experimental Results of Varying Deposition Conditions

The first part of this study was concerned with the influence of the deposition variables on the kinetics of the process. Figure 3 shows the effect of  $SiCl_4$  partial pressure on the deposition rate with constant  $NH_3$  partial pressure. The mol fraction of  $SiCl_4$  was varied from  $7 \times 10^{-5}$  to  $2 \times 10^{-3}$  while the  $NH_3$  mol fraction was kept at  $4 \times 10^{-2}$ . The slope of the curve illustrated in Fig. 3 is approximately 0.8.

The effect of changing the  $NH$  partial pressure at constant  $SiCl_4$  partial pressure was studied. The mol fraction of the  $NH_3$  was varied from  $4 \times 10^{-3}$  to  $7 \times 10^{-2}$  while the mol fraction of the  $SiCl_4$  was held at  $2 \times 10^{-4}$ . It appeared that varying the  $NH_3$  concentration had no effect on the deposition rate. However, even at the lowest  $NH_3$  concentration there was still an order of magnitude more ammonia than silicon tetrachloride. A second set of conditions was then

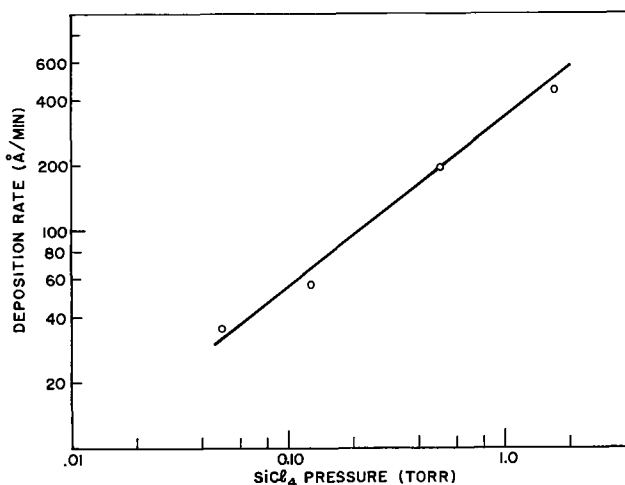


Fig. 3. Effect of  $SiCl_4$  partial pressure on deposition rate (at 1000°C and  $NH_3$  partial pressure of 28 Torr).

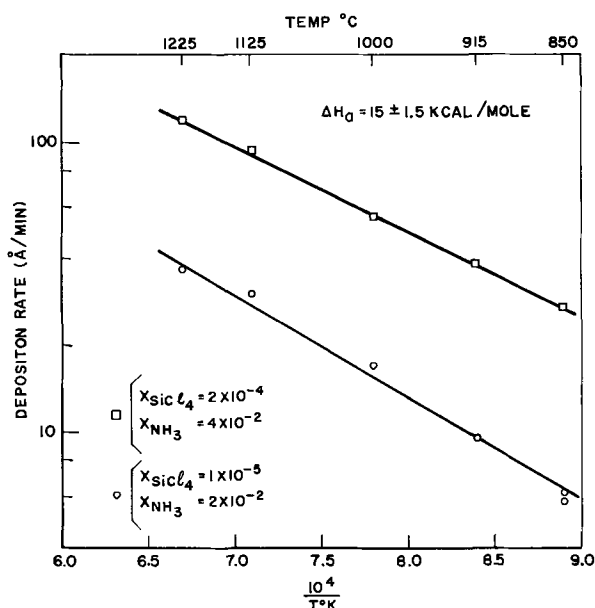


Fig. 4. Temperature dependence of silicon nitride deposition at  $2 \times 10^{-4} : 4 \times 10^{-2}$  and  $1 \times 10^{-5} : 2 \times 10^{-2}$  mol fractions, respectively, of  $\text{SiCl}_4 : \text{NH}_3$ .

chosen, where the  $\text{NH}_3$  mol fraction was varied from  $2 \times 10^{-3}$  to  $4 \times 10^{-2}$  and the  $\text{SiCl}_4$  mol fraction was maintained at  $2 \times 10^{-3}$ , a factor of 10 higher than in the previous conditions. Again there was no marked effect even when the mol ratio of  $\text{NH}_3$  to  $\text{SiCl}_4$  fell to unity.

The free energy ( $\Delta G^\circ$ ) of the reaction of  $\text{SiCl}_4$  plus  $\text{NH}_3$  to form silicon nitride (see Table I) is negative almost down to room temperature. Figure 4 shows the results of varying the deposition temperature at two different vapor phase concentrations of reagents. The apparent activation energy ( $\Delta H_a$ ) obtained was  $15 \pm 1.5$  kcal/mol.

Silicon nitride films were deposited between  $550^\circ$  and  $1225^\circ\text{C}$  with films ranging in thickness from  $500\text{\AA}$  to  $2\mu$ . The  $2\mu$  thick layer caused a slight bending of  $0.010$  in. thick substrates concave upward; under  $300\times$  magnification, hairlike cracks were readily visible in this film. However, a film  $1.8\mu$  thick deposited on silicon caused no bending of the substrate even though cracks were seen in the film when it was examined under  $300\times$  magnification. When this film was exposed to a water-amine-pyrocatechol etching system (23) at  $95^\circ\text{C}$  for 30 min, additional hairlike cracks started to appear (see Fig. 5). It was possible to observe the

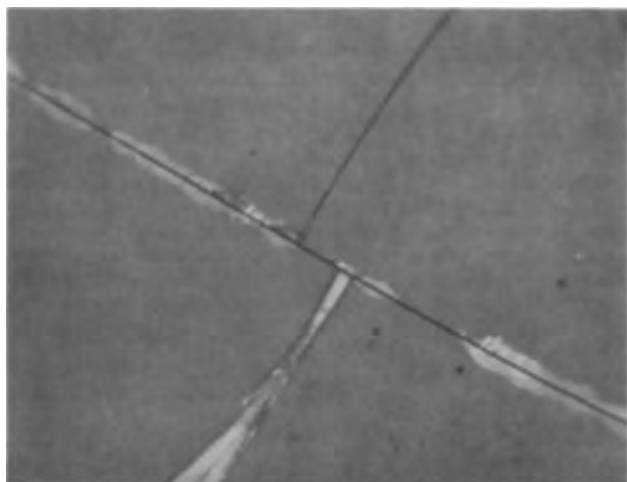


Fig. 5. Photomicrograph of  $1.8\mu$  thick film with "cracks" after it has been etched with water-amine-pyrocatechol system. (Magnification ca.  $200\times$ .)

"growth" of these new cracks as etching proceeded. The crack from lower left to center appeared first and then started to get broader before the crack from upper left to lower right appeared. Still later, the crack from center to upper right appeared, and at this point the etching was terminated. The reason for the way these cracks appeared is not known at this time, but one possible explanation might be the relief of strain by preferential stress corrosion of the sample. Films  $4000\text{\AA}$  thick or less did not show any cracks either before or after exposure to the water-amine-pyrocatechol etching system.

Figure 6 is a plot of the etch rate in concentrated (49%) HF of the samples deposited for the upper curve of Fig. 4. Note that as the deposition temperature decreased the deposition rate decreased but the etch rate of the samples increased.

Optical transmission studies, with a Xenon lamp as a source, were performed on a  $4000\text{\AA}$  thick silicon nitride film deposited on a sapphire substrate; the effective band gap of the film was found to be  $5.6 \pm 0.2$  ev.

In an attempt to identify the crystal nature and chemical composition of the deposited films, transmission electron diffraction and infrared absorption measurements were made. The electron diffraction patterns obtained on films deposited at all the temperatures studied showed only very diffuse rings, which could not be identified, and which indicated that the films were always amorphous. The infrared spectrum obtained on films deposited at  $550^\circ$  and  $1000^\circ\text{C}$  showed the characteristic Si-N band (13) (see Fig. 7). However, it is clearly seen that the films grown at these two temperatures are not identical. This is not surprising in light of the possible mechanisms for the reaction of  $\text{SiCl}_4$  with  $\text{NH}_3$ .

#### Discussion of Deposition Kinetics

The mechanism involved in the deposition of a nitride film from  $\text{SiCl}_4$  and  $\text{NH}_3$  is not understood at this time. Sneed and Brasted (24) indicate that the reactions involved in the formation of silicon nitride are

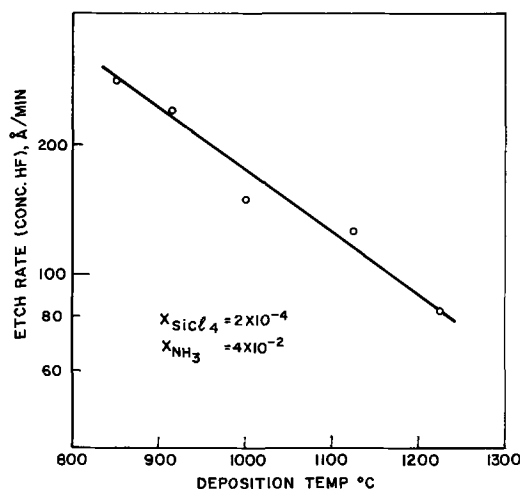
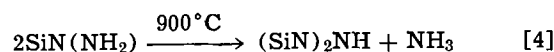
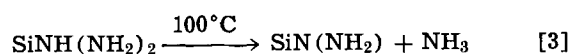
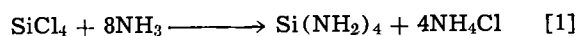


Fig. 6. Etch rate in concentrated HF of silicon nitride films deposited at different temperatures.

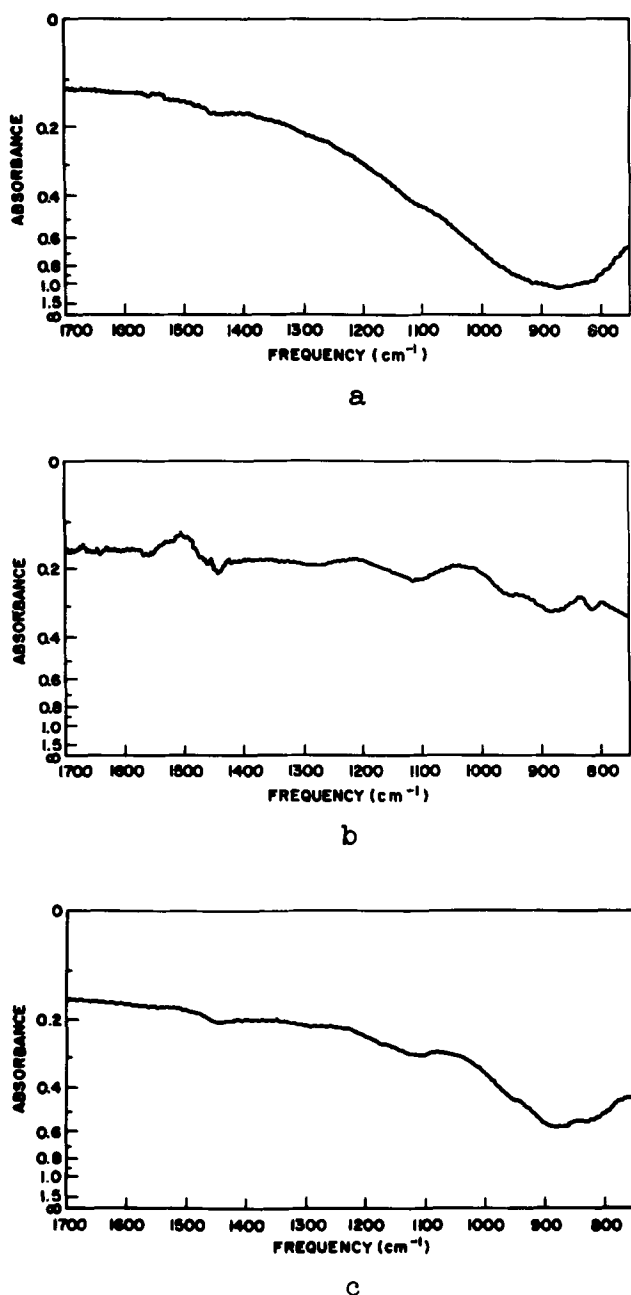
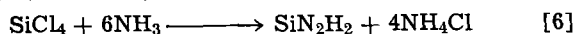


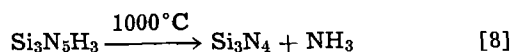
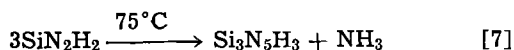
Fig. 7. Infrared analysis spectra: a, spectrum of film deposited at 1000°C; b, silicon substrate blank; c, spectrum of film deposited at 550°C.



Billy (9) claims, however, that at room temperature



which, on continued heating, yields  $\text{Si}_3\text{N}_4$  by stepwise loss of  $\text{NH}_3$  schematically represented by



There is a discrepancy between Billy and Sneed and Brasted about the temperature necessary to obtain the  $\text{Si}_3\text{N}_4$  form; Billy claims that  $\text{Si}_3\text{N}_4$  can be achieved at 1000°C, while Sneed and Brasted say that 1200°C is required.

Billy notes that  $\text{Si}_3\text{N}_4$  can be obtained in the pure form at 550°C by thermally decomposing pure  $\text{SiN}_2\text{H}_2$ , but he also notes that the presence of  $\text{NH}_3$  or  $\text{NH}_4\text{Cl}$  will have a strong influence on the decomposition

mechanism. We have also seen an influence of  $\text{NH}_4\text{Cl}$  on the deposition kinetics. During our depositions, a white powdery material formed on the upper and lower portions inside of the reactor wall. X-ray analysis showed it to be an impure form of  $\text{NH}_4\text{Cl}$ , possibly containing silicon amine compounds but definitely having no silicon oxide, chloride, nitride, or oxynitride. The reactor wall in the area immediately around the pedestal was clear and uncoated. If three or more depositions were attempted without a cleaning of the reaction chamber, the  $\text{NH}_4\text{Cl}$  built up on the reactor wall would begin to flake off onto the silicon substrate. It was therefore instituted as standard procedure that the reactor tube and pedestal shield be cleaned after every run.

In order that the influence of  $\text{NH}_4\text{Cl}$  might be studied, a series of measurements was performed starting with a clean-walled reactor. Silicon tetrachloride and nitrogen were admitted into the reaction chamber while the substrate temperature was maintained at 1000°C. No visible deposit was obtained on the silicon after 30 min under these conditions. Ammonia was then admitted to the reaction chamber in addition to the silicon tetrachloride plus nitrogen, and both the silicon substrate and the walls were coated. The nitride-coated silicon slice was then removed after the reactor was cooled and purged; the  $\text{NH}_4\text{Cl}$  was not cleaned from the reactor walls. A new silicon slice was then placed in the reaction chamber. Again, after the normal nitrogen purge of the system, only nitrogen and silicon tetrachloride were introduced, and this time a very slow deposition of nitride was observed on the silicon slice. These findings indicate that the material deposited on the walls contributes  $\text{NH}_3$  to the ambient.

Another influence of  $\text{NH}_4\text{Cl}$  was observed when the wall of the reaction tube was separately heated with heating tape to 300°-350°C during a deposition. The deposition rate was found to increase by a factor of 5 over that obtained under the equivalent cold-wall conditions.

It is impossible at this time to expound further on the possible reaction mechanism, since no detailed analytical measurements have been made on the film or on the gaseous reaction products.

### Results of Electrical Measurements

The dielectric strength was found to range from about 0.5 to  $1 \times 10^7$  v/cm for all the films tested and to be independent of contact area, film thickness, or conductivity type of the substrate. Samples that were exposed to a water-amine-pyrocatechol etching system at 95°C for 30 min had a negligible pinhole count.<sup>3</sup> This is in agreement with the observed absence of area dependence of breakdown, which might be expected to occur in the presence of defects of the type reported by Lopez (26). Insulating films deposited by other processes have frequently shown a rather strong contact area dependence of dielectric strength.

The absence of a film thickness effect (in the range 1000-6000Å) for the dielectric strength (27) can be explained by the fact that the films were amorphous in structure (28), as was revealed by electron diffraction studies. The dielectric strength was also about the same whether the contact was made positive or negative, although usually the negative polarity was used. Inasmuch as some degree of time dependence of breakdown was found at either polarity, and in view of the rather high current levels sustained prior to breakdown, it appears likely that the true intrinsic value of dielectric strength for these films is somewhat higher than the  $1 \times 10^7$  v/cm value quoted above. Varying the rate of application of potential by a factor of 10 did not change the breakdown levels.

<sup>3</sup> The water-amine-pyrocatechol etching system has been shown to be capable of delineating pinholes or potential pinholes in silicon nitride films (25).

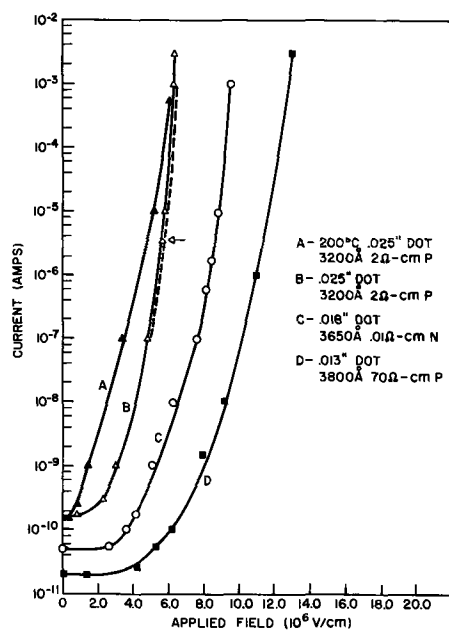


Fig. 8. Curve A, sample M92B—3200Å thick film on a 2 ohm-cm, p-type substrate with a 0.025 in. diameter gold dot and negative polarity on the gold (200°C). Curve B, sample M92B—3200Å thick film on a 2 ohm-cm, p-type substrate with a 0.025 in. diameter gold dot and negative polarity on the gold (room temperature). Curve C, sample M76A—3650Å thick film on a 0.01 ohm-cm, n-type substrate with a 0.018 in. diameter gold dot and negative polarity on the gold (room temperature). Curve D, sample M87A—3800Å thick film on a 70 ohm-cm, p-type substrate with a 0.013 in. diameter gold dot and negative polarity on the gold (room temperature).

In the measurement of dielectric strength, when the applied field reached about  $3 \times 10^6$  v/cm, a rather steep rise in conduction was observed. In Fig. 8 the log of current has been plotted against applied field for several samples; curves B, C, and D show the increase in conduction for three different film samples, all at room temperature, and with negative polarity on the contact dot.<sup>4</sup> The difference in relative levels of these curves at low fields is thought to be due to difference in capacitance. Film thickness for the three samples increases, contact area decreases, and hence capacitance decreases, from left to right. Since potential is being applied by the voltage ramp technique, the current is equal to the charge derivative with respect to time. In other words, the relatively flat portions of the curves observed below a field of about  $3 \times 10^6$  v/cm represent charging current. The conduction phenomena observed at higher fields is probably not related to dielectric failure or thermal breakdown (29) (except possibly in a very small range lying very close to the intrinsic dielectric strength), since it does not cause permanent loss of normal insulating properties of the film. With reference to curve B of Fig. 8, the voltage ramp was stopped when the field reached  $5.6 \times 10^6$  v/cm (arrow), and conduction remained at a level of  $3.5 \times 10^{-6}$  amp for 10 min. Thereafter, the voltage ramp was restarted and the conduction curve was retraced about 10 times between  $10^{-7}$  amp and  $10^{-3}$  amp (dashed portion of the curve). Breakdown eventually occurred when the field was increased to  $6.4 \times 10^6$  v/cm; conduction just prior to breakdown was well in excess of 3.0 ma (full scale of our meter). High conduction phenomena in nitride films have also been observed by Doo and Nichols (30) in films obtained from silicon hydride

<sup>4</sup> The negative polarity was originally chosen for this measurement in an attempt to avoid the type of gradual time-dependent breakdown previously reported (29) for atmospheric-pressure, steam-grown  $\text{SiO}_2$  films. When a few tests were performed on the nitride with the opposite polarity, results similar to those reported here were obtained.

and ammonia and by Hu and Gregor (31) in reactively sputtered nitride films.

In an attempt to learn something of the mechanism of conduction, the sample from which the data for curve B were obtained was heated to 200°C and curve A was obtained. The displacement of the curve to the left at 200°C would seem to rule out impact ionization or avalanche multiplication as the mechanism of conduction; if the latter were responsible one would expect the shift to be in the other direction (32). Tests performed at liquid nitrogen temperature indicate that the high conduction at high fields can be virtually eliminated at low temperature. For one sample tested, with an applied field of  $8.3 \times 10^6$  v/cm, a conduction of  $1.2 \mu\text{a}$  at room temperature decreased to 0.005 na at liquid nitrogen temperature. This would tend to rule out both field emission and impact ionization as mechanisms of conduction. The mechanism tentatively proposed at the present time is deep-trap ionization by field-assisted thermal excitation (Frenkel-Poole effect) (33). The fact that silicon nitride films can show the type of conduction observed here can perhaps be explained by the presence of mechanical strain in the films, as suggested by results obtained with the water-amine-pyrocatechol etching system (see Fig. 5), or by the presence of impurity atoms. It is known that the density of isolated levels or deep traps increases with mechanical strain, with the presence of foreign atoms, and with rise in temperature (34).

The prebreakdown conduction phenomena reported here are not believed to be of the type associated with moisture, since the conduction appears to be only slightly responsive to varying percentages of relative humidity. Furthermore, heating generally causes an increase rather than a decrease in conduction for a given applied potential.

On a good steam-grown oxide on silicon, surface charge densities of  $2-4 \times 10^{11}$  charges/cm<sup>2</sup> and surface state densities of about  $2 \times 10^{11}$  states/cm<sup>2</sup> are obtained from a combination of conductance and capacitance measurements (19, 20). Figure 9 is the result of an MIS capacitance-voltage sweep made on a double dielectric layer (gold-silicon nitride-silicon dioxide-silicon) where the nitride was deposited on top of 1000Å of steam-grown oxide. Note that the value of  $3 \times 10^{11}$ /cm<sup>2</sup> for the sum of surface charge plus surface state density (19) indicates that the deposition of the nitride had no deleterious effects on the surface properties of the already existing Si-SiO<sub>2</sub> interface. For comparison, the normal values of surface charge plus surface state densities obtained when the nitride is deposited on bare silicon at a deposition temperature of 1000°C range from  $7-18 \times 10^{11}$ /cm<sup>2</sup> (see Fig. 10). Samples which have low surface charge densities generally also have low surface state densities. Values of surface charge and surface state densities are found to be fairly uniform among different contact dots on the same sample. Figure 11 is a plot for a nitride deposited on bare silicon at 850°C; the value of  $16 \times 10^{11}$ /cm<sup>2</sup> for the surface charge plus surface state density is

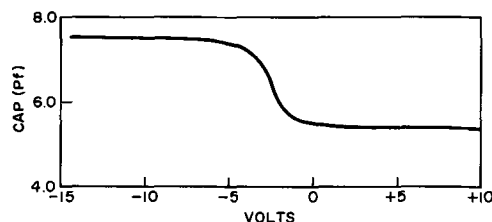


Fig. 9. MIS capacitance curve of a 0.010 in. diameter gold dot on a double dielectric layer (1850Å nitride on 1000Å oxide). The nitride was deposited at 1000°C and the silicon was 1 ohm-cm, p-type. The dielectric constant of the composite layer measures 5.0 and the SC + SS density is  $3 \times 10^{11}$ /cm<sup>2</sup>.

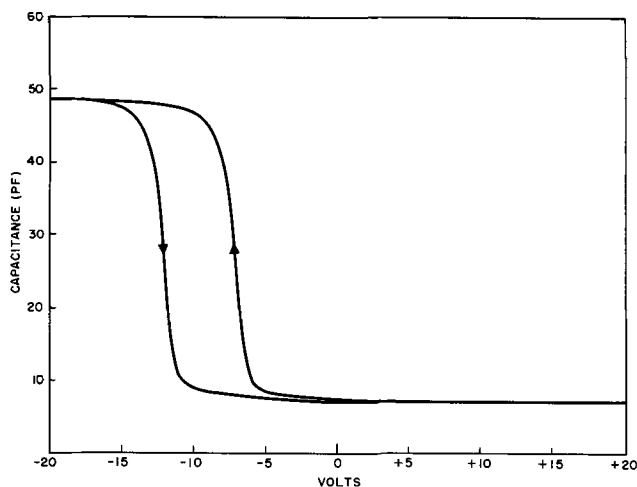


Fig. 10. MIS capacitance curve of a 0.015 in. diameter gold dot on a 1500Å thick nitride layer deposited on 35-40 ohm-cm, p-type silicon at 1000°C. The dielectric constant is 7.3 and the SC + SS density is  $17 \times 10^{11}/\text{cm}^2$ .

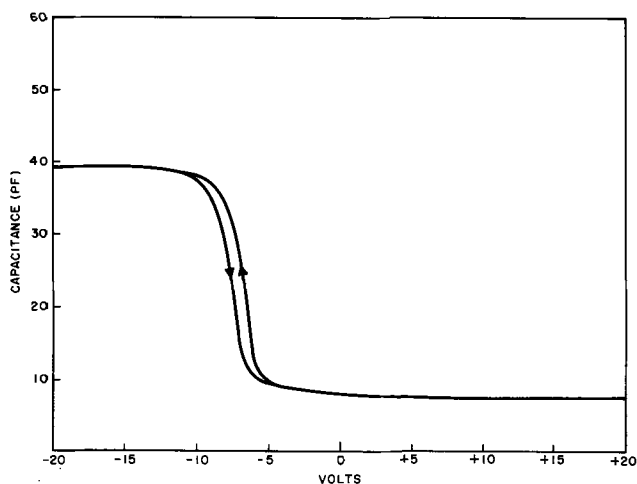


Fig. 11. MIS capacitance curve of a 0.015 in. diameter gold dot on a 1750Å thick nitride deposited on 35-40 ohm-cm, p-type silicon at 850°C. The dielectric constant is 7.1 and the SC + SS density is  $16 \times 10^{11}/\text{cm}^2$ .

comparable with those obtained on films grown at 1000°C.

In Fig. 10 and 11, there are indications of an instability in the passivation capabilities of the nitride as evidenced by the hysteresis loop in the capacitance-voltage plot. Carrier injection from the silicon, with subsequent trapping in the nitride, is probably one of the reasons for this behavior (35). In comparison, the data in Fig. 9 are typical of the stability seen in good oxide passivation of a silicon surface. It is still too early in the development of the nitride deposition work to say that this phenomenon is an intrinsic property of silicon nitride rather than a reflection of the level of technology at this time. It is believed that further development is needed to provide a better understanding of the process variables which influence conditions at the silicon-silicon nitride interface.

The value of dielectric constant, computed from the maximum capacitance values of the MIS capacitance curves, ranged from about seven to eight.

No charge storage of the type ascribed to ion drift in  $\text{SiO}_2$  (21, 22) could be found for any of the films tested.

Radioactive sodium drift experiments were carried out at 400°C with +2 to +8v applied to the contact dots for 1 min each. Radiotracer analyses showed that these films provide a barrier to sodium drift under

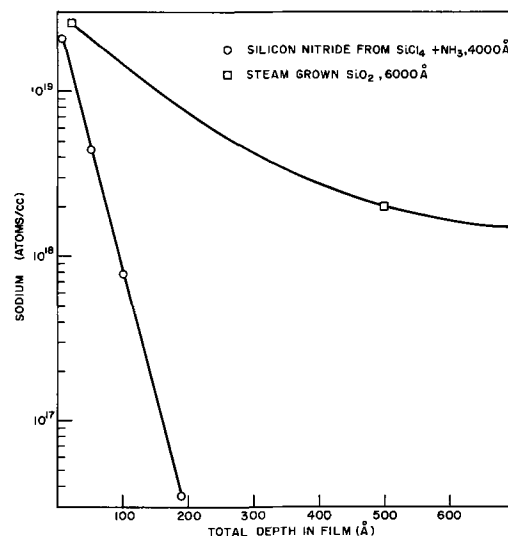


Fig. 12. Thermal diffusion of Na at 600°C into a steam-grown silicon dioxide film and into a silicon nitride film deposited at 1000°C. Courtesy of J. V. Dalton.

the conditions of voltage, time, and temperature described. Incremental etching and counting after drifting showed that all active sodium was removed with <100Å of the film. Tests conducted in the same manner on  $\text{SiO}_2$  films have shown that sodium drifts through the film and piles up at the Si-SiO<sub>2</sub> interface (36).

Thermal diffusions of Na were carried out at 600°C for 22 hr on the silicon nitride films. Diffusion profiles of the diffused samples showed that thermal diffusion takes place to a much smaller degree than in atmospheric-pressure steam-grown  $\text{SiO}_2$  (Fig. 12). Incremental etching and radiotracer counting of the silicon nitride films after diffusion of the  $\text{Na}^{22}/\text{Na}^{23}$  tracer source showed that all active sodium was removed with <200Å of the film.

### Discussion of Electrical Measurements

The panacea for complete surface passivation and control still has not been found. Silicon nitride does provide a better diffusion mask than silicon dioxide against unwanted impurities, but a penalty must be paid in that surface state and surface charge densities are higher with the former material. Generally, this process has yielded numbers for surface charge plus surface state densities of  $7\text{--}18 \times 10^{11}/\text{cm}^2$  when the deposition was done at 1000°C. Surface charge plus surface state densities of  $10\text{--}16 \times 10^{11}/\text{cm}^2$  were not uncommon when the deposition temperature was dropped to 850°C. It is possible that improvements might result from additional work on the process, but for the present the nitride films seem to have at least one half an order of magnitude more surface charge plus surface state densities than good oxide films. Additionally, the problem of hysteresis effects might also respond to improvements in processing.

### Conclusions

It has been demonstrated that a dielectric film can be deposited very easily on a silicon substrate by reacting  $\text{SiCl}_4 + \text{NH}_3$  at elevated temperatures. Infrared spectra of the films and some of their electrical and optical properties have been determined. The use of the films as protective coatings and as diffusion masks is clearly indicated.

Although some of the kinetics of the process have been determined, the mechanism is still far from clear.

### Acknowledgment

It is a pleasure to thank J. P. Luongo for the infrared measurements; Miss D. Margel for the electron

diffraction and x-ray analyses; G. P. Carey and P. A. Byrnes for MIS capacitance and conductance measurements; A. Frova for the bandgap measurement; and T. M. Buck, S. M. Sze, and M. J. Rand for many helpful suggestions.

Manuscript received June 23, 1967; revised manuscript received Jan. 22, 1968. This paper was presented at the Philadelphia Meeting, Oct. 9-14, 1966, as Abstract 148.

Any discussion of this paper will appear in a Discussion Section to be published in the December 1968 JOURNAL.

#### REFERENCES

- M. M. Atalla, E. Tannenbaum, and E. J. Scheibner, *Bell System Tech. J.*, **38**, 749 (1959).
- C. J. Frosch and L. Derick, U. S. Pat. 2,802,760; *This Journal*, **104**, 547 (1957).
- F. P. Heiman and S. R. Hofstein, *Electronics*, **37**, 50 (1964).
- E. H. Snow, A. S. Grove, B. E. Deal, and C. T. Sah, *J. Appl. Phys.*, **36**, 1664 (1965).
- Dutch Pat. 6,405,186, November 1964; British Pat. 1,006,803, October 1965.
- N. C. Tombs, H. A. R. Wegener, R. K. Wheeler, B. T. Kenney, and A. J. Coppola, Digest of Technical Papers, 1966 International Solid State Circuits Conference, **9**, 58 (1966).
- J. V. Dalton, *This Journal*, **113**, 165C (1966).
- V. Y. Doo, *IEEE Trans. Electron Devices*, **ED-13**, 561 (1966).
- M. Billy, *Ann. Chem.*, **4**, 795 (1959).
- W. Kaiser and C. D. Thurmond, *J. Appl. Phys.*, **30**, 427 (1959).
- V. Y. Doo, D. R. Nichols, and G. A. Silvey, *This Journal*, **113**, 1279 (1966).
- H. F. Sterling and R. C. G. Swann, *Solid-State Electronics*, **8**, 653 (1965).
- S. M. Hu, *This Journal*, **112**, 260C (1965).
- "Vapor Deposition," C. F. Powell, J. H. Oxley, and J. M. Blocher, Jr., Editors, p. 612, John Wiley & Sons, Inc., New York (1966).
- P. Wang, *Sylvania Technologist*, **11**, 50 (1958).
- W. A. Pliskin and E. E. Conrad, *IBM J. Res. Dev.*, **8**, 43 (1964).
- E. A. Corland and H. Wimpfheimer, *Solid-State Electronics*, **7**, 755 (1964).
- F. Reizman, *J. Appl. Phys.*, **36**, 3804 (1965).
- A. S. Grove, B. E. Deal, E. H. Snow, and C. T. Sah, *Solid-State Electronics*, **8**, 145 (1965).
- E. H. Nicollian and A. Goetzberger, *Bell System Tech. J.*, **46**, 1055 (1967).
- M. Yamin and F. L. Worthing, *This Journal*, **111**, 62C (1964).
- M. Yamin, *IEEE Trans. Electron Devices*, **ED-12**, 88 (1965).
- R. M. Finne and D. L. Klein, *This Journal*, **111**, 63C (1964).
- M. C. Sneed and R. C. Brasted, "Comprehensive Inorganic Chemistry," Vol. 5, p. 173, D. Van Nostrand Co., New York (1959).
- F. M. Finne, Private communication.
- A. D. Lopez, *This Journal*, **113**, 89 (1966).
- F. Forlani and N. Minnoja, *Physica Status Solidi*, **4**, 311 (1964).
- K. W. Plessner, *Proc. Phys. Soc.*, **60**, 243 (1948).
- F. L. Worthing, *This Journal*, **112**, 68C (1965).
- U. Y. Doo and D. R. Nichols, *ibid.*, **113**, 212C (1966).
- S. M. Hu and L. V. Gregor, *ibid.*, **113**, 213C (1966).
- C. R. Crowell and S. M. Sze, *Appl. Phys. Letters*, **9**, 242 (1966).
- S. M. Sze, *J. Appl. Phys.*, **38**, 2951 (1967).
- J. J. O'Dwyer, "The Theory of Dielectric Breakdown of Solids," p. 6, Clarendon Press, Oxford (1964).
- S. M. Hu, D. R. Kerr, and L. V. Gregor, *Appl. Phys. Lett.*, **10**, 97 (1967).
- T. M. Buck, F. G. Allen, J. V. Dalton, and J. D. Struthers, Paper presented at IEEE Silicon Interface Specialists Conference, Las Vegas, Nev., November 1965.

## Phosphors Based on Rare Earth Phosphates Fast Decay Phosphors

R. C. Ropp\*

Westinghouse Electric Corporation, Bloomfield, New Jersey

#### ABSTRACT

Phosphors based on rare earth phosphates and activated by Ce<sup>+3</sup> can be prepared with efficiencies comparable to the previously known P-16 phosphor as well as having operating maintenance characteristics essentially equivalent to it. In addition, the rare earth phosphate phosphors have decay times nearly three times faster than this commercial material. These new materials may open applications in electronic devices not feasible before.

Decay time of luminescent materials is important in many electronic applications, but has little significance in others. For example, it is not critical in 60-cycle fluorescent lamp operation, but is of major concern for devices such as a flying-spot-scanner since it limits the rapidity of rescan of the device.

Decay time can be classified in two broad categories, exponential and logarithmic, the former being proportional to  $e^{-t}$  and the latter to a power function such as  $t^{-2}$  (1). Many luminescent materials possess an exponential decay so that it is common to express a time constant as  $1/e$  (time to decay to 37% of the original intensity,  $I_0$ ), or, alternately, time to decay to 10% of  $I_0$ . Common decay times range from a few milliseconds (e.g., parity forbidden spin reversal of Mn<sup>+2</sup>) to several hundred nanoseconds (e.g., allowed

dipole transitions). Fast decay phosphors in the nanosecond range have usually involved the Ce<sup>+3</sup> activator particularly for cathodoluminescent materials. P-16, a widely used phosphor, is a calcium magnesium silicate activated by Ce<sup>+3</sup> and has a decay time of about 120 nsec. A phosphor with still faster decay time also involved the Ce<sup>+3</sup> activator and was described by Struck (2). Recently, Blasse and Brill, have also described Ce<sup>+3</sup> in Y<sub>3</sub>Al<sub>5</sub>O<sub>12</sub> (3) as a fast decay material.

In 1941, the emission of Ce<sup>+3</sup> in 29 different hosts was surveyed by Kroger and Bakker (4). Next followed a survey of ultraviolet emitting phosphors for fluorescent lamp application in 1947 by Clapp and Ginther (5). A fairly comprehensive study of fast decay phosphors for flying spot cathode-ray tubes was made in 1951 by Brill and Klasens (6). The most recent survey covers ultraviolet emission but does not

\* Electrochemical Society Active Member.



mention decay time (7). The present paper presents a survey of the rare earth phosphates, activated by  $Ce^{+3}$ , with particular reference to decay time and emission properties.

### Experimental Methods

**Preparation of phosphors.**—Phosphors were prepared by precipitating solutions of the appropriate rare earths with a dilute solution of phosphoric acid. Mixtures of the ions were made, including a soluble salt of the activator, before precipitation. An excess of phosphate was maintained at all times by adding the rare earth solutions to the phosphoric acid solution. Because of the method of preparation, no mixing or blending steps were necessary prior to firing to obtain a uniform and homogeneous composition. In general, a hydrated product was obtained, but the degree of hydration was a function of the nature of cations present, concentration of reagents, and temperature employed during the course of precipitation. The materials as produced were then fired to form the phosphor composed of the desired solid solution of phosphates. Firing in air was accomplished in open silica crucibles placed at temperature in a large globar furnace.

**Measurements.**—Excitation and emission spectra of photoluminescence were obtained with the aid of a commercial spectrofluorimeter (8) which provided a constant energy beam over the range of 20,000–50,000  $cm^{-1}$  (5000–2000Å) and recorded energy corrected spectra directly. Resolution of the instrument varied from a few angstroms in the ultraviolet to about 10Å in the red region of the spectrum. Intensity data were obtained by instrumental integration of the emission bands by means of an integrator directly attached to the recorder.

Most of the cathode-ray intensity data were obtained in a demountable vacuum system consisting of an electron gun and a turntable carrying the phosphor samples, all located in an evacuated glass chamber. The tetrode gun had a tungsten anode and was located about 20 in. from the final anode. Normal operating voltage was about 20 kv with a beam spot size of 5 mm. The phosphors, located in 1.0-cm holes, were viewed one at a time from the bombarded size by means of a first surface 45° plane mirror, a quartz mirror, and a quartz lens. No charging effects from the defocused beam were observed. Decay time was measured in a separate apparatus employing a pulsed electron beam having a rise time of ½ nsec. Emission from the phosphor caused a response in a separate photomultiplier which was displayed on an oscilloscope. Resolution was not limited by the time-constant of the experimental apparatus.

### Experimental Results

Both  $LaPO_4$  and  $GdPO_4$  are monoclinic and possess the monazite structure;  $YPO_4$  is tetragonal and has the xenotime structure (9).  $Ce^{+3}$  in each, or any combination of the three compounds, yields both photo- and cathodoluminescence, characteristic of the structure. Shown in Fig. 1 are photoluminescence spectra for phosphors containing 5 g-a/o (gram-atomic per cent) of  $Ce^{+3}$  per mol of phosphate. Note that the emission bands peak in the ultraviolet as expected, but that their position is a function of structure and composition. The emission peaks of  $Ce^{+3}$  in  $GdPO_4$  and  $LaPO_4$  are near 3200°, whereas in  $YPO_4$ , they are nearer 3500Å.

The excitation bands are more difficult to analyze. It was shown previously (10) that the excitation bands which appear at highest energy in  $La_2O_3:Gd$  and  $Y_2O_3:Gd$  could be attributed to cationic exciton absorption. A similar explanation was made for  $LaPO_4:Gd$  and  $YPO_4:Gd$  spectra in a prior paper (11) because of identical energy positioning. For  $YPO_4:Ce$  and  $LaPO_4:Ce$  phosphors, the highest energy bands might be caused by absorption due to formation of

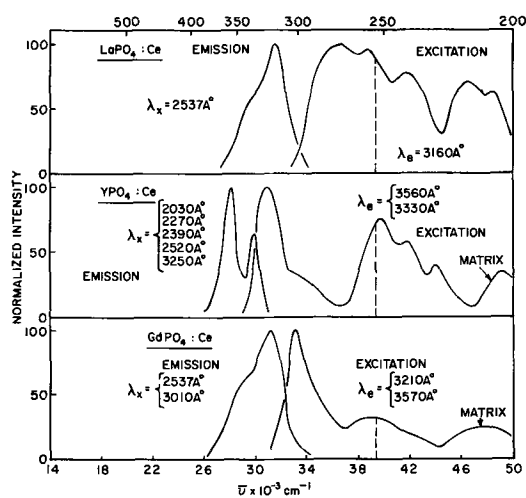


Fig. 1. Photoluminescence of some cerium-activated rare earth phosphates.

exciton states or they may be due to crystal field effects on the  $4f^1 \rightarrow 5d^1$  transition of  $Ce^{+3}$ . In addition, these bands could also be attributed to upper excited states of  $Ce^{+3}$  and might well include such transitions as  $4f^1 \rightarrow 6s^1$ .

However, in  $GdPO_4:Ce$  a further solution of the excitation processes can be presented. Excitation in the  $4f^7$  levels (transition:  $^8S_{7/2} \rightarrow ^6I_J$ ) causes both  $Gd^{+3}$  and  $Ce^{+3}$  emission, the latter from energy transferred from excited  $Gd^{+3}$  centers. This can be demonstrated more clearly by considering the effects of  $Ce^{+3}$  concentration in  $GdPO_4$  (typical spectra are given in Fig. 2). At 0.01 g-a/o of  $Ce^{+3}$ , only  $Gd^{+3}$  excitation bands are seen as evidenced by the fact that each produces both  $Gd^{+3}$  and  $Ce^{+3}$  emission. The band at 3105Å is the typical emission found in all  $Gd^{+3}$  containing phosphors (i.e.,  $^6P_J$  levels). However, at 2.5 g-a/o  $Ce^{+3}$ , the  $Ce^{+3}$  band at 3000Å produces only typical  $Ce^{+3}$  emission, whereas the  $Gd^{+3}$  excitation bands at 2740 and 2380Å produce both  $Gd^{+3}$  and  $Ce^{+3}$  emission. Thus, for the various phosphors shown in Fig. 1, one is led to the conclusion that each excitation band at lowest energy is probably due to  $Ce^{+3}$  excitation.

As a photoluminescent material,  $YPO_4:Ce$ , the most efficient phosphor, had an integrated output of only 36% of the commercial  $Ba_3SiO_5:Pb$  phosphor when excited by 2537Å and measured under identical conditions, as shown in Fig. 3.

Cathode-ray excitation produces spectra nearly identical to those from ultraviolet excitation except that the relative intensities of these phosphors vary somewhat more for the former than for the latter mode of excitation. The intensities shown in Fig. 4 are relative to one another whereas those of Fig. 1 were normalized so that the spectra could be more easily compared. Note that the spectra of  $YPO_4:Ce$  and  $LaPO_4:Ce$  are about equal in output intensity but

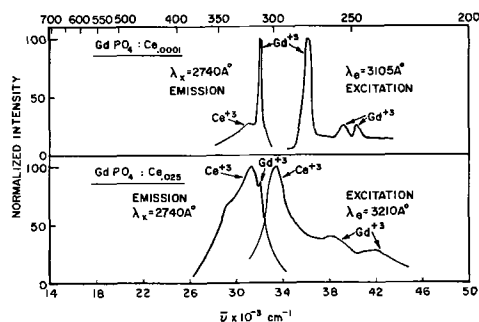


Fig. 2. Photoluminescence of cerium-activated gadolinium phosphate phosphors.

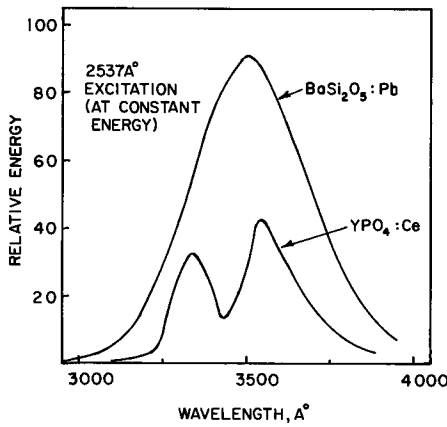


Fig. 3. Radiometric comparison of ultraviolet emitting phosphors

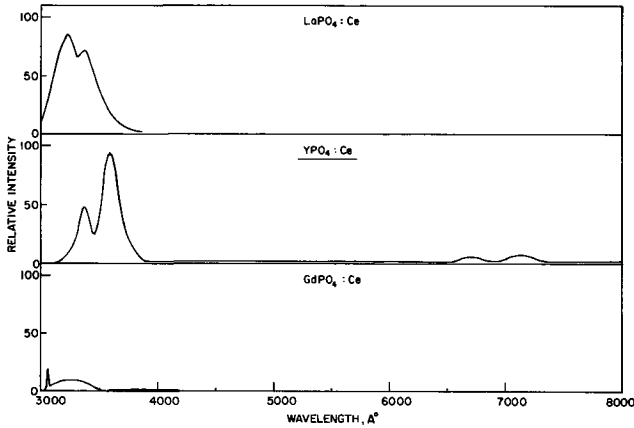


Fig. 4. Cathodoluminescence of  $Ce^{+3}$  activated phosphors

that of  $GdPO_4:Ce$  is much lower. Thus, in a device such as a cathode-ray tube,  $YPO_4:Ce$  should be much superior to the others when used in combination with an ordinary glass face-plate whose wavelength cutoff is usually about  $3300\text{\AA}$ . That this is true is shown in Fig. 5. Figure 5A shows the relative intensity of  $LaPO_4:Ce$  compared to a standard P-16 phosphor. Figure 5B shows the same phosphor when viewed through a glass face-plate while Fig. 5C shows a  $YPO_4:Ce$  phosphor as compared to the same P-16 phosphor, viewed through a similar glass face-plate of a 5-in. cathode-ray tube.

As shown in Fig. 6 for photoluminescence, the optimum activator concentration for the  $LaPO_4$  and

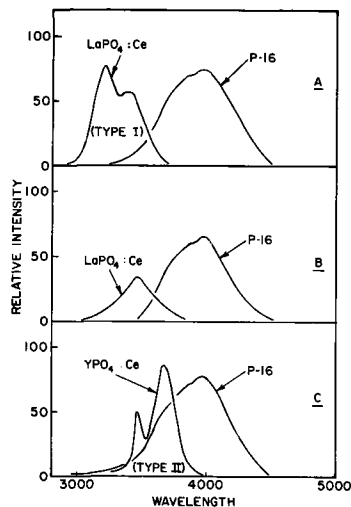


Fig. 5. Relative cathodoluminescence of  $Ce^{+3}$  activated rare earth phosphates.

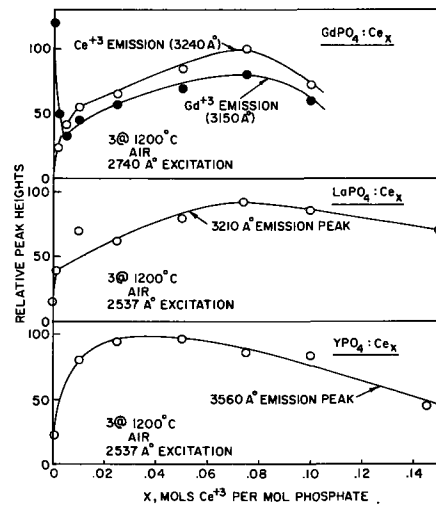


Fig. 6. Optimum activator concentration

$GdPO_4$  compounds is about 7.5 g-a/o  $Ce^{+3}$  whereas it is about 5.0 g-a/o in the  $YPO_4$  material. Thus, 6.0 g-a/o  $Ce^{+3}$  represents a reasonable average for the three systems.

In the binary Y-Gd system, as shown in Fig. 7, the  $GdPO_4:Ce_{0.06}$  phosphor has about 10% of the output of the  $YPO_4:Ce_{0.06}$  phosphor as measured by comparison of peak heights. In the ternary Y-Gd-La system, as shown in Fig. 8, two types of emission appear, one

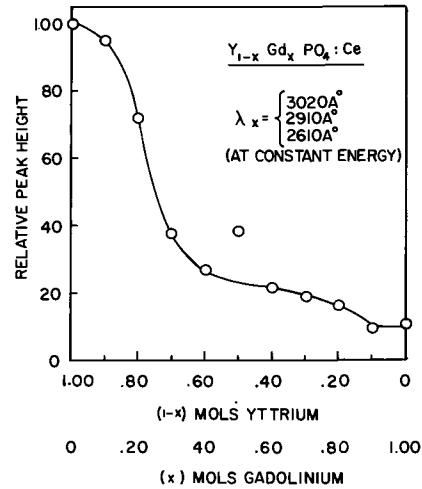


Fig. 7. Relative efficiency of  $Ce^{+3}$  activated rare earth phosphates.

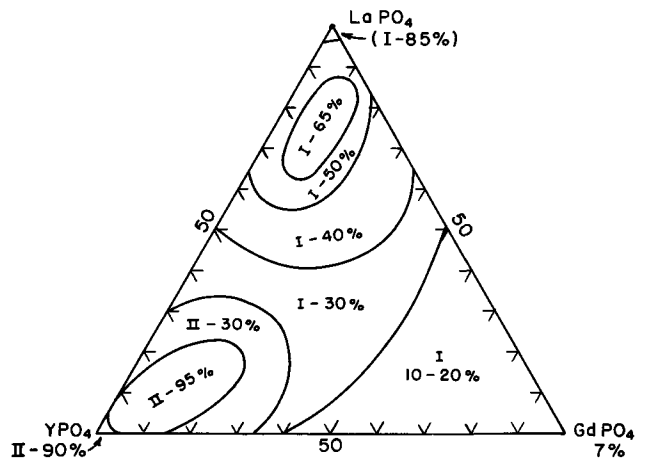


Fig. 8. Luminescent intensity in the ternary system. Emission spectra: type I,  $LaPO_4:Ce$ ; type II,  $YPO_4:Ce$ .

similar to that of  $\text{LaPO}_4:\text{Ce}$  and the other to that of  $\text{YPO}_4:\text{Ce}$ . In this system, the relative peak heights of the ternary compositions were compared under constant energy excitation. In this way, a direct comparison of output was obtained even though wavelength positions of the emission bands changed.

It is interesting to find that no more than 10-15%  $\text{GdPO}_4$  can be tolerated in these systems without adversely affecting the over-all output. The limits of composition, to obtain the best cathodoluminescent phosphor as given in Fig. 8 for the ternary system are:

$$\begin{array}{l} \text{Y}_u \text{Gd}_v \text{La}_w \text{PO}_4 : \text{Ce}_x \\ \hline 95\% > u > 60\% \\ 20\% > v > 0\% \\ 25\% > w > 0\% \\ 15\% > x > 2\% \end{array}$$

At the  $\text{Y}_{0.80}\text{Gd}_{0.10}\text{La}_{0.10}\text{PO}_4:\text{Ce}_{0.06}$  composition, the decay time to  $1/e$  was found to be 40 nsec, when compared to a standard P-16 phosphor whose decay time was measured to be 114 nsec, as shown in Fig. 9. These results were obtained using a gated oscilloscope with photomultiplier, having a  $\frac{1}{2}$  nsec rise time and a 2 nsec pulse width. The decay time of the  $\text{LaPO}_4:\text{Ce}$  phosphor was also measured and found to be 32 nsec. Thus, structure does not seem to have a major effect on decay time.

The operating maintenance efficiency of these phosphors was determined to be similar to that of the standard P-16 phosphor, as shown in Fig. 9. A loss of about 50% of the original intensity occurs within 30 min of initial operation under the operating conditions employed for these cathode-ray tubes. This loss

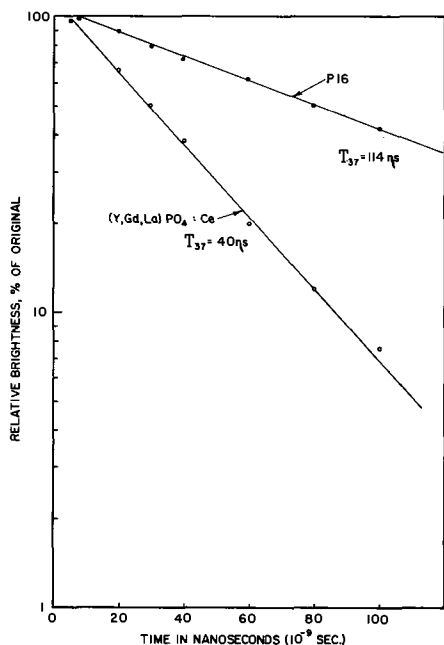


Fig. 9. Comparison of decay time of two phosphors

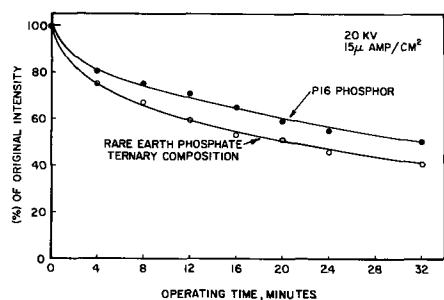


Fig. 10. Comparison of maintenance of efficiency of  $\text{Ce}^{+3}$  activated phosphors.

indicated is much larger than those encountered under normal operating conditions. Taylor *et al.* (12) have studied various P-16 phosphors and concluded that the poor maintenance of P-16 phosphors in general was due to a surface degradation of the silicate host materials. In view of the results presented herein, it seems more logical that the operating loss is due to a change in the state of the  $\text{Ce}^{+3}$  activator rather than a change in the host material, particularly since equivalent results were seen and one was a phosphate and the other a silicate.

## Discussion

It has been shown that phosphors based on rare earth phosphates, and activated by  $\text{Ce}^{+3}$ , can be prepared with an output rivaling the P-16 phosphors as well as possessing essentially equivalent operating maintenance characteristics in a cathode-ray tube. In addition, the rare earth phosphate phosphors have decay times nearly three times faster than the best known commercial material P-16.

We can compare the emission properties of these phosphors with those described by Struck (2), who also found fast decay properties for  $\text{Ce}^{+3}$  in  $\text{LaPO}_4$  and  $\text{YPO}_4$ . Struck found identical emission properties for both of these matrices, in contrast to the results presented herein. In Struck's phosphors, the main emission peak occurred close to 3200Å. However, he prepared his materials by solid-state reaction of oxides and phosphates, a method which is certain to produce small amounts of meta and polyphosphates, as has been shown by the extensive and comprehensive work of Thilo (13). In contrast, precipitation from solution produces stoichiometric phosphates and completely different emission properties for  $\text{YPO}_4:\text{Ce}$ . The  $D_{2d}$  site symmetry (14) has a major effect on the transition probabilities so that the lower energy emission band contains the greater part of the total emission energy in  $\text{YPO}_4:\text{Ce}$  while in  $\text{LaPO}_4:\text{Ce}$ , the opposite is true. Since the site symmetry in  $\text{LaPO}_4:\text{Ce}$  is likely to be lower, this leads one to believe that Struck's results could be ascribed to a lower site symmetry in his  $\text{YPO}_4:\text{Ce}$  phosphor, particularly because of the remarkable correspondence of all of his emission bands. One of the probable causes for his results for  $\text{YPO}_4:\text{Ce}$  is nonstoichiometry (*i.e.*, lower symmetry cation site) attendant on the method of preparation employed.

In regard to application, we have found the  $\text{YPO}_4:\text{Ce}$  phosphor to be useful in a one-gun beam-indexing color television tube where the P-16 phosphor cannot be employed because of excessive decay times. In this tube, which is similar to one described previously (15), a mosaic of red-, green-, and blue-emitting-vertical-phosphor-stripes are arranged in a repetitive manner. This screen is aluminized, and a vertical pattern of  $\text{YPO}_4:\text{Ce}$  stripes is superimposed. The ultraviolet emission caused when the electron beam scans past the  $\text{YPO}_4:\text{Ce}$  stripe is picked up by a photomultiplier, and the signal generated is used to modulate the incoming color signals to position the electron beam on the desired color stripe. At the television frequencies employed, a nanosecond decay phosphor is mandatory in order to pinpoint the beam position during each sweep across the screen. The use of the  $\text{YPO}_4:\text{Ce}$  phosphor also obviated the requirement of a quartz window in the tube (and the attendant problems in installing it) in order to pick up the ultraviolet signal. In such a system, we obtained "white" screen brightnesses of 165 ft-L, which is approximately 300% of the current commercial production models.

## Acknowledgment

The author is indebted to E. Chen for phosphor preparation, to B. Tartaglio for cathodoluminescent measurements, and Dr. C. K. Lui Wei for x-ray measurements.

Manuscript received Aug. 29, 1967; revised manuscript received Nov. 20, 1967.

Any discussion of this paper will appear in a Discussion Section to be published in the December 1968 JOURNAL.

## REFERENCES

1. A. J. Dekker, "Solid-State Physics," Prentice Hall, Englewood, N. J. (1958).
2. C. W. Struck, U. S. Pat. 3,104,226 (May, 1961).
3. G. Blasse and A. Brill, *Appl. Phys. Letters*, **II**, 53 (1967).
4. F. A. Kroger and J. Bakker, *Physica*, **8**, 628 (1941).
5. H. G. Clapp and R. J. Ginther, *J. Opt. Soc. Amer.*, **37**, 355 (1947).
6. A. Brill and H. A. Klasens, *Philips Research Repts.*, **7**, 421 (1952).
7. J. W. Gilliland and M. S. Hall, *Electrochem. Technol.*, **4**, 378 (1966).
8. Model 195—Perkin-Elmer Corp., Norwalk, Conn.
9. F. Weigel, V. Scherer, and H. Henschel, *J. Amer. Ceram. Soc.*, **486**, 342 (1965); R. C. L. Mooney, *J. Chem. Phys.*, **16**, 1003 (1948).
10. R. C. Ropp, *This Journal*, **111**, 311 (1964).
11. R. C. Ropp, Papers presented at the Cleveland Meeting of the Society, May 1-6, 1966, as Abstracts 20 and 21.
12. R. C. Taylor, S. A. Ward, and R. E. Rutherford, Jr., *Appl. Phys. Letters*, **6**, 128 (1965).
13. See, for example, E. Thilo, *Angew. Chem.*, **4** 1061 (1965) for a comprehensive review.
14. R. W. G. Wyckoff "Crystal Structures," 2nd ed. vol. 3, p. 15, Interscience Publishers, New York (1965).
15. J. D. Bowker (assigned to RCA), U.S. Pat. 3,164,744, Jan. 5, 1965.

## Mixed Valence Europium Phosphors

W. A. McAllister\*

Advanced Development Department, Westinghouse Electric Corporation, Bloomfield, New Jersey

## ABSTRACT

Replacement of lanthanum in  $\text{LaPO}_4:\text{Eu}$  phosphors by barium-lithium pairs ( $\text{La}_{1-2x}\text{Ba}_x\text{Eu}_x\text{Li}_x\text{PO}_4$ ) leads to interesting emission characteristics: (i) line emission typical of  $\text{Eu}^{+3}$  for all ultraviolet excitation but most pronounced at short wavelength; (ii) A blue band for excitation wavelengths longer than 266 nm, for certain values of  $x$ ; (iii) a uv band prominent under the same conditions favoring the blue emission. Results of x-ray and microscopic examination indicate a single-phase material. It is concluded that the line emission is due to an  $\text{Eu}^{+3}$  center which receives energy from the host, the bands to different  $\text{Eu}^{+2}$  centers.

The characteristic that makes trivalent rare earth ions attractive as activators in phosphor and laser applications, intense emission in a narrow spectral region, is a barrier to gross spectral shifts. Thus, while local site symmetry can alter the ratios of the intensities of the lines, the perceived colors are in the same range, e.g., orange-red for  $\text{Eu}^{+3}$ , green for  $\text{Tb}^{+3}$ . Drastic spectral changes are associated with changes in oxidation state of the rare earths. Thus  $\text{Eu}^{+2}$  typically has band emission peaked at shorter visible wavelengths than the red lines of  $\text{Eu}^{+3}$ . Coexistence of both species in the same host has not been reported often since the preparative techniques favoring trivalent and divalent europium involve oxidizing and reducing atmospheres, respectively. Jaffe and Banks (1) did include an emission spectrum with both band and line characteristics for hydrogen fired  $\text{CaO}:\text{Eu}$  in a paper on europium activated oxides and sulfides. Similar results, cited herein, were noted when barium-lithium combinations were substituted for lanthanum in  $\text{LaPO}_4:\text{Eu}$ -type phosphors using the raw mix formulation  $\text{La}_{1-2x}\text{Ba}_x\text{Eu}_x\text{Li}_x\text{PO}_4$ . The relative importance of the different emission characteristics, line and band, was found to be a function of europium concentration and excitation energy.

## Experimental

Phosphors were prepared by firing raw mixes of Lindsay Chemical (99.9%)  $\text{La}_2\text{O}_3$ ,  $\text{Eu}_2\text{O}_3$ , and Mallinckrodt  $\text{Li}_2\text{CO}_3$ ,  $\text{BaCO}_3$ , and  $\text{NH}_4\text{H}_2\text{PO}_4$  in an atmosphere consisting of nitrogen-2 v/o (volume per cent) hydrogen at 1250°C, using three 1-hr firings with grinding between firings. In the range  $x = 0.02$  to 0.20 the products were single phase materials in which emission properties varied with excitation wavelength and the magnitude of  $x$ . Details of the emission and

excitation spectra were examined at room temperature and with 254, 298, and 312 nm excitation wavelengths using a facility described previously (2). Reflectance characteristics were compared with a  $\text{BaSO}_4$  standard, in integrating spheres attached to a Cary Model 15 double beam spectrophotometer. X-ray powder diagrams were made using a Philips instrument with Geiger counter detector.

## Results

Phosphors with  $x = 0.06$  to 0.14 exhibited emission in (i) sets of lines in the red with peak intensities at 700, 610, and 595 nm, (ii) a blue band peaked at 480 or 420 nm, (iii) a uv band centered at 385 nm. The relative importance of these spectral features was a function of exciting wavelength and composition. These relationships are summarized as relative numerical intensities of emission peaks in Table I and, in part, by the emission spectra of Fig. 1. (Where the sets of lines are represented by the envelopes. These were not resolved further, the emphasis here being on

Table I. Relative plaque output of emission peaks for  $\text{La}_{1-2x}\text{Ba}_x\text{Eu}_x\text{Li}_x\text{PO}_4$  phosphors

Excitation wavelength, nm	Emission peak wavelength, nm	Relative intensity			
		$x=0.06$	0.10	0.12	0.14
254	385	1	1	14	28
	480	2	1	7	15
	595	250	228	195	174
298	385	1	7	202	220
	420	0	50	0	0
	480	14	12	167	200
	595	34	33	18	15
312	385	1	14	231	260
	420	0	63	0	0
	480	11	17	216	250
	595	2	7	13	19

\* Electrochemical Society Active Member.

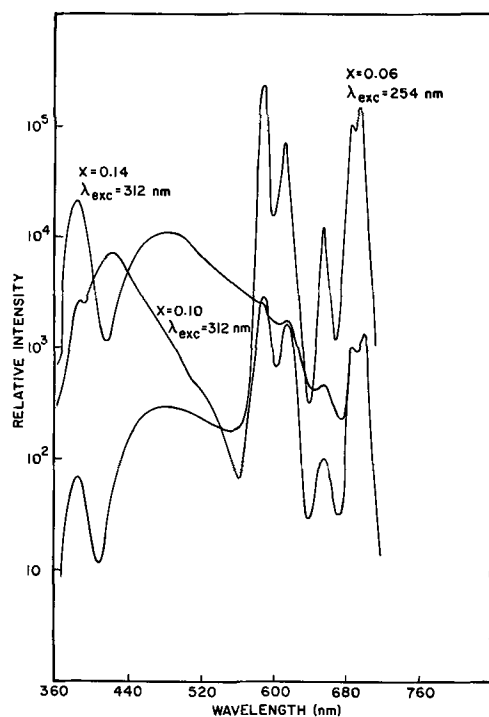


Fig. 1. Emission spectra of  $\text{La}_{1-2x}\text{Ba}_x\text{Eu}_x\text{Li}_x\text{PO}_4$  phosphors

the appearance of  $\text{Eu}^{+3}$  and  $\text{Eu}^{+2}$  in the same host rather than on the levels within  $\text{Eu}^{+3}$ .) In the latter presentation, a number of curves were omitted for clarity. Those remaining serve to illustrate the influence of europium concentration and excitation wavelength on emission, it being evident that, in general, high europium concentration and long uv excitation favor the band, and low europium concentration and short wave uv excitation the line, emissions. There is, however, an exception for the peaks under long wave excitation at 312 nm (see Table I), both band and line intensities increasing with concentration although the change is not so pronounced for the latter.

An explanation for this behavior may be found in Fig. 2, the excitation spectrum for emission peaked at 595 nm. This curve strongly resembles a similar one reported for  $\text{LaPO}_4:\text{Eu}$  phosphor (3) and consists of a broad band at short uv wavelengths with structure in the region from 300 to 400 nm. One such peak is at about 312 nm where the band emissions of our phosphors were excited most effectively. The result is the small contribution to the line emission noted above. The excitation spectra for the bands were also determined, the findings being summarized in Fig. 3 and the following comments: (A) The excitation bands for 385 and 420 nm emission peaks are essentially identical. (B) These excitation spectra overlap that of the

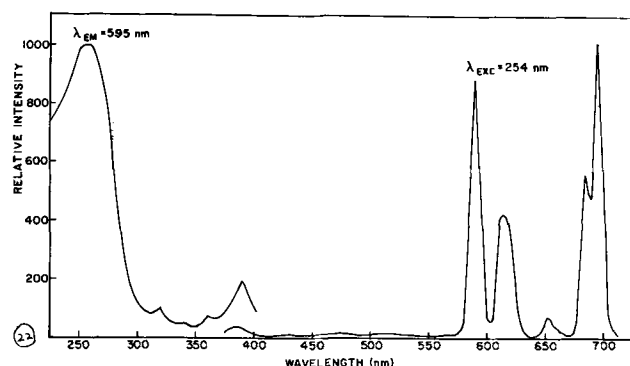


Fig. 2. Excitation spectrum for line emission in  $\text{La}_{0.72}\text{Ba}_{0.14}\text{Eu}_{0.14}\text{Li}_{0.14}\text{PO}_4$  phosphor.

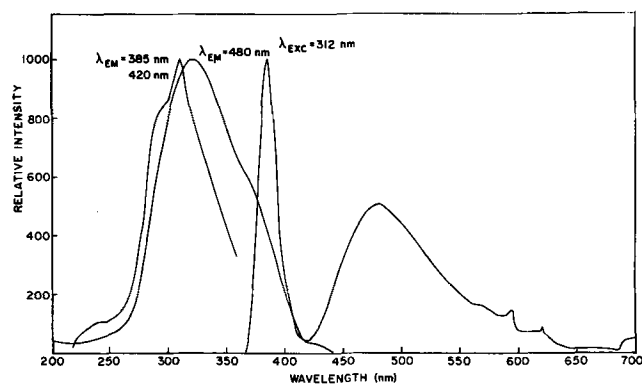


Fig. 3. Excitation spectra for emission bands in  $\text{La}_{0.72}\text{Ba}_{0.14}\text{Eu}_{0.14}\text{Li}_{0.14}\text{PO}_4$  phosphor.

480 nm emission peak and both lie within the wavelength range 200-400 nm in which  $\text{Eu}^{+3}$  emission is excited. (C) The 385 nm emission band overlaps the excitation band for emission peaked at 480 nm, but not for that peaking at 420 nm.

Thus all emissions are present to some extent for incident radiation from 200 to 400 nm and the uv and blue band emissions appear together as a result of overlapping excitation spectra. The reasons for the appearance of a band peaked at 420 nm remained unclear so materials in which either barium or europium was omitted were prepared. In Table II we see that, for samples without europium, there is a new emission centered at 335 nm but only for short wave excitation. (The excitation and emission spectra for this band are shown in Fig. 4.) Band emissions are very weak and line and 385 nm uv peaks are totally absent. Samples without barium also have no uv emission, while the line emission is absent for long wave excitation; the most prominent feature in these formulations is the 420 nm band.

The absorption characteristics were next examined, using reflectance measurements on the powders. The diffuse reflectance curves for phosphors with both barium and europium, in the uv region (Fig. 5) are in general agreement with data for  $\text{LaPO}_4:\text{Eu}$  (3). Materials without europium did not absorb well in the short wave region while those without barium absorbed best throughout the entire interval.

### Discussion

The line emission in this host is essentially a duplicate of that presented earlier for  $\text{LaPO}_4:\text{Eu}$  (3). The major peaks, 595 and 700 nm, are due to the  $^5\text{D}_0 - ^7\text{F}_1$  magnetic dipole and  $^5\text{D}_0 - ^7\text{F}_4$  electric dipole transitions, respectively, while 610 nm emission is due to the  $^5\text{D}_0 - ^7\text{F}_2$  electric dipole transition. The occurrence of these lines, in appreciable intensities, in the both  $\text{LaPO}_4$  host and our modified material, is interesting. Recent work on crystal structure sensitivity of  $\text{Eu}^{+3}$  emission (4) associates prominent 610 and 700 nm emission with occupation of sites lacking a center of inversion symmetry ( $\text{YAl}_3\text{B}_4\text{O}_{12}:\text{Eu}$ ), strong 595 nm emission in a host ( $\text{Ba}_2\text{GdNbO}_6$ ) with a center of inversion. The presence of all three in  $\text{LaPO}_4:\text{Eu}$  suggests several different crystallographic sites for the activator.

Table II. Relative plaque output of emission peaks for  $\text{La}_{1-2x}(\text{Ba} \text{ or } \text{Eu})_x\text{Li}_x\text{PO}_4$  phosphors.

Excitation wavelength, nm	Emission peak wavelength, nm	Relative intensity			
		0.06 Ba	0.12 Ba	0.06 Eu	0.12 Eu
254	335	155	119	0	0
	420	1	1	24	1
	480	2	1	3	4
	595	0	0	7	2
312	420	1	1	24	6
	480	0	1	4	7

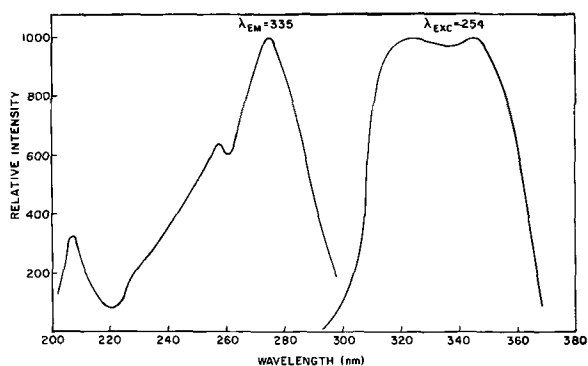


Fig. 4. Excitation and emission of  $\text{La}_{1-2x}\text{Ba}_x\text{Li}_x\text{PO}_4$  phosphors

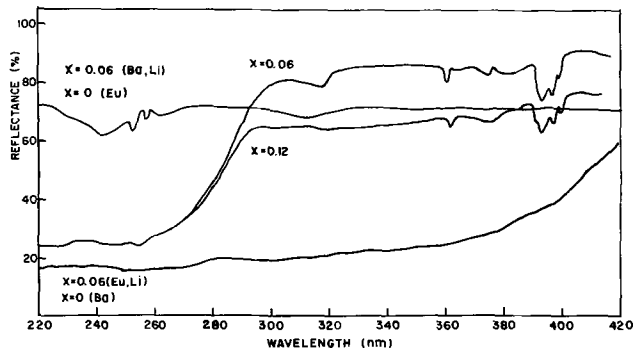


Fig. 5. Diffuse reflectance spectra for  $\text{La}_{1-2x}\text{Ba}_x\text{Eu}_x\text{Li}_x\text{PO}_4$  phosphors.

The crystal structures of rare earth phosphates have been reported (5, 6), both hexagonal and monoclinic forms being important. The mineral monazite, the  $\text{LaPO}_4:\text{Eu}$  and our barium modification all have the monoclinic structure, with over-all symmetry  $P2/n(C_{2h})$ . The rare earth in monazite is coordinated to the corners of four different phosphate groups by short (2.46Å) bonds and to two additional tetrahedra by four longer (2.66Å) bonds. Thus the local site has inversion symmetry and the strong 595 nm emission is expected for europium in such sites. The appearance of emission expected for sites lacking inversion symmetry must mean that replacement of lanthanum by europium in  $\text{LaPO}_4:\text{Eu}$  produces two types of sites, one having a small deviation from inversion symmetry.

The emission bands noted in  $\text{La}_{1-2x}\text{Ba}_x\text{Eu}_x\text{Li}_x\text{PO}_4$  are to be associated with the presence of  $\text{Eu}^{+2}$ . Such divalent europium emission bands have been reported with peaks at 480 nm in oxides and with various peaks in the range 400-600 nm in halides and silicates (7). This flexibility suggests extension to the near uv as reasonable. Further the excitation peak for the 385 (and 420) nm band is at 310 nm, near the 320 nm absorption peak for  $\text{Eu}^{+2}$  ( $\text{EuCl}_2$ ) in water (8). Interestingly the other broad absorption band found in the same investigation has a maximum at 248 nm so that short wave excitation of the  $\text{Eu}^{+2}$  centers is possible and (see Fig. 1) observed.

There remains the 420 nm emission band for consideration. Since it has an intensity in samples without barium which can be an appreciable fraction of the value noted in phosphors with both europium and barium, the emission must be due to isolated europium centers. While these are primarily  $\text{Eu}^{+2}$  centers, the data in Table II show that there is also 595 nm line emission in samples containing europium alone. Increased excitation wavelength and low europium concentration favor the blue band emission. The structure evident in the emission spectra where this band is pronounced (Fig. 1) indicate that it appears in addition to, rather than instead of, the 385 and 480 nm emission. This implies a second phase but none was de-

tected in the x-ray powder patterns or on microscopic examination under long and short wave excitation. Etching with mineral acids also did not disclose a surface phase different from the bulk material. The appearance of this peak at excitation wavelength-concentration combinations for which the line and band features are changing rapidly may signify disordering of the species substituting for host lanthanum.

The uv band emission peaked at 335 nm in  $\text{La}_{1-2x}\text{Ba}_x\text{Li}_x\text{PO}_4$  phosphors is not evident when europium is also present. The range covered by the band, 310-360 nm, coincides with that in which the other europium band and line emissions are well excited and cannot be isolated when europium is included. Also absorption in europium-containing materials is much better in the range where this host band is excited. The appearance of emission on introduction of Ba-Li pairs does indicate a change in the host favoring absorption in the short wave uv, where phosphates are usually transparent.

While the appearance of  $\text{Eu}^{+2}$  band emission is most simply explained by the use of slightly reducing atmosphere, the number of such bands demands some qualifying statement. A pertinent observation is the absence of any band emission when strontium or calcium were used for barium in a similar series of phosphors. Since the reduction of europium depends on the availability of an electron the appropriate differences between barium and the other alkaline earths, must be sought. One such comparison, that of orbital radii (9) and energy level, is given below with  $\text{La}^{+3}$  included. From the standpoint of energy level and ra-

Chemical species	Orbital radius, Å	Orbital
$\text{Ba}^{+2}$	0.87	5p
$\text{Sr}^{+2}$	0.68	4p
$\text{Ca}^{+2}$	0.54	3p
$\text{La}^{+3}$	0.819	5p

dius the barium is the best match for  $\text{La}^{+3}$ . Further the larger radius of  $\text{Ba}^{+2}$  permits greater overlap with nearly  $\text{O}^{2-}$  ions when barium replaces lanthanum and, as barium (and europium) concentration increases the possibility of the Ba-O-Eu configuration does also.

Now the spectral properties of europium have been investigated and the importance of charge transfer from the  $\text{O}^{2-}$  anion of the absorbing group to  $\text{Eu}^{+3}$  established for both liquids (10) and solids (11). This includes  $\text{LaPO}_4:\text{Eu}$  (3) and, in view of the similarity in  $\text{Eu}^{+3}$  excitation and emission in the two systems, the barium-containing materials we have prepared. This tendency of the oxygen to transfer an electron to europium coupled with the greater overlap of barium with the oxygen may lead to complete transfer, i.e., reduction of  $\text{Eu}^{+3}$  to  $\text{Eu}^{+2}$ , in configurations where barium and europium are separated by an oxygen anion. Exchange between cations separated by an anion have been used to correlate bonding with type of magnetic behavior observed (12) and extended to include optical phenomena such as luminescence quenching (13) and efficiency (14) in rare earth activated solids. It is proposed that the appearance of band emission here is due to a similar mechanism.

#### Acknowledgment

The writer wishes to express his gratitude for the spectral measurements of W. A. Thornton and R. J. Wisniewski and the x-ray diffraction results provided by C. K. Lui Wei.

Manuscript received Sept. 14, 1967; revised manuscript received Dec. 7, 1967. This paper was presented at the Dallas Meeting, May 7-12, 1967, as Abstract 76.

Any discussion of this paper will appear in a Discussion Section to be published in the December 1968 JOURNAL.

## REFERENCES

1. P. M. Jaffe and E. Banks, *This Journal*, **102**, 518 (1955).
2. W. A. Thornton, Paper presented at the San Francisco Meeting of the Society, May 10-14, 1965, Extended Abstracts, Abstract 38.
3. W. L. Wanmaker, A. Bril, J. W. ter Vrugt, and J. Broos, *Philips Research Repts.*, **21**, 270 (1966).
4. G. Blasse, A. Bril, and W. C. Nieuwpoort, *J. Phys. Chem. Solids*, **27**, 1587 (1966).
5. R. C. L. Mooney-Slater, *Z. Krist.*, **117**, 371 (1962).
6. R. W. G. Wyckoff, *Crystal Structures*, **III**, 33 (1965).
7. H. G. Jenkins and A. H. McKeag, *This Journal*, **97**, 415 (1950).
8. F. D. S. Butement, *Trans. Faraday Soc.*, **44**, 617 (1948).
9. J. T. Waber and D. T. Cromer, *J. Chem. Phys.*, **42**, 4116 (1965).
10. C. K. Jorgensen, *Mol. Phys.*, **5**, 271 (1962).
11. G. Blasse and A. Bril, *Solid State Commun.*, **4**, 373 (1966).
12. See, for example, J. B. Goodenough, *Mol. Designing Mater. Devices 1965*, 42, and references cited therein.
13. L. G. Van Uitert and L. F. Johnson, *J. Chem. Phys.*, **44**, 3514 (1966).
14. G. Blasse, *J. Chem. Phys.*, **45**, 2356 (1966).

## Zinc Oxide and Zinc-Cadmium Oxide Phosphors

W. Lehmann\*

Westinghouse Research Laboratories, Pittsburgh, Pennsylvania

### ABSTRACT

Zinc oxide phosphors may emit in four different bands, the ultraviolet near-edge emission, the common green band (possibly involving sulfur), a yellow-orange band due to selenium, and a red to near infrared band due to ammonia. About 10% of ZnO can be replaced by CdO with a corresponding shift, to lower energies, of the optical absorption edge, of the near-edge emission, and of the green emission. The possibility of an impurity activation due to anion substitution is discussed.

The best known luminescence of zinc oxide consists of a rather broad and structureless band in the green centered at about 2.4-2.45 eV. Partial replacement of ZnO by MgO and resulting shift of the green emission toward blue was reported by Smith(1). We have investigated the influence of a similar partial replacement of ZnO by CdO which does not seem to have been reported before.

Zinc oxide itself may emit in, at least, four different emission bands which are shown in Fig. 1. They are:

(a) The near-edge emission, a narrow and somewhat irregularly shaped band in the near-ultraviolet with the peak at about 3.18-3.20 eV at room temperature which is near the optical absorption edge of ZnO (~3.25 eV).

(b) The common green emission band whose origin is still a matter of considerable controversy [a discussion of it is given in ref. (2)].

(c) A yellow-orange band with the peak at 1.95-2.0 eV which appears in the presence of selenium (3, 4).

(d) A red to infrared emission band with the peak at about 1.55 eV which does not seem to have been reported before. We observed this emission in nominally pure ZnO fired in NH<sub>3</sub> at 1000°-1100°C. Similar fringes in either H<sub>2</sub> or N<sub>2</sub> are ineffective.

Our work on the influence of a gradual replacement of ZnO by CdO was limited to the first two of these four bands. The phosphors were prepared by firing either ZnO (luminescent grade purity) or intimate mechanical mixtures of ZnO and CdCO<sub>3</sub> (reagent grade) under conditions facilitating the one or the other emission band.

The green emission of ZnO is known to require slightly reducing firing conditions (5) and is observed to be enhanced by the presence of traces of sulfur (1, 3, 6). However, and in contrast to ZnO, an addition of a trace of sulfur to (Zn,Cd)O gives only poor results. Apparently, the sulfur reacts mainly with the cadmium and keeps it separate as CdS. Therefore, the (Zn,Cd)O phosphors were fired, without deliberate

addition of sulfur, in argon, at about 1100°C. Addition of iodine to facilitate particle growth is permissible and was not observed to have an effect on the emission spectrum which, in every case, consists of a single broad band corresponding to the green band of ZnO with little or no contribution of the near-edge emission.

The preparation conditions used to obtain near-edge emission in (Zn,Cd)O phosphors were those reported for ZnO phosphors (7). This technique completely isolates the near-edge emission with no detectable other emission bands.

Pure CdO ordinarily occurs in the cubic NaCl lattice. It is reported to be soluble in hexagonal ZnO (wurtzite lattice) only up to 4.9% (8). We observed CdO to be soluble in ZnO up to about 10 m/o (molar per cent) as determined by x-ray analysis, by optical reflection spectra, and by luminescence emission spectra. X-ray diffraction spectra of some samples are shown in Fig. 2 where separate lines, corresponding to the NaCl lattice of CdO, are visible at 15%, but not at 10% or below, of CdO added to the ZnO. Higher amounts of added CdO remain undissolved as separate phase which is clearly visible also at the dark body color of the samples. Evaluation of the x-ray spectra permits one to determine mean nearest neighbor dis-

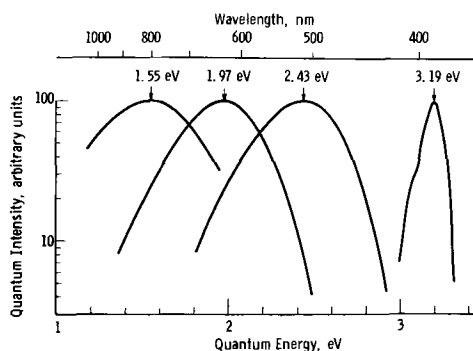


Fig. 1. Four luminescence emission bands observed in ZnO phosphors.

\* Electrochemical Society Active Member.

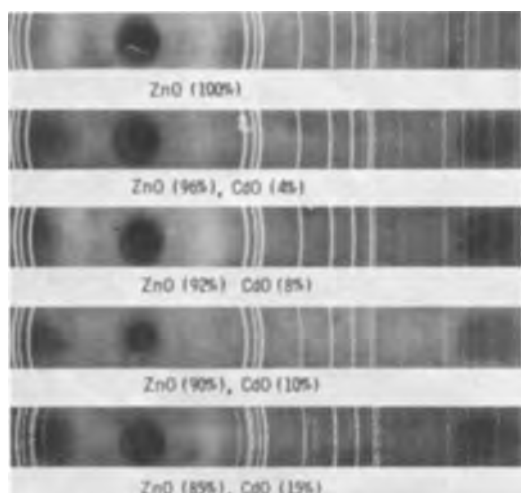


Fig. 2. X-ray diffraction spectra of (Zn,Cd)O

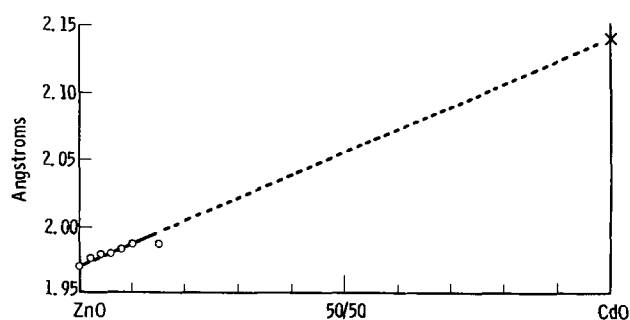


Fig. 3. Next-neighbor distances of hexagonal (Zn,Cd)O; o = measured and x = hypothetical.

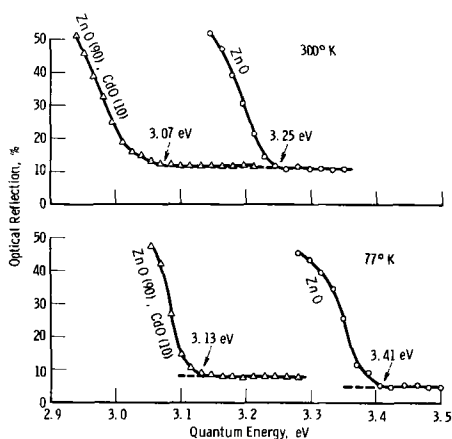


Fig. 4. Optical reflection spectra of ZnO and of ZnO (90%)-CdO (10%).

tances in the lattice. Plotted as a function of the CdO concentration in Fig. 3, they are all, within the accuracy of these measurements, on a straight line connecting the values for ZnO (1.97Å) and the, in reality nonexistent, hexagonal CdO (2.14Å).<sup>1</sup> Hence, Vegard's law is fulfilled at least within the limited range of solubility.

Gradual replacement of ZnO by CdO causes the quantum energy corresponding to the optical absorption edge (or whatever is measured as such under ordinary conditions) to decrease. As a consequence, pure ZnO ordinarily is white, but a solid solution of 90% ZnO-10% CdO is slightly yellow in body color. Some optical reflection spectra demonstrating this shift of the absorption edge are given in Fig. 4.

<sup>1</sup> Determined from the sum of tetrahedral standard radii, Zn = 1.31Å, Cd = 1.48Å, O = 0.66Å.

The approximate peak position of the near-edge emission as a function of the CdO concentration is shown in Fig. 5 and compared with the corresponding shift of the absorption edge. Both curves are approximately parallel. While the near-edge emission of ZnO is in the near ultraviolet, that of a (Zn,Cd)O phosphor containing 10% of CdO is in the visible violet. Two measured actual emission spectra are given in Fig. 6. Gradual replacement of ZnO by CdO causes also the green ZnO emission to move towards lower quantum energies, i.e., toward yellow (Fig. 7). Measured spectra of ZnO, of a (Zn,Cd)O containing 10% of CdO and, for comparison, of a (Zn,Mg)O phosphor containing 20% of MgO, are shown in Fig. 8.

Conclusions to the origin or luminescence in ZnO phosphors may be drawn from these results. Various models have been proposed in the literature linking either the near-edge emission, or the common green

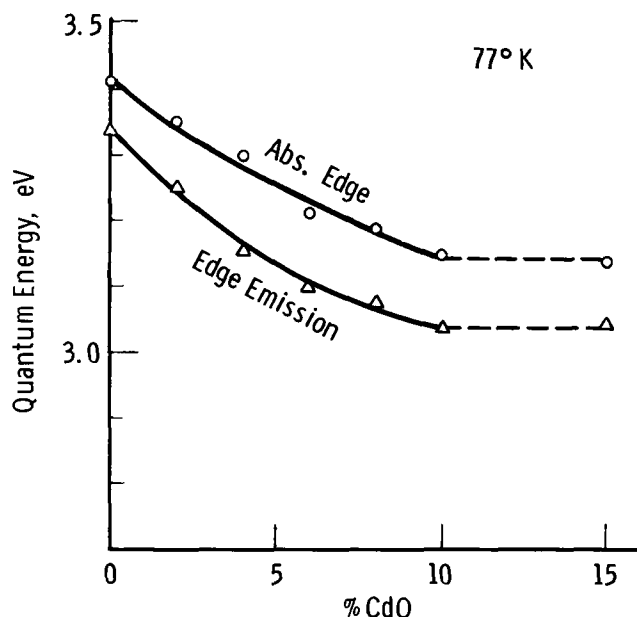


Fig. 5. Optical absorption edge and center of near-edge emission (excited by ultraviolet of 365 nm at 77°K) of (Zn,Cd)O as function of the CdO concentration.

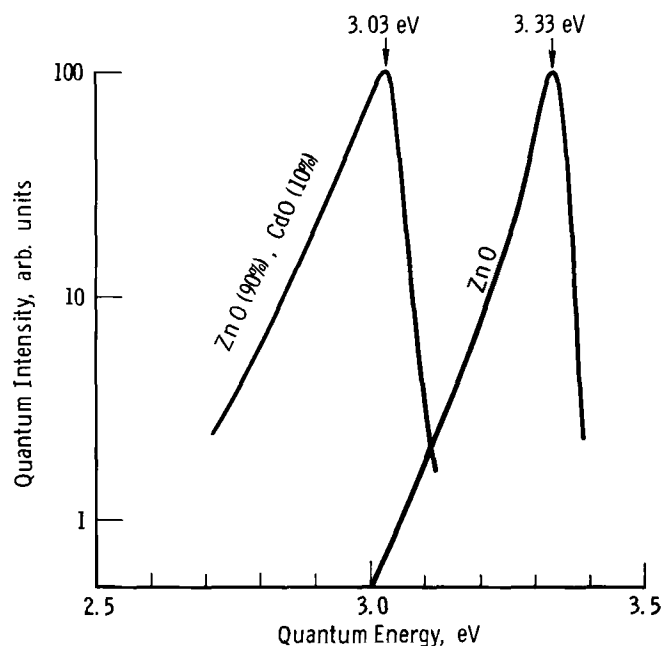


Fig. 6. Near-edge emission spectra of ZnO:Ga and of ZnO (90%)-CdO (10%):Ga excited by ultraviolet of 365, nm at 77°K.



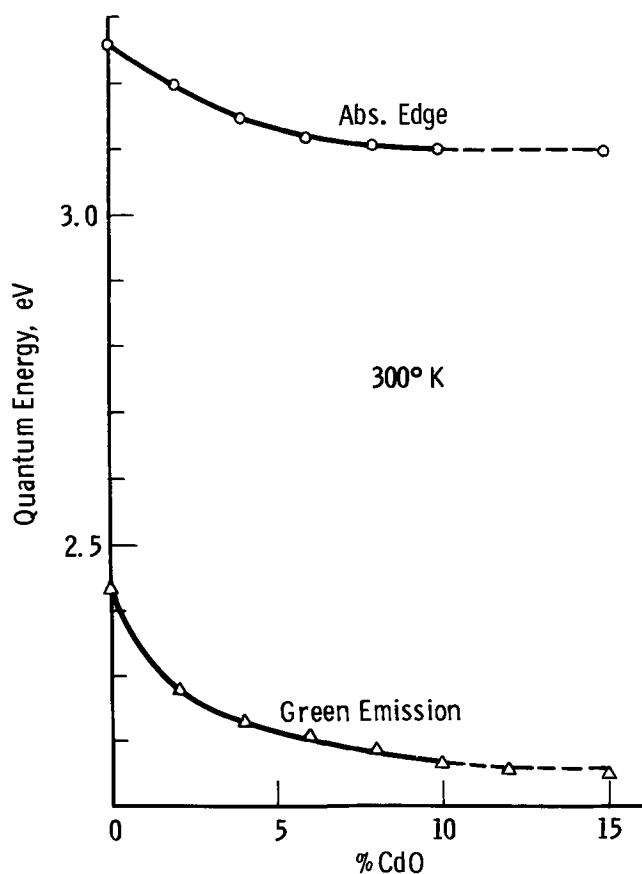


Fig. 7. Optical absorption edge and peak position of the "green" emission (excited by ultraviolet of 365 nm, at room temperature) of  $(\text{Zn,Cd})\text{O}$  as function of the CdO concentration.

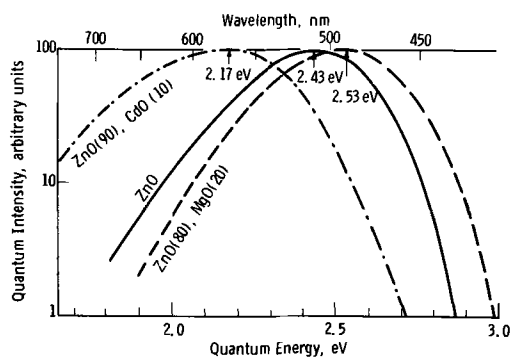


Fig. 8. "Green" emission band spectra of ZnO, of ZnO (90%)-CdO (10%), and of ZnO (80%)-MgO (20%), all excited by ultraviolet of 365 nm at room temperature.

emission, or the yellow-orange emission of ZnO to native lattice defects (*e.g.*, oxygen vacancies) but there seems to be little agreement between the authors. Alternatively, it has been proposed that the green emission band of ZnO might be due to traces of sulfur dissolved in the ZnO lattice (3), and a correlation between the intensity of the green emission and deliberately added sulfur (1, 3, 6) and similar correlations between the yellow-orange emission and deliberately added selenium (3, 4, 6), and between the infrared band and the ammonia atmosphere during firing, undoubtedly do exist. The observation of at least some green emission in ZnO to which no sulfur was intentionally added is not considered to be a sure criterion since sulfur may easily be present in all ordinary "pure" ZnO to start with, or in the carbon black recommended by Leverenz (5), or even in the air, especially of a laboratory. Traces of sulfur in green emitting ZnO are not easily analyzed and may be present only in the ppm range.

The valence band of the predominantly ionic ZnO is mainly determined by the anion, *i.e.*, oxygen. Sulfur and selenium are isoelectronic to oxygen. If they are dissolved in ZnO substituting for oxygen, their effect may be to split states out of the valence band into the forbidden band gap, and particular emission may be due to an electron transition between such state and one of the band edges. Luminescence due to an isoelectronic anion impurity in a II-VI compound, CdS:Te, is known already (9). A similar situation is proposed for the red emission which appears to involve nitrogen and hydrogen (since firing in pure nitrogen, or in pure hydrogen, are ineffective) and which is proposed to be due to N-H pairs. A nitrogen replacing an oxygen atom in ZnO would be an acceptor, an interstitial hydrogen is a donor, consequently, a pair of both would be electrically as neutral as a sulfur or selenium substituting for an oxygen atom.

Gradual replacement of zinc by cadmium shifts the green ZnO emission towards lower energy similar to a corresponding of many emission bands in  $(\text{Zn,Cd})\text{S}$  phosphors which fairly unambiguously can be understood on the basis of a Schön-Klasens type of recombination (10). Hence, at least the green ZnO emission appears to be due to an electron transition from or near the conduction band edge into a valence state of the sulfur located above the upper edge of the valence band of the ZnO. The same probably holds also for the yellow-orange emission due to selenium and for the infrared emission due to ammonia although corresponding investigations involving a gradual replacement of zinc by cadmium are not yet made. The near-edge emission of ZnO and of  $(\text{Zn,Cd})\text{O}$  seems to behave differently in some respects, and its mechanism is still too uncertain to be discussed here.

A more practical consideration concerns the availability of ZnO-type phosphors of various emission colors due to gradual replacement of up to 10 m/o of ZnO by CdO. This shifts the extremely fast near-edge emission of n-type doped ZnO (7) out of the near ultraviolet into the visible violet. The energy efficiency of catholuminescence seems to be little affected by this shift, and although it is not too high (estimated: 1-2%), these materials may be useful in applications where high speed of response ( $\sim 10^{-9}$  sec or shorter) is imperative. By contrast, the efficiency of catholuminescence of green ZnO ( $\sim 6-7\%$ ) reduces to about 2-3%, at best, as soon as some ZnO is replaced by CdO. This lower efficiency of yellowish  $(\text{Zn,Cd})\text{O}$  (made without sulfur) compared to green ZnO (made with sulfur) seems to be due to the resistance of sulfur to be dissolved in the material whenever cadmium is present. At the moment, it is not known whether the situation can be improved.

Manuscript received Oct. 20, 1967; revised manuscript received Nov. 15, 1967. This paper was presented at the Dallas Meeting, May 7-12, 1967, as Abstract 28.

Any discussion of this paper will appear in a Discussion Section to be published in the December 1968 JOURNAL.

#### REFERENCES

1. A. L. Smith, *This Journal*, **99**, 155 (1952).
2. A. Pfahnl, *ibid.*, **109**, 502 (1962).
3. S. M. Thomsen, *J. Chem. Phys.*, **18**, 770 (1950); U. S. Pat. 2,573,817.
4. L. Y. Markowski and N. S. Orshanskaya, *Optics and Spectroscopy*, **9**, 40 (1960).
5. H. W. Leverenz, "An Introduction to Luminescence of Solids," p. 67, New York-London (1950).
6. Confirmed in our laboratory.
7. W. Lehmann, *Solid-State Electronics*, **9**, 1107 (1966).
8. Gmelin's Handb. Anorg. Chem., 8 Edition "Cadmium," p. 431.
9. A. C. Aten and J. H. Haanstra, *Phys. Lett.*, **11**, 97 (1964).
10. W. Lehmann, *This Journal*, **113**, 449, 788 (1966); **114**, 83 (1967).

# Doping of Epitaxial Silicon Films

W. H. Shepherd

Fairchild Semiconductor, Research and Development Laboratory, Palo Alto, California

## ABSTRACT

The doping of epitaxial silicon layers deposited by the hydrogen reduction of  $\text{SiCl}_4$  has been studied. The dopants used were phosphorus, arsenic, and antimony introduced as the trichlorides. In each case for fixed dopant to silicon ratios in the gas phase the film resistivity was found to increase with rising temperature and decrease with increasing growth rates. The results are explained by a model which takes into consideration both the transfer and thermodynamic properties of the reactor system. An analysis of the results then leads to values for the activity coefficients for phosphorus, arsenic and antimony in silicon.

In general, control of resistivity in epitaxial silicon films has not presented any serious problems and, as a result, there has been no strong incentive to investigate the mechanisms involved. Only Raichoudhury and Fergusson (1) have attempted an analysis. Wang *et al.* (2) showed that for a constant arsenic/silicon ratio in the gas phase the resistivity of layers deposited by the hydrogen reduction of  $\text{SiCl}_4$  was sensitive to temperature and to growth rate, but they made no serious attempt to establish the reasons. Nuttall (3) presented similar data for phosphorous and antimony, but again was unable to provide a good explanation for his results. In this paper, a model is proposed which is felt to be of general application. It is tested here for the specific case of layers deposited by the hydrogen reduction of  $\text{SiCl}_4$  and doped with phosphorus, arsenic, or antimony using trihalide sources of the impurities.

## Theory

The resistivity of an epitaxial layer is determined by the relative rates at which silicon and dopant atoms are added to the film. A previous paper (4) considered the processing governing the deposition of silicon by hydrogen reduction of  $\text{SiCl}_4$  in horizontal reactors. Here it will be assumed that the "deposition" of dopant at the silicon surface can be treated in the same manner. It is in order then to review briefly the silicon deposition process.

### Rate of Deposition of Silicon

Figure 1 shows film growth rate plotted logarithmically against  $1/T$   $^\circ\text{K}^{-1}$  for the small, six-wafer horizontal reactor used in this work. This relationship is typical, qualitatively at least, of most multiwafer reactors using hydrogen reduction of  $\text{SiCl}_4$ . The region at lower temperatures in which the growth rate varies exponentially as  $1/T$   $^\circ\text{K}^{-1}$  is called the kinetic region since it is thought that at these temperatures the rate-limiting process is the chemical reaction at the silicon surface. As the temperature is raised the chemical reaction rate increases rapidly, the surface concentration of  $\text{SiCl}_4$  falls, and the concentration gradient of  $\text{SiCl}_4$  normal to the surface steepens in order to meet the requirements of the faster surface reaction. A point is eventually reached where the surface concentration of  $\text{SiCl}_4$  is so much smaller than the bulk concentration that a further decrease in its value produces no noticeable increase in the concentration gradient. In this condition  $\text{SiCl}_4$  is being transferred from the gas stream at the maximum rate possible. It is now the transfer properties of the gas stream which determine the over-all deposition rate, and since these properties vary only slowly with temperature the mass-transfer region is characterized by a very low-temperature sensitivity of growth rate. In Fig. 1 a broken line shows how the growth rate should vary if transport limited throughout the temperature range (4).

In ref. (4) (Eq. 19) a model was developed to describe the deposition process in the mass transfer region. According to this model the rate of deposition,  $G$ , is given by an equation of the form

$$G = \Psi_s x_s - A \{ (1 + 2\Psi_s x_s)^{1/2} - 1 \}^2 \quad [1]$$

The first term on the R.H.S. of the equation represents the flux of silicon toward the growing surface as  $\text{SiCl}_4$  while the second term allows for the fact that silicon is lost from the surface as  $\text{SiCl}_2$ . In Eq. [1]  $\Psi_s$  is a gas transfer coefficient for  $\text{SiCl}_4$  in  $\text{H}_2$  and has the same units as those chosen for  $G$ , e.g.,  $\mu \text{ min}^{-1}$ , since  $x_s$  is the mole ratio of  $\text{SiCl}_4$  in the initial, unreacted gas stream and is dimensionless. The parameter  $A$  contains both thermodynamic and transfer terms but is essentially temperature independent and a constant for a specific deposition system.

For growth rates less than  $1.5 \mu \text{ min}^{-1}$  the second term can be neglected with a resultant error of only a few per cent and even at  $2.5 \mu \text{ min}^{-1}$  the error incurred is less than 20%. For simplicity then it will be assumed for the purposes of this paper that the growth rate is given simply by the first term in Eq. [1], and hence is linear in  $\text{SiCl}_4$  concentration, at least in the mass transfer region.

In the kinetic region the dependence of growth rate on concentration has not been determined. However the rate may be expressed in the form

$$G = f(T, x_s) \Psi_s x_s \quad [2]$$

where  $f$  is a function of temperature and possibly of  $\text{SiCl}_4$  concentration also. The growth rate *vs.* temperature data of Fig. 1 were obtained at a mole ratio of  $\text{SiCl}_4$  of 0.0048 and by conducting the experiments in the present work at the same concentration, (actually at a mole ratio of 0.0050),  $f$  can be determined empirically as the ratio of the actual growth rate to that expected for a mass transfer controlled process at

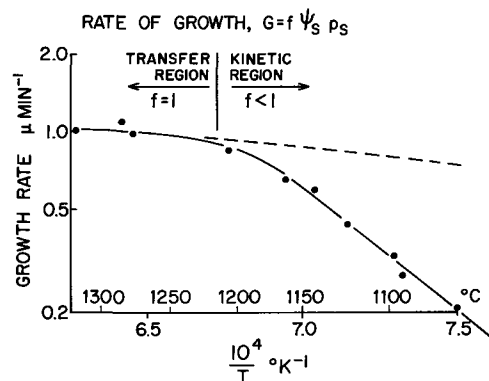
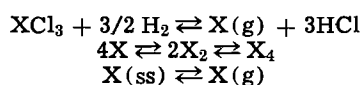


Fig. 1. Temperature dependence of silicon deposition rate for  $\text{SiCl}_4$  concentration of 0.48 m/o.

the same temperature (i.e., as indicated by the broken line). Actually then, Eq. [2] can be regarded as a general one in which  $f = 1$  in the mass transfer region.

#### Deposition of Dopant

The treatment adopted here parallels that used to develop the model for epitaxial deposition of silicon. That is, it is assumed that the reduction of the dopant compound takes place only at the heated surface, i.e., not in the gas phase or on the reactor walls, that all surface reactions are fast so that rate processes are mass transfer controlled, and that all dopant species at the surface, whether in the silicon or in the adjacent gas phase, are in thermodynamic equilibrium. The assumption that the rate processes are transfer controlled throughout the temperature range employed and that for none of the dopants is there a kinetic region such as observed for silicon is reasonable in view of the ease with which all of the pertinent chlorides are reduced in hydrogen at temperatures well below those of concern in this work. The surface equilibria of concern here are



where  $\text{X} = \text{P, As, or Sb}$  and  $\text{X(ss)}$  represents the dopant in solution at the silicon surface. Volume diffusion in the solid will be ignored. Thermodynamic data (5) indicate that for the experimental conditions used the reduction of the compounds,  $\text{XCl}_3$ , is essentially complete and further that for arsenic and antimony the only gaseous elemental species of interest at the silicon surface are monatomic. For phosphorus, particularly at the lower end of the experimental temperature range, both  $\text{P}$  and  $\text{P}_2$  should be considered, but since the only phosphorus doping data amenable to analysis were taken at the very upper limit of temperature, i.e.,  $1340^\circ\text{C}$ , it happens that in this case also only the monatomic species need be considered.

The situation then is that dopant compound transfers to the surface where it is completely reduced to monatomic elemental dopant. Some of this dopant is incorporated in the growing silicon film while some remains in the gas phase adjacent to the surface and in equilibrium with its solution in the silicon. Since there is a gradient of elemental dopant out from the surface, loss occurs from the surface to the bulk gas stream. In a steady state, which will be assumed to occur instantaneously, the material balance for dopant at the surface requires that the rate of transfer toward the surface in the form of the halide equals the rate of uptake by the film plus the rate of loss in the elemental form to the gas stream.

The rate of transfer of dopant halide to the surface per square centimeter, assuming a model analogous to that for silicon deposition, is

$$F_D = n\psi_D x_d \quad [3]$$

where  $x_d$  is the mole ratio of halide in the gas stream,  $\psi_D$  is the transfer coefficient for the halide in hydrogen, and  $n$  is an integer denoting the number of atoms of dopant per molecule of halide. Since  $n = 1$  for all the halides used, it will be omitted from subsequent equations. With  $\psi_D$  in  $\mu \text{ min}^{-1}$  the flux of dopant  $F_D$  has the same units.

The rate of transfer of elemental dopant away from the surface ( $F_E$  ( $\mu \text{ min}^{-1}$ )) is (ref. 4, Eq. 9)

$$F_E = \psi_E x_E \quad [4]$$

where  $x_E$  is the mole ratio of element in the gaseous equilibrium region close to the surface and  $\psi_E$  the transfer coefficient for elemental dopant.

The rate of incorporation of dopant in the film,  $F_I$ , can be written again in  $\mu \text{ min}^{-1}$ , as

$$F_I = GR_s \quad [5]$$

where  $R_s$  is the atom ratio of dopant in the silicon at the silicon-gas interface. Since we have identical numbers of atoms per cubic centimeter for dopant and silicon the film thickness ratio is identical with the atom ratio.

One further relationship is necessary. It has been assumed that equilibrium exists between gaseous and dissolved dopant, and since both are in monatomic dispersion and in general the solutions are dilute so that Henry's law may be applied, the equilibrium can be expressed in the form.

$$x_E = \gamma R_s \quad [6]$$

In all experiments the ambient pressure was 1 atm so that  $x_E$  is equivalent to a partial pressure of gaseous monatomic dopant in atmospheres and if, for the present purposes, unit activity of the dopant is defined as 1 atm pressure of monatomic species then  $\gamma$  is the activity coefficient for the dopant in silicon.

The dopant material balance previously enunciated is otherwise stated as

$$F_D = F_I + F_E$$

Substituting from Eq. [3] through [6] and rearranging gives

$$\alpha = \frac{R_s}{R_G} = \frac{1}{f(1 + \psi_E \gamma / G)} \frac{\psi_D}{\psi_S} \quad [7]$$

where  $R_G$  is  $x_d/x_s$  the atom ratio of dopant to silicon in the initial gas stream and  $\alpha$  is a distribution coefficient defined in the same manner as that used in conventional crystal growth from a melt. From Eq. [7] it appears that the effects to be investigated are mainly described by the term  $(\psi_E \gamma) / G$  and appear when this term is larger than unity. The behavior of  $\alpha$  for different magnitudes of  $\psi_E \gamma / G$  is considered briefly now.

(a) If  $(\psi_E \gamma) / G \ll 1$ , Eq. [7] simplifies to

$$\alpha = \frac{1}{f} \cdot \frac{\psi_D}{\psi_S} \quad [8]$$

In the mass transfer region where  $f = 1$  the distribution coefficient is simply the ratio of the transfer coefficients for dopant and silicon, and it is not influenced by growth conditions. Further, since the transfer coefficients probably do not differ by much more than a factor of two at the most, it is possible to predict that  $\alpha$  should have values in the range 0.5-2.0. In the kinetic range  $f$  becomes small and  $\alpha$  may increase above this range.

(b) At the other extreme when  $(\psi_E \gamma) / G \gg 1$ , Eq. [7] becomes

$$\alpha = \frac{1}{f} \cdot \frac{G}{\psi_E \gamma} \cdot \frac{\psi_D}{\psi_S} \quad [9]$$

which, since  $G = f\psi_S x_s$ , can be further reduced to

$$\alpha = \frac{\psi_D}{\psi_E} \cdot \frac{x_s}{\gamma} \quad [10]$$

As before  $\psi_D / \psi_E$  can be expected to be close to unity and to remain constant, but now  $\alpha$  is directly proportional to the concentration of  $\text{SiCl}_4$ ,  $x_s$ , and inversely proportional to the activity coefficient  $\gamma$  and hence is very much affected by growth conditions.

(c) The third situation is that in which  $\psi_E \gamma / G \cong 1$ . In this case  $\alpha$  may tend toward situation (a) or (b) depending on the exact conditions of growth.

The critical factor determining the magnitude of  $\psi_E \gamma / G$  is  $\gamma$ . Changing dopants will not affect  $\psi_E$  greatly and though, in principle  $G$  is infinitely variable, in practice growth rates are normally maintained within a narrow range, e.g., 0.3-1.0  $\mu / \text{min}$ . The activity coefficient,  $\gamma$ , however, may be varied over several orders of magnitude either as a function of temperature or dopant. Thus if  $\gamma$  is very large, i.e., the dopant evaporates readily from silicon, then the situa-

tion illustrated in (b) pertains and the distribution coefficient,  $\alpha$ , is sensitive to growth parameters. If  $\gamma$  is small so that the dopant has no tendency to re-evaporate from the silicon, then the situation in (a) holds and  $\alpha$  is insensitive to growth conditions.

### Experimental Details

The experiments were carried out in a small, six-wafer horizontal reactor previously described (4). The arrangement used then was modified by replacing the evaporative  $\text{SiCl}_4$  source with a liquid feed source. The  $\text{SiCl}_4$  flow was metered through a Fischer-Porter 1/16-08 size meter. This feed method was employed in order to maintain a constant atom ratio of dopant to silicon in the gas mixture in the simplest manner. The  $\text{SiCl}_4$  was doped in all cases with the trichloride of the element to be used, i.e., with  $\text{PCl}_3$ ,  $\text{AsCl}_3$ , or  $\text{SbCl}_3$ . First, a master solution was prepared by adding a known volume, approximately 0.5 ml, of the chloride to 1000 ml of undoped  $\text{SiCl}_4$  (better than 100 ohm-cm n-type) in a fused quartz flask. This was shaken and allowed to stand for 24 hr to ensure mixing. The solutions doped with arsenic and antimony were then chemically analyzed and found to be within 20% of the expected concentrations. In the case of the phosphorus master solution, analysis was considered to be too inexact to be worthwhile. The master solutions were diluted further in the same manner to produce the final mixtures. The atom ratios of dopant to silicon used were: phosphorus  $1.1 \times 10^{-6}$ ; arsenic  $1.2 \times 10^{-6}$ ; antimony  $8.8 \times 10^{-6}$ .

Epitaxial layer resistivities were determined from V/I and groove and stain measurements on 15-20 $\mu$  thick deposits grown on boron doped substrates of approximately 1 ohm-cm p-type. Quoted resistivities and growth rates were averaged from measurements on three wafers. Temperatures were measured optically and corrected by amounts varying from 140°C at the highest temperature used to 100°C at the lowest.

### Results

**General discussion.**—Figure 2 shows the influence of deposition temperature on layer resistivity. All experiments were conducted at a constant  $\text{SiCl}_4$  concentration of 0.5 m/o (mole per cent) ( $\cong 1.0 \mu \text{min}^{-1}$  at 1250°C) rather than a constant growth rate, since this was experimentally simpler to control. Phosphorus exhibits virtually no change, antimony, a very marked increase in resistivity with rising temperature, while arsenic is intermediate in behavior. In Fig. 3, the distribution coefficients calculated from the resistivity data are plotted vs. deposition temperature. The most notable feature is the very low value of  $\alpha$  for antimony doping. Reference to the theoretical discussion of Eq. [7] through [10] indicates that for antimony in silicon  $\gamma$  is large and is the predominant factor in  $\alpha$ , for phosphorus  $\gamma$  is small, while for arsenic  $\gamma$  has an intermediate value.

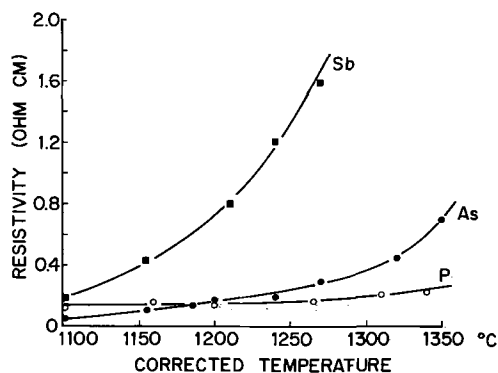


Fig. 2. Temperature dependence of epitaxial layer resistivity for  $\text{SiCl}_4$  concentration = 0.5 m/o ( $\cong 1 \mu \text{min}^{-1}$  at 1250°C).

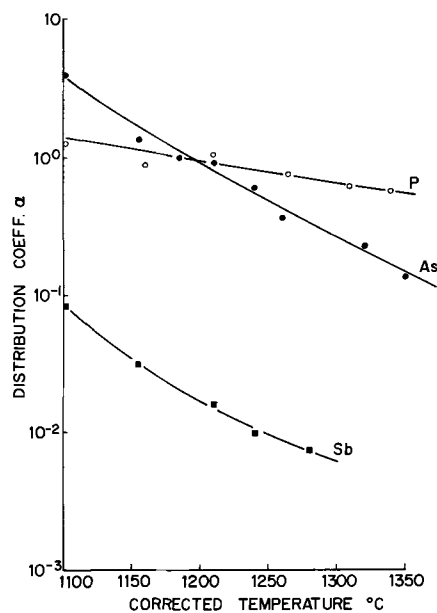


Fig. 3. Temperature dependence of  $\alpha$  for P, As, and Sb.  $\text{SiCl}_4$  concentration 0.5 m/o ( $\cong 1 \mu \text{min}^{-1}$  at 1250°C).

Figure 4 presents data on the influence of film growth rate on layer resistivity at temperatures in the mass transfer region. For the phosphorus study, a higher than normal temperature had to be employed to obtain readily observable effects. The distribution coefficients calculated from these data are plotted as a function of growth rate in Fig. 5. The results are consistent with those obtained from the temperature dependence of  $\alpha$  on the basis of the proposed doping mechanism. Thus, from Eq. [8] if  $\gamma$  is small,  $\alpha$  should tend to a limiting value, probably in the range 0.5-2.0 at high growth rates. This is observed for phosphorus. If  $\gamma$  is large,  $\alpha$  becomes small and directly proportional to growth rate. The data for antimony satisfy these conditions. For arsenic, the data appear to show a slight curvature, but insufficient to be conclusive and indicate no close approach to a limiting value.

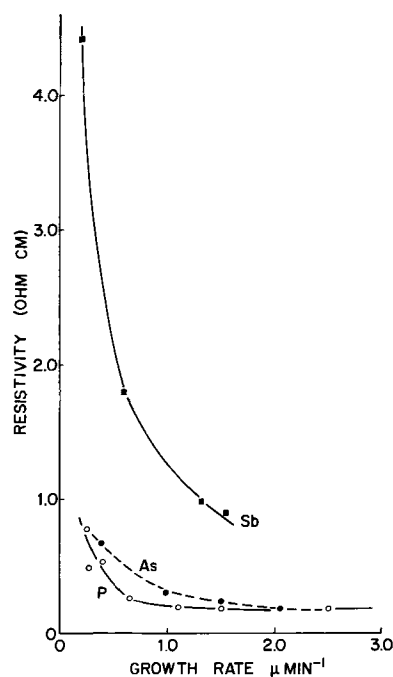


Fig. 4. Growth rate dependence of epitaxial layer resistivity for P(1340°C), As(1240°C), and Sb (1270°C).

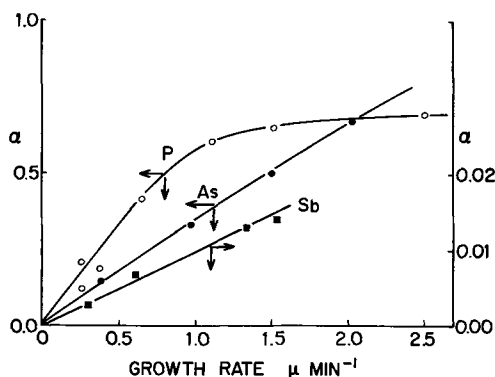


Fig. 5. Growth rate dependence of  $\alpha$  for P(1340°C), As(1240°C), and Sb(1270°C).

Calculation of activity coefficients.—Equation [7] can be rearranged to give

$$\gamma = \frac{\Psi_D}{\Psi_E} \left( \frac{1}{\alpha} - \frac{\Psi_S}{\Psi_D} \cdot f \right) x_s \quad [11]$$

This is a convenient form to employ for analysis of the  $\alpha$  vs. temperature data which were obtained for a constant  $x_s$ . The terms in this equation can be evaluated except for  $\Psi_E$  which cannot be separated from  $\gamma$  using any of the present measurements.

For antimony,  $\alpha < 10^{-1}$  at all temperatures investigated, and  $\gamma$  may be approximated from the simplified relationship

$$\gamma = \frac{\Psi_D}{\Psi_E} \cdot \frac{x_s}{\alpha} \quad [12]$$

For phosphorus and arsenic, it is necessary to evaluate the term  $(\Psi_S/\Psi_D) \cdot f$ .

The value of  $f$  can be obtained from Fig. 1 as previously indicated and for phosphorus  $(\Psi_S/\Psi_D)$  can be determined from the high growth rate limit of  $\alpha$  in Fig. 5. However, for phosphorus, the term  $1/\alpha - \Psi_S/\Psi_D \cdot f$  is very much smaller than  $1/\alpha$  or  $\Psi_S/\Psi_D \cdot f$  and the present data are insufficiently accurate to permit a worthwhile analysis except at the highest temperatures used.

For arsenic,  $\Psi_S/\Psi_D$  cannot be obtained from Fig. 5 since no rate limit of  $\alpha$  is observed. However, Eq. [7] may be written in the form

$$\frac{1}{\alpha} = \gamma \cdot \frac{\Psi_E}{\Psi_D} \cdot f \Psi_S \cdot \frac{1}{G} + \frac{\Psi_S}{\Psi_D} \cdot f \quad [13]$$

Hence, a plot of  $\alpha^{-1}$  vs.  $G^{-1}$  should be linear with an intercept on the  $\alpha^{-1}$  axis equal to  $(\Psi_S/\Psi_D) \cdot f$  (in the mass transfer region). Such a plot is shown in Fig. 6 from which a value of  $(\Psi_S/\Psi_D) \approx 0.4$  is measured. This would give the high-growth-rate limit for  $\alpha$ , if it could be achieved, as 2.5 which is reasonable.

Activity coefficients, or at least values of  $(\Psi_E/\Psi_D) \cdot \gamma$ , can be obtained also from Fig. 5, for the temper-

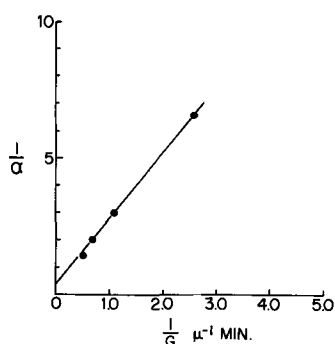


Fig. 6. Plot of  $1/\alpha$  vs.  $1/G$  for As doping at 1240°C

ature used. As the growth rate tends to zero,  $\alpha$  in all cases is given by Eq. [10] so that

$$\frac{d\alpha}{dx_s} = \frac{\Psi_D}{\Psi_E} \cdot \frac{1}{\gamma} \quad [14]$$

But in the mass transfer range  $G = \Psi_S x_s$  hence

$$\gamma \cdot \frac{\Psi_E}{\Psi_D} = \left( \Psi_S \frac{d\alpha}{dG} \right)^{-1} \quad [15]$$

where  $\Psi_S \approx 230 \mu \text{ min}^{-1}$  (4). Using Eq. [15] a value of  $(\Psi_E/\Psi_D) \cdot \gamma$  was calculated for phosphorus at 1340°C, and using Eq. [11] and [12] similar calculations were made for arsenic and antimony over a range of temperatures. The results are plotted in Fig. 7 as  $(\gamma \Psi_E/\Psi_D)$  vs.  $1/T \text{ K}^{-1}$ . We may reasonably make the assumption  $\Psi_E/\Psi_D = 1$ , and as for other ratios of gaseous transfer coefficients the uncertainty introduced should not exceed a factor of 2-3.

The phosphorus data points represented by open squares are calculated from the diffusion data of Coupland, (6), which related surface concentration to pressure of phosphorus vapor and hence can be analyzed to give  $\gamma$ . The data are in surprisingly good agreement with the single point (open circle) obtained in this work.

The data for arsenic and antimony plot linearly in Fig. 7 as they should if they represent activities, and all data are in the expected relative order, i.e.,  $\gamma_{\text{As}} > \gamma_{\text{Sb}} > \gamma_{\text{P}}$  (7).

Although the experiments have been performed using only the chlorides of the doping elements, the proposed doping model, if correct, shows that essentially the same results will be obtained regardless of the compounds used, e.g., hydrides. This is substantiated by the work of Wang *et al.* (2) for  $\text{AsH}_3$  and will still be true if the compound is unstable enough to decompose on the reactor walls so that the dopant passes through in elemental form. This may not be so obvious but an analysis similar to that presented above shows it to be so. Minor differences will result because of different transfer coefficients for various doping compounds but the basic characteristics are determined by the activity coefficient of the dopant which is not dependent on the doping compound employed.

#### Acknowledgments

The author is indebted to J. Ruiz for the experimentation and to many colleagues for helpful discussions.

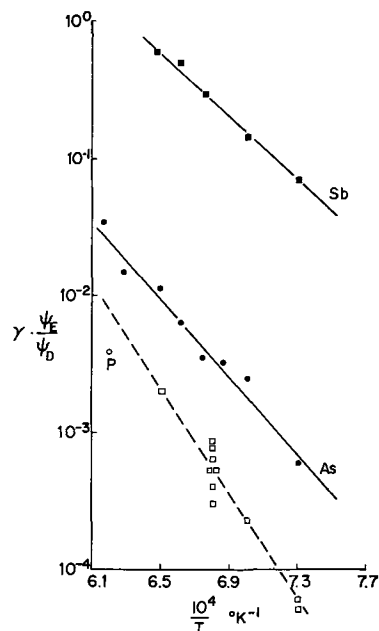


Fig. 7. Arrhenius plot of  $\gamma$  for P, As, and Sb in silicon (assuming  $\Psi_E/\Psi_D = 1$ ).

Manuscript received July 27, 1967; revised manuscript received ca. Dec. 5, 1967. This paper was presented at the Philadelphia Meeting, Oct. 9-14, 1966, as Abstract 192.

Any discussion of this paper will appear in a Discussion Section to be published in the December 1968 JOURNAL

## REFERENCES

1. P. Raichoudhury and R. R. Fergusson, Paper presented at the Cleveland Meeting of the Society, May 1-6, 1966, as Abstract 37.
2. P. Wang, U. S. G. Res. Rep, Ad 601343 April 1964.
3. R. Nuttall, *This Journal*, **111**, 317 (1964).
4. W. H. Shepherd, *This Journal*, **112**, 988 (1965).
5. (a) JANAF Thermochemical Data Tables, Compiled by Dow Chemical Co.; (b) Thermodynamic Properties of the Elements, Stull and Sinke, Advances in Chemistry Series No. 8 (1956).
6. M. J. Coupland, *Proc. Phys. Soc.*, **73** (4), 577 (1959).
7. S. E. Bradshaw and A. I. Mlavsky, *J. Electronics*, **2**, 134 (1956).

## Effects of Back-Melting on the Dislocation Density in Single Crystals: GaSb

R. S. Mroczkowski,<sup>1</sup> A. F. Witt,\* and H.C. Gatos\*

Department of Metallurgy and, Center for Materials Science and Engineering, Massachusetts Institute of Technology, Cambridge, Massachusetts

## ABSTRACT

A pronounced reduction in dislocation density was observed in gallium antimonide single crystals after partial back-melting and controlled resolidification. The distribution of dislocations in the parent crystals and regrown sections was studied by etch-pit counting and x-ray topography (Lang method). The observed reduction in dislocation density was explained in terms of the dislocation distribution in the parent crystal and the geometry and thermal conditions of the back-melting process.

A back-melting process has been employed recently for studying the formation of heterojunctions and mixed single crystals of different III-V compounds (1, 2). Since the geometry of the resolidification process and the associated thermal conditions differ from those encountered in Czochralski and other crystal growth techniques it was decided to study the influence of these contrasting growth conditions on the crystalline perfection of the regrown material. Accordingly, single crystal wafers of gallium antimonide were partially melted and regrown with the unmelted rest of the original wafer acting as substrate. These types of conditions are similar to those encountered in the traveling solvent method (3). This paper reports some interesting results concerning density and distribution of dislocations in regrown single crystal wafers.

## Experimental Procedure

Gallium antimonide wafers (1.5 x 2 x 3 mm) with their large faces of (110), (211), and (111) orientation, were chemically etched in a modified CP-4 etchant (5HNO<sub>3</sub> conc.; 3CH<sub>3</sub>COOH; 3HF 48%) and placed between two carbon strip heaters (6 x 1 x 70 mm at a horizontal separation of 10 mm) with independent power supplies. The heaters were installed in a glass chamber in which the back-melting experiments were conducted in a hydrogen atmosphere of about 10 mm Hg overpressure. The back-melting and resolidification processes were observed through an externally mounted binocular microscope with a long working distance objective. During the back-melting experiments the upper carbon strip was first heated to about 1200°C. The resulting temperature gradient between the heated strip and the nonheated lower strip (on which the gallium antimonide was placed) just initiated back-melting of the wafer. By means of a controlled current through the lower strip the temperature gradient between the strips could be adjusted in such a way that the location of the solid-melt interface could be kept in any desired position and could also

be moved at controlled rates. In this way any portion of the gallium antimonide wafer could be melted. After the appropriate region was melted, controlled resolidification was initiated by reversing the melting procedure, i.e., the current through the lower strip was reduced at a rate appropriate for the desired resolidification rate; the actual regrowth rates varied between 1 and 10 in./hr. It was observed that within this range the structural characteristics of the regrown material were independent of the actual growth rate.

The density and distribution of dislocations in the parent crystal and the regrown sections were investigated by etch-pit counting and by x-ray topography employing the Lang technique (4). Etch-pit counting was carried out in a plane normal to the regrowth axis after the wafer was mechanically polished with 0.03 $\mu$  alumina and etched with the above mentioned modified CP-4. The etch-pit distribution was examined by light microscopy under the appropriate magnification. X-ray topography was performed using a Lang camera and an x-ray microfocus unit. Standard Lang transmission geometry was employed. In all instances Ag, K- $\alpha$  radiation was used and the images recorded on nuclear emulsions.

## Results

In a series of experiments gallium antimonide wafers were subjected to back-melting and regrowth with the solid-melt interface normal to the <211> direction. Since the semiconductor melt under the given experimental conditions is only subjected to gravity and surface tension it always assumes the shape of a distorted spherical segment. Because of volume expansion during solidification the regrown single crystals assume a dome-like shape. The regrown wafers were mounted in plastic, polished to expose a (111) plane, and finally etched to reveal dislocations and other defects.

Figure 1 is a photomicrograph of an etched single crystal in which the upper part has been regrown. The lowest position of the crystal-melt interface during the back-melt process can readily be recognized as a curved remelt line which sharply delineates areas

\* Electrochemical Society Active Member.

<sup>1</sup> Present address: RCA Research Laboratories, Somerville, New Jersey.

of high and rather low dislocation densities. Etch-pit counting revealed a varying dislocation density ranging from  $10^3$  to  $10^4$  dislocations per square centimeter in the parent crystal below the remelt line and a dislocation density of close to zero in the adjacent regrown section above the remelt line. Not shown in Fig. 1 is the uppermost part of the regrown crystal in which the dislocation density is very high (due to very rapid solidification), exceeding that of the parent crystal. Since the detection of dislocations in the form of etch-pits requires that individual dislocations intersect the surface under consideration, the absence of dislocation etch-pits in the regrown section could not be considered as indicating complete absence of dislocations.

A (220) x-ray topograph of a regrown crystal of the above series of experiments is shown in Fig. 2. In this topograph the regrown section can be readily differentiated from the parent crystal by the drastic change in dislocation density. However, the dislocation density in the upper part is not as low as appears in Fig. 1. Most of the dislocations in the regrown section are

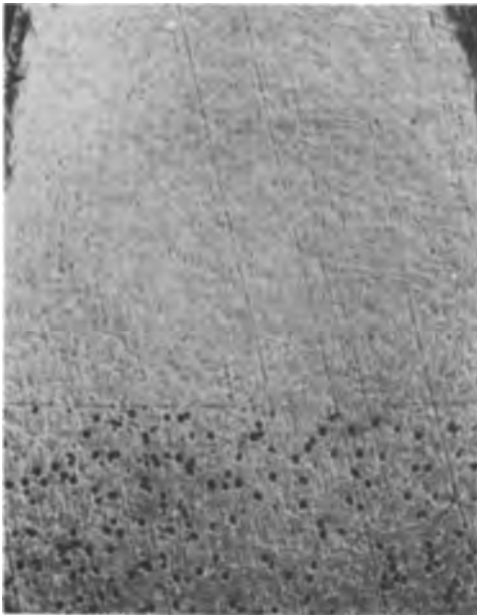


Fig. 1. Dislocations in parent crystal and regrown section of a gallium antimonide wafer. The curved remelt line separating the two regions is clearly visible. The (111) plane shown is normal to the regrowth axis. Magnification ca. 105X.



Fig. 2. X-ray topograph of partially regrown gallium antimonide wafer. The regrown region exhibits a marked decrease in the dislocation density; Ag,  $K\alpha$  radiation; (220) reflection. Magnification ca. 20X.

observed to run nearly parallel to the regrowth axis and do not intersect the (111) plane on which the etch-pit count was performed.

The relationship between the dislocations in the parent gallium antimonide and the regrown crystals was further investigated by successively regrowing the same wafer in two perpendicular directions, as indicated in Fig. 3. In the first stage of this experiment the section left of the remelt line A (Fig. 3a) was regrown. The wafer was subsequently ground flat on one side, rotated on the heating strip and again remelted perpendicular to the original remelt direction, thus producing the remelt line B (Fig. 3a) on the regrown wafer. A topograph of such a twice regrown single crystal is shown in Fig. 3b. In region I, the unmelted parent crystal, the dislocation density is very high. Regions II and III which were both regrown only once exhibit the previously discussed reduction in dislocation density. Region IV which was twice regrown in different directions shows that the second regrowth process led to a further reduction in the density of dislocations. The very high dislocation density observed in the upper part of Fig. 3b is the result of turbulent, rapid growth which is always observed in the final stages of the resolidification process.

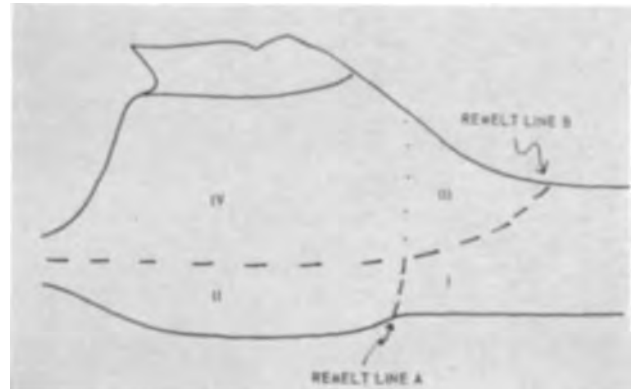


Fig. 3a. Schematic diagram of a twice regrown gallium antimonide wafer corresponding to x-ray topograph of Fig. 3b. A and B are the remelt lines resulting from the first and second back-melting experiments respectively. Region I represents the original parent crystal; region II was once regrown during the first back-melt experiment, region III was once regrown during the second back-melt experiment. Region IV was regrown twice in different directions.

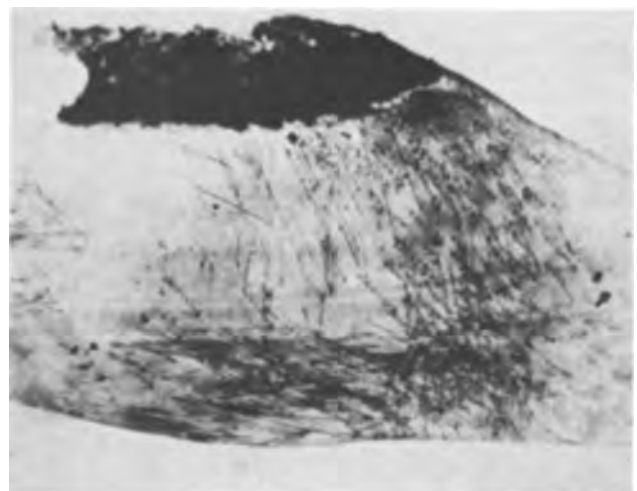


Fig. 3b. X-ray topograph of twice regrown gallium antimonide wafer (corresponding schematic is shown in Fig. 3a). Note the very low dislocation density in the twice regrown section (area IV in Fig. 3a) Ag,  $K\alpha$  radiation; (220) reflection. Magnification ca. 25X.



Fig. 4. X-ray topograph of a gallium antimonide wafer exhibiting a high density of dislocations. Two sets of dislocations can be observed. One set of rather long dislocations appears aligned along the  $\langle 111 \rangle$  growth direction, the other consists of a network of dislocation loops. Ag,  $K\alpha$  radiation (220) reflection. Magnification ca. 40X.

### Discussion

In crystals grown from the melt two types of dislocations are usually observed. The dislocations of the one type propagate from the seed and are generally long and straight. In the second type belong dislocations which are introduced by thermal stresses encountered in crystal growth systems. These latter dislocations assume complex shapes [tangles (5)] and frequently appear as loops or partial loops. They can readily be differentiated from the long and rather straight dislocations previously discussed. The density of dislocations ( $\rho$ ) caused by thermal stress, has been related to the deviation from the average thermal gradient (6),  $\delta\Delta T$  in the growth system as follows

$$\rho = \frac{1}{a} \alpha \delta\Delta T$$

where  $a$  is the lattice constant and  $\alpha = da/dT$  the coefficient of thermal expansion.

While the exact origin of individual dislocations cannot be determined unambiguously because of their complex movement under different stresses, some pertinent observations can be made. Figure 4 is a topograph of a poor quality gallium antimonide single crystal exhibiting a very high dislocation density. Many of the dislocations are straight and aligned along the  $\langle 111 \rangle$  growth direction. On the other hand, a large number of randomly oriented complex shaped dislocations can be observed which are apparently due to the presence of thermal and solidification stresses. The observed reduction of the dislocation density in partially regrown single crystal wafers is attributed to two factors. First all dislocations which originate and terminate within the region subjected to back-melting are eliminated and are not regenerated during the resolidification process. Second, the small size of the wafer and the absence of constraints on the solid-liquid system result in resolidification under significantly reduced thermal and mechanical stress (com-

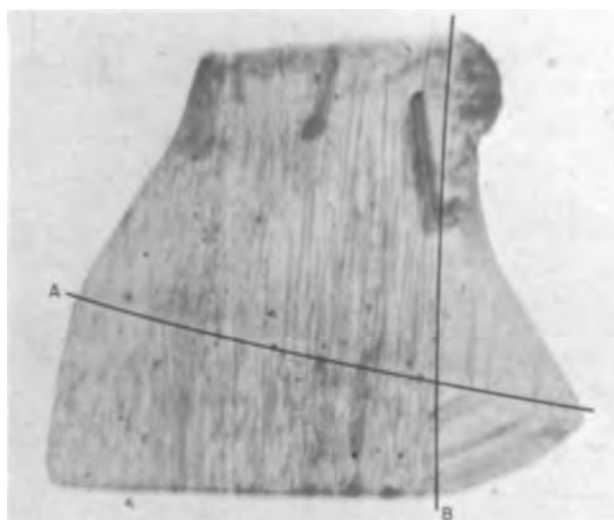


Fig. 5. X-ray topograph of a twice remelted gallium antimonide wafer of low dislocation density. Back-melting in the direction of the original growth axis (remelt line A) resulted in a material exhibiting essentially the original dislocation density. The second remelt experiment (from right to left) normal to the original growth axis (remelt line B) led to a noticeable reduction in dislocation density. Ag,  $K\alpha$  radiation, (220) reflection. Magnification ca. 25X.

pared to the conditions in Czochralski pulling systems) and are responsible for the absence of stress induced dislocations. The dislocation density in the regrown region is determined by the propagation of dislocations present in the parent crystal with a component along the regrowth direction. Apparently the orientation of the propagated dislocations is largely dependent on their orientation in the parent crystal. In this regard the experiment illustrated in Fig. 5 is of particular interest. Here regrowth along the original growth axis did not noticeably reduce the dislocation density whereas regrowth normal to the growth direction of the parent crystal resulted in substantial reduction in dislocation density.

The type of solidification discussed here under the virtual absence of thermal stresses could prove most useful for the detailed study of dislocation elimination and propagation.

### Acknowledgment

This work was supported by the Advanced Research Projects Agency under Contract SD-90.

Manuscript received Oct. 23, 1967; revised manuscript received ca. Dec. 3, 1967.

Any discussion of this paper will appear in a Discussion Section to be published in the December 1968 JOURNAL.

### REFERENCES

1. D. E. Hinkley, R. H. Rediker, and M. C. Lavine, *Appl. Phys. Letters*, **5**, 110 (1964).
2. R. S. Mroczkowski, M. C. Lavine, and H. C. Gatos, *Trans. AIME*, **233**, 456 (1965).
3. W. G. Pfann, *ibid.*, **203**, 961 (1955); A. I. Mlavski and M. Weinstein, *J. Appl. Phys.*, **34** [9], 2885 (1963).
4. A. R. Lang, *Acta Met.*, **5**, 358 (1957).
5. A. E. Jenkinson and A. R. Lang, "Imperfections in Crystals," p. 471, Interscience Publisher, Inc., New York (1962).
6. J. Friedel, "Dislocations," p. 205, Addison-Wesley Press (1964).



# Diffusion from a Plane, Finite Source into a Second Phase with Special Reference to Oxide-Film Diffusion Sources on Silicon

A. E. Owen<sup>1</sup> and P. F. Schmidt\*<sup>2</sup>

Westinghouse Research and Development Center, Pittsburgh, Pennsylvania

## ABSTRACT

A model is set up for the diffusion from a source of finite thickness into an adjacent second phase of semi-infinite extent. With the principal assumption of no diffusion in or out of the system, a solution is obtained for the diffusion profile in the second phase. It is also assumed that the diffusion coefficients are independent of concentration, but segregation at the inter-phase boundary is taken into account and so also, to a first approximation, is the possibility of precipitation or reaction at the interface. The model predicts a change in the profile from an ERFC to Gaussian shape depending on whether the diffusion length in the source is much less than or much greater than its thickness, i.e., as the diffusion time increases.

The theoretical predictions of the model are compared to tracer diffusion results from phosphorus doped anodic oxide sources on silicon. These experiments were carried out with unprotected (no undoped SiO<sub>2</sub> film covering the source) oxide sources in a sealed quartz tube. Thus the phosphorus initially lost by out-diffusion could not escape from the system altogether, and it is shown that these conditions approximated the boundary condition of no out diffusion. The diffusion results obtained in this way are in agreement with the model.

In recent years interest has grown in the use of doped oxide films as diffusion sources for device fabrication in semiconductors (1-6). These sources can be deposited by a variety of means, such as anodization, pyrolytic decomposition, or reactive sputtering, and offer the advantages of control of the dopant concentration and of low deposition temperatures which do not alter pre-existing diffusion profiles in the semiconductor substrate. Anodic oxidation also provides very accurate control of the oxide thickness and the possibility of depositing the diffusion source only in the windows of a diffusion mark. Electrophoretic deposition of doped oxides (7) is interesting from the materials point of view since it is practically unlimited in its scope as to substrates or dopants. The present paper solves the diffusion equations for the two-phase system: very thin oxide source/semi-infinite substrate, subject to the idealized assumptions of no loss of dopant to the ambient by out-diffusion and of concentration independent diffusion coefficients. Segregation coefficients at the oxide/semiconductor interface, as well as precipitation or compound formation at this interface, however, are taken into account.

The concentration dependence of phosphorus<sup>3</sup> diffusivity in silicon is well known (8-10), and could be taken into consideration in the calculations; very little, however, is known about the strong concentration dependence of phosphorus diffusivity in phosphosilicate glass and in phosphorus doped SiO<sub>2</sub> (11). In the present paper the diffusion coefficients are regarded as concentration independent. This assumption may not be as severe a limitation on the usefulness of the theory as it might appear at first glance, precisely because of the very strong concentration dependence of diffusivity in the oxide. The diffusivity is relatively high in the phosphosilicate composition range (20) but drops sharply just outside this range to very small values of diffusivity in pure SiO<sub>2</sub>. Probably very little phosphorus is supplied by the oxide source to the sil-

icon substrate after the diffusivity in the oxide has become strongly concentration dependent due to the beginning of depletion of the source; from this point on the amount and profile of phosphorus already in the silicon will determine the further development of the profile in the silicon. The strong concentration dependence of diffusivity in the oxide will thus show up mostly as a reduced effective concentration of dopant originally contained in the oxide source.

While the theory proposed is still only an approximation, it is a step closer to being exact than existing theories since it does not treat the oxide source as an infinitely thin plane source. For very short diffusion times, as long as the oxide source is not yet being depleted, it will act like an infinite source, and the resulting profile in the substrate will be a complementary error function (ERFC); for long diffusion times, it may be regarded as an infinitely thin plane source. The effect of the diffusion parameters (oxide thickness, ratio of diffusivities in oxide and substrate, segregation coefficient, and compound or precipitate formation) on the shape of the diffusion profile as a function of time forms the main body of this discussion. It is easy to show that the important parameter, which governs the transition from ERFC to Gaussian is the diffusion length for the impurity in the oxide, i.e.,  $\sqrt{D_1 t}$  (where  $D_1$  is the diffusion coefficient for the impurity in the oxide, and  $t$  is the diffusion time).

## Model and Solution of the Diffusion Equations

To regard the anodic oxide film as equivalent to a plane source is to assume that the impurity can diffuse across the oxide in times short compared with the diffusion time. The validity of such an assumption would obviously depend on the relationship between the diffusion coefficient in the oxide, oxide thickness, and diffusion time. Such an approximation is not expected to be appropriate in all circumstances therefore, and in any more general analysis it is necessary to consider a two-phase system taking into account the properties of the oxide film. The model adopted is shown schematically in Fig. 1, in which phase 1 represents the oxide and phase 2 the silicon. The oxide has a thickness  $l$  (measured negatively from zero), a concentration-independent diffusion coefficient  $D_1$

\* Electrochemical Society Active Member.

<sup>1</sup> Present address: Department of Electrical Engineering, University of Edinburgh, Scotland.

<sup>2</sup> Present address: Bell Telephone Laboratories, Inc., Allentown, Pennsylvania.

<sup>3</sup> The experimental work included in this paper deals exclusively with phosphorus; in principle, the theory applies to the diffusion of any other dopant as well.

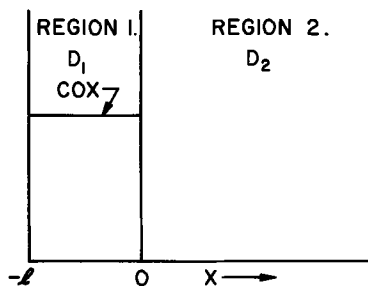


Fig. 1. Theoretical model for the anodic oxide diffusion source. Region 1 represents oxide with uniform initial concentration of phosphorus  $C_{ox}$  and diffusion coefficient  $D_1$ . Region 2 represents silicon with zero initial concentration of phosphorus and diffusion coefficient  $D_2$ .

for the impurity and an initial uniform<sup>4</sup> concentration of impurity  $C_{ox}$ . The silicon extends from zero to infinity, has a zero initial impurity concentration and a concentration-independent diffusion coefficient for impurity  $D_2$ . The diffusion equations for the system of Fig. 1 are therefore

in region 1

$$\frac{\partial^2 C_1}{\partial x^2} - \frac{1}{D_1} \frac{\partial C_1}{\partial t} = 0 \quad [1]$$

in region 2

$$\frac{\partial^2 C_2}{\partial x^2} - \frac{1}{D_2} \frac{\partial C_2}{\partial t} = 0 \quad [2]$$

and these have to be solved simultaneously with the initial conditions

$$C_1 = C_{ox}; -l < x < 0, t = 0 \quad [3]$$

$$C_2 = 0; x > 0, t = 0 \quad [4]$$

The boundary conditions have been chosen as follows

$$\text{At } x = -l, \frac{dC_1}{dx} = 0 \quad [5]$$

At

$$x = 0, D_1 \frac{dC_1}{dx} = D_2 \frac{dC_2}{dx} \quad [6]$$

and

$$C_1 = mC_2 \quad [7]$$

At

$$x = \infty, C_2 = 0 \quad [8]$$

Boundary conditions [6], [7], and [8] are straightforward and physically reasonable. Condition [6] simply expresses the continuity of flux and [7] the segregation of impurity at the interface, with a segregation coefficient  $m$ . Boundary condition [5], however, which requires that there is no flow of impurity from the oxide to the ambient or *vice versa* requires particular consideration. At first sight this would seem to be an unrealistic condition, but there are indications that it is a fair approximation under the conditions of the experiments described in ref. (1), in which unprotected (cf. below) oxide sources were used in conjunction with sealed quartz diffusion tubes of small volume; in the case of protected oxide sources [see ref. (2)], boundary condition (5) holds almost exactly. Evidence for these points will be mentioned below.

Surprisingly, a complete solution of the diffusion problem set out in Fig. 1 and Eq. [1] to [8] does not appear to have been given before. Carslaw and Jaeger (12) quote ref. (13) for the temperature at the interface of a hot magmatic intrusion into a cold rock (*i.e.*, a parameter corresponding to the concentration  $C_0$  at the silicon-oxide interface) but solutions correspond-

ing to concentration profiles are not available. It should be remarked in passing, therefore, that although the model used here is only an approximation for the oxide film diffusion source situation, it does provide an exact solution (subject to concentration-independent coefficients) to the problem of diffusion from a source sandwiched between two semi-infinite media of a second phase, *i.e.*, two of the models drawn in Fig. 1 placed back-to-back.

Using the Laplace transformation (12) the simultaneous partial differential Eq. [1] and [2] have been solved for the concentration in the phase 2,  $C_2$ , subject to the initial conditions [3] and [4] and the boundary conditions [5] to [8]. The solution is

$$C_2 = \frac{C_{ox}}{2} \frac{(1-\alpha)}{m} \left[ \sum_0^{\infty} (-1)^n \alpha^n \operatorname{erfc} \frac{(2Rln+x)}{2\sqrt{D_2 t}} - \sum_0^{\infty} (-1)^n \alpha^n \operatorname{erfc} \frac{(n+1)2Rl+x}{2\sqrt{D_2 t}} \right] \quad [9]$$

in which  $C_{ox}$ ,  $D_2$ ,  $l$ , and  $m$  have already been defined,  $t$  is the diffusion time, and  $x$  is the depth at which the concentration is  $C_2$ . The parameters  $R$  and  $\alpha$  are given by

$$R = \sqrt{(D_2/D_1)} \quad [10]$$

and

$$\alpha = \frac{(R/m) - 1}{(R/m) + 1} \quad [11]$$

For the purpose of computation Eq. [9] has been expressed in terms of dimensionless parameters

$$\frac{C_2}{C_{ox}} m = \frac{(1-\alpha)}{2} \left[ \sum_0^{\infty} (-1)^n \alpha^n \operatorname{erfc} \frac{[2(R/m)n+x/lm]}{2\sqrt{D_2 t/ml}} - \sum_0^{\infty} (-1)^n \alpha^n \operatorname{erfc} \frac{[2(R/m)(n+1)+x/lm]}{2\sqrt{D_2 t/ml}} \right] \quad [12]$$

Equation [12] has been programmed and the concentration ( $C_2/C_{ox}$ )  $m$  computed as a function of distance ( $x/lm$ ) for various values of time ( $\sqrt{D_2 t/ml}$ ) and the parameter ( $R/m$ ). The diffusion Eq. [12] has the important property that the concentration profile in the phase 2 changes shape from ERFC to Gaussian according to the relationship between the time parameter ( $\sqrt{D_2 t/ml}$ ) and the parameter ( $R/m$ ). For instance, for a given ( $R/m$ ) the profile changes from ERFC to Gaussian as the diffusion time increases and, conversely, for a constant time ( $\sqrt{D_2 t/ml}$ ) the profile changes from Gaussian to ERFC as ( $R/m$ ) increases. In actual practice it is to be expected, of course, that ( $R/m$ ) remains constant while the diffusion time is varied, but for convenience in illustration the change in shape of the profile is shown in Fig. 2 for a constant ( $\sqrt{D_2 t/ml}$ ) = 5 with ( $R/M$ ) varying. Also plotted in Fig. 2 are points corresponding to true Gaussian and ERFC curves, and it will be noticed that the profile of Eq. [12] is approximately intermediate between Gaussian and ERFC when

$$\frac{\sqrt{D_2 t}}{ml} = \frac{R}{m} \quad [13]$$

Substituting for  $R$  ( $=\sqrt{D_2/D_1}$ ) and rearranging gives the set of conditions: if

$$\sqrt{D_1 t} < l, \text{ profile tends to ERFC} \quad [14a]$$

$$\sqrt{D_1 t} \approx l, \text{ profile is intermediate} \quad [14b]$$

$$\sqrt{D_1 t} > l, \text{ profile tends to Gaussian} \quad [14c]$$

Thus the shape of the profile in the phase 2 depends, in fact, only on the diffusion time and the characteris-

<sup>4</sup>It is shown in ref. (1) that the initial distribution of phosphorus in an anodically grown oxide is, in fact, practically uniform.

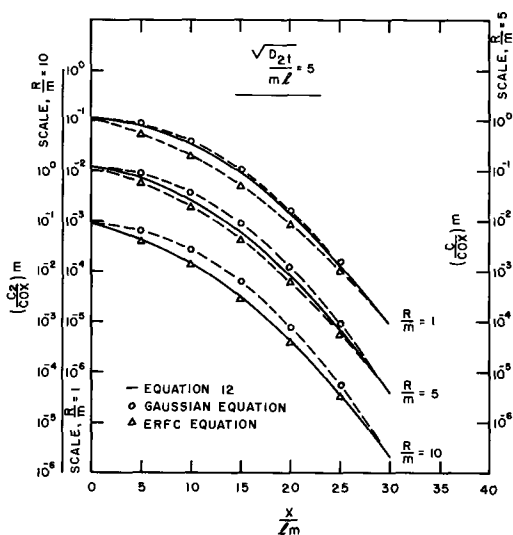


Fig. 2. Illustrating the change from Gaussian to ERFC form of the profile predicted by Eq. [12] as  $R/m$  varies at constant time,  $(\sqrt{D_2t/ml}) = 5$ .

tics of phase 1 (the oxide). When the diffusion length of impurity in the oxide,  $\sqrt{D_1t}$ , is much less than the thickness of the oxide  $l$  the oxide tends to behave as an infinite source (ERFC), but when the diffusion length is much greater than the thickness of the oxide, it tends to behave as an infinitely thin plane source (Gaussian). Physically these conditions are perfectly reasonable and could have been anticipated from the remarks made at the beginning of this section. Another way of looking at this is to regard the "effective" thickness of the oxide as depending upon time and, through the diffusion coefficient, on temperature.

In device fabrication the impurity surface concentration in the silicon,  $C_o$ , is an important parameter, and this has been plotted in a reduced form in Fig. 3. The surface concentration expressed as  $[(C_o/C_{ox})m]$  is given as a function of time,  $(\sqrt{D_2t/ml})$ , for various values of the parameter  $(R/m)$ . The surface concentration can be written analytically by putting  $(x/lm) = 0$  in Eq. [12] and simplifying, leading to

$$\frac{C_o}{C_{ox}} M = \frac{(1-\alpha)^2}{2} \sum_{n=1}^{\infty} (-\alpha)^{n-1} \operatorname{erf} \frac{nl}{\sqrt{D_1t}} \quad [15]$$

This equation shows that the time variation of the surface concentration depends only on the diffusion time and the characteristics of the oxide. At a given value of  $(R/m)$  the surface concentration is independent of time for very small values of time; in this region the

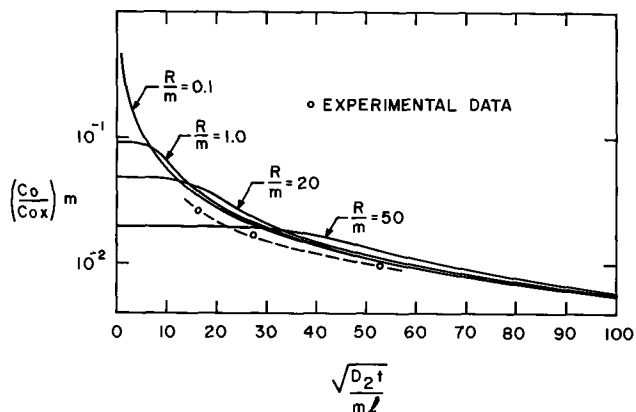


Fig. 3. Surface concentration as a function of time for different values of  $R/m$  according to Eq. [12]. Also shown for comparison are some experimental points.

oxide will behave as an infinite source. As the time parameter  $(\sqrt{D_2t/ml})$  approaches  $(R/m)$  the surface concentration begins to decrease slowly at first and then more rapidly when  $(\sqrt{D_2t/ml}) = (R/m)$ . When  $(\sqrt{D_2t/ml}) \gg (R/m)$  the surface concentration decreases linearly with the inverse of  $(\sqrt{D_2t/ml})$ , and in this region the oxide behaves as an infinitely thin plane source. Note also that in this region the surface concentration depends only slightly on  $(R/m)$  whereas in the ERFC region it depends strongly on  $(R/m)$ .

The bulk of the work reported in ref. (1), (2), and (14) is concerned with the use of phosphorus-doped anodic oxide films as diffusion source. In early diffusion experiments with P-32 labeled phosphorus, sectioning of the silicon after diffusion revealed the presence of a sharp spike of phosphorus within the first 1-2,000Å of the silicon surface. The material in this spike was subsequently identified as silicon phosphide precipitates by Schmidt and Stickler (15), who also give some examples of the diffusion profile in the Si. Later work (16) showed that precipitates of SiP forming during the initial stages of diffusion on silicon surfaces of any orientation (17, 18) tend to become especially large on (110) surfaces and do not disappear even at long diffusion times; the phosphorus incorporated into these precipitates is lost for the diffusion process. Since the silicon bars, on which experimental work reported here was carried out, had their large surfaces (110) oriented, the SiP precipitates must have formed readily, and this fact presumably accounts for the shift to lower concentrations of the phosphorus diffusion profile observed in the early tracer runs (cf. Fig. 3).

Irrespective of the mechanism by which precipitates or compounds are formed at the interface, their formation results in a certain fraction of the phosphorus flux crossing the oxide/silicon interface being retained at the interface. If such a process takes place, the boundary condition [6] for flux continuity across the oxide/silicon interface must be modified; assuming that the fraction  $K$  of flux retained at the interface is a constant, this boundary condition becomes

$$D_1 \frac{dC_1}{dx} + K D_1 \frac{dC_1}{dx} \Big|_{x=0} = D_2 \frac{dC_2}{dx} \quad [16]$$

Solving the same equations with the boundary condition [16] in place of [6] again leads to Eq. [12] but now the parameter  $\alpha$  is given by

$$\alpha = \frac{(R/m) - (1-K)}{(R/m) + (1-K)} \quad [17]$$

Thus, when  $K$  is zero (no spike formation) Eq. [12] is unchanged as it obviously should be; when  $K = 1$  (all the phosphorus retained at the interface)  $\alpha = 1$  and  $C_2 = 0$ , i.e., there is no diffusion into the silicon, again as expected. The effect of  $K$  in Fig. 3 is to make  $(R/m)$  appear larger than it would otherwise be in the absence of spike formation, i.e., to lower the curves and reduce their slope slightly.

### Discussion: Relevance to Anodic Oxide Diffusion Sources

The theoretical work described herein was initiated during the early stages of development of doped anodic oxide sources (1), when nondoped anodic oxide films, grown on top of the doped source<sup>5</sup> as a protection against out-diffusion, were not yet available. Subsequently it was found that these protective oxide covers, a few hundred angstroms thick, act as complete barriers to out-diffusion into the ambient for any time-temperature diffusion conditions of practical interest (2). This masking ability is, of course, a consequence of the very strong concentration dependence

<sup>5</sup>The anodic formation of nondoped oxide on top of a doped oxide is possible because the anodization of silicon proceeds by cation migration (1).

of phosphorus diffusivity in pure  $\text{SiO}_2$ . In the heavily doped source, on the other hand, the phosphorus diffusivity is relatively high, so that most of the phosphorus has diffused into the silicon before the protective oxide cover is penetrated by phosphorus diffusing outward.

Oxide diffusion sources with protective oxide covers thus come very close to the boundary condition [5] of no diffusion across the oxide/ambient interface; the amount of phosphorus diffusing into the pure  $\text{SiO}_2$  cover is negligible compared to the amount diffusing into the Si substrate. Unfortunately, the experimental work described in ref. (2) was oriented toward process development, and the diffusion times chosen were either not short enough to demonstrate the transition from an ERFC to a Gaussian profile, or not long enough to show the predicted deviation of junction depth from a square-root of time dependence at long diffusion times. This became clear only after conclusion and evaluation of the tracer results; while the results obtained in [2] are not at variance with the theory proposed here, they could not be used to prove the correctness of the theory.

The only tracer work in which very short and very long diffusion times were used are the early tracer runs, made with unprotected oxide sources in sealed small quartz tubes. In these experiments there was an initial very fast loss of phosphorus from the outer surface of the oxide; however, this phosphorus could not escape from the sealed system, and for longer diffusion times there actually occurred some reabsorption of phosphorus from the gas phase by the oxide. The amount of phosphorus reabsorbed was, however, small compared to that left in the system oxide + silicon after the initial fast out-diffusion, and for practical purposes the assumption of "no out-diffusion" appears to be valid after the first 5-10 min of heat-treatment, as will be discussed in more detail below.

It should be noted that the experimental results are quoted only to show that they are not in disagreement with the proposed theory; they are not assumed to prove its validity. Specifically, it should also be noted that the results quoted are not representative of the potential usefulness of doped oxide sources; for practical applications, the reader is referred to ref. (1-6).

Evidence for the approximate validity of boundary condition [5] in the experimental work (unprotected oxide sources about  $1500\text{\AA}$  thick; doping level in the oxide up to  $4 \times 10^{21}/\text{cc}$ ; argon filled quartz tubes; diffusion temperatures of typically  $1175^\circ\text{C}$ ) is then given in Fig. 4 where the amount of phosphorus (in atoms/ $\text{cm}^2$ ) in the silicon, that which remains in the oxide, and the total in oxide plus silicon, is plotted as a function of the square-root of time at  $1175^\circ\text{C}$ . The data of Fig. 4 were obtained from experiments using P-32 as a tracer. Note that the vertical ordinate has been compressed and should, on this scale, extend to three or four times the height shown. These data show that during the very early stages of diffusion there is an extremely rapid loss of phosphorus from the oxide. At times still short compared with the experimental diffusion times, this out-diffusion apparently ceases, however, and eventually there is actually an increase in total phosphorus with time, i.e., there is some in-diffusion. The increase at longer diffusion times, however, is relatively small. The assumption of no out-diffusion implicit in boundary condition (5) therefore appears to be experimentally justifiable at least for comparatively long diffusion times. Support for this was provided by another experiment made under similar conditions in which the phosphorus in the silicon and oxide was measured for diffusion times between 5 and 90 min (in increments of 5 min), and it was found that after the first 5-10 min the total amount of phosphorus in oxide plus silicon became practically constant, i.e., a condition equivalent to Eq. [5].<sup>6</sup> Yet fur-

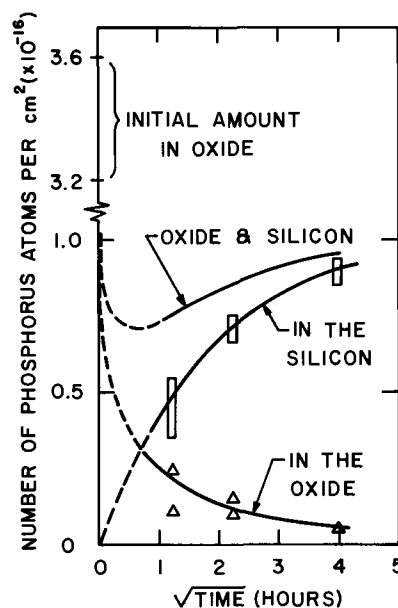


Fig. 4. Amount of phosphorus found in the silicon, the amount remaining in the oxide, and the total in oxide and silicon as a function of diffusion time.

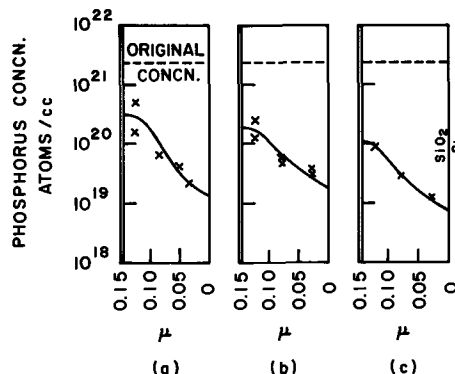


Fig. 5. Phosphorus profiles in oxide after diffusion: (a)  $1\frac{1}{2}$  hr at  $1175^\circ\text{C}$ ; (b) 5 hr at  $1175^\circ\text{C}$ ; (c) 15  $9/10$  hr at  $1175^\circ\text{C}$ .

ther supporting evidence is to be found in the phosphorus profiles in the oxide, determined after diffusion, by etching oxide away in a step-wise fashion, and counting the radioactive P-32 removed. Three such profiles are shown in Fig. 5; in each case the oxide was grown by the method of ref. (1), to a thickness of  $1450\text{\AA}$  and was found to have a phosphorus concentration before diffusion of  $2.2\text{--}2.5 \times 10^{21}$  atoms/ $\text{cm}^3$ . The original phosphorus concentration is shown by the horizontal lines in Fig. 5. Figures 5(a), 5(b), and 5(c) correspond to diffusion times of 1.5, 5, and 15.9 hr at  $1175^\circ\text{C}$  in an argon-filled sealed quartz tube. The data of Fig. 5 are not very accurate, due to some nonuniformity in the local dissolution rate of the oxide, and the profile has deliberately been drawn in horizontal at the outer surface to conform with boundary condition [5], but at least they fairly conclusively indicate a situation corresponding to no out-diffusion. The effective concentration of phosphorus in the oxide,  $C_{ox}$  will, of course, be less than that initially present. According to the data of Fig. 4 about 80% of the original phosphorus is lost from the oxide-silicon system and consequently in the samples of Fig. 5, for instance,  $C_{ox}$  would be approximately  $5 \times 10^{20}$  atoms of phosphorus  $\text{cm}^{-3}$ , as indicated.

The fact that the phosphorus concentration at the outer surface of the oxide remained high for all diffusion times is undoubtedly due to the sealed tube operation; it would not have remained high in an open flow system. Diffusion of phosphorus into the dense quartz of the tube walls is very slow, so that out-

<sup>6</sup> The authors are indebted to their colleague, T. W. O'Keefe, for carrying out these measurements.

diffusion will have practically stopped as soon as saturation of the gas phase and internal tube surfaces with  $P_2O_5$  occurred. Eventually some of the phosphorus pentoxide on tube walls and in the gas phase becomes available for back-in-diffusion as the concentration in the oxide source drops due to diffusion into the Si substrate.

Note that the diffusion must be carried out in an inert ambient: diffusion in air would lead to the formation of new oxide at the  $SiO_2/Si$  interface, and to a much more complicated situation.

It is not quite clear which factor is mostly responsible for the approximate constancy of the total amount of phosphorus in oxide plus silicon after the first 5-10 min of heat-treatment. It may be due to a relatively slow transport of phosphorus across the outer oxide surface due to a shallow diffusion gradient, but it is also possible that the outer surface of the oxide underwent a drastic structural change during the initial stage of rapid out-diffusion of phosphorus, and that the diffusivity of phosphorus in this surface layer became strongly different from its initial value.

An assessment of Eq. [12] can be obtained from a comparison of predicted junction depths and surface concentrations with those obtained experimentally. The samples of Fig. 5, for instance, were prepared on 2 ohm-cm p-type material, and gave the junction depths plotted on a reduced scale, as a function of time, in Fig. 6. In obtaining this figure the diffusion coefficient of phosphorus in silicon at 1175°C was taken to be  $10^{-12}$  cm<sup>2</sup>/sec (19), oxide thickness  $l = 1450\text{Å}$ , and  $m$  was taken as 0.3. (In six samples  $m$  was found experimentally to vary between 0.2 and 0.4 with a mean of approximately 0.3). From the data of Irvin (20) the base concentration of 2 ohm-cm p-type silicon is  $7.00 \times 10^{15}$  atoms/cc and thus, at the junction, the dimensionless concentration parameter of Eq. [12] has a value

$$\frac{C_B}{C_{ox}} m \approx 4 \times 10^{-6}$$

where  $C_{ox}$  has been given the effective value for the samples of Fig. 5 (i.e.,  $5 \times 10^{20}$  atoms/cc) and  $C_B$  is the concentration at the junction. Predicted values for the junction depth were then obtained graphically by plotting  $(C/C_{ox})m$  vs. the reduced depth  $x/lm$  for various values of the time parameter  $\sqrt{D_2t/ml}$  at particular values of  $(R/m)$ , and reading off the depth corresponding to the above reduced concentration. Theoretical curves obtained in this way for  $(R/m)$  equal to 10 and 20 are also drawn in Fig. 6, and the

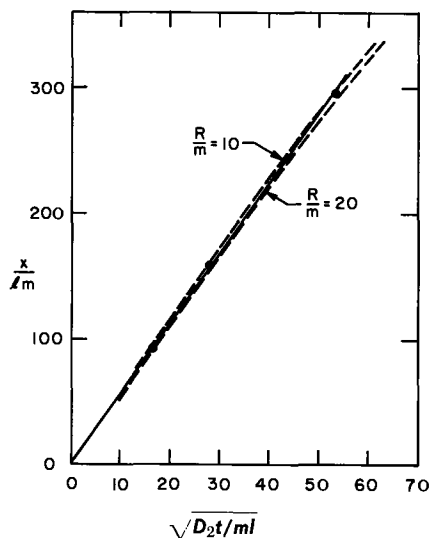


Fig. 6. Junction depths as a function of time in terms of the parameters of Eq. [12]. Comparison with the predictions of Eq. [12] with  $(R/m) = 10$  and 20 and base concentration corresponding to  $(C/C_{ox})m \approx 4 \times 10^{-6}$ .

experimental points fall roughly between these two curves. Two features of Fig. 6 should be noted in passing. First, the theoretical curves begin to deviate from the linear dependence on square-root of time and at longer diffusion times this deviation becomes even more marked. And second, for  $(R/m)$  values in this range the junction depth-time relationship is not very sensitive to  $(R/m)$ .

Now according to Sah, Sello, and Tremere (21)  $R$  is very nearly 3 at temperatures of 1100° and 1150°, but for an unspecified amount of phosphorus in the oxide. A value of  $R = 3$  at 1175°C would, therefore, seem reasonable and hence, using the value of  $m = 0.3$ , quoted above

$$R/m = 10$$

The experimental points plotted in Fig. 6 suggest that  $(R/m)$  is a little larger than this, say about 15, but the nature of the comparison is such that this discrepancy is hardly significant, and the experimental data can be considered consistent with the model. Thurston, Tsai, and Kang (11) report, however, that  $R$  is rather sensitive to the amount of phosphorus in the oxide and also possibly, depending on the actual concentration, on temperature. In the present experiments the oxide contained about 5 w/o (weight per cent) of phosphorus and from the data of Thurston *et al.* a value in the region of 5 would be appropriate for  $R$  at 1175°C, whence

$$R/m \approx 16$$

This agrees rather well with the experimental results of this paper although it must be pointed out that according to ref. (11) much larger values of  $R$ , and hence  $R/m$ , are possible. Thus, the value of  $(R/m) = 10$  would seem to represent a lower limiting value, and without knowing precisely what is the appropriate concentration of phosphorus in the oxide a more definite estimate cannot be made.

The experimental surface concentrations for the same samples are plotted, again in dimensionless form, in Fig. 3. As anticipated earlier, these samples, like those of ref. (15), showed a "spike" in the phosphorus concentration at the surface; this spike was neglected in arriving at the measured surface concentrations plotted in Fig. 3. The experimental points show about the right time dependence for a value of  $(R/m)$  in the range 10 to 20 implied by the results of Fig. 6 and tentatively suggested by the data discussed above. In magnitude, however, the points are somewhat lower than expected. The reasons for this are almost certainly connected with the formation of the spike for, as already shown, the removal of a fraction of the flux at the interface would have the effect of lowering the theoretical curves of Fig. 3. Qualitatively such an adjustment would bring the experimental points into better agreement with the predictions.

Finally, it should be pointed out that the trend of the experimental results presented in Fig. 3 and 6 lead one to expect that the concentration profiles in the silicon should be nearly Gaussian, especially at the longer diffusion times. As was mentioned early in this paper this is not unexpected, and the profile shape resulting from anodic oxide diffusion sources is examined in ref. (14).

### Conclusions

The solution of the two-phase diffusion problem given in this paper, exact where the diffusion coefficients are independent of concentration and out-diffusion can be neglected, may be approximately applicable to the more complex practical situation for diffusion from doped (anodic) oxides on silicon. For the samples discussed in this paper, nonprotected oxide sources diffused in a sealed tube at 1175°C, there appears to be an intermediate range of diffusion time (i.e., 1½ hr to perhaps 15 or 16 hr) in which the assumption of no-flow across the oxide-ambient interface is reasonably justified. Under these conditions sat-

atisfactory agreement is found between the predictions of the model and measured parameters such as the junction depth. In the particular samples studied here the concentration profile in the silicon is expected to be nearly Gaussian, especially at the longer diffusion times. A Gaussian profile is not always to be expected, however, and the theoretical model shows that the important quantity is the diffusion length  $\sqrt{D_1 t}$ , in the oxide. When the diffusion length is small compared with the thickness of the oxide (i.e., short diffusion times) an ERFC profile will result.

#### Acknowledgments

This work was carried out while the authors were members of the Westinghouse Research Laboratories, Pittsburgh; they are indebted to the company for providing facilities, and to several of their former colleagues for cooperation and assistance during all phases of the work. Particular thanks are due to Miss Freedman and Mr. Heath of the Mathematics Department for programming and computing the diffusion equation. Dr. O'Keefe was responsible for the out-diffusion experiment mentioned in the text and Mr. Roney assisted with the other experiments.

Manuscript received Aug. 30, 1967; revised manuscript received ca. Dec. 12, 1967.

Any discussion of this paper will appear in a Discussion Section to be published in the December 1968 JOURNAL.

#### REFERENCES

1. P. F. Schmidt and A. E. Owen, *This Journal*, **111**, 682 (1964).
2. P. F. Schmidt, T. W. O'Keefe, J. Oroshnik, and A. E. Owen, *ibid.*, **112**, 800 (1965).
3. H. Becke, D. Flatley, W. Kern, and D. Stolnitz, *Trans. Metallurg. Soc. AIME*, **230**, 307 (1964).
4. H. Kunz, D. Clerc, and D. Jahn, *Brown Boverly Rev.*, **53**, 34 (1966).
5. J. Scott and J. Olmstead, *RCA Rev.*, **26**, 357 (1965).
6. W. V. Münch, *IBM J. Res. Dev.*, **10**, 438 (1966); *Solid State Electronics*, **9**, 619 (1966).
7. Westinghouse Electric Corp., Research Lab., ASTIA Report 473801, dated November 1965.
8. E. T. Handelman, *Solid State Electronics*, **2**, 123 (1961).
9. S. Maekawa, *J. Phys. Soc. Japan*, **17**, 1592 (1962).
10. J. J. Chang, *IEEE Trans. Electron Devices*, **ED-10**, 357 (1963).
11. M. O. Thurston, J. C. C. Tsai, and K. D. Kang, ASTIA Report AD 261 201 (1961).
12. H. C. Carslaw and J. C. Jaeger, *Conduction of Heat in Solids*, 2nd Edition, p. 236 (OUP).
13. T. S. Lovering, *Bull. Geol. Soc. Amer.*, **47**, 87 (1936).
14. T. W. O'Keefe and P. F. Schmidt, To be published.
15. P. F. Schmidt and R. Stickler, *This Journal*, **111**, 1188 (1964).
16. T. W. O'Keefe, P. F. Schmidt, and R. Stickler, *ibid.*, **112**, 878 (1965).
17. E. Kooi, *ibid.*, **111**, 1383 (1964).
18. H. Garski, *Z. Naturforsch.*, **22a**, 6 (1967).
19. C. S. Fuller and J. A. Ditzenberger, *J. Appl. Phys.*, **27**, 544 (1956).
20. I. Fränz, H. Langheinrich, and K. H. Löcherer, *Telefunken-Z.*, **37**, 194 (1964).
21. J. C. Irvin, *Bell Syst. Tech. J.*, **41**, 387 (1962).
22. C. T. Sah, H. Sello, and D. A. Tremere, *J. Phys. Chem. Solids*, **11**, 288 (1959).

## The Close-Spaced Growth of Degenerate P-Type GaAs, GaP, and Ga(As<sub>x</sub>, P<sub>1-x</sub>) by ZnCl<sub>2</sub> Transport for Tunnel Diodes

P-A. Hoss,<sup>\*1</sup> L. A. Murray, and J. J. Rivera<sup>2</sup>

*Electronic Components and Devices, Radio Corporation of America, Somerville, New Jersey*

#### ABSTRACT

A close-spaced growth system is described in which zinc chloride is used as both the transport agent and the doping source to grow GaAs, GaP, and Ga(As<sub>x</sub>, P<sub>1-x</sub>) epitaxial layers on GaAs substrates. Uniform transport and doping is obtained by situating resistively heated molten zinc chloride on both sides of the inductively heated close-space furnace. Degenerate GaAs layers with areas of 10 cm<sup>2</sup>, thicknesses of 1 mm, and reproducible doping levels of 5 x 10<sup>19</sup> cm<sup>-3</sup> were used to produce up to 1600-amp tunnel diodes.

In the development of high current tunnel diodes uniformly doped wafers of degenerate GaAs 8-12 cm<sup>2</sup> in area are needed. Melt grown crystals do not show sufficient reproducibility of doping or adequate uniformity in these dimensions. The close-spaced growth of epitaxial GaAs has been discussed by a number of authors (1-5). Using H<sub>2</sub>O or HCl as the transport agent this method has produced rapid growth rates (circa 1 mm/hr). A close-spaced inductive furnace (6) has the ability to accept the 10 cm<sup>2</sup> undoped GaAs substrates for epitaxial growth. In these systems doping was achieved by incorporation of n-type dopants such as Se, S, and Te in the source material. Our attempts to grow p-type GaAs using zinc in this manner resulted in n-type layers and loss of the "volatile" zinc to the hydrogen ambient. This paper discusses a new open-tube method of uniformly introducing zinc chloride vapor into the close-spaced furnace for the

p-type epitaxial growth of GaAs, GaP, and their alloys on undoped GaAs substrates, and the use of grown GaAs and Ga(As<sub>0.8</sub>P<sub>0.2</sub>) in making tunnel diodes.

#### Apparatus

The apparatus used is shown diagrammatically in Fig. 1. The close-spaced radio frequency induction furnace (6) is composed of two series-connected, flat-wound copper coils geometrically parallel, as shown. These are powered by a 10 kw generator either at 450 kc, or at 3 Mc. The coils couple to a pair of carbon susceptors placed in a quartz reaction tube of 4.3 x 1.3 cm<sup>2</sup> cross section. The susceptors heat the source and substrate, which are themselves separated by 1 mm thick molybdenum spacers. The required source-substrate temperature difference is obtained by mechanically moving the pair of RF coils vertically toward or away from the pair of susceptors. Temperatures are monitored by means of electrically isolated molybdenum sheathed thermocouples imbedded in the susceptors. One thermocouple electronically main-

\* Electrochemical Society Active Member.

<sup>1</sup> Present address: TRW Electronics, 14520 Aviation Boulevard, Lawndale, California, 90260.

<sup>2</sup> Present address: Burroughs Corporation, Plainfield, New Jersey.

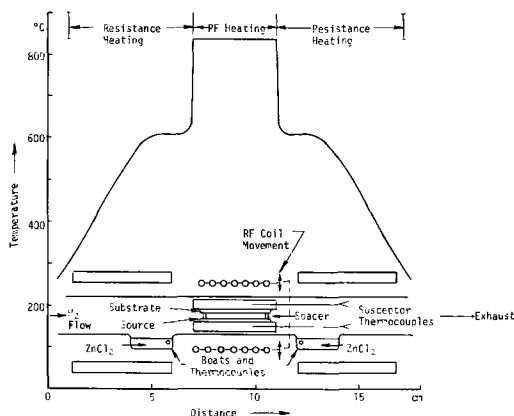


Fig. 1. Close space RF furnace with resistively heated side furnaces and temperature profile at start of growth.

tains the substrate susceptor to within  $1^{\circ}\text{C}$  of the growth temperature by controlling the RF generator with a differential amplifier, magnetic amplifier and saturable reactor series. At low hydrogen flows the source susceptor tracks to within  $2^{\circ}\text{C}$  of the temperature required. At each end, the rectangular quartz tube is depressed 1 cm to form 4 cm x 2 cm boats to contain the zinc chloride. Into the side of each boat a thin tube is fused so that its tip is surrounded by the liquid zinc chloride at operating temperatures. The tubes accept thermocouples which electronically control the cylindrical resistance furnace around each boat to within  $4^{\circ}\text{C}$  of its desired temperature. All furnaces can be reproducibly located such that the temperature gradient along the tube is maintained from run to run. Uniformity of the susceptors to within  $2^{\circ}\text{C}$  is periodically checked with a pyrometer. The temperature profile shown in Fig. 1 was obtained by inserting a molybdenum sheathed thermocouple from each end and profiling the running furnaces with the susceptors at equal temperature in nitrogen, but without the source and substrate present. The sharp temperature change in the region between the susceptor and the ambient nitrogen is probably due in part to heat conduction along the 60 mil OD molybdenum sheath. The sheath is grounded, eliminating RF pick-up in the thermocouple circuits as checked by rapid turn off and on of the RF generator at operating power. Furthermore, molybdenum appears inert to the reaction atmosphere.

### Procedure

The GaAs substrates are melt grown, undoped, and angle-cut  $2\text{--}3^{\circ}\text{C}$  off the (111) plane to give up to  $10\text{ cm}^2$  in area. Growth takes place on the chemically polished  $(\bar{1}\bar{1}\bar{1})$  plane. The back (111) side has been previously coated with  $\text{SiO}_2$  from the thermal decomposition of ethyl orthosilicate to reduce decomposition of the backs during the growth of 1 mm layers.

The GaAs and GaP sources were single-crystal or polycrystalline undoped wafers 1-2 mm thick. The  $\text{Ga}(\text{As}_x, \text{P}_{1-x})$  sources were wafers of pressed and sintered mixtures of pure GaAs and GaP powders. X-ray diffraction from copper radiation is used to measure the alloy composition with change in d-spacing. The (111) plane was used for sintered powders and the (444) plane for single crystals.

Zinc chloride has been shown capable of transporting GaAs (8) in a closed-tube system and the effectiveness of zinc as a p-dopant for GaAs is known. Zinc chloride was found well suited for close-spaced transport when treated to reduce its moisture content. CP zinc chloride, as purchased, is stored at  $140^{\circ}\text{C}$  under mechanical vacuum of  $30\text{--}50\mu$ . It is loaded while still warm, and just prior to the run the zinc chloride and susceptors-substrate-source assembly are held at  $300^{\circ}\text{C}$  in flowing hydrogen for 5 min. This

bakeout virtually eliminates hillocks on the epitaxial layers, possibly caused by gallium oxide inclusions.

After bakeout the hydrogen flow is adjusted to  $10\text{--}30\text{ cm}^3/\text{min}$  through the  $4.3 \times 1.3\text{ cm}^2$  rectangular tube cross section of which  $2.4\text{ cm}^2$  is occupied by the susceptors-source-substrate cross section. The GaAs source is then heated to  $840^{\circ}\text{C}$  with GaAs substrate  $10^{\circ}\text{--}20^{\circ}$  higher to etch off some of the substrate. Simultaneously the zinc chloride is heated to approximately  $430^{\circ}\text{C}$ . After etching the temperature is inverted, with the source held at  $840^{\circ}$  and the substrate at  $800^{\circ}\text{C}$ . For the growth of  $\text{Ga}(\text{As}_x, \text{P}_{1-x})$  with  $0 < x \leq 1$  the source is held at  $950^{\circ}$  and the substrate at  $910^{\circ}\text{C}$ .

### Experimental Results

The growth rates and resistivity of GaAs and GaP grown by close-spaced transport depend on the temperature of the zinc chloride, the hydrogen flow, the source and substrate temperatures, and the spacing between them. The system has been operated at no hydrogen flow, but the flow range of  $10\text{--}30\text{ cc/min}$  resulted in a reduction of hillocks on the surface. At these low hydrogen flows the zinc chloride still achieves near saturation, based on growth rate and doping level comparisons with no flow. The GaAs substrate temperature of  $800^{\circ}\text{C}$  for GaAs growth and  $910^{\circ}\text{C}$  for GaP and phosphide-arsenide alloys were found high enough to give satisfactory growth with no tendency to polycrystallinity. The source temperature  $40^{\circ}$  higher was picked to achieve growth rates in the range of  $100\ \mu/\text{hr}$  under the condition of growth for thick layers for tunnel diodes. While not studied in detail, the growth rate can be halved to doubled by reducing or increasing the temperature of the source, with little effect on this high doping level. The observed change in growth rate of GaAs with change in the zinc chloride temperature is shown in Fig. 2. Thickness was measured by a micrometer before and after the run. A  $5000\text{\AA}$  silicon dioxide layer deposited from the thermal decomposition of ethylorthosilicate eliminates back etching of the substrate during growth and the thicknesses measured agree well with measurements between the top of the layer and the substrate where the spacers had prevented growth. The observed change in doping level with changes in zinc chloride temperature was also studied for GaAs, as seen in Fig. 3.

Carrier concentrations are determined by the plasma resonance technique (7). This method gives zinc concentrations in GaAs reproducible to about 3% by IR reflectance in the  $2 \times 10^{19}$  to  $9 \times 10^{19}$  carriers/ $\text{cm}^3$  range. Since the plasma resonance measurement covers a circle about 4 mm in diameter, this method is also used to measure the doping uniformity of layers. An

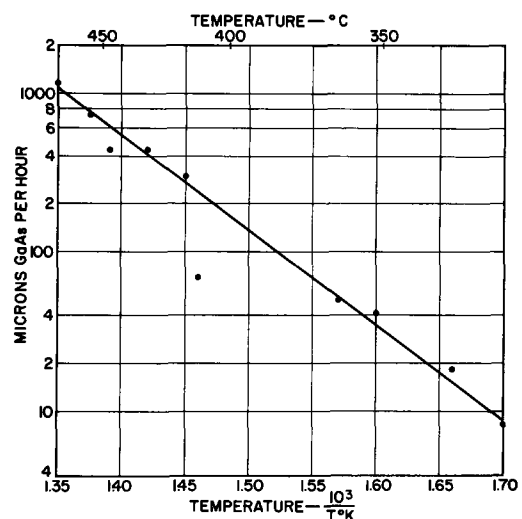


Fig. 2. GaAs growth rate as a function of zinc chloride temperature

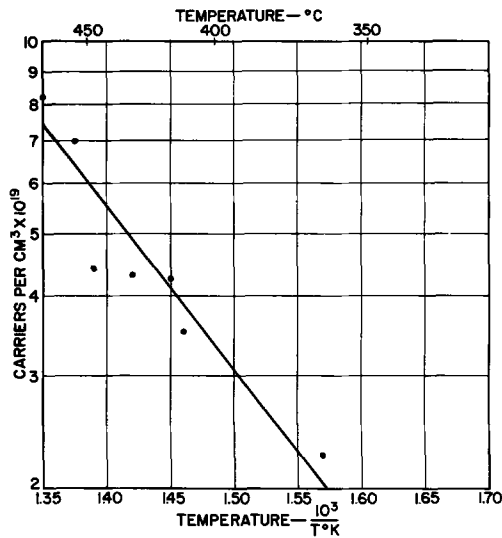


Fig. 3. GaAs doping level as a function of zinc chloride temperature

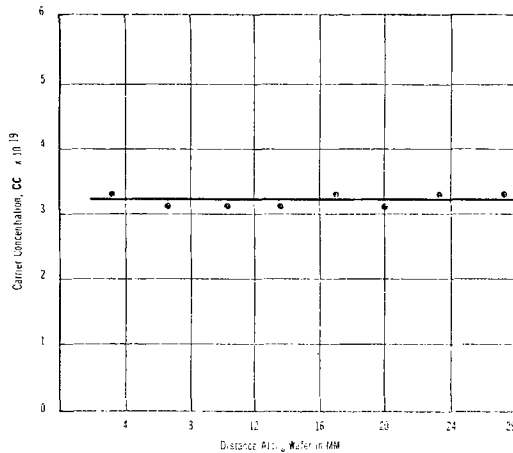


Fig. 4. Doping variation across a large area GaAs grown layer

example of the high degree of doping uniformity obtainable is shown in Fig. 4, as measured along a 28 mm line of a 32 x 22 mm wafer. The run-to-run reproducibility of zinc doping GaAs was checked out on 19 consecutive runs with temperature and flow settings unchanged. The minimum wavelengths as read by plasma resonance and the equivalent carrier concentrations are shown in Table I. The average is  $5.5 \times 10^{19}$  carriers/cm<sup>3</sup> and the average deviation 13%. The Hall mobilities of the GaAs layers varied from 40 to 50 cm<sup>2</sup>/v-sec in the zinc concentration of 3 to 5 x

Table I. Minimum wavelengths as read by plasma resonance and equivalent carrier concentrations

Run	$\lambda$ Min in microns	$N \times 10^{19}$ carriers/cm <sup>3</sup>
1	5.7	4.2
2	5.4	5.1
3	5.3	5.5
4	5.3	5.5
5	5.3	5.5
6	5.3	5.5
7	5.4	5.1
8	5.5	4.7
9	5.2	5.9
10	5.6	4.5
11	5.5	4.7
12	5.0	6.9
13	5.1	6.5
14	5.2	5.9
15	5.8	3.9
16	5.2	5.9
17	5.2	5.9
18	5.8	3.9
19	5.2	5.9

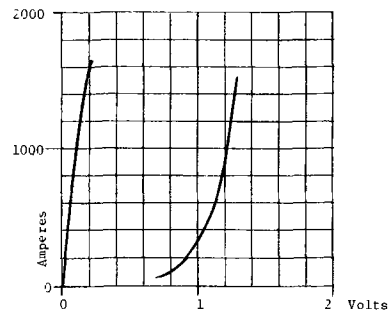


Fig. 5. Current-voltage plot of a high current GaAs tunnel diode 200 amp/division, 0.2 v/division.

$10^{19}$  carriers/cm<sup>3</sup>. The Hall mobility of a zinc doped Ga(As<sub>0.8</sub>P<sub>0.2</sub>) sample was 30 cm<sup>2</sup>/v-sec.

**Tunnel Diode Fabrication**

Epitaxial layers 0.6 to 1.0 mm thick with concentrations of 5 to 6 x 10<sup>19</sup> carriers/cm<sup>3</sup> were used to fabricate tunnel diodes. A contact is placed on the top grown (111) surface by lapping it flat, coating with sintered gold, nickel plating the gold, and evaporating another sintered gold layer. The wafer is then reversed and the original GaAs substrate, on the (111) side, lapped off and the wafer polished to a final thickness of 0.4-0.5 mm. A tin-lead dot about 6 cm<sup>2</sup> in area is then alloyed into the (111) surface to form the junction and top contact. The diode is then soldered to its package with Au-Ga-Zn alloy and tested. Figure 5 shows the current voltage trace of such a tunnel diode. Electrical characteristics are as follows:  $I_P = 1640$  amp;  $V_P = 0.21$ v;  $V_F = 1.3$ v;  $I_V = 60$  amp;  $V_V = 0.64$ v.

Smaller tunnel diodes were similarly fabricated from Ga(As<sub>0.8</sub>P<sub>0.2</sub>) wafers.  $I_P/I_V$  ratios up to 30:1 were achieved.

**Discussion**

The authors' previous experience has shown the need for low carrier gas flows if uniformity of growth is to be maintained in close-spaced transport and the reactants kept between the source of substrate. For tunnel diodes where a high doping level is also required, the use of a zinc chloride source on each side allows for low flows without sacrificing doping uniformity. Since the growth rate and doping level were found reproducibly dependent on the zinc chloride temperature, the temperature of the liquid zinc chloride must control the partial pressure of the zinc chloride in the high-temperature region of the furnace. The growth rate can be adjusted independently by means of the source and substrate temperatures.

**Acknowledgments**

The authors are indebted to P. D. Gardner, P. M. Britt, and Mrs. E. M. Strouse for fabricating and measuring the tunnel diodes and for valuable suggestions and discussions. They also thank R. D. Miller, J. S. Doyle, and A. G. Salerno for their assistance during this program.

The authors gratefully acknowledge the support of the Air Force Aeropropulsion Laboratory, Research and Technology Division, Air Force System Command, USAF.

Manuscript received Oct. 8, 1965; revised manuscript received ca. Dec. 11, 1967. This paper was presented in part at the Washington Meeting, Oct. 11-15, 1964, as Abstract 161.

Any discussion of this paper will appear in a Discussion Section to be published in the December 1968 JOURNAL.

**REFERENCES**

1. F. H. Nicoll, *This Journal*, **110**, 1165 (1963).
2. E. Sirtl, *J. Phys. Chem. Solids*, **24**, 1285 (1963).
3. P. H. Robinson, *RCA Rev.*, **24**, 574 (1963).
4. G. E. Gottlieb and J. F. Corboy, *RCA Rev.*, **24**, 585 (1963).



5. H. Flicker, B. Goldstein, and P-A. Hoss, *J. Appl. Phys.*, **35**, 2959 (1964).
6. P-A. Hoss and L. A. Murray, Paper presented at the Washington Meeting of the Society, Oct. 11-15, 1964, Extended Abstract 161.
7. L. A. Murray, J. J. Rivera, and P-A. Hoss, *J. Appl. Phys.*, **37** 4743 (1966).
8. N. Holonyak, D. C. Jillson, and S. F. Bevacqua, "Metallurgy of Semiconductor Materials," Metallurgical Society Conference V. 15, p. 49, John Wiley & Sons, Inc., New York (1962).

## The Effects of Growth Rate on the Thermoelectric Properties of $\text{Bi}_2\text{Te}_3\text{-Sb}_2\text{Te}_3\text{-Sb}_2\text{Se}_3$ Pseudoternary Alloys

W. M. Yim and E. V. Fitzke

RCA Laboratories, Princeton, New Jersey

### ABSTRACT

The effects of growth rate on the thermoelectric properties of n- and p-type  $\text{Bi}_2\text{Te}_3\text{-Sb}_2\text{Te}_3\text{-Sb}_2\text{Se}_3$  pseudoternary alloys have been investigated and correlated with microstructures. The results show that higher values of the figure of merit ( $Z$ ) are invariably associated with lower growth rates and hence greater homogeneity. For both n- and p-type alloys, the improvement in  $Z$  was as large as 50% when the growth rate was reduced from about 6 to 0.6 cm/hr. However, the growth-rate dependence of individual thermoelectric parameters was not the same for both alloys. For the n-type alloy, which is a single-phase alloy, slow growth rates resulted in an increase in the Seebeck coefficient, and a decrease both in the lattice thermal conductivity and electrical resistivity. For the p-type alloy, the variations with growth rate in the Seebeck coefficient and, to a lesser extent, in the lattice thermal conductivity were similar to those for the n-type alloy. However, its electrical resistivity increased with decreasing growth rates, and this was shown to be associated with the presence of a Te-rich second phase in the p-type alloy. Consistent with this interpretation are the results of an annealing study of these alloys.

The figure of merit of a thermoelectric material is often lowered by the presence of compositional and microstructural inhomogeneities in the material (1). These inhomogeneities are, in large part, related to growth conditions used for the material's preparation. Although the importance of optimum growth condition is generally recognized, only a few detailed studies (2) have been made in the past to elucidate the role of growth variables on the thermoelectric properties.

In this paper, we shall present the results obtained in a study of the effects of various growth rates on the thermoelectric properties of n- and p-type  $\text{Bi}_2\text{Te}_3\text{-Sb}_2\text{Te}_3\text{-Sb}_2\text{Se}_3$  pseudoternary alloys (3) grown by the Bridgman technique. The presentation of the results will include the metallographic observation of microstructures, and the dependence on growth rate of the Seebeck coefficient, electrical resistivity, and thermal conductivity at room temperature. Included also in this paper are the results of the effects of annealing at 390°C on the room temperature thermoelectric properties of these alloys.

It will be shown that lower growth rates result in better homogeneity and higher figures of merit for both n- and p-type alloys. However, the growth-rate dependence of their individual thermoelectric parameters is not the same, and this difference will be related to the difference in the microstructure of n- and p-type alloys, in particular, to the presence of a second phase in the latter alloy. These results will be corroborated by the annealing study.

### Experimental Procedure

An n-type composition  $(\text{Bi}_2\text{Te}_3)_{75}(\text{Sb}_2\text{Te}_3)_{20}(\text{Sb}_2\text{Se}_3)_5$  doped with 0.16 w/o (weight per cent)  $\text{SbI}_3$ , and a p-type composition  $(\text{Sb}_2\text{Te}_3)_{70}(\text{Bi}_2\text{Te}_3)_{25}(\text{Sb}_2\text{Se}_3)_5$

Key words: thermoelectric alloys;  $\text{Bi}_2\text{Te}_3\text{-Sb}_2\text{Te}_3\text{-Sb}_2\text{Se}_3$  alloys; microstructures; thermoelectric properties; effects of growth rate; effects of annealing.

containing 2 w/o excess Te were used for the present study.<sup>1</sup>

In the preparation of the alloys, high-purity (99.999%) component elements were used, and these were obtained from the American Smelting and Refining Company. The alloys were grown by a vertical Bridgman method with freezing rates ranging from 0.24 to 7.6 cm/hr but under a constant temperature gradient of  $\sim 25^\circ\text{C}/\text{cm}$  in the melt near the freezing interface. The resulting ingots, 0.7 cm in diameter and 18 cm long, consisted of coarse grains, whose cleavage characteristics suggested a preferred orientation with their (111) cleavage planes generally aligned with the long axis of the ingots, and this was particularly true for slowly grown ingots.

The metallographic observation of microstructure was made on sections cut perpendicular to the long axis of the ingots. The etchant used for the n-type material was 20%  $\text{HNO}_3$  in  $\text{H}_2\text{O}$ , and that for the p-type material was 1  $\text{HNO}_3\text{-2 HCl-2}$  saturated  $\text{K}_2\text{S}_2\text{O}_8$  in  $\text{H}_2\text{O}$ .

The measurements of electrical resistivity  $\rho$ , Seebeck coefficient  $Q$ , and thermal conductivity  $\kappa$  were made on short cylinders, 0.7 cm diameter and about 0.7 cm long. The electrical or temperature gradient was applied in the direction of the axis of the cylinder, which was the growth direction of the ingot and, as a result of the preferred growth, this direction coincided approximately with a direction perpendicular to the [111] trigonal axis of the crystallites. The mea-

<sup>1</sup>All compositions are in mole per cent unless otherwise specified, and they represent starting compositions. It should be noted that the above compositions do not correspond to the alloys of the highest figures of merit found in the pseudoternary system. The best n-type alloy is  $\text{SbI}_3$ -doped  $(\text{Bi}_2\text{Te}_3)_{90}(\text{Sb}_2\text{Te}_3)_5(\text{Sb}_2\text{Se}_3)_5$ , and the best p-type alloy is excess Te-doped  $(\text{Sb}_2\text{Te}_3)_{72}(\text{Bi}_2\text{Te}_3)_{25}(\text{Sb}_2\text{Se}_3)_3$ , having room temperature figures of merit  $3.2 \times 10^{-3}$  and  $3.4 \times 10^{-3}$  deg<sup>-1</sup>, respectively (3). Nevertheless, the results presented in this paper are representative of n-type materials in the  $\text{Bi}_2\text{Te}_3$ -rich end and p-type materials in the  $\text{Sb}_2\text{Te}_3$ -rich region of the pseudoternary alloys.

surement techniques have been given in detail in previous papers (3, 4). The measurements of these individual thermoelectric parameters provided a direct determination of the materials figure of merit,  $Z = Q^2/\kappa \cdot \rho$ .

A selected group of n- and p-type specimens was annealed in a partial pressure of Ar at 390°C for a duration as long as 1000 hr. The annealing temperature chosen was, as will be shown later, slightly lower than the melting point of a second phase present in the p-type material. The thermoelectric properties of each specimen were measured at room temperature before and after the annealing treatment. In addition, room temperature Hall coefficients were measured on a few representative slow-grown samples to study the effect of annealing on the carrier concentration and mobility. Hall specimens were prepared by cleaving the bulk material, and had typical dimensions of 7x2x0.3 mm. The direction of magnetic field was perpendicular to, and the current was parallel to, the cleavage plane.

In all measurements, specimens were taken from approximately the same location of ingots, ~ 6 cm from the first portion to freeze.

### Effects of Growth Rate

**Microstructure.**—The compound semiconductors  $\text{Bi}_2\text{Te}_3$ ,  $\text{Sb}_2\text{Te}_3$ , and  $\text{Sb}_2\text{Se}_3$  form pseudoternary solid-solution alloys over a wide range of compositions except in the neighborhood of large  $\text{Sb}_2\text{Se}_3$  concentrations (5). The phase diagrams of  $\text{Bi}_2\text{Te}_3$ - $\text{Sb}_2\text{Te}_3$  (6) and  $\text{Bi}_2\text{Te}_3$ - $\text{Sb}_2\text{Se}_3$  (7) show that the equilibrium distribution coefficient of  $\text{Sb}_2\text{Te}_3$  in  $\text{Bi}_2\text{Te}_3$  and that of  $\text{Sb}_2\text{Se}_3$  in  $\text{Bi}_2\text{Te}_3$  are nearly equal to unity. Therefore, the present materials, when undoped, are pseudoternary alloys of approximately uniform compositions along the length of ingots. For the n-type alloy used in the present study, the amount of  $\text{SbI}_3$  added was within its solubility limit of about 0.2 w/o in the  $\text{Bi}_2\text{Te}_3$ -rich pseudoternary alloys; hence, the present n-type alloy is a single-phase material. The distribution of the dopant appeared generally uniform, as inferred from a straight resistance-scan trace along the ingot except for the first and last 2-cm portions to freeze. For the present p-type alloy, the Te addition exceeded the solubility limit of about 0.2 w/o and therefore the p-type alloy is a two-phase material. Although the equilibrium distribution coefficient of Te in the  $\text{Sb}_2\text{Te}_3$ -rich pseudoternary alloys is less than one, the distribution of second phase was fairly uniform along the ingot except again near the first and last portions to freeze.

In Fig. 1, microstructures of fast-grown, n- and p-type alloys (a and c) are compared with those of slow-grown alloys (b and d). It is clearly seen that at the slow growth rates one obtains an improvement in the microstructural homogeneity.

**(N-type alloy).**—The n-type alloy, when slowly grown (~ 0.6 cm/hr), is a homogeneous material of large grain size, as evident from typical cleavage cracks running obliquely through the middle of Fig. 1(b). These cracks were introduced during polishing in one grain, and the dark area at the top of the photomicrograph is a portion of another grain. By contrast, the fast-grown (~ 4 cm/hr) n-type alloy consists of a lamellar structure, as shown in Fig. 1(a). These are probably the regions of severely varying composition, but are to be distinguished from second phase such as that present in the p-type alloy [Fig. 1(c) and 1(d)].

The lamellar structure is probably associated with constitutional supercooling (8). During growth of multicomponent alloys under a constant temperature gradient, unless the growth rate is sufficiently slow, constitutional supercooling would occur with ensuing compositional segregation. This appears to be the case for the fast-grown n-type alloy shown in Fig. 1(a). By using a slow growth rate, the constitutional super-

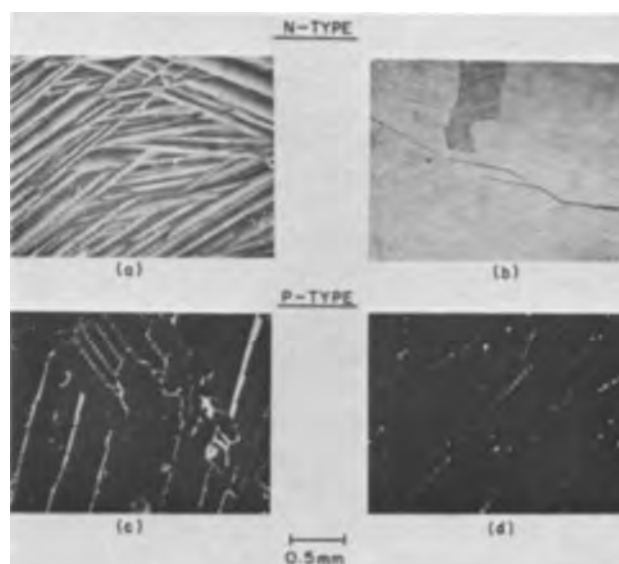


Fig. 1. Growth rate ( $R$ ) dependence of microstructures on n-type  $\text{SbI}_3$ -doped  $(\text{Bi}_2\text{Te}_3)_{75}(\text{Sb}_2\text{Te}_3)_{20}(\text{Sb}_2\text{Se}_3)_5$  and p-type excess Te-doped  $(\text{Sb}_2\text{Te}_3)_{70}(\text{Bi}_2\text{Te}_3)_{25}(\text{Sb}_2\text{Se}_3)_5$  alloys: (a) fast-grown n-type,  $R = 3.8$  cm/hr,  $Z = 1.4 \times 10^{-3}$  deg $^{-1}$ ; (b) slow-grown n-type,  $R = 0.57$  cm/hr,  $Z = 2.1 \times 10^{-3}$  deg $^{-1}$ ; (c) fast-grown p-type,  $R = 7.6$  cm/hr,  $Z = 2.2 \times 10^{-3}$  deg $^{-1}$ , and (d) slow-grown p-type,  $R = 0.64$  cm/hr,  $Z = 3.1 \times 10^{-3}$  deg $^{-1}$ . All taken on ingot cross sections.

cooling was avoided, as in Fig. 1(b). The effect on microstructure of different temperature gradients with a constant growth rate was not investigated. However, the effect of increasing the temperature gradient would be, as is well known (8), essentially similar to that of lowering the growth rate.

**(P-type alloy).**—The p-type alloy is, as stated above, a two-phase material consisting of a pseudoternary  $\text{Sb}_2\text{Te}_3$ - $\text{Bi}_2\text{Te}_3$ - $\text{Sb}_2\text{Se}_3$  solid-solution matrix and a second phase, which appears as lamellae on an etched cross section. An electron-probe analysis showed that the second phase was composed of approximately 90 a/o (atomic per cent) Te with small amounts of Bi, Sb, and Se. The melting point of this second phase was found by DTA to be about 415°C, as compared with ~ 450°C for pure Te. From these observations, it appears that the second phase is a eutectic rich in Te. It is interesting in this connection to note that the second phase, whether it resulted from the excess addition of Te or Se, melted at about the same temperature. This shows that in both cases the second phase is similar in composition, indicating that Se preferentially enters into solid solution, and rejects from it the Te-rich second phase (3, 4).

There is a marked difference in the microstructure, especially in the second phase, between fast- and slow-grown p-type alloys. At a growth rate of about 8 cm/hr, the second phase appears as thick lamellae along cleavage planes and grain boundaries, as in Fig. 1(c). At a much lower growth rate of 0.6 cm/hr, the second phase precipitates as thin discontinuous lamellae dispersed in the matrix, as in Fig. 1(d).

**Thermoelectric properties.**—The growth-rate dependence of the thermoelectric properties at 300°K of n- and p-type pseudoternary alloys is shown in Fig. 2(a) (Seebeck coefficient  $Q$ ), 2(b) (electrical resistivity  $\rho$ ), 2(c) (measured total thermal conductivity  $\kappa_{\text{total}}$ , and lattice thermal conductivity  $\kappa_{\text{ph}}$ ), and 2(d) (figure of merit  $Z$ ). The lattice thermal conductivity was obtained from the measured total thermal conductivity by using the relation,  $\kappa_{\text{total}} = \kappa_{\text{el}} + \kappa_{\text{ph}}$  where  $\kappa_{\text{el}}$  is the electronic thermal conductivity and no ambipolar contribution was assumed. The electronic contribution was calculated from the Wiedemann-Franz relation,

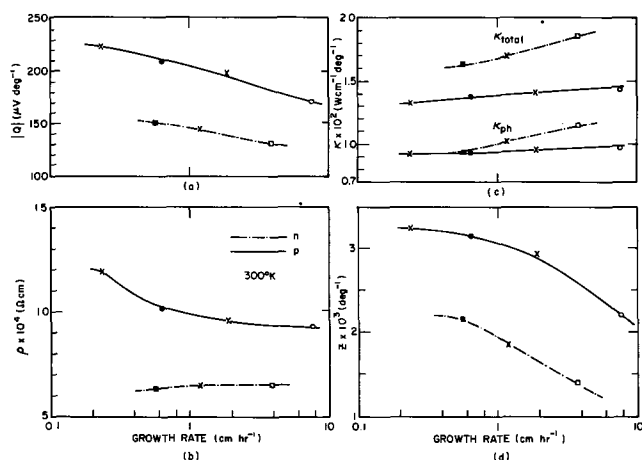


Fig. 2. Growth-rate dependence of thermoelectric properties at 300°K of n-type  $Sb_{13}$ -doped  $(Bi_2Te_3)_{75}(Sb_2Te_3)_{20}(Sb_2Se_3)_5$  and p-type excess Te-doped  $(Sb_2Te_3)_{70}(Sb_2Te_3)_{25}(Sb_2Se_3)_5$  alloys: (a) The Seebeck coefficient ( $Q$ ), (b) electrical resistivity ( $\rho$ ), (c) total thermal conductivity ( $\kappa_{total}$ ) and lattice thermal conductivity ( $\kappa_{ph}$ ); and (d) figure of merit ( $Z$ ).

for which the Lorentz number corresponded to the simple case of acoustical lattice scattering and non-degeneracy,  $2(k/e)^2$ , where  $k$  is the Boltzmann constant and  $e$  is the electronic charge.

For both the n- and p-type alloys,  $Q$  increases, and  $\kappa_{total}$  and  $\kappa_{ph}$  decrease, with decreasing growth rate  $R$ . The variations in  $\rho$  with  $R$  are, however, not the same for both materials:  $\rho$  of the n-type decreases, while that of the p-type alloy increases, with decreasing  $R$ .

In general, in a given material where doping impurities are fully ionized, one would expect the electrical resistivity to decrease as the material becomes more homogeneous. The change in  $\rho$  of the n-type alloy [Fig. 2(b)] shows this to be the case, since a greater inhomogeneity is associated with a slower growth rate, as shown by the microstructure in Fig. 1(b). However, the observed change in  $\rho$  of the p-type alloy cannot be explained on the basis of homogeneity alone.

It has been shown (3) that Te acts as a donor in the p-type alloy, and therefore the Te atoms in solid solution would raise the electrical resistivity of the p-type matrix by compensation. However, it is not the resistivity of the matrix that alone is responsible for the  $\rho$  of the bulk. A single-phase p-type alloy having the same major composition as the present one, when doped with a maximum soluble amount of Te of about 0.2 w/o, showed only a slight increase in  $\rho$  to  $7.5 \times 10^{-4}$  ohm-cm from the undoped value of  $6.5 \times 10^{-4}$  ohm-cm. With further additions of Te, the second phase started to precipitate, but the bulk  $\rho$  increased regularly with corresponding increase in  $Q$  up to an onset of the intrinsic conduction. Thus, the Te-rich second phase was essential in controlling the resistivity of the p-type alloy.<sup>2</sup>

The second phase at slow growth rates appears as thin, discontinuous lamellae [Fig. 1(d)] as contrasted to thick, continuous lamellae [Fig. 1(c)] at fast growth rates. While no simple explanation is available, it may be that the higher  $\rho$  for the slowly grown p-type alloy is due to the discontinuous nature of the second phase, in addition to a larger Te concentration in the matrix because of more time available for the solution of Te atoms. This is corroborated by annealing results, the discussion of which will follow shortly.

The present result on the growth-rate dependence of  $\rho$  of the p-type alloy is in disagreement with the result of Cosgrove *et al.* (2), who reported that the resistivity of a p-type material decreased with decreasing growth rate. The composition of their p-type

alloy was  $BiSbTe_3$  doped with 0.56 w/o Se or, in the pseudoternary notation, the material corresponded approximately to a solid solution of  $(Bi_2Te_3)_{50}(Sb_2Te_3)_{48}(Sb_2Se_3)_2$  containing 1 w/o excess Te, most of which would appear as a second phase. Because of this difference in the alloy composition, a direct comparison of the previous and the present results is difficult to make.

Cosgrove *et al.* (2) did not report the presence of a second phase, but they did detect n-type regions in the p-type matrix by thermal probing. It is possible that the n-type regions were of a similar nature to the Te-rich second phase, although in the present work the relatively small dimensions of the second phase rendered the thermal-probe technique unsuccessful.

The increase in  $Q$  for the p-type alloy with decreasing  $R$  is to be expected [Fig. 2(a)], since in an extrinsic semiconductor the Seebeck coefficient is approximately proportional to  $\ln \rho$ . Thus, the increase in  $Q$  for the p-type alloy can be accounted for by the corresponding increase in  $\rho$ . For the n-type alloy, the observed variation in  $Q$  with  $R$  is contrary to what one would expect from the change in  $\rho$ . It was first pointed out by Airapetians (1) that compositional inhomogeneities can substantially reduce the Seebeck coefficient and, at the same time, increase the thermal conductivity of a thermoelectric material by "circulating currents." As a consequence, the inhomogeneities lead to a lower figure of merit for the material. The increase in  $Q$  of the n-type alloy, in spite of a decrease in  $\rho$ , may be ascribed to an improvement in the material's homogeneity with decreasing growth rate.

The measured total thermal conductivity, as well as the lattice thermal conductivity, decreased with decreasing growth rate, as shown in Fig. 2(c). For the n-type alloy, the  $\kappa_{ph}$  decreased by about 20% when  $R$  was reduced from 4 to 0.6 cm/hr. By comparison, the  $\kappa_{ph}$  of the p-type alloy decreased only 5% on reducing  $R$  from 8 to 0.6 cm/hr.

Circulating currents tend to enhance heat transport; hence, a material containing second phase may exhibit a higher thermal conductivity than a similar material without the second phase. However, there is an additional effect on heat transport of the second phase, which tends to decrease the thermal conductivity. In a two-phase material, the possibility exists that sub-microscopic precipitates or crystalline defects, such as arrays of dislocations present at the phase boundaries, may cause significantly the scattering of phonons. Thus, the phonon scattering by these defects would modify the extent of increase in the thermal conductivity arising from circulating currents. Since the present two-phase p-type alloy is already imperfect, even when prepared under most ideal conditions [for instance, a dislocation density of  $10^{10} \sim 10^{11}$  cm<sup>-2</sup> (2) would be required to maintain lattice registry between the second phase and matrix], variations in the growth rate would not drastically alter the defect density. The fact that the  $\kappa_{ph}$  of the p-type alloy is nearly independent of  $R$  suggests this may be the case. Therefore, it appears that the contribution of the circulating currents is relatively small for the present materials, especially for the p-type alloy, over the range of growth rates used. The changes in  $\kappa_{ph}$  for the present case are in no way as large (by a factor of two) as those reported by Cosgrove *et al.* (2) for p-type  $BiSbTe_3$  doped with Se.

The changes in  $Q$ ,  $\rho$ , and  $\kappa$  with different growth rates are reflected in the figures of merit, as seen in Fig. 2(d). The figures of merit of the n- and p-type alloys were significantly improved by using slow growth rates: the resulting improvement in  $Z$  for both materials is more than 50%. The factors contributing the most to this improvement are the increase in  $Q$  and the reduction in  $\kappa_{ph}$  for the n-type, and the increase in  $Q^2/\rho$  for the p-type alloy. The results shown in Fig. 2(d) demonstrate clearly the important role of optimum growth conditions in achieving high figures of merit.

<sup>2</sup> The increase in  $\rho$  with increasing excess Te addition may alternatively be explained by the assumption that the second phase depletes the matrix of Bi and Sb (acceptors), and thus causes a decrease in the hole concentration in the material.

## Effects of Annealing

The changes in the room temperature thermoelectric properties of annealed specimens are shown in Fig. 3(a) ( $Q$ ), 3(b) ( $\rho$ ), 3(c) ( $\kappa_{\text{total}}$  and  $\kappa_{\text{ph}}$ ), and 3(d) ( $Z$ ). It is interesting to note that the rate of the changes is generally greater during the first 10-hr than longer-time annealing. As in Fig. 2, the broken curves are for n-type and the full curves are for p-type alloys. For ease of reference, the same symbol for each individual data point was used in Fig. 3 as in Fig. 2. For example, a full circle at zero annealing time in Fig. 3 corresponds to the same p-type alloy grown at 0.6 cm/hr shown by the full circle in Fig. 2. Also included in Fig. 3 (open triangles) are the annealing data of slow-grown, single-phase, undoped, p-type alloy having the same major composition as the Te-doped alloy.

For fast-grown n-type alloy,  $Q$  increased while  $\rho$  and  $\kappa_{\text{ph}}$  decreased; thus,  $Z$  increased with annealing in a manner similar to the effects of decreasing the growth rate. Although no apparent change in microstructure was observed, this improvement must be related to a partial homogenization of segregated structures. As might be expected, the slowly grown n-type alloy showed essentially no change upon annealing in its thermoelectric properties.

For Te-doped p-type material, annealing resulted in an increase in  $Q$  and  $\rho$ , while  $\kappa_{\text{ph}}$  remained unchanged for both the fast- and slow-grown alloys; hence, there was a slight improvement in  $Z$ . These changes in the thermoelectric properties are again reminiscent of the effects of lowering the growth rate.

Since the single-phase, undoped, p-type alloy showed essentially the same properties before and after the annealing, the increase in  $Q$  and  $\rho$  of the Te-doped alloy must have resulted from the presence

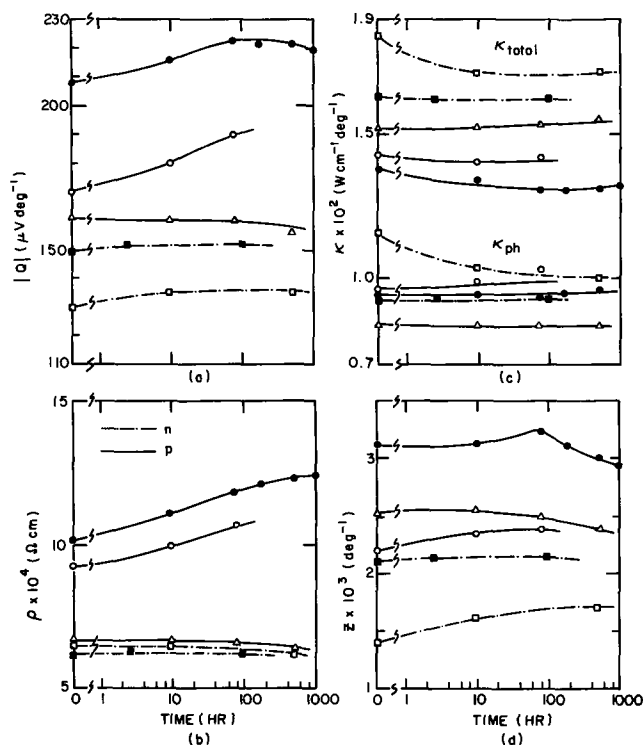


Fig. 3. Variations in thermoelectric properties at 300°K of n-type  $\text{Sb}_{13}$ -doped ( $\text{Bi}_2\text{Te}_3)_{75}(\text{Sb}_2\text{Te}_3)_{20}(\text{Sb}_2\text{Se}_3)_5$ ; p-type undoped, and excess Te-doped ( $\text{Sb}_2\text{Te}_3)_{70}(\text{Bi}_2\text{Te}_3)_{25}(\text{Sb}_2\text{Se}_3)_5$  with annealing time: (a) the Seebeck coefficient ( $Q$ ); (b) electrical resistivity ( $\rho$ ); (c) total thermal conductivity ( $\kappa_{\text{total}}$ ) and lattice thermal conductivity ( $\kappa_{\text{ph}}$ ), and (d) figure of merit ( $Z$ ). ( $\circ$ ) excess Te-doped p-type,  $R = 7.6$  cm/hr; ( $\bullet$ ) excess Te-doped p-type,  $R = 0.64$  cm/hr; ( $\Delta$ ) undoped p-type,  $R = 0.64$  cm/hr; ( $\square$ )  $\text{Sb}_{13}$ -doped n-type,  $R = 3.8$  cm/hr; and ( $\blacksquare$ )  $\text{Sb}_{13}$ -doped n-type,  $R = 0.57$  cm/hr.

Table I. Effect of annealing on room temperature carrier concentration and mobility

	Anneal. time, hr	Carrier conc., $10^{18}/\text{cm}^3$	Mobility, $\text{cm}^2/\text{v} \cdot \text{sec}$
p-type	0	2.3	271
	73	1.9	280
n-type	0	7.0	143
	100	6.8	149

p-type: doped with 2 w/o excess Te, grown at 0.64 cm/hr; n-type: doped with 0.16 w/o  $\text{Sb}_{13}$ , grown at 0.57 cm/hr.

of the Te-rich second phase in the doped alloy. It is most probable that on annealing some re-resolution of Te takes place, which causes a decrease in the hole concentration and results in an increase in  $\rho$  and  $Q$ . The metallographic examination, however, revealed no change in the microstructure after annealing. This is reasonable in view of the following simple argument.

If one assumes that each Te atom acts as a singly ionized donor, and that the hole mobility is independent of annealing, then one can calculate the change in the hole concentration corresponding to the change in  $\rho$ . The number of Te atoms that must dissolve in order to effect the experimentally observed  $\rho$  change, was calculated to be negligibly small as compared with that present in the second phase. Thus, one would not expect to see any change in the structure metallographically. The same conclusion was also arrived at from the calculation of the change in  $Q$  on annealing, with the assumption that  $Q$  is inversely proportional to logarithm of the carrier concentration. A slight decrease in  $Q$  and  $Z$  for the slow-grown p-type alloy beyond 100-hr annealing may be due to evaporation of Te from the specimen, as evidenced sometimes from a thin, shiny film deposit on the inside wall of quartz ampoule.

In a material such as the present p-type alloy, it is difficult to obtain reproducible Hall data because of the presence of second phase. Nevertheless, the data shown in Table I<sup>3</sup> indicate that the changes with annealing in  $Q$  and  $\rho$  of slowly grown p-type alloy were due mostly to a change in the carrier concentration, resulting presumably from the Te re-resolution. For slowly grown n-type alloy, the Hall data show that there was essentially no change in the carrier concentration, nor in the mobility.

## Conclusions

The effects of various growth rates on the thermoelectric properties of n- and p-type  $\text{Bi}_2\text{Te}_3$ - $\text{Sb}_2\text{Te}_3$ - $\text{Sb}_2\text{Se}_3$  pseudoternary alloys have been investigated and correlated with microstructures. The results show that higher values of the figure of merit are invariably associated with lower growth rates and hence greater homogeneity. For both n- and p-type alloys, the improvement in the figure of merit was as large as 50% when the growth rate was reduced from about 6 to 0.6 cm/hr. However, the growth rate dependence of individual thermoelectric parameters was not the same for both alloys.

For the n-type alloy, which is a single-phase material, slow growth rates resulted in an increase in the Seebeck coefficient, and a decrease both in the lattice thermal conductivity and electrical resistivity. These changes are what one would expect from an improvement in the material's homogeneity with decreasing growth rate, since the deleterious effects of circulating currents would diminish as material's homogeneity improves. For the p-type alloy, which is a two-phase material, the variations with growth rate in the Seebeck coefficient and, to a lesser extent, in the lattice thermal conductivity were similar to those in the n-

<sup>3</sup> The carrier concentration was calculated with the assumption of simple spherical band structure, and the mobility reported here is the Hall mobility,  $R_H \cdot \sigma$ , where  $R_H$  is the Hall coefficient and  $\sigma$  is the electrical conductivity.

type alloy. However, slow growth rates resulted in an increase in its electrical resistivity. The resistivity increase in the p-type alloy was interpreted on the basis of Te re-resolution from the Te-rich second phase present in the alloy. Consistent with this interpretation are the results of an annealing study of these alloys. The annealing effects, while less pronounced, were essentially similar to those brought about by variations in the growth rate.

#### Acknowledgments

The authors are grateful to E. J. Stofko and T. V. Pruss for their valuable contributions in materials preparation and thermoelectric measurements. Constructive comments by F. D. Rosi during the course of this work are gratefully acknowledged.

Manuscript received Dec. 5, 1967.

Any discussion of this paper will appear in a Discussion Section to be published in the December 1968 JOURNAL.

#### REFERENCES

1. S. V. Airapetiants, *Soviet Phys.—Tech. Phys.*, **2**, 429 (1957); S. V. Airapetiants and M. S. Bresler, *ibid.*, **3**, 1778 (1958).
2. G. J. Cosgrove, J. P. McHugh, and W. A. Tiller, *J. Appl. Phys.*, **32**, 621 (1961); R. W. Ure, Jr., *ibid.*, **33**, 2290 (1962).
3. W. M. Yim, E. V. Fitzke, and F. D. Rosi, *J. Materials Sci.*, **1**, 52 (1966).
4. F. D. Rosi, B. Abeles, and R. V. Jensen, *J. Phys. Chem. Solids*, **10**, 191 (1959).
5. I. Teramoto and S. Takayanagi, *J. Phys. Chem. Solids*, **19**, 124 (1961).
6. M. J. Smith, R. J. Knight, and C. W. Spencer, *J. Appl. Phys.*, **33**, 2186 (1962).
7. V. G. Kuznetsov and K. K. Palkina, *Russ. J. Inorg. Chem.*, **8**, 624 (1963); also, A. Matsumura, Private communication.
8. See, for example, B. Chalmers, "Principle of Solidification," John Wiley & Sons, Inc., New York, (1964).

## Technical Note



### Eu<sup>+2</sup> Activation in Some Alkaline Earth Strontium Phosphate Compounds

M. V. Hoffman\*

Lighting Research Laboratory, General Electric Company, Cleveland, Ohio

The fluorescence of divalent europium has received increased attention recently, and a number of phosphors emitting in the blue or ultraviolet region have been described. The efficiency and the narrow spectral distribution of Eu<sup>+2</sup>-activated phosphors make them attractive for use in reprographic and black light applications and for ultraviolet emission in cathode-ray tubes. Nazarova (1) found cathodoluminescence in Sr<sub>3</sub>(PO<sub>4</sub>)<sub>2</sub>, α and β Sr<sub>2</sub>P<sub>2</sub>O<sub>7</sub> and Sr(PO<sub>3</sub>)<sub>2</sub>, all with Eu<sup>+2</sup> activation. In another group of strontium compounds, Gorbacheva (2) found that Eu<sup>+2</sup> did not enter the β (Sr,Mg)<sub>3</sub>(PO<sub>4</sub>)<sub>2</sub> structure completely unless very strong reducing conditions were used, and this gave yellow emission. She also found blue emission with Eu<sup>+2</sup> in SrMg<sub>2</sub>(PO<sub>4</sub>)<sub>2</sub>. More recently, Wanmaker and ter Vrugt (3) have reported that divalent europium responds efficiently to ultraviolet excitation in alkaline earth pyrophosphates and showed that the strontium compounds were the most efficient. They described Sr<sub>2</sub>P<sub>2</sub>O<sub>7</sub>:Eu and Sr<sub>0.8</sub>Mg<sub>1.2</sub>P<sub>2</sub>O<sub>7</sub>:Eu and showed that they are efficient phosphors with narrow emission bands.

As pointed out by Wanmaker and ter Vrugt, the Sr compounds are suitable potential host lattices for Eu<sup>+2</sup> activation because of the similarity of ionic radii (Sr<sup>+2</sup> 1.13Å, Eu<sup>+2</sup> 1.17Å). In addition to a site for Eu<sup>+2</sup> substitution, the host lattice should have chemical stability in the nonoxidizing atmospheres required to place Eu in the site as a divalent cation and also the absence of a site or structure which will hold Eu in its preferred trivalent state.

A group of compounds which illustrate these requirements are found in the ternary systems SrO-MgO-P<sub>2</sub>O<sub>5</sub> and SrO-ZnO-P<sub>2</sub>O<sub>5</sub>, and these were exam-

ined with Eu<sup>+2</sup> activation. The orthophosphate joins of these systems have been described previously by Sarver, Hoffman, and Hummel (4). The compounds on these joins are the true ternary orthophosphates, SrMg<sub>2</sub>(PO<sub>4</sub>)<sub>2</sub> and SrZn<sub>2</sub>(PO<sub>4</sub>)<sub>2</sub>, and the stabilized high-temperature forms, or β form of Sr<sub>3</sub>(PO<sub>4</sub>)<sub>2</sub>, which are found only in the ternary region. These systems also contain the compounds SrMgP<sub>2</sub>O<sub>7</sub>, Mg<sub>3</sub>Sr<sub>2</sub>P<sub>4</sub>O<sub>15</sub>, and SrZnP<sub>2</sub>O<sub>7</sub>. The compatibility triangles are shown in Fig. 1 and 2. No solid solutions were found except in the β orthophosphate regions.

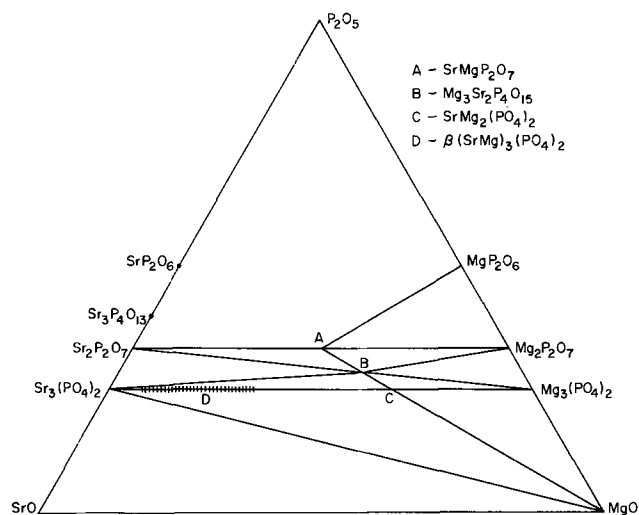


Fig. 1. Compatibility triangles in part of SrO-MgO-P<sub>2</sub>O<sub>5</sub> system

\* Electrochemical Society Active Member.

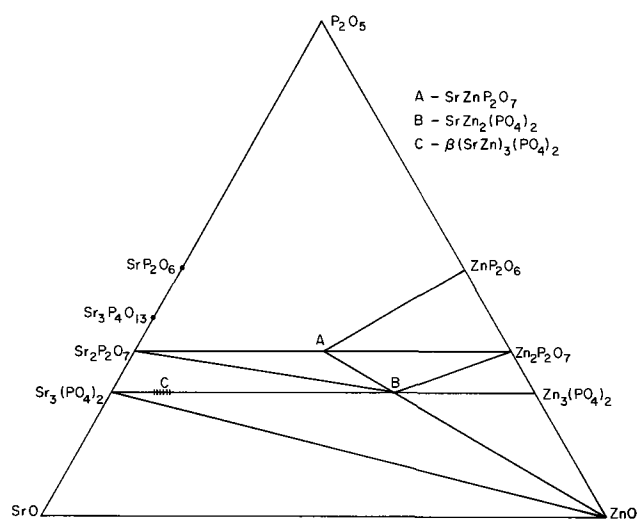


Fig. 2. Compatibility triangles in part of SrO-ZnO-P<sub>2</sub>O<sub>5</sub> system

The x-ray diffraction data for these compounds are shown in the Appendix.

#### Phosphor Preparation

The starting materials used in these experiments were SrHPO<sub>4</sub>, SrCO<sub>3</sub>, MgNH<sub>4</sub>PO<sub>4</sub>·H<sub>2</sub>O, MgCO<sub>3</sub>, ZnO, (NH<sub>4</sub>)<sub>2</sub>HPO<sub>4</sub>, and Eu<sub>2</sub>O<sub>3</sub>, all of purity normally used in phosphor manufacture. The europium was used either as the oxide or coprecipitated with the strontium compounds. The materials were mixed dry and fired in air at temperatures of from 900° to 1100°C, depending on the composition used. Samples containing a large amount of (NH<sub>4</sub>)<sub>2</sub>HPO<sub>4</sub> were fired initially at 550°C for several hours, milled, and then refired at a higher temperature. The final firing was in a flowing nonoxidizing atmosphere, usually a mixture of less than 1% H<sub>2</sub> in N<sub>2</sub>. Other atmospheres such as mixture of CO and CO<sub>2</sub> can also be used satisfactorily.

#### Measurements

The identifications of these compounds and their determination when present as minor, second phases in the various phosphor preparations were made by x-ray diffraction, using the General Electric XRD-5 with CuK<sub>α</sub> radiation. The emission spectra were obtained with a corrected, direct recording spectrometer with a grating monochromator (5). The excitation response between 120 and 300 nm was determined with a vacuum monochromator and is relative to sodium salicylate. The reflectance spectra in this region were determined on the same instrument and are relative to CaF<sub>2</sub>. This standard is used because it has a higher reflectivity in the ultraviolet than MgO and also is more stable with time. The method used to measure the excitation and reflectance below 300 nm has been described by Johnson (6).

The reflectance measurements in the visible and near ultraviolet regions were made on a Cary 14 spectrophotometer and are also relative to CaF<sub>2</sub>. In the Cary 14, monochromatic light is directed on to the sample, and the photocell detects all wavelengths coming from the sample; i.e., reflected light of the incident wavelength and also any fluorescence emitted by the sample, if it is excited by the incident light. The instrument is modified to measure reflectance of materials fluorescing in the visible by the insertion of a Corning 7-54 filter between the sample and the detector when measuring in the ultraviolet region. Fluorescence in the ultraviolet is transmitted by the 7-54 filter and is recorded as a rise in the reflectance curve at the exciting wavelengths. The Cary 14 is extremely sensitive in this region and can be used to detect weak ultraviolet fluorescence. With phosphors as efficient as those reported here, the interference of the fluorescence is too large to obtain meaningful reflectance

Table I. Summary of fluorescence spectra

Compound	Emission peak 254 nm excitation nm	Half width nm	Relative peak height
SrMgP <sub>2</sub> O <sub>7</sub> :0.02Eu	393	26	100
αSr <sub>3</sub> (PO <sub>4</sub> ) <sub>2</sub> :0.01Eu	405	43	60
αSr <sub>2</sub> P <sub>2</sub> O <sub>7</sub> :0.18Eu	415	40	47
Sr <sub>3</sub> P <sub>4</sub> O <sub>13</sub> :0.02Eu	415	60	20
SrMg <sub>2</sub> (PO <sub>4</sub> ) <sub>2</sub> :0.02Eu	410	47	18
Mg <sub>3</sub> Sr <sub>2</sub> P <sub>4</sub> O <sub>15</sub> :0.02Eu	440	—	5

curves below 400 nm. The instrument, as modified by the insertion of the 7-54 filter, was used to determine the presence or absence of ultraviolet fluorescence, and to give a qualitative measure of the excitation.

#### Results

The incorporation of Eu<sup>+2</sup> is possible in all of the strontium compounds in these systems, resulting in strong absorption bands in the ultraviolet region. The emission and excitation spectra are dependent on the composition and structure of the host lattice. Table I summarizes the fluorescence spectra found for the more efficient phosphors in these systems.

Of the orthophosphate compounds, only αSr<sub>3</sub>(PO<sub>4</sub>)<sub>2</sub>:Eu<sup>+2</sup> is efficient. Nazarova (1) reported an emission peak at 425 nm under cathode-ray excitation. We measured the emission at 405 nm under 254 nm excitation. The SrMg<sub>2</sub>(PO<sub>4</sub>)<sub>2</sub> compound is much less efficient, peaks at 410 nm, and is excited by radiation below 260 nm. The spectral distribution curves of these two phosphors are shown in Fig. 3. The compound, Mg<sub>3</sub>Sr<sub>2</sub>P<sub>4</sub>O<sub>15</sub>, is the least efficient and peaks at 440 nm, with the major excitation below 250 nm.

The SrZn<sub>2</sub>(PO<sub>4</sub>)<sub>2</sub> and SrZnP<sub>2</sub>O<sub>7</sub> compounds are strongly absorbing with Eu<sup>+2</sup> present, but have no visible or ultraviolet fluorescence. The reflectance curves show no evidence of ultraviolet emission under any excitation, Fig. 4. Measuring the reflectance and excitation of SrZn<sub>2</sub>(PO<sub>4</sub>)<sub>2</sub>:Eu between 140 and 300 nm with the vacuum monochromator also showed no emission and 75-85% absorption in this region.

The substitution of Eu in the β(SrMg)<sub>3</sub>(PO<sub>4</sub>)<sub>2</sub> compound gave both blue and red emission from the two valence states of Eu and showed Eu<sup>+3</sup> absorption lines, even when fired in an atmosphere of 5% H<sub>2</sub> in N<sub>2</sub>.

The β structure is stabilized by the incorporation of a divalent cation such as Mg, Ca, Zn, or Cd in the orthophosphate stoichiometry (4) and should be expected to accept Eu<sup>+2</sup> without difficulty in the Sr site. The β structure, however, can also be stabilized by a trivalent cation, such as Al<sup>+3</sup>, and this stoichiometry falls on the Sr<sub>3</sub>(PO<sub>4</sub>)<sub>2</sub>-AlPO<sub>4</sub> join, resulting in a de-

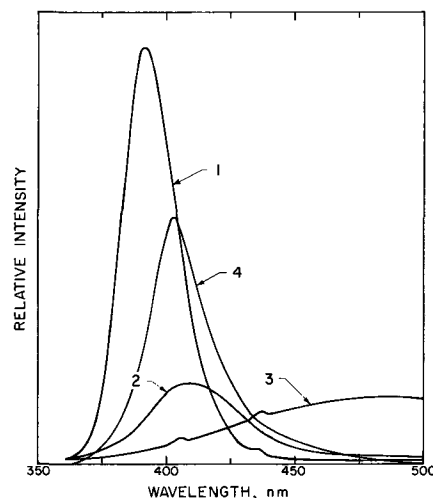


Fig. 3. Spectral distribution, 2537Å excitation: curve 1, SrMgP<sub>2</sub>O<sub>7</sub>:0.02Eu<sup>+2</sup>; curve 2, SrMg<sub>2</sub>(PO<sub>4</sub>)<sub>2</sub>:Eu<sup>+2</sup>; curve 3, MgWO<sub>4</sub>; curve 4, αSr<sub>3</sub>(PO<sub>4</sub>)<sub>2</sub>:0.01Eu.

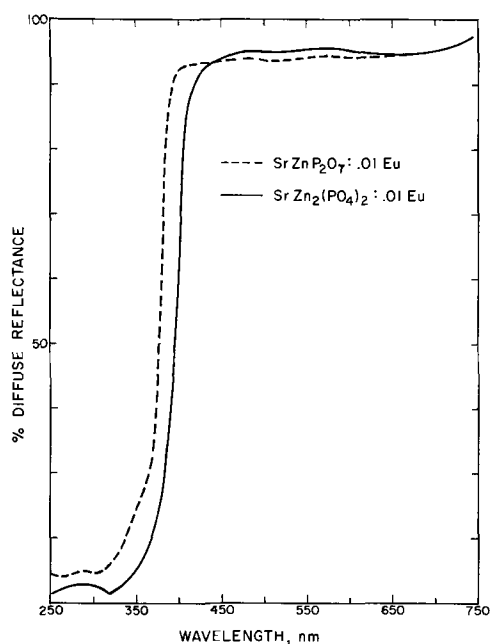


Fig. 4. Diffuse reflectance curves,  $\text{SrZnP}_2\text{O}_7:0.01\text{Eu}^{+2}$  and  $\text{SrZn}_2(\text{PO}_4)_2:0.01\text{Eu}^{+2}$ .

fect structure (7). The substitution of  $\text{YPO}_4$  also forms a compound with an x-ray diffraction pattern very similar to Al-stabilized  $\beta$   $\text{Sr}_3(\text{PO}_4)_2$  and may also be the  $\beta$  form. The presence of both blue and red fluorescence suggests that Eu has substituted for  $\text{Sr}^{+2}$  and is also present as  $\text{Eu}^{+3}$ , plus a cation vacancy. Both types of substitution may be present in the same structure, but more likely, the presence of  $\text{Eu}^{+3}$  has moved the composition into a two-phase region of  $\beta$   $(\text{Sr},\text{Mg})_3(\text{PO}_4)_2$  and a  $\beta$ -type structure stabilized with  $\text{Eu}^{+3}$ .

The ternary pyrophosphate  $\text{SrMgP}_2\text{O}_7$  is the most efficient phosphor found in these systems, as shown in Table I. The compatibility relationships show that this compound does not accept  $\text{Mg}_2\text{P}_2\text{O}_7$  or  $\text{Sr}_2\text{P}_2\text{O}_7$  in solid solution, i.e., compositions on the join on either side of  $\text{SrMgP}_2\text{O}_7$  will be two-phase material. The luminescent data and the x-ray diffraction pattern given in ref. (3) for the composition  $\text{Sr}_{0.8}\text{Mg}_{1.2}\text{P}_2\text{O}_7:\text{Eu}$  reflect the presence of more than one phase. The inclusion of  $\text{Mg}_2\text{P}_2\text{O}_7$  with  $\text{SrMgP}_2\text{O}_7$  has no effect on the  $\text{Eu}^{+2}$  emission other than a decrease of the measured intensity due to dilution with an inert material. Composition high in  $\text{Sr}_2\text{P}_2\text{O}_7$ , however, affect the emission and absorption much more strongly than the relative intensities of the two phosphors would indicate.  $\alpha\text{Sr}_2\text{P}_2\text{O}_7$  accepts considerable  $\text{Eu}_2\text{P}_2\text{O}_7$  in solid solution and reaches its peak fluorescence intensity at compositions between  $\text{Sr}_{1.9}\text{Eu}_{0.1}\text{P}_2\text{O}_7$  and  $\text{Sr}_{1.8}\text{Eu}_{0.2}\text{P}_2\text{O}_7$ , or about five to ten times the amount found to be optimum in other  $\text{Eu}^{+2}$ -activated phosphors. When mixtures containing  $\text{Sr}_2\text{P}_2\text{O}_7$  and  $\text{SrMgP}_2\text{O}_7$  are prepared with  $\text{Eu}^{+2}$ ,  $\text{Sr}_2\text{P}_2\text{O}_7$  preferentially accepts the activator, and the emission of  $\text{Sr}_2\text{P}_2\text{O}_7:\text{Eu}^{+2}$  at 415 nm is present in much greater proportion than the compound itself.

The peak fluorescence intensity in the ternary pyrophosphate is found between the composition  $\text{Sr}_{0.99}\text{Eu}_{0.01}\text{MgP}_2\text{O}_7$  and  $\text{Sr}_{0.90}\text{Eu}_{0.10}\text{MgP}_2\text{O}_7$ , with almost constant intensity between  $\text{Sr}_{0.99}\text{Eu}_{0.01}\text{MgP}_2\text{O}_7$  and  $\text{Sr}_{0.95}\text{Eu}_{0.05}\text{MgP}_2\text{O}_7$ . This phosphor peaks at 393 nm under long and short ultraviolet and under cathode-ray excitation. The reflectance curve from the Cary 14 shows considerable emission under 360 nm excitation and strong fluorescence below 325 nm. The true excitation and reflectance curves in the region from 140 to 300 nm are shown in Fig. 5.

The response to excitation between 120 and 300 nm was compared to sodium salicylate, which is constant between the region of 230 to 330 nm, and has a quan-

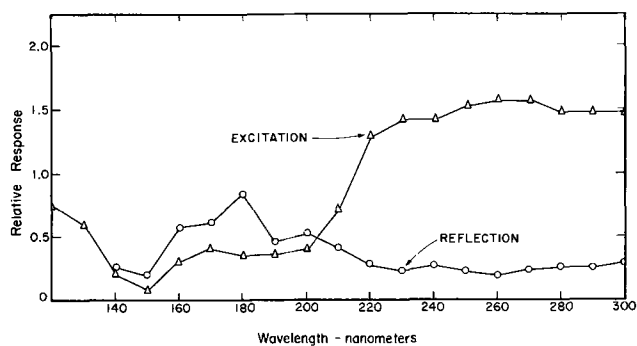


Fig. 5.  $\text{SrMgP}_2\text{O}_7:0.02\text{Eu}$  phosphor:  $\Delta$  excitation relative to  $\text{NaC}_7\text{H}_5\text{O} = 1$ ;  $\circ$  reflectance relative to  $\text{CaF}_2 = 1$ .

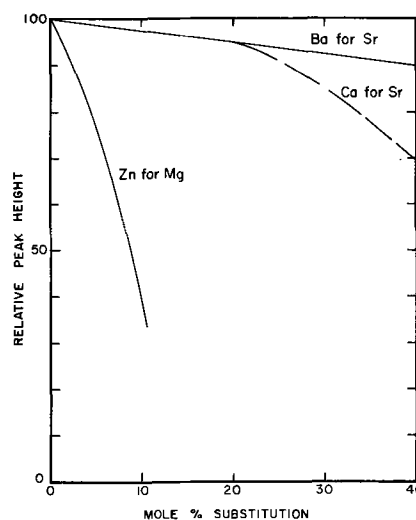


Fig. 6. Relative intensity of 393 nm peak for cation substitution in  $\text{SrMgP}_2\text{O}_7:0.02\text{Eu}^{+2}$ .

tum yield of 64% (8, 9). From this comparison,  $\text{SrMgP}_2\text{O}_7:\text{Eu}$  is almost constant over the range 220-300 nm and has a quantum yield of 90-95%.

#### Cation Substitution

$\text{SrMgP}_2\text{O}_7$  has two sites for cation substitutions, and a wide range of solid solutions are possible. Complete solid solution is probably between  $\text{SrMgP}_2\text{O}_7$  and  $\text{BaMgP}_2\text{O}_7$  and between  $\text{SrMgP}_2\text{O}_7$  and  $\text{SrZnP}_2\text{O}_7$ . Partial substitution of Ca for Sr can be made although the analogous compound  $\text{CaMgP}_2\text{O}_7$  does not exist. The effect on the  $\text{Eu}^{+2}$  emission was measured for substitutions of these cations, and the changes in peak height of the 393 nm emission are shown in Fig. 6. At least 20 mole % of Ba can be substituted without an appreciable change in the peak intensity. With 40% substitution, the brightness is decreased only about 10%, but the compound with complete substitution,  $\text{BaMgP}_2\text{O}_7:\text{Eu}$ , emits at 400 nm, with about 10% of the efficiency of the  $\text{SrMgP}_2\text{O}_7$  analogue. With the substitution of  $\text{Ca}^{+2}$ , a smaller cation, the intensity is decreased and the emission peak is shifted to longer wavelengths (Fig. 7). Substitutions of 10% Zn for Mg changed the absorption edge of the lattice to 390 nm, and the intensity of the emission decreased by about 50%.

#### Acknowledgments

The author would like to thank Dr. R. L. Brown, T. E. Lusk and B. Walsh for the emission and excitation data. The samples were prepared and measured by R. P. Kattler.

Manuscript received Nov. 30, 1967; revised manuscript received ca. Jan. 29, 1968. This paper was presented at the Boston Meeting, May 5-9, 1968, as Abstract 59.

Any discussion of this paper will appear in a Discussion Section to be published in the December 1968 JOURNAL.

## APPENDIX

X-Ray Diffraction Patterns, CuK $\alpha$  Radiation

SrMgP <sub>2</sub> O <sub>7</sub>			Mg <sub>3</sub> Sr <sub>2</sub> P <sub>4</sub> O <sub>15</sub>			SrZnF <sub>2</sub> O <sub>7</sub>		
2 $\theta$	d	I	2 $\theta$	d	I	2 $\theta$	d	I
12.7	6.99	26	12.4	7.13	4	12.75	6.93	23
13.9	6.37	54	15.1	5.86	5	13.7	6.46	9
17.6	5.04	10	15.5	5.71	7	13.85	6.39	18
18.1	4.90	6	15.7	5.64	13	19.90	4.46	9
19.9	4.46	6	19.5	4.55	4	21.80	4.07	18
21.0	4.23	14	20.1	4.47	3	22.80	3.90	3
21.4	4.15	17	21.5	4.13	2	23.60	3.77	4
22.5	3.95	16	23.55	3.77	57	25.80	3.45	7
23.5	3.79	14	24.9	3.57	2	26.80	3.32	100
24.4	3.65	45	25.9	3.44	2	27.40	3.25	67
25.6	3.48	10	26.6	3.35	23	28.34	3.15	25
26.8	3.33	100	27.7	3.22	53	29.00	3.08	63
27.2	3.28	70	29.45	3.03	63	30.20	2.96	46
28.2	3.16	70	30.3	2.95	11	30.90	2.89	42
29.2	3.06	70	32.0	2.79	100	33.50	2.67	24
30.1	2.97	36	32.85	2.73	28	33.70	2.66	28
30.8	2.90	66	34.4	2.61	11	34.60	2.59	30
33.1	2.70	46	35.4	2.53	12	35.50	2.53	12
33.8	2.65	60	37.8	2.38	17	36.20	2.48	2
34.5	2.60	37	38.7	2.33	14	36.95	2.43	12
35.6	2.52	20	39.0	2.31	7	39.20	2.30	16
39.4	2.29	46	39.6	2.27	6	39.60	2.27	16
41.0	2.20	30	41.0	2.20	15	40.50	2.22	4
41.8	2.16	7	41.7	2.16	4	41.08	2.19	18
43.6	2.08	13	42.9	2.11	23	41.62	2.17	11
44.2	2.05	64	44.7	2.03	3	44.08	2.05	44
45.7	1.99	30	46.3	1.96	3	44.07	2.03	9
46.1	1.97	24	46.9	1.94	5	45.96	1.97	37
			47.4	1.92	3	47.0	1.93	7
			48.35	1.88	29			
			49.0	1.86	3			
			49.3	1.85	6			
			50.1	1.82	16			
			50.8	1.80	29			

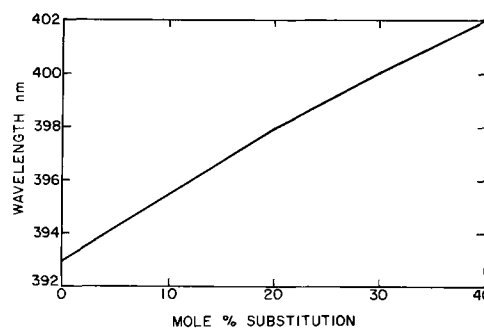


Fig. 7. Shift of peak position with Ca substitution for Sr in SrMgP<sub>2</sub>O<sub>7</sub>:02Eu<sup>+2</sup>.

## REFERENCES

1. V. P. Nazarova, *Bull. Acad. Sci. USSR, Phys. Ser.*, **25**, 323 (1961).
2. N. A. Gorbacheva, *ibid.*, **30**, (1966).
3. W. L. Wanmaker and J. W. ter Vrugt, *Philips Research Repts.*, **22**, 355 (1967).
4. J. F. Sarver, M. V. Hoffman, and F. A. Hummel, *This Journal*, **108**, 1103 (1961).
5. R. L. Brown, *Illum. Eng.*, **61**, 230 (1966).
6. P. D. Johnson, *J. Opt. Soc. Amer.*, **51**, 1235 (1961).
7. Ref. (4) and unpublished work, J. F. Sarver and M. V. Hoffman.
8. N. Kristianpoller and R. A. Knapp, *Appl. Optics*, **3**, 915 (1964).
9. N. Kristianpoller, *J. Opt. Soc. Amer.*, **54**, 1285 (1964).



# Physical-Chemical Studies of KOH-ZnO Electrolytes

W. H. Dyson,<sup>†</sup> L. A. Schreier,\*  
W. P. Sholette,\* and A. J. Salkind\*

E.S.B. Inc. Research Center, Yardley, Pennsylvania

## ABSTRACT

Physical-chemical studies of the electrolyte system KOH-ZnO in the range 30-46% aqueous KOH are described. Vapor pressures at 100°-145°C were obtained in sealed bombs equipped with gauges. Electrical conductivities of samples were measured at 10°, 25°, and 55°C. ZnO solubilities over the range 10°-145°C were determined by analysis of KOH solutions saturated with ZnO; a special solubility apparatus was constructed to obtain samples at temperatures above 100°C.

The aim of this study was to obtain fundamental physical-chemical data for the KOH-ZnO electrolyte system, for use in the development of heat-sterilizable silver-zinc cells. The region of interest for this application included electrolyte concentrations of 35, 40, and 45% KOH, sterilization temperatures of 125°, 135°, and 145°C, and operating temperatures in the range of 10°-55°C.

Vapor pressures of aqueous KOH above 100°C have been previously obtained by extrapolation of data taken below 100°C (1) or by comparison with a reference liquid (2). Electrical conductivities have been reported for KOH solutions at several temperatures by Klochko and Godneva (3), and for ZnO-saturated KOH at 25°C by Dirkse (4). Solubility of ZnO in KOH has been studied by Dirkse for the range -30° to 44°C (4).

In the present work, the following are included: (I) Direct measurements of the vapor pressure of 30-46% KOH solutions in the temperature range of 100°C to 145°C. (II) Conductivity data at 10°, 25°, and 55°C for 35-46% KOH solutions containing varying levels of dissolved ZnO from zero concentration to saturation. (III) Studies of ZnO solubility in 35-46% KOH for several temperatures in the range of 10°-145°C.

In general, reagent grade ZnO powder was dissolved in KOH solutions of various concentrations to make electrolytes for these measurements. Analysis for ZnO content was made by titrating  $Zn^{++}$  with 0.1M EDTA to the xylene orange endpoint (pH 5.0-5.5), and for KOH by titrating  $K^+$  with sodium tetraphenylborate solution using an amperometric endpoint detection. Limits of experimental error were  $\pm 0.05\%$  ZnO and  $\pm 0.25\%$  KOH. Individual experimental details will be given in the respective sections to follow.

## Vapor Pressure

Vapor pressures were measured in sealed nickel bombs heated in an oil bath. These bombs were constructed from 2.5 in. diameter nickel pipe nipples, 8 in. long, and nickel pipe couplings. Both items were cut in half and a round, nickel plate heliarc welded to all cut surfaces, thereby making two bombs with caps. Pressures were read on 3 in. dial ammonia gauges with 0-100 psig range. These were connected to the cap through  $\frac{1}{4}$  in. stainless steel fittings and tubing. The parts were assembled using Teflon pipe tape which helped to seal and prevent galling. The oil baths were Blue M, Model MOD-115A, which operated over the range 0-180°C and maintained temperature to within  $\pm 0.5^\circ C$ . The "oil" used was Blue M High Temperature Ucon Fluid.

<sup>†</sup> Electrochemical Society Associate Member.

\* Electrochemical Society Active Member.

Key Words: dissolution rate, ZnO in aq. KOH; electrical conductivity, aq. KOH and aq. ZnO-KOH; potassium hydroxide, aq. electrolytes; silver-zinc cells, heat sterilizable; solubility, ZnO in aq. KOH; vapor pressure, aq. KOH; zinc oxide, in aq. KOH.

Initial experiments showed that aqueous KOH, directly in contact with nickel, yielded the same pressure at the elevated temperatures as when contained in a Teflon or polypropylene liner. Pressures in the sealed bomb were read directly in psig and corrected for increase in pressure of entrapped air with temperature. Minor corrections were also applied for expansion of electrolyte and for change of solution concentration due to transfer of water to the vapor phase. Figure 1 presents an Othmer-type plot (5) for vapor pressure of KOH solutions at sterilization temperatures. This plot also includes values obtained from the International Critical Tables (1) for temperatures of 100°C and below.

The Othmer method presupposes constancy of the ratio of molar latent heats of the liquid under study and a reference liquid, according to the equation

$$\log P = (L/L') \log P' + C$$

where  $P$  and  $P'$  are the vapor pressures of the liquid being studied (KOH solution) and the reference liquid ( $H_2O$ ),  $L$  and  $L'$  are their molar latent heats, and  $C$  is an integration constant. The data show that the Othmer treatment of vapor pressure for this system is valid up to and including the highest sterilization temperature.

Experiments with KOH-ZnO solutions yielded no consistent pattern of vapor pressure vs. ZnO concentration at the sterilization temperatures. In fact, within limits of experimental error ( $\pm 0.5^\circ C$ ;  $\pm 0.25\%$  KOH;  $\pm 15$  mm Hg) there was no effect of ZnO dissolution on the vapor pressures of the KOH solutions.

## Conductivity

Electrical conductivities of aqueous KOH and KOH-ZnO solutions were measured using a 50 ml conduc-

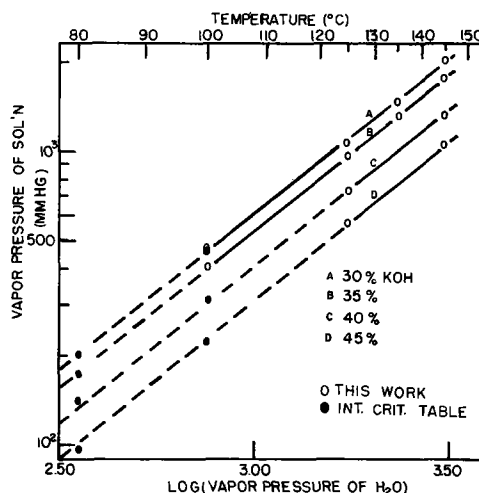


Fig. 1. Othmer-type plot; vapor pressure of KOH solutions

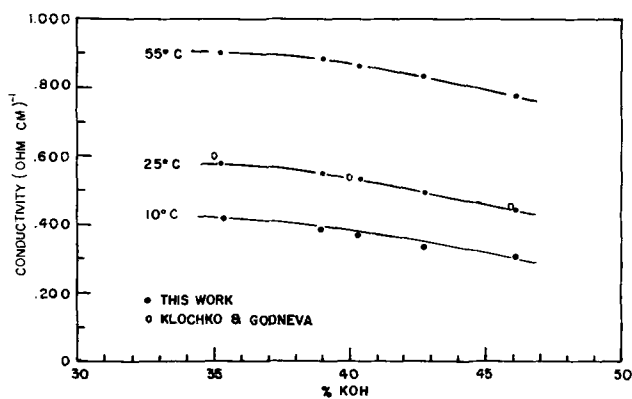


Fig. 2. Conductivity of KOH solutions

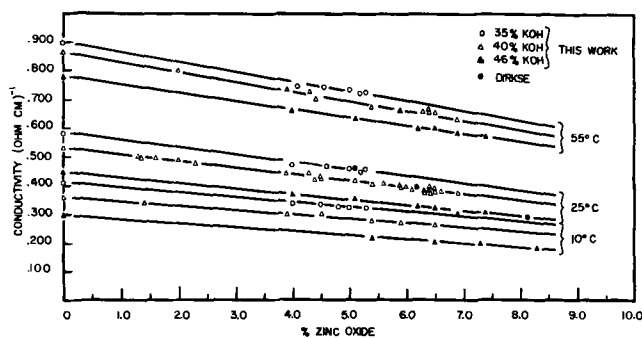


Fig. 3. Conductivity of KOH-ZnO solutions

tivity cell and a Wayne-Kerr Universal Bridge with low impedance adaptor. The cell was immersed in a temperature-controlled water bath until the resistance for a given electrolyte at a given temperature became constant. Calibration and cell-constant determination were periodically checked using a 1 demal KCl standard solution.

Conductivities of pure KOH solutions at three temperatures are plotted in Fig. 2, which includes data for 25°C from Klochko and Godneva (3). Figure 3 gives data on KOH-ZnO conductivities for the same temperatures. Each line of Fig. 3 begins with the conductivity of pure KOH of a given concentration; the conductivity then decreases slightly with increasing addition of ZnO (expressed as final weight per cent ZnO in the given initial KOH solution). A large number of data points were determined for 40% KOH at 25°C to indicate the experimental accuracy of the measurements. Conductivity points from the data of Dirkse (4) are included for ZnO-saturated solutions at 25°C.

#### Solubility

Preliminary experiments for determining the rate of ZnO dissolution in KOH at sterilization temperatures were run in the sealed nickel bombs, or in similar bombs of stainless steel when magnetic stirring was to be used. In the latter case, the bombs contained Teflon inserts to prevent corrosion of the stainless steel by the hot caustic solutions.

The dissolution of ZnO into aqueous KOH at 145°C as a function of time is plotted in Fig. 4. For each run of this experiment, sufficient ZnO powder was added to 100 ml of a given KOH concentration to yield 8% ZnO in the final solution if all were to dissolve. No stirring was employed; samples for analysis were siphoned from the supernatant solution after the bombs were allowed to cool to room temperature. Dissolution of ZnO in the electrolyte under these conditions increased with time and with KOH concentration. However, in similar experiments with stirring during the heating period, the time dependence was not present and all solutions appeared to be saturated with ZnO at room temperature, even after short heating times. Furthermore, even when samples were unstirred dur-

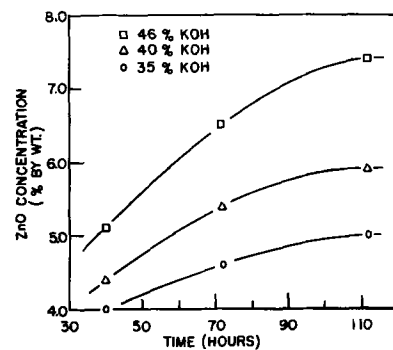


Fig. 4. Dissolution of ZnO in KOH at 145°C

ing sterilization, a simple physical mixing of the electrolyte and undissolved ZnO followed by a centrifugation of this mixture yielded solutions which were saturated with ZnO to the same level as those which had been stirred for the whole time. These room temperature solubility values, which agreed with those obtained by dissolution of excess ZnO in KOH at 25°C with stirring, are given in Table I.

The above experiments indicated that the rate of ZnO dissolution in KOH is rapid when stirring is employed, but is strongly time dependent in unstirred systems in which diffusion of the soluble species away from the solid-electrolyte interface is a significant factor. A further experiment was devised to confirm this point. Eight 75 ml samples of 40% KOH, containing varying quantities of ZnO powder, were shaken for one minute each at 25°C and then immediately centrifuged and the solutions analyzed. The results are plotted in Fig. 5, in which "ZnO mixed with KOH" signifies sufficient ZnO to yield the final % ZnO indicated if all were to dissolve. The actual amount of ZnO dissolved for a given amount present increases linearly at low ZnO and levels off with increasing excess ZnO as saturation is approached.

In many of the dissolution rate experiments, Tyndall effect observations showed that colloidal dispersion accompanied the dissolution of ZnO. By comparing analyses of clear saturated solutions with those of saturated solutions having heavy Tyndall effects, it was determined that the amount of ZnO in colloidal form was very small and could be neglected in comparison to the amount in solution.

The following conclusions were reached as a result of the dissolution rate experiments:

1. Dissolution of ZnO powder in KOH is rapid when stirring or mixing is used.
2. Dissolution may be slow in unstirred solution due to (a) small quantity of ZnO surface exposed to electrolyte, and (b) limited diffusion of dissolved species away from the solid-liquid interface.
3. The diffusion-limited nature of the dissolution of ZnO in aqueous KOH, and the resulting stratification effect in unstirred electrolyte, is more pronounced the higher the KOH concentration.
4. Colloidal dispersion may occur when excess ZnO is present; however, the quantity in colloidal form is small compared to that in solution.

Initial experiments for determining equilibrium solubilities were run for the range 10°-95°C. Excess ZnO was added to solutions saturated at room temperature in stoppered flasks. These were immersed in a water-bath at the desired temperature and agitated for two days or longer, then allowed to settle until no Tyndall

Table I. Solubility of ZnO in KOH at 25°C

Initial % KOH	Final % ZnO
46	8.3
40	6.5
35	5.2

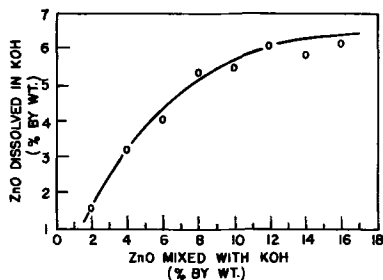


Fig. 5. Dissolution of ZnO into 40% KOH at 25°C

effect was observable in the supernatant solution. Samples of the solution were then siphoned for analysis. Results indicated little or no variation of ZnO solubility with temperature, i.e., the quantity of ZnO dissolved in each KOH concentration was the same over the entire temperature range as listed in Table I. To check this further, a plot of literature data [listed as % Zn vs. % K in the equilibrium saturated solutions by Dirkse (4)] was made and is shown in Fig. 6. The solid line is drawn for the 25°C data; ZnO solubility increases with KOH concentration along this smooth curve up to about 36% K (corresponding to about 52% KOH), then decreases rapidly with increasing KOH concentration above this point. The data for other temperatures fall along this curve, but the "critical region" of KOH concentration differs for each temperature, as indicated by the broken lines in Fig. 6. For the range of KOH concentration of interest in the present studies, viz. 35-45% initial KOH (or about 23-30% K in the final saturated solution), Fig. 6 suggests that ZnO solubility is temperature independent or very nearly so for all temperatures above 0°C.

In order to ascertain whether the temperature invariance of ZnO solubility in aqueous KOH extends up to sterilization temperatures, a special solubility apparatus was constructed as illustrated in Fig. 7. It consisted of two sealed stainless steel bombs with Teflon liners, connected by a nickel siphon tube for isolating and transferring a small sample of saturated

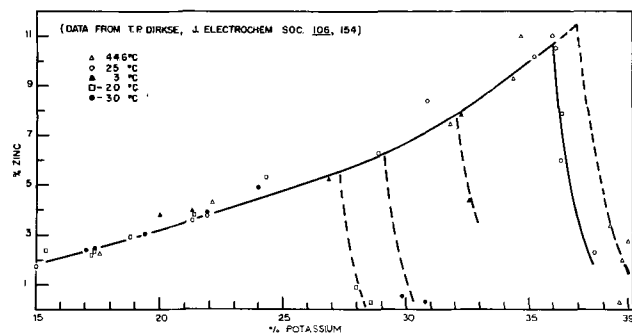


Fig. 6. Composition of saturated KOH-ZnO solutions

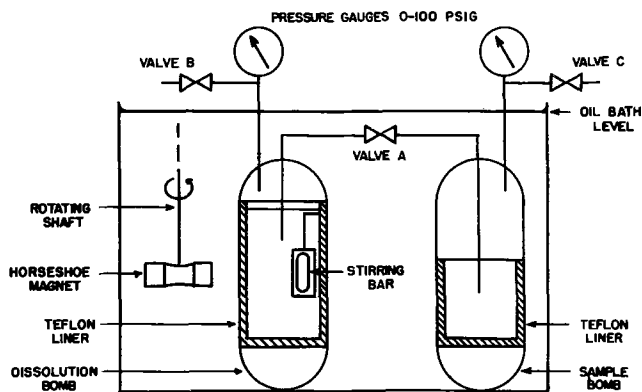


Fig. 7. Schematic of solubility apparatus

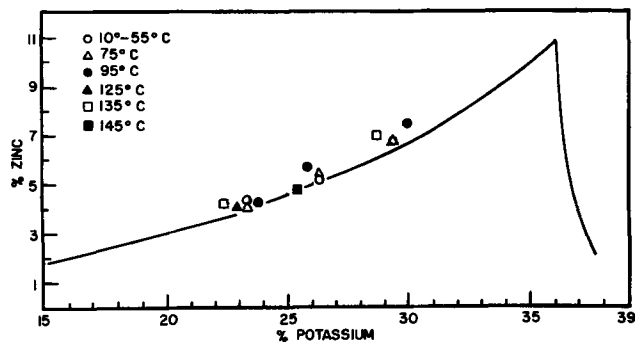


Fig. 8. Composition of saturated KOH-ZnO solutions

solution. Valves and fittings were Monel, and gaskets were Teflon. For a given solubility determination, KOH saturated with ZnO at room temperature was placed together with excess ZnO into the dissolution bomb. The apparatus was then assembled in sealed condition with all valves closed, and brought up to temperature in the oil bath. The solution was stirred at least 48 hr to assure attainment of equilibrium, using a magnetic stirrer suspended by silver wire and activated by a rotating horseshoe magnet external to the bomb. After allowing the excess suspended ZnO to settle for a minimum of 48 hr, a valve "A" was opened and a sample of the saturated solution was transferred through the siphon tube; the excess vapor pressure in the dissolution bomb relative to the empty sample bomb was sufficient to accomplish this transfer. When both bombs reached the same pressure, valve "A" was closed; the oil bath was then allowed to cool to room temperature and the sample removed for analysis.

Results of solubility experiments for all temperatures are plotted in Fig. 8. The 25°C curve from Fig. 6 is included in Fig. 8 for comparison. The data from this work confirms that there is little or no temperature dependence of ZnO solubility in aqueous KOH in the range of 35-46% KOH and 10°-145°C.

### Discussion

Baker and Trachtenberg have recently reported conductivity and solubility data for KOH and ZnO-KOH solutions over the temperature range -66° to 36°C (6). These data are in agreement with our results, which are referred to in their article under JPL Contract 951296 (their reference 1). Also described in our original reports are a number of experiments showing the applicability of the fundamental data to sterilizable Ag-Zn cells. The important observations and conclusions of the latter studies are given in the latest contract summary report (7).

The findings of this study suggest a number of possible areas for future investigations which could be of theoretical and practical importance. More sensitive techniques would allow the detection of small changes in vapor pressure of KOH with dissolution of ZnO, which, in turn, could be related to solution activity, etc. Extension of these measurements to low KOH concentrations would also be of interest, especially since a theoretical treatment would be feasible in that region. Finally, diffusion measurements and studies of colloidal properties for this system would be desirable.

### Acknowledgments

The authors wish to express their appreciation to Mr. Ted Heyman for carrying out much of the experimental work. This work was performed for the Jet Propulsion Laboratory, California Institute of Technology, sponsored by the National Aeronautics and Space Administration under Contract NAS7-100.

Manuscript received Oct. 24, 1967; revised manuscript received Feb. 23, 1968. This paper was presented at the Chicago Meeting, Oct. 15-19, 1967, as Abstract 32.

Any discussion of this paper will appear in a Discussion Section to be published in the December 1968 JOURNAL.

## REFERENCES

1. International Critical Tables, Vol. 3, p. 373.
2. Solvay Technical and Engineering Service Bulletin No. 15, p. 26 (1960).
3. M. A. Klochko and M. M. Godneva, *Russ J. Inorganic Chem.* IV, 2127 (1959).
4. T. P. Dirkse, *This Journal*, **106**, 154 (1959).
5. D. F. Othmer and R. Gilmont, "Kirk-Othmer Encyclopedia of Chemical Technology," 1st Edition, Vol. 14, p. 611.
6. C. T. Baker and I. Trachtenberg, *This Journal*, **114**, 1045 (1967).
7. Jet Propulsion Laboratory Contract No. 951296, Interim Summary Report to Sept. 30, 1967, p. 19-35.

## The Kinetics of Adsorption, Surface Reaction, and Electrochemical Oxidation of Propane on Platinum in Hydrofluoric Acid

Elton J. Cairns,\*<sup>1</sup> Adrian M. Breitenstein,<sup>2</sup> and Anthony J. Scarpellino<sup>3</sup>

General Electric Research and Development Center, Schenectady, New York

## ABSTRACT

The rate of adsorption of propane on platinum in 37 m/o HF at 30°C has been measured using single linear voltage sweep techniques as a complement to earlier studies at 90°C. The surface coverage by hydrocarbon species was measured as a function of adsorption time and potential. The rate of adsorption follows Langmuir kinetics with a third-order dependence on free surface. The rate of reaction of the initial adsorbate at 90°C to form a highly electroactive species (type I) was also measured, and found to be proportional to the surface coverage of the initial adsorbate (type II) and the square of the fraction free surface. The subsequent rate of electrochemical oxidation of type I was proportional to the surface coverage of type I and to free surface. Values for the kinetic parameters are reported, and the results are discussed in terms of a proposed mechanism for the over-all oxidation process.

Because of the strong current interest in direct hydrocarbon fuel cells, the study of the kinetics and mechanism of the anodic oxidation of saturated hydrocarbons is of immediate importance.

At present, hydrocarbon fuel cells require the use of platinum as the electrocatalyst in strong acid electrolytes at temperatures above about 90°C (1-8). The choice of the most appropriate acid electrolyte requires that the anion not be specifically adsorbed on the platinum electrocatalyst, since this would block the adsorption of hydrocarbon molecules. This requirement eliminates HCl, HBr, and HI from further consideration. The acid must also be thermally stable and must not react directly with hydrocarbons; this eliminates HNO<sub>3</sub>, concentrated HClO<sub>4</sub>, and H<sub>2</sub>SO<sub>4</sub> (except  $\leq 3N$ ,  $\leq 100^\circ\text{C}$ ) (9). Weak acids must be eliminated because of low conductance and high concentration overvoltages. The final choice seems to be between H<sub>3</sub>PO<sub>4</sub> (4-6) and HF (2, 3, 7, 8) as suitable electrolytes. Some anion of phosphoric acid adsorbs to an appreciable extent on platinum reducing the over-all rate of hydrocarbon oxidation and complicating the study of these processes. On the other hand, the fluoride anion is adsorbed to only a small extent or not at all (10, 11), providing for a maximum extent and rate of hydrocarbon adsorption and electrochemical oxidation.

Because of the above considerations, HF was chosen as the electrolyte for a study of the behavior of hydrocarbons at platinum anodes. Propane was chosen as the saturated hydrocarbon of first interest because it has been shown to react rapidly in fuel cells (1-4, 6-9) and because it is the smallest hydrocarbon molecule containing the characteristic paraffin CH<sub>2</sub> group. In order better to understand the hydrocarbon fuel cell, with

the hope of finding a substitute for platinum, it was decided that a detailed study of the kinetics and mechanism involved in the over-all anodic oxidation process for propane was of interest. It is desirable to study such a complex process by separating it, so far as possible, into the various individual steps which make up the process, starting with the adsorption step, proceeding to surface reactions and finally to the steps which produce carbon dioxide and hydrogen ions.

The adsorption of methane (12) and ethane (13, 14) onto platinum from perchloric acid has been investigated at temperatures below those which correspond to good fuel cell performance. Gilman (13) found that the adsorption process for ethane was second order in free surface, and first order in ethane concentration. The same adsorbates (15), plus propane (15-17) and butane (15) were studied in phosphoric acid, but no kinetic information was obtained because the adsorption process was diffusion-limited. Butane coverage has been measured on platinum electrodes in sulfuric acid (18, 19), but no rate expressions were reported. The adsorption of some unsaturated hydrocarbons such as ethylene (20, 21) and acetylene (21) on platinum has been studied, but the rates were diffusion-limited, so only steady-state coverage information is available.

The first portion of this study showed that the rate of propane adsorption on platinum in hydrofluoric acid at 90°C is consistent with Langmuir kinetics, third order in free surface at both 0.2 and 0.3v vs. a reversible hydrogen electrode in the same electrolyte (rhe) (22). The formation of a highly electroactive species from the initially adsorbed "propane" was also reported (22). This paper extends the adsorption rate studies down to 30°C and provides a kinetic analysis of a surface reaction and the rate-determining electrochemical step in the over-all anodic process.

### Experimental

The electrochemical studies of the rate of propane adsorption and surface reaction were carried out in

\* Electrochemical Society Active Member.

<sup>1</sup> Present address: Argonne National Laboratory, Argonne, Illinois.

<sup>2</sup> Present address: Materials & Processes Laboratory, General Electric Company, Schenectady, New York.

<sup>3</sup> Present address: Pratt & Whitney Aircraft, East Hartford, Connecticut.

an all-polytetrafluoroethylene (PTFE) three-compartment electrochemical cell, described in detail in ref. (22). The cell was mounted in a forced convection air thermostat which controlled the air stream temperature to within  $\pm 0.1^\circ\text{C}$ ; control of the electrolyte temperature was better.

The working electrode was a smooth platinum wire 0.146 cm in diameter with an exposed portion 1.034 or 0.960 cm long having a hemispherical end. The surface of the electrode was carefully polished by the procedure given in ref. (22). The "true" surface area of the polished electrode was determined by cathodic hydrogen deposition during a linear cathodic voltage sweep, applied via a potentiostat and function generator. With the assumption that  $220 \mu\text{C}/\text{cm}^2$  is the charge required for the cathodic deposition of hydrogen prior to hydrogen evolution, the true area was found to be  $0.5467 \text{ cm}^2$  for the larger electrode and  $0.474 \text{ cm}^2$  for the smaller one, corresponding to a roughness factor of 1.15.

The highly purified electrolyte solution was 37 m/o HF, prepared from quartz-redistilled water and Mallinckrodt analytical reagent grade 48 w/o HF, in all-PTFE apparatus by the procedure described in ref. (22).

All gases used in the electrochemical apparatus were first saturated with electrolyte solution vapor at the appropriate temperature by passing them through electrolyte-containing bubblers made of Pt and PTFE. The propane was Matheson instrument grade, 99.5% min purity and Phillips research grade, 99.97%; both gave identical results. Argon, 99.998% min. purity, oxygen removed, was used as an inert atmosphere during blank determinations and electrode area measurements.

The electrochemical measurements were performed with a Wenking fast-rise potentiostat, a function generator, a potentiometer, a dual-beam X-Y oscilloscope with differential preamplifiers, and a camera. The wiring diagram and additional details have been presented elsewhere (22).

Before each experiment, the working electrode was given a pretreatment consisting of ten alternate anodic and cathodic potentiostatic pulses of 10-15-sec duration (portion A of the voltage sequence in Fig. 1) in order to bring the electrode to a reproducible condition and prevent the accumulation of hydrogen or oxygen in the vicinity of the electrode. Next, the electrode was protected for the later adsorption step by the rapid formation of a protective oxide layer at 1.6v for 6 sec (portion B of voltage sequence). The potential was then stepped to 1.2v in order to maintain the oxide layer while the appropriate mass transport conditions were established (portion C of voltage sequence). During portion C, propane (or argon) was bubbled over the electrode, with stirring (400 rpm) for 60 sec, after which bubbling was stopped, and stirring was continued for 1 min ( $90^\circ\text{C}$ ) or 2 min ( $30^\circ\text{C}$ ) to sweep any gas bubbles away from the electrode. Finally, the desired mass transport conditions were established: quiescent, propane-saturated electrolyte.

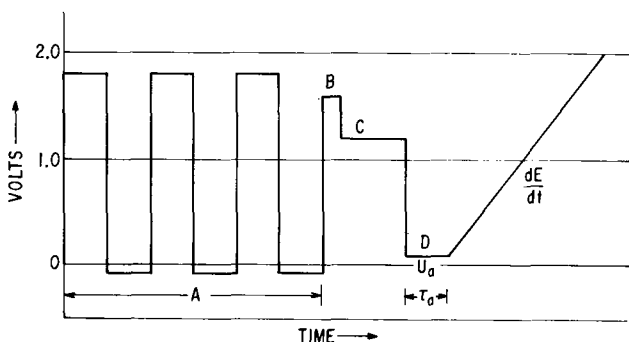


Fig. 1. Voltage sequence for measurement of propane adsorption

The potential of the working electrode was then stepped to the adsorption potential,  $U_a$ , at which the oxide layer was quickly reduced ( $\sim 2 \text{ msec}$ ), and propane was adsorbed for time  $\tau_a$  (portion D of voltage sequence). After time  $\tau_a$  a linear anodic (or cathodic) voltage sweep was applied. The current-voltage trace during the voltage sweep period (see Fig. 1) was photographed from the oscilloscope screen, yielding a permanent record of the current required for the oxidation of the species on the electrode surface (or for the cathodic deposition of hydrogen in the presence of adsorbate). Blank experiments were performed in the presence of argon for use in data reduction. This procedure is explained in more detail in ref. (22) and is similar to that used by Gilman (13) in related investigations.

Various anodic and cathodic sweep experiments were performed as a function of adsorption time  $\tau_a$  (0.01 — 3600 sec), adsorption potential  $U_a$  (0.2 and 0.3v), sweep speed  $dE/dt$  (0.1 — 100 v/sec), and temperature ( $30^\circ$  and  $90^\circ\text{C}$ ). The objective was to determine the rates of propane adsorption and surface reactions, if any, as a function of potential and temperature. The further objective of measuring the rate of anodic oxidation was best achieved by the use of high-area fuel cell electrodes under otherwise similar experimental conditions.

The steady-state anodic oxidation rate for propane was measured at  $90^\circ\text{C}$  as a function of potential by means of an all-PTFE apparatus already described (2,3). These results were used in conjunction with steady-state surface coverages for examination of possible kinetic expressions, as described in a later section of this paper.

### Results and Analysis

As pointed out before (22, 23), it is necessary that the current-voltage trace in the presence of the surface species resulting from propane adsorption be highly reproducible and significantly different from the "blank" trace in the presence of argon. Furthermore, the difference between the traces must be a measure of the amount of material on the electrode surface. This has been shown to be the case for propane on platinum in hydrofluoric acid (22).

A sample trace for propane adsorbed on platinum at 0.3v (vs. r.h.e) in 37 m/o HF at  $30^\circ\text{C}$  for  $\tau_a = 480 \text{ sec}$  is shown in Fig. 2, together with the blank trace in the presence of argon. The difference between the areas under the two traces in the interval between 0.5v and the point where they merge near 1.7v at  $90^\circ\text{C}$  and near 1.8v at  $30^\circ\text{C}$  is called  $Q$ , and has the units of charge (coulombs). This charge can have several components

$$Q = 1.8_{0.5} Q_{\text{HC}} + \Delta Q_{\text{dl}} + \Delta Q_{\text{O}} + Q_{\text{diff}} \quad [1]$$

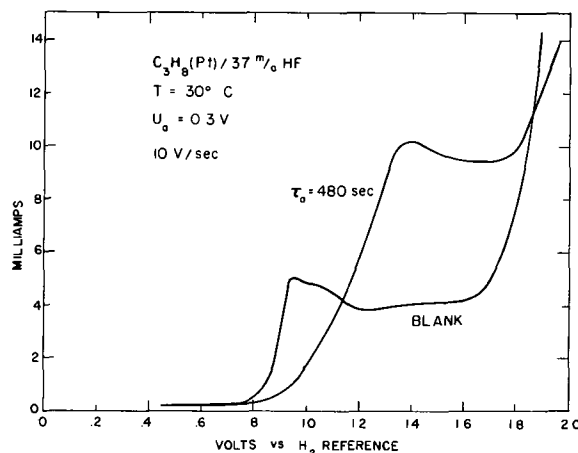


Fig. 2. Current-voltage traces for 480 sec of propane adsorption on Pt in 37 m/o HF at  $30^\circ\text{C}$  and the corresponding blank trace (argon instead of propane).

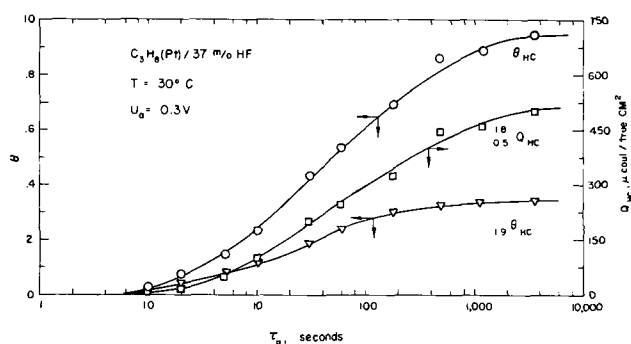


Fig. 3. Surface coverage due to propane adsorption at 0.3v, 30°C, as a function of adsorption time.

The value of  $^{1.8}_{0.5}Q_{HC}$ , the charge required to oxidize the hydrocarbon species on the electrode in the interval 0.5-1.8v vs. rHe after adsorption for time  $\tau_a$ , is the desired quantity. It is evaluated by subtracting the three relatively small terms  $\Delta Q_{dl}$ ,  $\Delta Q_0$ , and  $Q_{diff}$  from  $Q$ , and/or performing experiments under conditions where one or more of these correction terms is zero. The term  $\Delta Q_{dl}$  is the change in the charge stored by the double layer as the linear voltage sweep is applied;  $\Delta Q_0$  corresponds to the change in the charge required to oxidize the surface of the electrode to the potential where the traces merge (about 1.7v at 90° and 1.8v at 30°C); and  $Q_{diff}$  accounts for any propane which diffused to the electrode surface from the bulk electrolyte and was oxidized during the anodic sweep, causing an increase in  $Q$ . Proper choice of sweep speeds plays an important part in minimizing the sizes of the correction terms. The method of evaluating  $\Delta Q_{dl}$ ,  $\Delta Q_0$ , and  $Q_{diff}$  is explained in detail in ref. (22). All of the correction terms were small compared to  $Q$ , so that the value of  $^{1.8}_{0.5}Q_{HC}$  could be obtained with good accuracy.

**Propane adsorption at 0.3v, 30°C.**—The conditions of 0.3v and 30°C were chosen for these experiments in order that the present results might be compared to those for 0.3v at 90°C in the same electrolyte on the same electrode (22). Qualitatively, the propane trace of Fig. 2 is significantly different from the corresponding trace for 90°C [Fig. 4, ref. (22)]. The main difference is that only one current peak is observed (near 1.4v) at 30°C while two were observed (near 0.8v and near 1.2v) at 90°C.<sup>4</sup> Because of this difference, no labeling of peaks (type I, type II, etc.) (22) is necessary, but the single peak observed at 30°C is analogous to the type II peak at 90°C.

The single peak at 30°C is analogous to the type II peak at 90°C because of the similarity in peak voltages (1.3 at 90°C vs. 1.4 at 30°C) (22) and because the peak at 30°C can be hydrogenation-desorbed as can the type II peak at 90°C (15, 24). The type I peak at 90°C, by contrast, appears at 0.8v and cannot be hydrogenation-desorbed to a large extent (15, 24, 26). Furthermore, by slowly increasing the temperature and repeating the anodic sweep experiment, the type I peak can be seen to "grow in," while the type II peak remains relatively unchanged (15, 25).

In order to select the appropriate sweep speed range for which  $Q_{diff}$  is negligible, the value of  $Q$  was determined for 0.1, 1, 10, and 100 v/sec at all adsorption times. The values of  $Q$  for each  $\tau_a$  were plotted against sweep speed, and plateaus were found in the range 0.7-20 v/sec, assuring no  $\Delta Q$  or  $Q_{diff}$  contributions in this range. The plateau values of  $Q$  yielded the  $^{1.8}_{0.5}Q_{HC}$  values used in the preparation of the adsorption curve of Fig. 3. The curves of total fractional surface coverage by hydrocarbon species,  $\theta_{HC}$ , and fractional coverage by hydrocarbon species at 1.9v,  $^{1.9}Q_{HC}$  are discussed below. The  $^{1.8}_{0.5}Q_{HC}$  data for the

full time range studied fall far below the amounts permitted by diffusion, hence, the adsorption process is kinetically limited at 30°C. The electrode approaches saturation coverage at  $\tau_a$  of 3600 sec, in contrast with a time of a few hundred seconds obtained at 90°C (22).

It was observed that some of the relatively slowly oxidized adsorbed hydrocarbon species remained on the electrode at potentials above the crossover point in Fig. 2. It was therefore necessary to obtain a measure of the amount of material remaining in order to determine the total surface coverage due to hydrocarbon species. The method previously developed for this purpose (22) depends on the fact that the rate of oxygen evolution at potentials near 1.9v is hindered by the presence of adsorbed species. The fractional decrease in oxygen evolution current was found to be equal to the fractional coverage by slowly (or difficultly) oxidized species:

$$^{1.9}\theta_{HC} = \frac{^{1.9}i_{Ar} - ^{1.9}i_{HC}}{^{1.9}i_{Ar}} \quad [2]$$

where  $^{1.9}i_{Ar}$  is the (oxygen evolution) current at 1.9v with argon present instead of propane (this is the same as  $^{1.9}i_{HC}$  at  $\tau_a = 0$ ), and  $^{1.9}i_{HC}$  is the current at 1.9v in the presence of adsorbed propane, as read from the voltage-sweep oscillogram (e.g., Fig. 2). The voltage 1.9 was chosen because it was found to be in the linear region of the Tafel plots for oxygen evolution. The plateau values of  $^{1.9}\theta_{HC}$  obtained for each  $\tau_a$  as a result of plotting  $^{1.9}\theta_{HC}$  against sweep speed were used to construct the curve shown in Fig. 3. Again, a saturation coverage is approached at 3600 sec.

In order to perform a kinetic analysis for the adsorption rate studies, it is necessary to know the total fractional surface coverage by hydrocarbon species,  $\theta_{HC}$ , as a function of adsorption time. This means that it is necessary to convert the  $^{1.8}_{0.5}Q_{HC}$  and  $^{1.9}\theta_{HC}$  information of Fig. 3 into a plot of  $\theta_{HC}$  vs.  $\tau_a$ . This was accomplished as follows: It is known from previous work on this system (22) that saturation coverage corresponds to a monolayer. Furthermore, the number of electrons (per surface site occupied) required for the oxidation of the more difficultly oxidized species (those still on the surface at 1.9v) is near 4 (21-23) (consistent with about one carbon per Pt site). Values of  $^{1.9}Q_{HC}$  vs.  $\tau_a$  were calculated using the expression

$$^{1.9}Q_{HC} = ^{1.9}n_{HC} ^{1.9}\theta_{HC} Q_{SH} \quad [3]$$

where  $^{1.9}n_{HC}$  is 4 electrons/site occupied and  $Q_{SH}$  is the charge required to deposit a monolayer of hydrogen on the Pt surface (220  $\mu\text{coulombs/true cm}^2$ ). The total charge required to oxidize all of the adsorbed hydrocarbon species on the electrode was calculated as the sum of  $^{1.8}_{0.5}Q_{HC}$  and  $^{1.9}Q_{HC}$ . This value was checked for consistency with the direct observations of  $Q_{HC}$  for higher temperatures. Good agreement was observed:  $Q_{HC, sat} = 850 \mu\text{coulombs/true cm}^2$  at 30°C vs.  $Q_{HC, sat} = 770 \mu\text{coulombs/true cm}^2$  for  $U_a = 0.3v$  and  $Q_{HC, sat} = 1090 \mu\text{coulombs/true cm}^2$  for  $U_a = 0.2v$ , both at 90°C. From the calculated  $Q_{HC}$  values,  $\theta_{HC}$  values were determined using the expression

$$\theta_{HC} = \frac{Q_{HC}}{Q_{HC, sat}} \quad [4]$$

These results were checked for reasonableness by calculating a value for  $n_{HC}$

$$n_{HC} = \frac{^{1.8}_{0.5}Q_{HC}}{\theta_{HC} - ^{1.9}\theta_{HC}} = \frac{^{1.8}_{0.5}Q_{HC}}{^{1.8}_{0.5}\theta_{HC}} \quad [5]$$

The value of  $n_{HC}$  calculated from Eq. [5], using all of the data was 3.77  $e^-/\text{site}$  obscured, in good agreement with the value 3.47 for  $n_{II}$  at 90°C, and a value of 3.71 obtained by Grubb and Lazarus (26) at 60°C in phosphoric acid. These checks do not prove that the  $n$  val-

<sup>4</sup> Additional experiments have shown the 0.8v peak to be absent at 60°C also.

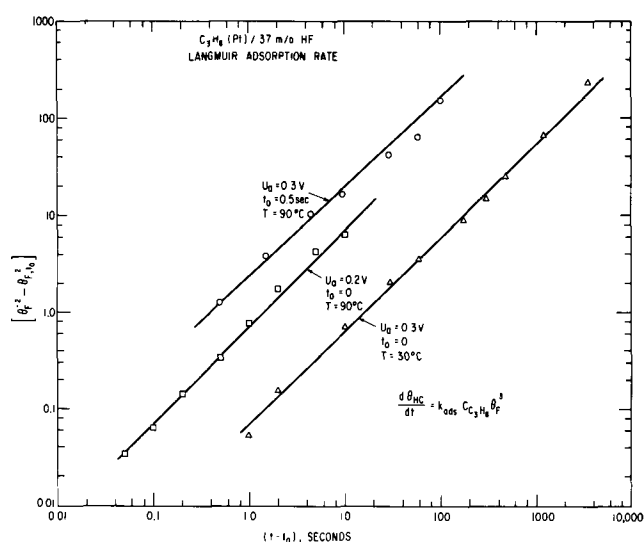


Fig. 4. Langmuir adsorption kinetic plot for the adsorption of propane on Pt in 37 m/o HF at 90°C for 0.2v and 0.3v, and at 30°C for 0.3v (vs. rhe).

ues are absolutely correct, but merely indicate that they are reasonable, and are consistent with the  $1.9\theta_{HC}$  and  $1.8_{0.5}Q_{HC}$  values measured. Furthermore, the assumption that  $\theta_{HC}$  is unity at long times is shown to be reasonable by the value of  $3.77 e^-/\text{site}$  for  $n_{HC}$ .

A plot of the  $\theta_{HC}$  values from Eq. [4] vs.  $\tau_a$  provides all of the information necessary for a kinetic analysis. In keeping with the results obtained for this system at 90°C, a test was made for Langmuir kinetics. The Langmuir rate law may be written as

$$\frac{d\theta_{HC}}{dt} = k_{ads}C_{HC}(1 - \theta_{HC})^m \quad [6]$$

where  $m$  is the order of reaction with respect to free surface and represents the number of surface sites involved in the rate-determining step of the adsorption process. In order to test the applicability of Eq. [6] to the results at 30°C, the following form of Eq. [6] was used

$$\log\left(\frac{d\theta_{HC}}{dt}\right) = \log(k_{ads}C_{HC}) + m \log(1 - \theta_{HC}) \quad [7]$$

A plot of  $\log\left(\frac{d\theta_{HC}}{dt}\right)$  (determined by graphical differentiation) vs.  $\log(1 - \theta_{HC})$  was found to yield a straight line over the full range of experimental values. The value of  $m$ , determined from the slope of the line, was 3.0 just as for 90°C; the value of  $k_{ads}C_{HC}$  was 0.035  $\text{sec}^{-1}$ . Equation [6] was integrated for  $m = 3$ , yielding

$$\theta_F^{-2} - \theta_{F,t_0}^{-2} = 2k_{ads}C_{HC}(t - t_0) \quad [8]$$

where  $\theta_F$  is the fraction of "free" surface, or  $(1 - \theta_{HC})$ . For the present experiments,  $\theta_{F,t_0} = 1$  when  $t_0 = 0$ .

A plot of  $\log\left(\frac{1}{\theta_F^2} - \frac{1}{\theta_{F,t_0}^2}\right)$  vs.  $\log(t - t_0)$  should yield a straight line of unit slope, the intercept of which is  $2k_{ads}C_{HC}$ . This plot, together with the results previously reported for 90°C is shown in Fig. 4. Note that all three lines are straight and have a slope of unity, indicating the applicability of Eq. [6] with  $m = 3$ . The values of  $k_{ads}C_{C_3H_8}$  obtained from Fig. 4 are listed in Table I, together with the measured value of  $C_{C_3H_8}$  at 90°C and an estimated value for 30°C.<sup>5</sup> The values of  $k_{ads}$  in the last column of Table I were obtained by dividing the entries in column 1 by those

<sup>5</sup> The solubility of propane in the HF azeotrope at 30°C was estimated from the measured value at 90°C using the known ratio of solubilities of propane in water and in the HF azeotrope.

Table I. Adsorption rate constants for propane on platinum in hydrofluoric acid azeotrope

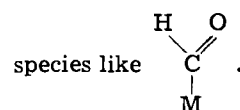
$$\frac{d\theta_{HC}}{dt} = k_{ads}C_{C_3H_8}(1 - \theta_{HC})^3$$

Conditions	$U_a$ , volts	$k_{ads}$ , $C_{C_3H_8}$ , $\text{sec}^{-1}$	$C_{C_3H_8}$ , moles/ $\text{cm}^3$	at $p_{C_3H_8}$ , mm Hg	S, m-mol l-atm	$k_{ads}$ , $\text{cm}^3/\text{mole-sec}$
90	0.2	0.35	$8.13 \times 10^{-8}$	425	0.145	$4.3 \times 10^6$
90	0.3	1.30	$8.13 \times 10^{-8}$	425	0.145	$1.6 \times 10^7$
30	0.3	0.035	$5.18 \times 10^{-7}$	742	0.53	$6.6 \times 10^4$

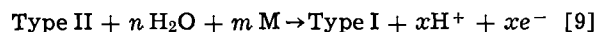
$\Delta H^\ddagger$  for adsorption at 0.3v = 20 kcal/mole.

in column 2. The apparent enthalpy of activation for adsorption at 0.3v was calculated from the last two entries in Table I, and was found to be 20 kcal/mole, a reasonable value for dissociative chemisorption, in which C-H bonds are broken.

Rate of formation of type I by surface reaction at 90°C.—It was found in the earlier portion of this study (22) that at temperatures near 90°C a peak near 0.8v appeared in the anodic sweep oscillogram. This peak (called type I) formed only after a significant fraction of the electrode was covered by adsorbed material (type II). The type I peak has also been observed by other investigators (12-15) and has been found to be only difficultly hydrogenation-desorbed. The results of a number of different indirect observations (12, 14, 16, 22, 24) indicate that the material represented by the type I peak is an oxygenated species, or group of species. The type I material found on Pt in HF at 90°C yielded during its oxidation 3 electrons/Pt site obscured, consistent with the idea of an oxygenated



Because of the fact that the type I peak for Pt exposed to  $C_3H_8$  in HF at 90°C formed after a significant fraction of the surface was covered by type II material (peak at 1.2v), and because the type I material is supposed to be partially oxygenated, one might propose a reaction such as



which corresponds to reactions [16a] and [16b] of ref. (22). If Reaction [9] is a reasonable representation of fact, then the rate expression for the formation of type I material should be

$$\frac{d\theta_I}{dt} = k_I \theta_{II} (1 - \theta_{HC})^{n+m} \quad [10]$$

where  $(1 - \theta_{HC})$  is the fraction of "free" surface, presumably covered by water or some related species (such as OH). The validity of Eq. [10] was tested by making use of  $\theta_{I,0.3}$  [the surface coverage of type I species, evaluated from a cathodic sweep experiment in the range 0.3-0.0v, as explained in ref. (22)],  $\theta_{II,0.3}$  [the surface coverage of type II species, obtained from cathodic sweep experiments in the range 0.3-0.0v, as explained in ref. (22)], and  $\theta_{HC}$  values of Fig. 9, ref. (22) for the preparation of a

plot of  $\log\left(\frac{1}{\theta_{II}} \frac{d\theta_I}{dt}\right)$  vs.  $\log(1 - \theta_{HC})$ . The plot was a straight line over the full range of time for which  $\theta_I$  values were available (0 - 180 sec), indicating that Eq. [10] is valid. The value of  $(n + m)$  obtained from the slope of the line was 2.0. As a final check, a plot of the integral form of Eq. [10] was prepared, as shown

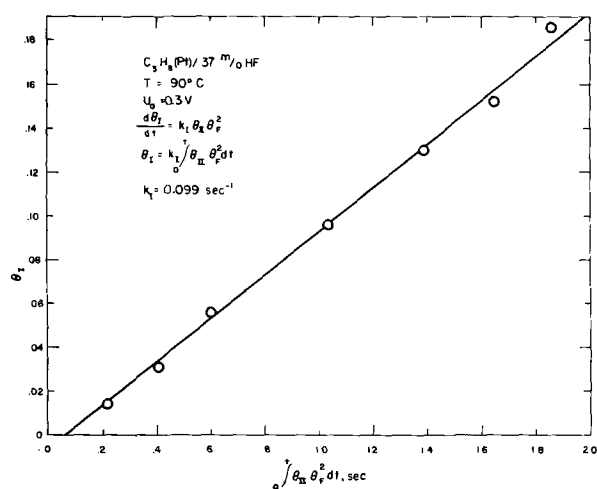


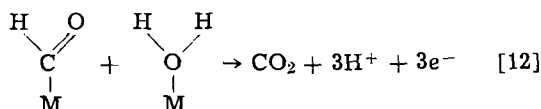
Fig. 5. Test of the integral form of the rate expression for the formation of type I. The slope of the straight line is the rate constant.

in Fig. 5. The slope of the straight line of Fig. 5 yields  $0.099 \text{ sec}^{-1}$  for the value of  $k_1$ . This analysis indicates that the surface reaction by which type I material is formed is second order in free surface and/or  $\text{H}_2\text{O}$  (or OH), and first order in type II.

*Rate of anodic oxidation of type I at 90°C.*—The last step in the over-all oxidation process for propane at potentials below 0.8v is the anodic oxidation of type I to form  $\text{CO}_2$  and  $\text{H}^+$



or



The anodic oxidation of type I is expected to involve one molecule of water and one "molecule" of type I, yielding the rate expression

$$i_1 = N F k_1 \theta_I (1 - \theta_T) \exp\left(\frac{\alpha n F}{RT} \eta\right) \quad [13]$$

In order to determine the applicability of Eq. [13], it is necessary to know the steady-state current density-voltage behavior in the potential range where essentially only type I (of carbonaceous species) is being oxidized (below about 0.8v), and the steady-state surface coverages of type I and total hydrocarbon species.

As discussed in the experimental section above, it was found necessary to observe steady-state current density-voltage characteristics by means of a high-area platinum black electrode, under experimental conditions otherwise identical to those used for the study of the smooth wire electrode at 90°C. The steady-state current density-voltage results are shown in Fig. 6, in Tafel plot form. The data of Fig. 6 are reproducible to within a few per cent in current density at a given potential or less than 10 mv at any current density over the range reported. Data from other electrodes parallel those of Fig. 6, but may be displaced by up to 10 mv. The steepness of the curve at the higher current densities is not related to mass-transport limitations, since electrodes of this type are capable of supporting  $500 \text{ ma/cm}^2$  when operated on propane at higher temperatures (2, 7). As might be expected from the knowledge that the surface coverage of all species is strongly potential-dependent, a straight line was not obtained (Fig. 6). If Eq. [13] is valid, a plot of  $\log\left(\frac{i}{\theta_I(1-\theta_T)}\right)$  vs.  $\eta$  (or  $E_{A-R}$  the voltage of the anode measured against rhe) should yield a

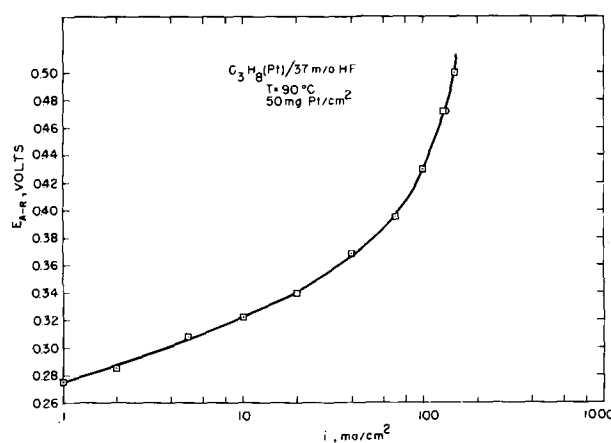


Fig. 6. Tafel plot of the steady-state voltage-current density data from a high-area Pt fuel cell electrode operating on  $\text{C}_3\text{H}_8$  at 90°C in 37 m/o HF.  $E_{A-R}$  is the resistance-free potential of the anode measured against a reversible hydrogen electrode in the same electrolyte.

straight line with a slope of  $(\alpha n F / RT)$ . It should be noted that a portion of the current reported in Fig. 6 is due to the oxidation of hydrogen resulting from the dissociative adsorption of the propane, as well as the hydrogen produced by subsequent dehydrogenation and oxidation steps, but this hydrogen contributes a constant fraction of the total current (8 electrons from hydrogen and 12 from carbon per propane molecule). This fact introduces a multiplicative constant to the right-hand side of Eq. [13]. Another factor to be considered in the test of Eq. [13] is the roughness factor of the high-area electrode, which also enters as a multiplicative constant on the right-hand side of the equation. These considerations make it difficult to determine a value for  $k_i$ , but do not interfere with the establishment of  $\alpha n$ .

The values of  $\theta_I$  and  $(1 - \theta_T)$  for use in Eq. [13] were obtained from the smooth electrode results reported in Fig. 5 of ref. (22) and some additional results. A summary of the surface coverages of all species at  $\tau_a = 300 \text{ sec}$  (essentially steady-state values) (22) is given in Fig. 7. The  $\theta$  values from Fig. 7, together with the steady-state current density-voltage values of Fig. 6 were used to prepare Fig. 8, a test of Eq. [13]. The use of surface coverage values from the smooth electrodes is justified here because of the parallelism in rate and extent of surface coverage by hydrocarbon species for the two types of electrodes (14). The straight line of Fig. 8 indicates the validity of Eq. [13]; the slope corresponds to an  $\alpha n$  value of 0.75. It is reasonable that the rate-determining step involves two electrons (probably the introduction of an oxygen atom to type I to form  $\text{CO}_2$ ), giving  $\alpha = 2$ ,  $n = 0.38$ . The value for  $k_i$  cannot be established because of the uncertainty in the surface roughness of the high-area electrode and the value of  $E_{A-R}$  (the potential of the hydrocarbon anode measured against a reversible hydrogen reference electrode) at which  $\eta$  is zero. If it is desired that  $k_i$  be expressed on the basis of the oxidation of type I only (i.e.,  $N = 3$ ,  $i_1 = 9/20 i$ ) then the value of  $E_{A-R}$  at  $\eta = 0$  must be known for type I. This is an inaccessible value, which prevents the quantitative evaluation of  $k_i$  on the basis of the reversible oxidation potential of type I.

### Discussion

The rate of adsorption of propane on platinum in 37 m/o HF at  $U_a = 0.3\text{v}$  and 30°C is proportional to the third power of the fraction of free surface available for adsorption, in agreement with the results for 90°C at adsorption potentials of 0.3 and 0.2v (vs. rhe). This is consistent with the involvement of three platinum surface sites in the rate-determining step for the



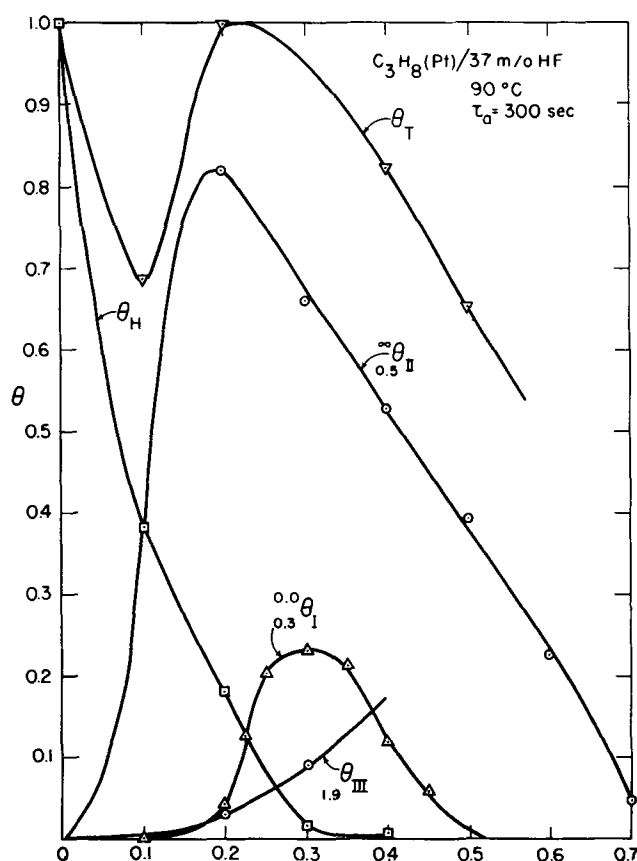
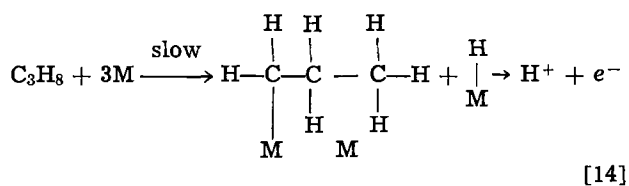


Fig. 7. Surface coverages of hydrogen and hydrocarbon species as a function of adsorption potential at 90°C and 300 sec adsorption time. These are essentially steady-state coverages.

adsorption of propane. It is conceivable that not all three sites are involved directly in the bonding; one or two may be sterically blocked from further participation in the adsorption process. Because of the fact that the Langmuir adsorption rate expression was obeyed over a wide range of surface coverages ( $0 < \theta < 0.95$ ), it is quite probable that the heat of adsorption changes little with surface coverage. The enthalpy of activation for adsorption at 0.3v in the temperature range 30° to 90°C was found to be 20 kcal/mole, consistent with dissociative chemisorption, such as



The adsorbed hydrogen atoms are quickly oxidized at 0.2 and 0.3v; the unbonded M indicates the possibility of sterically blocked surface sites. The rate of adsorption increases with temperature and is higher at 0.3 than at 0.2v. Both of these effects are expected, the former because the adsorption process is dissociative, the latter because the product hydrogen atoms are quickly removed, enhancing the rate of adsorption. The rate constants are summarized in Table I.

After the dissociative chemisorption of propane, the adsorbate probably dissociates further, yielding more hydrogen (which is consumed) and becomes more firmly bonded to the electrode surface. This can cause straining of the carbon-carbon bonds which may result in fragmentation. These processes may be indicated

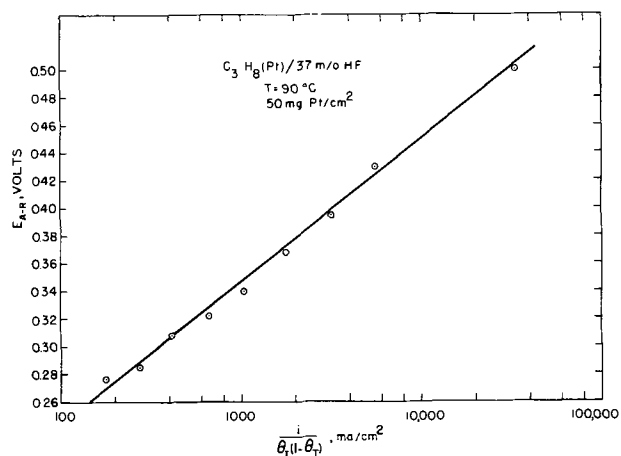
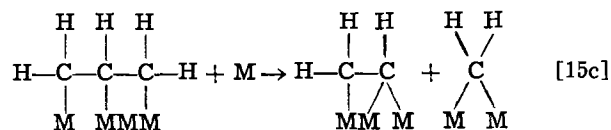
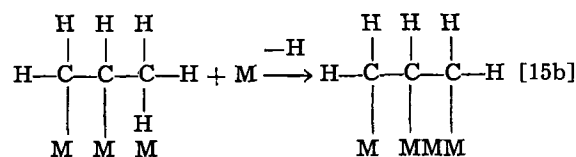
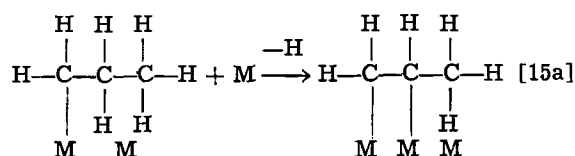


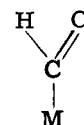
Fig. 8. Test of Eq. [13] using the current-density voltage data for the over-all rate of oxidation of propane shown in Fig. 6 where the rate-determining step is given by reaction [12], and the surface coverages were taken from Fig. 7. The slope of the straight line corresponds to  $\alpha n = 0.75$ .

schematically as follows



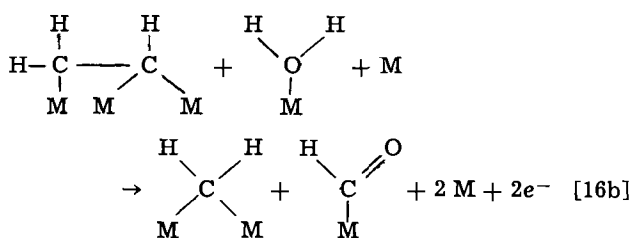
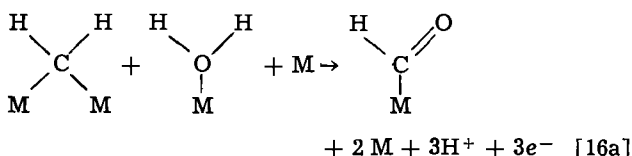
All of these species are considered to be representative of what has been called type II, i.e., the peak near 1.2v at 90°C, and the only peak (at 1.4v) at 30°C. All of the products in reactions [15a], [15b], and [15c] are of the type which can be hydrogenation-desorbed, yielding saturated hydrocarbons. The calculated number of electrons required for oxidation (to  $CO_2$  and  $H^+$ ) of the product species for the above reactions per surface site obscured is: 4.25  $e^-/H$  site for reaction [15b], in good agreement with 4.5  $e^-/H$  site observed for type II at  $U_a = 0.2v$ , 90°C; 3.40  $e^-/H$  site for reaction [15c], compared to 3.47  $e^-/H$  site observed for type II at  $U_a = 0.3v$ , 90°C and 3.77  $e^-/H$  site at  $U_a = 0.3v$ , 30°C. These comparisons serve to indicate that reactions [15a], [15b], and [15c] are reasonable postulates for the identity of the type II material over the range 30°-90°C, and 0.2-0.3v.

Another type of surface reaction occurs at temperatures above about 60°C (15, 25): a partial oxidation, producing a material which is not hydrogenation-desorbed to an appreciable extent, and which is readily oxidized. This material, called type I, is formed at potentials above about 0.15v (22), and causes an anodic peak in the oscillograms at 0.8v at 90°C (22). The charge required for oxidation of the type I material is 2.95  $e^-/H$  site (22), consistent with a stoichiometry such as



which requires 3 electrons per surface site for oxidation to  $\text{CO}_2$  and  $\text{H}^+$ .

As shown above in the Results section, the rate of formation of type I is proportional to the surface coverage of type II and to the square of the fraction free surface. Since type I is a single-carbon species (14, 22, 24) and is singly oxygenated, it is likely that only one water molecule is involved in its formation. It is further likely that an additional "free" surface site is required to accept the hydrogen atoms from type I and  $\text{H}_2\text{O}$  and provide for their conversion to protons. It is therefore suggested that the second order dependence on "free" surface is actually first order in adsorbed  $\text{H}_2\text{O}$  (or OH) and first order in surface available for hydrogen acceptance, corresponding, for example, to the equations



The rate expression for the above processes is

$$\frac{d\theta_I}{dt} = 0.099 \theta_{II} (1 - \theta_{HC})^2 \quad [17]$$

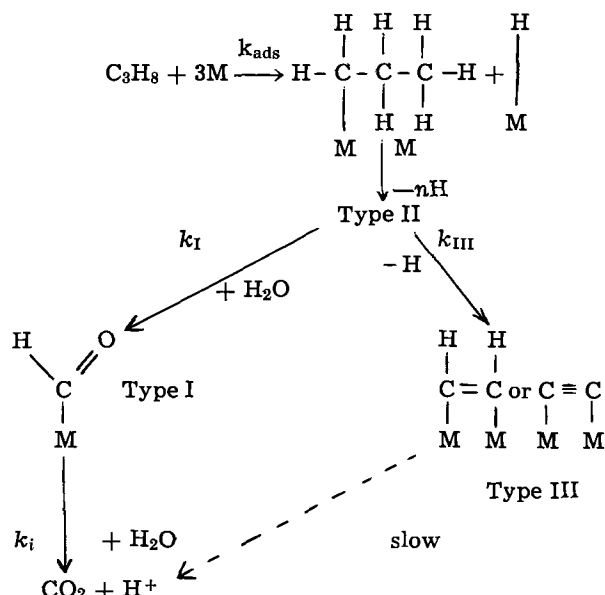
for 0.3v (vs. r.h.e.) at 90°C.

The subsequent oxidation of type I to  $\text{CO}_2$  and  $\text{H}^+$  is a process requiring 3  $\text{e}^-/\text{H}$  site, suggesting reaction [12], and its corresponding rate expression, Eq. [13], which was verified using a high-area electrode

$$i = s N F k_i \theta_I (1 - \theta_T) \exp\left(\frac{\alpha n F}{RT} \eta\right) \quad [18]$$

where  $N = 20$  for the over-all oxidation process for propane,  $s =$  the surface roughness,  $\sim 4000$ ,  $k_i =$  the reaction rate constant for reaction [13],  $\text{sec}^{-1}$ ,  $\alpha = 0.38$ , and  $n = 2$ .

All of the above results and those reported previously (22) suggest an over-all reaction scheme for the anodic oxidation of propane



The type III material is a highly dehydrogenated carbon-rich residue which forms slowly and covers less than 0.1 of the surface at 90°C (22). It can be oxidized to  $\text{CO}_2$  relatively slowly at high potentials ( $>1.8\text{v}$ ) and is generally an undesirable side-product. The desired path, which is the main one for propane at 90°C is the left-hand one. At temperatures below 60°C, the rate of formation of type I is extremely slow; therefore only the adsorption rate was determined at 30°C.

In general, no significant current densities have been measured for saturated hydrocarbons on high-area fuel cell electrodes under conditions where type I does not form at significant rates. It appears that one of the requirements for reasonable performance in fuel cells is a high rate of formation of type I, which can then be oxidized rapidly at acceptable overvoltages. This suggests that the search for more effective electrocatalysts for fuel cells consuming saturated hydrocarbons should concentrate on those materials which catalyze the equivalent of reactions [16a] and [16b] for the hydrocarbon of interest.

### Conclusions

1. Propane is adsorbed on platinum in 37 m/o hydrofluoric acid at a rate which is dependent on potential and surface coverage. The rate law is third order in free surface at 0.2 and 0.3v vs. r.h.e., and at 30° and 90°C. The apparent enthalpy of activation for the adsorption is 20 kcal/mole.

2. A highly electroactive species (type I) is formed from the type II adsorbate at 90°C by reaction with water (or OH). The reaction is first order in adsorbate (type II) and second order in free surface (consistent with first order dependence on water and first order dependence on hydrogen acceptance sites). The rate is a function of temperature and potential.

3. The final current-producing reaction is first order in type I, first order in free surface, and has an  $\alpha n$  value of 0.75 at 90°C. The surface coverage results from measurements on smooth electrodes are compatible with the current-voltage results from high-area electrodes.

4. The results suggest that successful electrocatalysts for the oxidation of saturated hydrocarbons must provide the dual function of promoting the conversion of adsorbed hydrocarbons to type I species, as well as the subsequent conversion of type I to  $\text{CO}_2$ .

### Acknowledgment

It is a pleasure to thank A. D. Tevebaugh for collaboration on the design, construction, and testing of the apparatus, for helpful discussions, and a critical review of the manuscript.

A portion of this work is a part of the program under contracts DA 44-009-AMC-479(T) and DA 44-009-ENG-4909, ARPA order No. 247 with the U. S. Army Mobility Equipment Research and Development Center, Fort Belvoir, Virginia, to develop a technology which will facilitate the design and fabrication of practical military fuel cell power plants for operation on ambient air and hydrocarbon fuels.

Manuscript received Dec. 11, 1967; revised manuscript received Jan. 31, 1968.

Any discussion of this paper will appear in a Discussion Section to be published in the December 1968 JOURNAL.

### REFERENCES

1. E. J. Cairns and G. J. Holm, Paper presented at Washington, D. C., Meeting of the Society, Oct. 11-15, 1964, as Abstract 30; see also *Extended Abstr. of the Battery Div.*, 9, 75 (1964).
2. E. J. Cairns, *This Journal*, **113**, 1200 (1966).
3. E. J. Cairns, in "Hydrocarbon Fuel Cell Technology," B. S. Baker, Editor, Academic Press, New York (1965).
4. W. T. Grubb and C. J. Michalske, in *Proc. 18th Ann. Power Sources Conf.*, PSC Publications Committee, Red Bank, N. J. (1964).

5. W. R. Epperly, in *Proc. 19th Ann. Power Sources Conf.*, PSC Publications Committee, Red Bank, N. J. (1965).
6. O. J. Adhart and A. J. Hartner, in *Proc. 20th Ann. Power Sources Conf.*, PSC Publications Committee, Red Bank, N. J. (1966).
7. E. J. Cairns and E. J. McInerney, *This Journal*, **114**, 980 (1967); see also *Extended Abstracts of The Industrial Electrolytics Div.*, **2**, 1 (1966).
8. E. J. Cairns, *Nature*, **210**, 161 (1966).
9. H. Binder, A. Köhling, H. Krupp, K. Richter, and G. Sandstede, *This Journal*, **112**, 355 (1965).
10. D. C. Grahame, *Chem. rev.*, **41**, 441 (1947).
11. A. N. Frumkin, in "Advances in Electrochemistry and Electrochemical Engineering," Vol. 5, p. 3, John Wiley & Sons, New York (1963).
12. L. W. Niedrach, *This Journal*, **113**, 645 (1966).
13. S. Gilman, *Trans. Faraday Soc.*, **61**, 2546 (1965).
14. L. W. Niedrach, S. Gilman, and I. Weinstock, *This Journal*, **112**, 1161 (1965).
15. L. W. Niedrach and M. Tochner, *ibid.*, **114**, 17 (1967).
16. S. B. Brummer, J. I. Ford, and M. J. Turner, *J. Phys. Chem.*, **69**, 3424 (1965).
17. S. B. Brummer and M. J. Turner, in "Hydrocarbon Fuel Cell Technology," B. S. Baker, Editor, Academic Press, New York (1965).
18. J. A. Shropshire and H. H. Horowitz, *This Journal*, **113**, 490 (1966).
19. R. J. Flannery and D. C. Walker, in "Hydrocarbon Fuel Cell Technology," B. S. Baker, Editor, Academic Press, New York (1965).
20. E. Gileadi, B. T. Rubin, and J. O'M Bockris, *J. Phys. Chem.*, **69**, 3335 (1965).
21. S. Gilman, in "Hydrocarbon Fuel Cell Technology," B. S. Baker, Editor, Academic Press, New York (1965).
22. E. J. Cairns and A. M. Breitenstein, *This Journal*, **114**, 764 (1967).
23. E. J. Cairns, A. M. Breitenstein, and A. J. Scarpellino, Paper presented at the Philadelphia Meeting of the Society, Oct. 9-14, 1966, as Abstract 1; see also *Extended Abstracts of the Battery Div.*, **11**, 1 (1966).
24. S. Gilman, *Trans. Faraday Soc.*, **61**, 2561 (1965).
25. E. J. Cairns and A. M. Breitenstein, in Semi-Annual Technical Summary Report No. 6, July-Dec., 1964, ARPA Order No. 247, Contract Nos. DA 44-009-ENG-4909 and DA 44-009-AMC-479(T), Gen. Elec. Co. to USA ERDL, Ft. Belvoir, Va., p. 4-104, ff.
26. W. T. Grubb and M. E. Lazarus, Paper presented at the Philadelphia Meeting of the Society, Oct. 9-14, 1966, as Abstract 6.

## Growth Characteristics of Iron Oxide Films Generated in Dilute Lithium Hydroxide Solution at 300°C

John B. Moore, Jr.,<sup>1</sup> and Robert L. Jones\*

*Naval Research Laboratory, Washington, D. C.*

### ABSTRACT

In the early stages of iron oxide growth on mild steel in pH 11 LiOH solution at 300°C, the oxide is largely oriented and grows at a rate and with a morphology dependent on the substrate grain orientation. After a certain film thickness is attained, however, the epitaxial oxide growing in the (001) Fe<sub>3</sub>O<sub>4</sub>//(001)α-Fe, [110] Fe<sub>3</sub>O<sub>4</sub>//[100]α-Fe orientation degenerates, leaving in its place a much thinner, fine-grained, randomly oriented "base film" partially covered by large solution-grown Fe<sub>3</sub>O<sub>4</sub> crystals. Experimental evidence indicates that the transformation is induced by stress generated within the epitaxial oxide as the film thickens. The two-phased oxide structure which exists after completion of the epitaxial oxide degeneration persists through oxidation periods of up to at least 300 hr. Observations of its growth behavior lead to the postulation of a growth mechanism in which iron passes through the base film into solution, subsequently to precipitate forming the upper surface crystals. It is shown possible, using this hypothesis, to derive a theoretical rate law which predicts that, in agreement with the experimentally determined corrosion rate data, the corrosion rate should decrease in a logarithmic fashion.

Research initiated by Potter (1) in England and Bloom (2) in the United States has shown that the morphology of iron oxide films generated on steel by attack of high temperature NaOH solution is apparently dependent on the physical system employed. Static corrosion tests at these two laboratories using alkali solutions of similar composition and run at the same temperatures produce oxide films which are chemically the same (Fe<sub>3</sub>O<sub>4</sub>), but structurally different. The Potter films have been examined by electron microscopy (3, 4) and scanning electron microscopy (5) as well as by standard metallographic techniques and it has been established that they have two layers. The inner layer adjacent to the metal is composed of tiny crystallites which come together to form a regular, adherent layer of uniform thickness which, although porous, is nonetheless protective. There is an irregular, poorly adhering, outer layer of much larger

tetrahedral crystals above this; this outer layer is thought to be largely nonprotective. Bloom films, on the other hand, appear to be single-layered, and made up of tightly bound, large Fe<sub>3</sub>O<sub>4</sub> crystals with well developed facets at the oxide/solution interface. These films are less porous and apparently more protective than Potter films. Previous morphological investigations of Bloom-type oxide films have been by metallographic cross-section and light microscopy only, however, and the work reported here, which involves a time sequence study by electron microscopy of the early stages of oxide film growth under Bloom's conditions, was undertaken to provide additional information concerning the physical structure of this type film and to elucidate, as far as possible, the mechanism by which it is generated.

The question as to why one physical form of oxide film or the other should be preferred with a given system has been taken up by Marsh (6) and more recently by Castle and Mann (7). There have also been electron microscopical investigations of the growth of

\* Electrochemical Society Active Member.

<sup>1</sup> Student Summer Trainee. Present address: Chemistry Department, Purdue University, Lafayette, Indiana.

oxide films on stainless steel in high temperature water (8,9) which are of interest in this general problem.

### Experimental

Most of the oxide films examined were formed on the interiors of sealed mild steel capsules filled completely with pH 11 LiOH aqueous solution following the technique devised by Bloom and Krulfeld (10), and heated at 300°C in a circulating air oven. The periods of heating ranged from 30 min to 12 days. A few films were grown on the interior walls of small autoclaves fabricated as described by Potter and Mann (1) using the same alkaline solution and temperature. Heating times in these experiments were generally less than 72 hr.

The capsules were fashioned from mild steel tubing of 0.020 in. wall thickness and 0.25 in. over-all diameter which was found, by analyses, to contain, in per cent, 0.09 C, 0.017 P, 0.032 S, 0.007 N, 0.57 Mn, 0.07 Si, 0.10 Cr, and 0.07 Ni. The autoclaves were made from 2 in. sections of 1 x 0.065 in. cold rolled steel pipe closed at each end with 1 x 0.125 in. caps machined from bar stock. These steels gave under analyses, in per cent, 0.23 C, 0.015 P, 0.038 S, 0.004 N, 0.85 Mn, 0.21 Si, 0.05 Cr and 0.05 Ni and 0.19 C, 0.004 P, 0.033 S, 0.004 N, 0.73 Mn, 0.01 Si, 0.06 Cr, and 0.05 Ni, respectively. The specimens were washed with hot detergent solution, degreased with trichloroethylene, and vacuum annealed at  $10^{-5}$ - $10^{-6}$  mm Hg pressure and 875°C for 1 hr before being cooled and exposed to the atmosphere. This vacuum-anneal pretreatment produces a very thin film of Fe<sub>3</sub>O<sub>4</sub>, which often gives evidence of a high degree of orientation, on the metal surface (11). The annealed specimens were stored in a closed container over anhydrous CaSO<sub>4</sub>.

The LiOH solutions were prepared with reagent grade LiOH and triply distilled water. Lithium hydroxide was chosen as the alkalizing agent in these experiments since Bloom's work has led to the conclusion that LiOH has certain advantages over NaOH and KOH as a boiler water additive (12). Exploratory runs with pH 11 NaOH, however, produced oxide films indistinguishable in the electron microscope from those formed with LiOH solutions, indicating that, with the dilute concentrations and short heating exposures employed here, the cation identity is probably not crucial to the film growth behavior observed.

Sections of oxide for electron microscopical examination were separated from the steel substrate by the iodine-methanol technique (13). When replicas were to be made, the platinum preshadowed carbon replicas of the oxide surface were prepared before the oxide films were stripped from the metal. The composite replica-iron oxide film was then floated on aqueous 20% HF solution which dissolved the oxide, with no visible damage to the replica, in just a few minutes.

Since we wished not only to follow the growth of the oxide film on the capsule wall, but also to determine whether its growth morphology could be related to the oxidation kinetics of the corrosion reaction, corrosion rate data were taken for six capsules in the hydrogen effusion apparatus built by Bloom (10). In this instrument, the corrosion rate is measured by monitoring the hydrogen which diffuses through the capsule wall, that hydrogen having originated in the reaction,  $3\text{Fe} + 4\text{H}_2\text{O} \rightarrow \text{Fe}_3\text{O}_4 + 4\text{H}_2$ . The measurements were made at 300°C using pH 11 LiOH in capsules prepared from the same material and in the same manner as described above.

### Results

An examination of oxide films stripped from the three different steels, that is, from the capsule interiors, and from the caps and walls of the autoclaves, indicates that the oxide morphology and growth pattern is qualitatively the same on all three surfaces, at least over the oxidation periods studied.

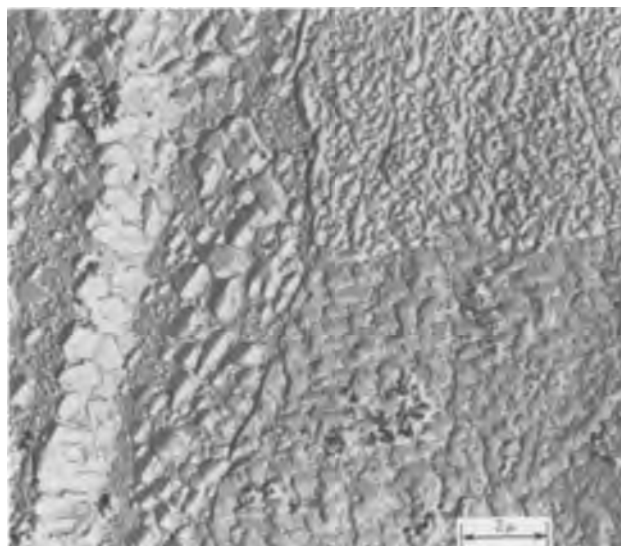


Fig. 1. Oxide morphologies developed after 2 hr at 300°C, pH 11 LiOH.

As the oxide film thickens, it becomes more coarsely crystalline, and characteristic morphologies develop on the different substrate grains as shown in Fig. 1. The oxide layer is often well oriented over the surface of an individual metal grain at this stage of film formation, and selected area diffraction from these films will reveal numerous "single crystal" diffraction patterns, of varying degrees of perfection, corresponding to several different oxide orientations. While the oxide in a given orientation does tend to exhibit a unique texture, as Fig. 1 would indicate, these textures do not seem to develop equally well for all orientations, and the establishment of a relationship between a particular oxide morphology and selected area diffraction pattern is difficult, except in one instance: oxide areas which have the distinctive morphology shown in the upper right corner of Fig. 1 always give electron diffraction patterns corresponding to the (001) plane of the spinel crystal structure (Fig. 4a).

Electron diffraction alone is not sufficient to distinguish between Fe<sub>3</sub>O<sub>4</sub> and  $\gamma$ -Fe<sub>2</sub>O<sub>3</sub>, or perhaps some cation deficient intermediate, in these circumstances, but, since this oxide exists and grows over several hours in an environment reported to produce Fe<sub>3</sub>O<sub>4</sub>, it is assumed to be Fe<sub>3</sub>O<sub>4</sub> which originally existed on the metal substrate in the epitaxial orientation, (001) Fe<sub>3</sub>O<sub>4</sub>//(001)  $\alpha$ -Fe,  $[\bar{1}\bar{1}0]$  Fe<sub>3</sub>O<sub>4</sub>// $[100]$   $\alpha$ -Fe (14). Bloom et al. (12) have found that LiFe<sub>5</sub>O<sub>8</sub>, which has a spinel structure very similar to Fe<sub>3</sub>O<sub>4</sub> and  $\gamma$ -Fe<sub>2</sub>O<sub>3</sub>, can be generated in this system, albeit at somewhat higher LiOH concentrations; this third possibility was ruled out, however, when microanalyses of stripped oxide films failed to show the presence of lithium.

This easily identified (001) oriented oxide, whatever its composition, makes an ideal specimen for following the course of oxide growth, and a study of these areas in oxide films generated with progressively increasing oxidation times (Fig. 2a-h; Fig. 2b and d are at higher magnifications than the rest of the series to show better the fine structure of the oxide film) reveals a most interesting phenomenon. The oxide in the (001) orientation evidently develops at a faster rate than that in other orientations, for areas of (001) oxide crystallites are detectable in films formed with as little as 30 min heating (Fig. 2a and b). It also grows in a different way, thickening in a uniform manner to form a compact, coherent layer while the oxide in non-(001) orientations consists of a thin film and discrete, widely separated larger crystals which appear to be considerably thicker than the film itself (Fig. 2c and d). The (001) epitaxial oxide continues

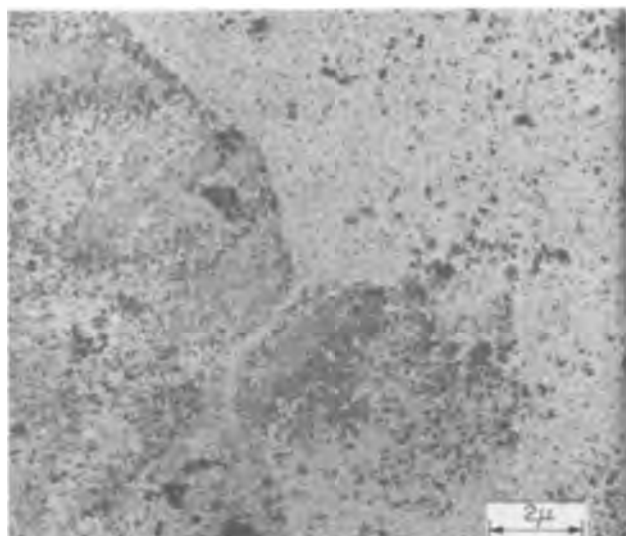


Fig. 2a

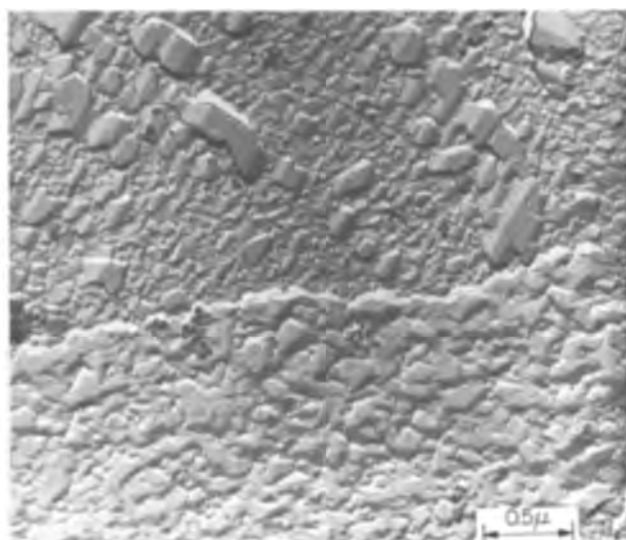


Fig. 2b

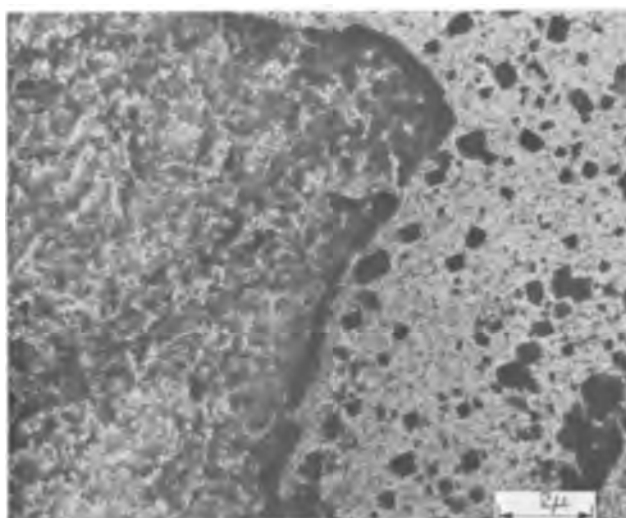


Fig. 2c

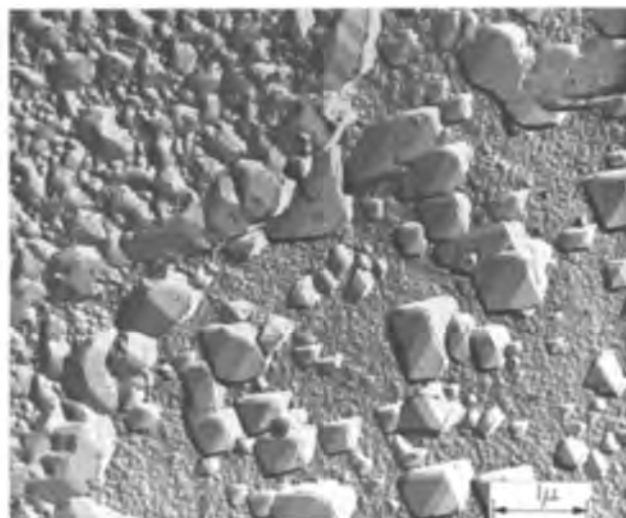


Fig. 2d

Fig. 2a-d. Time sequence series of electron micrographs showing the iron oxide film at progressive stages of development. The left column shows the oxide after (2a) 30 min and (2c) 2 hr at 300°C, pH 11 LiOH; the right column, replicas of the oxide upper surface at corresponding times.

to thicken with extended capsule heating and, as shown in Fig. 2e and f (6 hr heating), the boundary between the two oxide types becomes quite distinct. At about this point, however, one notices, in scanning across the oxide film, that the relative percentage of the surface area covered by the (001) oxide is definitely reduced, and more so than could be explained by fluctuations between individual specimens. Furthermore, if oxide films from longer heating periods are examined, the (001) oxide morphology is found to be almost completely absent. These facts lead to the conclusion that after a certain limiting thickness is reached, the epitaxial (001) oxide must undergo a transformation, or perhaps more descriptively, a degeneration which removes it from the capsule surface. This conclusion is supported by the appearance of the residual (001) oxide in Fig. 2f and particularly in Fig. 3 where two areas of epitaxially oriented oxide are just being engulfed in the final stages of the transformation.

The manner in which this transformation occurs suggests that it is stress induced and that the process

is initiated only after some minimum amount of stress has been generated within the epitaxial oxide, presumably as a result of the increase in oxide thickness. If selected area diffraction patterns are taken just inside the boundary of a degenerating oxide region and then just outside of it, that is, on an area of the surface which had been previously covered by the oriented oxide, they (Fig. 4a and b, respectively) show that the transformation involves, in addition to a marked decrease in oxide thickness, a decided oriented-to-unoriented transition of the surface oxide. No quantitative value for the epitaxial oxide thickness requisite for the commencement of the transformation process can be given, but the process itself is observed to begin after 2 to 6 hr heating and to be largely completed after 24 hr at temperature.

No other transformations of this nature were discovered when films from periods of heating longer than this were examined; the only visible change in the oxide morphology being a continually increasing coverage of the specimen surface by large, fully faceted crystals (Fig. 2g and h) which have been identified in previous work as  $\text{Fe}_3\text{O}_4$ . One noteworthy finding here, however, was that the thin oxide film next to the metal, the "base" film, which remains visible between the larger crystals, apparently changes little or not at all in thickness as the oxidation periods become longer. This conclusion was reached by comparing the

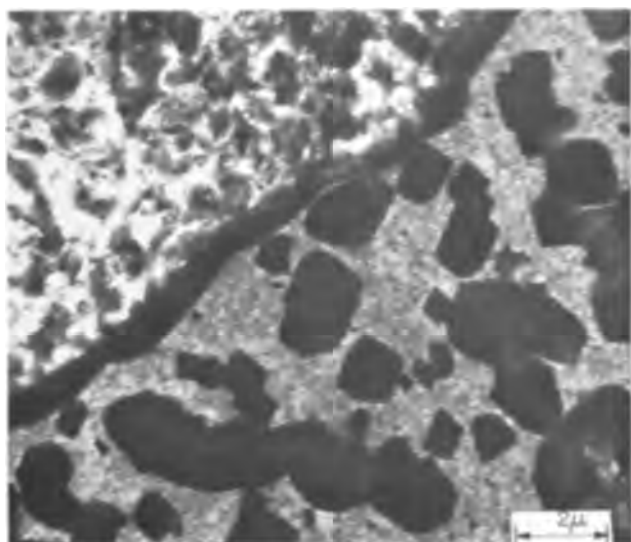


Fig. 2e

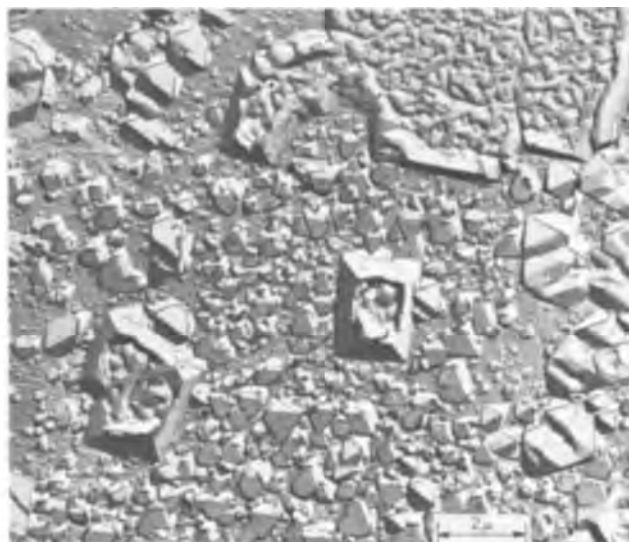


Fig. 2f

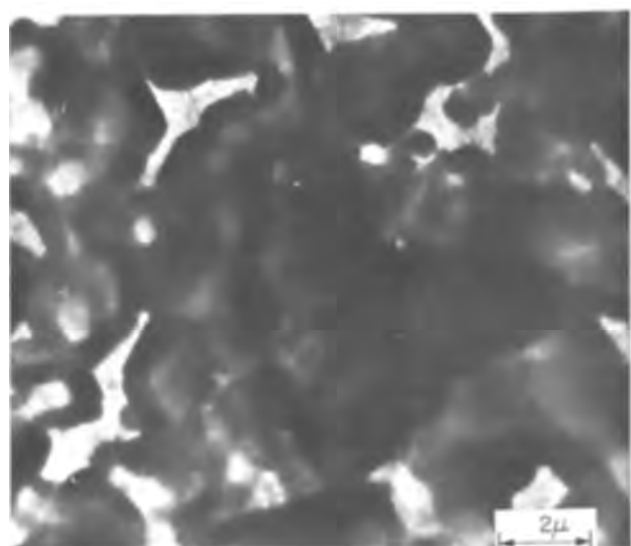


Fig. 2g

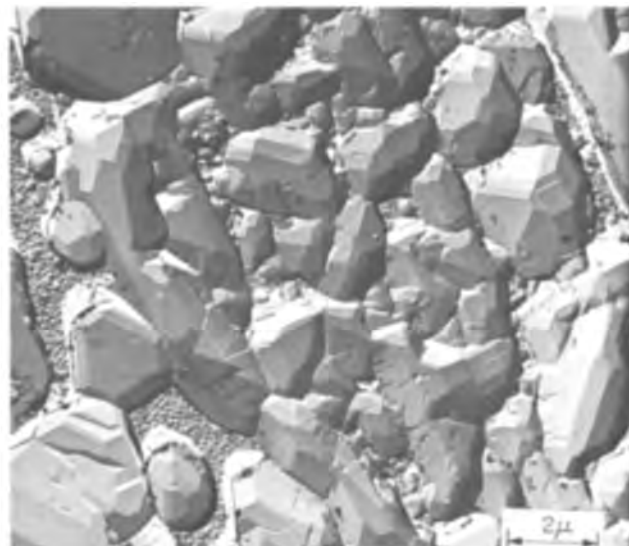


Fig. 2h

Fig. 2e-h. Time sequence series of electron micrographs showing the iron oxide film at progressive stages of development. The left column shows the oxide after (2e) 6 hr and (2g) 96 hr at 300°C, pH 11 LiOH; the right column, replicas of the oxide upper surface at corresponding times.

relative degree of electron transmittancy of base films formed with different heating times as, for example, in Fig. 2e where the time was 6 hr and Fig. 2g where it was 96 hr. While this technique is strictly applicable only for amorphous films, in instances such as this, where the films are composed of small, randomly oriented crystallites and the intensity losses due to diffraction are a direct function of film thickness, a good indication of relative film thicknesses can be obtained from a comparison of transmitted intensities provided, of course, that the electron microscope settings are not changed between specimens.

Replicas of the base film (Fig. 2h) reveal that it has still another distinctive property. After extended periods at 300°C (say, 50 hr and longer), the individual crystallites at the upper surface of this film, which show definite crystallographic forms with shorter heating times, become rounded and pebble-like and occur only over a rather limited size range (approximately 300-500Å). The appearance of the "equilibrium" base film is the same not only over the whole surface of a given specimen, but also between specimens of different steel composition from both the autoclave and capsule systems, indicating that this pebble-like texture is characteristic of the base film.

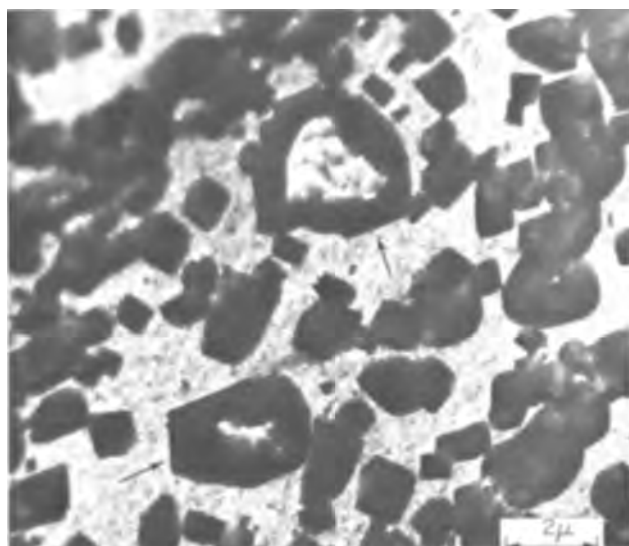


Fig. 3. Two areas of epitaxial oxide in the final stages of transformation after 6 hr at 300°C, pH 11 LiOH.



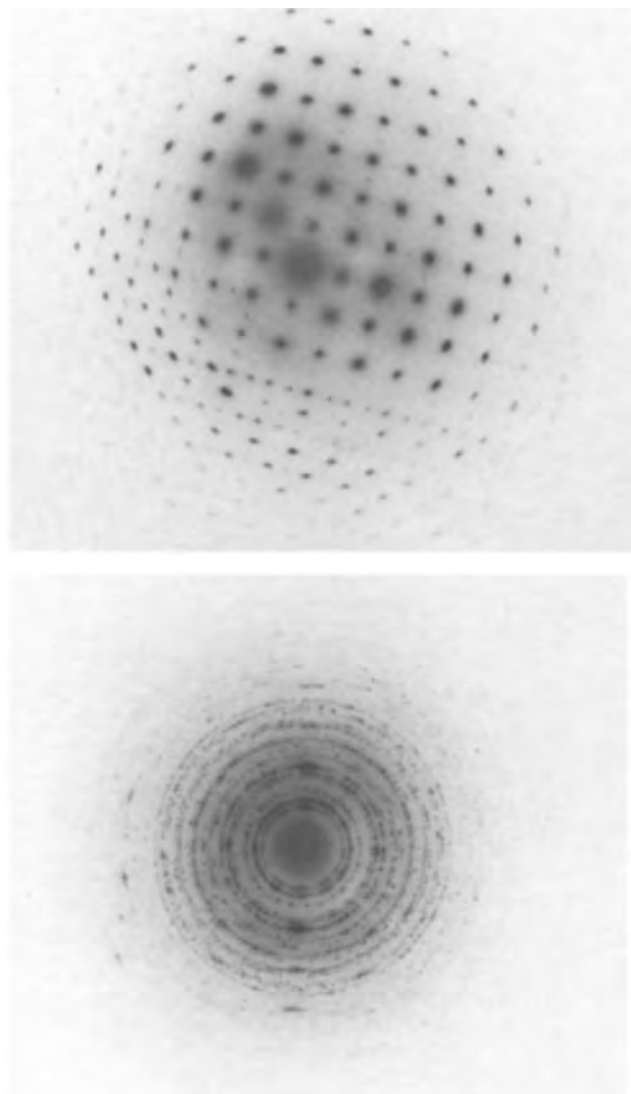


Fig. 4. Selected area diffraction patterns from epitaxial (4a, top) and transformed (4b, bottom) oxide areas.

Since the well developed facets of the larger upper crystals are a strong indication that they are formed by precipitation from solution, presumably on top of the base film, several attempts were made to show that there is in fact a polycrystalline layer between these crystals and the metal substrate by mechanically dislodging the crystals in question to reveal the underlying stratum. These upper crystals adhere so tenaciously, however, that if a dislodging force is applied, as by burnishing the oxide film *in situ* on the capsule wall with the end of a wooden rod, they will shear across the main crystal body rather than be dislodged.

The points in Fig. 5 represent the arithmetic mean of corrosion rate data from five capsules (one capsule of the original six leaked). The individual curves all have the same general form and, at 190 hr, they are all within  $\pm 5\%$  of the mean value shown. A logarithmic curve can be fitted to these averaged data points with good precision using the empirical method of Champion and Whyte (15). This fit may not be quite as meaningful as Fig. 5 would lead one to believe, however, for the derived logarithmic equation indicates an oxide film thickness of approximately 1500Å at  $t = 0$ , a value most likely too high by a factor of five or more. On the other hand, it is known that the hydrogen effusion technique employed here tends to give high results at short corrosion times because a certain amount of gas is desorbed from the capsule's exterior as it comes to temperature (10).

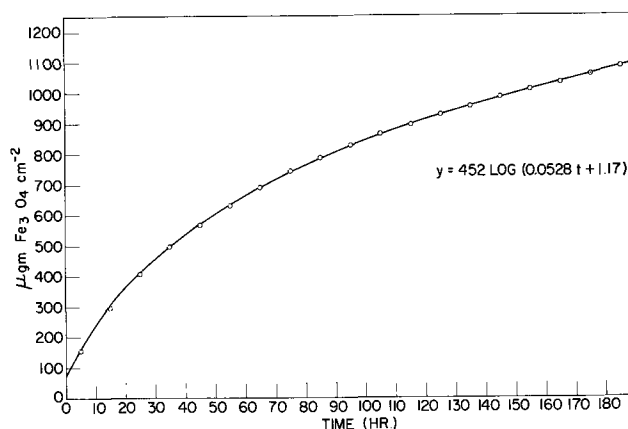


Fig. 5. Oxidation of low carbon steel in pH 11 LiOH at 300°C

### Discussion

Two distinct aspects of oxide film growth in high temperature LiOH solution have been revealed which will, for clarity, be discussed separately. These concern the degeneration of the epitaxially oriented (001) iron oxide, an event occurring in the earlier stages of film formation, and the two-phased, double-layered structural configuration which the oxide film assumes as this process is completed.

*Mechanism of epitaxial oxide transformation.*—In considering possible mechanisms for the epitaxial oxide degeneration, note needs be made of the recent experiments of Grauer and Feitknecht (16). They found that the protectiveness of air-formed oxide films on iron (these were strongly oriented) against attack by chromate solution increased with film thickness up to a certain point, but then decreased drastically. This loss of protective ability was attributed to the appearance of pores or fissures in the oxide film. They observed further that corrosive attack then proceeded in such a way that sections of the original oxide were undermined and displaced from the specimen surface, leaving in their place a very thin, randomly oriented, passive  $\text{Fe}_3\text{O}_4$  film.

A sufficient number of our observations run parallel to those of Grauer and Feitknecht to suggest that we may be observing two different manifestations of one basic phenomenon. We see, for example, electron diffraction patterns (Fig. 6) very much like the one published by these authors to show the degree of orienta-

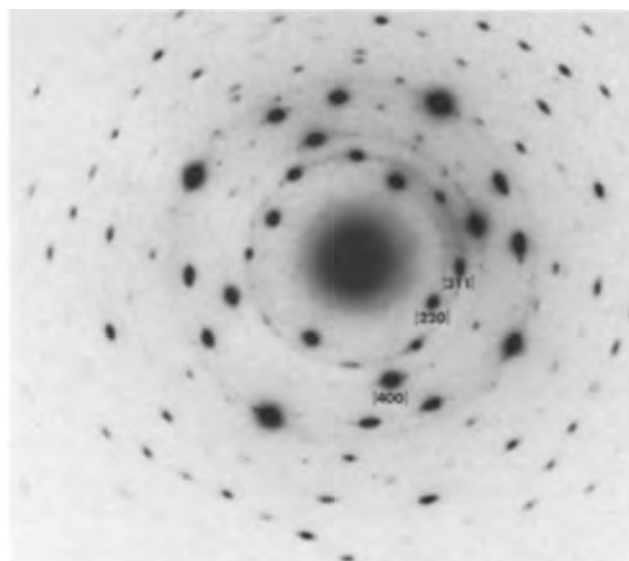


Fig. 6. Selected area diffraction pattern from an area of nucleating crystallites in an iron oxide film after 30 min at 300°C, pH 11 LiOH.

tion existing in their air-grown films when we examine areas of crystallite nucleation (Fig. 2a) in films grown in our capsules during short (30 min) heating exposures. These patterns are of some interest themselves for, while they resemble the (001) projection of the spinel reciprocal lattice, they cannot be indexed on this basis because of the presence of additional, anomalous diffraction spots, particularly those corresponding to the (311) planes of the spinel lattice. Reports of similar diffraction patterns from oxide films on iron or steel have been made previously and several hypothesis as to the origin of the (311) spots have been advanced (17-20). The one point of agreement seems to be that these patterns are associated with the process of nucleation of oriented oxide crystals on the specimen surface. For our own part, we observe that as the areas of oriented oxide thicken with extended heating, they cease to show this type of pattern, and yield instead the simple (001) spinel pattern (Fig. 4a).

Drawing from this background, we envision the following chronological sequence for the growth and subsequent transformation of epitaxial (001) iron oxide in the Bloom capsule system. A vacuum-anneal pretreatment such as the specimen tubing receives tends to produce an oriented  $\text{Fe}_3\text{O}_4$  film on the iron surface (11); this effect would be especially strong for (001) Fe grains where the favorable epitaxial orientation, (001)  $\text{Fe}_3\text{O}_4$ //(001)  $\alpha$ -Fe,  $[\bar{1}10]$   $\text{Fe}_3\text{O}_4$ // $[100]$   $\alpha$ -Fe, is possible. When the capsules are filled with LiOH solution, some  $\text{Fe}_3\text{O}_4$  may dissolve (21), but since the volume of capsule is small, the dissolution likely does not go to completion. With the commencement of heating, the residual film, still oriented, begins to develop further, with both the rate and morphology of this development dependent on the substrate grain orientation (Fig. 1). The growth rate of (001) iron oxide is apparently higher than that of iron oxide in other orientations (Fig. 2d), and a compact, coherent, and relatively thick layer of oxide soon builds up in this orientation. Stress mounts within this oxide layer as its thickness increases until finally the film fails, producing pores and fissures that permit the LiOH solution access to the underlying metal. Corrosive attack occurs then at the stressed metal/oxide interface so as to cause the oriented oxide to be replaced by a much thinner, finely crystalline, randomly oriented iron oxide film in a manner analogous to that reported by Grauer and Feitknecht. The displaced oxide dissolves, either at the time of displacement or later, since it is in a sealed capsule at high temperature, and then precipitates as secondary crystals on the underlying randomly oriented base film.

While the postulated stress-induced fissures could appear at random sites, e.g., above occlusions, etc., in the epitaxial oxide film, our experimental evidence is that attack usually initiates at the outer perimeter of a (001) epitaxial oxide area and proceeds inward. This is explainable if one assumes that the oxide grows thickest just above the substrate grain boundary, and that fissures would therefore be more likely to appear first in this region. The inward march of the transformation reaction results finally in a total engulfment, or "swallowing up" of the oriented oxide (indicated by arrows) as shown in Fig. 3.

Our electron micrographs also show that an encircling ring of larger crystals, which are apparently reprecipitated  $\text{Fe}_3\text{O}_4$ , is always present about a degenerating (001) oxide region. These secondary crystals arise presumably because the solution in this vicinity is heavily saturated with iron ion species, either from dissolution of the original oxide or fresh corrosive attack on the exposed metal surface, and the freshly formed base film just beyond the epitaxial oxide boundary represents the nearest stable site for nucleation and crystal growth from solution. As the

degenerating oxide recedes across the specimen surface, more or less continuous segments of the encircling ring should be left behind, since these crystals are nonmobile; and, indeed, strands of surface crystals which may be evidence of such a phenomenon are often found, as in the lower portion of Fig. 2e and at the right side of Fig. 3, near the epitaxial oxide boundary. These residual crystal strands might be better delineated and more abundant except for the fact that they are initiated in a supersaturated environment under nonequilibrium conditions and hence likely to be subject to further recrystallization themselves.

*Development of two-phased oxide film.*—The overall appearance of the two-phased film which develops with degeneration of the epitaxial oxide, and the manner in which the base film comes to be more and more covered by large  $\text{Fe}_3\text{O}_4$  crystals as the corrosion reaction progresses, strongly suggest that iron passes through the base film and into solution, subsequently to precipitate on the base film surface. This mechanism for the formation of oxide films on iron in high temperature aqueous media has, in fact, been proposed by Castle and Mann (7), who showed that by varying the factors which control the degree of saturation immediately at the corroding surface, one could apparently grow either Bloom films (no stirring, high saturation) or Potter-Mann films (stirring or iron ion sink, low saturation). If this theory is correct, the large surface crystals, formed by precipitation on a randomly oriented film, should themselves be randomly oriented; our electron micrographs reveal, however, that in certain areas the facets of the individual crystals are well aligned (Fig. 2h). There is no reason to expect crystals precipitating from solution onto a truly polycrystalline, randomly oriented substrate to nucleate and grow with a three-dimensional orientation, and the alignment displayed by these crystals needs explanation if the dissolution-precipitation mechanism is to be considered valid.

A similar type of orientation has been found by Field and Holmes (3) for Potter-Mann films, and they have published a metallographic cross-section micrograph of the oxide film (their Fig. 10) which clearly shows that, in this case, a polycrystalline layer better than  $5\mu$  thick exists between the metal grain and the oriented upper oxide crystal. In a discussion of this phenomenon, these authors pointed out that it seemed to be related to the fact that the specimen had been annealed, since oriented upper crystals occurred only with annealed surfaces and never with abraded surfaces.

A review of our electron micrographs brings forth two possibilities for the origin of the aligned surface crystals observed in our oxide films, neither of which would necessarily preclude the idea that the two-phased film grows primarily through dissolution-precipitation. The areas of crystal alignment are apparently associated with underlying metal grains, since we find instances of abrupt change in the direction of alignment across lines which probably represent the substrate grain boundaries, and different growth patterns are observed, depending on whether the metal grain is (001) or non-(001) oriented.

Many of the tiny crystallites which make up the early, very thin oxide films on non-(001) grains (upper half of Fig. 2b) are aligned, presumably by epitaxial forces. While these oxide films may therefore be considered to be partially epitaxially oriented, the areas of orientation are small and separated from one another, and apparently sufficient stress does not develop, in subsequent thickening of the oxide film, to cause a disorienting transformation in this grouping of oriented crystals. If it happens that the crystal alignment is such that planes giving preferred growth from solution are favorably oriented, then this set of crystals can act as nuclei for the development of



aligned secondary crystals; moreover, since precipitation from solution, under these circumstances, represents a low-stress mode of crystal growth, the precipitated secondary crystals may grow to appreciable size while still maintaining their alignment. It appears then that aligned secondary crystals occur on non-(001) grains because the nucleation sites, rather than being randomly situated, are actually oriented themselves from the very beginning of the growth process.

The initial oxide growth process on (001) substrate grains, on the other hand, is such that stress is produced within the oxide film and a transformation takes place that removes the original oxide, replacing it with a new polycrystalline and randomly oriented film. Can oriented growth of precipitated crystals occur on this surface? There is experimental evidence to indicate that it can. In Fig. 2e, for example, a number of the smaller surface crystals appearing on the freshly formed base film show a simple crystallographic form and a range of size which suggests that they are most likely newly nucleated and growing secondary crystals. Furthermore, the edges of many of these crystals are aligned, providing a clear indication that oriented growth is taking place here. The implications of this finding are uncertain. It may be simply that the transformation does not remove every vestige of orientation in the (001) oxide layer and that some crystallites of the great number constituting the base film remain in register with the substrate and hence with each other. This idea is supported by an examination of the base film diffraction pattern (Fig. 4b) which reveals a slight tendency to residual preferred orientation. Or, it may represent still another instance where an oriented species is observed to nucleate in a previously amorphous or randomly oriented surface film; such observations are not uncommon in gaseous oxidation experiments, having been reported by, among others, Gulbransen for iron oxide films (22), Bartlett for aluminum oxide films (23), etc. Whatever the source of these oriented crystallites, it may be expected that, although they may grow initially by recrystallization within the oxide film, they will eventually switch over to growth from solution and thus lead to the generation of large oriented upper crystals on (001) metal grains.

While these hypothesis may rationalize the presence of oriented secondary crystals in the films studied here, it is not obvious that the same arguments could be applied to explain the appearance of the oriented upper surface crystals found by Field and Holmes (3) where the polycrystalline layer between surface crystal and substrate is fully  $5\mu$  thick. How the surface crystals maintain orientation with the substrate through an intervening layer of such thickness remains a crucial, but unresolved question in the development of theories of oxide film formation in high temperature aqueous solution.

Although none of our conclusions are contingent upon a knowledge of the film structure under the large secondary crystals, it has been tacitly implied in these discussions that as the crystal being formed from solution grows laterally over the base film, the crystallites of this film are not incorporated into the body of the larger crystal, i.e., that a polycrystalline phase remains between the precipitated crystal and the metal below. There is as yet no experimental proof of this; the assumption is made through analogy with the work of the Potter and Mann group who have observed that the upper surface crystals never incorporate the inner polycrystalline layer. Extensions of the upper crystal down into the polycrystalline region are sometimes found however (3) and it may be that the adherence displayed by the secondary crystals in our capsule system results from a mechanical locking-in effect that such extensions would provide.

*Significance of evolved oxide structure.*—Two noteworthy characteristic properties are displayed by the base film once the two-phased structure is fully established: its upper surface takes on a distinctive pebble-like texture, and the film itself comes to a certain limiting thickness beyond which it will not grow. These properties are invariant, as far as can be seen, over the surfaces of the several different specimens examined, and it appears therefore that they are independent of such factors as substrate grain orientation, minor variations in alloy composition, and slight differences in surface pretreatment. Work with anodically passivated metals has shown that noncrystallographic oxide growth such as this occurs when the rate-determining step is diffusion through the passivating oxide film (24). Moreover, it may be noted that while the base film qualities seem unusual at first sight, they are just those that would be expected for an oxide film being simultaneously generated at the oxide/metal interface and dissolved at the oxide/solution interface. The film then would come to a limiting thickness as the rates of the two competing reactions become equal, and its outer surface, which is being continually renewed, would develop a morphology determined predominantly by the dissolution process. Oxide formation at the oxide/metal interface would initially be the faster reaction, but as the oxide film thickens, this reaction, controlled by solid state diffusion of reactants to or from that interface, would slow until its rate just equals that of the dissolution reaction at the oxide surface.

This hypothesis concerning the generation of the base film, which has been developed from observations of the growth behavior of the oxide, turns out to be quite similar to a mechanism of formation for passive oxide films advanced by Vetter (25); he explains the small but constant corrosion current which "passive" films exhibit by proposing that there is dissolution of the passive film, and that the rate of the anodic formation of the passive oxide and of its dissolution become equal at some given (and constant) film thickness. This, and the fact that the passive oxide films isolated by Grauer and Feitknecht (16) show essentially the same characteristics as our base film (they also being finely crystalline, randomly oriented films which remain at apparently constant thickness and show no substrate grain orientation dependence) give reason to believe that what we have described phenomenologically as the base film may actually be a high temperature passive oxide film.

There remains to be considered whether or not the oxide film morphology which has been revealed in this work can be correlated with the kinetic rate data taken during the formation of the film. We see first, from the smoothness of the curve in Fig. 5, that the degeneration of (001) epitaxial oxide either does not entail evolution of appreciable quantities of hydrogen, or takes place over such a small percentage of the specimen surface area that its effect on the over-all corrosion rate is negligible. Second, we note that the curve is logarithmic. Logarithmic reaction rate curves for the water/iron corrosion system have several times in the past been associated with the blocking of pores in the oxide film, so it is of interest to see if evidences of a pore blocking mechanism can be found here. No pores are visible in our electron micrographs, but this, of course, does not preclude the existence of pores smaller than the limit of resolution of the electron microscope (which may be as high as  $50\text{\AA}$  with these specimens), or of pores which follow a tortuous and nondirect route through the film. We can assume though that if there are pores in our oxide films, they are most likely in the base film. There is, however, no indication of any change in this film such as would suggest that pores are being blocked as the reaction progresses, i.e., the base film does not become thicker nor does it become more or less finely

crystalline. The one change that is observed during this period is that the base film is being increasingly covered with thick, adherent  $\text{Fe}_3\text{O}_4$  secondary crystals. Since these crystals are, from every indication, protective, this would suggest that the smooth decrease of the corrosion rate with time occurs not because pores are being blocked within the base film, but because more and more of this reactive film is being covered by shielding  $\text{Fe}_3\text{O}_4$  crystals.

The passing of cations through an oxide film to precipitate as discrete crystals at the solution/oxide surface is formally equivalent to the passing of cationic vacancies in the opposite direction through the film to congregate as cavities at the oxide/metal interface. Furthermore, in both cases, the oxidizing species is forbidden access to the underlying metal at the site of the cavity or crystal, and the effective surface area capable of continuing the corrosion reaction is thus reduced. It is possible therefore to adopt the derivation made for the new logarithmic law which is obeyed when cavities occur at the metal/oxide interface (26), making allowance for the fact that the oxide base film here remains at constant thickness, and show that the logarithmic nature of the corrosion rates observed in these studies can be accounted for in terms of the covering of an underlying oxide film by precipitating crystals, and that the oxide growth morphology and kinetic rate data are, in this sense, mutually consistent.

### Summary

In the growth of oxide films on annealed polycrystalline mild steel in high temperature pH 11 LiOH solution, the initial films tend to be epitaxially related to the substrate grains and to develop characteristic morphologies on the various grain orientations. The (001) oxide morphology is particularly distinctive and it has been possible to follow the growth and subsequent degeneration of this epitaxial species in detail. The degeneration of the (001) oxide begins only after a certain oxide thickness is attained, a fact suggesting that the transformation results from stress generated within the epitaxial oxide as its thickness increases.

The oxide film that exists after the epitaxial oxide has been transformed appears to consist of two layers, first a thin, finely crystalline, randomly oriented base film and above that, an incomplete layer of much larger, thicker crystals which are presumably solution-grown  $\text{Fe}_3\text{O}_4$ . The upper surface of the base film shows a pebble-like texture that is very uniform from point to point on the specimen. This surface is apparently made up of rounded crystallites which are somehow held to a very restricted size range (300-500Å). Furthermore, it appears that the base film comes to and remains at some limiting thickness as the corrosion reaction proceeds. Both of these observations have been interpreted as indicating that the base film is being simultaneously formed at the oxide/metal interface and dissolved at the solution/oxide interface, the film's upper surface texture resulting from the dissolution process and its limiting thickness coming about as the rates of the competing reactions become equal.

All indications are that, once this stage is reached, further film growth occurs by the passage of iron ions through the base film into solution to subsequently precipitate as large  $\text{Fe}_3\text{O}_4$  surface crystals, and the only change detected in the oxide film structure after this is a continually increasing coverage of the base

film by the upper crystal layer. Our corrosion rate data reveal a logarithmic decrease in the oxidation rate over this same time period which suggests that the precipitated crystals are protective and that the corrosion rate decreases as more crystals come down and the remaining area of exposed base film is reduced. This hypothesis is supported by the fact that one can, using the physical model proposed here, derive a theoretical rate equation which indicates that the corrosion rate curve should indeed be logarithmic.

### Acknowledgments

The authors wish to express their appreciation to O. R. Gates who analyzed our specimens, to G. N. Newport and E. D. Osgood who furnished valuable technical assistance, and to Dr. M. C. Bloom who provided many helpful discussions during the course of this work.

Manuscript received Nov. 20, 1967; revised manuscript received ca. Feb. 9, 1968.

Any discussion of this paper will appear in a Discussion Section to be published in the December 1968 JOURNAL.

### REFERENCES

1. E. C. Potter and G. M. W. Mann, 1st Intl. Cong. Metal. Corr., p. 417, London (1961).
2. M. C. Bloom, G. N. Newport, and W. A. Fraser, *This Journal*, **111**, 1343 (1964).
3. E. M. Field and D. R. Holmes, *Corr. Sci.*, **5**, 361 (1965).
4. E. M. Field, R. C. Stanley, A. M. Adams, and D. R. Holmes, 2nd Intl. Cong. Metal. Corr., p. 829, New York City (1963).
5. J. E. Castle and H. G. Masterson, *Corr. Sci.*, **6**, 93 (1966).
6. T. F. Marsh, *This Journal*, **113**, 313 (1966).
7. J. E. Castle and G. M. W. Mann, *Corr. Sci.*, **6**, 253 (1966).
8. M. Warzee, J. Hennaut, M. Maurice, and Ph. Berge, *Rev. Met. Mem. Sci.*, **62**, 239 (1965).
9. J. M. Francis and W. H. Whitlow, *J. Nucl. Matl.*, **20**, 1 (1966).
10. M. C. Bloom and M. Krulfeld, *This Journal*, **104**, 264 (1957).
11. P. B. Sewell, E. G. Brewer, and M. Cohen, *J. Phys. Chem.*, **67**, 2008 (1963).
12. M. C. Bloom, M. Krulfeld, and W. A. Fraser, *Corrosion*, **19**, 327t (1963).
13. W. H. J. Vernon, F. Wormwell, and T. J. Nurse, *J. Chem. Soc.*, **1939**, 621.
14. A. T. Gwathmey and K. R. Lawless, "The Surface Chemistry of Metals and Semiconductors," H. C. Gatos, Editor, p. 483, John Wiley & Sons, New York (1960).
15. F. A. Champion and M. Whyte, *J. Inst. Metals*, **75**, 737 (1949).
16. R. Grauer and W. Feitknecht, *Corr. Sci.*, **6**, 313 (1966).
17. A. Fursey, *Nature*, **207**, 747 (1965).
18. D. J. Dyson and S. R. Keown, *ibid.*, **209**, 707 (1966).
19. M. Cahoreau and M. Gillet, *Rev. Met. Mem. Sci.*, **63**, 976 (1966).
20. C. L. Foley, J. Kruger, and C. J. Bechtoldt, *This Journal*, **114**, 994 (1967).
21. D. Gilroy and J. E. O. Mayne, *Brit. Corr. J.*, **1**, 102 (1965).
22. E. A. Gulbransen, W. R. McMillan, and K. F. Andrew, *J. Metals*, **6**, 1027 (1954).
23. R. W. Bartlett, *This Journal*, **111**, 903 (1964).
24. J. M. West, "Electrodeposition and Corrosion Processes," p. 104, D. Van Nostrand & Co., London (1965).
25. K. G. Vetter, *This Journal*, **110**, 597 (1963).
26. U. R. Evans, "The Corrosion and Oxidation of Metals," p. 836, Arnold, London (1960).

# A Study of Living and Dead Yeast Cells Using Dielectrophoresis

Joe S. Crane and Herbert A. Pohl\*

Department of Physics, Oklahoma State University, Stillwater, Oklahoma

## ABSTRACT

Using a simple new physical technique, dielectrophoresis, living cells can rapidly be distinguished from dead ones, and collected separately. A detailed study using yeast cells is reported here. A comparative study of the dielectrophoresis of aqueous suspensions of living and dead yeast (*Saccharomyces cerevisiae*) was made over a range of frequencies, aqueous conductance, field strength, and time. The amount collected in a given period was observed to increase with field strength and aqueous resistivity except in the highest ranges where a reverse trend occurs. At high field strengths reversal of collection occurs (i.e., dispersion). The frequency responses of living and dead cells are different, enabling remarkably selective collection of living cells from a mixture of living and dead cells. Cells collected in this manner survive.

Dielectrophoresis can be defined as the motion of a neutral particle due to the action of a nonuniform electric field on its permanent or induced dipole moment. In the past, the phenomenon has been applied primarily to inanimate matter (1-5). Recently however, living yeast cells have also been investigated; a qualitative description of their dielectrophoresis was given (6). The present paper describes the more quantitative aspects of yeast cell behavior.

The apparatus used consisted of a pin-plate electrode system, mounted in a shallow cylindrical well which had been cut in a lucite plate. It has been described previously in detail (6). An aqueous suspension of yeast cells was placed in the well and an a-c voltage applied across the electrodes. It was found that the cells migrated towards the pin and collected there in chains parallel to the field lines. The length of these chains, or "yield," was determined microscopically after a given time and was used as a measure of the effectiveness of the field. It was found to be a function of applied voltage, frequency of the applied voltage, suspension resistivity, cell concentration, and time of collection.

The voltages were supplied either by an audio oscillator-amplifier combination or a specially designed 2.55 MHz source. Voltage was measured with a Hewlett Packard Type 410B vacuum tube voltmeter. The suspension resistivity was determined using a parallel plate probe as an arm of a Wheatstone bridge at a frequency of 1 KHz. An auxiliary capacitor was used in parallel with the variable arm of the bridge to improve the null. The resistance thus measured was converted to resistivity by comparison to the corresponding resistance of a 0.01N solution of KCl which has a known resistivity. The optical density of the suspension of cells was measured on a colorimeter, and this in turn was transformed into cell concentration through the use of a conversion curve. The curve was obtained by making a direct, microscopic cell count for various optical densities.

The yeast (*Saccharomyces cerevisiae*) was grown in a fluid peptone-dextrose broth. To prepare a suspension for study, the yeast cells were mixed with deionized water (distilled water passed through an ion exchange resin). The suspension was centrifuged and the supernatant liquid poured off. More deionized water was added, the suspension was mixed thoroughly, and again centrifuged. This washing procedure was continued until the desired specific resistivity was obtained. Dead cells were obtained by autoclaving viable cells and prepared for study by rinsing, etc., as for live cells.

After a suspension with the desired concentration and resistivity had been prepared, 0.060 cc of it was

placed into the electrode well, filling it. With the voltage and frequency preselected, the field was applied across the electrodes for a given length of time. The accompanying graphs (Fig. 1-5) show some typical results.

In general the movement of the cells is not always precisely in the direction of the field lines, as would normally be expected, but instead there is usually some accompanying motion of the liquid. When this motion becomes turbulent, the collected chains can be moved along the pin or even removed from it. This violent action very probably accounts for the drop in collection at high voltages and at high resistivities, shown in Fig. 1 and 2. The peaks that occur in the frequency curves of Fig. 3 are not due to such stirring however, but rather to the changing force on the cells as the frequency is varied.

The most significant point indicated by the data is that shown in Fig. 3. That is, at frequencies about 1 MHz and above, live cells are collected but dead ones are not. In fact dead cells, which had been collected at a lower frequency, were allowed to remain on the pin, and when the 2.55 MHz source was applied, they were immediately expelled from the pin and a clear zone was created around it.

As a visual check of the selectivity at these conditions, a suspension of dead cells was stained with crystal violet and then mixed with an approximately equal concentration of unstained live cells. When the field was applied to this mixture, the live cells collected quite readily but the stained dead cells were virtually unaffected. Under these conditions, dead cells, even if

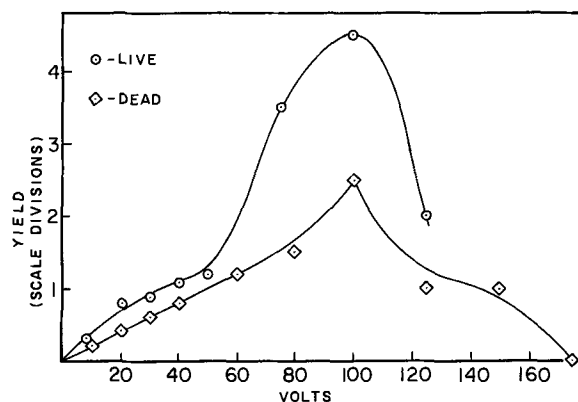


Fig. 1. Relative yield of yeast cells collected as a function of voltage across electrodes. Live cells collected at 100 kHz. with suspension resistivity,  $\rho$ , of  $1.6 \times 10^5$  ohm-cm. Dead cells collected at 10 kHz,  $\rho = 2.0 \times 10^5$  ohm-cm.

\* Electrochemical Society Active Member.

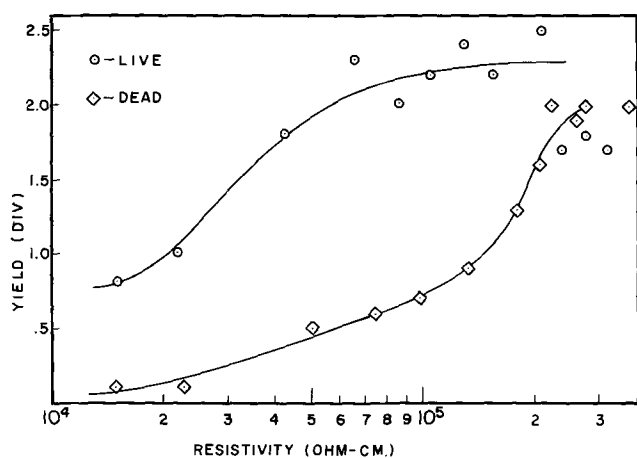


Fig. 2. Relative yield of yeast cells collected as a function of suspension resistivity. Live cells collected at 100 kHz and 50 rms volts applied; dead cells collected at 10 kHz and 30 rms volts applied.

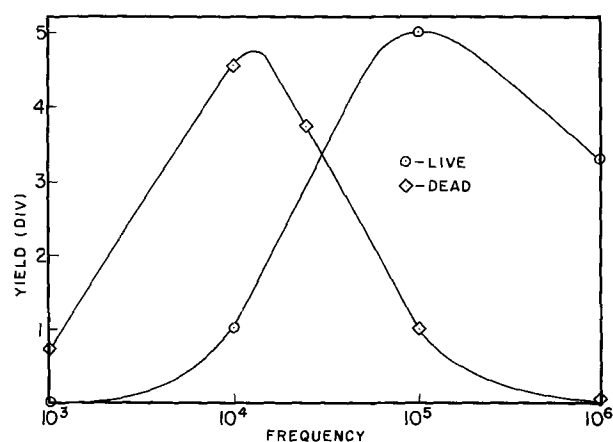


Fig. 3. Relative collection of yeast cells as a function of frequency. Voltage applied, 100v rms,  $\rho = 1.3 \times 10^5$  ohm-cm.

hit by live cells travelling toward the electrode, merely ricocheted aside and were not carried on in by the more intense field around the live cells.

A remaining problem with this method of separating cells is that of removing the cells once they have been separated, without remixing them. Since the electrode well is so small, the introduction of an instrument, such as a syringe needle, for extracting the cells causes considerable disturbance of the medium, knocking many of the collected cells off the pin. However, by the careful introduction of a capillary action micropipet, (0.01 cc) the disturbance can be minimized and most of the cells can be satisfactorily removed. An alternate solution to this problem might be a continuous flow process, wherein the suspension moves between the electrodes as part of a continuous stream. Preliminary studies of this method are being made.

There are several interesting observations concerning cell movement which are so far unexplained. One of these is the stirring motion in the system. It usually consists of two circular currents on either side of the pin. Their common current between the pin tip and the plate moves toward the pin in some cases and away from the pin in others. For some conditions, such as high frequency with high resistivity, there may even be no stirring at all. The determining factors are not yet clearly understood.

Another occurrence deserving comment is that some of the cells, having once been attracted toward the pin, will suddenly experience a considerable repulsive force either just prior to or immediately after touching the pin. This occurs while many of the other cells are collecting normally and experiencing no repulsion. Most

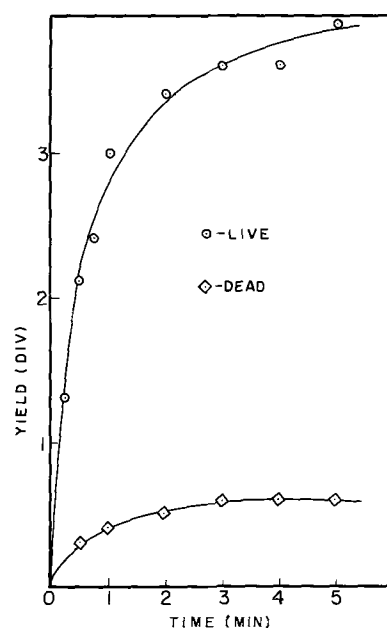


Fig. 4. Relative collection of yeast cells as a function of time. Live cells collected at 2.55 MHz, 120 rms volts,  $\rho = 2.2 \times 10^5$  ohm-cm. Dead cells collected at 100 kHz, 30 rms volts,  $\rho = 2.0 \times 10^5$  ohm-cm.

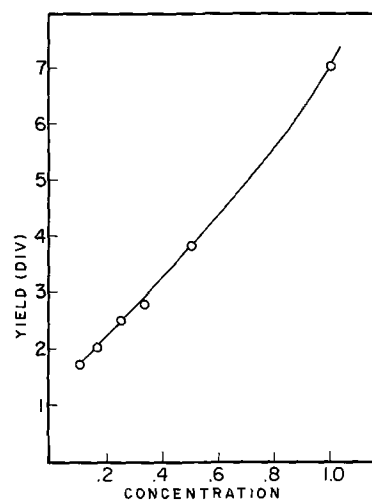


Fig. 5. Relative collection yield of live yeast cells as a function of suspension concentration. Concentration in relative units ( $1.0 \cong 4.6 \times 10^6$  cells/cm<sup>3</sup>). Collection made at 10 kHz, 10 rms volts,  $\rho = 2.0 \times 10^6$  ohm-cm for 2 min at each conc.

of the repulsion occurs at the tip of the pin where the field strength is the greatest which would indicate that there may be some charge transfer taking place.

Finally, at almost any frequency, a few of the collected cells can be seen to be rotating at a few revolutions per second. As the frequency is varied, these cells will stop rotating and others will begin. This is an unexpected result since in a uniform isotropic sphere, an induced dipole in a nonuniform electric field experiences no torque (7). One possible explanation is that the cell rotates as a means of conducting current along its surface (3).

To see if the collected cells were yet viable, the collection was run until complete as evidenced by the lack of free cells in the aqueous regions (about 7-8 min). The collected cells were removed from the pin electrode by the micropipet technique described above. The collected cells bred actively in nutrient agar cultures. We conclude that the dielectrophoretic treatment did not noticeably affect the viability of the yeast cells. Although yeast cells appear to survive readily

the entire history of the separation, it seems very likely that this will not generally be true for all species, for few species are able to withstand prolonged contact with deionized water. One obvious improvement in the technique which is still under study is the use of innocuous solutes such as dextrose, sucrose, glycerine, etc., which can render the deionized medium more satisfactorily isoosmotic to the suspended organisms.

The precise cause of the greater dielectrophoretic response of living cells as compared to dead cells is yet to be learned. It may lie simply in the greater conductiveness or free ion content of the living cells, or it may lie in the more effective double charge layers of the living cells. In our judgment, the latter cause appears more likely to be dominant. It is probable that the sheaths of counter ions in the liquid regions within and without the cells and next layers of their opposites bound more rigidly to cell structures will act as pliable, easily deformed charge clouds, and that these charge clouds readily interact with an external field to produce the high effective polarizabilities of the living cells. The problem is under active investigation. There are, it is recognized, many degrees of "deadness" or "death" recognizable or eventually recognizable in organisms. It is hoped that dielectrophoretic separabil-

ity will help in arriving at sharpened distinctions, not only among degrees of deadness or death, but also between normal and abnormal living cells.

#### Acknowledgment

The authors express their sincere thanks to the National Institutes of Health, U.S. Public Health Service for their grant in support of this research.

Manuscript received Nov. 28, 1967; revised manuscript received Jan. 29, 1968. This paper was presented at the Chicago Meeting, Oct. 15-19, 1967, as Abstract 154.

Any discussion of this paper will appear in a Discussion Section to be published in the December 1968 JOURNAL.

#### REFERENCES

1. H. A. Pohl, *J. Appl. Phys.*, **22**, 869 (1951); **29**, 1182 (1958).
2. H. A. Pohl, *Sci. Amer.*, **203**, 107 (1960).
3. H. A. Pohl and J. P. Schwarz, *J. Appl. Phys.*, **30**, 69 (1959); *This Journal*, **107**, 383 (1960).
4. H. A. Pohl and C. E. Plymale, *ibid.*, p. 390; H. A. Pohl, *ibid.*, p. 386.
5. W. F. Pickard, *Prog. Dielectrics*, **6**, 3 (1965).
6. H. A. Pohl and I. Hawk, *Science*, **152**, 647 (1966).
7. L. Page, "Introduction to Theoretical Physics," p. 382, D. Van Nostrand Co., New York (1952).

## Some Properties of Electroless Cobalt

Allan S. Frieze,<sup>1</sup> Richard Sard, and Rolf Weil\*

Department of Metallurgy, Stevens Institute of Technology, Hoboken, New Jersey

#### ABSTRACT

The nucleation of electroless cobalt deposits, their microstructures and hardnesses, the development of fiber axes and the shape of x-ray diffraction lines, from which information about particle size, lattice-fault densities, and microstrain was obtained, were studied. The results are explained in terms of growth inhibition by codeposited phosphorus. Data obtained from the analysis of x-ray diffraction-line shapes of some cobalt electrodeposits are appended.

Chemically deposited (electroless) cobalt-phosphorus films are of interest primarily because of their magnetic properties. Therefore, the relationships between the magnetic properties and the plating variables (1-7) and, to some extent, the microstructure (1-3), as observed electron microscopically using replicas have been studied previously. However, there has been no study of the structure and properties of Co-P deposits from a metallurgical viewpoint. The purpose of this communication is to report the results of such a study of the nucleation of the deposits, their microstructures and hardnesses as related to their chemical composition, the development of the preferred orientations and the shape of x-ray diffraction lines, which yielded information about microstrains, lattice faulting, and particle size.

#### Experimental Procedure

**Nucleation.**—For the study of the nucleation of cobalt-phosphorus deposits, thin amorphous carbon films served as the substrates. In experiments, which are discussed later, glass and acetate were used as substrates. No difference in the structure of thin deposits was observed when either carbon, glass, or acetate substrates were used. The carbon films were prepared by evaporation on eighth-inch diameter, 200 mesh grids previously covered with a nitrocellulose film,

which had been cast on water. After the carbon evaporation, the plastic film was dissolved. The carbon substrates were sensitized as described by Judge *et al.* (6) and then immersed for various times in baths containing 35 g/l CoSO<sub>4</sub> × 7H<sub>2</sub>O, 35 g/l Na<sub>3</sub>C<sub>6</sub>H<sub>5</sub>O<sub>7</sub> × 2H<sub>2</sub>O, 70 g/l (NH<sub>4</sub>)<sub>2</sub>SO<sub>4</sub>, and 5, 10, 25, 40 g/l NaH<sub>2</sub>PO<sub>2</sub> × H<sub>2</sub>O. The pH was adjusted to 8.7 ± 0.15 with NH<sub>4</sub>OH. The baths were operated at 75° and 90°C within 3°C. The deposits on the carbon substrates were examined directly in the electron microscope (Hitachi HU-11) immediately after drying. Transmission microscopy, selected-area and high resolution diffraction were employed.

**Structure of continuous films.**—For the study of the structure of continuous films, glass slides were the substrates. The preplating treatment, the bath compositions, and temperatures were the same as were used for the studies of the nucleation stage on carbon films. By controlling the deposition time, samples varying in thickness from 0.05 to 2μ were obtained. The deposition potential *vs.* a standard calomel electrode was recorded continuously during the plating on the glass substrates. The electrode was connected by means of a glass capillary filled with the plating solution and with the tip about 2 mm from the deposits surface. Initially, as the glass was nonconducting, the potential was zero. As a cobalt layer developed, the potential increased and then leveled off to a constant value, which was reproducible and was therefore considered representative of the plating conditions.

† Electrochemical Society Student Member.

\* Electrochemical Society Active Member.

<sup>1</sup> Present address: Becton, Dickinson and Company, Rutherford, New Jersey.

*X-ray diffraction studies.*—The fiber axes of the samples plated on glass were determined by the method of Clark and Simonsen (8). After the fiber axis was identified, the intensity of the x-rays diffracted by the plane normal to it was recorded in some cases with a counter to give a quantitative measure of the degree of preferred orientation.

In addition, four samples about  $1.5\mu$  thick with phosphorus contents of about 1, 2, 3, and 5% were deposited on acetate sheets, which were subsequently removed from the deposit by immersion in methyl-ethyl ketone. These samples were used to determine the microstrains and particle sizes according to the method of Warren and Averbach (9-10). In order to have a sample of sufficient thickness to obtain measurable diffracted intensities from the higher order diffraction lines, which are preferable for the Warren-Averbach method, a ten-layer thick assembly was placed in a special fixture which held them flat.

The Warren-Averbach method of determining the particle size and microstrain has been described in numerous publications. Therefore, only the pertinent parts will be briefly discussed. The diffracted intensity,  $P$ , is measured as a function of the Bragg angle,  $\theta$ , at regular intervals for two or more diffraction lines, preferably multiple orders from the same set of lattice planes. The shape of the broadened peaks as compared to those of an annealed sample is expressed in terms of a Fourier series. The annealed sample corrects for the broadening due to the instrumentation. Thus, the data are in terms of

$$P(\theta) = K \sum_L A_L \exp[-4\pi i L \lambda^{-1} (\sin\theta - \sin\theta_0)] \quad [1]$$

where  $L$  is the distance normal to the reflecting planes,  $A_L$  the Fourier coefficients,  $\lambda$  the wavelength of the x-radiation,  $\theta_0$  the Bragg angle corresponding to the average interplanar spacing, and  $K$  a proportionality constant. It is then assumed that the Fourier coefficients,  $A_L$  are the product of two terms

$$A_L = A_L^{PF} x A_L^S \quad [2]$$

where  $A_L^{PF}$  are the particle-size coefficients and  $A_L^S$  are the microstrain coefficients. It was shown by Warren (10) that only the strain coefficients are a function of the interplanar spacing. If the distribution of microstrains,  $\langle \epsilon \rangle$  is Gaussian, they are related to the Fourier coefficients by

$$\ln A_L^S = -2\pi^2 L^2 \langle \epsilon_L^2 \rangle d^{-2} \quad [3]$$

Therefore, by combining Eq. [2] and [3], the Fourier coefficients,  $A_L$ , are related to the strain by

$$\ln A_L = \ln A_L^{PF} - 2\pi^2 L^2 \langle \epsilon_L^2 \rangle d^{-2} \quad [4]$$

Thus a graph of  $\ln A_L$  vs.  $d^{-2}$  should be a straight line where the intercept is  $\ln A_L^{PF}$  and the slope is proportional to the square of the microstrain,  $\langle \epsilon_L^2 \rangle$ . In order to construct such a graph, the diffraction peaks of at least two sets of lattice planes with different values of  $d$  must be determined. The microstrains and particle dimensions which are determined by this analysis are in the direction perpendicular to the diffracting planes. If the two quantities are isotropic, data from any two or more sets of planes can be used in the analysis. If the particle size and strain vary with crystallographic directions, several orders of diffraction of the same set of planes should be used.

The separation of the broadening due to lattice faults and particle size from the coefficients,  $A_L^{PF}$ , can be performed in hexagonal metals by the following equations (10), which hold for planes with the Miller indices,  $(hkl)$ , as noted:

If  $(h-k) = 3N \pm 1$  and  $l$  is odd,

$$\left[ -\frac{dA_L^{PF}}{dL} \right]_{L=0} = \frac{1}{D} + \frac{|l|d}{c_0^2} (3\alpha + \beta) \quad [5a]$$

If  $(h-k) = 3N \pm 1$  and  $l$  is even,

$$\left[ -\frac{dA_L^{PF}}{dL} \right]_{L=0} = \frac{1}{D} + \frac{|l|d}{c_0^2} (3\alpha + 3\beta) \quad [5b]$$

If  $(h-k) = 3N$ ,

$$\left[ -\frac{dA_L^{PF}}{dL} \right]_{L=0} = \frac{1}{D} \quad [5c]$$

In Eq. [5],  $\alpha$  is the deformation-fault probability,  $\beta$  the growth-fault probability,  $D$  the particle-size dimension, and  $N$  an integer. It can be readily seen that Eq. [5b] and [5c] become identical if  $l$  is zero. As the second-order lines from many planes are often too weak to be usable in the analysis, it is necessary to assume isotropic strains and particle sizes. This assumption has been found (11) to be valid for cobalt powder and should also hold for electrodeposits because of the requirements for continuity in sheet. If isotropic strains and particle sizes are assumed,  $\alpha$  and  $\beta$  can be calculated from first-order lines from planes with the three types of indices set forth in Eq. [5]. Frequently a further assumption is necessary when even the first-order lines which satisfy the condition of Eq. [5b] are too broad. Christian and Swann (12) pointed out that such broadening results if  $\beta$  is large. It must then be assumed that  $\alpha$  is negligible and  $\beta$  is calculated from two sets of diffraction-line data. Then for example, the  $\{10\bar{1}0\}$ - $\{20\bar{2}0\}$  pair can yield data on strain and the actual particle size,  $D$ , as these lines do not broaden due to faulting. The  $\{10\bar{1}1\}$  line can yield a particle-size term with faulting. The faulting probability,  $\beta$ , can then be obtained by substituting the value of  $D$  obtained from the  $\{10\bar{1}0\}$ - $\{20\bar{2}0\}$  pair in Eq. [5a].

The experiments were conducted in a GE XRD6 x-ray-diffraction unit using filtered cobalt radiation. The analysis of the data required some minor alterations from the previously outlined procedure. An annealed cobalt sample invariably contains some face-centered-cubic phase and the faults associated with it. Thus, the diffraction lines from cobalt planes, which broaden due to faults, cannot be used for the determination of the instrumental broadening. Wagner and Aqua (13) suggested that annealed materials with similar absorption characteristics give essentially the same diffraction-peak shape at a given Bragg angle. Copper appeared to be a suitable substitute for annealed cobalt to determine the instrumental-broadening correction. Experiments to show the validity of this substitution are described in the Appendix. Table I shows the copper peaks which were used for the instrumental-broadening correction for the corresponding cobalt lines of the samples under consideration.

The cobalt lines which were used for the calculations of the microstrains were those diffracted by the planes perpendicular to the preferred orientation. The second-order lines of these planes were the only ones sufficiently intense so as to be usable in the analysis. Thus the  $\{0002\}$ - $\{0004\}$  pair was analyzed for the samples with 1% phosphorus which had a  $\langle 0001 \rangle$  fiber axis and the  $\{10\bar{1}0\}$ - $\{20\bar{2}0\}$  pair for the three other samples, which had  $\langle 10\bar{1}0 \rangle$  fiber axes. The  $K_{\alpha 1}$  and  $K_{\alpha 2}$  diffraction peaks were separated analytically by the Rachinger (14) method. The growth-fault probability was

Table I. Copper diffraction peaks used to correct cobalt peaks for instrumental broadening

Copper peak	Cobalt peak
(111)	(0002)
(222)	(0004)
(111)	(10 $\bar{1}$ 0)
(311)	(20 $\bar{2}$ 0)



calculated using the  $\{10\bar{1}1\}$  diffraction line. The microstrains were calculated at  $L = 30\text{\AA}$  for all samples. At smaller values of  $L$ , the Fourier coefficients become inaccurate because they are greatly affected by the background-radiation level, which cannot be selected with great precision.

**Hardness.**—To get an estimate of the hardness, indentations were made on the ten-layer thick composites with a one-gram load in a microhardness tester with a Vickers indenter.

### Results

The study of nucleation of Co-P on the carbon film showed that deposition occurred on the products of the  $\text{SnCl}_2\text{-PdCl}_2$  treatment. The electron-microscope examination of the carbon films which were only sensitized, showed that the products were not uniformly distributed over the surface as seen in Fig. 1a. The initial deposits of Co-P had a similar appearance, as shown in Fig. 1b, thus indicating that Co-P was nucleated on the products of the preplating treatments. As the deposition progressed, the distribution of the Co-P particles became more uniform. The number of particles depended on the plating conditions. Figure 2 shows the structure after 30-sec immersion in the electroless-cobalt solutions. Figure 2a shows the structure which resulted from deposition in the solution containing 10 g/l  $\text{NaH}_2\text{PO}_2 \cdot x\text{H}_2\text{O}$  at  $75^\circ\text{C}$ ; the sample represented by Fig. 2b was plated at  $90^\circ\text{C}$ . More nuclei formed at  $70^\circ\text{C}$  and the particles are smaller. Figures 2c and 2d show the structures developed in a bath containing 40 g/l  $\text{NaH}_2\text{PO}_2 \cdot x\text{H}_2\text{O}$  at  $75^\circ$  and  $90^\circ\text{C}$ , respectively. The number and the size of the particles appear not to have been significantly affected by the tem-

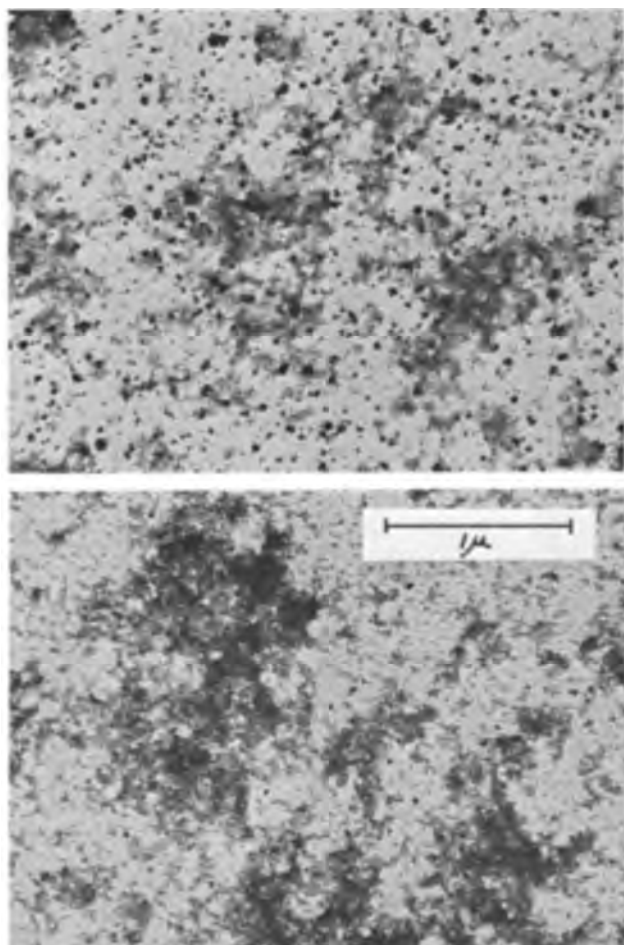


Fig. 1. Transmission electron micrographs of nucleation on carbon film: a. (top) after sensitization; b. (bottom) after sensitization and Co-P plating.

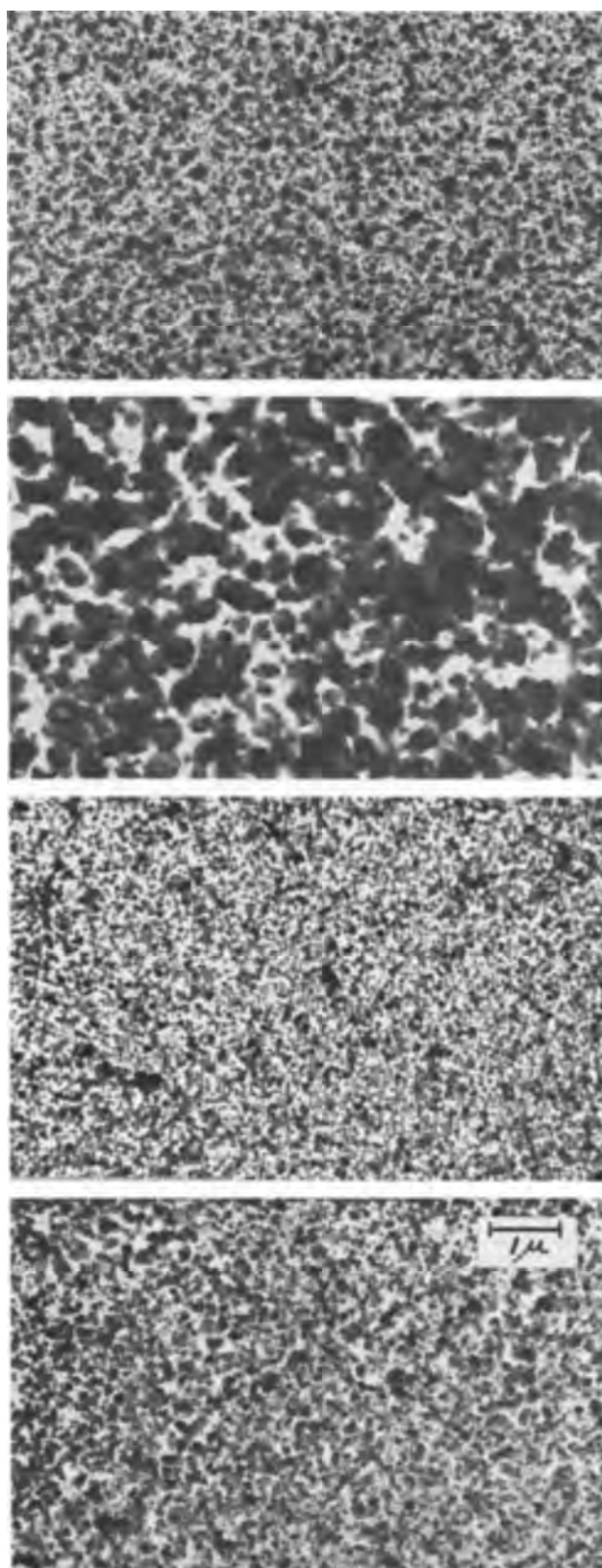


Fig. 2. Transmission electron micrographs of Co-P growth on carbon film: a. (top) plated at  $75^\circ\text{C}$  in bath containing 10 g/l  $\text{NaH}_2\text{PO}_2 \cdot x\text{H}_2\text{O}$ ; b. (next to top) plated at  $90^\circ\text{C}$  in bath containing 10 g/l  $\text{NaH}_2\text{PO}_2 \cdot x\text{H}_2\text{O}$ ; c. (next to bottom) plated at  $75^\circ\text{C}$  in bath containing 40 g/l  $\text{NaH}_2\text{PO}_2 \cdot x\text{H}_2\text{O}$ ; d. (bottom) plated at  $90^\circ\text{C}$  in bath containing 40 g/l  $\text{NaH}_2\text{PO}_2 \cdot x\text{H}_2\text{O}$ .

perature and are similar to Fig. 2a. The results from the baths containing 20 g/l  $\text{NaH}_2\text{PO}_2 \cdot x\text{H}_2\text{O}$  were very similar to those shown in Fig. 2c and 2d. Electron diffraction studies of all these samples indicated that

the  $\langle 0001 \rangle$  direction was predominantly perpendicular to the surface. It was also found that palladium particles from the sensitizing treatment tended to have  $\{111\}$  planes parallel to the surface.

After the samples became continuous, they assumed a structure characteristic of the orientation, which in turn was determined by the plating conditions. In the bath containing 5 g/l sodium hypophosphite at  $90^\circ\text{C}$ , the  $\langle 0001 \rangle$  direction continued to be predominantly perpendicular to the surface. The degree of preferred orientation increased with thickness. The degree of preferred orientation became more pronounced the higher the temperature and the lower the hypophosphite content of the baths. The microstructure which developed consisted of relatively large crystallites separated by crevices as shown in Fig. 3. Whenever the phosphorus content of the deposit was below 2%, the structure shown in Fig. 3 occurred. At higher phosphorus contents, in the range of 2 to 5%, an acicular structure shown in Fig. 4 was formed. This structure was associated with a  $\langle 10\bar{1}0 \rangle$  fiber axis.

The thickness at which the change occurred from the  $\langle 0001 \rangle$  axis, which all the initial nuclei possessed, to the  $\langle 10\bar{1}0 \rangle$  preferred orientation which developed in the samples with higher phosphorus contents, was determined from a graph of thickness *vs* the ratio of the diffracted intensity to background of the  $\{0002\}$  and  $\{10\bar{1}0\}$  peaks. The thickness was determined by fluorescent analysis. By taking the ratio of the diffracted intensity to background, a correction for the variation due to thickness was made. In a random co-

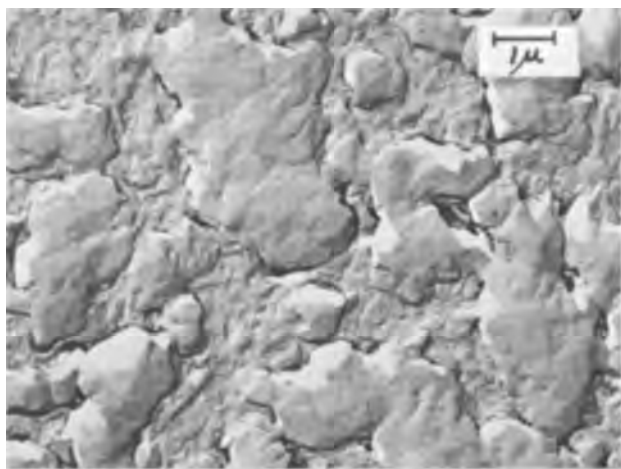


Fig. 3. Electron micrograph of replica showing structure associated with  $\langle 0001 \rangle$  fiber axis.

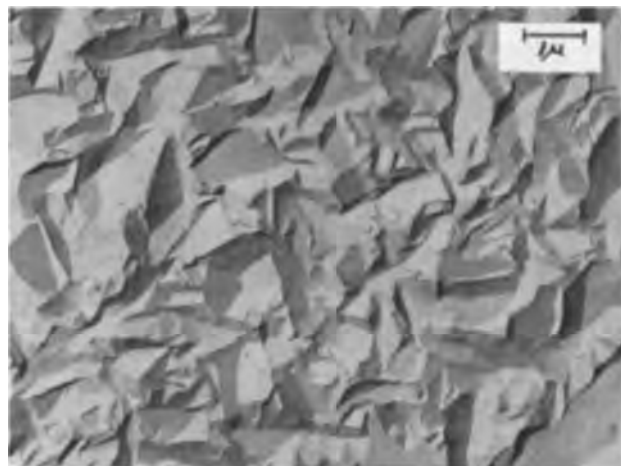


Fig. 4. Electron micrograph of replica showing structure associated with  $\langle 10\bar{1}0 \rangle$  fiber axis.

balt sample, the diffracted intensities from  $\{0002\}$  and  $\{10\bar{1}0\}$  planes are nearly equal. In the cobalt deposits, initially, the  $\{0002\}$  peak was the most intense. At a thickness of about 1000Å, the relative intensity from the two planes was essentially the same. Samples thicker than 1000Å with phosphorus contents above 2% had more intense  $\{10\bar{1}0\}$  lines. Thus, it appears that the change in the fiber axis occurred at about 1000Å. The microstructure as observed by replicas confirmed this result.

The deposition potential of the samples having the structure shown in Fig. 3 varied from 0.78 to 0.83v. The potential decreased with decreasing hypophosphite content of the bath and increasing temperature. The samples which exhibited the structures shown in Fig. 4 were deposited at potentials between 0.85 and 0.88v.

The results of the analysis of the x-ray line shapes by the Warren-Averbach method and the hardness tests are listed in Table II. It is seen that the samples with the  $\langle 0001 \rangle$  fiber axis have a larger particle size, fewer faults, and a lower hardness than those with the other fiber axis. The hardnesses of all samples and the microstrains of deposits with the  $\langle 10\bar{1}0 \rangle$  fiber axis increase with increasing phosphorus content. The particle size appears to remain constant for those samples with the  $\langle 10\bar{1}0 \rangle$  fiber axis. The macrostress as observed from the tendency of the samples to bend, was compressive for all four samples. The samples with the  $\langle 0001 \rangle$  fiber axis were only slightly stressed, whereas the others curled up after removing the substrate.

### Discussion

The nuclei of the products of the sensitizing treatment, in particular those of palladium, were expected according to the Bravais law to form with the closest packed planes,  $\{111\}$  parallel to the surface, as was observed. Cobalt depositing epitaxially on the palladium would then have the  $\{0001\}$  plane parallel to the surface. The observed  $\langle 0001 \rangle$  fiber axis in the nucleation stage probably developed in this way.

The development of a fiber axis characteristic of the plating conditions can be explained by assuming that phosphorus acts as a growth inhibitor. When the phosphorus concentration at the metal-solution interface is low, growth can continue predominantly laterally, i.e., with the  $\langle 0001 \rangle$  direction perpendicular to the surface. Such free growth would lead to the relatively large crystals that were observed. The crevices, seen in Fig. 3, are probably regions of higher phosphorus content, because the structure there resembles that of a deposit with higher phosphorus content. The crevices probably form because the phosphorus content at the metal-solution interface increases as the reduction reaction proceeds. The crevices were observed at thicknesses exceeding 1000Å. Further evidence that a composition difference existed between the crevice regions and the larger crystals was obtained from the fact that on exposure to moisture, corrosion occurred preferentially at the edges of the crevices. It is interesting that the  $\langle 0001 \rangle$  fiber axis and its accompanying microstructure were not observed by Sard, Schwartz, and Weil (15) in cobalt electroplated under a number of different conditions.

Table II. Analysis of x-ray line shapes and hardness tests

Sample No.	Fiber axis	Approximate phosphorus content, %	Particle size, D (Å)	Microstrain, $\langle \epsilon_{0001} \rangle^{1/2}$ (%)	Growth-fault probability, $\beta$	Hardness, kg/mm <sup>2</sup>
1	$\langle 0001 \rangle$	1	200	0.15	0.09	120
2	$\langle 10\bar{1}0 \rangle$	2	100	0.11	0.25	160
3	$\langle 10\bar{1}0 \rangle$	3	100	0.15	0.22	320
4	$\langle 10\bar{1}0 \rangle$	5	100	0.22	0.17	380



According to the theory proposed by Reddy (16), as applied to hexagonal metals, the {0001} plane should tend to be perpendicular to the surface when growth is inhibited. The least inhibited outgrowth (16) should occur when the closest packed direction is perpendicular to the surface, which would lead to a  $\langle 11\bar{2}0 \rangle$  fiber axis. This fiber axis, which was frequently observed in electrodeposited cobalt (15), was not observed in the electroless variety. The  $\langle 10\bar{1}0 \rangle$  direction which also lies in the {0001} plane is not close packed. Therefore, the deposits with the  $\langle 10\bar{1}0 \rangle$  fiber axis can be considered to have experienced a more inhibited outgrowth. The  $\langle 10\bar{1}0 \rangle$  fiber axes were also observed in electrodeposited cobalt (15) and resulted in a similar microstructure to that shown in Fig. 4. The reasons for the relationship between fiber axis and microstructure in cobalt deposits were discussed by Sard, Schwartz, and Weil (15).

The growth-fault probabilities which are listed in Table II are the highest ever reported for cobalt. As the growth-fault probability is the reciprocal of the number of planes between faults, it appears that sample 2 had a fault on the average of every fourth lattice plane. The faulting probability in cold-worked cobalt has been reported to be 0.05 to 0.1 (17). Electrodeposited cobalt, which is discussed in the Appendix to this paper, has maximum values of  $\beta$  of about 0.1 which are about the same as those of the low-phosphorus, electroless deposit. The reason for the high fault densities is apparently connected with the co-deposition of phosphorus. However, the mechanism by which phosphorus causes the faults is as yet unknown.

The particle size of the low-phosphorus sample is about the same as that of electroplated cobalt; the particle sizes of the samples 2, 3, and 4 are smaller. In all instances the particle size determined from the x-ray line-shape analysis is smaller than that observed by transmission electron microscopy of thin foils. The difference, which was discussed by Hofer *et al.* (18), results because the former measurement is the dimension of the coherently diffracting domain which may not appear as a grain in the electron microscope. Except for sample 4, the microstrains are about the same as those measured in electroplated cobalt and are also similar to those observed by Mitra and Halder (19) in cold-worked cobalt. The results of the hardness tests are in accord with the assumption that phosphorus acts as a growth inhibitor. There appeared to be no precipitation hardening as the equilibrium second phase,  $\text{Co}_2\text{P}$  was not observed.

### Conclusions

1. Cobalt-phosphorus deposits are nucleated on the products of the preplating treatments. The size and density of nuclei depends on the temperature of baths with low hypophosphite contents. In baths with higher hypophosphite contents the size and number of nuclei are relatively constant.

2. The initial nuclei which deposited on palladium-activated surfaces appear to have the basal plane of the hexagonal lattice predominantly parallel to the substrate. Samples thicker than about 1000Å assume a fiber axis which depends on the amount of codeposited phosphorus. Phosphorus contents below 2% result in a  $\langle 0001 \rangle$  orientation. When the phosphorus content is between 2 and 5%, a  $\langle 10\bar{1}0 \rangle$  fiber axis is observed.

3. The surface structure of the deposits is determined by the fiber axis. Those deposits with  $\langle 0001 \rangle$  orientations show lateral growth with relatively large grains that are often separated by crevices. An acicular structure is observed when there is a  $\langle 10\bar{1}0 \rangle$  fiber axis.

4. The deposition potential of samples with  $\langle 0001 \rangle$  fiber axes is lower than that with  $\langle 10\bar{1}0 \rangle$ . The struc-

tures can therefore be explained in terms of phosphorus acting as a growth inhibitor.

5. The highest growth-fault density observed in any cobalt sample to date is present in some of those obtained by electroless deposition. The strain, particle size, and hardness results tend to confirm the role of phosphorus as a growth inhibitor.

### Acknowledgments

The study of electroless cobalt was submitted by A. Frieze to the faculty of Stevens Institute of Technology in partial fulfillment of the requirements for the degree of Master of Science (Metallurgy). This work was supported by the International Business Machine Corporation, Poughkeepsie, New York, and their permission to publish it is gratefully acknowledged. The computer program for the evaluation of the Fourier coefficients was supplied by Dr. R. J. DeAngelis, University of Kentucky.

Manuscript received Nov. 29, 1967; revised manuscript received Feb. 12, 1968. This paper was presented at the Philadelphia Meeting, Oct. 9-14, 1966, as Abstract 117.

Any discussion of this paper will appear in a Discussion Section to be published in the December 1968 JOURNAL.

### APPENDIX

#### X-ray Line Shape Analysis of Some Cobalt Electrodeposits

A high density of lattice faults was observed by transmission electron microscopy in an earlier study (15) of electroplated cobalt. It was pointed out at that time that the fault density could be determined quantitatively by an analysis of x-ray diffraction profiles. The results of this analysis are reported here.

Five samples were selected from those studied previously (15) for analysis by the Warren-Averbach method, which was discussed in the part of this paper which dealt with electroless cobalt. The first criterion for selecting the specimens was the presence of a measurable diffraction line of the type which is broadened by faulting. Only the samples with the pseudorandomly oriented grains (they were random except that there were relatively few with the basal plane parallel to the substrate) satisfied this condition. Most of the electrodeposits had  $\langle 10\bar{1}0 \rangle$  and  $\langle 11\bar{2}0 \rangle$  fiber axes and hence there were very few grains with the planes of the type which broaden due to faulting, parallel to the surface. Whereas, this condition could be changed by tilting the specimen with respect to the x-ray beam, the broadening which resulted from the altered geometry made the peaks unsatisfactory for quantitative analysis. Of the samples with the pseudorandom structure, those with the broadest diffraction lines were selected.

The diffraction lines of annealed copper filings and those of annealed cobalt which do not broaden due to faulting were used for the instrumental-broadening correction. It was found that both sets of results agreed within experimental error. The results of the Warren-Averbach analysis of the x-ray diffraction lines, together with the plating conditions under which the selected deposits were produced are listed in Table III. The diffraction lines used to obtain the graphs of  $\ln A_L$  vs.  $d^{-2}$  (Eq. [4]) are also listed in Table III. The instrumental-broadening correction in each instance was made with the nearest diffraction line of the annealed copper sample.

As the samples which were selected had the broadest peaks, the particle sizes, fault densities, and strains listed in Table III were probably higher than the average for the cobalt samples of the earlier study (15). The fault density appears to be somewhat higher than that of cold-worked cobalt, but as already pointed out, not as high as that of the electroless variety. The reason for the lower value of the second sample is not known. The fault densities, which indicate a growth fault on the average of every ten to sixteen atom layers, agree with the electron-microscopic observations (20). There is some indication of a larger par-

Table III. Results of Warren-Averbach analysis of x-ray diffraction lines, and plating conditions

Bath composition		Current density, amp/dm <sup>2</sup>	Particle size, D (Å)	Microstrain $\langle \epsilon_{110}^2 \rangle^{1/2}$ (%)	Growth-fault probability, $\beta$	Diffraction lines used for calculating $A_{110}$ , <sup>1,2</sup> and $\langle \epsilon_{110}^2 \rangle$
Moles/liter CoSO <sub>4</sub> × 7H <sub>2</sub> O	Moles/liter CoCl <sub>2</sub> × 6H <sub>2</sub> O					
—	1.25**	2.5	300	0.17	0.09	(10 $\bar{1}$ 0), (1 $\bar{1}$ 20), (1 $\bar{1}$ 22)
—	1.25*	5.0	300	0.10	0.06	(10 $\bar{1}$ 0), (1 $\bar{1}$ 20), (1 $\bar{1}$ 22)
0.625	0.625*	0.5	300	0.12	0.09	(10 $\bar{1}$ 0), (2020)
0.625	0.625*	0.1	200	0.17	0.09	(10 $\bar{1}$ 0), (1 $\bar{1}$ 20), (0002), (1 $\bar{1}$ 22)
1.136	0.114***	2.5	450	0.11	0.10	(10 $\bar{1}$ 0), (1 $\bar{1}$ 20), (1 $\bar{1}$ 22)

\* Had face-centered cubic material present.

\*\* pH was 3.5, for all others pH was 2.0

\*\*\* Plated at 60°C, all others plated at room temperature.

particle size for the sample plated at the elevated temperature, as would be expected. No conclusions about the effect of the plating variables are warranted because of the few data available.

The samples marked with an asterisk in Table III were found to have some face-centered-cubic phase present as determined from the presence of the {200} line by x-ray diffraction. It is interesting to note that the fault densities of these samples is not higher than that of the others as would have been expected.

#### REFERENCES

1. R. D. Fisher and W. H. Chilton, *This Journal*, **109**, 485 (1962).
2. L. D. Ransom and V. Zentner, *ibid.*, **111**, 1423 (1964).
3. J. S. Judge, J. R. Morrison, D. E. Speliotis, and G. Bate, *ibid.*, **112**, 681 (1965).
4. Y. Moradzadeh, *ibid.*, **112**, 891 (1965).
5. J. S. Judge, J. R. Morrison, and D. E. Speliolis, *ibid.*, **113**, 547 (1966).
6. J. S. Judge, J. R. Morrison, D. E. Speliolis, and J. R. De Pew, *Plating*, **54**, 503 (1967).
7. R. D. Fisher and W. H. Chilton, *ibid.*, **54**, 537 (1967).
8. G. L. Clark and S. H. Simonsen, *This Journal*, **113**, 424 (1965).
9. B. E. Warren and B. L. Averbach, *J. Appl. Phys.*, **21**, 595 (1950).
10. B. E. Warren, "Progress in Metal Physics," Vol. 8, B. Chalmers and R. King, Editors, Pergamon Press, New York (1959).
11. N. C. Halder and G. A. Mitra, *Phil. Mag.*, **8**, 1985 (1963).
12. J. W. Christian and P. R. Swann, "Alloying Behavior and Effects in Concentrated Solid Solutions," T. G. Massalski, Editor, Gordon and Breach Science Publishers, New York (1965).
13. C. N. J. Wagner and E. N. Aqua, "Advances in X-Ray Analysis," Vol. 7, W. M. Mueller, G. Mallet, and M. Fay, Editors, Plenum Press, New York (1963).
14. W. A. Rachinger, *J. Sci. Instruments*, **25**, 254 (1948).
15. R. Sard, C. D. Schwartz, and R. Weil, *This Journal*, **113**, 424 (1966).
16. A. K. N. Reddy, *J. Electroanalytical Chem.*, **6**, 141 (1963).
17. T. R. Anantharaman and J. W. Christian, *Acta Cryst.*, **9**, 479 (1956).
18. E. M. Hofer, L. F. Chollet, and H. E. Hintermann, *This Journal*, **112**, 1145 (1965).
19. G. B. Mitra and N. C. Halder, *Acta Cryst.*, **17**, 817 (1964).
20. C. D. Schwartz, Master's Thesis, Stevens Institute of Technology (1964).

## Electrodeposition of Bright Copper from Copper Sulfate Solutions by Addition of Cyanide Ion

S. Venkatachalam<sup>1</sup> and C. A. Winkler

McGill University, Montreal, Quebec, Canada

#### ABSTRACT

Small concentrations of cyanide ion in copper sulfate solutions, in the presence of either gelatin or cystine, enable the electrodeposition of bright copper, provided the current density is appropriately controlled. Cyanide ion, alone, added to the sulfate solution, causes marked depolarization, and this is strongly accentuated when gelatin or cystine is present. A polarization of about  $240 \pm 10$  mv was associated with maximum brightness of the deposits. Experiments with radioactive cystine and cyanide suggest that a 1:1 complex of the two might be involved in the production of bright deposits. The results seem to be explicable if it is assumed that orientation at the surface is necessary for brightness, and that cyanide ion is capable of acting as an "electron bridge," either alone or in the complex.

The relations between the light-reflecting property, or brightness, the electrolytic polarization, and the structure of an electrolytic deposit have been the subjects of many investigations. In most of the work addition agents, when used, were chosen empirically, since there is still no generally accepted theory to explain the various observations made during the formation of bright electrodeposits. The older theories of

Blum (1) and Bancroft (2), which assume adsorption of brighteners on the cathode, have been further developed by others. Some of these (3-6) have assumed kinetic adsorption on the active centers, while others (7-10) have assumed preferential adsorption on defined faces of the growing microcrystals.

In general, brighteners are not only adsorbed as such on the cathode surface, but may also undergo transformation during electrolysis. The transformation of organic addition agents at the electrode is of particular

\* Electrochemical Society Active Member.

<sup>1</sup> National Research Council of Canada Postdoctoral Fellow.

interest, since the reflectivity of the deposit may then be caused, not by the brighteners initially present, but by the products of their electrochemical reduction or oxidation (11).

Gelatin has been the most commonly used brightener, and the reflectivity of copper deposits in its presence has been studied (3, 12, 13). The behavior in such systems may be markedly altered by the simultaneous presence of halide ion, particularly  $\text{Cl}^-$ , which, in certain ratios to the gelatin, may exert a depolarizing action, or change the brightness of the deposit [e.g., (4)].

Since  $\text{CN}^-$  ion is generally recognized as having some properties similar to the  $\text{Cl}^-$  ion, and since the use of cyanide baths is well known for deposition of several metals, it seemed of interest to investigate the effect of adding  $\text{CN}^-$  to the acid copper sulfate electrolyte generally used for the electrowinning of copper. The studies were extended to include the simple amino acid, cystine, as an addition agent, since it has been found to behave in this capacity in a manner somewhat similar to the more complex gelatin molecule, including similar effect of added  $\text{Cl}^-$  ion (6).

### Experimental

The cell used for the polarization measurements is shown in Fig. 1. It was made of Lucite tubing of 32 mm ID and 155 mm long, cemented into a square anode compartment at the top, in such a way that 2 mm of the tube protruded into the anode compartment. The anode was an annulus of copper, 42 mm ID and 10 mm high, that dipped into electrolyte contained in the channel between the protruding tube and the outer wall of the anode compartment. The copper cathode was bolted to a flange that was cemented to the bottom of the cell, with a butyl-rubber annular gasket between the two to prevent leakage. The total superficial area of cathode exposed to the solution was 8  $\text{cm}^2$ .

Polarization measurements were made with the familiar probe technique and a recording potentiometer. The reflectivity of the plated surface was measured in a parallel beam of light, operated with stabilized line voltage, and projected on to the sample held in a fixed position at  $45^\circ$  to the light beam, in a light-tight box. The reflected light was received on a photocell, the current from which was recorded on a microammeter.

In some experiments, the electrolyte contained  $^{35}\text{S}$ -labelled cystine and  $^{14}\text{C}$ -labelled potassium cyanide. The activity of the plated samples was determined in a windowless  $\beta$ -proportional counter.

A "standard" electrolyte had the composition:  $\text{CuSO}_4 \cdot 5\text{H}_2\text{O}$ , 125 g/l (British Drug Houses, A.R. grade);  $\text{H}_2\text{SO}_4$ , 100 g/l (A.R. grade). The water was twice distilled. Copper sulfate from the same manufactured lot, and a constant volume (150 ml) of electrolyte, were used in all experiments, and measurements were all made at  $25^\circ \pm 0.1^\circ\text{C}$ . Before any experiment was made with electrolyte containing an additive, the cathode was cleaned and brought to a

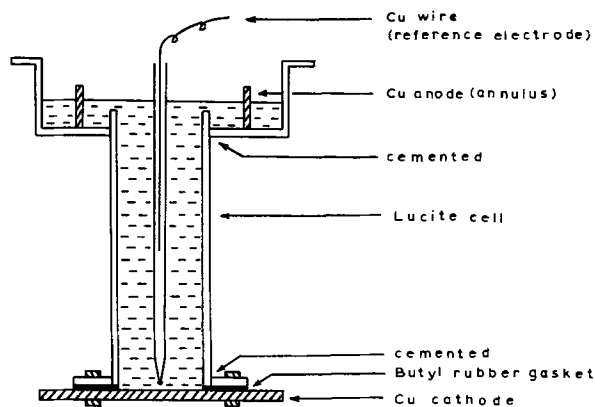


Fig. 1. Diagram of apparatus

"steady-state" surface condition by deposition under rigidly controlled conditions, as described in an earlier publication (12). The additives used, singly or in pairs, included: gelatin,  $\text{CN}^-$  ( $\text{KCN}$ ), cysteine, cystine, methionine,  $\alpha$ -alanine,  $\text{SO}_3^-$  ( $\text{K}_2\text{SO}_3$ ),  $\text{Cl}^-$  ( $\text{KCl}$ ), dithiodiglycolic acid, 2-aminothiazole and  $\text{CNS}^-$  ( $\text{KCNS}$ ).

### Results

**Gelatin with cyanide.**—Addition of various amounts of cyanide ion to the standard electrolyte decreased the polarization from 100 mv ("standard surface" value) to 30 mv (Fig. 2A). In the presence of gelatin, the depolarization by  $\text{CN}^-$  was as much as 200 mv. The cathode deposits showed increasing brightness as the concentration of cyanide ion was decreased. Experiments were therefore made in which the cyanide concentration was kept arbitrarily constant at 0.2 mg/l, and the gelatin concentration was varied from 50 to 200 mg/l. From the results (Fig. 3A), it is apparent that a maximum brightness was attained with about 100 mg/l gelatin, at the C.D. used (2 amp/ $\text{dm}^2$ ).

Experiments were then made in which this maximum gelatin/ $\text{CN}^-$  ratio, i.e., 500/1 was kept constant, while the total amount of the two additives was varied, at current densities in the range 0.5-5 amp/ $\text{dm}^2$ . The maximum brightness then depended on both the amount of the two additives and the current density (Fig. 3B).

**Cystine and related compounds with cyanide.**—Substitution of cystine for gelatin gave the results shown in Fig. 2B and 4A. Cystine behaved in a similar manner to gelatin, but the depolarization due to  $\text{CN}^-$  was less pronounced. As with gelatin, maximum brightness was obtained at a particular ratio of cystine/ $\text{CN}^-$  (roughly 80/1) for a C.D. of 3 amp/ $\text{dm}^2$ .

The effects on reflectivity and polarization of C.D. and  $\text{CN}^-$  concentration, in the presence of cystine, are shown in Fig. 3C and 5A. The close similarity with gelatin +  $\text{CN}^-$  is again apparent; maximum brightness depends on both the ratio of the two additives and the current density.

The effect of  $\text{CN}^-$  was also studied with other compounds that contain the functional groups that are present in cystine, e.g., methionine (an amino acid with a sulfur atom),  $\alpha$ -alanine (an amino acid without a sulfur atom), dithiodiglycolic acid (no amino group, but a -S-S- group). The results are presented in Fig. 2C and 4B. Methionine, like gelatin and cystine, markedly increased the polarization above that of the standard surface;  $\alpha$ -alanine had less effect. Depolarization by  $\text{CN}^-$  was considerably less with these compounds than with gelatin or cystine. The reflectivities of the deposits were not altered by any of these com-

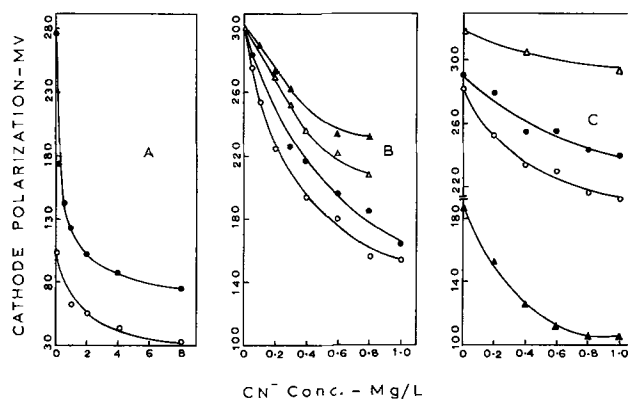


Fig. 2. Effect of cyanide ion concentration on cathode polarization, in the presence of other addition agents. A,  $\circ$  no gelatin,  $\bullet$  100 mg/l gelatin; B,  $\circ$  10 mg/l cystine,  $\bullet$  20 mg/l cystine,  $\triangle$  40 mg/l cystine,  $\blacktriangle$  80 mg/l cystine; C,  $\circ$  10 mg/l methionine,  $\bullet$  20 mg/l methionine,  $\triangle$  80 mg/l methionine,  $\blacktriangle$  20 mg/l  $\alpha$ -alanine.

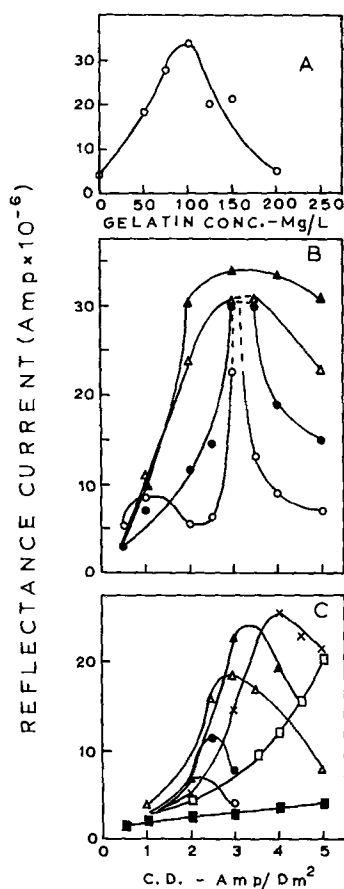


Fig. 3. Effect of current density and  $\text{CN}^-$  concentration on the reflectivity of the deposit, in the presence of gelatin or cystine. A,  $\circ$  0.2 mg/l  $\text{CN}^-$  concentration, 2 amp/dm<sup>2</sup>; B,  $\circ$  25 mg/l gelatin, 0.05 mg/l  $\text{CN}^-$ ,  $\bullet$  50 mg/l gelatin, 0.10 mg/l  $\text{CN}^-$ ,  $\triangle$  75 mg/l gelatin, 0.15 mg/l  $\text{CN}^-$ ,  $\blacktriangle$  100 mg/l gelatin, 0.20 mg/l  $\text{CN}^-$ ; C,  $\circ$  20 mg/l cystine, 0.05 mg/l  $\text{CN}^-$ ,  $\bullet$  20 mg/l cystine, 0.10 mg/l  $\text{CN}^-$ ,  $\triangle$  20 mg/l cystine, 0.2 mg/l  $\text{CN}^-$ ,  $\blacktriangle$  20 mg/l cystine, 0.3 mg/l  $\text{CN}^-$ ,  $\times$  20 mg/l cystine, 0.5 mg/l  $\text{CN}^-$ ,  $\square$  20 mg/l cystine, 0.8 mg/l  $\text{CN}^-$ ,  $\blacksquare$  20 mg/l cystine, 1.0 mg/l  $\text{CN}^-$ .

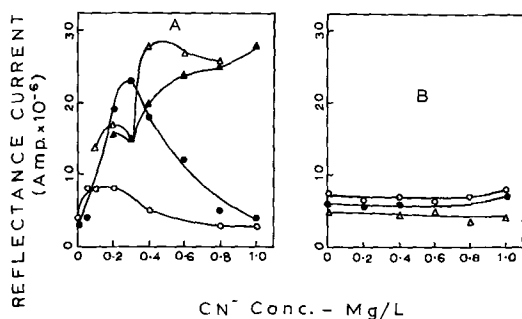
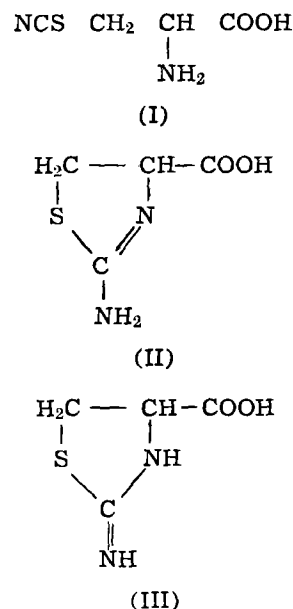


Fig. 4. Effect of cyanide ion concentration on the reflectivity of the deposit. A,  $\circ$  10 mg/l cystine, 3 amp/dm<sup>2</sup>,  $\bullet$  20 mg/l cystine, 3 amp/dm<sup>2</sup>,  $\triangle$  40 mg/l cystine, 3 amp/dm<sup>2</sup>,  $\blacktriangle$  80 mg/l cystine, 3 amp/dm<sup>2</sup>; B,  $\circ$  10 mg/l methionine, 3 amp/dm<sup>2</sup>,  $\bullet$  80 mg/l methionine, 3 amp/dm<sup>2</sup>,  $\triangle$  20 mg/l  $\alpha$ -alanine, 3 amp/dm<sup>2</sup>.

pounds in combination with the  $\text{CN}^-$ . Dithiodiglycolic acid itself behaved as a depolarizer, the values being 45-85 mv at current densities of 1-4 amp/dm<sup>2</sup>, and its behavior was not affected by the presence of  $\text{CN}^-$ . A combination of 20 mg/l methionine, a polarizer like cystine, and 1.4 mg/l dithiodiglycolic acid with 0.2 mg/l of  $\text{CN}^-$  did not alter much either the polarization values or the nature of the deposit (c.f. Table I).

**Cystine with  $\text{SO}_3^-$  and  $\text{Cl}^-$ .**—Sulfite ion is more nucleophilic in a kinetic sense than cyanide ion in reaction with cystine, and like  $\text{CN}^-$ , it is capable of

breaking the -S-S- bond easily (14). However, in the concentration range from 0.2 to 2 mg/l, it was without effect on the nature of the deposit when it was present with cystine (20 mg/l) in the electrolyte. Similar additions of chloride ion, which acts as a depolarizer in the presence of gelatin (4), had no effect on the deposit in the presence of cystine (20 mg/l) other than to cause some depolarization. Similarly, KCNS (0.2 - 0.5 mg/l) and 2-aminothiazole (20 mg/l) were without effect on the deposit, although they possess structures that are somewhat similar to those of the products formed when  $\text{CN}^-$  reacts with cystine (15-18), i.e.,  $\beta$ -thiocyanoalanine (I), 2-aminothiazole-4-carboxylic acid (II) or the equivalent 2-imino-4-thiazolidine carboxylic acid (III).



The data for these several systems are shown in Table I.

**Inclusion of cystine and  $\text{CN}^-$  in the deposit.**—The relative extents to which cystine and  $\text{CN}^-$  were included in the deposit were determined with electrolyte to which had been added cystine with  $^{35}\text{S}$  and  $\text{CN}^-$  with  $^{14}\text{C}$ . The total thickness of copper deposited was kept constant for all the experiments. The results are shown in Fig. 5B.

When cyanide alone was present in the solution, the amount of  $^{14}\text{C}$  included in the deposit remained constant irrespective of the current density. On the other hand, when cystine alone was present, retention of  $^{35}\text{S}$  decreased markedly up to 3 amp/dm<sup>2</sup>, beyond which the value remained constant. Also, when inactive cystine was present in conjunction with active cyanide, the activity of the deposit was rather precisely that corresponding to the inclusion of  $^{35}\text{S}$ , which strongly suggests that each cystine molecule included in the deposit carried with it one  $^{14}\text{CN}^-$  ion.

### Discussion

The results of the present study may be explained if it is assumed that some form of orientation at the surface is essential for brightness. The orientation might, but perhaps need not, correspond to exposure of only one particular crystal plane. That orientation, to produce a surface of relatively constant characteristics, as a condition for brightness is suggested by the almost constant polarization ( $240 \pm 10$  mv), at a C.D. of 2 amp/dm<sup>2</sup>, that characterized deposits of maximum brightness.

The action of gelatin, or cystine, or methionine alone, in increasing the polarization can be explained if it is assumed that these compounds are adsorbed on the active centers, thereby reducing the area of the cath-

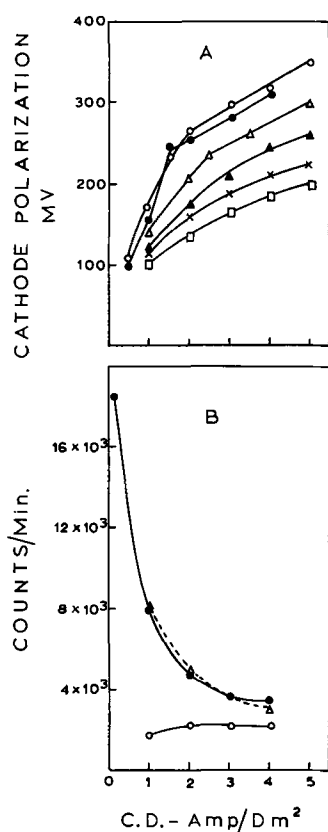


Fig. 5. Effect of current density and  $\text{CN}^-$  concentration on the cathode polarization, and the adsorption of  $^{35}\text{S}$  and  $^{14}\text{C}$ , in the presence of cystine. A,  $\circ$  20 mg/l cystine, no  $\text{CN}^-$ ,  $\bullet$  20 mg/l cystine, 0.05 mg/l  $\text{CN}^-$ ,  $\triangle$  20 mg/l cystine, 0.2 mg/l  $\text{CN}^-$ ,  $\blacktriangle$  20 mg/l cystine, 0.5 mg/l  $\text{CN}^-$ ,  $\times$  20 mg/l cystine, 0.8 mg/l  $\text{CN}^-$ ,  $\square$  20 mg/l cystine, 1.0 mg/l  $\text{CN}^-$ ; B,  $\circ$   $\text{CN}^-$  0.3 mg/l,  $^{14}\text{C}$  0.5  $\mu\text{C}/150$  ml,  $\bullet$  cystine 20 mg/l,  $^{35}\text{S}$  0.49  $\mu\text{C}/150$  ml,  $\triangle$  cystine 20 mg/l,  $\text{CN}^-$  0.3 mg/l,  $^{14}\text{C}$  0.5  $\mu\text{C}/150$  ml.

ode at which electron transfer may be readily effected, with a consequent increase in true current density, hence in polarization. On the other hand, the depolarization effect of  $\text{CN}^-$  alone can be explained in the manner suggested by Heyrovsky for the chloride ion (19), i.e., it might decrease the activation energy for the electron transfer by forming an intermediate "complex" of the type, electrode- $\text{CN}^-$ - $\text{Cu}^+$ , in which the cyanide ion acts as an "electron bridge."

While gelatin or cystine might be assumed to act mainly by adsorption at active centers (e.g., peaks), as might be demonstrated by autoradiography (20), it might well be that  $\text{CN}^-$  is adsorbed in a less specific way on the cathode surface. This would mean that,

in the presence of  $\text{CN}^-$ , deposition of metal at the peaks would be mainly through an intermediate complex of the type,  $\text{CN}^-$ -cyst- $\text{Cu}^+$ , while deposition on other parts of the surface would be through a  $\text{CN}^-$  bridge alone, with a smaller activation energy. The  $\text{CN}^-$  ion would then act as a depolarizer both in the absence and in the presence of the organic addition agent, as observed.

Maximum brightness of the deposit, corresponding to maximum orientation of the atoms in the surface, might require an optimal ratio of  $\text{CN}^-$  to cystine (or gelatin) to be present in the cathode film. This would suggest that, as found experimentally, different current densities should be necessary to achieve maximum brightness, corresponding to this particular concentration ratio in the film, as the concentrations of  $\text{CN}^-$  and cystine (or gelatin) are altered in the body of the solution. If the orientation were disturbed by an excess of cystine in the cathode film, a condition that might prevail at low current densities and high cystine to  $\text{CN}^-$  ratio in the solution, a bright deposit would not be obtained. On the other hand, with an excess of  $\text{CN}^-$  in the film, such as might be realized at high current densities and lower cystine to cyanide ion ratios in the solution, the copper ion would deposit directly through the  $\text{CN}^-$  bridge, and a coarser grained, rather than bright deposit, should result. It is also possible that too high current densities would tend to prevent bright deposits by promoting a rate of deposition greater than that with which orientation of the atoms in the deposit can occur.

The composition of a possible complex between cystine (or gelatin) and  $\text{CN}^-$  is suggested by the experiments with  $^{35}\text{S}$ -cystine and  $^{14}\text{CN}^-$ . Since the same activity was obtained, at different current densities, with the active cystine alone as with inactive cystine +  $^{14}\text{CN}^-$ , it would appear that the complex involved in the deposition process contains  $^{35}\text{S}$  and  $^{14}\text{C}$  in a 1:1 ratio, corresponding to a cystine- $\text{CN}^-$  complex of the same ratio.

#### Acknowledgment

This paper is a contribution from the Department of Chemistry, McGill University, Montreal, with financial assistance of the National Research Council of Canada.

Manuscript received Nov. 21, 1967; revised manuscript received Jan. 30, 1968.

Any discussion of this paper will appear in a Discussion Section to be published in the December 1968 JOURNAL.

#### REFERENCES

1. W. Blum, *Trans. Am. Electroplater's Soc.*, **23**, 266 (1913).
2. W. Bancroft, *Trans. Am. Electroplater's Soc.*, **36**, 213 (1919).

Table I. Mutual effects of polarizers and depolarizers on the polarization and reflectivity of the deposit

Addition agents	Current density, amp/dm <sup>2</sup>							
	1		2		3		4	
	Pol	Ref	Pol	Ref	Pol	Ref	Pol	Ref
Dithiodiglycolic acid (20 mg/l)	48	2.5	48	3	61	3.5	85	3
Dithiodiglycolic acid (20 mg/l) + $\text{CN}^-$ (0.3 mg/l)	45	2.5	50	3	69	3.2	80	2.5
Methionine (20 mg/l) + $\text{CN}^-$ (0.2 mg/l) + dithiodiglycolic acid (1.4 mg/l)	113	3	184	3	240	3	270	3
Cystine (20 mg/l) + $\text{SO}_3^{2-}$ (0.2 mg/l)					299	4		
Cystine (20 mg/l) + $\text{SO}_3^{2-}$ (0.4 mg/l)					303	5		
Cystine (20 mg/l) + $\text{SO}_3^{2-}$ (0.8 mg/l)					300	4.5		
Cystine (20 mg/l) + $\text{SO}_3^{2-}$ (1.0 mg/l)					302	4.5		
Cystine (20 mg/l) + $\text{Cl}^-$ (0.2 mg/l)					293	4		
Cystine (20 mg/l) + $\text{Cl}^-$ (0.4 mg/l)					288	4.5		
Cystine (20 mg/l) + $\text{Cl}^-$ (1.0 mg/l)					267	4		
Cystine (20 mg/l) + $\text{Cl}^-$ (2.0 mg/l)					237	3.5		
CNS <sup>-</sup> (0.2 mg/l)	31	3.5	58	3.5	81	3	90	3.5
CNS <sup>-</sup> (0.5 mg/l)	—	—	—	—	77	2	83	2
2-aminothiazole (20 mg/l)	46	3	94	3.5	157	5	204	5.5
Cystine (20 mg/l) + CNS <sup>-</sup> (0.2 mg/l)	—	—	170	2	237	2.5	260	2.5
Cystine (20 mg/l) + 2-aminothiazole (20 mg/l)	174	3.5	260	5.5	300	2.5	340	3.5

3. W. Gauvin and C. A. Winkler, *Can. J. Res.*, **B21**, 125 (1943).
4. W. Mandelcorn, W. B. McConnell, W. Gauvin, and C. A. Winkler, *This Journal*, **99**, 84 (1952).
5. V. Hospadaruk and C. A. Winkler, *J. Metals*, **5**, 1375 (1953).
6. A. J. Sukava and C. A. Winkler, *Can. J. Chem.*, **33**, 961 (1955).
7. K. Ekler and C. A. Winkler, *ibid.*, **33**, 1756 (1955).
8. S. C. Barnes, *Electrochim. Acta.*, **5**, 79 (1961).
9. G. G. Storey and S. C. Barnes, *J. Inst. Metals*, **90**, 336 (1961-62).
10. S. C. Barnes, *This Journal*, **111**, 296 (1964).
11. D. R. Turner and G. R. Johnson, *ibid.*, **109**, 798 (1962).
12. W. Gauvin and C. A. Winkler, *Can. J. Res.*, **A21**, 37 (1943).
13. W. Gauvin and C. A. Winkler, *ibid.*, **B21**, 81 (1943).
14. O. Gawron, "Chemistry of Organic Compounds," Vol. 2, Chap. 14, p. 362, Pergamon Press, New York (1966).
15. A. Schöberl and R. Hamm, *Chem. Ber.*, **81**, 210 (1948).
16. W. N. Aldrich, *Biochem. J.*, **48**, 271 (1951).
17. H. Behringer and P. Zillikens, *Ann. Chem.*, **574**, 140 (1951).
18. A. Schöberl, M. Kawohl, and R. Hamm, *Chem. Ber.*, **84**, 571 (1951).
19. J. Heyrovsky, *Discussions Faraday Soc.*, **1**, 212 (1947).
20. S. E. Beacom and B. J. Riley, *This Journal*, **106**, 309 (1959).

## Structural Characteristics of the Oxide on the (111) of Copper<sup>1</sup>

J. V. Cathcart\* and G. F. Petersen

*Metals and Ceramics Division, Oak Ridge National Laboratory, Oak Ridge, Tennessee*

### ABSTRACT

Cuprous oxide films, 25 to approximately 500Å thick, formed on the (111) of copper were studied by x-ray, electron microscopic, and ellipsometric techniques. The films were characterized in terms of their surface topography, epitaxial strains, mosaic spread, mosaic size, and their orientation relationships with the substrate metal. The films were demonstrated to contain large numbers of structural defects which could act as paths of easy diffusion, and a correlation was shown to exist between the rate of oxidation of the (111) of copper and the extent of these paths of easy diffusion in the oxide. Estimates were made of the effective grain-boundary width and diffusion coefficient in Cu<sub>2</sub>O, and it was concluded that substantial material transport could occur *via* these paths of easy diffusion.

One of the most notable features of the oxidation of metal single crystals is the marked oxidation rate anisotropy exhibited by these materials including those with cubic crystal structures. A good example of this behavior is furnished by copper (1) which at 250°C shows an order of magnitude difference between the oxidation rates of its most rapidly and most slowly oxidizing orientations. Various authors have suggested that the anisotropy of atomic packing on different crystal planes or the variation of work function with crystal plane might account for the observed results; however, objections can be raised to both these ideas. In recent papers, (2) we pointed to the existence of a correlation between the oxidation rate anisotropy of copper and a corresponding anisotropy of the extent of paths of easy diffusion through the growing oxide films. The present paper is a report of an additional correlation between the rate of oxidation of the (111) of copper and the degree of "lattice disregistry"<sup>2</sup> in the oxide film.

### Experimental Procedures and Results

The copper specimens used in this study were sliced from a 1-in. diameter single-crystal rod at such an angle as to expose a (111) surface. After mechanical polishing through 4/0 grade emery paper, the crystals were electropolished in 60% H<sub>3</sub>PO<sub>4</sub> and washed for 10 min in running distilled water. Just prior to oxidation the specimens were annealed in H<sub>2</sub> for 1 hr at 500°C to reduce the superficial oxide on their surfaces. They were then oxidized in purified oxygen at 200°C and a pressure of approximately 500 Torr. The all-glass apparatus in which the oxidation was carried out was

equipped with optical flats so that a continuous set of oxide thickness measurements could be made with an ellipsometer during the oxidation process.

Twelve specimens were prepared and examined using an x-ray technique developed by Borie and Sparks (3-5). The oxide on all specimens was highly oriented, and the epitaxial relationship between the oxide and metal was the same as that reported by previous authors (6), *viz.*, the (111)<sub>Cu<sub>2</sub>O</sub> || (111)<sub>Cu</sub>. The three <110><sub>Cu</sub> lying in the plane of the metal surface were parallel to the corresponding <110><sub>Cu<sub>2</sub>O</sub> which lie in the plane of the film. There are two ways in which these conditions may be met, thus resulting in twin-related orientations in the oxide. In the first or "parallel" orientation, the oxide and metal lattices are completely parallel to each other. The "antiparallel" orientation may be derived by a 180° rotation of the oxide lattice about its surface normal.

Since the twinning plane in this case is the (111), incoherent twin boundaries with components normal to the film surface must exist within the oxide. These boundaries produce regions of disorder within the oxide lattice and comprise an important fraction of the total "lattice disregistry" within the oxide.

The results of these measurements are summarized in Fig. 1. Nine of the 12 rate curves fell in a scatter band at the top of the graph. The other three specimens exhibited a marked reduction in oxidation rate. A complete rate curve was determined only for one of these three samples, a single thickness measurement being made on each of the others after the completion of oxidation.

The x-ray work revealed that the oxide on the nine specimens whose oxidation rates were essentially the same consisted of approximately equal quantities of parallel and antiparallel orientations. On the slow rate specimens, on the other hand, 78-90% of the oxide was in the antiparallel orientation. The x-ray results thus

\* Electrochemical Society Active Member.

<sup>1</sup> Research sponsored by the U. S. Atomic Energy Commission under contract with the Union Carbide Corporation.

<sup>2</sup> The term "oxide lattice disregistry" is used in this paper to mean the disorder existing in the oxide lattice as the result of the presence of dislocation arrays or grain boundaries which can act as paths of easy diffusion.

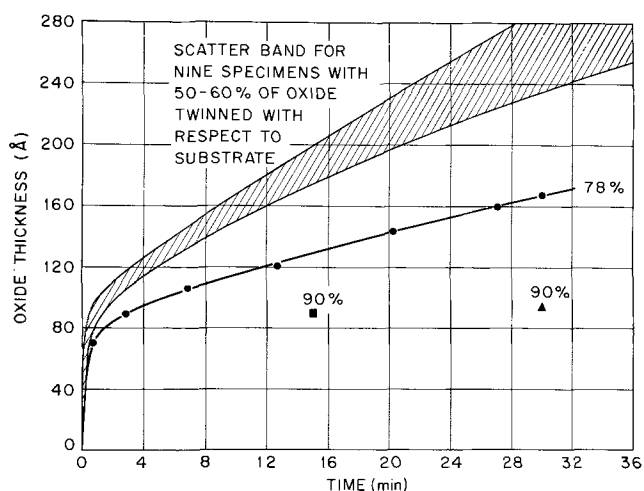


Fig. 1. Oxidation rate curves for the (111) of copper at 200°C and 500 Torr oxygen. The figures on the graph refer to the percentage of oxide present in the antiparallel orientation.

make it clear that those crystals exhibiting relatively small rates of oxidation were also those for which the extent of incoherent twin boundaries in the oxide was smaller, that is, those films in which a single orientation of the oxide predominated, in this case, the antiparallel orientation.

A trace of  $\text{CCl}_4$  (approximately 1 ppm) was present in the oxidation chamber in at least two of the three slow-rate runs, and this change in the orientation distribution in the oxide was undoubtedly related to the presence of  $\text{CCl}_4$  or some other surface contaminant.

### Discussion

These data along with a few earlier results allow one to construct a model for the oxide film on the (111) of copper. The features of the model may be summarized as follows:

**Surface topography.**—Electron microscope studies of surface replicas and stripped oxide films showed the existence of relatively minor thickness inhomogeneities in the oxide films in the thickness range 100–1000Å for oxidation at approximately 1 atm oxygen and at a temperature of 150°–250°C. Within this thickness range, at least to a first approximation, the films may be treated as a layer of uniform thickness.

**Epitaxial strains.**—With the possible exception of earliest stages of oxidation, the oxide lattice, because of epitaxial forces, is expanded normal to the plane of its surface and compressed in that plane. The x-ray study gave a quantitative expression for these strains in terms of average d-spacing values measured normal to the film surface. The thinnest films (approximately 25Å) were virtually unstrained, their lattice parameter being essentially that of bulk  $\text{Cu}_2\text{O}$ . With increasing thickness, however,  $d_{111}$  increased rapidly and passed through a shallow maximum (2).

**Strain gradient.**—Strain broadening of the (111) and (222) Bragg peaks indicated the existence of a strain gradient within the oxide. In analogy to the previously discussed case of the oxide on the (110) of copper, it was presumed that the strain gradient results from the relief of epitaxial strains within the films through the production of an array of growth dislocations in the films (5).

**Mosaic spread.**—These growth dislocations plus the small misorientations (both tilt and twist) introduced into the oxide during oxidation produce a mosaic structure in the oxide. The mosaic spread, defined in terms of the width at half-maximum intensity of a (111) rocking curve for the films, is smallest for the thinnest films, increasing from a value of 2° at 100Å

to about 7° at 500Å. Dark field electron microscopy of oxide stripped from the (111) indicated an average diameter for the mosaic blocks of 50–100Å.

**Oxide orientations.**—As indicated above, two different, twin-related orientations occurred in the oxide. There are two general ways in which these orientations may be distributed in the film: the orientation of each mosaic block may be fixed by that of the nucleus from which it grows. The oxide would then consist of columns of oxide, some having the parallel, others the antiparallel orientation. This condition, hereafter referred to as “columnar twinning,” is illustrated schematically in Fig. 2a. On the other hand, stacking faults may occur in the oxide causing repeated twinning in each mosaic block. This arrangement we have called “laminar twinning,” and it is shown schematically in Fig. 2b.

At the present time we are able to make only a rather ambiguous choice between these two alternatives. The x-ray results are inconclusive on this point; however, low-pressure oxidation studies by Lawless and Mitchell (7) suggest that the columnar twin model may be more correct. Electron micrographs of specimens oxidized at  $p_{\text{O}_2} = 10\mu$  and 400°C revealed well-formed, three-sided pyramids of oxide on the surfaces of the specimens. Both orientations of the oxide are clearly evident, but each pyramid appears to be almost perfectly formed. Such morphology would be crystallographically impossible if “laminar twinning” occurred.

It is debatable, however, that the results of oxidation at a pressure of 10 $\mu$  can be extrapolated to 1 atm. Thus for the moment no clear answer can be given the question of the precise distribution of the two oxide orientations in  $\text{Cu}_2\text{O}$  films. Whatever this distribution may be, the film will, in any case, be rich in incoherent twin boundaries. Such boundaries are almost as effective as preferred diffusion paths as ordinary high angle grain boundaries (8). Thus the presence of twin-related orientations in the oxide on the (111) automatically leads to the formation of extensive numbers of “paths of easy diffusion” in the oxide films.

**Diffusion effect.**—Crucial to the postulate of the importance of these paths of easy diffusion in the oxide film is the demonstration that the volume of such regions in combination with the appropriate diffusion coefficient is large enough to transport a significant quantity of material through the oxide. No information is available regarding the relative values of the vol-

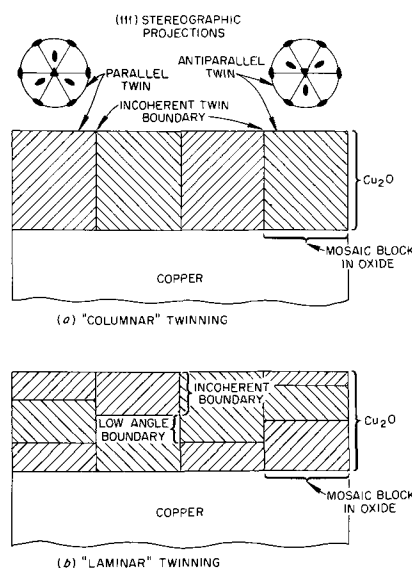


Fig. 2. Schematic representation of the distribution of twins in the oxide on the (111) of copper.

ume and grain-boundary diffusion coefficients,  $D_v$  and  $D_{gb}$ , respectively for  $\text{Cu}_2\text{O}$ ; however, in general  $D_{gb} \gg D_v$ . For metals, values of  $D_{gb}/D_v$  on the order of  $10^6$  have been reported; e.g., for self-diffusion in silver (9) at  $500^\circ\text{C}$ ,  $D_{gb}/D_v = 4 \times 10^6$ . Similar large values for this ratio have been reported for ionic compounds:  $10^6$  for anion self-diffusion in  $\text{NaCl}$  at  $500^\circ\text{C}$  (10),  $10^2$  for oxygen diffusion in  $\text{Al}_2\text{O}_3$  at  $1500^\circ\text{C}$  (11), and  $10^1$  for Ni in  $\text{MgO}$  at  $1715^\circ\text{C}$  (12). Furthermore, the activation energy for grain-boundary diffusion is generally 1/2 to 2/3 that for volume diffusion (13); thus  $D_{gb}/D_v$  should increase with decreasing temperature. Given the relatively low oxidation temperatures used for our copper specimens, it is reasonable to conclude that for  $\text{Cu}_2\text{O}$  at  $200^\circ\text{C}$ ,  $D_{gb}$  exceeds  $D_v$  by a substantial factor, probably several orders of magnitude.

The second parameter, knowledge of which is needed for our arguments, is the fraction of the total oxide volume associated with the grain boundaries; i.e., the volume fraction of the oxide for which  $D_{gb}$  is the valid diffusion coefficient. Estimates of grain boundary widths,  $\delta$ , given in the literature vary from as low as 5 to  $10^4$  Å with most of the more recent results for ionic compounds favoring comparatively wide grain boundaries. For metals the grain boundaries appear to be very narrow (12), but in ionic compounds the influence of grain boundary may extend large distances into adjacent grains; for example, an effective grain-boundary width of 200 Å was estimated for  $\text{NaCl}$  (10), and, for  $\text{MgO}$  values of  $\delta$  in the range of microns have been reported (12).

As indicated above, the diameter of the mosaic blocks in the (111) oxide films was approximately 100 Å. If the grain-boundary width in  $\text{Cu}_2\text{O}$  films is as high as  $10^2$  or  $10^3$  Å,  $D_{gb}$  will obviously hold for the entire volume of the oxide. On the other hand, if the effective width of the grain boundary is only 10 Å, roughly 20% of the oxide will be associated with grain boundaries. Thus it becomes apparent that grain-boundary diffusion could contribute significantly to material transport through the film for  $D_{gb}/D_v$  as small as 10, and for  $D_{gb}/D_v$  approximately  $10^3$ , grain-boundary diffusion may well be the dominant mechanism for material transport. These conclusions are also consistent with a theoretical analysis by Gibbs (14) of the influence of oxide grain boundaries on diffusion-controlled oxidation.

### Summary

In summary, our x-ray studies of the oxide on the (111) of copper demonstrated that these films con-

tained large numbers of structural defects which may act as paths of easy diffusion. A correlation was shown to exist between the rate of oxidation of the (111) and the extent of these paths of easy diffusion. Finally on the basis of reasonable assumptions concerning grain-boundary widths and diffusion coefficients, it appears that very considerable amounts of material transport could occur across the oxide via these paths of easy diffusion.

### Acknowledgment

The authors wish to thank C. J. Sparks and R. E. Pawel for much valuable assistance and discussion during the course of this research.

Manuscript received Aug. 28, 1967; revised manuscript received ca. Feb. 12, 1968.

Any discussion of this paper will appear in a Discussion Section to be published in the December 1968 JOURNAL.

### REFERENCES

1. F. W. Young, J. V. Cathcart, and A. T. Gwathmey, *Acta Met.*, **4**, 145 (1956).
2. J. V. Cathcart, G. F. Petersen, and C. J. Sparks, *Memoires Scientifiques Rev. Metallurg.*, **62**, 11 (1965); J. V. Cathcart, G. F. Petersen, and C. J. Sparks, "Oxidation Rate and Oxide Structural Defects," *Proceedings, Sagamore Conference on Physical and Chemical Characteristics of Surfaces and Interfaces*, 1967, University of Syracuse Press, Syracuse, N.Y.
3. B. S. Borie, *Acta Cryst.*, **13**, 543 (1960).
4. B. S. Borie and C. J. Sparks, *ibid.*, **14**, 569 (1961).
5. B. S. Borie, C. J. Sparks, and J. V. Cathcart, *Acta Met.*, **10**, 691 (1962).
6. K. R. Lawless and A. T. Gwathmey, *ibid.*, **4**, 153 (1956). A. T. Gwathmey and K. R. Lawless, "The Surface Chemistry of Metals and Semiconductors," pp. 483-521, John Wiley & Sons, New York (1960).
7. D. F. Mitchell, *The Low Pressure Oxidation of Copper Single Crystals*, Dissertation, University of Virginia, 1965.
8. D. Whitwham and P. Lacombe, "The 'Coherent' and 'Incoherent' Grain Boundaries in the Twins of Cubic Metals," *Fourth Metallurgy Colloquium*, France, pp. 161-182.
9. D. Turnbull and R. E. Hoffman, *Acta Met.*, **2**, 419 (1954).
10. L. W. Barr, I. M. Hoodless, J. A. Morrison, and R. Rudham, *Trans. Faraday Soc.*, **56**, 697 (1960).
11. Y. Oishi and W. D. Kingery, *J. Chem. Phys.*, **33**, 480 (1960).
12. B. J. Wuensch and T. Vasilos, *J. Am. Ceram. Soc.*, **47**, 63 (1964).
13. D. W. James and G. M. Leak, *Phil Mag.*, **12**, 491 (1965).
14. G. B. Gibbs, *Corrosion Sci.*, **7**, 165 (1967).



# Electrochemistry of Fused Lithium Perchlorate

Udo Anders and James A. Plambeck\*

Department of Chemistry, University of Alberta, Edmonton, Alberta, Canada

## ABSTRACT

The limiting reactions which occur during electrolysis of fused lithium perchlorate are shown to be  $\text{Li}^+ + e^- \rightarrow \text{Li}^\circ$  and  $\text{ClO}_4^- \rightarrow \frac{1}{2}\text{Cl}_2 + 2\text{O}_2 + e^-$  at the cathode and anode, respectively. The otherwise explosive reaction between the lithium metal generated and the fused perchlorate was prevented by alloying the lithium with silver. A cathodic peak observed at  $-1.5\text{v}$  with respect to a  $\text{Ag(I)/Ag}$  electrode is attributed to the reaction  $\text{ClO}_4^- + 2e^- \rightarrow \text{ClO}_3^- + \text{O}^-$ . Unlike the analogous peak process observed in fused nitrates, the electron:chlorate ratio is not 2:1 even though the expected 2:1 electron:oxide ratio is obtained. This and other behavior is explained on the basis of an oxide and peroxide-catalyzed decomposition of perchlorate and chlorate. Attempts were made to anodize metals into the melt; in no case except silver (for which the expected Nernstian behavior was observed) was this possible, oxide formation being generally observed instead.

While different nitrate melts have received much attention during the past years (1-9) little is known about the electrochemistry of fused perchlorates. Bombi and co-workers (10) established the Nernstian behavior of the  $\text{Ag(I)/Ag}$  electrode in fused  $\text{LiClO}_4$  during a solubility study of silver halides in this melt. Denning and Johnson (11) employed platinum and copper electrodes in fused  $\text{LiClO}_4$ . The copper electrode became coated with oxide as soon as it was inserted into the melt. During cathodic polarization of a platinum electrode, black oxide formation, an increase in the size of this electrode (attributed to  $\text{Li-Pt}$  alloy formation), and gassing were observed. When the current was switched off the material formed at the cathode reacted explosively with the melt.

Apart from the molten state,  $\text{LiClO}_4$  has been the object of studies in organic media. Maki and Geske (12) electrolyzed a 0.1M solution of  $\text{LiClO}_4$  in acetonitrile and obtained from the anode compartment an ESR signal which they assigned for a  $\cdot\text{ClO}_4$  radical. Cauquis and Serve (13) reinvestigated the electrolysis of  $\text{LiClO}_4$  in the different solvent nitromethane and essentially confirmed the earlier results of Maki and Geske.

## Experimental

**Solvent.**—Lithium perchlorate stands out among the perchlorates as being the only one that is stable in the molten state. It melts without decomposition at  $247^\circ\text{C}$  and does not begin to show an appreciable decomposition rate until the temperature is raised over  $400^\circ\text{C}$  (14). All experiments reported in this paper were done at  $260^\circ \pm 10^\circ\text{C}$ .

The  $\text{LiClO}_4$  used was anhydrous reagent grade (Amend Chemical Company). It was dried under high vacuum for 3 days at  $150^\circ\text{C}$ . It was then melted and purged with dry chlorine for 30 min to remove any remaining oxidizable impurities (15); during this time the original dark melt became completely clear. This process was followed by nitrogen purging for 12 hr in order to remove the chlorine from the system. During the experiments nitrogen purging was kept up at a slow rate in order to keep the melt free from traces of water. The initial chloride content was in the range of  $2 \times 10^{-4}$  moles/kg melt. It did not increase to more than  $1 \times 10^{-2}$  moles/kg melt during the time of the investigations, as shown by argentometric titration.

**Apparatus.**—The cell consisted of a Pyrex vessel with 24/40 and 14/20 standard taper joints. Pyrex feed-through tubes to which sintered glass disks of D porosity (Ace Glass Company, Vineland, New Jersey) were fused served as isolation compartments. Holes in the feed-through wall above the melt level

maintained equal pressure between the compartments and cell. The electrodes, each of which was kept in a separate isolation compartment, were silver wires (reference and working electrodes), other metal wires (for anodization studies), and platinum microelectrodes. The heating unit consisted of a heating mantle and a heating tape regulated by variable transformers. For mass spectrometric samples, a Pyrex U-type cell was constructed in which the anode and cathode compartments were separated by a sintered glass disk. The two electrodes were connected to tungsten leads sealed through the compartment tops. The cathode was a massive silver electrode while platinum served as the anode. Tubes leading through liquid nitrogen traps to a vacuum manifold were connected to both electrode compartments.

The voltammetric scans were performed with an Anotrol Model 4100 Potential Controller (Magna Electronics) using a platinum microelectrode, sealed in glass and ground flush, of  $0.9 \text{ mm}^2$  geometrical area. An Anotrol 4510 Scan Unit was used in combination with a EUW-20A (Heath Company) Multispeed Recorder. A Model IV Coulometric Current Source (E. H. Sargent and Company) was used for the anodization of metal electrodes.

**Chemicals.**—The  $\text{Li}_2\text{O}$  (Alfa Inorganics, Inc.),  $\text{Na}_2\text{O}_2$  (calorific grade, Allied Chemical),  $\text{LiClO}_4 \cdot 3\text{H}_2\text{O}$  (reagent grade, G. F. Smith Chemical Company), and  $\text{KOH}$  (analytical grade, British Drug Houses) were used as received. Samples of  $\text{LiNO}_3$  (Alfa Inorganics, Inc.),  $\text{KClO}_3$  (reagent grade, Nichols Chemical Company), and  $\text{KHSO}_4$  (reagent grade, Fisher Scientific) were vacuum-dried over magnesium perchlorate before use. Metal wires were cleaned mechanically and dried with acetone before use.

**Procedure.**—A reference electrode based on the  $\text{Ag(I)/Ag}$  couple (about 0.2M or 0.1M) was generated coulometrically for each experiment, and all potentials in this paper are given with reference to this electrode. Nernstian behavior corresponding to a one-electron change was observed for silver in this solvent on oxidation and reduction, in agreement with the work of Bombi and co-workers (10). Oxide was determined by acidimetric titration of the hydroxide formed after hydrolysis of the contents of a compartment, and chloride was determined by conventional argentometric titration. The method of Chen (16) was used to determine small amounts of  $\text{ClO}_3^-$  in the presence of large amounts of  $\text{ClO}_4^-$ ; the same method indicated the absence of  $\text{ClO}_2^-$  and  $\text{ClO}^-$  in all samples.

## Results and Discussion

Voltammetric scans of the pure  $\text{LiClO}_4$  melt with a platinum microelectrode gave the curve shown in

\* Electrochemical Society Active Member.

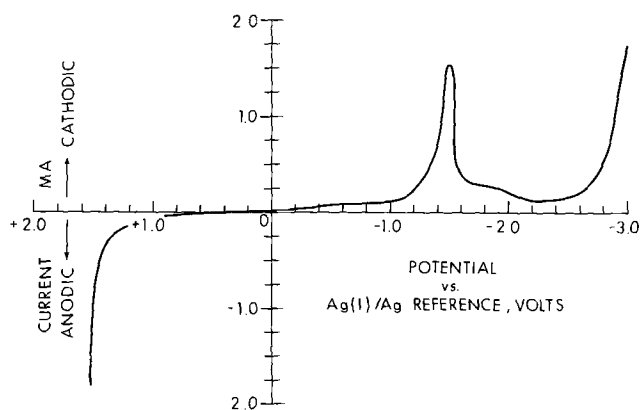


Fig. 1. Voltammogram of fused lithium perchlorate. Platinum microelectrode, geometrical area 0.9 mm<sup>2</sup>.

Fig. 1. At the anode the limiting electrode reaction occurs at +1.7v, the rising portion being spread out over approximately 0.3v. The cathodic limiting reaction occurs at -2.7v. There is an additional cathodic peak at -1.5v.

The cathodic limiting reaction is the deposition of lithium metal. Since pure lithium metal reacts explosively with the lithium perchlorate solvent (11) and since cathodic lithium deposition was inevitable during the investigation, it was necessary to reduce the activity of the lithium formed to as low a value as possible. It was found that alloy formation with silver served well for this purpose provided large enough silver electrodes and low enough current densities were used; current densities were approximately 0.1 amp/cm<sup>2</sup> and the total current approximately one meq/cm<sup>2</sup>. This alloy formation reduced but did not completely halt the reaction between lithium and the melt; gentle gas evolution was continuous and the amount of lithium found in the silver was less than that calculated from coulombs passed. Platinum and tungsten electrodes did not show as large a capacity for lithium metal and explosions occurred with both.

The over-all process for the anodic limiting reaction appears to be  $\text{ClO}_4^- \rightarrow 2 \text{O}_2 + \frac{1}{2} \text{Cl}_2 + e^-$ . The slow curvature of the voltammogram as the anodic limiting process begins to occur may indicate an irreversible reaction (17) or other complication. The gases produced at the anode during electrolysis of pure  $\text{LiClO}_4$  in the U-type cell were pumped off under vacuum and trapped with liquid nitrogen. Mass spectrometric analysis on a MS-9 spectrometer (Associated Electrical Industries) showed no fragments containing Cl-O bonds. Only chlorine was detected.

There is a very small but reproducible wave at  $E_{1/2} = -0.5\text{v}$ , which by analogy with nitrate systems (18) is probably due to residual traces of water. Except for this, the only voltammetric feature visible between the anodic and cathodic limiting reactions was a cathodic peak at -1.5v. This appeared similar to the peak observed in fused nitrates. The nitrate peak was interpreted (1, 2, 9) as due to the process  $\text{NO}_3^- + 2e^- \rightarrow \text{NO}_2^- + \text{O}^-$ . In nitrate melts the ratio  $e^-:\text{NO}_2^-:\text{O}^-$  was found to be 2:1:1. In a perchlorate melt the analogous process would be  $\text{ClO}_4^- + 2e^- \rightarrow \text{ClO}_3^- + \text{O}^-$ . When compartments of fused  $\text{LiClO}_4$  were electrolyzed at the peak potential of -1.5v, the  $e^-:\text{O}^-$  ratio found was 2.1, standard deviation 0.2, to one. No reproducible  $e^-:\text{ClO}_3^-$  ratio was observed, although comparison of the IR spectra (Perkin-Elmer 337, Nujol mull) of electrolyzed and unelectrolyzed  $\text{LiClO}_4$  revealed a new band at 970 cm<sup>-1</sup> which (by comparison with a known sample of  $\text{KClO}_3$ ) is due to the  $\text{ClO}_3^-$  ion (19). Chloride ion was also always present as shown by reaction with silver nitrate.

Attempts were made to determine the source of the peak by addition of reagents. Addition of  $\text{H}^+$  (as

$\text{KHSO}_4$ ) or  $\text{OH}^-$  (as  $\text{KOH}$ ) produced no apparent change in the peak. Addition of  $\text{ClO}_3^-$  (as  $\text{KClO}_3$ ) also produced no change in the peak, indicating that it could not be due to the reaction  $\text{ClO}_3^- + 2e^- \rightarrow \text{ClO}_2^- + \text{O}^-$ ; in fact, this reaction does not seem to occur within the decomposition range of the melt. Addition of  $\text{H}_2\text{O}$  (as  $\text{LiClO}_4 \cdot 3\text{H}_2\text{O}$ ) showed a small increase in the peak and violent evolution of a water vapor.

The similarity between the cathodic peak observed in this study and those observed in nitrate melts (1, 9) suggested the possibility of similar thermal equilibria in nitrate and perchlorate melts,  $\text{NO}_3^- \rightleftharpoons \text{NO}_2^- + \frac{1}{2} \text{O}_2$  and  $\text{ClO}_4^- \rightleftharpoons \text{ClO}_3^- + \frac{1}{2} \text{O}_2$ , both producing oxygen. The dissolved oxygen formed might then be the material which undergoes electrochemical reduction,  $\frac{1}{2} \text{O}_2 + 2e^- \rightarrow \text{O}^-$ , explaining the 2:1 electron:oxide ratio. However, although addition of  $\text{NO}_3^-$  (as  $\text{LiNO}_3$ ) increased the cathodic current in the peak region, careful examination indicated that the  $\text{NO}_3^-$  and  $\text{ClO}_4^-$  peaks were different although quite close in potential (Fig. 2), so that they in fact correspond to different processes. These peaks are not, then, due to dissolved oxygen. To prove this, the melt was saturated with dry oxygen gas; this had no effect on the height or position of the peak.

The major difficulty in the assignment of the peak to the  $\text{ClO}_4^- + 2e^- \rightarrow \text{ClO}_3^- + \text{O}^-$  reaction was clearly that no consistent  $e^-:\text{ClO}_3^-$  ratio was found for the electrolysis of fused  $\text{LiClO}_4$ , unlike the nitrate melts in which the expected 2:1 ratio was obtained. Chlorate was always present but generally in amounts less than expected (Table I). Decomposition of the perchlorate solvent would cause inconsistent  $e^-:\text{ClO}_3^-$  ratios as observed, chlorate being an intermediate in the decomposition, and also account for the observed chloride. Since the expected ratio of  $e^-:\text{O}^-$  was ob-

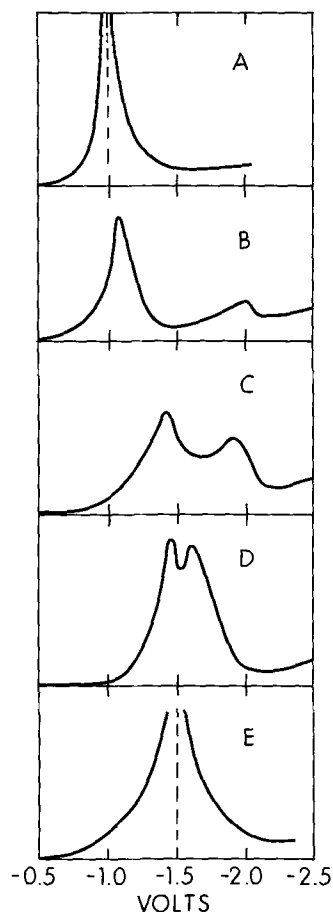


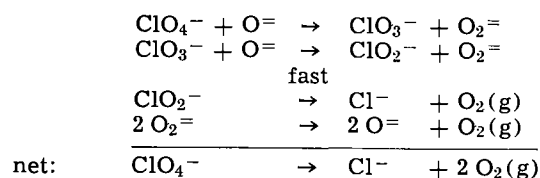
Fig. 2. Voltammetric peak detail. A, pure  $\text{LiNO}_3$ ; B, C, D,  $\text{LiClO}_4$  with decreasing amounts of  $\text{LiNO}_3$ ; E, pure  $\text{LiClO}_4$ .

Table I. Stoichiometry of cathodic peak

Mequivalents electricity	OH <sup>-</sup> , mmoles	ClO <sub>3</sub> <sup>-</sup> , mmoles	Cl <sup>-</sup> , mmoles
0.34		0.024	
0.90		0.023	
0.013		0.012	
3.3	2.9		1.6
3.4			3.0
3.4			4.1
3.1	2.8		1.7
1.8			0.38
1.7	1.8	1.25	0.27
1.4	1.2	0.29	0.22
1.8	2.0	0.70	0.31
1.8	1.8	3.7	0.28
0.26	0.27		0.040

tained, oxide could not be generated or used by this decomposition process; if involved, oxide must act as a catalyst. The gas evolved during electrolysis is therefore the oxygen produced by the oxide-catalyzed decomposition of chlorate and perchlorate to chloride. To test this, O<sup>=</sup> was added (as Li<sub>2</sub>O); obvious decomposition began at once and continued for at least 12 hr. Since the addition of OH<sup>-</sup> (as KOH, which seems highly soluble in fused LiClO<sub>4</sub>) did not induce the catalytic decomposition, water was added (as LiClO<sub>4</sub> · 3H<sub>2</sub>O) to samples in which obvious decomposition was occurring. Gas evolution ceased immediately, as would be expected if the decomposition were oxide-catalyzed; the addition of water would remove the oxide: H<sub>2</sub>O + O<sup>=</sup> → 2OH<sup>-</sup>. Additional evidence for an oxide-catalyzed decomposition is that the freshly generated oxides of magnesium and aluminum produced as discussed below also catalyzed melt decomposition although to a much lesser degree. It is well known that addition of metal oxides produces decomposition of both chlorate and perchlorate melts to chloride (14, 20, 21).

The catalytic decomposition which sets in after the O<sup>=</sup> is formed could occur by the following mechanism



The postulated peroxide intermediate has been found in heated samples of LiClO<sub>4</sub>-Li<sub>2</sub>O by Markowitz and Boryta (14). Addition of peroxide (as Na<sub>2</sub>O<sub>2</sub>) to the LiClO<sub>4</sub> melt induced immediate obvious decomposition as expected. It was also demonstrated that the reaction 4ClO<sub>3</sub><sup>-</sup> → 3ClO<sub>4</sub><sup>-</sup> + Cl<sup>-</sup> does not occur at an appreciable rate in the absence of oxide at this temperature; the addition of 250 mg of KClO<sub>3</sub> to a compartment containing approximately 5g of fused LiClO<sub>4</sub> did not result in any chlorate decomposition at 260°C after 6 hr as shown by analysis.

A peculiarity of fused LiClO<sub>4</sub> is that other than silver no metals could be anodized to form the corresponding ions. The fact that metals cannot be anodized into solution has also been found in the case of the nitrate melts. By addition of transition metal nitrates and chlorides to a nitrate melt a few metal ions could be brought into solution (5). This approach was not possible in fused LiClO<sub>4</sub>; all added transition metal nitrates or chlorides produced oxides immediately. Some of the metal-metal oxide couples are of relatively stable potential; for example Mg/MgO at -2.1v with a fluctuation of 40 mv over a period of hours. Some typical potentials of metals in contact with a LiClO<sub>4</sub> melt are listed in Table II.

Most metals form visible oxide layers with the exception of rhodium, iridium, and platinum which do not appear to form oxide layers even at high current densities. The behavior of the different metals tested is summarized in Table II. The behavior of thallium was

Table II. Metal behavior in fused lithium perchlorate

Metal	Potential against Ag(I)/Ag, v	Oxide formation (without current)	Oxide formation (with current)
Mg	-2.1	Massive	Massive
Al	-0.4	Film	Massive
Ti	Unstable	Film	Film
V	Unstable	Film	Massive
Fe	Unstable	Massive	Massive
Co	+0.4	Massive	Massive
Ni	+0.4	Massive	Massive
Cu	Unstable	Massive	Massive
Zn	-0.7	Massive	Massive
Zr	Unstable	Film	Massive
Nb	Unstable	Film	Massive
Mo	Unstable	Film	Massive
Rh	Unstable	None	Noble
Pd	Unstable	Thin film	Film
Ag	0.0 (def.)	None	Forms Ag <sup>+</sup>
Cd	-0.5	Massive	Massive
W	Unstable	Film	Film
Re	Unstable	Dissolves	Dissolves
Ir	Unstable	None	Noble
Pt	Unstable	None	Noble
Au	Unstable	None	Thin film*
Hg	Unstable	None	Massive
Tl	-1.4	None	See text
Pb	-1.0	Massive	Massive
U	Unstable	Massive	Massive

\* Only at high current density; otherwise noble.

unusual; the area of metal exposed to air formed black oxide as expected, while the area of metal exposed to the melt remained bright. On anodization, thallium was visibly lost from the wire, the surface remaining bright. Nernstian behavior was not observed; the potentials assumed after successive anodizations were stable but no reproducible Nernst slopes could be obtained, values of *n* ranging from 1.6 to 2.9. Analysis of the hydrolyzed melt for thallium (22) gave an e<sup>-</sup>:Tl ratio of about 1:1. This behavior would suggest the formation of a thallium oxide soluble in fused lithium perchlorate.

The reason for this oxide formation with most metals could well be the lower solvation energy of metal ions in fused perchlorates (and presumably also fused nitrates) as compared with fused chlorides (23) in which anodization of many metals is successful. To gain stabilization which is not available from the poorly coordinating perchlorate anion, the metal cation presumably adds oxygen by breaking Cl-O bonds in a neighboring ClO<sub>4</sub><sup>-</sup> anion.

### Acknowledgment

The authors are grateful to the National Research Council of Canada for financial assistance in the form of an Operating Grant (J.A.P.) and NRC Scholarship (U.A.).

Manuscript received Dec. 11, 1967; revised manuscript received Feb. 21, 1968. This paper was presented at the Boston Meeting, May 5-9, 1968, as Abstract 274. The paper is taken from the thesis of one of the authors (U. A.) submitted to the Faculty of Graduate Studies, University of Alberta, Edmonton, Alberta, in partial fulfillment of the requirements for the Ph.D. degree.

Any discussion of this paper will appear in a Discussion Section to be published in the December 1968 JOURNAL.

### REFERENCES

- H. S. Swofford, Jr., and H. A. Laitinen, *This Journal*, **110**, 814 (1963).
- H. S. Swofford, Jr., and P. G. McCormick, *Anal. Chem.*, **37**, 970 (1965).
- A. Conte and S. Casadio, *Ric. Sci.*, **36**, 433 (1966).
- A. Conte and S. Casadio, *ibid.*, **36**, 488 (1966).
- G. A. Mazzocchin, G. G. Bombi, and M. Fiorani, *Ric. Sci.*, **36**, 338 (1966).
- A. J. Arvia, A. J. Calandra, and M. E. Martins, *Electrochim. Acta*, **11**, 963 (1966).
- R. B. Escue, T. H. Tidwell, and D. K. Dickie, *J. Electroanal. Chem.*, **12**, 220 (1966).
- A. J. Arvia, A. J. Calandra, and M. E. Martins, *Electrochim. Acta*, **12**, 347 (1967).

9. H. E. Bartlett and K. E. Johnson, *This Journal*, **114**, 64 (1967).
10. M. Fiorani, G. G. Bombi, and G. A. Mazzocchin, *J. Electroanal. Chem.*, **13**, 167 (1967).
11. K. F. Denning and K. E. Johnson, *Electrochim. Acta*, **12**, 1391 (1967).
12. A. H. Maki and D. H. Geske, *J. Chem. Phys.*, **30**, 1356 (1959).
13. G. Cauquis and D. Serve, *Compt. rend.*, **262C**, 1516 (1966).
14. M. M. Markowitz and D. A. Boryta, *J. Phys. Chem.*, **69**, 1114 (1965).
15. D. L. Maricle and D. N. Hume, *This Journal*, **107**, 354 (1960).
16. Tung-ho Chen, *Anal. Chem.*, **39**, 804 (1967).
17. P. Delahay, "New Instrumental Methods in Electrochemistry," p. 76, Interscience Publishers Inc., New York (1965).
18. M. Peleg, *J. Phys. Chem.*, **71**, 4553 (1967).
19. F. A. Miller and C. H. Wilkins, *Anal. Chem.*, **24**, 1253 (1952).
20. F. C. Mathers and J. W. H. Alfred, *Trans. Electrochem. Soc.*, **42**, 285 (1922).
21. M. M. Markowitz, D. A. Boryta, and H. Stewart, *J. Chem. and Eng. Data*, **9**, 573 (1964).
22. "Scott's Standard Methods of Analysis," Sixth Ed., N. H. Furman, Editor, Vol. I, p. 1053, Van Nostrand, New York (1962).
23. J. A. Plambeck, *J. Chem. and Eng. Data*, **12**, 77 (1967).

## Mass Spectrometric and Torsion Effusion Studies of the Evaporation of Liquid Selenium

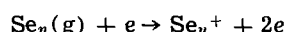
R. Yamdagni and R. F. Porter

*Department of Chemistry, Cornell University, Ithaca, New York*

### ABSTRACT

The composition of selenium vapor evaporating from liquid selenium has been studied mass-spectrometrically using single and double-oven type Knudsen effusion cells. The appearance potentials have been determined for various molecular species ( $\text{Se}_n$ ,  $n = 1$  to 8). The heats of vaporization of  $\text{Se}_2$ ,  $\text{Se}_5$ ,  $\text{Se}_6$ ,  $\text{Se}_7$ , and  $\text{Se}_8$  at 625°K have been obtained and the heat of fusion of selenium has been derived. The average molecular weight of the selenium vapor has been determined from the simultaneous measurements of vapor pressure by Knudsen and torsion effusion methods.

The molecular composition of the gaseous species evaporating from elemental selenium has been a subject of interest for several years. It has been known for some time from vapor density studies (1a-d) that polymeric species are present in the saturated vapor. Mass spectrometric studies of Goldfinger and co-workers (2) indicated that species  $\text{Se}_n$  with  $n$  as high as eight are formed in evaporation. The key problem in interpreting mass spectral data is to analyze the ion current for each species  $\text{Se}_n^+$  with respect to contributions from the simple ionization process



and from ion fragmentation processes that produce  $\text{Se}_n^+$  from a precursor of higher molecular weight than  $\text{Se}_n$ . Recently two papers based on mass spectrometric studies have appeared. Fujisaki (3) studied the evaporation from solid selenium and Berkowitz and Chupka (4) examined the vapor over the solid and liquid.

The work presented in this paper is a result of an experimental program to investigate the evaporation of liquid selenium. Where possible comparison of the results with those of Fujisaki *et al.* (3) and Berkowitz and Chupka (4) will be made.

### Experimental

Mass spectra of selenium vapor effusing from Knudsen-type oven were observed with a 10 in., 60°, direction-focusing mass spectrometer. The procedure is similar to that described in earlier work (5) except for the location of the Knudsen cell with respect to the mass spectrometer. Figure 1 shows the experimental arrangement. Pyrex cells were used for studies up to about 450°C. A few observations with quartz cells were made up to about 800°C, near the normal boiling point of selenium. The cells were heated by a resistance-type furnace that extended about 1 in. over either end of the chamber to provide uniform tem-

peratures. Temperatures were recorded with a chromel-alumel thermocouple. The effusion hole was produced by puncturing the thin glass wall of the cell with a fine tungsten wire (0.008 in. diameter). The opening was checked after the system was under vacuum by applying a "Tesla Coil" discharged near the orifice. For a separate series of experiments the cell was modified by allowing this sample compartment to extend outside the primary heating element. With this arrangement the extension containing a selenium sample could be heated when the main cavity was empty thus permitting independent control of the vapor pressure and vapor temperature (*i.e.*, the double-oven procedure).

In most cases the identification of  $\text{Se}_n^+$  species could be made by comparing the isotope structure observed for each mass grouping with that calculated from the normal isotopic abundances of Se species. For species higher than  $\text{Se}_6^+$ , the isotope structure was not completely resolved but sufficient to ensure identification.

A movable shutter located between the ion source and the cell was used to distinguish ions produced

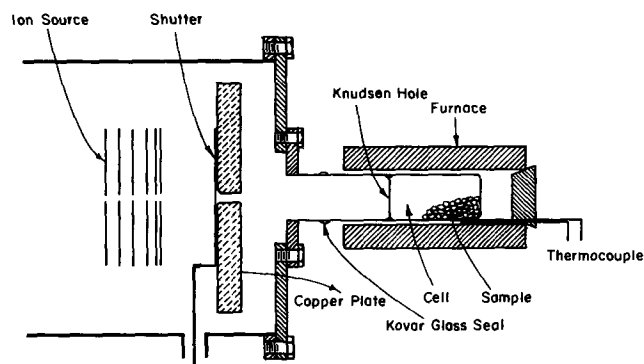
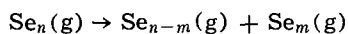


Fig. 1. Knudsen cell-mass spectrometer assembly

from selenium vapor from those appearing in the background. All ion intensities reported in this paper are those obtained from the shutter effect. Selenium samples (6) with reported purity of 99.999% were used.

### Results

A mass spectrum of the various products evaporated from liquid selenium at 600°K, showing relative ion intensities for species  $\text{Se}^+$  through  $\text{Se}_8^+$  for 75v electron energy is presented in Table I. Higher molecular weight species  $\text{Se}_9^+$  and  $\text{Se}_{10}^+$  were too low in intensity for meaningful comparisons. Appearance potentials for  $\text{Se}_n^+$  are given in Table II. Our results are consistently higher than those observed by Fujisaki *et al.* (3) and by Berkowitz and Chupka (4) but indicated a similar trend in values for  $\text{Se}_2^+$  to  $\text{Se}_8^+$ . At present we do not attach any quantitative significance to the differences in appearance potential values from the three independent determinations. We should note that much of this discrepancy is probably a consequence of variations in methods of determining threshold voltages and methods of voltage calibration. Analysis of ion fragmentation pattern was made from a series of observations of ion intensities as selenium pressure was changed at constant temperature for each ion species. In Fig. 2 we show the change in the  $\text{Se}_2^+/\text{Se}_n^+$  ratio as temperature of the selenium source is changed to effect a change of pressure in the sampling chamber. As the pressure is lowered at constant temperature, the thermodynamic effect is to shift the reaction



to the right. If the pressure is lowered in gradual steps the concentration of molecular species should diminish in the sequence from high values of  $n$  to low values. If an observed ion  $\text{Se}_n^+$  is produced by fragmentation from a molecule of higher molecular weight, the  $\text{Se}_n^+$  should decrease in the same proportion as other ions having the same molecular precursor. We note that as the total pressure decreases  $\text{Se}_8^+$  and  $\text{Se}_7^+$  decrease rapidly but at different rates relative to  $\text{Se}_2^+$  while  $\text{Se}_5^+$  and  $\text{Se}_6^+$  are still observable. We also note that the intensities of  $\text{Se}_3^+$  and  $\text{Se}_4^+$  do not change appreciably relative to that of  $\text{Se}_5^+$  and  $\text{Se}_6^+$ . This suggests a precursor relationship of  $\text{Se}_3^+$  and  $\text{Se}_4^+$  with  $\text{Se}_5^+$  and  $\text{Se}_6^+$ . At very low pressures only  $\text{Se}_2^+$  and  $\text{Se}^+$  could be detected and under no conditions could either  $\text{Se}_3^+$  or  $\text{Se}_4^+$  be detected in the absence of

Table I. Mass spectrum of selenium vapor ( $T = 600^\circ\text{K}$ )

Ion	Relative ion intensity*
$\text{Se}^+$	19.5
$\text{Se}_2^+$	100.0
$\text{Se}_3^+$	23.2
$\text{Se}_4^+$	14.4
$\text{Se}_5^+$	37.7
$\text{Se}_6^+$	41.3
$\text{Se}_7^+$	15.4
$\text{Se}_8^+$	2.1

\* Selenium sample contained in Pyrex Knudsen cell.

Table II. Appearance potentials for  $\text{Se}_n^+$  ion species produced by electron bombardment of selenium vapor

Ion	Ref. (4) data, v	Ref. (3) data, v	Present results, v
$\text{Se}^+$	—	—	$11.5 \pm 0.3$
$\text{Se}_2^+$	$9.2 \pm 0.1$	—	$9.8 \pm 0.3$
$\text{Se}_3^+$	$10.4 \pm 0.3$	$11.6 \pm 0.3$	$11.7 \pm 0.3$
$\text{Se}_4^+$	$10.1 \pm 0.3$	$10.9 \pm 0.2$	$11.4 \pm 0.3$
$\text{Se}_5^+$	$8.6 \pm 0.2$	$9.2 \pm 0.2$	$9.5 \pm 0.3$
$\text{Se}_6^+$	$8.8 \pm 0.2$	$9.08 \pm 0.05$	$9.5 \pm 0.3$
$\text{Se}_7^+$	$8.3 \pm 0.2$	$8.87 \pm 0.05$	$9.5 \pm 0.3$
$\text{Se}_8^+$	$8.6 \pm 0.2$	$8.97 \pm 0.05$	$9.4 \pm 0.3$

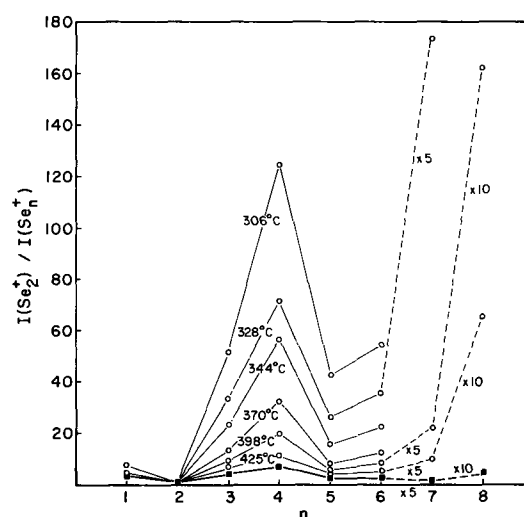


Fig. 2. Change of  $\text{Se}_2^+/\text{Se}_n^+$  in double-cell experiment when the pressure in sampling chamber is varied. Solid squares represent single cell results at  $T = 325^\circ\text{C}$ .

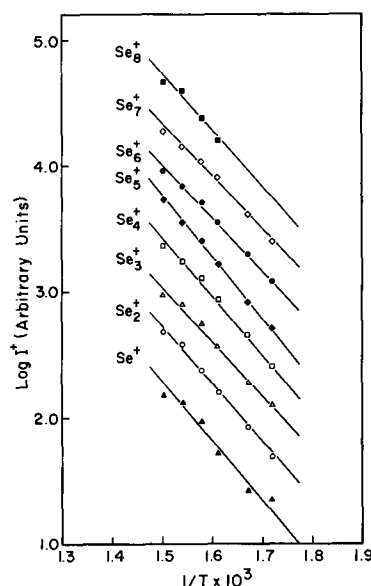


Fig. 3. Temperature dependence of  $\text{Se}_n^+$  ion intensities

$\text{Se}_5^+$  and  $\text{Se}_6^+$ . Considering the effects with change of pressure and low appearance potentials for  $\text{Se}_2^+$ ,  $\text{Se}_5^+$ ,  $\text{Se}_6^+$ ,  $\text{Se}_7^+$ , and  $\text{Se}_8^+$  relative to  $\text{Se}^+$ ,  $\text{Se}_3^+$ , and  $\text{Se}_4^+$  it is concluded that the former species arise primarily from molecular precursors with corresponding molecular formulas while the latter group is produced in fragmentation processes.

Temperature dependence measurements for  $\text{Se}_n^+$  species are shown in Fig. 3. The Clapeyron equation may be applied directly to the data for  $\text{Se}_2^+$ ,  $\text{Se}_5^+$ ,  $\text{Se}_6^+$ ,  $\text{Se}_7^+$ , and  $\text{Se}_8^+$  since, for these species, we can set the partial pressures of  $\text{Se}_n$  proportional to the ion intensity of  $\text{Se}_n^+$ . From the slopes of the curves we derive heats of vaporization of  $\text{Se}_n(\text{g})$  ( $n = 2, 5, 6, 7$ , and  $8$ ) given in Table III. Berkowitz and Chupka (4) measured the heats of reaction  $m \text{Se}_n(\text{g}) = n \text{Se}_m(\text{g})$ , and from their data we calculated heats of vaporization also listed in Table III.

### Discussion

Several values for the heat of fusion of selenium were calculated from the differences in heats of sublimation reported by Fujisaki *et al.* (3) and heats of vaporization determined in the present work. For these calculations the heat capacity for condensed selenium was taken from the Tables by Stull and Sinke (7) and

Table III. Comparison of heats of vaporization of  $\text{Se}_n(\text{g})$  species with data of ref. (4); values in kcal/mole at  $T = 625^\circ\text{K}$

Molecule	Ref. (4) data	Present results
$\text{Se}_2$	28.3	22.8
$\text{Se}_5$	25.8	23.1
$\text{Se}_6$	19.9	20.0
$\text{Se}_7$	20.9	20.2
$\text{Se}_8$	21.0	21.6

Table IV. Data for calculation of the heat of fusion of selenium

Species	(Temp. Coeff.) <sub>subl.</sub> <sup>a</sup> kcal/mole	(Temp. Coeff.) <sub>vap.</sub> <sup>b</sup> kcal/mole	$\Delta(\text{Temp. Coeff.})/n$ <sup>c</sup> kcal/g-atom
Se	(34.7)	23.2	10.76
$\text{Se}_3$	(35.2)	22.8	5.19
$\text{Se}_3$	(36.0)	20.8	4.09
$\text{Se}_4$	(34.8)	21.4	2.47
$\text{Se}_5$	37.2	23.1	2.05
$\text{Se}_6$	34.9	20.0	1.75
$\text{Se}_7$	39.6	20.2	2.09
$\text{Se}_8$	41.2	21.6	1.79

<sup>a</sup> Fujisaki *et al.* (3) data, values at  $T = 298^\circ\text{K}$ .

<sup>b</sup> Present results, values at  $T_{\text{AV}} = 625^\circ\text{K}$ .

<sup>c</sup> Values at  $T = 490^\circ\text{K}$ .

for  $\text{Se}_5(\text{g})$ ,  $\text{Se}_6(\text{g})$ ,  $\text{Se}_7(\text{g})$ , and  $\text{Se}_8(\text{g})$  were estimated as 25.0, 31.0, 37.0, and 43.0 cal deg<sup>-1</sup>. The average value of  $\Delta H_{\text{fusion}}$  from the four sets of data ( $\text{Se}_5$ ,  $\text{Se}_6$ ,  $\text{Se}_7$ , and  $\text{Se}_8$ ) is  $1.9 \pm 0.2$  kcal/g-atom (Table IV) which is higher than the value of 1.3 kcal/g-atom reported by ref. (7) and is lower than the value of 2.3 kcal/g-atom obtained by ref. (4). The widely divergent values of  $\Delta(\text{Temperature Coefficient})/n$  for Se,  $\text{Se}_2$ ,  $\text{Se}_3$ , and  $\text{Se}_4$  reaffirms the importance of ion fragmentation processes for  $\text{Se}^+$ ,  $\text{Se}_2^+$ ,  $\text{Se}_3^+$ , and  $\text{Se}_4^+$  (at least in solid-vapor equilibrium) while  $\text{Se}_5^+$ ,  $\text{Se}_6^+$ ,  $\text{Se}_7^+$ , and  $\text{Se}_8^+$  arise from direct ionization processes.

Although there is generally good agreement between our measured heats of vaporization of  $\text{Se}_5$ ,  $\text{Se}_6$ ,  $\text{Se}_7$ , and  $\text{Se}_8$  and previously published data, a disagreement exists in the data for  $\text{Se}_2$ . One problem centers about the interpretation of the degree of ion fragmentation to form  $\text{Se}_2^+$  from higher molecular weight precursors in the mass spectrometer. Berkowitz and Chupka (4) concluded that  $\text{Se}_2^+$  arises largely from ion fragmentation processes and that the concentration of  $\text{Se}_2$  in the vapor is quite low. This conclusion was based in part in trying to reconcile the high degree of association of selenium indicated by vapor density experiments (1a-d) with their own mass spectrometric observations. However, taken collectively, the mass spectrometric studies may be interpreted to show that  $\text{Se}_2^+$  observed in the mass spectrum of selenium vapor at temperatures of  $600^\circ\text{K}$  or higher arises largely by simple ionization of  $\text{Se}_2$ . The evidences are as follows:

1. The observed ratios of  $\text{Se}_2^+/\text{Se}_6^+$  and  $\text{Se}_2^+/\text{Se}_5^+$  depend on vapor temperature as shown in Table V. This could not arise if a simple ion-precursor relationship existed between  $\text{Se}_6$  and  $\text{Se}_2$  or between  $\text{Se}_5$  and  $\text{Se}_2$  in the higher temperature experiments. Considering the  $\text{Se}_2^+/\text{Se}_6^+$  and  $\text{Se}_2^+/\text{Se}_5^+$  values of ref. (2) and (3) it can be seen that the contributions made to the  $\text{Se}_2^+$  by  $\text{Se}_6$  and  $\text{Se}_5$  in the present case, cannot be more than 14 and 29%, respectively.

Table V. Ion intensity data pertinent to the formation of  $\text{Se}_2^+$  by ion fragmentation

Temp., °K	Condensed phase	$\text{Se}_3^+/\text{Se}_6^+$	$\text{Se}_2^+/\text{Se}_5^+$	Reference
448	Solid	0.33	0.77	(3)
473	Solid	0.25	0.65	(2)
544	Liquid	2.75	3.15	(4)
600	Liquid	2.42	2.65	Present work

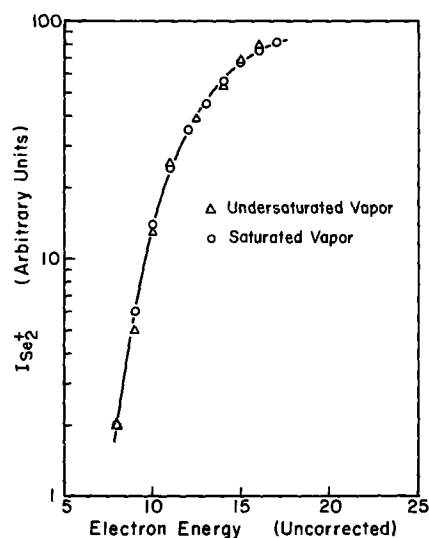


Fig. 4. Comparison of appearance potential data for  $\text{Se}_2^+$  obtained from saturated and undersaturated selenium vapor.

2. The appearance potential curve for  $\text{Se}_2^+$  obtained in experiments with the saturated vapor is nearly superimposable on the curve obtained when the system is undersaturated and  $\text{Se}_2$  is the major molecular species (Fig. 4). No structure is evident on the curve to show a break or discontinuity due to onset of a second ionization process. Fujisaki *et al.* (3) noted a break in the appearance potential curve of  $\text{Se}_2^+$  and concluded that even at low temperatures some  $\text{Se}_2$  is observable in the vapor from the solid.

With these considerations we may estimate the heat of formation of  $\text{Se}_2(\text{g})$  by the third-law procedure. In this calculation we assume that  $\text{Se}_2(\text{g})$  constitutes between 10 and 100% of the vapor at  $625^\circ\text{K}$ . Combining entropy and heat capacity data for  $\text{Se}(\text{s},1)$  and  $\text{Se}_2(\text{g})$  [taken from ref. (3) and corrected with our value for  $\Delta H_{\text{fusion}}/T_m$ ] and the vapor pressure data (see Appendix) we obtain the limits in  $\Delta H_{\text{vap}}^\circ$  for  $\text{Se}_2(\text{g})$  of 27.6 to 25.0 kcal/mole at  $625^\circ\text{K}$ . The value of  $\Delta H_{\text{fusion}}/T_m$  given by Berkowitz and Chupka (4) changes these limits to 27.0 to 24.4 kcal/mole, respectively. From these calculations it appears that  $\Delta H_{\text{vap}}^\circ$  of  $\text{Se}_2$  obtained from temperature dependence data is a lower limit. This could happen even if a small fraction of  $\text{Se}_2^+$  was formed by fragmentation of higher molecular species with low temperature coefficients. Therefore, taking both sets of data into account we recommend a value of  $25.5 \pm 2.5$  kcal/mole for  $\Delta H_{\text{vap}}^\circ$  of  $\text{Se}_2(\text{g})$  at  $625^\circ\text{K}$ .

#### Acknowledgment

Use of the facilities of the Cornell Materials Science Center (The Advanced Research Projects Agency Contract) is gratefully acknowledged. This work was supported by a grant from the Xerox Corporation.

Manuscript received Nov. 22, 1967; revised manuscript received Feb. 1, 1968.

Any discussion of this paper will appear in a Discussion Section to be published in the December 1968 JOURNAL.

#### REFERENCES

- 1 a. G. Preuner and I. Brockmoeller, *Z. Phys. Chem.*, **81**, 129 (1912); b. K. Neumann and E. Lichtenberg, *ibid.*, **A184**, 89 (1939); c. K. Niwa and Z. Shibata, *J. Faculty Sci. Hokkaido Univ., Japan*, Ser. III, **III**, 53 (1940); d. V. V. Illarionov and L. M. Lapina, *Doklady Akad. Nauk.*, **114**, 1021 (1957).
2. P. Goldfinger, M. Ackerman, and M. Jeunehomme, Final Technical Report Contract AF 61(052)-19, January 1959.
3. H. Fujisaki, J. B. Westmore, and A. W. Tickner, *Can. J. Chem.*, **44**, 3063 (1966).

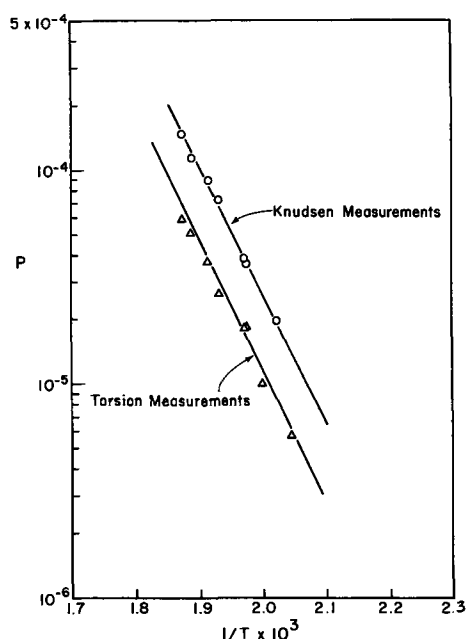


Fig. 5. Vapor pressure data for liquid selenium

- J. Berkowitz and W. A. Chupka, *J. Chem. Phys.*, **45**, 4289 (1966).
- R. F. Porter and F. A. Grimm, "Mass Spectrometric Studies of the Photochemical Oxidation of Diborane," *Advances in Chemistry Series*, To be published.
- Obtained from Alfa Inorganics Inc., Beverly, Mass.
- D. R. Stull and G. C. Sinke, "Advances in Chemistry Series," **18**, 179 (1956).
- P. K. Lee and R. C. Schoonmaker, "Condensation and Evaporation of Solids," p. 379, Gordon and Breach, New York (1964).
- A. W. Searcy and R. D. Freeman, *J. Chem. Phys.*, **23**, 88 (1955).

#### APPENDIX

Auxiliary experiments were designed to determine the vapor pressure of selenium in the temperature range overlapping that of mass spectrometric observations. The experimental apparatus is very similar to that described by Lee and Schoonmaker (8). The cell ( $1\frac{1}{4} \times \frac{5}{8} \times \frac{5}{8}$  in.) was made of graphite and had two circular  $\frac{1}{2}$  in. diameter hollow compartments drilled symmetrically on both sides of the suspension axis. The selenium sample was placed in the cell and the compartments were sealed with graphite lids. One effusion hole was located in diagonally opposite walls of each compartment. The holes were tapered off and made conical in shape to make length of channel to radius of hole ratio  $L/r$  negligible. The cell was suspended by a 0.002 in. diameter tungsten wire. The filament and the cell assembly was enclosed inside four molybdenum shields to reduce loss of heat and maintain uniform temperature. The temperature was measured by a chromel-alumel thermocouple placed very near to the cell. The angle of twist of the fiber, produced by

Table VI. Vapor pressure of liquid selenium determined by Knudsen effusion and torsion methods

Temperature, °K	Pressure, atm. $\times 10^5$	
	Knudsen	Torsion
489	—	0.571
494	1.983	—
500	—	1.007
506	3.669	1.834
507	3.897	1.808
517	—	2.036
518	7.196	—
522	8.986	3.737
529	11.271	5.138
533	14.962	5.900

the effusing vapor, was measured by the image of a light spot on a 100 cm circular scale. The image was formed by a small mirror and lens arrangement attached to the suspension system. A permanent C type magnet was used for damping the oscillation of suspension fiber. The entire system was enclosed in a Pyrex bell jar resting on a stainless steel plate. Pressures lower than  $10^{-5}$  mm were maintained inside the bell jar throughout the experiment.

The average molecular weight of vaporizing selenium species was determined from measurements of vapor pressures determined simultaneously by Knudsen and torsion methods as discussed by Searcy and Freeman (9). Pressures in the two cases are given by

$$P_k = W(2\pi RT/M)^{1/2}/k(a_1 + a_2)$$

and

$$P_T = 2D\theta/(q_1a_1 + q_2a_2)f$$

where  $W$  is the rate of effusion in g/sec;  $M$  the molecular weight of effusing species;  $k$  the Clausing factor (taken as unity);  $a_1, a_2$  the area of orifices in square centimeters;  $D$  the torsion constant [determined by the procedure used by ref. (9)];  $\theta$  the angle of twist of the suspension fiber;  $q_1, q_2$  the moment arms in centimeters; and  $f$  the Searcy-Freeman factor (taken as unity).

Results of a series of selenium vapor pressure measurements utilizing the torsion and Knudsen effusion techniques are illustrated graphically in Fig. 5. It was assumed in treating the Knudsen data, only for the purpose of calculations, that Se was the effusing species. Data given in Table VI may be used to calculate, for several temperatures, the average molecular weight ( $M^*$ ) of the vapor from the expression

$$M^*/M_{Se} = (P_k/P_T)^2$$

where  $M_{Se}$  is 78.96.

The temperature dependence data were fitted to a least squares analysis to give

$$\log P_k(\text{atm}) = 7.556 - \frac{6066}{T}$$

$$\log P_T(\text{atm}) = 7.233 - \frac{6093}{T}$$

From these equations we derive at  $T = 510^\circ\text{K}$  an average  $M^*/M_{Se} = 5.6 \pm 0.5$  which compares well with the value of  $5.4 \pm 0.3$  obtained by ref. (1c).

# Measurement of the Gravitational Component of Cell Potential in Molten Salts

Paul Duby\*<sup>1</sup> and Herbert E. Townsend, Jr.\*<sup>2</sup>

Department of Metallurgy and Laboratory for Research on the Structure of Matter,  
University of Pennsylvania, Philadelphia, Pennsylvania

## ABSTRACT

The gravitational component of cell potential has been investigated in a molten salt electrolyte by measuring the emf of a gravity cell in the earth's field. Two silver electrodes were placed at the ends of a 0.5m long tubular cell containing molten silver nitrate. The experiments were carried out by recording the changes of potential difference as changes in height difference between the electrodes were effected by rotating the cell in a vertical plane. An experimental value of  $6.75 \pm 0.05 \mu\text{V}/\text{m}$  was obtained for the gravitational emf per unit height at  $230^\circ\text{C}$  in good agreement with a theoretical result of  $6.78 \mu\text{V}/\text{m}$  as predicted by thermodynamic equations. The emf of a gravity cell has also been measured with a mixture of silver nitrate and silver chloride as the electrolyte. In this case, it is a function of the relative anionic transport numbers of the constituents of the melt and the new experiment is suggested as an alternate method for investigating electrical transport.

When an electrochemical cell consisting of two identical electrodes and an electrolyte is placed in a gravitational field in such a way that the electrodes are at a different level, an electrical potential difference is generated which is the gravitational component of cell potential. This effect was first observed by Colley (1), it was investigated further by Des Coudres (2) at the end of the past century, and it is described in detail by MacInnes (3). More recently, Grinnell and Koenig (4) carried out similar experiments with an improved technique for measuring the potential difference. Their results confirmed the theory and they obtained reliable values for the transport numbers in aqueous solutions of potassium iodide. Des Coudres (5) and Tolman (6) observed a greatly enhanced effect by substituting a centrifugal field of force for the gravitational field. MacInnes and co-workers (7) also carried out an investigation of the effect of centrifugal fields. All these studies, however, concerned aqueous electrolytes.

The purpose of the present investigation is to show that the same effect can be observed in fused salt systems and to determine if the measurement of the electromotive force generated by a gravitational or a centrifugal field can yield some information about transport properties of the melt. As a preliminary step, gravitational cells have been investigated, which consist of silver electrodes in pure silver nitrate or in a mixture of silver nitrate and silver chloride. The present paper is devoted to describing the experimental technique and demonstrating that the measured potential difference is actually the gravitational component of cell potential as predicted by the theoretical equations. This effect will be called gravitational emf or gravity emf.

With mixtures of molten salts, as is the case with aqueous electrolyte solutions, the gravitational emf depends on the transport numbers and partial molar volumes of the various ionic species. In the case of a single molten salt, however, the emf depends solely on the densities of the salt and the electrode. Thus, the magnitude of the emf of a gravitational cell with a single molten salt as the electrolyte can be readily predicted.

Let us consider the simple case of a cell which is made of two metallic electrodes M which behave re-

versibly towards the metallic ion in the molten salt MX, and let there be a level difference  $h_2 - h_1$  between these two electrodes. The free energy of the single molten salt MX, which is assumed to be in thermal and hydrostatic equilibrium, is not a function of the vertical coordinate in a gravitational field since the difference in potential energy is cancelled by the energy difference which results from the difference in hydrostatic pressure. Two metallic electrodes, however, which are located at different levels and which have a density different from that of the melt, are not in thermodynamic equilibrium since the difference between their potential energies does not equal the energy difference associated with the difference in hydrostatic pressure. For example, if the density of the metal is greater than that of the melt, the upper electrode has a greater free energy and it exhibits a negative electrical potential relative to the lower one. Indeed, if the two electrodes are connected by an electronic conductor outside the cell, an electric current flows such that the metal dissolves from the upper electrode and deposits on the lower one.

The mathematical description of this gravitational cell can be approached by two methods. The quasi-equilibrium derivation based on classical thermodynamics was presented by MacInnes (3) while Fitts (8) has shown that the same result is obtained by the nonequilibrium thermodynamics approach, using Onsager's reciprocal relation. For the simple case considered here, the classical approach is simpler, and it has the advantage of being more closely related to the physical picture of the phenomenon.

For the cell consisting of two reversible electrodes of the same metal M at different levels  $h_1$  and  $h_2$  in a single salt MX, which we represent by



the over-all effect of passing an electrical current is the removal of metal from one electrode and the deposition on the other. The displacement of salt, which results from the electrolytic transport, causes no change in the free energy of the system, so that the only contribution to a variation of the free energy is due to the transport of metal. Assuming that the temperature and chemical composition are uniform and constant, the total free energy variation is

$$dG_M = V_M dP + M_M g dh \quad [1]$$

where  $G_M$  is the Gibbs free energy of one gram-equivalent of the metal,  $M_M$  is the equivalent mass,  $V_M$  is

\* Electrochemical Society Active Member.

<sup>1</sup> Present address: Henry Krumb School of Mines, Columbia University, New York, N. Y.

<sup>2</sup> Present address: Homer Research Laboratories, Bethlehem Steel Corporation, Bethlehem, Pa.



the equivalent volume,  $P$  is the pressure,  $h$  is the coordinate in the gravitational field, and  $g$  is the local gravitational acceleration.

In a fluid in hydrostatic equilibrium, the pressure gradient is  $dP = -\rho_{MX}gdh$ , where  $\rho_{MX}$  represents the density of the molten salt electrolyte. Equation [1] can be integrated for a finite level difference  $\Delta h = h_2 - h_1$

$$\Delta G_M = (M_M - \rho_{MX}V_M)g \Delta h \quad [2]$$

The equilibrium cell potential  $\Delta E$  is

$$\Delta E = \frac{-1}{F} (M_M - \rho_{MX}V_M)g \Delta h \quad [3]$$

All the parameters in the above equation are well-known, and the value of the emf of a gravitational cell can be predicted for a single fused salt. If the electrolyte is a mixture, however, an additional variation in free energy of the system results from the electrical transport of the various species, and the gravitational emf becomes a function of the transport numbers. If the electrode reaction remains the same and if the single salt is replaced by a mixture of salts  $MX_i$  having a common cation, the passage of electric current causes the migration of anions at different rates and eventually results in a concentration change as observed in the Hittorf-type experiment. This effect can be described by defining the mass transport number  $T_{X_i}$  as the number of gram-equivalents of the ion constituent  $X_i$  which are transported per faraday from anode to cathode during electrolysis. A mass balance shows that, in addition to the transport of one gram-equivalent of metal per faraday from anode to cathode, there is a net transport of  $T_{X_i}$  gram-equivalents of each salt  $MX_i$  in the mixture. The contribution of each of the components of the mixture to the total free energy change  $\Delta G$  is given by a term similar to the right-hand side expression of Eq. [2] multiplied by the corresponding mass transport number.

$$\Delta G = (M_M - \rho_m V_M)g \Delta h + \sum_{i=1}^n T_{X_i}(M_{MX_i} - \bar{V}_{MX_i}\rho_m)g \Delta h \quad [4]$$

where  $\rho_m$  is the density of the mixture,  $M_{MX_i}$  is the equivalent mass of the salt  $MX_i$  and  $\bar{V}_{MX_i}$  is the partial equivalent volume of the salt  $MX_i$ .

The derivation of a similar equation for aqueous electrolytes is given by MacInnes (3). A more sophisticated presentation by Koenig and Grinnell (9) includes a thorough discussion of the assumptions of the quasi-equilibrium approach, as well as the relation between the emf of a gravity cell and the transport parameters from a Hittorf-type experiment.

For the simple case of a mixture of  $AgNO_3$  and  $AgCl$ , the emf of the gravitational cell can be written after some straightforward algebraic substitutions.

$$\Delta E = -\frac{g}{F} (M_{Ag} - \rho_m V_{Ag} + \phi \cdot \tilde{M}) \Delta h \quad [5]$$

where

$$\phi = T_{Cl}N_{AgNO_3} - T_{NO_3}N_{AgCl}$$

$$\tilde{M} = \frac{1}{V_m} (M_{AgCl}\bar{V}_{AgNO_3} - M_{AgNO_3}\bar{V}_{AgCl})$$

$V_m$  is the molar volume of the mixture;  $N_{AgCl}$  and  $N_{AgNO_3}$  are the mole fractions.  $\phi$  is the function introduced by Aziz and Wetmore (10) in order to describe the results of transport experiments in which the concentration change is measured after the passage of a given amount of electricity.

### Experimental

Although the measurement of the gravitational component of cell potential with a molten salt electrolyte

is similar in principle to the measurement with an aqueous electrolyte, the fact that the experiment must be carried out at elevated temperature requires a significantly different technique which is discussed below in some detail.

*Principle of the measurement.*—The importance of separating the effect of the gravitational field from other phenomena and especially the effect of small temperature differences is illustrated by the following comparison. The emf of the gravitational cell, predicted by Eq. [3] for the system silver-silver nitrate at 230°C, equals 6.78  $\mu V/m$  of level difference. The thermal emf of the same system, in contrast, is 330  $\mu V/^\circ C$  (11) at the same temperature. A temperature difference of about  $10^{-3}^\circ C$  between two electrodes placed at one meter level difference would accordingly cause an error of 5% on the value of the gravitational component of cell potential, if an equilibrium measurement were attempted. The construction of a vertical furnace having a 1-meter zone in which the temperature is uniform within  $10^{-3}^\circ C$ , or alternatively, the precise measurement of temperature differences within  $10^{-3}^\circ C$  in order to correct for the thermal emf, are both difficult approaches owing to practical considerations.

It has been found that changes in electromotive forces resulting from changes in an external constraint can be measured in the presence of a much larger thermal emf by recording the electrical response to a sudden variation of the external constraint. This technique was applied successfully to the measurement of a pressure-induced electromotive force of the order of a few microvolts in a similar system (12).

The method of varying the external constraint, used by various investigators for measurements of gravitational emf in aqueous solutions, namely connecting two half-cells by a flexible tube containing the electrolyte and measuring the equilibrium potential difference before and after altering their relative position by a system of ropes and pulleys, is not practical at higher temperature. The technique, which is adopted instead, consists of changing the vertical distance between electrodes at both ends of a salt-filled tube by rotating the whole assembly in a vertical plane. In this manner, only the relative position of the electrodes in the earth's gravitational field is varied very rapidly, while the difference in temperature or surface condition of the electrodes remains unchanged or varies much more slowly.

*Apparatus.*—The cell is represented on Fig. 1. It consists of a 1-in. OD,  $\frac{3}{8}$ -in. ID extruded Teflon tubing threaded at both ends. The electrodes are disks of  $\frac{1}{2}$ -in. diameter machined from high-purity (99.99%) silver, and they are held in position by the Teflon stoppers which thread into the tube and form a salt-tight seal. Teflon was chosen as the container material because such a seal can be easily formed, and the cell can be opened and resealed many times. Teflon is chemically inert and its mechanical properties are adequate up to about 260°C.

The significant features of the furnace are the  $\frac{1}{4}$ -in. wall thickness copper pipe upon which the resistance windings (insulated by several layers of asbestos paper) are wound, and the small, independently controlled windings at both ends which compensate for greater heat losses at those regions. These features are sufficient to provide a region roughly 0.5 meter in length in which the temperature is uniform within  $1.5^\circ C$ , a value found quite adequate for the experiment. A constant-voltage transformer, several autotransformers and an on-off time-proportioning temperature controller are used to regulate the temperature of the furnace within  $\pm 0.25^\circ C$  for durations of several hours. The fairly large heat capacity of the whole furnace further insures that any variation of temperature with time is very slow.

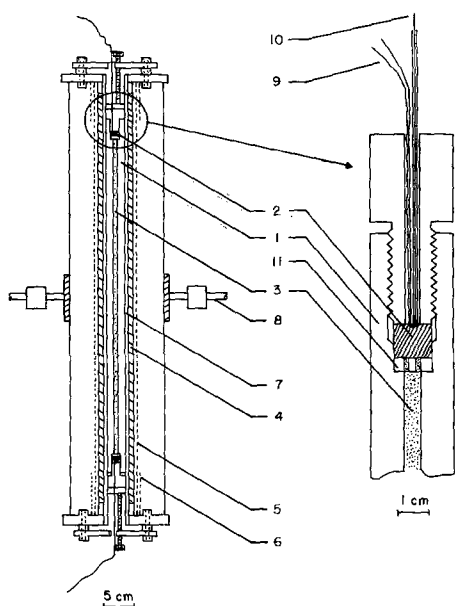


Fig. 1. Cell and furnace for measuring the emf of a gravitational cell. 1, Teflon cell; 2, silver electrodes; 3, molten salt; 4, copper pipe; 5, main resistance winding; 6, end winding; 7, Pyrex tube; 8, spindle and bearing; 9, chromel-alumel thermocouple; 10, tungsten wire; 11, electrode shield.

The furnace is held at the mid-point of its longitudinal axis by a collar which is supported on two bearings, such that the whole assembly can rotate in a vertical plane. A circular index plate has five pairs of holes which, when fitted with  $\frac{1}{2}$ -in. dowells, stop the movement of a manually turned crank at angles of  $30^\circ$ ,  $90^\circ$ ,  $180^\circ$ , and  $270^\circ$  from the horizontal starting position. Thus, by rotating the furnace through angles determined by the placing of pegs in the index plate, quick and well-defined rotations of the cell in a vertical plane result, from which the changes in height difference between the electrodes can be calculated accurately, if their distance is known. Because of the large expansion coefficient of Teflon, this distance was measured for each run by means of two rigid tungsten wires which are soldered into each electrode and extend to the outside of the furnace, supported along their length by an alumina tube.

The tip of a chromel-alumel thermocouple is soldered into each electrode. This has a twofold function of measuring the temperature and providing two alternative leads for measurement of the cell emf. A Keithley model 150A microvoltmeter ( $10^7$  ohms input impedance at  $10 \mu\text{V}$  full-scale sensitivity) amplifies the small emf changes which are then recorded with a strip-chart recorder. The two instruments are calibrated together at the time of the experiment with a Keithley model 260 nV source which remains in series with the cell during both measurement and calibration so as not to change the impedance of the circuit while performing different functions. Although the specified accuracy of the calibrating device is only  $\pm 0.5\%$ , it was compared to a Honeywell model 2768 microvolt potentiometer and found to agree with the more precise instrument within its specified accuracy of  $0.005 \mu\text{V}$ .

**Procedure.**—The electrolyte was prepared by fusing Baker reagent grade  $\text{AgNO}_3$  and holding it for several hours at  $250^\circ\text{C}$  to drive off any residual water. For the mixture, the appropriate amount of Baker reagent grade  $\text{AgCl}$  was added, after weighing in semidarkness. The melt was filtered through medium-porosity fritted glass under a partial vacuum. Filling the cell was found to be critical and extreme care was taken so that no air bubble would be trapped inside the cell.

Prior to actual measurement, the cell and furnace were kept in a horizontal position for several hours until thermal equilibrium was attained. This was necessary for two reasons. First, the mean temperature of the system required time to stabilize, during which temperature changes along the length of the furnace, which were not in phase, produced significant drifting thermal emfs. Second, the temperature profile prior to a measurement had to be adjusted since small temperature gradients in the salt near the electrodes would cause some heat convection and significant and rather fast temperature variations at the electrodes upon rotation of the cell. A similar effect results from the displacement of small solid particles or small gas bubbles in the melt. In addition to the precautions observed in filling the cell, filtering the melt and minimizing temperature gradients, convective effects were decreased by reducing the diameter of the cell immediately in front of the electrode. This was achieved by placing two Teflon disks with two small holes ( $1/20$ -in. diameter) to shield the electrode as shown in Fig. 1.

In general, the potential difference between the two electrodes could be kept to less than  $200 \mu\text{V}$ . This residual difference could easily be cancelled by opposing it by the built-in zero-suppress d-c power supply of the microvoltmeter, and the subsequent measurements of the gravitational emf were made by using one of the more sensitive ranges of the instrument; which in most cases, was  $10 \mu\text{V}$  full scale.

### Results and Discussion

The gravitational emf is a very small effect which must be investigated in the presence of other larger emfs, and it is important to present a method for identifying it without any doubt. Its measurement is based on the observation of the electrical response to a change of the cell position in the earth's gravitational field, and the interpretation of such a signal must be discussed in some detail.

A typical tracing of the actual recorded potential difference between the two electrodes is shown on Fig. 2. During the time preceding point A, the cell remains stationary in its initial position and the cell voltage is essentially constant. During the time interval from A to B, or about 1 sec, the cell is rotated through an angle  $\theta$  to a new position where it is held until time C, or about 3 to 6 sec. Time C and D is spent in rotating the cell back to its original position, where it remains thereafter.

The shape of these recorded signals suggests that they are the sum of three superimposed changes in

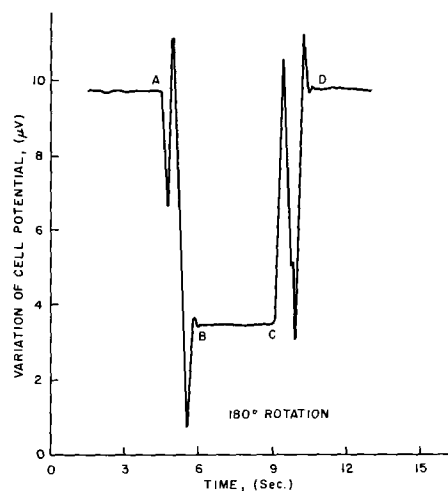


Fig. 2. Illustration of gravitational emf measurement by continuous potential recording. From A to B, the cell is rotated  $180^\circ$  from a vertical position; from C to D, it is restored to its initial position. Cell length: 48.16 cm; electrolyte:  $0.88 \text{ AgNO}_3 + 0.12 \text{ AgCl}$ ; temperature:  $230^\circ\text{C}$ .

potential difference. The first effect is due to random electrical noise in the circuit and to slow thermal drifts caused by gradual changes in temperature difference between the two electrodes or at other electrical connections. With good thermal insulation of the system, these drifts are typically less than  $0.1 \mu\text{V}/\text{sec}$ , and they appear linear during the relatively short time of a measurement.

The second contribution to the total signal is attributed to magnetic induction. It is observed during the motion of the furnace from time A to B and C to D, and it is due to induced currents when the loop formed by the cell and its lead wires are rotated in such a manner as to change the net enclosed magnetic flux. The amplitude of this signal and its shape depends on the position of the furnace relative to the magnetic field in the laboratory and the angular velocity of the assembly. It can be minimized by decreasing the area of the loop and by changing its position in the field, but it is difficult to suppress completely.

The third contribution to the composite signal is the gravitational component of cell potential. It should ideally be a square wave if the rotation of the furnace is fast compared to the recorder speed. It can be determined by measuring the vertical difference between two parallel lines drawn through the steady-state portions of the signal, i.e., AD and BC. The potential of the electrode which assumes the higher position after rotation becomes more negative, and this is in qualitative agreement with the physical picture and the equations derived earlier.

Figure 3 is a typical plot of the change in cell potential as a function of the change of the vertical component of electrode separation calculated from the angle of rotation. Each circle encloses the range of three to ten separate measurements. All series of data at a given temperature were found to be linear and to pass through the origin within the experimental uncertainty. The slope of the line corresponds to the gravitational component of cell potential per unit height.

Initially several combinations of cell length and diameter were considered. In general, the same value of the ratio  $\Delta E/\Delta h$  was observed regardless of length or diameter, although the precision of the data was found to improve with increasing length and decreasing diameter. Presumably, the greater effect associated with a longer cell and the decreased convection associated with thinner cells can account for these differences in precision.

The use of a plot of  $\Delta E$  vs.  $\Delta h$  is not the most accurate method for calculating the gravitational emf per unit height. Indeed, for several reasons the measurement of a number of  $180^\circ$  vertical to vertical rotations is preferable and yields a more reliable value. First, the electrical signal is larger, and so is the signal to noise ratio. Second, the rate of change of the

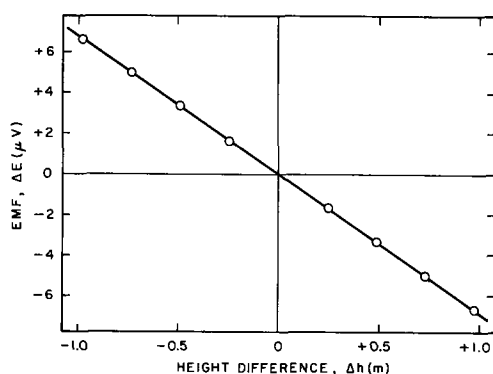


Fig. 3. Measured emf vs. height difference. Cell length: 48.94 cm; electrolyte:  $\text{AgNO}_3$ ; temperature:  $222^\circ\text{C}$ ; slope =  $\Delta E/\Delta h = 6.74 \mu\text{V}/\text{m}$ .

vertical component of electrode separation is minimum at the vertical position and maximum at the horizontal one. Hence, any error due to poor alignment of the angular control device with respect to the true vertical is minimized in measurements involving vertical initial and final positions. Third, the vertical component of separation between the faces of the parallel-aligned electrodes is subject to an uncertainty related to the inside cell diameter, which is also minimum in the vertical position of the cell.

A large number of the  $180^\circ$  vertical to vertical measurements were performed in a temperature range from the melting point of the salt up to about  $260^\circ\text{C}$ . After correction for instrument calibration and cell length, they were fitted to a linear function of temperature by the least squares method. At first, all the measurements were taken into account. Some of the recorded signals, however, were more difficult to read on the chart, as was typically the case when the thermal drift was greater than usual. In order to screen out these readings, in an unbiased fashion, they were disregarded if their difference from the mean exceeded five times the probable error. This criterion corresponds to disregarding data which have a probability less than one chance in one thousand of being valid, assuming a Gaussian distribution. This procedure is rather conservative and the reliability of the experimental technique is evidenced by the fact that it resulted in rejection of less than five per cent of the raw data. Figure 4 represents the measured gravitational emf per unit height as a function of temperature for pure silver nitrate and for a mixture of 12 m/o of silver chloride in silver nitrate. The final best lines are, respectively

for  $\text{AgNO}_3$

$$-\frac{\Delta E}{\Delta h} = 6.75 + 0.15 \times 10^{-3} (t - 200) \quad (\text{st. dev.} = 0.05) \quad [6]$$

for 0.88  $\text{AgNO}_3$  + 0.12  $\text{AgCl}$

$$-\frac{\Delta E}{\Delta h} = 6.73 + 0.47 \times 10^{-3} (t - 200) \quad (\text{st. dev.} = 0.03) \quad [7]$$

where  $t$  is the temperature in  $^\circ\text{C}$ , the emf is in microvolts and the height in meters.

The error resulting from the calibration of the electrical instruments and the error on the length of the cell are both of the order of  $0.005 \mu\text{V}/\text{m}$ , which is small compared to the standard deviation reported above. The latter is accordingly a good estimate of the precision of the final value for the emf per unit height.

The temperature dependence is small, but it is in qualitative agreement with the value obtained by

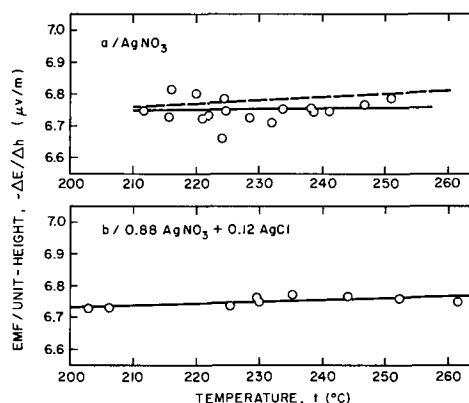


Fig. 4. Gravitational emf per unit height vs. temperature for pure silver nitrate (a) and for a mixture of silver nitrate and silver chloride (b); — least squares lines through experimental points (Eq. [6] [7]); — — — theoretical line (Eq. [8]).

application of Eq. [3]. Using data from Spooner and Wetmore (13) for the density of silver nitrate, and calculating the equivalent volume of silver from its expansion coefficient (14), the predicted value of the emf per unit height as a function of temperature is

$$-\frac{\Delta E}{\Delta h} = 6.75 + 1.0 \times 10^{-3} (t - 200) \quad [8]$$

This line has also been represented on Fig. 4 and the agreement with our experimental data is well within the range of the precision of the measurement.

In the case of a mixture, Eq. [5] can be used to calculate the transport function  $\phi$ . At 230°C, for instance, using a value of 4.034 g/cm<sup>3</sup> for the density of the mixture, as estimated by extrapolation of higher-temperature data (13), and assuming that the molar volume is a linear function of composition, one gets  $\phi = +0.02$ . The error on  $\phi$ , which corresponds to a standard deviation of 0.03  $\mu$ V/m on the emf per unit height is  $\pm 0.01$ . The errors on the density and partial equivalent volumes should be small in general (0.1%), but they are difficult to estimate here on account of the extrapolation.

The present value of  $\phi$  must be compared with Hill and Wetmore's result  $\phi = +0.05 \pm 0.01$  for the same mixture at 270°C (15),<sup>3</sup> and with  $\phi = -0.02$  which can be computed from data obtained by Monse (16), for 34 m/o AgCl at 250°C. Our result is within the range defined by these two investigations and, notwithstanding the extrapolation of density data, we think it is more reliable. The value of  $\phi = +0.02$  reported here corresponds to a mobility of the chloride ion constituent (relative to silver) equal to 80% of the mobility of the nitrate, and this result is consistent with the fact that, in many fused salt mixtures, the mobilities of like-charged ions are not very different (17).

In conclusion, the excellent agreement of the measured data with the values obtained by a theoretical relation for the pure salt is a definite indication that the observed phenomenon is actually the gravitational component of cell potential. The comparison of our data with other published values of  $\phi$  for a mixture shows that it is possible to obtain some information on the transport numbers by this type of measurement.

It is clear from Eq. [5] that the function  $\phi$  will eventually be calculated by the difference of two quantities which are of similar magnitude: the experimental emf of the gravitational cell and the expression  $(M_M - \rho_m V_M)g/F$ . The relative precision on  $\phi$  will not be very high, but this is due to the fact that  $\phi$  is usually a small quantity which represents the deviation from an ideal situation of equal anion mobilities. As shown by Hill and Wetmore's discussion of their data, the sign and the order of magnitude of  $\phi$  are sufficient to provide some interesting information about the conducting species in the melt.

The use of gravitational cell measurements instead of a Hittorf-type experiment for obtaining values of  $\phi$  offers several advantages. First, and most important, it is an instantaneous equilibrium measurement. The reading itself is carried out in a few seconds, during

which no temperature variation, and especially, no concentration change, can occur. Second, the measurement is rather simple and does not depend upon very accurate chemical analysis.<sup>4</sup> Setting up the experiment requires some care, but most problems were indeed solved and they have been discussed earlier in some detail. The condition, however, for obtaining good transport data is the knowledge, with sufficient accuracy, of the densities of the mixtures and the partial molar volumes in the temperature range. This information is not yet available for the system silver nitrate-silver chloride, but we expect that a more complete study of it will be the subject of a further communication.

#### Acknowledgments

This study is a contribution from the Laboratory for Research on the Structure of Matter, University of Pennsylvania, supported by the Advanced Research Projects Agency, Office of the Secretary of Defense.

Manuscript received Aug. 3, 1967; revised manuscript received ca. Jan. 24, 1968. This paper was presented at the San Francisco Meeting, May 9-13, 1965, as Abstract 100.

Any discussion of this paper will appear in a Discussion Section to be published in the December 1968 JOURNAL.

<sup>4</sup>The advantage can be fully appreciated only by a discussion of the errors involved in practice when Hittorf-type experiments are performed with fused salts. As an example, Duke, Laity, and Owens (18) report that, in their investigation of nitrate mixtures, about 90% of their raw data had to be disregarded.

#### REFERENCES

1. R. Colley, *Pogg. Ann.*, **157**, 370 (1876); *ibid.*, **157**, 624 (1876).
2. Th. Des Coudres, *Ann. Phys. Chem.*, **57**, 232 (1896).
3. D. A. MacInnes, "The Principles of Electrochemistry," Chap. 9, Dover, New York (1961).
4. S. W. Grinnell and F. O. Koenig, *J. Am. Chem. Soc.*, **64**, 682 (1942).
5. Th. Des Coudres, *Ann. Phys. Chem.*, **49**, 284 (1893).
6. R. C. Tolman, *Proc. Am. Acad. Arts Sci.*, **46**, 109 (1910); *J. Am. Chem. Soc.*, **33**, 121 (1911).
7. D. A. MacInnes and B. Roger Ray, *J. Am. Chem. Soc.*, **71**, 2987 (1949); *Rev. Sci. Ins.*, **20**, 52 (1949); D. A. MacInnes, *Proc. Am. Phil. Soc.*, **97**, 51 (1953); D. A. MacInnes and M. O. Dayhoff, *J. Chem. Phys.*, **20**, 1034 (1952).
8. D. D. Fitts, "Nonequilibrium Thermodynamics," p. 125, McGraw Hill Book Co., New York (1962).
9. F. O. Koenig and S. W. Grinnell, *J. Phys. Chem.*, **44**, 463 (1940).
10. P. M. Aziz and F. E. W. Wetmore, *Can. J. Chem.*, **30**, 779 (1952).
11. B. R. Sundheim and J. Rosenstreich, *J. Phys. Chem.*, **63**, 419 (1959).
12. P. Duby and H. H. Kellogg, *This Journal*, **110**, 349 (1963).
13. R. C. Spooner and F. E. W. Wetmore, *Can. J. Chem.*, **29**, 777 (1951).
14. "Metal Handbook," 8th ed., p. 1063, American Society for Metals, Novelty, Ohio (1961).
15. S. Hill and F. E. W. Wetmore, *Can. J. Chem.*, **32**, 864 (1954).
16. E. Monse, *Z. Naturforsch.*, **12a**, 526 (1957).
17. R. W. Laity and C. T. Moynihan, *J. Phys. Chem.*, **67**, 723 (1963).
18. F. R. Duke, R. Laity, and B. Owens, *This Journal*, **104**, 299 (1957).

<sup>3</sup>These authors define  $\phi$  as a function of transport fractions which have a sign opposite to that of our mass transport number. In order to get the same sign for the function  $\phi$ , we have interchanged the subscripts 1 and 2 in their expression of  $\phi$ .

## A Study of the Dissipation Factor ( $\tan \delta$ ) of Corrosion Product Films Formed on Aluminum Alloys in Hot Sodium Chloride Solution

W. H. Anthony

Metals Research Laboratories, Olin Mathieson Chemical Corporation, New Haven, Connecticut

Electrochemical studies of corroding aluminum surfaces are complicated by the corrosion process itself which continually increases the surface roughness and renders such quantities as capacitance per unit area and corrosion current density virtually indeterminate. The dissipation factor has the advantage that it is area independent because it is proportional to the product of capacitance and resistance whose area dependencies cancel each other out.

Breckenridge (1) recognized that vacancies in an ionic crystal are a source of dielectric loss. McMullen and Pryor (2) created additional point defects in an anodic film on aluminum by raising its temperature and by substituting hydroxyl ions for oxygen ions in the oxide lattice. In both cases, the dielectric loss increased significantly.

Keir, Heine, and Pryor (3) have observed that anodic films on aluminum become more conductive as a result of exposure to sodium chloride solutions. They explained the result by an exchange of chloride ions from the solution for oxygen ions in the oxide lattice. Such areas in the aluminum oxide film containing substantial chloride ions may later become pitting sites due to the increased mobility of aluminum ions through them.

The defect density in an aluminum oxide film may be altered by the introduction of impurity cations resulting from the presence of alloying elements in the aluminum substrate; these defects may in turn affect corrosion processes in a fashion somewhat similar to chloride ions. The present study has as its object the determination of the effect of cation impurities in the surface oxide film resulting from the presence of alloying elements in the metallic substrate on the dissipation factor of corrosion product films and on the corrosion rates of selected commercial aluminum alloys.

### Experimental Procedure and Results

**Bridge measurements.**—The experimental arrangements are shown diagrammatically in Fig. 1. The measuring cell carried a number of masked sheet specimens of the alloys under study immersed in sodium chloride solution at equal distances from each other and from the axis of a large cylindrical aluminum counter electrode.

The samples and the counter electrode were connected to terminals to which the "unknown" leads of a Wayne Kerr B221 transformer ratio arm bridge could be attached. Measurements of the parallel capacitance and the reciprocal of the parallel resistance of the measuring cell were carried out at a frequency of 100 cps. Measurements of the series resistance of the measuring cell were carried out at 10 and 20 kcps, using the Wayne Kerr Q221 low impedance adapter.

The external frequency source used was a General Radio Type 1210-C Unit R.C. oscillator capable of supplying a pure sinusoidal signal from 20–200,000 cps.

The detector used was a General Radio Type 1232-A tuned amplifier and null detector operable over the same frequency range. The signal amplitude passing through the measuring cell was limited to 10 mv peak to peak, and no more than three measurements were carried out during a 12-day run to minimize the somewhat remote possibility of damage to the corrosion films. The amplitude of the signal was monitored by a Type 536 Tektronix cathode-ray oscilloscope.

The following assumptions were made in determining the dissipation factor of the corrosion films on the alloy specimens:

1. The double layer capacitance and the counter electrode capacitance were in series with the specimen capacitance.
2. Both the double layer capacitance and the counter electrode capacitance were so large that their reciprocals could be neglected in the series capacitance formula.
3. The series resistance of the counter electrode was so small that it could be neglected in comparison with the specimen series resistance.
4. The impedance of the measuring cell could be represented by the network shown in Fig. 2. This network has the property of giving a linear plot of series resistance against the reciprocal of the signal frequency if the film impedance is mainly capacitive. Linear plots of this type having a common intercept on the resistance axis were obtained by Young (4) for series resistance measurements on anodic films formed on niobium. Young interpreted the intercept on the resistance axis as a pure solution resistance.
5. It is assumed that a corrosion film on aluminum consists of a thin stratum of oxide between the metal and a much thicker amorphous hydrated layer. The entire dielectric properties reside in this oxide layer, and the amorphous hydrated layer contributes nothing to the dielectric properties. Support for this assumption comes from experiments with boehmite films on aluminum (5) whose thickness computed from their interference colors were of the order of several thou-

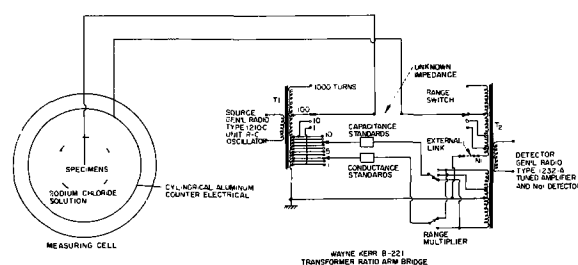


Fig. 1. Arrangements for measuring dissipation factor ( $\tan \delta$ ) of corroding aluminum alloy specimens parallel analog transformer ratio arm bridge.

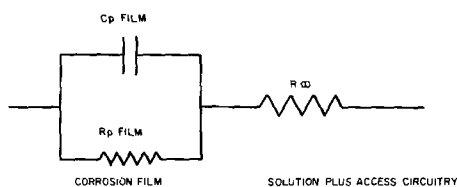


Fig. 2. Equivalent electrical circuit representing the measuring cell impedance.

sands of angstroms, but whose thickness computed from capacitance bridge measurements were under a hundred angstroms. Obviously, the thick boehmite films contributed nothing to the dielectric properties of the aluminum surface films.

As the measuring frequency was increased, the capacitative path in the film had much lower reactance than the resistive path so that ultimately at infinite frequency the impedance of the measuring cell became simply the pure resistance of the solution in the measuring cell and the access circuitry in agreement with Young. This fact is represented in the diagram by using the symbol  $R_{\infty}$  for the ohmic resistance of the solution plus access circuitry.

The value of  $R_{\infty}$  was thus obtained by extrapolating a plot of the series resistance vs. the reciprocal frequency to a zero value of the reciprocal frequency.

Calculation of the dissipation factor of the corrosion film was then performed by converting the parallel components of the measuring cell impedance to series components by the following formulas

$$C_s = \frac{(1 + \omega^2 C_p^2 R_p^2) C_p}{\omega^2 C_p^2 R_p^2} \quad [1]$$

$$R_s = \frac{R_p}{1 + \omega^2 C_p^2 R_p^2} \quad [2]$$

where  $C_p$  and  $R_p$  are parallel components of the measuring cell impedance and  $C_s$  and  $R_s$  are the corresponding series components.

The  $\tan \delta$  or dissipation factor of the corrosion film was then calculated from the formula

$$\tan \delta = \omega C_s (R_s - R_{\infty}) \quad [3]$$

Various thicknesses of  $4 \times \frac{3}{4}$  in. sheet specimens of alloys under study were masked to expose a  $\frac{1}{2}$  cm<sup>2</sup> window using a polyester backed adhesive tape.

The samples were mounted in the measuring cell with the exposed windows immersed in  $\frac{1}{2}$ M sodium chloride thermostatically controlled at 90°C. The exposed samples and the entire counter electrode assembly were immersed in the solution which was protected from evaporation by means of a layer of molten paraffin. At the end of the experiment, which lasted 13 days, the oxygen content was found to be 2 ppm by a modified Winkler method (6).

**Materials.**—Five commercial alloys, whose analysis is shown in Table I, were selected for study because a considerable amount of information about their susceptibility to corrosion in salt solutions and sea water has been published (7, 8).

**Corrosion tests.**—Duplicate  $1\frac{1}{2} \times 1$  in. sheet samples of the same group of alloys were subjected to corrosion tests; surface pretreatment was as follows: (a) immerse in 5% aqueous sodium hydroxide at 70°C

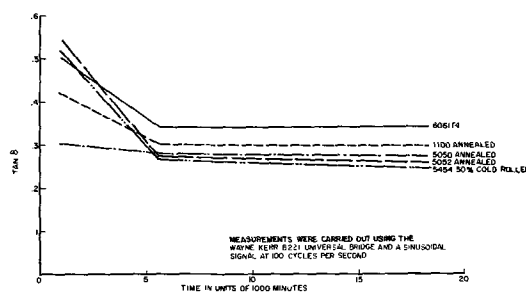


Fig. 3. Loss tangents of corrosion films on various commercial aluminum alloys exposed to  $\frac{1}{2}$ M sodium chloride at 90°C; oxygen content 2 ppm.

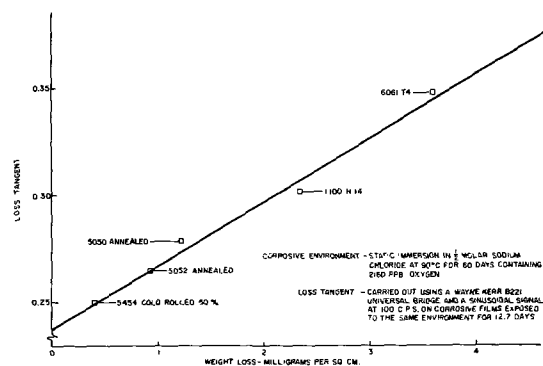


Fig. 4. Corrosion rates of commercial aluminum alloys correlated with loss tangents of corrosion films.

for 1 min; (b) rinse in distilled water; (c) immerse in cold 50% aqueous nitric acid for 10 sec; (d) rinse in distilled water; (e) dry with absorbent paper tissues.

The samples were weighed and then suspended for 60 days in  $\frac{1}{2}$ M sodium chloride at 90°C under a layer of molten paraffin. The oxygen content at the end of the test period was found to be 2 ppm as in the dissipation factor experiments. At the end of the experiment the samples were cleaned in a chromic-phosphoric solution and reweighed.

**Results.**—Figures 3 and 4 show plots of  $\tan \delta$  values vs. time and vs. corrosion weight loss. It is apparent that after an initial higher value,  $\tan \delta$  declines to a value close to its final measured value in 5000 min. There is a very close correlation between the final  $\tan \delta$  value and the weight loss in a fixed time of exposure. It should also be noted that the 5XXX series alloys 5454, 5052 have relatively low corrosion rates compared to alloy 1100 and 6061-T4.

Figure 5 shows a plot of the final  $\tan \delta$  value against the magnesium content of the alloys studied. With the conspicuous exception of alloy 6061 which has a higher copper and silicon content than the 5XXX series alloys, the  $\tan \delta$  value is almost inversely proportional to the magnesium content.

### Discussion

Our observation that 5XXX series alloys have superior corrosion resistance to 6061-T4 in hot aerated brine is corroborated by the work of Bohlmann (7) who found that 5XXX series alloys 5052 and 5454 had superior corrosion resistance to 6061-T4 in circulating

Table I. Elemental composition of commercial aluminum alloys used in the investigation

Alloy	Silicon	Iron	Copper	Manganese	Magnesium	Chromium	Zinc	Titanium
5454-H16	0.11	0.22	0.04	0.84	3.90	0.09	0.02	0.009
5052-O	0.10	0.35	0.05	0.04	2.20	0.17	0.03	0.015
5050-O	0.12	0.48	0.03	0.03	1.53	0.01	0.02	0.018
1100-H14	0.11	0.64	0.12	0.012	0.01	<0.002	<0.01	0.009
6061-T4	0.61	0.43	0.35	0.08	1.10	0.15	0.03	0.021

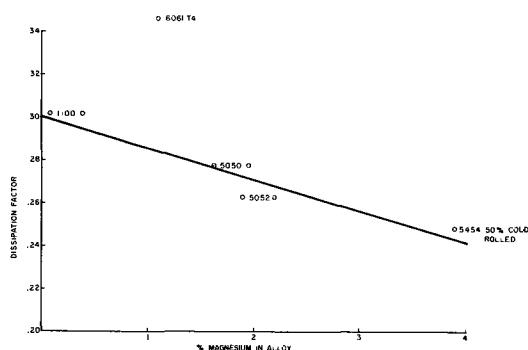


Fig. 5. Relationship between the magnesium content and the dissipation factor;  $\frac{1}{2}M$  sodium chloride at  $90^{\circ}C$ .

brine at  $300^{\circ}F$  based on weight loss measurements. Summerson, Pryor, Keir, and Hogan (8) measured the pit depth distributions of alloys 5052-H34, 5050-H34, and 6061-T4 after immersion in subtropical sea water. The 5XXX series alloys were found to have fewer and shallower pits in general than alloy 6061-T4.

Our results indicate also that a close relationship exists between the weight loss of aluminum alloys and the dissipation factor of their corrosion product films. We have also suggested that this dissipation factor is proportional to the density of defects in the dielectric layer at the metal interface known as the barrier layer.

### Conclusions

The dissipation factors of corrosion films on commercial aluminum alloys were found to be linearly related to their rates of corrosion in hot sodium chloride solution containing 2 ppm of dissolved oxygen.

5XXX series alloys containing magnesium had corrosion rates and dissipation factors which were inversely proportional to their magnesium content.

Alloy 6061-T4 was found to lose more weight and its corrosion film had a higher dissipation factor than the 5XXX series alloys.

### Acknowledgment

The author wishes to acknowledge the help of Mrs. Catherine Meyer who performed the Bridge measurements and for valuable help and advice from Drs. M. J. Pryor, J. A. Ford, and W. Wolfe, Jr.

Thanks are also made to the Aluminum Division of Olin Mathieson Chemical Corporation for permission to publish this work.

Manuscript received Aug. 10, 1967; revised manuscript received ca. Feb. 23, 1968.

Any discussion of this paper will appear in a Discussion Section to be published in the December 1968 JOURNAL.

### REFERENCES

1. R. G. Breckenridge, *J. Chem. Phys.*, **16**, 959 (1948).
2. J. J. McMullen and M. J. Pryor, "The Relation Between Passivation, Corrosion and the Electrical Characteristics of Aluminum Oxide Films," First International Congress on Metallic Corrosion, April 10-15, 1961.
3. M. A. Heine, D. S. Keir, and M. J. Pryor, *This Journal*, **112**, 24 (1965).
4. Laurence Young, *Trans. Faraday Soc.*, **51**, Part 4, 1250 (1955).
5. M. A. Heine, Private communication.
6. E. C. Potter and J. F. White, *J. Appl. Chem.*, **285**, Parts I, II, III, (1957).
7. E. G. Bohlmann, ORNL-3391, US-4-Chemistry, TID-4500 (28th Ed.), Reactor Chemistry Division, Annual Progress Report ending Jan. 31, 1964, Oak Ridge National Laboratory, Oak Ridge, Tenn.
8. T. S. Summerson, M. J. Pryor, D. S. Keir, and R. J. Hogan, Second Pacific Area Meeting Papers, ASTM Special Technical Publication No. 197, Metals, 157 (1957).

## The Double Layer Capacitance in Aqueous Solution

### III. Polycrystalline Tin

N. A. Hampson and D. Larkin

Chemistry Department, Loughborough University of Technology, Leicestershire, England

Recently differential capacitance measurements at silver(1) and cadmium(2) electrodes have been reported. This note records similar measurements with polycrystalline tin electrodes.

### Experimental

The Schering bridge, electrolytic cell, and purification procedure has been described elsewhere (1, 3). Electrodes ( $7.92 \times 10^{-2}$  cm<sup>2</sup> superficial area) were prepared from 99.999% tin supplied by Johnson Matthey and Company and sheathed in polyethylene (3).

Electrodes were polished mechanically on roughened glass lubricated with water. In most cases electrodes were also electrochemically etched (10 ma/cm<sup>2</sup>, 10% HClO<sub>4</sub>). After washing in double distilled water electrodes were introduced into the electrolytic cell without drying.

Electrolyte pH adjustments were made by the replacement of  $\sim 1/10$ th of the electrolyte by 0.01M HClO<sub>4</sub>.

### Results

Electrometric measurements indicated that outside the potential limits  $\sim -1.6v$  NHE to  $\sim -0.2v$  NHE considerable faradaic current flowed. There was an

almost ideally polarizable region from  $-0.6$  to  $-0.3v$ .

Changes in differential capacitance,  $C_L$ , during the initial stages of electrode/electrolyte contact time were small. Irrespective of electrode pretreatment a 5% reduction in  $C_L$  from the first available value to the stable value after 5 min was typical,  $C_L$  values were stable for at least 24 hr thereafter.

Figure 1 shows typical results of capacitance measurements on stable electrodes. At any potential in the experimental potential range the difference between  $C_L$  values characteristic of etched replicate electrodes was within  $\pm 5\%$  of the mean. Electrodes which had only been mechanically polished had  $C_L$  values  $\sim 25\%$  greater than corresponding etched electrodes.

In neutral solution differential capacitance curves contained a local capacitance maximum at  $-0.75v$ . In acid electrolytes the local maximum occurred at  $\sim 0.6v$  and was not so pronounced. A capacitance minimum occurred at  $\sim -0.4v$  with acid electrolytes which became more pronounced at greater dilution. In the most dilute electrolytes investigated this minimum occurred at  $-0.43 \pm 0.02v$ . The minimum was absent in neutral electrolytes. No hysteresis was observed either in neutral or acid electrolytes. Capacitance curves could be

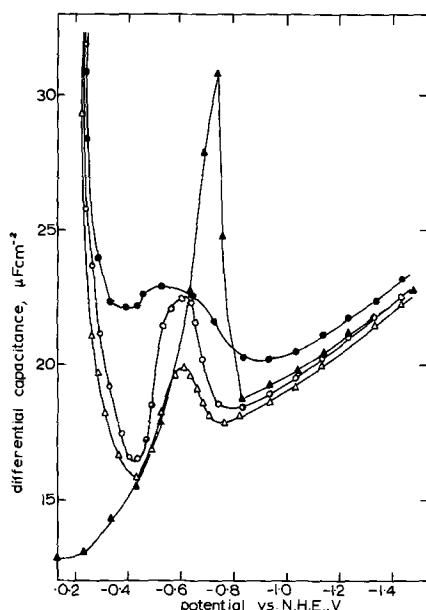


Fig. 1. Differential capacitance curves for polycrystalline tin in perchlorate electrolytes. 1 kHz; 23°C.  $\blacktriangle$ , 0.1M NaClO<sub>4</sub>, pH, 6.6-7;  $\bullet$ , 0.1M NaClO<sub>4</sub>, pH, 3-3.2;  $\circ$ , 0.007M NaClO<sub>4</sub>, pH, 3-3.3;  $\triangle$ , 0.0007M NaClO<sub>4</sub>, pH, 3-3.2.

traversed indefinitely in either direction without any irreversible changes taking place.

Figure 2 shows the extent of frequency dispersion at an electrolytically etched electrode. The extent of this dispersion was similar with electrodes only mechanically polished.

### Discussion

The differential capacitance curves in both neutral and acid solutions are very similar at negative potentials while at positive potentials marked differences occur. The general tendency of the capacitance at positive potentials in neutral solutions to approach low values is in contrast to the normal behavior of metals at the extremities of their polarizable region where an increase in the differential capacitance is invariably observed, as with tin in acid solutions. This effect is probably due to the formation of an oxide or hydroxide film as the electrode assumes more positive potentials (the hydrogen ions in the acid solution preventing this happening until even more positive potentials are reached). The peak which appears at about  $-0.7v$  in the capacitance curves in neutral solution is probably due to the oxide or hydroxide film developing or being removed (depending on the direction of the potential sweep) giving rise to a pseudo-capacitance similar to those observed when organic compounds are adsorbed on mercury. Increases in the electrolyte resistance were also noted at  $\sim -0.7v$  in neutral solution during potential sweeps which were absent in the acid solutions, such effects are indicative of structural changes in the metal-aqueous solution interphase. In the experimentally polarizable region (zero or very limited d-c flow) the most likely cause is film formation.

The steep rise in  $C_L$  at  $\sim -0.2v$  in acid electrolytes presumably marks the potential at the point of lattice dissolution.

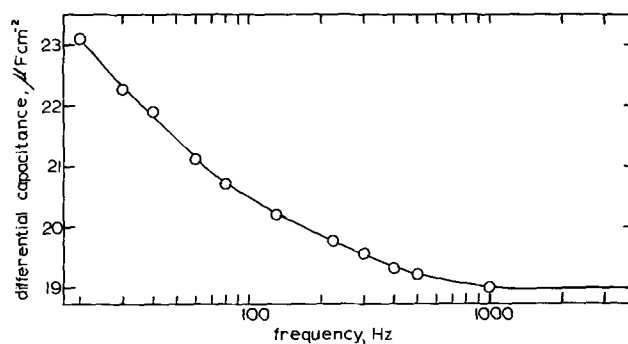


Fig. 2. Dispersion of capacitance with frequency: 0.007M NaClO<sub>4</sub>; pH, 3-3.3; 23°C;  $E_{li}$ ,  $-0.68v$ .

The shapes of the differential capacitance curves in acid electrolytes are similar to those observed with mercury. The capacitance curves form a family which exhibit a minimum. This minimum becomes more pronounced with dilution. These observations indicate that the capacitance curves in acid electrolytes correspond to the tin/electrolyte interphase uncomplicated by adsorption. The capacitance minimum, under these conditions, indicates the potential of zero charge (p.z.c.).<sup>1</sup> If the thermionic work function of tin is taken as 4.1v and that of mercury as 4.5v then the p.z.c. might be expected to be in the region of  $-0.6v$  NHE. The experimental capacitance minimum occurs at  $-0.43 \pm 0.02v$ . This compares well with  $-0.46v$  from capacitance minimum (4) and  $-0.36v$  by dipping (5).

The value of the capacitance obtained in pH  $\sim 3$  solutions are similar to those of mercury under corresponding conditions. Thus it is likely that the true area of the tin electrode is close to the superficial area. [c.f., cadmium (2)]

The small dispersion of frequency is probably explained by a minor degree of surface roughness and heterogeneity as discussed by de Levie (6) and Ramaley and Enke (7).

### Acknowledgment

One of the authors (D. L.) thanks the Science Research Council for financial support throughout these investigations (Parts I-III).

Manuscript received Nov. 9, 1967; revised manuscript received ca. Feb. 26, 1968.

Any discussion of this paper will appear in a Discussion Section to be published in the December 1968 JOURNAL.

<sup>1</sup> See ref. (1) for further comments on this point.

### REFERENCES

1. N. A. Hampson, D. Larkin and J. R. Morley, *This Journal*, **114**, 817 (1967).
2. N. A. Hampson, and D. Larkin, *ibid.*, **114**, 933 (1967).
3. J. P. G. Farr and N. A. Hampson, *Trans. Faraday Soc.*, **62**, 3494 (1966).
4. J. E. B. Randles reported by M. A. V. Devanathan and B. V. K. S. R. A. Tilak, *Chem. Rev.*, **65**, 635 (1965).
5. B. Jakuszewski and Z. Kozłowski, *Roczniki Chem.*, **36**, 1837 (1962).
6. R. de Levie, *Electrochim. Acta*, **10**, 113 (1965).
7. Louis Ramaley and C. G. Enke, *This Journal*, **112**, 947 (1965).



# Charge-Transfer Complexes and Electrochemical Cells— Coal Batteries

R. A. Friedel

United States Department of the Interior,  
Bureau of Mines, Pittsburgh Coal Research Center, Pittsburgh, Pennsylvania

The discovery that charge-transfer complexes can be used in electrochemical cells has been reported (1, 2). The electrical properties of encapsulated solid-state cells involving various donor substances complexed with iodine and with two other acceptor molecules, tetracyanoethylene (TCNE) and tetracyanoquinodimethane (TCNQ), placed between magnesium and an inert electrode have been described (2). After the initial report on this work (1) it occurred to us that our experience with the charge-transfer complexing ability of coals (3) could possibly be applied to making batteries from coal complexes. Similar batteries were produced from pellets 1 mm thick and 22 mm in diameter of iodine plus various coals mounted between magnesium and copper disks. Open-circuit voltage (ocv) as high as 1.9v and short-circuit current densities (sccd) as high as 14 ma/cm<sup>2</sup> were obtained; also, an anthracite coal was found to produce an ocv of 0.8v and a sccd as high as 50  $\mu$ a/cm<sup>2</sup>. Details will be reported later. The work on coal-iodine and other iodine batteries led us to suspect that: (i) the existence of a charge-transfer complex as such has little to do with the generation of potential and current; (ii) the presence of water is essential to the operation of the batteries; and (iii) water is a reactant, not a catalyst.

On the question of whether a charge-transfer complex is necessary, we found that batteries made from iodine with a variety of coals, ranging from lignite to meta-anthracite, differed only slightly in their electrical characteristics. Also, batteries prepared from pellets of iodine plus clay (kaolinite) and iodine plus paraffin (n-C<sub>20</sub>H<sub>42</sub>) performed just as capably as batteries involving charge-transfer complexes (Table I gives the maximum ocv and sccd for several batteries). In fact, iodine alone between magnesium and platinum or copper electrodes performed very well. Our data indicate that formation of a charge-transfer complex is not necessary for the generation of electric potential and current in iodine batteries. The electron donor in the complex serves essentially as a diluent; thus, the method of preparation of the complex is expected to be unimportant, as Gutman *et al.* reported (2). However, any diluent, including donor substances, can influence the rate at which molecular iodine becomes available for the battery reaction.

Charge-transfer complexes, in themselves, generally do not function as solid-state batteries when placed between appropriate electrodes at room temperature. Tetrachloroquinone ("Chloranil"), or stable com-

plexes made with it, are appropriate examples of inactive components (Table I). It appears that charge-transfer complexes are active battery components only if they contain a moiety that can react with magnesium, such as I<sup>-</sup>, TCNE<sup>-</sup>, and TCNQ<sup>-</sup>.

A variety of batteries have been assembled under dry conditions and operated at 44 to 48% humidity; maximum ocv and sccd values are given in Table I. Most of these batteries were assembled with magnesium and copper electrodes. Platinum in place of copper produces somewhat higher ocv and sccd, but battery operation is similar.

Gutman *et al.* noted the large increase in current when they added large amounts of liquid water to their charge-transfer complexes, but both ocv and sccd decreased drastically in a few minutes. They also noted that the effect of minute amounts of water on cell performance was unknown (2). Tables II-V present ocv and sccd data for iodine batteries, Mg/I<sub>2</sub>/Pt, showing variations with time and the large effect of water. The batteries represented by the data of Table II were prepared under dry conditions and then operated at a humidity of 45%. Table III presents data for a battery prepared under dry conditions and sealed in a 1-liter glass jar containing room air; the amount of water in the 1-liter jar was 0.009g (humidity, 48%). The values of ocv and sccd were measured by means of copper wires sealed into the lid of the desiccator; values are lower than those of Table II because of the lower amount of available water. Table IV represents an operating battery for which 0.02g of water vapor was added to the 1-liter container; both ocv and sccd increased immediately, the more drastic change occurring for the sccd.

Table V demonstrates the striking effect on a battery of removing the source of water completely, by operating an iodine battery in a desiccator. Batteries desiccated include: 1, I<sub>2</sub>; 2, perylene-I<sub>2</sub>; 3 n-C<sub>20</sub>H<sub>42</sub>-I<sub>2</sub>.

Table I. Performance of iodine batteries. Maximum open-circuit voltages and short-circuit current densities, humidity 44-48%

	Weight ratio I <sub>2</sub> : Donor	Maximum ocv, v	Maximum sccd, $\mu$ a/cm <sup>2</sup>
Mg/Kaolinite-I <sub>2</sub> /Cu	1:5	1.80	6,000
Mg/nC <sub>20</sub> H <sub>42</sub> -I <sub>2</sub> /Cu	1:5	1.80	3,000
Mg/I <sub>2</sub> /Cu	I <sub>2</sub> , 100%	1.80	20,000
Mg/I <sub>2</sub> /Pt	I <sub>2</sub> , 100%	2.00	75,000
Mg/Perylene-I <sub>2</sub> /Cu	1:2	1.90	500
Mg/Pittsburgh coal-I <sub>2</sub> /Cu	1:5	1.70	7,000
Mg/Tetrachloroquinone/Cu	T, 100%	0	0
Mg/Tetrachloroquinone-coal/Cu	1:1	0	0
Mg/Tetrachloroquinone-naphthalene/Cu	1:1	0	0

Table II. Effect of high water content. Iodine battery operated in laboratory air at high humidity. Mg/I<sub>2</sub>/Pt battery, 20°C, 45% humidity

Time, hr	Ocv, v	Sccd, $\mu$ a/cm <sup>2</sup>
0	1.50	1.0
3.5	1.70	9,000
17.4	1.80	35,000
21.5	1.95	75,000
41	1.90	15,000
43.4	1.85	12,500
137	2.00	10,000
161	1.85	2,500
290	1.77	1,000
362	1.99	750
468	1.75	400
516	1.80	400

Table III. Effect of low water content. Iodine battery operated in a sealed 1-liter glass jar containing laboratory air with 0.009g water vapor. Mg/I<sub>2</sub>/Pt battery, 20°C, humidity 48%

Time, hr	Ocv, v	Sccd, $\mu$ a/cm <sup>2</sup>
0	1.40	2.3
1	1.70	49
19	1.55	2500
43	1.50	2500
67	1.50	2200
75	1.70	1800

Table IV. Effect of the addition of water to an operating iodine battery placed in a sealed 1-liter glass jar. 0.02 cc of water were added during operation. Mg/I<sub>2</sub>/Pt battery, 23°C, 48% humidity

	Time, hr	Ocv, v	Scdd, $\mu\text{a}/\text{cm}^2$
	0	1.45	1.4
	0.5	1.50	2.6
	1.25	1.50	1.8
	2.00	1.42	1.3
0.02 cc H <sub>2</sub> O inserted in jar	2.17		
	2.35	1.57	85
	2.40	1.59	270
	3.10	1.52	10,000
	4.65	1.51	7,500
	5.80	1.50	4,000
	6.40	1.50	3,000
	6.70	1.50	3,000
	7.75	1.50	2,750
Removed from jar into room.	7.80		
Humidity, 48%	7.85	1.50	4,000
	7.95	1.53	8,000
	8.50	1.58	15,000
	9.00	1.57	25,000
	9.30	1.55	22,500

Table V. Extreme effect of water on an iodine battery. Iodine battery operated alternately at zero humidity (desiccation) and high humidity. Mg/I<sub>2</sub>/Cu/battery, 20°C, 45% humidity\*

	Time, hr min		Ocv, v	Scdd, $\mu\text{a}/\text{cm}^2$
Placed in desiccator:	0		1.27	5.0
	4.5		0.86	0.018
	93.0	35	0.10	0.001
Removed from desiccator:	93.0	37	0.70	0.008
	96.0		1.60	800.0
	138.5		1.75	17,500.0
	166.0		1.70	17,500.0
	408.0		1.20	2,500
Replaced in desiccator:	429.0		0.90	50.0
	501.0		0.50	0.09
	816		0.25	0.006
Removed from desiccator:	1344		0.50	17.5
	1440		1.00	1,050
	1848		1.20	125.0

\* Similar behavior was observed for Mg/I<sub>2</sub>/Pt.

In some cases batteries prepared in a dry box were placed immediately in a desiccator. Initially, small ocv and scdd were produced, presumably due to traces of water remaining in the dried battery components; then, both ocv and scdd decreased rapidly toward zero. On re-exposure to atmospheric humidity high ocv and scdd were rapidly attained. This cycle was repeated with similar results (Table V). Batteries were also prepared under dry conditions, were exposed

to the atmosphere and permitted to develop high ocv and scdd. Then, desiccation produced the same result as described above. Ocv of zero and scdd as low as  $2 \times 10^{-10}$  amp were measured on desiccated batteries. In all cases after removal from desiccation the batteries immediately developed ocv and scdd, the magnitude of which depended principally on the amount of water (humidity) made available to the battery and, to a less extent, on the age of the battery. Water is absolutely essential to operation of the batteries. The cells studied by Gutman *et al.* were encapsulated (2) but not sealed; water vapor presumably was able to enter their cells.

Water is not merely a catalyst in the battery operation; it participates directly in the battery reaction and is decomposed. We discovered this by collecting gas emitted from shorted batteries placed in closed containers. The gas produced is pure hydrogen. Thus any general equation for the battery reactions must include the decomposition of water.<sup>1</sup> Hydrolysis reaction(s) are apparently involved with the resulting formation of H<sup>+</sup>, followed by  $2\text{H}^+ + 2e \rightarrow \text{H}_2$ . When a battery is shorted in the presence of water vapor the uptake of water is extremely rapid. The electrolyte quickly becomes wet and the evolution of hydrogen becomes rapid. Under low humidity conditions the same reactions are less obvious but undoubtedly occur, including the evolution of hydrogen and rapid absorption of the available water.

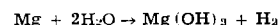
#### Acknowledgment

The author is grateful for the help of A. F. Logar and Dr. H. W. Sternberg.

Manuscript received Oct. 9, 1967.

Any discussion of this paper will appear in a Discussion Section to be published in the December 1968 JOURNAL.

<sup>1</sup> We believe that the over-all electrode reaction is essentially



with a theoretical potential of 1.86v. Filter paper soaked with an aqueous solution of molecular iodine and placed between magnesium and platinum electrodes produced the same ocv that were obtained with the iodine batteries.

#### REFERENCES

1. Anonymous, *Chem. and Eng. News*, **44**, 20 (1965).
2. F. Gutman, A. M. Hermann, and A. Renbaum, *This Journal*, **114**, 323 (1967).
3. R. A. Friedel and J. A. Queiser. Preprints, Fuel Chem. Div., Am. Chem. Soc. Meeting, Sept. 1966, New York, vol. 10, No. 3, pp. 1-6.

## On the Activity of Platinum Catalysts in Solution

### III. Facets on Flame-Formed Platinum Spheres

Theodore B. Warner\*

Naval Research Laboratory, Washington, D. C.

In a recent study of factors affecting the activity of platinum electrodes, it was noted that thermal treatments could change this activity markedly (1). Activity was monitored by measuring the rate of the reaction of hydrogen, dissolved in solution and in the electrode, with oxygen present on the surface of the electrode. The thermal treatments involved heating the platinum bead in an H<sub>2</sub>/O<sub>2</sub> flame until it was molten, and then recrystallizing. When the cooling rate through the freezing point was slow, platinum beads had a characteristic appearance, nominally spherical with numerous well-developed flat regions. Such electrodes exhibited relatively high activity compared

with those having more irregular surfaces and fewer or no flat regions.

Many studies using other metals, particularly Ag and Cu, have demonstrated that small spherical single crystals can be formed by recrystallizing the metal under the proper conditions (2, 3). Kaishev and Mutaftshiev (4) formed platinum single crystal spheres by melting and refreezing the ends of previously prepared single-crystal fragments. It appeared probable that the flat regions observed here were crystallographically significant and hence that there might be a correlation between electrode activity for this reaction and degree of crystal perfection. The purpose of this study was to determine whether the flats did have crystallographic significance, and if so, what

\* Electrochemical Society Active Member.

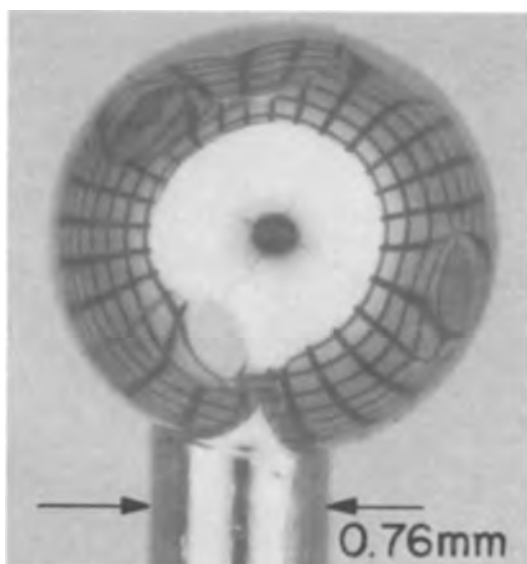


Fig. 1. Flame-formed platinum bead. A regularly arrayed grid has been optically projected onto the surface to reveal facets. Magnification  $\approx 40\times$ . Photograph by A. C. Simon.

crystal faces predominated. This was of interest not only because of the correlation with activity, but because of the very simple procedure by which these spheres could be formed.<sup>1</sup>

### Experimental Results

The platinum bead was examined by optical goniometry; it was mounted in approximately the same position shown in Fig. 1. To obtain better definition of surface details on the bright, reflective bead, the photograph shows the reflection from the bead surface of a grid of regularly spaced lines. Deviations from sphericity are indicated by irregularities in the reflected pattern. The pattern was obtained by mounting the bead in the center of a white, right circular cylinder marked with a black grid of parallel lines. Illumination was projected downward through a translucent planar surface, marked with a lighter rectangular grid, that appears as a bright circle in the photograph. Views of the surface from other angles have appeared elsewhere (5).

The angles between the flat faces were measured using a two-circle optical goniometer constructed according to the design of Barrett and Levenson (6). The poles were plotted on a 20 cm Wulff net graduated at  $2^\circ$  intervals. Goniometer readings were measured to the nearest  $0.5^\circ$  and were precise to  $\pm 0.5^\circ$ . The observed stereographic projection was rotated, using standard techniques (7) to coincide with a standard projection of poles of a cubic crystal and the data are shown in this form in Fig. 2. The solid points are observed poles on the front face of the projection, the open point at A is an observed pole on the rear face, and point B was the surface normal as mounted. Five  $\{111\}$  faces and three  $\{100\}$  faces were observed. The angular distances between all possible pairs of poles were measured using the Wulff net and compared with the angles expected in a perfect cubic crystal (8). The maximum deviation was  $1.7^\circ$ ; the standard deviation of an individual measurement was  $0.87^\circ$ . The  $\{111\}$  faces were all large and of the characteristic lenticular shape clearly visible in Fig. 1. The  $\{100\}$  faces were tiny and of the same shape. Within the precision of the method all of the faces were perfectly flat.

A specific search was made for emerging  $\{110\}$  faces at predicted positions. None was found, although the

<sup>1</sup> They were formed by melting an end of clean 0.030 in. diameter 99.99% pure platinum wire as received, undoubtedly polycrystalline, in a hand oxyhydrogen torch. Temperature was lowered by gradually reducing oxygen content of the flame over a period of 3-5 min.

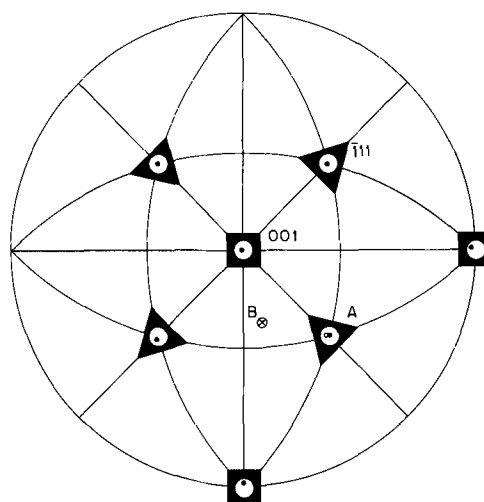


Fig. 2. Standard (001) stereographic projection of cubic crystal with observed data superimposed at relevant poles. Two poles are plotted at point A, one on the rear face. The surface normal was located at point B.

perfection of the spherical surface would have made identification easy even for a very small face.

The entire surface was repeatedly scanned for faces in other positions, which would be found if the crystal were a twin, or if several interpenetrating crystals were present. No such facets were found. This search was prompted by an anomalous region, visible at the top of the sphere in Fig. 1, that did not have the characteristic shape of an emerging face and was neither flat nor part of the sphere surface. Close microscopic examination showed this to be a tiny dimple, in all probability a shrinkage cavity formed in the last stages of bead solidification.

### Conclusions

The flat regions observed on a platinum sphere formed by melting the end of a wire in an  $H_2/O_2$  flame and slowly cooling the molten bead until resolidified were crystallographically significant. The large facets were  $\{111\}$  faces and the small ones were  $\{100\}$  faces of a platinum single crystal.

### Acknowledgments

The author wishes to thank Jeanne Burbank for suggesting the experimental technique, for making available her goniometer, for numerous helpful discussions concerning goniometry and crystallography, and for a critical reading of the manuscript. He also thanks Sigmund Schuldiner for helpful discussions concerning this work and Albert Simon for devising the technique and obtaining the photographs in Fig. 1.

Manuscript received Feb. 12, 1968.

Any discussion of this paper will appear in a Discussion Section to be published in the December 1968 JOURNAL.

### REFERENCES

1. T. B. Warner, S. Schuldiner, and B. J. Piersma, *This Journal*, **114**, 1120 (1967).
2. R. Piontelli, G. Poli, and G. Serravalle in "Transactions of the Symposium on Electrode Processes," E. Yeager, Editor, p. 67, John Wiley & Sons, New York (1961), and see references quoted therein.
3. D. K. Roe and H. Gerischer, *This Journal*, **110**, 350 (1963).
4. R. Kaishev and B. Mutafshiev, *Z. physik. Chem.*, **204**, 334 (1955).
5. T. B. Warner, S. Schuldiner, and B. J. Piersma, *This Journal*, **115**, 163 (1968).
6. C. S. Barrett and L. H. Levenson, *Trans. AIME*, **137**, 76 (1940).
7. C. S. Barrett, *ibid.*, **124**, 29 (1937).
8. C. S. Barrett and T. B. Massalski, "Structure of Metals," 3rd ed., pp. 40-42, McGraw Hill, Inc., New York (1966).

## Transient Voltage Changes Produced in Corroding Metals and Alloys

Warren P. Iverson<sup>1</sup>

Fort Detrick, Frederick, Maryland

The formation of "hollow whiskers" by the action of slightly acidified potassium ferricyanide and ferrocyanide solutions on metals and alloys (1) appeared to indicate that corroding metals produce bursts of metal ions from various point anodes. Since these bursts of ions appeared to be of a sporadic nature, it seemed possible that there might be transient fluctuations of the electrical charge on the metal. The present communication reports on the detection of such fluctuations in electrical charge.

The circuit shown in Fig. 1 was used. The voltmeter was of the high impedance type (11 megohms) with a chopper stabilized circuit. The electrodes consisted of an inert auxiliary electrode of platinum foil (1 x 4.5 cm) connected to a platinum wire and the test electrode, whose corrosion was to be studied. Various strips of metals and alloys were used as the test electrode. The cell and electrodes were placed in a grounded copper-jacketed chamber to control the temperature and provide a shield from stray currents. The corroding metals or alloys investigated were aluminum, aluminum alloys (2025 and 7075), magnesium ribbon, iron, mild steel (1010), and zinc, and each exhibited voltage fluctuations whose frequency and amplitude depended on the metal being studied. The fluctuations from pure aluminum, the two aluminum alloys, and magnesium were generally extremely rapid (1 to 2 or more per sec) and greater than 100  $\mu\text{V}$  in amplitude. Using a low input impedance audio amplifier with the platinum and the corroding electrode connected directly across the input, a wide range of fluctuations in the audio range could be heard with a loud speaker. Voltage fluctuations from corroding iron, steel, and zinc were slower (1 to 3 or less per 5-min interval) and less in amplitude (<50 or 60  $\mu\text{V}$ ). The fluctuations in the potential appeared to be directly related to the corrosion, because the addition of an inhibitor caused them to disappear. Likewise, a non-corroding metal (platinum) was studied (in this case both electrodes were platinum) no fluctuations were observed. As an example, Fig. 2 shows the voltage fluctuations in a 1010 mild steel coupon partly immersed in distilled water plus 0.1% NaCl and the effect of a corrosion inhibitor, sodium nitrite (2), in causing these fluctuations to disappear. Similar inhibitor effects were observed with aluminum in the presence of nitrates (3).

To account for these voltage fluctuations, it is postulated that they are caused by minute transient changes in the electrical charge on the electrode produced as a result of cathodic and anodic reactions during the corrosion process, the charge at any small interval of time representing the resultant charge of both reactions. The imbalance of charge may also be due to

transient changes in cathodic or anodic areas. If, for example, a corroding metal assumes a temporary increase in negative charge, the electrons would charge the plate of the capacitor in contact with it. An equal or opposite charge would develop on the other plate (flow of electrons away from the plate) thereby causing a difference in measurable potential across the resistance. The electrons might be expected to dissipate through the resistor to the platinum electrode and be removed as a result of reduction of the cations or neutral species in the solution. During a transient decrease in negative charge on the metal and capacitor plate, the flow of electrons would be from the platinum electrode, as a result of oxidation of the anions or neutral species in solution, to the other capacitor plate, again developing a measurable potential across the resistor. If no change in the charge occurs on the test electrode, no measurable potential is developed across the resistor. This is apparently the case for a non-corroding electrode such as platinum or a less noble metal in the presence of an inhibitor for the initial charge on the capacitor soon dissipates, and the measurable potential drops to zero. The time for the voltage developed across the resistor to decrease to zero appears to be directly related to the initial charge in the capacitor and the R.C. time constant and inversely related to the electrolyte concentration.

Investigations of these voltage fluctuations appear to offer much promise for the detection and study of the corrosion process and for the study of corrosion inhibitors. Thus far, these fluctuations give a qualitative "fingerprint" characterization of corrosion processes occurring in different metals and alloys. They also offer a very simple way to detect the efficacy of inhibitors, being able to detect corrosion instantane-

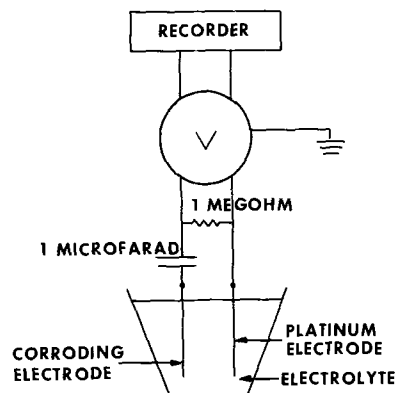


Fig. 1. Corrosion cell and circuit for detecting potential variations in corroding metals and alloys.

<sup>1</sup> Present address: National Bureau of Standards, Washington, D. C.

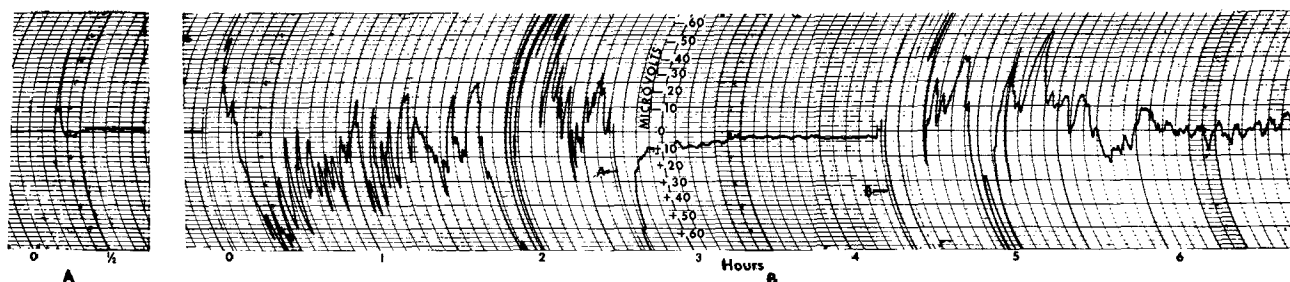


Fig. 2. Recorder trace of potential fluctuations. Chart speed 3 in/hr. A, Completely immersed platinum electrode (1 x 4.5 cm) in 0.1% NaCl solution; conductivity, 0.22 mhos; platinum electrode 1 cm from completely immersed auxiliary electrode, 25°C. B, Partially immersed (5.5 cm) 1010 steel electrode (1.3 x 18 cm) corroding in 0.1% NaCl solution; electrode 1 cm from completely immersed auxiliary electrode, 25°C. Chart A, electrodes transferred to fresh 0.1% NaCl solution plus 1% NaNO<sub>2</sub>; Chart B, electrodes transferred to fresh 0.1% NaCl solution.

ously. Further analysis of the voltage fluctuations, which is currently underway, will be required to relate them quantitatively to the corrosion rate and to determine the origin of the frequency and amplitude difference that differs with each metal.

#### Acknowledgment

The author thanks Mr. Lee Miller, Fort Detrick, for technical assistance.

Manuscript received Dec. 11, 1967.

Any discussion of this paper will appear in a Discussion Section to be published in the December 1968 JOURNAL.

#### REFERENCES

1. W. P. Iverson, *Nature* **213** (5075), 486 (1967).
2. H. H. Uhlig, "Corrosion and Corrosion Control," pp. 231-232, John Wiley & Sons, Inc., New York (1963).
3. G. C. Blanchard and C. R. Goucher, *Develop. Ind. Microbiol.* **6**, 95 (1964).

## The Direct Observation of Barrier Layers in Porous Anodic Oxide Films

G. C. Wood, J. P. O'Sullivan, and B. Vaszko

*Corrosion Science Division, Department of Chemical Engineering, University of Manchester Institute of Science and Technology, Manchester, England*

Earlier electron microscopical studies (1, 2) indicated that porous anodic oxide films on aluminum contain fine, regular, almost cylindrical pores, penetrating a close-packed hexagonal cellular structure as far as the barrier layer. The electrolyte appeared to determine the pore diameter while the forming voltage decided the barrier layer and cell wall thicknesses, although these features were not observed directly. Subsequently it was suggested (3), without visual evidence, that regular pores do not exist and that current is carried through a hydrogen-bonded structure between submicrocrystallites of anhydrous alumina, the degree of hydration increasing with the distance from the metal. Recent electron microscopy (4), however, supported a fibrous film structure, the fibers being hollow oxide cylinders containing water and anions.

The ability to observe the barrier layer and porous structure in section in some detail would assist considerably in resolving these anomalies. The only known previous attempt (5) led to a postulate that the barrier layer forms, by the interaction of liquid metal and oxygen, to a thickness independent of voltage. The present communication describes the initial results of a direct examination of barrier layer and pore and cell structures for films formed in a phosphoric acid electrolyte at high voltage.

Electropolished 99.99% aluminum specimens were anodized at 85, 100, or 115v for 1 hr in 4, 15, or 25% phosphoric acid at 25°C. Further experiments involved sharply increasing or decreasing the anodizing voltage after 30 min and removing the specimens when various parts on the resulting current/time transient curves had been reached. Films were fractured and di-

rect carbon replicas, shadowed with a platinum/carbon mixture, obtained from the surfaces and sections.

Figure 1a shows a section through the metal and film at the interface and, despite debris, the scalloped film base, cell structure, and pores are clearly visible. In Fig. 1b the film is separated from the metal, but the now classical conception of the film is clearly revealed. Some variation in apparent cell and pore diameters is to be expected, due to the different fracture planes present. Pores can undoubtedly be seen (2) despite statements to the contrary (6). In this particular micrograph they appear at about their "ideal" size, calculated on the assumption that the cell diameter is equal to twice the barrier layer thickness plus the pore diameter (1).

Average film dimensions from a number of such micrographs are shown in Table I. Due to variations in apparent pore diameter next to the barrier layer, the ideal pore diameter has been calculated as described.

Certain general conclusions may be drawn:

1. The classical film model (1, 2) is largely confirmed although the relationships derived (1) may not exactly hold.
2. The barrier layer thickness is proportional to the voltage, the ratio being about 10 Å/v in all cases.
3. The cell size also varies directly with the voltage, although the proportionality constant differs from previously (1).
4. The calculated pore diameter of 570-820Å, which agrees quite closely with the observed values (700-800Å) from Fig. 2, is considerably larger than the 330Å given previously. This was also found for films

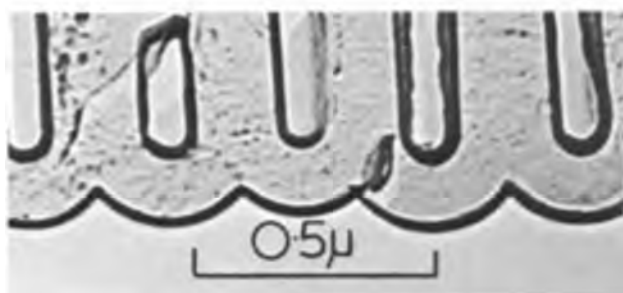


Fig. 1. Electron micrographs of sections through anodic films formed in 4% w/v phosphoric acid at 120v. (a, top) Film attached to the metal; (b, bottom) Detached film showing the barrier layer and pore structure.

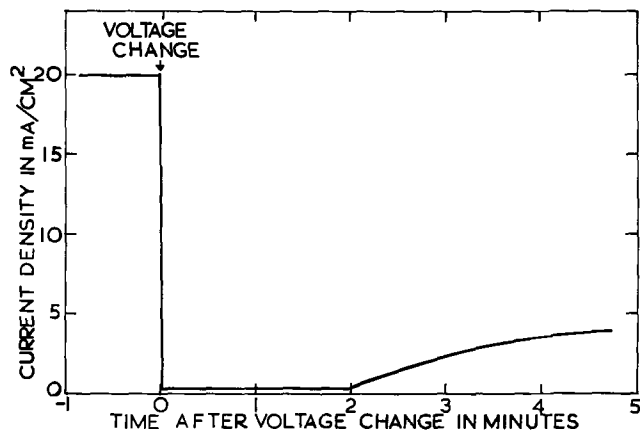
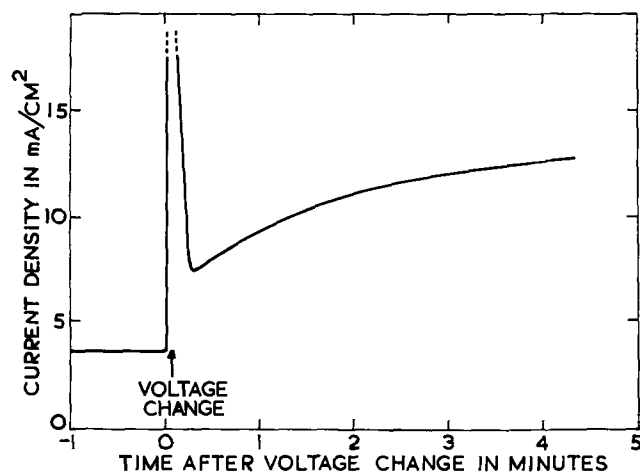


Fig. 2. Current density/time curves obtained on (a, top) increasing the voltage from 87 to 117.5v; (b, bottom) decreasing the voltage from 117.5 to 87v.

Table I. Cell, pore, and barrier layer dimensions in anodic films

Voltage	Acid concentration	Barrier layer thickness	A/v	Cell size A	Calculated pore diameter A
	% W/v	A			
87	4	860	9.9	2360	640
103	4	990	9.6	2800	820
117.5	4	1270	10.8	3330	790
87	15	860	9.9	2400	680
87	25	840	9.7	2250	570

formed in sulfuric acid. It should be noted that the previous workers (1) used a method involving a substantial extrapolation from anodizing voltage data and gave no direct measurements.

The size and irregularity of the pores increased as the outer surface was approached. Cells became more fibrous in appearance (4) and pores occasionally merged, divided, or ceased to function. Replicas from the outer film surface gave pore diameters of 600-1400Å for 4% acid, while pores merged for 15% acid and an extremely rough surface with cavities was apparent for 25% acid. This was indicative of pore widening and eventual gross dissolution.

Of particular interest are the results obtained when anodizing was halted, before steady-state conditions had been achieved, after a rapid superimposed voltage increase or decrease. The resulting current-time curves were of the form shown in Fig. 2a and 2b. Increasing the voltage (Fig. 2a) led to a rapid increase in



Fig. 3. Electron micrographs of sections through anodic films formed in 4% w/v phosphoric acid (a, top) 10 min after changing from 87 to 117.5v, showing pore joining and termination; (b, bottom) 13 min after changing from 117.5 to 87v, showing pore branching and incipient pore formation.

barrier layer thickness during the current surge and subsequent decline. Indeed the barrier layer overshot its expected thickness before subsequently thinning to its ideal value. The cell size increased more slowly and reached its expected value without overshooting at about the same time the barrier layer reached its expected thickness. There was some evidence that further thinning of the barrier layer then occurred. During the redevelopment of the cell base pattern certain pores combined and/or ceased to function as current carriers (Fig. 3a), so that the equilibrium number was established.

During the reverse experiment, a recovery period was experienced before the current rose from substantially zero to the steady state value (Fig. 2a). Electron microscopy indicated that barrier layer thinning (probably field-assisted) may have occurred during this period, despite the low current. Again a redistribution of pores and cells was required, in this case an increase in number. Figure 3b shows pores dividing into two and sometimes three branches, although not all the incipient pores continued to function. Presumably there may have been more initial pore branches when the three-dimensional situation is considered. The directional branching must have occurred by field-assisted dissolution in the outer part of the barrier layer, when the voltage was changed. Presumably the local field, temperature, and hydrogen-bonded structure determined which pores persisted. The final pore and cell dimensions after a voltage change appeared partly determined by the pore and cell distribution in the outer film as well as the final anodizing conditions. It is also likely that initial transient period prior to conventional steady-state anodizing has similar influences.

The work, which is continuing, provides strong evidence for certain aspects of the classical geometrical model. However, it must be recognized that prolonged electrolyte action increases porosity and alters the nature of the hydrogen-bonded structure in the outer parts of the film. The pore splitting and merging behavior gives some support to the concept of a transition region in the outer part of the barrier layer and of the porous layer immediately above it exerting some influence.

#### Acknowledgment

The authors are indebted to Professor T. K. Ross for the provision of facilities and to Dr. C. J. L. Booker for some interesting discussions on this subject.

Manuscript received Dec. 4, 1967.

Any discussion of this paper will appear in a Discussion Section to be published in the December 1968 JOURNAL.

#### REFERENCES

1. F. Keller, M. S. Hunter, and D. L. Robinson, *This Journal*, **100**, 411 (1953).
2. C. J. L. Booker, J. L. Wood, and A. Walsh, *Brit. J. Appl. Phys.*, **8**, 347 (1957).
3. J. F. Murphy and C. E. Michelson, Proc. of Conference on Anodizing Aluminium, University of Nottingham, September 1961, Aluminium Development Association, London (1962), p. 83.
4. H. Ginsberg and K. Wefers, *Metall.*, **17**, 202 (1963).
5. H. Akahori, *J. Electromicroscopy Japan*, **10**, 175 (1961).
6. F. P. Zalivalov, M. N. Tyukina, and N. D. Tomashov, *J. Russ. Phys. Chem. Soc.*, **35**, 429 (1961).

## Stability of Chemically Deposited Magnetic Thin Films with Time and Temperature

G. Wm. Lawless

Technical Institute, University of Dayton, Dayton, Ohio

Commercial adaptation of chemically deposited magnetic thin films, both hard and soft, seems to be nearing reality. Their suitable magnetic memory characteristics on variety of substrates has been amply demonstrated in numerous references (1-4). However, little seems to have been reported on such potentially troublesome areas as reproducibility, wear characteristics, creep, stress, magnetostriction, and aging, or stability with time and temperature. A study of this last noted property, aging or stability with time and temperature, is reported here.

Low coercive force NiCoP films were deposited from the solution composition as given in Table I. Details of deposition and solution operating characteristics have been previously reported (4), along with deposit composition studies. No analytical data are presented for this initial reporting since only one series of samples was prepared for each temperature level, and film composition would naturally have to be consistent prior to any extended research in this area. However, it may be recorded that past experience indicated that the reported solution, operating at 8.0 pH and 80°, characteristically produces low coercive force NiCoP films of 45-52% Ni, less than 5% P, and balance Co.

The films were deposited to various thicknesses on 5-mil phosphor bronze disks, 1.905 cm in diameter. Film thickness was determined by weight-density measurements with the NiCoP density taken as 8.7

g/cm<sup>3</sup>. All films were anisotropic, and the reported coercive force is taken along the easy axis. They were exposed in a still air atmosphere at temperatures of 25°, 65°, and 100°, periodically removed, cooled, and their magnetic properties evaluated. Relative humidity was not specifically controlled in the ambient environment of the samples, but their containing oven was located in an air-conditioned laboratory wherein the relative humidity variation was probably in the 50-70% range. Of particular interest was the variation in coercive force. Figures 1, 2, and 3 display this variation for samples of comparable thicknesses. One immediately observes that the deposit stability with time (change of coercive force), is a function of both the initial thickness (or initial coercive force) and the ambient temperature. For example, a 2000Å deposit exhibited little change in coercive force after 500 hr at 25°, but at 100° after 500 hr of exposure its coercive force had more than doubled. Similar results were observed for all thicknesses, but the thinner the

Table I. Basic solution formulation

Constituents	g/l
NiSO <sub>4</sub> · 6H <sub>2</sub> O	25.0
CoSO <sub>4</sub> · 7H <sub>2</sub> O	17.65
Na <sub>2</sub> C <sub>2</sub> H <sub>3</sub> O <sub>7</sub> · 2H <sub>2</sub> O	80.0
(NH <sub>4</sub> ) <sub>2</sub> SO <sub>4</sub>	40.0
H <sub>3</sub> PO <sub>2</sub>	18.83
8.0 pH	75°-95°C

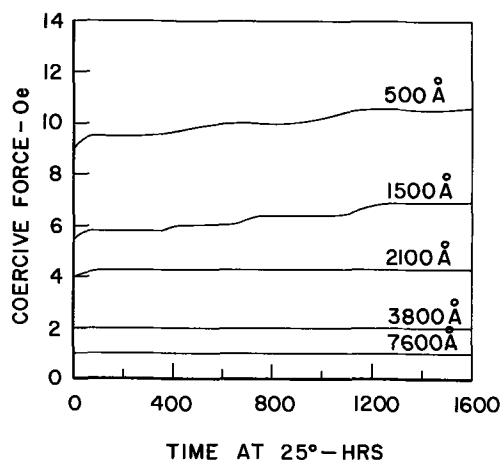


Fig. 1. Variation in coercive force

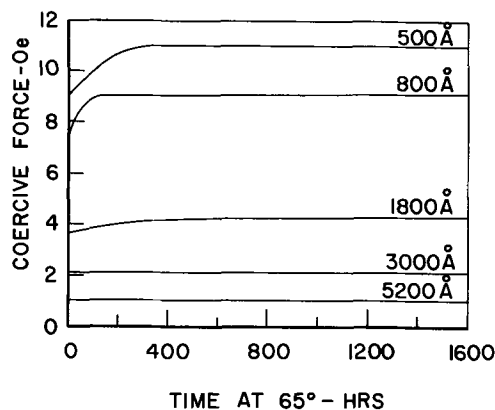


Fig. 2. Variation in coercive force

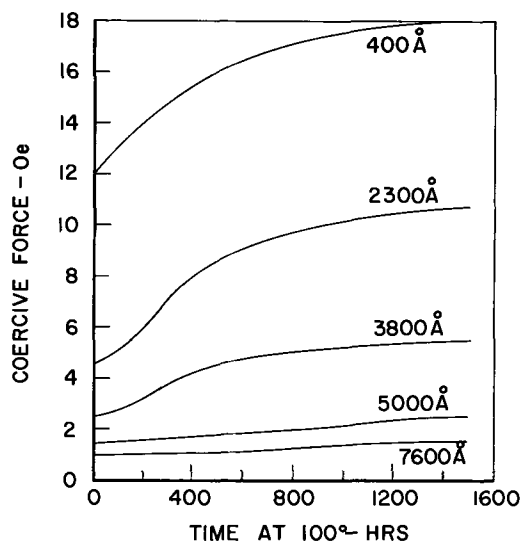


Fig. 3. Variation in coercive force

Saturation flux remained unchanged throughout the test period for all samples.

As somewhat of an addendum to this work, the high coercive force chemically deposited Co-P film, previously developed by Fisher and Chilton (1), was also investigated at 100° for a continuous time period of 1100 hr. Approximately 3000Å of the Co-P was applied to a commercially available polyimide film of 2 mil thickness. Four such samples were investigated. Periodic examination of the hysteresis loop of the deposits revealed no change in B-H characteristics over the 1100 hr test period. The coercive force of these test samples was approximately 400 oe in a 1000 oe drive field.

Manuscript received Oct. 11, 1967, revised manuscript received Feb. 6, 1968.

Any discussion of this paper will appear in a Discussion Section to be published in the December 1968 JOURNAL.

#### REFERENCES

1. R. D. Fisher and W. H. Chilton, *This Journal*, **109**, 485 (1962).
2. R. J. Heritage and M. T. Walker, *J. Elect. and Control*, **7**, 542 (1959).
3. V. Zenther, *Plating*, **52**, 868 (1965).
4. G. Wm. Lawless and R. D. Fisher, *ibid.*, **54**, 709 (1967).

deposit, the more pronounced was the rise in coercive force with time and temperature.

At the exposure temperatures of 25° and 65° the deposits seemed to reach an equilibrium state within 2000 hr, but at 100° exposure the coercive force of all samples (up to 7600Å thickness) continued to increase after 2000 hr.

An interesting stepwise pattern of increasing coercive force was observed on the thinner deposits at 25° exposure, suggesting perhaps a time-temperature equilibrium relationship. But this effect, however real or significant, failed to appear at the higher exposure temperatures.

## DISCUSSION

### SECTION



This Discussion Section includes discussion of papers appearing in the *Journal of The Electrochemical Society*, Vol. 114, No. 4, 5, 7, 10, and 12 (April, May, July, October, and December).

#### Solid-State Electrochemical Cells Based on Charge Transfer Complexes

F. Gutmann, A. M. Hermann, and A. Rembaum  
(pp. 323-329, Vol. 114, No. 4)

**Ashok K. Vijh**<sup>1</sup>: The interesting work reported above includes mechanistic conclusions which are not entirely sustained by a further analysis of the experimental results. It is stated that initial discharge of the iodide ions on the magnesium anode is the rate-deter-

<sup>1</sup> Sprague Electric Co., North Adams, Massachusetts.

mining stage (rds) in the over-all reaction. This conclusion is based principally on one piece of experimental evidence, namely, that at low over-voltages, a straight line is obtained between current and voltage and that for a freshly prepared cell, the exchange current density and thence, the stoichiometric number,  $\nu$ , obtained from this straight line has a value approximately equal to two (Fig. 4). The value of  $\nu = 2$  for the electrode reaction reported needs some further discussion and important points are developed below:

1. If the exchange current density,  $i_0$ , obtained by the extrapolation of the Tafel relation from Fig. 3 of the authors (for the freshly prepared cell) is used for the evaluation of  $\nu$  through Eq. [3] of the authors, a value of approximately 12 for the  $\nu$  may be



obtained. This is a frequently used procedure<sup>2</sup> and checks the validity of  $\nu$  obtained solely from the data used in constructing the linear current-potential relation, observed at low over potentials and reported in Fig. 4.

2. If the value of  $\nu$ , for the freshly prepared cell, is obtained by another procedure discussed by Bockris<sup>2</sup> in which transfer coefficients (reported for the present reaction by the above authors in their paper) and thence the Tafel slopes for the anodic and the corresponding cathodic reaction are utilized,  $\nu$  will attain value other than two. This procedure, however, is valid only if both the anodic and the corresponding cathodic reaction have the same mechanism.

3. Again, if the value of  $\nu$  for the freshly prepared cell is estimated by still another procedure, mentioned by Green<sup>3</sup> through the approximate use of data in Fig. 3 and 4 of the authors,  $\nu$  will have a value somewhere between 8 and 12.

4. Adopting the authors' procedure and data for evaluating  $\nu$  for the "aged" cell, a value of  $\nu$  approximately equal to unity may be obtained. It is probably unlikely that an aging period of three days would change the mechanism of the electrode process.

In conclusion, it is believed that it is purely fortuitous that for the particular data (i.e., for the fresh cell) chosen by the authors coupled with the procedure of evaluating  $\nu$  used by them in which both  $i_0$  and  $(d\eta/di)_{i \rightarrow 0}$  (and thence  $\nu$ ) are obtained from the same primary data (Fig. 4, circles), a value of two for the  $\nu$  is obtained. This, however, is quite meager and ambiguous an evidence for proposing reaction mechanism, especially when some degree of corrosion is probably involved as a competing reaction in the present case. The fundamental premise on which the interpretations of the authors are based is that, at higher current densities, the reaction is activation controlled (Fig. 3 and 5). However, a linear potential-log [current] relationship observed over less than half a decade of current densities (Fig. 3) is hardly a "Tafel line" or an evidence for activation control. In Fig. 3, probably a linear relation exists between current and potential (cf. Fig. 7), giving from the slope, the ohmic resistance of the cell. This would imply that the electrode process is probably diffusion-controlled. This suggestion is somewhat emphasized by the theoretically untenable and anomalously high values of the "Tafel Slopes" as deduced from Fig. 3. Again, a substantial accumulation of reaction products on the electrode, as demonstrated by the authors in the present electrode reaction, would rather strongly support a diffusion-controlled mechanism.<sup>4</sup>

### The Alkaline Manganese Dioxide Electrode, I. The Discharge Process

David Boden, C. J. Venuto, D. Wisler, and R. B. Wylie  
(pp. 415-417, Vol. 114, No. 5)

**S. Ghosh**<sup>5</sup>: In ref. (8) of the above paper the authors refer to one of our papers.<sup>6</sup> About our observations on the initial dilation of gamma MnO<sub>2</sub> during the initial stages of this discharge, the possible explanation for this dilation as observed by us was also quoted in the discussion part of this paper. Further, it is emphasized that "this process continues until the lattice is strained to the point at which it becomes unstable and crystallizes to a more stable phase" has been remarked. I would like to refer to my recent publication from the laboratory of Professor Brenet on this particular point.

<sup>2</sup> J. O'M. Bockris and A. K. S. Huq, *Proc. Roy. Soc.*, 237A, 277 (1956); J. O'M. Bockris, in "Modern Aspects of Electrochemistry," Vol. 1, Edited by J. O'M. Bockris and B. E. Conway, Butterworths, London (1954).

<sup>3</sup> M. Green in "Modern Aspects of Electrochemistry," Vol. 2, p. 397, Edited by J. O'M. Bockris, Butterworths, London (1959).

<sup>4</sup> B. E. Conway, "Theory and Principles of Electrode Processes," Ronald Press, New York (1965).

<sup>5</sup> Indian Standards Institution, Manak Bhavan, 9, Bahadur Shah Zafar Marg, New Delhi 1, India.

<sup>6</sup> J. P. Brenet and S. Ghosh, *Electrochim. Acta*, 7, 449 (1962).

Further I would like to refer to one of my publication<sup>7</sup>, wherein I have tried to explain a generalized approach about the mechanism on depolarization of metallic oxides in a cell system. In this paper, I attempted to propose that the "bound water incorporation in the crystal lattice" has a relation with the activity of the nonstoichiometric metallic oxide. The dilation of the crystal lattice has a definite bearing as the pronotonic acidity coupled with hydration is an important factor in determining the polarizability of the compound. I would like to refer to my thesis for my doctorate of science submitted to the University of Strasbourg in December 1966 under the guidance of Professor Brenet, wherein I compared and established different physicochemical techniques like x-ray defraction, electron defraction, magnetic susceptibility, and by chemical analysis about the water incorporation in the crystal lattice of gamma manganese dioxide and alpha and beta lead dioxide. Below are listed a few publications by Professor Brenet which will clarify further the discharge process as we now think for the manganese dioxide.<sup>8,9</sup>

### D. Boden, C. J. Venuto, D. Wisler, and R. B. Wylie:

The authors would like to express their appreciation to Dr. Ghosh for kindly pointing out this additional information. In our work, no attempt was made to determine either the degree of hydration of the crystal lattice or its effect on the electrochemical or crystallographic behavior of the manganese dioxide. The initial part of the discharge, where the lattice dilation occurs, is of great interest and, undoubtedly, further work should be done to determine the nature of the reactions taking place in this region.

### The Role of Hydrogen Peroxide in Oxygen Reduction at Platinum in H<sub>2</sub>SO<sub>4</sub> Solution

A. Damjanovic, M. A. Genshaw, and J. O'M. Bockris  
(pp. 466-472, Vol. 114, No. 5)

**A. L. Juliard**<sup>10</sup> and **C. C. Liang**<sup>11</sup>: We have read with deepest interest this excellent paper showing by the rotating disk-ring method that hydrogen peroxide is not formed as an intermediate in the reduction of oxygen at the platinum electrode in pure sulfuric acid aqueous solution.

However, we are suprised that the authors did not mention in this well documented paper that Liang and Juliard<sup>12</sup> came to the same conclusion using a cyclic-voltammetric method two years earlier.

There is no doubt that the eventual presence of hydrogen peroxide as intermediate can be more sensitively determined by the rotating disk-ring method, than by cyclic-voltammetry. Nevertheless, with the Liang-Juliard technique hydrogen peroxide could be detected if this compound covered more than 1% of the surface of the electrode. Since this was not the case, these authors concluded that the formation of hydrogen peroxide could not be held responsible for the overpotential of reduction of oxygen at platinum in sulfuric acid solutions.

### A. Damjanovic, M. A. Genshaw, and J. O'M. Bockris:

We regret that we did not cite the work of Liang and Juliard in our paper involving the detection of H<sub>2</sub>O<sub>2</sub>. At the time of writing the paper, we did not consider that the potentiodynamic method would have the sensitivity attributed to it.

<sup>7</sup> S. Ghosh, *Electrochem. Soc. Japan*, 34, 38 (1966).

<sup>8</sup> J. Brenet, Fifth Symposium on Sources of Energy, Brighton 1966.

<sup>9</sup> L. Balewski and J. Brenet, Presented at Philadelphia Meeting of the Society, October 9-14, 1966, Abstract No. 38.

<sup>10</sup> Green Acres, Bryn Mawr, Pennsylvania.

<sup>11</sup> P. R. Mallory & Co., Inc., Burlington, Massachusetts.

<sup>12</sup> A. L. Juliard and C. C. Liang, *Nature*, 207, 629 (1965); *J. Electroanal. Chem.*, 9, 390 (1965).

## Potential of Aluminum in Aqueous Chloride Solutions

T. Hagyard and W. B. Earl (pp. 694-698, Vol. 114, No. 7)

**A. K. Vijh and R. S. Alwitt**<sup>13</sup>: We believe that certain aspects of the above paper need further discussion as some of the conclusions reached by the authors are at variance with our recent work<sup>14</sup> and some previous data.<sup>15, 16</sup> The important points are developed below.

1. These authors have obtained the Tafel plot for the hydrogen evolution reaction (her) (Fig. 6 in the above mentioned paper) by choosing the electrode potential reached at a given current density in a galvanostatic charging curve after 1- $\mu$ sec. This procedure of obtaining a steady-state potential-log (rate) relationship (i.e., the Tafel plot) from a nonsteady-state transient (i.e., the charging curve) at a fixed time is not sound theoretically.<sup>17</sup> However, when initial discharge step is the rate-determining stage with a consequently negligible consumption of charge in the pseudo-Faradaic process, this procedure should give results comparable to those obtained under steady state, especially at higher current densities. However, appreciable discrepancies do arise between our results (obtained by conventional steady-state procedure) (Fig. 1) and those of the present authors for the transfer coefficients,  $\alpha$ , Tafel slopes,  $b$ , constant  $a$  of the Tafel equation and the potential regions for the her in general (Table I). In case of the results shown in Fig. 1, presence of spontaneous surface oxide is thermodynamically impossible.<sup>18</sup> Furthermore, if spon-

Table I.

Parameter	Hagyard and Earl	Vijh <sup>1</sup>
Tafel slope, $b$	$2.3 \times 5 RT/F$	$2.3 \times 2 RT/F$
$\alpha$	0.21	0.51
$a$	-2.21v	-1.012v
Potential region for her	More cathodic than ca.-1.3v	Less cathodic than ca.-1.0v

<sup>1</sup> Our results were obtained over pH range 0.1-4.4 (Fig. 1) and were calculated for pH 3.2 for the pH-dependent quantity,  $a$ , in this table;  $a$  is the constant in the empirical form of the Tafel equation  $\eta = a - b \log i$ .

taneous surface oxide were involved, the discrepancies between the results in Fig. 1 and those of the present authors would be expected in the direction opposite to the one observed<sup>17</sup> e.g., a higher Tafel slope in the presence of oxide. This is because of the kinetic participation of surface oxides in the activation controlled charge transfer event on the electrode, cathode in the present argument.

2. In Fig. 5d of these authors, a cathodic charging curve obtained at very high current density ( $> 7 \times 10^{-1}$  amp  $\cdot$  cm<sup>-2</sup>) is shown to contain some "blips" which have been interpreted as "molecular hydrogen formation of an explosive or chain type." The "blips" probably are vigorous bubble formation and are a usual problem in transients involving high-current densities. Perhaps the authors could explain what they mean by the "explosive" formation of molecular hydrogen.

3. It is stated that the oxide films are formed in aqueous solution, after the first millisecond, due to contamination by dissolved oxygen or impurities. However, a look a Pourbaix's Atlas<sup>18</sup> shows that the presence of oxide on aluminum in the pH range 5-8, approximately, arises due to a spontaneous process since oxide-covered aluminum is the configuration of minimum free energy and hence maximum stability. At the pH used by the authors (pH 3.2), no spontaneous oxide formation should occur, and hence the attempt of the authors to "outrun" the spontaneous, fast, formation of oxide is quite irrelevant. Also, presence or absence of dissolved contaminants is quite secondary as far as spontaneous oxide formation is concerned, and, is not the origin of oxide on aluminum, as these authors seem to assume.

4. It is claimed that no previous data exist either on the her or anodic dissolution on oxide-free aluminum. The authors are apparently unaware of the studies on the her by Pecherskaya and Stender<sup>14</sup> in 2N H<sub>2</sub>SO<sub>4</sub> and by Hickling and Salt in 1N HCl.<sup>15</sup> In these two solutions, existence of spontaneous oxide is thermodynamically impossible (see Pourbaix's Atlas).

5. These authors did not use a Luggin probe between the working and the reference electrode. At higher current densities (ca.  $> 1 \times 10^{-2}$  amp  $\cdot$  cm<sup>-2</sup>) this would tend to introduce significant IR drop, thus introducing unknown errors in the potential values quoted. Also, since anode and cathode have not been separated in the experimental arrangement of these authors, reaction products from the counter electrode would act as depolarizers on the working electrode resulting, again, in unreliable potential values. This criticism is particularly serious in any studies on the her.

6. An important parameter of electrode kinetics, namely, potential of zero charge, has been used in an entirely incorrect sense. It is concluded, by these authors, that the aluminum electrode when dipped in an aqueous solution on open circuit would achieve an initial potential approximately identical with the potential of zero charge for aluminum in that solution (unknown). This misleading statement may be rectified by consulting any of the standard reviews on electrode kinetics.<sup>17</sup>

- <sup>13</sup> Sprague Electric Co., North Adams, Massachusetts.  
<sup>14</sup> A. K. Vijh, *J. Phys. Chem.*, 72, 1148 (1968).  
<sup>15</sup> A. G. Pecherskaya and V. V. Stender, *Russ. J. App. Chem.*, 19, 1302 (1946).  
<sup>16</sup> A. Hickling and F. W. Salt, *Trans. Faraday Soc.*, 36, 1126 (1940).  
<sup>17</sup> B. E. Conway, "Theory and Principles of Electrode Processes," Ronald Press, New York (1965); see also "Progress in Reaction Kinetics," Vol. IV, G. Porter, Editor, Pergamon Press, New York (1966).  
<sup>18</sup> J. O'M. Bockris, "Modern Aspects of Electrochemistry," Vol. I, J. O'M. Bockris and B. E. Conway, Editors, Butterworths, London (1954).  
<sup>19</sup> P. Delahay, "Double Layer and Electrode Kinetics," Interscience, New York, 1965.  
<sup>20</sup> A. K. Vijh and B. E. Conway, *Chem. Revs.*, 67, 623 (1967).  
<sup>21</sup> M. Pourbaix, "Atlas D'Equilibres Electrochimiques," p. 168, Gauthier-Villars and Co., Paris (1963).

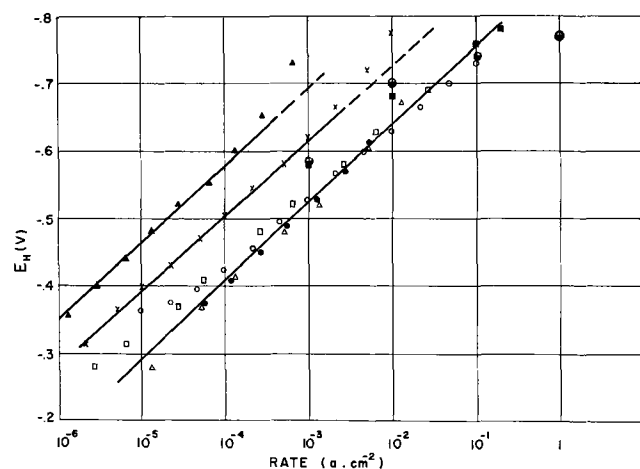


Fig. 1. Tafel plots for her on oxide-free aluminum in the following acidic solutions (ref. 14): ● 0.2N H<sub>2</sub>SO<sub>4</sub> (pH = 0.94); ○ 0.5N H<sub>2</sub>SO<sub>4</sub> (pH = 0.59); △ 0.86N H<sub>2</sub>SO<sub>4</sub> (pH = 0.37); □ 1.7N H<sub>2</sub>SO<sub>4</sub> (pH = 0.1); × 1N CH<sub>3</sub>COOH (pH = 2.4); ▲ 2N CH<sub>3</sub>COOH + 1N NH<sub>4</sub>COOCH<sub>3</sub> (pH = 4.4); and ■ 2N H<sub>2</sub>SO<sub>4</sub> (pH = 0.04), ref. (15); ● 1N HCl (pH = 0.1), ref. (16).

## Notes:

- (1) Tafel relationships are apparently independent of pH in the range 0.1-0.94. However, scatter in the points makes it difficult to draw any definite conclusions.
- (2) Results in Refs. (15) and (16) are unreliable due to impurities in the solutions etc. (see Ref. 14)

**T. Hagyard and W. B. Earl:** Contrary to the assertion of Vijn and Alwitt, the measurements of potential recorded in our Fig. 6 were not transients but as can be seen from our Fig. 5a the potential reached equilibrium in less than 1 msec. and has been observed to remain substantially unchanged over many seconds. This is clearly stated in our third paragraph and on p. 696 second column.

We cannot be expected to accept the criticism that our results do not agree with their unpublished results without having the opportunity of judging the reliability of their technique. It seems pertinent, however, that the results from the two papers which they quote in their Fig. 1, of which we were well aware, were considered by Bockris [our ref. (5)] and by us to be unreliable because of surface contamination. It is probably not a coincidence that these Tafel lines shown in Fig. 1 as purporting to be for hydrogen discharge on aluminum are almost coincident with the Tafel lines produced by the same authors for hydrogen discharge on iron. Iron is a very common impurity and a negligible amount (about  $10^{-9}$  moles/cm<sup>2</sup>) would suffice for a monolayer on the aluminum surface. The quoted authors did not even pre-electrolyze their solutions.

For conventional over voltage measurements even pre-electrolysis can be effective only if the auxiliary cathode is brought for a long period to a potential at least as negative as that to be reached by the test electrode and then only if the rate of deposition of impurities is greater than their rate of introduction from the anode and all parts. It is our contention that these conditions cannot be met for a reactive metal like aluminum which has a reversible potential around -1.7v. We consider that measurements of hydrogen over voltage on such metals must be carried out in times that are short compared with the time constant for the arrival of a monolayer of impurity atoms from the bulk of the solution. For our experiments A.R KCl was used with Fe = 0.002% max. and the time required for the transport to the electrode surface by molecular diffusion of sufficient ferrous iron to form a monolayer of iron would be 7 sec. if the maximum iron impurity were actually present. Our measurements were made in milliseconds and were thus free from any conceivable effect of impurities in solution. This is one of the main advantages of our method.

If the plots in their Fig. 1 represented a bare aluminum surface then at e.g., -0.5v anodic dissolution of the aluminum would be rapid and add its quota to the cathodic current. From our Fig. 4 a current of 1 a/cm<sup>2</sup> would be contributed from this source and  $10^{-5}$  a/cm<sup>2</sup> (their Fig. 1) from the external current which was presumably what they measured. Obviously the situation was much more complex than they assumed but it can be explained by our more recent work, yet to be published, without contravening the results in our present paper.

The criticism that the Pourbaix diagram for aluminum proves that aluminum oxide cannot exist on the metal at pH 3.2 is invalid and is due to a lack of understanding of the use of such diagrams. The diagram only shows that at equilibrium e.g., at pH 2 and unit aluminum ion concentration, the oxide, if formed, would dissolve to form a solution of the salt. Oxide formation from the metal is accompanied by a very great decrease in free energy and if it occurs faster than dissolution of the oxide in the acid, then oxide will remain on the surface. We have evidence, to be published in due course, that bare aluminum does in fact react chemically with our solutions at pH 3.2 in some 200  $\mu$ s producing an oxide layer of undetermined nature. Slow dissolution of aluminum oxide film in aluminum chloride solutions with the formation of presumably basic salts has been studied by one of us [J. Appl. Chem., 9, 323 (1959)]. The dissolution equilibrium depends on concentration and pH and our use

of pH 3.2 for most of our work was specifically to minimize oxide dissolution and basic salt formation under expected conditions close to the electrode surface.

Their suggestion (2) that the "blips" to which we referred were due to hydrogen bubble formation is hardly consistent with the fact that each "blip" corresponded with the passage of current approximately equal to one atomic layer of hydrogen. Although the point seems to us to be a minor one, we see no reason to retract "explosive" as applied to a surface process taking place, as can be seen dimly in our figure, in about 100  $\mu$ s and possibly involving most of the surface atoms in that time interval.

### A Generalized Expression for the Tafel Slope and the Kinetics of Oxygen Reduction on Noble Metal and Alloys

D. S. Gnanamuthu and J. V. Petrocelli (pp. 1036-1041, Vol. 114, No. 10)

**U. R. Evans**<sup>19</sup>: The new measurements provide welcome positive results, and two negative conclusions are also valuable, since they serve to clear the ground of encumbrances. These are (a) it is not possible to determine reaction mechanisms by means of  $b_c$  and  $i_0$  and (b) there is no apparent relationship of the number of holes in the d-band with the activity in NaOH or with  $b_c$  in H<sub>2</sub>SO<sub>4</sub> and NaOH.

Probably self-polarization, leading to a mixed potential, as envisaged by Hoar<sup>20</sup>, accounts for the failure to realize the reversible potential in absence of external current. But the main cause of the departure from rectilinear relationship between  $\eta$  and  $\log i$  is probably the fact that the cathodic reaction proceeds only on a few small favorable points. The approach resistance to a circular area of radius  $\tau_1$  slightly exceeds

$$\int_{\tau_1}^{\infty} \frac{\omega dr}{2\pi r^2} \quad \text{or} \quad \frac{\omega}{2\pi\tau_1}$$

where  $\omega$  is the specific resistance. If  $\tau_1$  is of atomic dimensions, this may easily exceed any other contribution to polarization and we may expect  $\eta$  to show a rectilinear relation with  $i$ , instead of with  $\log i$ . Such a rectilinear relation has been found for the cathodic reduction of oxygen on iron<sup>21</sup>; also in fuel-cell studies<sup>22</sup>, a long straight limb is often found on plotting  $i$  against  $\eta$ .

Some evidence that the cathodic reaction does occur mainly on isolated spots was provided by early corrosion studies of iron<sup>23</sup>, based on the ferroxyl indicator, although less clear-cut than the evidence that the anodic reaction starts locally and then spreads out. More instructive is the demonstration<sup>24</sup> that, on partly immersed specimens, much of the cathodic reaction occurs on the barely damp zone above the waterline; this entails a large ohmic resistance and would be unthinkable if the whole of the meniscus-zone area was available for the cathodic reduction of oxygen.

The restriction of cathodic reduction to favored spots is a feature of the pseudosplitting mechanism<sup>25</sup>, which explains the established facts better than any of the sixteen rival mechanisms conveniently arranged in Table I. The difficulty of understanding the reduction of O<sub>2</sub> to 2OH<sup>-</sup> (or to H<sub>2</sub>O) has always been that at some stage a splitting of the O<sub>2</sub> molecule would seem to be needed. In the gas-phase this splitting is a rare occurrence, except at high-temperatures, since

<sup>19</sup> 19 Manor Court, Grange Road, Cambridge, England.

<sup>20</sup> T. P. Hoar, Proc. Roy. Soc., (A) 142, 628 (1933).

<sup>21</sup> U. R. Evans and T. P. Hoar, Proc. Roy. Soc., (A) 137, 345 (1932) (see Fig. 14, p. 363).

<sup>22</sup> G. W. Walkden, Batteries, 2, 265 (1964).

<sup>23</sup> U. R. Evans, Metal Industry, London, 29, 481 (1926) and subsequent work unpublished.

<sup>24</sup> P. Hersch, Nature, 180, 1407 (1951).

<sup>25</sup> U. R. Evans, "Corrosion and Oxidation of Metals," Arnold (1960). Supplementary Volume, now in press, Part II, Section XIV, Theory II.

Table I. Stages in Pseudosplitting

ADSORBED OXYGEN MOLECULE

1 H O H O H O O O H O H O

METAL OR OXIDE

2 H O H O H O O O H O H O H O

3 H O O H O H O O O H O H O H O

4 H O O H O H O H O H O H O O H O

5 H O H O H O H O H O H O H O H O

ATOMIC LEDGE

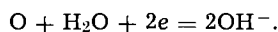
HIGH ← LOW

← KINK

$O + H_2O + 2e = 2OH^-$

it demands 117 kcal. On certain oxide surfaces, the energy demand is much lower: only 23.5 kcal is needed on a  $Cu_2O$  surface, where the affinity between  $Cu_2O$  and the one O atom (giving 2 CuO) allows the other O atom to become free and mobile<sup>26</sup>; this makes splitting an important occurrence at about 200°C, but that mechanism can hardly be in operation in the ordinary corrosion cell. In contrast pseudosplitting can lead to well separated O atoms without any relative movement of the two atoms of the original  $O_2$  molecule. It involves no *ad hoc* assumption, but only the well-recognized fact that hydrogen switching is an easy reaction, being often invoked to explain why the apparent mobility of  $OH^-$  and  $H_3O^+$  ions (which can switch H with a neighboring  $H_2O$  molecule as a Grotthus reaction), is greater than the true mobility of ions which must really thread their way through the crowd; also it explains why acid and alkali, mixed together, immediately neutralize one another.

If an oxygen molecule attaches itself to a surface carrying a carpet of OH groups, (Table I, Stage 1), the switch of hydrogen allows the production of uncovered O atoms at sites which travel about at random (Stages 2, 3, and 4), until at last (Stage 5) a position is reached (perhaps a kink-site where the neighboring OH groups are on the wrong level) less favorable to acquisition of H from a neighboring OH than from a water molecule in the liquid; this requires two electrons and constitutes the essential cathodic reaction



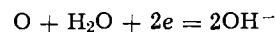
Such a mechanism not only shows why a straight line is obtained on plotting  $E$  against  $i$ , not against  $\log i$ , but also explains the fact that in some cases the current produced is more nearly proportional to  $\sqrt{p}$  than to  $p$  (the oxygen-pressure). For the wandering uncovered O-sites will sometimes meet, producing uncovered pairs which could be in equilibrium with the  $O_2$  of the gas-phase. Early measurements<sup>27</sup> of the corrosion of iron specimens partly immersed in salt solutions showed the corrosion-rate in oxygen to vary between 2.39 and 2.65 times that in air;  $\sqrt{5}$  is 2.23.

The mechanism also explains why efficient fuel cells generally use as electrolyte concentrated alkali or concentrated acid (where an analogous wandering is possible). It is not easy to obtain efficiency with a near-neutral liquid where the necessary chains of OH or  $H_3O$  will rarely occur. Some authorities believe that the failure of fuel cells containing near-neutral liquid is due to rapid changes of pH when current passes;

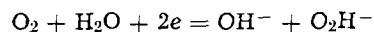
<sup>26</sup> W. E. Garner, T. J. Gray, and F. S. Stone, *Disc. Faraday Soc.*, **8**, 246 (1950).

<sup>27</sup> U. R. Evans, *J. Chem. Soc.*, 1929, 111.

no doubt that can be a serious cause of polarization, but experiments made with buffer solutions<sup>28</sup> would seem to have been only partly successful. A possible objection to the use of a near-neutral electrolyte is that pseudosplitting will be a rare occurrence, so that instead of



we may often get



where  $O_2H^-$  is the anion of hydrogen peroxide. Now hydrogen peroxide is often detected in the corrosion of zinc and aluminum; the fact that on metals of variable valency it is not detected may be due to its speedy catalytic decomposition on corrosion products. It is also often reported in fuel-cell reactions, but, if formed, is a sign of inefficiency, since the Pourbaix diagram<sup>29</sup> shows that the presence of appreciable  $H_2O_2$  concentration involves a drop in the emf to little more than half the theoretical value. A fuel cell which does not contain corrosive acid or unpleasant alkali would be welcome; but it will call for a mechanism to repress or replace the pseudosplitting mentioned above.

**D. S. Gnanamuthu and J. V. Petrocelli:** We welcome Dr. Evans' discussion and find his proposed mechanism very interesting. Such a mechanism certainly could account for more favorable energetics and deserves serious consideration.

#### Silver Oxide Electrode Processes

T. P. Dirkse, D. DeWit, and R. Shoemaker (pp. 1196-1200, Vol. 114, No. 12)

**J. J. Lander<sup>30</sup>:** The possibility of ion pair formation in concentrated solutions of KOH was suggested based on the following treatment<sup>31</sup> of the data for viscosity<sup>32</sup> and for conductivity<sup>33</sup> of KOH solutions at 25°C in the range 0.6 to 13.4 molar. If it is assumed that conductivity will be a direct function of the concentration and an inverse function of the viscosity and that no other factors are involved, then one may calculate the function  $\eta \lambda / C$  from the measured data to determine its constancy. The accompanying Table I shows the data. The function  $\eta \lambda / C$  is shown to be constant within an average  $\pm 1\%$  over the range 0.6 to 4.0M. Then, as concentration increases, the value of the function decreases, passes through a minimum at about 10M, and rises to the original value at 13.4M. This is interpreted to mean that extent of association is constant in the range 0.6 to 4.0M and that only ionic velocities are changing due to the viscosity increase. The decrease in the value of  $\eta \lambda / C$  above 4.0M could then be due to a greater extent of association (ion

<sup>28</sup> M. Beltzer, *Nature*, **213**, 64 (1967); *This Journal*, **114**, 1200 (1967).

<sup>29</sup> M. Pourbaix, "Atlas of Electrochemical Equilibria in Aqueous Solutions," p. 108, Pergamon Press, Fig. 1.

<sup>30</sup> Delco-Remy Division of General Motors Corp., Anderson, Indiana.

<sup>31</sup> AFAPL-TR-67-107, First Annual Technical Report on Contract Nr. AF 33 (615)-3487, August 31, 1967, p. 30-31.

<sup>32</sup> Hitchcock and McIlhenny, *Ind. and Eng. Chem.*, **27**, 466.

<sup>33</sup> L. S. Darken and H. F. Mier, *J. Am. Chem. Soc.*, **64**, 621 (1942); M. A. Klochko and M. M. Godneva, *J. Inorg. Chem. (USSR)*, **4** (9), 2127 (1959).

Table I. The function  $\eta \lambda / C$  for KOH solutions at 25°C

Concentration moles per liter	$\eta$ Centipoise	$\lambda$ (ohm-cm) <sup>-1</sup>	$\eta \lambda / C$
0.6	0.91	0.130	0.198
0.8	0.93	0.170	0.197
1.0	1.00	0.200	0.200
1.5	1.03	0.295	0.204
2.0	1.10	0.360	0.198
4.0	1.40	0.575	0.201
6.0	1.83	0.640	0.195
8.0	2.42	0.620	0.187
9.0	2.82	0.583	0.182
10.0	3.30	0.541	0.178
11.0	4.00	0.505	0.184
12.0	4.83	0.460	0.184
13.0	6.20	0.405	0.193
13.4	7.00	0.387	0.202

pairing) or decreased ionic velocities due to some cause over and above viscosity, or both. The reason for the minimum and the return to the original value at 13.4M is not clear.

**The Effect of Anodic Films on the Gaseous Oxidation of Tantalum, II. Films Formed in Phosphoric Acid Solutions**

R. E. Pawel (pp. 1222, Vol. 114, No. 12)

**D. A. Vermilyea**<sup>34</sup>: The magnitude of oxygen transport observed in these studies, along with the activation

<sup>34</sup> Research and Development Center, General Electric Co., Schenectady, New York.

energies deduced, allow an estimate of the concentration of defects in anodic films on tantalum. For example, for the 1000Å film formed in Na<sub>2</sub>SO<sub>4</sub> the oxygen flux at 500°C was about  $6 \times 10^{-11}$  gram atoms cm<sup>-2</sup> sec<sup>-1</sup>. The diffusion coefficient should not be much larger than the value obtained from  $D = 10^{-1} \exp(-43000/RT)$ , or about  $10^{-13}$  cm<sup>2</sup> sec<sup>-1</sup>. From the steady state diffusion law the concentration difference across the film is found to be  $6 \cdot 10^{-3}$  moles cm<sup>-3</sup>. Since Ta<sub>2</sub>O<sub>5</sub> itself is present at only  $1.8 \cdot 10^{-2}$  mole cm<sup>-3</sup> the defect concentration is evidently extremely high.

# Anodization of Vanadium in Acetic Acid Solutions

R. G. Keil<sup>1</sup> and R. E. Salomon

Chemistry Department, Temple University of the Commonwealth System of Higher Education,  
Philadelphia, Pennsylvania

## ABSTRACT

Uniform anodic vanadium tetroxide films of controlled thickness have been grown on vanadium in acetic acid-sodium tetraborate solutions containing small quantities of water. The film composition was established using Faraday's law and EPR and ATR spectroscopy. The anode reaction was found to be 100% efficient in the production of vanadium(IV) oxide. The lack of oxygen evolution was attributed to reduced water activity as a result of its interactions with the acetic acid. Information concerning the nature of the film was obtained.

The growth of anodic oxide films on several metals in nonaqueous media has been studied (1,2). The primary reasons for using nonaqueous anodizing solutions are to reduce the fraction of the anodic oxidation product dissolving during film growth (3) and to increase the current efficiency of the film formation process. In some instances, where the oxidation product is readily soluble in an aqueous environment, the use of a nonaqueous media may be the only way to grow an anodic film on that metal in solution (1, 4).

In 1957, Johansen, Adams, and Van Rysselberghe (5) studied the growth of anodic oxide films on a host of metals, including vanadium, in an aqueous boric acid-ammonia solution, pH 8. The study covered only potentials below the oxygen evolution potential using apparent current densities of 0 to 100  $\mu\text{a}/\text{cm}^2$ . For vanadium, a curve characteristic of that obtained for a material in which film growth occurred was not obtained. The authors concluded that for vanadium either an extremely porous film is produced or the oxidation product is rapidly undergoing dissolution. Little else is known about the anodic behavior of vanadium. With aqueous solutions the film tends to go into solution as vanadyl ions when anodization is attempted. Young (6) suggests that anodic films on vanadium might be grown in partly nonaqueous solutions. If an anodic film could be grown on vanadium, determination of the current efficiency of the anode reaction and the effect of repeated film growth upon the metallic substrate surface could be determined owing to the solubility of the vanadium oxides in water (7).

## Experimental

High-purity (99.94%), single-pass zone refined vanadium in both rod ( $\frac{3}{8}$  in. diameter) and foil (0.005 in.) form was purchased from the Materials Research Corporation. According to the supplier, the impurity content was in parts per million: O(200), N(50), H(3), C(150), Fe(50), Ni(10), Mg(5), Si(50), Mn(5), and Mo(50). Glass tubes were sealed to the vanadium metal with epoxy cement. Electrical connection to the external circuit via platinum wire was effected using mercury contacts. Picien wax (mp 80°C) was used as a "stopping off" compound. The molten wax was applied over a 100v anodic film and allowed to solidify gradually. The wax was subsequently removed from the surface of interest by rubbing that surface with a Kimwipe, saturated with toluene.

Prior to film growth the vanadium electrode was abraded, utilizing, first 2/0, then 3/0 and finally 4/0 emery paper. The abrasion was done on a Buehler Ltd. Metallurgical Polishing Wheel. The sample was then etched sparingly (15-30 sec) in a 1:1 water-nitric acid (70% assay) solution. Electrodes etched for long periods, greater than 3 min, showed visual evidence of grain boundary formation. An electrode

with grain boundaries was reabraded. Immediately prior to anodization the electrode was washed, first with absolute alcohol, then with anhydrous acetic acid, and finally with a portion of the anodizing solution. The electrode surface was not allowed to come into direct contact with the atmosphere after the etch step had been completed. Anodic brightening (18-20) of the vanadium metal surface occurred when anodization was attempted in a 95% ethanol-borax solution.

*Apparatus.*—The solvents, glacial acetic acid, ethanol, and glycerol, each containing either borax, sodium acetate, or lithium nitrate were tried as anodizing solutions to determine if they would support the growth of an anodic film on vanadium. Only electrolyte solutions of acetic acid, containing water, supported the growth of an anodic film. Anodic polarization of vanadium in solutions composed of other solvents resulted in dissolution of tetravalent vanadium. An anodizing solution in which a small fraction of the anodic oxidation product underwent dissolution during film growth and in which nonhomogeneous field effects (due to the low conductivity of the solution) were absent was desired. These requirements were met when an acetic acid solution 2.0M in water and 0.020M in  $\text{Na}_2\text{B}_4\text{O}_7$  was used. The conductivity of this solution was 79 micro-(ohm-cm)<sup>-1</sup>. In order that the conductivity of the hygroscopic acetic acid solution would not change significantly during the course of film growth, an anodization cell was constructed which would effectively isolate the anodizing solution from the atmosphere (Fig. 1). For at least 5 min prior to and during film growth the anodizing solution in the cell was purged with nitrogen through a glass frit at a rate sufficient to produce stirring action. The nitrogen was bubbled through traps containing about 100 ml of the anodizing solution prior to and on leaving the anodization cell. The cell was kept in a constant temperature bath. Liquid platinum paint obtained from Englehard Industries, Inc., Liquid Gold Division, was used to make the working cathode and the reference electrodes, as well as the electrical connection for both to the external circuit.

A constant formation current was maintained through the changing resistive load by using a current limiting resistor, together with a gas tube in series with a Keithley Model 241 calibrated high voltage power supply. The current through the circuit was calculated after measuring the potential across a standard resistance with a Leeds and Northrup potentiometer. The potential of the anode with respect to the platinum reference was measured with a Keithley Model 621R electrometer, the output of which was fed into a recorder. Constant current film growth was studied as a function of the apparent current density (100-1014  $\mu\text{a}/\text{cm}^2$ ), electrode separation and temperature (20°-45°C). A Sorensen Nobatron Model 300B power supply was used as a source of voltage for constant voltage film growth. For constant voltage film

<sup>1</sup> Present address: E. I. du Pont de Nemours and Company Inc., Jackson Laboratory, Deepwater, New Jersey 08023.

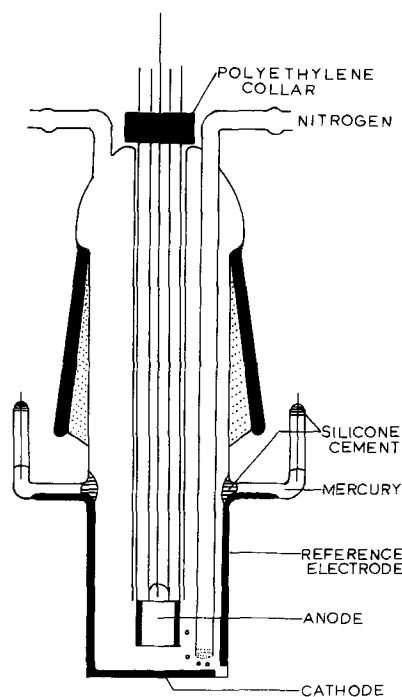


Fig. 1. Anodization cell

growth, a small separation (1 mm) was maintained between the vanadium anode and the platinum cathode in order to minimize the solution voltage drop. Films were grown to various formation voltages and then dissolved and analyzed for total vanadium.

**Analytical.**—The amount of vanadium present in a sample was determined using the colorimetric method of Talvite (8) in a slightly modified form. The method involved complexing pentavalent vanadium with 8-hydroxyquinoline in a chloroform medium. The following modifications were incorporated: (a) the film was quantitatively dissolved by immersing the electrode for 200 sec in distilled water (pH 6.6), (b) the vanadium present was oxidized to the pentavalent state with potassium peroxydisulfate, and (c) acetate ion in the sample was destroyed. A 200 sec immersion time was found experimentally to be sufficient to remove completely even the thickest film and make

negligible any contribution due to further oxidation and dissolution of the electrode. Vanadium was not detected after immersing a freshly prepared vanadium electrode in distilled water for 200 sec. The vanadium (IV) ion was oxidized to the pentavalent state with a 1% potassium peroxydisulfate solution. The excess  $S_2O_8^{2-}$  was destroyed by boiling the solution. Acetate ion interfered with the analysis in that it hindered rapid development of the vanadium-8-hydroxyquinoline complex. Therefore, the acetate was destroyed prior to complexing by evaporating a nitric acid solution of the vanadium ion to dryness. Pentavalent vanadium ion was quantitatively extracted from the aqueous phthalate buffered (pH 4.0) solution by complexing it with a 0.5% 8-hydroxyquinoline in a chloroform solution that was free of alcohol. The per cent transmittance was measured at 5500Å in a Beckman DU spectrophotometer. The solution followed Beer's law between 1 and 50  $\mu\text{g}$  of vanadium per milliliter of chloroform solution. The extinction coefficient was  $6.96 \times 10^4 \text{ cm}^3/\mu\text{g}$ .

**Identification of the anodic film.**—A study was made to determine the composition of the anodic film. Since the electrolysis was performed in acetic acid, the possibility existed that the film was vanadyl acetate. X-ray diffraction patterns were obtained to (a) determine whether the film was crystalline, and (b) identify the anodic oxidation product. The diffraction patterns were obtained using a Debye-Hull-Scherrer diffraction camera and a General Electric Model X-RD-6 x-ray diffraction apparatus. Copper  $K\alpha$  radiation was used. The plate voltage on the copper target was 40 kv. The plate current was 20 ma. Copper  $K\beta$  radiation was effectively removed by passing the diffracted radiation through a strip of nickel foil. Samples were usually rotated for periods of 1½ hr while exposed to radiation. Determination of the crystal structure of the anodic film was attempted three ways: (a) scraping a portion of the anodic film and running it in a quartz capillary, (b) *in situ* diffraction of an anodic film on a thin piece of vanadium wire, and (c) *in situ* diffraction of an anodic film on vanadium foil. During sample preparation and irradiation an inert ambient was maintained around the sample by purging a polyethylene bag around the camera with helium. The diffraction results are shown in Table I. Most of the lines were due to the vanadium metal substrate. However, seven very weak lines were obtained for higher formation voltage films which did not match any of the vanadium oxide or oxyhydroxide com-

Table I. X-ray diffraction results for anodic films on vanadium

Sample	Scrappings from anodic film	Anodic film on vanadium wire	Anodic film on vanadium wire	Anodic film on vanadium foil (wedge)	Vanadium metal lines	Unassigned lines
Formation voltage	10	50	100	50		
Exposure time (hr)	1.5	2.1 8.56 (s, broad)	6.3 8.63 (s, broad)	3.5 6.87 (vw) 4.76 (vw) 3.90 (vw) 3.13 (vw) 2.12 (vw)	8.84 (s, broad)	4.76
Diffraction lines obtained		2.12 (m)	2.12 (m)	1.78 (vw) 1.66 (vw) 1.51 (m) 1.23 (s) 1.15 (vw) 1.07 (w) 0.954 (m) 0.871 (w) 0.807 (m)	1.50 (m) 1.23 (s)	3.90 3.13 1.78 1.66 1.36 1.15
				0.954 (s) 0.870 (s) 0.807 (s)	0.954 (m) 0.872 (m) 0.808 (s)	

(s) strong; (m) medium; (w) weak; (vw) very weak.

pounds reported in the literature (9-11). The observed structure is attributed to regions of the film which are in a pseudo-ordered state. The line intensity indicates the structure is short range.

Attenuated Total Reflectance (ATR) spectra of the anodic films were obtained with a Perkin-Elmer Model 337 double beam, recording spectrophotometer in the spectral region 4000 to 400  $\text{cm}^{-1}$ . It was equipped with a Model 12 double beam internal reflection attachment supplied by Wilks Scientific Corporation, South Norwalk, Connecticut. The films were grown to formation voltages between 1 and 75v. On completion of film growth, the film was removed from the anodizing solution in a nitrogen atmosphere, thoroughly wiped with a Kimwipe, and dried in a stream of warm nitrogen. The spectrum was then run using standard procedures (12) on a ThBr-ThI plate (refractive index = 2.5). The complete infrared spectrum of a 50v film between 4000 and 400  $\text{cm}^{-1}$  is shown in Fig. 2. Newly grown anodic films were found to dissolve readily in distilled water. However, if the film was stored for a few days in a nitrogen atmosphere and then immersed in distilled water, it dissolved very slowly. The ATR spectrum of an aged film was found to be featureless (Fig. 3) in the spectral region 4000 to 400  $\text{cm}^{-1}$  with the exception of two bands at 1015 and 975  $\text{cm}^{-1}$ . Comparison of an ATR spectrum of the anodizing solution (Fig. 4) with those of freshly prepared and aged films shows that the structure in Fig. 2, except for the bands at 1015 and 975  $\text{cm}^{-1}$  is due to components of the anodizing solution, principally acetic acid monomer (13) and dimer (14-16), incorporated into the freshly prepared film. For band identification purposes the infrared transmission spectra of the vanadium oxides, obtained from Alpha Inorganics Co., was further substantiated from x-ray diffraction data. Comparison of the spectra shows a good match be-

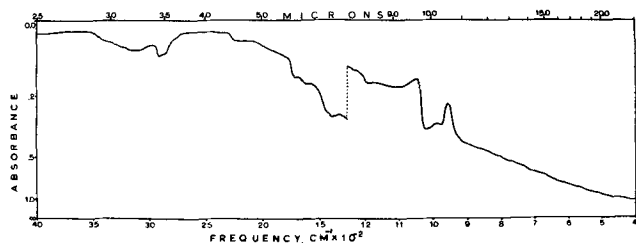


Fig. 2. ATR spectrum of a 50v anodic film between 4000 and 400  $\text{cm}^{-1}$ .

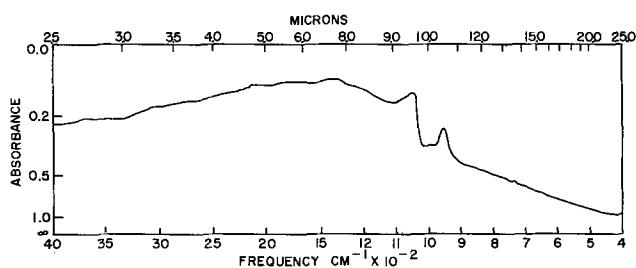


Fig. 3. ATR spectrum of an aged 50v film between 4000 and 400  $\text{cm}^{-1}$ .

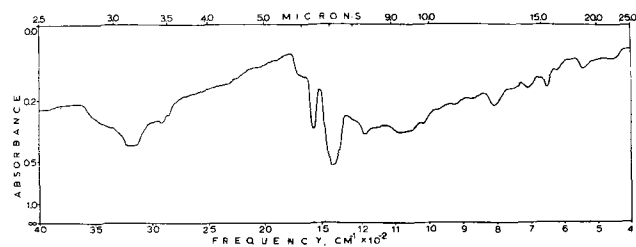


Fig. 4. ATR spectrum of the anodizing solution between 4000 and 400  $\text{cm}^{-1}$ .

tween the ATR spectra of the anodic film and the pellet spectra of  $\text{V}_2\text{O}_4$ . An interesting region in the anodic film spectra occurs at frequencies below 975  $\text{cm}^{-1}$  where the continued increase in absorbance of light with wavelength is probably due to absorption by the vanadium metal (12, 17) substrate. A linear increase in film penetration with wavelength is expected.

Electron Paramagnetic Resonance (EPR) spectra of dissolved anodic films contained the well-known signal of the vanadyl ion. A Varian dual-channel paramagnetic resonance spectrophotometer Model 4500 with a  $\text{TE}_{104}$  mode dual cavity was used for the 9.5 kilomegacycles/sec resonance absorption measurements. The magnetic field was controlled by a Fieldial regulator V-FR-2100. 1,1-Diphenylpicrylhydrazyl (DPPH) was used as a standard for "g" measurements as well as an internal standard for determining the concentration of paramagnetic species in a given sample. EPR spectra were obtained for anodic films which were dissolved into an aqueous 0.1M sulfate-bisulfate buffer solution, pH 1.9. The buffer solution was purged with nitrogen for 10 hr to remove all oxygen prior to use. A given film was grown to a desired voltage and on completion of growth the electrode was dried in a nitrogen atmosphere and dissolved in a known volume of buffer solution. A portion of this solution was drawn up by capillary action into each of three capillary tubes and the tubes sealed using a small flame. The solution was kept in the center of the tube until the sealing step had been completed in order to prevent solution evaporation and vanadium oxidation. Standard solutions of vanadyl ion were prepared from vanadyl sulfate,  $\text{VOSO}_4 \cdot x\text{H}_2\text{O}$ . A calibration curve (peak height vs. vanadyl ion concentration) was prepared. The concentration of paramagnetic ions in a sample containing a dissolved anodic film was obtained by comparing the peak height in its EPR spectrum with the calibration curve prepared from the standard vanadyl ion solutions. Knowledge of the volume of buffer used to dissolve the anodic film together with the concentration enable calculation of the total vanadyl ion to be performed. The spectra were identified as those of the vanadyl ion by comparing the g-values obtained from an EPR spectrum of a known vanadyl solution ( $g = 2.0021$ ) with that of the dissolved film. The total amount of vanadyl ion in a given sample was determined as a function of the formation voltage. The dependence was linear. The slope was 0.0178  $\mu\text{moles}$  of vanadyl ion per square centimeter per formation volt.

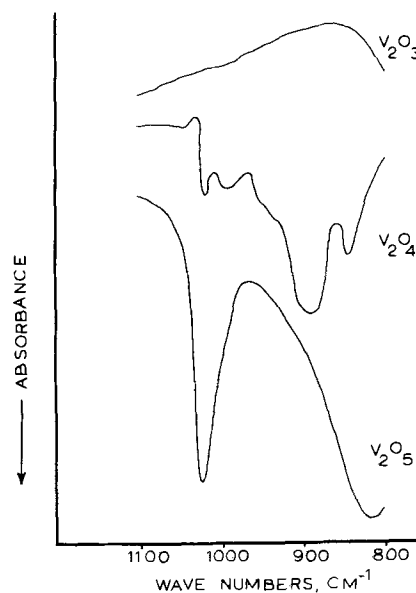


Fig. 5. Transmission spectra of known vanadium oxides in a KBr matrix between 1100 and 800  $\text{cm}^{-1}$ .



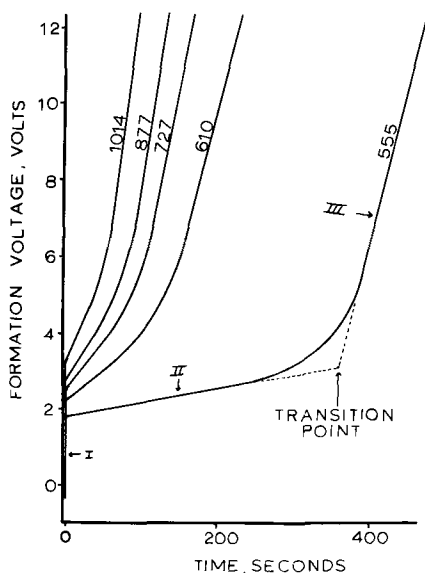


Fig. 6. Constant current growth curves at 25°C for various formation current densities.

**Constant current film growth.**—The growth curves obtained at 25.0°C using various formation current densities and an anode-working cathode separation of 8 mm are shown in Fig. 6. The growth curves obtained when using the painted platinum strip as the reference electrode were identical to those obtained when a saturated calomel Luggin-capillary reference electrode was used. However, the rest potential of the vanadium anode with respect to the platinum strip and the calomel reference electrode was found to be  $-0.12$  and  $0.14$ v, respectively, and invariant with time. Apparently the exchange current density across the platinum strip was sufficient to enable it to assume a stable potential. There are three regions of interest on a given constant current growth curve, *viz.*, (I) the initial transient and film growth below (II) and above (III) the transition point (T.P.). The intersection of an extension of the two straight line portions of the constant current growth curve was designated the transition point. When film growth commenced, the anode potential increased sharply from its zero current value. The initial transient, which was linearly dependent on the growth current density and the anode-cathode separation, was attributed to the ohmic voltage drop across the anodizing solution. The effect of polarization on the double layer, *i.e.*, initial charging of the double layer, was considered minimal. After the initial transient, the potential of the anode slowly increased (region II) in a linear fashion with time due to the growth of the film. Unless the specific resistance of the newly formed layers of the anodic film is changing, the slope of the growth curve is proportional to the rate of film growth. After a time, the slope of the growth curve increased and remained at this higher value (region III) until film breakdown commenced.

The total charge passed to reach the transition point was a function of the apparent current density, increasing linearly with decreasing formation current density. Below  $600 \mu\text{A}/\text{cm}^2$  however, large increases in the charge required to reach the transition point were found. An analysis of the anodizing solution for vanadium showed that vanadium was dissolving during the course of film growth when the potential of the anode was less than the transition potential. The formation voltage was obtained by subtracting the initial transient from the potential of the anode when film growth was stopped. Vanadium was detected colorimetrically in the greenish-blue anodizing solution. The fraction of the anodic oxidation product dissolving decreased with increasing formation current density (Table II). The second linear slope of the con-

Table II. Fraction of anodic oxidation product dissolving as a function of apparent current density at 25.0°C for film growth\* up to the transition potential

Current density, $\mu\text{A}/\text{cm}^2$	Transition potential, v	Fraction dissolving
555	3.4	0.95
610	3.8	0.86
727	4.6	0.82
877	5.0	0.79
1014	5.7	0.72

\* Anode-working cathode separation, 8 mm.

stant current growth curve (region III) was found to depend linearly on the formation current density (Fig. 7). A determination of the fraction of oxidized vanadium dissolving after the transition point was made. A vanadium electrode was anodized at  $555 \mu\text{A}/\text{cm}^2$  to a formation voltage of 20v. Then the anodization cell was cleaned, fresh anodizing solution added, and the electrode further anodized to a formation voltage of 100v over a period of 15 min. Afterward, the anodizing solution was analyzed for vanadium; however, none was found. Similar results were obtained when the process was repeated using other formation current densities.

The apparent oxidation state of anodically oxidized vanadium, defined as the ratio of the number of Faradays passed to grow the film to the number of moles of vanadium found in the film, was calculated. The average oxidation state of a vanadium ion in the film was  $4.00 \pm 0.06$  (Table III). The apparent oxidation state was neither a function of the formation voltage nor of the formation current density. Gas evolution at the anode was not observed. An anodic film could not be grown at 25.0°C if the formation current density was less than about  $450 \mu\text{A}/\text{cm}^2$ . Below this value the potential of the anode did not increase beyond about 1v. Film growth was found to be increasingly difficult at higher temperatures. In general, the minimal current density required to grow a film increased with increasing temperature. Film growth above 45°C was not possible using a formation current density of  $900 \mu\text{A}/\text{cm}^2$ .

During film growth under constant current conditions, the potential of the anode increased until a certain film thickness was attained. At that potential, film breakdown began. The formation voltage to which a film could be grown before film breakdown occurred was found to depend markedly on the quantity of water in the anodizing solution. Specifically, for sodium borate-acetic acid solutions five and two molar

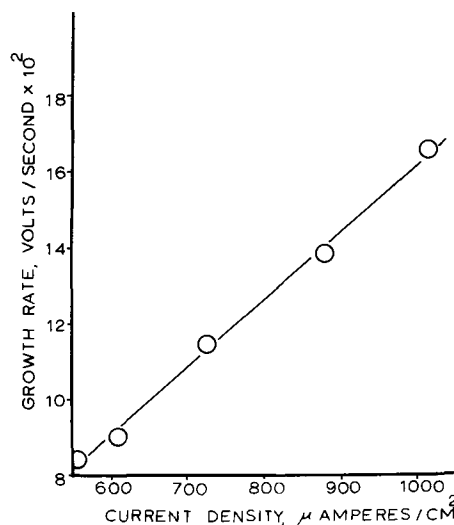


Fig. 7. Rate of film growth as a function of the formation current density at 25°C.

Table III. Apparent oxidation state of the vanadium anodic oxidation product for various formation voltages

Formation current density, $\mu\text{A}/\text{cm}^2$	Formation voltage, v	Total vanadium, $\mu\text{moles}$	Total charge passed, $\mu\text{Faradays}$	Apparent oxidation state
555	3.4	0.381	1.51	3.97
610	3.8	0.145	0.583	4.06
727	4.6	0.135	0.545	4.03
877	5.0	0.115	0.464	4.04
1014	5.7	0.105	0.413	3.93
555	18	0.197	0.816	4.14
497	39	0.831	3.34	4.02
727	44	0.504	1.94	3.86
520	50	0.850	3.39	3.99
727	61	0.811	3.29	4.06
727	75	0.992	3.94	3.98
727	85	1.12	4.41	3.94

in water, films could be grown to 25 and 110v, respectively. The dependence of the film breakdown potential on the amount of water in the anodizing solution is quite striking.

**Constant voltage film growth.**—Anodic films were grown under constant voltage conditions to various formation voltages. In all constant voltage work the anode-working cathode separation was 1 mm. A typical constant voltage growth curve is shown in Fig. 8. The initially large current density across the electrode surface as film growth commenced decreased rapidly until it reached a limiting value of  $0.15 \text{ ma}/\text{cm}^2$ . The optical thickness of the film was recorded (Table IV) and the amount of vanadium anodically oxidized in a film of given formation voltage determined colorimetrically. The dependence of the amount of vanadium anodically oxidized on the formation voltage was found. A least squares determination for the linear relationship was found to be  $0.0170 \mu\text{moles}$  of vanadium per square centimeter per formation volt.

### Discussion of Results

**Oxidation state of the vanadium in the film.**—Within experimental error, the apparent oxidation state of the vanadium in the anodic film,  $4.00 \pm 0.06$ , was invariant with the formation voltage and the formation current density. The significance of the result is that the oxidation state of the oxidized vanadium is not a function of the potential of the substrate vanadium. This result sets the maximum oxidation state for the vanadium in the anodic film, but does not identify the film as vanadium (IV) because part of the charge

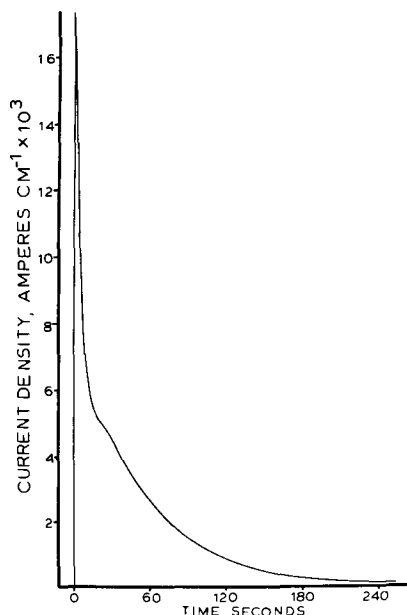


Fig. 8. Constant voltage growth curve for a 40v anodic film at 25°C.

Table IV. Film thickness data for constant voltage film growth obtained by comparing the film interference color with that on a barium stearate stepgauge

Formation voltage, v	Film interference color	Corresponding thickness of barium stearate, $\mu\text{in.}$
4.0	V. lt. brown	<3
7.0	Lt. brown	
13.0	Dark blue	5
15.0		6
19.0	Silver blue	<8
27.0	Yellow	9
32.0	Orange-yellow	
35.0	Reddish-orange	
39.0	Dark red	11
42.0	Purple	12
43.0	Blue	13
45.0	Greenish-blue	14
50.0	Green	15

passed could be producing gas at the anode. Gas evolution at the anode was not observed and as we shall see did not, in fact, occur.

The significance of the EPR results is that the dependence of the amount of vanadyl ion on the formation voltage was experimentally found to be  $0.0178 \mu\text{moles}/\text{cm}^2/\text{formation volt}$  and that this quantity was equal, within experimental error, to the dependence of the total amount of vanadium in the anodic film on the formation voltage, i.e.,  $0.0170 \mu\text{moles}/\text{cm}^2/\text{formation volt}$ . This data, together with the fact that the apparent oxidation state was 4.0, shows the anodization process is 100% efficient in the production of tetravalent vanadium. If the anodic oxidation product were composed of a vanadium(II) species, when dissolved, the vanadium ion would reduce water and go to the trivalent state. Further oxidation, i.e., oxidation of vanadium(III) ion would not be thermodynamically favored in the absence of dissolved oxygen in the solution. Experimentally, an EPR signal was not observed when stock solutions of either pentavalent or trivalent vanadium ion in the buffer solution were treated similarly. The anodic oxidation product was further identified by comparing the transmission spectra of the known vanadium oxides in a KBr matrix with the ATR spectra of anodic films. Comparison showed the anodic film was  $\text{V}_2\text{O}_4$  and that no vanadium(V) oxide was present in the film. The facts that: (a) the anodic film dissolved to form the paramagnetic  $\text{VO}^{2+}$  ion, (b) the ATR spectra of the anodic films matched that of  $\text{V}_2\text{O}_4$ , (c) the apparent oxidation state of the vanadium in the film was 4.0 and invariant with formation voltage, (d) the dependence of the paramagnetic vanadyl ion was equal to the dependence of the total vanadium on formation voltage, and (e) gas evolution at the anode was not observed, permits conclusive identification of the anodic oxidation product as  $\text{V}_2\text{O}_4$ . Oxygen for the anodic film was most likely provided by the water in the anodizing solution because an anodic film could not be formed on the vanadium unless water was present, regardless of the formation current density or the voltage applied to the anode. Lack of oxygen evolution in the acetic acid solutions might be due in part to the low activity of water in the anodizing solutions as a result of strong interactions (25-27) between water and acetate ion. The role of water in the film growth process is under investigation.

The production of vanadium tetroxide as a result of anodic oxidation is not predicted thermodynamically. The available data for vanadium in aqueous media is only approximate when applied to this work. However the  $E_h$ -pH diagram of Pourbaix (28) shows that  $\text{V}_2\text{O}_4$  and  $\text{V}_2\text{O}_3$  are stable in the region of stability of water. The oxidation state which is produced as a result of anodization is dependent on the metal/film interface potential difference (EMF), a parameter which is not measurable in this instance. However, if it were no more than about 0.4v,  $\text{V}_2\text{O}_4$  would be produced.

**Nature of the anodic film.**—The absorption bands in the transmission spectrum of  $\text{V}_2\text{O}_4$  were centered at

1020 and 990  $\text{cm}^{-1}$  while the corresponding bands in the ATR spectra were centered at 1015 and 975  $\text{cm}^{-1}$ . The shift suggests an amorphous film structure. However, in the region of an absorption band the refractive index is not represented well by the Cauchy (21, 22) relationship. Large quantities of electromagnetic energy are dissipated in the vicinity of an absorption band, since a resonance condition exists in which induced dipole moments in the medium are approximately in phase with the electromagnetic field (23). The refractive index of the film was not determined. If the refractive index of the film were close to that of the KRS-5 prism in the region of the absorption, then there is no angle of incidence at which internal reflection can take place and nearly all the energy will pass into the sample. The recorded internal reflection absorption band will be very strong but broadened toward long wavelengths and hence, distorted as compared to that measured by transmission. The degree of crystallinity of the film, therefore, cannot rest solely on the spectral data which is indicative of an amorphous structure. As previously indicated, x-ray diffraction patterns of the anodic films exhibited very weak lines after lengthy exposure to the radiation. These very weak lines also indicate the films are amorphous or very slightly crystalline.

Three pieces of experimental data should now be considered. First, the infrared results (Fig. 2-4) show that the acetic acid, incorporated into the film during film growth, evaporates from the film after a relatively short time. Second, a hump appears on the constant voltage growth curve. Third, the final leakage current density, 0.15  $\text{ma}/\text{cm}^2$ , was 1000 times larger than that found for anodic films formed on some other valve metals (24). The comparative speed with which the acetic acid evaporated suggests it might have been located along channels in the film. The onset of a porous "channel" structure during the early stages of film growth would account for these experimental results.

*Electrochemical kinetic considerations.*—At any time during constant current film growth, the film thickness,  $D_f$ , is given by the expression

$$D_f = D_f^0 + Bt \quad [1]$$

where  $D_f^0$  (cm) is the film thickness prior to anodization (here  $D_f^0 = 0$ ),  $B$  is the film growth rate, in centimeters per second, and  $t$  is the time of film growth. Here  $B$  is given by

$$B = \frac{dD}{dt} = \frac{iM}{nFS} \quad [2]$$

where  $M$  is the molecular weight,  $n$  is the electrode reaction valence,  $S$  is the density of the film, and  $i$  is the apparent formation current density. The film thickness and potential rate of increase is related by

$$\frac{iM}{nFS} = \frac{1}{E} \frac{dV}{dt} \quad [3]$$

where  $E$  is the field strength and  $V$  is the potential of the vanadium electrode with respect to the reference. The film growth rate dependence on the apparent formation current density is plotted in Fig. 7. The

dependence is linear. For constant current growth, a linear dependence of the growth rate on the current density necessitates that the field be constant over the range of current densities investigated. The electrostatic field across the anodic film was calculated for a given growth rate and apparent current density using Eq. [3], and a density of 4.34  $\text{g}/\text{cm}^3$  for the anodic film. The calculated field was constant within experimental error. The average field was  $3.2 \pm 0.2 \times 10^6 \text{v}/\text{cm}$ .

Manuscript received Sept. 28, 1967; revised manuscript received Jan. 16, 1968. This work was done in partial fulfillment of the requirements for the Ph.D. degree at Temple University.

Any discussion of this paper will appear in a Discussion Section to be published in the December 1968 JOURNAL.

#### REFERENCES

1. S. Zwerdling and S. Sheff, *This Journal*, **107**, 338 (1960).
2. E. Rajjola and A. W. Davidson, *J. Am. Chem. Soc.*, **78**, 556 (1956).
3. J. A. Davies, B. Domeij, J. P. S. Pringle, and F. Brown, *This Journal*, **112**, 675 (1965).
4. J. B. Story, *ibid.*, **112**, 1107 (1965).
5. H. A. Johansen, G. B. Adams, and P. Van Rysselberghe, *ibid.*, **104**, 339 (1957).
6. L. Young, "Anodic Oxide Films," Academic Press Inc., New York (1961).
7. R. G. Keil and R. E. Salomon, *This Journal*, **112**, 643 (1965).
8. N. A. Talvite, *Anal. Chem.*, **25**, 604 (1953).
9. W. Klemm and L. Grimm, *Z. anorg. Chem.*, **250**, 42 (1942).
10. N. Schonberg, *Acta Chim. Scand.*, **8**, 221 (1954).
11. G. Anderson, *ibid.*, **8**, 1599 (1954).
12. N. J. Harrick, *Ann. New York Acad. Sci.*, **101**, 928 (1963).
13. F. Douville, C. Duval, and J. Lecomte, *Compt. rend. acad. sci.*, **212**, 953 (1941).
14. M. M. Davies and G. B. Sutherland, *J. Chem. Phys.*, **6**, 755 (1938).
15. J. Grove and H. Willis, *J. Chem. Soc.*, Part II, 877 (1951).
16. M. Flett, *ibid.*, 962 (1951).
17. J. Picht, *Abhandl. Deut. Akad. Wiew. Berlin*, **2**, 5 (1955).
18. T. P. Hoar, *Nature*, **165**, 64 (1950).
19. L. Young, *Acta Met.*, **5**, 711 (1957).
20. D. A. Vermilyea, *ibid.*, **5**, 492 (1957).
21. R. S. Longhurst, "Geometrical and Physical Optics," John Wiley & Sons, Inc., New York (1957).
22. F. A. Jenkins and H. E. White, "Fundamentals of Physical Optics," McGraw-Hill Book Co., New York (1937).
23. W. W. Wendlandt and G. B. Hecht, "Reflectance Spectroscopy," John Wiley & Sons, Inc., New York (1966).
24. F. Keller, M. S. Hunter, and D. L. Robinson, *This Journal*, **100**, 411 (1953).
25. V. Vitagliano and P. A. Lyons, *J. Am. Chem. Soc.*, **78**, 4538 (1956).
26. E. I. Holt and P. A. Lyons, *J. Phys. Chem.*, **69**, 2341 (1965).
27. R. A. Robinson and R. H. Stokes, "Electrolyte Solutions," Butterworths, London (1959).
28. M. J. N. Pourbaix, CEBELCOR, RT 29 (1956).

# Electric Conduction through Thin Insulating Langmuir Film

Shiro Horiuchi,<sup>1</sup> Jiro Yamaguchi, and Kiyooki Naito

Faculty of Engineering Science, Osaka University, Toyonaka, Osaka, Japan

## ABSTRACT

Electric conduction through calcium stearate Langmuir films of several monomolecular layers has been studied. The devices are prepared by transferring monolayers of stearic acid spread on an aqueous surface to an evaporated tin electrode on a glass substrate and evaporating the upper electrode. Tunnel emission is observed when the aluminum upper electrode is negatively biased and Schottky emission is observed when the lower electrode is negatively biased. The trapezoidal energy barrier model of Simmons adequately accounts for the details of current-voltage-temperature characteristics. The observed barrier height at the stearate and tin interface is 0.8 eV and that at the stearate and aluminum interface is 1.3 eV.

There has been a considerable revival of interest in electrical conduction through thin film insulator, since Mead proposed the "hot" electron devices which operated with hot electrons injected through thin (100Å) insulating film by quantum mechanical tunneling (1).

In order to inject hot electrons with good efficiency and controllability, such a film must be thin, homogeneous, uniform in thickness, and have excellent dielectric properties. Most of experimental studies on the electron transport through thin insulating films sandwiched between metals have been made on oxide grown on base electrode metals because of their uniformity and compactness. Mechanisms such as tunneling (2, 3), Schottky emission (4), field and thermal ionization of traps and impurities (5), etc. have been proposed to explain the observed characteristics.

However, it is known that Langmuir films of certain organic materials behave as good insulators and are easily obtained using the classical process developed by Langmuir and Blodgett (6, 7). It appeared to be an attractive problem to employ these monolayers as an insulating barrier between metal electrodes, because the metal-insulator-metal sandwich would have a definite barrier thickness predicted by the length of a molecule and number of monomolecular layers.

A pioneering and extensive study on Ba and Ca stearate monolayers has been made by Handy and Scala, and their results show promising properties of the Langmuir films as an insulating barrier for the observations of electron tunneling phenomena (8). The metal-insulator-metal sandwich prepared by them exhibited highly nonlinear and thickness-dependent voltage-current characteristics. However, the barrier heights at the electrodes and the explanation of the observed temperature dependence were not given.

It is the purpose of this paper to give details of the voltage and temperature dependences of the current through the calcium stearate monomolecular films sandwiched between aluminum and tin electrodes.

## Experimental Procedures

Metal-insulator-metal structure were fabricated as follows. Monomolecular films were deposited on evaporated tin films on a microscope slide using the Langmuir-Blodgett technique. A 0.005 mol solution of calcium carbonate or barium chloride in deionized water was brought to pH 9 by hydrochloric acid for the flotation medium. Oleic acid was used as the piston oil. Transfer was performed at 0.2-2.0 cm/sec. Counter electrodes of tin or aluminum were used to give junctions in the order of 1 mm<sup>2</sup>.

Capacitance measurement at 1 kc was made on all junctions prior to the V-I characteristic measure-

ment in order to check incompletely insulating junctions which had ohmic characteristics. Capacitance values of good junctions on a slide glass showed fairly good agreement with each other, but the scatter from slide to slide was up by a factor of 2. Capacitance of a junction with 29 layers of monomolecular film was also measured as a function of frequency. It was independent of frequency over the range of 1 kc to 1 Mc. The dielectric constant was calculated from the capacitance using the stearate monomolecular layer thickness of  $\approx 24\text{Å}$ . It was estimated to be 2.5 which is in agreement with bulk value and was used to estimate image potential in the analysis of experimental results.

Current voltage characteristics of the junctions were obtained with d-c voltage at temperatures from 200° to 350°K. When a constant voltage was applied, a large amount of transient current was observed, which decayed approximately in proportion to  $1/t$ . The transient current was proportional to applied voltage, while the steady-state current increased exponentially with increasing voltage. Plots of V-I characteristics were made with the steady state values.

## Results and Discussion

Figure 1 shows a typical result of the V-I characteristics observed in the Al-Ca stearate-Sn junction. When the lower tin metal electrode is negatively biased, the observed current,  $I_1$  is strongly temperature-dependent above 200°K but nearly independent

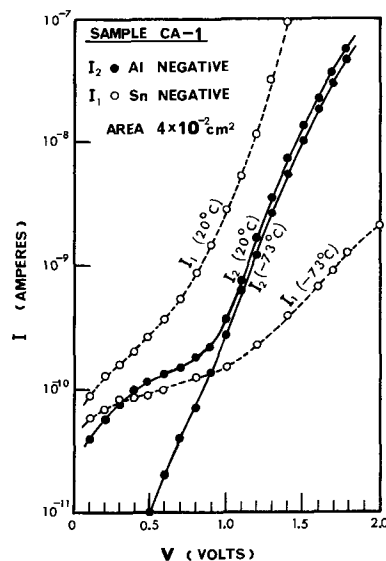


Fig. 1a. Plot of  $I_1$  and  $I_2$  vs.  $V$  for the Sn-Ca stearate (3 monomolecular layer)-Al junction (with 3 layers of insulating monomolecular film). Black dots and white circles indicate  $I_2$  and  $I_1$ , respectively.

<sup>1</sup> Present address: Central Research Laboratory, Matsushita Electric Industrial Co., Ltd., Kadoma, Osaka, Japan.

Key words: Conduction through Thin Langmuir films.

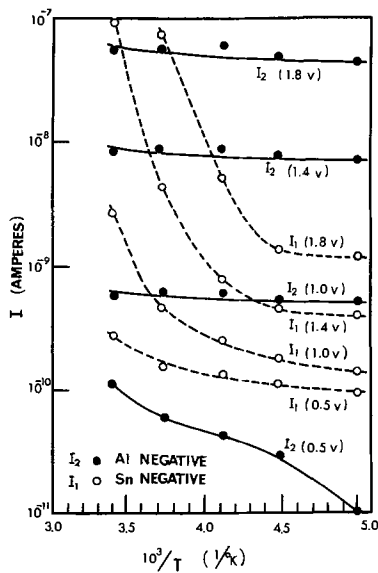


Fig. 1b. Plot of  $I_1$  and  $I_2$  vs.  $1/T$  for the Sn-Ca stearate junction

on the temperature below 200°K. In contrast to  $I_1$ , the current  $I_2$  which was observed when the upper aluminum electrode was negatively biased, is independent of temperature in the temperature range studied. Similar characteristics were observed for Al-Ba stearate-Sn junctions. The presence of a temperature-dependent current  $I_1$  and a temperature independent current,  $I_2$  in the same junction suggests that more than one mechanism of electron transfer is operative.

In contrast to these asymmetric junctions, the Sn-Ca stearate-Sn junction showed symmetrical V-I characteristics to the polarity of applied voltage as shown in Fig. 6. The dependence on electrode material suggests that the dominating conduction mechanisms would be barrier limited.

It is well known that the rate limiting mechanism of electron transfer through extremely thin insulating films will be tunneling emission and Schottky emission. Trapezoidal barrier models have been used by Pollack *et al.* to explain the observed V-I characteristics with tunnel and Schottky emissions (9, 10). A similar model is proposed here for the Al-stearate-Sn sandwich system. Simmons has derived the expressions for the thermionic emission (11) and tunnel emission (12) between dissimilar electrodes including the effect of image potential.

The results of Schottky emission can be summarized by the following relations for the trapezoidal barrier shown in Fig. 2.

$$J_1 = AT^2 \exp \left( -\frac{\phi_1}{kT} + \frac{\{14.4[7 + Ks(eV - \Delta\phi)]\}^{1/2}}{kTKs} \right) \quad [1]$$

$$J_2 = AT^2 \exp \left( -\frac{\phi_1}{kT} - \frac{\{14.4[7 + Ks(eV + \Delta\phi)]\}^{1/2}}{kT \cdot Ks} \right) \quad [2]$$

where  $\phi_1$  and  $\phi_2$  are barrier heights between metals and an insulator and  $\Delta\phi_1 = \phi_2 - \phi_1$  ( $\phi_2 > \phi_1$ ),  $s$  is the insulator thickness, and  $K$  is the specific dielectric constant.  $J_1$  and  $J_2$  are the net current flowing in the system when the electrode of lower work function is negatively and positively biased, respectively. From these equations, it is easily seen that Schottky emission will be observed at room temperature when the electrode of the lower barrier height is negatively biased, if the lower barrier height,  $\phi_1$  is 1 eV or less. However, the thermionic emission is hardly observed when the electrode of lower work function is positively biased because the ratio  $J_1/J_2$  is as large as  $10^8$ , if  $\Delta\phi$  is 0.5 eV.

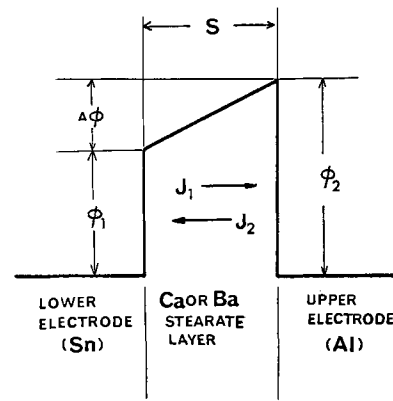


Fig. 2. Trapezoidal energy barrier. Direction of arrows labeled with  $J_1$ ,  $J_2$  indicates that of net electron flow when the lower electrode is negatively and positively biased, respectively.

From the results shown in Fig. 1, only a tunneling process is assumed for  $I_2$ . A Fowler-Nordheim plot of  $I$  at 200°K gave a straight line above  $1/V = 1.2$  ( $v^{-1}$ ). In Fig. 3, a theoretical curve for  $J_2$  obtained by calculation based on Simmons' equations using a dielectric constant of 2.5 is shown together with the experimental values. A reasonable fit can be obtained with the assumed barrier parameters of  $\phi_1 = 0.8$  eV,  $\Delta\phi = 0.5$  eV, and  $s = 23\text{\AA}$ . However, in order to obtain the fit shown here, the effective area of the samples was adjusted to values between  $10^{-8}$  and  $10^{-10}$  of the geometrical area. The assumed barrier heights  $\phi_1 = 0.8$  eV and  $\phi_2 = 1.3$  eV are in good agreement with those obtained from the Schottky plots of  $I_1$  as shown later, but the thickness of barrier for electron tunneling is much smaller than that predicted from the number of transferred layers and estimated from capacitance measurement. The relatively low barrier height of  $\phi_1$  suggests Schottky emission over the barrier. It is considered that the temperature dependence of  $I_1$  shown in Fig. 1b consists of Schottky component  $I^*_1$  and temperature independent component  $I_{10}$ .  $I^*_1$  was obtained by reducing  $I_{10}$ , current values at the lowest temperature from  $I_1$ . Examination of Eq. [1] suggests a plot of  $\ln I^*_1$  vs.  $(eV - \Delta\phi)^{1/2}$  as shown in Fig. 4 with  $\Delta\phi = 0.5$  eV and  $T = 268^\circ\text{K}$ . From the slope and Eq. [1], we obtain  $Ks = 170\text{\AA}$ . The barrier thickness,  $68\text{\AA}$  obtained by dividing  $Ks$  with  $K = 2.5$  is not far from the value,  $75\text{\AA}$  predicted from the number of transferred monomolecular layers.

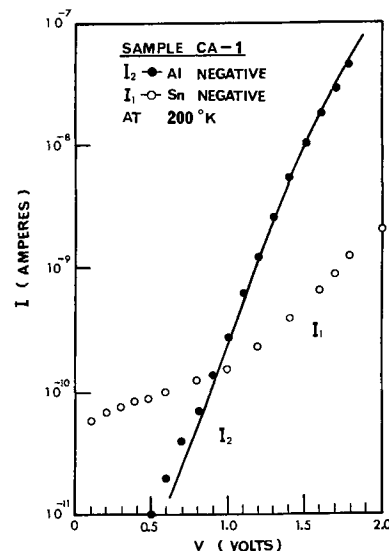


Fig. 3. Plot of  $I_2$  vs.  $V$  for sample CA-1 at 200°K. Solid curve is a fit of  $I_2$  to Simmons' tunneling equation assuming  $s = 23\text{\AA}$ ,  $K = 2.5$ ,  $\phi_1 = 0.8$  eV, and  $\Delta\phi = 0.5$  eV.

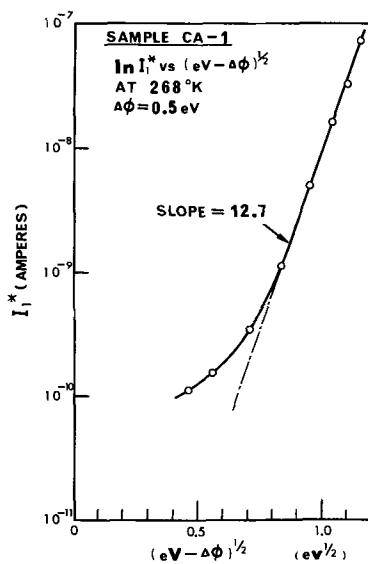


Fig. 4. Plot of  $I_1^*$  vs.  $(eV - \Delta\phi)^{1/2}$  for sample CA-1 at 268°K with  $\Delta\phi = 0.5$  eV.

Equation [1] also suggests the plot of  $\ln(I_1^*/T^2)$  vs.  $1/T$  at constant applied voltage as indicated in Fig. 5. From the slope,  $\phi_1$  is calculated to 0.78 eV by using  $K_s = 170\text{\AA}$ . This value is in good agreement with the value of  $\phi_1$  determined from the voltage dependence of tunnel current  $I_2$ .

In Fig. 6, V-I characteristics and its temperature dependence of the Sn-Ca stearate-Sn junction are shown. A marked difference of the characteristic from that shown in Fig. 1 is the symmetrical characteristic to the polarity of applied voltage. For the case of the Sn-Ca stearate-Sn junction, barrier heights at the metal-stearate interfaces are the same for both the upper and lower electrodes, and a rectangular barrier model will be applicable. By the use of Simmons' tunneling equations for similar electrodes (13), a reasonable fit to the experimental plots is obtained with  $\phi (= \phi_1 = \phi_2) = 0.8$  eV,  $s = 44\text{\AA}$  and  $K = 2.5$ . Barrier height at the Sn-Ca stearate interfaces is in agreement with the corresponding one of the trapezoidal barrier for the Al-stearate-Sn junction. However, analysis of temperature dependent current at higher temperature was not successful. Currents at higher temperature were unstable and could not be used to obtain reliable temperature dependence. A similar analysis to Fig. 5 gave a smaller thermal barrier height of 0.5 eV. These results are summarized in Table I together with the data obtained on the Al-Ba stearate-Sn junction.

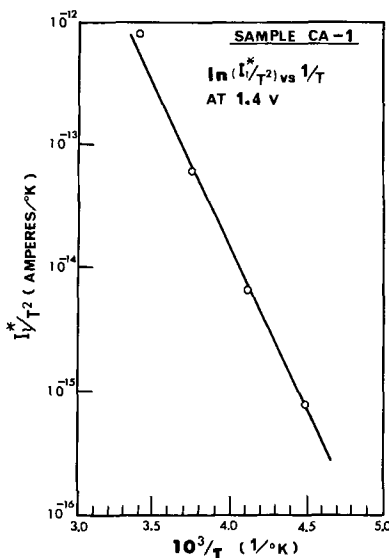


Fig. 5. Plot of  $I_1^*/T^2$  vs.  $1/T$  for sample CA-1 at 1.4v

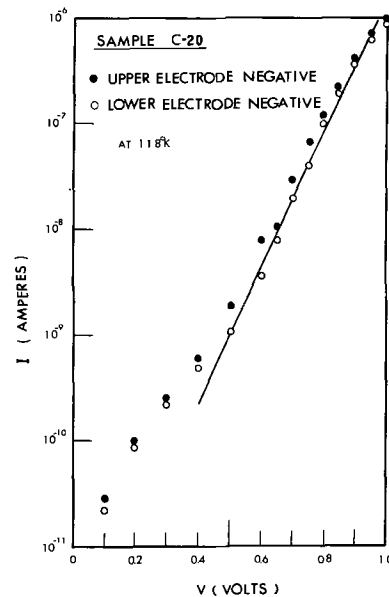


Fig. 6a. Plot of  $I_1$  and  $I_2$  vs.  $V$  for the Sn-Ca stearate-Sn junction. White circles and black dots indicate  $I_1$  and  $I_2$ , respectively. Solid curve in the Fig. 6a is a fit of  $I_2$  to Simmons' equation assuming  $s = 44\text{\AA}$ ,  $K = 2.5$ , and  $\Delta\phi = 0.8$  eV.

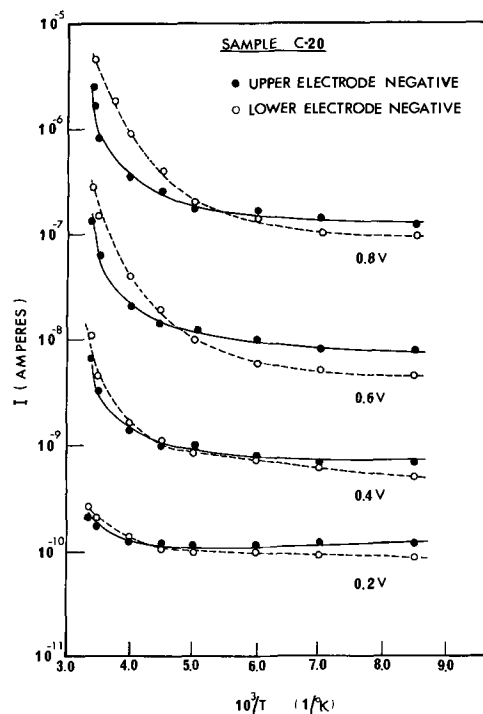


Fig. 6b. Plot of  $I_1$  and  $I_2$  vs.  $1/T$  for the Sn-Ca stearate-Sn junction.

Consequently, it has been shown that the temperature and voltage dependence of the current satisfies the Schottky emission mechanism and that the voltage dependence of the low-temperature current is as predicted by tunneling. Barrier heights between the stearate and aluminum and tin obtained by the above analysis are self-consistent and 1.3 and 0.8 eV, respectively.

However, there are two problems remaining in the analysis. One is the difference of barrier thicknesses determined from tunneling current and Schottky current. The other is the barrier height difference of  $\phi_1$  and  $\phi_2$ . As shown in Table I, the barrier thickness obtained from the Schottky current is in reasonable agreement with the value predicted from the number of transferred layers by assuming the length of cal-

Table I. Barrier parameters obtained from analysis based on tunnel and Schottky emission mechanisms

Sample No.	Construction of junction	Number of layers	Predicted thickness of insulator, Å	Tunnel ( $I_2$ )			Schottky ( $I_1^*$ )		
				$\phi_1$ (ev)	$\phi_2$ (ev)	s (Å)	$\phi_1$ (ev)	$\phi_2$ (ev)	s (Å)
CA-1	Sn-Ca stearate-Al	3	71.4	0.8	1.3	23	0.78	1.28	68
BA-3	Sn-Ba stearate-Al	3	71.4	0.8	1.3	22	0.79	1.29	84
C-20	Sn-Ca stearate-Al	4	94.2	0.8	0.8	44	0.5	0.5	—

cium stearate molecule to be 23.8Å (14), while the barrier thickness obtained from the barrier parameters which showed the best fit to the experimental plots of tunneling current disagreed with the former value. This is not surprising. Even for the sample with multistearate layers with which we believe complete coverage has been attained, there will be significant local inhomogeneity in thickness. If there are voids or pin holes in the transferred monolayers, some of them in the outer layers will be filled with metal when the upper electrode is evaporated. Most of the tunneling current will pass through such voids as tunneling emission is more strongly dependent on the barrier thickness than Schottky emission. The fact that the effective area to fit the experimental values of  $I_2$  to the calculated current density is small by a factor of  $10^{-8} \sim 10^{-10}$  seems to support the presence of such conduction patches.

The barrier height determined from the above analysis indicates that the work function of tin is smaller than that of aluminum. This is in contradiction with the values of work functions given by Michaelson (15). However, through use of published values of barrier heights between several kinds of metals and semiconductors, Geppert *et al.* derived preferred values of work functions (16). According to their values, the work function of tin is 0.15 ev lower than that of aluminum, but the difference is not large enough to explain our experimental value, i.e.,  $\Delta\phi = 0.5$  ev.

Another possible cause of the higher barrier height at aluminum electrode is a thin oxide layer at the interface. When tin is coated with calcium or barium stearate, a certain amount of water is entrapped either at the tin surface or in the stearate layers. Deposition

of aluminum forms an active layer which is capable of reacting with trapped water and forming at the aluminum-stearate interface a layer of oxide limited to perhaps one or two atom layers in depth. The aluminum-aluminum oxide barrier is known to be about 1.5 ev, and the effect of image force lowering for such a thin layer would reduce apparent barrier height to the observed value. The barrier diagram for the case would be as shown in Fig. 7 by assuming no trapped charge at the interfaces. However, the current predicted by the model shown in Fig. 7 increases very steeply with increasing voltage, if the thickness of the stearate is assumed to be equal to that obtained from the slope of  $\ln I_1^*$  vs.  $V^{1/2}$ . As a result, conduction patches with thinner effective barrier thickness must be taken into consideration in order to interpret the experimental results. Measurements on the Au-Ca stearate-Sn junctions were tried in order to avoid possible formation of aluminum oxide but were not successful because all the samples prepared showed ohmic characteristics with very small resistance. These problems, therefore, have not been resolved by the present investigation.

#### Acknowledgment

The authors are grateful to Mr. O. Sueta for the set up of the apparatus for layer transfer and the preliminary experimental measurements. The assistance of Mr. O. Furuya is also acknowledged.

Manuscript received Aug. 29, 1967; revised manuscript received Feb. 26, 1968. This paper was presented at the Electrets Symposium at the Chicago Meeting, Oct. 15-19, 1967, as Abstract No. 132.

Any discussion of this paper will appear in a Discussion Section to be published in the December 1968 JOURNAL.

#### REFERENCES

1. C. A. Mead, *J. Appl. Phys.*, **32**, 646 (1961).
2. D. Meyerhofer and S. A. Ochs, *ibid.*, **34**, 2535 (1963).
3. S. R. Pollack and C. E. Morris, *ibid.*, **35**, 1503 (1964).
4. P. R. Emtage and L. Tantraporn, *Phys. Rev. Letters*, **8**, 267 (1962).
5. C. A. Mead, *Phys. Rev.*, **128**, 2088 (1962).
6. I. Langmuir, *Proc. Roy. Soc.*, **170A**, 1 (1939).
7. K. B. Blodgett and I. Langmuir, *Phys. Rev.*, **51**, 964 (1937).
8. R. M. Handy and L. C. Scala, *This Journal*, **113**, 109 (1966).
9. S. R. Pollack and C. E. Morris, *J. Appl. Phys.*, **35**, 1503 (1964).
10. W. E. Flannery and S. R. Pollack, *ibid.*, **37**, 4417 (1966).
11. J. G. Simmons, *ibid.*, **35**, 2472 (1964).
12. J. G. Simmons, *ibid.*, **34**, 2581 (1963).
13. J. G. Simmons, *ibid.*, **34**, 1793 (1963).
14. G. L. Clark, P. R. Sterrett, and P. W. Leppla, *J. Am. Chem. Soc.*, **57**, 330 (1935).
15. H. B. Michaelson, *J. Appl. Phys.*, **21**, 536 (1950).
16. D. V. Geppert, A. M. Couley, and B. V. Dore, *ibid.*, **37**, 2458 (1966).

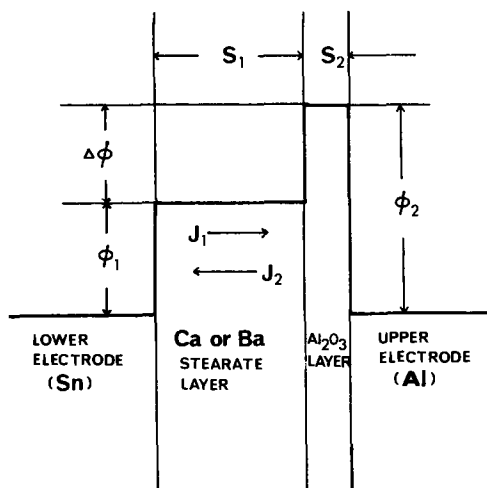


Fig. 7. Energy barrier of Al-Al<sub>2</sub>O<sub>3</sub>-Ca stearate-Sn junction

# Red Electroluminescent (Zn, Cd)(S, Se)-Type Phosphors

T. Hariu, T. Seki, K. Miyashita, and M. Wada

Department of Electronic Engineering, Tohoku University, Sendai, Japan

## ABSTRACT

Red light emitting electroluminescent phosphors in the (Zn,Cd)(S,Se):Cu system were investigated. The best red electroluminescent phosphor is obtained by firing (0.9Zn,0.1Cd)(0.1S,0.9Se) adding Cu,  $5 \times 10^{-3}$  g-atom/mole and the same coactivator concentration at  $1000^\circ \sim 1100^\circ\text{C}$ . Electroluminescent and photoluminescent properties of phosphors of various composition were interpreted by curves illustrating the energy level variation with composition in solid solution, which is obtained by considering nearest-neighbor effects, and a temperature quenching factor in electroluminescence. From similar considerations, the variation of luminescent properties of phosphors of given composition, containing given luminescent centers, can be predicted, and the critical frequency of excitation when developing electroluminescent phosphors of a given color is presented.

A (Zn,Cd)(S,Se) system as red light emitting electroluminescent (EL) phosphors has been developed for a part of its composition by Palilla and Baid (1), Matsuo *et al.* (2), Mironov and Markovskii (3), and Kolomoitsev *et al.* (4) in the course of our investigation, and earlier by Hegyi *et al.* (5), Larach *et al.* (6), Gelling *et al.* (7), and others, but it seems that a unified discussion on firing condition and EL properties has not been achieved. For example, the optimum firing condition differs from composition to composition, and parameters involved in EL characteristics vary with composition. Thus a question arises, "how shall we expect the possibility of (Zn,Cd)(S,Se) as long wavelength light emitting phosphors?"

Solid solutions have been extensively prepared recently to change energy gap continuously for the purpose of matching the exciting or the emitting energy. In this system, a knowledge about the impurity energy level variation with composition as well as about the energy gap variation is indispensable, for the former is undoubtedly very sensitive to optical and electrical properties.

In this paper we tried to give a systematic discussion on the above problem, and to give basic considerations on the impurity energy level variation in this system in connection with them.

## Phosphor Preparation

The (Zn,Cd)(S,Se) system has two crystal forms, varying with composition and firing temperature. The brightness variation with composition is sometimes referred to as being the difference in crystal form (7-12). Thus this variation, although a little affected by activator and coactivator, is depicted in Fig. 1 with a sample composition which is expected to emit red light, because of its approximately linear variation of band gap and photoluminescent results.

Cu was added in the form of  $\text{CuSO}_4$ , with selected concentrations of 1.2 and  $5 \times 10^{-3}$  g-atom/mole. Cl was mainly used as coactivator in the form of  $\text{NH}_4\text{Cl}$  with the same concentration as Cu and 5 and 10 m/o (mole per cent) respectively. A mixed powder material containing the above impurity was dried and fired in a nonflowing  $\text{N}_2$  atmosphere at  $900^\circ$ ,  $1000^\circ$ , and  $1100^\circ\text{C}$ .

## Results

The peak wavelength of emission spectral distribution of all samples was about  $680 \text{ m}\mu$ . Figure 2 shows the brightness variation with composition. Because firing conditions have different effects on the phosphors with different host crystal compositions, the maximum value of brightness is also plotted (curve B). A dot on the left side is of a sample obtained by two-step firing (13). Also shown are the measured crystal forms. All the samples have nearly equal equivalent lattice constants  $a_H = 3.99$  and  $c_H = 6.51\text{\AA}$ . A

similar tendency of variation in brightness was observed for phosphors of the same composition containing Cu and Mn as activators.

The optimum concentration of Cu is different with composition: a lower concentration ( $1 \times 10^{-3}$  g-atom/mole) for composition near (Zn,Cd)S, but brighter EL phosphor with composition near ZnSe requiring a higher concentration ( $5 \times 10^{-3}$ ). In the latter phosphor, the concentration of coactivator higher than Cu has a minor effect on EL brightness (up to a few per cent) but makes a breakdown at lower voltage. However, in the former the concentration of coactivator higher than Cu ruins EL brightness, but a decrease in the breakdown voltage was not observed. Higher firing temperature ( $1000^\circ \sim 1100^\circ\text{C}$ ) is good for all compositions.

The frequency dependence variation with composition is shown in Fig. 3. Phosphor that contains more Se as host crystal constituent is characterized by a more superlinear dependence.

The luminescence brightness depends on voltage in accordance with the usually observed law [ $B = B_0 \exp(-c/V^{1/2})$ ]. The variation in c-value with composition is shown in Fig. 4, which indicates a smaller c-value for phosphor with composition near ZnSe.

The brightness variation with time is shown in Fig. 5 with composition as a parameter. This indicates that phosphor with composition near (Zn,Cd)S shows a quick decrease with time. The maintenance of the best phosphor in Fig. 2 is shown in Fig. 6. A similar initial increase in brightness shown in this figure was observed in phosphors of all compositions washed in NaCN aqueous solution.

The photoluminescent emission spectra are shown in Fig. 7. Curve A is an emission spectrum at room

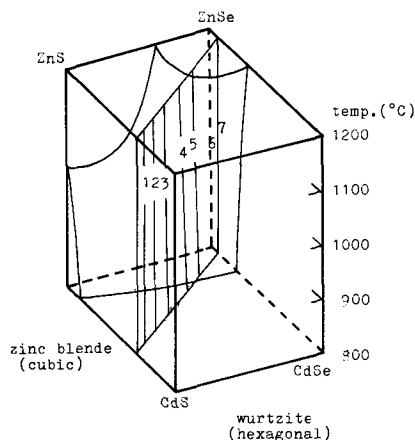


Fig. 1. Crystal structure and investigated composition for red EL phosphor.



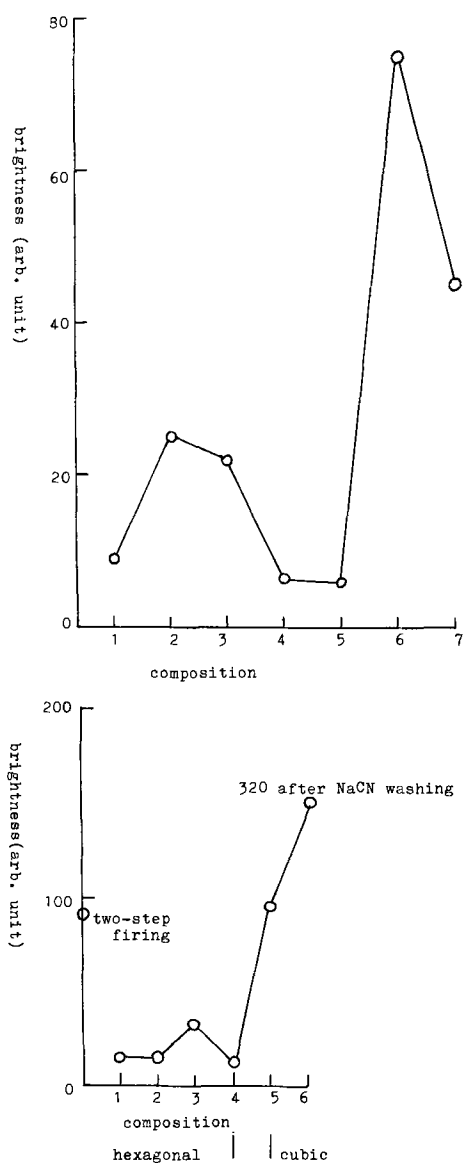


Fig. 2. (a, top) Brightness variation with composition; applied voltage 1 kc, 700v; firing temperature 900°C, Cu :  $2 \times 10^{-3}$  g-atom/mole, Cl :  $4 \times 10^{-3}$  g-atom/mole. (b, bottom) Brightness variation with composition (maximum value), applied voltage 1 kc, 700v.

temperature which is common to all compositions with a minor difference. The figure shows that the short wavelength emission band shifts to the shorter wavelength as the composition approaches the ZnSe side.

Figure 8 shows the photoluminescent brightness dependence on temperature, in which it is seen that the luminescence of a phosphor containing more Se was quenched at lower temperature. Phosphors containing a considerable amount of both elements as anion constituent (S and Se) show a slow decay of luminescence with rising temperature, which is not a temperature quenching characteristic of a single band, but a superposed characteristic of some different emission bands characterized by different quenching temperatures. This situation is shown in Fig. 9 using samples of composition No. 5 in Fig. 1, measured with a fixed wavelength scale of the spectrometer.

**Discussion**

*Impurity level variation in solid solution.*—The problem of impurity level variation in (Zn,Cd) (S,Se) solid solution has also been treated by Lehmann (14), based on ionic bonding and the Schoen-Klasen model. The model discussed here is based on the association model, to which were added further aspects relating to impurity level variation.

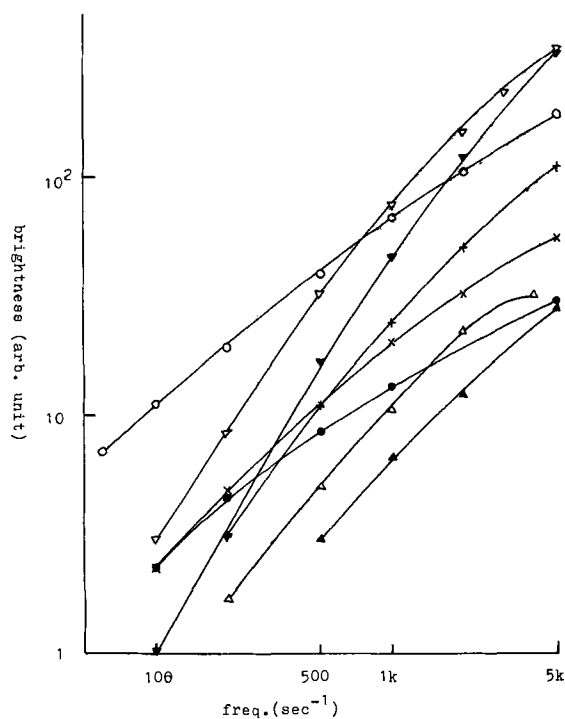


Fig. 3. Frequency dependence variation with composition, applied voltage 700v, composition: ○ (two-step firing), ● 1, × 2, + 3, △ 4, ▲ 5, ▽ 6, ▽ 7.

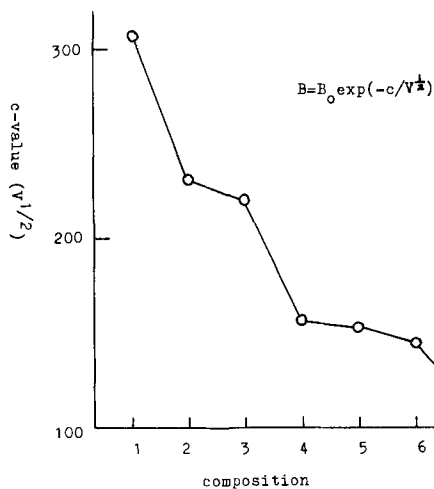


Fig. 4. c-Value variation with composition, applied frequency 1 kc.

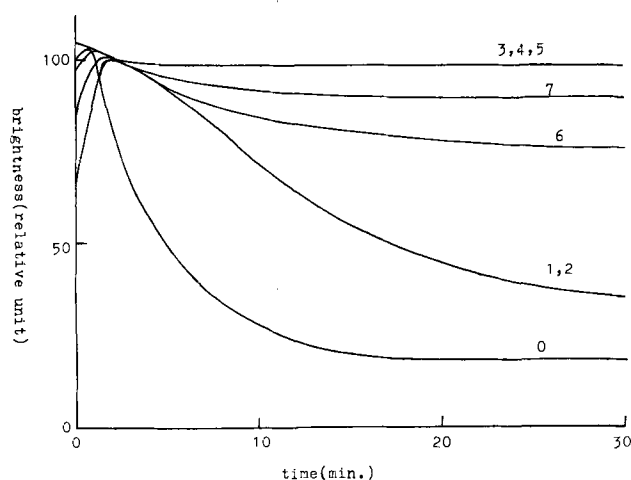


Fig. 5. Maintenance variation with composition. Number indicates composition in Fig. 1 (0: two-step firing), applied voltage 1 kc, 500v.

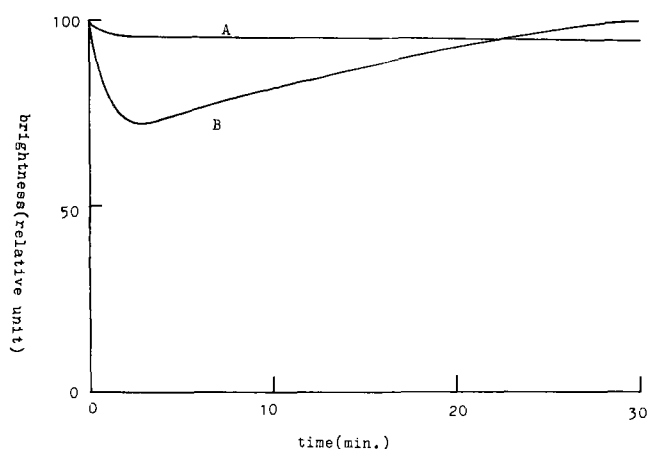


Fig. 6. Maintenance of  $(9\text{ZnSe}) (1\text{CdS}) : \text{Cu}(5 \times 10^{-3})$ ,  $\text{Cl}(5 \times 10^{-3})$ ,  $1100^\circ\text{C}$  firing. B: after NaCN washing. Applied voltage 1 kc, 500v.

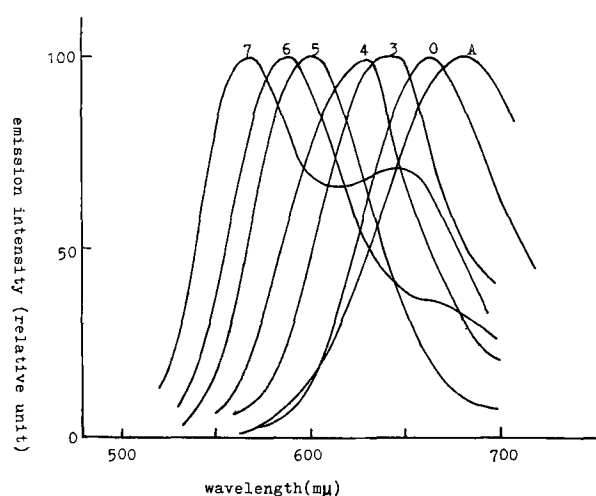


Fig. 7. Photoluminescent spectrum variation with composition. A: at room temperature, common to all compositions with a minor difference. Curves numbered are of each composition at  $-110^\circ\text{C}$ .

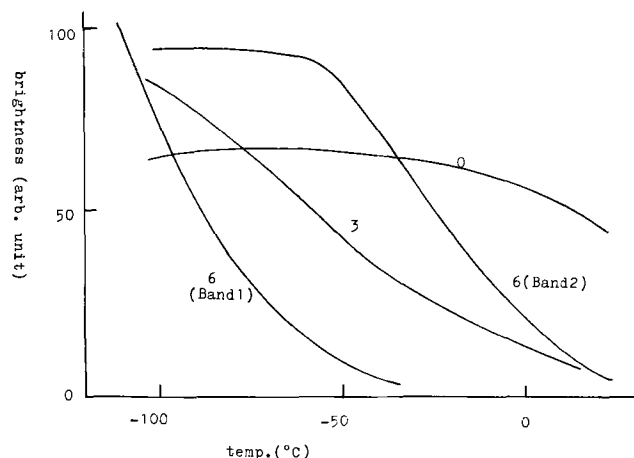


Fig. 8. Photoluminescent brightness dependence on temperature. Number indicates composition in Fig. 1.

Of the three models for luminescent center; Schoen-Klasen, Lambe-Klick, and association, the last is the most reasonable with  $(\text{Zn,Cd}) (\text{S,Se})$ -type phosphors, for the following reasons:

(A) There are two emission bands (the short and long wavelength band which will be referred to later as band 1 and band 2, respectively) in this type of phosphor activated with Cu and coactivated with halogen or group III elements. The variation in emis-

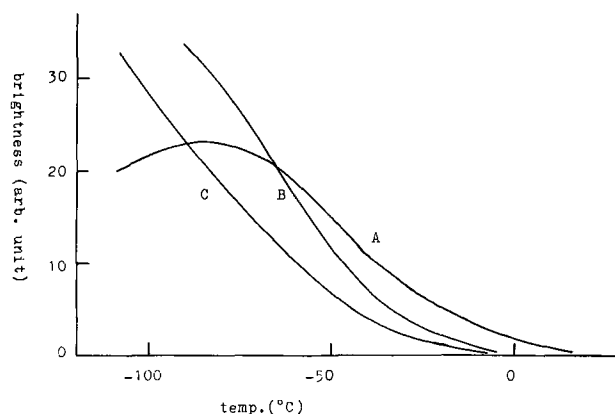


Fig. 9. Photoluminescent brightness dependence on temperature of composition 5. Wavelength: A-660  $m\mu$ , B-620  $m\mu$ , C-600  $m\mu$ .

sion spectrum with activator and coactivator concentration can be explained by the association model; the lower energy emission band is strong at the activator concentration equal to that of coactivator.

(B) Both emission bands have the same optical quenching spectra, which indicate that the ground states for both bands have the same energy difference from the valence band.

(C) In the EL brightness dependence on voltage [ $B = B_0 \exp(-c/V^{1/2})$ ], both bands have the same  $c$ -value. This fact indicates that excitation energy involved is the same (15)<sup>1</sup>. The latter two discussions have been given by Curie (16).

The basic idea on the impurity level variation is as follows:

*Deep impurity level.*—A wave function of an electron forming a deep impurity level is localized, and in the first approximation the impurity energy level is determined by the impurity ion to which that electron belongs and its nearest neighbors. Thus in the solid solution between crystals to which the same anion belongs, e.g., ZnS and CdS, an energy level of an impurity, a substitute for a cation, does not vary relative to the energy band formed by anions;  $S^{-2}$  in ionic bonding model expressions. On the contrary, if a different anion belongs to this, the situation is different. The impurity level splitting in the latter case was treated by Fonger (17) by using  $\text{Zn}(\text{S,Se})$ .

*Shallow impurity level.*—A wave function of an electron forming a very shallow impurity level is approximated by a hydrogen-like model.

The above ideas lead to a schematic shown in Fig. 10 illustrating the impurity level variation in  $(\text{Zn,Cd}) (\text{S,Se})$  solid solution.

*Discussion of experimental results.*—The energy level variation in the sample composition prepared here is shown in Fig. 11, which is obtained from the vertical section of Fig. 10. The observed variation of emission spectra in Fig. 7 agrees with this; band 1 shifts to a shorter wavelength as the composition approaches ZnSe, while band 2 is almost unvaried.

The variation in quenching characteristics is also explained by the above model, as well as the slow decay in the case of phosphors containing a considerable amount of both anions.

The frequency dependence variation in EL with composition and temperature is explained by considering the temperature quenching factor of EL to be  $[1 + D \exp(-E_c/kT)/f]^{-1}$  (18, 19), ( $E_c$ , the activation energy of temperature quenching),  $E_c$  varying as shown in Fig. 10 and 11.

The variation in emission spectra with frequency and temperature arises from the same effect. That is, at sufficiently low temperature at which quenching oc-

<sup>1</sup> This cannot be a justification of the association model, unless the main excitation is a direct one of luminescent center and not a host excitation.

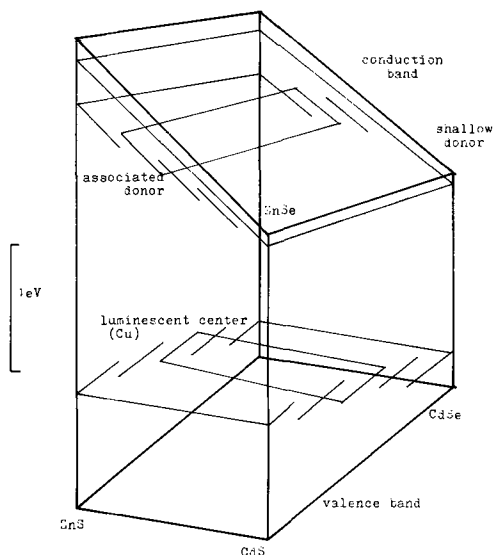


Fig. 10. Energy level diagram for (Zn, Cd) (S, Se) system

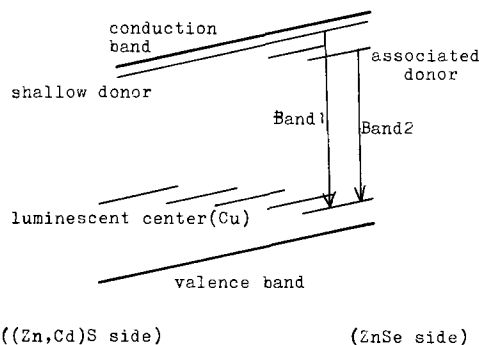


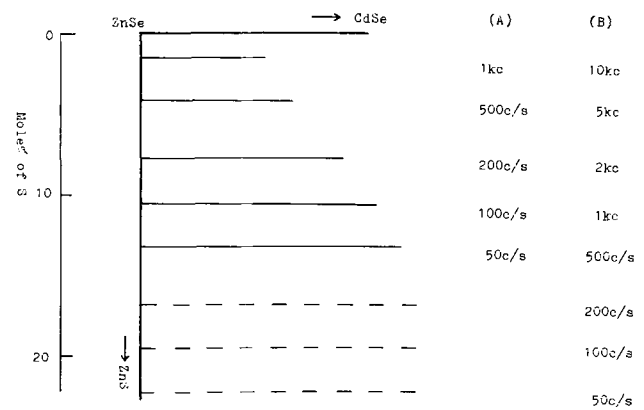
Fig. 11. Schematic energy level diagram for prepared samples

curs in neither band, the emission spectrum variation is not observed except in the change due to cross section of donors, band gap variation, half width variation of emission spectrum, etc. In the temperature region at which quenching occurs, the emission band of the smaller  $E_c$  increases relatively with increasing frequency and falling temperature. Of course, when the emission band which is not due to the delayed recombination, e.g., the Mn band, coexists, the contribution of this band to the emission spectrum variation is to be considered by the same temperature quenching factor as photoluminescence, i.e.,  $[1 + \nu \exp(-E_c/kT)]^{-1}$ . In the latter case the emission spectrum variation with applied voltage is observed to be owing to the differences of the  $c$ -value.

(Zn,Cd)(S,Se) as EL phosphors emitting longer wavelength light.—Red EL phosphors whose composition is near (Zn,Cd)S, made by modified firing technique (20, 13), are superior to those whose composition is near ZnSe, especially under low excitation frequency. The former, however, shows a rapid deterioration, which seems to be due to deep traps because the deteriorated phosphors recover after a day or so without excitation. Further trials, e.g., introducing shallow donors, are expected for improvement.

Under high excitation frequency (a few kilocycles), fairly good red EL phosphors were obtained by using a composition near ZnSe, but the brightness decrease under low frequency excitation is inevitable on account of temperature quenching.

Critical frequencies for application can be determined by defining them as  $f=f_1$  when  $q$  (temperature

Fig. 12. Critical frequencies for application of (Zn, Cd) (S, Se) as EL phosphor. (A) frequency for  $q = 1/2$ , (B) frequency for  $q = 9/10$ .

quenching factor) =  $1/2$  and  $f=f_2$  when  $q \approx 9/10$  [ $(D/f) \exp(-E_c/kT) = 0.1$ ], which are shown in Fig. 12 for room temperature, and  $D=10^8 \text{ sec}^{-1}$  (19), using band 2 (band of higher quenching temperature) and approximating step-like energy level variation with composition by linear variation. This figure indicates the composition to choose of EL phosphors of given color and of given excitation frequency.

#### Acknowledgment

The authors wish to thank Professors T. Takahashi, S. Yoshida, and Y. Shibata for valuable discussions and their continued interest in these investigations.

Manuscript received Nov. 28, 1967; revised manuscript received Jan. 29, 1968.

Any discussion of this paper will appear in a Discussion Section to be published in the December 1968 JOURNAL.

#### REFERENCES

1. F. C. Palilla and D. H. Baird, *This Journal*, **109**, 1162 (1962).
2. T. Matsuo *et al.*, Report of EL Committee of Japan (1964).
3. I. A. Mironov and L. Ya. Markovskii, *Optics and Spectrosc.*, **16**, 285 (1963).
4. F. I. Kolomoitsev *et al.*, *ibid.*, **15**, 44 (1963).
5. I. J. Hegyi, S. Larach, and R. E. Shrader, *This Journal*, **104**, 717 (1957).
6. S. Larach and R. E. Shrader, *RCA Rev.*, **20**, 532 (1959).
7. W. G. Gelling and J. H. Haanstra, *Philips Research Repts.*, **16**, 371 (1961).
8. A. Wachtel, *This Journal*, **107**, 602 (1960).
9. W. Lehmann, *ibid.*, **108**, 607 (1961).
10. A. Dreeben, *ibid.*, **110**, 1045 (1963).
11. D. W. G. Ballentyne, *ibid.*, **107**, 807 (1960).
12. D. W. G. Ballentyne and B. Ray, *Physica*, **27**, 337 (1961).
13. T. Hariu *et al.*, *J. Electrochem. Soc. Japan*, **33**, 793 (1965).
14. W. Lehmann, *This Journal*, **113**, 449, 788 (1966).
15. J. Mattler and T. Ceva, "Luminescence of Organic and Inorganic Materials," p. 537, H. P. Kallmann and G. M. Spruch, Editors, John Wiley & Sons Inc., New York (1962).
16. D. Curie, "Luminescence in Crystals," Mathuen Co. Ltd., London, and John Wiley & Sons Inc., New York (1963), Dunod of Paris (1960).
17. W. H. Fonger, *Phys. Rev.*, **137**, A1038 (1965).
18. H. F. Ivey, "Electroluminescence and Related Effects," ("Advances in Electronics and Electron Physics," Sup. 1), Academic Press, New York (1963).
19. Unpublished.
20. W. Lehmann, *This Journal*, **110**, 759 (1963).

# Fluorescent Properties of Alkaline Earth Aluminates of the Type $MAI_2O_4$ Activated by Divalent Europium

Frank C. Palilla,\* Albert K. Levine,<sup>1</sup> and Maija R. Tomkus

*The Bayside Laboratory, Research Center of  
General Telephone and Electronics Laboratories, Bayside, New York*

## ABSTRACT

The luminescent characteristics of alkaline earth aluminates activated by divalent europium have been investigated. Ultraviolet excitation of these compounds can occur through the host lattice and from the  $4f^7$  ground state to excited states of the  $4f^7$  and  $4f^65d^1$  electronic configurations of divalent europium. The emissions involve  $4f-5d$  transitions as evidenced by the broadness of the spectra, sensitivity to structure, and sensitivity to temperature. Evidence is also presented that the  $Eu^{2+}$  occupies cationic-lattice sites. The performance details of these phosphors in fluorescent lamps are described.

Considerable attention has been devoted recently to the fluorescence of trivalent europium because of the high efficiency of several Eu-activated systems under both cathode ray and ultraviolet excitation and because its relatively simple fluorescence spectrum makes it amenable to theoretical mechanism studies (1). This paper discusses the fluorescence properties of divalent europium with emphasis on its high efficiency as a green and blue emitter when incorporated in certain aluminate lattices. The optical properties of the divalent and trivalent ions of europium differ considerably in several respects, and these differences relate primarily to the degree of interaction with the lattice. Unlike the sharp emission lines obtained from  $Eu^{3+}$ , the emission from  $Eu^{2+}$  is broad and structureless.

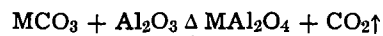
Investigations of visible-emitting phosphors based on divalent europium have been reported by a number of workers, dating back to 1934 (2). Attention has also been devoted to the question of the mechanism of the fluorescence process. Freed and Katcoff (3) report that the fluorescence spectrum of  $Eu^{2+}$  in  $EuCl_2$ - $SrCl_2$  solutions consists of broad diffuse bands with an underlying structure that becomes evident at low temperatures. The intense violet-blue fluorescence band which they report has a maximum at 406 nm. Freed and Katcoff furthermore state that the  $Eu^{2+}$  spectrum is particularly sensitive to the crystalline environment. They propose that the principal features of the  $Eu^{2+}$  spectrum are accounted for by the presence, in activated states, of an electron in outer shells (such as  $5d$ ,  $6s$ ,  $6p$ , or the lattice). Butement (4) proposed a similar mechanism for the  $EuCl_2$ - $SrCl_2$  system. The later work of Jenkins and McKeag (5) on europium-activated alkaline earth silicates and the work of McClure and Kiss (6) on rare-earth-activated cubic crystals support this view. Reinfeld and Glasner (7) have recently supplemented the work of previous investigators by a study of the absorption and fluorescence spectra of  $Eu^{+2}$  in alkali halide crystals. The absorption spectrum of  $Eu^{2+}$  contains two broad absorption bands in the ultraviolet, peaking at about 250 and 330 nm, which they too attribute to the  $4f^7 \rightarrow 4f^65d^1$  transition resulting from the splitting of the  $5d$  orbitals by the crystal field. In 1946  $SrAl_2O_4$  was reported as a phosphor host by Froelich (8) who used Mn as an activator. He obtained red fluorescence with long u.v. excitation, but no fluorescence with short u.v. excitation. In 1963 a Belgian patent (9) described broad green emission from this host when activated by europium and synthesized in

a reducing atmosphere. No performance features were discussed, however, nor was a study of the effect of cationic species described.

This paper describes an investigation of the alkaline earth aluminates activated by divalent europium with emphasis on  $SrAl_2O_4:Eu$ . The materials show outstanding response to both long and short u.v. excitation and moderate response to cathode ray excitation. The emission intensity and distribution are shown to be functions of the alkaline earth cationic species. The spectral shifts are attributable to the different crystal field environments of the europium in the various structures obtainable within the  $MO \cdot Al_2O_3$  composition (where  $M = Mg, Ca, Sr, \text{ or } Ba$ ).

## Experimental Procedure

The phosphors are synthesized by dry blending  $MCO_3$  (where  $M = Mg, Ca, Sr, \text{ or } Ba$ ),  $Al_2O_3$ , and  $Eu_2O_3$ , according to the equation



A slight excess of  $Al_2O_3$  is preferable (0.7-0.9 M/Al). A reducing atmosphere of forming gas ( $H_2-N_2$ ),  $H_2$ , or  $NH_3$  is preferred over CO with a firing temperature of  $1200^\circ-1750^\circ C$  for a few hours. When the phosphors are prepared in this manner, a Eu concentration of about 3-5 m/o (mole per cent) for Mg, Sr, and Ba aluminates and 0.1 m/o for  $CaAl_2O_4$  has been found to be optimum, giving products which fluoresce very efficiently under u.v. excitation. X-ray diffraction studies indicate that the major phase present is  $MAI_2O_4$  with some  $Al_2O_3$  in excess. The phosphors tend to decompose in water with a consequent diminution in fluorescence efficiency. X-ray examination shows that one of the decomposition products is  $3MO \cdot Al_2O_3 \cdot 6H_2O$ .

The emission spectra are given in terms of relative energy. This was accomplished by using a NBS 1000w quartz-iodine lamp as an internal reference as described by Avella, Sovers, and Wiggins (10).

## Results and Discussion

The aluminates prepared as described above are well crystallized and the powders produce sharp x-ray patterns. However, the crystalline habit is not well defined. Attempts to obtain uniform particles and a narrow size distribution were unsuccessful. While the structures of Ba and Mg aluminates are known (11), those of Ca and Sr aluminates are still not well characterized (12). The two sites available for incorporating Eu are either the  $Al^{3+}$  sites or the  $M^{2+}$  sites.  $Al^{3+}$  is small (0.50Å) but  $M^{2+}$  ranges in size from 0.65 to 1.35Å. Taking the case of  $Sr^{2+}$ , which is almost

\* Electrochemical Society Active Member.

<sup>1</sup> Present address: Richmond College of the City University of New York, Staten Island, New York 10301.

equal in size to  $\text{Eu}^{2+}$  (1.13 to 1.12Å), x-ray diffraction patterns show no crystal lattice distortions supporting the latter site preference ( $\text{Sr}^{2+}$  sites). This, of course, is based on the assumptions that all of the added Eu is incorporated in the crystal lattice and that substitutions up to 8 m/o Eu in a site which would be only slightly distorted by differences in ionic size would show up in the diffraction pattern.

The phosphors, when synthesized in a reducing atmosphere, are greenish in body color. The excitation spectrum of  $\text{SrAl}_2\text{O}_4:\text{Eu}$ , obtained by the method of Eby (13) which corrects for instrumental effects and records excitation spectra in terms of relative efficiency, is presented in Fig. 1. The Mg, Ca, and Ba analogs have closely similar excitation spectra. The strong absorption above 350 nm is consistent with the observed energy level scheme for absorption by  $\text{Eu}^{2+}$  having a  $4f^7$  electronic configuration (14), but the absence of fine structure also indicates absorptions into  $4f^65d^1$  levels which have been lowered by the incorporation of  $\text{Eu}^{2+}$  in a crystalline matrix; the broad absorption that peaks between 240-270 nm is consistent with the energy level scheme for absorption by  $\text{Eu}^{2+}$  having a  $4f^65d^1$  electronic configuration (14); the broad absorption below 200 nm may well represent absorption directly into the host lattice. Since no sharp lines are observed in the emission spectra, the transitions to the ground state must originate in levels of the  $4f^65d^1$  configuration. If absorption occurs into an energy level of the  $4f^7$  configuration above the band or emitting levels of  $4f^65d^1$ , radiationless transition to this latter level occurs prior to the final luminescent transition.

The emission colors range from blue for  $\text{CaAl}_2\text{O}_4:\text{Eu}$  to green for  $\text{SrAl}_2\text{O}_4:\text{Eu}$  with the Mg and Ba analogs peaking at intermediate wavelengths. Figure 2 shows the broad-band character of the emissions, providing evidence that europium is present in the divalent state. The fact that the emissions do not shift in the order of increasing ionic radius of the cation may be due to the different environment about the  $\text{Eu}^{2+}$  in each of the four compounds. The whole spectral range of peaks from 440-520 nm can be obtained by appropriate alkaline earth cationic combinations.

The broadness of the emission band indicates an interaction between the host and the activator which can be attributed to the presence of an excited electron in an outer shell of the  $\text{Eu}^{2+}$  ion. The transitions correspond to  $4f-5d$  transitions. The oscillator strengths of these transitions are orders of magnitude higher than those for the normally weak and shielded  $4f-4f$  transitions of the trivalent Eu ion. The luminescence spectrum of  $\text{Eu}^{2+}$  is also more sensitive to temperature quenching. The luminescence peak of  $\text{SrAl}_2\text{O}_4:\text{Eu}$  at  $-196^\circ\text{C}$  is about 20% more intense than that at room temperature. This result is consistent with the expectation that in luminescent processes involving interaction with the lattice, lattice vibrations which lead to

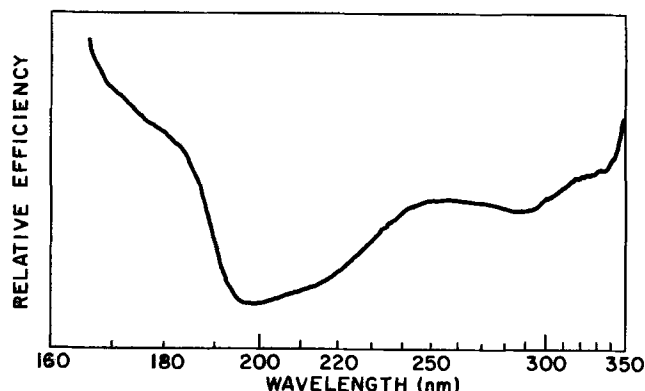


Fig. 1. Excitation spectrum of  $\text{SrAl}_2\text{O}_4:\text{Eu}$  corrected for instrumental variables.

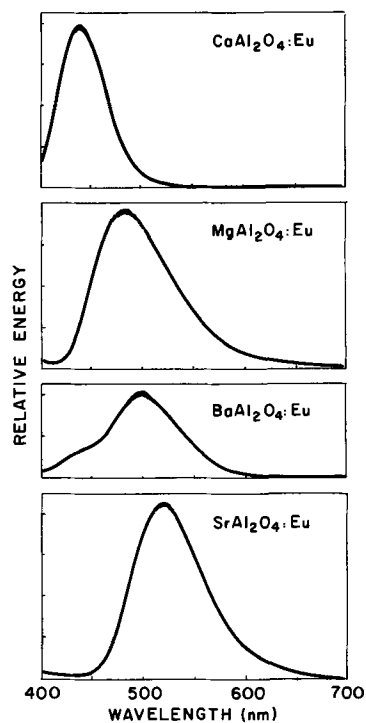


Fig. 2. Emission spectra of alkaline earth aluminates corrected for instrumental variables.

dissipative interactions are minimized by reduced temperatures. The emission spectrum at liquid  $\text{N}_2$  temperature shows a shoulder on the principal emission, indicating a relatively weak, broad emission band near 450 nm. This does not appear to be lattice emission since no appreciable fluorescence is obtained from the unactivated host material.

Additional evidence that the transitions involved are not confined to the  $4f$  shell of  $\text{Eu}^{2+}$  comes from the excitation spectrum of  $\text{SrAl}_2\text{O}_4:\text{Eu}$ . The feeble excitation band of  $\text{SrAl}_2\text{O}_4$  is broad and peaks at 270 nm; the excitation band of  $\text{SrAl}_2\text{O}_4:\text{Eu}$  is broad and peaks near 350 nm (Fig. 1). The shift in excitation peak indicates that Eu plays the principal role in excitation, while the broadness indicates that this excitation is not restricted to  $4f-4f$  transitions.

Outside of the spectral details described here, there has been little other direct or unambiguous evidence for the presence of divalent europium in this system. A sample of  $\text{SrCl}_2:\text{Eu}$  was prepared, and it was found that the emission consists of a narrow band which peaks at about 410 nm, and which appears to show some structure at liquid  $\text{N}_2$  temperatures. An EPR spectrum, shown in Fig. 3, conclusively established the presence of divalent europium. A similar study was made on  $\text{SrAl}_2\text{O}_4:\text{Eu}$  and  $\text{SrAl}_2\text{O}_4$  and the corresponding traces are shown in Fig. 3b and 3c, respectively. The smeared out band observed in the  $\text{SrAl}_2\text{O}_4:\text{Eu}$  spectrum is real and may be due to  $\text{Eu}^{2+}$ , but the hyperfine structure of  $\text{Eu}^{2+}$  was not observed, even with samples of low activator concentration and more sensitive operating conditions. The hyperfine  $\text{Eu}^{2+}$  structure has, however, been observed with the system  $\text{SrO}\cdot\text{Al}_2\text{O}_3\cdot\text{SiO}_2:\text{Eu}$  (Fig. 3d) which was prepared in an identical manner and which shows the same broad emission characteristics. The inability to observe this ERP structure in  $\text{SrAl}_2\text{O}_4:\text{Eu}$  may be attributed to a site of extremely low symmetry for the  $\text{Eu}^{2+}$ , or even to its presence in more than one site.

It may be significant to note that when the phosphors are prepared in an oxidizing atmosphere, red emission is observed instead of the blue to green emission observed when a reducing atmosphere is used during preparation. It may also be significant that the red and blue to green emission (together with a corresponding

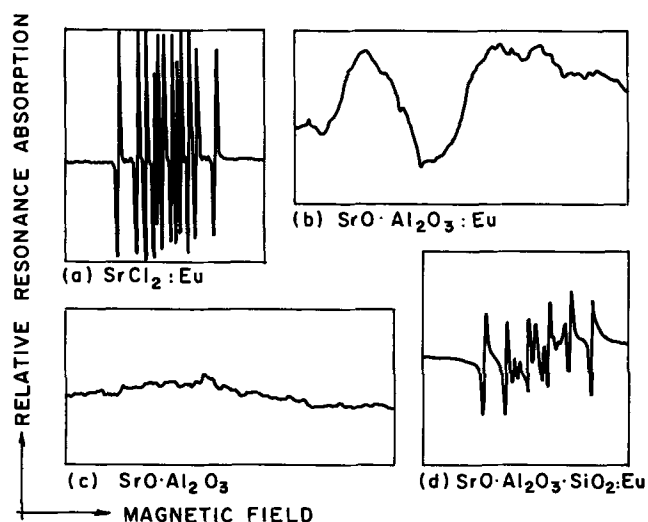


Fig. 3. EPR spectra of (a)  $\text{SrCl}_2:\text{Eu}$ , (b)  $\text{SrO}\cdot\text{Al}_2\text{O}_3:\text{Eu}$ , (c)  $\text{SrO}\cdot\text{Al}_2\text{O}_3$ , and (d)  $\text{SrO}\cdot\text{Al}_2\text{O}_3\cdot\text{SiO}_2:\text{Eu}$ .

white and greenish body color, respectively) is reversible; thus, a phosphor that emits red after refiring in an oxidizing atmosphere will emit green if refired again in a reducing atmosphere. The  $\text{Eu}^{3+}$  emission lines, however, are different depending on whether the phosphor (taking in this case  $\text{SrAl}_2\text{O}_4:\text{Eu}$ ) is fired first in air or first in  $\text{H}_2$  and then air. All the lines present in the latter are also present in the former. The sample fired solely in air, however, has extra emission lines suggesting that the Eu in this case has also been incorporated in a separate phase of  $\text{Al}_2\text{O}_3$  which is present in excess.

Because of their high luminescence efficiency these phosphors are of interest for lighting applications. In this connection it is useful to compare  $\text{SrAl}_2\text{O}_4:\text{Eu}$  with  $\text{Zn}_2\text{SiO}_4:\text{Mn}$  which is commercially used in fluorescent lamps. Both of these phosphors have their emission peak near 520 nm; however, their excitation maxima occur at different wavelengths. At the peak excitation of the aluminate (near 350 nm) the silicate responds only feebly. On the other hand, the intensity of the aluminate emission is 75% of that of the silicate when they are excited at the peak of the latter (254 nm). Additional results were obtained by exciting the phosphors with the total u.v. output of a low-pressure mercury discharge germicidal lamp with dominant emission at 254 nm and a medium pressure S-4 lamp with dominant emission at 365 nm. Brightness readings were obtained by use of a 1P21 photomultiplier in combination with a Wratten 106 filter. The results are presented relative to  $(\text{Zn}_{0.7}\text{Cd}_{0.3})\text{S}:\text{Ag}$ , which also has its emission peak at 520 nm.

	LPMV lamp	MPMV lamp
$(\text{Zn}_{0.7}\text{Cd}_{0.3})\text{S}:\text{Ag}$	100	100
$\text{Zn}_2\text{SiO}_4:\text{Mn}$	310	4
$\text{SrAl}_2\text{O}_4:\text{Eu}$	315	120

In actual fluorescent lamps, where response to the total u.v. radiation from the mercury discharge becomes

significant, the  $\text{SrAl}_2\text{O}_4:\text{Eu}$  exceeds  $\text{Zn}_2\text{SiO}_4:\text{Mn}$  in both lumen output and in maintenance characteristics. For example 40-w lamps containing  $\text{SrAl}_2\text{O}_4:\text{Eu}$  yield 3343 lumens after 117 hr of operation; this level of brightness represents 96.5% of initial lamp output.

The emission of  $\text{SrAl}_2\text{O}_4:\text{Eu}$  is quenched at elevated temperatures. At 300°C the emission intensity is down to about 10% of its room temperature intensity. When the phosphor is allowed to cool, however, the intensity returns to its original level. After prolonged heating at 500°C in air, the reaction is no longer reversible. This is true of all the other alkaline earth aluminates as well.

The phosphors are further characterized by a rapid initial decay followed by a long persistence at a very low light level. Thus the  $\text{SrAl}_2\text{O}_4:\text{Eu}$  phosphor decays to 1/10 of initial brightness in 10  $\mu\text{sec}$  but has a low-level persistence which lasts many seconds. The cathode ray response of the described alkaline earth aluminates is moderate and yields 20-30% of the response from  $(\text{Zn},\text{Cd})\text{S}:\text{Ag}$  cathode ray standards of matching emission color.

#### Acknowledgments

The authors are grateful to J. Ragusin for assistance in the preparation of the samples, to Dr. J. Rosenthal for EPR spectra, to Dr. C. Wiggins for corrected emission spectra, and to Dr. O. Sovers for useful discussions on mechanism. The authors appreciate the assistance of D. Howell in the preparation of this manuscript.

Manuscript received Dec. 18, 1967; revised manuscript received ca. Feb. 28, 1968. This paper was presented at the Boston Meeting, May 5-9, 1968, as Abstract 54.

Any discussion of this paper will appear in a Discussion Section to be published in the December 1968 JOURNAL.

#### REFERENCES

1. F. C. Palilla, Keynote Address presented at the Dallas Meeting, May 7-12, 1967, Extended Abstracts, 16, 68, *Electrochem. Tech.*, 6, 39 (1968).
2. H. Haberlandt, B. Karlik, and K. Prziabram, *Sitzber. Akad. Wiss. Wein Math.-Naturwiss. Klasse, Abt. IIa*, 143, 151 (1934).
3. S. Freed and S. Katcoff, *Physica*, 14, 17 (1948).
4. F.D.S. Butement, *Trans. Faraday Soc.*, 44, 617 (1948).
5. H. G. Jenkins and A. H. McKeag, *This Journal*, 97, 415 (1950).
6. D. S. McClure and Z. Kiss, *J. Chem. Phys.*, 39, 3251 (1963).
7. R. Reisfeld and A. Glasner, *J. Opt. Soc. Amer.*, 54, 331 (1964).
8. H. C. Froelich, U. S. Pat. 2,392,814, Jan. 15, 1946.
9. Belgium Pat. 1,347,459, Nov. 18, 1963. Also issued as H. Lange, U. S. Pat. 3,294,699, December 27, 1966.
10. F. J. Avella, O. J. Sovers, and C. S. Wiggins, *This Journal*, 114, 613 (1967).
11. R.W.G. Wykoff, "Crystal Structures," 2nd ed., vol. 3, John Wiley & Sons, New York (1965).
12. F. P. Glasser and L. S. Dent Glasser, *J. Am. Ceram. Soc.*, 46, 377 (1963).
13. J. E. Eby, Paper presented at the Toronto Meeting, May 3-7, 1964, Abstract 27.
14. G. H. Dieke and H. M. Crosswhite, *Appl. Optics*, 3, 675 (1963).

# Anodic Dissolution of Heavily Doped N-Type Ge in Aqueous Solutions

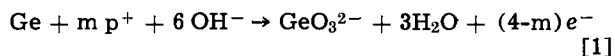
R. Gereth<sup>1</sup> and M. E. Cowher

IBM Watson Research Center, Yorktown Heights, New York

## ABSTRACT

The anodic dissolution of n-type Ge in aqueous solutions is generally assumed to be hole-production-rate limited. Investigations of Ge half-cell reactions, which revealed the significance of the minority carrier density for the dissolution process, have been performed in the past only with lightly doped, n-type Ge electrodes having donor concentrations of less than  $3 \times 10^{16} \text{ cm}^{-3}$ . The present experiments cover the entire resistivity range of available Ge single-crystal material. In the case of heavily doped, n-type Ge with a donor concentration above  $2 \times 10^{18} \text{ cm}^{-3}$ , no evidence of electrolytic current density limitation attributable to a hole deficiency at the semiconductor surface is detected over the voltage range employed between the Ge electrode and the electrolyte. It is suggested that the anodic dissolution of heavily doped, n-type Ge is governed by a conduction band mechanism, *i.e.*,  $\text{Ge} \rightarrow \text{Ge}^{4+} + 4e^-$ , and that, therefore, no holes are required for the dissolution process. This hypothesis is consistent with previous observations that heavily doped, n-type Ge can be electropolished without illumination and with the results of this work showing that the corrosion potential of heavily doped, n-type Ge electrodes cannot be explained on the basis of a minority carrier controlled "quasi-photovoltaic effect."

More than a decade ago Brattain and Garrett (1) published their classical paper, "Experiments on the Interface Between Germanium and an Electrolyte." Following this pioneering work, many other scientists have looked into the dissolution behavior of Ge in aqueous solutions in order to gain new insight into surface effects and to find practical means of preparing mirror-smooth semiconductor surfaces applicable for device fabrication. As a result of these investigations,<sup>2</sup> it is generally assumed that the anodic dissolution of n-type Ge in aqueous solutions requires holes. Consequently, the anodic dissolution of n-type Ge in alkaline solutions is described in the literature (2, 4-7) by the following equation



The parameter  $m$  was found (7) to vary in n-type Ge between 2 and 3.6, depending on the doping level and on the amount of holes available, and to reach 4 for p-type Ge. Equation [1] illustrates that  $m$  holes have to be present for the reaction to occur, while  $(4-m)$  electrons are simultaneously produced. This means that n-type Ge dissolves *via* a combination of valence band and conduction band mechanisms.<sup>3</sup> In accordance with this model it was found, for example, that lightly doped, n-type Ge can be electropolished only if extra holes are supplied by illuminating the Ge wafer with an intense light source (8) and that the corrosion potential of lightly doped, n-type Ge in an alkaline solution containing an oxidizing agent can be explained (6) on the basis of a minority carrier controlled quasi-photovoltaic effect.

On the other hand, it has been stated that heavily doped, n-type Ge can also be electropolished (8) without illumination,<sup>4</sup> a result which is inconsistent with the hypothesis that the hole production is the rate-limiting factor for the anodic dissolution process of n-type Ge (10). In addition, it was recently observed (1) that the corrosion potential  $U_k$  of n-type Ge as a function of hole concentration exhibits an un-

expected extremum, *i.e.*,  $-U_k$  increases with an increase in doping level up to a donor concentration of approximately  $2 \times 10^{17} \text{ cm}^{-3}$  and decreases with an increase in donor concentration beyond this value. For more details see the section on Corrosion Potential  $U_k$  of Ge Electrodes.

It is the purpose of this paper to show that two different mechanisms seem to govern the anodic dissolution behavior of lightly and of heavily doped, n-type Ge. All previous investigations of Ge half-cell reactions, which revealed the significance of holes for the dissolution process of n-type Ge, have been performed only with lightly doped, n-type Ge (1, 4, 5, 7, 12-16) having donor concentrations below  $3 \times 10^{16} \text{ cm}^{-3}$ . The present investigations cover n-type Ge single-crystal material with resistivities ranging from 3 to 0.0008 ohm-cm. Previously reported experiments involving high resistivity, n-type and p-type Ge electrodes have been partly repeated for basis of comparison and will be included in the following sections. Current-voltage characteristics of Ge electrodes immersed in alkaline solutions and alkaline solutions containing an oxidizing agent will be presented. The results of the present experiments suggest that the anodic dissolution of heavily doped, n-type Ge is governed by a conduction band mechanism and that no holes are required for the dissolution process.

## Experimental Arrangement

The simple apparatus used for studying the Ge half-cell reactions in aqueous solutions is illustrated in Fig. 1. The Ge electrode potential was measured against a commercially available saturated calomel reference electrode using a high impedance voltmeter. A platinum foil was used as an auxiliary current electrode. All half-cell measurements were done with the Ge samples in the dark and with the electrolyte covered by a dry  $\text{N}_2$  atmosphere. The Ge wafers were cut from crucible grown crystals and were mechanically lapped on one side and chemically polished (17) on the other. The latter surface was exposed to the electrolyte. A metal film was evaporated on the lapped backside of the wafers and alloyed with the Ge to ensure reliable ohmic contact. Most test samples had (111) oriented surfaces and were doped either with Sb or Ga with the exception of the 0.0008 ohm-cm sample which was doped with As.

<sup>1</sup> Present address: AEG—Telefunken, Hellbronn, Germany.

<sup>2</sup> For a review see Gerischer (2) and Turner (3) and the references given there.

<sup>3</sup> Oxidation in its simplest form can either occur by absorbing a hole,  $\text{A} + \text{p}^+ \rightarrow \text{A}^+$  (valence band mechanism), or by emitting an electron,  $\text{A} \rightarrow \text{A}^+ + e^-$  (conduction band mechanism).

<sup>4</sup> Similar observations (8, 9) have been made during the electropolishing of heavily doped, n-type Si material with resistivities below 0.01 ohm cm.

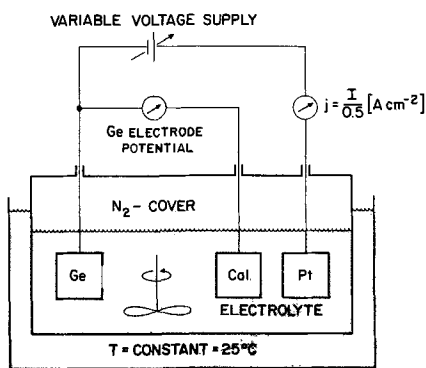


Fig. 1. Corrosion potential apparatus

To facilitate the current-voltage measurements, a special sample fixture was designed which is illustrated in Fig. 2. It consists of two parts: the sample holder and a special measuring jig. The Ge wafers are black-waxed on a hot-plate between two microscope glasses containing circular holes of 0.5 cm<sup>2</sup> area. Due to surface tension a thin film of black wax runs underneath the cover glasses ensuring a tight assembly. The excess black wax in the glass openings can easily be rinsed off using standard organic solvents. By this means, a well-defined area (0.5 cm<sup>2</sup>) of the Ge wafer can then be exposed to the electrolyte. The sample holder is attached to the actual measuring jig by a vacuum-chuck arrangement. A standard o-ring ensures a good seal. This set-up has the advantage that the assembly of the Ge wafer onto the microscope glasses, which play the role of mask and handle, can be performed on a hot-plate away from the rest of the sample fixture. Thus, one sample can be mounted while another is attached to the sample fixture and used for current-voltage measurements. Hence, replacing one sample on the fixture with another takes only a matter of seconds. It just requires releasing the vacuum, taking one sample off, and replacing it with a premounted sample.

### Experimental Results

First, measurements of the corrosion potential  $U_k$  of n-type and p-type Ge will be described. Then the observed current-voltage characteristics of selected Ge electrodes in alkaline solutions with and without an oxidizing agent will be reported. The term "I/V characteristic" will from now on be used to refer to the current-voltage characteristics of the Ge electrodes.

**Corrosion potential  $U_k$  of Ge electrodes.**—Figure 3 shows the results of the  $U_k$  measurements. The corrosion potential was measured potentiometrically vs. a saturated calomel reference electrode. All  $U_k$  values listed in Fig. 3 were measured on Ge electrodes immersed in an electrolyte composed of 0.1M  $K_3[Fe(CN)_6]$ , 0.1N NaOH, and 1.0N  $NaNO_3$ . This elec-

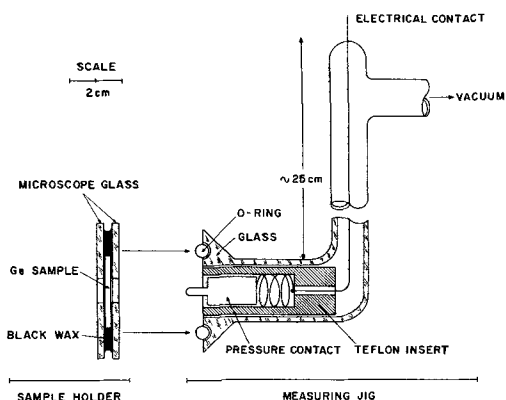


Fig. 2. Sample fixture for electrolytic current-voltage measurements.

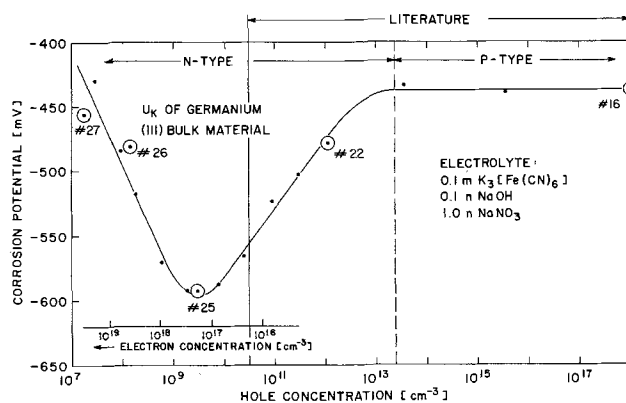


Fig. 3. Corrosion potential of Ge electrodes measured at +25°C vs. a saturated calomel reference electrode.

trolyte was chosen because in a similar composition, it had already been studied extensively by other investigations (2). The data for lightly doped, n-type Ge and for p-type Ge agree very well with previously published results (6). However, the linear relation, shown there, between  $U_k$  and the logarithm of the hole concentration does not hold for heavily doped, n-type Ge and an unexpected minimum<sup>5</sup> can be seen in the  $U_k$  vs. hole concentration curve at a donor concentration of approximately  $2 \times 10^{17}$  cm<sup>-3</sup>.

The minimum  $U_k$  value in Fig. 3 is not characteristic for samples with (111) surface orientation. The effect was also observed with (110) and (100) oriented samples and with acid solutions. The individual  $U_k$  readings were extremely stable and could be reproduced within the accuracy of  $\pm 3$  mv over a period of several months. The data shown in Fig. 3 was taken without stirring the electrolyte and at a constant electrolyte temperature of  $25 \pm 0.1^\circ\text{C}$ . The  $U_k$  readings themselves have a temperature sensitivity of, typically, 2 mv/ $^\circ\text{C}$ .

Gerischer and Beck (6) assumed for their model explaining the logarithmic dependence of  $U_k$  on hole concentration that both electrons and holes are required for the anodic dissolution process of n-type Ge. To determine why their hypothesis fails for predicting  $U_k$  of heavily doped, n-type Ge and to understand better the Ge dissolution mechanism, Ge test samples were selected whose  $U_k$  readings fall into areas, left and right, with respect to the minimum  $U_k$  value in Fig. 3. The  $U_k$  value of one test sample coincides very closely with the "minimum  $U_k$  value." The samples are distinguished by circles around the corresponding data points and are comprised of one p-type sample (No. 16); one high resistivity, n-type sample (No. 22); one lightly doped, n-type sample (No. 25); and two heavily doped, n-type samples (No. 26, No. 27). The Ge half-cell reactions of these samples were measured in alkaline solutions with and without an oxidizing agent; the results obtained are presented below.

**I/V characteristics of Ge electrodes.**—Figure 4 shows current-voltage measurements obtained on Ge samples whose resistivities are listed in the upper left corner of the drawing and which were immersed in a 0.1N NaOH solution containing 1.0N  $NaNO_3$ . The current density is plotted vs. electrode potential. Note that the two samples No. 22 and No. 25, both belonging to the group of "lightly doped Ge," exhibit small ( $< 1$  ma/cm<sup>2</sup>) anodic limited current densities, which do not depend on stirring the electrolyte as has been reported previously (2). The I/V characteristic of the most heavily doped n-type sample No. 27 is almost identical with that measured on the p-type electrode. Both

<sup>5</sup> It should be noted that the "minimum" in Fig. 3 actually corresponds to the largest negative corrosion potential value measured.  $U_k$  of Ge is negative with respect to the calomel reference electrode and the ordinate in Fig. 3 is calibrated in the conventional way, with increasing negative mv-values listed from top to bottom.



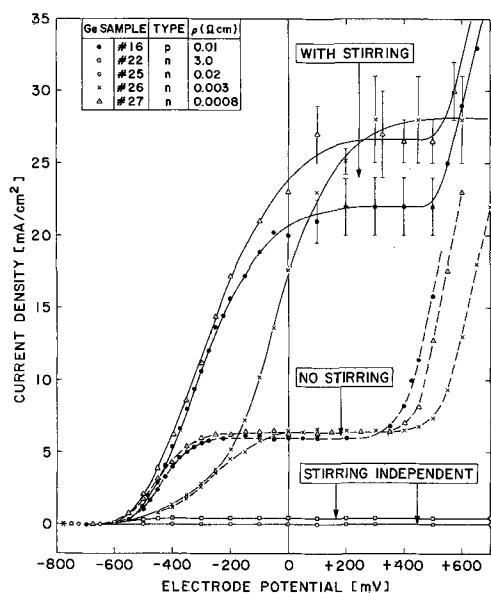


Fig. 4. Current-voltage characteristics of Ge electrodes immersed in a 0.1N NaOH solution containing 1.0N NaNO<sub>3</sub>.

samples show for Ge electrode potentials between  $-250$  and  $+300$  mv an anodic current plateau much larger in magnitude, however, than that measured for the lightly doped, n-type samples. In addition, this current-density plateau can be drastically increased by stirring the electrolyte or by varying its pH value. This indicates that the current-density plateau is caused by the limited OH ion supply from the electrolyte (5, 16). The stirring action was not uniform in the electrolyte; consequently, fluctuations were encountered when the current-density plateau was reached. For current densities below this value, the current-voltage readings were extremely constant. The renewed current density increase above an electrode potential of approximately  $+0.4$ v is thought to be caused by an increased OH ion supply due to H<sub>2</sub>O electrolysis (14).

To substantiate further the observation that p-type and heavily doped, n-type Ge electrodes show very similar I/V characteristics, the anodic limited current density of the samples was measured for a fixed anodic bias of  $-100$  mv and with no stirring as a function of electrolyte temperature. The results are plotted semi-logarithmically in Fig. 5 vs. the reciprocal electrolyte temperature.

Figure 5 shows that the anodic saturation current density in lightly doped, n-type Ge increased approximately three times for each  $10^\circ$  temperature increment. The heavily doped, n-type Ge electrode behaves exactly like the p-type electrode; both exhibit only a slightly temperature sensitive current density.

The half-cell measurements were extended to a redox system, i.e., an electrolytic cell in which the Ge electrodes are immersed into an alkaline solution containing the oxidizing agent  $K_3[Fe(CN)_6]$  (see Fig. 6). This is the same electrolyte used for measuring the corrosion potentials plotted in Fig. 3. Consequently, the corrosion potentials  $U_k$ , as reported in Fig. 3, are identical with those Ge electrode potentials in Fig. 6 belonging to zero external current. Thus, one can extract  $U_k$  values from I/V measurements via the intersect of the I/V curves with the abscissa. For reasons which will become apparent in the discussion section, it is of great interest to find out how the electrode potentials of the I/V curves in Fig. 6 belonging to zero current density, depend on the concentration of the oxidizing agent in the electrolyte. The experimental answer to this question is given in Fig. 7 and 8 for three selected Ge electrodes. In each case the entire I/V curve was measured for different  $K_3[Fe(CN)_6]$  concentrations (0.005, 0.02, 0.06, and

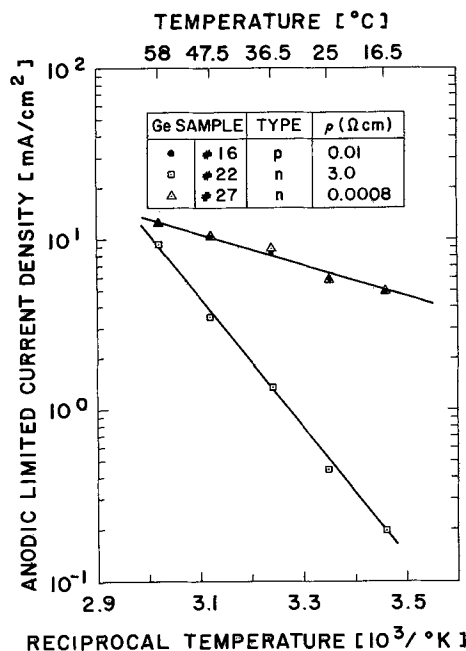


Fig. 5. Anodic limited current density, measured at a fixed Ge electrode bias of  $+100$  mv vs. the temperature of the electrolyte.

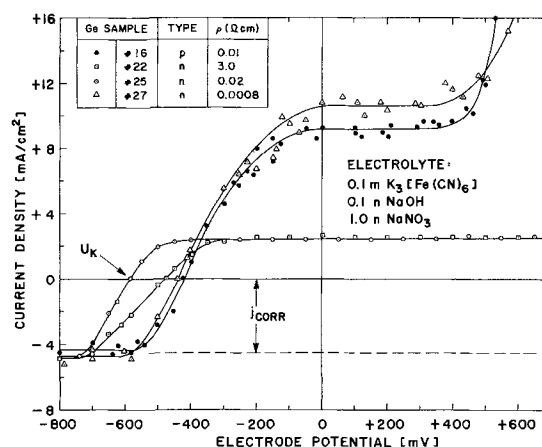


Fig. 6. Current-voltage characteristics of Ge electrodes immersed in a stirred redox-system.

0.1M) in the unstirred electrolyte yielding different  $j_{corr}$  values (0.08, 0.4, 1.5, and 3.0 ma/cm<sup>2</sup>, respectively). However, only the corresponding  $U_k$  vs.  $j_{corr}$  values are plotted in Fig. 7 and 8.

Figures 7 and 8 are arranged by plotting current density semilogarithmically vs. electrode potential. Two kinds of experimental results are shown: solid symbols are used to report the  $U_k$  vs.  $j_{corr}$  studies as outlined above. The open symbols represent regular I/V measurements carried out in an unstirred electrolyte containing 0.1M  $K_3[Fe(CN)_6]$ . This time, however, the Ge dissolution current density rather than the total externally measured current density was plotted.<sup>6</sup> In other words, the open symbols in Fig. 7 and 8 show how the current density through the Ge electrodes increases from the value of the cathodic limited plateau as a function of increasing external electrode potential.

The results from both kinds of measurements can be approximated by one curve for each the p-type and the heavily doped, n-type Ge in Fig. 7. Gerischer and Beck (6) have already reported the same observation for p-type Ge. For the high resistivity n-type Ge,

<sup>6</sup> From the work of Beck and Gerischer (4, 7) one can assume that the externally measured current density represents the difference between the Ge dissolution current density and  $j_{corr}$ .

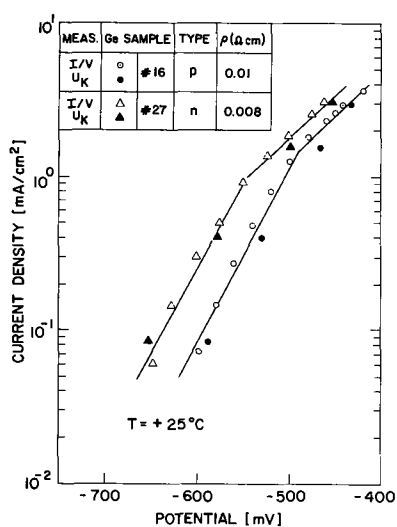


Fig. 7. Dissolution and corrosion current density as a function of electrode and corrosion potential respectively for p-type and heavily doped, n-type Ge.

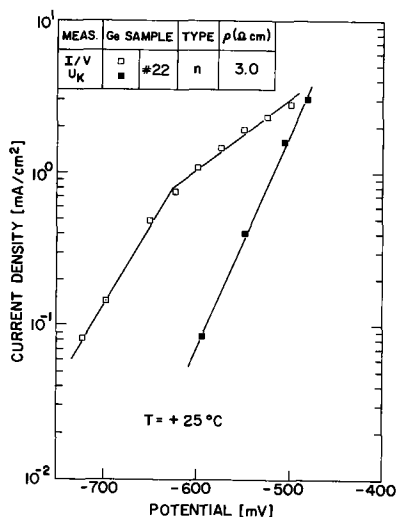


Fig. 8. Dissolution and corrosion current density as a function of electrode and corrosion potential, respectively, for lightly doped, n-type Ge.

however, the two current-voltage curves differ drastically (see Fig. 8). For example, at an electrode potential of  $-600$  mv the Ge dissolution current density differs by more than one order of magnitude from the corrosion current density belonging to a  $U_k$  value of  $-600$  mv.

### Discussion

The current density through the Ge electrodes as a function of increasing electrode potential first follows in Fig. 4 and 6 the following pattern: first no Ge dissolution, then an exponential current increase followed by a current plateau, which is hole-diffusion-rate limited for the lightly doped, n-type samples and OH-ion-diffusion-rate limited for both the p-type and the heavily doped, n-type samples. The transition between the exponential branch of the I/V characteristic and the plateau region occurs smoothly. It is, therefore, unlikely that the larger magnitude of the plateau current density in the case of heavily doped n-type Ge is due to additional carriers generated by an avalanche process in the breakdown region of a surface inversion layer (12).

Additional confirmation that the anodic dissolution process of heavily doped, n-type Ge does not depend on the minority carrier density can be gained from the temperature sensitivity of the anodic limited current

density presented in Fig. 5. The strong exponential increase in the anodic limited current density as a function of electrolyte temperature is, for the 3 ohm-cm, n-type Ge electrode quantitatively the same as is known for the temperature dependence of the saturation current in a reversed biased Ge pn junction. Uhler (13) has previously reported the same temperature variation of the anodic-saturation current for the case of a 5.5 ohm-cm, n-type Ge electrode immersed in a 10% KOH solution. These observations suggest that the anodic dissolution current is governed in high resistivity, n-type Ge by the equilibrium concentration of minority carriers, i.e., the concentration of holes. On the other hand, the weak temperature sensitivity in the anodic current-density plateau of p-type and heavily doped, n-type electrodes could be accounted for by an increased OH-ion-diffusion rate from the electrolyte to the semiconductor surface.

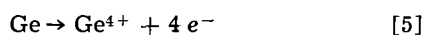
The Tafel plots shown in Fig. 7 and 8 substantiate the above described differences in dissolution behavior between heavily and lightly doped Ge. Gerischer (2) has pointed out that p-type Ge behaves exactly like metals under cathodically controlled corrosion conditions. Therefore, the relation between the corrosion potential and the corrosion current density is the same as between electrode potential and the dissolution current density. Compare the location of the solid dots and open circles in Fig. 7. For high resistivity, n-type Ge, however, complication arises by an incomplete balance of minority carrier injection into the electrode surface causing an additional potential drop (6). This explains the fact that, for a given current density, the corrosion potential (solid squares) and the electrode potential (open squares) are widely different in Fig. 8.

In the case of the heavily doped, n-type Ge electrode, one finds no deviation (see open and solid triangles in Fig. 7) from the corrosion behavior known to occur in metals and p-type Ge. This is indicative that the corrosion behavior of heavily doped, n-type Ge is majority carrier controlled.

Gerischer's model (6) explains the corrosion potential of n-type Ge on the basis of two major assumptions, viz., the existence of a surface inversion layer and the importance of both kinds of carriers for the Ge anodic dissolution process. Both assumptions, however, are not valid for the case of heavily doped, n-type Ge. At room temperature, n-type Ge becomes degenerate at a donor concentration of approximately  $2 \times 10^{18} \text{ cm}^{-3}$ , making the existence of a surface inversion layer unlikely for donor concentrations greater than this value. In addition, the experimental results discussed in the previous section have shown that the anodic dissolution of heavily doped, n-type Ge requires only the presence of one kind of carrier, viz., electrons. These considerations suggest that the minimum in the  $U_k$  curve of Fig. 3 is caused by the beginning of a transition region at the end of which n-type Ge becomes degenerate and the mode of anodic dissolution changes from a hole to an electron controlled mechanism. The I/V characteristic of sample No. 25 (0.02 ohm-cm, n-type;  $2 \times 10^{17}$  donors  $\text{cm}^{-3}$ ) shows, in Fig. 4, a barely detectable anodic limited current density ( $< 50 \mu\text{a}/\text{cm}^2$ ), which is hole-diffusion-rate limited. The  $U_k$  of the same sample, however, is not quite as large as expected from an extrapolation of  $U_k$  values measured on more lightly doped, n-type Ge electrodes (see Fig. 3). This is indicative of the beginning of the transition region as defined above. On the other hand, the I/V characteristic of sample No. 26 (0.003 ohm-cm, n-type;  $3.5 \times 10^{18}$  donors  $\text{cm}^{-3}$ ) exhibits in Fig. 4 evidence of an intermediate state. The anodic current plateau is, through this sample, no longer minority carrier-concentration controlled although it is reached at a larger electrode potential than observed for either the p-type or the 0.0008 ohm-cm, n-type electrode. Experiments in which the corrosion potential was used as a tool to measure high surface concentrations ( $C_0 \sim 6 \times 10^{19} \text{ cm}^{-3}$ ) of n-type

diffused Ge layers have shown (11, 19) that the  $U_k$  curve of Fig. 3 can even be linearly extrapolated beyond the data point corresponding to the most heavily doped bulk sample investigated. For example, the above-mentioned diffused n-layer was doped with  $6 \times 10^{19}$  As atoms  $\text{cm}^{-3}$  at the surface according to sheet resistance measurements. This layer showed a corrosion potential of  $-400$  mv immediately after the sample had been immersed in the electrolyte. However, one might speculate that, in the region of extremely high impurity level,  $U_k$  becomes also a function of the specific doping element present.

The results of the present investigations have demonstrated that the anodic dissolution behavior of lightly and heavily doped, n-type Ge is different. Therefore, it seems reasonable to divide the range of n-type Ge material for considering its dissolution behavior into two groups (20), namely, into  $n^-$  and  $n^+$  Ge. The unexpected minimum of  $U_k$  apparent in Fig. 3 for n-type Ge with a donor concentration of  $2 \times 10^{17}$   $\text{cm}^{-3}$  suggests using this donor concentration as a "dividing line" between  $n^-$  and  $n^+$  Ge. For  $n^-$  Ge, the  $m$  values are those reported in the literature (7); for  $n^+$  Ge, however, specifically for degenerately doped Ge with a donor concentration above  $2 \times 10^{18}$   $\text{cm}^{-3}$  at room temperature, an  $m$  value of zero must be postulated because no holes are required for the dissolution process, as shown by the present investigations. This suggests that the dissolution of heavily doped, n-type Ge is given phenomenologically by a conduction band mechanism



Equation [5] states that heavily doped n-type Ge is oxidized by giving off 4 electrons.

It can be speculated that heavily doped, n-type Si might also follow a different dissolution mechanism, i.e., a minority-carrier-concentration independent mechanism in contrast to the data available in the literature for lightly doped, n-type Si. This model might shed some light on the confusion about the anomalous dissolution process in Si.

#### Acknowledgment

The authors thank Dr. A. Reisman for his interest and support and Dr. T. O. Sedgwick for many stimu-

lating discussions. They are grateful to J. M. Green for his assistance in editing the manuscript.

Manuscript received Sept. 5, 1967; revised manuscript received Feb. 13, 1968.

Any discussion of this paper will appear in a Discussion Section to be published in the December 1968 JOURNAL.

#### REFERENCES

1. W. H. Brattain and C. G. B. Garrett, *Bell System Tech. J.*, **34**, 129 (1955).
2. H. Gerischer, "Advances in Electrochemistry and Electrochemical Engineering," Vol. 1, pp. 139-232, P. Delahay, Editor, Interscience Publishers, New York-London (1961).
3. D. R. Turner, "The Electrochemistry of Semiconductors," pp. 155-204, P. J. Holmes, Editor, Academic Press, London-New York (1962).
4. F. Beck and H. Gerischer, *Z. Elektrochem.*, **63**, 943 (1959).
5. F. Beck and H. Gerischer, *ibid.*, **63**, 500 (1959).
6. H. Gerischer and F. Beck, *Z. Physik. Chem. N.F.*, **23**, 113 (1960).
7. H. Gerischer and F. Beck, *ibid.*, **24**, 378 (1960).
8. M. V. Sullivan, P. L. Klein, R. M. Finne, L. A. Pompliano, and G. A. Kolb, *This Journal*, **110**, 412 (1963).
9. D. Baker and J. R. Tillman, *Solid-State Electronics*, **6**, 589 (1963).
10. J. F. Dewald, "Semiconductors," pp. 727-752, N. B. Hannay, Editor, Reinhold Publishing Corp., New York (1959).
11. R. Gereth, *This Journal*, **113**, 318C (1966).
12. D. R. Turner, *ibid.*, **103**, 252 (1956).
13. A. Uhler, *Bell System Tech. J.*, **35**, 333 (1956).
14. H. Gerischer and F. Beck, *Z. Physik. Chem. N. F.*, **13**, 389 (1957).
15. H. Gerischer, *Anales fis. quim.*, **56B**, 535 (1960).
16. H. V. Harten, R. Menning, and G. Schwandt, *Phillips Tech. Rev.*, **26**, 127 (1965).
17. A. Reisman and R. L. Rohr, *This Journal*, **111**, 1425 (1964).
18. O. Madelung in "Handbuch der Physik," Vol. 20, pp. 161, Berlin-Goettingen-Heidelberg (1957).
19. R. Gereth and M. E. Cowher, To be published.
20. R. Gereth and M. E. Cowher, Recent News Paper presented at the Dallas Meeting of the Society, May 7-12, 1967.

## Pyrolytic Deposition of Silicon Dioxide in an Evacuated System

J. Oroshnik<sup>1</sup>\* and J. Kraitchman<sup>2</sup>

Westinghouse Research Laboratories, Pittsburgh, Pennsylvania

#### ABSTRACT

The formation of silicon dioxide films by the low-temperature (750°C) decomposition of tetraethoxysilane in an evacuated system was studied. The performance of the system was investigated and the film characteristics evaluated. After a simple thermal treatment most of the properties of the deposited oxides were comparable to those of thermally grown oxides.

In the fabrication of semiconductor devices silicon dioxide films are used for a variety of purposes. Various techniques of producing these films have been investigated. While very good quality oxides are produced by the thermal oxidation of silicon, film production by other deposition techniques offers several potential advantages when compared with the thermal

growth of films. Thicker films can be achieved at lower temperatures and in shorter times. The substrate is not consumed during the process. The film can be produced on substrates other than silicon.

One deposition technique that has been investigated involves the pyrolytic decomposition of various silane compounds (1-3). In this technique an open tube system in which a carrier gas is used to bring the silane vapor into the decomposition region was commonly employed. The pyrolytic oxides produced by this technique were reported to have physical and chem-

\* Electrochemical Society Active Member.

<sup>1</sup> Present address: Corning Glass Works, Raleigh, North Carolina.

<sup>2</sup> Present address: Glass Research Center, PPG Industries, Pittsburgh, Pennsylvania.

ical properties similar to those of thermally grown oxides. However, recent studies (4) have indicated that there are significant differences between the properties of these pyrolytic oxides and thermal oxides, and for many device applications the quality of these pyrolytic oxides is inferior to those of thermal oxides.

Pyrolytic oxides have also been produced in an evacuated system (5), but no extensive evaluation of the performance of this system or the properties of the oxides have been reported. In this study an evacuated deposition system was used to produce pyrolytic oxides, the performance of the system evaluated, and the properties of the pyrolytic oxides determined.

### Experimental

A schematic diagram of the deposition system is shown in Fig. 1. The central region of the reaction tube was maintained at a temperature of 750°C. Silicon wafers were placed on a 6-in. long quartz boat which was then inserted into the reaction tube. After pumping the system down to a pressure of 15–30 $\mu$ , tetraethoxysilane (tetraethylorthosilicate) vapor was admitted to the system. On completion of a run the vapor flow was stopped, but pumping on the reaction tube was continued for 5 min to remove the remaining vapor and gaseous decomposition products. The reaction tube was then isolated from the cold trap, back-filled with nitrogen, and the samples removed.

To investigate the performance of the system, runs were made in which 1-in. diameter silicon wafers were placed at the ends and in the center of the quartz boat. The boat position was changed from run to run. In some of the runs a needle valve was used to control the rate of delivery of the silane vapor to the reaction tube. At maximum delivery rate (needle valve by-passed) deposition rates of about 300 Å/min were obtained. The results of some typical runs are shown in Fig. 2. The region of most uniform deposition was displaced from the furnace center toward the input end. At the maximum delivery rate the displacement was about 2 in. As would be expected at lower delivery rates, the region of most uniform deposition became broader and was displaced still further toward the input end. However, in all cases the region of uniform deposition was sufficiently broad so that no appreciable variation (less than 50Å) occurred in the oxide thickness on the 1-in. wafers. Multibeam interference measurements on a few samples showed that, for the purposes described above, the oxide thickness could be estimated by comparison of interference colors with a calibrated step gauge constructed of thermally grown oxides on silicon. This rapid and nondestructive comparison technique was used for routine thickness determinations.

### Results

**Etch rate.**—Pyrolytic silicon oxides produced by other techniques have been reported to etch more rapidly than thermal oxides (4). The pyrolytic oxides produced by the vacuum deposition technique used

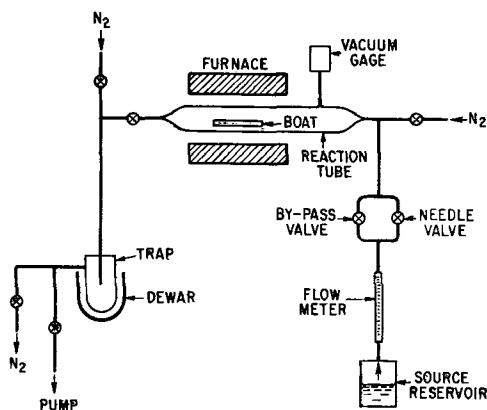


Fig. 1. System used for the deposition of pyrolytic oxides

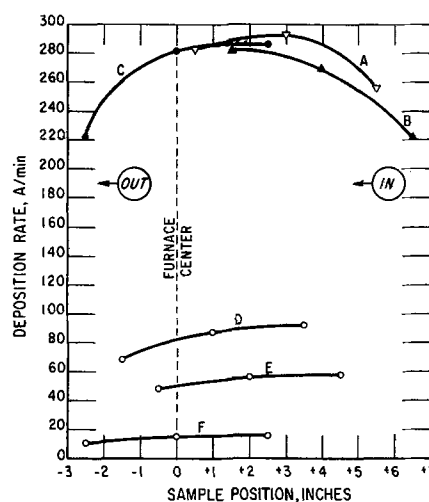


Fig. 2. Deposition of pyrolytic silicon dioxide. The results illustrated by curves A, B, and C were obtained with the silane vapor delivered at the maximum rate (needle valve by-passed). In the runs illustrated by curves D, E, and F the delivery rate was controlled with a needle valve and monitored with a flow meter. In arbitrary units the flow meter readings were (D) 14.5; (E) 9.8; (F) 5.0.

here were also found to behave in a similar manner. These oxides were observed to etch at the rate of 10–15 Å/sec in P-etch (15 parts of 49% hydrofluoric acid, 10 parts of 70% nitric acid, and 300 parts of water).

It has also been shown that a simple thermal treatment of other pyrolytic oxides increases their density, reduces their etch rate, and improves other properties of these films (4). The oxides produced in this investigation were subjected to a thermal treatment of 10–15 min in wet oxygen (bubbled through water kept at 95°C) at 800°C. The effects of this thermal treatment on vacuum deposited pyrolytic oxides appeared similar to those produced on other pyrolytic oxides. Subsequent to this thermal treatment the densified pyrolytic oxides had etch rates of 2 Å/sec. This value is indistinguishable from that of thermally grown oxides. Thermal treatment with dry oxygen at 800°C for periods as long as 1 hr yielded incompletely densified pyrolytic oxides as evidenced by etch rates of 4 Å/sec and higher.

**Thermal treatment and oxide thickness.**—In earlier work in which pyrolytic oxide films of the order of 1 $\mu$  thick were studied, it was reported that the thickness of the films decreased after thermal treatment (4). In this investigation, films of the order of 0.1 $\mu$  thick have also been studied. Both thickness increases and decreases have been observed following thermal treatment. In particular, films about 0.25 $\mu$  thick exhibited no significant change in thickness after thermal treatment. Thinner films, e.g., about 0.15 $\mu$ , become thicker. Thicker films, e.g., about 0.35 $\mu$ , become thinner.

These observations require no revision of the ideas expressed previously (4) that the film shrinkage is due to densification caused by the thermal treatment. To explain these results it is only necessary to recognize that during the thermal treatment the film simultaneously grows thicker due to thermal oxidation.

The magnitude of these effects can be estimated as follows: The thermal oxidation of silicon can be described by a combination of linear and parabolic rate expressions (6–11). At 800°C in wet oxygen, and for oxides less than 0.5 $\mu$  thick the oxidation behavior is essentially linear and, hence, structural differences between the pyrolytic and thermal oxides would be expected to have a negligible effect on the growth characteristics. We can, therefore, obtain an adequate estimate of the amount of oxide growth that occurs during the thermal treatment by assuming the pre-ex-

Table I. Calculated thickness changes due to thermal treatment

Original thickness, $\mu$	Change in thickness, $\mu$		Net
	Growth <sup>a</sup>	Densification <sup>b</sup>	
0.15	0.010	-0.006	+0.04
0.25	0.010	-0.010	0.00
0.35	0.009	-0.014	-0.05

<sup>a</sup> Calculated using a linear rate constant of 0.05  $\mu$ /hr, a parabolic rate constant of 0.1  $\mu^2$ /hr, and for an oxidation time of 0.25 hr at 800°C in wet oxygen.

<sup>b</sup> Calculated on the basis of a 4% film shrinkage during the thermal treatment.

isting pyrolytic oxide to be equivalent to a thermal oxide of the same thickness.

For these calculations, the linear and parabolic rate constants can be determined with adequate accuracy from available data (7, 12). The results of these calculations are given in the second column of Table I. The last column gives the predicted values due to the combined effects of the growth values in the second column and the shrinkage values in the third column. In agreement with our experimental observations these calculations indicate that a significant increase in the film thickness should be observed only on films thinner than 0.15 $\mu$ , while a significant decrease in film thickness should be observed only on films thicker than 0.35 $\mu$ .

**Masking properties.**—While pyrolytic silicon dioxide was found to be a good diffusion mask for boron and phosphorus, contamination doping from the oxide can be a serious problem. In our initial work using a commercial grade of tetraethoxysilane, calculations made using sheet resistance and junction depth measurements (13) indicated contamination doping levels as high as 10<sup>18</sup> per cc were present in the silicon substrate after diffusion. Subsequent work using a purified form of the silane reduced the contamination level to the order of 10<sup>15</sup> to 10<sup>16</sup> per cc. Although contamination levels of this magnitude are quite acceptable in most instances, there are cases where it would not be satisfactory.

**Optical properties.**—The infrared spectra of the pyrolytically deposited oxides indicated that the amount of water present in the oxides (as evidenced by the O-H stretching band in the 3 $\mu$  region) was not significantly different from that found in thermally grown oxides. The Si-O stretching vibration in the 9 $\mu$  region was found to have its peak at 9.35 $\mu$ . However, after densification the peak shifted to 9.3 $\mu$ . This position is indistinguishable from the position found for this peak in thermally grown oxides.

Ellipsometric measurements on the oxides yielded values of 1.44-1.45 for the refractive index. After densification the measurements yielded values of 1.45-1.46. Thermally grown oxides measured by the same technique were found to have a refractive index of 1.46.

**Electrical properties.**—The electrical resistivity and breakdown strength of the pyrolytic oxides were found to be lower than in thermal oxides; the dielectric constant was higher. However, after thermal treatment the properties of the oxides were not significantly different from those of the thermal oxides. Table II summarizes the various electrical properties

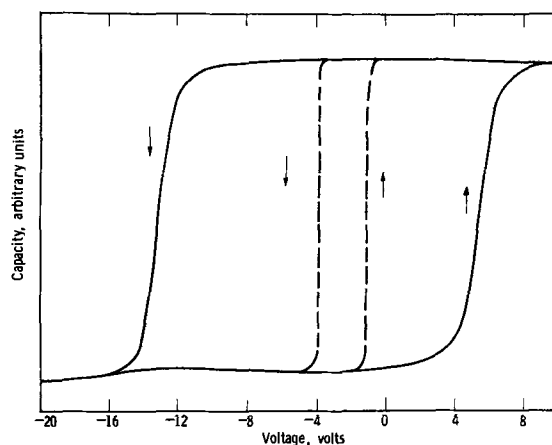


Fig. 3. MOS capacitance-voltage characteristics. Densified pyrolytic oxide 3000 $\text{Å}$  thick on 15 ohm-cm n-type silicon. Voltage is potential of metal contact with respect to silicon substrate. Solid curve, bias swept at normal rate; dashed curve, bias swept very slowly.

of these oxides and some of the other properties discussed previously.

The capacitance-voltage characteristics of metal-oxide-semiconductor (MOS) capacitors fabricated using the pyrolytic oxide were also studied. The small-signal high-frequency (100 kc/sec) capacitance (14, 15) was measured as a function of applied d-c bias. The flat band potential of these capacitors was very large (about -80v), indicating the presence of a high surface state charge density and/or fixed or mobile space charges in the oxide. After densification, the flat band potential was significantly smaller. However, the C-V characteristics then exhibited hysteresis effects. This is illustrated by the curve shown in Fig. 3. When the applied d-c bias is swept at a rate of 0.5-1.0 v/sec, the large hysteresis loop shown by the solid line is obtained. As the sweep rate is reduced, the hysteresis loop narrows as indicated by the dashed line. While it is not clear whether the presence of very mobile ions or other processes are responsible for these effects, it is evident that the MOS characteristics of these pyrolytic oxides are inferior to those of high-quality thermally grown oxides.

### Summary

The deposition of silicon dioxide films by the pyrolytic decomposition of tetraethoxysilane in an evacuated system was investigated. Various performance parameters of the system were studied. Films were deposited at rates as low as 10  $\text{Å}/\text{min}$  and as high as 300  $\text{Å}/\text{min}$ . The oxide films exhibited no significant variation in thickness over a 1-in. diameter wafer.

Various properties such as etch rate, infrared spectra, refractive index, resistivity, breakdown strength, dielectric constant, and capacitance-voltage characteristics of the pyrolytic oxides were measured. While there were a number of significant differences between the properties of these low-temperature pyrolytic oxides and those of thermally grown oxides, most of these differences vanished when the pyrolytic oxides were given a simple thermal treatment.

When subjected to the thermal treatment, thin pyrolytic oxides increased in thickness, while thick pyro-

Table II. Silicon dioxide properties

Oxide	Etch rate (P-etch), $\text{Å}/\text{sec}$	Infrared spectra (Si-O stretching band), $\mu$	Refractive index	Resistivity, ohm-cm	Breakdown strength, v/cm	Dielectric constant
Pyrolytic	10-15	9.35	1.44-1.45	0.01-1 $\times 10^{15}$	4 $\times 10^6$	5.5-6.5
Densified pyrolytic	2	9.3	1.45-1.46	0.1-5 $\times 10^{16}$	5-7 $\times 10^6$	4.0-4.5
Thermal	2	9.3	1.46	0.1-5 $\times 10^{16}$	5-10 $\times 10^6$	3.5-4.0

lytic oxides decreased in thickness. Calculations showed that the observed thickness changes resulting from the thermal treatment could be satisfactorily accounted for by the simultaneous growth of new oxide, plus densification of the pyrolytic oxide.

The thermal treatment was also found to lower the large flat band potential observed on MOS structures fabricated with the pyrolytic oxide to values comparable to those obtained on MOS capacitors fabricated with thermally grown oxides. The magnitude of the hysteresis effects observed in the C-V characteristics of MOS capacitors fabricated using the thermally treated pyrolytic oxide was found to be dependent on the rate at which the bias voltage was swept.

The pyrolytic oxides were also found to have diffusion masking properties comparable to those of thermally grown oxides. When prepared using a purified form of the silane, the contamination levels produced by pyrolytic oxide diffusion masks were reduced to levels of about  $10^{15}$  to  $10^{16}$  per cc.

#### Acknowledgment

The authors wish to thank T. W. O'Keeffe for valuable discussions and assistance in some of the measurements. They are indebted to W. K. Sheets and N. J. Roney for assistance in the experimental work. This work was supported in part by the U. S. Air

Force Avionics Laboratory, Air Force Systems Command, U. S. Air Force.

Manuscript received Sept. 5, 1967; revised manuscript received ca. Feb. 8, 1968.

Any discussion of this paper will appear in a Discussion Section to be published in the December 1968 JOURNAL.

#### REFERENCES

1. E. L. Jordan, *This Journal*, **108**, 478 (1961).
2. J. Klerer, *ibid.*, **108**, 1070 (1961).
3. J. Klerer, *ibid.*, **112**, 503 (1965).
4. W. A. Pliskin and H. S. Lehman, *ibid.*, **112**, 1013 (1965).
5. J. E. Sandor, Paper presented at the Los Angeles meeting of the Society, May 6-10, 1962.
6. B. E. Deal, *This Journal*, **110**, 527 (1963).
7. B. E. Deal and A. S. Grove, *J. Appl. Phys.*, **36**, 3770 (1965).
8. A. G. Revesz, K. H. Zaininger, and R. J. Evans, *Appl. Phys. Letters*, **8**, 57 (1966).
9. P. J. Burkhardt and L. V. Gregor, *Trans. Met. Soc. AIME*, **236**, 299 (1966).
10. W. A. Pliskin, *IBM J. Res. Develop.*, **10**, 198 (1966).
11. T. Nakayama and F. C. Collins, *This Journal*, **113**, 706 (1966).
12. H. C. Evitts, H. W. Cooper, and S. S. Flaschen, *ibid.*, **111**, 688 (1964).
13. J. C. Irvin, *Bell System Tech. J.*, **41**, 387 (1962).
14. K. Lehovc, A. Slobodskoy, and J. L. Sprague, *Phys. Status Solidi*, **3**, 447 (1963).
15. D. R. Kerr, *IBM J. Res. Develop.*, **8**, 385 (1964).

## Autodoping of Epitaxial Silicon

W. H. Shepherd

*Fairchild Semiconductor, Research and Development Laboratory, Palo Alto, California*

#### ABSTRACT

It is assumed that autodoping of epitaxial silicon films grown on heavily doped n-type substrates occurs by transfer of the elemental dopant from the backside of the wafer into the gas phase and subsequently into the depositing film. The processes governing the rate of transfer of autodopant into the film are considered and a quantitative relationship derived for the impurity profile in the film. The relationship gives a satisfactory explanation of autodoping from arsenic doped substrates and shows why antimony is so much to be preferred as a substrate dopant.

The resistivity of an epitaxial silicon film is influenced by two principle contamination factors: (a) the dopant transferred from the substrate into the growing film by way of the gas phase, and (b) background contamination from the reactor and impurities introduced with the feed gases. For the great majority of presently required film resistivities background contamination is no problem. Dopant transfer from the substrate, however, or autodoping as it is generally termed, is often a highly important factor determining the choice of substrate dopant and resistivity. There has been some discussion in the literature (1, 2) concerning the manner in which the dopant transfers from substrate to film with the recent consensus being that a significant amount is transferred by way of the gas phase. Joyce (2) has shown that for n-type dopants halide formation is unnecessary since transfer occurs when the substrates are heated in hydrogen alone. This is not surprising since n-type dopants P, As, and Sb are all readily volatile at epitaxial deposition temperatures and need not form halides to enter the gas phase. Furthermore, available thermodynamic data do not support halide transfer mechanisms. Boron is different since its vapor pressure is so low that elemental transfer is negligible. In this case thermodynamic data do support transfer as BCl. The

present paper, however, is concerned specifically only with arsenic autodoping.

In another paper (3) the author presents data on the activity coefficients for n-type dopants in silicon and discusses the mechanisms of deliberate doping. From these considerations it is apparent that arsenic is the best test vehicle for n-type autodoping studies. Antimony has so slight an autodoping effect that it is not normally detectable above background contamination. Phosphorus, under the expected growth conditions, evaporates from the backside of the silicon substrate in dimeric form making analysis of out-diffusion from the silicon complex.

#### Theory

Once deposition begins, the exposed face of the wafer is assumed to be sealed rapidly by the growing film and is not a source of dopant for contamination of the system (4). The back surface of the wafer is uncoated throughout the run and remains a continuing source of autodopant. The qualitative description of the process then is that dopant diffuses from the backside of the wafer in elemental form, mixes, and is diluted in the main gas stream of the reactor and dopes the epitaxial deposit in the usual way.

To obtain a quantitative picture the following assumptions are made:

(A) The dopant evaporates from the back of the wafer in monatomic form, and immediately adjacent to the surface equilibrium exists between the dopant in the gas and in the silicon, i.e., there is no surface barrier to evaporation.

(B) The dopant mixes completely with the main gas stream and remains monatomic.

(C) At the surface of the growing epitaxial layer the dopant is again in equilibrium between gas and solid phases, and the rate of incorporation is not in any way controlled by kinetic processes at the surface.

*Evaporation of dopant from the substrate.*—Since the dopant is in monatomic form in both the gas phase and the solid state, the equilibrium for the dopant in the two phases can be written

$$x_D = \gamma R_s \tag{1}$$

where at an ambient pressure of one atmosphere  $x_D$  is the mole fraction of dopant in the gas phase,  $R_s$  is the mole fraction in the silicon surface, and  $\gamma$  is an activity coefficient dependent only on temperature. If it is assumed that the evaporation is from the front of the wafer rather than the back, the flux of dopant from the gaseous surface region,  $F_D$ , is

$$F_D = \Psi_D \cdot x_D \tag{2}$$

where  $\Psi_D$  is a gaseous transfer coefficient with units of atoms  $\text{cm}^{-2} \text{sec}^{-1}$  (5).

For evaporation from the back of the wafer the rate will be restricted to a degree which is difficult to estimate. For the present this restriction can be represented by a multiplying factor,  $\lambda$ , less than one so that the effective transfer coefficient becomes  $\lambda\Psi_D$ . The flux of dopant from the backside of the wafer is

$$\begin{aligned} F_D &= \lambda\Psi_D\gamma R_s \\ &= \lambda\Psi_D \frac{\gamma C_s}{N} \end{aligned} \tag{3}$$

where  $C_s$  is the concentration of dopant, in atoms  $\text{cm}^{-3}$ , in the silicon surface (backside), and  $N$  is the density of atoms in the silicon lattice, i.e.,  $5 \times 10^{22}$  atoms  $\text{cm}^{-3}$ . Equation [3] states that the flux of dopant is proportional to the surface concentration,  $C_s$ . Under this boundary condition the solution of the problem of diffusion within the substrate is of a well-known form (6) and is

$$F_D = \theta C_B \exp\left(\theta^2 \frac{t}{D}\right) \operatorname{erfc}\left(\theta \frac{\sqrt{t}}{\sqrt{D}}\right) \tag{4}$$

where  $\theta = \lambda\Psi_D\gamma/D$ ,  $t$  is time in seconds, and  $D$  the diffusion coefficient for the dopant in silicon expressed in  $\text{cm}^2 \text{sec}^{-1}$ .  $\theta$  has units of velocity, in this case  $\text{cm sec}^{-1}$ .  $C_B$  is the initial concentration of dopant in the substrate.

*Incorporation of autodopant in the epitaxial film.*—If the total wafer area is  $A \text{ cm}^2$  (counting backside only), the rate of evaporation of autodopant into the reactor gas stream is  $AF_D$  atoms  $\text{sec}^{-1}$ . Hence, for a main stream hydrogen flow rate of  $H$  molecules  $\text{sec}^{-1}$  the mole ratio of autodopant in the stream, assuming complete mixing, is  $AF_D/H$ .

It is assumed that the gaseous dopant in contact with the surface of the growing film is in thermodynamic equilibrium with the impurity component of the crystal the mole fraction of dopant in the gas is, after Eq. [1], equal to  $\gamma R_F = \gamma C_F/N$  where  $R_F$  and  $C_F$  refer to instantaneous atom ratios and concentration of dopant in the surface of the silicon. The mole fraction of autodopant in the gas stream, which for present purposes may be considered as dopant deliberately added to the initial gas stream is  $AF_D/H$ . From previous papers (5, 3) the average flux of dopant from the gas to the wafer surfaces can be written as the difference between the initial bulk concentration and

the equilibrium surface concentration times a transfer coefficient for the dopant. This leads to

$$\text{Dopant Deposition Rate} = \Psi'_D \left( \frac{AF_D}{H} - \frac{\gamma C_F}{N} \right) \tag{5}$$

The transfer coefficient  $\Psi'_D$  is the same one used in Eq. [2] and [3] except that now it is expressed in  $\mu\text{min}^{-1}$  rather than in atoms  $\text{cm}^{-2} \text{sec}^{-1}$ . In making this transformation it must be recognized that since the dopant enters the silicon lattice the atom density of the dopant "film" is that of the parent lattice, i.e.,  $5 \times 10^{22}$  atoms  $\text{cm}^{-3}$ . If the atom fraction of dopant in the film is  $R_F$  and the silicon growth rate is  $G \mu\text{min}^{-1}$  then the rate of deposition of dopant is given by  $GR_F = GC_F/N$ . Equating this with Eq. [5] and rearranging gives

$$C_F = \frac{NA F_D}{H \left( \frac{G'}{\Psi_D} + \gamma \right)} \tag{6}$$

The expression for  $F_D$  (Eq. [4]) can be written

$$F_D = \theta f(t) C_B \tag{7}$$

where  $f(t) = \exp(\theta^2 t/D) \operatorname{erfc}(\theta \sqrt{t}/\sqrt{D})$  is mainly a function of time since  $\theta^2/D$  is not strongly temperature dependent. The temperature dependence of  $\theta$  is due to the activity coefficient  $\gamma$  (Eq. [4]) so that the temperature sensitivity of  $\theta^2/D$  is represented by  $\gamma^2/D$ . Both  $\gamma$  and  $D$  vary with temperature according to the familiar relationship  $\exp(-\Delta H/RT)$ . It is experimentally observed (3) that for arsenic, phosphorus and antimony in silicon  $\Delta H_A \approx \Delta H_D/2$ . Hence  $\theta^2/D$  is temperature insensitive. Substituting for  $F_D$  in Eq. [6], replacing  $H$  with  $H'$  which has practical units of liters  $\text{min}^{-1}$ , and evaluating the numerical factors in  $N$  and  $H$  gives the film/substrate doping ratio as

$$\frac{C_F}{C_B} = \frac{120 A \theta f(t)}{H' \left( \frac{G}{\Psi'_D} + \gamma \right)} \tag{8}$$

For a constant set of growth conditions, the term  $f(t)$  which varies from  $1 \rightarrow 0$  as  $t$  goes from  $0 \rightarrow \infty$  describes the profile in the film. All of the parameters in Eq. [8] are known or can be estimated reasonably well except for  $\lambda$  which has to be established empirically.

In Fig. 1, the function  $\exp x^2 \operatorname{erfc} x$  is plotted against  $x$ . When  $x = \theta(t/D)^{1/2}$  this function is  $f(t)$ . Thus for  $x < 0.1$ ,  $f(t) = 1$ , and for  $x > 1.0$   $f(t) = 1/2x$ .

Putting  $x = \theta(t/D)^{1/2}$  and substituting these approximations into Eq. [8] gives

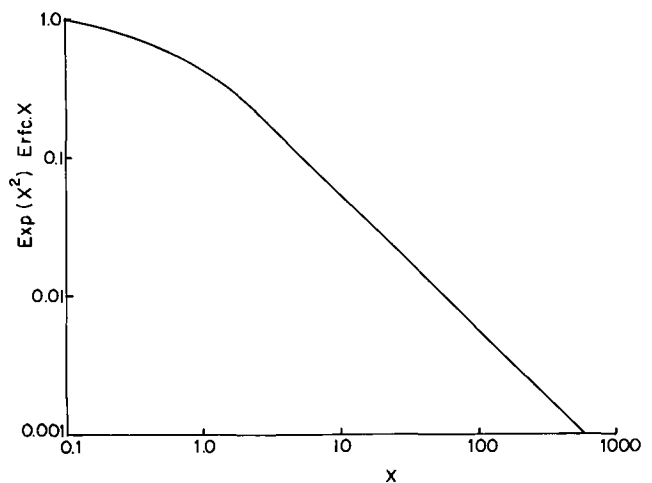


Fig. 1. Plot of  $f(x) = \exp x^2 \operatorname{erfc} x$  against  $x$

for  $\theta(t/D)^{1/2} < 0.1$

$$C_F = \frac{120 A \theta}{H' \left( \frac{G}{\Psi_D} + \gamma \right)} \quad [9a]$$

for  $\theta(t/D)^{1/2} > 1.0$

$$\frac{C_F}{C_B} = \frac{60 A}{H' \left( \frac{G}{\Psi_D} + \gamma \right)} \cdot (D/t)^{1/2} \quad [9b]$$

From the above relationship we see that initially the level of autodoping is independent of time. During this period the loss of dopant is rate controlled by gas transfer from the wafer surface, and the surface concentration  $C_s$  is not substantially below the bulk concentration  $C_B$ . At longer times when  $C_s \ll C_B$  the condition is reached when dopant evaporates from the surface as fast as it can diffuse there, and solid-state diffusion in the silicon becomes the rate-limiting process. In this condition the autodoping is proportioned to  $t^{-1/2}$ . Approximate calculations show that for arsenic and antimony the time independent phase is so brief that it is not of practical significance.

Since the evaporation of impurity from the back of the wafer is independent of the growth process, at least as far as the model is concerned, the time  $t$  in the above expressions is actually the time of heat-treatment. If the reactor is raised quickly to temperature and deposition is begun immediately, then  $t$  is essentially the growth time. It is more normal, however, to etch the wafers prior to growth; and this is usually carried out at a higher temperature, 1300°C, rather than 1200°C. This can be allowed for by replacing  $t$  in the above relationships by  $(t + t_E)$ , where  $t$  now is the actual growth time and  $t_E$  is an effective pre-heat time at the growth temperature. The value of  $t_E$  is obtained from

$$\{\theta f(t_E)\}_{T_G} = \{\theta f(t_H)\}_{T_H} \quad [10]$$

where  $T_G$  = growth temperature,  $T_H$  = etch temperature, and  $t_H$  = length of etch or preheat cycle.

For the present situation where the etch cycle is 5 min at 1300°C, the growth is at 1200°C, and the dopant is arsenic, it turns out that  $t_E < 1$  min, and in the following analyses it has been ignored.

### Experimental Procedures

All experimental data were obtained using deposition by hydrogen reduction of  $\text{SiCl}_4$  in a conventional horizontal reactor. The arsenic doped substrates had resistivities in the range 0.013-0.015 ohm-cm (i.e.,  $C_B = 1.8 - 2.4 \times 10^{18}$  atoms  $\text{cm}^{-3}$ ) and were approximately 1 in. in diameter. They were prepared for epitaxy by chemical etching. Twenty were used in each run. Also included were two  $p^-$  test chips ( $\sim 80$  ohm-cm) and three 2.0 ohm-cm n-type phosphorus doped test wafers. The  $p^-$  wafers were used to obtain approximate values for the level of autodoping and for the epitaxial thickness from junction depth and V/I measurements. The n-type wafers were for the purpose of comparison with  $n^+$  wafers and for impurity profiling close to the substrate-epitaxial layer interface. Where etching was carried out, HBr was used at a temperature of 1300°C (1200°C optical), the rate of etching was 0.35  $\mu/\text{min}$ , and the time was 5 min. The main  $\text{H}_2$  flow rate was 50 liters/min at room temperature and at atmospheric pressure. All depositions were made at 1200°C (1100°C optical).

Impurity profiles in the epitaxial films were obtained from the capacitance-voltage characteristics of shallow, boron diffused, mesa diodes. The diffused junction depth was  $\sim 1\mu$ , and this is allowed for in all the reported results. Film thicknesses were measured on the  $n^+$  substrates by IR techniques, a correction of  $-1\mu$  being applied in all cases. For lightly doped test

wafers, the thickness was taken from a neighboring  $n^+$  wafer. In some instances the epitaxial layers were thin enough and sufficiently lightly doped for the impurity profiles to be determined into the diffusion tail from the substrate. In these cases the position of the profile relative to the substrate film interface could be established most accurately.

**Results.**—Some general autodoping characteristics observed in the experiments will be summarized before examining the principal features in detail.

1. Analysis of many impurity profiles showed the autodoping to be essentially the same over all wafers within a factor of about two. This indicates a degree of mixing along the reactor length which might seem surprising. However, the tilt of the boat produces a slight suction effect beneath it, and a reverse flow of gas can be observed below the boat when small oxide flakes are present in a deliberately contaminated reactor. This apparently causes substantial mixing of the gases.

2. The level of autodoping is similar on  $n^+$  and  $n$  wafers in the same run. There is, apparently, a slightly lesser effect on  $n$  wafers, but the observed differences are generally within a factor of two between  $n^+$  and  $n$  wafers, and are not very significant. It does, however, correlate with the following observation.

3. There is a trend toward higher autodoping at the edge of  $n^+$  wafers. The variation from center to edge is generally within a factor of two. Because of this, the impurity profiles, when reported for  $n^+$  wafers, have been taken near the center of the wafer.

Figure 2 shows profiles taken on five wafers from a single run. This run included no etch or preheat cycle. All profiles have been adjusted along the distance axis using the outdiffusion tails. The solid line is obtained from the theory in a manner described below.

Figure 3 shows profiles taken on five wafers from a 2-hr run. In this instance the wafers were etched prior to deposition. The first 6-min growth was carried out at 0.75  $\mu/\text{min}$ , and the next 114-min growth at 0.13  $\mu/\text{min}$ . The solid line is from the theory.

The points in Fig. 3 cover part of a growth cycle between 40 and 100 min, while those in Fig. 2 cover the first 15 min. Combining the two sets of data, it should be possible to test Eq. [8] and evaluate the unknown parameter,  $\lambda$  (Eq. [3]).

In Eq. [8],  $\lambda$  appears in  $\theta$  and  $f(t)$ ; all other parameters can be evaluated. The values used for these parameters are:  $C_B = 2 \times 10^{18}$  at.  $\text{cm}^{-3}$ ;  $H' = 50$  liters

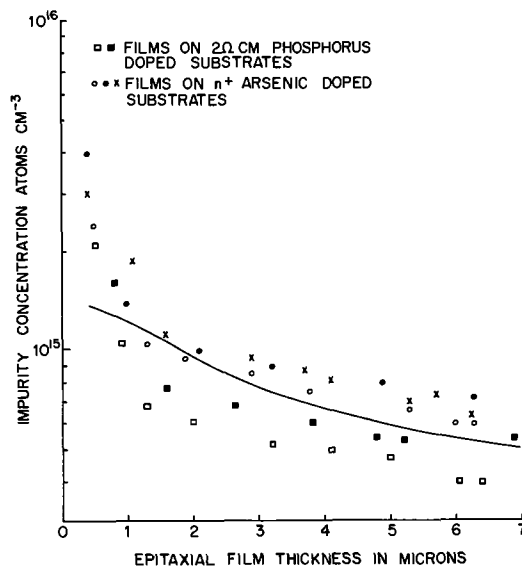


Fig. 2. Impurity profiles on epitaxial films grown at 1200°C (corrected) and  $0.55 \mu\text{min}^{-1}$  for 15 min. Substrate doping level,  $C_B = 2 \times 10^{18}$  at.  $\text{cm}^{-3}$ .



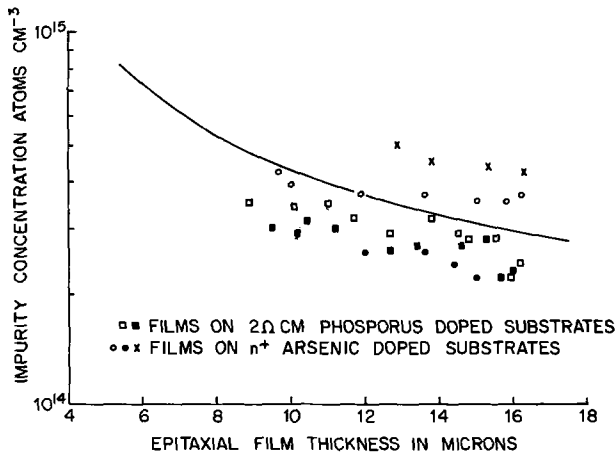


Fig. 3. Impurity profiles on epitaxial films grown at 1200°C (corrected) for 6 min at 0.75  $\mu\text{min}^{-1}$  and 114 min at 0.13  $\mu\text{min}^{-1}$ . Wafers were etched for 5 min at 1300°C before deposition. Substrate doping  $C_B = 2 \times 10^{18}$  at.  $\text{cm}^{-3}$ .

$\text{min}^{-1}$ ;  $A = 100 \text{ cm}^2$ ;  $\Psi_D = 1.3 \times 10^{19}$  at.  $\text{cm}^{-2} \text{ sec}^{-1}$ ;  $\Psi'_D = 150 \mu\text{min}^{-1}$ ;  $\gamma = 3.5 \times 10^{-3}$ .

The value of the activity coefficient for As in silicon at 1200°C is taken from previous work (3). The value for the gaseous transfer coefficient for arsenic,  $\Psi_D$ , is taken to be the same as that for  $\text{SiCl}_4$  in the same reactor (5) and is probably uncertain by a factor of two. Using the quantities as defined above, values of  $\theta f(t)$  have been calculated for the data points in Fig. 2 and 3, except for those close to the substrate film interface in Fig. 2. In Fig. 4, values of  $\theta f(t)$  are plotted vs. the corresponding values of  $t^{1/2}$ . The points in the plot should lie on a line corresponding in slope, although not in absolute value, to some portion of the plot in Fig. 1 since the time dependence arises only from  $f(t)$  ( $f(x) = f(t)$  for  $x = \theta\sqrt{t/D}$ ). A reasonable correspondence can be found with the linear portion of Fig. 1 as demonstrated by the solid line in Fig. 4. This means that  $\theta\sqrt{t}/\sqrt{D} > 1.0$ . The actual value of  $\theta$ , and hence  $\lambda$ , can be obtained for the line in Fig. 4 by iteration. Thus,  $\theta f(t) = 1.7 \times 10^{-8}$  for  $t^{1/2} = 1.5 \text{ min}^{1/2}$ . Knowing the diffusion coefficient,  $D$ , for arsenic in silicon ( $D = 2.5 \times 10^{-13} \text{ cm}^2 \text{ sec}^{-1}$  at 1200°C)  $f(t)$  can be calculated for any assumed value of  $\theta$  and for  $t^{1/2} = 1.5$  from Fig. 1 and the product  $\theta f(t)$  then compared with  $1.7 \times 10^{-8}$ . Carrying this process through leads to  $\lambda \approx 0.04$ , i.e., the effective transfer rate by gaseous diffusion from the back surface of a 1-in.

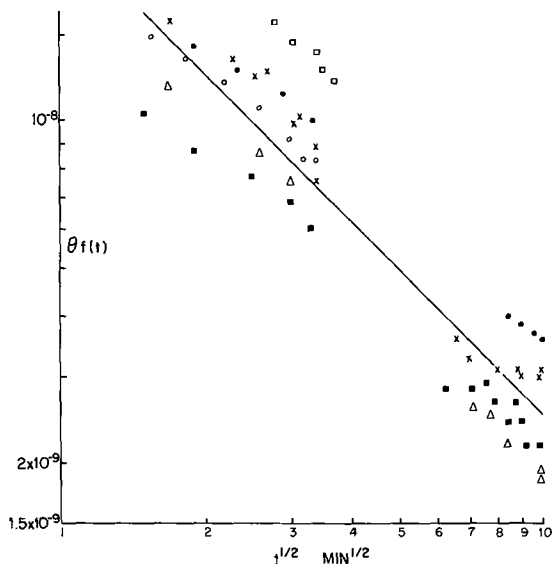


Fig. 4.  $\theta f(t)$  vs.  $t^{1/2}$  for data presented in Fig. 2 and 3

wafer is approximately 1/25 of that from an exposed surface. Values of  $\theta f(t)$  from Fig. 4 were used to calculate the theoretical impurity distributions shown in Fig. 2 and 3.

Using published diffusivities for antimony, values of  $\gamma$  from ref. (3), and  $\lambda = 0.04$ , an autodoping profile for antimony has been calculated and compared with that for arsenic in Fig. 5. The predictions are that, for film thicknesses commonly of interest, antimony is much less of a problem than arsenic. This is in agreement with known facts. Generally, the differences between arsenic and antimony are further magnified by the use of arsenic for high substrate doping levels not attainable with antimony because of its limited solubility.

In the 2-hr slow growth run, Fig. 3, the diode profiling did not reach closer to the substrate than about 9  $\mu$ . To obtain a profile closer to the substrate, one of the 2 ohm-cm n-type wafers was etched in a slow chemical etch to leave, hopefully, about 7-8  $\mu$  of the epitaxial layer. Diodes were made on the remaining film, and an interesting, though in retrospect predictable, effect was observed (2). Two profiles from this wafer are shown in Fig. 6. Both demonstrate a very definite peak in the n-type dopant concentration at what must be the substrate-film interface, since the profiles level off at a concentration close to that ex-

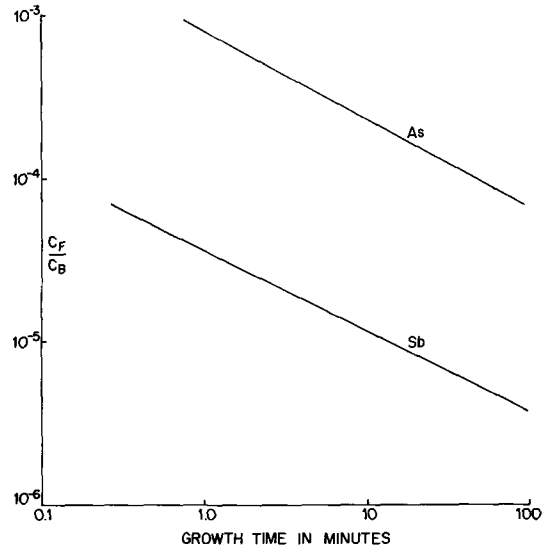


Fig. 5. Comparison of antimony autodoping with that caused by arsenic as estimated using Eq. [8].

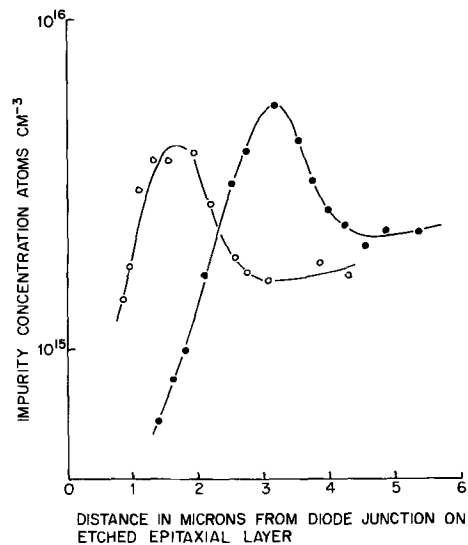


Fig. 6. Impurity profiles close to substrate film interface on 2 ohm-cm n-type substrates from run shown in Fig. 3.

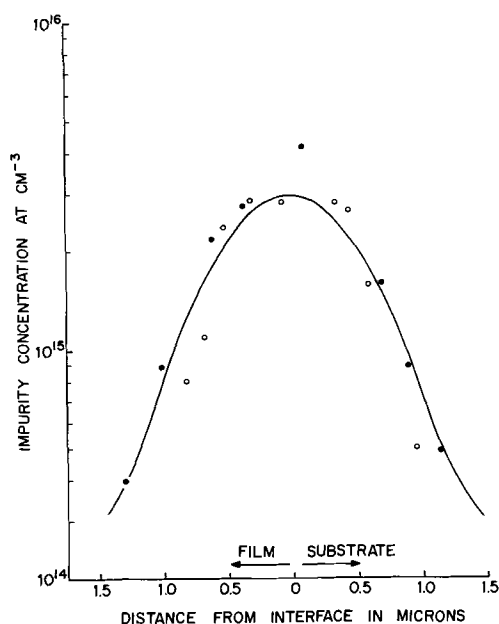


Fig. 7. Comparison of impurity profiles of Fig. 6 with Gaussian profile calculated for arsenic "predeposition."

pected for the substrate. This effect can be explained either by the presence of an n-type contaminant on the wafers prior to deposition or to a predeposition with arsenic prior to growth. Such a predeposition can be expected to occur during the preheat cycle, even when etching is taking place, because of the arsenic present in the gas stream, either from evaporation from the substrates or released by the etching process. If this is the correct explanation, the concentration distribution should be close to Gaussian because the length of the growth cycle considerably exceeded that of the preheat cycle and should correspond to that expected for arsenic. To determine the exact profiles, the contribution of the outdiffusion tail from the substrate (phosphorus doped) was first subtracted, assuming the original substrate doping levels of  $2.5 \times 10^{15}$  at.  $\text{cm}^{-3}$  for the upper curve and  $2.0 \times 10^{15}$  for the lower. The data from the two profiles, adjusted so that the maxima of the two curves coincide on the distance

axis, are plotted in Fig. 7. The solid line is a Gaussian profile plotted from the known time and temperature and the diffusivity of arsenic. The fit is excellent.

A consequence of this kind of predeposition is that test wafers of opposite conductivity type to the film being deposited cannot always be used reliably for determining the resistivity of the epitaxial deposit.

### Conclusions

It has been assumed that autodoping is a process involving gaseous transfer of dopant from the backside of the substrate into the epitaxial film. From this premise, a simple theory appears to present a satisfactory explanation of the axial autodoping profiles observed on  $n^+$  arsenic doped wafers.

If the above assumption is correct, sealing of the backside of the substrate wafer with, for example, an  $\text{SiO}_2$  layer should significantly reduce the level of autodoping. Such an effect was clearly established by Joyce *et al.* (2). These authors, in the same paper, also showed that most transfer of substrate dopant to their test wafers occurred during the pregrowth heat-treatment. At this stage, the front surface of the substrate is exposed so that their observation is an expected one. However, pregrowth transfer, except by way of contamination of the reactor, will not influence the doping in the epitaxial film on the  $n^+$  substrates. The effect close to the substrate-film interface on lightly doped test wafers has already been demonstrated.

Manuscript received July 27, 1967; revised manuscript received Jan. 13, 1968. This paper was presented at the Philadelphia Meeting, Oct. 9-14, 1966, as Abstract 190.

Any discussion of this paper will appear in a Discussion Section to be published in the December 1968 JOURNAL.

### REFERENCES

1. C. O. Thomas, D. Kahng, and L. C. Manx, *This Journal*, **109**, 1055 (1962).
2. B. A. Joyce, J. C. Weaver, and D. J. Maule, *ibid.*, **112**, 1100 (1965).
3. W. H. Shepherd, *ibid.*, **115**, 541 (1968).
4. A. Grove, *et al.*, *J. Appl. Phys.*, **36**, 802 (1965).
5. W. H. Shepherd, *This Journal*, **112**, 998 (1965).
6. Crank, "Mathematics of Diffusion," p. 34, Oxford University Press (1957).

## Radiotracer Studies of Ion Implanted Profile Build-Up in Silicon Substrates

K. E. Manchester

Research and Development Laboratories, Sprague Electric Company, North Adams, Massachusetts

### ABSTRACT

Injection of radiotracer markers at varying fractions of the total implanted dose has provided information on dose dependence of "channeling" in silicon substrates. The implanted profile (total) variation with substrate orientation agrees with that previously reported for electrically active impurities which was determined by junction delineation. Comparison of marker profiles shows a reduction of about 1/10 in impurity ion concentration at three times the depth of the peak of the distribution and about 1/20 the concentration at four times the depth of the peak of the distribution after  $2 \times 10^{13}$  ions/ $\text{cm}^2$  have impinged on the substrate. A greater fall-off in channeled ions is found when the dose was increased to  $5 \times 10^{14}$  ions/ $\text{cm}^2$ .

Doping of semiconductors by injection of impurity ions is an important technique that is being extensively investigated (1). It has been shown that p-n junction properties of implanted structures after a mild thermal treatment are comparable to those of thermally diffused structures (2).

Two important observations one makes when characterizing implanted junctions are: (I) During the anneal which is necessary to optimize and stabilize electrical properties, the p-n junction is observed to move deeper into the substrate. This can be as much as  $0.3\mu$  for an initial depth of  $0.6\mu$ . (II) The depths of

the junctions are much deeper than calculated by existing theory for amorphous solids and they are dependent on substrate orientation.

If this technique is to be used to produce semiconductor devices, it is necessary to characterize the concentration profile of injected ions. To do this, it is necessary to understand the anneal process. The anneal conditions are thermally mild, *i.e.*, 600°C-10 min for phosphorus implanted p-type silicon, and 800°C-15 min for boron implanted n-type silicon. The junction movement suggests either a damage enhanced impurity atom movement or a change in the substitutional/interstitial ratio of injected impurity atoms.

The orientation effect has previously been reported in terms of junction depth as a function of ion energy in the three primary orientations (3). It was found that the deepest junctions for identical implant conditions are found in (110) oriented silicon with depths in the (111) and (100) oriented substrates about equivalent.

The work to be presented here is an investigation of the effect of annealing on implanted profiles and the "channeling" phenomena by a radiotracer technique. The work was initiated by earlier experimental results obtained in this laboratory on profiles of implanted ions by differential sheet conductivity. Integration under the electrical profile accounts for about 80% of the ions striking the sample as measured by beam current.

The experiments to be discussed here were designed to determine the disposition of the remaining 20% of the impinging ions, *i.e.*, are they present as interstitials or have they been lost during the implant, perhaps by sputtering. Unfortunately, this question was not answered; however, valuable information on profile build-up has been derived from our measurements and is discussed herein.

### Experimental

All specimens were implanted with 40 keV  $^{31}\text{P}$  phosphorus ions. A single 40 keV "marker" of approximately  $10^{11}$  ions/cm $^2$  of radioactive  $^{32}\text{P}^+$  was implanted in each specimen after a predetermined number of  $^{31}\text{P}^+$  ions had been implanted. After the marker implantation was complete,  $^{31}\text{P}$  ions were implanted until the total dose of  $5 \times 10^{14}$  ions/cm $^2$  was injected. Three different series were examined in which the implantation sequence was: (a)  $\sim 10^{11}$  ions/cm $^2$   $^{32}\text{P}^+$  followed by  $5 \times 10^{14}$  ions/cm $^2$   $^{31}\text{P}$ ; (b)  $2 \times 10^{13}$  ions/cm $^2$   $^{31}\text{P}^+$  followed by  $\sim 10^{11}$  ions/cm $^2$   $^{32}\text{P}^+$  followed by  $4.8 \times 10^{14}$  ions/cm $^2$   $^{31}\text{P}^+$ ; and (c)  $5 \times 10^{13}$  ions/cm $^2$   $^{31}\text{P}^+$  followed by  $\sim 10^{11}$  ions/cm $^2$   $^{32}\text{P}^+$  followed by  $4.5 \times 10^{14}$  ions/cm $^2$   $^{31}\text{P}^+$ . Handling hazards determined the upper limit of  $^{32}\text{P}^+$ , which could be implanted. It also determined equipment modifications to do the implants.  $^{32}\text{P}$  decays by emission of a 1.7 meV  $\beta$  and has a half life of 14.3 days.

The basic equipment for these experiments was an isotope separator at the Oak Ridge National Laboratory. It is shown schematically in Fig. 1. Ions are generated in the source, accelerated by an electrode system, dispersed according to  $e/m$  by the magnetic field perpendicular to the plane of the beam and impinged on the substrates in the receiver.

The source charge was prepared by irradiating a 2-g sample of red phosphorus with thermal neutrons until 4 Curies of  $^{32}\text{P}$  were produced. The charge was allowed to cool 6 days to reduce short-lived isotope levels to that which could be safely handled.

The source charge container was designed to allow it to be inserted into the source through a vacuum lock and manipulated to break the ampule containing the phosphorus when the charge container was in position.

The receiver was a special design shown in Fig. 2-4. Figure 2 shows the rotatable substrate drum being inserted into the vacuum lock just behind the isolating ball valve. Figure 3 shows the sample drum in position

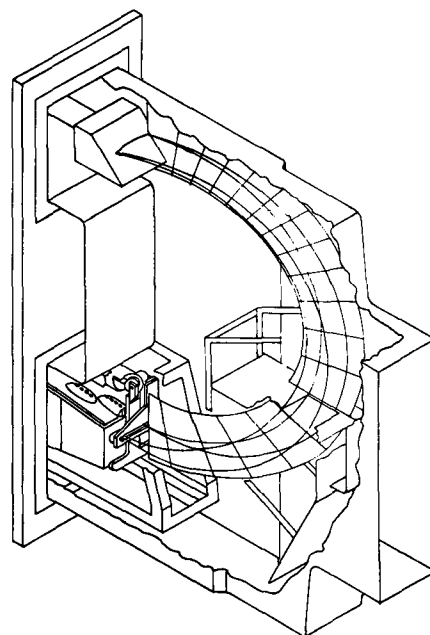


Fig. 1. Schematic of isotope separator



Fig. 2. Receiver design showing vacuum port for loading sample holder.

in the vacuum system with the index plate removed. During the implantation, the drum is rotated at a fixed speed. Because of the rotary motion, the surfaces of samples are not always normal to the beam, but vary from  $+7^\circ$  to  $-7^\circ$  from the normal. Note the beam entrance slot and the probe just below. Three rows of samples are contained on each drum with twelve samples in each row. Figure 4 shows the index plate in position. Note the double set of indexing slots spaced about 0.8 in. apart in the vertical direction to uncover one row of samples at a time and the probe just below the slot which exposed the sample to the beam. The position of the bottom slot was one mass unit below the upper slot. The purpose of this arrangement was to provide a method of monitoring the  $^{32}\text{P}^+$  beam current by observing the  $^{31}\text{P}^+$  current on the probe. A number of assumptions were involved in this measurement, such as equivalent efficiency of ionization for the two isotopes and also a uniform beam current density across each beam so that the current of  $^{32}\text{P}^+$  ions was the  $^{31}\text{P}^+$  ion current multiplied by the isotope ratio ( $5 \times 10^{-6}$ ). Unfortunately, there were gross errors in these assumptions, which are pointed out in Table I. This table indicates how the row activity varied with position, thus indicating inhomogeneity in the beam. Maximum activity indicated for the middle row is two



Fig. 3. Receiver design showing sample positioning in beam



Fig. 4. Receiver design showing beam current monitoring technique.

orders of magnitude low based on the calculated activity from  $10^{11}$  ions/cm<sup>2</sup>. This discrepancy would not allow a material balance to be made; however, qualitative inspection of profiles provides valuable information.

All samples were implanted with 40 keV ions, both  $^{32}\text{P}^+$  and  $^{31}\text{P}^+$  with all other parameters held constant with the exception of orientation and the fraction of total dose implanted before the marker was injected.

All samples were analyzed in depth by uniformly removing silicon layers of known thickness by the anodic oxidation technique described by Busen and Linzey (4). The activity of each layer was determined by counting the solution of the dissolved oxide. Residual activity was also monitored as a cross check. All count data were corrected for background and also corrected for decay to the time of the implantation.

Table I. Variation in raw activity when primary beam current density adjusted to constant value

Run Position	1	2	3
	Activity cts/min	Activity, cts/min	Activity, cts/min
1	828	12076	1226
2	901	14018	1852
3	1350	12408	1229
4	741	13815	1602
5		12498	1206
6	1000	11441	1113
7	801	12500	1569
8	1030	11689	1209

### Results

In Fig. 5 the influence of the annealing process on impurity movement is shown. Four implantations were made under identical conditions in (100) oriented p-type silicon. Two of these implants were annealed at 600°C for 10 min before profile determination. The other two were processed without thermal treatment. It can be seen that the four sets of data points are fitted by the same curve. It can be concluded that gross diffusion to move the junction  $0.2\mu$  as observed by delineation (5) has not occurred and that this movement is a reflection of a change in the substitutional/interstitial ratio of the injected atoms. Other important features of Fig. 5 are the buried peak which occurs at the depth calculated by theory (6) and the depth at which unit activity occurs.

Figure 6 is the profile of an identical implant in (111) oriented p-type silicon. Here again,  $2 \times 10^{13}/\text{cm}^2$  of  $^{31}\text{P}^+$  were introduced before the tracer marker. This profile is similar in nature to the profile in Fig. 5. Within experimental error, they are the same. Both have unit activity at 3000Å. Here again, notice the peak of the distribution which falls at 500Å in good agreement with Lindhard-Scharff-Schiott theory.

Figure 7 is an identical implant in (110) oriented p-type silicon. Here the "tailing" in the distribution becomes noticeable when compared to the profiles for the (100) and (111) orientations. Unit activity is found 1000Å deeper at 4000Å. The peak is again at 500Å. Comparing the depths for unit activity, it is seen that the depth in the (110) oriented material is 33% deeper than either the (111) or (100) oriented material. This compares favorably with the 31% deeper junction

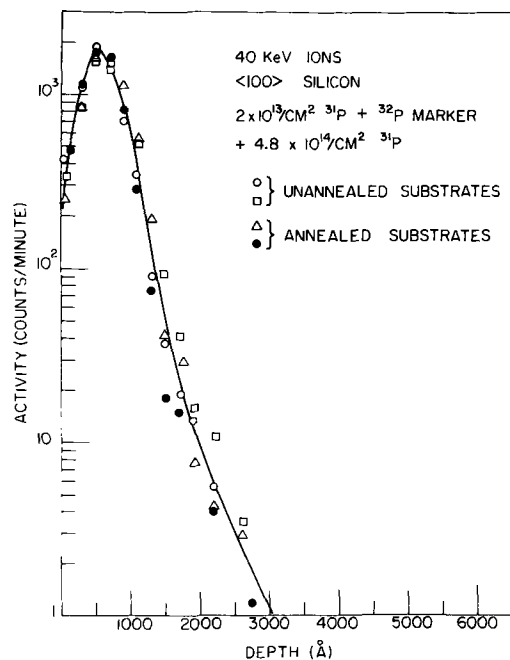


Fig. 5. Activity profile of  $^{32}\text{P}^+$  marker in (100) silicon injected after  $2 \times 10^{13}/\text{cm}^2$   $^{31}\text{P}^+$  and the effect of annealing.

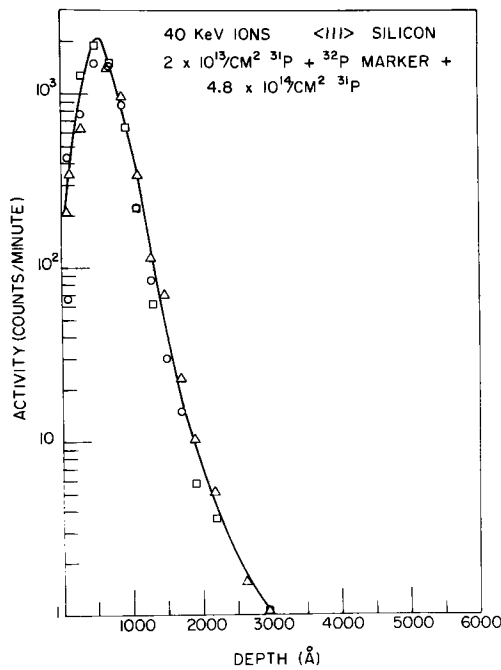


Fig. 6. Activity profile of  $^{32}\text{P}^+$  marker in (111) silicon injected after  $2 \times 10^{13}/\text{cm}^2$   $^{31}\text{P}^+$ .

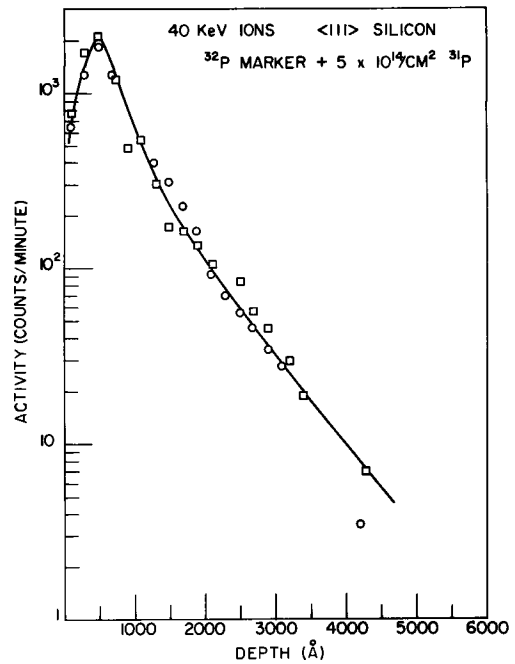


Fig. 8. Activity profile of  $^{32}\text{P}^+$  marker in (111) silicon injected before  $^{31}\text{P}^+$  dose.

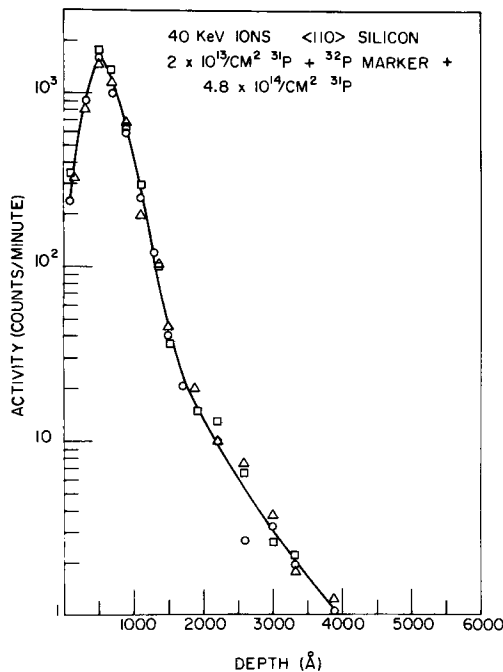


Fig. 7. Activity profile of  $^{32}\text{P}^+$  marker in (110) silicon injected after  $2 \times 10^{13}/\text{cm}^2$   $^{31}\text{P}^+$ .

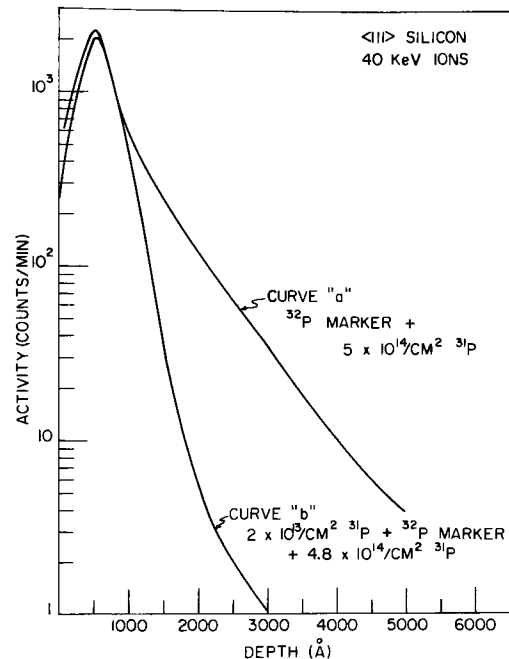


Fig. 9. Comparison of activity profiles of  $^{32}\text{P}^+$  marker in (111) silicon when injected before and after  $2 \times 10^{13}/\text{cm}^2$   $^{31}\text{P}^+$ .

depth by delineation for 40 keV  $\text{P}^+$  ions in the (110) direction when compared to the other two directions (2).

The profile in Fig. 8 results when the  $^{32}\text{P}^+$  marker is injected first in (111) oriented silicon. Here it is seen that the channeling tail extends deep into the substrate with unit activity occurring almost 2000 Å deeper than previously found when  $2 \times 10^{13}$  ions/ $\text{cm}^2$  of  $^{31}\text{P}^+$  are initially injected. A comparison of the two profiles is shown in Fig. 9 and it can be seen that the fraction of channeling ions or the range of channeling ions has been markedly reduced.

Data for marker profiles injected after  $5 \times 10^{13}$  ions/ $\text{cm}^2$  of  $^{31}\text{P}^+$  indicate a further fall off in channeling; however, this reduction is not as dramatic as the initial one. These data have been obtained from samples with much lower initial activity, thus, the

profiles can only reflect the trend. Figure 10 is a comparison for the (110) direction of implant and Fig. 11 is a comparison for the (100) direction.

### Conclusion

In conclusion, it can be stated that:

1. "Channeling" down an open crystalline direction is definitely concentration dependent. It appears that after  $2 \times 10^{13}$  ions/ $\text{cm}^2$  have been injected either the channels have been blocked by interstitials (either impurity atom or dislodged host atom) or sufficient damage has occurred at the surface to effectively present an amorphous surface to incoming ions.

2. The annealing conditions necessary to restore structure and stabilize electrical properties do not cause a measurable diffusion such as one might conclude from the observed junction movement. The experiments indicate that the injected ion profile is

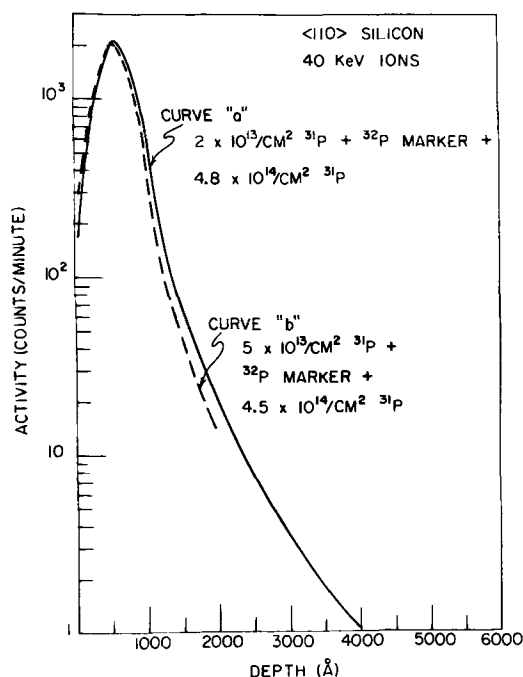


Fig. 10. Comparison of activity profiles of  $^{32}\text{P}^+$  marker in (110) silicon injected after  $2 \times 10^{13}/\text{cm}^2$  and  $5 \times 10^{13}/\text{cm}^2$   $^{31}\text{P}^+$ .

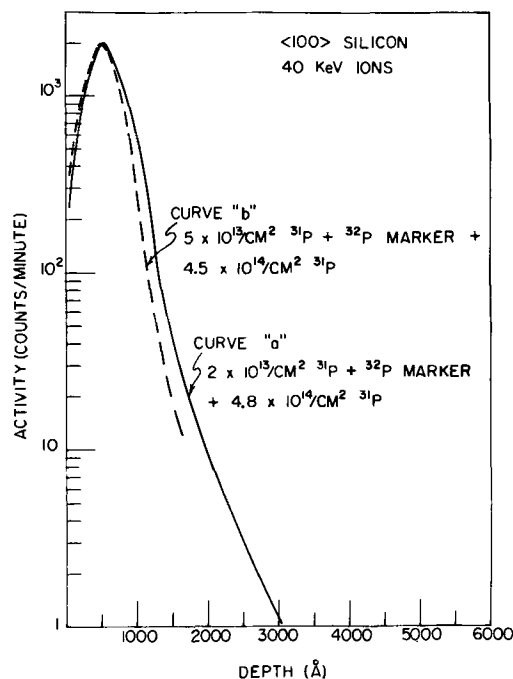


Fig. 11. Comparison of activity profiles of  $^{32}\text{P}^+$  marker in (100) silicon injected after  $2 \times 10^{13}/\text{cm}^2$  and  $5 \times 10^{13}/\text{cm}^2$   $^{31}\text{P}^+$ .

constant during the annealing process within the error of the experiment. Therefore, the junction movement must result from a change in the substitutional/interstitial ratio for the injected ions.

3. The experimental range for 40 keV phosphorus ions in silicon, which is defined by the location of the buried peak, agrees well with the value calculated by Lindhard's theory for amorphous substrates. This is within reason, since the implantations, which provided the data for the profiles, were made by rotating the samples through an angle of  $\pm 7^\circ$  to the beam direction. Thus, only a small fraction of the incoming ions were injected in a channeling direction. At all other times, the substrate exhibited varying degrees of opaqueness to the ion beam.

#### Acknowledgment

The author is deeply indebted to Mr. Gerald Alton of the Oak Ridge National Laboratory and Mr. Ernest LaFlamme of Sprague Electric Research and Development Center for their assistance in carrying out the experiments described herein.

Manuscript received Dec. 20, 1967; revised manuscript received Feb. 16, 1968. This paper was presented at the Chicago Meeting, Oct. 15-19, 1967.

Any discussion of this paper will appear in a Discussion Section to be published in the December 1968 JOURNAL.

#### REFERENCES

1. L. N. Large and R. W. Bicknell, *J. Mat. Sci.*, **2**, 589 (1967).
2. K. E. Manchester and C. B. Sibley, *Trans. AIME*, **236**, 379 (1966).
3. K. E. Manchester, C. B. Sibley, and G. Alton, *Nuc. Inst. and Methods*, **38**, 169 (1965).
4. K. M. Busen and R. Linzey, *Trans. AIME*, **236**, 306 (1966).
5. K. E. Manchester, Proceedings of Second International Electron and Ion Beam Conference (1966) in press; K. E. Manchester, *SCP and SST*, **9**, No. 9 48 (1966).
6. J. Lindhard, H. M. Scharff, and H. E. Schiott, *Kgl. Danske Videnskab. Selskab. Mat.-Fys. Medd.*, **33**, No. 14 (1963).

## The Influence of Thermal $\text{SiO}_2$ Surface Constitution on the Adherence of Photoresists

Robert O. Lussow

IBM Components Division, East Fishkill Facility, Hopewell Junction, New York

#### ABSTRACT

The adherence of certain commercial photoresists with thermal  $\text{SiO}_2$  was found to depend on the surface constitution of the  $\text{SiO}_2$ . Thermal  $\text{SiO}_2$  surfaces were modified to contain: (i) adsorbed molecular water, (ii) appreciable concentration of silanol groups, or (iii) predominantly siloxane structure. The adherence of Kodak photoresists KPR-2, KTFR, and KMER with each of these surface types was evaluated.

In the production of certain microelectronic devices, selected areas of oxidized silicon are protected from chemical etching with photopolymer coatings called photoresists. The etchant removes the oxide layer from the unprotected portion of the surface. The desired

access hole configuration has sides almost perpendicular to the substrate surface. In some cases, however, the etched holes show considerable taper or rounding at the upper edge. Since the etchants normally used do not attack the photoresist, this defect is ascribed to a

failure of the adhesion between the polymer and the oxide. A breakdown of the bonding allows the etchant solution to penetrate the interface between the oxide and photoresist and to attack the originally protected SiO<sub>2</sub> (1).

Attempts to improve the bonding of organic materials to SiO<sub>2</sub> surfaces have centered around the use of surface precoating techniques. The predominant method used, in microelectronics as in other unrelated fields, is based on reacting organohalosilanes with the SiO<sub>2</sub> (2-6). The layer produced serves as the bonding surface for the polymeric material. A recent paper by Bergh (1) has shown that there is a correlation between the water wettability of the SiO<sub>2</sub> surface and the adherence of these surfaces with a commercial photoresist. He found that as the water wettability of the surface increased, the adherence decreased. Bergh concluded that the presence of silanol-type surface groups caused the increase in wettability, with the attendant decrease in adherence. The choice of the organohalosilanes for surface precoatings implicitly supports this conclusion. The work reported here was undertaken to define more clearly the surface structure of thermal SiO<sub>2</sub> and its influence on the adherence of selected photoresists.

### Silicate Composition

SiO<sub>2</sub> is composed of silicon atoms in tetrahedral coordination with oxygen atoms. The surface of an ideal silica surface would be composed of silicon-oxygen or siloxane bridges. Real silica surfaces have been shown to contain outwardly disposed hydroxyl or silanol groups on their surfaces (2, 3, 5, 7, 8).

The surface hydroxyl groups are thermally stable up to temperatures of about 600°C, where sintering begins to occur (9, 10). These silanol-group sites have been shown to be capable of forming coordination or hydrogen-type bonds with molecular water (7-9, 11-13). NMR studies have shown that other surface sites on silica are also capable of forming similar bonds (13). This strongly held water can be removed by heating at high temperatures and using low pressures or long drying times (7, 9, 12). Physically bound water, on the other hand, can be readily removed at moderate temperatures and normal pressures.

### Experimental

**Silicon oxides.**—The surfaces used for these experiments were thin layers of SiO<sub>2</sub> prepared by oxidation of n-type epitaxial silicon. The oxide layers were grown on 1.25-in.-diameter circular silicon slices by thermal oxidation at 970°C in alternating atmospheres of steam and dry oxygen. The resulting oxide layers were about 6000Å thick.

The oxides were cleaned by immersion in hot, concentrated sulfuric and chromic acids, and then rinsed with deionized water. The excess water was blown from the surface and the samples dried for 10 min at 110°C. This was followed by outgassing at 50°C for 30 min in a vacuum oven whose pressure was about 100 milliTorr. The surface condition at this point is referred to as the "initial" condition.

The prepared oxide surfaces were modified by a variety of treatments. Chemical attack by water and acids, and exposure to nitrogen or steam at elevated temperatures were used. The sequence and details of each modification procedure will be discussed below. The modified oxides were subsequently outgassed in a vacuum oven at 50°C for 30 min at about 100 milliTorr pressure.

**Photopolymers.**—Commercial photoresists marketed by the Eastman Kodak Company were used. Three different types were evaluated: (i) Kodak Photo Resist, Type 2 (KPR-2), (ii) Kodak Thin Film Resist (KTFR), and (iii) Kodak Metal Etch Resist (KMER). The processing of the photoresist coatings was done in accordance with the manufacturer's recommendations (14).

**Oxide wettability measurements.**—The wettability of the oxide surfaces was measured by using 4.0 x 10<sup>-6</sup> liter droplets of boiled, 5 x 10<sup>-4</sup> mhos deionized water. The relative wettability of the surfaces was determined by the equilibrium spread size of the water droplets on the respective surfaces. The wettability of each sample is reported as the average diameter, *D<sub>T</sub>*, of four droplets, one placed in each quadrant of the surface. The details of this method have been presented elsewhere (15).

**Evaluation of adherence.**—"Adherence" used in this context is defined as previously discussed by Bergh (1), and was evaluated by the resolution of a pattern etched into the SiO<sub>2</sub> layer. The pattern used for this evaluation was a two-dimensional array of alternating rectangles and circles; approximately 2000 figures were etched into each oxidized silicon slice. The etchant was a hydrofluoric acid solution buffered with ammonium fluoride to attain an etch rate of 1000 Å/min. The quality of the etched patterns was examined microscopically at 100X. Good adherence of the photoresist to the SiO<sub>2</sub> gave patterns with sharp edges; poor adherence was evidenced by color fringes at the periphery of the etched holes, indicating a gradation in oxide thickness. The adhesive quality is reported as the percentage figures in the etched array showing color fringes around their periphery.

### Results and Discussion

The surface structures of a series of thermally oxidized silicon slices were modified by various wet oxidation and hydrolysis techniques. The wettability of these samples was measured before and after the surface treatments and after a subsequent vacuum outgassing. The oxidation and hydrolysis conditions and typical wettability data are summarized in Table I. The surface treatments caused the wettability of all samples to increase. The subsequent vacuum outgassing of the samples treated with H<sub>2</sub>O, HNO<sub>3</sub>, and H<sub>2</sub>SO<sub>4</sub> reduced their respective wettability to values close to those obtained prior to the surface treatments. For the samples treated with the HF-NH<sub>4</sub>F mixture, the final outgassing reduced the wettability, but the ultimate values were greater than those measured before chemical treatment.

A second series of thermally oxidized silicon slices was subjected to the thermal treatments in air. The water wettability of these samples was measured after heating at each of the temperatures indicated in Table II. The results summarized in Table II show that the wettability increases with temperatures up to 450°C. At 650°C the wettability decreased and did not change further upon heating at 750°C. After the treatment at 750°C, the same samples were heated again at 350°C. This latter treatment increased the wettability to a value consistent with the previous lower temperature data.

Another series of thermally oxidized silicon slices was exposed at 350° and 500°C to flowing nitrogen streams containing varying concentrations of water vapor. Table III shows the water wettability of these

Table I. Effect of wet oxidation and hydrolysis treatments on the water wettability of thermal SiO<sub>2</sub>

Treatments <sup>a</sup>	Wettability, <i>D<sub>T</sub></i> , in.		
	Initial	After treatment	After outgas
DI H <sub>2</sub> O	0.130	0.180	0.127
Boil 30 min	0.133	0.168	0.128
HNO <sub>3</sub> (conc)	0.128	0.140	0.126
35°C, 10 min	0.134	0.149	0.129
Buffered HF <sup>b</sup>	0.129	0.286	0.142
25°C, 30 sec	0.130	0.240	0.139
H <sub>2</sub> SO <sub>4</sub> (conc)	0.127	0.158	0.127
95°C, 10 min	0.122	0.155	0.125

<sup>a</sup> Following treatment, the samples were rinsed in deionized water, blown off and dried at 110°C.

<sup>b</sup> HF buffered with NH<sub>4</sub>F to attain an etch rate of 1000 Å/min.

Table II. Water wettability of thermal SiO<sub>2</sub> after thermal treatments in air

Temperature <sup>a, b</sup> , °C	Wettability, D <sub>T</sub> , in.	
	Sample 1	Sample 2
Initial	0.138	0.147
185	0.148	0.149
250	0.160	0.159
450	0.170	0.163
650	0.147	0.149
750	0.148	0.148
350	0.176	0.170

<sup>a</sup> Samples remained at each temperature for 30 min.

<sup>b</sup> After each wettability measurement and prior to the subsequent thermal treatment, the samples were dried for 10 min at 110°C.

Table III. Effect of water vapor at 350° and 500°C on the water wettability of thermal SiO<sub>2</sub>

Treatment <sup>a, b</sup>	Wettability, D <sub>T</sub> , in.		
	Initial	After treatment	After outgas
Dry N <sub>2</sub> , 2.0 cfm	0.126	0.138	0.132
350°C, 0.5 hr	0.126	0.144	0.132
N <sub>2</sub> sat'd with H <sub>2</sub> O, 2.0 cfm <sup>c</sup>	0.125	0.146	0.132
350°C, 0.5 hr	0.124	0.148	0.133
Steam/N <sub>2</sub> , 2.0 cfm <sup>d</sup>	0.127	0.145	0.136
350°C, 0.5 hr	0.129	0.146	0.133
Steam/N <sub>2</sub> , 1.0 cfm <sup>d</sup>	0.123	0.152	0.132
500°C, 0.5 hr	0.126	0.151	0.140
Steam/N <sub>2</sub> , 1.0 cfm <sup>d</sup>	0.126	0.152	0.146
500°C, 1.0 hr	0.124 <sup>e</sup>	0.153	0.144
	0.126 <sup>e</sup>	0.162	0.140
Dry N <sub>2</sub> , 2.0 cfm	0.124	0.157	0.139
750°C, 0.5 hr	0.144 <sup>e</sup>	0.112	
	0.139 <sup>e</sup>	0.111	

<sup>a</sup> Treated nitrogen streams were preheated to furnace temperature, and then passed over the heated samples.

<sup>b</sup> All samples were cooled to room temperature in dry N<sub>2</sub> at end of treatment.

<sup>c</sup> Saturated by bubbling through 25°C water.

<sup>d</sup> Nitrogen was swept through the vapor phase of a steam generator.

<sup>e</sup> The same samples were used for the 500°C, steam/N<sub>2</sub> and the 750°C, dry N<sub>2</sub> treatments.

samples before treatment, after treatment, and after the final vacuum outgassing. In all cases, the exposure to nitrogen-water vapor at the elevated temperatures increased the wettability. The wettability after exposure was independent of the partial pressure of water vapor at 350°C, but increased with temperature. The wettability after treatment at 500°C showed a very slight increase when the exposure time was raised from 0.5 to 1.0 hr. Vacuum outgassing the treated samples decreased their wettability, but not to the initial values.

Two of the vacuum outgassed samples from the 1.0-hr, steam-nitrogen, 500°C exposure were heat treated for 0.5 hr at 750°C in dry nitrogen. The results of this treatment are also included in Table III. The initial wettability reported for these samples is the final outgassed wettability measured after the 500°C steam-nitrogen exposure. The 750°C heat treatment decreased the water wettability of these surfaces to values lower than those measured on the "initial" samples.

Two methods of sample drying were compared. After the surface treatments previously described, each group of samples was divided into two sets. One set was vacuum outgassed at 50°C, and the second set was desiccated over silica gel for 55 days. The 500°C, steam-nitrogen samples that were desiccated were subsequently vacuum outgassed at 50°C. The water wettability of these surfaces after each drying step is reported in Table IV. The wettability changes with surface treatment were consistent with those reported for the same treatments in Tables I and III. Prolonged desiccation of the prepared samples reduced the wettability to almost the same extent as the vacuum outgassing technique.

Table IV. Comparison of surface drying techniques

Treatment	Wettability, D <sub>T</sub> , in.			
	Initial	After treatment	After dessiccation	After outgas
H <sub>2</sub> SO <sub>4</sub> (conc) <sup>a</sup>	0.127	0.174	0.134	—
95°C, 10 min	0.122	0.179	—	0.127
HF-NH <sub>4</sub> F mixture <sup>a</sup>	0.129	0.322	0.143	—
25°C, 30 sec	0.130	0.325	—	0.142
DI H <sub>2</sub> O <sup>a</sup>	0.130	0.190	0.135	—
Boil, 30 min	0.132	0.180	—	0.127
Steam/N <sub>2</sub> , 1.0 cfm <sup>b</sup>	0.126	0.162	0.145	0.140
500°C, 30 min	0.124	0.157	0.142	0.139

<sup>a</sup> Following treatment, the samples were rinsed in flowing DI water for 5 min, blown off with N<sub>2</sub>, and air oven dried 10 min at 110°C.

<sup>b</sup> Samples were cooled to room temperature in dry N<sub>2</sub>.

It is shown by these experiments that the wettability of SiO<sub>2</sub> surfaces can be modified by the treatments and procedures described above: (a) an increase when samples are subjected to wet oxidation and hydrolysis or gas phase oxidation with water vapor, and (b) a partial reversal of increases when the surfaces are vacuum outgassed or desiccated for prolonged periods. In some cases the wettability of the vacuum outgassed surfaces was further reduced by heat treatments at temperatures in excess of 650°C. Comparing the wettability behavior of these samples with the known surface structures of SiO<sub>2</sub>, it is possible to deduce the surface constitution of the modified, thermally oxidized silicon surfaces used in this study.

The increase in water wettability that was reversed by vacuum outgassing or desiccating suggests the presence of strongly adsorbed molecular water. Physically adsorbed water would have been removed by the low temperature oven drying before the wettability measurements. The oxidation conditions used on these samples did not grow a significant amount of additional oxide (16-18). The first step in the oxidation of silicon by water is adsorption of a film of water (19). This mechanism implies that wettability increases that occur after gas phase oxidation should be independent of the partial pressure of water vapor in the gas phase. This was observed with the 350°C gas phase oxidations (Table III). The strongly adsorbed molecular water would be held to the surface by coordination or hydrogen-type bonding. This water was removed at low temperatures at an appreciable rate only when reduced pressures were used.

The wettability changes of the samples treated with the buffered hydrofluoric acid or gas phase oxidations at elevated temperatures were not completely reversed on vacuum outgassing. The permanent increase in wettability is attributed to the formation of additional silanol (Si-OH) groups on the silica surfaces. These are formed by hydrolysis of surface fluoride compounds in the reaction with HF (6, 8), or the thermal oxidation of silicon with water vapor (19). The silanol groups decomposed when heated to temperatures greater than 650°C (Tables II and III), and the elimination of water resulted in a surface comprised of siloxane (Si-O-Si) structure. The variation in initial wettability of the sample surfaces is attributed to variations in the silanol content or in the surface roughness factor (20) produced during the growth of the original oxide layer.

The chemical constitution of these SiO<sub>2</sub> surfaces can be classified into three different types. Type 1 surfaces are those with molecular water strongly bound to the solid. Type 2 surfaces contain an appreciable amount of silanol groups, but no adsorbed molecular water. Type 3 surfaces consist of predominantly siloxane structure with no adsorbed molecular water. These three types are illustrated schematically in Fig. 1.

The influence of these surface structures on adherence with KPR-2 is illustrated in Table V. The surfaces were prepared as described in the table. The same procedure was used on all samples for KPR-2



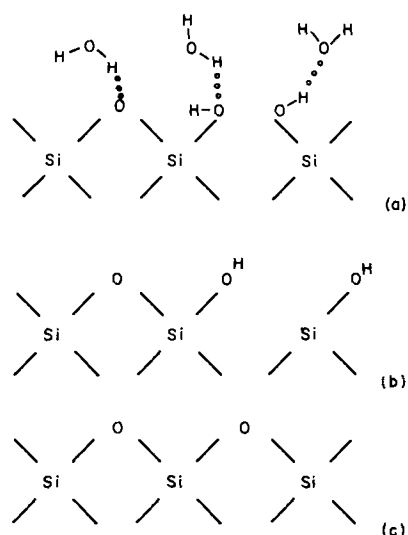


Fig. 1. Schematic representation of thermal SiO<sub>2</sub> surface structures. (a) Type 1, with adsorbed molecular water; (b) Type 2, containing silanol groups, no adsorbed molecular water; and (c) Type 3, predominantly siloxane structure, no adsorbed molecular water.

processing, etching, and adhesion evaluation. The data of Table V summarize the SiO<sub>2</sub> wettability values after each surface treatment, the surface type of the samples to be etched, and the adhesion performance. Poor adherence resulted when surfaces with the Type 1 structure were used. Both Type-2 and Type-3 surfaces showed good adherence with KPR-2. It should be noted that a high water wettability does not necessarily preclude poor photoresist adherence with the SiO<sub>2</sub> surfaces (6). Samples with wettability as high as  $D_T = 0.19$  in., corresponding to a contact angle of less than 10 arc degrees, show good adherence with KPR-2 if the surface is not of Type 1. This is seen in the data from the samples treated with buffered HF.

Table V. Adhesion of KPR-2 on thermal SiO<sub>2</sub>

Surface treatment <sup>a</sup>	Surface structure	Wettability $D_T$ , in.	Adherence, % defects
H <sub>2</sub> SO <sub>4</sub> (conc, 95°C, 10 min)	Type 1	0.172	10
H <sub>2</sub> SO <sub>4</sub> (conc, 95°C, 10 min)	Type 1	0.177	20
Desiccated <sup>b</sup>	Type 2	0.134	0
Vacuum outgassed <sup>c</sup>	Type 2	0.152	0
Vacuum outgassed <sup>c</sup>	Type 2	0.148	0
DI water (boil, 30 min)	Type 1	0.149	80
DI water (boil, 30 min)	Type 1	0.154	80
Desiccated <sup>b</sup>	Type 2	0.135	0
Vacuum outgassed <sup>c</sup>	Type 2	0.143	5
Vacuum outgassed <sup>c</sup>	Type 2	0.147	5
Buffered HF (25°C, 1 min)	Type 1	0.254	20
Buffered HF (25°C, 1 min)	Type 1	0.264	20
Vacuum outgassed <sup>c</sup>	Type 2	0.160	0
Vacuum outgassed <sup>c</sup>	Type 2	0.187	0
NH <sub>4</sub> OH (conc, 50°C, 10 min)	Type 1	0.169	10
NH <sub>4</sub> OH (conc, 50°C, 10 min)	Type 1	0.170	10
Vacuum outgassed <sup>c</sup>	Type 2	0.143	0
Vacuum outgassed <sup>c</sup>	Type 2	0.143	0
Steam/N <sub>2</sub> (500°C, 1 hr) + Vacuum outgassed <sup>c</sup>	Type 2	0.146	0
Steam/N <sub>2</sub> (500°C, 1 hr) + Vacuum outgassed <sup>c</sup>	Type 2	0.144	0
Dry N <sub>2</sub> (750°C, 1 hr)	Type 3	0.112	0
Dry N <sub>2</sub> (750°C, 1 hr)	Type 3	0.111	0
None <sup>d</sup>	Type 1	0.132	20
None <sup>d</sup>	Type 1	0.132	10
Vacuum outgassed <sup>c</sup>	Type 2 or 3	0.124	0
Vacuum outgassed <sup>c</sup>	Type 2 or 3	0.111	0

<sup>a</sup> All samples in each series were subjected to the specified oxidation and/or hydrolysis treatments.

<sup>b</sup> Desiccated over silicon gel for 55 days.

<sup>c</sup> Outgassed at 50°C for 30 min under about 100 milli-Torr pressure.

<sup>d</sup> These samples were taken directly from the oxidation furnace; they were not acid cleaned or vacuum outgassed prior to the initial wettability measurement.

Table VI. Adhesion of KTR and KMER on thermal SiO<sub>2</sub>

Surface treatment	Surface structure	$D_T$ , in.	Photoresist	Adherence, % defects
Boil, DI H <sub>2</sub> O	Type 1	0.174	KTR	100
Boil, DI H <sub>2</sub> O	Type 1	0.172	KTR	100
Vacuum outgassed <sup>a</sup>	Type 2	0.147	KTR	100
Vacuum outgassed <sup>a</sup>	Type 2	0.146	KTR	100
750°C, N <sub>2</sub> <sup>b</sup>	Type 3	0.111	KTR	0
750°C, N <sub>2</sub> <sup>b</sup>	Type 3	0.109	KTR	0
Boil, DI H <sub>2</sub> O	Type 1	0.152	KMER	0
Boil, DI H <sub>2</sub> O	Type 1	0.159	KMER	0
Vacuum outgassed <sup>a</sup>	Type 2	0.129	KMER	0
Vacuum outgassed <sup>a</sup>	Type 2	0.133	KMER	0
750°C, N <sub>2</sub> <sup>b</sup>	Type 3	0.114	KMER	0
750°C, N <sub>2</sub> <sup>b</sup>	Type 3	0.123	KMER	0

<sup>a</sup> All samples in each series were boiled in DI H<sub>2</sub>O before vacuum outgassing for 30 min at 50°C under 100 milli-Torr pressure.

<sup>b</sup> The samples baked in N<sub>2</sub> at 750°C for 1 hr were first treated as in (a) above.

The adherence of photoresists KTR and KMER to these three surface structures was examined in a similar manner. The evaluation of KTR and KMER adherence is given in Table VI. The data shown are for the surface treatment, surface type, photoresist used, and adherence of each sample. The adherence of KTR was poor on surface Types 1 and 2, but good on surface Type 3. KMER adherence was unaffected by these variations in surface structure.

### Conclusions

Three types of SiO<sub>2</sub> surface structures were deduced from wettability changes caused by various surface treatments. Type 1 surface structures contain a strongly adsorbed layer of molecular water. Type 2 surfaces have a significant amount of silanol groups present, but no adsorbed molecular water. Type 3 surfaces consist of predominantly siloxane structure without adsorbed molecular water. The water wettability alone of these surfaces is not sufficient to predict their adhesion performance. SiO<sub>2</sub> adherence with photoresists is determined by the surface structure of the oxide (which also affects the wettability). Kodak Photo Resist Type 2 does not adhere well to surfaces containing appreciable amounts of adsorbed molecular water, but its adherence is unaffected by silanol or siloxane surface structures. Adsorbed molecular water or silanol surface groups have a detrimental effect on the adherence of Kodak Thin Film Resist. The adherence of Kodak Metal Etch Resist is independent of the SiO<sub>2</sub> surface structures investigated here.

### Acknowledgments

The author wishes to thank Mr. L. H. Wirtz and Miss B. J. Kriscka for assistance in making these measurements, and Dr. H. A. Levine for many helpful discussions.

Manuscript received Oct. 19, 1967; revised manuscript received Feb. 1, 1968. This paper was presented at the Chicago Meeting, Oct. 15-19, 1967, as Abstract 179.

Any discussion of this paper will appear in a Discussion Section to be published in the December 1968 JOURNAL.

### REFERENCES

1. A. A. Bergh, *This Journal*, **112**, 457 (1965).
2. R. K. Iler, "The Colloid Chemistry of Silica and Silicates," Cornell University Press (1957).
3. J. A. Cunningham, L. E. Sharif, and S. S. Baird, *Electrochem. Technol.*, **1**, 242 (1963).
4. J. G. Koelling and K. E. Kolb, *J. Chem. Soc.*, **1**, 6 (1965).
5. A. V. Kiseler, Vortrage Originfassung Zwischenstaatlich Kongress, Grenzflaechenaktive Stoffe (Cologne), **2**, 391 (1960).
6. B. Schwartz, *This Journal*, **106**, 871 (1959).
7. P. C. Carman, *Trans. Faraday Soc.*, **36**, 964 (1940).
8. W. A. Weyl, *Glass Industry*, **28**, 231 (1947).
9. W. K. Lowen and E. C. Broge, *J. Phys. Chem.*, **65**, 16 (1961).

10. I. Shapiro and I. M. Kolthoff, *J. Amer. Chem. Soc.*, **72**, 776 (1950).
11. S. S. Baird, Conference on Clean Surfaces, New York Academy of Science, 869 (1963).
12. H. W. Fox, E. F. Hare, and W. A. Zisman, *J. Phys. Chem.*, **59**, 1097 (1955).
13. V. I. Kulividze, N. M. Ievskaya, T. S. Egorova, V. F. Kiselev, and I. D. Sokolov, *Kinetika i Kataliz*, **3**, 91 (1962); Chem. Abstr. **57** 16023d (1962).
14. "Photosensitive Resists for Industry," Industrial Data Book P-7, Eastman Kodak Co., Rochester, N. Y. (1962).
15. R. O. Lussow, L. H. Wirtz, and H. A. Levine, *This Journal*, **114**, 877 (1967).
16. S. P. Zhdanov, Proc. Conference on the Structure of Glass (Leningrad 1953), Eng. Trans, I. Academy of Sci. USSR Press, p. 125 (1958).
17. W. A. Pliskin, Unpublished data, International Business Machines Corp. (1964).
18. B. E. Deal and A. S. Grove, *J. Applied Phys.*, **36**, 3770 (1965).
19. W. Eitel, "Physical Chemistry of Silicates," University of Chicago Press, p. 342 (1954).
20. R. N. Wentzel, *Ind. Eng. Chem.*, **28**, 988 (1936).

## Geometrical Stability of Shallow Surface Depressions During Growth of (111) and (100) Epitaxial Silicon

C. M. Drum and C. A. Clark

*Bell Telephone Laboratories, Inc., Allentown, Pennsylvania*

### ABSTRACT

The shapes and positions of shallow (500Å) depressions on silicon substrates undergo changes during the growth of epitaxial silicon deposited by the hydrogen reduction of SiCl<sub>4</sub>. Control of this distortion is important for the proper registration of diffusion masks in the fabrication of junction isolated integrated circuits. Data are presented on the shape distortion of surface depressions and the lateral displacements of the edges of these depressions; the effects of surface orientations in the vicinity of (111) and (100), the temperature of the deposition, and the orientation of surface depressions relative to symmetry planes in the lattice are included. Symmetrical displacements of small magnitude (~2.5μ for an 8μ epitaxial layer) can be obtained for one pair of sides of rectangular depressions on surfaces 3° off (111) toward a nearest (110); depressions are obliterated during growth onto surfaces very near (111), and surfaces off (111) toward a nearest (100) produce diffuse, highly distorted figures. For exact (100) surfaces, symmetrical and small displacements can be obtained with both pairs of sides of the rectangular depressions; the sharpness of the boundaries of depressions on (100) surfaces is strongly dependent on the temperature of the epitaxial deposition. Large pits associated with stacking faults on (111) surfaces can be qualitatively understood in terms of distortion of the small groove which occurs at the fault-surface intersection. Generally, knowledge of the anisotropy of the growth rate along with knowledge of the symmetry of the lattice provide a qualitative understanding of the crystallographic dependence of the distortion phenomenon.

During the course of work on the growth of epitaxial silicon for the fabrication of integrated circuits, we have made a study of the geometrical stability of shallow surface depressions during the growth process. The shallow, flat-bottomed depressions were bounded by steps approximately 500Å in height, and it was entirely expected that changes would occur in the shapes and positions of these steps during the growth of epitaxial layers approximately 80,000Å thick (8μ). For example, well known theories of crystal growth include the concept of atoms being incorporated into a growing crystal at favored sites on the surface (1), e.g., monatomic steps or kinks in these steps; thus at low supersaturations, low-indexed surfaces of a crystal could grow by the lateral spreading of these steps. The shallow depressions of interest in the present work had as their boundaries steps several orders of magnitude higher than monatomic steps, thereby exposing some regions with crystallographic orientations different from that of the substrate. Therefore, since the growth rate is known to vary with orientation (2), this provides an additional reason for anticipating that the depressions might undergo changes in shape during growth.

The problem of the stability of the figures arose in the following manner. One method for the fabrication of p-n junction-isolated integrated circuits involves the deposition of n-type epitaxial films onto p-type

substrates. These substrates contain a pattern of highly doped N<sup>+</sup> regions which serve to lower the collector series resistance. Electrical isolation between regions is obtained by diffusing p-type region through the epitaxial layer. The mask for this isolation diffusion must be properly registered, and a sequence of processing steps for accomplishing this is shown in Fig. 1. As indicated on Fig. 1, after the N<sup>+</sup> regions are diffused by standard techniques, the silicon exposed by the windows is re-oxidized thermally. Then, prior to epitaxial growth, all the oxide is removed with HF, leaving shallow depressions in the silicon surface which identify the positions of the N<sup>+</sup> regions. The ideal situation after epitaxial growth is depicted on the left of Fig. 1, in which the depressions after epitaxy faithfully identify the positions of the N<sup>+</sup> buried layers. However, the problem which led to this investigation is illustrated in the section to the right on Fig. 1; namely, the shallow depressions can be laterally displaced during epitaxial growth as drawn. This displacement can in some cases be greater than 25μ and subsequent misalignment of the P<sup>+</sup> isolation diffusion may result in shorting of the P<sup>+</sup> and N<sup>+</sup> regions.

The distortion of the depressions has been found to be strongly dependent on the crystallographic orientation of the surfaces, which is not surprising in light of the known variations in growth rate with orienta-

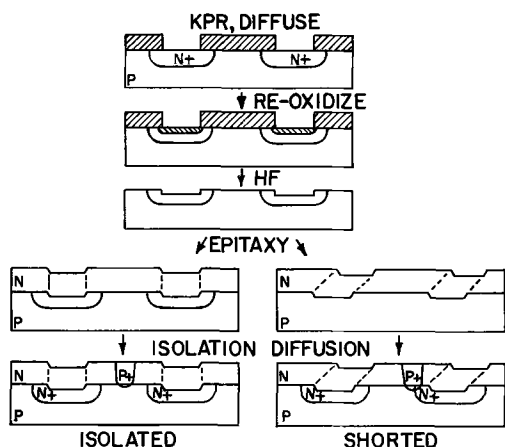


Fig. 1a. Processing steps for producing shallow depressions at the sites of diffused regions.

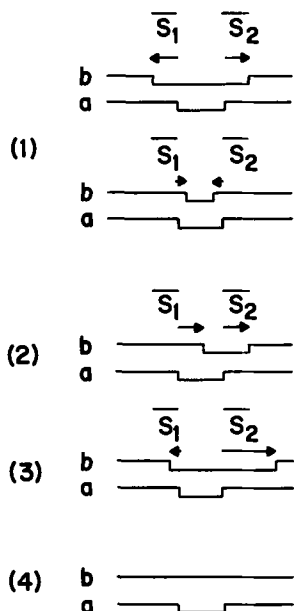


Fig. 1b. Cross-sections through substrate (a) and epitaxial surfaces (b), illustrating four cases. 1. Symmetrical distortion, 2. nonsymmetrical distortion without change of size, 3. nonsymmetrical distortion with change of size, 4. obliteration or washout.

tion (2). Throughout this paper, we denote the orientation of the large surface of a slice as being near either the particular (111) plane or the particular (100) plane. Previously, Benjamin and Patzner (3) reported that the pattern distortion was reduced by using slices oriented  $>2^\circ$  off (111), and Boss and Doo (4) reported that it was important to use slices with normals oriented  $3^\circ$  to  $5^\circ$  off [111] toward a nearest  $\langle 110 \rangle$ . This conclusion is generally in agreement with our data contained herein. Boss and Doo mentioned that distortion of depressions 1000 to 2000Å deep can also be minimized with near (111) wafers by reducing the growth rate below  $0.5\mu/\text{min}$ , although they did not specify whether this was accomplished by reducing the temperature or the concentration of reactants. In this connection, it is also noteworthy that Tung (2) has reported that low growth rates, obtained by adjusting the concentration of  $\text{SiCl}_4$ , would yield more perfect surfaces on substrates oriented close to (111); he found that surface pyramids did not grow when the growth rate was less than  $0.4\mu/\text{min}$ , and also that these pyramids did not grow when the substrates were misoriented from (111).

We have found that steps  $\sim 500\text{\AA}$  high generally suffer less change of shape than steps  $1500\text{\AA}$  high, even with properly oriented substrates. In addition, we report a significant influence of the temperature of the

epitaxial deposition, both for near (111) and for (100) surfaces. We have also found that the orientation of the steps relative to mirror planes of symmetry in the lattice is an important variable to consider in producing depressions whose boundaries have symmetrical displacements relative to the edges of the buried layers.

To facilitate later discussion, we define four possible types of distortion, illustrated in Fig. 1b. Cross-sections are drawn to indicate the relative positions of the depressions in the substrate and epitaxial surfaces. The first situation is called "symmetrical distortion," in which case the displacements of the steps are symmetrical about the center. Thus  $\bar{S}_1 = -\bar{S}_2$  in 1 of Fig. 1b. There is no displacement of the center of the figure. The width of the figure may increase or decrease, as shown. The next case is called "nonsymmetrical distortion without change of size." Here there is a net shift of the center of the figure, and the displacement vectors are equal,  $\bar{S}_1 = \bar{S}_2$ . The third case is "nonsymmetrical distortion with change of size," with  $|\bar{S}_1| \neq |\bar{S}_2|$ . The last case illustrates "obliteration" or "washout" of the surface feature.

When considering an entire rectangular depression, the phrase "a pair of sides" will refer to a pair of parallel sides of the rectangle. One pair of sides may in practice become distorted differently from the other pair, so information about both is necessary to completely specify the distortion. We refer to individual surface figures as flat-bottomed depressions or as pits, as appropriate. We use the word *pattern* to denote an array of individual geometrical figures.

### Experimental Details

All of the epitaxial films were grown by the hydrogen reduction of  $\text{SiCl}_4$  at a mole fraction of about 1% unless otherwise stated, and at specified temperatures near  $1200^\circ\text{C}$  with growth rates in the vicinity of  $1\mu/\text{min}$  (5). The substrate slices were placed either directly on the inductively heated susceptor or on a thin quartz wafer on the susceptor. Temperatures were measured by optical pyrometry, correcting for emissivity according to the data of Allen (6). The angular misorientations of the slices from (111) were measured within about 20 min of arc with x-ray goniometry (7), and the directions of the misorientations were determined by Laue back reflection x-ray photographs.

The substrate slices were cut from 4 to 10 ohm-cm, boron-doped ingots. They were mirror polished, cleaned, oxidized at  $1100^\circ\text{C}$ , and antimony was diffused at  $1250^\circ\text{C}$  through windows opened in the oxide by standard photolithography techniques. The last 10 min of the diffusion step was a thermal oxidation with dry oxygen in order to create shallow depressions in the silicon exposed by the windows. Some slices were prepared without the antimony diffusion, i.e., shallow depressions were formed by a short oxidation after windows were opened. Prior to epitaxial growth, all oxide was removed and the surfaces were hydrophobic.

The numerical results herein refer to depressions about  $500\text{\AA}$  deep as measured by interferometry, and to epitaxial thicknesses of about  $3\mu$ . All of the surface observations were made with interference contrast microscopy (8) which provides considerable contrast at steps of small height.

### Distortion and Displacement on Surfaces near (111)

A pattern of circular shallow depressions (Fig. 2a) was used in order to observe the distortion for every possible orientation of steps on a given slice. The circles generally became oval-shaped figures after epitaxial deposition, as shown in Fig. 2b-c. To characterize this change of shape, we define the "shape distortion" to be the difference in the principal diameters of the ovals; some data on the shape distortion as a function of surface orientation and growth tem-

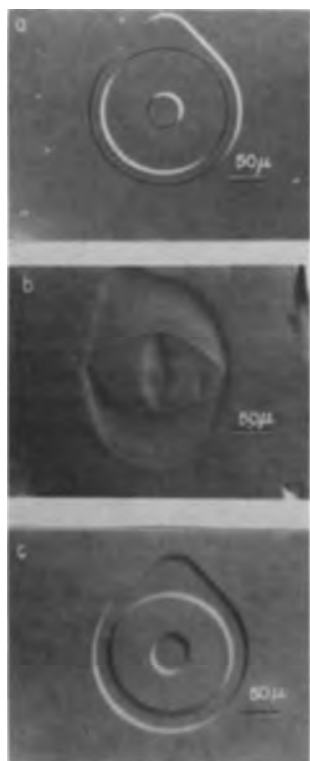


Fig. 2. Undistorted circular depression  $\approx 500\text{\AA}$  deep in silicon substrate (a), and same feature after epitaxial deposition on substrates  $1^\circ$  (b), and  $3^\circ$  off (111) toward a nearest {110} (c). Interference contrast micrographs.

perature are shown in Fig. 3. The general features of the data are the following: (i) there is a discontinuity in the distortion at the exact (111) position, since patterns on surfaces very close to (111) could not be recognized after deposition; (ii) the shape distortion decreased with angular orientation off (111) and was generally lower at higher growth temperatures; and (iii) there was always some measurable distortion.

There are some further details which are important, since there are many ways to misorient a surface off (111). It will become apparent later in this section that symmetry conditions will play a part in determining the most useful way to orient a surface off (111). The exact (111) surface has 3-fold symmetry with three mirror planes in the lattice normal to (111), and this symmetry is reduced with a surface that is slightly off (111). It is possible to retain one of these mirror planes normal to the surface, so that two-fold symmetry is retained. The two ways of doing this are included in the data of Fig. 3, i.e., surfaces  $\theta$  degrees off (111) toward a nearest {100} denoted  $111-\theta^\circ-100$ , and likewise, surfaces off (111) toward a nearest {110}, denoted  $111-\theta^\circ-110$ . From Fig. 3 it is clear that  $111-\theta^\circ-110$  surfaces exhibited lower distortion, less temperature dependence of the distortion and sharper edges. We also experimented with several other ways to orient surfaces off (111), and the results showed the same general decrease in distortion with misorientation. The greatest distortion occurred on  $111-\theta^\circ-100$  surfaces.

A distorted surface pattern should be accompanied by lateral displacement of a step on the epitaxial surface relative to the edge of the buried layer. To measure this displacement, patterns with rectangular features were used; these patterns contained a small alignment feature in the shape of a T, which served as a monitor of the distortion of the surface feature. Figure 4 consists of data on the width of the stem of the T after epitaxial growth plotted against the lateral shift of one side of a depression, as revealed by angle lapping and staining. These points were taken from slices whose orientations ranged from  $\frac{1}{2}^\circ$  to  $4^\circ$  off

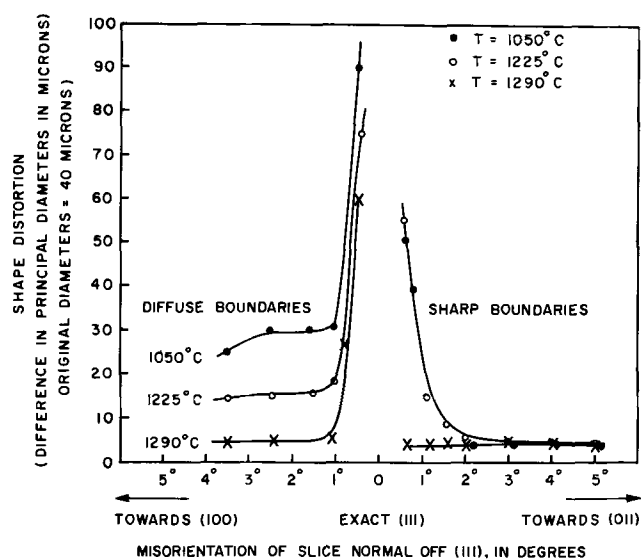


Fig. 3. Shape distortion vs. surface orientation near (111)

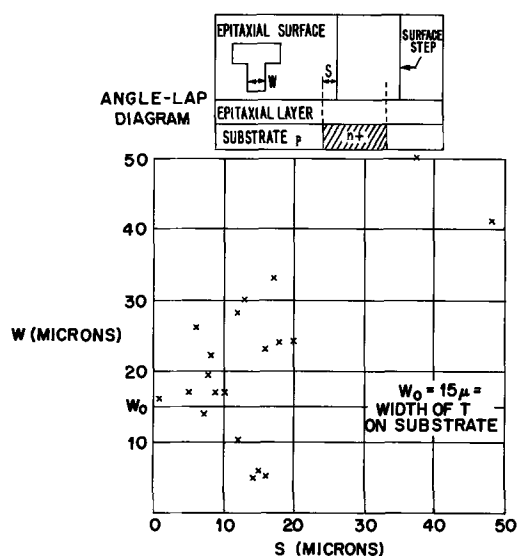


Fig. 4. Width of a standard surface figure (T) vs. displacement of edge of rectangular figure relative to the edge of the buried layer.

[111] in random directions. As expected, the displacement generally increased with deviations of the width of the stem of the T from its original value. However, a number of points show W close to its original value  $W_0$ , but with a displacement S of approximately  $10\mu$ . These data suggest that an undistorted depression is necessary but not sufficient to ensure that the edges of the depression are precisely ( $\pm 2.5\mu$ ) registered relative to the edges of the buried layer.

According to the data of Fig. 3, the  $111-\theta^\circ-110$  surfaces will provide more control over the shape distortion than the other orientation shown in Fig. 3. We may ask just how small will the lateral displacement be on such a surface, or how precisely can a step be grown relative to the buried layer? It is now clear that the crystallographic orientations play a very important role in the lateral displacement of the depressions, i.e., in the lateral growth at the small steps. Since the original surface feature is symmetrically positioned relative to the buried layer, as drawn in Fig. 1, the ideal situation after epitaxial growth would also be for the figure and buried layer to be symmetrical. To achieve this, opposite sides of a shallow pattern should have identical crystallographic orientations; this will be the case if there is a mirror plane of symmetry in the lattice, normal to the slice and parallel to the edge of the depression.

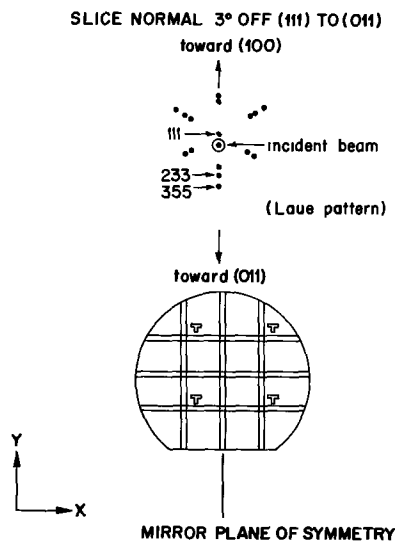


Fig. 5. Drawing of Laue x-ray pattern from a silicon slice with a  $111\text{-}3^\circ\text{-}110$  surface, and drawing of rectangular surface features with one pair of sides parallel to the mirror plane of symmetry normal to the surface of the slice.

With  $111\text{-}\theta^\circ\text{-}110$  surfaces, as shown in Fig. 5, one orientation of steps in a depression may be aligned parallel to the one mirror plane which is normal to the surface. We experimented with slices oriented  $3^\circ$  off (111) toward a nearest  $\{110\}$ , denoted  $111\text{-}3^\circ\text{-}110$ , and verified that the resultant displacements of the steps parallel to the mirror plane were symmetrical and small ( $\sim 2.5\mu$ ), as shown in Fig. 6. However, other steps in the rectangular figure were not parallel to a mirror plane of symmetry, and the displacements were not symmetrical, as illustrated. A typical value of the maximum displacement for these steps was  $14\mu$  or 1.7 times the epitaxial thickness. In this case the net displacement of the center of the surface figure relative to the buried layer reproducibly occurred in the  $[11\bar{2}]$  direction, using conventional notation (7).

If, with  $111\text{-}3^\circ\text{-}110$  surfaces, the steps were oriented at  $45^\circ$  to those indicated in Fig. 5, we found that sharp figures were grown; however, the displacements were approximately equal to the film thickness but the steps were not symmetrically displaced relative to the buried layer. In this case, neither pair of sides were distorted symmetrically. For reproducible results, it appears necessary to control both the orientation of the pattern and of the slice. One method for routinely accomplishing this is to grind a flat section on the ingot

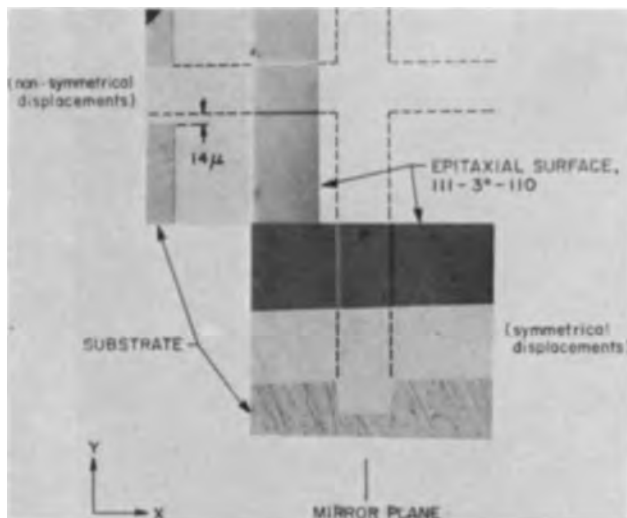


Fig. 6. Double angle-lap and stain of a slice oriented as in Fig. 5. The displacements were symmetrical for only one pair of sides.

prior to slicing, so that each slice has a  $\{112\}$  flat as shown in Fig. 5. Then the orientation of each slice may be determined by inspection.

#### Patterns on (100) Surfaces

From symmetry considerations, one expects to obtain symmetrical distortion of both pairs of sides of rectangular depressions on exact (100) surfaces. We have experimented with figures whose sides were parallel to the  $\langle 011 \rangle$  directions. Again, it was found that the temperature of deposition had a significant effect on the nature of the distortion, independent of the concentration of  $\text{SiCl}_4$ . At  $1240^\circ\text{C}$ , the resultant depressions had very sharp boundaries and were undistorted. Angle-lapped sections showed that both sets of sides of the depressions were symmetrically shifted by small ( $\sim 2.5\mu$ ) amounts relative to the buried diffusion.

However, at lower temperatures such as  $1215^\circ$  and  $1185^\circ\text{C}$ , much less sharp boundaries resulted. This was an effect of temperature and not an effect of concentration, over the range 0.4 to 1.7 m/o (mole per cent)  $\text{SiCl}_4$ .

These results were obtained on slices with surfaces within 15 min of (100). A complete graph of lateral displacement as a function of orientation off (100) has not been plotted, but a few examples of nonsymmetrical shifts for surfaces  $2^\circ$  off (100) have been observed.

#### Other Effects

Vapor phase HCl etching of silicon is a well established method of final substrate preparation, which generally allows more perfect epitaxial layers to be grown. We found that negligible distortion took place on  $111\text{-}3^\circ\text{-}110$  surfaces during either 1 or 10 min HCl etching at  $1290^\circ\text{C}$  and 1% HCl in  $\text{H}_2$ . Some distortion did result, however, on surfaces closely oriented to (111).

The distortion of depressions does not depend on the presence of a high concentration of dopant; this has been demonstrated by producing shallow patterns in undiffused substrates. The resultant distortions after epitaxial growth showed the same orientation dependence as those on diffused slices. Occasionally the process of antimony diffusion by means of  $\text{Sb}_2\text{O}_3$  in nitrogen produces a rough surface, believed to be associated with precipitation of a second phase. In this event, the boundaries of the diffused regions were "distorted" prior to epitaxial growth, and some distortion after epitaxial growth was thus inevitable.

A few experiments were carried out with deeper ( $1500\text{\AA}$ ) depressions, produced by longer oxidations after diffusion. Their boundaries after epitaxial deposition showed less sharpness than those obtained with  $500\text{\AA}$  depressions, even when other variables such as orientation and growth conditions were identical. Thus, the use of deeper depressions appears to be accompanied by unnecessary complications which do not aid in controlling the distortion phenomenon.

We have no evidence that gas flow conditions have any influence on the distortion. All of the epitaxial layers of this work were grown on horizontally rotating pedestals heated by induction. Several runs were made with a set of identically oriented slices, positioned in a variety of ways on the pedestal; the results showed no effect of the position on the pedestal on the distortion.

#### Effect of Surface Orientations Near (111) on Pits at Stacking Faults

The fact that stacking faults can be detected with interference contrast microscopy on as-grown surfaces of epitaxial silicon (9) indicates that a small surface disturbance occurs at the site of the stacking fault-surface intersection. There are generally two components to this surface irregularity; (i) a well-defined triangular figure (or portions thereof) whose dimensions are directly related to the film thickness, and (ii) a less-sharply defined pit, which can vary

greatly in size and shape. We believe that the origin of these figures is as follows. During growth, there will be a tendency for the surface to become thermodynamically equilibrated since atoms are mobile on the surface; a groove would then form at the intersection of the stacking fault and the surface. This process could be called "stacking-fault grooving," in analogy with the well-known grain boundary grooving which occurs in metals (10). The groove forms so that the energy of the crystal is lowered; at equilibrium, the tension of the stacking fault will be equilibrated by components of the surface tension of the exposed surface at the groove. This grooving would explain the presence of the triangular part of the figure, whose shape will be essentially unaffected by changes in orientation near (111). Next, this groove which is a depression in the surface, will suffer distortion during growth; this distortion is very dependent on surface orientations near (111). Thus the small effect of grooving is enhanced by distortion. In some cases, this distortion-part of the surface figure can be a very large pit, as illustrated in Fig. 7a; the stacking faults at one end of the pit are revealed after a brief Sirtl etch (11) as shown in Fig. 7b. As expected, the largest of these pits occurred on surfaces which gave the greatest distortion, i.e., surfaces off (111) toward a nearest {100}. Also, the various grooves at a single stacking fault triangle became distorted differently, and those grooves which tended to expose regions of exact (111) surfaces became distorted the most. For diffused diodes, some data indicate that these large pits associated with stacking faults have undesirable electrical effects; Orr (12) has measured the reverse voltage at 10  $\mu$ a (breakdown voltage) of diffused diodes on a slice containing large pits at stacking faults. For the particular case he studied, the

results were that diodes with large pits had very low breakdown voltages ( $\sim 10$ v) and diodes without the pits had higher breakdown voltages ( $\sim 60$ v). Further details suggested that low breakdown resulted from a combined effect of the pits and the stacking faults. These very large pits at stacking faults may be eliminated by either reducing the fault density or by using substrates which are oriented off (111) toward a nearest {110}. Also, higher growth temperatures reduce the size of the pits, since the distortion is reduced. Generally, very small pits accompany stacking faults on 111-3°-110 surfaces, as shown in Fig. 7c. Also, no large pits on (100) surfaces have been observed to accompany stacking faults.

### Discussion

It is evident that the distortion is greatly influenced by the crystallographic orientations involved; presumably, an important reason is the anisotropy of the growth rate. A possible qualitative explanation for the temperature dependence of the distortion is a decrease in the anisotropy of the growth rate at higher temperatures. This temperature dependence of the anisotropy has apparently not been studied experimentally, but it is known that many components of the growth process are temperature dependent, e.g., surface diffusion coefficients, nucleation rates, and densities of kink sites.

From experimental data for epitaxial silicon (2), it is known that the growth rate has a cusped minimum at (111) and little or no minimum at (100) or (110). This immediately gives a qualitative understanding of the necessity to orient the surface off the (111) position; since (111) is the slowest growing surface, the growth rate normal to a (111) slice will be very slow compared to the growth of the different crystallographic orientations exposed at the edges of a depression. Thus these figures become obliterated during growth. We have directly observed this process through a microscope equipped with a hot-stage deposition chamber, and the obliteration of figures on surfaces very close to (111) took place quickly, during the first micron of growth. To achieve a higher growth rate normal to the slice, one orients the surface off (111). The choice of the direction off (111) is dictated by experimental data such as that in Fig. 3, together with symmetry considerations.

The observation that some depressions increase their width during growth suggests that preferential etching of material occurs at some steps. It is known (5) that etching of silicon substrates takes place with high (>0.28) mole fractions of  $\text{SiCl}_4$  in  $\text{H}_2$ , and it is generally believed that some etching occurs as a basic part of the growth process at lower concentrations. The present results merely suggest that this etching effect is also dependent on orientation.

This study of the distortion phenomenon has also led to some understanding of the origin of surface topographical defects in general, as illustrated by the example of pits at stacking faults. For a surface free from topographical irregularities, the present results suggest that high temperatures and/or carefully controlled surface orientations are important factors, in addition to the more commonly recognized factors such as substrate perfection and cleanliness.

In conclusion, it appears that knowledge of the epitaxial growth rates as a function of crystallographic orientation, along with knowledge of the symmetry of the lattice are important factors in understanding the distortion in a qualitative manner. Quantitative details on the temperature dependence, the magnitude of the distortion, and the magnitude of the displacements can only be obtained by experiment. In practice, symmetrical and small (approximately  $2.5\mu$ ) displacements can be obtained for both pairs of sides of rectangular depressions on (100) surfaces and for one pair of sides of depressions on 111-3°-110 surfaces.

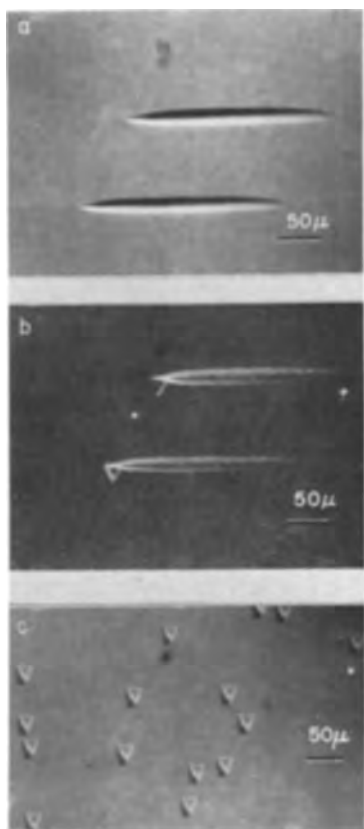


Fig. 7. Pits associated with epitaxial stacking faults on silicon surfaces near (111). Fig. 7a. Surface off (111) toward a nearest {100}. Interference contrast. Fig. 7b. Same area as a, after a brief Sirtl etch. Fig. 7c. Surface off (111) toward a nearest {110}. Interference contrast.

### Acknowledgments

We are grateful to M. D. Patterson for the photolithographic and diffusion work, and to V. E. Hauser and E. R. Helfrich for the epitaxial depositions.

Manuscript received Nov. 27, 1967; revised manuscript received ca. Jan. 27, 1968. This paper was presented at the Dallas Meeting, May 7-12, 1967, as a Recent News Paper.

Any discussion of this paper will appear in a Discussion Section to be published in the December 1968 JOURNAL.

### REFERENCES

1. W. K. Burton, N. Cabrera, and F. C. Frank, *Phil. Trans. Roy. Soc. (London)*, **A243**, 299 (1950).
2. S. K. Tung, *This Journal*, **112**, 436 (1965); S. Mendelson, *J. Appl. Phys.*, **35**, 1570 (1964).
3. C. E. Benjamin and E. J. Patzner, Recent News Paper presented at Electrochemical Society, San Francisco, May 1965.
4. D. W. Boss and V. Y. Doo, Abstract 186, Extd. Abstracts, Electronics Division Electrochemical Society, **15**, 59 (1966).
5. H. C. Theuerer, *This Journal*, **108**, 649 (1961).
6. F. G. Allen, *J. Appl. Phys.*, **28**, 1510 (1957).
7. E. A. Wood, "Crystal Orientation Manual," Columbia University Press, 1963.
8. G. Nomarski and A. R. Weill, *Rev. Met. (Paris)*, **52**, 121 (1955).
9. R. H. Dudley, *J. Appl. Phys.*, **35**, 1360 (1964).
10. G. L. J. Bailey and H. C. Watkins, *Proc. Phys. Soc.*, **B63**, 350 (1950); W. W. Mullins, *J. Appl. Phys.*, **28**, 333 (1957).
11. E. Sirtl and A. Adler, *Z. Metallkde*, **52**, 529 (1961).
12. S. R. Orr, Unpublished data.

## Technical Notes



### Scanning Electron Microscopy of Twin Structures in Silicon Web Dendrite Crystals

G. H. Schwuttke and E. K. Brandis

IBM East Fishkill Laboratories, Hopewell Junction, New York

The scanning electron microscope (SEM) has recently been introduced as a new tool to examine and study defects in semiconductor devices (1-3). An outstanding feature of the SEM is its high resolution combined with large depth of focus. More recently the application of the SEM as a refined "probe" has been described (4,5). Specifically, its ability to locate regions of avalanche breakdown in devices has been the subject of several papers (6,7). This note describes the application of the SEM to problems of crystal growth and shows its usefulness for the detection of twin structures in silicon web dendrite crystals.

In general, the detection or location of twins in crystals is relatively easily accomplished through chemical etching. Chemical etching followed by optical inspection is also quite useful for the study of twin structures in semiconductor crystals; however, the interpretation is difficult or sometimes impossible if the twins are spaced as closely as in web dendrite crystals.

Faust and John (8) have shown that the inspection of fractured web crystal surfaces can give reliable information of the true twin structures as long as it is possible to view fractured surfaces directly and the twin spacing is within microscopic resolution.

For submicroscopic twin spacing the electron microscope replication technique has been shown to be very successful and reliable (9). However, this technique is relatively complicated and time consuming.

Such difficulties do not exist for the scanning electron microscope. The electron optics of the SEM provide a large depth of field, many times that of the light microscope. The crystals are inspected directly making cumbersome replication unnecessary. Consequently, the exact surface topography of the crystal is easily explored, and submicron twin lamellae can be detected.

The cleavage planes of silicon are the {111} planes. Skillful cleavage of silicon breaks the crystal on the cleavage planes. This technique works also quite well for thin web and micron web (8). A diagram of the

cleaved section of web dendrite is shown in Fig. 1. The crystallographic indices of the twinned segments are referred to the parent crystal.

For the inspection of such surface structures the SEM is operated in the secondary electron collection mode (4). In this mode of operation the contrast in the SEM topograph depends on the efficiency of secondary electron collection. A (111) cleavage surface appears either bright or dark depending on its position relative to the SEM signal detector. The cleavage plane is bright if secondary electrons are readily collected and the plane appears dark if the position of the signal detector relative to the crystal plane is such that no or fewer electrons are collected (for instance in the shadow side of the plane). From the bright/dark contrast in the SEM topograph the twin structure is easily deduced.

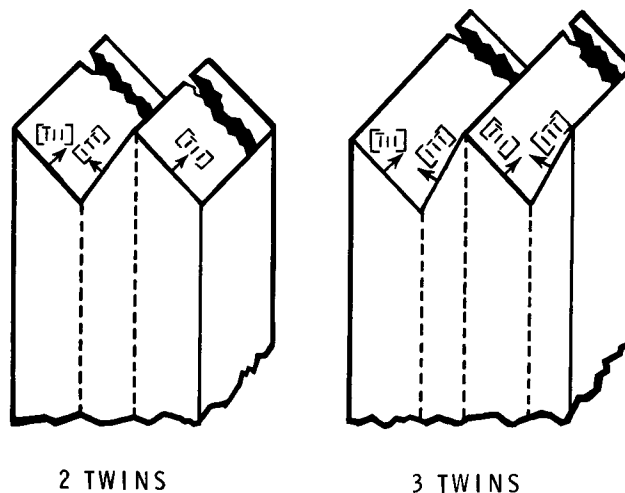


Fig. 1. Diagram of cleaved web dendrite structure



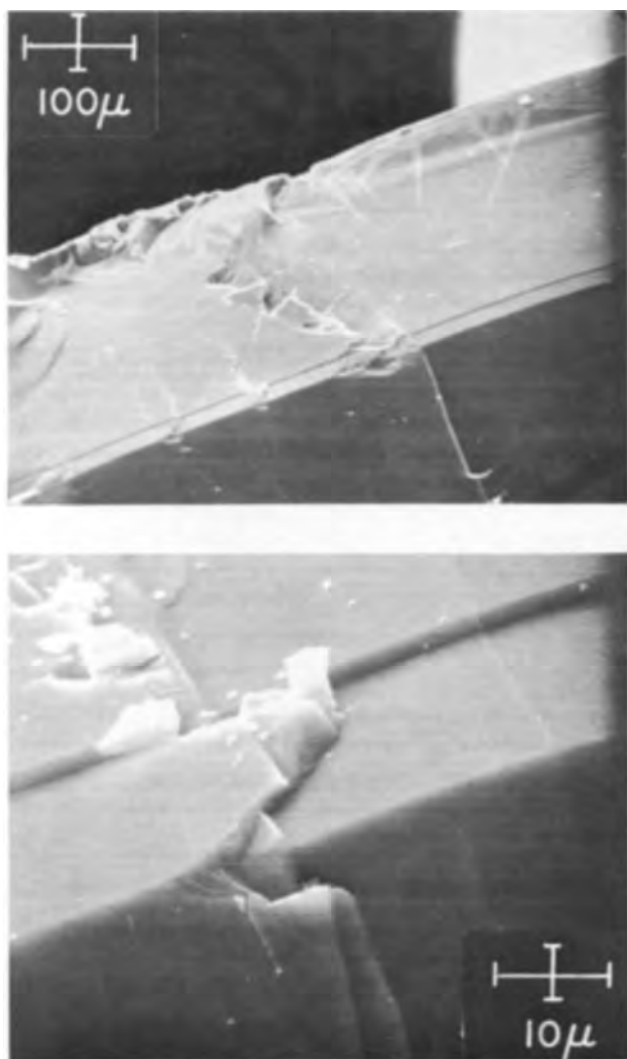


Fig. 2. SEM topograph of cleaved cross section of web dendrite revealing twin structure: (a) (top)  $100\mu$ ; (b) (bottom)  $10\mu$ .

The effect of twin lamellae present in cleaved silicon web dendrite crystals on SEM contrast is shown in Fig. 2a and 2b. Figure 2a is the SEM topograph of the cleaved cross section of such a crystal. Magnification is low, approximately 140X. However, a thin black line indicates the presence of a twin lamellae. This is seen much better at higher magnification. In Fig. 2b, the same crystal area is viewed at a magnification of approximately 2800X. Note the three-dimensional contours displayed in the SEM topograph.

To establish the validity of SEM contrast interpretation SEM topographs of cleaved web dendrites were correlated with electron microscopy results obtained through the replica technique of Stickler (9), specifically developed for the investigation of silicon surfaces. An example of such a correlation is shown in Fig. 3a and 3b. Figure 3a represents the electron transmission micrograph and Fig. 3b is the SEM topograph. The electron micrograph and the SEM micrograph do not show exactly the same area of the web dendrite surface because this is rather difficult to achieve. However, the areas depicted in these two micrographs are located reasonably close to each other and the twin structure is continuous in these areas. The agreement between the two measurements is obvious. Confidence in the SEM method for the inspection of twin structure in web dendrites has been established through numerous measurements.

A systematic investigation of fractured web dendrite crystals by optical and SEM microscopy has shown that optical inspection alone may not always be sufficient to reveal the true twin structure. An example

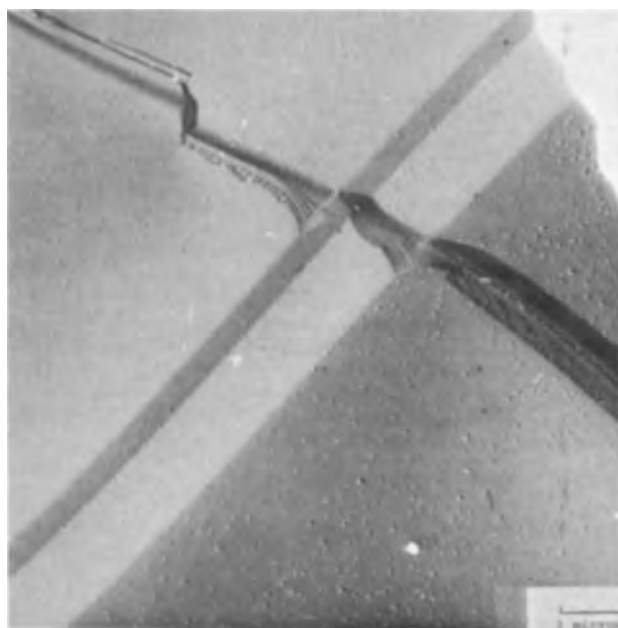


Fig. 3a. Electron microscope replica of fractured web dendrite crystal showing twin lamellae.

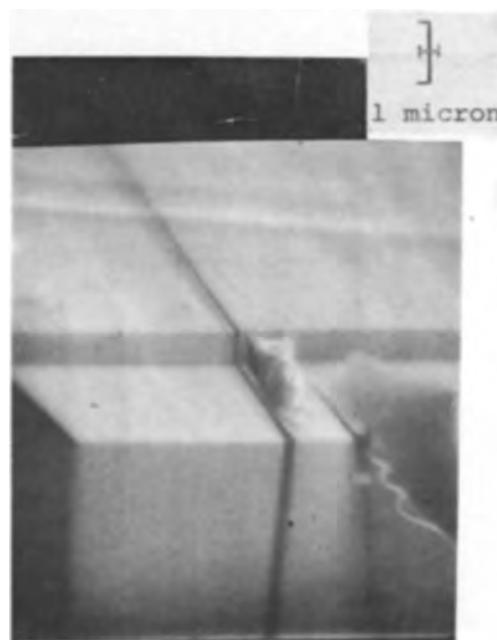


Fig. 3b. SEM micrograph of crystal shown in Fig. 3a

of this is presented in Fig. 4a and 4b. The photomicrograph presented in Fig. 4a is an optical picture of a multiple (submicron) twin structure. The corresponding SEM micrograph is shown in Fig. 4b at a magnification of approximately 7000X. In the optical photomicrograph we recognize only two grooves while in the SEM topograph multiple twinning is clearly evident.

For a quantitative evaluation of SEM pictures the foreshortening of the SEM image as seen on the cathode ray tube must be considered.

#### Acknowledgment

The authors are indebted to Dr. O. C. Wells for his assistance in recording the SEM topographs and also to Mr. D. Cameron and Mrs. F. Ordonez for the skillful electron microscopy. Part of this work was sponsored under Government Contract AF 16(628)-5059.

Manuscript received June 29, 1967; revised manuscript received Feb. 15, 1968. This paper was presented



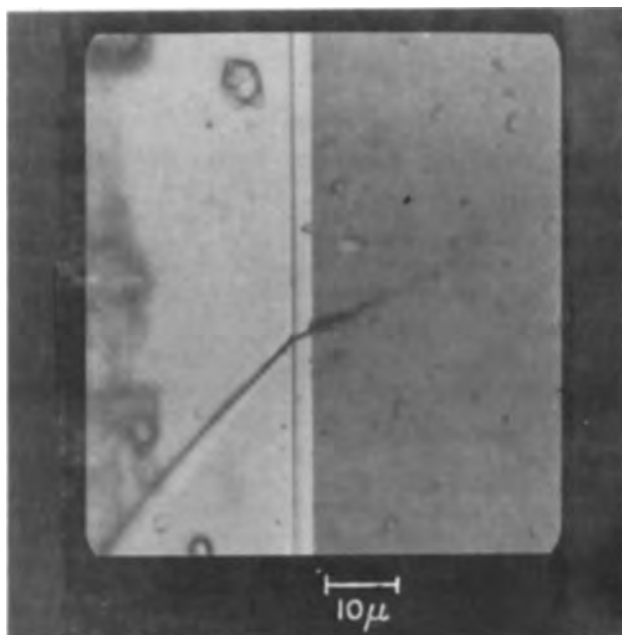


Fig. 4a. Optical micrograph of crystal area shown in Fig. 4b

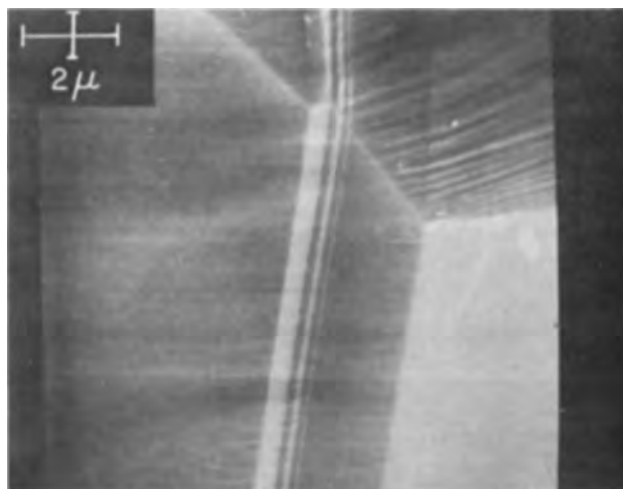


Fig. 4b. SEM topograph showing multiple twin structures in web dendrite crystal.

at the Dallas Meeting, May 7-12, 1967, as a Late News Paper.

Any discussion of this paper will appear in a Discussion Section to be published in the December 1968 JOURNAL.

#### REFERENCES

1. J. J. Lander, T. M. Buck, H. Schreiber, Jr., and J. R. Mathews, *Appl. Phys. Letters*, **3**, 203 (1963).
2. W. Czaja and G. H. Wheatley, *J. Appl. Phys.*, **35**, 2782 (1964).
3. W. Czaja and J. R. Patel, *ibid.*, **36**, 1476 (1965).
4. T. E. Everhard, O. C. Wells, and R. K. Matta, *This Journal*, **111**, 929 (1964) also T. E. Everhard, O. C. Wells, and C. W. Oatley, *J. Electron. Control*, **7**, 97 (1959).
5. W. F. B. Neve, K. A. Hughes, and P. R. Thornton, *J. Appl. Phys.*, **37**, 1704 (1966).
6. I. G. Davies, K. A. Hughes, D. V. Sulvay, and P. R. Thornton, *Solid State Electronics*, **9**, 275 (1966).
7. N. F. B. Neve, D. V. Sulvay, K. A. Hughes, and P. R. Thornton, *Trans. Electron Devices*, **ED-13**, 639 (1966).
8. J. W. Faust, Jr., and H. F. John, *This Journal*, **117**, 562 (1962).
9. R. Stickler, *J. Sci. Instruments*, **41**, 523 (1964).

## Preparation and Properties of Amorphous Germanium Nitride Films

Haruo Nagai and Tatsuya Niimi

*Electrical Communication Laboratory, Nippon Telegraph and Telephone Public Corporation, Musashino-shi, Tokyo, Japan*

Compared to much work on silicon nitride films for passivation of silicon devices, there are only a few reports about the compounds between germanium and nitrogen,  $\text{Ge}_3\text{N}_2$  and  $\text{Ge}_3\text{N}_4$  (1-3).

In this paper a new method of preparation of amorphous germanium nitride film, using the reaction of germanium tetrachloride and ammonia, and some properties of the film are reported.

#### Experimental

The apparatus used for the deposition of the germanium nitride film was similar to an rf-heated silicon epitaxial deposition system widely used, in which the deposition was carried out on a hot substrate crystal placed on a heated molybdenum pedestal held in the center of a vertical fused silica tube. As  $\text{GeCl}_4$  reacts with  $\text{NH}_3$  at room temperature and produces  $\text{Ge}(\text{NH})_2$  and  $\text{NH}_4\text{Cl}$ , the two reactants must be introduced separately onto the hot substrate where the reaction takes place. The vapor of  $\text{GeCl}_4$  was carried into the system by purified hydrogen gas passing over liquid  $\text{GeCl}_4$  stored in an evaporator kept at  $0^\circ\text{C}$ .

The ammonia gas used was of high purity and dried by passing through a KOH column and a cold trap kept at  $-22^\circ\text{C}$  before introduction into the reaction

tube. The substrate surface was (111) single crystal germanium or silicon, mirror polished and etched with CP4. After the temperature of the substrate was raised to the reaction temperature in hydrogen, ammonia and germanium tetrachloride were introduced into the reaction tube.

#### Results

It was possible to form the films in the temperature range from  $400^\circ$  to  $600^\circ\text{C}$ . The deposited films were uniform, transparent, and adherent to the substrates. Above  $600^\circ\text{C}$ , the epitaxial growth of germanium was observed, and below  $400^\circ\text{C}$ , the growth of the film was too slow to be observed. The effect of the substrate temperature on the deposition rate is shown in Fig. 1 for a typical reactant concentration, giving an activation energy of 17 kcal/mole.

When the concentration of  $\text{GeCl}_4$  was varied from 0.1 m/o (mole per cent) to 0.6 m/o, the deposition rates remained almost unchanged, if the reaction temperature and the concentration of  $\text{NH}_3$  were kept constant. The thickness of the film, required for the determination of the deposition rate, was measured by the optical interference technique using mercury light ( $5461\text{\AA}$ ), and, at the same time, the refractive indices of the films were determined to be  $2.06 \pm 0.06$ , which are marked

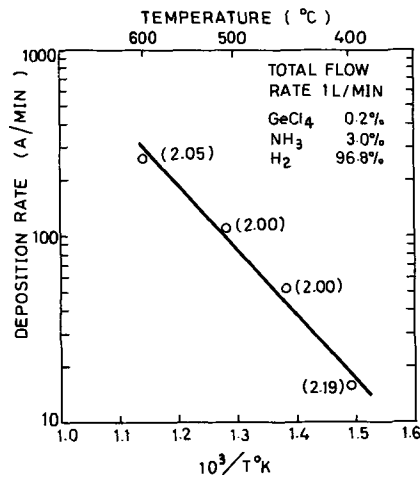


Fig. 1. Temperature dependence of the deposition rate of the film. Numbers in parentheses are refractive indices.

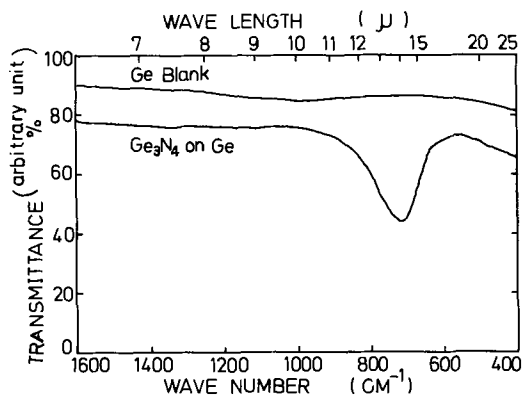


Fig. 2. Infrared transmission curve for the film on germanium

at several growth points along the experimental curve in Fig. 1. No correlation was found between the value of refractive indices of the films and deposition conditions. The infrared absorption spectra of the films showed the broad band of absorption with a peak between 720 and 750  $\text{cm}^{-1}$ , and qualitatively the peak was found to move toward the lower frequency side at the samples deposited at higher temperatures. In Fig. 2 is shown a typical absorption spectrum taken on a sample having a film of thickness 2870 Å deposited at 600°C on an n-type 40 ohm-cm germanium substrate crystal.

X-ray and electron diffraction show that the films deposited were amorphous. Figure 3 is a typical reflection electron diffraction pattern for the film mentioned in Fig. 2.

It is reported, that above 700°C germanium reacts with ammonia and forms  $\text{Ge}_3\text{N}_4$  crystal which has a mixed structure of  $\alpha$ - and  $\beta$ -phases (4).

The infrared absorption spectrum of the crystal prepared by the above method shows sharp absorption peaks at 770 and 730  $\text{cm}^{-1}$ , the later corresponding to the absorption of  $\alpha$  phase  $\text{Ge}_3\text{N}_4$  crystal (5), and the absorption peaks of the films reported here are near these values. The chemical analyses of the films were not performed, but from these facts, the films deposited were considered to be amorphous  $\text{Ge}_3\text{N}_4$ . Generally the films were slightly soluble in water, con-



Fig. 3. Electron diffraction pattern for the film

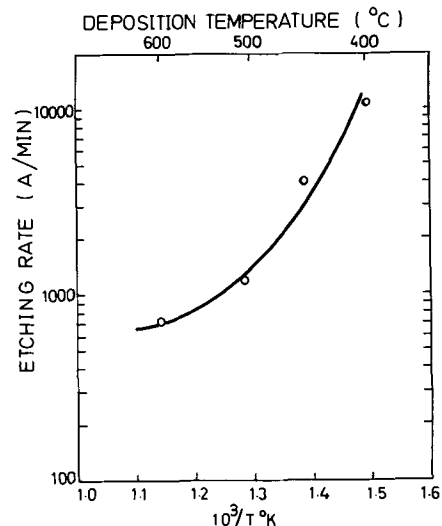


Fig. 4. Dependence of the etching rate of the film by 46% HF at 20°C on the deposition temperature. Reactant concentration is the same as the case of Fig. 1.

centrated  $\text{HCl}$ ,  $\text{H}_2\text{SO}_4$ ,  $\text{H}_3\text{PO}_4$ , and  $\text{NaOH}$  solution, but rapidly dissolved in concentrated  $\text{HF}$  and  $\text{HNO}_3$ .

The dissolution rate decreased with the higher growth temperature of the films and Fig. 4 shows an example of the results in 46%  $\text{HF}$  at 20°C. When the film was kept at or above 600°C in hydrogen, the thickness of the film was reduced rapidly, and in  $\text{Ar}$  or  $\text{N}_2$ , the films were decomposed slowly.

The electrical resistivity of the films was very high, ranging from  $10^{14}$  to  $10^{16}$  ohm-cm.

Manuscript received Jan. 29, 1968.

Any discussion of this paper will appear in a Discussion Section to be published in the December 1968 JOURNAL.

#### REFERENCES

1. W. C. Johnson, *J. Am. Chem. Soc.*, **52**, 5160 (1930).
2. R. Storr, A. N. Wright, and C. A. Winkler, *Can. J. Chem.*, **40**, 1296 (1962).
3. M. D. Lyutaya, G. V. Samsonov, and O. T. Khorpyakov, *Z. Neorgam. Khim.*, **9**(7), 1529 (1964).
4. S. N. Ruddleden and P. Popper, *Acta Cryst.*, **11**, 465 (1958).
5. Y. Igarashi, K. Kurumada, and T. Niimi, *Japan. J. Appl. Phys.*, **7**, 300 (1968).

## Some New Classes of Efficient $\text{Eu}^{2+}$ -Activated Phosphors

G. Blasse, W. L. Wanmaker, and J. W. ter Vrugt

N. V. Philips' Gloeilampenfabrieken, Eindhoven-Netherlands

The absorption and fluorescence of the  $\text{Eu}^{2+}$  ion in solids is well known. The fluorescence usually consists of an emission band in the short-wavelength part of the visible region (1). Some of the  $\text{Eu}^{2+}$ -activated alkaline-earth silicates have been reported to show efficient fluorescence (2). Recently the efficient, green fluorescence of  $\text{SrAl}_2\text{O}_4\text{-Eu}^{2+}$  was mentioned in a patent (3). The purpose of this communication is to report on some new classes of efficient  $\text{Eu}^{2+}$ -activated photoluminescent phosphors, whose emission spreads over the region 390-520 nm. More detailed information is published elsewhere (4-6).

Samples were prepared by standard ceramic methods firing in an atmosphere of nitrogen containing 5% of hydrogen. Optical measurements were performed as described before (7). The host lattices involved are the following: (a) alkaline-earth pyrophosphates ( $\text{Me}_2^{2+}\text{P}_2\text{O}_7$ ), (b) alkaline-earth aluminates of the magneto-plumbite type ( $\text{Me}^{2+}\text{Al}_{12}\text{O}_{19}$ ), (c) alkaline-earth magnesium silicates of the types  $\text{Me}_2^{2+}\text{MgSi}_2\text{O}_7$  (e.g., akermannites) and  $\text{Me}_3^{2+}\text{MgSi}_2\text{O}_8$  (merwinites), and (d) alkaline-earth aluminates with tridymite-like structure ( $\text{Me}^{2+}\text{Al}_2\text{O}_4$ ). All these compounds can be easily doped with divalent europium. In this way phosphors are obtained with a high efficiency under 254 and 365 nm excitation. The efficiency for cathode-ray excitation is not so high (although comparable to those of  $\text{Ce}^{3+}$ -activated phosphors). The color of the emission varies from blue to green and depends strongly on the host lattice used and to a lesser extent on the choice of the alkaline earth ion (or the composition of a mixture of alkaline earth ions). It is therefore possible to prepare phosphors with a specific emission peak in the region 390-520 nm by an appropriate choice of the chemical composition of the host lattice.

Table I shows data on the fluorescence of some of the new materials. Figure 1 gives the spectral energy distribution of one example out of every class of the host lattices. The emission region 395-440 nm is covered by the pyrophosphate and aluminate phosphors with general formulas  $\text{Me}_2\text{P}_2\text{O}_7\text{-Eu}$  and  $\text{MeAl}_{12}\text{O}_{19}\text{-Eu}$ , the region 440-475 nm by the silicate phosphors with formula  $\text{Me}_3\text{MgSi}_2\text{O}_8\text{-Eu}$ , the region 440-510 nm by the

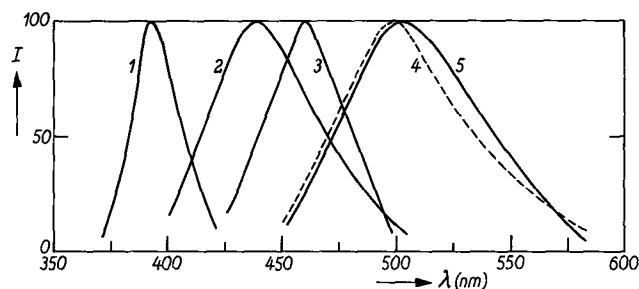


Fig. 1. Spectral energy distribution of the emission of: 1.  $\text{Sr}_{10}\text{Mg}_{12}\text{P}_2\text{O}_7\text{-Eu}^{2+}$ , 2.  $\text{BaAl}_{12}\text{O}_{19}\text{-Eu}^{2+}$ , 3.  $\text{Sr}_3\text{MgSi}_2\text{O}_8\text{-Eu}^{2+}$ , 4.  $\text{Ba}_3\text{MgSi}_2\text{O}_7\text{-Eu}^{2+}$  (broken line), and 5.  $\text{BaAl}_2\text{O}_4\text{-Eu}^{2+}$ . 254 nm excitation. Along the ordinate the relative radiant power per constant wavelength interval (I) is plotted.

silicate phosphors with formula  $\text{Me}_2\text{MgSi}_2\text{O}_7\text{-Eu}$ , and the region 500-520 nm by the aluminate phosphors with formula  $\text{MeAl}_2\text{O}_4\text{-Eu}$ . The optimum  $\text{Eu}^{2+}$ -concentration amounts to roughly 2-5 a/o (atom per cent). For further details the reader is referred to other papers (4-6).

Manuscript received Dec. 15, 1967. This paper was presented at the Boston Meeting, May 5-9, 1968, as Abstract 56.

Any discussion of this paper will appear in a Discussion Section to be published in the December 1968 JOURNAL.

### REFERENCES

1. D. S. McClure, "Electronic Spectra of Molecules and Ions in Crystals," Solid State Reprints, Academic Press, New York (1959).
2. H. G. Jenkins and A. H. McKeag, *This Journal*, **97**, 415 (1950); Brit. Pat. 544,160, 1942.
3. U. S. Pat. 3,294,699, 1966.
4. W. L. Wanmaker and J. W. ter Vrugt, *Philips Res. Repts*, **22**, 355 (1967) (pyrophosphates).
5. G. Blasse, W. L. Wanmaker, J. W. ter Vrugt, and A. Bril, *ibid.*, **23**, 189 (1968). (silicates).
6. G. Blasse and A. Bril, *ibid.*, **23**, 201 (1968). (aluminates).
7. A. Bril and W. L. Wanmaker, *This Journal*, **111**, 1363 (1964).

Table I. Some data on new  $\text{Eu}^{2+}$ -activated phosphors

Composition*	Position of maximum of emission band (nm)	Quantum efficiency, %		Reflection, %, 254 nm	$T_{50}^{**}$ , °K	Radiant energy efficiency for cathode-ray excitation, %, 20 kv
		250-270 nm excitation	Maximum value in u.v. region			
$\text{Sr}_{10}\text{Mg}_{12}\text{P}_2\text{O}_7\text{-Eu}$	395	55	65	13	490	3.5
$\text{Sr}_2\text{P}_2\text{O}_7\text{-Eu}$	420	65	65	14	470	4.5
$\text{SrAl}_{12}\text{O}_{19}\text{-Eu}$	395	40	55	44	370	1.5
$\text{BaAl}_{12}\text{O}_{19}\text{-Eu}$	435	40	70	65	525	2.5
$\text{Sr}_3\text{MgSi}_2\text{O}_7\text{-Eu}$	470	35	40	20	305	1.5
$\text{Ba}_3\text{MgSi}_2\text{O}_7\text{-Eu}$	500	60	75	26	465	3.0
$\text{Sr}_3\text{MgSi}_2\text{O}_8\text{-Eu}$	460	35	60	11	520	3.0
$\text{Ba}_3\text{MgSi}_2\text{O}_8\text{-Eu}$	440	50	80	8	350	0.5
$\text{SrAl}_2\text{O}_4\text{-Eu}$	520	45	55	17	380	1.5
$\text{BaAl}_2\text{O}_4\text{-Eu}$	505	50	60	20	380	2.0

\*  $\text{Eu}^{2+}$ -concentration 2 a/o.

\*\*  $T_{50}$  is the temperature at which the light output of the phosphor has decreased to 50% of the value measured at liquid  $\text{N}_2$  temperature.

# Crystallographic Phase Transformation of Ferric Fluoride

W. J. Croft and M. Kestigian\*

*Sperry Rand Research Center, Sudbury, Massachusetts*

Ferric fluoride ( $\text{FeF}_3$ ) was reported originally to possess the rhombohedral  $\text{AlF}_3$ -type structure (1). More recent work has shown (2, 3) that the structural unit actually is a bimolecular rhombohedral cell (space group  $R\bar{3}c$ ) with the fluorine atoms in slightly distorted hexagonal closest packing. The metal atoms occupy certain octahedral interstices and form a rhombohedrally distorted simple cubic superlattice. The unimolecular rhombohedral pseudocell reported by Hepworth *et al.* (2) has an angle  $\alpha = 88.22^\circ$  which indicates the small degree of distortion from the cube.

Crystals prepared by vapor transport are morphologically orthogonal in outline, appearing as cubes or cubes elongated on one fourfold axis. Examination in plane-polarized light indicates these crystals to be anisotropic and to show extinction at approximately  $45^\circ$  to the elongated (fourfold) axis. Each morphological crystal consists of several units, each of which shows extinction at  $45^\circ$  to the pseudocube [100] edge.

Many of the crystals have a fibrous appearance with the fiber axes at  $45^\circ$  to the elongation direction of the crystal. These fibers extinguish parallel to the polarization directions of the microscope. By tilting various crystals it is observed that the C-axis elongated fibers are clustered in groups or bundles with each bundle having its axis parallel to one of the four  $\langle 111 \rangle$  directions of the pseudocubic form of the crystal.

The present study has also observed crystallographic reflections with  $h + k + l$  odd (superlattice reflection) which Hepworth *et al.* (2) report and cite as evidence of the bimolecular rhombohedral unit cell.

\* Electrochemical Society Active Member.

The crystals were heated on the stage of a polarizing microscope. A Leitz heating stage was used with the sample being held on a transparent, fused quartz plate. The heating chamber was continuously flushed with dry helium which had previously passed through a liquid nitrogen trap. If care was not taken to avoid oxygen, the crystals turned from green to brown when held at temperatures above  $350^\circ$ , indicating that oxidation was taking place. At  $410^\circ\text{C} \pm 5^\circ$  the crystals became isotropic. This is a reasonable transformation although the twinning became much more complex by cycling through this transformation. The room temperature x-ray diffraction pattern reappeared after the heating cycle was complete.

## Conclusion

Crystals of anhydrous ferric fluoride ( $\text{FeF}_3$ ) have been formed by sublimation and grow in the cubic crystallographic symmetry. These crystals have been shown to undergo a phase transformation to a rhombohedral unit cell at  $410^\circ \pm 5^\circ$ . This crystallographic phase transformation prevents the growth of large single crystals by the usual methods.

Manuscript received Feb. 19, 1968.

Any discussion of this paper will appear in a Discussion Section to be published in the December 1968 JOURNAL.

## REFERENCES

1. F. Ebert, *Z. Anorg. Chem.*, **196**, 375 (1931).
2. M. A. Hepworth, K. H. Jack, R. D. Peacock, and G. J. Westland, *Acta Cryst.*, **10**, 63 (1957).
3. K. H. Jack and V. Gutmann, *ibid.*, **4**, 246 (1951).

# The Effect of Moisture on the Aluminum-Silica Reaction

Ronald Silverman

*The Bayside Laboratory, Research Center of  
General Telephone & Electronics Laboratories Incorporated, Bayside, New York*

Considerable interest has been focused recently on the reactivity of aluminum on silica because of the extensive use of these materials in integrated micro-circuit components. Aluminum is used as the contact and conduction metallization, while silica is used as the diffusion mask and insulator. Many investigators have shown that production devices may become degraded during processing and during life as a result of a reaction between aluminum and silica. Working with aluminum heat-treated in contact with thermally grown silica, Lehman (1), Berger (2), and Schnable (3) found that different reaction rates were obtained in various atmospheres. Cratchley and Baker (4), working with silica fibers coated with aluminum, found lower reaction rates than those obtained with the thermal grown silica substrates.

The different reaction rates between Al and  $\text{SiO}_2$  which were observed by the previous investigators may have been due to the variations in the moisture content of the heat-treatment atmosphere and/or the

type of silica substrate. In the present work, the influence of different substrate on the rate of reaction of  $\text{Al/SiO}_2$  composites was studied from  $400^\circ$ - $625^\circ\text{C}$  for 1 to 21 hr. The substrates investigated were as follows: fused silica,  $\text{H}_2\text{O}$  content nil;  $0.5\mu$  thick dry oxygen grown silica films,  $\text{H}_2\text{O}$  content nil; and  $0.5\mu$  thick steam grown silica films,  $\text{H}_2\text{O}$  content 0.1 w/o (5); moisture content of various atmospheres was 1-10,000 ppm  $\text{H}_2\text{O}$ .

Samples were prepared by evaporating 99.999 pure Al at  $10^{-6}$  Torr on to the substrates. Typically  $0.2\mu$  thick films were deposited in a pattern that provided lateral contacts for a four-point resistance determination. The width of the resistance strip was 0.15 cm, and the potential was measured over a distance 0.325 cm. Except for the reduced pressure ( $10^{-6}$  Torr) runs, all samples, at least two for each run, were heat-treated in a  $2\frac{1}{2}$ -in. ID Inconel muffle furnace through which argon, air, hydrogen, nitrogen, or oxygen flowed at the rate of approximately  $10\text{ ft}^3/\text{hr}$ . The dew point

Table I. Reactions of aluminum on silica for various heat-treatment conditions for 1 hr

Heat treatment, Temp, °C	Atmosphere	Moisture, ppm	Electrical resistance, ohms		$\left(1 - \frac{R_1}{R_2}\right) \times 100\%$	X-ray phases	Visual observation	
			Initial	Final				
1)	400	10 <sup>-9</sup> Torr	—	0.19	0.19	0	*	No change.
2)	600	10 <sup>-9</sup> Torr	—	0.19	0.20	5	*	No change.
3)	625	10 <sup>-9</sup> Torr	—	0.20	0.23	13	Al, amorphous silica.	Slight dulling of surface.
4)	550	air	10,000-20,000	0.18	0.18	0	*	No change.
5)	600	air	10,000-20,000	0.18	4600	100	Si, amorphous silica.	Uniform darkening, no free Al.
6)	400, 500, 550	H <sub>2</sub>	>10	0.20	0.20	0	*	No change.
7)	600	H <sub>2</sub>	>10	0.20	5000	100	Si, amorphous silica.	Uniform darkening, no free Al.
8)	400, 500, 575	argon	6.5	0.20	0.20	0	*	Slight change.
9)	600	argon	6.5	0.20	4700	100	Al very weak, Si, amorphous silica.	Uniform darkening, no free Al.
10)	600	argon	2.5	0.17	68	100	Al, amorphous silica.	Spotty darkening free Al; reaction.
11)	400, 500	N <sub>2</sub>	2.5	0.17	0.17	0	*	No change.
12)	600	N <sub>2</sub>	2.5	0.17	3.80	96	Al, weak Si, amorphous silica.	Spotty reaction at edges and interior.
13)	600	N <sub>2</sub>	1.7	0.17	0.17	0	*	No change.
14)	600	O <sub>2</sub>	<1.0	0.21	1.20	83	Weak Al, amorphous silica.	Free Al, slight darkening, light colored film on Al.

\* Not determined.

of each gas as it entered the furnace was determined, and the ppm H<sub>2</sub>O content was obtained from published dew point vs. moisture content curves. After each treatment the samples were examined visually, and standard x-ray diffraction techniques were used to determine the phases present on reacted fused silica samples. To determine the percentage of the film which had reacted, the electrical resistance after each treatment was measured. An increase in the resistance was attributed to a decrease in the thickness of Al due to reaction with the silica. This appears to be justified since a change in sample color and/or the incidence of a new phase in the x-ray diffraction pattern was observed when a resistance change occurred.

The effect of heat-treatment temperature, atmosphere, and moisture content on the initial ( $R_1$ ) and final ( $R_2$ ) resistance, the percentage of the change in thickness of the reacted film  $(1 - R_1/R_2) 100\%$ , the x-ray phases detected, and the results of visual observations are given in Table I for the 1-hr-treated fused-silica samples. Little or no reaction was detected on samples fired for 1 hr at temperatures up to 575°C (samples 1,4,6,8,11) in any atmosphere. At 600°C, the extent of reaction increased significantly with increased atmospheric moisture for both oxygen-containing and inert atmospheres. The aluminum films were completely reacted in atmospheres containing 6.5 ppm H<sub>2</sub>O (samples 5,7,9) or more, and even in the presence of 2.5 ppm H<sub>2</sub>O, most of the aluminum film (10,12) was consumed. *In vacuo* (2) or in nitrogen (13) containing 1.7 ppm moisture, no reaction was observed. Unexpectedly, the reaction in pure oxygen (14) did not totally consume the Al film, while as little as 6.5 ppm moisture in argon (9) caused complete reaction. The moisture content has a greater effect than the free oxygen in the heat-treatment ambient in influencing the reaction rate. In vacuum (3) at 625°C only a 13% decrease may have been due to slight reaction or to a small amount of evaporation, as evidenced by a slight dulling of the surface.

As expected, all x-ray patterns showed the broad peak, characteristic of amorphous silica. In addition, lines characteristic of Si were found in the x-ray diffraction pattern for several of the reacted films. These films (5,7,9,12) were generally darker (less free Al) than the other films and, as shown earlier, had the greatest resistance. The light-colored film found on the 600°C oxygen treated sample (14) could not be identified with x-ray diffraction analysis.

The magnitude of the resistance, i.e., 4600-5000 ohms, of the completely reacted couples (5,6,9) cannot

be explained on the basis of a continuous Al film; the calculation of the thickness of Al corresponding to this resistance results in the meaningless value of 10<sup>-9</sup> cm. To study this further, resistance measurements of six heavily reacted films were made at +25°, -70°, and -196°C. The resistance in all cases was found to increase with a decrease in temperature and plots (log R vs. 1/T) were straight lines indicative of nonmetallic conduction. The activation energy for the conduction process was calculated to be 0.012 ± 0.004 ev.

The resistance changes for Al films on the three different substrates are tabulated in Table II for 550° and 600°C treatment times from 1 to 21 hr and moisture in the treatment atmosphere from 1 to 10,000 ppm H<sub>2</sub>O. The results showed that there was a small tendency toward greater resistivity change on the steam grown silica samples compared to the fused or the dry-oxygen grown samples. Couples heated at 550°C for 1 hr exhibited no change in resistance regardless of substrate type. However, beyond this period, increases in resistance were found; the rate of change increased with increased moisture in the treatment atmosphere. An abrupt rate increase occurred between 1 and 2.5 ppm H<sub>2</sub>O. In 2.5 ppm H<sub>2</sub>O the Al films were almost totally reacted within 21 hr. In 10,000 ppm H<sub>2</sub>O, total film reaction was obtained between 5 and 21 hr.

At 600°C no reaction was found after the 1-hr treatment in ambients containing 1 ppm H<sub>2</sub>O for all three

Table II. Kinetics of Al/SiO<sub>2</sub> reaction

Material	Heat-treatment conditions, Temp, °C	Ambient H <sub>2</sub> O, ppm*	Percentage of Al reacted (1 - R <sub>1</sub> /R <sub>2</sub> ) 100%		
			1 hr	5 hr	21 hr
Steam-grown silica	550	<1	0	3.0	17
	550	1	0	4.0	18
	550	2.5	0	45	84
	600	<1	0	100	—
	600	1	0	100	—
Dry-oxygen- grown silica	550	<1	0	3.5	7
	550	1	0	0	6
	550	2.5	0	7	88
	600	<1	0	100	—
	600	1	0	100	—
Fused silica	550	<1	0	3.5	7
	550	1	0	0	16
	550	2.5	0	3.5	34
	550	10,000	0	49	100
	600	<1	0	100	—
	600	1	0	100	—

\* N<sub>2</sub>, 1 ppm H<sub>2</sub>O; argon, 2.5 ppm H<sub>2</sub>O; air, 10,000 ppm H<sub>2</sub>O; vac, <1 ppm.

substrates. However, between 1 and 5 hr the Al was totally reacted in even these relatively dry atmospheres on all substrates. This is believed to be due to the incidence of the Al-Si eutectic (577°C) which should accelerate the process, as suggested by Cratchley (4).

The results of these experiments suggest that the moisture content of the heat-treatment atmosphere and of the substrates used significantly affected the reaction rate between Al and SiO<sub>2</sub>. These H<sub>2</sub>O contents may have been sufficiently different in the previous investigators work to account for the discrepancies found.

Darkening occurred first at the edges of the film patterns. Therefore, in all probability, an ambient silica-aluminum reaction took place initially. Complete darkening occurred concomitant with a disappearance of elemental aluminum and the growth of a Si phase. It can be deduced that the Al reduced SiO<sub>2</sub> to Si with the formation of an aluminum oxide. The specific oxide could not be identified, since no diffraction patterns characteristic of an Al-oxide were found. The resistance and temperature coefficient of resistance of the completely reacted films indicates that a layer of nonmetallic material was formed. It does not appear

likely that its conduction could be attributed to ionic conduction since the activation energy was too low (6). The type of conduction process involved would have to be determined by other experimentation.

Manuscript received Nov. 6, 1967; revised manuscript received Feb. 29, 1968.

Any discussion of this paper will appear in a Discussion Section to be published in the December 1968 JOURNAL.

#### REFERENCES

1. H. S. Lehman, *IBM Journal R & D*, **8**, 422 (1964).
2. W. M. Berger, *et al.*, "Reliability Phenomena in Aluminum Metallization on Silicon Dioxide; Physics of Failure in Electronics," Vol. 4, M. E. Goldberg and J. Vaccaro, RADC Series in Reliability, (1966) p. 1.
3. G. Schnable and R. Keen, "Study of Contact Failures in Semiconductor Devices," RADC TR 66-165 (1966), p. 138.
4. D. Cratchley and A. A. Baker, *Amer. Cer. Soc. Bull.*, **46**, 2, 191 (1967).
5. A. J. Moulson and J. P. Roberts, *Trans. Brit. Ceram. Soc.*, **59**, 388 (1960).
6. D. A. Vermilyea, "Kinetics of Ion Motion in Anodic Oxide Films, Non-Crystalline Solids," p. 328, J. D. Frechette, J. Wiley & Sons, New York (1960).

## DISCUSSION SECTION



This Discussion Section includes discussion of papers appearing in the *Journal of the Electrochemical Society*, Vol. 114, No. 2, 4, and 9 (February, April, and September).

### Travelling Solvent Defects on Silicon Wafers

E. Biedermann (pp. 207-208, Vol. 114, No. 2)

**C. H. L. Goodman**<sup>1</sup>: The defects referred to by Biedermann were in fact discussed six years ago<sup>2</sup> and, as pointed out then, have the same origin as the submelting-point melting patterns on silicon and other materials described still earlier by Pearson and Treuting.<sup>3</sup> In connection with<sup>2</sup> it was later found that the relevant contamination was definitely due to residues left by the water used for washing. These residues could be almost eliminated by using deionized water doubly distilled in a quartz-glass apparatus for the final wash, and preventing this drying freely on the surface of the specimen by wiping the latter clean with hard, ash-free, filter paper.

More recently, at these laboratories, Stewart<sup>4</sup> has developed a Soxhlet isopropyl alcohol washing technique, for gallium arsenide, which completely prevents the development of surface melt patterns, or what Biedermann terms "nails" (we prefer "tadpoles") on heating.

The formation of surface melt patterns should indeed be a general phenomenon with surface-contaminated solids: see for example Danilov's work with silver<sup>5</sup>, Haneman's with InSb<sup>6</sup>, or, for that matter, Stewart's with GaAs.<sup>4</sup>

**E. Biedermann**: I thank Dr. Goodman very much for having drawn my attention to the series of much earlier papers on the submelting point melting patterns on silicon and other materials. No doubt, our

"nails" are physically the same phenomenon. As to the chemical composition of the impurities involved they are, however, clearly of another origin with a much lower melting point of the eutectic pellets. We also observed the "submelting-point globules," but we did not take the trouble to identify their chemical composition, since they do not show up at the common process temperatures of epitaxial growth or diffusion cycles in the usual silicon planar technology.

### Vacuum Thermal Etching of Germanium and Silicon Surfaces

G. J. Russell and D. Haneman (pp. 398-403, Vol. 114, No. 4)

**J. Pfeifer**<sup>7</sup>: In the paper on "Epitaxial Growth of Germanium on Germanium Substrates Cleaned and Heated by Electron Bombardment" published in the *Physica Status Solidi*<sup>8</sup> the electron bombardment on (111) surface of germanium substrates by electron beam of 500 and 1000v was described. In the temperature range of 650°-800°C the morphological properties of the substrate agreed with the observations of Russell and Haneman on (111) Si at 1100°C. With the rise of temperature the average linear dimension of the etch pits increases, whereas their density decreases. The surface microtopography did not change qualitatively almost up to the melting point. In the vicinity of the melting point the surface area of the pits increases in such an extent that the pits are overlapping. The photomicrograph taken by Jona of heat-treated Ge surfaces proves this observation.<sup>9</sup> Even on surfaces on which evaporation was compensated by vapor deposition, no worm-formation could be detected.

Figure 1. displays a Ge surface (111) just below the m.p. The sample was bombarded by electrons of 1000v for 12 min. The surface evaporation was compensated by vapor deposition originating from a separate Ge source. The background vacuum amounted

<sup>1</sup> Materials Synthesis Group, Standard Telecommunication Laboratories, Harlow, Essex, England.

<sup>2</sup> C. H. L. Goodman, *Solid State Electronics*, **3**, 72 (1961).

<sup>3</sup> G. L. Pearson and R. G. Treuting, *Acta Cryst.*, **11**, 397 (1958).

<sup>4</sup> C. E. Stewart, *Solid State Electronics*, **10** (1967).

<sup>5</sup> V. N. Danilov, *Kristallografiya*, **7**, 154 (1962).

<sup>6</sup> D. Haneman, *J. Appl. Phys.*, **31**, 217 (1960).

<sup>7</sup> Research Institute for Technical Physics of the Hungarian Academy of Science, Budapest, Ujpest 1, Pf 76, Hungary.

<sup>8</sup> J. Pfeifer, *Phys. stat. sol.*, **17**, K15 (1966).

<sup>9</sup> F. Jona, *Appl. Phys. Letters*, **6**, 205 (1965).

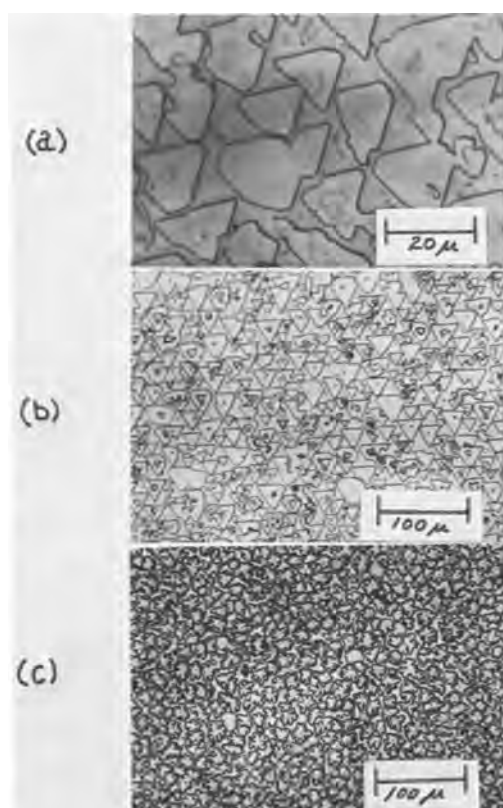


Fig. 1. Electron bombarded (111) Ge surface in the vicinity of the m.p.

to  $4 \times 10^{-9}$  Torr and even during the electron bombardment the pressure was less than  $1 \times 10^{-7}$  Torr. It might be supposed that the island-like contamination in the interior of the hillocks (Fig. 1a) is some sort of a conglomerate caused by oxide contamination as described by Russell and Haneman in connection with the worm-formation. Figure 1b displays the same sample as Fig. 1a in a smaller magnification, whereas Fig. 1c displays the warmest part of the sample. The melting process, the beginning of which might be observed in Fig. 1a already, produced the drop-like contraction of the hillocks as shown in Fig. 1c.

These results do not seem to support the suggestion according to which the undersaturation might be the only reason for the worm-formation. It is more probable that the topographical conditions in the vicinity of the m.p. are caused by surface contaminations. The contamination of the surface of the sample partly occurs during its chemical preparation. In a vacuum system the samples might be contaminated secondarily by the residual gases and by other heated parts of the work-chamber; in various vacuum systems the heat treated surfaces might be different.

**G. J. Russell and D. Haneman:** The principal point raised by Pfeifer is that triangular etch pits were observed on a heated (111) Ge surface even though some deposition of vapor "from a separate Ge source" was occurring. This is contrasted to the conclusion obtained in the cited paper that worm shaped rather than triangle shaped pits tend to form in the presence of much returning vapor. As detailed in the paper, the amount of such returning vapor, or degree of undersaturation, is a critical factor in determining the shape of the etch pits on vacuum heated (111) Ge surfaces. Pfeifer's findings are not inconsistent with ours provided the return of Ge vapor in her experiments did not compensate the loss beyond the critical amount, i.e., the geometry and temperatures of the two crystals and the other surroundings are of significance in

analyzing the results of such experiments. We stress again the importance of fully detailing the condition of the surroundings of a heated Ge surface in order to properly estimate the degree of undersaturation that is maintained, and hence account for etch figures.

### Activation Energies in the Chemical Etching of Semiconductors in $\text{HNO}_3\text{-HF-CH}_3\text{COOH}$

A. F. Bogenschütz, W. Krusemask, K. H. Löcherer, and W. Musinger (pp. 970-973, Vol. 114, No. 9)

**B. Schwartz and K. L. Lawley**<sup>10</sup>: We find that the interpretation of the data used in Fig. 3 raises some questions in our minds. It has been very well established in the literature<sup>11,12</sup> of the existence of diffusion limitation in the etching of silicon in certain composition regions of this reagent system. However, diffusion limitation in the etching of germanium by this same chemical system has not been so clearly established<sup>13</sup> except, possibly, in very high  $\text{HNO}_3/\text{HF}$  mol ratios.<sup>14</sup>

Many investigators who have studied the etching of semiconductors in this reagent system have found numerous cases where the temperature dependence of the etching rate could be expressed by more than one "apparent" activation energy. Camp<sup>15</sup> did an excellent analysis of this situation to show how one could explain this type of dependence on the basis of sequential controlling mechanisms becoming predominant in different temperature ranges. We believe that such is the case for the germanium data of the author's Fig. 3. We have replotted their data and include, as the solid line (see our Fig. 1), their straight line interpretation. It is our contention that the data are better described by at least two straight lines as shown by the dotted lines on the figure. From a least squares analysis of the data, the temperature dependences appear to be 3.5 and 7.5 kcal/g-mol in the high and low temperature regions, respectively.

In a number of papers on the chemical etching of germanium<sup>15,16</sup>, it was noted that a breaking curve of the shape shown in the accompanying plot, would

- <sup>10</sup> Bell Telephone Laboratories, Inc., Murray Hill, N. J. 07974.  
<sup>11</sup> B. Schwartz and H. Robbins, *This Journal*, **108**, 365 (1961).  
<sup>12</sup> D. L. Klein and D. J. D'Stefan, *This Journal*, **109**, 37 (1962).  
<sup>13</sup> B. Schwartz and H. Robbins, *This Journal*, **111**, 196 (1964).  
<sup>14</sup> T. E. Burgess, *This Journal*, **109**, 341 (1962).  
<sup>15</sup> P. R. Camp, *This Journal*, **102**, 586 (1955).  
<sup>16</sup> B. Schwartz, *This Journal*, **114**, 285 (1967).

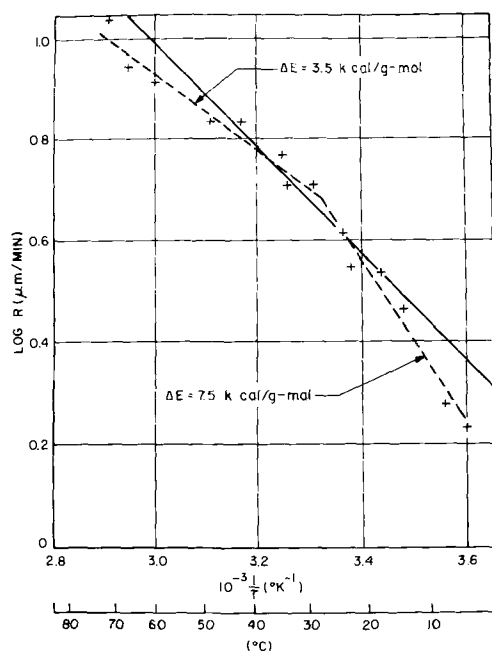


Fig. 1. Plot of the logarithm of the etch rate as a function of the reciprocal of the absolute temperature.

have to be described by a reciprocal sum relationship. This mathematical form makes it difficult to extract the true activation energy.

We recommend, therefore, that Messrs. Bogenschütz *et al.*, consider that though the viscosity comparison with etching of silicon may be valid, their analysis of the germanium system is invalid. In addition, we propose that one of the possible explanations for the breaking curve as seen in this work, might be a shift from a physisorption to a chemisorption rate limiting step on the surface and that the temperature dependencies being observed are really related to this mechanism shift.

**A. F. Bogenschütz, W. Krusemark, K. H. Löcherer, and W. Mussinger:** We are pleased to note the interest of B. Schwartz and K. L. Lawley on our experiments and

their interpretation of the results. Although the Si etching system we investigated is not completely identical with the systems quoted by B. Schwartz and K. L. Lawley, an activation energy of the same order of magnitude was found, thus confirming the results of Schwartz and Lawley, and expressing the conclusions in general terms.

For the Ge etching process Schwartz and Lawley suggest a breaking ( $\log R - 1/T$ ) curve. The results published in the literature so far deviate widely from each other. Further clarifying investigations will prove very useful.

Our work was directed principally towards finding a possible relationship between the etching velocity of a system and the viscosity of an etching solution in order to predict the etching behavior of other systems by means of viscosity measurements.



# Charging the Silver Oxide Electrode with Periodically Varying Current

## III. 60 CPS Asymmetric A.C.

Charles P. Wales

Naval Research Laboratory, Washington, D. C.

### ABSTRACT

The discharge capacity of sintered silver electrodes in KOH solutions was improved 40-50% when the prior charge was made by a 60 cps asymmetric a.c. composed of two opposing half-wave currents 180° out of phase, rather than a constant charge current, both at the 20-hr rate in 35% KOH at 25°C. Commercial Ag-Zn cells containing similar silver electrodes gave capacity increases of 15-25% under the same conditions. Capacity depended on the proportion of charge and discharge components of the a.c. Capacity improvements were smaller when net charge current was at the 6-hr rate, when charge current was composed of 60 cps half-wave reverse current superimposed on constant charge current, or when the KOH concentration was increased. No significant improvement occurred when the charge with reverse current followed a series of discharges at the 1-hr rate.

An advantage of the silver oxide electrode used in alkaline storage batteries is its ability to be discharged at high current densities. To obtain the full capacity of which the electrode is capable, common practice has been to charge (anodically oxidize) the electrode at a relatively low current density. Previous work at this laboratory has shown that when pulses of charge current are superimposed on a steady charging current, the capacity of the subsequent discharge of a silver electrode can be greater than the capacity obtained by a constant current at the same rate (1). It has also been shown that, when charge current is interrupted periodically throughout a charge, the result can be either increased discharge capacity or faster recharging (2). The present work was undertaken to determine the effects of brief discharge periods during charges. The effects of relatively long discharges will be reported separately.

In the electroplating industry brief current reversal has been used for depolarization and for the periodic reverse current plating process. The effect of superimposing alternating current on direct current has been studied by a large number of investigators. A review of the earlier work was given by Halla (3). Some of the more recent work is covered by Rius *et al.* (4) and the references cited therein. Many of these investigations have dealt with depolarization while gas was being evolved at inert electrodes.

Several reports have been made on effects of charging batteries with an alternating current. The use of a.c. superimposed on direct current for recharging Leclanché primary cells without getting needles of zinc or large amounts of gas was proposed by Beer (5). In a similar way Romanov *et al.* (6) used asymmetric a.c. for charging cells which contained zinc negative electrodes to prevent dendritic zinc from forming and causing damage. Romanov (7) reported several changes after asymmetric a.c. was used for charging pressed silver powder electrodes: the total capacity of the following discharge increased, and the AgO/Ag<sub>2</sub>O potential plateau during discharge was shorter in length and at a lower potential than usual. The electrolyte concentration was not specified. Romanov reported that the use of a constant charge current resulted in AgO that was concentrated at the grid and able to show the AgO potential on discharge, but the use of a.c. resulted in a uniform distribution of AgO throughout the electrode (8). Flerov (9) used sintered silver electrodes in 1.40 sp gr KOH and found

that if a sufficiently large a.c. was superimposed on the steady charging current, the AgO/Ag<sub>2</sub>O discharge potential plateau was eliminated completely, but in contrast to the results of Romanov (7, 8), the total discharge capacity was unchanged. Flerov attributed the lowered discharge potential to diffusion in the solid phase being impeded by cations of alkali metal which had been introduced into the silver oxides during the a-c charge. Rather different results were reported recently for smooth silver electrodes. When an a.c. was superimposed on a constant charging current, the capacity of a smooth silver electrode in 10N KOH was unchanged unless current exceeded a high value that was critical (10). If current during the anodic half-period reached at least 10 ma/cm<sup>2</sup>, then true surface area and discharge capacity of the electrode both increased greatly but the AgO/Ag<sub>2</sub>O discharge potential plateau was not shortened, although this plateau contained an additional plateau if current of the preceding charge exceeded the critical value. The increased capacity was attributed partly to increased surface area and partly to formation of AgO with a different structure than the common AgO.

Thus there is disagreement as to whether or not capacity of a silver electrode can be increased when brief discharge periods occur during a charge, and disagreement as to the causes for the observed changes. The present work describes the results of charging silver electrodes with two types of charge current which had brief periods of current reversal.

### Experimental Procedure

Test cells were made with one of two sizes of sintered silver plaques, depending on the size available when the cells were constructed. The plaques were either 30.5 x 63.5 x 0.8 mm or 41.5 x 38.0 x 0.8 mm. The sintered silver had an average weight of 7.9 or 5.8g, respectively, not including the grid of expanded silver metal. This weight of sintered silver corresponds to a theoretical electrode capacity of 3.9 or 2.9 amp-hr, respectively. The electrodes were wrapped individually with cellulosic separator material, instead of being wrapped in pairs as is the common practice in Ag-Zn cells. The separator was folded around the electrode in such a way that five layers of separator covered both sides of the electrode. The separator was held in place by wrapping with a small Ag wire and was open only at the top of the electrode. The sintered Ag plaques and the separator has been manufactured for use in commercial Ag-Zn storage batteries.

Key words: silver oxide electrode, capacity, charge current, storage batteries.

\* Electrochemical Society Active Member.

The wrapped Ag electrodes were used as both test electrodes and counter electrodes, and were about 2 cm apart in a cell. Each test cell contained one test electrode. Five of the test cells contained one counter electrode and one cell contained two connected in parallel, placed on each side of the test electrode. Microscopic examination of similar Ag electrodes at various states of charge showed that the electrodes were highly porous and, at the 20-hr rate of charge and discharge, having only one side of the electrode face the counter electrode did not favor reaction at that side (11). The test cells contained an excess of either 35% KOH or 50% KOH as the electrolyte and an Ag/Ag<sub>2</sub>O reference electrode. Since a counter electrode was being reduced at the same time as a test electrode was being oxidized, and *vice versa*, little gas was produced in a cell except at the end of charge and discharge. All work was done at  $25^\circ \pm 1^\circ\text{C}$ .

As in the previous work (1, 2) the constant current which resulted in a complete charge or discharge in approximately 20 hr was arbitrarily taken as the standard, or normal, charge and discharge current. Capacity of the test cells decreased during the early charge-discharge cycles and then became relatively constant. After the tenth cycle, the same current was used for the rest of the study of these cells and corrections were not made for deviations in charge or discharge time from 20 hr. Complete normal charges (using the 20-hr rate as defined above) were alternated with complete charges which used one of the reversal conditions. Two types of charge current which had brief periods of current reversal were used. One type was obtained by taking a half-wave rectified current derived from commercial 60 cps alternating current and superimposing this half-wave current in the discharge direction onto a larger constant charge current. The waveform of this current is shown as B in Fig. 1. The second type was obtained by combining two half-wave 60 cps rectified currents which were  $180^\circ$  out of phase and which flowed in opposite directions through resistances of different values (D in Fig. 1). Both of these charge currents were types of 60-cycle asymmetric a.c. with forward components larger than reverse components. Only one set of reversal conditions was used in any given charge.

All charges were continued until oxygen evolution was occurring and potential had stopped changing rapidly. The final charge potential was about 510-530

mv positive to the Ag/Ag<sub>2</sub>O reference electrode when the 20-hr rate of constant charge current was used. Constant current charge input was usually 1 or 2% greater than the capacity of the following discharge. After a charge was finished, a cell was immediately discharged at approximately the 20-hr rate of constant current to a final potential which was 300 mv negative to the Ag/Ag<sub>2</sub>O reference. In a few cases that are specifically noted, a cell was discharged at the 1-hr rate to a final potential which was 500 mv negative.

To minimize variations in cell capacity the discharge capacities of the four normal cycles (20-hr constant current charge and discharge) that were nearest each discharge were averaged. This moving average was then taken as the normal capacity at that particular point in the life of a cell and is the capacity referred to whenever normal capacity is mentioned. The capacity of each discharge was calculated as a per cent of this varying average. Thus, the discharge capacity which followed a charge with current reversals could be compared to a value which was representative of actual cell capacity, regardless of changes in normal capacity over the life of a cell.

Some charges with current reversals which resulted in increased test cell capacity were tried with one model of a commercial Ag-Zn secondary cell. The commercial cells contained either 35 or 45% KOH. Typical electrolyte analysis has been given earlier (2). Each commercial cell had four sintered silver electrodes of the same size as the test electrodes which had a theoretical capacity of 2.9 amp-hr and had five zinc electrodes. The silver electrodes limited cell capacity and gave a theoretical cell capacity of about 11.5 amp-hr, although the nominal rated cell capacity given by the manufacturer was only 5 amp-hr. The Ag-Zn cells were charged individually until cell potentials reached 2.05v. Complete charges at the 20-hr rate of constant current (as defined above) were alternated with charges which had current reversals. The cells were discharged at the 20-hr constant current to 1.10v. Since capacity of these cells varied from one charge-discharge cycle to the next, the 20-hr current was recalculated after each constant current cycle and a different current used for the following cycle whenever actual charge and discharge time had deviated greatly from 20 hr.

## Results

Before any charges with a periodically reversed current were tried, the cells were charged and discharged by the 20-hr constant current until capacity became relatively constant. During the first two charge-discharge cycles of a new test cell, capacity of the electrodes was often as high as 70 to 80% of the capacity theoretically possible for the silver active material. Then capacity decreased until, after 8-10 cycles, it became relatively constant in the range 45-60% of theoretical capacity, usually averaging 50-56% of the theoretical capacity in 35% KOH and about 10% lower in 50% KOH.

Capacity of the commercial Ag-Zn cells also changed with use, but not in the same way as the test cells changed. Thirteen commercial cells were used. Eleven reached a maximum capacity that was 68-79% of the theoretical value, and the other two reached 62 and 64%. The commercial cells which contained 45% KOH always gave the maximum discharge capacity after either the initial or second charge, but the cells which contained 35% KOH did not reach a maximum until charge 5 to 8. After reaching this maximum, the capacity of the commercial Ag-Zn cells gradually declined during the remainder of their lives. Ten of the Ag-Zn cells contained 45% KOH. These cells gave only 4 to 21 (an average of 11) charge-discharge cycles before they developed internal short circuits. A cell was discarded after it developed a noticeable short circuit, as evidenced by unsteady charging potentials and failure to reach 2.05v during charge. The

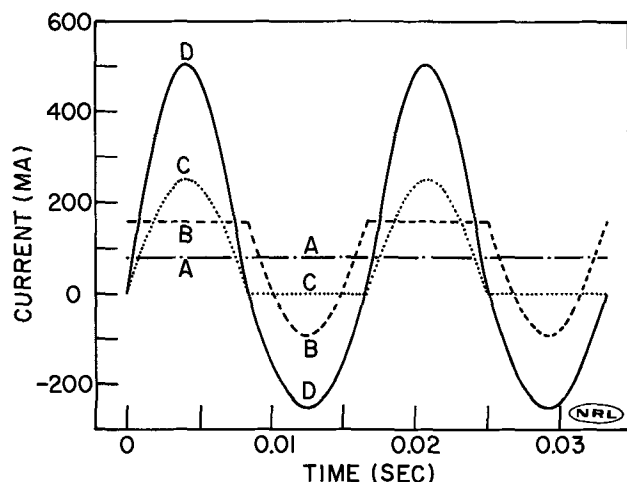


Fig. 1. Comparison of constant current to several charge currents derived from 60 cps a.c. For each example the net charge current was equivalent in coulombs per unit time to a constant current of 80 ma. A, constant current; B, constant forward current with half-wave rectified a.c. superimposed in reverse direction; C, half-wave rectified a.c.; D, half-wave forward current with half-wave reverse current superimposed  $180^\circ$  out of phase with forward current. The ratio of forward component to reverse component was 2:1 for both B and D.

three commercial Ag-Zn cells, which differed from these ten cells only in the electrolyte concentration of 35% KOH, did not develop noticeable short circuits and were still in good condition when work was completed, after having undergone from 23 to 53 cycles apiece.

Charge acceptance of a silver electrode could be increased over the amount obtained from a constant charge current if the electrode was charged with a constant current which had half-wave rectified 60 cps alternating current superimposed in the discharge direction (B in Fig. 1). When this type of current was used, with net current equivalent in coulombs per unit time to the 20-hr rate of constant charge current, a distinct increase in discharge capacity was obtained from the test cells which contained 35% KOH (Table I). The improvement was insignificant, however, in 50% KOH or when commercial Ag-Zn cells were used (Table I).

Previous work has shown that a charge with half-wave rectified a.c. (C in Fig. 1) can give a greater capacity to a silver oxide electrode than a charge with constant current (2). This work was extended by the use of half-wave rectified 60 cps a.c. in the charge direction which had a smaller half-wave rectified 60 cps a.c. in the discharge direction superimposed on alternate half-cycles (D in Fig. 1). Compared to results when constant current was used for a charge, this asymmetric a.c. gave relatively large capacity increases with the silver electrodes in test cells which contained 35% KOH and gave smaller but definite capacity increases with the commercial Ag-Zn cells (Table II). The effect of varying the a.c. frequency was not studied.

The effective current, when using an asymmetric a.c. derived from commercial a.c., was the numerical value of the constant current which would produce the same quantity of electrochemical products as the asymmetric a.c. The effective current could be calculated by taking the average (arithmetic mean) of the instantaneous a.c. values. The effective current was not the root-mean-square value of the a.c. (the numerical value of a constant current which would produce the same heat or power as the a.c.). It can be shown mathematically that the asymmetric current, obtained by combining two half-wave currents which flowed in opposite directions, had components which reached peak values approximately  $\pi$  times as large as constant currents that were equivalent in cou-

**Table I. Discharge capacity of silver oxide electrodes following charges with 60 cps asymmetric a.c. obtained by superimposing half-wave rectified a.c. in reverse direction onto constant charge current. Net charge current was equivalent to 20-hr rate of constant current**

Magnitude of a.c. components (multiple of 20-hr current)		Discharge capacity (% of normal capacity)			
		Test cells		Commercial cells	
Forward	Reverse	35% KOH	50% KOH	35% KOH	45% KOH
1.0	0.0	100*	100*	100*	100*
1.5	0.5	119.5 120.0 129.3 123*	102.0 107.4 105*		
2.0	1.0	112.9 121.0 127.4 120*	100.9 101.8 101*	98.3 102.1 104.1 102*	99.3 101.6 109.3 103*
3.0	2.0	132.6 142.6 143.1 139*	99.2 107.1 103*	102.4 102.7 102.8 103*	103.3 105.3 104*

\* Average.

**Table II. Discharge capacity of silver oxide electrodes following charges with asymmetric a.c. obtained by combining two half-wave 60 cps currents which flowed in opposite directions and were 180 degrees out of phase. Net charge current was equivalent to 20-hr rate of constant current**

Magnitude of a.c. components (multiple of 20-hr current)		Discharge capacity (% of normal capacity)			
		Test cells		Commercial cells	
Forward	Reverse	35% KOH	50% KOH	35% KOH	45% KOH
1.0	0.0	123.7 130.3 132.6 129*	99.5 102.0 101*	101.1 103.5 102*	97.4 100.8 99*
1.5	0.5	140.9 149.6 145*	99.3 103.4 101*		
2.0	1.0	129.6 149.0 161.5 147*	95.4 100.2 98*	110.2 114.6 120.5 115*	109.7 111.5 111.7 111*
3.0	2.0	147.8 153.3 160.2 154*	90.1 93.1 92*	121.6 121.8 127.2 124*	101.7 112.8 113.1 109*
5.0	4.0	118.8 135.6 141.7 151.2 137*		117.9 118.5 118*	

\* Average.

lombs per unit time to these half-wave components (Fig. 1).

Capacity tends to decrease as charge rate increases. Figure 2 shows capacities obtained after complete charges of sintered silver electrodes at various rates of constant current, with the 20-hr rate taken as a reference point. Sixty cps asymmetric a.c. of the type shown as D in Fig. 1 was tried at the 6-hr rate of charge using the test cells (Table III). When the reverse component was low, there was little or no improvement over the capacity obtained following a constant current charge at the 6-hr rate (Fig. 2) or following a charge by a half-wave current at the 6-hr rate (Table III, reverse component 0.0). Capacity of a charge at the 6-hr rate was improved when both components of the asymmetric a.c. were large.

This asymmetric a.c. was used at the 6-hr rate for a few charges of the commercial silver-zinc cells. The results resembled those shown in Table III except that improvement was not as large. For example, three charges at the 6-hr rate which used 6 times the 20-hr rate for the forward component and 3 times for the reverse component gave an average capacity in 35% KOH that was 96% of the normal capacity, while a

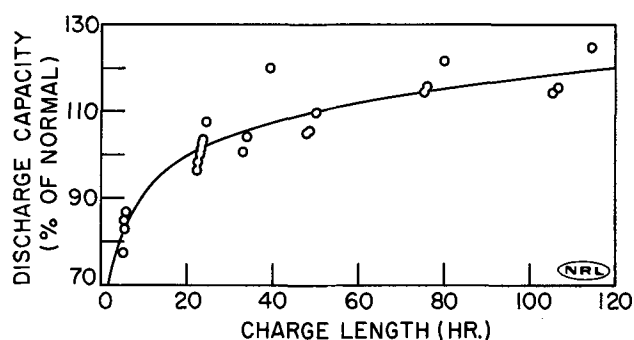


**Fig. 2. Dependence of discharge capacity of silver oxide electrodes on the rate of constant current used for charge. Electrolyte was 35% KOH at 25°C.**

Table III. Discharge capacity of silver oxide electrodes in 35% KOH, following charges with an asymmetric a.c. obtained from two half-wave 60 cps currents 180 degrees out of phase. Net charge current was equivalent to 6-hr rate of constant current

Magnitude of a.c. components (multiple of 20-hr current)		Discharge capacity (% of normal capacity)
Forward	Reverse	
3.0	0.0	69.2
		78.3
		89.8
		99.7
		84*
4.0	1.0	75.2
		75.9
		76.6
		99.5
		82*
5.0	2.0	76.4
		81.5
		95.0
		96.6
		87*
6.0	3.0	96.9
		101.6
		108.4
		102*
9.0	6.0	96.4
		107.9
		127.3
		111*

\* Average.

constant current at the 6-hr rate gave an average capacity that was 84% of the normal. In 45% KOH capacity was not this large, but showed the same type of improvement. In 45% KOH charges at the 6-hr rate gave an average 81% of normal capacity with the same asymmetric a.c. and 69% of normal with constant charge current.

Potentials of silver electrodes in the test cells are shown in Fig. 3 for a few of the discharges following charges which used 60-cycle asymmetric a.c. at the 20-hr rate. The shape of the first discharge plateau was not completely reproducible. Potential of this plateau was noticeably lower after the forward component of the charge a.c. had been half-wave rectified a.c. than after the forward component had been constant current. The first discharge plateau tended toward lower potentials as the forward and reverse

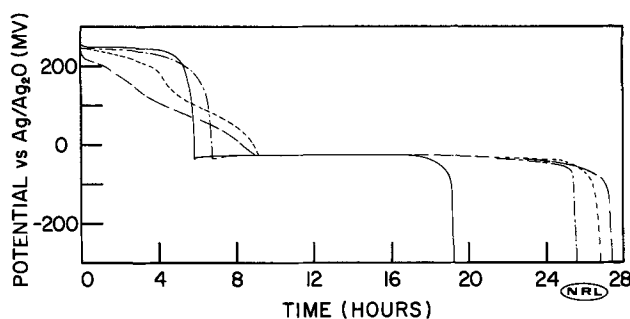


Fig. 3. Constant current discharges of silver oxide electrodes in 35% KOH. Net current of previous charge was at or equivalent to 20-hr rate of constant current. Solid line, discharge after constant current charge; dash and dot line, after 60 cps half-wave rectified a.c. charge; short dash line, after charge by 60 cps asymmetric a.c. with constant forward component of 3 times the 20-hr rate and half-wave reverse component of 2 times the 20-hr rate; long dash line, after charge by 60 cps asymmetric a.c. with half-wave forward component of 3 times the 20-hr rate and half-wave reverse component of 2 times the 20-hr rate.

components of the previous charge both increased, with net charge current remaining constant. These changes in discharge potentials, following a charge with asymmetric a.c., were observed with commercial silver-zinc cells containing 35 or 45% KOH and with the test cells containing 35% KOH. In 50% KOH, however, the discharge potentials were the same as after a constant current charge.

Interruption of the reverse current component for a few seconds resulted in different charge potentials after current was resumed. The net charge current was increased by interrupting the reverse current component. The net charge current fell back to the normal value after resuming the reverse current, but charging potentials became lower than they were before interruption. This drop in potential was similar to the potential drops observed after pulses of charge current were added to a constant charge current (1). These results suggest that the beneficial results of the two types of charge might be combined, but this was not pursued further.

As already mentioned, cycles with normal charges alternated with cycles having reversals. Sometimes, for no apparent reason, a constant current charge at the 20-hr rate gave a capacity that differed rather widely from the normal capacity. It seemed likely that these differences could be a result of changes that had occurred during the preceding cycle, in which charge current had been reversed. The current composed of two half-wave rectified currents (D in Fig. 1) was the charge current most likely to be followed by a 20-hr constant current charge-discharge cycle which had unusual capacity. There was, nevertheless, no increase or decrease in capacity following a constant current charge which correlated consistently with this or any other of the charges with reversals.

*Discharge rate.*—For the results that have already been given, capacity was measured at the 20-hr discharge rate. There were also three series of charge-discharge cycles in which fully charged silver electrodes were discharged in 35% KOH at the 1-hr rate. Each series consisted of 13-45 consecutive complete discharges at the 1-hr rate following completion of charges at the 20-hr rate. The first discharge at the 1-hr rate gave slightly less capacity than was obtained at the 20-hr discharge rate. As charges at the 20-hr rate and discharges at the 1-hr rate were repeated, discharge capacity gradually increased for 5 or 6 cycles and often exceeded normal capacity. The length of the AgO/Ag<sub>2</sub>O potential plateau decreased during the first few discharges at the 1-hr rate until, finally, the AgO/Ag<sub>2</sub>O potential plateau no longer appeared on discharge. At the same time the Ag/Ag<sub>2</sub>O charge plateau was becoming longer until it reached approximately 1.6 to 2.1 times its normal length, with almost 50% of the charge taking place at the Ag/Ag<sub>2</sub>O plateau. The final potential of the oxygen evolution plateau gradually increased in this period.

After charges at the 20-hr rate and discharges at the 1-hr rate became relatively reproducible, charges were tried under some of the reversal conditions that had proven most beneficial earlier. These conditions no longer increased capacity significantly. For example, the test cells were charged with currents of the types shown in B and D of Fig. 1, having the ratio 3:2 for charge component to discharge component with net charge current equivalent to the 20-hr constant current, but capacity of the subsequent discharge of the test cells at the 1-hr rate was only 100-102% of capacity following a constant current charge.

After resuming the 20-hr discharge rate, it was noted that the electrode had not discharged completely at the 1-hr rate. Ten to 30% additional capacity could be removed at the 20-hr rate following a discharge at the 1-hr rate. Normal cycles revealed several changes from conditions before the series at the 1-hr rate. Capacity had increased 15 to 40%, and the AgO/Ag<sub>2</sub>O

discharge plateau was only 1/3 to 2/3 its normal length. Capacity declined to approximately its former value in 10 cycles. The length of the  $\text{AgO}/\text{Ag}_2\text{O}$  discharge plateau is given in Fig. 4 for normal cycles before and after discharges at the 1-hr rate. As this plateau gradually increased, the amount of charge that took place at the  $\text{Ag}/\text{Ag}_2\text{O}$  plateau gradually decreased back to its former value.

### Discussion

A larger increase in capacity can be obtained from a silver electrode by using an asymmetric a.c. for the charge current than by using the charge methods tried earlier (1, 2). Table II shows that capacities more than 50% larger than normal resulted from charging with a 60 cps asymmetric a.c. composed of two half-wave currents. Capacity increases were smaller, however, when silver electrodes were charged in 35% KOH by an asymmetric a.c. which was obtained by superimposing a half-wave 60 cps current in the discharge direction onto a larger constant charge current (Table I). This difference is not surprising because a half-wave charge current without reversal gave approximately 29% more capacity than a constant charge current (Tables I and II, reverse component 0.0). When forward and reverse half-wave currents were combined, a part of the beneficial effect of reversal was obtained, in addition to the benefit from the rapidly pulsating charge current. Note that the waveform, when a half-wave 60 cps reverse current was superimposed on a constant charge current, was rather different from the waveform of the current obtained by combining two opposing half-wave currents (B and D in Fig. 1). The current reached much larger forward and reverse values for the same net charge current when the two half-wave currents were used.

As a general rule, the capacity of a secondary cell will decrease as charge rate increases. A silver electrode, charged in 35% KOH with constant current at the 6-hr rate, gave a discharge capacity which averaged 83% of the normal capacity (Fig. 2). Previous work has shown that close to 100% of normal capacity could be obtained at the 6-hr rate when a silver electrode was charged with unidirectional current that flowed 1/4 or 1/8 of the time with 60 periods of current flow per second (2). By charging at the 6-hr rate with asymmetric current type D in Fig. 1 which had a sufficiently large reverse component, capacity was obtained which exceeded the normal capacity and was 1/3 greater than the capacity obtained by a constant current at the 6-hr rate (Table

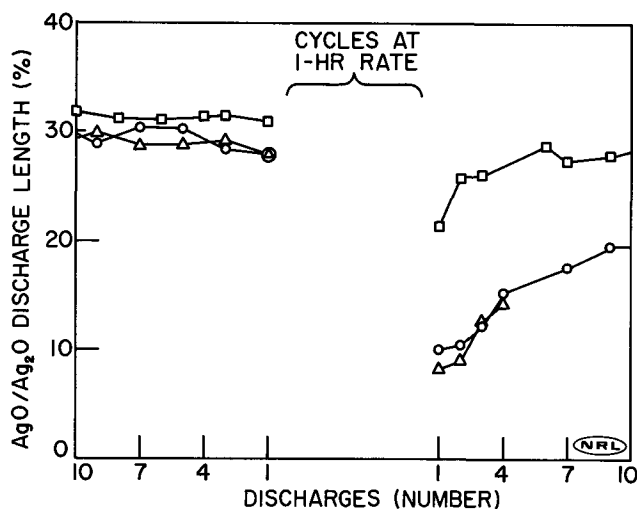


Fig. 4. Per cent of discharge that took place before  $\text{Ag}_2\text{O}/\text{Ag}$  potential was reached after charges at 20-hr rate in 35% KOH at 25°C. Results are given for discharges at the 20-hr rate immediately before (at left) and immediately after (at right) a series of 13 (□), 22 (△) or 45 (○) complete discharges at the 1-hr rate.

III). Although slow charges with this asymmetric a.c. gave a larger capacity than rapid ones, a rapid charge with asymmetric a.c. is valuable if it is important that charge time be small.

After commercial Ag-Zn cells which contained 35% KOH were charged with asymmetric a.c. composed of two half-wave currents, their discharge capacity was markedly larger than the capacity obtained from commercial cells by the other charge methods (Table II). This type of asymmetric a.c. also gave an increased capacity with commercial Ag-Zn cells which contained 45% KOH. Although the capacity increase was relatively small, it was the only time that the commercial Ag-Zn cells which contained 45% KOH showed a definite improvement when charged with periodically varying current. The test cells which contained 50% KOH did not give significantly increased capacity after a charge with either type of asymmetric a.c. This lack of improvement was consistent with the previous results; cells containing 50% KOH never showed the improvement which could be obtained in 35% KOH by charging with a varying current (1, 2).

Compared to a normal charge with constant current, several changes were observed during a charge with asymmetric 60-cycle a.c. The  $\text{Ag}/\text{Ag}_2\text{O}$  potential plateau was shorter than normal for a charge, the  $\text{Ag}_2\text{O}/\text{AgO}$  plateau was longer than normal, and the potential rise to the oxygen evolution plateau was slower than usual. The rapidly fluctuating current was, of course, accompanied by fluctuating cell potentials. As the silver electrode became more completely charged, its potential could exceed the oxygen evolution potential while the charge component of the a.c. reached its maximum value, particularly when a large charge component was used. A part of the current being consumed in gas evolution resulted in a lower current efficiency than the efficiency which was obtained with a constant charge current. The rates of asymmetric a.c. used did not result in a marked increase in cell temperature over the usual warming. One can speculate that charges with asymmetric current could shorten cell life, especially if the components of the current were large with respect to the net effective current. Shorter cell life was not observed, but the experimental method (alternating normal charges with charges having current reversals) would somewhat mask a shortening of life if the harmful effect was weak.

It is believed that the increased capacity that was obtained when the silver electrodes were charged with a 60 cps asymmetric a.c. was mainly the result of the transient high charge currents. The peaks in charge current were closely followed by peaks in potential. When charge potential reached a maximum, there may have been additional oxidation of Ag particles that were already completely surrounded with an oxide coating. Crystal lattice dimensions indicate that there is a large expansion of the crystal as metallic silver is oxidized to  $\text{Ag}_2\text{O}$ . There is only a slight additional increase in volume as  $\text{Ag}_2\text{O}$  is oxidized to  $\text{AgO}$ , but the lattice is distorted as dimensions change in going from face-centered cubic to monoclinic crystals. Microscopic examination of silver electrodes indicated that  $\text{AgO}$  crystals tend to form in larger sizes than do  $\text{Ag}_2\text{O}$  crystals, that during a charge the  $\text{AgO}$  crystals partially or completely fill much of the electrode surface and many internal cavities, and that a thin layer of  $\text{Ag}_2\text{O}$  always separates the  $\text{AgO}$  from the Ag (11). When charge potential reached a maximum, possibly additional  $\text{Ag}_2\text{O}$  formed below the  $\text{AgO}$  coating as oxygen penetrated the coating under the influence of this high potential, and then the  $\text{AgO}$  coating cracked as a result of expansion beneath it. Cracks in the  $\text{AgO}$  coating would allow the electrolyte to penetrate nearer to the metallic silver, and oxidation could continue at lower charge potentials. Another possible, but less likely, factor was that cracking may have resulted from stresses set up by

the rapid formation of oxides when the forward current reached peak values. The reverse current may tend to relieve stresses, however. Although cracking would decrease concentration gradients within the electrode and allow more silver to oxidize, cracking could possibly have the disadvantage of isolating some of the oxidized silver from good electrical contact with the conducting grid.

In addition to the increased capacity, another notable change that was observed following a charge with 60 cps asymmetric a.c. was the tendency for potentials to be lower than usual in the early part of a discharge (Fig. 3). The proportion of the total discharge that took place before potential reached the  $\text{Ag}_2\text{O}/\text{Ag}$  plateau remained approximately the same as it had been following a normal charge. As mentioned earlier, the potential of the initial discharge plateau was lower following a charge with asymmetric a.c. which had large forward and reverse components than it was following a charge at the same net current which had smaller components. These results suggested that if sufficiently large forward and reverse components had been used, the initial potential plateau would disappear, as has been reported to occur (9). Discharges lasted close to 30 hr after the charges which gave greatly increased capacity (Fig. 3) because the discharge current was kept at the 20-hr rate, as defined by capacity following a constant current charge. If a higher discharge rate had been used following the asymmetric a.c. charges which had large components, the initial potential plateau would probably have disappeared at a much lower discharge current than the current required for the plateau to disappear following a normal charge.

Differences in the structure of the charged active material can account for a discharge following an asymmetric a.c. charge having less of an initial potential plateau than a discharge following a constant current charge. Increased concentration gradients of oxygen ions and lowered conductivity could occur in the active material of an electrode with an unusually large proportion of the Ag converted to oxide. Lowered discharge potentials could result from oxygen ions moving through oxide layers that were thicker than usual. Concentration gradients in the electrode would gradually decrease while the AgO coating was being reduced. Conductivity improves after Ag begins to form during a discharge (12). Although the present work has confirmed the report of Romanov that a charge with asymmetric a.c. gave increased capacity (7), the explanation of Romanov for the low initial discharge potential plateau following an asymmetric a.c. charge cannot be accepted (8). Microscopic examination of sintered electrodes during constant current charge and discharge (11) indicated that the reactions did not take place preferentially at the grids as Romanov reported. Perhaps the pressed powder electrodes of Romanov had poorer conductivity than the sintered electrodes used in the present work.

Since current was high for only a fraction of a second during a charge with asymmetric 60-cycle a.c., unduly large concentration gradients did not form in the electrolyte unless large a.c. components were used. Large concentration gradients would form if the current had been kept at its maximum value and would limit the amount of oxidation during a charge. This effect is greatest in very concentrated KOH, where the mobility of the hydroxyl ion becomes most limiting. Therefore, when 60 cps asymmetric a.c. that had large forward and reverse components was used, the charge acceptance was usually poorer in 45% and 50% KOH than it was in 35% KOH for the same current (Tables I and II).

The differences between results with the commercial Ag-Zn cells and the test cells were probably due mainly to different concentration gradients. It is doubtful that the presence or absence of zinc was important because an excess of zinc was present and,

therefore, the silver electrode limited the cell capacity. The commercial cells were tightly packed and had little free electrolyte. This arrangement should result in concentration gradients near the electrode surface being larger in the commercial cells than they were in the test cells at the same current density. Therefore the commercial cells showed less improvement after a charge with reversals than the test cells showed.

It was reported that after a sheet silver electrode had been oxidized by a 50 cps asymmetric current and anodic current density had exceeded a critical value (much higher than the current densities used in the present work with sintered silver electrodes) an x-ray diffraction pattern of the electrode showed a different intensity distribution than was usual for AgO (10). The explanation given was that  $\text{Ag}_2\text{O}_3$  had formed during the anodic pulses at high current density and then decomposed to AgO, and that this AgO had a form imposed by the decomposition of  $\text{Ag}_2\text{O}_3$  rather than by the underlying silver base. It is interesting to note, however, that the x-ray pattern given in (10) resembled rather closely the pattern reported for a tetragonal AgO (13). The tetragonal AgO was reported to be an intermediate phase between  $\text{Ag}_2\text{O}$  and monoclinic AgO when silver metal was oxidized by ozone. Close comparison of the x-ray diffraction patterns could not be made because neither (10) nor (13) gave tabular values for the patterns. Nevertheless one can speculate that perhaps ozone, or some related oxygen species, may be produced at sufficiently high potentials and oxidize metallic silver or  $\text{Ag}_2\text{O}$  to the tetragonal AgO. In the present work, using relatively low currents, potentials were below the value required to produce ozone.

*Discharge rate.*—The lack of improvement when discharges were done at the 1-hr rate was consistent with results reported earlier. After a series of discharges at the 1-hr rate, a silver electrode gave a relatively high per cent of the capacity theoretically possible. Under these conditions a charge with repeated open-circuit periods, which usually resulted in improved capacity, gave only about the same capacity as a constant current charge (2) because the form of silver in the electrode varied with the rate of reduction (14). Fast reduction of the silver oxides resulted in smaller crystals of silver, and rapidly produced silver probably had a larger number of imperfections. These smaller crystals could be charged more readily. Therefore, a charge following several fast discharges can have more capacity than a charge following a slow discharge. The observed gradual increase in capacity during a series of cycles with fast discharges indicated a progressive decrease in particle size of the silver active material. The small particles had a larger surface area, and more  $\text{Ag}_2\text{O}$  formed before charge potential rose to the  $\text{Ag}_2\text{O}/\text{AgO}$  plateau.

The high oxygen evolution potential at the end of a charge, following discharges at the 1-hr rate, indicated that concentration gradients or resistance under these conditions was higher than usual. Higher resistance could result from the finer particles being in poorer contact with each other because a larger than usual proportion of silver had been oxidized. Effects of concentration gradients and resistance become more important at high rates of discharge. The oxide particles were not all reduced before discharge potential dropped to the cutoff value. Capacity was probably limited more by incomplete reduction than by charge acceptance during discharges at the 1-hr rate. It was likely, therefore, that the form of charge current was less important under these conditions than under slow discharge rates. When the slow discharge rate was resumed, particle size increased during the next few cycles, as indicated by the gradually declining capacity and by the potential plateaus gradually recovering their former proportions.

### Conclusions

Charge acceptance was increased markedly, under certain conditions, when current was reversed periodically during a charge. Highest capacity was obtained after a charge by a 60 cps asymmetric a.c. composed of two opposing half-wave rectified currents 180° out of phase, with the reverse component two-thirds as large as the forward component. When test cells containing 35% KOH were charged with this current at the 20-hr rate, one-half more capacity could be obtained than the capacity which resulted from a constant current charge at the same rate. This a.c. used at the 6-hr rate gave one-third more capacity than a constant current at the same rate. When commercial silver-zinc cells containing 35% KOH were charged with this asymmetric a.c., they gave less improvement than the test cells but more capacity than they gave with other charge methods. Improvement decreased with increasing KOH concentration. A discharge following an asymmetric a.c. charge which gave improved capacity showed less AgO/Ag<sub>2</sub>O potential plateau than usual, probably as a result of increased concentration gradients within the electrode. The charges with periodic reversals were not effective in increasing capacity after a series of discharges at the relatively high current of the 1-hr rate. Under these conditions capacity was probably limited more by incomplete reduction during discharge than by charge acceptance.

Manuscript received Nov. 3, 1967; revised manuscript received March 1, 1968. This paper was presented at the Chicago Meeting, Oct. 15-19, 1967, as Abstract 42.

Any discussion of this paper will appear in a Discussion Section to be published in the June 1969 JOURNAL.

### REFERENCES

1. C. P. Wales, *This Journal*, **111**, 131 (1964).
2. C. P. Wales, *ibid.*, **113**, 757 (1966).
3. F. Halla, *Z. Elektrochem.*, **35**, 838 (1929).
4. A. Rius, J. Llopis, and F. Colom, Proc. 6th Meeting Intern. Comm. Electrochem. Thermodynam. and Kinet., p. 280, Butterworths, London (1955).
5. E. Beer, U. S. Pat. 2,752,550 (1956).
6. V. V. Romanov, P. D. Lukovtsev, G. N. Kharchenko, and P. I. Sandler, *Zh. Prikl. Khim.*, **33**, 1556 (1960).
7. V. V. Romanov, *Vestn. Elektroprom.*, **31** No. 9, 26 (1960).
8. V. V. Romanov, *Zh. Prikl. Khim.*, **34**, 1312 (1961).
9. V. N. Flerov, *ibid.*, **37**, 580 (1964).
10. G. Z. Kazakevich, I. E. Yablokova, and V. S. Bagotskii, *Elektrokhim.*, **2**, 1055 (1966).
11. C. P. Wales and A. C. Simon, To be published.
12. B. D. Cahan, J. B. Ockerman, R. F. Amlie, and P. Ruetschi, *This Journal*, **107**, 725 (1960).
13. A. S. McKie and D. Clark, "Batteries" (Proc. 3rd Intern. Symp., Bournemouth, England) p. 285, Pergamon Press, New York (1963).
14. C. P. Wales and J. Burbank, *This Journal*, **112**, 13 (1965).

## Chemical Identification of Adsorbed Species in Fuel Cell Reactions

### I. Propane Oxidation

H. J. Barger, Jr., and M. L. Savitz\*

United States Army Mobility Equipment Research & Development Center, Fort Belvoir, Virginia

#### ABSTRACT

The cathodic desorption products resulting from the reaction of propane at a fuel cell electrode were identified and studied as a function of potential. The ratio of cathodically desorbable material to nondesorbable material was measured at three potentials and compared to similar data obtained for a platinum wire electrode.

Since the demonstration that hydrocarbons oxidize at a fuel cell electrode to give carbon dioxide (1), there has been considerable interest in the elucidation of the over-all reaction mechanism with the hope that the information gained could lead to more reactive and lower cost catalysts. From the work of Gilman (2), Niedrach *et al.* (3), and Brummer *et al.* (4), who used mainly C<sub>2</sub> or C<sub>3</sub> compounds as the reactant, evidence has been obtained for several types of intermediates on the electrode surface. Depending on potential of adsorption, there was a species thought to contain C and H which could be removed by cathodic pulsing, designated CH<sub>α</sub>, another CH material not removed by cathodic treatment which was suggested to be polymeric, CH<sub>β</sub>, and a more highly oxidized substance called O type which was thought to contain at least one C-O bond (4c). Either a flamed platinum wire with a geometrical area of approximately 0.1 cm<sup>2</sup> (2, 4) or 0.20 cm diameter Teflon-bonded platinum black electrode (3) was used in taking these data. Thus, the total amount of adsorbed material was much too small to permit chemical identification of the de-

sorption products. In order to obtain larger amounts of the desorption products, larger electrodes using platinum black catalysts were tried. Grubb (5) found that on cathodic hydrogenation after adsorption at 0.2 and 0.4v, followed by galvanostatic pulsing for 50 min, methane and ethane were obtained in sufficient quantities to be detected by gas chromatography. This is in marked contrast to the work of Shropshire and Horowitz (6) who found only butane starting material after cathodic treatment of their electrode. With these discrepancies in mind, we decided to restudy the cathodic desorption products obtained from the reaction of propane at a fuel cell electrode.

#### Experimental

The cell used in taking the data is shown schematically in Fig. 1.<sup>1</sup> A Teflon o-ring and an electrode backing were placed against the glass cell in circular groove. Against the backing was placed a commercially available American Cyanamid Type LAA-25 electrode consisting of 25 mg/cm<sup>2</sup> platinum black and

<sup>1</sup> Dr. W. T. Grubb, General Electric Company, was very helpful in the initial design of the cell.

\* Electrochemical Society Active Member.



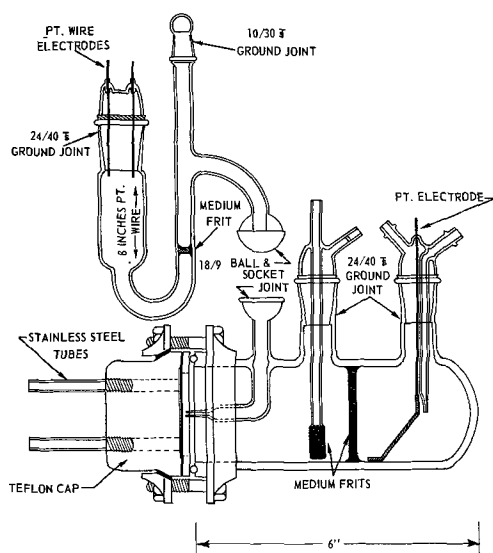


Fig. 1. Schematic diagram of electrochemical cell

25 w/o (weight per cent) Teflon pressed together on a tantalum screen. A Teflon coating on the gas side prevented electrolyte leakage. Immediately behind the electrode was a 1/16-in. gas space milled out of a Teflon block. The potential of the working electrode, active geometric area 20.3 cm<sup>2</sup>, was measured against an autogenous hydrogen electrode (7a) by means of a Luggin capillary fixed 1 mm from the working electrode. The autogenous hydrogen electrode was found to have a potential 40 mv cathodic to the hydrogen electrode in agreement with Giner's results on similar electrodes (7b). All reported potentials are against the autogenous hydrogen electrode. The counter electrode, a 58.2 cm<sup>2</sup> geometric area with a platinum loading of 35 mg/cm<sup>2</sup>, was folded to fit into its compartment which was separated from the working electrode by a glass frit. High-purity helium 99.995% and instrument grade propane 99.5% minimum purity were purchased from the Matheson Company. No organics other than propane could be detected in this gas with the flame ionization detector of the Perkin Elmer 154 D Gas Chromatograph. The electrolyte, 85% H<sub>3</sub>PO<sub>4</sub> Fisher reagent grade, was purified by treatment with 1 volume of hydrogen peroxide for 2 volumes of acid following the procedure of Savitz (8). Untreated electrolyte gave results similar to treated electrolyte. Figure 2 shows the schematic of the circuit used for adsorption and dehydrogenation studies. Potentials were set and controlled by a Wenking 62TRS potentiostat and monitored with a Keithley 610A Electrometer. Two sets of 1.3v batteries were connected in series with the potentiostat through a ten turn potentiometer for manually setting the potential steps used in electrode pretreatment. A model CK 18-3 Kepco power supply was used for anodically and cathodically

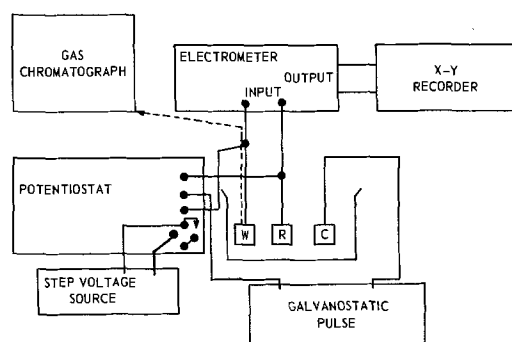


Fig. 2. Circuit diagram for adsorption and dehydrogenation studies.

pulsing the working electrode. Products obtained on cathodic pulse were examined with a Perkin-Elmer 154 D gas chromatograph using a flame ionization detector and a 6 ft Poropak column at 100°C. Product identification was assured by comparison of retention times with Poropak specification literature (9) and with known compounds. Voltage time curves were obtained on a Hewlett-Packard 7000 A X-Y recorder. The cell was maintained at 100°C ± 1 in a Fisher oven.

A typical run using the gas chromatograph would be as follows. First the working electrode was pretreated for the reasons described by Brummer (4a) and Gilman (10). The electrode was held at 1.35v relative to the hydrogen electrode until the current as monitored on the potentiostat no longer changed over a 5-min period. The current at this point was usually between 5 and 20 ma anodic for the total cell, and the time necessary to reach this point was about 3-5 min. Helium which passed over the electrode during this time was stopped, and propane was used instead at a flow rate of 5 to 10 cc/min, the same as for He. Next the potential was lowered to 0.05v by throwing a switch changing the batteries and resistance in series with the potentiostat. There was a lag time of about 20 sec from the time the switch was thrown until the potential reached 0.05v. Again the electrode was held at this potential until the current no longer changed. This usually took about 20 min at which point the cathodic current would be between 150 and 300 ma. Then the working electrode was held at the potential where adsorption was to be studied. When the current no longer changed, often after 45 min (11), the electrode was swept with helium. The current became cathodic or more cathodic depending on potential. During this time the effluent was monitored with the gas chromatograph. After passing helium through the cell for 10 min, a large amount of propane was still being swept from the electrode, but no methane or ethane was observed. A mercury relay, when triggered, switched from the potentiostatic circuit to galvanostatic circuit with which a cathodic current of 1.5 amp was applied to the working electrode. Methane/ethane ratios were found to be independent of the current between 1.5 and 2 amp and whether the pulse was galvanostatic or potentiostatic. The helium effluent was sampled 1½ min after pulsing. This time was very critical if desorption products were to be found. The time reflects the length of the line between the cell and the gas chromatograph and the rate of the helium sweep. Varying amounts of methane and ethane as well as a sizable amount of propane were observed depending on the potential. No normalization of the areas corresponding to methane and ethane concentration was made. The sequence used for gas chromatographic measurements is shown in Fig. 3.

To determine the relative amounts of desorbable and nondesorbable intermediates on the fuel cell electrode, an anodic galvanostatic pulse was used to examine the surface of the electrode. The charging curves were followed with an XY recorder. The electrode was pretreated as above and, when the current no longer changed at the potential being studied, helium was swept through the cell. After a given length of time

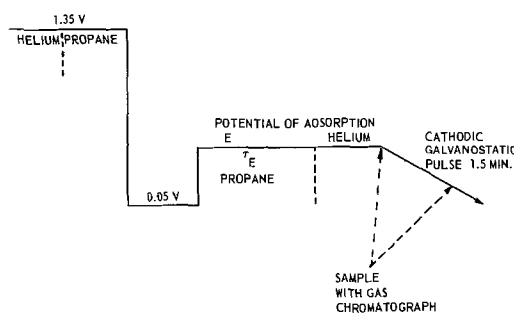


Fig. 3. Potential sequence used in gas chromatographic studies



under helium, the electrode was either anodically pulsed with a galvanostatic current of 2 amp or was potentiostatically lowered to 0.05v for 3 min, after which time the potential was raised back to the original potential of adsorption for 2 min and anodically pulsed as above. Times under helium,  $T$ , were measured exactly and varied to 30 min. A comparison of the background curve, obtained by pretreating and holding the electrode at the potential of interest under helium followed by an anodic pulse, with the curve without the cathodic treatment, gave the amount of charge obtained from the oxidation of all the surface species on the electrode at the time of the pulse. Similarly the anodic charging curve obtained after the cathodic treatment, when compared with the background, gives the amount of charge needed to oxidize the noncathodically desorbable material. The actual charge was obtained by measuring the difference in time between the background charging curve and the anodic charging curve as obtained above at 1.85v and multiplying this value by the current of the galvanostatic pulse. The voltage, 1.85, was chosen because oxygen evolution generally occurred between 1.8 and 1.9v (12). The slopes of the curves in the 1.5-1.9v range were nearly parallel so little error was introduced in picking this value.

Since the working electrodes used here are large and of a complex nature, it was seen that absolute numbers varied from experiment to experiment. However the trends which were observed were real and readily reproducible.

### Results and Discussion

Brummer and Turner (4) have shown that on a platinum wire the absolute amounts of desorbable and nondesorbable intermediates vary with potential. In this work we observe a variance in the composition of the desorbable intermediates as shown by the relative amount of methane compared to ethane seen after a cathodic pulse. The ratio is seen to be very dependent on potential. Propane is not used in this comparison because it is slowly removed from the gas space and the electrode. This propane would be indistinguishable from that resulting from the cathodic hydrogenation of  $C_3$  species on the surface. Undoubtedly the  $C_1$  and  $C_2$  species continue to react while under the long helium sweep, but since there was a large amount of propane on the surface and the current no longer changed, the relative amounts of methane and ethane obtained were felt to be representative of the relative amounts of the species on the surface while propane was passing through the gas space. Although trace amounts of methane and ethane were sometimes observed while sweeping with propane, all were eliminated by sweeping with helium prior to the cathodic pulse. In Fig. 4 there are three voltage regions to be considered. The desorbable  $C_1$  species as measured by the methane is seen to increase from a very small percentage relative to the  $C_2$  species at 0.2-0.3v to approximately one third of the total desorbable  $C_1$ - $C_2$  at 0.35-0.5v and then decreases at higher potentials. Adsorption at open circuit, 0.3-0.35v, gave similar methane-ethane ratios to those obtained on potentiostatic adsorption at 0.3. Since at the low potentials, 0.2 and 0.3v, the relative amounts of the  $C_1$  species is small, these species are probably more reactive than the  $C_2$  species or are incompatible with the surface at these potentials. The possibility that the  $C_1$  intermediates might be dimerizing to give  $C_2$  intermediates is ruled out because no butanes, pentanes, or hexanes were observed on gas chromatographic analysis. These higher molecular weight compounds would have resulted from the interaction of  $C_1$ ,  $C_2$ , or  $C_3$  intermediates.<sup>2</sup> As the voltage is increased to 0.35-0.5v, the

<sup>2</sup> It must be remembered that, when  $C_1$  intermediates are mentioned, methane is not the adsorbed compound in mind. Rather the  $C_1$  species might be thought of as a methine, methylene, or methyl fragment representing three, two, and one bonds between carbon and the surface or a combination of the possibilities. The actual structure of these intermediates is being determined by labelling experiments now in progress.

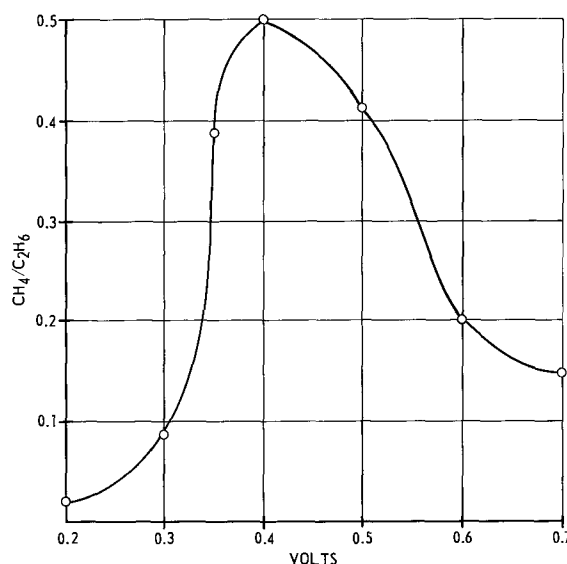


Fig. 4. Ratio of methane to ethane as a function of potential

amount of methane relative to the ethane increases. At these potentials, there is perhaps enough driving force available for the more reduced  $C_2$  species to contribute to the current. Finally at 0.6 and 0.7v, the methane-ethane ratio decreases. This is hard to rationalize, but might be explained by a change in the platinum surface as suggested by Schuldiner (13). The high dependence of the methane/ethane ratio on potential was demonstrated in another way by adsorbing at 0.7v and lowering the potential to 0.2v while sweeping with helium just prior to the cathodic pulse. On pulsing the methane/ethane ratio for 0.2 was observed. Similarly adsorption at 0.2 and switching to 0.7v prior to pulsing gave results expected for 0.7 not for 0.2.

A galvanostatic anodic pulse with and without prior cathodic treatment after adsorption at a potential was used to differentiate between the amounts of cathodically desorbable and nondesorbable materials. These techniques, used extensively earlier by Brummer and Turner (4c, d) are shown schematically in Fig. 5 and 6. Results, as reflected in the amount of charge obtained, varied markedly depending on the time under helium sweep before the anodic pulse espe-

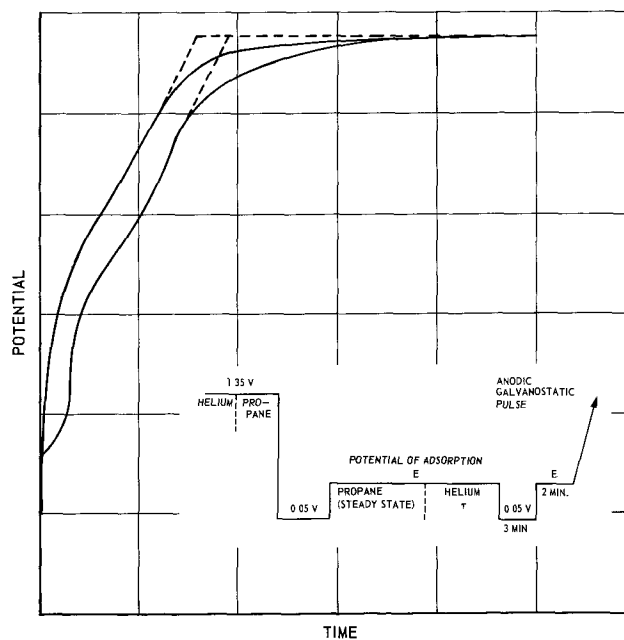


Fig. 5. Anodic charging curve with cathodic treatment

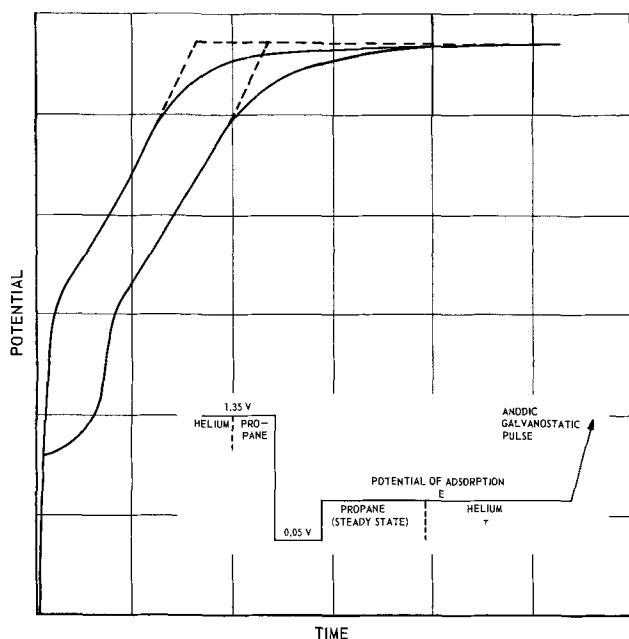


Fig. 6. Anodic charging curve without cathodic treatment

cially at 0.4v. Thus some of the surface species continued to react under helium at 0.4v so the amount of charge observed after anodic pulse would be smaller than the amount on the electrode when the helium sweep began. To minimize this oxidation, the potential was lowered from 0.4 to 0.2v just prior to sweeping with helium. Less charge was obtained than when the potential was held at 0.4v. It was then observed chromatographically that methane came off the surface in moving the potential from 0.4 to 0.2v. This was shown after all traces of methane and ethane had been removed by helium at 0.4. Again the high dependence of the composition of the desorbable intermediates on potential is demonstrated. The problem of determining the relative amount of desorbable to nondesorbable material at steady state, just prior to He sweep, was solved by sweeping with helium for differing times at the potential of adsorption prior to pulsing and then extrapolating the charge obtained to zero time. As expected from the chromatographic results, the 5-min point was usually off the line because excess propane was still being swept out of the lines, electrode, etc. The extrapolated desorbable/nondesorbable ratios are 3.6, 0.96, 0.44 for 0.2, 0.3, and 0.4v, respectively. Using a smooth platinum wire, Brummer obtained  $CH\alpha/O$  type- $CH\beta$ , ratios for propane of 0.4, 0.4, 0.4, for 0.2, 0.3, and 0.4v (4d) and 1.6, 1.3, 1.2 for hexane (15).<sup>3</sup> At 0.2 and 0.3v where the net current is cathodic, the total amount nondesorbable material does not change with time as evidenced by the zero slope of the time-charge curves (Fig. 7 and 8). However at 0.4v, where there is an anodic current, Fig. 9, nondesorbable material is reacting much faster than the desorbable material (Fig. 10).

These results may be explained by assuming that the oxidation of the nondesorbable species to  $CO_2$  is slow at 0.2 and 0.3v and is replenished by the desorbable intermediates as fast as  $CO_2$  is being formed, keeping the total nondesorbable concentration constant. Another possibility is that the nondesorbable species is changing very slowly, if at all, at 0.2 and 0.3v, and the desorbable intermediates react to give  $CO_2$  by another reaction pathway or come off the electrode as an alkane, alcohol, alkene etc.

<sup>3</sup> There is no evidence presented in this work which indicates the nondesorbable material contains a carbon oxygen bond but this seems to be a reasonable assumption on the basis of Niedrach's work (3).

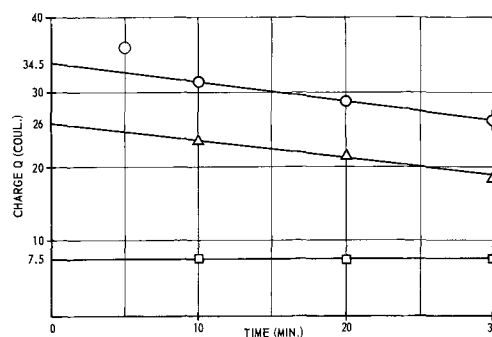


Fig. 7. Charge vs. time curves for adsorbed species at 0.2v:  $\circ$  = total Q at 0.2v;  $\square$  = nondesorbable at 0.2v;  $\triangle$  = desorbable at 0.2v.

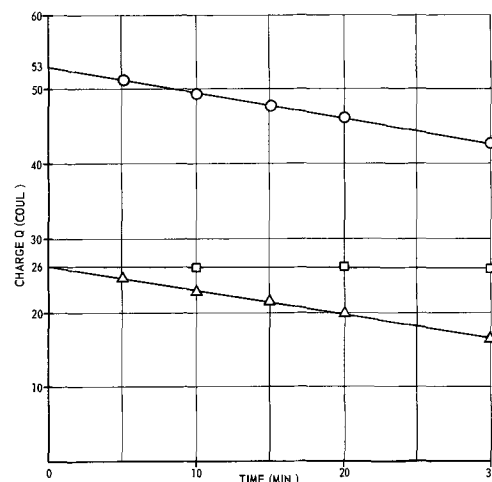


Fig. 8. Charge vs. time curves for adsorbed species at 0.3v:  $\circ$  = total Q at 0.3v;  $\square$  = nondesorbable at 0.3v;  $\triangle$  = desorbable at 0.3v.

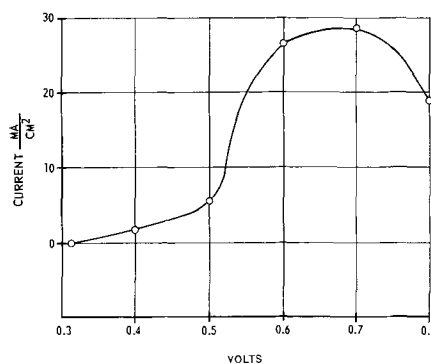


Fig. 9. Polarization curve for the LAA-25 electrode on propane

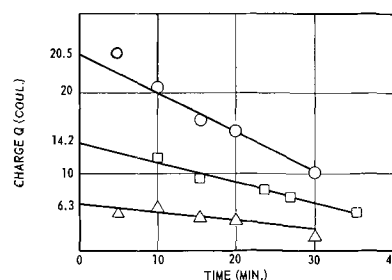


Fig. 10. Charge vs. time curves for adsorbed species at 0.4v:  $\circ$  = total Q at 0.4v;  $\square$  = nondesorbable at 0.4v;  $\triangle$  = desorbable at 0.4v.

### Conclusions

1. The composition of the desorbable species on the surface is highly dependent on potential and changes rapidly when the potential is varied.

2. There is a qualitative similarity between a platinum wire electrode and a fuel cell electrode in that, with propane as a reactant, cathodically desorbable and nondesorbable intermediates are observed. A more detailed comparison shows that the relative amounts of these intermediates differ in the dependence on potential for the two electrodes.

### Acknowledgment

The interest and helpful suggestions of Dr. S. B. Brummer, Tyco Laboratories, are gratefully acknowledged.

Manuscript received May 8, 1967; revised manuscript received March 1, 1968.

Any discussion of this paper will appear in a Discussion Section to be published in the June 1969 JOURNAL.

### REFERENCES

1. W. T. Grubb and L. W. Niedrach, Proceeding from the 17th Annual Power Sources, p. 69, May 1963.
2. S. Gilman, *Trans. Faraday Soc.*, **61**, 2561 (1966).
3. L. W. Niedrach and M. Tochner, *This Journal*, **114**, 17 (1967) and references cited therein.
- 4a. S. B. Brummer, J. I. Ford, and M. J. Turner, *J. Phys. Chem.*, **69**, 3424 (1965).
- b. S. B. Brummer and M. J. Turner, "Hydrocarbon Fuel Cell Technology," p. 409, B. S. Baker, Editor, Academic Press, New York (1965).
- c. S. B. Brummer and M. J. Turner, Paper presented at the Philadelphia Meeting of the Society, Oct. 9-14, 1966, as Abstract 6.
- d. S. B. Brummer and M. J. Turner, *J. Phys. Chem.*, **71**, 2825 (1967).
5. W. T. Grubb in General Electric Report No. 6 on Contracts DA-44-009-AMC-479(T) and DA-44-009-ENG-4909.
6. J. A. Shropshire and H. H. Horowitz, *This Journal*, **113**, 490 1351 (1966).
- 7a. J. Giner, *J. Electrochem. Soc.*, **111**, 376 (1964).
- b. J. Giner, Private communication.
8. M. L. Savitz, R. L. Januszski, and G. R. Frysinger, "Hydrocarbon Fuel Cell Technology" p. 443, B. S. Baker, Editor, Academic Press, New York (1965).
9. Waters Associates Inc., 61 Fountain Street, Framingham, Mass. in "Poropak", p. 7.
10. S. Gilman, *J. Phys. Chem.*, **67**, 78 (1963).
11. See also E. Gileadi, G. Stoner, and J. O'M. Bockris in University of Pennsylvania Report 7 Sept.-6 April 66 on Contract DA-44-009-AMC-469(T).
12. For a similar way of obtaining charge from charging curves see ref. (4b).
13. S. Schuldiner and T. B. Warner, *This Journal*, **112**, 212 (1965).
14. S. B. Brummer and M. J. Turner, *J. Phys. Chem.*, **71**, 3494 (1967).

## The Surface Roughening of a Cu-Au Alloy during Electrolytic Dissolution

Howard W. Pickering

Edgar C. Bain Laboratory for Fundamental Research, United States Steel Corporation, Research Center, Monroeville, Pennsylvania

### ABSTRACT

During anodic dissolution of Cu 10 a/o (atomic per cent) Au (Cu10Au) alloy the polarization capacity increases with time by a factor of 20 to >100; the factor is higher, the higher the current density in the range investigated (1-5 ma/cm<sup>2</sup>). The polarization capacity can be considered to be approximately proportional to the surface area of the electrode. The capacity and thus the surface area increases by more than an order of magnitude during the first minute of dissolution; further increase proceeds at an ever decreasing rate, so that after about 15 min the surface area no longer changes appreciably with additional amounts of dissolution. A decreasing influence of the time of electrolysis on the magnitude of the surface area is understood in terms of the occurrence of a surface smoothing (aging) process which becomes increasingly more important with increase in the area. Aging is also indicated to occur when the current is interrupted; the capacity decreases sharply at an ever decreasing rate. After 1 hr aging is virtually complete, and the area, although decreased by about a factor of two from that existing just prior to interruption of the current, is still at least 10 times greater than that existing at the start of anodic dissolution. A decrease in surface area after the current is cut off is in accord with the data of Wagner and others for analogous conditions. Extrapolation of the measured capacity to zero time of electrolysis gives an approximation of the double layer capacity for Cu10Au of 30  $\mu\text{f}/\text{cm}^2$ .

In two previous papers (1,2) it was shown that, during anodic dissolution of Cu from Cu-Au alloy at room temperature, Au is not ionized and that enrichment of Au in the alloy occurs. Accordingly Cu diffuses from the bulk alloy toward the alloy-environment interface and Au diffuses in the opposite direction. Volume diffusion in the presence of given supersaturations of mono- and divacancies was analyzed theoretically and concluded to proceed *via* divacancies. For analogous conditions of diffusion Harrison and Wagner (3) have theorized that a plane solid-liquid

interface is not stable. In accord with this result they have observed during preferential dissolution of Cu from solid Cu-Ni alloys in liquid Ag at 1000°C that a highly ragged interface is formed. In particular they have observed wedges filled with liquid metal protruding into the interior of the alloy. Similarly roughening of the surface and penetration of electrolyte into the alloy may be expected when Cu is preferentially dissolved from Cu-Au alloy. Formation of a porous layer during anodic dissolution of Cu-Au has been reported by various authors (4-8); and in one case in-

dividual pores were observed and measured at a few hundred Å diameter by transmission electron microscopy (8). It is the purpose of this paper to obtain a measure of the extent of surface roughening with the help of measurements of the polarization capacity during anodic dissolution of Cu from Cu-Au alloy.

Polarization capacity measurements have been made by Bowden and co-workers (9) for a determination of the roughness of various metallic surfaces. Measurements of this kind have also been used in order to determine the decrease in the true surface area of silver obtained by cathodic reduction of silver chloride by Wagner (10), by Gerischer and Tischer (11), and by Jaenicke and Schilling (12). Measurements may be made with an alternating current in a bridge circuit (11, 12). In particular an alternating current can be superimposed on a predetermined direct current by which the rate of dissolution is determined. For the experimental conditions used by Gerischer *et al.* (11, 12) the measured capacity approximated the differential double layer capacity of the Ag electrode and as such gave a direct measure of its change in surface area with time. The relevant concepts underlying these measurements and those presented in this paper, where in addition one has a faradaic impedance due to the passage of a direct current by which the rate of dissolution of Cu is determined, are contained in the next section.

### General Procedure

Polarization capacity measurements at 24°C were conducted in order to determine approximately the increase in true surface area which occurs when Cu is anodically dissolved from Cu 10 a/o Au (Cu10Au) alloy in 1M H<sub>2</sub>SO<sub>4</sub>. In addition capacity measurements were continued after the current was interrupted in order to examine the possibility that a decrease in true surface area occurs due to the surface migration of atoms and related processes.

*Theory of the capacity measurement.*—The impedance  $Z$  of a circuit between a Cu-Au electrode subject to anodic polarization and a counter electrode comprises the impedance  $Z_1$  of the Cu-Au electrode, the ohmic resistance  $R_e$  of the electrolyte, and the impedance  $Z_2$  of the counter electrode in series

$$Z = Z_1 + R_e + Z_2 \quad [1]$$

In order to simplify the evaluation it is desirable that  $R_e$  and  $Z_2$  be small in comparison to  $Z_1$ . Since  $Z_1$  and  $Z_2$  are inversely proportional to the surface areas of the respective electrodes, it is expedient to make the surface area of the counter electrode much larger than that of the Cu-Au electrode, *e.g.*, one may use a quasi-spherical Cu-Au electrode of radius  $r_1$  of about 0.05 cm surrounded at a distance of about 5 cm by a platinized platinum gauze as the counter electrode. Under these conditions the resistance of the electrolyte is

$$R_e \simeq \frac{1}{4\pi\sigma r_1} \quad [2]$$

where  $\sigma$  is the specific conductivity of the electrolyte, which is supposed to be fairly high so that  $R_e$  is low.

The factors which determine the impedance of an electrode have been discussed by various authors (13-31). For the present investigation, considerable simplification may be introduced. In particular, contributions to  $Z_1$  corresponding to concentration polarization may be considered to be negligible in the case of irreversible dissolution, *i.e.*, when the electrode is at least 0.1v more noble than the equilibrium potential of pure copper in the electrolyte. Also in the case of an alloy from which the less noble component is dissolved, one can neglect differences in the local current density along the outer surface of the electrode in accord with considerations due to Hoar and Agar (32) and to Wagner (33, 34), because the product of the conductivity of the electrolyte and the slope of the po-

tential-current density curve is much greater than the radius of the quasi-spherical electrode.

According to Grahe (19) the impedance  $Z_1$  of the Cu-Au electrode may be represented by a faradaic and a nonfaradaic impedance in parallel. The faradaic impedance comprises an ohmic resistance and a pseudo-capacitance as well. The nonfaradaic impedance is that of the differential double layer capacity  $C_{1d}$ . With increasing frequency of the alternating current the nonfaradaic impedance decreases more and more, whereas the faradaic impedance in parallel remains finite. The over-all impedance  $Z_1$  is equal to the reciprocal of the sum of the admittances in parallel, each of which in turn is equal to the reciprocal of the faradaic and nonfaradaic impedance. Thus, at sufficiently high frequencies,  $Z_1$  becomes practically equal to the nonfaradaic impedance. Representing the impedance of a capacity by an imaginary term, one has

$$Z_1 = -\frac{j}{\omega C_{1d}} \quad [3]$$

where  $j = (-1)^{1/2}$  and  $\omega = 2\pi f$  with  $f$  as the frequency (Hz) of the alternating current. Use of Eq. [3] presupposes conditions where the resistance of the electrolyte in the porous layer of the alloy does not affect the current distribution and does not make a significant contribution to the total impedance.

Substitution of Eq. [2] and [3] in Eq. [1] for  $Z_2 \ll 1$  yields

$$Z = \frac{1}{4\pi\sigma r_1} - \frac{j}{\omega C_{1d}} \quad [4]$$

Equation [4] is the equation for the impedance of a circuit with the ohmic resistance  $R_e = 1/4\pi\sigma r_1$  in series with the differential double layer capacitance  $C_{1d}$  (see Fig. 1 for circuit analog). To test the applicability of Eq. [4] for finite frequencies one may conduct measurements of the real and the imaginary part of the impedance  $Z$  at various frequencies in order to find the frequency above which the real part of  $Z$  is essentially independent of  $\omega$  and the imaginary part is inversely proportional to  $\omega$ .

The differential double layer capacity  $C_{1d}$  is in essence proportional to the true surface area of the Cu-Au electrode. Thus, under conditions where Eq. [4] holds, the imaginary part of the impedance  $Z$  is inversely, and the differential double layer capacity directly, proportional to the true surface area. One has therefore the following relation for the determination of the ratio between the true surface area  $A_1$  of a Cu-Au electrode at time  $t'$  and that at  $t''$

$$\frac{A_1(t'')}{A_1(t')} \simeq \frac{\text{Im } Z_1(t')}{\text{Im } Z_1(t'')} \simeq \frac{C_{1d}(t'')}{C_{1d}(t')} \quad [5]$$

This relation implies that the capacity per unit true surface area is essentially independent of alloy composition and of the true current density. Actually since the capacity per unit true surface area may vary to some extent, Eq. [5] can be used only as an approximation. Nevertheless measurement of the polarization capacity would seem to be an appropriate method for obtaining order-of-magnitude changes in surface area while current is passed. It, unlike other methods such as BET measurements, provides measurement during the experiment itself; hence, changes in surface area which may occur when the current is cut off and spurious contributions which may arise during preparations for using other methods are not part of the measured value.

*Experimental arrangement.*—For measurement of the real and imaginary parts of the impedance of a Cu10Au electrode, the circuit shown schematically in Fig. 1 was used in accord with recommendations made by Gerischer (31). In essence it is a slight modification of the circuit used by Gerischer and Tischer (11)

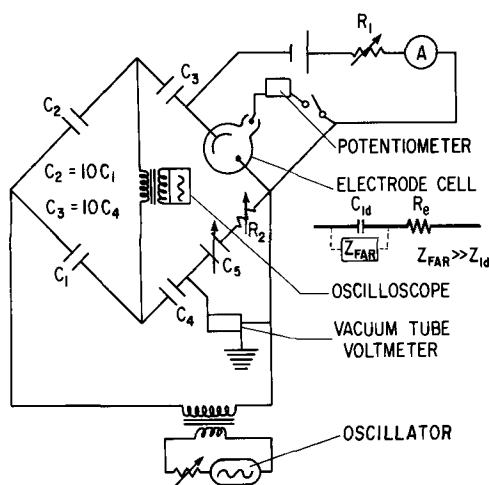


Fig. 1. Circuit for measuring the impedance

for investigations on silver deposits obtained by cathodic reduction of silver chloride. Since the direct current to be applied to the Cu10Au electrode is low, the circuit producing the direct current consists of a battery yielding a rather high voltage of 200v and a variable resistor  $R_1$  in series. Since  $R_1$  is necessarily large the alternating current flows practically only between the test and counter electrodes even without inductances in the d-c circuit as used by Gerischer and Tischer (11). In addition capacitors  $C_3 \approx C_2$  and  $C_4 \approx C_1$  were placed in series with the Cu-Au test electrode and the balancing circuit, respectively. Hence, when the capacitance of the Cu-Au test electrode becomes much larger than  $C_2$  the impedance of the branches containing the test electrode and the balancing elements remains approximately equal to the impedance of their corresponding branches containing the standard capacitors  $C_2$  and  $C_1$ ; otherwise stray impedance would interfere seriously. For this reason, too, the circuit was completely shielded. Capacitances  $C_3$  and  $C_4$  also prevented the flow of direct current from the cell to the other branches of the bridge. Sensitivity remained adequate even at the highest capacity of the Cu-Au electrode, about 50  $\mu\text{f}$ . For  $C_2 = 10 C_1$  and  $C_3 = 10 C_4$ , the double layer capacity  $C_{1d}$  was obtained as  $C_{1d} = 10 C_5$  after the bridge had been balanced. The reference electrode was then switched into the circuit and the potential measured. The circuit was tested and calibrated by making impedance measurements as a function of frequency for capacitors ranging from 0.5 to 50  $\mu\text{f}$  in series with a 7-ohm resistance substituted for the electrode circuit in the unknown branch of the bridge. A Hewlett-Packard 200 CD oscillator provided an alternating current signal over a wide range of frequency. A Tektronix type 543 oscilloscope with a type E amplifier served as the null instrument. The equivalent circuit used for balancing the bridge consisted of Cornell-Dubilier decade capacitors with a range of 0.001-11.111  $\mu\text{f}$  in 0.001  $\mu\text{f}$  increments in series with a General Radio resistor of low inductance rating with a range of 0.1-1000.1 ohm in 0.1 ohm increments. In order to be within the range of a virtually linear relation between current and voltage the root-mean-square amplitude of the a-c voltage across the cell was maintained at 0.003v with the help of a Hewlett-Packard 400D vacuum tube volt meter. A frequency of 30 kHz was chosen for the actual measurements on the basis of preliminary impedance data obtained as a function of frequency on Cu10Au electrodes before and after anodic dissolution, which showed that for this frequency, Eq. [4] was approximately satisfied.

The capacity measurement was made in a Pyrex cell, Fig. 2. A semicylindrical counter electrode made of platinized-platinum gauze was centered 5 cm from a

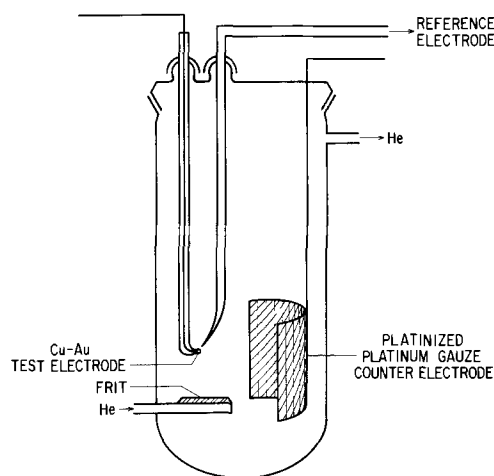


Fig. 2. Cell used for the polarization capacity measurements

quasi-spherical Cu10Au test electrode with a radius of 0.05 cm. The electrolyte, 1M  $\text{H}_2\text{SO}_4$ , was made from reagent-grade acid and doubly distilled water of conductivity  $3 \times 10^{-7}$  mho-cm $^{-1}$ . Pre-purified He was passed through the solution to eliminate oxygen. The reference cell was a mercury-mercurous sulfate electrode in contact with 1M  $\text{H}_2\text{SO}_4$ . The potentials are reported relative to the standard hydrogen electrode (SHE).

The test electrodes were machined from Cu10Au alloy which had been vacuum-melted from metals of 99.999% Cu and 99.995% Au, homogenized in an evacuated Vycor capsule at 700°C for 4 days, and swaged. They were then sealed with an epoxy cement in finely drawn Pyrex tubes with somewhat less than a hemisphere of surface exposed. A photograph of the electrode at 50X facilitated measurement of its geometrical area. Electrical contact was provided by a copper wire previously soldered to the stem of the electrode which passed along the inside of the tube. Surface roughness resulting from the machining operation was reduced by mechanically polishing to the extent that at 50X the surface had a high gloss and was virtually free of scratches. In order to establish that the high degree of cold work in the specimen did not unduly influence the area increase, a few preliminary runs were made with Cu10Au electrodes which were in the annealed condition (1 hr at 700°C in an evacuated capsule and no mechanical polish). The results for the annealed and for the cold worked samples were not significantly different.

## Results

The capacity measured during anodic dissolution of Cu from Cu10Au increases sharply with time, rising in 10-20 min by a factor of 20 to > 100 depending on the current density. As anodic dissolution continues the capacity eventually levels off and may even decrease. When the current is interrupted the capacity again changes appreciably, decreasing sharply at an initially high but ever decreasing rate. Figure 3 illustrates this behavior for Cu10Au electrodes anodically dissolving at a current density of 1 or 3 ma/cm $^2$ .

From additional capacity data for other current densities it was established that (a) for a given time of electrolysis the capacity is higher the higher the current density and (b) as one proceeds from a current density of 1-5 ma/cm $^2$  the capacity increases to higher and higher values prior to leveling off, with the result that more than a one-hundredfold increase in capacity was measured for Cu10Au electrodes dissolving at 4 or 5 ma/cm $^2$ .

The capacity data appear in Fig. 3 also in terms of the ratio of the measured capacity to the initial capacity,  $C_0$ , where  $C_0$  is obtained by extrapolation to zero time of the capacity measured during anodic dis-

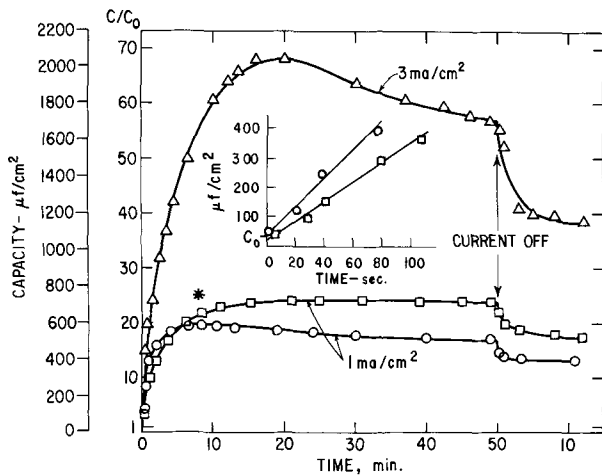


Fig. 3. Capacity measured during anodic dissolution and the ratio of the measured capacity to the initial capacity  $C_0$  for Cu10Au electrodes dissolved in 1M  $H_2SO_4$  at 1 ma/cm<sup>2</sup> (O and □) and 3 ma/cm<sup>2</sup> (Δ).  $C_0$  is obtained by extrapolation to zero time of the capacity measured at the very early stages of dissolution as shown in the insert for the runs at 1 ma/cm<sup>2</sup>. \* indicates the  $C/C_0$  calculated from the BET measurement of area for a Cu10Au electrode which had been dissolved at 1 ma/cm<sup>2</sup> for 8 min.

solution. A reasonably good extrapolation was possible at 1 ma/cm<sup>2</sup> since at very early stages of anodic dissolution a plot of capacity vs. time is nearly linear as may be seen in the insert of Fig. 3. The average initial capacity obtained in this manner from data of several Cu10Au electrodes is  $C_0 \sim 30 \mu f/cm^2$  with a rather poor reproducibility of about  $\pm 50\%$ .

Auxiliary calculations by Wagner (35) show that during the run with the current density  $i = 10^{-3}$  amp/cm<sup>2</sup> the resistance of the electrolyte in the porous zone of the sample was much less than the absolute magnitude of the double layer impedance and, therefore, use of Eq. [3] is justified. Values of  $C_{1d}$  reported for  $i = 3 \cdot 10^{-3}$  amp/cm<sup>2</sup>, however, are somewhat uncertain in view of the contribution of the resistance of the electrolyte in the pores especially at higher depths of penetrations after 5 min. The uncertainty does not seem to be excessive since values of  $C_{1d}$  measured after termination of the run depend only slightly on frequency above 20 kHz (Fig. 5).

Figure 4 shows capacity data for a Cu10Au electrode, where the current of 3 ma/cm<sup>2</sup> was cut off at an early stage of anodic dissolution while the capacity was still rising at a high rate. The decrease in capacity after the current is interrupted occurs mainly

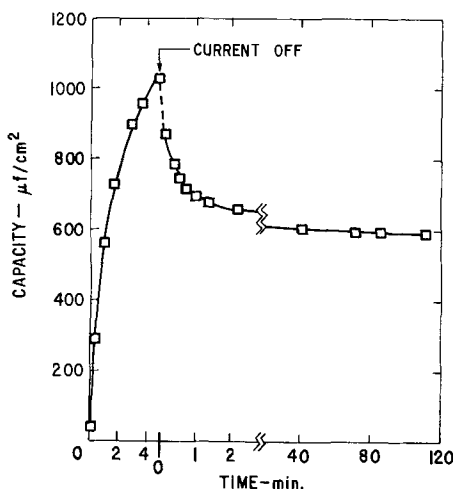


Fig. 4. Capacity of a Cu10Au electrode measured during and after dissolution in 1M  $H_2SO_4$  at 3 ma/cm<sup>2</sup>, illustrating a sharp decrease in capacity when the current is cut off.

within a few minutes; after 1 hr virtually no further change occurs, and the capacity, although decreased by about a factor of two from that existing just prior to cut-off of the current, is still greater by an order of magnitude than at the start of anodic dissolution when the surface was essentially plane.

As standard procedure the capacity and resistance were measured as a function of frequency both before and after anodic dissolution in order to confirm that Eq. [4] was approximately satisfied. These capacity data are shown in Fig. 5 for the electrodes whose capacity during anodic dissolution is reported in Fig. 3; above about 20 kHz the capacity is nearly independent of frequency over a wide range. The resistance behaved similarly, decreasing from a high value at low frequencies to a final value of about 7 ohm for frequencies above 20 kHz.

While current is passing the potential remains fairly constant within  $\pm 20$  mv. After interruption of the current the potential decreases to a less noble value. Potential data obtained during and after anodic dissolution at 1 and 3 ma/cm<sup>2</sup> are shown in Fig. 6.

Discussion

From Eq. [5] and the capacity data the surface area of the Cu10Au electrode is seen to increase by a factor of 20 to  $> 100$  when Cu is anodically dissolved from Cu10Au alloy. On the basis of other investigations (1, 2) which show that anodic dissolution of Cu from Cu-Au alloys occurs via interdiffusion in the alloy, roughening of the surface was to be expected, in accord with theory and experimental data for analogous conditions [Harrison and Wagner (3)].

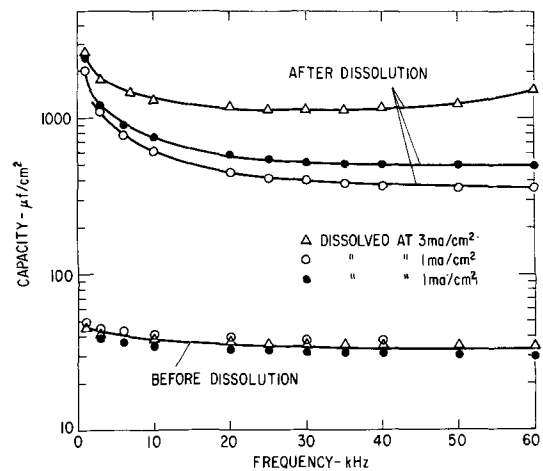


Fig. 5. Capacity measured before and after dissolution as a function of the frequency of the alternating current for the three Cu10Au electrodes of Fig. 3, illustrating an extended region of frequency over 20 kHz where the capacity is nearly independent of frequency.

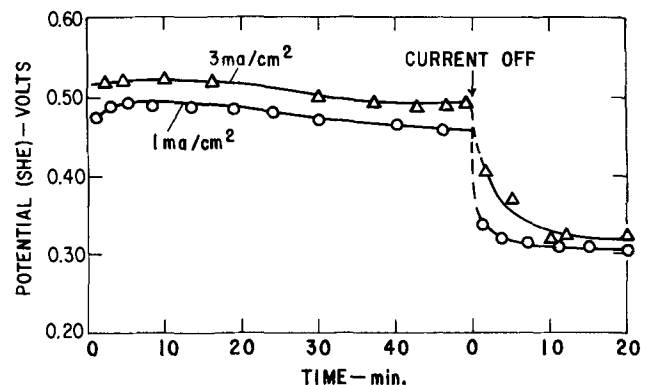


Fig. 6. Potential measured during and after dissolution of two Cu10Au electrodes in 1M  $H_2SO_4$  at 1 ma/cm<sup>2</sup> (O) and 3 ma/cm<sup>2</sup> (Δ).

The eventual leveling-off of the capacity suggests that the rate of increase of the surface area decreases until the total area no longer changes appreciably with time even though dissolution of Cu continues. This is understood in terms of an increasing participation of a second process (aging) which tends to reduce the area (35). Initially the surface area increases rapidly, the rate being determined mainly by the rate of Cu dissolution. As dissolution continues and the surface area becomes large, aging becomes more important in determining the net change in surface area; i.e., when roughening has occurred to a considerable extent, there will be significant amounts of Au-rich alloy especially near the original alloy-electrolyte interface where aging may occur in virtually complete absence of Cu dissolution. A net decrease in area in these regions which eventually becomes comparable to the amount of new surface formed near the base of the channels where dissolution of Cu mainly occurs, would explain how a surface area which initially increases sharply finally becomes only a weak function of the time of electrolysis.

When the direct current is cut off and anodic dissolution ceases, the capacity sharply decreases as reported in the data of Fig. 3 and especially 4. The potential also changes appreciably when the current is cut off (Fig. 6). Some data of Bockris and Conway (36) would seem, however, to indicate that the effect of potential on double layer capacity is small for the experimental conditions employed in this investigation. They found that the differential double layer capacity of Cu in 1N H<sub>2</sub>SO<sub>4</sub> becomes a weaker and weaker function of potential as the frequency is increased; at 5 kHz, the highest frequency employed, the differential double layer capacity was virtually independent of potential in the range -100 to 300 mv. Even so, values obtained from Eq. [5] after the current is shut off are somewhat uncertain. A decrease in surface area which occurs after the current is cut off is understandable in terms of continued aging which now proceeds in the complete absence of the metal dissolution and the accompanying formation of new surface.

The occurrence of an aging process is in accord with the data of Wagner (10), of Gerischer and Tischer (11), and of Jaenicke and Schilling (12) for analogous conditions. They observed a decrease in the surface area of silver obtained by cathodic reduction of silver chloride and attributed it to the surface migration of atoms and related processes. Aging during and after anodic dissolution of Cu from Cu-Au alloys may proceed similarly.

The fact that appreciable changes in the surface area may occur when the current is interrupted (as shown in Fig. 3 and 4), shows the desirability of *in situ* measurements of changes of area during anodic dissolution. Measurement of the polarization capacity provides a convenient way to do this especially when only approximate determination of changes in surface area is needed.

It was confirmed by the BET method that the change in surface area may be approximately determined from measurements of the polarization capacity. After dissolution at 1 ma/cm<sup>2</sup> for 8 min the BET area of a Cu<sub>10</sub>Au electrode was found to have increased by about a factor of 25, or something less than twice the increase determined by the polarization capacity (see Fig. 3).<sup>1</sup> Further experimentation is desirable in order to confirm the proposed aging mechanism.

#### Acknowledgment

The author is greatly indebted to Professor Dr. Carl Wagner of the Max-Planck Institut für Physikalische Chemie for suggesting the investigation and making

<sup>1</sup> For comparison of the BET area with the area determined from the capacity, one should note that a decrease in surface area occurs after the current is shut off (i.e., prior to the BET measurement) and that reaction products may remain even after extensive rinsing of the sample. The latter would tend to give a BET area on the high side.

available an unpublished memorandum containing the pertinent theoretical concepts and suggestions on the experimental arrangement. He also gratefully acknowledges helpful discussions with Doctors C. A. Johnson, N. P. Louat, and R. P. Frankenthal, the skillful assistance of Messrs. P. J. Byrne, H. A. Hughes, and E. A. Fischione and the aid of Dr. H. A. Podgurski for the BET area determination, all of this laboratory.

Manuscript received Sept. 5, 1967; revised manuscript Feb. 13, 1968.

Any discussion of this paper will appear in a Discussion Section to be published in the June 1969 JOURNAL.

#### REFERENCES

- H. W. Pickering and C. Wagner, *This Journal*, **114**, 698 (1967).
- H. W. Pickering, *ibid.*, **115**, 143 (1968).
- J. D. Harrison and C. Wagner, *Acta Met.*, **7**, 722 (1959).
- L. Graf, *Metallforschung*, **2**, 193, 207 (1947).
- L. Graf, *Z. Metallkunde*, **40**, 275 (1949).
- H. Gerischer and H. Rickert, *ibid.*, **46**, 681 (1955).
- R. Bakish and W. D. Robertson, *Trans. AIME*, **206**, 1278 (1956).
- H. W. Pickering and P. R. Swann, *Corrosion*, **19**, 369t (1963).
- F. P. Bowden and E. K. Rideal, *Proc. Roy. Soc. (London)*, **A120**, 59, 80 (1928); F. P. Bowden and E. A. Conner, *ibid.*, **127**, 317 (1930); F. P. Bowden and K. E. W. Grew, *Discussions Faraday Soc.*, **1**, 91 (1947).
- C. Wagner, *This Journal*, **97**, 71 (1950).
- H. Gerischer and R. P. Tischer, *Z. Elektrochem.*, **58**, 819 (1954).
- W. Jaenicke and B. Schilling, *ibid.*, **66**, 563 (1962).
- P. Dolin and B. Ershler, *Acta Physicochim. U.R.S.S.*, **13**, 747 (1940).
- B. Ershler, *Discussions Faraday Soc.*, **1**, 269 (1947).
- A. N. Frumkin, *ibid.*, **1**, 57 (1947).
- D. C. Grahame, *J. Am. Chem. Soc.*, **63**, 1207 (1941).
- D. C. Grahame, *ibid.*, **68**, 301 (1946).
- D. C. Grahame, *Chem. Rev.*, **41**, 441 (1947).
- D. C. Grahame, *This Journal*, **99**, 370C (1952).
- J. E. B. Randles, *Discussions Faraday Soc.*, **1**, 11 (1947).
- J. E. B. Randles and K. W. Somerton, *Trans. Faraday Soc.*, **48**, 937 (1952).
- H. Gerischer, *Z. physik. Chem.*, **198**, 286 (1951).
- H. Gerischer, *ibid.*, **201**, 55 (1952).
- H. Gerischer, *Z. physik. Chem. N.F.*, **1**, 278 (1954).
- C. N. Reilly, High Frequency Methods, in P. Delahay, "New Instrumental Methods in Electrochemistry," pp. 319 ff., Interscience Publishers, New York (1954).
- P. Delahay, "The Study of Fast Electrode Processes by Relaxation Methods, in: *Advances in Electrochemistry and Electrochemical Engineering*," Vol. 1, pp. 233 ff., P. Delahay and C. W. Tobias, Editors, Interscience Publishers, New York (1961).
- K. Vetter, "Elektrochemische Kinetik," Springer-Verlag, Berlin (1961).
- J. O'M. Bockris, The Mechanism of the Electrodeposition of Metals, in "Modern Aspects of Electrochemistry," Vol. 3, J. O'M. Bockris and B. E. Conway, Editors, pp. 224 ff., Butterworth, London (1964).
- E. Gileadi and B. E. Conway, The Behavior of Intermediates in Electrochemical Catalysis in "Modern Aspects of Electrochemistry," Vol. 3, *loc. cit.*, pp. 347 ff.
- P. Delahay, "Double Layer and Electrode Kinetics," Interscience Publishers, New York (1965).
- H. Gerischer, *Z. Elektrochem.*, **58**, 9 (1954).
- T. P. Hoar and J. N. Agar, *Discussions Faraday Soc.*, **1**, 162 (1947).
- C. Wagner, *This Journal*, **98**, 116 (1951).
- C. Wagner, *ibid.*, **107**, 445 (1960).
- C. Wagner, Private communication.
- J. O'M. Bockris and B. E. Conway, *J. Chem. Phys.*, **28**, 707 (1948).

# The Oxidation of Niobium in the Temperature Range 450°-720°C

J. S. Sheasby

Faculty of Engineering Science, The University of Western Ontario, London, Ontario, Canada

## ABSTRACT

The oxidation properties of niobium were studied in the temperature range 450°-720°C at oxygen pressures 1-760 Torr. Particular emphasis was placed on correlating the morphology of the reaction products with the oxidation kinetics. During the initial, approximately parabolic oxidation period the scale appears compact, and at the transition from parabolic to linear kinetics the scale blisters and cracks. Scale formed during linear oxidation grows in a series of crude layers. From the relationships determined between the rate of oxidation and the thickness of the oxide layers, it is deduced that the rate of oxidation is controlled at all times by the diffusional properties of the oxide layer in contact with the metal phase. The sensitivity of the rate of oxidation to oxygen pressure is ascribed to the pressure sensitivity of the underlying parabolic rate constant of formation of the niobium pentoxide, and to a lesser extent to changes in the width of the oxide layers with the rate of their formation. The inversion in the temperature coefficient of the oxidation reaction as the temperature is lowered from 625°-600°C is associated with the disappearance of layers of NbO and NbO<sub>2</sub> from the reaction zone and the appearance of a metastable platelet phase.

The oxidation behavior of niobium has been studied by many workers, and the literature was reviewed most recently by Seybolt (1). Niobium exhibits unusual oxidation features, for at each temperature and oxidation pressure the oxidation rate is found to follow a complex series of time laws. This paper describes an investigation into the oxidation behavior of niobium in the temperature range 450°-720°C, at oxygen pressures near atmospheric, for times from 2 min to several hours. At times shorter than this, or for the equivalent oxygen uptake at lower pressures, Hurlen (2) reports that the oxygen rate is time independent. At reaction times longer than several hours a second breakaway reaction has been reported by Kolski (3) and by McLintock and Stringer (4).

The field under study is characterized by a time independent rate (linear reaction rate law), which is usually preceded by a short period of approximately parabolic behavior. The linear reaction rate is pressure-sensitive and also decreases in magnitude as the temperature is increased from 600° to 625°C. The major part of the weight gain is associated with the formation of niobium-pentoxide although oxygen is also consumed by the formation of lower or suboxides and by solution in the metal phase. Whereas there is good agreement between previous studies on the rates of oxidation and types of time laws observed at various oxidation conditions, there is no agreement as to the physical events and the nature of the rate controlling steps associated with each stage. Particular areas of disagreement are: (i) the reaction products formed during parabolic oxidation, and the rate controlling step; (ii) the mechanism of the transition from parabolic to linear oxidation kinetics; (iii) the rate-controlling step during linear oxidation; (iv) the mechanism of the rate inversion at 600°C.

Previous workers (2, 4, 5) have considered the high pressure sensitivity of the oxidation rate and the linear oxidation kinetics indicative of equilibrium oxygen adsorption at an interface, followed by a phase boundary controlled reaction. However, Sheasby, Wallwork, and Smeltzer (6) have recently shown that in the temperature range 720°-825°C the niobium pentoxide scale grows protectively, and that the parabolic rate constant of its formation is pressure sensitive, thus permitting the pressure sensitive linear oxidation kinetics to be rate controlled by a barrier film mech-

anism. This paper describes the results of an investigation into this possibility.

## Experimental

Specimens were cut in the form of squares approximately 1.1 cm<sup>2</sup> from sheet 1 mm thick produced by Fansteel. The specimens were prepared for oxidation by abrasion up to 600 grade silicon carbide paper, followed by electropolishing for 30 sec in a nitric acid -30% hydrofluoric acid electrolyte at 24v using a carbon cathode.

The kinetics of oxidation were examined using a volumetric apparatus. Experimental runs were initiated by admitting oxygen to a specimen brought to temperature under vacuum. Previous estimates of specimen self-heating for this procedure gave an initial rise above the furnace temperature of about 30°C. The specimens then cooled to a steady value in about 4 min to about 2°-3°C above the furnace temperature. For most of the experiments an oxygen pressure of 380 Torr was used, and at this pressure a 1 cm movement of the mercury bead corresponds to an oxygen uptake of approximately  $1.4 \times 10^{-5}$  g/cm<sup>2</sup>. At least two runs were made at each temperature, and the rate constants so determined usually agreed to better than 10%. After oxidation all the specimens were examined metallographically. To obtain minimum loss of oxide the specimens were plunged while still hot into cold-mounting compound.

## Experimental Results

*Kinetic results.*—A series of specimens was oxidized at 380 Torr at approximately 25°C intervals over the temperature range 450°-720°C to a weight gain of about 0.01 g/cm<sup>2</sup>. Further specimens were oxidized as required for specific times, temperatures, and oxygen pressures.

A typical weight gain curve in which initial protective behavior breaks away to a time-independent reaction rate is shown in Fig. 1. A plot of (weight gain)<sup>2</sup> vs. time for the protective period gives a good fit to a straight line intersecting the time axis close to the origin. The weight gain curves for the series of specimens oxidized at 380 Torr were analyzed for values of the reaction rate constants  $Kp_v$  and  $Kl_v$ . Where  $Kp_v$ , the parabolic reaction rate constant, and  $Kl_v$ , the linear reaction rate constant, are defined by



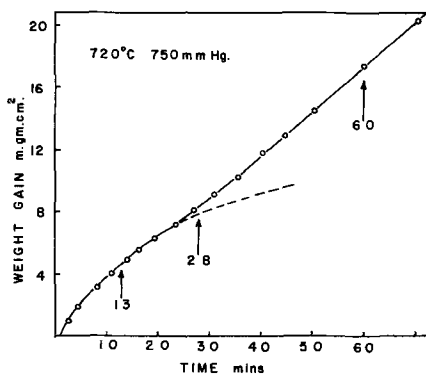


Fig. 1. Oxidation of niobium at 720°C, 750 Torr

the equations

$$w^2 = Kp_v t + a$$

$$w = Kl_v t + b$$

respectively;  $w$  is the weight of oxygen absorbed at time  $t$ , and  $a$  and  $b$  are reaction constants.

It was found that below approximately 610°C the protective period is too short to obtain a parabolic rate constant, and below 550°C, after the initial deviations of approximately 10-min duration, the reaction rate tends to decrease slowly as oxidation proceeds, Fig. 2. This latter behavior has been reported previously by Ayimore *et al.* (7) and by Cox and Johnston (8) and will be discussed later. Values of the linear rate constant  $Kl_v$  agree well with previous investigations (Fig. 3), and in particular a decrease in reaction rate is noted as the oxidation temperature is increased from 600° to 622°C. Values of the parabolic

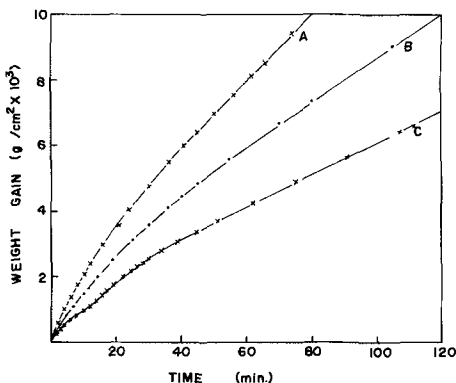


Fig. 2. Oxidation of niobium at 520°C. Curve A, 760 Torr; curve B, 380 Torr; curve C, 150 Torr.

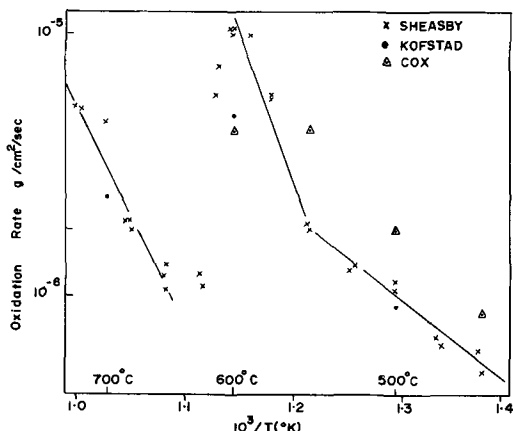


Fig. 3. Dependence of the linear rate of oxidation of niobium at 380 Torr on temperature. X This investigation, interpolated values of ● Kofstad *et al.* (13), and Δ Cox *et al.* (7).

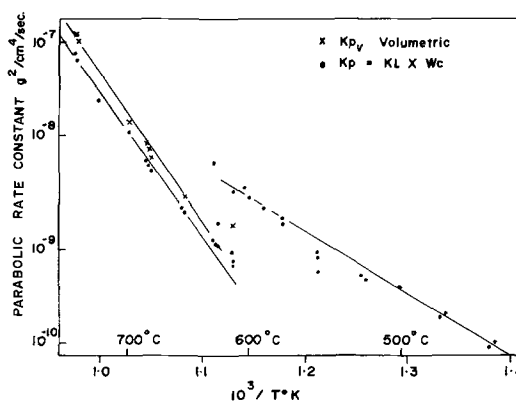


Fig. 4. Dependence of the derived and measured parabolic rate constants of oxidation of niobium at 380 Torr on temperature.

rate constant  $Kp_v$  are shown in Fig. 4. No other values have been reported for these reaction conditions.

**Metallographic results.**—The principal reaction product in the range 10-760 Torr 450°-720°C is  $\gamma$ -niobium pentoxide as designated by Terao (9). Layers of NbO and NbO<sub>2</sub> are present at the metal surface on specimens reacted above 620°C. Below 600°C these oxides are absent and are replaced by a platelet phase tentatively identified as the suboxide NbO<sub>z</sub> as designated by Norman (10). The appearance or nonappearance of the equilibrium diagram oxides NbO and NbO<sub>2</sub> depends on the time, temperature, and pressure of oxidation, and also on the local radius of curvature of the metal-oxide interface. For instance, as shown in Fig. 5, for a specimen reacted at 626°C in 380 Torr oxygen, NbO and NbO<sub>2</sub> are stable on the main faces of the specimen, but not at the specimen corners. The reaction conditions necessary for the formation of NbO and NbO<sub>2</sub> are the subject of a current study and will be reported later.

In cross section the niobium pentoxide layer tends to be thicker at specimen corners and edges than on the

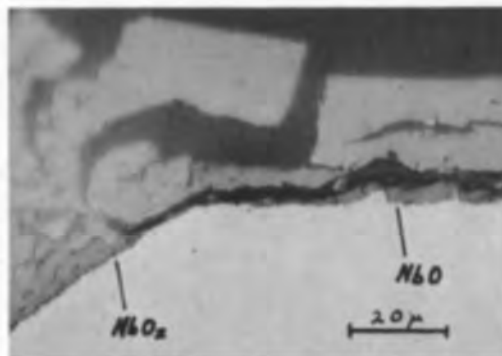


Fig. 5. Cross section of specimen oxidized at 380 Torr, 626°C for 65 min., showing abnormal edge effect. Magnification A (top) ca. 100X, B (bottom) ca. 525X.



Fig. 6. Cross section of specimen oxidized at 380 Torr, 575°C for 32.5 min, showing normal edge effect. Magnification 125X.

main faces (Fig. 6), thus preventing too literal an interpretation of the reaction rate constants measured by the volumetric apparatus. The niobium-pentoxide layer on all the specimens contains lenticular fissures parallel to the metal surface giving the scale a laminar appearance. When the scale is formed from niobium containing platelets these fissures or pores tend to be aligned, running at an angle of about 60° to the metal surface and occurring in pairs to give a chevron pattern superimposed on the laminations (Fig. 7). This chevron pattern of pores probably has the same origin as the similar structure in tantalum pentoxide scales described and discussed by Stringer (11).

Laminations in niobium pentoxide scale layers formed from NbO and NbO<sub>2</sub> are thicker than those formed from niobium containing platelets. Lowering the oxidation pressure or raising the temperature tends to increase the thickness of these laminations so that above 725°C the oxide is not layered (6). When viewed in polarized light the oxide scales formed at the higher temperatures are seen to be composed of columnar crystals with the long axis normal to the plane of the laminations, Fig. 8d. Similar structures have been observed in scales formed at lower temperatures, but in general the layer widths and oxide grain size are too small to make observation possible. The columnar grains are continuous over many laminations, indicating that when the oxide layered renucleation of oxide crystals was not necessary. In fact, in only rare instances in the several hundred specimens examined, has a structure been observed in which new oxide grains appear to have nucleated beneath a pore.

Several series of specimens were oxidized for various lengths of time at specific temperatures and oxygen pressures. Photomicrographs of one such series oxidized at 720°C in oxygen at 760 Torr for times of 13, 28, 68, and 100 min are shown in Fig. 8 (a-d), and the associated weight gain curve in Fig. 1. The scale is black during the period of the first parabola and in cross section appears compact, Fig. 8a. Deviation from the parabola is accompanied by the appearance of

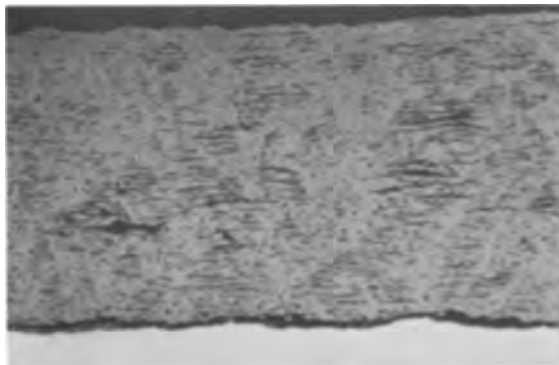


Fig. 7. Cross section of specimen oxidized at 750 Torr, 600°C for 120 min, showing chevron markings superimposed on the laminations. Magnification 100X.

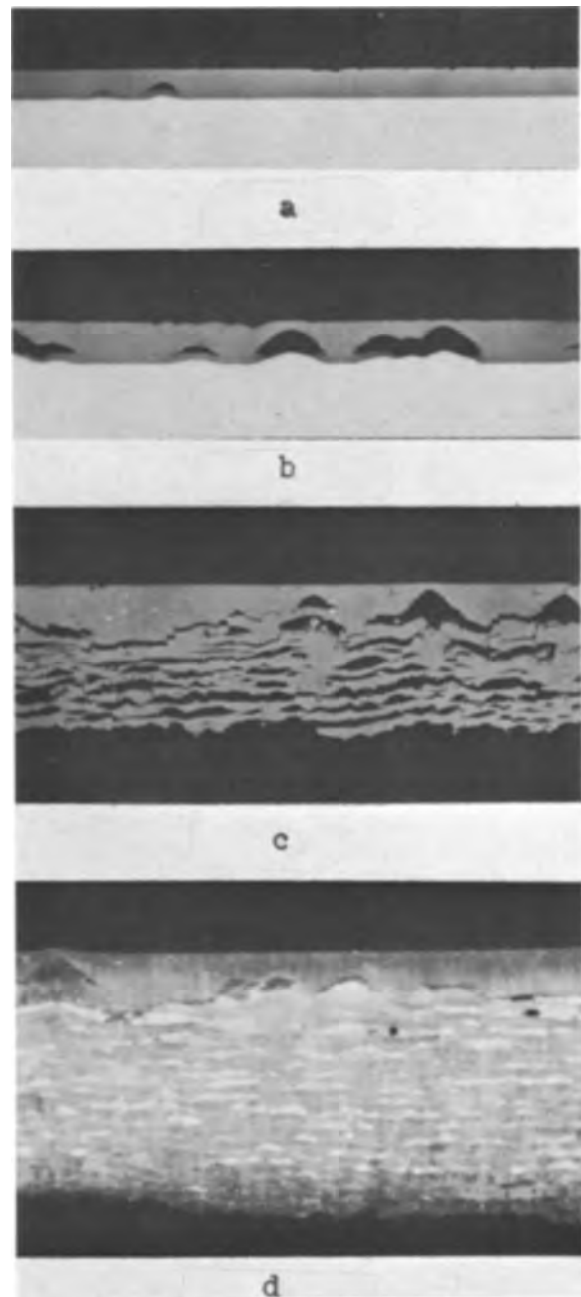


Fig. 8. Cross sections of specimens oxidized at 720°C 760 Torr: a, 13 min; b, 28 min; c, 68 min; d, 100 min. Polarized light. Magnifications 75X.

yellow blisters on the scale, which in cross section are seen to be regions where the scale has become detached from the metal and reacted with oxygen to become stoichiometric, Fig. 8b. It is to be noted that the pores act as barriers to further oxidation, and that until the oxide cracks between the blisters a second layer does not form. Growth of the new coherent layer continues until it in turn blisters, and the cycle repeats. The first two of three layers often form sufficiently in phase to be evident in the kinetic curves. Later, all traces of unevenness are lost and the reaction rate is linear.

Other series reacted at lower temperatures showed similar relationships between the morphology of the reaction product and the associated weight gain curve. However, below 600°C the shortness of the period of initial nonlinear behavior, combined with the uncertainties introduced by the technique of starting the reaction and overheating of the specimen when first introduced to oxygen, prevents quantitative analysis

of either the volumetric or the metallographic measurements.

**Analysis.**—Because of the correlation between the morphology of the oxide scale with the variations in the weight-gain curve it is proposed that this oxidation reaction is an excellent example of the class of oxidation reactions known as “paralinear.” The layered oxide scale emanates from the growth of the oxide to a critical thickness, cracking, and regrowth. Throughout this cycle the rate of reaction is controlled by diffusion across the layer of oxide that is in the process of growing.

The columnar grain structure of the layered oxide indicates that there is no pause in the oxidation reaction associated with the nucleation of new oxide layers. On the other hand, the layer of oxide in contact with the metal phase was not observed to be significantly thicker than the other layers, though cooling cracks make this observation less certain. It follows that the linear oxidation rate  $Kl_o$  should be related by the mean layer width  $W_c$  to the underlying parabolic rate constant  $Kp$  for the reaction (12), according to the equation

$$Kp = Kl_o \times W_c$$

This parabolic rate constant should have the same value as that of the parabolic oxidation at the start of the reaction as measured either by the volumetric apparatus ( $Kp_v$ ) or metallographically. Furthermore, even though the local linear rate constants  $Kl_o$  and lamination thicknesses as determined metallographically can vary from point to point on a specimen, the parabolic rate constant derived using the equation above should have the same value.

Measurements of the width of laminations in the niobium pentoxide scale were made at several points on all specimens. It must be emphasized that particularly at the lower temperatures the scale layers are not clearly defined making it extremely difficult to measure  $W_c$  with any accuracy. Determinations from the specimen shown in Fig. 6 are given in Table I where it can be seen that the derived parabolic rate constants tend to increase as the local linear rate constant increases. The higher values are associated with the curved regions of the specimen and could have been caused by two effects. First, the scale could have cracked closer to the metal at these points, and second, measurements made at 750°C showed that the parabolic rate constant of oxidation on a convex metal surface could be enhanced 30% above that on a flat surface. Apart from sites of more extreme edge oxidation, values of  $Kp$  derived from metallographic measurements taken from around a specimen generally agreed to within 30% of a mean value. The derived parabolic rate constants of all the specimens reacted at 360 Torr as a function of  $(1/T^\circ K)$  are shown in Fig. 4. Two lines can be drawn on this plot, the high-temperature line corresponding to specimens with layers of NbO, and the low-temperature line to specimens with platelets. The data points at about 610°C, between the two lines, were obtained from specimens in which platelets formed initially, and only later in the reaction did a layer of NbO stabilize. In

certain specimens this dual oxidation behavior persisted to the end of the run, Fig. 5, and values of  $Kp$  could be taken corresponding to the two extremes.

### Discussion

From the morphological and kinetic evidence presented the oxidation behavior of niobium in the temperature range 450°–820°C and pressure range 1–760 Torr agrees both qualitatively and quantitatively with a “repeated-parabolic” or “paralinear” scaling model. Differences in scaling behavior as the temperature is lowered are to a large extent caused by a decreased plasticity of the oxide. Above about 750°C the oxide does not layer, and consequently the over-all reaction rate is essentially parabolic (6). At an oxygen pressure of 380 Torr at 720°C the oxide grows protectively to a thickness of about 40 $\mu$ , and as the temperature is lowered to 625°C the protective thickness is reduced to about 13 $\mu$ . Below 600°C, the initial oxide grows to a thickness of only a few microns before failing, possibly because the platelets promote cracking. During this period of oxidation the niobium pentoxide scale layer is growing by a mechanism in which oxygen is the predominate diffusing species. This is evidenced by the sustained appearance of polishing defects from the initial preparation on the free oxide surface. Calculations show that in this phase of the reaction less than 5% of the weight gain of a specimen is associated with oxygen solution in the metal phase and the formation of sub or lower oxides. This value decreases as the reaction proceeds.

After the onset of scale layering the reaction rate is observed to be essentially linear. The excellent agreement between the measured and calculated parabolic rate constants above 625°C, Fig. 4, confirms that the rate of oxidation under these conditions is controlled by the transport properties of the layer of oxide in contact with the metal phase. That is, the linear rate of oxidation is not due to phase boundary control, but is the result of a repeated parabolic process. Below 625°C, such direct confirmation of the oxidation mechanism is not available. However, the correlation of the metallographic observations with inflections in the rate curve, and the analysis of the enhanced oxidation at specimen corners strongly supports the continued operation of a paralinear mechanism. There are no values in the literature with which these calculated parabolic rate constants can be directly compared, although they appear to be approximately one order of magnitude faster than those of Gulbransen and Andrew (13). It is noted that below 625°C the oxides NbO and NbO<sub>2</sub> are not present at the metal oxide interface as required in their description of the oxidation reaction by Cox and Johnston (8), by Inouye (14), and by Blackburn (15).

The initial parabolic rate constants are known to be sensitive to the oxidizing pressure (6). Further, it has been observed both in this study and that of Kofstad and Kjøllesdal (16), that the thickness of scale laminations tends to increase as the oxidation pressure is reduced. Hence the variation of both the linear rate of reaction and the calculated parabolic rate is considered to emanate from these causes and not as a result of phase boundary control.

At temperatures below 550°C, at some time well after breakway, the rates of reaction tend to change slowly to lower values. For example, in Fig. 2B, the rate of reaction of a specimen reacted at 520°C at 380 Torr after 120 min has fallen to 0.6 that of the rate at 20 min. This behavior has been reported previously (7), and was considered to be due to a thickening of the barrier film. This could occur in two ways; the average lamination thickness  $W_c$  could increase, or the lamination thickness could remain constant but the point at which a new lamination forms could move further from the metal-oxide interface. Examination of oxidized specimens showed no evidence of a change in lamination width greater than 0.85, whereas a change of 0.6 is required for the first mechanism. The

Table I. Scale measurements on a specimen oxidized at 575°C at an oxygen pressure of 380 Torr for 32.5 min. Linear reaction rate as determined volumetrically,  $Kl_v$ ,  $5.16 \times 10^{-6}$  g.cm<sup>2</sup>/sec

No. of layers	Layer thickness $W_c$ , $\mu$	Local linear rate of oxidation, $Kl$ g/cm <sup>2</sup> /sec	Parabolic rate constant $Kp = Kl \times W_c \times 1.56$ g <sup>2</sup> /cm <sup>4</sup> /sec
19	2.4	$3.6 \times 10^{-9}$	$1.4 \times 10^{-8}$
25	2.2	$4.4 \times 10^{-9}$	$1.5 \times 10^{-8}$
30	2.2	$5.2 \times 10^{-9}$	$1.7 \times 10^{-8}$
34	2.1	$5.8 \times 10^{-9}$	$1.9 \times 10^{-8}$
43	1.9	$6.7 \times 10^{-9}$	$2.0 \times 10^{-8}$
50	1.9	$7.4 \times 10^{-9}$	$2.2 \times 10^{-8}$
63	1.7	$8.3 \times 10^{-9}$	$2.2 \times 10^{-8}$
111	1.8	$1 \times 10^{-8}$	$4.4 \times 10^{-8}$

second mechanism requires the lamination of oxide adjacent to the specimen to be up to 1.3 times thicker than the average. However, the laminated structure is not sufficiently well defined, particularly near the metal-oxide interface where cooling effects are most disruptive, for such a judgment to be made. An alternative mechanism is proposed by Cox and Johnston (8) to explain this reduction in rate, in which the reaction is partially stifled by restriction of the gas flow due to the growth of the porous outer scale. In growing the porous structure is altered so that the restriction the scale presents to the gas attains a limiting value. Subsequent oxidation would then obey a linear rate law and show an almost linear dependence of the rate on gas pressure. A central feature of their arguments is that the pressure sensitivity of the reaction is a consequence of the porous plug character of the scale, and not due to subsequent phase boundary or transport steps. However, it can be seen in Fig. 2, that oxidation is pressure sensitive from the start of reaction, that is before a porous plug has been formed. Hence it is considered that resistance to oxidation caused by the detached scale laminations is only of secondary importance.

One of the most prominent characteristics of the oxidation behavior of niobium is the decrease in reaction rate of specimens as the temperature is increased from 600°-625°C. This behavior is most evident in the values of the derived parabolic rate constant, where association with the lower temperature line correlates with platelets in the specimen, and association with the high-temperature line correlates with NbO (and probably NbO<sub>2</sub>) at the metal-oxide interface. The platelet phase has been considered in some detail by Cox and Sheasby (17), concluding that the platelets are a metastable phase, and that they form during reaction and not while the specimen is being cooled to room temperature. These conclusions are based on the following arguments.

1. Norman, Kofstad, and Krudtaa (18) noted that platelets only form from supersaturated solutions of oxygen in niobium, and they could not prepare an oxide with the same structure as the platelets by melting together the appropriate quantities of metal and pentoxide.

2. On certain specimens reacted just above 600°C it is possible for platelets to form at one point on a specimen and for layers of NbO and NbO<sub>2</sub> to form at another. The niobium pentoxide scale formed above the platelet phase is always much thicker than that formed above the layers of lower oxides. Typical microhardness traces beneath two such regions are shown in Fig. 9. Theoretical diffusion gradients were

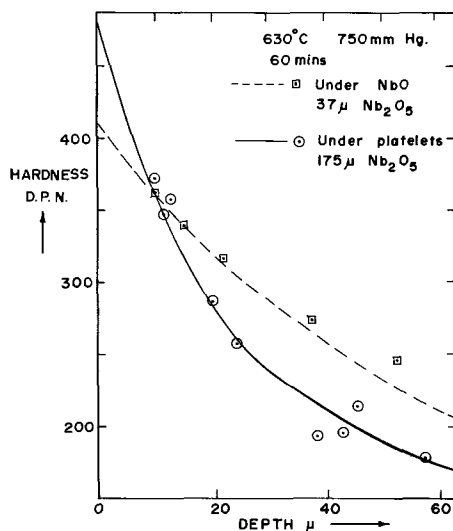


Fig. 9. Microhardness gradients under two different regions of the same specimen.

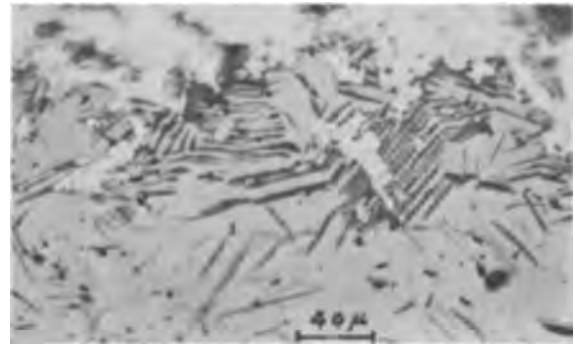


Fig. 10. Taper section of niobium oxidized at 600°C at an oxygen pressure of 750 Torr for 60 min, showing a band of platelets in the metal phase; taper ratio approx. 10:1. Magnification 250X.

calculated assuming a linear rate of interface motion, varying only the hardness value corresponding to the oxygen concentration at the metal-oxide interface to optimize the fit to the experimental points. As NbO is the stable phase, the hardness of the metal in contact with it, i.e., at zero depth on the broken curve, corresponds to the equilibrium level of saturation of oxygen in niobium. The hardness value under the platelet phase extrapolates to a higher hardness value at the surface, indicating that the metal is supersaturated with oxygen in this region. As platelets are only found within the supersaturated zone they are a metastable phase.

3. Platelets have never been observed beneath a continuous layer of NbO.

4. If platelets are present at the end of oxidation, traces of their previous existence in the metal, as described by Stringer (11) for oxidized tantalum, are observable in the layered niobium-pentoxide. Further, particularly in taper sections, it often appears that the center of single platelets has been consumed by the advancing metal-oxide interface, Fig. 10. It is improbable that platelets nucleating independently during cooling would so often lineup with each other on either side of a region of pentoxide.

The presence of platelets in the reaction zone can therefore be taken as evidence that the metal is supersaturated with oxygen with respect to NbO, the next stable phase on the equilibrium diagram. It follows that in these circumstances the niobium-pentoxide adjacent to the metal phase will be supersaturated with niobium. The oxidation rate has been shown to be controlled by the diffusional properties of the niobium-pentoxide layer in contact with the metal phase. Hence it is proposed that the increase in oxidation rate observed above the platelet phase is due to the enhanced oxygen concentration gradient present in the niobium-pentoxide under these conditions.

#### Acknowledgments

The author is grateful to Mr. E. Kohn for his assistance with the experimental work. The research was supported by the National Research Council of Canada and The University of Western Ontario.

Manuscript received Feb. 16, 1968.

Any discussion of this paper will appear in a Discussion Section to be published in the June 1969 JOURNAL.

#### REFERENCES

1. A. U. Seybolt, *Advances in Physics*, **12**, 1 (1963).
2. T. Hurlen, *J. Inst. Metals*, **89**, 273 (1960-61).
3. T. L. Kolski, *Trans. ASM*, **55**, 119 (1962).
4. C. H. McLintock and J. Stringer, *J. Less Common Metals*, **2**, 233 (1960).
5. D. W. Bridges and W. M. Fassell, *This Journal*, **103**, 326 (1956).
6. J. S. Sheasby, G. R. Wallwork and W. W. Smeltzer, *ibid.*, **113**, 1225 (1966).

7. D. W. Aylmore, S. J. Gregg, and W. B. Jepson, *ibid.*, **107**, 495 (1960).
8. B. Cox and T. Johnston, *Trans. Met. Soc. AIME*, **227**, 36 (1963).
9. N. Terao, *Japan, J. Appl. Physics*, **2**, 156 (1963).
10. N. Norman, *J. Less Common Metals*, **4**, 52 (1962).
11. J. Stringer, *ibid.*, **11**, 111 (1966).
12. J. Stringer, *Met. Rev.*, **11**, 113 (1966).
13. E. A. Gulbransen and K. F. Andrew, *This Journal*, **105**, 4 (1955).
14. H. Inouye, "Columbium Metallurgy," p. 649, Metals Society, AIME, Conf. 1960.
15. P. E. Blackburn, *This Journal*, **109**, 1142 (1962).
16. P. Kofstad and H. Kjollesdal, *Trans. Met. Soc. AIME*, **221**, 285 (1961).
17. G. W. Cox, Ph.D. Thesis, University of N.S.W. (1963).
18. N. Norman, P. Kofstad, and O. J. Krudtaa, *J. Less Common Metals*, **4**, 124 (1962).

## Insulator-Induced Conduction

Jerry M. Cantril and H. A. Pohl\*

*Department of Physics, Oklahoma State University, Stillwater, Oklahoma*

### ABSTRACT

The presence of insulating particles, even those of higher resistivity than the liquid, was found to increase electrical conduction in several dielectrical liquids. We believe this to be a general effect which will occur if the particles have a higher dielectric constant than the liquid. In particular, we observed in several highly purified liquids (C Cl<sub>4</sub> and toluene) that the current conducted across a cylindrical electrode system was considerably enhanced when highly purified solids (*e.g.*, polyvinyl chloride, quartz, or sulfur) were held against the smaller inner electrode by dielectrophoretic force. A theory for the effect is given. It emphasizes the effect of local field concentration (field-focussing) by the particles. This "focussing" of the field in the liquid acts to enhance carrier concentration and conduction since the conduction is in the nonohmic space-charge-limited regime.

Solid particles with a dielectric polarization higher than that of the surrounding liquid medium are pulled dielectrophoretically into regions of highest field strength. This effect has been used to accomplish separations of solid particles in nonuniform electric fields (1-4). The present study has sought to inquire experimentally as to what effect the deposition of solid material might have on electrical conduction through the liquid.

The effects of particles on electrical conduction processes in liquids are as yet incompletely known. Conductive particles such as iron or wet particles such as moist clay are known to play an important role in dielectric breakdown of liquids (6, 7). The role of insulating material particles in conduction in dielectric liquids is less well known, especially at voltages well below breakdown values. Electrophoretic phenomena involving the charging of particles and their subsequent discharge after migration to an electrode are well recognized (6, 7). Kok (6) has expressed the opinion that particles, themselves of an insulating nature, have a negligible effect on current flow in liquid dielectrics and that their effect would be indistinguishable from the background ionic current. Pohl and Schwar (3) have suggested that rotational Brownian motion of suspended particles may enhance current flow by rotationally transporting deposited ions from the medium on the surface of the particles. The effect on conduction due to insulating particles resting at an electrode has not been studied. In the case of purely ohmic conduction one would expect the presence of particles of lower conductivity than the liquid to block current flow. Yet the earlier experiments of Pohl and Schwar had indicated that the opposite might occur, and that the presence of insulating particles could enhance current flow in dielectric liquids. The present work was undertaken to examine more quantitatively the experimental facts and to derive a theoretical understanding of them.

A somewhat distantly related phenomenon is known to occur in glow discharge tubes. When the cathode is entirely covered with a thin film of insulating material

(5) a current increase is observed. The explanation proposed was that a positive space charge was formed either inside or at the surface of the insulating material, the positive charge being supplied by positive ions from the gas plasma in the tube. The resultant high field in the insulating layer pulled electrons through it, some of which are emitted with high velocity into the conducting gas. This effect, as we shall see, is different in an essential way from that which we shall discuss for particles. The particles produce a three-dimensional perturbation in the electric field, the film produces only a one-dimensional one, and different mechanisms are called into play.

The present experiments were conducted with particles held to an electrode in a nonuniform field by the action of dielectrophoretic force. Great care was taken with regard to purity of the liquids and the suspended particles. A combination of exhaustive recycled sorption and electrical de-ionization was used in a sealed test cell to achieve very high purity and a high degree of reproducibility. The experiments, broadly speaking, were done using a slightly modified form of dielectrophoretic technique with cylindrical geometry (1-4). Polyvinyl chloride (PVC), sulfur, and silicon dioxide were used as solids, carbon tetrachloride and carbon tetrachloride-toluene mixtures were used as liquids.

### Experimental

*Test system.*—A schematic diagram of the test system is shown in Fig. 1. The cell was designed so that the purification system was integral with it. The purification system comprised two parts; a sorption bed of 6-12 mesh silica gel in the lefthand chamber of the Pyrex glass cell, and a set of three concentric cylindrical stainless steel electrodes in the righthand chamber. The latter electrodes were connected as shown to a 45v battery. The central chamber served as the test chamber. The sintered glass filter beneath the central test chamber had a maximum pore size of 40-60 $\mu$ , while that under the sorption bed had a maximum pore size of 170-200 $\mu$ . The whole cell was 21.6 cm high and 14.0 cm wide. The chambers were constructed of

\* Electrochemical Society Active Member.

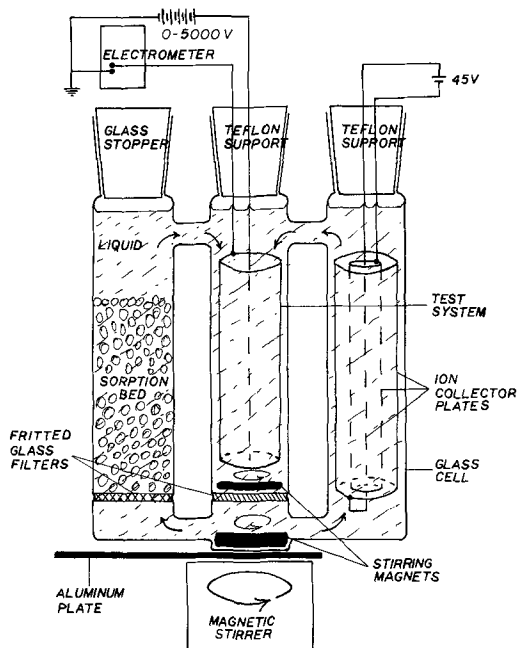


Fig. 1. Schematic diagram of test cell and circuits

35 mm Pyrex glass tubing. The distance from the tops of the filters to the bottoms of the upper two sidearms was 14 cm. Two stirring magnets whose function will be described below sat in the cell. The lower magnet was Teflon encased and was 0.64 cm by 1.92 cm overall. The magnet in the central chamber was Pyrex glass encased and was 0.41 cm by 2.44 cm over-all.

The cell was mounted in a 20 x 44 x 8 cm aluminum box. The box, to complete its shielding function, was fitted with a brass screen door and grounded. The box with its cell enclosed sat in a clear plastic envelope through which passed dry nitrogen to provide a dry inert atmosphere. This assembly was mounted on a magnetic stirrer drive. An aluminum plate was inserted between the stirrer drive and the box to aid dissipation of the heat generated by the stirrer motor. Electrical leads ran from the test cell, through the box wall and the plastic envelope to the test circuit. The entire assembly and test circuit sat in a second shielding cage. The 45v battery was mounted inside the inner shielding box as shown.

The test electrode assembly is shown diagrammatically in Fig. 2. The outer electrode consisted of 2.16 cm ID Pyrex glass tubing provided with an inside transparent conductive tin oxide coating, using the technique of Gomer (8). The stainless steel electrode (which here was never used separately) had an outside diameter of 1.98 cm and an ID of 1.82 cm. The center wire electrode was 22 B. & S. gauge platinum wire, of 0.644 mm diameter. The hollow bolt shaft and nut assembly was used to apply tension to the center wire. The holes and slots in the Teflon spacers allowed the liquid to circulate through the test region during purification.

The test voltages were provided by a bank of Burgess U 320 batteries (nominally 510v each) whose voltages were measured before and after each run with an Aryton Mather Static voltmeter. The current was measured with a Kieithley 610B electrometer. The whole system sat in an electrical cage for shielding and operator safety. The box, cage, and the low side of the electrometer were all at a common ground potential.

**Materials and procedures.**—The solids used were purified PVC, sulfur, and silicon dioxide (quartz). The liquid used for the PVC tests was a mixture of 5.5 to 3 volume ratio of carbon tetrachloride and toluene, chosen to have a density slightly less than that of the powder. Pure carbon tetrachloride alone

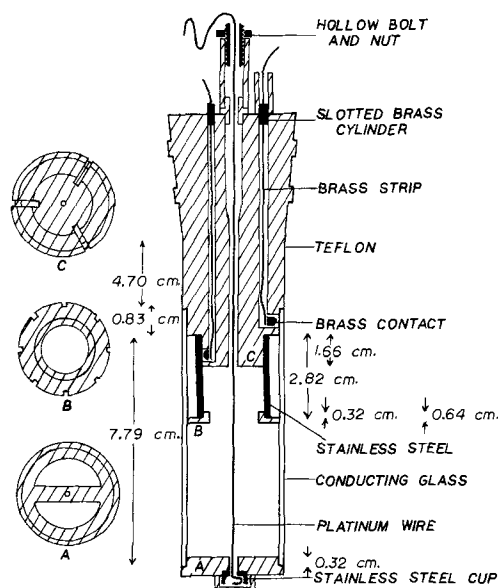


Fig. 2. Cross section of test electrode system with views of spacers showing slots and holes for circulation of liquid.

was used for the tests with sulfur and silicon dioxide. The liquid samples used were at least of reagent grade purity. They were stored over solid anhydrous silica gel in a dry box when not in use. The powder samples were stored and dried as a thin layer over anhydrous calcium sulfate for at least one week before use.

The PVC sample, obtained from Bordon Chemical Company, was partially purified by extracting for 12 hr with distilled water to remove impurity salts, then by extracting with reagent grade  $\text{CCl}_4$  for another 12 hr to remove organic impurities. The powder was then dried and sieved to pass 80 mesh screen and stop on 100 mesh screen, then stored in the desiccator. The silicon dioxide was first washed with concentrated HCl, then repeatedly with distilled water, then cp acetone, dried, ground, sized to 80-100 mesh range, and stored dry.

Sulfur was recrystallized 3 times from reagent grade  $\text{CS}_2$ , dried, sized to 80-100 mesh range, and stored dry.

The test cell was loaded by putting the powder sample into the center chamber of the cell, then filling the cell with the desired liquid. After loading and mounting the cell, the lower magnetic stirrer was caused to spin and pump the liquid through the purification loops and test cell. The liquid portion passing through the sorption bed was chemically cleaned. The liquid portion through the ion collector plates was electrically purified by the plating out of the residual ions, in a manner suggested by Streier (9).

Purity was tested periodically by observing the current flow at 300v. The upper (glass-encased) magnet could be selectively activated to follow the larger lower one by running the stirrer drive at low speed. When the desired optimum of purity had been achieved, the liquid was electrically "conditioned" by applying the total voltage of the battery bank across the test system until the current had decreased to an essentially steady value. After conditioning the liquid, a current versus voltage curve was taken while decreasing the voltage in steps. The full voltage was then reapplied and the original curve either rechecked or the powder was caused to be stirred up into the central test chamber by activating the upper stirrer bar. When the powder sample had been pulled dielectrophoretically to the center electrode, another current-voltage curve was taken while again decreasing the voltage in steps as before. On shunting the electrodes, the powder would fall from the center wire allowing the test to be repeated. All results re-

ported here are with the center wire serving as the anode.

Current-voltage readings were taken in the following way. After the attainment of "steady-state" conditions at full voltage as described above, the voltage was decreased in steps by switching out batteries. As each battery was removed and the (reduced) voltage re-applied an initial current peak of temporary nature was observed. Typically a new steady state was reached in 1 hr at each voltage, and the data recorded. The temporary current surge was typically two to four times the final steady-state readings. The instrument error was such as to give a precision of  $\pm 1.2 \times 10^{-13}$  amp.

### Results

A typical set of results is shown in Fig. 3 for a 0.110g sample of 80-100 mesh PVC. After the current-voltage curve for the liquid alone was taken, a second current reading at the highest voltage closely checked the first. (Note the slightly higher circled point at near 5000v.) The powder sample was then stirred up into the test region and allowed to collect at the center wire, then a current-voltage curve obtained with the powder in place on the center electrode. Finally the cell was discharged by shunting, the powder allowed to fall back to the base of the central cell out of the field, full voltage reappplied, and a current reading taken (blacked in circular point near 5000v) on the liquid alone. This reading was typically slightly higher than before on the pure liquid but much lower than with the powder present at the electrode surface. A last point was taken (blacked-in triangle) with the powder again at the electrode surface, completing the proof that the presence of the insulating particles on the electrode did indeed enhance current flow. Closely similar results were obtained in numerous other runs with PVC, sulfur, and  $\text{SiO}_2$ .

The sheath formed at the center wire was observed with a 10 x travelling microscope and had the appearance of villous streamers formed by the powder granules. There was a relatively even vertical distribution of adherence. The maximum sheath diameter was about four times the central wire diameter. The streamers, or "pearl chains" as they have been called arise because of the intensification of the field in the neighborhood of each particle and the resultant dielectrophoretic force between particles along the field lines.

### Discussion

The observed enhancement of current flow caused by the presence of insulating particles cannot be accounted for by the simple argument that the central electrode is just bigger. For an ohmic system the resistance,  $R$ , of a cell with cylindrical electrodes (neg-

lecting end effects) is

$$R = \frac{\rho}{2\pi L} \ln (r_2/r_1)$$

where  $\rho$  is the specific resistivity of the liquid,  $L$  is the cell length, and  $r_2$  and  $r_1$  are the radii of the outer and inner conductors. The current was increased by a factor of about 3 over most of the voltage range when particles were present. To account for such a large factor by enlargement of the central electrode (as if by a conductive layer!) would require the effective diameter of the central electrode to be increased by 10.5 fold. The powders examined were, however, not conductive, but were insulators of a specific resistivity as high as or higher than that of the liquid, and present in a layer such as to be only fourfold greater in diameter than the central wire. Clearly electrode "enlargement" in the simple ohmic sense cannot account for the observed effect.

We suggest instead that the current enhancement by the particles is due to field intensification at their boundaries. In all cases considered here, the particles are of higher dielectric constant than the liquid medium. The particles are pulled dielectrophoretically into the regions of highest field intensity where they tend locally to intensify the field even further. If, for example, the charge carriers originate in the liquid itself by field dissociation (whether of trace impurities or of solvent molecules) then the field enhancement due to the presence of the particles will increase the charge carrier production and, hence, the current (see Fig. 4).

In the following we will find it more convenient to speak of the conductance of the system instead of the total current. Figure 5 shows the conductances of

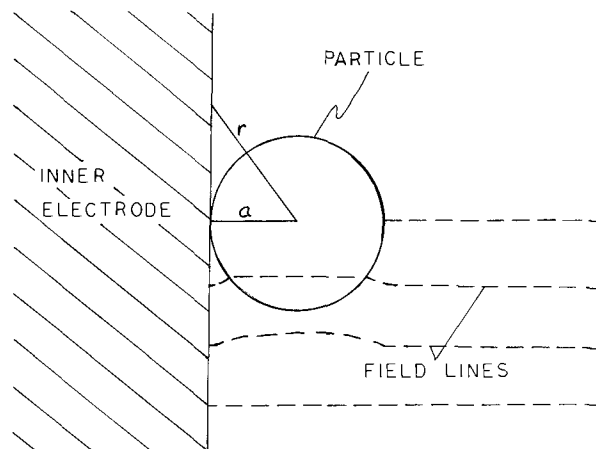


Fig. 4. Sketch of particle at center electrode showing field intensification.

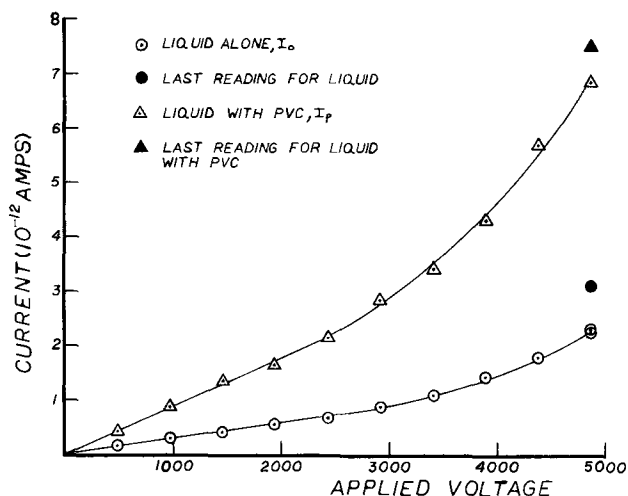


Fig. 3. Current vs. voltage curves for liquid alone and liquid with 80-100 mesh size PVC.

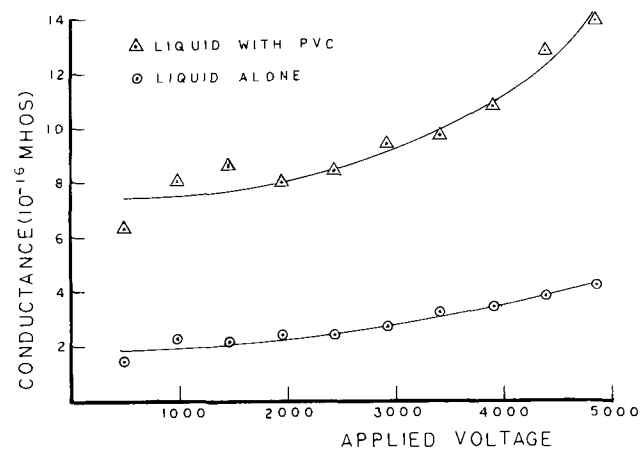


Fig. 5. Conductance vs. voltage for liquid alone,  $\odot$ ; and that for liquid with 80-100 mesh size PVC,  $\triangle$ .



the system for the 80-100 mesh size PVC run. It is seen that the conductances in both cases are strongly dependent on the applied voltage. To account for the conduction increase we assume a reasonable functional dependence of the conductance of the liquid on the electric field. We then calculate a field enhancement parameter for the case of particles being present. We assume the conductivity  $\sigma_o$  is composed of two terms, a constant term  $\sigma_{oc}$  and a field dependent term  $\sigma(\vec{E})$  where  $\vec{E}$  is the electric field.  $\sigma_{oc}$  may be interpreted as the residual conductivity resulting from impurities and background radiation and/or cosmic radiation. The functional form of  $\sigma(\vec{E})$  is derived by assuming that the energy stored in the field over a distance  $l_o$  aids in the ionization of charge carriers. The conductivity may be written as

$$\sigma(\vec{E}) = qn\mu$$

where  $n$  is the concentration of carriers,  $q$  is the charge of the carrier, and  $\mu$  is the mobility of the carrier in the medium. The field energy over the distance  $l_o$  affecting carrier birth is

$$E = ql_o|\vec{E}|$$

We can now write  $n$  as

$$n = n_o \exp\left(\frac{ql_o|\vec{E}|}{2kT}\right)$$

where  $k$  is Boltzmann's constant and  $T$  is the absolute temperature. The field dependent conductivity can then be written

$$\sigma(\vec{E}) = \sigma_{oo} \exp\left(\frac{ql_o|\vec{E}|}{2kT}\right) \quad [1]$$

where

$$\sigma_{oo} = q\mu n_o$$

We are interested in the region around the center electrode since this is where the particles are deposited and cause the greatest field distortions. In the case of liquid only being in the system, the electric field at the center electrode is

$$\mathcal{E}_o = |\vec{E}| = \frac{V}{r_1 \ln(r_2/r_1)}$$

where  $V$  is the total applied voltage,  $r_1$  is the radius, and  $r_2$  is the inner radius of the outer electrode. Equation [1] may now be written as

$$\sigma(\vec{E}) = \sigma_{oo} \epsilon_o \exp(\alpha_o V)$$

where

$$\alpha_o = \frac{ql_o}{2kT} \frac{1}{r_1 \ln(r_2/r_1)}$$

The total conductivity may now be written as

$$\sigma_o = \sigma_{oc} + \sigma_{oo} \exp(\alpha_o V) \quad [2]$$

The current density is

$$|\vec{j}_o| = \sigma|\vec{E}| = \sigma_{oc}\mathcal{E}_o + \sigma_{oo}\mathcal{E}_o \exp(\alpha_o V)$$

Integrating over the surface area  $S$  of the center electrode we have for the total current

$$\begin{aligned} I_o &= \int_s j_o dS \\ &= \int_s \sigma_{oc}\mathcal{E}_o dS + \int_s \sigma_{oo}\mathcal{E}_o \exp(\alpha_o V) dS \\ &= \sigma_{oc}\mathcal{E}_o S + \sigma_{oo}\mathcal{E}_o \exp(\alpha_o V) S \end{aligned} \quad [3]$$

since  $\sigma_{oc}$ ,  $\epsilon_o$ ,  $\alpha_o$ ,  $V$  and  $\sigma_{oo}$  are constant over the surface. For the conductance  $G_o$  of the system we may now write

$$\begin{aligned} G_o &= I_o/V \\ &= \frac{\sigma_{oc}\mathcal{E}_o S}{V} + \frac{\sigma_{oo}\mathcal{E}_o}{V} \exp(\alpha_o V) S \\ &= G_{oc} + G_{oo} \exp(\alpha_o V) \end{aligned} \quad [4]$$

For the case of particles being present the expression for the total current is similar to [3]

$$I_p = \int_s \sigma_{oc}\mathcal{E}_p dS + \int_s \sigma_{oo}\mathcal{E}_p \exp\left(\frac{ql_o\mathcal{E}_p}{2kT}\right) dS$$

where  $\mathcal{E}_p$  is the electric field at the surface of the center electrode when particles are present. For purposes of convenience we rewrite  $I_p$  as

$$\begin{aligned} I_p &= \sigma_{oc}\mathcal{E}_o \int_s \frac{\mathcal{E}_p}{\mathcal{E}_o} dS + \sigma_{oo}\mathcal{E}_o \int_s \frac{\mathcal{E}_p}{\mathcal{E}_o} \exp\left(\frac{ql_o\mathcal{E}_o}{2kT} \frac{\mathcal{E}_p}{\mathcal{E}_o}\right) dS \\ &= \sigma_{oc}\mathcal{E}_o \int_s \frac{\mathcal{E}_p}{\mathcal{E}_o} dS + \sigma_{oo}\mathcal{E}_o \int_s \frac{\mathcal{E}_p}{\mathcal{E}_o} \exp\left(\alpha_o \frac{\mathcal{E}_p}{\mathcal{E}_o} V\right) dS \end{aligned}$$

where the definitions  $\sigma_{oc}$ ,  $\sigma_{oo}$ ,  $\mathcal{E}_o$ , and  $\alpha_o$  are as before. The conductance of system when particles are present may now be written as

$$\begin{aligned} G_p &= I_p/V \\ &= \frac{\sigma_{oc}\mathcal{E}_o}{V} \int_s \frac{\mathcal{E}_p}{\mathcal{E}_o} dS + \frac{\sigma_{oo}\mathcal{E}_o}{V} \int_s \frac{\mathcal{E}_p}{\mathcal{E}_o} \exp\left(\alpha_o \frac{\mathcal{E}_p}{\mathcal{E}_o} V\right) dS \\ &= G_{pc} + G_{op} \exp(\alpha_p V) \end{aligned} \quad [5]$$

$G_{pc}$ ,  $G_{op}$ , and  $\alpha_p$  are the parameters of the conductance curve when particles are present and may be obtained from the data. The conduction enhancement is characterized by the difference between  $\alpha_o$  and  $\alpha_p$ . We now calculate  $\alpha_p$  knowing  $\alpha_o$ ,  $G_{oo}$ , and  $G_{op}$  and compare this value with the experimental value. Using the second terms on the right-hand sides of Eq. [4] and [5]

$$\alpha_p = \ln \left[ \frac{G_{oo} \int_s \frac{\mathcal{E}_p}{\mathcal{E}_o} \exp\left(\alpha_o \frac{\mathcal{E}_p}{\mathcal{E}_o} V\right) dS}{G_{op} S} \right] \quad [6]$$

For simplicity we now assume an even distribution of identical particles over the surface of the electrode. The surface averaged factor in [6] may then be calculated over an effective area for one particle instead of over the whole electrode surface. The problem remaining is to determine  $\mathcal{E}_p/\mathcal{E}_o$  and the surface of integration. We assumed the solution of the well-known problem of the dielectric sphere in a homogeneous field. For the surface of integration we chose a plane tangent to the sphere and to the electrode surface as shown in Fig. 4. Using these assumptions,  $\mathcal{E}_p/\mathcal{E}_o$  over the surface can be shown to be

$$\begin{aligned} \mathcal{E}_p/\mathcal{E}_o &= \left\{ 1 + 2 \left( \frac{\epsilon_2 - \epsilon_1}{\epsilon_2 + 2\epsilon_1} \right) \left( \frac{a}{r} \right)^3 \left[ 3 \left( \frac{a}{r} \right)^2 - 1 \right] \right. \\ &\quad \left. + \left( \frac{\epsilon_2 - \epsilon_1}{\epsilon_2 + 2\epsilon_1} \right) \left( \frac{a}{r} \right)^6 \left[ 3 \left( \frac{a}{r} \right)^6 + 1 \right] \right\}^{1/2} \end{aligned}$$

where  $\epsilon_2$  and  $\epsilon_1$  are the dielectric constants of the solid and liquid, respectively,  $a$  is the radius of the particle, and  $r$  is the distance from the center of the sphere to a point on the plane.

The calculation for  $\alpha_p$  was carried out for the 80-100 mesh size PVC for a voltage of 5000v. The average particle diameter was taken to be 0.0163 cm, the relative dielectric constants of the liquid and solid to be 2.29 and 12.0, respectively,  $G_{oo}$  to be  $1.19 \times 10^{-16}$  mhos,  $\alpha_o$  to be  $2.91 \times 10^{-4}/v^{-1}$ , and  $G_{cp}$  to be  $3.66 \times 10^{-17}$  mhos. The integration was carried out over a circular area whose radius was twice the radius of the sphere.

With this, it was then possible to obtain the desired result, i.e., an *a priori* evaluation of  $\alpha_p$  by use of Eq. [6].

The value of  $\alpha_p$  obtained by this *a priori* calculation was  $6.2 \times 10^{-4} \text{ volt}^{-1}$ . This value is in rather satisfactory agreement with that found experimentally ( $6.1 \times 10^{-4} \text{ volt}^{-1}$ ). In view of the simplifications used in the calculation, this consonance with experiment lends support to the theory presented. We regard



theory presented as recognizedly a first approximation in interpretation. Further work, both experimental and theoretical is called for.

#### Acknowledgment

The authors acknowledge with appreciation the support of the Research Foundation of Oklahoma State University in this research study.

Manuscript received Nov. 28, 1967; revised manuscript received March 1, 1968. This paper was presented at the Chicago Meeting, Oct. 15-19, 1967, as Abstract 152.

Any discussion of this paper will appear in a Discussion Section to be published in the June 1969 JOURNAL.

#### REFERENCES

1. H. A. Pohl, *J. Appl. Phys.*, **29**, 1182 (1958).
2. H. A. Pohl and J. P. Schwar, *J. Appl. Phys.*, **30**, 69 (1959).
3. H. A. Pohl and J. P. Schwar, *This Journal*, **107**, 383 (1960).
4. H. A. Pohl and C. E. Plymale, *ibid.*, **107**, 390 (1960).
5. A. M. Slettin, "Spray Discharge," Encyclopaedic Dictionary of Physics, Vol. 2, p. 445, Pergamon Press, New York (1961).
6. J. A. Kok, "Electrical Breakdown of Insulating Liquids," Interscience Publishers Inc., New York (1967).
7. A. H. Sharbaugh and P. K. Watson, "Conduction and Breakdown in Liquid Dielectrics," Progress in Dielectrics, **4**, J. Birks and J. Hart, Editors, p. 201, New York (1960).
8. R. Gomer, *Rev. Sci. Inst.*, **29**, 993 (1953).
9. M. P. Strier, "The Dielectric Properties of Liquids Under a Small D. C. Bias," (Paper presented to the 1962 Conference of Electrical Insulation of the National Academy of Science held at Hershey, Pa. Technical Report, Thomas A. Edison Lab., McGraw Edison Co.

## Thermodynamic Properties of Molten Mixtures of Nickel Chloride with Some Alkali Halides

Drannan C. Hamby and Allen B. Scott\*

Department of Chemistry, Oregon State University, Corvallis, Oregon

#### ABSTRACT

Thermodynamic properties including the activity coefficient and the partial molar free energy, enthalpy, and entropy of mixing have been determined for the solute  $\text{NiCl}_2$  in the solvents  $\text{KCl}$ ,  $\text{NaCl}$ ,  $\text{LiCl}$ , and 1:1  $\text{NaCl-KCl}$ . The values of the properties were established by measuring the reversible emf of cells of the type



where  $M$  represents an alkali metal cation. Cell emf's were determined over a range of concentration from approximately  $10^{-4}$  to  $4 \times 10^{-1}$  mole fraction of solute and temperatures ranging from the melting points of the solvents to  $900^\circ\text{C}$ . The experimentally determined entropy of mixing has been compared with calculated values based on several microstate models. Reference electrodes of the type



which utilized solid porcelain as a bridge, were immersed in the same melts, and allowed continuous monitoring of chlorine electrode potentials as solute concentration varied.

In a preliminary study of electrode designs the  $\text{AgCl}$  formation cell



was studied as a function of temperature. Several electrode designs were tested for both the chlorine and metal electrodes. The relationship between cell emf and temperature was found to be in agreement with that established by Senderoff and Mellors.

The electrowinning and electrofining of Ni from fused salt baths has received attention in this and other laboratories in recent years (1, 2). This interest has led, in the present case, to a study of several cells of the type



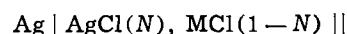
where

$$N = \frac{\text{moles solute}}{\text{moles solvent} + \text{moles solute}}$$

and  $\text{MCl}$  is  $\text{KCl}$ ,  $\text{NaCl}$ , 1:1  $\text{NaCl-KCl}$ , or  $\text{LiCl}$ , for the purpose of establishing cell potentials as a function of both temperature and solute concentration. By utilizing supplementary thermochemical data and making proper choices of standard and reference states, the cell data have been used to calculate solute activity

coefficients as well as partial molar free energies, enthalpies and entropies of mixing of  $\text{NiCl}_2$  in the various solvents. The magnitude of the latter quantity,  $\bar{S}$ , may be predicted theoretically on the basis of various microstate models, and a comparison of theoretically and experimentally derived entropies of mixing has been made.

Reference electrodes of the type

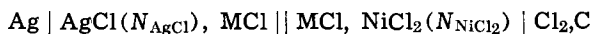


similar to those described by Lamb and Labrie (3) and by Littlewood (4) were placed in the cells described above. The solvent,  $\text{MCl}$ , was always the same on both sides of the membrane. This arrangement allowed measurement of the quantity

$$\Delta E' = E'_{\text{Ag}} - E_{\text{Ag}}$$

\* Electrochemical Society Active Member.

where  $E'_{Ag}$  and  $E_{Ag}$  are emf's for the cell



in the respective cases  $N_{NiCl_2} \neq 0$  and  $N_{NiCl_2} = 0$ . This information is useful in establishing the limits of NiCl<sub>2</sub> concentration over which one may convert potentials measured with the Ag reference electrode to potentials based on the chlorine reference electrode without correcting for junction effects.

The AgCl formation cell



which has received attention in several laboratories, was studied in a preliminary investigation of electrode designs. Of primary interest in this work was the demonstration of chlorine electrode reversibility and the effectiveness of various methods of shielding the metal electrode from direct attack by chlorine.

### Experimental

Two AgCl formation cells and six cells involving NiCl<sub>2</sub> as a solute were tested. These will be referred to as cells A and B and cells I through VI, respectively. Solvents in cells I through VI were KCl, NaCl, 1:1 molar NaCl-KCl, LiCl, LiCl, and KCl, respectively.

The outer cell envelope consisted of two parts, a closed-end Vycor tube and a Pyrex top. The Vycor tube was 64 mm in diameter, 45 cm long, and flanged at the open end; the Pyrex top, also made of 64 mm tubing, had a matching ground flange and tubular openings through which electrodes, a thermocouple, and a sampling tube could be introduced into the cell. When the cell was assembled, the glass flanges were separated by an O ring and clamped together by means of metal clamps. The various cell components, which entered through the cell top, were coupled by means of rubber tubing of appropriate sizes to the tubular openings in the Pyrex top. An inner crucible of Vycor, or Ultra Carbon Company UF-4-S graphite in the case of the AgCl formation cell, was used as the melt container.

Each cell tested utilized two chlorine electrodes, one of each design illustrated in Fig. 1. The graphite rod was 1/4 in. diameter Ultra Carbon Company grade UF-4-S. The porous parts were machined from National Carbon Company, grade 60, porous graphite. The Vycor sheath served to prevent shorting of the electrodes, provided mechanical strength, and defined the path of the Cl<sub>2</sub> into the melt. Air tightness at the top of the sheath was insured by application of a high-melting wax in the liquid state while maintaining a vacuum in the sheath. Pretreatment of the electrodes

consisted of dipping in dilute HF, rinsing, immersion in boiling dilute HCl, rinsing, and then heating to 800°C in Cl<sub>2</sub> for several hours.

Chlorine and HCl gas were Matheson Company "high purity." The gases were passed over Mg(ClO<sub>4</sub>)<sub>2</sub> before entering the cell. The gas delivery system was glass except for a few inches of rubber tubing near the cell top. Chlorine flow was measured by means of a Manostat Corporation, model M9142C flowmeter in the gas line. Gases left the cell through a sulfuric acid trap, the entry tube of which was immersed just below the surface of the acid.

Metal electrodes were 0.020 in. wire obtained from A. D. McKay and described as 99.9+ % pure. The electrodes were cleaned by abrasion with emery paper and wiping with an acetone-dampened cloth. Various designs of Vycor protection tubes for the metal electrodes are shown in Fig. 1. All of the designs were tested in the AgCl formation cell; design D was later utilized for all nickel electrodes. The capillaries were from 0.1 to 0.5 mm in diameter and about 1 cm long. The open ended tube, A, was used only in conjunction with a graphite crucible which provided a shallow well into which the lower end of the tube was received. An atmosphere of dry argon was maintained over the melt inside the Ni electrode protection tubes.

The Ag reference electrodes used in this work utilized a 1/2 in. diameter McDanel porcelain tube as a solid electrolyte. Metallic contact to the silver electrode was made by fusion to platinum inside a small-diameter alumina tube; thus, the silver-air interface was eliminated and electrode stability was improved. An inert atmosphere over the Ag reference electrodes was not found to be necessary.

The salts used in this work were:

AgCl. Mallinckrodt, reagent grade AgCl was oven dried in air and fused under chlorine in the presence of carbon.

NaCl and KCl. Reagent grade materials were further purified by passage through ion exchange columns (5). Before use the salts were vacuum desiccated, oven dried at 120°C in air for many hours, then placed in the cell and gradually heated and melted under continuous chlorine flow in the presence of carbon (6).

LiCl. Reagent grade material was used. Two methods of dehydration were attempted: (a) Cell IV. Aspirator pumping and heating under flowing argon to 400°C, followed by fusion under flowing chlorine in the presence of carbon. (b) Cell V. More extensive vacuum pretreatment consisting of approximately 24 hr at pressures from 0.2 to 0.7 mm Hg combined with intermittent purging of the cell with dry HCl while slowly bringing the cell temperature to 500°C. The salt was then fused under HCl and chlorinated in the presence of carbon.

NiCl<sub>2</sub>. Reagent grade NiCl<sub>2</sub> · 6H<sub>2</sub>O was oven dried in air at 130°C, ground in a porcelain mortar, and subsequently dried for at least 4 hr under anhydrous HCl at 400°C. The salt was transferred to weighing bottles in a glove bag under nitrogen and subsequently stored in a desiccator until used. Transfer to the cell involved brief exposure to the atmosphere.

Electrolytes utilized in the Ag reference electrodes were prepared from the purified NaCl and KCl and from reagent grade LiCl and AgCl. The salts were weighed out in the desired proportions and fused and chlorinated in the presence of carbon for at least one hour. The melts were drawn into clean, dry, Vycor rods from which they were removed as the solid and stored under CCl<sub>4</sub>.

The furnace was a Marshall Company test furnace, 16 in. in length with a 3 in. diameter throat. Power was supplied to the furnace with a West, Model JSB Control. Cell temperatures were determined by means of a calibrated Chromel-Alumel thermocouple housed in a 6 mm Vycor sheath immersed in the melt. The measuring thermocouple was calibrated in freezing

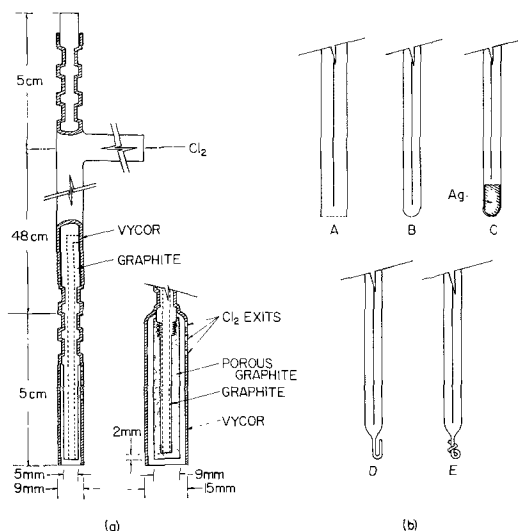


Fig. 1.(a) Chlorine electrode designs; Fig. 1(b) Vycor protection tubes for metal electrodes.

aluminum, supplied by the N.B.S., and by comparison against an L&N Pt, Pt-10% Rh thermocouple, Model 8710-B-K2002. Temperature measurements were observed to vary as much as 3° due to different positioning of the thermocouple in the bath. Since this is estimated to be greater than the degree of uncertainty involved in the calibration the uncertainty in temperature is taken to be  $\pm 3^\circ$ .

Emf measurements were made with a Systems Research Corporation differential voltmeter, Model 5501. This instrument was checked periodically against a laboratory standard Eppley cell.

Thermoelectric effects associated with the electrodes in the absence of electrolyte were determined experimentally *in situ* for each pair of electrodes using powdered graphite as an electrical connection at the hot junction. Thermoelectric potentials developed by various pairs of Ni-to-graphite electrodes differed by  $\pm 2$  mv.

The cell and electrodes were cleaned by rinsing in boiling 1N HCl, and rinsing at least twice with distilled water and dried under flowing chlorine at 800°C for several hours. The cell was then cooled and solvent (2 moles) added to the crucible. After melt preparation was complete, solute was added and cell potentials were measured as a function of temperature, the usual sequence being intermediate, high, and low temperatures. Linearity and reproducibility of the cell emf as a function of temperature was taken as one indication of reversible behavior. Nickel electrodes were left in the melt only long enough for steady potentials to be obtained, usually a few minutes.

After each potential measurement a melt sample was taken by means of a flamed 6 mm Vycor tube. Nickel was determined spectrophotometrically in aqueous solution as the tetracyano complex (7). Aqueous solutions of known concentration of NiCl<sub>2</sub> were used to establish the absorbance curve. The method of least squares was applied to determine the best relationship between absorbance and concentration for 18 known samples. The standard deviation,  $\sigma$ , from the least squares line was  $\sigma = 4 \times 10^{-3}$  absorbance units. Bath samples were usually diluted to give absorbance values between 0.200 and 0.700. Thus, the limit of error (99% confidence level) of bath concentrations calculated on the basis of one sample is taken to be  $2.6 \sigma = 0.010$  absorbance units or approximately  $\pm 3\%$  of bath concentration for intermediate absorbance values. Usually three potential measurements and three samples were taken at each nominal concentration. The analytical data were averaged to establish the bath concentration.

Solute additions were made both electrolytically and as the dry powder. A positive pressure of chlorine or inert gas was maintained in the cell at all times and care was taken to open the cell to air for only minimal lengths of time in carrying out changes of electrodes, solute additions, and sampling operations.

Some modifications were made in equipment or procedure as the work progressed. For the most part these were aimed at decreasing the possibility of atmospheric contamination of the melt during cell operation: (a) mechanical stirring (Ni cells only) using a Teflon bearing at the cell top was discontinued after cell III; (b) provision of an air lock at the top of the cell for sampling was provided after cell III; (c) in the initial experiment with KCl the metal electrode compartment was changed after each potential measurement. Subsequently, this compartment was changed as infrequently as possible. Equalization of melt concentration inside and outside the metal electrode compartment was achieved by purging with dry argon and allowing the compartment to refill.

## Results

*The AgCl formation cell.*—The results from work on the AgCl formation cells A and B are illustrated in

Fig. 2, 3, and 4. The cell emf's have been corrected for thermoelectric effects.

Polarization of the chlorine electrodes (Fig. 2) as a test of electrode reversibility was carried out by passing current between the chlorine electrode and an auxiliary graphite electrode. Potential differences were measured between the chlorine electrode and a non-current-carrying Ag electrode (design C, Fig. 1). Only resistive polarization was evident, and hysteresis ef-

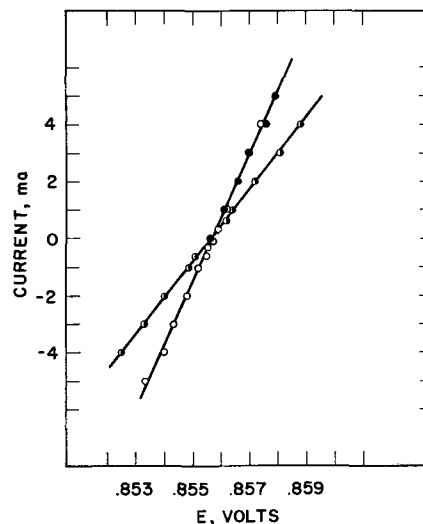


Fig. 2. Polarization data for two chlorine electrodes. Porous electrode design: ●, increasing positive current, ○, decreasing positive current. Nonporous electrode design: ● decreasing positive current.

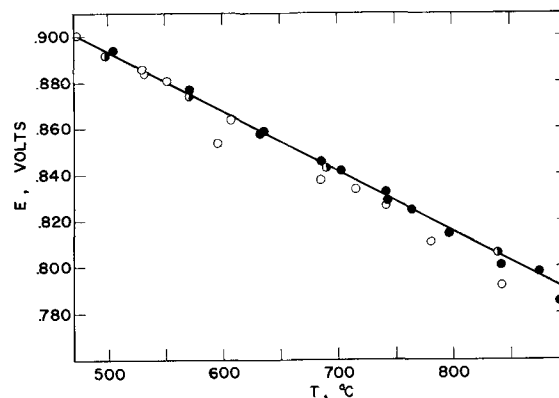


Fig. 3. Cell voltage,  $E$ , for AgCl formation cell A; Ag electrode housed in protection tube C, ●, tube B, ●, tube A, ○. The solid line represents the data of Senderoff and Mellors.

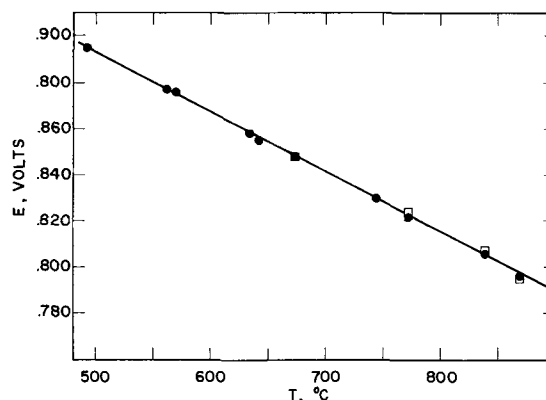


Fig. 4. Cell voltage,  $E$ , for AgCl formation cell B; Ag electrode housed in protection tube C, ●, tubes D or E, □. The solid line represents the data of Senderoff and Mellors.

fects were absent to within ±1 mv. Potential differences between unpolarized chlorine electrodes of different design in the same cell were generally less than 1 mv.; short term (order of seconds) fluctuations were of the order of 0.1 mv. No dependence of chlorine electrode potential on design could be established.

The flow rate of chlorine was varied by factors up to 30 to 1, but the effect upon the emf was always less than 1 mv. Termination of chlorine flow was made apparent within minutes by a decrease in cell emf; however, the cell emf's regained their initial values within minutes after resumption of Cl<sub>2</sub> flow. Intermediate Cl<sub>2</sub> flow rates were adopted as standard.

The effect on cell emf of the degree of shielding of the Ag electrode is illustrated in Fig. 3. Cells utilizing Ag electrodes housed in the open well protection tube (A, Fig. 1) gave emf's which were scattered, and on the average, less than those observed by Senderoff and Mellors (8) whereas cells utilizing Ag electrodes housed in constricted or "scavenged" (B, C, Fig. 1) tubes were found to yield cell emf's more in agreement with Senderoff and Mellors' data.

The data in Fig. 4 were obtained from a freshly prepared cell (cell B) utilizing scavenged or capillary (D and E, Fig. 1) protection tubes. The agreement with Senderoff and Mellors' data is excellent.

*The cells Ni | NiCl<sub>2</sub>, MCl | Cl<sub>2</sub>, C.*—Current reversibility of the chlorine electrodes used in each cell was verified; curves similar to those shown in Fig. 2 resulted in all cases. Potential differences between chlorine electrodes of different design in the same cell were near 1 mv, or less, with short term fluctuations of the order of 0.1 mv. Current reversibility of the Ni electrodes was verified in cells II through VI at NiCl<sub>2</sub> concentrations near  $N = 10^{-2}$ . An example of these tests is shown in Fig. 5.

The data from each cell were plotted as cell emf,  $E$ , vs. temperature at each concentration. From these curves, emf's were read at a series of fixed temperatures to prepare the graphs shown in Fig. 6. Below  $N = 10^{-2}$ ,  $E$  at constant temperatures may be represented by

$$E = a - b \log N$$

where  $b = 2.303 RT/2F$ . The solid straight lines in Fig. 6 were drawn with slopes  $b$  below  $N = 10^{-2}$  and the intercept  $a$  was chosen to give the best fit with the data points for  $N < 10^{-2}$ . Table I gives the values of the constants  $a$  and the average deviations of the data

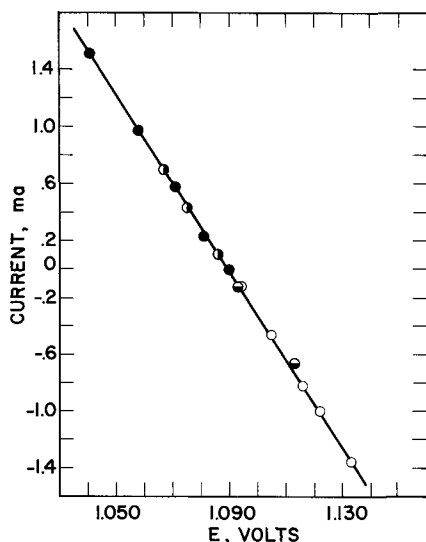


Fig. 5. Polarization of a nickel electrode; cell II, NaCl solvent,  $N_{NiCl_2} = 8.3 \times 10^{-3}$ . Positive current was first increased across the electrode-electrolyte interface, ●, then decreased ○. Negative current was then increased, ○, and subsequently decreased ●.

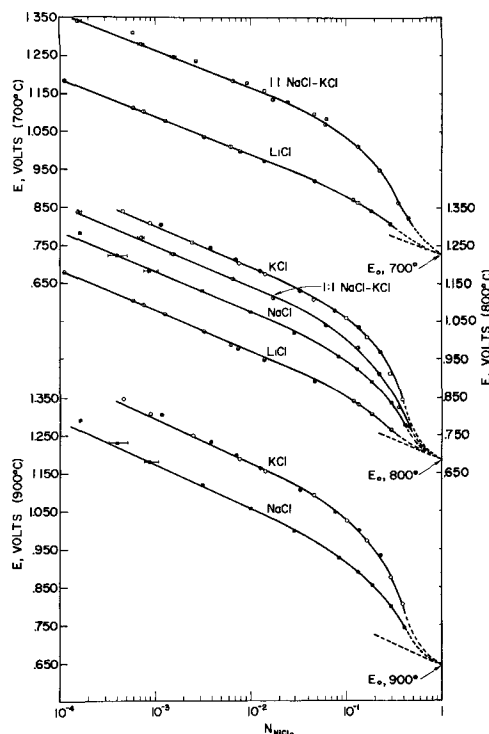


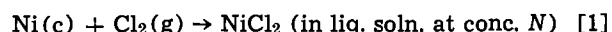
Fig. 6. Cell emf,  $E$ , vs.  $\log N_{NiCl_2}$  at 700°, 800°, and 900°C. Cell I, KCl solvent, ●; cell II, NaCl solvent, ■; cell III, 1:1 NaCl-KCl solvent, ○; cell IV, LiCl solvent, ⊙; cell V, LiCl solvent, ⊕; cell VI, KCl solvent, ○. Earlier data of Flengas and Ingrahm 705°C, □. Uncertainty in concentration is indicated by extended bars where the magnitude of the uncertainty exceeds the size of the symbol representing the data point.

points from the straight lines in the low concentration range.

An attempt was made to obtain cell data at  $N < 10^{-4}$ ; however, stable emf's (i.e., short-term fluctuations in  $E$  less than 1 mv) were not achieved in this concentration range. Furthermore, the variation of  $E$  with temperature was usually nonlinear, uncertainties in concentration were large, and the values of  $E$  were larger than would be predicted on the basis of the data at higher concentrations. These effects are attributed to the appreciable solubility of chlorine in these melts and to the presence of impurities, e.g., oxygen, in the cell which seriously effect the nickel electrode potential when the exchange current for the desired reaction is low.

For NaCl, KCl, and NaCl-KCl melts, the electrolyte containers and glass cell components were observed to suffer only slight surface etching during experiments lasting as long as seven days. In the case of LiCl, rapid etching of glass components was noted for melts prepared by both techniques mentioned above. However, the rate of attack was observed to decrease as NiCl<sub>2</sub> concentration increased, becoming insignificant as solute concentration passed  $10^{-4}$  mole fraction. Evidently, oxygen was removed by precipitation as NiO (9, 10).

The thermodynamic functions for the cell reaction



have been calculated on the basis of the definitions

Table I. Values of the constants  $a$

	$a$ , °C			Avg dev., mv		
	700	800	900	700°C	800°C	900°C
LiCl	0.798	0.759		2	2	
NaCl		0.864	0.824	5	5	8
KCl		0.982		3	3	6
1:1 NaCl-KCl	0.973	0.930	0.946	2	4	

$$\lim_{N \rightarrow 1} \frac{a}{N} = 1$$

$$a = N\gamma$$

where  $a$ ,  $N$ , and  $\gamma$  refer to the solute,  $\text{NiCl}_2$ . Thus, the standard and reference states of the solute are chosen as the pure liquid with the properties of the pure liquid at the temperature of the experiment. The partial molar Gibbs function of mixing and the partial molar enthalpy and entropy of mixing are given by

$$\bar{G} = -nFE - \Delta G^\circ$$

$$\bar{H} = \Delta H - \Delta H^\circ$$

$$\bar{S} = nF \left( \frac{\partial E}{\partial T} \right)_P - \Delta S^\circ$$

where  $\Delta G^\circ$ ,  $\Delta H^\circ$ ,  $\Delta S^\circ$  are the standard changes for reaction [1]. The excess free energy of mixing is given by

$$\bar{G}^E \equiv \bar{G} - RT \ln N = RT \ln \gamma$$

Equations describing the temperature dependence of  $\Delta G^\circ$  and  $\Delta H^\circ$  have been derived with the aid of the thermochemical data tabulated by Wicks and Block (11) and Kubaschewsky and Evans (12).

$$\Delta H^\circ = 6.14 \times 10^4 + 9.35T$$

$$- 1.05 \times 10^{-3}T^2 - 0.68 \times 10^5T^{-1}$$

$$\Delta G^\circ = 6.14 \times 10^4 + 9.19T - 2.15T \log_{10}T$$

$$+ 1.05 \times 10^{-3}T^2 - 0.34 \times 10^5T^{-1}$$

Calculated values of  $\Delta G^\circ$ ,  $\Delta H^\circ$ , and  $\Delta S^\circ$  at selected temperatures are listed in Table II. The curves of Fig. 6 have been extrapolated to  $N = 1$ ,  $E^\circ$ , on the basis of the values of  $\Delta G^\circ$  at the temperature of the experiment. These values of  $E^\circ$  are shown in Fig. 6. Values of  $E^\circ$  calculated on the basis of the earlier compilation of Hamer *et al.* (13) lie more than 100 mv higher than those used here and are in conflict with the present cell data.

Table II. Calculated values of  $\Delta H^\circ$ ,  $\Delta G^\circ$ ,  $\Delta S^\circ$ 

	650°C	700°C	750°C	800°C	850°C	900°C
$\Delta H^\circ$ (kcal)	-53.8	-53.4	-53.0	-52.7	-52.3	-52.0
$\Delta G^\circ$ (kcal)	-34.7	-33.6	-32.7	-31.6	-30.7	-29.7
$\Delta S^\circ$ (eu)	-20.7	-20.3	-19.8	-19.7	-19.2	-19.0
$E^\circ$ (v)	0.756	0.727	0.709	0.685	0.675	0.644

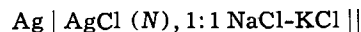
Emf values were read at selected concentrations from the curves of Fig. 6 and used to calculate the values of the functions given in the Tables III through VI. Values of  $\bar{S}$  given in tables are smoothed values based on graphs of  $\Delta S$  as a function of concentration.

*Ag reference electrodes.*—The Ag reference electrodes incorporated in cells III, IV, and VI are described in Table VII.

$E'_{\text{Ag}}$  was found to be independent of  $N_{\text{NiCl}_2}$  up to  $N_{\text{NiCl}_2} = 10^{-2}$ . Values of  $E'_{\text{Ag}}$  given in the table are average values, corrected for thermoelectric emfs, taken over the duration of the experiment  $E'_{\text{Ag}} - E_{\text{Ag}}$ , at  $\text{NiCl}_2$  concentrations up to  $N_{\text{NiCl}_2} = 10^{-2}$ . The maximum limits of deviation from the averages are given. Values of  $\Delta E'$ , that is,  $E'_{\text{Ag}} - E_{\text{Ag}}$ , were detectable at higher  $\text{NiCl}_2$  concentrations; these values are plotted in Fig. 7.

### Discussion

Various aspects of the behavior of nickel electrodes in fused media have been studied by other investigators (14-19). Equilibrium electrode potentials in 1:1 NaCl-KCl have been measured by Flengas and Ingrahm (14, 15) and some of their data may be compared with the present results. Flengas and Ingrahm used the reference electrode



where the double line represents an asbestos fiber, to measure the potential of the Ni electrode as a function of  $\text{NiCl}_2$  concentration up to  $N = 6.2 \times 10^{-2}$  at 705°C in 1:1 NaCl-KCl. In an independent experiment the potential of the reference electrode was compared with that of the chlorine electrode in the same solvent. Thus, potential differences between nickel and chlo-

Table III. NaCl solvent, cell II

$N_{\text{NiCl}_2}$	E (volts)		$\bar{G}$ (kcal)		$\bar{G}^E$ (kcal)		$\gamma$		$\bar{S}$ (eu)	$\bar{H}$ (kcal)
	800°C	900°C	800°C	900°C	800°C	900°C	800°C	900°C	800°C	800°C
0.00100	1.182	1.172	-22.9	-24.4	-8.2	-8.3	$2.14 \times 10^{-2}$	$2.88 \times 10^{-2}$	+18.5	-3.5
0.00300	1.132	1.117	-20.6	-21.8	-8.2	-8.3	$2.14 \times 10^{-2}$	$2.82 \times 10^{-2}$	+14.1	-5.5
0.00700	1.092	1.073	-18.8	-19.8	-8.2	-8.2	$2.14 \times 10^{-2}$	$2.95 \times 10^{-2}$	+12.2	-5.7
0.0200	1.043	1.020	-16.5	-17.3	-8.2	-8.2	$2.18 \times 10^{-2}$	$2.95 \times 10^{-2}$	+9.7	-6.4
0.0500	0.993	0.965	-14.2	-14.8	-7.8	-7.8	$2.56 \times 10^{-2}$	$3.46 \times 10^{-2}$	+7.5	-6.2
0.0700	0.972	0.942	-13.2	-13.8	-7.6	-7.6	$2.88 \times 10^{-2}$	$3.88 \times 10^{-2}$	+6.7	-6.0
0.100	0.947	0.914	-12.1	-12.5	-7.2	-7.1	$3.46 \times 10^{-2}$	$4.80 \times 10^{-2}$	+5.3	-6.4
0.150	0.912	0.878	-10.5	-10.8	-6.4	-6.4	$4.89 \times 10^{-2}$	$6.51 \times 10^{-2}$	+3.8	-6.4
0.200	0.883	0.848	-9.1	-9.4	-5.7	-5.7	$6.91 \times 10^{-2}$	$8.90 \times 10^{-2}$	+3.0	-5.9
0.250	0.857	0.822	-7.9	-8.2	-5.0	-5.0	$9.79 \times 10^{-2}$	$1.18 \times 10^{-1}$	+2.8	-5.0
0.300	0.833	0.797	-6.8	-7.1	-4.3	-4.3	$1.36 \times 10^{-1}$	$1.92 \times 10^{-1}$	+2.6	-4.1
0.350	0.808	0.773	-5.7	-6.0	-3.4	-3.5	$2.01 \times 10^{-1}$	$2.23 \times 10^{-1}$	+2.2	-3.4
0.400	0.783	0.748	-4.5	-4.8	-2.6	-2.7	$3.01 \times 10^{-1}$	$3.16 \times 10^{-1}$	+1.9	-2.7

Table IV. KCl solvent, cell VI

$N_{\text{NiCl}_2}$	E (volts)		$\bar{G}$ (kcal)		$\bar{G}^E$ (kcal)		$\gamma$		$\bar{S}$ (eu)	$\bar{H}$ (kcal)
	800°C	900°C	800°C	900°C	800°C	900°C	800°C	900°C	800°C	800°C
0.00100	1.301	1.292	-28.4	-29.9	-13.7	-13.8	$1.65 \times 10^{-3}$	$2.70 \times 10^{-3}$	+17.7	-9.5
0.00300	1.250	1.236	-26.1	-27.3	-13.7	-13.8	$1.65 \times 10^{-3}$	$2.72 \times 10^{-3}$	+14.2	-10.9
0.00700	1.212	1.193	-24.3	-25.3	-13.7	-13.8	$1.61 \times 10^{-3}$	$2.75 \times 10^{-3}$	+12.0	-11.5
0.0200	1.162	1.140	-22.0	-22.9	-13.7	-13.8	$1.66 \times 10^{-3}$	$2.74 \times 10^{-3}$	+8.9	-12.5
0.0500	1.108	1.085	-19.5	-20.3	-13.1	-13.4	$2.14 \times 10^{-3}$	$3.25 \times 10^{-3}$	+6.6	-12.5
0.0700	1.087	1.059	-18.5	-19.1	-12.9	-12.9	$2.40 \times 10^{-3}$	$3.89 \times 10^{-3}$	+5.9	-12.2
0.100	1.060	1.027	-17.3	-17.7	-12.4	-12.3	$3.01 \times 10^{-3}$	$5.12 \times 10^{-3}$	+4.5	-12.5
0.150	1.023	0.983	-15.6	-15.6	-11.5	-11.2	$4.49 \times 10^{-3}$	$8.13 \times 10^{-3}$	+3.3	-12.1
0.200	0.989	0.946	-14.0	-13.9	-10.6	-10.2	$7.00 \times 10^{-3}$	$1.27 \times 10^{-2}$	+3.0	-10.8
0.250	0.957	0.910	-12.5	-12.3	-9.6	-9.6	$1.12 \times 10^{-2}$	$2.09 \times 10^{-2}$	+2.5	-9.9
0.300	0.923	0.873	-11.0	-10.6	-8.4	-7.8	$1.94 \times 10^{-2}$	$3.64 \times 10^{-2}$	+2.4	-8.5
0.350	0.882	0.832	-9.1	-8.7	-6.8	-6.2	$4.05 \times 10^{-2}$	$7.00 \times 10^{-2}$	+2.1	-6.9
0.400	0.838	0.792	-7.1	-6.8	-5.1	-4.7	$9.14 \times 10^{-2}$	$1.34 \times 10^{-1}$	+1.6	-5.4

Table V. NaCl-KCl solvent, cell III

$N_{\text{NiCl}_2}$	$E$ (volts)		$\bar{G}$ (kcal)		$\bar{G}^E$ (kcal)		$\gamma$		$\bar{S}$ (eu)	$\bar{H}$ (kcal)
	700°C	800°C	700°C	800°C	700°C	800°C	700°C	800°C	700°C	800°C
0.00100	1.263	1.248	-24.7	-26.0	-11.3	-11.2	$2.92 \times 10^{-3}$	$5.16 \times 10^{-3}$	+18.2	-6.8
0.00300	1.217	1.198	-22.5	-23.7	-11.3	-11.3	$2.90 \times 10^{-3}$	$5.10 \times 10^{-3}$	+12.7	-10.1
0.00700	1.181	1.158	-20.9	-21.8	-11.3	-11.2	$2.93 \times 10^{-3}$	$5.16 \times 10^{-3}$	+10.5	-10.6
0.0200	1.134	1.110	-18.7	-19.6	-11.2	-11.2	$3.15 \times 10^{-3}$	$5.14 \times 10^{-3}$	+8.1	-10.9
0.0500	1.086	1.058	-16.5	-17.2	-10.7	-10.8	$3.95 \times 10^{-3}$	$6.33 \times 10^{-3}$	+6.5	-10.3
0.0700	1.064	1.034	-15.5	-16.1	-10.3	-10.4	$4.79 \times 10^{-3}$	$7.54 \times 10^{-3}$	+5.7	-10.0
0.100	1.037	1.004	-14.2	-14.7	-9.8	-9.8	$6.35 \times 10^{-3}$	$1.01 \times 10^{-2}$	+4.7	-9.7
0.150	1.000	0.962	-12.5	-12.8	-8.9	-8.7	$1.03 \times 10^{-2}$	$1.67 \times 10^{-2}$	+3.7	-8.9
0.200	0.968	0.927	-11.0	-11.2	-7.9	-7.7	$1.65 \times 10^{-2}$	$2.68 \times 10^{-2}$	+2.7	-8.2
0.250	0.933	0.894	-9.4	-9.6	-6.8	-6.7	$3.02 \times 10^{-2}$	$4.39 \times 10^{-2}$	+1.7	-7.8
0.300	0.902	0.865	-8.0	-8.3	-5.7	-5.7	$5.32 \times 10^{-2}$	$6.85 \times 10^{-2}$	+1.7	-6.5
0.350	0.868	0.835	-6.4	-6.9	-4.4	-4.7	$1.04 \times 10^{-1}$	$1.12 \times 10^{-1}$	+1.7	-5.1
0.400	0.847	0.808	-5.5	-5.7	-3.7	-3.7	$1.48 \times 10^{-1}$	$1.75 \times 10^{-1}$	-0.3	-6.1

Table VI. LiCl solvent, cell IV

$N_{\text{NiCl}_2}$	$E$ (volts)		$\bar{G}$ (kcal)		$\bar{G}^E$ (kcal)		$\gamma$		$\bar{S}$ (eu)	$\bar{H}$ (kcal)
	700°C	800°C	700°C	800°C	700°C	800°C	700°C	800°C	800°C	800°C
0.00100	1.088	1.078	-16.6	-18.1	-3.2	-3.4	0.189	0.204	+16.7	-0.2
0.00300	1.043	1.028	-14.5	-15.8	-3.3	-3.4	0.184	0.201	+13.6	-1.3
0.00700	1.007	0.988	-12.8	-14.0	-3.3	-3.4	0.186	0.204	+10.7	-2.6
0.0200	0.963	0.940	-10.8	-11.8	-3.3	-3.4	0.186	0.201	+7.7	-3.6
0.0500	0.920	0.895	-8.8	-9.7	-3.0	-3.3	0.207	0.214	+6.1	-3.2
0.0700	0.902	0.876	-8.0	-8.8	-2.9	-3.1	0.228	0.231	+5.4	-3.0
0.100	0.883	0.853	-7.1	-7.7	-2.7	-2.8	0.251	0.266	+4.7	-2.7
0.150	0.857	0.823	-5.9	-6.4	-2.3	-2.3	0.313	0.339	+3.8	-2.4
0.200	0.838	0.800	-5.1	-5.3	-1.9	-1.9	0.366	0.417	+2.9	-2.2
0.250	0.822	0.780	-4.3	-4.4	-1.6	-1.4	0.430	0.516	+1.9	-2.4
0.300	0.806	0.763	-3.6	-3.6	-1.2	-1.0	0.525	0.621	+0.2	-3.4

rine electrodes may be calculated from Flengas and Ingrahm's data. Corrections for thermoelectric effects were included in a later publication (15); however, the polarity of the stated correction for a Ni, Ni-Ag, Pt combination is opposite that expected on the basis of the tabulated (20) thermal emfs of various elements relative to platinum. Flengas and Ingrahm's data without thermoelectric corrections has been included in Fig. 6. It is believed that proper correction for thermoelectric effects would bring the two sets of data into agreement at concentrations near  $10^{-2}$  mole fraction.

Flengas and Ingrahm observed a non-Nernstian slope, 0.107 as opposed to an expected 0.097, in their work with the Ni electrode. Similar effects have been reported by Maricle and Hume (16) in polarographic work and a tendency toward high emf values at low concentrations was observed in the present work. The authors believe that this tendency is due to a mixed potential at the nickel electrode arising from the presence of small amounts of oxygen in the cell. Attention is called to the difference in the data for cells I and VI, Fig. 6, both involving KCl solvent. Changes in experimental procedures decreased the possibility of oxygen contamination of the cell and resulted in decreased values of cell emf at low NiCl<sub>2</sub> concentrations.

Yang and Hudson (21) reported on the error involved in calculating the emf for a cell containing the chlorine electrode from that of a cell in which the chlorine electrode was replaced by the Ag|AgCl, MCl|| reference electrode. Here we have shown, by direct measurement, that the potential difference between the reference electrode and the chlorine electrode is constant for  $N_{\text{NiCl}_2} < 10^{-2}$  (Fig. 7). Thus, potentials arising from differences in chloride ion activity on either side of the membrane and from the membrane itself are constant at sufficiently low NiCl<sub>2</sub>

concentration. If this result is taken to be valid generally, the Ag | AgCl, MCl || reference electrode may be reliably used in place of the chlorine electrode to study, at low concentrations, solutes such as FeCl<sub>2</sub>.

It is also of importance that the data of Fig. 7 indicate no measurable change of the chlorine electrode potential with solute concentration up to  $2 \times 10^{-2}$  mole fraction solute unless there are compensating effects that render  $\Delta E'$  negligible below this concentration.

The measure of solute deviation from ideal behavior, on the basis of the chosen standard and reference states, is given by the excess partial molar free energy,  $\bar{G}^E = RT \ln \gamma$ . The magnitude of  $\bar{G}^E$  at any fixed solute concentration varies with solvent in the order KCl > NaCl-KCl > NaCl > LiCl which follows the order established in numerous previous studies which include the solutes PbCl<sub>2</sub>, CdCl<sub>2</sub>, ZnCl<sub>2</sub>, MgCl<sub>2</sub>, CeCl<sub>3</sub>, FeCl<sub>2</sub>, BeCl<sub>2</sub>, in the alkali chlorides (22, 24). The order of variation of  $\bar{G}^E$  with solvent is commonly explained on the basis of a competition for anions between the solute and solvent cations. The solvent cation of largest charge-to-size ratio, Li<sup>+</sup>, is considered to be the most effective competitor for chloride ions, and its presence results in the smallest degree of bonding between the solute cations and solvent anions.

Table VII. Ag reference electrodes

Cell	$N_{\text{AgCl}}$	Solvent	$E'_{\text{Ag}}$	
			700°C	800°C
III	$6.6 \times 10^{-2}$	1:1 NaCl-KCl	$1.063 \pm 6$ mv	
IV	$7.3 \times 10^{-2}$	LiCl	$0.978 \pm 2$ mv	
VI	$5.5 \times 10^{-2}$	KCl		$1.136 \pm 4$ mv

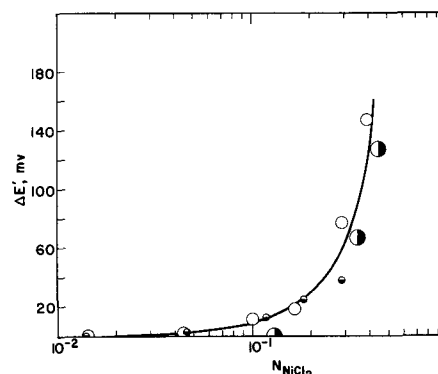


Fig. 7. Values of  $\Delta E' = E'_{\text{Ag}} - E_{\text{Ag}}$  vs.  $\log N_{\text{NiCl}_2}$ . Sizes of the symbols representing the data points were chosen to reflect the limits of deviation given in Table VII. Symbols are related to cells and solvents as in Fig. 6.

A comparison of  $\overline{G}^E$  for  $\text{NiCl}_2$  and  $\text{MgCl}_2$  in  $\text{KCl}$  and in  $\text{NaCl-KCl}$  mixture is of interest (Fig. 8) because of the similarity in the ionic size of nickel and magnesium ions. The crystal radii of hexacoordinated  $\text{Ni}^{2+}$  and  $\text{Mg}^{2+}$  ions are 0.69 and 0.66 Å, respectively (24). In Fig. 8 our results for  $\text{NiCl}_2$  are compared with those of Neil and Clark (25) for  $\text{MgCl}_2$ . Except at concentrations below  $N = 0.1$ , where  $\text{NiCl}_2$  is significantly less ideal, the two solutes exhibit about the same departure from ideality. There is good evidence (25-29) that both nickel and magnesium exist as chloro-complexes in the alkali chloride melts; this is likely a major cause of nonideal behavior both with respect to the heat of mixing and the entropy of mixing. We return to this point later in connection with the entropy of mixing.

In Fig. 9 the variation of the partial molar entropy of mixing of  $\text{NiCl}_2$ ,  $\overline{S}$ , is shown as a function of  $\log N_{\text{NiCl}_2}$ , for all of the solvents investigated. If the solutions of  $\text{NiCl}_2$  in the alkali halides are ideal, then according to Raoult's law, we can assert that  $\overline{S}$  follows the equation

$$\overline{S} = [\partial \Delta S_{\text{mix}} / \partial n_{\text{NiCl}_2}]_{T,p,n_{\text{MCl}}} = -R \ln N_{\text{NiCl}_2} \quad [2]$$

where  $\Delta S_{\text{mix}}$  is the ideal entropy of mixing and  $n$  is the number of moles. The ideal curve is shown as the solid

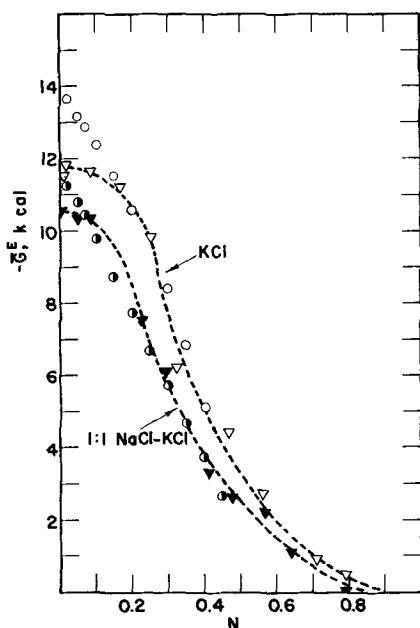


Fig. 8. Excess partial molar free energy,  $\overline{G}^E$ , vs. mole fraction for the solutes  $\text{MgCl}_2$ ,  $\nabla$ ,  $\nabla$ , and  $\text{NiCl}_2$ ,  $\circ$ ,  $\circ$  in the indicated solvents at  $800^\circ\text{C}$ . The  $\text{MgCl}_2$  data are those of Neil.

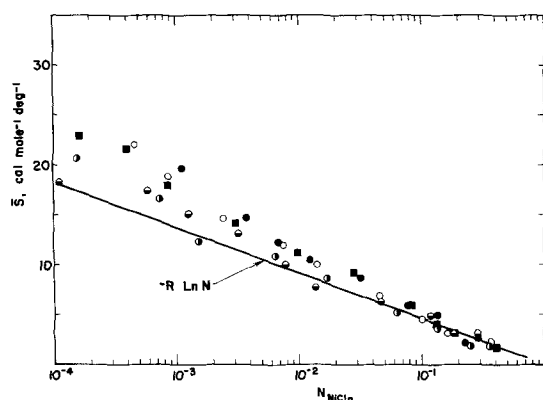


Fig. 9. Partial molar entropy of mixing for  $\text{NiCl}_2$ ,  $\overline{S}$ , as a function of  $\log N_{\text{NiCl}_2}$ , compared with the value predicted on the basis of the Temkin model. Symbols are related to cells and solvents as in Fig. 6.

line in Fig. 9. The deviations from ideality are not severe, probably lying within the experimental error in the case of the  $\text{LiCl}$  solutions. Deviation is most pronounced in  $\text{KCl}$  solutions, with  $\text{NaCl}$  and  $\text{NaCl-KCl}$  solutions intermediate.

Several causes for nonideal mixing suggest themselves and merit comment. First there is the excess entropy of mixing, present even in the case of perfect random mixing, which derives from the temperature coefficients of the intermolecular interaction energies. This is usually small, and in any case can only be found empirically. In the absence of specific chemical interactions, e.g., complex formation, it may be shown that incorporation of cation vacancies to balance the excess charge of the  $\text{Ni}^{2+}$  ion and maintain a pseudo-lattice structure leads to nonideality. The degree of departure from ideality depends on the degree of association between  $\text{Ni}^{2+}$  and the vacancy. The formation of a complex also leads to a deviation from [2] as shown below; in addition, vacancy incorporation may also occur together with complex formation, with the possibility of vacancy association, so that the functional dependence of  $\overline{S}$  on  $N_{\text{NiCl}_2}$  may be extremely complicated even if simple models are used for the statistical calculation of the configurational entropy.

Lattice models for the mixing of liquid  $\text{NiCl}_2$  with a liquid alkali halide (in which the formation of halo-complexes is not considered) have been reviewed (22, 30), and lead to the following results:

(a) Temkin model:  $\overline{S} = -R \ln N$ ; (b) vacancy model:  $\overline{S} = -2R \ln N'$ ; (c) associated vacancy model

$$\overline{S} = -R[-N'_s + \ln N' - (N'^2_s/Z) \ln 2]$$

where  $N = N_{\text{NiCl}_2} = n_{\text{Ni}} / (n_{\text{Ni}} + n_s)$ ,  $N' = 2n_{\text{Ni}} / (2n_{\text{Ni}} + n_s)$ ,  $N'_s = 1 - N'$ , with  $n_{\text{Ni}}$  and  $n_s$  representing the number of moles of  $\text{NiCl}_2$  and the number of moles of the alkali halide, respectively, and  $Z$  is the number of nearest cation sites surrounding a cation site. We take  $Z = 4$  for molten alkali halides (31).

In each case the assumption has been made that only one anion,  $\text{Cl}^-$ , exists in solution; thus, its mole fraction is unity, and there is no anion contribution to the partial molar configurational entropy. The Temkin entropy is calculated from the number of ways one can distribute a given number of distinguishable sites among a certain number of cations; no provision is made for charge compensation in the case of mixing mono- and divalent cations. The entropy of the Temkin model is that of an ideal mixture. The vacancy model allows for charge compensation by requiring that one vacant site be created per divalent cation, but assumes no association between vacancies and divalent cations. The associated vacancy model, on the other hand, assumes complete association.

In Fig. 10, the observed values of  $\overline{S}$ , plotted against  $\log N_{\text{NiCl}_2}$ , are compared with the predictions of models (b) and (c). The data are clearly inconsistent with the vacancy model, but agree about as well with the associated vacancy model as with the Temkin model. This is not surprising, as the slope of  $\overline{S}$  calculated for the associated vacancy case vs.  $N'$ , is, except at  $N' > 0.2$ , virtually indistinguishable from that of  $\overline{S}$  calculated for the ideal case vs.  $N$ .

We turn next to the effect of complex formation. The absorption spectrum of  $\text{NiCl}_2$ - $\text{KCl}$  solutions bears a close resemblance to that of crystalline  $\text{Cs}_2\text{ZnCl}_4$  in which  $\text{Cs}_2\text{NiCl}_4$  is isomorphically substituted (26), which is good evidence that tetrahedral  $\text{NiCl}_4^{2-}$  complexes exist in the solutions. The same species is also found in  $\text{RbCl}$  and  $\text{CsCl}$  (32). The coordination geometry is evidently considerably altered in  $\text{NaCl}$  and  $\text{LiCl}$  (26, 32, 33). In  $\text{LiCl}$ , for example, an octahedral form appears to exist in equilibrium with the tetrahedral form (33). A pronounced distortion also occurs in  $\text{KCl}$  solutions to which a third electrolyte such as  $\text{ZnCl}_2$  is added (34). One may assume that a high concentration

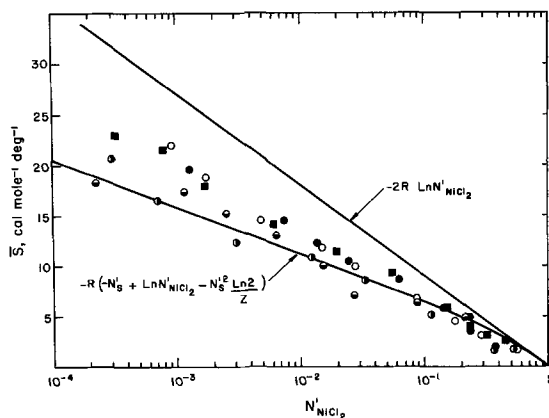
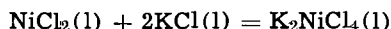


Fig. 10. Partial molar entropy of mixing for NiCl<sub>2</sub>,  $\bar{S}$ , as a function of  $\log N'_{\text{NiCl}_2}$ , compared with values predicted on the basis of the vacancy and associated vacancy models. Symbols are related to cells and solvents as in Fig. 6.

of NiCl<sub>2</sub> itself would have an effect similar to addition of ZnCl<sub>2</sub> on the coordination geometry of NiCl<sub>4</sub><sup>2-</sup>. For simplicity, we consider only the tetrahedral case, applicable strictly only to NiCl<sub>2</sub> in KCl among the solutions we report on here. Further, we anticipate that, at high NiCl<sub>2</sub> concentration, even in KCl the assumption of tetrahedral coordination about nickel may be subject to later modification; however, here we will assume the tetrahedral complex to be the only nickel species present at all compositions having  $N_{\text{NiCl}_2} < 1/3$ , that is, the composition corresponding to the double salt K<sub>2</sub>NiCl<sub>4</sub>.

Let us consider the mixing to occur in two steps. The first is the formation of the complex liquid salt according to



The second step consists of mixing the complex liquid salt with an excess of KCl to give the desired solution. Let the entropy change for the complex salt formation be  $\Delta S'$ . The partial molar entropy of K<sub>2</sub>NiCl<sub>4</sub> for mixing K<sub>2</sub>NiCl<sub>4</sub> with KCl will then be given by

$$\begin{aligned} \bar{S}_{\text{K}_2\text{NiCl}_4} &= [\partial \Delta S_{\text{mix}} / \partial n_{\text{K}_2\text{NiCl}_4}]_{T,p,n_{\text{KCl}}} \\ &= nF \left( \frac{\partial E}{\partial T} \right)_p - \Delta S^{\circ} - \Delta S' = \bar{S} - \Delta S' \end{aligned}$$

where  $n_{\text{KCl}}$  is the number of moles of KCl in excess of that consumed in forming the double salt. For pure liquid K<sub>2</sub>NiCl<sub>4</sub> (that is, at  $N_{\text{NiCl}_2} = 1/3$ ),  $\bar{S}_{\text{K}_2\text{NiCl}_4}$  is zero, and  $\Delta S'$  is thus just the value of  $\bar{S}$  at  $N_{\text{NiCl}_2} = 1/3$ . According to Fig. 9,  $\Delta S'$  is about 2 cal/mole deg. This is not far from the value for ideal mixing of NiCl<sub>2</sub> and KCl; this may be largely fortuitous, as  $\Delta S'$  certainly must be composed of significant contributions from vibrational frequency changes as the complex ion is formed from NiCl<sub>2</sub>.

For the second step, that is, mixing of K<sub>2</sub>NiCl<sub>4</sub> with more KCl, we may again obtain certain results based on ideal mixing or on pseudolattice models of the kind already discussed.

For ideal mixing,  $\bar{S}_{\text{K}_2\text{NiCl}_4}$  is given by

$$\bar{S}_{\text{K}_2\text{NiCl}_4} = -R \ln N_1$$

where  $N_1$ , the mole fraction of K<sub>2</sub>NiCl<sub>4</sub>, is given by

$$N_1 = n_{\text{Ni}} / (n_s - n_{\text{Ni}}) = N / (1 - 2N)$$

Note that  $N_1$  can exceed unity; if so, however, the solution is then a mixture of K<sub>2</sub>NiCl<sub>4</sub> and NiCl<sub>2</sub>. The partial molar entropy of mixing for NiCl<sub>2</sub>, is, then, according to the assumption of ideal mixing of K<sub>2</sub>NiCl<sub>4</sub> with KCl, given by

$$\bar{S} = \Delta S' - R \ln N_1$$

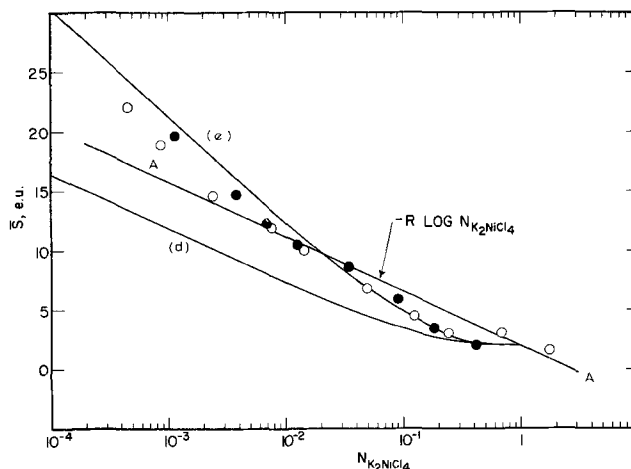


Fig. 11. Partial molar entropy of mixing for NiCl<sub>2</sub> in KCl as a function of  $\log N_{\text{K}_2\text{NiCl}_4}$ , compared with predictions based on ideal mixing of K<sub>2</sub>NiCl<sub>4</sub> with KCl (curve A) and models (d) and (e) as indicated (see text). See Fig. 6 for symbols.

In Fig. 11, the observed values of  $\bar{S}$  for NiCl<sub>2</sub> in KCl are presented as a function of  $N_1$ , together with the ideal-mixing curve drawn so as to pass through  $\Delta S' = 2.00$  eu at  $N_1 = 1.00$ . The considerable deviation from the ideal curve for  $N_1 > 0.1$  is not unexpected, since both K<sub>2</sub>NiCl<sub>4</sub> and KCl contribute K<sup>+</sup> ions to the mixture.

Next we consider some pseudolattice models for the mixing of K<sub>2</sub>NiCl<sub>4</sub> with KCl, as follows:

(d) The NiCl<sub>4</sub><sup>2-</sup> ion replaces one K<sup>+</sup> ion and four surrounding Cl<sup>-</sup> ions on the KCl pseudolattice. The excess charge of nickel is not compensated by vacancies. This model is physically identical to the Temkin model (a) with, however, the restriction that two additional K<sup>+</sup> ions are added to the lattice for each NiCl<sub>4</sub><sup>2-</sup> ion added. The partial molar entropy of mixing, for K<sub>2</sub>NiCl<sub>4</sub>, is

$$\bar{S}_{\text{K}_2\text{NiCl}_4} = -R \ln N_1 (N_1 + 1)^2 + R \ln (2N_1 + 1)^3$$

This model, although plausible, has some questionable features in addition to the artificiality of assigning lattice positions to ions in the liquid state. The coordination number of K<sup>+</sup> in fused KCl is about four (31), and it may be inferred from the isotropic properties of the liquid that the coordination is tetrahedral, but the Cl-Cl distance in the solvent is probably larger than that in the complex (26, 31) so that the fit of the complex upon the pseudolattice is not very close.

(e) The NiCl<sub>4</sub><sup>2-</sup> is accommodated as in (d), but one vacancy is created on the positive-ion sublattice for each NiCl<sub>4</sub><sup>2-</sup> ion. In this case  $\bar{S}_{\text{K}_2\text{NiCl}_4}$  is given by

$$\bar{S}_{\text{K}_2\text{NiCl}_4} = -2R \ln \frac{8N_1(N_1 + 1)}{(3N_1 + 1)^2}$$

(f) If the vacancies in model (e) are assumed to be completely associated with the complex ions, the result differs, as before, only slightly from that of model (d).

On Fig. 11 are also shown curves for  $\bar{S}$  corresponding to the predictions based on model (d) and (e), with  $\Delta S' = 2.00$  eu. The observed values for KCl are most nearly in accord with model (e). It is noteworthy that all the pseudolattice models investigated predict the observed negative deviation from ideal mixing for  $N > 0.10$ . Comparison of the data for the LiCl, NaCl, and NaCl-KCl solutions (Fig. 9) with the calculated curves of Fig. 11 will show that models (d) and (e) apply about as well to these cases as do models (a) and (c). For clarity, and because of doubt about the actual nature of complexes in these solutions, we have not included these data on Fig. 11.



Although the number of plausible models which may be tested is large (including, for example, those in which complex ions are distributed on the anion sublattice either with or without vacancy-compensation) the examples above suffice to allow us to state some conclusions.

First, the entropy-of-mixing data, which we estimate to be within about  $\pm 2$  eu, is insufficiently accurate, and the calculated entropies insufficiently sensitive to variations in the model, to permit one to select unambiguously the most representative model for each of these solutions.

Second, the Temkin or ideal model for mixing  $\text{NiCl}_2$  with the alkali halides (as well as the associated vacancy model) is satisfactory for  $\text{LiCl}$ , but less so for  $\text{NaCl}$ ,  $\text{KCl}$ , and  $\text{NaCl-KCl}$ , while the vacancy model is unsatisfactory for any of the solutions.

Third, the entropy of mixing in  $\text{KCl}$  is reasonably consistent with the predictions based on a model in which tetrahedral  $\text{NiCl}_4^{2-}$  complex ions and an equal number of positive-ion vacancies are distributed on the cation pseudolattice.

#### Acknowledgments

The initial encouragement by W. J. Kroll to undertake this research, and his continued interest is acknowledged with thanks. The authors are also indebted to D. A. Nissen, K. Stern, R. D. Walker, and Robert Stromatt for useful discussions and information, and to the Tektronix Foundation for valued support.

Manuscript received Nov. 30, 1967; revised manuscript received March 19, 1968. This paper was taken from the Ph.D. thesis of one of the authors (D.C.H.), Oregon State University, 1968.

Any discussion of this paper will appear in a Discussion Section to be published in the June 1969 JOURNAL.

#### REFERENCES

- D. A. Nissen, Ph.D. Thesis, Oregon State University, 1964.
- T. A. Sullivan, B. E. Barton, and F. R. Cattoir, To be published.
- R. J. Labrie and V. A. Lamb, *This Journal*, **106**, 896 (1959).
- R. Littlewood, *Electrochim. Acta*, **3**, 270 (1961).
- W. J. Fredericks, F. E. Roaztoczy, and J. Hatchett, Final Report. SRI Project # PAU-3523.
- D. L. Maricle and D. N. Hume, *This Journal*, **107**, 354 (1960).
- T. S. Soine, M. S. Thesis, Oregon State University, 1957.
- S. Senderoff and G. W. Mellors, *Rev. Sci. Instr.*, **29**, 151 (1958).
- H. A. Laitinen and B. B. Bhatia, *This Journal*, **107**, 705 (1960).
- H. Bloom and J. W. Hastie, "Molten salts as solvents," in "Non-Aqueous Solvent Systems," T. C. Waddington, Editor, p. 377, Academic Press, New York (1965).
- C. Wicks and F. Block, *U. S. Bur. Mines Bull.*, **605**, 85 (1963).
- O. Kubashewski and E. L. Evans, "Metallurgical Thermochemistry," 2nd ed., John Wiley & Sons, Inc., New York (1956).
- W. J. Hamer, M. S. Malmberg and B. Rubin, *This Journal*, **103**, 8 (1956).
- S. N. Flengas and T. R. Ingrahm, *Can. J. Chem.*, **35**, 1245 (1957).
- S. N. Flengas and T. R. Ingrahm, *This Journal*, **106**, 714 (1959).
- D. L. Maricle and D. N. Hume, *Analyt. Chem.*, **33**, 1189 (1964).
- R. Littlewood, *Electrochim. Acta*, **4**, 155 (1961).
- Y. K. Delimarskii and N. V. Vlasyuk, *Ukrain. Khim. Zhur.*, **28**, 688 (1962).
- H. A. Laitinen and C. H. Liu, *J. Am. Chem. Soc.*, **80**, 1015 (1958).
- American Institute of Physics Handbook, McGraw-Hill, New York, 1957, p. 4-8.
- L. Yang and R. G. Hudson, *This Journal*, **106**, 986 (1959).
- M. Blander, Editor, "Molten Salt Chemistry," Interscience, New York (1964).
- C. Beusman, ORNL 2323 (1957).
- L. H. Ahrens, *Geochim. et Cosmochim. Acta*, **2**, 155 (1952).
- D. E. Neil and H. M. Clark, *J. Chem. and Eng. Data*, **10**, 21 (1965).
- D. M. Gruen and R. L. McBeth, *J. Phys. Chem.*, **63**, 393 (1959).
- F. M. Hornyak, *J. Am. Chem. Soc.*, **79**, 5435 (1957).
- H. Flood and S. Urnes, *Z. Elektrochem.*, **59**, 834 (1955).
- O. J. Kleppa and F. G. McCarty, *J. Phys. Chem.*, **70**, 1249 (1966).
- T. Forland, *Discussions Faraday Soc.*, **32**, 122 (1961).
- H. A. Levy and M. D. Danford in ref. (22), p. 118.
- G. P. Smith and C. R. Boston, *J. Chem. Phys.*, **43**, 4051 (1965).
- J. Brynestad, C. R. Boston, and G. P. Smith, *ibid.*, **47**, 3179 (1967).
- C. A. Angell and D. M. Gruen, *J. Phys. Chem.*, **70**, 1601 (1966).

# On the Mechanism of Anodic Chlorate Formation in Dilute NaCl Solutions

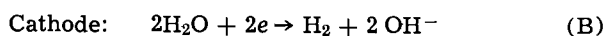
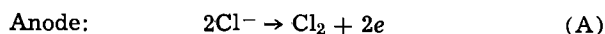
N. Ibl\* and D. Landolt\*<sup>1</sup>

Department of Industrial and Engineering Chemistry,  
Swiss Federal Institute of Technology, Zurich, Switzerland

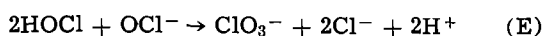
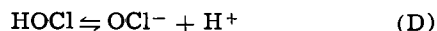
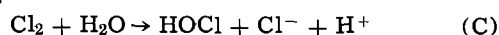
## ABSTRACT

The rates of anodic chlorate formation were measured under a variety of well-defined hydrodynamic conditions. In dilute NaCl solutions (<0.1M) these rates are up to 60 times larger than those calculated for mass transport control as hitherto postulated. The rates of chlorate formation were calculated using a model which involves the coupling of mass transfer with a chemical reaction (chlorine hydrolysis) proceeding in the diffusion layer. The agreement between the calculated and the experimental values is satisfactory. The model used describes adequately the mechanism of anodic chlorate formation in the range of conditions investigated. In dilute NaCl solutions the rate of chlorate formation is governed by the kinetics of the chlorine hydrolysis. At higher chloride concentrations equilibrium may limit the hydrolysis and the mechanism of the process then changes accordingly.

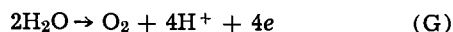
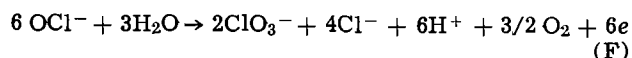
Chlorate is manufactured industrially by electrolysis of neutral sodium chloride solutions in cells without a diaphragm. The reactions taking place in a chlorate cell were formulated by Foerster and Mueller (1, 2) as follows:



Solution:



Anodic loss reactions:<sup>2</sup>



Reaction (G) plays a minor role, as long as the solution does not become too alkaline, or the chloride concentration too low.<sup>3</sup> According to reactions (E) and (F) chlorate may be formed in two ways, either by a purely chemical reaction of the hypochlorite ion with hypochlorous acid in the bulk solution (chemical chlorate formation) or by electrochemical oxidation of the hypochlorite at the anode under simultaneous oxygen evolution (anodic chlorate formation). If all chlorate is formed by the chemical reaction (E), six Faradays are consumed in the oxidation of one mole chloride to chlorate. This is said to correspond to a maximum current efficiency  $\tau_{\text{ClO}_3}$  of 100%. If all chlorate is formed by reaction (F) the current efficiency cannot be higher than 66.7% since one third of the current is used for the evolution of oxygen.

Only little is known about the rate-determining step of the anodic loss reaction (F) which limits the current efficiency in technical cells. As was already observed by Foerster (2) the concentration of hypochlorite in the bulk solution increases during electrolysis until a steady state is reached (see Fig. 2). According to this author there is approximate proportionality between the rate of oxygen evolution result-

ing from reaction (F) and the hypochlorite concentration in the solution, both for the steady and the unsteady state (2). This was confirmed later by Knibbs and Palfreeman (4). From a discussion of Foerster's results, de Valera (5) and Beck (6) concluded that the anodic chlorate formation is controlled by the mass transport of the hypochlorite from the bulk solution toward the anode. In his treatment of Foerster's data, Beck took into account the complication that under transport control the rate of chlorate formation and therefore the rate of oxygen evolution should increase somewhat faster than would correspond to proportionality with the hypochlorite concentration, because the thickness  $\delta$  of the diffusion layer decreases when the stirring by the gas bubbles becomes stronger owing to a faster gas evolution. Whereas Foerster worked mainly with platinum electrodes, Hammar and Wranglén (7) have recently made a comprehensive study of the rate of oxygen evolution in chlorate electrolysis with graphite electrodes. They also found that the rate of oxygen evolution is proportional to the hypochlorite concentration if the influence of the gas bubbling on  $\delta$  is taken into account, and they concluded that mass transport of the hypochlorite is the rate-determining step of the anodic chlorate formation.

Most of the afore-mentioned experiments of the literature were carried out with concentrated NaCl solutions (>1M). Recently, Selvig and Ibl made measurements in dilute solutions where the rates of chlorate formation were up to ten times larger than those expected for a diffusion controlled process (8). The latter values were calculated from the measured oxygen evolution rate by means of the following correlation for mass transfer at gas evolving electrodes, given by Ibl and Venczel (9, 11).

$$k_L = \frac{DV^{0.5}}{1.50 \times 10^{-3}}$$

where  $k_L$  = mass transfer coefficient (cm/sec);  $D$  = diffusion coefficient (cm<sup>2</sup>/sec);  $V$  = gas evolution rate (cm<sup>3</sup>/cm<sup>2</sup> min).

Electrolyzing acid sodium chloride solutions of various concentrations, Selvig found a strong dependence of the steady state hypochlorite concentration on the chloride concentration. Figure 1 shows results similar to those of Selvig, but obtained in slightly alkaline solutions (10). Steady-state hypochlorite concentrations and chlorate formation rates are given for a variety of experiments performed by electrolyzing sodium chloride solutions of various concentrations at constant current density in the absence of forced con-

\* Electrochemical Society Active Member.

<sup>1</sup> Present address: Lawrence Radiation Laboratory, University of California, Berkeley, California.

<sup>2</sup> Loss reactions at the cathode may be suppressed almost entirely by adding small amounts of potassium bichromate to the solution (3).

<sup>3</sup> Formation of perchlorate is another possible anodic loss reaction. It may occur at platinum electrodes but under extreme conditions only.

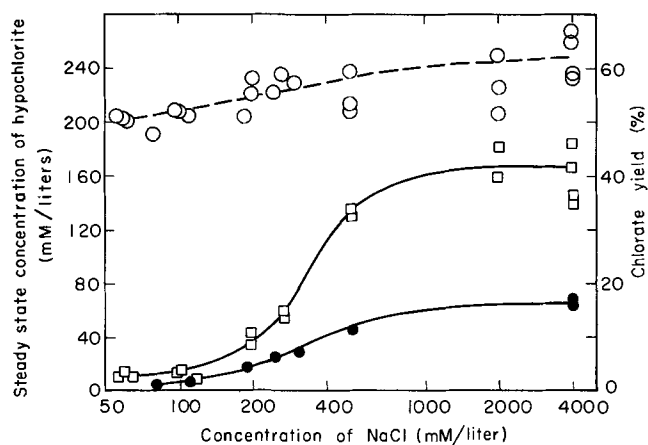


Fig. 1. Steady-state hypochlorite concentrations and chlorate formation rates at various chloride concentrations in unstirred solutions: ● hypochlorite concentration,  $i = 5$  ma/cm<sup>2</sup>; □ hypochlorite concentration,  $i = 20$  ma/cm<sup>2</sup>; ○ chlorate yield,  $i = 5$  ma/cm<sup>2</sup>;  $i = 20$  ma/cm<sup>2</sup>.

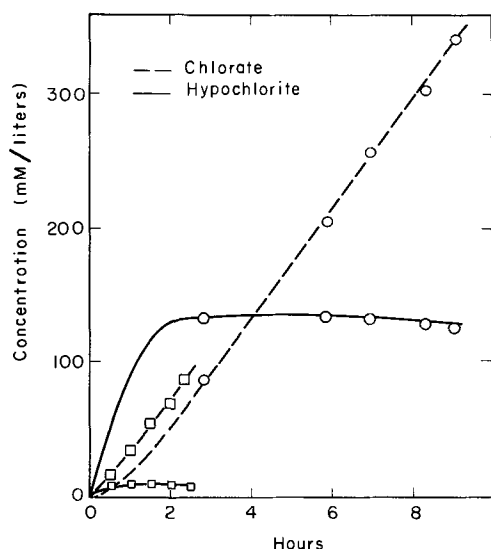


Fig. 2. Variation of hypochlorite and chlorate concentration with time during electrolysis of NaCl solution: ○ concentration of NaCl = 4 mole/liter; □ concentration of NaCl = 0.05 mole/liter, maintained approximately constant during experiment.

vection.<sup>4</sup> Bichromate was added to the solution to reduce cathodic losses. pH and chloride concentration were kept constant by adding concentrated HCl or NaOH during the experiments. Hypochlorite and chlorate concentrations were followed over time by potentiometric titration (see below). Oxygen and hydrogen evolution rates in the steady state were measured using a standard oxygen absorption method.

The history of a typical experiment is shown in Fig. 2. Starting with no hypochlorite in the solution hypochlorite is built up in the bulk at the beginning of the experiment. Gradually more chlorate is formed until a steady state is reached after some time when hypochlorite concentration and chlorate formation rate remain constant. The steady-state values given in Fig. 1 as a function of the NaCl concentration show a sharp decrease in the hypochlorite concentration at chloride concentration below about 400 mM/liter. On the other hand, the chlorate formation rate decreases only slightly, the decrease being possibly due to increased oxygen evolution according to reaction (G).

<sup>4</sup> The cell was constructed in a way to allow circulation of the electrolyte for good mixing. It contained two graphite electrodes (AGLX 58, Union Carbide) of 100 cm<sup>2</sup> surface area. The electrolyte volume was between 170 and 200 ml.

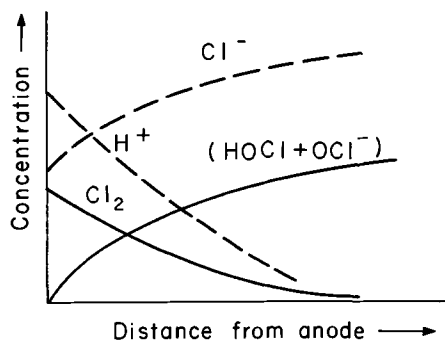


Fig. 3. Concentration profiles near the anode (schematically)

All the experiments of the literature mentioned so far were carried out without external stirring, the only convection present being that due to gas evolution and to the density differences in the solution. The hydrodynamic conditions were thus not well defined, and an accurate comparison with theoretical relationships is therefore difficult. This also applies to Selvig's results. However, in the latter case the discrepancy with the values calculated for mass transport control are so large that at least under the conditions of Selvig's experiments, the rate of chlorate formation can hardly be interpreted in terms of mass transport alone. Furthermore, the results of Fig. 1 (i.e., the large difference between the steady-state hypochlorite concentration measured in dilute and concentrated NaCl solutions in spite of the almost unchanged rate of chlorate formation) strongly suggest that the kinetics of chlorate formation are more complicated than would correspond to a simple transport mechanism. In the mass transfer theory of chlorate formation, as hitherto developed in the literature, only the diffusion of the hypochlorite toward the anode is considered, without taking into account the possible influence of the kinetics of the hypochlorite formation, i.e., it is more or less tacitly assumed that the chlorine hydrolysis [reaction (C)] does not take place in the diffusion layer but only in the bulk solution and does not affect the rate of the anodic chlorate formation. However, as we have pointed out in an earlier paper (11), the chlorine hydrolysis is a relatively fast reaction. One should therefore expect that it takes place within the diffusion layer, close to the anode where the chlorine is generated. In the next section the rate of chlorate formation will be calculated using a model which involves the coupling of mass transfer with a chemical reaction (chlorine hydrolysis) in the diffusion layer, and in a later section the computed values will be compared with measurements carried out under well-defined hydrodynamic conditions.

#### Theoretical

Schematic concentration profiles near the anode as they may be expected according to the reactions (A) and (F) are shown in Fig. 3; chloride and hypochlorite<sup>5</sup> are consumed at the anode and must therefore be transported towards it. Molecular chlorine and hydrogen ions are generated and must be transported away from the anode.

The differential equations describing the system are obtained from a balance of mass for an infinitely small volume element in the diffusion layer. Neglecting migration we may write the general equation

$$\frac{\partial c_i}{\partial t} = -U \nabla c_i + D_i \nabla^2 c_i + R_i \quad [1]$$

where  $c_i$  = concentration of species  $i$  (mole/cm<sup>3</sup>) where  $i = 1$  stands for molecular chlorine,  $i = 2$  for hydrogen ion,  $i = 3$  for hypochlorite (sum of hypo-

<sup>5</sup> It is assumed that the dissociation equilibrium of the hypochlorous acid is established infinitely fast, and the term hypochlorite is used here as the sum of hypochlorous acid and hypochlorite ions.

chlorite ions and hypochlorous acid);  $t$  = time (sec);  $U$  = velocity vector (cm/sec);  $D_i$  = diffusion coefficient of species  $i$  (cm<sup>2</sup>/sec);  $R_i$  = rate of production of species  $i$  by chemical reaction (mole/cm<sup>3</sup> sec).

In applying Eq. [1] to our system, the following simplifications were made: The steady state only ( $\partial c/\partial t = 0$ ) was considered. The concept of a stagnant diffusion layer was used, thereby dropping the convection term and only considering the dimension perpendicular to the electrode. The chlorine hydrolysis was treated as a first order irreversible reaction following the rate law

$$-\frac{dc_1}{dt} = kc_1$$

The differential equation for the chlorine profile in the diffusion layer thus becomes

$$D_1 \frac{d^2c_1}{dx^2} - kc_1 = 0 \quad [2]$$

Boundary conditions are:  $x = 0$ ;  $D_1(dc_1/dx) = -i\phi_1/2F$ ; and  $x = \delta$ ,  $c_1 = 0$ . The first boundary condition states that the chlorine flux at the anode surface is proportional to the density of the current used for the oxidation of chloride ions to chlorine ( $\phi_1$  = fraction of total current used for reaction A). The second boundary condition states that the chlorine concentration in the bulk is essentially zero as it may be expected if the solution is neutral. Equation [2] was first applied to the calculation of the chlorine profile at the anode by Beck (12). Its solution may be expressed as an exponential function<sup>6</sup>

$$c_1 = \frac{i\phi_1}{2FD_1a} \exp(-ax) \quad \text{with } a = \sqrt{\frac{k}{D_1}} \quad [3]$$

Equation [3] holds for the case where the thickness of the layer in which the chemical reaction occurs, is small as compared with the thickness  $\delta$  which the diffusion layer would have under the same hydrodynamic conditions but without a concomitant chemical reaction. Hydrogen ion and hypochlorite concentration profiles are calculated by integrating the equations

$$D_2 \frac{d^2c_2}{dx^2} + kc_{1(x)} = 0 \quad [4]$$

$$D_3 \frac{d^2c_3}{dx^2} + kc_{1(x)} = 0 \quad [5]$$

in which  $c_{1(x)}$  can be expressed by means of Eq. [3]. Equation [4] implies that all the hydrogen ions generated in the diffusion layer result from reaction (C), i.e., that no hydrogen ions are produced by reaction (D). This is a reasonable assumption since in the present model the diffusion layer is quite acid (see below) and the dissociation constant (13) of HClO is  $4 \times 10^{-8}$  mole/liter at 25°C, so that all the hypochlorite is virtually present as HClO in the diffusion layer. Boundary conditions for Eq. [4] are  $D_2(dc_2/dx) = i\phi_2/F$  at  $x = 0$  and  $c_2 = 0$  at  $x = \delta$ . The flux of the hydrogen ions at the anode surface is given by the density of current corresponding to the evolution of oxygen according to reactions (F) and (G) ( $\phi_2$  = fraction of total current used for oxygen evolution).<sup>7</sup> For a neutral solution the hydrogen ion concentration in the bulk solution is virtually zero. Boundary conditions for Eq. [5] are:  $c_3 = 0$  at  $x = 0$  and  $c_3 = c_0$  at  $x = \delta$ . Outside the diffusion layer the hypochlorite

<sup>6</sup> The exact solution of Eq. [2] is

$$c_1 = \frac{i\phi_1}{2FD_1a} \left( \frac{e^{-ax}}{1 + e^{-2a\delta}} - \frac{e^{ax}}{1 + e^{2a\delta}} \right) \quad (3')$$

which for  $a\delta \gg 1$  takes the form of Eq. [3]. The assumption  $a\delta > 1$  must be made anyhow if the convection term of the fundamental differential Eq. [1] is to be neglected in the integration.

<sup>7</sup> The boundary condition at the interface implies the validity of the stoichiometry of the anodic chlorate formation given by reaction (F). This question will be discussed in the section on Experimental results.

concentration equals the bulk concentration which may be determined experimentally. The hypochlorite concentration at the interface is taken as zero, i.e., it is assumed that it is oxidized at the limiting rate. At potentials where  $\text{Cl}^-$  is discharged this assumption appears justified since various authors (2, 4) have reported that hypochlorite reacts at substantially less positive potentials than  $\text{Cl}^-$ .

The corresponding solutions of Eq. [4] and [5], describing the concentration profiles of hydrogen ion and hypochlorite in the diffusion layer, are

$$c_2 = \frac{i\phi_1}{2FD_2a} (e^{-a\delta} - e^{-ax}) + \frac{i(\delta - x)}{FD_2} \left( \frac{\phi_1}{2} + \phi_2 \right) \quad [6]$$

$$c_3 = \frac{i\phi_1}{2FD_3a} (1 - e^{-ax}) + \frac{x}{\delta} \left\{ c_0 - \frac{i\phi_1}{2FD_3a} (1 - e^{-a\delta}) \right\} \quad [7]$$

The hypochlorite flux at the anode, which corresponds to the rate of anodic chlorate formation, is obtained by differentiating Eq. [7] at  $x = 0$

$$j_h = -D_3 \left( \frac{dc_3}{dx} \right)_{x=0} = \frac{i\phi_1}{2F} \left( \frac{1}{a\delta} - 1 \right) - D_3 \frac{c_0}{\delta} - \frac{i\phi_1}{2Fa\delta} e^{-a\delta} \quad [8]$$

The above calculations show that the chlorine hydrolysis proceeding within the diffusion layer has two consequences: (i) the pH in the diffusion layer, being already lower than that of the bulk solution due to the electrochemical hydrogen ion generation by reaction (F) and (G), is lowered even further by the chemical reaction as may be verified by comparing the hydrogen ion concentration at the anode surface calculated by Eq. [6] with that expected for a diffusion controlled process according to

$$(c_2)_{x=0} = \frac{i\phi_2\delta}{D_2F} \quad [6']$$

To illustrate the increased acidity of the diffusion layer we calculate from Eq. [6] the concentration of the  $\text{H}^+$  ions at the interface for the conditions of the experiment B indicated in Table I. With  $k = 6.3 \text{ sec}^{-1}$  ( $t = 13^\circ$ );  $D_1 = 10^{-5} \text{ cm}^2 \text{ sec}^{-1}$  and  $D_2 = 5 \times 10^{-5} \text{ cm}^2 \text{ sec}^{-1}$  we obtain  $(c_2)_{x=0} = 2.65 \times 10^{-2}$  mole/liter. If we make the corresponding calculation with Eq. [6'], i.e., without taking hydrolysis into account, we get  $(c_2)_{x=0} = 1.83 \times 10^{-2}$  mole/liter. (ii) The concentration gradient of hypochlorite at the anode is increased [Eq. (8)], and hence the rate of anodic chlorate formation becomes higher than expected for a process controlled by diffusion alone.

The shape of the hypochlorite concentration profile in the stagnant diffusion layer is illustrated in Fig. 4. Curve 1 in Fig. 4 was calculated from Eq. [7] for the data of experiment B (Fig. 2) which are given in Table I. The values of the diffusion coefficients of chlorine and hypochlorite were assumed as  $10^{-5} \text{ cm}^2/\text{sec}$ ; the rate constant of the chlorine hydrolysis at  $13^\circ\text{C}$  was obtained by interpolation of literature values (14) as  $6.3 \text{ sec}^{-1}$ . The dotted line in Fig. 4 represents the concentration profile for a diffusion controlled process. It follows from the two curves that the hypochlorite concentration in the diffusion layer is shifted upward by the chemical reaction and a steeper concentration gradient at the anode results. Curve 2 illustrates the interesting fact that the concentration in the diffusion layer may even exceed the bulk concentration. It was calculated in the same way as curve 1 but under the assumption of zero bulk hypochlorite concentration. The concentration max-

Table I. Data of experiments A and B used in the calculation of concentration profiles and equilibrium concentrations

	A	B
Sodium chloride concentration (mole/liter)	4.0	0.056
Current density (ma/cm <sup>2</sup> )	20	20
Average temperature (°C)	20	13
Average pH	9.3	9.0
Steady-state hypochlorite concentration (mM/liter)	134	10
Steady-state chlorate formation rate (mole/cm <sup>2</sup> sec)	$20 \times 10^{-9}$	$17.6 \times 10^{-9}$
Current efficiency for chlorate formation (%)	57.8	50.8
Thickness of diffusion layer (cm) calculated from oxygen evolution rate	$1.1 \times 10^{-3}$	$0.9 \times 10^{-2}$

imum within the diffusion layer may be interpreted in such a way that in the absence of hypochlorite in the bulk solution part of the hypochlorite generated within the diffusion layer reacts at the anode and part of it diffuses toward the bulk. In the absence of hypochlorite losses in the bulk curve 2 does not represent a true steady state, because the bulk concentration increases with time. The steady-state approach is appropriate, however, for large bulk volumes, where the hypochlorite concentration changes only very slowly. In the absence of hypochlorite losses other than anodic, a true steady state would be reached when the bulk hypochlorite concentration reaches a value equal to the corresponding maximum concentration of the diffusion layer.

In order to test the above ideas about the mechanism of anodic chlorate formation, chlorate formation rates were measured under well defined conditions of hydrodynamic flow, of pH, and of temperature.

#### Experimental Procedure and Apparatus

The experimental set-up is shown schematically in Fig. 5a. The electrolyte was pumped continuously through a channel cell at flow rates between 10 and 160 cm/sec. The Lucite cell (Fig. 5b) contained compact impregnated graphite electrodes (EK 200 Ringsdorf, Germany) with smooth surfaces of a length (in the direction of flow) of 5, 10, or 20 cm, the breadth being 5 cm in all cases. A diaphragm (porous polyethylene) could be inserted between anode and cathode. The distance between anode and cathode (or diaphragm) was 2.25 or 9 mm. Potentials at the anode were measured vs. a saturated calomel electrode using a backside capillary drilled through the graphite. If a diaphragm was inserted in the cell, the cathodically evolved hydrogen could escape from a glass tube connected to a mercury valve. The temperature of the system was kept low by means of a cryostat in order

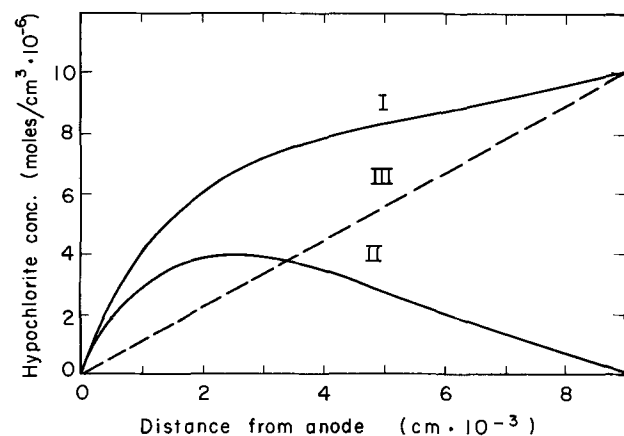


Fig. 4. Calculated hypochlorite concentration profiles in the diffusion layer (experiment B). Curve I,  $c_0 = 10 \times 10^{-6}$  mole/cm<sup>3</sup>, curve II,  $c_0 = 0$ , both curves, diffusion coupled with chemical reaction, and curve III, diffusion controlled process,  $c_0 = 10 \times 10^{-6}$  mole/cm<sup>3</sup>.

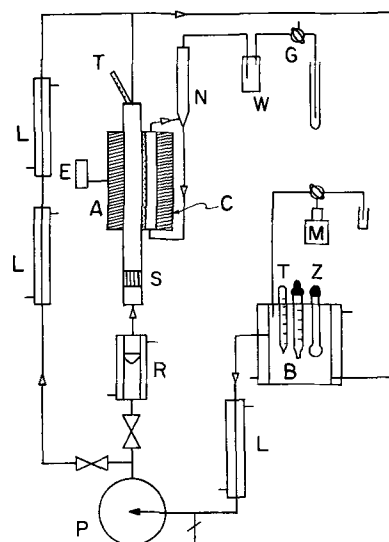


Fig. 5a. Experimental set-up for continuous flow electrolysis. A, anode; B, bulk reservoir; C, cathode; D, diaphragm; E, reference electrode; F, backside capillary; G, gas outlet; L, cooling device; M, buret for automatic pH control; N, pressure compensating tube; P, pump; R, rotameter; S, channels for quieting the flow; T, thermometer; W, gas washing bottle; Z, glass electrode.

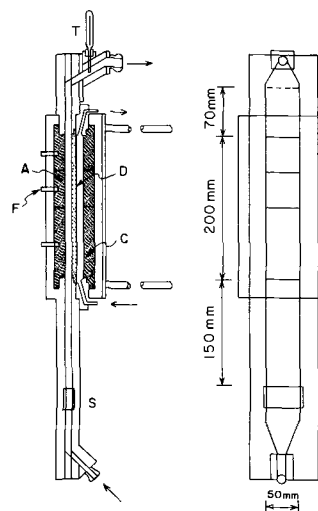


Fig. 5b. Flow cell. For caption see Fig. 5a

to suppress the chemical chlorate formation (reaction E). Most experiments were performed at a constant temperature of  $7^\circ \pm 0.5^\circ\text{C}$ . The pH of the electrolyte was measured with a glass electrode. It was kept constant by automatically adding conc NaOH or conc HCl with the help of an "Impulsomat" (Metrohm, Herisau, Switzerland). The flow rate was measured with a rotameter and regulated by two PVC valves and a bypass. A nonpulsating ceramic pump was used (Chemiepumpenbau, Zofingen, Switzerland). The flow of the solution was quieted by passing through 20 to 80 channels, 2 mm in diameter, drilled through Lucite block S. The whole system contained no metallic parts in contact with the electrolyte. The electrolyte volume used varied from 1.6 to 2.0 liter. The electrolysis was performed at constant current density, usually 5 ma/cm<sup>2</sup>.<sup>8</sup> The absence of chemical chlorate formation during the experiments was confirmed by circulating hypochlorite solutions in the flow system under the same conditions, but in the absence of current, and measuring hypochlorite and chlorate concentrations as a function of time.

<sup>8</sup> Further details of the experimental arrangement and of the results are given in the thesis of one of the authors (10).

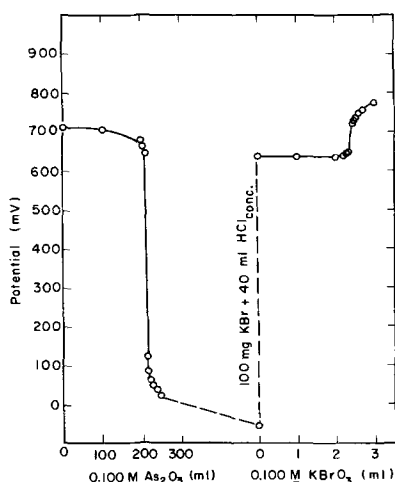


Fig. 6. Potentiometric titration of hypochlorite and chlorate

**Analytical.**—Two samples of 2 ml were taken from the electrolyte solution at suitable intervals. One sample served for the determination of the chloride ion concentration by a conventional titration method using silver nitrate as titrant and potassium bichromate as indicator. In the second sample the sum of the concentrations of hypochlorite, hypochlorous acid, and molecular chlorine and the concentration of chlorate were determined using an improved potentiometric titration method, based on a procedure given by Norkus and Prokopchik (15). These authors determined hypochlorite by potentiometric titration with  $As_2O_3$ . The chlorate was then reduced by excess  $As_2O_3$  by heating the sample for several minutes to  $90^\circ C$  after  $OsO_4$  has been added as catalyst. The excess arsenic oxide was titrated with potassium bromate solution using methyl orange as indicator [cf. Peters and Deutschländer (16)].<sup>9</sup> In our experiments the following procedure was found to give rapid and sufficiently accurate results: After the addition of some 1N sodium bicarbonate solution to the sample, hypochlorite was titrated potentiometrically with a solution of usually 0.05 or 0.005 mole/liter  $As_2O_3$ . A 100 ml beaker containing a platinum ring electrode and a calomel electrode with ceramic double diaphragm was used. Before each run the platinum electrode was immersed briefly in conc sulfuric acid containing chromate. After reaching the hypochlorite endpoint excess arsenic oxide was added, then some potassium bromide (about 30 mg) and a volume of chemically pure concentrated hydrochloric acid approximately equal to the solution volume already present. The solution which had to contain now at least 20% HCl was then allowed to stand for 3 to 5 min. After that time the excess  $As_2O_3$  was titrated potentiometrically with  $KBrO_3$ . The relative potential change was followed using a potentiometer range of 0–140 mv. The shape of the potentiometric titration curves is illustrated in Fig. 6. The accuracy of the chlorate concentration values determined by the described method was better than  $\pm 2\%$  for chlorate concentrations not smaller than 0.001 mole/liter. In view of its great importance for the present study the analytical procedure was tested in some detail. A more complete report of the experiments carried out has been given elsewhere (10).

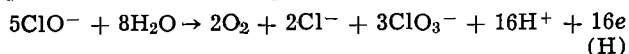
### Experimental Results

In each run the change of the hypochlorite concentration with time was followed, until a steady state

<sup>9</sup> Norkus and Prokopchik give a procedure by which  $ClO_2^-$  can be determined in the same sample. Hypochlorite is then titrated in alkaline medium, chlorite in neutral medium with  $OsO_4$  as catalyst. The complete determination of hypochlorite, chlorite, and chlorate was found by us to be rather uncertain and lengthy, because of the slowness of potential changes in alkaline medium. The determination of chlorite was not necessary, however, in our experiments, since tests showed that in chlorate electrolysis chlorite is never present in measurable amounts.

with a constant hypochlorite concentration was reached (Fig. 2). The values of the hypochlorite concentrations and of the rates of chlorate formation measured in the steady state with dilute NaCl solutions are summarized in Table II. Measured and calculated rates of chlorate formation are compared in Table III in terms of the corresponding hypochlorite fluxes at the anode.

The linking of the rate of chlorate formation with the hypochlorite flux at the anode requires the knowledge of the stoichiometry of the anodic chlorate formation. According to reaction (F) three moles of hypochlorite, oxidized anodically, yield one mole of chlorate. Stoichiometric ratios different from those given by reaction (F) have been found by Rius and Llopis (17, 18). According to these authors their experiments fit best the equation



In this case only 1.7 moles of hypochlorite are needed to yield 1 mole chlorate. It seems that reaction (F) applies to acid baths, reaction (H) to strongly alkaline solutions. The great influence of pH on the stoichiometry of the anodic chlorate formation is apparent from Foerster's results (2) as well as from those of Rius and Llopis (17, 18). It was also observed in a series of stoichiometric measurements carried out in our laboratory. Now, we have seen that with the model discussed earlier the pH at the interface is quite low. We therefore use the stoichiometric ratios given by reaction (F). The formation of one mole chlorate then corresponds to the diffusion of three moles of hypochlorite to the anode. We thus have  $j_e = 3v_{ClO_3}$ , where  $v_{ClO_3}$  is the measured rate of chlorate formation (mole  $cm^{-2} sec^{-1}$ ). We will regard  $j_e$  as an experimental value of the hypochlorite flux at the interface.

The hypochlorite flux for a diffusion controlled process (without influence of a chemical reaction) may be calculated from the bulk concentration  $c_0$  by

$$j_d = -D_3 \frac{c_0}{\delta}$$

For the case that mass transfer is coupled with a first order chemical reaction (chlorine hydrolysis) the hypochlorite flux at the anode  $j_h$  is related to the bulk concentration by Eq. [8]. In the calculation of  $j_d$  and  $j_h$  the diffusion coefficient of hypochlorite was assumed as  $10^{-5} cm^2/sec$  since no measured values were available in the literature. The value of the rate constant for chlorine hydrolysis at  $7^\circ C$  was interpolated from an Arrhenius plot given in ref. (14) as  $k = 3.6 sec^{-1}$ . The diffusion layer thickness was evaluated experimentally by measuring limiting currents for the reduction of ferricyanide to ferrocyanide at various flow rates. The measurements were performed at  $25^\circ C$  with a solution containing 0.05 mole/liter potassium ferricyanide, 0.01 mole/liter potassium ferrocyanide, and 1.0 mole/liter potassium chloride. The cell geometries and electrodes were the same as in the chlorate experiments. Figure 7 shows Nusselt numbers calculated from the measured limiting currents according to

$$Nu = \frac{i_0 L}{F c_{Fe} D_{Fe}}$$

as a function of the Reynolds number  $Re = uL/v$ , where  $i_0$  = limiting current density;  $L$  = length of electrode<sup>10</sup> (here always 20 cm);  $F$  = Faraday con-

<sup>10</sup> For fully developed channel flow the quantity  $L^* = 4 \frac{\text{cross section}}{\text{perimeter}}$  would be more appropriate in forming the dimensionless numbers  $Nu$  and  $Re$  than the quantity  $L$  which is used in describing the flow past a flat plate. Since in the chlorate experiments the ratio electrode area/electrolyte volume must not be too small, the entrance length in our experiments was usually shorter than that required for the two hydrodynamic boundary layers to merge. The calculated value of the average diffusion layer thickness is not affected by the choice of the characteristic length as long as only experiments performed under equal geometrical conditions are compared as it was done here.

Table II. Constant current electrolysis of dilute NaCl solutions under forced convection

No.	Cl <sup>-</sup> , mole/liter	T <sub>s</sub> , °C	pH	u, cm/sec	i, ma/cm <sup>2</sup>	E <sub>a</sub> , mv v. SCE	Gap width, mm	c <sub>st</sub> , mM/liter	v <sub>ClO<sub>3</sub></sub> , mole/cm <sup>2</sup> sec × 10 <sup>-9</sup>	τ <sub>ClO<sub>3</sub></sub> , %
1	0.046	0.0	4.0	13	1	1580	9	1.95	0.93	53.7
2	0.055	0.0	1.9	13	1	1560	9	1.50	0.72	41.6
3	0.037	3.2	3.1	13	5	1620	9	5.4	3.56	41.2
4	0.047	0.3	9.0	13	5	1600	9	6.4	4.30	49.8
5	0.130	2.2	9.0	13	5	1580	9	14	5.41	62.7
6	0.047	7.8	2.0	13	5	1580	9	1.4	3.32	38.4
7	0.052	7.0	2.0	13	5	1610	9	0.5	1.72	19.8
8	0.05	7.0	9.0	13	5	1680	9	1.0	2.07	23.9
9	0.05	7.0	9.0	13	5	1670	9	1.6	2.94	34.0
10	0.05	7.0	9.0	13	5	1660	9	1.2	2.87	33.2
11	0.1	7.0	9.0	13	10	1720	9	~3	7.11	41.0
12	0.073	7.0	9.0	44	5	1530	9	1.3	3.39	39.2
13	0.053	7.0	9.0	44	5	1550	9	0.3	1.71	19.7
14	0.083	7.0	9.0	44	5	1580	9	1.0	2.84	32.8
15	0.052	7.0	2.0	44	5	1610	9	0.8	2.70	31.2
16	0.052	7.0	2.3	154	5	1700	2.25	0.4-0.3	2.01	23.3
17	0.055	7.0	2.1	154	5	1740-1900	2.25	(0.2)	1.77	20.4
18	0.053	7.0	9.2	153	5	1700	2.25	0.3-0.25	2.35	27.2
19	0.1	7.0	9.0	145	10	1810	2.25	0.7	6.06	35

Cl<sup>-</sup>, average value of chloride concentration in the steady state; the chloride concentration was held constant by adding conc NaCl periodically; T<sub>s</sub>, average cell temperature; variations in cell temperature with time  $\leq \pm 0.5^\circ$ ; pH: during the experiment the pH could vary  $\pm 0.3$  due to the automatic regulation; u, linear flow velocity; i, current density; E<sub>a</sub>, steady-state anode potential (given values are rounded average values, since the potentials were not always constant during an experiment); gap width, distance between anode and diaphragm; c<sub>st</sub>, measured total steady-state concentration of hypochlorous acid and chlorine; v<sub>ClO<sub>3</sub></sub>, chlorate formation rate in the steady state determined from the slope of chlorate concentration vs. time curves; τ<sub>ClO<sub>3</sub></sub>, current efficiency of chlorate formation related to the reaction Cl<sup>-</sup> → ClO<sub>3</sub><sup>-</sup> + 6e (6F per mole ClO<sub>3</sub><sup>-</sup> = 100%).

stant; c<sub>Fe</sub> = concentration of ferricyanide; D<sub>Fe</sub> = diffusion coefficient of ferricyanide in 1N KCl at 25°C, equal to  $0.7 \cdot 10^{-5}$  cm<sup>2</sup>/sec (19); u = linear flow velocity; ν = kinematic viscosity of the solution (equal to  $0.85 \cdot 10^{-2}$  cm<sup>2</sup>/sec for 1N KCl) (20).

From Fig. 7 average thicknesses of the diffusion layer were calculated for chlorate experiments of corresponding Reynolds numbers, according to  $\delta = L/NU$ . In the evaluation of Re the kinematic viscosity of a 0.05 N-sodium chloride solution at 7°C was taken as  $1.42 \cdot 10^{-2}$  cm<sup>2</sup>/sec (20, 21).

Table III. Comparison between measured and calculated chlorate formation rates

No.	δ, cm × 10 <sup>-2</sup>	c <sub>o</sub> , mole/cm <sup>3</sup> × 10 <sup>-6</sup>	j <sub>e</sub> , mole/ cm <sup>2</sup> sec × 10 <sup>-9</sup>	j <sub>a</sub> , mole/ cm <sup>2</sup> sec × 10 <sup>-9</sup>	j <sub>h</sub> , mole/ cm <sup>2</sup> sec × 10 <sup>-9</sup>	j <sub>e</sub> /j <sub>a</sub>	j <sub>e</sub> /j <sub>h</sub>
1	1.8	1.95	2.79	1.08	3.49	2.6	0.8
2		0.47	2.16	0.26	2.13	8.3	1.0
3		4.5	10.68	2.50	11.74	4.3	0.9
4		6.4	12.90	3.55	14.71	3.6	0.9
5		14	16.23	7.78	21.82	2.1	0.7
6		0.42	9.96	0.23	9.27	43.3	1.1
7		0.14	5.16	0.08	4.76	64.5	1.1
8		1.0	6.21	0.56	6.19	11.1	1.0
9		1.6	8.82	0.89	8.89	9.9	1.0
10		1.2	8.61	0.67	8.48	12.9	1.0
11		3.0	21.33	1.67	21.02	12.8	1.0
12	0.74	1.3	10.17	1.76	9.66	5.8	1.1
13		0.3	5.13	0.41	4.40	12.5	1.2
14		1.0	8.52	1.35	7.97	6.3	1.1
15		0.22	8.10	0.30	6.60	27.0	1.2
16	0.24	0.08	6.03	0.33	3.16	18.3	1.9
17		0.05	5.31	0.21	2.70	25.3	2.0
18		0.25	7.05	1.04	4.35	6.8	1.6
19	0.26	0.70	18.18	2.69	11.63	6.8	1.6

δ Average thickness of diffusion layer, calculated from limiting current measurements for ferricyanide reduction.

c<sub>o</sub> Concentration of hypochlorite and hypochlorous acid in the steady state. c<sub>o</sub> is related to the total concentration of chlorine, hypochlorous acid, and hypochlorite c<sub>st</sub> by

$$c_o = \frac{K_1 c_{st}}{(Cl^-)(H^+) + K_1} \times 10^{-3} \text{ [mole/cm}^3\text{]}$$

where K<sub>1</sub> is the equilibrium constant of the chlorine hydrolysis

$$K_1 = \frac{(HOCl)(Cl^-)(H^+)}{(Cl_2)} \text{ in mole}^2\text{/liter}^2$$

j<sub>e</sub> Hypochlorite flux at the anode determined from experimentally measured chlorate formation rates:  $j_e = 3v_{ClO_3}$  [cf. reaction (F)].

j<sub>a</sub> Hypochlorite flux at anode calculated from steady-state hypochlorite concentration assuming a diffusion controlled process:  $j_a = -D_3 c_o / \delta$ .

j<sub>h</sub> Hypochlorite flux at anode calculated by taking into consideration the chlorine hydrolysis within the diffusion layer (Eq. [8]).

### Discussion of Results

Table III shows that the ratio  $j_e/j_a$  strongly varies with the conditions and is always much larger than 1. The experimental rate of chlorate formation is up to 64 times larger than the value calculated for transport control without influence of a chemical reaction. This confirms our earlier results (8, 11) and is strong evidence that under the conditions of the experiments in Table II the rate of anodic chlorate formation is not controlled by a simple mass transport of hypochlorite by diffusion and convection from the bulk to the anode.<sup>11</sup> The calculation considering the influence of the chlorine hydrolysis in the diffusion layer, on the other hand, fits the experimental results much better; the ratio  $j_e/j_h$  remains nearly constant and is close to 1, except for very high flow rates. This departure from the value of 1 observed at high flow rates is not surprising, however. In the fundamental differential equation for the mass transport (Eq. [1]) the convection term was dropped before carrying out the integration which finally yielded the relationship  $j_e/j_h$  (Eq. [8]). This procedure can lead to a good ap-

<sup>11</sup> Mass transfer due to migration, although not entirely negligible in some of the experiments, played a minor role, since excess chloride was always present in the solution. Also the uncertainty in the assumption of a value of the diffusion coefficient does not alter the conclusions, since the uncertainty is expected to be smaller than a factor of 2 whereas  $j_a$  and  $j_h$  differ by an order of magnitude. Furthermore, if the estimated value of D was wrong,  $j_e/j_a$  would be different from 1 but would be constant in a transport controlled process.

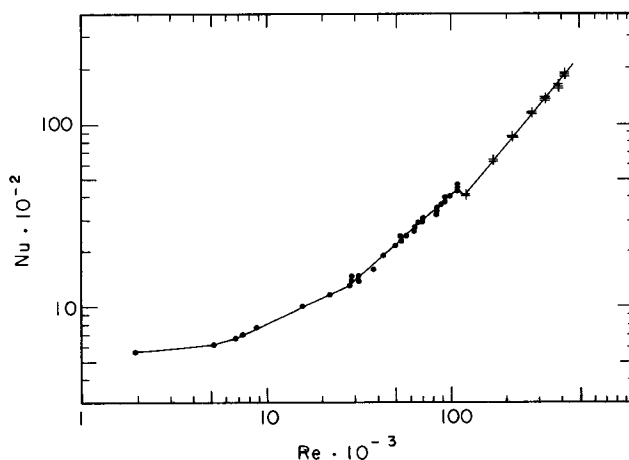


Fig. 7. Evaluation of mass transfer conditions in flow cell by measuring limiting current for the reduction of ferricyanide. O gap width 9 mm, + gap width 2.25 mm.

proximation only if the thickness  $\delta_R$  of the zone in which the hydrolysis takes place (reaction layer) is small as compared to the normal thickness which the diffusion layer would have in the absence of a chemical reaction. Let us consider as representative for  $\delta_R$  the distance from the anode at which the chlorine concentration has dropped to 1% of its value at the interface.<sup>12</sup> With  $k = 3.6 \text{ sec}^{-1}$  we obtain for this distance (from Eq. [3]) a value of  $3.8 \times 10^{-3} \text{ cm}$ . At flow rates of 13 and 44 cm/sec this is smaller than the normal thickness of the diffusion layer  $\delta$ , but not at flow rates of 145 and 154 cm/sec (Tables II and III). These two latter flow rates are precisely those at which the ratio  $j_e/j_h$  becomes substantially larger than 1.

From all this we can conclude that the model involving the coupling of mass transfer with a first order chemical reaction proceeding in the diffusion layer describes adequately the mechanism of anodic chlorate formation under the conditions of the experiments of Table II and Table III. In dilute NaCl solutions the rate of the anodic chlorate formation is governed by the kinetics of the chlorine hydrolysis in the immediate vicinity of the electrode.

In concentrated NaCl solutions, however, the ratio  $j_e/j_h$  is systematically substantially smaller than 1 (23) and, as we have seen in Fig. 1, the steady-state bulk concentration of hypochlorite is much larger than in dilute solutions. This suggests that the mechanism of chlorate formation is not the same in dilute and concentrated NaCl solutions: The model developed in this paper appears to be restricted to dilute solutions. This can be readily understood by considering the chemical equilibrium of reaction (C) in the diffusion layer.<sup>13</sup> For the purpose of illustration the equilibrium HOCl concentration at the point where the HOCl concentration reaches a maximum in the diffusion layer, is calculated for the two experiments A and B listed in Fig. 2 and Table II. The bulk hypochlorite concentration is assumed to be zero in both cases. The distance from the anode at which the maximum is located, is obtained by differentiating Eq. [7] and setting  $dc_3/dx = 0$ ,

$$X_m = -\frac{1}{a} \ln Z$$

with

$$Z = \frac{1}{a\delta} (1 - e^{-a\delta}) - \frac{2c_0 D_3 F}{\delta i \phi_1}$$

The corresponding numerical values are  $X_m = 2.18 \times 10^{-3} \text{ cm}$  for A and  $2.49 \times 10^{-3} \text{ cm}$  for B. The hydrogen ion concentrations at  $X_m$  are  $25.89 \times 10^{-3} \text{ mole/liter}$  for A and  $19.98 \times 10^{-3} \text{ mole/liter}$  for B, calculated from Eq. [6], setting  $\phi_2 = 1 - \phi_1$  and  $D_2 = 5 \times 10^{-5} \text{ cm}^2/\text{sec}$ . The equilibrium concentration of HOCl is given by

$$(\text{HOCl})_{\text{eq}} = \frac{K(\text{Cl}_2)}{(\text{Cl}^-)(\text{H}^+)}$$

where  $K \approx 3 \times 10^{-4} \text{ mole}^2/\text{liter}^2$  at the temperature of the experiments (22). Setting for the chlorine concentration the maximum possible value corresponding to the saturation concentration  $(\text{Cl}_2)_{\text{sat}} \approx 0.06 \text{ mole/liter}$  one obtains the maximum possible values of the

<sup>12</sup> The definition of the thickness of the reaction layer is somewhat arbitrary. One can also define an effective thickness of the reaction layer in a way quite similar to the definition of the usual effective or equivalent thickness of the adhering diffusion layer of Nernst. From Eq. [3] it can be easily derived that the effective thickness of the reaction layer is equal to  $0.5\sqrt{D_1/k}$  if the influence of convection is entirely disregarded. With  $D = 10^{-5} \text{ cm}^2 \text{ sec}^{-1}$  and  $k = 3.6 \text{ sec}^{-1}$  this effective thickness is about  $2 \times 10^{-3} \text{ cm}$ . Comparison with the values of  $\delta$  shown in Table III leads to the same conclusions as above, i.e. that the departure of  $j_e/j_h$  takes place at flow rates which appear as very reasonable from the viewpoint of the simplifications made.

<sup>13</sup> The outlined considerations based on the dependence of the rate of the chlorine hydrolysis and of the hydrolysis equilibrium in the diffusion layer on chloride concentration and pH may explain why there has to be a difference in the bulk hypochlorite concentration in dilute and concentrated chloride solutions. But there are also differences between the two cases with respect to the electrode reactions which will be discussed elsewhere (23).

HOCl equilibrium concentration at  $X_m$

$$c_{3 \text{ eq}} = 0.17 \times 10^{-6} \text{ mole/cm}^3 \quad (\text{A})$$

$$c_{3 \text{ eq}} = 16.1 \times 10^{-6} \text{ mole/cm}^3 \quad (\text{B})$$

These concentrations may then be compared to the concentrations at  $X_m$  calculated from Eq. [7] for a first order irreversible reaction

$$c_{3h} = 3.69 \times 10^{-6} \text{ mole/cm}^3 \quad (\text{A})$$

$$c_{3h} = 3.88 \times 10^{-6} \text{ mole/cm}^3 \quad (\text{B})$$

Comparison shows that for the dilute sodium chloride solution (experiment B) the value  $c_{3h}$  lies well below the equilibrium value. In concentrated sodium chloride solution (experiment A), on the other hand, the value of  $c_{3h}$  is about 20 times larger than the equilibrium value. The above comparison illustrates the fact that in concentrated NaCl solutions the chlorine hydrolysis cannot proceed in the diffusion layer in the same way as in dilute solutions, because the equilibrium value is reached much earlier and the hydrolysis is therefore stopped. Our study of the concentrated solutions will be reported in more detail in a subsequent paper (23).<sup>14</sup>

#### Acknowledgments

The authors wish to thank A. Frei for helpful discussions. This work was supported by the Robert Gnehm Fonds of the Swiss Federal Institute of Technology and the Schweizerischer Aluminium Fonds, Zurich, and also by the United States Atomic Energy Commission.

Manuscript received Dec. 6, 1967; revised manuscript received March 19, 1968. This paper was presented at the Cleveland Meeting, May 1-6, 1966, as Abstract 168.

Any discussion of this paper will appear in a Discussion Section to be published in the June 1969 JOURNAL.

<sup>14</sup> A summary of the results obtained with dilute and concentrated solutions has been recently given elsewhere (24).

#### REFERENCES

1. F. Foerster, *Elektrochem. wässriger Lösungen*, 3. Aufl. (1922).
2. F. Foerster, *Trans. Am. Electrochem. Soc.*, **46**, 23 (1924).
3. E. Müller, *Z. Elektrochem.*, **5**, 469 (1899).
4. N. V. S. Knibbs and H. Palfreeman, *Trans. Faraday Soc.*, **16**, 402 (1920).
5. V. de Valera, *ibid.*, **49**, 1338 (1953).
6. T. Beck, paper presented at the Indianapolis Meeting of the Society, April 30-May 3, 1961 as Abstract 125.
7. L. Hammar and G. Wranglén, *Electrochim. Acta*, **9**, 1 (1964).
8. A. Selvig, Thesis ETH, Zurich, Prom. Nr. 3268 (1962).
9. N. Ibl and J. Venczel, Paper presented at the Cleveland Meeting of the Society, May 1-6, 1966 as Abstract 94. J. Venczel, Thesis ETH, Zurich, Prom. Nr. 3019 (1961).
10. D. Landolt, Thesis ETH, Zurich, Prom. Nr. 3673 (1965).
11. N. Ibl, *Chem. Ing. Techn.*, **35**, 353 (1963).
12. T. Beck and N. Ibl, Unpublished correspondence (1962/63).
13. J. W. Ingham and J. Morrison, *J. Chem. Soc.*, **8**, 1200 (1933).
14. C. W. Spalding, *A.I.Ch.E. Journal*, **8**, 685 (1962).
15. P. K. Norkus and A. Yu. Prokopchik, *Zhur. Anal. Khim.*, **16**, 336 (1961).
16. K. Peters and E. Deutschländer, *Apoth. Z.*, 594 (1926).
17. A. Rius and J. Llopis, *Anales Fis. quim.*, **41**, 1030, 1282, 1395 (1945).
18. J. Llopis, *ibid.*, **42**, 41 (1946).
19. D. Jahn and W. Vielstich, *This Journal*, **109**, 849 (1962).
20. *Handbook of Chemistry and Physics*, 43rd ed., D. C. Hodgman, R. C. West, and S. M. Selby, Edi-



tors, Chemical Rubber Publishing Co., Ohio (1961).  
 21. Landolt-Börnstein, *Phys. Chem. Tab.*, 1, 138 (1923).  
 22. R. E. Connick and Y. T. Chia, *J. Am. Chem. Soc.*, **81**, 1280 (1959).

23. D. Landolt and N. Ibl, To be published in *Electrochim. Acta*.  
 24. N. Ibl and D. Landolt, *Chem. Ing. Tech.*, **39**, 706 (1967).

## Technical Notes



### The Hydrothermal Corrosion and Recrystallization of Noble Metals

V. G. Hill

*Tem-Pres Research, Inc., A Carborundum Subsidiary, State College, Pennsylvania*

During a research program on the hydrothermal growth of oxide crystals, it was observed that in some cases the solutions used dissolved parts of the noble metal liners of the autoclaves and produced small crystals of these metals. The understanding and preventing of this type of corrosion is important because it is necessary to protect the autoclaves from the corrosive solutions often used by containing them inside noble metal liners. The deterioration of the liner often results in the loss of the autoclave by the escape of the solution through holes formed in the liner. The increased application of the hydrothermal method, particularly with concentrated solutions for the growth of various single crystals including some higher valence compounds and nonstoichiometric oxides, makes this an urgent problem.

The growth of metal crystals by the hydrothermal technique is also of interest because there are few reported examples of the application of the method for producing metal crystals hundreds of degrees below their melting points (1, 2). Levinson and Carter obtained silver crystals during the growth of  $\alpha\text{-Al}_2\text{O}_3$  using 4N NaOH as the hydrothermal solution. Similar results were obtained by Monchamp, Putzbach, and Nielsen (3) during the growth of ruby and  $\text{Y}_3\text{Fe}_5\text{O}_{12}$  from  $\text{K}_2\text{CO}_3$  solution and ZnO crystals using 5M KOH as the hydrothermal solution. They found that the crystallization of the silver liner could be prevented by suspending in the solution a small piece of the metal whose oxide is being grown.

We found that silver, gold, and platinum dissolved in some hydrothermal solvents and grew as small crystals. In the case of silver, 4N KOH solution dissolved and recrystallized it at an appreciable rate in the presence of only small amounts of oxygen at temperatures above 400°C. The solution of the metal occurred in the nutrient part of the vessel where a liquid phase (KOH solution) was present. The growth of the silver crystals was primarily in the liquid phase, particularly at the interface of the liquid and vapor phases. This suggested that silver was much less soluble in the vapor phase than in the liquid. The crystals grew out from the walls of the vessel toward the center and were up to 5 mm in length. The silver crystals were of rhombic outline. These rhombs were often elongated forming laths, or grew as stepped clusters to form hollow rhombs (Fig. 1). Confirmation of the role of oxygen was obtained by comparing the results obtained from runs in which oxygen was deliberately introduced with those made in an oxygen-free environment. The former yielded copious silver dendrites, while the latter did not produce any silver crystals at all. The presence of only a small amount of oxygen

in the vessels resulted in a slower growth rate, but much better crystals. Silver was also attacked and recrystallized by 2N LiCl solution. The results appear to be similar to those produced by KOH solutions.

The best gold crystals were formed by the attack of 2N LiCl on the walls of the sealed gold capsules at temperatures between 350° and 450°C. Most of the crystals were needles, but a few were cube faces truncated by octahedron faces (Fig. 2). Roughly similar results were obtained with NaCl solution, but the degree of attack was much less. KCl solutions barely attacked it. HCl solutions also attacked gold in the presence of oxygen. Platinum was attacked by LiCl solutions, but much less so than either gold or silver, and in fact only a thin coating of platinum was deposited on the walls of the gold tube used to contain the reactants.

The attack on the silver by alkali hydroxide was due to the presence of oxygen in the vessel. The transport mechanism was probably through the formation of an unstable oxide. In reactions with amphoteric oxides in an alkali hydroxide solution, oxygen can be readily eliminated by suspending a small piece of the corresponding metal of the oxide in the alkaline solution. The hydrogen produced combined with any oxygen in the vessel and made the environment reducing. In other cases, a simple hydrogen generator was placed inside the autoclave. This was a sealed platinum tube crimped in the center initially to separate the charge of sodium hydroxide solution and metallic zinc. When the autoclave was heated, the contents of the tube expanded and reacted. The hydrogen gener-

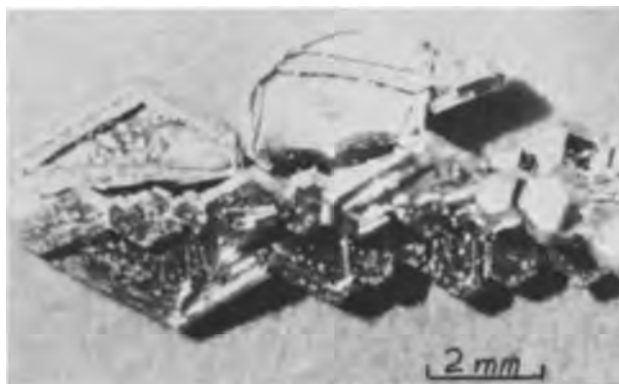


Fig. 1. Hydrothermally grown silver crystals

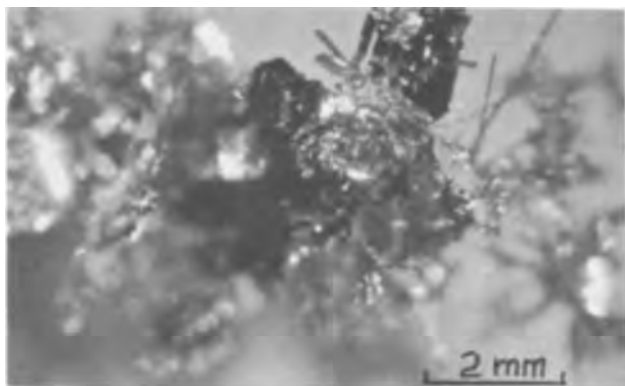


Fig. 2. Hydrothermally grown gold crystals

ated diffused through the walls of the tube into the autoclave. Attack on the silver by the strong alkali did not occur in a reducing environment. It is essential that the last traces of free oxygen be eliminated from the vessel. The amount of metal needed for the scavenging of all the oxygen can be reduced by making up the solution with freshly boiled water and flushing out the autoclave with nitrogen.

The crystallization of gold in chloride solutions appears to be related to the increase in the activity of oxygen with temperature. In fact, the experimental evidence suggests that oxygen becomes a very strong oxidizing agent, and may severely corrode gold under certain conditions. It should be pointed out however that although the attack on gold increases with increased oxygen pressure, very little oxygen is required to initiate the attack. It is thus possible for gold to be transported across a thermal gradient and redeposited in the presence of only trace amounts of oxygen. The mechanism of the reaction is probably due to the formation of complex gold halide anions which decompose to give metallic gold. The mechanism

of the attack on platinum appears to be also related to the change in activity of the oxygen with temperature. The result is much less severe than in the case of either silver or gold.

Other metals and alloys are also dissolved and re-crystallized by solutions under hydrothermal conditions. For example, the alloy, Stellite 21, which is used to fabricate the autoclaves was attacked by KOH solution in some runs and small cobalt crystals grew in the cooler parts of the vessel.

These results serve to emphasize the limitations in the use of noble metal liners in current hydrothermal research. These are more suitable for work under reducing rather than oxidizing conditions. The use of halogens, particularly chlorides, should be avoided. Platinum appears to be best for working under oxidizing conditions, but the severity of attack may increase under high oxygen pressures, particularly in runs of long duration. Silver appears to be the most serviceable in strongly alkaline solutions under reducing conditions.

#### Acknowledgments

The author wishes to express his thanks to Dr. R. I. Harker for his interest in the work and for critically reading the manuscript. This work was done as part of a research project on hydrothermal crystal growth sponsored by the U.S. Air Force Materials Laboratory, Wright-Patterson Air Force Base, Ohio. Mr. Paul W. Dimiduk was the Project Engineer.

Manuscript received July 31, 1967; revised manuscript received March 26, 1968.

Any discussion of this paper will appear in a Discussion Section to be published in the June 1969 JOURNAL.

#### REFERENCES

1. J. Wyart, *Discussions Faraday Soc.*, **5**, 323 (1949).
2. S. Levinson and F. L. Carter, *This Journal*, **113**, 756 (1956).
3. R. R. Monchamp, R. C. Puttbach, and J. W. Nielsen, *ibid.*, **113**, 1133 (1966).

## A Stress Corrosion Cell for Uniaxial Tensile Tests

F. H. Cocks and W. M. Krebs\*

*Tyco Laboratories, Inc., Waltham, Massachusetts*

There is at present great interest in studying the phenomenon of stress corrosion cracking, particularly in aluminum and titanium alloys, and a variety of test methods are being used to determine the susceptibility of metals to failures of this kind (1, 2). Most of these methods may be considered as either constant strain or constant load tests. In almost all cases what is measured, in addition to electrochemical data such as current density or potential, is the time to failure or to the first appearance of surface cracks. In constant load tests a weight is hung from the specimen either directly or through levers. In the more usual constant strain tests, the specimen is bent to a fixed radius or loaded uniaxially by a bolt and nut mechanism. These methods have the advantage of simplicity of construction so that they are well suited to situations where large numbers of samples are to be tested and multiple testing jigs are necessary. They fail, however, to take advantage of the greater amount of information concerning mechanical properties that can be obtained through the use of modern tensile testing equipment. To utilize to the full extent the capabilities of the model TTDL Instron Universal Testing Machine a special stress corrosion cell was built. Although designed for use with an Instron, this cell can equally

well be used with any vertical tensile machine having a 6-in. clearance, or for any constant deadweight load experiment. As will be discussed, this cell has the particular advantage of being fully sealed from the atmosphere and has facilities for thermostating and for mass transport control.

The cell consists, as shown schematically in Fig. 1 and in the photographs of Fig. 2, of a heavy walled Pyrex tube, fitted with smaller inlet and outlet tubes which terminate in ball joints. The working volume is about 70 ml. The inlet tube is fitted with a perforated ring of glass which directs the incoming flow uniformly against the gauge section of the specimen. Provision for controlled stirring is not commonly provided in stress corrosion studies, but it has been found that under certain circumstances the stirring rate can be an important variable (3). The outlet has an extension tube which is bent upward to draw off any gas produced during the corrosion process. The solution is circulated by means of a Masterflex peristaltic pump<sup>1</sup> operating on Viton tubing and connected to the system via Teflon tubing and ground glass ball joints. Before entering the cell, this solution is thermostated by being passed through a water-jacketed

\* Electrochemical Society Active Member.

<sup>1</sup> Cole-Parmer Institute and Equipment Corporation, Chicago, Illinois.

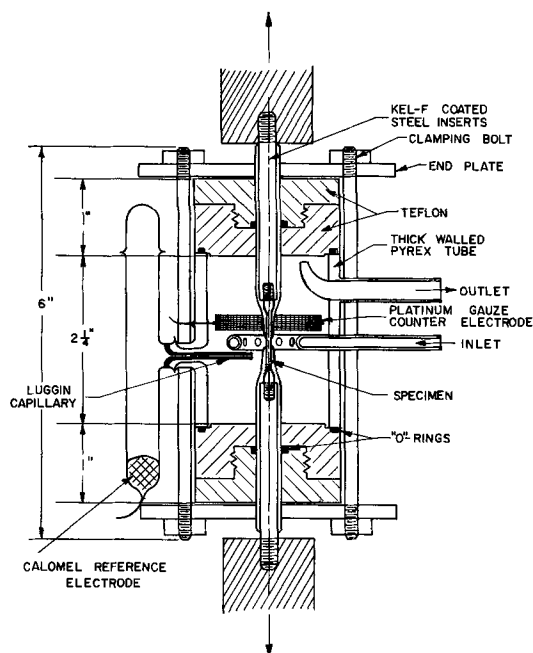


Fig. 1. Schematic diagram of the stress corrosion cell

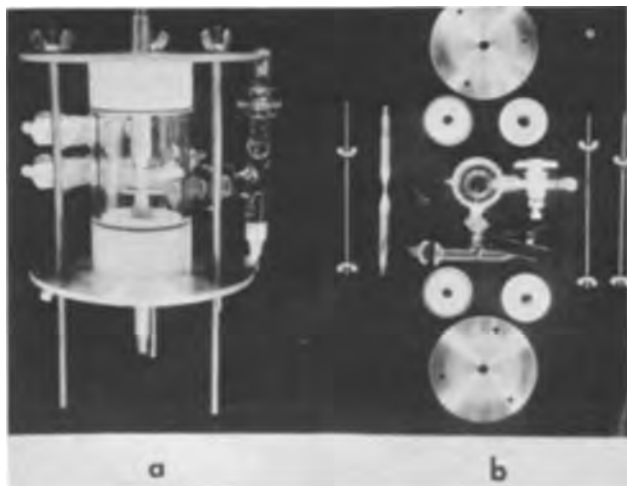


Fig. 2. Stress corrosion cell (a) as assembled, including specimen, and (b) disassembled.

reaction kettle. There it is also deoxygenated by purging with nitrogen before being pumped into the cell itself. Using a Haake<sup>2</sup> thermostat to control the temperature in the jacket, the cell has been operated with solution temperatures up to 75°C. The peristaltic pump system is completely reversible and can supply continuously variable flow rates of from 0 to 700 cc/min.

A ring of fine mesh platinum screen serves as the counter electrode. The reference electrode, against which the specimen potential is measured, is contained in a separate unit which is joined to the cell via an O-ring joint. From this reference electrode a Luggin capillary extends into the cell close to the working electrode. This capillary not only reduces the "uncompensated" resistance between the reference and working (specimen) electrode, but also virtually eliminates agitation in the reference compartment due to stirring in the body of the cell. Such a design also permits the rapid and easy exchange of reference electrodes as would be required, for example, in changing from chloride to sulfate solutions.

<sup>2</sup> Poly Science Corporation, International Division, Evanston, Illinois.

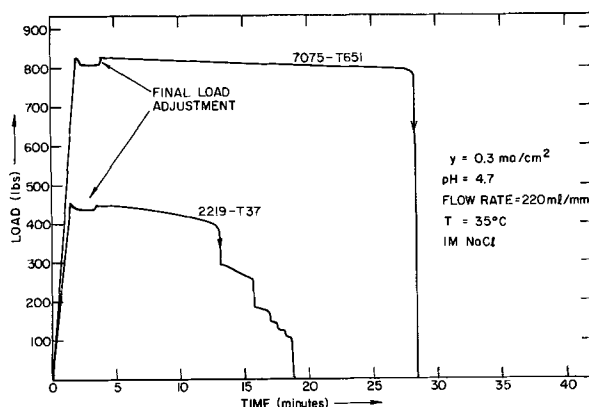


Fig. 3. Load vs. time during stress corrosion tests on the aluminum alloys 2219-T37 and 7075-T651.

The sample itself is a short 1½-in. standard tensile specimen which is threaded at each end into ⅜-in. steel extension rods. By using small specimens, samples from the short transverse direction of rolled material can be tested, and this is usually the direction of interest in stress corrosion studies. This assembly, sample and grips, is dipped into a molten mixture of Kel-F No. 200 and No. 210 waxes to mask off all but a ⅜-in. section on the gauge length, to which corrosion is consequently restricted. Masking the grips is necessary in order to eliminate corrosion of the steel extension rods. These are passed through the Teflon end pieces of the cell by means of deformable O-ring seals, as shown in Fig. 1. Because the end pieces are threaded, these seals can be independently tightened even after the cell is fully assembled (Fig. 2). The Teflon end pieces are also sealed onto the flat ends of the cell by means of O-rings together with three long bolts which pass through circular aluminum clamping plates at each end of the cell. The O-ring seals have been found to be extremely effective, and leakage of solution does not occur, even after violent specimen failure. The use of a sealed and purged system eliminates effects due to dissolved air or oxygen<sup>3</sup> and is, therefore, an improvement over other cells for use with testing equipment which have been open to the air (4). By using standard tensile bar samples, many of the problems associated with the use of wire specimens are avoided (3, 5).

In operation, the cell is mounted vertically in the Instron by threading the steel extension rods into tensile grips. The current through the cell (between working and counter electrodes) is monitored on a multirange strip chart recorder, and the load applied to the sample is continuously monitored by means of the Instron load cell. The strain is calculated from the known cross-head position. With this apparatus, it has been possible to make constant strain, continuous straining, and variable strain rate tests. The latter two types of tests in particular can provide information, especially on oxide film ductility (6), which cannot be obtained either from constant strain or constant dead weight load tests alone. By continuously monitoring the load, the amount of stress relaxation which occurs before failure can be quantitatively determined. This is a useful parameter because the stress is a critical factor in determining the time to failure, and if considerable relaxation occurs, the time to failure will be greatly increased. This could lead to an erroneous conclusion as to susceptibility, if not taken into account. Also, any discontinuities, such as might occur during sudden crack propagation, can be observed.

Figure 3 shows results obtained using this system. Here, the applied load vs. time during a stress corro-

<sup>3</sup> As was noted by Dr. H. Lee Craig at the workshop on stress corrosion held at the Naval Air Materials Laboratory, Philadelphia, June 6-7, 1967, the change in solubility of dissolved oxygen can account for most of the temperature dependence reported for stress corrosion of aluminum alloys.

Table I. Nominal compositions and yield strengths of the aluminum alloys 7075-T651 and 2219-T37

Alloy	Nominal composition	Yield strength, psi
7075-T651	Al-5.6 Zn-2.5 Mg-1.6 Cu-0.3 Cr	73,000
2219-T37	Al-6.3 Cu-0.3 Mn-0.18 Zr-0.1 V-0.06 Ti	44,000

sion test was measured for two different aluminum alloys, 7075-T651 and 2219-T37. The properties and compositions of these alloys are shown in Table I. The initial applied stress in each case was 90% of the 0.2% offset yield stress. Each test was carried out in 1M NaCl buffered to a pH of 4.7 with acetic acid and sodium acetate and corrosion was carried out galvanostatically with a current density of 0.3 ma/cm<sup>2</sup>. It is evident that there are different modes of failure of each alloy.

For 7075-T651, failure is catastrophic, and only a very brief period of rapidly decreasing load immediately preceding failure can be seen. Hence, a single stress corrosion event occurred, *i.e.*, once the crack reaches a critical length it causes immediate (probably purely mechanical) failure.

For 2219-T37, however, failure occurs in a stepwise manner, with several points of discontinuous load change separated by regions in which the load decreases relatively slowly. This stepwise failure can be interpreted in two ways; on the one hand, the intermittent decreases in load could represent discontinuous propagation of a single crack; alternatively, they could represent the periodic initiation of new cracks. To determine which of these possibilities was correct, specimens of high-purity Al-4 Cu alloy were prepared. After solution heat-treatment for 6 hr at 520°C, these specimens were quenched and aged for 20 hr at 200°C to render them susceptible to stress corrosion cracking. The 6-hr solutionization treatment gave rise to sufficiently large grain size (0.2 mm) that the mode of crack propagation could be observed directly. The specimens were also cut so as to have a rectangular cross section with a width to thickness ratio of six to one, thus allowing the progress of crack propagation to be observed over the full length of specimen life. These specimens cracked in the same stepwise manner as did the commercial 2219-T37 specimens, and in each case failure was observed to propagate via a single crack. The regions of discontinuous fall in load were observed to coincide with the advancement of a crack along a grain boundary. Similarly, the intervening regions of relatively slowly decreasing load resulted from the halting of crack advance at grain boundary intersections. It could be concluded, therefore, that cracking occurs in this alloy by a periodic-electrochemical-mechanical mechanism (7), and that the electrochemical stage is associated with the reinitiation of mechanical failure at grain boundary intersections.

This stress corrosion cell, and the capability of the Instron for setting load or strain, are particularly useful in a relatively new area of interest, of great relevance to stress corrosion, recently brought out by the work of Bubar and Vermilyea (6). In their preliminary studies they explored oxide ductility on a number of metals; the rupture of surface oxides is of crucial importance to many theories of aluminum stress corrosion. In our system studies of the oxide film ductility on aluminum alloys were made by varying the strain, while the specimen was under potentiostatic control. The principle of the method is as follows: If the oxide is completely nonductile, increasing the strain results in its continual rupture. This exposes oxide film-free metal surface. The process of "repairing" the surface via its anodic oxidation will then give rise to a current which adds to the steady corrosion current. With a ductile oxide, the film thins and rupture will occur sometime after the strain is

applied, depending on the ductility. The rate of current increase after this point will be not only a function of the rate of film rupture, but also will depend on the rate of film repair.

Figure 4 presents results obtained on a tensile specimen of 2219-T37 which had been potentiostatically controlled at a sufficiently anodic potential to result in a corrosion current of about 0.4 ma/cm<sup>2</sup>. The strain was applied after the current had become nearly steady. Unloading was carried out at the same strain rate as the loading. Slight load relaxation (creep) occurred during the period of constant strain. Thus, the time required for unloading was slightly smaller than that for loading. From Fig. 4, the delay between the time at which the load was applied and the point at which the current increased can be seen to correspond to a strain of  $1.5 \times 10^{-3}$ . Beyond this point the increase in current with time is unmistakable. The rate of increase in current with strain (time) does not remain constant but increases. At constant strain there is a small decrease in the current, which becomes very rapid as the sample is unloaded. The final current is approximately the same as that before the strain was applied. We should emphasize that the specimen of 2219-T37 underwent less than a 1% change in exposed area during straining, which alone is insufficient to account for the factor of two change in the current.

It is evident, therefore, that during straining the oxide film becomes less protective through thinning and/or fracture. This metal undergoes rapid dissolution and there is an increase in current. Repair of the film at these cracks undoubtedly occurs, but the low rate of current decrease at constant strain indicates that this repair occurs only slowly and inefficiently in chloride. The decrease in current upon unloading corresponds to the closure of these fissures. Had the sample been plastically deformed substantially such a process would have been markedly retarded. From the length of time between loading and current increase, at least an indication of the over-all strength of the oxide film can be obtained. It is thought that the oxide film is of a different character above grain boundaries and precipitate phases than above the solutionized matrix. This technique promises to provide a quantitative picture of these properties.

These experiments are indicative of the range of this technique. Using it, we can expect critical tests of oxide rupture theories of stress corrosion and detailed studies of flaws in their passive layers. Further studies on age-hardened aluminum alloys are in progress.

In summary, we have described a new stress corrosion cell. This cell has the advantages of being sealed, leak-free, easy to assemble, and suitable for electrochemical measurements under controlled load and strain conditions. With this cell we have explored the mode of cracking of two aluminum alloys. Specifically, we have shown that in the Al-Cu system, cracks

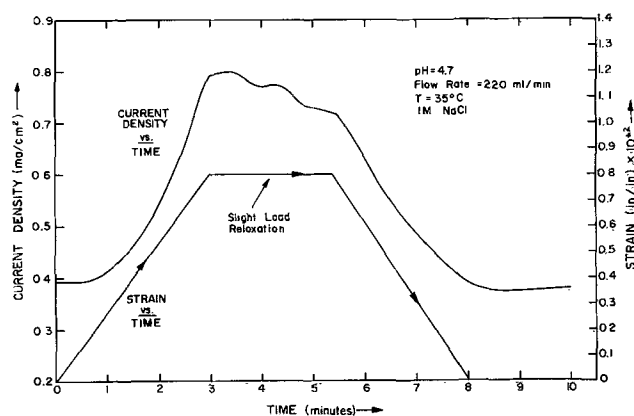


Fig. 4. Relation between strain and current density for 2219-T37.

progress rapidly along grain boundaries but can be halted at grain boundary intersections. Exploratory experiments have indicated the application of this system to the study of oxide ductility and film repair.

#### Acknowledgments

The authors wish to express their appreciation to J. F. Russo for his skillful assistance in the construction of this cell. This work was supported by the National Aeronautics and Space Administration, G. C. Marshall Space Flight Center, Huntsville, Alabama, on contract No. NAS 8-20297.

Manuscript received July 24, 1967; revised manuscript received Feb. 19, 1968.

Any discussion of this paper will appear in a Discussion Section to be published in the June 1969 JOURNAL.

## The Role of Gaseous Oxygen during HNO<sub>3</sub> Treatment of Platinum

Stuart G. Meibuhr\*

Research Laboratories, General Motors Corporation, Warren, Michigan

The nitric acid treatment (1-3) of bright Pt has been found to give a Pt electrode that will exhibit the reversible O<sub>2</sub> electrode potential of 1229 mv (4) in sulfuric acid and in phosphoric acid solutions (3). The treated, bright Pt electrode also has been shown to exhibit a higher double layer capacity (5) and a lower cathodic polarization (2, 6) than an untreated Pt electrode. The increased activity of the treated electrode has been maintained for several days despite severe cathodic polarization (6). Vacuum fusion analysis indicated a greater amount of oxygen to be associated with treated Pt than with untreated Pt (6); however, the quantity of nitrogen remained virtually unchanged.

The work reported here was concerned with the question of whether atmospheric oxygen was the source of the excess oxygen previously found in HNO<sub>3</sub> treated Pt.

The open-circuit oxygen potentials of three Pt wires were measured with an electrometer in a 3.25M H<sub>2</sub>SO<sub>4</sub> solution contained in a three-compartmented glass cell maintained at room temperature. Experiments were performed in triplicate. The electrolyte was preelectrolyzed cathodically and anodically at 200 ma/cm<sup>2</sup> in a manner similar to one described before (7). The H<sub>2</sub> counter and reference electrode was a small piece of American Cyanamid Company's AA-1 electrode material that was spot-welded to a Pt wire.

All three test electrodes were cleaned by repeated flaming followed by quenching in HNO<sub>3</sub>. After cleaning, the electrodes were washed well. The electrodes were then sealed in glass tubing with polypropylene. This technique was simpler than sealing the Pt wire directly to glass. Electrode number 1 was tested immediately without HNO<sub>3</sub> treatment. Electrodes 2 and 3 were HNO<sub>3</sub> treated for 4 days in a closed system. Electrode 2 was treated in acid through which oxygen was bubbled. This procedure simulated the open-air treatment described earlier (1). Electrode 3 was

\* Electrochemical Society Active Member.

#### REFERENCES

1. H. L. Logan, "The Stress Corrosion of Metals," John Wiley & Sons, Inc., New York (1967).
2. F. A. Champion, "Corrosion Testing Procedures," 2nd ed., John Wiley & Sons, Inc., New York (1965).
3. T. P. Hoar and J. J. West, *Proc. Roy. Soc.*, **A268**, 304 (1962).
4. T. R. Beck, Solid State Physics Lab., Boeing Scientific Research Lab., Seattle, Wash., Report D1-82-0554, July 1966.
5. T. P. Hoar and J. G. Hines, *J. Iron Steel Inst.*, **182**, 124 (1956).
6. S. F. Bubar and D. A. Vermilyea, *This Journal*, **114**, 882 (1967).
7. F. H. Keating, "Symposium on Internal Stresses in Metals and Alloys," p. 311, Institute of Metals, London (1948).

Table I. Results of open-circuit voltage measurements

Electrode	Potential, mv	Stability, hr
1	1060 ± 10	> 8
2	1225 ± 5	> 8
3	1225 ± 5	48

treated in acid through which argon was bubbled to exclude oxygen.

The measured open-circuit potentials of the three types of electrodes are listed in Table I. The difference between types 1 and 2 or 3 shows that the cleaning process did not affect the results. Because the potential of electrodes 2 and 3 was identical,<sup>1</sup> the oxygen found previously (6) in the HNO<sub>3</sub> treated Pt did not come from the atmosphere. The only possible source of the oxygen is the electrolyte.

Manuscript received Feb. 12, 1968; revised manuscript received March 19, 1968.

Any discussion of this paper will appear in a Discussion Section to be published in the June 1969 JOURNAL.

<sup>1</sup> Electrodes 2 and 3 also showed a similarity in their resistance to potential decay when hydrogen gas replaced oxygen.

#### REFERENCES

1. J. P. Hoare, *This Journal*, **110**, 1019 (1963).
2. J. P. Hoare, *ibid.*, **112**, 849 (1965).
3. R. Thacker and J. P. Hoare, *ibid.*, **113**, 862 (1966).
4. W. M. Latimer, "Oxidation Potentials," 2nd ed., p. 39, Prentice-Hall, New York (1952); A. J. de Bethune and N. A. S. Loud, "Standard Aqueous Electrode Potentials and Temperature Coefficients," Clifford Hampel, Skokie, Ill. (1964).
5. J. P. Hoare, *Nature*, **204**, 71 (1964).
6. J. P. Hoare, S. G. Meibuhr, and R. Thacker, *This Journal*, **113**, 1078 (1966).
7. R. Thacker, "Hydrocarbon Fuel Cell Technology," B. S. Baker, Editor, p. 525 Academic Press, Inc., New York (1965).

# The Use of Discontinuous Metal Films in Determining the Rate of Formation of Very Thin Oxide Films

Francis P. Fehlner

Research and Development Laboratories, Corning Glass Works, Corning, New York

## ABSTRACT

A new method for determining the low-temperature oxidation-rate constants of metals has been developed. The method is based on measuring the change in d-c resistance of a discontinuous metal film when it is exposed to oxygen. Values of the logarithmic oxidation-rate constant ( $10^{-9}$  cm) for zirconium (1.8-10.3), titanium (0.2-4.0), niobium (0.8-3.2), and nickel (0.2-2.0) have been determined under the following conditions: 77°-298°K and  $10^{-6}$  to  $10^{-8}$  Torr oxygen.

A new method has been developed to measure the tarnishing rate of a metal at or below room temperature. The method is based on the change in d-c resistance of a discontinuous metal film when it is exposed to a reactive gas such as oxygen. Using this method, oxidation rates for titanium (1, 2), nickel (2), and zirconium (3) have been found which are smaller than rates obtained by other investigators. In the present work, the low-temperature oxidation of niobium is examined.

This new technique is a direct outgrowth of a detailed study of the electrical properties of discontinuous thin films of metals on glass (1-3). Formation of such films occurs initially by the nucleation of discrete islands which, after a certain growth period, coalesce into a physically continuous film. For example, a metal film may be deposited on a glass substrate by evaporation in a vacuum system. The condensing atoms exhibit large surface mobilities, arising primarily from their still-high kinetic energy. The magnitude of this mobility will depend on the materials involved and on the temperature and condition of the substrate. The migrating atoms undergo mutual collisions, resulting in the formation of clusters and embryos. Finally, large stable islands of metal are formed on the glass surface. These islands subsequently grow both horizontally and vertically until they coalesce into a continuous film. If metal evaporation is halted before the islands join together, a discontinuous film is left on the glass surface. Pashley (4, 5) and others have described this process in much greater detail.

Discontinuous metal films have several outstanding electrical characteristics which differentiate them from thicker films, although film conductivity in both cases can be explained on the basis of electron transport. The temperature coefficient of resistance for discontinuous films is negative; they show a decrease in a-c resistance with increasing frequency, and their mode of electron transport is by tunneling of electrons from island to island through insulating gaps.

There has been a continuing discussion of the role of thermionic emission *vs.* tunneling in the electron transfer process, but for the present study, the "activated tunneling" mechanism proposed by Neugebauer and Webb (6, 7) best fits the experimental conditions in a quantitative manner. The following equation is a condensed version of their expressions for film conductivity in terms of the geometrical characteristics and energy considerations of the islands and gaps (Fig. 1).

$$\sigma = Ad\phi^{1/2} \exp \left[ -\frac{\epsilon}{kT} - Bd\phi^{1/2} \right] \quad [1]$$

where  $\sigma$  = film conductivity, A, B = constants dependent on island size,  $k$  = Boltzmann constant,  $d$  = interisland distance,  $\phi$  = energy barrier to electron

transfer,  $\epsilon$  = activation energy for conduction, and  $T$  = temperature.

In the study of oxygen adsorption on titanium (1, 2), nickel (2), and zirconium (3), the relationships between  $\sigma$ ,  $\phi$ , and  $d$  in Eq. [1] were examined. In brief, it was found that the initial chemisorption of an oxygen monolayer caused an increase in  $\phi$ , while the subsequent oxidation of the metal islands led to an increase in  $d$ . Both changes caused a decrease in  $\sigma$  or, conversely, an increase in film resistivity  $\rho$ .

The increase in  $d$  occurring during film exposure to oxygen can be directly related to the low-temperature oxidation-rate constant by combining the empirical expression (8a)

$$s = K \log (at + t_0) \quad [2]$$

where  $s$  = oxide thickness,  $t$  = time,  $K$  = oxidation rate constant,  $a$ ,  $t_0$  = constants, with the assumption that the interisland distance after oxidation equals the interisland distance prior to oxidation plus twice the oxide thickness. This is illustrated in Fig. 1, where the small correction due to the oxide-metal volume ratio has been ignored. Under the conditions of large interisland distances and long exposure times, the following equation has been derived (3) for determining  $K$

$$\frac{\Delta \log \rho}{\Delta \log t} = 8.06 \times 10^7 \phi^{1/2} K \quad [3]$$

where  $\Delta$  has been used in place of the differential.

The determination of  $K$  from Eq. [3] requires both low pressures and low temperatures, so that the reaction will proceed slowly. At oxygen pressures below  $10^{-6}$  Torr, both the formation of an oxygen monolayer and the oxidation process have been observed. From the latter, rate constants for the low-temperature oxidation of titanium (1, 2), nickel (2), zirconium (3), and niobium have been calculated. The resulting rate constants are smaller than those obtained by other investigators (see Table I). This difference can be attributed to the restrictive experimental conditions of  $10^{-8}$  to  $10^{-6}$  Torr, and 77°-298°K.

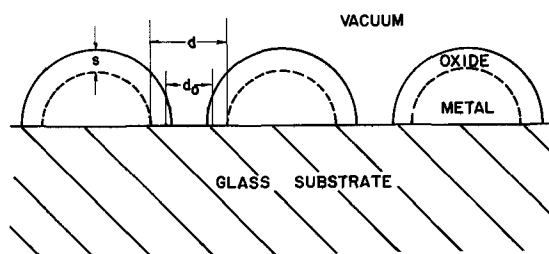


Fig. 1. Idealized cross section of a discontinuous thin film of metal;  $s$ , oxide thickness;  $d$ , interisland distance.

Table I. Comparison of experimental values for low-temperature oxidation-rate constants

Metal	Temp. range, °K	This work		Temp. range, °K	Literature		Refer.
		K, $10^{-9}$ cm	$E_a$ , kcal mole $^{-1}$		K, $10^{-9}$ cm	$E_a$ , kcal mole $^{-1}$	
Nickel	77-298	0.2-2.0	0.2	195-299 293	3-11 10	1.5 —	(26) (27)
Niobium	$\approx 50$ -298	0.8-3.2	0.01	—	—	—	—
Titanium	77-298	0.2-4.0	0.2	298 298	65 60	— —	(23) (28)
Zirconium	77-298	1.8-10.3	0.3	323-373	39-59	1.9	(23)

The discontinuous film method does not work well with low-melting-point metals, such as copper or aluminum (2), unless the metal film is first stabilized against thermal rearrangement. Such island rearrangement is responsible for a change in film resistivity which interferes with the resistivity change caused by oxygen exposure.

### Experimental Method

An ultrahigh-vacuum system was used for the experiments, to avoid contamination of the films before they were exposed to oxygen. The basic parts of the stainless-steel, copper-gasketed system are shown in Fig. 2. An 8-hr bakeout at 225°C led to a base pressure of  $10^{-9}$  Torr. Pressure readings taken with the Bayard-Alpert ion gauge were corrected to the substrate position.

Evaporations were carried out at  $2 \times 10^{-8}$  Torr from tungsten filaments. The films were deposited on Corning Code 7059 glass substrates held at the temperature at which the experiment was to be run. The only exception was the  $\approx 50^\circ\text{K}$  run in which film deposition took place at 77°K. Initial film resistance was used as a measure of film reproducibility, since the temperature coefficient of resistance for the films was close to zero. The metals were better than 99.9% pure. The films used in the present study were almost continuous, since films made up of very small islands would be completely oxidized during the formation of a monolayer of oxygen. Further experimental details are to be found in ref. (2) and (3).

### Results

The present work on the low-temperature oxidation of niobium illustrates the potential of the discontinuous thin film method. The log-log dependence of niobium film resistance on time at constant oxygen pressure is shown in Fig. 3, 4, and 5. Substrate temperatures were 297°, 77°, and  $\approx 50^\circ\text{K}$ , while the oxygen pressure was  $9 \times 10^{-8}$  Torr in all but one case. Initial film resistance was  $\approx 11$  kohm sq $^{-1}$  except in Fig. 5 where a value of 715 kohm sq $^{-1}$  was used. No unusual effects (3) due to heat of adsorption or impurities were encountered. The sudden rise in resistance caused by monolayer formation was followed by the log-log linear behavior resulting from island oxidation.

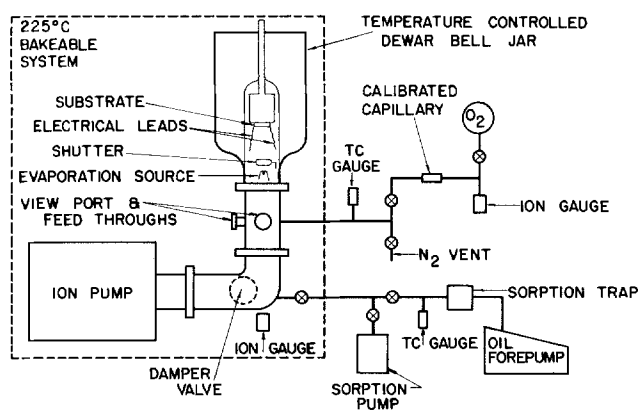


Fig. 2. Ultrahigh-vacuum system used for film evaporation, d-c resistance measurements, and oxygen exposure.

The slight increase in resistance with time found during the blank runs was due to adsorption of residual gases remaining in the vacuum chamber. This was especially true during the cool-down period for the  $\approx 50^\circ\text{K}$  runs.

The value of the change in niobium work function caused by oxygen adsorption is still unknown. Hence, the value of  $\phi$  in Eq. [3] was estimated to be 5 eV from comparison with the behavior of other refractory metals (9). Values of the rate constant  $K$  were then calculated from the slope of the  $\log R - \log t$  plots.

The value of the low-temperature oxidation-rate constant for niobium is compared with values for other metals in Table I. The relative oxidation rates follow the order:  $\text{Zr} > \text{Ti} > \text{Nb} > \text{Ni}$ . The rates found in the present work, when compared with those determined by other investigators, are found to be lower by a factor of approximately ten. The experimental activation energy shown in Table I is very small and may actually be zero, since the small difference in film structure caused by changes in deposition temperature was not taken into account.

### Discussion

The manner in which oxide films form at low temperature is still subject to various interpretations since definitive experimental data is lacking. Several theories (8b) have been developed to account for observations which include no oxygen diffusion into the metal (10), logarithmic kinetics (8a), and a very thin, adherent oxide film. The proposed mechanisms are

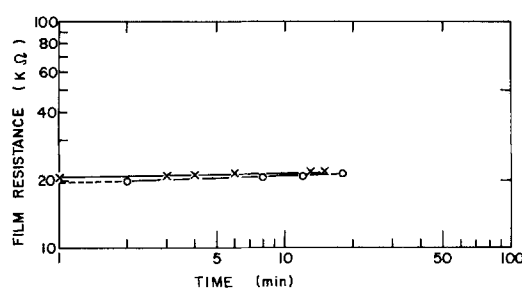


Fig. 3. Blank runs for niobium films in a vacuum of  $5 \times 10^{-9}$  Torr. X, Nb1A-1 at 297°K, O, Nb2A-1 at 77°K.

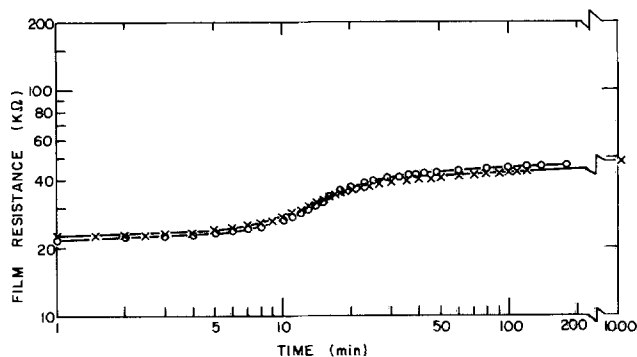


Fig. 4. Change in niobium film resistance caused by oxygen exposure at  $9 \times 10^{-8}$  Torr. X, Nb1A-1 at 297°K; O, Nb2A-1 at 77°K.



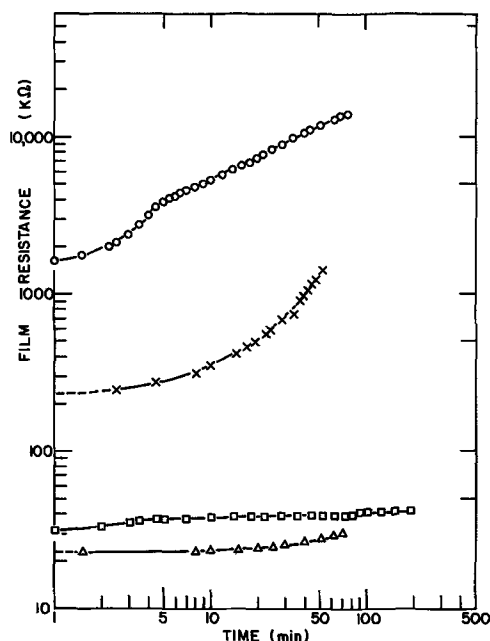


Fig. 5. Change in niobium film resistance caused by oxygen exposure at  $\approx 50^\circ\text{K}$ . X, cool down and O, oxygen run for Nb4A-1 at  $9 \times 10^{-8}$  Torr.  $\Delta$ , cool down and  $\square$ , oxygen run for Nb3A-1 at  $2 \times 10^{-7}$  Torr.

similar, since they all depend on electron transfer from the metal to oxygen adsorbed on the oxide surface. The electric field set up by the resulting charge separation causes ions to migrate through the oxide with a subsequent increase in oxide thickness.

The proposed oxidation mechanisms differ in the choice of a rate-limiting process: ion or electron transport. Cabrera and Mott (11) consider ion migration through the oxide under the influence of the electric field to be the most important process. Hauffe and Ilshner (12) hold that electron tunneling through the oxide is initially rate limiting with ion migration becoming subsequently more important. Fromhold and Cook (13) postulate a transition from ionic to electronic rate control. Uhlig (14) interprets the process as electron transfer across the metal-oxide interface, with a subsequent buildup of space charge in the oxide. These varied approaches to low-temperature oxidation predict either a direct or indirect logarithmic relationship between oxide thickness and time during the early stages of reaction, with a change in kinetics occurring after formation of a thin oxide film (in the range, 20-100Å thick). A direct logarithmic relationship (12, 14) is often observed, although the closely related inverse relationship is also possible (11). However, it is very difficult to differentiate experimentally between these two logarithmic relationships (15). Hence, the direct logarithmic expression has been adopted in the present work.

The interpretation of the experimental curves is based on the assumption that the Neugebauer-Webb conduction mechanism in discontinuous thin films involves direct tunneling from island to island through the vacuum gap. As a result, the sudden rise in resistance from B to C in Fig. 6 is interpreted as being due to an increase in the work function of the metal island surfaces. In other words, a monolayer of oxygen forms. The subsequent log-log linear portion of Fig. 6 (C to D) is then due to the oxidation of the islands.

Recently (16-19) conduction in discontinuous thin films has been reinterpreted in terms of electron tunneling from island to island through the substrate. This does not change the form of the conduction equation (Eq. [1]) but it does change the interpretation of the energy barrier  $\phi$ . No longer is  $\phi$  the vacuum work function of the metal islands, but it becomes the barrier to electron transfer at the metal-substrate in-

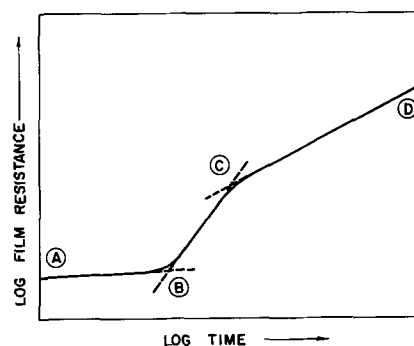


Fig. 6. Change in film resistance caused by oxygen exposure at constant pressure.

terface. Adsorption of a monolayer of oxygen can no longer affect film conductivity since  $\phi$  is not changed. However, oxidation of the metal islands still causes an increase in interisland distance and, as a result, an increase in film resistance. Hence, rate constants determined using Eq. [3] are still valid.

If substrate conduction is assumed, Fig. 6 must be reinterpreted. A to B now represents monolayer formation; B to C, a fast oxidation with a transition at C to a slow oxidation. These two oxidation rates may well correspond to the regions of ionic and electronic control postulated by Fromhold and Cook (13).

It is still too soon to discard the vacuum tunneling hypothesis, since substrate conduction has been shown to hold only for films with large interisland distances. The films used in the present work have very small interisland distances, so that it is still possible for direct tunneling to occur through the vacuum gaps (17). Experiments to resolve this point should be carried out in the near future. In any case, values of  $K$  calculated from the C to D linear portion of Fig. 6 would only be affected by a factor of two ( $\phi^{1/2}$ ) if the initial portion of the curve were reinterpreted.

The oxidation rate constants in Table I are based on an increase in the size of the interisland gaps and hence may be compared with the slow oxidation rate constants obtained by other investigators. The values of the oxidation rate constants found using the present method are smaller than those reported in the literature. Various factors can account for this difference.

Oxygen pressure was not an important variable in the discontinuous thin film work, but the range in which the pressure varied ( $10^{-6}$  to  $10^{-8}$  Torr) was far removed from that used to obtain the literature values (5-760 Torr) in Table I. Cabrera (20) has pointed out that pressures below  $10^{-4}$  Torr can lead to a reduction in the number of negatively charged oxygen ions adsorbed at the oxide-oxygen interface. As a result, the Mott potential and consequently the rate of oxidation will be reduced. Grimley (21) has also commented on this aspect of the oxidation process.

Low-temperature oxidation rates measured in high vacuum could not be found in the literature, so the effect of a ten-decade decrease in oxygen pressure can only be based on the present work. If the measured variation in  $K$  is attributed to oxygen pressure alone, then the rate constant must vary directly with the logarithm of pressure.

The above relationship may not be completely correct, since there is another factor which can modify the rate constant. Much published work has been done in a poorly controlled environment or at best, in a poor vacuum. It has been well established (8c, 15, 22, 23) that water vapor can affect the oxidation behavior of a metal, both decreasing and increasing the rate depending on conditions. Revesz (24) has also pointed out the influence of sodium and/or hydroxyl ions in increasing the rate of thermal oxidation of silicon. In fact Revesz and Evans (25) feel that silicon oxidation is normally an impurity controlled process.



Hence, the elimination of water and other impurities from the ultrahigh-vacuum work may well have changed the oxidation process, thereby reducing the oxidation rate.

### Summary

The oxidation of discontinuous metal films offers a simple and sensitive method for measuring low-temperature oxidation rate constants. The advantages of the method include control of variables such as impurities and heat of adsorption which can change the experimentally measured rates. These factors must be eliminated, or at least controlled, since they do not appear in the theoretical expressions for oxidation rate constants.

In addition, the surface structure of the metal can be controlled, and even single crystal surfaces can be utilized in films grown by epitaxial techniques. Uniform island size can be obtained by annealing the films for a long time, provided, of course, that the vacuum is high enough to prevent formation of a monolayer of gas.

The discontinuous film method is limited to the examination of tarnishing reactions, i.e., to temperatures below  $\approx 500^\circ\text{K}$ . Experimental techniques are relatively difficult, and all the interfering effects, such as film rearrangement, have not yet been eliminated. Despite these complications, the method offers a powerful tool for measuring tarnishing rates under very difficult conditions of pressure and temperature. Refinements in both theory and practice will allow the experimental results to be directly related to the microscopic parameters used in deriving reaction rate constants.

### Acknowledgment

Thanks are due J. R. Hutchins and P. A. Tick for critically reading the manuscript and R. C. Fisk for aiding in the performance of the experiments.

Manuscript received Oct. 24, 1967; revised manuscript received March 15, 1968.

Any discussion of this paper will appear in a Discussion Section to be published in the June 1969 JOURNAL.

### REFERENCES

1. F. P. Fehlner, *Nature*, **210**, 1035 (1966).
2. F. P. Fehlner, *Trans. 3rd Intern'l. Vac. Cong.*, Vol. II, p. 691, Pergamon Press, Oxford, 1966.
3. F. P. Fehlner, *J. Appl. Phys.*, **38**, 2223 (1967).
4. D. W. Pashley, *Adv. Phys.*, **14**, 327 (1965).
5. D. W. Pashley, *J. Vac. Sci. Tech.*, **3**, 156 (1966).
6. C. A. Neugebauer and M. B. Webb, *J. Appl. Phys.*, **33**, 74 (1962).
7. C. A. Neugebauer, *Trans. 9th Symp. Amer. Vac. Soc.*, p. 45, MacMillan Co., New York (1962).
8. O. Kubaschewski and B. E. Hopkins, "Oxidation of Metals and Alloys," Butterworths, London (1962), a) p. 35, b) p. 102, c) p. 156.
9. V. S. Fomenko, "Handbook of Thermionic Properties, Electronic Work Functions, and Richardson Constants of Elements and Compounds," Plenum Press Data Div., New York, 1966, pp. 69-71, 118-120.
10. S. Nakamura and E. W. Müller, *J. Appl. Phys.*, **36**, 3634 (1965).
11. N. Cabrera and N. F. Mott, *Rep. Prog. Phys.*, **12**, 163 (1948-49).
12. K. Hauffe and B. Ilschner, *Z. Elektrochem.*, **58**, 382 (1954).
13. A. T. Fromhold, Jr., and E. L. Cook, *Phys. Rev.*, **158**, 600 (1967).
14. H. H. Uhlig, *Acta Metallurg.*, **4**, 541 (1956).
15. H. P. Goddard, *This Journal*, **114**, 354 (1967).
16. R. M. Hill, *Nature*, **204**, 35 (1964).
17. C. A. Neugebauer and R. H. Wilson, "Basic Problems in Thin Film Physics," R. Niedermayer and H. Mayer, Editors, p. 579, Van den Hoeck and Ruprecht, Göttingen (1966).
18. D. S. Herman and T. N. Rhodin, *J. Appl. Phys.*, **37**, 1594 (1966).
19. A. A. Milgram and C. Lu, *ibid.*, **37**, 4773 (1966).
20. N. Cabrera, *Phil. Mag.*, **40**, 175 (1949).
21. T. B. Grimley, *Discussions Faraday Soc.*, **28**, 223 (1959).
22. B. E. Deal and A. S. Grove, *J. Appl. Phys.*, **36**, 3770 (1965).
23. V. V. Andreeva and E. L. Alekseeva, *Zh. Prikl. Khim.*, **35**, 1175 (1962).
24. A. G. Revesz, *Phys. Status Solidi*, **19**, 193 (1967).
25. A. G. Revesz and R. J. Evans, *Trans. IEEE*, **ED 14**, 789 (1967).
26. J. J. Chessick, Yung-Fang Yu, and A. C. Zettlemoyer, "Solid/Gas Interface," Proc. 2nd Intern. Conf. Surface Activity, p. 269, Butterworths, London (1957).
27. Ch. Weissmantel, *Werkstoffe u. Korrosion*, **13**, 682 (1962).
28. G. Hass and A. Bradford, *J. Opt. Soc. Amer.*, **47**, 125 (1957).

## Refractive Indices of ZnO, ZnS, and Several Thin-Film Insulators

J. C. Burgiel, Y. S. Chen, F. Vratny,\* and G. Smolinsky

Bell Telephone Laboratories, Incorporated, Murray Hill, New Jersey

### ABSTRACT

Optical constants of ZnO and ZnS near the band edges have been measured with an interference technique. Measurements on ZnO were performed on dielectric coated single crystals while those in ZnS were performed on thin films. Using a related method, we have also determined the refractive indices of insulating thin films of Ta<sub>2</sub>O<sub>5</sub>, Nb<sub>2</sub>O<sub>5</sub>, Si<sub>3</sub>N<sub>4</sub>, and a glow-discharge deposited silicone polymer. The significant features are discussed and related to the work of others.

Increasing studies of luminescence in II-VI semiconducting compounds have made detailed knowledge of the optical constants of these materials essential. Furthermore, efforts toward the development of luminescent devices using these compounds have made information concerning the optical constants of certain

Key words: refractive indices, insulator films, thin films, ZnO, ZnS.

\* Electrochemical Society Active Member.

dielectric films desirable. We have investigated at room temperature the II-VI compounds ZnO and ZnS together with thin films of the insulators Si<sub>3</sub>N<sub>4</sub>, Ta<sub>2</sub>O<sub>5</sub>, Nb<sub>2</sub>O<sub>5</sub>, and a glow-discharge deposited silicone polymer (1).

For ZnO we have measured both the real and imaginary parts of the ordinary refractive index as a function of wavelength at energies above as well as below

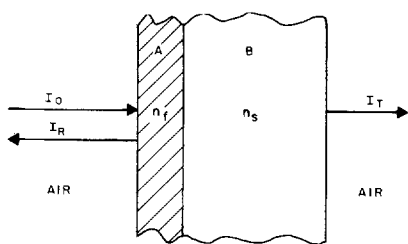


Fig. 1. Schematic diagram of samples used for determining the optical properties of the thin film. The optical properties of the substrate are known in this case.

the band gap. While there exist measurements of the refractive index below the band gap (2, 3), we believe our results are the first for the region near and above the band gap. For ZnS we have extended and corrected existing data on the real part of the refractive index in the region above the band gap. While ZnO measurements were performed on single crystal material (4), the ZnS measurements were performed on evaporated and crystallographically oriented sputtered films (5).

We have also measured the refractive indices of insulating thin films of chemically deposited  $\text{Si}_3\text{N}_4$  (6), reactively sputtered  $\text{Ta}_2\text{O}_5$  and  $\text{Nb}_2\text{O}_5$  (7), and a glow-discharge deposited silicone polymer. These measurements were performed over the respective wavelength regions in which these materials are transparent. These films are interesting because of their applications not only in electroluminescent cells, but also in light-trapping and waveguiding structures for use in second-harmonic generation and optical mixing (8), and in possible lasers.

### Methods

The optical constants reported here were determined from light interference in either the transmission or the reflection spectra of thin films. Previous workers (9-14) have employed such methods extensively to determine the optical constants of various materials. Our experiments can be divided into two categories, transparent film on transparent bulk substrates and on absorbing substrates.

*Transparent film on transparent bulk substrate.*—Figure 1 depicts a schematic diagram of a typical sample: a thin film A of thickness  $d$  on a bulk substrate B. Since both A and B are nonabsorbing, they are characterized by their respective refractive indices,  $n_f$  and  $n_s$ . The transmittance is given by (14)

$$T = \frac{I_T}{I_0} = \left\{ \frac{r_B^2}{1 - r_B^2} + \frac{1 + (r_A \cdot r_{AB})^2 - 2r_A r_{AB} \cos \phi}{(1 - r_A^2)(1 - r_B^2)} \right\}^{-1} \quad [1]$$

where  $r_A = \frac{n_f - 1}{n_f + 1}$ ,  $r_B = \frac{n_s - 1}{n_s + 1}$ ,  $r_{AB} = \frac{n_f - n_s}{n_f + n_s}$ , and

$\phi = \frac{4\pi n_f d}{\lambda}$  with  $\lambda$  being the wavelength of the incident light.

When  $\phi = m\pi$ , or equivalently when

$$\lambda_m = \frac{4n_f d}{m} \quad (m = 1, 2, 3, \dots) \quad [2]$$

the transmittance goes through a maximum or a minimum depending upon whether  $(-1)^m r_{AB}$  is positive or negative. Also the transmittance of this sample at  $m = 2, 4, 6, \dots$  can be shown to be equal to that of the substrate alone, and in turn gives an excellent check on the uniformity of the deposited film.

In a region in which  $n_f$  and  $n_s$  do not vary too rapidly with  $\lambda$ , the ratio of transmittance at neighboring maximum and minimum is given by

$$\frac{T_{\max}}{T_{\min}} = 1 + \frac{4r_A |r_{AB}| (1 - r_B^2)}{(1 - r_A |r_{AB}|)^2 - (r_A - |r_{AB}|)^2 r_B^2} \quad [3]$$

This function contains only two variables, i.e.,  $n_s$  and  $n_f$ ; therefore, given one, the other can be determined from the measured value of the ratio at a particular  $\lambda_m$ . Thus given the values of  $n_s$ , the film thickness  $d$  as well as the values of  $n_f$  as a function of  $\lambda$  can be determined through Eq. [2] and [3].

The fact that the wavelength at which the extremes occur can be accurately read and that the ratio of  $T_{\max}/T_{\min}$  does not require absolute measurements makes this method quite accurate for measuring  $n_f$  and  $d$ . This type of experiment can also be carried out using a measurement of reflection.

*Transparent film on absorbing substrate.*—Figure 2 gives the schematic diagram of a typical sample: a thin transparent film A of thickness  $d$  and index of refraction  $n_f$ , on a substrate C, bulk or film, whose optical constants are  $n_s$  and  $k_s$ , the latter being the extinction coefficient. In this case, the values of  $n_f(\lambda)$  are known either using the method of the previous section or from the literature; the unknowns are  $n_s(\lambda)$  and  $k_s(\lambda)$ .

The reflectivity at normal incidence is given by (9)

$$R = \frac{I_R}{I_0} = \frac{r_A^2 + |r_{AC}|^2 - 2r_A |r_{AC}| \cos(\phi + \theta)}{1 + r_A^2 |r_{AC}|^2 - 2r_A |r_{AC}| \cos(\phi + \theta)} \quad [4]$$

where  $r_A$  and  $\phi$  have already been defined, and where

$$|r_{AC}| e^{i\theta} = \frac{n_f - n_s + ik_s}{n_f + n_s - ik_s} \quad [5]$$

From Eq. [5] one obtains

$$|r_{AC}|^2 = 1 - \frac{4(n_s/n_f)}{\left(1 + \frac{n_s}{n_f}\right)^2 + \left(\frac{k_s}{n_f}\right)^2} \quad [6]$$

and

$$\theta = \tan^{-1} \frac{k_s/n_f}{1 - \frac{n_s}{n_f}} + \tan^{-1} \frac{k_s/n_f}{1 + \frac{n_s}{n_f}} \quad [7]$$

Experimentally, the quantities  $R$  and  $\theta$  can be determined from the reflectivity spectrum; the former is trivial and the latter is determined from the relationship

$$\frac{4\pi n_f d}{\lambda_m} + \theta = m\pi \quad [8]$$

at the extreme of the spectrum.  $n_f(\lambda)$  is already known and the thickness  $d$  can be determined from the  $n_f d$  product in a region where both film and substrate are transparent. Once  $R$  and  $\theta$  are known at various  $\lambda_m$ 's the values of  $n_s$  and  $k_s$  can be determined with the aid of a computer.

This method does rely on the absolute magnitude of the reflectivity; however, it does not contain the error one usually gets from a Kramers-Kronig anal-

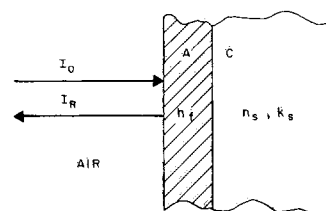


Fig. 2. Schematic diagram of samples used for determining the optical properties of the substrate. The optical properties of the thin film are known in this case.

Table I.

Material	Method of preparation	Unknowns	Section of paper describing measurements	Substrate or overlying film
Ta <sub>2</sub> O <sub>5</sub>	Reactive rf-sputtering	<i>n</i>	*	Sapphire
Nb <sub>2</sub> O <sub>5</sub>	Reactive rf-sputtering	<i>n</i>	*	Sapphire, quartz
Si <sub>3</sub> N <sub>4</sub>	Pyrolytic reactor of SiH <sub>4</sub>	<i>n</i>	*	Sapphire
Silicone polymer	Glow-discharge deposition	<i>n</i>	*	Sapphire, KTaO <sub>3</sub>
ZnO	Bulk single crystal	<i>n, k</i>	‡	Ta <sub>2</sub> O <sub>5</sub> and ZnS films
ZnS	rf-Sputtering, evaporation	<i>n, k</i>	*†	Sapphire, Si <sub>3</sub> N <sub>4</sub> film on sapphire

\* Transparent film on transparent bulk substrate.

† Transparent film on absorbing substrate.

ysis of the reflectivity spectrum arising from either insufficient coverage or from important nearby optical structure.

To assume good sensitivity and accuracy using this method, it is necessary that  $n_t$  and  $n_s$  not be too different and that  $k_s$  not be very large; in other words, as can be seen from Eq. [5],  $|\tau_{AC}|$  should not be near unity. This method therefore should be very good in determining the optical constants of the II-VI compounds near the band edge using dielectric films of similar refractive indices, but is not well suited for studying these constants in metals or in some of the homopolar semiconductors (12, 13).

### Results

Details concerning our samples are listed in Table I.

**Insulating films.**—An important problem arising in the production of certain insulating films is reproducibility. Slight variations in preparation conditions can cause variations in the properties of the resulting films. These problems are well under control for Ta<sub>2</sub>O<sub>5</sub> (7), Si<sub>3</sub>N<sub>4</sub> (6), and ZnS (5).<sup>1</sup> The glow-discharge technique used in preparing our silicone polymer films seems relatively free from such difficulties. Our Nb<sub>2</sub>O<sub>5</sub> films, however, were deposited under preliminary conditions and further experiments are necessary to show that we have indeed achieved reproducible films.

The refractive indices of our Ta<sub>2</sub>O<sub>5</sub> and Nb<sub>2</sub>O<sub>5</sub> sputtered films are plotted in Fig. 3. For both oxides our measured refractive indices are about 10% smaller than corresponding results for anodic films of these same materials (15). This discrepancy is well outside our limits of error and we conclude that for Ta<sub>2</sub>O<sub>5</sub> and Nb<sub>2</sub>O<sub>5</sub>, anodic and sputtered films are optically quite different.

The refractive indices for Si<sub>3</sub>N<sub>4</sub> and the silicone polymer are plotted in Fig. 4. Our results for Si<sub>3</sub>N<sub>4</sub>

<sup>1</sup> We have studied more than a dozen ZnS films and found excellent consistency and reproducibility. In particular, below the band gap at least, we get the same results for both sputtered and evaporated films; this fact alone argues strongly that the properties of our film are not being affected by variations in our method of deposition.

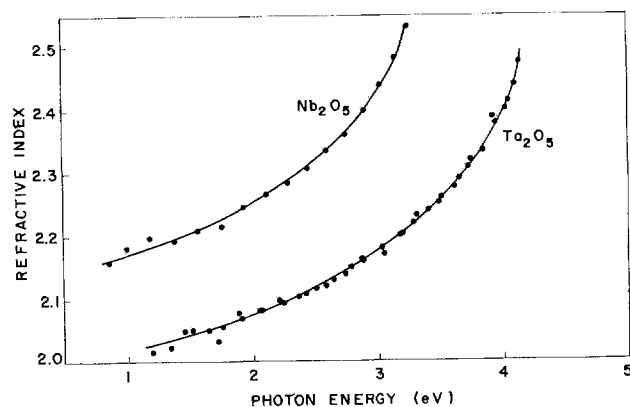


Fig. 3. Refractive indices of Ta<sub>2</sub>O<sub>5</sub> and Nb<sub>2</sub>O<sub>5</sub> sputtered films

are in good agreement with the value  $n = 2.00$  to  $2.05$  obtained by Bean *et al.* (16) at a wavelength of 5461 Å.

The refractive index of the silicone polymer was measured for films deposited on two optically very different substrates, KTaO<sub>3</sub> (17) and Al<sub>2</sub>O<sub>3</sub>. This was necessary in order to resolve the ambiguity arising because in this case Eq. [3] has two possible solutions. It seems worth mentioning that the glow-discharge method of preparing polymer films (1) is a very simple one requiring relatively little specialized equipment. Using this method, polymer films can be produced from most reasonably volatile organic compounds; and by changing the raw materials, it is possible to tailor the properties of the resulting film.

ZnO.—Figure 5 shows  $n$  and  $k$ , the real and imaginary parts of the ordinary complex refractive index, for ZnO for photon energies ranging from 2 to 4 eV. The measurements were made by coating the ZnO single crystal (4) with a thin film of Ta<sub>2</sub>O<sub>5</sub>, the refractive index of which is obtained from Fig. 3. At energies sufficiently below the band gap of ZnO that  $k$  is very small,  $\theta$  in Eq. [8] is zero. From the magnitude of the interference fringes, and from the shift in their positions, *i.e.*, from the value of  $\theta$ , we are able to determine both  $n$  and  $k$  for the ZnO substrate. The chief uncertainty in this procedure is the slight possibility that due to different surface mobility or to somewhat different heat transfer conditions the Ta<sub>2</sub>O<sub>5</sub> film deposited on ZnO may have a slightly different density than the Ta<sub>2</sub>O<sub>5</sub> deposited on sapphire. For this reason we have also performed the experiment using a sputtered ZnS film in place of the Ta<sub>2</sub>O<sub>5</sub> to determine the refractive index of ZnO below 3.0 eV. The results are also given in Fig. 5 and are in reasonable agreement with those from Ta<sub>2</sub>O<sub>5</sub> coated

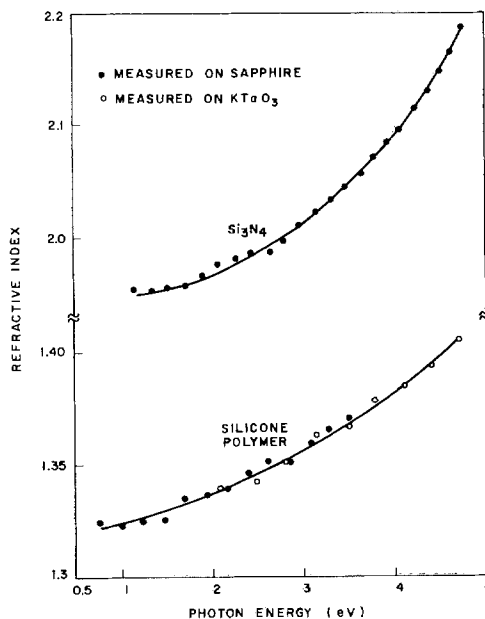


Fig. 4. Refractive indices of Si<sub>3</sub>N<sub>4</sub> and silicone polymer thin films.

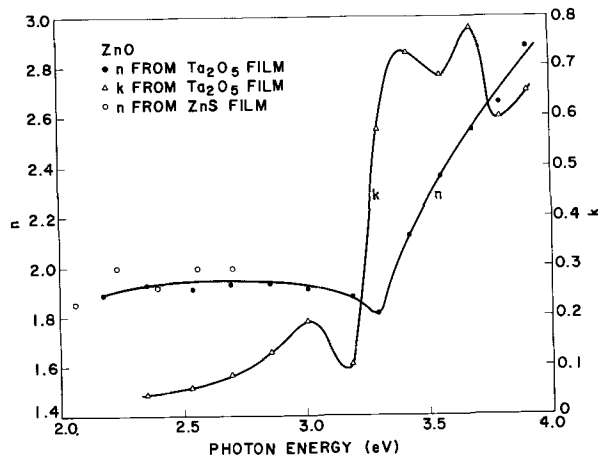


Fig. 5. Real and imaginary parts of the ordinary complex refractive index ( $\bar{n} = n + ik$ ) of ZnO.

samples. The refractive index at 2.5 eV is 1.94 as compared to 2.05 in ref. (3).

The structure between 3.0 and 4.0 eV in the curves of Fig. 5 is an interesting new feature of ZnO. Admittedly our data points are too far apart to adequately resolve this structure, however we are continuing our studies of this phenomenon. Neither of the authors of ref. (2) and (3) give results to this high an energy. It is tempting to associate the peaks in  $k$  at 3.4 and 3.7 eV with exciton transitions (18, 19). Unfortunately extrapolation of the temperature dependence of the  $A$  ( $n = 1$ ) exciton (19) to room temperature is at best an uncertain procedure; however, if such an extrapolation is made, the numbers appear reasonable. We hope that an experiment of ours currently in progress will clarify the nature of this structure.

ZnS.—There is serious disagreement between the results of Coogan (20) and of Hall (21) for the refractive index of thin ZnS films at energies about 3 eV. Both sets of data were obtained from fitting the transmission and the reflection spectra of thin ZnS films. The data of Coogan show significant structure at 4.4 eV, while those of Hall increase monotonically with photon energy. We have applied the method described in this paper to determine the refractive index of ZnS films, both sputtered and evaporated. The results are given in Fig. 6. Data below 3.0 eV was obtained from ZnS films on c-cut sapphire substrates. No difference was found between the sputtered films (predominantly cubic ZnS with the (111) plane in the plane of the film) and the evaporated films. Data above 3.5 eV was obtained using [sapphire] — [ $\text{Si}_3\text{N}_4$  film] — [ZnS film] samples by the method stated in the section on Transparent film on absorbing substrate. Both types of sample yielded similar results. Although the results above the ZnS gap are somewhat scattered, it is certain that they are much closer to those of Hall than of Coogan. Recently, similar results were reported by Cardona (22) in a Kramers-Kronig analysis of the reflectivity spectra of ZnS single crystals, both cubic and hexagonal.

#### Symbols

- $d$  = film thickness.  
 $k$  = extinction coefficient.  
 $k_s$  = extinction coefficient of substrate.  
 $m$  = integer giving the order of reflectivity or transmittance extremum.  
 $n$  = refractive index  
 $n_f$  = refractive index of thin film.  
 $n_s$  = refractive index of substrate.  
 $R$  = reflectivity of entire sample.

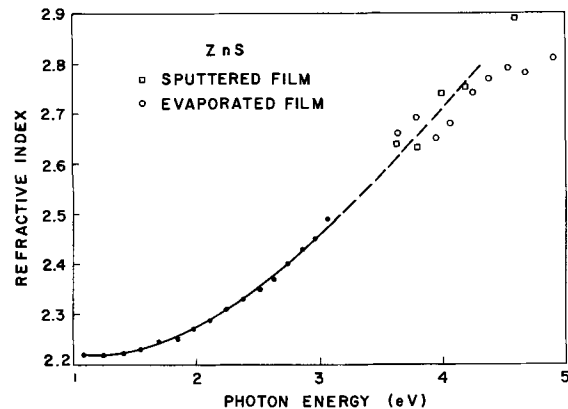


Fig. 6. Refractive index of ZnS thin films. Below the band gap the results for both sputtered and evaporated films agree; however, above band gap some differences occur.

- $r_{AB}$  = complex reflectance of interface between material A and B.  
 $T$  = transmittance of entire sample.  
 $\theta$  = phase of complex reflectance.  
 $\lambda$  = wavelength of incident light.  
 $\lambda_m$  = wavelength corresponding to extremum of order  $m$ .  
 $\phi = (4\pi n_f d) / \lambda$

Manuscript received Jan. 8, 1968; revised manuscript received ca. March 5, 1968. This paper was presented at the Boston Meeting, May 5-9, 1968, as Abstract 18.

Any discussion of this paper will appear in a Discussion Section to be published in the June 1969 JOURNAL.

#### REFERENCES

- G. Smolinsky, To be published.
- Erich Mollwo, *Z. Angew. Phys.*, **6**, 257 (1954).
- W. L. Bond, *J. Appl. Phys.*, **36**, 1674 (1964).
- E. D. Kolb, *J. Am. Ceram. Soc.*, **47**, 9 (1964).
- G. A. Rozgonyi and W. J. Polito, Private communication.
- V. Y. Doo, D. R. Nichols, and G. A. Silvey, "Late News" paper at Buffalo, N. Y., Meeting of the Society, Oct. 1965; V. Y. Doo, *IEEE Trans.*, **ED-13**, 561 (1966).
- F. Vratny, *This Journal*, **114**, 505 (1967); *J. Am. Ceram. Soc.*, **50**, 283 (1967).
- G. E. Smith, To be published, *J. Quantum Electronics*, May 1968.
- R. L. Mooney, *J. Opt. Soc. Am.*, **35**, 574 (1945).
- J. F. Hall and H. F. C. Ferguson, *ibid.*, **45**, 74 (1955).
- P. J. Lenngrans, *ibid.*, **41**, 714 (1951).
- J. M. Bennet, E. J. Ashley, and H. E. Bennet, *Appl. Opt.*, **8**, 961 (1965).
- D. K. Burge, *ibid.*, **8**, 967 (1965).
- "Physics of Thin Films," p. 69, G. Hass, Editor, Academic Press, New York (1963).
- L. Young, "Anodic Oxide Films," pp. 78-86 and pp. 187-190, Academic Press, London and New York (1961).
- K. E. Bean, P. S. Gleim, R. L. Yeakley, and W. R. Runyan, *This Journal*, **114**, 733 (1967).
- This refractive index as a function of wavelength for  $\text{KTaO}_3$  is given by S. H. Wemple, *Phys. Rev.*, **137**, A1575 (1965).
- D. G. Thomas, *J. Phys. Chem. Solids*, **15**, 86 (1960).
- Y. S. Park, C. W. Litton, T. C. Collins, and D. C. Reynolds, *Phys. Rev.*, **143**, 512 (1966).
- C. K. Coogan, *Proc. Phys. Soc., London*, **70**, 845 (1957).
- J. F. Hall, *J. Opt. Soc. Am.*, **46**, 1013 (1956).
- M. Cardona and G. Harbeke, *Phys. Rev.*, **137**, A1467 (1965).

# Equilibria and $\text{Eu}^{2+}$ Luminescence of Subsolidus Phases Bounded by $\text{Ba}_3\text{MgSi}_2\text{O}_8$ , $\text{Sr}_3\text{MgSi}_2\text{O}_8$ , and $\text{Ca}_3\text{MgSi}_2\text{O}_8$

Thomas L. Barry

*Sylvania Lighting Center, Sylvania Electric Products, Inc., Danvers, Massachusetts*

## ABSTRACT

The incorporation of divalent europium in the compounds  $\text{Ca}_3\text{MgSi}_2\text{O}_8$ ,  $\text{Sr}_3\text{MgSi}_2\text{O}_8$ , and  $\text{Ba}_3\text{MgSi}_2\text{O}_8$  produces phosphors of high luminescence yield. These phosphors respond well to both long and short wavelength ultraviolet excitation, as well as to cathode ray bombardment. The peak of the emission band occurs at progressively shorter wavelength and narrows as the radius of the major alkaline earth ion (Ca, Sr, or Ba) is increased. A  $1200^\circ\text{C}$  isotherm on compositions intermediate to  $\text{Sr}_3\text{MgSi}_2\text{O}_8$  and  $\text{Ba}_3\text{MgSi}_2\text{O}_8$  shows a complete series of crystalline solutions to exist at this temperature. Using an orthorhombic cell the d-spacings of the (222) reflection vary continuously from 1.956 Å for  $\text{Sr}_3\text{MgSi}_2\text{O}_8:\text{Eu}^{2+}$  to 2.012 Å for  $\text{Ba}_3\text{MgSi}_2\text{O}_8:\text{Eu}^{2+}$ . The emission spectra of these samples, however, vary in a discontinuous manner. Complete crystalline solution is likewise observed in a  $1200^\circ\text{C}$  isotherm for compositions intermediate to  $\text{Sr}_3\text{MgSi}_2\text{O}_8$  and  $\text{Ca}_3\text{MgSi}_2\text{O}_8$ . Here the d-spacings of the (222) reflection from the orthorhombic cell vary continuously from 1.909 Å for  $\text{Ca}_3\text{MgSi}_2\text{O}_8:\text{Eu}^{2+}$  to 1.956 Å for  $\text{Sr}_3\text{MgSi}_2\text{O}_8:\text{Eu}^{2+}$ . Again the peak of the emission spectra varies discontinuously with composition even for the complete crystalline solution series.

Emission spectra and x-ray diffraction data collected on samples prepared in the  $1200^\circ\text{C}$  subsolidus isotherm intermediate in composition to  $\text{Ca}_3\text{MgSi}_2\text{O}_8$  and  $\text{Ba}_3\text{MgSi}_2\text{O}_8$  show an intermediate compound to be formed. This compound  $\text{BaCa}_2\text{MgSi}_2\text{O}_8$  has luminescent properties which more closely resemble those of the calcium end-member. Several compositions were prepared in the subsolidus,  $1200^\circ\text{C}$ , isothermal, ternary section bounded by  $\text{Ca}_3\text{MgSi}_2\text{O}_8$ ,  $\text{Sr}_3\text{MgSi}_2\text{O}_8$ , and  $\text{Ba}_3\text{MgSi}_2\text{O}_8$ . The samples prepared show the major feature of the section to be a large single phase region. In general, broadening of spectral energy distributions is observed as compositions move into the ternary section. All the compositions prepared resulted in phosphors of relatively high efficiency.

Several other works on subsolidus equilibria cover various parts of the phase data presented here. Klasens, Hoekstra, and Cox (1) in an extensive work on lead activation of ternary silicates mention the complete crystalline solubility of ( $\text{Ba}_3\text{MgSi}_2\text{O}_8$  and  $\text{Sr}_3\text{MgSi}_2\text{O}_8$ ) and ( $\text{Ca}_3\text{MgSi}_2\text{O}_8$  and  $\text{Sr}_3\text{MgSi}_2\text{O}_8$ ). They also report that x-ray data from a 1:1 composition between  $\text{Ca}_3\text{MgSi}_2\text{O}_8$  and  $\text{Ba}_3\text{MgSi}_2\text{O}_8$  prepared subsolidus shows that substantial  $\text{Ca}^{2+}$  in  $\text{Ca}_3\text{MgSi}_2\text{O}_8$  can be replaced by  $\text{Ba}^{2+}$ , while very little  $\text{Ba}^{2+}$  in  $\text{Ba}_3\text{MgSi}_2\text{O}_8$  can be replaced by  $\text{Ca}^{2+}$ . Regarding the fluorescence of the compounds they report all three to be of little importance. Aside from Pb, they tried many of the other usual activators such as Mn, Tl, Bi, Sb, Sn, etc., in the ternary compounds. Although some did show a weak fluorescence, none of the others led to phosphors of any appreciable efficiency.

Nadachowski and Grylicki (2) in a study of the phase equilibria in the  $\text{Ba}_2\text{SiO}_4\text{-Ca}_2\text{SiO}_4\text{-Mg}_2\text{SiO}_4$  system reported two compounds,  $\text{BaMgSiO}_4$  and  $\text{BaMg}_3\text{Si}_2\text{O}_8$ , existed in the bounding system  $\text{Ba}_2\text{SiO}_4\text{-Mg}_2\text{SiO}_4$ , which they represent as binary. They did not report the compound  $\text{Ba}_3\text{MgSi}_2\text{O}_8$ . One ternary compound ( $\text{BaCa}_2\text{MgSi}_2\text{O}_8$ ) was reported to exist in the system.

Argyle (3) redid the phase relations in the  $\text{BaO-MgO-SiO}_2$  system. He reports the compound  $\text{Ba}_3\text{MgSi}_2\text{O}_8$  found earlier by Klasens *et al.* (1) but not by Nadachowski and Grylicki (2). X-ray data from his work and that of Klasens state that the com-

pound  $\text{BaMg}_3\text{Si}_2\text{O}_8$  reported by Nadachowski and Grylicki is really a mixture of  $\text{BaMg}_2\text{Si}_2\text{O}_7$  and  $\text{MgO}$ .

## Experimental

**Starting materials.**—The alkaline earth carbonates of the large alkaline earth ions and the silicic acid used in this study were luminescent grade chemicals. The basic magnesium carbonate was a Mallinckrodt analytical reagent containing less than 0.005% sulfate as an impurity. The europium oxide was of 99.9% purity. Analysis of the europium oxide, as given by the American Potash and Chemical Corporation, showed only trace amounts of other rare earth ions. The ammonium chloride used was a commercially available reagent grade chemical. Assays were run on basic magnesium carbonate, manganese carbonate, and silicic acid to allow compensation for sorbed water in formulating the blends.

**Preparation of starting mixtures.**—Starting mixtures were prepared by dry blending the appropriate proportions of the raw materials in a model 8000 Spex Mixer/Mill for 15 min. The addition of a few glass beads to the raw blend greatly facilitates the mixing process.

**Firing procedure.**—The blended mixtures were fired in alumina boats at  $600^\circ\text{C}$  in air. This firing initiates the decomposition of the alkaline earth carbonates and reaction with the ammonium chloride flux.

The prefired samples were then fired at  $1200^\circ\text{C}$  in an atmosphere of 4 parts nitrogen to 1 part hydrogen. Firing times of 2 to 12 hr and temperatures ranging between  $1100^\circ$  and  $1300^\circ\text{C}$  were used at various times,

**Key words:** Phosphors alk earth silicates, emission spectra, europium ( $2+$ ) activation, fluorescence europium ( $2+$ ), equil subsolidus, energy transfer Eu ( $2+$ ) to Mn ( $2+$ ), luminescence alk earth silicates.

the routine combination being 4 hr at 1200°C. After firing the samples were allowed to cool to room temperature in the reducing atmosphere.

The optimum flux concentration was about 0.20 moles of  $\text{NH}_4\text{Cl}$  per mole of silicic acid. The presence of the  $\text{NH}_4\text{Cl}$  flux effects both the reaction rate and the luminescence of a particular composition at a given temperature. Samples fired without flux yield a product of considerably poorer crystallinity, as evidenced in x-ray diffraction patterns, and give emission curves much broader and substantially less intense than that characteristic of the equilibrium assemblage.

**Characterization of products.**—Both fast ( $2^\circ/\text{min}$ ) and slow ( $0.25^\circ/\text{min}$ ) scans using a Norelco x-ray diffractometer with filtered  $\text{CuK}\alpha$ -radiation were useful in phase identification. Fluorescent properties (excitation spectra and spectral energy distribution curves) were determined using equipment and techniques, which have been fully described elsewhere (4).

### Results and Discussion

**End-member phases.**—The three compounds which delimit the compositions covered in this study all produce highly efficient, narrow band, blue emitting phosphors when activated by divalent europium. They exhibit a brilliant blue fluorescence when excited by u.v. radiation or cathode rays. They respond well to 2537Å radiation as well as to radiation from a blacklite lamp, which has a broad u.v. spectrum from 3250 to 4000Å. These phosphors possess band widths about one-third as wide as most commercial blue phosphors. Activator concentrations between 0.005 and 0.10 atom fraction europium were all found to produce efficient phosphors. A value of 0.04 was commonly used in this study. The spectral properties of these phosphors are given in Table I. The intensity factors given in Table I are the product of the peak height, the scale factor, and the width at half height. The factors given for individual members of the compositional series include experimental variables. They are only a qualitative measure of intensity variations and are given in order to compare the compounds themselves and also subsequent compositions to follow. Figure 1 gives the spectral energy distribution curves for the three compounds run at different instrument settings, as indicated by the intensity factors. The narrowing of the emission band and the shifting to shorter wavelengths as the ionic radius of the major alkaline earth ion is increased is obvious in these curves.

Figure 2 gives plots of peak wavelength vs. the ionic radii of the large alkaline earth ions. Plots are given for both Ahrens' and Goldschmidt radii. Both plots indicate a nearly linear relationship with a slight positive deviation for one set of radii and a slight negative deviation for the other. This indicates the structures of the three compounds to be quite closely related if not isomorphous. Klasens *et al.* (1) reported that an isomorphous relationship appeared to exist for  $\text{Ca}_3\text{MgSi}_2\text{O}_8$ ,  $\text{Sr}_3\text{MgSi}_2\text{O}_8$ , and  $\text{Ba}_3\text{MgSi}_2\text{O}_8$ . They thus indexed the x-ray lines for all three compounds on the basis of an orthorhombic cell. Their cell dimensions for the three orthorhombic cells are given in Table II. An earlier work by Nurse (5) states that merwinite,  $\text{Ca}_3\text{MgSi}_2\text{O}_8$ , is monoclinic with cell dimensions

$$a_0 = 10.77, b_0 = 9.20, c_0 = 13.26\text{Å}; \beta = 91^\circ$$

In addition Argyle (3) states that x-ray patterns of

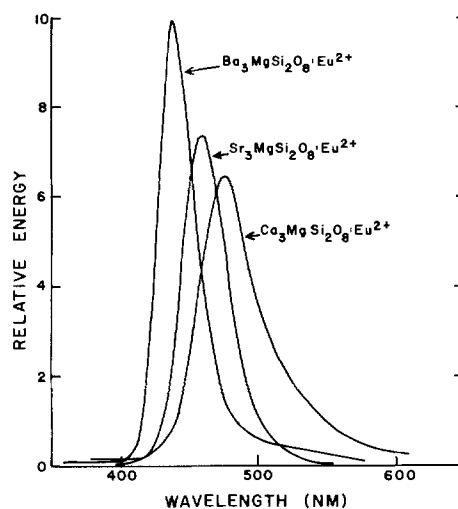


Fig. 1. Spectral energy distribution curves for  $\text{Ba}_3\text{MgSi}_2\text{O}_8:\text{Eu}_{0.04}^{2+}$ ,  $\text{Sr}_3\text{MgSi}_2\text{O}_8:\text{Eu}_{0.04}^{2+}$ , and  $\text{Ca}_3\text{MgSi}_2\text{O}_8:\text{Eu}_{0.04}^{2+}$  (2537Å excitation).

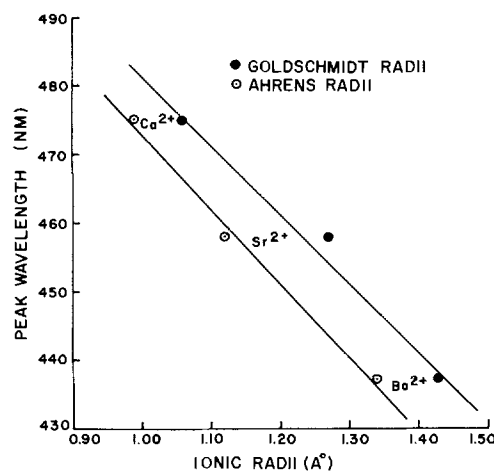


Fig. 2. Peak wavelength vs. ionic radii of large alkaline earth ions.

$\text{Ca}_3\text{MgSi}_2\text{O}_8$  and  $\text{Ba}_3\text{MgSi}_2\text{O}_8$  were not sufficiently alike for them to have the same structures. Using the orthorhombic cell of Klasens for  $\text{Ca}_3\text{MgSi}_2\text{O}_8$ , lines from this compound were used to assign indices to lines in  $\text{Ba}_3\text{MgSi}_2\text{O}_8$ . These indices were then used to obtain lattice parameters for the orthorhombic cell. However, these lattice parameters could not be used successfully to index all the remaining lines.

The diffraction data collected in this study agreed with the works of Nurse (5) and Argyle (3). The monoclinic distortion of the orthorhombic structure was very clearly in evidence in some of the crystalline solution phases prepared. However, the orthorhombic cells proposed by Klasens *et al.* (1) approximate the true structures fairly closely, as the monoclinic distortions are slight, and were used in assigning indices to the x-ray peaks used in defining crystalline solubility in this study. The monoclinic distortion was very pronounced in the  $\text{Ca}_3\text{MgSi}_2\text{O}_8$ - $\text{Sr}_3\text{MgSi}_2\text{O}_8$  complete solution series and slight in the  $\text{Ba}_3\text{MgSi}_2\text{O}_8$ - $\text{Sr}_3\text{MgSi}_2\text{O}_8$  series.

Table I. Fluorescent data on compounds

Phosphor composition	Wavelength of maximum emission, nm	Width of band at half intensity, nm	Intensity factor
$\text{Ca}_3\text{MgSi}_2\text{O}_8:\text{Eu}_{0.04}^{2+}$	475	52	21.8
$\text{Sr}_3\text{MgSi}_2\text{O}_8:\text{Eu}_{0.04}^{2+}$	458	39	50.3
$\text{Ba}_3\text{MgSi}_2\text{O}_8:\text{Eu}_{0.04}^{2+}$	437	31	60.5

Table II. Cell dimensions for three orthorhombic cells

	$a_0$ , Å	$b_0$ , Å	$c_0$ , Å
$\text{Ca}_3\text{MgSi}_2\text{O}_8$	5.2	9.2	6.8
$\text{Sr}_3\text{MgSi}_2\text{O}_8$	5.4	9.6	7.2
$\text{Ba}_3\text{MgSi}_2\text{O}_8$	5.5	9.8	7.6

The subsolidus  $\text{Ba}_3\text{MgSi}_2\text{O}_8$ - $\text{Sr}_3\text{MgSi}_2\text{O}_8$  join.—A subsolidus isotherm at  $1200^\circ\text{C}$  was run on samples prepared at 10 m/o (mole per cent) intervals for compositions varying between  $\text{Ba}_3\text{MgSi}_2\text{O}_8$  and  $\text{Sr}_3\text{MgSi}_2\text{O}_8$ . Using the (222) reflection from the orthorhombic cell, described above, the change in x-ray d-spacing with composition was followed. This plot is given in Fig. 3. The continuous variation in d-spacing of the (222) reflection from a value of  $1.956\text{\AA}$  for  $\text{Sr}_3\text{MgSi}_2\text{O}_8$  to  $2.012\text{\AA}$  for  $\text{Ba}_3\text{MgSi}_2\text{O}_8$  shows complete crystalline solution to exist between these two compounds. Spectral energy distribution curves were obtained on these samples when divalent europium was employed as the activator. The variation of peak wavelength with composition is given in Fig. 4. This figure shows that the replacement up to 50 m/o of  $\text{Ba}^{2+}$  by  $\text{Sr}^{2+}$  in  $\text{Ba}_3\text{MgSi}_2\text{O}_8$  has essentially no effect on the position of the emission band. However, broadening of the band does occur. Beyond the 50-50 composition on up to  $\text{Sr}_3\text{MgSi}_2\text{O}_8$  the emission peak does shift in a fairly continuous manner with composition and the width of the emission band narrows. The fluorescent data obtained on the samples prepared are given in Table III.

The scatter of the points in the 30-50 m/o  $\text{Ba}_3\text{MgSi}_2\text{O}_8$  region in Fig. 3 and 4 is due to the presence of a small amount of a nonequilibrium second phase, which is not characteristic of this join. Extreme examples of the formation of metastable phases which can arise when compositions along this join are sought are given below.

Since this join has previously been established as one of complete crystalline solution (1), the spectral energy distribution (S.E.D.) curves for finished phosphors, activated by divalent europium, should

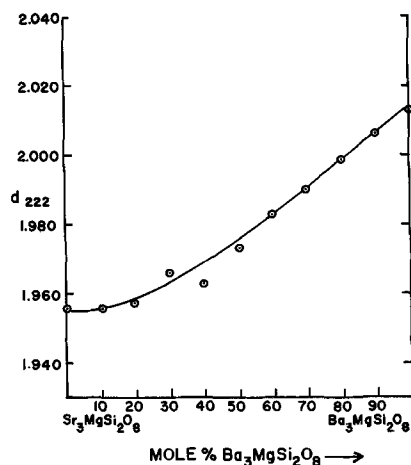


Fig. 3. X-ray d-spacing vs. composition for  $\text{Sr}_3\text{MgSi}_2\text{O}_8$ - $\text{Ba}_3\text{MgSi}_2\text{O}_8$  crystalline solutions.

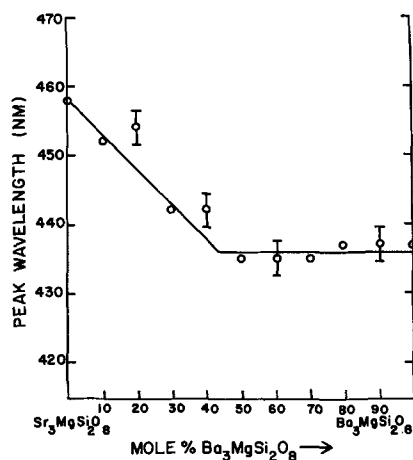


Fig. 4. Peak wavelength vs. composition for  $\text{Sr}_3\text{MgSi}_2\text{O}_8$ - $\text{Ba}_3\text{MgSi}_2\text{O}_8$  crystalline solutions.

Table III. Fluorescent data on compositions in the subsolidus region between  $\text{Ba}_3\text{MgSi}_2\text{O}_8$  and  $\text{Sr}_3\text{MgSi}_2\text{O}_8$

$\text{Sr}_3\text{MgSi}_2\text{O}_8$	Mole per cent $\text{Ba}_3\text{MgSi}_2\text{O}_8$	$\lambda_{\text{peak}}$ , nm	$W_{1/2}$ , nm	Intensity factor
100	0	458	39	50.3
90	10	452	47	87.4
80	20	454	46	80.0
70	30	442	47	59.2
60	40	442	46	93.8
50	50	435	42	40.3
40	60	435	40	90.0
30	70	435	38	69.5
20	80	437	36	66.3
10	90	437	34	63.2
0	100	437	31	60.5

yield single band emissions, intermediate to those of the two end-members as presented above. When two compositions represented by the following formulations ( $\text{Ba}_2\text{Sr}$ ) $\text{MgSi}_2\text{O}_8$  and ( $\text{BaSr}_2$ ) $\text{MgSi}_2\text{O}_8$  were prepared, S.E.D. curves showed a double peak which was in direct contrast to the single peak observed for other members prepared along this join. This so-called doublet, in the case of ( $\text{Ba}_2\text{Sr}$ ) $\text{MgSi}_2\text{O}_8$ , is actually composed of two overlapping bands in the blue region (due to one of the metastable phases and the equilibrium crystalline solution) and a band in the green region due to the second metastable phase. However, these formulations may be represented by other joins which intersect the  $\text{Sr}_3\text{MgSi}_2\text{O}_8$ - $\text{Ba}_3\text{MgSi}_2\text{O}_8$  join at the respective points. Thus, other phases, which are indicative of this other join, may form metastably. This is exactly what happens to these two mixtures. Thus, instead of forming a single phase crystalline solution which may be formulated as ( $\text{Ba}_2\text{Sr}$ ) $\text{MgSi}_2\text{O}_8$ , two additional phases ( $\text{BaMgSiO}_4$  and  $\text{SrBaSiO}_4$ ) form metastably and these are readily seen in the S.E.D. curves, since the spectra obtained for the fired sample contains peaks of the two metastable components and differs from the single peak which is characteristic of the crystalline solution. The same holds for the ( $\text{BaSr}_2$ ) $\text{MgSi}_2\text{O}_8$  formulation except different phases are metastably formed. This was quickly established, as all the compounds as well as other selected compositions have been prepared and S.E.D. curves obtained for each sample.

This trend is not so easily observed in x-ray diffraction patterns of these compositions because of poor crystallinity of the metastable phases formed and the resultant low intensity broad lines of the patterns obtained. Also, reheating the initial samples obtained by firing 3 hr at  $1200^\circ\text{C}$  in 20%  $\text{H}_2$  for 12 hr more in the same atmosphere and at the same temperature greatly diminished the intensity of the emission peaks of the metastable phases and increased that of the stable crystalline solution.

Various compounds have been employed as starting materials in preparation of the crystalline solutions in this system. Drastic changes in the kinetics have been observed with different starting materials formulated to yield the identical result after firing. In samples prepared incorporating a hydrated magnesium silicate,  $\text{MgO}\cdot 2.5\text{SiO}_2\cdot 1.5\text{H}_2\text{O}$ , as a starting material equilibrium was difficult to obtain in many instances even by prolonged heating ( $\sim 60$  hr at  $1200^\circ\text{C}$ ). However, when this compound is replaced in the blend by basic magnesium carbonate ( $3\text{MgCO}_3\cdot \text{Mg}(\text{OH})_2\cdot 3\text{H}_2\text{O}$ ) plus partially decomposed silicic acid ( $\text{SiO}_2\cdot \text{XH}_2\text{O}$ ), equilibrium was obtained within 4 hr at  $1200^\circ\text{C}$ , except for the specific compositions previously noted. The same type of metastable relations observed above apply here.

The subsolidus  $\text{Ca}_3\text{MgSi}_2\text{O}_8$ - $\text{Sr}_3\text{MgSi}_2\text{O}_8$  join.—The  $1200^\circ\text{C}$  subsolidus isotherm run between these compounds also showed a join of complete crystalline solution. The variation of the (222) reflection with composition, again on the basis of the orthorhombic cell, resulted in a continuous curve varying from  $1.956\text{\AA}$  for  $\text{Sr}_3\text{MgSi}_2\text{O}_8$  to  $1.909\text{\AA}$  for  $\text{Ca}_3\text{MgSi}_2\text{O}_8$ . This plot is

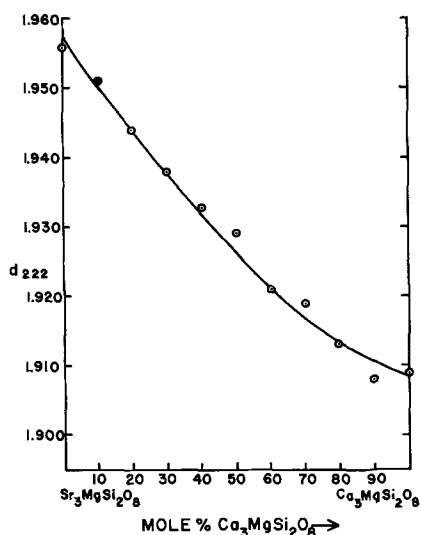


Fig. 5. X-ray  $d$ -spacing vs. composition for  $\text{Sr}_3\text{MgSi}_2\text{O}_8$ - $\text{Ca}_3\text{MgSi}_2\text{O}_8$  crystalline solutions.

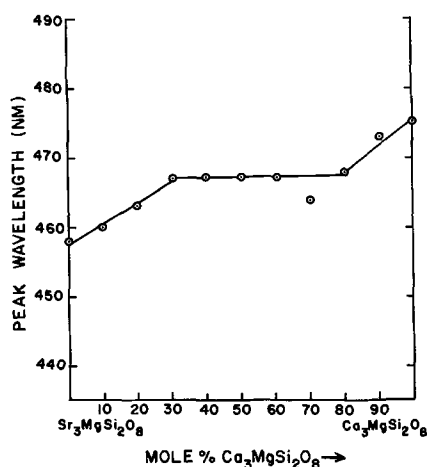


Fig. 6. Peak wavelength vs. composition for  $\text{Sr}_3\text{MgSi}_2\text{O}_8$ - $\text{Ca}_3\text{MgSi}_2\text{O}_8$  crystalline solutions.

given in Fig. 5. A curve of the emission wavelength at maximum intensity vs. composition (for divalent europium activation) is given in Fig. 6. This shows that emission peak to be sensitive to composition in the regions near the end-members. The center of the diagram shows a large compositional region (30 to 80 m/o  $\text{Ca}_3\text{MgSi}_2\text{O}_8$ ) in which both the position and width of the emission peak are relatively insensitive to composition. The data on the fluorescent samples are given in Table IV. In general, the intensity factors above show a substantial increase in fluorescent output for the crystalline solution phases.

*The subsolidus  $\text{Ca}_3\text{MgSi}_2\text{O}_8$ - $\text{Ba}_3\text{MgSi}_2\text{O}_8$  join.*—Evaluation of both x-ray and fluorescent (S.E.D.) data collected on samples prepared in the subsolidus region

between the compounds  $\text{Ca}_3\text{MgSi}_2\text{O}_8$  and  $\text{Ba}_3\text{MgSi}_2\text{O}_8$  revealed the existence of an intermediate compound. The chemical formula of this compound is  $\text{BaCa}_2\text{MgSi}_2\text{O}_8$  and its x-ray pattern is distinctly different from that of either  $\text{Ca}_3\text{MgSi}_2\text{O}_8$  or  $\text{Ba}_3\text{MgSi}_2\text{O}_8$ . The spectral energy distribution curve of this compound (when divalent europium is employed as the activator) although different from both compounds is more similar to that of  $\text{Ca}_3\text{MgSi}_2\text{O}_8:\text{Eu}^{2+}$ .

X-ray diffraction studies of subsolidus compositions intermediate to  $\text{Ba}_3\text{MgSi}_2\text{O}_8$  and  $\text{Ca}_3\text{MgSi}_2\text{O}_8$  indicate a very limited solubility of  $\text{Ca}_3\text{MgSi}_2\text{O}_8$  in  $\text{Ba}_3\text{MgSi}_2\text{O}_8$  probably of the order of 10 m/o. Patterns of compositions between 10 and 40 m/o  $\text{Ca}_3\text{MgSi}_2\text{O}_8$  exhibit two distinct phases, one a  $\text{Ba}_3\text{MgSi}_2\text{O}_8$  crystalline solution and the other a  $\text{BaCa}_2\text{MgSi}_2\text{O}_8$  crystalline solution. Between 40 and 80 m/o  $\text{Ca}_3\text{MgSi}_2\text{O}_8$ , a large single phase region with the  $\text{BaCa}_2\text{MgSi}_2\text{O}_8$  structure exists. From 80 m/o  $\text{Ca}_3\text{MgSi}_2\text{O}_8$  on up to the pure compound itself two crystalline phases co-exist, one a  $\text{BaCa}_2\text{MgSi}_2\text{O}_8$  crystalline solution, and the other essentially pure  $\text{Ca}_3\text{MgSi}_2\text{O}_8$ . The fluorescent data on these samples are given in Table V.

It can be seen in the table that the emission peak broadens from the compound  $\text{Ca}_3\text{MgSi}_2\text{O}_8$ , narrows again with further increase in the  $\text{Ba}_3\text{MgSi}_2\text{O}_8$  concentration, rebroadens, and is finally very sharp for the pure  $\text{Ba}_3\text{MgSi}_2\text{O}_8$  compound. It has been reported by Klasens *et al.* (1) that a substantial amount of  $\text{Ca}^{2+}$  can be replaced by  $\text{Ba}^{2+}$ , while little  $\text{Ca}^{2+}$  seems to be taken up by  $\text{Ba}_3\text{MgSi}_2\text{O}_8$ . If these data represented the complete picture of what occurs between these two ternary orthosilicate compounds, then the two crystalline solution fields would be separated by a two phase region in which two crystalline solution phases (varying in amount with composition) would be in equilibrium with one another at a constant temperature. Thus, it would not be possible for an intermediate composition to yield an emission spectrum with a band any narrower than that of the sum of the two crystalline solutions in equilibrium at the given temperature. The narrowing of the emission spectrum for the intermediate compositions evidenced in Table V clearly demonstrates that this is not the case. The fluorescence spectra of the divalent europium incorporated in these specimens make obvious the intermediate compound formed. The divalent europium employed in this study yields more efficient phosphors with spectral energy distributions which are much more definitive as an aid in interpreting the phase relations for these compositions than the divalent lead employed by Klasens *et al.* (1). A search of the literature revealed this intermediate compound ( $\text{BaCa}_2\text{MgSi}_2\text{O}_8$ ) had been reported in a phase equilibrium study of the so-called ternary system  $\text{Ba}_2\text{SiO}_4$ - $\text{Mg}_2\text{SiO}_4$ - $\text{Ca}_2\text{SiO}_4$  by Nadachowski and Grylicki (2).

*Ternary compositions bounded by  $\text{Ca}_3\text{MgSi}_2\text{O}_8$ ,  $\text{Sr}_3\text{MgSi}_2\text{O}_8$ , and  $\text{Ba}_3\text{MgSi}_2\text{O}_8$ .*—Several divalent europium activated fluorescent compositions have been prepared at  $1200^\circ\text{C}$  in the orthosilicate plane bounded by the compounds  $\text{Ca}_3\text{MgSi}_2\text{O}_8$ ,  $\text{Sr}_3\text{MgSi}_2\text{O}_8$ , and  $\text{Ba}_3\text{MgSi}_2\text{O}_8$ . The compositions studied are represented by lines joining one pure compound with the 1:1 com-

Table IV. Fluorescent data on compositions in the subsolidus region between  $\text{Ca}_3\text{MgSi}_2\text{O}_8$  and  $\text{Sr}_3\text{MgSi}_2\text{O}_8$

Mole per cent $\text{Ca}_3\text{MgSi}_2\text{O}_8$	Mole per cent $\text{Sr}_3\text{MgSi}_2\text{O}_8$	$\lambda_{\text{Peak}}$ , nm	$W_{1/2}$ , nm	Intensity factor
100	0	475	50	15.5
90	10	473	63	41.6
80	20	468	60	68.4
70	30	464	58	83.5
60	40	467	50	78.0
50	50	467	48	82.2
40	60	467	48	63.3
30	70	467	48	46.1
20	80	463	44	42.2
10	90	460	42	47.8
0	100	458	39	50.3

Table V. Fluorescent data on composition in the subsolidus region between  $\text{Ca}_3\text{MgSi}_2\text{O}_8$  and  $\text{Ba}_3\text{MgSi}_2\text{O}_8$

$\text{Ca}_3\text{MgSi}_2\text{O}_8$	$\text{Ba}_3\text{MgSi}_2\text{O}_8$	$\lambda_{\text{Peak}}$ , nm	$W_{1/2}$ , nm	Intensity factor
100	0	475	52	21.8
90	10	472	74	50.2
80	20	460	77	83.2
70	30	450	64	88.2
60	40	443	56	53.8
50	50	443	51	47.4
40	60	443	52	40.6
30	70	450	61	26.2
20	80	455	78	51.5
10	90	460	90	59.4
0	100	437	31	60.5



position between the other two compounds. In general, broadening of spectral energy distributions of intermediate compositions occurs as we move away from the compositions representing the pure compounds. This can be seen in Table VI which gives the emission peak and the width at half height for compositions intermediate to  $\text{Sr}_3\text{MgSi}_2\text{O}_8$  and  $\text{Ba}_3\text{MgSi}_2\text{O}_8$ .

Table VII presents the same data for compositions intermediate to  $\text{Ca}_3\text{MgSi}_2\text{O}_8$  and the 1:1 composition between  $\text{Ba}_3\text{MgSi}_2\text{O}_8$  and  $\text{Sr}_3\text{MgSi}_2\text{O}_8$ .

The data obtained for samples prepared along the third join between  $\text{Ba}_3\text{MgSi}_2\text{O}_8$  and 1:1 composition between  $\text{Ca}_3\text{MgSi}_2\text{O}_8$  and  $\text{Sr}_3\text{MgSi}_2\text{O}_8$  are tabulated in Table VIII.

The data in Tables VI-VIII indicate that if the divalent europium ( $r^{2+} = 1.12\text{\AA}$ ) is substituting for the large divalent alkaline earth ions, the emission spectra, in regard to shifting and broadening, are least sensitive when the dominant alkaline earth ion is larger than divalent europium as in the case of  $\text{Ba}^{2+}$  ( $r^{2+} = 1.34\text{\AA}$ ), most sensitive when it is smaller as  $\text{Ca}^{2+}$  ( $r^{2+} = 0.99\text{\AA}$ ), and intermediate when the disparity is minimum such as for  $\text{Sr}^{2+}$  ( $r^{2+} = 1.12\text{\AA}$ ) (6).

X-ray diffraction patterns of the compositions run in this study indicate very extensive ternary crystalline solution to exist. Only a single phase was present in the ternary compositions presented here.

#### Co-activation with Manganese

Attempts at incorporating both divalent europium and divalent manganese in the three bounding phases of this study were conducted. Manganese alone does not activate these compounds. Previous works on co-activation in alkaline earth phosphate systems have reported such phenomena (7, 8). It was found that co-activation with europium and manganese occurred quite efficiently in the compound  $\text{Ba}_3\text{MgSi}_2\text{O}_8$ . An S.E.D. curve showing both europium and manganese emission is given in Fig. 7. A substantially less efficient co-activation was found in the S.E.D. curves of the compounds  $\text{Ca}_3\text{MgSi}_2\text{O}_8$  and  $\text{Sr}_3\text{MgSi}_2\text{O}_8$ . The S.E.D. curves for the three compounds (activated by divalent europium alone) given in Fig. 1 show the large variation in peak position for the three compounds. The peak for  $\text{Ba}_3\text{MgSi}_2\text{O}_8$  falls at a considerably lower wavelength than the other two. The wavelength at which maximum intensity occurs may be the key to co-activation for the europium-manganese pair

Table VI. Fluorescence data on ternary crystalline solution phases

Composition	$\lambda_{\text{Peak}}$	$W_{h/2}$ , nm
$\text{Sr}_3\text{MgSi}_2\text{O}_8$	458	39
$(\text{Sr}_{2.25}\text{Ba}_{0.375}\text{Ca}_{0.375})\text{MgSi}_2\text{O}_8$	457	51
$(\text{Sr}_{1.50}\text{Ba}_{0.75}\text{Ca}_{0.75})\text{MgSi}_2\text{O}_8$	450	58
$(\text{SrBaCa})\text{MgSi}_2\text{O}_8$	443	53
$(\text{Ba}_{1.5}\text{Ca}_{1.5})\text{MgSi}_2\text{O}_8$	443	51

Table VII. Fluorescence data on ternary crystalline solution phases

Composition	$\lambda_{\text{Peak}}$	$W_{h/2}$ , nm
$\text{Ca}_3\text{MgSi}_2\text{O}_8$	475	52
$(\text{Ca}_{2.25}\text{Sr}_{0.375}\text{Ba}_{0.375})\text{MgSi}_2\text{O}_8$	462	74
$(\text{Ca}_{1.50}\text{Sr}_{0.75}\text{Ba}_{0.75})\text{MgSi}_2\text{O}_8$	450	58
$(\text{CaSrBa})\text{MgSi}_2\text{O}_8$	443	53
$(\text{Ba}_{1.5}\text{Sr}_{1.5})\text{MgSi}_2\text{O}_8$	433	42

Table VIII. Fluorescence data on ternary crystalline solution phases

Composition	$\lambda_{\text{Peak}}$	$W_{h/2}$ , nm
$\text{Ba}_3\text{MgSi}_2\text{O}_8$	437	31
$(\text{Ba}_{2.25}\text{Sr}_{0.375}\text{Ca}_{0.375})\text{MgSi}_2\text{O}_8$	445	46
$(\text{Ba}_{1.5}\text{Sr}_{0.75}\text{Ca}_{0.75})\text{MgSi}_2\text{O}_8$	440	48
$(\text{BaSrCa})\text{MgSi}_2\text{O}_8$	443	53
$(\text{Ca}_{1.5}\text{Sr}_{1.5})\text{MgSi}_2\text{O}_8$	467	48

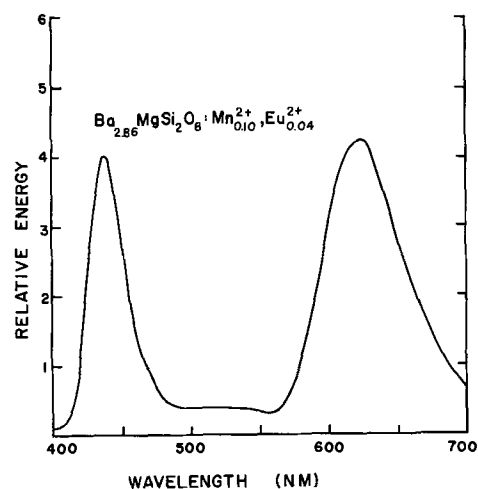


Fig. 7. Spectral energy distribution curve showing co-activation with  $\text{Eu}^{2+}$  and  $\text{Mn}^{2+}$  in  $\text{Ba}_3\text{MgSi}_2\text{O}_8$ .

in these compounds. It was also observed that the wavelength at which maximum intensity of the manganese emission occurs shifts to longer wavelength as the average ionic radius of the large alkaline earth ion is decreased by substitution of ( $\text{Sr}^{2+}$ ), or ( $\text{Sr}^{2+} + \text{Ca}^{2+}$ ) for  $\text{Ba}^{2+}$ . Examples illustrating this shifting are given in Table IX.

Figure 8 shows the decrease in europium emission as the manganese concentration is increased and a corresponding increase in the manganese emission up to the point where concentration quenching sets in. This type of relationship is characteristic of an energy transfer process.

#### Conclusion

Divalent europium activation of  $\text{A}_3\text{MgSi}_2\text{O}_8$  phases (where A = Ca, Sr, and Ba, or any combination of the three) has produced a series of narrow band, high-luminescent yield phosphors in which the emission band can be shifted over the blue region of the spectrum. These phosphors have potential application in photocopy devices where the energy delivered must fall within specific wavelength limits. They may also find application as color correction phosphors, as they are capable of supplying more energy at the key wavelengths necessary to achieve the desired result. This would also allow some variations in the other phosphors in the blend because of the narrow spectral region covered by the blue color corrector.

This work agrees with that of Klasens *et al.* (1) on the complete crystalline solubility of ( $\text{Ba}_3\text{MgSi}_2\text{O}_8$  and  $\text{Sr}_3\text{MgSi}_2\text{O}_8$ ) and ( $\text{Sr}_3\text{MgSi}_2\text{O}_8$  and  $\text{Ca}_3\text{MgSi}_2\text{O}_8$ ). In these two pseudobinary systems where complete crystalline solution exists, the luminescence of intermediate phases has been shown to be enhanced. Also, the emission wavelength at which maximum intensity occurs does not vary in a continuous manner even for the systems with complete crystalline solution. However, the divalent europium served as a more definitive probe in establishing the existence of the compound  $\text{BaCa}_2\text{MgSi}_2\text{O}_8$  not reported by them in the  $\text{Ca}_3\text{MgSi}_2\text{O}_8$ - $\text{Ba}_3\text{MgSi}_2\text{O}_8$  pseudobinary system.

Reaction kinetics are greatly affected by the starting materials and also may be characteristic for specific compositions.

Table IX. Emission data on some  $\text{Eu}^{2+}$ ,  $\text{Mn}^{2+}$  co-activated crystalline solution phases

Composition	Blue band $\lambda_{\text{Peak}}$ , nm	Red band $\lambda_{\text{Peak}}$ , nm
$\text{Ba}_{2.86}\text{MgSi}_2\text{O}_8:\text{Eu}_{0.04}^{2+}, \text{Mn}_{0.10}^{2+}$	437	620
$(\text{Ba}_{2.11}\text{Sr}_{0.75})\text{MgSi}_2\text{O}_8:\text{Eu}_{0.04}^{2+}, \text{Mn}_{0.10}^{2+}$	437	645
$\text{Ba}_{1.36}\text{Sr}_{0.75}\text{Ca}_{0.75})\text{MgSi}_2\text{O}_8:\text{Eu}_{0.04}^{2+}, \text{Mn}_{0.10}^{2+}$	443	670
$\text{Sr}_{2.86}\text{MgSi}_2\text{O}_8:\text{Eu}_{0.04}^{2+}, \text{Mn}_{0.10}^{2+}$	458	685
$\text{Ca}_{2.86}\text{MgSi}_2\text{O}_8:\text{Eu}_{0.04}^{2+}, \text{Mn}_{0.10}^{2+}$	475	>700

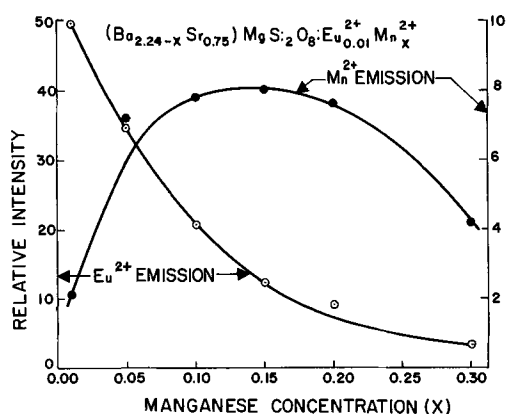


Fig. 8. Effect of manganese concentration on the energy transfer in  $(\text{Ba}_{0.224-x}\text{Sr}_{0.75})\text{MgSi}_2\text{O}_8:\text{Eu}_{0.01}^{2+}, \text{Mn}_x^{2+}$ .

Co-activation with manganese produces a phosphor with two distinct emission bands. One characteristic of the particular composition activated by europium alone and a second band in the red region of the spectrum whose position may be regulated by the formulation of A in  $\text{A}_3\text{MgSi}_2\text{O}_8$ . The spectral energy distribution curves of these co-activated phosphors (Fig. 7) conform fairly well to the action spectra of chlorophyll synthesis and photosynthesis. Thus, they may potentially be useful as "Gro-Lux" phosphors. This possibility is enhanced because of the latitude allowed in shifting both the blue and red emission bands.

### Acknowledgments

The author wishes to express his thanks to Dr. K. H. Butler and Dr. M. J. B. Thomas for their encouragement and valuable discussions during the course of this investigation. Appreciation is also extended to Mr. A. Rudis for the preparation and spectral determinations on many of the samples and to Miss M. Skeadas for the x-ray diffraction data.

Manuscript received Feb. 9, 1968; revised manuscript received March 18, 1968.

Any discussion of this paper will appear in a Discussion Section to be published in the June 1969 JOURNAL.

### REFERENCES

1. H. A. Klasens, A. H. Hoekstra, and A. P. M. Cox, *This Journal*, **104**, 93 (1957).
2. F. Nadachowski and M. Grylicki, *Silikat. Tech.*, **10**, 79 (1959).
3. J. F. Argyle, Ph.D. Thesis, The Pennsylvania State University, 1963; Univ. Microfilms (Ann Arbor, Michigan), Order No. 64-1378, 201 pp.
4. J. E. Eby, Paper presented at the Toronto Meeting, May 3-7, 1964, Abstract No. 27.
5. R. W. Nurse, Proceedings of the Third International Symposium on the Chemistry of Cement, London 1952, p. 63. Cement and Concrete Association, London (1954).
6. L. H. Ahrens, *Geochim. cosmochim. Acta*, **2**, 155 (1952).
7. N. A. Gorbacheva, *Izvest. Akad. Nauk, SSSR, Phys. Ser.*, **30**, 1521 (1966).
8. W. L. Wanmaker and J. W. ter Vrugt, *Philips Res. Repts.*, **22**, 355 (1967).

## Fluorescence of Uranium-Activated Compounds with Rocksalt Lattice

G. Blasse

Philips Research Laboratories, N. V. Philips' Gloeilampenfabrieken, Eindhoven, Netherlands

### ABSTRACT

The green fluorescence of the following phosphors is reported:  $\text{Li}_3\text{NbO}_4\text{-U}$ ,  $\text{Li}_3\text{SbO}_4\text{-U}$ ,  $\text{Li}_2\text{SnO}_3\text{-U}$ ,  $\text{LiScO}_2\text{-U}$ , and  $\text{MgO-U}$ . Their crystal structures are based on the rocksalt lattice. It is found that for increasing lithium content of the host lattice the position of the maximum of the emission band shifts to shorter wavelengths and the quantum efficiency increases. This relation is discussed. Concentration quenching occurs at low activator concentration.  $\text{Y}_6\text{WO}_{12}\text{-U}$  with regular  $\text{UO}_6$  octahedra emits also in the green. For some other compounds red emission was found. Green uranium emission is assigned to  $\text{UO}_6$  groups and uranyl ( $\text{UO}_2$ ) groups, red emission to  $\text{UO}_4$  groups. It is shown that this assignment is consistent with the structural data for a large number of uranium-activated oxides. Energy transfer was observed between the uranium center and  $\text{Eu}^{3+}$ . Addition of  $\text{Cr}^{3+}$  or  $\text{Rh}^{3+}$  quenches the uranium fluorescence drastically.

The fluorescence of hexavalent uranium centers is well known. In glasses this fluorescence is usually ascribed to the uranyl ( $\text{UO}_2^{2+}$ ) group (1). In solids two types of emission occur, viz., green and/or red emission. This difference was earlier noted by Kröger (2), who ascribed the green emission to uranyl groups and the red emission to uranate groups (i.e., hexavalent uranium ions substituted at a crystallographic site of the host lattice, for example, for tungsten). Runciman (3), however, ascribed the green emission of  $\text{CaO-U}$  and  $\text{Ca}_2\text{MgWO}_6\text{-U}$  to the uranate ( $\text{UO}_6$ ) group.

Gobrecht and Weiss (4) investigated thoroughly the uranium-activated scheelites and concluded that the green emission originates from the uranyl group and the red emission from the uranate ( $\text{UO}_4$ ) group. Effi-

cient green uranium fluorescence in the solid state was reported by Leonov (5) for  $\text{Li}_4\text{WO}_5\text{-U}$  and  $\text{Li}_4\text{MgWO}_6\text{-U}$  and by Mooney (6) for  $\text{Li}_6\text{Mg}_5\text{Sb}_2\text{O}_{13}\text{-U}$ . These host lattices are related to the rocksalt lattice. Therefore we decided to investigate the uranium fluorescence in other compounds with rocksalt-like lattices. On the other hand we looked for a host lattice that could offer only a regular octahedral coordination for hexavalent uranium in order to study the emission of regular  $\text{UO}_6$  groups.

### Experimental

Samples were prepared by usual ceramic methods, firing intimate mixtures of highly pure oxides and/or carbonates in air at  $950^\circ$  for lithium-containing ma-

materials and at 1350° for  $Y_6WO_{12}$ . Uranium was used as uranyl nitrate or acetate and introduced into the host lattice according to stoichiometric equations, using  $Li^+$  as charge compensator if necessary (e.g.,  $W^{6+} \rightarrow U^{6+}$ ,  $5Nb^{5+} \rightarrow 4U^{6+} + Li^+$ ,  $5Sn^{4+} \rightarrow 3U^{6+} + 2Li^+$ ,  $5Mg^{2+} \rightarrow U^{6+} + 4Li^+$ , etc.).

The uranium concentration was varied from 0.1 to 1.0 a/o (atomic per cent) per formula unit of the host lattice. Samples were checked by x-ray analysis. The performance of the optical measurements has been described elsewhere (7).

### Results

The following uranium-activated materials were studied:  $Li_3NbO_4-U$ ,  $Li_3SbO_4-U$ ,  $Li_2SnO_3-U$ ,  $LiScO_2-U$ ,  $MgO-U$ ,  $LiNbO_3-U$ ,  $LiSbO_3-U$ ,  $NaSbO_3-U$ , and  $Y_6WO_{12}-U$ . Only  $Li_3NbO_4-U$  shows a green fluorescence of reasonable intensity at room temperature.  $Li_3SbO_4-U$  and  $Li_2SnO_3-U$  show a weak green fluorescence and  $LiSbO_3-U$  a weak orange fluorescence at room temperature. The other compounds do not fluoresce at room temperature, but they fluoresce at liquid  $N_2$  temperature. The emission color of the last group of materials is green, except for  $NaSbO_3-U$  which shows an orange fluorescence. The excitation source in all these cases is long- and/or short-wave ultraviolet radiation.

The spectral energy distribution of the emission of part of the samples studied is given in Fig. 1-3. Tables I and II indicate the position of the maximum of the

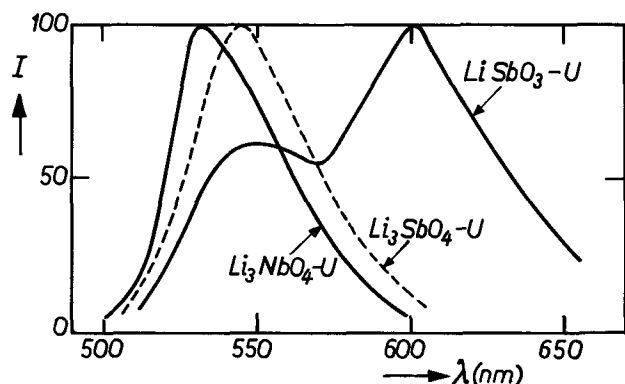


Fig. 1. Spectral energy distribution of the fluorescence at room temperature of  $Li_3NbO_4-U$ ,  $Li_3SbO_4-U$ , and  $LiSbO_3-U$  (365 nm excitation). Along the ordinate the radiant power per constant wavelength interval ( $I$ ) has been plotted in arbitrary units.

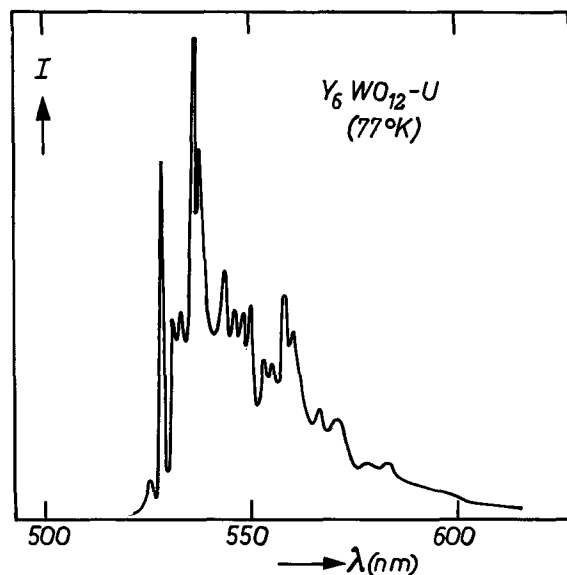


Fig. 2. Spectral energy distribution of the fluorescence at 77°K of  $Y_6WO_{12}-U$ . For  $I$  see Fig. 1.

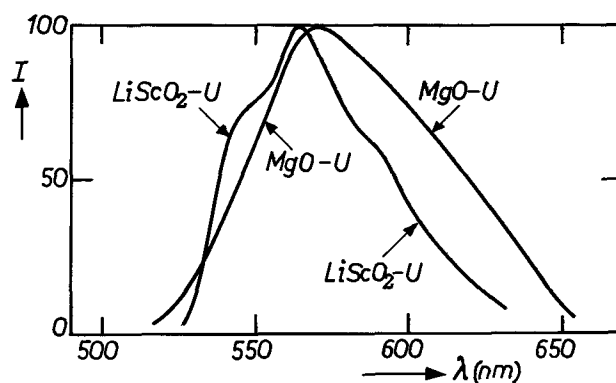


Fig. 3. Spectral energy distribution of the fluorescence at 77°K of  $LiScO_2-U$  and  $MgO-U$ . For  $I$  see Fig. 1.

emission band of all phosphors studied. The quantum efficiency of the fluorescence of the more efficient phosphors at room temperature is given in Table I.

The excitation spectrum of the green fluorescence of  $Li_3NbO_4-U$  is given in Fig. 4 and resembles that of  $Li_6Mg_5Sb_2O_{13}-U$  (6). Under cathode-ray excitation  $Li_3NbO_4-U$  shows blue and green emission with an energy conversion factor of about 1%. This blue emission was also observed for the unactivated  $Li_3NbO_4$  (8), so that energy transfer from host lattice (niobate group) to uranium center is inefficient.

The variation of quantum efficiency with uranium concentration was studied for  $Li_3NbO_4-U$ . The highest observed quantum efficiency in the u.v. region amounts to 45%, 30%, and 20% for uranium concentrations of 0.1, 0.5, and 1.0 a/o per formula unit  $Li_3NbO_4$ , respectively. Although values for still lower U-concentrations varied too much to give reliable data, it is clear that concentration quenching of the fluorescence occurs at very low concentrations. For increasing U-content the emission band becomes

Table I. Position of the maximum of the emission band and maximum quantum efficiency in the u.v. region of some uranium-activated materials with rocksalt-like lattices.

Composition <sup>a</sup>	Maximum emission band, nm	Maximum quantum efficiency, %	Reference
$Li_4MgWO_6-U$	514	~30 <sup>b</sup>	5
$Li_4WO_6-U$	520	~60 <sup>b</sup>	5
$Li_6Mg_5Sb_2O_{13}-U$	523	~45 <sup>b</sup>	6
$Li_3NbO_4-U$ (Li)	530	45	
$Li_3SbO_4-U$ (Li)	545	30	
$Li_2SnO_3-U$ (Li)	550	10	
$LiScO_2-U$ (Li)	565 <sup>c</sup>	<sup>d</sup>	
$MgO-U$ (Li)	570 <sup>c</sup>	<sup>d</sup>	

<sup>a</sup> Uranium concentration 0.1 a/o per formula unit; charge compensator between parentheses.

<sup>b</sup> Values estimated from literature data.

<sup>c</sup> At 77°K.

<sup>d</sup> No emission at room temperature; weak emission at 77°K.

Table II. Color and/or position of the maximum of the emission band of the uranium fluorescence in some mixed metal oxides.

Composition <sup>a</sup>	Emission values in nm	Remarks	Reference
$LiSbO_3-U$ (Li)	Orange (550 and 600)	Weak at room temp	This work
$LiNbO_3-U$ (Li)	Green (~550)	Only at 77°K	This work
$NaSbO_3-U$ (Na)	Orange (610)	Only at 77°K	This work
$Y_6WO_{12}-U$	Green (~540)	Only at 77°K	This work
$CaWO_4-U$	Green + red		2, 4
$CdWO_4-U$	Red (625)		2, 3
$MgWO_4-U$	Red (590 and 610)		2
$Li_2WO_4-U$	Green (540)		5
$Li_3PO_4-U$	Green		2
$CaO-U$	Green		3
$Ca_2MgWO_6-U$	Green		3

<sup>a</sup> Charge compensator between parentheses.

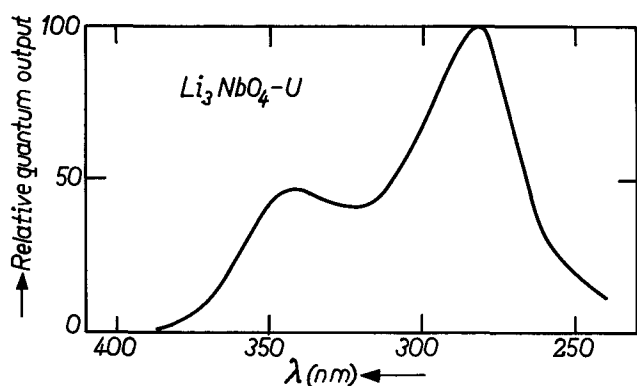


Fig. 4. Relative excitation spectrum of the emission with  $\lambda > 500$  nm of  $\text{Li}_3\text{NbO}_4\text{-U}$ .

steeper on the short-wavelength side and its maximum shifts to longer wavelength.

Energy transfer from the uranium center  $\text{Eu}^{3+}$  was observed in  $\text{Li}_3\text{SbO}_4\text{-U}$ , Eu. The excitation spectrum of the  $\text{Eu}^{3+}$  fluorescence shows also the uranium excitation bands of  $\text{Li}_3\text{SbO}_4\text{-U}$  [these are similar to these of  $\text{Li}_3\text{NbO}_4\text{-U}$  (Fig. 4)]. Energy transfer from the uranyl group to  $\text{Eu}^{3+}$  in glasses and solutions has been observed before (9, 10).

Addition of  $\text{Cr}^{3+}$  or  $\text{Rh}^{3+}$  to  $\text{Li}_3\text{NbO}_4\text{-U}$  or  $\text{Li}_3\text{SbO}_4\text{-U}$  quenches the fluorescence drastically. On addition of 0.5 a/o of  $\text{Cr}^{3+}$  per formula unit  $\text{Li}_3\text{SbO}_4\text{-U}$  (1 a/o), for example, the light output of the uranium fluorescence decreases to 5%. For the same  $\text{Rh}^{3+}$  concentration this figure is 35%.  $\text{Rh}^{3+}$  shows weak absorption bands at 400 and 525 nm in  $\text{Li}_3\text{NbO}_4$  and at 345 and 460 nm in  $\text{Li}_3\text{SbO}_4$ .

### Discussion

*Compounds with rocksalt-like lattices.*—A number of the host lattices investigated have the rocksalt structure or a structure based on a superstructure of this structure (ordering of cations):  $\text{MgO}$  has rocksalt structure,  $\text{Li}_2\text{SnO}_3$  (12),  $\text{Li}_3\text{SbO}_4$  (13), and  $\text{Li}_4\text{WO}_5$  (14) have ordered rocksalt structures. Table I shows that the uranium emission of these compounds shifts to longer wavelengths and the quantum efficiency decreases for decreasing lithium content of the host lattice.

$\text{Li}_4\text{MgWO}_6\text{-U}$  and  $\text{Li}_6\text{Mg}_5\text{Sb}_2\text{O}_{13}\text{-U}$  are also included in this table for the following reason.  $\text{Li}_4\text{MgWO}_6$  is a compound in the system  $\text{Li}_4\text{WO}_5\text{-MgO}$ . Both compounds have rocksalt structure and the cations involved have about equal radii. Therefore the structure of  $\text{Li}_4\text{MgWO}_6$  is probably also of the rocksalt type. In the analogous  $\text{Re}^{6+}$  system it has indeed been found that  $\text{Li}_4\text{ReO}_5$  as well as  $\text{Li}_4\text{MgReO}_6$  have rocksalt-like structures (12, 15).  $\text{Li}_6\text{Mg}_5\text{Sb}_2\text{O}_{13}$  is a composition in between  $\text{MgO}$  and  $\text{Li}_3\text{SbO}_4$  (both with rocksalt structure and cations with equal radii), so that the structure of this compound can probably also be described as a superstructure of the rocksalt structure. From Table I it follows that only  $\text{Li}_4\text{MgWO}_6\text{-U}$  seriously disagrees with the correlation mentioned above.

The correlation of Table I recalls two other correlations given by us before: for niobates the quantum efficiency at room temperature, and the quenching temperature, of the fluorescence increases if the absorption edge (and the emission band) shifts to shorter wavelength (8, 16); for  $\text{Eu}^{3+}$ -activated mixed metal oxides the quantum efficiency and the quenching temperature of the  $\text{Eu}^{3+}$  fluorescence increase if the charge-transfer absorption band of the  $\text{Eu}^{3+}$ -center shifts to shorter wavelengths (17, 18). We could account for these correlations by assuming that charge-transfer absorption bands move to shorter

wavelengths if the potential field at the  $\text{O}^{2-}$  ion due to the cations increases. This assumption is not unreasonable. In the present case it can only be relevant if a charge-transfer process is indeed involved in the uranium fluorescence. For the uranyl group it has been shown that this is the case (19). The lowest absorption band is ascribed to an electron transfer from the highest filled molecular orbital (m.o.) of the complex (which is localized mainly on the oxygen ions) to the lowest empty molecular orbital (which consists mainly of the 5f orbital of the uranium ion). It seems probable that this is also the case for uranium centers in oxides (uranate groups). The highest filled m.o. is a nonbonding oxygen orbital, the lowest empty m.o. is the 5f orbital [ $\text{U}^{5+}$  in the solid state has  $5f^1$  configuration; see, e.g. (20)]. The nonbonding orbitals and the 5f orbital will not depend strongly on the type of uranium center, so that their energy difference is mainly determined by the field at the oxygen ions (the higher this field, the lower the oxygen orbitals are situated).

Elsewhere we have shown that for ordered structures the potential field at the  $\text{O}^{2-}$  ions around the higher charged cations is always relatively high (8). We feel, therefore, that the results of Table I are in a physical sense closely connected with our results for niobates and europium-activated oxides in spite of the chemical differences. If the  $\text{Li}^+$  content of the host lattice increases, the cationic charge is distributed less homogeneously. The field at a part of the anions becomes stronger, the charge transfer bands shift to shorter wavelengths, and the fluorescence efficiencies and quenching temperatures increase. Since these relations can now no longer be considered to be accidental, further investigation of them seems highly desirable.

We will now discuss the nature of the fluorescent center in these compounds with rocksalt lattice. In view of the green fluorescence of the uranyl group it is tempting to assign the green fluorescence of the present phosphors to uranyl groups as well. It is difficult, however, to imagine how the  $\text{U}^{6+}$  ion can be introduced in the rocksalt lattice as a linear  $\text{UO}_2$  group. Moreover the  $\text{U}^{6+}$  ion in oxides is not in all cases present in the form of a  $\text{UO}_2$  group. In  $\text{CaUO}_4$  and  $\text{UO}_3$  (21) one can clearly distinguish separate  $\text{UO}_2$  groups. In  $\text{Li}_4\text{UO}_5$ , however,  $\text{UO}_6$  octahedra are present with four shorter and two longer U-O distances (22) and in  $\text{Y}_6\text{UO}_{12}$  even regular  $\text{UO}_6$  octahedra have been found (23).  $\text{Y}_6\text{WO}_{12}$  is isomorphous with  $\text{Y}_6\text{UO}_{12}$ . For this reason we decided to study  $\text{Y}_6\text{W}_{1-x}\text{U}_x\text{O}_{12}$ , because materials of this composition will contain regular  $\text{UO}_6$  octahedra.

*Color of the uranium emission in oxides.*—The emission of  $\text{Y}_6\text{WO}_{12}\text{-U}$  (Fig. 2) consists of a broad band in the green with a pronounced structure. Runciman (3) also observed structure in the uranium emission of  $\text{CaO}$ ,  $\text{Ca}_2\text{MgWO}_6$ , and other compounds. The emission band of  $\text{Li}_3\text{NbO}_4\text{-U}$  shows also structure at liquid nitrogen temperature. These phenomena will not be discussed in this paper. What is of interest here is that the emission is in the green part of the spectrum. This shows that green uranium emission originates not only from uranyl groups ( $\text{UO}_2^{2+}$ ), but also from  $\text{UO}_6$  octahedra. Only Runciman (3) seems to have recognized this fact. The red uranium emission must then be ascribed to  $\text{UO}_4$  groups. In Table II which contains also a number of data from the literature the emission color of a number of uranium-activated phosphors are compared. We will attempt to correlate these with the crystal structure.

Compounds with rocksalt lattice show green uranium fluorescence without exception. This lattice consists of a cubic close-packed array of anions in which all the octahedral holes are occupied by cations. In this situation it is very unfavorable for a cation to occupy one of the tetrahedral holes, since each tetrahedral hole has a large number of occupied octahedral holes

at short distances ( $\sim 1.8\text{\AA}$ ). No crystal structures are known that are based on a close-packing with not only all octahedral but also part of the tetrahedral holes occupied (21, 24). In accordance with this, no red  $\text{UO}_4$  emission is observed. Since the rocksalt lattice does not give favorable opportunities for linear  $\text{UO}_2$  groups, it seems probable that the emission from uranium-activated compounds with rocksalt lattice is due to  $\text{UO}_6$  groups, *i.e.*, the  $\text{U}^{6+}$  ion occupies the normal crystallographic sites of the cations.

$\text{LiNbO}_3$ ,  $\text{LiSbO}_3$ , and  $\text{NaSbO}_3$  have a structure based on a hexagonal close-packed array of anions with two thirds of the octahedral holes filled (21). The distribution of the cations among these holes is different for the three compounds. In these structures the  $\text{U}^{6+}$  ion can occupy octahedral holes. However, occupation of tetrahedral holes is not so unfavorable as in the rocksalt lattice, because not every tetrahedral hole is surrounded by a large number of octahedral ions at short distances (compounds with crystal structures in which part of the octahedral and part of the tetrahedral sites are occupied are well-known, *e.g.*, spinels and olivines). It is therefore not surprising that the uranium-emission color is green in  $\text{LiNbO}_3\text{-U}$  ( $\text{UO}_6$  groups), green and red in  $\text{LiSbO}_3\text{-U}$ , ( $\text{UO}_6$  and  $\text{UO}_4$  groups; see Fig. 1), and red in  $\text{NaSbO}_3\text{-U}$  ( $\text{UO}_4$  groups). Why the emission color is different for these three cases cannot be explained at the moment. However, there are at least no serious objections against the presence of  $\text{UO}_4$  groups in this structure.

In the uranium activated scheelites (*e.g.*,  $\text{CaWO}_4$ ) red and green fluorescence have both been observed. In our interpretation the red emission is due to  $\text{UO}_4$  groups ( $\text{U}^{6+}$  on a  $\text{W}^{6+}$  site). The scheelite structure has a large number of unoccupied octahedral holes the centers of which are situated midway between each pair of next-nearest tungsten neighbors. We propose, therefore, that the green uranium emission in scheelites is due to  $\text{UO}_6$  groups which are formed by occupation of the empty octahedral holes by  $\text{U}^{6+}$  ions. This is at least as probable as the assumption of the interstitial uranyl groups proposed by Gobrecht and Weiss (4).

In wolframites (*e.g.*,  $\text{CdWO}_4$  and  $\text{MgWO}_4$ ) only red uranium fluorescence has been observed. In all the papers in the literature this emission is assigned to a  $\text{UO}_4$  group. This agrees with the present hypothesis. However, the  $\text{W}^{6+}$  ion in the wolframite structure is in six-coordination. Two explanations can be offered: (a) only half of the octahedral holes in the hexagonal close-packed array of  $\text{O}^{2-}$  ions of this structure are occupied, so that the  $\text{U}^{6+}$  ion may occupy tetrahedral sites, and (b) the  $\text{WO}_6$  octahedron is strongly elongated in the wolframite structure. In  $\text{CdWO}_4$  for example, the  $\text{W}^{6+}$  ion has four  $\text{O}^{2-}$  ions at 1.80-1.87 $\text{\AA}$  and two  $\text{O}^{2-}$  ions at 2.22 $\text{\AA}$  (25). For  $\text{NiWO}_4$  these values are 4 x 1.79 $\text{\AA}$  and 2 x 2.19 $\text{\AA}$  (26). If  $\text{U}^{6+}$  substitutes for  $\text{W}^{6+}$  on a  $\text{W}^{6+}$  site, something like a  $\text{UO}_4$  is formed.

$\text{Li}_2\text{WO}_4$  and  $\text{Li}_3\text{PO}_4$  have both structures with the metal ions in four coordination. The oxygen lattice of  $\text{Li}_2\text{WO}_4$  (phenacite structure) is not close-packed and contains large octahedral holes in which the  $\text{U}^{6+}$  ion would fit. This possibility was previously suggested by Van Arkel (27). The green fluorescence of  $\text{Li}_2\text{WO}_4\text{-U}$  would then be due to centers of this type. The structure of  $\text{Li}_3\text{PO}_4$  is again based on a hexagonal close-packed array of  $\text{O}^{2-}$  ions (28). Half of the tetrahedral holes are occupied, whereas the octahedral holes are empty. The  $\text{U}^{6+}$  ion can therefore occupy octahedral sites (green luminescence as found experimentally).

In conclusion we see that the assignment of green emission to  $\text{UO}_6$  and uranyl groups and of red emission to  $\text{UO}_4$  groups does not contradict the structural data and that it is not necessary in many cases to assume interstitial uranyl groups to explain a green emission. This assignment is the same as proposed by

Runciman (3) but differs from that given by Kröger (2) and Gobrecht and Weiss (4).

*Concentration quenching.*—From our results it follows that concentration quenching of the uranium emission occurs at low uranium concentration ( $<1$  a/o) as has been observed before by other workers [see, *e.g.* (4)]. Dexter and Schulman (29) have proposed a theory of concentration quenching. They assume that energy is transferred from activator to activator center until it reaches a sink or is emitted as radiation. Therefore the efficiency of the energy transfer between the activator centers is one of the factors determining the critical concentration at which concentration quenching starts [see also (30)]. Dexter and Schulman estimate this critical concentration at 0.1-1.0 a/o, if the transitions involved are allowed electric dipole transitions.

From the fact that the emission band of  $\text{Li}_3\text{NbO}_4\text{-U}$  moves to longer wavelengths and becomes steeper on the short wavelength side we conclude that the energy transfer occurs partly radiatively (self-absorption).  $\text{Li}_3\text{NbO}_4\text{-U}$  in fact shows an absorption band peaking at about 500 nm (data from diffuse reflection spectra), so that the energy overlap of emission and absorption band is large. This is required for radiative transfer. Moreover it is very probable that the transfer will also occur by nonradiative electric dipole-dipole interaction, since the optical strength of the transition involved is by no means weak (charge-transfer) and the energy overlap large.

In conclusion we see that the energy transfer from one uranium center to another is efficient and that the critical concentration for quenching is therefore low.

*Energy transfer to other centers.*—Finally we shall briefly discuss some other cases of energy transfer which were observed during this investigation.

Under short-wave u.v. and especially cathode-ray excitation the phosphor  $\text{Li}_3\text{NbO}_4\text{-U}$  emits not only a green fluorescence, but also a strong blue fluorescence. The latter emission originates from the host lattice itself (8). It may therefore be concluded that the energy transfer from host lattice to uranium center is far from efficient. This follows also from the excitation spectrum of the fluorescence (Fig. 4): the excitation band of the host lattice at about 240 nm is absent. There are two possible reasons for this inefficient transfer: (a) Transfer through the host lattice will not be efficient, since the energy overlap condition is badly fulfilled: the emission band of  $\text{Li}_3\text{NbO}_4$  almost fails to overlap the absorption band (8). A similar phenomenon has been observed for  $\text{YNbO}_4\text{-Eu}$ , where large amounts of Eu are needed to quench the niobate emission (31). However, the total quantum efficiency (of niobate and  $\text{Eu}^{3+}$  emission) remains constant. This points to inefficient energy transfer through the niobate lattice. Since in our case the activator concentration is necessarily low to prevent concentration quenching, this effect will be important. (b) It is also possible that energy transfer from niobate group to uranium center is not very efficient, since the  $\text{Li}_3\text{NbO}_4$  emission (peaking at 370 nm) lies in between two absorption bands of the uranium center (peaking at 500 nm at 340 nm). The energy overlap with these two bands is certainly not sufficient to allow transfer over large distances, so that the transfer through the host lattice indeed determines the total transfer efficiency from host lattice to activator. The situation is contrary to that in  $\text{Li}_3\text{NbO}_4\text{-Cr}$ , where the transfer from niobate to  $\text{Cr}^{3+}$ -center is extremely efficient (32). This explains why a very small amount of  $\text{Cr}^{3+}$  ions quenches the niobate emission completely, although the transfer through the lattice is inefficient.

In  $\text{Li}_3\text{SbO}_4\text{-U}$ , Eu transfer from the uranium center to  $\text{Eu}^{3+}$  was observed. It was shown above that the transfer between the uranium centers is efficient. The transfer from uranium center to  $\text{Eu}^{3+}$  is possible, since the uranium emission overlaps the  $^5\text{D}_1$  and  $^5\text{D}_0$  levels

of the  $\text{Eu}^{3+}$  ion (at about 525 and 580 nm, respectively). In view of the low optical strength of the transitions involved this transfer does probably not occur by electric multipole interaction but by exchange interaction. This was also found for the uranyl  $\rightarrow \text{Eu}^{3+}$  transfer in solutions (10) and other transfer processes to  $\text{Eu}^{3+}$  (33).

The strong quenching effect of  $\text{Cr}^{3+}$  on the fluorescence of  $\text{Li}_3\text{NbO}_4\text{-U}$  will be partly due to efficient energy transfer from the uranium center to  $\text{Cr}^{3+}$ . The uranium emission (530 nm) overlaps the intense, broad charge-transfer band of the  $\text{Cr}^{3+}$  center in  $\text{Li}_3\text{NbO}_4$  (380 nm) reasonably well (32). Both optical transitions are of a charge-transfer type and are therefore allowed electric-dipole transitions, so that transfer by electric dipole-dipole interaction is expected to be efficient. The shape of the emission band of the uranium center does not depend on the  $\text{Cr}^{3+}$  concentration. Therefore we exclude radiative transfer.

The quenching effect of  $\text{Rh}^{3+}$  is less than that of  $\text{Cr}^{3+}$ . The uranium emission overlaps the  $\text{Rh}^{3+}$  absorption in  $\text{Li}_3\text{NbO}_4$  at 525 nm very well, but the optical strength of this absorption is expected to be much lower than that of the absorption of  $\text{Cr}^{3+}$  in  $\text{Li}_3\text{NbO}_4$  (in the case of  $\text{Rh}^{3+}$  we are concerned with a parity-forbidden d-d transition, viz.,  ${}^1\text{A}_{1g} \rightarrow {}^1\text{T}_{1g}$ ). This weaker interaction causes a less efficient transfer.

In the case of  $\text{Li}_3\text{NbO}_4\text{-U,Rh}$  and especially of  $\text{Li}_3\text{NbO}_4\text{-U,Cr}$  it must be kept in mind that under short-wave as well as under long-wave u.v. excitation part of the exciting energy is already absorbed directly by the  $\text{Rh}^{3+}$  and  $\text{Cr}^{3+}$  centers, so that even without any energy transfer at all the green uranium output is expected to decrease with the addition of  $\text{Cr}^{3+}$  or  $\text{Rh}^{3+}$ .

Finally we note that the crystal-field splitting of the  $\text{Rh}^{3+}$  ion in  $\text{Li}_3\text{NbO}_4$  is relatively small. From the position of the two absorption bands we find the following approximate values for  $\Delta$  (crystal-field splitting) and B (electrostatic interaction parameter):  $\Delta = 17,500 \text{ cm}^{-1}$  and  $B = 400 \text{ cm}^{-1}$ . For  $\text{Li}_3\text{SbO}_4$   $\Delta = 20,000 \text{ cm}^{-1}$  and  $B = 450 \text{ cm}^{-1}$ . The calculation procedure has been described previously (34). For  $\text{Al}_2\text{O}_3\text{-Rh}$  these values are  $26,400 \text{ cm}^{-1}$  and  $400 \text{ cm}^{-1}$ , respectively (34). Low values of the crystal-field splitting of  $\text{Cr}^{3+}$  in niobates were observed and have been discussed elsewhere (32).

#### Acknowledgment

The author is greatly indebted to Dr. A. Bril, who obtained all the optical data reported.

Manuscript received Feb. 13, 1968; revised manuscript received March 19, 1968. This paper was presented at the Boston Meeting, May 5-9, 1968, as Abstract 47.

Any discussion of this paper will appear in a Discussion Section to be published in the June 1969 JOURNAL.

#### REFERENCES

1. G. E. Rindone, "Luminescence of Inorganic Solids," p. 430, P. Goldberg, Editor, Academic Press, New York (1966).
2. F. A. Kröger, "Some Aspects of the Luminescence of Solids," Chap. IV, Elsevier Publishing Co., New York (1948).
3. W. A. Runciman, *Brit. J. Appl. Phys., Suppl. No. 4*, S 78 (1955).
4. H. Gobrecht and W. Weiss, *Z. Physik*, **140**, 139 (1955).
5. Yu. S. Leonov, *Opt. Spectroscopy*, **9**, 145 (1960), and **10**, 357 (1961).
6. R. W. Mooney, *This Journal*, **108**, 1110 (1961).
7. A. Bril and W. L. Wanmaker, *ibid.*, **111**, 1363 (1964).
8. G. Blasse and A. Bril, *Z. Physik, Chem., N. F.*, **57**, 187 (1968).
9. L. G. de Shazer and A. Y. Cabezas, *Proc. I.E.E.E.*, **52**, 1355 (1964).
10. J. L. Kropp, *J. Chem. Phys.*, **46**, 843 (1967).
11. R. Hoppe, *Z. Anorg. Chem.*, **339**, 130 (1965).
12. G. Lang, *ibid.*, **348**, 246 (1966).
13. G. Blasse, *ibid.*, **326**, 44 (1963).
14. G. Blasse, *ibid.*, **331**, 44 (1964).
15. P. P. Pfeiffer, Thesis, Karlsruhe, 1963.
16. G. Blasse, *J. Chem. Phys.*, In press.
17. G. Blasse, *ibid.*, **45**, 2356 (1966).
18. G. Blasse and J. de Vries, *This Journal*, **114**, 875 (1967).
19. S. P. McGlynn and J. K. Smith, *J. Molec. Spectroscopy*, **6**, 164 (1961).
20. S. Kemmler Sack, E. Stumpp, W. Rüdorff, and H. Erfurth, *Z. Anorg. Chem.*, **354**, 287 (1967).
21. A. F. Wells, "Structural Inorganic Chemistry," Third edition, Clarendon Press, Oxford (1965).
22. H. Hoekstra and S. Siegel, *J. Inorg. Nucl. Chem.*, **26**, 693 (1964).
23. S. F. Bartram, *Inorg. Chem.*, **5**, 749 (1966).
24. E. W. Gorter, XVII Internat. Kongress für reine und angewandte Chemie, München, 1959, Band I.
25. A. P. Chichagov, V. V. Ilyukhin, N. V. Belov, *Doklady Akad. Nauk, SSSR*, **166**, 87 (1966).
26. R. O. Keeling, *Acta Cryst.*, **10**, 209 (1957).
27. A. E. van Arkel, "Moleculen en Kristallen," p. 272, van Stockum, 's Gravenhage (1961) (In Dutch).
28. J. Zemann, *Acta Cryst.*, **13**, 863 (1960).
29. D. L. Dexter and J. H. Schulman, *J. Chem. Phys.*, **22**, 1063 (1954).
30. G. Blasse and A. Bril, *This Journal*, To be published.
31. W. L. Wanmaker, A. Bril, J. W. ter Vrugt, and J. Broos, *Philips Res. Repts.*, **21**, 270 (1966).
32. G. Blasse, *J. Inorg. Nucl. Chem.*, **29**, 1817 (1967).
33. G. Blasse and A. Bril, *J. Chem. Phys.*, **47**, 1920 (1967).
34. G. Blasse and A. Bril, *This Journal*, **114**, 1306 (1967).

# Electroluminescent Properties of ZnSe-Type Phosphors

T. Hariu, T. Seki, K. Miyashita, and M. Wada

Department of Electronic Engineering, Tohoku University, Sendai, Japan

## ABSTRACT

Electroluminescent properties of ZnSe-type phosphors, including host crystals of modified compositions, were examined, especially temperature dependence and Mn-band characteristics. The variation in frequency dependence with temperature and composition was interpreted by considering the temperature quenching factor of electroluminescence,  $q = [1 + (D/f) \exp(-E_c/kT)]^{-1}$  ( $E_c$ , the activation energy of temperature quenching). On the contrary, the Mn-band, which is not due to the delayed recombination, did not have a superlinear frequency dependence, even in the temperature quenching region. Consideration in which the  $c$ -value was assumed to be constant with time was not sufficient to explain the  $c$ -value variation in each band with temperature and frequency, and the excitation process characteristics obtained by the Mn-band.

The mechanism of electroluminescence (EL) investigated so far has been based mainly on the experimental results of ZnS. The results of host crystals with different compositions (Zn,Cd)(S,Se) will add further aspects to the discussion of the mechanism in the sense that the parameters involved, *e.g.*, the position of luminescent centers and donors in energy diagram, can be changed continuously.

In the case of EL, contrary to the photoluminescence (PL), the excitation occurs in the different course of time of recombination. Contrary to this fact, generally observed characteristics involve both of them, at least in the case of light emission from the Cu center. On the contrary, properties of light emission from the Mn center are characterized by the excitation process and the same recombination process as that of PL, because the excited electron does not become free and therefore the recombination is not delayed.

This paper describes EL properties of ZnSe-type phosphors including host crystals of modified compositions, paying special attention to effects of temperature and the Mn band.

## Experimental Procedure

Phosphor preparation procedure has been described in another paper (1). Light emission from an EL cell in a vacuum chamber was measured using a Hitach EPU-2 type spectrometer and R136 photomultiplier. The phosphors were bound with paraffin, the electric property of which is almost constant up to room temperature.

## Results

Emission spectra are shown in Fig. 1. ZnSe:Cu,Cl has two emission bands with peak wavelength at 530 and 640 m $\mu$  (which will be called band 1 and band 2, respectively). In addition to them, ZnSe:Cu, Mn, Cl has the Mn band with peak wavelength at about 585m, which is the same as the Mn band in ZnS, though in contradiction with the results in literature (2). Emission color varies with excitation frequency in the temperature range where temperature quenching occurs, *i.e.*, high frequency and low temperature make band 1 increase. In the temperature range where band 1 has been quenched, the emission color did not change with frequency and temperature up to about 0°C, although temperature quenching of the Mn band occurred in this range. Above this temperature at which band 2 begins to be quenched, high frequency and low temperature make band 2 greater compared with the Mn band. High applied voltage makes the Mn band greater relatively.

The activation energy of quenching of PL ( $B = B_0 / [1 + \nu \exp(-E_c/kT)]$ ) obtained from the brightness dependence on temperature is shown in Table I for each band.

Frequency dependence of emission intensity of EL for each band is shown in Fig. 2 for ZnSe:Cu,Cl and in Fig. 3 for ZnSe:Cu,Mn,Cl. As for band 1 and band 2, in the temperature range in which temperature quenching occurred, the intensity increased superlinearly with frequency as expected. However, the intensity of the Mn band increased a little sub-linearly in the whole temperature range measured, even in the range in which temperature quenching occurred.

As expected, in the case where some Se in the crystal base was substituted with S and the quenching temperature was made higher, the temperature at which superlinear increase would appear became higher, as shown in Fig. 4 for the sample composed of 10% substitution for Se.

In connection with the frequency dependence, the temperature dependence of brightness was measured with frequency as parameter, shown in Fig. 5 for ZnSe:Cu,Cl and in Fig. 6 for the Mn band in ZnSe:Cu,Mn,Cl.

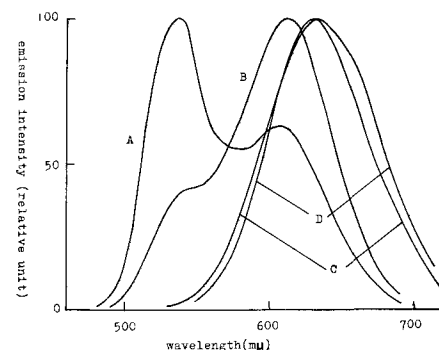


Fig. 1(a). Emission spectra of ZnSe:Cu, Cl. Curve A, -100°C, 10 kc; curve B, -100°C, 1 k(kHz); curve C, 12°C, 10 k(kHz); curve D, 12°C, 1 k(kHz).

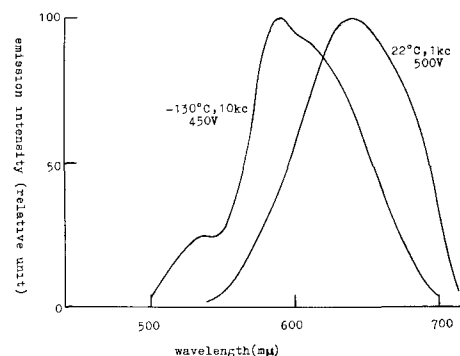


Fig. 1(b). Emission spectra of ZnSe:Cu, Mn, Cl

Table I. Activation energy of quenching

Sample	Emission band	$E_c$ , ev
ZnSe:Cu,Cl	Band 1	0.17
	Band 2	0.29
ZnSe:Cu,Mn,Cl (9.5ZnSe) (0.5CdSe) :Cu,Cl	Mn band	0.39
	Band 1	0.17
	Band 2	0.29
(9ZnSe) (1CdS) :Cu,Cl	Band 1	0.25
	Band 2	0.35

Luminescence intensity depended on voltage according to the law usually observed in ZnS ( $B = B_0 \exp(-c/V^{1/2})$ ), with  $c$ -value variation with frequency and temperature shown in Tables II, III, and IV. In ZnSe-type phosphors, the  $c$ -value tended to increase with frequency, and decrease with temperature, but it tended to increase at near room temperature. This tendency was not found in the sample composed of 10% substitution for Se, as shown in Table III. Voltage dependence of emission intensity for the Mn band and band 2 of (9ZnSe) (1CdS):Cu,Mn,Cl is shown in Fig. 7. For the Mn band, the  $c$ -value changed to a greater value at about 500v, but the smaller  $c$ -value is still greater than that of band 2.

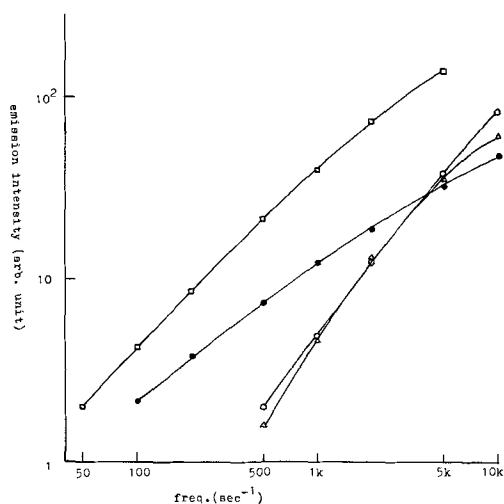


Fig. 2. Frequency dependence variation of ZnSe:Cu, Cl. ○ Band 1,  $-100^\circ\text{C}$ ; ● band 2,  $-100^\circ\text{C}$ ; □ band 2,  $-40^\circ\text{C}$ ; △ band 2,  $28^\circ\text{C}$ ; applied voltage, 400v.

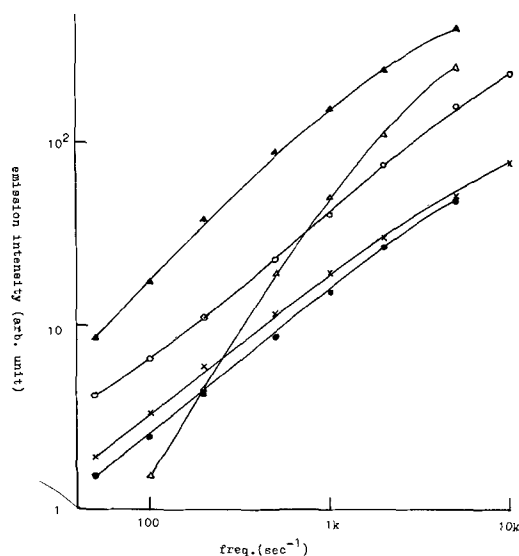


Fig. 3. Frequency dependence variation of ZnSe:Mn, Cl. (No relation among ordinate positions of curves.) Band 2: ▲  $-12^\circ\text{C}$ , △  $25^\circ\text{C}$ ; Mn band: ×  $-130^\circ\text{C}$ , ●  $12^\circ\text{C}$ , ○  $25^\circ\text{C}$ ; applied voltage, 450v.

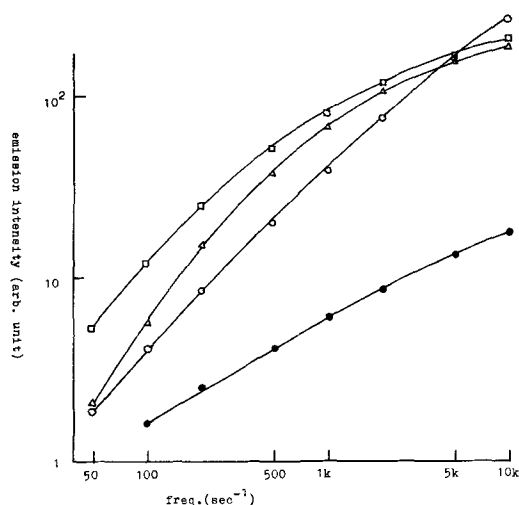


Fig. 4. Frequency dependence variation of (9ZnSe) (1CdS):Cu, Cl. ○ Band 1,  $-130^\circ\text{C}$ ; ● band 2,  $-130^\circ\text{C}$ ; □ band 2,  $4^\circ\text{C}$ ; △ band 2,  $23^\circ\text{C}$ ; applied voltage, 450v.

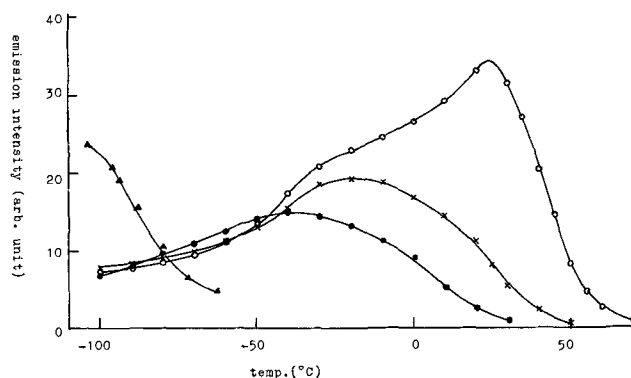


Fig. 5. Temperature dependence of EL intensity of ZnSe:Cu, Cl. ▲ Band 1, 10 kHz, 350v; ○ band 2, 10 kHz, 300v; × band 2, 2 kHz, 350v; ● band 2, 500 Hz, 450v.

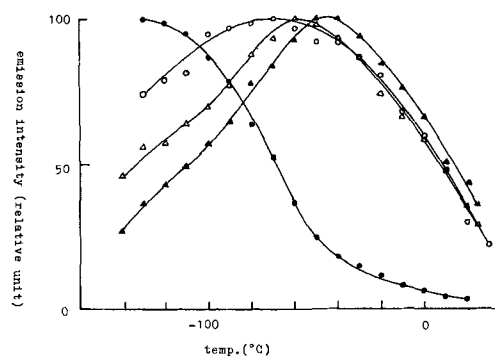


Fig. 6. Temperature dependence of EL intensity of the Mn band in ZnSe:Cu, Mn, Cl. ● Photoluminescence; ▲ 10 kHz, 400v; △ 1 kHz, 400v; ○ 100 Hz, 450v.

## Discussion

**Excitation process.**—The voltage dependence of brightness allows us to discuss the excitation process. The familiar relation between brightness and voltage

$$B = B_0 \exp(-c/V^{1/2}) \quad [1]$$

which is deduced theoretically by considering the supply of primary electrons, and the probability of impact ionization in the Mott-Schottky type barrier region (3), can explain the experimental results. A small deviation from [1] does not provide sufficient information to find out how primary electrons are supplied: tunneling from  $\text{Cu}_2\text{S}$  phase, thermally or





$$-\frac{dN_c^+}{dt} = SvnN_c^+ \quad [4]$$

where  $N_c^+$  is the unoccupied emission center,  $S$  the capture cross section,  $n$  the density of electron in the conduction band, and  $v$  the thermal velocity of free electron. This equation also applies to the case where the emission process is the transition from donor state to emission center, if the unoccupied donor is easily occupied.

Considering that generally  $n \gg N_c^+$  (monomolecular recombination), it can be written as follows

$$N_c^+ = N_{co}^+ \exp\left(-\frac{t}{\tau}\right) \quad [5]$$

where  $\tau = 1/Svn \approx \text{const.}$ , and  $N_{co}^+$  is the number of excited emission centers. Consequently, the emission intensity per unit time  $B$  is expressed as follows

$$B = N_{co}^+ f \left[ 1 - \exp\left(-\frac{1}{\tau f}\right) \right] \quad [6]$$

which is apparently the same result as that of Zalm (3), Thornton (6), and Miyashita (5). Of course, in the low frequency region

$$B \propto f \quad (\tau f \ll 1) \quad [7]$$

As the temperature rises, holes begin to escape from the emission center and  $N_{co}^+$  decreases with time after excitation at the following rate

$$-\frac{dN_c^+}{dt} = \nu N_c^+ \exp(-E_c/kT) \quad [8]$$

If we simplify the process so that recombination will not occur during  $t = 0 \sim t = mT_o/4$  and will begin at  $t = mT_o/4$ , as shown in Fig. 9, the decreased excited emission center  $N_{co}^+$  is calculated as follows

$$N_{co}^+ = N_{co}^+ \exp\left(-\frac{\gamma mT_o}{4}\right) = N_{co}^+ \exp\left(-\frac{D\gamma}{f}\right) \quad [9]$$

where  $\gamma = \nu \exp(-E_c/kT)$

In the recombination process

$$-\frac{dN_c^+}{dt} = \gamma N_c^+ + SvnN_c^+ = \left(\gamma + \frac{1}{\tau}\right) N_c^+ \quad [10]$$

and a similar calculation as the above leads to

$$B \propto N_{co}^+ f \frac{1}{\gamma + \frac{1}{\tau}} \left[ 1 - \exp\left\{-\left(\gamma + \frac{1}{\tau}\right) / f\right\} \right] \quad [11]$$

The temperature quenching factor  $q$  affecting brightness dependence on frequency at the low-frequency region is obtained by expanding Eq. [9] as follows

$$q = [1 + (D/f) \exp(-E_c/kT)]^{-1} \quad (D\gamma/f < 1) \quad [12]$$

This result was also suggested by Ivey (7). Equation [12] indicates that superlinear characteristics are ob-

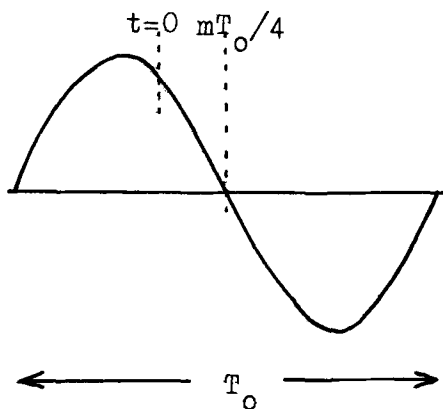


Fig. 9. Simplification of process

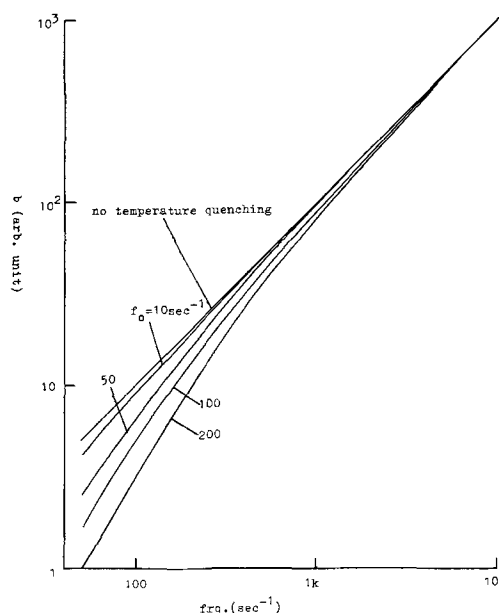


Fig. 10. Effect of temperature quenching on frequency dependence [ $b=f/(1+f_o/f)$ ].

served, as expected. In Fig. 10 frequency characteristics are given for several values of  $f_o = D \exp(-E_c/kT)$ .

Using Fig. 5 and Eq. [12], an approximate value of  $D$  is obtained from the temperature at which brightness is half of the maximum, to be  $\sim 10^8 \text{ sec}^{-1}$ . This is reasonable, considering  $\gamma = 10^8 \sim 10^9 \text{ sec}^{-1}$  (8-10).

It is noted that the above consideration of temperature quenching applies to the frequency characteristics of the delayed recombined emission center as the Cu center, but not to the Mn center; that is, superlinear dependence should not be observed even if temperature quenching occurs, as shown in Fig. 3. This result also suggests that energy transfer from the Cu center to the Mn center does not occur in this case and the Mn center is excited directly. It is clear here that characteristics of the Mn band enables us to look into the excitation process.

#### Acknowledgment

The authors wish to thank Professors T. Takahashi, S. Yoshida, and Y. Shibata for valuable discussions and their continued interest in these investigations.

Manuscript received Nov. 28, 1967; revised manuscript received ca. Feb. 21, 1968.

Any discussion of this paper will appear in a Discussion Section to be published in the June 1969 JOURNAL.

#### REFERENCES

1. T. Hariu, T. Seki, K. Miyashita, and M. Wada, *This Journal*, **115**, 638 (1968).
2. S. Asano *et al.*, Paper presented at the Spring meeting of Soc. of Appl. Phys. of Japan, Abstract p. 317 (1965).
3. P. Zalm, *Philips Research Repts.*, **11**, 417 (1956).
4. J. Mattler and T. Ceva, "Luminescence of Organic and Inorganic Materials," H. P. Kallmann and G. M. Spruch, Editors, p. 537, John Wiley & Sons Inc., New York (1962).
5. K. Miyashita, Thesis, Tohoku University, 1961.
6. W. A. Thornton, *Phys. Rev.*, **102**, 38 (1956); **103**, 1585 (1956).
7. H. F. Ivey, "Electroluminescence and Related Effects," "Advances in Electronic and Electron Physics," sup. 1, Academic Press, New York (1963).
8. G. F. Garlick and A. F. Gibson, *Proc. Roy. Soc.*, **A188**, 485 (1947).
9. G. F. Garlick and M. H. F. Wilkins, *ibid.*, **A184**, 408 (1945).
10. J. T. Randall and M. H. F. Wilkins, *ibid.*, **A184**, 366 (1945).

# Impurity Distribution in Single Crystals

## IV. Growth Characteristics and Impurity Incorporation During Facet Growth

K. Morizane,<sup>1\*</sup> A. F. Witt,\* and H. C. Gatos\*

Department of Metallurgy and Center for Materials Science and Engineering,  
Massachusetts Institute of Technology, Cambridge, Massachusetts

### ABSTRACT

Impurity heterogeneities in the "core" region of InSb single crystals pulled from the melt were shown to be sensitive to thermal asymmetry, the location of the facet in the crystal, and the orientation of the facet relative to the growth axis. This behavior was explained assuming that the lateral growth rate which controls the incorporation of impurities in the core region is markedly modified by the extent of kinetic supercooling.

Theoretical treatments of the effective impurity distribution ( $k_{\text{eff}}$ ) during crystal growth are based on two different operating mechanisms. According to one, partition equilibrium is assumed at the solid-liquid growth interface and the effective impurity incorporation is considered as a process controlled by solute diffusion in the melt (1-4). The other mechanism postulated specific adsorption and solute diffusion in the solid immediately upon solidification as the principal parameters controlling the impurity incorporation (5, 6). This latter point of view was formulated to account for the observed orientation dependence of the effective distribution coefficient (5). It also explained differences in the growth rate dependence of  $k_{\text{eff}}$  for donor and acceptor impurities in semiconductor crystals; this behavior cannot be explained readily by solute diffusion in the melt.

At the time the above theories were published the "facet effect" had not as yet been discovered (7-9). Its discovery revealed that facet growth leads to a "core" formation which constitutes a major impurity heterogeneity in semiconductor crystals such as Ge, InSb, and others. This effect is most likely responsible for the earlier observed orientation dependence of  $k_{\text{eff}}$ . In the core the actual impurity concentration is reported (10) to differ in some systems by almost an order of magnitude from the rest of the crystal. Furthermore, the extent of coring may vary widely depending on growth conditions (11). For this reason all experimentally determined effective distribution coefficients reported prior to the discovery of the facet effect should be considered with caution.

The presence of macroscopic (111) growth facets on InSb single crystals pulled from the melt led to the conclusion that impurity cores are formed as a result of nonequilibrium conditions prevailing during impurity incorporation at the facet ( $k_{\text{interface}} \neq k_0$ ). These conditions were related to specific adsorption (6) in conjunction with lateral layer growth. The many attempts to examine the actual morphology of the growth interface (detection for example, of growth steps) by rapid removal of the growing crystal from the melt were not completely conclusive because of solidification of the layer of melt adhering to the crystal during removal. More direct information concerning the shape of the growth interface and facet growth was first obtained by Dikhoff (9) in his investigation of rotational impurity striations in core regions of doped germanium and silicon crystals.

The purpose of the present communication is to reconsider "facet growth" and the associated mechanism of impurity incorporation in the light of the recent findings on microscopic growth rates and the microscopic distribution of impurities as revealed by high resolution etching techniques (12).

### Experimental Findings Regarding Facet Growth

In a recent study concerned with the determination of microscopic growth rates in InSb single crystals by means of "rate striations" it was shown that under constant pulling rate (with and without rotation) the microscopic rate of growth in the facet region (core region) remains virtually constant in contrast to the rate in the off-facet region which exhibits rather pronounced growth rate fluctuations. These findings are shown in Fig. 1 where an "off-core" to "on-core" transition region of an InSb single crystal grown with seed rotation is depicted.

It was found in the present investigation that, depending on growth conditions, the core regions usually exhibit impurity fluctuations of varying geometric configuration. In single crystals pulled with seed rotation the intensity of these concentration fluctuations appears to increase with thermal asymmetry and is most pronounced in the core periphery. In all instances these fluctuations exhibit the periodicity of seed rotation; however, their detailed pattern depends on the location and relative orientation of the growth facet. Under "ideal" growth conditions (*i.e.*, the pulling direction coincides with the  $\langle 111 \rangle$  crystallographic direction) the facet (core) appears in the center of the crystal and normal to the growth direction. At slow rotational rates (about 10 rpm for pulling rates in the vicinity of 1 iph), the impurity fluctuations assume a helical pattern (Fig. 2). In crystals in which the growth direction deviates by an

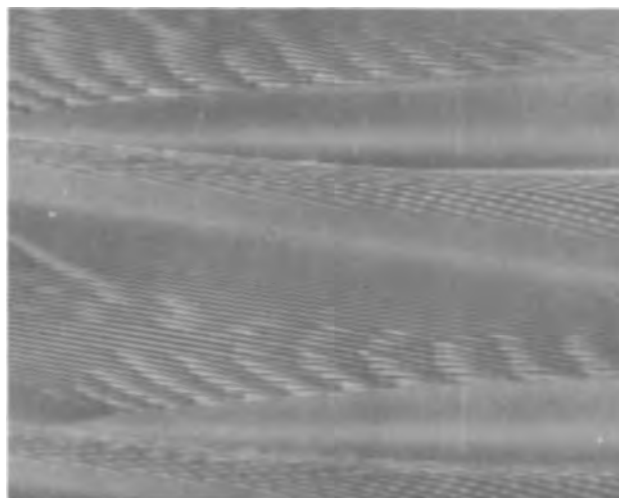


Fig. 1. Off-core to core transition region in InSb single crystal. Note the microscopic growth rate fluctuations in the off-core region and the constancy in growth rate in the core region. Magnification 900X.

\* Electrochemical Society Active Member.

<sup>1</sup> Present address: Texas Instruments Inc., Dallas, Texas.

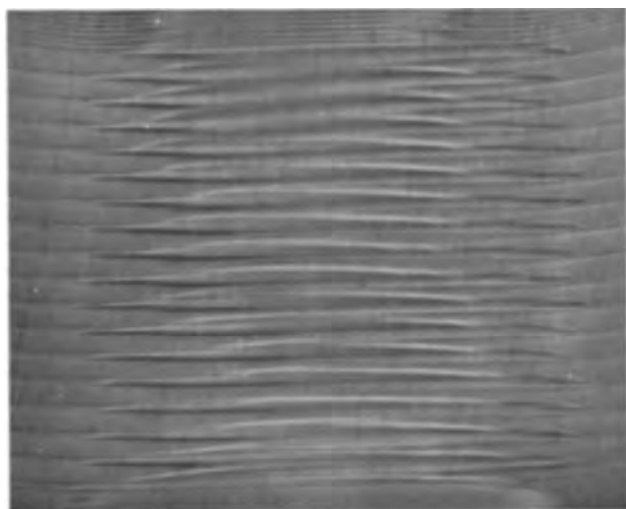


Fig. 2. Rotational impurity striations in the core region of an InSb single crystal. The helical pattern is characteristic of slow rates of rotation (4 rpm) (in centrally located facets). See text. Magnification 12X.

order of degrees from the  $\langle 111 \rangle$  direction, the (111) growth facet is shifted from the crystal center. The corresponding rotational core heterogeneities no longer exhibit a helical pattern but instead a more or less pronounced banded structure (Fig. 3). In either case, the heterogeneities are not associated with corresponding fluctuations in the vertical growth rate. As demonstrated unambiguously by means of rate striations (13) the microscopic rate of growth in the core is virtually constant.

Single crystals pulled without seed rotation exhibit nonrotational striations which are continuous across the off-core and the core regions but have no helical component (Fig. 4). Here again, the fluctuations in impurity concentration are associated with growth rate fluctuations in the off-core region whereas in most instances no corresponding microscopic growth rate variations are observed in the core region. Very small growth rate variations occasionally observed in the core region are invariably much smaller than those in the off-core region.

#### Discussion

A comparison of the impurity distribution in the off-core and in the core regions of single crystals pulled from the melt reveals differences in impurity

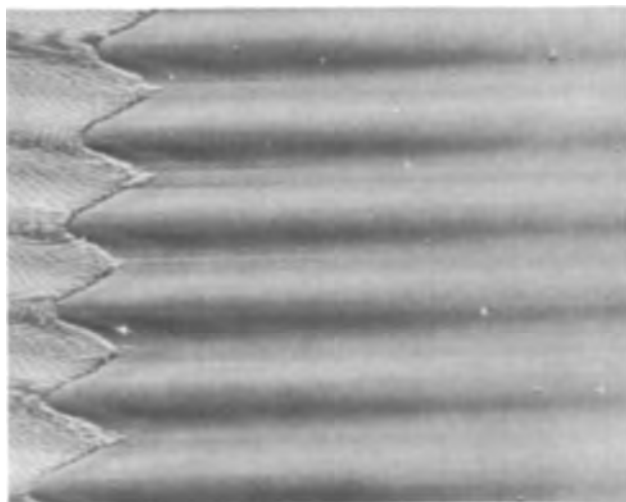


Fig. 3. Rotational impurity striations in the core region of an InSb single crystal. The observed band-like pattern is characteristic of rotational pulling with the growth facet shifted from the center to the periphery of the crystal. Magnification 90X.

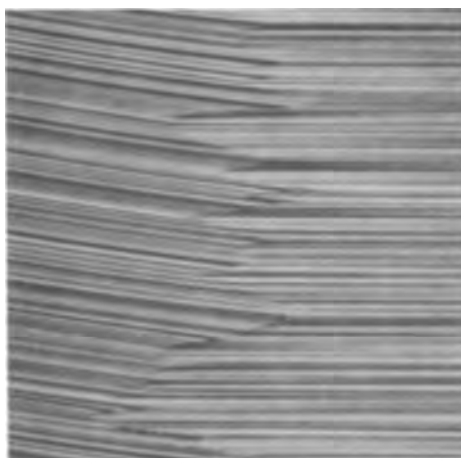


Fig. 4. Nonrotational impurity striations in InSb single crystal. Note the continuity of striations across the off-core and the core region. Magnification 40X.

incorporation which indicate the operation of different growth mechanisms in the two regions.

Employing rate striations (13) it was demonstrated that in the presence of thermal asymmetry (which can never be completely eliminated) the off-core region grows at varying growth rates. These growth rate fluctuations are responsible for the observed rotational impurity striations, i.e., the parameter primarily controlling the effective impurity distribution is the microscopic growth rate.

In the core region of crystals pulled with rotation it has been reported (10) that the impurity concentration is substantially greater than in the off-core region. Yet it has been recently shown (13) that the microscopic rate of growth in the core region is in most instances smaller (never greater) than in the off-core region. Thus, if the controlling parameters of crystal growth and impurity incorporation were the same in both regions, then a decreased impurity concentration would be expected in the core region. The increased impurity concentration in the core was attributed (6) to a rapid sheet growth across the facet which leads to an increased nonequilibrium incorporation of impurities. According to this treatment the rate of the sheet growth is independent of the speed of movement of the isotherms and dependent only on the rate of incorporation of liquid atoms into the growing solid and the rate of dissipation of the latent heat of fusion. Accordingly, the concentration of impurities should be uniform across the facet.

As shown in the present and earlier results (13) the impurity concentration, however, can vary markedly across the facet. In fact the patterns of impurity heterogeneities observed in the core region of crystals grown under rotation are sensitive to thermal asymmetry, the location of the core in the crystal and the orientation of the facet relative to the growth axis. This behavior cannot be explained by any of the proposed theories of impurity incorporation during facet growth.

Moreover it has been shown theoretically (14) and experimentally (13) that rotational striations in pulled crystals are caused and controlled by thermal asymmetry. In the presence of thermal asymmetry the temperature at the facet-melt interface (region of kinetic supercooling) must vary asymmetrically about the axis of rotation, as shown schematically in Fig. 5. The observed nonuniform impurity incorporation across the growth facet can thus be related to a nonuniform lateral growth rate resulting from the nonuniform interfacial temperature. Under usual growth conditions the location and shape of the solidification isotherm remains geometrically fixed (14). Thus, nonrotational pulling under thermally asymmetric conditions will result in a radial decrease in impurity dis-

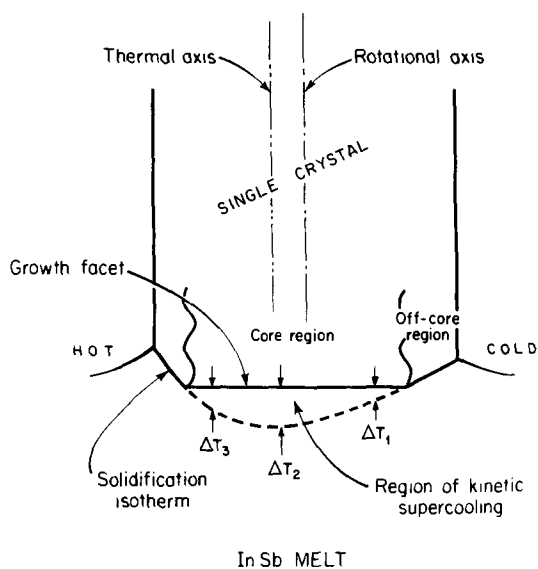


Fig. 5. Schematic presentation of thermal conditions across the growth facet in the presence of thermal asymmetry. Note varying amount of kinetic supercooling ( $\Delta T_2 > \Delta T_3 > \Delta T_1$ ).

tribution emanating from the thermal axis. Convectively induced temperature fluctuations in the melt near the growth interface (15) will result in random changes in the amount of supercooling at the facet and, thus, in the formation of random nonrotational striations although the vertical growth rate remains virtually constant.

Under the above interface configuration it is apparent that in crystals pulled with seed rotation the periodic displacement of the thermal axis about the axis of rotation will result in the observed helical patterns of rotational striations (Fig. 2). If the direction of pulling does not coincide with the say,  $\langle 111 \rangle$  crystallographic direction, then the facet is not exactly horizontal and thus it does not rotate on its own plane. With such a deviation of the facet from the horizontal position the axis of rotation does not intersect the facet at its center. For relatively excessive deviations (of the order degrees) the axis of rotation will not intersect the facet at all and thus the conditions leading to the formation of the helical patterns of impurity fluctuations in the core no longer prevail. The

impurity fluctuations must then assume the observed band-like pattern (Fig. 3).

### Summary

In summary, it was shown that in crystals pulled from the melt (in the present case InSb) the mechanism of facet growth is significantly different from that prevailing in the off-facet region. The incorporation of impurities in the facet region is controlled by the lateral growth rate. This rate was taken to be affected by the profile of kinetic supercooling and its fluctuations. On this basis the experimentally observed impurity fluctuations in the core region were satisfactorily explained.

### Acknowledgment

This work was supported by the National Science Foundation under Contract GK-1653.

Manuscript received Feb. 6, 1968; revised manuscript received ca. March 14, 1968. This paper was presented at the Dallas Meeting, May 7-12, 1967, as Abstract 95.

Any discussion of this paper will appear in a Discussion Section to be published in the June 1969 JOURNAL.

### REFERENCES

1. J. A. Burton, W. P. Slichter, J. D. Struthers, and E. D. Kolb, *J. Chem. Phys.*, **21**, 1991 (1953).
2. C. Wagner, *J. Metals*, **200**, 154 (1954).
3. V. G. Smith, W. A. Tiller, and J. W. Rutter, *Can. J. Phys.*, **33**, 723 (1955).
4. K. F. Hulme, *Proc. Phys. Soc. (London)*, **368**, 393 (1955).
5. R. N. Hall, *J. Chem. Phys.*, **57**, 836 (1953).
6. A. Trainor and B. E. Bartlett, *Solid State Electronics*, **2**, 106 (1961).
7. K. F. Hulme and J. B. Mullin, *Phil. Mag.*, **4**, 1286 (1959).
8. W. P. Allred and R. K. Willardson, Paper presented at the Chicago Meeting of the Society, May 1-5, 1960, as Abstract 88.
9. J. A. M. Dikhoff, *Solid State Electronics*, **1**, 202 (1960).
10. J. B. Mullin, *Electrochem. Soc. Mtg. Abstr.*, **9**, 176 (1960).
11. K. F. Hulme and J. B. Mullin, *Solid State Electronics*, **5**, 211 (1962).
12. A. F. Witt, *This Journal*, **114**, 298 (1967).
13. A. F. Witt and H. C. Gatos, *ibid.*, **115**, 70 (1968).
14. K. Morizane, A. F. Witt and H. C. Gatos, *ibid.*, **114**, 738 (1967).
15. A. Müller and M. Wilhelm, *Z. Naturforsch.*, **19a**, 254 (1964).

# Accommodation of Lattice Mismatch at Heterojunctions

R. S. Mroczkowski,<sup>1</sup> A. F. Witt,\* and H. C. Gatos\*

Department of Metallurgy and Center for Materials Science and Engineering,  
Massachusetts Institute of Technology, Cambridge, Massachusetts

## ABSTRACT

The accommodation of lattice mismatch at heterojunctions grown by back-melting and subsequent regrowth was investigated employing the InSb-GaSb system. Single crystals of either GaSb or InSb served as the one component (substrate) of the heterojunctions and the regrown part was an alloy of the general formula  $Ga_xIn_{1-x}Sb$ . The lattice mismatch at the heterojunction was varied by varying the composition of the regrown alloy. It was found that the accommodation of the lattice mismatch takes place by the generation of dislocations the number of which is consistent with a simple linear lattice model.

The recent interest in the electrical properties of semiconductor heterojunctions has precipitated the need for studying the structural aspects of such junctions. In a previous report (1) we have discussed the implications of the phase diagram of the binary (or pseudobinary) system involved. Attempts to study dislocation distribution and propagation across such heterojunctions made it apparent that the density of dislocations originating at the heterojunction was too high for any meaningful examination. A first step in approaching the study of dislocations at heterojunctions was the investigation of their behavior at "homojunctions" formed by back-melting under conditions prevailing during the formation of heterojunctions (2). It was shown that the thermal conditions during back-melting do not lead to the formation of new dislocations. In the back-melted portion of the crystal all of the observed dislocations originated in the parent crystal.

In the light of these results and the unique characteristics of semiconductor heterojunctions it was felt that it would be of interest to study the dependence of the density of dislocations at the plane of the grown heterojunctions on the lattice mismatch between the two component semiconductors. The lattice mismatch would be varied by varying the composition of  $Ga_xIn_{1-x}Sb$  solid solutions grown in single crystal form on single crystal substrates of either InSb or GaSb.

## Experimental Techniques

The heterojunctions consisting of pure GaSb, or pure InSb, and  $Ga_xIn_{1-x}Sb$  alloys were prepared as follows: the single crystal rectangular substrate, say GaSb, measuring  $1\frac{1}{2} \times 2 \times 3$  mm, was positioned between two resistively heated carbon strips. A small piece of InSb was placed on the substrate. The upper strip was first heated to approximately  $1000^\circ C$  and held at this temperature. In this way the InSb piece and the upper surface of the substrate were melted. The lower strip was then heated in a carefully controlled manner until just the desired amount of the substrate could be melted. At that moment the melting process was arrested and regrowth allowed to occur by decreasing the power input in the lower and then the upper carbon strip. By employing different size pieces of InSb and remelting the same amount of the GaSb substrate it was possible to grow  $Ga_xIn_{1-x}Sb$  of varying composition on a GaSb substrate.

Since the melting point of GaSb ( $706^\circ C$ ) is appreciably higher than that of InSb ( $525^\circ C$ ) it was found that heterojunctions of  $Ga_xIn_{1-x}Sb$  on InSb substrates

could not be prepared satisfactorily by melting pure GaSb pieces onto the InSb. The molten interface could not be controlled and the regrowth process was erratic. The difficulties were, to a large extent, overcome by employing pieces of an alloy of approximately 50% GaSb-50% InSb which were placed on the InSb substrates. In this way the same procedure as for the GaSb substrates could be followed.

From the relative amounts of the melted substrate and alloying material it was possible to obtain only an estimate of the alloy composition at the heterojunctions. The actual composition was determined by means of electron probe microanalysis.

Dislocations and their networks were studied by etching and by x-ray techniques employing a Lang camera. The etchant employed was a 5:3:3 mixture by volume of concentrated  $HNO_3$ , concentrated HF and glacial acetic acid, respectively. A microfocus x-ray source was employed in conjunction with the Lang camera to obtain the x-ray transmission topographs. The various  $\langle 220 \rangle$  reflections of  $AgK\alpha$  radiation were recorded on Ilford nuclear emulsion plates.

## Results and Discussion

A typical photomicrograph of an alloy heterojunction is shown in Fig. 1. The substrate (lower part) is GaSb and the alloy at the heterojunction contains 0.4% In ( $Ga_{0.996}In_{0.004}Sb$ ). It is seen that the back-melt interface is delineated by an increased concentration of dislocation etch pits resulting from the accommodation of the existing lattice mismatch. No such line of dislocation pits was observed at the interface of par-

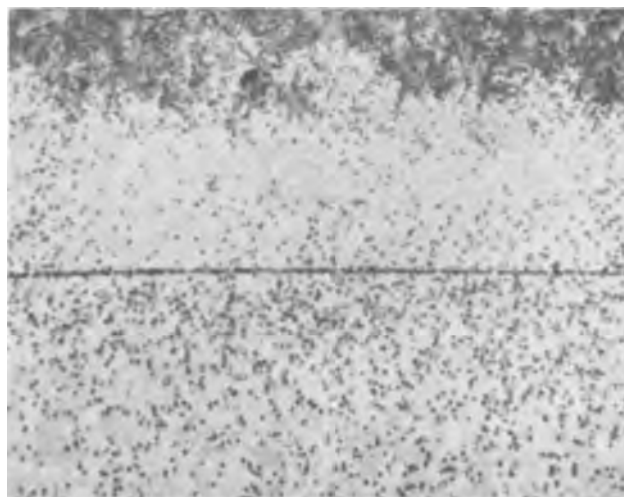


Fig. 1. Dislocations across an alloy heterojunction of  $Ga_{0.996}In_{0.004}Sb$  (top section) on a GaSb substrate. Magnification ca. 150X.

\* Electrochemical Society Active Member.

<sup>1</sup> Present address: RCA Research Laboratories, Somerville, New Jersey.

tially melted and regrown single crystals (2) (homojunctions). It is further seen in Fig. 1 that these dislocation pits are also present in the regrown region. No such pits were evident in the regrown region near the homojunctions (2). It was indicated that in the case of the homojunctions no dislocations were formed during the regrowth process apparently because no thermal stresses were present. Among the dislocations in the substrate crystal only those which had a component parallel to the direction of regrowth propagated into the regrown section. In the present case a fraction of the dislocations generated to accommodate the lattice mismatch are propagated in the regrown region. At some distance from the interface there is a marked increase in dislocation density apparently resulting from the increased concentration of In [consistent with the GaSb-InSb phase diagram (3)] which imposes the accommodation of an increased lattice mismatch.

An x-ray topograph is shown in Fig. 2. The substrate is again GaSb (lower part) and the In content at the junction is 0.8% ( $\text{Ga}_{0.992}\text{In}_{0.008}\text{Sb}$ ). The heterojunction is clearly visible. However, the dislocation network is not seen since the dislocation lines are predominantly parallel to the interface. As in the case of the "homojunction" (2) here, also, dislocations with their lines primarily parallel to the direction of solidification are propagated indicating that no dislocations are generated in the regrowth region as a result of thermal stresses. The black area at some distance from the interface is again due to the increased In content resulting in an increase in dislocation density to accommodate the increased lattice mismatch. The x-ray topograph of Fig. 3 was taken parallel to the junction interface. The dislocation networks at the heterojunctions not visible in Fig. 2 are visible here as a crossed grid. The spacing in the grid is not completely uniform, apparently reflecting a lack of complete uniformity in composition on a microscale. The InSb content at the interface was too low to be measured by electron probe microanalysis.

The dislocation density expected for the accommodation of an abrupt lattice mismatch in single crystal growth can be readily calculated on the basis of a simple linear lattice model. If onto a linear lattice, with a constant  $a_0$ , another lattice with a constant  $a_0 + \delta$ , where  $\delta$  is a positive increment, is epitaxially superimposed, a dislocation will be required to obtain perfect registry of the lattices every  $n$  unit cells where  $n$  is calculated from the self-explanatory relationship

$$(n+1)a_0 = n(a_0 + \delta) \quad [1]$$

or

$$n = a_0/\delta \quad [2]$$

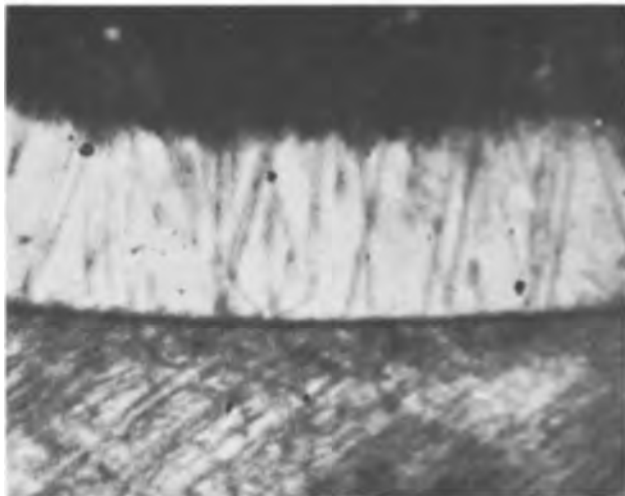


Fig. 2. X-ray topograph of an alloy heterojunction of  $\text{Ga}_{0.992}\text{In}_{0.008}\text{Sb}$  (top) on a GaSb substrate;  $\text{AgK}\alpha$  radiation, (220) reflection. Magnification ca. 40X.

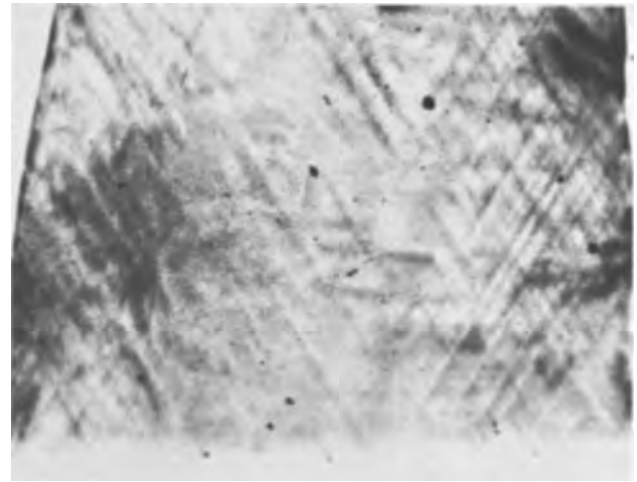


Fig. 3. X-ray topograph of an alloy heterojunction shown in the plane of the interface. The crossed dislocation grid is considered to be due to the accommodation of the lattice misfit; the In content in the  $\text{GaInSb}$  alloy grown on GaSb was too small to be determined analytically;  $\text{AgK}\alpha$  radiation (220) reflection. Magnification ca. 40X.

The dislocation spacing,  $\Delta$ , is then given by

$$\Delta = na_{uvw} \quad [3]$$

where  $a_{uvw}$  is the lattice translation in the  $\langle uvw \rangle$  direction. For example  $a_{110} = \sqrt{2}a_0$ . In general

$$a_{uvw} = Sa_0 \quad [4]$$

where  $S$  is a geometric relation between the  $\langle uvw \rangle$  direction and the  $[100]$  direction. Thus,

$$\Delta = nSa_0 \quad [5]$$

and from Eq. [2]

$$\Delta = Sa_0^2/\delta \quad [6]$$

In the alloy heterojunctions of the present investigation the polished surface used for the dislocation count was parallel to a (111) crystallographic plane, the growth axis was parallel to a  $\langle 211 \rangle$  direction and the melt interface was parallel to a  $\langle 110 \rangle$  direction. Accordingly,  $S$  in the present case is  $\sqrt{2}$  giving

$$\Delta = \sqrt{2}a_0^2/\delta \quad [7]$$

Assuming the Vegard law is obeyed in this system it is apparent that

$$\delta = a_0(\text{InSb}) - a_0(\text{GaSb}) = 6.485 - 6.095 = 0.390 \text{ \AA} \quad [8]$$

and for the alloys

$$\delta = \delta_{100\%} (1/100) (\text{InSb}\%) = 3.90 \times 10^{-3} (\text{InSb}\%) \text{ \AA} \quad [9]$$

Then,  $\Delta$ , can be expressed in terms of the molar per cent of InSb in the alloy

$$\Delta = \sqrt{2}a_0^2/\delta = \sqrt{2}(6.095)^2/3.90 \times 10^{-3} (\% \text{InSb}) = 1.34/(\text{InSb}\%)$$

where  $\Delta$  is in microns.

The dislocation spacing in the present alloy heterojunctions was determined by etch pit counting at 1000X. Typical photomicrographs of some GaSb based heterojunctions are shown in Fig. 4. The experimentally measured dislocation spacings and the calculated values are plotted for comparison in Fig. 5.

The quantitative agreement between the calculated and experimental dislocation spacings is quite good. The experimental spacings tend to be somewhat less than the calculated values. This result suggests that





Fig. 4a. Photomicrograph of alloy heterojunctions,  $\text{Ga}_{0.9965}\text{In}_{0.0035}\text{Sb}$  on GaSb. Magnification 300X.

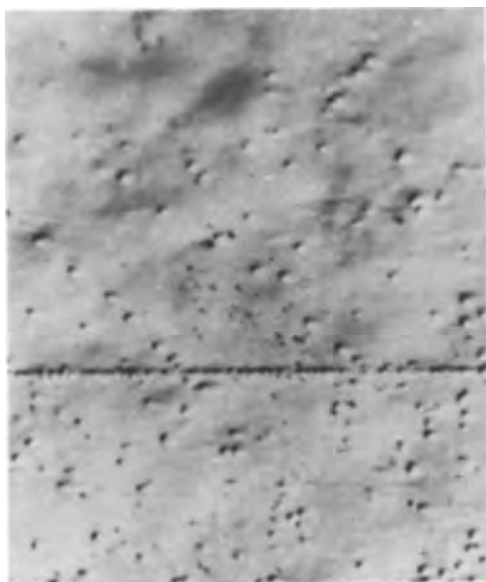


Fig. 4b. Photomicrograph of alloy heterojunctions,  $\text{Ga}_{0.992}\text{In}_{0.008}\text{Sb}$  on GaSb. Magnification 300X. Note increased density of dislocations at the junctions with increased InSb content in both a and b.

little, if any, of the lattice mismatch is accommodated by strain, after the model of van der Merwe (4). The somewhat smaller experimental dislocation spacing than the calculated values may be attributed to some dislocation generation during the growth process. The

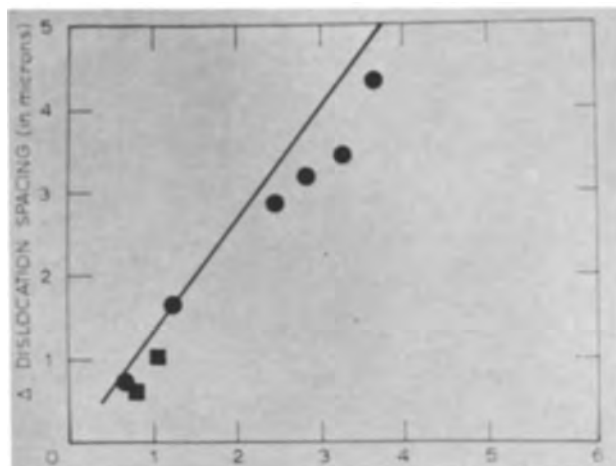


Fig. 5. Dislocation spacing vs. the reciprocal of alloy composition: ● (% In Sb)<sup>-1</sup>; ■ (% Ga Sb)<sup>-1</sup>.

thermal expansion coefficients of the substrate and the alloy are slightly different, and thus some thermal stresses may occur on cooling. The dislocation network at the interface and the dislocation propagation from the substrate provide the dislocation interactions necessary for Frank Read sources which can then be activated by the differential thermal expansion stresses. Such dislocation generation might account for the dislocations observed near the remelt interface in alloy heterojunctions and which are not associated with the accommodation of the lattice mismatch. It will be recalled that no dislocations are observed near the remelt interface in back-melted GaSb wafers (homojunctions) where no differences in thermal expansion or interface dislocation networks exist.

#### Acknowledgment

This work was supported by the Advanced Research Projects Agency under contract SD-90.

Manuscript received Feb. 6, 1968; revised manuscript received March 14, 1968.

Any discussion of this paper will appear in a Discussion Section to be published in the June 1969 JOURNAL.

#### REFERENCES

1. R. S. Mroczkowski, M. C. Lavine, and H. C. Gatos, *Trans. AIME*, **233**, 456 (1965).
2. R. S. Mroczkowski, H. C. Gatos, and A. F. Witt, *This Journal*, **115**, 747 (1968).
3. J. C. Wooley, "Compound Semiconductors," vol. I, p. 3, R. K. Willardson and H. L. Georing, Editors, Reinhold Publishing Corp., New York (1962).
4. J. H. van der Merwe, "Thin Single Crystal Films," p. 165, M. H. Francombe and H. Sato, Editors, MacMillan Co., New York (1964).



# The Distribution Coefficient of Oxygen in Germanium

W. D. Edwards

Defence Research Telecommunications Establishment, Ottawa, Ontario, Canada

## ABSTRACT

An indirect method has been used to obtain a value for the distribution coefficient of oxygen in germanium. The method requires a knowledge of the distribution coefficient of aluminum in germanium and also information upon the state of oxidation of aluminum in germanium. If aluminum oxide in liquid germanium is assumed present as  $Al_2O_3$  then a distribution coefficient  $k$  for oxygen in germanium of 0.11 is indicated.

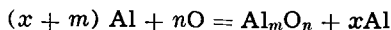
The effects of oxygen dissolved in germanium have been studied by a number of people (1, 2). The presence of oxygen can lead to a change from p to n type when the germanium is subjected to heating cycles such as are involved in the production of alloy type devices. Recently Fox (3) has shown that the presence of oxygen in germanium is detrimental to the production of lithium drifted gamma-ray spectrometers from such germanium.

It is therefore of interest to know the distribution coefficient of oxygen between liquid and solid germanium. The effective distribution coefficient of oxygen at the growth rate used is given by

$$k_{\text{eff}} = C_S / C_L$$

where  $C_S$  and  $C_L$  are the oxygen concentrations in the germanium solid and liquid, respectively. While the concentration of oxygen in solid germanium is readily calculated from the optical absorption coefficient at  $11.7\mu$  the concentration of oxygen in liquid germanium is not easily ascertained. An indirect method has therefore been used to obtain the oxygen concentration in liquid germanium and thence the distribution coefficient.

An equilibrium oxygen concentration is established in a germanium melt and this is then removed by the addition of aluminum. A reaction of the form



takes place. Both reaction products are subsequently incorporated into the growing crystal. While the aluminum dopes the germanium p type in the normal manner the aluminum oxide does not dope the crystal (4).

The amount of aluminum added to the melt,  $(x + m)Al$ , is known and from resistivity and Hall coefficient measurements the quantity,  $xAl$ , may be calculated. Hence the amount of aluminum neutralized by the oxygen,  $mAl$ , is known and from this the required concentration of the oxygen in the germanium melt may be calculated.

## Experimental

Germanium crystals were grown at 1 mm/min and 30 rpm in the  $\langle 111 \rangle$  direction by the Czochralski method. Intrinsic grade germanium was used and was contained in a fixed carbon crucible which was heated by a slotted carbon heater. The whole enclosure was continually flushed by helium maintained at 1 atm pressure.

After the growth of an initial portion of crystal, to allow for a check on the residual impurity concentration, see Fig. 1, section one, oxygen was slowly added to the system. This was continued for 15 min in order to establish an equilibrium oxygen concentration in the melt. Sufficient aluminum was then added to the melt, see Fig. 1, to both neutralize the oxygen in the melt and to dope the melt p type. The oxygen supply

Key words: Germanium, oxygen in germanium, distribution coefficient of oxygen in germanium.

was cut off a few seconds before the aluminum was added. Previous work (5) on crystals doped with oxygen alone has shown that there is no significant change in the oxygen content of the crystal grown in the first minute after the oxygen supply is cut off. The reaction between the aluminum and oxygen in the melt was rapid. To reduce the possibility of the oxidation of the aluminum by the oxygen still in the helium-oxygen atmosphere the system was evacuated to approximately  $10^{-5}$  Torr within minutes of the aluminum addition. Crystal growth was continued at the 1 mm/min rate for approximately 50 min and then the crystal was withdrawn from the melt. The crystal was cooled to room temperature over a 2-hr period.

The crystal was sectioned to provide samples for resistivity plots by the two probe method, infrared measurements to determine the oxygen concentration, and for Hall coefficient and conductivity measurements. Etching studies on the sectioned crystal established that the solid-to-liquid interface shape was very slightly convex toward the liquid.

## Results and Discussion

Kaiser and Thurmond (6) have shown that oxygen in germanium gives rise to a sharp optical absorption at  $11.7\mu$ . The magnitude of the absorption coefficient,  $\alpha$ , at this wavelength has been shown to be proportional to the oxygen concentration, the relationship being (7)

$$\alpha = 1 \text{ cm}^{-1} \equiv 1.25 \times 10^{17} \text{ oxygen/cc}$$

where  $\alpha$  is in units of  $\text{cm}^{-1}$ . This relationship was obtained by comparison of the infrared absorption coefficient with the corresponding concentrations obtained directly by vacuum fusion analysis. Corbett *et al.* (8) have shown that the absorption at  $11.7\mu$  is

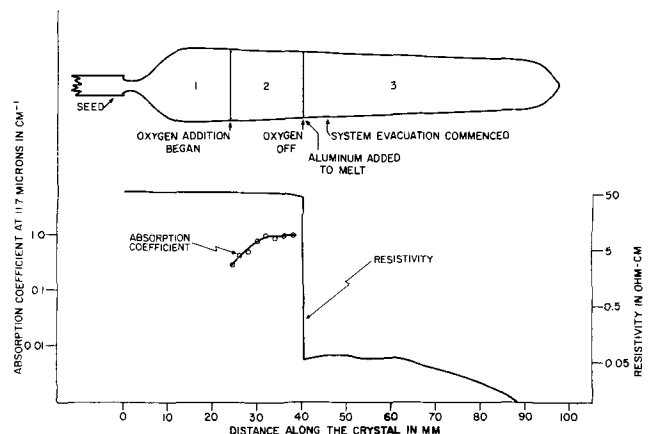


Fig. 1. Plots of resistivity and absorption coefficient vs. distance along the crystal. The relevant position in the crystal is indicated. The growth rate was 1 mm/min. The effective distribution coefficient at this growth rate, is given by  $\frac{C_S}{C_L} = \frac{\text{column three value}}{3/2 (\text{column seven value})}$

Table I.

1 Crystal	2 Absorption coefficient, cm <sup>-1</sup>	3 Oxygen conc. in the solid, No/cm <sup>3</sup>	4 Measured Al conc. in solid, No/cm <sup>3</sup>	5* Calculated Al conc. in liquid, No/cm <sup>3</sup> of equivalent solid	6* Added Al conc. in liquid, No/cm <sup>3</sup> of equivalent solid	7* Al conc. Col. 6 - Col. 5, No/cm <sup>3</sup> of equivalent solid	8 Distribution coeff. assum- ing Al <sub>2</sub> O <sub>3</sub>
85	1.4	1.75 × 10 <sup>17</sup>	3.68 × 10 <sup>17</sup>	5.03 × 10 <sup>17</sup>	1.48 × 10 <sup>18</sup>	9.7(7) × 10 <sup>17</sup>	0.11(9)
86	0.98	1.22 × 10 <sup>17</sup>	8.45 × 10 <sup>16</sup>	1.16 × 10 <sup>18</sup>	1.93 × 10 <sup>18</sup>	0.77 × 10 <sup>18</sup>	0.10(5)
87	0.36	4.5 × 10 <sup>16</sup>	6.2 × 10 <sup>17</sup>	8.5 × 10 <sup>17</sup>	1.11 × 10 <sup>18</sup>	2.6 × 10 <sup>17</sup>	0.11(5)

\* Columns 5, 6, and 7 are expressed in these units to avoid the introduction of the density ratio of liquid to solid germanium.

due to interstitial oxygen. Provided that  $\alpha < 1 \text{ cm}^{-1}$ , errors due to the presence of oxygen in other forms remain small (5).

Samples were cut from section two of the crystal, see Fig. 1, and their absorption coefficients,  $\alpha$ , were measured. The values obtained are plotted in Fig. 1. It is seen that the addition of oxygen for a period of 15 min is sufficient to establish an equilibrium oxygen concentration in the growing crystal. At this concentration the presence of donors due to the oxygen (5) is barely detectable as a small reduction of the resistivity below the intrinsic value. The values of  $\alpha$  for the slices taken immediately prior to the cut-off of the oxygen supply, for three different crystals, have been entered in column two of Table I. From these values of  $\alpha$  the oxygen concentration in the solid,  $C_S$ , may be calculated. The values found are given in column three of Table I.

Hall coefficient and conductivity measurements were made in the temperature range 77°-373°K on samples cut from section three, see Fig. 1, of the crystals. The aluminum acceptor concentrations in the solid were calculated from these measurements. The aluminum acceptor concentrations in the material grown just after aluminum doping of the liquid are entered in column four of Table I. The equivalent concentrations in the liquid, based on the assumption of a distribution coefficient for aluminum of 0.073 (9), are entered in column five. In column six are the total aluminum concentrations in the liquid calculated from the known melt volumes and amounts of aluminum actually added.

When the aluminum is oxidized it no longer acts as a p-type dopant. The amount of aluminum that has been oxidized is given by the differences between that which was added to the melt and that which was calculated from the Hall coefficient measurements on the crystal as present in the melt, i.e., the difference between columns six and five of Table I. This difference is given in column seven and is the amount of aluminum required to "getter" the oxygen present in the liquid in concentration  $C_L$ .

Although the inclusion of the aluminum oxide in the germanium crystal has been demonstrated (5), the aluminum-to-oxygen ratio has not been measured. The quantitative analysis for aluminum and oxygen at a few parts per million or less in germanium is marginal. With the assumption that the formula for the aluminum oxide formed is Al<sub>2</sub>O<sub>3</sub> a value for  $k_{\text{eff}}$  for oxygen in germanium,  $C_S/C_L$ , is readily calculated. The values found are given in column eight of Table I.

The value found for  $k_{\text{eff}}$  is approximate and is probably a minimum value. We have a condition of dynamic equilibrium which involves oxygen exchange at the interface between the melt and furnace atmos-

phere. As a result the oxygen content in the melt is probably not uniform. As the method described gives an average value for the oxygen concentration in the melt, this is a source of uncertainty. When the aluminum is added to the melt impurity oxides may well be reduced but as the germanium used was intrinsic grade this source of error should be very small. Another more serious source of error is the unknown contribution of the oxygen present in the furnace atmosphere before the evacuation takes place. The rate of oxidation of the aluminum in the melt immediately after aluminum doping and before evacuation takes place is not excessive, see Fig. 1, and the error due to this is not expected to be more than several per cent. An accurate calculation of the equilibrium value of the distribution coefficient (10), i.e., the value for an infinitely slow growth rate, is not feasible at the present time because of the many uncertainties in the parameters involved, e.g., the diffusion coefficient of oxygen in liquid germanium.

In summary, the distribution coefficient of oxygen in germanium for a crystal growth rate of 1 mm/min is approximately 0.11. This value is calculated on the assumption that the formula for the aluminum oxide formed is Al<sub>2</sub>O<sub>3</sub>, and that the distribution coefficient of aluminum in germanium is 0.073.

#### Acknowledgment

The author wishes to thank Mr. W. A. Hartman for his help in measuring the optical absorption coefficient.

Manuscript received Dec. 14, 1967; revised manuscript received March 8, 1968.

Any discussion of this paper will appear in a Discussion Section to be published in the June 1969 JOURNAL.

#### REFERENCES

1. J. Bloem, C. Haas, and P. Penning, *J. Phys. Chem. Solids*, **12**, 22 (1959).
2. C. S. Fuller, W. Kaiser, and C. D. Thurmond, *The Physics and Chem. of Solids*, **16**, 161 (1960).
3. R. J. Fox, *IEEE Trans. Nucl. Sci.*, NS-13, 367 (1966).
4. W. D. Edwards, *J. Appl. Physics*, **34**, 2497 (1963).
5. W. D. Edwards, *ibid.*, To be published, 1968.
6. W. Kaiser and C. D. Thurmond, *ibid.*, **32**, 115 (1961).
7. E. J. Millet, L. S. Wood, and G. Bew, *Brit. J. Appl. Physics*, **16**, 1593 (1965).
8. J. W. Corbett, R. S. MacDonald, and G. D. Watkins, *J. Phys. Chem. Solids*, **25**, 873 (1964).
9. F. A. Trumbore, E. M. Porbanski, and A. A. Taglia, *ibid.*, **11**, 239 (1959).
10. J. A. Burton and W. P. Slichter, "Transistor Technology," vol. 1, p. 71, D. Van Nostrand Co. Inc., New York (1958).

# The Synthesis and Epitaxial Growth of GaP by Fused Salt Electrolysis

J. J. Cuomo\* and R. J. Gambino

IBM Watson Research Center, Yorktown Heights, New York

## ABSTRACT

Single crystals of GaP have been deposited epitaxially on silicon substrates ( $\langle 111 \rangle$ ,  $\langle 100 \rangle$ , and  $\langle 110 \rangle$ ) by fused salt electrolysis. A  $100\mu$  thick layer of GaP was cathodically deposited at a current density of  $50 \text{ ma/cm}^2$  from a fused salt solution consisting of  $2 \text{ NaPO}_3$ ,  $0.5 \text{ NaF}$ , and  $0.25 \text{ Ga}_2\text{O}_3$ , maintained at  $800^\circ\text{C}$ . The deposits have been doped, both p- or n-type, during growth by adding small concentrations of  $\text{ZnO}$  or  $\text{Na}_2\text{SeO}_4$  into the solution. Electroluminescent p-n junctions have also been fabricated by growing a layer of one carrier type, then overgrowing a layer of the other carrier type. Preliminary experiments on the deposition of AlP and ZnSe indicate that the fused salt electrolysis method can be applied to the synthesis of many compound semiconductors.

Considering the nature of electrodeposition, it is somewhat surprising that electrolytic techniques have not been utilized more frequently in the technology of crystal growth. One of the essential features of all methods of single crystal growth is a small, controlled displacement of the system from thermodynamic equilibrium in the direction of the desired solid phase. This condition can be obtained in an electrolytic cell by applying a potential slightly greater than the equilibrium potential for the reaction of interest. The rate of growth, moreover, is simply dependent on the current density and the current efficiency of the electrode reaction. In addition, since the growth is constrained to occur at an electrode, the seeding and geometry of the crystal should be more readily controllable.

High quality single crystals of a few metals, notably silver and copper (1) have been prepared electrolytically from aqueous solutions. A number of intermetallic compounds have been obtained as small, randomly oriented single crystals during the course of their synthesis from fused salts (2-4) but, in general, electrolytic methods have rather rarely been applied to single crystal growth. Single crystals of a number of oxides, such as vanadate spinels (5) and  $\text{Mn}_2\text{O}_3$  (6), have been grown electrolytically, but these methods apparently depend on changes in the oxidation state of the molten salt solvent rather than on electrodeposition so that they are not pertinent to the present discussion.

This paper deals with the synthesis and epitaxial crystal growth of GaP by electrodeposition from fused salt solutions. GaP was studied because of its importance as an electroluminescent device material and because it is representative of a whole class of large band gap III-V and II-VI semiconductors. This work demonstrates the feasibility of growing single crystals of GaP by fused salt electrolysis of sufficient quality to be of interest for electronic device applications. The experimental approach was to study the cathode deposits obtained by the electrolysis of several molten salt solutions. After achieving the synthesis of GaP, single crystal substrates were used as the cathode and the operating conditions necessary for epitaxial crystal growth were determined. The products were studied primarily by x-ray diffraction and metallographic methods. In a few cases spectrochemical analysis and electrical properties studies were made.

## Experimental Procedure

A schematic of the apparatus is shown in Fig. 1. It consists of a quartz chamber heated by a resistance

\* Electrochemical Society Active Member.

furnace. A graphite crucible, which contains the melt, is placed within the chamber. Electrical contact was made to the crucible which also serves as the anode of the cell.

Two types of cathodes were used. In the synthesis experiments, the cathode consisted of a  $\frac{1}{4}$  in. diameter, spectrographic grade graphite rod which was immersed into the melt to a depth of about 1 in. In the crystal growth experiments, single crystal wafers, usually of silicon, were used as the cathode. Substrates with  $\langle 111 \rangle$ ,  $\langle 110 \rangle$ , and  $\langle 100 \rangle$  crystallographic orientations were used. The wafers were attached to a graphite rod, which provided electrical contact to the wafer by means of the assembly shown in the inset of Fig. 1. With this assembly, approximately  $10 \text{ cm}^2$  of a 1.25 in. diameter wafer could be exposed to the solution. During this investigation both constant current and constant voltage supplies were used to obtain the electrodeposits. The compositions (in molar ratio) used to effect the synthesis and epitaxial growth of GaP were as follows:

1.  $2.0 \text{ NaPO}_3$ ,  $0.5 \text{ NaF}$ , and  $0.125$  to  $0.25 \text{ Ga}_2\text{O}_3$
2.  $1.2 \text{ LiCl}$ ,  $0.8 \text{ KCl}$  (eutectic composition),  $0.1 \text{ Ga}_2\text{O}_3$ , and  $0.2 \text{ NaPO}_3$
3.  $1.0 \text{ NaCl}$ ,  $1.0 \text{ KCl}$ ,  $0.05 \text{ Ga}_2\text{O}_3$ , and  $0.1 \text{ NaPO}_3$ .

The chemicals used were of reagent grade with the exception of  $\text{Ga}_2\text{O}_3$  which had a purity of 99.999%.

In all compositions, the sodium metaphosphate and gallium oxide act as the source of phosphorus and gallium respectively. In the first composition the sodium metaphosphate also acts as the solvent. The latter two

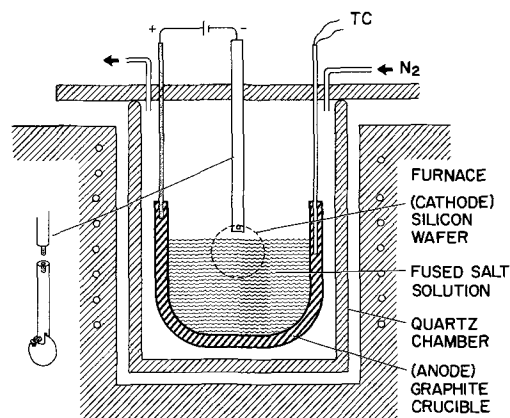


Fig. 1. Schematic of the apparatus for the preparation of GaP by fused salt electrolysis.

compositions allow for lower temperature operation and compatibility with quartz. The sodium metaphosphate bath will severely attack quartz, and it was therefore necessary to use graphite crucibles for this system. It was found that a thin layer of pyrolytic graphite on the inner wall of the quartz crucible would also act as an effective barrier against sodium metaphosphate attack. A dry, inert atmosphere was provided largely to prevent the oxidation of the graphite components and to prevent moisture from reacting with the melt.

The procedure used was to add the premixed composition to the crucible, allow the contents to come up to a predetermined temperature under an inert atmosphere, then lower the substrate into the melt with the potential on. The graphite portion of the cathode should not be introduced into the melt for this will produce a dendritic mass of GaP on the graphite making it difficult to remove the substrate.

When the deposition was completed, the substrate was slowly removed from the bath. This procedure allows for most of the solution that has been dragged out with the substrate to run off and for the phosphate glass that forms on the surface to cool slowly thus preventing cracking of the epitaxial layer.

The gallium phosphide layer was readily removed from the silicon substrate by dissolving the silicon in a solution of  $\text{HNO}_3$  and HF. The GaP surface was protected from the etch by a coating of apiezon wax which was also used to bond the wafer to an alumina disk for support. The dissolution of the silicon is rapid, whereas GaP is only slowly attacked by the etchant. After the silicon was removed, the epitaxial layer of GaP was detached from the alumina-supporting wafer with trichlorethylene. Thorough rinsing with trichlorethylene, then acetone, and finally with water and alcohol produced clean crystals. When a single wafer of silicon was used as a substrate, it was somewhat difficult to expose the silicon to the etch because it was covered on both sides with GaP. On occasion, the wafer split parallel to its surface exposing a silicon surface so that the above technique was readily employed. If two silicon wafers, back to back, are used as a substrate, the subsequent removal of the silicon from the GaP is greatly facilitated.

## Results

Some of the operating parameters and results of experiments with the  $\text{NaPO}_3$ -NaF solutions are shown in Table I. In the initial experiments, a graphite rod

was employed as a cathode and the deposits consisted of polycrystalline GaP of various grain size and shape. Powdery yellow deposits were obtained at high cell currents (i.e., 5000 ma) and rather coarsely crystalline products with crystallites up to 0.1 mm diameter and 0.5 mm long were produced at cell currents of about 100 ma. The bath was operated at temperatures between 800° and 1000°C. The lower limit was determined by the liquidus temperature of the mixture which became a clear liquid at about 750°C. The melt begins to vaporize quite rapidly at about 1000°C so this temperature was selected as an upper limit. Within this temperature range, the quality of the GaP product appears to be fairly independent of temperature.

At low cell voltages, below about 0.6v, no solid products were observed at the cathode but a gas, believed to be phosphorous vapor, was evolved. When the cell was operated in air, bubbles of this gas ignited on reaching the surface of the melt, resulting in a puff of white smoke, indicating the presence of phosphorous vapor. At higher voltages, about 0.6v, GaP is deposited at the cathode as well as phosphorous vapor. The cell current increases rapidly with increasing cell voltage at about this value of cell voltage.

It was found that p or n doping of the GaP deposit can be achieved by incorporating small amounts of compounds of the appropriate doping elements in the bath. Zinc in the form of ZnO was used for p-type doping. Selenium in the form of  $\text{Na}_2\text{SeO}_4$  and tellurium in the form of  $\text{Na}_2\text{TeO}_3$  were used to produce n-type doping. Table I shows some of the concentrations used and the effect on the resulting GaP layers. Experiments 4A and 4B were run under identical conditions with the exception of the cell potential. From the photoluminescence results it appears that the dopant concentration in the product depends on the cell voltage as well as on the concentration of the dopant in the bath.

The initial results, which showed that rather large crystallites of GaP could be deposited from this bath, suggested that with suitable control of nucleation, single crystals could be obtained. The method seemed well suited for an epitaxial growth approach if a suitable substrate could be found which would also serve as a cathode. Silicon was selected because of its availability as high quality single crystal wafers, crystallographic compatibility with GaP, high electrical conductivity, and high melting point. Epitaxial single crystal layers of undoped GaP were obtained when the graphite cathode was replaced by a silicon wafer

Table I. Typical GaP deposition experiments with  $\text{NaPO}_3$ -NaF melts

No.	Melt composition			Temp, °C	$E_{\text{cell}}$ , v	$I_{\text{cell}}$ , ma	Time, hr	Cathode composition	Orientation	Cathode products
	$\text{NaPO}_3$ , moles	NaF, moles	$\text{Ga}_2\text{O}_3$ , moles							
1	2	1/2	1/6	850	5.00	5000	3/4	Graphite	Random (polycrystal)	Fine yellow powder
2	2	1/2	1/4	900	0.60	100	16	Graphite	Random (polycrystal)	Yellow dendrites, needles and small crystals
3	2	1/2	1/4	900	2.00	900	4	Graphite	Random (polycrystal)	Yellow dendrites
4A	2	1/2	1/4 + 0.1g ZnO	800	1.00	1500	1	Graphite	Random (polycrystal)	GaP which showed bright red luminescence at 77°K
4B	2	1/2	1/4 + 0.1g ZnO	800	0.70	300	1	Graphite	Random (polycrystal)	GaP which showed very weak luminescence at 77°C
5	2	1/2	1/4	900	1.50	400	15	Si	<111>	Epitaxial layer of GaP
6	2	1/2	1/4	1000	0.62	200	25	Si	<111>	25μ thick epitaxial layer with thicker polycrystal layer
7	2	1/2	1/4	800	1.50	390	15	Si	<111>	50μ thick epitaxial layer
8	2	1/2	1/4 + 0.5g ZnO	800	0.91	450	20	Si	<111>	100μ thick Zn-doped layer
9	2	1/2	1/4 + 0.5g ZnO	800	0.90	360	15	Si	<100>	80μ thick epitaxial layer
10	2	1/2	1/4	800	0.35	200	15	Ge	Random (polycrystal)	GaP layer with Ge precipitate
11	2	1/2	1/4	800	0.64	260	14	Ge	<111>	25μ thick epitaxial layer—dark brown in color
12	2	1/2	1/4 + 0.5g ZnO	800	2.50	430	15	GaP n-type	Random (polycrystal)	Very thin epitaxial layer
13	2	1/2	1/4 + 0.5g ZnO	800	0.75	410	16	GaP	<110>	20μ epitaxial layer
14	2	1/2	1/4 + 0.5g ZnO	850	0.90	55	1	GaP	Poly—large grain	Epitaxial p-type overgrowth found
15	2	1/2	1/4 + 0.5g ZnO	850	0.96	64	10	GaP	Poly—large grain	Epitaxial p-type overgrowth found
16	2	1/2	1/4 + 0.5g ZnO	850	1.02	250	4	Si	<100>	p-type GaP epitaxial
17	2	1/2	1/4 + 0.59 $\text{Na}_2\text{SeO}_4$	850	1.10	800	13	Si	<100>	Epitaxial GaP
18	2	1/2	1/4 + 0.59 $\text{Na}_2\text{SeO}_4$	900	1.33	470	4	Si	<111>	n-type GaP epitaxial deposit
19	2	1/2	1/4 + 0.59 $\text{Na}_2\text{TeO}_3$	810	1.08	400	6	Si	<111> <100>	n-type epitaxial growth

with  $\langle 111 \rangle$  orientation. Typically the deposits consisted of an epitaxial layer about  $25\mu$  thick which was covered with a rather dendritic, polycrystalline overgrowth. The GaP single crystal was usually cracked in many places along cleavage planes. Subsequent experiments were aimed at obtaining thicker single crystal layers, eliminating the polycrystalline overgrowth, and reducing the number of cracks.

The rate of growth of the epitaxial layer is rapid initially,  $10\text{--}20\ \mu/\text{hr}$ , but decreases with time. This time dependence may be related to the relatively high electrical resistivity of the GaP which causes a substantial voltage drop across the product layer. Eventually, the potential at the surface of the GaP layer may become too low for GaP synthesis. The fact that doped GaP, which has a lower resistivity, grows to a greater thickness tends to support this argument (see sample 8, Table I).

The amount of polycrystalline overgrowth was somewhat reduced by using orientations other than  $\langle 111 \rangle$  such as  $\langle 100 \rangle$  and  $\langle 110 \rangle$  substrates. Doping, however, had an even more noticeable effect on the smoothness of the growth surface. For example, Zn-doped GaP on  $\langle 111 \rangle$  Si was essentially free of overgrowth and uniform in thickness. Undoped GaP was found to vary in carrier type from point to point on the surface, and this nonuniformity could contribute to dendritic growth.

Cracking of the GaP layer was substantially reduced by carefully cooling the crystal layer after its removal from the molten salt bath. When the electrolysis was completed, the cathode was raised out of the melt and left suspended just above the melt surface in the hot zone of the furnace. The furnace power was turned off and the crystal allowed to cool with the furnace over a period of several hours. The crystal was removed from the furnace when the temperature reached  $300^\circ\text{--}400^\circ\text{C}$ .

Figure 2 is a photomicrograph of a GaP crystal taken with transmitted light. The crystal was removed from the silicon substrate by the method described previously. The characteristic  $\langle 111 \rangle$  cleavage planes of the crystal are indicative of epitaxial growth of the GaP on the Si substrate with the same orientation. Figure 3 shows a cross-sectional view of a cleaved wafer taken with transmitted light. The silicon-GaP interface is clearly seen and is sharp. The layer above the epitaxial GaP is the dendritic overgrowth. The thickness of the epitaxial GaP layer is about  $100\mu$ .

A back reflection Laue pattern of a GaP crystal removed from the silicon substrate is shown in Fig. 4. The substrate had a  $\langle 111 \rangle$  orientation and as can be seen from the three-fold symmetry of the pattern, the GaP also has a  $\langle 111 \rangle$  orientation. The crystalline quality is good as indicated by the sharpness of the spots in the pattern.



Fig. 2. Photomicrograph taken with transmitted light of  $\langle 111 \rangle$  surface of epitaxially-grown GaP. Magnification ca. 18X.

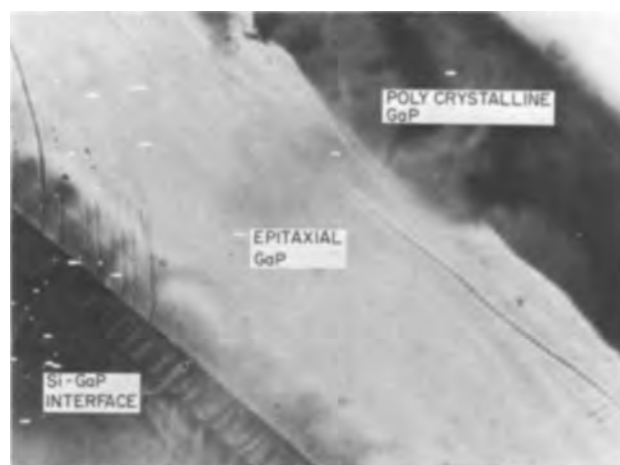


Fig. 3. Photomicrograph of a cross-sectional view of a cleaved wafer. The GaP is about  $100\mu$ . Magnification 110X.

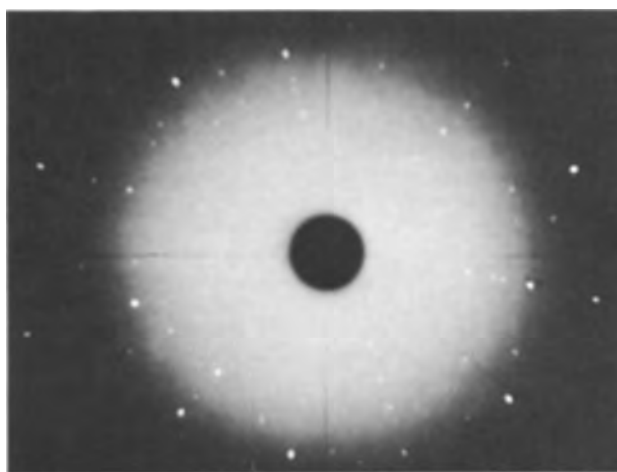


Fig. 4. Back reflection Laue pattern of epitaxial GaP

The lattice constant of the GaP prepared by this process was determined by the powder method using silicon as an internal standard. The value measured was  $5.4504 \pm 0.0008\text{\AA}$  in good agreement with the previously reported value  $5.447 \pm 0.006\text{\AA}$  (17).

The results of an emission spectrographic analysis of the GaP are shown in Table II. Sample A was measured with the silicon substrate attached to the GaP. Sample B had the substrate removed by the process previously described. The low silicon concentration in sample B is somewhat surprising in view of the fact that silicon substrates were used and considering that reagent grade NaF typically has 0.10%  $\text{Na}_2\text{SiF}_6$  as an impurity. Apparently, the deposition potential of silicon from this melt is so high that it does not electrodeposit with the GaP. The relatively high gold concentration in sample A may be explained by the fact that gold plated tweezers were used in handling the GaP wafers after growth. As can be seen by comparing sample A and B the impurity elements which are high in one sample are at very low levels or not detected in the other sample. This leads to the conclu-

Table II. Spectrographic analysis of GaP in a/o

Impurity	Sample A (with substrate)	Sample B (without substrate)
Si	Major	0.001
Au	0.01	N.D.
Mg	0.01	0.001
Fe	N.D.	0.01
Al	0.05	N.D.
Cu	0.001	0.001

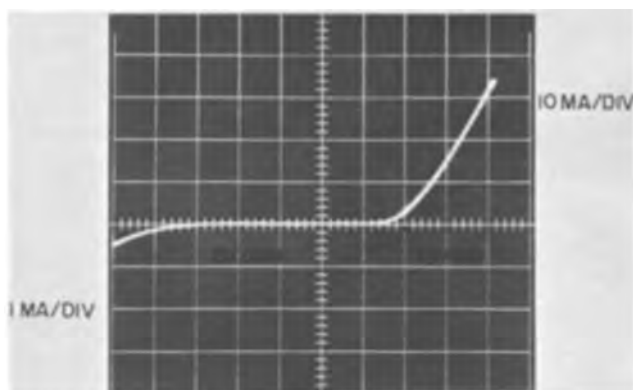


Fig. 5. I.V. characteristics of a GaP diode prepared by fused salt electrolysis.

sion that certain impurities, for example Mg and Al which deposit at high potentials, can be avoided by using lower cell voltages. The heavy metal impurities, which deposit at very low potentials, can probably be removed by a preplating treatment. The gallium phosphide product is relatively pure considering the purity of the starting materials and crucibles.

The resistivity, Hall mobility, and carrier concentration of sample 9 (see Table I) were determined by the van der Pauw method. An indium-gold alloy was used to make contact to the GaP crystal. The room temperature measurements on p-type GaP show  $\rho = 0.0703$  ohm-cm;  $\mu = 27$  cm<sup>2</sup>/v-sec;  $N_a - N_d = 3.3 \times 10^{18}$  carriers/cc. The value of the Hall mobility suggests a total impurity concentration ( $N_a + N_d$ ) of the order of  $10^{19}$ /cc.

Electrodeposited overgrowths on GaP substrate-cathodes were obtained using wafers of GaP cut from Bridgeman-grown crystals (8). The deposits consisted of a thin epitaxial layer about  $20\mu$  thick covered by a thicker polycrystalline overgrowth. The epitaxial layer was thickest near the electrical contact to the wafer, indicating a large potential gradient in the plane of the wafer. The deposited layer was doped p-type by adding ZnO to the solution and the wafer was n-type so that a p-n junction was formed. The diode characteristics of such a junction are shown in Fig. 5. The turn-on voltage is about 1.8v. The light emitted from these diodes was red both at room temperature and at 77°K. The efficiency was estimated to be of the order of  $10^{-4}$ . Light-emitting diodes were also prepared by the solution regrowth technique (9) on electrodeposited GaP chips. The light emitted from these diodes was usually orange-red. In these preliminary experiments, the feasibility of fabricating light-emitting diodes has been demonstrated but not optimized.

The main emphasis of this work was on the NaPO<sub>3</sub> melt compositions; the two other molten salts mentioned previously were, however, studied briefly. Alkali halide mixtures were selected as the solvents because of their low melting points, compatibility with quartz, and high decomposition potentials (10). Gal-

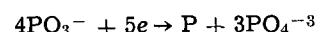
lium oxide and sodium metaphosphate were dissolved in these molten salts. The melt compositions studied and some typical results are shown in Table III.

The cathode product from both the NaCl-KCl and the LiCl-KCl solutions was a mixture of Ga and GaP. Apparently in these solutions Ga deposits at a lower potential than phosphorus, at least when the Ga<sub>2</sub>O<sub>3</sub> and NaPO<sub>3</sub> concentrations in the solutions are those shown.

Evidence of epitaxial growth of GaP from the LiCl-KCl eutectic solution was obtained in that small oriented triangles were observed to form on the <111> silicon substrate-cathode. A possible explanation for the fact that the GaP deposited only in isolated spots is that the silicon wafer was passivated by a layer of SiO<sub>2</sub> and the GaP only grew at the location of pin holes in the passive layer. In the fluoride-containing melt, the SiO<sub>2</sub> layer is probably quickly dissolved but since the chloride melts do not attack quartz, the SiO<sub>2</sub> layer would not be removed by contact with the solution.

### Discussion

The exact mechanism for the formation of GaP by fused salt electrolysis was not explicitly studied during the course of this investigation; however, a number of tentative conclusions about the mechanism can be drawn from the observations presented under Results. The evidence suggests that in the NaPO<sub>3</sub>-NaF electrolyte, GaP is formed by the codeposition of the elements at the surface of the cathode, with phosphorus in excess. The fact that the deposits are coherent epitaxial layers supports the codeposition-surface reaction mechanism. The cathode reaction which liberates gallium is most probably the reduction of Ga<sup>+3</sup> ions to metal. The reduction of metaphosphate ions to elemental phosphorus at the cathode is more difficult to explain, particularly because it occurs at such a low cell potential. Yocom (4) has proposed the following cathode reaction



based largely on the observations that phosphorus and sodium orthophosphate were the cathode products observed after the electrolysis of a NaPO<sub>3</sub> melt. He concluded, therefore, that the reduction does not take place through the intermediate formation of sodium. The glassy phase, which surrounds the cathode and the GaP product after electrolysis in our experiments, is also believed to be Na<sub>3</sub>PO<sub>4</sub>.

Plots of cell voltage vs. cell current were found to be useful for establishing the necessary conditions for codeposition. The curves for the metaphosphate melt had the general shape shown in Fig. 6. The low potential portion of the curve is believed to be due to the metaphosphate cathode reaction. If the cell is operated at voltages that correspond to this portion of the curve, phosphorus is evolved but no GaP deposits. At a somewhat higher cell potential, the slope of the curve increases fairly sharply and GaP begins to deposit. The voltage at which the change in slope occurred varied slightly with melt composition, tempera-

Table III. Deposition experiments with alkali halide melts

Melt composition	Temp, °C	$E_{\text{cell}}$ , v	$I_{\text{cell}}$ , ma	Time, hr	Cathode composition	Cathode orientation	Cathode products
1 NaCl, 1 KCl, 0.1 Ga <sub>2</sub> O <sub>3</sub> , 0.2 NaPO <sub>3</sub>	800	1.55	300	17	Graphite	Poly	Mixture of GaP and Ga metal
1 NaCl, 1 KCl, 0.1 Ga <sub>2</sub> O <sub>3</sub> , 0.2 NaPO <sub>3</sub>	800	1.30	190	18	Si	<111>	Yellow polycrystalline deposits on Si
1.2 LiCl, 0.8 KCl, 0.05 Ga <sub>2</sub> O <sub>3</sub> , 0.1 NaPO <sub>3</sub>	600	1.70	20	19	Graphite	Poly	Ga metal
1.2 LiCl, 0.8 KCl, 0.05 Ga <sub>2</sub> O <sub>3</sub> , 0.1 NaPO <sub>3</sub>	600	0.72	150	18	Graphite	Poly	GaP deposit
1.2 LiCl, 0.8 KCl, 0.05 Ga <sub>2</sub> O <sub>3</sub> , 0.1 NaPO <sub>3</sub>	550	2.05	155	24	Si	<111>	Much Ga metal, very little GaP. GaP present as oriented, isolated triangles up to $10\mu$ thick
1.2 LiCl, 0.8 KCl, 0.15 SeCl <sub>4</sub> , 0.15 ZnCl <sub>2</sub>	550	0.96	150	1	Si	<111>	Oriented triangles
1.2 LiCl, 0.8 KCl, 0.15 SeCl <sub>4</sub> , 0.15 ZnCl <sub>2</sub>	520	1.8	110	1	Si	<111>	Reddish microcrystals

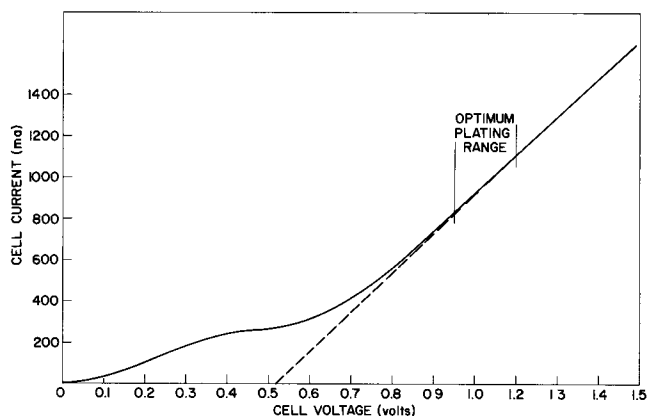


Fig. 6. Typical dependence of cell current on cell voltage for the sodium metaphosphate bath with graphite electrodes.

ture, and the experimental setup used. However, the break in the current-voltage curve was a reliable indication of the minimum voltage for GaP formation. At the beginning of each run, therefore, a current-voltage curve was plotted and the operating voltage set at a value somewhat above the change in slope.

The cathode reactions in the halide melts are apparently different in that the GaP product is sometimes contaminated with elemental gallium (see Table III). The deposition potential of gallium is apparently lower than that of phosphorus in the compositions studied. The halide solutions warrant further investigation because they have a number of desirable properties. Their lower melting temperatures are advantageous from the point of view of experimental flexibility: for example it might be possible to use germanium substrates with a lower melting halide solution. The problem of thermal shock cracking would also be greatly reduced by a lower operating temperature. Perhaps most important from the point of view of semiconductor technology is the fact that the halides are relatively easy to purify and are in fact commercially available in high purity form.

The deposition potentials of many elements from halide melts have been determined in recent years (11, 12). This data should be useful in extending the method of fused salt electrolysis to other III-V and II-VI compounds. The metaphosphate solution is not as readily extended to other compounds other than phosphides. We have shown that AlP and InP are obtained from the metaphosphate melt when  $\text{Ga}_2\text{O}_3$  is replaced by  $\text{Al}_2\text{O}_3$  or  $\text{In}_2\text{O}_3$ . ZnSe and ZnTe have been deposited epitaxially on Si from halide melts (see Table III). The success of these initial experiments suggests that most of the III-V and II-VI compounds can be deposited by fused salt electrolysis.

A number of applications for the method of fused salt electrodeposition suggest themselves. In device

fabrication especially, the flexibility and controllability of an electrolytic method should find applications. It should be possible, for example, to produce p-n junctions in the growing crystal simply by changing the cell potential. Plating through masks also appears to be feasible, at least in the halide melts, using  $\text{SiO}_2$ , for example, as a mask material.

The method of fused salt electrolysis may have a substantial economic advantage over other methods of semiconductor device fabrication. Conventional methods require the separate steps of extracting and purifying the constituent elements, growth of single crystals, slicing the crystals into wafers, and doping the wafers to produce a p-n junction. The method of fused salt electrolysis accomplishes the extraction, crystal growth, and junction formation in one operation. This method may become important therefore in such areas as the production of electroluminescent devices and the fabrication of solar cells (13).

#### Acknowledgment

The authors wish to express their appreciation to S. Blum for providing GaP substrates, C. Kelly and M. Lorentz for fabricating and characterizing diodes, and J. Woods for the electrical measurements. The technical assistance of Miss J. Bartivic, H. G. Schaefer, and R. Wnuk is gratefully acknowledged.

Manuscript received Dec. 26, 1967.

Any discussion of this paper will appear in a Discussion Section to be published in the June 1969 JOURNAL.

#### REFERENCES

1. H. E. Buckley, "Crystal Growth," Vol. 142, p. 97, John Wiley & Sons, Inc., New York (1951).
2. M. Chêne, *Compt. rend.*, **3**, 571 (1938).
3. L. Andrieux and M. Doderio, *ibid.*, **19**, 753 (1934).
4. P. N. Yocom, The Preparation of Transition Metal Phosphides by Fused Salt Electrolysis, University Microfilms, Ann Arbor, Michigan (1958).
5. D. B. Rogers, A. Ferretti, and E. J. Delaney, Solid State Research, Lincoln Laboratory, M.I.T., Lexington, Mass., June, 1964.
6. E. Banks and E. Kostiner, *J. Appl. Phys.*, **37**, 1423 (1966).
7. W. B. Pearson, "A Handbook of Lattice Spacings and Structures of Metals and Alloys," Pergamon Press, New York (1958).
8. S. E. Blum and R. J. Chicotka, *This Journal*, **114**, 146C (1967).
9. M. R. Lorenz and M. Pilkuhn, *J. Appl. Phys.*, **37**, 4094 (1966).
10. H. A. Laitinen, W. S. Ferguson, and R. A. Osteryoung, *This Journal*, **104**, 516 (1957).
11. S. N. Flengas and T. R. Ingraham, *Canadian J. Chem.*, **36**, 1103, 1662 (1958).
12. H. A. Laitinen and J. W. Pankey, *J. Am. Chem. Soc.*, **81**, 1053 (1959).
13. F. Daniels, *American Scientist*, **55**, 34 (1967).



# Si-SiO<sub>2</sub> Fast Interface State Measurements

Dale M. Brown\* and Peter V. Gray

General Electric Company, Research & Development Center, Schenectady, New York

## ABSTRACT

The low-temperature (77°K) MOS-C(V) curves previously utilized to measure the number of fast interface states are analyzed. Quantitative variations in the number of fast states with variations in crystal orientation, oxidation atmosphere, vacuum and hydrogen annealing, together with some results of MOS-FET vacuum annealing are presented. For instance, high-temperature vacuum annealing of oxidized silicon wafers is shown to be capable of producing a very high density of donor and acceptor type fast interface state levels of the type previously identified by measuring MOS-C(V) flat-band voltage at low temperatures. These results suggest that these bands of donor and acceptor levels arise from a single type of defect which is electrically amphoteric.

Cooling MOS samples to low temperatures and measuring resultant changes in the samples' flat band voltage as determined from capacitance *vs.* voltage [C(V)] curves has previously been shown to be a simple and direct method of measuring the number of fast interface state levels at the Si-SiO<sub>2</sub> interface (1). This method, of course, normally detects only those states between the high- and low-temperature Fermi levels. In order to scan both sides of the band gap, these experiments were performed on identically oxidized pairs of n- and p-type samples. The results of these previous experiments suggested that the acceptor- and donor-type interface state levels detected using these sample pairs are caused by a single type of defect which is electrically amphoteric. The amphoteric nature of the fast interface defect discussed in ref. (1) and the symmetry of the interface state levels suggests that they can be thought of as being levels taken out of the conduction and valence band continuum by the discontinuities experienced by the Si bonds at the surface. In order to explain the increases in surface channel conductance that occurred when thermal oxides were formed in dry O<sub>2</sub> and subsequently annealed in H<sub>2</sub> or whenever steam oxidation was performed, Balk has proposed that a fast interface state consists of an oxygen vacancy defect at the Si-SiO<sub>2</sub> interface whose chemically unsaturated bonds can be saturated with H which in turn causes the annihilation of the fast state (2).

The charge within these fast interface states at any particular value of surface potential must not be confused with the amount of fixed charge,  $Q_{so}$ .  $Q_{so}$  has usually been determined by measuring the room temperature MOS-C(V) flatband voltage. This type of determination for  $Q_{so}$  is, of course, correct only in the absence of fast interface states even at measurement frequencies high enough to eliminate all the fast state capacitance if interface states are present. In fact, it is very difficult to distinguish, especially for very low values of surface charge, the fixed charge component and the fast interface state component from one another. This is because such a separation requires detailed information about the nature and distribution of fast states. The fixed charge has been attributed to positive alkali ion contamination, oxygen ion vacancies and/or excess positively charged Si at the Si-SiO<sub>2</sub> interface, or even in some special instances to negative ion complexes.

It is the purpose of this paper to explain the low-temperature (77°K) MOS-C(V) curves utilized to measure the total number of fast states and to show how the number of fast states can be varied over a very wide range. For instance, the dependence of the interface state density on how "wet" the oxide is has often been alluded to but never directly measured.

Furthermore, if fast surface states are due to the presence of unsaturated Si bonds at the interface, their number should be greatly increased by vacuum annealing since the reduction of SiO<sub>2</sub> by Si should produce more unsaturated bonds at the interface and/or the vacuum annealing might also eliminate any Si-H bonding within the oxide.<sup>1</sup> In addition, experiments with MOS-FETs show that fast interface states when present inhibit surface inversion and drastically reduce the mobility of the free carriers in the channel.

## Experimental Techniques

One ohm-cm n- and p-type wafers 2.5 cm in diameter and 0.15 cm thick were lapped and etched in white etch<sup>2</sup> and rinsed in distilled H<sub>2</sub>O. Following this treatment they were placed in a double-walled quartz thermal-oxidation chamber. The complete oxidation system is shown schematically in Fig. 1. The oxygen used for oxidation was an extra dry grade<sup>3</sup> but was initially passed through a quartz tube heated to 1000°C by a simple resistance furnace. This preheating preburned any hydrocarbons present in the oxygen, and the resulting water was trapped. Known amounts of H<sub>2</sub>O could then be introduced by subsequently passing this dry O<sub>2</sub> through water (or ice) and a trap, both of which were held at fixed temperatures. In this manner the O<sub>2</sub> oxidation atmosphere could be varied between 1 atm O<sub>2</sub> + 80 ppm H<sub>2</sub>O and 0.9 atm O<sub>2</sub> + 10<sup>5</sup> ppm H<sub>2</sub>O. The O<sub>2</sub> dew point was measured at the exhaust of the oxidation chamber. After oxidizing the samples at 1000°C for either 2 or 3 hr depending on orientation, the sealed oxidation chamber was removed from the oxidation furnace and allowed to cool in the oxidation atmosphere. The resultant oxides were about 1200Å thick.

Vacuum annealing could be performed by placing one of these previously oxidized samples inside a Si vacuum furnace. This is shown in Fig. 2. The Si furnace cavity was enclosed in a quartz bell jar which is attached to a high vacuum ion pump system and the Si furnace was heated by an RF induction heater. The sample's temperature was monitored by using a Pt-Pt 10% Rd thermocouple connected to a potentiometric recorder<sup>4</sup> through an RF filter.

Al dots about 2 mm in diameter were formed on the surface of the oxide by evaporating Al from a W filament through a nonintegral metal mask. The wafers were not heated during the formation of the Al dots or at any time previous to the taking of C(V) curves. The C(V) curves were then measured at 300° and

<sup>1</sup> A number of possible reactions which could occur within oxides and alter the number of interface states has been extensively discussed by E. Kooi, *IEEE Transactions on Electron Devices*, 13, 238 (1966); E. Kooi and M. V. Whelan, *Appl. Phys. Letters*, 9, 314 (1966).

<sup>2</sup> Three parts HNO<sub>3</sub> to 1 part HF.

<sup>3</sup> Matheson Company, extra dry grade oxygen.

<sup>4</sup> Leeds and Northrup Speedomax H.

\* Electrochemical Society Active Member.



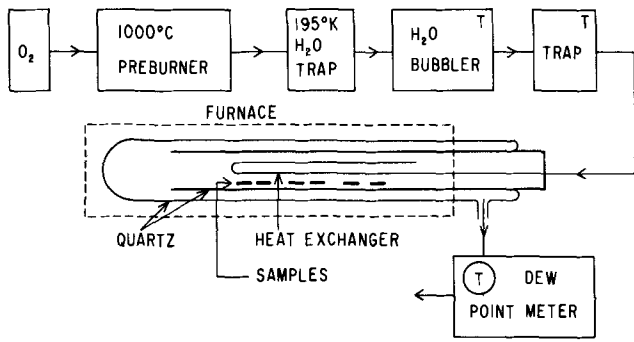


Fig. 1. Oxidation apparatus. The internal quartz heat exchanger is used to preheat the oxidation ambient before it enters the sample chamber. The H<sub>2</sub>O bubbler and trap both at temperature T are used to introduce fixed amounts of H<sub>2</sub>O into the O<sub>2</sub> stream.

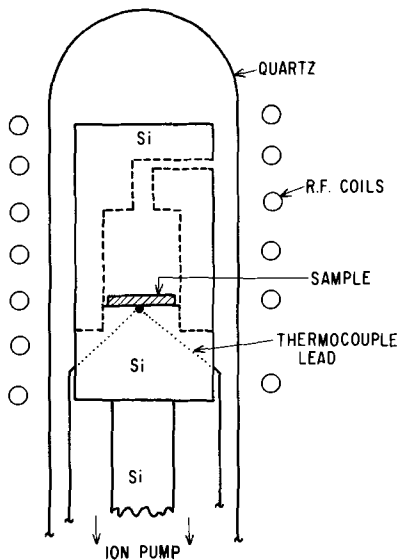


Fig. 2. High-purity Si high vacuum RF furnace used to vacuum anneal oxidized samples.

78°K to determine the number of fast interface states produced by the initial oxidation or by subsequent vacuum annealing.

The C(V) curves were obtained by using a continuously recording capacitance vs. voltage bridge which utilizes a lock in amplifier<sup>5</sup> as a phase detector and a-c to d-c converter. A schematic diagram of this apparatus is shown in Fig. 3. The a-c signal frequency was either 100 or 150 kc unless otherwise noted.

**Results**

**C(V) curve analysis.**—A typical set of room temperature and liquid nitrogen temperature C(V) curves is shown in Fig. 4. Also presented are the calculated C(V) curves using methods of analysis described later in the text.

The 300°K curve of Fig. 4 resembles the theoretical MOS-C(V) curve for no interface states and shows little evidence of the  $\sim 10^{13}/\text{cm}^2$  states actually present. The "flat band capacitance" in this sample does not occur at the flat band condition but actually for about 0.1 ev of band bending (slight depletion). This is because the 100 kc capacitance due to interface states,  $C_{FS}$ , is quite large at this point. And by the time that the true flat band condition is reached, the interface state capacitance is so large that the total capacitance is nearly that of the oxide,  $C_o$ . There are two evidences of this high interface state density at room temperature. (A) The C(V) plot is frequency dependent with the "apparent" flatband voltage moving in the negative voltage direction as the frequency

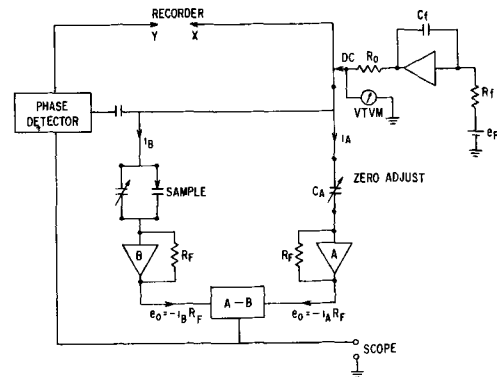


Fig. 3. Schematic diagram of continuous scanning MOS-C(V) bridge.

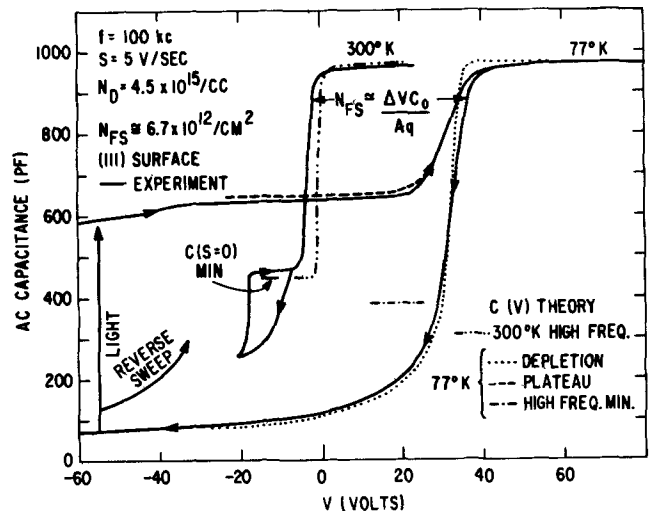


Fig. 4. Representative set of 300° and 77°K MOS-C(V) curves for samples with large amounts of fast interface states. The 300°-77°K curve voltage shift,  $\Delta V$ , gives the number of fast states  $N_{FS} \approx \Delta VC_o / Aq$  where  $C_o$  is the oxide capacity,  $A$  is the electrode area, and  $q$  is the electronic charge; 5 v/sec sweep speed. Experimental curves are solid lines, calculated are dashed and dash-dotted (see Fig. key). All theoretical curves are for  $\phi_{MS} = 0$  and  $Q_{so} = 0$ . 300°K curve assumes  $N_{FS} = 0$ . But the 77°K depletion curve is appropriately displaced in voltage.

is decreased and (B) if the vertical scale is greatly expanded near  $C_o$ , and C(V) is plotted between -10 and +70v bias the variations in interface state capacitance and that due to surface accumulation can be observed.

The 77°K plot of C(V) exhibits two phenomena not seen at 300°K, namely very strong hysteresis and photosensitivity effects. Most pronounced is a "ledge" of nearly constant capacitance shown in Fig. 4 from +20 to -40v which will occur whenever the bias is swept from negative to positive values. The ledge occurs over the same bias range as the plotted hysteresis loop made up of the lower outgoing trace and the plateau return trace. Both indicate that over this bias range the sample is not in thermodynamic equilibrium. During the plotting of this ledge, interface states below the Fermi level are being filled with electrons from the conduction band. The nearly constant capacitance corresponds to the degree of band bending (depletion) required to provide electrons at the surface to fill interface states at the voltage sweep speed. Thus, increasing the sweep speed will slightly increase the ledge capacitance since electrons are required at a greater rate and depletion type band bending must accordingly decrease. The nature of this ledge in no way gives information about the distribution of interface states even though its extent does depend on the total number present. It is, in fact, possible to observe a similar plateau or ledge and hys-

<sup>5</sup> Princeton Applied Research JB-5.

teresis loop (but at negative bias) in samples with no interface states if the surface is initially inverted. In this case, electrons are being provided to recombine with surface valence band holes and the ledge capacitance is slightly smaller than shown here. In the present sample, the ledge extends from large negative bias values whenever the surface is inverted by sweeping the sample to negative bias values and waiting for electrons to accumulate at the surface. Of course, this process can be enhanced by the presence of light or by going to sufficient fields to produce avalanching.<sup>6</sup>

On the lower trace shown in Fig. 4 the surface goes into strong depletion at 77°K because once the traps have become charged by sweeping the sample into accumulation they require minority carriers (holes) for neutralization. Therefore, as the charge on the field plate is reduced, the charge trapped in the fast interface state traps creates a strong internal field which forces the surface into depletion. This, of course, is a nonthermal equilibrium condition because the quasi-Fermi level is pinned above the charged acceptor states at the Si-SiO<sub>2</sub> interface. This condition can be maintained for hours because of the extremely small number of holes present in the n-type material at 77°K. Flashing light on the sample produces hole-electron pairs and the holes rapidly recombine with the negatively charged acceptor interface states which in turn extinguishes the internal field and the depletion region collapses. The capacity therefore rises toward the plateau value.

All of the effects observed here for this n-type MOS structure are also observed (with appropriate sign changes) for p-type samples. The number of fast states is of course approximately given by the voltage spacing between the 300° and 78°K flatband voltages.<sup>7</sup> This is indicated by the equation in Fig. 4 where  $N_{FS}$  is the number of fast states in the upper half of the band gap between the 300° and 78°K Fermi levels and  $\Delta V$  is the change in flatband voltages.<sup>8</sup>

The experimental curves shown in Fig. 4 were obtained by sweeping the sample past -60v where a type of avalanche breakdown repeatedly occurred which is not well understood because at this point the oxide became conductive enough to load the sweep circuit. This type of 77°K surface carrier generation, which stresses the oxide without destructively breaking it down, apparently produces the spacing between the capacitance curves above the plateau which are traced as the flatband condition is approached from the left and as the sample is swept away from accumulation into strong depletion. This spacing has been observed to decrease and even disappear in some samples if the extent of the voltage sweep is limited and the plateau is reached from the depletion curve either by reversing the direction of sweep or by illuminating the sample. Continuous illumination with strong light maintains a level of capacitance near the plateau value for both the outgoing and returning trace but this does not imply that the samples' capacitance in this case is even close to the thermal equilibrium value. A great

variety of curves can be obtained from samples of this nature at low temperatures depending on how the traces and retracings are made. But Fig. 4 amply illustrates all the main features of these situations.

As described above, the low-temperature ledge capacitance is controlled by the rate at which free carriers can fill interface states or by the rate of recombination of holes and electrons near the surface through recombination centers. And in fact, the primary recombination centers for carriers near the surface may be these fast interface state levels whenever they are present. An analytical formulation for the value of the interface state ledge capacitance is given below.

The rate of interface state filling is controlled by the interface state capture cross section  $\sigma$ , and the free carrier concentration,  $n$ , at the interface

$$1/\tau = \sigma \bar{v} n \quad [1]$$

where  $\bar{v}$  is the average free carrier thermal velocity. The instantaneous surface current is then

$$i_s = N n \sigma \bar{v} q \quad [2]$$

where  $N$  is the number of surface states not in equilibrium, and  $q$  is the electronic charge. This current can be related to the rate at which one adds charge to the interface during the filling of these states

$$i_s = C_o \frac{dV}{dt} = C_o S \quad [3]$$

where  $C_o$  is the capacitance of the dielectric layer and  $S$  is the sweep speed.

Since  $n = AT^{3/2}e^{-q\phi_s/kT}$  where  $A$  is the effective density of states divided by  $T^{3/2}$  and  $q\phi_s$  is the energy difference between the majority carrier band edge and the Fermi level at the surface, the surface potential which establishes the low temperature capacitance plateau is given by

$$\phi_s = \frac{kT}{q} \ln \left[ \frac{AT^{3/2}N\sigma\bar{v}q}{C_o S} \right] \quad [4]$$

Notice that the value of surface potential required to fill the fast states decreases as the sweep speed increases (the band edge moves towards the Fermi level). This, in turn, means that the ledge capacitance will increase slightly as the sweep speed increases. The ledge or plateau capacitance should also increase slightly as the empty interface states are filled, that is, as  $N$  in Eq. [4] decreases.

This analysis is compared with experiment in Fig. 4. The procedure for this comparison was as follows. The material used in these studies was specified as being  $1 \pm 0.25$  ohm-cm.<sup>9</sup> However, the actual surface concentration was determined by using the value of the 300°K zero sweep speed high-frequency minimum capacitance,  $C_{min}(S=0)$ , shown in Fig. 4. (The set of equations used to compute the differential capacitance curves are presented in the Appendix.) This value of  $N_D$  was then utilized in the  $C(V)$  equations to compute the 77°K depletion curve and the 77°K capacitance plateau. The fact that the theoretical depletion curve fits the experimental data so well is an indication that this particular sample is not heavily compensated with boron. If it were, the  $N_D-N_A$  value near the surface would be higher than that many depletion lengths away from the surface. This is because boron is segregated out of the surface during thermal oxidation (4).

The fit between the experimental ledge capacitance and the one calculated using Eq. [4] is within experimental error.<sup>10</sup> Furthermore, the slow increase in the capacitance, which occurs along the plateau as the empty interface states near the conduction band edge

<sup>6</sup> Similar 78°K  $C(V)$  curves have just recently been described by A. B. Kuper, E. Greenstein, and H. P. Caban-zeda. Recent News Paper given at the Chicago Meeting of the Society, Oct. 16, 1967. Electronics Division Abstract RN-3. Minority carrier generation by avalanche breakdown in MIS capacitors has also been observed by A. Goetzberger and E. H. Nicollian, *Appl. Phys. Letters*, 9, 444 (1966).

<sup>7</sup> The approximation here is largely due to the difficulties in determining the 300°K flatband voltage when  $N_{FS}$  is very large. This is because the fast state capacitance shifts the apparent flatband voltage (see text). The degree of uncertainty in  $N_{FS}$  can be estimated by examining n-type samples if we assume that the oxide space charge in all samples is positive or zero,  $Q_{so} \geq 0$ . For example, measurements on an n-type sample with  $N_{FS} \approx 5 \times 10^{12}/\text{cm}^2$  give an apparent 300°K flatband voltage at  $10^5$  and  $10^7$  Hz of -5 and -2v, respectively, but +28v at 78°K for both frequencies. The maximum error in  $N_{FS}$  is therefore about 20% if it is assumed that  $Q_{so} = 0$ . Because of this difficulty the  $Q_{so}$  values quoted in this article are approximate and are labeled " $Q_{so}$ ".

<sup>8</sup> Another method of detecting interface states which is based on measuring the conductive component of the MOS varactor impedance has been described by Nicollian and Goetzberger (3). This method is particularly effective for measuring interface state densities near the middle of the band gap and when the total number of interface states is low.

<sup>9</sup> TI LOPEX—Texas Instruments, Inc., Dallas, Texas.  $1 \pm 0.25$  ohm-cm n-type corresponds to an  $N_D-N_A = (5.8 \pm 1.8) \times 10^{15}/\text{cc}$ .

<sup>10</sup> The capture cross section and average thermal velocity used in these calculations are those used by Nicollian and Goetzberger (3):

$\sigma_n = 1 \times 10^{-15} \text{ cm}^2$  and  $\bar{v} = 10^7 \times (T/300^\circ\text{K})^{1/2}$ .

are filled, is also accounted for. Variations in the height of the plateau with sweep speed have also been verified; however, this correlation is not shown here.

The calculated 77°K high frequency minimum ledge capacitance (equilibrium theory) is also shown in Fig. 4. This was done to emphasize the fact that this capacitance, which is determined and maintained by minority carrier surface inversion, is very difficult to achieve at this low temperature. In fact, no practical combinations of sweep speed and/or illumination levels can be expected to maintain it while the MOS applied voltage is varied.

*$N_{FS}$  Variations with oxidation atmosphere ( $O_2 + H_2O$ ) and surface orientation.*—The variation in fast interface state density as a function of ppm  $H_2O$  added to the oxidation atmosphere can be found from Fig. 5, 6, and 7 which are plots of flatband voltage [assuming  $C_{FS}$  (150 kc)  $\approx 0$ ] for sample temperatures of 300° and 78°K for a range of  $H_2O$  concentrations between 80 and  $10^5$  ppm. Figure 5 gives the data for (111) orientated crystal surfaces, Fig. 6 gives it for (110) surfaces and Fig. 7 gives the data for (100) surfaces. Although the samples were all about  $1200 \pm 100\text{\AA}$  in thickness the data have been normalized for 1000Å of oxide. Note that the numbers of fast in-

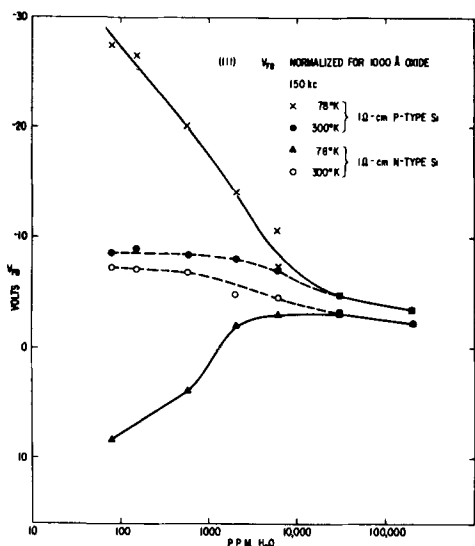


Fig. 5. Flatband voltages for (111) 1 ohm-cm n- and p-type oxidized Si wafers at 300° and 78°K vs. ppm  $H_2O$  added to oxygen oxidation ambient.

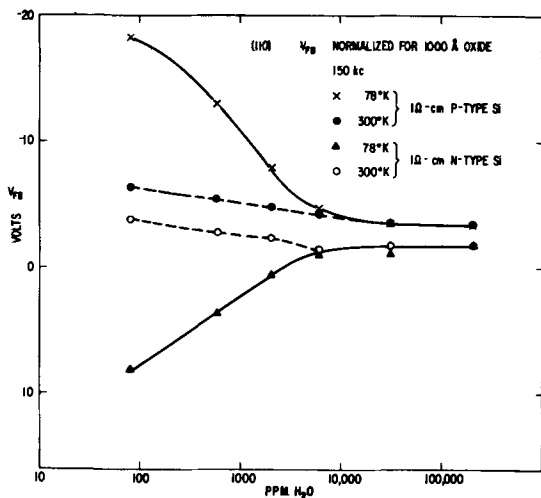


Fig. 6. Flatband voltages for (110) 1 ohm-cm n- and p-type oxidized Si wafers at 300° and 78°K vs. ppm  $H_2O$  added to oxygen oxidation ambient.

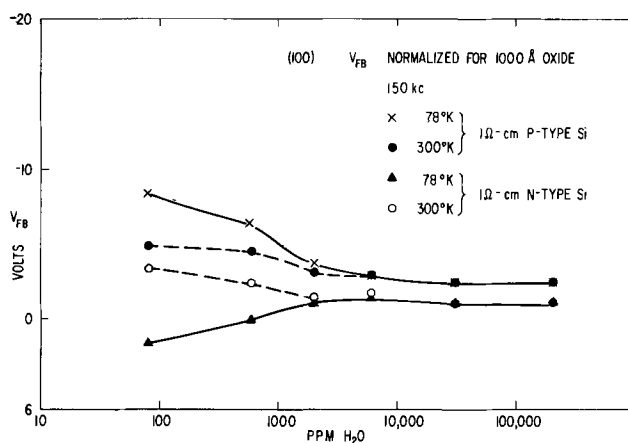


Fig. 7. Flatband voltage for (100) 1 ohm-cm n- and p-type oxidized Si wafers at 300° and 78°K vs. ppm  $H_2O$  added to oxygen oxidation ambient.

terface states as measured by the change in flatband voltage between 300° and 78°K occur in almost identical numbers for any pair of n- and p-type samples oxidized in the same ambient. This holds for each of the three orientations. The number of fast states in both halves of the band gap increase monotonically as the oxygen is dried out. At 30,000 ppm  $H_2O$ , the fast state density,  $N_{FS}$ , is  $\leq 10^{10}/\text{cm}^2$  while for lower concentrations it increases until at the 80 ppm  $H_2O$  level  $N_{FS}$  is about  $3.8 \pm 0.3 \times 10^{12}/\text{cm}^2$  for n- and p-type (111) samples,  $2.5 \times 10^{12}/\text{cm}^2$  for (110) samples and  $9.3 \pm 2 \times 10^{11}/\text{cm}^2$  for (100) samples.<sup>11</sup>

*Increases in  $N_{FS}$  with vacuum annealing.*—As pointed out previously, vacuum annealing could be expected to produce even larger amounts of interface states by producing more unsaturated Si bonds through the reduction of  $SiO_2$  by Si at the  $SiO_2$ -Si interface and/or by elimination of Si-H bonds. The results of some high-temperature vacuum annealing experiments (pressure  $\sim 5 \times 10^{-7}$  Torr) done on a variety of (111) samples are shown in Table I. Samples 1 and 2 are identically treated n- and p-type samples. Notice that the additional vacuum annealing treatment has greatly increased the fast interface state density in these two samples, and yet the number of donor and acceptor levels still appear in almost identical numbers. Vacuum annealing can also increase the number of fast states in "wetter" oxides too, as is shown by the results obtained from sample 3. Sample 4 is a dry oxide that was first vacuum annealed and then  $H_2$  annealed, and the results show that  $H_2$  annealing eliminates the fast interface state defects as originally proposed by Balk (2). As mentioned previously, an exact interpretation of the "apparent" room temperature flatband condition is made difficult when the number of interface states is very large and the measuring frequency is too low to eliminate interface state capacity. However, the  $Q_{50}$  values in Table I indicate that  $H_2$  annealing which eliminates the states does not increase the amount of fixed positive charge. Therefore, the enhanced surface inversion observed by Zaininger and Warfield using  $H_2$  annealed p-type MOS varactors (5) was probably caused by the elimination of the fast interface states produced by the initial dry oxidation.

These results therefore show that the respective donor and acceptor fast state levels appear in equal numbers (within experimental accuracies) on identically treated pairs of p- and n-type samples. This fact is necessary to conclude that the fast state defect center is electrically amphoteric. It is not sufficient,

<sup>11</sup> It is interesting to note that the oxide growth rate is virtually unaffected by additions of water below 10,000 ppm  $H_2O$ . This fact can also be deduced from the wet and dry oxide growth rate constants given by B. E. Deal and A. S. Grove, *J. Appl. Phys.*, **36**, 3770 (1965).

Table I. Results of vacuum and H<sub>2</sub> annealing\*

Sample**	Initial oxide			Vacuum anneal				H <sub>2</sub> anneal		
	O <sub>2</sub> oxidation ppm H <sub>2</sub> O	N <sub>FS</sub>	"Q" <sub>so</sub> /q	Anneal, °C	hr	N <sub>FS</sub>	"Q" <sub>so</sub> /q	Anneal	N <sub>FS</sub>	"Q" <sub>so</sub> /q
1. n-type	80	32	16	1100	2	140	3.4			
2. p-type	80	41	20	1100	2	110	6.5			
3. p-type	6000	8.0	13	800	2	70	18			
4. p-type	80	—	—	1100	2	—	—	800°C, 1 hr	≤0.1	8.7

\* N<sub>FS</sub> and "Q"<sub>so</sub>/q in units of 10<sup>11</sup>/cm<sup>2</sup>. For an explanation of "Q"<sub>so</sub> see footnote 7.

\*\* 1 ohm-cm (111) Si.

however. One could still maintain that only one type of level occurs in either n or p-type samples. To prove that both types of levels appear in a single sample, it is necessary to look at inverted surfaces.

**Effects of N<sub>FS</sub> on surface inversion.**—Figure 8 shows a schematic picture of how the fast interface state levels in the minority carrier half of the band gap are charged whenever the surface is inverted. In this case, the surface of n-type Si has been inverted to produce a p-type channel. This, of course, is the surface condition required to turn on a p-channel enhancement mode MOS-FET. Charging these defect states is expected to have two effects: increase the threshold voltage, and reduce the channel carrier mobility by charge scattering (6). In order to demonstrate this effect clearly, a p-channel enhancement mode MOS-FET was fabricated. The threshold and carrier channel mobility as determined by measuring the small a-c signal channel conductance are shown in Table II. The thresholds given in Table II are defined as the gate voltage at which the surface conductivity of the channel is 1 μmho/square. The initial 300°K characteristics were: threshold -6v and channel mobility, 190 cm<sup>2</sup>/v-sec as determined by the slope of the channel conductance curve well beyond threshold. (It is assumed that well beyond threshold all the fast states are filled and that all the additional charge added to the surface adds free mobile charge to the channel.) The Al contacts were next removed and the device vacuum annealed at 1000°C to produce a large number of interface states. After reapplying the Al contacts the device characteristics were redetermined. Initially the 300° and 78°K thresholds were -6 and -7v, respectively, and N<sub>FS</sub> ≈ 4 × 10<sup>10</sup>/cm<sup>2</sup>. (Even without fast states, about a 1v shift in threshold is

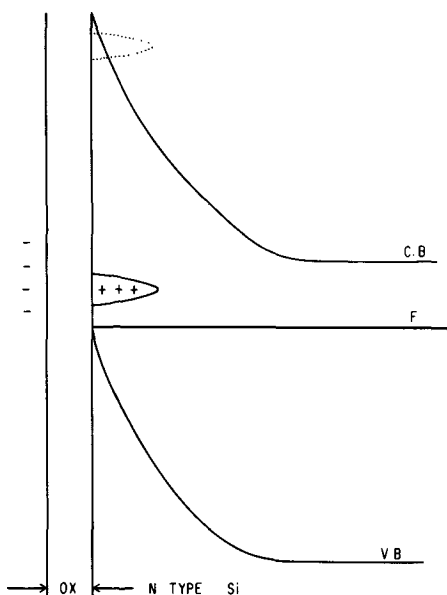


Fig. 8. Schematic representation of how the fast interface state levels in the minority carrier half of the forbidden band are charged when the surface is inverted. In this case, n-type Si bulk material is inverted to produce a p-type surface.

expected for this change in temperature because  $kT$  at 77°K is much smaller and because of the shift in bulk Fermi level.) Following vacuum annealing, the LN<sub>2</sub> threshold had increased to -34v which indicates a N<sub>FS</sub> ≈ 5.9 × 10<sup>12</sup>/cm<sup>2</sup>, and the LN<sub>2</sub> channel mobility has decreased from 340 to 45 cm<sup>2</sup>/v-sec. The room temperature characteristics are now greatly degraded giving a threshold of -18.5v and a channel mobility of only 60 cm<sup>2</sup>/v-sec. Thus, as expected, surface inversion now requires additional surface charge to charge the defect centers, which when charged, greatly decrease the channel carrier mobility by introducing large amounts of additional scattering.<sup>12</sup> The temperature dependence of the mobility has also been altered. Before annealing, the channel mobility increased with decreasing temperature which suggests that phonon scattering was dominant; after annealing, however, the mobility at 78°K is slightly lower than it is at 300°K. This suggests that charged interface states reduce the channel mobility by coulomb potential scattering of the free carriers in the channel.

### Summary

The technique of cooling samples to 77°K and measuring the resultant shift in flatband voltage has been shown to be an excellent method of detecting and measuring the total number of fast states between the 300° and 77°K Fermi levels. And in fact, the range of detection is approximately 0.1 to greater than 200 × 10<sup>11</sup>/cm<sup>2</sup>. The 77°K C(V) curves have been explained and analyzed, and the so-called 77°K plateau or ledge capacitance explained. The results show that the fast interface state donor and acceptor levels always appear in nearly equal numbers. For example, the number of acceptor and donor levels measured on similarly treated n- and p-type samples, respectively, are essentially equal before and after their number has been greatly increased by vacuum annealing. These same levels are eliminated by H<sub>2</sub> annealing. These defect centers when present can drastically raise even the room temperature performance of MOS-FETs since their production has been shown to alter the threshold and greatly reduce the channel mobility of a MOS-FET. Furthermore, these two sets of defect levels are observed to delay both surface

<sup>12</sup> The presence of interface states is of course also apparent in the difficulty of attaining the characteristic very low-frequency surface inversion curve in standard MOS varactors. However, it is more difficult to make this effect in varactors as quantitative as the measurement of FET thresholds at low temperatures.

Table II. Vacuum annealed Mos-fet\* characteristics

T, °K	Initial characteristics, N <sub>FS</sub> ≈ 4 × 10 <sup>10</sup> /cm <sup>2</sup>		After vacuum anneal, <sup>b</sup> N <sub>FS</sub> ≈ 5.9 × 10 <sup>12</sup> /cm <sup>2</sup>	
	Threshold, <sup>†</sup> v	Channel mobility, <sup>‡</sup> cm <sup>2</sup> /v-sec	Threshold, v	Channel mobility, cm <sup>2</sup> /v-sec
300	-6	190	-18.5	60
78	-7	340	-34	45

\* 1 ohm-cm n-type (111) Si substrate, p-channel enhancement mode MOS-FET.

† 1 μmho/square.

‡ As determined by slope of channel conductance curve vs. gate voltage well beyond threshold (see text).

<sup>b</sup> 1000°C, 1-hr vacuum anneal.

accumulation and surface inversion.<sup>13</sup> All these results suggest that these levels are caused by a single type of defect which is electrically amphoteric.

### Acknowledgments

The authors wish to acknowledge the fine technical help given by George Charney, Cliff Circe, and Lloyd Keifer in preparing wafers and in running the oxidation and vacuum systems used in this study.

Manuscript received Nov. 20, 1967; revised manuscript received March 4, 1968. This paper was presented in part at the Philadelphia Meeting, Oct. 9-14, 1966, as Recent News Paper 13.

Any discussion of this paper will appear in a Discussion Section to be published in the June 1969 JOURNAL.

<sup>13</sup> Preliminary experiments on self-registered Mo gate MOS-FETs (D. M. Brown, W. Engeler, M. Garfinkel, P. V. Gray, Recent News Paper presented at the Chicago Meeting of the Society, Oct. 16, 1967, Electronics Div. Abstract RN-7) also show this correlation. That is, large shifts in MOS-FET threshold and in the MOS-C(V) flatband condition have been observed to occur simultaneously when the samples are cooled. Furthermore, as these shifts are reduced by hydrogen annealing, the FET thresholds are lowered, and the channel mobilities are increased.

### REFERENCES

1. P. V. Gray and D. M. Brown, *Appl. Phys. Letters*, **8**, 31 (1966).
2. P. Balk, Paper presented San Francisco Meeting of the Society May 9-13, 1965, as Abstract 109.
3. E. H. Nicollan and A. Goetzberger, *Bell System Tech. J.*, **46**, 1055 (1957).
4. B. E. Deal, A. S. Grove, E. H. Snow, and C. T. Sah, *This Journal*, **112**, 308 (1965).
5. E. H. Zaininger and G. Warfield, *Proc. IEEE*, **52**, 972 (1964).
6. E. Arnold and G. Abowitz, *Appl. Phys. Letters*, **9**, 344 (1966).
7. R. H. Kingston and S. F. Neustadter, *J. Appl. Phys.*, **26**, 718 (1955).
8. D. R. Frankl, *Solid State Electronics*, **2**, 71 (1961).
9. A. S. Grove, B. E. Deal, E. H. Snow, and C. T. Sah, *ibid.*, **8**, 145 (1965).
10. C. G. B. Garrett and W. H. Brattain, *Phys. Rev.*, **99**, 376 (1955).
11. R. Linder, *Bell System Tech. J.*, **41**, 803 (1962).
12. P. M. Marcus, *IBM Journal*, **8**, 496 (1964).
13. R. Stratton, *Proc. Phys. Soc. (London)*, **B68**, 746 (1955).
14. R. Seiwatz and M. Green, *J. Appl. Phys.*, **29**, 1034 (1958).

### APPENDIX

#### Analytical Model for the Semiconductor Surface Varactor<sup>14</sup>

A brief presentation of the equations used to compute the theoretical C(V) curves in the text follows.

Several analytical papers have appeared which have treated various aspects of the surface properties of semiconductors with varying degrees of accuracy and completeness. Specialized solutions for the electric field at the semiconductor's surface have been presented by Kingston and Neustadter (7) for the case of fully ionized impurity states and nondegenerate free carrier distribution. These specialized solutions of Kingston and Neustadter have been used by Frankl (8) and by Grove, Deal, Snow, and Sah (9) to develop MOS capacitance calculations. Similar sets of equations have been developed by Garrett and Brattain (10), Lindner (11), and also by Marcus (12) who has included the effects of the hypothetical midband gap interface states. Stratton (13) has developed a specialized solution for the surface field for the limiting case of extreme degeneracy. Seiwatz and Green (14) have presented an exact equation for the surface field using Fermi-Dirac functions, and their equation is similar to ours in this respect. However, they did not develop the appropriate equations for the capacitance of the MOS varactor.

<sup>14</sup> Partial reproduction of "MOS Science and Technology, I. Analytical Model for the Semiconductor Surface Channel and the MOS Varactor and Field Effect Transistor," by D. M. Brown and P. V. Gray; General Electric Report No. 67-C-026, March (1967).

The assumptions are that: (i) the semiconductor bulk band structure can be characterized by parabolic bands and a density of states effective mass and a forbidden energy gap, all of which are continuous in value right up to the insulator-semiconductor interface; (ii) thermodynamic equilibrium holds throughout the semiconductor; and (iii) the insulator and insulator-semiconductor interface is perfect and does not contain any electronic traps nor does the insulator contain any ionic space charge.

The development of the formula for the electric field at the surface of the semiconductor for any degree of band bending parallels that given by Seiwatz and Green (14). The only difference is that the zero of energy in our calculations is taken at the valence band edge whereas Seiwatz and Green use the so-called intrinsic Fermi level which is very close to the middle of the forbidden band. Having zero energy at a band edge simplifies the situation somewhat.

The surface field is calculated by integrating Poisson's equation. The surface field is supported by a space charge region near the semiconductor's surface. The charge density,  $\rho$ , is given by

$$\rho = \rho_D - \rho_A + q(p-n) \quad [\text{A.1}]$$

where  $\rho_A$  and  $\rho_D$  are the densities of ionized acceptors and donors, and  $p$  and  $n$  are the densities of electrons and holes given by

$$n = A_C T^{3/2} F_{1/2}(U - E_G) \quad [\text{A.2}]$$

and

$$p = A_V T^{3/2} F_{1/2}(-U) \quad [\text{A.3}]$$

where  $E_G = \epsilon_G/kT$  is the reduced band gap,  $U$  is the reduced potential and

$$A_i = 2(2\pi m_i^* k/h^2)^{3/2} \quad \begin{array}{l} i = C(\text{conduction band}) \\ i = V(\text{valence band}) \end{array} \quad [\text{A.4}]$$

is the density of states divided by  $T^{3/2}$  with  $m_i$  being the density of states effective mass and  $F_{1/2}$  is the Fermi Dirac integral to the 1/2 order.<sup>15</sup> Fixed charge densities of ionized impurities are

$$\rho_A = qN_A [1 + 2 \exp(E_A - U)]^{-1} \quad [\text{A.5}]$$

$$\rho_D = qN_D [1 + 2 \exp(U + E_D - E_G)]^{-1} \quad [\text{A.6}]$$

where  $N_A$  and  $N_D$  are the density of acceptors and donors, respectively, and  $E_A$  and  $E_D$  their activation energies measured from the nearest band edge divided by  $kT$ .

Integrating Poisson's equation gives the semiconductor surface field

$$\epsilon_S^2 = \frac{8\pi}{K_S} kT \left\{ N_A \ln \left| \frac{2 + \exp(U_S - E_A)}{2 + \exp(U_B - E_A)} \right| \right. \quad [\text{A.7}]$$

$$\left. + N_D \ln \left| \frac{2 + \exp(E_G - E_D - U_S)}{2 + \exp(E_G - E_D - U_B)} \right| \right.$$

$$\left. + A_C T^{3/2} [F_{3/2}(U_S - E_G) - F_{3/2}(U_B - E_G)] \right.$$

$$\left. + A_V T^{3/2} [F_{3/2}(-U_S) - F_{3/2}(-U_B)] \right\}$$

where  $\epsilon_S$  is in statvolts/cm and  $U_S = q\phi_s/kT$  and  $U_B = q\phi_B/kT$  are the reduced surface and bulk potentials, respectively, and  $K_S$  is the semiconductor's dielectric constant. The total net semiconductor space charge is then

$$Q_S = K_S \epsilon_S / (4\pi) \quad [\text{A.8}]$$

The semiconductor's differential a-c capacitance is given by differentiation of Eq. [A.8]. This gives

$$C_S (\text{low frequency}) = - \frac{\partial Q_S}{\partial \phi_S} = \frac{q}{\epsilon_S} \left\{ N_A [1 + 2 \exp(-U_S + E_A)]^{-1} \right. \quad [\text{A.9}]$$

$$\left. - N_D [1 + 2 \exp(U_S + E_D - E_G)]^{-1} \right. \left. + A_C T^{3/2} F_{1/2}(U_S - E_G) - A_V T^{3/2} F_{1/2}(-U_S) \right\}$$

statfarads/cm<sup>2</sup>

<sup>15</sup> J. S. Blakemore, "Semiconductor Statistics," Pergamon Press, New York (1962). Blakemore's  $\mathcal{F}$  is used here.

Equation [A.9] then is the capacitance equation for the low-frequency limit because it includes the contributions of all charges to the differential a-c capacitance.

At sufficiently high frequencies, minority carriers cannot respond to the a-c signal, but as the surface is inverted by the d-c bias, the depletion width increases toward a maximum. This maximum occurs when the concentration of minority carriers at the surface is large enough to determine the size of the depletion region. In other words, at high frequencies, the minority carriers act like fixed charges concentrated at the surface. Deal *et al.* (4) have decided that this maximum depletion width occurs when the surface potential reaches the value

$$U_S = E_G - U_B \quad [A.10]$$

This is a guess which is based on physical reasoning. It agrees quite well with experiment. When this condition is reached, the depletion width and the high-frequency capacity remain constant. A solution for the high-frequency capacity can be obtained by dropping one of the two last terms, the minority carrier term, in Eq. [A.9] and specifying that for the inversion region, the semiconductor space charge capacity is constant and is equal to

$$C_S(U_S) = C_S(E_G - U_B) \quad [A.11]$$

The depletion capacity occurs when minority carriers cannot accumulate near the surface even in the bias range corresponding to inversion. This occurs,

for instance, when the MOS bias is rapidly switched from an accumulation value to an inversion value, and the capacitance is measured before minority carriers can accumulate at the surface; this case can also occur if the oxide leaks electrically. This transient non-equilibrium condition gives rise to a very wide depletion region, and evaluations for this situation are obtained by dropping the minority carrier terms in Eq. [A.7] and [A.9] and making evaluations for very large amounts of band bending.

The MOS capacitance is given by

$$C(U_S) = \frac{C_o C_S(U_S)}{C_o + C_S(U_S)} \quad [A.12]$$

where  $C_S(U_S)$  is any one of the three semiconductor capacities described above, and  $C_o$  is the capacitance of the dielectric.  $C_S$  is, of course, dependent on the applied voltage. The applied voltage for any given value of surface potential is

$$V(U_S) = (kT/q)(U_S - U_B) - Q_S/C_o + \phi_{MS} \quad [A.13]$$

where  $\phi_{MS}$  is the metal-semiconductor work function difference.

These equations are easily programmed for computer calculations of  $C(V)$  using the surface potential,  $\phi_s$ , which specifies the amount of semiconductor band bending at the surface, as the running variable. Such a set of straightforward and exact solutions for the MOS surface capacitance varactor is perhaps easier to understand and use than the specialized analytical solutions developed by others.

## Preparation of High-Purity Nickel

### II. Zone Melting

R. R. Soden and V. J. Albano

*Bell Telephone Laboratories, Incorporated, Murray Hill, New Jersey*

#### ABSTRACT

Nickel single crystals have been prepared by electron beam float zone melting with resistance ratios ( $R_{273^\circ\text{K}}/R_{4.2^\circ\text{K}}$ ) of 4000. These ratios were obtained by the selective removal of carbon by an oxygen treatment during the zone melting of specially prepared electrolytic nickel. Our data suggest that carbon and iron have a nearly equal contribution to the residual resistivity of Ni ( $\cong 4 \times 10^{-10}$  ohm-cm/atomic ppm). Thus, the total carbon and iron content of nickel, neglecting all other contributions to the residual resistance, must be less than 5 atom ppm to obtain a 4000 resistance ratio. Several commercial sources of nickel were zone melted and found to contain too much iron to approach this purity level.

Very high-purity metal single crystals are necessary for experiments directed toward an understanding of their intrinsic electronic properties. For this end, we have employed electron beam zone melting, together with chemical purification techniques, to obtain nickel single crystals of purities heretofore not obtained. One result of this work is that galvanomagnetic measurements by Reed and Fawcett (1) were allowed to be made to obtain information regarding the electronic structure of nickel.

The major requirement of a metal for high-field Fermi surface measurements is that  $\omega_c \tau \gg 1$ , where  $\omega_c$  is the cyclotron frequency for the electron and  $\tau$  is the electron relaxation time. Since  $\omega_c$  is proportional to the magnetic field strength which is applied to a sample and  $\tau$  is inversely proportional to the resistivity of the metal, either large fields must be available or the purity of the metal must be improved to lower the residual resistivity and thus increase  $\tau$ . It is now more feasible to increase the purity of the metal than to obtain the very high fields that are required.

Resistance ratios ( $R_{273^\circ\text{K}}/R_{4.2^\circ\text{K}}$ ) as high as 4000 have been obtained on nickel single crystals. These crystals were prepared by the floating zone melting of specially prepared electrolytic nickel. The preparation of this high-purity electrolytic nickel has been previously described (2). Resistance ratio data for zone melted commercial nickels are also reported and compared with the above data. The effect of carbon and iron on the ratio is reported and discussed.

#### Experimental

*Evaluation of purity.*—The primary difficulty in an investigation of this type is determining the impurities which contribute significantly to the residual resistivity. We employed spark spectra, vacuum fusion, and mass spectra analytical techniques to obtain data to complement the resistance ratio information.

*Source material, zone melting, and crystal growth.*—High-purity nickel was obtained from various commercial sources as sponge and rod. Table I contains the emission spectrographic analysis on these mate-

Table I. Concentration of impurities in ppm by weight in starting Ni samples

Source	Cu	Al	Mg	Si	Fe	Ca	C
1	<1	1.0	1.0	4.0	7.0	<1	—
2	0.25	6.3	7.0	3.4	7.5	2.0	—
3	0.35	4.5	4.3	3.4	2.9	2.0	—
4	1.1	6.0	2.7	<0.1	7.6	1.7	—
BTL Electrolytic	0.5	N.D.	0.9	0.9	1.3	N.D.	~50

rials, as well as the electrolytic nickel prepared in these laboratories. The approximate carbon content of the as-plated electrolytic nickel is also shown. The carbon present in this material is thought to be due to pickup during the purification of the electrolyte. Nickel from source 1 was in the form of prefabricated rods ¼ in. diameter by 6 in. long. Nickel from sources 2, 3, and 4 were in sponge form. The preparation of the electrolytic nickel was previously described and was in the form of rods or rectangular plates of various dimensions.

The sponge materials were preformed into ¼ x ¼ x 3 in. bars by pressing at approximately 30,000 psi in a hardened steel die. The bars were not fragile and could be suspended in the zone melting apparatus without presintering.

The electrolytic nickel plates required cutting into rods. After cutting, the rods were vigorously etched with a 50% H<sub>2</sub>O-50% H<sub>2</sub>SO<sub>4</sub> anodic etch to remove iron which may have been picked up during cutting and washed with deionized water. Electrolytic nickel already in the form of rods was also subjected to this cleaning treatment.

The vacuum float zone melting apparatus employed in this work has been described (3). However, for this work, the rf coil was replaced by an electron gun which consists of a circular 0.0115-in. diameter thoriated tungsten filament and molybdenum focusing plates on the top and bottom. A mechanically driven variac control similar to that described by Schadler (4) was used to control the emission current.

All the nickel samples were suspended in the vacuum station from a quartz hook by cutting a notch in the top of a given sample and attaching a loop of 10 mil nickel wire of good purity. The bottom of each sample was placed in contact with a nickel rod which was held by an adjustable chuck. Focusing plates for the gun were selected on the basis of the experiment being conducted and usually had openings of 1 to 2 times the sample diameter. Before the start of zone melting, the sample was electron beam welded to the nickel crystal. Zone melting of the sample was started ½ in. up from the weld. Progressive melting-in from the surface of the rod was usually done on each sample to remove gaseous contaminants which were initially present in most of the materials. Up to ten passes were made on the samples at rates of either 0.001 or 0.0005 in./sec. The vacuum ranged between 2 x 10<sup>-5</sup> and 4 x 10<sup>-7</sup> mm of Hg depending on the contaminants present in the nickel and/or on the diameter of the rod.

### Results

Purification by zone melting can take place by selective vaporization and/or segregation. The ease of removal of a solute impurity from a host metal by selective vaporization can be qualitatively estimated from the available thermodynamic data (5). Table II shows the equilibrium vapor pressures  $p_i^*$  at 1725°K, for the impurities which were detected in our original nickel samples (Table I). Assuming that the partial pressure,  $p_i$  of the impurity in the vapor is given by  $X_i p_i^*$  (ideal solution), where  $X_i$  is the atom fraction, selective vaporization may occur when  $(p_i^* X_i) / (p_{Ni} X_{Ni}) > 1$ . That is, selective vaporization resulting in purification may occur when the escaping tendency of the impurity is greater than that of the solvent. On this basis, the third column in

Table II. Equilibrium vapor pressures ( $p_i^*$ ) at 1725°K for impurities detected in the original nickel samples compared to the vapor pressure of pure nickel

Impurity	$p_i^*$ atm	$X_i = \frac{p_{Ni} X_{Ni}}{p_i^*}$
Ni	4.3 x 10 <sup>-6</sup>	—
Cu	2.4 x 10 <sup>-4</sup>	0.018
Al	8 x 10 <sup>-4</sup>	0.0054
Mg	>5	<10 <sup>-6</sup>
Si	2 x 10 <sup>-6</sup>	1
Fe	1.15 x 10 <sup>-5</sup>	0.37
Ca	~1	<10 <sup>-6</sup>

Table II shows the approximate limiting impurity level obtainable by selective vaporization. It appears that only Mg and Ca can be removed from nickel to a low level by selective vaporization. If the growth conditions were such that the amount of vaporization of Ni from the molten zone was increased, the impurity elements Fe, Cu, and Si could be concentrated.

Purification by segregation appears to be limited for the materials studied in this work because the segregation coefficients for the impurities encountered are apparently unfavorable. However, we will show that selective oxidation, in addition to selective vaporization, coupled with floating zone melting, is effective in obtaining nickel having high resistance ratios.

#### Initial Results on Electrolytic Nickel

Table III shows representative  $R_{273^\circ K} / R_{4.2^\circ K}$  data on zone melted electrodeposited nickel obtained early in this investigation. It is important to note the large variation in ratio even though the metallic impurity contents on these materials, based on emission spectroscopy, were not initially very different in all the samples.

The data on plate IV, which was the first material investigated, were particularly baffling. The plate was approximately 6 x 3 x ⅛ in. thick. The edges were rounded due to the higher effective current density during plating and had a diameter of ~3/16 in. Each section was zone refined separately. Although the as-plated material showed only a slight increase in resistance ratio from top to bottom, the ratios of the zone melted rods were completely inconsistent compared to the starting ratios.

#### Initial Results on Commercial Nickels

Zone melting of commercial nickel samples, the analysis of which is given in Table I, was done concurrently with the electrolytic nickel. Results are shown in Table IV. Increasing the number of zone passes did not affect the ratios so dramatically as in

Table III. Resistance ratios for representative electrolytic nickel samples

Form of electrodeposit	As-deposited	Number of zone melting passes		
		1	3	6
Plate IV				
Bottom edge	748	2177		
Interior	649	622	1430	1276
Top edge	523	226		
Rod	345	240		190
Rod	933	1375		655
Rod	870	1530		840

Table IV. Resistance ratios for commercial nickels after two zone melting passes

Source	Original form of material	Number of zone melting passes		
		2	4	6
1	Rod			
2	Sponge	870		
3	Sponge	1400	1350	
4	Sponge	2000		
		1540		1450



the case of the electrolytic samples. Also, the zone melting behavior was different. Large fluffy deposits were found on the focusing plates of the electron gun assembly which were not observed during the zoning of the electrolytic nickel. An x-ray powder pattern was taken of this deposit. It revealed approximately 80-90% nickel and 10-20% nickel oxide (estimated by relative line intensity). Since the surfaces of the zone refined rods were not smooth, several samples were sectioned, electropolished in  $H_2O-H_2SO_4$ , electro-etched, and examined. A cellular-type microstructure was observed which was not found in the zone melted electrolytic nickel. A cellular structure is a consequence of impurity segregation during unidirectional solidification. Since the sponge nickel samples contained adsorbed oxygen and the electron beam interacts with back streaming diffusion pump oil to form a polymer on the nickel surface (6), oxygen and carbon were suspected as serious contaminants. Even additional trapping in the chamber was insufficient to prevent carbon pickup. Several samples were analyzed for carbon to test this hypothesis; results are summarized in Table V.

The amount of carbon present did not correlate exactly with the resistance ratios since other impurities were present in varying amounts, but the trend toward increasing ratio with decreasing carbon content was in the proper direction. It was thus apparent that carbon must be removed to ascertain better the effect of metallic impurities on the resistance ratios.

#### Removal of Carbon

The removal of carbon from nickel by the use of oxygen during vacuum zone melting is relatively easy due to the following fortuitous circumstances:

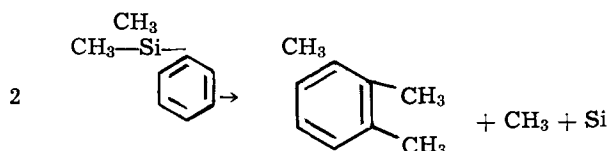
1. Nickel can be readily oxidized.
2. Oxygen is soluble in nickel to the extent of 1 w/o (weight per cent) at its melting point.
3. The free energy change for the reaction of carbon with oxygen is much more negative than that of nickel with oxygen. Thus, the removal of carbon by oxygen is thermodynamically favorable.

Prior to zone melting, the nickel rods were heated at  $900^\circ C$  in air forming a coating of green NiO on the rod surface. This treatment results in an oxygen pickup of up to 1 w/o depending on the rod diameter. During the first pass or two, the heat input is controlled manually since the high oxygen content makes the molten zone somewhat unstable. A metallographic cross section of this part of a zone melted nickel rod shows a uniform NiO precipitate in the nickel matrix. Repeated zone melting was continued until the surface of the molten zone became stable and the surface of the rod appeared smooth. At this stage, no precipitate was observed metallographically. It thus takes 4 to 6 zone passes at 0.001 in./sec to remove the oxygen. A typical analysis of the zone melted nickel after the above treatment shows <20 atom ppm carbon and <8 atom ppm oxygen. By utilizing the above treatment, the resistance ratio of electrolytic nickel having the lowest metallic impurity content was raised from ~500 to 4000.

Increasing the number of zone melting passes beyond 6 now results in a decrease in the resistance ratio of the nickel, an observation made earlier. This is probably due to pickup of carbon from the diffusion pump oil vapor which now is important since there is

little excess oxygen present for oxidation of the carbon. The Octoil "S," which had been used as the diffusion pump oil, was therefore changed to DC-704 oil to decrease the carbon pickup. This silicone oil has a lower vapor pressure and was deemed to be less prone to fractionation problems. Indeed, the ratio did not decrease, after reaching a maximum, as rapidly with this oil. However, we were not able to restore the high ratio by re-oxidation and zone melting as we could when the pure hydrocarbon oil was used. This result suggested silicon contamination from the DC-704 oil. In addition, more passes were required to remove all the nickel oxide which suggested that oxygen removal is also enhanced by the higher concentration of hydrocarbon vapors in the system when pumped with Octoil "S."

Shapiro (7) performed residual gas analysis to determine the decomposition reaction for DC 704 oil and found the reaction to be



Thus silicon appears to be readily available for contamination of nickel. However, we have not performed any analysis to determine the amount of silicon contamination. It appears that the choice of diffusion pump oil is important for purification of nickel, therefore it would appear that an oilless vacuum system may be desirable for achieving even higher ratios for Ni.

#### Results of Removal of Both Carbon and Oxygen

The analysis of the electrolytic nickel before zone melting showed carbon contents of 20-100 atom ppm (2). Since the amounts of the metallic impurities did not correlate with the resistance ratios shown in Table III, it was postulated that the as-plated materials contained a carbon-to-oxygen ratio which depended on the current density at the particular region of the electrodeposit. This thought was also suggested by the anomalous results shown in Table III for the electrodeposited plate number four after zone melting. In order to verify this, sections of plate IV having low resistance ratios were oxygen treated and then zone melted. Resistance ratios of 3200 to 3500 were consistently obtained. Thus, it appears that an oxygen-bearing compound of nickel is being obtained at the high current density areas of the plate and it reacts with the carbon during zone melting. The amount of reaction, of course, depends on the concentration of oxygen. An alternative explanation is that stratification of metallic impurities was occurring in the plating bath. However, our observation of the effect of carbon appears to eliminate this as a plausible explanation.

Mass spectroscopic analysis of the nickel having a 4000 ratio had shown the sum of the metallic impurities to be about 1 atom ppm and hence the resistance ratio seemed to be dependent on the carbon content; therefore, to determine the effect of carbon on the resistance ratio, several samples of source 2 nickel sponge with a resistance ratio of 1500 were mixed with various amounts of spectroscopically pure carbon. The samples were compacted and given one zone pass. The resistance ratio was obtained for each sample. They were then analyzed for carbon. Figure 1 shows the plot of these data. From the slope of the curve and the resistivity of nickel at  $273^\circ K$ , a contribution to the residual resistance of  $3.0 \times 10^{-10}$  ohm-cm per atomic ppm carbon in nickel is obtained.

Figure 2 shows a plot of the reciprocal of resistance ratio vs. concentration in parts per million for iron in nickel. The accurate fit of the points reflects the sensitivity of the analysis for iron in nickel and the dominant contribution of iron to the helium temperature resistivity once the carbon content is minimized: The

Table V. Comparison of resistance ratio vs. carbon content for various samples

Sample	Number of passes	$R_{273^\circ K}/R_{1,3^\circ K}$	Carbon content in weight ppm
Electrolytic	0	554	94
Rod 23	1	1530	41
Electrolytic	1	685	63
Rod 37	6	800	12
Source 2	1	1500	28
Source 3	1	2000	5



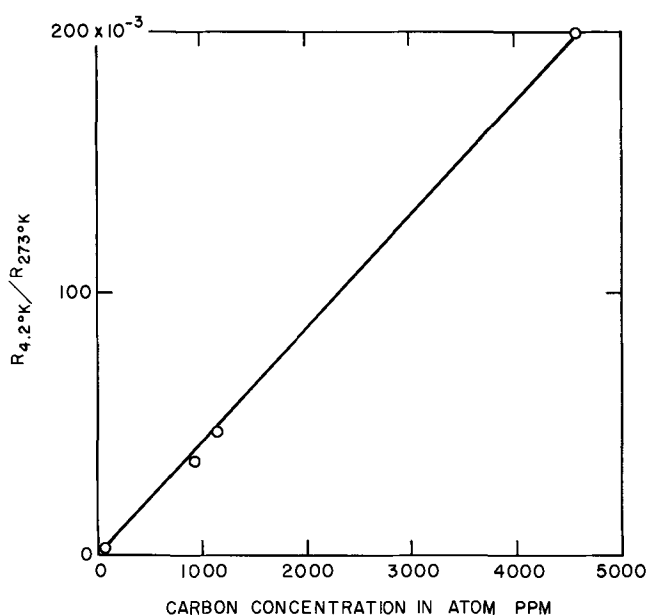


Fig. 1. Plot of the reciprocal of the resistance ratio vs. carbon concentration in commercial sponge nickel.

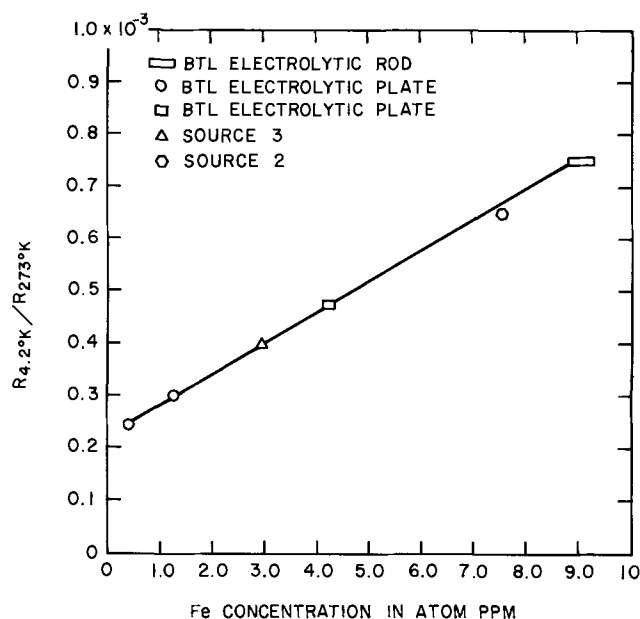


Fig. 2. Plot of the reciprocal of the resistance ratio vs. iron concentration. Each Ni sample was given an oxygen treatment to bring the C content to the same level.

six points represent different nickel samples all of which have had the same oxygen treatment to remove carbon. Each nickel sample was obtained from the various sources as noted. The contribution to the helium temperature resistivity of nickel per atom ppm Fe is calculated from this curve to be  $4 \times 10^{-10}$  ohm-cm. It appears that carbon and iron are equally as effective in scattering electrons in Ni.

#### Discussion

Since electrolyte purification techniques coupled with electroplating reduces the total metallic impurities to about 1 atom ppm in nickel, it is desirable to consider more closely what may be inhibiting attainment of a much higher resistance ratio.

A generalization of Matthiessen's rule would make one suspect that ratios much larger than 4000 can be obtained for Ni. However, some transition metals show appreciable deviations from a  $T^5$  scattering law, i.e., their resistivities vary more slowly than  $T^5$ . This has the effect in nickel of perhaps limiting the resistance ratio, as defined by  $R_{273^\circ\text{K}}/R_{4.2^\circ\text{K}}$ , by a significant lattice contribution at 4.2°K. This contribution is given as about  $5 \times 10^{-10}$  ohm-cm at 4.2°K (8). By simply dividing this number into the room temperature resistivity of nickel, a ratio no better than 13,000 is expected if lattice scattering is the dominant mechanism.

According to Matthiessen's rule the residual resistivity ( $\rho_r$ ) is related to the thermal contribution ( $\rho_L$ ), the chemical contribution ( $\rho_i$ ), and the contribution due to physical imperfections ( $\rho_D$ ) by the relation  $\rho_r = \rho_L + \rho_i + \rho_D$ . The value of  $\rho_{4.2^\circ\text{K}}$  for our nickel with a 4000 ratio is  $2 \times 10^{-9}$  ohm-cm. Using this value and the value obtained for the thermal contribution (8), the following expression is obtained

$$\rho_i + \rho_D = 15 \times 10^{-10} \text{ ohm-cm}$$

Several investigators (9) have shown the average resistivity contribution per dislocation line to be of the order of  $10^{-19}$  ohm-cm. Well annealed metal crystals usually contain about  $10^7$  lines per  $\text{cm}^2$ . Thus, the contribution of the physical imperfections to the residual resistivity, assuming that the dislocations are the only type of defect of importance, will be small and  $\rho_i$  will be of the order of  $15 \times 10^{-10}$  ohm-cm. Since carbon is the major contaminant in our materials, it is the only impurity which we presently consider important. Therefore,  $\rho_i = 3 \times 10^{-10} C_c$  where  $C_c$  is the carbon concentration in atom ppm so that our material having a ratio of 4000 appears to have 5 atom ppm of carbon present. This carbon level is below the capability of present analytical detection techniques. To double the ratio will require a carbon content of about 2 atom ppm or in more conventional notation approximately 0.4 ppm by weight. The attainment of this carbon level cannot be obtained in an oil system.

#### Acknowledgment

The authors would like to thank E. Buehler and E. Berry for their early contribution to this work. The mass spectra analysis performed by D. L. Malm and the resistance ratio measurements by G. F. Brenner are gratefully acknowledged, as are many helpful discussions with W. A. Reed. Thanks are also due to J. H. Wernick for discussions and comments on the manuscript.

Manuscript received Oct. 27, 1967; revised manuscript received ca. March 4, 1968.

Any discussion of this paper will appear in a Discussion Section to be published in the June 1969 JOURNAL.

#### REFERENCES

1. W. A. Reed and E. Fawcett, *J. Appl. Phys.*, **35**, (1964).
2. V. J. Albano and R. R. Soden, *This Journal*, **113**, 511 (1966).
3. E. Buehler, *AIME Trans.*, **212**, 694 (1958).
4. H. W. Schadler, "The Art and Science of Growing Crystals," J. J. Gilman, Editor, (1963).
5. Hultgren *et al.*, "Selected Values of Thermodynamic Properties of Metals and Alloys" (1963).
6. L. Holland *et al.*, *Rev. Sci. Inst.*, **34**, (1963).
7. H. Shapiro, "High Vacuum Technology, Testing and Measurement Meeting," June 8-9, 1965, p. 149.
8. G. K. White and R. J. Tainsh, *Phys. Rev. Letters*, **19**, 166 (1966).
9. P. Gregory *et al.*, *Metallurgia*, **70**, 71 (1966).

# Selected Area Electron Diffraction Study of Twinned $\alpha$ -Fe<sub>2</sub>O<sub>3</sub> Bladelike Platelet Growths on Iron

Richard L. Tallman\* and Earl A. Gulbransen\*

Westinghouse Electric Corporation, Research and Development Center, Pittsburgh, Pennsylvania

## ABSTRACT

The structure of  $\alpha$ -Fe<sub>2</sub>O<sub>3</sub> bladelike platelets formed on iron at 450°C in atmospheres containing both water vapor and a trace of oxygen was studied. Single crystal electron diffraction patterns show the blade axis to be  $[\bar{1}120]$ . The collection of all of the patterns indicates a structure of twinned crystals whose orientations are related by mirroring on the blade face plane,  $(\bar{1}101)$ . Arguments are presented in favor of a growth mechanism involving the diffusion of iron atoms or ions along the twin interface to the tip, where reaction occurs with oxygen.

When annealed or cold-worked iron is reacted with water vapor atmospheres containing a trace of oxygen at 400°C, pointed bladelike oxide platelets form and predominate over whisker growths (1, 2). These oxide platelets are about 150Å thick, 2500-6000Å wide at the base, and grow to lengths up to 100,000Å. Electron diffraction patterns show the platelets to be  $\alpha$ -Fe<sub>2</sub>O<sub>3</sub> (1, 2). Bigot (3) and Talbot and Bigot (4) in a recent study suggest that the bladelike oxide platelets are cubic  $\gamma$ -Fe<sub>2</sub>O<sub>3</sub>. Numerical data to substantiate this were not presented, however.

This paper presents: (i) new selected area electron diffraction studies on iron oxide bladelike platelets; (ii) evidence that the bladelike platelets consist of twinned oxide crystals of  $\alpha$ -Fe<sub>2</sub>O<sub>3</sub>; and (iii) a likely growth mechanism for bladelike oxide platelets on iron. A similar study has been made of  $\alpha$ -Fe<sub>2</sub>O<sub>3</sub> whisker growths in iron oxidation (5, 6).

## Experimental

A number of 99.99% pure iron wires carefully oxidized in a mixture of 10% water vapor and 90% argon containing a trace of oxygen (from the system and the <0.005% in commercial argon) were available from earlier studies (1). Before oxidation the iron wires had been carefully annealed and cleaned. Bladelike platelets have been found in our laboratory to grow in atmospheres ranging at least to 3% water in oxygen, where rounded whisker growths predominate. Such platelets have been obtained in our laboratory in many experiments over a period of years, on specimens of high-purity irons from Battelle, the National Bureau of Standards, and Westinghouse ("Puron" iron), and on a less pure iron from Armco.<sup>1</sup> Annealing, cleaning, and oxidation procedures have varied. Annealing at 850°-890°C commonly resulted in grain dimensions in the range 10-200 $\mu$ . Some effort has been made to find out how the controlled variables produce effects on the growths. The results obtained, however, are not sufficient to show that the whisker and platelet growths obtained do not result from some impurity effect, or do not show impurity effects.

An RCA EMU-3D electron microscope with selected area diffraction was used at 100 kV electron energy. The relative rotation of the selected area electron diffraction patterns was determined by use of the selected area images and the selected area diffraction patterns of asbestos fibers.

## Results and Discussion

*Description of the bladelike platelets.*—Figure 1 shows an electron micrograph of an assembly of bladelike oxide platelets formed on annealed pure iron when reacted in 10% water vapor and 90% argon con-

taining a trace of oxygen for 25 hr at 400°C. Bladelike platelets grown under other reaction conditions using water vapor and oxygen exhibit similar lengths, thicknesses, and ratios of width to length. Differences are found in the tip shapes, in the presence of striated growth patterns on the faces, and in the presence of curvature in the plane of the oxide platelet. Electron diffraction analyses of many of these platelets suggest that all of such platelets have essentially the same structure.

Figure 2 shows a selected area diffraction pattern for a number of bladelike platelets at one edge of an oxidized wire. Such fiber texture patterns are satisfactorily indexed by the  $\alpha$ -Fe<sub>2</sub>O<sub>3</sub> cell. Measurements on these patterns provide the instrument constant (effectively the scale in Å<sup>-1</sup>) for the selected area diffraction patterns from specimens at the same distance from the objective lens. This use of the platelets as a standard was justified by the establishment in an earlier study (2) that the platelets are  $\alpha$ -Fe<sub>2</sub>O<sub>3</sub>. In that work, no lenses were used between the specimen and the plate, and patterns of a standard were used to establish the instrument constant. The  $d$ -spacings calculated from the measured dimensions of the platelet diffraction patterns are all  $\alpha$ -Fe<sub>2</sub>O<sub>3</sub>  $d$ -spacings (2).

The possibility that a metallic impurity is concentrated in these growths has not been eliminated because only small changes in lattice dimensions would

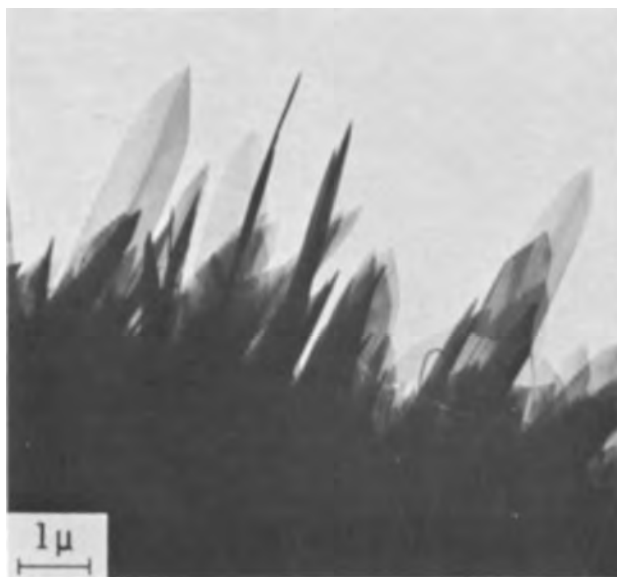


Fig. 1. Pointed bladelike platelets at the edge of an iron wire after 24 hr at 450°C in 10% H<sub>2</sub>O in argon with a trace of oxygen.

\* Electrochemical Society Active Member.

<sup>1</sup> American Rolling Mills Company, Middleton, Ohio.

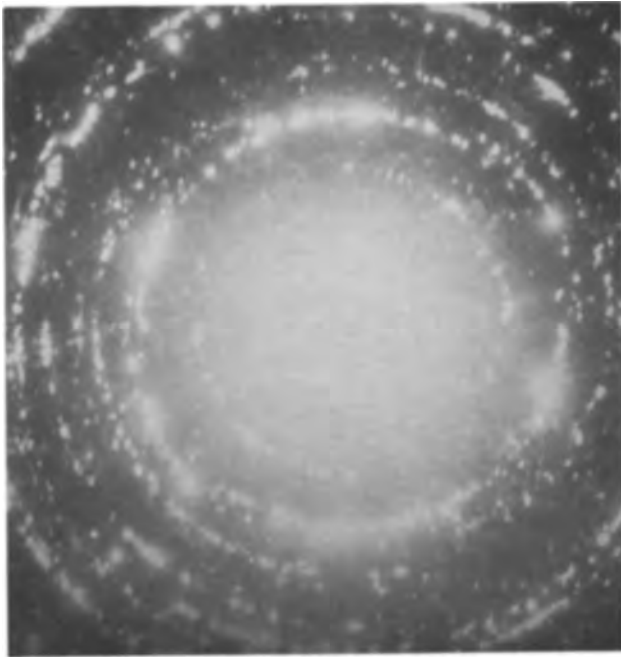


Fig. 2. Selected area mode,  $\alpha$ -Fe<sub>2</sub>O<sub>3</sub> pointed bladlike platelets at the edge of a wire.

result for some impurities. (A special analytical technique would be required to obtain the platelet analysis.)

Table I shows the  $d_{hkl}$  values, the intensities, and the three indexing systems for  $\alpha$ -Fe<sub>2</sub>O<sub>3</sub>. The conventional structural rhombohedral P and hexagonal index systems and the face-centered rhombohedral F or morphological system are given (5, 6). The geometry of the rhombohedral F lattice is readily understood as a small distortion of cubic geometry. The indices used, unless otherwise indicated, refer to the rhombohedral F system.

In Fig. 2 the regions of greatest intensity lie in the 202 ring. Arcs of weak 111 reflections together with possible 111 spots, both forbidden, are apparent near the center.

Table I.  $\alpha$ -Fe<sub>2</sub>O<sub>3</sub>- $d$ -values, intensities (6) and indices

I/I <sub>0</sub>	$d_{hkl}$ <sup>b</sup>	Indices		
		Hexagonal hkil	Rhomb. P hkl	Rhomb. F hkl
—	4.5790 <sup>a</sup>	0003	111	111
—	4.1536 <sup>a</sup>	1011	100	111
25	3.6795	0112	110	200
100	2.6973	1014	211	202
50	2.5158	1120	101	220
—	2.3240 <sup>a</sup>	0115	221	311
2	2.2895	0006	222	222
30	2.2050	1123	210	311
—	2.1519 <sup>a</sup>	0221	111	311
2	2.0768	2022	200	222
40	1.8398	0224	220	400
—	1.7893 <sup>a</sup>	1017	322	313
—	1.7071 <sup>a</sup>	2025	311	313
60	1.6933	1126	321	402
4	1.6353	2131	201	331
—	1.6016	1232	211	420
6	1.5976	0118	332	422
—	1.5263 <sup>a</sup>	0009	333	333
35	1.4851	2134	310	422
—	1.4582 <sup>a</sup>	0227	331	511
35	1.4525	3030	211	242
—	1.4126	1235	320	511

<sup>a</sup> Absent for  $\alpha$ -Fe<sub>2</sub>O<sub>3</sub>—for hh0l: 1 = 2m required.

<sup>b</sup> Calculated from the hexagonal dimensions (7),  $a = 5.0317$ ,  $c = 13.737\text{\AA}$ .

*Selected area diffraction patterns.*—Eight different selected area patterns have been indexed. Six of these are shown in Fig. 3, 4, and 5. The axis of the blades was found to be  $[110]$ , i.e.,  $[\bar{1}\bar{1}20]$  and  $[\bar{1}01]$  in the conventional structural hexagonal and rhombohedral systems, respectively. This axis is the fiber axis of the fiber texture patterns from surfaces with dense growths of blades.

The most striking characteristic of the blade diffraction we would characterize by continuous reciprocal lattice rods normal to the blade face. This face is  $(11\bar{1})$ , and the rods show a distorted hexagonal pattern corresponding to the three-fold symmetry of the  $\langle 111 \rangle$  body diagonal of a cube. Figure 6 shows at lower left the nearly hexagonal electron diffraction pattern, or cross section of the reciprocal lattice, obtained with the beam normal, or nearly normal, to the blade face as in Fig. 3a. None of the unindexed spots of Fig. 3a can be ascribed to double diffraction. All the rods produce spots in all the patterns, and all the spots correspond to rods. This experimental fact we have indicated in Fig. 6 by showing continuous rods. Some, but not all, of the unindexed spots, of patterns in general, can be indexed as double diffraction spots. Thus the diffraction patterns in general result from a tilt of the rods in the beam and are based on a correspondingly distorted and enlarged hexagon. To be precise, however, the curvature of the reflecting sphere results in the rows of the pattern being concave in the direction of the tilt of the blade face from the position normal to the beam.

The concept of a reciprocal lattice rod seeming to be sufficiently broad, we have used it to describe the diffraction spot positions, as distinct from its use in describing a theoretical result. The theoretical result most commonly referred to, loosely, by the reciprocal lattice rod is the absolute square of the shape transform of a thin crystal. The first zero of the shape transform, limiting the extent of its principal maximum from the index point, is at the reciprocal of the crystal thickness (8). The weak diffraction spots we do not index do not result from this theoretical extension of the principal maxima. Whether a theoretical calculation of the intensities from subsidiary maxima can be devised to predict the intensities of these observed spots we cannot say.

Hirsch *et al.* (9), referring to the extension of reciprocal lattice points, state, "No reliable estimate of the absolute length of these spikes can be given, because for all but the smallest of crystals the heavy scattering causes a breakdown of the kinematical diffraction treatment." The  $\alpha$ -Fe<sub>2</sub>O<sub>3</sub> platelets are so thin that the diffraction effects should be essentially kinematic.

Hirsch *et al.* (10) show a diffraction pattern from (111) gold film very much like that of Fig. 3a. Pashley and Stowell (11) found the anomalous spots of this pattern to give dark field images of the double positioning twin boundaries. Such boundaries are essentially parallel to the beam, whereas the  $\alpha$ -Fe<sub>2</sub>O<sub>3</sub> boundaries are essentially perpendicular to the beam (otherwise they would have been observed). Pashley and Stowell suggest that the unindexed spots may be double diffraction even in the absence of the required primary beams. This suggestion seems to rely on a dynamic interaction between beams traveling parallel to the boundary. Nevertheless, it may be that the interface and/or the surface structures of the  $\alpha$ -Fe<sub>2</sub>O<sub>3</sub> platelets are involved in the anomalous diffraction we find.

The angle measured between the tip edges of the blade image compares well with the angle calculated for the blade projection from the blade orientation in the beam, which can be calculated from the dimensions of the pattern. In this way, the tip edge directions have been confirmed by measurements on several blade images and diffraction patterns.

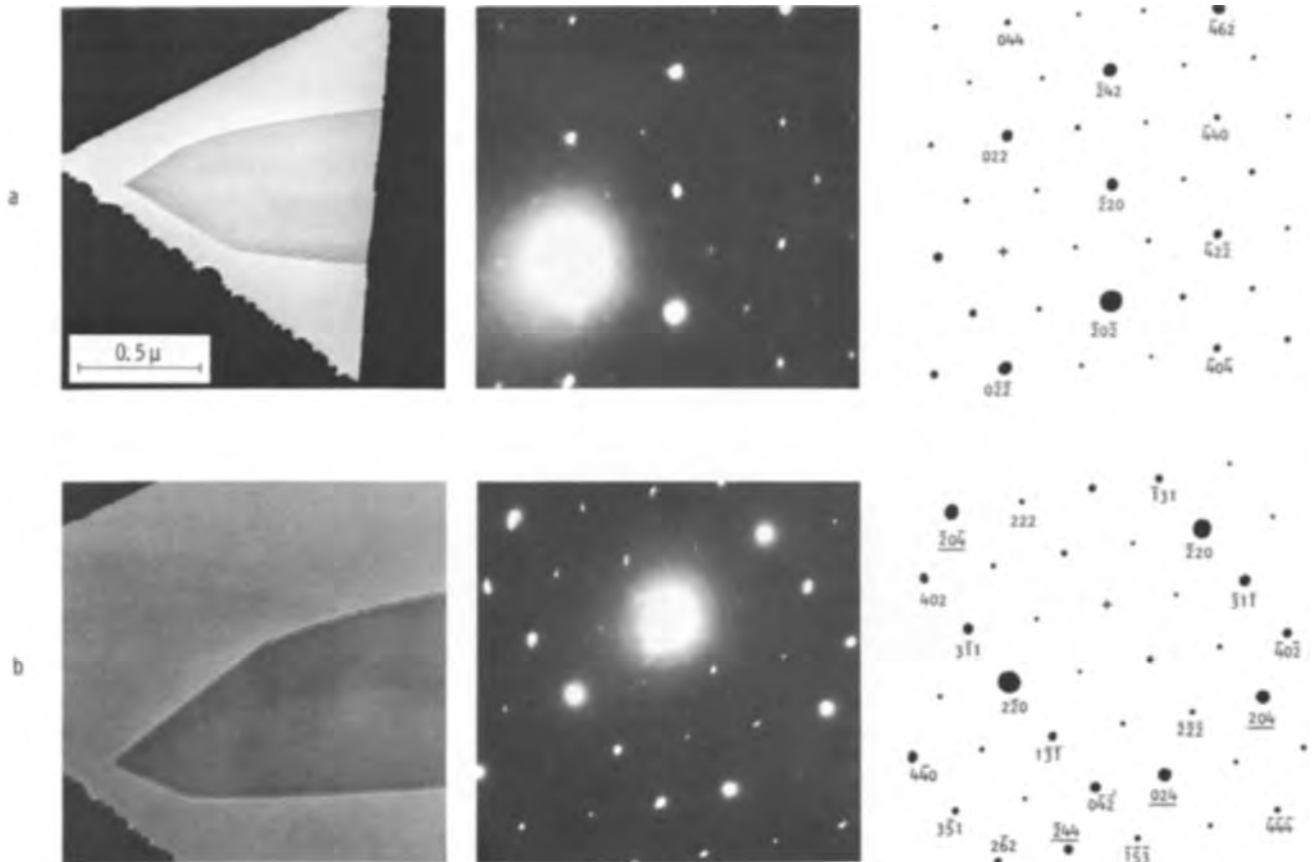


Fig. 3. Selected area electron diffraction of  $\alpha$ - $\text{Fe}_2\text{O}_3$  platelets, indexed with face-centered rhombohedron,  $\alpha = 85.7^\circ$ . Images rotated  $+145$  to  $148^\circ$  relative to diffraction.

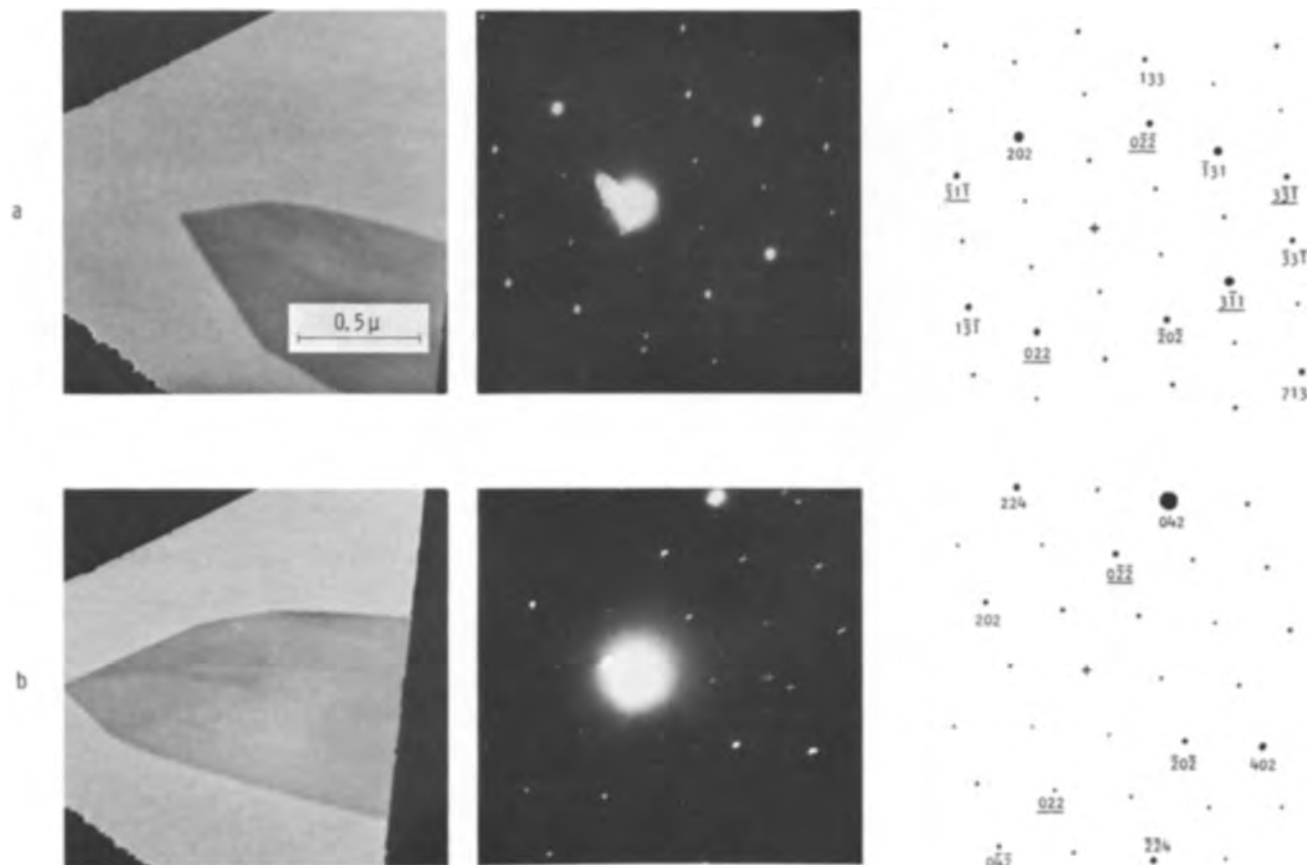


Fig. 4. Selected area electron diffraction of  $\alpha$ - $\text{Fe}_2\text{O}_3$  platelets, indexed with face-centered rhombohedron,  $\alpha = 85.7^\circ$ . Images rotated  $+145$  to  $148^\circ$  relative to diffraction.

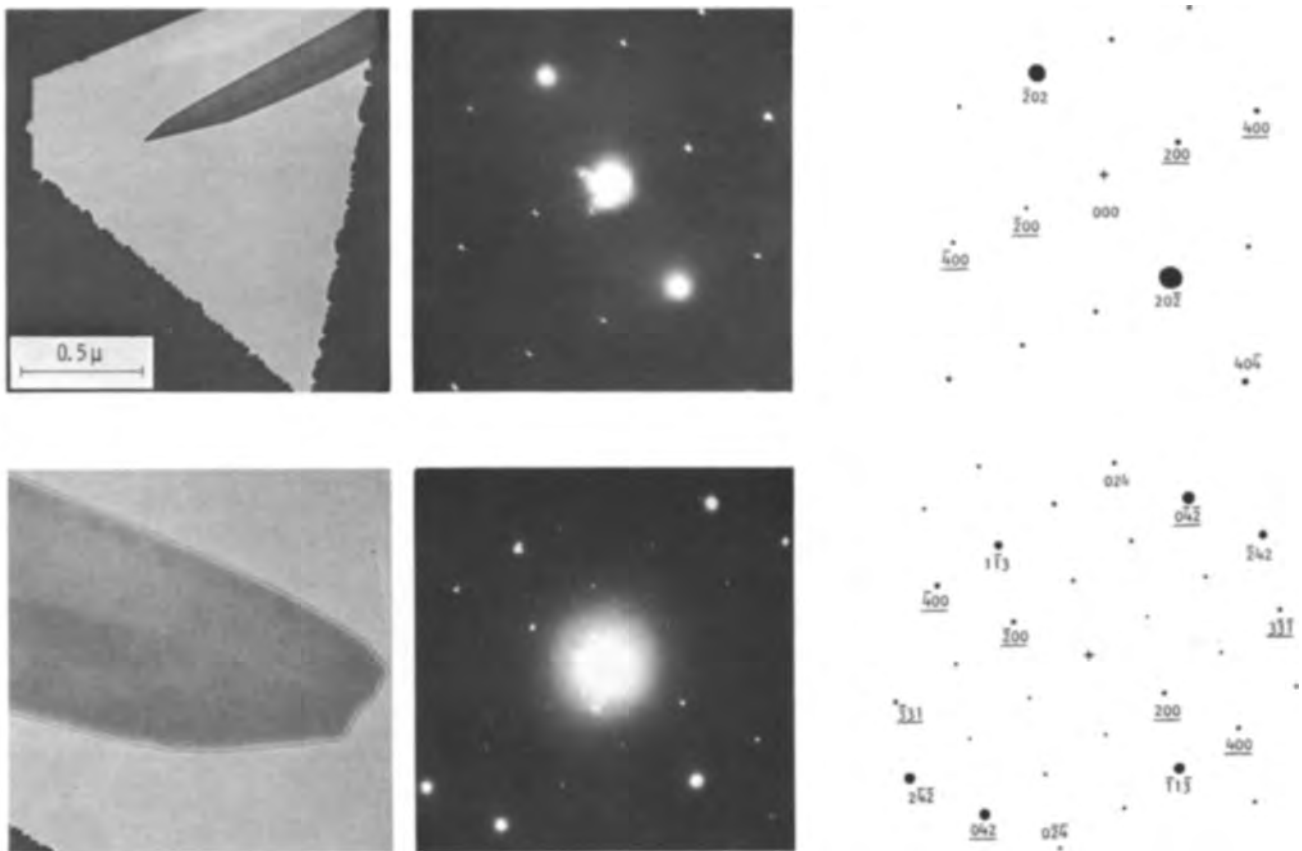


Fig. 5. Selected area electron diffraction of  $\alpha\text{-Fe}_2\text{O}_3$  platelets, indexed with face-centered rhombohedron,  $\alpha = 85.7^\circ$ . Images rotated  $+ 145$  to  $148^\circ$  relative to diffraction.

The indexing of the selected area diffraction patterns can be accomplished with the aid of a reciprocal lattice model, together with drawings of each twinned reciprocal lattice net normal to the growth axis. Each drawing, or net, corresponds to a row of spots of the diffraction pattern, a row normal to the projection of the blade axis onto the diffraction pattern; and each rod of a drawing, to a point in the corresponding row.

Figure 3a shows the pattern obtained when the beam is nearly normal to the blade face, also illustrated in Fig. 6. Figure 3b shows the pattern when the blade is tilted about its axis so that the beam is nearly normal to the threefold axis. The twin indices, where they are necessary, are underlined in all these patterns.

Figure 4a results from a slight tilt of the blade approximately about  $[11\bar{2}]$  (normal to the blade axis and

in the blade face). It is thus closely related to Fig. 3a in dimensions and indexing. Figure 4b results from a slightly greater tilt approximately about  $[11\bar{2}]$ . The four central indexed spots are indexed the same in each case. Such anomalies are explained as follows: Only two geometrical (infinitesimal) points and the origin can lie on the reflecting sphere at once, and in general none lie exactly on the sphere (except the origin). The extent along the rods of the interference regions associated with the index points is believed to be the principal cause of the high intensities observed in so many spots. No tilting of the specimen stage was attempted; the patterns are for different blades as they were found.

The pattern of Fig. 5a shows indexed point rows at a little less than  $90^\circ$  which would be found normal to one another (and indexed otherwise) in the untwinned lattice. Extreme distortion of the hexagonal pattern is illustrated in this figure. The "first layer line" in this pattern passes through  $\bar{2}02$  and  $200$ . Figure 5b shows another distorted hexagonal pattern. In this pattern,  $\bar{4}00$  to  $400$  is the zero layer line.

We conclude that most of the selected area diffraction patterns can be indexed only by the use of two crystals whose orientations are related by mirroring on the blade face plane  $(11\bar{1})$ . The blade face has the corresponding indices,  $(\bar{1}101)$  and  $(010)$ , using the conventional structural hexagonal and rhombohedral unit cells. The twinning is not required in indexing the patterns for a few special orientations, e.g., Fig. 3a. In order that the indices given refer to right-handed coordinate systems, the twin orientations are related by a twofold rotation about the normal to the twin plane.

The  $\alpha\text{-Fe}_2\text{O}_3$  bladelike platelet morphology is shown in Fig. 7. In Fig. 7, we use the more conventional

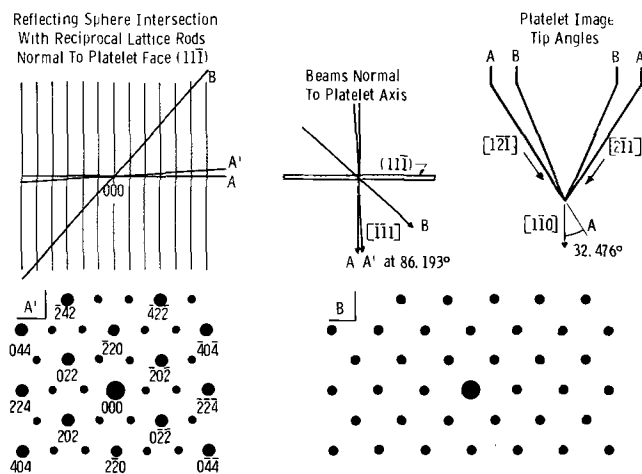


Fig. 6. Indexed spots in net normal to  $[111]$  ( $\alpha\text{-Fe}_2\text{O}_3$  rhombohedral F indexing); all other spots also observed.

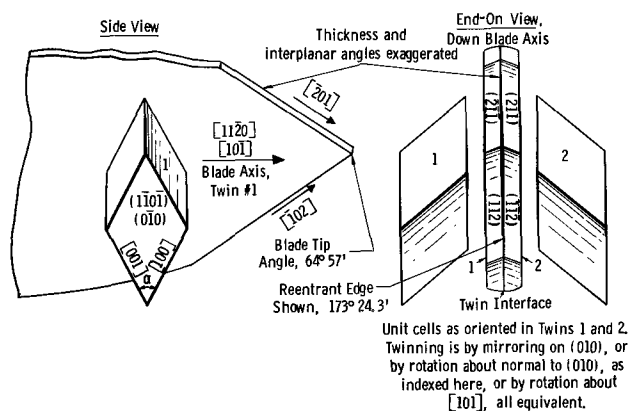


Fig. 7.  $\alpha$ - $\text{Fe}_2\text{O}_3$  pointed bladelike platelet morphology (actual number of twins is undetermined). Structural rhombohedral unit cell pictured,  $a = 5.4228\text{\AA}$ ,  $\alpha = 55^\circ 17'$ .

structural rhombohedral unit cell for presenting the results. The blade face and blade axis are indexed also by the structural hexagonal unit cell.

The orientation of the twins is shown in Fig. 7. The blade tip angle, roughly determined from electron micrographs, indicates that the blade tip edges can be described as follows: In the face-centered rhombohedral  $F$  unit cell, the blade tip edges lie along  $[\bar{1}2\bar{1}]$  and  $[2\bar{1}\bar{1}]$  directions. The blade tip angle is calculated to be  $64^\circ 57'$ , which compares to the  $60^\circ$  angle found in the cubic system. Figure 6 shows the blade tip edges lying along  $[20\bar{1}]$  and  $[\bar{1}0\bar{2}]$  in the structural rhombohedral unit cell.

The two blade tip edge directions are equivalent, but not with respect to the blade. The tip edge directions given are the intersections of planes in mirror orientation to one another which intersect in reentrant edges at one tip edge and nonreentrant edges at the other. These planes are indexed  $(202)$  and  $(0\bar{2}\bar{2})$  in the face-centered rhombohedral system, planes which are normal to  $(11\bar{1})$  in the cubic system. Figure 7 shows the indexing of the tip edge in the structural rhombohedral unit cell. The reentrant edge angle is  $173^\circ 24.3'$ .

**Discussion of platelet morphology.**—General features of the bladelike platelet structure remain undetermined. First, the number of twins has not been determined. There may be more than one twin interface. Second, the atomic structure of the twin interface has not been determined. It is not known whether a mirror plane exists in the structure. Third, the tip faceting has not been observed. The planes shown as facets in Fig. 7 do not necessarily occur as facets.

The asymmetry of the tip could explain an asymmetrical tip image for the case of a two-twin blade. For three twins, the structure would have a twofold axis along its length, so that no asymmetry in the tip would be predicted.

Many blade images show a line down the center to the tip with usually uniform but different transmission of electrons on opposite sides of the line. This line appears to be the trace of the tip point. The asymmetry of the tip may result in a thickness difference because the growth mechanisms at the two tip edges are not identical. For example, growth steps may nucleate more readily at the reentrant edge. That the center line results only from the tip growth mechanism is suggested by the absence of this line for blades with rounded tips. The features of the blade faces result from thickness contrast and some thickness variations are traces of the tip edges.

Except for the effect of the apparent thickness variation across the center line, the uniform thickness contrast of the well-formed unbent blades and the bend contours of the few highly bent blades suggest nothing more

complex than the simple twinned morphology. The dark field images obtained show either the whole blade in nearly uniform contrast or bend contours, further confirming that the twins extend across the whole surface of the blade.

**More anomalous diffraction.**—In addition to the reciprocal lattice rods on which lie all the  $\alpha\text{-Fe}_2\text{O}_3$ -indexed points, it appears from weak unindexed spots that parallel to each of these rods are two satellite rods. These satellite rods are positioned along the blade axis at one sixth of the repeat distance between the index rods. The reflections associated with these rods appear slightly elongated normal to the blade axis.

**Comparison with previous morphological studies.**—Bigot (3) and Talbot and Bigot (4) failed to analyze correctly their selected area electron diffraction patterns of  $\alpha\text{-Fe}_2\text{O}_3$  bladelike platelets. Bigot (3) attributes diffraction patterns of bladelike platelets to  $\gamma\text{-Fe}_2\text{O}_3$  without presenting numerical data. They comment that the pattern dimensions are too small for the  $(0001)$  structural hexagonal plane of  $\alpha\text{-Fe}_2\text{O}_3$  (for which, pattern rows would be at  $60^\circ$ ). Their indexing corresponds to a beam direction along  $[\bar{1}10]$  of cubic  $\gamma\text{-Fe}_2\text{O}_3$  (pattern rows at  $54^\circ 44'$ ).

The relative pattern dimensions are, however, only slightly distorted from those to be expected for orientation of the beam parallel to the  $\alpha\text{-Fe}_2\text{O}_3$   $[\bar{1}10]$  face-centered rhombohedral direction. A curvature of the rows parallel to  $[\bar{1}120]$  or  $[\bar{1}10]$ , (structural hexagonal and rhombohedral  $F$  indices, respectively) results from the angle of the beam to the reciprocal lattice rods. This curvature is expected for a thin  $\alpha\text{-Fe}_2\text{O}_3$  crystal with  $(11\bar{1})$  faces and with the beam along  $[\bar{1}10]$ . The direction of curvature indicates the  $(11\bar{1})$  orientation in the beam. The misalignment of the beam from  $[\bar{1}10]$  is not in the  $(1120)$  structural hexagonal plane as the symmetry of the intensities is lost and the pattern is skewed, or sheared, two degrees. The angle of  $022$  to  $422$  in the  $(011)$  plane of the cubic system is  $54^\circ 44'$ , whereas the corresponding angles by Bigot's indexing measured in Bigot's pattern are about  $51^\circ 25'$  and  $54^\circ 30'$ . The corresponding angles in  $\alpha\text{-Fe}_2\text{O}_3$  should be  $53^\circ 49'$ . The measured angles differ from  $53^\circ 49'$  as a result of the skewed nature of the pattern. This distortion also results in discrepancies of up to 3% in the relative  $d$ -spacings calculated from the pattern.

The corresponding spacings for  $\gamma\text{-Fe}_2\text{O}_3$  are about 13–16% greater than those for  $\alpha\text{-Fe}_2\text{O}_3$ . It would appear that such a variation in the instrument constant for selected area diffraction was accepted by Bigot in indexing the pattern as  $\gamma\text{-Fe}_2\text{O}_3$ .

Some of the details of the intensities in Bigot's pattern are not simply interpreted; but otherwise, the pattern is indexed by  $\alpha\text{-Fe}_2\text{O}_3$ . Twinning is neither required nor precluded by this indexing.

**Novel character of the  $\alpha\text{-Fe}_2\text{O}_3$  platelet structure.**—Palache *et al.*, (12) state that lamellar twinning on  $\{10\bar{1}\}$  is common in natural corundum ( $\alpha\text{-Al}_2\text{O}_3$ , sapphire) and natural hematite ( $\alpha\text{-Fe}_2\text{O}_3$ ). The indices used are morphological hexagonal and are the indices of the morphological rhombohedral surfaces  $\{100\}$ . The twinning we have studied in  $\alpha\text{-Fe}_2\text{O}_3$  bladelike platelets is on the structural rhombohedral surfaces. These are the morphological hexagonal  $\{02\bar{2}\}$  and morphological rhombohedral  $\{11\bar{1}\}$  planes.

We have not found any evidence in the literature for growth twinning on the rhombohedral planes of the structural rhombohedron for  $\alpha\text{-Fe}_2\text{O}_3$  or isomorphous minerals. We conclude that this is not a common twinning relation for the crystal growth mechanisms of minerals, which involve some type of deposition. We suggest that if the bladelike platelet growth proceeded by a surface transport mechanism, the same morphology would be found in minerals.

Scanning electron microscopy (13) has provided micrographs of hematite platelets a few microns thick and about  $10\mu$  across. These platelets grew in many orientations on mild steel in a 7-hr oxidation in 13% sodium hydroxide solution at  $300^\circ\text{C}$  and also by anodic polarization in sodium hydroxide solutions. The morphology of these platelets was not described, but their somewhat equilateral triangular appearance suggests the common (0001) tabular habit.

*Transport mechanisms for platelet growth.*—The bladelike platelets we believe to grow by the internal transport of iron to the tip. Takagi (14) has observed that such growths grow from the tip. The blades are too perfect to have been formed by extrusion. Surface diffusion seems highly unlikely because growth should occur readily in areas closer to platelet bases. Some arguments for internal diffusion in such growths we have given in more detail in previous publications (5, 6).

An additional and more powerful argument can be based on Coble's data on the shrinkage of  $\alpha\text{-Fe}_2\text{O}_3$  compacts on sintering (15). Coble shows that the shrinkage rate is limited by the iron lattice diffusion process. Surface diffusion would reduce the surface area which provides the driving force for the shrinkage, thereby decreasing the apparent iron lattice diffusion coefficient. An upper limit on the surface diffusion coefficient for iron can be estimated from Coble's data at  $750^\circ\text{C}$  to be  $10^4$  to  $10^6$  times smaller at  $750^\circ\text{C}$  than the surface diffusion coefficient required to provide the iron transport for the growth at  $1\text{-}100\text{\AA}$   $\text{sec}^{-1}$  of  $\alpha\text{-Fe}_2\text{O}_3$  whiskers and platelets.

It can be argued that the presence of  $\text{Fe}_3\text{O}_4$  or  $\gamma\text{-Fe}_2\text{O}_3$  may provide for whisker and platelet growth a surface transport mechanism not present in the sintering experiments on pure  $\alpha\text{-Fe}_2\text{O}_3$ . And further, that any sites for growth on the  $\alpha\text{-Fe}_2\text{O}_3$ ,  $\gamma\text{-Fe}_2\text{O}_3$ , and  $\text{Fe}_3\text{O}_4$  surfaces other than those producing the whisker and platelet growth may be poisoned. These arguments seem excessive to us.

In the case of platelets, the limited thickness can readily be understood as a result of internal diffusion along a plane interface. Platelet thickness would be expected to taper from the base if platelets grew by surface diffusion. Platelet surfaces, as revealed by thickness contours, are commonly at least slightly imperfect, so that further growth could occur readily; but platelets generally appear uniform in thickness along the lengths observed.

The model for growth of blade-shaped oxide platelets is shown in Fig. 7. The platelet must contain one or more twin interfaces. These provide paths for the internal diffusion of iron atoms which results in the growth.

The flat elongated structure of the bladelike platelets indicates that there are several ionic diffusion coefficients operating. The lattice diffusion of iron normal to the blade face is small, so that the blade remains thin. The transport at the twin interface and normal to the blade axis may be greater; so that the blade grows more broad as it grows longer. The transport at the twin interface and along the blade axis is greatest, so that the blade grows long. Transport over the tip surface is small, so that the blade grows thin.

We have reported in an earlier work (1) that in dry oxygen and in water vapor atmospheres with a trace of oxygen, oxide whiskers are the first growths to be observed. In water vapor atmospheres with a trace of oxygen, only bladelike platelets are found later in the oxidation process. The platelets may ob-

struct the view of the original whisker growths. No platelets grow in water vapor free of oxygen. The whiskers are distinguished from the platelets by their whiskerlike shape. These shape differences are believed to correspond to structural differences we have determined, the whiskers having axial screw dislocations without twinning (5), and platelets having twinning without dislocations. The role of water vapor in the growth mechanism remains to be determined.

### Summary

The bladelike iron oxide platelets observed by electron microscopy to have grown so as to extend out of the oxide film on the surface of pure iron have been studied. Electron diffraction from the oxidized surface by large numbers of these growths is characteristic of  $\alpha\text{-Fe}_2\text{O}_3$ . Such fiber-texture patterns show the fiber axis to be  $[\bar{1}120]$ , in agreement with the selected area electron diffraction patterns. The latter show also that the blades are twinned on the blade face plane, the (010) structural rhombohedral surface. The straight edges at the blade tip have prominent crystallographic directions. The asymmetry of the blade image in outline and in contrast corresponds to the asymmetry of the twinned structure.

Anisotropy in the diffusion of iron in the twin interface, together with apparently negligible lattice diffusion of iron, is believed to result in the blade shape. Iron leaving the interface at the tip is incorporated into growth on the tip edge surfaces.

Determination of the nature of the growth site and the driving forces would permit a more satisfactory appraisal of the significance of these growths.

Manuscript received Sept. 8, 1967; revised manuscript received ca. Feb. 6, 1968. This work was supported in part by the Office of Naval Research under Contract No. Nonr-4949(00).

Any discussion of this paper will appear in a Discussion Section to be published in the June 1969 JOURNAL.

### REFERENCES

1. E. A. Gulbransen and T. P. Copan, *Discussions Faraday Soc.*, **28**, 229 (1959).
2. E. A. Gulbransen, *Mem. Sci. Rev. Met.*, **62**, 253 (1965).
3. J. Bigot, *ibid.*, **60**, 5 (1963).
4. S. Talbot and J. Bigot, *ibid.*, **62**, 261 (1965).
5. R. L. Tallman and E. A. Gulbransen, *This Journal*, **114**, 1227 (1967).
6. E. A. Gulbransen and R. L. Tallman, "Chemical Physics of Surface Reactions of Metals," May 31, 1967, AD-653-723, Clearinghouse, Springfield, Va.
7. ASTM X-ray Powder Data File, Card 13-534 (1964), Aravindakshan and Ali.
8. B. K. Vainshtein, "Structure Analysis by Electron Diffraction," E. Feigl and J. A. Spink, Editors, pp. 32-36, The Macmillan Co., New York (1964).
9. P. B. Hirsch, A. Howie, R. B. Nicholson, D. W. Pashley, and M. J. Whelan, "Electron Microscopy of Thin Crystals," p. 129, Butterworths, Washington (1965).
10. *Ibid.*, p. 307.
11. D. W. Pashley and M. J. Stowell, *Phil. Mag.*, **8**, 1605 (1963).
12. C. Palache, H. Berman, and C. Frondel, "The System of Mineralogy," 7th Ed., Vol. I, pp. 519-534, John Wiley & Sons, Inc., New York, (1944).
13. J. E. Castle and H. G. Masterson, *Anti-Corrosion*, **1**, 6 (1966).
14. R. Takagi, *J. Phys. Soc. Japan*, **12**, 1212 (1957).
15. R. L. Coble, *J. Am. Ceram. Soc.*, **41**, 55 (1958).





## Sr<sub>3</sub>(PO<sub>4</sub>)<sub>2</sub>-Tb, A Bluish-White Emitting Cathode-Ray Phosphor with a Long Decay Time

A. Brill, W. L. Wanmaker, and J. W. ter Vrugt

N. V. Philips' Gloeilampenfabrieken, Eindhoven, Netherlands

When terbium-activated phosphors are excited with ultraviolet radiation or cathode rays, the terbium ion is raised from the <sup>7</sup>F<sub>6</sub> ground state into the <sup>5</sup>D<sub>3</sub> or higher levels. Generally speaking emission is only found from the lower lying <sup>5</sup>D<sub>4</sub>-level, corresponding to the transitions <sup>5</sup>D<sub>4</sub> → <sup>7</sup>F<sub>j</sub> (j = 0–6). The blue emission originating from the transitions <sup>5</sup>D<sub>3</sub> → <sup>7</sup>F<sub>j</sub> has been found by Van Uitert (1) in CaWO<sub>4</sub>-Tb and Ca<sub>1-2x</sub>Na<sub>2x</sub>Tb<sub>2</sub>WO<sub>4</sub>, especially for low terbium concentrations, by Nelson (2) for SiO<sub>2</sub>-Tb and by Blasse and Brill (3) for LaOBr-Tb and YOCl-Tb. For high Tb concentrations the large transition probability <sup>5</sup>D<sub>3</sub> → <sup>5</sup>D<sub>4</sub> with high activator concentration was ascribed by Pearson, Peterson, and Northover (4) to a transfer process: the transition of an electron from the <sup>5</sup>D<sub>3</sub> to the <sup>5</sup>D<sub>4</sub> level of one ion is matched by the promotion of an electron from the <sup>7</sup>F<sub>6</sub> to the <sup>7</sup>F<sub>0</sub> level of another ion, the corresponding energies being about equal.

In this paper we report on the blue cathodoluminescence and photoluminescence of Sr<sub>3</sub>(PO<sub>4</sub>)<sub>2</sub>-Tb phosphors, which were not described before. Nazarova (5) studied the influence of Tb-addition on the Eu<sup>2+</sup> luminescence in Sr<sub>3</sub>(PO<sub>4</sub>)<sub>2</sub>-Eu<sup>2+</sup>, whereas the photoluminescence of Sr<sub>3</sub>(PO<sub>4</sub>)<sub>2</sub> activated with Tb + Sn or Cu was described in a patent (6). In another patent (7) the influence of Tb addition on the luminescence of Dy activated alkaline earth phosphates was reported.

### Experimental

The phosphors were prepared by heating twice an intimate mixture of luminescent grade SrHPO<sub>4</sub>, SrCO<sub>3</sub>, and TbPO<sub>4</sub> for 2 hr at temperatures ranging from 1100° to 1400°C in a slightly reducing atmosphere. In between the two firings the mixture was ground. Up to firing temperatures of 1350°C only the α-Sr<sub>3</sub>(PO<sub>4</sub>)<sub>2</sub> phase was found. Above this temperature also the β-phase appears (8). With 0.32g at. terbium added per mole of Sr<sub>3</sub>(PO<sub>4</sub>)<sub>2</sub>, diffraction lines from a new phase appears in the x-ray diagrams. The optical properties of the phosphors were determined in a way described already before (9).

### Results and Discussion

With ultraviolet (uv) excitation the maxima in the excitation spectra are located below 240 nm for both the α- and the β-Sr<sub>3</sub>(PO<sub>4</sub>)<sub>2</sub>-Tb.

With the 254 nm line of a low pressure mercury discharge lamp they are only weakly excited. Especially the emission originating from the <sup>5</sup>D<sub>3</sub>-level was very poor. The intensities of the <sup>5</sup>D<sub>4</sub> → <sup>7</sup>F<sub>4</sub>, <sup>7</sup>F<sub>5</sub> and <sup>7</sup>F<sub>6</sub> emissions are nearly independent on the crystal structure of the host lattice and on the terbium concentration.

With cathode-ray excitation, however, also a strong emission from the higher lying <sup>5</sup>D<sub>3</sub>-level was observed up to high terbium concentrations [more than 0.32g at. per mole Sr<sub>3</sub>(PO<sub>4</sub>)<sub>2</sub>] as may be seen from Fig. 1 and Table I. The lines originating from the <sup>5</sup>D<sub>3</sub>-level are found near 380 nm (<sup>5</sup>D<sub>3</sub> → <sup>7</sup>F<sub>6</sub>), 415 nm (<sup>5</sup>D<sub>3</sub> → <sup>7</sup>F<sub>5</sub>),

440 nm (<sup>5</sup>D<sub>3</sub> → <sup>7</sup>F<sub>4</sub>), and 460 nm (<sup>5</sup>D<sub>3</sub> → <sup>7</sup>F<sub>3</sub>). Longer wavelength <sup>5</sup>D<sub>3</sub>-fluorescence, if present, is obscured by the <sup>5</sup>D<sub>4</sub> → <sup>7</sup>F<sub>6</sub> emission.

Due to the presence of both the <sup>5</sup>D<sub>4</sub> and the <sup>5</sup>D<sub>3</sub>-emission Sr<sub>3</sub>(PO<sub>4</sub>)<sub>2</sub>-Tb shows a bluish-white fluorescent color with cathode-ray excitation. The radiant efficiency (*i.e.*, the energy conversion efficiency, see Table I) is high for an oxidic phosphor, but it is much lower than those of ZnS-Ag and (Zn, Cd) S-Ag, which are normally used in TV receiving tubes (10). The highest value we obtained was 8% for the α-phase phosphor (the β-phase phosphors had a lower efficiency, less than 1%). Because of the emission near 380 nm, the radiant efficiency of the fluorescence emitted in the visible region is lower, *viz.*, about 6%.

Another interesting property of the Sr<sub>3</sub>(PO<sub>4</sub>)<sub>2</sub>-Tb phosphor is the behavior of the rise and decay times of the <sup>5</sup>D<sub>3</sub> and <sup>5</sup>D<sub>4</sub> emission. The lower the probability of the <sup>5</sup>D<sub>3</sub> → <sup>5</sup>D<sub>4</sub> transition, the stronger is the blue <sup>5</sup>D<sub>3</sub> emission, the longer its decay and the slower the rise of the green <sup>5</sup>D<sub>4</sub> emission due to the slower population of the latter level. This is demonstrated in Fig. 2, where a pulse of cathode rays is irradiating the phosphor. The blue emission has its maximum at the end of the exciting pulse as is normally found, but the maximum of the green emission shows a delay of 2 msec with respect to the end of the pulse. Theoretically (11) this delay δ is

$$\delta = [\tau(^5D_4) \cdot \tau(^5D_3) / \{\tau(^5D_4) - \tau(^5D_3)\}] \cdot \ln[\tau(^5D_4) / \tau(^5D_3)]$$

where τ(<sup>5</sup>D<sub>3</sub>) and τ(<sup>5</sup>D<sub>4</sub>) are the decay times of the <sup>5</sup>D<sub>3</sub>- and <sup>5</sup>D<sub>4</sub>-emissions. These have been measured separately and are found to be 4 and 9 msec, respectively. The formula gives a still larger delay (*viz.* 5 msec) than experimentally observed. Similar results

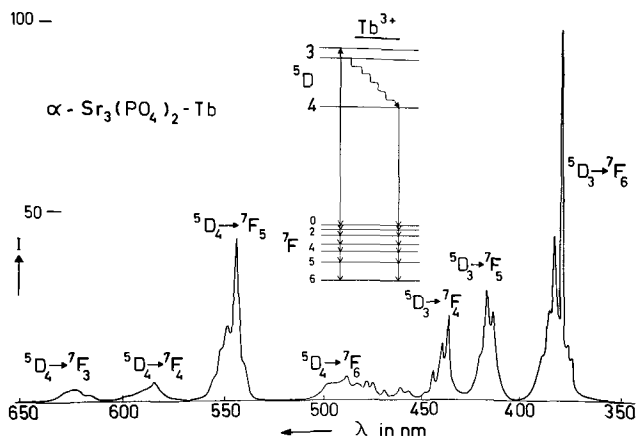


Fig. 1. Emission spectrum of α-Sr<sub>2.86</sub>(PO<sub>4</sub>)<sub>2</sub>-0.08 Tb with cathode-ray excitation. Along the ordinate the radiant power (I) per constant wavelength interval has been plotted in arbitrary units.



Table I. Properties of  $\alpha$ -Sr<sub>2.98-1.5x</sub>(PO<sub>4</sub>)<sub>2-x</sub> Tb phosphors

x	Rad. eff. C.R. exc. (20 kv) in %		
	Total	<sup>5</sup> D <sub>3</sub> → <sup>7</sup> F <sub>j</sub> (blue and uv)	<sup>5</sup> D <sub>4</sub> → <sup>7</sup> F <sub>j</sub> (mainly green)
0.01	3.5	2.5	1
0.02	4	3	1
0.04	6	4.5	1.5
0.12	6.5	5	1.5
0.15	6.5	4.5	2
0.21	7	5	2
0.24	6	4	2

were found by us (12) in Eu<sup>3+</sup>-activated phosphors, in which also a delay for the emission originating from the lowest excited level (<sup>5</sup>D<sub>0</sub>) was observed.

In the cases where a long decay time is desired, for instance for reducing flicker (13) in television pictures,  $\alpha$ -Sr<sub>3</sub>(PO<sub>4</sub>)<sub>2</sub>-Tb offers interesting possibilities. Since the color is bluish-white and the efficiency reasonable it can be usefully applied for example in monitor tubes.

#### Acknowledgments

The authors wish to express their thanks to Mr. J. G. Verlijdsdonk and Mr. G. J. R. A. Tops for preparing the phosphors; and to Mr. J. de Poorter for the optical measurements on the phosphors.

Manuscript received March 26, 1968. This paper was presented at the Boston Meeting, May 5-9, 1968, as Abstract 33.

Any discussion of this paper will appear in a Discussion Section to be published in the June 1969 JOURNAL.

#### REFERENCES

1. L. G. van Uitert, *J. Chem. Phys.*, **32**, 1161 (1960).  
L. G. van Uitert, *ibid.*, **44**, 3514 (1966).
2. W. F. Nelson, "Physics of Noncrystalline Solids," p. 625, J. A. Prins, Editor, North Holland Publishing Co., Amsterdam (1965).

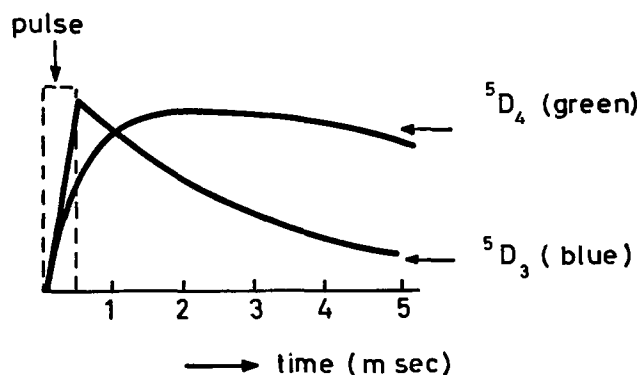


Fig. 2. Rise and decay curves of the <sup>5</sup>D<sub>3</sub> → <sup>7</sup>F<sub>j</sub> and <sup>5</sup>D<sub>4</sub> → <sup>7</sup>F<sub>j</sub> emissions in  $\alpha$ -Sr<sub>2.86</sub>(PO<sub>4</sub>)<sub>2</sub>-0.08 Tb.

3. G. Blasse and A. Bril, *Philips Research Repts.*, **22**, 481 (1967).
4. A. D. Pearson, G. E. Peterson, and W. R. Northover, *J. Appl. Phys.*, **37**, 729 (1966).
5. V. P. Nazarova, *Bull. Acad. Sci. U.S.S.R. Phys. Ser.*, **25**, 323 (1961).
6. British Pat. 882,347, 1961.
7. U. S. Pat. 2,427,728, 1946.
8. J. F. Sarver, M. V. Hoffman, and F. A. Hummel, *This Journal*, **108**, 1103 (1961).
9. A. Bril and W. L. Wanmaker, *This Journal*, **111**, 1363 (1964).
10. A. Bril in "Luminescence of Organic and Inorganic Materials," Kallmann and Spruch, Editors, J. Wiley & Sons, New York, London (1962). A. Bril and H. A. Klasens, *Philips Res. Repts.*, **7**, 401 (1962).
11. M. J. Weber and R. F. Schaufele, *J. Chem. Phys.*, **43**, 1702 (1965).
12. A. Bril, W. C. Nieuwpoort, W. L. Wanmaker, G. Blasse, and C. D. J. C. de Laat, Int. Conf. on Luminescence, Budapest 1966.
13. J. Haantjes and F. W. de Vrijer, *Wireless Engineer*, **28**, 40 (1951).

## Effects of Vapor Composition on the Growth Rates of Faceted Gallium Arsenide Hole Deposits

Don W. Shaw

Materials Science Research Laboratory, Texas Instruments Incorporated, Dallas, Texas

In an earlier study (1) it was demonstrated that GaAs could be epitaxially deposited in holes etched into GaAs substrates. These deposits had faceted upper surfaces which were extraordinarily smooth. When viewed by Nomarski interference contrast microscopy (2) the surfaces were apparently stepless. The same results were obtained using an electron microscope with shadowed replicas.

Due to the availability of semi-insulating GaAs, it is possible to use this selected area technique to produce planar integrated circuit structures (3). In this case holes etched into a semi-insulating substrate would be refilled with semiconducting GaAs of the desired electrical properties. Obviously it is important to be able to control the morphologies of the hole deposits, e.g., to be able to stop the deposition when the upper surface of the hole deposit is nearly flush with the surrounding substrate surface. In ref. (1) it was found that by depositing in holes etched into {111}B substrates this condition was fulfilled. However, later studies showed that this was not true for all reactor systems or designs. With some deposition conditions the {111}B hole deposits were as high as 30-50 $\mu$  above the substrate surface.

In view of the above, a study of the effects of vapor composition on the growth rates of faceted GaAs deposits was undertaken. The principal goal of this investigation was to define conditions necessary to obtain GaAs hole deposits of the desired morphologies. However, the faceting nature of GaAs hole deposits also allowed a study of GaAs epitaxial deposition rates on precisely defined orientations (facets). The mechanism which accounts for facet formation with hole deposits has been previously described in detail (1). Growth on these facets may be considered as growth on relatively "stepless," precisely oriented surfaces.

The investigation was divided into four parts. First, a series of runs was made using the "arsenided gallium" (Ga/AsCl<sub>3</sub>/H<sub>2</sub>) deposition system, and growth rates were obtained for each of the four major orientations ({111}A, {111}B, {110}, {100}). This was to establish a reference point using a well-known, reliable deposition system and to develop our experimental techniques so that reproducible growth rate data could be obtained. Next, the deposition rates were studied as a function of the Ga/As ratio with the total molar flux (GaCl and As<sub>4</sub>) held constant. For this and the remaining parts of the study an elemental dep-

osition system was employed which will be described later. In the third phase of the investigation the effect of the GaCl concentration on the deposition rate was studied at a constant As<sub>4</sub> concentration. Finally, the effects of the As<sub>4</sub> concentration were studied at constant GaCl concentration.

### Experimental

Chromium doped substrates, oriented to <0.5° from the principal direction, were employed for all runs. The substrates were polished with sodium hypochlorite on a rotating Pellon cloth in the manner described by Reisman and Rohr (4). A 3000-3500Å silica etch and deposition mask was applied by the oxidative TEOS process and circular windows, 3 and 6 mils in diameter, were cut into the mask. Holes 3-6μ deep were then etched into the substrate at the sites defined by the mask windows. Sodium hypochlorite (Clorox) was used to etch holes in {111}A substrates. For all other orientations either a 1:1000-Bromine:Methanol or 0.7M H<sub>2</sub>O<sub>2</sub>-1.0M NaOH solution (5) was employed. The holes were always etched just prior to deposition.

The deposition conditions employed with the "arsenided gallium" system were identical with those previously described (1).

For the vapor composition studies the reactor design illustrated in Fig. 1 was utilized. The purity of the elemental source materials was rated at 99.9999%. Gallium is transported as GaCl formed by the reaction of HCl with the Ga source which is maintained at 900°C. Experimental transport measurements showed that essentially 1 mole of GaCl is formed for each mole of HCl entering the Ga source zone at this temperature. Consequently the amount of the gallium species in the vapor was computed from the HCl flux over the gallium source. Hydrogen chloride was generated by the reduction of redistilled AsCl<sub>3</sub> by H<sub>2</sub> in a reduction tube filled with crushed quartz (6). The temperature of this tube was 950°C. The HCl flux was computed from the flow rate of H<sub>2</sub> through the bubbler and the vapor pressure of AsCl<sub>3</sub> at the bubbler temperature. The AsCl<sub>3</sub> bubbler was always placed in a water filled Dewar to prevent temperature fluctuations.

The amount of arsenic in the vapor stream was computed from the flow rate of H<sub>2</sub> over the arsenic source and the vapor pressure of arsenic at the source zone temperature. The vapor pressure of arsenic was calculated from the following equation (7)

$$\log P_{As_4} = \frac{-6777}{T} + 10.559$$

where  $P_{As_4}$  is the arsenic vapor pressure (Torr) and  $T$  is the absolute temperature. Complete saturation of the H<sub>2</sub> carrier gas with arsenic is assumed in calculating the arsenic content in the vapor stream. The temperature variation along the length of the arsenic source boat was less than three degrees. The arsenic source temperature was varied between 435° and

485°C depending on the desired vapor pressure. A substrate temperature of 825°C was used in all cases unless otherwise specified. The substrate holder was capable of holding four 1 x 1 cm slices inclined at an angle of approximately 45° from the tube axis.

All depositions were made under conditions in which the amount of extraneous deposition on the substrate holder, the deposition mask, and the surrounding tube walls was minimized or eliminated altogether. When deposition occurs only on the substrate and not on the surrounding areas which are at the same temperature, the reactions which lead to deposition may then be described as catalyzed by the substrate surface. In addition, it was found that the deposition rate is significantly reduced by the presence of extraneous GaAs on the tube walls. This is probably due to depletion of reactant species from the vapor stream by the extraneous material.

The deposition rate measurements were obtained by measuring the height of the upper surface facets above the substrate surface. Usually 10-15 facets were measured on each slice with the average value being recorded. An interferometer was used to measure facet heights less than 6μ. White light was used to follow the fringes from the substrate surface to the facet surface. The facet heights above 6μ were measured by the change of focus technique with a microscope micrometer scale. In this case high magnifications and wide objective apertures were used to minimize depth of field. The accuracy of this technique was estimated to be ±2μ while a precision of ±1μ was obtained. The depth of the hole did not significantly influence the measured facet growth rates. This is because the holes fill from the walls inward as well as from the bottom upward so that a small peripheral facet forms early in the deposition around the top of the hole. The parameter of interest was the height of this facet above the substrate surface. Thus it was not necessary to fill the hole completely to obtain a valid measurement [e.g., see Fig. 8 of ref. (1)]. Only those hole deposits with smooth surface facets were utilized for measurements.

### Results and Discussion

The effects of orientation on the facet growth rates were first investigated with the "arsenided-gallium" system. Table I shows the results for four runs in which the seed holder was loaded with specimens of each of the four orientations. The position of the {111}B as the slowest growing orientation is also observed with systems using precompounded GaAs source material (8-10). Bobb *et al.* (11) determined epitaxial growth rates as a function of substrate orientation with the arsenided gallium system using large area substrates. They found the rates to be in the ratio 5:2:2:1—{111}A:{100}:{110}:{111}B. This agrees qualitatively with the results shown in Table I. However, the rate differences are much more pronounced for faceted deposition than for the large area deposition. This is probably due to the increased emphasis on nucleation of new growth steps with faceted epitaxial growth. Due to small orientation errors, steps are inherently present in the substrate prior to deposition. During large area deposition, growth of the epitaxial

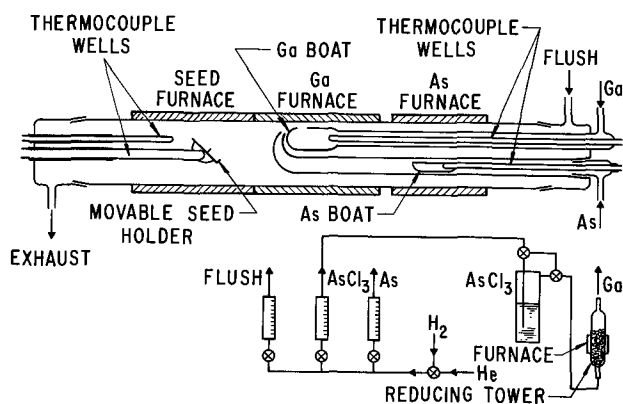


Fig. 1. Separate source apparatus for gallium arsenide deposition

Table I. Effects of substrate orientation on deposition rate with the arsenided gallium system

Run designation	Time, hr	{111}A	{100}	{110}	{111}B
F-424	0.61	34	12	6	0.7
F-430	0.67	42	11	9	1.1
F-448	1.00	62	15	4	1.3
F-469	1.00	66	17	8	1.5
		{111}A	{100}	{110}	{111}B
Average rate μ/hr		60	16	8	1.5
Relative rates		40	10	5	1

layer in the direction perpendicular to the substrate is considered to be the result of the lateral propagation of these growth steps over one another. However, with limited area deposition such as observed with the hole deposits, the growth steps may propagate across the entire area before very many new growth steps are formed (1). Thus growth on facets should be more dependent on the rate of growth step nucleation than on the rate of propagation of steps already formed. This is also consistent with the absolute deposition rates.

During the next series of experiments the Ga/As ratio was varied while the total molar flux ( $\text{GaCl} + \text{As}_4$ ) was held constant. Within experimental error no pronounced effects on the growth rate were observed with either  $\{100\}$  or  $\{110\}$  as the Ga/As ratio was varied from 0.5 to 11. However, the Ga/As ratio was found to influence the deposition rates strongly on the polar  $\{111\}$  facets. This is illustrated for the  $\{111\}$ B in Fig. 2. The rate decreases gradually with decreasing Ga/As ratios down to a value of approximately 2:1 after which the rate decreases more rapidly. It is only at Ga/As ratios  $< 1:1$  that the  $\{111\}$ B facet growth rate drops below  $2\mu/\text{hr}$ . This defines the conditions necessary to obtain planar type selected area deposits with  $\{111\}$ B substrates—relatively low Ga/As ratios. In contrast to the  $\{111\}$ B, the  $\{111\}$ A facet growth rates show a negative dependence on the Ga/As ratio, i.e., the growth rate decreases with increasing Ga/As ratio. This is illustrated by Fig. 3. Indeed, with a Ga/As ratio of 11:1 the  $\{111\}$ A facet growth rate is less than  $2\mu/\text{hr}$ . Thus it would be possible to fabricate planar selected area structures using  $\{111\}$ A substrates if the Ga/As ratio were high.

In another series of depositions the  $\text{As}_4$  flux was held constant at a value of  $6.1 \times 10^{-5}$  mole/min while the GaCl flux was varied between  $5.0 \times 10^{-5}$  and  $30 \times 10^{-5}$  mole/min. The results are shown in Fig. 4 for all four orientations. Each orientation exhibits increasing deposition rates with increasing GaCl flux. The  $\{111\}$ A rate is apparently considerably more sensitive to variations in the GaCl flux than the other orientations. The nonpolar  $\{110\}$  and  $\{100\}$  facet growth rates exhibit similar dependencies on the GaCl flux.

Figure 5 presents a log-log plot of the deposition rate for  $\{100\}$  and  $\{110\}$  facets vs. the  $\text{As}_4$  flux at constant GaCl flux. As can be seen, the rates are independent of the  $\text{As}_4$  flux, and the deposition may be described as zero order with respect to the arsenic species. Comparison of the absolute rate values with those from Fig. 4 shows that the rates are approximately those predicted from the GaCl flux. Note from Fig. 4 and 5 that there is always approximately a factor of ten difference between the rates of  $\{100\}$  and  $\{110\}$  facets. The effects of varying the  $\text{As}_4$  fluxes on the growth rates of the polar  $\{111\}$  facets are shown in

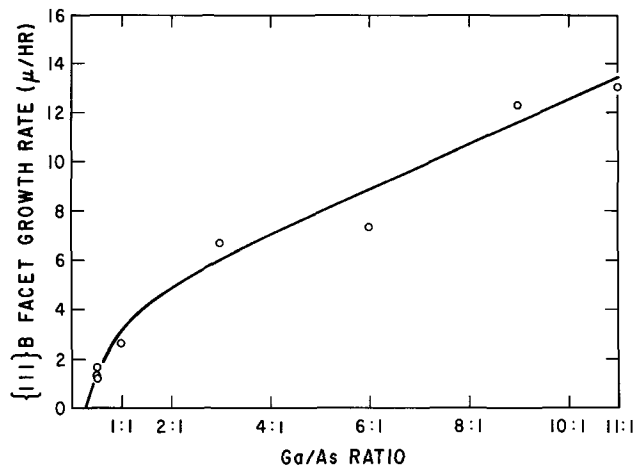


Fig. 2. Variation in  $\{111\}$ B facet growth rate as a function of the Ga/As ratio.

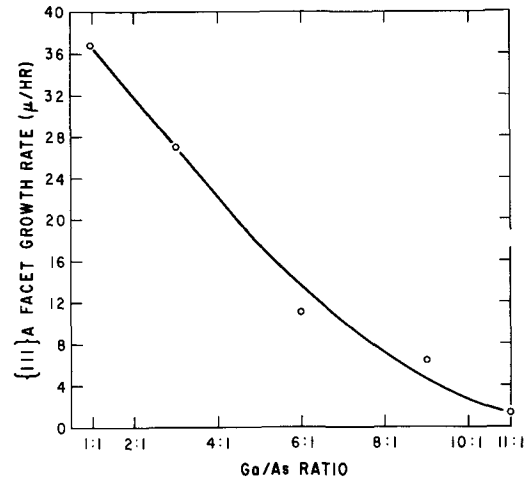


Fig. 3. Variation in  $\{111\}$ A facet growth rate as a function of the Ga/As ratio.

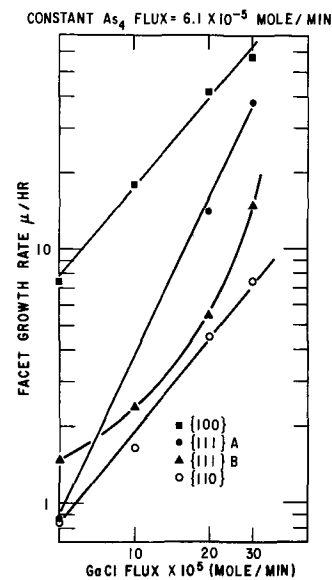


Fig. 4. Variation in facet growth rates as a function of the GaCl flux.

Fig. 6. The  $\{111\}$ A rate exhibits a normal dependence on the  $\text{As}_4$  flux, while the  $\{111\}$ B rate shows a negative dependence on the  $\text{As}_4$  flux, i.e., its growth rate is inhibited by increasing  $\text{As}_4$  concentrations. Although two lines of different slope are drawn through the points in Fig. 6, the dependence may not be linear. The experimental accuracy does not exclude a nonlinear relationship.

Surface catalyzed reactions may be divided into the following series of steps: (a) mass transport of the reactants up to the catalyst (crystal) surface, (b) adsorption of the reactants on the surface, (c) reactions of the adsorbed species on the surface, (d) surface diffusion of the species to steps and incorporation into the lattice, and (e) mass transport of the products away from the surface. With respect to steps c and d, it should be noted that the adsorbed reactants may also diffuse to the crystal step and then react at that site. If any step is significantly slower than the others it becomes the rate limiting step. If any one of the mass transport steps were the rate-limiting step, the reaction rate would be strongly influenced by the flow rate but would be relatively independent of substrate orientation (12). Since in all of the experiments described above the rate was strongly orientation dependent, it is probable that the deposition rate is not mass transport limited. This indicates that the rate is probably determined by either an adsorption-desorp-

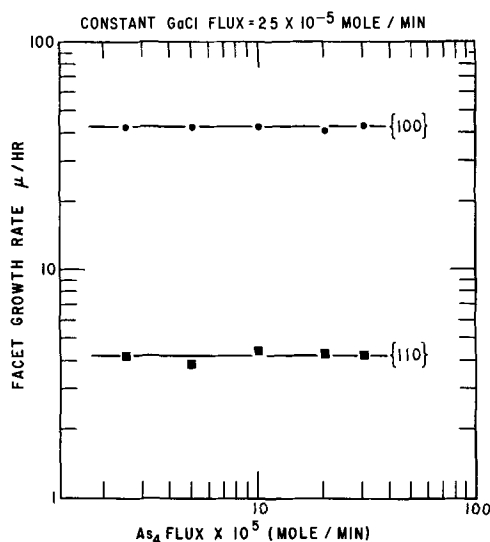


Fig. 5. Variation in {100} and {110} facet growth rates as a function of the arsenic flux.

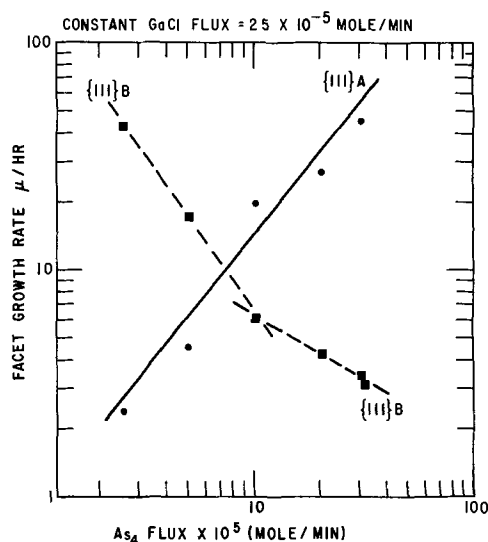


Fig. 6. Variation in {111}B and {111}A facet growth rates as a function of the arsenic flux.

tion process or by the surface reaction itself. In order to completely describe the epitaxial mechanism, many more experiments would be required.

The negative growth rate dependence of the {111}B facets on the arsenic concentration explains the necessity of having low Ga/As ratios in order to obtain low {111}B facet growth rates. The initial step in the nucleation of a {111}B layer is addition of a singly bonded gallium. However, at high arsenic concentrations the arsenic species may compete with the gallium species for surface sites.

The deposition rate of {111}A facets exhibited a positive dependence on both the gallium and the arsenic species. However, as is shown by Fig. 3, the deposition rate decreased with increasing Ga/As ratio. This appears to be a contradiction until it is realized that while the Ga/As ratio increased it did so by a small increase in the GaCl flux and a relatively large decrease in the As<sub>4</sub> flux. Thus at a ratio of 2:1 the GaCl flux was  $29.3 \times 10^{-5}$  mole/min and the As<sub>4</sub> flux was  $3.9 \times 10^{-5}$  mole/min. When the Ga/As ratio was increased to 11:1 the GaCl flux was increased to  $32.2 \times 10^{-5}$  mole/min, while the As<sub>4</sub> flux decreased to  $0.73 \times 10^{-5}$  mole/min. This also explains the relative independence of the {100} and {110} facet growth rates on the Ga/As ratio for that series of experiments. The data shown in Fig. 6 indicate that it would be possible to use the {111}A orientation for planar selected area deposition if relatively low arsenic concentrations were employed.

The relatively high {100} rates and the independence of the rate on the arsenic concentration makes it the least desirable orientation for planar hole deposition. The high {100} growth rates are probably due to the ease of nucleation of {100} layers. In every case the addition of atoms onto a {100} surface results in double bonded atoms. It is again stressed that nucleation of new layers is considerably more important with facet growth than with the usual large area deposition.

#### Acknowledgment

Appreciation is expressed to Mr. D. G. Vieaux, Jr., for his assistance with the experimental work. Thanks are also extended to Dr. L. G. Bailey for helpful discussions of possible deposition mechanisms. The initial portions of this work were supported by the Air Force Avionics Laboratory, Electronics Technology Division, under Contract AF 33(615)-2101.

Manuscript received Feb. 2, 1968; revised manuscript received April 3, 1968.

Any discussion of this paper will appear in a Discussion Section to be published in the June 1969 JOURNAL.

#### REFERENCES

1. D. W. Shaw, *This Journal*, **113**, 904 (1966).
2. G. Nomarski and A. R. Weill, *Rev. Metallurg.*, **52**, 121 (1955).
3. E. W. Mehal, R. W. Haisty and D. W. Shaw, *Trans. Met. Soc. AIME*, **233**, 596 (1965).
4. A. Reisman and R. Rohr, *This Journal*, **111**, 1425 (1965).
5. D. W. Shaw, *ibid.*, **113**, 958 (1966).
6. E. W. Mehal and G. R. Cronin, *Electrochem. Technol.*, **4**, 540 (1966).
7. Landolt-Bornstein, *Zahlenwerte, und Funktionen*, Vol. 2a, p. 11, Springer-Verlag, Berlin (1960).
8. F. V. Williams, *This Journal*, **111**, 886 (1964).
9. R. R. Moest, *ibid.*, **113**, 141 (1966).
10. D. Effer, *ibid.*, **113**, 1020 (1966).
11. L. C. Bobb, H. Holloway, K. H. Maxwell, and E. Zimmerman, *J. Phys. Chem. Solids*, **27**, 1679 (1966).
12. E. G. Bylander, *This Journal*, **109**, 1171 (1962).

# Dependence of Sheet Resistance on SiO<sub>2</sub> Masking Geometry in Diffused Si Regions

J. P. Décosterd, D. Chauvy, and K. Hübner\*

Centre Electronique Horloger S. A., Neuchâtel, Switzerland

We have observed systematic differences in sheet resistance within the same IC chip depending on the width of the SiO<sub>2</sub> strip surrounding a particular diffusion window. A large meander-type boron diffused resistor of several hundred squares with line width and spacing of 10 $\mu$ , will show up to 20% lower sheet resistance than a short straight resistor surrounded by wide SiO<sub>2</sub> stripes. This applies for diffusion conditions as they are commonly used for resistors and bases in IC's. Under special conditions the difference can be much more pronounced.

In a series of specific experiments, including various masking patterns, we could convince ourselves, that the observed effect is not due to: (a) leakage current, (b) lateral impurity diffusion within the Si, (c) variation in SiO<sub>2</sub> thickness, (d) corner effects in resistor surface geometry, (e) particular surface preparation including chemical HNO<sub>3</sub> preoxidation, (f) any process following the predeposition, (g) choice of a particular diffusion system, (h) choice of a particular impurity (effect observed for boron and phosphorus, other doping elements not investigated). The effect does however depend on: (i) SiO<sub>2</sub> strip width around the diffusion window, (ii) size of the masking window, in particular line width of a diffused resistor, (iii) predeposition time.

Samples for the experiments reported below were prepared from 1-2 ohm cm, (111) orientation, n-type wafers. Customary cleaning procedures were employed, the final chemical treatment before oxidation or predeposition being an HF or buffered HF dip, respectively.

Oxidation was carried out at 1200°C in a 90-min wet, 5-min dry O<sub>2</sub> cycle, with the water temperature for the wet O<sub>2</sub> being 95°C. The type of masking pattern for the boron predeposition employed to obtain the results of Fig. 2 and 3 is shown in Fig. 1. It consists of 8 simple one-line windows for diffused resistors measuring 200 $\mu$  in length and 10 $\mu$  in width. The ends are formed by 50 x 50 $\mu$  square pads for the Al contacts. The individual resistors differ only in the width (not thickness) of the surrounding SiO<sub>2</sub> strip delineating the diffusion windows. This width of SiO<sub>2</sub> varies in Fig. 1 from 4 $\mu$  for the resistor in the upper left hand corner to 150 $\mu$  for the second resistor from the left in the bottom row. Each resistor is therefore surrounded by a different SiO<sub>2</sub> strip width. The space between these oxide surfaces surrounding each resistor is bare silicon. The photoresist used was centrifuged KMER.

The boron predeposition for most experiments was carried out in a Pt box system with a pure liquid B<sub>2</sub>O<sub>3</sub> glass as a source in a dry N<sub>2</sub> ambient, at 910°C. Control runs made in a more conventional BBr<sub>3</sub> liquid source system at 950°C yielded the same results. Right after boron predeposition contact windows were cut and Al evaporated from a stranded tungsten wire. After photoetching the remaining Al was alloyed at 578°C in N<sub>2</sub> for 6 min to assure good contact.

Typical results for a predeposition cycle likely to be used for a base diffusion are shown in Fig. 2. Plotted is sheet resistance in ohms per square as a function of the width of the surrounding masking oxide. The point for SiO<sub>2</sub> width equal to zero is the four-point probe measurement taken on the back side of the wafer.

The scatter indicated is for all chips measured on an entire wafer, the points being the averages. It is clearly visible that the width of the SiO<sub>2</sub> strip surrounding the diffused resistors influences sheet resistance by about 17%. The wider the SiO<sub>2</sub> strip surrounding the diffused silicon, the higher is the sheet resistance or the lower is the electrically active impurity concentration. For the conditions represented in Fig. 2 sheet resistance becomes constant for SiO<sub>2</sub> widths larger than about 50 $\mu$ .

This result expresses what we have been observing on diffused resistors in integrated circuits. Large me-

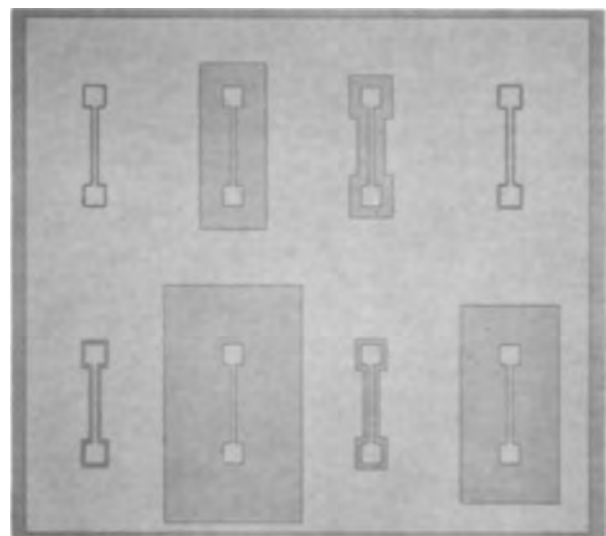


Fig. 1. Test pattern for SiO<sub>2</sub> mask used to obtain the resistor geometries whose characteristics are shown in Fig. 2 and 3. Total chip size is 1700 x 1600 $\mu$ ; resistors are 200 x 10 $\mu$  with SiO<sub>2</sub> masking bands ranging from 4 to 150 $\mu$ .

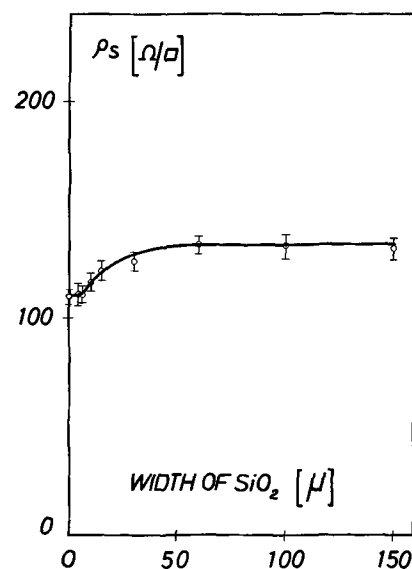


Fig. 2. Sheet resistance in ohms per square vs. width of the SiO<sub>2</sub> masking band surrounding the diffused resistors. Predeposition was carried out in a BBr<sub>3</sub> system at 950°C for 20 min.

\* Electrochemical Society Active Member.

Key words: diffusion in Si, masking against diffusion, sheet resistance of diffused layers.

ander-type resistors have very little  $\text{SiO}_2$  surface between individual lines of the same resistor. Their sheet resistance is therefore lower than that of a simple one-line resistor with large  $\text{SiO}_2$  surfaces around it.

We have no specific model to explain our experiments, but suggest the following mechanisms which might account for most of our observations:

The affinity of the dopants ( $\text{B}_2\text{O}_3$ , but also  $\text{P}_2\text{O}_5$ ) to deposit on the  $\text{SiO}_2$  surface is larger than for the bare Si. This leads to a disturbance of the dopant distribution in the gas phase close to the edge of a diffusion window, where the oxide is thus preventing the  $\text{B}_2\text{O}_3$  molecules from depositing on the Si.

The molecules of the dopants deposited on the bare Si diffuse laterally on the Si surface to the oxide so that only part of these molecules supply doping atoms to the bulk.

Precipitation of the dopants in the Si on crystal imperfections in the strained regions along the edges of the diffusion windows cannot be ruled out. It is conceivable that less crystal disorder and therefore less precipitates are generated along the window edges, if the surrounding oxide frame is very narrow. This would explain our findings without further postulates.

To examine this last mechanism we varied the  $\text{SiO}_2$  thickness from 2500 to 20,000 Å, which should influence the strain generated, and found no influence. In separate experiments we established that lateral diffusion is a sensitive test to determine the presence of crystal imperfections at window edges. They reduce the lateral diffusion close to the surface of boron and enhance that of phosphorus. This is in agreement with the diffusion behavior of these elements along small angle grain boundaries in Si and suggests the presence of dislocations along the window edges. All our measurements presented here have been carried out on surfaces which exhibit a normal lateral diffusion behavior. It can therefore be assumed, that no excessive crystal disorder is responsible for the effect reported, but precipitation phenomena cannot be excluded as a possible mechanism to explain our observations.

Furthermore we established experimentally that:

(A) The effect is more pronounced if the predeposition time is small. Boron predepositions were carried out for only 3 min at 910°C. The results are shown in Fig. 3. While in Fig. 2 the difference in sheet resistance for  $\text{SiO}_2$  width of  $4\mu$  and  $150\mu$  was 17%, it is 26% in Fig. 3.

For such short predeposition times the resulting diffusion length is much smaller than the surface dimensions of the patterns. Two-dimensional diffusion effects can therefore be excluded as explanation. For longer predeposition times (60 and 120 min) the effect gradually gets smaller.

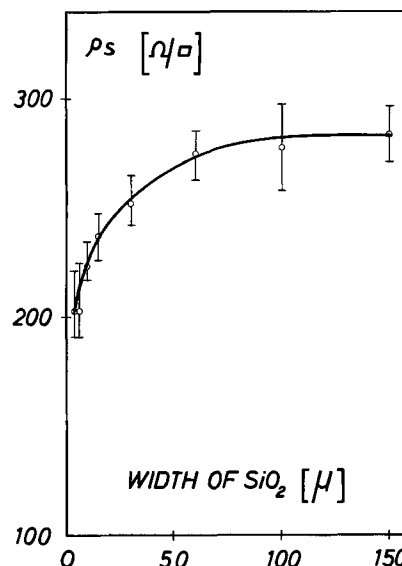


Fig. 3. Same measurement as in Fig. 2, but for a predeposition in a Pt box system with  $\text{B}_2\text{O}_3$  as a source at 910°C for 3 min.

A chemical  $\text{HNO}_3$  preoxidation does not attenuate the effect. This observation however is not in good agreement with our first proposed model.

One would also expect for the models suggested the line width of the diffused resistors to influence the observed effect. We also could confirm this point experimentally and repeatedly on a set of one-line resistor pairs of different line and  $\text{SiO}_2$  width. The effect gets smaller the wider the resistor lines are.

In conclusion we can state that we have found experimental evidence of  $\text{SiO}_2$  masks influencing sheet resistance during B (and P) predeposition in Si. The effect is most pronounced for small windows (order  $10\mu$ ) and short predeposition times.

#### Acknowledgment

The authors express their sincere thanks to R. Guye, who has actually discovered this effect in his IC work and contributed to its better understanding in many stimulating discussions.

Manuscript received Jan. 22, 1968; revised manuscript received March 3, 1968. This paper was presented at the Chicago Meeting, Oct. 15-19, 1967, as Late News Paper 16.

Any discussion of this paper will appear in a Discussion Section to be published in the June 1969 JOURNAL.

# Double Layer Capacitance of Zinc Electrodes in KOH Solutions

T. P. Dirkse\* and R. Shoemaker

Calvin College, Grand Rapids, Michigan

## ABSTRACT

The double layer capacitance of amalgamated and nonamalgamated zinc electrodes has been measured in a range of KOH solutions at room temperature. The presence of zincate ions and of surface active materials modifies the capacitance values. There appears to be some correlation between the extent to which a surface active material modifies the double layer capacitance and its effectiveness in increasing the cycle life of the zinc electrode.

In zinc-alkaline batteries the zinc electrodes are usually amalgamated. This is done to improve the stand or shelf-life characteristics of the zinc electrode. Amalgamation raises the hydrogen overvoltage on zinc and thus reduces considerably the corrosion rate of zinc in highly alkaline solutions. However, amalgamation does more than raise the hydrogen overvoltage. It also modifies the anodic behavior of the zinc (1). It was suggested that this is due to a change in the surface of the zinc electrode. As a result, the anodic reaction may proceed by a somewhat different mechanism at these amalgamated electrodes (1). The work reported here was undertaken in an effort to get more information about this suggested mechanism.

One way to obtain information about the electrode/electrolyte interface is to measure the double layer capacitance at the electrode. This is difficult with an electrochemically active electrode such as zinc. Passage of current alters the nature of the electrode surface. Furthermore, any current used in making double layer capacitance measurements may also be accompanied by Faradaic current, i.e., chemical changes. In spite of this difficulty, attempts to measure double layer capacitance were nonetheless made because similar work with the silver electrode had proven fairly successful (2).

## Results

The method used was the one suggested by McMullen and Hackerman (3). The electrode surface was the cross-sectional area of a 0.063 in. diameter zinc wire encased in a Teflon tube. Further experimental details have been described earlier (2). The square wave frequency was 50,000 Hz, and the value of the current was of the order of 0.1 ma.

Some typical results are given on Fig. 1 and 2. The arrows on these figures designate the open circuit potential of the electrode in that solution. The values for the nonamalgamated zinc electrodes, Fig. 1, are in good agreement with those obtained by others (4). The reproducibility is also good for an electrode such as zinc.

One outstanding feature of these results is that amalgamation alters the surface characteristic of the zinc electrode. The presence of zincate ions alters the values at potentials cathodic to that at open circuit. This is to be expected because at these potentials metallic zinc is deposited and this introduces an appreciable Faradaic current which has the effect of increasing the value of the calculated double layer capacitance.

At potentials anodic to the open circuit value there is a marked difference in the behavior of amalgamated and nonamalgamated electrodes. The amalgamated electrodes give values close to the generally accepted ones ( $20 \mu\text{f}/\text{cm}^2$ ). It should be noted here that no correction was made for a roughness factor for zinc. Consequently, the data reported in Fig. 1 and 2 are

somewhat higher than the actual values for the non-amalgamated zinc.

A summary of the results is presented on Fig. 3. The capacitance values plotted on this graph are those obtained at the open circuit potential of the zinc electrode in that electrolyte. There is a maximum in the double layer capacitance values at 30-35% KOH for both types of electrodes. The presence of zincate ion has no effect on amalgamated electrodes but has a slight effect on nonamalgamated zinc.

In recent years it has been found that certain surface active materials increase the cycle life of the zinc electrode (5). The double layer capacitance of zinc electrodes was also measured in the presence of some such materials, Fig. 4-6. Ordinarily, the presence of Emulphogene BC-610 does not shift the equilibrium potential as much as is shown in Fig. 6. These open circuit or equilibrium potentials were somewhat random. There was no zincate in these solutions. However, there is a tendency to shift the equilibrium potential to more positive values. This phenomenon has been observed by others also (6).

## Discussion

At potentials cathodic to the open circuit value, the difference between amalgamated and nonamal-

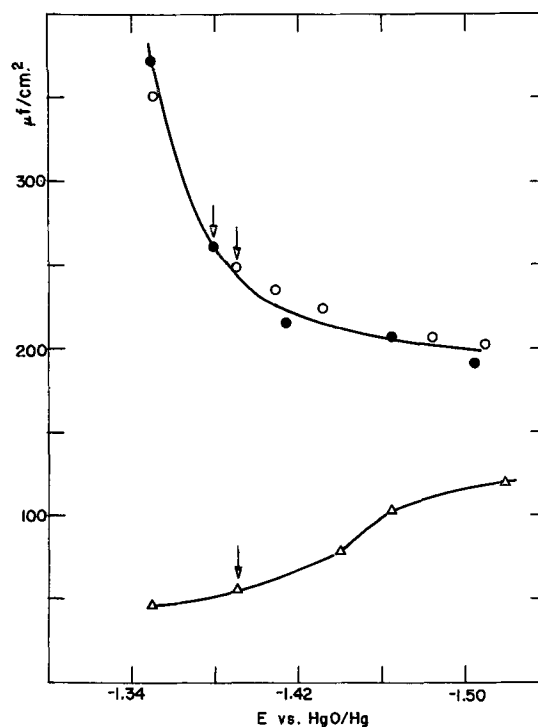


Fig. 1.  $dI_c$ -potential curve for zinc electrodes in 40% KOH. Circles, zinc (2 separate runs); triangles, amalgamated zinc.

\* Electrochemical Society Active Member.

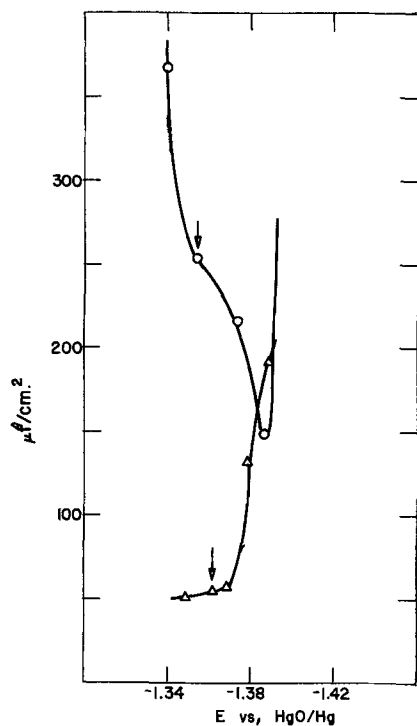


Fig. 2. *dlc*-potential curve for zinc electrodes in 40% KOH saturated with ZnO. Symbols same as for Fig. 1.

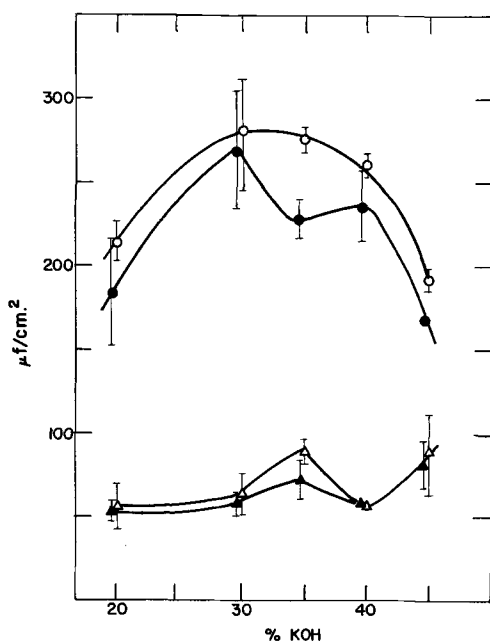


Fig. 3. *dlc*-potential curves for zinc electrodes on open circuit. Circles, zinc; triangles, amalgamated zinc; open symbols, no zincate; closed symbols, saturated with ZnO.

gated electrodes decreases. This is noted particularly in zincate-free solutions where the reduction of zincate cannot occur. As the potential of the electrode increases in the anodic direction, the difference in behavior of the two types of electrodes increases.

The behavior represented on Fig. 1 is consistent with other work on the anodic and cathodic processes of the zinc electrode (1). The effect of amalgamation on the overvoltage for the zinc/zincate reaction and on the limiting current density at the zinc electrode is more pronounced for the anodic than for the cathodic processes.

The double layer capacitance value can be considered as the current necessary to bring about a given

rate of voltage change on the electrode. The current necessary to do this, then, is much greater for the nonamalgamated electrodes. This can be explained by assuming the adsorption of  $\text{OH}^-$  ions on the zinc adatoms (4). It is then more difficult to increase the potential of the zinc electrode anodically. It follows from this that no such adsorption (or a considerably smaller amount) takes place at amalgamated electrodes. Amalgamation may make the surface of the zinc more like a liquid, i.e., more homogeneous. It may remove screw dislocations and other imperfections. As a result there are no adatoms (adsorbed atoms with a low coordination number) on an amalgamated surface (1).

The variation of the double layer capacitance with KOH concentration, Fig. 3, has been noted before (2) and will be discussed in another paper. The presence of zincate ion has but little effect on the double layer capacitance, Fig. 3. There appears to be a slight difference at the nonamalgamated electrodes, but most of this is within the experimental uncertainty. The biggest difference is in 35% KOH. This difference is real but no satisfactory explanation for it is available.

The effect of additives to the electrolyte is especially interesting. The presence of maleic anhydride was found to have no significant effect on the cycle life of the zinc electrode. In the presence of this material the double layer capacitance of zinc electrodes was not changed except for some displacement, Fig. 4.

The use of Igepal CO-730 did not increase the cycle life of the zinc electrode (5). It did have an effect on the shape of the double layer capacitance curve of the nonamalgamated zinc electrode, Fig. 5. The double layer capacitance value is lower and it does not rise as abruptly at anodic potentials.

The cycle life of the zinc electrode was increased most by the use of Emulphogene BC-610 (5). Cell failure was often due to loss of zinc electrode capacity rather than to the formation of shorts (dendrites). Emulphogene BC-610 also had the greatest effect on the double layer capacitance of both types

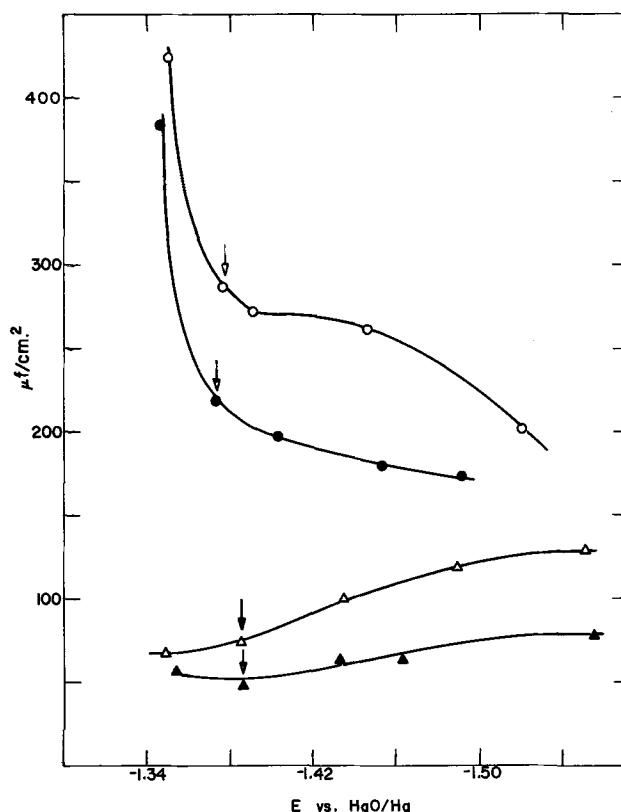


Fig. 4. *dlc*-potential curve for zinc electrodes in 30% KOH. Circles, zinc; triangles, amalgamated zinc; open symbols, no additive; closed symbols, 0.01% maleic anhydride.



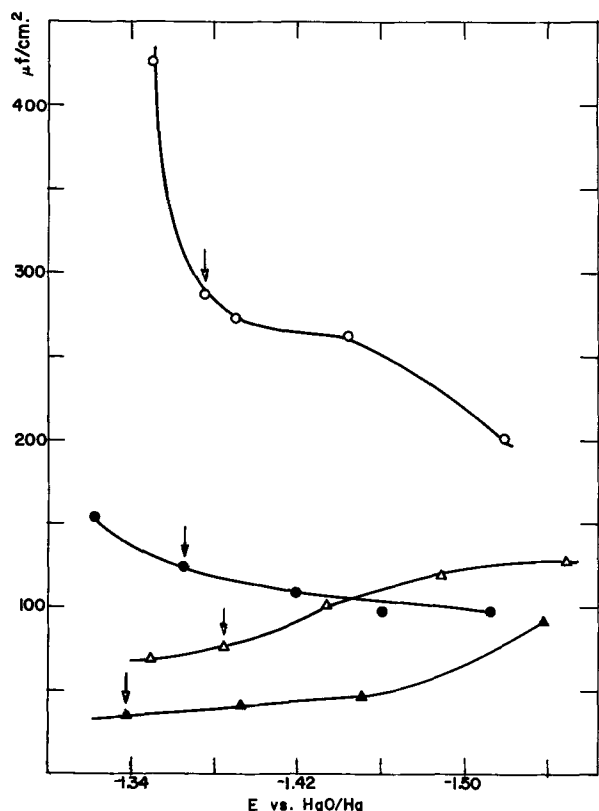


Fig. 5. *d/c*-potential curve for zinc electrodes in 30% KOH. Circles, no additive in the electrolyte; triangles, saturated with Igepal CO-730; open symbols, zinc; closed symbols, amalgamated zinc.

of zinc electrodes, Fig. 6. It altered the shape of the curve for the nonamalgamated electrodes completely and even lowered that of the amalgamated electrodes significantly.

These phenomena can again be accounted for in terms of surface adsorption. The surface active materials are adsorbed on the electrode surface. The Igepal CO-730 and the Emulphogene BC-610 are preferentially adsorbed on the electrode surface, the latter more so. This displaces or prevents  $\text{OH}^-$  ion adsorption. In fact, with Emulphogene BC-610, Fig. 6, the double layer capacitance of the nonamalgamated electrode becomes similar to that of the amalgamated electrode.

Such preferential adsorption of the surface active materials is undoubtedly associated with the increased cycle life of the zinc electrodes. The adsorption of the additives takes place on the most active reaction sites and prevents electrochemical reaction from occurring preferentially at these sites. This may prevent or delay the growth of zinc dendrites, which is a common mode of failure in the silver-zinc batteries. The anodic reaction mechanism may also be changed somewhat (1). The adsorption of the surface active materials at the preferred reaction sites forces the electrochemical reaction to take place over the rest of the electrode surface. This results in a more complete electrochemical use of the entire electrode surface instead of only certain parts of the surface. Thus treeing and dendrite growth are at least delayed.

In silver-zinc batteries the zinc electrodes are amalgamated. Consequently, if the above explanation is correct, it would appear unsuited to account for the extended cycle life of these batteries. However, it is likely that during cycling the deposits of zinc formed on charge are not amalgamated, at least to the extent of the original electrode. As a result, the

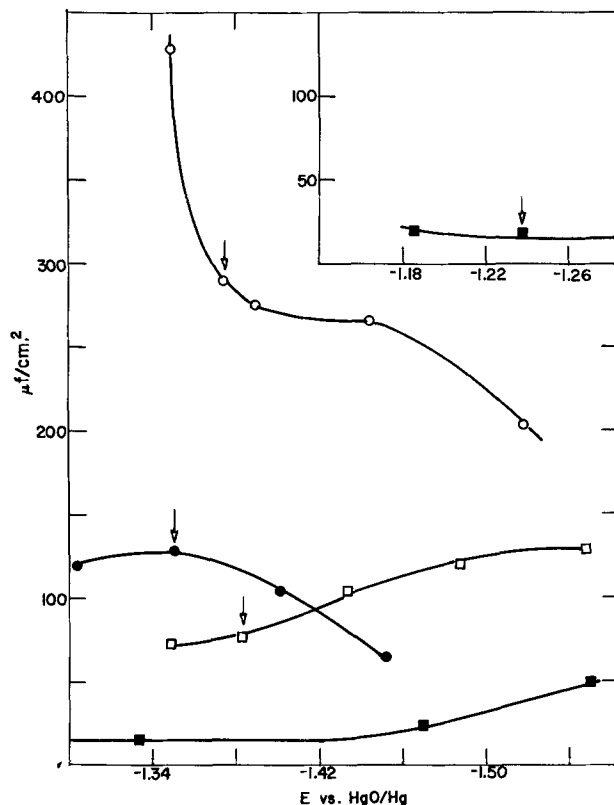


Fig. 6. *d/c*-potential curve for zinc electrodes in 30% KOH. Circles, zinc; squares, amalgamated zinc; open symbols, no additive; closed symbols, saturated with Emulphogene BC-610.

beneficial effects of amalgamation then cease to exist as cycling continues. Under such conditions it is very likely possible that the surfactants then exert their beneficial effect on the nonamalgamated or slightly amalgamated zinc deposits, and in this way serve to extend the cycle life of the zinc electrodes.

As a practical matter, the results reported here suggest that, in seeking additives to improve the zinc electrode behavior, the measurement of the double layer capacitance of the zinc electrode in the presence of such additives may serve as a useful tool in selecting substances which will be most effective. Furthermore, the results of this work are consistent with the mechanisms that have previously been suggested for the anodic zinc processes (1, 4).

#### Acknowledgment

The work reported here was supported by the U.S. Air Force Aero Propulsion Laboratories.

Manuscript submitted Jan. 17, 1968; revised manuscript received April 12, 1968.

Any discussion of this paper will appear in a Discussion Section to be published in the June 1969 JOURNAL.

#### REFERENCES

1. T. P. Dirkse, D. De Wit, and R. Shoemaker, *This Journal*, **114**, 447 (1967).
2. T. P. Dirkse, D. De Wit, and R. Shoemaker, *ibid.*, **114**, 1196 (1967).
3. J. J. McMullen and N. Hackerman, *ibid.*, **106**, 341 (1959).
4. J. P. G. Farr and N. A. Hampson, *Trans. Faraday Soc.*, **62**, 3493 (1966).
5. J. A. Keralla and J. J. Lander, Paper delivered at the Chicago Meeting, Oct. 15-19, 1967, as Paper 37.
6. L. Milicka and M. Miadokova, *Z. phys. Chem. (Leipzig)*, **236**, 231 (1967).

# Self-Discharge in Alkali Metal-Containing Bimetallic Cells

J. C. Hesson, M. S. Foster, and H. Shimotake

Argonne National Laboratory, Argonne, Illinois

## ABSTRACT

The self-discharge rate of a concentration cell is considered to be due to the dissolution and ionization of alkali metal atoms in the fused-salt electrolyte. Assuming that an equilibrium exists between dissolved alkali metal atoms and alkali metal ions and electrons, an expression was derived which relates the self-discharge rate as a function of current. This expression was used to construct graphs showing the effect of cell current on the self-discharge rate for a variety of conditions. It is demonstrated that the open-circuit potential of such a cell will be less than that predicted from theoretical thermodynamic considerations.

Thermally regenerative bimetallic cells with alkali metal anodes have been considered as a means to convert heat energy into electrical energy (1-4). In these cells, the anode consists of an alkali metal such as lithium, sodium, or potassium, and the cathode consists of a binary alloy of the alkali metal and a more noble metal, such as lead, bismuth, or tin. An electrolyte consisting of a mixture of molten salts of the anode alkali metal is used. The open circuit potentials of such cells have been used to calculate the thermodynamic properties of binary alloys (5-7).

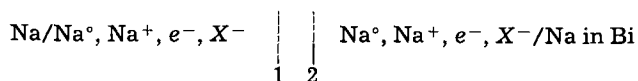
In this laboratory, it has been noted that, in the case of sodium-bismuth bimetallic cells using a molten sodium fluoride-sodium chloride-sodium iodide electrolyte, a non-faradaic or "irreversible" transfer of sodium from the anode to the cathode takes place. Since this transfer of sodium takes place without producing an electrical current in the external circuit, it is also called self-discharge of the cell. The self-discharge rate is much too large to be explained simply by the diffusion of dissolved sodium atoms through the electrolyte. In addition, it has been noted that the rate of self-discharge decreases as the current drawn from the cell is increased.

## Theoretical Analysis

In order to explain the observed self-discharge rate and its anomalous behavior with current, a theoretical analysis has been made. In this analysis, it is assumed: (a) that the self-discharge of the cell is in part due to electronic conductivity of the electrolyte which in turn results from dissolved alkali metal, and (b) that an equilibrium exists between dissolved alkali metal atoms and alkali metal ions and electrons.

We shall consider the cell of unit cross sectional area with parallel anode and cathode. The electrolyte thickness is  $L$  cm and it is postulated that no convective stirring takes place in the electrolyte.

The concentration cell to be considered is typified by the sodium-bismuth cell:



where all concentration changes occur in the region between the imaginary boundaries 1 and 2. The electrolyte immediately adjacent to the anode will be saturated with sodium metal, and the solubility of sodium is defined to be  $X_{\text{Na}}^A$ . The electrolyte immediately adjacent to the cathode will also contain dissolved sodium. Since the activity of sodium in the cathode alloy is much less than the activity of sodium in the anode, the concentration of sodium in the elec-

trolyte adjacent to the cathode,  $X_{\text{Na}}^C$ , will be much less than  $X_{\text{Na}}^A$ .

In the region between 1 and 2, the equivalent current density of sodium atoms, in amp/cm<sup>2</sup>, through the electrolyte and toward the cathode will be

$$i_o = \frac{-FD\rho X_{\text{Na}}}{MRT} \frac{d\mu_{\text{Na}}}{dx} \quad [1]$$

where  $F$  is the Faraday constant,  $D$  the effective diffusion coefficient of sodium atoms,  $\rho$  the density of the electrolyte solution,  $X_{\text{Na}}$  the mole fraction of sodium dissolved in the electrolyte,  $M$  the molecular weight of the electrolyte solution,  $R$  the universal gas constant,  $T$  the absolute temperature,  $\mu_{\text{Na}}$  the chemical potential of sodium due to concentration effects, and  $x$  the distance toward the cathode from the anode-electrolyte interface. The partial current density of sodium ions,  $i_i$ , is

$$i_i = \frac{-\kappa_i}{F} \frac{d\mu_i}{dx} - \kappa_i \frac{d\psi}{dx} \quad [2]$$

where  $\kappa_i$  is the partial sodium ion conductivity of the electrolyte (assumed constant),  $\mu_i$  the chemical potential of the sodium ions due to concentration effects, and  $\psi$  the local electric potential in the electrolyte. The partial electrical current density due to electrons in the electrolyte,  $i_e$ , is

$$i_e = \frac{\kappa_e}{F} \frac{d\mu_e}{dx} - \kappa_e \frac{d\psi}{dx} \quad [3]$$

where  $\kappa_e$  is the partial electronic conductivity of the electrolyte and  $\mu_e$  the chemical potential of the dissolved electrons. Note that the current carried by electrons is considered to be positive when the electrons themselves flow toward the anode (in the negative direction of  $x$ ). The total electrical current density,  $i$ , is the sum of the partial currents

$$i = i_i + i_e = \frac{1}{F} \left( \kappa_e \frac{d\mu_e}{dx} - \kappa_i \frac{d\mu_i}{dx} \right) - (\kappa_i + \kappa_e) \frac{d\psi}{dx} \quad [4]$$

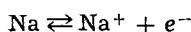
The apparent self-discharge rate is

$$J_{\text{Na}}^* = i_o - i_e = (i_o + i_i) - i \quad [5]$$

It is assumed that steady-state conditions apply at any fixed current, i.e., (i) the current through any plane bisecting the electrolyte and parallel to the electrode-electrolyte interfaces is constant, and (ii) the total number of sodium nuclei in the electrolyte is constant. Therefore, Eq. [5] shows that  $J_{\text{Na}}^*$  is independent of position and is constant for a given  $i$ .

The dissolved sodium atoms in the electrolyte are assumed to be in equilibrium with sodium ions and

electrons, and, therefore, from the equilibrium



we know

$$\mu_{\text{Na}} = \mu_i + \mu_e \quad [6]$$

Equations [4] and [6] may be combined to yield the expression

$$\frac{d\mu_e}{dx} = \frac{\kappa_i}{\kappa_i + \kappa_e} \frac{d\mu_{\text{Na}}}{dx} + \frac{F i}{\kappa_i + \kappa_e} + F \frac{d\psi}{dx} \quad [7a]$$

This equation may be combined with Eq. [3] to eliminate the dependence of  $i_e$  on  $\psi$

$$i_e = \frac{\kappa_i \kappa_e}{F(\kappa_i + \kappa_e)} \frac{d\mu_{\text{Na}}}{dx} + \frac{\kappa_e i}{\kappa_i + \kappa_e} \quad [7b]$$

The concentration of sodium atoms dissolved in the electrolyte is small, allowing us to use dilute solution theory.

If the activity coefficient of sodium atoms dissolved in the fused electrolyte is constant for the dilute solutions involved, we may write

$$\frac{d\mu_{\text{Na}}}{dx} = RT \frac{d(\ln X_{\text{Na}})}{dx} \quad [8]$$

Bredig's results (8) suggest that for dilute solutions of sodium in molten sodium halides, the partial electronic conductivity,  $\kappa_e$ , is proportional to the mole fraction of sodium metal in the solution, or

$$\kappa_e = K_e X_{\text{Na}} \quad [9]$$

Using these assumptions and the basic differential relationships, the following equation is obtained

$$J_{\text{Na}}^* = - \left[ \frac{FD\rho}{M} + \frac{K_e RT \kappa_i}{F(\kappa_i + K_e X_{\text{Na}})} \right] \frac{dX_{\text{Na}}}{dx} - \frac{K_e X_{\text{Na}} i}{(\kappa_i + K_e X_{\text{Na}})} \quad [10]$$

As the imaginary boundaries 1 and 2 are considered to approach the electrode-electrolyte interfaces, Eq. [10] may be integrated to yield

$$J_{\text{Na}}^* + i = \left[ \frac{\kappa_i RT}{FL} + \frac{FD\rho \kappa_i i}{LMK_e(i + J_{\text{Na}}^*)} \right] \ln \left[ \frac{J_{\text{Na}}^* \kappa_i + (J_{\text{Na}}^* + i)K_e X_{\text{Na}}^A}{J_{\text{Na}}^* \kappa_i + (J_{\text{Na}}^* + i)K_e X_{\text{Na}}^C} \right] + \frac{FD\rho(X_{\text{Na}}^A - X_{\text{Na}}^C)}{LM} \quad [11]$$

Two interesting cases of Eq. [11] may be mentioned. If the current,  $i$ , in the external circuit is zero, then

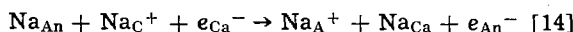
$$J_{\text{Na}}^* = q_0 = \frac{\kappa_i RT}{FL} \ln \left( \frac{\kappa_i + K_e X_{\text{Na}}^A}{\kappa_i + K_e X_{\text{Na}}^C} \right) + \frac{FD\rho(X_{\text{Na}}^A - X_{\text{Na}}^C)}{LM} \quad [12]$$

and if the self-discharge rate,  $J_{\text{Na}}^*$  is zero

$$i = p_0 = \left[ \frac{\kappa_i RT}{FL} + \frac{FD\rho \kappa_i}{LMK_e} \right] \ln \left( \frac{X_{\text{Na}}^A}{X_{\text{Na}}^C} \right) + \frac{FD\rho(X_{\text{Na}}^A - X_{\text{Na}}^C)}{LM} \quad [13]$$

These equations will be used later in demonstrating some typical results of this treatment.

The cell reaction producing current in the external circuit may be written



where the subscripts An and Ca refer to the anode and cathode themselves and A and C to the electrolyte immediately contiguous with the anode and cathode,

respectively. The Gibbs free energy change,  $\Delta G$ , for reaction [14] is

$$\Delta G = (\mu_{\text{Na,Ca}} - \mu_{\text{Na,An}}) + (\mu_{\text{i,A}} - \mu_{\text{i,C}}) + F(\psi_{\text{A}} - \psi_{\text{C}}) + (\mu_{\text{e,An}} - \mu_{\text{e,Ca}}) - F(\psi_{\text{An}} - \psi_{\text{Ca}}) \quad [15]$$

Because the chemical potentials of electrons in the anode and cathode,  $\mu_{\text{e,An}}$  and  $\mu_{\text{e,Ca}}$ , are only a function of concentration (9) and are very nearly equal, we may write

$$\mu_{\text{e,An}} = \mu_{\text{e,Ca}} \quad [16]$$

Likewise, because the composition of the electrolyte varies only slightly

$$\mu_{\text{i,A}} = \mu_{\text{i,C}} \quad [17]$$

The cell terminal voltage is defined as

$$E = \psi_{\text{Ca}} - \psi_{\text{An}} \quad [18]$$

Thus, if only equilibrium processes take place,  $\Delta G = 0$ , and Eq. [15] becomes

$$\Delta G = (\mu_{\text{Na,Ca}} - \mu_{\text{Na,An}}) + F(\psi_{\text{A}} - \psi_{\text{C}}) + FE = 0 \quad [19]$$

Writing the theoretical thermodynamic open-circuit potential,  $E^\circ$ , as

$$E^\circ = -\frac{1}{F} (\mu_{\text{Na,Ca}} - \mu_{\text{Na,An}}) \quad [20]$$

and substituting into Eq. [19] results in

$$E = E^\circ + (\psi_{\text{C}} - \psi_{\text{A}}) \quad [21]$$

Combining Eq. [4] and [7], we find

$$d\mu_i = \frac{\kappa_e}{\kappa_i + \kappa_e} d\mu_{\text{Na}} - F d\psi - \frac{F i}{\kappa_i + \kappa_e} dx \quad [22]$$

Using the definition of  $J_{\text{Na}}^*$  in Eq. [10], we convert Eq. [22] to the integrable equation

$$d\mu_i = -\frac{F}{\kappa_i} \left[ (J_{\text{Na}}^* + i) dx + \frac{FD\rho}{M} dX_{\text{Na}} \right] - F d\psi \quad [23]$$

Integrating from  $x = 0$  to  $x = L$  and using Eq. [17]

$$\psi_{\text{C}} - \psi_{\text{A}} = -\frac{1}{\kappa_i} \left[ (J_{\text{Na}}^* + i) L + \frac{FD\rho}{M} (X_{\text{Na}}^C - X_{\text{Na}}^A) \right] \quad [24]$$

The terminal voltage of the cell is, in general, given by

$$E = E^\circ - \frac{1}{\kappa_i} (J_{\text{Na}}^* + i) L - \frac{FD\rho}{\kappa_i M} (X_{\text{Na}}^C - X_{\text{Na}}^A) \quad [25]$$

Several interesting results of Eq. [25] may be noted. One of these is the fact that the open-circuit terminal voltage of the cell is less than the theoretical thermodynamic open-circuit potential by an amount

$$E - E^\circ = -\frac{q_0 L}{\kappa_i} - \frac{FD\rho}{\kappa_i M} (X_{\text{Na}}^C - X_{\text{Na}}^A) = -\frac{RT}{F} \ln \left( \frac{\kappa_i + K_e X_{\text{Na}}^A}{\kappa_i + K_e X_{\text{Na}}^C} \right) \quad [26]$$

Therefore, it is not possible to measure the theoretical thermodynamic open-circuit potential of the above cell by direct means.

Another is the fact that the terminal voltage of the cell when the self-discharge rate is zero is

$$E = -\frac{FD\rho}{MK_e} \ln \frac{X_{\text{Na}}^A}{X_{\text{Na}}^C} \quad [27]$$

where we have utilized the assumptions that equilibrium exists and the activity coefficient is constant so that

$$E^\circ = -\frac{RT}{F} \ln \frac{X_{\text{Na}}^C}{X_{\text{Na}}^A} \quad [28]$$

Equation [27] shows that a negative terminal voltage will exist when the self-discharge rate is reduced to zero.

**Results**

Equation [11] was solved by putting it into the form

$$\frac{L}{\kappa_i} J_{Na}^* = \frac{1}{1+N} \left[ \frac{RT}{F} + \frac{FD\rho N}{MK_e(1+N)} \right] \ln \left[ \frac{1 + (1+N) \frac{K_e X_{Na}^A}{\kappa_i}}{1 + (1+N) \frac{K_e X_{Na}^C}{\kappa_i}} \right] + \frac{FD\rho(X_{Na}^A - X_{Na}^C)}{\kappa_i M(1+N)} \quad [29]$$

where  $N = i/J_{Na}^*$ . Values of  $N$  were assumed and values of  $L/\kappa_i J_{Na}^*$  and  $Li/\kappa_i$  were calculated for values of  $K_e X_{Na}^A/\kappa_i$  of 0.4, 0.8, and 1.6. For a temperature of 858°K, values of  $X_{Na}^A/X_{Na}^C$  of 10, 100, 1000, and 10,000 were chosen. By Eq. [28] these values of  $X_{Na}^A/X_{Na}^C$  correspond to  $E^\circ$  values of 0.1702, 0.3404, 0.5107, and 0.6809v, respectively. Other constants assumed for these calculations were:

- $\rho = 2.5 \text{ g/cm}^3$
- $M = 105$  (typical for NaF-NaCl-NaI mixtures) g/mole
- $D = 1 \times 10^{-4} \text{ cm}^2/\text{sec}$  (the Stokes-Einstein equation gives  $2.01 \times 10^{-5}$  and the Eyring equation,  $1.9 \times 10^{-4}$ )
- $K_c = 100, 200, 400 \text{ ohm}^{-1} \text{ cm}^{-1}$
- $X_{Na}^A = 0.004 \text{ mole/mole}$
- $\kappa_i = 1 \text{ ohm}^{-1} \text{ cm}^{-1}$

The calculated values of  $LJ_{Na}^*/\kappa_i$  and  $Li/\kappa_i$  are shown in Fig. 1, 2 and 3. It was noted that contributions by the terms involving  $FD\rho/M$  in Eq. [29] are negligible. This result indicates that the self-discharge rate is due

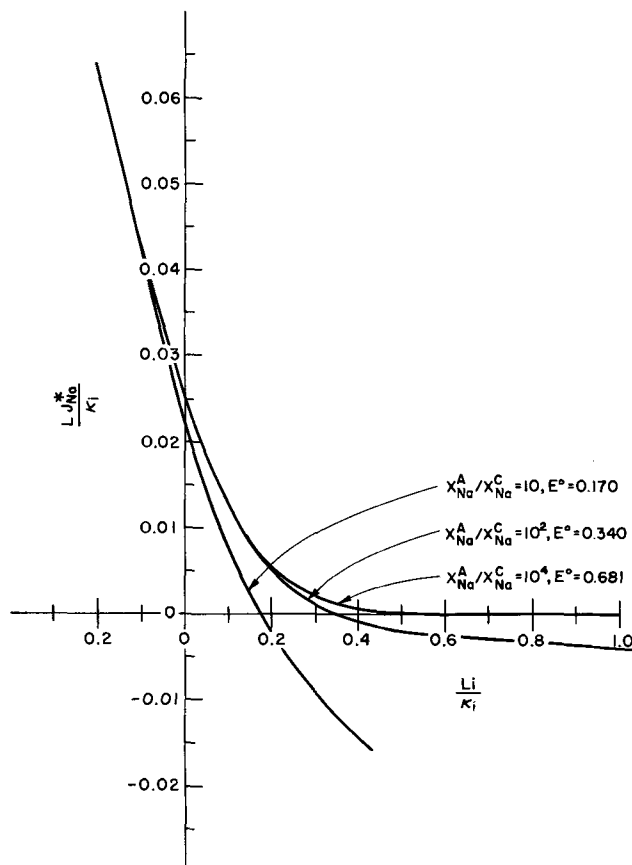


Fig. 1. Theoretical self-discharge rate as a function of cell current density.  $K_e/\kappa_i = 100$ ,  $K_e X_{Na}^A = 0.4$ ,  $X_{Na}^A = 0.004$ .

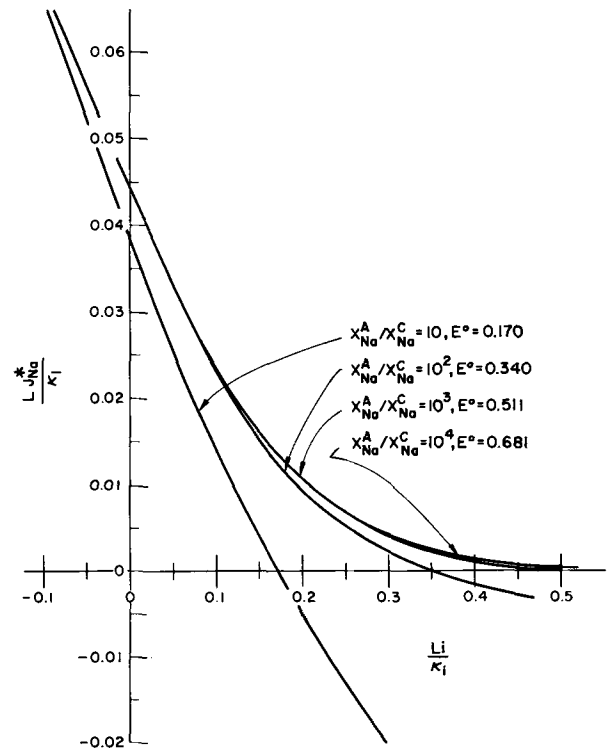


Fig. 2. Theoretical self-discharge rate as a function of cell current density:  $K_e/\kappa_i = 200$ ,  $K_e X_{Na}^A = 0.8$ ,  $X_{Na}^A = 0.004$ .

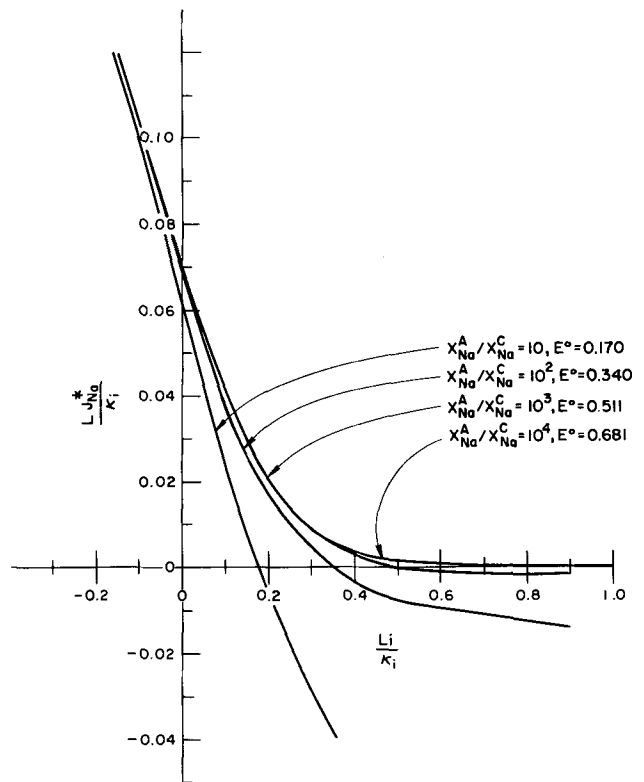


Fig. 3. Theoretical self-discharge rate as a function of cell current density:  $K_e/\kappa_i = 400$ ,  $K_e X_{Na}^A = 1.6$ ,  $X_{Na}^A = 0.004$ .

primarily to the electronic conductivity of the electrolyte solution and not to the diffusion of neutral sodium. Further, it was noted that the self-discharge rate decreases with increasing cell current.

The variation of  $X_{Na}$  (mole fraction of sodium dissolved in the electrolyte) with distance,  $x$ , from the anode-electrolyte interface was computed for  $i = 0$  ( $J_{Na}^* = q_0$ ) and  $J_{Na}^* = 0$  ( $i = p_0$ ); for  $K_e X_{Na}^A/\kappa_i = 1$ ; and for  $X_{Na}^A/X_{Na}^C = 10$  and 10,000. These values

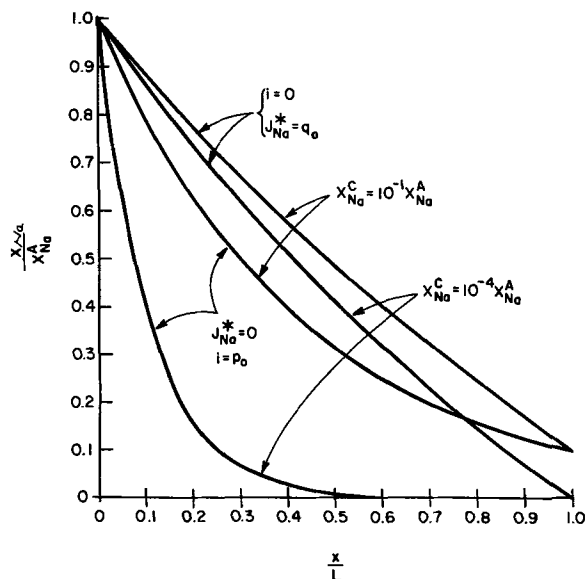
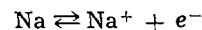


Fig. 4. Calculated sodium concentration in the electrolyte as a function of distance from anode:  $\frac{K_e}{\kappa_1} = 250$ ,  $\frac{K_e X_{Na}^A}{\kappa_1} = 1$ ,  $X_{Na}^A = 0.004$ .

are shown in Fig. 4 as  $X_{Na}/X_{Na}^A$  vs.  $x/L$ . It can be seen from the figure that the concentration of dissolved sodium in the vicinity of the anode decreases more rapidly than elsewhere as the cell current is increased.

The efficiency of solid-electrolyte fuel cells has been discussed by Takahashi *et al.* (10). They assumed that the electronic component of the conductivity of the electrolyte is always uniform. Therefore, the electronic current in the electrolyte must decrease linearly with increasing current output.

Similarly, Suski and Kubisz (11) discuss the current efficiency of the electrolysis of molten sodium chloride with a liquid metal after assuming that all sodium atoms in the electrolyte are there by diffusion through the boundary layer. No allowance is made for the equilibrium ionization reaction



in the electrolyte. Thus, their treatment attributes a greater portion of the self-discharge to the diffusion term and gives a linear change of self-discharge with cell current. It can be seen from Fig. 1 and Eq. [25] that the terminal cell voltage predicted by our treatment will not be linearly dependent on  $i$ . The results of our theory are in qualitative agreement with experimental results, and a paper covering the experiments and their comparison with theory is being prepared.

Manuscript submitted Oct. 13, 1967; revised manuscript received April 15, 1968. This paper was presented at the Chicago Meeting, Oct. 15-19, 1967, as Paper 19. The work reported in this paper was performed at Argonne National Laboratory, operated by the University of Chicago under the auspices of the U. S. Atomic Energy Commission, Contract No. W-31-109-eng-38.

#### REFERENCES

1. B. Agruss, *This Journal*, **110**, 1097 (1963).
2. R. E. Henderson, "Liquid Metal Cells", in "Fuel Cells—A CEP Technical Manual," p. 17, AICHE (1963).
3. J. C. Hesson and H. Shimotake, "Thermodynamic and Thermal Efficiencies of Thermally Regenerative Bimetallic and Hydride EMF Cell Systems," in "Advances in Chemistry Series," C. E. Crouthamel and H. L. Recht, Editors, Am. Chem. Soc., Washington, D. C., In press.
4. R. E. Henderson, B. Agruss, and C. Caple, "Energy Conversion for Space Power," Vol. 3, p. 411, Academic Press, Inc., New York (1961).
5. M. S. Foster, S. E. Wood, and C. E. Crouthamel, *Inorg. Chem.*, **3**, 1428 (1964).
6. M. S. Foster and C. C. Liu, *J. Phys. Chem.*, **70**, 950 (1966).
7. M. S. Foster, C. E. Crouthamel, and S. E. Wood, *ibid.*, **70**, 3042 (1966).
8. M. A. Bredig, "Mixtures of Metals with Molten Salts," in "Molten Salt Chemistry," M. Blander, Editor, John Wiley and Sons, Inc., New York (1964).
9. J. G. Kirkwood and I. Oppenheim, "Chemical Thermodynamics," p. 206, McGraw-Hill Book Company, Inc., New York (1961).
10. T. Takahashi, K. Ito, and H. Iwahara, *Electrochem. Acta*, **12**, 21 (1967).
11. L. Suski and K. Kubisz, *ibid.*, **12**, 1161 (1967).

## Correction

In the paper "Accommodation of Lattice Mismatch at Heterojunctions" by R. S. Mroczkowski, A. F. Witt, and H. C. Gatos which was published in the July 1968 issue of the *Journal* (Vol. 115, pp. 750-752) the Ac-

nowledgment should read as follows: "This work was supported by the Office of Naval Research under Contract Nonr-3963(05) and by the Advanced Research Projects Agency under Contract SD-90."

# Critical Potentials for Pitting Corrosion of Ni, Cr-Ni, Cr-Fe, and Related Stainless Steels

J. Horvath<sup>1</sup> and H. H. Uhlig\*

Department of Metallurgy and Materials Science,  
Massachusetts Institute of Technology, Cambridge, Massachusetts

## ABSTRACT

Critical pitting potentials for the binary Cr-Fe and Cr-Ni alloys in 0.1N NaCl become more noble (correspondingly more resistant to pitting) with increasing Cr content, particularly in the region 25-40% Cr and 10-20% Cr, respectively. The potentials for 57.8% Cr-Fe and pure Cr fall within the transpassive region. Ni containing 3.2% Mo, to the contrary, shows a lower (more active) critical potential; higher per cent Mo-Ni alloys appear to fall within the transpassive region corroding anodically as  $\text{MoO}_4^{--}$  plus  $\text{Ni}^{++}$  without pitting. Ni alloyed with 15% Cr-Fe shifts the potential in the noble direction; Mo alloyed with 15% Cr, 13% Ni stainless steel has a similar but even greater effect. At 0°C, 15% Cr, 13% Ni stainless steel exhibits a potential 0.5v more noble than at 25°C, corresponding to greatly increased resistance to pitting. This shift is less pronounced for the stainless steels containing Mo; in fact, at or above 1.5% Mo, the critical potentials at 0°C are below those at 25°C. In 0.1N NaBr, alloyed Mo shifts the potentials slightly in the active direction, contrary to a marked noble shift in 0.1N NaCl. At 0°C the potentials are still more active. These trends correlate with observed pitting for 15% Cr, 13% Ni stainless steel and the similar alloy containing 2.4% Mo in 10%  $\text{FeBr}_3$  both at 0° and 25°C. Absence of pitting is observed in 10%  $\text{FeCl}_3$  at 0°C for 15% Cr, 13% Ni stainless steel, but not for the similar alloy containing 2.4% Mo, which pits. The over-all results are explained on the basis of competitive adsorption at the metal surface and an effect of temperature on the structure of the double layer.

The concept of a critical potential above which passive alloys are liable to pitting corrosion in halide solutions, but below which they resist pitting, presumably for an indefinite period of exposure, has been described by several investigators. This subject was reviewed, among others, in an earlier paper by Kolotyркиn (1) and briefly by Leckie and Uhlig (2). The latter reported the effect of various environmental factors on the observed critical potentials of 18-8 stainless steel in NaCl solutions.

In view of the electrochemical mechanism of pit initiation and growth, it is concluded that pitting should be observed in aerated halide solutions, e.g., sea water, only in those metals and alloys whose critical potentials lie below the reversible oxygen electrode (approximately 0.8v in air). This is supported by data of Table I listing critical potentials for several metals in 0.1N NaCl. In sea water (approximately 0.5N NaCl) these values (1, 2) would be expected to be a few centivolts more active. Metals such as Cr and Ti, therefore, having critical potentials above 1v successfully resist pitting corrosion in aerated sea water in contrast to the other listed metals with values below 0.8v. The only exceptions that may arise in practice result from crevices at which stagnant electrolyte of higher  $\text{Cl}^-$  concentration accumulates because of electrochemical transport (lowering the critical potential) and, more importantly, of lower pH and dissolved  $\text{O}_2$  concentration causing localized breakdown of passivity (7). In general, the more noble the critical potential, the more resistant is the metal to pitting attack. But how fast pits grow once initiated usually depends on rate of the cathodic reaction, which in aerated NaCl is dependent on rate of  $\text{O}_2$  diffusion and reduction. The over-all rate, in turn, is a function of available total cathode surface (8) and conductivity of the electrolyte.

In this paper, the effect of alloying on the critical potentials of the Cr-Fe-Ni-Mo system in aqueous NaCl solution is reported, first as exhibited by several binary

alloys and then by some of the ternary and quaternary alloys of the usual stainless alloy compositions. Data also include an interesting, perhaps unexpected, effect of temperature on the critical potentials of stainless steels containing alloyed Mo.

## Experimental Procedure

Alloys were prepared in the laboratory from pure components by vacuum melting in dense alumina crucibles. After allowing A or He to enter the furnace the melt was drawn into 7 mm diam Vycor tubes and quenched in water. The ingots were homogenized in A or He, usually at 1050°-1100°C for several hours after which each composition was determined chemically. Ingots of Ni-Cr, Ni-Mo, and Cr-Fe were cold rolled to 0.25 cm, then annealed at 1000°-1050°C and water quenched. The Cr-Fe alloys containing more than 40% Cr were difficult to roll or swage, hence electrodes were machined directly from the homogenized ingot. Ingots of the lower % Cr-Fe alloys and of the stainless steels were swaged to about 0.45 cm diam rods, annealed at 1050°C, and water quenched.<sup>2</sup> All electrodes measured approximately 2 cm long and were either 0.4 cm diam or 0.5 cm wide by 0.2 cm thick. They were mounted as described earlier (2) by a threaded member allowing attachment to a nickel

<sup>2</sup> A subsequent anneal after quenching to avoid intergranular attack was not necessary because of low carbon content (0.001-0.002%).

Table I. Critical pitting potentials for various metals in 0.1N NaCl, 25°C\*

Metal	Critical potential, v	Reference
Al	-0.45	(3)
Ni	0.28	Present data
18-8	0.26**	(2)
Zr	0.46	(1)
Cr	>1.0	(4)
Ti	>1.0	(5, 6)

\* Estimated from data for various  $\text{Cl}^-$  concentrations.

\*\* This value is characteristic of one commercial composition. Higher values are usually obtained for pure alloys as described later in this paper.

\* Electrochemical Society Active Member.

<sup>1</sup> Institute of General and Physical Chemistry, University of Szeged, Szeged, Hungary.

wire. The electrode was firmly pressed by means of the wire against a glass tube separated by a Teflon gasket, assuring exposure of only the electrode, Teflon, and glass surface to the electrolyte. The electrodes were abraded to a final 3/0 emery paper, and pickled usually in 15%  $\text{HNO}_3$ , 5%  $\text{HF}$  at  $80^\circ\text{C}$  for 5 min to remove the cold worked surface.

Iron used for the melts was electrolytic grade, first deoxidized then decarburized in  $\text{H}_2$  to approximately 0.001-0.002% C. Chromium was of special high purity obtained from Union Carbide Company. Carbonyl nickel was made available by courtesy of The International Nickel Company. Molybdenum was 99.9% and for some few alloys it was spectroscopic grade, but without differing results.

The electrolyte for most experiments was 0.1N NaCl deaerated with purified nitrogen (passed over Cu at  $450^\circ\text{C}$ ), but without flow of nitrogen during the time of actual measurements. The Pyrex cell, fitted with ground glass joints as described previously (2), was located in an air thermostat maintained at  $25^\circ \pm 0.2^\circ\text{C}$ , which could also be adjusted to constant temperatures higher or lower than room temperature. A Wenking potentiostat was employed in conjunction with a chart recorder. The electrolyte was usually maintained above the Teflon gasket-electrode interface. Several comparative measurements were made holding the electrolyte below the Teflon gasket allowing a meniscus to form at the gas-liquid interface. Under conditions of continuous potential sweep, such critical potentials were found in general to be higher (more noble) than for total immersion. However, for long-time or steady-state conditions, values tended to focus on the same potential for partially or totally immersed electrodes, hence in view of the shorter times needed to achieve steady state under conditions of total immersion, it was this procedure which was usually followed. Pitting was observed to initiate preferably at the Teflon-electrode interface, but was not restricted to such areas in long-time polarization runs.

The experimental procedure was to first polarize the electrode potentiostatically at the least noble potential within the passive region for at least 15 min in order to achieve steady-state passivity. The potential was then advanced in stages of 50 mv, allowing 5 min between each change. Initially the current decreased or remained constant after each potential adjustment, but eventually a steadily increasing current at some potential  $V_c$  indicated the onset of pitting (or of transpassivity). Steady-state values  $V_c$  were obtained subsequently by holding the potential for long times at a fixed value and then observing pitting or the lack of it under a low power microscope. The lowest potential for which pitting could not be observed after a 10-hr or longer period of constant polarization was considered to be the steady-state value  $V_c$ . Reproducibility was in the order of  $\pm 5$  mv.

## Results

**Binary alloys.**—Values of the steady-state critical potentials  $V_c$  for binary Cr-Fe alloys in 0.1N NaCl at  $25^\circ\text{C}$  are shown in Fig. 1. Similar potentials  $V_c$  obtained by changing potentials in 50 mv increments at 5-min intervals were only slightly more noble. Measurements began at 12% Cr because the alloys below this composition exhibited less or no passivity and hence localized breakdown of passivity, leading to pitting, did not occur under present experimental conditions. Values of  $V_c$  rise rapidly in the region of 25-40% Cr indicating appreciably greater resistance to pitting at and above this composition range. Some pitting was observed for the 48.8% Cr-Fe alloy, but not for 57.8% Cr-Fe nor for pure Cr. The latter electrodes corroded uniformly with production of  $\text{CrO}_4^{--}$  (transpassivity).

Although the general shape of the curve is the same, data for Cr-Fe alloys reported by Kolotytkin (1) in 0.1N NaCl show more noble values in the range  $>25\%$

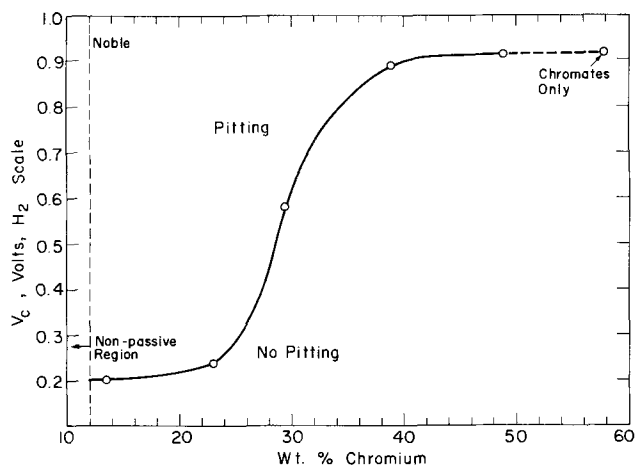


Fig. 1. Critical pitting potentials for Cr-Fe alloys in 0.1N NaCl,  $25^\circ\text{C}$ .

Cr. These differences can probably be ascribed to use of more rapid polarization rates than we used, which shifted potentials prematurely into the transpassive region accompanied by  $\text{CrO}_4^{--}$  formation. The reported observation by Steigerwald (9) that anodic pitting in 0.1N NaCl does not occur on chromized steel surfaces containing above 29% Cr is not readily explained. Perhaps again, lack of steady state conditions in his experiments, which were achieved in our measurements only through long-time polarization runs, may be accountable for the discrepancy.

Values of steady state potentials  $V_c$ , and also of non-steady state values  $V_c$  obtained as described earlier, for Cr-Ni alloys in 0.1N NaCl are shown in Fig. 2. Because Ni itself is passive, measurements for this alloy series began with 0% Cr. Values of  $V_c$  rise to more noble values especially within the range 10-20% Cr. Pitting was observed for all compositions including the maximum 29.4% Cr alloy. Measurements were not extended to higher Ni compositions because a two-phase alloy region forms which complicates interpretation of any potential trend.

The Mo-Ni alloys behave quite differently as is shown by potentiostatic polarization curves of Fig. 3. The corrosion potentials, corrosion behavior, and galvanostatic anodic polarization of these alloys have been reported previously (10). Pure nickel exhibits a normal critical potential  $V_c$  at 0.3v, above which pitting occurs. The polarization curve beyond  $V_c$  is almost linear up to a current density of  $0.4 \text{ ma/cm}^2$  and no oscillations are observed. Addition of 3.2% Mo to nickel lowers the value of  $V_c$  to about 0.2v and the potential increases abruptly just above  $0.1 \text{ ma/cm}^2$ .

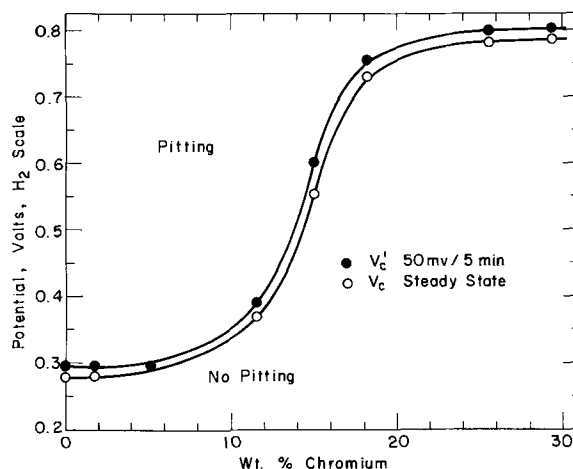


Fig. 2. Critical pitting potentials for Cr-Ni alloys in 0.1N NaCl,  $25^\circ\text{C}$ .

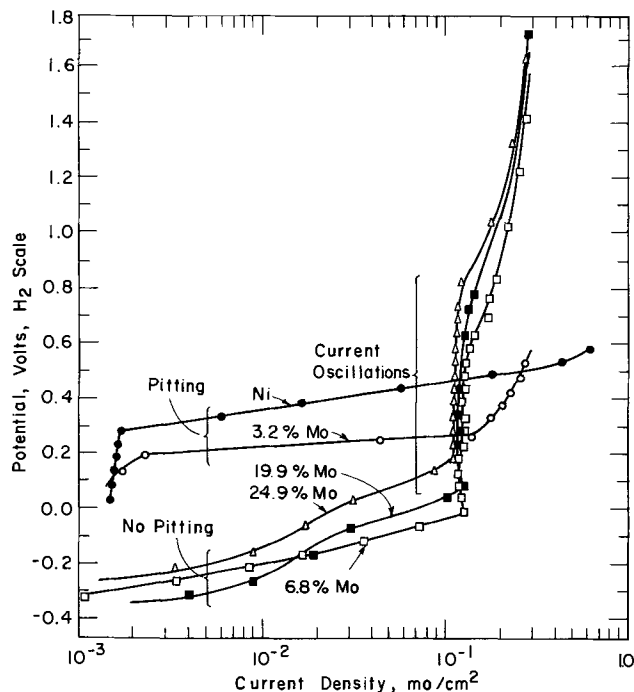


Fig. 3. Potentiostatic anodic polarization curves for Mo-Ni alloys in 0.1N NaCl, 25°C.

Alloys containing still larger Mo additions show no break, but exhibit instead an increasing current for small increments of potential beginning at values as active as  $-0.3\text{v}$ . No pitting was observed in alloys of 6.8% or higher Mo content. A long-time run during the initial period of polarization showed only a dark film, probably molybdenum oxide, covering the electrode surface. At about  $0.1\text{ ma/cm}^2$ , current oscillations occur, the peak values of which are indicated in Fig. 3. These cease at about  $0.9\text{v}$ , but the potential continues to rise steeply. It is concluded that  $\text{MoO}_4^{--}$  forms beginning at the potentials corresponding to current oscillations accompanied by periodic breakdown and formation of passivity, until on reaching a still higher potential range, conditions become stabilized. The upturn of potential at  $0.1\text{ ma/cm}^2$  for the 3.2% Mo-Ni alloy is probably also the result of  $\text{MoO}_4^{--}$  formation. The Pourbaix diagram (11) for pure molybdenum, for example, shows that molybdate formation at pH 7 begins at about  $-0.4$  to  $-0.5\text{v}$  in line with the formation of molybdates in the Ni-Mo alloys beginning at somewhat more noble values. Although molybdenum was detected by chemical analysis of the anolyte after polarization of the Mo-Ni alloys, it was not easy to determine its precise valence. However, the probability that molybdate formation is the cause of current oscillations in the  $0-0.9\text{v}$  range is supported by similar oscillations observed for the 15% Cr, 13% Ni stainless steel (Fig. 4) caused by chromate formation in the potential range of  $0.7-1.55\text{v}$ . The Pourbaix diagram for pure Cr (12) at pH 7 shows that  $\text{CrO}_4^{--}$  forms beginning at  $0.5-0.6\text{v}$  which is expectedly lower but in reasonable correspondence with the lower limit of the observed oscillations for the stainless alloy.

#### Cr-Fe-Ni Stainless Steels

The solid solution ternary 15% Cr alloys containing increasing amounts of alloyed Ni were prepared by H. Feller who reported their passive properties in  $1.28\text{N H}_2\text{SO}_4$  (13). The critical potentials for these alloys in  $0.1\text{N NaCl}$  at  $25^\circ\text{C}$  shift in the noble direction as Ni increases (Fig. 5). The shift is not as large as for equivalent Cr additions, but the potential change correlates with the well-known improved corrosion and pitting resistance of high Ni stainless steels in chloride media as compared to the nickel-free or low-nickel stainless steels.

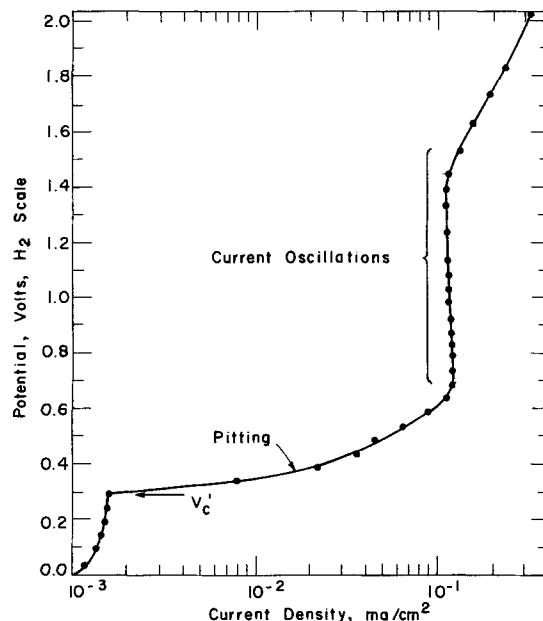


Fig. 4. Potentiostatic anodic polarization curve for 15% Cr, 13% Ni stainless steel in 0.1N NaCl, 25°C.

Kolotyrykin (1) also reported more noble critical potentials for Cr-Ni-Fe stainless steels with increasing Ni content.

Alloyed Mo up to 2.4% in a 15% Cr, 13% Ni stainless steel at  $25^\circ\text{C}$  similarly shifts the critical potential toward more noble values (Fig. 6). The change of potential is relatively greater than for corresponding Ni additions, and accompanies the well-known improved resistance of the Mo-containing stainless steels (e.g. Type 316) to pitting corrosion in chlorides. According to Tomashov *et al.* (14),  $V_c$  becomes still more noble with increasing amounts of alloyed Mo above 2.4%. The quantitative interpretation of data for high Mo stainless steels is complicated, however, by the formation of a multiphase structure. The present alloys, relatively low in Cr and high in Ni, were chosen to preserve a single-phase structure, as was confirmed by metallographic examination.

The potentiostatic behavior of the 1.43% Mo stainless steel is shown in Fig. 7. Here current oscillations begin at the somewhat lower potential of  $0.55\text{v}$  compared to  $0.7\text{v}$  for Mo-free stainless steel (Fig. 4) and reach a similar upper value of  $1.5\text{v}$ . It is likely that both  $\text{MoO}_4^{--}$  and  $\text{CrO}_4^{--}$  form in this potential range.

Hospadaruk and Petrocelli (15) apparently obtained more active values of  $V_c$  in  $0.5\text{N NaCl}$  for commercial 18-8 (Type 301), 18% Cr-Fe and 17% Cr, 13% Ni, 2.2% Mo (Type 316) stainless steel than are indicated

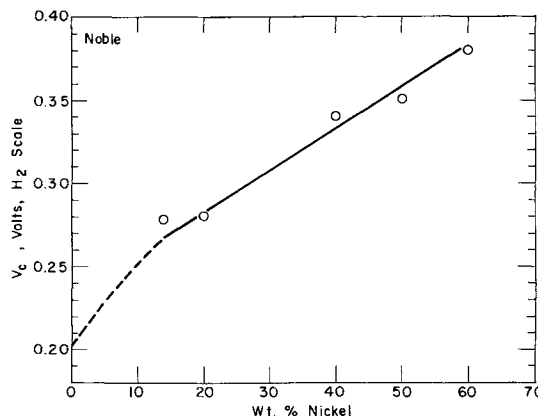


Fig. 5. Critical pitting potentials for 15% Cr-Fe alloys with increasing Ni content, in  $0.1\text{N NaCl}$ ,  $25^\circ\text{C}$ .



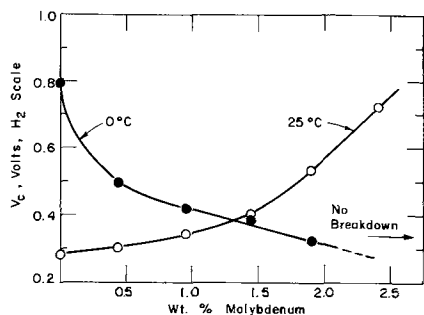


Fig. 6. Critical pitting potentials for 15% Cr, 13% Ni stainless steel with increasing Mo content, in 0.1N NaCl, 25°C and 0°C.

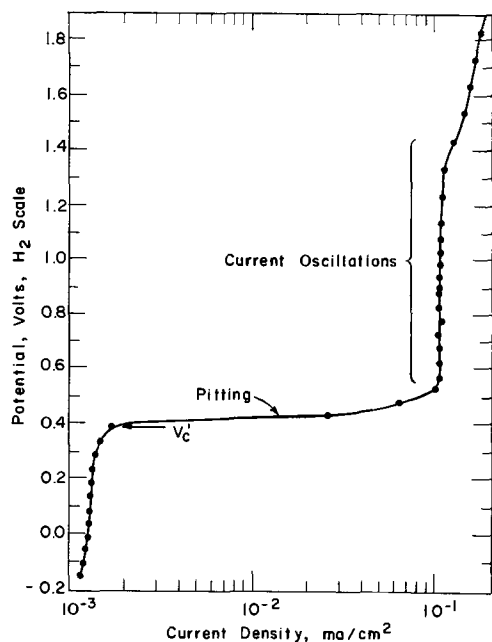


Fig. 7. Potentiostatic anodic polarization curve for 15% Cr, 13% Ni, 1.43% Mo stainless steel in 0.1N NaCl, 25°C.

by our values in 0.1N NaCl. Although their data do not support an effect of Cl<sup>-</sup> concentration on  $V_c$  for 18-8, previous data of Leckie and Uhlig (2) show a shift of 0.07v in the active direction on going from 0.1 to 0.5N NaCl. This shift explains a large part of the difference in their results and those presently reported. It should be mentioned in addition that their use of austenitic alloys slowly cooled from the annealing temperature causes some degree of carbide precipitation and chromium depletion along grain boundaries. This effect would tend to artificially shift measured critical potentials in the active direction and, according to our experience, would also appreciably decrease reproducibility of the measurements.

At 40°C, values of  $V_c$  for the 15% Cr, 13% Ni stainless steel approximate those at 25°C. At 0°C, however,  $V_c$  shifts to the markedly more noble value of 0.78v (Fig. 6) which is 0.5v more noble than the value at 25°C. This appreciable shift was first reported for 18-8 by Leckie and Uhlig (2) who made the prediction, later confirmed, that pitting of 18-8 would not occur in 10% FeCl<sub>3</sub> at 0°C because the oxidation-reduction potential of 10% FeCl<sub>3</sub> is below the observed critical potential at this temperature.

Unexpectedly, the addition of Mo to stainless steel is found to reduce the shift in the noble direction occurring at 0°C. For the 1.3% Mo alloy, the values of  $V_c$  at 0°C and 25°C are the same, and for 2% Mo the value at 0°C approximates that for the Mo-free stainless steel at 25°C. At 0°C the 2.4% Mo alloy reaches the transpassive state and no definite critical potential is observed. Instead, current increases continu-

ously with potential and the electrode corrodes uniformly. Pitting can be induced, however, if the alloy is polarized to a value approaching 0.6v. Accordingly the alloy containing 2.4% Mo immersed in 10% FeCl<sub>3</sub> at 0°C, for which the oxidation-reduction potential lies above 0.6v, showed definite pitting after two days, contrary to the behavior of the alloy without Mo which was free of pitting. In similar tests at 25°C, the 2.4% Mo alloy did not pit within two days (it probably would have for longer time exposure), but the alloy free of Mo was pitted.

It was observed (16, 17) some years ago that the molybdenum-containing stainless steels, although relatively resistant to pitting in ferric chloride, tend to pit in much shorter time in equivalent bromide solutions. The critical potentials conform to this observation as shown in Fig. 8. The value of  $V_c$  (0.54v) for the 15% Cr, 13% Ni alloy in 0.1N NaBr at 25°C is 0.26v more noble than in 0.1N NaCl, hence pitting of this composition alloy is less pronounced in bromides than in chlorides. However, on adding molybdenum to the 15% Cr, 13% Ni steel, values of  $V_c$  change only slightly, tending toward more active values. This is in contrast to a marked shift in the noble direction in chloride solutions, hence pitting in >2% Mo stainless steels, as observed, is more pronounced in bromides than in chlorides. At 0°C, the value of  $V_c$  in bromides for the Mo-free stainless steel is definitely below the value at 25°C, opposite to the pronounced more noble shift observed in chlorides. The critical potential tends to decrease still further on addition of 0.43% Mo. Indefinite results are obtained at 1.43% Mo or above, no well established critical potentials being observed. Apparently the transpassive state of the Mo stainless steels is reached at relatively low potentials and the alloys corrode generally without pitting. Pitting, as before, could be induced by polarizing to a potential in the region of 0.6v. These trends of critical potential were confirmed by two-day pitting tests in 10% FeBr<sub>3</sub> solutions, pitting occurring at 0° and at 25°C for the 0%, 1.4%, and 2.4% Mo alloys.

### Discussion

The basic mechanism accounting for the critical potential appears to be one of Cl<sup>-</sup> adsorbing competitively with oxygen of the passive film for sites on the metal surface. As the potential is made more noble, Cl<sup>-</sup> ions move into the double layer of the electrode surface, eventually reaching at the critical potential the concentration required to displace adsorbed oxygen (or an oxygen-H<sub>2</sub>O complex) at favored locations. Adsorbed Cl<sup>-</sup> greatly reduces the overvoltage for anodic dissolution of metal, compared to the situation for adsorbed oxygen, thereby initiating a pit. This is essentially the mechanism described by Leckie and Uhlig (2), the Russian school (1) and by Brauns and

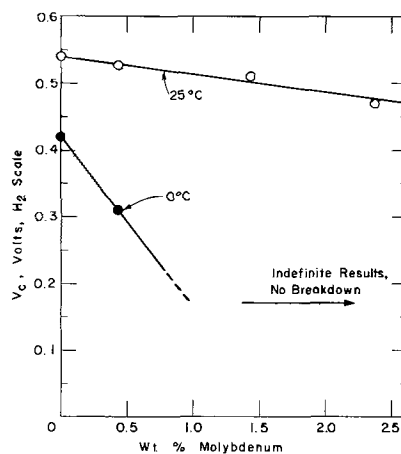


Fig. 8. Critical pitting potentials for 15% Cr, 13% Ni stainless steel with increasing Mo content in 0.1N NaBr, 25°C and 0°C.

Schwenk (18). A different model requiring penetration and breakdown of a supposed metal oxide passive film was described by Streicher (17) and by Hoar, Mears, and Rothwell (19).

According to the adsorption model, the observed more noble values of  $V_c$  for Cr-Fe alloys with increasing Cr content is ascribed to the increasing affinity of the alloys for oxygen compared to  $\text{Cl}^-$ . Since the Flade potential is a measure of passive film stability (20), it also changes with Cr content but in the negative or more active direction. The sharp rise of  $V_c$  at 25-40% Cr shown in Fig. 1 compared to the similar pronounced decrease of Flade potential at 10-30% Cr reported by King and Uhlig (21) suggests, however, that increased stability of the passive film is only one factor affecting  $V_c$ ; the relative affinity of the alloy for  $\text{Cl}^-$  is also a factor.

When  $V_c$  becomes sufficiently noble to overlap the transpassive region,  $\text{CrO}_4^{--}$  plus  $\text{Fe}^{+++}$  are produced as anodic products, and corrosion of the electrode surface may then proceed uniformly with little or no localized attack. Hence the 57.8% Cr-Fe alloy, and probably higher Cr alloys including pure Cr as well, do not pit at the noble potentials corresponding to pronounced rise of current in the potentiostatic curves, but they corrode uniformly instead. Whether pitting occurs in any of the Cr-Fe alloys at some potential within the transpassive region probably depends on whether  $V_c$  is exceeded for a particular alloy, the rate of stirring, and whether the uniform corrosion rate by  $\text{CrO}_4^{--}$  formation exceeds the rate of localized corrosion. Since pitting was observed in some Cr-Fe alloys and also in some of the Cr-Ni alloys polarized well into the transpassive region, it is apparently possible for  $\text{Cl}^-$  to adsorb despite simultaneous  $\text{CrO}_4^{--}$  formation. However, the two ions adsorb competitively and it is expected that for a sufficiently high surface concentration of  $\text{CrO}_4^{--}$ , adsorption of  $\text{Cl}^-$  would be less probable and  $\text{CrO}_4^{--}$  would act as a pitting inhibitor in the same sense as do other anions, e.g.,  $\text{SO}_4^{--}$ ,  $\text{ClO}_4^-$ , and  $\text{NO}_3^-$  (2).

Steigerwald (9) noted that >30% Cr-Fe alloys are resistant to pitting on immersion in 10%  $\text{FeCl}_3 \cdot 6\text{H}_2\text{O}$  at room temperature for 10 days. The measured oxidation-reduction potential of 18-8 in 10%  $\text{FeCl}_3$  inhibited with 5%  $\text{NaNO}_3$  to avoid pitting (which does not affect oxidation-reduction kinetics of  $\text{Fe}^{+++} \rightleftharpoons \text{Fe}^{++}$ ) (22) is about 0.8v (23). Lack of pitting is consistent with reported values of  $V_c$  shown in Fig. 1 equal to or greater than 0.8v at or above approximately 34% Cr.

The same considerations mentioned above apply to increasing values of  $V_c$  for Cr-Ni alloys (Fig. 2). In the 15% Cr-Fe series, alloyed Ni shifts  $V_c$  in the noble direction perhaps because Ni, for one reason, has less affinity for  $\text{Cl}^-$  than does Cr. This is shown by the relative free energies of formation for the metal chlorides (Table II). Molybdenum, similarly, but to a greater extent, shifts  $V_c$  of the 15% Cr, 13% Ni alloy series both because of decreased affinity of Mo for  $\text{Cl}^-$  and because of its increased affinity for oxygen. It is probable furthermore that the greater tendency of the Mo stainless steels to pit in bromide compared to chloride solutions corresponds to a relatively higher affinity of Mo for  $\text{Br}^-$ , although corresponding free energy data are not available.

The situation becomes more complex at low temperatures where the shift of  $V_c$  may be large but

where relative affinities are not expected to differ appreciably from those applying at room temperature. However, the structure of the double layer is probably sensitive to temperature, as for example occurs through relative hydration of ions in the outer and perhaps also the inner Helmholtz layers, as well as through hydration of the passive film itself. In other words, it is plausible that the relatively greater hydration of both the passive film and adsorbed ions (altering their effective radii) at low temperatures changes both concentration of ions in the double layer and their critical separation from oxygen of the passive film, thereby affecting conditions for competitive adsorption. Hence the critical potential is also changed, the direction of which is sensitive to specific chemical affinities, in particular accounted for by alloyed Mo. Any alternative mechanism based on relative ease of penetration of ions through a supposed passive oxide film brought about by similar temperature changes is considered to be less plausible.

#### Acknowledgment

The present research was aided by a grant from the Office of Saline Water, U.S. Department of the Interior. One of us (J. H.) is grateful for the award of a fellowship by the Ford Foundation. H. P. Leckie contributed some of the preliminary data and in particular the final data appearing in Fig. 5.

Manuscript submitted Nov. 29, 1967; revised manuscript received ca. April 30, 1968. This paper was presented at the Chicago Meeting, Oct. 15-19, 1967, as Paper 77.

Any discussion of this paper will appear in a Discussion Section to be published in the June 1969 JOURNAL.

#### REFERENCES

1. Ya. Kolotyrlin, *Corrosion*, **19**, 261t (1963).
2. H. Leckie and H. Uhlig, *This Journal*, **113**, 1262 (1966).
3. H. Kaesche, *Z. Physik. Chem. N. F.*, **34**, 87 (1962).
4. N. Greene, C. Bishop, and M. Stern, *This Journal*, **108**, 836 (1961).
5. N. Hackerman and C. Hall, *J. Phys. Chem.*, **57**, 262 (1953).
6. F. Posey and E. Bohlmann, Second Symp. on Fresh Water from the Sea, Athens, Greece, May 1967.
7. H. Uhlig, *This Journal*, **108**, 327 (1961).
8. O. Ellis and F. LaQue, *Corrosion*, **7**, 362 (1951).
9. R. Steigerwald, *ibid.*, **22**, 107 (1966).
10. H. Uhlig, P. Bond, and H. Feller, *This Journal*, **110**, 650 (1963).
11. M. Pourbaix, "Atlas of Electrochemical Equilibria in Aqueous Solutions," p. 275, Pergamon Press, New York (1966).
12. Ref. 11, pp. 262-264.
13. H. Feller and H. Uhlig, *This Journal*, **107**, 864 (1960).
14. N. Tomashov, G. Chernova, and O. Marcova, *Corrosion*, **20**, 166t (1964).
15. V. Hospadaruk and J. Petrocelli, *This Journal*, **113**, 878 (1966).
16. H. H. Uhlig and J. Wulff, *Trans. A.I.M.E., Iron and Steel Div.*, **135**, 494 (1939).
17. M. Streicher, *This Journal*, **103**, 375 (1956).
18. E. Brauns and W. Schwenk, *Archiv. Eisenhüttenw.*, **32**, 387 (1961).
19. T. Hoar, D. Mears, and G. Rothwell, *Corros. Sci.*, **5**, 279 (1965).
20. H. Uhlig, "Corrosion and Corrosion Control," pp. 61-62, John Wiley & Sons, Inc., New York (1963).
21. P. King and H. Uhlig, *J. Phys. Chem.*, **63**, 2026 (1959).
22. M. Stern, *This Journal*, **104**, 559, 600 (1957).
23. H. Leckie, Unpublished data.
24. W. Latimer, "Oxidation Potentials," Prentice-Hall, New York (1952).

Table II. Free energies of formation, 25°C (24)

	Kcal
$\text{CrCl}_2$ (c)	-85.2
$\text{NiCl}_2$ (c)	-65.1
$\text{MoCl}_2$ (c)	-34.6
$\text{MoO}_4^{--}$ (aq.)	-218.8
$\text{CrO}_4^{--}$ (aq.)	-176.1

# Thermodynamic Properties of the Oxides of Fe, Ni, Pb, Cu, and Mn, by EMF Measurements

G. G. Charette<sup>1</sup> and S. N. Flengas\*

Department of Metallurgy and Materials Science, University of Toronto, Toronto, Ontario, Canada

## ABSTRACT

A "closed system" solid electrolyte electrochemical cell has been designed to investigate the thermodynamic properties of metal oxides. The measurements with this cell are free of mixed potentials arising from nonequilibrium oxygen pressure conditions in the electrode compartments. The oxide systems investigated include Ni-NiO, Pb-PbO<sub>(S,L)</sub>, Cu-Cu<sub>2</sub>O, Cu<sub>2</sub>O-CuO, Fe-Fe<sub>x</sub>O, Fe<sub>y</sub>O-Fe<sub>3</sub>O<sub>4</sub>, Fe<sub>3</sub>O<sub>4</sub>-Fe<sub>2</sub>O<sub>3</sub>, MnO-Mn<sub>3</sub>O<sub>4</sub>, and Mn<sub>3</sub>O<sub>4</sub>-Mn<sub>2</sub>O<sub>3</sub>.

Calculation of equilibria involving oxide phases at high temperatures is often handicapped by the lack of reliable thermodynamic data on free energies. Most of the standard free energies of formation for oxides available in the literature have been calculated from enthalpies and heat capacities measured calorimetrically or from gas-solid equilibrium-type measurements. Quite often the high-temperature heat capacities are obtained by extrapolation from lower temperature data or estimated using semi-empirical rules. Calculations based on calorimetric data are often contradictory and include the rather wide error limits of the various thermal quantities involved in the calculation. For example, the free energies of formation of the oxides PbO, NiO, FeO, and Cu<sub>2</sub>O given by Kubaschewski and Evans (1), have an estimated uncertainty of  $\pm 3$ ,  $\pm 2$ ,  $\pm 3$ , and  $\pm 1$ , kcal/mole of oxide, respectively. Also, the free energies for these oxides found in thermodynamic tabulations by Wicks and Block (2) differ from the average values given by Kubaschewski and Evans (1) by about 1 kcal.

More recently, electrochemical measurements with galvanic cells using solid oxide electrolytes made possible the direct determination of free energies at elevated temperatures with a higher degree of accuracy. Particularly, the pioneering work by Kiukkola and Wagner (3) has demonstrated the usefulness of the solid solutions of calcium and zirconium oxides as selective oxygen anion electrolytes. These electrolytes have been used in solid oxide electrochemical cells to separate the two electrode compartments, to screen the electronic conductivity of the oxides at high temperatures, and to establish electrochemical contacts which are free of junction potentials. The systems investigated so far by this technique include the oxides of Ni (3-15, 21, 23), Fe (3-7, 9-12, 14-22), Cu (3, 4, 8, 12, 23), Pb (4, 8, 12), Mn (6), and many others.

These measurements have been conducted by the "open cell stacked pellet" technique described by Kiukkola and Wagner (3). In this method the indicating electrode consisted of a pelletized and sintered mixture of the metal-metal oxide system under investigation separated from the reference electrode by a pellet of the zirconia-calcia diaphragm. The reference electrode was another metal-metal oxide system of known free energy of formation. Most of these cells were operated under flow using an inert gas common for both electrodes.

Blumenthal and Whitmore (6) used the common open cell stacked pellet technique in a stream of purified inert gas along with a ZrO<sub>2</sub> based electrolyte to measure the systems Fe<sub>3</sub>O<sub>4</sub>-Fe<sub>2</sub>O<sub>3</sub> and MnO-Mn<sub>3</sub>O<sub>4</sub> between 750° and 1050°C. Their ranges of scatter amounted to  $\pm 5$  mv with the latter and  $\pm 7$

mv with the former, approximately two to four times the scatter observed by workers working with more conventional oxide systems.

Rezukhina *et al.* (24) modified the usual technique slightly and operated their cells under vacuum.

Rapp (7) determined the free energy of formation of MoO<sub>2</sub> from Mo using as reference half-cells the systems Fe-Fe<sub>x</sub>O and Ni-NiO along with ZrO<sub>2</sub> (0.15 CaO) as the solid electrolyte. When his cell was constructed simply by pressing together flat metal oxide and electrolyte tablets, he noted that the cell voltage was about 35 mv too low and very dependent on helium flow rate. His later results were greatly improved by fabricating the electrolyte in an H-form and fitting the sintered metal-metal oxide cylinders into each side.

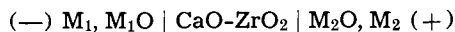
Roeder and Smeltzer (9) mounted their stacked pellets of electrodes and electrolyte independently from the furnace assembly. Finally, Steele and Alcock (4) developed a cell whereby the two electrodes could be kept separate by pressing one side of the electrolyte against the open polished end of an alumina tube. Separate flows of inert gas were maintained within and without the alumina tube, thereby giving each half-cell compartment an independent oxygen potential. It is doubtful, however, whether the electrolyte to alumina contact could make the gas atmospheres over the two compartments truly independent of each other.

Although emf measurements have yielded much higher accuracies ( $\pm 100$ -200 cal) than available calorimetric data ( $\pm 1$ -3 kcal), some measurements on identical systems do not agree among themselves or show an abnormal scatter of points. Several workers have mentioned some practical difficulties encountered while measuring emf's with solid electrolyte cells, especially the variation of the cell emf while varying the rate of flow of inert gas, and the eventual drift in the potential after operating a cell for long periods of time at high temperatures. Such difficulties become particularly severe where the difference in oxygen pressures above the two metal-metal oxide pellets is large or when one of the oxides has a relatively high equilibrium oxygen pressure. This may explain why the typical open cell stacked pellet technique has not been as successful on oxide systems such as Fe<sub>3</sub>O<sub>4</sub>-Fe<sub>2</sub>O<sub>3</sub>, Cu<sub>2</sub>O-CuO, and MnO-Mn<sub>3</sub>O<sub>4</sub> (6).

The free energy for a spontaneous exchange reaction of the type



where M<sub>1</sub>O and M<sub>2</sub>O are the metal saturated phases of the two oxides, may be obtained directly from the emf of the following solid oxide electrochemical cell



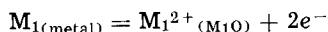
The over-all reaction may be realized electrochemi-

\* Electrochemical Society Active Member.

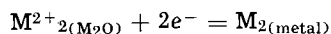
<sup>1</sup> Present address: Quebec Iron and Titanium Corporation, Sorel, Quebec, Canada.

cally by considering either cationic or anionic half-cell reactions. Upon passage of two Faradays of electricity a cationic model predicts the following charge transfer operations

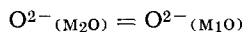
(a) at the (–ve) electrode:



(b) at the (+ve) electrode:



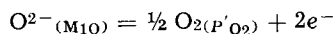
(c) oxygen anion transfer through the CaO-ZrO<sub>2</sub> membrane



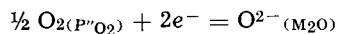
The over-all cell reaction (A) is:  $M_1 + M_2\text{O} = M_2 + M_1\text{O}$ .

In the anionic model the half-cell reactions are written as:

(a) at the (–ve) electrode:



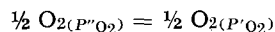
(b) at the (+ve) electrode:



(c) oxygen anion transfer through the CaO-ZrO<sub>2</sub> membrane:



The over-all cell reaction (B) is:



where  $P''_{O_2}$  and  $P'_{O_2}$  are the partial pressures of oxygen present over the oxide phases M<sub>2</sub>O and M<sub>1</sub>O, respectively. For the derivation it is assumed that the transport number of oxygen anions through the zirconia membrane is unity.

The cell potential  $E_A$ , for cell reaction (A), is given by the well-known expression

$$E_A = - \left[ \frac{\Delta G^\circ_{f, M_1O} - \Delta G^\circ_{f, M_2O}}{2F} \right] \quad [2]$$

where,  $\Delta G^\circ_{M_1O}$  and  $\Delta G^\circ_{M_2O}$ , are the standard free energies for the formation of the oxides M<sub>1</sub>O and M<sub>2</sub>O at the temperature of the measurement. Written in this manner, the cell appears to be a galvanic cell.

The cell potential  $E_B$ , for reaction (B), is given as

$$E_B = - \frac{RT}{2F} \ln \left[ \frac{P'_{O_2}}{P''_{O_2}} \right]^{1/2} \quad [3]$$

The cell in this case appears to be an oxygen concentration cell and the net cell reaction is the transfer of oxygen from the high- to the low-pressure side. The metallic electrodes are taken as truly inert electrodes. The two equations, [2] and [3], represent the same potential

$$E = E_A = E_B$$

only when the oxygen pressures over the oxide phases correspond to the true equilibrium pressures. For this case Eq. [3] may be converted to Eq. [2] by introducing the well-known relationship for the standard free energy of formation of an oxide

$$\Delta G^\circ_{f, MO} = - RT \ln (P_{O_2})^{1/2}_{\text{eq.}} \quad [4]$$

It appears, therefore, that under equilibrium oxygen pressure conditions the half-cell reactions could be described in terms of either the cationic or the anionic processes, and a cell of this type could be considered as either a galvanic or an oxygen concentration cell. However, if the oxygen content of the atmosphere surrounding each compartment is not at equilibrium with the metal-metal oxide system present, the measured

cell potential is not necessarily the thermodynamic potential of the system.

Considering the case of the open cell stacked pellet assembly used by previous investigators, it is unlikely that such cells could be operated under truly equilibrium conditions. For a given "purified" argon atmosphere, the oxygen level in the inert gas should cause either oxidation of the metal or reduction of the oxide. These effects should be more pronounced at the outer edges of the electrode pellets where charge transfer operations are also taking place, and in effect an oxygen potential gradient should be expected to exist within each compartment soon after starting an experiment. Although the magnitude of this effect cannot be estimated, it is evident that the potentials obtained under such conditions are best described as mixed potentials (25), and their departure from the true equilibrium values should depend on the nonequilibrium conditions and the self-adjusting capacity of each metal-metal oxide system.

Preliminary experiments in this investigation with a Pt, Fe<sub>2</sub>O<sub>3</sub>-Fe<sub>3</sub>O<sub>4</sub> open-type electrode have shown the validity of these considerations. The potentials in this system were found to drift with time when the flow rate of helium was kept constant and were also dependent on the flow rate of the gas.

For this reason the measurements reported in this paper were obtained with a "closed cell" designed to operate under truly equilibrium oxygen pressure conditions. These cells have been found to be extremely stable and could function for periods of several weeks without any detectable change in their emf. The present technique was first used on systems which had been successfully investigated previously, such as the Fe-Fe<sub>2</sub>O<sub>3</sub>, Ni-NiO, Fe<sub>2</sub>O-Fe<sub>3</sub>O<sub>4</sub>, and Cu-Cu<sub>2</sub>O, and was then used to obtain accurate data on the more doubtful systems Fe<sub>3</sub>O<sub>4</sub>-Fe<sub>2</sub>O<sub>3</sub>, Pb-PbO, MnO-Mn<sub>3</sub>O<sub>4</sub>, Mn<sub>3</sub>O<sub>4</sub>-Mn<sub>2</sub>O<sub>3</sub>, and Cu<sub>2</sub>O-CuO.

The calcia-doped zirconia electrolyte is a purely ionic conductor only within a specified range of oxygen pressures for each temperature. Measurements, therefore, were obtained only with oxide systems compatible with the oxygen pressure requirements.

Along with the results of the present investigation, data from various other sources are also shown for comparison when necessary. All information derived from the present work is tabulated in the form of free energy equations and sigma-functions.

## Experimental

The most important piece of equipment in the present study was a 24 in. long tube of calcia-stabilized zirconia, commercially available from the Zirconium Corporation of America. The tube can be described as having one closed end (flat) an OD of 1/2 in., an ID of 3/8 in., and a nominal wall thickness of 1/16 in. It is impervious and has been certified helium leak tested to  $5 \times 10^{-7}$  or less standard cc/sec at room temperature by the manufacturing company. In addition, all tubes used in the present investigation were subjected to helium leak detection tests in this laboratory, using a Veeco Mass Spectrometer Leak Detector (Model MS-9). The tubes were of the Zircoa-B grade material for which the following typical chemical analysis is given in weight per cent: 93.5 (ZrO<sub>2</sub> + HfO<sub>2</sub>), 4.8 CaO (10 m/o [mole per cent]), 0.62 SiO<sub>2</sub>, 0.25 MgO, 0.10 Fe<sub>2</sub>O<sub>3</sub>, 0.18 Al<sub>2</sub>O<sub>3</sub>, 0.11 TiO<sub>2</sub>. The material is described as being fully stabilized in the cubic crystal configuration and able to retain its crystal structure, even on repeated cycling, to its melting point (approximately 2625°C). Under experimental conditions of repeated heating and cooling the tubes behaved very well since no cracking due to thermal shock was ever detected, and there was no evidence of chemical attack from the various oxides used as electrode materials. Conductivity measurements on the tube material, performed in this laboratory by Etsell (26), could not detect any oxygen pressure effect on the conductivity

in an oxygen pressure range from 1 to  $10^{-18}$  atm and for temperatures up to  $1080^{\circ}\text{C}$ . In addition, McClaine and Coppel (27) have reported similar observations for the electrolyte containing 95 m/o  $\text{ZrO}_2$  and 5 m/o  $\text{CaO}$ .

Anticipating the results of the present investigation, the emf's measured with these commercially available tubes for the well-known systems Ni-NiO and  $\text{Fe-Fe}_x\text{O}$ , agreed within  $\pm 1$  mv with the results of Kiukkola and Wagner (3), Steel and Alcock (4), and others who utilized zirconia doped with 15 m/o  $\text{CaO}$  which is well established for its ionic behavior. Accordingly, it may be said with confidence that the zirconia material used in the present investigation was behaving like an ionic membrane permeable only to oxygen anions.

The cell design used for the emf measurements is shown in Fig. 1. It consists of two half-cell compartments separated by the calcium oxide stabilized zirconia diaphragm, both sealed under vacuum. The inner reference electrode is the closed-end zirconia tube containing the loosely packed nickel-nickel oxide powder. The top of this tube is closed by a tight fitting bell-shaped Pyrex tube which supports a tungsten electrode connection sealed into the glass. The bell is connected to the zirconia tube with De Khotinsky cement. The nickel electrode is a  $\frac{1}{8}$  in. diameter nickel rod pressed against the nickel oxide powder by means of a heavy spring and an aluminum insulating rod of  $\frac{1}{4}$  in. diameter.

The assembled Ni-NiO half-cell is first evacuated using the side arm tube shown in the diagram, heated to  $100^{\circ}\text{-}200^{\circ}\text{C}$ , and then the tube is flame-sealed under vacuum. The outer half-cell contains either a different metal-metal oxide system or a mixture of two different oxides of the same metal and an inert platinum foil electrode. The loosely packed oxides are contained in impervious thoria or recrystallized alumina crucibles placed inside a flat-bottom quartz tube. The top of this tube is again sealed with De Khotinsky cement to a larger bell-shaped Pyrex tube which supports two tungsten lead wire connectors sealed into glass.

The entire cell is assembled by inserting the Ni-NiO reference half-cell into the empty thoria or alumina crucible, pressing it against the Pt foil electrode, and packing the free volume of the crucible with the oxide mixture under investigation. The zirconia tube is kept tightly against the platinum foil by means of a second

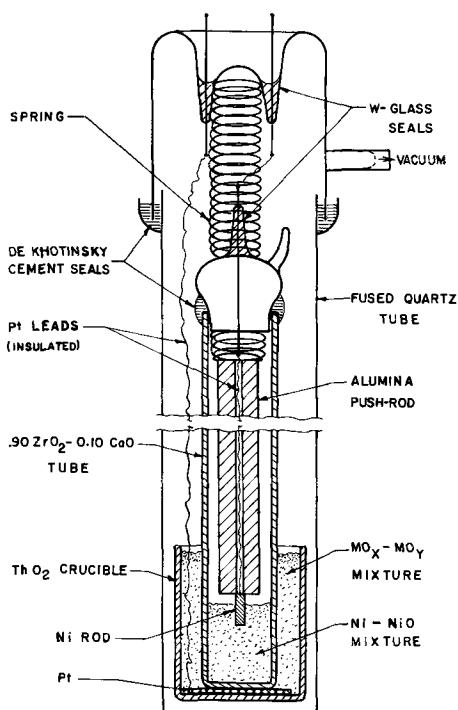


Fig. 1. Closed cell for emf measurements

metal spring inserted between the inner and the outer bells. All electrode connections are silver soldered. Finally, the outer bell is cemented in place by melting the De Khotinsky cement in the ring container shown on the diagram, and the cement is allowed to solidify while pressing the outer bell against the spring. Then the outer compartment is also evacuated from a side arm tube and flame-sealed under vacuum.

For some of the more volatile systems, like  $\text{PbO}$ , vaporization losses could be minimized by sealing the compartment while under a pressure of argon gas not exceeding 100 mm Hg. The upper part of the cell, where the cement seals are located, remains at room temperature during measurements, as only the bottom 8 in. are in the furnace.

Cell runs below  $1150^{\circ}\text{C}$  were conducted in chromel wire wound electrical furnaces, controlled to  $\pm 1^{\circ}\text{C}$  using temperature controllers and thermocouples. Electric field effects were eliminated by shielding the interior of the furnaces with grounded Inconel tubing. Cell temperature measurements were taken on the outer wall of the cell at the level of the Ni-NiO powder using calibrated Pt-13% Rh thermocouples. Cell potentials were measured using a calibrated Radiometer pH meter connected to a scale expander that allowed the emf's to be read to  $\pm 0.1$  mv. All potential readings were corrected for thermal emf's, measured separately.

The runs which included measurements up to  $1300^{\circ}\text{C}$  were conducted in a platinum wound furnace of large heat capacity without metal shielding. Reading the emf's, in this case, required a temporary power shut-off. However, less than  $1^{\circ}\text{C}$  was lost during this time. The high-temperature version of the cell used in this furnace required only one modification: replacement of the outer quartz tubing with a closed-end impervious alumina tube. In addition, both compartments were evacuated and partially filled with argon before sealing. Radiation baffles and water cooling were also required at the top.

The elimination of mixed potentials in the "closed cell" technique can be attributed to two main factors:

1. The use of hermetically sealed half-cell compartments, where oxygen can reach an equilibrium pressure approaching as closely as possible that of the M-O system in the compartment. To this end a large excess of metal-metal oxide powder mixture is present to ensure that the system is capable of adjusting itself to the equilibrium conditions at the temperature of the electrodes. Thus, any excess oxygen due to desorption or diffusion through the quartz container should combine with the excess metal present.

2. The use of a "buried Pt electrode" imbedded at the bottom of the thoria crucible in the outer compartment and pressed directly against the zirconia electrolyte.

This technique gave a rapid cell response and highly stable potentials over periods of times occasionally exceeding two to three weeks.

## Results and Discussion

The results of the present investigation are plotted in Fig. 2 to 10, indicating at times the order in which the readings were taken (e.g. Fig. 3, 7-9). Least-squares lines were computed using a standard computer program and drawn through the points. The equation for each least-squares line is given in Table I along with the maximum deviation of the experimental results from the calculated line (i.e., the range, in  $\pm$ mv). In Table I may also be found the values for the free energies of oxidation as a function of temperature for all the systems investigated.

Data from a number of investigators have also been plotted along with our results, being converted when necessary using the emf measurements from the present investigation. The purpose in this listing is not to establish a complete review of thermodynamic values

Table I. Thermodynamic data

Reactions (O <sub>2</sub> is the gas at 1 atm)	Temperature range, °K	Cell potential E = A - BT (mv) (T is °K)		Standard deviation, mv	Maximum deviation, mv	Standard free energy change (cal) $\Delta G^{\circ}_R = A' + B'T$ (T is °K)		Estimated accuracy** (cal)
		A	B			A'	B'	
Ni (S) + 1/2 O <sub>2</sub> = NiO (S)	911-1376	1.210.83	0.43993	±0.57	±1.0	-55,844	20.290	±50
Pb (L) + 1/2 O <sub>2</sub> = PbO (S)	772-1160	1.114.48	0.49950	±1.30	±2.4	-51,400	23.037	±110
Pb (L) + 1/2 O <sub>2</sub> = PbO (L)	1160-1371	987.85	0.38941	±0.51	±0.8	-45,560	17.960	±40
Fe (S) + NiO (S) = FeO (S) + Ni (S)	903-1540	154.13	-0.10400	±0.61	±0.9	-7,108	-4,797	±50
3FeO (S) + NiO (S) = Fe <sub>3</sub> O <sub>4</sub> (S) + Ni (S)	949-1272	405.34	0.19644	±0.47	±0.7	-18,694	9,083	±35
Ni (S) + 3Fe <sub>2</sub> O <sub>3</sub> (S) = 2Fe <sub>3</sub> O <sub>4</sub> (S) + 2NiO (S)	967-1373	-69.44	-0.29425	±1.00	±1.5	3,203	-13,571	±70
Ni (S) + Cu <sub>2</sub> O (S) = NiO (S) + 2Cu (S)	924-1328	346.68	0.07046	±0.19	±0.3	-15,989	3,249	±15
Ni (S) + 2CuO (S) = NiO (S) + Cu <sub>2</sub> O (S)	892-1320	531.16	-0.05102	±0.14	±0.3	-24,497	-2,353	±15
Ni (S) + Mn <sub>3</sub> O <sub>4</sub> (S) = NiO (S) + 3MnO (S)	992-1393	58.27	-0.13648	±0.39	±0.6	-2,687	-6,295	±30
Ni (S) + 3Mn <sub>2</sub> O <sub>3</sub> (S) = 2Mn <sub>3</sub> O <sub>4</sub> (S) + NiO (S)	884-1126	622.99	-0.03735	±2.12	±3.0	-28,732	-1,722	±140
Fe (S) + 1/2 O <sub>2</sub> = FeO* (S)	903-1540	—	—	—	—	-62,952	15,493	±100
3FeO (S) + 1/2 O <sub>2</sub> = Fe <sub>3</sub> O <sub>4</sub> * (S)	949-1272	—	—	—	—	-74,538	29,373	±85
2Fe <sub>3</sub> O <sub>4</sub> (S) + 1/2 O <sub>2</sub> = 3Fe <sub>2</sub> O <sub>3</sub> * (S)	967-1373	—	—	—	—	-59,047	33,861	±120
2Cu (S) + 1/2 O <sub>2</sub> = Cu <sub>2</sub> O* (S)	924-1328	—	—	—	—	-39,855	17,041	±65
Cu <sub>2</sub> O (S) + 1/2 O <sub>2</sub> = 2CuO* (S)	892-1320	—	—	—	—	-31,347	22,643	±65
3MnO (S) + 1/2 O <sub>2</sub> = Mn <sub>3</sub> O <sub>4</sub> * (S)	992-1393	—	—	—	—	-53,157	26,585	±80
2Mn <sub>3</sub> O <sub>4</sub> (S) + 1/2 O <sub>2</sub> = 3Mn <sub>2</sub> O <sub>3</sub> * (S)	884-1126	—	—	—	—	-27,112	22,012	±190

\*Calculated from emf data.

\*\* The accuracy quoted is that calculated from the maximum deviations from the computed least squares lines. For calculations based on two consecutive cell reactions, the corresponding limits of accuracy have been accumulated.

or to search for wide variations in previously published data, but simply to compare the results from the present investigation with those that have been obtained more recently or quoted more liberally.

**Ni-NiO system.**—The system investigated represents the oxygen saturated metal phase in equilibrium with the metal saturated oxide phase. However, Ni-saturated NiO is known to be stoichiometric (28), and solid Ni metal dissolves very little oxygen until 1438°C (29), which contributes to making the Ni-NiO system ideal as a reference electrode for use with solid electrolytes at temperatures between 500° and 1400°C. The present results are in reasonably good agreement with other data. The standard free energies of formation of NiO calculated from thermochemical data have tended to agree increasingly with equilibrium measurements in the last few years, e.g., ±200 to ±500 cal at 1000°C (30, 2, 31-33) as shown in part by Chipman (34). The values of Coughlin (35) and Kubaschewski and Evans (1), however, are out by as much as 1.7 kcal at 1000°C.

The materials used in the present work were high-purity INCO nickel analyzing 99.9%+ Ni and NiO powder of Fisher Certified Reagent grade. The two were mixed in roughly equal amounts, added to the ZrO<sub>2</sub>+CaO tube and lightly pressed in the bottom. The cell described in Fig. 1 was operated with pure oxygen flowing in the outer compartment and hence the standard free energy of formation of pure NiO from pure Ni and oxygen at 1 atm was directly obtained. The results shown in Fig. 2 indicate the high accuracy (±50 cal) of the present investigation. The measurements obtained herein are in excellent agreement with Alcock and Belford (8) and Elliott and Gleiser (36). The Ni-NiO system was therefore chosen as a standard reference electrode for nearly all subsequent emf determinations.

**Pb-PbO system.**—The system investigated represents the oxygen saturated liquid metal phase in equilibrium with the metal saturated oxide phase. According to Hansen (29) PbO is a stoichiometric compound up to its melting point, reported variously as being

from 885° to 897°C (1, 2, 37-38). Richardson and Webb (39) reported that molten lead dissolved up to 1.04 a/o (atomic per cent) O at 900°C, 1.79 a/o O at 1000°C, and 2.89 a/o O at 1100°C. On the other hand, Barteld and Hofmann (40) and Sano and Minowa (41) independently reported different solubility values, e.g., 0.12 a/o O at 900°C, 0.10 a/o O at 800°C, and 0.04 a/o O at 700°C. Hence, the solubility of oxygen in liquid lead is still unresolved.

In view of the relatively high vapor pressures of Pb and PbO at elevated temperatures, it was believed that the present technique would be particularly suited for the determination of the free energy of formation for PbO from pure Pb and oxygen. A mixture of yellow PbO (Fisher Certified Reagent) and of Pb (British Drug Houses Certified) was placed inside the ZrO<sub>2</sub> tube and pure oxygen flowed in the outer com-

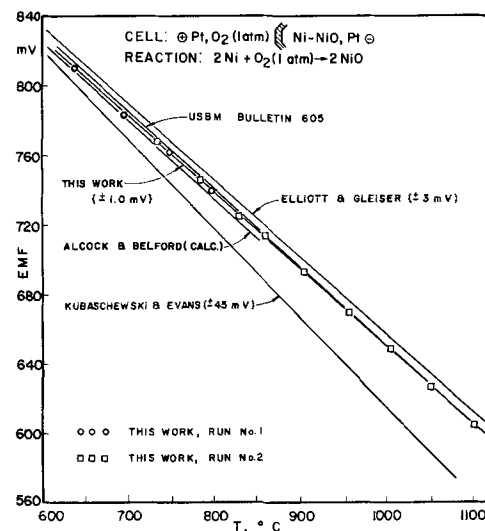


Fig. 2. Temperature dependence of emf for the Ni, NiO system

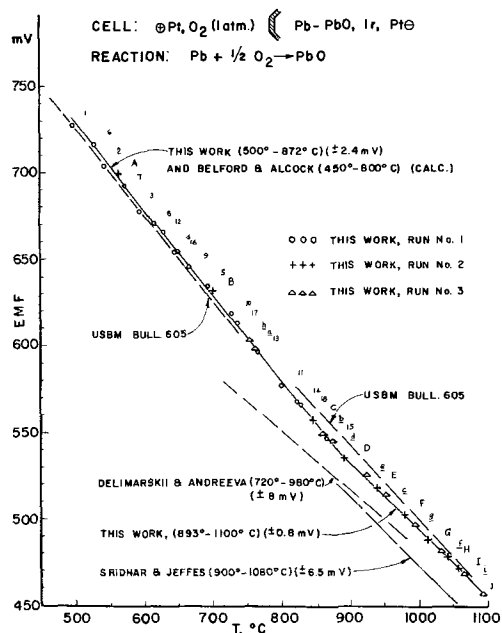


Fig. 3. Temperature dependence of emf for the Pb, PbO system

partment. In place of the Ni rod, an iridium wire served to establish electrical contact with the Pb-PbO since Ir has been shown to be insoluble in molten Pb (39).

Our data from three runs are shown in Fig. 3 along with those of several other investigators. The free energies of formation of solid PbO are available from several sources both thermochemical (1, 2, 42) and electrochemical (8). These have tended to agree well recently ( $\pm 150$  cal at  $1000^\circ\text{K}$ ) with few exceptions (1). On the other hand,  $\Delta G^\circ_f$  values for liquid PbO are in complete disagreement. On considering the results of Kvyatkovskii *et al.* (43), Delimarskii and Andreeva (44), Wicks and Block (2), JANAF (42), Elliott and Gleiser (36), Sridhar and Jeffes (45), and Matsusita and Goto (12), many of which are plotted and compared in Fig. 3, one finds a general spread of values of at least 2000 cal. For solid PbO, the results obtained are in good agreement with Belford and Alcock (8, 13), and with Wicks and Block (2).

**Fe-Fe<sub>x</sub>O system.**—The system represents the iron saturated Wüstite phase, as defined in the Fe-O phase diagram (46, 47). The triple point, where the Fe, Fe<sub>x</sub>O, and Fe<sub>3</sub>O<sub>4</sub> phases coexist was located by Vallet and Racciah (47) to be at  $611^\circ\text{C}$ . Thus, the system was investigated in the temperature range  $630^\circ\text{--}1270^\circ\text{C}$ , using the high-temperature cell arrangement in a Pt furnace. The starting materials in the outer compartments consisted of a mixture of electrolytic iron powder (Fisher) to which a small amount of Fe<sub>2</sub>O<sub>3</sub> powder (Fisher Certified) had been added. The results of this investigation are plotted in Fig. 4.

In general, the Ni-NiO/Fe-FeO cell has always been the most successful with solid electrolytes, as can be seen from the excellent agreement with several other publications (3, 4, 7, 9, 10, 21) with the exception of the data given by Wicks and Block (2).

**Fe<sub>2</sub>O-Fe<sub>3</sub>O<sub>4</sub> system.**—The system investigated represents the oxygen saturated Wüstite phase in equilibrium with metal saturated magnetite, as defined by the Fe-O phase diagram (46).

The magnetite (Fe<sub>3</sub>O<sub>4</sub>) was prepared by reducing Fe<sub>2</sub>O<sub>3</sub> (Fisher Certified) in a stream of CO/CO<sub>2</sub> (1:4) at  $900^\circ\text{C}$  for  $1\frac{1}{2}$  hr. The resulting material, crushed to  $-200$  mesh, was 99.9% magnetic. A mixture of this magnetite and of electrolytic iron powder (Fisher) was prepared in such proportions as to yield equal weights of FeO and Fe<sub>3</sub>O<sub>4</sub> at  $800^\circ\text{C}$ . The emf values (9, 11, 21), however, do not show as high a degree of agreement as might have been expected in this system, particularly at the higher temperatures. The occur-

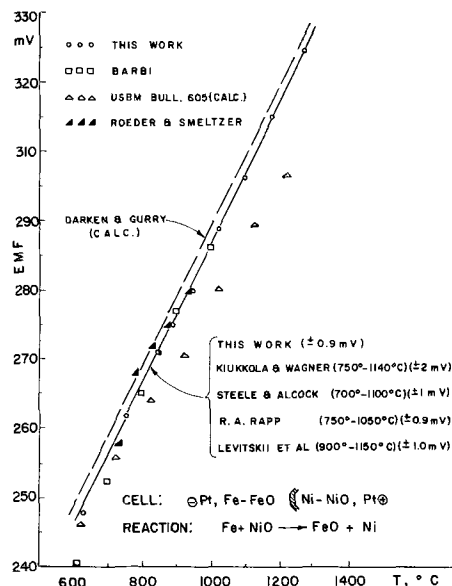


Fig. 4. Temperature dependence of emf for the system Ni, NiO-Fe, FeO.

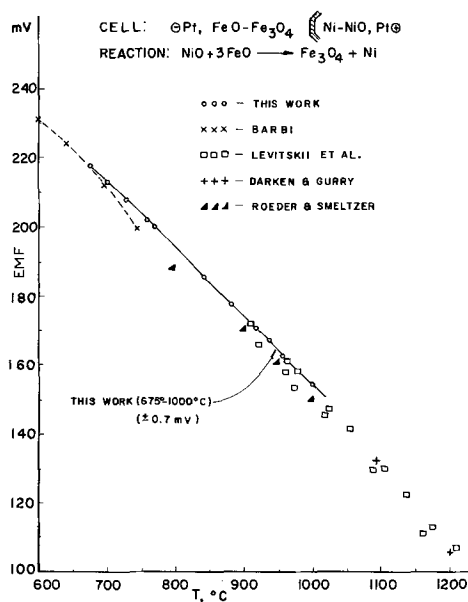


Fig. 5. Temperature dependence of emf for the system Ni, NiO-FeO, Fe<sub>3</sub>O<sub>4</sub>.

rence of mixed potentials in the other work is a strong possibility. Other data have also been plotted for comparison (46).

**Fe<sub>3</sub>O<sub>4</sub>-Fe<sub>2</sub>O<sub>3</sub> system.**—The system represents the oxygen saturated magnetite phase in equilibrium with hematite, as defined in the Fe-O phase diagram.

Magnetite, as produced in the manner described above, was mixed in equal proportion with hematite powder (Fe<sub>2</sub>O<sub>3</sub> Fisher Certified) and added to the ThO<sub>2</sub> crucible. The measurements obtained are plotted in Fig. 6. Although the range ( $\pm 1.5$  mv) is wider compared to the other systems investigated presently, the accuracy achieved by this investigation on the Fe<sub>3</sub>O<sub>4</sub>-Fe<sub>2</sub>O<sub>3</sub> system is greater than anything hitherto attainable in the temperature region of  $700^\circ\text{--}1100^\circ\text{C}$ . Except for Blumenthal and Whitmore's work (6), no other emf results are available. Mixed potentials are strongly suspected in the latter's investigation, and the disagreement with the present results is significant. Norton (48) and Salmon (49) used oxygen dissociation pressure measurements to obtain their values.

Because of the slow rates of reoxidation of magnetite, particularly after sintering above  $875^\circ\text{C}$ , a long

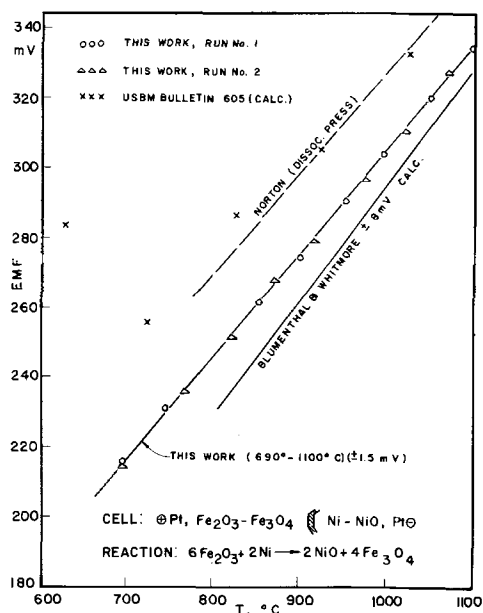


Fig. 6. Temperature dependence of emf for the system Ni, NiO- $\text{Fe}_3\text{O}_4$ ,  $\text{Fe}_2\text{O}_3$ .

time was required to return to the equilibrium pressure of oxygen in a closed system on lowering the temperature. In practice, a much shorter period of time was required to obtain equilibrium with an increasing temperature (decomposition of  $\text{Fe}_2\text{O}_3$ ). Hence, most of the measurements reported with this system were obtained on increasing the temperature.

It should be noted that free energies tabulations for the Fe-O system based on thermochemical information (1, 2, 36, 50, 51) differ from equilibrium measurements by 100-500 cal for  $\text{Fe}_x\text{O}$  and  $\text{Fe}_3\text{O}_4$ , and by as much as 1000 cal for  $\text{Fe}_2\text{O}_3$ .

**Cu-Cu<sub>2</sub>O system.**—The Cu-O phase diagram (52) indicates that the phases  $\text{Cu}_2\text{O}$  and CuO are of fixed composition up to their melting points and that Cu dissolves a negligible amount of oxygen below 1065°C.

An equal amount of Fisher Certified cuprous oxide powder was mixed and added to a crucible in the outer compartment. The results appear in Fig. 7 along with

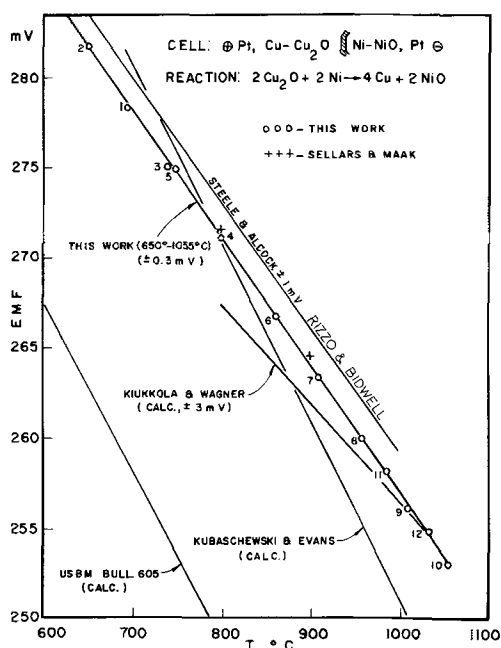


Fig. 7. Temperature dependence of emf for the system Ni, NiO-Cu,  $\text{Cu}_2\text{O}$ .

other emf (3, 4, 23, 65) and calorimetric (1, 2, 66) work. The agreement is fairly good among several values, particularly between those of (4), (23), (65), (66) and of the present investigation. Again the data found in Bulletin 605 of the U.S. Bureau of Mines and in Kubaschewski and Evans' tabulations (1) are in disagreement with the present work.

The recent calorimetric work by Mah *et al.* (66), where new Cp values have been obtained, shows a remarkable agreement with the equations given in Table I, the maximum deviation being 32 cal between 900°C and 1300°K for  $\Delta G^\circ_f$ . The cell design used by (65) was in some aspect similar to the present one.

**$\text{Cu}_2\text{O}$ -CuO system.**—Because of the high equilibrium pressures of oxygen involved, the present technique was particularly well suited. The cupric oxide utilized was of the Fisher Reagent grade. A very high degree of accuracy and reproducibility is evident from the plot of our experimental values in Fig. 8. The agreement amongst various workers (48, 53, 54, 55, 64) is also reasonably good. The data given in Bulletin 605 of the U.S. Bureau of Mines (2) are again in disagreement with the present work.

Mah's (6) values for the  $\Delta G^\circ_f$  of CuO again agree very well with the present ones. Between 900° and 1300°K the maximum difference is 57 cal/mole CuO. The work of Bidwell (64) also compares very well with the present results, and his experimental technique was similar in part.

**MnO-Mn<sub>3</sub>O<sub>4</sub> system.**—Although each of the previous metal oxide systems has a well-defined metal-oxygen phase diagram, this is not the case for the Mn-O system. Considerable disagreement exists concerning the stoichiometry of the various phases at different temperatures (56-60). It is not the purpose of this paper to suggest a Mn-O phase diagram, but simply to determine the free energy changes occurring from one oxide phase to the next, providing that there is no ambiguity as to which phases are involved. It is widely known that MnO,  $\text{Mn}_3\text{O}_4$ ,  $\text{Mn}_2\text{O}_3$ , and  $\text{MnO}_2$  exist as stable crystalline phases and can be converted to one another by suitable adjustments of temperature and oxygen partial pressure.

The manganese oxide with the approximate Mn:O ratio of 1:1 was prepared by decomposing  $\text{MnCO}_3$  (Fisher Reagent grade) in vacuum at 475°C. The manganese oxide corresponding to the approximate composition  $\text{Mn}_3\text{O}_4$  was prepared by decomposing  $\text{MnO}_2$  (Baker Analyzed Reagent) at 850°C in vacuum for 3 hr. Equal amounts of MnO and  $\text{Mn}_3\text{O}_4$  were mixed

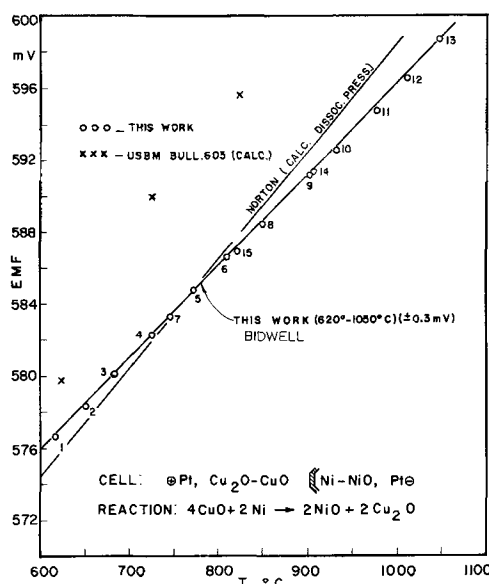


Fig. 8. Temperature dependence of emf for the system Ni, NiO- $\text{Cu}_2\text{O}$ , CuO.



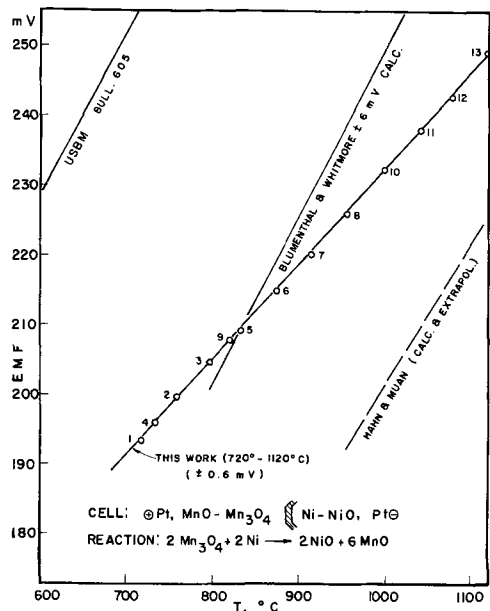


Fig. 9. Temperature dependence of emf for the system Ni, NiO-Mn, Mn, Mn<sub>3</sub>O<sub>4</sub>.

and packed in a crucible in the outer cell compartment. The two oxide phases were held long enough at each temperature to allow the emf values to stabilize completely and the equilibrium compositions to be established, the MnO phase being saturated with oxygen and the Mn<sub>3</sub>O<sub>4</sub> phase with Mn. Approaching the various temperature settings from opposite directions yielded a straight line, as illustrated by the results of this investigation in Fig. 9. Next to the Cu-Cu<sub>2</sub>O and Cu<sub>2</sub>O-CuO systems, the present MnO-Mn<sub>3</sub>O<sub>4</sub> system appears to be the most successful of those investigated. This is in contrast with the scatter evident in the emf results of Blumenthal and Whitmore (6), where mixed potentials are suspected and with the wide variations in other investigations (2, 58). The more recent results of Kim, Wilbert, and Marion (61), using a cobalt oxide resistance wire to measure low oxygen pressures in a gas, leads one to wonder whether metastable Mn-O phases are involved, or whether their method itself was subject to large errors.

**Mn<sub>3</sub>O<sub>4</sub>-Mn<sub>2</sub>O<sub>3</sub> system.**—Mn<sub>2</sub>O<sub>3</sub> powder was prepared by heating MnO<sub>2</sub> (Baker Analyzed Reagent) in air at 880°C for 18 hr. The resulting sinter was ground to -325 mesh and mixed with an equal amount of Mn<sub>3</sub>O<sub>4</sub> powder prepared as previously described. The two manganese oxides were packed in a crucible in the outer compartment of the cell and held at six different temperatures for periods of time up to a week. The emf response appeared to be very sluggish compared to previously described systems. Figure 10 is a plot of emf against temperature for the present Mn<sub>3</sub>O<sub>4</sub>-Mn<sub>2</sub>O<sub>3</sub> system. As may be ascertained from Fig. 10, a great deal of disagreement exists between authors concerning this system (55, 58, 61-63). From the work of Schmahl and Stemmler (62) at higher temperatures, it would seem possible that one of the two phases involved is a metastable one, thus explaining the scatter in the various data, particularly those obtained by the transportation method (55) at low temperatures. On the contrary, the present method allows for equilibration over long periods of time at high temperatures and should be considered the most accurate.

**Sigma-function calculations.**—The present experimental values have been combined with calorimetric data to calculate the sigma functions for all the metal-oxygen systems investigated. The sigma-function calculations are given in Table II.

By the nature of its derivation, the plot of sigma against 1/T should always give a straight line. Any

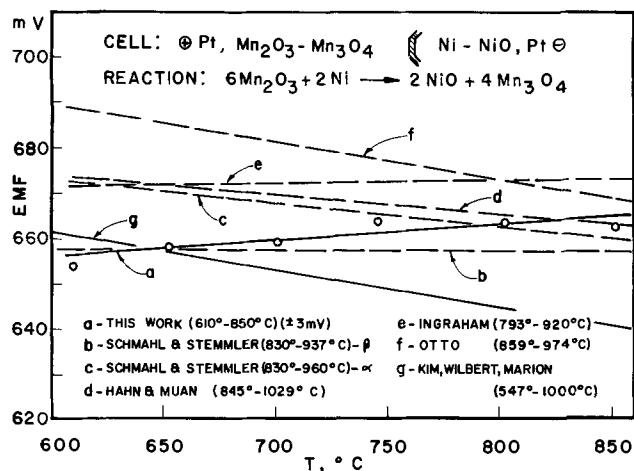


Fig. 10. Temperature dependence of emf for the system Ni, NiO-Mn<sub>2</sub>O<sub>3</sub>, Mn<sub>3</sub>O<sub>4</sub>.

deviations from linearity would indicate either (a) errors in the evaluation of the electrochemical potentials determined herein, or (b) experimental errors in the existing heat capacity data and in their temperature dependence, or both. A survey of the results given in Table II indicates that the functions are linear with fairly low standard deviations. The largest standard deviation can be found with the Pb-PbO<sub>(s)</sub> system, probably because of low accuracy in the heat capacity data.

The integration constant  $\Delta H^\circ$  of the sigma-function calculation can be used directly to calculate the standard heats of formation at 298°K. The heats of formation obtained in this manner have been compared with calorimetric values listed in Kubaschewski and Evans (1), Wicks and Block (2), and Elliott and Gleiser (36) and are listed in Table III. The agreement is excellent in most cases except for the Pb-O and the Fe-O systems which are not shown in the table. For the latter the calculation involves the numerous phase changes occurring in this system, and it is also possible that, due to the long extrapolations involved, small discrepancies in the heat capacity data could have a pronounced effect in the calculation of the heats of reactions at 298°K. The recent value of  $-40,830 \pm 300$  cal/mole published by Mah *et al.* (66) for  $\Delta H^\circ_f$  (Cu<sub>2</sub>O) compares well with the present value of  $-41,030$  cal/mole at 298°K.

### Conclusions

An emf technique, using a solid electrolyte tube of 10 m/o CaO-stabilized zirconia, has been developed to measure the pressure of oxygen above two metal-oxygen phases in equilibrium, where two half-cells are allowed to build up their own equilibrium oxygen pressure independently. This technique eliminates mixed potentials and provides for reproducible, accurate, and stable emf readings over periods of several weeks. Furthermore, it provides truly static measurements, thus allowing equilibrium conditions to be established.

The emf measurements have yielded accurate standard free energies of formation of NiO (911°-1371°K), PbO (772°-1371°K), FeO (903°-1540°K), Cu<sub>2</sub>O (924°-1328°K), and of Fe<sub>3</sub>O<sub>4</sub> (949°-1272°K), Fe<sub>2</sub>O<sub>3</sub> (967°-1373°K), CuO (892°-1320°K), Mn<sub>3</sub>O<sub>4</sub> (992°-1393°K), and Mn<sub>2</sub>O<sub>3</sub> (884°-1126°K) from the lower metal oxides. The data are compared with previously reported measurements, and the accuracy of the previously existing data is discussed in the light of the present results. Sigma-function calculations substantiate the claim of accuracy for the present work.

### Acknowledgments

The authors are indebted to Professor H. U. Ross of this Department for helpful discussions. The financial

Table II. Sigma-function calculations

Reaction (with O <sub>2</sub> gas at 1 atm)	Temperature range of mea- surement (°K)	$\Sigma = \frac{\Delta H^\circ}{T} + I^*$		Maximum deviation (cal/°K)	Standard deviation (cal/°K)	Temperature range** of calculation (°K)
		(cal °K)	I (cal/°K)			
Ni + ½O <sub>2</sub> = NiO (β) (γ)	911-1376	-57,437	32.804	±0.053	±0.028	633-1725
Pb + ½O <sub>2</sub> = PbO (L) (yellow)	772-1145	-52,510	23.726	±0.156	±0.074	762-1159 (mp)
Pb + ½O <sub>2</sub> = PbO (L) (L)	1166-1371	-51,009	52.046	±0.025	±0.017	1159-1371
α-Fe + ½O <sub>2</sub> = FeO (Wüstite)	903-1031	-64,685	46.891	—	—	298-1033
β-Fe + ½O <sub>2</sub> = FeO (Wüstite)	1120-1163	-61,640	1.162	±0.013	±0.005	1033-1179
γ-Fe + ½O <sub>2</sub> = FeO (Wüstite)	1219-1540	-65,704	39.800	±0.024	±0.017	1179-1674
3FeO + ½O <sub>2</sub> = β-Fe <sub>3</sub> O <sub>4</sub> (S)	949-1272	-80,731	97.635	±0.040	±0.027	900-1650
2/3β-Fe <sub>3</sub> O <sub>4</sub> + 1/6O <sub>2</sub> = β-Fe <sub>2</sub> O <sub>3</sub>	967-1040	-22,362	33.301	±0.018	±0.012	900-1050
2/3β-Fe <sub>3</sub> O <sub>4</sub> + 1/6O <sub>2</sub> = γ-Fe <sub>2</sub> O <sub>3</sub>	1094-1373	-19,102	1.265	±0.023	±0.013	1050-1730
2Cu + ½O <sub>2</sub> = Cu <sub>2</sub> O (S) (S)	924-1328	-41,030	17.170	±0.024	±0.013	298-1357 (mp Cu)
½Cu <sub>2</sub> O + ¼O <sub>2</sub> = CuO (S) (S)	892-1320	-17,939	31.526	±0.015	±0.011	298-1502 (mp Cu <sub>2</sub> O)
Cu + ½O <sub>2</sub> = CuO (S) (S)	892-1320	-38,419	40.077	±0.034	±0.023	298-1357 (mp Cu)
3MnO + ½O <sub>2</sub> = α-Mn <sub>3</sub> O <sub>4</sub> (S)	992-1393	-53,531	13.540	±0.050	±0.026	298-1445 (T.P.-Mn <sub>3</sub> O <sub>4</sub> )
2/3α-Mn <sub>3</sub> O <sub>4</sub> + ½O <sub>2</sub> = Mn <sub>2</sub> O <sub>3</sub> (S)	884-1126	-10,181	11.940	±0.040	±0.028	298-1350

$$* \Sigma = -\frac{nFE}{T} + \Delta a/nT + \frac{\Delta bT}{2} - \frac{\Delta C}{2T^2}$$

where  $E$  is the potential for the reaction, and the heat capacity data have been obtained consistently from Kelley's tabulations (37) with the exception of those of the copper oxides which come from Mah *et al.*'s work (66).

\*\* "Temperature range" represents the maximum temperature range to which the calculation is applicable, as determined by the stability of the phases present in the reaction.

Table III. Comparison of the heats of formation at 298°K obtained from the sigma-function calculations with other existing data

Oxide	$-\Delta H^\circ_f, 298^\circ\text{K}$ (kcal/mole)			E & G (36)
	Sigma	K & E (1)	W & B (2)	
Cu <sub>2</sub> O (S)	41.030	40.0	40.8	41.8
CuO (S)	38.420	37.1	37.5	38.3
Mn <sub>3</sub> O <sub>4</sub>	329.5*	331.4	331.4	331.4
Mn <sub>2</sub> O <sub>3</sub>	220.7*	229.2	229.2	229.2
NiO	57.44	57.5	57.3	57.3

\* A value of 92.0 kcal/mole has been used for  $-\Delta H^\circ_f$  of MnO (1, 2, 36)

aid of the Ford Foundation and of the National Research Council of Canada to one of the authors (G. G. C.) and of the National Research Council of Canada in providing equipment funds is also gratefully acknowledged.

Manuscript submitted Nov. 6, 1967; revised manuscript received March 11, 1968.

Any discussion of this paper will appear in a Discussion Section to be published in the June 1969 JOURNAL.

#### REFERENCES

- O. Kubaschewski and E. Evans, "Metallurgical Thermochemistry," Pergamon Press, London (1958).
- C. E. Wicks and F. E. Block, U. S. Bureau of Mines, Bull. 605 (1963).
- K. Kiukkola and C. Wagner, *This Journal*, **104**, 379 (1957).
- B. C. H. Steele and C. B. Alcock, *Trans. AIME*, **233**, 1359 (1965).
- H. Schmalzried, *Z. Elektrochem.*, **66**, 572 (1962).
- R. N. Blumenthal and D. H. Whitmore, *J. Am. Ceram. Soc.*, **44**, 508 (1961).
- R. A. Rapp, *Trans. AIME*, **227**, 371 (1963).
- C. B. Alcock and T. N. Belford, *Trans. Faraday Soc.*, **60**, 822 (1964).
- G. A. Roeder and W. W. Smeltzer, *This Journal*, **111**, 1074 (1964).
- G. A. Barbi, *J. Phys. Chem.*, **68**, 1025 (1964).

- G. A. Barbi, *Trans. Faraday Soc.*, **62**, 1589 (1966).
- Y. Matsushita and J. Goto, *J. Fac. Eng., Tokyo Univ.*, **27**, 217 (1964).
- T. N. Belford and C. B. Alcock, *Trans. Faraday Soc.*, **61**, 443 (1965).
- M. Hock, A. S. Iver, and J. Nelken, *J. Phys. Chem. Solids*, **23**, 1463 (1962).
- N. Birks, *Nature*, **210**, 407 (1966).
- H. Peters and G. Mann, *Z. Elektrochem.*, **63**, 244 (1959).
- Ya. I. Gerasimov, *et al.*, *Russ. J. Phys. Chem.*, **36**, 180 (1962).
- G. A. Barbi, *J. Phys. Chem.*, **68**, 2912 (1964).
- H. Schmalzried, *Z. Physik. Chem.*, **25**, 178 (1960).
- V. N. Drobyshev, T. N. Rezhukhina, and L. A. Tarasova, *Russ. J. Phys. Chem.*, **39**, 70 (1965).
- V. A. Levitskii, T. N. Rezhukhina, and V. G. Dneprova, *Elektrokhim.*, **1**, 933 (1965).
- R. E. Carter, *J. Am. Ceram. Soc.*, **43**, 448 (1961).
- C. M. Sellars and F. Maak, *Trans. AIME*, **236**, 457 (1966).
- T. N. Rezhukhina, V. I. Lavrent'ev, V. A. Levitskii, and F. A. Kuznetsov, *Russ. J. Phys. Chem.*, **35**, 671 (1961).
- "Encyclopedia of Electrochemistry," C. A. Hampel, Editor, Reinhold Publishing Corp., New York (1964).
- T. H. Etsell, M.A.Sc. Thesis, "Electrical Conductivity Measurements on La<sub>2</sub>O<sub>3</sub>-CaO and Other Solid Oxide Electrolytes," University of Toronto (1966).
- L. A. McClaine and C. P. Coppel, *This Journal*, **113**, 80 (1966).
- E. M. Levin, C. R. Robbins, and H. F. McMurdie, in "Phase Diagrams for Ceramists," M. K. Resor, Editor, American Ceramic Soc., Columbus, Ohio (1964).
- M. Hansen, "Constitution of Binary Alloys," McGraw-Hill, Inc., New York (1958).
- "Fuel Cells," Vol. II, G. J. Young, Editor, Reinhold Publishing Corp., New York (1963).
- M. Watanabe, *Sci. Rep. Imp. Tohoku Univ.*, **1**, **22**, 436 (1933).
- R. Fricke and G. Weitbrecht, *Z. Elektrochem.*, **48**, 87 (1942).
- R. N. Pease and R. S. Cook, *J. Am. Chem. Soc.*, **48**, 1199 (1926).
- J. Chipman, *Pure and Applied Chem.*, **5**, 669 (1962).
- J. P. Coughlin, U. S. Bur. of Mines Bull. 542 (1954).

36. J. F. Elliott and M. Gleiser, "Thermochemistry for Steelmaking," Vol. I, Addison-Wesley Publishing Co., New York (1960).
37. K. K. Kelley, U. S. Bur. of Mines Bull. 584 (1960).
38. E. N. Rodigina, K. Z. Gomel'skii, and V. F. Luginina, *Russ. J. Phys. Chem.*, **35**, 884 (1961).
39. F. D. Richardson and L. E. Webb, *Trans. Inst. Min. Metall.*, **64**, 529 (1954).
40. K. Barteld and W. Z. Hofmann, *Erzbergb. Metallhuttenu.*, **5**, 102 (1952).
41. K. Sano and E. Minowa, *Mem. Fac. Eng. Univ. Nagoya, Japan*, **5**, 80 (1953).
42. JANAF Thermochemical Tables, PB-168370, Clearinghouse for Federal Scientific and Technical Information, Springfield, Va., 1965.
43. Kvyatkovskii, Esin, Abdeev and Khan, *Vestnik. Akad. Nauk. Kazakh. S.S.R.*, **16**, 19 (1960).
44. Yu. K. Delimarskii and V. N. Andreeva, *Zh. Neorg. Khim.*, **5**, 1800 (1960); *Russ. J. Inorg. Chem.*, **5**, 873 (1960).
45. R. Sridhar and J. H. E. Jeffes, *Trans. Inst. Min. Metall.*, **76**, C44 (1967).
46. L. S. Darken and R. W. Gurry, *J. Am. Chem. Soc.*, **67**, 1398 (1945).
47. P. Vallet and P. Raccach, *Mem. Sc. Rev. Met.*, **LXII** (i), 1 (1965).
48. F. J. Norton, General Electric Res. Lab. Report No. 55-RL-1248, March 1955, Schenectady, N. Y.
49. O. Salmon, *J. Phys. Chem.*, **65**, 550 (1961).
50. M. Olette and M. F. Ancey-Moret, *Rev. Met.*, **60**, 569 (1963).
51. "The Making, Shaping and Treating of Steel," H. E. McGannon, Editor, 8th ed., pp. 258-60 U. S. Steel Corp. (1964).
52. R. Vogel and W. Pocher, *Z. Metallkunde*, **21**, 333 (1929).
53. F. H. Smyth and H. S. Roberts, *J. Am. Chem. Soc.*, **42**, 2582 (1920).
54. *Ibid.*, **43**, 1061 (1921).
55. K. Hochgeschwender and T. R. Ingraham, *Can. Met. Quarterly*, **6**, 71 (1967).
56. M. LeBlanc and G. Wehner, *Z. Physik. Chem., Abt. A*, **168**, 59 (1934).
57. T. E. Moore, M. Ellis and P. W. Selwood, *J. Am. Chem. Soc.*, **72**, 856 (1950).
58. W. C. Han and A. Muan, *Am. J. Sc.*, **258**, 66 (1960).
59. M. W. Davies and F. D. Richardson, *Trans. Faraday Soc.*, **55**, 604 (1959).
60. C. Klingsberg and R. Roy, *J. Am. Ceram. Soc.*, **43**, 620 (1960).
61. D. Q. Kim, Y. Wilbert, and F. Marion, *Compt. rend.*, **262C**, 756 (1966).
62. N. G. Schmahl and B. Stemmler, *This Journal*, **112**, 365 (1965).
63. E. M. Otto, *ibid.*, **111**, 88 (1964).
64. L. R. Bidwell, *ibid.*, **114**, 30 (1967).
65. F. E. Rizzo, L. R. Bidwell and D. F. Frank, *Trans. Met. Soc. AIME*, **239**, 593 (1967).
66. A. D. Mah, *et al.*, USBM RI 7026, September, 1967.

## The Experimental Requirements for Making Accurate High Pressure Conductance Measurements on Aqueous Solutions with Pt-in-Glass Cells

A. B. Gancy\* and S. B. Brummer\*

*Tyco Laboratories, Inc., Waltham, Massachusetts*

### ABSTRACT

Experimental procedures are described for obtaining accurate high pressure coefficients of conductance of dilute aqueous solutions of strong electrolytes ( $\geq 2$  mM) in the ranges 1-2250 atm and 3°-55°C. Procedures are developed such that an over-all accuracy of 0.1% in the high pressure conductance is obtained. It is shown that in order to obtain reproducible and accurate results great attention must be paid to the stability of the electrode seal through the body of the conductance cell. Pt foil of suitably small cross section has been sealed to the Pyrex cell wall using soft glass and ten intermediate grades. It is shown that this produces an electrode seal which is leak-free and stable over the entire range of temperature and pressure studied. Also incorporated into the seal is a multiple-wire cage design which imparts high mechanical stability to the external electrode terminals. A capillary cell is described which is compensated for anisotropic distortion under pressure and which is suitable for precise measurements with solutions more concentrated than 5 mM. It is shown that the cell constant variation with pressure, and the effects of anisotropic distortions of the electrodes under pressure, can be determined to within 0.02% for this and other compensated electrode configurations. The errors arising from contamination of the solutions with impurities are described. It is shown that a typical weak electrolyte impurity must be kept below ~1% of the (~2 mM) salt concentration if an over-all accuracy of 0.1% is to be attained at 2000 atm. Similarly, the concentration of dissolved O<sub>2</sub> must be maintained below ~50  $\mu$ M for a 2 mM salt solution.

The present research effort is directed at exploring very accurately the temperature and pressure coefficients of the limiting ionic conductance of aqueous solutions. The aim is to develop a treatment of the limiting ionic mobility involving transition state parameters along the lines suggested earlier (1-4). Experimentally, this involves the accurate determination of the conductance of dilute (1-20 mM) salt solutions in the range 0°-55°C and 1-2300 atm. For the mean-

ingful interpretation of the activation parameters, an accuracy of 0.1% is required.

Since ionic conductance is one of the most characteristic properties of electrolyte solutions and can readily be measured with high accuracy (~0.01%), this would not appear to be a difficult experimental problem. At high pressures, however, despite much interest, the data in the literature are very discordant and discrepancies of up to several per cent have been

\* Electrochemical Society Active Member.

observed, even in simple cases.<sup>1</sup> Some of the reasons which have been suggested to account for this variability are solution contamination<sup>2</sup> and variations of cell constant with pressure (10-12). In the present work we have explored these sources of errors and have shown how to eliminate them to the extent that the required 0.1% accuracy can be attained.

### Experimental

Much of the substance of this communication represents the testing of experimental procedures; these are described in the results section. The general procedures of containing the pressure and of measuring resistances (<0.05%) were described earlier (3). As before, pressure was generated by pumping oil with a hydraulic pump (Pressure Products, Inc., Hatboro, Pennsylvania). A significant improvement is in the measurement of pressure ( $\pm 3$  atm) on a Bourdon tube gauge (Heise Gauge Company, Newtown, Connecticut). Pressure vessels were thermostated to better than 0.01°C, although the absolute temperature was known only to 0.02°C.

Solutions were made from recrystallized salts in ion-exchange water (resistivity  $\geq 10$  megohm-cm). Before use, they were carefully deaerated. The high pressure conductance cells were filled by manipulating the solutions with helium gas in a closed, glass apparatus. These cells were inverted into Pyrex cups containing instrument grade mercury. The Hg functioned as the pressure transmitting fluid and prevented solution interaction with the hydraulic fluid.

### Results and Discussion

**High pressure Pt-in-Pyrex electrode seals.**—As will become apparent, a major reason for the irreproducibility and inaccuracy of high pressure conductance measurements is the inadequacy of electrode seals. Some of the earliest investigations of high pressure solution conductance utilized Pt-to-glass electrode seals (13, 14). Before the development of Pyrex, the glass used in making the cells was probably a Jena glass. Specific mention of glass type was made by Körber (15) who used "Jena Gerateglas." The thermal expansion coefficients of Pyrex, Gerateglas, and Pt are 3.3,  $\sim 4.8$ , and  $9.0 \times 10^{-6}/^\circ\text{C}$ , respectively, so that the modern day use of Pyrex instead of Jena glass should result in only a very slightly poorer seal. Yet, no mention was made in those papers of problems in obtaining accurate and reproducible conductance data originating from the Pt-glass seal. More recently, Hamann *et al.* (9-16) have demonstrated the use of conventional Pt-glass conductance cells to 3000 atm, with no mention of electrode seal problems. Most of the aims of our study can be achieved by working at pressures below 3000 atm and there seemed no reason not to use the high pressure conductance cell employing the conventional Pt-Pyrex electrode seals that have so frequently been described (2, 3, 9, 13-17).

The first results were disappointing. Specifically, it was found that after a pressure cycle the solution resistance did not return to the initial 1 atm value to within the desired 0.1%. Deviations of several tenths of a per cent were not uncommon, and they were generally in the direction of increasing resistance. In addition, the glass around the Pt was often observed to have cracked after a high pressure cycle and we were sometimes able to detect droplets of hydraulic oil inside the cells, especially after operating at the higher temperatures. Another problem was that the electrode seals were not stable to routine handling and electrodes often parted from the surrounding glass. It was evident that while such seals might have been adequate for the early investigations, where

highly dilute solutions were rarely examined, they are not acceptable for an accurate study. It is also apparent that some of the irreproducibility in the literature (5-7) may have been due to problems associated with Pt-glass electrode seals.

Several alternatives to the conventional Pt-in-Pyrex cell are available: One possibility would be to use soft glass instead of Pyrex. This is not generally favored for, although the use of soft glass may have solved the electrode seal problem, the contamination of dilute solutions through attack of the glass is expected. Zisman (8) did not use a Pt-glass seal but projected the electrodes through a layer of oil covering the electrolyte. The oil also functioned as the pressure transmitting medium. This method has been criticized (5, 8, 9) on the grounds that contamination may be introduced into the solution *via* the oil. Horne *et al.* (18) used a similar method. One possibility, following Jamieson (19), is to use a Teflon-bodied cell. This has the advantage that the electrode seals survive high pressures, due to the high compressibility of Teflon and consequently its high deformability around the Pt. On the other hand, this same high deformability leads to considerable uncertainties in knowing the cell constant as a function of pressure (10). Ellis (6) sought to solve this problem by using a Teflon-bodied cell in which the electrodes were fixed not to the body of the cell, but to a glass former inside the Teflon cylinder. To avoid distortion of the electrodes under pressure, electrical connection was made by passing fine platinum wire through the Teflon wall. The pressure coefficient of the cell constant was then largely determined by the compressibility of the glass, which is well-known. Although this technique would appear to be adequate, the results still showed considerable scatter (up to 0.3%). A variation on this design has recently been described (22).

Ovenden (11) took a different approach. He used Pt-in-Pyrex cells but sought to overcome the difficulties with the electrode seals. As is well-known, a channel is left between the Pt and the Pyrex, because of different coefficients for contraction on cooling. On compression and decompression, this channel closes and opens again ("breathes"). To narrow the channel, Ovenden sealed very thin Pt foil (5 x 40 mils) within the glass instead of the more usual heavier wires. This narrower channel should mitigate erratic changes in solution concentration. Rigidity was effected by joining the 5 mil foil to stout (40 mil) Pt wires which projected from the glass. An over-all accuracy of 0.1% was claimed.

An effort therefore was made to reproduce Ovenden's seal. Instead of using 5 x 40 mils foil, we used 10 mil wire having 4 mm sections pressed into 6 x 12 mil foil. These, being smaller, should function even better than Ovenden's foil. Four such wires were used per electrode. They were fashioned into a cage which terminated at the electrode inside the cell and at the electrical lead terminal outside (Fig. 1a). This cage provides for seals on fine wires, while at the same time it maintains a low electrical impedance. It has the particular advantage that any stresses inevitably applied to the external wire, in making electrical connections, etc., cause the wire to bend but not to break. Such stresses are not transmitted to the glass, and the annoying problem of glass cracking and chipping so common to ordinary seal designs is avoided. Using this design, we have also never experienced a cracking of the glass around the seal upon the application of pressure, a frequent occurrence in our experience with other configurations, including Ovenden's.

This seal showed no signs of oil intrusion over the experimental ranges 3°-55°C and 1-2250 atm. The reproducibility of the conductance data was also much improved. However, we noticed a downward drift of the resistance in one or more of the five cells used per experiment. This drifting phenomenon was ob-

<sup>1</sup> Much of the early work has been reviewed by Hamann (5). The discordant nature of the results in the literature has been brought out by Ellis (6) and by Horne *et al.* (7).

<sup>2</sup> Hamann (6) comments on solution contamination by the pressure-transmitting oil in Zisman's work (8), and the reaction of electrolytes with the pressure-transmitting Hg in the work of Buchanan *et al.* (9).

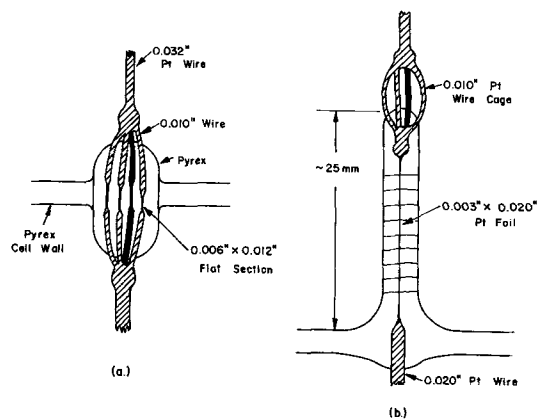


Fig. 1. Improved Pt-glass electrode seals; (a) cage structure for mechanical stability; (b) graded glass seal.

served most often at the highest temperatures ( $55^{\circ}\text{C}$ ) and was never experienced below  $25^{\circ}\text{C}$ . Exhaustive tests showed that such drifting was not due to localized heating within the cell during the electrical measurements. In one cell which contained three electrodes, such that any of three electrode pairs could be measured, it was found that one pair yielded constant resistance values while the other two pairs drifted. Thus, the drifting was not caused by accidental contamination of the cell solution.

It was observed that when the filled conductivity cells utilizing the Ovenden-type Pt-Pyrex seals were allowed to stand on the laboratory bench for several days, a salt crust appeared at the external seal. Correspondingly, the level of the Hg sealant rose within the cell neck. This indicates that there is capillary action past the seal. This same leaking could occur during the experiment itself within the oil-filled pressure vessel. In this case, however, instead of the solution's evaporating, it could creep along the glass cell exterior. Leaking could therefore result in a parallel impedance to the solution which would lower the measured cell resistance and would probably vary in an unpredictable fashion as the exterior solution film becomes more or less widespread. To test this parallel impedance hypothesis, a series of badly behaving cells was removed from the pressure vessel and given a thorough external washing. Resumption of the measurements showed the complete absence of the drifting phenomenon and a general increase of each cell resistance.

Because the seal in Ovenden's work was made around larger foil, the problem should have been more severe. He did not report the effect, however. We believe that this was because he used a gas rather than an oil hydraulic fluid. Hence his leaking electrolyte would evaporate rather than accumulate. His Pt-in-Pyrex seals were evidently adequate for gas-filled pressure systems. They can also be used for oil-filled systems, but this entails periodic removal of the cells for washing. It should be mentioned that Howard (12), who used an oil-filled pressure system, refills his Pt-Pyrex cells after each and every pressure cycle, although the reason for this enormously time consuming process is not given. A more acceptable solution is to lessen even further the clearance between the Pt and the glass. This can be accomplished by using very small cross-sectional Pt, which is very hard to work with, or with graded glass seals.

We have successfully sealed 3 x 20 mil foils through 10 grades of glass from Pyrex on the inside of the cell, to soft glass on the outside. The linear coefficient of expansion of soft glass ( $8.8 \times 10^{-6}^{\circ}\text{C}^{-1}$ ) compares closely with that of Pt ( $9.0 \times 10^{-6}^{\circ}\text{C}^{-1}$ ). The 3 x 20 mil foil can be routinely sealed without cracking of the intermediate glasses on cooling. Although these materials are compatible with respect to thermal expansion, however, there is still an appreciable divergence between the compressibilities of Pt and glass.

For this reason, a ribbon of foil wider than about 20 mil often failed under pressure. This size foil worked well up to 2250 atm, the highest pressure employed. The seal is shown in Fig. 1 (b). As before, the cage design is retained at the outside of the seal to avoid putting mechanical stresses on the seal during handling and electrical connection. Cells with these electrode seals showed no salt crust or rise in the level of the mercury sealant during standing, filled, for several weeks. Resistances were steady during measurement and, after a pressure cycle, the initial value is almost invariably reproduced to within 0.1% (Fig. 2). Such stability was found at all experimental temperatures and over the period of several weeks required to carry out 10 pressure cycles. We emphasize this long-term stability, since there is a major saving of time if we can avoid periodic washing or refilling of the cells.

We have demonstrated the reproducibility of given cells in terms of self-consistency. A more convincing test would be to show how well different cells agree with one another. Figure 3 shows the pressure coefficients of conductance for RbCl at  $20^{\circ}\text{C}$ . All five cells contained the same 6.4 mM solution. The consistency is excellent and within the 0.1% required. This result is typical of literally hundreds of data points and is in sharp contrast with the aforementioned discrepancies in the literature (5-7).

Another convincing test of cell performance is to measure the concentration dependence of the pressure coefficient of conductance in a group of cells. We have shown that the resistance ratio  $R_i/R_P$  should vary linearly with  $\sqrt{C_i}$  and that the slope of this relation should agree with that calculated from the Debye-Hückel limiting (21) law. Figure 4 shows plots for LiCl solutions at  $25^{\circ}\text{C}$  at 1000 and 2000 atm. We see that deviations of the experimental points from linearity are well within 0.1% and that the  $R_i/R_P$

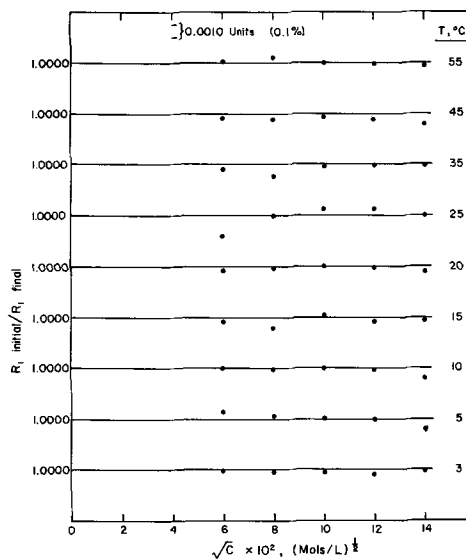


Fig. 2. The RbCl system: reproducibility of the resistance measurements after pressure cycling.

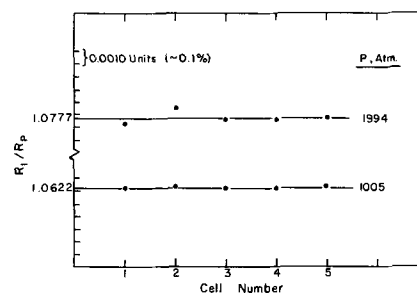


Fig. 3. The RbCl system: reproducibility of the conductance ratios at  $20^{\circ}\text{C}$ ;  $c = 6.4 \text{ mM}$ .

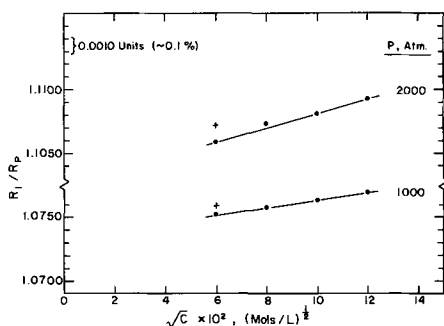


Fig. 4. The LiCl system: concentration dependence of the pressure coefficient of conductance at 25°C [ $+$  represents measurement made with a rod-ring cell. The other data points refer to the capillary cell configuration (see text)]

vs.  $\sqrt{C_1}$  relations are appropriately linear. The slopes are 0.026 and 0.054 (liters/equiv.)<sup>1/2</sup> at 1000 and 2000 atm, respectively, in excellent agreement with those calculated from the limiting law, 0.031  $\pm$  0.005 and 0.056  $\pm$  0.005 (21) (liters/equiv.)<sup>1/2</sup>.

There can be little doubt then that these Pt-in-Pyrex seals are suitable for extrapolation of data to infinite dilution with a precision within 0.1%. To obtain this accuracy, however, some attention must be given to the change of the cell constant with pressure.

*Variation of cell constant with pressure.*—As mentioned, this is a serious problem for Teflon cells. For glass cells, the expected variation is  $\sim 0.1\%$  per 1000 atm (6) and only becomes important when high accuracy is required. This change of cell constant with pressure assumes isotropic compression of the glass and no anisotropic distortions of the electrode geometry due to differential compression of the electrode-glass seal. Ovenden (11) was concerned about the latter effect and suggested a configuration using a ring electrode and a coaxial rod (Fig. 5b). With this configuration, it was argued, circular symmetry should minimize the effects of possible small displacements of the rod relative to the ring. Ovenden also assumed that this configuration leads to a negligible change of cell constant with pressure as a result of isotropic compression. Howard (12) claimed to demonstrate this point by comparing the rod and ring cell with the parallel plate configuration (Fig. 5a); his results showed scatter of up to 0.4%, however. In our view, the cell constant of this configuration should vary with pressure, as a result of the isotropic compression of Pt (0.01% per 1000 atm).

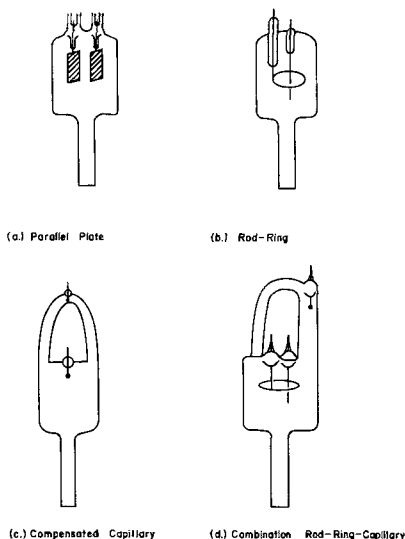


Fig. 5. High pressure conductance cells

The problem with the rod and ring configuration is that with solutions of concentrations above about 5 mM, it yields resistances which are too low for convenient measurement. For this reason we have constructed a compensated capillary cell (Fig. 5c). Any effects of distortions of the electrode geometry should be minimized by this configuration. We would expect the constant of this cell to be determined by the linear compressibility of Pyrex, or  $\sim 0.1\%$ /1000 atm. Figure 5(d) shows a combination cell incorporating both configurations, whereby very accurate comparisons of the two cell types were made using the same solution at the same time. In Fig. 6 we show the quotient of the rod-ring and capillary cell data as a function of pressure, at various temperatures. It is evident that this quotient increases linearly with pressure, essentially independent of temperature. The slope of the line in Fig. 6 is  $0.70 \times 10^{-6}$  atm<sup>-1</sup>. To a good approximation, this should be equal to the difference between the compressibilities of Pyrex and Pt. According to Bridgman, the mean linear compressibilities of Pyrex (22) and Pt (23) over the temperature and pressure range of our experiments are 0.975 and  $0.114 \times 10^{-6}$  atm<sup>-1</sup>, respectively. The difference between these compressibilities,  $0.86 \times 10^{-6}$  atm<sup>-1</sup>, is in good agreement with our data; the discrepancy is equivalent to an uncertainty of 0.03% at 2000 atm.

It is clear then that the two types of cell can be used together for solutions of different concentrations but that different allowances must be made for the variation of their cell constants with pressure. Indeed, this is essential to do when we are exploring the concentration dependence of the pressure coefficient of conductance since errors of 0.1–0.2% in lower concentration ranges would lead to serious errors in extrapolating to infinite dilution (Fig. 4). The results of Fig. 6 also show that scatter from anisotropic distortion of the electrodes, etc. is less than  $\pm 0.02\%$  up to 2250 atm.

*Errors arising from solution contamination.*—There can be little doubt that many of the problems in early work arose from inadequacies in cell construction. Solution contamination from hydraulic fluid or from Hg pressure seals has been blamed for some of the difficulties, however, and some examination of this problem seems called for. We consider contamination with the following materials: strong electrolytes, Hg, weak electrolytes, and O<sub>2</sub>.

Minor strong electrolyte impurities with strong electrolyte subject salts obviously pose no problem. This is especially the case as the pressure coefficients of the conductance of most strong electrolytes are similar in magnitude (24).

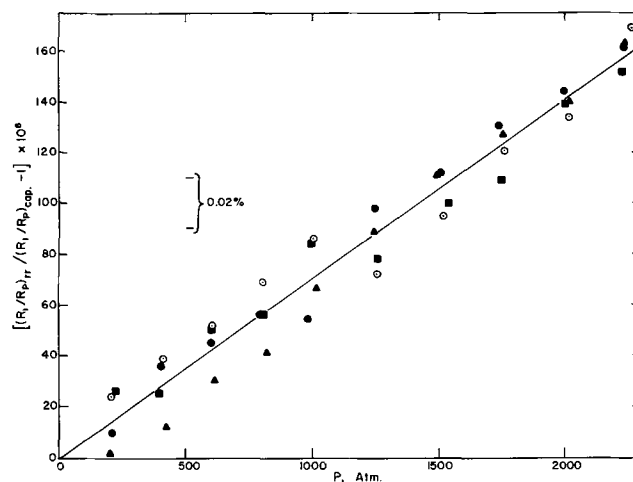


Fig. 6. Relative pressure coefficients of the rod-ring and capillary cells, NaCl system;  $c = 3.6$  mM ( $\odot$ —35°C;  $\square$ —25°C;  $\triangle$ —10°C;  $\bullet$ —3°C).

Hg contamination has been blamed for irreproducibility in high pressure measurements, particularly in acid solutions (5, 8, 9). However, appreciable Hg dissolution in nonoxidizing media in the absence of  $O_2$  is not thermodynamically possible. Even in the presence of a fully air-saturated solution (see later), the effect (presumably *via* Hg solubility) is relatively minor and could not have been responsible for the most significant errors in the literature.

Normally, one would not need to worry about the effects of minor weak electrolyte impurities when making measurements with strong electrolytes. An exception is in measuring the pressure coefficient of conductance. This arises because weak electrolytes dissociate extensively at higher pressures (9). Ellis was the first to point out that this poses a problem for the case of  $CO_2$  in equilibrium water (6). To examine the extent of this effect, we deliberately doped 2.5 and 4.9 mM KCl solutions with 2 ppm of  $CH_3COOH$ . The pressure coefficients of the conductance of such solutions were compared with those of the corresponding uncontaminated KCl solutions. Results are shown in Fig. 7.

It is seen that the pressure coefficient of the contaminated solutions is higher than that of the uncontaminated solutions, and that the deviation increases linearly with pressure. The displacement of the contaminated solution data is such as to suggest that the dissociation constant of  $CH_3COOH$  increases by about 1.6 at 2000 atm. Hamann and Strauss (16) obtained a ratio of 2.3. According to these results, we must restrict the weak electrolyte impurity to less than 0.5 ppm ( $CH_3COOH$  equivalent), at a salt concentration of 2 mM, to obtain our required accuracy of 0.1%. Ion-exchange water, which may contain weak electrolyte, is evidently adequate in this respect. These data also show that in discussing the possible effects of contamination, it is not sufficient just to show, as has sometimes been done, that the 1 atm solution resistance is constant under the given treatment since large changes can occur under pressure.

In a further series of experiments, LiCl and  $(Et)_4NCl$  solutions were deliberately saturated with  $CO_2$ -free air. The following observations were made: The resistance of the aerated cell, in contrast to all the others, drifted slowly downward during the first few days after loading. When the drifting had apparently stopped, the first pressure cycle was carried out; during the ascending part of this cycle the pressure coefficient for the aerated solution was slightly too high ( $<0.1\%$ ). Upon lowering the pressure, the resistance of this solution fell  $\sim 0.5\%$ . In subsequent pressure cycles, the pressure coefficient for aerated solutions was low by about 0.06% per 1000 atm (Fig. 8).

Our tentative explanation of these phenomena is that initial reaction between Hg and  $O_2$  produces soluble mercury entities which supersaturate the

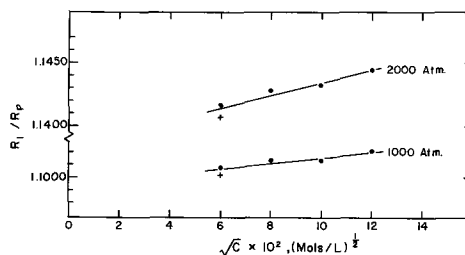


Fig. 8. The LiCl system: effect of solution aeration upon the pressure coefficient of conductance at 15°C (+ aerated solution).

solution (25). This is not unreasonable since  $Hg_2Cl_2$ , for example, does supersaturate when Hg is anodized at low current densities in HCl (26). When the pressure is lowered, the solution cools and the supersaturated salt crystallizes. Some such catastrophic fall in resistance (up to 0.5% in 2 mM solution) on cooling was always observed with aerated solutions. Once this had happened and all the  $O_2$  in the solution had been used up, however, the solution behavior was nearly normal with respect to pressure coefficient (Fig. 8). In our opinion, it is preferable to deaerate the solutions in order to avoid the aforementioned initial erratic behavior; at least, one should keep the  $O_2$  concentration to about 20% of its normal air-saturated level ( $\sim 50 \mu M$ ) to attain an accuracy of 0.1% in the pressure coefficient during all stages of the measurement.

### Summary

Methods of obtaining high pressure ( $>2000$  atm) coefficients of the conductance of dilute aqueous solutions ( $\geq 2$  mM) of strong electrolytes with an overall accuracy of 0.1% are described.

An important requirement to obtain reproducible and accurate results is the Pt-in-graded glass seal. The criterion for a stable, leak-free seal is that the Pt to be sealed is in the form of a thin strip of foil (0.003 x 0.020 in.). A novel cage structure for the seal, which combines good mechanical strength with small sealing diameters, is described.

A compensated capillary cell is described which is suitable for measurements with solutions  $\geq 5$  mM. This cell is compared with Ovenden's rod and ring configuration (11), and it is shown that correction for the variation of cell constants with pressure can be made within 0.02%. Anisotropic distortion errors are within this limit.

The effects of solution contamination are discussed. It is shown that weak electrolyte impurities (acetic acid or equivalent) in a 2 mM salt solution must be kept below  $\sim 1$  mole % of the salt concentration to maintain an accuracy of 0.1% in the conductance at 2000 atm. Similarly,  $O_2$  contamination must be kept below 50  $\mu M$ .

### Acknowledgments

We are pleased to thank Mr. H. Lingertat for assistance with the experimental work. This work was supported by the Office of Saline Water under Contracts OSW 14-01-0001-425 and 14-01-0001-966.

Manuscript submitted Feb. 29, 1968; revised manuscript received April 30, 1968.

Any discussion of this paper will appear in a Discussion Section to be published in the June 1969 JOURNAL.

### REFERENCES

1. S. B. Brummer and G. J. Hills, *Trans. Faraday Soc.*, **57**, 1816 (1961).
2. S. B. Brummer and G. J. Hills, *ibid.*, **57**, 1823 (1961).
3. S. B. Brummer, *J. Chem. Phys.*, **42**, 1636 (1965).
4. S. B. Brummer, *ibid.*, **42**, 4317 (1965).
5. S. D. Hamann, "Physico-Chemical Effects of Pressure," Chap. 7, Butterworths, London (1957).
6. A. J. Ellis, *J. Chem. Soc.*, 3689 (1959).

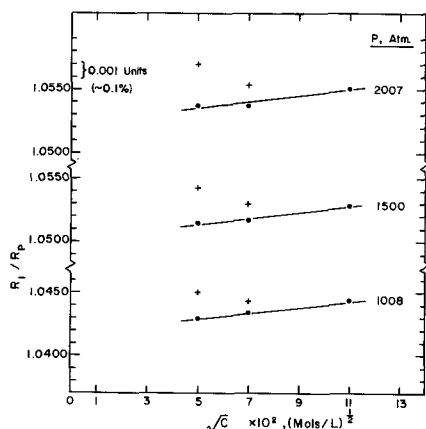


Fig. 7. The KCl system: effect of HAc contamination upon the pressure coefficient of conductance at 35°C (+ 2 ppm HAc).

7. R. A. Horne, B. R. Myers, and G. R. Frysinger, *ibid.*, **39**, 2666 (1963).
8. W. A. Zisman, *Phys. Rev.*, **39**, 151 (1932).
9. J. Buchanan and S. D. Hamann, *Trans. Faraday Soc.*, **49**, 1425 (1953).
10. C. E. Weir, *J. Res. Natl. Bur. Standards*, **53**, 245 (1954).
11. P. J. Ovenden, Thesis, Univ. of Southampton, 1965.
12. B. Howard, Thesis, Univ. of London, 1963.
13. J. Fink, *Ann. Phys.*, **26**, 481 (1885).
14. A. Bogojawlensky and G. Tammann, *Z. Phys. Chem.*, **27**, 457 (1898).
15. F. Körber, *ibid.*, **67**, 212 (1909).
16. S. D. Hamann and W. Strauss, *Disc. Faraday Soc.*, **22**, 70 (1956).
17. G. J. Hills, P. J. Ovenden, and D. R. Whitehouse, *ibid.*, **39**, 207 (1965).
18. R. A. Horne and G. R. Frysinger, *J. Geophys. Res.*, **68**, 1967 (1963).
19. J. C. Jamieson, *J. Chem. Phys.*, **21**, 1385 (1953).
20. D. A. Lown and Lord Wynne-Jones, *J. Sci. Instruments*, **44**, (12), 1038 (1967).
21. S. B. Brummer and A. B. Gancy, To be published.
22. P. W. Bridgman, *Amer. Jour. Sci.*, **110**, 359 (1925).
23. P. W. Bridgman, *Proc. Amer. Acad.*, **58**, 166 (1923).
24. G. Tammann, *Z. Physik. Chem.*, **17**, 725 (1895).
25. I. M. Kolthoff and J. J. Lingane, "Polarography," 2nd Ed., Vol. II, p. 553, John Wiley & Sons, Inc., New York (1965).
26. J. G. Ives and G. J. Janz, "Reference Electrodes," Chap. 3, G. J. Hills and D. J. G. Ives, Editors, Academic Press, New York (1961).

## Technical Notes



### Differences between the Combustion of Aluminum Droplets in Air and in an Oxygen-Argon Mixture

J. L. Prentice

*The Michelson Laboratories, U. S. Naval Weapons Center, China Lake, California*

and L. S. Nelson

*Sandia Laboratory, Albuquerque, New Mexico*

When aluminum droplets were burned during free fall in air and in its nitrogen-free analog, 20% oxygen in argon, keeping other conditions identical, marked differences between the combustions appeared and will be described in this communication.

Each droplet,  $377\mu$  in diameter, was prepared and ignited by exposing a small square of aluminum foil to a focused, millisecond pulse of radiation from a Nd-glass laser as described elsewhere (1). The squares of foil, 1.02 mm on a side and  $20\mu$  thick, were supported at the laser focus on crossed aluminum fibers. The air was obtained from a cylinder (Matheson, special dry), while the oxygen-argon mixture was made as used from ultra high purity cylinder gases (Linde). In both cases, the gaseous atmospheres were at a total pressure of  $625 \pm 5$  Torr, and were flowing upward slowly through a windowed combustion chamber 11 cm on each side and 36 cm high.

The experiments were performed in a manner that permitted observation of the light emitted by the burning particles from ignition to burn-out. The emission of radiation was recorded by high-speed photography, as a time exposure with a 102 x 127 mm view camera, and with an RCA 7102 (S-1 surface) photomultiplier-oscilloscope combination. A narrow band interference filter that peaked at  $8300\text{\AA}$  was placed before the photomultiplier, which viewed the falling particle from a distance of 3.7m. In a number of experiments, 2.5 mm-wide semi-opaque tapes spaced 38 mm apart were placed horizontally across the front window of the combustion chamber. Each time the particle passed behind a tape, a dip formed in the oscilloscope trace. These dips allowed us to correlate distance of fall with both combustion time and the intensity of light emitted by the burning droplet.

Time-exposed photographs of the trajectories of droplets burning in the two atmospheres are shown in Fig. 1a and 1b. The trace from the droplet that burned

in air was uneven with scalloped edges in the upper part and showed side traces and swerving in the lower part. In the nitrogen-free combustion, however, the trace was somewhat broader and shorter, but with smooth edges. High-speed photography has shown that the traces with scalloped edges are caused by spinning particles, while the side traces and swerving are associated with jetting and/or fragmentation of the droplets. Drops without spin had even traces.

The photomultiplier records of the light emitted by the particles burning in the two atmospheres were also different as shown in Fig. 2a and b. In air there usually was an initial rise of about 15 msec duration after which the trace oscillated rapidly. After a gradual second increase there was a very irregular emission of light which decayed altogether at about 275 msec for the droplet diameter used here. Although the gross features of each oscilloscope record were similar the individual traces varied greatly from experiment to experiment, especially in the frequency of oscillation.

In the 20% oxygen-argon atmosphere, however, the trace rose sharply after the laser pulse, and then decayed smoothly over a somewhat longer time of 400 msec. The peak intensity was about 12% greater than for the droplet that burned in air. Also, two irregularities were seen in this trace: the change in slope at about 200 msec, and the tiny peaks just before extinction. The over-all shape of the curve as well as the irregularities were reproducible when the experiments were repeated.

Distances of fall were determined from the dips on traces similar to those in Fig. 2a and 2b, and have been plotted in Fig. 3 against the square of time. The straight line has been drawn for a body in vacuo accelerating gravitationally from rest, where the distance is  $gt^2/2$ . The droplets fell slightly faster than gravitational at the beginning of the oxidation in both atmos-





Fig. 1. Time-exposed track photographs of  $377\mu$ -diameter aluminum droplets as they burned in free fall (a, left) in air and (b, right) in a mixture of 20% oxygen in argon, with total gas pressures in both cases at 625 Torr. Short traces emanating from holder arise from tiny droplets formed from crossed aluminum fiber support. Note the typical erratic trace that appears when an aluminum droplet burns in air.

pheres but then gradually slowed as time increased. The droplet that burned in 20% oxygen-argon fell more slowly than the droplet that burned in air and virtually stopped before the light emission died out.

When the droplets were allowed to impact glass plates at similar stages of the combustions in the two atmospheres, marked differences again appeared, as shown in the photomicrographs in Fig. 4. Here the droplet that had burned in the oxygen-argon mixture was a bare aluminum sphere surrounded by a circular smoke pattern. (The sphere had an indentation, presumably due to contraction on freezing.) The droplet that had been ignited in air, however, showed a glass-like hemispherical cap attached to one side of the aluminum sphere, forming a pronounced bilobate structure. Also, for the combustion in air, the smoke pattern on the glass plate was definitely nonsymmetric, being confined to the area nearest the aluminum end of the particle.

We now attempt to explain the following characteristics of the burning aluminum droplets: (i) the droplets spin in air but not in  $O_2/Ar$ ; (ii) the droplets jet in air but not in  $O_2/Ar$ ; (iii) the droplets radiate less intensely in air than in  $O_2/Ar$ ; (iv) the droplets fall more rapidly in air than in  $O_2/Ar$ . We suggest tentatively that the accumulation of the cap-like lobe of condensed phase product during combustion in air but not in  $O_2/Ar$  is responsible for the variations in behavior in each case.

Since the substitution of argon for nitrogen in the gas mixture was the only difference between the two systems reported here, nitrogen may be participating in the combustion as a reactive species. Recently, Michel *et al.* (2) have obtained aluminum oxynitrides

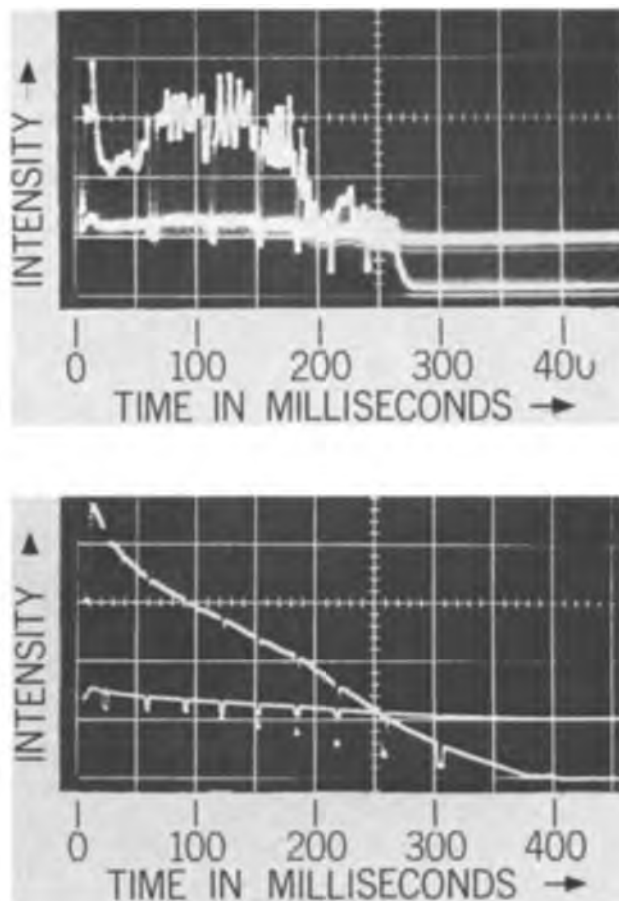


Fig. 2. Oscilloscope records of RCA 7102 photomultiplier output when it viewed  $377\mu$ -diameter aluminum droplets burning (a, top) in air and (b, bottom) in a mixture of 20% oxygen in argon at a total pressure of 625 Torr. Central traces were recorded with second beam of dual beam oscilloscope at an amplification 0.1 that used for other trace. Sharp dips in trace were formed as droplet passed behind strips of tape placed horizontally across front of combustion chamber. Intensity scales are identical in both traces.

by melting a mixture of alumina and aluminum in air with an induction heater. The similarity of their system to the one reported here suggests that the product which accumulates on aluminum droplets burning in the presence of nitrogen likewise might be some aluminum-oxygen-nitrogen species of as yet undetermined composition. [An analogous reaction occurs when zirconium droplets burn in air (3).] The assumption (4) that the product lobe of the bilobate configuration shown in Fig. 4a is aluminum oxide should be examined carefully in view of the experimental findings reported here.

Comparison of Fig. 1a and b and 4a and b indicates that an uneven track due to a spinning particle is recorded when condensed-phase product accumulates on the droplet's surface, while the even, smooth-edged trace appears when this product is absent. A possible explanation of this behavior is that when the product is present, an aerodynamically unstable situation arises, owing to the dissymmetry of the bilobate particle and the directional, possibly turbulent, vaporization of the aluminum. This could result in the observed spin. When the product lobe is absent, however, the droplet burns stably and spin is not observed.

The jetting seen toward the bottom of Fig. 1a when the specimen burns in air also may arise from the accumulated lobe of product. When quenched specimens similar to the one shown in Fig. 4a are examined with an optical microscope, considerable frothiness is seen in the product globule. Later in the burning, the frothiness is less evident, but larger bubbles appear,

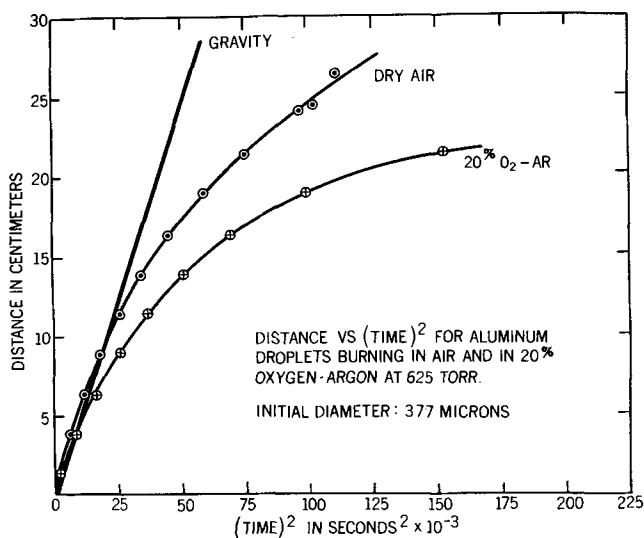


Fig. 3. Distance of fall plotted against the square of time for aluminum droplets burning in air and in a mixture of 20% oxygen in argon at a total pressure of 625 Torr. Initial droplet diameter was 377  $\mu$ .

some of which seem to have burst at the surface. Both the frothiness and the larger bursting bubbles suggest gas-related processes which may cause the jets and fragmentation seen in Fig. 1a. Again, when there is no product lobe present, the jets and fragmentations are likewise absent.

The lower radiant emission from the droplets that burned in air (Fig. 2a and b) may be caused by an incomplete flame front around the droplets, due to reduced and directional vaporization of aluminum. Thus, if the smoke patterns shown in Fig. 4 are true indicators of the shape and magnitude of the flame that surrounds the burning droplet, the droplets that burned in air had only an approximately hemispherical flame zone, while those that burned in the oxygen-argon mixture had a fully spherical flame zone. Since it is thought that the radiation in burning aluminum droplets emanates mainly from the cloud of incandescent smoke particles formed in the combustion (5), it is not surprising that the peak light intensity measured photoelectrically is lower for the droplets that burned in air, where the product lobe seems to block roughly half of the flame front, than for droplets that burned in O<sub>2</sub>/Ar, where the complete flame front is present.

Perturbation of the symmetrical cloud of particles by the product cap may also explain the greater rate of fall of droplets that burn in air than in O<sub>2</sub>/Ar (Fig. 3). If it can be assumed that the cloud of hot gases that surrounds the particle adds a drag or buoyancy force opposed to gravity, it is possible that the more spherical cloud formed in O<sub>2</sub>/Ar would give rise to a slower rate of fall than would the partially spherical cloud thought to accompany the droplet while burning in air.

A paradox arises, however, when burning times in the two atmospheres are compared (see Fig. 2a and b). Thus, if the rate of vaporization of aluminum is reduced when the droplet burns in air, due to the presence of the product lobe on the droplet's surface, the over-all burning time might be expected to be longer in air than in O<sub>2</sub>/Ar. Actually the droplet burns to extinction of light emission more rapidly in air than in O<sub>2</sub>/Ar. A possible explanation for this is that in air, both oxygen and nitrogen can act as oxidizers. Then since the effective oxidizer concentration is greater, the droplet can reach a state of complete oxidation more rapidly in air than in O<sub>2</sub>/Ar. Perhaps in air, part of the reaction with the atmosphere occurs in the vapor phase flame front, while the rest is associated with the product lobe, where oxygen and ni-

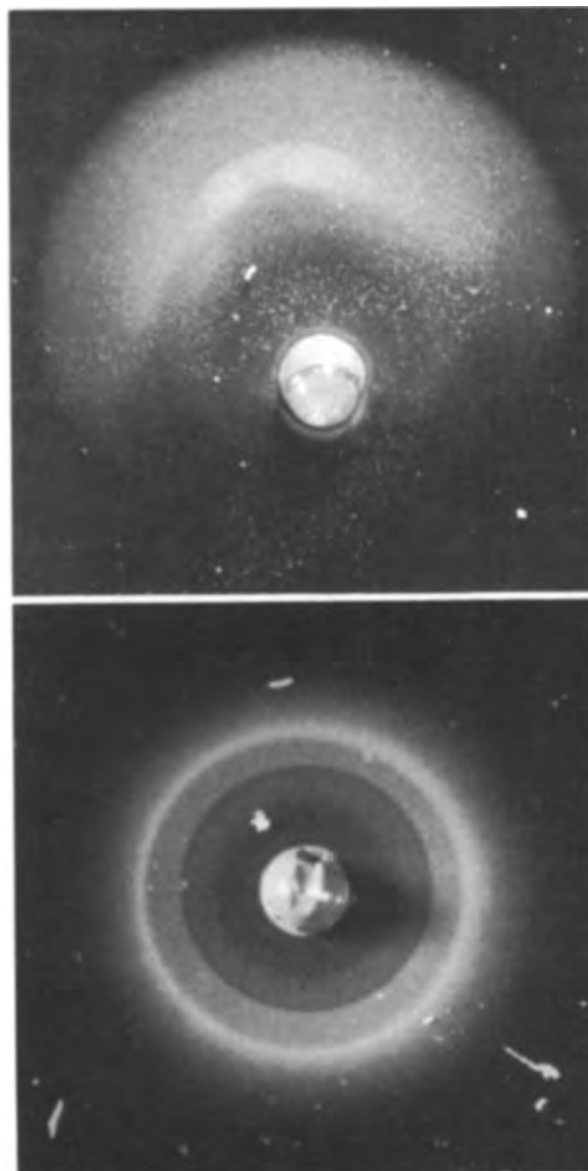


Fig. 4. Photomicrographs of aluminum droplets that had impacted glass plates during combustion (a, top) in air and (b, bottom) in a mixture of 20% oxygen in argon. Note the bilobate structure of the droplet that had burned in air, and the bare metallic appearance of the droplet that had burned in O<sub>2</sub>/Ar.

trogen pass into the lobe from the gas phase and aluminum oxidizes at the metal-product interface.

It should be emphasized that the explanations given here for the behavior of burning aluminum droplets are mostly speculative. Obviously, more study must be devoted to the basic chemical questions that arise in this work, namely, what is the nature of the product lobe, and why does it collect in the one atmosphere but not in the other. Nevertheless, these results strongly suggest that earlier work on the combustion of metal droplets in oxygen mixed with nitrogen or other reactive gases [e.g., flame ignition studies (6)] should be reexamined for possible complications due to transient or end-products other than the simple metal-oxygen compounds usually assumed to form.

#### Acknowledgment

This work was supported jointly by the U. S. Naval Weapons Center under NASA W.O. No. 6032 and by the U. S. Atomic Energy Commission. The skilled experimental assistance of Mr. N. L. Richardson is gratefully acknowledged.

Manuscript submitted Nov. 22, 1967; revised manuscript received April 29, 1968.

Any discussion of this paper will appear in a Discussion Section to be published in the June 1969 JOURNAL.

## REFERENCES

1. L. S. Nelson, N. L. Richardson, and J. L. Prentice, *Rev. Sci. Instruments*, **39**, 744 (1968).
2. D. Michel, M. Perez y Yorba, and R. Collongues, *Compt. Rend. C263*, 1366 (1966).
3. L. S. Nelson, *Science*, **148**, 1594 (1965).
4. See, for example, Review by H. C. Christensen, R. H. Knipe, and A. S. Gordon, *Pyrodynamics*, **3**, 91 (1965).
5. F. G. Brockman, *J. Opt. Soc. Am.*, **37**, 652 (1947).
6. See, for example, references cited by A. Macek, Eleventh Symposium (International) on Combustion, Berkeley, California, 1966, pp. 203-214, The Combustion Institute, Pittsburgh, Pennsylvania (1967).

## On the Mechanism of Oxidation of Cobalt Between 750° and 1000°C Using Inert Gold Spheroidal Markers

J. P. Foster\* and R. J. Reynik\*\*

Department of Metallurgical Engineering, Drexel Institute of Technology, Philadelphia, Pennsylvania

For the oxidation mechanism of cobalt there is conflicting evidence between thermogravimetric, electrical conductivity, and self-diffusion on the one hand, and marker studies on the other. The purpose of this note is to clarify the discrepancies associated with these marker studies.

Since the kinetics of oxidation is parabolic, the Wagner defect reaction theory is applicable. According to thermogravimetric (1, 2) and electrical conductivity studies (1) the exponent of the oxygen partial pressure dependence is positive, and Wagner's theory states that the oxide is a p-type semiconductor. Thus its defect structure can be either cation vacant or anion interstitial. Further, the oxygen partial pressure dependence for the diffusion of Co<sup>60</sup> in CoO is the same as that for the oxidation of Co to CoO. This indicates that the defect structure of CoO is cation vacancies.

Marker studies of the oxidation of Co are not in agreement with the above conclusions. Investigators using nichrome (3) and Pt (4) wires as markers report the final marker positions at the interface between the gray outer CoO scale and the brown, inner CoO scale. This interface between the two layers is coincident with the original metal surface (4). Hence these investigators (3, 4) conclude the outer layer is formed by the diffusion of Co ions and the inner brown CoO layer is supplied by O ion diffusion through the outer layer. The investigators (2) using a radioactive Pt slurry and Al<sub>2</sub>O<sub>3</sub> particles (5) on Co at 1200°C report no inner brown CoO scale, hence only observe a single layer, and final marker locations at the metal|gray CoO interface. They conclude that gray CoO forms by cobalt ion diffusion through oxide scale vacancies. This failure to observe an inner brown CoO scale is contrary to data reported by Phalnkar (3). No marker results have been reported below 900°C, where Co<sub>3</sub>O<sub>4</sub> forms together with gray CoO (but not brown CoO).

### Experimental

All details of specimen preparation and experimental technique are identical to that previously reported (6), except as noted. Three different weights of gold (Table I) were vapor-deposited onto carefully prepared as-cast cylindrical cobalt specimens. The gold films again spheroidized at 400°C. Gold-marked and unmarked specimens were simultaneously oxidized in static air at 750°, 850°, and 1000°C, for times in multiples of 24 hr, up to 144 hr.

### Results

For all specimens, the final marker location is at a well-defined demarcation line within the gray CoO

scale (see Fig. 1). On adjacent sides of the demarcation line, and yet completely within the gray CoO scale, there appears a compact CoO scale and a small void CoO scale, respectively. With the exceptions of the inert spheroids appearing within the inner CoO scale, the differences in spheroidal sizes (corresponding to different quantities of deposited gold film), and minor variations in random void appearances, the microstructures for the gold-marked and unmarked specimens were identical. Gold is soluble in Co (7). However, the size of the spheroids, depends solely on the initial quantity of deposited gold. Once formed, the spheroids remained approximately constant (Fig. 2) for different oxidation temperatures and times. If the gold spheroids were soluble in Co to any large extent, their size would necessarily decrease with increasing oxidation time. But this was not observed, hence gold spheroids can be used as inert markers in oxidation studies.

### Discussion

No comparison of final marker location is possible at 750° or 850°C. At 1000°C the final location of the gold spheroidal markers does not agree with the locations reported using nichrome (3) or Pt (4) wires and Al<sub>2</sub>O<sub>3</sub> particles (5). This difference is due to fragmentary contact of these markers with the original metal surface (8). The vapor deposited spheroidal gold layer has excellent surface contact. Disagreement with the radioactive Pt slurry on Co at 1200°C is probably due to the fact that a brown, inner CoO scale was not observed.

A more serious disagreement in final marker location at 750°, 850°, and 1000°C is with the predicted results of thermogravimetric, electrical conductivity, and self-diffusion studies. Since gray CoO is cation deficient, one would expect the final marker location to be found at the metal|oxide interface. However, this failure of inert markers to be found at metal|oxide interfaces is not confined to the cobalt system. In ox-

Table I. Weights of gold evaporated, and impurities\* in as-cast cobalt

Oxidation temperature, °C	Weight of Au, g
750	0.0121
	0.0283
	0.0735
850	0.0346
	0.0097
1000	0.0970

\* Graduate Student, Department of Metallurgical Engineering.  
\*\* Associate Professor, Department of Metallurgical Engineering.

\* <0.001 Cu, <0.001 Pb, <0.001 Mg.  
Spectrographic analysis courtesy of the Naval Air Engineering Center, Philadelphia, Pa.

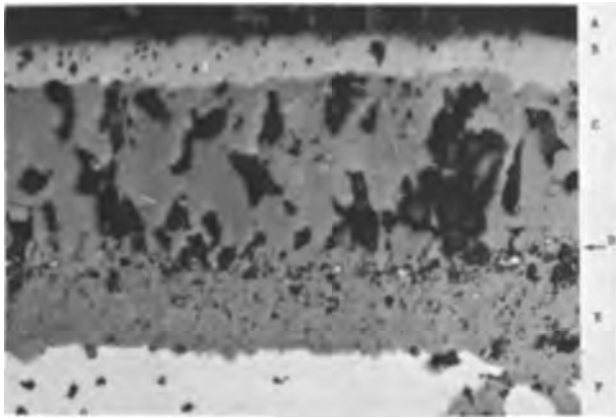


Fig. 1. Co specimen marked with 0.0283g gold and oxidized at 750°C for 120 hr. Magnification 1500X. Unetched. A, bakelite; B,  $\text{Co}_3\text{O}_4$ ; C, compact gray  $\text{CoO}$ ; D, spherical gold marker; E, small void gray  $\text{CoO}$ ; F, Co metal.

oxidation studies involving Ni (9) and in the sulfidation of Cu (10) and Ag (11) (all of which have been established as cation deficient), the final marker positions were always found at a position corresponding to the demarcation line observed in the present cobalt studies. It is proposed that the oxidation of Co to gray  $\text{CoO}$  follows a similar mechanism (12) to that proposed to describe the formation of  $\text{NiO}$ ,  $\text{CuS}$ , and  $\text{AgS}$ . Plastic flow at the metal|oxide interface is insufficient to remove the vacancies arriving as a consequence of cation migration. Cracks result at this interface, and this leads to a detachment of the marker from the metal|oxide interface causing it to be found at the demarcation line.

#### REFERENCES

1. B. Fisher and D. Tannhauser, *This Journal*, **111**, 1194 (1964).
2. R. E. Carter and F. D. Richardson, *Trans. AIME*, **203**, 336 (1955).
3. C. A. Phalnikar, E. B. Evans, and W. M. Baldwin, Jr., *This Journal*, **103**, 429 (1956).
4. A. Preece and G. Lucas, *J. Inst. Metals*, **81**, 219 and 731 (1951-1952).
5. F. S. Pettit and J. B. Wagner, Jr., *Acta. Met.*, **12**, 41 (1964).
6. J. P. Foster and R. J. Reynik, *Appl. Phys. Letters*, **9**, 148 (1966).
7. M. Hansen, "Constitution of Binary Alloys," McGraw-Hill Publishing Co., New York (1958).
8. S. Mrowec and T. Werber, *Acta. Met.*, **8**, 819 (1960).
9. J. A. Sartell and C. H. Li, *J. Inst. Metals*, **90**, 92 (1961-1962).
10. S. Mrowec and T. Werber, *Acta. Met.*, **7**, 696 (1959).
11. J. Mikulski, S. Mrowec, and T. Werber, *Bull. Acad. Polon. Sci. Cl. III*, **7**, 737 (1959).
12. P. Kofstad, "High-Temperature Oxidation of Metals," Chap. 5, John Wiley & Sons, Inc., New York (1966).

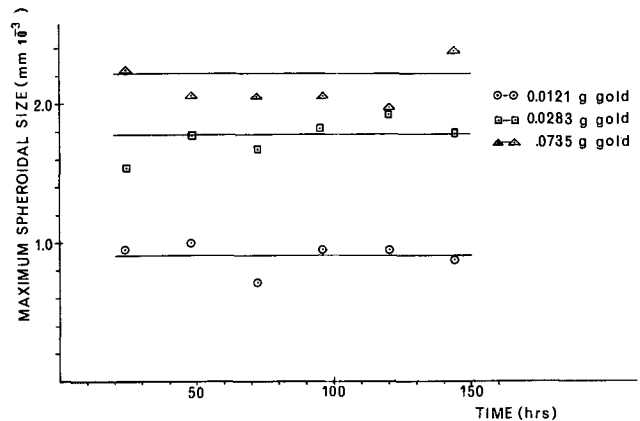


Fig. 2. Maximum gold spheroidal size as a function of oxidation time at 750°C for different weights of gold.

## Structure and Morphology of Electrodeposited Molybdenum Dendrites

Cletus J. Bechtoldt, Fielding Ogburn,\* and J. Smit

National Bureau of Standards, Washington, D. C.

The structure and morphology of electrodeposited dendrites have been the subject of a number of investigations (1). None of these studies, however, contain information on electrodeposited body centered cubic (bcc) dendrites. Recently this laboratory had the opportunity to examine electrodeposited molybdenum dendrites. The purpose of this note is to report on that study, particularly with respect to the twin structure phenomenon.

The dendrites, contributed by Senderoff, had been removed from the edges of cathodes on which molybdenum had been deposited. Deposition was made from a molten fluoride system similar to that described in a patent (2). Dendrites are not a normal product of this process and ceased to form after continued electrolysis. These molybdenum specimens were examined using Weissenberg, precession, back-reflection Laue, and divergent beam x-ray techniques and by optical goniometric and microscopic methods.

#### Observations

Precession patterns, one example of which is shown in Fig. 1, indicated that the dendrites had two ori-

entations with a common  $\langle 111 \rangle$  direction parallel to the direction of growth. Diffraction symmetry was that for the usual twin relation in a bcc lattice. Back-reflection Laue patterns showed the bounding facets parallel to the direction of growth to be  $\{110\}$  planes. Rotation of the dendrites about the growth axis produced clear signals at precise  $60^\circ$  intervals on an optical goniometer, consistent with the lateral surfaces being  $\{110\}$  planes.

The x-ray diffraction patterns were unusually sharp for electrodeposited material. A back reflection pseudo-Kossel pattern, Fig. 2 (divergent x-ray beam technique), revealed a crystal having a high degree of perfection. Each element of an ellipse in the pseudo-Kossel pattern represents diffraction from a different area on the dendrite. The degree of perfection of the dendrite is indicated by the sharpness and by the absence of irregularities on the curved elements in the pattern.

A typical molybdenum dendrite is shown in Fig. 3. The dendrites are characterized by flat-appearing lateral surfaces and a basically hexagonal cross-section. Frequently a cleft appears near the growing tip. The largest dendrites are approximately 20 mm long

\* Electrochemical Society Active Member.



Fig. 1.  $110$  zero level precession pattern of molybdenum dendrite showing twin structure. Respective orientation shown by solid and broken lines.

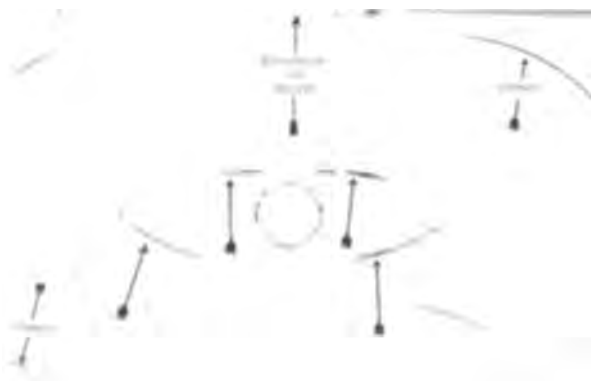


Fig. 2. Back reflection pseudo-Kossel pattern showing degree of perfection of molybdenum dendrite. Cu radiation, 10 cm specimen to film distance taken on  $\{110\}$  surface containing twin boundary. Fragments of  $\{321\}$  ellipsoids are indicated by arrows.

and 2 mm wide. Many of the specimens are marked by striations on the lateral surfaces as shown in Fig. 4. These striations change direction on crossing from one lateral surface to another. Measurement of the angles formed by the striations on two adjacent surfaces with the common edge of these surfaces show them to be traces of  $\{100\}$  planes within one degree. The lateral surfaces of the dendrites appear to diverge gradually in the direction of growth, yet optical and diffraction examinations (alignment by auto collimator) indicated these surfaces to be parallel to the growth axis. The striations apparently mark successive growth layers which result in the appearance of divergence.

The striations show a change of direction on certain of the lateral surfaces in addition to the change in direction previously noted at the intersection of the lateral surfaces. In both cases the change in direction results in the formation of a herringbone pattern. When observed on a lateral surface the union of the striations in the herringbone pattern (that portion that would ordinarily be taken as a backbone) forms a quasi-boundary. This boundary is made up at times of short straight segments having a definite angular shape. At other times the boundary between the twins appears (microscopically) as a continuously curving line more characteristic of a grain boundary. Back-reflection Laue patterns obtained from a beam cen-

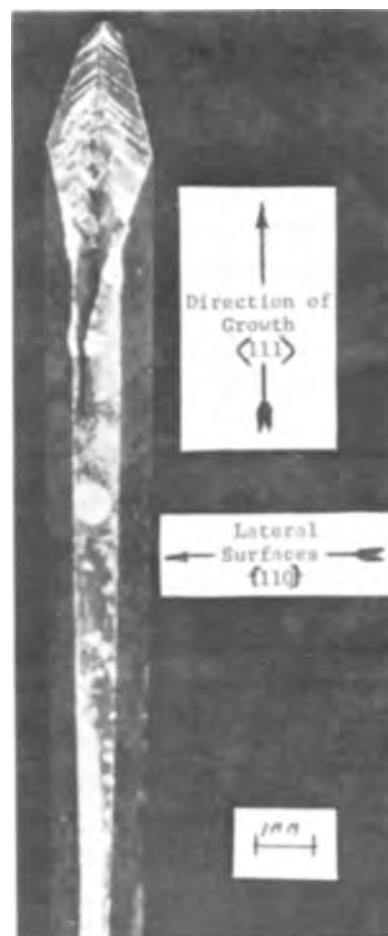


Fig. 3. Typical molybdenum approximately 20 mm long by 2 mm wide. A crevice near the tip is shown.

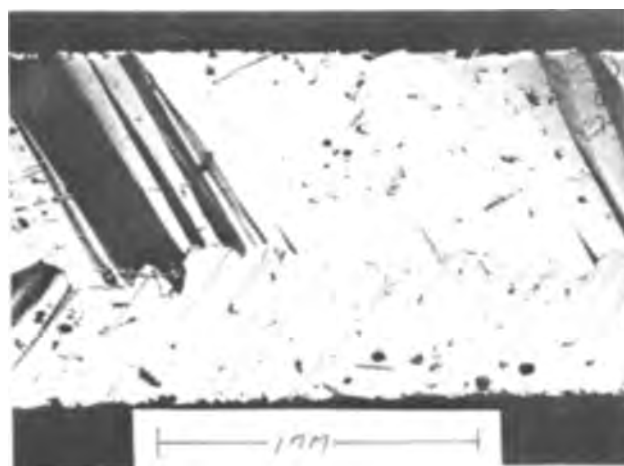


Fig. 4. Lateral face of molybdenum showing herringbone pattern and juncture of twin orientations.

tered on the boundary always showed a twin structure. At times the boundary crosses from one lateral surface to an adjacent surface, extending the full length of the dendrite. A second boundary can always be found on one of the other exterior surfaces. Figure 5 is an optical photomicrograph showing the boundary between the twinned crystals in a section taken perpendicular to the growth axis.

A common feature of these dendrites is a cleft or crevice near the tip and elongated voids in the interior. These voids and crevices always occurred between the two crystals of twin orientation and, in effect, are a broadening of the boundary. Careful optical examination of the surfaces of the crevices and



Fig. 5. Photomicrograph of a section of a molybdenum dendrite taken normal to the direction of growth showing internal juncture of twin orientations. A void contained in the boundary is shown.

voids revealed cubically shaped corners and  $\{110\}$  facets, the latter not always parallel to the direction of growth. Frequently the growth on one surface in the crevice overlapped those on an adjacent surface. The boundaries containing the angular shapes previously mentioned apparently arise due to continued growth and filling of these crevices.

The features of the growth tips varied substantially. Essentially the tip, containing step-like surfaces, starts as a point and grows to ultimately form a hexagonally shaped shaft. Optical goniometer measurements made on many of the tips showed them to contain numerous facets lying between the  $\{100\}$  and  $\{110\}$  planes on a 100 zone (see Fig. 6). The most prominent facets on the tip are  $\{100\}$  facets. Following the  $\{100\}$  facets in prominence were other extremely narrow facets making small angle steps along the  $\{100\}$  zone from the prominent  $\{100\}$  facets toward the  $\{110\}$  lateral bounding surfaces. These facets stopped abruptly  $10^\circ$  to  $14^\circ$  before the  $\{110\}$  lateral surface. Several distinct sequences of this kind appeared between the  $\{100\}$  planes of the growing tip and the bounding  $\{110\}$  lateral surfaces. To obtain increased resolution, the dendrites were mounted on a two circle goniometer and examined using a modified bench-type metallurgical microscope and a point light source. Long, slender facets differing by as little as half a degree were observed.

A detailed optical examination of the morphology of the as-grown tip of the dendrite was also under-



Fig. 6. The location of observed facets on the tip of molybdenum dendrites shown on a stereograph projection in the growth direction. Heavy lines indicate location of optical reflections along 100 zones.

taken. However, at the high magnification the depth of focus was much too shallow to permit accurate measurements of the growth front facets. In view of the possibility that the tips had been altered or damaged since growth, this examination was abandoned. However, the extreme tip on several dendrites was carefully polished mechanically and then electropolished. This produced a minute cross-section nearly normal to the direction of growth, as shown in Fig. 7. The configuration displayed on the tip section suggests traces of  $\{112\}$  composition planes forming a zig-zag. The angles between segments are approximately  $60^\circ$ , which is the angle between two  $\{112\}$  planes parallel to the direction of growth. The segments were perpendicular to a  $\{110\}$  bounding facet. Each segment is about 0.005 mm long and the distance between terminal points of the zig-zag is as long as 0.05 mm. At greater distances the boundary degenerates into the grain-like boundary previously described.

#### Discussion

Electrodeposited dendrites frequently appear to grow by the same mechanism as crystals pulled from supercooled solutions where a higher nucleation rate is achieved at a twin plane reentrant edge. In a recent paper, Faust and John (3) cited the following requirements or conditions as necessary to achieve crystal growth by the twin plane reentrant edge mechanism.

1. The embryo nucleus must contain one or more twin planes.
2. The growth front of the material must be faceted.
3. The reentrancies must be indestructible, *i.e.*, any initial reentrancy must not fill in to form a closed figure bounded by planes and sharp corners.
4. The twin plane must intersect one or more stable facets at an angle different from  $90^\circ$ .
5. The direction of growth must lie in the twin plane.

Presently these requirements are known to be met by dendrites with structures in the cubic, hexagonal, and orthorhombic crystal systems. Specifically, in the cubic system, only fcc dendrites having the copper, diamond, and zinc blend-type structures have been observed to fulfill the requirements. Molybdenum dendrites of the W-type structure with a body centered cubic lattice may represent a new structure that meets these conditions. Requirements 1 and 5, discussed in the preceding section, are met inasmuch as the molybdenum dendrites are twinned and the direction of growth is within the  $\{112\}$  composition plane.

The dendrites are well faceted and there is strong circumstantial evidence and hence is presumed their growth fronts are faceted (requirement 2). Direct evidence, positive or negative, however, could not be obtained.

Accepting the presumption that the growth front has stable facets (likely to be  $\{110\}$ ) the zig-zag configura-

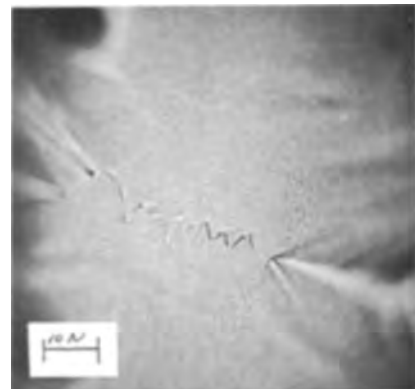


Fig. 7. Photomicrograph of a molybdenum dendrite near the extreme tip showing  $\{112\}$  composition planes of the twin boundary formed.

tion provides for self perpetuation (requirement 3). This can be seen if we consider what would happen if the reentrant angles at the two composition planes filled in. New facets would develop and new reentrant angles would form probably within the acute angles between the zigs and zags. Continued growth at these new reentrant angles would reestablish the original facets at the composition planes. Continued growth in the new reentrant angle would establish a new set of reentrances, probably the original set, ignoring the {111} planes which do not form stable facets. Lastly there are a number of facets in a [100] zone which are not 90° to the composition plane, as called for by requirement 4. It seems reasonable for one of these to form at the growing tip.

These specimens appear to be examples of dendritic growth of a bcc material by the twin plane reentrant edge mechanism. This is consistent with the observations that all the dendrites grew in the <111> direction. The intersection of the boundaries in Fig. 7 have a <111> direction and if the intersecting boundaries are essential to the growth mechanism, the dendrites must grow in the same direction. The growth direction is also facilitated, or may even be determined, by the six lateral, closest packed slowest growing 110 facets.

#### Acknowledgment

The authors wish to acknowledge the cooperation of Dr. S. Senderoff of the Parma Research Laboratory, Union Carbide Corporation, in contributing the molybdenum dendrites for this investigation.

Manuscript submitted April 2, 1968; revised manuscript received May 13, 1968. This paper was presented at the Philadelphia Meeting, Oct. 9-14, 1966, as Paper 116.

Any discussion of this paper will appear in a Discussion Section to be published in the June 1969 JOURNAL.

#### REFERENCES

1. G. Wranglen, *Trans. Royal Inst.*, Tech. No. 92 (1955).  
J. W. Faust, Jr. and H. E. John, *This Journal*, **108**, 109 (1961); **110**, 463 (1963).  
F. Ogburn, B. Paretzkin, and H. S. Peiser, *Acta Cryst.*, **17**, 774 (1964).  
F. Ogburn, *This Journal*, **111**, 870 (1964).  
F. Ogburn, C. J. Bechtoldt, J. B. Morris, and A. de Koranyi, *ibid.*, **112**, 574 (1965).  
J. Smit, F. Ogburn, C. J. Bechtoldt, *ibid.*, **115**, 371 (1968).
2. G. W. Mellors and S. Senderoff, Canadian Patent 688,546, Electrodeposition of Refractory Metals, June 9, 1964, Example Number XXXII, p. 36.
3. J. W. Faust, Jr. and H. F. John, *J. Phys. Chem. Solids*, **25**, 1407 (1964).

## Brief Communication



### The Solubility of Silver (II) Oxide in Alkaline Solutions

Arthur Fleischer\*

Consultant, Orange, New Jersey

The solubility of AgO in potassium hydroxide solutions has been reported by Dirkse and Wiers (1) up to 5M KOH and by Hills (2) up to 12M KOH. The authors of both papers indicated that the solubility curve as a function of KOH concentration at 25°C was the same as that for the solubility of silver (I) oxide, Ag<sub>2</sub>O. Amlie and Ruetschi (3) indicated that there was an uncertainty with regard to the solubility of AgO. They considered the coincidence in the solubilities of the two oxides to be rather suspicious, citing that Dirkse *et al.* (1) did not show that the dissolved species was bivalent. Subsequently Hills (2) refers to the "proven presence of a higher valent species."

Application of the phase rule throws light on this problem of the apparently identical solubilities of the two silver oxides. Let an excess of these two oxides, Ag<sub>2</sub>O and AgO, be added to a potassium hydroxide solution for the determination of the silver concentration in the solution phase. At equilibrium, the system will consist of four phases, namely two solid phases representing the silver oxides, a solution (or liquid) phase, and a gas phase; the latter accommodates the equilibrium oxygen and water vapor pressures. The system will also have four components which may be selected as the compounds, Ag<sub>2</sub>O, AgO, KOH, and H<sub>2</sub>O, or any other four combinations which will yield all phases in any proportion.

The insertion of these values in the phase rule equation,  $P + F = C + 2$ , with the number of phases,

\* Electrochemical Society Active Member.

$P$ , equal to the number of components,  $C$ , yields 2 as the number of degrees of freedom,  $F$ . Experimentally, these two degrees of freedom are used up by selecting temperature and KOH concentration as the independent variables. Thus, the system is made invariant and the solubility or any other property of the system is fixed. In other words, it may be said that the activity of the silver species is fixed for any selection of temperature and KOH concentration in this system.

The published solubility curve for AgO in KOH solutions as a function of KOH concentration must therefore be interpreted as corresponding to the presence of two solid phases, namely AgO and Ag<sub>2</sub>O. This condition is not difficult to postulate for the cited work in view of the known instability of AgO at ambient temperature. On standing in the presence of KOH solution, AgO loses oxygen with the formation of Ag<sub>2</sub>O (1, 2).

Manuscript submitted April 15, 1968; revised manuscript received ca. May 2, 1968.

Any discussion of this paper will appear in a Discussion Section to be published in the June 1969 JOURNAL.

#### REFERENCES

1. T. P. Dirkse and B. Wiers, *This Journal*, **106**, 284 (1959).
2. S. Hills, "Extended Abstracts of the Battery Division," Vol. 6, p. 9, The Electrochemical Society, Inc., New York (1961).
3. R. F. Amlie and P. Ruetschi, *This Journal*, **108**, 813 (1961).



# Chemical Reactions Involving Holes at the Zinc Oxide Single Crystal Anode

W. P. Gomes,<sup>1</sup> T. Freund, and S. R. Morrison

Stanford Research Institute, Menlo Park, California

## ABSTRACT

The anodic oxidation of various reactants dissolved in water was studied on a zinc oxide single-crystal electrode by electrical techniques. It was found that only a few substances inject electrons into the conduction band. However, many reactants are oxidized by holes, which are created in the crystal by illumination: A class of two- or multi-equivalent reducing agents, called current-doubling agents, undergoes oxidation by a two-step mechanism in which reaction with a hole leads to the formation of a radical-type intermediate, which then injects an electron in the conduction band. Relative hole reactivities for different reagents were determined by making current measurements during competitive oxidation of current-doubling and noncurrent-doubling reactants. The reactivity of different radical-type intermediates toward oxidizing agents was investigated. Experimental support is given for the idea that a common intermediate, the hydrogen atom, is formed during the oxidation of many organic current-doubling species. Differences in behavior depending on the crystal face are discussed.

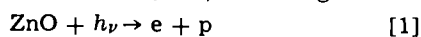
Since the initial work of Brattain and Garrett (1) on the electrochemistry of germanium, there has been considerable interest in the behavior of semiconductor electrodes, as indicated by reviews by Gerischer (2), Boddy (3), and Myamlin and Pleskov (4). The first extensive investigation on the zinc oxide/electrolyte system in the absence of any reactant was made by Dewald (5). Cathodic reduction reactions on single-crystal zinc oxide were studied by Dewald (6), Freund and Morrison (7), and Lohmann (8). An effect called "current doubling" was reported by Morrison and Freund (9) in connection with the anodic behavior of aqueous formate ion on an illuminated zinc oxide electrode; the authors attributed it to the formation of a radical-type intermediate on the crystal surface and showed the role of this radical in the photocatalytic oxidation of formate by oxygen.

In the present contribution, the generality of the current-doubling effect for many multi-equivalent reducing agents is demonstrated. This new electrochemical effect can be utilized for studying reactions between electronic charge carriers of the solid and reactants at the surface, and between sorbed radicals and oxidizing species. We believe that these studies are pertinent to the field of heterogeneous catalysis (9), since charge transfer processes can be important steps in adsorption and chemical reactions on semiconductor catalysts. The current-doubling results are useful for predictions (10) of catalytic activity and selectivity.

## Method

In an aqueous electrochemical cell containing a zinc oxide electrode under anodic bias, a negligibly low current is observed in the dark in chemically inert solutions as well as in solutions containing various reducing agents. In Fig. 1, the band model of zinc oxide in an anodic condition is represented, including the surface. The lack of dark electron injection suggests that the energy level associated with the sorbed species is situated below the bottom of the conduction band, e.g., R.

When zinc oxide is illuminated with the light of  $\lambda < 385 \text{ m}\mu$  (the band gap is 3.2 eV), electron-hole pairs are formed within the crystal, according to



where e represents an electron in the conduction band

and p a hole in the valence band. Under anodic bias, only holes will move toward the surface. Therefore the flux of holes to the surface is primarily dependent on the bulk properties of the crystal and on the photon flux. The rate of oxidation reactions should be determined by the hole current at the surface and therefore be independent of the nature of the reducing agent in solution. The same current was observed experimentally at constant light intensity in electrochemically inert solutions as well as in the solutions of all one-equivalent and many two- or multiequivalent reducing agents. This current was found to be proportional to the light intensity and to increase only slightly with increasing anodic bias. When no reducing agent is present in solution, it has been shown (8, 11) that the reaction involved is the anodic photodissolution of zinc oxide resulting in the oxidation of the lattice oxide ion.

With some two- or multiequivalent reducing agents such as formate ion, the external anodic current,  $J$ , was found to approach  $2J_p$ . The mechanism suggested (9) is illustrated by Fig. 1. The assumption is that the one-equivalent oxidation of the current-doubling agent R will lead to the formation of a radical-type species  $R^+$  with an electron energy level above the bottom of the conduction band. Thus  $R^+$  can inject an electron into the semiconductor. This process is expressed by the surface reactions



where p is a hole in the valence band and e is an electron in the conduction band. Reactions [2] and

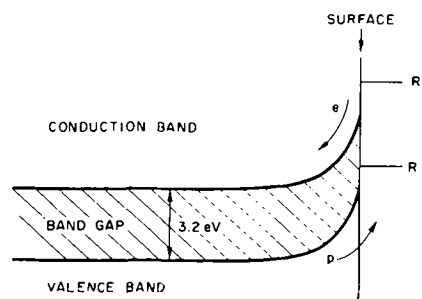


Fig. 1. The band model of ZnO with anodic bias

<sup>1</sup> Atholl McBean Fellow, 1966-1967. Permanent address: Laboratorium voor Kristallografie en Studie van de Vaste Stof, Rijksuniversiteit Gent, Belgium.



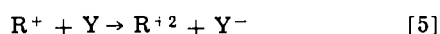
[3] represent<sup>2</sup> the two-equivalent oxidation of R. If a one-equivalent reducing agent is present, no process equivalent to reaction [3] may occur.

Thus, in principle, the anodic current  $J$  will have one of two values, either  $J_p$  or  $2J_p$ . The  $J_p$  case occurs without any reducing agent or with a one-equivalent reducing agent, and the  $2J_p$  case occurs with a current-doubling agent.

The mechanism of current doubling represented by reactions [2] and [3] suggests that two different types or reagents, when added to a solution of a current-doubling agent, could lower the steady-state rate of reaction [3] and thus lower the measured current  $J$ . The first, "X-type," reagents are reducing agents which are oxidized by holes solely. If X is, for instance, a one-equivalent reducing agent, its oxidation will be represented by



The competition between reactions [4] and [2] would lead to a decrease in the rate of the electron injection reaction. The second, "Y-type," reagents are oxidizing agents that react with the radical  $R^+$  according to the surface reaction



where the reduction of Y is assumed to be one-equivalent. The competition between reactions [5] and [3] would also lead to a decreased electron injection. It has previously been reported (9) that  $O_2$  acts as a Y-type reagent with respect to the current-doubling agent, formate ion, and the process was called "quenching."

These competitive reactions can be used to obtain qualitative and quantitative information about the behavior of various species at the zinc oxide anode. By current measurements with solutions containing current-doubling agents as a function of the addition of reagents of unknown behavior, species that are electrochemically active at the zinc oxide electrode can be detected. This is particularly useful for determining if a reducing agent exhibits X-type behavior, since X-type substances by themselves do not affect the photocurrent. The electrochemical activity of oxidizing agents toward sorbed radicals can also be detected by the decrease of the photocurrent due to current-doubling substances, i.e., quenching by Y-type substances. Previously (7) the electrochemical activity of oxidizing agents in the absence of reducing agents has been studied using a capacitance-current method. Quantitative current measurements during competitive reaction between current-doubling agents and other reactants, in steady-state conditions, can provide information about relative hole reactivities of various reactants and about relative reactivities of different radical-type species at the zinc oxide surface. This paper describes the results of quantitative current measurements for the purpose of determining relative hole reactivities and radical reactivities.

### Experimental

The apparatus consisted essentially of an electrochemical cell, an electrical measuring circuit, and a light source. The cell contained a zinc oxide single crystal as one electrode, a platinum working electrode, a saturated calomel reference electrode, and an electrolyte. The electrical circuit allowed the measurement of the voltage of the zinc oxide vs. SCE, the current through the zinc oxide, and the capacitance between the zinc oxide and platinum electrodes. The light source was an incandescent microscope lamp. Details have been given elsewhere (7, 9).

Zinc oxide single crystals about 5 mm in diameter and 1 mm thick, cut perpendicular to the c-axis, were obtained from Minnesota Mining and Manufacturing

<sup>2</sup> The possibility should not be excluded that, in some cases, reaction [2] gives more than one product and one of these is the injecting species.

Company. In most experiments, the (000 $\bar{1}$ ) face was in contact with the electrolyte. This face was prepared by lapping, and the lapping damage was then removed by etching for about 15 sec in concentrated HCl solution, which rapidly attacked the (000 $\bar{1}$ ) face, allowing its identification (12). Subsequently, the crystal was kept for several hours in 85%  $H_3PO_4$ , which we found to be a good polishing agent for the (000 $\bar{1}$ ) face. When the (0001) face was studied, the sequence of reagents was reversed, since 85%  $H_3PO_4$  preferentially attacks the (0001) face and concentrated HCl solutions polish it.

Most experiments were carried out on two zinc oxide samples, whose donor densities were on the order of  $10^{17} \text{ cm}^{-3}$  as determined by capacitance-voltage measurements (5). The surface area of the crystal in contact with the electrolyte ranged between 5 and 10 mm<sup>2</sup>. Except in the experiment with  $O_2$  as a reagent,  $N_2$  was bubbled through the solutions to remove dissolved  $O_2$  before each measurement. In experiments that involved current measurements during exposure to light, the gas bubbling was interrupted at regular intervals to read the current, until a constant current value was obtained. Unless otherwise stated, measurements were performed at +1.0v vs. SCE and at room temperature.

### Results

*Current-doubling agents.*—The following species have been found to show current doubling: arsenic (III), cyanide, borohydride, sulfide, formate, binoxalate, tartrate, acetaldehyde, and many aliphatic alcohols, such as methanol, ethanol, 1- and 2-propanol, 1-butanol, 1,2-ethanediol, and 1,2,3-propanetriol. It should be noted that neither oxalate ion nor 2-methyl-2-propanol exhibits current-doubling.

According to Reactions [2] and [3], for a solution of a current-doubling agent, the current should be  $J = 2J_p$  ( $J_p$  being determined at the same light intensity and voltage with a solution free of current-doubling agent). Experimentally,  $J$  is often found to be somewhat less than twice the hole current. If we define the electron current  $J_e$  by

$$J_e = J - J_p \quad [6]$$

this means that often  $J_e/J_p < 1$ . A competition with the anodic dissolution of zinc oxide could be the cause of this effect. The value of  $J_e/J_p$  depends on the nature and concentration of the current-doubling agent, in some cases on the pH of the solution (e.g.,  $J_e/J_p$  increases with pH in the case of alcohols), and in all cases on the crystal face exposed,  $J_e/J_p$  being much higher on the (000 $\bar{1}$ ) than on the (0001) face. The experimental conditions for quantitative work were chosen so that several current-doubling agents would have values of  $J_e/J_p$  equal or close to unity. In all the experiments discussed below, the (000 $\bar{1}$ ) face was in contact with the solutions and unless otherwise specified, the solutions were 1M in KCl and 0.05M in KOH.

*Competitive oxidation of current-doubling and non-current-doubling reducing agents.*—The following current-doubling agents were used:  $CH_3OH$ ,  $C_2H_5OH$ ,  $2-C_3H_7OH$ ,  $(CHOH-COO^-)_2$  as  $(CHOHCOOK)_2$ , and  $BH_4^-$  as  $KBH_4$ . The following noncurrent-doubling "X-type" reagents were used:  $Br^-$  as  $KBr$ ,  $SO_3^{2-}$  as  $Na_2SO_3$ , and  $I^-$  as  $KI$ .

*Current as a function of the concentration of X.*—The variation of the current  $J$  has been studied as a function of the concentration of noncurrent-doubling reducing agent, [X], in solutions of constant concentration of current-doubling agent, [R]. A typical result is presented in Fig. 2, where  $J_p/J_e$  has been plotted vs. [X]. A straight line is obtained, indicating a relationship

$$J_p/J_e = 1 + \alpha[X] \quad [7]$$

where  $\alpha$  is a constant. In cases where  $J_p/J_e > 1$  at

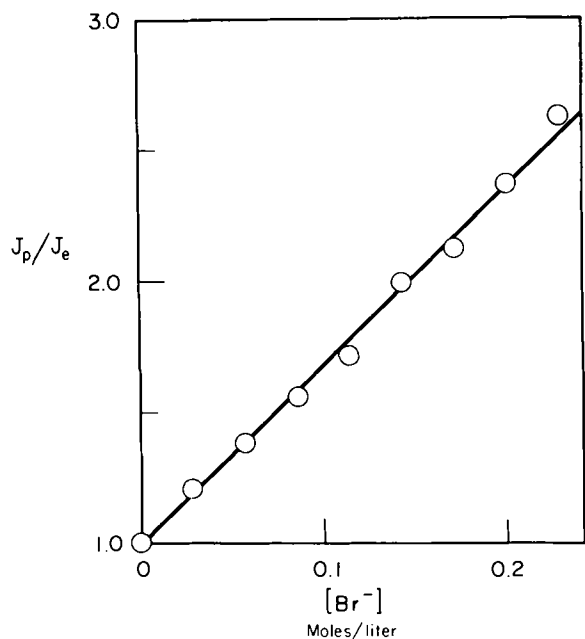


Fig. 2. Ratio of hole to electron currents,  $J_p/J_e$ , vs. concentration of bromide ion in solution in 0.01M  $C_2H_5OH/1M$  KCl/0.05M KOH.

$[X] = 0$ , a linear dependence of  $J_p/J_e$  on  $[X]$  is also found. A relationship of the type given by Eq. [7] appears to be obeyed in any of the combinations of one of the current-doubling agents with one of the noncurrent-doubling agents listed above.

*Current as a function of the concentration of R.*—Methanol and ethanol show the simplest quantitative behavior. In Fig. 3 the results are plotted as values of  $J_p/J_e$  vs. the ratio  $[X]/[R]$ , for three different experiments in which R was 0.02M, 0.1M, and 0.5M  $CH_3OH$  and in which X, being  $I^-$ , was added so that the ranges of  $[X]/[R]$  covered were the same. This procedure was chosen to avoid very narrow as well as very wide ranges of  $[X]/[R]$ , corresponding with very small and very large changes in  $J_p/J_e$  respectively,

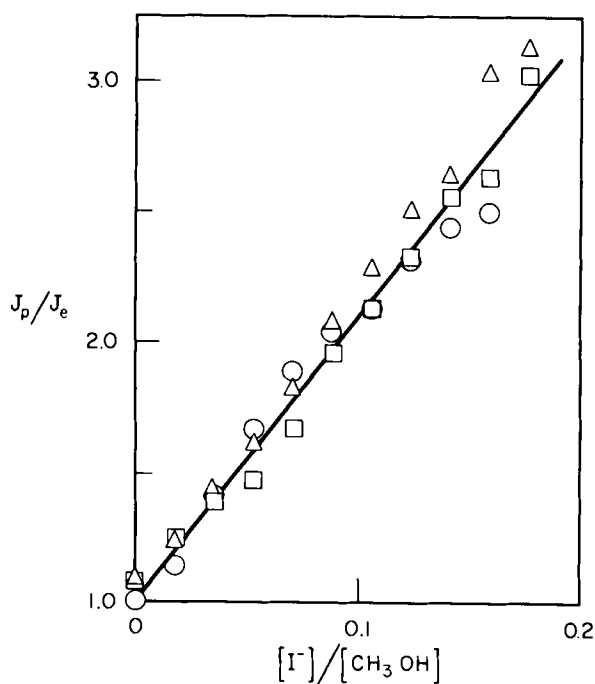


Fig. 3. Ratio of hole to electron currents,  $J_p/J_e$ , vs. ratio of solution concentration of iodide to methanol.  $[I^-]/[CH_3OH]$ , in 1M KCl/0.05M KOH.  $\circ$  0.5M  $CH_3OH$ ,  $\triangle$  0.1M  $CH_3OH$ ,  $\square$  0.02M  $CH_3OH$ .

since both situations are subject to comparatively large experimental errors. It is seen in Fig. 3 that the following relationship holds

$$(J_p/J_e) = 1 + \beta[X]/[R] \quad [8]$$

where the reactivity ratio  $\beta$  is a constant. Relationship [8] has been found to be obeyed for ethanol as well as for methanol. The data are independent of the order of mixing.

Table I gives the values of  $\beta$  determined from separate experiments. In cases where  $J_p/J_e > 1$  for  $[X] = 0$ , a corrected value of  $J_p$  was used for the calculation of  $\beta$ . This correction was based on the assumption that a constant fraction of the holes, determined from the  $J_p/J_e$  value at  $[X] = 0$ , reacts by another pathway than that involving X and R, e.g., anodic dissolution of zinc oxide. In no case was the correction more than 25%. For  $SO_3^{2-}$ , a correction was made, when necessary, for a small dark injection current that was sometimes observed. Of the many substances investigated, only dithionite gave a high dark injection current. This dark current might be associated with the known (13) dissociation to the radical ion  $SO_2^{\cdot-}$ ; radicals may be expected to have an energy level above the bottom of the conduction band. The values of  $\beta$  are independent of the light intensity and the crystal as shown in Table I.

Relationship [7] seems to be more generally applicable than the more restrictive relationship [8]. In contrast to methanol and ethanol, the following substances obey [7] but not [8]: 2-propanol, tartrate ion, and borohydride ion. The nonconstancy of  $\beta$  is shown in Table I. For two  $(CH_3)_2CHOH$  vs.  $I^-$  experiments, changing the alcohol concentration by a factor of 10 resulted in a change of  $\beta$  by a factor of 3. In the case of tartrate ion,  $\beta$  is constant for iodide and sulfite but not for bromide. While borohydride was investigated at only one concentration, nonsimple behavior is illustrated by the  $\beta$  values with the three X substances. For sulfite and iodide the values are almost equal, in contrast to the other current-doubling agents where they differ by more than a factor of 4. For bromide, even at the solubility limit, no effect was found on current-doubling by borohydride.

*Qualitative results.*—By observing the current in alcohol solutions on addition of various reactants, it was established that, in addition to the reducing agents mentioned above, acetone, oxalate, and 2-methyl-2-propanol are oxidized by holes, whereas chloride, acetate, and phthalate are electrochemically inert.

*Quenching of current-doubling by an oxidizing agent.*—The number of systems suitable for quantitative studies is restricted here by the requirement that the oxidizing agent Y should react with the sorbed radical-type intermediate  $R^+$ , but not with the current-

Table I. Values for the reactivity ratio,  $\beta$

Substance	R	Molarity	Br <sup>-</sup>	X SO <sub>3</sub> <sup>2-</sup>	I <sup>-</sup>	
CH <sub>3</sub> OH		0.02-0.5	0.14	2.8	12	
			0.16		11	
			0.12		11	
C <sub>2</sub> H <sub>5</sub> OH		0.01-0.4	0.07	1.5	5.2	
			0.10	1.5	5.5	
				1.3	6.0	
			1.1 <sup>a</sup>			
(CH <sub>3</sub> ) <sub>2</sub> CHOH		0.01	0.08	1.5	5.5	
					0.1	13
					0.1	17
(CHOHCOO <sup>-</sup> ) <sub>2</sub>		0.01	0.23	5.1	20	
			0.01		21	
			0.05		22	
			0.05		21	
			0.05		21	
BH <sub>4</sub> <sup>-</sup>		0.001	0.000	0.33	0.38	
					0.42	

<sup>a</sup> 10 x higher light intensity.

<sup>b</sup> Different crystal.

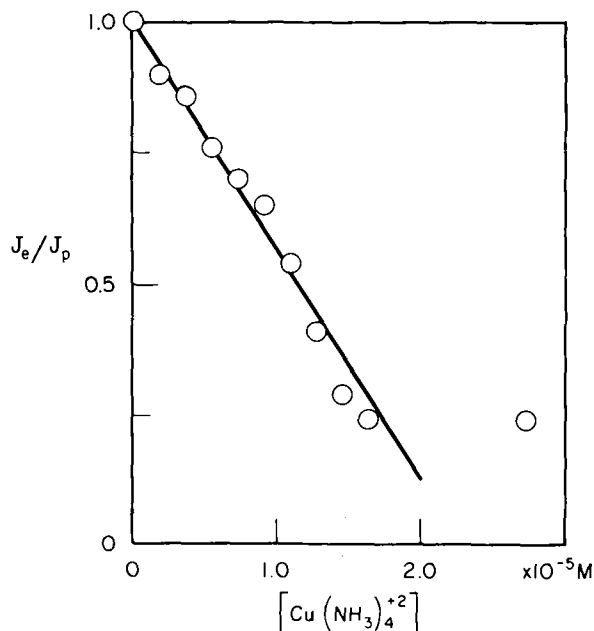


Fig. 4. Ratio of electron to hole currents,  $J_e/J_p$  vs. copper (II) concentration in solution,  $[Cu(NH_3)_4^{+2}]$  for 1M  $C_2H_5OH/1M$  KCl/0.05M KOH.

doubling agent R; this eliminates, for instance, systems such as alcohol-permanganate or borohydride-ferricyanide. A Y-type reagent for which this requirement is met with respect to alcohols and formate as current-doubling agents is the tetramminecopper(II) ion. A typical quenching curve in which  $J_e/J_p$  is plotted against  $[Cu(NH_3)_4^{+2}]$  is shown in Fig. 4, indicating a relationship

$$J_e/J_p = 1 - \gamma[Y] \quad [9]$$

where  $[Y]$  is the concentration in solution and  $\gamma$  is a constant. Relationship [9] appears to be valid for the system  $Cu(NH_3)_4^{+2}$  vs. all current-doubling agents investigated, namely, methanol, ethanol, 2-propanol, and formate. In the cases in which the initial value (absence of Y) of  $J_e/J_p < 1$ , the same type of relationship holds, with the same value of  $\gamma$ , but of course with a different intercept. Relationship [9] was usually found to be obeyed down to about  $J_e/J_p = 0.2$ .

In Table II, values of the quenching coefficient,  $\gamma$ , are listed for different combinations of experimental conditions. It can be seen that  $\gamma$  is independent of the nature and concentration of the current-doubling agent, the hole current  $J_p$ , the light intensity  $I$ , and the zinc oxide crystal used.

Some work was also done with dissolved  $O_2$  as a quenching agent. The concentration of dissolved oxygen was varied by bubbling  $N_2-O_2$  mixtures of known composition through the solutions. The amount of quenching in alcohol solutions, even when saturated with  $O_2$  at 1 atm pressure, was, however, insufficient to permit drawing any quantitative conclusions.

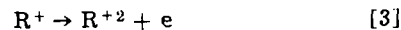
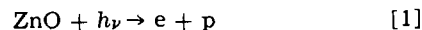
### Discussion

*Competitive oxidation of current-doubling and non-current-doubling agents.*—A theoretical expression that

Table II. Quenching coefficients for tetramminecopper (II)

Current-doubling agent R	[R] (moles/l)	$J_p$ (nA)	Crystal No.	$\gamma$ (in $10^4$ l/mole)
$CH_3OH$	0.1	100	34	5.7
$C_2H_5OH$	0.1	100	34	5.4
$C_2H_5OH$	0.1	1000	34	4.5
$C_2H_5OH$	0.1	100	35	5.9
$C_2H_5OH$	1	100	34	4.8
$C_2H_5OH$	1	1000	34	4.8
$C_2H_5OH$	1	100	35	6.2
$(CH_3)_2CHOH$	0.1	100	34	4.9
HCOO-	0.1	100	35	5.9
HCOO-	1	100	35	4.7

accounts for the experimental relationship [8], valid in the case of  $CH_3OH$  and  $C_2H_5OH$ , can be derived as follows. Consider the reactions



where R is assumed to be a two-equivalent, and X a one-equivalent reducing agent. Since reaction [1], whose rate is determined by the light intensity, is the rate-determining step, a steady state in p and  $R^+$  may be assumed. Considering that the currents are proportional to the rates, we can write

$$J_p/J_e = \{k_R[R_{ad}][p] + k_X[X_{ad}][p]\}/k_R[R_{ad}][p] \quad [10]$$

where  $k_R$  and  $k_X$  are the rate constants of reactions [2] and [4], respectively,  $[R_{ad}]$  and  $[X_{ad}]$  are the surface concentrations of sorbed R and X, and  $[p]$  is the formal hole concentration at the surface. If independent sorption of X and R according to linear sorption isotherms is assumed, which usually implies low degrees of coverage, relationship [10] becomes

$$J_p/J_e = 1 + (K_X/K_R) ([X]/[R]) \quad [11]$$

where  $K$ , the hole reactivity constant, is equal to the product of the sorption and the rate constants and the brackets refer to concentrations in solution. Relationship [11] is in agreement with the experimental expression [8], whereby

$$\beta = K_X/K_R \quad [12]$$

It should be pointed out that our use of a formal hole concentration on the surface should not be taken as evidence for the existence of sorbed holes in the sense of adsorbed chemical species. Conceptually, the hole in the valence band and the electron in the conduction band arise from ideas restricted to the bulk of the zinc oxide near, but not on, the surface. Experimentally, only flow rates of these carriers within the solid are measured. In the kinetic formulation given above, no problems arise with the use of a formal concentration on the surface because of the same dependence on both  $J_e$  and  $J_p$ .

From the values of  $\beta$  listed in Table I, relative values of hole reactivity can be calculated for all the reactants involved. For instance, a value of  $K$  for sulfite relative to iodide is found by dividing the  $\beta$  values obtained from sulfite vs. methanol and iodide vs. methanol. An important observation is that the same value is found, as required by theory, from the data involving ethanol. Similarly,  $K$  for the bromide relative to iodide can be calculated in two ways. Values of  $K$  as determined with different titrants are listed in Table III, where, arbitrarily,  $K = 100$  is chosen by iodide. By inserting the  $K$  values for iodide, sulfite, and bromide in the data of Table I,  $K$  values for methanol and ethanol are deduced in three ways. From Table III, it can be seen that all results are independent of the way they have been determined. This provides confidence in the competition concept and in the quantitative values of relative hole reac-

Table III. Hole reactivities

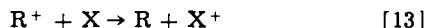
Species	K	Titrant
I-	100	—
$SO_3^{2-}$	23	$CH_3OH$
	23	$C_2H_5OH$
Br-	1.2	$CH_3OH$
$CH_3OH$	1.5	$C_2H_5OH$
	10	Br-
	8	$SO_3^{2-}$
	8	I-
$C_2H_5OH$	16	Br-
	18	$SO_3^{2-}$
	18	I

tivities. Thus, while it has not been possible to evaluate the absolute hole reactivity of a substance, it has been shown that unique reactivities can be assigned to several substances.

We shall now discuss the cases where relationship [8] does not hold. For 2-propanol, the dependence of  $\beta$  on  $[R]$  can be explained by a nonlinear isotherm. Relative values for  $K_X$  can still be found by comparing  $\beta$ -values calculated from experiments in which the 2-propanol concentrations are the same. By normalizing the data from row 3 of Table I to  $K_{I^-} = 100$ , we find  $K_{SO_3^{2-}} = 27$  and  $K_{Br^-} = 1.5$ , in fair agreement with the values calculated from the methanol and ethanol experiments. It may be remarked here that this result would not agree with another model for the sorption of X and R, which also results in a relationship of the type given by [11]. This model assumes complete coverage and competition for the same surface by X and R. Indeed, anomalies in the sorption of 2-propanol would, with these assumptions, lead to deviations in the  $[X]$  dependence.

With tartrate,  $K_{SO_3^{2-}}$  is 24; the behavior with  $Br^-$  cannot be interpreted at this time. With borohydride, the  $K$ -values for  $SO_3^{2-}$  and  $I^-$  are about equal, whereas the value for  $Br^-$  is zero. We think this could result from reduction of the oxidation products of the noncurrent-doubling reactants by  $BH_4^-$ , a powerful reducing agent, followed by electron injection from the radical product of  $BH_4^-$ . The net result with  $BH_4^-$  is a decrease, or the complete disappearance, of the influence of the noncurrent-doubling agent on  $J_p/J_e$ , since an electron-injection radical is produced independent of the  $[Br^-]$ . The oxidation products of  $Br^-$  are likely to be more reactive toward reducing agents than are the ones of  $I^-$ ; the oxidation products of  $SO_3^{2-}$  are probably not reactive at all.

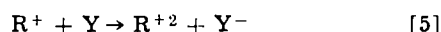
Our results exclude an alternate mechanism for competitive oxidation by holes, in which the oxidation reaction of the noncurrent-doubling agent would be



Indeed, the current-concentration relationship in this case would not include any dependence on  $[R]$ , in contradiction with experimental observation (relationship [8]).

#### Quenching of Current Doubling by an Oxidizing Agent.

—The current-concentration characteristics of the Y-type reagent  $Cu(NH_3)_4^{+2}$  with three alcohols and formate ion can be described in terms of a competition between the conduction band and the oxidizing agent Y for the electron of the photoproduced radical  $R^+$ . These surface reactions can be represented as



The experimental result, Eq. [9], can be written to show that  $(J_p - J_e)/J_e$ , the ratio of chemical oxidation [14] to electron injection [3], equals the ratio  $\gamma[Y]$  to  $\{1 - \gamma[Y]\}$  where  $[Y]$  refers to concentration in solution and  $\gamma$  is a constant independent of light intensity and copper ion concentration. At least formally, this current-concentration relationship describes chemical oxidation by Y of the intermediate and inhibition by Y of the electron injection process. While we are still uncertain of the detailed interpretation of these results, some general characteristics seem to be clear. First, the ratio of chemical oxidation to inhibition by Y is independent of the rate of generation of the intermediate  $R^+$ . Second, the electrical results are independent of the concentration of R. Third, the value of  $\gamma$  is the same for the four different R substances investigated. The last characteristic is particularly noteworthy, since the implication is an identical rate-determining process for all four R substances. This may arise from the rate expression

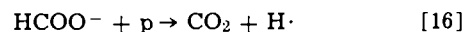
being independent of R or from the generation of a common intermediate from all four R substances. We favor the latter explanation, with the intermediate,  $H\cdot$ , as  $R^+$ . In the next section chemical support for the idea of the hydrogen atom as a common intermediate will be given.

It should be noted that the possibility of the  $Cu(NH_3)_4^{+2}$  effect resulting from the reduction of the  $Cu(II)$  by conduction band electrons was ruled out by the absence of a cathodic current in the dark at the same voltage.

*Chemical considerations.*—In the foregoing section it was suggested that the radical-type intermediate formed during the oxidation of different alcohols and formate ion could be the hydrogen atom. For a primary alcohol, for instance, the two-equivalent oxidation would be the surface reactions<sup>3</sup>



In the case of formate, the first oxidation step would be



This hypothesis of  $H\cdot$  being the common electron injector in many current-doubling reactions is supported by the following chemical evidence: (I) For 12 of the current-doubling agents, the oxidation can be considered as a dehydrogenation. (II) Binoxalate,  $C_2O_4H^-$ , exhibits current doubling, whereas oxalate  $C_2O_4^{2-}$  is oxidized by two holes. (III) Acetaldehyde shows current doubling, and acetone is oxidized by a hole mechanism. (IV) 2-Methyl-2-propanol,  $(CH_3)_3COH$ , which has no  $\alpha$ -hydrogen, is oxidized without current doubling, in contrast with the primary and secondary alcohols investigated.

It was assumed that the oxidation of R is two-equivalent and that of X one-equivalent. No chemical analyses were made in order to support this hypothesis. In the case of 2-propanol, the electrical data indicated that the oxidation is two-equivalent. The argument is as follows. The two-equivalent oxidation product of 2-propanol is acetone. Our experiments show that acetone is oxidized solely by holes. Since at least two holes must be involved per acetone molecule, the ratio  $J_e/J_p$  could not be more than 1:3 if 2-propanol were oxidized beyond acetone. Experimentally,  $J_e/J_p$  for 2-propanol was found to be near unity, implying that the acetone formed must be desorbed. The small amount present on the surface because of the sorption equilibrium would not have any noticeable influence on the current doubling. For the other reactants investigated, our results do not provide evidence concerning desorption following the first oxidation step. The oxidation product at the electrode could, for instance, be  $I(O)$  as  $I_2$  or  $I(+1)$  as  $OI^-$  in the case of  $I^-$ , and  $S(+V)$  as  $S_2O_6^{2-}$  or  $S(+VI)$  as  $SO_4^{2-}$  in the case of  $SO_3^{2-}$ .

The lack of knowledge about the absolute amounts sorbed makes it impossible to isolate the rate constants for oxidation by holes from the experimental values of  $K$ . The type of numerical data available at present has a practical significance in that they allow certain predictions about selective oxidation of mixtures of reactants in contact with illuminated zinc oxide, not only in anodic, but also in catalytic conditions. Indeed, illuminated zinc oxide has been shown (14, 15) to be a catalyst for the reaction between oxygen and several of the reagents under investigation (alcohols, formate, oxalate) with formation of  $H_2O_2$ . Considering the mechanism suggested for one of these reactions (9), a direct correlation is likely to exist between the relative oxidation rates in a mixture of such reactants and the relative  $K$  values determined under anodic conditions.

<sup>3</sup> It is assumed here that the alcohols sorb in the form of the alcoholate anions; this view is supported by the pH dependence of current doubling with alcohols.

Manuscript submitted March 14, 1968; revised manuscript received April 25, 1968.

Any discussion of this paper will appear in a Discussion Section to be published in the June 1969 JOURNAL.

## REFERENCES

1. W. H. Brattain and C. G. B. Garrett, *Bell System Tech. J.*, **34**, 129 (1955).
2. H. Gerischer, *Adv. in Electrochemistry and Electrochem. Eng.*, **1**, 139 (1961).
3. P. J. Boddy, *J. Electroanal. Chem.*, **10**, 199 (1965).
4. V. A. Myamlin and Yu. V. Pleskov, "Electrochemistry of Semiconductors," Plenum Press, New York (1967).
5. J. F. Dewald, *J. Phys. Chem. Solids*, **14**, 155 (1960).
6. J. F. Dewald, in "Surface Chemistry of Metals and Semiconductors," p. 205, John Wiley & Sons, Inc., New York (1960).
7. T. Freund and S. R. Morrison, *Surface Science*, **9**, 119 (1968).
8. F. Lohmann, *Ber. Bunsenges.*, **70**, 87 (1966).
9. S. R. Morrison and T. Freund, *J. Chem. Phys.*, **47**, 1543 (1967).
10. T. Freund, S. R. Morrison, and W. P. Gomes, Proc. IV International Congress on Catalysis (1968).
11. K. Hauffe and J. Range, *Ber. Bunsenges.*, **71**, 690 (1967).
12. G. Heiland, P. Kunstmann, and H. Pfister, *Z. Physik*, **176**, 485 (1963).
13. R. G. Rinker, T. P. Gordon, D. M. Mason, and W. H. Corcoran, *J. Phys. Chem.*, **63**, 302 (1959).
14. T. R. Rubin, J. G. Calvert, G. T. Rankin, and W. MacNevin, *J. Am. Chem. Soc.*, **75**, 2850 (1952).
15. V. I. Veselovskii and D. M. Shub, *Zh. Fiz. Khim.*, **26**, 509 (1952).

## Intrinsic Stress in Evaporated Metal Films

E. Klokholm and B. S. Berry

International Business Machines Corporation, Watson Research Center, Yorktown Heights, New York

## ABSTRACT

The sign and magnitude of the intrinsic stresses observed in evaporated metal films cannot be predicted from *a priori* knowledge. In an effort to correlate the observed intrinsic stress,  $S$ , with other physical parameters,  $S$  has been measured in films of fifteen different metals. The stress was measured *in situ* by the cantilevered substrate technique. The films were evaporated from an electron bombarded source in vacuums of  $10^{-6}$  to  $10^{-7}$  Torr onto glass substrates at room temperature. Under these conditions the intrinsic stress was generally found to be tensile, though exceptions were observed. The data obtained indicate that films of metals with higher melting temperatures and larger shear moduli have intrinsic stresses which approach a magnitude roughly equal to 0.01 of the shear modulus. It is suggested that such high values of stresses are generated by the annealing and constrained shrinkage of disordered material buried behind the advancing surface of the growing films. Reduction of the stress is predicted when surface rearrangements preempt the need for extensive subsequent internal annealing. This proposal is considered in the relation to the experimental observation that the intrinsic stress is small when the ratio of the (absolute) substrate and melting temperatures exceeds  $\frac{1}{4}$ .

The existence of large internal stress in thin films is of considerable importance in the use and application of thin films in microcircuit technologies. These stresses can cause film rupture, loss of adhesion, substrate cracking, and changes in the physical and chemical properties of the films. For films which have been deposited on substrates at temperatures above or below the temperatures at which the film is to be used, the internal stress consists of two terms. One of these is a thermal stress due to the difference in the thermal expansion of the film and the substrate. The second stress, generally called the intrinsic stress, is apparently a fundamental result of the manner of growth of the thin film. In the work presented here we will be concerned only with the intrinsic stress in films deposited on glass substrates at or near room temperature. It will become apparent that the intrinsic stress is often larger than the yield stress in bulk materials.

### Experimental

In an effort to correlate the intrinsic stress,  $S$ , with other physical parameters, the stress has been measured as a function of film thickness in 15 different metals deposited on glass substrates at room temperature. The cantilevered substrate technique was used to measure  $S$ . In this technique one end of a glass substrate is rigidly clamped in a fixed mount. The free end is connected to the arm of an electronic microbalance. A deflection,  $D$ , of the free end produces

an output from the microbalance which is proportional to  $D$ . A film deposited on one side of the substrate results in a deflection proportional to the bending moment exerted on the substrate by the film. The bending moment is in turn proportional to  $Sd$  where  $d$  is the film thickness and  $S$  is the average stress in the film. The sense of  $D$  is a direct indication of the kind of stress in the film. For a film deposited on the underside of the substrate, an upward  $D$  indicates a compressive stress in the film; a tensile stress causes a downwards deflection. To calibrate the substrate in order to obtain  $Sd$  from  $D$ , it is only necessary to note the response of the microbalance caused by the application of a known weight to the free end of the substrate. The sensitivity of the stress measuring instrumentation is such the  $Sd$  from 50 to greater than  $10^5$  d/cm can be continuously measured over the entire range. Finally, to obtain  $S$  from  $Sd$ , an independent measurement of the film thickness is necessary. The film thickness was determined from a calibrated oscillating quartz crystal film thickness monitor. The crystal monitor was calibrated by measuring the thickness of a film interferometrically and relating this thickness to the change in the resonant frequency of the quartz crystal. The entire apparatus is mounted in the upper portion of an oil pumped, liquid nitrogen trapped, 18-in. bell jar evaporator. An electron gun was used as the evaporation source; evaporation rates were from 2 to 5Å/sec. Chamber pressures during film

deposition were  $10^{-6}$  to  $10^{-7}$  Torr. The substrates prior to deposition were at room temperature; however, during deposition the substrate temperature increased by about  $25^{\circ}\text{C}$ . In order to maintain the temperature within this limit, the films had to be deposited sequentially in steps of about  $25\text{\AA}$ .

### Results and Discussion

The data for  $Sd$  as a function of  $d$  are presented in Fig. 1, 2, and 3. The thickness dependence of the average stress, calculated from these results using the definitional relationship  $S \equiv (Sd)/d$  for uniform continuous films, is shown in Fig. 4, 5, and 6. It should be noted that these plots magnify considerably small irregularities of doubtful significance which occur near the foot of the  $Sd$  vs.  $d$  curves. To avoid this region of uncertainty, relative comparisons of the stress in

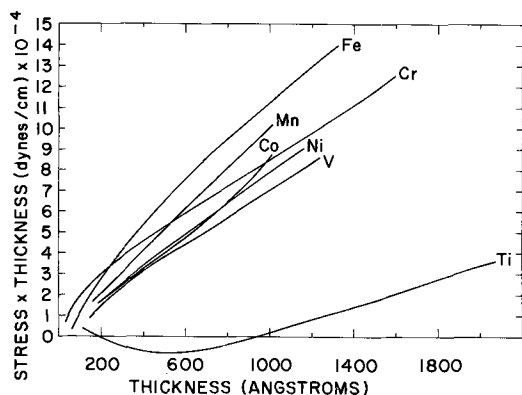


Fig. 1. Stress-thickness product as a function of film thickness for Fe, Mn, Cr, Co, Ni, V, and Ti.

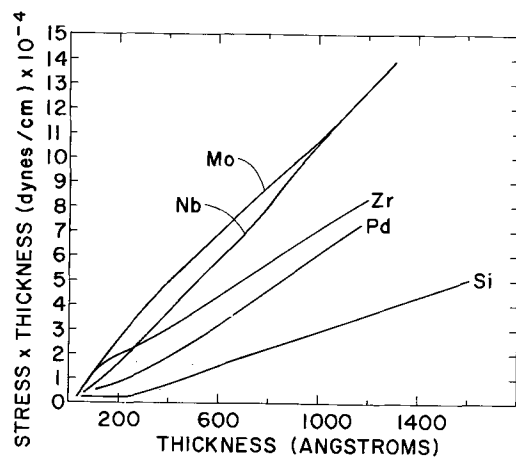


Fig. 2. Stress-thickness product as a function of thickness for Mo, Nb, Zr, Pd, and Si.

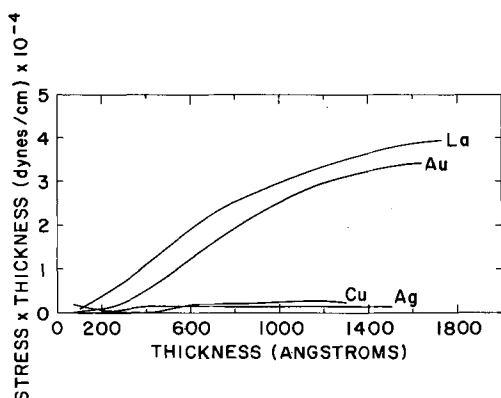


Fig. 3. Stress-thickness product as a function of film thickness for La, Au, Cu, and Ag.

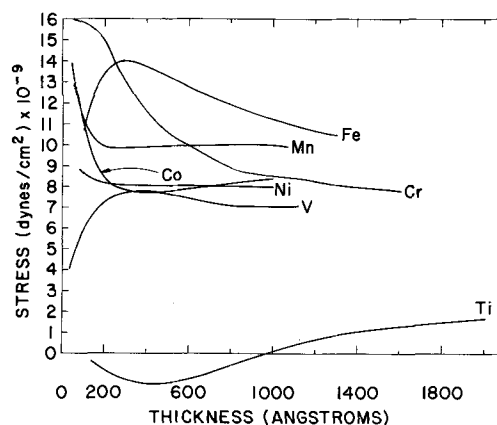


Fig. 4. Stress for the metals in Fig. 1 as a function of film thickness.

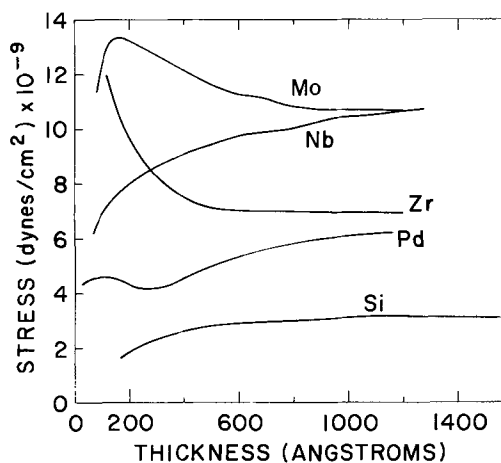


Fig. 5. Stress for the metals in Fig. 2 as a function of film thickness.

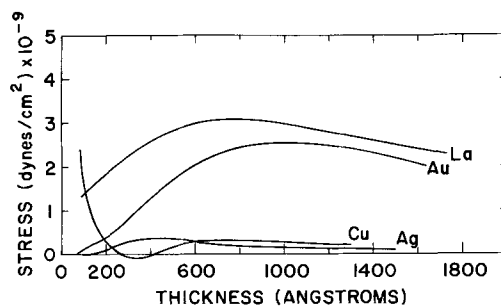


Fig. 6. Stress for the metals in Fig. 3 as a function of film thickness.

different materials have been made at a film thickness of  $1000\text{\AA}$ . This information is given in Table I, together with values of melting point  $T_m$  and shear modulus  $\mu$ . Figure 7 shows the dependence of the data in Table I on position in the periodic table. The stress in Zr, Nb, V, Ti, Co, and Mn evaporated films have not been previously reported. Stress in the films of the other metals have been reported, and the values of  $S$  given here are in agreement with those quoted in the reviews by Hoffman (1-4).

From the above data, two empirical conclusions are possible; first, the stress in the harder, more refractory metals is very large, about  $10^{10}$  dynes/cm<sup>2</sup>, while in the softer, more fusible metals, Cu, Ag, Au, and La,  $S$  varies from about  $5 \times 10^9$  to less than  $10^9$  dynes/cm<sup>2</sup>. Second, there is a systematic gradation in the form of the  $Sd$  vs.  $d$  curves. The  $Sd$  for the softer, more fusible metals of Fig. 3 rises from a small value to either a broad maximum or to approximately a constant value. For most of the remaining metals of

Table I. Stress in different materials, also melting point and shear modulus.

Atomic No.		$T_m$ Melting temp. °K	$S \times 10^{-9}$ (d/cm <sup>2</sup> ) 1000Å films	Shear modulus $\mu \times 10^{-11}$ (d/cm <sup>2</sup> )
1.				
22	Ti	1930	0	4.1
23	V	2130	7	4.7
24	Cr	2120	8.5	9
25	Mn	1520	9.8	7.8
26	Fe	1810	11	8.4
27	Co	1770	8.4	7.8
28	Ni	1710	8	7.8
29	Cu	1360	0.6	4.6
2.				
40	Zr	2135	7	3.7
41	Nb	2740	10.5	3.7
42	Mo	2900	10.8	12
46	Pd	1830	6	4.6
47	Ag	1235	0.2	2.8
3.				
57	La	1190	3	1.5
79	Au	1340	2.6	2.8

Fig. 1 and 2,  $Sd$  increases almost linearly with  $d$ . A notable exception is  $Sd$  for Ti films which inexplicably is at first in compression, and at about 1000Å changes to tension with increasing  $d$ .

It is evident from Fig. 7 that some degree of correlation exists between  $S$ ,  $\mu$ , and  $T_m$ . The correlation of  $S$  jointly with  $\mu$  and  $T_m$  seems to be better than with  $T_m$  and  $\mu$  considered separately. As an empirical rule, it appears that, if  $T_m < 1500^\circ\text{K}$  and  $\mu \leq 4 \times 10^{11}$  d/cm<sup>2</sup> simultaneously, then the stress is relatively small, and  $Sd$  does not continuously increase with  $d$ . On the other hand, for  $T_m > 1500^\circ\text{K}$  and  $\mu \geq 4 \times 10^{11}$  d/cm<sup>2</sup>, the stress is large ( $\cong 0.01\mu$ ) and  $Sd$  increases linearly with  $d$ .

It is of interest to consider now the incremental stress,  $S_i$ , defined as the local slope at a point on the  $Sd$  vs.  $d$  curve

$$S_i \equiv \Delta Sd / \Delta d$$

This stress can be interpreted as the stress produced in an incremental layer  $\Delta d$  at the free surface of the film. In the refractory metals  $Sd$  is roughly linear in  $d$  and therefore  $S_i$  and the stored elastic energy density remains constant. Furthermore, since  $S_i$  is almost independent of  $d$ , an essentially uniform stress must also be present in such films. On the other hand,  $S_i$  in the more fusible metals first increases to a maximum, and decreases towards zero (or even changes sign), and hence the stored elastic energy decreases with  $d$  after the first few hundred Angstroms. The stage of decreasing  $S_i$  is thought to indicate that the stress in such films is due primarily to stresses at the film-substrate interface. For an idealized model (5), it has been shown that the interfacial stresses should decrease as  $1/d$ . In the thick, high melting point films, however, the observation that  $S_i$  is both large and approximately independent of thickness leads to the

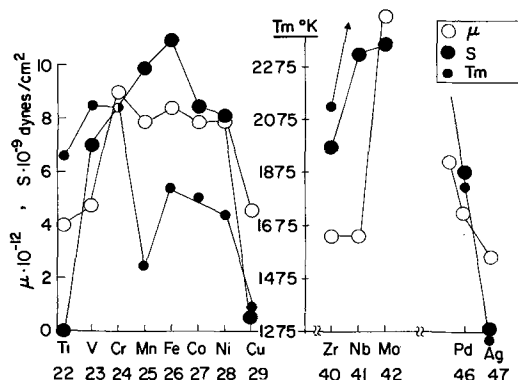


Fig. 7. Stress in 1000Å films plotted as a function of atomic number for comparison with the melting temperature  $T_m$  and the shear modulus  $\mu$ .

conclusion that in this case the dominant contribution to the stress is not caused by interfacial effects but is caused by a second contribution whose magnitude is dependent on the deposition process.

It is suggested that this second contribution to the intrinsic stress (which we shall refer to as the growth stress) originates from the annealing and attendant shrinkage of disordered material buried behind the advancing surface of the growing film. The disordered material is envisaged to have a structure and density lying between the two extremes represented by a perfect crystal and a highly defective supercooled liquid. Consequently, any annealing which produces a more nearly perfect crystalline arrangement results in an attendant shrinkage strain which would occur isotropically if it were free to occur without restraint. Shrinkage in the plane of the film is, however, inhibited by the substrate, with the result that an isotropic stress is generated in the plane of the film. To account for the magnitude of the largest stresses encountered in this work ( $S_{\max} \cong 0.01\mu$ ) it is only necessary to postulate that annealing tends to produce a maximum density increase of a few per cent, which seems quite reasonable in view of its similarity to the density increase produced by freezing a liquid metal.<sup>1</sup> Further, since annealing will produce the same value of  $S_i$  in each incremental layer of the film, this explanation for the stress is consistent with the required prediction that the  $Sd$  vs.  $d$  curve should be approximately linear in all cases where the growth stress is the dominant contribution to the total intrinsic stress. It should also be noted that since the rough proportionality between  $S_{\max}$  and  $\mu$  implies that the maximum shrinkage strain has an approximately constant value of 1%, we infer that the maximum density change produced by annealing is also roughly constant from one material to another.

One of the most important features of any model for the origin of the growth stress is the insight it yields into the factors which may govern the dependence of the stress on the temperature of the substrate. In the present model, the stress is postulated to occur as a result of an internal rearrangement behind the growing surface of the film. It follows that if the rearrangement involves a thermally activated process, it could be inhibited (and the stress prevented from developing) by deposition on a substrate held at a sufficiently low temperature. However, since this temperature can be expected to be comparable with the very low temperatures needed to deposit an amorphous film (4.2°K or less for pure metals), we conclude that in the present experiments the annealing always proceeds very rapidly to completion, so that the magnitude of the growth stress reflects only the amount of disorder initially present on a surface layer before it becomes buried by the condensation of succeeding layers. For the purpose of rough estimation, consider a film growing under steady-state conditions at a rate  $R_0$  monolayers/sec. On the average, the atoms are exposed on the surface for a time  $R_0^{-1}$ , which in the present experiments is about 1 sec. We suppose that in this interval thermally activated movements occur in a manner tending to improve the crystalline order of the surface, and that these occur at a rate  $\Gamma$  given by an Arrhenius relationship (6), of the type

$$\Gamma = \nu_0 \exp - \frac{Q}{RT_s} \quad [1]$$

where  $\nu_0$  is a frequency factor,  $Q$  is an activation energy,  $R$  is the gas constant, and  $T_s$  the absolute substrate temperature. On this basis it can be argued that a high growth stress corresponds to the condition  $\Gamma \ll R_0$ , and a low stress to the condition  $\Gamma \gg R_0$ . Taking the order of magnitude of  $\nu_0$  as  $10^{14}$  sec<sup>-1</sup>, the effective transition temperature corresponding to

<sup>1</sup> It is interesting to note that for the case of gallium, a metal which expands on freezing, Buckel (7) has found the stress to be compressive in as-deposited films.

$\Gamma = R_0$  occurs when

$$\frac{Q}{RT_s} = 32 \quad [2]$$

Writing now, by analogy with an empirical rule for self-diffusion (6), that  $Q$  is proportional to the melting point  $T_m$ , i.e., that

$$Q \approx KT_m \quad [3]$$

Eq. [2] becomes

$$\frac{KT_m}{RT_s} \approx 32 \quad [4]$$

An examination of the experimental data indicates that the growth stress apparently decreases in the neighborhood of  $T_m/T_s \approx 4.5$ . Inserting this value in Eq. [4] yields  $K \approx 13$  cal/mole/°C. Since this value of  $K$  is about 0.4 of the  $K$ -value necessary to fit Eq. [3] to self-diffusion data, we obtain the result that  $Q$  in Eq. [1] is only 0.4 of that for self-diffusion. An activation energy of this magnitude is consistent with a mechanism involving surface diffusion and/or the movement of vacancies. Either one or both of these processes could provide a means for removing the disorder from the surface of the film, and hence govern the temperature dependence of the growth stress.

In summary, the present observations are believed to demonstrate that the intrinsic stress in metallic films should generally be regarded as being composed of two contributions. One of these is thought to be produced by the mismatch at the film-substrate interface, while the other contribution, the growth stress, is believed to result from the annealing and shrinkage of disordered material behind the surface of the growing film. A distinguishing feature of these two contributions is the different manner in which they cause the average stress to vary with film thickness. The

growth stress is predicted to be highly temperature dependent, and to become small when  $T_s/T_m \gtrsim 1/4$ .

#### Acknowledgments

The authors are indebted to Mr. Walter Pritchett for his invaluable assistance in the stress measurements, and especially to Dr. A. S. Nowick for suggesting a connection between defect annealing and stress generation in thin films.

Manuscript submitted Jan. 15, 1968; revised manuscript received April 4, 1968. This paper was presented at the Dallas Meeting, May 7-12, 1967, as Paper 55.

Any discussion of this paper will appear in a Discussion Section to be published in the June 1969 JOURNAL.

#### REFERENCES

1. R. W. Hoffman, "Thin Films," H. G. F. Wilsdorf, Editor, pp. 99; American Society for Metals, Cleveland (1964).
2. R. W. Hoffman, "The Use of Thin Films in Physical Investigations," J. C. Anderson, Editor, p. 261, Academic Press, New York (1966).
3. R. W. Hoffman, "Physics of Thin Films," G. Hass and R. E. Thun, Editors, Vol. 3, p. 211, Academic Press, New York (1966).
4. R. W. Hoffman, "Measurement Techniques for Thin Films," B. Schwartz and N. Schwartz, Editors, p. 312, The Electrochemical Society, Inc., New York (1967).
5. J. H. van der Merwe, *J. Appl. Phys.*, **34**, 117 (1963).
6. See for instance, P. G. Shewmon, "Diffusion in Solids," p. 65, McGraw-Hill Book Co., New York (1963).
7. G. Günther and W. Buckel, "Basic Problems in Thin Film Physics," R. Niedermayer and H. Mayer, Editors, p. 231, Vandenhoeck and Ruprecht Göttingen (1966).

## Ion Mobility in Crystals of a Mixed-Alkali Ferrite: $K_xNa_{1-x}Fe_7O_{11}$

K. O. Hever\*

Scientific Laboratory, Ford Motor Company, Dearborn, Michigan

#### ABSTRACT

A mixed alkali hexagonal ferrite phase  $K_{0.87}Na_{0.13}Fe_7O_{11}$ , is reported. The unit cell and crystal density show it to be closely related to the known phase,  $KFe_{11}O_{17}$ . In the temperature range 200°-500°C the  $Na^+$  ions are immobile, but the  $K^+$  ions exchange rapidly and completely with  $Na^+$  from molten salt. The self-diffusion coefficients for  $K^+$  in  $K_{0.87}Na_{0.13}Fe_7O_{11}$ , and  $Na^+$  in  $NaFe_7O_{11}$ , have been determined as a function of temperature. Exchange from aqueous solution was found to be inhibited. The mobility of alkali ions in these crystals also leads to dielectric loss effects. It is suggested that the new phase has a defect structure.

In a recent publication the exchange and self-diffusion of the sodium ion in beta-alumina have been reported (1). Beta-alumina has been given the formula  $Na_2O \cdot 11Al_2O_3$  (2) and the potassium ferrite,  $K_2O \cdot 11Fe_2O_3$ , is considered to be isomorphous with it (3). It was the purpose of this work to investigate  $K^+$  ion mobility in potassium ferrite.  $K_2O \cdot 11Fe_2O_3$  is one of four closely related phases that have been reported to exist in the  $K_2O$ - $Fe_2O_3$  system. If a particular phase is represented as  $K_2O \cdot \kappa Fe_2O_3$  then the values of  $\kappa$  reported are 5 (4), 6 (5), 7 (6-8), and 11 (8, 9). Of these phases the  $\kappa = 5$  compound is rhombohedral while the others are hexagonal. The unit cell dimensions, proposed unit cell formulae, calculated den-

sities and experimental densities have been summarized previously (4). The two end members,  $KFe_{11}O_{17}$  ( $\kappa = 11$ ) and  $KFe_5O_8$  ( $\kappa = 5$ ) have both been reported as products of cooling a melt of KF and  $\alpha$ - $Fe_2O_3$ , but neither has been prepared by heating  $K_2CO_3$  or  $KNO_3$  with  $\alpha$ - $Fe_2O_3$ , this technique yielding the compounds of intermediate composition ( $\kappa \approx 6$  or 7). The apparent dependence of the product on the method of preparation has led to an expression of doubt (5) as to the existence of the phase  $\kappa = 11$ , while other authors (8) maintain that it does exist, but is metastable with respect to the  $\kappa = 7$  compound above 700°C.

The preparation of two crystal types,  $M_2O \cdot 7Fe_2O_3$  and  $M_2O \cdot 5Fe_2O_3$ , where  $M^+$  represents the sum of

\* Electrochemical Society Active Member.



alkali ions present as  $\text{Na}^+$  and  $\text{K}^+$ , is reported below. Both types of crystals were obtained by cooling  $\text{Na}_2\text{O}$ ,  $\text{K}_2\text{O}$ ,  $\text{Fe}_2\text{O}_3$  melts. Recourse to this melt followed the failure of several attempts to employ the KF melt method. The crystals obtained from KF were not reproducible in composition and were too small to analyze singly.

**Crystal preparation.**—A melt of molar composition  $2\text{Na}_2\text{O} \cdot \text{K}_2\text{O} \cdot 6\text{Fe}_2\text{O}_3$  was cooled at the rate of  $5^\circ\text{C}/\text{hr}$  from  $1250^\circ$  to  $1100^\circ\text{C}$  and then rapidly to room temperature. After removal of the solid from the platinum crucible, the crystals were extracted by dissolution of the melt component in boiling 100% nitric acid. The crystal form was that of thin platelets up to  $\sim 0.5$  cm in diameter. Single crystal and batch analyses were identical and corresponded to the formula  $\text{M}_2\text{O} \cdot 7\text{Fe}_2\text{O}_3$  where  $\text{M}^+ = 0.87 \text{K}^+ + 0.13 \text{Na}^+ \dots \{1\}$

The crystal density at  $30^\circ\text{C}$  was found to be 4.29. An attempt to reduce the amount of sodium in the crystals by exchange from molten  $\text{KNO}_3$  at  $400^\circ\text{C}$  led to an unchanged chemical analysis, even after five days of immersion, indicating that the  $\text{Na}^+$  ions were immobile. The exchange of  $\text{K}^+$  for  $\text{Na}^+$  by immersion of the crystals in molten  $2\text{NaNO}_2 \cdot \text{NaNO}_3$  eutectic at  $300^\circ\text{C}$  was found to be rapid ( $\sim 50\%$  exchange in a few minutes) and the final crystal composition, obtained after five days of immersion with several melt changes, corresponded to the formula  $\text{M}_2\text{O} \cdot 7\text{Fe}_2\text{O}_3$  where  $\text{M}^+ \cong 99.5\% \text{Na}^+ \dots \{2\}$

From the inability to exchange the sodium ions of crystals {1} it was thought that the crystals might involve two phases with perhaps an alkali-rich phase microdispersed in the major component phase. From the absence of lines that could not be indexed on the hexagonal unit cell:  $a = 5.931\text{\AA}$ ,  $c = 23.74\text{\AA}$  and from the consistency of the crystal composition after partial dissolution in acid, the material is presumed to have a single phase. The difference between  $\text{Na}^+$  and  $\text{K}^+$  mobilities is probably due to their different ionic sizes.

The dissolution experiments were performed, at room temperature, with 20% hydrochloric acid and crystals which had been ground to less than  $40\mu$  in size. After partial dissolution, the crystals were washed with water and treated with hot 20% KOH solution to replace protons that had entered the crystal by exchange. The composition of the crystals was found to be unchanged from {1}. The process of dissolution in acid, washing in alkali and chemical analysis was repeated. Again no change of composition was detected.

A rhombohedral mixed-alkali ferrite was found to crystallize together with small crystals of  $\alpha\text{-Fe}_2\text{O}_3$  when a melt of molar composition  $34\text{Na}_2\text{O} \cdot \text{K}_2\text{O} \cdot 74\text{Fe}_2\text{O}_3$  was cooled slowly. Large single crystals could be removed from the melt by hand, and their composition was found to correspond to the formula  $\text{M}_2\text{O} \cdot 5\text{Fe}_2\text{O}_3$  where  $\text{M}^+ = 0.89 \text{Na}^+ + 0.11 \text{K}^+$ . No other phases could be detected from the x-ray spectrum which could be completely indexed on the non-primitive hexagonal unit cell:  $a = 5.937\text{\AA}$ ,  $c = 35.77\text{\AA}$ . Most crystals were small and irregularly shaped and therefore unsuitable for self-diffusion measurements. They lost alkali when in contact with hot nitric acid and decomposed to  $\alpha\text{-Fe}_2\text{O}_3$  when heated in air above  $300^\circ\text{C}$ .

**Self-diffusion of alkali ions in crystals {1} and {2}.**—The self-diffusion of  $\text{K}^+$  in crystals {1} and  $\text{Na}^+$  in crystals {2} was measured at various temperatures by observation of the rate of loss from the crystals of  $\text{K}^{42}$  radioisotope into an inactive  $\text{KNO}_3$  or  $\text{KSCN}$  melt, and  $\text{Na}^{22}$  radioisotope into an inactive  $\text{NaNO}_2/\text{NaNO}_3$  melt, respectively. The crystals had previously been equilibrated with an active melt, and comparison was made between the activity of the equilibrated crystal and the activity of the crystal after immersion in the

inactive melt. All activity measurements were made in the direction perpendicular to the plane of the platelet, i.e., perpendicular to the plane of diffusion (1) so that corrections for absorption of radiation by the crystal were unnecessary.

$\text{K}^{42}$  was obtained in solid  $\text{KNO}_3$  by neutron irradiation at the Phoenix reactor of the University of Michigan. The  $\text{Na}^{22}$  was purchased from a commercial source. A  $\beta$ -particle Geiger counter was utilized for radioactivity measurements.

In order to determine diffusion constant ( $D$ ) values it was assumed that no serious error would be introduced by using the equation (10) for fractional loss of ions as a function of time ( $t$ ) for diffusion from an infinitely long cylinder of radius  $r$  into a bath of infinite volume

$$M(t)/M_{(\infty)} = 1 - 4\sum_{n=1}^{\infty} \frac{1}{\alpha_n^2} \exp(-D\alpha_n^2 t/r^2)$$

where  $M(t)/M_{(\infty)}$  is the fractional loss of radioactivity of the crystals and  $\alpha_n$  are the  $n^{\text{th}}$  roots of the zero order Bessel equation,  $\alpha_1 = 2.405$ ,  $\alpha_2 = 5.520$ ,  $\alpha_3 = 8.654$ , etc. The above equation was acceptable for diffusion in the platelets because their layer structure leads to radial diffusion only [this has been elegantly illustrated for " $\beta$ -alumina" previously (1)]. It was found that when the edge of platelet was obstructed by epoxy cement, exchange does not occur. The melts were stirred during exchange to maintain a near-zero concentration of radioactive tracer in them, and results were found to be independent of the rate of stirring. Interpolation from a curve (15) of  $M(t)/M_{(\infty)}$  vs.  $(Dt/r^2)^{1/2}$  gave, for measured  $M(t)/M_{(\infty)}$ , a value of  $Dt/r^2$ . An average value of  $r^2$  was determined from the area of the crystal obtained by planimeter integration from a photograph of the crystal taken through a microscope.  $D$  values were obtained at various temperatures and the activation energy determined (Fig. 1). The activation energies for  $\text{K}^+$  and  $\text{Na}^+$  self-diffusion in the ferrite crystals were found to be  $(7.21 \pm 0.3)$  and  $(13.7 \pm 0.7)$  kcal/mole, respectively, and the pre-exponential factors  $1.05 \times 10^{-3}$  and  $1.48 \text{ cm}^2/\text{sec}$ , respectively. Exchange from an aqueous solution of alkali ion was not observed even after 20 hr at  $84^\circ\text{C}$  for 1-2 mm diameter crystals either in the sodium case or in the potassium case, indicating that the apparent diffusion constants were less than  $10^{-11} \text{ cm}^2/\text{sec}$ . Room temperature diffusion of  $\text{Na}^{22}$  in crystals {2} was measured by diffusing a small amount of  $\text{Na}^{22}$  into one end of an approximately rectangular crystal; this was achieved by dipping the end of the crystal into a high

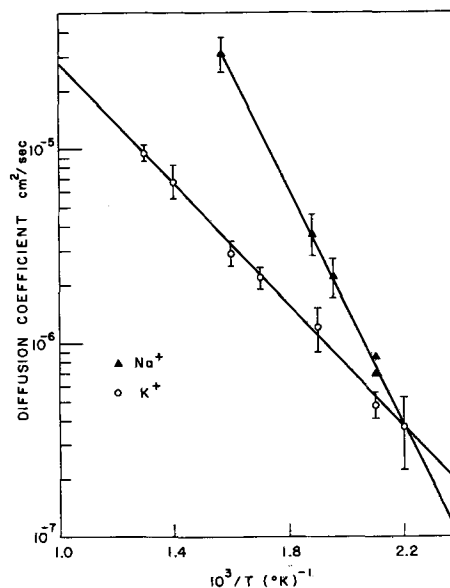


Fig. 1. Self-diffusion of  $\text{K}^+$  and  $\text{Na}^+$  ions in  $\text{M}_2\text{O} \cdot 0.7\text{Fe}_2\text{O}_3$  crystals.

specific activity  $\text{NaNO}_3$  melt ( $\sim 1$  mc in 50 mg) after protection of the other sides with an epoxy cement. After immersion for about 8 sec, the crystal was rapidly cooled to room temperature and the activity profile along the longest axis of the crystal estimated by shielding a portion of the crystal by 0.05 cm thick platinum foil and counting the exposed area. With 30% of the area at the "hot" end exposed, a count rate of 4,100 cpm was observed compared to a total count rate of 4,350 cpm for 100% exposed. Assuming that the platinum foil absorbed all  $\beta$  rays, but allowed complete transmission of  $\gamma$  rays, and noting the 0% exposed count of 310 cpm, we can state that at least 15/16 of the total count was observable in a 30% area at the hot end. This allows the increase in activity of a 30% exposed area at the cold end with time to be treated as the one-dimensional diffusion in a rod of length  $l$  cm of uniform cross section from an instantaneous source placed at the hot end ( $x = 0$ ). The required expression for fractional increase of activity at time  $t$ ,  $[M(t)/M(x)]$ , for an exposed fraction of length  $\Delta x$  is

$$\frac{M(t)}{M(x)} = 1 + \frac{2}{\pi} \sum_{n=1}^{\infty} \frac{(-1)^n}{n} \frac{1}{\Delta x} \exp(-Dn^2\pi^2t/l^2) \sin(n\pi\Delta x)$$

This expression was summed by computer and a curve constructed of  $M(t)/M(x)$  against  $Dt$  for  $\Delta x = 0.3$  and  $l = 0.30$  cm. From the observed  $M(t)/M(x)$  value (correcting for background)  $Dt$  can be interpolated for several values of  $t$ . A plot of this  $Dt$  value against  $t$  gave a straight line which, due to the approximate nature of the assumption of instantaneous source, did not pass through the origin. The experimentally determined  $M(t)$  vs.  $t$  plot and the  $Dt$  vs.  $t$  plot appear in Fig. 2. The slope of this plot gave a value for  $D$  of  $2.6 \times 10^{-8}$  cm<sup>2</sup>/sec.

**Dielectric loss measurements.**—Additional evidence for ionic mobility was provided by measurement of dielectric loss for the crystals {1} and {2} undertaken by R. Radzilowski of this laboratory. The crystals were ground to between 100 to 200 mesh and mixed with powdered  $\alpha$ -alumina in the ratio 1:3 by weight, respectively. This powder was loosely packed between two concentric aluminum cylinders 2.3 mm apart and 13 cm long, with a mean diameter of  $\sim 2$  cm. The capacity and  $\tan \delta$  values were measured on a type 716-C General Radio Capacitance (Schering) bridge as a function of temperature at frequencies of 100, 1000, and 10,000 Hz. The  $C \tan \delta$ -temperature curves exhibited loss maxima (Fig. 3 and 4) and from a plot of  $\ln$  (frequency) against reciprocal temperature for the three points of maximum loss the activation energy

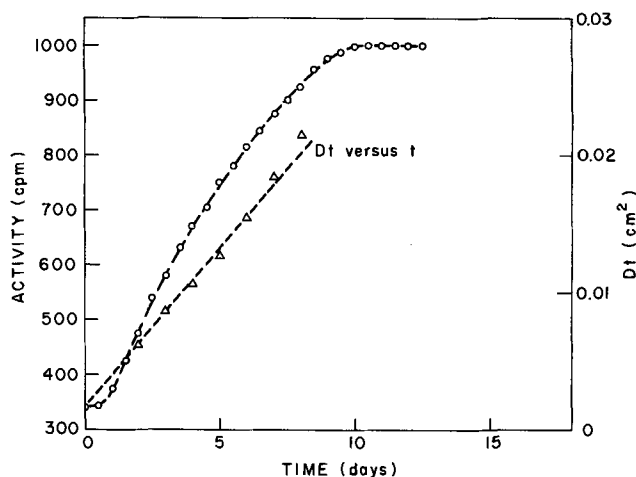


Fig. 2. Room temperature  $\text{Na}^{22}$  diffusion along a rectangular crystal of  $\text{Na}_{20.7}\text{Fe}_2\text{O}_3$ ; activity of exposed length vs. time.

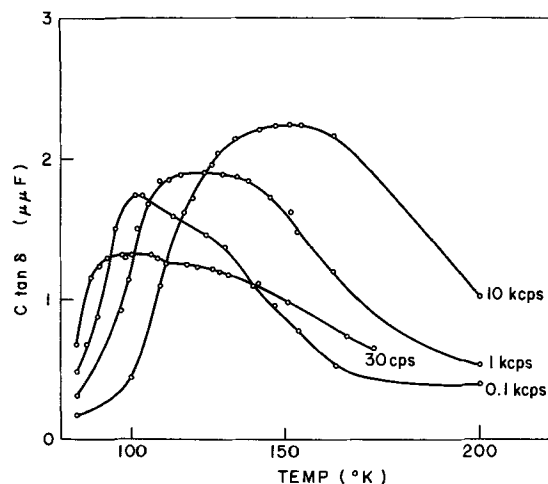


Fig. 3. Dielectric loss curves,  $C \tan \delta$  vs. temperature for 25 w/o of crystals {1} in  $\alpha$ -alumina (cps = Hz).

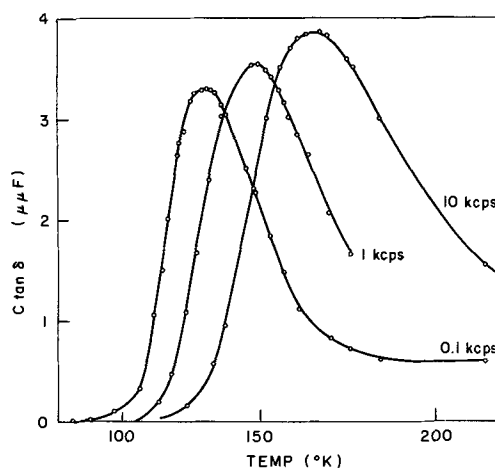


Fig. 4. Dielectric loss curves,  $C \tan \delta$  vs. temperature for 25 w/o of crystals {2} in  $\alpha$ -alumina (cps = Hz).

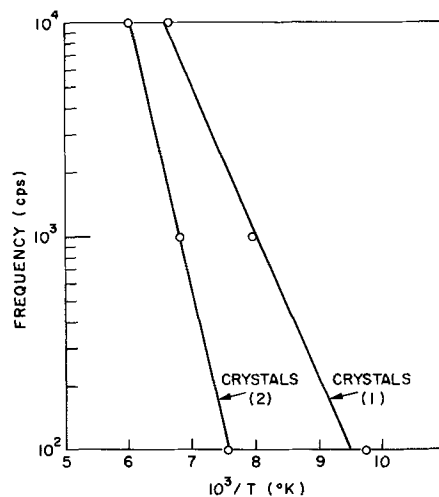


Fig. 5. Frequency of maximum dielectric loss against reciprocal temperature.

was determined (Fig. 5). The activation energies were  $(2.94 \pm 0.5)$  kcal/mole for crystal {1} and  $(5.87 \pm 0.6)$  kcal/mole for crystal {2}. These values are substantially lower than the high-temperature activation energies for diffusion of 7.2 and 13.7 kcal/mole, respectively.

Thus these ferrite crystals show dielectric loss behavior similar to that of  $\beta$ -alumina crystals reported earlier (1). It is believed that the loss is of the Max-

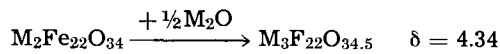
well-Wagner type (14) which is the type to be expected from the presence of mobile changes. The discrepancy between activation energies determined from the tracer technique and dielectric loss curves is, at the moment, unexplained. The dielectric loss behavior will be the subject of a later paper.

### Discussion

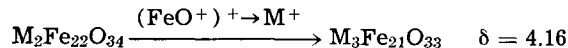
The crystal structure of the compound  $\text{KFe}_{11}\text{O}_{17}$  ( $\kappa = 11$ ) has been discussed previously (3, 12, 13). The compound may be viewed as a substitutional solid solution of  $\text{K}_2\text{O}$  in  $\alpha\text{-Fe}_2\text{O}_3$  ( $\text{O}^-$  by  $\text{K}^+$ ) and the unit cell as a hexagonal superlattice of the spinel arrangement of  $\alpha\text{-Fe}_2\text{O}_3$  (12). The structures of the other potassium ferrite phases  $\kappa = 5, 6, 7$  are unknown. The corresponding sodium compounds are also unknown. The significant feature of the structure of  $\text{KFe}_{11}\text{O}_{17}$  with respect to ion mobility is that the  $\text{K}^+$  ions occur in layers of low density relative to the material between layers (9). Although the author has not been able to prepare crystals of  $\text{KFe}_{11}\text{O}_{17}$ , crystals of a mixed alkali ferrite,  $\text{K}_{0.87}\text{Na}_{0.13}\text{Fe}_7\text{O}_{11}$ , have been prepared.

A comparison of the data relating to  $\text{KFe}_{11}\text{O}_{17}$  and  $\text{K}_{0.87}\text{Na}_{0.13}\text{Fe}_7\text{O}_{11}$ , given in Table I shows the close similarity of the unit cell dimensions and experimental densities of the two compounds. Three alternative ways in which the compounds might be related, while preserving the unit cell dimensions, are given below. The theoretical densities ( $\delta$ ), calculated from the known unit cell volume and proposed unit cell formulae, are also given.

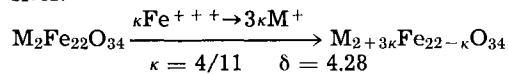
(a) Interstitial solid solution of  $\frac{1}{2}\text{M}_2\text{O}$  per unit cell.



(b) Substitutional solid solution.



(c) A defect structure with statistical occupation of  $\text{Fe}^{3+}$  sites.



Since the chemical composition,  $\text{M}_20.7\text{Fe}_2\text{O}_3$  where  $\text{M} = 0.87\text{K}^+ + 0.13\text{Na}^+$ , is slightly closer to alternatives (b) and (c) than to (a), and since only alternative (c) is consistent with the experimental density of 4.29, a defect structure is indicated. Although this argument is speculative it does suggest that order-disorder phenomena should be looked for in the alkali ferrite compounds. It is possible that an ordered defect compound has already been made by Roth and Cooper (7) who report the  $\text{K}_20.7\text{Fe}_2\text{O}_3$  'a' axis as 10.287 which is larger, by a factor of  $\sqrt{3}$ , than that normally observed.

The experiments to detect ion mobility in  $\text{M}_20.7\text{Fe}_2\text{O}_3$  crystals show the following features.

Table I. Comparison of the phases  $\text{KFe}_{11}\text{O}_{17}$  and  $\text{K}_{0.87}\text{Na}_{0.13}\text{Fe}_7\text{O}_{11}$

Unit cell		Proposed unit cell formula	Calc.	Exp.	Reference
a(Å)	c(Å)				
5.932	23.80	$\text{K}_2\text{Fe}_{22}\text{O}_{34}$	4.24	4.24	(8)
5.932	23.74	$\text{K}_2\text{Fe}_{22}\text{O}_{34}$	4.25	4.30	(9)
5.931	23.74	See text	See text	4.29	This work

1. Alkali ion mobility is high, the self-diffusion coefficients of  $\text{Na}^+$  and  $\text{K}^+$  at  $300^\circ$  are in the range  $10^{-5}$  to  $10^{-6}$   $\text{cm}^2/\text{sec}$  which is comparable to ion mobilities in  $\beta$ -alumina (1) and of the same order as ion mobilities in aqueous solution at room temperature. In the temperature range  $200^\circ\text{-}500^\circ\text{C}$  the diffusion constants of  $\text{K}^+$  and  $\text{Na}^+$  ions can be described as a function of temperature by Arrhenius equations. Although the activation energy for the  $\text{Na}^+$  is approximately twice that of ion  $\text{K}^+$  the pre-exponential factor is larger by a factor of  $10^3$ . The net effect is a higher mobility for  $\text{Na}^+$  than for  $\text{K}^+$ .

2. The room temperature  $\text{Na}^+$  diffusion coefficient of  $2.6 \times 10^{-8}$   $\text{cm}^2/\text{sec}$  is larger than the value of  $\sim 1.6 \times 10^{-10}$   $\text{cm}^2/\text{sec}$  predicted by extrapolation of the high-temperature  $D$  values down to room temperature. The discrepancy between these two values probably reflects a changeover from a high activation energy to a lower activation energy with decreasing temperature. The low values of the activation energy of  $\text{Na}^+$  and  $\text{K}^+$  for dielectric loss compared to those for diffusion also support a change of activation energy with temperature.

3. The exchange of  $\text{K}^+$  and  $\text{Na}^+$  between aqueous solution and the crystals, at  $85^\circ\text{C}$ , was not observed. The inhibition of exchange must occur at the solution-crystal interface since the diffusion constant within the crystal, for  $\text{Na}^+$  at room temperature, was measurable.

### Acknowledgment

The author is indebted to Dr. J. T. Kummer and Dr. Y. Yao for help in planning the experiments, to Dr. W. Pierson for the use of his laboratory facilities and to Mr. R. Radzilowski for performing the dielectric loss measurements.

Manuscript submitted Dec. 13, 1967; revised manuscript received March 22, 1968.

Any discussion of this paper will appear in a Discussion Section to be published in the June 1969 JOURNAL.

### REFERENCES

- J. T. Kummer and Y. Yao, *J. Inorg. Nucl. Chem.*, **29**, 2453 (1967).
- C. A. Beevers and M. A. S. Ross, *Z. Kristallogr.*, **97**, 57 (1934).
- V. Adelskold, *Arkiv Kemi, Min. Geol.*, **12A**, 1 (1938).
- C. J. M. Rooymans, C. Langerais, and J. A. Schuilkes, *Solid State Communications*, **4**, 85 (1965).
- R. Scholder and M. Mansmann, *Z. anorg. u. allgem. Chem.*, **321**, 246 (1963).
- W. L. Roth and F. E. Luborsky, *J. Appl. Phys.*, **35**, 966 (1964).
- W. L. Roth and A. S. Cooper, *General Electric Rep.* 60, RL-2461 M.
- Y. Otsubo and K. Yamaguchi, *Nippon Kagaku Zasshi*, **82**, 676 (1961).
- E. W. Gorter, *Philips Research Repts.*, **9**, 363 (1954).
- R. M. Barrer, "Diffusion In and Through Solids," Macmillan Publishing Co., New York (1941).
- J. Crank, "Mathematics of Diffusion," Clarendon Press, Oxford (1956). 1st ed., p. 59, integration of equation 4.58 with  $h/l \rightarrow 0$ .
- A. D. Wadsley, *Rev. Pure Appl. Chem.*, **5**, 165 (1955).
- J. J. Went, G. W. Rathenau, E. W. Gorter, and G. W. van Oosterhaut, *Philips. Tech. Rev.*, **13**, 203 (1952).
- V. V. Daniel, "Dielectric Relaxation," Academic Press, New York (1967).
- J. Crank, "Mathematics of Diffusion," Clarendon Press, Oxford (1956), 1st ed., curve numbered "0", p. 72.

# A Solid-State Electrochemical Cell Based on Ion Conductive Ceramics

K. O. Hever\*

Scientific Laboratory, Ford Motor Company, Dearborn, Michigan

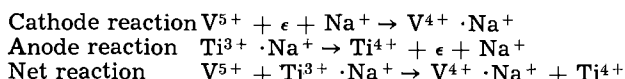
## ABSTRACT

A solid-state electrochemical cell has been devised using a ceramic ion conducting electrolyte and ceramic electrodes which are simultaneously ion and electron conducting. Charge/discharge of the cell occurs without chemical phase change and the reaction of the cell to an electric current is therefore capacitive. The origin of the capacitance is discussed in terms of the crystal structure of the ceramic used and the transient electrical characteristics described in terms of diffusion theory. Possible applications are suggested.

This paper reports an attempt to construct a secondary battery offering the advantages associated with ceramic materials. Mechanical and electrical stability leading to a long cycle life, operation over a wide temperature range, ease of construction, and cheapness of materials are the principal advantages ceramic materials offer.

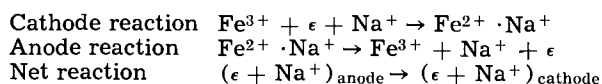
An ionically conducting solid which has electronic conduction properties by virtue of a transition element in more than one valency state contained in its structure provides a solid-state electrode. Two such electrodes in contact with a solid permeable only to ions constitute a solid-state electrochemical cell. If the transition metals involved at each electrode are different, the primary energy storage mechanism will be associated with a solid-state oxidation-reduction. Example 1 illustrates this case.

### Example 1



In example 1 the transition metal ions are immobile and the  $Na^+$  ions mobile. The  $O^=$  ions of the ceramic are required only as host ions and do not take part in the reactions. Since the electrodes contain both the mobile electrons ( $\epsilon$ ) associated with donor ions and mobile  $Na^+$  ions they are written together as ion pairs ( $V^{4+} \cdot Na^+$ ,  $Ti^{3+} \cdot Na^+$ ). On discharge the  $Na^+$  ions flow from anode to cathode through the electrolyte and an equal number of electrons flow from anode to cathode through the external circuit. If the two electrodes are identical in composition, the cell will not exhibit a spontaneous voltage, but an electrostatic capacity to store energy will exist. Example 2 illustrates this case; a voltage will develop on charging the cell as  $Na^+$  ions and electrons are progressively removed from the anode and added to the cathode.

### Example 2



The ceramic electrodes which can be used to construct solid-state cells must allow ionic and electronic conductivity. An additional requirement is that the crystal structure must allow some degree of non-stoichiometry since ions have to be added or removed from the lattice without change of phase.

The requirements of ionic conductivity and non-stoichiometry appear to restrict useful materials to those transition metal oxides that can be made to crystallize in "tunnel" or "layer" structures in the presence of alkali. These compounds have been dis-

cussed in a review article (8) and typical examples are the vanadium bronzes, tungsten bronzes (tunnel), and alkali ferrites (layer). Ionic conduction has been established for the layer compounds  $\beta$ -alumina (7),  $Na_2O \cdot 11 Al_2O_3$ , and the mixed alkali ferrite  $(K,Na)_2O \cdot 7Fe_2O_3$  (15). This paper describes the preparation and properties of two electrochemical cells that depend for their operation on the ion conducting properties of these layer compounds. Alkali ion mobility in these compounds is a consequence of their unique crystal structure (11) in which the alkali ions are arranged in layers separated by blocks of atoms arranged in the manner of spinel. Although this structure has been proposed in terms of the compounds  $Na_2O \cdot x Al_2O_3$  (9) and  $K_2O \cdot x Fe_2O_3$  (1, 6, 10) where  $x = 11$ , compounds in which  $x = 6$  or 7 have been reported as having the same characteristic x-ray spectrum (2-5). The cells are of the type discussed under example 2 above in which the electrodes are of identical composition when the cell is discharged.

## Experimental Technique

The ceramic compositions of electrodes and electrolytes are given below, the powder x-ray diagrams indicated that the dominant phase present in each case was isomorphous with  $\beta$ -alumina.

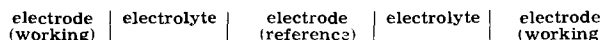
	Mobile ion (presumed)	Electrolyte	Electrodes
Cell (a)	$Na^+$	"M Brick"	$Na_2O \cdot 5 (Fe_{0.95}Ti_{0.05}AlO_3)$
Cell (b)	$K^+$	$1.3K_2O \cdot 0.2Li_2O \cdot 10Al_2O_3$	$1.3K_2O \cdot 0.2Na_2O \cdot 10 (Fe_{1.9}Ti_{0.1}O_3)$

In cell (a) the electrolyte consisted of "M" brick which is a commercially available, fusion cast,  $\alpha$ -alumina,  $\beta$ -alumina eutectic. Preliminary experiments to produce electrodes having the characteristic x-ray spectrum of  $\beta$ -alumina by sintering mixtures of  $Na_2CO_3$ ,  $\alpha$ - $Fe_2O_3$ , and  $TiO_2$  failed. Inclusion of  $\alpha$ - $Al_2O_3$  in the electrode mixture produced materials having the desired x-ray spectrum. Presumably these materials contained substantial quantities of a sodium  $\beta$ -aluminate-ferrite solid solution (12).  $Ti^{4+}$  ions acted as doping agents causing the sintered material to show ferromagnetism and an n type thermoelectric effect. It was presumed that  $Ti^{4+}$  gave rise to  $Fe^{2+}$  donor ions, in the major phase of the ceramic, by charge compensation in the manner described for doped  $\alpha$ - $Fe_2O_3$  (13). A ceramic powdered material of composition  $Na_2O \cdot 5 (Fe_{0.95}Ti_{0.05}AlO_3)$  was prepared by mixing the appropriate proportions of  $Na_2CO_3$ ,  $\alpha$ - $Fe_2O_3$ ,  $TiO_2$ , and  $\alpha$ - $Al_2O_3$  powders and heating the mixture at  $1000^\circ C$  for 1 hr. The powder was then mixed with a binder, "carbowax," in benzene solution and the benzene was removed by evaporation. Approximately 0.4g of powder was compacted in a hydraulic press under a pressure of 20,000 lb/in.<sup>2</sup>, yielding a pellet of  $\frac{1}{2}$  in. diameter and 1 mm thick. The binder was then removed by heating the pellet at  $700^\circ C$  for 1 hr.

\* Electrochemical Society Active Member.

Two such pellets were placed on either side of a 2 mm thick,  $\frac{3}{8}$  in. square of "M" brick and the whole object wrapped in 0.0005 in. thick platinum foil. The sandwich in foil was then heated at 1400°C for 1 hr, cooled to room temperature, and the foil cut away to cover only the end electrode area to which it had bonded during the firing process.

A three-electrode cell using the materials of cell (a) was constructed by placing three electrode disks and two electrolyte squares in the sequence



The whole object was then wrapped in platinum foil and sintered as above.

In cell (b) it was found necessary to include  $\text{Na}_2\text{O}$  in the electrode components and  $\text{Li}_2\text{O}$  in the electrolyte components in order to promote sintering. The electrolyte disk was prepared from the appropriate proportions of  $\text{K}_2\text{CO}_3$ ,  $\text{Li}_2\text{CO}_3$ , and  $\alpha\text{-Al}_2\text{O}_3$  by the technique previously described and then sintered at 1960°C for  $\frac{1}{2}$  hr in a gas fired furnace. To limit the loss of alkali the disk was fired in a crucible containing a powder of the same composition. The electrodes were prepared and sintered onto the electrolyte disk as before.

Electrical measurements were made under conditions of potential control. The cell arrangement and a block diagram of the apparatus is shown in Fig. 1. The cell was clamped between two spring loaded platinum disks and the leads soldered into the glass metal seals of a Pyrex container. The Pyrex container was heated by a tube furnace and the cell temperature measured by a thermocouple touching the electrolyte disk. Current was supplied to the cell from the Wenking potentiostat and was measured by the voltage developed across the series decade resistance box,  $R_2$ . This voltage was displayed on a Honeywell "Elektronik 17" strip chart recorder equipped with voltage suppression. The integrated value of charge passed through the cell was measured by a Weston Instrument voltage integrator in parallel with the decade resistance box  $R_1$ . To measure the a-c impedance of the cell as a function of frequency a mechanical sinusoidal generator was inserted into the reference circuit of the potentiostat which was set to maintain zero potential difference between anode and reference electrodes. The generator was constructed from a 1.5v battery, a 20 kohm sinusoidal potentiometer, a synchronous motor, and a speed reducer. The output was continuous up to 1v at a choice of frequencies 1, 0.5, 0.2, 0.1, 0.05, . . . 0.001 cycles/min. Higher frequencies were obtained

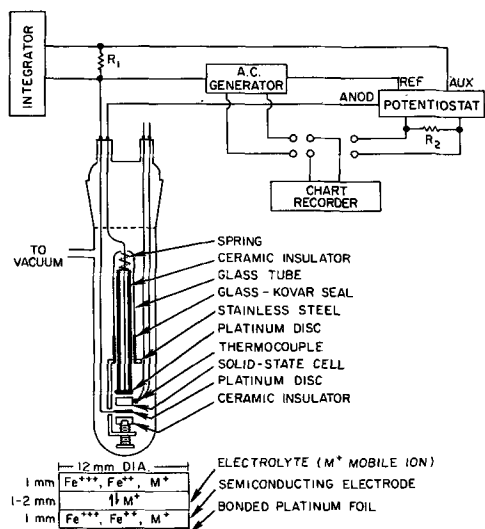


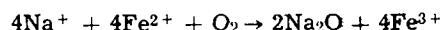
Fig. 1. Experimental arrangement for measurement of electrical properties of solid-state battery.

from an electronic oscillator. The cell impedance was calculated by division of the peak to peak generator voltage by the peak to peak output current of the potentiostat.

Measurements were made after the Pyrex container had been evacuated to a pressure of less than  $10^{-4}$  Torr, although the electrical characteristics were not dependent on the atmosphere pressure over periods of time up to 20 hr. Since the electrical characteristics of the two cells were qualitatively the same the experimental results are discussed in detail with reference to cell (a), the results for cell (a) and cell (b) are then compared.

### Results and Discussion

**Steady-state charge-voltage characteristic.**—The steady-state charge-voltage characteristic appears in Fig. 2 for cell (a) at 300°C. It was obtained by measurement of the charge required to increase, successively, the steady-state potential in 0.1v increments. It can be seen from Fig. 2 that up to 0.6v the device acts as an 18 Farad capacitor, but at voltages greater than 0.6v the capacitance decreases, i.e., the device is nonlinear. On open circuit a rate of loss of potential of about 1/3 mv/hr was observed, equivalent to an internal shorting resistance of  $\sim 3 \times 10^5$  ohms. This shorting may be due to the dissipative reaction caused by residual air,



which leads to a decrease in the quantity of mobile sodium. Such a loss would cause a loss of potential if the cell is regarded as a capacitor.

In order to estimate the capacitance of a cell, each electrode may be regarded as a parallel plate condenser where one set of plates are the  $\text{M}^+$  conducting layers and the other set are the spinel blocks containing the  $\text{Fe}^{++}$  donor ions. Each electrode can then be charged by electrons flowing into the semi-conducting spinel blocks and ions flowing between these blocks. 1 cc of the material would then have a capacitance of the order of

$$2 \times \frac{\text{Number of blocks/cm}}{\frac{1}{2} (\text{Distance between blocks})} \times 0.9 \times 10^{-13} \text{ Farad}$$

i.e.,

$$2 \times \frac{10^7}{2 \times 10^{-8}} \times 0.9 \times 10^{-13} \sim 80 \text{ Farads/cc}$$

For an electrode volume of 0.1 cc then, assuming a single phase material, capacitance  $\sim 8\text{F}$ . Two such electrodes in series would give a capacitance of  $\sim 4\text{F}$ , which is of the same order of magnitude as the experimental value (18F). Also, on this model, the ca-

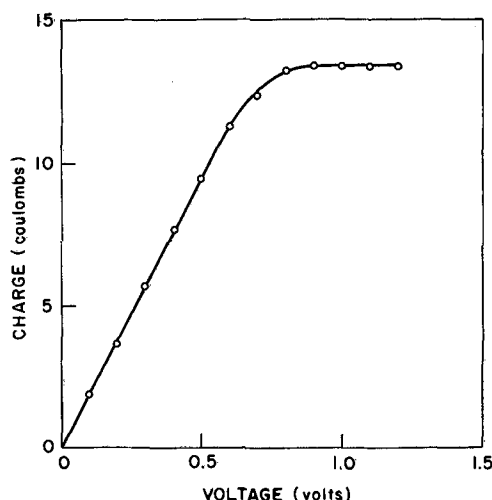


Fig. 2. Steady-state charge-voltage characteristic of  $\text{Na}^+$  solid-state battery at 300°C.

capacitance ( $C$ ) should decrease with temperature due to the thermal expansion of the electrodes.

Values obtained for the temperature coefficient of steady-state voltage at constant charge  $(\partial V_o/\partial T)_Q$  where  $T$  is the temperature in  $^{\circ}\text{C}$ , were

$(\partial V_o/\partial T)_Q$ v/ $^{\circ}\text{C}$	$V_o$ v	$\frac{1}{V_o} (\partial V_o/\partial T)_Q$ $(^{\circ}\text{C})^{-1}$
$2.0 \times 10^{-4}$	0.34	$5.9 \times 10^{-4}$
$1.4 \times 10^{-4}$	0.26	$5.7 \times 10^{-4}$
$1.1 \times 10^{-4}$	0.17	$6.7 \times 10^{-4}$
		Ave. = $6.1 \times 10^{-4}$

Since  $C \propto 1/l$  where  $l$  = spacing of layers,  $C \times l$  = constant. With  $CV_o = Q$  = constant, then

$$\frac{1}{C} \frac{\partial C}{\partial T} = -\frac{1}{V_o} \frac{\partial V_o}{\partial T} = -\frac{1}{l} \frac{\partial l}{\partial T}$$

Since  $(1/l) (\partial l/\partial T)$ , the coefficient of expansion, is unlikely to have a value much greater than  $10^{-5}$ , thermal expansion alone seems insufficient to explain the effect of temperature on voltage at constant charge.

In order to establish which electrode is limiting the charging process and causing nonlinearity of the  $Q$ - $V_o$  characteristic in the high voltage region (0.6-1.0v) the three-electrode device was charged to a controlled voltage between the working electrodes and their potentials was then measured with respect to the reference electrode. Figure 3 shows the steady state  $Q$ - $V_o$  characteristics for each electrode, at  $300^{\circ}\text{C}$ , where the

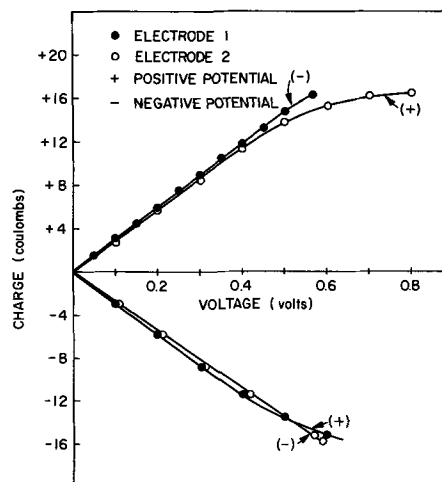
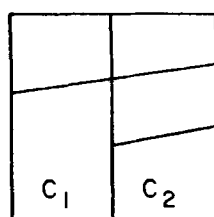


Fig. 3. Steady-state single electrode potentials vs. charge for a three electrode cell with  $\text{Na}^+$  as mobile ion at  $300^{\circ}\text{C}$ .

assuming an infinitely thin electrolyte can be modified, rigorously, for finite thickness of electrolyte.

A case which is suitable for comparison to experiment is the solution of the diffusion equation for short times ( $Dt/h^2 < 0.2$ , where  $h$  is the electrode thickness) i.e., the semi-infinite case,  $-\infty < \kappa < \infty$ :



$$\kappa = -h \quad \kappa = 0 \quad \kappa = +h$$

Impermeable surfaces

Permeable interface

Boundary conditions

$$t = 0 \quad c = c_1 \quad \kappa < 0 \quad V = V_o$$

$$c = c_2 \quad \kappa > 0$$

$$t = \infty \quad c = \frac{(c_1 + c_2)}{2} \quad V = 0$$

voltage plotted is the absolute value of potential difference between the electrode and the reference (center) electrode. No current was withdrawn from this reference electrode at any time. Figure 3 shows that it is the positive electrode which is limiting the charging process independent of the direction of the current flow. This might be expected since at some point in the charging process the positive electrode will lose all its  $\text{Fe}^{++}$  donors and become electronically insulating at which time the charging process must stop.

**Charge-time characteristics, potential control.**—Figure 4 shows  $q$  vs.  $\sqrt{t}$  plots for cell (a) at  $300^{\circ}\text{C}$  and successive voltage jumps ( $\Delta V$ ) of 100 mv. The linearity of the  $q$  vs.  $\sqrt{t}$  characteristics indicate that the speed of response to an impressed field is diffusion controlled. By combining the solution of the one dimensional diffusion equation  $\partial c/\partial t = D \partial^2 c/\partial \kappa^2$ , where  $D$  is the mutual diffusion coefficient of the two mobile species, with the experimentally determined relationship,  $Q = CV_o$ , equations describing the electrical characteristics of the cell can be obtained. It will be assumed that  $D_1/D_2$  approaches unity or zero, where  $D_1, D_2$  are the self-diffusion coefficients of the two mobile species.

The validity of the diffusion equation will not be disturbed by the presence of an electrolyte of finite thickness since charge transport within the electrolyte can occur only by migration and not by diffusion. This fact is a consequence of the existence of only one species of charge carrier, the alkali ion, in  $\beta$ -alumina (7). Thus the presence of the electrolyte affects the electrical characteristics only as a series resistance and the solutions of the diffusion equation obtained

The solution of the semi infinite case when  $D$  is independent of  $c$  is

$$c = \frac{(c_1 + c_2)}{2} - \frac{(c_1 - c_2)}{2} \operatorname{erf} \left( \frac{\kappa}{2\sqrt{Dt}} \right),$$

$$\left( \frac{\partial c}{\partial \kappa} \right)_{\kappa=0} = \frac{-(c_1 - c_2)}{2\sqrt{Dt\pi}}$$

From Fick's first law and for a univalent mobile ion

$$\frac{i}{F} = -D \left( \frac{\partial c}{\partial \kappa} \right)_{\kappa=0}$$

where  $i$  = current per unit area,  $F$  = the Faraday in coulombs per mole, and  $c$  is expressed in mole/cm<sup>3</sup>.

From the steady-state relationship  $Q = CV_o$

$$\frac{(c_1 - c_2)}{2} Fh = CV_o$$

By combining these equations

$$i = \frac{CV_o}{h} \sqrt{\frac{D}{\pi t}}$$

and on integration therefore

$$q = \frac{2CV_o}{h} \sqrt{\frac{Dt}{\pi}}$$

The analysis can be generalized to any two equilibrium states by expressing the time dependent part of the general solutions as  $\Delta c \cdot \operatorname{erf} (\kappa/2\sqrt{Dt})$  where  $\Delta c$  is the change in concentration for any value of  $\kappa$  between  $t = 0$  and  $t = \infty$ . Relating  $\Delta c$  to the difference in voltage ( $\Delta V$ ) between the two equilibrium states

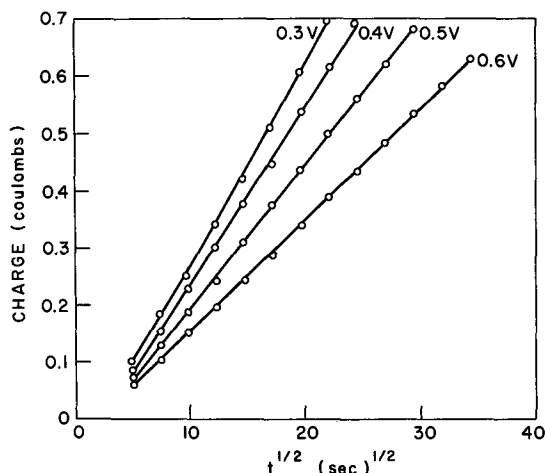


Fig. 4. Charge vs.  $(\text{time})^{1/2}$  for  $\text{Na}^+$  solid-state battery at  $300^\circ\text{C}$  under  $t=0$  potential drop of 0.1v from voltage indicated.

existing at  $t = 0$  and  $t = \infty$  by  $\Delta cFh = C\Delta V$  then the expression for  $q$  becomes

$$q = \frac{2C\Delta V}{h} \sqrt{\frac{Dt}{\pi}} \quad [1]$$

Equation [1] can be corrected for the finite electrolyte resistance,  $R$  ohms/cm<sup>2</sup>, by replacing  $\Delta V$  by  $\Delta V - iR$  and using  $i = dq/dt$ . Then Eq. [1] becomes, by successive approximation

$$q = \frac{\frac{2C\Delta V}{h} \sqrt{\frac{Dt}{\pi}}}{1 + \frac{RC}{h} \sqrt{\frac{D}{\pi t}}} \approx \frac{2C\Delta V}{h} \sqrt{\frac{Dt}{\pi}} - \frac{2C^2\Delta VDR}{h^2\pi} \quad [2]$$

From the slope and intercept of the  $q$  vs.  $\sqrt{t}$  curves, therefore,  $D$  and  $R$  can be determined if  $C$  is known from the steady state  $Q$  vs.  $V_0$  characteristic.  $R$  can also be determined by a high-frequency a-c measurement or from the value of the initial discharge current.  $R$  was found to be  $\sim 30$  ohms/cm<sup>2</sup>. The calculated values of  $D$  are plotted against voltage in Fig. 5. The values of  $D$  decrease with increasing voltage, i.e., decrease with increasing difference of concentration of mobile ion between anode and cathode.

The fact that  $D$  values are not independent of concentration is to be expected if the mechanism of alkali ion diffusion involves interstitial sites or vacancies since the extent to which such sites are occupied will be a function of over-all concentration. The addition of ion-electron pairs would be expected to alter the electrostatic energy and hence the unit cell dimensions

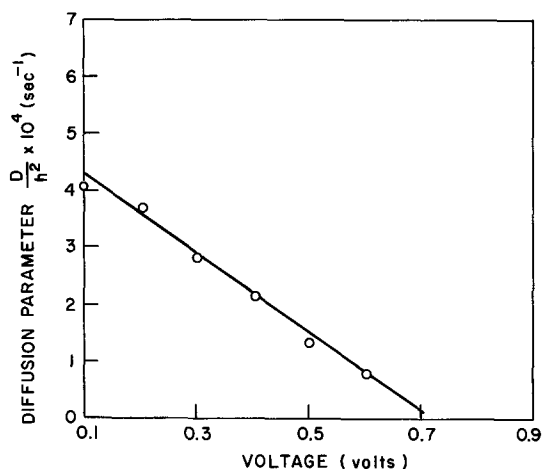


Fig. 5. Variation of diffusion parameter with voltage of  $\text{Na}^+$  solid-state battery at  $300^\circ\text{C}$ .

of the material. Evidence that self-diffusion coefficients of  $\beta$ -alumina are sensitive to the concentration of unoccupied sites and to the  $c$  axis dimension has been presented previously (7). Since the measured diffusion coefficient will be controlled primarily by the electrode of lowest individual  $D$  value the slope of Fig. 5 is in the expected direction. The fact that the measured value becomes negligibly small at high voltages probably reflects the fact that one electrode has become virtually impermeable due to one or both of the above effects.

For long times,  $Dt/h^2 > 0.2$ , the solution of the diffusion equation in series form can be used to yield expressions for current and charge as a function of time.

$$i = \frac{2C\Delta VD}{h^2} \sum_{n=1,3}^{\infty} \exp\left(\frac{-n^2\pi^2\tau}{4}\right) \text{ where } \tau = Dt/h^2$$

$$q = \frac{8}{\pi^2} C\Delta V \left( \sum_{n=1,3}^{\infty} \frac{1}{n^2} - \sum_{n=1,3}^{\infty} \frac{1}{n^2} \exp\left(\frac{-n^2\pi^2\tau}{4}\right) \right)$$

Thus the electrical characteristics measured near the steady-state condition can be described with two parameters,  $C$  and  $D/h^2$ , whereas the electrical characteristics measured far from the steady state can be described with one parameter,  $C/h\sqrt{D}$ . This result is seen to be a general one by calculating the response of the cell under other experimental conditions, e.g., constant current operation or alternating current operation.

**Constant load discharge characteristics.**—Figure 6 shows the constant load voltage-time curve for 1K and 5K ohm loads for cell (a) at  $300^\circ\text{C}$ , from a starting potential of 1v. The theoretical energy density of the device is  $\frac{1}{2} \times 18 \times (\frac{1}{2})^2 \sim 2$  joule/cc ( $\frac{1}{2} CV^2$  where  $C$  = capacity per unit volume,  $V = \frac{1}{2}v$ ), or, for a specific gravity of 4 g/cc, 240 joules/lb. This theoretical energy density is of the order of 0.2% of that afforded by conventional wet batteries which also have the advantage of constant voltage operation. The power density is limited by the internal resistance of the battery, which is about 30 ohms, at  $300^\circ\text{C}$ , and maximum power output is therefore  $\approx 0.25$  w/lb.

However no effort was made to prepare more highly conductive ceramic parts by variation of composition or sintering conditions, and it should be possible to improve these considerably. The instantaneous internal resistance of the device was equivalent to a resistivity  $\sim 60$  ohm cm at  $300^\circ\text{C}$ , probably all of this resistance residing in the electrolyte. An electrolyte resistivity of  $\sim 5$  ohm cm at  $300^\circ\text{C}$  can be prepared (14). Reduction of the electrolyte thickness from the present 2 mm down to  $\sim 0.5$  mm is also possible with present experimental techniques.

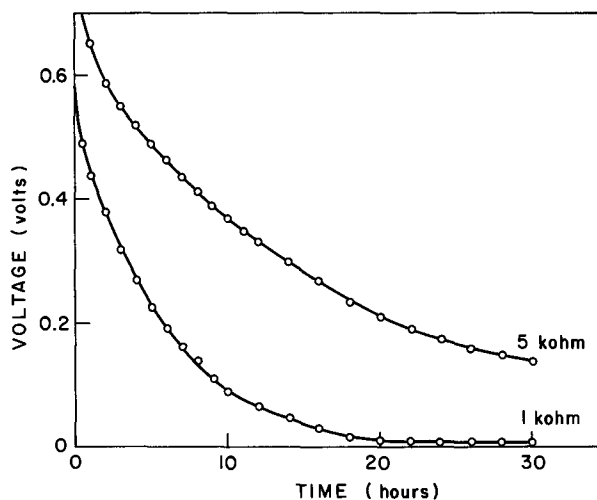


Fig. 6. Discharge (voltage-time) characteristic for  $\text{Na}^+$  solid-state battery at  $300^\circ\text{C}$  from a  $t=0$  voltage of 1v under 1-kohm and 5-kohm loads.

**A-C impedance characteristics.**—Figures 7, 8 show the variation of impedance ( $Z$ ) with frequency ( $w/2\pi$ ) for cell (a) at 500°C. The applied voltage was 100 mv peak to peak. The low-frequency range investigated was necessitated by the large capacitance involved, a phase angle of 45° occurred at a frequency  $\sim 1$  cpm. Measurements were taken after transient effects had become negligible. The a-c impedance measurements are consistent with equations developed from the solution of the diffusion equation with the appropriate bounding conditions.

$$\frac{\partial c}{\partial t} = D \frac{\partial^2 c}{\partial \kappa^2}$$

Assume the solution  $c = f(\kappa) e^{i\omega t}$  where  $i = \sqrt{-1}$ . Then

$$\frac{\partial^2 c}{\partial \kappa^2} = a^2 c \text{ where } a = \left( \frac{i\omega}{D} \right)^{1/2}$$

The general solution is

$$c = [A_1 \cosh(a\kappa) + A_2 \sinh(a\kappa)] e^{i\omega t}$$

$$\frac{\partial c}{\partial \kappa} = a[A_1 \sinh(a\kappa) + A_2 \cosh(a\kappa)] e^{i\omega t}$$

From the boundary conditions

$$\kappa = \pm 0 \quad c = \pm c_0 e^{i\omega t} \quad \text{therefore } A_1 = \pm c_0$$

$$\kappa = \pm h \quad \frac{\partial c}{\partial \kappa} = 0 \quad \text{therefore } A_2 = -\frac{c_0 \sinh(ah)}{\cosh(ah)}$$

Assuming that  $Fh c_0 e^{i\omega t} = CV$  and  $i = -FD \left( \frac{\partial c}{\partial \kappa} \right)_{\kappa=0}$  then

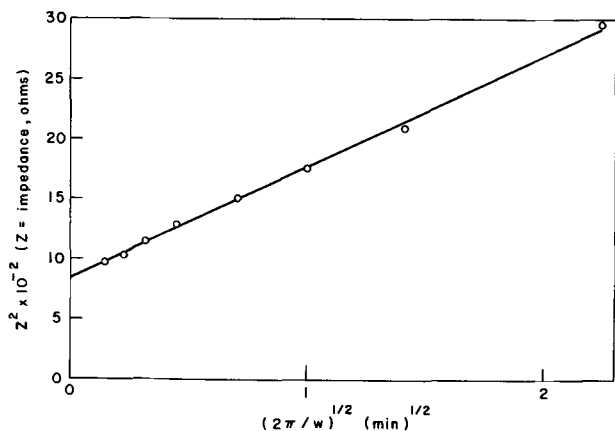


Fig. 7. Dependence of impedance on frequency for frequencies  $w/2\pi \cong 0.2$  cpm for  $\text{Na}^+$  solid-state battery at 500°C.

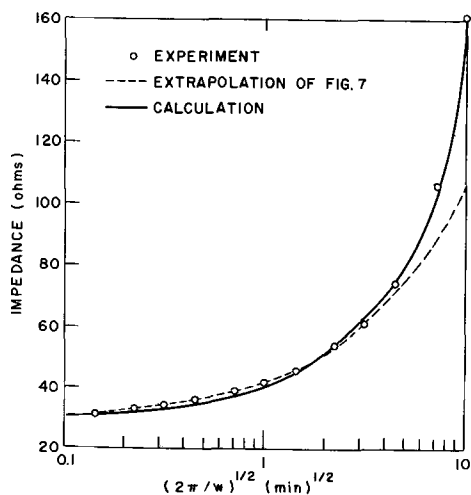


Fig. 8. Variation of solid-state battery impedance with frequency ( $w/2\pi$ ) for  $\text{Na}^+$  solid-state battery at 500°C.

$$i = \frac{DCa}{h} \cdot \frac{\sinh(ah)}{\cosh(ah)} \cdot V$$

and the impedance is given by

$$z = \frac{\cosh(ah)}{\sinh(ah)} \cdot \frac{h}{CDA}$$

Replacing "a" by  $\left( \frac{i\omega}{D} \right)^{1/2}$  and noting  $\sqrt{i} = (1+i)/\sqrt{2}$  then

$$z = \frac{h}{C} \left( \frac{2}{wD} \right)^{1/2} (F_1 - iF_2) \quad [3]$$

where

$$2F_1 = \frac{\sinh(2w'h) - \sin(2w'h)}{\cosh(2w'h) - \cos(2w'h)}$$

$$2F_2 = \frac{\sinh(2w'h) + \sin(2w'h)}{\cosh(2w'h) - \cos(2w'h)}$$

and  $w'$  is a reduced frequency parameter

$$w' = \left( \frac{w}{2D} \right)^{1/2}$$

the total cell impedance ( $Z$ ) includes the in-phase electrolyte resistance  $R$

$$Z^2 = R^2 + \frac{2Rh}{C} \left( \frac{2}{wD} \right)^{1/2} F_1 + \frac{h^2}{C^2} \frac{2}{wD} (F_1^2 + F_2^2) \quad [4]$$

The shapes of the functions  $F_1$  and  $F_1^2 + F_2^2$  are shown in Fig. 9, 10.

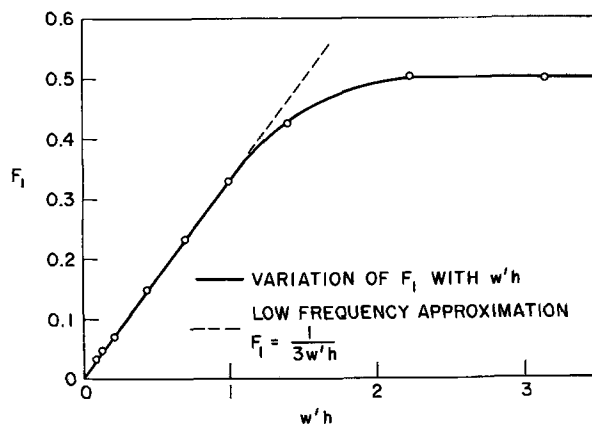


Fig. 9. Variation of  $F_1$  with  $w'h$

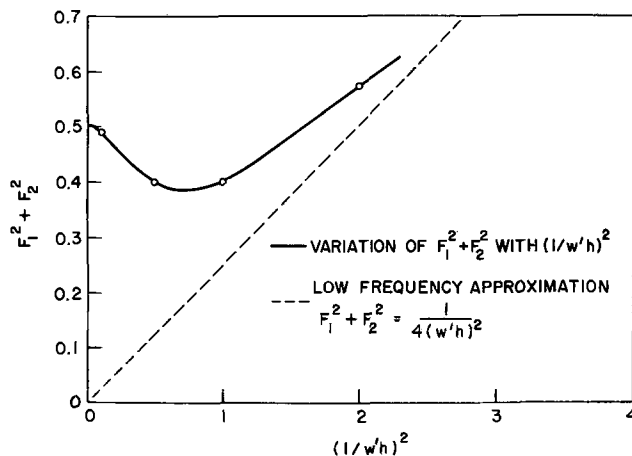


Fig. 10. Variation of  $F_1^2 + F_2^2$  with  $(1/w'h)^2$



Two limiting cases occur

1.  $w'h \rightarrow 0$  i.e. (low frequency  $F_1 \rightarrow \frac{1}{3} w'h$   
 (high  $D$  value  
 (low  $h$  value  $F_1^2 + F_2^2 \rightarrow \frac{1}{4(w'h)^2}$

when

$$Z^2 = R^2 + \frac{2}{3} \frac{Rh^2}{CD} + \frac{1}{w^2 C^2} + \frac{1}{9} \frac{h^4}{C^2 D^2}, w'h < 0.5 \quad [5]$$

2.  $w'h \rightarrow \infty$  i.e. (high-frequency  $F_1 \rightarrow 0.5$   
 (low  $D$  value  
 (high  $h$  value  $F_1^2 + F_2^2 \rightarrow 0.5$

when

$$Z^2 = R^2 + \frac{Rh}{C} \left( \frac{2}{Dw} \right)^{1/2} + \frac{h^2}{C^2 Dw}, w'h > 2 \quad [6]$$

Qualitatively the impedance is in accord with Eq. [5] and [6],  $Z^2$  increasingly linearly with  $(2\pi/w)^{1/2}$  and rising rapidly at about  $w/2\pi = 0.05$  cpm ( $\sim 10^{-3}$  Hz). If  $w'h$  is put at  $\sim 2$  for the changeover point of the two limiting cases, then for  $w/2\pi = 10^{-3}$  Hz,  $D/h^2 \sim 7 \times 10^{-4} \text{ sec}^{-1}$ . From the value of the slope of Fig. 7, 120 ohm<sup>2</sup> sec<sup>1/2</sup> then  $C (D/h^2)^{1/2} \sim 0.14F \text{ sec}^{-1/2}$  and, therefore,  $C \sim 5F$ . Better estimates of the values of  $D/h^2$  and  $C$  were obtained by a least squares fitting method of Eq. [4] to the experimental points, the values obtained were  $D/h^2 = 1.3 \times 10^{-3} \text{ sec}^{-1}$  and  $C = 6.6F$ . The calculated curve and experimental points appear in Fig. 8 for the whole frequency range measured (50-0.01 cpm).

Figures 11 to 14 show the electrical characteristics of cell (b) at two temperatures: 300°, 500°C. The capacitance and diffusion parameter ( $D/h^2$ ) values are shown together with those of cell (a) in Table I.

The values of diffusion coefficient ( $D$ ) obtained from Table I by putting  $h = 0.1$  cm are of the same order of magnitude as those obtained by radioactive tracer techniques on single crystals of alkali aluminates (7) and ferrites (15) and of the same order as those observed in aqueous solution at room temperature.

The discrepancy in Table I between  $C$  and  $D/h^2$  values obtained by different electrical methods probably reflects the breakdown of the simplifying assumptions used in developing Eq. [1] to [6].

*Practical Applications*

It is doubtful that the power density of a ceramic cell could be increased sufficiently to provide a useful secondary battery unless high-temperature operation were a necessity.

The practical applications of the device considered as a capacitor rather than a battery are: (A) an electronic integrator for integrations over long periods of

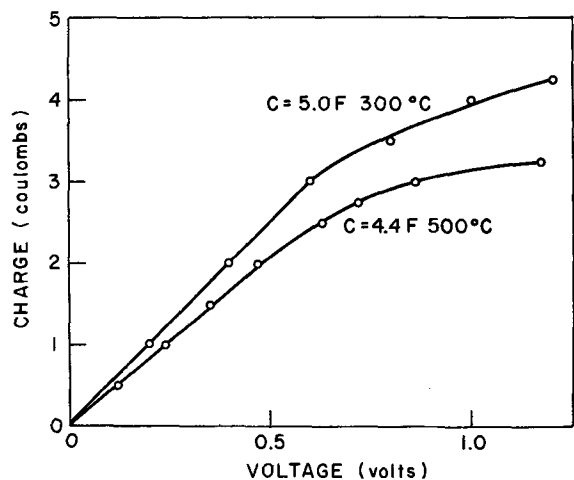


Fig. 11. Steady-state charge-voltage characteristic of K<sup>+</sup> solid-state battery at 300°, 500°C.

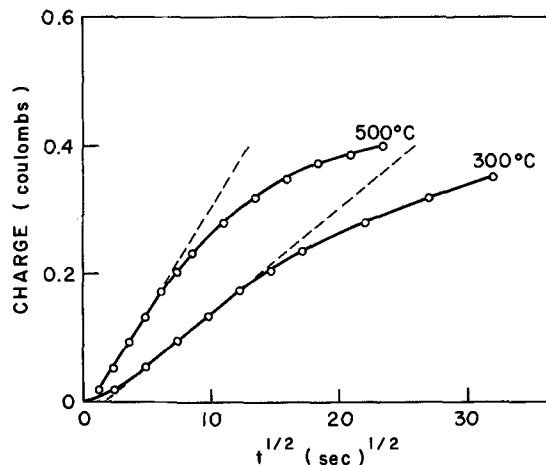


Fig. 12. Charge vs. (time)<sup>1/2</sup> for K<sup>+</sup> solid-state battery for 0.1v potential step at t=0 for two temperatures.

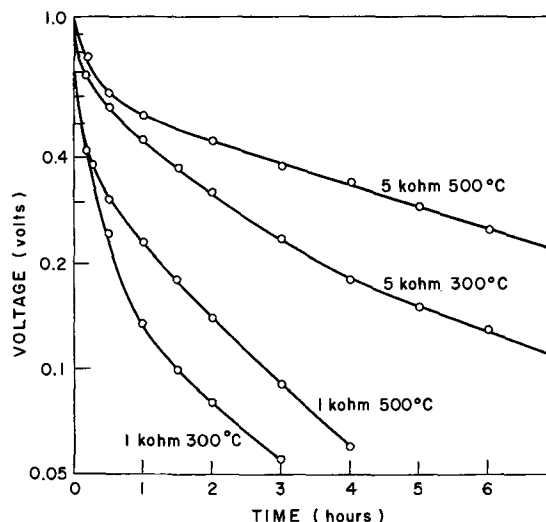


Fig. 13. Discharge (voltage-time) curve for K<sup>+</sup> solid-state battery at two temperatures (300°, 500°C) and two loads (1, 5 kohm).

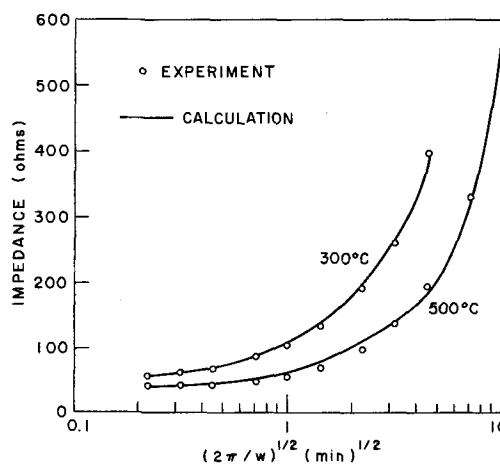


Fig. 14. Variation of K<sup>+</sup> solid-state battery impedance with frequency at 300°, 500°C.

time; (B) as a capacitor in filter circuits for d-c smoothing, phase correction, etc.

In (A) the main criteria would be stability, reliability and price; the present device offers advantages in reliability and price, but stability has not been fully investigated.

In (B) the power factor as a capacitor greatly detracts from its usefulness, power losses arise from the electrolyte resistance (independent of frequency) and

Table I. Capacitance values and diffusion parameter values for Na<sup>+</sup> and K<sup>+</sup> solid-state batteries

Cell	°C	C, F	D/h <sup>2</sup> , sec <sup>-1</sup>	Method of measurement
(a)	300	19	4 × 10 <sup>-1</sup>	Q-V <sub>0</sub> and q-√t curves
(a)	500	6.6	1.3 × 10 <sup>-3</sup>	A-C impedance
(b)	300	5.0	8.4 × 10 <sup>-1</sup>	Q-V <sub>0</sub> and q-√t curves
		2	4.4 × 10 <sup>-1</sup>	A-C impedance
(b)	500	4.4	4.3 × 10 <sup>-3</sup>	Q-V <sub>0</sub> and q-√t curves
		1.7	2.1 × 10 <sup>-3</sup>	A-C impedance

from the electrode resistance (increase with frequency). These losses may be reduced for a given frequency of operation by reduction of electrode thickness  $h$  (causing  $w'h$  to decrease) and by reduction of the electrolyte resistance. This could be achieved, possibly, by using a porous sintered body of low particle size in a solution of the appropriate alkali metal ion, the solution may have to be nonaqueous in view of the inhibition of ion exchange in aqueous solutions. Vacuum deposited thin films may be of use, but again a low resistance electrolyte is needed. The necessity of low operating voltage is a disadvantage to the device as compared to other capacitors, but the use of low voltage equipment is common (batteries, transistors), also the device does not polarize (compare electrolytic capacitors). Finally, the nonlinearity of the  $q$  vs.  $V$  characteristic seems of little use, as tunable capacitors have found application only at microwave frequencies. However its existence does offer, in principle, the construction of other circuit elements such as amplifiers and rectifiers.

#### Acknowledgment

The author is greatly indebted to Dr. J. T. Kummer of this laboratory, whose ideas initiated and guided the work.

Manuscript submitted Dec. 13, 1967; revised manuscript received March 22, 1968.

Any discussion of this paper will appear in a Discussion Section to be published in the June 1969 JOURNAL.

#### REFERENCES

1. C. J. M. Rooymans, C. Langerais, and J. A. Schulkes, *Solid State Commun.*, **4**, 85 (1965).
2. R. Scholder and M. Mansmann, *Z. anorg. u. allgem. Chem.*, **321**, 246 (1963).
3. W. L. Roth and F. E. Luborsky, *J. Appl. Phys.*, **35**, 966 (1964).
4. W. L. Roth and A. S. Cooper, *General Electric Rep.* **60**, RL-2461 M.
5. Y. Otsubo and K. Yamaguchi, *Nippon Kagaku Zasshi*, **82**, 676 (1961).
6. E. W. Gorter, *Philips Research Repts.*, **9**, 363 (1954).
7. J. T. Kummer and Y. Yao, *J. Inorg. Nucl. Chem.*, **29**, 2453 (1967).
8. A. D. Wadsley, *Rev. Pure Appl. Chem.*, **5**, 165 (1955).
9. C. A. Beevers and M. A. S. Ross, *Z. Kristallogr.*, **97**, 57 (1934).
10. V. Adelskold, *Arkiv Kemi, Min. Geol.*, **12A**, No. 29, 1 (1938).
11. J. J. Went, G. W. Rathenau, E. W. Gorter, and G. W. van Oosterhaut, *Philips Tech. Rev.*, **13**, 203 (1952).
12. H. Saalfeld, *Z. anorg. u. allgem. Chem.*, **291**, 117 (1957).
13. F. J. Morin, Monograph 3116 Bell Telephone System "Oxides of the 3d Transition Metals."
14. J. T. Kummer, and N. Weber, "A Sodium-Sulfur Secondary Battery," presented at the Automotive Engineering Congress, Detroit, Mich., January 1967.
15. K. Hever, *This Journal*, **115**, 826 (1968).

## Foil Electrets and Their Use in Condenser Microphones

G. M. Sessler and J. E. West

Bell Telephone Laboratories, Incorporated, Murray Hill, New Jersey

#### ABSTRACT

New results are reported on polarization and depolarization characteristics of foil electrets made of polyester, fluorocarbon, polycarbonate, and polyimide. The foils (¼ to 1-mil thick) are polarized by exposure to d-c fields at high temperatures. Use of a depolarization technique made it possible to measure for the first time separately the decay characteristics of homocharge and heterocharge of foil electrets. Time constants for the homocharge decay of foil electrets at room temperature were found to be about 0.1 years for polyimide, one year for polyester, and more than 100 years for fluorocarbon and polycarbonate. The relaxation times of the heterocharge on polyester and fluorocarbon electrets at room temperature vary from 0.1 to 1 year. These results are compared with other data on the net decay of both charges, derived in part from measurements at room temperature taken over a five-year period and in part by extrapolating high-temperature data. All time constants depend somewhat on preconditioning of the electrets after forming. Condenser microphones built with fluorocarbon and polycarbonate foil electrets are expected to show little change in sensitivity over periods of the order of 100 years.

Electrets formed of disks of dielectric material have been known for a long time. It was not until 1962, however, that the polarization of thin films (about 1 mil thick or less) was reported in the literature (1). The first film electrets or foil electrets were made of polyester and had time constants of the charge decay of the order of one year. The polarization of dielectric films with substantially longer charge lifetimes, however, was reported only recently (2). Foil electrets, while having basically the same electrical properties as disk electrets, differ from these in their me-

chanical behavior, due to the flexibility of the foil. This flexibility turns out to be very important when foil electrets are used in condenser microphones, since it causes the microphone sensitivity to remain constant even if the polarization of the electret decays somewhat with time (2). Condenser microphones with foil electrets exhibit also a higher capacitance per unit area than transducers with disk electrets.

In this paper, we will discuss some new results on the polarization and depolarization characteristics of foil electrets, as determined by research in our lab-

oratory over the past years. Although many different polymers were investigated, emphasis is placed on those foil materials for which extensive measurements at room temperature have been obtained. This allows us to determine decay characteristics directly at room temperature and to compare these data with various results extrapolated from high-temperature measurements. In the final part of this paper, we will present the continuation of our long-term sensitivity measurements on electret microphones.

### Polarization and Measurement of Foil Electrets

Foil electrets have been polarized in our laboratory using a variety of dielectric materials, such as polyester,<sup>1</sup> fluorocarbon,<sup>2</sup> polyimide,<sup>3</sup> and polycarbonate,<sup>4</sup> usually 0.25-1 mil thick. The polarization is achieved by heating the foils to temperatures up to 150°C (polyester) or 230°C (polyimide, fluorocarbon, and polycarbonate) and exposing them to electrical fields between 10 and 100 kv/cm, as described elsewhere (2). The foil may also be interposed between two sheets of dielectric during the polarization process. In this case a higher polarizing voltage may be used.

The polarization of a thermoelectret consists in general of hetero- and homocharge. According to Gross and de Moraes (3), the homocharge is due to a surface effect involving the transfer of charge through the dielectric-electrode interface. Thus the homocharge consists of space charges located close to the surfaces of the dielectric. The heterocharge is due to a volume effect and can consist of a volume polarization caused by the orientation of dipoles or of a space charge polarization due to a migration of ions over distances comparable to the thickness of the sample. The heterocharge can also be caused by a migration of charge carriers over microscopic distances (3).

Two methods were employed to measure the polarity and the quantity of the surface charge on foil electrets. For most of the measurements, a dissectible capacitor (4) in connection with a ballistic galvanometer was used (2). Condenser plates of various sizes were utilized to determine the total charge on a foil as well as its spatial distribution.

Surface charges of foil electrets incorporated into microphones or loudspeakers have also been measured indirectly by a modified dynamic capacitor (5) method. The latter method, when applied to an electret microphone, uses an external d-c bias which is adjusted to a value  $V_B$  for which the microphone, exposed to a sound field, shows zero electric output (1). In the case of an electret loudspeaker, an external d-c bias in addition to a signal voltage is applied; here, the external voltage is adjusted to a value  $V_B$  for which the acoustic output of the loudspeaker consists only of the second harmonic of the signal voltage (6). In both cases, the surface charge  $q$  can be determined from the equation (7)

$$V_B = - (4\pi/\epsilon) qd \quad [1]$$

where  $\epsilon$  is the dielectric permittivity of the foil and  $d$  is the foil thickness. Equation [1] shows that the bias  $V_B$  does not depend on the thickness of the air gap between the electret foil and the back electrode of the transducer.

Measurements performed by these methods show that foil electrets, when formed with an air gap, generate fields corresponding to a net homocharge, i.e., the homocharge is the predominant charge in this case. However, when sheets of dielectric are interposed between foil and electrodes during the forma-

tion process, the foils exhibit occasionally an apparent heterocharge. On nonmetallized electrets, the charges on the two surfaces were found to have opposite sign and to be of comparable magnitude. Most electrets have an initial surface charge of a few  $10^{-8}$  C/cm<sup>2</sup>.

### Depolarization Experiments

More information about the nature of the charge on foil electrets can be gained from depolarization experiments (4) in which the foil electret is discharged between two metal disks in contact with the foil surfaces at elevated temperatures.

The depolarization current of a 1-mil polyester electret having initially a homocharge with a surface density of  $q_1 = 2.1 \times 10^{-8}$  C/cm<sup>2</sup> is shown in Fig. 1. The foil was polarized six days prior to the discharge experiment. The net discharge current shows a positive sign in the temperature range from about 70° to 105°C. This polarity corresponds, for the particular setup used in the experiment, to the depolarization of a heterocharge. The integrated positive current yields a charge density of  $1.6 \times 10^{-8}$  C/cm<sup>2</sup> (disk area 32 cm<sup>2</sup>). Considering the air gaps between foil and metal plates (7), this corresponds to a heterocharge density of  $q_2 = 4.0 \times 10^{-8}$  C/cm<sup>2</sup>. When the depolarization current reached zero at  $T = 105^\circ\text{C}$ , the foil was cooled down to room temperature. Then, using a dissectible capacitor, its surface charge was determined to be  $q_3 = 2.8 \times 10^{-8}$  C/cm<sup>2</sup> which is smaller than the expected value  $q_1 + q_2 = 6.1 \times 10^{-8}$  C/cm<sup>2</sup>. The difference has to be attributed to an external decay of part of the homocharge through the disk-electret interface. In this case, internal depolarization of the homocharge is negligibly small below 105°C.

The depolarization of the electret was then continued and carried to higher temperatures. At temperatures from 100° to 140°C, the discharge current has negative sign, indicating the internal decay of a homocharge. The surface charge density, as obtained from the integrated negative current, is  $2.4 \times 10^{-8}$  C/cm<sup>2</sup>, which is slightly below  $q_3$ , indicating some additional interfacial decay. The foil was found to be completely discharged after this phase of the depolarization experiment.

From Fig. 1 we can determine the time constants for heterocharge and internal homocharge decay. The results are discussed below.

Depolarization experiments on fluorocarbon and polycarbonate electrets show qualitatively the same results, although fluorocarbon usually does not exhibit a large heterocharge. The temperature range for depolarization of the homocharge on these materials is higher than for polyester.

### Decay of the Surface Charge at Elevated Temperatures

The decay processes for space charges and dipole alignments on electrets are controlled by the conductivity of the foil material and by its dielectric relaxation, respectively. In most organic substances, the temperature dependence of the conductivity  $\sigma$  can be

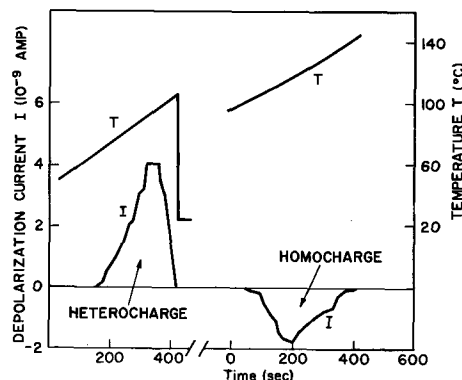


Fig. 1. Net depolarization current for a 1-mil polyester electret. The time dependence of the temperature is also shown.

<sup>1</sup> Available under the tradename "Mylar A" and "Mylar C" from E. I. du Pont de Nemours and Co., (Inc.).

<sup>2</sup> Available under the tradename "Teflon" and "Teflon FEP" from E. I. du Pont de Nemours and Co., (Inc.).

<sup>3</sup> Available under the tradename "H-film" from E. I. du Pont de Nemours and Co., (Inc.).

<sup>4</sup> Manufactured under the name "K-1 polycarbonate" by Eastman Chemical Products, Inc. Bis-Phenol A Polycarbonate with low and high molecular weight was also supplied by Natvar Corporation and Farbenfabriken Bayer A. G., respectively.

expressed (8) by  $\sigma = \sigma_0 \exp(-E_1/kT)$ , where  $E_1$  is an activation energy. The time constant  $\tau_1$  of the homocharge decay is given by  $\tau_1 = \epsilon/4\pi\sigma$ , where  $\epsilon$  is the dielectric constant (2). For a dipole alignment, the temperature dependence of the relaxation time  $\tau_2$  can also be expressed by a relation  $\tau_2 = \tau_0 \exp(-E_2/kT)$ . This suggests Arrhenius plots  $\log(\sigma/\sigma_0) = -E_1/kT$  and  $\log(\tau_2/\tau_0) = -E_2/kT$  to determine time constants over a range in which the activation energies and  $\sigma_0$  and  $\tau_0$  do not change substantially.

Time constants at elevated temperatures have been obtained by two different methods. In one method (which we may call the current method), the foil electret is exposed to increasing temperatures between two disk electrodes in close contact to the foil surfaces, and the depolarization current is measured as a function of temperature (see previous section). The time constant  $\tau(T)$  at a temperature  $T$  reached at time  $t_1$  can then be obtained from the current  $I(t_1)$  at that temperature and the remaining quantity of charge  $Q(t_1)$  by the equation

$$\tau(T) = Q(t_1)/I(t_1) = \left( \int_{t=t_1}^{\infty} I(t) dt \right) / I(t_1) \quad [2]$$

Time constants obtained from such measurements for polyester and FEP fluorocarbon electrets are shown in Fig. 2 as a function of  $1/T$ . As expected,  $\log \tau$  is found to be proportional to  $1/T$ . If extrapolated to room temperature, the time constant for the homocharge decay of polyester is 1.5 years while that for the heterocharge decay is about 0.5 years. Activation energies may be determined from the slopes of the lines in Fig. 2. For the homocharge decay, the activation energies below and above the glass transition temperature of polyester at  $80^\circ\text{C}$  are apparently not too different. This is evident from the fact that the extrapolated time constant of the homocharge decay corresponds to that found directly at room temperature (see below) for the net charge decay.

For the homocharge decay of FEP fluorocarbon at room temperature, Fig. 2 yields an extrapolated time constant of about 50 years, corresponding again to that found directly at room temperature (see below). The

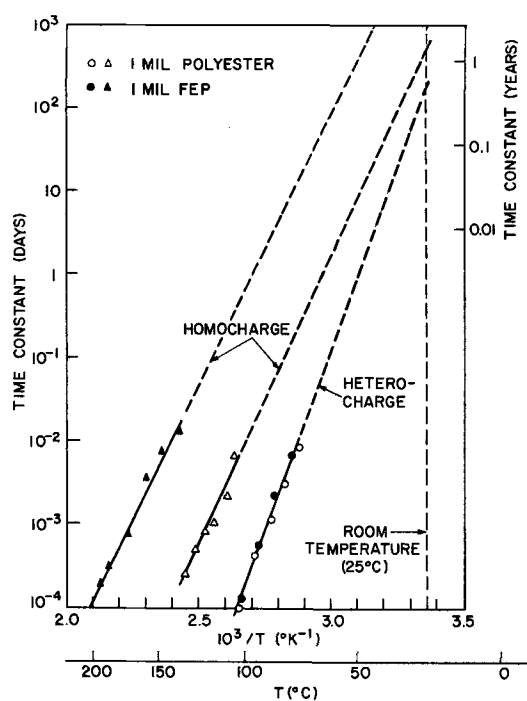


Fig. 2. Time constant of the homocharge and heterocharge decay of 1 mil polyester and FEP fluorocarbon electrets as a function of inverse temperature. Data for polyester were obtained from the depolarization current measurements shown in Fig. 1. Extrapolated time constant for FEP homocharge decay is 50 years.

time constant of the heterocharge decay at room temperature is found to be 0.5 years and is thus about equal to the dielectric relaxation time (9).

Homocharge and heterocharge decays are therefore of different nature. The heterocharge is thus expected to consist either of a dipole orientation or of a charge migration over microscopic distances (3) rather than of a space-charge polarization associated with a homocharge. On fluorocarbon, the heterocharge is apparently due to a dipole alignment and only important for some time after polarization of the electret. Later, only the homocharge prevails on this foil.

The second method for determining time constants at elevated temperatures consists of measurements of the surface charge before and after the electret has been exposed to temperatures above room temperature (charge method). In this case, the foil is heated either suspended freely or making contact to metal surfaces.

In Fig. 3 the time constants of the net charge decay of 1-mil polyester, H-film, fluorocarbon, and polycarbonate electrets, as determined with the charge method, are shown as a function of  $1/T$ . The foils were subjected to some aging at elevated temperatures after polarization, resulting in a loss of about 50% of the original electret charges, before these measurements were taken. This aging increases the measured time constants considerably. The polycarbonate foils were also baked before polarization in order to remove moisture. Measurements taken at room temperature are also included if available.

In Fig. 3, the straight line extrapolation of the time constants for polyester and FEP fluorocarbon electrets agrees well with the results obtained at room temperature (see below) indicating relatively constant activation energies in the temperature range under consideration. The time constant of FEP fluorocarbon seems to be about 100 years at room temperature. KI polycarbonate has also an extrapolated lifetime of about 100 years at room temperature; direct measurements at this temperature (see below) yield a time constant of the order of 10 years or more. H-film is clearly represented by two or more straight lines, indicating a change in activation energy at about  $100^\circ\text{C}$ .

Due to preheating, most of the heterocharge was removed prior to these experiments. The measured time

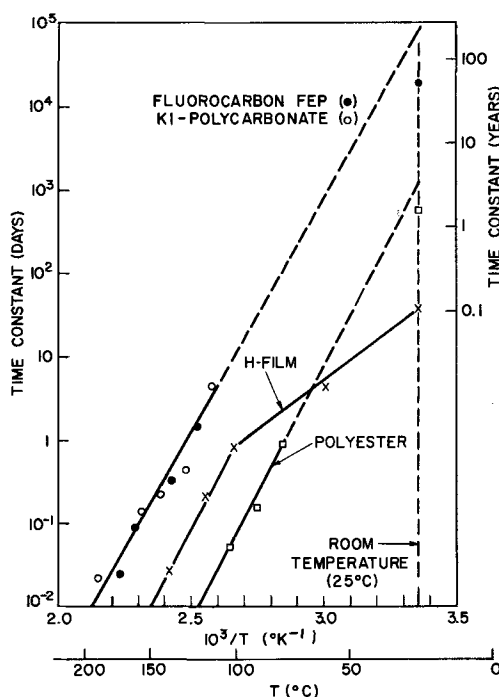


Fig. 3. Time constant of the net surface charge decay of 1-mil polyester, H-film, FEP fluorocarbon, and KI polycarbonate electrets as a function of inverse temperature. Data obtained by heating electrets freely suspended in air.

constants are therefore those related to the homocharge decay. They agree well with the corresponding time constants obtained with the current method.

The two methods discussed above differ in some important respects. First, the current method allows an independent measure of the time constants of homocharge and heterocharge decay as long as the depolarization of the two charges takes place in different temperature ranges. Measurement of both time constants is much more difficult with the charge method, where one can usually not assess the heterocharge decay in the presence of a large homocharge.

Another difference between the two methods is obvious when extrapolations to room temperature are considered. Results on the time constants of homocharge and heterocharge decay obtained with the current method at elevated temperatures can be extrapolated to room temperature by Arrhenius-plots if, as has been previously mentioned, the activation energies do not change substantially over the temperature range of interest and the temperature dependence of the time constants is essentially exponential. On the other hand, the charge method allows, under these conditions, only an extrapolation of the time constant of the longer lasting charge. Even this is only possible if this charge has a substantially greater lifetime than the other charge over the entire temperature range of interest and if the shorter-lasting charge is initially removed by aging.

A third difference is that the current method provides a good contact between the foil and the metal disks. Thus, some of the homocharge may decay externally through the plates. In the charge method this may be avoided by suspending the foil freely in air. The two methods yield therefore somewhat different information.

#### Surface Charge Decay of Foil Electrets at Room Temperature

The decay of the surface charge of foil electrets as a function of time at room temperature is shown in Fig. 4 and 5 for several polyester, fluorocarbon, polycarbonate, and H-film electrets. Previous measurements (2) have been extended to periods of about five years with the foils stored unshorted and in normal room atmosphere. Aging at elevated temperatures after polarization (to remove less resistant charges) was not applied to these foils. All foils have an initial surface charge of a few  $10^{-8}$  C/cm<sup>2</sup>. Most of the decays are nonexponential.

For polyester, the time "constant" of the decay has initial values of about 0.2 years and increases to about one year. For fluorocarbon and fluorocarbon FEP, the

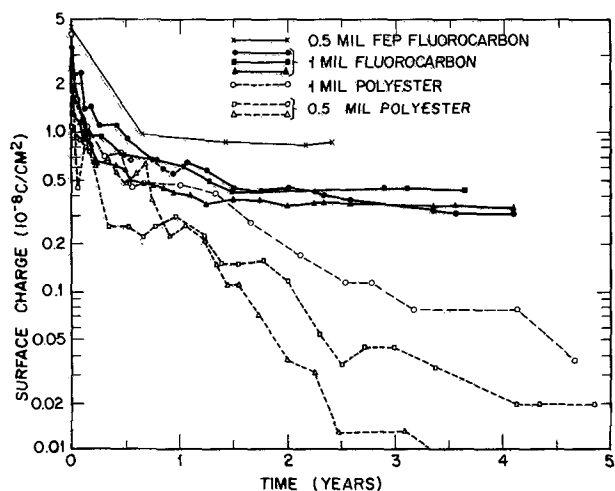


Fig. 4. Variation of surface charge of several fluorocarbon and polyester electrets at room temperature. Electrets kept unshorted. The electrets were not aged at elevated temperatures after polarization.

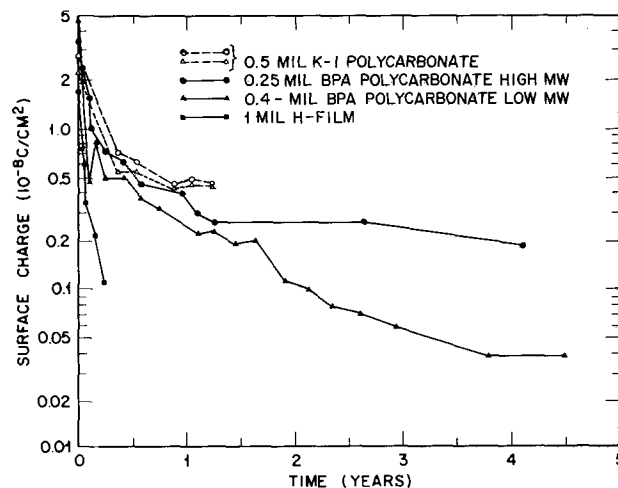


Fig. 5. Variation of surface charge on H-film, KI polycarbonate and BPA polycarbonate of high and low molecular weight at room temperature. Electrets kept unshorted. The electrets were not aged at elevated temperature after polarization.

time constants over the last year of the measurements are about twenty and fifty years, respectively. BPA-polycarbonate has time constants of about two to ten years, while KI polycarbonate, although only measured over a period of about 1.5 years, seems to have a lifetime of more than 10 years. H-film has a time constant of only 0.1 years. The small fluctuations superimposed on the decays are probably due to environmental changes. Aged foils show initially larger time constants.

Existing theories of the time variation of electret charges (10), which take into consideration the resistive decay of the homocharge and the thermal relaxation of the dipole polarization, predict a time-dependence of the surface charge given by

$$q(t) = A_1 \exp(-t/\tau_1) - A_2 \exp(-t/\tau_2) \quad [3]$$

where  $t$  is time,  $\tau_1$  and  $\tau_2$  are the time constants for homocharge and heterocharge decay and  $A_1$  and  $A_2$  are constants depending on  $\tau_1$  and  $\tau_2$  and the relative amount of both charges. These theories can, however, not account for the observed temporal increase of the time "constants" of the surface charge decay, since they assume a field-independent conductivity of the foil material. Another assumption is that the dipole polarization decays independent of the electric field. Both assumptions are, however, known to be invalid for fields larger than  $10^3$  v/cm.

In foil electrets with surface charges of the order of  $10^{-8}$  C/cm<sup>2</sup>, the field strength  $E$  in the sample is between  $10^4$  and  $10^5$  v/cm. Since the conductivity of many organic materials increases (8) strongly with  $E$  in this range, we expect a nonexponential decay of the surface charge with a temporal increase of its time constant, as observed in the experiments (see Fig. 4 and 5).

The nonexponential character of the decay is enhanced due to the fact that the surface charge density of the foil is not constant over the entire area. An example is shown in Fig. 6. Similar results have also been obtained elsewhere (11). Thus areas with high surface charge density will lose their charge at a faster rate than areas with low density. A third reason for expecting nonexponential decays is that the conductivity of the foil material is not uniform over the entire surface. Thin dielectric foils seem to consist of small domains having different electrical properties. This has been substantiated by measurements of the dielectric strength of polymers (12). Thus it is possible that the time constant for the charge decay of foil electrets is first determined by domains having relatively small volume resistivity. After these domains have lost most of their charge, other domains having larger volume resistivity will determine

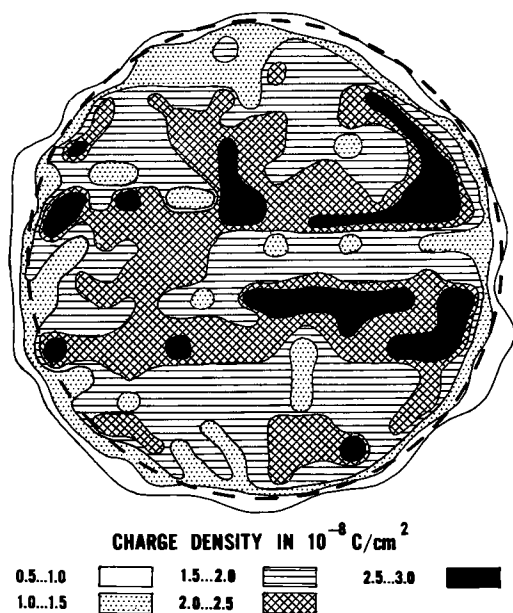


Fig. 6. Surface charge density on a 1 mil polyester electret polarized two days prior to measurements. Dashed circle, polarized area; diameter 7.4 cm.

the rate of the decay. A fourth factor causing nonexponential decays may be the difference between external and internal decay rates of the homocharge.

The increase of the time constant of the decay is also responsible for the somewhat different results obtained in Fig. 3 and 4. While the time constant of FEP fluorocarbon electrets at room temperature was found by extrapolation (see Fig. 3) to be about 200 years, it seems to be only about 50 years when measured directly at room temperature (see Fig. 4). Indications are, however, that the time constants in Fig. 4 and 5 will further increase with time and will finally reach the higher values determined in Fig. 3.

The conductivity for polyester, as determined from the initial slope in Fig. 4, is of the order of  $10^{-19}$  (ohm cm) $^{-1}$ . This is, as expected, somewhat smaller than the value of  $10^{-18}$  (ohm cm) $^{-1}$ , obtained with standard methods by using fields greater than those corresponding to surface charges of  $10^{-8}$  C/cm $^2$ .

### The Electret Microphone

The diaphragm in the electret microphone consists of a foil electret covered with an optically thin metal layer on one side. The foil electret is stretched across a metallic backplate with the metal side facing out. A sound wave impinging on the microphone changes the air layer between foil and backplate and thus disturbs the electric fields. This gives rise to a voltage across a terminating resistor. Details on microphone construction and performance are given elsewhere (2).

The decay of the sensitivity of various polyester and fluorocarbon microphones is shown in Fig. 7. Measure-

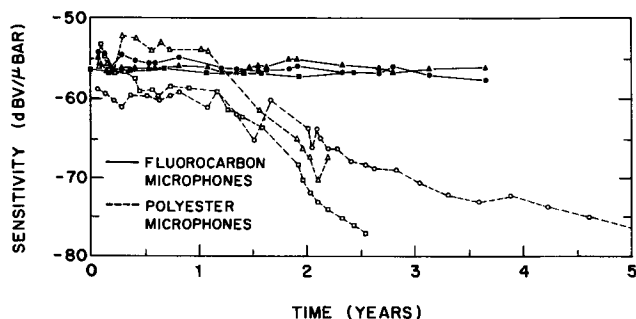


Fig. 7. Sensitivity of various fluorocarbon and polyester electret microphones as a function of time, under normal environmental conditions.

ments have now been extended to periods of up to five years with the microphones stored in normal room atmosphere. The polyester systems show a relatively constant sensitivity for a period of about 1 year. Thereafter, the sensitivity decreases more or less exponentially with time constants from one to two years, corresponding to the time constants found for the decay of the net surface charge. The fluorocarbon systems exhibit smaller fluctuations in sensitivity and show no decay for the time measured (about 4 years). The foils used in these microphones were not aged at elevated temperatures after polarization. Obviously, such aging is not necessary for constant sensitivity of fluorocarbon systems.

Thus, the decay of the surface charge, as evident from Fig. 4 and 5, is not reflected in a corresponding loss in microphone sensitivity. The apparent difference in foil and microphone behavior has been explained previously (2) by a mechanical slackening of the foil which compensates for some time the drop in sensitivity expected due to the charge decay. This compensating mechanism is effective as long as the voltage corresponding to the surface charge is within a range over which the sensitivity does not depend very much on the bias [see Fig. 7 of ref. (13)]. Later, the sensitivity decreases proportional with the surface charge. The compensation is only possible because of the flexibility of the thin foils used in these microphones.

### Conclusions

Various methods have been used to measure time constants of the charge decay of foil electrets. A method utilizing measurements of the depolarization current at elevated temperatures (current method) made it possible for the first time to determine separately the decay characteristics of homo- and heterocharge of foil electrets. In many cases, results on the time constants of homo- and heterocharge decay at elevated temperatures can be extrapolated to room temperature by Arrhenius-plots. Other measurements of the life-times were made by determining the change in net surface charge of the electret after repeated exposure to elevated temperature (charge method). This method measures therefore the net decay of homo- and heterocharge. As has been shown above, an extrapolation to room temperatures is in this case at best possible for the longer-lasting charge. Time constants of the net surface charge decay have also been determined directly at room temperature.

Measurements performed with the different methods yield similar results. In some cases, the time constants and activation energies obtained from these measurements allow to determine the nature of the polarization.

The forming of fluorocarbon and polycarbonate foil electrets, which have time constants of the charge decay of about 100 years, made possible electret microphones with correspondingly long lifetimes.

### Acknowledgment

The authors are grateful to Dr. G. L. Link and Dr. S. Matsuoka for stimulating discussions.

Manuscript submitted Sept. 6, 1967; revised manuscript received April 8, 1968. This paper was presented at the Electret Symposium at the Chicago Meeting, Oct. 15-19, 1967, as Paper 140.

Any discussion of this paper will appear in a Discussion Section to be published in the June 1969 JOURNAL.

### REFERENCES

1. G. M. Sessler and J. E. West, *J. Acoust. Soc. Am.*, **34**, 1787 (1962).
2. G. M. Sessler and J. E. West, *ibid.*, **40**, 1433 (1966).
3. B. Gross and R. J. De Moraes, *J. Chem. Phys.*, **37**, 710 (1962).
4. B. Gross, *Am. J. Phys.*, **12**, 324 (1944); B. Gross, *J. Chem. Phys.*, **17**, 866 (1949).
5. L. A. Freedman and L. A. Rosenthal, *Rev. Sci. Instrum.*, **21**, 896 (1950).

6. G. M. Sessler and J. E. West, in Proc. Fourth Intern. Congress Acoustics, Copenhagen, 1962, Paper N55.
7. G. M. Sessler, *J. Acoust. Soc. Am.*, **35**, 1354 (1963).
8. C. B. G. Garrett, "Organic Semiconductors," in "Semiconductors," N. B. Hannay, Editor, pp. 634-675, Reinhold Publishing Corp., New York (1959).
9. D. W. Mc Call, D. C. Douglass, and D. R. Falcone, To be published.
10. A. N. Gubkin, *Sov. Physics, Techn. Phys.*, **2**, 1813 (1958).
11. A. L. Di Mattia, Private communication.
12. G. L. Link, Private communication.
13. W. Kuhl, G. R. Schodder, and F. K. Schroeder, *Acustica*, **4**, 519 (1954).

## Phosphors Based on Rare Earth Phosphates

### I. Spectral Properties of Some Rare Earth Phosphates

R. C. Ropp\*

Westinghouse Electric Corporation, Bloomfield, New Jersey

#### ABSTRACT

Spectral properties of rare earth phosphate phosphors are presented and compared to rare earth oxide phosphors studied previously. It is shown that changing to a phosphate host does not affect the wavelengths produced, but has a major effect on the total energy efficiency as well as the intensity of the emission lines produced relative to one another. The latter observation is attributed to site symmetry effects on transition probabilities from an emitting energy level.

The lanthanides have been found in various natural states, some of which include the mineral monazite, which has the approximate composition  $(\text{Ce}, \text{La})\text{PO}_4$ , and xenotime, which is primarily an yttrium phosphate. Despite the wide occurrence of these minerals, little is known concerning the spectral properties of the pure rare earth phosphates or specific rare earth phosphates activated by small quantities of other rare earths. Phosphors as  $\text{CePO}_4$  (1) and  $\text{EuPO}_4$  (2) have been prepared, and more recently single crystals of rare earth orthophosphates have been described (3), yet remarkably little has appeared in the literature concerning the fluorescence properties of these materials.

Perhaps the most extensive discussion to date has been presented by Brill and Wanmaker (4) on the physical properties of  $\text{GdPO}_4:\text{Eu}$  as well as the luminescence properties of  $\text{EuPO}_4$ . Details of preparation, decay times, diffraction patterns, and quantum efficiencies were given, but the discussion was limited to gadolinium phosphate as a matrix. In later publication, Brixner and Flournoy (5) mention some of the properties of the  $\text{GdPO}_4:\text{Eu}$  phosphor and compare the emission of  $\text{Eu}^{+3}$  in different hosts. However, with these exceptions, a description of the fluorescence properties of rare earth phosphates has not been available heretofore.

Rare earth orthophosphates, in addition to being found in nature, have been synthesized in the laboratory by fusion methods (6), hydrothermal crystallization from aqueous solutions (7, 8), and chemical reaction (9-11). Phosphates of the cerium subgroup (La to Gd) have been found to possess the monoclinic monazite structure (isomorphous with  $\text{SrCrO}_4$ ), while those of the yttrium subgroup (Dy to Lu) have the tetragonal xenotime structure (isomorphous with  $\text{ZrSiO}_4$ ).

Prior discussions by the author have been concerned with the fluorescence of rare earth oxide phosphors (12, 13). The present work is an extension of a survey of the spectral properties of rare earth phosphors in which the properties of rare earth phosphates will be compared with those of corresponding rare earth oxides.

#### Experimental Methods

**Preparation of phosphors.**—The nitrates (or the oxides dissolved in concentrated nitric acid) of the

requisite rare earths were dissolved to form 0.40-2.0M solutions, depending on the particular preparation desired. Mixtures of the ions in solutions were made and the activators were maintained at a 5 m/o (mol per cent) concentration. Because of the method of preparation, no mixing or blending steps were necessary prior to firing to obtain uniform and homogeneous materials. Phosphoric acid was employed as the source of soluble phosphate and was diluted in requisite proportions so that an excess of phosphate was maintained at all times. The materials as produced were fired in air to form the phosphor composed of the desired solid solution of phosphates.

Thermogravimetric analyses of typical raw materials obtained are shown in Fig. 1. The precipitation conditions yielded  $\text{LaPO}_4 \cdot \frac{1}{2}\text{H}_2\text{O}$ , whereas  $\text{YPO}_4 \cdot \text{H}_2\text{O}$  was obtained under the same conditions.

**Measurements.**—Excitation and emission spectra were obtained with the aid of a commercial instrument having two monochromators. The excitation monochromator provided a constant energy excitation beam over the range of 20,000-50,000  $\text{cm}^{-1}$ . Either monochromator could be programmed separately to

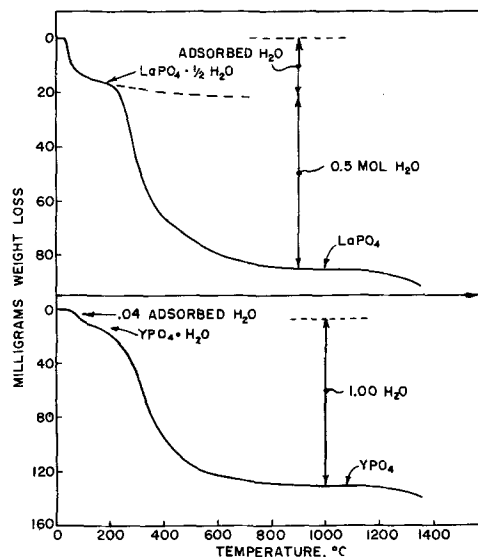


Fig. 1. Thermal decomposition of precipitated rare earth phosphates

\* Electrochemical Society Active Member.

provide excitation or emission spectra. In the case of multiple fluorescence peaks, a separate excitation spectrum was obtained and compared to the others. In most cases they were identical, but in a few cases they were not, as detailed below. Emission spectra were obtained directly, already corrected for instrumental energy losses and photomultiplier response. Resolution in the instrument varied from a few angstroms in the ultraviolet to about 10Å in the red region of the spectrum.

### Experimental Results

The rare earth phosphate phosphors prepared in this study were precipitated as crystalline stoichiometric materials. In considering the rare earth phosphates as phosphors, two possibilities present themselves. One involves rare earth phosphate compositions such as  $\text{ErPO}_4$  or  $\text{HoPO}_4$ , and the other, specific rare earth phosphates containing small amounts of "unlike" rare earth cations as activators, i.e.,  $\text{LnPO}_4:\text{X}$ . Of the two, the latter type of phosphor would be expected to produce the most intense fluorescence. A study of the absorption excitation, and fluorescence properties of  $\text{LnPO}_4$  materials will be the subject of a subsequent report (Part II).

In the case of the  $\text{LnPO}_4:\text{X}$  type of phosphor, Ln must include only those cations containing paired electrons, i.e.,  $\text{Y}^{+3}$  or  $\text{La}^{+3}$ , since unpaired electrons give rise to vibronic coupling processes and possess intermediate levels for cascading of energy to produce infrared and phonon emission (14).

**Relative intensities of emission.**—In observing the spectroscopic properties of the rare earths, Dieke and co-workers (15) have shown that rare earths such as  $\text{Pr}^{+3}$ ,  $\text{Nd}^{+3}$ ,  $\text{Ho}^{+3}$ , and  $\text{Er}^{+3}$  possess numerous intermediate f-electron energy levels, so dissipation of excitation energy by a cascade process can result in up to three possible modes: (i) infrared photon emission (low energy); (ii) phonon emission; and (iii) visible photon emission (high energy). Thus, only the intermediate trivalent cations, such as  $\text{Sm}^{+3}$ ,  $\text{Eu}^{+3}$ ,  $\text{Tb}^{+3}$ , and  $\text{Dy}^{+3}$ , would be expected to produce room temperature fluorescence in the visible region of the spectrum because of the relatively wide gaps which appear between their energy levels.

The data obtained and given in Table I show that this is indeed the case and that the same relative pattern of intensity is followed in the phosphates as observed for the oxides, namely, that  $\text{Sm}^{+3}$ ,  $\text{Eu}^{+3}$ ,  $\text{Tb}^{+3}$ , and  $\text{Dy}^{+3}$  produce the strongest visible emission intensity. However, the total emission intensity is a function of the matrix as well as the activator, as will be shown below. In general, phosphates are lower in both intensity and quantum efficiency than the corresponding oxide phosphors.

**Europium-Activated rare earth phosphates.**—The excitation and emission properties of the europium-activated rare earth phosphates are given in Fig. 2. There are five sets of emission lines, three of major intensity and two of low intensity, as well as minor

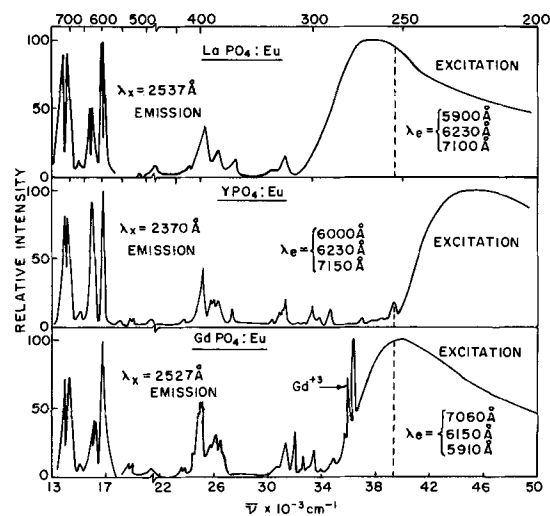


Fig. 2. Europium activated rare earth phosphates

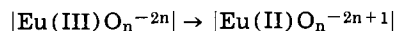
variations in the emission wavelengths as a function of matrix composition. A comparison of the emission of  $\text{Eu}^{+3}$  in  $\text{YPO}_4$  and  $\text{Y}_2\text{O}_3$  is made in Fig. 3. Emission lines are observed in the same general region of the spectrum for both the oxide and the phosphate phosphors, with the exception that the emission at  $7100 \text{ \AA}$  in  $\text{YPO}_4:\text{Eu}$  now contains a considerable part of the total emission energy. In Fig. 3, the emission spectra are plotted as to indicate that the same transitions occur but that the relative emission energy in each is a function of the matrix and site symmetry.

A comparison of the emission intensities can be made as follows:

Phosphor	Excitation, Å (constant energy)	Integrated emission output ( $\mu$ watts)	Quantum efficiency, %
$\text{Y}_2\text{O}_3:\text{Eu}_{0.05}$	2537	306 (100%)	72
$\text{YPO}_4:\text{Eu}_{0.05}$	2370	140 (45.8%)	38

The integrated emission output was obtained by instrumental integration of the emission curves.

The excitation spectra are the more interesting of the measured properties. The usual low level peaks resulting from transitions between the  $4f^6$  energy levels of  $\text{Eu}^{+3}$  occur below  $34,000 \text{ cm}^{-1}$ . In the  $\text{GdPO}_4:\text{Eu}$  phosphor, excitation of the  $\text{Gd}^{+3}$  levels ( $^8\text{S}_{7/2} \rightarrow ^6\text{I}_J$ ) can also be seen. In addition, there are broad excitation bands which occur at various wavelengths, depending on the matrix in which  $\text{Eu}^{+3}$  finds itself. These are the charge-transfer bands, typical for the  $\text{Eu}^{+3}$ -oxygen center (16), for which indirect evidence has been presented by the author and co-workers (17). The mechanism can be written



Close examination of the excitation spectra leads to the conclusion that structure has a significant effect on these charge-transfer states. This is explained as

Table I. Relative emission peak at constant energy excitation

Activator (0.05 mol)	Color	Excitation wave- length (Å)	Comparison of main emission peak heights		
			$\text{LaPO}_4$	$\text{YPO}_4$	$\text{GdPO}_4$
$\text{Eu}^{+3}$	Orange	2290	81	90	101
$\text{Sm}^{+3}$	Red	3680	3	2	5
$\text{Dy}^{+3}$	Yellow	3540	10	13	3
$\text{Tb}^{+3}$	Green	3780	34	17	11
$\text{Pr}^{+3}$	Green	2280	1	1	1.5
$\text{Gd}^{+3}$	U.V.	2760	67	180 (est.)	—
$\text{Er}^{+3}$	Greenish red	2580	1	1	1.2
$\text{Ho}^{+3}$	—	—	—	N.D.*	—
$\text{Nd}^{+3}$	—	5620	—	Very low intensity	—
$\text{Yb}^{+3}$	—	—	—	N.D.*	—

\* Not detected (between 2800 and 7400 Å).

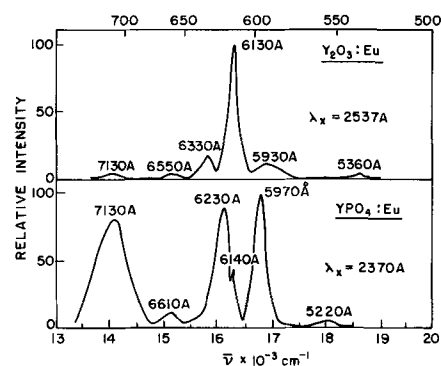


Fig. 3. Fluorescent properties of  $\text{Eu}^{+3}$  activated phosphors



follows: In  $\text{GdPO}_4$  and  $\text{LaPO}_4$ , which have the Monazite structure (monoclinic-site symmetry of cation is  $C_1$ ) the broad excitation peak occurs at  $2570\text{\AA}$  for the former and  $2650\text{\AA}$  for the latter, whereas in yttrium phosphate, which has the xenotime structure (tetragonal-site symmetry of  $\text{Y}^{3+}$  is  $D_{2d}$ ) a different peak position near to  $2370\text{\AA}$  is observed and only a narrow low intensity  $4f^6$  excitation line can be seen at  $2537\text{\AA}$  (the dotted line). Thus structure (oxygen symmetry around the  $\text{Eu}^{+3}$  in a cation site) plays a major role in determining the positions of these broad bands.

Since it has already been demonstrated that matrix excitation bands in the more ionic oxide hosts occur at  $45,500\text{ cm}^{-1}$  ( $2198\text{\AA}$ ),  $47,600\text{ cm}^{-1}$  ( $2100\text{\AA}$ ),  $58,100\text{ cm}^{-1}$  ( $2079\text{\AA}$ ) for the lanthanum, gadolinium, and yttrium oxides, it is likely that the broad excitation bands of the present phosphors are not related to exciton mechanisms, particularly in view of the evidence presented in the next section.

**Gadolinium-activated rare earth phosphates.**—When solid solutions containing 5 m/o gadolinium phosphate in lanthanum phosphate or yttrium phosphate are prepared and spectral properties measured, the results shown in Fig. 4 are obtained. There is a single set of emission lines near to  $32,000\text{ cm}^{-1}$  caused by the  ${}^6P_1 \rightarrow {}^8S_{7/2}$  transition within the  $\text{Gd}^{3+}$  ion. The excitation bands at  $36,000\text{ cm}^{-1}$  represent the transitions  ${}^8S_{7/2} \rightarrow {}^6I_7$ , while the low intensity bands at  $40,000$  and  $44,000\text{ cm}^{-1}$  are probably caused by upper  $4f^7$  electron-excited state transitions within the  $\text{Gd}^{3+}$  ion. There are also two other bands at  $46,400\text{ cm}^{-1}$  ( $\text{LaPO}_4$ ) and  $49,000\text{ cm}^{-1}$  ( $\text{YPO}_4$ ), whose existence have very interesting implications. Because they disappear when measured at liquid nitrogen temperature, and because of their similarity to intense bands measured previously in oxide phosphors (12, 13), I have surmized that these excitation bands represent cation exciton bands, rather than charge transfer bands between cations and oxygen sites. In the oxide phosphors, these bands were called "matrix" bands and were present in all phosphors irrespective of activator. The positions of the bands were dependent on the nature of the cation indicating that these bands involved cationic rather than anionic sites. A change from oxide to phosphate adversely affects the intensity but not the position of these bands. If the bands were charge-transfer bands, they should get stronger in the phosphates, as compared to the oxides. Experimentally, the reverse occurs. Note that a change in structure and point symmetry [cubic oxide ( $C_{2v}$ ) to tetragonal ( $D_{2d}$ ) or monoclinic ( $C_1$ ) phosphate] has no effect on the positions of these bands contrary to the effect observed for  $\text{Eu}^{+3}$ -oxygen charge-transfer bands, as given above.

**Cerium-Activated rare earth phosphates.**—The trivalent ion,  $\text{Ce}^{+3}$ , has an electronic structure containing one  $4f$  electron, and as an activator, generally results in phosphors having broad-band ultraviolet emission. In the rare earth phosphates, the emission bands of  $\text{Ce}^{+3}$  are not unlike those found for other materials.

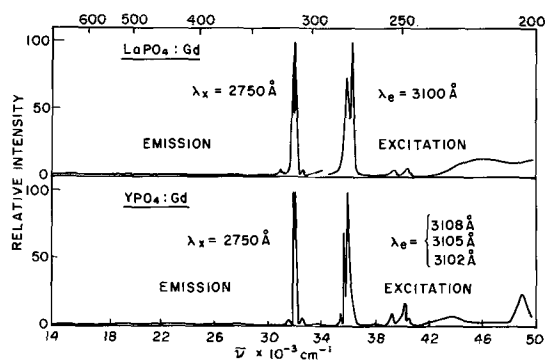


Fig. 4. Gadolinium activated rare earth phosphates

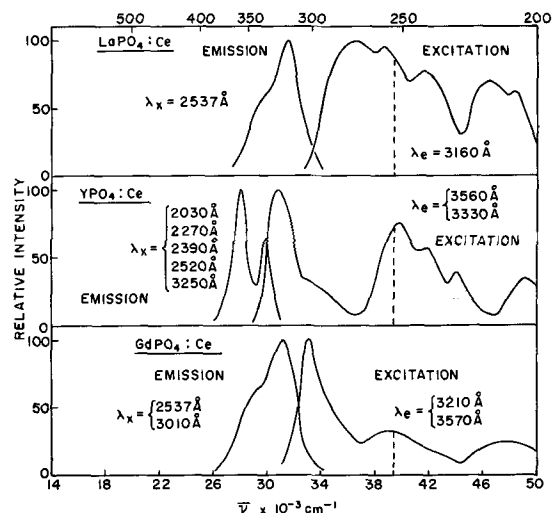


Fig. 5. Cerium activated rare earth phosphates

The spectral properties of these phosphors are shown in Fig. 5 where differences in the emission band produced by  $\text{Ce}^{+3}$  are emphasized. In the monazite structure ( $\text{LaPO}_4$  and  $\text{GdPO}_4$ ) emission bands peaking at about  $3150\text{--}3200\text{\AA}$  are seen. However, in the xenotime structure ( $\text{YPO}_4$ ), two emission bands are produced at  $3300$  and  $3550\text{\AA}$ .

The excitation bands are interesting in that they show considerable variation. For example, in  $\text{LaPO}_4$ , the excitation bands arise from the excited state of the activator and probably involve crystal field splitting of the  $5d$  excited state. It is noteworthy that the excitation spectra of  $\text{LaPO}_4:\text{Ce}$  and  $\text{GdPO}_4:\text{Ce}$  are quite different in spite of the similarity in structure and, therefore, point symmetry at the  $\text{Ce}^{+3}$  site. These materials (18) are fast decay phosphors ( $\sim 40 \times 10^{-9}$  sec).

**Terbium activated rare earth phosphates.**—The spectral properties of terbium activated rare earth phosphates are given in Fig. 6. Nearly the same emission spectra are seen for all of the phosphors. However, major differences are observed for the excitation bands because of the crystal field affect on the  $4f \rightarrow 5d$  transition. In  $\text{YPO}_4:\text{Tb}$  there are two excitation bands, depending on which emission line is being observed. Three separate samples of  $\text{YPO}_4:\text{Tb}$  were measured and found to give identical results, leaving little doubt that the data presented in Fig. 6 represent a reasonably accurate picture of the excitation spectra observed for  $\text{YPO}_4:\text{Tb}$ . Such behavior is unusual.

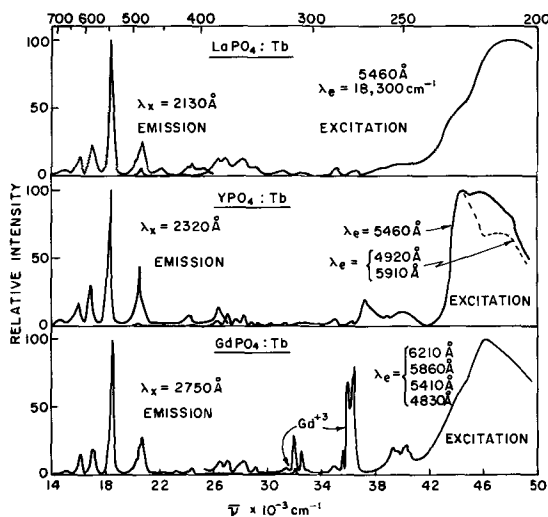


Fig. 6. Terbium activated rare earth phosphates

For the  $\text{LaPO}_4:\text{Tb}$  phosphor, the usual low level excitation bands due to transitions between the  $4f^8$  electron energy levels were seen, as well as the broad band peaking at about  $46,000\text{ cm}^{-1}$ , an activator  $4f \rightarrow 5d$  excitation transition. The side band at about  $44,000\text{ cm}^{-1}$  which appears in  $\text{LaPO}_4:\text{Tb}$  is probably due to upper energy transitions of  $\text{Tb}^{3+}$ . In  $\text{GdPO}_4:\text{Tb}$ , a broad band at  $46,200\text{ cm}^{-1}$  appears, in addition to the usual  $\text{Gd}^{3+}$  excitation levels. It becomes apparent that the  $\text{Tb}^{3+}$  ( $4f \rightarrow 5d$ ) excitation bands are the only bands observed in these phosphors, in contrast to the oxide systems in which exciton mechanisms were the major feature. As will be shown in a later paper, drastic changes in the excitation bands occur as the Tb becomes 100%, as in  $\text{TbPO}_4$ .

**Dysprosium-activated rare earth phosphates.**—In the rare earth phosphates, dysprosium produces a yellow emission which consists of two groups appearing at 4800 and 5740 Å (see Fig. 7). Changes in the matrix produce slight changes in the position of these emission peaks. The position of the emission lines of dysprosium in the rare earth phosphates is not as greatly affected by the matrix as is that of cerium, terbium, or europium (having  $4f \rightarrow 5d$  and charge-transfer mechanism, respectively). In the monazite structures ( $\text{LaPO}_4:\text{Dy}$  and  $\text{GdPO}_4:\text{Dy}$ ), the major emission lines occur at about 4730 and 5740 Å, while in the xenotime structure ( $\text{YPO}_4:\text{Dy}$ ), there is a shift of about 100 Å to the longer wavelengths. The excitation spectra are easily recognized as being essentially excitation transitions within the  $4f^9$  multiplets of  $\text{Dy}^{3+}$ . The identity of the broad excitation bands beyond  $46,000\text{ cm}^{-1}$  remains unknown. The major excitation band in  $\text{GdPO}_4:\text{Dy}$  is due to transitions within the  $\text{Gd}^{3+}$  ion.

**Holmium and erbium activated rare earth phosphates.**— $\text{Ho}^{3+}$  did not produce any measurable fluorescence in the rare earth phosphates. Wavelengths between 2900 and 8400 Å were scanned, using various excitation wavelengths, but if fluorescence was produced, it was below the limit of the detection of the instrument.

The emission intensity of  $\text{Er}^{3+}$  was extremely weak but measurable and consisted of a major line at 4010 Å with others at 4700 and 5290 Å. Other than this, the spectra were featureless, such that they are not presented herein. In  $\text{GdPO}_4:\text{Er}$ , the major emission line at 3100 Å is caused by transitions within the  $\text{Gd}^{3+}$  cation. There are also very low-level-intensity emission lines due to  $\text{Er}^{3+}$ .

**Neodymium and praseodymium activated rare earth phosphates.**—The intensity of emission of  $\text{Nd}^{3+}$  was found to be very weak, such that the spectra of the  $\text{GdPO}_4:\text{Nd}$  phosphor could not be measured. In  $\text{YPO}_4:\text{Nd}$  and  $\text{LaPO}_4:\text{Nd}$ , only one emission line at

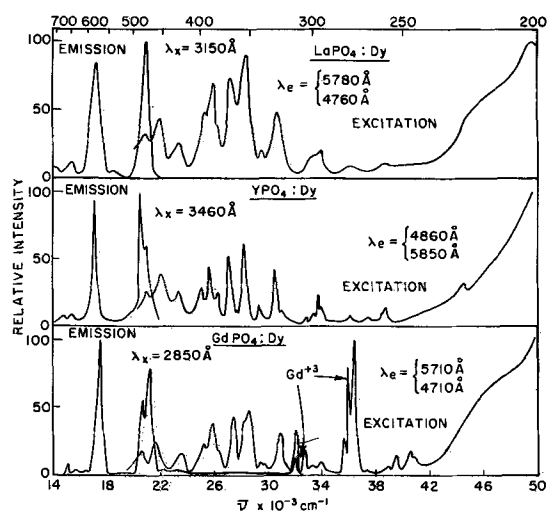


Fig. 7. Dysprosium activated rare earth phosphates

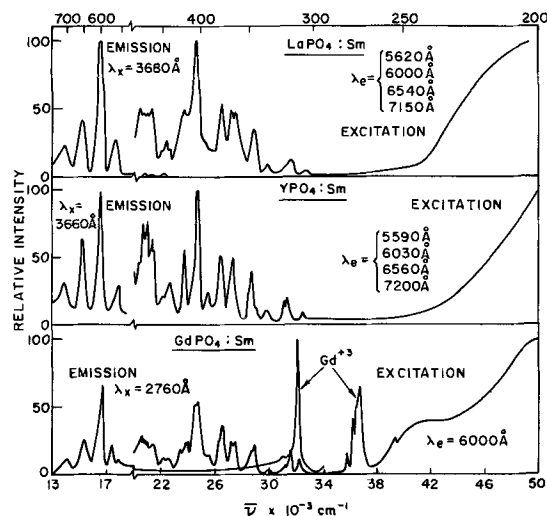


Fig. 8. Samarium activated rare earth phosphates

7240 and 7200 Å, respectively, was observed. Excitation is maximum in the green region of the spectrum.

Phosphors activated by  $\text{Pr}^{3+}$  produced fluorescence too weak to measure.

**Samarium activated rare earth phosphates.**— $\text{Sm}^{3+}$  produces a series of four emission lines in the visible region of the spectrum, as shown in Fig. 8. A slight shift toward longer wavelengths was observed for  $\text{YPO}_4:\text{Sm}$  (xenotime structure) as compared with  $\text{LaPO}_4:\text{Sm}$  (monazite structure). The excitation spectra consist mostly of narrow bands between 3000 and 5000 Å, caused by interlevel transitions of  $4f^5$  electrons within the  $\text{Sm}^{3+}$  ion. No broad bands due to the  $\text{Sm}^{3+}$  were noted. In  $\text{GdPO}_4$ , the major lines and major excitation bands are caused by transitions within  $\text{Gd}^{3+}$ , including that at  $36,600\text{ cm}^{-1}$ .

**Thulium activated rare earth phosphates.**— $\text{Tm}^{3+}$  produces an ultraviolet emission line at 3680 Å in  $\text{LaPO}_4$ , and at 3660 Å in  $\text{YPO}_4$ , as shown in Fig. 9. This spectrum differs considerably from that found for  $\text{Tm}^{3+}$  in the rare earth oxides. In  $\text{Y}_2\text{O}_3:\text{Tm}$ , a blue emission line at  $21,700\text{ cm}^{-1}$  was dominant, whereas in  $\text{YPO}_4:\text{Tm}$ , the major emission line is positioned at  $28,700\text{ cm}^{-1}$ . The excitation spectrum generally consists of narrow bands representing transitions within the  $\text{Tm}^{3+}$  ion. In  $\text{GdPO}_4:\text{Tm}$  the major emission line is due to transitions within the  $\text{Gd}^{3+}$  ion. The excitation band of  $\text{Gd}^{3+}$  is likewise the major feature in the excitation spectrum.

### Discussion of Results

It has been shown that the brightest phosphors are the rare earth phosphates activated by  $\text{Gd}^{3+}$ ,  $\text{Eu}^{3+}$ , or  $\text{Tb}^{3+}$ .  $\text{Dy}^{3+}$  may be classified as possessing intermediate intensity, but the other activators produce only a very low degree of fluorescence. Of immediate interest is a comparison of the fluorescent peaks produced in the phosphates and in the oxides. It is obvious from Fig. 3 that the same transitions which produce fluorescence in the  $\text{Y}_2\text{O}_3:\text{Eu}$  phosphor take place in the phosphate as well. However, the emission of  $\text{Tb}^{3+}$  does not show as great a variation as noted for  $\text{Eu}^{3+}$ . The major emission lines as a function of host lattice are given for the various activators in Table II. Only those lines containing a major portion of the emission energy (50%) are cited, with the exception of a few, such as  $\text{Sm}^{3+}$ , where a single emission line contains but 15-25% of the total energy. Also noted are those activators, such as  $\text{Dy}^{3+}$ , whose emission spectra change considerably as a function of host lattice.

It may be concluded that structure and site symmetry are the major factors which determine the amount of energy concentrated in any transition that results in fluorescence. Some activators are materially

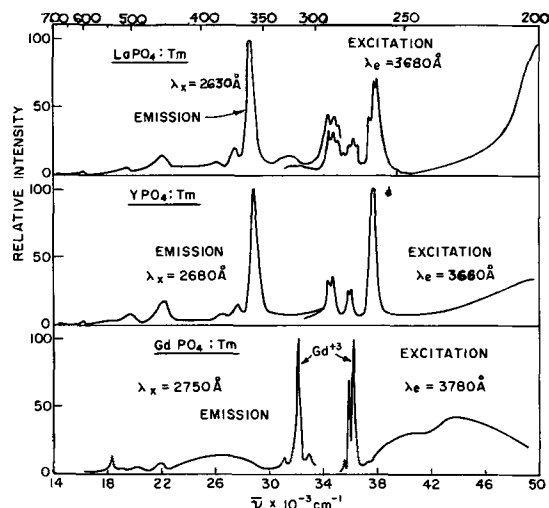


Fig. 9. Thulium activated rare earth phosphates

affected by the matrix, while others such as  $Gd^{+3}$  or  $Tb^{+3}$ , do not show significant changes in emission when incorporated into a cubic lattice ( $Y_2O_3-C_{2v}$ ) as compared to a tetragonal lattice ( $YPO_4-D_{2d}$ ). It is apparent that the same transitions occur for most activators, but that the relative amount of energy concentrated in each is a function of site symmetry.  $Eu^{+3}$  shows the most variation, as presented in Table III. Blasse *et al.* (21) have also commented on this in regard to the  $Eu^{+3}$  ion as an activator.

Of the excitation spectra, only  $Eu^{+3}$  and  $Tb^{+3}$  show broad bands, denoting perturbation of electronic states (charge-transfer and  $4f \rightarrow 5d$  transitions, respectively) by the electric field of the host lattice. Only the po-

sition of the bands change in the phosphates, as compared to the oxides.

$Y_2O_3:Eu$  has a quantum efficiency of 72% (22) and  $YPO_4:Eu$  has a quantum efficiency of 38%. Brill and Wanmaker (4) report a quantum efficiency of 28% for  $GdPO_4:Eu$ . Thus, we can conclude that the incorporation of  $Eu^{+3}$  into what is presumably a more covalent matrix results in a phosphor only 50% as efficient as that produced when  $Eu^{+3}$  is incorporated into a more ionic host such as  $Y_2O_3$ .

The most probable explanation is: (a) europium in oxygen-dominated lattices forms a charge-transfer center with its nearest neighbor oxygen atoms, *i.e.*,  $Eu^{+3}O_n^{-2n}$ . This accounts for the relatively high optimum activator concentrations observed by many authors (15 m/o in  $Y_2O_3$ ), in contrast to the other rare earths (14); (b) in phosphates, it is already known by ESR measurements that the oxygen atoms are tightly bound within the  $PO_4$  group. Therefore, they would not be expected to be available for sharing to form a charge-transfer center with  $Eu^{+3}$ . Since the high efficiency associated with  $Eu^{+3}$  arises because of these Laporte-allowed transitions, rather than from the  $4f \rightarrow 4f$  forbidden transitions, it is not surprising that the inclusion of  $Eu^{+3}$  in a lattice wherein the oxygen orbitals are bound more tightly and are less polarizable, has the effect of producing a phosphor of lower efficiency.

### Acknowledgment

The author is indebted to J. Grasso and E. Chen for preparation of materials to the Dr. C. K. Lui Wei for x-ray diffraction measurements.

Manuscript submitted Nov. 10, 1967; revised manuscript received *ca.* April 1, 1968. This paper was presented at the Cleveland Meeting, May 1-6, 1966, as Paper 32.

Any discussion of this paper will appear in a Discussion Section to be published in the June 1969 JOURNAL.

Table II. Effect of matrix: major emission lines of rare earth activators

Activator	Oxides			Phosphates		
	Y Å	Gd Å	La Å	Y Å	Gd Å	La Å
$Ce^{+3}-4f^1$	N.D.*	N.D.*	N.D.*	3650	3210	3160
$Pr^{+3}-4f^2$	511	N.D.*	N.D.*	N.D.*	N.D.*	N.D.*
$Nd^{+3}-4f^3$	N.D.*	N.D.*	N.D.*	7200	N.D.*	7200
	5740	5750	5890	5890	5740	5620
$Sm^{+3}-4f^5$	5870	6180	6030	6030	6000	6000
	6110	6670	6660	6660	6540	6540
	6250	6950	7200	7100	7150	7150
$Eu^{+3}-4f^6$	6130	5120	6210	6250	5910	5900
				7150	7060	7100
$Gd^{+3}-4f^7$	3140		3160	3100	—	3100
$Tb^{+3}-4f^8$	5400	5470	5440	5460	5410	5460
	4870					
	4950					
$Dy^{+3}-4f^9$	5380	5750	5720	4860	4710	4760
	5720			5840	5710	5780
$Ho^{+3}-4f^{10}$	5500	5500	5470	N.D.*	N.D.*	N.D.*
			5560			
	4720					
$Er^{+3}-4f^{11}$	5320	5530	5270			
	5590	5590	5440	4020	4010	4010
$Tm^{+3}-4f^{12}$	N.D.*	N.D.*	3680	3460	—	3480
			4610			

\* Not detected.

Table III. Comparison of  $4f^6$  transitions responsible for fluorescence

Transitions	$Y_2O_3:Eu$ (cubic)		$YPO_4:Eu$ (Tetragonal)	
	Lines observed $cm^{-1}$	Relative energy %	Lines observed $cm^{-1}$	Relative energy %
$^3D_0 \rightarrow ^7F_4$	14,030	3.4	14,030	24.6
$^3D_0 \rightarrow ^7F_3$	15,270	2.7	15,130	3.9
$^3D_1 \rightarrow ^7F_4$	15,800	12.2	16,050	27.0
$^3D_0 \rightarrow ^7F_2$	16,310	68.1	16,290	12.9
$^3D_0 \rightarrow ^7F_1$	16,860	9.5	16,750	30.0
$^3D_0 \rightarrow ^7F_0$	18,660	4.1	19,160	1.6

### REFERENCES

- F. A. Kroger and J. Baker, *Physica*, **8**, 628 (1941).
- H. Lange, *Ann. Phys.*, **32**, 361 (1938).
- R. S. Feigelson, *J. Am. Ceram. Soc.*, **47**, 257 (1964).
- A. Brill and W. L. Wanmaker, *This Journal*, **111**, 1363 (1964).
- L. H. Brixner and P. A. Fluorney, *ibid.*, **112**, 303 (1965).
- W. Florence, *Jahrb. Mineral.*, **II**, 102 (1898); see also M. A. Dubein, *Compt. rend.*, **107**, 622 (1888).
- M. K. Carron, C. R. Naeser, H. J. Rose, and F. A. Hildebrand, U. S. Geol. Survey Bull., **1036N**, 253 (1958).
- M. K. Carron, M. E. Morse, and K. J. Murata, *Am. Mineral.*, **43**, 985 (1958).
- R. C. L. Mooney, *J. Chem. Phys.*, **16**, 1003 (1948).
- R. C. L. Mooney, *Acta Cryst.*, **3**, 337 (1950).
- H. Schwartz, *Z. anorg. u. allgem. Chem.*, **323**, 44 (1963).
- R. C. Ropp, *This Journal*, **111**, 311 (1964).
- R. C. Ropp *ibid.*, **112**, 181 (1965).
- R. C. Ropp, Proceeding of the Fifth Rare Earth Conference Ames, Iowa (Sept. 1965), To be published.
- G. H. Dicke and L. A. Hall, *J. Chem. Phys.*, **25**, 465 (1957).
- C. K. Jorgensen, Proceedings of the Fifth Rare Earth Conference, Ames Iowa (1965), To be published; See also H. J. Borchardt, *Loc. cit.* (1965).
- R. C. Ropp, E. E. Gritz, P. H. Haberland, and D. E. U. Ridout, *Electrochem. Technol.*, **4**, 24 (1966).
- R. C. Ropp, *This Journal*, **115**, 531 (1968).
- G. H. Dieke and H. M. Crosswhite, *Appl. Optics*, **2**, 675 (1963).
- D. S. McClure and Z. J. Kiss, *J. Chem. Phys.*, **39**, 325 (1963).
- G. Blasse, *ibid.*, **45**, 2356 (1966).
- R. C. Ropp, *Ill. Eng.*, **60**, 530 (1965).

# Growth of ZnSe-ZnTe Solid Solutions in Te<sub>2</sub> Atmosphere

M. Aven, R. B. Hall,<sup>1</sup> and J. S. Prener\*

General Electric Research and Development Center, Schenectady, New York

## ABSTRACT

The solid-vapor equilibria in the Zn-Se-Te system are examined under conditions of near-stoichiometry and under excess chalcogen pressure. It is shown that the best conditions for growing ZnSe<sub>x</sub>Te<sub>1-x</sub> crystals of uniform composition occur in the presence of intentionally added excess Te. The crystallographic and compositional characteristics of doped and undoped ZnSe<sub>x</sub>Te<sub>1-x</sub> crystals grown in vacuum and in the presence of excess Te are described.

There are nine possible ternary compound combinations involving a pair of Zn or Cd chalcogenides. All of these, with the exception of CdS-CdTe and ZnS-ZnTe have been reported to be miscible in the solid state in all proportions (1). The combinations having a common chalcogen atom, *e.g.*, ZnS-CdS (2) or ZnSe-CdSe (3) have been grown from the vapor phase as single crystals without serious segregation problems during the growth. Of the combinations having a common metal, the sulfo-selenides, *e.g.*, CdS-CdSe (4, 5), have also been obtained in unsegregated single crystal form. The seleno-tellurides, *i.e.*, CdSe-CdTe (6) and ZnSe-ZnTe (7-10), on the other hand, have shown considerable tendency toward segregation into Se and Te-rich components during growth from both the melt and vapor phase. Some improvement in vapor phase synthesis of ZnSe-ZnTe crystals was achieved by a two-step procedure (11) in which polycrystalline but relatively unsegregated boules were first grown by a modified Piper-Polich technique (12) using a fast growth rate (~0.4 mm/hr), followed by their epitaxial regrowth on ZnSe single crystal seed plates at a slower growth rate (~0.1 mm/hr). Although boules having reasonably uniform single crystalline sections as large as 0.3 cm<sup>3</sup> had been grown by this technique, the poorly defined relationship between the composition of the charge and the grown crystal, and the tendency toward polycrystallinity in the last-grown end of the boule made it desirable to look for better techniques for the growth of ZnSe<sub>x</sub>Te<sub>1-x</sub> crystals. The incentive for this effort has been the unique property of ZnSe<sub>x</sub>Te<sub>1-x</sub> among the wide band gap II-VI compounds of being synthesizable in both p- and n-type forms, which makes it suitable as a material for light-emitting and semiconducting p-n junction devices.

The present report will describe a vapor phase synthesis method in which ZnSe<sub>x</sub>Te<sub>1-x</sub> crystals are grown in an excess Te atmosphere using a very small temperature gradient. The method has yielded boules having good compositional uniformity, reproducibility in the Se/Te ratio, and very few large angle grain boundaries. It will be shown that these results cannot be derived from equilibrium thermodynamics of the ZnSe<sub>x</sub>Te<sub>1-x</sub> solid-vapor system, and that kinetic factors have to be considered in trying to understand the behavior of the system.

## Experimental Technique

The starting materials for the ZnSe<sub>x</sub>Te<sub>1-x</sub> crystal growth have been ZnSe powder obtained from GE Chemical Products Plant, Merck Company, Eagle-Picher Company, or synthesized in this Laboratory; and ZnTe powder obtained from Eagle-Picher Company or synthesized in this Laboratory. No significant dif-

ferences in the growth habit or crystalline perfection were found between the crystals grown from the materials obtained from these various sources.

The powders were dry mixed by passing them a few times through a No. 90 mesh silk screen, and pre-fired at 850°C in flowing purified H<sub>2</sub> for 1-2 hr. If desired, nonvolatile dopants such as Li were added to the powder mix in the form of aqueous solutions prior to the H<sub>2</sub>-firing step. Volatile dopants such as P were best added during the next step, which involved sintering the pre-fired powder in closed tubes under a Te pressure of about 5 x 10<sup>-2</sup> atm. The sintering, performed at temperatures between 925° and 1025°C for times ranging from 60 to 80 hr, increased the bulk density of the pre-fired powder from about 40% to between 80 and 95% of the bulk density of the ZnSe<sub>x</sub>Te<sub>1-x</sub>. The sintered powder compact was then transferred to a growth tube containing a ZnSe<sub>x</sub>Te<sub>1-x</sub> seed crystal, and enough Te to give about 5 x 10<sup>-2</sup> atm Te pressure at the growth temperature. The tube was evacuated, the charge and the seed positioned at the opposite ends of the tube, and the system transferred to the growth furnace.

As shown in Fig. 1, the initial position of the tube in the growth tube was such as to effect a thermal etching of the seed crystal, the temperature difference between the seed end and the charge end of the tube being approximately 7°C. After about one quarter of the seed had etched away, the tube was repositioned, with the seed now in a region approximately 5°C cooler than the bulk of the charge. In this position growth on the seed occurred at the rate of approximately 100 mg/day in 7 mm ID growth tubes and 200 mg/day in 10 mm ID growth tubes at 5 x 10<sup>-2</sup> atm Te pressure. A few runs attempted at higher Te pressures showed that the growth was extremely slow under such conditions.

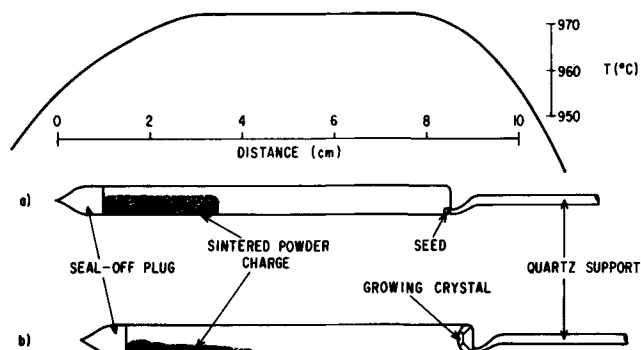


Fig. 1. Temperature profile, geometry of the growth tube, and the location of the charge and the seed in (a) the seed etch position, and (b) the growth position. Tube diameter, 7 mm; tube length, 7.5 cm; weight of charge, 2g.

<sup>1</sup> Present address: University of Delaware, Newark, Delaware.

\* Electrochemical Society Active Member.

The temperature gradient between the seed and the charge was kept low for two reasons. First, in order to have the system as close as possible to thermodynamic equilibrium conditions (see Discussion) large temperature gradients were to be avoided. Second, the minimum temperature difference at which spontaneous nucleation was found to occur is 18°C. Hence, in order to avoid spurious nucleation on the walls of the quartz tube and to have the growth confined exclusively to the seed crystal, the temperature gradient between the seed and the charge had to be kept below 18°C. Small temperature gradients for the closed tube growth of II-VI compound crystals have also been recommended by Shiozawa and Jost (3) on the basis of their experience with the growth of ZnSe-CdSe solid solutions.

### Results

Table I intercompares the starting compositions, the x-ray lattice constants, and the compositions of the grown crystals of a few representative growth runs in the presence and in the absence of excess Te. The relative amounts of Se and Te in the grown crystals were calculated from their lattice constants on the basis of the data of Larach *et al.* (13). The lattice constants were determined from x-ray powder patterns on approximately 5 mg (crushed) pieces cut from the grown boules. The first line in the table represents data obtained for the remaining charge, and the nose and the rear portion of a 1.2 cm long crystal having a diameter of about 2 mm. The constancy of the  $x$ -values over this distance demonstrates the uniformity in composition parallel to the growth direction. The next line of data is for a flat cylinder-shaped crystal 3 mm thick and 7 mm in diameter, with samples taken from its upper, middle, and lower portions. The close agreement between the values of  $x$  for these samples indicate that the composition is also uniform in the direction perpendicular to the direction of growth. The third line, representing the data for a crystal grown without the addition of extra Te, shows the large disparity between a piece taken from the left-over charge and two portions of the grown crystal. A significant variation in composition is also seen in the data for a crystal grown without the addition of extra Te, but under  $5 \times 10^{-2}$  atm pressure of argon. The beneficial effect of the Te addition on the uniformity of composition is also evidenced by the considerably sharper x-ray diffraction lines for the first two crystals (standard deviations in the lattice constant determinations for the individual pieces range from 0.0002 to 0.0006 Å) as compared with the third (standard deviation 0.002 Å).

Figure 2 shows a photograph of a ZnSe<sub>0.30</sub>Te<sub>0.70</sub> crystal. It was grown in a direction approximately normal to the plane of the photograph. The large face on the right is a (110) face; its Laue spot pattern, shown in Fig. 3 demonstrates a fairly good short range crystalline perfection. The growth steps clearly visible on this face indicate that the growth of the crystal is occurring in the  $\langle 110 \rangle$  direction, having possibly started from a screw dislocation at the apex of the triangular area at the right hand side of the (110) face [cf. ref. (3)].

Figure 4 illustrates the relationship between the initial compositions of doped and undoped mixed powders of ZnSe and ZnTe, and the compositions of the boules grown from them. There appears to be no

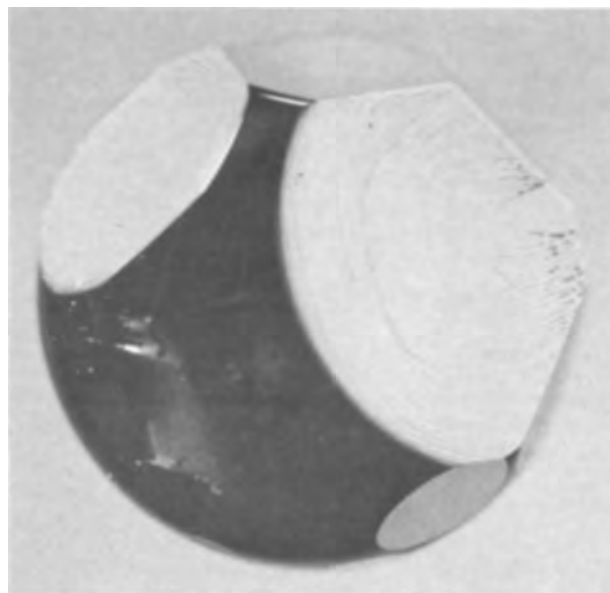


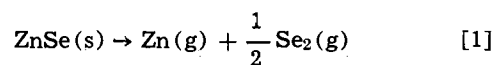
Fig. 2. Photomicrograph of a ZnSe<sub>0.30</sub>Te<sub>0.70</sub> crystal. The faces at the right and upper left are (110), the one on top is (100). Magnification, 10X.

systematic difference between the behavior of the doped and undoped crystals. All points lie below the (dashed) line representing equal  $x$  values in the charges and the grown crystals, indicating that the crystals have always a somewhat higher Te content than the charge from which they were grown. This may be a consequence of having had to make a compromise between the maximum tolerable Te pressure and a reasonable growth rate (higher Te pressures presumably favoring a closer correspondence between the charge and crystal compositions). The solid line represents a least squares fit of the data and the points corresponding to pure ZnTe and ZnSe to a polynomial of the form  $x_c = a + bx_p + cx_p^2$ , where  $x_c$  indicates the composition of the grown crystal, and  $x_p$  that of the mixed powders of ZnSe and ZnTe. The standard deviation of the data points from this line ( $a = 0.0063$ ,  $b = 0.673$ ,  $c = 0.319$ ) is 0.03.

### Discussion

The most important quantity characterizing the evaporation rate of a solid is the magnitude of the constant  $K_p$  which expresses the equilibrium between the solid and its vapor.

Investigations by several workers (14, 15) have shown that the vapor over subliming binary II-VI compounds consists almost entirely of separate metal and chalcogen species, with no evidence of any molecular compounds. The equilibrium between solid ZnSe and the vapor phase over it can then be written as<sup>2</sup>



The equilibrium constant for this reaction is

$$K_p^{\text{ZnSe}} = p_{\text{Zn}} \cdot p_{\text{Se}_2}^{1/2} \quad [2]$$

<sup>2</sup> For the present discussion we will neglect the presence of the higher molecular weight Se molecules, i.e., Se<sub>4</sub>, Se<sub>6</sub>, Se<sub>8</sub>, etc.

Table I. Lattice constant and composition values of some ZnSe<sub>x</sub>Te<sub>1-x</sub> crystals

Starting composition (x)	Pressure of excess Te or Ar (atm)	Lattice constant (Å)				Composition (x)			
		Charge	Piece A	Piece B	Piece C	Charge	Piece A	Piece B	Piece C
0.30	$5 \times 10^{-2}$ Te	5.9731	5.9848	5.9809	—	0.31	0.28	0.29	—
0.30	$5 \times 10^{-2}$ Te	—	5.9731	5.9773	5.9743	—	0.31	0.30	0.31
0.30	None	5.769	6.064	5.996	—	0.78	0.09	0.26	—
0.55	$5 \times 10^{-2}$ Ar	5.79	5.97	6.00	—	0.74	0.32	0.25	—

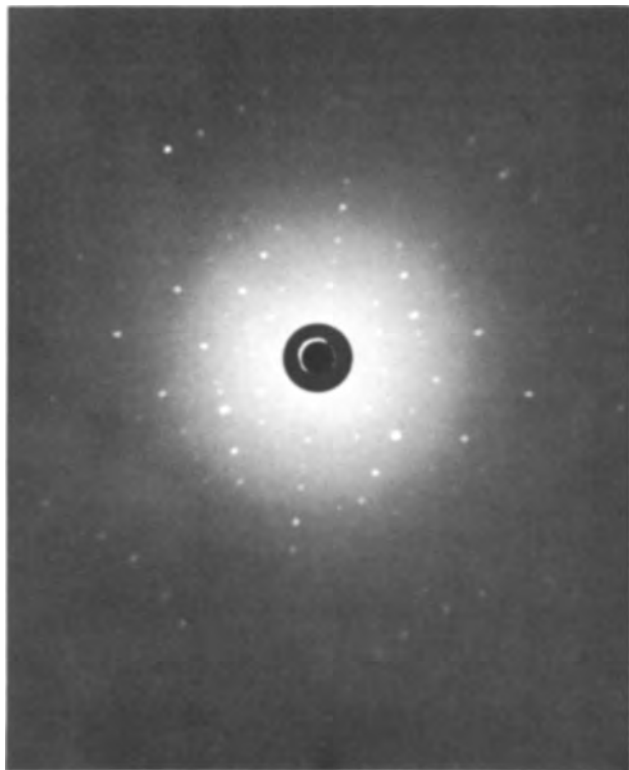


Fig. 3. X-ray diffraction pattern of a (110) face of the  $\text{ZnSe}_{0.30}\text{Te}_{0.70}$  crystal shown in Fig. 2.

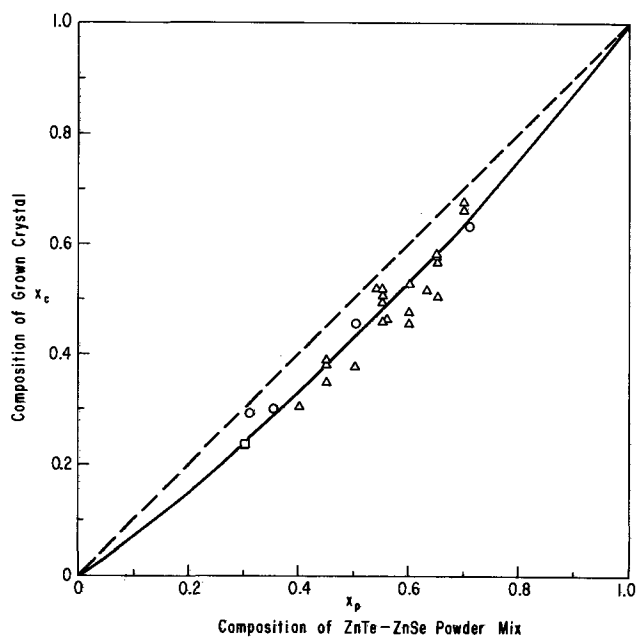
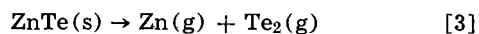


Fig. 4. Relationship between the initial composition of the mixed powders of ZnSe and ZnTe,  $x_p$ , and the composition of the crystals grown from them,  $x_c$ . Circles, undoped; triangles, doped with P; square, doped with Li. The dashed line corresponds to the relationship  $x_c = x_p$ , the solid line represents a least squares fit to  $x_c = a + bx_p + cx_p^2$ .

Similarly, for ZnTe, we have



$$K_p^{\text{ZnTe}} = p_{\text{Zn}} \cdot p_{\text{Te}_2}^{1/2} \quad [4]$$

Table II lists the equilibrium constants,  $K_p$ , at 970°C for the chalcogenides of Zn and Cd. Examination of the equilibrium constants for the pairs ZnS-ZnSe or CdS-CdSe, for example, shows that they are roughly

Table II. Equilibrium constants ( $K_p = p_{\text{Met.}} \cdot p^{1/2}_{\text{Chalc.}}$ ) Zn and Cd chalcogenides

Compound	( $K_p$ ) 970°C
ZnS	$2.0 \times 10^{-6}$
ZnSe	$4.7 \times 10^{-6}$
CdS	$3.7 \times 10^{-4}$
ZnTe	$5.0 \times 10^{-4}$
CdSe	$5.1 \times 10^{-4}$
CdTe	$4.0 \times 10^{-3}$

within a factor of two of each other. This indicates that the volatilities of the two compounds making up the pair are very close to each other, and that there should be no serious segregation problems in growing  $\text{ZnS}_x\text{Se}_{1-x}$  or  $\text{CdS}_x\text{Se}_{1-x}$ . Indeed, as was mentioned in the introduction, these solid solutions have been obtained in good quality single crystal form. The equilibrium constants for ZnSe and ZnTe, on the other hand, differ by almost a factor of a hundred, indicating that these compounds have quite different volatilities.

Suppose we have a quantity of  $\text{ZnSe}_x\text{Te}_{1-x}$ , with, say,  $x = 0.5$  in a sealed evacuated tube. To the first approximation, the vapor pressures of Zn and  $\text{Te}_2$  can be assumed to be equal to those over the more volatile compound making up the solid solution, i.e., ZnTe. At 970°C these vapor pressures are  $p_{\text{Te}_2} = 4.1 \times 10^{-3}$  atm and  $p_{\text{Zn}} = 8.2 \times 10^{-3}$  atm, respectively. This relatively high pressure of Zn will, by virtue of Eq. [2], suppress the pressure of  $\text{Se}_2$  to about  $10^{-7}$  atm. The saturated vapor over the evaporating  $\text{ZnSe}_x\text{Te}_{1-x}$  will thus contain Zn and  $\text{Te}_2$  in the ratio of 2/1, whereas the Zn to  $\text{Se}_2$  ratio is about  $2/10^{-4}$ . The consequence of this is, of course, the preferential evaporation of ZnTe out of the charge, with a corresponding enrichment with respect to ZnSe, as has been found to be the case experimentally.<sup>3</sup>

This qualitative conclusion is in accord with thermodynamic calculations based on a model which assumes that (i) both the evaporating solid and the growing crystal are in thermodynamic equilibrium with the gas phase in its immediate vicinity, (ii) there is no gradient in total pressure, (iii) Zn,  $\text{Se}_2$ , and  $\text{Te}_2$  are the predominant gaseous species, and (iv) that the  $\text{ZnSe}_x\text{Te}_{1-x}$  is close to stoichiometric. The solution of the integral equation expressing the composition of the growing crystal as a function of the fraction of charge evaporated based on this model predicts that the growing crystal should start out considerably richer in ZnTe than the initial composition of the evaporating charge and that, as the growth proceeds, the later-grown parts of the crystal should become increasingly richer in ZnSe. If an appropriate term expressing the presence of excess Te is introduced into the integral equation, it is found, however, that the addition of Te makes no difference in the degree of segregation.<sup>3</sup> This contradicts the experimental evidence presented.

This finding as well as the past experience of several workers shows that care has to be exercised in applying equilibrium thermodynamics to the growth of II-VI compounds. As shown recently by Toyama (16) the rate of material transport in the growth of II-VI compounds can either be limited by the vaporization and condensation processes, or by the gaseous diffusion along the growth tube. The vaporization rate can generally not be calculated from the Herz-Knudsen-Langmuir equations using equilibrium constant data. For CdS, for example, Somorjai and Epsen (17) find that its vacuum evaporation rate is only about a tenth of that calculated from the equilibrium constant and is a strong function of the stoichiometry of the compound. The suggested reasons for this are

<sup>3</sup> We are not presenting the development of the appropriate mathematical formalism in this paper because, although quite straightforward, it involves quite lengthy algebraic manipulations and because it did not lead to a realistic representation of the system studied.

surface reactions involving rearrangement, association and dissociation of surface atoms before vaporization. The surface reaction is often the slow step in the evaporation sequence and is followed by rapid desorption of surface species. Similar interactions involving among other things, temperature and pressure-dependent "sticking coefficients," occur in the condensation process at the cold end of the growth tube. These relationships are expected to be even more complex when more than two atomic species are present, as is the case with solid solutions, and when the deviation from stoichiometry is as large as is encountered in tellurides under excess Te pressure.

In examining the possible effect of excess Te on the way in which thermodynamic equilibrium is established in the ZnSe<sub>x</sub>Te<sub>1-x</sub> system, the role of the SeTe gaseous species should be considered. The phase diagram of the Se-Te system indicates miscibility in all proportions in the liquid state. This suggests that the vapor phase over liquid Se-Te solutions contains SeTe molecules in concentration comparable to that of Se<sub>2</sub> and Te<sub>2</sub>. As far as the ZnSe<sub>x</sub>Te<sub>1-x</sub> system is concerned, it can be shown that the ratio of  $p_{\text{Se}_2}$  to  $p_{\text{Te}_2}$  is

$$\frac{p_{\text{Se}_2}}{p_{\text{Te}_2}} = (K_p^{\text{ZnSe}}/K_p^{\text{ZnTe}})^2 (x/1-x)^2$$

whereas the ratio of  $p_{\text{SeTe}}$  to  $p_{\text{Te}_2}$  can be written as

$$\frac{p_{\text{SeTe}}}{p_{\text{Te}_2}} = (K_p^{\text{ZnSe}}/K_p^{\text{ZnTe}}) (x/1-x) K_p^{\text{Se}_2} K_p^{\text{Te}_2} / (K_p^{\text{SeTe}})^2$$

where

$$K_p^{\text{Se}_2} = p_{\text{Se}}/p_{\text{Se}_2}^{1/2}$$

$$K_p^{\text{Te}_2} = p_{\text{Te}}/p_{\text{Te}_2}^{1/2}$$

$$K_p^{\text{SeTe}} = p_{\text{Se}}^{1/2} p_{\text{Te}}^{1/2} / p_{\text{SeTe}}^{1/2}$$

Using these equations at 970°C for  $x = 0.5$  gives  $p_{\text{Se}_2}/p_{\text{Te}_2} = 10^{-4}$ , and  $p_{\text{SeTe}}/p_{\text{Te}_2} = 10^{-2}$  [ $K_p^{\text{Se}_2} K_p^{\text{Te}_2} / (K_p^{\text{SeTe}})^2$ ]. As  $K_p^{\text{SeTe}}$  is not available from literature, we will consider the cases where  $(K_p^{\text{Se}_2} K_p^{\text{Te}_2})^{1/2} / K_p^{\text{SeTe}} < 1$  and  $(K_p^{\text{Se}_2} K_p^{\text{Te}_2})^{1/2} / K_p^{\text{SeTe}} > 1$ . In the former case  $p_{\text{SeTe}}/p_{\text{Te}_2} < 10^{-2}$ , i.e., the ratio of the total Se to total Te in the gas phase is still very small. If, however,  $(K_p^{\text{Se}_2} K_p^{\text{Te}_2})^{1/2} / K_p^{\text{SeTe}}$  should be substantially larger than unity, the ratio  $p_{\text{SeTe}}/p_{\text{Te}_2}$  may get large enough to provide a better balance between the supply of Se and Te to the gas phase, with an accompanying reduction in the degree of segregation. Since the addition of Te cannot change the magnitude of the equilibrium constants this would, of course, be true in the presence as well as in the absence of excess Te, if the system is close to equilibrium in both cases.

It is possible, however, that there exist kinetic limitations to the formation of SeTe species in the vacuum growth conditions. It could be, for example, that in the absence of excess Te the formation of SeTe species by a surface reaction is improbable because the surface Zn-Se bonds are much stronger than the surface Zn-Te bonds, and the probability of formation of SeTe by a gaseous collision between Se<sub>2</sub> and Te<sub>2</sub> molecules is low because of low partial pressure ( $10^{-7}$  atm) of Se<sub>2</sub>. The addition of excess Te would increase both the gaseous collision frequency between Se<sub>2</sub> and Te<sub>2</sub>, and may additionally modify the reactions on or near the surface of the evaporating charge in such a way as to promote the formation of the SeTe species.

Two other factors besides the enhanced formation of the SeTe species may contribute to the improvement of the uniformity of ZnSe<sub>x</sub>Te<sub>1-x</sub> crystals grown in Te atmosphere. First, calculations have shown that under equilibrium conditions the tendency to segregate decreases with decreasing temperature difference between the charge and the growing crystal. As the presence of a denser gas atmosphere is expected to enhance the heat exchange between the charge and the crystal, the temperature gradient in the presence of Te should be less than in vacuum. That the segregation

was not quite as severe in argon atmosphere as it was in vacuum (see Table I) may be due to the same effect. Second, it has been demonstrated (18) that chalcogen self-diffusion rate in II-VI compounds increases with the vapor pressure of chalcogen over the solid compound. The intermixing of Te and Se atoms in the growing crystal by solid state diffusion would therefore proceed at a faster rate in Te atmosphere than in vacuum. Which of these factors is the dominant one will have to be resolved by further experimental work.

### Summary

When ZnSe<sub>x</sub>Te<sub>1-x</sub> crystals are grown in vacuum, one finds that the first-grown portions of the crystals are invariably richer in ZnTe than the later grown portions and that the charge becomes increasingly richer in ZnSe as the growth proceeds. This undesirable feature can be largely eliminated by growing the crystals with deliberate addition of excess Te to the growth tube. Various sections of the crystals grown under such conditions were subjected to lattice constant determination by x-ray diffraction analysis, and were found, in most cases, to differ from each other by no more than  $x = \pm 0.01$ . Only slight enrichment of the grown crystals with respect to ZnTe as compared to the charge material was observed. The degree of enrichment, as well as the uniformity in composition of the grown crystals was found to be independent of the species, and the concentration of the sometimes added dopants, Li and P.

### Acknowledgments

The ideas presented in this paper evolved from discussions with Professors J. Mitchell and H. H. Woodbury, whose contribution to the present work is herewith gratefully acknowledged. We also want to thank L. M. Osika for the extensive x-ray work on the ZnSe<sub>x</sub>Te<sub>1-x</sub> crystals carried out under his supervision. W. Garwacki assisted in the preparation of the ZnSe and ZnTe powders, and in the growth of the ZnSe<sub>x</sub>Te<sub>1-x</sub> crystals. The work reported in this paper was sponsored in part by the AFCRL Contract No. 19(618)-4976.

Manuscript received April 19, 1968.

Any discussion of this paper will appear in a Discussion Section to be published in the June 1969 JOURNAL.

### REFERENCES

1. See, e.g., M. R. Lorenz in "Physics and Chemistry of II-VI Compounds," M. Aven and J. S. Prener, Editors, p. 112, North-Holland, Amsterdam (1967).
2. See, e.g., E. A. Davis, R. E. Drews, and E. L. Lind, *Solid State Comm.*, **5**, 573 (1967), and E. L. Lind and E. A. Davis, Submitted to *This Journal*.
3. L. R. Shiozawa and J. M. Jost, Research on II-VI Compound Semiconductors, Final Technical Report, Contract No. AF-33(657)-7399, U.S.A.F. Aeronautical Research Laboratories, 1965, p. 44.
4. L. R. Shiozawa, S. S. Devlin, and J. M. Jost, Research on II-VI Compound Semiconductors, 9th Quarterly Report, Contract No. AF-33(616)-3923, U.S.A.F. Aeronautical Research Laboratories, 1959.
5. N. I. Vitrikhouskii and I. B. Mizetskaya, *Soviet Phys. Solid State*, **1**, 912 (1959).
6. A. D. Stuckes and G. Farrell, *J. Phys. Chem. Solids*, **25**, 477 (1964).
7. A. G. Fischer and W. H. Fonger, Investigation of Two-Carrier Electroluminescence, Scientific Report No. 3, U.S.A.F. Cambridge Research Laboratories, Contract No. AF-19(628)-3866, 1965, p. 6. This report describes the growth of ZnSe<sub>x</sub>Te<sub>1-x</sub> crystals from melt, using a rapid quench technique to prevent segregation.
8. M. Aven and W. Garwacki, *Appl. Phys. Letters*, **5**, 160 (1964).
9. G. Mandel, F. F. Morehead, and P. R. Wagner, II-VI Laser Material Study, Final Report, Project



- DEFENDER Contract NONR-4216(00), 1964, p. 66.
10. Y. Tsujimoto, T. Nakajima, and Y. Onodera, Proc. Joint Meeting Jap. Phys. Soc. and Jap. Soc. Appl. Phys. Tokyo, May 1967.
11. M. Aven, R. N. Hall, L. M. Rosenberg, and H. H. Woodbury, New Solid State Device Concepts, Scientific Report No. 3, U.S.A.F. Cambridge Research Laboratories, Contract No. AF-19(628)-4976, 1965, p. 11.
12. W. W. Piper and S. Polich, *J. Appl. Phys.*, **32**, 1278 (1961).
13. S. Larach, R. E. Shrader, and C. F. Stocker, *Phys. Rev.*, **108**, 587 (1957).
14. R. F. Brebrick and A. J. Strauss, *J. Phys. Chem. Solids*, **25**, 441 (1964).
15. P. Goldfinger and M. Jeunehomme, *Trans. Faraday Soc.*, **59**, 2851 (1963).
16. M. Toyama, *Jap. J. Appl. Phys.*, **5**, 1204 (1966).
17. G. A. Somorjai and D. W. Epsen, *J. Chem. Phys.*, **11**, 1389 (1964); *ibid.*, p. 1394.
18. See, for example, H. H. Woodbury in "II-VI Semiconducting Compounds," Proceedings Internat. Conf., Providence, R. I., 1967, D. G. Thomas, Editor, W. A. Benjamin, New York, p. 244.

## Epitaxial Growth of Zinc- and Cadmium-Doped Gallium Phosphide by Gallium Chloride Vapor Transport

Lars C. Luther and D. D. Roccasecca

*Bell Telephone Laboratories, Incorporated, Murray Hill, New Jersey*

### ABSTRACT

Zinc- and cadmium-doped gallium phosphide crystals have been grown by an open tube halogen transport process at 805°-875°C. The zinc-doping varied from  $10^{17}$  to  $10^{19}$  cm<sup>-3</sup> while cadmium could be incorporated at levels ranging from  $10^{16}$  to  $10^{18}$  cm<sup>-3</sup>. We observed a linear dependence of zinc and cadmium concentration on the partial pressure of the dopant in the growth ambient. This linear dependence is evidence for a nonequilibrium, kinetically controlled process. The structural and electrical properties are compared with the properties of crystals grown by the wet hydrogen process. A study of the gallium consumption as a function of experimental variables yielded a Ga to PCl<sub>3</sub> ratio of  $2.5 \pm 0.2$ , independent of PCl<sub>3</sub> feed rate and carrier gas flow. A ratio of 2.64 is predicted from thermodynamic data provided the species GaCl<sub>2</sub>(g) can be neglected in the initial reaction between HCl and Ga.

At the present time the open tube vapor transport technique used to produce large single crystals of gallium phosphide relies on two sets of volatile gallium compounds: the oxide (Ga<sub>2</sub>O) and the halides. In the moist hydrogen system (1) the oxide is the transporting medium. For the halogen systems (2-5) conditions are created to preferentially form the mono-halide which subsequently disproportionates to give the phosphide and the trihalide. In this study of the chloride-phosphide system the reactants were phosphorus trichloride and elemental gallium.

### Experimental

Pure phosphorus trichloride was obtained from Asarco Intermetallics Company (6). Other starting materials were 99.9999% gallium from Alusuisse and zinc and cadmium from United Mineral and Chemical Company, both 99.9998%. Tank hydrogen was used as carrier gas. The apparatus consists of a quartz furnace tube connected by means of ground quartz joints and Beckman Teflon tube fittings to a phosphorus trichloride bubbler and flowmeters. A schematic is given in Fig. 1. The hydrogen carrier gas was passed over a platinum catalyst followed by a phosphorus pentoxide absorber to suppress the oxygen content. A high loss, low temperature furnace was placed upstream of the one-zone principal furnace to vaporize the dopant. The partial pressure of the dopant was determined from weight loss measurements of the dopant source boat (quartz). The gallium source (50g) was heated in a 125 mm boron nitride boat.

The gallium arsenide seed crystals supplied by Monsanto and Asarco Intermetallics Company, were in the form of (111) oriented 0.4 mm thick slices cut from undoped, boat-grown ingots. Preparation of the seed crystals consisted of a 5-12 min etch at 85°C in mixture of concentrated sulfuric acid, water, and 30%

hydrogen peroxide (3:1:3). During the etching about 0.1 mm of material was removed. Often a highly polished (111) Ga surface was obtained while the (111) As face became wavy. A similar etchant (3:1:1) is often used under milder conditions to produce etch pits on the gallium face in order to differentiate between (111) faces. The more drastic conditions employed here result in a faster dissolution of material on both faces and reduce the preferential dissolution near imperfections. The primary objective of the etch was to remove mechanical damage. A highly perfect polish of the substrate was not deemed essential for epitaxial growth.

The seed crystals had the dimensions 32 by 16 mm. They were placed Ga-face up on an L-shaped quartz support at an angle of about 30° to the flow direction. Only the bottom and top edges of the crystal were in contact with the quartz support. The gallium boat

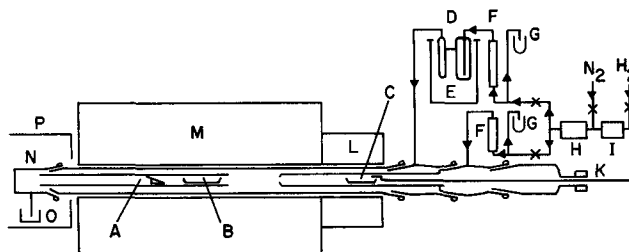


Fig. 1. Schematic diagram of apparatus for halogen transport of GaP. Arrows indicate direction of gas flow. A, GaAs seed; B, Ga boat; C, Cd boat; D, PCl<sub>3</sub> bubbler; E, Dewar; F, flowmeter; G, overflow pressure regulator; H, P<sub>2</sub>O<sub>5</sub> absorber; I, Pt catalyst; K, push rod; L, high loss furnace; M, principal furnace; N, bubbler cap; O, oil bubbler; P, exhaust.



was placed in a 21 mm ID quartz tube in a region corresponding to the flat zone of the furnace, 7.5 cm upstream of the seed. The 15 cm long flat zone was maintained at 935°C controlled to within  $\pm 1^\circ\text{C}$  while the seed spanned a temperature gradient of  $70^\circ\text{C}$  centered at  $840^\circ\text{C}$ . The quartz tube with gallium source and seed was pushed into the furnace with nitrogen flowing. The furnace tube was then closed with a bubbler cap. After a 10 min heat-up period the atmosphere in the furnace was changed to hydrogen and after an additional period of 10 min a  $\text{PCl}_3$ -carrying, second hydrogen stream which bypassed the cadmium or zinc source was admitted. The dopant source boat was pushed into the high loss furnace after allowing  $\frac{1}{2}$  hr of growth. Cadmium or zinc vapor is carried by the dry hydrogen stream into the main furnace where it is mixed into the  $\text{PCl}_3/\text{H}_2$  stream at about  $800^\circ\text{C}$  before passing over the gallium boat.

In a leak free system the atmosphere in the furnace would remain clear. Though a glass plate in the bubbler cap condensation of  $\text{GaCl}_2$  could be observed. Persistent formation of heavy white smoke after admission of  $\text{PCl}_3$  signalled the presence of oxygen or moisture and polycrystalline growth.

Unless effects of feed and flow rate variation were being studied the flow rates of the two feeding hydrogen streams were kept constant: 140 cc/min dry hydrogen and 100 cc/min hydrogen bubbled through  $0^\circ\text{PCl}_3$ . Epitaxial growth was usually allowed to continue for 6-10 hr during which a 1 mm thick layer was deposited under standard conditions. Longer runs proved unprofitable because large amounts of gallium chloride accumulated and clogged the reaction tube.

Flowmeters were calibrated by measuring the rate of motion of soap films in glass tubes. In separate experiments the vapor pressure of  $\text{PCl}_3$  was determined by weight loss to be 36 mm at  $0^\circ\text{C}$ . The hydrogen carrier gas was found to be saturated even at flow rates higher than any used for crystal growth.

A large number of experimental data on the rate of consumption of the two initial reactants, Ga and  $\text{PCl}_3$  was collected. The rate of consumption of Ga in mM/min was determined by dividing the weight loss of the source by the duration of the run. The  $\text{PCl}_3$  rate of consumption in mM/min was obtained from the average flow rate of hydrogen saturated with  $\text{PCl}_3$  at  $0^\circ\text{C}$ . In the presence of a liner tube with an estimated furnace tube clearance of 0.5 to 1 mm a small amount of HCl and  $\text{P}_4$  from the decomposition of  $\text{PCl}_3$  may bypass the gallium source and remain unreacted. Since the mole ratio of the reactants is an important characteristic of the system, special experiments were carried out in which the gallium boat and the seed were placed directly into the furnace tube. In four such runs in which the  $\text{PCl}_3$  feed rate was varied from 0.073 to 0.26 mM/min the Ga/ $\text{PCl}_3$  mole ratio did not deviate significantly from the mean of the ratios obtained in the experimental runs in which a liner tube was used.

An experimental analysis of the cool effluent gas in these special runs was made. The gas was passed through a dry ice trap to remove  $\text{GaCl}_3$  and the remaining HCl was absorbed in an alkaline solution. The total amount of unreacted HCl carried over in a run could then be determined by precipitation as  $\text{AgCl}$  and was found to correspond to a vapor pressure of  $3 \times 10^{-4}$  atm or to 0.5% of the reacted  $\text{PCl}_3$ .

### Results and Discussion

**Crystal growth and perfection.**—The best crystals grown by the halogen transport process were about 1 mm thick with  $45^\circ$  bevelled edges on the (111) A or Ga growth face as shown in the upper crystal of Fig. 2 together with a typical water vapor transported crystal. The as-grown halogen transported crystal is transparent because the GaAs substrate was etched off during the deposition process. The other crystal was lapped to remove the GaAs substrate. The pits seen on

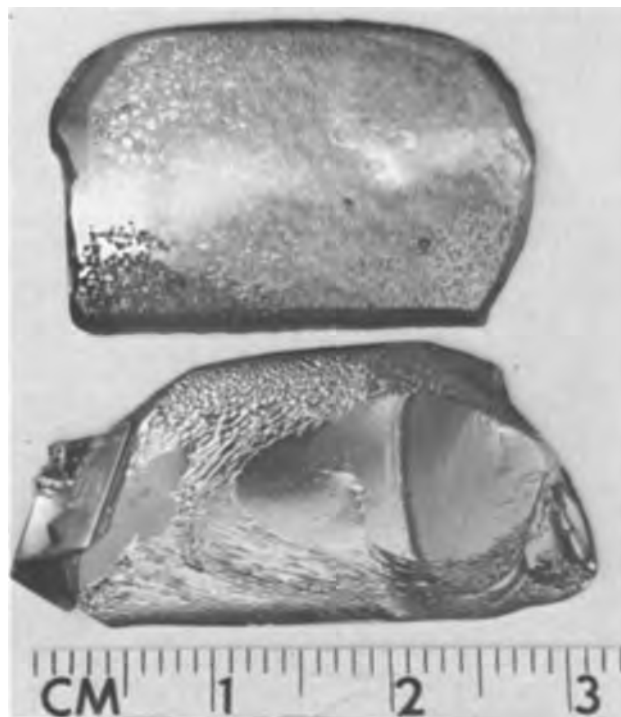


Fig. 2. Single crystals of GaP grown by vapor transport on GaAs seeds. The upper crystal is grown by halogen transport and is here shown as grown. The lower crystal is grown by the moist hydrogen method and displays typical flats, terraces and, at the left, non-epitaxial growth. The GaAs substrate has been removed from the lower crystal by lapping.

the lower left of the growth side of the halogen transported crystal are characteristic of the "hot" end. With higher  $\text{PCl}_3$  feed rates this pitting could be eliminated but instead polycrystalline growth occurred at the "cold" end. Note that the dense pitting seen in the upper left part is on the backside. Even the best "flats" grown by halogen transport have a mosaic structure characterized by relatively large flats inclined at small angles to an average plane. In comparison the flats developed in the wet hydrogen process are more nearly perfect but generally smaller.

Several crystals were grown on the (111) B or As face of seed crystals. Typically the final crystal face would show large, axially symmetric hillocks (a cobble stone, rather than fish scale pattern). In comparing epitaxial growth on the A and B faces a significant orientation effect on sulfur doping was noted. The sulfur was unintentionally introduced through the use of low-purity  $\text{PCl}_3$  in initial experiments. Crystals grown from the sulfur contaminated  $\text{PCl}_3$  were n-type with a carrier concentration between  $10^{16}$  and  $10^{17}$   $\text{cm}^{-3}$ . The C-line (7) due to sulfur appeared in the spectrum. With a cadmium pressure of several Torr, low mobility, p-type crystals could be obtained if epitaxial growth occurred on the A face. If, however, growth took place on the B face the epitaxial layer would be n-type. Thus from an atmosphere containing both sulfur and cadmium n- and p-type crystals can be grown depending upon seed orientation. A strong orientation effect on donor doping has previously been discussed by Groves (8).

Usually the epitaxial layer grown on the (111) A face was thicker at the cold end. In some cases it was twice as thick as the hot end. Since the seed crystal was oriented within  $\frac{1}{2}^\circ$  the final growth face was considerably off (111).

Inclusions were rarely observed in the halogen transported GaP and, in contrast to wet hydrogen transported material, voids were never encountered. The GaAs seed was extensively and irregularly etched and converted to a brittle layer of porous GaP. During

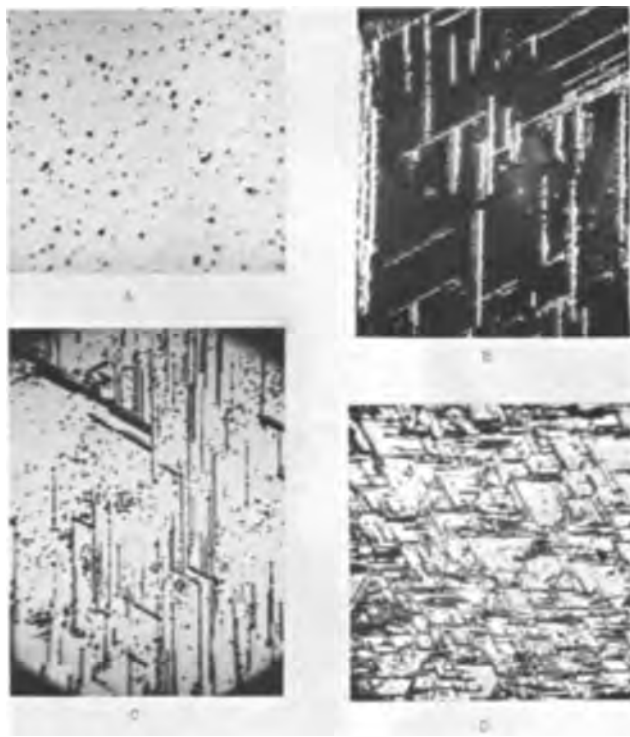


Fig. 3. Photomicrographs of etched GaP. The etchant is a mixture of hot chromic and hydrofluoric acids in the presence of silver ions. All magnifications ca. 60X. A, wet hydrogen transported, (111)B; B, halogen transported, (111)A, dark field; C, halogen transported, (111)A; D, halogen transported, (111)B, same crystal as C.

longer runs the seed evaporated completely and the exposed backside of the GaP crystal began to erode.

Figure 3 is a collection of photomicrographs of etched GaP surfaces. The etchant used is a mixture of 1g chromic acid in 2 ml of water, 1 ml hydrofluoric acid, and 8 mg silver nitrate (9). The crystals are etched for ½ to 1 hr at 90°C. Water vapor grown GaP (111) B faces shown in Fig. 3A respond to the etchant with individual etch pits. In Fig. 3B and C virgin (111) A faces of halogen transported GaP typically show rows of overlapping etch pits in two out of three symmetry directions with few randomly distributed individual etch pits. The (111) B face shown in Fig. 3D was prepared by lapping the heavily pitted backside of a halogen transported crystal, polishing it with chlorine bubbling through methanol, and then etching it in the chromic acid etchant as above.

The etch grooves appearing on micrographs Fig. 3B, 3C, and 3D probably correspond to stacking faults. Wet hydrogen transported material never showed such etch grooves on either growth or substrate face. We therefore conclude that wet hydrogen transported material possesses a higher degree of structural perfection. Comparison of micrographs Fig. 3C and 3D which show the response of the growth and substrate side of the same crystal suggests that there is a reduction in the number of stacking faults during growth. However, the difference in defect density may also have been brought about by a difference in the effectiveness of the etch to reveal faults on the two polar faces.

The higher degree of structural imperfection in the halogen transported GaP is perhaps related to the difference in growth conditions. The halogen transported crystals studied here were grown at a temperature 200°C lower than the moist hydrogen grown material. Since the moist hydrogen grown crystals also grow more slowly it was interesting to evaluate the effect of growth rate on etch behavior for halogen transported GaP. Here it was found that although the growth rate could be varied by a factor of ten no

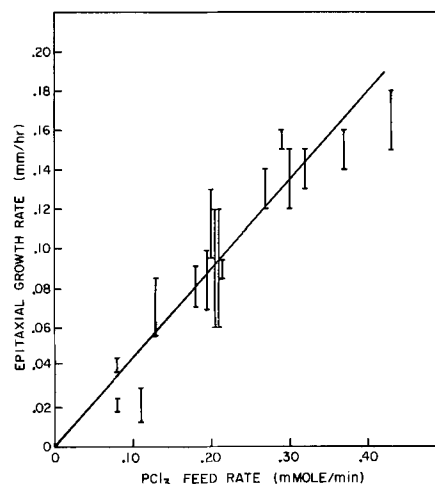


Fig. 4. Growth rate of epitaxial GaP under the following experimental conditions: seed temperature; 840°C in a gradient of 18°C/cm, carrier gas flow 0.240 l/min in a 21 mm ID quartz tube, PCl<sub>3</sub> feed rate variable.

significant change in the appearance of etched growth surfaces was observed.

The thickness of the epitaxial deposits was measured at different points and divided by the growth time in order to obtain an average growth rate. Experiments showed this to be a meaningful number. Two crystals grown at the same PCl<sub>3</sub> feed rate but over different periods of time (3 and 6 hr) gave the same growth rate. Figure 4 indicates that the macroscopic growth rate depends linearly on the PCl<sub>3</sub> feed rate even up to the highest feed rates used. Feed rates exceeding 0.4 mM/min tended to give polycrystalline deposits. The vertical spread in the data collected on Fig. 4 reflects the higher growth rates at the colder end of the crystal.

Resistance measurements of doped GaP crystals were made by the Van der Pauw method. The contacts used were Au and W wire pressure contacts to gallium dots or directly to the crystal. By applying d-c pulses the contacts could be made ohmic. The ohmic behavior of the contact resistances was verified by varying the applied current in the measuring circuit.

*Transport mechanism.*—In a recent paper Seki and Araki (10) have given a detailed theoretical analysis of the GaP-Cl<sub>2</sub>-H<sub>2</sub> system. They calculated the partial pressures of all important species [ignoring GaCl<sub>2</sub>(g)] and presented the results graphically as functions of temperature and hydrogen-chlorine ratio at a selected set of conditions. At high temperatures (>1100°K) only HCl, GaCl, P<sub>2</sub>, and P<sub>4</sub> were found to be present in the gas phase in significant amounts. At lower temperatures (<900°K) the species HCl, GaCl<sub>3</sub>, and P<sub>4</sub> predominated. In order to explain our data we have made a simplified analysis of the same system using the same sources (11-13) of thermodynamic information as Seki and Araki. This was necessary because their results were obtained for a set of representative conditions which differed somewhat from our experimental conditions.

By independently varying the flow rates of dry hydrogen and PCl<sub>3</sub>-saturated hydrogen the PCl<sub>3</sub> feed rate was varied while keeping the total carrier gas flow constant. Alternately the PCl<sub>3</sub> feed rate was kept constant while the total carrier gas flow rate was varied. The Ga/PCl<sub>3</sub> consumption ratios determined experimentally in these two sets of experiments are summarized on Fig. 5 and Table I. The ratio is independent of PCl<sub>3</sub> feed rate and total carrier gas flow rate. The average ratio determined from 34 measurements is 2.5 with a standard deviation of 0.2. The data from the special runs in which no liner tube was used are included on Fig. 5 and indicate that there is negli-

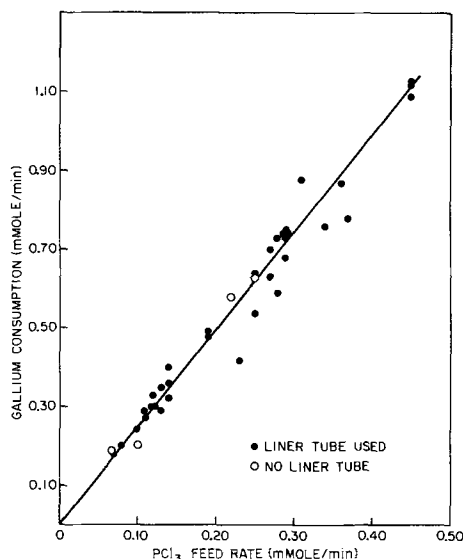


Fig. 5. Gallium/ $\text{PCl}_3$  consumption ratio as a function of  $\text{PCl}_3$  feed rate. The straight line drawn through the data points represents the average ratio 2.5. The standard deviation is 0.2.

gible bypass of reactants as discussed in the experimental section.

During a transport run the gallium source boat is heated in a phosphorus partial pressure several orders of magnitude higher than the decomposition pressure of GaP which is  $8 \times 10^{-6}$  atm at  $1200^\circ\text{K}$  (14). One might therefore have expected to find extensive conversion of gallium to GaP. When the gallium source is pulled out of the reaction zone after a run, a skin of GaP can be observed to form during cooling. However, upon digestion of the gallium it is found that there is no GaP precipitate in the source boat other than the skin on the surface. The weight of this skin corresponds closely to the solubility (14) of phosphorus in gallium at the source temperature. We can therefore rule out the possibility that conversion of gallium to GaP is prevented by slow diffusion of phosphorus in gallium. There is no GaP precipitate on or in the gallium during the run. This conclusion is important in the subsequent argument.

The  $\text{PCl}_3$  carried into the reaction chamber by the hydrogen carrier gas is decomposed according to the equation



Even at room temperature the equilibrium of this reaction lies far to the right. Slow kinetics, however, prevent phosphorus deposition in the cold zone of the apparatus. At higher temperatures the phosphorus tetramers dissociate



Table I. Gallium and  $\text{PCl}_3$  consumption rates and ratio vs. total carrier gas flow

Total carrier gas flow, cc/min	Gallium consumption, mM/min	$\text{PCl}_3$ consumption, mM/min	Mole ratio
180	0.69	0.28	2.5
175	0.73	0.29	2.5
190	0.70	0.27	2.6
220	0.64	0.25	2.6
225	0.63	0.25	2.5
260	0.54	0.25	2.2
315	0.74	0.29	2.6
320	0.74	0.29	2.4
325	0.68	0.29	2.4
360	0.63	0.27	2.3
365	0.73	0.28	2.6
380	0.75	0.29	2.6

From the phosphorus balance equation

$$p_{\text{PCl}_3} = 4p_{\text{P}_4} + 2p_{\text{P}_2} = \frac{36}{760} \frac{100}{240} \text{ atm} = 2 \times 10^{-2} \text{ atm}$$

which together with

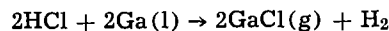
$$K_2 (1200^\circ\text{K}) = 10^{-2}$$

yields the pressures of the two species in the reaction zone

$$p_{\text{P}_2} = 5 \times 10^{-3} \text{ atm}$$

$$p_{\text{P}_4} = 2.5 \times 10^{-3} \text{ atm}$$

One of the initial reactions in the hot zone is undoubtedly



$$K_3 = \frac{p^2_{\text{GaCl}} p_{\text{H}_2}}{p^2_{\text{HCl}}} \quad [3]$$

At  $1200^\circ\text{K}$  the equilibrium coefficient is so large ( $10^4$ ) that one would expect quantitative conversion of the HCl provided the gallium source in the reaction zone is long enough. However, in the presence of phosphorus at a pressure higher than the decomposition pressure of GaP, solid GaP should coexist with the gallium. The following reaction must therefore be considered.



$$K_4 = \frac{p^2_{\text{GaCl}} p_{\text{H}_2} p_{\text{P}_2}}{p^2_{\text{HCl}}} \quad [4]$$

Let the superscript  $i$  denote incoming pressure while unscripted  $p$  denotes equilibrium pressure. If HCl and GaCl are the only chlorine-containing species in the reaction zone

$$p_{\text{HCl}} = p^i_{\text{HCl}} - p_{\text{GaCl}}$$

Typical experimental conditions are

$$p_{\text{H}_2} \simeq 1 \text{ atm}$$

$$p_{\text{P}_2} = 5 \times 10^{-3} \text{ atm}$$

and  $K_4(1200^\circ\text{K}) = 2.5 \times 10^{-1}$ . At equilibrium in the presence of solid GaP

$$p^i_{\text{HCl}} - p_{\text{GaCl}} = \frac{p_{\text{GaCl}} \times 1 \times (5 \times 10^{-3})^{1/2}}{(2.5 \times 10^{-1})^{1/2}}$$

$$p_{\text{GaCl}} = \frac{p^i_{\text{HCl}}}{1.14}, \quad p_{\text{HCl}} = 0.12 p^i_{\text{HCl}}$$

It is apparent from Eq. [4] that solid GaP will precipitate when the HCl pressure drops below the equilibrium value. Since this is not observed to happen in the experiment

$$p_{\text{HCl}}(\text{exp}) \geq 0.12 p^i_{\text{HCl}}$$

from which follows that the gallium consumption is

$$\frac{\text{moles Ga}}{\text{min}} \leq \frac{\text{moles PCl}_3}{\text{min}} 3(1-0.12)$$

or

$$\frac{\text{Ga}}{\text{min}} \leq 2.64 \frac{\text{moles}}{\text{min}}$$

$$\frac{\text{moles}}{\text{min}} \text{ PCl}_3$$

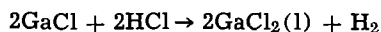
It may be argued that the absence of GaP precipitate is not significant since supersaturation could have occurred. Another observation is relevant here. A small amount of GaP was placed in a boat immediately down stream to the gallium source within the constant temperature zone. During two normal runs only negligible amounts of GaP were consumed (0.38 and 0.06g compared to gallium losses of 20 and 15g). This

indicates that the phosphorus-saturated gallium is very close to being in equilibrium with solid GaP.

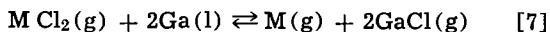
The theoretical consumption ratio was derived for a given phosphorus pressure. However, the variation of the ratio with  $\text{PCl}_3$  feed rate is small. Over the experimentally used range of  $\text{PCl}_3$  feed rates (0.10 to 0.45 mM/min) the theoretical Ga/ $\text{PCl}_3$  consumption ratio calculated from Eq. [2] and [4] varies from 2.73 to 2.54. Such a variation is within experimental error and therefore not evident.

In the above discussion we have made the important assumption that only HCl and GaCl are present in the reaction zone in significant amounts. The pressure of  $\text{GaCl}_3$  is indeed negligible as shown by Seki and Araki (10). The absence of the dihalide has been assumed in previous discussions (10, 13, 15, 16). The agreement observed in this study between the theoretical Ga/ $\text{PCl}_3$  ratio (neglecting  $\text{GaCl}_2$ ) and the experimental value can be used as evidence that no significant amount of dichloride is present in the Ga-Cl system at 1200°K if the system studied was at equilibrium. We believe that equilibrium was established on the strength of the data collected in Table I and Fig. 5 according to which the Ga/ $\text{PCl}_3$  ratio is constant for a wide range of feed and flow rates.

In the experimental section it was pointed out that the HCl partial pressure of the effluent gases was negligible. Since a significant fraction (0.12) of the incoming HCl does not react with the gallium, according to the analysis presented above, there must be subsequent reactions taking place in the seed region further downstream. One such reaction may be



**Distribution of dopants.**—Because the dopants passed over the gallium boat in the reaction zone, some loss of dopant to the gallium source must have occurred in these experiments. The metal vapor (Zn or Cd) will react to form the gaseous chloride immediately after mixing with the hydrogen chloride gas. Subsequently, upon passing over the gallium boat, a reduction will occur



where  $\text{M} = \text{Zn}, \text{Cd}$ . Using the thermodynamic data for  $\text{ZnCl}_2(g)$  and  $\text{CdCl}_2(g)$  given in ref. (17), together with those for  $\text{GaCl}(g)$  from ref. (13), the equilibrium constants at 1200°K for reaction 7 were calculated. For an experimental GaCl pressure of  $5 \times 10^{-2}$  atm it was found that half of the zinc and virtually all the cadmium would be present in the elemental state at equilibrium. This would in turn result in a solution of dopant in the gallium source. An estimate of the required equilibrium concentrations of dopant in the gallium source was made on the basis of Raoult's law. The total amount of zinc or cadmium required to saturate the gallium source in both cases turned out to be about 3% of the total amount of dopant transported during the run. Thus the loss of dopant to the gallium source is negligible.

**Zinc-doping.**—The electrical properties of several zinc-doped samples were studied in detail by Casey and Ermanis (18). From their data, the bulk of which will be published elsewhere, we selected the room temperature Hall mobility. A straight line has been drawn through the experimental points displayed in Fig. 6. There is no theoretical significance attached to this straight line; it is helpful in obtaining interpolated mobilities for samples for which only the room temperature resistivity is known. Using these estimated mobilities with the measured resistivities, the plot of Fig. 7 was constructed, showing the room temperature hole concentration as a function of the zinc partial pressure of the growth ambient.

Several crystals were cleaved into smaller pieces and samples were taken from opposite ends of the crystal to study the effect of the temperature gradient

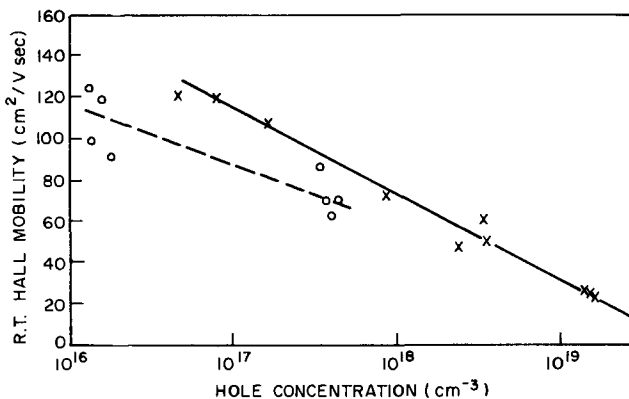


Fig. 6. Room temperature Hall mobility as a function of hole concentration of Zn-doped GaP(X) and Cd-doped GaP(O).

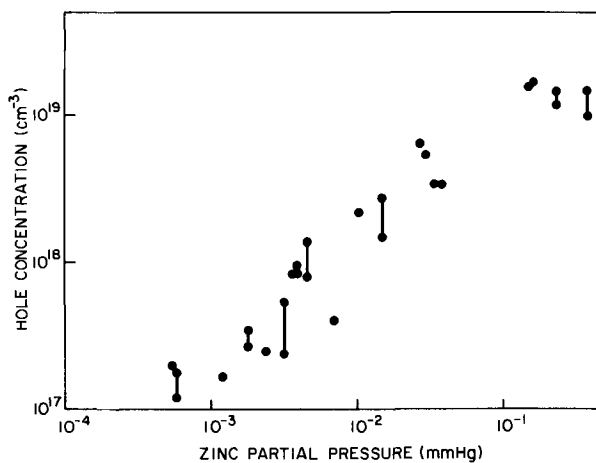


Fig. 7. Hole concentration of Zn-doped GaP as a function of Zn partial pressure of growth ambient.

on the doping. In Fig. 7, data from the same crystal are connected by straight vertical lines. Although a spread in the resistivities is noticed, no systematic variation with growth temperature could be observed. In this respect, the zinc-doped crystals differed notably from the cadmium-doped crystals, which will be described below.

Casey and Ermanis (18) analyzed the temperature dependence of the hole concentration of several zinc-doped crystals in terms of a three parameter model (ionization energy and zinc and donor concentrations). For these samples the measured hole concentration and the estimated total zinc concentration are given as follows: ( $4.2 \times 10^{16}$ ,  $8.1 \times 10^{16}$ ), ( $1.6 \times 10^{17}$ ,  $3.0 \times 10^{17}$ ), ( $7.0 \times 10^{17}$ ,  $3 \times 10^{18}$ ), ( $2.3 \times 10^{18}$ ,  $6 \times 10^{18}$ ), ( $3.3 \times 10^{18}$ ,  $8 \times 10^{18}$ ) all in  $\text{cm}^{-3}$ . For one of these samples the total zinc concentration was determined experimentally by neutron activation analysis and found to agree with the curve fitting estimate to within a few per cent.

Wet chemical analyses of two heavily zinc-doped GaP crystals were performed. The analytical method developed by Luke (19) employs coprecipitation of zinc with copper as carbamates. The precipitate is filtered off and analyzed directly on the micropore filter using x-ray spectrochemical analysis. Three samples from one crystal were used to obtain a total zinc concentration of  $6.0 \pm 0.2 \times 10^{18} \text{ cm}^{-3}$  and hole concentrations of  $3.9$  and  $4.9 \times 10^{18} \text{ cm}^{-3}$ . Similarly, another crystal contained  $2.0 \pm 0.1 \times 10^{19} \text{ cm}^{-3}$  zinc and yielded hole concentrations of  $1.2$  and  $1.5 \times 10^{19} \text{ cm}^{-3}$ .

The estimates of Casey and Ermanis (18) and the results of the chemical analysis show that the total zinc concentration consistently is two to three times larger than the hole concentration over the entire doping range. We conclude from Fig. 7 that the zinc con-

centration increases linearly with the zinc partial pressure of the growth ambient.

The room temperature mobilities of the halogen transported GaP crystals were found to be identical within experimental error with those of zinc-doped crystals grown by wet hydrogen transport (20). For both materials the mobility dropped from  $100 \text{ cm}^2/\text{v-sec}$  at a doping level of  $2 \times 10^{17} \text{ cm}^{-3}$  [holes to  $50 \text{ cm}^2/\text{v-sec}$  at a doping level of  $2 \times 10^{18} \text{ cm}^{-3}$  (holes)]. This indicates that the difference in structural perfection observed by means of etch-studies does not noticeably influence the room temperature Hall mobility.

**Cadmium doping.**—One of the low cadmium-doped samples was studied thoroughly by Ermanis and Casey (21). From the temperature dependence of the Hall mobility and the resistivity they calculated:  $N_A = 2.3 \times 10^{16} \text{ cm}^{-3}$ ,  $N_D = 7.5 \times 10^{15} \text{ cm}^{-3}$ , hole concentration at room temperature  $1.0 \times 10^{16} \text{ cm}^{-3}$ , Hall mobility at room temperature  $120 \text{ cm}^2/\text{v-sec}$ , maximum Hall mobility ( $\sim 80^\circ\text{K}$ )  $1600 \text{ cm}^2/\text{v-sec}$ , and a cadmium ionization energy of 0.09 eV.

Room temperature mobilities obtained on several samples were used with the measured resistivities to calculate hole concentrations. Figure 6 shows a plot of Hall mobilities vs. hole concentration. Comparison of these room temperature mobilities with those of zinc-doped GaP crystals shows that the scatter of the mobility data is larger for the Cd-doped crystals and that the mobilities at a given hole concentration are higher for the zinc-doped crystals. These observations could be explained by a larger amount of compensation in the Cd-doped crystals. The dashed line of Fig. 6 was used to convert resistivity measurements obtained on other samples to hole concentrations. The hole concentrations obtained in this manner were then plotted as a function of the cadmium partial pressure of the growth ambient, Fig. 8. The spread in the hole concentrations at low cadmium pressures is significant. Several of the crystals were cleaved into smaller pieces and samples were taken from hot, cold, and intermediate regions. Data from the same crystal are connected by straight lines. In all cases the colder regions had a higher hole concentration than the  $70^\circ\text{C}$  hotter front edge of the crystal. Samples from the center gave intermediate values. With higher cad-

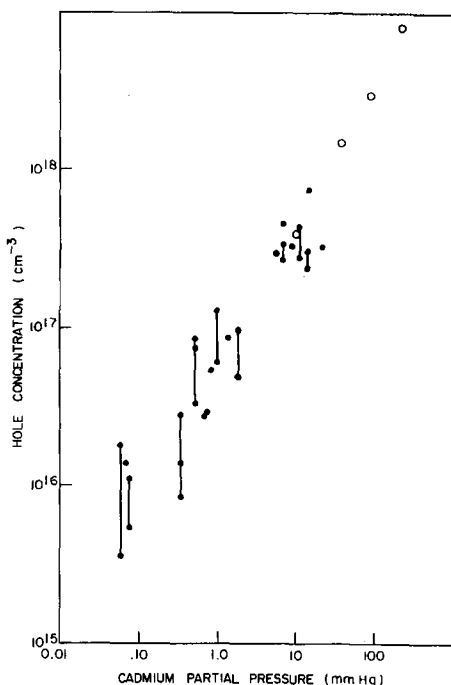


Fig. 8. Hole concentration of cadmium-doped epitaxial GaP as a function of cadmium partial pressure [● data of this study, ○ data of Alferov *et al.* (16)].

mium pressures the concentration variation narrowed down considerably.

For comparison, data obtained by Alferov *et al.* (22) are included on Fig. 8. Their crystals were grown epitaxially by a closed tube vapor transport technique using  $\text{CdCl}_2$  as dopant. The exact growth temperature is not known. Some of the samples grew at temperatures as low as  $730^\circ\text{C}$ . The growth rate was 10 times slower than that of the crystals described here.

The fact that Alferov *et al.* used different growth temperatures yet obtained the same linear dependence of hole concentration for a given cadmium partial pressure is compatible with our observation that for high cadmium pressures growth temperature differences are unimportant.

Using the experimental ionization energy of 0.09 eV and a hole mass of  $0.5m_e$  one may calculate the total cadmium concentration. For a hole concentration of  $1 \times 10^{18} \text{ cm}^{-3}$  a total cadmium concentration of  $6 \times 10^{18} \text{ cm}^{-3}$  is obtained, while at the  $10^{16} \text{ cm}^{-3}$  level practically all the cadmium is ionized. When the theoretically calculated correction factors were applied to the hole concentrations of Fig. 8 the cadmium concentration data plotted in Fig. 9 resulted. The line drawn through the data points has a slope of unity.

**Incorporation of dopant.**—The total acceptor concentration is expected to equal the ionized acceptor concentration at the growth temperature. At equilibrium, for an extrinsic semiconductor, one expects a square root dependence of the ionized acceptor concentration on the partial pressure of the doping impurity. Such a square root dependence has been observed for zinc-doped GaP both in solution (23) and at  $1080^\circ\text{C}$  in moist hydrogen vapor growth (20). Thus the first power dependence displayed in Fig. 7 and 9 is surprising.

Consider the possibility that in the halogen transport system described, growth rates are fast enough so that the incorporation of acceptor is not an equilibrium process. Nonequilibrium effects on doping have been noted previously. Orientation effects have been described by Williams (24) and Moest (25) for GaAs crystals grown from the vapor and for GaP by Groves (8). In our case, assume specifically that the equilibrium between cadmium or zinc atoms adsorbed on the growing surface and those incorporated in the bulk of the crystal is not established because diffusion of the dopants is slow. To check whether this is a reasonable assumption, we may compare diffusion and growth rates for the zinc-doped GaP grown at  $1080^\circ\text{C}$  with those of zinc- and cadmium-doped crystals grown at  $880^\circ\text{C}$ .

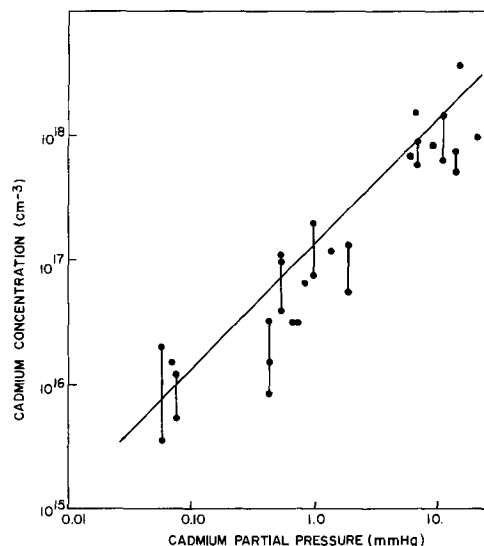


Fig. 9. Total cadmium concentration of cadmium-doped epitaxial GaP as a function of cadmium partial pressure.

Table II. Comparison of diffusion coefficients and growth rate

	D (cm <sup>2</sup> /sec)	Growth rate (cm/sec)
Zn in GaP (1080°C)	$3 \times 10^{-9}$	$3 \times 10^{-6}$
Cd in GaP (880°C)	$1 \times 10^{-12}$	$3 \times 10^{-5}$
Zn in GaP (880°C)	$3 \times 10^{-10}$	$3 \times 10^{-5}$

No data are available on the diffusion of cadmium in GaP. In GaAs, however, parallel studies of both zinc and cadmium diffusion have been made (26). The diffusion activation energies for zinc and cadmium were found to be equal, while the pre-exponential factor  $D_0$  for zinc was much higher than for cadmium. This suggests that the mechanism of diffusion is the same for both impurities. Using the  $D_0$  ratio for Cd and Zn diffusion in GaAs as an estimate for the corresponding quantity for GaP and assuming that the activation energies for Zn and Cd diffusion also are identical in GaP, we can estimate a diffusion coefficient for Cd in GaP to be used below 900°C.

$$D(\text{Cd in GaAs}) = 0.05 \times e^{-2.43/kT} \text{ cm}^2/\text{sec} \quad [\text{Ref. (26)}]$$

$$D(\text{Zn in GaAs}) = 15 \times e^{-2.43/kT} \text{ cm}^2/\text{sec} \quad [\text{Ref. (26)}]$$

$$D(\text{Zn in GaP}) = 7.5 \times 10^{-8} C^{0.45} e^{-2.50/kT} \quad [\text{Ref. (27)}]$$

$$= 27 \times e^{-2.50/kT} \text{ cm}^2/\text{sec} \text{ for } C = 10^{19} \text{ cm}^{-3}$$

$$D(\text{Cd in GaP}) = 0.1 \times e^{-2.50/kT} \text{ cm}^2/\text{sec} \quad [\text{Estimated}]$$

We can now compare diffusion coefficients and growth rates, Table II. The differences in diffusion coefficients and growth rates at the two temperatures suggests that the processes of impurity incorporation may be qualitatively different in the two cases. Zinc incorporated at 1080°C can be homogeneously distributed throughout the crystal during growth. Cadmium and zinc incorporated at 880°C diffuse too slowly to equilibrate with the ambient pressure. The cadmium or zinc concentration of the bulk crystal reflects the density of dopant atoms adsorbed on the growing surface. Even the ten times slower growth rates employed by Alferov *et al.* are not slow enough to ensure equilibrium concentrations.

#### Acknowledgments

We are grateful to H. C. Casey for the permission to use selected data prior to publication, to F. Ermanis for Hall measurements, and to Miss S. Vincent for the chemical analysis. The assistance of H. C. Montgomery in making Hall measurements is gratefully acknowledged. We wish to thank F. A. Trumbore, K. L. Lawley, C. J. Frosch, and L. J. Varnerin for comments and valuable suggestions.

Manuscript submitted March 18, 1968; revised manuscript received April 15, 1968. This paper was presented at the Boston Meeting, May 5-9, 1968, as Paper 101.

Any discussion of this paper will appear in a Discussion Section to be published in the June 1969 JOURNAL.

#### REFERENCES

1. C. D. Thurmond and C. J. Frosch, *This Journal*, **111**, 184 (1964).
2. G. R. Antell and D. Effer, *ibid.*, **106**, 509 (1959).
3. I. Akasaki, M. Hashimoto, T. Hara, Paper presented at the Dallas Meeting, May 7-12, 1967 as Abstract 100, Extended Abstracts.
4. W. G. Oldham, *J. Appl. Phys.*, **36**, 2887 (1965).
5. G. S. Kamath and D. Bowman, *This Journal*, **114**, 192 (1967).
6. *Electronics*, **40** (13), 192 (1967).
7. D. G. Thomas, M. Gershenzon, and J. J. Hopfield, *Phys. Rev.*, **131**, 2397 (1963).
8. W. O. Groves, Crystal Growth, Supplement to J. Phys. Chem. Solids, Proc. Internat'l. Conf. on Crystal Growth, Boston, 1966, pp. 669-672.
9. M. S. Abrahams and C. J. Buiochi, *J. Appl. Phys.*, **36**, 2855 (1965).
10. H. Seki and H. Araki, *Jap. J. Appl. Phys.*, **6**, 1414 (1967).
11. D. R. Stull, G. C. Sinke, "Thermodynamic Properties of the Elements," Amer. Chem. Soc., Series (1956).
12. JANAF, "Interim Thermochemical Tables," Vol. 2, Thermal Laboratories, Dow Chemical Co.
13. R. R. Fergusson and T. Gabor, *This Journal*, **111**, 585 (1964).
14. C. D. Thurmond, *J. Phys. Chem. Solids*, **26**, 785 (1965).
15. D. Effer and G. R. Antell, *This Journal*, **107**, 252 (1960).
16. D. Effer, *ibid.*, **112**, 1020 (1965).
17. A. Glassner, "The Thermochemical Properties of the Oxides, Fluorides and Chlorides to 2500°K," ANL-5750, Argonne National Laboratory.
18. H. C. Casey and F. Ermanis, To be published.
19. C. L. Luke, To be published in *Anal. Chim. Acta*.
20. L. C. Luther, Unpublished.
21. H. C. Casey and F. Ermanis, Unpublished.
22. Zh. I. Alferov, V. I. Korol'kov, M. K. Trukan, and S. P. Chaschin, *Sov. Phys. Solid State*, **7**, 1915 (1966).
23. F. A. Trumbore, H. G. White, M. Kowalchik, R. A. Logan, and C. L. Luke, *This Journal*, **112**, 782 (1965).
24. F. V. Williams, *ibid.*, **111**, 886 (1964).
25. R. R. Moest, *ibid.*, **113**, 141 (1966).
26. B. Goldstein, *Phys. Rev.*, **118**, 1024 (1960).
27. L. I. Chang and G. L. Pearson, *J. Appl. Phys.*, **35**, 374 (1964).

# Formation of Thick Semi-Insulating GaAs Films by Flash Evaporation

T. B. Light, E. M. Hull, and R. Gereth<sup>1</sup>

IBM Watson Research Center, Yorktown Heights, New York

## ABSTRACT

Highly oriented films of semi-insulating GaAs, up to 40  $\mu\text{m}$  thick, have been grown on single crystal Ge and semi-insulating GaAs substrates using a modified flash evaporation process. The GaAs films were obtained by flash evaporation of chromium doped GaAs powder with excess As admixed. The quality of the evaporated films was evaluated for degree of crystallinity using x-ray diffraction, and for resistivity using spreading resistance measurements. The voltage-current characteristics have also been determined. Both the degree of polycrystallinity and the resistivity of the evaporated GaAs films are dependent on the substrate temperature and the ratio of As:GaAs in the source material. A maximum in film resistivity *vs.* substrate temperature is observed which coincides with a structural change from polycrystalline to highly oriented growth. Optimum film growth conditions are typically represented by an As:GaAs volume ratio of 1:1 in the source material and by substrate temperatures between 525° and 575°C. At substrate temperatures above 575°C, the measured spreading resistance of the films drops sharply even though they are increasingly oriented.

The successful epitaxial growth of smooth Ge layers on semi-insulating GaAs substrates (1,2) makes it possible to consider dielectric isolation for integrated circuits using Ge devices. Isolated planar structures of Ge on semi-insulating GaAs can be fabricated by etching islands of Ge and then back-filling with an insulator. A potentially useful technique for achieving this backfilling is via a flash evaporation method. Such a technique for depositing films of GaAs has indeed been reported by Richards *et al.* (3). Because of the incongruent manner in which GaAs evaporates, it has been suggested by Muller and Richards (4) that the stoichiometry of the films could be best controlled by the addition of As to the source material. No reference has, however, been found regarding the use of Cr doped semi-insulating GaAs as a source material for flash evaporation of semi-insulating GaAs layers.

The present work describes the use of Cr doped semi-insulating GaAs, with As added, in a "reactive" flash evaporation mode to obtain layers of semi-insulating GaAs. The results of electrical and structural evaluation are presented.

## Experimental Procedure

**Preparation of GaAs Layers.**—The apparatus used is shown schematically in Fig. 1. Powdered (40-60 mesh size) chromium doped high resistivity GaAs source material, with powdered As admixed, is fed from a micrometer screw operated metering device into a vibrating feed trough. The barrel of the feed device is rotated to provide a tumbling action for uniform powder feed. The powder drops from the feed trough through a tantalum guide (collimating) funnel and a tantalum guide tube, then into the input opening of an enclosed and shielded tantalum high temperature box source. Inside the box source, the particles encounter a surface at 45° to the angle of incidence. They are deflected from this surface toward the exit and vaporized. The vaporized GaAs is baffled before reaching the exit opening which is positioned beneath the substrate holder. The box source heater is surrounded by a water cooled jacket so that extended runs can be made in the vacuum system without excessive radiant heating effects. The substrate is mounted onto a tantalum substrate heater using molybdenum spring clips.

The guide funnel and guide tube are necessary to limit the amount of GaAs powder which is diverted

by back streaming vapor. A guide tube connected directly to the input opening of the source heater is not desirable because a temperature gradient due to radiation losses develops along the tube between the source and the opening. Consequently, a certain portion of the guide tube would reach a critical temperature at which As evaporates rapidly, leaving a liquid Ga film behind. This film is capable of entrapping GaAs powder which could block the entrance to the source boat eventually. To avoid this problem, the guide tube was supported on an open framework above the source heater shield. In this way, the "critical" temperature zone is located within the gap between the guide tube and the source heater input opening. The standard evaporation conditions were as follows: (i) rate of deposition, (0.05-0.15)  $\mu\text{m}/\text{min}$ ; (ii) source temperature, 1325°C (505w); (iii) source to substrate distance, 10 cm; (iv) pressure during evaporation,  $10^{-5}$  Torr initially, decreasing to  $4 \times 10^{-6}$  Torr; (v) deposition time, 90 min (vi) substrates used, (110) Ge, (110) and (111) Cr doped semi-insulating GaAs. If excess As powder were not added to the GaAs source powder, deposition times of only 10 min duration were possible, using many combinations of source designs and temperatures, before a film of excess Ga accumulated on the substrate. Excess As vapor has also been introduced by using a separate controlled temperature oven type source.

**Structural characteristics.**—The structure of the layers has been characterized by x-ray diffraction techniques in order to determine whether they were

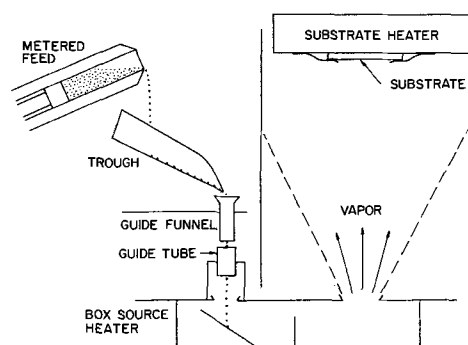


Fig. 1. Schematic representation of flash evaporation feed, source, and substrate.

<sup>1</sup> Present address: AEG-Telefunken, Heilbronn, Germany.



polycrystalline or highly oriented. The wafers were mounted in a Debye-Scherrer powder camera with the incident x-ray beam intersecting the film surface at a small angle from horizontal. This geometry was chosen to maximize the diffracting volume of the layer relative to the substrate diffracting volume. The occurrence and nature of the observed powder pattern lines or Laue spots can be used as an indicator of the degree of polycrystallinity or preferred orientation in the layers.

**Electrical characteristics.**—The relative resistivities of the layers were determined by measuring the spreading resistance using two fine tungsten probes in contact with the layer surface. (The measured resistance is thus twice the spreading resistance for one probe.) For the case of a semi-infinite piece of material the spreading resistance,  $R_s$ , is related to the resistivity,  $\rho$ , by the relation  $R_s = \rho/2d$ ; where  $d$  is the diameter of the contact area [see ref. (5)]. For a layered structure, such as a film on a substrate, with resistivities  $\rho_f$  and  $\rho_s$ , respectively, the spreading resistance also depends on the layer thickness and the substrate resistivity. In the case of Ge substrates,  $\rho_s \ll \rho_f$ . The Ge substrate shunts part of the current and thus lowers the effective spreading resistance. This effect increases with decreasing thickness. In the case of semi-insulating GaAs substrates,  $\rho_s \cong \rho_f$  and the relation  $R_s = \rho/2d$  is a reasonable approximation. The factor  $2d$  was determined approximately by making both four terminal and spreading resistance measurements on the same samples of semi-insulating GaAs. Very clean surfaces are necessary to avoid surface shunting effects.

The maximum applied voltage for spreading resistance determination was 5v. Voltage-current characteristics were investigated using the same probe configuration and using applied voltages up to 90v. A Tektronix model 575 transistor curve tracer was used to determine breakdown voltage up to a maximum of 200v.

**Deposition parameters investigated.**—Two kinds of experiments were carried out. In the first set the volumetric ratio of As powder to GaAs powder in the source material was varied, keeping the metered feed rate constant and using a substrate temperature of 625°C. In the second set of experiments the substrate temperature was varied for two constant volume ratios of As to GaAs, namely 1:1 and 1:5.

## Results

**Ratio of As to GaAs.**—The volume ratio of As to GaAs in the source material was varied from 1:10 to 2:1, while keeping the substrate temperature constant at 625°C. All ratios less than 1:2 resulted in polycrystalline films. All ratios greater than 1:2 yielded highly oriented films. The spreading resistance of the films did not vary by more than an order of magnitude for any ratio except the smallest (1:10). The latter resulted in films having significantly lower resistances.

**Substrate temperature.**—The spreading resistance as a function of substrate temperature during film deposition is shown in Fig. 2. The solid lines are for (110) oriented GaAs substrates and the dashed line is for (110) oriented Ge substrates. The vertical bars represent the range of spreading resistance data observed for each sample. The Cr doped semi-insulating GaAs used for source and substrate material had a spreading resistance in the range  $1-3 \times 10^{10}$  ohms ( $10^8$  ohm cm range). The ratios 1:1 and 1:5 listed in Fig. 2 refer to the As to GaAs volume ratios used in the source material.

A feature common to all of the curves in Fig. 2 is the increase of the spreading resistance with substrate temperature up to a maximum value at a characteristic temperature, and a very rapid fall off at higher substrate temperatures. In all cases the characteristic temperature region correlates with a change in the

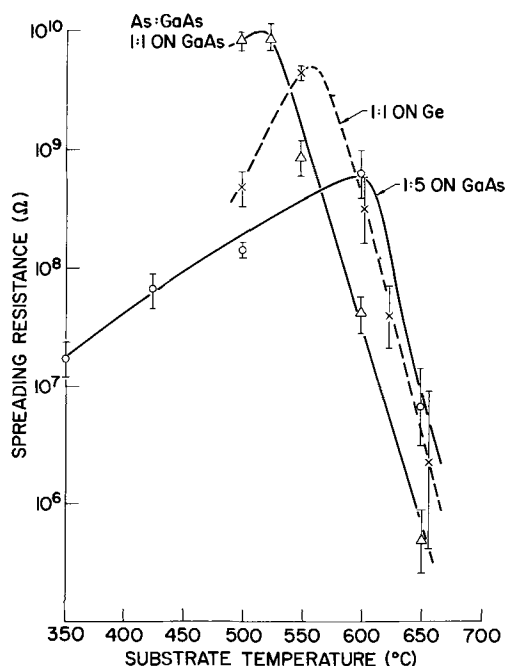


Fig. 2. Spreading resistance vs. substrate temperature for deposits on Ge (dashed line) and on GaAs (solid lines), using two different volume ratios of As:GaAs in the source.

film structure from a polycrystalline to an oriented state. The film structure will be discussed in greater detail below. One can see from Fig. 2 that the onset of oriented growth on GaAs substrates occurs at a 75°C higher substrate temperature if the As to GaAs volume ratio in the source is decreased from 1:1 to 1:5. It is also evident that the substrate temperature must be raised by 40°C to achieve oriented growth on a Ge substrate using a 1:1 source As/GaAs ratio. The following results all refer to films made using a 1:1 source As/GaAs ratio.

**Structure.**—Typical x-ray powder pattern results are shown in Fig. 3 for substrate temperatures below and above the polycrystalline-oriented growth characteristic temperature range. The greater line broadening observed for the lower temperature deposit indicates a smaller particle size.

Deposits were also made on (111) GaAs substrates and Fig. 4 shows the surface of an oriented deposit formed at a substrate temperature of 625°C.

The amount of Cr in the deposited layers was determined by spark source mass spectrometry and was found to be the same as in the source material ( $\sim 3 \times 10^{17}/\text{cm}^3$ ).

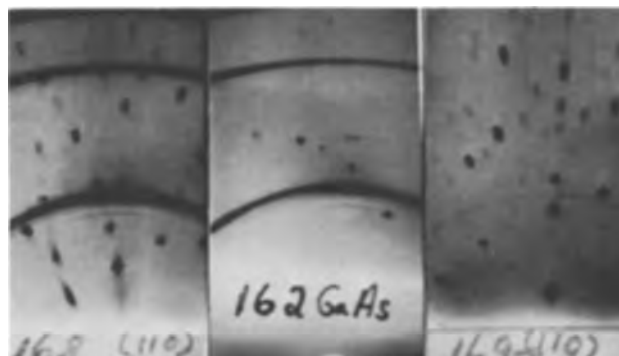


Fig. 3. Typical Debye-Scherrer powder patterns (region of 111, 220 and 311 reflections only) for deposits made on GaAs substrates using substrate temperatures of (a)  $\sim 450^\circ\text{C}$ , (b)  $\sim 500^\circ\text{C}$ , and (c)  $\sim 625^\circ\text{C}$ ; and a source As/GaAs ratio of 1:1.



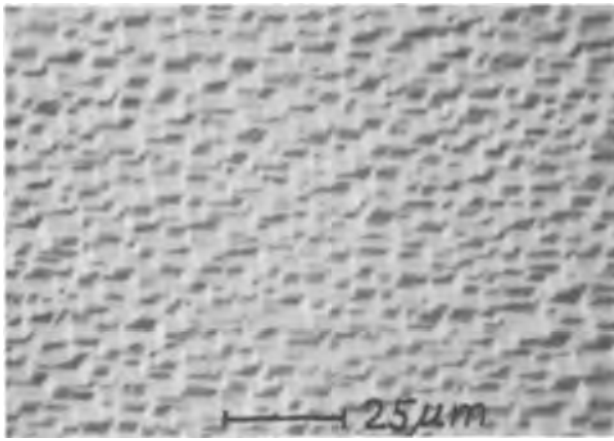


Fig. 4. Surface of deposit on (111) GaAs surface using a substrate temperature of 625°C, and a source As/GaAs ratio of 1:1.

**Electrical characteristics.**—Figure 5 shows current-voltage characteristics that were measured for layers deposited on semi-insulating GaAs substrates at different substrate temperatures. Log  $V$  vs. log  $I$  is linear for voltages up to 90v, and the slope is nearly unity indicating essentially ohmic behavior for those films deposited at 575°C and lower. For a given voltage, the current decreases with increasing deposition temperature to a minimum and then increases rapidly. This corresponds to the spreading resistance behavior shown in Fig. 2. The behavior is no longer linear beyond 2v for films deposited at 625°C.

The current-voltage characteristics of layers deposited under optimum conditions (highest spreading resistance and oriented growth) on Ge and semi-insulating GaAs substrates are compared with those of bulk Cr doped semi-insulating GaAs in Fig. 6. The increasingly larger currents with increasing voltage for the layer on the Ge substrate is interpreted as due to the effect of the low resistivity Ge substrate on the spreading resistance measurements as discussed ear-

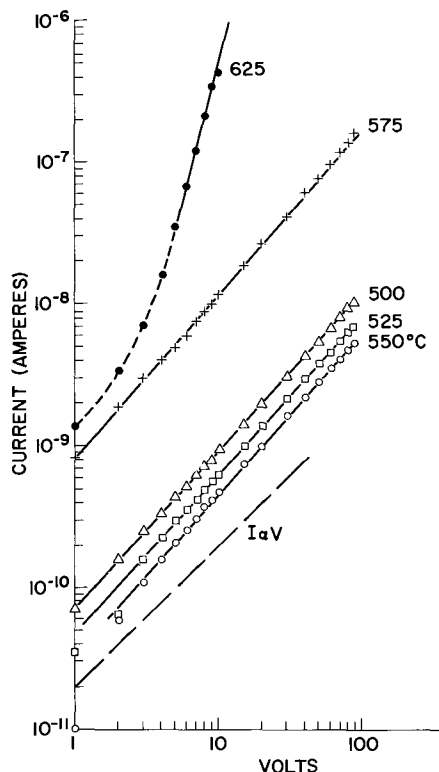


Fig. 5. Log current vs. log voltage for deposits on GaAs substrates using substrate temperatures in the range 500°-625°C, and a source As/GaAs ratio of 1:1.

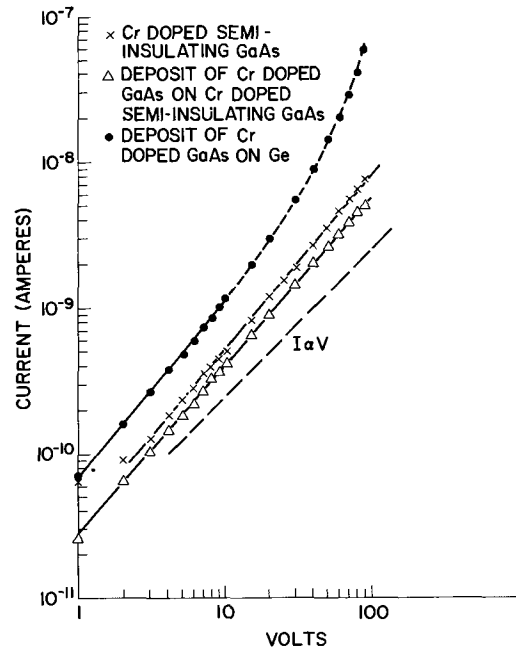


Fig. 6. Log current vs. log voltage for deposits made under optimum conditions on Ge and GaAs substrates, compared with bulk Cr doped semi-insulating GaAs.

lier. The breakdown voltage for layers on semi-insulating GaAs substrates is greater than 200v. These current-voltage characteristics indicate that the deposited layer behaves in a similar manner to the bulk material. They are also consistent with the results published by Haisty and Hoyt (6) for bulk Cr doped semi-insulating GaAs, using electron injecting contacts, except that these authors observed an  $I \propto V^3$  region at higher voltages.

Further work is in progress concerning the effects of annealing in different ambients on the properties of Cr doped semi-insulating GaAs in both bulk and film samples. This work also encompasses an effort to understand the effect of substrate temperature on spreading resistance in the region of rapidly decreasing spreading resistance. The results will be the subject of a forthcoming paper.

### Conclusions

Thick highly oriented layers of Cr doped semi-insulating GaAs can be grown on GaAs and Ge substrates by reactive evaporation, in which excess As powder is added to Cr doped GaAs powder evaporated in the flash evaporation mode. Optimum film growth conditions are represented by substrate temperatures between 525° and 575°C and by a 1:1 volume ratio of As to GaAs in the source material. Judging from the close similarity of the current-voltage characteristics, the conduction mechanism in the film appears to be the same as in bulk Cr doped semi-insulating GaAs.

### Acknowledgments

We wish to thank R. L. Rohr, J. A. Petriello, and C. X. Duncombe for wafer lapping and polishing, and J. Angilello for suggesting and implementing the x-ray diffraction low angle powder pattern technique. The authors greatly appreciate the technical assistance of Miss S. A. Sharpe at all stages of preparing and characterizing the GaAs films.

Manuscript submitted March 1, 1968; revised manuscript received ca. April 15, 1968. This paper was presented at the Chicago Meeting, Oct. 15-19, 1967 as Paper 162.

Any discussion of this paper will appear in a Discussion Section to be published in the June 1969 JOURNAL.

## REFERENCES

1. M. Berkenblit, A. Reisman, and T. B. Light, Presented at the Chicago Meeting, Oct. 16-18, 1967, Abstract 160.
2. A. Papazian and A. Reisman, *ibid.*, Abstract 159.
3. J. L. Richards, P. B. Hart, and L. M. Gallone, *J. Appl. Phys.*, **34**, 3418 (1963).
4. E. K. Muller and J. L. Richards, *ibid.*, **35**, 1233 (1964).
5. R. G. Mazur and D. H. Dickey, *This Journal*, **113**, 255 (1966).
6. R. W. Haisty and P. L. Hoyt, *Solid State Electronics*, **10**, 795 (1967).

## Behavior of Dislocations in Silicon Semiconductor Devices: Diffusion, Electrical

J. E. Lawrence

*Fairchild Semiconductor, Division of Fairchild Camera & Instrument Corporation, Palo Alto, California*

### ABSTRACT

Stationary dislocations did not influence the diffusion of boron to a measurable extent in tests conducted to amplify the dislocation-core diffusion effect and the vacancy source action of the fixed dislocations in silicon. In contrast, moving dislocations contributed to large enhanced diffusion effects apparently by acting as sources of excess vacancies. Very high concentrations of stable dislocations, without impurity precipitates, have very slight effects on p-n junction reverse currents ( $\sim +2X$ ), transistor gain ( $\sim -0.2X$ ), and the storage time ( $\sim -3X$ ) of nongold doped npn transistors. Unstable dislocations are slightly more electrically active than low energy stable dislocations. The precipitation of metallic contaminants such as copper can greatly alter the electrical properties of dislocations. Devices formed in material with few dislocations are more likely to degrade due to metal precipitate formation. The degradations attributed to metal precipitates are large p-n junction reverse currents, emitter to collector short circuits and wide variations in transistor gain.

Discontinuities in a periodic lattice may be centers at which nonuniform solute diffusion can occur and significant electrical activity can be generated. Dislocations are of particular interest since they consist of a chain of discontinuities which, it has been proposed, may provide a preferential path for solute and charge migration over great distances within a semiconductor material. Unanimous agreement does not exist for the manner and extent to which dislocations influence solute diffusion in disordered silicon. A dislocation core diffusion mechanism has been advanced by Queisser *et al.* (1) and Kartensen (2), who investigated solute diffusion along the grain boundaries of semiconductor bicrystals. These investigators considered low angle grain boundaries as consisting of planar arrays of dislocations after a model proposed by Bragg (3) and Burgers (4). Other workers have reported that stationary dislocations produced by bending (5) and loading (6) single crystals do not contribute to a measurably enhanced solute diffusion. Dislocations forced to move under the influence of an externally applied force have been shown to contribute to enhance solute diffusion effects (6,7).

General agreement does not exist for the manner and extent to which dislocations influence the electrical characteristics of npn transistors. This is due in part to the difficulty of separating the contribution of dislocations from the often associated effects of point defects and impurity precipitates. The low-temperature deformation of silicon creates generation-recombination centers which annihilate quickly at 300°C (8). These centers are very likely point defects for similar electrical activity and annealing properties which have been found for Frenkel defects formed by electron bombardment (9). A single, large impurity precipitate has been shown to cause much greater p-n junction reverse currents than a large cluster of very small precipitates (10). However, all precipitates whether tightly packed units or not could be ex-

pected to be more active electrically than a dislocation free of impurity precipitation. The early reports on lattice disorders in germanium concluded that dislocations do influence the generation-recombination and mobility of free charges (11).

The present work was conducted to determine the manner and extent to which stationary and moving dislocations influence solute diffusion during thermal treatments commonly used in the fabrication of simple double-diffused npn transistors. The second purpose of this investigation was to determine the extent to which (a) stable dislocations, (b) newly formed unstable dislocations, and (c) dislocations with associated impurity precipitates, influence p-n junction reverse currents, transistor gain, and the storage time of nongold-doped npn transistors. The terms "stable" and "stationary" in this discussion refer to dislocations which do not exhibit a detectable movement during the thermal treatments necessary for device fabrication. In contrast, "unstable" dislocations are defined as those which move extensively during a thermal treatment.

### Experimental Procedure

The test material consisted of (111) silicon wafers growth doped with phosphorus to 20-50 ohm-cm n-type. The starting wafers were cut from dislocation-free ingots and chemically polished to remove the random lattice damage generated during the wafer shaping treatments. In this investigation, dislocations were created in otherwise disorder-free material by either thermal quenching, mechanical loading, or solute diffusion.

A gettering procedure was employed which renders undesired junction degrading metals electrically inactive without introducing the gettering agent to the silicon lattice (12). This was achieved by forming a phosphorus glass on the surface of the SiO<sub>2</sub> film which covered both sides of a silicon test wafer.

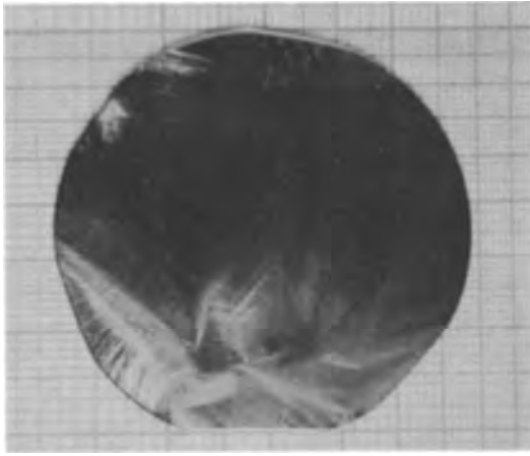


Fig. 1. Preferential etch delineated distribution of low energy stable dislocations. The light region contains  $> 5 \times 10^7$  disl/cm<sup>2</sup>; the dark region contains  $< 10^3$  disl/cm<sup>2</sup>.

The thermal quenching treatment produced greater than  $5 \times 10^7$  disl/cm<sup>2</sup> in one region of a wafer while leaving the remainder of the wafer with fewer than  $10^3$  disl/cm<sup>2</sup> as shown in Fig. 1. This treatment consisted of repeatedly inserting and extracting a standing test wafer from a 1270°C furnace. The quenched wafers were then annealed at 1270°C to allow the newly formed dislocations to obtain a low energy state. The quenching act produced a thermal gradient at which the top of the wafer cooled 500°C the first second while the portion of the wafer in contact with the quartz boat cooled at 20°C/sec, as determined by an optical pyrometer. The dislocations which formed to relieve this thermally induced lattice stress generally lay in the crystal's inclined {111} planes. The resulting dislocation arrays passed from one wafer face to the opposite wafer surface. These wafers were used to analyze the effects of stable dislocations on solute diffusion and the electrical properties of semiconductor devices.

The effects of moving dislocations on solute diffusion was investigated by externally stressing a wafer during a 1200°C boron diffusion treatment. The loading apparatus used to stress a silicon wafer at 1200°C consisted of a silicon stylus with silicon weights and a quartz stabilizing assembly (6). The loading tests were performed by placing the silicon stylus on the (111) surface of n-type wafers into which boron had been diffused to a depth of  $\frac{1}{2}\mu$  from a constant source. The silicon wafer with the weighted pin in position was then placed in the 1200°C furnace for the diffusion test. This high-temperature loading treatment created  $>4 \times 10^9$  disl/cm<sup>2</sup> in a highly localized region beneath the weighted stylus.

High concentrations of diffused solutes were also used to generate the lattice stress necessary for dislocation formation and motion. This source of moving dislocation was discussed in earlier papers considering their effect on single (13) and double diffused structures (7). An interaction between the possible influences of stationary and moving dislocations on boron diffusion was investigated by forming double diffused npn structures in wafers such as that shown in Fig. 1.

The effect of new unstable dislocations on the reverse current of a p-n junction was investigated on test structures where the concentration of dislocations in a junction's depletion region was governed by the strain relaxation mode within the diffused region. It has been shown (13) that diffusion induced stresses are relieved by the formation of either of two distinct types of dislocation networks within the diffused region: hexagonal networks of predominantly edge dislocations, or arrays of concentric loops. In those cases where the hexagonal networks are generated within the diffused region, extensive arrays of unstable loops

are simultaneously formed outside the diffused region. In contrast, no such arrays are formed outside the diffused regions in those cases where concentric loop networks are generated within the diffused region.

The single and double diffused structures used to determine the electrical effects of stable dislocations were formed by the planar diffusion of low concentrations of boron and phosphorus to avoid the electrical effects associated with boron or phosphorus precipitates. The quantity of diffused boron in the base regions was near  $Q \simeq 2 \times 10^{15}$ /cm<sup>2</sup>. Similarly, the phosphorus emitter concentrations were near  $Q \simeq 1 \times 10^{16}$ /cm<sup>2</sup>. The depth of boron penetration in the single and double diffused structures was generally  $5.5\mu$ . Two phosphorus emitter depths were used: (i)  $X_{je} = 5.0\mu$  to create a narrow basewidth punch-through limited structure and (ii)  $X_{je} = 1.0\mu$  to create a structure with a  $4.5\mu$  basewidth.

Copper was introduced to some test wafers to determine the effect of copper on devices formed in highly dislocated material as well as in material relatively free of dislocations. The junction-degrading metal was introduced after the electrical characteristics of "clean" devices had been determined. The gas transfer method of copper diffusion described earlier (10) was employed. The actual concentration of copper in the test wafers was not resolved, though it was likely above the solubility limit at 1100°C since precipitation did occur.

The extent of enhanced p-n junction penetration was determined by comparing the depths of stain-delineated boundaries resolved by counting interference fringes on low angle grooved sections. Electrical measurements of the transistor gain and emitter-to-collector reverse bias characteristics (14) supported the sensitivity ( $\pm 0.1\mu$ ) of the data acquired by the p-n junction staining method of junction delineation.

#### Experimental Results: Diffusion

The diffusion of boron at a constant 1200°C into a wafer similar to that shown in Fig. 1 showed no detectable enhanced diffusion due to stationary dislocations. Likewise, the diffusion of boron into similar material during a thermal treatment in which the wafer temperature was repeatedly cycled between 1200° and 30°C also failed to exhibit an enhanced diffusion effect from stationary dislocations. In each test the depths of stained p-n junction were equal (within  $0.1\mu$ ) in both regions with  $> 5 \times 10^7$  stable disl/cm<sup>2</sup> and with  $< 10^3$  disl/cm<sup>2</sup>. Phosphorus was diffused into these boron-diffused wafers to form narrow basewidth npn transistors with  $X_{jb} = 5.5\mu$  and  $X_{je} = 5.0\mu$ . No diffusion spikes were delineated. Electrical measurements indicated very good uniformity of transistor gain and an absence of emitter-to-collector shorts in the narrow basewidth npn transistors with the above widely different concentrations of stationary dislocations. These electrical measurements indicate the absence of any diffusion anomalies beyond the resolving power of the p-n stain delineation technique employed.

The contribution of moving dislocations to solute diffusion was analyzed in this investigation by determining the extent of enhanced diffusion of boron in a lattice undergoing dynamic lattice deformation during loaded-lattice diffusion tests. The initial 10 min of the loading tests provided a condition for boron diffusion in a localized region containing moving dislocations. After the initial 10 min the dislocations which had moved due to the external stress became comparatively stationary (6). The results of the loading tests, presented in Fig. 2, identify boron solutes as exhibiting a significantly enhanced penetration within the locally deformed region which formed to relieve the externally applied stress.

Lattice stresses generated by diffused dopants were employed to determine if moving dislocations interacted with pinned stationary dislocations to create a measurable net effect on solute diffusion. Earlier work (13) had identified the quantity of diffused boron re-

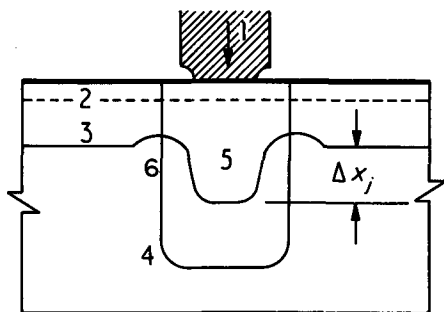


Fig. 2A. Dislocation-dependent boron diffusion effect achieved in the 1200°C loaded lattice diffusion tests. Schematic diagram illustrating: 1, weighted silicon stylus; 2, penetration of boron prior to loading; 3, penetration of boron outside stressed region; 4, periphery of locally deformed lattice; 5, enhanced diffusion of boron within deformed lattice; and 6, retarded penetration of boron at periphery of deformed lattice.

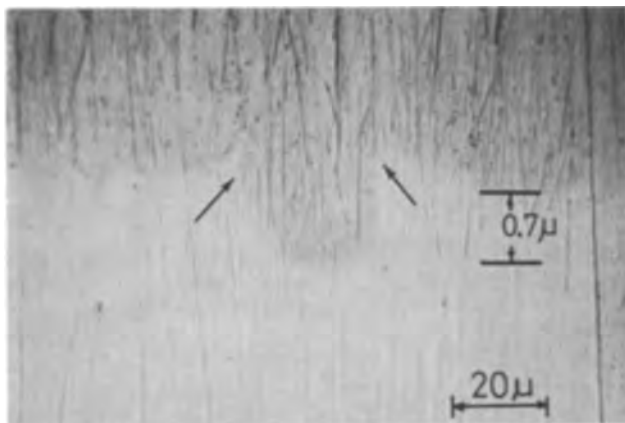


Fig. 2B. Stain delineated boron penetration front in region represented schematically in Fig. 2A.

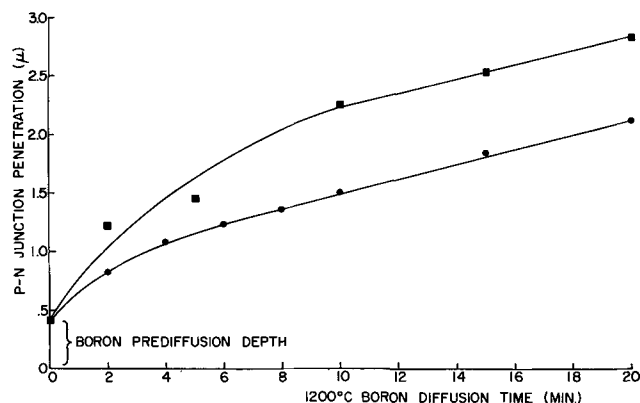


Fig. 2C. Boron penetration rate during loaded lattice diffusion tests for region 3 in Fig. 2A (lower curve) and region 5 in Fig. 2A (upper curve).

quired to strain silicon sufficiently to form and move dislocations beyond the dopant diffusion front as being  $Q \cong 2.6 \times 10^{16}$  boron/cm<sup>2</sup>. Test structures were formed by diffusing very high concentrations of boron, i.e.,  $Q > 3 \times 10^{16}$ /cm<sup>2</sup>, into wafers containing widely different concentrations of stationary dislocations, such as that shown in Fig. 1. The results of these tests disclosed the same amount of enhanced base diffusion associated with moving dislocations regardless of the concentration of pinned stationary dislocations, viz.,  $> 5 \times 10^7$ /cm<sup>2</sup> or  $< 10^3$ /cm<sup>2</sup>. The electrical analysis of these wafers disclosed transistor gain uniformity and an absence of emitter-to-collector short circuits which would indicate the absence of any localized enhanced

diffusion fronts below the resolving power of the metallographic analysis, viz., 0.1μ.

#### Experimental Results: Electrical

The contribution of (a) stable dislocations, (b) newly formed unstable dislocations, and (c) copper precipitates at dislocations to the reverse current of p-n junctions was determined on structures deeply diffused (5μ) with boron. Wafers of the type shown in Fig. 1 were used to determine the electrical effects of low energy stable dislocations. The reverse I-V characteristics of p-n junctions formed in dislocation-free material coincided with the curve obtained from junctions formed in regions with a uniform distribution of  $10^3$  disl/cm<sup>2</sup> (5 disl/device). P-N junctions with a uniform distribution of  $> 5 \times 10^7$  disl/cm<sup>2</sup> ( $2.5 \times 10^5$  disl/device) were found to have slightly greater than two times the reverse currents of similar p-n junctions formed in dislocation-free material. The reverse I-V characteristics of typical p-n junctions containing high and low concentrations of low energy stable dislocations appear in Fig. 3.

Also shown in Fig. 3 is a typical curve of the I-V characteristics of a p-n junction which contained newly formed, unstable dislocations in initially "dislocation-free" material; i.e., the initial material was free of dislocation etch pits after SIRTLE etching. These dislocations were formed to relieve the stress generated by a high concentration of diffused boron. The p-n junctions with newly formed, unstable dislocations in their depletion regions had higher reverse currents than similar p-n junctions without such lattice disorder in their depletion regions.

Copper impurities which precipitate at a dislocation and obtain a tightly packed configuration contribute to very high reverse currents as shown in Fig. 3. Such electrically active precipitates commonly form when the only crystalline disorder is localized near the wafer surface and copper is abundant. However, the addition of copper to a highly dislocated wafer, such as that shown in Fig. 1, contributed to only approximately five times the reverse current of a copper-free, low disorder p-n junction.

The contribution of low energy, stable dislocations to the electrical characteristics of narrow and wide basewidth npn transistors was investigated by recording the base-collector leakage, transistor gain, and storage time. The results of this analysis are tabulated in Table I. The percentage differences between the parameter values in each column were observed for three duplicate tests. The actual parameter values in Table I are the mean values of twenty units made in both highly and lowly dislocated portions of the same wafer. The measured parameter values were within 50% of the mean value in all cases. The base-collector junctions of transistors

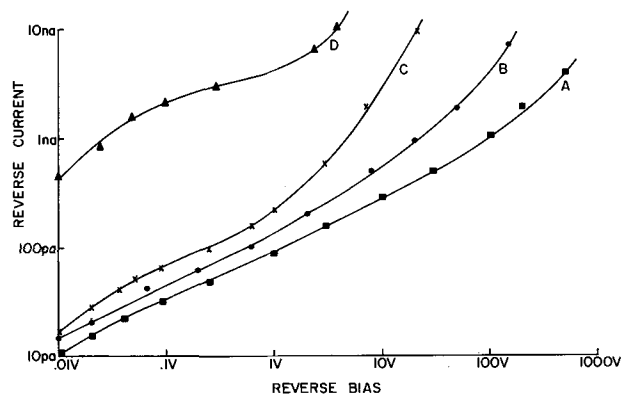


Fig. 3. Log *I* vs. log *V* characteristics of p-n junctions with different amounts of crystalline disorder: Curve A, disorder free or with  $< 10^3$  stable disl/cm<sup>2</sup>; curve B,  $> 5 \times 10^7$  stable disl/cm<sup>2</sup>; curve C,  $10^7$  unstable disl/cm<sup>2</sup>; curve D, tightly packed copper precipitate.

Table I. Typical values representing slight influence of  $> 5 \times 10^7$  stable disl/cm<sup>2</sup> on base-collector currents ( $I_{BC}$ ), transistor gain ( $\beta$ ), and storage time ( $\tau_s$ ) of nongold doped npn structures

	$I_{BC}$ at 150v p-n junctions, na	$\beta(I_B = 100\mu a)$ wide basewidth	$\beta(I_B = 100\mu a)$ narrow basewidth	$\tau_s$ narrow basewidth, $\mu s$	$\tau_s$ wide basewidth, $\mu s$
Units with $> 5 \times 10^7$ disl/cm <sup>2</sup>	6.7	2.9	201	0.49	0.63
Units with $< 10^8$ disl/cm <sup>2</sup>	3.0	3.2	274	1.66	1.1

formed in a lattice with  $> 5 \times 10^7$  disl/cm<sup>2</sup> were found to have approximately two times the reverse current at 150v compared to similar transistors formed in a portion of the same wafer having  $< 10^8$  disl/cm<sup>2</sup>. Similarly, transistors in the highly dislocated regions were found to have slightly lower transistor gains and storage times than identical transistors formed in the near dislocation-free portions of the same wafers. The contributions of new unstable dislocations to the transistor parameter values were considered to be a constant for all regions of the same wafer and therefore should not appear in the difference in parameter values attributed to the low energy, stable dislocations tabulated in Table I. The concentration of new unstable dislocations was assumed uniform since their necessary formation condition, i.e., solute concentration, was assumed to be constant. Whereas, the concentration of stable dislocations was not uniform since the initial quench/anneal treatment successfully created a difference of four orders of magnitude.

The addition of copper to narrow basewidth npn structures in near dislocation-free material contributed to the random development of emitter-to-collector short circuits and widely differing transistor gains. Copper precipitates were delineated in the base regions of transistors in such wafers. The similar addition of copper to narrow basewidth npn structures which had  $> 5 \times 10^7$  disl/cm<sup>2</sup> in the starting material contributed to fewer devices failing due to emitter collector short circuits and widely differing transistor gains than found in the less dislocated structures.

### Discussion

The above results show considerable differences as to the influence of dislocations on solute diffusion and the electrical characteristics of semiconductor devices. The following discussion will attempt to describe why (a) moving dislocations contributed to large enhanced diffusion effects; (b) stationary dislocations did not influence solute diffusion to a measurable extent; (c) dislocations free of large precipitates were quite electrically inactive; and (d) metallic contaminants were less electrically active in highly dislocated material than in dislocation-free material.

Moving dislocations were found to contribute to an enhanced diffusion of boron in the loaded-lattice diffusion tests. This was deduced from the observation that enhanced boron diffusion occurred beneath the weighted stylus only during the period of great dislocation motion after which the dislocations became comparatively stationary. These stationary dislocations of concentration  $> 4 \times 10^9$  disl/cm<sup>2</sup> did not enhance the diffusion of boron after the initial 10 min of loaded-lattice diffusion within the experimental limits of the measurements used, as shown in Fig. 2C. The contour of the boron penetration front just outside the periphery of the localized region of great lattice disorder exhibits a slight retardation. This area is identified by No. 6 in the schematic diagram in Fig. 2A and by the arrows in the micrograph in Fig. 2B. The retarded penetration cannot be attributed to the movement of the solute atoms being directly influenced by dislocation motion since the region of retarded penetration is relatively free of dislocations (6). However, this effect is associated with dislocations since it occurs only during the period of great dislocation motion. The retarded penetration of boron outside the locally deformed region and the enhanced penetration of boron in the region of great dislocation motion

could be explained by a mechanism which related these abnormal diffusion effects to excess vacancies generated by moving dislocations. These vacancies will have a net flux out of the localized cylinder of moving dislocations. The boron solutes around the locally deformed region will have a net flux into the deformation cylinder, thus depleting the surrounding region of boron dopants.

Dislocations which move by climbing will generate vacancies by the atomic shifts shown in the schematic diagrams in Fig. 4. These illustrations show how the translation of a substitutional atom to the dislocation core will create a dislocation jog, an element of climb, and a vacancy. This model has been discussed in detail by Thomson and Balluffi (15). The movement of a dislocation by gliding may not contribute to vacancy formation since no atomic movement away from the glide plane is required.

Stationary dislocations were not found to influence the diffusion of boron or phosphorus in tests employing stable dislocations. Since boron and phosphorus diffuse by the vacancy mechanism in silicon (16), a model justifying the absence of a diffusion effect dependent on stationary dislocation in a system of continually changing temperature must explain the absence of a net vacancy action of stationary dislocations. Three considerations seem possible. One consideration is that the vacancy-source action of a stationary dislocation during its heating period is equal to the vacancy sink action of the same dislocation during the cooling period of the diffusion cycle. By this hypothesis, the enhanced diffusion of boron near a dislocation during wafer heating would be countered by the retarded diffusion of boron near a dislocation during wafer cooling. Another possibility is that the vacancies generated at the wafer surface saturate the boron diffused region quickly, thus rendering the vacancy source action of stationary dislocations within the crystal insignificant relative to boron diffusion. This might occur if the diffusion of vacancies is many times faster than the diffusion of boron. However, this is not the case since the diffusion coefficient of boron (17) at 1200°C is nearly six times greater than the reported self-diffusion of a silicon (18). The third, and most likely, explanation for the absence of a measurable vacancy action of stationary dislocations suggests the

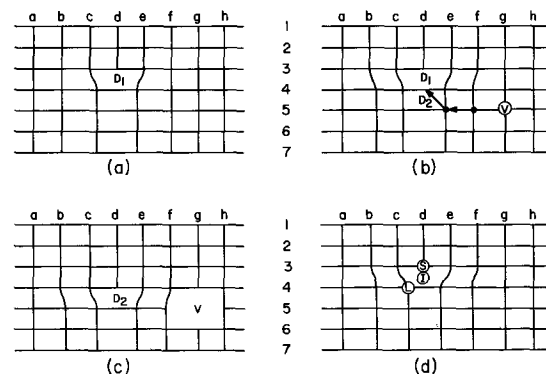


Fig. 4. Schematic representation of a dislocated crystal lattice: (a) dislocation lying perpendicular to drawing with core at  $D_1$ ; (b) atom shifts required to form a jog  $D_2$  and vacancy "V"; (c) new dislocation core position  $D_2$  and vacancy "V" following jog formation; (d) likely positions of Cottrell-captured "S" small impurities, "L" large impurities, and "I" very small impurities.

dislocations do not form jogs for vacancy formation due to their being pinned by a "Cottrell"-captured impurity, as illustrated in Fig. 5(D), and hence cannot climb. An unpinned dislocation could form a jog and contribute a vacancy to a system without an externally applied force.

Cottrell's model (19) concerns the strain energy interaction between impurities of size different from silicon and edge dislocations. The region around an edge dislocation is one of both lattice tension and compression. Therefore, both large (Sb, Ga) and small (B, P, O) impurities, relative to silicon, would be attracted to the dislocation to achieve a lower combined-energy of lattice distortion. The interaction energy between the dislocation and the impurity varies inversely with distance but should be felt over large distances depending on the wafer temperature.

Stationary dislocations were not found to contribute to enhanced solute diffusion by providing a preferential path for the passage of small solutes. The dislocation core diffusion model very likely did not dominate the diffusion process due to an impurity clogging action of the type proposed by Ruoff and Balluffi (20). The Cottrell capture of an impurity by a dislocation would restrict the size of the dislocation core, thus restricting the passage of diffused dopant impurities.

Boron diffusion tests were performed in a system containing moving dislocations within a background of stationary dislocations to determine if the two dislocation states would interact in a manner which would cause an additional dislocation-dependent solute diffusion effect. Two interactions seem possible: first, the excess vacancies generated by moving dislocations could be annihilated at the stationary dislocations before they influence boron diffusion. This would be detected as a reduction of the enhanced boron diffusion compared to that caused by newly formed dislocations sweeping through otherwise dislocation-free material. Second, the lattice stress which causes the dislocations to move could cause the stationary dislocations to oscillate and thus generate an additional source of vacancies. This would contribute to an enhanced boron diffusion greater than that associated with moving dislocations in a system free of stable dislocations. However possible these two models may be, the boron diffusion test results did not support the existence of an interaction between stable dislocations and the effect of moving dislocations on boron diffusion in silicon. Thus, it is very likely that the stationary dislocations were firmly pinned and not capable of any vacancy action.

Because of the very small influence of dislocations on the reverse current, transistor gain, and storage time of nongold-doped npn transistors observed in this work, this discussion of the electrical activity of dislocations in semiconductor devices will be quite general. The slight increase in electrical activity of devices with  $>5 \times 10^7$  low energy, stable dislocations/cm<sup>2</sup> could be due to (a) the dislocations providing a path for channeling injected minority carriers through a p-n junction's depletion region or (b) the dislocations creating current by the generation-recombination process. A common denominator for both of these causes for excess reverse current is an energy level associated with the dislocation. Shockley (21) and Read (22) proposed a model for the electrical activity of dislocations in semiconductors based on dangling bonds at the core of dislocations having some edge component. The space charge barrier surrounding a dislocation may have a dominant effect in determining the hole-electron recombination characteristics as reported recently by Morrison (23). The contribution of a channel current to the reverse current of a p-n junction would be reduced by an interruption in the sequence of dangling bonds. Dislocations which have not been fully annealed would be expected to have far more dangling bonds than a fully annealed dislocation. The dislocation with the fewest

dangling bonds is the most stable and, by the Shockley-Read model, is less electrically active. Hornstra (24) has shown that high-temperature annealing can provide for the diffusion of vacancies and interstitials which can transform an edge dislocation with atoms having two dangling bonds to an edge dislocation with no dangling bonds.

The foregoing model relating the electrical characteristics of a dislocation to dangling bonds has been considered by some to be a highly restricting model (25, 26). Read had shown that pure edge dislocations should have a maximum number of dangling bonds while pure screw dislocations would have no dangling bonds. By this model, edge dislocations would be highly charged while screw dislocations would have no charge. This hypothesis does not appear to agree with recent experimental work using bicrystals and compound semiconductors. The latter work identified both edge and screw dislocations as having similar charges (26). Heine (26) has proposed a general model for charge accumulation at dislocations in semiconductors which attributes an energy level to localized atomic strain at a dislocation. This model and the earlier "dangling bond" model behave, electrically, similarly in that the lattice strain about a nonannealed dislocation is greater than the localized lattice deformation which surrounds an annealed dislocation.

The high reverse currents of p-n junctions in nonannealed dislocated material reported in this work can be attributed to large lattice strain and dangling bonds associated with individual dislocations. Similarly, the lower reverse currents associated with stable dislocations can be attributed to a reduction in lattice strain and fewer dangling bonds.

The influence of dislocations on the generation-recombination of electrons and holes in transistor structures has been of great interest since Chynoweth and Pearson (27) reported that avalanche breakdown microplasmas occurred preferentially at dislocations in silicon p-n junctions. They also reported dislocations as contributing to enhanced internal field emission and, consequently, a soft reverse characteristic. Recent investigations (10, 13) using lightly doped n-type silicon have shown that microplasma emission and soft reverse characteristics are caused by tightly packed precipitates in a junction's depletion region, not simply lattice disorders. Precipitates are believed to cause localized high electric fields, thus making it likely for both avalanche breakdown and field emission. Copper precipitates in this investigation were found to cause emitter-collector shorts and a variability of transistor gain. Interesting, though, is the low level of electrical parameter variability associated with copper when the metal was added to highly dislocated wafers. This is attributed to the large concentration of available copper precipitation sites away from the transistor's depletion regions in highly dislocated material. In nearly disorder-free material, copper is attracted to the diffused regions of a transistor since these regions contain the only available precipitation sites.

The principal conclusion from this study is that dislocations in starting material do not significantly influence p-n junction reverse currents, transistor gain, and the storage time of finished nongold-doped semiconductor devices.

#### Acknowledgment

The author wishes to express his appreciation to Dr. R. N. Tucker for his stimulating suggestions during the development of this investigation. The continuing interest in this work provided by Dr. H. Sello made this investigation possible. The experimental assistance of Miss B. Johnston in all phases of this work was very helpful.

Manuscript submitted Jan. 22, 1968; revised manuscript received March 26, 1968. This paper was presented at the Chicago Meeting, Oct. 15-19, 1967, as Paper 174.

Any discussion of this paper will appear in a Discussion Section to be published in the June 1969 JOURNAL.

## REFERENCES

- H. J. Queisser, K. Hubner, and W. Shockley, *Phys. Rev.*, **123**, 1245 (1961).
- F. Karstensen, *J. Electron. Control*, **3**, 305 (1957).
- W. L. Bragg, *Proc. Phys. Soc.*, **52**, 54 (1940).
- J. M. Burgers, *ibid.*, **52**, 23 (1940).
- L. S. Heldt and J. N. Hobstetter, *Acta Met.*, **11**, 1165 (1963).
- J. E. Lawrence, *Brit. J. Appl. Phys.*, **18**, 405 (1967).
- J. E. Lawrence, *J. Appl. Phys.*, **37**, 4106 (1966); *Bull. Am. Phys. Soc.*, **11**, 401 (1966).
- H. Kressel and A. Elsea, *Solid-State Electron.*, **10**, 213 (1967).
- R. G. Fletcher and W. L. Brown, *Phys. Rev.*, **92**, 591 (1953).
- J. E. Lawrence, *This Journal*, **112**, 796 (1965).
- For a review, see W. Bardsley, "Progress in Semiconductors," Vol. 4, A. F. Gibson, R. E. Burgess, and F. A. Kröger, Editors, John Wiley & Sons, Inc., New York (1960).
- J. E. Lawrence, *Trans. TMS-AIME*, **242**, 484 (1968).
- J. E. Lawrence, *This Journal*, **113**, 819 (1966).
- R. L. Berry, Private communications.
- R. M. Thomson and R. W. Balluffi, *J. Appl. Phys.*, **33**, 803 (1962).
- C. S. Fuller and J. Z. Ditzenberger, *ibid.*, **27**, 544 (1965).
- A. D. Kurtz and R. Yee, *ibid.*, **31**, 303 (1960).
- W. R. Wilcox and T. J. LaChappelle, *ibid.*, **35**, 240 (1964).
- A. H. Cottrell, "Dislocations and Plastic Flow in Crystals," p. 134, Oxford University Press, London (1953).
- A. L. Ruoff and R. W. Balluffi, *J. Appl. Phys.*, **34**, 1845 (1963).
- W. Shockley, *Phys. Rev.*, **91**, 228 (1953).
- W. T. Read, Jr., *Phil. Mag.*, **45**, 775 (1954).
- S. R. Morrison, *Phys. Rev.*, **104**, 619 (1956).
- J. Hornstra, *J. Phys. Chem. Solids*, **5**, 129 (1958).
- V. Celli, A. Gold, and R. Thomson, *Phys. Rev. Letters*, **8**, 96 (1962).
- V. Heine, *Phys. Rev.*, **146**, 568 (1966).
- A. G. Chynoweth and G. L. Pearson, *J. Appl. Phys.*, **29**, 1103 (1958).

## Structure and Sodium Migration in Silicon Nitride Films

J. V. Dalton\* and J. Drobek

Bell Telephone Laboratories, Incorporated, Murray Hill, New Jersey and Allentown, Pennsylvania

## ABSTRACT

Silicon nitride films deposited on silicon substrates by several techniques were studied. Electron diffraction studies of the films revealed that films varied in crystallite size from  $<10$  to  $\sim 100\text{\AA}$ . Radiotracer diffusion experiments using  $\text{Na}^{22}$  as diffusant revealed that the smaller crystallite films were better barriers to sodium diffusion than the larger crystallite films. Field enhanced drift of sodium was not observed in any of the silicon nitride films regardless of crystallite size. Silicon nitride films composed of large crystallites appeared to etch faster than smaller crystallite films in dilute buffered hydrofluoric acid.

Thin films of silicon nitride are of interest in the fabrication of semiconductor devices because they have been found to be relatively impermeable to the highly mobile ionic species which degrade devices using silicon dioxide as an insulating or passivating film (1,2) Sodium, because of its high mobility and common occurrence as contamination, is a common cause of instabilities in these devices (3-5).

Several methods of depositing silicon nitride films have been reported (6-9). The object of this investigation was to determine to what extent and in what ways silicon nitride is superior to silicon dioxide in inhibiting the movement of sodium. During the investigation silicon nitride films deposited by a variety of techniques were studied, and within each deposition technique conditions were varied to yield films of slightly different physical properties. A large number of such variations were studied; experiments and results reported are sufficient to detail the advantages and disadvantages of silicon nitride as compared to silicon dioxide.

Films of silicon nitride over silicon dioxide and mixed oxide-nitride films were not studied during this investigation; in fact, efforts were made to exclude oxides from all films studied by using specially dried gases and moisture free conditions.

### Deposition of Silicon Nitride Films

Thin films of silicon nitride may be deposited on silicon substrates by several techniques including:

- Pyrolytically by the reaction of  $\text{SiH}_4$  and  $\text{NH}_3$  (6).

- Pyrolytically by the reaction of  $\text{SiCl}_4$  and  $\text{NH}_3$  (7).
- Microwave plasma deposition (silicon sputtered through a nitrogen plasma) (8).
- D-C plasma deposition (silicon halide vapor in a nitrogen plasma) (9).

Several parameters may be varied in each of these deposition systems: temperature, flow rate, plasma density, etc. Only those parameters which influence the ability of the film to block sodium motion are discussed in this paper.

The silicon nitride films studied during this investigation were deposited on the (111) face of high resistivity (5-50 ohm-cm) silicon wafers  $> 0.75$  in. in diameter and 0.010 in. thick. Substrate preparation include a mechanical lap followed by a mechanical polish and in some cases a chemical polish. Wafers were given typical semiconductor preoxidation cleaning immediately before silicon nitride film deposition.

### Electron Diffraction Studies

Glancing angle electron diffraction photographs were taken of the surface of each film using an RCA type EMD2 electron diffraction unit operated at 50 kv. The film was then etched in small increments, and after each etch a diffraction pattern was recorded. In this manner the structural characteristics of the film (degree and type of crystallinity) were mapped as a function of film thickness.

The structure of silicon nitride has been studied by Forgeng and Decker (10). Accurate values of the interplanar spacings obtained from powder as well as single crystal samples are available. Both  $\alpha$  and  $\beta$   $\text{Si}_3\text{N}_4$  have several high intensity reflections which are

\* Electrochemical Society Active Member.



specific for one or the other type. Therefore,  $\alpha$ ,  $\beta$  or  $\alpha$ - $\beta$  forms of  $\text{Si}_3\text{N}_4$  can be identified (15). The evidence that  $\alpha$   $\text{Si}_3\text{N}_4$  forms first on elemental silicon in a nitriding atmosphere was established by a number of experiments carried out by Turkdogan *et al.* (15). As the reaction proceeds the  $\alpha$ - $\text{Si}_3\text{N}_4$  now in direct contact with the gaseous phase is converted to  $\beta$ - $\text{Si}_3\text{N}_4$ . Turkdogan's experiments were conducted at 1450°C.

Crystallite size in the film was determined by line broadening in the diffraction pattern; the lines (rings) become broader if there are too few coherently scattering atoms to yield sharp rings or spots. For electron diffraction the following expression for crystallite diameter ( $\sigma$ ) is used

$$\sigma = \frac{C}{\Delta S}$$

where  $C = L\lambda$  (camera constant),  $L$  = distance from specimen to photographic plate,  $\lambda$  = wavelength used,  $\Delta S$  = line broadening.

The possible error in our estimation of crystal size is  $\pm 15\%$ . The mass penetration depth of a 50 keV electron is  $\sim 3 \times 10^{-3} \text{ gcm}^{-2}$ . For silicon nitride (density  $\approx 3$ ) this yields a total penetration of  $10^{-3} \text{ cm}$ . Effective penetration for diffraction studies is less than total penetration because of scattering. In glancing angle electron diffraction the effective penetration in amorphous or small crystallite films has been found to be about 1% of the total penetration, in our case,  $10^{-5} \text{ cm}$  or 1000Å; this is the penetration along the beam. The angle of incidence of the beam with the surface of the film was varied between 0.02 and 0.1 radians. Therefore, the beam penetration in the direction normal to the surface was about 20-100Å. A more detailed discussion of the interaction of electron beams with thin films has been presented by Calbick (11).

#### Radiotracer Experiments

Movement of sodium in the nitride films was studied by deliberately contaminating the films with radioactive sodium, etching the film in small increments and counting the  $\gamma$  activity remaining in the sample after each etch. The sodium contaminated samples were treated in two general ways. They were either heated to cause the sodium to diffuse through the films or they were heated while a field was applied to enhance the sodium motion.

The isotope used in the tracer studies was  $\text{Na}^{22}$  ( $T_{1/2} = 2.60$  years). The isotope was purchased as an acid solution of  $\text{NaCl}$  and total sodium concentration was specified by the vendor, New England Nuclear Corporation. This permitted calibration of activity with total sodium content of the solution so that a specific gamma emission from a sample could be converted to a specific sodium concentration. This method does not account for unintentional  $\text{Na}^{23}$  contamination of the sample. However, intentional contamination was approximately 100 times higher than the level of unintentional  $\text{Na}$  contamination measured at these laboratories by Buck *et al.* (5).

Sodium<sup>22</sup> was detected and counted by means of a  $3 \times 3$  in. well-type Na I (Th activated) scintillation crystal connected to a Technical Measurement Corporation Model 102 analyzer. Sensitivity was typically  $3.0 \times 10^{10}$  sodium atoms/count/min and background was usually 50 counts/min. The 0.51 MeV peak of  $\text{Na}^{22}$  was traced and an energy range of 0.491 to 0.520 MeV was counted in order to maximize the sample to background activity. In order to minimize the statistical error of the measurements and yet complete the studies in a reasonable period of time each count was made for 60 min or 10,000 counts whichever came first. The standard deviations in the concentration plot (Fig. 1) show that this system yields statistically significant concentration points.

Autoradiographs were taken of samples after application of the radioactive sodium, after diffusion,

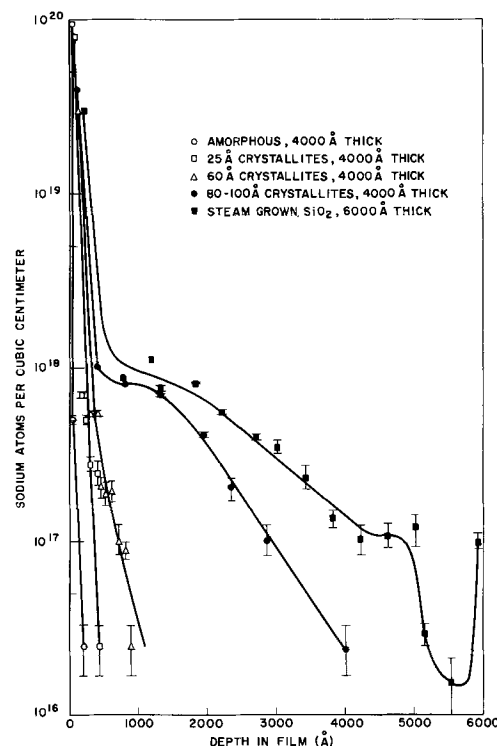


Fig. 1. Sodium diffusion profiles in silicon nitride and silicon dioxide.

after field enhanced drift, and at any step where it was desirable to determine uniformity of  $\text{Na}^{22}$  distribution across the surface of the sample or, in the case of drift experiments, to study localized field enhancement of diffusion. All autoradiographs were obtained by placing the sample in direct contact with Kodak No-screen x-ray film for a length of time sufficient to yield a high contrast picture.

**Diffusion Experiments.**—Sodium was applied to the silicon nitride films ( $1 \text{ cm}^2$ ) by evaporation in a vacuum from a platinum boat (at 1000°C) on which a few drops of tracer solution had been dried. This method was found to yield a relatively uniform sodium deposition. After deposition of the sodium the wafers were heated to 600°C for 22 hr in forming gas (85% nitrogen, 15% hydrogen). After diffusion, the wafers were water washed, autoradiographed, and incrementally etched in HF. Activity was counted after each etch until no activity above background remained in the sample.

**Drift experiments.**—For field enhanced diffusion (drift) experiments sodium was applied to silicon nitride films in the same manner as for the diffusion experiments. Gold dots were vacuum evaporated over the sodium and silver was evaporated onto the exposed silicon back surface of the wafer to provide contacts. A potential was applied to most of the dots on a wafer (20-30 square dots, 0.025 in. on a side), one at a time, with +4v (on the gold dots) for 1 min each. Field strengths ranged from  $7 \times 10^4$  to  $1 \times 10^5$  v/cm under these conditions. Most drift experiments were done while the samples were at 400°C in room air; however, some experiments were done at higher temperatures, some in forming gas, and some at higher voltages. The total time that a sample was at elevated temperature during these field enhanced diffusion experiments was 60-90 min. Current flow was recorded while the potential was applied, and on some dots I-V scans were run over a range of -4 to +4v to confirm the absence of charge storage effects normally seen in  $\text{SiO}_2$  films (12).

The samples were counted before and after removal of the metal contacts with aqua regia and after further



water washing. Autoradiographs were taken to determine if the sodium had diffused into the silicon nitride under the dots. The nitride film was then removed by HF in small increments, counting after each etch until all the active sodium was removed.

**Etching.**—The silicon nitride films were etched in dilute buffered hydrofluoric acid (13). In most cases a wafer was quartered so that diffusion, drift, and diffraction studies could be made on the same film. Etch rates were determined during the diffraction studies and also during the drift and diffusion experiment; results agreed well.

Film thickness measurements were made during the diffraction experiments using a spectrophotometer (14) and during the diffusion and drift experiments by comparison with a color chart.

### Experimental Results

**Diffraction.**—Electron diffraction studies revealed that the silicon nitride films varied considerably in crystallite size and structure.  $\alpha$ ,  $\beta$ , and  $\alpha\beta$  mixtures of silicon nitride were found. Crystallite sizes ranged from  $< 10$  to  $\sim 100\text{\AA}$ . Films of crystallites  $< 20\text{\AA}$  will arbitrarily be called amorphous.

Pyrolytically deposited (silane or silicon tetrachloride) films were usually amorphous; however, if these films were deposited at temperatures  $< 900^\circ\text{C}$  on improperly cleaned substrates they were crystalline and invariably  $\alpha$   $\text{Si}_3\text{N}_4$ . The crystallite size in these crystalline, pyrolytic films ranged from 20–40 $\text{\AA}$ .

The structure of  $\text{Si}_3\text{N}_4$  films prepared by d-c plasma discharge was also studied. Several of them were crystalline; some were amorphous. These crystalline films ranged from 20–80 $\text{\AA}$  in crystallite size and were usually  $\beta$  or  $\alpha$ - $\beta$  mixtures. Occasionally  $\alpha$   $\text{Si}_3\text{N}_4$  which forms first and then a transition form  $\alpha$  to  $\beta$  (15) was observed at the interface.

Microwave plasma deposited films were usually crystalline ( $\alpha$  or  $\alpha\beta$ ), and average crystallite size ranged from 40 to several hundred angstroms.

The diffraction studies also revealed that the films were not uniform in crystallite size throughout their thickness. Some went from amorphous at the top to crystalline at the  $\text{Si}$ - $\text{Si}_3\text{N}_4$  interface, but more often they were amorphous at the interface and crystalline at the top. These transitions in crystallite size may be partly attributed to contamination or fallout in the reaction vessel or the gas streams providing nucleation sites for the formation of large crystallites.

**Diffusion.**—The ability of sodium to penetrate the silicon nitride films was found to be related to the crystallite size of the film. Sodium was found to diffuse more easily into the films composed of larger crystallites. Figure 1 shows four diffusion profiles of Na in silicon nitride films of different crystallite sizes. A diffusion profile of Na in steam grown  $\text{SiO}_2$  [from ref. (5)] is shown on the same plot for comparison. The  $\text{SiO}_2$  diffusion conditions were identical to the nitride diffusion conditions. In silicon nitride films where the crystallite size changed in the interior of the film sodium diffusions were carried out twice, once at the outer surface and on another piece after etching to the point where a significant difference in crystallite size was detected by electron diffraction. In these experiments the same relationship was observed; that is, the films composed of larger crystallites were penetrated more easily by Na.

**Drift.**—No field enhancement of the diffusion of sodium was detected in any of the silicon nitride films studied regardless of crystallite size or type. In some cases sodium activity remained after removal of the metal contacts and thorough washing, but autoradiographs showed that this remaining activity was a random spottiness or in some cases a uniform darkening of the film due to slight diffusion of sodium at the elevated temperature. Temperatures as high as  $700^\circ\text{C}$ , voltages as high as 10v, or ambients of nitrogen or forming gas or any permutation of these

conditions did not cause enhanced motion of the sodium into the film.

Figure 2a shows a drawing of a silicon nitride coated wafer with a gold dot pattern applied. Figure 2b is the autoradiograph of this sample after removal of the gold dots and water washing of the surface. Most of the activity of drifted silicon nitride films was removed by water washing. The general darkening of this picture is due to background radiation. The larger dark spots, indicating  $\text{Na}^{22}$  activity do not correspond to the positions of the dots which had been subjected to the +4v, but may be due to nonuniform sodium deposition or flaws in the film.

In contrast, Fig. 3a, b depicts the dot patterns and autoradiograph of a 6000 $\text{\AA}$   $\text{SiO}_2$  film [from ref. (5)]. Deposition and drift conditions were identical to those for the nitride sample. In this case an image of each dot which had seen the +4v is reproduced in the autoradiograph. Incremental etching and counting of this film revealed that 90% of the  $\text{Na}^{22}$  was within 800 $\text{\AA}$  of the  $\text{Si}$ - $\text{SiO}_2$  interface. Autoradiographs taken after several etching steps showed that the activity patterns shown in Fig. 3b persisted throughout the film.

**Etch rate.**—Etch rates of silicon nitride films in dilute HF were found to be related to crystallite size in the film. Amorphous films were the slowest etching. Figure 4 is a plot of etch rate vs. crystallite size for several silicon nitride films. The fast etching of the

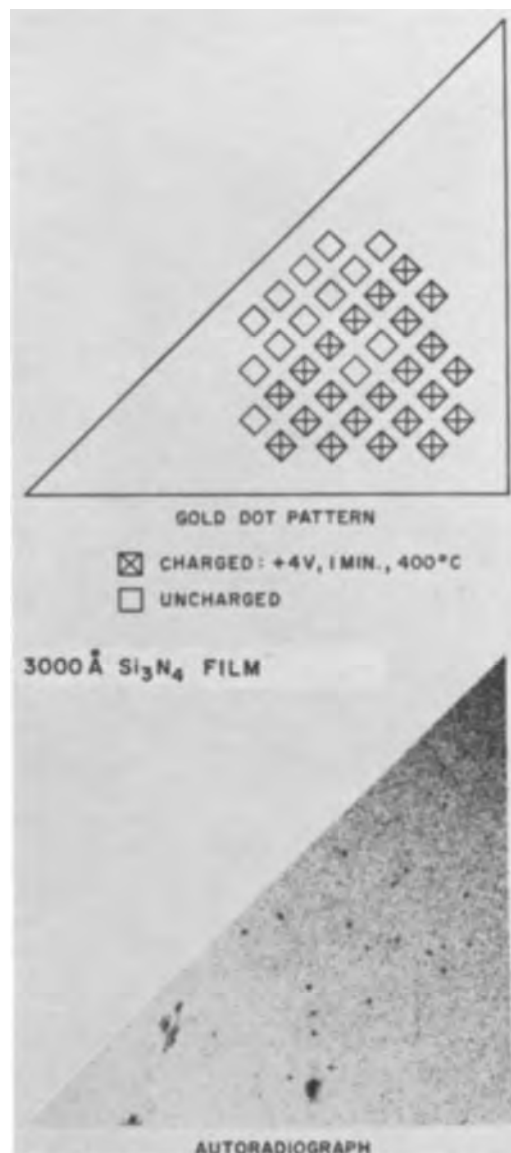


Fig. 2a (top). Gold dot pattern on silicon nitride film; b (bottom) autoradiograph after removal of gold dots.

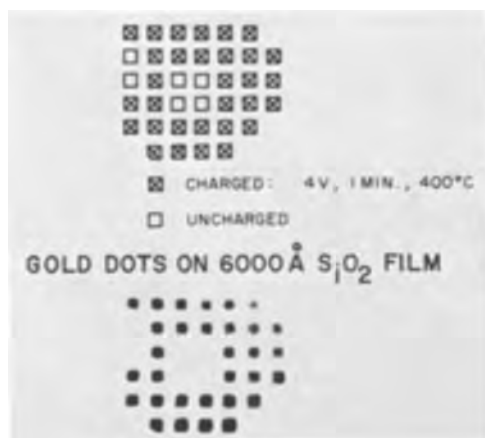


Fig. 3a (top) Gold dot pattern on silicon dioxide film; b (bottom) autoradiograph after removal of gold dots.

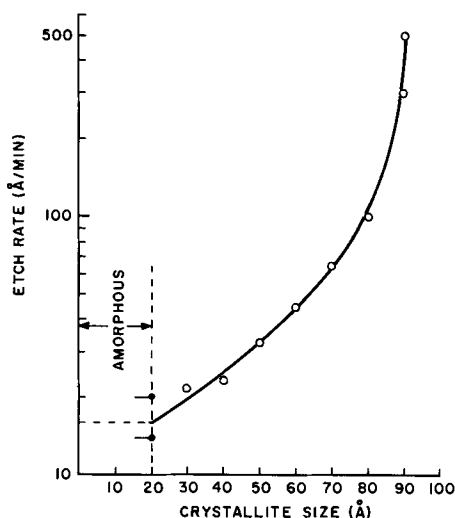


Fig. 4. Etch rate vs. crystallite size of silicon nitride films

more crystalline films may be caused by diffusion of the etchant along grain boundaries and actual lifting of crystallites. Evidence for this type of etching was seen in the crystalline films; pitting and nonuniform preferential etching occurred.

It has been reported (16) that the etch rate of silicon nitride films is strongly dependent on the oxygen content of the film. No evidence for the presence of oxygen was found in the pyrolytic films either by infrared or scanning electron beam analysis; however, the plasma films were found to contain 1% oxygen by weight. This level of oxygen is quite low and moreover this same 1% was found in a group of plasma films which had a wide range of etch rates.

**Error analysis.**—Standard deviations are indicated as flags on each plotted point on distribution plots (Fig. 1).

The error in estimation of film thickness by comparison with a color chart is approximately  $\pm 50\text{\AA}$  for each point.

### Summary and Conclusions

Electron diffraction studies revealed that pyrolytically deposited silicon nitride films were amorphous except when deposited on dirty substrates. D.C. plasma deposited films, we observed, were both amorphous and crystalline. Microwave plasma deposited silicon nitride films were usually crystalline.

Etch rate and sodium penetration were related to crystallite size in the films. Films composed of large crystallites were found to be more easily penetrated by sodium (under our diffusion conditions) and generally faster and less uniformly etched than films composed of small crystallites.

Grain boundaries may be considered as surfaces whose atomic arrangement is irregular. Several authors have reported that diffusion proceeds more rapidly in grain boundaries than in the body of the grains (17-22). Moreover, it has been reported that diffusion enhancement is greater in wide grain boundaries (18) which are usually associated with large crystallites. We therefore conclude that the increase in sodium diffusion with grain size (within the range of crystallite sizes observed,  $\sim 20$  to  $\sim 100\text{\AA}$ ) is due to rapid diffusion in wide grain boundaries. The apparent high etch rate and pitting of the large crystallite films is probably caused by etchant penetrating the wide grain boundaries and lifting out crystallites.

The field enhanced drift experiments on silicon nitride films indicate that these films, regardless of deposition technique, provide a barrier to sodium drift under the conditions of voltage, time and temperature described.

### Acknowledgments

The authors are indebted to T. M. Buck and R. Jaccodine for their encouragement and many helpful discussions.

Manuscript submitted Nov. 27, 1967; revised manuscript received ca. April 2, 1968.

Any discussion of this paper will appear in a Discussion Section to be published in the June 1969 JOURNAL.

### REFERENCES

1. E. H. Snow, A. S. Grove, B. E. Deal, and C. T. Sah, *J. Appl. Phys.*, **36**, 1664 (1965).
2. J. R. Mathews, W. A. Griffin, and K. H. Olson, *This Journal*, **112**, 899 (1965).
3. E. Yon, W. H. Ko, and A. B. Kuper, *IEEE Trans.*, **ED-13**, 276 (1966); paper presented at Buffalo, N. Y., Meeting of the Society, To be published.
4. H. G. Carlson, C. R. Fuller, and J. Osborne, "Physics of Failure in Electronics IV," 390 (1966) (CFSTI—Dept. of Commerce), H. G. Carlson et al., *ibid.*, **V**, 265 (1967).
5. T. M. Buck, F. G. Allen, J. V. Dalton, and J. D. Struthers, *This Journal*, **114**, 862 (1967), presented at IEEE Silicon Interface Specialists Conference, Las Vegas, Nevada, Nov. 1965.
6. V. Y. Doo, D. R. Nichols, and G. A. Silvey, *This Journal*, **113**, 1279 (1966).
7. M. J. Grieco, F. L. Worthing, and B. Schwartz, *This Journal*, **115**, 525 (1968).
8. J. R. Ligenza and E. I. Povelonis, Private communication; Process Described for  $\text{SiO}_2$  at the Washington Meeting of the Society, Oct. 11-15, 1964, as Paper 138.
9. W. C. Erdman and A. Androshuk, Paper presented at the Philadelphia Meeting of the Society, Oct. 9-14, 1966, as Recent News Paper 3.
10. W. D. Forgeng and B. F. Decker, *Trans. Met. Soc., AIME*, 343-348 (1958).
11. C. J. Calbick, Interaction of Electron Beams with Thin Films, *Physics of Thin Films*, 11 (1964).
12. M. Yamin, *IEEE Trans.*, **ED-12**, 88-96 (1965).
13. "Bell Etch,"  $\sim 8\%$  HF, Etches Atmospheric Pressure Stream Grown  $\text{SiO}_2$  at 1000Å/min.
14. F. Reizman, *J. Appl. Phys.*, **36**, 3804 (1965).
15. E. T. Turkdogan, P. M. Bills, and V. A. Tippet, *J. Appl. Chem.*, **8**, May 1958.
16. D. M. Brown, P. V. Gray, F. K. Heumann, H. R. Phillip, and E. A. Taft, *This Journal*, **115**, 311 (1968).
17. M. R. Achter, L. S. Birks, and E. J. Brooks, *J. Appl. Phys.*, **30**, 1825 (1959).
18. A. E. Austin and N. A. Richard, *ibid.*, **32**, 1462 (1961).
19. "Electron Probe Microanalysis," L. S. Birks, pp. 147-154.
20. D. B. Wittry, paper presented at AIME Meeting, Boston, Mass., August 1959.
21. J. Philibert and H. Bizouard, *Rev. Met. (Paris)*, **56**, 187 (1959).
22. R. E. Smallman, "Modern Physical Metallurgy," 2nd ed., Butterworths, London (1963).

# A Study on Making Abrupt Heterojunctions by Solution Growth

Kazuhiro Kurata and Tadamasa Hirai

Central Research Laboratory, Hitachi Ltd., Kokubunji, Tokyo, Japan

## ABSTRACT

Ge-Si and Ge-GaAs abrupt heterojunctions without intermediate layers have been fabricated by a new alloying technique which was developed from metallographic consideration on the base-solvent-solute ternary phase system in solution growth. The alloying was carried out under the condition of no penetration occurring at the interface between the base crystal and the molten alloy. To maintain this condition, the compositions of the starting alloy which would be melted on the base crystal were selected as follows. The Ag-Ge alloy containing 45 atomic % Ge and the Al-Ge alloy containing 40 atomic % Ge were melted on Si and GaAs wafers respectively. The rectifying V-I characteristics and the results of the junction capacitance measurements showed that these junctions were abrupt and the crystallized Ge layers were heavily doped with solvent metals.

Since the work of Kroemer (1, 2), epitaxial heterojunctions between two semiconductors have aroused great interest. Many applications which have been proposed for these junctions are, for example, wide bandgap emitter transistors (3, 4), majority carrier rectifiers (5), high speed and window effect photo-detectors (6), and optical transistors (7).

Conventional methods which have been reported for producing these junctions are the vapor phase depositions. Recently they have also been obtained by the regrowth from liquid phases. Wei and Shewchun (8) have reported the electrical properties of alloyed heterojunctions between Ge and Si in which the former is fully melted on the latter. A simple technique to make heterojunctions where only the interface between the two semiconductors is melted has been reported by Rediker *et al.* (9) and Hinkley *et al.* (10).

On the other hand, Takeda *et al.* (11) have reported the phase diagram for the pseudobinary system Ge-GaAs determined by means of thermal analysis, microscopic observation, and x-ray microanalysis. They have shown that it was of a simple eutectic type, and the eutectic point lay at 15 m/o (mole per cent) GaAs, and its temperature  $865^{\circ} \pm 2^{\circ}\text{C}$  stood lower than the melting points of both semiconductors.

Therefore, it is impossible to make a metallographically perfect heterojunction between Ge and GaAs by a simple alloying technique. If the Ge crystal which is in contact with the GaAs crystal is heated to a temperature above the eutectic point, both crystals begin to melt at the contact region, and then the eutectic composition of GaAs-Ge molten solution is formed. Therefore the eutectic solid layer is formed between the recrystallized Ge and GaAs layers when the melt is cooled. In fact, intermediate layers like this have been observed by some researchers (12, 13).

In the present work, a metallographic analysis of the preparation of the alloy or the solution growth heterojunctions was made, and the conditions to guarantee making abrupt heterojunctions with no other undesirable junctions near the interface between two semiconductors were described. The results of the analysis were experimentally applied to producing Ge-Si and Ge-GaAs junctions.

## Principle of the Method

Desirable properties of the alloy-melt on the base wafer for making single crystal heterojunctions by a simple alloying technique, shown in Fig. 1, are as follows: (I) the alloy shown in Fig. 1a should contain a considerable amount of semiconductor  $S_1$  which is to be crystallized on the base wafer  $S_2$ , to ensure a satisfying growth rate without constitutional super-

cooling. (II) The base semiconductor  $S_2$  in Fig. 1b should not dissolve into the alloy-melt on it in order that the crystallized layer in Fig. 1c will make neither a eutectic structure nor a regrown homojunction between  $S_1$  and  $S_2$ .

The conditions ensuring the above properties are occasionally satisfied by the selection of the components and composition of the melt. When the alloy-melt which was composed of C% of metallic solvent M and (100-C)% of semiconductor  $S_1$  as a solute contacts with the base semiconductor  $S_2$ , the necessary conditions of "no penetration" can be seen in the phase diagram of the ternary M- $S_1$ - $S_2$  alloy system, as shown in Fig. 2.

In the binary M- $S_1$  system, if the melt of this composition is cooled down to the temperature of  $t$  from a higher temperature, then the solute  $S_1$  begins to crystallize as the primary crystal.

In the ternary M- $S_1$ - $S_2$  system, however, the composition C can vary along the line C  $S_2$  with dissolution of  $S_2$ , if the liquidus temperatures on this line are equal to  $t$  or lower than  $t$ . Figure 2a shows that this composition-dominating line C  $S_2$  contacts with the "pond" (hatched region) at the one point C, and so the composition of the melt is kept at C. Here the "pond" means a region which is enclosed with an equitemperature line at the liquidus point  $t$  of the binary M- $S_1$  alloy with the initial concentration C.

In the case of Fig. 2b, however, the line C  $S_2$  which is dominating the mole ratio of  $S_1$  vs. M in the ternary M- $S_1$ - $S_2$  system so as to be C by initial contents of  $S_1$  and M, crosses the pond at two parts and even more, and so the alloy melt dissolves the base crystal  $S_2$ . Therefore the concentration C moves toward  $S_2$  along the line C  $S_2$ , then to the another portion C' which is also on the equitemperature line of  $t$ . In this case, it is clearly impossible to crystallize  $S_1$  on  $S_2$  as a primary crystal by cooling, and we can make neither abrupt heterojunctions nor epitaxial growths.

In conclusion, the necessary conditions for the alloying technique have been shown above. The experi-

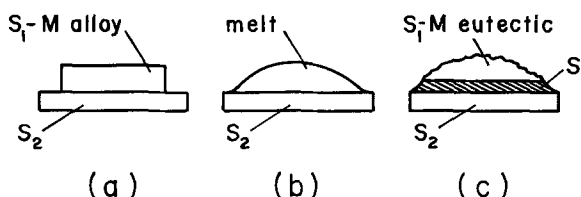


Fig. 1. Simple alloying technique for making single crystal heterojunction between  $S_1$  and  $S_2$ .

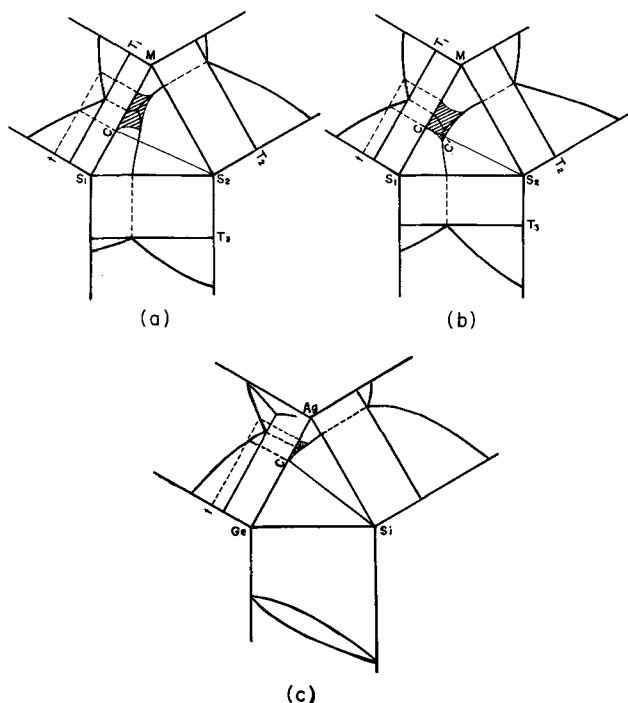


Fig. 2. Necessary condition of "no penetration" for making alloy or solution growth heterojunctions between  $S_1$  and  $S_2$ .

mental determination of the ternary phase diagrams, however, must be difficult. Therefore it was assumed from each of the three binary systems as shown in Fig. 2c.

#### Fabrication of Ge-Si Heterojunction

As shown in Fig. 3a, the Ge-Si alloy system exhibits a complete solid solubility, and the lowest solidus temperature in this system is equal to the melting point of Ge. Therefore, to prevent the dissolving of the base Si, it is essential that the eutectic temperatures of the Si-M and Ge-M systems are lower than the melting point of Si and that the alloying temperature is still lower than the eutectic line of the Si-M system.

Figure 3b and c show the composition of the initial solution C, in which case Ag is used as solvent and C is free to be selected by its solidus point  $t$  within the range of the temperature difference  $\Delta T$  between the two eutectic lines.

An Ag-Ge alloy containing 40 a/o (atomic per cent) Ge, whose liquidus point is  $750^\circ\text{C}$ , was prepared by vacuum melting of the pure elements in a quartz ampoule and quenching in water. The alloy was rolled to the thickness of  $1 \sim 3$  mm, and then cut into many pieces whose sizes were about  $8 \times 8$  mm each. Single crystal silicon wafers which had (111) surfaces were used as the base. The wafers were lapped mechanically to be approximately 0.5 mm thick with silicon carbide abrasives, and then etched in CP4 (4 parts  $\text{HNO}_3$ , 3 parts  $\text{CH}_3\text{COOH}$ , 3 parts  $\text{HF}$ ) to get a mirror finish. After rinsing in deionized water, the wafers were dried and broken into about  $10 \times 10$  mm pieces suitable for the alloy procedure.

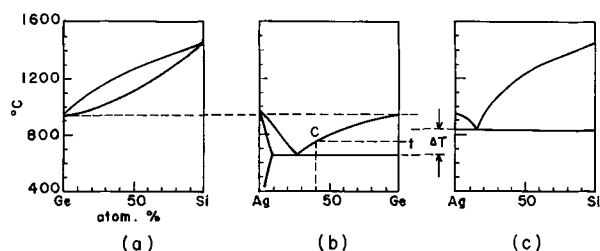


Fig. 3. The temperature difference,  $\Delta T$ , between two alloy systems  $S_1$ -M and  $S_2$ -M.

The alloying was carried out by placing a silicon wafer on an Ag-Ge alloy piece which was placed on a quartz disk in a vertical type electric furnace as shown in Fig. 4. In order to obtain good wetting between the silicon and the alloy melt, the alloying was carried out in an atmosphere of dry argon mixed with hydrogen as high as 20%. The alloy process consisted of heating to  $770^\circ\text{C}$ , which is a little higher than the liquidus point of the alloy, and slow cooling to  $650^\circ\text{C}$ . To ensure a completely homogeneous solution, the melt was kept at  $770^\circ\text{C}$  for 30 min. After fusion, the melt was cooled at the rate of  $100^\circ\text{C/hr}$  to the eutectic temperature of the Ag-Ge system, and then the electric power was turned off.

By this procedure, single crystal germanium layers over 0.5 mm thick were epitaxially crystallized on the (111) surfaces of the silicon seeds. The growth rates were approximately 0.4 mm/hr rather faster than the travelling solvent method. Figure 5 shows a polished cross section of the junction. The front of the grown germanium layer was parallel to the (111) surface of the seed, and often exhibited crack-like regions which were presumably formed during cooling from the liquidus temperature, because of constitutional supercooling of the solution.

Figure 6a shows several terraces which were formed at the front of the grown layer. The areas of the terraces were hexagonal. Figure 6b shows a cross section of one of the terraces by lapping and polishing parallel to the junction area. It is probable that the concentration of solute germanium in the Ag-Ge alloy solution was decreased near the crystallizing front during the cooling and then the terrace structure was formed.

#### Fabrication of Ge-GaAs Heterojunction

Ag and Al were tested as the solvents in this experiment. Although the phase diagrams between each solvent and the gallium arsenide are unknown, the eutectic temperatures appearing on both phase diagrams of Ag-Ge and Al-Ge alloy system are fairly lower than the melting point of the elements as shown in Fig. 7. Ag is an acceptor impurity in Ge, but its influence is negligibly small, because the solid solubilities of Ag in Ge are only  $4 \times 10^{13}$  to  $3.5 \times 10^{14}$  atoms/cm<sup>3</sup> at  $700^\circ \sim 800^\circ\text{C}$ . Although the solid solubility of Al in Ge is much higher, the Al is a neutral impurity to the base GaAs. The composition of the

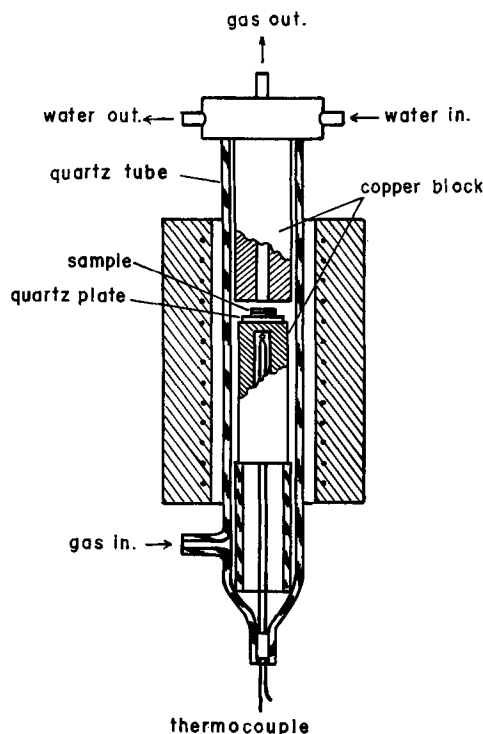


Fig. 4. Furnace for alloying

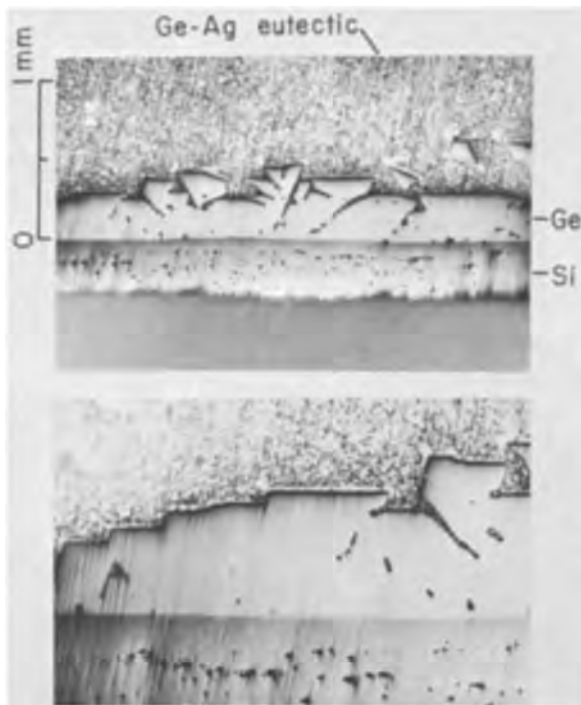


Fig. 5. Polished cross section of the Ge-Si heterojunction

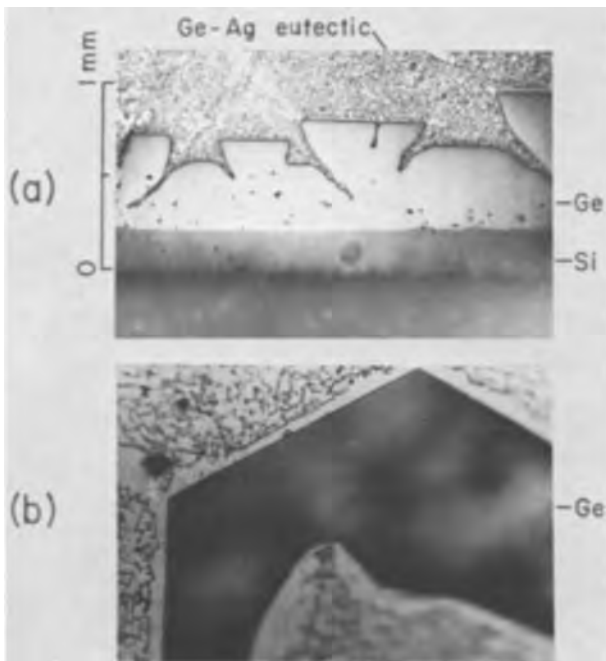


Fig. 6. Terrace structures formed at the front of the grown Ge layer.

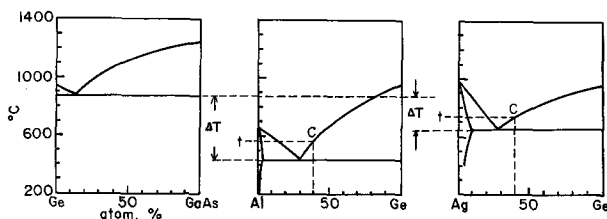


Fig. 7. Phase diagrams of the alloy systems GaAs-Ge, Al-Ge, and Ag-Ge.

Ag-Ge alloy was the same as that used in the fabrication of Ge-Si junctions.

For another purpose, an Al-Ge alloy containing 40 a/o Ge, whose liquidus temperature was 560°C, was prepared by vacuum melting in a graphite crucible.

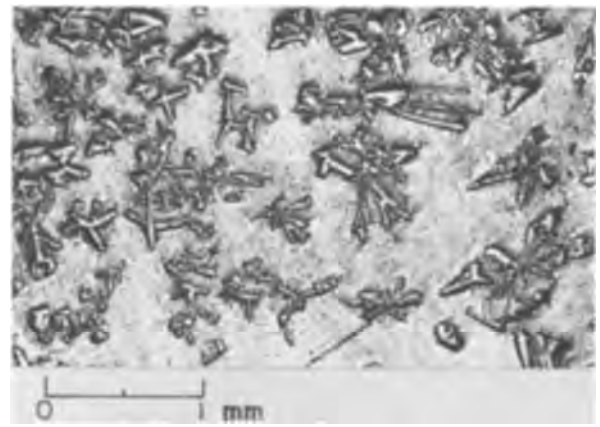


Fig. 8. Photomicrostructure of the Al-Ge (40 a/o) alloy quenched in water from 600°C.

Figure 8 shows a photomicrograph of the structure of the alloy quenched in water from 600°C. As the dendritic primary crystallites were suitably distributed in the matrix of eutectic, the average composition was ensured when the alloy was rolled and cut into small pieces suitable for the alloy process.

The seed GaAs was used in the form of 0.5 ~ 1.0 mm thick wafers whose areas were approximately 6 x 6 mm. In order to remove surface damage, the wafers were etched and polished chemically in a 2 : 2 : 1 volumetric mixture of H<sub>2</sub>SO<sub>4</sub>, H<sub>2</sub>O<sub>2</sub>, and H<sub>2</sub>O. These wafers were cut from a single crystal ingot grown by the free surface method (14).

Similar procedures were taken to crystallize the germanium layers on the gallium arsenide seeds from the solutions. Initially, the alloy on the seeds was fully melted at a temperature higher than its liquidus point, and cooled slowly to near the eutectic temperature for crystallization and then allowed to cool spontaneously to room temperature. The initial heating for the Ag and Al solutions were 770°C for 0.5 hr and 580°C for 0.5 hr, respectively. The cooling rate for crystallization was about 200°C/hr. All these cycles were carried out in an atmosphere of dry argon.

After the junction had been formed, several samples were cross-sectioned by mounting them in a casting resin and lapping them with silicon carbide abrasives. A mirror finish was obtained by mechanical polishing with diamond paste.

Figure 9 shows a polished cross section of the Ge-GaAs heterojunction fabricated by crystallization of Ge from the Al-Ge alloy solution. Striations appearing in the GaAs region were caused by mechanical lapping. The polyphase region consists of small primary crystallites and matrix eutectics of the Ge-Al system, which indicates the same structure as that in the photograph of Fig. 8. Since the luster of polished germanium was considerably different from that of gallium arsenide, it was relatively easy to distinguish between the two semiconductors. The junction appeared as an interface line, and the transition from

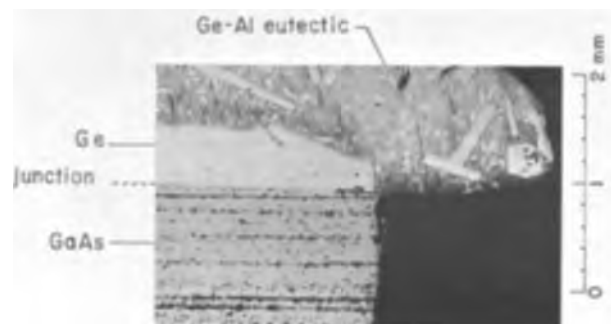


Fig. 9. Polished cross section of the Ge-GaAs heterojunction fabricated by crystallization of Ge from the Al-Ge alloy solution.



Fig. 10. Polished cross section of the Ge-GaAs junction fabricated by crystallization of Ge from the Al-Ge alloy solution. (Higher magnification).

gallium arsenide to germanium was abrupt. Higher magnifications of the junction region, as in Fig. 10, will show that no intermediate layers exist, such as eutectics between the two semiconductors.

However, in the case of the Ag-Ge alloy melt, an intermediate phase layer between the seed gallium arsenide and the crystallized germanium was formed, as shown in Fig. 11, and its magnified photograph in Fig. 12. From this result, it is supposed that a eutectic line of the Ag-GaAs alloy system may exist at a lower temperature than expected, and so the necessary conditions described in Fig. 2 are not satisfied in this case.

#### Electrical Measurements

The capacity and current-voltage characteristics of the Ge-GaAs heterojunctions have been measured. In the case of the Ge-Si junction, it was difficult to fabricate the diodes by the method we used because of the largeness of the junction area which tended to cause an electrical short through the crack-like regions in the grown layer of germanium.

The diodes used in this experiment were made from the heterocrystal wafers fabricated by the method described above. The wafers were cut into approximately 2.5 x 2.5 mm chips by an ultrasonic cutting machine, and then ohmic electrical contacts were achieved as shown in Fig. 13. In this figure, the junction is clearly seen as the interface between the two

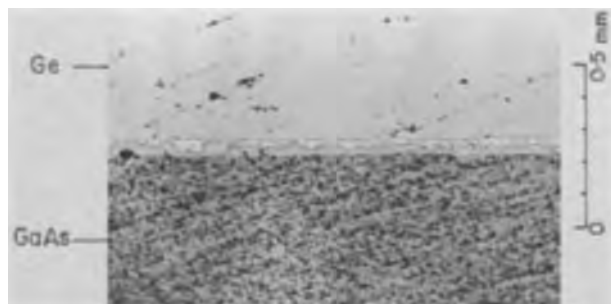


Fig. 11. Polished cross section of the Ge-GaAs structure fabricated by crystallization of Ge from the Ag-Ge solution.

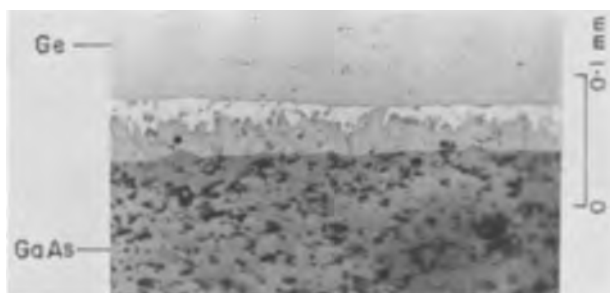


Fig. 12. Polished cross section of the Ge-GaAs structure fabricated by crystallization of Ge from the Ag-Ge solution. (Higher magnification).

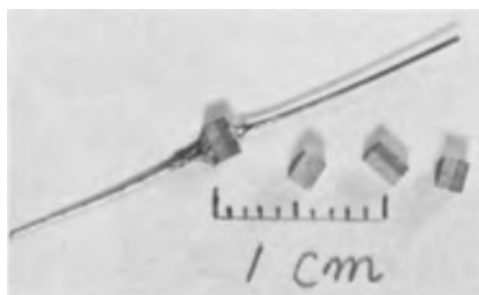


Fig. 13. Diodes made from the heterocrystal wafers

different lusters. The ohmic contact to the n-type base GaAs region was achieved by the following procedure: (i) electroplating with Sn onto the lapped surface, (ii) electroplating with Ni onto the Sn, and then, (iii) soldering the Ni to a copper lead wire with ordinary Pb-Sn solder. The contact to the opposite side of the junction, which was the Al-Ge eutectic alloy surface, was achieved by soldering to the copper lead wire or a conventional diode header with aluminum chloride as a flux.

In the case of the Ge-Si junction, chemical plating with Ni to the n-type base Si and soldering with Pb-Sn alloy to the Ag-Ge eutectic side were done.

The base crystals used were n-type GaAs wafers of 0.002 ohm-cm and n-type Si wafers of 5 ohm-cm. After fabrication, the diodes were carefully coated with Apiezon wax except the junction region. They were then etched chemically and rinsed with deionized water.

Typical I-V characteristics of these diodes observed on a curve tracer are shown in Fig. 14 and 15. Both junctions have a soft breakdown, and their breakdown voltage increases with decreasing temperature as expected of a Zener breakdown. Because of high doping of Al in the Ge layer, the diffusion voltages in the forward characteristic of Ge-GaAs junction, 0.8v at 300°K and 1.0v at 77°K are somewhat higher than those measured for the vapor grown junctions by Anderson (5).

The circuit used to measure the low current I-V characteristics of the Ge-GaAs diodes is shown in Fig. 16. A Boonton model 74C capacitance bridge was used to measure the C-V characteristics of the Ge-GaAs structures at the frequency of 100 kHz.

#### Results and Discussion

The low current I-V characteristics measured at 300° and 77°K of typical Ge-GaAs p-n heterojunction diodes fabricated by this method are shown in Fig. 17. Forward conduction occurred in all junctions when the Ge was biased positively, as was the case with Ge-Si p-n heterojunctions. From the ordinary diode theory, the current-voltage characteristics can be described by the following empirical formula

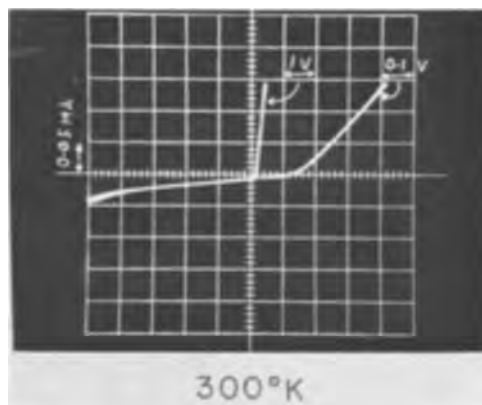


Fig. 14. Typical I-V characteristics of the Ge-Si heterojunction diodes observed on a curve tracer, at 300°K.

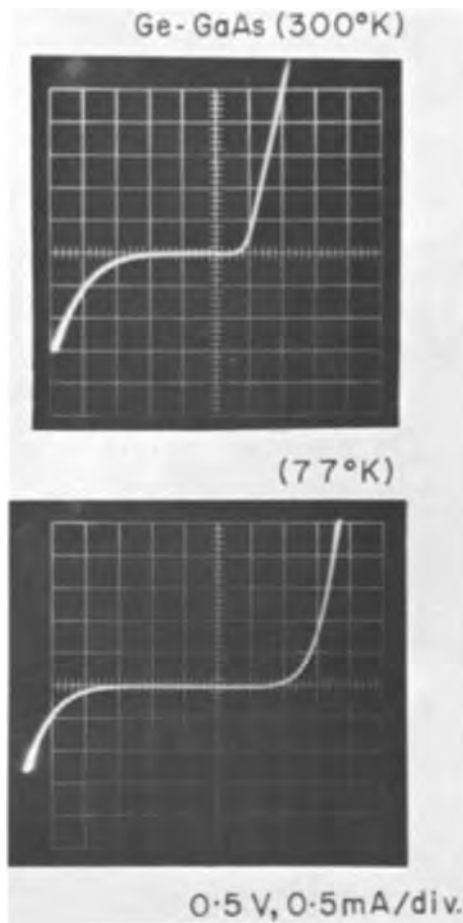


Fig. 15. Typical I-V characteristics of the Ge-GaAs diodes observed on a curve tracer, at 300° and 77°K.

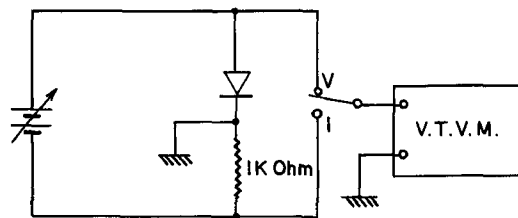


Fig. 16. Circuit used to measure the low current I-V characteristics of the Ge-GaAs diodes.

$$I = I_0 [\exp (qV/\eta kT) - 1] \quad [1]$$

where  $I_0$  is the saturation current and  $\eta$  is a nondimensional coefficient. From the formula, the forward and the reverse current of the junctions can be written as follows

$$I \approx I_0 \exp (qV/\eta kT) \text{ (forward)} \quad [2]$$

$$I \approx I_0 \text{ (reverse)} \quad [3]$$

The nondimensional coefficient  $\eta$  depends on the conduction mechanism, and it takes the value 1 or 2 with the diffusion or recombination current respectively. The values obtained from the forward characteristics shown in Fig. 17 were  $\eta = 1.67$  for 300°K and  $\eta = 7.50$  for 77°K. Although the room temperature value can be explained as a combination of diffusion and recombination current, the value for 77°K cannot be explained. As can be seen from Fig. 17, the forward current for both diodes varies as seen in

$$I = I_0 \exp (\alpha V) \quad [4]$$

where  $\alpha$  is relatively independent of temperature.

$$\alpha \approx 2.0 \sim 2.3 \quad (77^\circ \sim 300^\circ\text{K}) \quad [5]$$

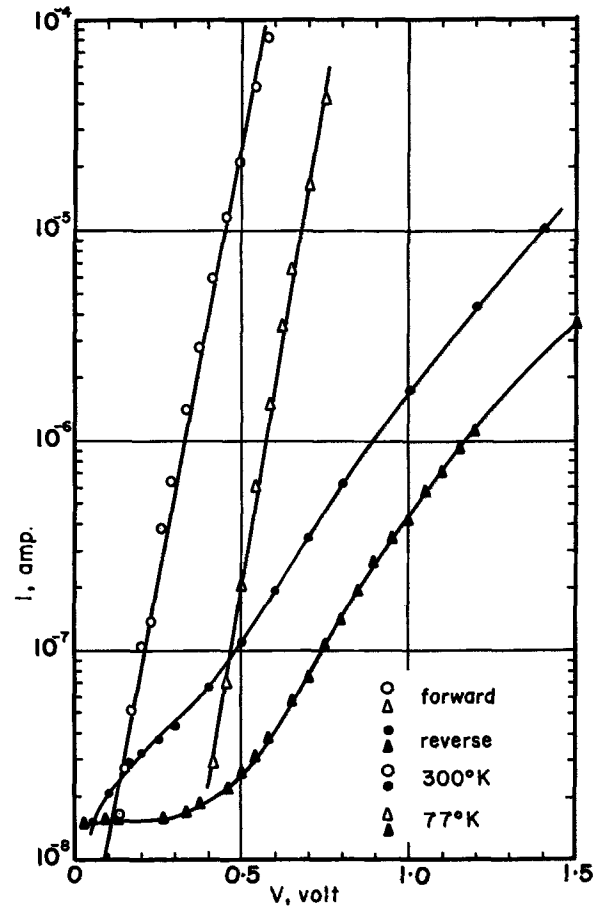


Fig. 17. Low current I-V characteristics of typical Ge-GaAs p-n heterojunction diodes.

Therefore, it rather may be possible to explain the current by a tunneling mechanism as described by Rediker *et al.* (9) for GaAs-GaSb interface-alloy heterojunctions.

The junction capacitance on the Ge-GaAs p-n heterodiodes was measured at room temperature as a function of bias voltage. Typical plots of  $C^{-2}$  vs.  $V$  for the two diodes are shown in Fig. 18. As can be seen from the figure, the capacitance varies as the reciprocal square root of the voltage, as expected of an abrupt junction.

As the grown germanium layer contains the concentration of the limit of solid solubility of aluminum which is as high as  $10^{20}$  atoms/cm<sup>3</sup>, it can be assumed that the depletion region is extended to the base GaAs region. The width of the depletion region  $w$  is

$$w = \left( \frac{2\epsilon V}{q N_D} \right)^{1/2} \quad [6]$$

$$w = \epsilon A/C \quad [7]$$

where  $A$  is the area of the junction and  $\epsilon$  is the dielectric constant of GaAs. Referring to Fig. 18, the capacities depending on bias voltage are

$$C = 2250 \text{ pF} \quad (\text{at } -2v)$$

and

$$C = 3670 \text{ pF} \quad (\text{at } 0v)$$

$$\text{As the junction area } A \text{ is } 4 \times 10^{-2} \text{ cm}^2$$

$$w = 1890 \text{ \AA} \quad (\text{at } -2v)$$

and

$$w = 1160 \text{ \AA} \quad (\text{at } 0v)$$

It may be possible to explain the forward current of the junction by means of tunneling.

### Summary

Metallographical considerations on the base-solvent-solute ternary phase system for solution growth



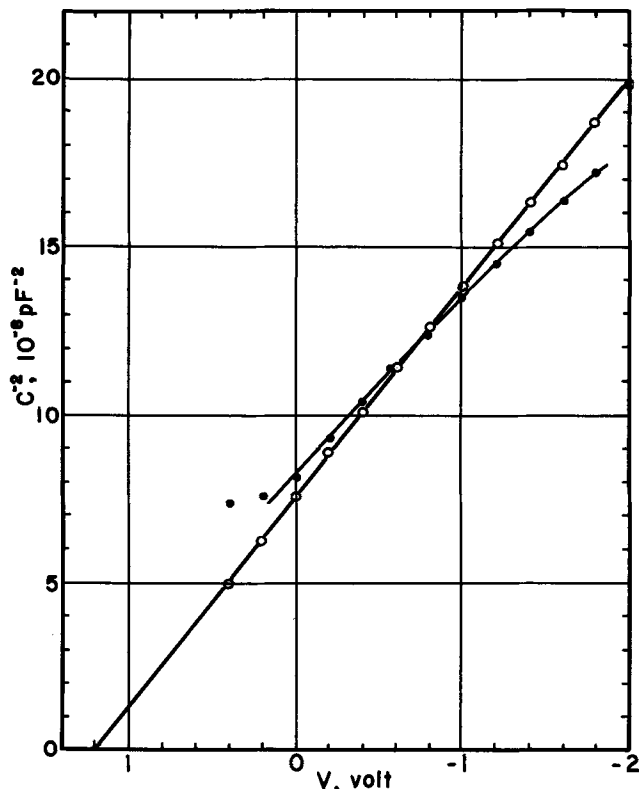


Fig. 18. Typical C-V characteristics of the Ge-GaAs p-n heterojunction diodes.

of heterocrystals were made, and the conditions to ensure a metallurgically perfect junction were described. From this result, Ge-Si and Ge-GaAs heterojunctions have been fabricated by crystallizing Ge from Ag and Al solutions onto the base crystals, using simple alloying techniques. The conditions employed were as shown in Table I, where M is the solvent metal;  $t$  is the liquidus point of the M-S<sub>1</sub> alloy used;  $T_1$ ,  $T_2$ , and  $T_3$  are the eutectic lines in the binary alloy systems of S<sub>1</sub>-M, S<sub>2</sub>-M, and S<sub>1</sub>-S<sub>2</sub>, respectively; and C is the content of S<sub>1</sub> in S<sub>1</sub>-M solution.

Microscopic observations of these junctions showed that there is no intermediate phase between the two semiconductors, and that the growth of the Ge layers may be epitaxial to the base crystals as shown in Fig.

Table I. Alloying conditions employed for making heterojunctions

Junction, S <sub>1</sub> on S <sub>2</sub>	M	$t$ , °C	$T_2$ , °C	$T_3$ , °C	C, a/o	$T_1$ , °C	Solubility, M in S <sub>1</sub>
Ge-Si	Ag	650	830	(937)	45	790	$10^{13}/\text{cm}^3$
Ge-GaAs	Al	424	660	865	40	550	$10^{20}/\text{cm}^3$

6. As the crystallized Ge layer is saturated with the solvent metals, the diffusion voltage in the forward drop of the I-V characteristic for the Ge-GaAs junctions is appreciably lower than that measured for vapor phase grown junctions, and the major mechanism of the current flow is found to be due to tunneling. The breakdown in the reverse characteristic of the junction is soft and of a Zener type. The C-V characteristics show that the junctions are abrupt, as expected from the metallurgical considerations.

#### Acknowledgments

The authors wish to thank Mr. Kodera for valuable discussions in the interpretation of electrical characteristics.

Manuscript submitted Nov. 27, 1967; revised manuscript received April 30, 1968.

Any discussion of this paper will appear in a Discussion Section to be published in the June 1969 JOURNAL.

#### REFERENCES

1. H. Kroemer, *Bull. Am. Phys. Soc.*, **2**, 143 (1956).
2. H. Kroemer, *R.C.A. Rev.*, **18**, 1332 (1957).
3. W. Shockley, U.S. Pat., 2,569,347 (1951).
4. H. Kroemer, *Proc. Inst. Radio Engrs.*, **45**, 1535 (1957).
5. R. L. Anderson, *Solid-State Electron.*, **5**, 341 (1962).
6. R. H. Rediker, T. M. Quist, and B. Lax, *Proc. IEEE*, **51**, 218 (1963).
7. R. F. Rutz, *ibid.*, **51**, 470 (1963).
8. L. Y. Wei and J. Shewchun, *ibid.*, **51**, 946 (1963).
9. R. H. Rediker, S. Stopek, and J. H. R. Ward, *Solid-State Electron.*, **7**, 621 (1964).
10. E. D. Hinkley, R. H. Rediker, and M. C. Lavine, *Appl. Phys. Letters*, **5**, (5), 110 (1964).
11. Y. Takeda, T. Hirai, and M. Hirao, *This Journal*, **112**, 363 (1965).
12. R. S. Mroczkowski, M. C. Lavine, and H. C. Gatos, *Trans. AIME, Met. Soc.*, **233**, 456 (1965).
13. H. Kasano and S. Iida, *Japan. J. Appl. Phys.*, **6**, (9), 1038 (1967).
14. K. Kurata, J. Shirafuji, and T. Endo, *Japan. J. Appl. Phys.*, **2**, 65 (1963).

## Brief Communication



### Self-Registered Molybdenum-Gate MOSFET

D. M. Brown,\* W. E. Engeler, M. Garfinkel, and P. V. Gray

General Electric Research and Development Center, Schenectady, New York

The use of Mo films as etch masks to pattern Si<sub>3</sub>N<sub>4</sub> films has been described previously (1). In this study, KPR and potassium ferricyanide etch<sup>1</sup> was used to first pattern the Mo film and the underlying Si<sub>3</sub>N<sub>4</sub> film was subsequently etched away and patterned by using concentrated HF (48%) which dissolves Si<sub>3</sub>N<sub>4</sub> but does not dissolve Mo. That the unique chemical prop-

erties of Mo can be used to form patterns in multiple layers of Mo, Si<sub>3</sub>N<sub>4</sub>, and SiO<sub>2</sub> has also been pointed out (2).

It is the purpose of this short article to show that Mo films can also be used as high temperature diffusion masks; and that this, in turn, makes it possible to fabricate self-registered enhancement mode MOSFETs by utilizing a portion of the Mo diffusion mask as the gate electrode.

\* Electrochemical Society Active Member.  
<sup>1</sup> 92g K<sub>3</sub>Fe(CN)<sub>6</sub>, 20g KOH, 300g H<sub>2</sub>O.



### Mo Film Diffusion Masking

Having shown the usefulness of Mo as an etch mask, we next turned our attention to the use of Mo as a diffusion mask to see if patterned Mo films could be utilized as diffusion masks against some of the standard silicon dopants at high diffusion temperatures. Mo, of course, is a refractory metal with a melting point of  $2600^{\circ}\text{C}$ . Diffusion experiments were done with films of Mo over thin films of thermal silicon dioxide to prevent the formation of  $\text{MoSi}_2$ . There was no danger of the Mo reducing the silicon dioxide film since silicon dioxide is more stable than any of the Mo oxides.

Figure 1 shows a result of this investigation by using angle lapping and staining to delineate the converted regions. The remaining portions of the Mo mask which is  $5000\text{\AA}$  thick are shown in the upper corners of the picture. This Mo film was deposited over  $1200\text{\AA}$  of thermal oxide grown on a 1 ohm-cm n-type silicon wafer. After patterning the Mo film, a thin layer of undoped oxide was deposited over the Mo pattern and diffusion was carried out for 16 hr at  $1100^{\circ}\text{C}$  in a closed tube using elemental boron. The diffused p-type material is stained almost black in the picture. And, indeed, we see that the Mo film is acting as a diffusion mask. The angle lapping and staining give a junction depth of  $6.3\mu$  wherever the Mo film was removed, whereas it is only  $1.1\mu$  deep under the Mo mask. Other experiments indicated that Mo films are an even better mask against phosphorus diffusion.

### Self-Registered Mo-Gate MOSFET

The next step was to make MOSFETs utilizing these discoveries. In this case Mo can be used as the metal gate electrode: Mo, after all, is a good metal with a room-temperature resistivity of only  $5\ \mu\text{ohm-cm}$ . Furthermore, by utilizing a Mo film as the diffusion mask to define source and drain, and subsequently as the gate electrode, two important things can be achieved. All critical alignment steps are eliminated during the fabrication of these devices since such a process automatically registers the source and drain junctions under the edges of the Mo gate electrode, and the devices can therefore be formed with a minimum of gate to source and drain region overlap which is important for the reduction of the gate to drain feedback capacitance. This, of course, increases the gain-bandwidth product of the device.

How this has been done is shown schematically in Fig. 2. First, we grow a high quality thin thermal oxide on a Si wafer; this oxide will subsequently be

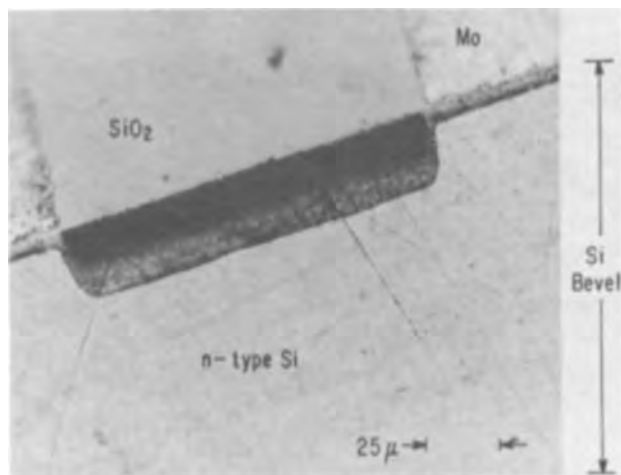


Fig. 1. Angle lapped and stained section showing Mo diffusion masking of boron. Underlying Si wafer is 1 ohm-cm n-type. Converted p-type regions are stained dark. Junction depth under oxide covered Si is  $6.3\mu$ ;  $1.1\mu$  under Mo-covered oxide. Bevel magnification is  $\approx 5X$ .

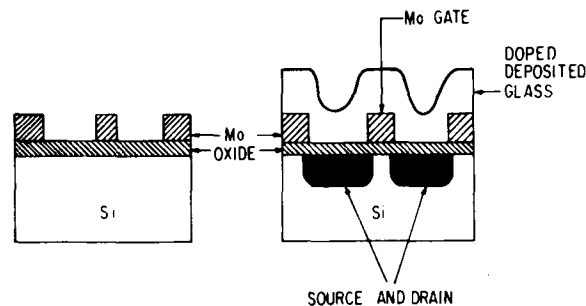


Fig. 2. Schematic diagram of fabrication steps used to make a type of self-registering Mo-gate MOSFET.

used as the gate dielectric. Next we deposit and pattern a Mo film to form the channel adjacent source and drain region patterns. We then deposit a doped glass which is utilized as the diffusion source and diffuse the dopant through the thermal oxide and into the Si to form the source and drain, thus achieving automatic self-registration of the source and drain junctions under the Mo gate. All that needs to be done to finish the device is to subsequently make contact to the source and drain and buried Mo gate. Contact apertures are etched in the deposited glass in the conventional manner using photoresist and buffered HF. Final metalization is also conventionally formed by patterning an evaporated metal film (e.g., Al).

In Fig. 3 we show a picture of a finished device with circular geometry. We have removed the Al contacts here; the gate buried within the oxide layers in this instance is a ring of Mo 1 mil wide. The source and drain regions are covered with glass. Showing within these regions are the dig-down apertures used to contact the FET's source and drain. Surrounding the device is glass-covered Mo. The deposited glass was doped with phosphorus, and the underlying wafer is 1 ohm-cm p-type silicon.

Figure 4 shows an angle lapped and stained device. The original p-type material is dark, and the diffused source and drain regions being n-type are light. Here

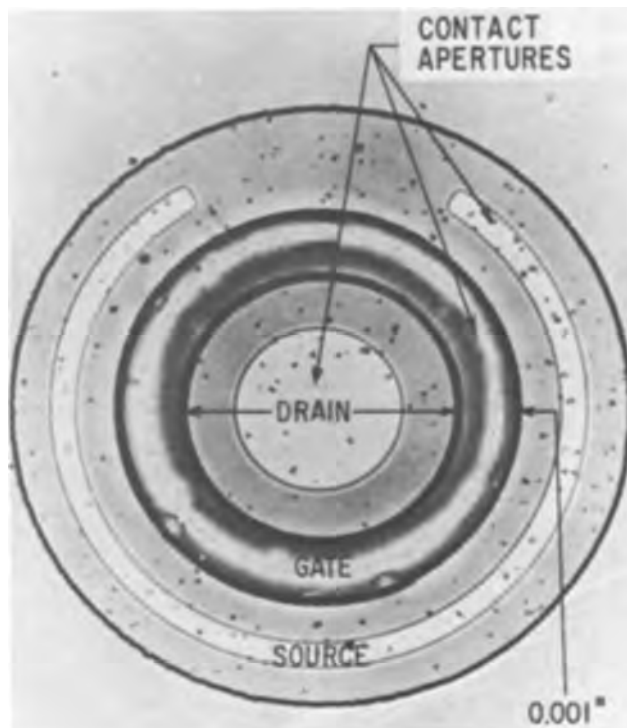


Fig. 3. Finished device. Al contacts removed. Buried Mo gate is a ring 1 mil ( $25\mu$ ) wide. Channel aspect ratio ( $W/L$ ) is 20. Small dots are remaining portions of Al contacts or colored glass crystallites in deposited glass.

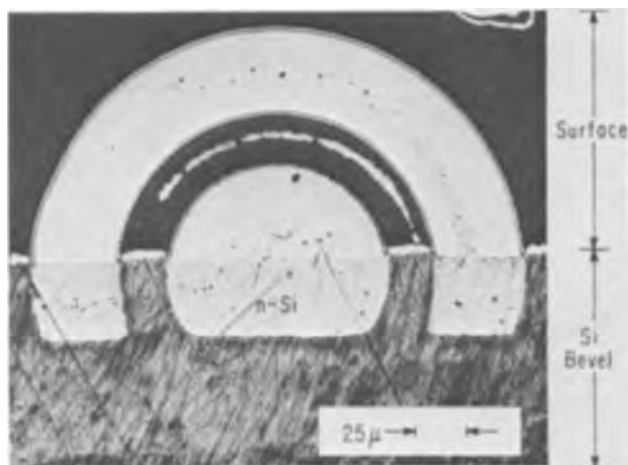


Fig. 4. Angle lapped and stained device like that of Fig. 3 showing automatic source and drain junction registration under edges of circular Mo gate electrode. Underlying wafer is 1 ohm-cm p-type Si (dark) and diffused n-type source and drain regions are light. Junction depth is  $2.5\mu$ . Bevel magnification is 17.6X.

we see the self-registry of the source and drain junctions with the Mo gate. The junction depth is about  $2.5\mu$ , whereas the source and drain region overlap with the Mo gate is  $2\mu$ .

These devices are n-channel enhancement mode and after  $H_2$  annealing exhibit low threshold voltages and have channel mobilities of  $200\text{--}400\text{ cm}^2/\text{v}\cdot\text{sec}$ . Some characteristic curves are shown in Fig. 5. The scale for the source to drain current is  $20\text{ }\mu\text{a}/\text{div}$  and for source-drain voltage it is  $1\text{ v}/\text{div}$  with gate steps starting at zero and increasing upwards at  $0.2\text{ v}/\text{step}$ . The  $20\mu$  threshold is about  $+0.8\text{v}$ . The MOS-C ( $V_G$ ) curve of the device whose characteristic curves are shown in Fig. 5 indicates a fixed charge,  $Q_{so}$ , of about  $1 \times 10^{12}/\text{cm}^2$ . A very small amount of channel current is observed at  $V_G = 0$ . Strong surface inversion occurs for  $V_G > 0$ .

#### Summary

These experiments have shown the following:

Thin films of Mo deposited upon thin oxides can mask against both phosphorus and boron.

Therefore, thin films of Mo can be used not only as etch masks to pattern silicon nitride and silicon dioxide films, but can also be used as diffusion masks and therefore be utilized to form converted conductivity-type regions within the underlying silicon by high temperature diffusion techniques.

The use of Mo films in this manner has some very substantial advantages in the fabrication of MOS-FETs:

1. Part of the Mo diffusion mask can be utilized subsequent to source-drain formation as the gate

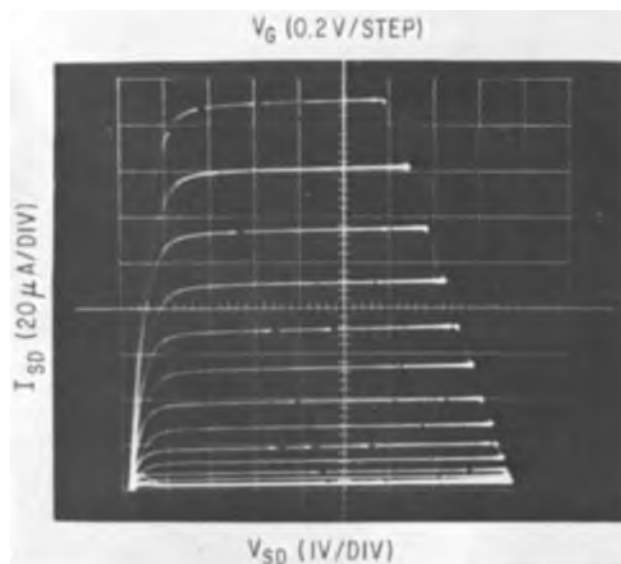


Fig. 5. Source-drain characteristic curves for n-channel enhancement mode device shown in Fig. 3. Scales are:  $I_{SD} = 20\mu\text{ amp}/\text{div}$ ;  $V_{SD} = 1\text{ v}/\text{div}$ ;  $V_G = +0.2\text{ v}/\text{step}$ , 12 steps.

electrode. This therefore: (a) provides for automatic self-registration of the source and drain junctions under the Mo gate for every MOSFET device on the wafer, (b) in turn this eliminates excessive feedback capacity, and (c) also eliminates the need for any critical mask alignments during FET processing.

2. Mo is easily patterned and the high resolution of the photoresist mask is readily transferred to the moly film, this has been shown previously (1).

3. Mo is a metal with a high conductivity, which means that contact to the gate electrode need not be extensive. That is, contact can be made at a single point and because of all of the above features, the Mo gate can therefore be very complicated in form in order to create devices with very large aspect ratios and large figures of merit.

Manuscript submitted March 10, 1968; revised manuscript received April 26, 1968. This paper was presented at the Chicago Meeting, Oct. 15-19, 1967, as a Recent News Paper, Electronics Div., Paper 7.

Any discussion of this paper will appear in a Discussion Section to be published in the June 1969 JOURNAL.

#### REFERENCES

1. D. M. Brown, W. E. Engeler, M. Garfinkel, and F. K. Heumann, *This Journal*, **114**, 730 (1967).
2. D. M. Brown, P. V. Gray, F. K. Heumann, H. R. Philipp, and E. A. Taft, *ibid.*, **115**, 313 (1968).

## Correction

In the paper "SiSiO<sub>2</sub> Fast Interface State Measurements" by Dale M. Brown and Peter V. Gray, which was published in Vol. 115, pp. 760-766, July 1968, on p. 764 the third from the last sentence in the Summary should read: "These defect centers when present can

drastically alter even the room temperature performance of MOSFETs since their production has been shown to raise the threshold and greatly reduce the channel mobility of a MOSFET."



### The Early History of the Electrodeposition and Separation of Particles

Myron Robinson

*Research-Cottrell, Incorporated, Bound Brook, New Jersey*

#### ABSTRACT

The existence of electrostatic forces of attraction had been known to classical antiquity, but the first reported observations in the electrostatics of airborne particles date from about 1600. Closely associated with studies of smoke and other fine suspended particles in an electric field was the discovery of the man-made corona discharge after 1670. A review is presented of the contributions of the very early investigators of electrodeposition, electroseparation, and the high-voltage discharge, among whom are some of the foremost names in the history of science: Gilbert, Boyle, Newton, Coulomb, and Faraday.

Electrostatic dust precipitation, liquid spraying, mineral separation, xerography, and other widespread applications of the electrodeposition and separation of particles are, for the most part, developments of the twentieth century. But as is commonly the case in the history of science, the essential phenomena had been demonstrated in principle long before an advancing technology provided the ancillary equipment required for effective commercial utilization.

The following survey briefly reviews the older historical background of the subject, from the earliest times to 1907, the year marking the first successful commercial application of electrostatic precipitation.

#### The Beginnings of Particle Electrostatics and the Discovery of the Corona Discharge

Thales of Miletus, one of the seven wise men of Greece and founder of the school whence Socrates came, is commonly mentioned as the discoverer of electrostatic attraction. This claim, particularly frequent in textbooks on electrostatics, is not, however, well documented by the literary remains available to us. No writings of Thales have survived, and it is to Diogenes Laertius, the third century biographer of the philosophers, that we are indebted for information on Thales' electrical "researches." In this connection, Diogenes notes simply that ". . . Aristotle and Hippias [Greek sophist, fifth century B.C.] say that he [Thales] attributed souls also to lifeless things, forming his conjecture from the nature of the magnet, and of amber" (1). Aristotle, on the other hand, speaks only of the animation of the magnet as an opinion that originated with Thales, and even of this he is not altogether certain: "Thales, too, apparently judging from the anecdotes related of him, conceived soul as a cause of motion, if it be true that he affirmed the loadstone to possess soul, because it attracts iron" (2).

Since the two foregoing quotations comprise the known evidence linking Thales to the discovery of electrostatic attraction, the association of Thales with amber may well have been an invention of Diogenes

800 years after the alleged event. That this could have been so is not strange, for the early writers closely associated electric and magnetic phenomena, often speaking of electricity as a kind of magnetism, and considering magnetic action the general case of attractive mechanism. As late as 1600, for example, William Gilbert, the "Galileo of magnetism," still preserved this already old tradition by having in his "De Magnete" (Fig. 1) a chapter entitled "On the Magnetic Coition," of which the first segment was subtitled "On the Attraction of Amber" (3).

It is clear, in any case, that the existence of electrostatic forces of attraction had been known to classical antiquity, for the observation that a rubbed amber attracts straws, dried leaves, and other light bodies ostensibly in the same way a magnet attracts iron is variously credited to Theophrastus (ca. 300 B. C.), Pliny (first century), and Solinus (third century), as well as other ancients, Greek and Roman (4). But owing to the deficiency of scientific method and to the absorbing interests of practical life, repeated accounts of electrostatic attraction from the earliest times to the advent of Gilbert, revealed little in the way of novelty either in observation or interpretation. Indeed, it remained for Gilbert to observe specifically that electrostatic forces could deflect particulate matter from an aerosol. Discussing the attractive power of amber, sulfur, diamond, and other "electric" (i.e., dielectrics) "when stimulated by friction," Gilbert reported that such materials would "entice smoke sent out by an extinguished light" (3). ("Electric" for-

REVIEW  
SECTION



Fig. 1. Title page of *De Magnete*. The text reads: "William Gilbert of Colchester, Physician of London, On the Magnet, Magnetic Bodies Also, and on the great magnet the earth; a new Physiology, demonstrated by many arguments & experiments. London, 1600."

merly designated a nonconductor. The term originated with Gilbert who applied it to substances capable of receiving a charge by rubbing. "Nonelectric" referred to a conductor.)

Three quarters of a century later the experiment was repeated by the Irish natural philosopher Robert Boyle (Fig. 2): "For having well-lighted a Wax-taper, which I preferred to a common Candle to avoid the stink of the snuff, I blew out the flame; and when the smoak ascended in a slender stream, held, at a convenient distance from it, an excited piece of Amber or a chafed Diamond, which would manifestly make the ascending smoak deviate from its former line, and turn aside, to beat, as it were, against the Electric, which, if it were vigorous would act at a considerable distance . . ." (5).

In both foregoing examples, the smoke was attracted to the dielectric either by virtue of a charge acquired by the particles in the incomplete combustion process, or as a result of the polarization of the electrically neutral particles in the nonuniform electric field surrounding the dielectric. Since a corona discharge was not used to impart a net charge to the particles, neither instance can be regarded as a true forerunner of electrostatic precipitation or liquid spraying in the conventional present-day sense. Nevertheless, Boyle may not have missed the mark by much. As Joseph Priestly informs us in his celebrated history of electricity, "Mr. Boyle got a glimpse, as we may say, of the electric light: for he found that a curious diamond . . . brought from Italy, gave light in the dark when it was rubbed against any kind of stuff; and . . . it became electrical" (6).

Together with his predecessors, Boyle noted the ability of amber to draw "not only Sand and Mineral Powders, but Filings of Steel and Copper, and beaten Gold it self." He supported the contention, first put forth by Gilbert, that magnets attract iron whereas amber "draws indifferently all bodies whatsoever" (6). There was at this early time, however, no mention of the possibility of electrostatic mineral separation,

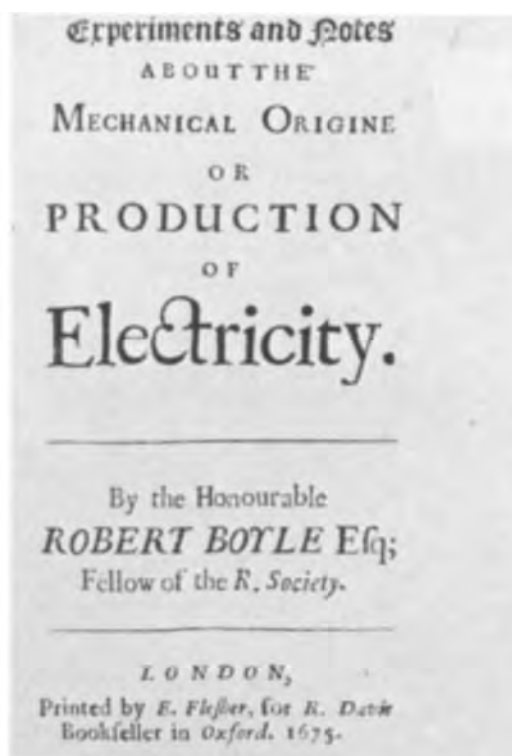


Fig. 2. Title page of Boyle's book treating his electrical researches. The term "mechanical" refers to the frictional origin of electricity. This was the first printed book on electricity to appear in English.

or any suggestion that particles of unlike physical characteristics might behave differently in the presence of amber.

Production of a substantial man-made corona could not have antedated the development of the high-voltage generating machine. A frictional machine consisting of a sulfur sphere mounted on a crankshaft was described in 1672 by Otto von Guericke, better known for his invention of the vacuum pump and Magdeburg hemispheres. The sulfur sphere was charged by rubbing the hand against it while it was rotated in a wooden frame (Fig. 3). Using this apparatus, von Guericke made the important discovery of the effectiveness of pointed conductors in attracting charged bodies. He noted further that the rubbed globe glowed in the dark and that when it was brought



Fig. 3. Von Guericke's frictional electrostatic machine is on the right. On the left, the burgomeister is demonstrating how a feather *a*, first charged by contact with the sphere, may be made to move about in the air as he chose. This is probably the earliest example of achieving the directed motion of a particle under the action of an electric field (7).

to the ear "roaring and crashings" were heard in it (7).

The experiments of Boyle and von Guericke were made about the same time, neither deriving advantage from the labors of the other. Their observations seem to be the earliest recorded of the corona discharge.

Von Guericke's frictional machine and subsequent improvements on it were to accelerate the progress of electrical science, but the more primitive charging methods lingered tenaciously. In 1709, Francis Hauksbee, curator of instruments for the Royal Society of London, reported that he had experienced a weak sensation of pressure, presumably the electric wind, by holding a charged tube close to his face (Fig. 4). Hauksbee's announcement of his discovery throws interesting light on the state of electrical knowledge and experimental technique at the time. "Having procured a Tube, or hollow Cylinder, of fine Flint Glass," he wrote, "about one Inch diameter, and thirty in length; I rubb'd it pretty vigorously with paper in my hand until it had acquired some Degree of Heat . . . When the Tube became hottest by the strongest Attrition, the Force of the [electrical] Effluvia was render'd manifest to . . . [the] Sense . . . of feeling. They . . . were plainly to be felt upon the Face or any other tender part, if the rubb'd Tube were held near it. And they seemed to make very nearly such sort of stroaks upon the Skin, as a number of fine limber Hairs pushing against it might be suppos'd to do. This vigorous Action of the Effluvia put me upon an attempt, to find in what manner such a motion was propagated, and in what figure or sort of track it went along. For which end I held the rubb'd Tube near the Flame of a Candle, Smoke, Dust and surfaces of Liquids; but without any manner of success."

Hauksbee's efforts to employ smoke-tracer and similar techniques to follow the flow pattern of the electric wind failed. In fact, he gives the impression that the drag force of the wind was so weak and the electric attractive force on the smoke particles and other substances so strong that the particles and liquid moved against the air current to deposit on

the tube. In Hauksbee's view this deposition confined the electric effluvia within the tube and thereby suppressed the wind: "For the small parts of Dust and Powders, the streams of Liquids, the oleaginous Fumes of Flame, and the like sort of parts of Smoke it self, immediately adher'd to the surface of the Tube, and so kept in the Effluvia: which therefore requir'd the assistance of a fresh Attrition to open their passage and give them vent again" (8).

Once again, the principle of the modern electrostatic sprayer or precipitator, the charging of particles to the same polarity as that of the discharge electrode and their subsequent repulsion from that electrode, was yet to be clearly demonstrated. It is possible, though, that a step in the right direction had already been taken by the savants of the Academy del Cimento of Tuscany, contemporaries of Boyle and von Guericke (Fig. 5). To these gentlemen "we are indebted for several observations on the subject of electricity," among them a report of 1667 that a stream of smoke rising near a piece of rubbed amber would in part "bend . . . and be arrested by the Amber and in part, as if reflected from a Glass . . . mount upwards." The attracted portion, "as the Amber cools, rises in *smoak* again, and vanishes" (9). The latter statement may be the first recognition of a frequent problem in commercial electrostatic precipitation, the failure of particles of low resistivity to adhere to a collecting electrode. The twin columns suggest the smoke is of mixed charge, particles of opposite sign being drawn off in different directions.

The splitting of a column of smoke in an electric field, a phenomenon vaguely reminiscent of the important Stark and Zeeman discoveries of a later period, has since been noted time and again in the literature. As late as 1839 Faraday regarded this experiment worthy of mention in his "Experimental Researches:" "If a smoking wax taper be held . . . towards a charged prime conductor . . . two currents will [often] form, . . . one . . . passing to the conductor, and the other . . . outwards, and from the conductor . . ." (10) (A prime conductor is a high-capacity, corona-free conductor for storing charge generated by an electrostatic machine. See Fig. 6.)

Shortly after Hauksbee, Isaac Newton performed a similar corona experiment. "The electric Vapour," he wrote, ". . . excited by the friction of the . . . [Sphere] against the Hand will . . . be put into such an agitation as to emit Light . . . and in pushing out of the . . . [Sphere] will sometimes push against the Finger so as to be felt" (11). No mention is made,

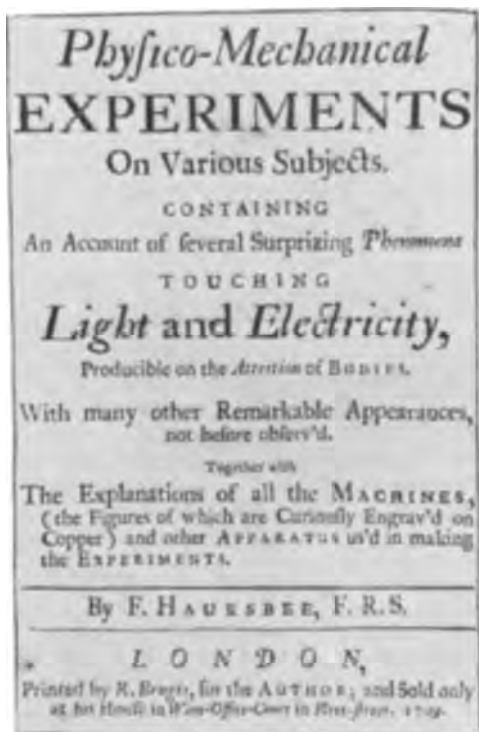


Fig. 4. Hauksbee's title page. The *Light* referred to is that emitted in an electrical discharge.



Fig. 5. English translation, authorized by the Royal Society of London, of "Saggi di naturali esperienzi" which originally appeared in Florence in 1667. The frontispiece illustrates the timelessness and universality of science: The personified Academy del Cimento is handing a copy of the *Essayes* to the seated Royal Society while Aristotle and the goddess of nature look on.

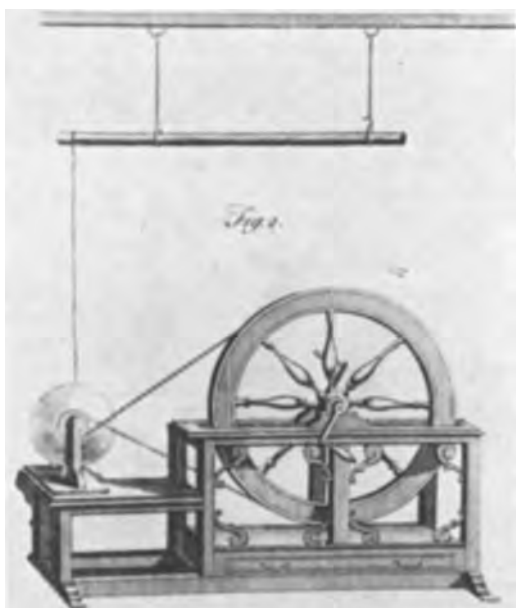


Fig. 6. A frictional electrostatic machine circa 1767 (16). The glass sphere at the left replaces von Guericke's sulfur ball. A fine chain dragging against the sphere transfers charge from the surface of the latter to the suspended prime conductor.

however, of the action of the "electric Vapour" on aerosols.

In 1746, the French philosopher Jean Antoine Nollet revealed his findings that electrified points displayed "brushes of light" (12). A year later, Benjamin Franklin revealed in a letter to his friend Peter Collinson of the Royal Society, "the wonderful effect of pointed bodies, both in drawing off and throwing off the electrical fire" (13). Nollet's and Franklin's observations were largely a rediscovery of a phenomenon noted earlier by von Guericke and long since forgotten. But this time, the corona discharge was to be established as a favorite subject of experimental study among the electrical investigators of the day. (The term "corona," with reference to a gaseous discharge, is of comparatively recent origin, commonly appearing in the literature only after 1900.)

In 1771, the Italian electrician-astronomer, Giambattista Becarria, succeeded where Hauksbee had not. "The movements that the electric wind can excite," he noted, ". . . repel the hot smoke of a candle just blown out, and if you present a strongly electrified point to the flame of a candle . . . the flame will . . . be repelled by the wind." Becarria thus seems to have been the first to bring about the repulsion of suspended particles from a high-voltage electrode by means of a corona discharge. However, he was concerned with observing the flow patterns of the electric wind issuing from a point and was apparently unaware that Coulombic forces as well as aerodynamic drag played a direct role in the repulsion of the particles. "It is false," Becarria asserted with but partial accuracy, "that it be the outflowing electrical matter that itself directly thrusts away the smoke, blows out the candle or . . . constitutes the electric wind, an opinion in which I see some people firmly persist" (14).

Experiments with a candle are not as straightforward as they may seem. Analysis is complicated by the ionized structure of the flame: the tip and mantle are positively charged whereas the core exhibits a surplus negative charge. Consequently, a candle flame may be subjected to conflicting electrostatic and aerodynamic forces in the presence of a point discharge.

#### Electrical Characteristics of Gasborne Particles

The electrical conductivity of dust and smoke particles, today a matter of chief importance in elec-

trodepositional devices, particularly precipitators and conductance separators, was early an object of scientific inquiry. In 1746 the English physician William Watson, "the most distinguished name in this period in the history of electricity," reported to the Royal Society that a charge is acquired by an insulated conductor placed in a column of smoke rising out of an electrified vessel of burning turpentine. The doctor's experimental set-up was quaintly animate: holding vessel or conductor at each end of the bizarre transmission line was an "electrified man" suitably isolated from ground. Watson concluded, with some surprise, "here we find the smoke of an originally-electric a conductor of Electricity" (15).

Nine years later, the subject was again brought to the attention of the Royal Society with an account of a modification of the foregoing experiment, but now yielding a contrary result. "Mr. Henry Eeles of Lismore in Ireland . . . electrified a piece of down, suspended in the middle of a long silk string, and made steam and smoke of several kinds pass . . . through it, and observed that its electricity was not in the least diminished, as he thought it would have been, if the vapour had been non electric, and consequently had taken away with it part of the electric matter with which the down was loaded" (16).

Eeles flatly concluded that "exhalations of all kinds are electrical [i.e., nonconducting]." Further clarification on this score awaited the Anglo-Italian electrical researcher Tiberius Cavallo. Repeating the smoke-attraction experiment, but using a charged metal sphere in place of his forerunners' rubbed dielectric, Cavallo wrote, in 1777, "the smoak . . . will be attracted by the electrified body and . . . form a kind of atmosphere about it. This atmosphere will remain for a few seconds . . . and gradually vanish, . . . diffus[ing] . . . itself into space." No previous performer of this now popular demonstration had offered an adequate explanation of the mechanism involved. Cavallo's views, on the other hand, are remarkably up to date and go so far as to reveal an appreciation of the concept of charging time constant: "The smoak is attracted by the electrified body . . . for the same reason that other bodies are attracted by it . . . It . . . is not immediately repelled, because it is a bad Conductor, and acquires Electricity very slowly; but having acquired a sufficient quantity . . . it begins to quit the electrified body, and ascending into the air, extends itself into a large space, in consequence of the repulsion existing between its own electrified particles" (17).

Elsewhere Cavallo proceeded to obtain a semi-quantitative measurement of aerosol conductivity. Suspending a cork-ball electrometer over the prime conductor of an electrostatic machine, he noted that the balls did not diverge. But putting "upon the prime conductor a wax-taper just blown out, so that its smoke may ascend to the electrometer . . . the balls . . . will immediately separate a little . . . which shows that smoke is a Conductor in a small degree" (18). (An electrometer is an instrument consisting of two cork balls suspended from a common point by insulating threads. Like charges on the balls cause them to diverge. See Fig. 7.)

A few decades later Michael Faraday could speak of "the power of particles of dust to carry off electricity in cases of high tension" as being "well known," (19) and cautions that high-voltage apparatus "be perfectly free from dust or small loose particles, for these very rapidly lower the charge and interfere on occasions when their presence and action would hardly be expected" (20).

#### The Dust Controversy and Gaseous Conductivity

The problem of the electrification of dust, without specific reference to intentional electrodeposition, played a curious role in the history of gaseous electronics. Coulomb, who in 1785 investigated the loss of electricity from a charged body suspended by in-



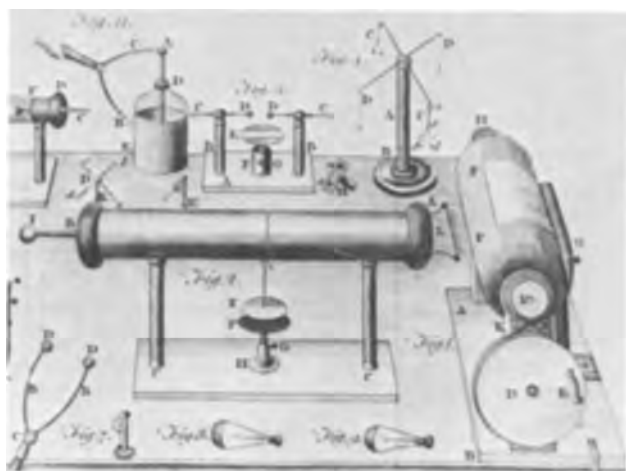


Fig. 7. Illustrations of Cavallo's apparatus (17). In the electrostatic machine, Fig. 1, the earlier manually rubbed glass sphere has been replaced by a cylinder F rubbed by a silk cushion G stuffed with hair. Charge is drawn off onto the prime conductor, Fig. 2, by means of the corona points L. Fig. 4 C shows a cork-ball electrometer.

sulating strings, thought that after allowing for leakage along the supports, some lost charge still remained to be accounted for by a convective discharge through the air (21). Convective discharge or electrical convection were the terms applied to the passage of electricity from one place to another by the motion of charge-bearing particles of ordinarily uncharged matter, e.g., gas molecules, dust, etc. Coulomb supposed that air particles in contact with a charged body acquired an electrical charge of the same sign as the body and that the particles were then repelled by the body. Accordingly, molecules of air could be charged with electricity, much like bits of metal.

Here and there an occasional question was raised regarding the validity of this charging theory. Faraday, though voicing some reservations, went along with the prevailing belief. Kinnersley and Franklin had objected more strongly. As Priestly tells us, "Mr. Kinnersley of Philadelphia, in a letter dated March 1761, informs his friend and correspondent Dr. Franklin, then in England, that he could not electrify anything by means of steam from electrified boiling water; from whence he concluded that, contrary to what had been supposed by himself and his friend, steam was so far from rising electrified that it left its share of common electricity behind" (16, 22).

In time, however, experimental data accumulated which seemed to be explicable only on the hypothesis that molecules of gases or vapors resisted electrification. Warburg in 1872, supported by Nahrwold in 1887, adduced compelling evidence that the loss of charge from an isolated electrified body could be accounted for by the presence of dust in the ambient air (23, 24). These researchers held that it was the dust and not the air striking the charged body that was responsible for carrying off the electricity. In this newer view the dust did not even have to be present in the original air. It might, it was believed, be given off by the charged conductors under investigation. Thus, Lenard and Wolf demonstrated in 1889 that when ultraviolet light fell on a negatively electrified platinum surface, a steam jet in the neighborhood of the surface showed by its change of color that the vapor had been condensed (25). Lenard and Wolf attributed the condensation of the jet to dust or metallic vapor emitted from the illuminated surface, the dust producing condensation by forming nuclei around which the water droplets coalesced. The experimenters were, of course, observing the photoemission of electrons from the metallic surface by means of a primitive cloud chamber. But being unaware of the existence of electrons or gaseous

ions and supposing that dust was indispensable to droplet condensation, Lenard and Wolf were led to conclude that the metal was disintegrating under the action of the light, the metallic vapor carrying off the negative electricity and leaving behind the positive. The belief that air molecules could not be charged was further supported by the experimental results of Blake in 1882 and Sohncke in 1888 (26, 27). These studies seemed to show that not only is there no electricity produced by the evaporation of an unelectrified liquid, but also that the vapor rising from an electrified liquid does not carry a charge. It was natural enough to argue that if molecules of vapor are capable of receiving a charge under any circumstances, they should be expected to do so in this case.

Lord Kelvin and Magnus MacLean further observed in 1894, "That air can be electrified either positively or negatively is obvious from the fact that an isolated spherule of pure water, electrified either positively or negatively, can be wholly evaporated in the air . . . This demonstrates an affirmative answer to the question, can a molecule of gas be charged with electricity? It shows that the experiments referred to as pointing to the opposite conclusion are to be explained otherwise" (28). Despite this, F. Braun could write as late as 1896, "The question of whether a gas can be electrified is answered mostly in the negative, at least among German investigators. All phenomena indicating the possibility of electrification can be explained by the presence of dust particles that might have been contained in the gas from the outset or else introduced during the process of electrification" (29). It was not long, however, before the last vestige of doubt on this score was eliminated. X-rays were discovered in 1895. Almost immediately J. J. Thomson, at the head of a brilliant group of young scientists at the Cavendish Laboratory of Cambridge, undertook to answer the question of how dust-free gases are made conductive by the new radiation. It was quickly found that gas rendered conducting this way lost all its conductivity when filtered through glass wool or traversed by a current-producing electric field. The conclusion was inevitable that gaseous conductivity was due to the presence of electrified particles. These particles were called ions by analogy with the term coined by Faraday in 1834 with reference to the charge carriers of electrolytic solutions (30).

### Practical Electrodeposition

Credit for the earliest electrodepositional device comprising both a corona discharge electrode and a particle-collecting surface belongs to a German teacher of mathematics, M. Hohlfeld. Having observed in thunderstorms that increased rainfall usually followed closely after lightning discharges, Hohlfeld speculated in 1820 that electric discharges simulated in the laboratory might produce a corresponding effect. Filling a bottle with smoke from burning paper, he "corked the bottle, passing through the cork a wire . . . extending to within three inches of the bottom of the bottle. The . . . [wire] was connected to . . . [an electrostatic machine] so that the electricity was silently transferred into the bottle and brought in contact with the smoke . . . With the passing of the first spark the smoke vanished, the water from the smoke appearing on the bottom of the bottle" (31).

Hohlfeld evidently thought that a spark discharge was required to achieve his purpose because he was trying to simulate thunder. That a (relatively) silent corona would accomplish the same result was reported 30 years later by C. F. Guitard, unaware that any attention had previously been drawn to the subject. In his words: "It . . . struck me, that if I brought a wire from an electrifying machine into . . . [a glass] cylinder [filled with tobacco smoke] the air would immediately become charged with electricity, which would cause each portion of smoke to fly to the

sides of the cylinder . . . The [experimental] effect produced was perfectly magical; the slightest turn of a small electrifying machine produced immediate condensation. It was astonishing to see how small a quantity of electricity produced a most powerful effect" (32).

Experimental studies of the behavior of aerosols in electric fields, with or without a corona discharge, are seen to have been pursued sporadically and largely independently by workers in several countries from 1600 on into the 19th Century. But not until 1883 do we find the proposal put forth (by Oliver Lodge, professor of physics at University College, Liverpool) that the charging and precipitation of dust in a corona might offer an effective means of suppressing atmospheric contamination (33). In 1870, John Tyndall, the British physicist whose name brings to mind the well-known light-scattering effect, had noted that a dust-free space formed over a hot body in strongly illuminated dusty air. Further study of this phenomenon, which is now known to be a consequence of differential molecular bombardment (radiometry), was undertaken by Oliver Lodge. Professor Lodge's lecture demonstrator, J. A. Clark, hypothesized that air streaming over a hot surface might become electrified by friction, and that from air so charged, dust could somehow be expelled. To test this supposition, a rod mounted in a smoke-filled box was raised to a few thousand volts. With the appearance of corona "a very violent and remarkable effect was noticed; the . . . [clear region] widened enormously and tumultuously and the whole box was rapidly cleared of smoke" (34). Electrical precipitation had once again been brought to light.

In a letter to *Nature* in 1883 in which he announced Clark's discovery, Lodge, unlike his predecessors, went on to suggest several practical ideas. "It is somewhat surprising," he noted, "considering the perfection to which electrostatic machines have been brought that they have not received any practical application. The electrical clearing of the air of smoke rooms, or of tunnels, is perhaps not an impractical notion. The close relationship between fogs, epidemics, &c., and the suspension of solid particles in the air, suggests the use of electrical means for sanitation and for weather improvement" (33).

Lodge's first thoughts centered on treatment of the already polluted atmosphere rather than on the true offender, the actual sources of pollution. A proposal that this latter approach might offer the solution to a vexing problem was made by Alfred Walker, a lead smelter who, with Lodge's advice, promptly undertook the construction of a full-sized precipitator at his furnaces in Bagillt in Wales (35, 36). Here, Lodge recalled years later, clouds of lead oxide fume had been escaping into the air "to the damage of the neighboring agriculture. But the method of producing high-tension electricity in those days was rather primitive, and by no means of an engineering character. [The 50-kv, 0.3-ma Wimshurst machines which had then only recently been developed, and of which much was expected, proved to be less than satisfactory for the application at hand.] Moreover, the difficulties of insulation were not properly appreciated. . . . It is doubtful if any real electrification was communicated to the flues, along which the hot, flaming, and smoky gases were rushing at a considerable pace from the smelting furnaces: so that the first attempt at practical application was unsuccessful, and . . . was discontinued" (37).

There is some question as to whether Walker would have succeeded in any case. Modern experience has shown that the highly resistive, finely divided, lead oxide fume is one of the most troublesome of aerosols to precipitate.

Lodge was not dismayed by the disappointing outcome of Walker's attempt. Over the ensuing years, with his son, he carried forward his researches. But despite his many large-scale experiments leading to

various improvements (e.g., introduction of the transformer and tube rectifier and development of suitable high-voltage insulators), the technical breakthrough on which the birth of a new industry hinged was to be made elsewhere.

The widespread publicity attendant on the investigations of Lodge and his associates stimulated activity by others. Over the next two decades, in addition to Walker's patents in half a dozen countries, additional patents and an occasional publication served to keep alive interest in the "electrical condensation" of smoke. It remained ultimately for Frederick Cottrell, professor of physical chemistry at the University of California, to bring to fruition the process of electrostatic precipitation that now bears his name. Avenues of technical communication open to Cottrell at the turn of the century were so far from adequate that not until he constructed his first commercial precipitator did he become aware of Lodge's work antedating his own by some 20 years. Cottrell himself appears to have had no clear-cut recollection of how the idea of precipitation came to him. Nevertheless, he fully acknowledged Lodge's priority and characteristically minimized his own considerable contribution (38). Writing in 1914 of his introduction to the subject, Cottrell had this to say: "Some eight years ago, while studying various methods for the removal of acid mists in the contact sulphuric process . . . the author had occasion to [independently] repeat the early experiments of Lodge and became convinced of the possibility of developing them into commercial realities. The subsequent work may fairly be considered as the reduction to engineering practice as regards equipment and construction of the fundamental process long since laid open to us by the splendid pioneer work of Lodge, a feat vastly easier to-day than at the time of Lodge and Walker's original attempt" (39).

In 1907, following impressive laboratory demonstrations, Cottrell set out "to duplicate these experiments on a scale some two hundred-fold larger. This was carried out . . . at the E. I. duPont de Nemours Powder Co. at Pinole, on San Francisco Bay, where the contact gases from one of their . . . sulphuric acid units were employed" (39). The operation was an unqualified success.

### Epilogue

Practical electrostatic precipitation on a commercial scale had been born. In a much broader sense, though, the accumulated effort of the preceding two millennia and more now heralded an era in which particulate electrodeposition and separation were to find commonplace and diverse application. The subsequent explosive industrial expansion of fine particle electrostatics calls to mind Lodge's prophetic words before the Royal Dublin Society in 1884: "Whether anything comes of it [electrodeposition] practically or not, it is an instructive example of how the smallest and most unpromising beginnings may, if only followed up long enough, lead to suggestions for large practical application. When we began the investigation into the dust-free spaces found above warm bodies we were not only without expectation, but without hope or idea of any sort, that anything practical was likely to come of it . . . [And so] it may happen that the yet unapplied and unfruitful results evoke a sneer, and the question . . . ["What good is it?"] the only answer to which question seems to be: No one is wise enough to tell beforehand what gigantic developments may not spring from the most insignificant fact" (40).

Developments in recent decades in the application of particle electrostatics have indeed been impressive: among typical electrodepositional or separating devices may be numbered mineral and foodstuff separators, electrostatic flock coaters and particle orientors, electrostatic painting, coating, and printing devices, gas and liquid filters, and still others. But



these achievements of the more recent past comprise a story of their own, one that is told, under appropriate headings, in other papers of this series.

### Acknowledgments

The author is indebted to George A. Carkhuff whose careful photographic work under adverse conditions provided the illustrations for this paper, and to the Institute of Electrical and Electronic Engineers and the American Institute of Physics in whose publications portions of this history have previously appeared.

Manuscript received Nov. 28, 1967. This paper was presented at the Chicago Meeting, October 15-19, 1967 as Abstract 144.

### REFERENCES

- Diogenes Laertius, "The Lives and Opinions of Eminent Philosophers," p. 15, Transl. C. D. Yonge, George Bell and Sons, London (1895).
- Aristotle, "De Anima," Book I, Chap. 2, p. 17, Transl. R. D. Hicks, Hakkert, Amsterdam (1965).
- W. Gilbert, "De Magnete," London, 1600. Engl. Transl. "William Gilbert of Colchester . . . on the Magnet," p. 46ff, The Gilbert Club, London (1900).
- "Photii Bibliotheca," Rothomagi, folio, col. 1040-1, cod. 242, 1653, cited by P. F. Mottelay, "Bibliographical History of Electricity and Magnetism," p. 7, Charles Griffin and Co., Ltd., London (1922).
- R. Boyle, "Experiments and Notes About the Mechanical Origine or Production of Electricity," pp. 13-4, London (1675).
- J. B. Secondat de Montesquieu, "Histoire de l'électricité," p. 141 (1746). Cited by ref. (16) *op. cit.*, 5th ed., p. 6 (1794).
- O. von Guericke, "Experimenta nova magdeburgica," pp. 147-50 and figures, Amsterdam (1672).
- F. Hauksbee, "Physico-Mechanical Measurements on Various Subjects," pp. 46-7, London (1709).
- "Saggi di naturali esperienze," Academia del Cimento, Florence, 1667. Engl. Transl. R. Waller, "Essays of Natural Experiments Made in the Academie del Cimento," pp. 128-132, London (1684).
- M. Faraday, "Experimental Researches in Electricity," London, Vol. 1, 1839, par. 1602.
- J. Newton, "Opticks," 2nd ed., pp. 315-6, London, (1718).
- J. A. Nollet, "Essai sur l'électricité des corps," Paris, 1746.
- A. H. Smith, "Writings of Benjamin Franklin," New York, Vol. 2, p. 303 (1905).
- G. Becarria, "Elettricismo artificiale," Turin, 1772, par. 781, 783.
- W. Watson, *Trans. Roy. Soc. London*, **10**, 296 (1746).
- J. Priestly, "History and Present State of Electricity," 1st ed., pp. 214-216 and figures, London (1767).
- T. Cavallo, "A Complete Treatise of Electricity in Theory and Practice," pp. 309-10, plate I, London (1777).
- Ref. (17), *op. cit.*, 4th ed., Vol. 1, p. 321 (1795).
- Ref. (10), *op. cit.*, par. 1569.
- Ibid.*, par 1201.
- C. A. de Coulomb, "Memoires de l'Academie des Sciences," p. 612, Paris (1785).
- E. Kinnersley, *Phil. Trans. Roy. Soc. London*, **53**, 84, (1763).
- E. Warburg, *Ann. Physik*, **145**, 578 (1872).
- R. Nahrwold, *ibid.*, **32**, 1 (1887).
- P. Lenard and M. Wolf, *ibid.*, **37**, 443 (1889).
- L. J. Blake, *ibid.*, **145**, 578 (1872).
- L. Sohncke, *ibid.*, **34**, 925 (1888).
- Lord Kelvin and M. MacLean, *Proc. Roy. Soc. London*, **56**, 84 (1894).
- F. Braun, *Ann. Physik*, **59**, 688 (1896).
- J. J. Thomson and E. Rutherford, *Phil. Mag.*, **42**, 392 (1896).
- M. Hohlfield, *Archiv Gesante Naturlehre*, **2**, 205 (1824).
- C. F. Guitard, *Mechanics Magazine*, **53**, 346 (1850).
- O. J. Lodge, *Nature*, **28**, 297 (1883).
- O. J. Lodge, *J. Soc. Chem. Ind.*, **5**, 572 (1886).
- A. A. Walker, Great Britain, Pat. 11,120, Aug. 9, 1884.
- A. O. Walker, *Engineering*, **39**, 627 (1885).
- O. J. Lodge, "Electrical Precipitation," pp. 21-40, Oxford University Press, London (1925).
- F. Cameron "Cottrell, Samaritan of Science," Doubleday, New York (1952).
- F. G. Cottrell, "Problems in Smoke, Fume and Dust Abatement," Publication 2307, Government Printing Office, Washington, D. C., 1914.
- O. J. Lodge, *Nature*, **29**, 610 (1884).

## SECTION NEWS

### Boston Section

The Boston Section held its second meeting of the 1967-1968 season at the Ledgemont Laboratory of the Kennecott Copper Corp., Lexington, Mass., on November 14, 1967.

Mr. Ralph B. Soper was presented with a Past-Chairman's pin in appreciation of his services in that office during 1966-1967.

The speaker for the evening was Ivor E. Campbell, Vice-President of The Electrochemical Society, who spoke on "Vapor Deposition, Past, Present, and Future." Dr. Campbell reviewed the development of vapor deposition processes, their present commercial status, and opportunities for further utilization. The relative advantages of chemical and physical vapor deposition were discussed as well as the relationship of these processes to other coating processes.

R. G. Donald,  
Secretary

### Cleveland Section

During the year 1967-1968 the Cleveland Section, as usual, has had a wonderful year of programs arranged by Program Chairman R. J. Brodd. Dinner meetings are held monthly on the second Tuesdays from September to June except in October and May when the National Meetings of the Society are in session.

The principle speakers and titles for meetings are as follows:

September—"Current Distribution on and in Porous Electrodes," R. J. Brodd, Union Carbide.

November—"Edison plus TEFLON—Application of New Material to Electrochemical Cells," G. Frysinger, U. S. Army Electronic-Command.

December—"A Chemical View of Semiconductors," D. Trivich, Wayne State University.

January—"Conduction and Electroluminescence in Oxide Films," T. W. Hickmott, I.B.M. Corp.

February—"Electrochemistry and Reactive Intermediates in Electrosynthesis in Nonaqueous Solvents," M. E. Peover, National Physical Lab., Teddington, England.

March—"The Influence of Adsorp-

tion on Electrode Reactions at the dropping Mercury Electrode," J. Kuta, Heyrovsky Polarographic Institute, Czechoslovakia.

April—"Between Science and Art—Recent Research in Nonaqueous Solvents and Electrochemical Calorimetry," R. T. Foley, American University.

The June meeting will be "Ladies Night" with a subject of general interest.

It has been a custom of the Cleveland Section to have a short after dinner talk at each meeting. The subjects for the year are of great variety, ranging from "Recent Advance on CdS Thin Film Cell," by W. Bower, "Comments on the World-Wide Chlorine Industry," L. E. Vaaler, "Some Recent Developments in Electroplating," K. Willson, to "Society Affairs," by Vice-President N. Corey Cahoon.

T. S. Lee,  
Secretary

### Detroit Section

The annual joint dinner meeting of the Detroit Section and the National Association of Corrosion Engineers was



### The Study of Surface Chemistry by the Mossbauer Effect\*

M. C. Hobson, Jr.

*Virginia Institute for Scientific Research, Richmond, Virginia*

To define a surface precisely is difficult, to measure its properties, arduous. A single crystal provides a close approximation to a known surface. But experimental difficulties obtain because of the minute amount of material provided by the surface atoms of a single crystal. If the knowledge of the surface geometry provided by single crystals can be abandoned, some of the difficulties can be overcome by dispersing the material in the form of microcrystals having high surface to bulk atom ratios. Samples of this type may or may not be supported on inert material with a high surface area, but, in either case, an increasing number of instrumental techniques become applicable to the study of surface chemistry by virtue of the increase in the quantity of surface atoms present. One of these, Mössbauer Effect spectroscopy, is capable of supplying us with much detailed information on surface structures; information often difficult, if not impossible, to obtain by any other experimental method.

The Mössbauer Effect is the name given to the recoilless emission and resonant reabsorption of low energy gamma rays, and was discovered by Rudolf Mössbauer in 1958. It was rapidly recognized as a powerful and versatile technique for the study of the physical properties of matter; particularly, for the study of the structure of solids. Since several excellent reviews have appeared recently on the basic physics of the technique only those points that apply to an understanding of the chemical information that can be obtained from the measurements will be discussed. Applications of the technique will include studies on the valence states of surface atoms, chemisorption on surfaces, size measurements on microcrystals, lattice dynamics of surface atoms and, an allied area, the structure of surface layers much more than one atom thick, but having properties that differ from the bulk.

The most important property of a Mössbauer gamma ray is its very narrow line width. The sharpness of the absorption band not only permits high resolution of hyperfine interactions, but it also permits a simple modulation technique for sweeping the gamma ray energy through resonance; namely, by using the Doppler Effect. By starting at zero velocity and moving the source or the sample relative to the other through a range of velocities to a maximum of a few mm/sec the gamma ray energy is modulated by many times its line width and spectra containing multiple resonance absorptions are readily observed. These resonance absorptions may be observed experimentally in either of two geometrical configurations as shown schematically in Fig. 1. Illustrated in diagram A is the usual arrange-

ment for studying thin samples by transmission. An absorption spectrum is obtained which manifests itself as a drop in the count rate on passing through resonance as the velocity is varied. As shown in diagram B the primary gamma radiation is not observed directly, but the absorbed gamma rays are observed on re-emission. A plot of count rate *vs.* velocity results in an increase in the count rate on passing through resonance and an emission spectrum is obtained.

There are some 34 or more elements for which the Mössbauer Effect has been observed and a number of others for which it is predicted. All together about half the elements in the periodic table should exhibit the effect, but, in practice, only a few elements can be studied readily outside of laboratories having very large radiochemical facilities. Currently the most useful isotopes are iron-57, tin-119, antimony-121, iodine-127, iodine-129, and gold-197. Unfortunately, the effect is not found in any of the lighter elements in the periodic table up through argon.

The changes that take place in Mössbauer spectra of different compounds of the same element are the result of hyperfine interactions between the nucleus and the extranuclear electrons. For chemical applications the most useful observables are the chemical shift, the electric quadrupole splitting, and the magnetic dipole splitting (Zeeman splitting). In discussing these we will assume the nuclear ground state has a spin of 1/2 and the excited state a spin of 3/2; a situation which occurs frequently among Mössbauer nuclei.

The chemical shift,  $\delta$ , is a consequence of the finite size of the nucleus. The common practice of assuming a point charge for the nucleus is not a valid approximation for this type of measurement. Since the gamma ray emitted by the nucleus represents a change in the electrostatic energy of the nucleus on going from a higher to a lower energy level those parameters which affect the nuclear energy levels will govern the energy of the gamma ray. One of these is the radius of the nucleus which is usually different for each energy level. The other is the electron density at the

REVIEW  
SECTION

\* This work was supported, in part, by the Air Force Office of Scientific Research, Grant No. AF-AFOSR-734-65.

Key words: Mössbauer Effect, surface chemistry, catalysis, thin films, corrosion.

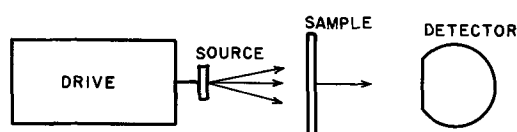


DIAGRAM A  
RESONANT ABSORPTION

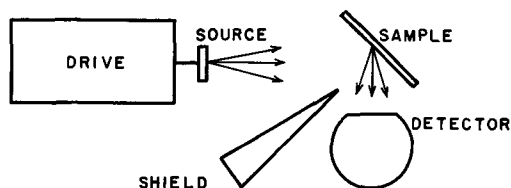


DIAGRAM B  
RESONANT SCATTERING

Fig. 1. Block diagrams of two experimental schemes. Diagram A shows the transmission scheme, and diagram B shows the scattering scheme.

nucleus resulting from its finite size. The relationships are given by

$$\delta = \left[ \frac{4}{5} \pi Z e^2 R^2 \right] \cdot \frac{\Delta R}{R} \cdot [\Delta |\psi_0|^2]$$

where the first term on the right is a collection of physical constants, the second, the change in the radius of the nucleus on going from the ground to the first excited state and the third, the difference between the wave function that gives the electron density at the nucleus of the source and the wave function that gives the electron density at the nucleus of the absorber. Therefore, the gamma ray energy is directly proportional to the electron density at the nucleus and the change in the radius of the nucleus on undergoing a transition. The change in radius is a characteristic of the isotope, but the electron density will vary with chemical changes that the element may undergo. The latter effect is produced primarily by s-electrons and indirectly by p and d-electrons via their screening effects on the s-electrons. The maximum change in the electron density at the nucleus on going from one valence state to another will not result in energy shifts large enough to measure directly, but it is relatively easy to measure the difference in the shifts between a standard and an unknown. Single crystals of sodium nitroprusside have been adopted by the National Bureau of Standards as reference material for Mössbauer studies on Fe-57. The term differential chemical shift,  $\delta_0$ , has been proposed for reporting spectral shifts relative to standard sodium nitroprusside.

When the nuclear spin quantum number,  $I$ , is greater than  $1/2$  the nucleus is not spherically symmetrical and the nuclear quadrupole moment takes on non-zero values. Coupling of this quadrupole moment with the gradient of an unsymmetrical electric field lifts the nuclear spin degeneracy and additional peaks appear in the spectrum. For the case of  $I = 3/2$ , the excited state of Fe-57, and an axially symmetric electric field gradient this energy level splits into an upper and lower level. The absorption peak splits into a symmetrical doublet and the magnitude of the splitting between the two peaks is a measure of the coupling of the excited nucleus with the electric field gradient. For this special, but often observed, case the energy difference between the two peaks is given by

$$\Delta E_Q = \frac{e^2 q Q}{2}$$

where  $Q$  is the nuclear moment and  $eq$  is the electric field gradient. These two quantities are independent and to obtain the value of one of them the other must be either calculated or measured by another experimental method; a situation similar to the interpretation of the chemical shift. Once the value of the nuclear quadrupole moment is established the splitting may be used to calculate the magnitude of the electric field gradient. The presence of more than one type of crystallographic site and the structure of the orbitals used in the bonding of the compound may be deduced from these data in some cases.

Finally, the presence of an internal magnetic field will cause a hyperfine Zeeman splitting of the nuclear energy levels similar to the splitting observed for unpaired extranuclear electrons in an applied magnetic field. Again consider the case of the iron  $1/2$  to  $3/2$  transition. The spin  $1/2$  level will split into two substates and the spin  $3/2$  split into four substates. The transitions are governed by the selection rules for magnetic dipole transitions; namely,  $\Delta m = 0, \pm 1$  and six equally spaced lines are observed. If an electric field gradient is superimposed on such a spectrum, the spacing between the peaks will no longer be equal. The effect is complex, and information on the quadrupole coupling cannot be deduced without independent knowledge of the crystal structure and the relationship between the electric field gradient and the magnetic field.

The problems associated with applying this technique to the study of surface structures are those generally applicable to all resonance absorption methods used in the investigation of surfaces. The amount of material on the surface is small compared to the bulk which makes it difficult to resolve those features in the spectrum unique to the surface structures. To overcome this measurements are made on very porous materials, or materials highly dispersed on the surface of porous materials. However, the Mössbauer Effect, by virtue of its radioactive nature, has a certain versatility not common to other spectroscopic methods. Not only can it be applied to systems of a highly dispersed nature, but the surfaces of single crystals can be studied as well. If the radioactive nuclei, that normally are the source of the  $\gamma$ -rays, are deposited on the surface of a single crystal in a monatomic layer or less, the structure and chemical bonding of the atoms in this surface source may be studied using a standard absorber. The former type of measurement has been carried out in our laboratory utilizing the Fe-57 isotope dispersed on alumina and on silica gel (1, 2).

Highly dispersed samples of metals or metal oxides are commonly prepared by impregnating a porous material; such as, silica gel or alumina, with a salt of the metal that can be readily decomposed thermally. The catalytically active surface is obtained by calcination followed by oxidation-reduction cycles as desired. Shown in Fig. 2 is a typical example of iron-on-alumina. The sample is 23% iron and the top spectrum is the initial preparation following a calcination at  $500^\circ\text{C}$ . In this form the iron exists as  $\alpha$ -ferric oxide with an average crystallite diameter of  $300\text{\AA}$  as determined by x-ray line broadening. The six line Zeeman pattern produced by the antiferromagnetic structure of the  $\alpha$ -Fe<sub>2</sub>O<sub>3</sub> is superimposed on a doublet in the center of the spectrum. The doublet has a differential chemical shift of  $+0.51$  mm/sec and a quadrupole splitting of  $1.07$  mm/sec. These values fall in the general range for high-spin ferric compounds, and the doublet is believed to represent  $\alpha$ -Fe<sub>2</sub>O<sub>3</sub> crystallites so small that the magnetic field has collapsed.

Reduction of the oxide to magnetite is easily done in flowing hydrogen at temperatures in the  $200^\circ$  to  $300^\circ\text{C}$  range. The identification of the magnetite struc-

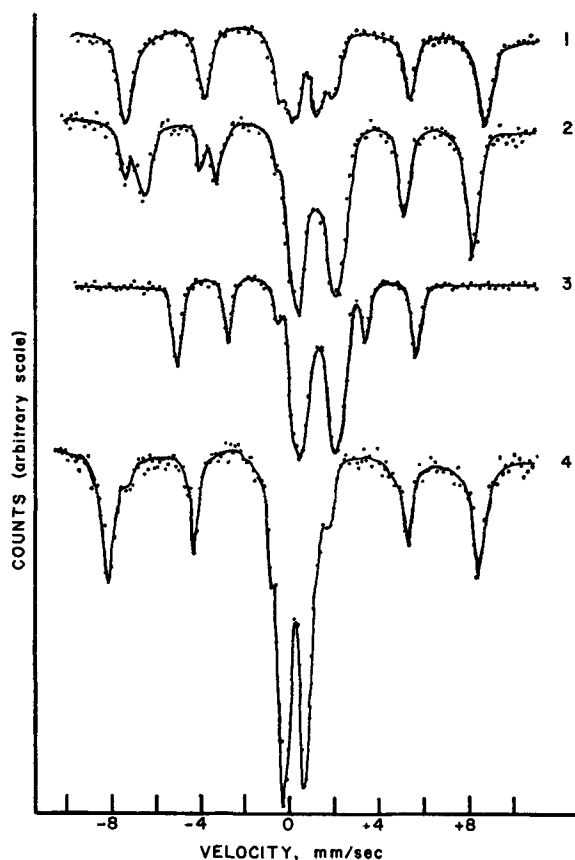


Fig. 2. Spectra of an  $\text{Fe-Al}_2\text{O}_3$  catalyst undergoing an oxidation-reduction cycle. 1. initial preparation, 2. partial reduction to magnetite, 3. completed reduction to metallic iron, and 4. re-oxidation to ferric oxide.

ture by the Mössbauer spectrum is evidenced by a splitting of the six line Zeeman pattern into two partially superimposed Zeeman patterns as seen in the second spectrum. Further reduction is more difficult, but the third spectrum in Fig. 2 is obtained after a prolonged treatment at  $500^\circ$  to  $600^\circ\text{C}$ . The change in the positions of the six lines of the Zeeman pattern indicates the formation of a metallic iron phase. At the same time the doublet has increased in relative size and shifted in a positive velocity direction. Its differential chemical shift is  $+0.98$  mm/sec and its quadrupole splitting is  $1.73$  mm/sec. These values and the relatively large size of the doublet indicate that a large fraction of the total amount of iron present is in the form of ferrous ions; probably, a ferrous oxide. Further treatment in flowing hydrogen does not change this spectrum. The phase containing the ferrous ions appears to be stabilized by the surface of the alumina making the complete reduction to the metallic state impossible. This state of affairs has been suspected in previous studies of supported iron catalysts, but never established since the ferrous phase has not been found in x-ray diffraction analysis of similar samples.

The fourth spectrum in Fig. 2 is obtained on re-oxidation of the sample. The positions of the peaks in the six line Zeeman pattern and the differential chemical shift and quadrupole splitting of the doublet are similar to the initial spectrum. However, the relative size of the doublet compared to the Zeeman pattern has changed drastically. Could it be that the structural details observable by Mössbauer spectroscopy will make it possible to determine the thermal history of any given sample? The deactivation of a catalyst during use is a continuing industrial problem. Irreversible structural changes as observed here certainly suggest that the technique may be useful as a quality control method and further investigation in this area seems worthwhile.

The surface effects can be made to stand out quite sharply by using very dilute solutions enriched in Fe-57 for the preparation of the samples. Very small crystallites that are highly dispersed over the surface can be obtained, and consequently a high surface to bulk atom ratio. In these samples only a doublet is obtained similar to the doublet in the middle of the bottom spectrum in Fig. 2. Usually the quadrupole splitting is large and the chemical shift less positive for the smaller crystallite sizes. On reduction in flowing hydrogen above  $400^\circ\text{C}$  the doublet transforms into an unsymmetrical triplet with a general shifting of the spectrum in a positive velocity direction as shown in the top spectrum of Fig. 3. This triplet appears to be the superposition of two doublets. The values of the differential chemical shift and quadrupole splitting for the one consisting of peaks 1 and 2 are characteristic of high-spin ferric ions, and for the other, peaks 1 and 3, high spin ferrous ions. On adsorption of ammonia spectrum B is obtained. Peak 2 has almost vanished and the splitting between peaks 1 and 3 has increased indicating additional polarization of the 3d electrons.

Kinetic studies on ammonia decomposition over iron catalysts indicate that dissociative chemisorption of ammonia takes place. If one assumes that ammine radicals are formed by chemisorption of ammonia on this catalyst, then peak 2 of spectrum A is probably produced by a high-spin ferric state. The ammine radical, with its strong tendency to donate electrons to the adsorption site, complexes with the 3d orbitals of the ferric ions and produces a high-spin ferrous complex on the surface, as indicated in spectrum B. The reversible nature of the surface complex is demonstrated by obtaining spectrum C on out-gassing the sample.

Adsorption on the surface has also been studied from the standpoint of the adsorbate instead of the adsorbent. Karasev and co-workers (3) adsorbed tetramethyl tin on  $\gamma$ -alumina and observed the

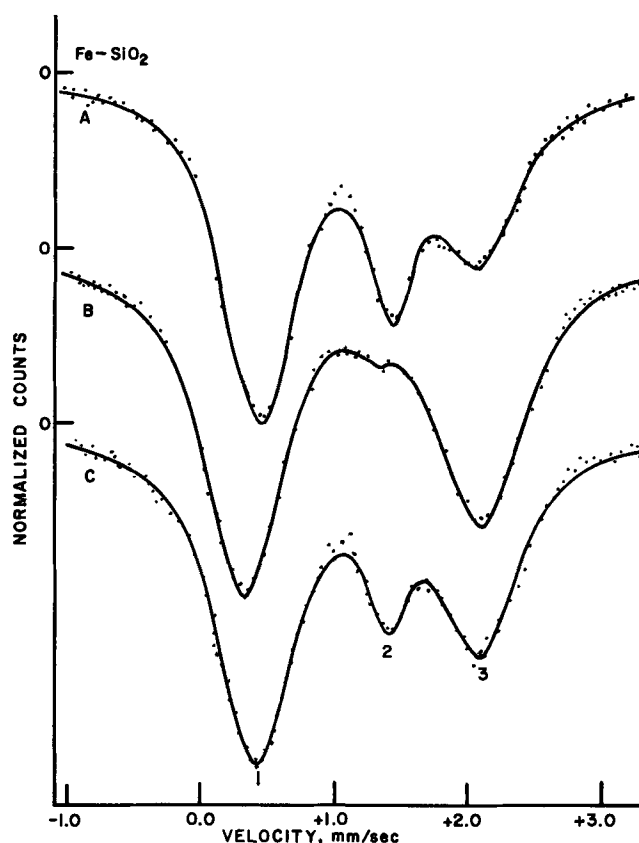


Fig. 3. Spectra of ammonia chemisorption on a highly dispersed  $\text{Fe-SiO}_2$  sample. (A) initial sample reduced in  $\text{H}_2$ , (B) after adding  $\text{NH}_3$  to 1.35 Torr, and (C) after outgassing at  $100^\circ\text{C}$ . (Ref. 2).

formation of a doublet. They interpreted this result in terms of two different chemisorbed species, each producing a singlet rather than the quadrupole splitting of one species to produce the doublet. One peak results from the reaction of the tetramethyl tin with surface hydroxyl groups with the formation of methane and leaving tin in a position on the surface normally occupied by an aluminum ion. The other peak is produced by dissociative chemisorption to form hydrogen and an aluminum-methyl-tin surface complex.

Similar studies could be made using volatile compounds of iodine for the adsorbate. Both I-127 and I-129 isotopes are usable for Mössbauer Effect studies. The technique is very attractive for further studies on the structure of surface complexes.

The catalytic activity of supported metals is more complex than would be expected for a simple picture of small crystallites of the metal resting on the surface of an inert support. To gain insight into the nature of these catalysts one needs to know the surface area of the metal and the size and size distribution of the metal crystallites. Magnetically ordered structures, such as iron and some of its oxides, produce six line Zeeman patterns. However, there is a critical size below which the magnetic ordering cannot be maintained and the six lines collapse into a doublet. Since this effect is also a function of temperature an average crystallite size can be obtained by observing the per cent area under the doublet *vs.* the Zeeman pattern in spectra similar to the bottom one in Fig. 2, and when the ratio is 1:1 a calculation of the size can be made. Kündig and co-workers (4) have developed this method and applied it to microcrystalline ferric oxide on silica gel. In fact, a number of Mössbauer studies have been made on microcrystalline materials, and many of these are discussed in ref. (4). With the exception of Kündig's extensive investigation, correlations with surface properties were not made directly, but only implied.

A second method, also proposed by Kündig, is based on the observation that the magnitude of the splitting of the doublet appears to increase with decreasing crystallite size. This is a particularly interesting observation since it would be usable for microcrystallites smaller than those which can be measured by x-ray line broadening, and it becomes important when all of the crystallites are so small that no Zeeman pattern is observed. We have proposed a simple mathematical model for calculating the average crystallite size from the magnitude of the quadrupole splitting observed for the doublet. The observed splitting is calculated as the weighted sum of the theoretical splitting produced in the iron nucleus of an iron ion on the surface with one oxygen ion removed from its coordination sphere plus the splitting of an ion in the bulk. The weighting factors consist of the ratio of the volume of a spherical shell containing the surface iron ions to the total volume and the volume of the rest of the interior of the sphere to the total volume. As the particles become smaller the amount of iron in the surface shell to that in the bulk becomes larger and, consequently, the splitting of the doublet increases. Kündig has made similar estimates, but obtained his results by an empirical fit of the data rather than calculation from a model. On plotting the results for known samples we find that the fit of the data to the theoretical curve is good for ferric oxide on silica gel, but only fair for ferric oxide on alumina. However, there is some question as to the extent of interaction with the support when the crystallite size becomes so small that a large fraction of the iron ions are on the surface of the crystallite. In both of the methods outlined above the result is critically dependent on the assumption that the observed doublet is produced by, and only by, the small size of the alpha-ferric oxide crystallites. Any interaction with the support has been ignored. This assumption is far from being firmly es-

tablished. Certainly, the changes found in the sequence of spectra in Fig. 2 demonstrate that one does not recover the identical starting material following an oxidation-reduction cycle. Since iron ions can replace aluminum ions in the alumina lattice it is not surprising that these drastic changes are observed for iron-on-alumina samples, but not for iron-on-silica samples. However, some features of the iron-on-silica spectra do change; such as, an increase in the splitting of the doublet on undergoing an oxidation-reduction cycle. It does not seem possible to derive these changes from a sintering process. The crystallites seem to be growing smaller rather than larger, contrary to expectations. Perhaps it will be necessary to abandon the concept of very small, highly dispersed crystallites, and correlate catalytic activity with the features of the spectra rather than structures derived from the spectra. The question begs further investigation.

The highly dispersed systems discussed so far suffer from a valid criticism. They cannot be considered as "clean" surfaces with known crystalline surface structure. For fundamental studies of bonding and lattice dynamics carefully prepared surfaces of single crystals must be used. It is possible to employ the Mössbauer Effect in the study of surfaces of single crystals by depositing the gamma ray source on the surface and using a known single line absorber; such as, a stainless steel foil. The only published work in this area has been reported by Burton and Godwin (5). They deposited Co-57 by vacuum evaporation on the surfaces of tungsten and silver and recorded the spectra of the gamma rays emitted in a direction normal to the surface and at an angle  $60^\circ$  from the normal. They considered three possible situations which would affect the recoil free fraction of the gamma ray emission. For a nucleus bound in a lattice the recoil free fraction will be smallest along the direction of largest displacement. In the bulk of a cubic crystal this will be isotropic and a single line is obtained which does not change with orientation of the crystal. If the nucleus is just in the surface, its largest displacement will be normal to the surface and the lowest intensity for the absorption peak will be normal to the surface. However, if the nucleus is on the surface, its largest displacement will be parallel to the surface and the intensity smallest in that direction.

The result obtained by Burton and Godwin for a polycrystalline tungsten surface is shown in Fig. 4. The observed spectrum is found to be the sum of three components with the middle line caused by atoms that diffused into the bulk. The doublet is the result of the coupling of the nuclear quadrupole moment with an electric field gradient axially symmetric to the normal of the surface. The asymmetry of the doublet may be attributed to the angular dependence of the intensities of the two transitions. The spectrum observed at  $60^\circ$  from the normal is similar, but the relative intensities of the components has changed. The decrease in the low velocity peak relative to the high velocity peak indicates that the electric field gradient is negative. When the experiment was repeated using the (310) surface of a single crystal of tungsten the bulk component disappeared. The lack of grain boundaries in the single crystal presumably prevents the diffusion into the bulk under the conditions of sample preparation.

Using a single crystal of silver as the substrate a broad peak was obtained, but no angular dependence was observed. The authors suggest that this might be caused by poor surface preparation, or by the collection of the cobalt atoms into small islands. The combination of Mössbauer Effect measurements and low energy electron diffraction measurements simultaneously on a given system of this type would be a natural extension of this work. The LEED measurements would indicate the type of surface lattice the evaporated cobalt atoms had formed, or if they had formed dispersed islands, and the Mössbauer measure-

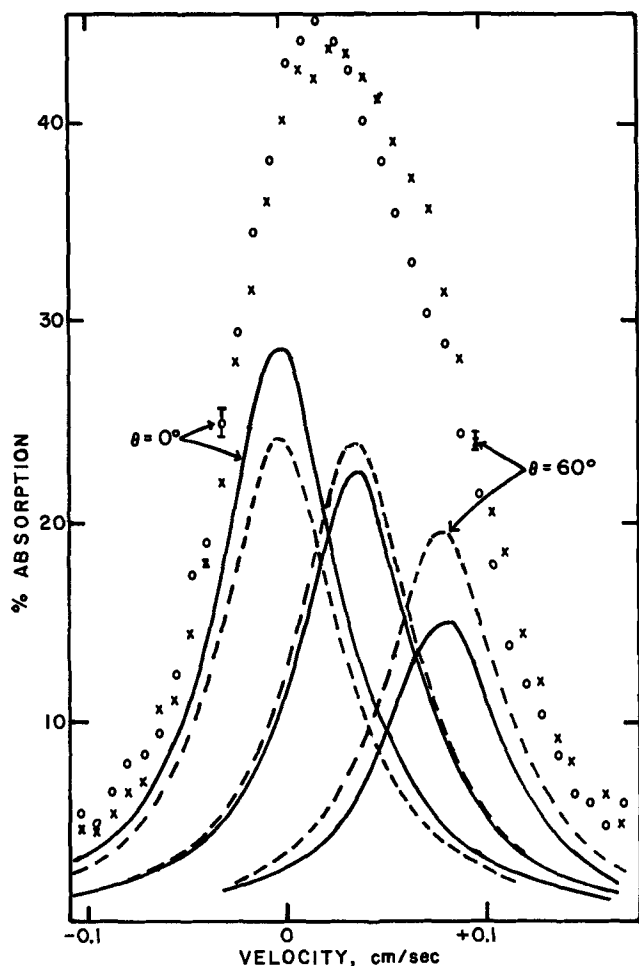


Fig. 4. Spectra of Co-57 vacuum evaporated onto polycrystalline tungsten, measured at 100°K. (Ref. 5).

ments would give information on the type of bonding and the magnitude of the lattice vibrations on the surface. At present the latter cannot be obtained with much precision from intensity measurements of LEED patterns. Although this approach has been suggested by several workers, nothing on these highly complementary measurements has, as yet, been reported in the literature.

Closely allied to the surface itself is the formation of thin films on a surface. These may be corrosion products, deposited material, or metallurgical samples that have been treated in some manner that is expected to change the structure of a surface layer relative to that of the bulk. For such samples an interesting modification of the experimental technique may be used to advantage.

Instead of observing the absorption of the gamma radiation on passing through the sample the detector is placed to one side of the sample and shielded from the gamma ray source. The nuclei that absorb the radiation have a short half-life in the excited state and then re-emit the radiation on decaying to the ground state. The detector observes the re-emitted radiation, and one obtains an emission spectrum as opposed to an absorption spectrum obtained by the usual technique of transmission. The low energy gamma rays that will reach the detector without additional scattering will be those from a thin surface layer. In the case of iron the thickness of the detected layer may be reduced many fold by preparing the sample with enriched Fe-57 on the surface.

It is seldom easy or desirable to prepare samples of optimum thickness for transmission spectra; e.g., 0.5 to 1.0 mils for iron, when studying corrosion or metallurgical processes. For thicker samples, if a

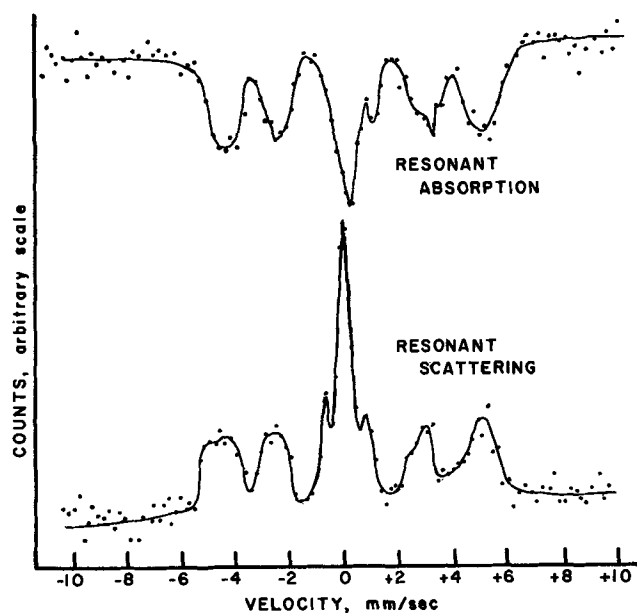


Fig. 5. Spectra of the same sample run in the two experimental modes illustrated in Fig. 1. Top corresponds to diagram A and bottom, to diagram B.

transmission spectrum can be obtained at all, the peaks will be broadened, and, consequently, there is a loss in resolution. In the backscatter method the resolution is inherently better for such samples since thickness broadening is not a factor. Comparison of the two methods is under study in our laboratory, and an example of a highly alloyed steel is shown in Fig. 5. The sample was approximately 4 mils thick. The loss in resolution from thickness broadening in the absorption spectrum compared to the emission spectrum is quite evident. A disadvantage which is not obvious in this illustration is the low counting rate that occurs in the backscatter geometry. Thus, it takes much longer to obtain an emission spectrum comparable to one obtained by transmission. Nevertheless, one can visualize a number of applications in which sample preparation is an important part of the experimental problem and the backscatter method the best answer. Publications from several laboratories working on this technique may be anticipated in the near future.

The application of Mössbauer Effect spectrometry to chemical problems is in its infancy, and this is particularly true in the studies on surface chemistry. The existing literature on its application to surface studies is, at best, meager. However, the examples discussed herein demonstrate the power of the technique for producing detailed information on structure and bonding in surfaces that would be difficult, if not impossible, to obtain by any other method. This additional information permits a deeper insight into the fundamental processes taking place in surface reactions. Exploitation is recommended.

Manuscript received Dec. 11, 1967; revised manuscript received Jan. 11, 1968. This manuscript was based on an invited lecture presented at the Chicago Meeting, October 15-19, 1967 as paper 69.

#### REFERENCES

1. M. C. Hobson and A. D. Campbell, *J. Catalysis*, **8**, 294 (1967).
2. M. C. Hobson, *Nature*, **214**, 79 (1967).
3. A. N. Karasev, Yu. A. Kolbanovskii, L. S. Polak, and E. B. Shlikhter, *Kinetika i Kataliz*, **8**, 232 (1967).
4. W. Kündig, K. J. Ando, R. H. Lindquist, and G. Constabaris, *Czech. J. Phys.*, **B17**, 467 (1967).
5. J. W. Burton and R. P. Godwin, *Phys. Rev.*, **158**, 218 (1967).

# The Scientific Society Through the Centuries<sup>1</sup>

Harry C. Gatos<sup>†</sup>

*Massachusetts Institute of Technology, Cambridge, Massachusetts*



I would like to share with you this evening some thoughts and observations on the scientific societies as they have functioned and evolved in years past. I found it rewarding to view the present day societies, including our own, in the light of their intellectual origins. Furthermore, I subscribe to the view that in planning the future there is much gain to be derived from examining the past.

In reflecting on, and tracing its origin, it becomes immediately apparent that the scientific society was the springboard for the scientific and engineering revolution that set apart the last three centuries from the rest of human history. In many important aspects it has served as the central stage on which the scientific tale has unfolded.

It is certainly tempting to ask whether such a stage was a predetermined consequence of the emerging science or whether it was conceived by some visionaries who proceeded to recruit potential protagonists and provided the catalytic actions necessary to overcome the barriers of past centuries. Although there is an element of rhetoric in such a question there is indeed much to ponder over in both of its parts.

The scientific society as we know it now was distinctly established in the second half of the seventeenth century. Within about ten years three major scientific societies were organized in Europe: the Accademia del Cimento of Florence in Italy (1657), the Royal Society in England (1660), and the Academy of Sciences in France (1666). The simultaneous appearance of these societies at this particular time was certainly not a statistical coincidence. We must view it as the natural product of the times and as a manifestation of a broader intellectual revolution.

Before we look at the prevailing over-all climate and the specific circumstances that brought about the launching of the scientific society, it should be interesting to take a brief look at the scientific activities during the preceding centuries.

Very early civilizations like the Mesopotamian, Egyptian, Chinese, and Greek achieved truly high intellectual and technological levels. Yet in those

civilizations the scientific method of deliberate experimentation to complement concepts and theories did not reach the stage of an organized effort and, thus, did not achieve critical dimensions.

Plato's Academy in the fourth century B.C. can be considered as the first formal effort for communicating knowledge, for exchanging thoughts and for carrying out scientific research. The topics dealt with extended through all aspects of pure and applied philosophy; subjects of scientific nature were treated within the framework of the prevailing philosophical patterns. The informal approach to intellectual exchange did, without doubt, reach its zenith during that golden age of Athens where very long discussions on all types of subjects were held over eating and drinking sessions. Such sessions of dining and wining are called in Greek, Symposia. I must observe that our present day Symposia have degenerated into just technical sessions.

During the second century B.C. the Greeks came very close to setting off the scientific revolution which was not destined to come about until many centuries later. Archimedes had shown the way to the experimental application of natural principles in measuring the density of irregularly shaped objects. He also applied scientific principles to military developments in defending Syracuse from the attacking Romans. During that period there were large public libraries in many cities, the most famous of which was at the Museum at Alexandria. This institution's four departments, mathematics, astronomy, medicine, and literature were functioning much like research institutes and were served by 400,000 volumes, or rather rolls, the largest library of the ancient world.

Here is how the editors of *Life* magazine refer to this period in their "Guide to Science" (1967). "Theoretical knowledge was increasing along with practical technology, and each was stimulating the other in the modern manner. The Greeks of the Second Century B.C. were entitled to feel that they lived in a wonderful age of discovery when nature was yielding on every side to the power of human intellect. If this spirit had been maintained the present era of explosive change, which began about 1600 A.D. might have begun 1700 years earlier and perhaps the earth's first colony on the moon would have spoken Greek."<sup>2</sup>

But that spirit was not maintained and the Greeks were conquered by the practical minded Romans. Then followed the early stages of Christianity encouraging mysticism rather than the scientific approach. Then followed the dark ages, then the middle ages: in all seventeen centuries of intellectual stagnation.

Through all these periods Europe's scientific needs were formally served by the Aristotelian scientific system which through the years became totally rigid. In fact Aristotle's teachings were turned into mummies and were, thus, deprived from either natural erosion or development. There lived great individuals with far reaching ideas and fertile minds but they could not change the course of events. The communities at large were rendered completely sterile to the seeding of new forward looking thinking. Roger Bacon in the 13th century was outstanding among the visionaries and came forth with truly revolutionary teachings. Nothing, he proclaimed, should be accepted except through open-eyed observation and experimentation. But great minds and great ideas need a ready

<sup>†</sup> Electrochemical Society Active Member.

<sup>1</sup> The Electrochemical Society Presidential Address, delivered at the Boston Meeting of the Society, May 7, 1968.

<sup>2</sup> Reprinted from Guide & Index of the *Life* Science Library, Time-Life Books, © Time Inc. 1967.



environment to take hold. Bacon's environment needed three more centuries of seasoning. In his time scientific knowledge was not communicated nor was it discussed in the open. In fact the scientists were a mixture of sorcerers and chemists working in secret laboratories on the "philosophers stone" which would turn base metals into gold and "the elixir of life" which would prolong life indefinitely.

A sharp change in the scientific attitude can unmistakably be observed about 1600 A.D. I do not believe that a complete analysis of all the evolutionary and revolutionary forces that brought about the change can be formulated. It is clear, however, that central to this change and to the scientific revolution that followed was the conscious introduction of the scientific experiment not only as a means for testing principles, laws, or theories, but also as an end in itself.

This experimental attitude heralded by Roger Bacon and practiced by the great Leonardo da Vinci was adopted by a number of master scientists and their disciples during the second half of the 16th and the first half of the 17th centuries. The realization of the merits of the experimental approach and of its complexities brought scientists together. They became anxious to join forces and thus better plan the experiment, construct the needed instruments and carry out the measurement. It was on this basis that the first formal scientific society was born in Italy in 1657, the Accademia del Cimento of Florence, which means the Academy of Experiment. Here nine scientists joined their efforts and their hopes to develop and construct instruments to acquire experimental skills and to establish fundamental truths. Although the Accademia del Cimento is usually considered as the forefather of the scientific societies there were earlier scientific organizations in Italy. Among them was the Accademia dei Lincei in Rome, organized in 1603. The academicians carried out studies on insects and plants and collected natural objects. Galileo became its member in 1609 and constructed a microscope for the society which was the first ever to be used in the study of zoology. The proceedings of the society *Gesta Lynceorum* represent a very early systematic record of scientific studies. But the death of the Society's founder and patron Duke Federigo Cesi in 1630 and the events that led to the condemnation of Galileo brought the Academy's functions to an end.

The Accademia del Cimento is certainly a descendent of the Accademia dei Lincei. The two Medici brothers that sponsored the Accademia del Cimento were pupils of Galileo and of Galileo's renown disciples Viviani and Torricelli. The meetings took place in the Medici residence in a room which was essentially a research laboratory with the most modern equipment of the day. In 1667, ten years of experiments and results were published in the "*Saggi di naturali esperienza fatte nel Accademia del Cimento.*" This is a remarkable account of original experiments performed with respectable accuracy. Instruments such as thermometers and hygrometers are described in detail. The pendulum is presented as a tool for the precise measuring of time. Experiments dealing with the variation of atmospheric pressure and vacuum are discussed. Many other experiments are recorded intended to test the views of thinkers like Galileo and Torricelli.

The Accademia del Cimento ceased to function ten years after its foundation. Like the earlier smaller academies, it did not survive its sponsors. Yet its charter, its activities, and its records constitute a milestone in the maturing of scientific thought. Remarkable among the Academy's functions was its contact with science outside Florence. Distinguished scientists in other parts of Italy as well as in France and in England were elected corresponding members. In this capacity they were in effective communication with the Academy, exchanging information on experimental results and discussing their significance.

The Accademia del Cimento like the societies that followed, was primarily dedicated to performing of experiments and obtaining accurate measurements. But at the same time it developed a definitive mechanism for exchanging and developing scientific thought, for submitting it to objective testing and for communicating the result to the scientific community at large.

In other parts of Europe the climate was now also ready for detached scientific inquiry. In England, Francis Bacon in his fable "New Atlantis" put forth a "Solomon's House" whose riches consisted of ideal laboratories for experimental research and whose fellows would investigate all branches of human knowledge. Francis Bacon was certainly an immense intellectual force in establishing free scientific thought.

The Royal Society in England was established in 1660 following a long series of informal meetings of men deeply concerned with experimental knowledge. It was conceived and organized as a scientific society by private individuals rather than by the state; King Charles II established by Charter the Society as a Royal Society in 1662. However, this formal act was a mere recognition of the Society's mission. Here is how one of its founders John Wallis describes the Society's early activities: "Our business was (precluding matters of theology and state affairs) to discourse and consider Philosophical Inquiries and such as related there unto: as Physick, Anatomy, Geometry, Astronomy, Navigation, Staticks, Magneticks, Chymicks, Mechanicks, and Natural experiment; . . . We then discoursed . . . on the improvement of telescopes, and grinding of glasses for that purpose, the weight of air, the possibility of impossibility of vacuities, and nature's abhorrence theory, the Torricellian experiment in quick silver, the descent of heavy bodies and the degrees of acceleration therein; and diverse other things of like nature."

In the preamble to the King's charter all of the founders dreams and labors were given Royal acceptance and blessing: "And whereas we are informed that a competent number of persons of eminent learning, ingenuity and honour, concurring in their inclinations and studies toward this employment, have for some time accustomed themselves to meet weekly and orderly to confer about the hidden causes of things, with a design to establish certain and correct uncertain theories in philosophy and by their labour in the disquisition of nature to prove themselves real benefactors to mankind; and that they have already made a considerable progress by diverse useful and remarkable discoveries, inventions and experiments in the improvement of Mathematics, Mechanics, Astronomy, Navigation, Physics, and Chemistry, we have determined to grant our Royal favour, patronage and all the encouragement to this illustrious assembly and so beneficial and laudable and enterprise."

Encouragement was, thus, granted but not the needed funds. Experiments considered of importance were still carried out at the meeting places largely at the members expense. At the same time the members and guests were urged to bring and demonstrate any experiments which they were performing on their own. Thus, Boyle demonstrated his famous experiments on gases and Dr. Clark demonstrated his studies of injecting liquid in the veins of animals. New instruments were presented to the Society by their inventors for its use like Newton's telescope, Huygens lens, and others. Furthermore, books written by its members were critically discussed and if found worthy of publication they were sponsored. Another important function of the Society was to acquire information on the prevailing philosophical and scientific systems in other lands through formal correspondence and planned voyages. Written records of foreign societies and of individual writers were translated, reviewed, and evaluated. An international exchange of ideas and results was now on a sound footing in England also.



The Royal Society made an early decision for the publication of a journal, but the plans did not materialize until its secretary undertook to publish monthly, as a private enterprise, the important communications made to the Society. Thus, in 1665, the first number of the *Philosophical Transactions* was published marking another milestone toward securing the foundation of the scientific revolution. Some time later Thomas H. Huxley wrote: "If all the books in the world except the *Philosophical Transactions* were destroyed, it is safe to say that the foundations of physical science would remain unshaken, and that the vast intellectual progress of the last two centuries would be largely, though incompletely recorded."

Before leaving the Royal Society of the 17th century I wish to underscore that its members discussed extensively the possibility of assuming educational responsibilities including the establishment of their College. The Society concluded that educational functions would detract from its research character or its dedication to the discovery of scientific truths and their practical applications. This decision was a far reaching one. It identified for all times the scientific society with original research and development.

A few years after the formation of the Royal Society the Academy of Sciences was organized in France, in 1666. Unlike the Royal Society, the French Academy was founded as a royal institution. It was funded by the royal treasury and its members were compensated like state servants. However, like its sister societies in other countries, the French Academy of Sciences was born in small private meetings of strong believers in the cause of science; it was then adopted by one of Europe's greatest monarchs Louis the 14th. During his reign, it developed into the major scientific institution in all of Europe.

Colbert is considered the spiritual father of the French Academy; he lived completely dedicated to its organization and functions. The membership was varied, ranging from broadly based scholars to men skilled in specific experimental studies. As with the other academies of the 17th century here also performing experiments was a major function and many famous scientists participated. Marriotte's studies of the phenomena of air pressure, Roemer's calculation of the velocity of light from the satellites of Jupiter, Huygen's development of the pendulum clock and the wave theory of light represent a small sampling of the Academy's work. The important happenings in the Academy including new instruments, new results, and new communications in general appeared in the *Journal of the Savants* which was published outside the Academy and edited by one of its members.

The French Academy with government funding became involved in activities which were too costly for the privately organized societies. The observatory of Paris built by the state at the recommendation of academicians was put under the Academy's complete direction. Similarly the Academy undertook expensive scientific expeditions for astronomical and other observations. Furthermore, it often sponsored foreign scientists to come to Paris and partake in experiments and discussions.

In Germany during the 17th century the pursuit of science and original experimental research did not reach the broad dimensions found in Italy, England, and France. There were of course learned societies functioning and great thinkers like Kepler and Leibniz were contributing to the rapidly advancing scientific thought. However, the first scientific society with the scope of the Royal Society and the French Academy of Sciences was not established until 1700.

Of the earlier societies that existed in Germany during the 17th century it is interesting to mention the Collegium Naturae Curiosorum founded in 1652 and still existing today. It was organized in Schweinfurt by a local physician and its mission was focused to advancement of medicine and pharmacy. Consistent with

the times, direct observation and experimentation were adopted as a means for progress. The society did not have its own laboratory for experimental research, but its members undertook on their own or were assigned by the president a topic for investigation. The results were discussed, corrected, and further elaborated before they were published. Within a few years the society's membership and activities extended beyond the limits of Schweinfurt. In 1677 the Emperor became its patron and by 1687 the Academy adopted the name of Academia Caesarea Leopoldina. Its periodic publication *Miscellanea Naturae Curiosorum* was most highly regarded not only in Germany but throughout Europe. The role of this Academy was certainly a limited one and evolved only about medicine. However, it was a role with subtleties of extraordinary importance. The Academy advocated and practiced the view that medicine must be based on scientific research and experimental observation. In those years medicine was even in greater need than the natural sciences to be liberated from mysticism and witchcraft.

The first broadly based scientific society in Germany was organized under circumstances appreciably different from those which prevailed earlier in other countries. By the end of the 17th century the financial factor had become a very important one in the life of scientific academies. Gottfried Leibniz in advocating the organization of scientific societies across Germany was well aware of this factor. Thus, in 1699, when the calendar was reformed from the Protestant to the Roman Catholic, he proposed to the Elector of Brandenburg that a monopoly of calendars be established and that the proceeds be used for the founding and support of a scientific society. The proposal was readily accepted. An interesting condition was imposed by the Elector, that German be the official language of the Society rather than Latin which was commonly used in scientific matters. The introduction of the vernacular into scientific writing in Germany and in other countries was an essential step in broadening the basis for communicating scientific findings.

In July, 1700, the charter was obtained and the Berlin Academy was established. The plans called for a library, an observatory and a research laboratory. Drawing on the experiences of the Royal Society and the French Academy of Sciences the organization and functions of the new academy were spelled out in great detail. There was a significant deviation, however, from the existing societies: the expressed intent of the Berlin Academy was to be concerned with things useful and not just with matters purely scientific. Agriculture, commerce, and manufacturing were to be central to the Academy's interests. This is perhaps the first organized participation of scientists in matters not entirely scientific.

In spite of the dedication of Leibniz and the Elector's support the Academy was slow in taking hold. The publication of the first volume of its proceedings *Miscellanea* did not appear until 1710. Soon after the Academy experienced additional difficulties when Frederick William I ascended to the throne of Prussia. He considered science effeminateness and thought Leibniz a totally unworthy individual. Leibniz remained unshaken in his beliefs and visions on the vital role of the scientific society in the growth of science and the well being of mankind. In his travels he brought his convictions to Russia and Austria where he found sympathetic and even grateful ears. In fact, he is responsible for the Academy of St. Petersburg which was officially founded in 1724. In Vienna he obtained an imperial protocol for the foundation of an Academy but the plan was finally defeated and the Academy of Vienna was not to be organized until the middle of the 19th century. Leibniz died disappointed; but his labors were not in vain. The Berlin Academy was to achieve a high place indeed among the learned

societies in Europe and contributed heavily in giving to science its modern status.

Here in America, during the colonial years the scientists were served by the Royal Society through correspondence or travel to England, and over the years a small number of distinguished colonists were elected members of the Royal Society: Cotton Mather, the three John Winthrops, James Bowdoin, Paul Dudley, Roger Williams, Zabdiel Boylston of New England; Benjamin Franklin, David Rittenhouse and John Morgan of Pennsylvania; William Byrd II, John Mitchell and John Tennent of Virginia; and Alexander Garden of South Carolina.

Several early attempts were made by the colonists to found local learned organizations. For example, in 1683, the Boston Philosophical Society was established which according to Cotton Mather was "A Philosophical Society of Agreeable Gentlemen who met once a Fortnight for a Conference upon Improvements in Philosophy and Additions to the stores of Natural History." But this society was very short lived like other early ones.

The master mind and main force behind the lasting foundation of learned organizations in this country was one of the greatest intellects it has produced, the Boston born, and Philadelphia raised Benjamin Franklin. In 1727 he formed his secret Junto, about which he wrote: "I had formed most of my ingenious acquaintance into a club of mutual improvement which we called Junto; we met on Friday evenings. The rules that I drew up required that every member, in his turn, should produce one or more queries on any point of Morals, Politics or Natural Philosophy, to be discussed by the company; and once in three months produce and read an essay of his own writing on any subject he pleased. Our debates were to be under the direction of the President, and were to be conducted in the sincere spirit of inquiry after truth without fondness of dispute or desire of victory."

Franklin kept his Junto a secret organization to protect it from intruders. He soon recognized, however, that the implications of a learned society were reaching far beyond the interests of their small select group. Accordingly, each member was encouraged to form a subsidiary club to function like the parent Junto. Several such clubs were successfully established. But a few years later, in 1743, he proposed the establishment of the American Philosophical Society and to this end he circulated throughout the colonies a memorandum with the title: "A Proposal for Promoting Useful Knowledge among the British Plantations in America." This memorandum said in part "That one society be formed of virtuosi or ingenious men, residing in the several colonies, to be called the American Philosophical Society, who are to maintain in constant correspondence. That these members meet once a month, or oftener, . . . to communicate to each other their observations and experiments, to receive, read and consider such letters, communications or queries as shall be sent from distant members, to direct the dispersing of copies of such communications, as are valuable, to other distant members in order to procure their sentiments there upon." The following year 1744, the American Philosophical Society came into existence and still functions as a distinguished learned society.

In the meantime the Junto club developed into the American Society Held at Philadelphia for Promoting Useful Knowledge. Then in 1769, it united with the American Philosophical Society under the new name, American Philosophical Society Held at Philadelphia for Promoting Useful Knowledge. This remains its official name to date although it is known with its shorter name, American Philosophical Society. During the 18th century, the Society played a very significant role in the advancement of science here and in Europe. In its observatory at the State House Yard, David Rittenhouse and his fellow astronomers secured the

first accurate data for determining the astronomical unit, that is the distance of the sun from the earth. The big clock that Rittenhouse devised for his experiments still runs in the Society's quarters in Philadelphia. Important communications in various scientific areas were discussed before the Society and the most brilliant minds here and abroad were honored with membership including the father of modern chemistry Antoine Lavoisier.

With the closing of the revolutionary war a new society was incorporated in Boston (1780) the American Academy of Art and Sciences which is still in existence with quarters in Newton, a suburb of Boston. John Adams provided the organizing force, and he was a charter member along with James Bowdoin, John Hancock, and Samuel Adams. Among the early elected fellows were George Washington, Benjamin Franklin, David Rittenhouse, and Thomas Jefferson. The objectives of the new Academy were similar to those of the other learned societies founded in the 17th and 18th century: Direct involvement in experimentation for the discovery of scientific truths, critical discussions of new discoveries and other matters of intellectual challenge which might contribute to the advancement of knowledge and (quoting from its charter) "may tend to advance the interest, honor, dignity and happiness of a free independent and virtuous people."

The National Academy of Science was founded in Washington much later, in 1863, with President Lincoln authorizing the Federal Charter. In its one century old life, the Academy has honored with membership the most distinguished scientists of the country. It has been a most important source emanating scientific guide lines to the government and to the scientific community at large.

I believe that before we pursue the scientific societies into the 19th and 20th centuries we should examine the orientation of the universities as intellectual centers in the light of the emerging detached scientific approach and with respect to the scientific societies.

The European universities of the 17th century had established a deeply rooted and closely guarded tradition in their instruction spectrum. Grammar, logic, and rhetoric were taught along with the four mathematical subjects—arithmetic, geometry, music, and astronomy. Natural philosophy was another major area of instruction, usually reserved for advanced studies. Similarly medicine and theology were treated as what we might call today post graduate subjects.

Although there were variations among the major European countries, by and large, mathematics consisted essentially in Euclid's work, astronomy was based on Ptolemy's writings, and natural philosophy was the contents of "Aristotle's Physica." As for medicine the writings of Galen and Hippocrates were heavily drawn upon. The whole intellectual activity within the university was most tightly bound to systems put forth many many centuries earlier.

The factors that kept the university in a sphere intellectually polarized to the distant past are not straight forward and we shall not pursue them here. We must recall, however, that the universities were generally under the auspices of the church. Accordingly, the theological faculties were the leading academic bodies and the key administrative positions were held by theologians. It is generally agreed that the theologians of the 17th century were not particularly suited to champion the cause of free scientific inquiry.

The conclusion is inescapable that the university of the 17th century could not possibly serve as a breeding ground for revolutionary minds nor as the home for the now insuppressible scientific method.

There were, of course, isolated instances of great minds being affiliated with universities like Isaac Newton who became a professor in Cambridge Uni-

versity. However, their short range impact on the over-all university activities was rather small. Such scholars took their creative work for discussion and criticism outside the university walls, and into the scientific societies. Great scientists like Bacon, Boyle, Huygens, Van Helmont, Kepler, Leibniz, Descartes, Pascal, Marriotte, and many others never became university faculty members.

It is significant to point out, however, that the universities did not enter in open polemics with the scientific societies and the new scientific attitude. They simply guarded the traditional curricula and resisted the infiltration of the new philosophies with great determination. The conservatism of the universities persisted through the 18th century. The statutes of Oxford University remained unchanged for three centuries (from 1570 to 1858) and those of the theological faculty of Bologna for over four centuries (from 1360 to 1783).

Clearly in the 17th century the scientific societies were the home of all that was science and its broad implications. They believed in original thought, they provided for complex and accurate experiments, they evaluated and recorded the results, they communicated the new information to the world, they studied applied aspects of sciences as pertaining to agriculture and commerce, and in all these ways they brought science to the conscience of the community at large.

I wish to quote from the book of Martha Ornstein on the "Role of Scientific Societies in the Seventeenth Century" (The University of Chicago Press, 1918): "These societies provided the advance guard of civilization in the second half of the seventeenth century. . . . They were the concentrated expression of the new spirit which was to gain the supremacy in the realm of thought and life. They typify this age drunk with the fullness of new knowledge, busy with the uprooting of superannuated superstitions, breaking loose from traditions of the past, embracing most extravagant hopes for the future. In their midst the spirit of minute scientific inquiry is developed; here the charlatany and curiosity of the alchemist and magician are transformed into methodical investigation; here the critical faculty is developed so that the disclosure of an error is as important as the discovery of a new truth; here exact observation is put as high-nay, higher-than generalization; here the individual scientist learned to be contented and proud to have added an infinitesimal part to the sum of knowledge; here, in short, the modern scientist was evolved."

By the end of the 18th century the conservatism of the university had noticeably succumbed to natural erosion. The Aristotelian system was quietly put aside. Chairs in Chemistry, in Physics, and other scientific disciplines were being created and occupied by individuals reared in the spirit of the scientific societies and committed only to free scientific inquiry. The metamorphosis was slow and perhaps painful but it was complete and the universities did in turn become the primary centers for science and technology. They built their observatories and their research laboratories. Universities such as that of Cambridge, Oxford, Paris, Berlin, Leipzig, Vienna, St. Petersburg, Leyden, Harvard, and many others became the homes and centers of activities of some of the brightest stars in the stardom of science. At the same time they trained new scientists to carry on the scientific search and to meet the new needs of the young industrial revolution.

Thus, in the 19th century the scientific society passed on the torch to the University; but it did not run out its course. The scientific societies remained the exciting forum for the presentation, evaluation and permanent recording of the new experimental and theoretical results. Their meetings continued to be,

and still are, the most fertile grounds for the cross-fertilization of ideas and results.

With the increasing numbers of scientists, and scientific centers, the scientific societies evolved to meet the new needs. The original academies had and still have a limited membership. It was only through one of the academicians that the formal presentation of new work could be made. Furthermore with the rapidly expanding areas of research the spectrum of scientific societies needed to be extended. Thus, new societies began to spin off the original ones and many were independently founded; they were devoted to one branch of science with a broader basis for membership. New members joined not just by invitation, as in the academies, but after requesting admission provided certain requirements were met. Thus, the Geological Society of London was established in 1807; the British Chemical Society, in 1841; the French Chemical Society in 1857; the German Physical Society in 1845; the American Chemical Society in 1876; the American Physical Society in 1899, and so on. The list has grown to very large numbers, perhaps to many thousands and it is still growing. Only a few weeks ago a new sister society was founded in England, the Society for Electrochemistry.

Our own Electrochemical Society was founded at the turn of the present century along the same pattern established two and one-half centuries earlier: the need for a new society was diagnosed by a few imaginative individuals who proceeded to transform an idea into a living mechanism. Six scientists from Pennsylvania addressed a circular letter dated October 19, 1901, to scientists in the United States, just as Benjamin Franklin had done 150 years before them in proposing the foundation of the first scientific society in this country. The letter pointed out that "The rapidly growing importance of the subject of electrochemistry and the want of suitable occasions in this country for the discussion of papers and questions pertaining thereto by those especially interested, have suggested the advisability of founding a National Electrochemical Society similar in its organization to the American Chemical Society and the American Institute of Electrical Engineers . . ."

As a result of this letter eleven electrochemists met in Philadelphia on November 1, 1901, and agreed to meet again in Philadelphia, in April, 1902; this time 52 individuals attended. It was at that meeting that the Society was formally founded under the name American Electrochemical Society. In 1930 the Society was incorporated and its name was shortened to the present name: The Electrochemical Society, Inc. Eliminating the word American from the name was consistent with the Society's international membership which now exceeds 4000.

It is in this general pattern that scientific academies and scientific societies continue to be formed: to meet an oncoming need and rise to the scientific and technological challenges of the times. The academies, like the National Academy of Sciences in Washington, have been and still are deeply involved in providing a vital interface between the government and science at large, in war and in peace. The scientific societies like ours provide for meetings to bring forth the new results, the new thoughts, and the new trends. They provide the great forum where young minds are stimulated and mature ones are challenged. They provide what I believe will continue to be central to the life of science and engineering, an opportunity for personal communication, for personal exchange of thought, for personal contact, and for good fellowship.<sup>3</sup>

<sup>3</sup> I wish to record my amazement at the large amount of literature available on the foundation and development of scientific societies. I have chosen not to present a list of references since numerous volumes with pertinent information and containing the quotations included here are widely available.

# Rates of Dissociation of $\text{Ag}_2\text{O}_2$

Earl M. Otto\*

National Bureau of Standards, Washington, D. C.

## ABSTRACT

The dissociation of  $\text{Ag}_2\text{O}_2$  into  $\text{Ag}_2\text{O}$  and  $\text{O}_2$  has been investigated over the temperature range from 22° to 100°C for the dry material, for water slurries, and for slurries in KOH solutions of concentrations from 1 to 13M. The method consisted in measuring the  $\text{O}_2$  volume while the dissociation was progressing, and in most cases very smooth curves were obtained when the volume of dry  $\text{O}_2$ , corrected to 0°C, 760 Torr, per gram of sample was plotted against time.  $\text{Ag}_2\text{O}_2$  in water had the lowest rate of evolution, dry  $\text{Ag}_2\text{O}_2$  had an intermediate rate, and  $\text{Ag}_2\text{O}_2$  in the high concentrations of KOH solution, such as are used in Ag-Cd cells, had the highest rate. The rates ranged from 0.0001 to 1.8 ml hr<sup>-1</sup> g<sup>-1</sup>.

Although in the past two decades considerable interest has been shown in silver-silver oxide cathodes in primary and secondary batteries and reports on the investigations have appeared in the chemical literature (1-5), there has been no extensive study of the instability of  $\text{Ag}_2\text{O}_2$  dry, wet with water, and wet with solutions of KOH. The presently reported study was undertaken because the author had been working with silver-cadmium cells stored at various temperatures for different periods of time and wished to understand better the reactions taking place during the cycling of these cells.

It has long been known that there is an oxide of silver wherein the valence of the silver is greater than unity. The chemically made product has an empirical formula of approximately  $\text{Ag}_2\text{O}_{1.97}$ , and the writer chooses to accept the evidence given by Cohen and Ostrander (6) (and certain references quoted by them) for the existence of  $\text{Ag}^{+3}$  and  $\text{Ag}^{+1}$  with the absence of  $\text{Ag}^{+2}$ . Hence the formula will be written herein as  $\text{Ag}_2\text{O}_2$ .

## Experimental

The study consisted in subjecting samples of chemically prepared  $\text{Ag}_2\text{O}_2$  to periods of standing in closed systems at room temperature, 30°, 50°, 70°, and 100°C. The oxide used came from three commercial sources. Samples from two of these were analyzed by the author by means of  $\text{O}_2$  evolution. The results indicated 95-97%  $\text{Ag}_2\text{O}_2$ . The results of Ag determinations on one sample by Cohen (6) and the assay supplied by one manufacturer were also within the 95-97% range. A commercial laboratory determined by the use of a mercury porosimeter that the one product had a total pore volume of 0.525 cm<sup>3</sup>/g, an area of 2.73 m<sup>2</sup>/g, and a real density of 7.74 g/cm<sup>3</sup> at 15,000 psi pressure. The media surrounding the samples were air, water, and KOH solutions of various concentrations ranging from 1 to 13M (5 to 50%) KOH. The volumes of  $\text{O}_2$  were measured over mercury, water, or the KOH solution, whichever was the most suitable and convenient.

Three types of apparatus were employed. For 30°, 50°, and some 70°C runs the apparatus previously used by the author (7) for determining the rates of gassing of dry cells was adopted, with 10 to 13g samples employed. For 100°C and the remaining 70°C runs the samples (1-2g) were placed in long, narrow-necked bulbs to which reflux condensers were attached. The bulbs were immersed in glycerine in a clear glass wide-mouth Dewar flask in which a heating element had been located. Current to the heating element was regulated by means of a mercury thermometer and a mercury-level sensing device set at the desired temperature. Delivery tubes from the tops of the condensers led to gas burettes and leveling bulbs filled

with water. For room temperature the best arrangement was to place the sample in an inverted polypropylene test tube having a one-holed rubber stopper through which passed a plastic tube to serve as a leveling device. A small hole was drilled in the bottom of the test tube and an inverted polypropylene measuring pipette attached to the test tube bottom by epoxy cement. The tip of the pipette was closed with the cement. As  $\text{O}_2$  evolved it moved upward into the pipette, displacing the KOH solution, where its volume could be measured easily.

The investigation was begun with  $\text{Ag}_2\text{O}_2$  in 11.6M KOH solution (44%) at 50°C, since this concentration of KOH is commonly used in Ag-Cd cells and cell temperatures are not expected to exceed 50°C. From these conditions the study was extended to lower and to higher concentrations to see if there is a concentration for maximum rate of oxygen evolution, just as there is such a concentration (6M) for specific conductance of KOH. Then the question arose as to the instability of  $\text{Ag}_2\text{O}_2$  at room temperature dry, wet with water, and wet with KOH solutions. Since the dissociation of  $\text{Ag}_2\text{O}_2$  was found to be slow at 50°C, it was decided to increase temperatures to as high as 100°C.

All volumes of  $\text{O}_2$  have been calculated on a dry basis and corrected to 0°C, 760 Torr. Water vapor pressures at the several temperatures and KOH concentrations were obtained by interpolations of plots of  $\log p$  vs.  $1/T$ , using the data given in the International Critical Tables. Rates of reaction are expressed in milliliters of dry  $\text{O}_2$  (STP) per hour per gram of  $\text{Ag}_2\text{O}_2$  at the stated temperature and concentration. In order to keep the number of graphs to a minimum and yet present in graphic form most of the recorded data, the dissociation curves have been grouped by like orders of magnitude of gas volumes for like periods of time.

The zero times of the experiments were the times at which temperature equilibration and water vapor saturation of the air in the closed systems were judged to have occurred.

The results of the major investigation are given in Fig. 1 to 6.

Attention should be called to illustrations of reproducibility of measurements. Curves 1-3 and 1-4 (the number before the hyphen refers to figure and the number after hyphen to curve) have essentially the same slope. Likewise, curves 2-1 and 2-2 are nearly the same. Curves 6-2 and 6-3 were obtained from the same materials and temperature, but with different arrangements of apparatus and slightly different conditions of experimentation. Another factor in this last case was the extremely small volume of oxygen evolved (0.6 ml). One would think that curves 4-1 and 4-2 should be similar. Apparently, however, company "B"  $\text{Ag}_2\text{O}_2$  released its  $\text{O}_2$  more slowly than did the company "A" material. Had the company "B"

Key words: silver oxides,  $\text{Ag}_2\text{O}_2$ ,  $\text{Ag}_2\text{O}$ , dissociation, rates, aqueous potassium hydroxide.

\* Electrochemical Society Emeritus Member.

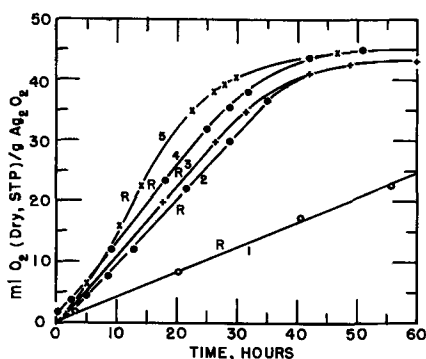


Fig. 1. Dissociation of  $\text{Ag}_2\text{O}_2$ . Curve 1, Dry  $\text{Ag}_2\text{O}_2$  100°C. Curve 2, 7.9M KOH 100°C. Curves 3, 4, 11.6M KOH 100°C. Curve 5, 13.2M KOH 100°C. R shows location, on this and succeeding figures, where the slope was calculated to give the rate of dissociation. All rates are for 1g samples. Complete dissociation of 96% pure  $\text{Ag}_2\text{O}_2$  should yield 43.3 ml dry  $\text{O}_2$  at 0°C, 760 Torr.

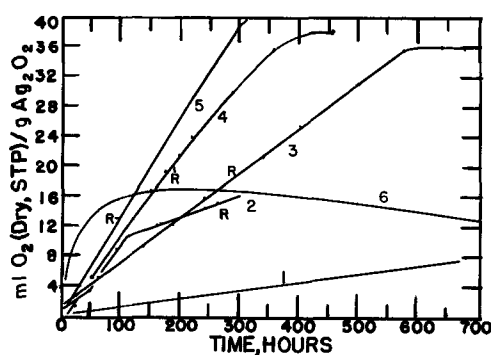


Fig. 5. Dissociation of  $\text{Ag}_2\text{O}_2$ . Curve 1, NOLTR 62-187, Figure 2 curve 5 40% KOH (10.0M) 32.2°C. Curve 2, Water (no KOH) 100°C. Curve 3, 11.6M KOH 70°C. Curve 4, 13.2M KOH 70°C. Curve 5, NOLTR 62-187 40% KOH (10.0M) 71°C. Curve 6, same as curve 3 except there is an additive of Ag equal to weight of  $\text{Ag}_2\text{O}_2$ .

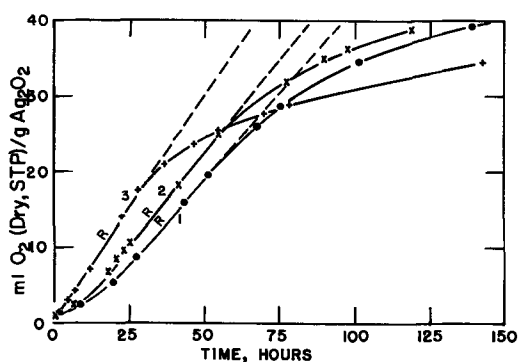


Fig. 2. Dissociation of  $\text{Ag}_2\text{O}_2$ . Curves 1, 2, Dry  $\text{Ag}_2\text{O}_2$  100°C. Curve 3, 4.0M KOH 100°C.

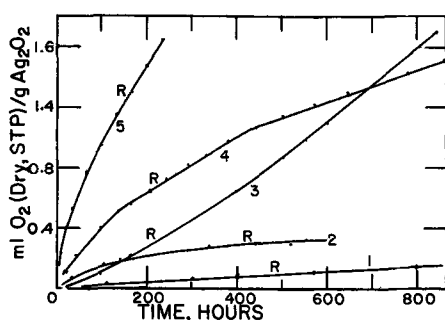


Fig. 3. Dissociation of  $\text{Ag}_2\text{O}_2$ . Curve 1, Water (no KOH) 50°C. Curve 2, 1.06M KOH 50°C. Curve 3, Dry  $\text{Ag}_2\text{O}_2$  50°C. Curve 4, 4M KOH 50°C. Curve 5, Charged positive plate (per g  $\text{Ag}_2\text{O}_2$ ) 11.6M KOH 50°C.

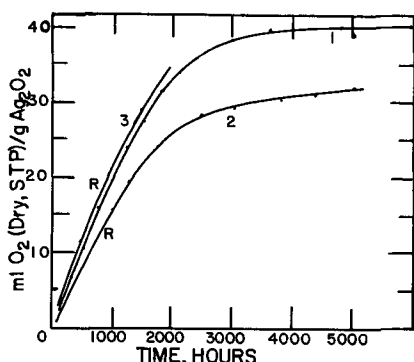


Fig. 4. Dissociation of  $\text{Ag}_2\text{O}_2$ . Curve 1, Company "A"  $\text{Ag}_2\text{O}_2$  in 11.6M KOH 50°C. Curve 2, Company "B"  $\text{Ag}_2\text{O}_2$  in 11.6M KOH 50°C. Curve 3, From U.S. Naval Ordnance Laboratory Technical Report NOLTR 62-187, Figure 2 curve 3 40% KOH (10.0M) 47.5°C.

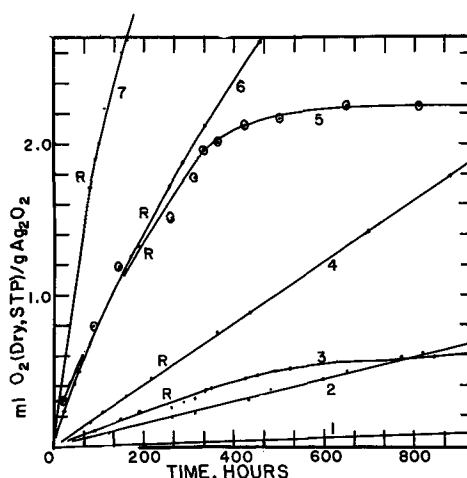


Fig. 6. Dissociation of  $\text{Ag}_2\text{O}_2$ . Curve 1, Charged positive plate (per g silver oxide powder) 11.6M KOH 25°C. Curves 2, 3, 11.6M KOH 22°C. (Two different set-ups.) Curve 4, 11.6M KOH 30°C. Curve 5, Additive of 1g Ag/1g  $\text{Ag}_2\text{O}_2$ , 11.6M KOH 22°C. Curve 6, 7.9M KOH 50°C. Curve 7, 7.9M KOH 70°C.

oxide been investigated a few thousand hours more, it might have yielded just as much  $\text{O}_2$  as the other oxide did.

In one instance a mixture of 47.4% Ag powder with 52.6%  $\text{Ag}_2\text{O}_2$  was allowed to dissociate in 11.6M KOH at 25°C. Surprisingly the initial rate per gram of  $\text{Ag}_2\text{O}_2$  was much greater than that of  $\text{Ag}_2\text{O}_2$  with no additive.<sup>1</sup> (See curve 6-5.) Apparently, metallic silver serves as a catalyst, but possibly only in the early stages of dissociation (the first 300 hr in this case). A similar observation was made with a 50% Ag/50%  $\text{Ag}_2\text{O}_2$  mixture at 70°C, except that the rate (which was five times that of  $\text{Ag}_2\text{O}_2$  having no Ag powder) began to decrease after 20 hr and came to zero at 240 hr and then the  $\text{O}_2$  began to be consumed. Curve 5-6 shows a plot of the data obtained. In another instance  $\text{Ag}_2\text{O}$  was used with 11.6M KOH at 45°C. In this instance a mercury lamp was placed adjacent to the reaction bulb containing the  $\text{Ag}_2\text{O}$  and caused to shine on the sample in order to give full opportunity for dissociation to be catalyzed by light energy. However, even in one month there was no evidence of oxygen evolution. This lack of oxygen evolution is somewhat in contrast to the observations reported elsewhere (5a): (i) that a greater amount of  $\text{O}_2$  was obtained than could be accounted for by the dissociation

<sup>1</sup> Wagner (5b) reported that  $\text{Ag}_2\text{O}_2$  ground with powdered Ag in a ball mill and let stand dry at room temperature was largely converted to  $\text{Ag}_2\text{O}$ .

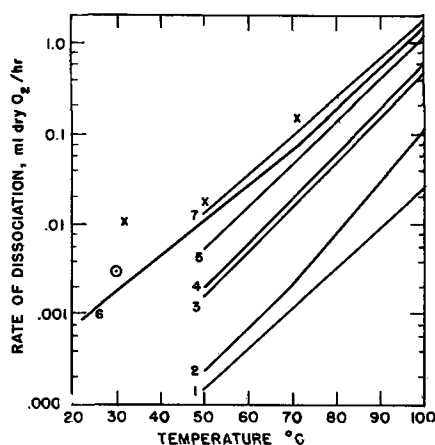


Fig. 7. Rates of dissociation of  $\text{Ag}_2\text{O}_2$ . Effect of temperature and KOH concentration. Curve 1, Water only. Curve 2, 1.06M KOH. Curve 3, Dry  $\text{Ag}_2\text{O}_2$  only. Curve 4, 4.0M KOH. Curve 5, 7.9M KOH. Curve 6, 11.6M KOH. Curve 7, 13.2M KOH. Circled dot, Amie and Rüetschi point. X's, NOL points for 11.6M. All rates are for 1g samples.

of  $\text{Ag}_2\text{O}_2$  into  $\text{Ag}_2\text{O}$ , and (ii) that free Ag was detected. The authors of ref. (5a) expressed concern about the possibility of gas leakage, but proved in one case that the leakage was inconsequential. In the present work Apiezon-T grease was the lubricant-sealant for all ground-glass joints and the presence of a continuous surface of the brown grease was sufficient evidence that no leaks ever occurred.

The positive plate material (with grid removed) of a fully charged silver-cadmium cell was heated in 11.6M KOH at 100°C until no more  $\text{O}_2$  was evolved. The time required was the same as that for  $\text{Ag}_2\text{O}_2$  but the volume of  $\text{O}_2$  indicated only about 40% of  $\text{Ag}_2\text{O}_2$ . This is in close agreement with the per cent of time the discharge of a cell is at the higher of the two voltage levels. At 25° and 50°C, positive plate material dissociated, on a per gram basis, at about one third the rate obtained for the 97%  $\text{Ag}_2\text{O}_2$  material.

Figure 7 and Table I give initial steady gassing rates calculated at regions "R" shown in Fig. 1 to 6. Table I also shows where the various curves may be found. In all figures the points shown on the curves are the actual experimental values. It can be seen that in most instances the curves consist essentially of lines drawn through the points.

Figure 8 gives the rates of  $\text{O}_2$  evolution plotted against the KOH concentration at 50° and 100°C. In the latter case a straight line is obtained, if the rate (unexplainably low) for 11.6M KOH is ignored. For 50°C, if the rate (unexplainably high) for 11.6M is also ignored, a smooth curve can be drawn through

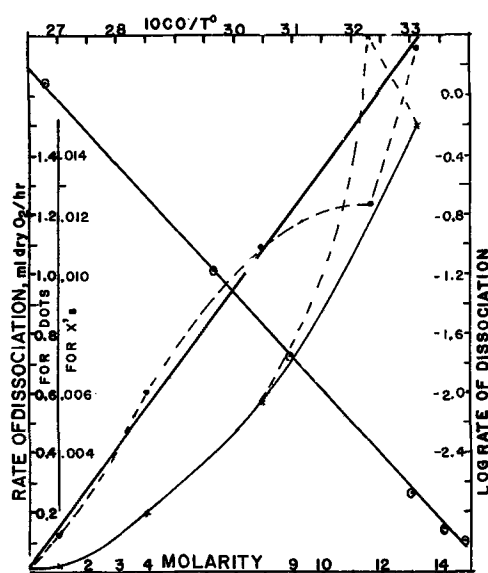


Fig. 8. Rates of dissociation of  $\text{Ag}_2\text{O}_2$ . Effect of concentration of KOH on  $\text{Ag}_2\text{O}_2$  at 100°C, shown by dots; at 50°C, shown by X's (use ordinates at left and abscissas at bottom). Effect of temperature on  $\text{Ag}_2\text{O}_2$  in 11.6M KOH shown by circled dots (use ordinates at right and abscissas at top).

the remaining 5 points. The behavior at 70°C is similar to that at 100°C but the line through the points is nearer to being straight.

The broken lines have been drawn to show the effect of not ignoring any of the data. Figure 8 also shows a plot of the log of the rate against  $1/T$ , but for 11.6M KOH only, since this is the only concentration which was used at all temperatures. A line through all the points is practically straight. This fact gives more credence to all rates determined with 11.6M KOH.

### Discussion

Since the rate of oxygen evolution is a direct function of the concentration of KOH, KOH must take part in the reaction, but since there are long periods of constant rate, the KOH must be regenerated to keep the concentration constant.

It is very noteworthy that many curves have straight line segments (i.e., constant slopes), indicating zero order or pseudo zero order reactions are taking place. Most remarkable is curve 5-3 where the rate of dissociation of  $\text{Ag}_2\text{O}_2$  in 11.6M KOH at 70°C remained constant for 24 days and then dropped to zero in about 5 more hours. The zero time of this graph does not indicate the beginning of  $\text{O}_2$  evolution, but merely when temperature equilibration was reached and the stop-

Table I. Initial steady rates of dissociation of  $\text{Ag}_2\text{O}_2$  (ml  $\text{O}_2$ /hr/g  $\text{Ag}_2\text{O}_2$ ) in various media at various temperatures

Temperature, °C	KOH, M					$\text{H}_2\text{O}$	Dry	Charged Ag plate KOH, M 11.6
	13.2	11.6	7.9	4.0	1.06			
22		0.0010 (6-2, 3)*						
25		0.0012				0.00001**	0.0001**	0.0001 (6-1)
30		0.0022 (6-4)						
50	0.015	0.018 (4-1)	0.0053 (6-6)	0.0020 (3-4)	0.00022 (3-2)	0.00015 (3-1)	0.0016 (3-3)	0.005 (3-5)
70	0.12 (5-4)	0.060 (5-3)	0.0022 (6-7)		0.002			
100	1.76 (1-5)	1.23 (1-3,4)	1.09 (1-2)	0.60 (2-3)	0.126	0.026 (5-2)	0.46 (1-1; 2-1,2)	***

\* In parentheses numbers before hyphen refer to figures and numbers after hyphen refer to curves where graphs of data may be found.

\*\* These are obtained by extrapolations of curves in Fig. 7.

\*\*\* Rate not obtained, but volume of  $\text{O}_2$  evolved indicated 41.5% of cathode to be  $\text{Ag}_2\text{O}_2$ .

cock over the Hg was closed. The controlling condition could hardly be the surface of the  $\text{Ag}_2\text{O}_2$  because this would have to be much less when 90% dissociation has taken place. The author is led to speculate that the dissociation reaction takes place in the dissolved portion of the  $\text{Ag}_2\text{O}_2$ . The KOH is thought to cause the  $\text{Ag}_2\text{O}_2$  to go into solution by a reaction such as



Then two  $\text{O}-\text{Ag}=\text{O}-$  ions dissociate and give  $\text{O}_2$  and two  $\text{AgO}^-$  ions. Needless to say these ions may really exist in hydrated forms, as  $\text{Ag}(\text{OH})_4^-$  and  $\text{Ag}(\text{OH})_2^-$ , respectively. The  $\text{AgO}^-$  may react with the  $\text{AgOH}$  to form  $\text{Ag}_2\text{O}$  and regenerate the  $\text{OH}^-$ . If the temperature is  $100^\circ\text{C}$ , it may be that the loss of oxygen takes place so fast that the solvent action demand is too great toward the end of the dissociation. Of course the rate of the solvent action necessarily is a function of the surface of the  $\text{Ag}_2\text{O}_2$ . At lower temperatures and low concentrations there could be concurrent side reactions which interfere with the progress of the dissociation. One of these could be the deposition of the  $\text{AgOH}$  or  $\text{Ag}_2\text{O}$  causing a blocking action. Curve 3-3 is odd in that the rate of dissociation increased perceptibly with time. (Note that this is  $\text{Ag}_2\text{O}_2$  with no added water or KOH.) Needless to say, the mechanism of this dissociation has to be different. It could be that moisture in the original sample is slowly lost and any residual ionic substances (e.g., KOH) accelerate dissociation of  $\text{Ag}_2\text{O}_2$ . Curve 3-4 is peculiar in that there appear to be three notably different slopes and the change of one to another takes place suddenly. No explanation is offered at present.

Curve 5-6 must be compared with curve 5-3 since the only difference is that the former resulted from addition of powdered Ag. Again it is the considered opinion that the free Ag has served to catalyze greatly the dissociation of  $\text{Ag}_2\text{O}_2$  into  $\text{Ag}_2\text{O}$  and  $\text{O}_2$ .  $\text{O}_2$  begins slowly to oxidize Ag to  $\text{Ag}_2\text{O}$ . At 240 hr these two reactions became equal and thereafter  $\text{O}_2$  was consumed faster than it was formed. No doubt this sequence of reactions would have continued until the available free Ag or the  $\text{O}_2$  became exhausted. This observation is in contradiction to NOLTR 62-187 where it is stated that some free Ag was produced simply by the dissociation of  $\text{Ag}_2\text{O}_2$  in 10N KOH at  $71^\circ\text{C}$ .

The slope of the curve shown by Amlie and Rüetschi (4b) for 40% KOH at  $30^\circ\text{C}$  in their Fig. 7 appears to be about  $0.003 \text{ ml hr}^{-1} \text{ g}^{-1}$ . This rate is shown in Fig. 7 as the  $\odot$  point. However, it is not known if the data of these investigators were calculated to a dry basis. The presently reported rate for 11.6M (44%) solution at  $30^\circ\text{C}$  is  $0.002 \text{ ml hr}^{-1} \text{ g}^{-1}$ .

The data given by the NOL investigators (5) are shown as curve 5-7, curve 4-3, and curve 5-5 for  $\text{Ag}_2\text{O}_2$  in 40% KOH at  $32.2^\circ$ ,  $47.5^\circ$ , and  $71^\circ\text{C}$ , respectively. The rates have been calculated and included in Fig. 7 as the

x points. The greatest discrepancy between the NOL data and the present author's data occurs in the lower temperature region. At the higher temperatures discrepancies may be due to different activities of different  $\text{Ag}_2\text{O}_2$  samples. The NOL report does not mention any corrections having been made for water vapor in the evolved oxygen.

### Conclusions

The rate of dissociation of  $\text{Ag}_2\text{O}_2$  increases markedly with KOH concentration up to 11.6M, but there is less effect at higher concentrations.

The rate of dissociation of  $\text{Ag}_2\text{O}_2$  is much greater at high temperatures than at low temperatures.

Dry  $\text{Ag}_2\text{O}_2$  presumably is unstable at room temperature and would largely decompose in a few years (5-10). It has approximately the same rate of dissociation as in 4.0M KOH.

The rate of dissociation is slowest when the  $\text{Ag}_2\text{O}_2$  is wet with water and hence, for longest shelf life of this substance unmixed with anything else, it should be stored this way.

### Acknowledgments

This work was supported in large part by NASA Goddard Space Flight Center. Thanks are due to M. Ames Chemical Works for furnishing most of the  $\text{Ag}_2\text{O}_2$ . The laboratory assistance given by Kenneth Kramer and William Seelig is much appreciated.

Manuscript submitted Oct. 30, 1967; revised manuscript received April 29, 1968.

Any discussion of this paper will appear in a Discussion Section to be published in the June 1969 JOURNAL.

### REFERENCES

- I. A. Denison, *This Journal*, **90**, 387 (1946).
- T. P. Dirkse and G. J. Werkema, *ibid.*, **106**, 88 (1959).
  - T. P. Dirkse and B. Wiers, *ibid.*, **106**, 284 (1959).
  - T. P. Dirkse, *ibid.*, **106**, 453 (1959).
  - T. P. Dirkse, *ibid.*, **107**, 859 (1960).
  - T. P. Dirkse, *ibid.*, **109**, 173 (1962).
- C. P. Wales and J. Burbank, *ibid.*, **106**, 885 (1959).
  - C. P. Wales, *ibid.*, **108**, 395 (1961).
  - C. P. Wales, *ibid.*, **109**, 1119 (1962).
- B. D. Cahan, J. B. Ockerman, R. F. Amlie, and P. Rüetschi, *ibid.*, **107**, 725 (1960).
  - R. F. Amlie and P. Rüetschi, *ibid.*, **108**, 813 (1961).
- F. M. Bowers, R. D. Wagner, N. R. Berlat, and G. L. Cohen, U. S. Naval Ordnance Laboratory Technical Report, NOLTR 62-187 (1962).
  - R. D. Wagner, NOLTR 64-214 (1964).
- G. L. Cohen and E. H. Ostrander, U. S. Naval Ordnance Laboratory Technical Report, NOLTR 64-13 (1964). See also G. L. Cohen and G. Atkinson, *Inorg. Chem.*, **3**, 1741 (1964).
- E. M. Otto and W. G. Eicke, *This Journal*, **104**, 199 (1957).



# Analysis of the Uhlig Defect Model of Oxidation Kinetics

A. T. Fromhold, Jr.\*

Department of Physics, Auburn University, Auburn, Alabama

## ABSTRACT

A self-consistent development is given of a model of oxidation kinetics in which growth rate is determined by thermionic emission of electrons over a potential barrier due to the metal-oxide work-function and modified by space charge due to trapped electrons in the oxide and compensating surface charge at the metal-oxide interface. The following expression is derived for the growth rate

$$dy(t)/dt = B_0 \exp\{-y(t)^2/y_0^2\}$$

where  $y(t)$  is the oxide film thickness at time  $t$ , and  $y_0 = (\epsilon kT/2\pi e^2 n_0)^{1/2}$  is the characteristic thickness at which a uniform concentration  $n_0$  of trapped electrons of charge  $-e$  attenuates the growth rate significantly at temperature  $T$ ,  $\epsilon$  is the relative dielectric constant of the oxide, and  $k$  is the Boltzmann constant. The parameter  $B_0 = \beta A' \exp(-e\phi/kT)$  can be considered to determine the time scale, where  $A'$  is the flux of electrons (or charge) in the parent metal which impinges on the potential barrier of height  $\phi$  represented by the oxide, and  $\beta$  is the volume of oxide formed per electron (or per unit of charge) which traverses the oxide film. This growth-rate expression clearly does not lead to a direct-logarithmic growth law. Moreover, the characteristic film thickness  $y_0$  at which rate is significantly attenuated is of the order of the Debye length, in contrast with the conclusion reached by Nwoko and Uhlig that space-charge effects should be much larger. A development of the activation barrier for electron emission illustrates that the electron affinity of adsorbed oxygen is not a factor in the activation energy for electron emission when the emission process is rate-limiting. This results in a modification of the time scale for the kinetics by many orders of magnitude relative to that of Uhlig and Nwoko. Finally, the nonzero ionic current will perturb the rate-limiting electron current; the "coupled currents" method previously developed by the present author, in which the currents are balanced by the surface charge field, is suggested to be appropriate for studying this effect.

An analysis of the kinetics of oxide film growth published by Uhlig (1) some ten years ago is based on the idea contained in the quotation (2), "When the oxidation rate, therefore, is controlled by electron flow from the metal, an increasing negative space charge (or decreasing positive space charge) obviously enters as an important factor in establishing the rate of electron flow, tending in general to slow down escape of electrons as the oxide grows, and, therefore, simultaneously slowing down escape of metal ions and the oxidation process itself." The kinetics of oxide growth were considered by Uhlig to be determined by the well-known semi-empirical equation (3) for electron current across the contact of a metal and a semi-conducting oxide

$$i = A' \exp(-e\phi/kT) \{\exp(ev'/kT) - 1\} \quad [1.1]$$

where  $A'$  is a constant,  $\phi$  is the metal-oxide work function,  $e$  is the electronic charge magnitude,  $v'$  is an applied voltage across the metal-oxide junction,  $k$  is Boltzmann's constant, and  $T$  is the absolute temperature. If  $\exp(ev'/kT)$  is much larger than unity, Eq. [1.1] reduces to

$$i \simeq A' \exp\{-e(\phi - v')/kT\} \quad [1.2]$$

Equation [1.2] is also applicable to certain cases for which  $ev'$  is negative, including that for the Uhlig model. (This is discussed in the section on Electron Activation Energies of the present paper.) The effect of space charge on the kinetics was introduced by considering  $v'$  in Eq. [1.2] to be the potential drop established across the film by space charge, which can be computed from Poisson's equation (4-7). For the sake of simplicity, the space charge was considered to be uniformly distributed throughout the oxide in the case of thin films; in the case of thick films, a diffuse region

of space charge was postulated in addition to the region of uniform space charge.

The basic idea that space charge exerts an important effect on oxidation rate is good. However, Uhlig's mathematical development of the model outlined above has been criticized (8) by the present author on the following points:

1. The position coordinate  $x$  in Poisson's equation of electrostatics was misinterpreted to be the total film thickness  $y(t)$ , which led to the application of physically meaningless boundary conditions. This misinterpretation is evidenced most clearly by the fact that the Uhlig treatment leads to a nonconservation of electrical charge during growth. In addition, numerical errors of several orders of magnitude are introduced into the computation of the space-charge electric field for a given defect concentration in the oxide film, so that space-charge effects for charged particle transport are predicted to be enormous relative to computations based on the proper application of Poisson's equation.

2. The electron affinity  $\tilde{v}$  of adsorbed oxygen at the oxide-oxygen interface was considered to reduce the activation energy for electron transfer from metal to adsorbed oxygen, thus effectively reducing the metal-oxide work function  $\phi$  at the metal-oxide interface by  $\tilde{v}$ . It was pointed out in the criticism that this can be true only for special cases; it cannot be generally true if one accepts the usual thermodynamic concept of an activation barrier.

3. Ionic transport was not included in the treatment. The present author argues that it is necessary to make assumptions regarding this matter even in cases for which electrons represent the rate-limiting species. That is, a concentration gradient of ions across the oxide represents a diffusion potential; this diffusion potential should contribute to the establishment of an

\* Electrochemical Society Active Member.



electrostatic potential across the oxide, especially whenever the ionic species is not rate-limiting as in the case of the Uhlig model.

In the discussion section of a paper by Nwoko and Uhlig (9) entitled "Logarithmic Oxidation Kinetics of Zinc," a rebuttal to the criticism (8) is given, and the original Uhlig treatment is employed in unmodified form to interpret experimental data. The present communication summarizes the results of a re-examination of the topic and attempts to clarify several misconceptions introduced by the rebuttal of Nwoko and Uhlig (9).

It is to be emphasized that the purpose of the present communication is not to present a new model of oxidation kinetics. Instead, it represents a clarification of the matter of the electron current over Schottky-type barriers appropriate for the Uhlig model. Such an electron current, when properly coupled (10, 11) with the ionic current according to our concept of the oxidation process, does provide the basis for a new model.

The section of the present paper on Poisson's Equation as Applied to an Oxide Film clarifies the matter of Poisson's equation as utilized to compute potentials in the oxide film; appropriate boundary conditions are employed to derive the growth equation appropriate for the Uhlig model. The section on Electron Activation Energies is a discussion of electron activation barriers; the relationship between such barriers and the free energy of electron transport through the oxide and the free energy of formation of the oxide is clarified therein. The section on the Possibility of Obtaining the Direct-Logarithmic Law constitutes an examination of (and effective argument against) two possible *ad hoc* hypotheses which can lead to a direct logarithmic growth law for the Uhlig model. The section on the Effect of the Ionic Current on the Electron Current due to Coupling treats the question of whether the ionic current can be validly ignored whenever the electronic current is rate-limiting. The section on the Misconceptions in Uhlig and Nwoko Paper is a clarification of misconceptions introduced in the paper of Nwoko and Uhlig (9), and the section, Conclusions, is a brief statement of the principal conclusions of the present work.

### Poisson's Equation as Applied to an Oxide Film

According to classical electromagnetic theory (4), Poisson's equation in Gaussian units is

$$\nabla^2\varphi = -4\pi\rho/\epsilon \quad [2.1]$$

where  $\varphi$  is the scalar electrostatic potential which can vary from point to point in the medium,  $\rho$  is the charge density which may also be a function of position in the medium,  $\epsilon$  is the relative dielectric constant of the medium, and  $\nabla^2$  is the Laplacian (5-7).

A planar oxide film of thickness  $y(t)$  is considered as a one-dimensional problem with the origin at the metal surface. The position in the oxide normal to the metal surface is represented by  $x$ . The electrostatic potential will be independent of position parallel to the metal surface, so that  $\varphi = \varphi(x)$  only. If trapped electrons (charge  $-e$ ) of density  $n(x)$  constitute the sole contribution to the space charge, as was assumed by Uhlig (1), then  $\rho = -n(x)e$ . Equation [2.1] in this case reduces to

$$\frac{d^2\varphi(x)}{dx^2} = \frac{4\pi n(x)e}{\epsilon} \quad [2.2]$$

This equation yields the electrostatic potential as a function of  $x$  for any arbitrary position in the planar oxide film. Clearly the independent variable  $x$  denoting the position in the film normal to the metal surface cannot be replaced in this equation by the total thickness  $y(t)$  of the film, as was done by Uhlig (12). The proper way to obtain the total electrostatic potential  $v'$  impressed across the film is to solve Eq. [2.2] for

the  $n(x)$  in question; then  $v'$  is given by the difference in  $\varphi(x)$  as evaluated at the interface  $x = y(t)$  and  $x = 0$

$$v' = \varphi(x)|_{x=y(t)} - \varphi(x)|_{x=0} \quad [2.3]$$

The effective voltage for electron emission is given by  $v'$  only when the maximum in the thermionic barrier occurs at or very near  $x = y(t)$ . This excludes the case where the barrier maximum occurs at (or very near)  $x = 0$ , and also excludes cases in which the barrier maximum occurs at some intermediate position in the oxide film. For the Uhlig model, however,  $v'$  as defined by Eq. [2.3] gives an adequate representation of the effective voltage for electron emission, as will be shown later in the present work.

Specification of the two boundary conditions for the second-order differential equation [2.2] at all time  $t$  must be made consistent with the physical situation at hand. Since the zero of potential is arbitrary, it can be chosen to be zero inside the parent metal. For the common case of a semiconducting oxide growing on a metal, there is no sudden discontinuity in potential across the metal-oxide interface. This is due to the relatively low conductivity of the semiconducting oxide relative to the metal, so the interfacial dipole layer with its accompanying potential discontinuity at the interface between two different metals is replaced in the case of a metal-oxide interface by a single surface-charge layer on the metal accompanied by a volume distribution of charge of the opposite sign in the oxide. The extent of the charge distribution in the oxide is given approximately by the Debye length  $L_D$  in the semiconducting oxide (13, 14)

$$L_D = (\epsilon kT/8\pi e^2 n_0)^{1/2} \quad [2.4]$$

where  $n_0$  is  $n(x)$  in the limit of a uniform charge distribution. This parameter  $L_D$  is approximately 27Å for  $n_0 = 10^{18} \text{ cm}^{-3}$  and approximately 27,000Å for  $n_0 = 10^{12} \text{ cm}^{-3}$ , assuming  $T = 300^\circ\text{K}$  and  $\epsilon = 10$ . Therefore the change in electrostatic potential which takes place from the interior of the metal to the interior of the semiconductor occurs gradually over a distance of the order of  $L_D$ , with no sudden discontinuity occurring within a lattice parameter or so of the metal-semiconductor interface. Therefore  $\varphi(0)$ , the potential in the oxide immediately adjacent to the metal interface, is for all practical purposes equal to the potential inside the interior of the metal, which is chosen to be the zero potential point. Hence  $\varphi(0) = 0$  can be chosen as one of the required physically meaningful boundary conditions for the present problem, although Eq. [2.3] shows that  $v'$  is actually independent of the choice of  $\varphi(0)$ . It should be noted that this boundary condition is independent of time of growth of the oxide and hence independent of the thickness of the oxide.

This specification of a boundary condition for the complete period of time over which oxidation occurs is necessary; otherwise the potential  $\varphi(x)$  would not be determined for the entire period of oxidation. This is a critical weakness of the Uhlig theory (1), where the boundary conditions on the potential are specified for only two values of the film thickness ( $y = 0$  and  $y = l$ , where  $l$  is a length determined by the criterion (15) that the field be "zero at the metal surface when the assumed thickness of the constant charge density film is  $l$ "). Since the boundary conditions are specified for only two film thicknesses, it follows immediately that they are specified for only two points in time, namely, the time at which oxidation begins and the time at which  $y(t)$  reaches the thickness  $l$ . The electrostatic potential utilized by Uhlig is therefore mathematically undefined.

A second boundary condition for the electrostatic potential could be the specification during the period of oxidation of the value of  $\varphi$  at any position  $x_0(t)$  (which may be constant or else specified as a function of time) other than  $x = 0$ , or it could be  $d\varphi/dx$  evaluated at such a position or at  $x = 0$ . The choice of a

second boundary condition valid for the period of oxidation is not an easy one in the Uhlig theory; it is somewhat more straightforward in the approach proposed by the present author (10), where ion transport is explicitly included in the formulation of the problem, and the surface-charge field  $-d\varphi(x)/dx|_{x=0}$  is determined as a function of film thickness  $y(t)$  by the coupling condition that the charge currents of the ionic and the electronic species must be equal in magnitude. No such coupling is present in the Uhlig theory; this constitutes the basis for the present author's criticism (8) that ionic transport is ignored in the Uhlig theory. To quote from Uhlig and Nwoko (9), "Furthermore, ionic transport was justifiably ignored in our treatment [reference 1] because it is considered to be the faster process during initial oxidation, with electron transfer being controlling." In the absence of coupling with the ionic current, and with an absence of experimental measurements for the total potential  $v'$  across the film (Eq. [2.3]), it seems clear that the second boundary condition must involve some reasonable assumption regarding either  $\varphi(x)|_{x=y(t)}$ ,  $-d\varphi(x)/dx|_{x=0}$ , or  $-d\varphi(x)/dx|_{x=y(t)}$ . The latter two quantities represent the electrostatic field  $E(x)$  at  $x = 0$  and  $x = y(t)$ , respectively.

Before making a specific choice of boundary condition, and thereby restricting the generality of all subsequent results, it is helpful to examine first the relationship between values of the electric field at different points in the film imposed by Poisson's equation. During film growth, the total charge of the system must be maintained constant; for oxidation of a charge-neutral metal, the total charge must therefore remain zero

$$q_0\sigma_0 + q_y\sigma_y - e \int_0^{y(t)} n(x) dx = 0 \quad [2.5]$$

where  $\sigma_0$  and  $\sigma_y$  are the surface densities of charged particles with charge per particle of  $q_0$  and  $q_y$  at  $x = 0$  and  $x = y$ , respectively. Therefore, one or both of the surface charge densities must vary with  $y(t)$ , which in turn represents a dependence of  $E(0)$  and/or  $E(x)|_{x=y(t)}$  on  $y(t)$  since according to elementary electrostatics and Eq. [2.2]

$$E(x) = -\frac{d\varphi(x)}{dx} = \frac{4\pi q_0\sigma_0}{\epsilon} - \frac{4\pi e}{\epsilon} \int_0^x n(x) dx \quad [2.6]$$

The combination of Eq. [2.5] and [2.6] yields the results

$$E(0) = 4\pi q_0\sigma_0/\epsilon \quad [2.7]$$

and

$$E(x)|_{x=y(t)} = -4\pi q_y\sigma_y/\epsilon \quad [2.8]$$

Clearly if the surface charge density  $q\sigma$  could be specified from physical considerations at either interface for the period of oxidation, the surface-charge fields at both interfaces would be given by the above equations for the period of oxidation for any  $n(x)$  appropriate for the system.

The matter of a proper choice for  $n(x)$  is a non-trivial matter. The  $n(x)$  is defined by Uhlig (1) as density of electrons in the oxide which are trapped at impurities or defects, thereby constituting an excess charge density in the oxide. Uhlig (1) makes the assumption that  $n(x)$  has a uniform value  $n_0$  for positions in the oxide less than a distance  $L$ , at which there is a discontinuity in  $n(x)$ , following which  $n(x)$  decreases exponentially with  $x$ . These distributions for  $n(x)$  as well as the assumed discontinuity are clearly *ad hoc* assumptions resulting in a two-stage growth law. Although each of these distributions may be physically realistic in certain limiting cases, the concept of an abrupt transition between the two is clearly nonphysical. Nwoko and Uhlig (9), in their section entitled "Cause of Two-Stage Oxidation Behavior," explain the abrupt transition as occurring at the point at which "the electrostatic energy in the outer oxide approaches the thermal energy  $kT$ ."

Clearly this represents some fundamental misunderstanding of the nature of a Boltzmann distribution, since this classical distribution adequately describes the competition between electrostatic and thermal energies, but contains no discontinuity of the type postulated by Uhlig. The present development will be based on the uniform distribution  $n_0$ , since this serves to illustrate the basic errors in the Uhlig treatment while retaining the advantages of simplified mathematical expressions. The corrected treatment can be readily extended to the case of a diffuse distribution of space charge (16). The value of  $n_0$  for a given physical system is assumed to be determined by experimental conditions of oxidation and sample preparation; the computed potentials with the corresponding space-charge effects can be compared with experimental studies of the kinetics.

With  $n(x) = n_0$ , Eq. [2.5] yields

$$q_0\sigma_0 + q_y\sigma_y = en_0 y(t) \quad [2.9]$$

and Eq. [2.6] yields

$$E(x) = -\frac{d\varphi(x)}{dx} = (4\pi q_0\sigma_0/\epsilon) - (4\pi e/\epsilon)n_0 x \quad [2.10]$$

A further integration of Eq. [2.10] and application of the previously developed boundary condition  $\varphi(0) = 0$  yields

$$\varphi(x) = -(4\pi q_0\sigma_0/\epsilon)x + (2\pi e/\epsilon)n_0 x^2 \quad [2.11]$$

Evaluation of Eq. [2.11] at  $x = y(t)$  and substitution into Eq. [2.3] yields

$$v' = -(4\pi q_0\sigma_0/\epsilon)y + (2\pi e/\epsilon)n_0 y^2 \quad [2.12]$$

According to the Uhlig theory it is the change in this potential with increasing  $y(t)$  that results in a retarding effect on the flow of electrons from metal to oxide which steadily increases with increasing  $y(t)$ , ultimately resulting in a limiting-thickness type growth law. It is quite informative to utilize Eq. [2.12] to compute realistic values for  $v'$ . The first term in Eq. [2.12] represents the surface-charge contribution to the potential across the film, while the second term represents the space-charge contribution. For example, assume that  $y(t)$  is 50 Å and  $n_0 = 0.24 \times 10^{18} \text{ cm}^{-3}$ , which are obtained from the data and analysis of Nwoko and Uhlig (9) for cold rolled zinc sheet (abraded, and etched in HCl) oxidized for approximately 450 min at 206°C in oxygen pressures in the neighborhood of 0.56 Torr. The value of the space-charge term in Eq. [2.12] is thus approximately  $\pm 5.4 \times 10^{-3} \text{ v}$  for  $\epsilon = 10$ . The corresponding ratio  $ev'/kT$  occurring in Eq. [1.2] at 206°C is approximately  $\pm 0.13$ . The term  $\exp(ev'/kT)$  differs from unity by only  $\approx 13$  parts in 100, so that the difference in current  $i$  for zero film thickness  $y(t)$ , for which  $v'$  is zero due to the lack of space charge, and the current  $i$  for  $y(t) = 50 \text{ Å}$ , is only 13%. In other words, the current as computed for the 50 Å film is 0.87 or 1.13 times the current with no space charge, so that the space charge for all practical purposes provides an insignificant attenuation of the current. This is in contrast to the conclusions of Nwoko and Uhlig (9) that the space charge has attenuated the current so markedly that the film has almost ceased to grow.

Up to this point, no boundary conditions have been utilized, so that the conclusions are generally valid under all conditions. The development can be carried no further, however, without some additional assumption which will allow the choice of the second boundary condition. The specification of either  $q_0\sigma_0$  or  $q_y\sigma_y$  for fixed  $n_0$  and for all  $y(t)$  would be sufficient, since Eq. [2.9] would then yield the surface-charge density at the opposite interface. The additional assumption which will be invoked at this point to fix the second boundary condition is that the electric charge  $q_y\sigma_y$  at the outer interface is a constant during the oxidation process. Although this is not in general accordance

with the concept of the oxidation process held by the present author (10, 11), it is apparently in accordance with the concept of Uhlig (15, 17) and therefore appears to be the most reasonable choice necessary to remove the arbitrariness in the matter of the second boundary condition for the Uhlig theory. To quote from the paper by Uhlig (15), "Interpretation of Volta potential measurements as described above assumes that electric charge at the air-oxide interface remains essentially constant, which is a reasonable assumption for constant partial pressure of oxygen; and that major change of potential is accounted for by changing electric charge in the thin oxide films." Since  $q_{y\sigma_y}$  thus is assumed independent of  $y(t)$ , it has the same value in the limit that  $y(t)$  approaches zero. Equation [2.9] thus yields  $q_{y\sigma_y} = -q_{o\sigma_o}|_{t=0}$ . However the point  $y(t) = 0$  corresponds to the bare metal, uncovered by oxide, and because the metal is initially charge-neutral,  $q_{o\sigma_o}|_{t=0}$  is zero. Hence  $q_{y\sigma_y}$  can be chosen to be zero initially, and also subsequently during the oxidation process, in complete accordance with the principles underlying the Uhlig formulation. (Since coupling between species is not considered in the Uhlig theory, any other choice would be either arbitrary or *ad hoc*.) For this case, Eq. [2.9] yields

$$q_{o\sigma_o} = en_0 y(t) \quad [2.13]$$

which when substituted into Eq. [2.12], yields

$$v' = -(2\pi en_0/\epsilon) y(t)^2 \quad [2.14]$$

This is the effective voltage, provided the maximum in  $\nabla(x)$  occurs at  $x_m \cong y(t)$ , as mentioned previously. Substituting Eq. [2.11] for  $\nabla(x)$  into the condition

$$\left. \frac{d\nabla(x)}{dx} \right|_{x=x_m} = 0 \quad [2.15]$$

yields

$$x_m = q_{o\sigma_o}/en_0 \quad [2.16]$$

Substitution of Eq. [2.13] into this expression then gives the result  $x_m = y(t)$ , thus satisfying the condition  $x_m \cong y(t)$ . It is therefore concluded that Eq. [2.14] represents a valid expression for the effective voltage for electron transport in the Uhlig model.

Substituting Eq. [2.14] into Eq. [1.2] gives

$$i = A' \exp(-e\phi/kT) \exp\{-y(t)^2/y_0^2\} \quad [2.17]$$

where

$$y_0 = (\epsilon kT/2\pi e^2 n_0)^{1/2} \quad [2.18]$$

The oxide growth rate is proportional to the electron current, so that

$$\frac{dy(t)}{dt} = \beta i \quad [2.19]$$

where  $i$  is given by Eq. [2.17] and  $\beta$  is the proportionality constant involving the volume of oxide formed for each electron which traverses the oxide film. Defining the quantity  $B_0$  as

$$B_0 = \beta A' \exp(-e\phi/kT) \quad [2.20]$$

the growth equation becomes simply

$$\frac{dy(t)}{dt} = B_0 \exp\{-y(t)^2/y_0^2\} \quad [2.21]$$

The parameter  $y_0$  defined by Eq. [2.18] can be seen to be equal to twice the Debye length  $L_D$  as given by Eq. [2.4]. Integration of Eq. [2.21] does not yield a direct-logarithmic growth law. It is therefore concluded that the Uhlig model does not properly yield a direct-logarithmic growth law (or a two-stage logarithmic growth law) unless additional assumptions are employed.

Furthermore, the thickness  $y_0$  at which the space charge begins to attenuate the growth rate appreciably, and also the pre-exponential factor  $B_0$ , differ by orders-of-magnitude from the corresponding quantities

$y'_0$  and  $B'_0$ , which occur in the Uhlig growth rate expression (18)

$$dy(t)/dt = B'_0 \exp\{-y(t)/y'_0\} \quad [2.22]$$

where

$$B'_0 = \beta A' \exp(-e\phi/kT) \exp(\tilde{v}/kT) \quad [2.23]$$

and

$$y'_0 = \epsilon kT/4\pi e^2 n_0 l \quad [2.24]$$

The newly introduced parameters are  $\tilde{v}$  and  $l$ . (The quantity  $\tilde{v}$  is to be carefully distinguished from the effective voltage  $v'$  given by Eq. [2.12].) The quantity  $\tilde{v}$  is defined somewhat ambiguously in the Uhlig theory

as follows (19): "...  $\tilde{v}$  is the apparent positive potential at the metal surface created by the growing oxide.

The term  $\tilde{v}$ , in general, is numerically equal to the potential difference between the metal-oxide interface and the oxide-oxygen interface for metal-oxide systems in which lattice diffusion of oxygen ions toward

the metal is negligible. As will be shown later,  $\tilde{v}$  is approximated by the electron affinity of oxygen adsorbed on the oxide; it is, therefore, a constant independent of oxide thickness and, like the work function, it is substantially independent of temperature." The value quoted for this parameter (20) is 3.6 ev. The quantity  $l$  is defined by Uhlig (15) as the assumed thickness of the constant charge density film at which the field is zero at the metal surface, and values deduced for this parameter (21) are of the order of 1,000 to 100,000 Å.

From Eq. [2.18], [2.20], [2.23], and [2.24]

$$y'_0/y_0 = y_0/2l = (\epsilon kT/2\pi e^2 n_0)^{1/2}/2l \quad [2.25]$$

and

$$B'_0/B_0 = \exp(\tilde{v}/kT) \quad [2.26]$$

For  $n_0 = 10^{16} \text{ cm}^{-3}$ ,  $\epsilon = 10$ ,  $T = 300^\circ \text{K}$ ,  $l = 10,000 \text{ Å}$ ,

and  $\tilde{v} = 3.6 \text{ ev}$ , the above ratios have the approximate values  $y'_0/y_0 \cong 0.03$  and  $B'_0/B_0 \cong \exp(140) \cong 10^{60}$ , which emphasizes the tremendous discrepancy between the predicted effects of space charge on growth rate, even neglecting the fact that the growth laws have a different functional form.

At this point, it is helpful to analyze the source of the parameter  $l$ , which is one of the two parameters which cause large excursions in the Uhlig theory relative to the present development. The parameter  $l$  comes about through the incorrect usage of  $y(t)$  in place of  $x$  in Poisson's equation, since a boundary condition was imposed at one very large film thickness  $y(t) = l$  corresponding to one point in time instead of at a point  $x_0(t)$  for the entire time of growth. The thickness  $l$  corresponded by definition to the point at which  $E(O) = 0$ . Referring to Eq. [2.7] and [2.9], it can be seen that if  $q_{y\sigma_y} = 0$  as was argued previously, then  $E(O)$  can never be zero for finite film thicknesses and nonzero values of  $n_0$  without violating the principle of conservation of total charge (Eq. [2.9]) for the system. That is, for nonzero space charge, the surface charge at the two interfaces must be equal and opposite to the total space charge for over-all charge conservation; this precludes the surface-charge density from being zero simultaneously at both interfaces for a nonzero value of  $n_0$ . This matter of nonconservation of total electrical charge immediately illustrates the necessity of a proper choice of boundary conditions.

The parameter  $\tilde{v}$  is the second quantity in the Uhlig theory which results in such a large difference from the present development. Basically it is claimed by Uhlig (1) that the electron affinity of adsorbed oxygen at the oxide-oxygen interface lowers the activation energy for electron transfer from the metal through the oxide, which therefore results in an in-

crease in the electron flux through the film by a factor of approximately  $\exp(140)$ . This matter, which is simply a confusion of the thermodynamic concepts of activation energy and free energy of reaction (22), is considered in detail in the following section.

### Electron Activation Energies

Referring to the standard activation barrier illustrated in Fig. 1, it can be seen that the activation energies for forward and reverse reactions are  $W_f$  and  $W_r$ , respectively, while the free energy change  $\Delta U$  for the reaction is  $\Delta U = W_r - W_f$ . The rate  $R_f$  of forward reaction is

$$R_f = n_f \nu_f \exp(-W_f/kT) \quad [3.1]$$

and the rate  $R_r$  of the reverse reaction is

$$R_r = n_r \nu_r \exp(-W_r/kT) \quad [3.2]$$

$n_f$  is the number of particles in the position of the first potential minimum,  $\nu_f$  is the attempt frequency of these particles, and  $W_f$  is the potential barrier height in the forward direction, while  $n_r$  is the number of particles in the position of the second potential minimum,  $\nu_r$  the attempt frequency of these particles, and  $W_r$  is the potential barrier height in the reverse direction. The net rate of the reaction is

$$R_{\text{net}} = R_f - R_r \quad [3.3]$$

which of course is zero in the limit of chemical equilibrium. For equilibrium, the forward and reverse rates are equal

$$n_f \nu_f \exp(-W_f/kT) = n_r \nu_r \exp(-W_r/kT) \quad [3.4]$$

so that

$$(n_r/n_f) = (\nu_f/\nu_r) \exp(\Delta U/kT) \quad [3.5]$$

Clearly the right-hand side has the standard form for an equilibrium constant (22) for the reaction, and this depends only on  $\Delta U$  and not on the individual values of  $W_f$  and  $W_r$ .

For a strongly nonequilibrium process, however, the reaction is predominantly in the forward direction. That is, at the start of the reaction,  $n_r = 0$ , so the net rate of the reaction is given by Eq. [3.1]. This involves only the activation energy  $W_f$ , and is independent of  $W_r$  and hence of  $\Delta U$ .

The oxidation of metals is clearly a strongly nonequilibrium process, at least so long as the oxidation proceeds, as evidenced by an appreciable growth rate of the oxide film. Hence the rate-limiting step for oxidation, which is postulated to be electron transport in the Uhlig theory, must be strongly nonequilibrium. Therefore, on the basis of the Uhlig theory, the rate of oxidation must be determined by the activation energy for electron transport in the forward direction instead of the free energy change  $\Delta U_e$  for electron transport through the oxide as postulated by Uhlig (1). Only in the case of theories based on ionic rate-limit-

ing transport does  $\Delta U_e$  become the important quantity for electron transport, since only then does the electronic species approach equilibrium. The free energy of formation of the oxide,  $\Delta U_{\text{oxide}}$ , does not occur explicitly in the rate equations, since this includes not only the free energy change  $\Delta U_e$  for transport of electrons through the oxide, but also includes the free energy change  $\Delta U_i$  for transport of an equivalent number of ions (i.e., equivalent in charge) through the film

$$\Delta U_{\text{oxide}} = \Delta U_e + \Delta U_i \quad [3.6]$$

This point does not seem to have been clarified previously in the literature; it represents a subject of much present-day discussion (23).

The relevant electron energy diagram is illustrated in Fig. 2. The diagram clearly is analogous to the schematic reaction barrier shown in Fig. 1 and discussed above. Initially the electrons are in the conduction band of the metal, with the oxide representing an activation barrier in the forward direction. With no electric fields in the system (Fig. 2a, 2b) the activation energy for electron transport in the forward direction is the metal-oxide work function  $\phi$ ; this parameter is the energy difference between the conduction band in the oxide and the Fermi level in the metal. The activation energy for electron motion in the

reverse direction is shown in Fig. 2a,b to be  $\tilde{v}$ , and the net energy change effected in electron transport from the Fermi level of the metal to the  $O^-$  state in

adsorbed oxygen is  $\Delta U_e = \tilde{v} - \phi$ . [Note that this is positive for Fig. 2a and negative for Fig. 2b. Mott (24) considers the former picture while Uhlig (25) prefers the latter.] The quantity  $\Delta U_e$  is unimportant for computing the net rate of electron transport, however, when this is the rate-limiting step for the process, as was argued for the reaction barrier in Fig. 1. Hence the activation energy in zero field in the Uhlig theory

should be  $\phi$  and not  $\phi - \tilde{v}$ , as was employed by Uhlig (19). With nonzero space charge, the activation barrier for electron transport is modified by the electrostatic potential in the oxide. Figure 2b is thus modified to the form illustrated in Fig. 2c or Fig. 2d. Figure 2c illustrates the case in which all compensating surface charge is located at the metal-oxide interface while

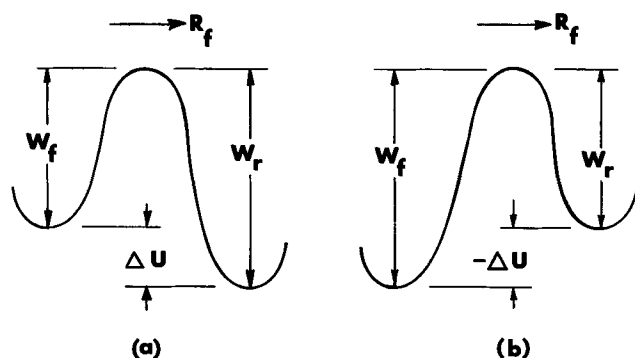


Fig. 1. Standard activation barriers  $W_f$  for the forward direction and  $W_r$  for the reverse direction. (a) Positive free energy change  $\Delta U$  for reaction in the forward direction. (b) Negative free energy change  $\Delta U$  for reaction in the forward direction.

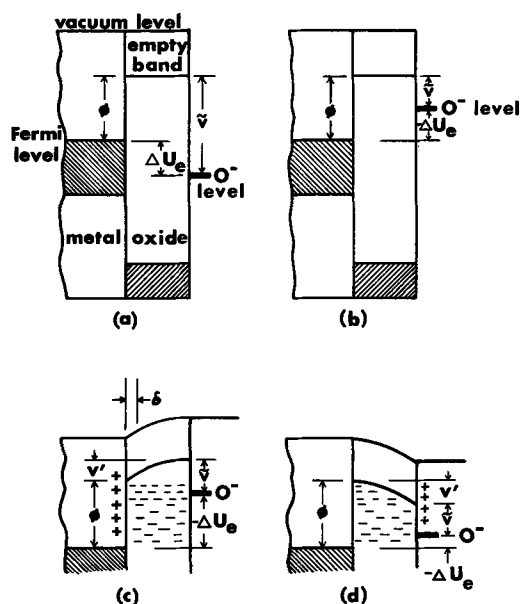


Fig. 2. Electron energy diagrams for metal-oxide-oxygen system. (a)  $O^-$  level below metal Fermi level. (b)  $O^-$  level above metal Fermi level. (c) Negative space charge with compensating positive charge at the metal-oxide interface. (d) Negative space charge with compensating positive charge at the oxide-oxygen interface.

Fig. 2d illustrates the case in which all compensating surface charge is located at the oxide-oxygen interface. It can be noted that the activation barrier in the forward direction is increased by  $v'$  for the case of Fig. 2c, but is unmodified in Fig. 2d. The activation barrier in the reverse direction is unchanged in Fig. 2c but increased by  $v'$  in Fig. 2d; these modifications of the reverse barrier are unimportant for the Uhlig theory, however, as argued above. [These conclusions must be modified slightly when image potentials are included (11); such complicating effects were neglected by Uhlig.] It is interesting to note that if surface charge at  $x = 0$  is ignored (Fig. 2d), the potential maximum occurs at  $x = 0$ , and the space charge contribution to the potential has no effect on the electron current. This emphasizes the importance of the surface charge. It is therefore seen that the Uhlig concept of trapped electrons causing a continuous increase in height of the activation barrier as the film thickness increases is most closely approximated by the case illustrated in Fig. 2c, so that the activation energy for this case is  $e(\phi - v') = e(\phi + |v'|)$ , a

quantity independent of the electron affinity  $\tilde{v}$  of adsorbed oxygen. For an electron flux  $A'$  with a Boltzmann-type distribution in energy (i.e., the high energy "tail" due to  $kT$  spreading of the Fermi-Dirac distribution function) incident on the barrier, the electron current over the barrier is given by

$$i = A' \exp\{-e(\phi - v')/kT\} \quad [3.7]$$

which is identical to Eq. [1.2]. This equation therefore represents a valid expression for the electron current in the Uhlig model provided there is no reverse electron current, i.e., no thermal excitation of electrons from filled  $O^-$  states at  $x = y(t)$  into the oxide conduction band toward the metal-oxide interface. This will indeed be the case if the electron current is rate-limiting, as in the Uhlig model, since the oxide growth is presumably being retarded due to a deficiency of electrons at the oxide-oxygen interface.

The physical situation represented by Fig. 2c is also the one in accordance with the Uhlig assumption of an unchanging surface charge at the oxide-air interface (15, 17). The development leading to the growth law of Eq. [2.21] represents this situation. The fact remains, however, that a direct-logarithmic growth law is not obtained, contrary to the development by Uhlig (1). In addition, the factor of  $\exp(140)$  introduced by the inclusion of  $\tilde{v}$  into the activation energy in the Uhlig development is definitely absent in the present development.

### On the Possibility of Obtaining the Direct-Logarithmic Law

The origin of the direct-logarithmic growth law in the Uhlig development rests on the fact that the parameter  $l$  introduced in the application of improper boundary conditions in Poisson's equation resulted in a very large term in  $v'$  which was linear in  $y$ , so that the quadratic term could be neglected. It can be seen from Eq. [2.14] that  $v'$  obtained in the present development is purely quadratic in  $y(t)$ , with no linear term; hence the growth law represented by Eq. [2.21] is not of the direct logarithmic form. A considerable effort was made in ref. (8) to find a physical situation for which a term linear in  $y(t)$  would be obtained for  $v'$ , so that the Uhlig result of a direct-logarithmic law could still be valid, albeit with greatly modified values of the parameters. To this end, an additional factor was introduced into the development, this being the electron tunneling distance or scattering length in the oxide. It is clear that the simple activation barrier theory discussed up to this point assumes that the electron is thermally excited from the Fermi level of the metal into the conduction band of the oxide, and the rate of transport deduced thereby presumes

that the electron neither penetrates the classically inaccessible region in the barrier nor is scattered in the conduction band of the oxide before surmounting the potential maximum. Clearly, both quantum-mechanical tunneling as well as electron scattering are real effects; it was therefore believed (8) that the introduction of one or the other of these factors could perhaps modify the physical picture in such a direction as to yield a direct-logarithmic growth law.

It is certain that a uniform space charge will always contribute a term to the potential which is parabolic in  $x$  (see Eq. [2.11]); the surface-charge field, however, contributes a term linear in  $x$ . Thus the total potential drop across the film is proportional to  $y(t)^2$  for the space charge contribution and is proportional to  $E(O)y(t)$  for the surface charge field. Therefore, one way to obtain a linear term in  $y(t)$  which is needed to obtain the direct-logarithmic growth law is for  $E(O)$  to be independent of  $y(t)$  and to be large relative to the space-charge term. However, neither of these conditions are met in the present development: The  $E(O)$  increases linearly with  $y(t)$  if all of the compensating surface charge is located at  $x = 0$  (see Eq. [2.7] and [2.9]), thus yielding a parabolic contribution [ $E(O)y(t) \propto y(t)^2$ ] to the potential; furthermore this term is of the same order of magnitude as the space charge term. If all compensating surface charge is located at  $x = y(t)$ , then  $E(O) = 0$  and again there is no large linear contribution to the potential. Hence, the assumption of a constant  $E(O)$  requires the introduction of some physical mechanism not now included in the Uhlig theory. In addition, it requires surface-charge fields much larger than the space-charge field in order to neglect properly the space-charge contribution to the potential; this in itself would be inconsistent with the basic hypothesis of Uhlig that space charge due to trapped electrons is the mechanism responsible for the direct-logarithmic growth kinetics. Nevertheless, this is essentially what was done in the Uhlig treatment (1), since the value of  $E(O)$  was computed from the criterion that the uncompensated charge at  $x = 0$  for all film thicknesses be equal in magnitude but opposite in sign to the total space charge in some film of arbitrary but enormous thickness  $l$  (of the order of  $10^4$  to  $10^5 \text{ \AA}$ ). Thus  $q_o\sigma_o$  was given the value  $en_ol$ , corresponding to  $E(O) = 4\pi en_ol/\epsilon$ . When this is coupled with the assumption that  $q_y\sigma_y$  is independent of film thickness, the condition for conservation of charge (Eq. [2.9]) is violated. Clearly this approach cannot be considered to be valid.

Another possible way in which a surface-charge contribution to the potential can be obtained which is linear in  $y(t)$  and which predominates over the space-charge term, and which has the additional advantage of being due entirely to a surface-charge at  $x = 0$  not exceeding the total space charge, is for the electrostatic potential effective in reducing the activation barrier to be that potential developed over a fixed distance  $\delta$  which is independent of  $y(t)$ . Admittedly this would be an *ad hoc* assumption, although it is perhaps not quite so artificial when one thinks of  $\delta$  as a maximum distance in the oxide characteristic of easy electron tunneling between traps or of electron scattering in the conduction band of the oxide.

For example, electron tunneling can occur quite readily through barriers 10-15Å in thickness for the barrier heights less than several electron-volts normally encountered in metal-oxide systems; thus sharp spikes and corners in the simplified electron energy diagrams illustrated in Fig. 2 can be ignored, since thermal excitation to an energy below the barrier maximum can still result in transport across the barrier provided the electron can tunnel readily through the classically disallowed region. This matter of combined mechanisms for electron transport has been formulated quite generally by Murphy and Good (26). In such a case, the effective activation energy may

well be modified by  $\tilde{v}$  (see Fig. 2b), as claimed by Uhlig, provided the film thickness is less than a distance  $\delta_{\text{tun}}$  characteristic of easy electron tunneling, i.e.,  $y(t) \lesssim 50\text{\AA}$ , since the classically disallowed region no longer represents the true activation barrier. However, easy electron tunneling precludes the possibility of rate being limited by electron emission, so the Uhlig theory would be inapplicable in this case.

For films much thicker than the characteristic scattering length  $\delta_s$  for electrons in the conduction band of the oxide, the electrostatic potential developed across the region ( $0 \leq x \leq \delta_s$ ) is almost entirely due to the surface-charge contribution for the case in which the distribution of space charge is uniform and the total compensating surface charge is located at  $x = 0$ . Furthermore the total space charge increases linearly with  $y(t)$ , so  $E(O)$  also increases linearly with  $y(t)$ . The potential drop across the region  $0 \leq x \leq \delta_s$  is closely approximated by  $-E(O)\delta_s$ , so that we have the desired result of a large linear term in  $y(t)$ . This was the approach employed in ref. (8) to obtain a direct-logarithmic growth law, although it was realized at that time and is reiterated now that the result is quite artificial because of the *ad hoc* assumptions involved. For example, the appropriate energy diagram is given by Fig. 2c; note that easy transport of electrons from  $x = 0$  to  $x = \delta_s$  does not guarantee subsequent transport through the film, since the transport of electrons from  $x = \delta_s$  to  $x = y(t)$  must take place against an opposing electric field.

In light of the above discussion, it is concluded that even the inclusion of additional physical considerations in the Uhlig theory does not lead to a direct-logarithmic growth law in any straightforward manner. Hence this growth law as based on the Uhlig postulates must be considered to be theoretically unfounded. The alternate growth law given by Eq. [2.21] is more in keeping with the basic postulates of the theory and with elementary electrostatics.

The physical and mathematical treatments by Uhlig (27) of the diffuse space charge distribution and the cubic equation, as well as the derivation of the Rideal-Jones relation, are based on reasoning similar to that which he utilized for the uniform space charge development and hence are subject to the same type of errors which have been pointed out above. In addition, many *ad hoc* manipulations and approximations are made by Uhlig (27, 28) which are neither mathematically nor physically justifiable. It is not worth the additional effort, and indeed is beyond the scope of the present communication, to consider these sections in detail.

### Effect of Ionic Current on Electron Current due to Coupling

The present author has proposed (10) a technique for obtaining the oxidation kinetics for formation of a coherent oxide on a metal whenever transport takes place by currents of the oppositely charged species through the oxide. This method consists in coupling the transport equations through the macroscopic electric field in the oxide, imposing the condition of equal charge currents as the criterion for obtaining the surface-charge field, and numerically or analytically integrating the system of equations. The hypothesis of equal charge currents utilized to obtain the surface-charge field is intuitively reasonable since this is the quasi-stable situation for a given film thickness in which the currents do not change the surface-charge field. This method has also been justified by numerical computations (29). Now, in the Uhlig model, the space-charge fields are presumed to be large, so that both current equations must include the effects of this nonhomogeneous space-charge field. This can be accomplished readily for the ionic species through an averaging technique (16), so that integrated current equations, although admittedly approximate, are still

available. A better approach would be to perform exact numerical computations.

Let us denote the electronic and ionic charge currents as  $i = -eJ_e$  and  $q_iJ_i$ , respectively, where the electronic and ionic charges are  $-e$  and  $q_i$ , and  $J_e$  and  $J_i$  are the corresponding particle currents. Then the "kinetic condition" of equal but opposite charge currents which determines  $E(O)$  as a function of film thickness  $y(t)$  is (11)

$$q_iJ_i - eJ_e = 0 \quad [5.1]$$

The dependence of  $E(O)$  on  $y(t)$  thereby obtained is to be substituted into one of the two currents  $J_i$  and  $J_e$  to obtain the growth rate

$$\frac{dy(t)}{dt} = R_cJ_c \quad [5.2]$$

where  $J_c$  is the rate-limiting particle current, and  $R_c$  is the volume of oxide formed per particle of the flux  $J_c$  which is transported from  $x = 0$  to  $x = y(t)$ . (In the Uhlig theory,  $\beta$  is related in a simple manner to  $R_c$ , depending on whether  $i$  and  $A'$  are interpreted to be charge or particle fluxes.)

In practice, the solution of the above equations must usually be performed numerically. This is the case for an ionic diffusion current coupled with the electron current treated in the preceding sections. The electrostatic potential obtained from combining Poisson's equation with the  $E(O)$  deduced utilizing this approach is designated the "kinetic potential" to reflect its function of equalizing the charge current magnitudes.

This "coupled currents" approach is considered to give a much more accurate picture of the kinetics than the conventional approach of assuming one current to be rate-limiting, and then integrating the corresponding growth equation by making some arbitrary (or *ad hoc*) assumption regarding the film-thickness dependence of the surface-charge field. For this reason, the integration of Eq. [2.21] and a computation of characteristic growth curves is not deemed advisable at this time. It is clear that Eq. [2.21] represents a growth law which has a sharper decrease in the growth rate in the neighborhood of  $y_0$  than the corresponding logarithmic growth law. The "coupled currents" approach has been utilized successfully (11, 30) for several models of the growth kinetics applicable at different temperature and film-thickness ranges, and is currently being utilized to obtain the kinetics for a model based on the presently discussed electron current. The results, together with appropriate comparisons with the predictions of Eq. [2.21] and experimental results, will be presented subsequently.

### Misconceptions in Uhlig and Nwoko Paper

Several misconceptions were introduced in the rebuttal given in the paper by Nwoko and Uhlig (9). The purpose of the present section is to counteract the most serious of these.

To quote from Uhlig and Nwoko (9): "In our opinion there is no physical or theoretical reason to believe that an electron entering the oxide at the metal-oxide interface cannot migrate through the conduction band of the oxide to the oxide-oxygen interface in order to ionize adsorbed oxygen, where indeed the electron must go if oxidation is to proceed. In a p-type oxide, a positive hole migrates through the oxide thickness in the opposite direction." This statement is completely inapplicable to the Uhlig theory of oxidation, which is based on the postulate that rate is limited by the transfer of electrons from the metal across the oxide, so that the rate-limiting step is the thermal excitation of electrons from the metal over the energy barrier represented by the oxide. Hence there cannot be a significant migration (i.e., simple diffusion or field-assisted diffusion) of electrons (or holes) in the conduction (or valence) band whenever



this theory is applicable. On the other hand, if the oxide is not of the insulator-type, but instead is a good electronic conductor or semiconductor, then the Uhlig model cannot be valid since ions instead of electrons will limit the growth rate. For example, this would be the case in Fig. 2a whenever the  $O^-$  levels are below the top of the filled valence band in the oxide; the electrons then flow from the filled band into the empty  $O^-$  levels, so that p-type semiconductor through the partially depleted valence band becomes possible. The Uhlig model is clearly inapplicable since electron emission does not then limit the rate.

Even if the oxide is an insulator-type oxide in which electrons (or holes) can be the rate-limiting species, the energy imparted to the electron (or hole) by thermal excitation will be lost on the average in a distance  $\delta_s$  if the oxide thickness  $y(t)$  is much greater than the electron scattering length  $\delta_s$  of electrons in the conduction band of the oxide (or holes in the valence band of the oxide). The electrons (or holes) must then be transported the remainder of the distance  $\delta_s \leq x \leq y(t)$  by some other transport process, and the Uhlig theory becomes inapplicable (30). Two processes can then possibly be effective: electric field migration, and diffusion under a concentration gradient. Electric field migration is definitely eliminated for the Uhlig theory, since the net field has polarity such as to drive electrons in the negative x-direction instead of in the positive x-direction [see Fig. 2c, which illustrates that in the Uhlig model electrons are required to migrate up a potential hill created by the electric field (30)]. Furthermore, in this case there is no electron concentration gradient created which can serve as a force to drive electrons up the potential hill, since, according to the Uhlig model, the electrons are rate-limited by thermal emission at the metal-oxide interface. Whenever rate is no longer limited by electron emission at the metal-oxide interface due to scattering of electrons in the conduction band of the oxide  $\{y(t) \gg \delta_s\}$ , the transport process can then become diffusion-controlled by the concentration gradient and space charge fields due to the scattered electrons. Such a mechanism, however, yields results (10) which must be entirely different from Eq. [2.21], the latter being applicable only for thermal excitation of electrons over an activation barrier.

A point which should be emphasized is that the parameter  $\tilde{v}$  is ineffective for the thermal emission process of the Uhlig theory regardless of whether the electron traverses the film in a one-step process, or whether thermal emission is effective only for a distance  $\delta_s$  before scattering, with subsequent diffusion under a concentration gradient. This confusion of the concept of activation energy for electron transport with the net free energy change which results from such transport is emphasized by a further quotation from Nwoko and Uhlig (9): "We consider that the activation energy for oxidation is equivalent to transfer of an electron from metal to oxide to oxygen adsorbed on oxide, given by  $e(\phi - \tilde{v})$  where  $e$  is the electronic charge,  $\phi$  is the metal work function  $\phi_0$  modified by amount  $\chi$  through contact with the oxide such that  $\phi = \phi_0 - \chi$ , and  $\tilde{v}$  is related to the electron affinity of adsorbed oxygen (approximately 3.6 eV). The total energy of electron transfer is increased by the growing more negative space charge in the oxide accounting for a decreasing oxidation rate as the oxide grows." Clearly the energy  $e(\phi - \tilde{v})$  is the free energy change and not the activation energy; confusion of such concepts is the source of the orders-of-magnitude discrepancy between predicted and physically reasonable effects of space charge on the growth kinetics in the Uhlig theory. As can be seen

from Fig. 2b, the free energy change  $e(\phi - \tilde{v})$  can be equal to the activation energy only if this quantity is positive and the electron traverses the classically disallowed region by tunneling, a process which is of importance only if the thickness  $y(t)$  is less than  $\delta_{\text{tun}} \leq 50\text{\AA}$ .

### Conclusions

The results of our careful re-examination of the Uhlig model and its original mathematical treatment are threefold:

1. Our conclusions remain unchanged that errors in the original Uhlig treatment lead to a prediction of space-charge effects which are orders of magnitude too large to be physically realistic for the space-charge concentrations in question.
2. The present consideration of electron tunneling distances and electron scattering lengths in the oxide fails to justify the appropriate *ad hoc* assumption necessary for obtaining a direct-logarithmic (or two-stage logarithmic) growth law from the Uhlig model; it is concluded, therefore, that such a growth law is presently theoretically unfounded for the case of oxide films too thick ( $\geq 100\text{\AA}$ ) for appreciable electron tunneling.
3. The perturbations to the surface-charge field, electronic current, and oxidation kinetics which are introduced by the current of the ionic species should be examined numerically by the "coupled currents" approach to the theory of oxidation kinetics to ascertain whether or not these effects can be validly neglected.

Manuscript submitted Jan. 29, 1968; revised manuscript received May 21, 1968.

Any discussion of this paper will appear in a Discussion Section to be published in the June 1969 JOURNAL.

### REFERENCES

1. H. H. Uhlig, *Acta Met.*, **4**, 541 (1956).
2. Ref. (1), p. 545.
3. H. Torrey and C. Whitmer, "Crystal Rectifiers," p. 80, McGraw-Hill Book Co., New York (1948).
4. J. D. Jackson, "Classical Electrodynamics," pp. 12, 13, 109, 615, 616, John Wiley & Sons, Inc., New York (1962).
5. P. M. Morse and H. Feshbach, "Methods of Theoretical Physics," p. 7, McGraw-Hill Book Co., New York (1953).
6. J. A. Stratton, "Electromagnetic Theory," p. 162, McGraw-Hill Book Co., New York (1941).
7. W. K. H. Panofsky and M. Phillips, "Classical Electricity and Magnetism," p. 9, Addison-Wesley Publishing Co., Reading, Mass. (1955).
8. A. T. Fromhold, Jr., *Nature*, **200**, 1309 (1963).
9. V. O. Nwoko and H. H. Uhlig, *This Journal*, **112**, 1181 (1965). In particular, see p. 1183.
10. A. T. Fromhold, Jr., *J. Chem. Phys.*, **41**, 509 (1964); *Bull. Am. Phys. Soc.*, **10**, 454 (1965).
11. A. T. Fromhold, Jr., and E. L. Cook, *Phys. Rev. Letters*, **17**, 1212 (1966); *Phys. Rev.*, **158**, 600 (1967); *Phys. Rev.*, **163**, 650 (1967).
12. Ref. (1), p. 547, Eq. [5].
13. N. Cabrera and N. F. Mott, *Rept. Progr. Phys.*, **12**, 163 (1949).
14. P. J. Holmes, "The Electrochemistry of Semiconductors," p. 86, Academic Press, New York (1962).
15. Ref. (1), p. 547.
16. A. T. Fromhold, Jr., *J. Chem. Phys.*, **40**, 3335 (1964).
17. See Fig. 3 of ref. (1), p. 549.
18. Ref. (1), p. 548, Eq. [11].
19. Ref. 1, pp. 547, 548.
20. Ref. 1, p. 552.
21. Ref. 1, p. 553, Table 3; ref. 9, p. 1183, Table 2.
22. S. Glasstone, K. J. Laidler, and H. Eyring, "The Theory of Rate Processes," p. 98, McGraw-Hill Book Co., Inc., New York (1941).
23. P. J. Jorgensen, *This Journal*, **114**, 820 (1967).
24. N. F. Mott, *Trans. Faraday Soc.*, **43**, 431 (1947).
25. Ref. 1, p. 544.

26. E. L. Murphy and R. H. Good, Jr., *Phys. Rev.*, **102**, 1464 (1956).  
 27. Ref. 1, pp. 549-551.  
 28. Ref. 1, pp. 552-553.
29. A. T. Fromhold, Jr., *J. Phys. Chem. Solids*, **24**, 1081 (1963).  
 30. E. L. Cook, MS thesis (unpublished), Auburn University (1965).

# Stress Corrosion Cracking of Titanium Alloys

## II. An Electrochemical Mechanism

T. R. Beck\*

Boeing Scientific Research Laboratories, Seattle, Washington

### ABSTRACT

Kinetic measurements were made under potentiostatic conditions for hydrogen ion reduction on and oxidation of newly generated surfaces of a titanium alloy in aqueous solutions. Approximate kinetic parameters were obtained during the growth of the first monolayer of oxide and for growth of thicker films. These kinetic data were used in an approximate model in an attempt to simulate the electrochemical events in a stress corrosion crack propagating through the titanium alloy in aqueous solution. The observed current flowing into a crack could be semiquantitatively accounted for in the model by oxidation of the crack walls. The oxide cracking and wedging mechanisms of crack propagation can be rejected in the model and, if the assumptions are valid, in the real metal. Further work will be required to define other mechanisms at the crack tip.

An experimental investigation of the effect of potential and various ions in aqueous solution on stress corrosion cracking (SCC) of titanium: 8% Al-1% Mo-1% V alloy (Ti:8-1-1) was reported in a prior paper (1). A similar effect of potential on the strength of another titanium alloy in seawater has also been reported (2). The purpose of the present paper is to present new data on kinetics of oxidation of freshly generated Ti:8-1-1 alloy surface and kinetics of hydrogen ion reduction thereon, and to illustrate how these data can be used in a preliminary interpretation of the electrochemistry in a propagating stress corrosion crack. A more rigorous analysis will follow in another paper (3).

The usual four SCC mechanisms were proposed at the start of this work as possibilities for titanium alloys (4):

1. A mechanism involving a titanium oxide:
  - (a) stepwise formation and fracture of brittle titanium dioxide layer at the tip of a crack;
  - (b) wedging of a crack by formation of titanium dioxide.
2. A mechanism involving hydrogen:
  - (a) stepwise formation and fracture of brittle surface hydride layer at the tip of a crack;
  - (b) precipitation of a hydride phase within the plastic zone due to a more rapid diffusion and/or easier nucleation, leading to a degradation of properties in this region.
3. Preferential anodic dissolution at specific electrochemically active sites at the tip of a crack.
4. A surface energy lowering mechanism involving adsorption of a species from the electrolyte phase in contact with the metal.

The electrochemical kinetics experiments and the analysis presented in the paper provide a basis for rejecting the brittle oxide and oxide wedging mechanisms for Ti:8-1-1 in aqueous solution as will be shown. Further work must be done before a definitive statement can be made about the applicability of mechanisms 2 through 4 to titanium alloys.

Unless otherwise stated, potentials are given in millivolts and the saturated calomel electrode (SCE)

is the zero standard of reference. A table of nomenclature is given.

### Experimental

Two types of kinetics experiments were made: studies of multiple monolayer (multilayer) oxide growth; and studies of growth of the first monolayer and of hydrogen ion reduction during the growth of the first monolayer. In addition, open-circuit mixed potentials for the monolayer oxide formation and hydrogen ion reduction were determined. All experiments were made with Ti:8-1-1 alloy in the mill-annealed condition, having the composition and properties previously listed (1).

The stress corrosion cracking specimens and cell previously described (1) were used in studies of multilayer oxide growth. The essential difference between the kinetics experiments and the previously described SCC experiments was that a higher cross-head velocity (0.5 cm/min) was used and a very rapid fracture at a higher load occurred. Current was recorded on an x-y plotter using an x-axis speed of 5 cm/sec at fracture. The experiments were run potentiostatically using a Wenking Model 6379TR potentiostat (1). The oxidation current to the new surface was that current measured after final fracture [Fig. 5, ref. (1)] corrected for the small current to the preexisting exterior surface. The specimens were usually anodized to minimize the correction for background current to the preexisting surface. In later experiments a Tektronix type 545 A oscilloscope and Polaroid camera were used to record the current transient at less than  $10^{-1}$  sec from fracture.

Kinetics of oxidation and hydrogen ion reduction on new metal surface during the formation of the first monolayer of oxide were studied in the smaller Teflon cell illustrated in Fig. 1. The smaller specimens were used to avoid excessively high currents from the high current density initial reactions. The new area generated for the two surfaces was approximately 0.05 cm<sup>2</sup>. A coating of epoxy resin was applied to the small specimens to avoid reaction on the preexisting surface. The resin was scored over the notch in the metal to localize the break in the resin and minimize adhesion failure and exposure of preexisting titanium surface.

\* Electrochemical Society Active Member.



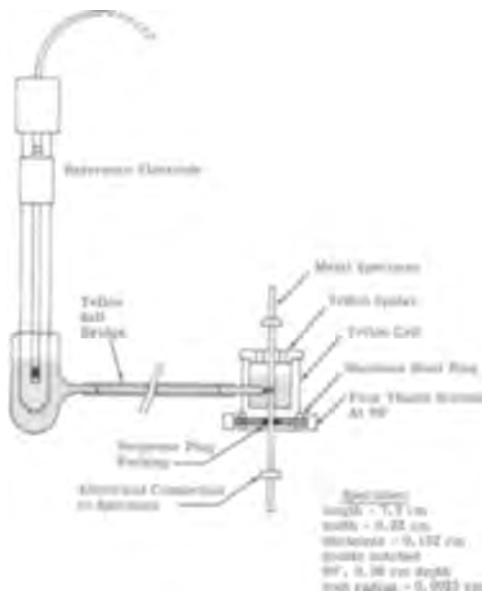


Fig. 1. Cell for monolayer kinetics experiments

A sudden break was caused by dropping a 45 kg (100 lb) weight connected through a 5:1 lever arm to the specimen. Travel of the lever arm was limited so that the new fracture surfaces separated by 1 to 2 mm. Movement of the lever arm closed a microswitch that triggered the sweep in the Tektronix type 545 A oscilloscope. The camera shutter was open on time exposure during the run.

Runs were made in 0.6M potassium chloride and concentrated (approx. 12M) hydrochloric acid. Concentrated HCl was used because initial analysis of events in a propagating stress corrosion crack indicated that the electrolyte becomes acid. The preliminary data thus far obtained are not precise, but nevertheless are suitable for order of magnitude estimates of oxidation current density, exchange current density, and mixed potential. Refinements to improve the accuracy of the experiments are underway.

The IR drop in the electrolyte between the new surfaces and the Luggin capillary tip at the high current densities observed threw some doubt into the precise value of the mixed potential as determined from the kinetics experiments. To avoid the IR drop, the mixed potential, just after fracture and exposure of new metal surface, was measured at open circuit with a Tektronix type 545 A oscilloscope. The input impedance was about  $10^6$  ohms so that the oscilloscope should have had little influence on an electrode with an initial current on the order of 5 ma ( $10^{-1}$  amp/cm<sup>2</sup> current density) and a high conductivity electrolyte.

## Results

**Multilayer oxide growth.**—Results of the kinetic experiments using the 2.54 cm wide 0.152 cm thick mill-annealed specimens are shown in Fig. 2. At a potential of 0 mv to SCE applied to the titanium specimen, the 0.6M chloride, bromide, and iodide solutions gave essentially the same current *vs.* time relationship. The initial, approximately horizontal, part of the curve corresponds to formation of about a monolayer of oxide ions. The charge density is ( $3.5 \times 10^{-1}$  amp/cm<sup>2</sup>) ( $2.5 \times 10^{-3}$  sec) =  $880 \times 10^{-6}$  coulomb/cm<sup>2</sup>. Monolayer coverage of oxide ion is equivalent to about  $425 \times 10^{-6}$  coulomb/cm<sup>2</sup> on the basal plane of  $\alpha$ -Ti assuming one double charged oxide ion per titanium atom. The difference between these two values may be due to surface roughness, parallel formation of soluble titanium species, and experimental error. Thereafter the current decays approximately with the reciprocal of time.

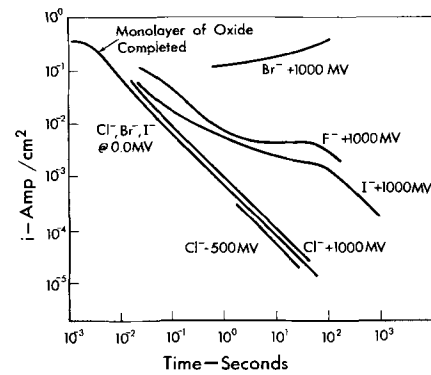


Fig. 2. Kinetic data on oxidation of Ti:8-1-1 in 0.6M halide solutions.

From the coincidence of the curves at a potential of 0 mv to SCE the same mechanism appears to apply for the chloride, bromide, and iodide solutions, assumed to be the oxidation of titanium by water. The current density *vs.* time relation is displaced toward higher current densities with increased positive potential in 0.6M chloride as expected.

Considerable deviations in the direction of increased current density were observed in 0.6M bromide and iodide solutions at a specimen potential of +1000 mv. This is consistent with observed onset of pitting corrosion (1), the rise of current density with time in 0.6M bromide apparently being due to increase in number and/or size of pits. Although specimens in iodide solution did not show visible evidence of pits to the eye in the specimen at +1000 mv, incipient pitting is suspected at a micro scale. Further studies on pitting corrosion of titanium will be reported elsewhere (5).

With 0.6M fluoride solution the current density *vs.* potential curves at +1000 mv and 0 mv (not shown) were considerably above the curves for chloride, consistent with the known corrosiveness of fluoride to titanium and the formation of soluble  $TiF_6^{2-}$  ions (6).

It is appropriate at this point to compare the data to the theoretical oxide growth rate based on the high-field conduction equation using constants for titanium available in the literature. The growth rate of an anodic oxide film starting from a molecular thickness is (7)

$$\frac{dt}{d\tau} = A(i - i_K) \quad [1]$$

where the current density can be expressed by the high-field conduction equation

$$i = i_0 \exp\left(\frac{\beta \Delta \phi}{t}\right) \quad [2]$$

A solution of these equations may be obtained for a plane electrode under potentiostatic conditions ( $\Delta \phi = \text{constant}$ ). Assuming that  $i \gg i_K$  during the initial period of film growth, gives

$$d\tau = - \left( \frac{\beta \Delta \phi}{A i_0} \right) \left[ \frac{d \ln I}{I (\ln I)^2} \right] \quad [3]$$

The solution to the right-hand term in brackets is available in tables (8).

The solution to Eq. [3] is compared to the experimental data for Ti:8-1-1 at 0 mv to SCE in Fig. 3. The following values were used in the constant in Eq. [3]:

$$\begin{aligned} A &= 4.85 \times 10^{-5} \text{ cm}^3/\text{coulomb for rutile.} \\ \beta &= 6 \times 10^{-6} \text{ cm/v [average experimental value for oxidation of commercially pure Ti (9)].} \\ i_0 &= 2 \times 10^{-13} \text{ amp/cm}^2 \text{ [average experimental value for oxidation of commercially pure Ti (9)].} \end{aligned}$$

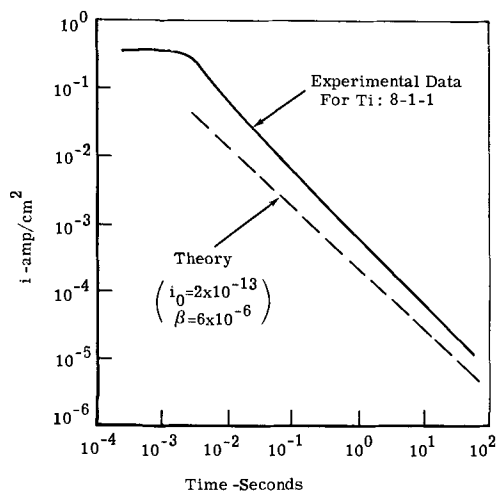


Fig. 3. Comparison of kinetic data on oxidation of titanium to theory using constants from literature.

$\Delta\phi = 1v$  [In neutral solution the reversible potential for titanium oxidation is about  $-1.5v$  vs. SCE (6). Assuming the Flade potential is  $0.5v$  (10) and neglecting the overpotential for the oxide to electrolyte reaction, which becomes small as the film thickness increases, gives  $\Delta\phi \approx 1v$  across the film for an applied potential of  $0v$  to SCE).

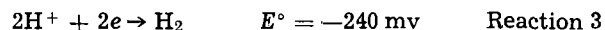
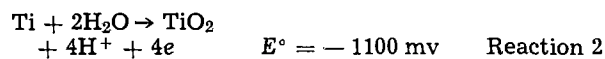
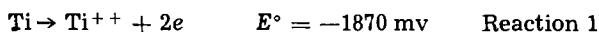
There appears to be a reasonable correspondence between the experimental data and the theory using the constants from Johanson *et al.* (9). It is therefore considered that the kinetic data for Ti:8-1-1 in chloride, bromide, and iodide at  $0$  mv in Fig. 3 represent the formation of titanium dioxide. The displacement of the experimental data for Ti:8-1-1 to higher current densities could be due to higher conductivity of the oxide corresponding to its higher defect concentration.

An alternate interpretation for the experimental current density for Ti:8-1-1 being above the theory as well as having a greater slope could be that there is a parallel corrosion current to form soluble titanium species. In other words,  $i \approx i_k$ . Thermodynamically the formation of soluble species appears very likely (11), and further work is underway to resolve this question.

**Growth of first monolayer of oxide and hydrogen ion reduction.**—Determining the kinetics of formation of the first monolayer of oxide and of hydrogen ion reduction on the newly generated bare metal surface was difficult in experiment and interpretation. The difficulties are due to the high current densities with resultant high ohmic drops in the electrolyte, the short time to complete the monolayer, and the possibility of more than one anodic reaction. Nevertheless some order of magnitude data for newly generated titanium surface, heretofore unavailable, were obtained for a concentrated HCl electrolyte.

According to the potential-pH diagram for titanium (11) divalent titanium ion is the thermodynamically stable species that should be formed by oxidation of titanium at the potentials used for the experiments in concentrated HCl. Titanium dioxide can form, however, at potentials positive to its reversible potential, also in the range of the experiments. Formation of  $TiO_2$  apparently blocks further rapid formation of  $Ti^{++}$ . Dissolution of oxide covered titanium in acid solution is known to proceed at relatively low rates (in the range of  $1-10 \mu a/cm$  at room temp) (12).

The reactions that are possible in the potential range of the experiments and their standard reversible potentials (SCE scale) are (6)



Formation of  $TiO$  ( $E^\circ = -1550$  mv) is an alternate to reaction 2 at high negative potentials. In the 12M HCl used, all of the potentials would be about  $64$  mv more positive. The range of potentials used in the experiments was  $-1050$  to  $-500$  mv. In this range it would appear that reaction 1 should be favored over reaction 2 because of a much larger driving force, but the titanium was observed to passivate. As will be seen from the quantity of charge passed and the rate of passivation it appears that reaction 1 proceeds at a rate of no greater order of magnitude than reaction 2. Because there was no way of determining the exact extent of reaction 1, it was not considered in the analysis. More sophisticated experiments will have to be devised to get rate data for reaction 1 on newly generated bare metal surface.

Typical current-time oscilloscope traces for potentiostatic experiments are shown in Fig. 4 for a net anodic current and a net cathodic current. In all of the experiments there was an initial peak (items 1 and 3) followed by a decay in current. Because the observed peak current densities were very high (about  $10^{-1}$  to  $1$  amp/cm<sup>2</sup>) it is assumed that the electrical double layer charging component (13) is a minor contribution. Furthermore, analysis of the data based on Reactions 2 and 3 gives a self-consistent picture.

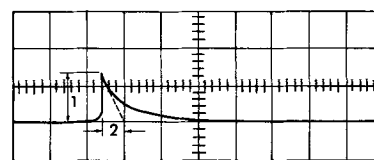
The net current density measured is, of course, the difference between the anodic and cathodic current densities

$$i = i_a - i_c \quad [4]$$

Near the mixed potential, where many of the experiments were conducted, the net external current is not a good measure of the actual current density, but there was an independent method of estimating the anodic current as described below.

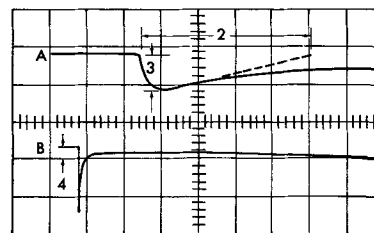
The initial decay in potential is assumed to be due to coverage by oxide. The potentials are far enough from the reversible that the kinetics can be described by the Tafel equation. Therefore

$$i_a = (1 - \theta) i_m \exp \left( \frac{\alpha_m n_m F \eta_m}{RT} \right) \quad [5]$$



a. Conc. HCl at  $-800$  mv (Net Anodic Current)

Vert.  $0.1$  v/cm (across  $10\Omega$ ),  
Horiz.  $2$  ms/cm



b. Conc. HCl at  $-960$  mv (Net Cathodic Current)

(A) Vert.  $0.1$  v/cm (across  $10\Omega$ ),  
Horiz.  $2$  ms/cm  
(B) Vert.  $0.05$  v/cm (across  $10\Omega$ ),  
Horiz.  $0.2$  sec/cm

Fig. 4. Current-time oscillographs. 1, Initial oxidation peak on bare Ti; 2, time to form oxide monolayer at initial oxidation current density; 3, Initial  $H^+$  reduction peak on bare Ti; 4,  $H^+$  reduction on  $TiO_2$ .

and

$$i_c = (1 - \theta) i_H \exp \left( \frac{\alpha_H n_H F \eta_H}{RT} \right) \quad [6]$$

It is assumed that Eq. [5] is valid for low coverage because a considerably increased overpotential would be needed to form oxide on oxide as compared to bare metal. The fraction coverage,  $\theta$ , is related to the anodic current by

$$\frac{d\theta}{d\tau} = \frac{i_a}{Q_o} \quad [7]$$

The value of the coulombic charge,  $Q_o$ , is based on a layer of adsorbed oxide ions or of  $TiO$ , assumed to be the precursor of  $TiO_2$ .

Extrapolation of the limiting slope at time zero of the current-time curves to zero current gives the time to form a monolayer at a constant current equal to the initial value (item 2, Fig. 4). The initial current density for oxide formation based on Eq. [7] is therefore

$$i_a = \frac{Q_o}{\tau_o} \quad [8]$$

If this analysis is correct, Eq. [8] should give the true anodic oxide current density, even in the mixed potential and net cathodic reaction regions.

Values of peak anodic current density (open circles) and of anodic current density calculated from Eq. [8] (closed circles) are plotted in Fig. 5. Although there is considerable scatter in the values from Eq. [8], as might be expected from a first derivative of experimental data and from changing surface potential due to changing IR drop, the agreement between the two values is reasonably good. The implication of this is that the order of magnitude of the rate of formation of  $Ti^{++}$  cannot be greater than the rate of formation of oxide. The dashed Tafel line was drawn with a slope of 120 mv/decade using an estimated IR drop correction described in the Appendix. The exchange current density,  $i_m$ , appears to be between  $10^{-2}$  and  $10^{-1}$  amp/cm<sup>2</sup>, but this must be a lower limit because of the uncertainty in estimating IR drop. By way of comparison for another active metal, Hagyard and Earl (14) obtained an exchange current density of about  $10^{-3}$  amp/cm<sup>2</sup> for oxidation of freshly cut aluminum surface in 1M KCl.

It could be questioned whether species other than oxide on the surface could cause the decrease in current density with time. That the rate of change of

coverage increases with potential in the positive direction indicates that it is not hydrogen. An adsorbed charged species such as  $Ti^{++}$  might have the observed effect on the kinetics (15), and its presence cannot be disproved based on the work done thus far. However, oxide is known to form and lead into multilayer growth so it appears to be the more likely species.

Values of peak cathodic current density (squares) are plotted in Fig. 6. The plateau current density after several seconds (item 4, Fig. 4) is also plotted (circles). This approximately steady-state current density on thinly oxidized surface was lower than the peak value by about an order of magnitude and is in fair agreement with extrapolations from lower current density hydrogen ion reduction on oxide covered titanium (12, 16). The net cathodic current shown in Fig. 4b went through a minimum, further evidence of a substantial initial anodic current component.

The mixed potential for hydrogen ion reduction and titanium oxidation on newly generated bare metal in 12M HCl appeared to be about -800 mv from Fig. 5 and 6. The initial open-circuit mixed potential observed in 12M HCl was in the range of -650 to -800 mv. Stern and Wissenberg (12) obtained a mixed potential on oxide covered surface in hydrogen-saturated 20% (2.3M)  $H_2SO_4$  of -720 mv (SCE). This appears to be a reasonable agreement between these values obtained in acid solution. Although the present work was done with solutions that were not de-aerated the current densities on bare metal (estimated from Fig. 5 and 6 are on the order of  $10^{-1}$  to 1 amp/cm<sup>2</sup>) were so much higher than the diffusion limited current density for oxygen reduction ( $\approx 10^{-5}$  amp/cm<sup>2</sup>) that the latter can be ignored.

### Discussion

The purpose here is to utilize the data obtained on kinetics of oxidation of newly generated titanium metal surface to interpret the electrochemistry in a stress corrosion crack. Results in the prior paper (1) showed that there is an electrochemical process involved in SCC of titanium alloy that affects velocity of crack propagation.

*Model.*—The configuration of the stress corrosion crack used in the analysis is shown in Fig. 7. A uniform small-angle crack from the mouth to the tip is assumed. Visual observation of crack opening and optical photomicrographs show that this is a reasonable assumption to a distance of  $10^{-4}$  cm from the crack tip. An angle of 3° or 0.05 radians is also a reasonable

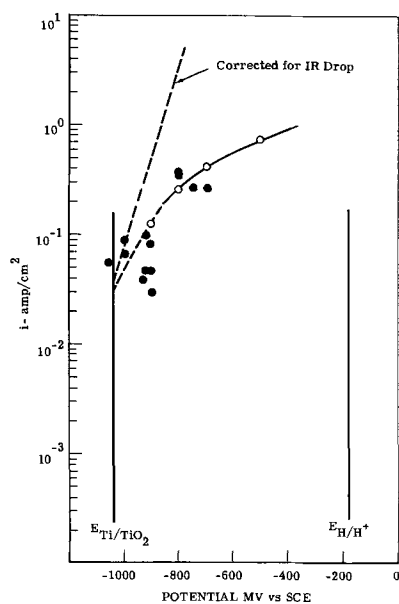


Fig. 5. Kinetics of oxidation of new Ti:8-1-1 surface in 12M HCl. (○ Item 1, Fig. 4; ● Eq. [5] and item 2, Fig. 4).

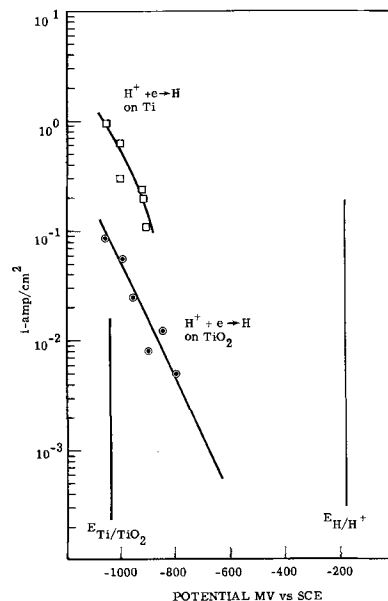
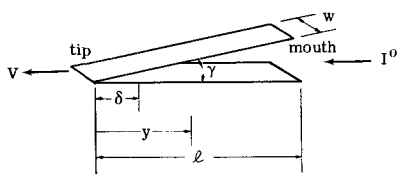


Fig. 6. Kinetics of  $H^+$  ion reduction on new Ti:8-1-1 surface in 12M HCl (□ Item 3, Fig. 4; ○ item 4, Fig. 4).



$w$  = thickness of metal specimen  
 $l$  = length of crack  
 $y$  = distance from tip  
 $\delta$  = length of zone with less than one monolayer of oxide  
 $\gamma$  = included angle of crack, radians  
 $I^o$  = current flowing into crack  
 $V$  = velocity of propagation

Fig. 7. Configuration of crack in metal used in the analysis

average from observed cracks. The crack propagates through the metal at a velocity  $V$  and a value of  $10^{-2}$  cm/sec will be chosen as a basis for calculation.

Based on the results of the oxidation kinetics studies on newly generated titanium surface the crack is divided into two parts; a "monolayer zone" from the tip to a position  $\delta$  where the first monolayer of oxide is completed, and a "multilayer zone" extending from  $\delta$  to the crack length. The high current density observed for reactions 2 and 3 at the mixed potential leads to the assumption that the mixed potential is established in the monolayer zone. With an applied potential more positive than the mixed potential, however, reaction 2 will dominate in the multilayer zone making the electrolyte in the crack become acid.

These assumptions are consistent with the observations that the zero-current intercept for a propagating crack occurs at about  $-800$  mv (1), as the mixed potential for reactions 2 and 3 is about  $-800$  mv in acid solution. A crack propagating at open circuit spontaneously approaches a potential of about  $-800$  mv from a previously potentiostated level either higher or lower than  $-800$  mv. Apparently the driving force for oxidation of the new titanium surface within the crack is so high that enough cathodic reaction occurs exterior to the crack that there is a net anodic acid-forming reaction within the crack at open circuit.

Only the oxidation of titanium is considered in this analysis as it is the major constituent in the alloy. The chemistry of other constituents may be delineated when kinetic data for oxidation of new surfaces of other alloys are obtained.

*Current for oxidation of walls of crack.*—In this simplified analysis a lumped current for the formation of the first monolayer of oxide will be used rather than considering the detailed kinetics. This is acceptable because the current for the formation of the first monolayer is a small fraction of the total current. This current required for formation of the first monolayer of oxide on the two walls of the crack is

$$I^s = 2wVQ_o \quad [9]$$

The actual value of  $I^o$  should be smaller than that calculated from Eq. [9] if there is some hydrogen ion reduction to establish a mixed potential.

The current flowing to the two walls in the multilayer zone can be described by

$$Iw = 2w \int_{\delta}^l i dy \quad [10]$$

The experimentally observed current density for oxide growth at a potential of 0 mv to SCE shown in Fig. 3 can be described approximately by the following expression

$$i = \frac{8.8 \times 10^{-4}}{\tau} \text{ amp/cm}^2 \quad [11]$$

Potential, of course, varies with position  $y$  in the crack and would thus affect the kinetic expression and

complicate the analysis, but the limiting case of a constant potential will be assumed sufficiently accurate for the present analysis. The "age" of the surface at a point  $y$  distance from the tip is

$$\tau(y) = \frac{y}{V} \quad [12]$$

Eliminating  $i$  and  $\tau$  from Eq. [10], [11], and [12] and solving gives

$$Iw = 2(8.8 \times 10^{-4}) wV \ln \frac{l}{\delta} \quad [13]$$

Combining Eq. [9] and [13] to obtain total anodic current gives

$$I^o = 2wV \left( Q_o + 8.8 \times 10^{-4} \ln \frac{l}{\delta} \right) \quad [14]$$

Appropriate values of the parameters can be put in Eq. [14] to test it in respect to observed current in SCC experiments. At a velocity of  $10^{-2}$  cm/sec in a 0.127 cm thick specimen the observed current is about  $25 \mu\text{a}$  for a crack length of about 0.1 cm [ref. (1), Fig. 12 and 13]. Using a value of  $Q_o = 4.25 \times 10^{-4}$  coulomb/cm<sup>2</sup> and an assumed value of  $\delta = 10^{-4}$  cm, based on the monolayer zone being near the mixed potential (Fig. 4), gives a calculated  $I^o = 16.5 \mu\text{a}$  from Eq. [14]. This is in reasonable (order of magnitude) agreement with experiment considering that there is some branching observed in actual stress corrosion cracks and that this is a very much oversimplified approach.

An interesting consequence of this analysis is that for the wedge-shaped crack geometry used in the model, the oxide mechanisms of crack propagation can be eliminated. Because the crack propagation velocity is high ( $\sim 10^{-2}$  cm/sec) the first monolayer is not complete on the wall for a considerable distance from the tip. This eliminates the concept of the brittle oxide film at the tip in the model. It can also be shown that the thickness of oxide that does form on the walls is small compared to the crack width, thus eliminating the oxide wedging mechanism in the model. Because the observed SCC current can be semi-quantitatively accounted for in the model, it is suggested that these oxide mechanisms are not involved in the SCC of titanium alloys in aqueous solutions. The work done thus far, however, is not definitive regarding the anodic dissolution, surface energy or hydride mechanisms.

*Potential drop in crack.*—The resistance of a uniform-resistivity electrolyte in a small constant-angle crack from the mouth to a position,  $y$ , is

$$R_e = \frac{\rho_e}{w\gamma} \ln \frac{l}{y} \quad [15]$$

Because the anodizing current falls off very rapidly with time (Fig. 3) or distance from first monolayer coverage, it can be assumed that most of the current flows to a region at a distance about the order of magnitude  $\delta$  from the tip. Therefore, the potential drop in the electrolyte in the crack would be

$$\Delta\phi \approx I^o R_e \quad [16]$$

Combining Eq. [14], [15], and [16] making the approximation that  $Q_o$  can be neglected compared to  $8.8 \times 10^{-4} \ln l/\delta$  gives

$$\Delta\phi \approx \frac{2(8.8 \times 10^{-4})\rho_e V}{\gamma} (\ln l/\delta)^2 \quad [17]$$

Using bulk resistivity of 15 ohm cm for 0.6M alkali halide (17), a crack angle of 0.05 radians,  $V = 10^{-2}$  cm/sec,  $l = 0.1$  cm, and  $\delta = 10^{-4}$  cm gives  $\Delta E = 0.25v$ . This can be compared to 0.5v in SCC experiments [ref. (1), Fig. 12] assuming the monolayer zone is at the mixed potential for reactions 2 and 3 in acid

solution. Again this appears to be a reasonable check for such an oversimplified model. Furthermore, Eq. [17] predicts a linear relationship between velocity and potential and Eq. [14] and [17] give a linear relationship between current and potential, in agreement with observations (1). However, there is one basic flaw; the increase in acidity of the electrolyte in the crack due to reaction 2 will give a considerably lower resistivity and thus a lower calculated potential drop. Therefore, it must be concluded that this simple analysis of the potential drop in a crack is inadequate.

**General.**—The lesson in this simple analysis of the electrochemistry on the walls of a stress corrosion crack is that the electrochemical conditions at the crack tip, where the decision of slip *vs.* fracture is made, may be very different than the macroscopic conditions outside of a crack. Because it is not possible to examine experimentally the microscopic conditions at the tip of a moving crack it would appear that a more rigorous analysis of the electrochemical kinetics and transport processes in a crack is in order (3). Some of the interrelationships between the potential and concentration gradients in a moving crack are illustrated qualitatively in Fig. 8.

As with the electrochemistry, the macroscopic stress and metallurgical conditions are different than those at atomic dimensions at the tip of a crack. It would seem that quantitative models which treat the transmission of stress and strain through the plastic zone around a crack tip to the metal atoms at the crack tip need to be developed. Some of the factors presumably involved are also listed in Fig. 8. Furthermore, Fig. 8 suggests that the complete solution to this interdisciplinary problem of stress corrosion cracking will require close cooperation between electrochemists, metallurgists, and mechanical engineers both in design of experiments and in theoretical analysis.

### Conclusions

Electrochemical kinetics experiments at constant applied potential on new surfaces generated by fast fracture of titanium: 8% Al-1% Mo-1% V alloy in 0.6M KCl and in 12M HCl showed

1. Growth of a passivating film after completion of the first monolayer appeared to be reasonably consistent with high-field conduction kinetics and literature values for  $i_0$  and  $\beta$  determined for thicker oxide films on titanium.
2. The exchange current density for formation of the first anodic monolayer in 12M HCl is on the order of  $10^{-2}$  to  $10^{-1}$  amp/cm<sup>2</sup> or larger.
3. The rate of hydrogen ion reduction on the bare metal surface is an order of magnitude or more higher than on oxide covered surface at the same applied potential.
4. A mixed potential is observed on open circuit with new surface that is compatible with hydrogen ion

reduction and titanium oxide formation and for which the current density of the anode and cathode current reactions appear to be on the order of  $10^{-1}$  to 1 amp/cm<sup>2</sup>.

An approximate model attempting to simulate the electrochemistry in a propagating stress corrosion crack, suggested by the kinetic data, showed:

5. The anodic current flowing into a propagating stress corrosion crack under potentiostatic conditions can be semiquantitatively accounted for in the model by anodic current to the walls of the crack.
6. The open-circuit potential of a propagating stress corrosion crack in Ti:8-1-1 coincides with the mixed potential for hydrogen ion reduction and titanium oxidation in an acid solution. It is suggested, based on the high current density at the mixed potential on bare metal surface, that the crack tip potential approaches this mixed potential.
7. The oxide wedging and brittle oxide mechanisms can be rejected in the model because the crack velocity is so high that the tip outruns the oxide. Because the observed SCC current can be semiquantitatively accounted for in the model, it is suggested that these oxide mechanisms are not involved in the SCC of titanium alloys in aqueous solutions. It is not possible based on the work completed thus far to pass judgment on the relevance of the hydrogen, anodic attack and adsorption mechanisms of SCC in titanium alloys.

A more rigorous analysis of the electrochemical mass transport and kinetic processes is presently underway as a consequence of the approximate analysis reported herein (3).

### Acknowledgment

The author is indebted to Drs. M. J. Blackburn and A. W. Smith for helpful discussion of mechanisms, and Mr. R. E. Lee for conducting the kinetics experiments.

This work was supported in part by NASA/Headquarters contract NAS 7-489.

Manuscript submitted Nov. 17, 1966; revised manuscript received ca. June 10, 1968. This manuscript was presented in part at the Philadelphia Meeting, Oct. 9-14, 1966, as Paper 69.

Any discussion of this paper will appear in a Discussion Section to be published in the June 1969 JOURNAL.

### REFERENCES

1. T. R. Beck, *This Journal*, **114**, 551 (1967).
2. N. G. Feige and T. Murphy, *Metals Engrg. Quart.*, **ASM**, **7**, 53 (1967).
3. T. R. Beck and E. A. Grens II, To be submitted to the *Journal*.
4. e.g., H. H. Uhlig, "Corrosion and Corrosion Control," p. 117-20, John Wiley & Sons, Inc., New York (1963) or H. L. Logan, "The Stress Corrosion of Metals," John Wiley & Sons, Inc., New York (1966).
5. T. R. Beck, Paper presented at the Chicago Meeting, Oct. 15-19, 1967, as Paper 76.
6. W. Latimer, "Oxidation Potentials," 2nd ed., Prentice-Hall, Englewood Cliffs, N. J. (1952).
7. K. Vetter, "Electrochemical Kinetics," (Translation), p. 767, Academic Press, New York (1967).
8. National Bureau of Standards, "Handbook of Mathematical Functions with Formulas, Graphs, and Mathematical Tables," M. Abramowitz and I. A. Stegun, Editors, pp. 245-248 (1964).
9. H. A. Johanson, G. B. Adams, and P. Van Rysselberghe, *This Journal*, **104**, 339 (1957).
10. K. Vetter, *ibid.*, pp. 748-54.
11. M. Pourbaix, "Atlas of Electrochemical Equilibria," pp. 213-22, Pergamon Press, New York (1966).
12. M. Stern and H. Wissenberg, *This Journal*, **106**, 759 (1959).
13. T. N. Andersen, R. S. Perkin, and H. Eyring, *J. Am. Chem. Soc.*, **86**, 4496 (1964).
14. T. Hagyard and W. B. Earl, *This Journal*, **114**, 694 (1967).
15. L. I. Antropov, "Kinetics of Electrode Processes and Null Points of Metals," Council of Scientific & Industrial Research, New Delhi, 1960.

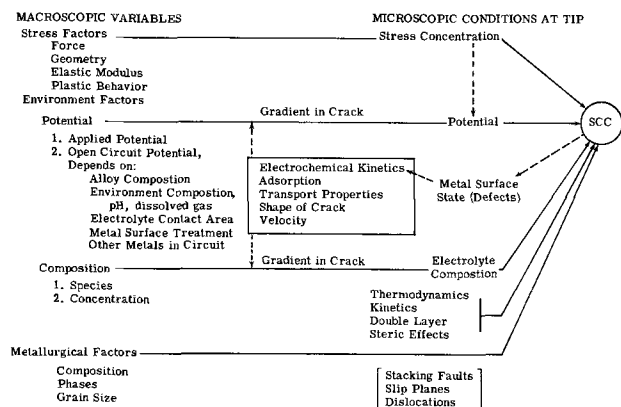


Fig. 8. Summary of stress corrosion cracking variables and mechanisms.

16. Ya. M. Kolotyркиn and P. S. Petrov, *Zhur. Fiz. Khim.*, **31**, 659 (1957).  
 17. International Critical Tables, McGraw Hill, New York (1933).

## NOMENCLATURE

- $A$  = constant for oxide,  $M_o/zF\rho_o$ , cm<sup>3</sup>/coulomb  
 $a$  = jump distance in oxide, cm  
 $F$  = Faraday, 96,500 coulomb/equiv or 23,060 cal/v equiv  
 $I$  = dimensionless current density,  $i/i_o$   
 $I$  = current, amp  
 $i$  = current density, amp/cm<sup>2</sup>  
 $i_H$  = exchange current density for hydrogen ion reduction  
 $i_K$  = corrosion current density  
 $i_m$  = exchange current density for oxide on bare metal  
 $i_o$  = exchange current density for high-field conduction  
 $l$  = crack length, cm  
 $\ln$  = logarithm base  $e$   
 $M$  = molecular weight, g/mole  
 $n$  = number of electrons in rate-determining step  
 $Q_o$  = charge density of monolayer, coulomb/cm<sup>2</sup>  
 $R$  = gas constant, 1.987 cal/deg mole  
 $R_c$  = resistance, ohms  
 $S$  = area, cm<sup>2</sup>  
 $T$  = absolute temperature, °K  
 $t$  = thickness of oxide, cm  
 $V$  = crack propagation velocity, cm/sec  
 $w$  = thickness of specimen, cm  
 $y$  = distance from tip, cm  
 $z$  = equiv/mole

## Greek Letters

- $\alpha$  = transfer coefficient, dimensionless  
 $\beta$  = constant in high-field conduction equation,  
 $\frac{\alpha z F a}{RT}$ , cm/volt  
 $\gamma$  = crack angle, radians  
 $\delta$  = length of monolayer zone, cm  
 $\eta$  = overpotential, v  
 $\theta$  = oxide coverage, dimensionless  
 $\rho_o$  = density, g/cm<sup>3</sup>  
 $\rho_c$  = resistivity, ohm cm  
 $\tau$  = time, sec  
 $\phi$  = potential, v

## Subscripts

- $a$  = anodic  
 $c$  = cathodic  
 $e$  = electrolyte  
 $H$  = hydrogen ion  
 $K$  = corrosion

- $m$  = bare metal surface  
 $o$  = oxide  
 $\delta$  = monolayer of oxide

## Superscripts

- $o$  = external  
 $w$  = walls of multilayer zone  
 $\delta$  = monolayer zone

Table I. Comparison of apparent resistance to calculated electrolyte resistance for new area = 0.05 cm<sup>2</sup>

Soln.	$\rho_c$ (17) ohm-cm	$R_{calc.}$ ohms	$R_{meas}$ ohms	Ratio $R_{meas}:R_{calc.}$
0.6M KCl	15	19	51 <sup>(a)</sup>	2.7
12M HCl	1.8	2.3	12 <sup>(a)</sup> 4.6 <sup>(c)</sup>	5.2 2.0

- <sup>(a)</sup> Anodic branch.  
<sup>(c)</sup> Cathodic branch.

## APPENDIX

An approximation to the resistance of the electrolyte in the kinetics experiments for the first layers of oxide is made here. A more rigorous treatment of this very complex current distribution problem does not appear to be justified. Assume that the two new square shaped surfaces formed are replaced by a sphere of equal area. The resistance of a spherical body of electrolyte surrounding the new surface to a counter electrode remotely removed would be

$$R_e = \frac{\rho_e}{4\pi r_1}$$

where

$$r_1 = \sqrt{\frac{S}{4\pi}}$$

Therefore

$$R_e = \frac{\rho_e}{2\sqrt{\pi S}}$$

It is evident that the actual resistance for the two new surfaces should be larger than this value because they face each other at close range giving interference of the current flow lines in solution and because the current density is not uniform across the surfaces. The ratio of apparent resistance from a plot of initial peak current vs. potential to calculated current is larger by a factor of 2 to 5 as shown in Table I. It is therefore concluded that the apparent resistance is largely IR drop in solution and that the initial current peak is limited in part by IR drop.

# Passivation of Anodic Reactions

Sigmund Schuldiner\*

Naval Research Laboratory, Washington, D. C.

## ABSTRACT

Extending the Wagner (1) definition of passivity to anodic reactions of chemical species on inert electrodes, it is shown that initiation of passivation of a Pt electrode for the hydrogen oxidation reaction can be explained by small amounts (fraction of a monolayer) of adsorbed anions. Anion adsorption can effectively reduce the active electrode area, but the major passivation effect is the poisoning of catalytic sites which retards the catalytic reaction so that in most of the region where passivation occurs the reaction rate is controlled by the increased free energy of activation with increased potential. The change in sign from positive to negative of the  $dE/d(\log i)$  kinetic relation can be explained by adsorption of a small number of anions and is limited when the active sites are essentially saturated. Desorbed oxygen atoms in addition to sulfate ions can have a strong effect on the catalytic activity of Pt for the hydrogen oxidation reaction. This concept may be extended to other retarded anodic reactions and to the passivation of iron in particular.

Wagner (1) has given the following phenomenological definition of passivity: "A metal may be called passive when the amount of metal consumed by a chemical or electrochemical reaction at a given time is significantly less under conditions corresponding to a higher affinity of the reaction (*i.e.*, a greater decrease in free energy) than under conditions corresponding to a lower affinity." An electrochemical example given by Wagner is that the steady-state rate of anodic dissolution of a metal in a given environment is lower at a more noble single electrode potential than at a less noble potential.

This definition of passivity has been extended by Gilroy and Conway (2) to include reactions other than the oxidation of metals. Oxidation reactions of chemical species at an inert metal surface also can decrease under conditions corresponding to a higher affinity of the reaction. A well-known example of this is the oxidation of hydrogen on a platinum electrode in sulfuric acid solution under an atmosphere of hydrogen gas (3). Under potentiostatic steady-state conditions (Fig. 1) as the overvoltage is increased in a noble direction the rate of hydrogen oxidation increases until a potential of 0.04v (*vs.* NHE) is reached. At increasingly noble potentials the current density (reaction rate) remains constant ( $i = 2 \text{ ma/cm}^2$ , true area) up to a potential of about 0.7v. At potentials greater than 0.7v the rate of oxidation of hydrogen decreases until a potential of 1.2v is reached. We (3) concluded that the decrease in the rate of hydrogen oxidation in this range was due to the adsorption of sulfate ion which caused an increase in the free energy of activation of the anodic hydrogen reaction. As the potential was changed from 0.7 to 1.2v the increased coverage of the Pt electrode with sulfate ion further retarded the reaction.

It was shown (3) that passivation of the hydrogen oxidation reaction in the potential range from 0.7 to 1.2v could not be due to the formation of oxygen species on the electrode surface. This is because the rate of the chemical reaction of such oxygen species on Pt with hydrogen would be orders of magnitude faster than their rate of formation. In addition, hydrogen oxidation is much faster than water oxidation. Hence, from 0.7 to 1.2v the existence of adsorbed oxygen atoms, other oxygen species or Pt oxides would be very short-lived and the accumulation of such species on the surface could not occur.

In passing, an explanation should be given as to why water will be rapidly oxidized to oxygen atoms which deposit on the Pt surface with a high current density anodic pulse starting at a potential of about

0.9v (4), whereas, at steady-state potentiostatic conditions, the rate of water oxidation is so slow (5) in the potential range from 0.7 to 1.2v and the rate of hydrogen oxidation and reduction of oxygen atoms with hydrogen is so fast (3) that oxygen atoms cannot exist on the surface in this potential range. A high current density anodic pulse only sees the hydrogen and water adsorbed on the Pt surface. These surface species are all very rapidly oxidized with high current density anodic pulses. Thus, water, or water fragments, which is strongly adsorbed on the Pt surface can be rapidly oxidized with such anodic pulses.

In short, the reactivity of species initially associated with a surface before a rapid current or voltage perturbation is applied may be quite different from the steady-state reactivity of like species or their parents coming to the surface from the solution. Another example of this is the very fast reaction of chemisorbed organic species under high current density pulses, organic species which react very slowly under steady-state conditions.

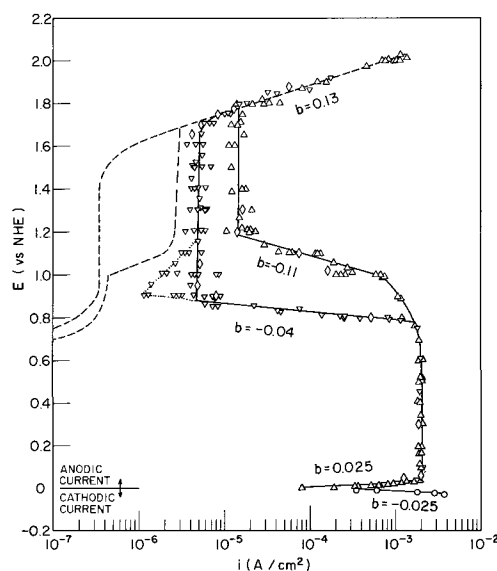


Fig. 1. Steady-state potentiostatic current density vs. potential relation on Pt in hydrogen-saturated 1M  $\text{H}_2\text{SO}_4$ .  $\text{H}_2$  flow rate  $> 1000 \text{ ml/min}$ :  $\circ$  cathodic current;  $\triangle$  anodic current, increasing applied potentials;  $\nabla$  anodic current, decreasing applied potentials. Broken line is relation in He-saturated solution (5), where hysteresis line to the right is for increasing applied potentials, to the left for decreasing applied potentials [from ref. (3)].

\* Electrochemical Society Active Member.

For the over-all reaction,



Following Parson's (7) analysis, and since at high anodic potentials the amount of coverage of the electrode with adsorbed H atoms will approach zero, the Langmuir adsorption isotherm is approximated, we can express the reaction rate as

$$i = kP_{\text{H}_2} \theta^n \exp(-\Delta G^\circ/RT) \exp(\alpha\phi F/nRT) \quad [2]^1$$

where  $k$  is a constant,  $P_{\text{H}_2}$  is the partial pressure of hydrogen,  $\theta$  is the effective fraction of sites on the Pt surface where oxidation can occur,  $n$  is the reaction order,  $\Delta G^\circ$  is the standard free energy of activation for the reaction when  $\phi = 0$ ,  $\phi$  is the inner potential difference between metal and solution,  $\alpha$  is the transfer coefficient,  $F$ ,  $R$ , and  $T$  are the faraday, gas constant, and Kelvin temperature, respectively. Under given conditions of concentration of reactants one would normally expect the exponential term containing the potential to determine the reaction rate,  $i$ . As the applied potential is increased the reaction rate will increase until a limiting condition is reached where the reaction rate will remain independent of increased potential. If under certain potential conditions, the reaction, or reaction mechanism, or the rate-controlling step of the over-all reaction changes, then  $\Delta G^\circ$  can change and therefore affect the current density. However, such a change is normally reflected in a change of Tafel  $b$  [=  $dE/d(\log i)$ ] slope rather than a retardation of the reaction rate. This is because the controlling free energy of activation of an anodic reaction is decreased as the potential is made more noble. However, under passivation,  $dE/d(\log i)$  changes from a positive to a negative value.

### Experimental Data

Figure 2 shows the number of coulombs of charge required to saturate a potentiostated Pt bead electrode with adsorbed oxygen atoms. The experiment was carried out in 1M  $\text{H}_2\text{SO}_4$  saturated with hydrogen at 1 atm. [The experimental conditions were the same as previously reported (3).] The  $q_0$  value is the number of  $\mu\text{coul}/\text{cm}^2$  of charge required to fill the available Pt sites with adsorbed oxygen atoms. This was determined by potentiostating the Pt electrode at a given potential, then very rapidly (1  $\mu\text{sec}$ ) switching from potentiostatic control to a high current density anodic charging pulse [see ref. (6) for instrumentation.]

Figure 2 shows that up to potentials of about 0.4v the number of sites on the Pt surface which can adsorb oxygen atoms remains constant and is equivalent to about one monolayer. At potentials more noble than 0.4v the number of available sites decreases and remains essentially constant at about 3/4 of the monolayer value between 0.6 and 0.7v. At potentials above 0.7v the number of available sites drops further and is equal to zero at about 1.5v. The decrease in available Pt sites apparently occurs in two phases. Whatever is causing the drop in available sites in the potential region between 0.4 and 0.6v does not affect the rate of hydrogen oxidation. However, at potentials beyond 0.7v the rate of hydrogen oxidation decreases. The cause of the hysteresis shown in both Fig. 1 and 2 is believed to be dermasorption of oxygen atoms at higher potentials (3). This dermasorbed oxygen decreases the number of surface sites which can adsorb oxygen (Fig. 2).

<sup>1</sup> This equation represents the various kinetic factors which may influence the measured current density. In fact, since in the potential region from 0.04 to 0.7v, current density is independent of potential, and if the rate-controlling mechanism remained the same above 0.7v, the only effect of potential may be on anion adsorption. Of importance is that because of the changes on the electrode surface induced by potential changes in the passivating region, the reaction rate is dependent primarily on the effective electrode area and a nominal free energy of activation required to oxidize hydrogen under the given surface states.

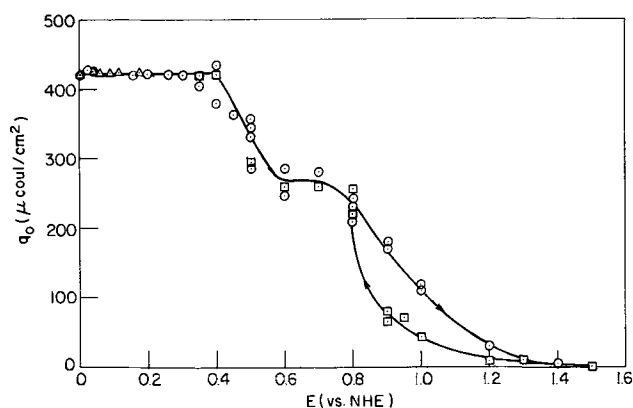


Fig. 2. Amount of oxygen formed on a potentiostated Pt electrode. 1M  $\text{H}_2\text{SO}_4$ ,  $P_{\text{H}_2} = 1$  atm. Anodic charging current density pulse = 1.8 a/cm<sup>2</sup>.

### Discussion

The data in Fig. 1 and 2 demonstrate that the onset of passivity is accompanied by a decrease in the number of sites available for oxygen atom adsorption with an anodic charging pulse. At 1.2v where a limiting current density is reached, the number of such sites is small. Since it was previously shown (3) that steady-state passivation due to oxygen species or oxide formation in a hydrogen-saturated sulfuric acid solution was not feasible, those sites which are unavailable for oxygen atom adsorption with a high current charging pulse are considered occupied by sulfate ions under steady-state potentiostatic conditions.

In the light of the Wagner definition of passivity and Eq. [2], we can conclude that two possible factors cause passivation of the hydrogen oxidation reaction. One is a decrease in the number of available active sites and the other is an increase in the free energy of activation for each increment of potential increase. The data in Fig. 2 indicate a drop in the number of sites available for oxygen atom adsorption between 0.4 and 0.6v, however there is no accompanying retardation of the hydrogen oxidation rate in this potential range (Fig. 1). This means that active hydrogen oxidation sites are not affected in this potential range. The potential-increasing arm in Fig. 1 shows a relatively small retardation of the hydrogen oxidation rate in the potential range from 0.7 to 1.0v followed by a sharp exponential decrease ( $b = -0.11$ ) from 1.0 to 1.2v. The potential decreasing arm of the data in Fig. 1 shows in the potential range from 0.9 to 0.75v a much higher dependence of reaction rate on potential ( $b = -0.04$ ).

For the rising potential range from 0.7 to 1.0v the fraction of available sites for oxygen atom adsorption (Fig. 2) changes from about 0.6 to 0.25. In this same potential range Fig. 1 (rising potentials) shows a decrease in hydrogen oxidation rate from  $2 \times 10^{-3}$  to  $7 \times 10^{-4}$  a/cm<sup>2</sup>. If we consider the change in available oxygen sites as a change in available reaction sites for hydrogen oxidation it will amount to a reduction in area of about 0.4, the accompanying reduction in reaction rate is about 0.35. In terms of Eq. [2], this amounts to a  $n \approx 1$  and satisfactorily explains the reduction in hydrogen oxidation rate on a change in  $\theta$ .

The changes in reaction rate from 1.0 to 1.2v on the increasing potential arm (Fig. 1) corresponds to a 0.2 reduction in sites available for oxygen deposition with a decrease in reaction rate by a factor of 50. The decreasing potential arm from 0.9 to 0.75v showed a 0.4 increase in sites with about a 1000 time increase in reaction rate. Neither the passivation in the linear log ( $b = -0.11$ ) increasing potential arm nor the activation in the linear log ( $b = -0.04$ ) decreasing potential arm can be attributed to the  $\theta$  term in Eq. [2]. This is based on the previous discussion of Fig. 2.



We can therefore conclude that the passivation in these potential ranges must be due to a condition where each small increment of potential causes a significant change in the free energy of activation,  $\Delta G^\circ$ , for the hydrogen oxidation reaction. The exponential term containing  $\Delta G$  must override the exponential potential term.

The number of catalytically active sites on a clean Pt electrode is very small (as is evident from the fact that the rate of the hydrogen reaction on Pt is very sensitive to trace amounts of impurities). It appears that on the increasing potential arm of Fig. 1 up to a potential of 1.0v, adsorption of sulfate ion merely blocks part of the catalytically active sites. At potentials above 1.0v, however, the sulfate ion must be so strongly adsorbed that it acts like a catalytic poison and causes a large increase in the free energy of activation for the hydrogen oxidation reaction. On the decreasing potential arm shown in Fig. 1 and in the potential range from 0.9 to 0.75v ( $b = -0.04$ ), the Pt contains a small amount of dermasorbed oxygen (3, 5). This trace of dermasorbed oxygen evidently has an important effect on the value of the free energy of activation. Dermisorbed oxygen in combination with adsorbed sulfate ion therefore acts as a very strong catalytic poison.

Uhlig (8) has for some time offered as an explanation of passivity the combined effects of chemisorbed oxygen species and resultant decreases in catalytic activity. Our work on the anodic oxidation of hydrogen on Pt confirms Uhlig's hypothesis and extends the possible catalytic poisons to anion adsorption.

### Conclusions

The data on the anodic oxidation of hydrogen on Pt evaluated in terms of the extended Wagner definition of passivity show that passivation can be initiated by small increases (a fraction of a monolayer) in the amount of anion adsorbed and that the passivation process is limited when the Pt surface is essentially saturated with these adsorbed anions. Small amounts of sorbed species may cause large changes in the free energy of activation for the reaction and lead to the conclusion that since the role played by active Pt sites is that of a catalyst for the hydrogen reaction, the adsorption of anions (and dermasorption of oxygen atoms) can effect a poisoning of active sites and a subsequent rate-controlling increase in the free energy of activation for the reaction.

One can extend this analysis to the passivation of iron. Here the dissolution of iron can be considered to involve a catalytic step which may be retarded by chemisorption of poisons at a given potential. The influence of oxygen species associated with the iron could also have a large effect.

The primary purpose of this paper is to demonstrate that the Wagner definition of passivation naturally leads to the conclusion that passivity, so defined, is initiated by adsorption of small amounts (a fraction of a monolayer) of species which can either reduce the active surface area or act as catalytic poisons. The primary effect for large passivation effects appears to be the adsorption of catalytic poisons which cause large increases in the free energy of activation of the reaction. The passivation process itself [ $b = -dE/d(\log i)$ ] is limited by saturation of the active sites with such poisons.

This, of course, does not mean that there are not other reasons and processes for slow oxidation reactions under other conditions. The value of the extended Wagner definition is that it leads to a reasonable explanation of an unusual kinetic occurrence, the reversal of the  $dE/d(\log i)$  slope.

### Acknowledgment

This research was partially supported by the Advanced Research Projects Agency of the Department of Defense as part of the ARPA Coupling Program on Stress-Corrosion Cracking (ARPA Order 878).

Manuscript submitted Jan. 30, 1968; revised manuscript received April 22, 1968. This paper was presented at the Montreal Meeting, Oct. 6-11, 1968 as Paper 389.

Any discussion of this paper will appear in a Discussion Section to be published in the June 1969 JOURNAL.

### REFERENCES

1. Carl Wagner, *Corrosion Science*, **5**, 751 (1965).
2. D. Gilroy and B. E. Conway, *J. Phys. Chem.*, **69**, 1259 (1965).
3. S. Schuldiner, *This Journal*, **115**, 362 (1968).
4. S. Schuldiner and R. M. Roe, *ibid.*, **110**, 332 (1963).
5. S. Schuldiner, T. B. Warner, and B. J. Piersma, *ibid.*, **114**, 343 (1967).
6. T. B. Warner and S. Schuldiner, *ibid.*, **114**, 359 (1967).
7. R. Parsons, *Trans. Faraday Soc.*, **54**, 1053 (1958).
8. H. H. Uhlig, *Z. Elektrochem.*, **62**, 700 (1958).  
H. H. Uhlig, "Corrosion and Corrosion Control," p. 78, John Wiley & Sons, Inc., New York (1964).

# Passivity in Cu-Ni-Al Alloys—A Confirmation of the Electron Configuration Theory

F. Mansfeld and H. H. Uhlig\*

Department of Metallurgy and Materials Science, Massachusetts Institute of Technology, Cambridge, Massachusetts

## ABSTRACT

Potentiostatic anodic polarization data show that a transition from active to passive state is observed for Ni-Cu and Ni-Cu-Zn alloys only when the 3d band of energy levels in the alloy is unfilled. At and above a critical alloy composition, electrons from Cu or Zn completely fill the d band and the passive state disappears. Previous data showed that the calculated critical composition comes close to the observed value assuming that alloyed Cu donates one electron and alloyed Zn two electrons per atom. Present measurements for the 45% Ni-Cu-Al ternary alloys show that Al contributes three electrons per atom. Secondary passivity, which is observed for pure nickel in a potential region noble to that for primary passivity, is similarly observed in the Cu-Ni-Al alloys, but again only when the d band of energy levels is unfilled. Potential decay curves confirm that a passive film, either in the primary or secondary region, exists only on alloys with an unfilled d band. Decay potentials corresponding either to secondary or to primary passivity (Flade potentials) are not greatly sensitive to aluminum content nor to the absolute number of electron vacancies. However, alloyed aluminum affects the passive current density for the 45% Ni ternary alloys accounting for a minimum at 2.35% Al.

The primary and secondary passive films are considered to have an adsorbed structure consisting mainly of oxygen in mono- or multilayers which increase the overvoltage for anodic dissolution of the alloy. The film corresponding to secondary passivity is less stable and presumably thicker than that corresponding to primary passivity. Both films are considered to be intermediates in the formation of stoichiometric metal oxides.

The present work on passivity in the Cu-Ni-Al alloys continues a research program on the general mechanism of passivity in metals and alloys. Osterwald and Uhlig (1) confirmed previous reports (2, 3) that there is a critical composition for passivity in the binary Cu-Ni alloys; Stolica and Uhlig (4) found later that there also exists a critical composition in the ternary Cu-Ni-Zn alloys. In both cases the critical compositions for passivity were determined by measuring anodic potentiostatic polarization curves in 1N H<sub>2</sub>SO<sub>4</sub> at 25°C.

According to the electron configuration theory of passivity (3), a metal or alloy should be capable of becoming passive so long as it has unfilled d-orbitals or an unfilled d band which favors chemisorption of oxygen. It is suggested that the chemisorbed oxygen markedly decreases the exchange current density thereby increasing the overvoltage for metal dissolution in the passive region. When the d band is filled, as in the nontransition metals, the overvoltage for anodic dissolution remains small, and the metal or alloy tends to form stoichiometric oxides in preference to chemisorbed oxygen films. Oxide films, if they form, are not thought to be a major source of corrosion protection.

From this it follows that the critical composition for passivity in Cu-Ni alloys should appear when the d electron vacancies in the 3d band of Ni at the surface of the alloy (0.6 vacancy per Ni atom plus 1 vacancy created by an adsorbed oxygen atom) are just filled by available donor electrons from Cu (one 4s electron per Cu atom). In other words, so long as the atomic ratio of Cu to Ni is smaller than 1.6, the alloy should be passive; otherwise it should be active. The same is true for the Cu-Ni-Zn alloys where passivity occurs so long as the atomic ratio holds:  $(\text{Cu} + 2\text{Zn})/\text{Ni} < 1.6$  where Zn donates two 4s electrons per atom. This was confirmed by the experiments of Stolica and Uhlig (4).

To explore the electron configuration theory further, Cu-Ni-Al alloys were prepared and both the

critical c.d. for passivity  $i(\text{crit})$  and the passive c.d.  $i(\text{pass})$  were measured by potentiostatic anodic polarization curves in 1N H<sub>2</sub>SO<sub>4</sub> at 25°C. Both saturation magnetic moments of Ni-Al alloys and the Hume-Rothery rules for structure of intermetallic compounds have shown that Al contributes 3 electrons to Ni compared to 2 electrons from Zn and 1 electron from Cu. It is predicted, therefore, that Cu-Ni-Al alloys should remain passive so long as the atomic ratio holds:  $(\text{Cu} + 3\text{Al})/\text{Ni} < 1.6$ ; otherwise the alloys should be active.

## Preparation of Alloys

In order to check the effect of alloyed Al on the passive properties of Cu-Ni alloys, two conditions must be met. The first is that the maximum added amount of Al should supply electrons sufficient to fill the surface d band of Ni; the second is that the added Al should not exceed solubility limits for a single-phase alloy, otherwise galvanic interaction of the separate phases tends to destroy passivity and complicates interpretation of the measurements. By referring to the binary phase diagrams, it was concluded that the required conditions were likely to be satisfied in alloys with 45 w/o (weight per cent) Ni, 1-9 w/o Al, balance Cu. Their single-phase structure was confirmed by examining polished and etched specimens under the microscope.

The alloys were prepared from electrolytic Cu, 99.99+ % Al and carbonyl Ni. They were melted in dense alumina crucibles under vacuum by induction heating. After filling the furnace with purified argon, the melt was drawn into 7 mm Vycor tubes and water quenched. The ingots were homogenized in argon at 950°C for 24 hr, swaged to 0.15 in. (0.39 cm) diameter, annealed in argon at 950°C for 1 hr, and then air cooled while remaining in an argon atmosphere within a quartz tube. They were swaged to a final 0.14 in. (0.37 cm) diameter then annealed and cooled as before.

The chemical analyses of the alloys are given in Table I which also lists values of the atomic ratios and per cent d band filled. The latter is obtained by di-

\* Electrochemical Society Active Member.

Table I. Composition of Ni-Al-Cu alloys

Cu		Ni		Al		Atomic ratio**	% d band filled
w/o	a/o	w/o	a/o	w/o	a/o		
54.60	52.67	45.33	47.33	—	—	1.11	69.6
53.38	50.69	(45.45)*	(46.71)	1.17	2.60	1.25	78.3
52.23	48.84	(45.42)	(45.99)	2.35	5.17	1.40	87.4
51.00	47.04	(45.51)	(45.40)	3.49	7.56	1.53	95.9
49.84	45.29	(45.51)	(44.77)	4.65	9.94	1.68	104.8
48.39	43.30	(45.65)	(44.14)	5.96	12.56	1.83	114.6
47.50	41.44	(45.36)	(43.88)	7.14	14.68	1.95	121.8
45.98	39.84	45.42	42.55	8.64	17.61	2.17	135.8

\* Values in brackets obtained by difference.

\*\* Atomic ratio =  $\frac{a/o \text{ Cu} + 3 a/o \text{ Al}}{a/o \text{ Ni}}$

% d band filled = atomic ratio  $\times 100/1.60$ .

viding the value of the atomic ratio by 1.6 and multiplying by 100. On this basis of calculation, assuming Al to contribute 3 electrons per atom, 4 alloys were prepared with an unfilled d band and 4 alloys with a filled d band.

#### Experimental Procedure

Electrodes from annealed rods were machined to cylinders approximately 1 cm long and 0.3 cm in diameter. They were cleaned in boiling benzene and pickled in conc. HCl at 90°C for 1 min which served to remove surface oxides.

The electrolyte consisting of 1N H<sub>2</sub>SO<sub>4</sub> was deaerated with N<sub>2</sub> which had been passed over Cu-turnings at 450°C. Nitrogen also served to stir the electrolyte before each polarization run until the corrosion potential became constant. All experiments were carried out in a constant temperature room at 25° ± 0.5°C, using a Wenking potentiostat and various recorders. The potentials were measured with reference to a saturated calomel electrode, 1N H<sub>2</sub>SO<sub>4</sub> salt bridge, but are reported on the standard hydrogen scale without correction for the small liquid junction potential.

#### Results

Polarization curves were obtained both with a continuous sweep rate of 20 mv/min, and also employing quasi-stationary measurements for which the potential was kept at a fixed value until the current was relatively constant for at least 2 min. For the latter, potentials were changed in steps of 20 mv in the active region and 40 mv in the passive and transpassive regions. Figure 1 shows potentiostatic anodic

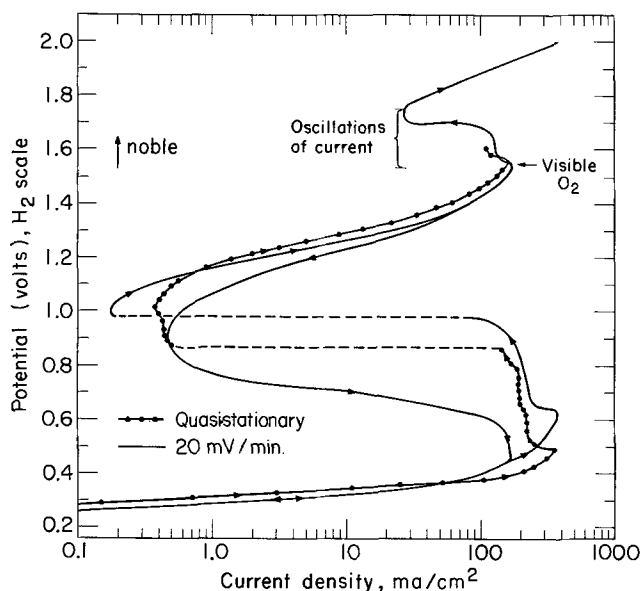


Fig. 1. Potentiostatic anodic polarization curves for 45.4% Ni-2.35% Al-Cu alloy in 1N H<sub>2</sub>SO<sub>4</sub>, 25°C.

polarization curves at 25°C obtained both ways for an alloy containing 2.35 w/o Al having an atomic ratio (Cu + 3 Al)/Ni equal to 1.40. All three curves have Tafel lines in the active region with a slope of approximately 30 mv. After reaching a maximum, the c.d. drops sharply to small values (200-500  $\mu\text{a}/\text{cm}^2$ ) in the passive region and increases again in the transpassive region with a slope of about 120 mv. At still higher potentials the c.d. drops again, conforming to a region of secondary passivity. At these noble potentials the current starts to oscillate and the first small bubbles of oxygen are observed. The oscillations stop when the minimum c.d. in the region of secondary passivity is reached. During the oscillations, black-appearing rings, presumably caused by transient oxides, pass over the surface of the electrode. While this happens the c.d. reaches a maximum and O<sub>2</sub> evolution a minimum. Each time a black ring disappears, O<sub>2</sub> evolution reaches a maximum. Secondary passivity is not unique to these alloys; it has also been observed in pure Ni (1, 5-9), Ni-Mo (10), Ni-Cr (11), and Fe-Cr alloys (12-14).

Shapes of the polarization curves depend in general on direction of potential sweep. Differences of this kind were also observed by Stolica and Uhlig (4) for the passive Cu-Ni-Zn alloys. A contributing factor could be a green-brown film, probably a salt layer, which is formed in the active region when the potential is changed from the corrosion potential to more noble values, but which becomes dislodged from the electrode surface when the maximum c.d. is reached. No such film is observed when the potential is changed from the passive to the active direction. It is also possible that the invisible passive film formed at more noble potentials is not completely disrupted when the potential is changed from the passive to active direction, thereby lowering the observed critical c.d. and corresponding potential.

Because the stepwise technique takes a long time, and corresponding corrosion of the test specimen therefore is rather high, we carried out most of our experiments with a compromise constant sweep rate of 20 mv/min. Figure 2 shows polarization curves for three of the Cu-Ni-Al alloys and also for pure Cu starting in the noble region at a potential slightly more active than the potential where oxygen evolution begins. The 45% Ni-Cu alloy with 0% Al and the alloy with 2.35% Al have an atomic ratio smaller than 1.6. They show a marked transition from passive to active state. The passive c.d.  $i(\text{pass})$ , defined as the minimum c.d. in the passive region, is smaller for the alloy containing Al. The alloy containing 4.65 w/o Al, on the other hand, has an atomic ratio greater than 1.6, and although it shows some small variations of current which are not reproducible as the potential is adjusted, it does not undergo a true

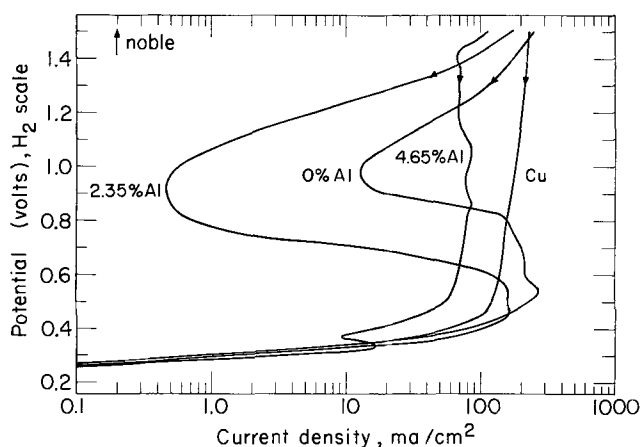


Fig. 2. Potentiostatic anodic polarization curves for Cu and for 45% Ni-Al-Cu alloys in 1N H<sub>2</sub>SO<sub>4</sub>, 25°C; 20 mV/min noble to active direction.

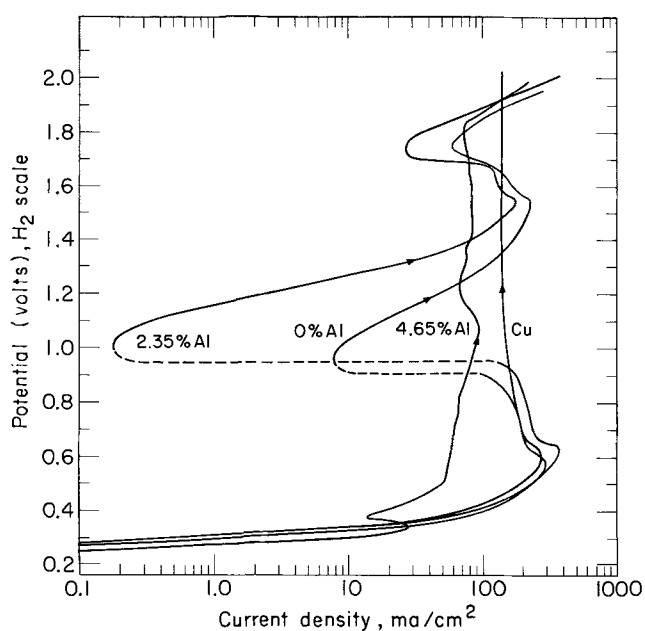


Fig. 3. Potentiostatic anodic polarization curves for Cu and for 45% Ni-Al-Cu alloys in 1N H<sub>2</sub>SO<sub>4</sub>, 25°C; 20 mv/min active to noble direction.

transition from passive to active state. It behaves similarly to Cu, the polarization curve of which is shown for comparison. The small loop appearing in the active region for the 4.65% Al alloy becomes smaller using slower sweep rates and disappears entirely with quasi-stationary measurements.<sup>1</sup> It is probably not related to any property of passivity. In Fig. 3 the results for the same alloys are presented with runs now starting in the active region. It can be seen that the alloys for which a passive current density is observed also exhibit a region of secondary passivity, contrary to the behavior of either the alloys which do not exhibit passivity, or of pure Cu.

In Fig. 4,  $i(\text{crit})$ , defined as the maximum value in the active region, and  $i(\text{pass})$  for all the alloys are plotted against the atomic ratio. Each point is the average value for 3 to 7 independent runs. Although the observed values of  $i(\text{crit})$  are lower for polarization runs going from the noble to active direction compared to the reverse direction, an observed  $i(\text{pass})$  exists only between 0% Al (at. ratio 1.11) and 3.49% Al (at. ratio 1.53). For higher Al alloys, only a maximum c.d. in the active region is detected which falls on the extrapolated line for  $i(\text{crit})$  values of lower Al alloys. The composition for intersection of  $i(\text{crit})$  and  $i(\text{pass})$  at which a passive c.d. is no longer observed is close to an atomic ratio of 1.6.

For the region of secondary passivity and for oxygen evolution, the behavior depends on alloy composition in a manner quite similar to that of normal passivity (Fig. 5). Only alloys with atomic ratios smaller than 1.6 which are correspondingly passive, show the phenomenon of secondary passivity. It is noted that addition of Al to Ni-Cu alloys lowers the c.d. which has to be reached in order to achieve secondary passivity. The minimum c.d. in this region corresponds to 2.35% Al, which is also the composition at which a minimum occurs in  $i(\text{pass})$ . The points plotted in Fig. 5 for the alloys with atomic ratio greater than 1.6 correspond to values where the c.d. starts to increase again and oxygen evolution begins.

It is significant that potential decay curves show discontinuities but only for alloys of atomic ratio < 1.6. A typical decay curve for the 45% Ni-2.35%

<sup>1</sup> In this particular potential region the current has a complicated time dependence following a prescribed change of potential. A thick, porous oxide is formed, which is not observed for the passive alloys.

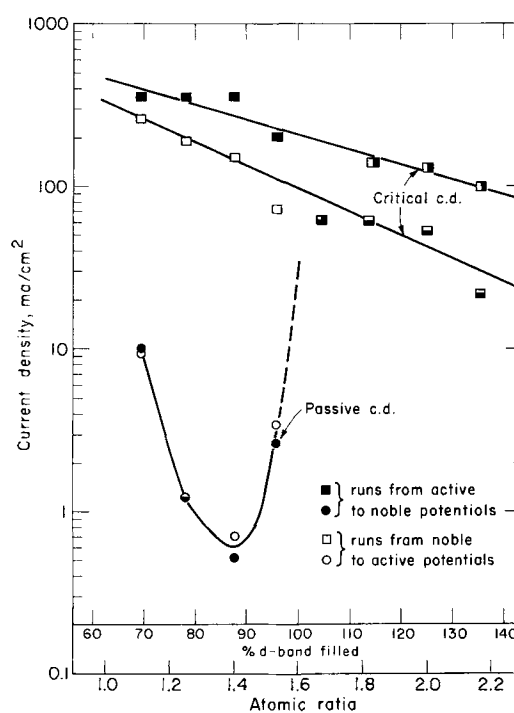


Fig. 4. Values of  $i(\text{crit})$  and  $i(\text{pass})$  for 45% Ni-Al-Cu alloys in 1N H<sub>2</sub>SO<sub>4</sub>, 25°C, showing passive behavior below but not above atomic ratio 1.6 (100% d band filled).

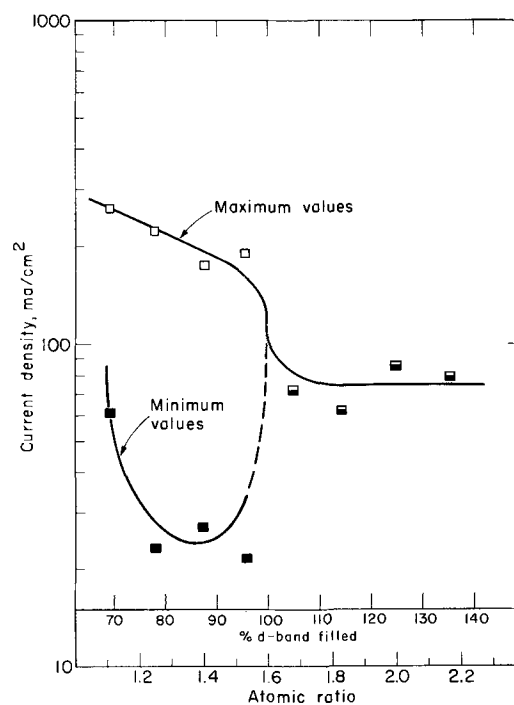


Fig. 5. Maximum and minimum current densities in the region of secondary passivity for 45% Ni-Al-Cu alloys in 1N H<sub>2</sub>SO<sub>4</sub>, 25°C, showing disappearance of secondary passivity above atomic ratio 1.6 (> 100% d band filled).

Al-bal. Cu alloy (atomic ratio 1.40) in 1N H<sub>2</sub>SO<sub>4</sub> at 1.5°C is shown in Fig. 6 starting from either the passive or transpassive region. The more noble potential at 1.7v corresponds to breakdown of the secondary passive film whereas 0.62v corresponds to breakdown of the primary passive film and hence the latter is the Flade potential. The secondary passive film breaks down independent of subsequent breakdown of the primary film. The decay curve is also shown for the 4.65% Al alloy (atomic ratio 1.68) showing a smooth transition from noble to active values and the com-

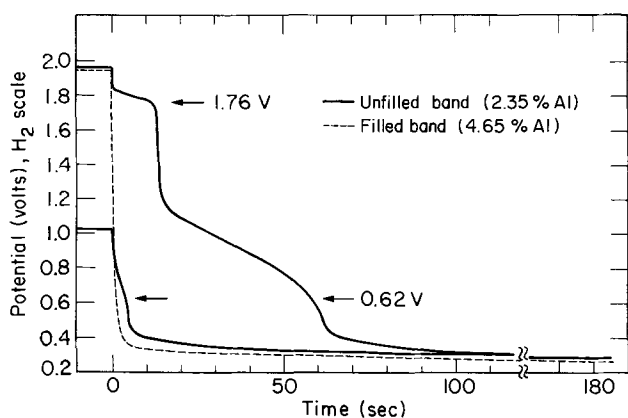


Fig. 6. Potential decay curves for 45.4% Ni-2.35% Al-Cu, atomic ratio 1.40 (unfilled d band) and 45.5% Ni-4.65% Al-Cu, atomic ratio 1.68 (filled d band) in 1N H<sub>2</sub>SO<sub>4</sub>, 1.5°C.

plete absence of any discernible change of slope marking breakdown of surface films.

A summary of the potential decay data at 1.5° and at 25°C is given in Table II. The lower temperature was chosen in addition to room temperature because of the more pronounced discontinuities in potential at 1.5°C resulting most likely from the greater stability of the passive film at low temperatures. Discontinuities were not observed for any of the alloys of atomic ratio >1.6 at either high or low temperatures. The relatively small observed temperature effect of Flade potential parallels the small temperature dependence noted previously for the Flade potentials of Fe (15) and of Ni (1).

### Discussion

The atomic ratio of approximately 1.6 separates alloys which exhibit a passive current density from those which do not, and it separates those alloys whose decay potentials show discontinuities corresponding to breakdown of passive films from those alloys whose potential decay curves do not show any discontinuities. Since the ratio 1.6 corresponds to 100% d band filled as described earlier, the original assumption that Al contributes 3 electrons per atom is confirmed. No other assumption of donor electrons leads to similar agreement. An atomic ratio >1.6 indicates that more donor electrons are available than are needed to fill electron vacancies (>100% d band filled).

The requirement of 3 electrons per Al atom to fill the d band, parallel to two electrons per Zn atom or 1 electron per Cu atom is considered to be a significant result.

Several incidental phenomena were observed which also deserve discussion. For example, the minimum in  $i(\text{pass})$  (Fig. 4) at 2.35% Al is also the approximate composition at which a minimum appears in the c.d. corresponding to secondary passivity (Fig. 5). This plus the fact that secondary passivity is observed only in alloys which have an unfilled d band lend support to the conclusion that whatever is the cause of secondary passivity, it is also related to the cause of

primary passivity. If the passive film has an adsorbed structure, as seems likely, rather than being composed of a diffusion-barrier stoichiometric metal oxide, then the film accounting for secondary passivity is also plausibly related to an adsorbed structure and its properties are tied in with the electron configuration of the underlying alloy.

In accord with quantitative data obtained for Ni in 1N H<sub>2</sub>SO<sub>4</sub> by Vetter and Arnold (5), an increasingly noble applied potential beyond the potential corresponding to  $i(\text{pass})$  but below secondary passivity is attended by increasing current accounted for entirely by increasing dissolution of metal ions. When the potential corresponding to secondary passivity is reached, an increased amount of adsorbed oxygen or a change in the structure of the adsorbed layers (including OH and H<sub>2</sub>O) making up the passive film acts to increase anodic overvoltage for metal dissolution. The current decreases, therefore, as observed. Vetter and Arnold's data show that this decrease cannot be attributed to an IR drop through an oxide film in view of the observed low resistivity of the film substance (<1 ohm-cm). On applying a still more noble potential, the current increases again attended predominantly by oxygen evolution. The average potential corresponding to minimum c.d. is  $1.74 \pm 0.03\text{v}$  and that corresponding to maximum c.d. is  $1.52 \pm 0.03\text{v}$  showing a slight trend toward more active values with per cent d band filled. At these noble potentials, the discharge of OH<sup>-</sup> or decomposition of adsorbed H<sub>2</sub>O to O<sub>2</sub> and H<sup>+</sup> becomes the preferred process, and hence oxidation of the alloy electrode tends to favor metal oxides rather than hydrated metal ions. The metal oxides are soluble, however, leading to momentarily visible black surface films, the presence or absence of which presumably causes the observed oscillations of c.d. and O<sub>2</sub> evolution.

For alloys with a filled d band, the rate of metal dissolution and oxide formation is not sensitive to potential throughout the noble region. Presumably in absence of an adsorbed film, the observed c.d., contrary to alloys with an unfilled d band, does not decrease under conditions corresponding otherwise to primary or secondary passivity. Visible dark porous oxides form in contrast to bright appearing surfaces characteristic of the passive alloys. The insensitivity of anodic processes to potential beyond the maximum c.d. suggests that the rate of reaction for non-passive alloys in the noble region is regulated by (i) an insulating barrier film whose thickness is more or less proportional to applied potential or by (ii) a slow process not involving electron transfer, e.g., acid dissolution of a metal oxide. The measured good conductivity of the passive film substance (5) on Ni and the corresponding good conductivity on the present alloys as indicated by Tafel behavior in the O<sub>2</sub> evolution region make (ii) a more likely explanation than (i).

In the binary Ni-Cu alloys, filling of the d band by electrons from alloyed Cu increases both  $i(\text{crit})$  and, even more,  $i(\text{pass})$  (1). Filling of the d band by electrons from alloyed Al, to the contrary, tends to decrease  $i(\text{crit})$  and also, at least up to a certain atomic ratio,  $i(\text{pass})$  as well. The potentials corresponding to  $i(\text{crit})$ , decrease on the noble-to-active polarization curves from about 0.52v for 0% Al (69.6% d band filled) to 0.41v for 3.49% Al (95.9% d band filled). Corresponding potentials for alloys with a filled d band marking a change of slope in the active region, fall between 0.45 and 0.53v with no discernible trend. Potentials corresponding to  $i(\text{pass})$  are 0.96v for 0% Al and 0.82v for 3.49% Al showing an almost linear relation with per cent d band filled. Explanations of these effects are complicated, and at present only speculative suggestions are possible. It might be said, for example, that alloyed Al appears to exert two opposing effects. The one is to increase  $i(\text{crit})$  and  $i(\text{pass})$  by reason of filling of the d band; the other is

Table II. Potentials (std. hydrogen scale) corresponding to change of slope in potential decay curves for 45% Ni-Al-Cu alloys in 1N H<sub>2</sub>SO<sub>4</sub>

(Avg of 3 runs)

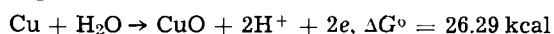
w/o Al	Atomic ratio	Flade potential		Potential of secondary passivity	
		1.5°C	25°C	1.5°C	25°C
—	1.11	0.65	0.73	1.75	1.74
1.17	1.25	0.63	0.75	1.75	1.72
2.35	1.40	0.62	0.66	1.74	1.71
3.49	1.53	0.60	0.67	1.75	1.71

to specifically impede dissolution rates by reason of the passive properties of Al itself. The latter effect might occur either through changes in activation energy for metal ion dissolution induced by alloyed Al, or perhaps through formation of  $\text{Al}_2\text{O}_3$  or similar films. At the noble potentials corresponding to passivity, the two opposing effects lead to a minimum in  $i(\text{pass})$ . The minimum is not observed with Ni-Zn-Cu alloys.

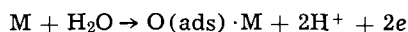
At less noble potentials and higher c.d. corresponding to transition from the active to passive state, the specifically retarding effect of Al dominates leading to a continuous decrease in  $i(\text{crit})$  with increasing alloyed Al. The opposite trend, that of increasing values of  $i(\text{crit})$ , is observed with alloyed Zn (4) or Cu (1). It should be noted that the effect of Al on  $i(\text{crit})$  is not related to d band structure because values for alloys with an unfilled d band fall on the same line as the maximum c.d. in the active region for alloys with a filled d band (Fig. 4). The appreciable change of  $i(\text{crit})$  with alloying additions may be taken as evidence that a critical c.d. does not result alone from concentration polarization, but that activation polarization and perhaps IR drop through surface films must also play a role.

The more noble Flade potentials for the alloys (Table II) than for pure Ni in 1N  $\text{H}_2\text{SO}_4$  (0.2v, 25°C) (1) imply that passivity in the alloys is less stable than for Ni (16). The surface film corresponding to secondary passivity in turn is less stable than the primary film and it decomposes at 1.7v leaving a residual primary passive film which decomposes at the Flade potential. The relatively small trend, if any, in the potentials corresponding to primary and secondary passivity, despite change of alloy composition, suggests that the stability of passive films in the 45% Ni-Al-Cu alloys is sensitive mostly to whether d electron vacancies exist, and not to the absolute number of d electron vacancies per atom.

The observed Flade potentials for the passive alloys in 1N  $\text{H}_2\text{SO}_4$ , pH 0.3, 25°C, are more noble than corresponds to a reaction such as



the standard potential (pH = 0) of which, as calculated from free energy data, is 0.57v. The corresponding potential for  $\text{Cu}_2\text{O}$  or NiO formation is 0.47 and 0.11v, respectively. The improbability of such reactions as a possible explanation of the Flade potential is also indicated by lack of an observed Flade potential in alloys with a filled d band, although their thermodynamic tendency to form  $\text{CuO}$ , NiO or similar oxide films differs but little from that of alloys of almost the same composition with an unfilled d band. The same considerations apply to formation of higher metal oxides as a possible cause of secondary passivity. Hence the reaction corresponding to the Flade potential is more likely



where  $\text{O}(\text{ads}) \cdot \text{M}$  represents the adsorbed passive film on metal M (of either less than monolayer or of multilayer dimensions, hence of unspecified ratio O to M) (17) and which forms only on alloys having an unfilled d band. The film forming in the region of secondary passivity is also assumed to have an adsorbed structure but of multilayer dimensions and probably of higher O to M ratio than in the primary film. In addition to adsorbed oxygen, it may also include mobile metal ions. A film of this kind is considered to be an intermediate, preceding formation of a stoichiometric higher metal oxide. Its structure does not appear to require incorporation of  $\text{SO}_4^{2-}$  or  $\text{S}_2\text{O}_8^{2-}$  ions, because secondary passivity was also observed in the 45% Ni-Cu and 45% Ni-2.35% Al-Cu alloys when anodically polarized in 1N  $\text{HClO}_4$  instead of 1N  $\text{H}_2\text{SO}_4$ . Details will be reported in a later paper.

### Acknowledgment

The authors are pleased to acknowledge support by the Shell Companies Foundation and by the Corrosion Research Council. They are grateful to David Duquette for help in preparing the alloys.

Manuscript submitted Feb. 6, 1968; revised manuscript received June 6, 1968. This paper was presented at the Chicago Meeting, Oct. 15-19, 1967, as Paper 54.

Any discussion of this paper will appear in a Discussion Section to be published in the June 1969 JOURNAL.

### REFERENCES

1. J. Osterwald and H. H. Uhlig, *This Journal*, **108**, 515 (1961).
2. H. Uhlig, *Trans. Electrochem. Soc.*, **85**, 307 (1944).
3. H. H. Uhlig, *Z. Elektrochem.*, **62**, 626 (1958).
4. N. Stolica and H. Uhlig, *This Journal*, **110**, 1215 (1963).
5. K. Vetter and K. Arnold, *Z. Elektrochem.*, **64**, 244 (1960).
6. N. Sato and G. Okamoto, *This Journal*, **110**, 605 (1963).
7. J. Osterwald and H. Feller, *ibid.*, **107**, 473 (1960).
8. E. Kunze and K. Schwabe, *Corr. Sci.*, **4**, 109 (1964).
9. R. Sayano and K. Nobe, *Corrosion*, **22**, 81 (1966).
10. P. Borggräfe and H. Feller, *Corr. Sci.*, **7**, 265 (1967).
11. J. Myers, F. Beck, and M. Fontana, *Corrosion*, **21**, 277 (1965).
12. M. Prazak, V. Prazak, and V. Cihal, *Z. Elektrochem.*, **62**, 739 (1958).
13. Th. Heumann and R. Schürmann, *Werkstoffe u. Korrosion*, **12**, 560 (1961).
14. R. Olivier, Proc. 6th Meeting Int. Com. Electrochem., Therm. and Kinetics, Portiers, p. 314 (1954).
15. F. Flade, *Z. Physik. Chem.*, **76**, 513 (1911).
16. "Corrosion and Corrosion Control," by H. Uhlig, pp. 59-62, John Wiley & Sons, Inc., New York (1963).
17. H. H. Uhlig, *Corrosion Sci.*, **7**, 325 (1967).

# Comparative Study of the Electrocrystallization of Tantalum and Niobium from Molten Fluoride Mixtures

Cl. Decroly,<sup>†</sup> A. Mukhtar, and R. Winand

Laboratory of Metallurgy and Electrochemistry, Free University of Brussels, Brussels, Belgium

## ABSTRACT

A comparison has been made of the electrocrystallization of tantalum and niobium from baths containing either KF and  $K_2TaF_7$  or KF and  $K_2NbF_7$ . The main purpose of the work was to determine why current efficiencies are generally much lower for niobium than for tantalum under the same experimental conditions. The phase diagram of the system KF- $K_2NbF_7$  has been drawn. Comparison with the diagrams of the system KF- $K_2TaF_7$  found in the literature does not give any evidence for a basic difference in the nature of the ionic species present in both types of baths. The results of the electrolyses performed have led to the following main conclusions: (A) An increase of the  $K_2NbF_7$  or  $K_2TaF_7$  content of the bath results in a considerable decrease of the current efficiency. This effect is much more striking for niobium than for tantalum. The grain size decreases also when the  $K_2NbF_7$  or  $K_2TaF_7$  content of the bath increases. (B) The current efficiency increases roughly with the cathodic current density while the grain size shows a very complex behavior against the same parameter. (C) The current efficiency decreases and the grain size increases when the length of the electrolysis increases. (D) The grain size decreases regularly when the temperature increases, while the current efficiency passes through a maximum at about 900°C.

Cathodic polarization curves drawn in both types of bath have shown a rather complex behavior of the ionic species to be discharged at the cathode. It appears that some part of the metallic deposit at the cathode is removed from it by the agitation of the bath and by its own weight and is redissolved in the bath through a chemical reaction giving rise to lower valency species. A part of these species is reoxidized at the anode, and another part of them participates again in the cathodic process. This phenomenon is much more effective for niobium than for tantalum in the same type of bath. All the experimental observations are interpreted in terms of this mechanism.

It is well known that tantalum and niobium have very similar chemical properties, so similar indeed that it is necessary to use very elaborate methods to separate them during the mineral and chemical processing of their ores.

It is thus quite astonishing that, while tantalum can be prepared economically by fused salt electrolysis, all the attempts to prepare niobium in the same way failed, the current efficiency being very low. It should of course be very interesting to know why there is such a big difference in the behavior of the two metals during the electrolysis. In this respect, although the literature (1) contains a rather large number of papers on the electrowinning of tantalum and niobium, it is rather difficult to draw any general conclusion from the published results. This is mainly due to the fact that most of the researchers have worked only on one of the two metals and generally under conditions so different that any valuable comparison of the results is impossible. It should be pointed out however that Chuk-Ching Ma (2) has studied the deposition of both tantalum and niobium in the same electrolytic cell, using a similar mixture for the electrolytic bath and the same washing technique to recover the metallic powders. He investigated the effect of current density and temperature on the particle size of these metals. In the case of tantalum, the bath contained 1 part potassium fluotantalate, 1 part potassium chloride, and 0.1 part tantalum pentoxide (by weight), while for niobium it contained 1 part fluoxyniobate ( $K_2NbOF_5$ ) and 1 part potassium chloride. Between 800° and 950°C, and with cathodic current densities from 10 to 40 amp/dm<sup>2</sup>, he found an increase of the grain size with the increase of temperature, while at high current densities the grains are finer than those obtained when working at lower values of this variable. However, this work does not give any information with regard to the current efficiencies. Moreover,

his results are in contradiction with those of Myers (3) concerning the effect of the current density on the grain size in the case of tantalum.

From another point of view, any complete study of electrocrystallization should be made in such a way as to enable one to establish a relation between the observed metallic crystals and the cathodic polarization curves (4) drawn under the same conditions as those under which the electrolyses were carried out. This seems perhaps more necessary in fused salts than in aqueous solutions (5), because of the rather large number of secondary factors which can influence the cathodic process. Among them, mechanical losses of the metal powder deposited at the cathode, redissolution of this metal in the bath, chemical reactions of the bath with the atmosphere of the furnace, and anode effect are certainly of considerable importance.

Therefore, although the cathodic mechanism of the electrodeposition of tantalum and niobium has already been studied by various authors (6-15), we cannot take the conclusions drawn in the literature as immediately useful for the interpretation of results of electrolyses done by other researchers.

We thus decided to start a research program with the purpose of ensuring a complete comparison of the electrocrystallization of the two metals. In order to simplify the problem as far as possible, we decided to study two similar all-fluoride baths, KF- $K_2TaF_7$  and KF- $K_2NbF_7$ , although it is evident from the literature that much better current efficiencies can be achieved when a certain amount of the oxide of the metal to be deposited is added to the bath and/or when some alkali chloride is present (16).

The present work being mainly a fundamental research, the economic aspects have been neglected in the attempt to obtain some information concerning the nature of the ionic species present in the bath. But we hope to have the opportunity in the near future to go further in this study by the investigation of the systems KF- $K_2TaF_7$ - $Ta_2O_5$  and KF- $K_2NbF_7$ - $Nb_2O_5$ , as

<sup>†</sup> Deceased.

well as  $\text{KF-KCl-K}_2\text{TaF}_7$  and  $\text{KF-KCl-K}_2\text{NbF}_7$  with or without additions of  $\text{Ta}_2\text{O}_5$  or  $\text{Nb}_2\text{O}_5$ .

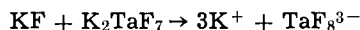
In the present paper, we will make successively the comparison between the systems  $\text{KF-K}_2\text{TaF}_7$  and  $\text{KF-K}_2\text{NbF}_7$  with regard to their phase diagrams and probable ionic species present in the liquid state, the influence of bath composition, current density, duration of the electrolysis and temperature on the current efficiency, particle size, and shape of the crystals obtained by electrolysis, and the cathodic polarization curves and probable cathodic mechanism of electrodeposition.

*Phase Diagrams of the Systems  $\text{KF-K}_2\text{TaF}_7$  and  $\text{KF-K}_2\text{NbF}_7$  and the Probable Ionic Species Present in the Melts of Each Mixture*

The phase diagram for the system  $\text{KF-K}_2\text{TaF}_7$  has been drawn by three groups of workers (17-19). While their results are not quite concordant, the general shape of the diagrams is the same. All the authors found a definite compound corresponding to the formula  $\text{KF}\cdot\text{K}_2\text{TaF}_7$  with a congruent melting point at  $776^\circ\text{--}780^\circ\text{C}$ . Two eutectic points are present in the diagrams. The first one is found at 22 to 25.5 m/o (mole per cent) of  $\text{K}_2\text{TaF}_7$  with a melting point included between  $718^\circ$  and  $727^\circ\text{C}$ . The second one is found at 70-79.5 m/o  $\text{K}_2\text{TaF}_7$ , with a melting point included between  $695^\circ$  and  $717^\circ\text{C}$ . The accuracy of the diagrams is said to be better on the side rich in  $\text{KF}$  than on the other one.

The phase diagram for the system  $\text{KF-K}_2\text{NbF}_7$  was not reported in the literature. Thus, we have drawn it by differential thermal analysis and by x-ray diffraction, according to the method previously used by one of the present authors (20), but somewhat improved in sensitivity and modified to cope with the corrosiveness of the melts. Our results were published recently (21). The phase diagram obtained is quite similar to that obtained for  $\text{KF-K}_2\text{TaF}_7$ . A definite compound corresponding to the formula  $\text{KF}\cdot\text{K}_2\text{NbF}_7$  is found, with a congruent melting point at  $760^\circ\text{C}$ . Two eutectic points are also found, the first one at 23 m/o  $\text{K}_2\text{NbF}_7$  with a melting point at  $723^\circ\text{C}$ ; the second one at 80 m/o  $\text{K}_2\text{NbF}_7$  with a melting point at  $707^\circ\text{C}$ .

Using the equation of the freezing point depression expressed in terms of Temkin's ionic mole fractions to analyze the alkali side of their phase diagram for  $\text{KF-K}_2\text{TaF}_7$ , Iuchi and Ono (17) suggested that the formation of the ionic species  $\text{TaF}_8^{3-}$  according to the reaction



is quite possible, the remaining ionic species being  $\text{K}^+$  and  $\text{F}^-$  ions. We have made the same calculations for the system  $\text{KF-K}_2\text{NbF}_7$ , and we came to the same conclusions as Iuchi and Ono. However, we are not completely convinced of the possibility of establishing without any doubt the nature of the ionic species present in the bath by this kind of calculations: all the possible modes of dissociation of the initial molecular compounds are not taken into consideration, and, finally, the decision concerning the type of ionic species present is a function of the accuracy of the determination of the liquidus curve of the phase diagram. We would thus prefer to say that the dissolution of  $\text{K}_2\text{TaF}_7$  and  $\text{K}_2\text{NbF}_7$  in  $\text{KF}$  occurs in such a way that only one new species seems to appear in the molten bath.

However, what is the most important for the comparison of the electrocrystallization of the two metals is that by the freezing point depression method, and, within its limits of accuracy, we did not find any noticeable difference between the two types of melts. This has been confirmed recently by spectrophotometry at high temperature on similar systems by Fordyce and Baum (22). They have found  $\text{TaF}_7^{2-}$  and  $\text{NbF}_7^{2-}$  to be the predominant species in the liquid.

### Experimental Study of Electrodeposition of Tantalum and Niobium from the Mixtures $\text{KF} + \text{K}_2\text{TaF}_7$ and $\text{KF} + \text{K}_2\text{NbF}_7$

*Apparatus.*—The main part of the apparatus has already been described elsewhere (5). We will recall here only its main characteristics and point out the few modifications that have been made.

Figure 1 shows a vertical section through the electrolytic cell of the interior of the furnace and its cover, with its accessories. The furnace is a water-cooled double-walled stainless steel vessel. It is vacuum tight so that the atmosphere can be controlled easily. The graphite crucible is heated by medium frequency induction (8000 Hz) and acts as the anode of the electrolytic cell. The cathode is a low carbon steel rod dipping in the bath. Since we did not find any suitable material to insulate the internal bottom part of the crucible, as we had in previous research (5), we were not able to ensure the cylindrical homogeneity of distribution of the current flow between the cathode and the anode.

The temperature of the bath is measured by two thermocouples protected by graphite-covered alumina sheaths dipping into the electrolytic bath. One of these thermocouples is used for the automatic temperature control which acts on the excitation of the medium frequency alternator.

The furnace is connected to a vacuum pump and also to argon bottles. Before reaching the furnace, argon is purified by passing successively through five tubes containing phosphoric oxide spread on glass wool, one tube containing copper turnings heated at  $500^\circ\text{C}$  and, finally, a second tube containing active calcium heated at  $450^\circ\text{C}$ .

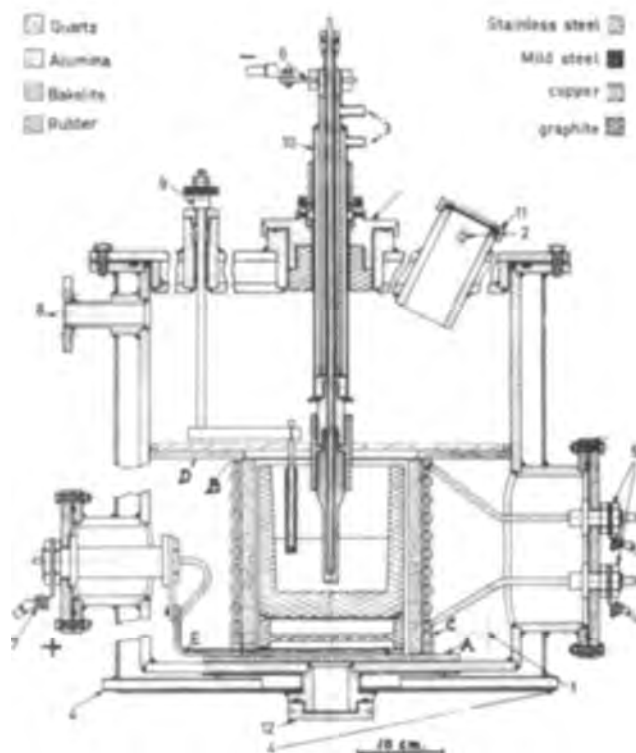


Fig. 1. Electrolytic furnace: 1, Main entry for argon; 2, auxiliary entry for argon; 3, entry (below) and exit (above) of the cooling water for the cathode assembly; 4, entry of the cooling water for the furnace body; 5, terminals for the medium frequency current; 6, negative pole for the electrolytic current; 7, positive pole for the electrolytic current; 8, exit for the gases (passage toward the cylinder); 9, assembly for the control and movements of the thermocouple rods; 10, cathode holding assembly; 11, viewing windows; 12, emptying orifice with its lid; A, quartz plate; B, quartz cylinder; C, quartz cylinder; D, quartz disk; E, water-cooled copper ring.



The direct current circuit for electrolysis is a very simple one. It is fed by a 20v — 500 amp dynamo with separate excitation, and contains the usual ammeter and volt meter.

**Experimental technique.—Raw materials.**—Potassium fluoride — p.a., E. Merck AG., Darmstadt.

Potassium fluotantalate ( $K_2TaF_7$ ), Fansteel-Hoboken, Antwerp (The analysis given by the manufacturers is: Ta > 45.5%; Nb < 0.01%; Ti < 0.01%; Si < 0.01%; Fe < 0.01%; W < 0.01%).

Potassium fluoniobate ( $K_2NbF_7$ ), Herman C. Stark, Berlin, Werk Goslar [No analysis is given, but it melts as a pure compound (21)].

Graphite, grade AGR, degassed thoroughly by heating under vacuum at a temperature 50°C higher than the working temperature.

**Description of an electrolysis run.**—After having placed a charge of 1500g of the required mixture of fluorides in the graphite crucible, the vessel is closed and the vacuum pump started. The charge is brought under vacuum to its melting point in about an hour. As soon as the charge begins to melt, the vacuum pump is stopped and purified argon is introduced into the furnace. When atmospheric pressure is reached, a flow of argon of 3 l/min is maintained. The cathode is then lowered into the bath under tension until it reaches a well-determined level, and the electrolysis is started. At the end of the experiment, the cathode is raised out of the bath, and the whole furnace is allowed to cool under purified argon.

No preelectrolysis is performed, because it could produce low valency ions in the bath prior to the start of the main electrolysis, thus changing the nature of the melt.

**Washing of cathodic deposits.**—After having tried different washing techniques described in the literature (1, 9, 16, 23, 24), we found (25) that the best method was as follows:

The deposits are broken by hammer and chisel and crushed in a mechanical crusher in the presence of a small amount of water. The crushed deposit is allowed to stay overnight in tap water; it is then crushed in a pebble mill. The fine metallic powder is washed for 1 hr with tap water in such a way as to ensure that only particles finer than 20 $\mu$  are lost.

Subsequent washing is done with hydrochloric acid of increasing concentrations (from 0.02 to 3N) in tap water. Finally, the powder is washed with distilled water and acetone before drying slowly under an infrared lamp. Only plastic jugs and beakers are used for the washing, to avoid any possible reaction of the fluorides with glass containers.

**Granulometric analysis and characteristic grain size.**—A standard Tyler sieves series was used, corresponding to mesh No. 28, 35, 48, 65, 100, 150, 200, 270, and 400.

Results have been plotted as the percentage of the different fractions retained between two sieves against the arithmetic mean diameter of the fraction. All the curves obtained have the same shape as the one represented on Fig. 2. To determine the characteristic grain diameter of the powder, a line is drawn from the maximum A of the curve parallel to the ordinate. Another line, parallel to the abscissa, is drawn from the center of the previous line cutting the curve at B and C. The center M of the segment BC gives the characteristic diameter  $\phi_{char}$  of the powder.

**Remarks concerning the current density  $J_c$  and the current efficiency  $r_c$ .**—The cathodic current density  $J_c$  is in fact the initial cathodic current density, unless otherwise stated.

The current efficiency  $r_c$  is based on the quantity of metal recovered after washing and is calculated by assuming that the valency of either tantalum or niobium is 5.

**Experimental program and results obtained.**—Influence of bath composition on current efficiency and

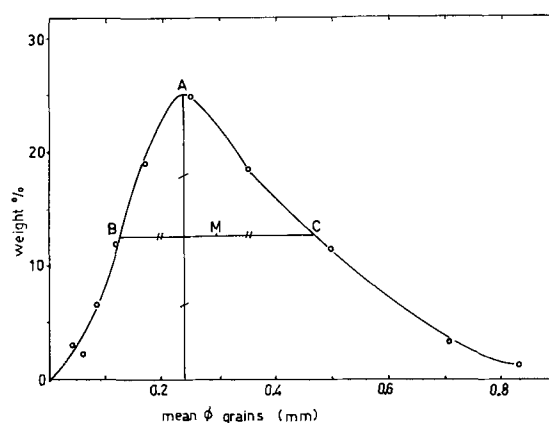


Fig. 2. Plot of a typical screen analysis showing the determination of the characteristic grain diameter ( $\phi_{char}$ ). Electrolyte, KF- $K_2TaF_7$  containing 25 m/o  $K_2TaF_7$ ; temperature, 900°C; initial cathodic current density, 480 amp/dm<sup>2</sup>; length of the electrolysis; corresponding to 177 amp hr.

**on characteristic grain diameter.**—All the experiments were carried out with the same initial current density of 400 amp/dm<sup>2</sup> corresponding to a current of 50 amp, the initial cathode area being 0.125 dm<sup>2</sup>. The bath temperature was kept near 900°C. All the electrolyses were performed with a quantity of electricity corresponding, at a theoretical current efficiency of 100%, to half depletion of the metal (tantalum or niobium) present in the bath. Thus, the duration of the electrolysis, and consequently the quantity of electricity passed through the cell, varied from one experiment to the other.

Figures 3 and 4 show the variation of the current efficiency and of the characteristic grain diameter against the molar composition of the bath. It can be seen that both  $r_c$  and  $\phi_{char}$  decrease when the initial content of tantalum or niobium of the bath increases. This effect is much more striking for niobium than for tantalum. From another point of view, the external aspect of the crystals gets worse when the tantalum or niobium content of the bath decreases.

It should be noted that the current efficiency falls almost to zero in the case of niobium as soon as the bath contains more than 25 m/o  $K_2NbF_7$ . It was also observed in this case that the steel cathode is severely corroded by baths containing more than 50 m/o  $K_2NbF_7$ . The color of the bath at the end of the electrolysis was yellowish green, while the walls of the

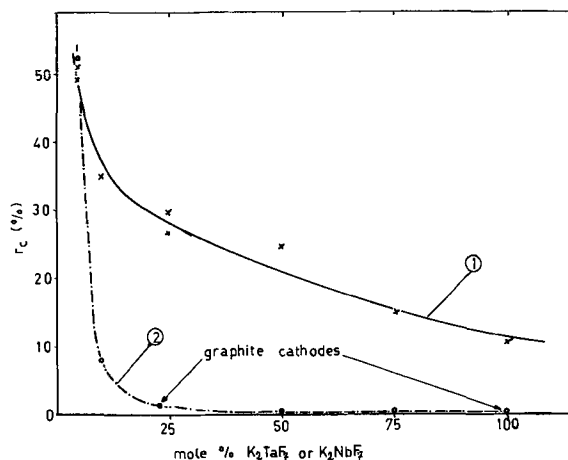


Fig. 3. Plot of the current efficiency against the molar composition of the baths for the systems KF- $K_2TaF_7$  (curve 1) and KF- $K_2NbF_7$  (curve 2). Weight of electrolyte, 1500 grains; duration, corresponding to half theoretical depletion of tantalum or niobium; initial cathodic current density, 400 amp/dm<sup>2</sup>; temperature, 900°C.

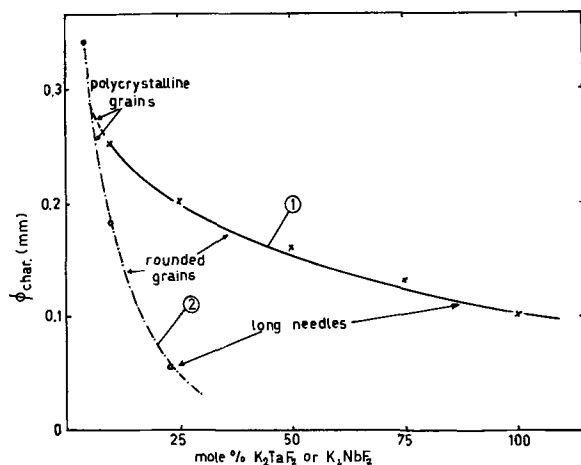


Fig. 4. Plot of the characteristic grain diameter against the molar composition of the baths for the systems  $KF-K_2TaF_7$  (curve 1) and  $KF-K_2NbF_7$  (curve 2); electrolysis conditions; see Fig. 3.

furnace were covered by a rather large quantity of a blue condensate.

At 10 m/o  $K_2NbF_7$ , these phenomena were practically negligible. In particular, the condensate on the walls of the furnace was white and in small quantity. It contained mainly  $K_2NbF_7$  and  $KF$ .

Two special runs were done with graphite cathodes and gave the same results as above stated, except for the yellowish color of the bath which was absent. It is thus probable that this color was due to an iron fluorocomplex whose formula is still unknown. On the other hand, it is probable that the blue condensate on the walls of the furnace contained some low valency niobium compound, such as  $NbF_3$ , but we did not succeed in identifying this compound by x-ray diffraction analysis. This point should be further investigated by additional research.

In the case of tantalum, no corrosion of the cathode was observed, and the condensate on the walls of the furnace remained always white. It seemed to contain essentially  $K_2TaF_7$  and  $KF$  and was produced in rather small quantity.

All the electrolyses described in this section were performed with anode effect. At the end of each run, the bath was covered by a black fluffy material consisting essentially of amorphous carbon.

*Influence of the initial cathodic current density on the current efficiency and on the characteristic grain diameter.*—The experiments were carried out with initial cathodic current density between 50 and 500 amp/dm<sup>2</sup>, at 900°C, and for a duration corresponding to the half theoretical depletion of the bath. For each type of baths, two compositions have been chosen: for  $KF-K_2TaF_7$ , 5 and 25 m/o  $K_2TaF_7$ ; for  $KF-K_2NbF_7$ , 5 and 10 m/o  $K_2NbF_7$ .

It was of course impossible to study the bath at 25 m/o  $K_2NbF_7$  because, as we have seen in the preceding section, it gives practically no deposit at all.

The plots shown on Fig. 5 and 6 are rather intricate; we will come back to this point in the general discussion at the end of the paper. We can see that the current efficiency increases with the cathodic current density in every case and that the results described in the preceding section are confirmed. Concerning the characteristic grain diameter, a problem arises due to the formation of polycrystalline grains. It is thus difficult to say whether the size of the true grains increases or decreases with the cathodic current density. In particular, in the case of the bath at 5 m/o  $K_2TaF_7$ , it is impossible to use the definition of the characteristic grain diameter as given above, because the shape of the distribution curve was not the usual one. The grains are coarser than in the other cases.

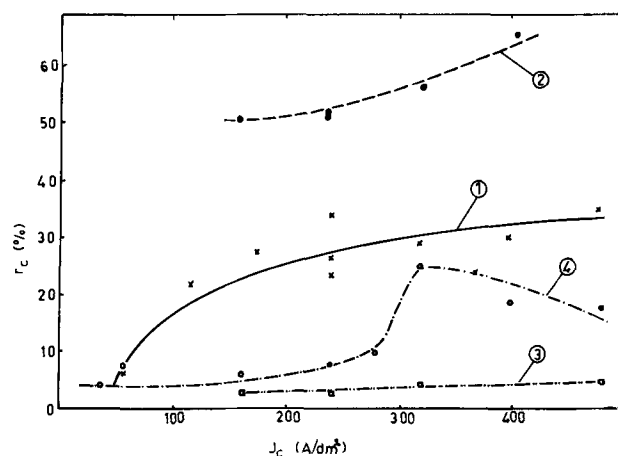


Fig. 5. Plot of the current efficiency against the initial cathodic current density for the following baths:  $KF-K_2TaF_7$  (75-25 m/o curve 1; 95-5 m/o, curve 2) and  $KF-K_2NbF_7$  (90-10 m/o curve 3; 95-5 m/o curve 4). Weight of electrolyte, 1500 grains; duration, corresponding to half theoretical depletion of tantalum or niobium; temperature, 900°C.

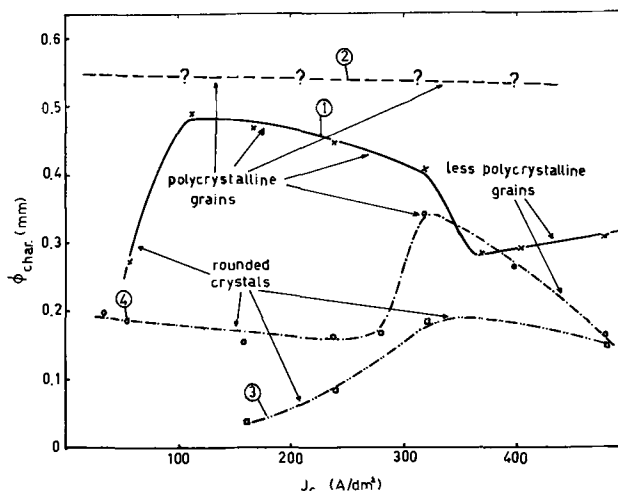


Fig. 6. Plot of the characteristic grain diameter against the initial current density for the following baths:  $KF-K_2TaF_7$  (75-25 m/o curve 1; 95-5 m/o curve 2) and  $KF-K_2NbF_7$  (90-10 m/o curve 3; 95-5 m/o curve 4); electrolysis conditions, see Fig. 5.

*Influence of duration of electrolysis on current efficiency and on characteristic grain diameter.*—The experiments were made with mixtures of  $KF-K_2TaF_7$  (75-25 m/o) and  $KF-K_2NbF_7$  (95-5 m/o) up to about two thirds of the theoretical depletion of the bath. Figures 7 and 8 show the results obtained under identical conditions for the two baths (initial cathodic current density, 240 amp/dm<sup>2</sup>; temperature, 900°C, 1500 gr. electrolyte).

It can be said that the two baths have roughly the same behavior: the current efficiency decreases and the grain size increases when the duration of the electrolysis increases. However, it should be noted that tantalum gives rise to polycrystalline grains which are bigger than those obtained for niobium. Moreover, the current efficiency is generally lower for niobium than for tantalum at equivalent percentages of the theoretical depletion of the bath.

*Influence of temperature on current efficiency and on characteristic grain diameter.*—The experiments have been run for  $KF-K_2TaF_7$  (75-25 m/o) and  $KF-K_2NbF_7$  (95-5 m/o) up to about 20-25% of the theoretical depletion of the bath. Figures 9 and 10 show the results obtained at 240 amp/dm<sup>2</sup> initial cathodic current den-

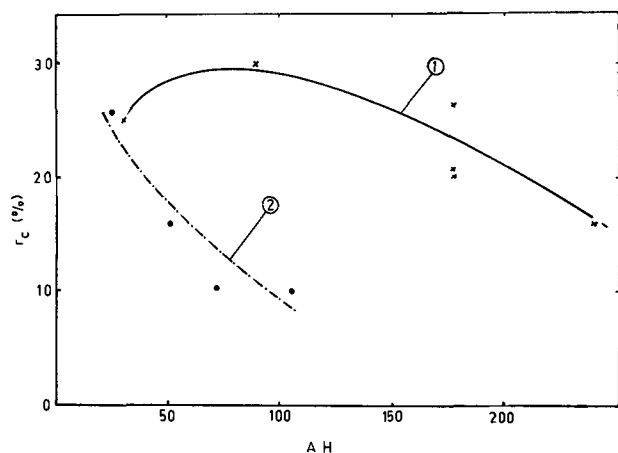


Fig. 7. Plot of the current efficiency against the duration of the electrolysis for following baths:  $\text{KF-K}_2\text{TaF}_7$  (75-25 m/o), curve 1;  $\text{KF-K}_2\text{NbF}_7$  (95-5 m/o), curve 2. Weight of electrolyte, 1500 grains; initial cathode current density, 240 amp/dm<sup>2</sup>; temperature, 900°C.

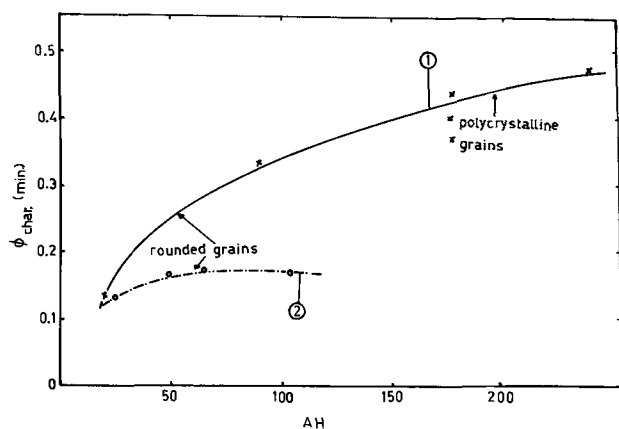


Fig. 8. Plot of the characteristic grain diameter against the duration of the electrolysis for the following baths:  $\text{KF-K}_2\text{TaF}_7$  (75-25 m/o), curve 1;  $\text{KF-K}_2\text{NbF}_7$  (95-5 m/o), curve 2. Electrolytic conditions; see Fig. 7.

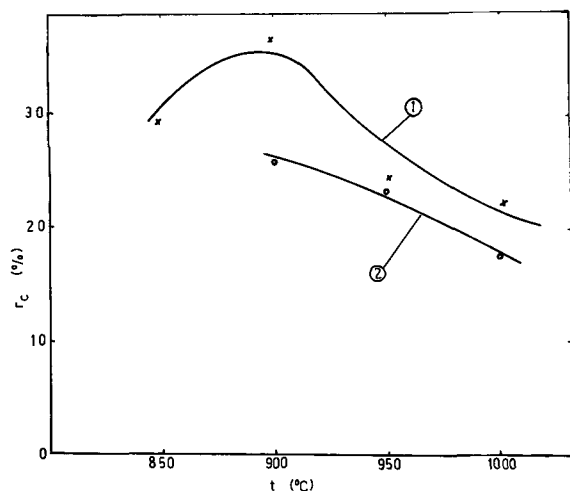


Fig. 9. Plot of the current efficiency against the temperature for the following baths:  $\text{KF-K}_2\text{TaF}_7$  (75-25 m/o), curve 1, and  $\text{KF-K}_2\text{NbF}_7$  (95-5 m/o), curve 2. Weight of the electrolyte, 1500 grains; initial cathodic current density, 240 amp/dm<sup>2</sup>. Duration of the electrolysis: corresponding to 50 amp hr for tantalum and to 25 amp hr for niobium, i.e., respectively, 25% and 18% of the theoretical depletion of the bath.

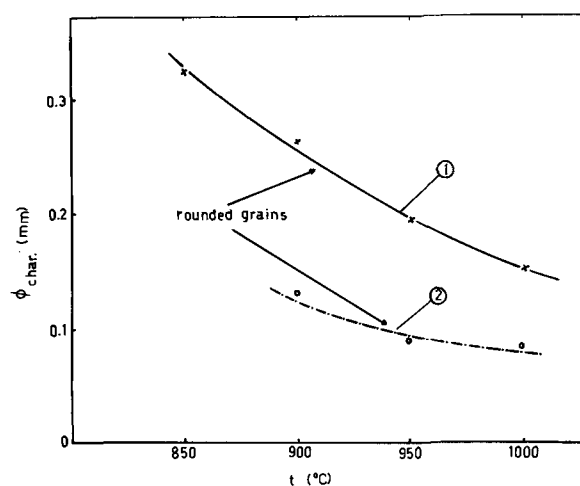


Fig. 10. Plot of the characteristic grain diameter against the temperature for the following baths:  $\text{KF-K}_2\text{TaF}_7$  (75-25 m/o), curve 1 and  $\text{KF-K}_2\text{NbF}_7$  (95-5 m/o), curve 2. Electrolysis conditions, see Fig. 9.

sity. The curve is limited to 900°C in the case of niobium because the bath melts at 840°C.

The two types of baths have the same behavior: the current efficiency seems to reach a maximum at about 900°C, while the grain size decreases regularly when the temperature increases.

#### Cathodic Polarization Curves for Deposition of Tantalum and Niobium from Pure Fluoride Baths

Cathodic polarization curves were drawn for the main baths used for the electrolyses described above using an "on" and "off" method to eliminate the ohmic drop between the cathode and the comparison electrode. The apparatus used has already been described previously by (5, 26) and has been used for other works similar to the present one (5, 13, 26-28). In this work, the rotating photographic recorder has been replaced by a Honeywell visicorder (29). The cathodic potentials measured just after switching off the current have been controlled in a few cases by making use of a double-beam Philips oscilloscope.

On the other hand, we have used comparison electrodes made of a silver wire dipping into a mixture of sodium chloride with 10 m/o silver chloride held in a boron nitride cylinder closed by a plug made of sintered boron nitride, bonded with a little sodium borate to ensure electrical conductivity (30).

Figure 11 summarizes the results obtained at 900°C for pure KF,  $\text{KF-K}_2\text{TaF}_7$  (75-25 m/o), fresh and after an electrolysis of 90 amp-hr and  $\text{KF-K}_2\text{NbF}_7$  (95-5 m/o), fresh and after an electrolysis of 60 amp-hr.

It can be seen that potassium is deposited at a potential of about 1.22v vs. the comparison electrode, and that the behavior of tantalum and niobium seems to be rather complex. We will come back to this problem in the general discussion.

#### General Discussion

*Electrochemical processes.*—In the present section, we shall see whether it is possible, on the basis of our experimental results, to give an answer to the question that we have put forward at the beginning of this paper: Why are the current efficiencies much lower for niobium than for tantalum under the same electrolysis conditions?

From the section on Phase Diagrams of the Systems it appears that the ionic species present in both types of baths ( $\text{KF-K}_2\text{TaF}_7$  and  $\text{KF-K}_2\text{NbF}_7$ ) should not be very different, at least at the beginning of the electrolysis. There must thus be another cause of the difference observed between tantalum and niobium in this respect.

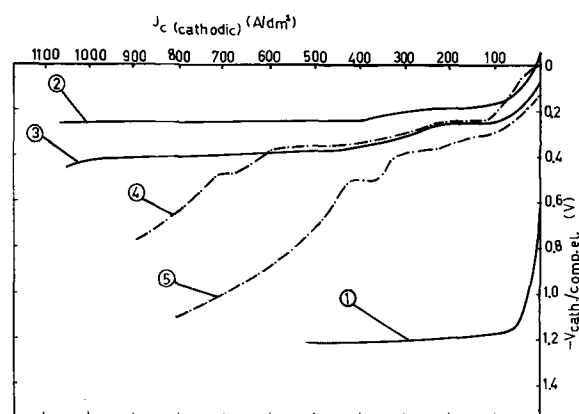


Fig. 11. Cathodic polarization curves for the deposition of: potassium, from pure KF (curve 1); tantalum, from  $\text{KF-K}_2\text{TaF}_7$  (75-25 m/o): fresh bath (curve 2) after an electrolysis of 90 amp hr (curve 3); niobium, from  $\text{KF-K}_2\text{NbF}_7$  (95-5 m/o): fresh bath (curve 4) after an electrolysis of 60 amp hr (curve 5). The ordinates give the potentials of the cathode against the "BN" comparison electrode ( $-V_{\text{cath/comp. el.}}$ ). The temperature is  $900^\circ\text{C}$ .

In fact, it is possible to explain all the experimental results in terms of the redissolution of the metal deposited at the cathode into the bath through a chemical reaction giving rise to lower valency species, this reaction being much more active for niobium than for tantalum.

Let us first consider the cathodic polarization curves of Fig. 11. Several authors (6-15) have found that the cathodic deposition of tantalum occurs through the medium of one reduced valency stage, while for niobium two intermediate reduced valency stages appear. However, these authors do not agree as to the charge of the metal ions in these several steps ( $\text{Ta}^{3+}$  or  $\text{Ta}^{2+}$ ;  $\text{Nb}^{4+}$ ,  $\text{Nb}^{3+}$  or  $\text{Nb}^{2+}$ ), nor do they agree about the corresponding ionic or molecular species. Even though it would be very interesting to have more detailed information on this problem, we do not think it necessary to discuss them more thoroughly at the present stage of our work.

Senderoff and Mellors (14, 15) have confirmed by chronopotentiometry that, in all-fluoride baths somewhat similar to those used in the present work ( $\text{LiF-NaF-KF} + \text{K}_2\text{NbF}_7$  or  $\text{K}_2\text{TaF}_7$ ), the deposition of tantalum or niobium occurs effectively through the above-mentioned intermediate steps. They are found as transients only and in a range of current density not exceeding  $35 \text{ amp/dm}^2$ . Thus it seems to us that, as our curves of polarization are drawn in such a way that they correspond to steady-state conditions as soon as the initial cathodic current density is higher than about  $50 \text{ amp/dm}^2$ , the observed potentials should correspond to the over-all reduction of the initial ionic species present in the bath to the metal and we should only observe one flat part on the curves before going up to the potential needed for the deposition of potassium, at least without making allowance for a secondary reaction. But, if we suppose that the cathodic deposit does not hold very tightly to the base metal, and that some part of the deposit is removed from it because of the bath agitation and its own weight,<sup>1</sup> then we must consider the possibility of a chemical reaction between the metal and the bath to form in the bulk of the melt the above-mentioned lower valency species.<sup>2</sup>

According to Senderoff *et al.* (14), tantalum metal is not attacked by  $\text{TaF}_7^{2-}$  in pure molten fluoride solutions. Instead, they have shown that a more oxidizing substance than  $\text{TaF}_7^{2-}$ , probably  $\text{Ta}^{6+}$  or a perfluoro-

compound, may be formed at the anode (31). This strong oxidizing substance, migrating and diffusing to the cathode, might be responsible, in the case of tantalum, for the dissolution of the metal to  $\text{TaF}_7^{2-}$  or  $\text{TaF}_2$ .

Anyway, the lower valency species can be partly re-oxidized at the anode, but they can of course take part in the cathodic process and give rise to a certain cathodic depolarization, at least as far as we do not exceed the limiting current density for their mass transfer from the bath to the cathode. According to this theory, we should thus observe two flat parts in the cathodic polarization curve for tantalum, and three for niobium. This is indeed the case.

The comparison between the polarization curves obtained for tantalum and niobium demonstrates that the limiting current density for the discharge of the lower valency species formed in the bulk of the bath is much higher for niobium than for tantalum, although the molar content in  $\text{K}_2\text{NbF}_7$  is five times lower than it is for  $\text{K}_2\text{TaF}_7$ . This suggests immediately that the secondary chemical reaction leading to the redissolution of the metal in the bath is much more active for niobium than for tantalum. Another point is that the current density limits for the deposition of the metal without depolarization or codeposition of potassium are much narrower for niobium than for tantalum. Finally, the comparison between the potential for the deposition of potassium and those observed for the deposition of tantalum and niobium without depolarization nor potassium codeposition leads to the conclusion that both metals seem to be deposited with a rather high overvoltage (about 0.7). This point should be investigated in another research program.

Let us now come back to the results of the electrolysis that we have performed.

We have found (Fig. 3) that the current efficiency decreases sharply with an increase of the molar content of the bath in  $\text{K}_2\text{TaF}_7$  or  $\text{K}_2\text{NbF}_7$ . This can certainly be explained by the redissolution chemical reaction that we have mentioned: it certainly will proceed at a higher speed if one of the components taking part in the reaction is present in higher concentration. Moreover, the long metallic needles that are observed at higher concentrations (Fig. 4) can probably be removed from the cathode more easily than the polycrystalline grains observed at low concentration. It appears clearly from Fig. 3 and 4 that the results are the same for both types of baths, but at much lower concentrations for  $\text{K}_2\text{NbF}_7$  than for  $\text{K}_2\text{TaF}_7$ . This certainly confirms our opinion that the redissolution chemical reaction occurs at a higher speed for niobium than for tantalum.

From another point of view, according to our hypothesis, we should observe an increase in current efficiency when the cathodic current density increases, at least as far as no potassium codeposition occurs. This is in fact what is shown on Fig. 5 (curves 1, 2, and 3). But for the bath at 5 m/o  $\text{K}_2\text{NbF}_7$ , it is probable that some potassium codeposition occurs at current densities higher than  $400 \text{ amp/dm}^2$ .

We can see in Fig. 7 that the current efficiency decreases when the duration of the electrolysis increases, at least after a certain length of time. This can be attributed to the fact that the mean cathodic current density for the whole electrolysis decreases with duration and this, according to Fig. 5, leads to a decrease in current efficiency in the range of current densities used in the experiments presented on Fig. 7. As the electrolysis goes on, the bath is progressively depleted in  $\text{K}_2\text{NbF}_7$  or  $\text{K}_2\text{TaF}_7$ , so that, according to Fig. 3, the current efficiency should, on the contrary, increase. These two opposite actions may account for the maximum observed in the case of tantalum.

Concerning the effect of temperature on current efficiency (Fig. 9), as the temperature increases the chemical reaction of redissolution proceeds faster; however, when the temperature is too low, the vis-

<sup>1</sup> In fact we have done an electrolysis with a small insulated graphite crucible hung under the cathode, and we have recovered a certain amount of metallic grains in it.

<sup>2</sup> In the case of niobium a blue color appears generally at the bottom of the bath, suggesting the presence of these reduced valency species in the bath.

cosity of bath increases and the deposited metal can be removed more easily from the cathode, so that a maximum could be observed on the curve, as it is the fact for tantalum. The decrease in current efficiency at low temperature could also be due to the lower speed of the mass transfer of the ions to be discharged to the cathode, leading thus to a partial codeposition of potassium.

We think we have been able to explain our experimental results in terms of the redissolution of the metal deposited at the cathode into the bath by a chemical reaction which is much more active for niobium than for tantalum. This is also in accordance with observations published recently (14, 15).

*Grain size and crystalline shape.*—We shall now discuss briefly the grain size and crystalline shape observed in terms of the general electrocrystallization theory (4, 5).

Generally, all the crystals observed are rounded grains or polycrystalline grains. This form of deposit occurs in fact at rather high overvoltages and correspond to the so called UD-type deposit (Unorientierter Dispersionstyp, *i.e.*, dispersed crystals, without any preferred orientation). Long needles, corresponding to the so called FI-type deposit (Feldorientierter Isolationstyp, *i.e.*, isolated crystals, oriented in the field), have only been found where the current efficiency was very low, because of the high concentration in  $K_2TaF_7$  or  $K_2NbF_7$  (see Fig. 4). This form of deposit can only be observed at low overvoltages, and it is probable that they are obtained through the lower valency species present in the electrolyte.

Concerning the variation of the grain size *vs.* the factors of the electrolysis, the discussion is somewhat difficult because of the formation on one hand of polycrystalline grains, and on the other, of very acicular crystals.

According to Fig. 4, the grain size seems to decrease when the concentration in the metallic ion to be discharged increases; this is of course the opposite of what could be expected from the theory: the germination speed should decrease and the growing speed of crystals should increase with an increase in concentration. The observations are somewhat confused because of the change in the nature of the grains obtained. Thus we think that the general theory still holds in our case, but that one should be extremely careful in the discussion of curves giving the characteristic grain diameter against any electrolysis factors: one should be sure, through microscopic examination, that the nature of the crystals did not change over the investigated range. In the case of Fig. 4, the polycrystalline grains observed at low concentration in  $K_2TaF_7$  or  $K_2NbF_7$  may be attributed to a high germination rate due to the rather high overvoltage. We have already explained the formation of the long needles observed at higher concentrations.

According to the theory, we should observe in Fig. 6 a decrease in the grain size with an increase in current density. In fact, the general behavior seems to be much more intricate. Again, we think that the theory is still valid, but we are not able to show it easily on a curve because of the formation of polycrystalline grains. These are found at rather high overvoltages, and they seem to be biggest in the range of current density where no cathodic depolarization occurs and where the codeposition of potassium does not occur.

Figure 8 shows, according to the theory, an increase in the size of the crystals with the duration of electrolysis, whereas Fig. 10 shows a decrease in the size of the crystals when the temperature increases, as can be expected when the inhibition is low.

Finally, from a practical point of view, it appears from Fig. 3 that it should, perhaps, be possible to deposit niobium from  $KF-K_2NbF_7$  baths with a rather good current efficiency, but that it should be necessary to work at a very low  $K_2NbF_7$  concentration, adding

continuously this compound in the immediate vicinity of the cathode.

### General Conclusions

We think that the reason for the low current efficiencies observed in the case of the electrodeposition of niobium from  $KF-K_2NbF_7$  is that some part of the niobium deposited at the cathode is removed from it by the agitation of the bath and by its own weight and is redissolved in the bath through a chemical reaction, giving rise to lower valency species. Some part of these species are reoxidized at the anode, and another part of them participate again in the cathodic process.

This phenomenon is much more effective for niobium than for tantalum in the same type of bath.

Further study should now be done with the same types of baths, but with the addition of  $Nb_2O_5$  or  $Ta_2O_5$ , and afterward in the presence of some alkaline chlorides.

### Acknowledgments

Our thanks are due to the Belgian Government which gave us a partial financial support. In particular, the subsistence of one of the authors was sponsored by the Pakistan Atomic Energy Commission from an O.C.D. scholarship given by the Belgian Government.

We are glad to acknowledge the help of the technicians of the laboratory, and especially of Mr. A. Verraghen.

Manuscript submitted Nov. 14, 1967; revised manuscript received May 28, 1968. This paper is part of the thesis presented by one of the authors (A.M.) in partial fulfillment of the requirements for the Ph.D. degree at the Free University of Brussels.

Any discussion of this paper will appear in a Discussion Section to be published in the June 1969 JOURNAL.

### REFERENCES

1. A. Mukhtar, Doctoral thesis in applied science, Free University of Brussels (1967) (ref. 72).
2. C. C. Ma, *Ind. Eng. Chem.*, **44**, 342 (1952).
3. R. H. Myers, *Proc. Aust. Inst. Min. Engrs.*, **144**, 297 (1946).
4. H. Fischer, "Elektrolytische Abscheidung und Elektrokristallisation von Metallen," Springer Verlag, Berlin (1954).
5. R. Winand, *Rev. Mét.*, **58**, 25 (1961); See also: "Contribution à l'étude de l'électrocristallisation en sels fondus et des phénomènes connexes—Application au cas du Zirconium," Thèse de Doctorat en Sciences Appliquées, Université Libre de Bruxelles, juin 1960.
6. P. Drossbach and F. Petrick, *Z. Elektrochem.*, **61**, 410 (1957).
7. I. D. Efros and M. F. Lantratov, *Zhur. Prikl. Khim.*, **36**, 2659 (1963).
8. V. M. Amosov, *Izv. Vyschikh Uchebn. Zavedenii, Tsvetn. Metal*, **8**, 110 (1965).
9. A. J. Kolk, Jr., M. E. Sibert, and M. A. Steinberg, "Technology of Columbium (Niobium)," p. 44 B. W. Gosner and E. M. Sherwood, Editors, John Wiley & Sons, New York (1958).
10. R. Gut, *Helv. Chim. Acta*, **43**, 830 (1960).
11. L. E. Ivanovskii and M. T. Krasil'nikov, "Electrochemistry of Molten and Solid Electrolytes," p. 41, Consultants Bureau Inc., New York (1961).
12. J. Dartnel, K. E. Johnson, and L. L. Shreir, *J. Less Common Metals*, **6**, 85 (1964).
13. C. Decroly and R. Winand, *ibid.*, **6**, 132 (1964).
14. S. Senderoff, G. W. Mellors, and W. J. Reinhart, *This Journal*, **112**, 840 (1965).
15. S. Senderoff and G. W. Mellors, *ibid.*, **113**, 66 (1966).
16. See ref. (1), and in particular: F. H. Driggs and W. C. Lilliendahl, *Ind. Eng. Chem.*, **23**, 634 (1931); C. W. Balke, *ibid.*, **27**, 1166 (1935); *Trans. Electrochem. Soc.*, **85**, 89 (1945); R. Monnier, Ph. Grandjean, J. Zahler, J. L. Blanc, and T. Toia, *Helv. Chim. Acta*, **44**, 1862 (1961); S. Nishimura, J. Moriyama, and I. Kushina, *Nippon Kogaya Kaishi*, **77**, 49 (1961);

- V. I. Konstantinov, S. I. Sklyarenko and E. A. Kholobes, *Poroshkovaya Metal.*, Akad. Nauk Ukr. SSR, **1**, 47 (1961);
- V. I. Konstantinov, K. M. Amosov, and E. A. Kholobes, *ibid.*, **5**, 42 (1961);
- E. Pruvot, French Pat. 1,199,033, Dec. 10 (1959);
- M. E. Sibert, USAEC Rep. AECU-3798 (1958);
- E. I. Gourovitch, *Zhur. Neorgan. Khim.*, **3**, 450 (1959);
- R. E. Cummings and F. R. Cattoir, U. S. Bureau of Mines, Rep. Invest. 6506 (9), (1964);
- G. W. Mellors and S. Senderoff, *This Journal*, **112**, 266 (1965);
- F. Van Goetsenhoven, *Mededel. Vlaam. Chem. Ver.*, **21**, 107 (1959);
- See also ref. (2), (3), and (9).
17. T. Iuchi and K. Ono, *Sci. Repts. Res. Inst., Tôhoku Univ.*, Ser. A, **13**, 456 (1961).
18. Ping-Hsim Ts'ui, N. P. Luzhnaya, and V. I. Konstantinov, *Zhur. Neorgan. Khim.*, **8**, 389 (1963).
19. I. D. Efros and M. F. Lantratov, *Zhur. Prikl. Khim.*, **37**, 2521 (1964).
20. R. Winand, *Ind. Chim. Belge, Comptes-Rendus du 31e Congrès International de Chimie Industrielle, Liège*, **1**, 744 (1958).
21. A. Mukhtar and R. Winand, *C. R. Acad. Sci. Paris*, **260**, (13), 3674 (1965).
22. J. S. Fordyce and R. L. Baum, *J. Chem. Phys.*, **44**, 1159, 1166 (1966); *J. Phys. Chem.*, **69**, 4335 (1965).
23. R. Monnier, Ph. Grandjean, and J. Zahler, *Helv. Chim. Acta*, **46**, 2966 (1963).
24. V. I. Amosov and V. M. Amosov, *Tsvetn. Metal.*, **35**, 72 (1962).
25. A. Mukhtar, Travail de fin d'études (Civil Engineer in Metallurgy), Free University of Brussels (1965).
26. R. Winand, *Electrochim. Acta*, **7**, 475 (1962).
27. R. Winand, *ibid.*, **8**, 53 (1963).
28. C. Decroly, A. Fontana and R. Winand, *Mémoires Scientif. Revue Mét.*, **61**, 287 (1964).
29. R. Winand, *Electrochim. Acta*, **11**, 581 (1966).
30. R. Winand, *C. R. Acad. Sci. Paris*, **264**, 649 (1967).
31. G. W. Mellors and S. Senderoff, *This Journal*, **112**, 642 (1965).

## Contact Resistance of Electroless Nickel on Silicon

Iwao Teramoto, Hitoo Iwasa, and Hideo Tai<sup>1\*</sup>

Research Laboratory, Matsushita Electronics Corporation, Takatsuki, Osaka, Japan

### ABSTRACT

The electric resistance of electroless nickel contacts to p-type silicon is investigated. The contact resistance increases by a factor of 100 when the resistivity of substrate silicon increases 10 times. It is also found that the contact resistance greatly increases on increasing the heat treatment temperature except for an intermediate temperature range between 450° and 600°C. The x-ray and chemical analyses show that the heat treatment at high temperatures causes a sharp increase in content of the nickel silicide phase accompanied by a decrease in the nickel phase. The observed change in contact resistance due to heat treatment is discussed in relation to the chemical transformations in the nickel-silicon-phosphorus system.

For fabrication of silicon devices, it has become increasingly important to establish processes for obtaining electrical contacts to silicon with an ohmic or very low resistance. The most successful contacts so far obtained are the vacuum deposition of a metal such as aluminum, gold, silver, nickel, or molybdenum onto the silicon surface, followed by heat treatment to diffuse in or to alloy with silicon. Hooper *et al.* (1) reported the contact resistances between silicon with a wide range of resistivities and several different metals which were evaporated in vacuum of  $10^{-5}$  Torr at substrate temperatures of 250°-300°C. They mention that the heat treatment after evaporation produces considerable lowering of the contact resistance in the case of nickel or palladium contacts while for most of the other metals changes in the contact resistance are small.

The electroless plating of nickel to silicon was first applied by Sullivan and Eigler (2) who reported that after annealing at a temperature above 400°C the contact resistance of electroless nickel greatly increases for p-type substrates while it decreases for n-type. The great majority of work on electroless nickel, however, has dealt with chemical reactions involved in the plating process or effects of incorporated phosphorus on the structure and mechanical properties of the film (3-6).

In this paper, chemical changes of the electroless nickel p-type silicon system on heat treatment are discussed in relation to the contact resistance.

### Experimental

Single crystals of p-type silicon with the carrier concentration of  $10^{18}$ - $10^{19}$  cm<sup>-3</sup>, which is of the order

of surface carrier concentration of practical diffused devices, were used. For the contact resistance measurement, the crystals were sawed into wafers and both surfaces of each wafer were lapped with 1200 mesh alumina to a thickness of about 200 $\mu$ . They were cleaned by degreasing, slight etching with a mixture of 5 parts of concentrated HNO<sub>3</sub> and 1 part of 48% HF, and rinsing with distilled water and methyl alcohol. The wafers were then stored in iso-propyl alcohol. Prior to plating, the wafer was dipped in NH<sub>4</sub>F solution (50%) for 30 sec and again rinsed thoroughly with methyl alcohol. This pretreatment was found to make the resultant contact resistance most reproducible. Since the thickness of plated films was not thick (about 1000Å) enough to obtain x-ray diffraction patterns on the surfaces, powdered silicon was plated in a similar way, but to a greater thickness for the x-ray and chemical analyses.

The detailed procedure and discussion of electroless nickel plating used are described elsewhere (7). The plating solution for making electric contacts to silicon consists of 30 g/l of NiCl<sub>2</sub>·6H<sub>2</sub>O, 50 g/l of NH<sub>4</sub>Cl, 65 g/l of (NH<sub>4</sub>)<sub>2</sub>HC<sub>6</sub>H<sub>5</sub>O<sub>7</sub>, 10 g/l of NaH<sub>2</sub>PO<sub>2</sub>·H<sub>2</sub>O, and 10 g/l of EDTA. Just before plating about 200 ml NH<sub>4</sub>OH was added to 1000 ml of the solution. The heat-treating of the nickel film plated onto silicon was performed in a flow of hydrogen (0.5 l/min), for 30 min in most cases. For contact resistance measurements, a second plating by conventional acidic solution was applied in order to facilitate soldering through which electric connections to outer copper plates were made. After the second plating, the silicon wafers were cut to 3 mm squares, each of which was sandwiched by 60/40 tin-lead solder pellets and copper plates outermost, being followed by soldering in a hydrogen flow at 340°C for 6 min. Possible protrusion

<sup>1</sup> Present address: Faculty of Engineering, Osaka University, Osaka, Japan.

sions of solder were removed by grinding all edges. A micrometer capable of 0.01 mm resolution was used for surface area measurement. The resistance, that is the d-c voltage drop between two outermost copper plates divided by the d-c current (0.1-1 amp) was then measured on this sample. The contact resistance in ohm-cm<sup>2</sup> was estimated by subtracting the resistance attributable to the bulk silicon from the measured resistance.

The chemical and x-ray analyses were performed on powder samples which were electroless nickel plated and heat treated in order to identify the phases present and determine the elemental composition.

### Results

The contact resistance was measured as a function of soldering temperature on the samples with hole concentration of  $1 \times 10^{18} \text{ cm}^{-3}$  and  $1 \times 10^{19} \text{ cm}^{-3}$ . The results are shown in Fig. 1. The electroless nickel films were heat-treated at a temperature of 450°C for 30 min. The contact resistance decreases with increasing soldering temperature, but at high temperatures a considerable amount of nickel may dissolve in the liquid solder. The solubility of nickel in the 60/40 tin-lead solder was determined by the chemical analysis of nickel in the solders which were equilibrated with solid nickel at constant temperatures and quenched. As shown in Fig. 2, the solubility of nickel in the liquid solder below 600°C is significantly lower than that in pure tin (8), and even than that in pure lead (9). Considering these two results concerning the soldering temperature, use was made of 340° or 400°C as the soldering temperature for further experiments.

Figure 3 represents the effect of carrier concentration in substrate silicon on the contact resistance. Heat-treating and soldering were made at 450° and 400°C, respectively. The contact resistance increases by a factor of  $10^2$  if the carrier concentration in substrate silicon is one order of magnitude lower. This result is comparable with the case of aluminum contact evaporated onto p-type silicon, reported by Hooper *et al.* (1), in which contact resistance of 0.005 ohm-cm silicon is higher and to 0.05 ohm-cm is lower than those of the respective present electroless nickel contacts. It is to be noted that a measurement of electroless nickel contact to n-type silicon with  $1 \times 10^{18}$  carriers  $\text{cm}^{-3}$  gave a contact resistance of  $2.5 \times 10^{-5}$  ohm-cm<sup>2</sup> which is remarkably lower than that of evaporated nickel contact.

The effect of heat-treating temperature on the contact resistance was studied and the result is shown in Fig. 4. The samples which contain  $1 \times 10^{18}$  holes  $\text{cm}^{-3}$

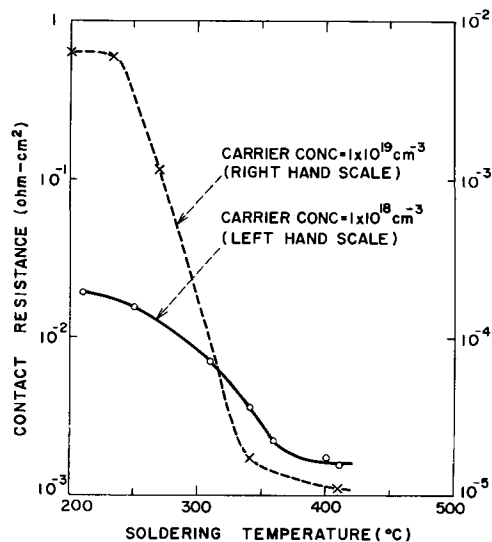


Fig. 1. Contact resistance of electroless nickel on silicon as a function of soldering temperature.

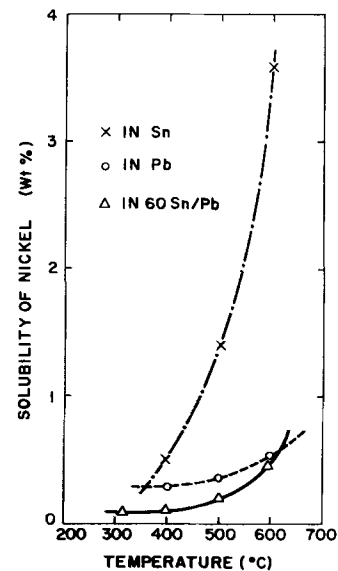


Fig. 2. Solubility of nickel in tin [after Hansen (4)], lead [after Elliott (5)] and 60/40 tin-lead solder.

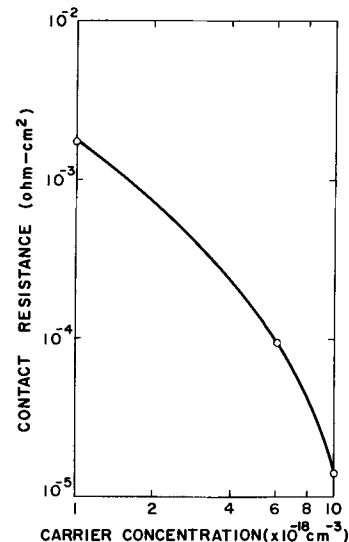


Fig. 3. Contact resistance of electroless nickel as a function of carrier concentration in silicon substrates.

were plated and followed by heat-treatment for a period of 30 min and soldering at 340°C. The contact resistance increases with increasing heat-treatment temperature except for the intermediate temperature range between 450°-600°C where it can be seen that the contact resistance is nearly independent of the temperature. This irregularity occurs in the temperature range, in which a peak and a steep increase of contact resistance were observed by Sullivan and Eigler for n-type and p-type silicon, respectively (2).

The present x-ray examination on the powder samples showed amorphous patterns for as-deposited electroless nickel, in accordance with the result of Goldenstein *et al.* (3), although proof of crystallinity by electron diffraction has been reported (4). After heat-treatment above 450°C, a new phase different from nickel or silicon was found, which was most probably NiSi on the basis of three peaks observed in the diffraction pattern. No Ni<sub>3</sub>P phase was detected. For the quantitative analysis of the NiSi phase, 40 w/o (weight per cent) of tungsten powder as a reference was admixed with the nickel-plated powder samples after heating. The diffraction intensity was measured on the (220) peak for tungsten and the (111) peak for nickel, and for NiSi the peak appearing at  $45.6^\circ$  of  $2\theta_{\text{CuK}\alpha}$  was used. Figure 5 shows the variation of

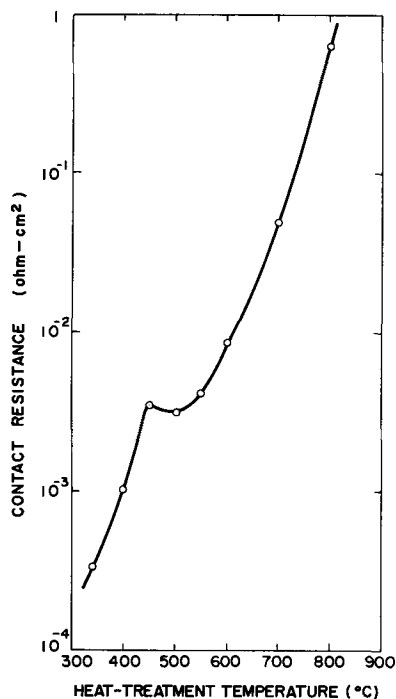


Fig. 4. Contact resistance of electroless nickel on silicon as a function of heat-treatment temperature.

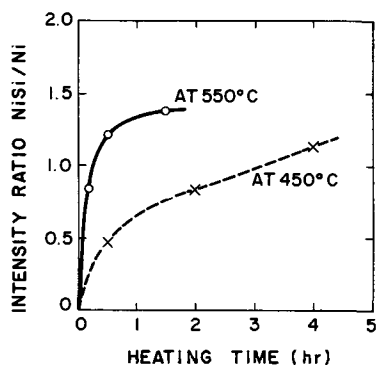


Fig. 5. Diffraction intensity ratio NiSi/Ni as a function of heating time.

NiSi content relative to nickel phase with the heating time, where the growth curves can be approximated by the logarithmic law. The x-ray intensity of NiSi and nickel phases as a function of heat-treatment temperature is shown in Fig. 6. As expected, the amount of NiSi sharply increases with increasing the heat-treatment temperature. On the other hand, the con-

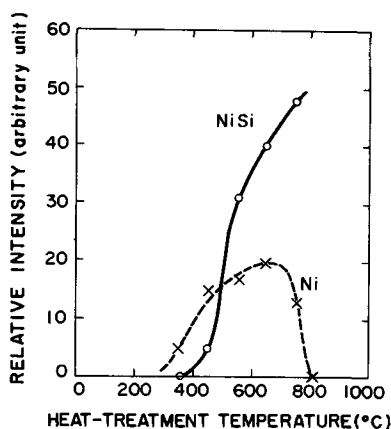


Fig. 6. Relative diffraction intensity of NiSi and Ni as a function of heat-treatment temperature.

tent of nickel phase passes through a broad peak in the vicinity of 600°C. Below the temperature of this peak, the amount of the nickel phase increases on increasing the heat-treatment temperature as a result of crystallization of amorphous nickel. Above the peak temperature, the content of the nickel phase approaches zero as the temperature is increased toward the value at which all of the nickel reacts with silicon to form nickel silicides.

The chemical analysis of nickel and phosphorus was made in two stages as follows. After the plated and heated silicon powders were immersed in aqua regia, the dissolved nickel and phosphorus were analyzed. These are named "soluble" elements. The undissolved powders were alkali-fused and dissolved in acid. The nickel and phosphorus in this acid solution were named "insoluble" elements. The results are shown in Fig. 7 and 8. At low heat-treatment temperatures almost all the nickel exists in "soluble" form, but the soluble nickel content goes down as a result of high temperature heating above 450°C where at the same time the insoluble nickel content increases. The apparent decrease of total nickel at high temperatures may be attributed to formation of a material unattacked by the alkali-fusion. This fact again suggests formation of the nickel silicides from the nickel phase, because the solid solubility of nickel in silicon, which may be in "insoluble" form, is far below these observed values. Figure 8 indicates that the content of "insoluble" phosphorus is invariably low, being comparable with the detectability in the present analysis, and that of "soluble" phosphorus is nearly proportional to the "soluble" nickel content. Thus it is suggested that most of the phosphorus component is associated with the "soluble" nickel regardless of possible formation of nickel phosphides. The decrease in the total phosphorus content above 600°C could be attributed to evaporation during heat treatment.

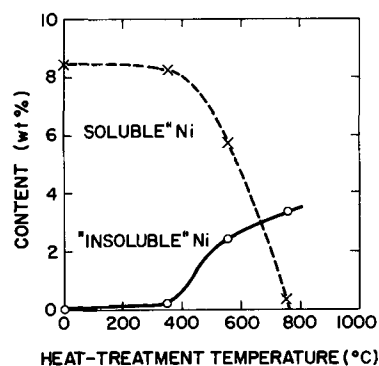


Fig. 7. Chemical analysis of nickel content "soluble" and "insoluble" in aqua regia (--- see text) as a function of heat-treatment temperature.

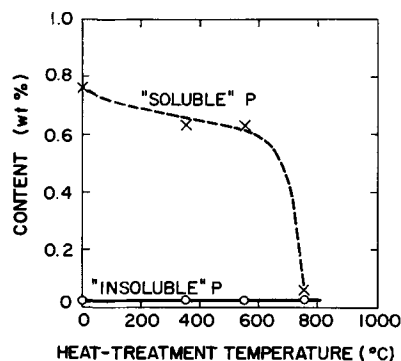


Fig. 8. Chemical analysis of phosphorus content "soluble" and "insoluble" in aqua regia (--- see text) as a function of heat-treatment temperature.

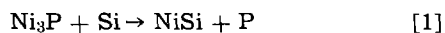


### Discussion

According to Hansen's phase diagram for the nickel-silicon system (8), there exist at least six intermediate compounds, of which NiSi is the silicon-richest one next to NiSi<sub>2</sub>. The latter compound is formed by a peritectic reaction which is usually quite slow in rate. This may be the reason that NiSi<sub>2</sub> was not detected by the present x-ray examination. Since nickel deposits on silicon substrates tend to become silicon rich at higher temperatures, it appears that nickel easily diffuses through the silicon lattice to form nickel silicides. This supposition is confirmed by the recent study of diffusion of nickel into silicon single crystals by Bonzel who obtained a diffusion coefficient at 450°C as large as 10<sup>-14</sup> cm<sup>2</sup>/sec (10).

As deposited the nickel-silicon interface comprises an intimate contact between the metal and the undisturbed semiconductor with no intervening layers. It was, in fact, observed that such a contact is unambiguously rectifying and has a reverse breakdown voltage of about 10v. By heat treatment below 450°C, nickel diffuses into the silicon substrate and creates an impurity gradient beneath the contact, which effectively impairs the rectifying property of the contact. However, since the solid solubility of nickel in silicon at a temperature below 450°C is deduced to be much lower than 10<sup>15</sup> atoms cm<sup>-3</sup> (11, 12), no "soluble" nickel was observed by the chemical analysis. According to Goldenstein *et al.* (3), on the other hand, phosphorus incorporated in the plated nickel film reacts with the nickel to form Ni<sub>3</sub>P at 300°C or above. Formation of this compound in the "soluble" film may effectively suppress the nickel diffusion into silicon, resulting in an increase in contact resistance with heat-treatment temperature.

Previous investigations as to the change in mechanical properties of electroless nickel during heat treatment have indicated that the equilibrium between nickel and Ni<sub>3</sub>P above 450°C is reached in as little as 30 min (3, 4). Approximately 30 w/o free nickel remains in the film after completion of the reaction with phosphorus to stoichiometric Ni<sub>3</sub>P, because the phosphorus content as deposited was found to be about 10 w/o in the present experiment. The observed facts regarding both the x-ray diffraction intensity corresponding to the NiSi phase and the "insoluble" nickel content increase above 450°C can be explained by the transformation of the free nickel remaining in the film to the NiSi phase. However, the room temperature resistivity of nickel silicides and the absolute value of thermoelectric power are so low that each of the silicides can be assumed to be either a metal or a degenerated semiconductor (13). Since the observed contact resistance is much higher than that estimated from the series resistance of silicides, the remarkable increase in contact resistance on heat treatment at temperatures above 600°C cannot be attributed to the NiSi formation from free nickel only. There is a further possibility for NiSi formation, *i.e.*



thus giving rise to a release of phosphorus. This assumption is based on an increase in free energies of formation of nickel phosphides with temperature (14), although they are still negative even at their melting points. It may be also supported by the fact that a remarkable decrease in hardness attributable to the Ni<sub>3</sub>P phase has been observed during heat treatment at temperatures above 450°C (4, 6). The released phosphorus could diffuse into the p-type silicon substrate, resulting in high contact resistance. This model explains the reported result that for the n-type substrate the contact resistance remarkably decreases during high temperature annealing (2). It is interest-

ing to note that if the effective hole concentration in the p-type substrate decreases by a factor of ten the contact resistance becomes 100 times higher as seen in Fig. 3. The solid solubility of phosphorus in silicon above 600°C is higher than 10<sup>19</sup> atoms cm<sup>-3</sup> (11, 12), but the diffusivity is not so high that the "insoluble" phosphorus content can be detected. The decrease of "soluble" phosphorus at temperatures higher than 550°C may be owing to evaporation of released phosphorus.

At the intermediate temperatures between 450° and 600°C no significant extent of phosphorus diffusion occurs because of the extremely small value of the diffusion coefficient, in accordance with the observed slight change in contact resistance. In this temperature range, the predominant chemical change is NiSi formation due to reaction of free nickel or Ni<sub>3</sub>P with substrate silicon, whereas phosphorus incorporated during plating can be assumed to have completely transformed to the Ni<sub>3</sub>P phase upon heat treatment for 30 min.

The above discussion can qualitatively explain all the results of x-ray and chemical analyses by regarding the free element and the Ni<sub>3</sub>P phase in the film as the "soluble" components and diffused elements into the substrate and the NiSi phase as the "insoluble" ones.

### Conclusion

The contact of electroless nickel plated onto p-type silicon has a rectifying character as deposited, but the resistance is greatly decreased by heat treatment at temperatures above 300°C as a result of the diffusion of nickel into the silicon substrate. From the practical point of view for obtaining a low contact resistance, it can be concluded that the most favorable temperature range of heat-treatment is between 450° and 600°C. Below 450°C no apparent NiSi phase is formed and consequently the mechanical contact may not be tight for the soldering process. Heat treatment at temperatures above 600°C brings forth a remarkable increase in contact resistance caused by diffusion of phosphorus into p-type silicon.

Manuscript submitted Mar. 29, 1968; revised manuscript received May 14, 1968.

Any discussion of this paper will appear in a Discussion Section to be published in the June 1969 JOURNAL.

### REFERENCES

1. R. C. Hooper, J. A. Cunningham, and J. G. Harper, *Solid-State Electronics*, **8**, 831 (1965).
2. M. V. Sullivan and J. H. Eigler, *This Journal*, **104**, 226 (1957).
3. A. W. Goldenstein, W. Rostoker, F. Schossberger, and G. Gutzeit, *ibid.*, **104**, 104 (1957).
4. A. H. Graham, R. W. Lindsay, and H. J. Read, *ibid.*, **109**, 1200 (1962); *ibid.*, **112**, 401 (1965).
5. J. P. Randin, P. A. Maire, E. Saurer, and H. E. Hintermann, *ibid.*, **114**, 442 (1967).
6. H. Mitani, K. Shoji, and T. Kanbe, *Kinzoku Hyomen Gijutsu*, **17**, 379 (1966).
7. H. Iwasa, M. Yokozawa, and I. Teramoto, *This Journal*, **115**, 485 (1968).
8. M. Hansen, "Constitution of Binary Alloys," 2nd ed., McGraw-Hill Book Co., New York (1958).
9. R. P. Elliott, "Constitution of Binary Alloys, First Supplement," McGraw-Hill Book Co., New York (1965).
10. H. P. Bonzel, *Phys. Stat. Sol.*, **20**, 493 (1967).
11. M. Yoshida and K. Furusho, *Japan. J. Appl. Phys.*, **3**, 521 (1964).
12. J. H. Aalberts and M. L. Verheijke, *Appl. Phys. Letters*, **1**, 19 (1962).
13. S. E. Mayer and A. J. Mlavy, "Properties of Elemental and Compound Semiconductors," H. C. Gatos, Editor, p. 261 (1959).
14. P. C. Ghosh and E. G. Hess, *Sci. Cult. (Calcutta)*, **28**, 386 (1962) not available to the authors; *Chem. Abstr.*, **58**, 2909 (1963).

# Anodic Oxidation of Hydrogen on Iron and Platinum in Sodium Hydroxide Solution

Sigmund Schuldiner\* and Clarence M. Shepherd\*

Naval Research Laboratory, Washington, D. C.

## ABSTRACT

In a rigorously controlled high-purity closed system, the electrochemical behavior of Fe and Pt electrodes for the hydrogen oxidation reaction showed marked differences both in the active and passive regions. The catalytic behavior of the two metals reflects the differences in metallic properties and anion adsorption. Iron was found to be a far better catalyst with a much less pronounced passive region. Iron corrosion was insignificant. Small amounts of platinum on iron strongly retarded hydrogen oxidation. Significant Pt dissolution and deposition on the iron working electrode was not found.

Recent work at this Laboratory (1, 2) has indicated that the passivation of the hydrogen oxidation reaction on platinum in acid solution is caused by anion adsorption. (Passivation is herein defined (2) as the anodic region in which  $dE/d(\log i)$  is negative). Anion adsorption initially caused rather moderate passivation effects due to the blocking of active sites in such a way as to cause a reduction in the effective electrode area. The major passivation effect, however, was due to a poisoning of catalytically active sites with strongly adsorbed anions and under proper conditions a combination of dermasorbed oxygen atoms and adsorbed anions.

The present work was undertaken to relate these findings to both Pt and Fe electrodes in alkaline solution. In addition, the question was considered of the effects of trace amounts of Pt deposited on pure iron in alkaline solutions on the behavior of the iron. This is an important question inasmuch as Pt counter and reference electrodes are commonly used in such experimental studies. Malachuk *et al.* (3) have indicated that anodic polarization of Pt in alkaline solutions can cause deposition of Pt on the working electrode.

## Experimental

The high-purity closed electrochemical system and experimental conditions were the same as reported (1, 4) with the exception that the solution was 0.2M NaOH. The working electrodes were a Pt wire (99.99%, 20 mil diameter, geometric area = 0.65 cm<sup>2</sup>); an Fe wire (fabricated from 3 pass electron beam zone refined iron with less than 4 ppm total metallic impurities, 20 mil diameter, geometric area = 0.65 cm<sup>2</sup>); and a similar Fe wire with about 1 cm of 3 mil Pt wire spot welded to the Fe wire and wound around its tip (Fe  $\gg$  Pt electrode). Each of these electrodes was connected to Pt leads and sealed off in lead-free soft glass tubes. The counter electrode was a large Pt gauze electrode. The reference electrodes were in an arm off the main cell compartment and were a calibrated miniature glass electrode and a Pd wire charged with hydrogen to a potential of about 50 mv positive to a hydrogen electrode in the same solution. This Pd-H wire electrode was used as the potentiostatic reference.

After the cell was cleaned with hot concentrated nitric acid, it was rinsed for at least 24 hr by continually distilling triply distilled water into it. About 100 ml of water was then distilled into the cell and cooled. A capsule of sodium metal (99.95% with <55 ppm heavy metals, sealed under argon) was broken in two and introduced into the cell under an atmosphere of purified helium. The two halves of the capsule were placed so that the open ends were at the bottom of the cell. Thus as sodium metal dissolved, the hydrogen gas generated filled the capsule ends and regulated the introduction of water into the capsule. This allowed a rather slow solution

of sodium metal. The resulting sodium hydroxide solution was 0.2M.

Before the Fe electrode was introduced into the cell, a Pt wire cathode was used with the Pt gauze electrode as an anode, and the solution was pre-electrolyzed at about 50 ma for several days under a pure helium atmosphere. On completion of the pre-electrolysis, the pre-electrolysis cathode was removed. Upon completion of the pre-electrolysis, the pre-electrolysis cathode was removed. The Pt electrode was then submitted to a potentiostatic polarization sequence of increasing and decreasing applied potentials until steady-state, reproducible values were obtained. This treatment took about 1 month. The helium flow was then replaced with hydrogen (purified by passing through heated Pd-Ag tubes). The potentials of the Pt wire, Pt gauze, and Pd wire were then determined against the glass electrode. After the Pt/H<sub>2</sub> electrodes reached their equilibrium values and the Pd wire was 50 mv positive to the Pt/H<sub>2</sub> potentials, the Fe wire (cleaned in 1M H<sub>2</sub>SO<sub>4</sub> and rinsed with triply distilled water) was introduced into the cell and was made the working electrode. After the open-circuit potential was determined, the gauze Pt electrode as the counter electrode and the Pd wire as the reference electrode were connected into the potentiostatic circuit. The glass reference electrode continuously monitored the potential on the Fe working electrode via a Keithley 610B electrometer. Current flow under potentiostatic conditions was determined with a Keithley 601 electrometer and recorded. Potentiostatic current-voltage curves were then determined after steady-state currents were achieved. Numerous runs under increasing and decreasing potential sequences were determined until reproducible results were obtained.

Similar measurements were made for a pure Pt wire working electrode. Another series of measurements was made with the iron wire with the small amount of attached Pt wire (Fe  $\gg$  Pt electrode).

While the electrodes were being held at a constant potential, the hydrogen (P<sub>H<sub>2</sub></sub> = 1 atm) flow was about 40 ml/min. When steady-state currents were obtained the hydrogen flow rate was increased to >1000 ml/min in order to minimize diffusion-controlled reaction rates. The currents shown in the figures were determined under these conditions. The temperature was 25° ± 2°C. All potentials were converted to the normal hydrogen electrode (NHE) scale.

## Experimental Results

The open-circuit potential for the Pt, Fe, and Fe  $\gg$  Pt electrodes were each the equilibrium potential of -0.78v for the H<sub>2</sub>O/H<sub>2</sub> reaction in the 13.2 pH, 0.2M NaOH solution. There was no visible sign of corrosion on the pure Fe wire even though the electrode was exposed for several weeks. However, the Fe  $\gg$  Pt electrode did show a very small amount of a yellowish brown corrosion product in the vicinity

\* Electrochemical Society Active Member.

of the Pt. Tests for iron in solution (thiocyanate) were always negative.

The steady-state potentiostatic current-voltage curves for the three working electrodes are shown in Fig. 1, 2, and 3. In each case there was some hysteresis on the decreasing potential sequence as compared to the increasing potential sequence. All of the electrodes showed Tafel regions at low anodic potentials where the rate of hydrogen oxidation was increased as the potential became more noble. At about  $-0.2\text{v}$  for the Pt electrode (Fig. 1) there was a sharp passivation and a large drop in hydrogen oxidation rate until a potential of about  $0.3\text{v}$  was reached. This was followed by a limiting current density of about  $3 \times 10^{-8}\text{ amp/cm}^2$  and at  $0.8\text{v}$  a Tafel region ( $b = 0.06$  slope) at which the predominant reaction is the oxidation of water to oxygen. The

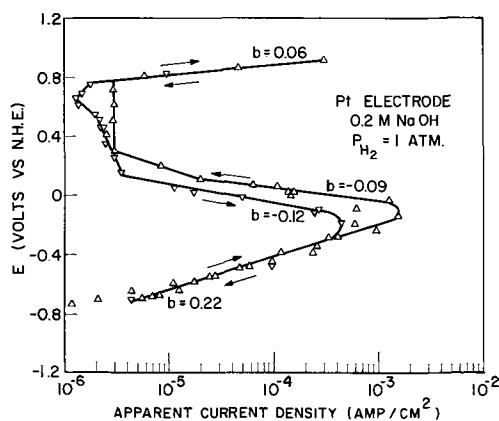


Fig. 1. Potentiostatic anodic current density vs. potential relation on Pt electrode.  $\Delta$ , increasing potential sequence;  $\nabla$ , decreasing potential sequence.

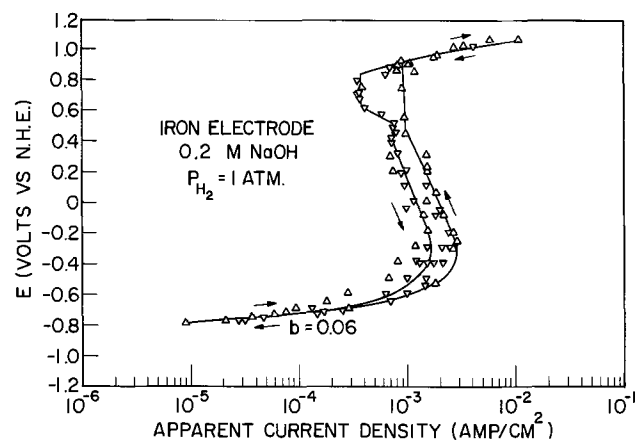


Fig. 2. Potentiostatic anodic current density vs. potential relation on Fe electrode. See Fig. 1 for meaning of symbols.

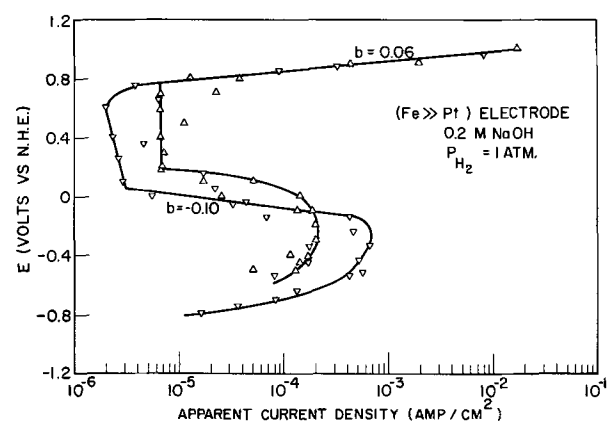


Fig. 3. Potentiostatic anodic current density vs. potential relation on Fe  $\gg$  Pt electrode. See Fig. 1 for meaning of symbols.

hysteresis for the decreasing potential sequence is most likely caused by dermasorbed oxygen (1, 4) until a potential of  $-0.3\text{v}$  where the hysteresis effect vanishes.

Figure 2 shows that the potentiostatic current-voltage relation for Fe is very different from that of Pt. The transition to a passive state is not as sharp, and the retardation of the hydrogen oxidation reaction in the passive region is rather moderate. An  $\text{O}_2$  formation region is reached at about  $0.9\text{v}$ . The hysteresis on the decreasing potential sequence may be due to either dermasorbed oxygen or an invisible layer of oxide. In any case, as the potential reaches about  $0.2\text{v}$  of the equilibrium value, the hysteresis becomes insignificant and the state of the iron surface is essentially the same as for the increasing potential sequence.

The data for the Fe  $\gg$  Pt electrode shown in Fig. 3 indicates that the very small relative area of Pt played a dominant role. The similarity to pure iron is evident at low potentials only.

### Discussion

The most striking feature of the potentiostatic current-voltage relations comparing pure Fe with Pt is the fact that Fe is a far more active electrode for the hydrogen oxidation reaction at all potentials. Figure 4 shows a comparison of the potentiostatic curves for the three working electrodes for an increasing potential sequence.

The effect of a small area of Pt on the Fe wire was to decrease its activity so that it behaved more like a Pt than Fe electrode. At low polarizations, however, the Fe  $\gg$  Pt electrode behaved more like the pure iron, especially in the decreasing potential sequence. The reduction in the limiting current density compared to both the Fe and Pt electrodes (Fig. 4) is surprising, but probably reflects the small amount of iron corrosion product formed near the Fe/Pt interface. It is evident from these experiments that trace amounts of Pt would have a marked effect on the electrode behavior of pure iron. It is evident also that under the experimental conditions using the high-purity system dissolution of Pt from electrodes during pre-electrolysis or during a run and the subsequent deposition of part of this Pt on the iron electrode must have been insignificant. There is, in fact, no evidence of Pt impurity affecting the results on the pure iron working electrode. Similarly there is no evidence of traces of iron in solution depositing on the Pt working electrode and affecting its behavior significantly.

The sharpness of the onset of passivity on the Pt electrode and the almost three orders of magnitude drop in hydrogen oxidation rate in this passive region ( $-0.1$  to  $0.3\text{v}$ ) indicate that the passivation is due primarily to the increase in the free energy of activation of the hydrogen oxidation reaction. This effect

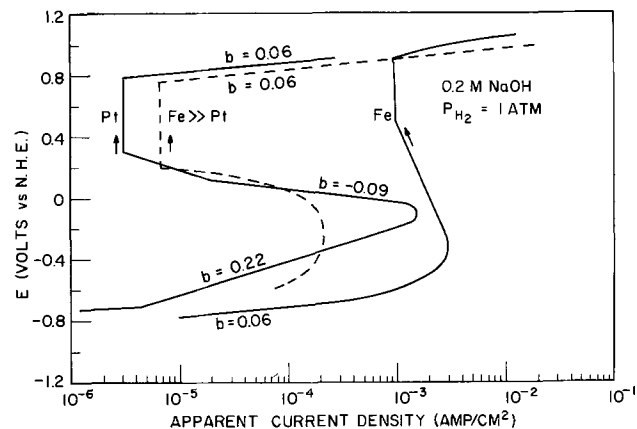


Fig. 4. Comparison of Pt, Fe, and Fe  $\gg$  Pt electrodes for increasing potential sequence.

is most likely due to the poisoning of catalytically active sites by anion ( $\text{OH}^-$ ) adsorption (2). The increase in activity in the potential range from about 0.1 to 0.0v for the decreasing potential sequence verifies this interpretation and, as in acid solution, shows the increased poisoning effect due to dermasorbed oxygen (2). These results are similar to those found for hydrogen oxidation passivation on Pt in sulfuric acid solution (1, 2) except that the alkaline solution results are more pronounced. This is evidently due to the higher heat of adsorption of  $\text{OH}^-$  over  $\text{SO}_4^{2-}$  ions. The much steeper Tafel slope ( $b = 0.22$ ) shown in Fig. 1, compared to the sulfuric acid result ( $b = 0.025$ ) reflects the fact that the rate-controlling step in alkaline solution is much more sensitive to polarization than in the acid. The 0.025 Tafel slope can be interpreted as a slow hydrogen dissociation to  $\text{H}_{\text{ad}}$  atoms, whereas the  $b = 0.22$  slope indicates that the rate is due to a complex hydrogen discharge. The hydrogen discharge must be affected by the sodium ions (5). The passivation as the potential becomes more noble indicates that the influence of adsorbed hydroxyl ions is probably not felt until the onset of passivity.

The surprisingly moderate passivation of the Fe electrode (Fig. 2) indicates that any anion adsorption or other effects at the passivation potential did not cause a poisoning of catalytically active sites and that the retardation of the hydrogen oxidation was due primarily to reduction in the active area (2) due to either weak anion adsorption or the formation of iron complexes with  $\text{OH}^-$  or other oxygen species. We do not, of course, know definitely that the iron electrode is free of oxide even at the open-circuit potential. However, the fact that it acts like a reversible hydrogen electrode and its low polarization eliminate the possibility of a high resistance oxide. Indeed, it is quite feasible that in the presence of hydrogen the iron is virtually free of oxides or oxygen species. The hydrogen equilibrium potential indicates an oxide-free metal, and the Tafel slope of 0.06 is likely due to a slow hydrogen discharge-controlled step. Additional work, however, is required to determine the state of the iron surface, both at the hydrogen equilibrium potential and under anodic polarization.

### Conclusions

This work has shown that the behavior of pure Pt and Fe electrodes under the rigorously controlled high-purity closed system environment is markedly different in both the active and passive hydrogen oxidation regions. The differences in catalytic behavior of the two metals are great, and their passivation behavior strongly reflect the differences in metallic properties and the influence of anion adsorption. No significant corrosion of iron was found, and iron was found to be a far better catalyst for the hydrogen oxidation reaction at all anodic potentials. Despite this the anion poisoning of catalytically active sites on iron was much less pronounced than on platinum. This means that anion adsorption has less effect on the surface states of iron than on platinum. Further work is required to define better the iron surface under the experimental conditions used so that its remarkable catalytic properties are understood. Under the conditions used, significant electrochemical effects due to dissolution and deposition of Fe or Pt on each other were not found.

### Acknowledgment

This research was supported by the Advanced Research Projects Agency of the Department of Defense as part of the ARPA Coupling Program on Stress-Corrosion Cracking (ARPA Order 878)

Manuscript submitted Feb. 21, 1968; revised manuscript received May 10, 1968. This manuscript was presented at the Montreal Meeting, Oct. 6-11, 1968, as Paper 333.

Any discussion of this paper will appear in a Discussion Section to be published in the June 1969 JOURNAL.

### REFERENCES

1. S. Schuldiner, *This Journal*, **115**, 362 (1968).
2. S. Schuldiner, *J. Electrochem. Soc.*, **115**, 897 (1968).
3. P. Malachuk, R. Jasinski, B. Burrows, and S. Carrol, Extended Abstracts J-I of the Battery Division, The Electrochemical Society Fall Meeting, Chicago, Oct. 15-20, 1967, p. 48.
4. S. Schuldiner, T. B. Warner, and B. J. Piersma, *This Journal*, **114**, 343 (1967).
5. S. Schuldiner, *ibid.*, **101**, 426 (1954).

## Solid Electrolyte Coulometry; Silver Bromide Electrolyte

John H. Kennedy and Fred Chen

*University of California, Santa Barbara, California*

and Andy Clifton

*Bissett-Berman Corporation, Santa Monica, California*

### ABSTRACT

The properties of a new type of coulometer utilizing a solid electrolyte have been investigated. The system consists of silver bromide electrolyte between a silver and a gold electrode. Coulombs of charge are recorded by plating silver on the gold electrode and then recovered by stripping the silver from the gold electrolytically. A voltage rise when the gold electrode is depleted of silver serves as the end-point indicator. Under carefully controlled conditions, more than 99% of the silver plated on the gold could be stripped off. However, long charging periods or idle periods between charging and stripping gave low results.

During recent years, considerable interest has developed in two fields, solid electrolyte materials (1-3) and miniature coulometers for integrating and timing circuit components (4). It has been the aim of this research to examine the problems associated with and

Key words: coulometer; coulometry; electrolyte; solid; silver bromide.

advantages of such devices, using solid electrolytes in place of the conventional liquid electrolytes.

The problems can be divided into three areas: (I) Preparation of solid electrolytes with acceptable conductivity over the required temperature range. (II) Achievement of high current efficiency over the required temperature range to yield cells with high

accuracy, long charge hold capability and also sufficient charge capacity. (III) Achievement of acceptable voltage cut-off characteristics for a practical system. This is primarily a function of electrode-solid electrolyte interface effects and electrolyte decomposition.

Of the many compounds which have been studied as solid electrolytes, silver compounds have two properties which make them attractive as silver coulometers; (i) conductivities are generally quite high compared to other solid materials, and (ii) conduction mechanism is via silver ion transference. Thus, it was concluded that initial studies should be made using silver compounds as electrolytes for coulometers.

The basic concept of these coulometers is quite simple. The system consists of a silver electrode, electrolyte, and gold electrode. An amount of silver is transferred electrolytically to the gold (charging operation). Then the silver is transferred back to the silver electrode (stripping operation). While silver remains on the gold electrode the system is essentially a silver-silver couple and the voltage is predominantly  $iR$  drop through the electrolyte. As the silver becomes depleted, the silver activity on the gold drops and the voltage begins to rise. Finally, when the silver is completely stripped off, the voltage may rise to over 1v as the gold begins to oxidize. This voltage rise can be used to activate a trigger circuit. When the charging and stripping operations are carried out at constant current, the process is used for timing. However, the voltage rise occurs when a specific number of coulombs have been transferred. Thus, when the charging cycle is carried out at variable current, integration can be accomplished by stripping at constant current

$$\int_0^{t_{\text{charge}}} i dt = i_{\text{strip}} t_{\text{strip}}$$

Since the process is electrolytic, the electrolyte must be an ionic conductor with a negligible electronic conductivity. Theoretically, if the same fraction of the current was electronic in both charge and strip, accurate timing could still be accomplished. However, any idle time between charging and stripping, called charge hold, would allow the electronic contribution to act as a short, changing the charge setting until the open-circuit voltage reached exactly zero. Also, in practice, the voltage drops are different for charge and strip because of electrode polarizations, which would cause the electronic contribution to be different. This consideration rules out pure  $\text{Ag}_2\text{S}$ ,  $\text{Ag}_2\text{Te}$ , and other silver compounds which are known to be electronic conductors, or have significant electronic contributions to their conductivity.

Silver halides, especially  $\text{AgI}$ , exhibit high conductivities and have been used in various solid electrolyte batteries (2, 5). Compounds of the type  $\text{MAg}_4\text{I}_5$  show conductivities similar to aqueous solutions (6, 7). On the other hand,  $\text{AgI}$  decomposes at 0.7v and thus, end-point signals would have to be significantly below this value to minimize electrolyte decomposition, and  $\text{KAg}_4\text{I}_5$  may not be stable at room temperature (7), which could cause undesirable time effects. Pure silver bromide has a low intrinsic conductivity,  $3 \times 10^{-8}$  mho-cm<sup>-1</sup> calculated at room temperature, but several studies have shown that higher conductivities can be achieved by the addition of impurities as doping agents. Especially effective are divalent ions,  $\text{Cd}^{++}$  (8) or  $\text{S}^{=}$  (9). Also, polycrystalline silver bromide exhibits much higher conductivities from grain boundary conduction (10). This study examines the characteristics of silver bromide as an electrolyte for solid electrolyte silver coulometers.

### Experimental

**Silver Bromide.**—Commercial  $\text{AgBr}$  (Matheson, Coleman, and Bell) was used for the studies labeled MC&B  $\text{AgBr}$ . Drying the material for 0, 2, 24, or 48 hr

was examined, but the results were identical. Bromine purification was used to eliminate reduced silver content. This was accomplished by contacting the material with bromine vapor at room temperature for  $\frac{1}{2}$  to 1 hr.

Silver bromide was also prepared from reagent grade  $\text{AgNO}_3$  and alkali bromide ( $\text{NaBr}$  and  $\text{KBr}$ ) by the following procedure. Solutions of 200 ml of approximately 1M  $\text{AgNO}_3$  and 1M  $\text{MBr}$  were mixed by pouring together into an empty beaker. The precipitate was digested near the boiling point for 1 hr and then allowed to stand for 12 hr. The silver bromide was filtered and dried for 3 hr at 135°C. Samples were prepared using stoichiometric ratios, 20% excess  $\text{AgNO}_3$ , and 10% excess  $\text{MBr}$ .

Silver bromide doped with  $\text{CdBr}_2$  was prepared by grinding together MC&B  $\text{AgBr}$  and  $\text{CdBr}_2$  [0.1, 0.2, 0.5 m/o (mole per cent)]. A preparation containing 0.2%  $\text{CdBr}_2$  was also prepared by heating the mixture at 280°C for 110 hr. No difference in results was observed.

Silver bromide doped with 0.2%  $\text{Ag}_2\text{S}$  was prepared by grinding the commercial materials together and heating at 280°C for 100 hr.

**Pellet preparation.**—Pellets were prepared with a Perkin-Elmer evacuable die, 0.5 in. diameter. As an example, 0.25g powdered silver (5-10 $\mu$ ) was pressed at 8000 psi followed by 0.50g silver bromide sample pressed at 8000 psi, and finally 0.50g powdered gold (5-15 $\mu$ ) pressed at 8000 psi. The whole pellet was then pressed under vacuum at 60,000 psi and held under these conditions for 1 min. After removal from the die, the edges of the pellet were sanded to remove any metal which would act as an electrical short.

Some of the pellets were sectioned and examined by photomicrography. The boundary lines between electrolyte and electrode were extremely sharp in all cases.

**Grain boundary examination.**—Grain size was determined for the  $\text{AgBr}$  electrolyte after pressing by etching the surface and examining microscopically. The surface was polished first with a metallurgical polishing wheel and then etched with a concentrated solution of sodium thiosulfate in water. The solution was rubbed on the silver bromide surface which was preferentially attacked along the grain boundaries.

**Electrode contacts.**—The first conductivity measurements were made by mechanically pressing gold and silver foils against the silver bromide pellet. The results were irreproducible and resistances were about 20,000 ohms for the normal pellet. The same pellets pressed between silver and gold powders had resistances of about 3000 ohms. The rest of the resistance when using foils was attributed to the electrode-electrolyte interface. This was also shown by the fact that the resistance was not linearly dependent on pellet thickness. All the work reported in this paper was done on pellets pressed between gold and silver powder. This method of electrode contact was reproducible, and the resistance was linearly dependent on pellet thickness.

In most cases, the pellets were then clamped between plastic plates containing metal lead wires. Pellets with spot-welded leads showed operating voltages which were pressure dependent after long periods of charge.

**Electrochemical measurements.**—A Beckman Electroscan-30 was used for controlled potential electrolysis, cyclic voltammetry, and recorded charge-strip cycles at constant current. Specialized test equipment with trigger circuit cut-off was provided by Bissett-Berman Corporation for constant current charge-strip cycles. This equipment was especially useful for long cycles because the current was automatically stopped when the voltage reached a predetermined value (0.5-0.8v). Although the Electroscan-30 is designed as a 3-electrode system, the pellets did not normally contain a reference, and

thus, all measurements are voltage drops between working anode and cathode. An experiment is described in which a silver reference was placed next to the working silver electrode to study electrode polarization.

### Results

**Resistivity measurements.**—Resistance of the pellets was measured with a General Radio No. 1650A Impedance Bridge using 1000 cycle a-c signal. The resistance consists of three terms, two electrode-electrolyte contacts and the electrolyte itself. Since the contact resistance should be independent of pellet thickness, resistance measurements on MC&B AgBr ( $\text{Br}_2$  purified) pellets of various thicknesses from 0.015 to 0.254 cm were made and are shown in Fig. 1. Within experimental error, the points lie on a straight line with the intercept at zero indicating little, if any, contact resistance.

The resistivity was about a thousand times smaller than that calculated from the intrinsic conductivity measured at higher temperatures. This result is in agreement with previous studies (10) which attributed the enhanced conductivity to grain boundary conduction. Silver bromide prepared from  $\text{AgNO}_3$  and alkali bromide gave widely varying results, and the resistance rose rapidly with time (Fig. 2). Heating the

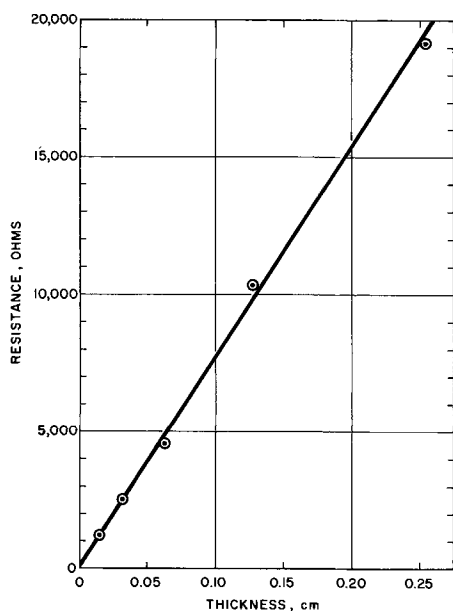


Fig. 1. Resistance of AgBr pellets, MC&B AgBr,  $\text{Br}_2$  purified

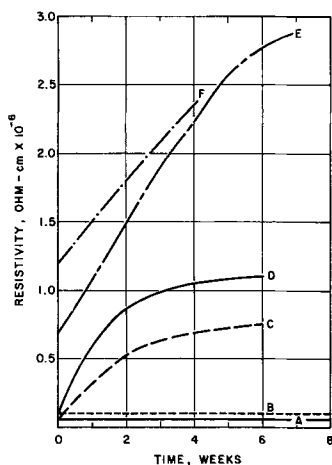


Fig. 2. Aging effects for AgBr pellets. (A) MC&B, no  $\text{Br}_2$  purification, (B) MC&B,  $\text{Br}_2$  purified, (C) Precipitated AgBr, NaBr, excess  $\text{Ag}^+$ ,  $\text{Br}_2$  purified, (D) Precipitated AgBr, NaBr, stoichiometric,  $\text{Br}_2$  purified, (E) Precipitated AgBr, KBr, excess  $\text{Ag}^+$ ,  $\text{Br}_2$  purified, (F) Precipitated AgBr, KBr, excess  $\text{Br}^-$ , no  $\text{Br}_2$  purification.

pellet to  $200^\circ\text{C}$  for 2-3 hr increased the resistivity up to  $6 \times 10^6$  ohm-cm. The heat treatment was not a drying effect; pellets made from AgBr powder dried at  $200^\circ\text{C}$  for 48 hr had resistances only slightly higher than the powder dried at  $130^\circ\text{C}$ . Pellets of commercial AgBr heated to  $100^\circ\text{C}$  for short periods of time showed little or no change in resistance when cooled to room temperature, but a marked increase to  $> 10^6$  ohm-cm occurred when treated at  $200^\circ\text{C}$ . The increase in resistance after heat treating was not due to an electrode-electrolyte interface effect, since thicker pellets showed a proportionate increase, too. The grain size of precipitated AgBr was 8-20  $\mu$  diameter while MC&B was 2.6-3.5  $\mu$  diameter. MC&B heated to  $200^\circ\text{C}$  had a grain size of 12-13.5  $\mu$ . Thus, it appeared that the larger the grain size, the lower the conductivity.

The resistivity of MC&B AgBr as a function of temperature is shown in Fig. 3 for the temperature range  $-40^\circ$  to  $+100^\circ\text{C}$ . At room temperature the resistivity compares closely with the freshly precipitated material of Shapiro and Kolthoff (10), but the slope was not as great, resulting in higher conductivities at low temperatures.

Samples of MC&B AgBr were treated with bromine vapor to eliminate the presence of reduced silver from photodecomposition. The powder turned from light green to bright yellow and was handled in the dark after the bromine treatment. The resistivity increased from  $0.60 \times 10^5$  to  $0.98 \times 10^5$  ohm-cm, but again no aging effects were observed at room temperature. In order to standardize preparative procedures, all samples, except where noted, were bromine treated to eliminate reduced silver.

Addition of 0.1-0.5%  $\text{CdBr}_2$  to MC&B AgBr decreased the conductivity 10-30%, while 0.2%  $\text{Ag}_2\text{S}$  increased the conductivity 10%. All of the samples, including MC&B AgBr, contained small amounts of sulfur, but there was no apparent correlation between sulfur content and conductivity. Addition of KBr decreased the conductivity markedly.

It is concluded that MC&B AgBr exhibits high conductivity primarily because of grain boundary conduction, since it loses the conductivity upon heat treating at  $200^\circ\text{C}$ . However, the crystallite surface properties must be less active than freshly precipitated AgBr, because room temperature annealing was not observed. Finally, it cannot be overlooked that small concentration of impurities, specifically  $\text{Ag}_2\text{S}$  and  $\text{Ag}_2\text{O}$ , may be enhancing the conductivity of the commercial AgBr and causing the surface passivity. In any case, the material gave reproducible results from bottle to bottle and showed no aging effects when kept below  $100^\circ\text{C}$ . Thus, it was a convenient material to use for solid electrolyte coulometry studies.

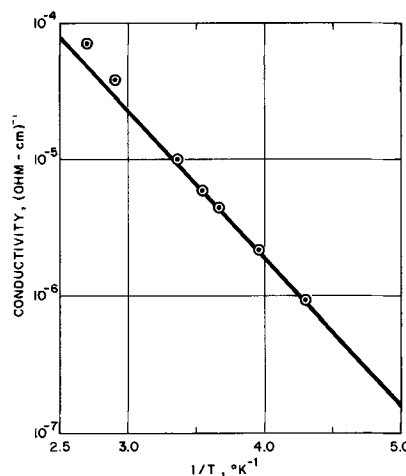


Fig. 3. Temperature dependence for AgBr conductivity, MC&B AgBr,  $\text{Br}_2$  purified.

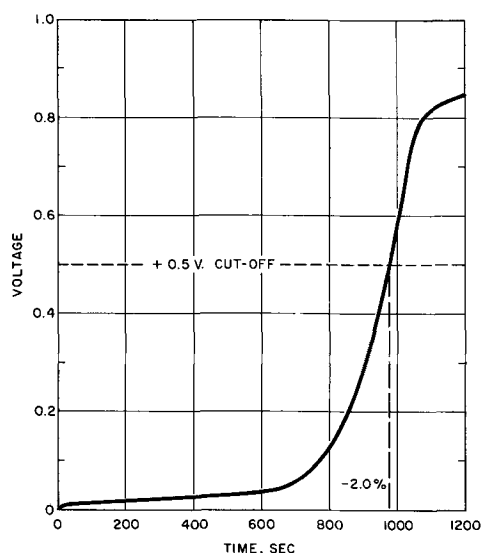


Fig. 4. Stripping curve for AgBr, MC&B AgBr, Br<sub>2</sub> purified. Charge: 1000 sec at 5  $\mu$ a; stripping current: 5  $\mu$ a.

**Charge-strip curves.**—The voltage drop during the stripping cycle should remain equal to  $iR$  until the gold surface becomes depleted of silver, at which time the voltage will rise until it reaches the Ag/AgBr, AuBr/Au potential plus  $iR$ , or until Br<sub>2</sub> discharge occurs at the Au electrode. Figure 4 shows a stripping curve for a charge of 1000 sec at 5  $\mu$ a. The gold surface had been oxidized to 500 mv vs. Ag before charging. As can be seen, the voltage starts to rise about 200 sec before the 500 mv end-point and reached the end-point at 980 sec, a -2% error.

During the charge cycle, the system is a silver-silver couple and the only voltage drop, in principle, should be from internal resistance. In practice, the voltage drop was somewhat higher than that predicted from a-c conductivity measurements because of polarization effects. Conductivity measurements taken at various stages of the charging cycle showed small changes in resistance (< 5%), but not enough to account for the voltage drop during d-c current flow. Polarization and increased resistance during long charge cycles was significant, the voltage sometimes rising to the decomposition voltage of the electrolyte.

**Cyclic voltammetry.**—Cyclic voltammetry was used to examine the electrode reactions which took place on the gold electrode. The pellet coulometers did not contain a reference electrode, and thus, the curves shown in Fig. 5 contain  $iR$  drop contribution. The silver electrode was assumed to be a stable reference electrode, since the curves were completed in less than 2-3 min which would not allow sufficient time to deplete the silver electrode of active sites. In general, three anodic peaks were observed before the final cut-off (Fig. 5). The anodic peak voltages corrected for  $iR$  drop were +0.095v, +0.30v, +0.63v while the final cut off was about +0.8v vs. the silver electrode. The first peak was usually observed on the first cycle only and would remain as only a shoulder on succeeding cycles. This peak was attributed to silver metal present on the gold being oxidized to AgBr. For a reversible couple, the peak voltage should be  $E_{1/2} + 0.028/n$ . The  $E_{1/2}$  value for silver oxidation is zero volts vs. the silver reference, and this shift to +0.067v probably indicates a lower silver activity on the gold compared to the pure silver electrode although irreversibility would also give rise to a voltage shift.

The final cut-off could be due to any of the following three reactions

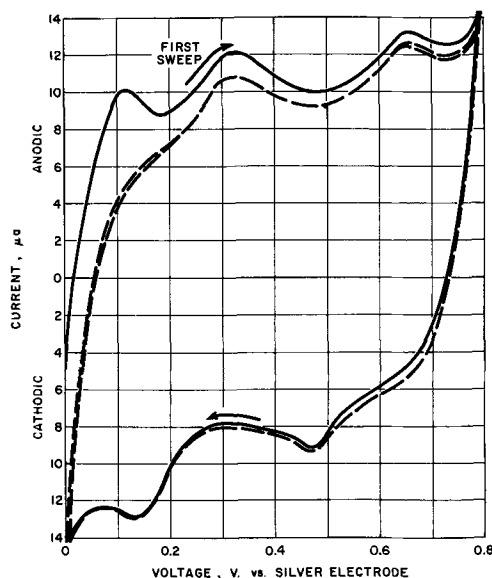
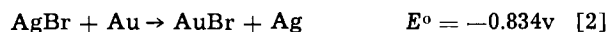
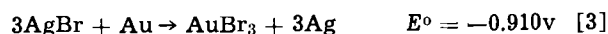
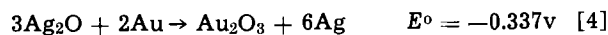


Fig. 5. Cyclic voltammetry, MC&B AgBr, no Br<sub>2</sub> purification, scan rate = 200 sec/v.



At high current densities all three may occur, but at equilibrium the most stable product would be AuBr.

The two small peaks at +0.30 and +0.63v were probably due to impurities. The following reactions are considered



The peak heights and positions were affected by scan rate, indicative of irreversibility. Also, the peak separation between anodic and cathodic scan was 0.14v (corrected for  $iR$  drop) for both peaks, again indicating irreversibility. It should be stressed that since a third reference was not present, voltage values are open to question, and with the irreversible nature, it is impossible to assign the peaks on the basis of voltage alone. However, addition of Ag<sub>2</sub>S to AgBr increased the peak height at +0.30v, which is compatible with reaction [6]. Also, addition of Ag<sub>2</sub>O did not increase the peak height at +0.30v, but introduced a new peak at +0.75v. Thus, it is concluded that the peak was caused by the presence of sulfide, and that the samples (both MC&B and precipitated AgBr) contained little or no Ag<sub>2</sub>O.

**Controlled potential electrolysis.**—Anodic stripping of the gold electrode at controlled potential was carried out to determine residual currents for the pellets. Current which flows at the cut-off voltage will determine the lower limit at which the coulometer can be used. In addition, the residual current can be used to calculate the upper limit of the electronic conductivity contribution. This limit was calculated by the method described by Ilschner (11) for single crystals of AgBr. The plateau region was not as well-defined for the polycrystalline material but little change in residual current was observed between 0.5 and 0.7v. The results in Table I show that the electronic conductivity for MC&B is about 0.2% of the total conductivity.

Controlled potential electrolysis was used to clean the pellet electrolytically prior to use and after a series of experiments. The technique was also used to recover silver charge on the gold electrode which was not found using constant current.



Table I. Residual current and leakage current results

Sample type	Residual current, at 0.7v, nanoamp	$k_{0'}^0$ , ohm <sup>-1</sup> cm <sup>-1</sup> $i_R \times 10^9$	Open-circuit time $T_{o.c.}$ , hr	Charge lost, $Q$ , $\mu\text{coul}$	Leakage current, $i_L = Q/T_{o.c.}$ , nanoamp
MC&B, 0.06 cm (thickness)	26	60	68	268	1.09
MC&B, 0.06 cm Br <sub>2</sub> purified	18	42	96	366	1.05
MC&B, 0.03 cm Br <sub>2</sub> purified	16	19	72	490	1.89
AgBr precipitated from NaBr, 0.06 cm	60	140	79	116	0.41
AgBr precipitated from KBr, 0.06 cm	34	79	144	314	0.61
MC&B, 0.2% CdBr <sub>2</sub> Br <sub>2</sub> , 0.06 cm	28	65	83	320	1.07
MC&B, 0.5% CdBr <sub>2</sub> Br <sub>2</sub> , 0.06 cm	28	65	141	497	0.98

**Leakage current.**—After a cell was driven to a high voltage (0.5–0.8v) the open-circuit voltage would decay slowly with time, and a number of  $\mu\text{coul}$  of charge had to be passed to return the cell to the original voltage. A representation of the process is shown in Fig. 6. The charge lost could be thought of as a leakage current and Table I shows the results for a number of AgBr pellets.

Several identical pellets (MC&B, Br<sub>2</sub> purified) were given waiting periods of 2–200 hr to determine charge lost as a function of time. The leakage current ( $i_L = Q/T_{o.c.}$ ) was higher at the beginning of the open-circuit period than at the end, indicating that the leakage current was a function of open-circuit voltage. Also, the leakage current was higher for pellets having closer electrode spacing, indicating that the leakage current was a function of cell resistance. These results are consistent with the idea of a small electronic contribution to the total conductivity. Since the leakage current was much lower than the residual current, the residual current must be predominantly ionic in nature. Based on the leakage current value, the electronic conductivity must be less than  $< 10^{-10}$  (ohm-cm)<sup>-1</sup> or 0.01% of the total conductivity for MC&B AgBr.

**Timing accuracy.**—Timing accuracy for the silver bromide coulometers was checked at currents of 1–100  $\mu\text{a}$  and for periods of 50–200 sec. This charge ranged from less than a monolayer (approximately 300  $\mu\text{coulombs}$ ) to about 70 atomic layers on the average. In the current range 5–50  $\mu\text{a}$ , the average error was less than  $\pm 1\%$  in almost all cases (Table II). At 1–2  $\mu\text{a}$  a positive error of about 25  $\mu\text{coul}$  was observed. The negative errors observed at high charge settings were shown to be predominantly silver remaining on the gold by stripping the gold at controlled potential, in which case the remaining  $\mu\text{coul}$  were recovered at very low current.

**Charge hold.**—Though the pellets showed high accuracy when stripping was carried out immediately, it is necessary that the charge be stored and stripped at a later time for most practical applications. Time at open-circuit between charging and stripping is called

charge hold. Silver bromide pellets gave negative errors as charge hold time increased. The results are shown in Fig. 7. Actually, the charge was not lost since the remaining silver could be removed at very low currents by using controlled potential electrolysis. This phenomenon is considered in detail in the discussion section.

**Charge capacity.**—Another practical consideration is the amount of charge which can be transferred to the gold and subsequently stripped without losing accuracy or shorting from silver growth. Table II shows that negative errors of 10% were observed with charges of 20,000  $\mu\text{coul}$  (5.56  $\mu\text{a-hr}$ ). Also, charge hold experiments indicated that negative errors were encountered as charge hold time increased (Fig. 7). Thus, it would be expected that negative errors would be observed when the cells were charged for long periods of time. Results shown in Fig. 8 confirm this prediction. Again the use of low currents, 1  $\mu\text{a}$ , was helpful in stripping the more inactive silver.

No shorting was observed up to 850  $\mu\text{a-hr}$  of charge transferred to the gold, and photomicrographs of the sectioned pellet showed a fairly smooth silver deposit on the gold. The thickness (9.27 $\mu$ ) was about three times that calculated from the amount of silver present (2.6 $\mu$ ), indicating that the silver layer was mixed with AgBr electrolyte. However, when an attempt was made to strip the silver from the gold, shorting occurred after half of the silver had been transferred. A thickness determination of silver on the gold after shorting gave the same results as the beginning. This would indicate that silver nearer the gold was being stripped first, leaving needles extending into the silver bromide. Needles growing on the silver electrode during the stripping operation would finally touch and short the cell. Needle growth on the silver must be much more pronounced, since the ratio of distances was about 50:1. The shorting needles were so thin that they were not detected under the microscope.

The operating voltage during long periods of charge would shift from the  $iR$  drop value to the decomposition voltage of the electrolyte. The time at which

Fig. 6. Controlled potential cleaning and charge leakage at open-circuit, MC&B AgBr, Br<sub>2</sub> purified.

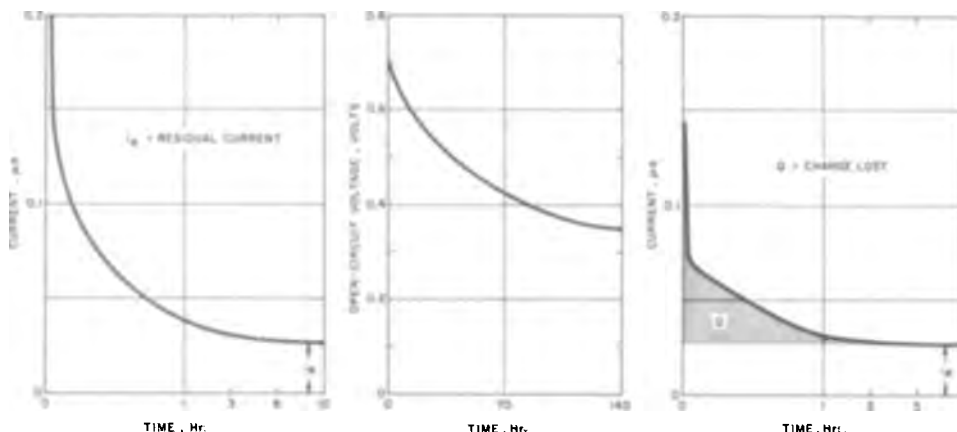




Table II. Timing accuracy for AgBr coulometers MC&amp;B AgBr

Current, $\mu\text{a}$	Charge time, sec					
	50		100		200	
	Avg. error, %	Avg. dev., %	Avg. error, %	Avg. dev., %	Avg. error, %	Avg. dev., %
1	+60.5	5.4	+26.2	2.4		
2	+17.8	2.4	+9.3	0.9		
5	+1.7	0.4	+0.9	0.6	-0.9	0.7
10	+1.7	0.8	0.0	1.2	+0.3	0.3
20	-0.2	0.3	-0.3	0.4	-0.1	0.6
50	-0.1	0.2	-0.1	0.3	-0.1	0.2
100	-0.2	1.0	-3.6	1.0	-10.3	0.3

Note: Results represent average of 8-10 determinations.

this voltage shift occurred depended on the current, clamping pressure and previous history of the pellet, but was 1-2 hr at 20  $\mu\text{a}$  for a fresh pellet (Fig. 9). Voltage measurements taken with an oscilloscope immediately after current interruption showed that only part of the observed high charging voltage was due to iR drop. The remainder was polarization with a very fast decay (half of the decay occurred during the first 20 msec). Charge transferred under these conditions showed the same type of negative error observed before the shift, i.e., no discontinuity in accuracy was found at the voltage shift point.

**Reference electrode experiments.**—In an effort to explain the high operating voltage during charge and the existence of seemingly inactive silver after storage, pellets were prepared with a gold and two silver electrodes by cutting the silver layer. One silver electrode was operated in the usual manner while

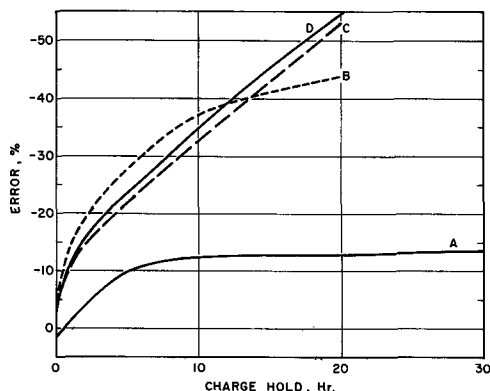


Fig. 7. Charge hold results. (A) MC&B AgBr dried powder,  $\text{Br}_2$  purified, 0.03 cm thick, (B) MC&B AgBr,  $\text{Br}_2$  purified, 0.06 cm thick, (C) MC&B AgBr, 0.2%  $\text{CdBr}_2$ ,  $\text{Br}_2$  purified, (D) MC&B AgBr, 0.5%  $\text{CdBr}_2$ ,  $\text{Br}_2$  purified.

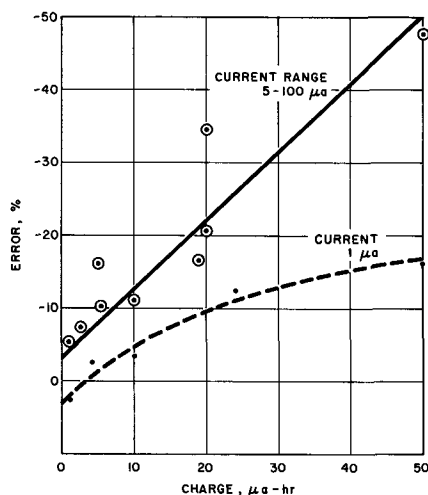


Fig. 8. Charge capacity results, MC&B AgBr,  $\text{Br}_2$  purified

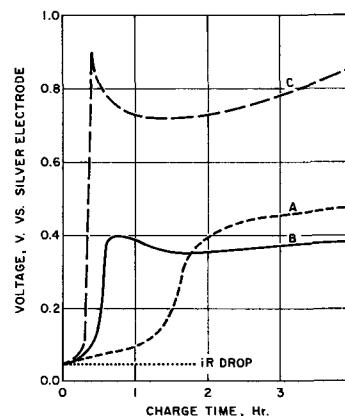


Fig. 9. Charge cycle polarization, MC&B AgBr,  $\text{Br}_2$  purified, current 20  $\mu\text{a}$ . (A) Fresh pellet, (B) Same pellet, 3 day idle period after 4 hr charge in (A), (C) Same pellet, 3 day idle period after four 4 hr charge periods.

the smaller section was used as a reference electrode. The potentials of the working silver and gold electrodes vs. the silver reference were recorded during charge and strip cycles.

At low currents ( $< 5 \mu\text{a}$ ), the voltage rise at the end of stripping was due to an increasing potential at the gold electrode as expected. However, polarization at the silver electrode was pronounced at higher currents during charge and some polarization was observed during stripping. Current interruption during charge showed a rapid decay to zero volts, while during stripping, decay was considerably slower.

No polarization ( $< 10$ -20 mv) was observed at the gold electrode during charge. Potential changes at the gold electrode during stripping occurred near the end-point, but the rise began earlier if a charge hold period had been present. A very slow decay took place when the current was interrupted.

Unclamped cells exhibited much larger voltages after long periods of charge which were pressure dependent. All of the voltage was accounted for by increased iR drop (checked by a-c conductivity measurement) and polarization at the silver electrode.

## Discussion

Although the solid electrolyte coulometer operated essentially as the simple concept predicted, several characteristics were observed which did not fit this picture. These were especially significant in the high charge capacity and charge hold experiments.

There are four electrochemical reactions which take place during operation. These are silver plating and stripping at the silver electrode, and silver plating and stripping at the gold electrode. In addition to contact problems when the cells were not clamped, reference electrode experiments indicated severe polarization while stripping silver from the silver electrode. Some polarization was also observed during silver plating at the silver electrode. These results suggest that only a small fraction of the silver electrode was available for electrolysis, and thus, high current densities at these few active sites greatly magnified concentration polarization effects. The high current density at a few sites on silver also explains the needle growth during stripping which caused shorting.

Electrodeposited silver is active (12) and would be deposited at active electrolyte sites. Thus, at the gold electrode, silver could be plated and stripped with high efficiency, provided the cycle time was short. When the charging time was long, or if a charge hold time was present, migrations in the electrolyte and on the silver surface allowed some of the silver to become inactive. This would contribute to the low results observed. This same effect was observed in aqueous solutions (13-15). Stripping at very low currents at controlled potential would allow much of this

silver to be recovered. After a charge-discharge cycle, electrodeposited silver would be present at the silver electrode and polarization should be less. This was also observed.

Another effect could cause low results during stripping. When large charges were used, the silver plate might be thick enough to allow under-cutting. That is, silver would be oxidized close to the gold leaving silver metal in the electrolyte region not connected electrically to the gold electrode. This silver would be lost permanently, and not recovered by controlled potential electrolysis. Under-cutting appeared to be significant (> 5% lost) only when charges of > 50-100  $\mu\text{a-hr}$  were attempted.

### Conclusion

Commercial AgBr (MC&B) when pressed between silver and gold metal powders exhibits adequate conductivity at room temperature to be useful as a solid electrolyte for coulometers. This conductivity appears to be predominantly along grain boundaries, but the material is sufficiently passive to show no room temperature annealing effects, and in fact, can be used at temperatures up to 100°C.

Silver coulometers containing AgBr as a solid electrolyte can be used under carefully controlled conditions. These conditions include current densities of 4-40  $\mu\text{a/cm}^2$ , preconditioning of the gold electrode to the cut-off voltage, charge capacities of 400-10,000  $\mu\text{coul/cm}^2$ , and immediate read-out (i.e., < 1 hr charge hold). Under these conditions, coulometer error will

be < 1%. Less stringent conditions can be applied if accuracy requirements are less demanding.

Manuscript submitted Feb. 9, 1968, revised manuscript received April 15, 1968.

Any discussion of this paper will appear in a Discussion Section to be published in the June 1969 JOURNAL.

### REFERENCES

1. K. Lehovc and J. Broder, *This Journal*, **101**, 208 (1954).
2. J. N. Mrgudich, *ibid.*, **107**, 475 (1960).
3. D. O. Raleigh, "Progress in Solid State Chemistry," Vol. 3, 83 (1966).
4. *Electronics*, **40**, No. 7, 186 (1967).
5. J. L. Weininger, *This Journal*, **105**, 439 (1958).
6. B. B. Owens and G. R. Argue, *Science*, **157**, 308 (1967).
7. J. N. Bradley and P. D. Greene, *Trans. Faraday Soc.*, **62**, 2069 (1966).
8. J. Teltow, *Ann. Phys., LPZ*, **5**, 63 (1949).
9. K. Lehovc and D. M. Smyth, U.S. Pat, 3,036,144, May 22, 1962.
10. I. Shapiro and I. M. Kolthoff, *J. Chem. Phys.*, **15**, 41 (1947).
11. B. Ilschner, *J. Chem. Phys.*, **28**, 1109 (1958).
12. W. M. Krebs and D. K. Roe, *This Journal*, **114**, 892 (1967).
13. J. J. Becker, *ibid.*, **111**, 480 (1964).
14. A. R. Nisbet and A. J. Bard, *J. Electroanal. Chem.*, **6**, 332 (1963).
15. J. W. Bixler and S. Bruckenstein, *Anal. Chem.*, **37**, 791 (1965).

## Membrane Potentials of Pyrex Glass Electrodes

R. H. Doremus

General Electric Research and Development Center, Schenectady, New York

### ABSTRACT

Potentials across Pyrex glass electrodes immersed in fused sodium-silver nitrates were measured. The membrane potential across the glass was small, so that the total cell potential was close to the electrode potential. The membrane potential showed a minimum at low silver concentration, which was attributed to the two-phase structure of the glass. These potentials were shown to be roughly consistent with the ion exchange theory for membrane potentials and measurements of ionic distribution and mobility in the Pyrex, although exact quantitative calculations of the potentials were not possible.

Several studies have been made of Pyrex borosilicate glass as a reference electrode for molten salts (1-6). However, in none of these papers was it made clear how much of the cell potential resulted from electrode potentials and how much from the glass. To test theories of the glass electrode potential it is important that the membrane potential of the glass itself be separately calculated and compared to the properties of the glass (7).

In the ion exchange theory the membrane potential of a glass electrode results from the exchange of ions between a solution and the glass (8, 9). This theory was found to be valid for a fused silica electrode in molten nitrates (7). In the present study membrane potentials across Pyrex glass electrodes immersed in fused sodium-silver nitrates were related to the ionic selectivity and mobility ratios in the glass.

Application of the equations for membrane potentials to Pyrex glass is complicated by phase separation in it. The presence of two phases in Pyrex has been deduced from electrical (10) and ion exchange measurements (11). Other borosilicate glasses show two phases in the electron microscope, but the scale of separation is too fine in Pyrex to be seen in this way. The membrane potential in Pyrex was apparently

influenced by the two phases present, and a completely satisfactory interpretation of the data was not possible.

### Equations for Glass Electrode Potentials

This section is based on a review article (9) which should be consulted for further details.

In the ion exchange theory the potential developed across a "fixed-charge" membrane with different solutions on either side of it can be separated into two portions, a phase boundary (Donnan or surface) potential and a diffusion potential. The surface potential arises because of differences in activities of ions between the solutions and the glass, while the diffusion potential results from differences in mobilities of different ions in the glass.

In most silicate glasses only monovalent cations can exchange and contribute to the membrane potential, so that present treatment is limited to these ions. The equilibrium distribution of A and B ions exchanging between solution and glass can be represented by the coefficient

$$K_{AB} = \frac{a'b''}{b'a''} \quad [1]$$

where  $a$  and  $b$  are the ionic activities in the solution (one prime) and the glass (two primes). The phase boundary potential depends on this selectivity coefficient, and the diffusion potential is determined by the ratio of mobilities  $u_B/u_A$  of the two ions in the glass. If a glass membrane separates two solutions 1 and 2 containing different ions A and B, the total membrane potential  $V_M$  in the case of constant activity coefficients and mobility ratio in the glass is (8, 9)

$$V_M = \frac{RT}{F} \ln \frac{a_1' + K_{AB}(u_B/u_A)b_1'}{a_2' + K_{AB}(u_B/u_A)b_2'} \quad [3]$$

where  $R$  is the gas constant,  $T$  the temperature, and  $F$  the Faraday. If the mobility ratio and activity coefficients of the ions in the glass are functions of concentration, the equations for the potential cannot be integrated without knowledge of the functionality. Even in this case the membrane potential is constant with time as soon as equilibrium between the solutions and glass surfaces is established and does not depend on the concentration profile of diffusing ions.

### Experimental Methods

Tubes of Pyrex glass of outside diameter 1.28 cm and wall thickness 0.11 cm were annealed at about 550°C and cooled slowly (1–2°/min) to room temperature. The composition of this glass was about 81% SiO<sub>2</sub>, 13% B<sub>2</sub>O<sub>3</sub>, 4% Na<sub>2</sub>O, 2% alumina, and small amounts of minor constituents. The Na<sub>2</sub>O concentration was found to be 4.22% with the flame photometer. The density of the glass at room temperature was 2.2 g/cm<sup>3</sup>.

The electrical potential across the glass was measured with the cell described previously (7, 9). An inner Pyrex tube contained pure molten silver nitrate, while the outer bath contained mixed silver-sodium nitrate in a fused silica cup. The composition of this solution was determined by weighing the salts as they were successively added to the outer melt. The electrodes were thin silver wires wound on fine silica tubes. Cell potentials were measured with a Keithley 610 B electrometer, or with a Rubicon potentiometer with the electrometer as a null indicator when more accuracy was desired. Cell potentials for a particular tube were reproducible to about ±1 mv. Temperatures were measured with a platinum: platinum-rhodium thermocouple immersed in the melt.

### Experimental Results and Discussion

To calculate the electrode potentials of the silver-silver nitrate electrodes, and thus to determine the membrane potentials of the glass from the total measured cell potentials, it was necessary to know the thermodynamic activities of the ions in the silver-sodium nitrate melts. Several investigators have measured the activity of silver ion in these melts (12–15); in ref. (12), (13) and (15) the following equation is given for the activity coefficient  $\gamma_{Ag}$  of this ion

$$\ln \gamma_{Ag} = \frac{840}{RT} X_{Na}^2 \quad [4]$$

where  $X_{Na}$  is the mole fraction of sodium nitrate in the melt. This result assumes negligible diffusion potentials in the cells with transference used to measure the electrode potentials. A very small diffusion potential was reported in ref. (15), using cells with and without transference. Application of the Gibbs-Duhem relation to Eq. [4] gives the following equation for the sodium ion activity coefficient

$$\ln \gamma_{Na} = \frac{840}{RT} X_{Ag}^2 \quad [5]$$

A somewhat lower value than 840 was found in ref. (14), and also in this reference and ref. (13) there is some evidence that Eq. [4] and [5] (implying a regular solution) do not apply over the whole concentra-

tion range. These small uncertainties do not affect the conclusions found here, except as noted below.

The total cell potentials measured for two different Pyrex tubes in various silver-sodium nitrate mixtures are given in Fig. 1. The electrode potentials  $V_e$  were calculated from the usual equation

$$V_e = \frac{RT}{F} \ln \frac{b_2}{b_1} \quad [6]$$

where the  $b$ 's are the thermodynamic activities of the silver ions in the two solutions, calculated from Eq. [4]. Since one solution was pure silver nitrate, it was taken as the standard state and considered positive, so that  $b_2 = 1$ . The calculated electrode potential as a function of ionic concentration is also shown in Fig. 1. The membrane potential  $V_m$  is the difference between the measured cell potential and the electrode potential and is plotted in Fig. 2.

If the activity data of Liquornik and Marcus (14) are used, the calculated electrode potential is up to 4

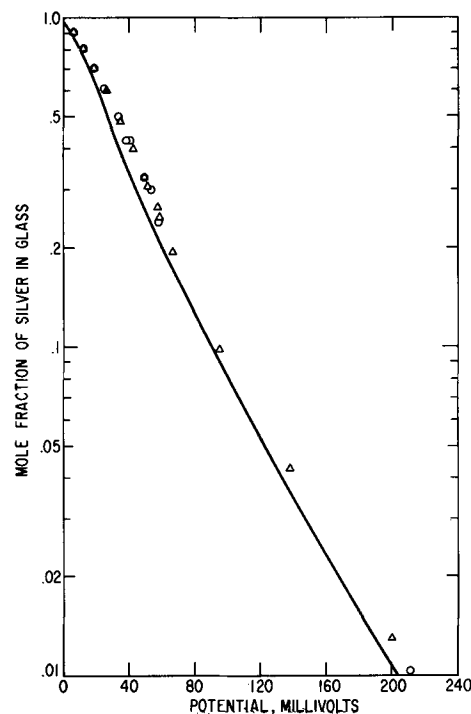


Fig. 1. Total measured cell potential at 340°C for two different Pyrex glass tubes containing pure silver nitrate and immersed in different silver-sodium nitrate solutions. Line, electrode potential calculated from Eq. [6].

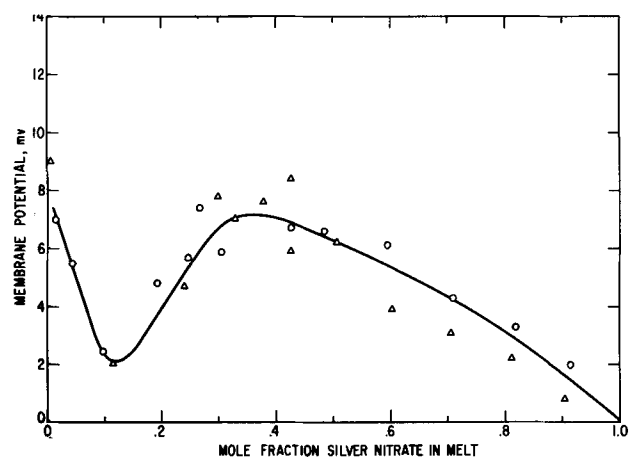


Fig. 2. Membrane potential of two Pyrex glass tubes containing pure silver nitrate and immersed in different silver-sodium nitrate solutions.

or 5 mv higher. While this is not a large fraction of the total potential, it does shift the membrane potentials at the lower silver concentrations to values 4 or 5 mv more negative, with progressively smaller shifts for higher silver concentrations. The general shape of the curve is not changed.

The membrane potentials shown in Fig. 2 are small, being only a few millivolts over the entire concentration range studied. This result is particularly striking at low silver concentrations, where the total measured potentials were larger than 200 mv. This small membrane potential implies that the product  $K_{\text{NaAg}}(u_{\text{Ag}}/u_{\text{Na}}) = p$  is close to one, if the melt is not too far from ideal thermodynamically. The value of  $p$  can also be estimated from the measured cell potential  $V$ , which is the sum of the electrode potentials  $V_e$  and the membrane potential  $V_M$ . From Eq. [3] and [6]

$$V = V_e + V_M = \frac{RT}{F} \left\{ \ln \frac{a_1 + pb_1}{a_2 + pb_2} + \ln \frac{b_2}{b_1} \right\} \quad [7]$$

or

$$\exp \frac{VF}{RT} = \frac{(a_1/b_1) + p}{(a_2/b_2) + p} \quad [8]$$

If the activities in solution 2 are held constant, a plot of  $\exp VF/RT$  against  $a_1/b_1$  should be a straight line. A plot of this kind for some of the present data is shown in Fig. 3. Since  $b_2 = 1$  and  $a_2$  is small, the slope of the line in Fig. 3 should equal to  $1/p$ , and the intercept unity. From the data in Fig. 3,  $p$  is about one.

However, the functional dependence of potential on melt concentration, shown in Fig. 2, does not fit Eq. [3] very well. This is because the plot of membrane potential in Fig. 2 is more sensitive to deviations from Eq. [3] than is the plot of total cell potential in Fig. 3, particularly for small membrane potentials. The minimum in the potential curve shown in Fig. 2 is not much beyond the experimental error, but it is believed to be real, since it was reproducible and was found on several different samples.

The equilibrium distribution of sodium and silver ions between nitrate melts and Pyrex was measured and reported elsewhere (11). The  $K_{\text{NaAg}}$  values of Eq. [1] calculated from these results are shown in Table I, using concentrations in the glass in place of activities. The resulting variation in  $K_{\text{NaAg}}$  at low silver concentrations shows that the glass was not ideal with respect to these ions, so that the concentrations are not equivalent to activities, particularly at lower silver concentrations. In ref. (11) this behavior was related to the two-phase nature of Pyrex glass, and it was shown that a simple model of two ideal phases

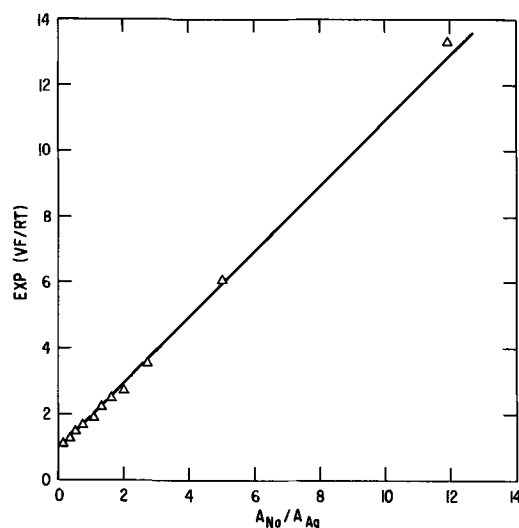


Fig. 3. Exponential of the measured cell potential as a function of melt activity ratio for a Pyrex tube containing silver nitrate and immersed in different silver-sodium nitrate melts.

Table I. Exchange of silver ions in a sodium nitrate melt with Pyrex glass

Mole fraction of silver nitrate in melt	Exchange coefficient, $K$
0.398	1.97
0.310	1.87
0.153	1.98
0.0475	2.05
0.0022	7.06
$3(10)^{-3}$	12.2

gives reasonable agreement with the data in Table I. In this model one phase is primarily sodium borosilicate, and contains 95% of the sodium ions in the unexchanged glass, while the second phase is high in silica and retains the rest of the sodium. It is the strong attraction of this silica phase for the silver ions that causes the change in  $K$  at lower silver concentrations.

The glass can be treated as a single nonideal phase; then the deviations shown in Table I are absorbed in activity coefficients of the ions in the glass. In this way a  $K'_{\text{NaAg}}$  that is constant and can be used in the equations for the membrane potential was found to equal 1.8 for the data in Table I (11). It was also found that the mobility ratio  $u_{\text{Ag}}/u_{\text{Na}}$  is about one in Pyrex when the mole fraction of silver in the glass is above about 0.2, and decreases for lower concentrations (16). Thus  $K'_{\text{NaAg}}(u_{\text{Ag}}/u_{\text{Na}})$  is not far from one at higher silver concentrations, in qualitative agreement with the values of  $p$  found above. It seems likely that the unusual dependence of the membrane potential on silver concentration shown in Fig. 2, as well as the difference between  $p$  and  $K'_{\text{NaAg}}(u_{\text{Ag}}/u_{\text{Na}})$ , are related to the two-phase nature of the Pyrex glass, but it was not possible to relate this dependence to the measured  $K'_{\text{NaAg}}$  and  $u_{\text{Ag}}/u_{\text{Na}}$  values in any simple way.

The temperature dependence for the total cell potential at different silver concentrations is shown in Fig. 4. The potential is proportional to  $RT/F$ , indicating that there is no large change in  $K'_{\text{NaAg}}$  or  $u_{\text{Ag}}/u_{\text{Na}}$  with temperature.

The low membrane potentials found suggest that the total potential of a cell with a Pyrex membrane immersed in a fused nitrate using silver-silver nitrate electrodes should follow Eq. [6] fairly well,

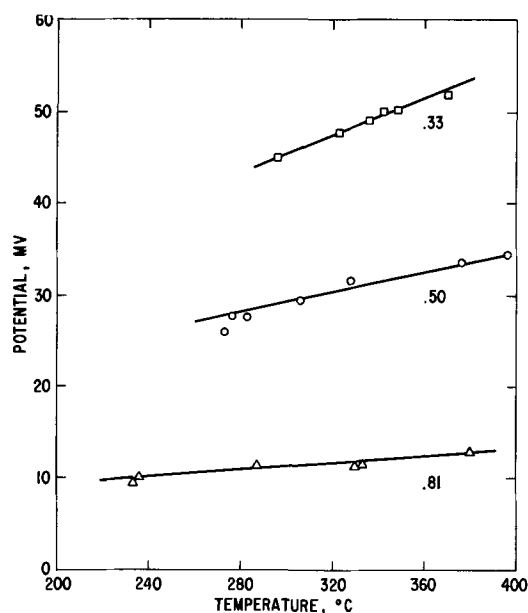
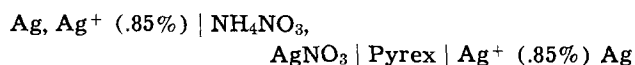


Fig. 4. Total measured cell potential for Pyrex glass tubes containing silver nitrate and immersed in silver-sodium nitrate solutions, as a function of temperature. The mole fraction of silver nitrate in the melt is noted on the graph.

especially at low silver concentrations. This agrees with the results of ref. (3) and (6).

In ref. (5) the cell



was studied. The two end solutions were ternary eutectics containing sodium, lithium, and potassium nitrates. For silver concentrations up to 12 mole % in the center compartment, a modification of Eq. [8] was obeyed, using concentrations instead of activities. A selectivity ratio of 0.32 was found for sodium and silver ions. However, this value is not directly comparable with the present  $p = 1$ , since the activities of sodium and silver ions may be quite different in ammonium nitrate than in mixed silver-sodium nitrate.

In further work these authors measured the potentials of cells similar to the present ones, using an equimolar sodium-silver nitrate melt inside the Pyrex tube (6). A plot of  $\exp(VF/RT)$  against  $a_1/b_1$ , using the authors' activity data, was close to a straight line, but showed some definite curvature. A value of about 0.8 for  $p$  was found. However, a plot of the membrane potential  $V_M$ , calculated from these data, as a function of melt composition shows deviations from expected behavior similar to those shown in Fig. 2, confirming the present results.

Manuscript submitted Feb. 27, 1968; revised manuscript received May 31, 1968.

Any discussion of this paper will appear in a Discussion Section to be published in the June 1969 JOURNAL.

#### REFERENCES

1. J. O. Bockris, G. J. Hills, D. Inman, and L. Young, *J. Sci. Instr.*, **33**, 438 (1956).
2. R. Littlewood, *Electrochim. Acta*, **3**, 270 (1961).
3. D. Inman, *J. Sci. Instr.*, **39**, 391 (1962).
4. G. W. Harrington and H. T. Tien, *J. Phys. Chem.*, **66**, 173 (1962).
5. K. Notz and A. G. Keenan, *ibid.*, **70**, 662 (1966).
6. A. G. Keenan, K. Notz, and F. L. Wilcox, *ibid.*, **72**, 1085 (1968).
7. R. H. Doremus, *ibid.*, **72**, (1968) (In print).
8. G. Karreman and G. Eisenman, *Bull. Math. Biophys.*, **24**, 413 (1962).
9. R. H. Doremus, "Diffusion Potentials in Glass," Chap. 4 in "Glass Electrodes for Hydrogen and Other Cations," p. 101, G. Eisenman, Editor, M. Dekker, New York (1966).
10. R. J. Charles, *J. Am. Ceramic Soc.*, **47**, 559 (1964).
11. R. H. Doremus, *J. Phys. Chem.*, **72**, 2665 (1968).
12. R. W. Laity, *J. Am. Chem. Soc.*, **79**, 1849 (1957).
13. M. Bakes, J. Guion, and J. P. Brenet, *Electrochim. Acta*, **10**, 1001 (1965).
14. M. Liquornik and Y. Marcus, Israel Atomic Energy Commission Report Conf. 742-2, June, 1964. Reported at CITCE Meeting, London, 1964.
15. J. A. A. Ketelaar, *J. Chim. Phys.*, **61**, 44 (1964).
16. R. H. Doremus, *Phys. Chem. Glasses*, **9**, (1968) (In print).

## Technical Notes



### Breakaway Oxidation Transition for a Zirconium-2.7 w/o Niobium Alloy

M. G. Cowgill,<sup>1</sup> S. H. Wong,<sup>2</sup> and W. W. Smeltzer\*

Department of Metallurgy and Materials Science, McMaster University, Hamilton, Ontario, Canada

The oxidation rates and the properties of the oxide films formed on a Zr-2.7 w/o Nb alloy in the temperature range 300°-500°C were shown to be dependent on the phases introduced into the metal by vacuum annealing and quenching from temperatures corresponding to the  $\beta$ -solid solution and the  $\alpha + \beta$  phase regions of the binary phase diagram (1,2). Martensitic specimens oxidized more rapidly than Widmanstätten alloys, the oxidation rate continually decreasing by formation of a protective film until a transition range was attained in which the rate subsequently increased to a maximum value associated with linear kinetics. The objective of the experiments reported here was to determine if  $\alpha$  and  $\beta$ -Zr could be distributed in the alloy by diffusion processes to influence the reaction kinetics within brief exposure periods at high temperatures in the range 870°-1000°C. It is demonstrated that this objective is feasible because, first, the solubilities of oxygen in the alloy phases differ by large factors, and second, the temperature coefficient for oxygen diffusion in  $\alpha$ -Zr is of a relatively high value.

The alloy was received as 2 mm thick sheet. Analyses for impurities, the oxygen content being 1100 ppm

maximum, and the method of specimen preparation by metallographic polishing have been reported (1). Specimens  $2 \times 2 \times 0.1$  cm were oxidized in oxygen at 400 mm Hg pressure in a volumetric apparatus (3). Once a specimen was in place, the assembly was evacuated at  $10^{-6}$  mm Hg for 4 hr at room temperature and the furnace at the reaction temperature then positioned about the reaction tube. After 15 min, oxygen was admitted to react with the specimen and its uptake was determined by means of the gas buret. The specimen after reaction was then rapidly cooled to room temperature by removing the furnace from the reaction tube. Oxidized specimen surfaces were examined by x-rays using a recording diffractometer and nickel-filtered copper radiation.

Results from the oxidation tests at 870°, 900°, 912°, 950°, and 990°C for exposures up to 170 min are presented in Fig. 1. At all temperatures, the curves were initially parabolic. At and below 912°, this type of oxidation for exposures up to 60 min was followed by a breakaway transition leading to more rapid reaction kinetics. Parabolic oxidation was obeyed up to the longest time observed at 950° and 990°. Those specimens oxidized at the three lower temperatures were characterized by a network of white on black oxide or white oxide while those specimens oxidized at 950° and 990° were black with white oxide only

\* Electrochemical Society Active Member.

<sup>1</sup> Present address: Atomic Power Division, Westinghouse Electric Corporation, Madison, Pennsylvania.

<sup>2</sup> Present address: Falconbridge Nickel Mines Ltd., Falconbridge, Ontario, Canada.

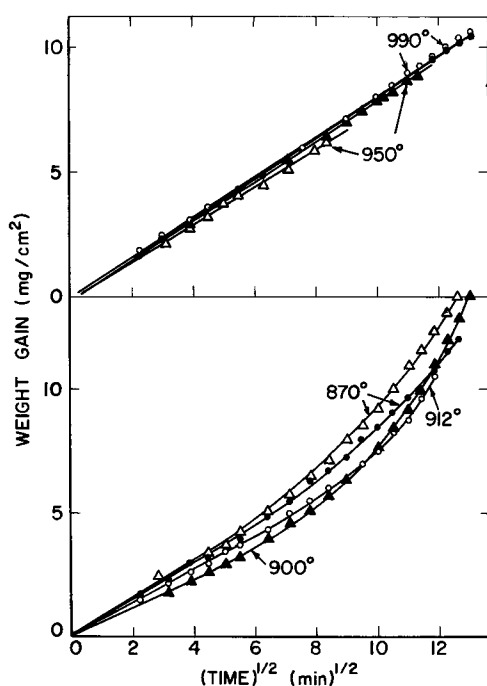


Fig. 1. Parabolic plots of oxidation data for a Zr-2.7 w/o Nb alloy at temperatures in the range 870°-990°C.

occurring along the edges, Fig. 2. A reflection at 2.94-2.95Å in addition to those for monoclinic zirconia was observed in the oxide x-ray diffraction pattern which could be indexed as a tetragonal oxide, an allotropic modification of zirconia or the mixed oxide  $6\text{ZrO}_2 \cdot \text{Nb}_2\text{O}_5$  (2).

Oxidation was associated with scale formation and oxygen solution in the metal. As illustrated in Fig. 3, specimens oxidized at 870° and 912° exhibited after transition from parabolic kinetics uneven oxide growths with many cracks present in the scale. In agreement with the findings of Richter *et al.* (4), a residual oxygen content of 1000 ppm in the alloy was sufficient to stabilize the  $\alpha$  and  $\beta$  phases at the temperature of 870°. The former phase in the specimen exposed at 900° appeared to form beneath the scale by oxygen diffusion at the reaction temperature. The photomicrograph of Fig. 4 illustrated the alloy microstructure developed beneath the oxide scale at these lower temperatures in greater detail.  $\beta$ -Zr was present over areas of the metal surface despite the precipitation of  $\alpha$ -Zr in the alloy matrix.

The reaction at 950° and 990° proceeded by parabolic kinetics without a breakaway transition as at the lower temperatures. Under these conditions, the scales formed on specimens were of relatively even thicknesses and of a compact structure, Fig. 5. An alloy microstructure at these temperatures was characterized by distinct layers of oxygen stabilized  $\alpha$ -Zr plates extending inwards from the metal surface into the  $\beta$ -Zr matrix.

These results are consistent with the reasoning that the different oxidation characteristics and alloy microstructures found at the extreme temperatures in the

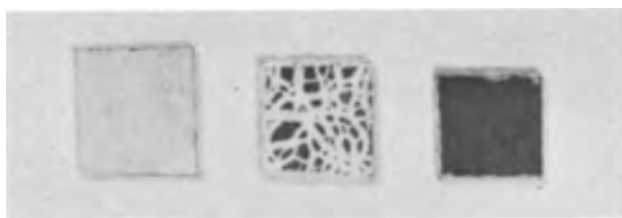


Fig. 2. Topographies of specimens oxidized for 170 min at 870°, 912°, and 990°C (left to right) (Magnification ca. 1.4X).

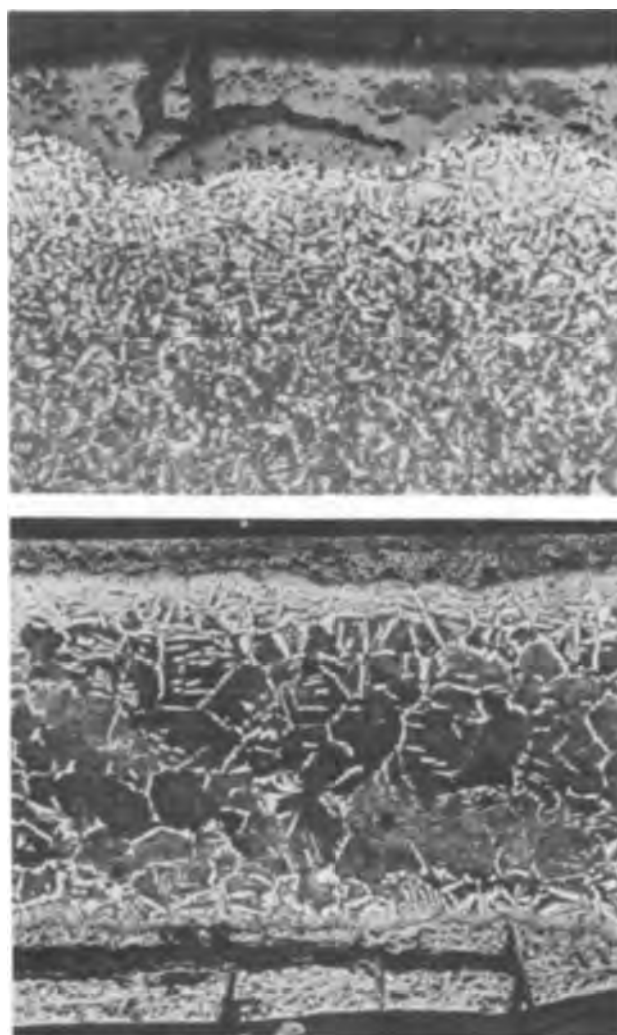


Fig. 3. Cross sections of specimens oxidized at 870°C for 170 min (top micrograph, 250X) and 900°C (bottom micrograph, 80X). White and dark phases in alloy represents  $\alpha$ -Zr and  $\beta$ -Zr, respectively.



Fig. 4. Alloy microstructure beneath oxide scale in specimen oxidized at 870°C (400X).

range 870°-990° were dependent on the oxygen solubilities and the rates for oxygen diffusion in the alloy phases. The solubility of oxygen in  $\beta$ -Zr is very low at 870° increasing to only 0.3 w/o at 1000° based on figures for unalloyed zirconium (5). Most of the oxygen entering the alloy therefore stabilizes and dissolves in

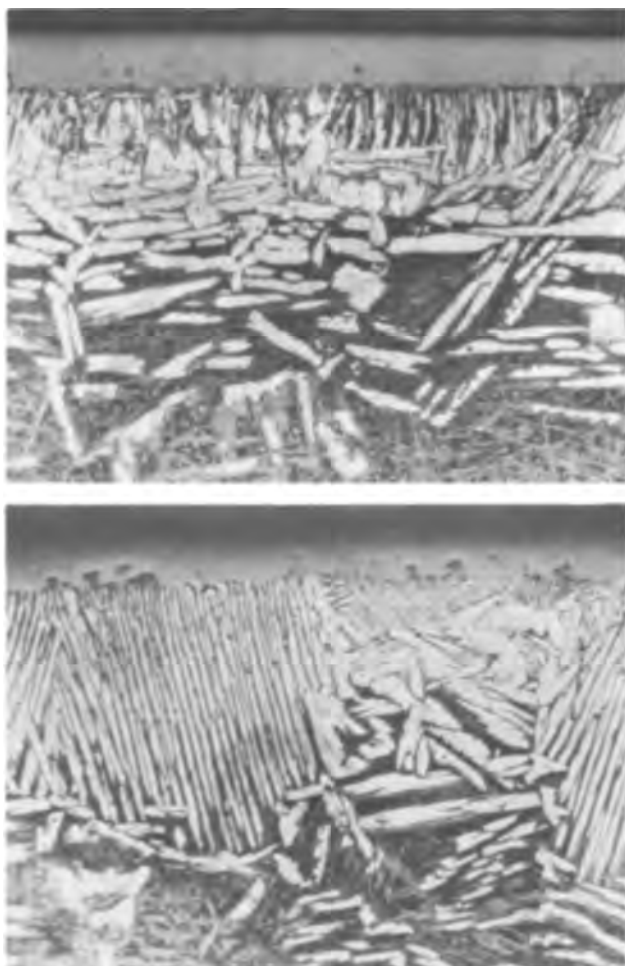


Fig. 5. Cross sections of specimens oxidized for 170 min at 950°C (top micrograph) and 990°C (bottom micrograph) (160X).

$\alpha$ -Zr, the solubility limit in this case being much larger and of the order of 7 w/o. Thus the alloy beneath the scale became a mixture of oxygen stabilized  $\alpha$  and  $\beta$ -Zr. The former phase has a low solubility for niobium, the maximum being about 1 w/o at the eutectic temperature of 610°C. Consequently, as  $\alpha$ -Zr is formed niobium segregates into the  $\beta$ -Zr matrix. The microstructure of the alloy at the metal/oxide interface then becomes dependent on the relative rates for diffusion of oxygen in  $\alpha$ -Zr and inward migration of the external scale.

The inward migration rates of the external scale at temperatures less than 912° were sufficiently rapid for  $\beta$ -Zr over relatively large areas surrounding the  $\alpha$ -Zr precipitates to remain in contact with a scale, its rapid oxidation leading to the breakaway oxidation transition (Fig. 4). On the other hand, oxygen diffusion becomes much more rapid at higher temperatures. The activation energies for oxygen diffusion in  $\alpha$ -Zr and the oxide scale formed on this metal phase are 52 and 29 kcal/g atom, respectively (7,8). Consequently, sufficient oxygen diffused into the alloy at temperatures higher than 950°C for stabilization of the distinct columnar layers of  $\alpha$ -Zr plates beneath the oxide scales,  $\beta$ -Zr being concentrated in narrow regions between these plates (Fig. 5). These regions, which would be enriched by segregated niobium if rapid boundary diffusion of metal did not occur, appeared to be of insufficient area for their oxidation to lead to a transition from parabolic kinetics. Accordingly, diffusion processes occurring during the breakaway oxidation transition of this alloy may be studied by investigating oxidation behavior for relatively brief exposures at high temperatures. It is also possible that quenched  $\beta$ -Zr specimens with a layer of  $\alpha$ -Zr plates formed in the alloy at and beneath its surface by oxygen solution may oxidize at slow rates for long exposures typical of Widmanstatten structures in the temperature range 300° - 500°C (1).

#### Acknowledgments

This research was completed under auspices of the Atomic Energy of Canada Limited and the Defence Research Board of Canada.

Manuscript submitted April 8, 1968; revised manuscript received ca. June 3, 1968.

Any discussion of this paper will appear in a Discussion Section to be published in the June 1969 JOURNAL.

#### REFERENCES

1. M. G. Cowgill and W. W. Smeltzer, *This Journal*, **114**, 1089 (1967).
2. M. G. Cowgill and W. W. Smeltzer, *ibid.*, **115**, 471 (1968).
3. G. R. Wallwork, W. W. Smeltzer, and C. J. Rosa, *Acta Met.*, **12**, 409 (1964).
4. H. Richter, P. Wincierz, K. Anderko, and U. Zwicker, *J. Less-Common Metals*, **4**, 252 (1962).
5. M. Hansen, "Constitution of Binary Alloys," p. 1079, McGraw-Hill Book Co., New York (1958).
6. C. E. Lundin and R. H. Cox, "The Determination of the Equilibrium Phase Diagram, Zirconium-Niobium," TID-11919 (1960).
7. G. V. Kidson, *Electrochem. Technol.*, **4**, 193 (1966).
8. J. Debuigne and P. Lehr, "Corrosion of Reactor Materials," Proceedings, p. 105, IAEA, Vienna (1962).

## Nucleating Ability of Grain Boundaries During Electrodeposition

T. Kilner<sup>1</sup> and A. Plumtree

Materials Science Laboratory, Department of Mechanical Engineering,  
University of Waterloo, Waterloo, Ontario, Canada

When crystallization occurs by the addition of successive layers of atoms, as in the electrodeposition of metals, the rate-controlling mechanism is the formation of nuclei for each new layer. If, however, sites are already present, growth may occur almost as fast as the atoms (or ions) arrive at the surface. The ideal condition for continuous and rapid growth of crystals

<sup>1</sup> Present address: Ontario Research Foundation, Sheridan Park, Ontario, Canada.

is that the growing faces shall always contain a self-perpetuating step or groove. Nucleation occurs readily in the step at the center-line of the groove, and atom layers then spread rapidly over the entire faces of the groove (1,2). A re-entrant groove is formed by the intersection of a twinned boundary with the growing interface (3). The presence of two or more twin boundaries in materials possessing face-centered or diamond-centered structures can produce a self-per-



petuating system of re-entrant grooves. For silver, therefore, it is not surprising that multiple twin boundaries have been observed in dendrites grown from fused salt electrolytes (4-7) and aqueous electrolytes (8-11).

Little is known, however, about the nucleating ability of a re-entrant groove formed by the intersection of the interface with high angle grain boundaries and also with annealing twins as opposed to growth twins. It is the purpose of this note to report the investigations made during the very early stages of electrodeposition of silver from an aqueous solution on a substrate containing both high angle grain boundaries and annealing twins.

Both cathode and anode were prepared from cold worked 99.98% silver. Sheet silver 0.010 in. thick cut in the form of a washer was used for the anode, whereas the cathodes were prepared from approximately 2 mm cubes annealed for one week at 900°C. By this means large grained cathode samples were produced, each containing approximately 10 grains/sample and numerous annealing twins. After silver soldering to copper wire for electrical connection, each cathode was mounted in a cold setting resin. The samples were then ground, mechanically polished down to 1/4 $\mu$  diamond paste, chemically polished using the solution of Gilpin and Worzala (12), and then etched to produce grain boundary grooves using the solution of Kilner and Plumtree (13). These silver cathodes were placed in a specially constructed cell, 2 cm deep by 3 cm in diameter, designed to fit under the objective lens of a Zeiss photomicroscope. A transparent Plexiglas lens shield was used to keep the solution (1M AgNO<sub>3</sub> + 2M NH<sub>4</sub>NO<sub>3</sub>) from touching the lens. By this arrangement, the objective lens could be immersed in the electrolyte to prevent the free surface from affecting image quality. The silver anode was made in the shape of a washer so that it would fit on the lens shield and allow photomicrographs to be taken of the cathode through the central hole.

Electrodeposition took place at room temperature using cell voltages ranging from 10 to 200 mv and currents from 0.1 to 25 ma. Current densities varied from approximately 0.001 to 2.5 amp/cm<sup>2</sup>. The solution was not stirred mechanically. Photomicrographs of the cathode were taken during the early stages of electrodeposition. Figure 1a and 1b show the freshly electrodeposited crystals as black spots on two different twinned substrates after 60 sec using a cell potential of 25 mv, current of 0.1 ma, and current density of 1 ma/cm<sup>2</sup>. Figures 1a and 1b indicate that preferential nucleation of silver crystals can occur at the high angle and twin boundaries. In the upper left section of each photograph which corresponds to the outer region of the cathode where the current density was higher due to anode shape, nucleation within the grains is quite noticeable. In this case, it is interesting to note that some crystal faces appear to be more receptive to nucleation than others. By comparing the number of new crystals along the random high angle grain boundaries, to those along twin boundaries, it becomes evident that the high angle grain boundaries offer better nucleation sites. This effect may be explained by the etchant producing a more pronounced groove and hence better nucleation site at these higher energy boundaries.

#### Acknowledgment

This work was sponsored by the National Research Council of Canada, Grant No. A-2770.



Fig. 1. Nucleation of silver at high angle grain and twin boundaries. The nuclei appear as black spots. Fig. 1a (top) Cell voltage 25mv, average current density 1 ma/cm<sup>2</sup>, etched. Magnification ca. 30X. Fig. 1b (below) Cell voltage 25 mv, average current density 1 ma/cm<sup>2</sup>, etched. Magnification ca. 28X.

Manuscript submitted April 1, 1968; revised manuscript received June 3, 1968.

Any discussion of this paper will appear in a Discussion Section to be published in the June 1969 JOURNAL.

#### REFERENCES

1. R. S. Wagner, *Acta Met.*, **8**, 57 (1960).
2. G. F. Bolling and W. A. Tiller, "Metallurgy of Elemental and Compound Semiconductors," p. 97, Interscience, Publishers, New York (1961).
3. I. N. Stranski, *Discussions, Faraday Soc.*, **5**, 69 (1949).
4. L. Yang, C. Chien, and R. G. Hudson, *This Journal*, **106**, 632 (1959).
5. J. W. Faust, Jr. and H. F. John, *ibid.*, **108**, 109 (1961).
6. A. M. Shams-El Din and G. Wranglen, *Electrochim. Acta*, **7**, 79 (1962).
7. T. B. Reddy, *This Journal*, **113**, 117 (1966).
8. M. Kikuchi and R. Yamazaki, *Denki Kagaku*, **33**, 283 (1965).
9. J. W. Faust, Jr., and H. F. John, *J. Phys. Chem. Solids*, **25**, 1409 (1964).
10. J. Smit, F. Ogburn, and C. J. Bechtoldt, *This Journal*, **115**, 371 (1968).
11. T. Kilner and A. Plumtree, To be published.
12. C. B. Gilpin and F. J. Worzala, *Rev. Sci. Inst.*, **35**, 229 (1964).
13. T. Kilner and A. Plumtree, *Trans. Met. Soc., AIME*, **239**, 129 (1967).



# The Analysis and Solubility of Cuprous Chloride in Hydrochloric Acid Solutions

John J. O'Connor, Anahid Thomasian, and Alton F. Armington

Air Force Cambridge Research Laboratories, Office of Aerospace Research,  
L. G. Hanscom Field, Bedford, Massachusetts

In a study on the crystal growth of CuCl (1), it has become necessary to determine the concentration of this material in the presence of HCl. Since the presence of the cuprous ion will interfere with the hydrogen ion determination, a method was devised in which both ions could be rapidly determined without interference.

## Analytical Procedure

In this procedure, the solution to be analyzed is diluted in a 250-ml beaker to about 40 ml. Oxygen is bubbled into the solution to convert the cuprous ion to cupric ion. The bubbling is continued for about 5 min after all the cuprous chloride precipitated by the dilution has dissolved and the solution has turned blue. After oxidation, the solution is titrated with 0.1F NaOH to an endpoint (measured by a pH meter) in the 4.5-4.8 pH range. After the titration, 3 additional ml of the NaOH solution is added, followed by 7 ml of 6F acetic acid, lowering the pH to about 2.5-3.0. Three grams of KI are added to the solution and the liberated  $I_3^-$  ion is titrated with 0.1F  $Na_2S_2O_3$ , using a starch indicator. Since, in the presence of oxygen, CuCl in HCl undergoes the following reaction



the number of millimoles of CuCl found must be added to the number of millimoles found in the NaOH titration in order to arrive at the true value of the hydrogen ion concentration. Reproducibility of duplicate samples was within 1%.

Several methods have been used to test the accuracy of the procedure. First, known amounts of CuCl and HCl were mixed in closed containers and analyses for hydrogen ion were made on the resulting solutions (Table I). No apparent trend can be found between the error and the concentrations used. Second, as there is no observable endpoint for the oxidation step, the solution must be oxygenated for sufficient time to ensure complete oxidation. Since HCl could conceivably be vaporized during this step, tests were made to determine if extensive treatment would cause any loss in hydrogen ion concentration. No loss in HCl could be detected even when oxygen was bubbled through the solution for 20 min after the appearance of the blue color. Finally, samples were analyzed for copper using both a standard technique and the technique described here. In the standard method, CuCl was oxidized with ferric ammonium sulfate and the resulting ferrous ion was titrated with standard potassium permanganate (2). Comparative results agreed within 1%.

Certain precautions are necessary when employing this procedure. First, sufficient time must be allowed during the oxygen addition to be certain that all cuprous ion is converted to cupric ion since only the cupric ion will react with KI to produce the  $I_3^-$  ion against which the thiosulfate is titrated. Since this method actually measures total copper, the presence of cupric ion will give erroneous results both for cuprous ion and hydrogen ion concentrations. Experiments have shown, however, that if the solution is colorless or only light yellow in color, the amount of cupric ion present will not cause a detectable

Table I. Comparison of calculated and experimental results from hydrogen ion concentration

	Calculated millimoles HCl/ml	Experimental millimoles HCl/ml
1.	0.953	0.954
2.	1.934	1.927
3.	2.771	2.799
4.	3.730	3.704
5.	4.663	4.607
6.	5.331	5.377
7.	6.375	6.426

error. Finally, care must be taken not to titrate beyond a pH of 4.5-4.8 during the hydrogen ion determination since beyond this point the formation of cupric hydroxide will interfere with the titration.

## Solubility of CuCl in HCl Solutions

Since the degree of saturation is important in a crystal growth study, a solubility curve was determined using the procedure outlined. A stock solution of 6F HCl saturated with CuCl was prepared at 30°C and cooled to room temperature (22°C). The test solutions were then prepared by diluting the stock solution to the desired formality. In all cases excess CuCl precipitated out. The solutions were held in closed vials containing copper turnings for three days with intermittent shaking. After allowing a day for the precipitate to settle to the bottom, samples of the supernatant were pipetted out for analyses.

The solubility of CuCl as a function of HCl formality is shown in Fig. 1. Since the method described here is not affected by the oxidation of the cuprous ion, the authors believe it to be more reliable than the previously published data (3) where the oxidation of the cuprous ion may have resulted in higher values for the solubility of CuCl. This could effect the determination in two ways. First, if the analyses were based on total copper, the amount of copper present as  $CuCl_2$  would be included. Second, the solubility of CuCl is increased when  $CuCl_2$  is present

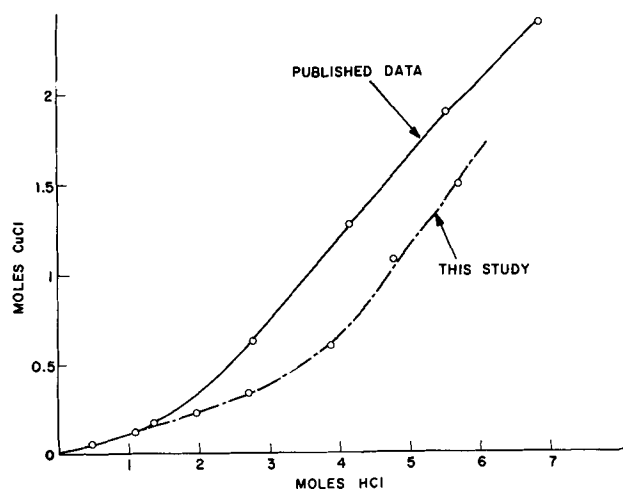


Fig. 1. Solubility of CuCl as a function of HCl concentration in water at 22°C. Moles in diagram are moles/liter.

Key words: Cuprous chloride, chemical complex, solubility analysis.

(4). This would increase the saturation value for CuCl.

Manuscript submitted Feb. 20, 1968; revised manuscript received ca. May 23, 1968.

Any discussion of this paper will appear in a Discussion Section to be published in the June 1969 JOURNAL.

#### REFERENCES

1. A. F. Armington and J. J. O'Connor, *Materials Research Bull.*, **2**, 907 (1967).
2. American Chemical Society Specifications for Reagent Chemicals, p. 136 (1950).
3. W. F. Linke, "Solubility of Inorganic and Metal Organic Compounds," 4th ed., Vol. 1, p. 925, van Nostrand Co., Princeton, N. J. (1958).
4. *Ibid.*, p. 927.

## Conductivity Cell for Use with Dense Gaseous Electrolytes

S. Naiditch, R. A. Williams, and K. P. Luke

*Unified Science Associates, Inc., Pasadena, California*

The principal problem in the measurement of conductivities of supercritical electrolytes is that of containing the electrolyte at the high temperatures and pressures involved. One approach is to use a cell with sufficient strength to withstand these conditions. This generally involves a massive steel cell having electrical insulators and a chemically inert lining to avoid reaction with the electrolyte (1). In our studies of supercritical electrolytes having ammonia ( $\text{NH}_3$ ) as the solvent, we have used a glass conductivity cell and avoided rupture of the cell by matching the internal pressure of the electrolyte with an external pressure. The critical properties of ammonia (132.9°C, 112 atm) are convenient for this method, while the use of glass simplifies the handling of ammonia and leads to a cleaner system than could be easily obtained with a metal cell.

In order to apply the required external pressure the cell must be placed in a high-pressure vessel and hence must be compatible with the interior dimensions of this vessel. In the present case the high-pressure chamber was 38 mm in diameter. The spatial restrictions made the use of a d-c conductivity measurement attractive, as difficulties due to high interelectrode capacitance would then be avoided. D-C measurements are best carried out using the four probe method (2) in which two electrodes produce a current through the electrolyte while two additional electrodes, positioned between the current carrying electrodes, are used to measure the voltage gradient set up in the electrolyte. The voltage measuring electrodes should be reversible in the electrolyte being investigated and no current should be drawn through them when the voltage is measured.

The cell is shown in Fig. 1. It is divided into four electrode compartments joined by the central cylindrical section, hereafter called the conductivity tube. The two extreme electrodes (1 and 4) are used to carry the current, which flows through the conductivity tube. The intermediate electrodes (2 and 3) measure the voltage across the middle section of the conductivity tube. This potential difference is measured through a pair of narrow slit apertures perpendicular to and encompassing the whole circumference of the conductivity tube.

The end portions of the conductivity tube serve to reduce end effects and to allow the current density to become constant and uniform through the middle section. The use of slits rather than holes for the measuring electrode serves to average out any non-uniformities still existing, as well as being much narrower for the same area. The cell constant is therefore geometrically well defined and can be taken as equal to  $K = 4L/(\pi d^2)$  where  $L$  is the separation of the measuring slits and  $d$  is the internal diameter of the tube.

Key words: Conductivity cell, dense gaseous electrolytes, supercritical electrolytes, ammonia.

The electrode leads are brought into the cell through tungsten-uranium glass seals. The electrode compartments are suitable for containing amalgam electrodes of the sort sometimes used in ammonia (3), in which case the tip of the tungsten feedthrough is left bare and completely immersed in the amalgam. If solid metal electrodes are to be used, platinum wire is fused to the tungsten. All of the tungsten and part of the platinum are covered with glass. The exposed platinum is then welded to the electrode material.

The freeze cup was used in the sealing-off operation after filling the cell with ammonia. The ammonia was condensed in the cell and held there with the cell at  $-78^\circ\text{C}$  in a dry ice, alcohol bath. Liquid nitrogen was poured into the freeze cup causing a plug of solid ammonia to form in the capillary. The system above this plug was then pumped to a high vacuum and the cell sealed off by fusion of the capillary above the freeze cup. This procedure allows the seal off to be made under high vacuum, reducing the impurities trapped in the cell. Its usefulness depends on the properties of the solvent being used.

The main problem in fabrication was making the conductivity tube, which must be sealed through the walls separating the electrode compartments without changing its internal dimensions. This was accomplished by collapsing a piece of ordinary glass tubing over a drill rod of the desired diameter by heating the tubing while maintaining a partial vacuum inside it. With the tube hot and the drill rod still inside, glass flanges were built up on the tube at the desired locations. These flanges were then sealed to the outer tubing and became the walls between the electrode

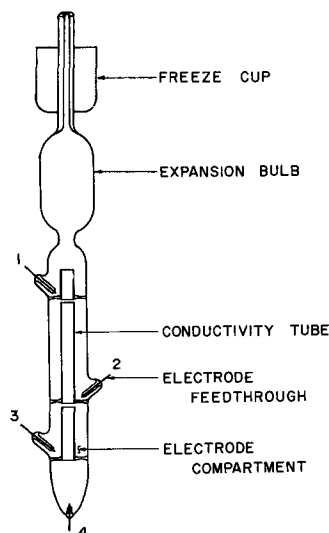


Fig. 1. Conductivity cell. Axis of cell is vertical in use

Table I. Effect of slit width on cell constant

Cell	d, cm	L, cm	W, cm	K, mhos/cm	K <sub>Hg</sub> , mhos/cm	K <sub>KCl</sub> , mhos/cm
A	0.4727	4.720	0.416	26.90	27.69	27.35
B	0.4747	4.774	0.041	26.98	26.94	25.56
C	0.4762	4.761	0.012	26.73	26.66	26.03

compartments. The different sections of the conductivity tube were held in alignment during cell fabrication by a carbon rod. When made in this way, the conductivity tube had a constant diameter over its whole length and could be made with very narrow voltage measuring slits.

The choice of slit widths is governed by the desired accuracy of the cell constant, the maximum allowable resistance between the measuring electrodes, and the requirement that good diffusion exist between the various parts of the cell. In order to examine the effect of slit width on the cell constant, three cells with different slit widths, *W* were built and the cell constants determined both geometrically and by measuring the cell resistance with known materials, namely, mercury and 1*N* KCl solution. Results are shown in Table I.

It is apparent that the slits in cell A, which are of about the same width as the diameter of the conductivity tube, are too wide for the geometrical cell constant to be meaningful. With cells B and C, however, the agreement between calculated and observed cell constants is good, particularly in the case of mercury. It should be noted that no special precautions were taken in the preparation of the KCl solution, ordinary reagent grade KCl and commercially bottled distilled water being the ingredients used. The conductivity of mercury is much less sensitive to the precautions taken than KCl solutions, and the values of the cell constant with mercury are therefore considered much more accurate. The tests indicate that for conductivity tubes whose length is much greater than their diameter, the use of voltage measuring slits of width 10% of the conductivity tube diameter or less will give a cell constant which can be easily calculated to better than ½%.

The cell has been used for conductivity measurements of solutions of AgNO<sub>3</sub> in NH<sub>3</sub> at temperatures well above the critical point of NH<sub>3</sub>. Figure 2 shows the voltage drop measured across the conductivity tube as a function of the cell current obtained with a supercritical AgNO<sub>3</sub>-NH<sub>3</sub> solution and using electrodes of high purity silver wire throughout. The linearity of the graph indicates that the cell is well behaved.

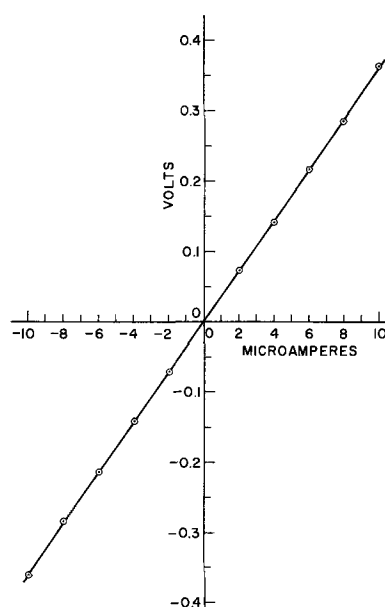


Fig. 2. Voltage drop across conductivity tube vs. cell current. Electrolyte is AgNO<sub>3</sub> at 0.02 moles/liter in dense gaseous NH<sub>3</sub> at 22 moles/liter and 151°C. Positive current flows upward.

The small emf (~ 1 mv) between the voltage probes may be due to surface impurities on the electrodes or to a small difference in the compositions of the electrolytes in the two electrode compartments. The cell used had 0.1 cm slits and a cell constant of 24 cm<sup>-1</sup>. Conductivity cells suitable for d-c measurements with dense gaseous electrolytes can thus be fabricated with the desired, geometrically defined cell constant.

#### Acknowledgment

This work was sponsored by National Aeronautics and Space Administration under Contracts NAS 7-437 and NAS 7-326.

Manuscript received Feb. 15, 1968.

Any discussion of this paper will appear in a Discussion Section to be published in the June 1969 JOURNAL.

#### REFERENCES

1. T. K. Fogo, S. W. Benson, and C. S. Copeland, *J. Chem. Phys.*, **22**, 212 (1954).
2. S. Glasstone, "Introduction to Electrochemistry," p. 47, D. Van Nostrand Co., Inc., New York (1942).
3. C. S. Garner, E. W. Green, and D. M. Yost, *J. Am. Chem. Soc.*, **57**, 2055 (1935).

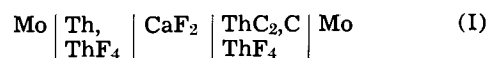
## Limitation of the Use of CaF<sub>2</sub> in Galvanic Cells for Thermodynamic Measurements due to the Onset of Electronic Conduction under Reducing Conditions

Carl Wagner\*

Max-Planck-Institut für physikalische Chemie, Göttingen, Germany

During the last ten years, galvanic cells involving solid electrolytes have been used with considerable success in order to obtain Gibbs energy data at elevated temperatures from measured emf values (1-3). Under highly reducing conditions an appreciable contribution of n-type electronic conduction in addition to ionic conduction may occur. Then the usual evaluation becomes invalid (4, 5) as has been discussed especially for ZrO<sub>2</sub>(+CaO) as solid electrolyte (6-8).

Also CaF<sub>2</sub> has been found to be a suitable solid electrolyte (9-13). For instance, the Gibbs energy change of the reaction Th + 2C = ThC<sub>2</sub> has been obtained from the emf of the cell (10)



The following calculation is made in order to find out under which conditions the onset of electronic con-

\* Electrochemical Society Active Member.

Table I. Effect of slit width on cell constant

Cell	d, cm	L, cm	W, cm	K, mhos/cm	K <sub>Hg</sub> , mhos/cm	K <sub>KCl</sub> , mhos/cm
A	0.4727	4.720	0.416	26.90	27.69	27.35
B	0.4747	4.774	0.041	26.98	26.94	25.56
C	0.4762	4.761	0.012	26.73	26.66	26.03

compartments. The different sections of the conductivity tube were held in alignment during cell fabrication by a carbon rod. When made in this way, the conductivity tube had a constant diameter over its whole length and could be made with very narrow voltage measuring slits.

The choice of slit widths is governed by the desired accuracy of the cell constant, the maximum allowable resistance between the measuring electrodes, and the requirement that good diffusion exist between the various parts of the cell. In order to examine the effect of slit width on the cell constant, three cells with different slit widths, *W* were built and the cell constants determined both geometrically and by measuring the cell resistance with known materials, namely, mercury and 1*N* KCl solution. Results are shown in Table I.

It is apparent that the slits in cell A, which are of about the same width as the diameter of the conductivity tube, are too wide for the geometrical cell constant to be meaningful. With cells B and C, however, the agreement between calculated and observed cell constants is good, particularly in the case of mercury. It should be noted that no special precautions were taken in the preparation of the KCl solution, ordinary reagent grade KCl and commercially bottled distilled water being the ingredients used. The conductivity of mercury is much less sensitive to the precautions taken than KCl solutions, and the values of the cell constant with mercury are therefore considered much more accurate. The tests indicate that for conductivity tubes whose length is much greater than their diameter, the use of voltage measuring slits of width 10% of the conductivity tube diameter or less will give a cell constant which can be easily calculated to better than ½%.

The cell has been used for conductivity measurements of solutions of AgNO<sub>3</sub> in NH<sub>3</sub> at temperatures well above the critical point of NH<sub>3</sub>. Figure 2 shows the voltage drop measured across the conductivity tube as a function of the cell current obtained with a supercritical AgNO<sub>3</sub>-NH<sub>3</sub> solution and using electrodes of high purity silver wire throughout. The linearity of the graph indicates that the cell is well behaved.

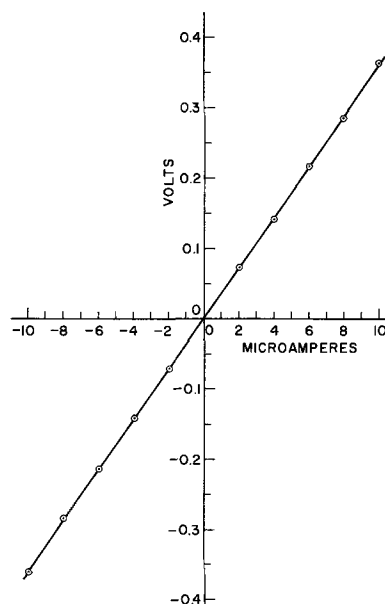


Fig. 2. Voltage drop across conductivity tube vs. cell current. Electrolyte is AgNO<sub>3</sub> at 0.02 moles/liter in dense gaseous NH<sub>3</sub> at 22 moles/liter and 151°C. Positive current flows upward.

The small emf (~ 1 mv) between the voltage probes may be due to surface impurities on the electrodes or to a small difference in the compositions of the electrolytes in the two electrode compartments. The cell used had 0.1 cm slits and a cell constant of 24 cm<sup>-1</sup>. Conductivity cells suitable for d-c measurements with dense gaseous electrolytes can thus be fabricated with the desired, geometrically defined cell constant.

#### Acknowledgment

This work was sponsored by National Aeronautics and Space Administration under Contracts NAS 7-437 and NAS 7-326.

Manuscript received Feb. 15, 1968.

Any discussion of this paper will appear in a Discussion Section to be published in the June 1969 JOURNAL.

#### REFERENCES

1. T. K. Fogo, S. W. Benson, and C. S. Copeland, *J. Chem. Phys.*, **22**, 212 (1954).
2. S. Glasstone, "Introduction to Electrochemistry," p. 47, D. Van Nostrand Co., Inc., New York (1942).
3. C. S. Garner, E. W. Green, and D. M. Yost, *J. Am. Chem. Soc.*, **57**, 2055 (1935).

## Limitation of the Use of CaF<sub>2</sub> in Galvanic Cells for Thermodynamic Measurements due to the Onset of Electronic Conduction under Reducing Conditions

Carl Wagner\*

Max-Planck-Institut für physikalische Chemie, Göttingen, Germany

During the last ten years, galvanic cells involving solid electrolytes have been used with considerable success in order to obtain Gibbs energy data at elevated temperatures from measured emf values (1-3). Under highly reducing conditions an appreciable contribution of n-type electronic conduction in addition to ionic conduction may occur. Then the usual evaluation becomes invalid (4, 5) as has been discussed especially for ZrO<sub>2</sub>(+CaO) as solid electrolyte (6-8).

\* Electrochemical Society Active Member.

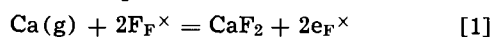
Also CaF<sub>2</sub> has been found to be a suitable solid electrolyte (9-13). For instance, the Gibbs energy change of the reaction Th + 2C = ThC<sub>2</sub> has been obtained from the emf of the cell (10)



The following calculation is made in order to find out under which conditions the onset of electronic con-

duction in  $\text{CaF}_2$  interferes with a straightforward thermodynamic evaluation of emf values.

According to Ure (14) pure  $\text{CaF}_2$  involves virtually equal concentrations of interstitial anions and anion vacancies. On exposure of  $\text{CaF}_2$  to Ca vapor, an excess of calcium is dissolved (15-18). As an analogue to the uptake of excess metal by alkali halides, one may formulate the chemical equation



where in accord with Kröger's notation (19)  $\text{F}_F^\times$  is a fluoride ion on a regular anion site and  $e_{F^\times}$  is an electron substituted for an anion also known as a color center (= F center). This interpretation of the structure of a color center is in accord with electron spin resonance investigations (20). Applying the law of mass action to the reaction in Eq. [1] it follows that the number of color centers per cubic centimeter,  $n_{e_{F^\times}}$ , is proportional to the square root of the partial pressure  $p_{\text{Ca}}$  of calcium, or the activity  $a_{\text{Ca}}$

$$n_{e_{F^\times}} \sim p_{\text{Ca}}^{1/2} \sim a_{\text{Ca}}^{1/2} \quad [2]$$

In addition to electrons trapped on anion sites, there is a small fraction of mobile excess electrons  $e'$  formed by the reaction



where  $V_F$  is an anion vacancy. The equilibrium condition is

$$\frac{n_{V_F} \cdot n_{e'}}{n_{e_{F^\times}}} = K \quad [4]$$

When an electrical field is applied, fluoride ions migrate as interstitials and via vacancies toward the anode. Likewise electrons migrate toward the anode. Thus the boundary between a colorless zone of virtually pure  $\text{CaF}_2$  and a colored zone of  $\text{CaF}_2$  involving an excess of calcium moves toward the anode at a velocity proportional to the electrical field strength. Observations may be evaluated in terms of the apparent mobility (16)  $u_{e_{F^\times}}$  of the color centers, which is related to the mobility  $u_{e'}$  of excess electrons by

$$n_{e_{F^\times}} \cdot u_{e_{F^\times}} = n_{e'} \cdot u_{e'} \quad [5]$$

In view of Eq. [3] to [5], the partial electronic conductivity  $\sigma_e$  of  $\text{CaF}_2$  with excess calcium may be written as

$$\sigma_e = n_{e'} \cdot u_{e'} \cdot e = n_{e_{F^\times}} \cdot u_{e_{F^\times}} \cdot e = n_{e_{F^\times}}^\circ \cdot u_{e_{F^\times}} \cdot e \cdot a_{\text{Ca}}^{1/2} \quad [6]$$

where  $e$  is the electronic charge and  $n_{e_{F^\times}}^\circ$  is the number of electrons substituted for fluoride ions per  $\text{cm}^3$  at  $a_{\text{Ca}} = 1$  corresponding to saturated calcium vapor. Thus the transference number  $t_e$  of electrons is found to be

$$t_e = \frac{\sigma_e}{\sigma_{\text{ion}} + \sigma_e} \cong \frac{\sigma_e}{\sigma_{\text{ion}}} = \frac{n_{e_{F^\times}}^\circ \cdot u_{e_{F^\times}} \cdot e}{\sigma_{\text{ion}}} a_{\text{Ca}}^{1/2} \quad \text{if } \sigma_e \ll \sigma_{\text{ion}} \quad [7]$$

where  $\sigma_{\text{ion}}$  is the ionic conductivity of pure  $\text{CaF}_2$ .

From Eq. [7] one may readily calculate values of  $a_{\text{Ca}}$  at which  $t_e$  is sufficiently low for neglect of electronic conduction in the thermodynamic evaluation of emf values, see Table I.

For the evaluation of Eq. [7], values of  $n_{e_{F^\times}}^\circ$  have been taken from Mollwo's paper (16). If, in view of results obtained by Lichter and Bredig (18) between 1060° and 1265°C a lower value of  $n_{e_{F^\times}}^\circ$  at 840°C is used in Eq. [7], higher values of  $a_{\text{Ca}}$  for  $t_e = 10^{-2}$  and  $10^{-3}$  are obtained. Thus values of  $a_{\text{Ca}}$  listed in Table I are to be considered as lower limiting values for the onset of electronic conduction.

As an example consider cell I where  $a_{\text{Ca}}$  on the left-hand side is determined by the virtual equilibrium

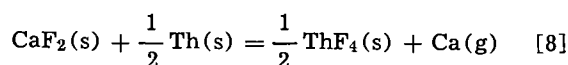


Table I. Calcium activities  $a_{\text{Ca}}$  for  $t_e = 10^{-2}$  and  $t_e = 10^{-3}$

Temp, °C	$n_{e_{F^\times}}^\circ$ (16) cm <sup>-3</sup>	$u_{e_{F^\times}}^\times$ (16)	$\sigma_{\text{ion}}$ (14) ohm <sup>-1</sup> cm <sup>-1</sup>	$a_{\text{Ca}}$ for $t_e = 10^{-2}$	$a_{\text{Ca}}$ for $t_e = 10^{-3}$
		cm <sup>2</sup> volt · sec			
600	$1 \cdot 10^{18}$	$2 \cdot 10^{-4}$	$1 \cdot 10^{-5}$	$1 \cdot 10^{-5}$	$1 \cdot 10^{-7}$
840	$2 \cdot 10^{20}$	$5 \cdot 10^{-4}$	$4 \cdot 10^{-3}$	$6 \cdot 10^{-6}$	$6 \cdot 10^{-8}$

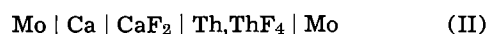
The reference state is solid calcium with  $a_{\text{Ca}} = 1$ . Thus  $a_{\text{Ca}}$  may be calculated from the standard Gibbs energies of formation (21)  $\Delta G_{\text{CaF}_2(s)}^\circ$  and  $\Delta G_{\text{ThF}_4(s)}^\circ$  of  $\text{CaF}_2$  and  $\text{ThF}_4$ , respectively,

$$\log a_{\text{Ca}} = \frac{\Delta G_{\text{CaF}_2}^\circ - \frac{1}{2} \Delta G_{\text{ThF}_4}^\circ}{2.30 RT} \quad [9]$$

Thus one obtains  $a_{\text{Ca}} = 6 \cdot 10^{-13}$  at 600°C and  $a_{\text{Ca}} = 4 \cdot 10^{-10}$  at 840°C. On comparing these values with values listed in Table I, it follows that electronic conduction in  $\text{CaF}_2$  equilibrated with Th +  $\text{ThF}_4$  is insignificant. On the right-hand side of cell I with a mixture of  $\text{ThC}_2$  and graphite, the thorium activity is less than unity, and accordingly  $a_{\text{Ca}}$  is still lower than the value on the left-hand side. Therefore, no significant interference due to partial electronic conduction is expected.

In other cells investigated by Heus and Egan (12) conditions are even more favorable since the metal fluorides involved such as  $\text{UF}_3$ ,  $\text{AlF}_3$ ,  $\text{NiF}_2$  have standard Gibbs energies of formation per equivalent which are less negative than that of  $\text{ThF}_4$  and, therefore, activities of calcium are much lower than in cell I. Conditions are somewhat less favorable at an electrode Mg,  $\text{MgF}_2/\text{CaF}_2$  since the Gibbs energy of formation of  $\text{MgF}_2$  per equivalent is more negative than that of  $\text{ThF}_4$  (12). Even in  $\text{CaF}_2$  equilibrated with Mg +  $\text{MgF}_2$  at 600°C,  $t_e$  is less than  $10^{-3}$ .

Electronic conduction in  $\text{CaF}_2$ , however, would interfere in cells involving metallic Ca with  $a_{\text{Ca}} = 1$  on one side, e.g., in the hypothetical cell



which has not been investigated so far.

#### Acknowledgment

The author wishes to thank Dr. J. J. Egan for critical comments.

Manuscript received March 28, 1968.

Any discussion of this paper will appear in a Discussion Section to be published in the June 1969 JOURNAL.

#### REFERENCES

1. K. Kiukkola and C. Wagner, *This Journal*, **104**, 308, 379 (1957).
2. H. Schmalzried, in "Thermodynamics," Proc. Symposium Vienna 1965, Vol. 1, p. 97, International Atomic Energy Agency, Vienna (1966).
3. D. O. Raleigh, "Progress in Solid State Chemistry," **3**, 83 H. Reiss, Editor, Pergamon Press, Oxford and New York (1966).
4. C. Wagner, *Proc. CITCE*, **7**, 361 (1957).
5. C. Wagner, "Advances in Electrochemistry and Electrochemical Engineering," Vol. 4, p. 1, Interscience Publishers, New York (1966).
6. H. Schmalzried, *Z. Elektrochem.*, **66**, 572 (1962).
7. H. C. Steele and C. B. Alcock, *Trans. AIME*, **233**, 1359 (1965).
8. J. W. Patterson, E. C. Bogren, and R. A. Rapp, *This Journal*, **114**, 752 (1967).
9. R. Benz and C. Wagner, *J. Phys. Chem.*, **65**, 1308 (1961).
10. J. Egan, *ibid.*, **68**, 978 (1964).
11. W. K. Behl and J. J. Egan, *This Journal*, **113**, 378 (1966).

12. W. J. Heus and J. J. Egan, *Z. physik. Chem. N. F.*, **49**, 38 (1966).
13. S. Aronson and A. Auskern, in "Thermodynamics," Proc. Symposium Vienna 1965, Vol. 1, p. 165, International Atomic Energy Agency, Vienna (1966).
14. R. W. Ure, *J. Chem. Phys.*, **26**, 1363 (1957).
15. L. Wöhler and G. Rodewald, *Z. anorg. Chem.*, **61**, 54 (1909).
16. E. Mollwo, *Nachr. Gesellsch. Wissensch. Göttingen, Math. Physik. Kl. N. F.*, **6**, 79 (1934).
17. H. Botinck, *Physica*, **24**, 639 (1958).
18. B. D. Lichter and M. A. Bredig, *This Journal*, **112**, 506 (1965).
19. F. A. Kröger, "The Chemistry of Imperfect Crystals," North-Holland Publishing Co., Amsterdam (1964).
20. J. Ahrend, *Phys. stat. sol.*, **7**, 805 (1964).
21. C. E. Wicks and F. E. Block, *Bureau of Mines Bull.* **605**, U. S. Government Printing Office, Washington, D. C. (1963).

## An Irreversible Photogalvanic Cell Utilizing Iron(III) and Iron(II) Oxalate

William M. Riggs and Clark E. Bricker

*The University of Kansas, Department of Chemistry, Lawrence, Kansas*

Since the photolysis of ferrioxalate solutions with light of wavelength of 4300Å and shorter results in the efficient reduction of iron(III) to iron(II) (1-3) this system can be used as the basis for a photogalvanic cell or to illustrate the Becquerel effect. The purpose of this note is to report the design and operating characteristics of such a cell.

If a platinum electrode is immersed in an iron (III) oxalate solution that is irradiated with light of a wavelength of 4300Å or shorter and a second platinum electrode is placed in another portion of the solution that is not exposed to radiation, a concentration cell will be established. Because of the increased iron(II) concentration around it, the electrode in the irradiated portion will assume a more negative potential than the other electrode and electrons will flow through an external circuit. When irradiation is stopped, the concentration cell will be depleted eventually by diffusion processes and the electrode reactions which will cause the flow of electrons to cease.

A U-shaped cell having a volume of approximately 240 ml with a sintered disk in the base of the U was filled with a solution that was 0.1M in iron(III), 0.1M in  $\text{H}_2\text{C}_2\text{O}_4$  and 0.5M in  $\text{H}_2\text{SO}_4$ . Platinum foil electrodes having an area of 4.7  $\text{cm}^2$  were placed in the arms of the cell. One side of the cell was shielded from the light while the other side was irradiated from a distance of about 8 in. with a 100w medium pressure mercury vapor lamp. After less than 10-min exposure, this cell developed a potential in excess of 0.5v on open circuit or produced a current of 0.3-0.4 ma through a resistance load of 600 ohms. Even though no provision was made for thermostating the cell, the temperature of the solution in the two arms of the U-tube was always within 5° of room temperature.

The variation of the electrical output of the photogalvanic cell with changes in the initial concentrations of reactants is summarized in Table I. These results suggest that any of the reactant concentrations can be varied over a five- to tenfold range without causing any major change in the electrical output. It is important, however, not to use too high a concentration of oxalic acid or too low a sulfuric acid concentration since solid ferrous oxalate will form under these conditions and coat the electrode in the irradiated compartment. This coating appears to decrease the efficiency of current passage by reducing the available electrode area.

In all cells with constant exposure, the maximum potential and maximum current develop in approximately 10 min and persist for 30 to 45 min. After this period, there is a slow decrease in these values as the concentration of iron(II) increases in the dark cell.

As long as excess oxalate remains in the irradiated cell, the iron(III) formed at the electrode will be rapidly photoreduced by oxalate, resulting in a constant iron(II) concentration in this compartment. The initial 10-min period during which the current and voltage rise to their maximum values corresponds to the time required for the initial reduction of iron (III) to iron(II) in the irradiated cell.

Increasing the electrode area by substituting platinum gauze for the platinum foil electrodes increases the current that can be obtained. Also, stirring the portion of the solution that is irradiated produces a tenfold increase in the current output.

To evaluate the increase in output obtainable with stirring and larger electrodes, a cell containing 0.1M iron(III), 0.1M  $\text{H}_2\text{C}_2\text{O}_4$ , and 0.5M  $\text{H}_2\text{SO}_4$  was irradiated and monitored continuously for 48 hr. The platinum gauze electrodes were shorted through a 20-ohm resistor, and the irradiated portion of the cell was stirred. The maximum current for the 48-hr period was 3.6 ma. The maximum power thus produced by the cell was  $9.8 \times 10^{-4}\text{w}$ , and the average power was  $2.6 \times 10^{-4}\text{w}$ . During the 48-hr period, a total of 624 coulombs passed through the external circuit.

It should be noted that since the free energy change of the reaction,  $2\text{Fe}(\text{C}_2\text{O}_4)^+ \rightarrow 2\text{Fe}^{++} + 2\text{CO}_2 + \text{C}_2\text{O}_4^{=}$ , is negative ( $\Delta G = -38.96$  kcal/mole) (4), the cell described is not a solar energy converter. The energy from the irradiation is necessary to overcome

Table I. Output of photogalvanic cell

[Fe <sup>+++</sup> ] moles/l	[H <sub>2</sub> C <sub>2</sub> O <sub>4</sub> ] moles/l	[H <sub>2</sub> SO <sub>4</sub> ] moles/l	Max. emf open circuit, v	Max. current through 600 ohms, ma	Max. power, w	Total current during 3 hr, coulombs
0.027	0.25	0.25	0.37	0.30	$5.4 \times 10^{-5}$	3.46
0.054	0.25	0.25	0.40	0.33	6.5	3.83
0.090	0.08	0.25	0.51	0.32	6.0	3.76
0.090	0.25	0.25	0.41	0.38	8.4	4.10
0.090	0.42	0.25	0.40	0.30	5.4	2.74*
0.090	0.25	0.05	0.46	0.30	5.4	3.31*
0.090	0.25	1.25	0.42	0.30	5.4	3.12
0.179	0.25	0.25	0.37	0.48	14.1	4.26
0.179	0.25	1.25	0.44	0.37	8.1	2.53
0.269	0.25	0.25	0.33	0.38	8.8	4.13

\* A comparatively large amount of  $\text{FeC}_2\text{O}_4$  precipitated during these runs.

Each set of data represents two runs, each of 3-hr duration. The first run was made with an open circuit so that the maximum potential could be measured; the second run with a  $600 \pm 1\%$  ohm resistor across the electrodes and the IR drop was monitored continuously. Both electrodes were platinum foil of 4.7  $\text{cm}^2$  area. All solutions were unstirred. All measurements on these cells were made with a Bausch and Lomb V.O.M. 5 recording vacuum tube voltmeter.

the activation energy of the reaction and then a fraction of the chemical energy becomes available to do electrical work.

Manuscript submitted May 1, 1968; revised manuscript received May 16, 1968.

Any discussion of this paper will appear in a Discussion Section to be published in the June 1969 JOURNAL.

## REFERENCES

1. C. G. Hatchard and C. A. Parker, *Proc. Roy. Soc. London*, **A235**, 518 (1956).
2. C. A. Parker and C. G. Hatchard, *J. Phys. Chem.*, **63**, 22 (1959).
3. W. M. Riggs and C. E. Bricker, *Anal. Chem.*, **38**, 897 (1966).
4. John B. Holden, Jr., Ph.D. Thesis, Princeton University (1961).

## Brief Communications



### The Specific Conductivity of Molten Lead Bromide

J. J. McNicholas\*

Brookhaven National Laboratory, Upton, New York

As part of a program to investigate the properties of the system lead, lead bromide and bromine, the specific conductivity of molten lead bromide was determined over the temperature range from 370° to 900°C at 1 atm.

Lead purity was 99.999%. This metal was cleaned in hydrobromic acid. The salt was prepared by direct chemical reaction from the elements. Silica glass was used as the container for the reaction since it had been previously shown to be completely resistant to chemical attack from molten lead, lead bromide and bromine simultaneously even at 900°C (1). Liquid bromine was 99.98% pure with a chlorine content below 20 ppm. The liquid was stored in equilibrium with the vapor in a Monel vessel submerged in a constant temperature water bath. This gave a constant pressure bromine source whose pressure level could be altered when desired by a change in the prescribed water bath temperature. The lead was slowly heated under vacuum until molten. When liquid it was observed to be shiny and clean. Bromine gas was admitted and the reaction was conducted at 900° until all lead had been reacted. The salt was cooled to circa 400°C, the vessel was evacuated and refilled with argon. The salt was then quenched under argon. Analysis of salt indicated 3 ppm Cu + Ni. The silica glass conductance cell is shown in Fig. 1. The design incorporated an external jacket which was filled with lead metal to insure temperature uniformity. The temperature control was better than  $\pm 0.25^\circ\text{C}$ . The inverted U-tube containing the salt used electrodes of tungsten welded to molybdenum ribbon-silica seals.

Conductance measurements were made using a General Radio 1608 Impedance bridge whose accuracy was 0.1% at 1000 Hz. The frequency was varied to 20 kHz but measured resistances did not change so all data was taken at 1 kHz. The terminal voltage was adjusted to 5-10 mv and the wave form was observed on an oscilloscope. Measurements were made with

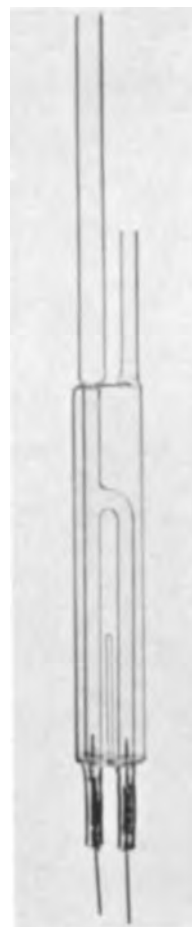


Fig. 1. Silica glass conductance cell

\* Electrochemical Society Active Member.

Key words: conductance, molten, fused, lead bromide, salt.

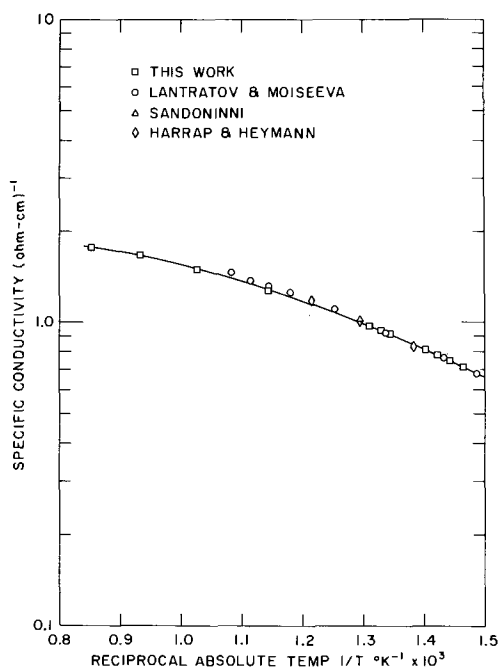


Fig. 2. Values of specific conductivity

increasing and decreasing temperature with excellent reproducibility of data. The cell constant determined at 25°C using 0.1N KCl was 63.3 cm<sup>-1</sup>. Values of the specific conductivity are plotted in Fig. 2 to provide a

comparison with ref. (2-4). This work extends the temperature range of measured conductance from 650° to 900°C which approaches the boiling point of the salt at 1 atm. A least squares fit to this experimental data gives

$$k = -2.918 + 7.162 \left( \frac{T}{1000} \right) - 2.696 \left( \frac{T}{1000} \right)^2$$

where  $k$  = conductivity —mho/cm and  $T$  = absolute temperature °K. The standard deviation was 0.0088.

#### Acknowledgment

The author wishes to thank Mr. William Horn who assisted in carrying out the experimental work.

This work was performed under the auspices of the United States Atomic Energy Commission.

Manuscript received June 4, 1968.

Any discussion of this paper will appear in a Discussion Section to be published in the June 1969 JOURNAL.

#### REFERENCES

1. J. J. McNicholas, BNL Report 9573.
2. M. F. Lantratov and O. F. Moiseeva, *Russ. J. Appl. Chem.*, **36**, 2201 (1963).
3. G. Sandoninni, *Gazz. Chim. Ital.*, **50I**, 289 (1920).
4. B. S. Harrap and E. Heymann, *Trans Faraday Soc.*, **51**, 259 (1955).

## Electrodeposition of Manganese from Aqueous Solution of MnBr<sub>2</sub>

Gianfranco Pistoia and Gianfranco Pecci

Istituto Elettrotecnico, Università di Roma, Rome, Italy

For the manufacture of storage batteries of high specific energy, an element of the type



would have some interest in that it can supply a theoretical energy of 560 whr/kg (considering only the electrode active materials) while that of the lead-acid batteries is 250 whr/kg.

The principal problem in this system is that of satisfactory electrodeposition of manganese, possibly in a cell of a single compartment, in order to avoid contributions to the internal resistance from the presence of diaphragms.

One can obtain deposits of manganese from baths of the chloride (1-4) or sulfate (4-9) salts, usually separating the anodic from the cathodic zone. When using MnBr<sub>2</sub> it is most important to be able to reduce the Br<sub>2</sub> content of the solution to the point where the corrosive effects at the cathode are minimal. By using an organic solvent such as bromoform, in which Br<sub>2</sub> is highly soluble (10), it is possible to obtain this condition. Naturally, one can later recover the Br<sub>2</sub> from the organic layer by physical methods.

The experimental technique consisted of performing the electrolyses in a cell of about 70 cm<sup>3</sup> volume containing 20 cm<sup>3</sup> CHBr<sub>3</sub> and 40 cm<sup>3</sup> MnBr<sub>2</sub> solution. Magnetic stirrers in both phases allowed a continuous exchange of the two layers through a perforated membrane of PVC. A solution containing 330 g/l of MnBr<sub>2</sub>

was preelectrolyzed for an hour in the presence of CHBr<sub>3</sub> using graphite electrodes and a current density of 8 amp/dm<sup>2</sup>. This treatment was necessary to eliminate certain impurities that tend to poison the metallic deposit.

After filtration the concentration of the solution was reduced to 315 g/l. This solution was then electrolyzed with graphite electrodes without additives. Dark deposits which did not adhere well to the electrodes were still obtained. On the addition of NH<sub>4</sub>Cl, which acts as a buffering agent on the pH and also increases the conductivity, only clearly metallic deposits were obtained. There was further improvement when small amounts of NH<sub>2</sub>OH·HCl (11) and of H<sub>2</sub>SeO<sub>3</sub> (4) (0.1 g/l) were added. The first acts as an antioxidant, giving a brightness to the deposits; the second affects the structure of the deposits, making it fine. The immersion of the cathode, immediately after electrodeposition, in a 5% solution of Na<sub>2</sub>Cr<sub>2</sub>O<sub>7</sub> (6) kept the deposit bright and shiny.

The quantity of added NH<sub>4</sub>Cl was determined empirically: when it was too small the deposits were unsatisfactory and the pH decreased rapidly; when in excess the current efficiency fell off, since one must work with a low current density. In Table I are shown the results obtained from solutions containing 20, 30, 40, and 50 g/l of NH<sub>4</sub>Cl at an initial pH 2.8-3.0 using graphite electrodes and varying the current density from 5.5 to 18 amp/dm<sup>2</sup>. On variation of the NH<sub>4</sub>Cl concentration it was always possible to obtain good

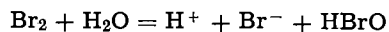


Table I. Manganese deposition from bromide bath: effect of current density and of ammonium chloride

MnBr<sub>2</sub>: 315 g/l; graphite electrodes (2.2 × 2.4 cm); initial pH, 2.8-3.0; temperature ~20°C; plating period, 10 min; quite vigorous agitation

NH <sub>4</sub> Cl, g/l	CD, (amp/dm <sup>2</sup> )	pH	Description of cathode deposit
20	5.5	3.4	Fairly bright, but darkens on standing
	9.0	3.3	Silver-gray, smooth, not compact
	14.0	2.7	Smooth, silver white, some darkening at the edges
	18.0	1.6	Very satisfactory in several places, dark in center
30	5.5	3.0	Silver in center, dark at the edges
	9.0	2.9	Fairly bright, some spots
	14.0	2.7	Smooth, silver-white, very satisfactory
	18.0	2.6	Bright only in one zone, quite spotted in the rest
40	5.5	3.1	Very poor deposit
	9.0	3.1	Smooth, compact but dull gray
	11.5	2.9	Silvery, compact, darkened in a narrow lateral band
	14.0	2.8	Satisfactory in center, dull at the edges
50	5.5	3.5	Bright, silvery, some streak
	9.0	3.4	Many dark streaks
	14.0	2.5	Quite darkened, metallic in only a few points

deposits, but one had, at the same time, to vary the current density for this purpose. In the range of concentration studied the optimum current seemed to diminish with the increase of NH<sub>4</sub>Cl concentration. The pH, after an initial increase, tended to drop in every case; however the rate of this change varied, depending on the concentration of NH<sub>4</sub>Cl. This behavior stems from an increase in concentration of Br<sub>2</sub> which is hydrolyzed as



In this initial investigation it was decided to examine more closely the solution of 30 g/l NH<sub>4</sub>Cl at a current density of about 14 amp/dm<sup>2</sup> and at an initial pH of 2.8-3.0. The purity of the deposits so obtained was determined by the method of Sandell, Kolthoff, and Lingane (11), based on the oxidation of Mn to HMnO<sub>4</sub> by (NH<sub>4</sub>)<sub>2</sub>S<sub>2</sub>O<sub>8</sub> in the presence of AgNO<sub>3</sub> catalyst and by titrating the HMnO<sub>4</sub> with a solution of sodium nitrite + sodium arsenite. The purity of the deposits so obtained was greater than 99.5%. On the other hand, since only traces of lead and iron were found on spectrographic analysis, we can infer that a total inhibition of oxidation would give a yield of 100% purity, i.e., the major impurities are oxidation products of the deposits.

The current efficiency with graphite (14 amp/dm<sup>2</sup>; initial pH = 2.9, final = 2.2; d.d.p. at the electrodes = 4.4v) was 63% after 10 min and 44% after 60 min. On platinum (best current density : 7.5 amp/dm<sup>2</sup>; initial pH = 3.0, final = 1.6; d.d.p. at the electrodes = 4.5v) the efficiency was 52% after 10 and 40% after 60 min. The decrease of the current efficiency with time can be attributed to the production of Br<sub>2</sub> which both changes the acidity of the bath and is itself corrosive (although most of this is extracted by the organic solvent). The ions Br<sub>3</sub><sup>-</sup> and Br<sub>5</sub><sup>-</sup> produced may also make an unwelcome contribution.

The physical state of the deposit is seen in Fig. 1, which shows a cross section of the deposit on graphite which appears to be both compact and uniform. The regular form of the surface layer suggests that the

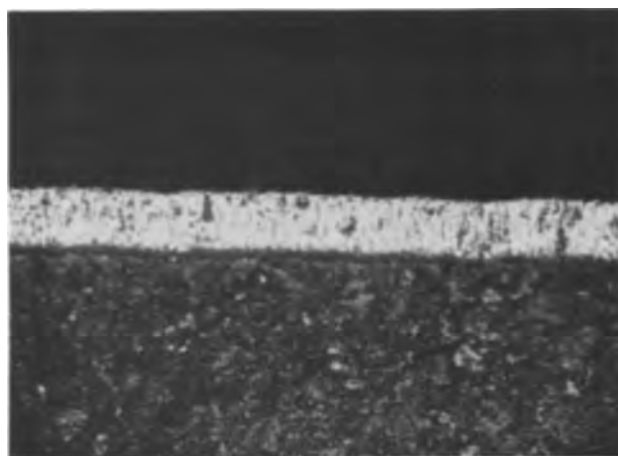


Fig. 1. Micrograph of a cross section of the manganese deposit on graphite. Original magnification 410X.

corrosive action of the Br<sub>2</sub> produced has been limited by its dissolution into the organic solvent.

At the present moment the advantages of this technique are: (a) the ability to produce deposits of Mn of high purity and good texture in a single-cell compartment; (b) the ability to isolate and recover the major part of the Br<sub>2</sub> formed.

A drawback of this technique is the relatively low current efficiency.

Further investigation is necessary, in particular the effect of pH, temperature, composition of the electrolyte, type of electrode, and stirring system are of interest.

#### Acknowledgment

The authors wish to thank Professor Ing. Mario DeRossi for his helpful suggestions and Dr. Roberto Bruno who made the micrograph.

This work was carried out under the sponsorship of the "Consiglio Nazionale delle Ricerche" under Contract No CNR 115.0860.0 1894.

Manuscript received May 13, 1968.

Any discussion of this paper will appear in a Discussion Section to be published in the June 1969 JOURNAL.

#### REFERENCES

- H. Oaks and W. Bradt, *Trans. Electrochem. Soc.*, **69**, 567 (1936).
- N. V. Koninklijke Nederlands Zoutindustrie, Neth. Appl. 6,501,844 (1966).
- V. Stender and Y. Loshkarev, *Zhur. Priklad. Khim.*, **36**, 1033 (1963).
- R. Dean, U. S. Pat. 2,798,038, July 2, 1957.
- Z. Yankelevich, *Mem. Inst. Chem. Acad. Sci. Ukrain. S. S. R.*, **6**, 19 (1939).
- C. Fink and M. Kolodney, *Trans. Electrochem. Soc.*, **71**, 287 (1937).
- W. Bradt and H. Oaks, *ibid.*, **71**, 279 (1937).
- H. Seymour, *Ind. Chem.*, **22**, 17 (1946).
- R. Kirk and D. Othmer, "Encyclopedia of Chemical Technology," Vol. VIII, p. 731, Interscience Publishers, Inc., New York (1952).
- W. Linke, "Solubilities of Inorganic and Metal-Organic Compounds," Vol. I, p. 447, D. Van Nostrand Co., Inc., New York (1958).
- R. Dean, U. S. Pat. 2,717,870, Sept. 13 (1955).
- E. Sandell, M. Kolthoff, and J. Lingane, *Ind. Eng. Chem. Anal. Ed.*, **7**, 256 (1935).

# Spectra of Some Rare Earth Vanadates

R. C. Ropp\*

Westinghouse Electric Corporation, Bloomfield, New Jersey

## ABSTRACT

Spectra of some rare earth activated  $\text{LnVO}_4$  phosphors, where Ln may be Y, Gd, or La, are presented. The most efficient phosphors, particularly in the  $\text{YVO}_4$  matrix, are those activated by  $\text{Sm}^{+3}$ ,  $\text{Eu}^{+3}$ , and  $\text{Dy}^{+3}$ . It is shown that  $\text{YVO}_4:\text{Dy}$  has an output efficiency comparable to commercial phosphors.  $\text{LaVO}_4:\text{Eu}$ , when properly prepared, has an output intensity exceeding that of  $\text{YVO}_4:\text{Eu}$ . The major energy absorption mechanism involves a charge transfer transition within the vanadate matrix from which energy is transferred *via* an exchange coupling mechanism resulting in excitation of the rare earth centers and subsequent emission of characteristic radiation.

The rare earth vanadates, *i.e.*,  $\text{LnVO}_4$ , where Ln may be Y, Gd, or La, are interesting as hosts for rare earth activators because the major excitation mechanism is considerably different from any previously reported in the literature. As pointed out in a prior paper on rare earth oxides (1), the cation in  $\text{LnVO}_4$  must possess a rare-gas configuration since unpaired electrons offer an alternate route for energy dissipation by spin coupling exchange rather than the desired photon-emission process.

A large number of recent papers on rare earth vanadates have appeared in the literature because of the adoption of  $\text{YVO}_4:\text{Eu}$  for color television and high pressure mercury vapor lamp applications. Among the more pertinent are those of VanUitert *et al.* (2), Brill *et al.* (3), Paililla *et al.* (4), Brixner *et al.* (5), and Blasse *et al.* (6). The present paper represents a continuation of the study of rare earth luminescence and the energy transport processes affecting these activators in various matrices.

## Experimental Methods

The raw materials were obtained as oxides in a pure form (described as at least 99.97% pure except for  $\text{Gd}_2\text{O}_3$  which was available only as 99.9% pure). The phosphors were prepared by mechanically mixing the desired coprecipitated rare earth oxalates with a suitable source of vanadium, usually  $\text{V}_2\text{O}_5$ , and firing the mixture in air for a few hours at a suitable temperature ranging between 800° and 1400°C, depending on the  $\text{V}_2\text{O}_5$  to  $\text{Ln}_2\text{O}_3$  ratio (7). Spectral measurements were obtained with a commercial spectrofluorimeter, Perkin Elmer Model 195, which measures excitation and emission spectra directly and presents them in a form already corrected for energy. Reflectance measurements were made with a double beam spectrophotometer, equipped with diffuse reflectance heads, coated with  $\text{BaSO}_4$ . A high intensity Xe-lamp was employed which provided ample radiation to operate at small slit widths so as to obtain high resolution.

A comparison of emission spectra was obtained by instrumentally integrating the spectra produced (via a Disc Instrument Model 303 integrator attached to the recorder) while illuminating the sample surface with a beam of ultraviolet radiation, monitored to maintain constant energy. Emission output could be directly compared on a microwatt basis.

X-ray measurements were made with a calibrated Philips-Norelco diffractometer using Ni-filtered Cu-K $\alpha$  radiation. Scanning rate was one degree  $2\theta$  per minute.

## Experimental Results

**Structure.**—Reviews of the literature on the structures of rare earth vanadates have been published recently (8, 9). Unit-cell dimensions observed in this work agreed closely with those of Schwarz (8).  $\text{YVO}_4$  and  $\text{GdVO}_4$  have the tetragonal Xenotime structure while  $\text{LaVO}_4$  has the monoclinic Monazite structure.

**Relative efficiencies.**—The addition of 5 m/o (mol per cent) rare earth activator to either  $\text{YVO}_4$ ,  $\text{GdVO}_4$ , or  $\text{LaVO}_4$ , resulted in emission characteristic of the rare earth. Very similar results were obtained in each of the three matrices, although there were individual differences, as noted below. Figure 1 shows the relative energy output in microwatts for each activator in  $\text{LaVO}_4$  and  $\text{GdVO}_4$  matrices. Note that the relative outputs of any given activator in these matrices are not materially affected by the excitation wavelengths used. (These outputs are not directly comparable for the two matrices because of the method of measurement, but are compared below for the several activators.)

$\text{YVO}_4$ , as a matrix, also has a moderate intensity blue emission band which is only slightly intensified at liquid  $\text{N}_2$  temperatures. Figure 2 shows the excitation-emission properties of  $\text{YVO}_4$  while Fig. 3 shows spectral properties of  $\text{YVO}_4:\text{Dy}$  at room and liquid nitrogen temperatures. The vanadate emission band is quenched at room temperature in favor of the rare earth line emission. This is good evidence for a phonon assistance mechanism since low temperatures, *i.e.*, phonon quenching, favors vanadate band emission. Very similar results were found for both the  $\text{Dy}^{+3}$  or  $\text{Sm}^{+3}$  ion in the  $\text{YVO}_4$  matrix, as exemplified by the emission band of  $\text{YVO}_4:\text{Dy}$  at 78°K (Fig. 3) and the excitation band of  $\text{YVO}_4:\text{Sm}$  at 78°K (Fig. 4), but at different activator concentrations. At 0.01 g-atom

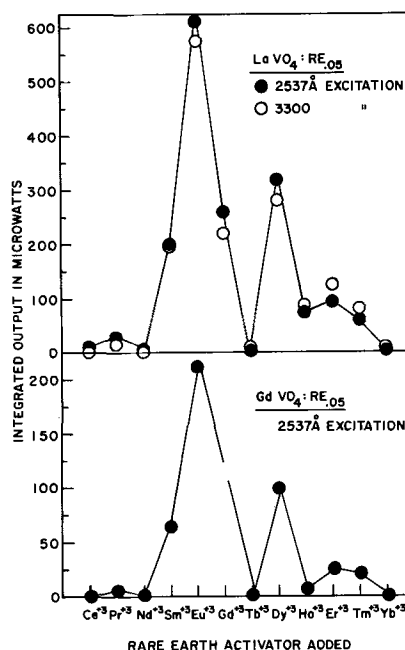
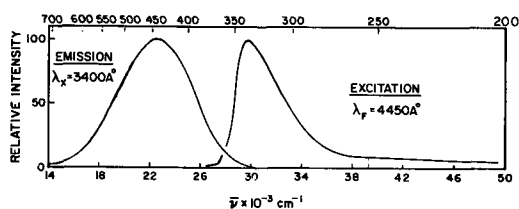
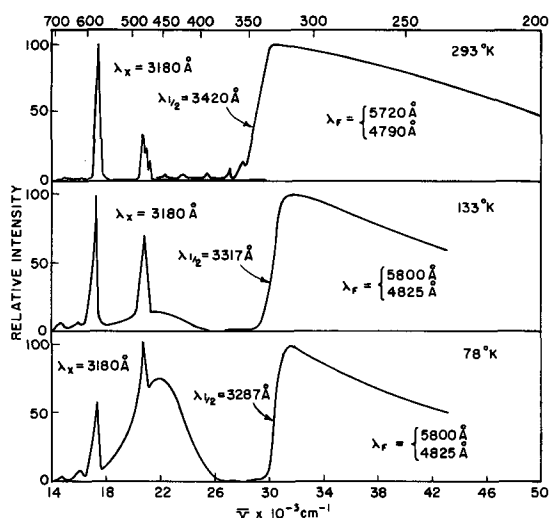
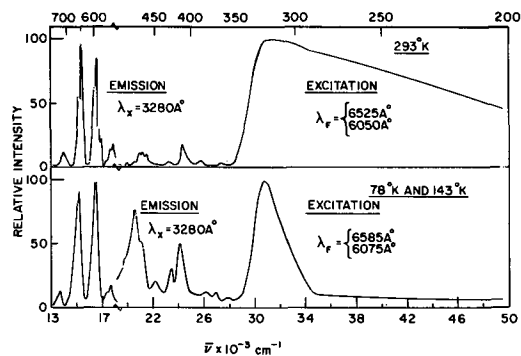


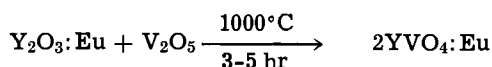
Fig. 1. Relative output of rare earth activators in  $\text{LnVO}_4$  matrices.

\* Electrochemical Society Active Member.

Fig. 2. Spectral properties of  $YVO_4$ —unactivatedFig. 3. Excitation-emission of  $YVO_4:Dy_{0.05}$  as a function of temperature.Fig. 4. Excitation-emission of  $YVO_4:Sm_{0.05}$  as a function of temperature.

$Dy^{3+}$ /mol  $YVO_4$  and at 0.005 g-atom  $Sm^{3+}$ /mol  $YVO_4$ , the spectra were very similar in that the vanadate band emission was noted at 78°K and the broad excitation band at 293°K changed at 78°K to a rather narrow band, similar to that of the pure  $YVO_4$  material. In general, it was found that the coupling between vanadate and the rare earth activator varied according to the ion present and its concentration. It is thus clear that the degree of energy transfer depends on the nature of the rare earth present, each rare earth having its own optimum concentration for maximum luminescent efficiency, as will be shown below.

**Effect of composition.**—The effect of composition on luminescence intensity may be demonstrated, using  $YVO_4:Eu$  as an example, in the following manner. Starting with  $Y_2O_3:Eu_{0.10}$  as shown in Fig. 5, the addition of  $V_2O_5$  causes the appearance of  $YVO_4$  according to the solid state reaction



The formation of  $YVO_4$  is proportional to the amount of  $V_2O_5$  added, a mixture of  $Y_2O_3$  and  $YVO_4$  being ob-

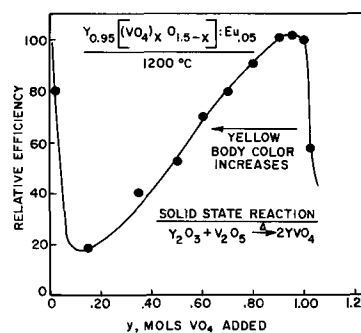
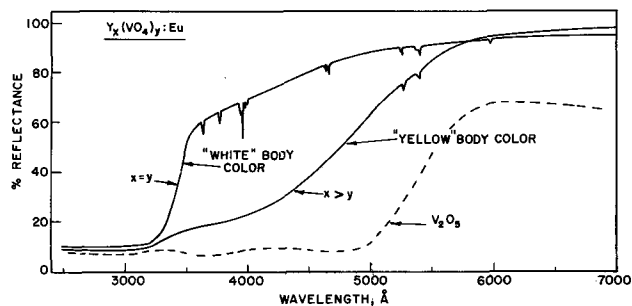
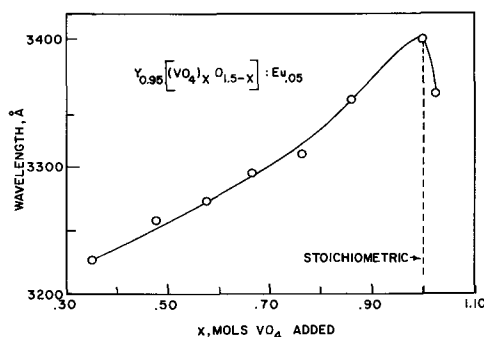


Fig. 5. Effect of phosphor composition on plaque brightness

served, according to x-ray diffraction analysis. The luminescence intensity decreases and then increases with vanadate concentration. The maximum intensity is observed near stoichiometry and then drops off when excess  $V_2O_5$  appears in the fired product. The stoichiometric vanadate has a "white" reflectance color which changes to a yellow color due to the appearance of an absorption band centered near 4000 Å, as shown in Fig. 6. The intensity of this band is inversely proportional to the vanadate content, the materials becoming more and more yellow in reflectance color as the vanadate decreases. Furthermore, the position of the absorption edge of vanadate is dependent on composition, as shown in Fig. 7. The excitation (or absorption) transition probably involves a charge transfer mechanism, such as:  $|(V^{5+}O_n^{-2n})| \rightarrow |(V^{4+}O_n^{-2n+1})|$ . The dependence of wavelength position on vanadium composition implies an interaction between vanadium centers.

**Rare earth spectra.**— $Ce^{3+}$  and  $Tb^{3+}$ .—Neither  $Ce^{3+}$  nor  $Tb^{3+}$  will activate any of the  $LnVO_4$  matrices ( $Ln = Y, Gd, \text{ or } La$ ). This behavior may be contrasted to the  $LnPO_4$  matrices, wherein  $Tb^{3+}$  produces a green emission of moderate intensity and  $Ce^{3+}$  produces a very strong ultraviolet emission (10). Since both matrices have the same structure, the difference must be related to the effect of the presence of the vanadate groups. It should be noted that these

Fig. 6. Reflectance spectra of  $YVO_4:Eu$  phosphorsFig. 7. Correlation of edge absorption with composition— $\lambda_{1/2}$  of vanadate excitation band shown.

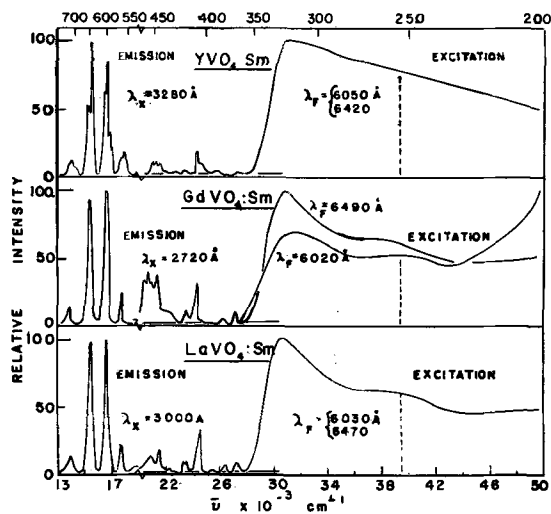


Fig. 8. Spectral properties of some rare earth vanadates

rare earths possess the same major energy transition, namely,  $4f^8 \rightarrow 4f^7 5d$  ( $Tb^{+3}$ ) and  $4f^1 \rightarrow 5d^1$  ( $Ce^{+3}$ ).  $Pr^{+3}$  and  $Nd^{+3}$ .— Both  $Pr^{+3}$  and  $Nd^{+3}$  produce a luminescence intensity so weak that measurement proved difficult. For this reason, the spectra are not included.  $Sm^{+3}$ .—Characteristic spectra consisting of four lines are produced by the  $Sm^{+3}$  activator in  $LnVO_4$  matrices, as shown in Fig. 8. The behavior of  $Sm^{+3}$  in the  $YVO_4$  matrix as a constant quantum emitter has already been commented upon (11). It is noteworthy that neither of the other matrices produces the same effect. In  $LaVO_4$ , the absorption edge of vanadate remains the prominent feature in the excitation spectrum for both of the major emission lines, whereas in  $GdVO_4$ , these same lines have dissimilar excitation spectra. This behavior can be interpreted as a difference in coupling between the vanadate and the  $Sm^{+3}$  excited states associated with the separate emission lines. The same phenomenon does not occur in  $YVO_4$  or  $LaVO_4$ . There is a considerable difference in comparative emission intensities, as shown in Table I. Thus, the most efficient phosphor is based on  $YVO_4$ . Also given, for comparison, is the  $YVO_4:Dy$  phosphor (see below). The optimum activator concentration for  $Sm^{+3}$  in  $LaVO_4$  is about ten times that required for the  $YVO_4$  matrix, as shown in Fig. 9. This behavior seems to be characteristic for the  $LaVO_4$  matrix.

$Eu^{+3}$ .—The inclusion of  $Eu^{+3}$  in  $LnVO_4$  matrices produces the typical red line emission, as shown in Fig. 10. The emission of  $Eu^{+3}$  in these matrices differs somewhat from oxide systems studied previously (1) in that the site symmetry in  $YVO_4$  splits the  ${}^7F_2$  level so that two narrow emission lines are observed instead of the one major line seen in the  $Y_2O_3$  phosphor for the  ${}^5D_0 \rightarrow {}^7F_2$  transition. A recent paper by Briffaut (12) analyzes the splitting of the  ${}^7F_2$  level by calculating the crystal field parameters using a  $42m$  symmetry. In our work, a total of five lines were observed for the  ${}^7F_2$  multiplet (spectrum not given) in agreement with the work by Briffaut. The major lines in  $YVO_4:Eu$  correspond to transitions between  ${}^5D_0$  and the  $A_1$  and  $B_1$  Stark levels of the  ${}^7F_2$  multiplet. According to Briffaut, these lines have electric dipole character,

Table I. Comparison of the output of  $Sm^{+3}$  in the three vanadate matrices

Phosphor	Emission color	Excitation wavelength			
		2537Å	%	3210Å	%
$LaVO_4:Sm_{0.025}$	Pink	57 $\mu$ watt	5.0	90 $\mu$ watt	8.0
$GdVO_4:Sm_{0.05}$	Orange	258	24		
$YVO_4:Sm_{0.0025}$	Orange	745	69	702	62
$YVO_4:Dy_{0.005}$	Yellow	1085	100	1126	100

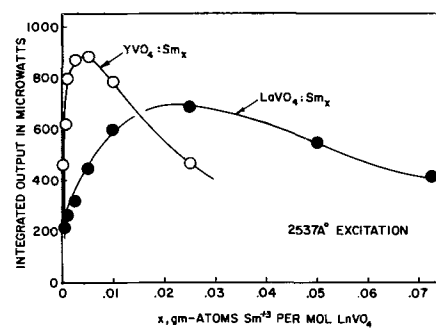


Fig. 9. Optimum activator concentrations in  $LnVO_4$  matrices

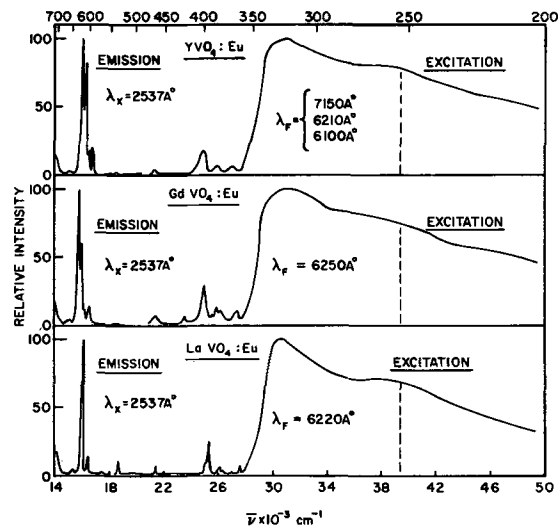


Fig. 10. Spectral properties of some rare earth vanadates

which accounts for their strong intensity in relation to the other Stark components.

Note, however, that the  $LaVO_4$  matrix (monazite structure) apparently does not cause the same splitting (see Fig. 10) since only one major line is seen. This is about the only notable effect in the  $Eu^{+3}$  spectra. The optimum activator concentration for  $Eu^{+3}$  in  $YVO_4$  is about 0.05 g-atom/mol  $YVO_4$  and for  $LaVO_4$  is about 0.10 g-atom/mol  $LaVO_4$ , as shown in Fig. 11 for ultraviolet excitation (the latter being shown for two exciting wavelengths). The relative emission intensities are given in Table II for the various  $Eu^{+3}$  phosphors employing constant energy excitation beam. Thus, although Palilla *et al.* (4) have stated that the low intensity of  $Eu^{+3}$  emission in  $LaVO_4$  is due to structure effects, it is obvious that this phosphor can be prepared so that it is just as efficient as those based on  $YVO_4$ .

$Dy^{+3}$ .—The incorporation of  $Dy^{+3}$  in  $LnVO_4$  matrices results in line emission composed of several Stark components, as shown in Fig. 12. The constant quantum emission behavior of  $Dy^{+3}$  in  $YVO_4$  has already been presented (11). Note that this behavior is not ob-

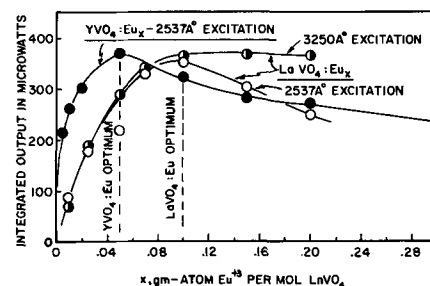


Fig. 11. Optimum activator concentration in  $LnVO_4$  matrices

Table II. Comparison of the output of  $\text{Eu}^{+3}$  in various matrices

Phosphor	Output, $\mu\text{watt}$ (2537Å excitation)	Per cent	Relative peak height
$\text{YVO}_4:\text{Eu}_{0.05}$	182	100	85
$\text{GdVO}_4:\text{Eu}_{0.05}$	152	84	69
$\text{LaVO}_4:\text{Eu}_{0.05}$	40	22	10
$\text{LaVO}_4:\text{Eu}_{0.10}$	186	102	87
$\text{Y}_2\text{O}_3:\text{Eu}_{0.10}$	219	120	100

served in  $\text{LaVO}_4$  or  $\text{GdVO}_4$ . The optimum activator concentration is, again typically, ten times larger in the  $\text{LaVO}_4$  matrix than it is in the  $\text{YVO}_4$  matrix, as shown in Fig. 13. (The ordinates in this figure are not comparable because of the method of measurement.) Even at the optimum level,  $\text{Dy}^{+3}$  produces a low efficiency in  $\text{LaVO}_4$  as may be seen by inspection of the data in Table III, which compares the relative efficiency of the various phosphors. In this case, the xenotime structure does seem to have a demonstrable effect on the luminescent intensity, as compared to the monazite structure ( $\text{LaVO}_4$ ). It has already been shown that interaction of activator sites, possibly through exchange effects, leads to self-quenching in  $\text{Y}_2\text{O}_3$  (13) at rather low concentrations of  $\text{Dy}^{+3}$ . Thus it is possible that the low luminescent intensity experienced for the  $\text{LaVO}_4$  matrix is due to the same effects.

Nevertheless,  $\text{Dy}^{+3}$  in  $\text{YVO}_4$  is remarkably efficient, as may be seen by inspection of Fig. 14. (The integrator employed for these measurements was originally designed for integration of lines such as those

Table III. Radiometric comparison of  $\text{Dy}^{+3}$  activated phosphors

Phosphor	Output 2537Å excitation, $\mu\text{watts}$	Per cent	Relative peak height
$\text{YVO}_4:\text{Dy}_{0.0025}$	237	100	94
$\text{GdVO}_4:\text{Dy}_{0.0025}$	250	105	96
$\text{LaVO}_4:\text{Dy}_{0.025}$	22	9	5

encountered in gas chromatography and should produce more accurate data for lines than for bands.) The  $\text{Dy}^{+3}$ -activated phosphors are at least as efficient as a commercial halophosphate phosphor, containing a high  $\text{Mn}^{+2}$  content so as to obtain a yellow emission color. Therefore, it would be expected that  $\text{YVO}_4:\text{Dy}$ , whose spectrum consists of 5720Å emission lines containing approximately 85% of the total output would produce a lamp of very high brightness, because the luminosity of these photons is very high. However, we achieved a rather disappointing result in that about 3000 lumens resulted after 100 hr burning in 40 watt fluorescent lamps, whereas the halophosphate phosphor produced a lamp with over 3400 lumens.

$\text{Er}^{+3}$  and  $\text{Ho}^{+3}$ .—Both of these activators produce characteristic line spectra in the  $\text{LnVO}_4$  matrices, as shown in Fig. 15 and 16. These spectra are similar to those seen for the  $\text{LnPO}_4$  matrices, except that the vanadate excitation band exists in the former. As a result, the  $\text{Er}^{+3}$  and  $\text{Ho}^{+3}$  activators are considerably more efficient in the  $\text{LnVO}_4$  lattices than in the  $\text{LnPO}_4$  lattices, due to absorption and transfer of energy within the vanadate centers. It is probable that the absorption coefficient of the vanadate matrix remains about the same, regardless of which activator is present, but in the case of  $\text{Er}^{+3}$  and  $\text{Ho}^{+3}$ , the exchange coupling coefficient is moderate to low, resulting in little energy transfer. The ground states of both of

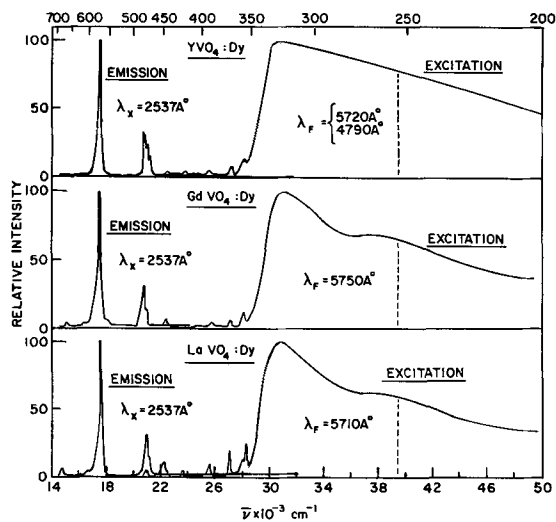


Fig. 12. Spectral properties of some rare earth vanadates

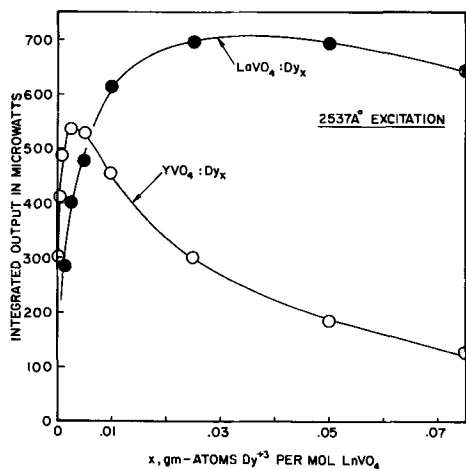


Fig. 13. Optimum activator concentration in  $\text{LnVO}_4$  matrices

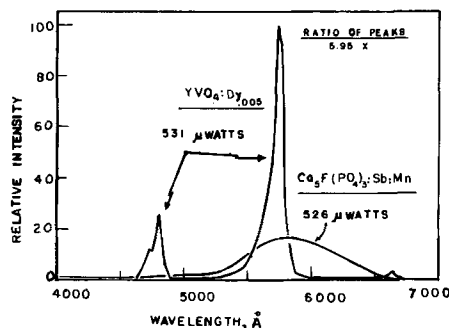


Fig. 14. Comparison of emission intensities— $\text{YVO}_4:\text{Dy}$  and yellow halophosphate.

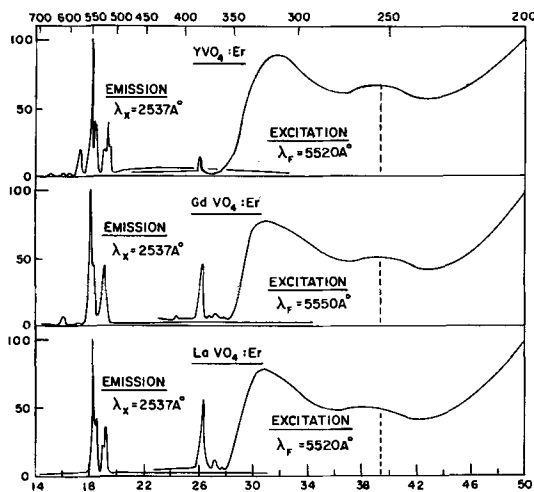


Fig. 15. Spectral properties of some rare earth vanadates

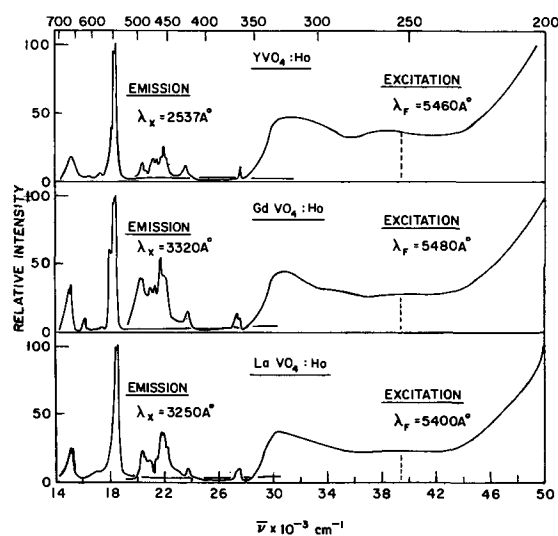


Fig. 16. Spectral properties of some rare earth vanadates

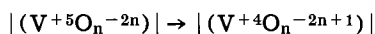
these ions are vibronically coupled to the lattice, a fact which further precludes high efficiency (13).

$\text{Tm}^{+3}$ .—The spectrum of  $\text{Tm}^{+3}$  in  $\text{LnVO}_4$  matrices consists of a single blue line at  $4500\text{\AA}$ , as shown in Fig. 17. The emission intensity is low (see Fig. 1). In  $\text{LnPO}_4$  matrices, the spectra were composed of the blue line and an ultraviolet line as well. The fact that only one line was observed in  $\text{LnVO}_4$  matrices must be attributed to the effect of local site symmetry on transition probabilities.

### Discussion

The spectra of various rare earth activators in  $\text{LnVO}_4$  matrices have been presented. The most efficient phosphors are those activated by  $\text{Eu}^{+3}$ ,  $\text{Sm}^{+3}$ , and  $\text{Dy}^{+3}$ .

The energy processes in these rare earth phosphors are considerably different from any previously reported by the author. The major absorption process occurs in the vanadate group probably via a charge transfer mechanism



Once the vanadate center becomes excited, it can either emit the energy as luminescence or transfer the energy to a rare earth center, which subsequently emits its own characteristic radiation. The latter mechanism is phonon regulated, as shown by the data given for  $\text{Sm}^{+3}$  and  $\text{Dy}^{+3}$  activated phosphors. It is particularly

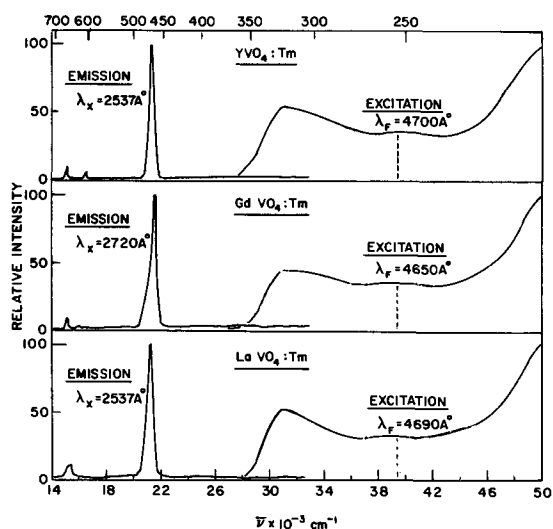
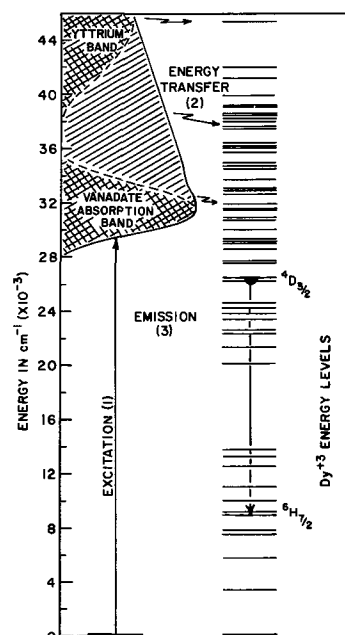


Fig. 17. Spectral properties of some rare earth vanadates

Fig. 18. Possible energy transport processes in  $\text{YVO}_4:\text{Dy}$  phosphors

noteworthy that  $\text{Eu}^{+3}$ , whose excitation mechanism can be classified as a charge transfer band, is the most efficient activator in the vanadate phosphors. In contrast, those activators involving a  $4f \rightarrow 5d$  transition as the main energy transition are not effective at all.

It is of interest to compare the present results which contradict those already published. Brixner and Abramson (5) showed line emission for  $\text{YVO}_4$  at  $300^\circ\text{K}$  and O'Conner (14) confirmed these observations. For a charge-transfer excitation mechanism, one expects a broad band emission at  $300^\circ\text{K}$ . The present results show a broad emission band for  $\text{YVO}_4$  and even in  $\text{YVO}_4:\text{Dy}$  or  $\text{YVO}_4:\text{Sm}$ , a broad emission band arises at  $78^\circ\text{K}$  because the  $|\text{VO}_4| \rightarrow \text{Ln}^{+3}$  energy transfer mechanism is hindered. Furthermore, the same 4800 and  $5720\text{\AA}$  lines, due to  $\text{Dy}^{+3}$  emission occur in the oxide and phosphate phosphors (1, 10). In all of the cases investigated by the author to date, the emission spectrum of  $\text{Dy}^{+3}$  has been distinctive, regardless of matrix. In addition, quantities as low as 10 ppm  $\text{Dy}^{+3}$  cause a moderate-intensity emission in  $\text{YVO}_4$ . Thus the prior data given by Brixner *et al.* and by O'Conner are incorrect and are due to impurity concentrations of  $\text{Dy}^{+3}$ .

Although Palilla and Levine (4) attribute the low output of  $\text{LaVO}_4:\text{Eu}$  to structural effects, we have shown that it can be prepared so that its output is as high as  $\text{YVO}_4:\text{Eu}$ .

For  $\text{Tb}^{+3}$  activated phosphors, no luminescence was noted in  $\text{LnVO}_4$  matrices ( $\text{Ln} = \text{Y, Gd, or La}$ ), where the initial  $\text{V}_2\text{O}_5/\text{Ln}_2\text{O}_3$  ratio was 1:1 or larger, prior to firing. At ratios less than 1:1, some  $\text{Tb}^{+3}$  emission was noted, particularly in  $\text{LaVO}_4$ , becoming greater as the ratio decreased. Thus, the results of Brill *et al.* (3) can be explained as activation of the oxide normally present in low  $\text{V}_2\text{O}_5/\text{Ln}_2\text{O}_3$  compositions but no activation of the vanadate.

Of those phosphors which behave as constant quantum emitters, it is interesting that such behavior implies that all of the upper energy excited states, of  $\text{Dy}^{+3}$  for example, may be coupled in the same manner to the emitting state. This is more easily seen by reference to Fig. 17. The transition from the  $4^1\text{D}_{3/2}$  state to the  $6^1\text{H}_{7/2}$  component of the ground state multiplet results in emission of  $5720\text{\AA}$  photons. Excitation occurs either in the vanadate absorption band or in the yttrium band, depending on energy. The exact positioning of the yttrium band remains uncertain, although it is shown in Fig. 17 near to  $2200\text{\AA}$ . That it

exists in the oxides has already been shown [ref. (1, 13)]. It is assumed to be present here.

The exact path of the energy transfer has not been proven. For example,  $44,000\text{ cm}^{-1}$  energy causes excitation in the yttrium band. This excited center may then decay by phonon processes to the vanadate band level, from which energy transfer may occur by phonon-regulated exchange processes to a  $\text{Dy}^{+3}$  level. Alternately, the excited yttrium center may exchange couple directly to an upper  $\text{Dy}^{+3}$  state, which would decay, again by phonon processes, to the  ${}^4\text{D}_{3/2}$  emitting state. However, in the latter mechanism, the emitting state is required to be coupled to all of the upper energy states of the  $\text{Dy}^{+3}$  ion, in the same manner, because of the constant quantum efficiency observed. In the former mechanism, the phonon-regulated exchange could occur via the  ${}^4\text{D}_J$  multiplet. The  ${}^4\text{D}_{1/2}$  level occurs near to  $31,000\text{ cm}^{-1}$  which could then relax to the emitting state  ${}^4\text{D}_{3/2}$ . The data presented herein are not sufficiently definitive to be able to delineate the correct mechanism. Whether the yttrium band is a charge transfer band remains uncertain, although an exciton band involving yttrium sites seems more likely, particularly because yttrium does not have a stable divalent state.

#### Acknowledgment

The author is indebted to G. Grasso and E. Chen for materials preparation and to Dr. C. K. Lui Wei for x-ray measurements.

Manuscript submitted Dec. 1, 1967; revised manuscript received May 15, 1968.

Any discussion of this paper will appear in a Discussion Section to be published in the June 1969 JOURNAL.

#### REFERENCES

1. R. C. Ropp, *This Journal*, **111**, 311 (1964).
2. L. G. VanUitert, R. R. Soden, R. C. Linares, and A. A. Ballman, *J. Chem. Phys.*, **36**, 702 (1962); *ibid.*, **36**, 1793 (1962).
3. A. Bril and W. L. Wanmaker, *This Journal*, **111**, 1363 (1964); A. Bril, W. L. Wanmaker, and J. Bross, *J. Chem. Phys.*, **43**, 311 (1965).
4. F. C. Palilla, A. K. Levine, and M. Rinkevics, *This Journal*, **112**, 776 (1965); A. K. Levine and F. C. Palilla, *Electrochem. Tech.*, **4**, 16 (1966).
5. L. H. Brixner and E. Abramson, *This Journal*, **112**, 70 (1964).
6. G. Blasse, *J. Chem. Phys.*, **45**, 2356 (1966).
7. Dutch Pat. No. 6,514,050, G. T. & E. Labs., N. Y. (1966).
8. H. Schwarz, *Z. anorg. allgem. Chem.*, **323**, 44 (1963).
9. V. S. Stubican and R. Roy, *Z. Krist.*, **119**, 342 (1963).
10. R. C. Ropp, *This Journal*, **115**, 841 (1968); paper presented at the Cleveland Meeting, May 1-6, 1966, as Paper 33.
11. R. C. Ropp, *J. Opt. Soc.*, **57**, 1240 (1967).
12. J. P. Briffaut, *C. R. Acad. Sc. Paris*, **262**, 562 (1966).
13. R. C. Ropp, Fourth Rare Earth Conference, Ames, Iowa, April 1966, paper No. 14, "Optimum Activator Concentrations in Rare Earth Oxide Phosphors," To be published.
14. J. R. O'Connor, *Trans. AIME*, **239**, 362 (1967).
15. R. C. Ropp, To be published.

## Vapor Phase Growth and Properties of Aluminum Phosphide

D. Richman

RCA Laboratories, Princeton, New Jersey

#### ABSTRACT

Aluminum phosphide epitaxial layers on Si and single crystal needles and platelets have been synthesized by a vapor transport reaction, utilizing the disproportionation of  $\text{AlCl}$ . Lattice constant determinations yielded a value of  $5.4625 \pm 0.0005\text{ \AA}$ . The optical band gap was found to be  $2.43 \pm 0.2\text{ eV}$ . Hall constant and resistivity measurements indicate that the as grown material is n-type with carrier concentrations in the  $1 \times 10^{18}$  range and mobilities of the value of  $70\text{ cm}^2/\text{v-sec}$ . Evidence was obtained for effects of variations in stoichiometry. The material as grown varies between pale yellow and a light green in color. Optical absorption studies revealed an infrared band in the green material with maximum absorption at  $11,800\text{ \AA}$ . The color could not be associated with the presence of foreign atoms. However, on annealing in vacuum at  $1000^\circ\text{C}$ , the color of the AlP changed from green to yellow, and the absorption band decreased in intensity. On annealing in a phosphorus atmosphere, these effects reversed.

Among the series of III-V compounds, the phosphides of boron, aluminum, and gallium are characterized by their high melting points and high dissociation pressures. These properties are known accurately only for GaP, the lowest melting of the three. Even for this material, its melting point of  $1467^\circ\text{C}$  and dissociation pressure of 35 atm are very high (1). For the other compounds, the melting points and pressures are even higher so that synthesis methods other than growth from the melt must be used.

One technique which appears to have great versatility is vapor phase synthesis. In this technique, gaseous species are reacted to form the solid of interest at temperatures and pressures considerably below those at the melting point of the solid. This approach has been used successfully for the synthesis

of GaAs from the elements as well as for the transport and epitaxial growth of Ge, Si, GaAs, GaP, and GaAs-GaP alloys.

Because of the difficulty in preparing single crystals of AlP(2), it is one of the least studied of the III-V compounds, and basic parameters such as band-gap and lattice constant are not well established. The use of vapor phase synthesis seemed to be well suited to overcome the difficulty of preparation, and therefore work was begun to synthesize single crystals of AlP of sufficient size to allow evaluation of the optical and electrical properties of this III-V semiconductor. In this research the chemical reactions in the vapor growth are different from that previously reported (2a), and more complete results concerning the properties of AlP are presented.

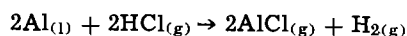
### Synthesis of AlP

The apparatus used for the synthesis of AlP is shown in Fig. 1. The use of an alumina reaction tube is necessary since AlCl reacts with quartz. Because alumina is not easily fabricated into various shapes, an apparatus with a straight-line geometry was used for these experiments. The procedure consisted of heating the reaction zone and the deposition zone to the desired temperature during a constant flow of hydrogen gas. When thermal equilibrium was established, the flow of HCl and PH<sub>3</sub> was started and with the H<sub>2</sub> was adjusted to give the desired concentration of gases in the two zones. It should be noted that the reactive gases were not mixed until they were in the deposition zone. This prevented reaction of the phosphorus with the liquid aluminum and the formation of AlP in the melt.

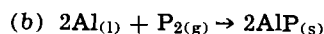
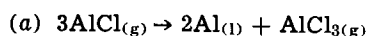
The gaseous aluminum halide species responsible for transport was determined for various temperatures and HCl flow rates, by metering the HCl flow and weighing the aluminum source before and after each run. Table I presents the results of several of these determinations.

The close one to one relationship between gram atoms of aluminum and moles of HCl indicates that AlCl is the molecular species responsible for the transport. Therefore, the equations for transport of aluminum and synthesis of AlP can be derived as follows:

(I) Source zone; high temperature



(II) Deposition zone; low temperature



The temperature of the deposition zone was held in the range 1200°-1250°C. The amount and rate of deposition could be controlled by varying the concentration of the AlCl in the deposition zone. This was done by varying the amount of hydrogen carrier gas that was introduced into the deposition zone through the PH<sub>3</sub> feed line. In this manner, deposition rates between 0 and 40 mg/cm<sup>2</sup>/hr could be obtained. The higher rates being obtained at high AlCl concentrations.

The two substrates used to nucleate growth were polished sapphire and silicon. The sapphire was used to support thin polycrystalline layers that would be suitable for optical absorption studies. Silicon was used as a substrate for the epitaxial growth of AlP. It was felt that, in this manner, large area single crystals of AlP could be prepared. In addition, needles and platelets of AlP were produced due to nucleation on the walls of the reaction tube. From these growths, samples were obtained for lattice constant determinations as well as samples suitable for optical absorption studies and electrical measurements, the results of which are described below.

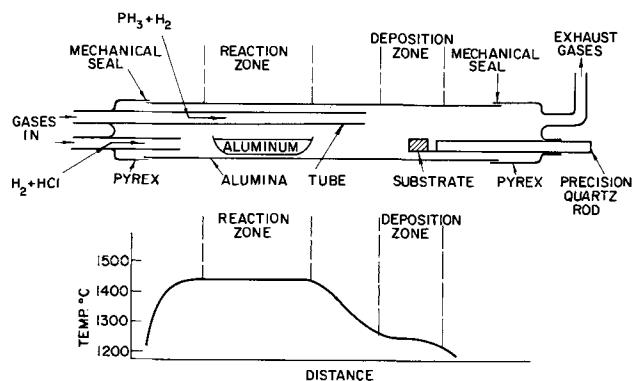


Fig. 1. Growth apparatus and temperature profile for AlP synthesis.

Table I. Consumption of aluminum as a function of temperature and moles of HCl used

Run	Temperature of aluminum source, °C	Wt. of aluminum lost from source, g	Gram atoms of aluminum consumed	Moles of HCl used
1	1420	0.84669	$3.14 \times 10^{-2}$	$3.16 \times 10^{-2}$
2	1330	0.81872	$3.04 \times 10^{-2}$	$3.16 \times 10^{-2}$
3	1507	0.85732	$3.18 \times 10^{-2}$	$3.16 \times 10^{-2}$
4	1460	0.52027	$1.93 \times 10^{-2}$	$2.06 \times 10^{-2}$
5	1470	1.25706	$4.66 \times 10^{-2}$	$6.15 \times 10^{-2}$

### Properties of AlP

**Lattice constant.**—Nine different samples of AlP comprising needles, platelets, and epitaxial material were submitted for x-ray lattice constant determinations. The results from all of these determinations yield a lattice constant for AlP of  $5.4625 \pm 0.0005\text{Å}$ . This is somewhat larger than the value of  $5.451\text{Å}$  reported by Addamiano (3), and is closer to, but smaller than, the value of  $5.467 \pm 0.002\text{Å}$  reported by Wang *et al.* (4).

**Optical properties.**—The bandgap of AlP has been reported to be either 2.42 eV (5) or 3.0 eV (6). A material of this bandgap should be a pale yellow. Observation of the material prepared here and elsewhere (3,4) indicates that some of the AlP is green. Emission spectrographic analysis shows no observable difference between the impurity content of the green and yellow crystals. A typical analysis shows the presence of Cu, Si, Mg, and Fe with the total impurity content in the 100-200 ppm range. In order to study this color difference, as well as to determine the optical band edge, absorption studies of polycrystalline layers on sapphire and unsupported single crystal platelets were undertaken. For this work, a Cary Model 14 double-beam spectrometer was used. Similar spectra were obtained from the supported and unsupported material. Figure 2 shows a typical spectrum for green AlP. The spectrum for yellow AlP lacks the band at  $11,800\text{Å}$ . The absorption in the region of the band edge does not increase rapidly. Such behavior is indicative of an indirect gap material, although more work must be done to establish this conclusion. The best fit to a plot of optical density vs.  $(h\nu - E_g)^2$  yields a bandgap of 2.43 eV at room temperature. One spectrum run at 77°K gave a shift in the band edge of  $260\text{Å}$  or 0.13 eV. This would indicate a liquid-nitrogen gap of 2.56 eV and so  $(dE/dT)_p = 5.8 \times 10^{-4} \text{ eV/deg}$ .

The effect of various heat treatments on the absorption band at  $11,800\text{Å}$  is shown in Fig. 3. It can be seen that vacuum annealing causes the intensity of the absorption band to decrease markedly. Also apparent is the increase in the band intensity on reheating in a phosphorus atmosphere. This behavior indicates that the color effects in AlP arise from non-stoichiometry, and most probably an excess of phosphorus leads to the green color. At present it has not

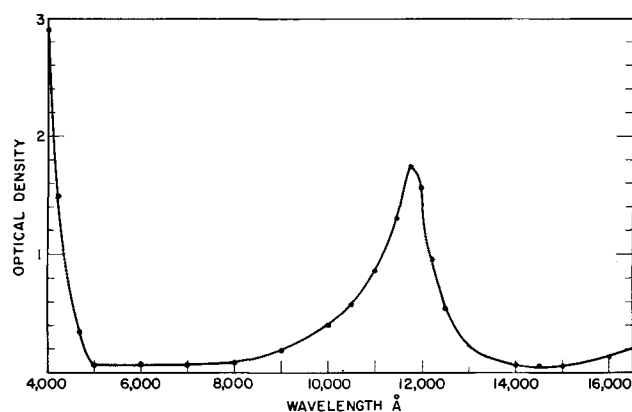


Fig. 2. Optical absorption spectrum of green AlP



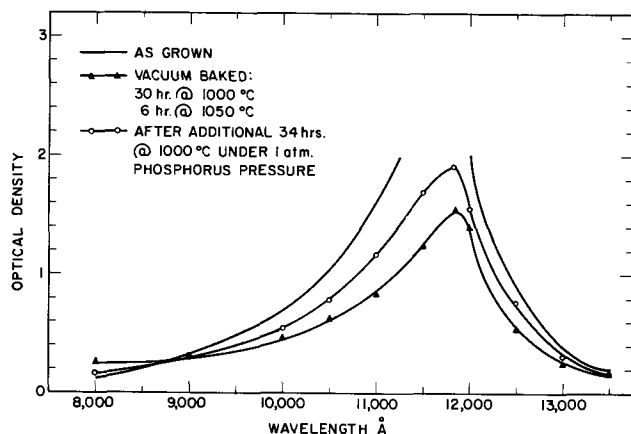


Fig. 3. Effects of various heat treatments on the infrared absorption band in green AIP.

been possible to correlate these optical effects with electrical measurements on this material. This is the first time that such evidence for deviations from stoichiometry have been observed in a III-V compound semiconductor.

**Electrical properties.**—Hall samples were shaped from single crystal needle specimens by hand lapping under dry kerosene. Ohmic contact to the AIP was achieved by ultrasonically soldering indium dots to the freshly prepared surface. All the AIP tested was n-type. Carrier concentrations were between  $4 \times 10^{17}$  and  $5 \times 10^{18}$  electrons/cm<sup>3</sup> with associated mobilities varying between 80 and 65 cm<sup>2</sup>/v-sec, respectively. No significant deionization was observed on cooling to liquid nitrogen temperature; however, a definite decrease of 20 to 50% of the room temperature mobility was observed in all cases.

Effects of annealing in vacuum could not be conclusively established. Preliminary findings indicate that a 45-hr anneal at 1090°C causes an increase in

carrier concentration by a factor of 2 or 3. For material with the lowest as-grown carrier concentration annealing resulted in a definite increase in the room-temperature and liquid-nitrogen mobilities. However, for the more heavily doped material the opposite effect was observed.

### Conclusion

The AIP is the first of the III-V compounds to show a reversible deviation from stoichiometry. This deviation is associated with the color of the material which varies from yellow to green with increasing phosphorus content. The bandgap of AIP is 2.43 eV and is an indirect transition. The low mobility for electrons in AIP is in agreement with this conclusion.

### Acknowledgments

The author would like to express his thanks to B. J. Seabury for technical assistance in the course of this work. This research was supported by the Advanced Research Projects Agency, Materials Sciences Office, under Contract No. SD-182.

Manuscript submitted April 19, 1968; revised manuscript received ca. May 15, 1968.

Any discussion of this paper will appear in a Discussion Section to be published in the June 1969 JOURNAL.

### REFERENCES

1. D. Richman, *J. Phys. Chem. Solids*, **24**, 1131 (1963).
2. A. Rabenau, "Compound Semiconductors, Vol. 1, Preparation of III-V Compounds," R. K. Willardson and H. L. Goering, Editors, Reinhold Publishing Corp., New York (1962).
- 2a. F. J. Reid, S. E. Miller, and H. L. Goering, *This Journal*, **113**, 467 (1966).
3. A. Addamiano, *Acta Cryst.*, **13**, 505 (1960).
4. C. C. Wang, M. Zaheeruddin, and L. H. Spinar, *J. Inorg. Nucl. Chem.*, **25**, 326 (1963).
5. H. G. Grimmeiss, W. Kischio, and A. Rabenau, *J. Phys. Chem. Solids*, **16**, 302 (1960).
6. "Semiconductors," p. 417, Ed. Hannay, Reinhold Publishing Corp., New York (1959).

# Electrical Characteristics of Silicon Nitride Films Prepared by Silane-Ammonia Reaction

George A. Brown, W. C. Robinette, Jr.,\* and H. G. Carlson\*

Texas Instruments Inc., Dallas, Texas

## ABSTRACT

The d-c conduction and complex dielectric constant of silicon nitride films prepared by silane-ammonia reaction have been studied as a function of the composition of the gaseous ambient in which they were formed. The d-c conductivity of the material increases sharply when the silane-ammonia ratio increases above 0.1. The increased conductivity is characterized by a lowering of the activation energy to about 1.0 eV from 1.5 eV for high resistivity nitride. The current-voltage characteristics display a  $\ln I-V^{1/2}$  dependence at high fields in the temperature range 200°-500°K. Measurement of the magnitude of the slope of this characteristic and its dependence on film thickness, index of refraction, temperature, and bias polarity suggests that conduction arises from field aided thermal ionization of trapping centers in the bulk of the film, the Poole-Frenkel effect. It is noted that the magnitudes of the slopes of the experimental  $\ln I-V^{1/2}$  plots, which are twice as large as Schottky emission slopes, are derivable within the framework of the Poole-Frenkel mechanism only under a special assumption regarding the statistics governing the occupancy of the traps.

The relative dielectric constant,  $\epsilon'_r$ , of the films has a constant value of approximately 7 for silane-ammonia ratios below 0.1 and increases gradually to about 10 for a silane-ammonia ratio of unity. Very small variations in  $\epsilon'_r$  with frequency and temperature were noted in the range of the measurements,  $5 \times 10^2 - 10^6$  Hz and 200°-500°K. Values of dielectric loss,  $\epsilon''_r$ , lower than  $10^{-3}$  have been observed for the low silane-ammonia ratio films, but these are also dependent on substrate surface preparation. An observed dependence of  $\epsilon''_r$  on sample area in some cases suggests the presence of localized film defects in the less carefully prepared samples. No structure in the loss-frequency-temperature characteristics of the material has been observed in the above-mentioned ranges of temperature and frequency that cannot be related to the d-c conductance of the silicon nitride or to the substrate resistance.

Electrical characteristics of silicon nitride films prepared by silane-ammonia reaction have been measured. Parameters studied include d-c conduction and complex dielectric constant as a function of composition of the gaseous ambient during film formation and of applied electric field and temperature during measurement.

The preparation of silicon nitride in thin films by the reaction of silane and ammonia in hydrogen diluent has been reported by several workers (1-4) and is one of several techniques by which films of the material have been formed (5, 6). While all of these films have certain similar characteristics, important differences exist (7). Indeed, as might be expected, the physical and electrical properties of films formed by silane-ammonia reaction have been found to vary with reactant composition during growth (2, 8, 9). In this work, samples formed from various silane-ammonia ratios in the gas were chosen to relate electrical characteristics to the parameters of film formation and to material properties.

The samples described in this study were prepared in the laboratory of Bean, Gleim, Yeakley, and Runyan (9), who have detailed many of the physical properties of the material. Deposition conditions for the films in the present study are given in ref. (9). All the films evaluated electrically were formed at  $850^\circ \pm 50^\circ\text{C}$  in a region of growth parameters found to produce amorphous films as determined by x-ray diffraction. Within the growth parameter region described by Bean *et al.*, it has been found that the physical and electrical characteristics vary only with the ratio of silane to ammonia in the gaseous ambient. No variation in behavior was found to result from changing film thickness or growth rate by varying total percentage of silane and ammonia in the gas

stream by a factor of two about normal levels while maintaining a fixed ratio.

Silicon nitride was formed on both molybdenum and silicon substrates. The silicon starting material varied from 0.01 to 5 ohm-cm n- and p-type of several crystal orientations and was usually etched in  $\text{H}_2\text{-HCl}$  vapor in situ immediately prior to film deposition. Commercial grade molybdenum sheet was cut into  $1 \times 2$  cm substrates and mechanically polished to a thickness of approximately  $260\mu$ . The substrates were degreased and cleaned prior to silicon nitride deposition.

The thickness of the deposited silicon nitride films ranged from 600 to 6000Å. The index of refraction and thickness of all samples used was measured with an ellipsometer using either a mercury arc source ( $\lambda = 5461\text{Å}$ ) or a laser source ( $\lambda = 6328\text{Å}$ ).

Capacitor structures for the electrical measurements were formed by vacuum evaporation of either aluminum or chromium on the surface of the nitride film and subsequent photolithographic definition of a pattern of circular dots ranging in area from  $1.8 \times 10^{-4}$   $\text{cm}^2$  to  $1.8 \times 10^{-2}$   $\text{cm}^2$ . None of the parameters in this study was found to depend on the metal contact material used.

Most of the electrical measurements were made on complete slices using a shielded probe in a darkened chamber. In some cases, however, 0.25 cm square chips were scribed and mounted in TO-60 headers for measurement.

## D-C Conduction

*Experimental results.*—The test set for d-c conduction measurements employed a resistance-programmed Kepco ABC 1000 voltage source and a Hewlett-Packard Model 425A micro-microammeter. For measurements at temperatures other than room temperature, a Statham SD-6 oven with temperature range between

\* Electrochemical Society Active Member.

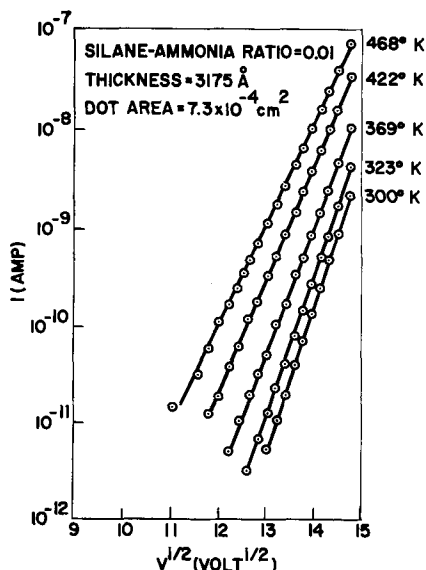


Fig. 1. Typical current-voltage-temperature data for a silicon nitride film.

200° and 575°K was used for packaged units, while a controlled ambient, hot stage probe chamber was used for slice-form studies in the range 300° to 500°K.

Current-voltage-temperature data representative of samples of all compositions studied are shown in Fig. 1. The silane-ammonia ratio for this sample is 0.01. From this  $\ln I-V^{1/2}$  plot, often called a Schottky plot, it is seen that the high field conduction in the temperature range from 300° to 468°K may be expressed as

$$I \sim I_0 \exp \left( \frac{\beta V^{1/2} - \Psi}{kT} \right) \quad [1]$$

where  $I$  is the measured current,  $V$  the applied voltage,  $\beta$  and  $\Psi$  are constants with temperature dependences to be explored,  $k$  is Boltzmann's constant, and  $T$  is the absolute temperature. The parameter  $\Psi$ , a low field activation energy for the current, is obtained from curves like those in Fig. 1 by extrapolation to the zero voltage intercept. The values of this intercept current,  $I_0$ , are shown plotted vs. reciprocal temperature in Fig. 2.

This activation energy is found to vary in value from about 1.5 eV for high resistivity silicon nitride samples like that shown in Fig. 1 to approximately 1 eV for

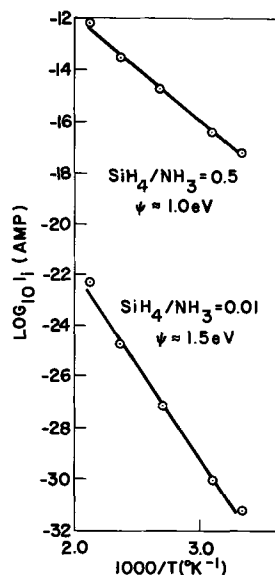


Fig. 2. Zero-volt-intercept current,  $I_0$ , plotted vs. inverse temperature, yielding activation energies for the conduction mechanism.

more conductive samples. Apparent activation energies as low as 0.5 eV have been observed for units characterized for a temperature dependent  $\beta$  in Eq. [1]. Such units will be discussed below. Measurements on capacitors varying in area as described above have established that this conduction is of a uniform, area-dependent nature. Hence the d-c resistivity of the films defined by the relation

$$\rho = \frac{E}{J} \quad [2]$$

can be determined from the data of Fig. 1.

It is found that the resistivity is a very strong function of the silane-ammonia ratio of the deposition ambient, as shown in Fig. 3 where the logarithm of the room temperature current density is plotted vs. the square root of the applied electric field for samples with silane-ammonia ratios of 0.01 to 1.2. Because of the strongly non-ohmic nature of these characteristics, the resistivity varies with field strength, and comparison of resistivities must be made at a fixed field. Figure 4 shows the d-c resistivity at  $E = 4 \times 10^6$  v/cm for films of the above-mentioned silane-ammonia ratio range. These values, like the refractive index and etch rate values reported by Bean *et al.*, saturate abruptly for silane-ammonia ratios of 0.1 and below. The dielectric strength of these films was found to be very close to  $10^7$  v/cm at room temperature for all the films, regardless of silane-ammonia ratio. It was observed that the uniformity of the d-c conduction data on molybdenum-substrate samples was in general inferior to that found with silicon substrates, although the form of the  $I-V$  relationship was unchanged. Residual

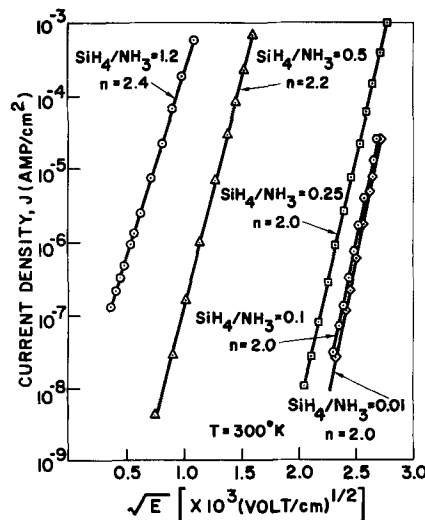


Fig. 3. Log current density plotted vs. the square root of the electric field, showing the dependence of conductance on silane-ammonia ratio.

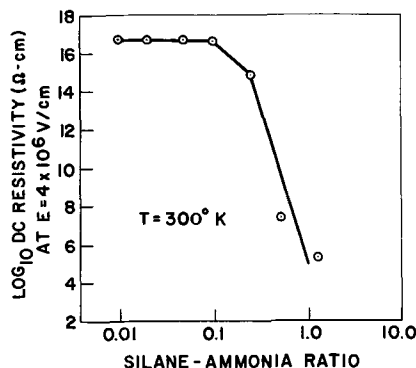


Fig. 4. The d-c resistivity of the silicon nitride films at an applied field of  $4 \times 10^6$  v/cm, as a function of silane-ammonia ratio.

irregularities on the molybdenum surface which could not be removed are thought to be the cause of this behavior. Because of the scatter in the molybdenum-substrate data, results obtained for films on silicon substrates are used in the quantitative characterization of the silicon nitride films.

*Model.*—On the basis of the strong dependence of the conductivity on film composition, independence of electrode materials and the analysis of the data to be given below, it is proposed that the conduction is electronic in nature and is limited by a bulk film mechanism. This mechanism is apparently a form of field-aided thermal ionization of trapping levels in the film, a process which in its simplest form is known as the Poole-Frenkel effect. The title arises from the work of Poole (10), who reported an exponential dependence of conductivity on applied electric field in mica and certain other insulators, and that of Frenkel (11), who proposed the model and derived the expression showing the  $\sigma \sim \exp(\beta E^{1/2})$  relationship. The mechanism has since been invoked by many workers studying conduction in thicker films of a variety of materials. Among them are Vermilyea (12) ( $ZrO_2$ ), Mead (13) ( $Ta_2O_5$ ), Hirose and Wada (14) (SiO), and Hartman *et al.* (15) (SiO). The applicability of the mechanism to silicon nitride films was pointed out by the authors (16), and other workers (17, 18) studying silicon nitride films fabricated by a variety of techniques have suggested this interpretation of their conductivity data.

The assumption of an electronic rather than ionic mechanism is based on experiments in which currents of  $10^{-3}$  amp/cm<sup>2</sup> of both polarities were maintained in samples for extended periods of time without observing any current decay due to ionic pileup near an electrode. Present data do not, however, permit differentiation between hole and electron currents. For definiteness, an electron transport mechanism will be assumed throughout the discussions.

The basic derivation of the Poole-Frenkel characteristics has appeared in the literature in brief form (11,12) and will not be presented here in detail. A few remarks will be made relative to the model.

Consider an occupied donor-like electron trap located in energy  $qU$  below the conduction band of an insulator as shown in Fig. 5. The main premise of the derivation is that under the influence of an applied electric field (indicated by the tilted bands of Fig. 5), an electron being excited from the trap is acted on by first, the applied field, and second, the coulomb attractive force of the positively charged center that it is escaping. The resultant of these two forces forms a potential distribution seen by the electron like that shown in the heavy line in Fig. 5.

Note the energy barrier that the electron must overcome to escape the center has been lowered by  $q\Delta U$ , making the escape more probable.

Frenkel showed that this potential barrier lowering,  $\Delta U_{p-f}$ , was given by

$$\Delta U_{p-f} = \left( \frac{qV}{\pi\epsilon d} \right)^{1/2}$$

where  $q$  = electronic charge,  $V$  = applied voltage across the film,  $\epsilon$  = dielectric constant of film, and  $d$  = film thickness. This may be compared with the case

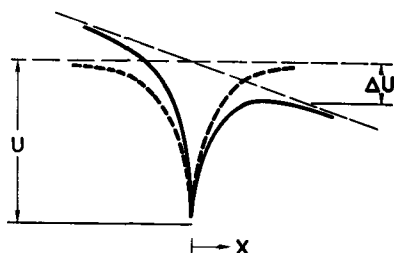


Fig. 5. Potential distribution acting on an electron escaping a donor-like trap.

of Schottky emission, the thermal excitation of carriers over an interfacial barrier lowered by the carrier's image force. Here a similar expression applies, with a barrier lowering,  $\Delta U_s$ , given by

$$\Delta U_s = \left( \frac{qV}{4\pi\epsilon d} \right)^{1/2}$$

where all quantities are as defined above. This quantity is a factor of two smaller than  $\Delta U_{p-f}$  because in the Schottky emission case, the carrier's image charge recedes as the carrier escapes the barrier, while in the Poole-Frenkel situation, the positively charged center is immobile.

The conductivity of a sample due to Poole-Frenkel emission was expressed by Frenkel (11) in the form

$$\sigma = \sigma_0 \exp[-q(U_{p-f} - \Delta U_{p-f})/2kT] \quad [3]$$

where  $U_{p-f}$  is the trap depth below the conduction band. The factor of two in the denominator of the exponent arises from a statistical description of the electron population above a donor-like center, under the assumption that at low temperatures, all the centers will be occupied by electrons (19). Thus the thermal activation energy for the low field conductivity is equal to one-half of the potential well depth. On the other hand, Schottky emission currents are commonly described by the expression

$$I = AT^2 \exp[-q(U_s - \Delta U_s)/kT]$$

where  $A$  = Richardson's constant,  $T$  = absolute temperature, and  $U_s$  = equilibrium barrier height. Thus it is seen that the magnitudes of the slopes of  $\ln I-V^{1/2}$  plots for normal Poole-Frenkel and Schottky emission are identical, since the factor of two in the denominator of Eq. [3] cancels the factor of two by which  $\Delta U_{p-f}$  exceeds  $\Delta U_s$ .

However, in the case of the Poole-Frenkel mechanism, a more general treatment is possible if it is postulated that the number of electrons available for excitation be smaller than the number of donor-like centers. The statistics describing the excited density in such a system were first worked out by deBoer and vanGeel (20) and Nijboer (21). Mott and Gurney (22) have outlined the derivation, and point out that such conditions might be expected to arise in a material containing an excess of its metallic ion over the stoichiometric requirement. This situation almost certainly applies to the films in this study formed at a high silane-ammonia ratio and could conceivably occur to some degree throughout the range of the investigation.

Following Mott and Gurney (19), consider a system of unit volume containing  $N$  donor-like centers located an energy  $E$  below the conduction band,  $N_e$  electrons available for excitations from these centers ( $N_e < N$ ), and  $n$  electrons of the  $N_e$  excited to the conduction band. Neglecting spin degeneracy, set  $N_c = (2\pi mkT/h^2)^{3/2}$ . Minimizing the free energy of the system with respect to the carrier concentration and assuming that only a small fraction of the available electrons will be excited to the conduction band leads to two possible expressions for the excited carrier density,  $n$ , depending on the relative magnitudes of the quantities  $n$  and  $(N - N_e)$ . If  $n \gg (N - N_e)$ , that is, the excited carrier density is greater than the electron deficiency of the donor-like centers,

$$n = \sqrt{N_e N_c} \exp(-E/2kT)$$

This expression is of the same form as that employed by Frenkel (11), and becomes exactly equivalent when the electron deficiency disappears,  $N_e = N$ . On the other hand, if  $n \ll (N - N_e)$ , that is, the electron deficiency of the donorlike centers is greater than the excited electron density, then this density becomes

$$n = \frac{N_e N_c}{N - N_e} \exp(-E/kT)$$

Note that there is no factor of two in the denominator of the exponential in this expression, and hence the low field thermal activation energy of the conductivity becomes equal to the energy difference between the donor-like levels and the conduction band. Therefore the Poole-Frenkel conductivity for the case of  $n \ll (N - N_e)$  is given by

$$\sigma = q\bar{\mu} \frac{N_e N_c}{N - N_e} \exp \left[ -q(U_{p-f} - \Delta U_{p-f})/kT \right]$$

$$\sigma = \sigma_o \exp \left[ q \left( \sqrt{\frac{qV}{\pi\epsilon d}} - U_{p-f} \right) / kT \right] \quad [4]$$

where  $\bar{\mu}$  = effective carrier mobility. The current-voltage relationship will be in this case

$$I = G_o V \exp \left[ q \left( \sqrt{\frac{q}{\pi\epsilon d}} V^{1/2} - U_{p-f} \right) / kT \right] \quad [5]$$

where  $G_o = \sigma_o A/d$ ,  $A$  = sample area, and  $d$  = sample thickness. The slope of a  $\ln I - V^{1/2}$  plot from Eq. [5] is seen to be twice as great as that for Schottky emission or the "normal" Poole-Frenkel effect. Hence in summary, a bulk-limited Poole-Frenkel effect may be characterized under the above generalization by a  $\ln I - V^{1/2}$  plot slope equal to 1 to 2 times the slope of a similar plot derived from Schottky emission in the same structure.

A treatment equivalent to that quoted above has recently been given by Mark and Hartman (23), who describe the electron deficiency of the donor-like centers in terms of partial compensation by an acceptor level. A multilevel model has also been discussed in this regard by Simmons (24).

**Data analysis.**—Equation [5], above, is of the same form as the empirical Eq. [1], with

$$\beta = \left[ \frac{q^3}{\pi\epsilon d} \right]^{1/2}$$

$$\Psi = q U_{p-f}$$

This fact is by no means sufficient evidence on which to conclude that the model represents a valid interpretation of the data, as is clear from the discussion above. Also, other choices beside simple Poole-Frenkel and Schottky emission mechanisms exist. O'Dwyer (25) has shown that conduction in thin dielectric structures in which carrier injection is due to either Schottky or Fowler-Nordheim emission can give rise to  $\ln I - V^{1/2}$  plots linear over many orders of magnitude of current. A combination of mechanisms, Schottky emission from the surface of agglomerated silicon particles imbedded in silicon monoxide films, has also been proposed by Johansen (26).

In order to justify the Poole-Frenkel interpretation, it is thus necessary to test all the dependences predicted in Eq. [5] experimentally, particularly with reference to the slope of the  $\ln I - V^{1/2}$  characteristics. The parameters available are seen to be the film thickness, dielectric constant (index of refraction), and temperature. The capability of varying the thickness and index of refraction by control of deposition parameters in the silane-ammonia reactor process as described by Bean *et al.* (9) facilitates the investigation.

It should be noted that the dielectric constant,  $\epsilon$ , enters the derivation only with reference to the field due to the ionized center. If the electron leaves the vicinity of the positively charged center before ionic polarization due to its creation can occur, as is likely, the optical dielectric constant, given by the square of the index of refraction, should be used here as is pointed out by Frenkel (11).

**Dependence of Schottky-plot slope on film thickness, index of refraction.**—The measured slopes of

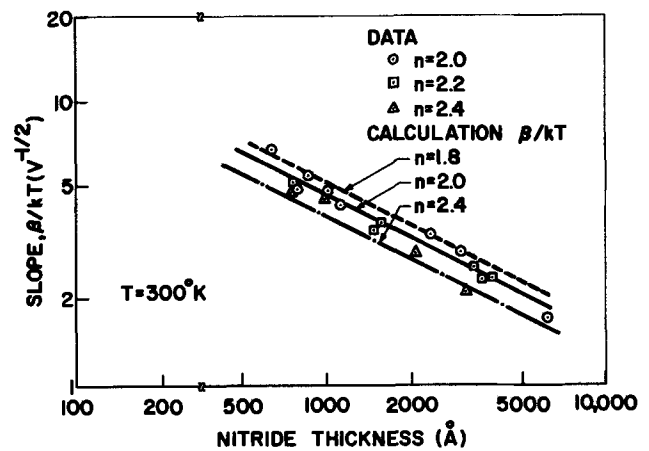


Fig. 6. Schottky plot slope at room temperature vs. silicon nitride film thickness. The points represent experimental data while the lines are calculated from Eq. [5].

$\ln I - V^{1/2}$  plots for samples of thickness between 600 and 6000 Å and indices of refraction of 2.0 to 2.4 are shown in Fig. 6. The values of thickness and index of refraction were obtained with an ellipsometer as described above. Superimposed on the data in Fig. 6 are three curves calculated from Eq. [5] using the relation  $\epsilon = n^2$  together with indices of refraction,  $n$ , of 1.8, 2.0, and 2.4. While there is scatter in the data it can be concluded that: (i) the predicted dependence of slope on film thickness is observed, (ii) for a given thickness, the films with higher indices of refraction have lower slopes, and (iii) all the experimental points lie within approximately 15% of the value predicted by Eq. [5]. There is an apparent trend toward experimental slope values about 10% higher than those predicted. A similar observation was made by Mead (13) for some of the thicker Ta<sub>2</sub>O<sub>5</sub> samples. He suggested that field intensification due to structural nonuniformities might cause this effect. For the silicon nitride films in the present case, the uniformity of current density measurements on metal dots of different areas indicates that if defects are controlling the conduction behavior, they must be uniformly distributed on a scale small compared to the dot sizes ( $1.8 \times 10^{-4} \text{ cm}^2 < A < 1.8 \times 10^{-2} \text{ cm}^2$ ). However, dielectric loss measurements to be discussed below do show an anomalous dependence on dot area for some slices, which might indicate the presence of defects. Defect density analysis on samples similar to those under study here, done by Tefteller (27) using an electrophoretic decoration technique, reveals densities of the order of  $10^2/\text{cm}^2$ . Assuming this value, a fair probability should exist of finding units free of these defects for all but the largest dot sizes.

With regard to the high slope values it should be noted that a decay in current lasting a few seconds to a minute or so was observed after increasing the applied voltage in the measurement of the current-voltage characteristics. While the measurements presented here are apparent steady-state values, if space charge regions associated with the contacts persist, their width will decrease the effective thickness of the films. This would cause the  $\ln I - V^{1/2}$  curve slopes to be anomalously high, as shown in Eq. [5].

Examination of the Poole-Frenkel effect expression, Eq. [5], shows that for accurate comparison, experimental values of the d-c conductance,  $I/V$ , should be plotted logarithmically vs.  $V^{1/2}$ . This has not been done for two reasons. First, for the great bulk of the films, those of fairly high resistivity, the correction makes a negligibly small change in the experimentally determined value of the curve slope, of the order of 1%. Second, it is found experimentally that for the most conductive films, where the division by  $V$  has the greatest effect on the form of the current characteris-

tics, in  $I-V^{1/2}$  plots are linear while  $\ln I/V$  vs.  $V^{1/2}$  plots depart from linearity to some degree.

The pre-exponential factor of  $V$  in the treatment leading to Eq. [5] arises from consideration of the average velocity of a carrier in transit of the film. The usual approach is to assign a constant mobility to the carriers. For an electron hopping model this mobility is of the form (28)

$$\bar{\mu} = \nu q \frac{R^2}{kT}$$

where  $\nu$  = attempt-to-escape frequency of electron in trap and  $R$  = hopping distance. Thus, the average carrier velocity is

$$\bar{\mu}E = \frac{\nu qR^2}{kT} \frac{V}{d}$$

where  $E = V/d$  = electric field strength in film and hence the pre-exponential portion of the Poole-Frenkel relationship, Eq. [5] is linear in applied voltage. A similar voltage dependence has been shown to apply to Schottky emission by Simmons (29) for the case of insulator thicknesses greater than the mean free path of the carrier.

On the other hand, Hill (30) has derived a modified Poole-Frenkel relationship on the basis of electron acceleration by the applied field between traps separated by a constant distance. This expression has a pre-exponential factor dependent on the square root of the applied field.

A model is conceivable in which the pre-exponential factor is independent of voltage if one chooses to assume both a fixed hopping distance and a mean escape time for the electrons from the trap that is much longer than the transit time between traps. However, such a model might be difficult to justify theoretically or verify experimentally.

**Temperature dependence.**—The general form of the temperature dependence of  $\ln I-V^{1/2}$  characteristics of these films was illustrated in Fig. 1. The variation of the slopes of some of these Schottky plots with temperature in the range 300°–470°C is illustrated in Fig. 7a for samples of various thicknesses and compositions. The  $T^{-1}$  lines drawn through the points indicate that the measured dependence is consistent with that predicted by Eq. [5] where a temperature-independent index of refraction and thickness are assumed. These measurements were made on slice-form samples in a controlled ambient hot stage. However, samples that had been scribed and broken into 0.25 cm chips and mounted in headers for measurement, displayed anomalous temperature dependences. Two examples are given in Fig. 7b. In particular, the upper curve of Fig. 7b is representative of four chips scribed from a slice that yielded the middle curve of Fig. 7a in the hot stage before scribing. It has been observed that the effect of scribing and breaking is to raise the level of conductance of a sample by a factor as great as 3 to 4 without changing the form of the  $I-V$  relationship. It is postulated that structural defects of some kind are propagated through the film during the scribe and break operation. The slopes of the room temperature Schottky plots are not usually changed. This is borne out in the case of the two curves referred to above in Fig. 7a and b, where the 300°K slope value is 4.2  $v^{-1/2}$  in each instance. This suggests that the observation of well-behaved  $\ln I-V^{1/2}$  dependences does not preclude the participation or even dominance of defects in the conductance characteristics.

The lower curve in Fig. 7b was observed on a scribed chip from a slice on which silicon nitride was deposited with a silane-ammonia ratio of 0.5. Analysis of  $I-V-T$  data on this sample revealed a thermal activation energy for conductance of 0.5 eV. Here again, the scribe and break operation is apparently the source of the behavior, since unscribed films of the same composition have consistently yielded activation energies of 1.0 eV (see Fig. 2) and temperature-independent values of  $\beta$ .

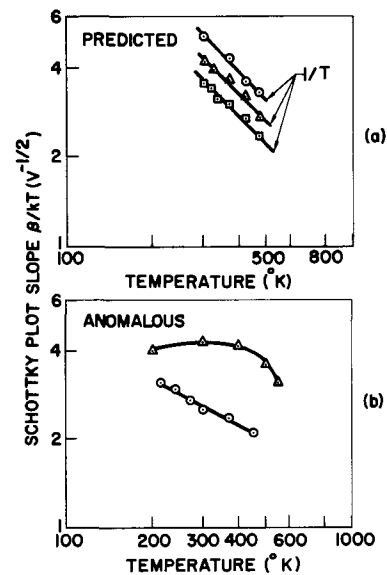


Fig. 7. Temperature dependence of the Schottky plot slopes of a variety of samples. (a) Slice-form measurements in agreement with Eq. [5]. (b) Anomalous results observed on scribed units.

**Polarity dependence.**—A typical example of the polarity dependence of the  $\log I-V^{1/2}$  characteristics is shown in Fig. 8. In general, it has been observed for metal-nitride-silicon structures that there is no consistent dependence of the slope of these plots on polarity, but that a slightly higher current is observed for a given applied voltage when the metal is positive rather than negative. Mead (13) has pointed out that a bulk-limited, thermal ionization mechanism, such as that proposed above, should have characteristics such that a plot of the negative vs. the positive voltage drop at a fixed current for samples of various thicknesses would have unity slope and abscissa intercept equal to twice the difference of the contact barrier heights. This situation is compared to one in which conduction is limited by field emission. In this latter case a plot of the type described above would have a slope proportional to the ratio of the contact barrier heights, to twice the difference of the contact barrier heights.

Such a plot for the aluminum-silicon nitride-silicon system is given in Fig. 9. The silane-ammonia ratio during fabrication of these films was 0.5, and thicknesses varied from 600 to 4000 Å. Positive and negative voltages at a current density of  $10^{-6}$  amp/cm<sup>2</sup> were extracted from  $\ln J-V^{1/2}$  plots made at room temperature.

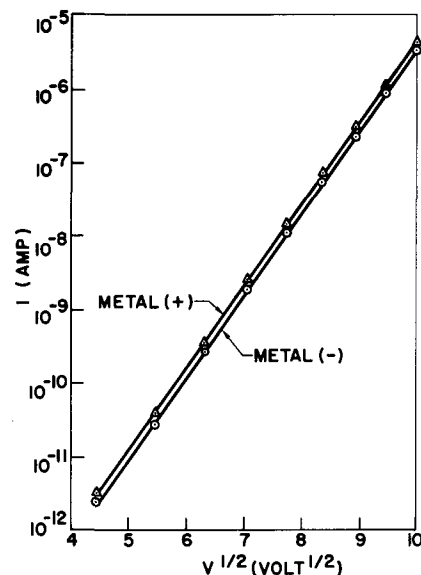


Fig. 8. Polarity dependence of d-c conduction data

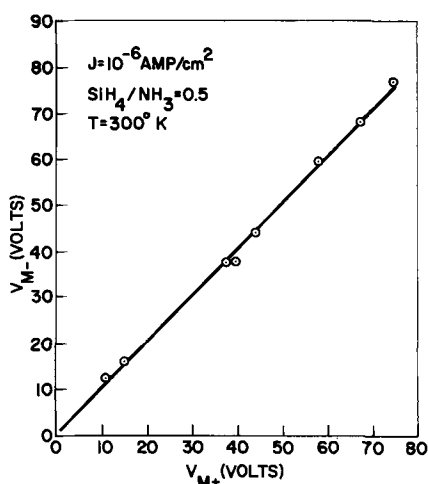


Fig. 9. Plot of the negative vs. positive voltage across samples of various nitride thickness at a fixed current density of  $10^{-6}$  amp/cm<sup>2</sup>. The unity slope is consistent with a bulk-limited transport mechanism.

It was determined that hysteresis effects were not of major importance in these results.

The line of unity slope passing very near the origin indicates that the data is consistent with the model proposed in this regard. Similar samples with chromium outer contacts yield points that fall along the same line.

**Pre-exponential factor.**—The value of the pre-exponential factor,  $I_0$ , in the experimental characteristics described in Eq. [1] can be determined by extrapolation of curves like those shown in Fig. 2 back to their ordinate intercepts.

Typically these values range from  $10^{-4}$  to  $10^{-1}$  amp/cm<sup>2</sup>. This is more than eight orders of magnitude smaller than the pre-exponential factor predicted for a Schottky emission mechanism in which the carrier mean free path is greater than the insulator thickness. In this case the value should be the Richardson constant, 120 amp/cm<sup>2</sup>, times the square of the absolute temperature. Application of the mobility limitation described by Simmons (29) would require mobility values of the order of  $10^{-8}$  cm<sup>2</sup>/v-sec to fit the model.

In general, the intercepts of high silane-ammonia ratio samples are larger than those of low ratio samples, within the limits given above. This is reasonable since in any model for the phenomenon like that proposed above, the pre-exponential factor should include the trap density.

### Complex Dielectric Constant

The response of a lossless dielectric to sinusoidal electrical excitation may be expressed as

$$J = i\omega\epsilon E \quad [6]$$

where  $J$  = current density,  $E$  = electric field strength,  $\omega$  = radian frequency,  $\epsilon$  = dielectric constant, and  $i$  = imaginary operator,  $\sqrt{-1}$ . If loss mechanisms are operative, resulting in an in-phase component of the current, these may be included in the formulation by definition of a complex dielectric constant

$$\epsilon^* \equiv \epsilon' - i\epsilon'' = (\epsilon'_r - i\epsilon''_r) \epsilon_0 \quad [7]$$

where  $\epsilon_0$  = permittivity of free space. The current density expression then becomes

$$J = i\omega(\epsilon' - i\epsilon'')E = \omega\epsilon''E + i\omega\epsilon'E \quad [8]$$

and it is seen that the real part of the current is proportional to the imaginary part of the dielectric constant,  $\epsilon''$ , while the real part of the dielectric constant,  $\epsilon'$ , describes the polarization or charge storage properties of the material. The physical mechanisms from

which these properties arise may be explored by measurement of the frequency and temperature dependence of these quantities (31, 32).

Such measurements have been made on the silicon nitride samples described above in the frequency range  $5 \times 10^2$  to  $10^5$  Hz and at temperatures from  $200^\circ$  to  $400^\circ\text{K}$ . A General Radio Model 1615A capacitance bridge fitted with a d-c voltage supply for sample biasing was employed. For samples on silicon substrates, a small bias was used to accumulate the silicon surface, increasing its capacitance. The bias was small enough that high-field effects were not induced in the dielectric, except in experiments designed to explore them, reported below. Samples on molybdenum substrates had voltage-independent characteristics, except for the high-field effects. The complex dielectric constant characterization of the silicon nitride was not dependent on the substrate material of the samples. The same probes and packaging techniques used for the conduction measurements were employed here.

**Real part,  $\epsilon'_r$ .**—The dependence of the real part of the complex dielectric constant of these silicon nitride films on silane-ammonia ratio in the reaction ambient is shown in Fig. 10. These measurements were made at a frequency of  $10^5$  Hz at room temperature. The values obtained were found to be very nearly frequency-independent in the range covered in these experiments. These results were derived from determination of capacitance-to-area ratios on slices with dots having four areas varying from  $7.3 \times 10^{-4}$  to  $1.8 \times 10^{-2}$  cm<sup>2</sup>, together with ellipsometric thickness measurement as described above. The error in the values is no more than  $\pm 5\%$ , and is limited by the variation of film thickness across a slice.

The saturated value of 7 for the relative dielectric constant at low silane-ammonia ratio is appreciably greater than the square of the index of refraction of the films, which is 4 in this region. This is evidence of appreciable atomic or orientational polarization in the material. The dependence of  $n^2$  on silane-ammonia ratio is very similar to that of  $\epsilon'_r$ , remaining smaller by a fairly constant amount. The location of the knee of the dielectric constant characteristic, at silane-ammonia ratios of 0.1-0.2, is like that of the  $n^2$  dependence and also of the static resistivity dependence, shown in Fig. 4. Etch rate studies done as a function of nitride preparation by Bean *et al.* (9) and by Harap (33) also indicate a change in material properties and behavior at this silane-ammonia ratio. It is thus postulated that all the above-mentioned characteristics are interrelated and attributable to the incorporation of excess silicon into the film structure at silane-ammonia ratios greater than about 0.1. These properties have been observed in films prepared in three reactors of differing configuration, so that it is believed that the results are descriptive of the nature of the

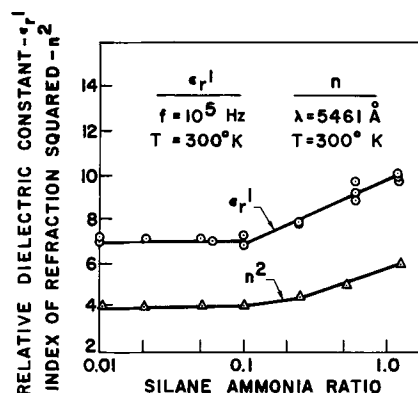


Fig. 10. Relative dielectric constant and the square of the index of refraction of silicon nitride films as a function of silane-ammonia ratio during growth.

chemical reaction involved and not merely the characteristics of a particular system.

The temperature dependence of the real part of the dielectric constant may be adequately described by a positive coefficient of approximately  $5 \times 10^{-4}/^\circ\text{K}$  between  $200^\circ$  and  $400^\circ\text{K}$  for films of low silane-ammonia ratio. At a silane-ammonia ratio of 0.5, the value of this coefficient increases to  $\sim 3 \times 10^{-3}/^\circ\text{K}$ .

**Dielectric loss,  $\epsilon''$ .**—Values of dielectric loss,  $\epsilon''$ , or loss tangent, the ratio  $\epsilon''/\epsilon'$ , were not as well behaved as the d-c conductance or  $\epsilon'$  measurements described above. On certain samples, predominantly those in which less care was taken in substrate surface preparation, an anomalous dependence of loss tangent on sample area was observed. Samples on substrates that were vapor etched in situ immediately prior to nitride deposition rarely exhibited this anomaly, but run-to-run variations in values obtained still precludes an exact characterization of a dielectric loss dependence on silane-ammonia ratio. Such a relationship is believed to exist, however, with values of  $\epsilon''$  at  $10^5$  Hz,  $300^\circ\text{K}$  of about  $10^{-3}$  for silane-ammonia ratios of 0.01 increasing to about  $3 \times 10^{-2}$  at a silane-ammonia ratio of unity.

Some typical examples of the frequency dependence of the dielectric loss characteristics are shown in Fig. 11. Curve (a) represents a sample with a degenerate n-type substrate while the curve (b) came from a sample having a 5 ohm-cm n-type substrate. Extension of the frequency range of measurement of curve (b) upward to 1 MHz shows that the high-frequency increase in  $\epsilon''$  is due to a component linearly dependent on frequency. Other experiments have shown that this difference between curves (a) and (b) is not due to the change in silane-ammonia ratio from 0.01 to 0.05, a region in which characteristics are constant.

Films on molybdenum substrates exhibit little or no frequency dependence as indicated by curve c. For a given film composition, however, the level of loss is generally somewhat higher for the molybdenum substrates than for the silicon. This may be related to the generally poorer finish of the molybdenum surface.

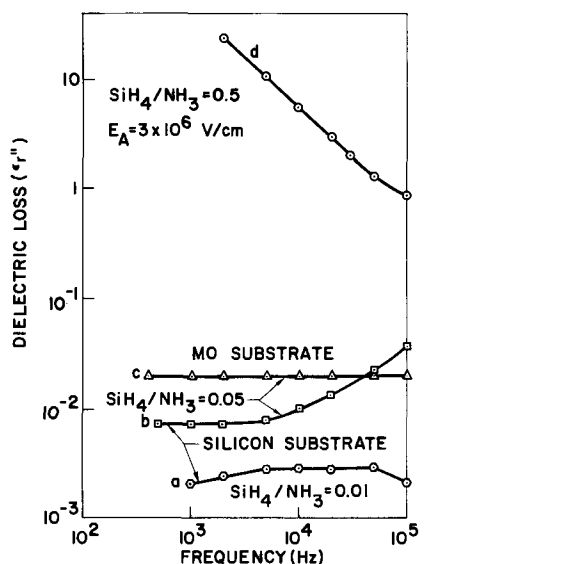


Fig. 11. Dielectric loss-frequency characteristics of various metal-nitride-silicon and metal-nitride-molybdenum structures. (a) Low silane-ammonia ratio nitride on degenerate silicon substrate. (b) Silicon nitride on 5 ohm-cm n-type silicon substrate. A small d-c bias used for (a) and (b) to accumulate the silicon surface. (c) Silicon nitride on moly substrate. This characteristic is bias-independent for low fields. (d) High field characteristic for a conductive silicon nitride film, displaying  $f^{-1}$  dependence. Here, bias polarity accumulates the silicon substrate.

If high electric fields are applied to the nitride film during measurement, a loss characteristic decreasing linearly with frequency like that shown in the curve (d) is observed. This low resistivity nitride sample was made with a silane-ammonia ratio of 0.5 and was biased with an electric field of  $3 \times 10^6$  v/cm, accumulating the silicon substrate. These characteristics can be understood by considering an equivalent circuit of the sample that includes a resistive component  $R_s$  due to the substrate in series with a parallel combination of a perfect capacitor  $C_i$  and a stationary resistance  $R_i$  representing the silicon nitride film. It can be shown that the dielectric loss-frequency characteristics of such a structure is given by the expression

$$\epsilon'' = \frac{(1 + \omega^2 R_s R_i C_i^2) d}{(1 + \omega^2 R_s^2 C_i^2) \omega R_i A} \quad [9]$$

where  $\omega$  = radian frequency,  $d$  = film thickness, and  $A$  = sample area, and it is assumed that  $R_s \ll R_i$ .

At low frequencies the  $\omega^2$  terms in brackets are much less than unity, leading to the simple  $\omega^{-1}$  expression involving the resistance of the insulator. Comparison of the  $R_i$  value derived from the  $\omega^{-1}$  component with the slope of a linear  $V$ - $I$  plot taken at the same bias level yields agreement with experimental error. Because of the nonlinear nature of the  $I$ - $V$  characteristic, the dynamic resistance of the films decreases with increased applied field strength. This is reflected in the loss-frequency characteristics given in Fig. 12, which shows the variation of the  $\omega^{-1}$  component of loss with increasing bias.

Because the insulator resistance in general is so much higher than the series substrate resistance, a range of frequency will exist in which the  $\omega^2$  term in the numerator of Eq. [9] will become larger than unity while the one in the denominator term remains smaller. In this regime, a linear increase in  $\epsilon''$  with frequency is predicted. Evaluating  $R_s$  from the value of the coefficient of the linear component of  $\epsilon''$  obtained from the extension of curve (b), Fig. 11, to 1 MHz yields a value of about 10 ohms, a reasonable value in terms of the parameters of the structure.

## Conclusions

It is felt that the results given above, taken together with those of Bean *et al.* (9), form a fairly consistent, unified picture of the behavior of silicon nitride films formed from the reaction of silane and ammonia.

Below a silane-ammonia ratio of 0.1 there is a range of ambient composition in which the physical and electrical properties of the material are invariant.

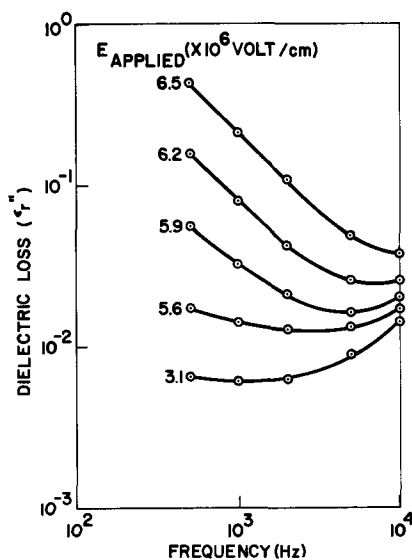


Fig. 12. Low frequency dielectric loss-frequency characteristics of a nitride film as a function of applied d-c field strength.



In this region, the films have a dielectric constant of  $7.0 \pm 0.1$ , very low loss, and a d-c resistivity of greater than  $10^{16}$  ohm-cm at fields below  $4 \times 10^6$  v/cm.

It is postulated that inclusion of excess silicon in the nitride films at silane-ammonia ratios above about 0.1 is responsible for the increase in dielectric constant and d-c conductivity observed. The increased conductivity is characterized by a lowering of the thermal activation energy for the process from 1.5 to 1.0 ev.

A second parameter effecting the conductance as well as the loss characteristics of the material is the scribe-and-break operation, which is assumed to act through the formation of structural imperfections or defects. Here the effect is an increase in conductivity by a factor of three or four without changing the form of the current-voltage relationship, and a dependence of dielectric loss on sample area in the range,  $1.8 \times 10^{-4} - 1.8 \times 10^{-2}$  cm<sup>2</sup>. The latter effect has also been observed in some cases in which silicon substrates were not vapor etched immediately prior to silicon nitride deposition and in cases in which molybdenum substrates were used.

The d-c conduction mechanism is found to be predominantly electronic, as opposed to ionic, under the conditions of these measurements. The choice of a model for the conduction data is based on the following considerations. First, the observation of well-behaved  $\ln I-V^{1/2}$  dependences which are linear over many orders of magnitude of current suggests the predominance of a single transport mechanism described by this relationship. Detailed measurements indicate that within experimental error the magnitude of the slope of the  $\ln I-V^{1/2}$  characteristics can be expressed as  $(q^3/\pi\epsilon d)^{1/2}/kT$ , where specific dependences upon film thickness,  $d$ ; dielectric constant,  $\epsilon = n^2$ ; and temperature,  $T$ , have been verified quantitatively. This slope value is larger by a factor of two than that predicted for Schottky emission or for the "normal" Poole-Frenkel effect as described by Frenkel (11). However, within the framework of the Poole-Frenkel effect, a condition may exist in which a slope value twice that found in the "normal" case is predicted. This condition implies a low-field thermal activation energy for conduction equal to the energy barrier for electron emission from the trap, instead of one-half the barrier as in the "normal" case. This higher slope value, which is in agreement with the experimental results, presented above, is the slope attributed to the Poole-Frenkel effect by many workers (13-15, 24, 26). It is not known whether these workers have tacitly assumed the physical conditions bringing about the change in activation energy (20, 23), or have merely misquoted Frenkel (11).

In the interpretation of the conduction data, the possibility of the interplay of competing transport mechanisms cannot be overlooked. Conduction results on the scribed material suggest the operation of a Poole-Frenkel type mechanism in which the centers are associated with structural defects in the nitride films. Also, in all samples, internal field emission of carriers trapped in centers like those described in Fig. 5 might be expected at lower temperatures where thermal excitation is inhibited. Some deviations from the  $\ln I-V^{1/2}$  dependence has been observed for samples at very high fields and low temperatures, but a satisfactory fitting of the data to a Fowler-Nordheim characteristic has not been possible at temperatures of 200°K and above.

#### Acknowledgment

The authors are indebted to their colleagues K. Bean, W. Tefteller, and R. Yeakley for sample preparation, to J. B. Coon and V. Harrap for many discus-

sions of the results, to T. E. Hartman for a copy of ref. (23) prior to publication, to C. E. Jones and R. Hickey for the ellipsometric measurements, to D. R. Collins for critically reading the manuscript, and to Roy W. Tucker and John McGraw for their technical assistance.

Manuscript submitted Feb. 15, 1968; revised manuscript received May 13, 1968. This manuscript was presented at the Philadelphia Meeting, Oct. 9-14, 1966, as Electronics Semiconductor Late News Paper 1.

Any discussion of this paper will appear in a Discussion Section to be published in the June 1969 JOURNAL.

#### REFERENCES

1. V. Y. Doo, D. R. Nichols, and G. A. Silvey, *This Journal*, **113**, 1279 (1966).
2. K. E. Bean, P. S. Gleim, and W. R. Runyan, Paper presented at the Philadelphia Meeting of the Society, Oct. 9-14, 1966, as Paper 147.
3. J. H. Scott and J. A. Olmstead, Paper presented at the Philadelphia Meeting of the Society, Oct. 9-14, 1966, as Paper 151.
4. C. H. Lee, T. L. Chu, and G. A. Gruber, Paper presented at the Philadelphia Meeting of the Society, Oct. 9-14, 1966, as Paper 154.
5. H. F. Sterling and R. C. G. Swann, *Solid State Electronics*, **8**, 653 (1965).
6. Symposium on Silicon Nitride, presented at the Philadelphia Meeting of the Society, Oct. 9-14, 1966, as Papers 146-163.
7. S. M. Hu, *This Journal*, **113**, 693 (1966).
8. V. Y. Doo and D. R. Nichols, Paper presented at the Philadelphia Meeting of the Society, Oct. 9-14, 1966, as Paper 146; and V. Y. Doo, D. R. Kerr and D. R. Nichols, *This Journal*, **115**, 61, (1968). This latter paper, which appeared while this manuscript was being prepared, reports silicon nitride properties and ambient composition dependences very similar to those found in the present study.
9. K. E. Bean, P. S. Gleim, R. L. Yeakley, and W. R. Runyan, *This Journal*, **114**, 733 (1967).
10. H. H. Poole, *Phil. Mag.*, **S.6**, **32**, #187, 112 (1916), and *ibid.*, **34**, #201, 195 (1917).
11. J. Frenkel, *Phys. Rev.*, **54**, 647 (1938).
12. D. A. Vermilyea, *Acta Met.*, **2**, 346 (1954).
13. C. A. Mead, *Phys. Rev.*, **128**, 2088 (1962).
14. H. Hirose and Y. Wada, *Japanese J. Appl. Phys.*, **4**, 639 (1965).
15. T. E. Hartman, J. C. Blair, and R. Bauer, *J. Appl. Phys.*, **37**, 2468 (1966).
16. G. A. Brown, W. C. Robinette, Jr., and H. G. Carlson, *This Journal*, **113**, 315C (1966).
17. S. M. Sze, *J. Appl. Phys.*, **38**, 2951 (1967).
18. S. M. Hu, D. R. Kerr, and L. V. Gregor, *Appl. Phys. Letters*, **10**, 97 (1967).
19. N. F. Mott and R. W. Gurney, "Electronic Processes in Ionic Crystals," 158ff, Oxford University Press (1940).
20. J. H. deBoer and W. C. vanGeel, *Physica*, **2**, 286 (1935).
21. B. R. A. Nijboer, *Proceedings of the Physical Society of London*, **51**, 575 (1939).
22. N. F. Mott and R. W. Gurney, "Electronic Processes in Ionic Crystals," p. 156, Oxford University Press (1940).
23. P. Mark and T. E. Hartman, *J. Appl. Phys.*, **39**, 2163 (1968).
24. J. G. Simmons, *Phys. Rev.*, **155**, 657 (1967).
25. J. J. O'Dwyer, *J. Appl. Phys.*, **37**, 599 (1966).
26. I. T. Johansen, *ibid.*, **37**, 499 (1966).
27. W. Tefteller, Private communication.
28. N. F. Mott, Paper presented at the Dallas Meeting of the Society, May 7-12, 1967, as Paper 16.
29. J. G. Simmons, *Phys. Rev. Letters*, **15**, 967 (1965).
30. R. M. Hill, "Thin Solid Films," Vol. 1, 39 (1967).
31. P. Debye, "Polar Molecules," Chemical Catalog Co. (1929).
32. H. Frohlich, "Theory of Dielectrics," Oxford University Press (1958).
33. V. Harrap, Private communication.

# The Diffusion of Nickel and Chlorine into P-Type Lead Telluride at 700°C

Thomas D. George<sup>1</sup> and J. Bruce Wagner, Jr.\*

Department of Materials Science and Materials Research Center, Northwestern University, Evanston, Illinois

## ABSTRACT

The diffusion of nickel and of chlorine into single crystals of p-type lead telluride has been measured at 700°C. When nickel and chlorine diffuse simultaneously, there is an interaction between them such that the concentration profile of the nickel exhibits a sharp minimum. In addition, a p to n junction is formed within the crystal, and both the minimum and the p-n junction migrate through the crystal in proportion to the square root of time. In the absence of chlorine, no minimum or p-n junction is formed by the in-diffusing nickel. In the presence of chlorine the diffusion coefficient was approximately  $2 \times 10^{-10}$  cm<sup>2</sup>/sec for the p-n junction and approximately  $9 \times 10^{-11}$  cm<sup>2</sup>/sec for the minimum in the nickel concentration.

Because of the effect small concentrations of impurities have on the electrical properties of semiconductors, a great deal of information has been collected on diffusion of impurities into these materials. In general, researchers have either applied the usual radiotracer technique or have followed the migration of a p-n junction if the impurity induces an electrical character different from the base material. In cases where p-n junction migration was used, it usually has been assumed that the penetration profile of the impurity resembled that obtained as a solution to Fick's law with the assumption of a constant diffusion coefficient. Cunnell and Gooch (1) were among the first to show that this type of penetration profile is not obtained for diffusion of zinc into gallium arsenide. Even though the migration of the p-n junction gave a straight line when plotted against the square root of time, the penetration profile for radioactive zinc showed that a constant value for the diffusion coefficient,  $D_{Zn}$ , could not be assumed. The problem of zinc diffusion into gallium arsenide has recently been analyzed by Casey, Panish, and Chang (2), who showed that  $D_{Zn}$  is a function of the zinc concentration and the activity coefficient of holes.

When two impurities are simultaneously diffused into gallium arsenide, there can be a striking interaction. Larrabee and Osborne (3) observed that when manganese and copper or when zinc and copper were simultaneously diffused into initially n-type GaAs, the concentration profile of copper exhibited a sharp minimum. The minimum appeared to migrate through the crystal with the square root of time. No minimum was observed when copper was diffused in the absence of manganese or zinc. Peart *et al.* (4) showed that essentially the same behavior was obtained when zinc was diffused into manganese-doped GaAs. The zinc concentration profile appeared to follow the expected error function type curve, but the manganese, which was initially uniform through the crystal, redistributed during the diffusion to produce a sharp concentration minimum behind the advancing zinc front. Peart *et al.* did not follow the redistribution as a function of time, but analyzed the results in terms of the Longini and Greene theory of ionization interaction between impurities in semiconductors (5). They concluded that if manganese behaves as an amphoteric impurity in GaAs, that it can act as either a donor or acceptor, a solubility minimum should exist just behind the advancing zinc front.

It is the purpose of the present paper to report another such impurity-impurity interaction, that of nickel and chlorine in lead telluride, and to show the

importance that experimental conditions play in the study of impurity diffusion in semiconductors.

## Experimental

Single crystals of lead telluride used in this investigation were grown by the Bridgman technique from the melt. The ingots were grown in quartz ampoules 7 mm ID. Each ingot weighed about 10g. Silver-doped ingots were grown in the same way. The silver was added in the form of a Pb-Ag alloy to give a final concentration of 0.05 m/o (mole per cent) Ag<sub>2</sub>Te in PbTe.

Wafers 2-3 mm thick were cleaved from the ingot and annealed approximately 100 hr at 700°C in a dynamic argon atmosphere. This treatment corresponds to equilibrating the crystal along the P(min) line. According to the P-T-x diagram of Fujimoto and Sato (6), crystals equilibrated in this way should be p-type. Checks with a hot probe showed that all crystals were p-type following the equilibration. Seebeck and Hall measurements made on the undoped crystals after annealing in argon indicated a carrier concentration of about  $2 \times 10^{18}$  holes/cm<sup>3</sup>. This value is somewhat higher than indicated by Fujimoto and Sato (6), but they made no measurements on samples equilibrated in argon. The P(min) line they reported was calculated from free energy of formation data.

Before carrying out the diffusion anneal, each wafer was ground flat on both faces. The thickness of each wafer was approximately 2 mm. The wafers were polished using 0.1 $\mu$  alumina on felt, and rinsed in a 1:1 volume mixture of acetic acid and 30% hydrogen peroxide to remove any oxide film. The radiotracer, nickel-63, was originally in an HCl solution which was neutralized with NH<sub>4</sub>OH. The tracer was applied either by allowing the neutral <sup>63</sup>NiCl<sub>2</sub> solution to evaporate to dryness on the wafer or by electroplating from the same solution. In either case the tracer was applied to only one face of the wafer. The chlorine-36 tracer was deposited on one face of the wafer by allowing a neutral solution of Ni<sup>36</sup>Cl<sub>2</sub> to evaporate to dryness.

Several experiments were carried out using <sup>63</sup>NiCl<sub>2</sub> as a vapor source. A drop of <sup>63</sup>NiCl<sub>2</sub> solution was placed in quartz wool and allowed to dry. The wool was placed in the bottom of the diffusion ampoule followed by a quartz spacer. The PbTe wafer was placed on the spacer so that the only source of nickel or chlorine was through the vapor.

Diffusion anneals were carried out at 700°C, either in flowing argon or in sealed ampoules evacuated to 10<sup>-6</sup> Torr. The total volume of each ampoule was less than 2 cm<sup>3</sup>.

\* Electrochemical Society Active Member.  
<sup>1</sup> NASA Trainee.

After the diffusion anneal the periphery of each wafer was ground down by approximately  $500\mu$  to reduce the edge effects in counting, and the wafer was mounted in a stainless steel ring. The nickel-63 and chlorine-36 activities were determined using the residual activity method in a flowing gas geiger detector with a window thickness of  $800\ \mu\text{g}/\text{cm}^2$ . After each layer was counted, a new surface was exposed by grinding off a thickness of  $2\text{--}10\mu$  using fine SiC paper and  $0.1\mu$  alumina on felt. The layer thickness was determined from changes in the focal point of a metal-lurgical microscope (400X) fitted with a dial gauge calibrated in microns. The thickness was taken from the average of three readings across the diameter of the wafer. After counting, the p-n character of the surface was determined with a hot probe attached to a microvoltmeter. The position of the p-n junction, when one formed, was determined by plotting the readings of the microvoltmeter *vs.* the penetration depth and drawing a smooth curve through the points.

### Results

The first attempt to study the diffusion of nickel into lead telluride was made on Ag-doped PbTe ( $\approx 1.9 \times 10^{19}$  Ag atoms/cm<sup>3</sup>). The <sup>63</sup>Ni was introduced by placing a drop of neutral <sup>63</sup>NiCl<sub>2</sub> solution on one face of the wafer and evaporating to dryness. The diffusion anneal was carried out in an evacuated ampoule. The results were striking in that the <sup>63</sup>Ni profile showed a sharp minimum followed by a region of relatively constant nickel concentration. Additional experiments showed that the minimum migrated through the crystal with the square root of time, and furthermore, the opposite face of the crystal showed a similar nickel concentration profile, even though the <sup>63</sup>Ni had been applied to only one face. These results (for a 12 hr diffusion anneal) are shown in Fig. 1. The diffusion coefficient for the migration of the minimum in the concentration profile was approximated by

$$D = x^2/t \quad [1]$$

where  $x$  is the position of the minimum relative to the initial surface, and  $t$  is the time of the diffusion anneal in seconds. A value of  $D_{\text{min}} = 4 \times 10^{-11}$  cm<sup>2</sup>/sec was obtained. In addition to the minimum in the concentration profile, a p-n junction was formed to the right, or at a deeper penetration in the crystal. No p-n junction migration rates were measured on the Ag-doped crystals.

In order to determine the origin of the minimum in the nickel concentration profile and the p-n junction, a series of experiments were designed to check out each of the experimental variables. For these experiments all crystals were undoped p-type PbTe,

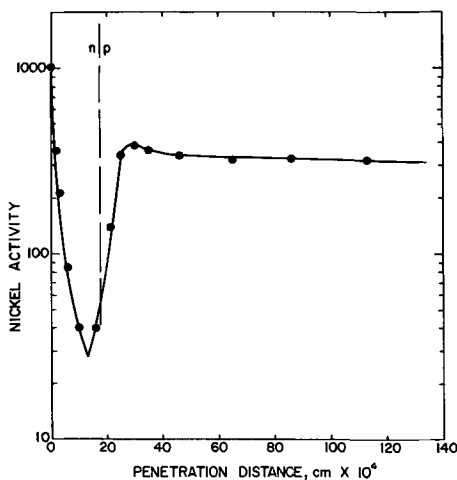


Fig. 1. Nickel profile for Ag-doped PbTe, 12 hr at 700°C (activity in counts per minute).

having initial carrier concentration of about  $2 \times 10^{18}/\text{cm}^3$ . All experiments were carried out at 700°C.

*Diffusion in an open system.*—To compare the diffusion of nickel in open and closed systems, several anneals were made in a dynamic argon atmosphere. Both electroplated <sup>63</sup>Ni and <sup>63</sup>NiCl<sub>2</sub> deposited on one face by evaporating a solution were used as diffusion sources. The initial <sup>63</sup>Ni activity was approximately the same for each set of experiments (100,000 counts/min). The results for the two different sources were the same. After a 24 hr anneal the nickel concentration profile could be represented by a curve of the type marked A in Fig. 2. The nickel concentration initially decreased relative to the concentration at the surface. At a depth of about  $20\mu$  the concentration became constant and remained so up to about  $20\mu$  from the opposite surface. The concentration of nickel near the opposite face of the wafer also showed a higher concentration than in the center of the wafer, even though no nickel was initially applied to this face. No p-n junction was formed under these experimental conditions. The crystals were entirely p-type, including the original surfaces, at the end of the diffusion anneal. This result is in contrast to the behavior observed by Bloem and Kröger (7) in their study of diffusion of nickel into PbS in the temperature range of 300°C. Bloem and Kröger reported that the crystal became n-type as the nickel diffused into it. No attempt was made to deduce a diffusion coefficient for nickel from the <sup>63</sup>Ni profiles in the present study.

*Diffusion in a closed system.*—Diffusion anneals were carried out in small evacuated ampoules. Both electroplated <sup>63</sup>Ni and <sup>63</sup>NiCl<sub>2</sub> deposited on one surface by evaporating a neutral solution were used as diffusion sources. The concentration profile from the electroplated nickel source was the same as those obtained in an open system (curve A of Fig. 1). When <sup>63</sup>NiCl<sub>2</sub> was used as the diffusion source, the nickel concentration profile shown in curve B of Fig. 2 was obtained for a 10 hr anneal. Note the existence of both a sharp minimum in the concentration profile and the p-n junction.

Using <sup>63</sup>NiCl<sub>2</sub> as the diffusion source, the time dependence of the position of the p-n junction and also the minimum in the nickel concentration profile were measured by varying the diffusion times from 2 to 24 hr. The results are shown in Fig. 3. Both the p-n junction and the minimum migrate in proportion to the square root of time, although not at the same rate. In addition the peak width containing the minimum

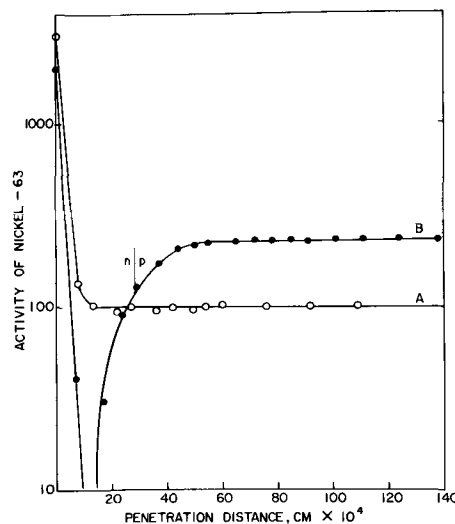


Fig. 2. The effect of chlorine on the closed-tube diffusion of nickel into PbTe (activity in counts per minute). A. Nickel electroplated onto one face of PbTe wafer, 0. Annealed for 24 hr. B. NiCl<sub>2</sub> deposited on one face of PbTe wafer, ●. Annealed for 10 hr.

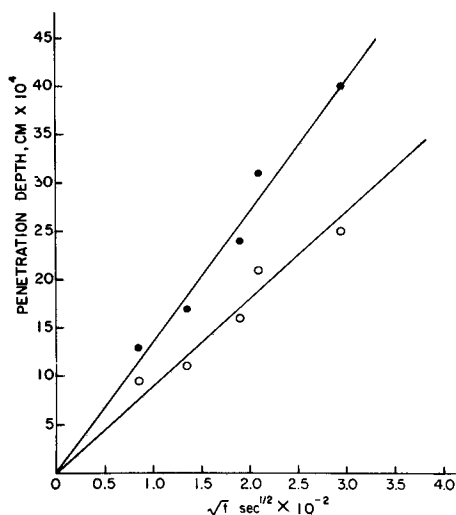


Fig. 3. Migration of [Ni] minimum and p-n junction through PbTe crystal, for  $^{63}\text{NiCl}_2$  deposited on wafer. —●— p-n junction. —○— [Ni] minimum.

became broader as the diffusion time was increased. Using Eq. [1] the values for the diffusion coefficients have been estimated as  $D_{p-n} = 2 \times 10^{-10}$  cm<sup>2</sup>/sec and  $D_{\text{min}} = 9 \times 10^{-11}$  cm<sup>2</sup>/sec.

**Results using  $^{63}\text{NiCl}_2$  vapor.**—Several experiments were carried out using  $^{63}\text{NiCl}_2$  which was not in direct contact with the PbTe crystal. A drop of  $^{63}\text{NiCl}_2$  solution was placed on quartz wool and allowed to dry. The quartz wool was placed in the bottom of the ampoule followed by a quartz spacer. The PbTe wafer rested on the spacer away from the quartz wool. The partial pressure of chlorine from the dissociation of  $\text{NiCl}_2$  is  $1.7 \times 10^{-6}$  Torr (8), and the vapor pressure of the  $\text{NiCl}_2$  molecule is on the order of 1 Torr (9, 10).

It was found that p-type PbTe can be converted to n-type by heating in an evacuated ampoule containing  $\text{NiCl}_2$  even when the  $\text{NiCl}_2$  is not in direct contact with the crystal. The position of the p-n junction as a function of annealing time is shown in Fig. 4, curve A. Curve B of Fig. 4 is the p-n junction migration data taken from Fig. 3 and shown for comparison. When  $\text{NiCl}_2$  is not in direct contact with the PbTe wafer, the best fit to the data points does not extrapolate back to zero at zero time. It is not known whether the difference is due to experimental error or due to some sort of time lag brought about by the fact that  $\text{NiCl}_2$  was not initially in direct contact with the sample. The amount by which the curve misses the origin corresponds to approximately 25 min.

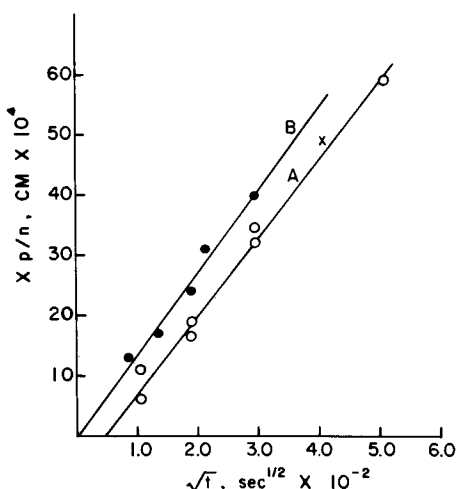


Fig. 4. Migration of p-n junction. —●—  $^{63}\text{NiCl}_2$  deposited on wafer (see Fig. 3). —○—  $^{63}\text{NiCl}_2$  from vapor. X  $\text{Ni}^{36}\text{Cl}_2$  (48 hr).

Crystals treated in this way had nickel-63 concentrations in the bulk which ranged from 25 to 50% of that found in crystals when  $^{63}\text{NiCl}_2$  was initially deposited onto a PbTe wafer. The nickel profiles seemed to have a minimum as was observed in samples described in section B above, but the activity was too low (on the order of 25–60 cpm above the background) to allow quantitative measurements to be made.

A parameter which could be measured easily was the initial surface activity of nickel after the diffusion anneal. These results are shown in Fig. 5. The concentration of nickel on the surface increases with the length of time of the diffusion anneal.

**Diffusion of chlorine.**—The concentration profile of chlorine was determined using  $\text{Ni}^{36}\text{Cl}_2$  deposited on one face of a PbTe wafer. Figure 6 shows the chlorine-36 distribution as well as the nickel-63 distribution obtained under similar conditions (24 hr anneals). With the counting equipment available it was not possible to obtain both profiles simultaneously because both  $^{63}\text{Ni}$  and  $^{36}\text{Cl}$  are  $\beta$ -emitters. The  $^{36}\text{Cl}$  profile is of the usual kind, i.e., it can be fitted to a plane source solution to Fick's law. The diffusion coefficient determined from the chlorine-36 profile was  $2.3 \times 10^{-10}$  cm<sup>2</sup>/sec. This value is essentially the same as found for the migration of the p-n junction.

**The effect of chlorine on nickel-doped PbTe.**—A wafer which had been previously diffused with  $^{63}\text{Ni}$  from an electroplated source (see Fig. 2, curve A) was ground down until the  $^{63}\text{Ni}$  activity was the same on both faces. This crystal was then placed in an evacuated ampoule containing  $^{63}\text{NiCl}_2$  and re-annealed for 24 hr at 700°C. The source and sample were not in con-

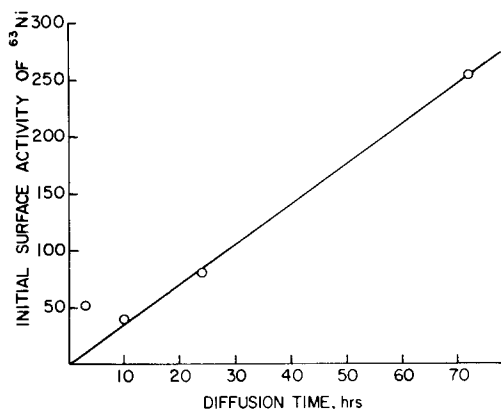


Fig. 5. Initial nickel-63 surface activity (counts per minute) after anneal in  $^{63}\text{NiCl}_2$  vapor.

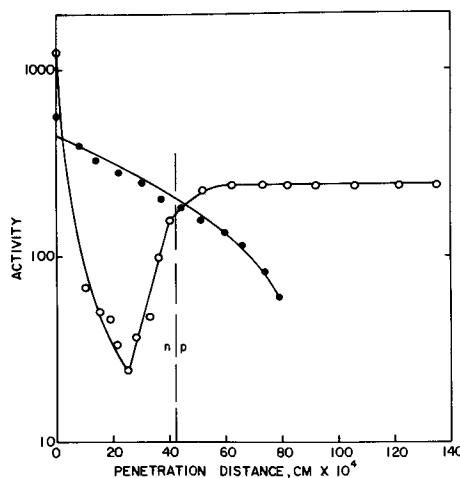


Fig. 6. Nickel-63 and chlorine-36 concentration profiles after 24 hr anneal, for  $\text{NiCl}_2$  deposited on one face of wafer. (activity in counts per minute). —○—  $^{63}\text{Ni}$ , —●—  $^{36}\text{Cl}$ .

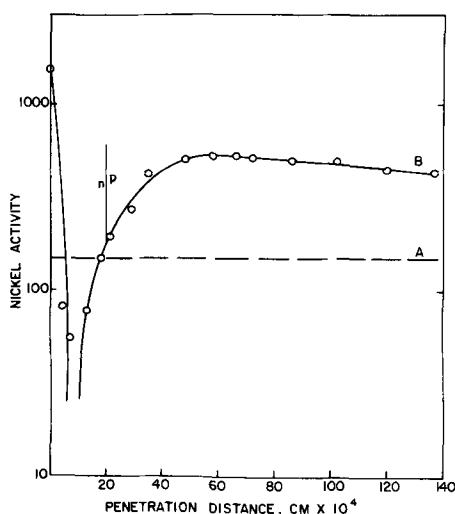


Fig. 7. Effect of chlorine on the distribution of nickel in nickel-doped PbTe (activity in counts per minute). A. Nickel-63 activity before anneal in  $^{63}\text{NiCl}_2$  vapor. Crystal p-type throughout. B. Distribution of nickel-63 after 24 hr in  $^{63}\text{NiCl}_2$  vapor.

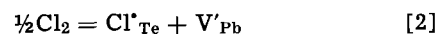
tact with each other but corresponded to the same arrangement as described in section C above. The results are shown in Fig. 7, where the dashed line A represents the approximate  $^{63}\text{Ni}$  activity before the re-anneal with the  $^{63}\text{NiCl}_2$  source. Curve B represents the distribution of nickel in the crystal after 24 hr. While it is almost certain that some nickel entered the crystal from the vapor, there has been an obvious redistribution of the nickel with an apparent increase in the nickel concentration, particularly at the surface. The opposite face of the wafer showed the same redistribution. The p-n junction was found just ahead of the minimum, although closer to the original surface than for samples initially containing no nickel. The p-n junction of curve B, Fig. 7 occurs at  $20\mu$ . For the same diffusion time (24 hr), the p-n junction for samples initially containing no nickel occurs at about  $40\mu$ .

### Discussion

The results obtained, while not representing a complete or quantitative picture of the interaction of chlorine and nickel in p-type lead telluride, allow a qualitative interpretation of this interaction. Several observations can be made based on the p-n behavior after diffusion and the relative rates of diffusion. First, the nickel can be assumed to occupy lead sites since interstitial nickel should produce n-type conductivity, but crystals into which nickel was diffused in the absence of chlorine retained their p-type character. Second, the chlorine is assumed to occupy tellurium sites since interstitial chlorine ions should produce p-type conductivity, in contrast to what is observed. Third, under the diffusion conditions imposed here, the nickel is assumed to migrate through the lattice via interstitials. This assumption is based on the mechanism proposed by Bloem and Kröger (7) following their low temperature studies of nickel diffusion in PbS. They proposed that nickel migrates via interstitials but occupies lead sites in the crystal. The n-type conductivity produced by the nickel was presumed to be due to that interstitial nickel which entered the lattice in excess of the available lead vacancies. The fact that in the present study nickel alone was not found to produce n-type conductivity may simply indicate a smaller nickel concentration in our crystals. The chlorine, on the other hand, is assumed to migrate via anion vacancies. This assumption is based partly on the magnitude of the diffusion coefficient for the p-n junction observed in this study and partly on the work of Fedorovick (11) who measured the tracer diffusion coefficient of chlorine-36 in

n-type PbSe and sodium-doped ( $\frac{1}{2}$  m/o  $\text{Na}_2\text{Se}$ ), p-type PbSe. He found that the energy of activation for diffusion in p-type material was 0.86 eV while in n-type it was 0.45 eV. At  $700^\circ\text{C}$  the diffusion coefficients for  $^{36}\text{Cl}$  calculated from Fedorovick's data are  $1 \times 10^{-10}$   $\text{cm}^2/\text{sec}$  for sodium doped, p-type crystals and  $7.5 \times 10^{-11}$   $\text{cm}^2/\text{sec}$  for n-type crystals. Assuming that chlorine migrates via anion vacancies, one would expect a higher diffusion coefficient in the case of the sodium-doped PbSe due to the larger number of anion vacancies in the doped material.

If a singly ionized chlorine atom enters the lattice and occupies an anion lattice site, it will produce the observed n-type conductivity because of the difference in valence states between the tellurium and chlorine. In order to preserve the electroneutrality of the crystal, however, one of two subsequent reactions must occur for each two chlorine atoms added. Either a tellurium interstitial must be produced or a lead vacancy created. The latter reaction will be assumed to occur as was also assumed by Koval'chik and Maslakorets from bromine in PbTe (12). In the Kröger-Vink notation this reaction can be represented by



assuming a singly ionized lead vacancy.

If nickel occupies vacancies on the lead sublattice, then an increase in the chlorine concentration, and hence an increase in the number of available lead vacancies, should signal an increase in the solubility of nickel in lead telluride. Qualitatively this is what is observed. Figure 7 shows the result of exposing a PbTe crystal containing nickel to a chlorine atmosphere. The surface concentration of nickel increases by nearly ten fold and there is a smaller increase in the nickel concentration to the right of the p-n junction. In addition, it was found that the surface concentration of nickel was a time dependent function when crystals of PbTe were exposed to  $^{63}\text{NiCl}_2$  vapor, see Fig. 5. This observation also supports the earlier assumption that chlorine causes the production of lead vacancies rather than tellurium interstitials. Some of the increase at the surface may be due to nickel being transferred from the vapor phase as was discussed in the previous section. By comparing the surface concentration of curve B in Fig. 7 with Fig. 5 it is seen that even accounting for vapor transport of nickel-63, there is still about a six fold increase in the surface concentration following the re-anneal.

The most important question of the minimum in the nickel concentration profile must now be examined. This involves both solubility and migration. The introduction of chlorine into the lattice necessitates the creation of lead vacancies. Concurrently, the lead ions in the lattice must migrate away from the created cation vacancies in the region of the passing chlorine front. Since the region near the surface of the crystal already contains a larger number of vacancies than the bulk crystal because of the migrating chlorine front, it is probable that the excess lead atoms would migrate back toward the surface of the crystal. An attempt was made to confirm this point by determining the diffusion profile of  $^{210}\text{Pb}$  into a crystal that was exposed to an atmosphere of  $\text{NiCl}_2$ . It was expected that there would be an observable effect on the  $^{210}\text{Pb}$  distribution curve. Within experimental error, however, the  $^{210}\text{Pb}$  concentration profiles obtained in the presence of  $\text{NiCl}_2$  were the same as those obtained when  $\text{NiCl}_2$  was not present. The fact that very little difference was observed in the  $^{210}\text{Pb}$  concentration profile may be due in part to the small variation in cation vacancy concentration across the PbTe phase field. According to Fujimoto *et al.* (6) the lead vacancy concentration varies by only a factor of three in going from the Pb/PbTe phase boundary to the Te/PbTe phase boundary. The effect of chlorine on the cation vacancy concentration in the present experiments

may be expected to be smaller than this factor of three.

All that is really required, however, to produce a minimum in the nickel concentration profile is that the migration of lead cations toward the surface be slower than the in-diffusion of chlorine. In this event, there will be a pile-up of cations behind the advancing p-n front. In this region, too, there will be a minimum in the number of available lead vacancies which nickel can occupy and a resulting decrease in the nickel concentration with a concurrent concentration increase at deeper penetration (Fig. 6). It was pointed out earlier that the position of the minimum nickel concentration and the advancing p-n front tend to move away from each other. That is, the p-n front migrates through the crystal faster than the minimum. This would be the case if the in-diffusion of chlorine were faster than the out-diffusion of the cations resulting from the required increase in cation vacancy concentration. Further, it was observed that the migration of the minimum in the Ag-doped PbTe was somewhat slower ( $D_{\min} = 4 \times 10^{-11}$  cm<sup>2</sup>/sec) than in undoped PbTe ( $D_{\min} = 9 \times 10^{-11}$  cm<sup>2</sup>/sec) as would be expected if cation vacancy migration were the controlling factor for the migration of the minimum.

Experiments in this laboratory indicate that in undoped crystals equilibrated under argon, the diffusion coefficient for <sup>210</sup>Pb is about  $2 \times 10^{-11}$  cm<sup>2</sup>/sec at 700°C. As mentioned earlier the presence of NiCl<sub>2</sub> in the ampoule does not appear to affect this result. Boltaks (13) gives the diffusion coefficient of tellurium as  $3 \times 10^{-10}$  cm<sup>2</sup>/sec at 700°C. In the absence of other influencing factors, then, anion migration is faster than cation migration in lead telluride at 700°C. While the simultaneous diffusion of nickel and chlorine cannot be fully explained in such simple terms, the relative migrative rates for the minimum in the nickel concentration profile and the p-n junction differ in the same direction as the two self-diffusion coefficients. ( $D_{\min} = 9 \times 10^{-11}$  cm<sup>2</sup>/sec,  $D_{p-n} = 2 \times 10^{-10}$  cm<sup>2</sup>/sec). Further it may be expected that any effect which retards anion migration will enhance cation migration.

One other observation was made which deserves comment. When nickel-63 alone was allowed to diffuse into PbTe under flowing argon, the nickel concentration was found to be higher near both surfaces of the wafer than in the bulk of the crystal. In the bulk of the crystal away from the surfaces the nickel concentration appeared to be uniform throughout the wafer. There are two possible explanations of these results. First it is possible that nickel migrates rapidly on the surface of PbTe and enters the crystal from the unplated surface after diffusing around the edge of the crystal. Alternatively the explanation may lie in a thermodynamic argument. If nickel behaves similarly to lead in the lattice as suggested by Kowal'chik and Maslakorets (12), then increasing the nickel concentration via diffusion would upset the defect equilibrium in the crystal. Specifically, nickel would decrease the cation vacancy concentration. At the same time, however, thermodynamics demands that the defect equilibrium constant (either the Schottky constant or Frenkel constant) be maintained. The crystal will begin changing its composition in order to satisfy the defect equilibrium constant. The cation vacancy concentration would be expected to begin increasing at the surface and migrate into the crystal. Since nickel appears to be very mobile at 700°C, it would then be expected to migrate to regions of higher vacancy concentrations, thus restoring the defect equilibrium both in the bulk of the crystal and near the surface.

### Summary

The diffusion of nickel and the simultaneous diffusion of nickel and chlorine from a NiCl<sub>2</sub> source have been studied in p-type lead telluride at 700°C. Marked

differences in the results were obtained depending on the experimental conditions employed.

When the diffusion anneal was carried out in an open system under flowing argon, the same results were obtained with both an electroplated <sup>63</sup>Ni source and when <sup>63</sup>NiCl<sub>2</sub> was deposited on one face of the crystal. Nickel diffuses through the lattice very rapidly. The nickel concentration was found to be higher on both faces of the wafer than in the bulk of the crystal even though nickel was initially deposited on only one face of the wafer. Under both of these experimental conditions, the crystal remained p-type throughout.

When diffusion anneals were carried out in a sealed ampoule two different results were obtained. When <sup>63</sup>Ni was electroplated onto one face of the PbTe wafer, the results were identical to those obtained in an open system. However, when <sup>63</sup>NiCl<sub>2</sub> was deposited on one face of the wafer by evaporation of the neutral solution, the <sup>63</sup>Ni concentration profile showed a sharp minimum followed by a region of relatively constant nickel concentration. The minimum in the <sup>63</sup>Ni profile was present near both faces of the wafer even though the <sup>63</sup>NiCl<sub>2</sub> was applied initially to only one face. The minima migrated through the crystal in proportion to the square root of time with an apparent  $D_{\min} = 9 \times 10^{-11}$  cm<sup>2</sup>/sec. In addition to the minimum in the nickel concentration profile, a p-n junction was formed at slightly deeper penetration in the crystal. The p-n junction also migrated through the crystal in proportion to the square root of time but with an apparent diffusion coefficient of  $2 \times 10^{-10}$  cm<sup>2</sup>/sec.

An experiment was carried out using a nickel-63 doped PbTe crystal. NiCl<sub>2</sub> was placed in the sealed ampoule but not in contact with the crystal. The <sup>63</sup>Ni concentration profile at the end of 24 hr was similar to those obtained when <sup>63</sup>NiCl<sub>2</sub> was evaporated onto an undoped crystal showing that the chlorine caused a redistribution of nickel behind the advancing chlorine front.

These results illustrate another impurity-impurity interaction in semiconductors and emphasize the role which experimental conditions play in altering diffusion in semiconductors.

### Acknowledgment

This work was supported by the U.S. Army Research office—Durham.

Manuscript submitted Jan. 15, 1968; revised manuscript received April 29, 1968. This paper was presented at the Boston Meeting, May 5-9, 1968, as Paper 71.

Any discussion of this paper will appear in a Discussion Section to be published in the June 1969 JOURNAL.

### REFERENCES

1. F. A. Cunnell and C. H. Gooch, *J. Phys. Chem. Solids*, **15**, 127 (1960).
2. H. C. Casey, M. B. Panish, and L. L. Chang, *Phys. Rev.*, **162**, 660 (1967).
3. G. B. Larrabee and J. F. Osborne, *This Journal*, **113**, 564 (1967).
4. R. F. Peart, K. Weiser, J. Woodall, and R. Fern, *Appl. Phys. Letters*, **9**, 200 (1966).
5. R. L. Longini and R. F. Greene, *Phys. Rev.*, **102**, 992 (1956).
6. M. Fujimoto and Y. Sato, *Japan J. Appl. Phys.*, **5**, 128 (1966).
7. J. Bloem and F. A. Kröger, *Philips Research Repts.*, **12**, 303 (1957).
8. A. Glassner, "The Thermochemical Properties of the Oxides, Fluorides and Chlorides to 2500°K," ANL-5750 U.S. Atomic Energy Commission.
9. R. C. Schoonmaker, A. H. Friedman, and R. F. Porter, *J. Chem. Phys.*, **31**, 1586 (1959).

10. H. Schafer, *Z. anorg. allgem. Chem.*, **278**, 300 (1955).  
 11. N. A. Fedorovick, *Soviet Phys.-Solid State*, **7**, 1291 (1965).  
 12. T. L. Koval'chik and Iu. P. Maslakovets, *Soviet Phys.-Tech. Phys.*, **1**, 2337 (1957).  
 13. B. I. Boltaks and Yu. N. Molhov, *ibid.*, **3**, 974 (1958).

## Epitaxial Deposition of Germanium onto Semi-Insulating GaAs

S. A. Papazian\* and A. Reisman\*

IBM Watson Research Center, Yorktown Heights, New York

### ABSTRACT

Smooth layers of epitaxial Ge have been grown on semi-insulating GaAs using the pyrolysis of  $\text{GeH}_4$ . Depositions were made between  $600^\circ$  and  $850^\circ\text{C}$  and the range most suitable for obtaining good growth was defined as  $650^\circ$ – $750^\circ\text{C}$ . Other factors affecting smoothness were substrate preparation, gas purity, and the total thickness of the deposit. The conductivity type profile of the deposits was determined using a traveling thermal probe on a beveled portion of the deposit, and it showed evidence of outdiffusion of both As and Ga from the substrate into the deposit in addition to As incorporation from the vapor phase. The semi-insulating properties of the GaAs wafers were measured before and after depositions, and it was found that no degradation of the resistivity occurred if the substrates were treated in a  $90\text{H}_2\text{SO}_4:5\text{H}_2\text{O}_2:5\text{H}_2\text{O}$  solution prior to depositions.

The recent interest in planar devices fabricated in Ge has prompted this investigation which is concerned with the possibility of defining a dielectric isolation scheme for this semiconductor. Since dielectric isolation approaches are expected to reduce stray capacitance effects encountered in junction isolated integrated circuits, a Ge/insulating substrate couple could be very useful if high quality epitaxy of Ge could be achieved. Semi-insulating GaAs is an attractive substrate for Ge because of the close match of the room temperature lattice constants ( $a_{\text{Ge}} = 5.6575\text{\AA}$ ,  $a_{\text{GaAs}} = 5.6533\text{\AA}$  (1)), and the apparent similarity in thermal expansion coefficients of the two materials (2).

The method used for depositing Ge epitaxially onto semi-insulating GaAs in this study was the pyrolytic decomposition of  $\text{GeH}_4$  in a  $\text{H}_2$  atmosphere according

to the reaction  $\text{GeH}_4(\text{g}) \xrightarrow{\text{heat}} \text{Ge}(\text{s}) + 2\text{H}_2(\text{g})$ . This reaction has been reported previously for deposition of Ge epitaxially onto Ge (3), onto conventional GaAs (4), and onto spinel (5), with some preliminary studies involving the use of semi-insulating GaAs (6).

The pyrolysis of  $\text{GeH}_4$  offers an advantage in the present instance over other deposition methods in that no possibility of vapor back-etching due to the presence of halogens or halogen acids exists. It has been found, for example, that in a  $\text{GeCl}_4$  reduction process for the deposition of Ge onto GaAs, extensive attack of GaAs occurs and degenerately doped n-type Ge layers result.

The purpose of this investigation was to define growth conditions necessary for achieving high quality Ge epitaxy on semi-insulating GaAs and to determine whether this process was amenable to controlled doping of the deposits, and if the high temperatures used were compatible with the semi-insulating properties of the GaAs.

### Experimental

The experiments were performed in a single wafer, vertical, flow type reactor shown in Fig. 1. Only quartz, Pyrex, and stainless steel have been used in constructing the system. Undoped  $\text{GeH}_4$ , obtained from the Matheson Company, enters the system at point A, after passing through a submicron filter to re-

move particulate matter. At point B the  $\text{GeH}_4$  is diluted with a small quantity of  $\text{H}_2$ . Part of this mixture is then introduced into the rest of the system at point C, the rest being bled out of a chimney and burned off. The  $\text{GeH}_4$ - $\text{H}_2$  mixture is diluted further with large quantities of  $\text{H}_2$  (which makes up most of the total flow rate through the reactor) at point D, before entering the reaction tube through a nozzle. This double dilution of  $\text{GeH}_4$  with  $\text{H}_2$  enables us to obtain good control over a wide range of  $\text{GeH}_4$  fluxes. Dopants can be introduced at points E and F. Of the two sources of  $\text{H}_2$  (Matheson, ultra high purity) seen in Fig. 1, the one passing through the Pd-Ag purifier is used for depositions while the other is used for continuous flushing of the system when not in operation. The pump line is used for evacuating the  $\text{GeH}_4$  lines before and after replacing  $\text{GeH}_4$  tanks. Failure to evacuate the lines thoroughly before and after exposure to the atmosphere resulted in coating of the lines with  $\text{GeO}_2$ .

The wafers are supported on a single crystal Ge pedestal which also acts as a susceptor for R. F. heating. The semi-insulating Cr doped GaAs wafers, which were obtained either from the Monsanto Company or from in-house crystal growing facilities, were polished in  $\text{NaOCl}$  using the method described by Reisman and Rohr (7). The single crystal Ge pedestals were etched in a  $5\text{HNO}_3:1\text{HF}$  solution, lapped and degreased in organic solvents after each run, and

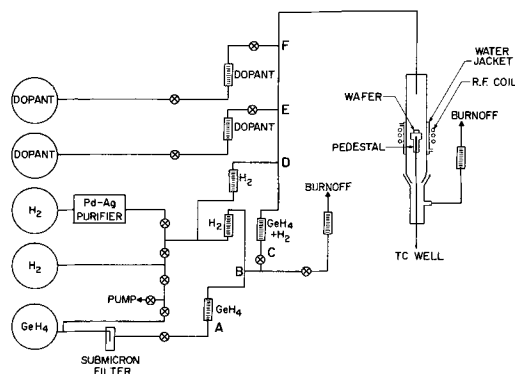


Fig. 1. Schematic representation of the  $\text{GeH}_4$  reactor

\* Electrochemical Society Active Member.



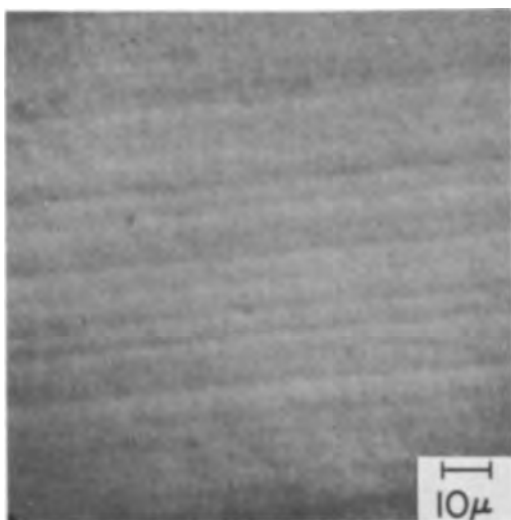


Fig. 2. Typical Ge deposit grown on semi-insulating GaAs;  $T_{\text{Growth}} = 650^{\circ}\text{C}$ , thickness  $\sim 8\mu$ .

cleaned ultrasonically in a  $1\text{NaOCl}:3\text{H}_2\text{O}$  solution just prior to depositions. The deposition temperature was measured and controlled via a thermocouple housed in a quartz well imbedded in the Ge pedestal. After loading the wafer, the system was flushed for a suitable length of time with purified  $\text{H}_2$  prior to a 30 min bake-out at the deposition temperature, after which  $\text{GeH}_4$  was admitted to the reactor. At the end of the depositions the  $\text{GeH}_4$  was turned off and the system flushed with purified  $\text{H}_2$  at temperature for approximately 20 min.

### Results and Discussion

Smooth layers of epitaxial Ge such as shown in Fig. 2 were grown on the (110) surface of semi-insulating GaAs under a variety of growth conditions. The pattern discernible in Fig. 2 is localized around slip lines in the  $\langle 1\bar{1}0 \rangle$ ,  $\langle 1\bar{1}\bar{2} \rangle$ , and  $\langle 1\bar{1}\bar{2} \rangle$  directions. The step height of this pattern is  $< 50\text{\AA}$  as was determined by using an interferometer with a laser attachment. The parameters affecting the surface quality of the epitaxial layers are discussed below.

**Effect of substrate preparation.**—The preparation of the GaAs substrates prior to depositions was found to be a very critical step. It was necessary to treat the NaOCl polished wafers in a  $90:5:5 = \text{H}_2\text{SO}_4:\text{H}_2\text{O}_2:\text{H}_2\text{O}$  solution just before epitaxy as described by Berkenblit *et al.* (8) in order to remove a possible residue left on the surface after polishing. The criticality of this step can be seen from a comparison of Fig. 2 and 3 showing two  $8\mu$  deposits grown under

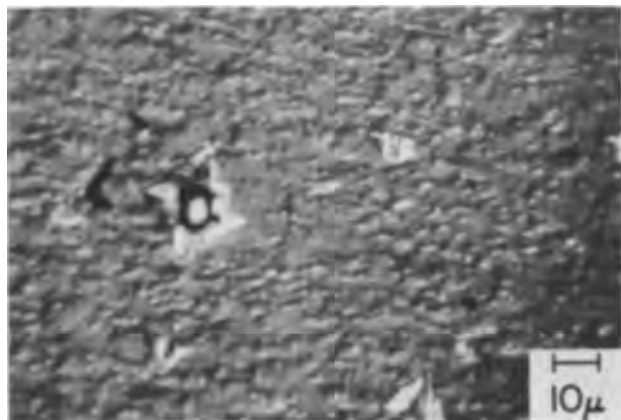


Fig. 3. Ge deposit grown on a semi-insulating GaAs substrate which was used without any additional treatment after NaOCl polishing.

identical conditions. The layer shown in Fig. 2 was grown using a substrate treated in  $90:5:5 = \text{H}_2\text{SO}_4:\text{H}_2\text{O}_2:\text{H}_2\text{O}$  solution whereas the substrate used in Fig. 3 was not treated following polishing.

**Effect of gas purity.**—The purity of both the  $\text{H}_2$  and the  $\text{GeH}_4$  had pronounced effects on surface quality. It was necessary, for instance, to purify the "ultra high purity"  $\text{H}_2$  further through a Pd-Ag diffuser, since failure to do so resulted in rough deposits. It was also important that the  $\text{GeH}_4$  be free of contaminants such as  $\text{B}_2\text{H}_6$ ,  $\text{HCl}$ ,  $\text{CO}_2$ ,  $\text{O}_2$ , and  $\text{H}_2\text{O}$  which were sometimes present in earlier  $\text{GeH}_4$  samples as by-products of the manufacturing process. These impurities caused undesirable nucleation and/or etching.

**Effect of total thickness of the deposit.**—The thicker a deposit, the more structured it became as can be seen on a  $20\mu$  deposit shown in Fig. 4. The growth pattern which is not very strong in deposits of up to  $10\mu$ , begins to affect surface quality above this thickness. The step height of the lines seen in Fig. 4 were measured to be approximately  $2000\text{\AA}$  by a Tally surf machine.

**Effect of deposition temperature.**—The temperature was found to be a most important parameter, since it not only affected the surface quality, but also the electrical characteristics of the deposits. Depositions were made between  $600^{\circ}\text{C}$ – $850^{\circ}\text{C}$  measured on the thermocouple, with surface temperatures approximately  $50^{\circ}$  lower, as was ascertained with an infrared pyrometer under simulated growth conditions. The temperatures mentioned in this paper refer to the values measured on the thermocouple. Good epitaxy, such as seen in Fig. 2, was achieved in the temperature range of  $650^{\circ}$ – $750^{\circ}\text{C}$ . However,  $750^{\circ}\text{C}$  was found to be a borderline case, since the results were erratic. Figure 5 depicts a deposit grown at  $600^{\circ}\text{C}$ . Its thickness,  $9\mu$ , is about the same as that of the deposit shown in Fig. 2, but faceted rather than smooth growth is observed. Figure 6, on the other hand, shows a  $4\mu$  deposit grown at  $775^{\circ}\text{C}$ . The structure on the surface consists of depressions, some of which extend through the deposit into the substrate as much as  $5\mu$ . Similar behavior is observed with thicker deposits grown at this temperature. It was observed, on beveling these layers, that the pits were coated by what is believed to be a Ge-Ga alloy. This assumption is based on the fact that a  $\text{H}_2$ -bake out of a GaAs wafer at ca.  $775^{\circ}\text{C}$  showed surface etching and evidence of liquid Ga droplets on the Ge pedestal, around the edge of the wafer. The fact that GaAs vaporizes incongruently above approximately  $680^{\circ}\text{C}$  (9,10) thus making the presence of a free Ga phase possible, supports this

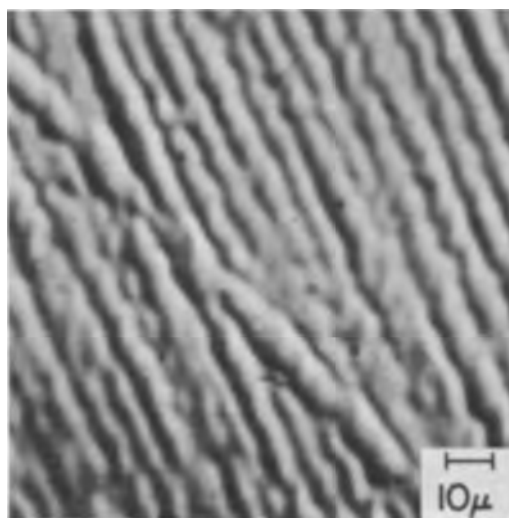


Fig. 4. Surface of a  $20\mu$  thick Ge deposit on semi-insulating GaAs





Fig. 5. Ge layer grown on semi-insulating GaAs at 600°C (thickness  $\sim 9\mu$ ).

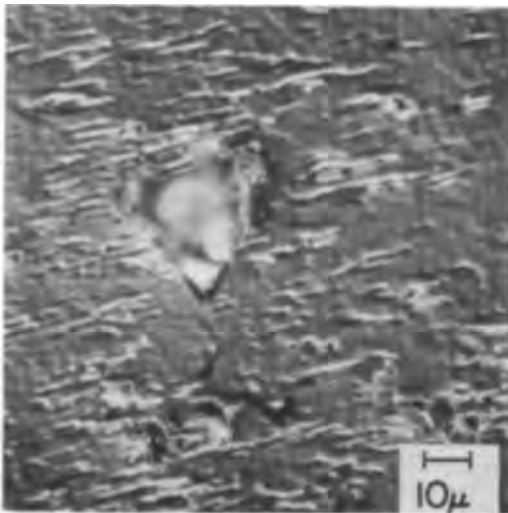


Fig. 6. Ge layer grown on semi-insulating GaAs at 775°C (thickness  $\sim 4\mu$ ).

interpretation. Depositions made at above 800°C resulted in extensive alloying of the GaAs substrate with both the Ge deposit and the pedestal.

*Effects of  $\text{GeH}_4$  concentration, growth rate, and total flow rate (or linear gas stream velocity).*—Results indicated that in the temperature range of 650°–700°C, varying the concentration, and therefore the growth rate, between 0.02–0.14%  $\text{GeH}_4$  by volume in  $\text{H}_2$  total flow rates ranging between 1.5–7 l/min, which corresponds to linear gas stream velocities of 150–720 cm/min at room temperature, does not affect surface quality.

In Fig. 7 and 8 growth rate *vs.* concentration curves are shown using two different techniques for varying the  $\text{GeH}_4$  concentration. The data for Fig. 7 were acquired using a constant input flow rate of  $\text{GeH}_4$  (constant flux) and varying the concentration by varying the flow rate of the diluent gas. The data points for this figure are therefore each at a different linear gas stream velocity. As might be anticipated, because the residency time of  $\text{GeH}_4$  molecules in the vicinity of the pedestal decreases with increasing linear gas stream velocity, the reaction efficiency decreases. At the higher flow rates, in addition, surface cooling probably plays a part in decreasing the growth rate. In Fig. 8, the data were acquired at constant total flow rate, the  $\text{GeH}_4$  concentration being varied by varying the  $\text{GeH}_4$  input flow rate. It is seen from Fig. 8

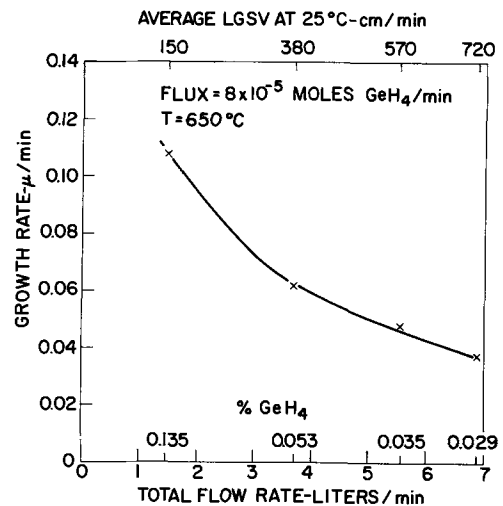


Fig. 7. Growth rate vs. total flow rate at constant  $\text{GeH}_4$  flux

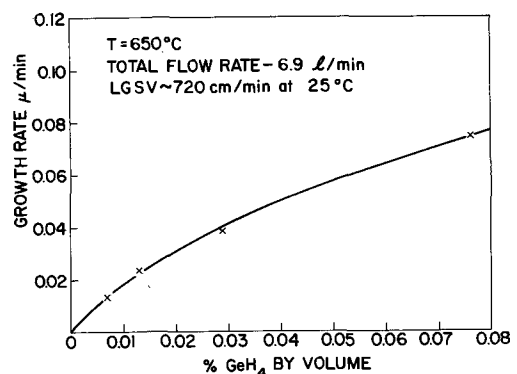


Fig. 8. Growth rate vs.  $\text{GeH}_4$  concentration at constant total flow rate.

that the curve is sublinear indicating that as the concentration is increased, the growth tends to become surface rather than mass transport controlled (11). Figure 9 shows a semi-log plot of growth rate as a function of  $1/T \times 10^3$  in the interval 600°–750°C using the conditions ca. 0.03%  $\text{GeH}_4$  at a total flow rate of 6.9 l/min. Since this flow rate is referenced to 25°C and 1 atm, the data of Fig. 9 are obviously each at a different linear gas stream velocity due to the temperature effect. Because of the latter and because the growth rate data do not cover even one decade, the apparent linearity of growth rate with  $1/T$  is considered fortuitous and not valid for obtaining an activation energy. Furthermore, since the data at 650°C and 0.03%, Fig. 8, appear to lie in a mass transport controlled region of growth, an extracted activation energy from Fig. 9 would not be related to the growth kinetics at the GaAs surface.

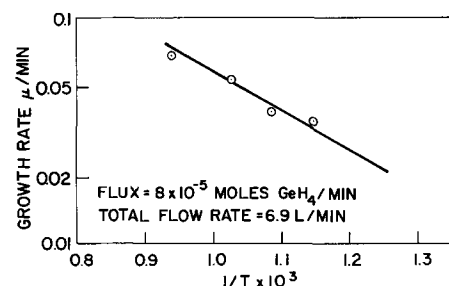


Fig. 9. Growth rate vs.  $10^3/T$  (concentration:  $\sim 0.03\%$   $\text{GeH}_4$  by volume).

At 750°C an apparent linear gas stream velocity effect was observed, where with decreasing total flow rates, surfaces became more structured. Since no flow rate effects were observed at the lower temperatures, this effect at 750°C may be attributed to differences in surface cooling, which was measured to be 15°-20°, between the highest and lowest flow rates, i.e., from 1.5 l/min to 7 l/min (linear gas stream velocity, 150 cm/min—720 cm/min at room temperature). Thus, at the low flow rates, the surface temperature is in the region where the onset of micro-alloying is suspected, whereas at the higher flow rates the surface is sufficiently cooled to place it in an insensitive temperature region.

**Random surface defects.**—The most commonly encountered random defect on the surface of the deposits is shown in Fig. 10. The flat, platelet type growths seen are attributed to imperfections on the starting substrate. In addition to this type of random defect, conglomerates of crystallites are also observed. These latter spurious nucleations seem to be due to dusting from the vapor phase. These random defects have been observed under all growth conditions. The density of these defects on deposits grown on Ge substrates is considerably less than on the GaAs.

**Crystalline perfection.**—The crystalline perfection of the deposits was determined by x-ray diffractometry using the method described by Cole and Stemple (12). Using this method, a perfection number is obtained which gives an indication of dislocations, strains, and other imperfections in the material. The x-ray perfection scale ranges from 1.45 for a perfect crystal to 6.0 for a mosaic crystal on (110) oriented single crystals. Both the GaAs substrates and the Ge deposits had perfection numbers ranging between 2-3.5 which, however, did not show an obvious dependence on either substrate preparation or on the growth parameters discussed.

**Electrical characteristics.**—The suitability of the GeH<sub>4</sub> pyrolysis process for controlled doping was investigated in an attempt to gain some insight into problems such as possible out-diffusion of As and/or Ga from the interface into the deposit and incorporation of As and/or Ga from the vapor phase during growth due to the incongruent vaporization of GaAs. The background impurity contribution from the undoped GeH<sub>4</sub> source and from the system was determined by depositing Ge onto high resistivity (~ 8 ohm-cm), p-type Ge substrates using similar conditions. The deposits were measured to be approximately 7 ohm-cm, p-type corresponding to a background im-

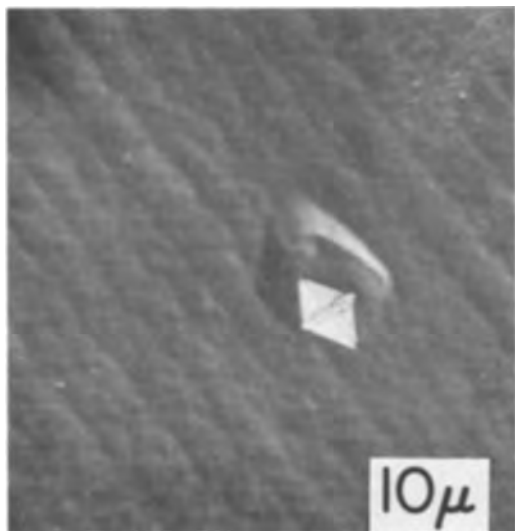


Fig. 10. Random defects encountered on Ge deposits grown on semi-insulating GaAs.

purity concentration of approximately  $4.5 \times 10^{14}$  acceptors/cc.

Ge deposits of up to approximately  $10\mu$  grown on semi-insulating GaAs below 750°C for most cases showed n-type surfaces. The resistivity, measured at the surface using a spreading resistance technique, varied between 0.05-0.2 ohm-cm, depending on growth conditions. However, a few growths were obtained in which regions of both n- and p-type conductivity were observed at the surface.

Deposits grown at 750°C, on the other hand, generally exhibited all p-type surfaces, with the exception of a few samples which showed either all n-type conductivity or both p- and n-type regions. Those deposits grown at above 750°C, where surface alloying occurred, were degenerately p-type. The occasional nonreproducibility of surface characteristics obtained on deposits below 750° and at 750°C indicates that more than one mechanism is responsible for impurities being incorporated into the growing layer.

Profiles of conductivity type throughout the deposit were next determined using a traveling thermal probe on beveled samples. A schematic representation of typical traveling thermal probe traces for deposits grown at temperatures lower than 750°C is shown in Fig. 11. As can be seen from this diagram, starting at the Ge/GaAs interface, a p-type layer extends into the deposit, approximately  $0.1\mu$ . This interface layer gives way to an n-type region that continues to the surface.

The following considerations are involved in interpreting the existence of such a profile. If we assume that only a fraction of the available As at the Ge/GaAs interface [ $\sim 4.6 \times 10^{14}$  As atoms/cm<sup>2</sup> on (110) GaAs] diffused into the Ge deposit, this amount would indeed be sufficient to account for all of the n-type impurities in the deposit, assuming the entire n-layer to have the same carrier concentration as the one measured at the surface. Furthermore, because of the vast difference in the diffusion constants of Ga and As in Ge, e.g., at 700°C,  $D_{As} \approx 2.5 \times 10^{-12}$  cm<sup>2</sup>/sec, whereas  $D_{Ga} \approx 5 \times 10^{-15}$  cm<sup>2</sup>/sec, the Ga moving into the deposit more slowly than the As would give rise to the small p-type layer detected at the interface. A comparison of the thickness of this layer with diffusion calculations supports this argument. However, the above argument does not explain all the data. For example, if we consider the duration of depositions (1-3 hr), the thickness of the deposits and the As diffusion constants involved, not all the n-type impurity can be attributed simply to out-diffusion from the GaAs surface. Because of the p-type nature of the impurities contributed from both the GeH<sub>4</sub> and the system, the only other source of n-type doping is believed to be As in the vapor resulting from GaAs dissociation. This dissociated As is then incorporated into the growing layer before the wafer is completely covered with deposited Ge. This As now serves as a second source for As diffusion in the deposit. Thus, it is assumed that both an interfacial out-diffusion of Ga and As plus a less systematic vapor phase impurity incorporation are responsible for the observed general conductivity type profile and surface conductivity type variations.

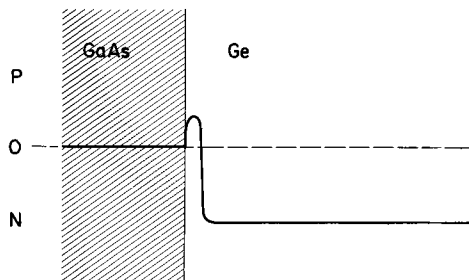


Fig. 11. Schematic representation of the conductivity type profile of Ge layers grown on semi-insulating GaAs at  $< 750^\circ\text{C}$ .

It was observed on thicker deposits, i.e.,  $> 16\mu$ , that the n-type region gave way finally to a p-layer that continued to the surface. This is attributed to the fact that once the wafer is completely covered with Ge, the only source of As is that out-diffusing at the GaAs-Ge interface in addition to that already incorporated from the vapor due to incongruent GaAs vaporization. At this point then, the  $\text{GeH}_4$  background impurity concentration of approximately  $10^{14}$  acceptors/cc is the only source of contamination and further growth is p-type in nature.

For depositions made at  $750^\circ\text{C}$  the above picture is somewhat unsatisfactory. The conductivity type profiles of the deposits in general again show the small p-type region at the Ge/GaAs interface leading into the n-type region, followed finally by the p-type top layer. This profile, however, is present on thin deposits, i.e.,  $5\text{-}10\mu$ . Furthermore, the surface p-type conductivity is much greater than could be supplied by the p-impurity present in the  $\text{GeH}_4$ ; while the latter would yield approximately 7 ohm-cm material, the surfaces were measured to be about 0.01 ohm-cm. A possible explanation is the following. During growth at  $750^\circ\text{C}$  and before the substrate is completely covered with Ge, the GaAs is vaporizing incongruently at a rapid rate with tiny pools of Ga forming on the Ge pedestal (possibly as a Ge-Ga alloy). In fact, such globules are visually observed on the pedestal after growth at higher temperatures. Once the wafer is overcoated with Ge, the pools of Ga on the pedestal now represent the primary source of contamination. This source exerts a sufficient vapor pressure to cause the heavy p-type doping. Even though the vapor pressure of Ga is very low at  $750^\circ\text{C}$ , it is sufficiently high for conducting p-type diffusions into Ge.

The deposits grown above  $750^\circ\text{C}$  which showed surface alloying were degenerately p-type throughout the deposit. The results given above imply that on depositions made below  $750^\circ\text{C}$ , the impurity levels are such that controlled doping can be obtained whereas at  $750^\circ\text{C}$  one would run into considerable difficulty.

*Semi-insulating properties.*—The compatibility of the  $\text{GeH}_4$  process with retention of semi-insulating properties of GaAs was investigated by measuring the spreading resistance of the substrates before and after deposition. The measurements after deposition were made by either etching islands in the deposit and measuring the spreading resistance between them, or by etching away the entire deposit and measuring the bare GaAs.

No degradation of the spreading resistance of the semi-insulating GaAs was observed if the substrates had been treated in the  $90\text{H}_2\text{SO}_4:5\text{H}_2\text{O}_2:5\text{H}_2\text{O}$  solution prior to deposition, regardless of growth condi-

tions in the deposition range  $650^\circ\text{-}750^\circ\text{C}$ . Some degradation was observed on as-polished substrates. This degradation was only a surface effect, however, since removal of several microns of the GaAs surface in the  $90\text{H}_2\text{SO}_4:5\text{H}_2\text{O}_2:5\text{H}_2\text{O}$  solution restored the semi-insulating properties of the substrate to their original value.

### Summary

It appears then, in summary, that smooth epitaxial Ge films of approximately  $10\mu$  can be deposited on semi-insulating GaAs in the temperature range of  $650^\circ\text{-}750^\circ\text{C}$  under a variety of growth conditions with good potential for controlled doping and without damaging the semi-insulating properties of the GaAs.

### Acknowledgment

The authors are greatly indebted to Messrs. M. Berkenblit and M. Sampogna for preparation of the substrates, Messrs. R. P. McGouey and B. J. Stoeber for their assistance with the experiments, Dr. A. G. Blachman and Mr. M. E. Cowher for the electrical characterizations, and Drs. T. B. Light and S. Krongelb for helpful discussions.

Manuscript submitted Feb. 2, 1968; revised manuscript received ca. May 8, 1968. This paper was presented at the Chicago Meeting, Oct. 15-19, 1967, as Paper 159.

Any discussion of this paper will appear in a Discussion Section to be published in the June 1969 JOURNAL.

### REFERENCES

1. Ann S. Cooper, *Acta Cryst.*, **15**, 578 (1962).
2. T. B. Light, M. Berkenblit, and A. Reisman, Presented at the Chicago Meeting, Oct. 16-18, 1967, as Paper 161.
3. E. A. Roth, H. Gossenberger, and J. A. Amick, *RCA Rev.*, **24**, 499 (1963).
4. R. L. Zanowick, Presented at the Buffalo Meeting, Oct., 1965, as Paper 120.
5. D. J. Dumin, *This Journal*, **114**, 749 (1967).
6. E. Clayton Teague and S. B. Watelski, Technical Report ECOM-02029-1, U. S. Army Electronics Command, Fort Monmouth, N. J.
7. A. Reisman and R. L. Rohr, *This Journal*, **111**, 12 (1964).
8. M. Berkenblit, A. Reisman, and T. B. Light, Presented at the Chicago Meeting, Oct. 16-18, 1967, as Paper 160.
9. V. J. Lyons and V. J. Silvestri, *This Journal*, **109**, 963 (1962). Private communication.
10. C. D. Thurmond, *J. Phys. Chem. Solids*, **26**, 785 (1965).
11. A. Reisman and M. Berkenblit, *This Journal*, **113**, 146 (1966).
12. H. Cole and N. R. Stemple, *J. Appl. Phys.*, **33**, 2227 (1962).

# Epitaxial Growth of Mirror Smooth Ge on GaAs and Ge by the Low Temperature $\text{GeI}_2$ Disproportionation Reaction

M. Berkenblit,\* A. Reisman,\* and T. B. Light

IBM Watson Research Center, Yorktown Heights, New York

## ABSTRACT

Ge epitaxial layers were grown by the  $\text{GeI}_2$  disproportionation reaction at  $350^\circ\text{C}$  on (110) semi-insulating GaAs and Ge substrates. The epitaxial surfaces are comparable in quality to those obtained by the higher temperature hydrogen reduction of  $\text{GeCl}_4$  on Ge substrates. Modifications of previously reported apparatus and growing conditions which lead to the enhanced surface qualities are described. These modifications include an increase in average linear gas stream velocity and  $\text{GeI}_2$  concentrations, improved substrate surface preparation techniques, and the protection of the wafer surface from spurious nucleation during the growth process.

There has been considerable recent interest in the use of planar Ge for ultra high performance switching circuit applications at these laboratories as well as for other device applications elsewhere. Ge grown on semi-insulating GaAs is being investigated as a starting material for an alternate, improved approach to device isolation over the presently employed junction isolation schemes. The Ge/GaAs system is potentially useful because of the apparent close structural match of the two materials, the semi-insulating properties of Cr doped GaAs, and the retention of these insulating properties during low temperature Ge deposition processes and subsequent device fabrication steps.

Among the potential methods for the deposition of Ge on GaAs (*i.e.*, pyrolytic reduction of the tetrahalide, decomposition of  $\text{GeH}_4$ , and the dihalide disproportionation reaction) the  $\text{GeI}_2$  disproportionation reaction is attractive because of the associated low temperatures. Notably, low temperature reactions have led in the past to poor surface qualities when compared to higher temperature processes. In addition, the surface characteristics showed a marked dependency on substrate orientation (1, 2).

This paper describes a method by which n- and p-type Ge epitaxial layers may be grown via the iodine process at a substrate temperature of  $350^\circ\text{C}$  on (110) semi-insulating GaAs and Ge substrates. The grown surfaces are mirror smooth and shiny, and are comparable to those obtained by the higher temperature hydrogen reduction of  $\text{GeCl}_4$  on Ge substrates. Changes in deposition parameters, improved substrate preparation and modifications of the apparatus previously reported on (2) are described which have led to the enhanced surface qualities. Of note also, is the fact that growth rates using the new procedure are comparable to those obtained in higher temperature epitaxial growth techniques.

## Experimental Procedure

**Flow and temperature.**—The Ge layers were grown in a horizontal system with a 1 in. diameter deposition chamber. The pertinent thermodynamics and basic flow system have been described earlier by the authors (2-4). The substrates were maintained at a temperature of  $350^\circ\text{--}355^\circ\text{C}$  and the Ge source bed was held at  $600^\circ\text{--}620^\circ\text{C}$ . A 15%  $\text{H}_2$ -85% He mixture was used as a carrier gas at an input flow rate of 915 cc/min which, expressed as a room temperature linear gas stream velocity at the substrate, is 190 cm/min. The  $\text{I}_2$  source for the HI generator was maintained at  $65^\circ\text{--}75^\circ\text{C}$  ( $\pm 0.2^\circ\text{C}$  at a given temperature) which encompasses a range of HI pressures of 11.0-20.5 Torr.

**Reagents.**—The carrier gas was mixed in the system (Matheson ultra pure  $\text{H}_2$  and He). Traces of  $\text{O}_2$  and  $\text{H}_2\text{O}$  were removed by passing this mixture through a heated Pt bed ( $450^\circ\text{C}$ ) in series with a liquid nitrogen freeze out trap. The HI generator used was the modified version described in ref. (5).

The Ge source material was Eagle-Picher intrinsic grade (40 ohm-cm or better). In order to extend the time between reloading Ge charges, a larger source bed was constructed to replace the one employed in the previously reported system. This new design also offers a more efficient reaction path through the crushed Ge to accommodate the higher flows employed in the present work. As shown in Fig. 1 the source bed was made up of a number of interconnected chambers in a 1 in. diameter tube. The openings in each chamber were positioned in such a way as to insure passage of the gas through the crushed Ge.

GaAs wafers were prepared both from Monsanto (horizontal Bridgeman) Cr doped and from Czochralski pulled Cr doped single crystals grown by S. Blum of our laboratories. Ge substrates, which were used as controls, were obtained from Czochralski pulled single crystals grown in house by C. Lent. Both the GaAs and Ge bulk single crystals were oriented to within  $0.5^\circ$  of the (110), sliced, lapped, and then polished using the  $\text{NaOCl}$  method of Reisman and Rohr (6). In the case of p-type Ge substrates, electropolishing in a KOH solution was used to assess effects of polishing on subsequent deposits. None were noted.

**Additional surface preparation.**—It was found that in order to obtain mirror smooth epitaxial deposits, both the GaAs and Ge wafers, after polishing and storage, required an additional chemical treatment immediately prior to being loaded into the epitaxial reactor. GaAs wafers were treated in a solution of  $90\text{H}_2\text{SO}_4:5\text{H}_2\text{O}_2:5\text{H}_2\text{O}$  (7, 8) in a hanging basket arrangement as shown in Fig. 2. The substrates were suspended in the solution in the basket, and stirring was effected via a rotating magnetic bar. The basket consists of a shallow quartz dish supported by rods and permits the cleaned wafer to be water quenched in



Fig. 1. Germanium source bed

\* Electrochemical Society Active Member.

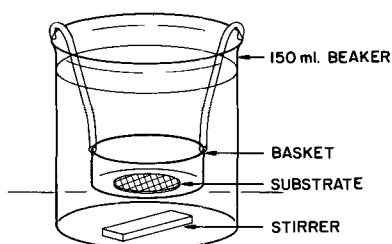


Fig. 2. Hanging basket used for cleaning GaAs substrates

situ immediately following the chemical treatment. A marked difference in surface texture was observed with different methods of agitation. For example, a pronounced degradation in the form of an orange peel texture results with the use of ultrasonic agitation in place of the method described.

Ge substrates, however, could be cleaned satisfactorily by a 90 sec treatment in a 3:1 solution of  $H_2O$ :NaOCl stock solution (5% available chlorine) using ultrasonic agitation. A final degree of surface cleaning was achieved by heating both the Ge and GaAs substrates, in situ, in a  $H_2$  ambient for 30 min ( $600^\circ C$  for GaAs and  $700^\circ C$  for Ge) prior to deposition.

One further factor that markedly affected deposit quality is the method employed for drying the substrates following chemical treatment and rinsing. If done improperly, it will invariably result in an epitaxial deposit marred by many surface imperfections. A procedure that yielded good results consistently is as follows. After chemical treatment, and quenching the chemical action in deionized water, the wafer is transferred from the etching basket to a vacuum chuck. During this transfer procedure a stream of deionized water is played on the wafer surface to prevent partial drying of the wafer. Simultaneously, the hosing action is stopped and a jet of high pressure clean nitrogen is directed onto the wafer surface to roll the water off. This enables almost instantaneous removal of liquid from the surface with a minimum amount of evaporation being permitted to take place. An example of the effects of a poor drying technique is shown in Fig. 3. In this case water was allowed to ball to the center of the substrate resulting in some drying of the edges before the surface was completely dried. Both photographs show the sharp difference in density of surface contamination. A grown layer on such a surface clearly replicates the two distinctly different areas.

**Vacuum chuck substrate holder.**—Previously, epitaxially deposited films were subject to the formation of large spurious overgrowths or "spikes" during the deposition process. Spikes as high as  $20\text{--}30\mu$  were observed on  $5\mu$  thick deposits when the substrates were placed face up in the horizontal deposition chamber. Because deposition in a disproportionation growth process is not confined to the substrate, but occurs on the walls of the reactor also, minute particles can flake off and serve as nuclei for these coarse protrusions. To eliminate the problem of dusting from the walls of the reactor and the attendant growth of spikes, a vacuum chuck was used to hold the substrate face down in the gas stream. The wafer holder, shown in Fig. 4, consists of a semicylindrical quartz piece and a support tube extending out of the system

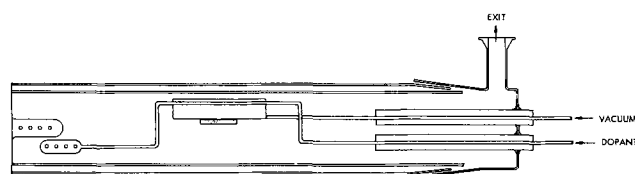


Fig. 4. Deposition chamber showing the position of vacuum chuck and dopant line.

to a vacuum line. The flat face is lapped and has a 25 mil vacuum orifice.

**Doping.**—Both n- and p-type Ge layers were grown using  $AsH_3$  and  $BI_3$ , respectively, as the dopant sources. The impurities were introduced into the system through a separate gas line as shown in Fig. 4.

### Experimental Results

In our earlier work, the low temperature HI-Ge vapor transport system was used at relatively low linear gas stream velocities (l.g.s.v.) and low hydrogen iodide vapor pressures (15-30 cm/min and HI in the range of 2-4 Torr). Velocities and concentrations were chosen so that the source was maintained at equilibrium, and deposition was in a quasi equilibrium or mass transport limited condition. Growth rates were in the range of  $0.3\text{--}0.8\ \mu/hr$ . The epitaxial films on (110) surfaces had a dull matte appearance that was unsuitable for application of small dimension photo-masking techniques. Deposits, exhibiting improved but still inadequate surface characteristics, were grown under these low growth rate conditions on several orientations other than the (110). The best surfaces under these conditions were obtained on wafers that were cut  $25^\circ$  off (100)  $\rightarrow$  (110).

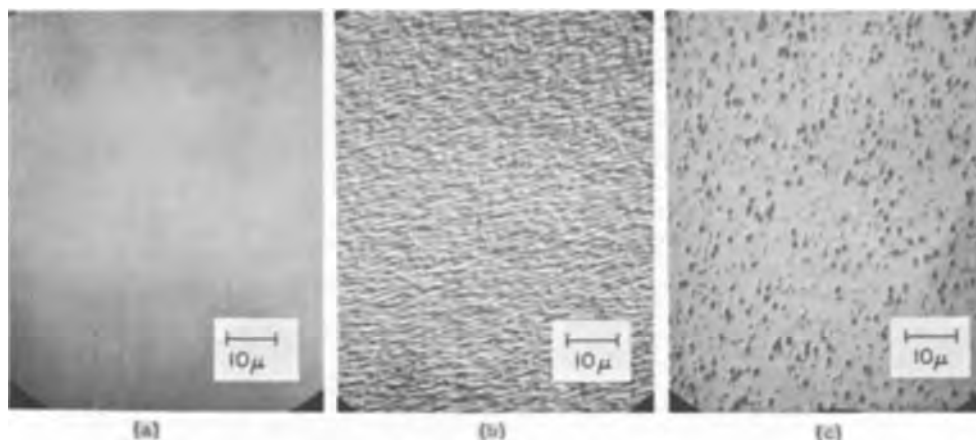
The first significant improvement in surface quality of deposits on (110) substrates was obtained by increasing both the l.g.s.v. and simultaneously increasing the vapor phase concentration of  $GeI_2$ . (As a matter of convenience the concentrations are expressed in terms of HI vapor pressures or temperature of the iodine source bed.) Attending these changes, the growth rate increased to a value ranging between 5 and  $10\ \mu/hr$  depending on the exact conditions of the experiment. This increase in growth rate was, however, less than would have been predicted theoretically (3) indicating a lowered efficiency of deposition. For example, the set of conditions leading to a  $10\ \mu/hr$  growth rate should have yielded a value of  $18\ \mu/hr$ . Such a result is not unexpected since with increasing l.g.s.v. and gas phase reactant concentration the deposition tends to become surface limited in the manner described by the authors (5). The improvement of surface smoothness coincident with changing the growth parameters in the direction of a surface rather than a mass transport regime is in clear distinction to observations made by Silvestri for hydrogen reduction of  $GeCl_4$  (9). In such a system he found that enhanced surface smoothness was directly related to maintaining the deposition in a mass transport controlled regime.

A range of operating conditions were determined which were suitable for obtaining mirror smooth surfaces. At a constant  $GeI_2$  concentration (11.0 Torr HI), depositions were of excellent quality in the l.g.s.v. range from 95 to 190 cm/min. No experiments were

Fig. 3. Example of poor drying technique.



Fig. 5(a, left). Surface obtained using full process; (b, center). surface obtained without pretreatment of substrate; (c, right). surface obtained using low l.g.s.v. and low  $\text{GeI}_2$  concentration.



conducted above 190 cm/min, and it was observed that at 50 cm/min surface quality had already degraded noticeably. At a constant velocity of 190 cm/min, smooth and shiny surfaces were obtained with HI pressures ranging between 5 and 35 Torr. Using HI pressures in the range 35 to 50 Torr resulted in visually mirror smooth surfaces which exhibited microscopic etch structures. The etching phenomenon at these higher HI pressures is believed to be due to incomplete equilibration at the Ge source.

In order to demonstrate the necessity for the several cleaning and growth condition steps described above, a series of  $5\mu$  layers of Ge were deposited on (110) semi-insulating GaAs. The three cases presented for comparison essentially summarize the over-all process. Figure 5a shows a surface obtained using the full process. Figure 5b is a micrograph of a deposit using all the critical procedures except that the substrate was not chemically treated prior to loading into the reactor. The deposit shown in Fig. 5c was obtained on a substrate which had the full cleaning procedure, but where both low l.g.s.v. and  $\text{GeI}_2$  concentration were employed for deposition. As is evident, only the surface obtained by employing all of the critical steps is shiny and smooth. The others vary in texture from hazy to dull matte.

Stacking faults were not observed either by interference contrast microscopy or by x-ray topography. In addition, the crystal perfection of the as-grown layers were equal to that of the starting substrate as determined by the x-ray crystallographic technique of Cole and Stemple (10).

Once conditions were established for obtaining reproducibly good Ge layers, the behavior of these layers in subsequent heating cycles (*i.e.*, oxide deposition, diffusions) was examined. Ge deposits on GaAs sub-

strates show signs of plastic deformation after heating to  $500^\circ\text{C}$  or higher. This behavior is attributed to strain due to a mismatch in the thermal coefficients of expansions between the GaAs substrates and the Ge epitaxial layers. Strain relief then occurs along slip planes during the heating cycle. An example of such slip line formation is shown in Fig. 6. As-grown layers were slip free, Fig. 5a.

Plastic deformation was not observed in Ge grown on Ge substrates, nor would it be expected if the strain is due to a thermal expansion mismatch. Ge grown on GaAs by the pyrolysis of  $\text{GeH}_4$  at  $650^\circ\text{C}$ , as reported by Reisman and Papazian (11), shows slip line formation after the initial deposition heat cycle.

Annealing or slow heat cycling did not appreciably change the extent of plastic deformation. A much thicker Ge deposit ( $33\mu$ ), than normally grown ( $5-10\mu$ ), shows the minimum decrease in crystal perfection after heating to above  $500^\circ\text{C}$ . The use of thin substrates ( $< 5$  mils) prevented slip line formation because the strain relief in such a structure occurs by elastic bending of the substrate.

A complete discussion of the plastic deformation characteristics of the epitaxial films and a calculation of the stress and extent of the thermal mismatch is discussed by the authors in a separate paper (12).

In an attempt to extend the usefulness of the deposition process, several experiments were performed on orientations other than (110). It was found that the growth conditions which provided mirror smooth deposits on (110) surfaces yielded structured surfaces on (111) and (100) oriented substrates. Since our interest at the present time is confined to (110) surfaces in conjunction with their use in fabricating Post Alloy Diffused transistors (13), no attempt was made to define growth parameters applicable to other orientations.

The Ge layers deposited in the undoped state were all n-type having a carrier concentration of the order of mid  $10^{14}$  to low  $10^{15}/\text{cc}$ . The preparation of more heavily doped n-type material is readily achieved with use of  $\text{AsH}_3$  as an arsenic source. The decomposition of  $\text{AsH}_3$  occurs at the growth temperatures employed and the addition of  $\text{AsH}_3$  to the vapor phase did not perturb the deposition process.

The use of  $\text{B}_2\text{H}_6$  as a p-type dopant source is standard in the high temperature  $\text{GeCl}_4$  process and was examined in the disproportionation growth.  $\text{B}_2\text{H}_6$  was found usable in obtaining deposits with resistivities varying between 1-0.005 ohm-cm under low growth rate conditions. However, at the growth rates arrived at for the present work, B addition via  $\text{B}_2\text{H}_6$  presented a problem. The maximum doping achieved was 0.02 ohm-cm and with further increase in  $\text{B}_2\text{H}_6$  concentrations the surface quality of the epitaxial deposits degraded.

At the low temperatures of the disproportionation reaction, the incorporation of B into the growing

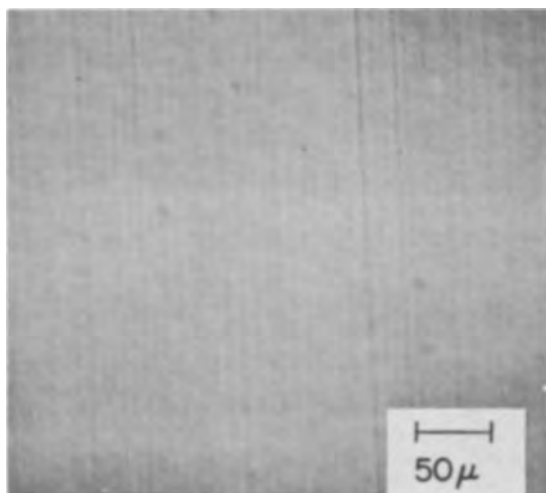


Fig. 6. Example of slip line formation

layer is assumed to occur via an intermediate formation of  $BI_3$  by the reaction of  $B_2H_6$  with HI (14, 15) in the gas stream. The  $BI_3$  yield is limited by the HI available in the gas stream and the efficiency of the reaction at the temperature of the epitaxial reactor. Therefore, in order to produce the necessary  $BI_3$  concentrations a large excess of  $B_2H_6$  is required which in turn perturbs the epitaxial reaction. To eliminate the dependence on this reaction, a source of  $BI_3$  was substituted for the  $B_2H_6$ . A range of concentrations were then obtained, sufficient for all doping levels required, by passing He or  $H_2$ -He mixtures at varying flow rates through a bed of solid  $BI_3$  maintained at room temperature. In the range of operation there was no degradation in surface quality with increasing  $BI_3$  concentrations.

Impurity concentration profiles were not measured. However, samples of Ge grown with high and low B concentrations on semi-insulating GaAs were angle lapped. Traveling hot probe measurements did not indicate the presence of any n-type regions near the interface. This implies a negligible back etching reaction. In addition, after etching the Ge deposit away, there was no measurable degradation of the insulating properties of the substrate material.

#### Summary

A low temperature process for the deposition of smooth and shiny Ge epitaxial layers at  $350^\circ C$  has been evolved. Each of the process steps are important and are necessary for good surfaces. These process steps include: (I) Chemical treatment to clean surfaces. (II) Rinsing and drying with care to avoid evaporative drying. (III) Holding the wafer in an upside down position during growth, to prevent dusting and attendant spike formation. (IV)  $GeI_2$  concentrations, expressed in terms of HI pressure, in the range 5-35 Torr. (V) Linear gas stream velocities, referred to room temperature, greater than 50 cm/min.

#### Acknowledgments

The authors wish to thank M. Sampogna for his assistance with the epitaxial reactor, and R. L. Rohr,

J. A. Petriello, and C. X. Duncombe for the polished substrates, and J. Angilello for the x-ray work.

Manuscript submitted Feb. 2, 1968; revised manuscript received ca. May 8, 1968. This paper was presented at the Chicago Meeting, Oct. 15-19, 1967, as Paper 160.

Any discussion of this paper will appear in a Discussion Section to be published in the June 1969 JOURNAL.

#### REFERENCES

1. J. C. Marinace, *IBM J. Res. & Dev.*, **4**, 248 (1960).
2. A. Reisman and M. Berkenblit, *This Journal*, **112**, 315 (1965).
3. A. Reisman and S. A. (Alyanaky) Papazian, *ibid.*, **111**, 1154 (1964).
4. A. Reisman, M. Berkenblit, and S. A. (Alyanaky) Papazian, *ibid.*, **112**, 241 (1965).
5. A. Reisman and M. Berkenblit, *ibid.*, **113**, 147 (1966).
6. A. Reisman and R. L. Rohr, *ibid.*, **111**, 1425 (1964).
7. M. V. Sullivan and L. A. Pompliano, *ibid.*, **108**, 60C (1961).
8. R. K. Willardson and H. L. Goering, "Compound Semiconductors," Vol. 1. "Preparation of III-V Compounds," Reinhold Publishing Corp. (1962); J. W. Faust, Jr., "Etching of the III-V Intermetallic Compounds."
9. V. J. Silvestri, Presented at the Chicago Meeting, Oct. 16-18, 1967, Abstract 163.
10. H. Cole and N. R. Stemple, *J. Appl. Phys.*, **33**, 227 (1962).
11. S. A. Papazian and A. Reisman, Presented at the Chicago Meeting, Oct. 16-18, 1967, Abstract 159.
12. T. B. Light, M. Berkenblit, and A. Reisman, *This Journal*, **115**, 969 (1968).
13. H. N. Yu and F. H. Dill, Presented at the Washington, D. C. IEEE Meeting, Oct. 18-20, 1967, Abstract 26.4.
14. A. E. Stock, "Hydrides of Boron and Silicon," Cornell Univ. Press (1933).
15. R. M. Adams, "Boron Metallo-Boron Compounds and Boranes," John Wiley & Sons, New York (1964).

## Plastic Deformation in Epitaxial Ge Layers Grown on Single Crystal Semi-Insulating GaAs

T. B. Light, M. Berkenblit,\* and A. Reisman\*

IBM Watson Research Center, Yorktown Heights, New York

#### ABSTRACT

The compatibility of Ge and GaAs, in terms of their temperature dependent mechanical properties, is described in this paper. Examination at room temperature of epitaxial Ge layers grown on wafers of single crystal, semi-insulating GaAs, at substrate temperatures of  $700^\circ C$  by pyrolytic dissociation of  $GeH_4$ , reveals evidence of plastic deformation immediately following the epitaxial deposition process. Plastic deformation is observed in epitaxial Ge layers grown at  $350^\circ C$ , by disproportionation of  $GeI_2$ , only after a subsequent annealing cycle to at least  $500^\circ C$ . The low substrate temperature Ge films, however, show elastic bending of thin substrates after deposition and cooling to room temperature. Based on these observations, it is possible to estimate the differential thermal expansion coefficient between Ge and GaAs ( $1 \times 10^{-6}/^\circ C$ ), and to use this result to estimate the critical shear stress for plastic deformation under low strain rate conditions ( $6.7 \times 10^7$  dynes/cm<sup>2</sup>). Interface dislocations are not observed.

The present work was prompted by observations made during the course of the work described by Papazian and Reisman (1), and by the present authors (2). Plastic deformation of the Ge epitaxial layers

grown on semi-insulating GaAs substrates was observed. This observation seemed inconsistent with the considerations that have motivated much work with the Ge/GaAs hetero-epitaxial system. These considerations, which were discussed by Amick (3) are: (i) same

\* Electrochemical Society Active Member.



crystal type; (ii) lattice parameter match within 1/10%; and (iii) indications of a good coefficient of thermal expansion match. The last assumption is questionable, at least as to whether the match is good enough.

In the present work, observations are made regarding the presence or absence of plastic deformation in Ge layers on GaAs substrates as a function of deposition temperature or annealing treatments. Slip line observations are correlated with the known slip planes and directions. Observations made from elastically bowed and plastically deformed samples are used to estimate the differential thermal coefficient of expansion between Ge and GaAs and to estimate the critical shear stress for Ge under low strain rate conditions.

### Experimental Procedure

The substrates used in this study were fabricated from Cr doped semi-insulating GaAs single crystals obtained from Monsanto or grown by S. E. Blum of this laboratory. (110) oriented substrates were prepared for epitaxial growth as described by Berkenblit *et al.* (2), and 5-10  $\mu\text{m}$  thick Ge epitaxial layers were grown using the  $\text{GeI}_2$  disproportionation reaction at 350°C (2) and the  $\text{GeH}_4$  pyrolytic decomposition reaction at 600°-700°C as described by Papazian and Reisman (1).

Slip steps resulting from plastic deformation were observed using the Nomarski interference contrast technique. This technique is capable of resolving step heights as small as 30Å (4). The presence of plastic deformation was inferred from the presence of slip steps. The validity of this inference was checked using x-ray topographs obtained with the scanning oscillator technique (5).

Elastic bowing of thin GaAs substrates after epitaxial Ge deposition was detected by measuring the surface profile across the front and back surfaces of the substrates before and after Ge deposition. A microscope with a 45X objective and vertical fine focus adjustment with 1  $\mu\text{m}$  scale divisions was used. The microscope stage was used to translate the wafer by 1 mm intervals as profile readings were made. The method was capable of determining profiles to within  $\pm 2 \mu\text{m}$ .

In some instances, Ge was selectively removed from the GaAs substrate using standard photolithographic masking techniques and etching with a 1:2 solution of 30%  $\text{H}_2\text{O}_2$  in water at a temperature of 40°C. The ratio of Ge to GaAs etch rates in this etchant is greater than 1800:1.

**Crystallographic considerations.**—Germanium plastically deforms by glide (slip) on the {111} planes, in the  $\langle 110 \rangle$  directions (6) (see Appendix.).

Figure 1 shows the situation as it applies to a (110) oriented wafer. Two {111} slip planes are perpendicular to the surface of the wafer along lines of intersection in the  $[\bar{1}12]$  and  $[\bar{1}\bar{2}1]$  directions (Fig. 1a), and two intersect the surface at 35° 16' along lines of intersection that are parallel and along the  $[\bar{1}10]$  direction (Fig. 1b).

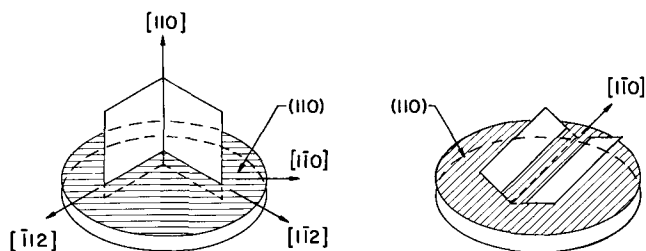


Fig. 1. Relationship between {111} slip planes and (110) surface of wafer. (a) {111} planes intersecting along lines in  $\langle 112 \rangle$  directions; (b) {111} planes intersecting along lines in  $\langle 1\bar{1}0 \rangle$  direction.

### Results

**Low-temperature deposition (350°C).**—After the Ge layer was grown (at 350°C) and the sample cooled to room temperature, no slip steps were observable. X-ray transmission topographs (Fig. 2) showed no evidence for plastic deformation or interface dislocations. The Ge layer was, however, in elastic compression. Figure 3 shows the profile of a 63  $\mu\text{m}$  thick GaAs wafer with a 10  $\mu\text{m}$  thick Ge epitaxial layer. Before deposition the profile was flat within  $\pm 2 \mu\text{m}$ . The maximum deflection in this case is 160  $\mu\text{m}$ . Assuming a mismatch of the thermal coefficients of expansion, the resulting configuration (Ge side convex) indicates that the GaAs has contracted a larger amount during cooling from the growth temperature. The GaAs exerts a compressive force on the Ge layer.

If a sample is heated to 500°C or above, either directly after growth at 350°C or after first cooling to room temperature, the Ge layer shows slip lines along the  $[\bar{1}10]$  direction as shown in Fig. 4. There are two resolvable sets of slip lines, with the lines of one set having the opposite contrast compared to those of the other set. The presence of two sets of slip lines is more clearly demonstrated if the surface is about 2° off orientation with respect to the (110) planes as shown in Fig. 5. In this case the light and dark contrast lines are not parallel. Consideration of Fig. 1b will show that if the wafer surface is not parallel to the (110) plane, the slip lines due to one set of planes (111) will not be parallel to the slip

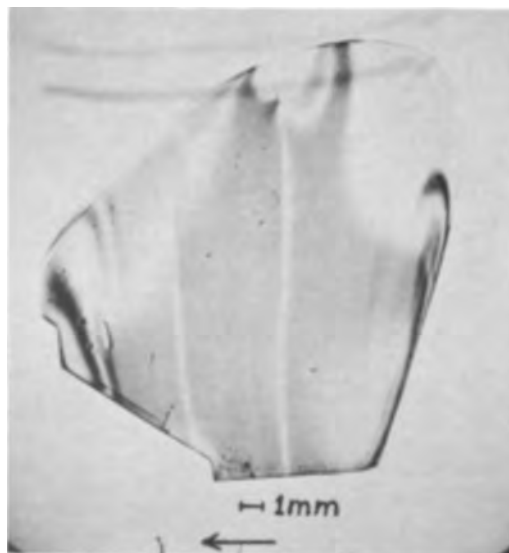


Fig. 2. Transmission (SOT) x-ray topograph of low-temperature Ge deposit (10  $\mu\text{m}$ ) on GaAs substrate (125  $\mu\text{m}$ ). The arrow indicates the direction of the  $[220]$  diffraction vector ( $\text{AgK}\alpha$  radiation).

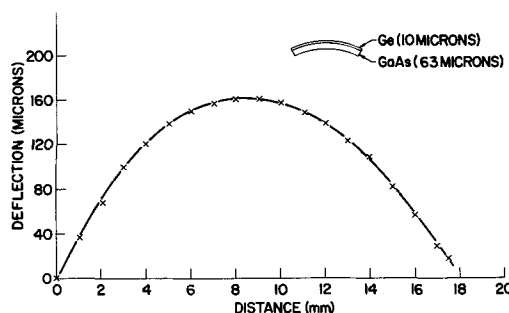


Fig. 3. Elastic deflection profile of low-temperature Ge deposit on a thin GaAs substrate.



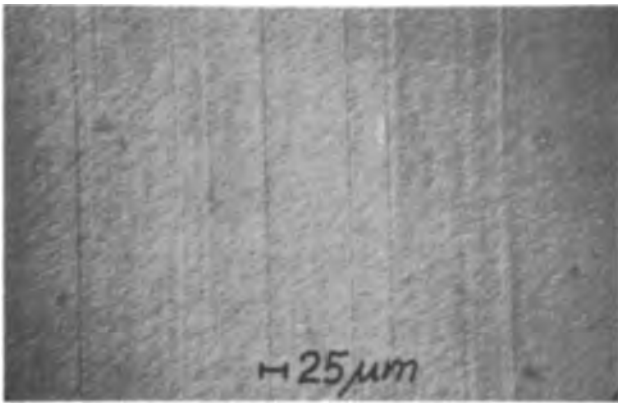


Fig. 4. Photomicrograph showing slip steps parallel to  $[1\bar{1}0]$  direction in low-temperature Ge deposit on GaAs substrate after heating to  $500^\circ\text{C}$ .

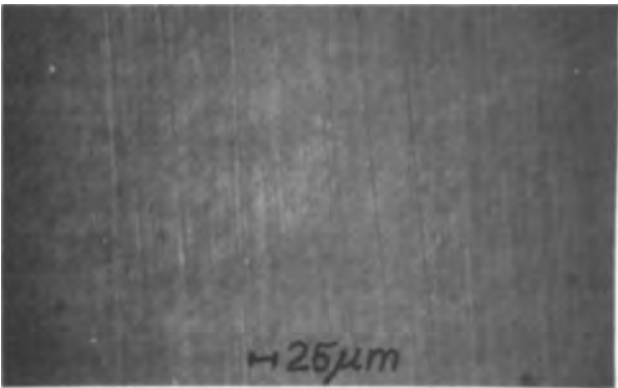


Fig. 5. Photomicrograph showing two nonparallel sets of slip steps in low-temperature Ge deposit on GaAs substrate  $2^\circ$  off orientation after heating to  $500^\circ\text{C}$ .

lines due to the other set of planes  $(1\bar{1}\bar{1})$ . This is true except when the line of intersection between the tilted surface and the  $(110)$  plane is the  $[1\bar{1}0]$  direction.

If the Ge layer is selectively removed from the GaAs substrate by masking and etching in  $\text{H}_2\text{O}_2$  solution (Fig. 6), the offsets of the slip lines at the  $10\ \mu\text{m}$  Ge-GaAs steps due to the  $35^\circ 16'$  inclinations of the  $\{111\}$  slip planes with respect to the  $(110)$  surface can be observed. Note that the light and dark contrast slip lines correspond to opposite offsets. In this figure, the slip steps are still visible on the GaAs surface. The 1800:1 ratio of Ge etch rate to GaAs etch rate and the length of exposure of the bare GaAs surface to the etch precludes the possibility that these steps are due

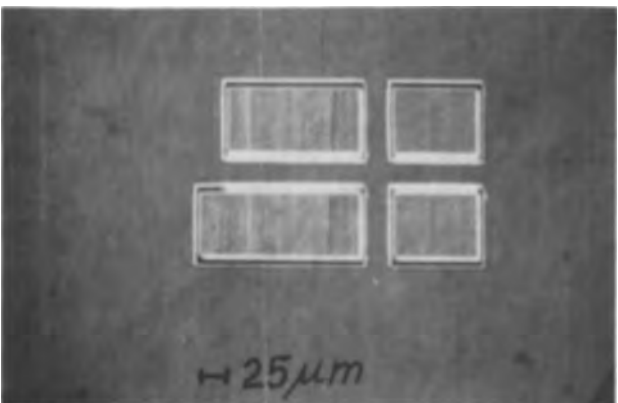


Fig. 6. Photomicrograph showing slip steps on original Ge deposit surface (4 islands) and on GaAs substrate surface after selective removal of Ge layer.

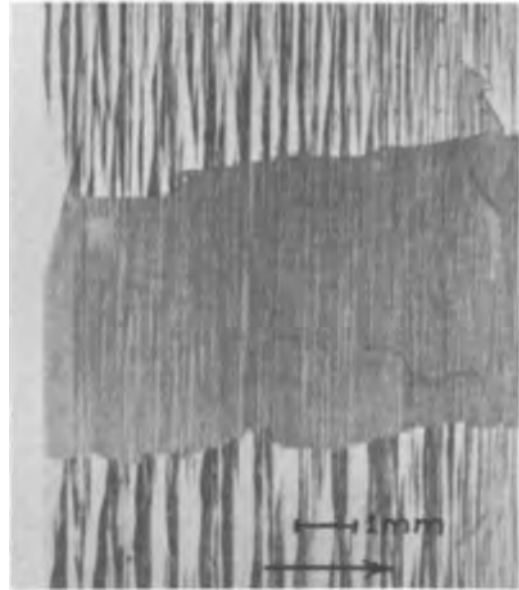


Fig. 7. Berg-Barrett reflection topograph of GaAs substrate with Ge layer selectively removed in center region. The arrow indicates the projection of the  $[333]$  diffraction vector onto the wafer surface ( $\text{CuK}\alpha$  radiation).

to replication of the surface topography, and the offset would not be observed if replication were occurring. Thus the presence of these slip steps on the GaAs surface indicates that the GaAs had been plastically deformed near the Ge/GaAs interface. A Berg-Barrett x-ray reflection topograph (Fig. 7) of a sample with the Ge layer removed in the central region confirmed that plastic deformation had occurred in the GaAs substrate.

*High-temperature deposition ( $600^\circ\text{--}700^\circ\text{C}$ ).*—In samples deposited at  $600^\circ\text{--}700^\circ\text{C}$ , three sets of slip steps were observed in the Ge layer after it was cooled to room temperature. This indicates that all four  $\{111\}$  slip planes were active at the higher temperatures. The slip steps due to the perpendicular slip planes,  $(\bar{1}11)$  and  $(111)$ , are more difficult to detect. The area in Fig. 8 has all three sets but only two can be seen clearly. An x-ray reflection topograph (Fig. 9) shows all three sets clearly.

### Discussion

The results can be summarized with the help of Fig. 10. The solid curve indicates schematically the variation with temperature of the critical stress for plastic yielding in the Ge layer. Assuming a difference in the thermal coefficients of expansion for Ge and GaAs, the dashed curves indicate schematically how the stress in the Ge layer would build up as the

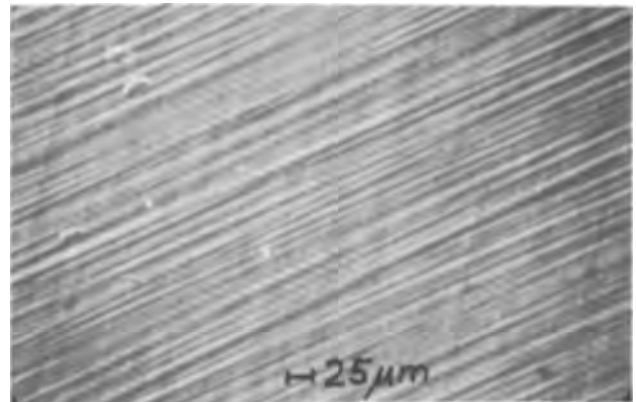


Fig. 8. Photomicrograph showing two visible sets of slip steps in high-temperature deposit of Ge on GaAs substrate; third set is not visible.

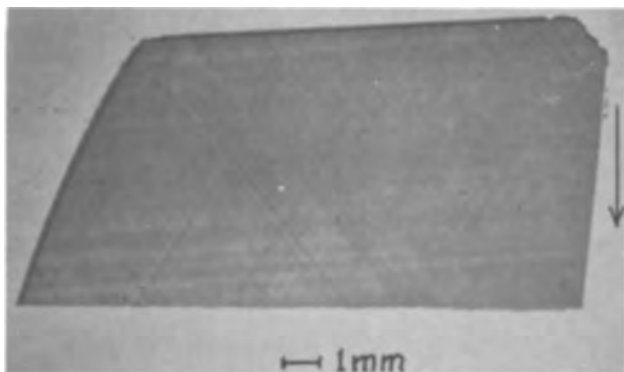


Fig. 9. Berg-Barrett reflection topograph of high-temperature Ge deposit on GaAs substrate. The arrow indicates the projection of the  $[333]$  diffraction vector onto the wafer surface (CuK $\alpha$  radiation).

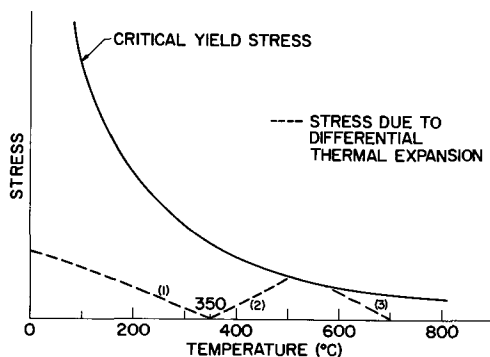


Fig. 10. Schematic showing behavior of critical yield stress and stress due to thermal expansion as a function of temperature. Solid line, schematic behavior of critical yield stress for Ge vs. temperature; dashed lines, stress due to differential thermal expansion between Ge and GaAs (assumed zero at deposition temperature).

temperature increases or decreases from the deposition temperature.

An elastic compressive stress was present after the sample had been cooled to room temperature after deposition at 350°C (curve 1). When the sample was heated from its deposition temperature of 350°C to higher temperatures (curve 2), a tensile stress was expected, and it has been determined that plastic yielding occurs at 500°C, *i.e.*, curve 2 intersects the critical yield stress curve at 500°C. If the Ge layer was deposited at high temperature and cooled to room temperature (curve 3), it was expected that the film would be stressed in compression and it has been determined that the film yields plastically at some relatively high temperature.

In the case of low-temperature Ge deposits heated to 500°C, plastic deformation occurred only by slip on two,  $(111)$  and  $(1\bar{1}\bar{1})$ , out of the four possible slip planes, whereas the high temperature Ge deposits plastically deformed by slip on all four  $\{111\}$  slip planes. This difference of behavior indicates that in the first case the critical shear stress (at 500°C) was exceeded in the  $(111)$  and  $(1\bar{1}\bar{1})$  slip planes only, while in the second case the critical shear stress (at approx. 600°C) was exceeded on all four slip planes. If the thermal coefficient of expansion mismatch provides the driving force for stress in the Ge layer, it can be assumed as a first approximation that the stress is confined to directions in the  $(110)$  plane.

From the discussion in the Appendix, and referring to Fig. 1, it is seen that the  $(\bar{1}\bar{1}\bar{1})$  and  $(1\bar{1}\bar{1})$  planes are perpendicular to the  $(110)$  plane (Fig. 1a). Considering the  $(\bar{1}\bar{1}\bar{1})$  plane, the component of stress in the  $[110]$  slip direction normal to the  $(110)$  plane is nominally zero. The components of stress in the  $[0\bar{1}\bar{1}]$  and  $[10\bar{1}]$

slip directions are in metastable equilibrium with the components in the  $[01\bar{1}]$  and  $[\bar{1}0\bar{1}]$  directions respectively so that there is no net slip, but this balance is easily upset by deviations from the assumed ideal situation. The same argument holds for the  $(111)$  plane.

The  $(111)$  and  $(1\bar{1}\bar{1})$  planes are at an angle of 35°16' with the  $(110)$  plane (Appendix). Considering the  $(111)$  plane, for example, there is a finite component of stress parallel to the  $[0\bar{1}\bar{1}]$  and  $[\bar{1}0\bar{1}]$  directions which gives rise to a shear couple acting across the slip plane. The resulting slip will cause slip steps parallel to the  $[1\bar{1}0]$  direction. The same argument holds for the  $(1\bar{1}\bar{1})$  plane except that the shear couple is reversed and a slip step of opposite sign will develop on the same surface and parallel to the  $[1\bar{1}0]$  direction.

The observed slip line configuration on the low-temperature Ge deposits heated to 500°C is that which would be expected from the above considerations. The observed slip on all four  $\{111\}$  slip planes for the high-temperature Ge deposit is probably the combined result of the lower critical yield stress at higher temperature and deviations from the idealized planar stress configuration assumed.

**Stress calculations.**—Some quantitative estimates of stress buildup and differential coefficient of expansion can be obtained from measurement of substrate bowing following deposition of low temperature films. Thus, the stress in the film can be calculated knowing the maximum substrate deflection. If it is then assumed that this stress is due to the differential coefficient of expansion,  $\Delta\alpha = \alpha_{\text{GaAs}} - \alpha_{\text{Ge}}$ , then  $\Delta\alpha$  can also be estimated from the maximum deflection. An estimate of the critical yield stress of the film at 500°C can then be obtained from this value of  $\Delta\alpha$ .

The formulas relating maximum deflection ( $\delta_{\text{max}}$ ),  $\Delta\alpha$  and the maximum stress ( $\sigma_{\text{max}}$ ) in bimetallic elements have been developed by Timoshenko (7). They hold for cases from thin films on thick substrates up to cases involving layers of equal thickness. Consequently, these equations are applicable to the present results where the ratio of film to substrate thickness is 10/63. The maximum deflection is given by

$$\delta_{\text{max}} = 3A \cdot \Delta\alpha \cdot \Delta T \cdot d^2/4(t_f + t_s) \quad [1]$$

where  $\Delta T$  is the temperature difference between the temperatures of deposition and measurement,  $d$  is the wafer diameter,  $t_f$  is the film thickness,  $t_s$  is the substrate thickness, and  $A$  is a function of the ratios  $t_f/t_s$  and  $E_f/E_s$ , where  $E$  is Young's modulus. For a measured deflection of 160  $\mu\text{m}$  and  $\Delta T = 325^\circ\text{C}$ , the estimated differential thermal expansion is  $\Delta\alpha = 1.2 \times 10^{-6}/^\circ\text{C}$ .

The maximum stress in the film,  $\sigma_{\text{max}}$ , is given by

$$\sigma_{\text{max}} = \frac{8 \delta_{\text{max}}}{d^2(1-\nu)} \left[ \frac{1}{6(t_f + t_s)t_f} (E_f t_f^3 + E_s t_s^3) + \frac{t_f E_f}{2} \right] \quad [2]$$

where the symbols have the same meaning as in Eq. [1], and  $\nu$  is Poisson's ratio (assumed the same for both materials and = 0.27). For the measured deflection of 160  $\mu\text{m}$  the estimated stress is  $\sigma_{\text{max}} = 4.8 \times 10^8$  dynes/cm $^2$ .

Equation [2] can be simplified by neglecting  $t_f$  compared to  $t_s$ , yielding Eq. [3] (8)

$$\sigma_{\text{max}} = \frac{4E_s t_s^2 \delta_{\text{max}}}{3(1-\nu)t_f d^2} \quad [3]$$

The calculation using this simplified relation results in the value  $\sigma_{\text{max}} = 5.1 \times 10^8$  dynes/cm $^2$  which is in excellent agreement with the result using Eq. [2].

Combining Eq. [1] and [3] yields an expression for the stress in terms of  $\Delta\alpha$  and  $\Delta T$ . An estimate of the

critical yield stress of the Ge film at 500°C can be made using the calculated differential thermal expansion ( $\Delta\alpha \approx 1 \times 10^{-6}/^\circ\text{C}$ ) and  $\Delta T = 150^\circ\text{C}$  (350°-500°C). The value estimated is  $1.9 \times 10^8$  dynes/cm<sup>2</sup>, which is equivalent to a critical resolved shear stress (i.e., component in the slip plane along the slip direction) of  $6.7 \times 10^7$  dynes/cm<sup>2</sup>. The estimated strain rate, which is calculated from the heating rate, is  $2 \times 10^{-6}$ /sec. The data of Bell and Bonfield (9) yields an extrapolated value of  $5.5 \times 10^7$  dynes/cm<sup>2</sup> at the same strain rate and temperature, for Ge with a dislocation density of approx.  $1 \times 10^6/\text{cm}^2$ .

**Relative coefficients of thermal expansion.**—Fig. 11 shows the available data for the coefficients of thermal expansion of polycrystalline Ge (solid line) and GaAs (dashed lines). The horizontal lines indicate that a constant value was quoted for the temperature range shown. The referenced data are for powdered (3, 10, 11) or polycrystalline (12, 13) specimens, except for the portion of the Ge curve below room temperature which was determined using a single crystal with  $\langle 100 \rangle$  orientation (14). The results given as a constant were determined by x-ray lattice parameter measurements (3, 10, 11), and the rest were determined using interference dilatometry.

The value,  $\Delta\alpha \approx 1 \times 10^{-6}/^\circ\text{C}$ , calculated above seems consistent with the GaAs data of Pierron, Parker, and McNeely (11) relative to the data for Ge. The data points shown in Fig. 11 were determined by Feder and Light (15) for a  $\langle 110 \rangle$  oriented single crystal of Cr doped semi-insulating GaAs, using a Fizeau type interferometer with a laser light source (16). The calculated value for  $\Delta\alpha$  is not consistent with the GaAs data of Feder and Light relative to the data for polycrystalline Ge. Efforts to obtain data for single crystal Ge above room temperature are in progress.

**Slip and lattice parameter mismatch.**—No evidence for mismatch dislocations, due to the small lattice parameter mismatch between Ge and GaAs, has been found in this study. Two previous studies have been concerned with the nature of imperfections in Ge/GaAs couples. Meieran studied GaAs layers on Ge substrates (17), and found slip which he concluded probably was due to the mismatch between lattice parameters. Krause and Teague studied Ge layers on semi-insulating GaAs substrates (18), and found effects that they concluded were due to misfit dislocations at the interface. In both cases the epitaxial deposition temperature was greater than 700°C. It is evident from the present study that plastic deformation due to the differential coefficient of thermal expansion is present in both of these previous studies. It is also evident from the present study that, if plastic deformation can be avoided by deposition at lower substrate temperatures, the presence of interface dislocations can be determined unambiguously.

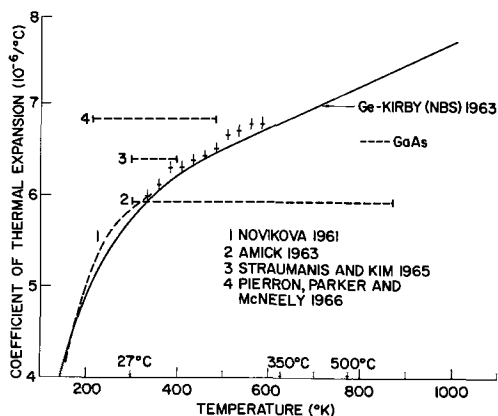


Fig. 11. Thermal coefficient of expansion as a function of temperature for Ge and GaAs.

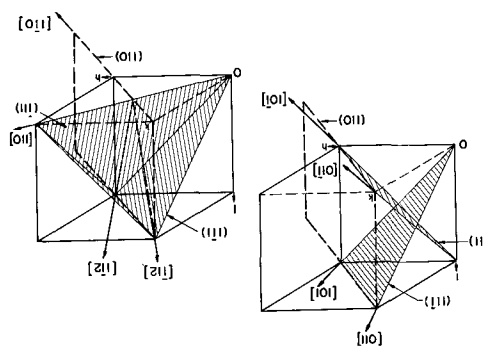


Fig. 12. Unit cubes showing relationship between  $\{111\}$  slip planes,  $\langle 110 \rangle$  slip directions, and  $(110)$  orientation of wafers.

X-ray topographs (Fig. 2) indeed show no evidence for interface dislocations and indicate that the interface is completely coherent.

### Conclusions

1. Ge layers deposited at low temperature (350°C) on semi-insulating GaAs substrates are not plastically deformed, but are under elastic compressive stress.
2. The low deposition temperature Ge layers plastically deform when heated to 500°C or above.
3. Ge layers deposited at higher temperatures (600°-700°C) are plastically deformed when observed at room temperature.
4. The driving force for stress is the differential coefficient of thermal expansion between Ge and GaAs.
5. Interface dislocations are not present at the Ge/GaAs interface.

### APPENDIX

**Diamond cubic structure, slip planes, and slip directions.**—There are four sets of  $(111)$  planes in the diamond cubic (Ge) crystal structure. These are the  $(111)$ ,  $(1\bar{1}\bar{1})$ ,  $(\bar{1}11)$  and  $(\bar{1}\bar{1}1)$  planes indicated by shading in Fig. 12a and 12b. The six-slip directions  $[0\bar{1}1]$ ,  $[\bar{1}01]$ ,  $[011]$ ,  $[101]$ ,  $[110]$  and  $[\bar{1}\bar{1}0]$  in Fig. 12a and 12b are indicated by arrows. The  $(110)$  plane, which corresponds to the wafer surface under observation, and its relation to the unit cubic cell is shown by the dashed outline which extends out of the cube. The  $(111)$  and  $(1\bar{1}\bar{1})$  planes, shaded in Fig. 12a, intersect the  $(110)$  plane along parallel lines in the  $[\bar{1}\bar{1}0]$  direction. The acute angle between either of these slip planes and the  $(110)$  plane is  $35^\circ 16'$ . The  $(\bar{1}11)$  and  $(\bar{1}\bar{1}1)$  planes, shaded in Fig. 12b, intersect the  $(110)$  plane along lines in the  $[\bar{1}\bar{1}2]$  and  $[\bar{1}12]$  directions, and are perpendicular to the  $(110)$  plane. These directions make an acute angle of  $54^\circ 44'$  with the  $[110]$  direction.

All of the  $\langle 110 \rangle$  slip directions, except the  $[110]$  direction, have a component perpendicular to the  $(110)$  plane and can thus give rise to slip steps observable on a  $(110)$  oriented surface. Slip on the  $(111)$  and  $(1\bar{1}\bar{1})$  planes would result in slip steps parallel to the  $[110]$  direction, and slip on the  $(\bar{1}11)$  and  $(\bar{1}\bar{1}1)$  planes would result in slip steps parallel to the  $[\bar{1}\bar{1}2]$  and  $[\bar{1}12]$  directions, respectively.

### Acknowledgments

The authors wish to thank Dr. A. Segmuller for preparing and interpreting the x-ray topographs, and Miss S. Sharpe and Mr. M. Sampogna for technical assistance.

Manuscript submitted Mar. 11, 1968; revised manuscript received June 7, 1968. This paper was presented at the Chicago Meeting, Oct. 15-19, 1967, as Paper 161.

Any discussion of this paper will appear in a Discussion Section to be published in the June 1969 JOURNAL.

## REFERENCES

1. A. Papazian and A. Reisman, *This Journal*, **115**, 961 (1968).
2. M. Berkenblit, A. Reisman, and T. B. Light, *ibid.*, **115**, 966 (1968).
3. J. A. Amick, *RCA Rev.*, **24**, 555 (1963).
4. G. Nomarski and A. R. Weill, *Rev. Metallurgie*, **52**, 121 (1955).
5. G. H. Schwuttke, *J. Appl. Phys.*, **36**, 2712 (1965).
6. H. G. Van Bueren, "Imperfections in Crystals," p. 613, North-Holland Publishing Co., Amsterdam (1960).
7. S. Timoshenko, *J. Opt. Soc. Am.*, **11**, 233 (1925).
8. R. W. Hoffman, "Physics of Thin Films," Vol. 3, p. 222, G. Hass and R. Thun, Editors, Academic Press, New York (1966).
9. R. L. Bell and W. Bonfield, *Phil. Mag.*, **9**, 9 (1964).
10. M. E. Straumanis and C. D. Kim, *Acta Cryst.*, **19**, 256 (1965).
11. E. D. Pierron, D. L. Parker, and J. B. McNeely, *ibid.*, **21**, 290 (1966).
12. S. I. Novikova, *Sov. Phys. Sol. State*, **3**, 129 (1961).
13. R. K. Kirby, AIP Handbook 2nd ed., Section 4f, pp. 4-64, McGraw-Hill Book Co., New York, (1963).
14. D. F. Gibbons, *Phys. Rev.*, **112**, 136 (1958).
15. R. Feder and T. B. Light, Submitted for publication.
16. R. Feder and H. P. Charbneau, *Phys. Rev.*, **149**, 464 (1966).
17. E. S. Meieran, *This Journal*, **114**, 292 (1967).
18. G. D. Krause and E. C. Teague, *Appl. Phys. Letters*, **10**, 251 (1967).

# Technical Notes



## Implantation and Detection of Low Energy Argon Ions in Silicon Single Crystals

James Comas<sup>1</sup> and Carmine A. Carosella

Naval Research Laboratory, Washington, D. C.

Although there have been many applications of the sputtering technique, *e.g.*, the production of thin semiconducting films, the cleaning of surfaces, and the formation of thin protective layers on solar devices, there is still much to be learned about the interaction between the bombarding primary and the target. The sequence of events leading to the ejection of surface atoms as the target is subjected to energetic gas bombardment has not yet been clearly established. One of the present problems in the construction of a consistent sputtering model is to determine the fate of the bombarding species.

Work focused on this aspect of the sputtering phenomenon has been based primarily on the detection of the released primary with a mass analyzer. Thermal desorption or resputtering the target with a different gas and recording the release of the first bombarding species are the methods usually employed. Primary release spectra obtained by Kornelson and Sinha (1), Erent and Carter (2), and Colligon and Leck (3) show peaks which are believed due to different trapping configurations and penetration depths. Re-emission investigations indicate that the damage produced by the bombarding species can act as trapping sites. Carmichael and Trendelenburg (4) have used ion induced re-emission to investigate the depth distribution of trapped atoms. From pumping speed measurements Winters (5) has obtained the sticking probability as a function of argon ion energy in the 80-300 ev range for Ni and Mo. This paper reports on a method of bombarding silicon in the 100-2200 ev range with argon and the detection of the implanted species *in situ*.

### Experiment

A schematic of the bombarding apparatus is shown in Fig. 1. The means of obtaining an argon plasma is similar to that previously used in sputtering experiments (6), the major difference being the extraction and further acceleration of the argon ions. The arrangement is placed in a 12-in. bell jar vacuum system which is evacuated with a 300 liter/sec frac-

tionating oil diffusion pump. The system is initially pumped down to a base pressure of about  $5 \times 10^{-6}$  Torr and then argon is leaked continuously into the system to a pressure of about  $5 \times 10^{-4}$  Torr. Electrons emitted from the tungsten filament F are accelerated through a slit in the ionization chamber I; the accelerating potential is adjusted (60v) to minimize the  $A^{++}$  content. This primary electron beam is collimated along the slit-filament alignment E-E by the magnetic field B (100 gauss). Under proper operating conditions a thermionically sustained, magnetically confined, arc discharge is struck and is spatially confined in the ionization chamber.

The stainless steel screen S, which is placed about 3 mm below the primary electron beam, acts essentially as a Langmuir probe when biased negative with respect to the plasma. Argon ions are drawn out of the plasma region, and those that pass through the screen are further accelerated between the screen and the target by applying a negative potential to the target with respect to the screen. A graphite ring is placed above the target and is at the same potential. This guard ring eliminates misleading edge effects and clearly defines the area of bombardment. With such an arrangement the bombarding energy range can be extended from 100 to 2200 ev with target currents in the order of 1-2 ma.

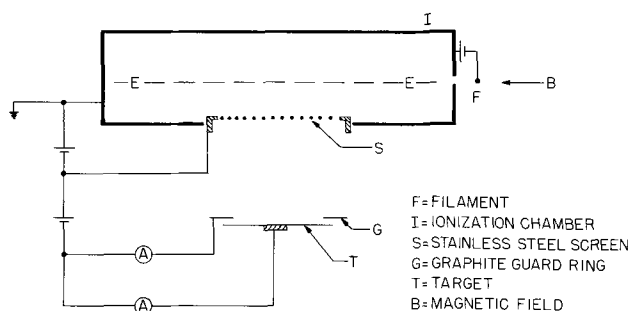


Fig. 1. Schematic of the bombarding apparatus

<sup>1</sup> NRC Postdoctoral Research Associate.

The targets used were thin (111) n-type (0.1 ohm cm) silicon wafers about 1 in. in diameter. They were chemically etched in a hydrofluoric, nitric, acetic acid solution and rinsed with ethyl alcohol prior to being sputtered. Aquadag was used to contact the samples to a stainless steel target mount. Various experiments, e.g., heating aquadag coated Si targets in an argon plasma, were performed to ensure that the observed argon was not due to adsorption by the contacts or the target. Erosion of a surface by noble gas bombardment releases trapped atoms, however, an equilibrium is soon reached between the trapping and implantation rates (3). Sputtering times were long enough to ensure an equilibrium condition between the impinging argon and the trapped argon being released as the surface is sputtered away. All samples were bombarded for 2 hr with a current of 1.3 ma.

After argon bombardment the targets were removed from the sputtering apparatus and placed in NRL's nuclear reactor for activation. The samples were placed in a neutron flux of  $10^{13}$  n/sec for 1 hr. The neutron activation produces  $A^{41}$ , which in the decay process emits a 1.293 gamma ray. A lithium-drifted germanium detector, used in conjunction with a multichannel analyzer, was used to obtain the gamma spectrum in this energy region. The system can resolve peaks 5 kev apart, which is sufficient to separate the only interfering gamma ray, a 1.265 Mev gamma from the decay of  $Si^{31}$ . To ensure that the counting geometry is the same for all samples they are placed in a Plexiglas holder fixed to the detector.

One of the main problems in making an absolute measurement of the argon content was in obtaining a suitable standard having the same geometry as the bombarded silicon. Containers for encapsulating air proved impracticable due to the masking of the argon signal by the container's high radioactivity. A method, very similar to that used by Woodman (7), was devised so as to irradiate air (0.94% argon) in a sealed quartz capsule and then to transfer the air into an evacuated glass container for counting. The glass container into which the irradiated air is transferred has approximately the same geometry as a silicon disk. A manometer was used to measure the air pressure in the transfer system. The activated argon in the irradiated air was counted in the same geometrical arrangement as the bombarded silicon. The activity of the argon in the container was then used as a standard to calculate the amount of trapped argon in the bombarded silicon samples.

### Results and Discussion

Typical data are shown in Fig. 2. The argon peak, identified by energy calibration of the detector with a  $Co^{60}$  source, as well as half-life measurements, is clearly resolved. Background counts due to the activation of natural argon by the reactor are eliminated by continuously flushing air from an external compressor through a sealed plastic bag surrounding the detector and sample, and by lead shielding. The initial

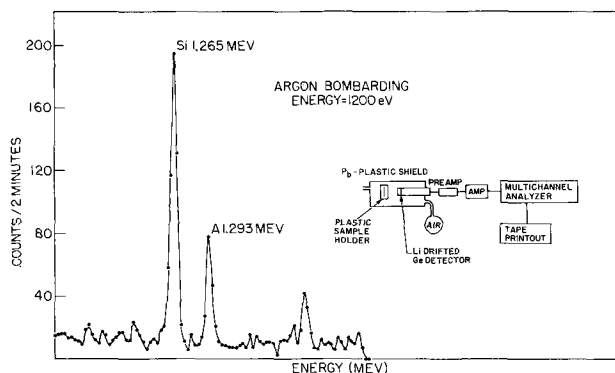


Fig. 2. Gamma ray spectrum of Si and A obtained from a Li drifted Ge detector 121 min after neutron activation.

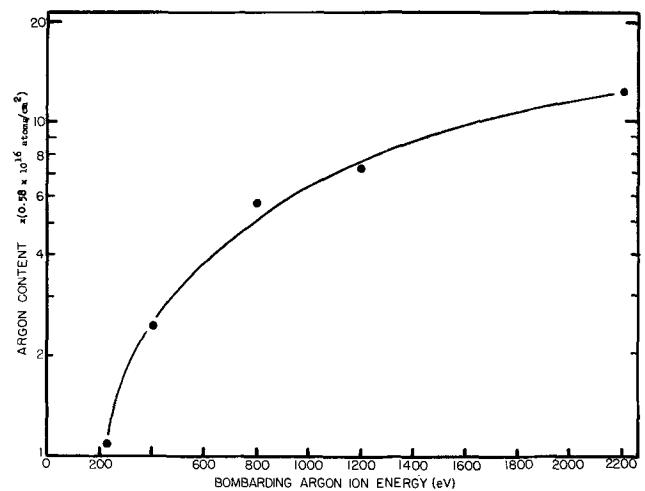


Fig. 3. Argon content in (111) Si vs. argon ion energy. Targets were bombarded for 2 hr with an argon ion beam of 1.3 ma.

argon activity in each sample is obtained from the extrapolation of half-life curves, the points being plotted as integrated argon peaks. It is estimated that the minimum amount of argon detectable is about  $10^{13}$  atoms.

Results of a series of bombarding experiments from 100 to 2200 ev are shown in Fig. 3. The argon content rises very sharply around 225 ev and appears to begin to reach a plateau around 2200 ev. No argon was detected at 100 ev. Winters, however, measured a sticking threshold at about 80 ev for  $A^+$  on Ni and Mo. At the present we are improving the sensitivity of the counting system and plan to investigate the low energy region in Si further.

The relative amount of argon trapped as a function of bombarding energy is consistent and reproducible. It is estimated, however, that a 20% error in the absolute argon content is possible due to errors in the calibration technique. At energies around 100 ev it may be that the argon does not penetrate far enough below the surface to be trapped. It may be that at low energies (around 100 ev) the sputtering process is a result of a surface rebounding mechanism as described by Harrison *et al.* (8). As the energy is increased the penetration depth is sufficient to cause disturbances several layers beneath the surface. The energy from these disturbances that reaches the surface can cause the ejection of a surface atom. The primary, having lost its energy in collisions with the target atoms, is trapped in an interstitial or substitutional position.

The data clearly show the applicability of the technique for the *in situ* measurement of trapped argon in sputtering studies. The possibility of subjecting the data to quantitative analysis allows one to calculate the probability of penetration as a function of bombarding energy.

### Acknowledgment

The authors wish to thank M. David Shores, Mr. Richard Vogt, and co-workers of the NRL Reactor Branch for their technical assistance and many helpful suggestions. Work on this paper was supported by NASA-Goddard Space Flight Center.

Manuscript submitted Feb. 19, 1968; revised manuscript received May 6, 1968. This manuscript was presented at the Chicago Meeting, Oct. 15-19, 1967, as Recent News Paper 34.

Any discussion of this paper will appear in a Discussion Section to be published in the June 1969 JOURNAL.

### REFERENCES

1. E. V. Kornelsen and M. K. Sinha, *Appl. Phys. Letters*, 9, 112 (1966).

2. K. Erents and A. Carter, *Vacuum*, **17**, 97, 215 (1967).
3. J. S. Colligon and J. H. Leck, Transactions 8 AVS National Vacuum Symposium, 1961, p. 275, Pergamon Press, Oxford (1962).
4. J. K. Carmichael and E. A. Trendelenburg, *J. Appl. Phys.*, **29**, 1570 (1958).
5. H. F. Winters, *J. Chem. Phys.*, **44**, 1472 (1966).
6. J. Comas and C. B. Cooper, *J. Appl. Phys.*, **37**, 2820 (1966).
7. F. J. Woodman, Windscale Reactor (England), Report No. A.R.D.C./P36 (1954).
8. D. E. Harrison, J. P. Johnson, and N. S. Levy, *Appl. Phys. Letters*, **8**, 33 (1966).

## Luminescence of $\text{Eu}^{3+}$ Activated Thorium, Alkali Metal Vanadates

H. L. Burrus and A. G. Paulusz

*Osram (G.E.C.) Research Laboratories, The General Electric Company Limited, Hirst Research Centre, Wembley, England*

Europium activated yttrium orthovanadate ( $\text{YVO}_4:\text{Eu}$ ) belongs to the class of host sensitized phosphors in which the exciting energy is absorbed mainly by the  $(\text{VO}_4)^{3-}$  groups and is subsequently transferred to the  $\text{Eu}^{3+}$  ion whence it is emitted as characteristic europium fluorescence (1). The efficiency of this process as a function of crystal structure has been discussed by Blasse (2). In  $\text{YVO}_4:\text{Eu}$  which has the zircon structure the transfer is particularly efficient (2). Other vanadates with this structure are therefore of interest in view of the current commercial applications of this phosphor in the television (3) and lighting industries (4). Such materials have been synthesized by Schwarz (5), and Avella has recently described the  $\text{Eu}^{3+}$  emission from compounds of the type  $\text{M}^{\text{IV}}\text{M}^{\text{II}}(\text{VO}_4)_2:\text{Eu}$  where  $\text{M}^{\text{II}}$  and  $\text{M}^{\text{IV}}$  are, respectively, divalent and tetravalent metals (6). We report here briefly on other vanadates with the zircon structure having the general formula  $\text{M}_2^{\text{IV}}\text{M}^{\text{I}}(\text{VO}_4)_3$ , where  $\text{M}^{\text{IV}}$  is thorium and  $\text{M}^{\text{I}}$  is a univalent alkali metal.

The materials were prepared by firing stoichiometric quantities of the appropriate luminescent grade oxides or carbonates with ammonium metavanadate in air at  $700^\circ\text{--}900^\circ\text{C}$  for up to 20 hr. X-ray diffraction examination of the products showed that  $\text{Th}_2\text{Li}(\text{VO}_4)_3$  and  $\text{Th}_2\text{Na}(\text{VO}_4)_3$  have the zircon-type crystal structure while the intended  $\text{Th}_2\text{K}(\text{VO}_4)_3$  proved to be a complex mixture of phases. The ionic radii of thorium (0.95Å) and sodium (0.95Å) are very close to that of yttrium (0.93Å). Lithium at 0.6Å is slightly smaller, but can fit into the structure quite well. Potassium (1.33Å) and the heavier alkali metals are apparently too large.

We briefly surveyed other possible compositions using in place of thorium the ions  $\text{Ge}^{4+}$ ,  $\text{Sn}^{4+}$ ,  $\text{Pb}^{4+}$ ,  $\text{Ti}^{4+}$ ,  $\text{Zr}^{4+}$  and  $\text{Ce}^{4+}$ , combining each in turn with  $\text{Li}^+$ ,  $\text{Na}^+$  and  $\text{K}^+$ . As the products in all cases were dark sintered masses, even when prepared with a 20% deficiency of vanadium, we did not examine them further.

When the thorium lithium and thorium sodium vanadates were prepared with a slight deficiency of vanadium the products had white body colors above  $300^\circ\text{C}$  but darkened rapidly on cooling below  $280^\circ\text{C}$ . As the change was reversible it may represent a phase transition at this temperature. Schwarz has found three phases in the system  $\text{PbTh}(\text{VO}_4)_2$  at different temperatures (5). The change can be prevented by incorporating an excess of cation (thorium and alkali metal), but as expected x-ray diffraction confirms the presence of excess thorium in the products.

The room temperature excitation and emission characteristics of the thorium lithium and thorium sodium compounds are compared with those of  $\text{YVO}_4$  in Fig. 1.

Under 365 nm excitation, the unactivated compounds give broad band yellowish green luminescence, peaking at 550 and 540 nm in the lithium and sodium compounds, respectively, and qualitatively similar to that reported for other vanadates (7). Addition of europium quenches this emission and gives rise to a brilliant  $\text{Eu}^{3+}$  spectrum similar in structure to that of  $\text{YVO}_4:\text{Eu}$ . However the lines are broadened approximately fivefold as was also reported by Avella for the II-IV vanadates. (Samarium and dysprosium give characteristic, but somewhat less intense emissions.) If europium is added according to the scheme  $2\text{Th}^{4+} + \text{M}^+ \rightarrow 3\text{Eu}^{3+}$ , charge compensation is unnecessary and the formula can then be written  $\text{Th}_{2-2x}\text{M}_{1-x}\text{Eu}_{3x}(\text{VO}_4)_3$ . The europium emission is at its brightest between  $x = 0.10$  and  $x = 0.25$ , with a maximum near  $x = 0.15$ . This is as expected for europium in the zircon structure according to the self-quenching mechanism proposed by Van Uitert and Johnson (8).

The excitation spectrum of  $\text{YVO}_4:\text{Eu}$  shows two prominent peaks at 320 nm and 250 nm. These have been ascribed to the first allowed electronic transition of the  $\text{VO}_4^{3-}$  group,  ${}^1\text{A}_1 - {}^1\text{T}_2$ , and a transition in the Y—O interaction center, respectively (1). The thorium lithium and thorium sodium compounds have excitation peaks at 330 and 336 nm respectively with a slight unresolved shoulder at approximately 275 nm.

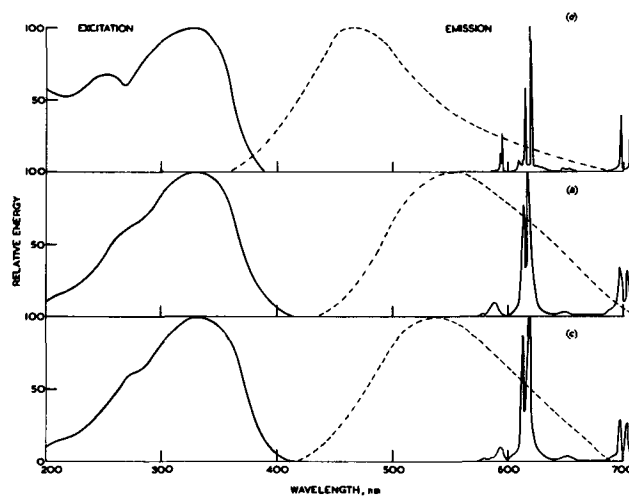


Fig. 1. Excitation and emission spectra of (a)  $\text{YVO}_4:0.05 \text{Eu}$ , (b)  $\text{Th}_2\text{Li}(\text{VO}_4)_3:0.15 \text{Eu}$ , (c)  $\text{Th}_2\text{Na}(\text{VO}_4)_3:0.15 \text{Eu}^{3+}$ . Dotted lines show the emission of the unactivated vanadates. All curves are normalized to 100 and discrete  $\text{Eu}^{3+}$  line absorptions have been omitted from the excitation spectra.

If the peaks correspond to the same transitions responsible for the  $\text{YVO}_4$  excitation spectrum, they have been shifted to longer wave lengths by 10-25 nm. The excitation at short wavelengths corresponding to the Y — O interaction in  $\text{YVO}_4$  is rather weak, and the phosphors are only poorly excited by 254 nm radiation and cathode rays.

Under 365 nm excitation,  $\text{YVO}_4:\text{Eu}$  shows a sharp increase in brightness as the temperature is raised. In all the complex vanadates we have examined there is a steady fall in brightness as the temperature is raised. An exception is  $\text{CaTh}(\text{VO}_4)$ , a compound reported by Avella (6), which peaks at about 160°C. However, the over-all brightness of this vanadate is rather poor. In contrast the thorium vanadates with lithium and sodium are much brighter than  $\text{YVO}_4:\text{Eu}$  at room temperature so that, although they fall in brightness with increasing temperature, they are about equal in brightness to  $\text{YVO}_4:\text{Eu}$  at 200°C. This is within the range of the bulb wall operating temperature of low wattage high-pressure mercury vapor lamps, so these phosphors could possibly find application for color correction in this type of lamp.

#### Acknowledgment

The authors are indebted to members of the Chemistry and Technical Services Division of the Hirst Research Centre for spectral and x-ray measurements.

Manuscript received May 16, 1968.

Any discussion of this paper will appear in a Discussion Section to be published in the June 1969 JOURNAL.

#### REFERENCES

1. R. K. Datta, *Trans. Metal Soc. AIME*, **239**, 355 (1967).
2. G. Blasse, *J. Chem. Phys.*, **45**, 2356 (1966).
3. A. K. Levine and F. C. Palilla, *Appl. Phys. Letters*, **5**, 118, (1964).
4. A. K. Levine and F. C. Palilla, *Appl. Optics*, **5**, 1467 (1967).
5. H. Schwarz, *Z. anorg. u. allgem. chem.*, **334**, 261 (1965).
6. F. J. Avella, *This Journal*, **113**, 855 (1966).
7. S. Rothschild, *Brit. J. Appl. Phys. Suppl.* **4**, S32 (1955).
8. L. G. Van Uitert and L. F. Johnson, *J. Chem. Phys.*, **44**, 3514 (1966).

## Fluorescence of $\text{Eu}^{2+}$ -Activated Barium Octaborate

G. Blasse, A. Brill, and J. de Vries

Philips Research Laboratories, N. V. Philips' Gloeilampenfabrieken, Eindhoven, Netherlands

A large number of  $\text{Eu}^{2+}$ -activated phosphors with high efficiencies for ultraviolet excitation have been reported recently by these laboratories (1-4). In this note the results of a study on the fluorescence of  $\text{Eu}^{2+}$ -activated alkaline earth borates are given. Five types of alkaline-earth borates exist, viz.,  $\text{Me}_3\text{B}_2\text{O}_6$  (Me = Ca, Sr, Ba),  $\text{Me}_2\text{B}_2\text{O}_5$  (Me = Ca, Sr),  $\text{MeB}_2\text{O}_4$  (Me = Ca, Sr, Ba),  $\text{MeB}_4\text{O}_7$  (Me = Ca, Sr, Ba), and  $\text{BaB}_8\text{O}_{13}$ . [For a list of these compounds see ref. (5)].

Only one efficient phosphor was found, viz.,  $\text{BaB}_8\text{O}_{13}:\text{Eu}^{2+}$ . This material shows a deep-blue emission under short-wavelength uv excitation.

#### Experimental

Samples were prepared by firing intimate mixtures of  $\text{CaCO}_3$ ,  $\text{SrCO}_3$ ,  $\text{BaCO}_3$ ,  $\text{Eu}_2\text{O}_3$ , and  $\text{H}_3\text{BO}_3$  as described before (5). The firing atmosphere consisted of  $\text{N}_2$  containing a few per cent of  $\text{H}_2$ . Samples were checked by x-ray analysis. The measurement of the optical properties was performed as indicated previously (6).

#### Results and Discussion

Samples of all the alkaline earth borates doped with 1 a/o of  $\text{Eu}^{2+}$  showed only weak fluorescence

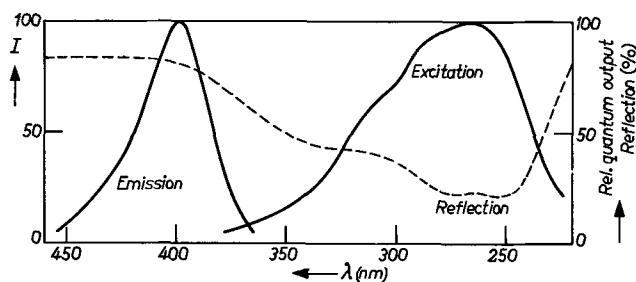


Fig. 1. Spectral energy distribution of the emission under 254 nm excitation, diffuse reflection spectrum and relative excitation spectrum of the emission of  $\text{Ba}_{0.99}\text{Eu}_{0.01}\text{B}_8\text{O}_{13}$ . The radiant power per constant wavelength interval ( $I$ ) is plotted in arbitrary units along the ordinate.

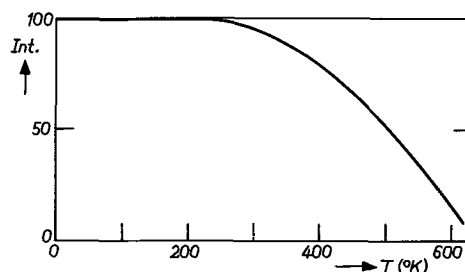


Fig. 2. Temperature dependence of the fluorescence of  $\text{Ba}_{0.99}\text{Eu}_{0.01}\text{B}_8\text{O}_{13}$  under 254 nm excitation.

under uv or cathode-ray excitation with one exception. Barium octaborate activated with  $\text{Eu}^{2+}$  ( $\text{Ba}_{1-x}\text{Eu}_x\text{B}_8\text{O}_{13}$ ) shows efficient blue fluorescence under 254 nm excitation. Figure 1 contains the spectral energy distribution of the emission, the diffuse reflection spectrum, and the relative excitation spectrum of the emission. The emission band peaks at about 400 nm. Because unactivated  $\text{BaB}_8\text{O}_{13}$  does not absorb in the uv region, the strong and broad absorption band in short-wavelength uv region must be due to the  $\text{Eu}^{2+}$  ion [ $4f \rightarrow 5d$  transition, see ref. (3)]. A strong excitation band corresponds with this absorption band. In view of the position of this band the phosphor is excited efficiently with 254 nm radiation.

The temperature dependence of the new phosphor (Fig. 2) is comparable to that of the best temperature-persistent  $\text{Eu}^{2+}$ -activated phosphors, for example  $\text{Sr}_{0.8}\text{Mg}_{1.2}\text{P}_2\text{O}_7:\text{Eu}^{2+}$  and  $\text{BaAl}_{12}\text{O}_{19}:\text{Eu}$  (4).

The energy efficiency for cathode-ray excitation (20 kv) of several samples varied between 0.5 and 1.0%. The quantum efficiency for 250-270 nm excitation of samples  $\text{Ba}_{1-x}\text{Eu}_x\text{B}_8\text{O}_{13}$  is 60% for values of  $x$  up to 0.01. For higher values of  $x$  the quantum efficiency decreases. For  $x = 0.02$ , for example, it is 45%.

In conclusion it can be stated that  $\text{BaB}_8\text{O}_{13}:\text{Eu}^{2+}$  is an efficient photoluminescent material.

Manuscript received May 13, 1968.



Any discussion of this paper will appear in a Discussion Section to be published in the June 1969 JOURNAL.

## REFERENCES

1. G. Blasse, W. L. Wanmaker, and J. W. ter Vrugt, *This Journal*, **115**, 673 (1968).
2. W. L. Wanmaker and J. W. ter Vrugt, *Philips Research Repts.*, **22**, 355 (1967).
3. G. Blasse, W. L. Wanmaker, J. W. ter Vrugt, and A. Bril, *ibid.*, **23**, 189 (1968).
4. G. Blasse and A. Bril, *ibid.*, **23**, 201 (1968).
5. W. L. Wanmaker and A. Bril, *ibid.*, **19**, 479 (1964).
6. A. Bril and W. L. Wanmaker, *This Journal*, **111**, 1363 (1964).

## The Hydrothermal Synthesis of Single Domain Lithium Niobate Crystals by Transport Reactions

V. G. Hill and K. Gerald Zimmerman

*Tem-Pres Research/The Carborundum Company, State College, Pennsylvania*

Lithium niobate single crystals are of interest because of the observed second harmonic generation and optical parametric effects. The successful growth of this material by high-temperature methods has been reported (1-5). Nassau and co-workers (4, 5) using the Czochralski technique, obtained large single domain  $\text{LiNbO}_3$  crystals by (a) the addition of low concentrations of  $\text{MoO}_3$  to the melt, (b) growth of the crystals in an electric field, and (c) poling polydomain crystals at  $1090^\circ\text{-}1210^\circ\text{C}$ . However, it is desirable to grow single domain  $\text{LiNbO}_3$  crystals at lower temperatures to determine if any further improvement in crystal quality can be achieved. The hydrothermal method is one approach.

The alternatives for hydrothermal growth of  $\text{LiNbO}_3$  single crystals were (a) the use of a mineralizer which will dissolve and transport  $\text{LiNbO}_3$  or (b) the formation of  $\text{LiNbO}_3$  by reacting phases whose bulk composition is along the join  $\text{LiNbO}_3\text{-H}_2\text{O}$ . Preliminary work with solutions of  $\text{NaOH}$ ,  $\text{KOH}$ ,  $\text{RbOH}$ ,  $\text{NH}_4\text{OH}$ ,  $\text{H}_2\text{SO}_4$ ,  $\text{HCl}$ ,  $\text{HNO}_3$ ,  $\text{HF}$ ,  $\text{LiCl}$ ,  $\text{NH}_4\text{Cl}$ , and  $\text{NH}_4\text{Cl-NH}_4\text{OH}$  as mineralizers resulted, in all cases, in the formation of new phases, and so the second alternative was the only choice. This technique is simply a controlled precipitation caused by reacting two solutions. It may be contrasted with the usual hydrothermal crystal growth method where a material is dissolved and transported in solution across a thermal gradient, and then precipitated. It is, however, desirable to refine the reaction so that only one phase can crystallize, and if possible, arrange the conditions so that the precipitation occurs as an overgrowth onto a seed. The latter arrangement will permit the growth of larger crystals once the basic techniques are established. The Tem-Pres hydrothermal research units (Model HR-1B), equipped with the cold seal "test tube" vessels, were used for the investigation. The reactions were done in sealed 5 and 10 mm gold tubes. The binocular and petrographic microscopes and x-ray diffractometer were used for the identification and characterization of the phases formed, including the crystals grown. The initial starting materials used were  $\text{Li}_2\text{CO}_3$  (99.9%),<sup>1</sup>  $\text{LiOH}\cdot\text{H}_2\text{O}$  (99.8%),<sup>1</sup>  $\text{Nb}_2\text{O}_5$  (99.9%).<sup>2</sup>  $\text{Li}_2\text{O}:4\text{Nb}_2\text{O}_5$  and  $3\text{Li}_2\text{O}:\text{Nb}_2\text{O}_5$  were prepared by firing stoichiometric mixtures of  $\text{Li}_2\text{CO}_3$  and  $\text{Nb}_2\text{O}_5$  at  $450^\circ\text{C}$  for two weeks and then slowly increasing the temperature to  $700^\circ\text{C}$ .

Lithium niobate was synthesized hydrothermally from  $\text{LiOH}$  and  $\text{Nb}_2\text{O}_5$ .  $\text{LiOH}\cdot\text{H}_2\text{O}$  was placed in a partially sealed 2.5-mm diameter gold tube. This tube was sealed inside a 5-mm diameter gold tube containing the calculated amount of  $\text{Nb}_2\text{O}_5$  to react stoichiometrically with the  $\text{LiOH}\cdot\text{H}_2\text{O}$  and also a small volume of water. The charge was reacted at temperatures between  $400^\circ$  and  $650^\circ\text{C}$ , and pressures up to 2 kb. The  $\text{LiNbO}_3$  crystals formed in these runs were always

of microscopic size and did not increase in size when the method of mixing the reactants were varied.

In an effort to control the rate of precipitation of  $\text{LiNbO}_3$  from solution by restricting the possible products and reaction paths, the use of other starting materials was tried.  $\text{Li}_2\text{O}:4\text{Nb}_2\text{O}_5$  and  $3\text{Li}_2\text{O}:\text{Nb}_2\text{O}_5$  were selected as the most suitable reactants. A (1:1) mixture of  $3\text{Li}_2\text{O}:\text{Nb}_2\text{O}_5$  and  $\text{LiOH}$  was placed in a 10-mm gold tube. The equivalent amount of  $\text{Li}_2\text{O}:4\text{Nb}_2\text{O}_5$  was then weighed into a 5-mm diameter gold tube. The 5-mm tube was suspended inside the 10-mm tube, sufficient water added to almost fill the 10 mm tube at temperature and pressure; then it was welded shut. The sealed tubes with contents were heated at temperatures between  $500^\circ$  and  $600^\circ\text{C}$  and 2 kb.  $\text{LiNbO}_3$  crystals measuring up to  $1 \times 0.2$  mm were formed in runs of two to three weeks duration (Fig. 1). These crystals were larger than those obtained by reacting  $\text{LiOH}$  with  $\text{Nb}_2\text{O}_5$ , showing that the rate of precipitation has been significantly decreased. Prolonged heating did not promote recrystallization since water was the only solvent remaining once the precipitation reaction had ceased. Attempts to slow down the precipitation rate further did not cause a noticeable improvement in crystal size. Similarly, satisfactory overgrowth on seeds was not achieved. The crystals formed were of high quality, and examination with a polarizing microscope indicated that they were single domain.

### Acknowledgment

This work was done as part of a research project on hydrothermal crystal growth sponsored by the U.S. Air Force Materials Laboratory, Wright-Patterson Air Force Base, Ohio. Mr. Paul W. Dimiduk was Project Engineer.

Manuscript submitted April 5, 1968; revised manuscript received June 3, 1968.



Fig. 1. Photomicrograph of hydrothermally grown single domain  $\text{LiNbO}_3$  crystals.

<sup>1</sup> Gallard-Schlesinger Chemical Manufacturing Corporation, Carle Place, New Jersey.

<sup>2</sup> A. D. MacKay, Inc., New York, New York.



Any discussion of this paper will appear in a Discussion Section to be published in the June 1969 JOURNAL.

## REFERENCES

1. B. T. Matthias and J. P. Remeika, *Phys. Rev.*, **76**, 1886 (1949).
2. A. A. Ballman, *J. Am. Ceram. Soc.*, **48**, 112 (1965).
3. S. A. Fedulov, Z. I. Shapiro, and P. B. Lodyzhenskii, *Kristallografiya*, **10**, 268 (1965).
4. K. Nassau and H. J. Levinstein, *Appl. Phys. Letters*, **7**, 69 (1965).
5. K. Nassau, H. J. Levinstein, and G. M. Lolocono, *J. Phys. Chem. Solids*, **27**, 989 (1966).
6. E. Ingerson and O. F. Tuttle, *Am. J. Sci.*, **245**, 313 (1947).
7. G. C. Kennedy and R. C. Newton, *Am. Min.*, **39**, 654 (1954).
8. R. C. Puttbach, R. R. Monchamp, and J. W. Nielsen, "Crystal Growth," H. Stephon Peiser, Editor, Pergamon Press, Symposium Publication Division, p. 569 (1967).

# Brief Communication



## Rate Characteristics of Constant Voltage Anodization of Yttrium

R. M. Goldstein and W. J. Pettit

McDonnell Company, St. Louis, Missouri

The constant voltage anodization of thin film yttrium for use in thin film capacitors has recently been reported (1). Since then more experimental data have been evaluated, and certain aspects of the anodization theory can be given.

The experimental procedure is as follows. Yttrium metal is electron-beam-evaporated through a metal mask on to a Corning 7059 slide. The resulting pattern of 18 metal leads is then masked by a nonconductive Alpha Stripecoat to prevent sparking at the air electrolyte interface, and anodized at 100v in an electrolytic cell. The cell consists of a platinum foil cathode, the slide as anode, another electrode in common with the anode to measure electrolyte voltage drop, and an electrolyte cooled to 1°C whose concentration is 6.4% ammonium pentaborate, 57.1% ethylene glycol, and 36.5% deionized water by weight. The voltage drop across the electrolyte and the current through the oxide film during anodization are monitored simultaneously by means of recorders of sufficiently high input impedance (1 Mohm) to avoid any appreciable loading. After the yttrium has been anodized, aluminum leads are evaporated so as to form 18 capacitors, each of area 0.02 cm<sup>2</sup>. The oxide thickness is calculated from the capacitance with an assumed dielectric constant of 17.1 (1).

From Fig. 1a, the initial current decay (less than 5 sec) may be represented by

$$I = I_s e^{-\alpha t} \quad [1]$$

where

$$\alpha = 0.18 \text{ sec}^{-1}$$

$$I_s = 250 \text{ mA/cm}^2$$

From Fig. 1b, the current at longer times (greater than 50 sec) may be represented by

$$I = I_L t^{-\beta} \quad [2]$$

where

$$\beta = 0.6$$

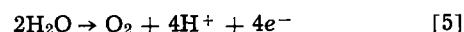
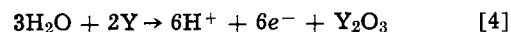
$$I_L = 30 \text{ mA/cm}^2$$

The measured current consists of ionic current,  $I_i(t)$ , and electronic current,  $I_e(t)$

$$I(t) = I_i(t) + I_e(t) \quad [3]$$

Only the ionic current contributes to the oxide growth. The two over-all reactions occurring at the

anode are



The former reaction takes place when there is ion motion through the oxide film. The latter reaction occurs especially at high voltages when the electrons from the oxygen ion are split off and pass through the film resulting in oxygen gas given off at the anode rather than anodization taking place. As the oxide becomes thicker, ionic transport becomes less and the electron current becomes more dominant.

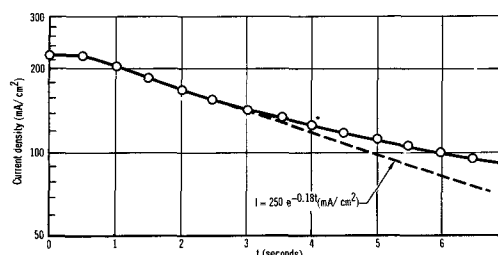


Fig. 1a. Short time current decay

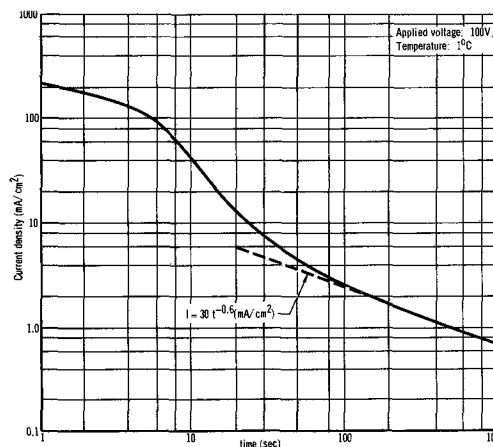


Fig. 1b. Total current decay

We relate the ionic current to the total current by means of the ionic efficiency,  $\eta(t)$

$$I_i(t) = \eta(t) I(t) \quad [6]$$

The ionic current may then be related to the oxide thickness by means of Faraday's law:

$$\int_0^t I_i(t) dt = x/\lambda \quad [7]$$

where

$$\lambda = \frac{M}{F(2z)\rho A}$$

$x$  = oxide thickness,  $M$  = molecular weight,  $z$  = effective valence of the yttrium ion,  $\rho$  = density of yttrium oxide,  $A$  = area of yttrium film,  $F$  = Faraday constant = 96,486.82 coulomb/mole.

As a first approximation to calculating the oxide thickness, assume the ionic efficiency to be independent of time. Then from Eq. [6] and [7]

$$\frac{dx}{dt} = \lambda\eta(t)I(t) \quad [8]$$

where  $I(t)$  is given by Eq. [1] or [2] depending on the time interval. Using a value of  $z=3$ , which is the value expected from the chemical half reaction, we have calculated the theoretically expected thicknesses of the oxide film for short time growth. These results, when compared with the experimental ones (Fig. 2) illustrate that the efficiencies are not independent of time and that for short times are much greater than one, e.g., they vary from 2.3 at 0.4 sec to 0.9 at 4.0 sec. The probable explanation for this result is that in the initial stages of anodization the effective valence of yttrium is less than three (incomplete ionization) or else that electrons are initially flowing through the oxide film unattached to the yttrium ions. This is in concurrence with the work by Dreiner, Lehovec, and Schimmel (2) on tantalum metal, except their hypothesis of efficiencies greater than one due to electron tunneling cannot be correct in our case as evidenced by the large oxide thickness (1000 Å) obtained in the first few seconds where our efficiencies are greater than one.

To establish the basis for short time current behavior we have plotted in Fig. 3 the logarithm of time as a function of reciprocal thickness. These data indicate that the short time growth is governed by a reciprocal logarithmic rate, i.e.,

$$1/x = A - B \ln t \quad [9]$$

where

$$A = 1.23 \times 10^{-3} \text{ \AA}^{-1}$$

$$B = 0.38 \times 10^{-3} \text{ \AA}^{-1}$$

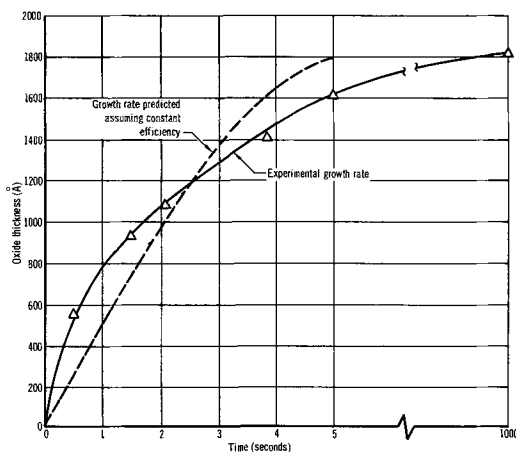


Fig. 2. Yttrium oxide growth rate

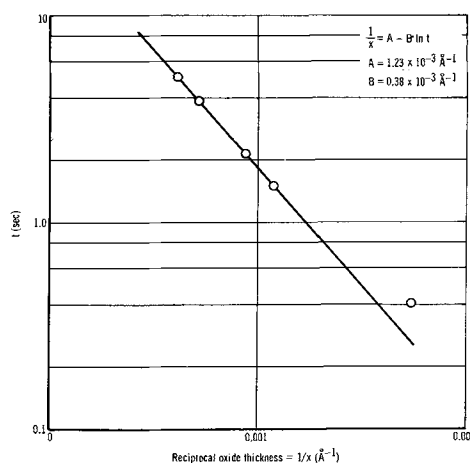


Fig. 3. Reciprocal logarithmic rate law for the anodization of yttrium metal.

Although this law is generally characteristic of thin tarnishing layers, a law of this type will occur if the two phase-boundary reactions, namely, (i) entry of a chemisorbed oxygen ion into a vacancy in the  $Y_2O_3$  at the yttrium oxide-electrolyte phase boundary or (ii) formation of an oxygen ion vacancy in the  $Y_2O_3$  at the yttrium oxide-yttrium phase boundary, proceed more quickly than the field transport of ionic defects leaving the latter as the rate determining step.

It is felt that after a very short time (5 sec) the phase boundary reaction probably becomes the limiting step. However, this law is only applicable to the point where the diffusion rate becomes comparable with the phase boundary reaction, which in the case of nonporous oxide growth is often so early in the reaction that the former is not observed (3).

In the long time range the theory of Dreiner *et al.* (2), which is developed from the Mott-Cabera equation and Faraday's law, the high field Frenkel defect model (4) and the "dielectric mosaic" theory (5) predict currents inversely proportional to time, while our experimental results predict a long time current decay proportional to  $t^{-0.6}$  (Eq. [2]). For these long times the growth rate is thought to be diffusion limited as evidenced by a small ionic efficiency and an ionic current approaching a  $t^{-0.5}$  dependence. This mechanism of current behavior is in agreement with Eq. [2].

The significance of this barrier oxide (16-18 Å/v) is that it can be grown rapidly enough (e.g., 1300 Å in 3 sec) and with superior electrical characteristics as field strength of  $4.4 \times 10^6$  v/cm (dry), dielectric constant of 17.1 and a low dissipation factor of 0.008 to find use as the dielectric in thin film capacitors.

#### Acknowledgment

This research was conducted under the McDonnell Independent Research and Development Program.

Manuscript submitted May 23, 1968; revised manuscript received June 16, 1968.

Any discussion of this paper will appear in a Discussion Section to be published in the June 1969 JOURNAL

#### REFERENCES

1. R. M. Goldstein, "Thin Film Yttrium Oxide Capacitors Formed by Electrochemical Anodization Techniques," Proceedings of the 1968 Electronic Components Conference, Washington, D. C. (May 1968).
2. R. Dreiner, K. Lehovec, and J. Schimmel, *This Journal*, **112**, 395 (1965).
3. K. Hauffe, "Oxidation of Metals," Plenum Press, New York (1965).
4. L. Young, "Anodic Oxide Films," Academic Press New York (1961).
5. M. J. Dignam, *This Journal*, **112**, 722 (1965).

# X-ray Study of the Active Materials in the Lead-Acid Storage Battery

Takewo Chiku\*

Toyota Central Research & Development Laboratories, Inc., Nagoya, Japan

## ABSTRACT

The structural change of the active materials in the lead-acid storage battery due to charge and discharge was examined by x-ray analysis. It is found that Pb and PbO<sub>2</sub> when charged are in a strained state which finds gradual release with time of discharge. The ratios of the integrated intensities Pb/PbSO<sub>4</sub> or PbO<sub>2</sub>/PbSO<sub>4</sub> in the negative and positive plates were measured, and it is pointed out that the value Pb/PbSO<sub>4</sub> in the fully charged state is closely connected to the life time of the battery, becoming very small with usage.

About three decades ago the present author (1) studied the active materials of negative plates in the lead-acid storage battery by an x-ray method and reported a slight change of the lattice constant of lead with time of discharge, which reached a minimum value at a period nearly corresponding to that of zero terminal voltage of the battery. The present author interpreted these results in terms of the generation of internal strains in the matrix. From a crystallographical point of view this phenomenon is thought to be very interesting inasmuch as it may throw light on the structural changes of lead crystals subjected to an electrochemical reaction. Unfortunately the experimental observation reported by Chiku seems to have been disregarded by many researchers, presumably because it appeared to be restricted to a problem in crystallography rather than to relate to a problem in electrochemistry.

The present study was carried out to reexamine Chiku's previous results by using recent techniques of x-ray analysis and to make a detailed observation of the internal structure of the active materials in the lead-acid storage battery as a function of progressive stages of charge and discharge.

## Experimental Procedure

Samples used for x-ray measurements were taken from the same type of commercial battery, described in another paper (2) at various stages of the discharge as shown in Fig. 1; they were put into a small polyethylene bag together with the electrolyte solution of the battery and were then mounted on a specimen holder; the size of specimen being of the order of 10 x 15 x 2 mm<sup>3</sup>. The thickness of polyethylene was 0.1 mm, and the total time to carry out an x-ray examination for one specimen took approximately 1 hr. The specimens prepared and examined in this manner will be referred to as "case 1" unless otherwise mentioned.

The change in interplanar spacing and in the integrated intensity of the specimens as a function of the depth from the surface was observed on specimens dried in vacuum at room temperature after having been washed in water to remove any measurable sulfate ion in the specimen. The specimens prepared and examined in this manner will be referred to as "case 2".

Measurements of x-ray diffraction were performed with the GF-D2 diffractometer made by Rigaku Denki Company in Japan using Cu-K $\alpha$  radiation, and profiles of various diffraction lines for Pb, PbO<sub>2</sub>, and PbSO<sub>4</sub> were measured as a function of progressive electrochemical reaction.

## Experimental Results

Figure 2a shows the changes in interplanar spacing of some lattice planes in lead crystals with time of

discharge in the negative plate, whereby the change of interplanar spacing of each measured (hkl) plane is referred to the change of the lattice parameter  $a_0$ . It will be seen from Fig. 2a that the interplanar spacings decrease gradually with time but that this decrease is different for different (hkl) planes, approaching the value of metallic lead irrespective of the type of (hkl) planes. This result agrees qualitatively with that reported previously (1). The interplanar spacing of PbO<sub>2</sub> in the positive plate also changes and with time of discharge approaches the interplanar spacing distance of each lattice plane of lead dioxide (tetragonal lattice:  $a$ , 4.941Å;  $c$ , 3.374Å). Figure 2b shows these results in which it should be noted that the change in lattice spacing with time of discharge is different for different planes, showing an anisotropy of lattice distortion in the crystal. The spacing of PbSO<sub>4</sub> created on both negative and positive plates changes slightly with progress in the reaction, showing a decreasing tendency toward the lattice spacing of lead sulfate with the time.

It is very interesting to note that Pb and PbO<sub>2</sub> in the state of charge are in a strained state, which is released gradually with time of discharge, or with decreasing terminal voltage in the battery.

At an early stage of discharge, the diffraction intensity of Pb was very weak, and some additional strong diffraction lines of unknown nature were detected. These additional diffraction lines could not be observed in the plate after a discharge of 2 hr. However, no measurable diffraction lines except those of Pb and PbSO<sub>4</sub> were found in the study of case 1. These results suggest that some unknown substances are produced during the process of sampling denoted by case 2.

Figure 3 shows the interplanar spacing of {111} and {200} as a function of the depth from the surface of the

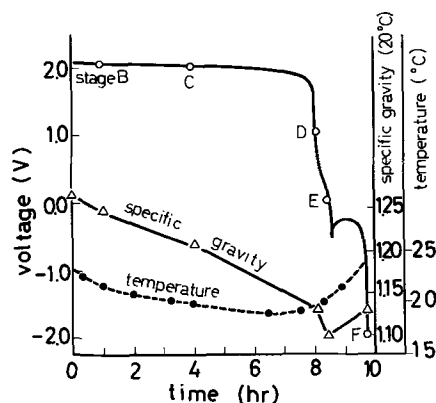


Fig. 1. Characteristic curves of discharge (at 4 amp) in the battery examined.

\* Electrochemical Society Active Member.

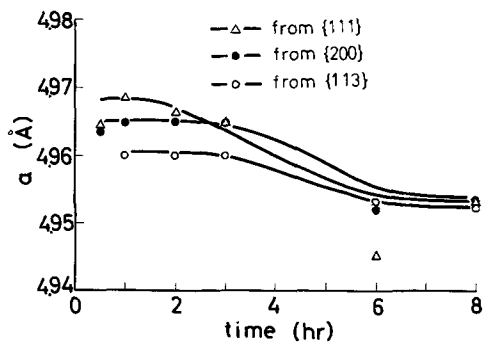


Fig. 2a. Changes of interatomic spacings of Pb in the negative plate with time of discharge, case 2.

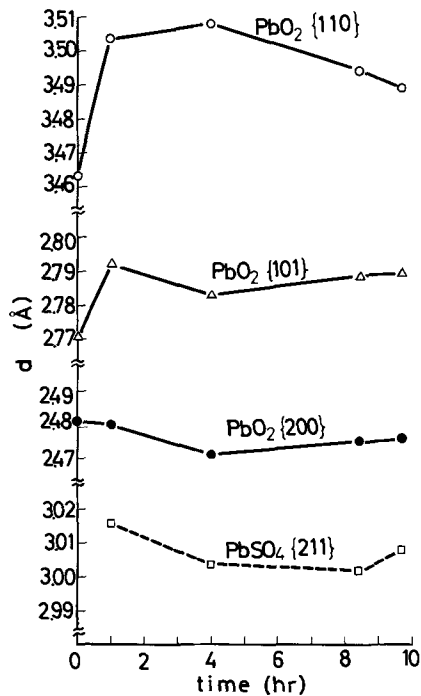


Fig. 2b. Changes of interatomic spacing of some (hkl) planes in  $PbO_2$  and  $PbSO_4$  in the positive plate with time of discharge, case 2.

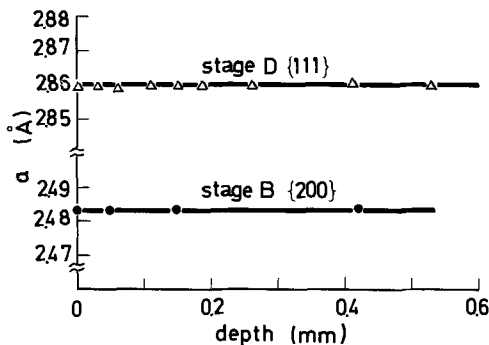


Fig. 3. Interatomic spacing of {111} and {200} in stages B and D of Pb in the negative plate as a function of the depth from the surface, case 2.

negative plate taken from stages B and D listed in Table I. It will be noted that the interplanar spacing remains constant irrespective of the depth. It is well known that the peak shift and the line broadening due to deformation are scarcely observable in lead because the recrystallization in lead crystal occurs even at room temperature. A slight increase of the integral breadth of the {200} diffraction, however, is obtained as shown in Fig. 4. This effect may be closely related

Table I. Dependence of Pb/ $PbSO_4$  in the fully charged state on the age of batteries

Integrated intensity	Pb{111}	Pb{200}	Pb{311}
	$PbSO_4\{211\}$	$PbSO_4\{211\}$	$PbSO_4\{211\}$
Battery			
New	$\infty$	$\infty$	$\infty$
Used	4.39	5.23	4.26
Old	1.27	1.85	1.50
Very old	0.26	0.61	0.77

to the nucleation and growth of  $PbSO_4$  during the process of discharge.

The integrated diffracted intensity of various (hkl) planes of the active materials in the negative and positive plate was measured as a function of time of discharge, the results of which are shown in Fig. 5a and 5b. The ratio of the integrated intensity of  $PbO_2$  to  $PbSO_4$  in the positive plate and that of Pb to  $PbSO_4$

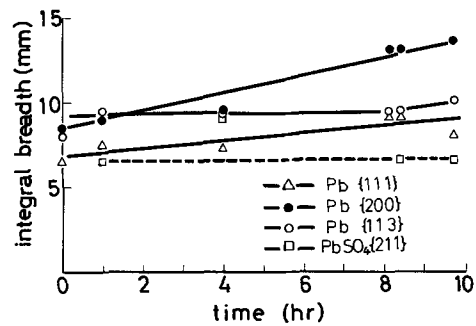


Fig. 4. Changes in the negative plate of the integral breadth of some diffraction lines of Pb and  $PbSO_4$ , case 1.

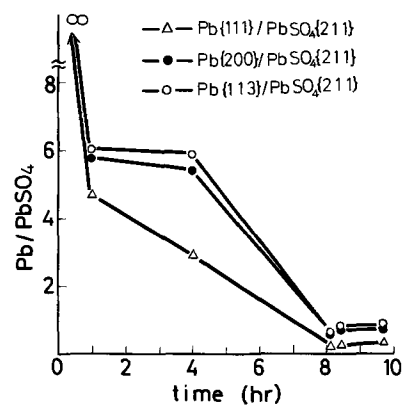


Fig. 5a. Dependence of Pb/ $PbSO_4$  in the negative plate on the time of discharge, case 1.

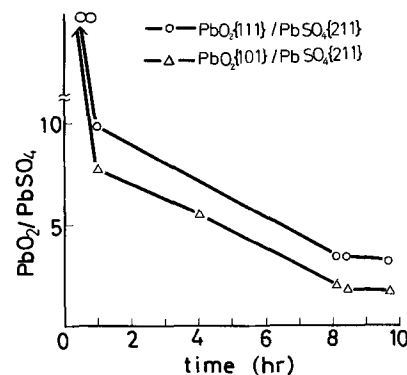


Fig. 5b. Dependence of  $PbO_2/PbSO_4$  in the positive plate on the time of discharge, case 1.

in the negative plate (notation Pb/PbSO<sub>4</sub> and PbO<sub>2</sub>/PbSO<sub>4</sub> are used unless otherwise stated) were plotted against the time of discharge and powders of Pb, PbO<sub>2</sub>, and PbSO<sub>4</sub> of extra pure reagents were used as standards to estimate the change which each active material undergoes with time. It can be seen from these results that Pb/PbSO<sub>4</sub> or PbO<sub>2</sub>/PbSO<sub>4</sub> decreases with time of discharge, at first very rapidly and then gradually and that after 10 hr, corresponding to the period of nearly zero terminal voltage, the value reaches about 0.5 for the negative plate and about 2.3 for the positive plate. These values do not correspond to the per cent changes of Pb, PbO<sub>2</sub>, and PbSO<sub>4</sub> in the negative or positive plate because the effect of absorption of x-rays due to PbSO<sub>4</sub> are not being considered in the present case.

One might expect that self-discharging in the battery may also bring about changes in the interatomic spacing, in the integral breadth, and in the integrated intensity of the active materials. Figure 6 represents the result obtained for the negative plate, from which may be seen, however, that the interplanar spacing remains virtually constant irrespective of the lapse of time. Figure 7 shows Pb/PbSO<sub>4</sub> for the negative plate calculated from the x-ray diffracted intensity, showing a similar tendency, but a very gradual decrease compared with that in the case of discharge. These results imply that the structural change of the active materials in the discharging process are different from those of the process of self-discharging.

The ratio PbO<sub>2</sub>/PbSO<sub>4</sub> in the positive or Pb/PbSO<sub>4</sub> in the negative becomes infinity at the fully charged state as shown in Fig. 5 and 7. These values, however, are thought to be a function of the numbers of repeti-

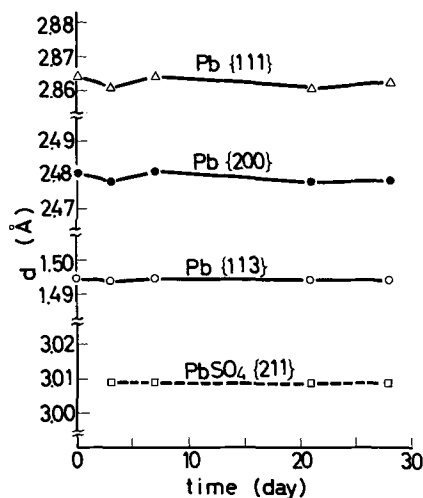


Fig. 6. Dependence of interatomic spacing of Pb and PbSO<sub>4</sub> in the negative plate on lapse of time, case 1.

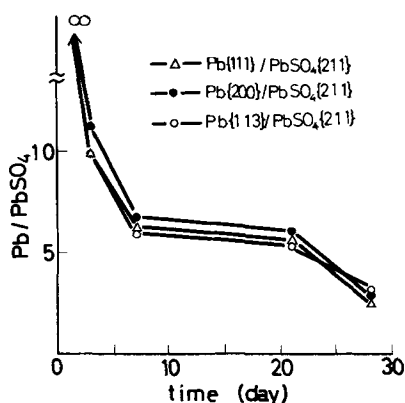


Fig. 7. Dependence of Pb/PbSO<sub>4</sub> in the negative plate on lapse of time, case 1.

tion of charges and discharges. Table I shows a decreasing tendency for Pb/PbSO<sub>4</sub> with time of battery usage.

### Discussion

As shown in Fig. 2a and 2b, a highly strained state is produced in the electrode plate due to charging which finds gradual release with time of discharge. An approximate value of the stored energy per unit volume in lead may be estimated from the elastic strains by the following consideration: Taking the lattice strain  $\left(\frac{a_0 - a}{a_0}\right)^2$  as the mean square strain, where  $a_0$  and  $a$  are the lattice constant of metallic lead and Pb as the active material, respectively,  $V$  is expressed by

$$V = \frac{3}{2} ES^2$$

where  $E$  is Young's modulus, and  $S$  the root mean square strain. Using the experimental data the result obtained turned out to be of the order of 0.05 cal/g.

The elastic stored energies of metals and alloys due to cold-working are usually within 0.1-0.5 cal/g (3, 4), and consequently the present elastic stored energy is small compared to values obtained for cold-worked specimens. The stored energy corresponding to the fully charged state was shown to be completely released when subjected to an anneal of 150°C for 1 hr in vacuum.

It is not known as yet how PbSO<sub>4</sub> crystallites nucleate and grow on Pb and how they dissolve during the process of discharging or charging. Burbank (5) studied the anodic oxidation of several compounds which existed in the positive plate of a lead-acid cell by electron microscopy and observed dendritic PbO<sub>2</sub> formed from PbSO<sub>4</sub>. Using an electron microscope the present author (6) recently observed the crystal growth of PbSO<sub>4</sub> on several kinds of crystal surfaces of lead. He found a dendritic growth of PbSO<sub>4</sub> crystallites, especially on the (100) plane of Pb crystal as the reaction progressed, but a shapeless growth when the specimen was merely soaked in the electrolytic solution. The results obtained in the present study suggest that the production of the lattice strain and its release may play an important part in solving the mechanism of the formation of PbSO<sub>4</sub> crystallites on Pb or PbO<sub>2</sub> resulting from the electrochemical reaction.

### Summary

Active materials in the lead-acid storage battery were examined by means of x-ray diffraction techniques, and the results were as follows:

1. The interplanar spacings of Pb, PbO<sub>2</sub>, and PbSO<sub>4</sub> in the electrode plate were changed with progressive discharge reaching at the period of nearly zero terminal voltage the spacing of metallic lead, lead dioxide, and lead sulphate, respectively.
2. The lifetime of a battery may be estimated from the value of Pb/PbSO<sub>4</sub>, the latter being small in old batteries even for the fully charged state.

### Acknowledgment

The author wishes to express his sincere thanks to Dr. K. Ninomiya and Dr. K. Nakajima for helpful discussion, and to Messrs. H. Haba and M. Kimura for their diligent aid throughout the course of the work.

Manuscript submitted Feb. 2, 1968; revised manuscript received June 21, 1968.

Any discussion of this paper will appear in a Discussion Section to be published in the June 1969 JOURNAL.

### REFERENCES

1. T. Chiku, *Toyoda-Kenkyû-Ihō*, 6, 15 (1939) (in Japanese).
2. T. Chiku, To be published.

3. P. B. Hirsch, "Progress in Metal Physics," Vol. 6, p. 236, Pergamon Press, New York (1956).
4. K. Nakajima, *Sci. Rep. Res. Inst. Tohoku Univ.*, 12, 309 (1960).
5. J. Burbank, "Power Source, Proceedings of the 5th International Symposium," p. 147 (1966).
6. T. Chiku, *et al.*, "The 8th Batteries Symposium," p. 88 (1967) (in Japanese).

## Charging the Silver Oxide Electrode with Periodically Varying Current

### IV. Intermittent Constant Current Reversals During Charge

Charles P. Wales\*

*Naval Research Laboratory, Washington, D. C.*

#### ABSTRACT

Sintered silver electrodes of the type used in storage batteries were charged by a constant current that was interrupted by periodic constant current discharges. Comparison to results from constant current charges showed a large capacity increase when the 20-hr constant charge current was reversed for 15 min out of every 60 min, but the total time required for a charge had increased greatly. Capacity could be improved a smaller amount, without charge time becoming excessive, by partly discharging the silver electrodes the first one or two times that potential reached a chosen value near the end of a constant current charge. In general, capacity improvement decreased as KOH concentration increased. Commercial silver-zinc cells always gave less improvement than the test cells.

Alkaline storage batteries containing silver oxide electrodes are used because of their high capacity compared to the more common storage battery systems. The discharge capacity of silver oxide electrodes is, however, strongly influenced by conditions of the preceding charge (anodic oxidation). Previous work at this Laboratory has shown several ways for charging silver electrodes that will give a capacity greater than the capacity obtained by a constant current charge. The electrode capacity can be increased if pulses of charge current are added to a constant charging current, using the proper conditions (1). Either increased capacity or faster recharging can result from interrupting the current periodically throughout a charge (2). The largest improvements were obtained following charges with 60 cps asymmetric sinusoidal a.c. derived from commercial a.c. (3). This asymmetric a.c. was composed of two half-wave rectified currents which flowed in opposite directions and were 180 degrees out of phase. Capacity improvements were smaller when silver electrodes were charged by an asymmetric a.c. which was obtained by superimposing a half-wave 60 cps current in the discharge direction on a larger constant charge current. The present work describes the results of relatively long constant current reversals which were separated by long periods of constant current charge.

#### Experimental Procedure

The test cells contained one of two sizes of sintered Ag plaques, depending on the size available when the cells were constructed. The plaques were either 30.5 x 63.5 x 0.8 mm or 41.5 x 38.0 x 0.8 mm. The sintered Ag had an average weight of 7.9 or 5.8g, respectively, not including the grid of expanded Ag metal. The weight of sintered Ag corresponds to a theoretical electrode capacity of 3.9 or 2.9 amp-hr, respectively. The electrodes were wrapped individually with cellulosic separator material, instead of being wrapped in pairs as is the common practice in Ag-Zn cells. The separator was folded around the electrode in such a way that 5 layers of separator covered both

sides of the electrode. The separator was held in place by wrapping with a small Ag wire and was open only at the top of the electrode. The sintered Ag plaques and the separator had been manufactured for use in commercial Ag-Zn storage batteries.

The wrapped Ag electrodes were used as both test electrodes and counter electrodes, and were about 2 cm apart. Each cell contained one test electrode. Five of the test cells contained one counter electrode and one cell contained two connected in parallel, placed on each side of the test electrode. Microscopic examination of similar Ag electrodes, at various states of charge, showed that the electrodes were highly porous and, at the relatively low cd's used, having only one side of these electrodes face the counter electrode did not favor reactions at that side (4). The test cells contained an excess of either 35% KOH or 50% KOH as the electrolyte and a Ag/Ag<sub>2</sub>O reference electrode. There was little gas production in a cell since a counter electrode was being reduced at the same time as a test electrode was being oxidized, and vice versa. All work was done at 25° ± 1°C.

As in the previous work (1-3) the constant current which resulted in a complete charge or discharge of the test electrode lasting approximately 20 hr was arbitrarily taken as the standard, or normal, charge and discharge current. Before any charges with a periodically reversed current were tried, the test cells were charged and discharged for 8 to 10 complete cycles at the 20-hr current, until capacity became relatively constant. After the tenth cycle, the same current was used for the rest of the life of these cells, and corrections were not made for deviations in charge and discharge time from 20 hr.

Complete normal charges (using the 20-hr rate as defined above) were alternated with complete charges which used one of two reversal conditions. Under one set of conditions, the current was reversed periodically during a charge at the 20-hr rate with the test electrode being discharged at the 20-hr rate for 0.01 to 15 min during this reversal period before the charge was resumed. These reversals were repeated throughout the charge at intervals varying from 1 min to 4 hr, with only one reversal length and interval used in any single charge. In another set of reversal

\* Electrochemical Society Active Member.

Key words: silver oxide electrode, discharge capacity, alkaline storage batteries, charge current.

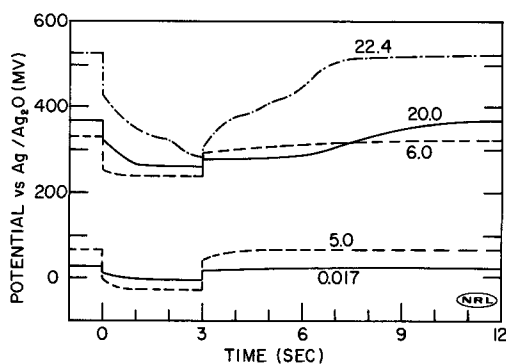


Fig. 1. Some excerpts of potentials measured in 35% KOH during a constant current charge of a silver electrode at the 20-hr rate with current reversed for 3 sec every 60 sec. Numbers by the curves give the total elapsed time in hours at the end of reversals for each excerpt.

conditions, the electrode was partly discharged the first two times that charge potential reached a chosen value near the end of a charge with up to 5% of the electrode capacity being removed in each of the two partial discharges. All charges were continued until oxygen evolution was occurring and potential had stopped changing rapidly. After a charge was completed, a cell was immediately discharged at approximately the 20-hr rate of constant current to a final potential which was 300 mv negative to the Ag/Ag<sub>2</sub>O reference. Charge and discharge currents were obtained from controlled power supplies.

To minimize variations in capacity the discharge capacities of the four normal cycles (20-hr constant current charge and discharge) that were nearest each discharge were averaged. This moving average was then taken as the normal capacity at that particular point in the life of a cell and is the capacity referred to whenever normal capacity is mentioned. The capacity of each discharge was calculated as a per cent of this varying average. Thus, the discharge capacity which followed a charge with current reversals could be compared to a value which was representative of actual cell capacity, regardless of changes in normal capacity over the life of a cell.

Some of the charges with current reversal which resulted in increased test cell capacity were tried with one model of a commercial silver-zinc secondary cell. The commercial cells contained either 35% KOH or 45% KOH. Each commercial cell had five zinc electrodes and four sintered silver electrodes of the same size as the test electrodes which had a theoretical capacity of 2.9 amp-hr. The silver electrodes limited cell capacity and gave a theoretical cell capacity of about 11.5 amp-hr, although the nominal rated cell capacity given by the manufacturer was only 5 amp-hr. The silver-zinc cells were charged individually

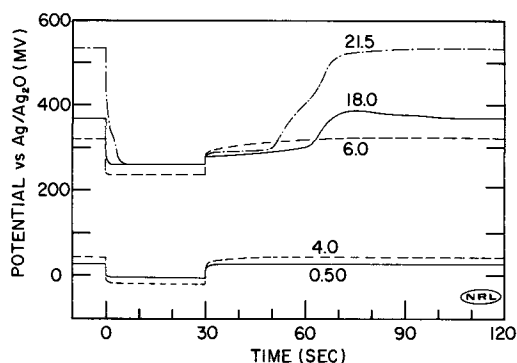


Fig. 2. Some excerpts of potentials measured in 35% KOH during a constant current charge of a silver electrode at the 20-hr rate with current reversed for 0.5 min every 30 min. Numbers by the curves give the total elapsed time in hours at the end of reversals for each excerpt.

until cell potential reached 2.05v. Complete charges at the 20-hr rate of constant current (as defined above) were alternated with charges which had current reversals. The cells were discharged at the 20-hr constant current to 1.10v. Since capacity of these cells varied from one charge-discharge cycle to the next, the 20-hr current was recalculated after each constant current cycle and a different current was used for the following cycle whenever actual charge and discharge time had deviated greatly from 20 hr.

## Results

Current reversals that were repeated every 1, 10, or 30 min during a constant current charge of a silver electrode had comparatively little effect on charge acceptance (Table I). In contrast, the relatively long reversal time of 15 min had a strong effect on charge acceptance when the reversal was repeated every 60 min (Table I). Since the reversal time of 15 min repeated every 60 min was effective for increasing capacity, this reversal was also tried with the commercial silver-zinc cells but the average discharge capacity obtained with 35% KOH was 114% of the normal capacity and with 45% KOH it was only 95% of normal capacity (averages of two measurements).

In a modification to shorten the time required for a complete charge, the silver electrodes in the test cells were discharged at the 6-hr rate for 5 min after every 45 min of charge at the 20-hr rate in 35% KOH. Three complete charges gave an average capacity only 102% of normal. This contrasts with the 143% average given in Table I for the same quantity of reversal done at the 20-hr rate after every 45 min of charge.

Except for the charges with 15 min reversals, the charges listed in Table I had potentials that tended to resemble each other. Figures 1 and 2 gave excerpts from two typical charges having periodic current reversals and show potentials during some of the brief reversals and potentials after charge was resumed. The five excerpts given on each figure show potentials from approximately the same five periods during a charge. The earliest portion (0.017 or 0.50 hr) shows the first reversal after the charge began. The second portion (5.0 or 4.0 hr) shows potentials obtained near the end of the Ag/Ag<sub>2</sub>O potential plateau of the charge, shortly before AgO began to form. The third portion (6.0 hr) shows potentials soon after the charge potential made the rapid rise to the Ag<sub>2</sub>O/AgO potential plateau. The fourth portion (20.0 or 18.0 hr) shows potentials obtained near the end of the Ag<sub>2</sub>O/AgO potential plateau. The final portion shown on Fig. 1 and 2 (22.4 or 21.5 hr) gives potentials after strong oxygen evolution was reached.

Figures 3 and 4 give excerpts of silver electrode potentials taken from two charges that had current

Table I. Discharge capacity of silver oxide electrodes following charges with periodic current reversal. Charge and discharge current were at 20-hr rate

Reversal time (% of total)	Reversal time (min)	Reversal repetition time (min)	Average discharge capacity (% of normal capacity)	
			35% KOH	50% KOH
0.67	0.2	30	98 [3]*	
1.0	0.01	1	102 [3]	
1.7	0.5	30	97 [2]	100 [2]
2.0	0.2	10	99 [3]	
3.3	1.0	30	99 [3]	
5.0	0.05	1	94 [2]	
5.0	0.5	10	111 [4]	99 [1]
6.25	15.0	240	95 [3]	
8.33	15.0	180	105 [3]	
10	1.0	10	87 [5]	
10	3.0	30	89 [3]	98 [1]
12.5	15.0	120	92 [5]	102 [1]
16.7	15.0	90	109 [7]	92 [1]
20	0.2	1	97 [3]	
20	2.0	10	101 [6]	98 [1]
25	15.0	60	143 [5]	77 [2]

\* Values in brackets give the number of measurements made.

reversed for 0.25 hr every 1.5 hr. As shown in Table I, this charge procedure gave a discharge capacity in 35% KOH that averaged 109% of the normal capacity. There was, however, considerable variation in the seven individual capacities that were averaged to give 109%. Four of the seven charges that had 0.25-hr reversals every 1.5 hr gave discharge capacities from 95 to 98% of normal capacity, but the other three charges gave 116, 128, and 133% of normal capacity. The discharges that gave 95 and 133% of normal capacity represented 58 and 79% of the capacity theoretically possible, respectively. The solid lines in Fig. 4 show that reversal potentials of a charge which gave improved capacity tended to be at successively lower values during the first half of a charge at the  $\text{Ag}_2\text{O}/\text{AgO}$  plateau (in contrast to reversals during a charge which gave normal capacity, shown by dashed lines), although the amount of  $\text{AgO}$  that was present on the electrode increased in this period. This resembles previous results when charge current was interrupted periodically throughout a charge (2). Under these conditions the open-circuit potentials also reached successively lower values as the amount of  $\text{AgO}$  present increased for half of a charge at the  $\text{Ag}_2\text{O}/\text{AgO}$  plateau.

It seemed likely that reversal had more effect near the end of a charge than in the earlier part of a charge, judging by potential changes observed during and after reversals. If the number of reversals were lowered, the time required for a complete charge of the silver electrode would be decreased, because the time spent in reversal and the charge time spent in replacing the capacity removed during reversal would both be decreased. Therefore, a series of charges were done in which current was reversed the first two times that a given electrode potential was reached. The potentials chosen were 400, 440, 480, and 510 mv vs. the  $\text{Ag}/\text{Ag}_2\text{O}$  reference electrode. These potentials were not reached until near the end of a charge.

Some of the results of partially discharging silver electrodes the first two times that a particular charge potential was reached are given in Table II. After the capacity removed by the reversal was replaced, additional charge was accepted before charge potential again reached the reversal point. Table II is arranged according to the additional charge accepted after the first reversal. The additional charge time was a better measure of capacity than was the average discharge capacity, because normal capacity after a constant current charge varied irregularly by several per cent. Since charges were done at the 20-hr rate of constant

Table II. Effect of reversing current the first two times that potential reached a particular value during a charge at the 20-hr rate. Charge potential of silver oxide electrode at reversal point was 440, 480, or 510 mv vs.  $\text{Ag}/\text{Ag}_2\text{O}$

Reversal rate of discharge (hr)	Reversal time (min)	Capacity removed by reversal (% of normal)	Average additional charge time (hr) <sup>a</sup>		Average discharge capacity after charge completion (% of normal)
			After first reversal	After second reversal	
20	30	2.50	3.18	0.31	116 [9] <sup>b</sup>
20	60	5.00	2.72	0.34	115 [4]
10	30	5.00	2.71	0.27	114 [4]
10	15	2.50	2.28	0.27	111 [7]
5	15	5.00	2.26	0.26	113 [4]
20	15	1.25	2.22	0.26	110 [6]
40	60	2.50	2.16	0.26	113 [4]
80	60	1.25	1.25	0.20	109 [4]
6.7	5	1.25	0.96	0.18	106 [7]
20	6	0.50	0.66	0.11	103 [5]
80	15	0.31	0.54	0.11	103 [4]
2	1.5	1.25	0.47	0.12	102 [7]
c	30	0.0	0.34	0.07	103 [3]
c	15	0.0	0.23	0.05	103 [3]
20	30	2.50	0.22 <sup>d</sup>	0.07 <sup>d</sup>	102 [4]
c	15	0.0	0.07 <sup>d</sup>	0.03 <sup>d</sup>	104 [3]

<sup>a</sup> Average time required for reversal point to be recovered after replacing capacity that was removed during the brief reversal.

<sup>b</sup> Values in brackets give the number of measurements made.

<sup>c</sup> Open-circuit stand.

<sup>d</sup> In 50% KOH solution. All other results were obtained in 35% KOH solution.

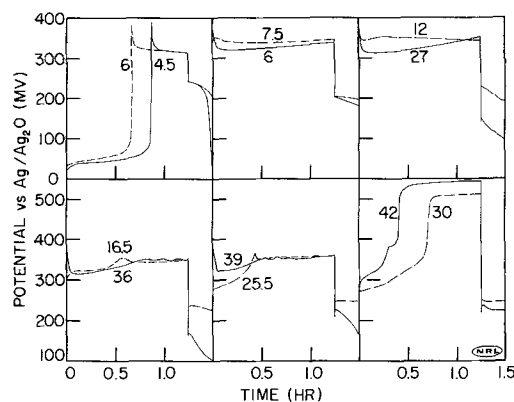


Fig. 3. Some excerpts of potentials measured in 35% KOH during two constant current charges of a silver electrode at the 20-hr rate. Charge current was reversed for 0.25 hr every 1.5 hr. Numbers by the curves give the total elapsed time in hours at the beginning of each excerpt. Charges produced 133% of normal capacity (solid lines) and 95% (dashed lines).

current, each additional hour of charge gave approximately 5% additional capacity. Table II includes a few open-circuit stands for comparison, although stands were quite ineffective for increasing capacity under these conditions. There was no significant difference between the results when the reversal potential was 440, 480, or 510 mv vs. the  $\text{Ag}/\text{Ag}_2\text{O}$  reference electrode; therefore, the results for these potentials are combined and summarized in Table II. Only five charges were done with 400 mv as the reversal potential, because the additional charge accepted when using this reversal potential was only 70 to 80% of the additional charge accepted at 440 to 510 mv. The results with 400 mv are not included in Table II. All reversal conditions listed in Table II resulted in increased capacity, although the increase was very small under some conditions.

The effect of two 30-min reversals at the 20-hr rate was tried with the commercial silver-zinc cells. The additional charge time in 35% KOH averaged 0.54 and 0.15 hr after the first and second reversals, respectively. These values were much less than the values obtained with the test cells in 35% KOH (top line of Table II). For the commercial silver-zinc cells containing 45% KOH, the additional charge averaged 0.21 and 0.08 hr after the first and second reversal, respectively.

## Discussion

The results obtained with relatively long reversals using a constant current (Table I) were, in general, markedly inferior to the results when the reverse current was derived from 60 cps asymmetric a.c. (3). No increase in capacity was obtained with most of

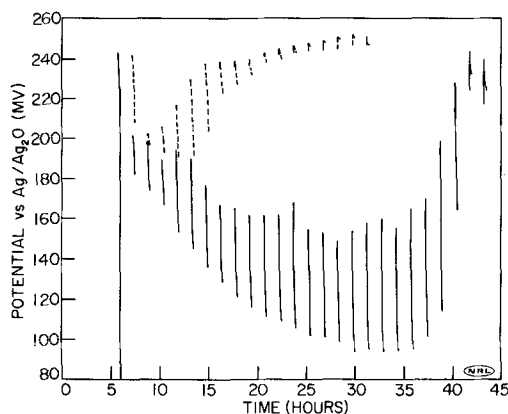


Fig. 4. Reversal potentials during the two charges shown in Fig. 3. Solid lines give reversal potentials during the charge which produced 133% of normal capacity and dashed lines give reversal potentials during the charge which produced 95%.



the long reversals that were tried. The only consistent and large increase came after a charge in which current was reversed for 15 out of every 60 min. This charge gave a capacity averaging 143% of the normal capacity, a value very close to the maximum capacity obtained following a charge in which current has held constant for long periods and then was increased for a few seconds (1). Approximately the same capacity was obtained when the electrode was charged by a rapidly pulsating unidirectional current (2), but a slightly larger capacity could be obtained following a charge with 60 cps asymmetric a.c. (3).

Although a large capacity was obtained by reversing the charge current for 15 out of every 60 min, a disadvantage of using long reversals was that the time required for a complete charge always exceeded 20 hr because of the necessity to replace the capacity removed during each reversal. Time could be shortened by having long charge periods between the reversal periods, but then it often happened that no reversal occurred near the end of a charge, at the point where potential changes during and after reversals seemed to indicate that reversals were most effective for increasing capacity. Although long reversals were the most beneficial reversals, not many charges with repeated discharges were tried in which over 1% of the capacity was removed with each reversal, because time required for a complete charge became excessive. For example, when the 20-hr charge current was used with current reversed for 15 out of every 60 min, 40 hr were required before a cell had a net charge of even 100% of normal capacity, and nearly 2.5 days were required for a complete charge. It should be noted, however, that the capacity averaging 143% of normal capacity obtained with this charge-discharge parameter was much larger than the 112% of normal capacity obtained after an electrode was charged using a steady constant current at the 2.5-day rate.

If maximum capacity is desired and total charge time is relatively unimportant, this charge with long reversals is preferable to a charge at a low constant current. If a constant discharge potential is desired, a low rate of constant charge current or the asymmetric a.c. (3) may be preferable. An electrode charged at a low current has less surface area than an electrode charged at a high current (5). The initial potential plateau during discharge of an electrode with small surface area is at a relatively low potential, because AgO on the surface is rapidly covered by Ag<sub>2</sub>O during discharge, judging by the results of x-ray diffraction (5); most of the discharge takes place at the Ag<sub>2</sub>O/Ag potential even though part of the current still is produced by the reduction of AgO. A low charge rate is preferable if the electrolyte concentration is high, for example 45 or 50% KOH. As charge current density increases, i.e., as charge time decreases, capacity falls more rapidly in concentrated KOH than in more dilute KOH. For example, when the commercial silver-zinc cells were charged at the 40-hr rate, a cell containing 45% KOH gave about 112% of normal (20-hr) capacity, while a cell containing 35% KOH gave only 105% of normal capacity.

Normal charge acceptance of a silver oxide electrode could be increased 15%, without charge time becoming excessive, by partially discharging the electrode once or twice near the end of a charge (Table II). The second reversal was not worth attempting unless a large amount of charge had been accepted after the first reversal. The additional charge after a second reversal was usually only 10 to 25% of the charge added after the first reversal. The few times that a third reversal was done at the same potential, added charge was less than it had been after the second reversal. Effectiveness of the reversals generally correlated with the amount of capacity removed. To obtain a capacity improvement that exceeded 10%,

the capacity removed during each reversal had to be over 1% of the normal electrode capacity. This result correlated with results found when reversals were repeated periodically throughout a charge (Table I). For a specific amount of reversal near the end of a charge, the rate of reversal current was also an important factor (Table II). Another important factor was electrolyte concentration. Although the added capacity was small under many of the conditions used, the recharge did always exceed the capacity removed during each of the two partial discharges.

Reports differ as to whether porous silver electrodes react first at the conducting grid or at the electrode surface. Romanov (6) used pressed silver powder electrodes and reported that the oxides were concentrated at the grid after a direct current charge. Dirkse (7, 8) reported that pellets of pressed Ag<sub>2</sub>O or AgO gave the potential of material next to the grid and not the potential of the bulk composition of the pellets. These results when pressed materials were used contrast with results obtained by x-ray diffraction of sintered silver electrodes (9) and of roughened sheet silver (5). Here the potentials were determined by the material on the surface, and oxidation of Ag<sub>2</sub>O and reduction of AgO took place initially on the surface of the electrode next to the solution. The newly formed oxide could be detected when it was present in a smaller amount than was necessary for detecting one component of a mixture by using x-ray diffraction. This indicated that when Ag<sub>2</sub>O was oxidized or AgO was reduced the initial formation must have been concentrated on the electrode surface. The initial formation of Ag<sub>2</sub>O on Ag was not detected as readily in x-ray diffraction patterns, because the initial oxidation occurred on the surface of silver particles which were distributed throughout the electrode. Similarly, the use of x-ray diffraction showed that when Ag<sub>2</sub>O was reduced relatively little Ag formed on the surface at first.

Microscopic examination of sintered silver electrodes has confirmed that the reactions are not concentrated at the grids. Microscopic examination of electrodes in various states of discharge indicated that Ag<sub>2</sub>O and Ag did not tend to form first at the grids and be concentrated there (4) nor did Ag<sub>2</sub>O and AgO tend to form first at the grids during a constant current charge (10). A large amount of unoxidized silver was still present in the vicinity of the grids at the end of a charge. Higher electrical resistance in some unsintered pressed powders may be the cause for the different behaviors that have been reported in the literature. All reactions may take place at the conducting grid with some pressed powder electrodes merely because there is less IR drop near the grid of these electrodes than there is at the electrode surface.

A large part of the silver had been oxidized to AgO by the time a normal charge of a sintered silver electrode ended, although substantial amounts of metallic silver remained with a thin coating of Ag<sub>2</sub>O separating the AgO from this Ag (4, 10). Much of the surface and many internal cavities were partially or completely filled with AgO crystals. When a nearly charged electrode was discharged briefly under the conditions in Table II, part of the AgO was converted to Ag<sub>2</sub>O. This reduction may have exposed some areas of the Ag<sub>2</sub>O-coated Ag that had been tightly covered by AgO crystals. Significant changes in crystal size and shape occur as the silver oxides are reduced or silver is oxidized (4, 10). AgO tends to form into much larger crystals than does Ag<sub>2</sub>O. Although the change in total volume is only slight as AgO is reduced to Ag<sub>2</sub>O, the crystal lattice is distorted as dimensions change in going from monoclinic to face-centered cubic crystals. Lattice dimensions indicate that a large expansion of the crystal occurs as metallic silver is oxidized to Ag<sub>2</sub>O and recent coulometric measurements have confirmed

that a large volume change occurs (11).

When a charge was resumed after a reversal near the end of a charge, current may have been divided between oxidizing the  $\text{Ag}_2\text{O}$  formed during the reversal and oxidizing  $\text{Ag}_2\text{O}$ -coated Ag that had been exposed where openings had formed in the AgO coating. A long reversal, during which relatively large amounts of AgO were reduced, probably exposed larger areas of  $\text{Ag}_2\text{O}$ -coated Ag than were exposed after short reversals. The excess of charge capacity over reversal capacity was, therefore, significantly larger after a long reversal than after a short reversal (Table II). Much of the current during a second reversal would probably reduce the same areas of AgO that were reduced after the first reversal. A second reversal was, therefore, much less effective than the first reversal in exposing Ag and promoting formation of additional AgO after the charge was resumed.

Although most of the periodic reversals repeated throughout a charge were not effective for increasing total charge capacity (Table I), the charges were of some interest because of the potentials observed. Figures 1 and 2 give potentials that were typical of all charges listed in Table I except for the charges with 15-min reversals. The potentials shown in Fig. 1 and 2 are generally similar, despite differences in reversal length, reversal repetition frequency, and per cent of time that current was reversed. During the early portion of the  $\text{Ag}_2\text{O}/\text{AgO}$  potential plateau, charge potential rose gradually after a reversal until a potential was reached which slightly exceeded the value measured just before reversal, and then potential slowly fell (Fig. 1 and 2). Later in the  $\text{Ag}_2\text{O}/\text{AgO}$  plateau the charge potential developed two steps after each brief reversal. During the first step the electrode charged at a potential only slightly above the  $\text{Ag}_2\text{O}/\text{AgO}$  equilibrium<sup>1</sup> until approximately 100% of the capacity lost during reversal had been replaced. Probably almost all current was oxidizing  $\text{Ag}_2\text{O}$  that had formed at readily accessible sites during the reversal. Then the reaction shifted to oxidation of sites which required more energy. Potential rose rapidly, passed through a maximum, and decreased slowly until a steady charging potential was reached again.

When current was reversed for 0.25 hr every 1.5 hr, the potential pattern obtained from the silver electrode during charges which gave improved capacity differed from the pattern during charges which gave normal capacity. During the charges which gave improved capacity, there was a potential maximum when charge current was resumed following each reversal at the  $\text{Ag}_2\text{O}/\text{AgO}$  potential plateau, except the final reversal before reaching oxygen evolution (solid lines in Fig. 3). Following these initial maxima, potentials fell to relatively low values during charges having improved capacity. There were only one or two such maxima during charges that gave normal capacity (dashed lines in Fig. 3) and the potential tended to have successively lower values as charge was resumed after each reversal. Charges having the highest capacity had low reversal potentials during most of the charge (Fig. 4) and high gas evolution potentials at the end of a charge (Fig. 3). A charge that gave the intermediate capacity of 116% had most reversal potentials in the range from 215 to 195 mv, intermediate between the two sets of values shown in Fig. 4. Thus, the relative discharge capacity that was going to be obtained could be predicted before this type of charge was half completed.

These potential changes during charges with relatively long reversals gave an indication of possible electrode conditions. After  $\text{Ag}_2\text{O}$  had started to oxidize to AgO, the first reversal began at a potential close to the  $\text{AgO}/\text{Ag}_2\text{O}$  equilibrium (Fig. 3, 4). At this time the electrode contained relatively large

amounts of  $\text{Ag}_2\text{O}$  and Ag, with a small amount of AgO present. Then, in the charges which gave improved capacity, came a series of reversals in which potentials were successively lower although increasing amounts of AgO were present on the electrode. Microscopic examination of electrodes during constant current charges indicated that all areas do not react simultaneously (10). AgO may form in one area while an adjacent area has no AgO. In charges with reversals which resulted in improved capacity, the AgO may have had a tendency to form a tighter coating or a thicker coating that blocked electrolyte channels more than usual and hindered ion movements. The successively lower discharge potentials probably resulted from a progressive hindrance to the reduction of AgO as the amount of AgO increased. The unusually low potentials during reversal were followed by charge potentials that began at a high value. Since the same amount of  $\text{Ag}_2\text{O}$  was produced during the reversal periods of both charges shown in Fig. 3, it was unlikely that the potential maxima on resuming charge were due to resistance of  $\text{Ag}_2\text{O}$ .

A change must then have occurred in the charges which gave improved capacity. Perhaps formation of AgO was initiated at new sites by the high potentials, or perhaps oxygen from the surface layers could penetrate deeper into the oxide layer under the influence of a high charging potential and could oxidize additional silver. When charge potential reached a maximum and then decreased, possibly the potential fall resulted from decreasing local current densities as AgO began to form in a larger number of sites, or possibly a blocking AgO coating cracked as a result of expansion as oxides formed below the AgO surface. Increased porosity would allow the electrolyte to penetrate nearer to the metallic silver that remained and result in decreased concentration gradients in the AgO layer. Charge potential fell to a value close to equilibrium values, lower than the potential of normal charges. Although the exact nature of the process is unknown, it apparently took place repeatedly and allowed more AgO than usual to be formed before diffusion through the AgO became sufficiently difficult that electrode potential rose to the oxygen evolution value. The few charges with periodic reversals which resulted in improved capacity (Table I) may have had charge and reversal periods proportioned correctly to give a potential maximum each time that charge was resumed.

After the initial potential maximum when charge was resumed, the charges which gave improved capacity often had additional smaller maxima as gradually rising potentials reached 351 to 355 mv (Fig. 3). Potentials dropped 4 to 10 mv after reaching the maxima and then again increased gradually. Many more of these slow potential fluctuations occurred in charges that gave the high capacity than in other charges. Charges at the 20-hr rate which gave normal capacity usually exceeded 355 mv only when potential made the sharp rise from the  $\text{Ag}/\text{Ag}_2\text{O}$  plateau to the  $\text{Ag}_2\text{O}/\text{AgO}$  plateau and again as potential rose slowly near the end of a charge (Fig. 1 and 2).

The differences between results with the commercial silver-zinc cells and the test cells were probably due mainly to different concentration gradients, but the exact nature of the process is unknown. The commercial cells were tightly packed and had little free electrolyte. This arrangement should result in concentration gradients near the electrode surface being larger in the commercial cells than they were in the test cells at the same current density. It is possible that zincate ions had diffused through the separator and reached the electrolyte which contacted the Ag electrodes, but it is doubtful that the presence or absence of zinc was an important factor.

### Summary

During charges of sintered silver electrodes of the type used in storage batteries, in one set of condi-

<sup>1</sup>The equilibrium potential of the  $\text{Ag}_2\text{O}/\text{AgO}$  couple vs.  $\text{Ag}/\text{Ag}_2\text{O}$  has been given as 261 mv (8) and as 262 mv (12).

tions periods of constant current charge were separated by shorter periods of constant current discharge. Current reversals lasting 0.01 to 3 min repeated every 1 to 30 min at the 20-hr rate had little effect on charge acceptance. Reversals of 15 min repeated every 60 min during a charge at the 20-hr rate increased capacity of test cells by an average of 43% in 35% KOH, but had the disadvantage of greatly increasing the total time required for a charge. Capacity was, however, much larger than the capacity obtained from an uninterrupted constant current charge requiring the same total time. More widely separated reversals of 15 min gave less improvement. Reversals seemed most effective for increasing capacity when they occurred near the end of a charge.

In another set of conditions, the silver electrodes were partly discharged the first two times that charge potential reached a chosen value near the end of a charge. Average capacity of test cells was improved by up to 16% without charge time becoming excessive. Effectiveness of reversals near the end of a charge correlated with the amount of capacity removed and was also affected by the rate of the reversal current. The second reversal gave much less added capacity than the first reversal gave.

In general, as KOH concentration increased, capacity improvement decreased. Commercial silver-zinc cells always gave less increase in capacity than the test cells gave.

Manuscript submitted Mar. 25, 1968; revised manuscript received June 12, 1968. This paper was presented at the Chicago Meeting, Oct. 15-19, 1967, as Paper 42.

Any discussion of this paper will appear in a Discussion Section to be published in the June 1969 JOURNAL.

#### REFERENCES

1. C. P. Wales, *This Journal*, **111**, 131 (1964).
2. C. P. Wales, *ibid.*, **113**, 757 (1966).
3. C. P. Wales, *ibid.*, **115**, 680 (1968).
4. C. P. Wales and A. C. Simon, NRL Rpt 6647, Jan. 9, 1968.
5. C. P. Wales and J. Burbank, *This Journal*, **112**, 13 (1965).
6. V. V. Romanov, *Zhur. Priklad. Khim.*, **33**, 2071 (1960).
7. T. P. Dirkse, *This Journal*, **107**, 859 (1960).
8. T. P. Dirkse, *ibid.*, **109**, 173 (1962).
9. C. P. Wales and J. Burbank, *ibid.*, **106**, 885 (1959).
10. C. P. Wales and A. C. Simon, To be published.
11. A. Langer and J. T. Patton, *This Journal*, **114**, 113 (1967).
12. J. F. Bonk and A. B. Garrett, *ibid.*, **106**, 612 (1959).

## A Coulogravimetric Investigation of the Zinc Electrode in Potassium Hydroxide

A. Langer\* and E. A. Pantier

Westinghouse Research Laboratories, Pittsburgh, Pennsylvania

#### ABSTRACT

The presented results obtained by weighing the zinc electrode in the electrolyte during the discharge cycle agree with data of others and explain why the capacity of the zinc electrode is a function of the amount of electrolyte used and roughly linearly dependent on the concentration of the potassium hydroxide up to about 10M. Previous results, that part of the zinc goes into solution, part is precipitated out as oxide or hydroxide, and that some adherent layer is formed which finally forces the potential of the plate to drop sharply, are substantiated on a more quantitative basis. The experiments also indicate that the relatively thick scale formed might not be the sole cause of the passivation phenomena.

The zinc electrode dissolves on discharge in an alkali electrolyte to form the tetrahydroxo zincate ion. This reaction was first proposed by Dirkse (1) and has been confirmed by such recent investigations as nuclear magnetic resonance (2) and infrared absorption spectra (3). Polynuclear forms, however, have been suggested from diffusion measurements (4). The formation of oversaturated solutions is favored by anodic action.

One can also observe that the surface of the electrode becomes covered during its working cycle, usually with a dark colored substance (5), and that a precipitate appears in the electrolyte. These solid substances have been identified as zinc hydroxides, oxides, or oxyhydroxides (6), but according to Feitknecht (7) there are many modifications of each. As the work of Flerov (8) indicates, only one form imparts passivity to the zinc electrode.

To gain some additional information about the behavior of the zinc electrode in potassium hydroxide electrolyte, coullogravimetric analysis was used. The underlying principle of the method has been described (9) and is based on the continuous weighing

of the electrode in the electrolyte during the discharge cycle of the zinc electrode. The weight loss, considering buoyancy, is correlated with other simultaneously recorded parameters such as the quantity of electricity passed and electrode potential.

For the recording of weight change, a torsion balance was converted for automatic weight registration. The current from the cell was passed through the torsion bands without any noticeable effect on the weighing (Fig. 1). The whole assembly including the cell was encased in an air-tight box. Thus, by maintaining a controlled atmosphere, the electrolyte was protected during long runs from the influence of carbon dioxide in air and from excessive evaporation. It should be mentioned that the hunting tendencies of the automatic weighing arrangement do impart small but noticeable vibrations to the sample which may slightly stir the solution, enough so that density gradients around the electrode might be minimized (10).

#### Experimental

The half cell consisted of a flat thin zinc sheet of high purity (Fisher Certified A.C.S.), with 100 cm total area counting both sides, and weighing about

\* Electrochemical Society Active Member.

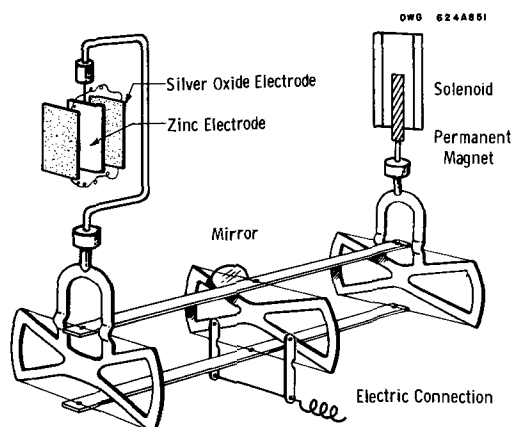


Fig. 1. Automatic weighing arrangement for coulgravimetry with torsion balance.

20g. Sintered silver plates of the same dimension (7 x 7 cm) but of large capacity by combining several plates in parallel were wrapped in cellophane and placed on both sides of the zinc. The spacing between the plates was rather narrow, so that 50 ml of the electrolyte, used throughout the experiments, completely covered the electrodes. Potassium hydroxide solutions, as carbonate free as possible, were prepared of different strength and the concentration determined by titration. These solutions were then saturated with zinc oxide (Fisher certified A.C.S.) by shaking for several days at room temperature. The zinc content was found polarographically after dilution of 1 or 2 ml to 50 ml with 1M KOH. Some care has to be exercised in the polarographic zinc determination, because the diffusion current decreases appreciably with increasing alkali concentration of the supporting electrolyte. Determinations of zinc were performed in a like manner on centrifuged solutions obtained after the cell ceased to function. Density of the electrolyte saturated with zinc oxide was also measured before and after the zinc electrode reacted in the discharge cycle until it became passivated. The results of these measurements are shown in Fig. 2. There was a noticeable increase in density of the electrolyte after the zinc plate was discharged. The values of density were used to apply the buoyancy corrections to the measured weight values. Similar data have already been published (11).

The silver electrode was always freshly charged and wrapped in new cellophane. A new zinc plate, abraded with fine steel wool and washed with acetone and water and new electrolyte, was also used for each experiment. An Hg/HgO reference electrode, connected by a bridge, confirmed that it was always

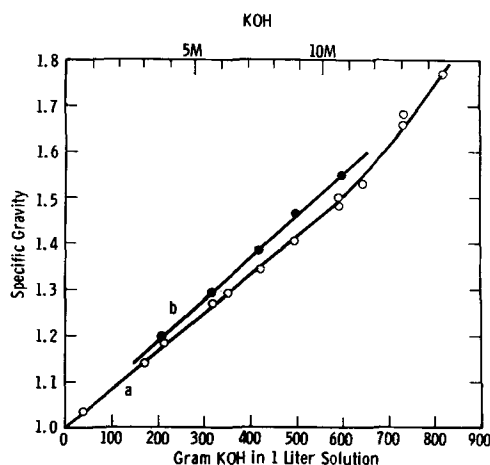


Fig. 2. Specific gravity of KOH solutions saturated with ZnO (a), saturated by discharging a zinc electrode until passivation (b).

the zinc electrode which failed in these experiments. The current flowing through the cell was calculated by Ohm's law from the continuously monitored potential across a calibrated 5.00 ohm resistance, which was also used to limit the discharge rate. The potentials across the resistance are represented by the upper graph A in Fig. 3, whereas the weight change as measured in the different electrolytes is shown by the lower graph B as a chronogravimetric relation. Just a few such relations are discussed.

Curve (a) represents a discharge in 40g KOH/liter. The current was low from the start and relatively little zinc was lost since the battery failed very early. Using 174g KOH/liter, it can be clearly seen that the weight of the electrode first decreases with time as shown in solid curve (b). From the ampere-hours passed one can also determine a theoretical curve for zinc loss by using Faraday's law, assuming no side reaction, and making correction for the buoyancy effect in the given electrolyte of known density. The dashed curve (b') was thus obtained. The two curves coincide at the beginning quite well but after a certain time the measured weight loss starts to decrease and the two curves deviate, until the zinc electrode loses no weight at all, although still delivering the same current as before. Only when the weight of the zinc plate actually starts to increase slightly does the potential and therefore the current output of the cell drop sharply, indicating that the electrode has reached a state of passivation.

An electrode in a solution of 213g KOH/liter behaved similarly, as indicated by curves c in Fig. 3. The total amount of reacted zinc was greater in this case. Again at the beginning of discharge, the electrode loses weight according to Faraday's law, but later the weight loss diminishes, finally leveling off. Only when the weight curve starts to bend upward is there a sharp drop in potential registered and the battery fails. From the current delivered, the weight loss should follow dashed curve c'.

The same trends can be observed with 310g KOH/liter and the electrode is active for a still longer time (Fig. 4, curve a). The upward swing in the weight curve forecasting the end of the reaction is no longer pronounced. At even higher electrolyte concentrations (490 and 595g KOH/liter) the electrode behaves somewhat differently as shown in the curves (b) and (c) of Fig. 4. The zinc electrode loses weight almost constantly during the entire discharge life and levels off only at the very end, followed by a sharp decrease in current output. The weight loss seems to proceed even at a slightly faster rate than calculated from the ampere-hours

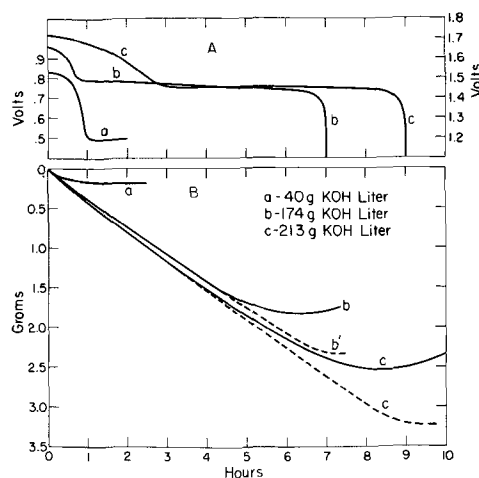


Fig. 3. A. Chronopotential relations across a 5 ohm bleeder resistor to calculate the current output. B. Chronogravimetric relations of the zinc electrode at different KOH concentrations. Solid line, as measured; dashed line, weight loss of zinc electrode calculated from coulombs passed with buoyancy corrections.

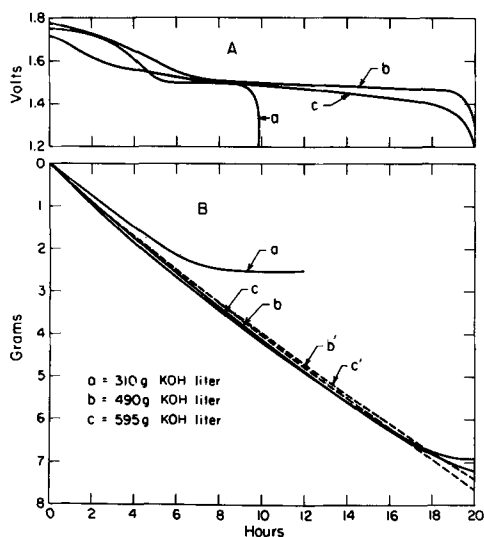


Fig. 4. A. Chronopotential relations across 5 ohm bleeder resistor. B. Chronogravimetric relations at different KOH concentrations. Solid line, as measured; dashed line, evaluated from A with buoyancy corrections.

delivered, as shown in dashed curves b' and c', which could mean an additional purely chemical attack, although no visible gas evolution was detected. The difference is not large enough to be caused by varying density factors. Still another phenomenon was noted. After some discharge had occurred, the weight loss did not proceed smoothly as in the beginning but in a rather irregular fashion. This behavior was traced to the formation of large blisters on the surface of the electrode which were flaking off, resulting in the erratic weight curve. Similar curves were obtained at higher concentrations of KOH but without a substantial increase in the amount of zinc reacted.

### Discussion

Let us correlate the concentration of the electrolyte with the weight loss of the electrode. First consider the leveling off of the weight curve. Figure 5 represents the idealized behavior of a zinc electrode in an electrolyte of 1.25 specific gravity, or about 5M. If a soluble complex is formed, the electrode should lose  $m = 1.22\text{g}$  of zinc for each ampere hour. Due to the buoyancy effect, taking into account the density of the zinc ( $d_{\text{Zn}}$ ) and the electrolyte ( $d_s$ ), the observed loss in the electrolyte will be only about 1g, calculated by the equation  $m^s = m(1 - d_s/d_{\text{Zn}})$ . In case ZnO were formed as an adhering compound, the increase in weight per ampere-hour would be close to 0.3g by weighing in air or, with buoyancy correction, an indicated increase of only 0.23g. Similar relations can be found for the formation of  $\text{Zn}(\text{OH})_2$  or any other compound, provided the density of the compound is known. Since at a certain time the balance registers no weight change, this must mean that the rate of zinc dissolution is equal to the oxide or hydroxide formation at the surface. We can easily calculate that at this point of no weight loss over 80% of the reacting zinc must be converted to a compound adhering to the electrode while less than 20% is still dissolving in the electrolyte.

Figure 6 shows the relation between potassium hydroxide concentration and the amount of Zn found in the electrolyte. This graph was derived from many more experiments of the type just described. It can be seen on the curve with circles that the amount of zinc dissolved in potassium hydroxide by shaking with zinc oxide is rising with increasing hydroxide concentration. At 800g KOH/liter, almost 180g Zn/liter is in the solution at room temperature. These

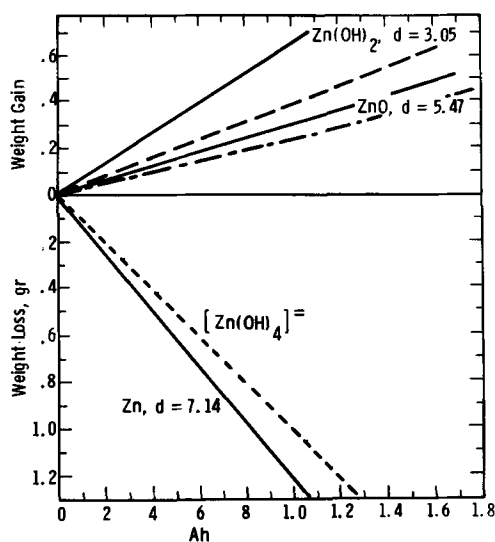


Fig. 5. Idealized behavior of a zinc electrode in an electrolyte of 1.25 density. Solid lines, weight change in air; dashed lines, weight change with buoyancy effect of electrolyte.

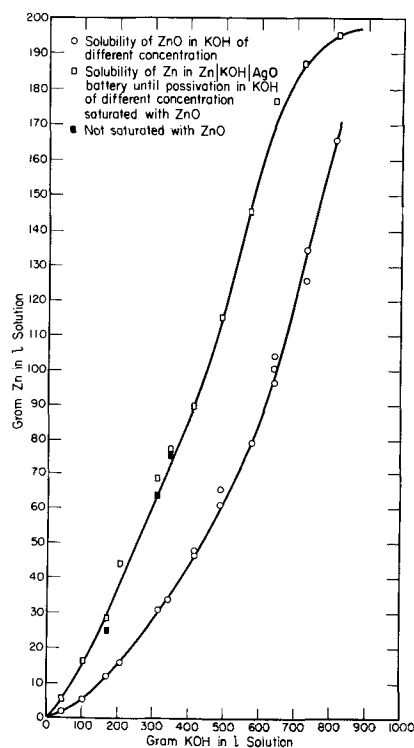


Fig. 6. Solubility of zinc oxide and of the zinc electrode in potassium hydroxide of increasing concentration.

results, of course, apply to the particular form of oxide used.

On the same graph the upper curve with squares is a plot of the zinc concentration in the electrolyte after the cell has been drained to the point of passivation. As can be noticed, quite an additional amount of zinc is present now in the electrolyte. Actually at lower KOH concentrations, almost the same amount of the zinc electrode dissolves during the discharge cycle as is derived from the solubility of zinc oxide directly. At higher KOH concentration this amount has diminished.

The increase in zinc concentration by battery action is usually referred to as the formation of a supersaturated solution. But under the prevailing conditions of relative stability one could consider, since the amount of zinc present in the solution is about twice the concentration of a ZnO-saturated solution, the formation of a soluble zinc-zincate ion or a complex

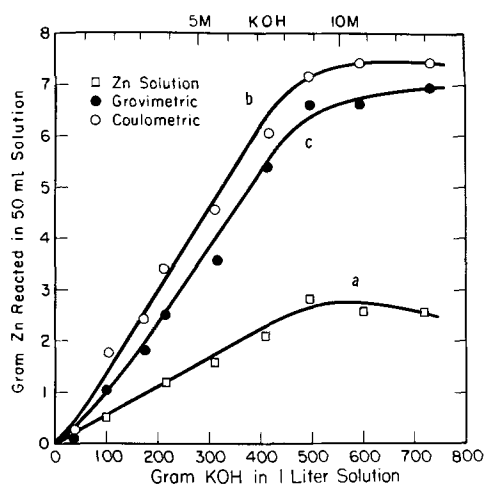


Fig. 7. Reaction of the zinc electrode as a function of KOH concentration.

of the type  $[\text{Zn}_2(\text{OH})_6]^-$  may also be possible. This complex only slowly decomposes to zinc oxide on standing. It should be mentioned that the same total amount of zinc in the electrolyte is obtained by anodic action whether one takes a zinc oxide saturated solution or an electrolyte initially free from zinc ions as indicated by the black squares. Without the zinc oxide dissolved, the capacity of the cell is correspondingly larger. This condition would be advantageous for primary batteries, but for fast recharging in secondary batteries it is advantageous to have an excess of zinc ions in the electrolyte.

If we now plot the difference between these two curves we obtain curve (a) indicated by squares in Fig. 7. This is the amount of zinc introduced into the electrolyte strictly by the dissolution of the zinc electrode into a zinc oxide saturated solution of potassium hydroxide. The circles (curve b) represent the amount of zinc reacted as calculated from the ampere-hours the battery has delivered. This latter value is as seen quite higher. Both are a function of electrolyte concentration as was indicated in previous findings by Shepherd (12) and Sanghi (13). The difference between the two curves must represent the amount of precipitated zinc compound, either adhering to the electrode, dispersed in the electrolyte, or settled to the bottom of the cell. The difference between the weight of the electrode as determined by direct weighing in the electrolyte with buoyancy correction (curve c, Fig. 7), and by calculating from Faraday's law must contain the weight of the zinc tied up as a precipitate adhering to the surface of the electrode. It is a relatively small fraction of the total as indicated on the graph and surprisingly constant through the large range of KOH concentra-

tions. The data are probably not too precise, but attempts to weigh the precipitate in the solution failed, because the compound was also dispersed within the cellophane wrapping around the silver. Also, partial disintegration of the adhering layer on the zinc plate, when taken out of the electrolyte, made the weighings of the zinc electrode in air before and after the reaction rather indecisive. One conclusion that can be drawn from Fig. 7 is that the zinc electrode does not derive its whole capacity from dissolution as zincate but a large portion by the formation of a nonadhering precipitate. The output of the cell increases markedly from low values with the increasing KOH concentrations and a maximum is reached at around 10M potassium hydroxide.

By the weighing procedure it was indicated that a surface layer must be formed which adheres at lower concentrations of potassium hydroxide KOH and peels off easily at high concentrations, in order to explain the leveling off of the weight curve as shown in Fig. 3 and 4. But this relatively thick layer cannot solely be responsible for the passivation of the electrode. The fact that passivation occurs rather abruptly and always when the weight-coulomb curve is on a slight increase might indicate that a thinner and denser layer is formed which blocks the electrochemical reaction. This film could be formed independently as a new phase on the surface of the zinc under the existing scale or by a recrystallization of the layer already present.

Manuscript submitted Feb. 13, 1968; revised manuscript received June 25, 1968. This paper was presented at the Philadelphia Meeting, Oct. 9-14, 1966, as Paper 46.

Any discussion of this paper will appear in a Discussion Section to be published in the June 1969 JOURNAL.

#### REFERENCES

1. T. P. Dirkse, *This Journal*, **101**, 328 (1954).
2. G. H. Newman and G. E. Blomgreen, *J. Chem. Phys.*, **43**, 2744 (1965).
3. J. S. Fordyce and R. L. Baum, *ibid.*, **43**, 843 (1965).
4. A. Brintzinger and J. Wallach, *Angew. Chem.*, **47**, 61 (1934).
5. T. P. Dirkse and F. De Haan, *This Journal*, **105**, 311 (1958).
6. K. Huber, *Z. Elektrochem.*, **62**, 675 (1958).
7. W. Feitknecht, *Werkstoffe und Korrosion*, **6**, 15 (1955).
8. V. N. Flerov, *Soviet Electrochem.*, **3**, 152 (1961), Consult. Bureau, New York.
9. A. Langer and J. Patton, *This Journal*, **114**, 113 (1967).
10. H. F. Eisenberg and H. F. Bauman, *ibid.*, **108**, 909 (1961).
11. T. P. Dirkse, *ibid.*, **106**, 154 (1959).
12. C. M. Shepherd, NRL Reports 3876, 4089, 5211.
13. Y. Sanghi and M. Fleischmann, *Proc. Ind. Acad. Sci.*, **46**, 309 (1957).

# Characterization of a Porous Graphite Cl<sub>2</sub> Electrode

Dominicus A. J. Swinkels\*<sup>1</sup> and Randall N. Seefurth<sup>2</sup>

General Motors Research Laboratories, Electric Powerplants Department, Indianapolis, Indiana

## ABSTRACT

An experimental grade of porous graphite known as Poco-AX has been characterized. The model previously developed for Cl<sub>2</sub> electrodes in fused LiCl was found to hold well under the conditions used. Although the material is 57% porous, its strength and machinability are excellent. Data are given for the pore size distribution, gas flow resistance, and electrical conductivity of the material. Performance as a Cl<sub>2</sub> electrode under various conditions of electrode thickness, Cl<sub>2</sub> pressure, and Cl<sub>2</sub> purity is described and compared with the theoretical model. It was demonstrated that current densities in excess of 10 amp/cm<sup>2</sup> can readily be obtained.

The requirements for gas diffusion fuel cell electrodes has led to the development and characterization of a variety of porous carbon and graphite materials (1, 2). Some of these materials have also been tested as Cl<sub>2</sub> electrodes for application in high power density and high energy density fused salt batteries such as the Li-Cl<sub>2</sub> battery (3, 4). The performance of various porous structures as Cl<sub>2</sub> electrodes in LiCl has been discussed in terms of the electrode porosity and pore size distribution (3) as well as the purity of the Cl<sub>2</sub> gas. The latter becomes particularly important when the porous carbon or graphite structure is optimized for high current density operations, since small amounts of inert impurities normally present in Cl<sub>2</sub> will then quickly build up in the electrode and poison it (5).

This paper reports on the characterization of a porous graphite known as Poco-AX,<sup>3</sup> which has demonstrated superior performance as a Cl<sub>2</sub> electrode in fused LiCl.

The AX grade is made by heating grade AC porous carbon to graphitization temperatures (2300°C) (6). The grade AC material has been previously described and tested for aqueous fuel cell applications (7). Both of these materials differ from the usual porous carbon and graphite materials in that they combine high porosity with very small pores and a very narrow pore size distribution. Table I shows a comparison with a more conventional material.

The materials from which AC and AX are prepared are considered proprietary by the manufacturer. The filler material used is smaller (less than 0.001 in. diameter) than that used in conventional graphites and the particles tend to be rounded (6). This seems to result in the narrower pore size distribution and the small pore size seen in AC and AX. Although no measurements have been made of the strength of these materials, general experience indicates that they are stronger than most porous carbons of similar porosity and can be machined to high tolerances. The graphitized material (AX) is preferred for use in high current density electrodes mainly because of its lower electrical resistivity. Therefore this material was tested extensively as a Cl<sub>2</sub> electrode in fused LiCl.

The pore size distribution of the AX material as determined by Hg intrusion measurements is shown in Fig. 1, together with a stepwise approximation which will be used in the theoretical treatment. The average tortuosity of the pores was determined by measuring the flow rate of N<sub>2</sub> through disks of the AX material at room temperature at various pressures across the disks and comparing them to calcu-

lated flow rates. The theoretical flow rates for a given porosity and pore size, taking into account both viscous (Poiseuille) flow and molecular streaming (Knudsen flow) (3), is given by

$$Q(r) = \phi(r) \left( \frac{\Delta P}{P} \right) \left[ \left( \frac{1.013 \times 10^6 r^2 (P_1 + P_2)}{16 \mu \tau t} \right) + \frac{4\delta r}{3\tau t} \left( \frac{2RT}{\pi M} \right)^{1/2} \right] \quad [1]$$

where  $Q(r)$  = the flow of gas in cc/sec through pores of radius  $r$  at pressure  $P$ ,  $\phi(r)$  = the volume of pores or radius  $r$  per cm<sup>3</sup> of electrode,  $P_1$  = the entrance pressure (atm),  $P_2$  = the exit pressure (atm),  $\Delta P = P_1 - P_2$ ,  $\mu$  = the gas viscosity (poise),  $\tau$  = the tortuosity of the pores,  $t$  = the thickness of the electrode (cm) in the direction of the gas flow,  $\delta$  = constant = 0.9,  $R$  = gas constant =  $8.317 \times 10^7$  erg/°K mole,  $T$  = temperature (°K), and  $M$  = the molecular weight of the gas.

The total theoretical flow rate through a piece of graphite with a range of different pore sizes is then given by

$$Q(\text{total}) = \sum_r Q(r) \quad [2]$$

The ratio of this calculated total flow using the step approximation of the pore size distribution to the experimentally determined flow leads to a tortuosity of 3.75. This is an unusually high tortuosity for so porous a material and is no doubt related to the method of manufacturing this material. It should be noted that the tortuosity found by a flow measurement heavily favors the tortuosity of the larger pores so that the tortuosity of the small pores may be quite different. However, a tortuosity of 3.75 will be used in all calculations.

## Cl<sub>2</sub> Electrode Model

A model has been developed describing the reaction kinetics at the porous graphite Cl<sub>2</sub> cathode (3). Because the fused LiCl electrolyte does not wet carbon or graphite, it is postulated that the reaction takes place in the interface region between the porous elec-

Table I. Comparison of porous carbon and graphite materials

	FC-11	Poco AC	Poco AX
Density, g/cm <sup>3</sup>	1.32	0.88	0.94
Resistivity, ohm-cm	0.005	0.010	0.004
Porosity, %*	35	56	57
Median pore diameter, $\mu$ *	5	1.4	1.4
Flow resistivity, mm Hg/cm	3**		16

\* Porosity as measured by Hg intrusion method; includes pores in the range of 100-0.035 $\mu$  in diameter.

\*\* "Carbon Electrodes for Fuel Cells." Pure Carbon Company Technical Bulletin No. 964, p. 2.

\* Electrochemical Society Active Member.

<sup>1</sup> Present address: B.H.P. Research Laboratories, Newcastle, New South Wales, Australia.

<sup>2</sup> Present address: General Motors Research Laboratories, Electric Powerplants Department, Warren, Michigan.

<sup>3</sup> Poco grade AX porous graphite is available in experimental quantities from Poco Graphite Inc., P. O. Box 1524, Garland, Texas 75041.



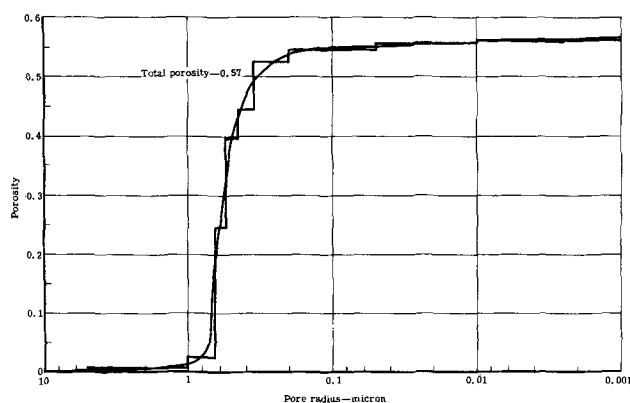


Fig. 1. Pore size distribution for POCO-AX graphite

trode and the electrolyte and not deep within the pores as is the case in most aqueous porous electrodes.

The over-all process at the Cl<sub>2</sub> electrode can be divided into the following five steps: (i) flow and diffusion of Cl<sub>2</sub> gas through the porous plug, (ii) dissolution of Cl<sub>2</sub> at the gas-liquid interface, (iii) diffusion of dissolved Cl<sub>2</sub> to the carbon-LiCl interface, (iv) dissociation and charge transfer, and (v) migration of Cl<sup>-</sup> ions into the bulk electrolyte. Steps (ii) and (v) are fast mass transport steps which have negligible effect on the polarization. Step (iv) occurs at the actual electrode-electrolyte interface and gives rise to the activation polarization. Steps (i) and (iii) give rise to the concentration polarization with the relative contribution of these two steps being determined mainly by the pore radius.

The maximum current density (amp/cm<sup>2</sup>) which a nonwetted electrode with pores of radius  $r$  (cm) can support is given by Eq. [3]

$$i_L(r) = \frac{AnFDKP_2\phi(r)}{r} \quad [3]$$

where  $A$  = constant  $\approx 8$ ;  $n$  = number of electrons, 2;  $F$  = Faraday, 96487 coul mole<sup>-1</sup>;  $D$  = diffusion coefficient of Cl<sub>2</sub> (in LiCl at 650°C  $D \approx 4 \times 10^{-5}$  sec<sup>-1</sup>);  $K$  = Henry's law constant, 10<sup>-6</sup> moles cm<sup>-3</sup> atm<sup>-1</sup> at 650°C;  $P_2$  = Cl<sub>2</sub> pressure at the gas-liquid interface; and  $\phi(r)$  = volume of pores of radius  $r$ /cm<sup>3</sup> of electrode.

The total current density for an electrode with a range of different pore sizes is then given by

$$i_L(\text{total}) = \sum_r i_L(r) \quad [4]$$

The partial pressure of Cl<sub>2</sub> at the gas-liquid interface ( $P_2$ ) is equal to the total pressure ( $P_T$ ) in the gas-stream feeding the electrode minus the pressure drop ( $\Delta P$ ) across the electrode and minus the partial pressure of impurities  $P_s(i)$  in the gas at the gas-liquid interface, i.e.,

$$P_2 = P_T - \Delta P - P_s(i) \quad [5]$$

The pressure drop  $\Delta P$  is determined by the flow resistance in the pores to the Poiseuille flow (viscous) and the Knudsen flow (molecular streaming).

For a single pore size,  $r$

$$\Delta P(r) = \frac{i_L R T L}{n F \phi(r)} \left[ \frac{16\mu}{1.013 r^2 [2P_T - \Delta P(r)]} + \frac{3}{48r} \left( \frac{\pi M}{1.6634T} \right)^{1/2} \right] \quad [6]$$

where  $R$  = gas const = 82.082 cm<sup>3</sup> atm deg<sup>-1</sup> mole<sup>-1</sup>, and  $L$  = pore length =  $\tau r$ .

For a piece of carbon with a variety of parallel flow paths of different radii, Eq. [6] becomes

$$\Delta P = \frac{1}{\sum_r \frac{1}{\Delta P(r)}}$$

The viscosity of Cl<sub>2</sub> gas ( $\mu$ ) used in Eq. [6] is given in centipoise by (8)

$$\mu = 1.4329 \times 10^{-4} + 4.6979 \times 10^{-5} T - 3.7158 \times 10^{-9} T^2 - 4.0541 \times 10^{-12} T^3 \quad [8]$$

The build-up of electroinactive impurities in flow-by electrodes, i.e., electrodes which have an excess of chlorine flowing behind the porous electrode to remove impurities from the electrode, has been previously treated (5) and is given by

$$P_s(i_L) = N_o P_T \exp \left( \frac{i_L R T \tau t}{n F P_T \phi_T D'} \right) \quad [9]$$

where  $P_s(i_L)$  = impurity pressure in the gas at the gas-liquid interface at the limiting current density  $i_L$  (amp/cm<sup>2</sup>),  $N_o$  = impurity mole fraction in the feed gas, and  $\phi_T$  = total porosity.

The diffusion coefficient  $D'$  for a binary gas mixture may be calculated (9) from

$$D' = \frac{0.001858 T^{(3/2)} \left( \frac{M_1 + M_2}{M_1 M_2} \right)^{1/2}}{\Omega_D P \left( \frac{\sigma_1 + \sigma_2}{2} \right)^2} \quad [10]$$

where  $T$  = temperature (°K),  $M_1$ ,  $M_2$  = molecular weights of the two gases,  $\sigma_1 \sigma_2$  = collision diameters (angstroms), and  $\Omega_D$  = collision integral available from tables.

For a mixture of Ar and Cl<sub>2</sub>,  $M_1 = 39.95$ ,  $M_2 = 70.91$ ,  $\sigma_1 = 3.418$ ,  $\sigma_2 = 4.115$ , and  $\Omega_D = 0.8652$ . This leads to  $D' = 0.84/P$ , where  $P$  = total pressure in atmospheres. This value of  $D'$  for the diffusion of impurities in the gas phase was entered in Eq. [9] and used in the calculations of the limiting current density for the POCO-AX graphite.

It is clear that  $P_2$  of Eq. [3] is a complex function of  $i_L$  and no explicit equation, therefore, can be written for  $i_L$ . A computer program was written to calculate  $i_L$  by an iteration process. The results of these calculations will be compared with the experimental data in the Discussion section. Inputs to the program consisted of the porosity and pore size distribution of the POCO-AX material and the various constants used in Eq. [1] to [10].

The pore size distribution was approximated by an 11 step staircase function also shown in Fig. 1. If we assume a random distribution of these pores throughout the bulk of the porous graphite then the same distribution will occur at any plane through the graphite such as the surface of the electrode. When current is drawn the total pressure in the pores is reduced and the electrolyte is drawn some distance into the larger pores thus contacting additional small pores. Since these small pores are very active (Eq. [3]) it is necessary to include them in the calculation of the limiting current density. This effective roughness due to penetration of LiCl into the larger pores was allowed for in the calculations by multiplying the number of small pores calculated from the measured porosity by a factor of 2 to 5. The effective roughness is really a variable quantity which should increase with increasing  $\Delta P$ . However, this added complexity of a variable roughness factor was not used. Table II shows the steps used in the computer program.

### Experimental Cells

Concentration polarizations were determined for POCO-AX porous graphite electrodes 1/8 in. and 1/16 in. thick at 1, 2, and 5 atm pressure each at 4 impurity levels.



Table II. Porosity-pore size steps used in computer calculations

Pore radius (microns)	Porosity
5.0	0.005
1.0	0.02
0.65	0.22
0.55	0.15
0.45	0.05
0.35	0.08
0.20	0.02
0.05	0.02*
0.01	0.015**
0.0025	0.015**
0.001	0.015**

\* Actual porosity  $\times 2$  to allow for effective roughness factor.  
 \*\* Actual porosity  $\times 5$  to allow for effective roughness factor.

A schematic diagram of the working parts of the cell used for these studies is shown in Fig. 2. LiCl electrolyte was contained in a Graph-i-tite A<sup>4</sup> crucible with a porous graphite bottom made of the Poco-AX test material. This porous graphite, to which Cl<sub>2</sub> or varying mixtures of Cl<sub>2</sub> and Ar could be fed, was the working electrode. A Graphite-i-tite A flow-by adaptor below the porous graphite disk ensured uniform gas flow past the entire inner electrode surface; a quartz tube on top of the electrode exactly defined the electrode area. The reference and counter electrodes were mounted concentrically. The reference electrode was electrically isolated by means of a quartz tube and was slipped inside a hollow counter electrode which was grooved to permit maximum surface area and slotted to prevent pressure differences between the inside and outside of the electrode. The entire assembly was placed inside a Vycor tube and heated by means of clamshell heaters outside the Vycor container for most of the 1 atm tests.

For the 2 and 5 atm tests, the Vycor tube was replaced by an outer stainless steel container (Type 316) with a Graph-i-tite A liner to protect the stainless steel from attack by hot Cl<sub>2</sub>. Flanges and cooling coils were welded on at both ends of the stainless steel pipe and the inside was bored out to a uniform circular diameter. A 0.5 in. wall Graph-i-tite A tube was machined to match the stainless steel pipe so that an average spacing of 0.010 in. existed between the graphite liner and the container. This space was filled with a suspension of Corning solder glass No. 7570 which was subsequently fused to provide an impervious coating between the graphite liner and the stainless steel.

Clamshell heaters around the center portion of the container provided the heat to raise the cell temperature to 650°C, while cooling coils near the flange cooled the ends sufficiently so that Teflon gaskets and insulators could be used. All gas lines to and from the cell were stainless steel tubing with Al<sub>2</sub>O<sub>3</sub> electrical isolators where necessary.

The gas mixtures used were prepared by mixing the required amounts of high purity Cl<sub>2</sub><sup>5</sup> and argon and checking the composition of the exit gas from the cell by gas chromatography.

#### Electrical Instrumentation

The method used to obtain polarization data was to pass a d-c current between the working and counter electrodes. This current was interrupted for less than 10<sup>-3</sup> sec about 10 times per second by means of a pulse generator, during which time the polarization was observed on an oscilloscope while no current flowed.

The over-all electrical circuit is shown in Fig. 3. The current flowing through the cell at any time is drawn from lead-acid batteries through the current controller. The working to reference electrode voltage

<sup>4</sup> Grade of dense graphite available from the Basic Carbon Corporation, Blank and Walmore Roads, Sanborn, New York 14132.  
<sup>5</sup> 99.975% pure Cl<sub>2</sub> available from Precision Gas Products, Inc., 817 East Linden Avenue, Linden, New Jersey 07036.

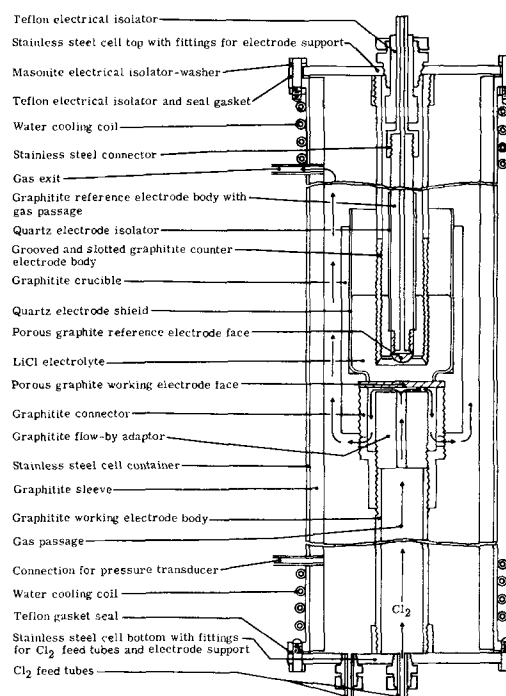


Fig. 2. Pressure test cell

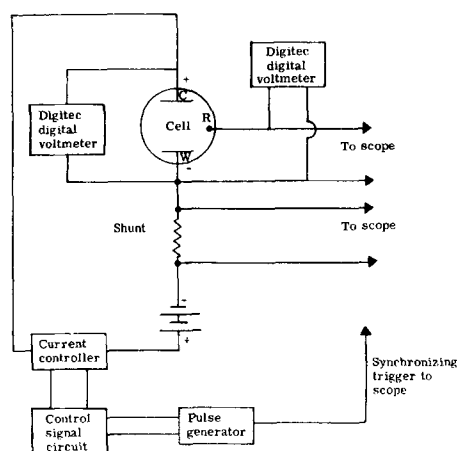


Fig. 3. Over-all electrical circuit: C, counter electrode; R, reference electrode; W, working electrode.

and the working to counter electrode voltage were monitored continuously on digital voltmeters.

Two current controllers of the same general design were used. The first one was capable of controlling currents up to 70 amp which was sufficient for the early one atmosphere part of the work. However, as the work progressed, it became necessary to use higher currents to produce the desired polarization and a 150 amp current controller was constructed. This controller was designed to allow currents up to 150 amp to be cut off in less than 100  $\mu$ sec. A simplified block diagram of the controller is shown in Fig. 4.

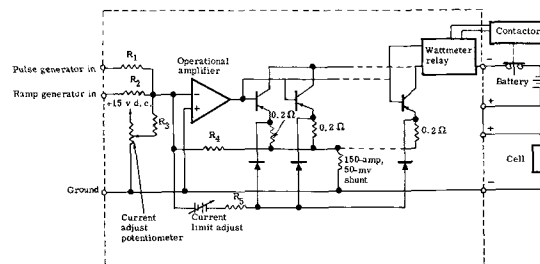


Fig. 4. Simplified diagram of the 150-amp current controller

Table III. Electrode performance data in amp/cm<sup>2</sup>

% Cl <sub>2</sub> →	1 atm				2 atm				5 atm				
	50	80	95	99+	50	80	95	99+	50	80	95	99+	
1/8-in. electrode	0.1 V	0.37	0.71	1.34	1.90	0.37	1.06	2.34	4.30	0.52	1.53	2.65	(5.40)
	0.2 V	0.48	0.94	1.58	2.46	0.47	1.24	2.60	5.87	0.59	1.70	3.04	(8.10)
	0.4 V	0.53	1.09	1.80	2.99	0.56	1.41	2.76	6.53	0.64	1.78	3.28	(11.40)
	0.6 V	0.56	1.16	1.87	3.29	0.62	1.48	2.90	6.76	0.67	1.89	3.39	(13.20)
	0.8 V	0.58	1.23	1.96	3.47	0.66	1.56	2.96	7.01	0.70	1.94	3.50	(14.50)
1/16-in. electrode	1.0 V	0.59	1.25	2.01	3.57	0.68	1.61	2.99	7.17	0.71	1.97	3.60	(15.45)
	0.1 V	0.47	1.02	1.73	2.98	0.60	1.59	3.24	(2.05)	0.71	1.91	3.89	(3.50)
	0.2 V	0.65	1.42	2.37	3.98	0.78	1.91	3.70	(4.30)	0.83	2.17	4.25	(6.63)
	0.4 V	0.76	1.68	2.86	4.87	0.90	2.16	4.12	(8.40)	0.91	2.32	4.42	(12.25)
	0.6 V	0.83	1.84	3.12	5.29	0.97	2.26	4.32	(11.33)	0.97	2.44	4.57	(17.40)
	0.8 V	0.86	1.89	3.21	5.59	1.00	2.33	4.43	(12.65)	1.00	2.49	4.66	—
	1.0 V	0.88	1.93	3.30	5.74	1.01	2.41	4.50	(13.15)	1.02	2.54	4.72	—

Current in the controller is provided by either a battery or low ripple d-c supply. Control of this current is accomplished by 15 germanium power transistors in parallel to provide reasonable power dissipating capabilities. Current flow through the 150 amp shunt provides a 0 to 50 mv current signal which is connected through feedback resistor R<sub>4</sub> to the operational amplifier input. A d-c voltage from the current adjust potentiometer and external signals from a ramp or pulse generator are also connected to the amplifier input.

Normal operation is to set the current adjust potentiometer to obtain the required steady-state current flow through the cell. The pulse and ramp signals are zero at this time. The output of the operational amplifier goes negative just enough to make the currents in R<sub>3</sub> and R<sub>4</sub> equal. If a negative pulse of sufficient amplitude is fed in, the output power transistors are turned off and the current through the cell is reduced to essentially zero.<sup>6</sup> The time required for the cell current to be turned off varies from 30 to 80 μsec depending on the initial d-c current flow, and the cell impedance.

#### Testing Procedure

After the cell was assembled, it was placed inside the furnace and connected to the gas feed system, the gas analysis system, and the electrical system. The cell was then purged with Ar and heated gradually to 400°C to remove any water vapor. Cl<sub>2</sub> was then purged through the cell and the temperature was increased to 650°C. The cell was kept at operating temperature with Cl<sub>2</sub> passing through it for 16-20 hr to treat the electrodes and purge the system. After this Cl<sub>2</sub> bake treatment was completed, the Cl<sub>2</sub> was flushed out with Ar, the reference electrode was removed, and the LiCl electrolyte was added to the cell through the hollow counter electrode. When the electrolyte had melted, the reference electrode was replaced in the cell. While the system was reaching thermal equilibrium, Cl<sub>2</sub> and Ar flows were started and adjusted to give the required gas composition as determined by the gas chromatograph. After all systems had reached equilibrium, sufficient current was passed to polarize the working electrode to 0.5v. The flow rates of the gases were then adjusted to give 100% excess Cl<sub>2</sub> over that required to support the current being drawn at 0.5v polarization while maintaining the gas composition. Data were taken after the new flow rates had been reached. The method used in taking data was to increase the current until the electrode showed various values of polarization between 0.1 and 1.0v as shown on the oscilloscope screen.

The oscilloscope trace was photographed and the concentration polarization was determined by extrapolating the recorded polarization back to the moment the current interruption started. This usually meant an extrapolation of 10<sup>-4</sup> sec which is the time required for the current to go to zero and for any activation polarization to decay.

<sup>6</sup> There is a small leakage current passing through the transistors at this time, but it is negligible through the current range in which measurements were taken.

#### Results

In this way, concentration polarization data were obtained for Poco-AX porous graphite electrodes 1/8 and 1/16 in. thick at total pressures of 1, 2, and 5 atm using gas mixtures containing 50, 80, 95, and 99.9% Cl<sub>2</sub>. Table III gives a summary of all the data. Each data point is the average of at least 10 determinations taken with both increasing and decreasing currents. All the data were obtained at a nominal temperature of 650°C. However, at high current densities the temperature rose unavoidably due to I<sup>2</sup>R, TΔS, and Iη heating in the cell. Since the temperature affects a number of the properties which determine the Cl<sub>2</sub> electrode performance, these higher temperature data are not strictly comparable to the 650°C data and are shown in brackets in Table III. At low polarizations, the 1/8 in. thick electrode performed better at 5 atm than the 1/16 in. thick electrode. Similar behavior has been observed in complete Li-Cl<sub>2</sub> cells. This is probably due to the greater penetration of electrolyte into the porous electrode due to a greater ΔP developed across the thicker electrode. Such increased penetration is equivalent to an increase in area; it results in improved performance in a manner similar to grooving the electrode.

#### Discussion

The concentration polarization data shown in Fig. 5 through 7 are of a form typical of concentration polarizations. For a plane electrode, the *i* - η relationship is

$$\eta = \frac{RT}{nF} \ln \left( \frac{i_L}{i_L - i} \right) \quad [11]$$

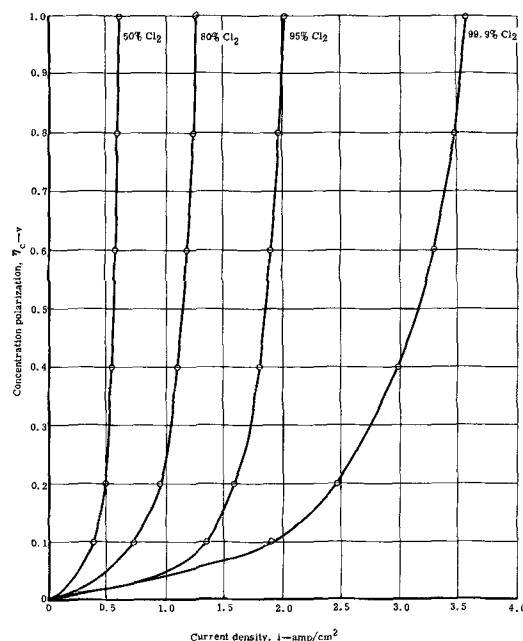


Fig. 5. Concentration polarization vs. current density for a 1/8-in. electrode at 1 atm.

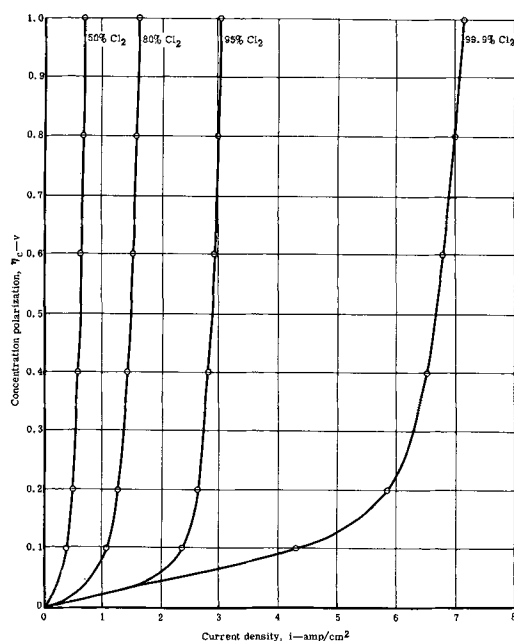


Fig. 6. Concentration polarization vs. current density for a  $\frac{1}{8}$ -in. electrode at 2 atm.

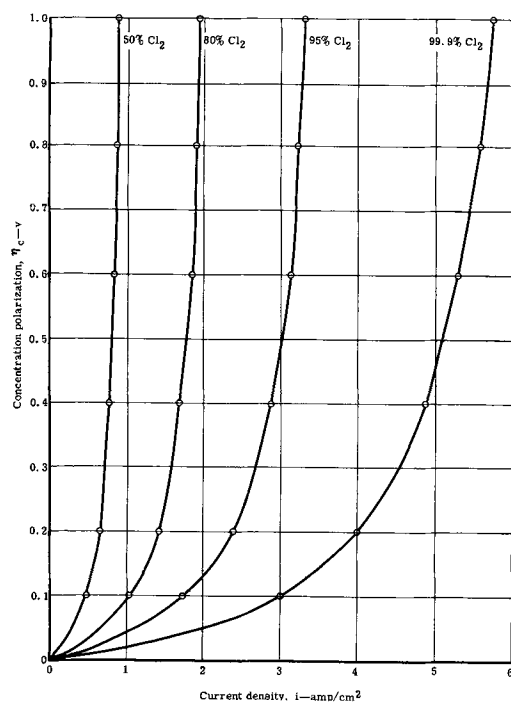


Fig. 7. Concentration polarization vs. current density for a  $\frac{1}{16}$ -in. electrode at 1 atm.

The smooth curves drawn through the experimental points in Fig. 5 through 7 have the same general shape as Eq. [11] but deviate in detail, particularly at high current densities. This is probably due to the fact that the electrode has a range of different pore sizes each with its own characteristic limiting current density. Therefore, the  $i - \eta$  relationship in this case is a complex average of a large number of individual relationships similar to Eq. [11]. The average would be a complex one since the pores of different sizes (and, therefore, different activities) are interconnected not only electronically through the graphite but also ionically through the electrolyte. They are also connected in the gas phase and, hence,  $\text{Cl}_2$  and impurities can flow and diffuse from one pore to another, and the average is not a simple average of parallel paths. No detailed theoretical treatment of the shape of the  $i - \eta$

Table IV. Comparison between calculated and experimental limiting current densities ( $i_L$ )

		1/8 in. electrode		1/16 in. electrode	
		Calculated $i_L$ (amp/cm <sup>2</sup> )	Experimental $i_L$ (amp/cm <sup>2</sup> )	Calculated $i_L$ (amp/cm <sup>2</sup> )	Experimental $i_L$ (amp/cm <sup>2</sup> )
$P_T = 1$ atm	99.9% $\text{Cl}_2$	2.79	3.15	4.84	5.10
	95% $\text{Cl}_2$	2.04	1.84	3.69	3.01
	80% $\text{Cl}_2$	1.22	1.13	2.27	1.77
	50% $\text{Cl}_2$	0.55	0.55	1.04	0.81
$P_T = 2$ atm	99.9% $\text{Cl}_2$	5.96	6.67	10.8	10.1
	95% $\text{Cl}_2$	2.83	2.82	5.39	4.26
	80% $\text{Cl}_2$	1.54	1.46	2.97	2.22
	50% $\text{Cl}_2$	0.67	0.60	1.29	0.95
$P_T = 5$ atm	99.9% $\text{Cl}_2$	7.25	12.4	14.2	14.9
	95% $\text{Cl}_2$	3.15	3.34	6.21	4.52
	80% $\text{Cl}_2$	1.70	1.83	3.34	2.39
	50% $\text{Cl}_2$	0.73	0.66	1.44	0.95

curve has been made. The theoretical treatment attempts to predict the limiting current density which can be obtained under various conditions of pressure, impurity level, and electrode thickness. The results of these calculations are compared with the experimental limiting current densities in Table IV. The experimental limiting current density is arbitrarily taken as the current density at 0.5v polarization which is obtained by interpolation from the experimental data in Table III.

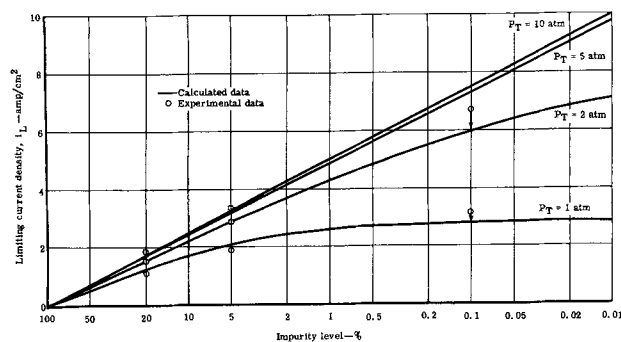


Fig. 8. Limiting current densities for a  $\frac{1}{8}$ -in. thick Poco-AX electrode.

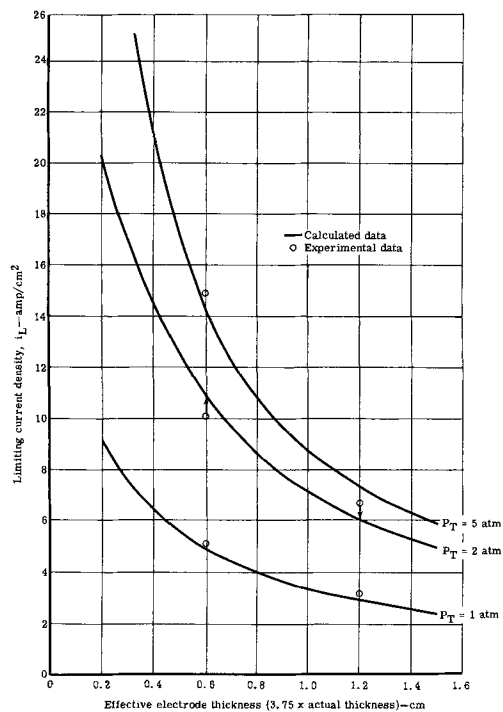


Fig. 9. Limiting current density at an impurity level of 0.1% for Poco-AX porous graphite.

For the  $\frac{1}{8}$  in. thick electrode, the agreement is within the precision of the experimental data, which is about  $\pm 10\%$  except for the 5 atm pure  $\text{Cl}_2$  points. For the  $\frac{1}{16}$  in. thick electrode, the calculated values of  $i_L$  are generally higher than the experimental data by 25 to 40%. A possible explanation of this is that for the thinner electrode the  $\Delta P$  developed across the electrode will be less. Therefore, the effective roughness of the electrode will be less since less electrolyte penetration will occur. By reducing the roughness factor used in the calculations from 5 to 3, the calculated values are reduced sufficiently so that the calculated limiting current densities are on the average high by only 12%. This is close to the precision of the experimental data. However, the roughness factor of 5 has been retained in the calculated values shown in the succeeding plots of  $i_L$  vs. various parameters. Figure 8 shows  $i_L$  for a  $\frac{1}{8}$  in. thick electrode as a function of pressure and impurity level, while Fig. 9 shows  $i_L$  at a fixed impurity level (0.1% impurities) as a function of pressure and electrode thickness. In each case, relevant experimental points are also shown. Figure 8 clearly shows that increasing the total pressure beyond 5 atm results in little or no improvement in electrode performance. Even pressure increases above 2 atm are only useful when the  $\text{Cl}_2$  contains less than 5% impurities. The effect of reducing electrode thickness is demonstrated by Fig. 9; however, lower values of  $i_L$  were often observed on the thinner electrodes due to the decreased effective roughness factor.

### Acknowledgment

This work was supported in part by the U.S. Air Force Aero Propulsion Laboratory, Wright-Patterson AFB, Ohio, under Contract No. AF33(615)-5343. The authors also wish to acknowledge the assistance of M. S. Lin in providing the specially designed gas chromatograph used in the  $\text{Cl}_2$  analysis and R. O. Whitaker and R. L. McNew in designing and building the current controllers.

Manuscript submitted April 11, 1968; revised manuscript received June 7, 1968.

Any discussion of this paper will appear in a Discussion Section to be published in the June 1969 JOURNAL.

### REFERENCES

1. R. R. Paxton, J. F. Demendi, G. J. Young, and R. B. Rozelle, *This Journal*, **110**, 932 (1963).
2. M. W. Reed and W. C. Schwemer, *ibid.*, **114**, 582 (1967).
3. D. A. J. Swinkels, *ibid.*, **113**, 6 (1966).
4. R. D. Weaver, Proceedings of the 19th Annual Power Sources Conference (May 1965), p. 113.
5. D. A. J. Swinkels, *This Journal*, **114**, 812 (1967).
6. R. D. Tait, Private communication.
7. M. W. Reed and R. J. Brodd, *Carbon*, **3**, 241 (1965).
8. "Thermophysical Properties Research Center Data Book," Vol. 2, Table 2030, Purdue University, Lafayette, Indiana (1966).
9. R. C. Reid and T. K. Sherwood, "The Properties of Gases and Liquids," pp. 268-269, McGraw-Hill Book Co., New York (1958).

## Behavior of Dimethyl Sulfitte as a Potential Nonaqueous Battery Solvent

N. P. Yao,<sup>†</sup> E. D'Orsay,<sup>1\*</sup> and D. N. Bennion\*

*Department of Engineering, University of California, Los Angeles, California*

### ABSTRACT

A potentially useful high energy battery electrolyte solvent, dimethyl sulfitte, was investigated. The conductivities, viscosities, and densities of sodium trifluoromethane sulfonate salt in dimethyl sulfitte are reported in the concentration range 0.01-0.20 mole  $\text{CF}_3\text{SO}_3\text{Na}/\text{Kg}$  solution and for the temperature range  $30^\circ\text{-}80^\circ\text{C}$ . The dielectric constant of dimethyl sulfitte is 22.5 at  $23.3^\circ\text{C}$ . Sodium trifluoromethane sulfonate is weakly ionized in this solvent yielding conductivities in the  $10^{-3}$  mho/cm range. Results of charging and discharging four different cell couples indicate this solvent is stable at cell potentials of over 4v vs. lithium.

One common feature of most nonaqueous organic solvents (1) which are stable with high energy density electrodes and which dissolve electrolytes is that they have functional groups containing a central carbon atom. Replacement of the central carbon atom by a sulfur atom, in either the plus four or six valence, generates a new class of organic solvents which are expected to yield equally useful properties. Physical and transport properties of the sulfur containing organic solvents have been recently explored (2, 3). The results indicate that many of the sulfur-containing organic solvents are potentially useful for high energy density battery applications. The properties of tetramethylene sulfoxide,  $(\text{CH}_2)_4\text{SO}$ , which is the sulfur analog of cyclopentanone,  $(\text{CH}_2)_4\text{CO}$ , has already been reported elsewhere (2). We report here some physical and transport properties of dimethyl sulfitte,  $(\text{CH}_3\text{O})_2\text{SO}$ , a sulfur analog of dimethyl carbonate,  $(\text{CH}_3\text{O})_2\text{CO}$ , and  $\text{CF}_3\text{SO}_3\text{Na}$ -dimethyl sulfitte mixtures.

Preliminary battery tests indicate that electrolyte solutions in dimethyl sulfitte can be used for secondary battery applications.

### Experimental

**Chemicals.**—Dimethyl sulfitte of high-purity grade was supplied by Eastman Organic Chemicals (Distillation Products Industries). They were unable to supply purity specifications except that it was prepared by a method described by Vogel and Cowan (13) in which thionyl chloride is reacted with methanol at  $0^\circ\text{C}$ . Karl Fisher titration (KFT) showed 196 ppm  $\text{H}_2\text{O}$  in the as-received material. A sample of the dimethyl sulfitte was distilled under 54 mm Hg nitrogen pressure at  $53^\circ\text{C}$ . The middle 75% of the material was retained for further tests. After purification, KFT showed 79 ppm water.

NMR spectra were run on the as received and purified dimethyl sulfitte. Using the carbon 13 peak as a calibration reference, two impurity peaks were observed at 18 and 85 Hz displaced from the principal dimethyl sulfitte peak. Each of these peaks represented

<sup>†</sup> Electrochemical Society Student Associate.

\* Electrochemical Society Active Member.

<sup>1</sup> Present address: SEV Marchal, Issy-les-Moulineaux, France.

just under 0.5% impurity or a total of 1% impurity. For the purified dimethyl sulfite the peak at 16 Hz disappeared while the 85 Hz peak remain unchanged.

Most of the results are reported for the as-received dimethyl sulfite. Check runs were made using purified dimethyl sulfite for viscosity, density, and specific conductance. Variations were within experimental uncertainty. A check on the solvent remaining in the bottle at the end of the experiments showed 300 ppm water.

Sodium trifluoromethane sulfonate ( $\text{CF}_3\text{SO}_3\text{Na}$ ) was synthesized in this laboratory by chemical conversion from barium trifluoromethane sulfonate which was supplied by Minnesota Mining & Manufacturing Company.  $\text{CF}_3\text{SO}_3\text{Na}$  was recrystallized twice from acetone, dried in vacuum for 24 hr, and was stored in a desiccator above silica gel. The melting point of  $\text{CF}_3\text{SO}_3\text{Na}$  was  $248^\circ \pm 1^\circ\text{C}$  which agrees well with that reported by Gramstad and Haszeldine (4),  $248^\circ\text{C}$ .

**Apparatus and equipment.**—The experimental cells and equipment for the measurement of melting point, dielectric constant, density, viscosity, and conductance were previously described (2). The same battery cell (2) was also used to test the charging and discharging characteristics for a number of battery couples. These couples were fabricated in the discharged condition and then activated electrochemically. In each case  $\text{LiClO}_4$  was the principle electrolyte, and Li was deposited and removed from an aluminum substrate at the negative. Copper ribbon mixed with  $\text{LiF}$ , Ag wire in a compartment saturated with  $\text{LiCl}$ , a mixture of  $\text{K}_2\text{SO}_4$  and graphite particles in a Pt cup, and a mixture of KI and graphite in a Pt cup were the four positives tested. The positive and negative compartments were separated by a glass frit.

### Results and Discussion

**Dimethyl sulfite.**—Dimethyl sulfite is a clear liquid at room temperature with typical ester-like odor. The melting point of dimethyl sulfite as determined in this laboratory is  $-141^\circ \pm 2^\circ\text{C}$ . The following physical properties are reported by Kyrides (5): boiling point is  $126^\circ\text{C}$  at 760 mm pressure and  $52^\circ\text{C}$  at 45 mm pressure, density is  $1.2073 \text{ g/cm}^3$  at  $24^\circ\text{C}$ , and the index of refraction is 1.4093 at  $20^\circ\text{C}$ . The dielectric constant of dimethyl sulfite as determined in this laboratory is  $\epsilon_{23.3} = 22.5 \pm 2\%$ . Specific conductance of dimethyl sulfite, as received, was  $1.8 \times 10^{-5} \text{ mho/cm}$ . Density data and viscosity data as functions of temperature were also determined and are presented in Fig. 1 and Fig. 2, respectively. The density value at  $24^\circ\text{C}$  as extrapolated from density data determined here agrees very well with the single reported value of  $d_{24} = 1.2073$  (5). The viscosity of dimethyl sulfite varies between 0.7715 (at  $30^\circ\text{C}$ ) and 0.4361 (at  $80^\circ\text{C}$ ) centipoise.

As a check on the effects of impurities, extra runs were made using purified dimethyl sulfite. There was

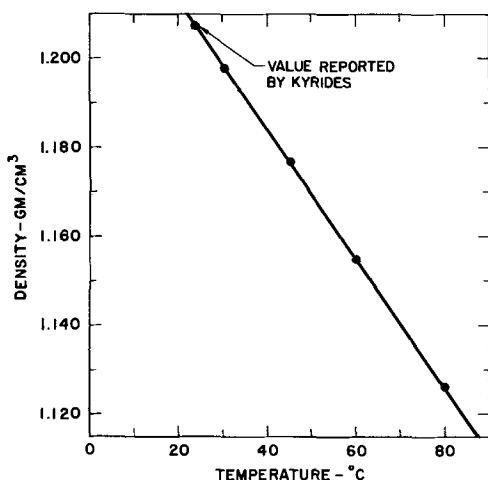


Fig. 1. Density of dimethyl sulfite as a function of temperature

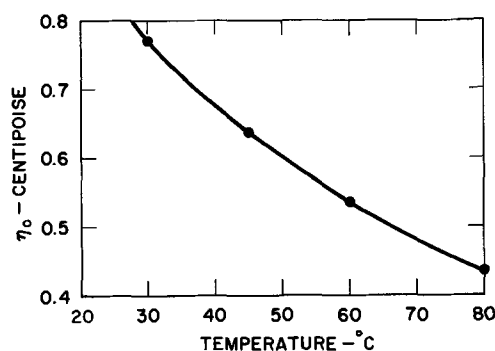


Fig. 2. Viscosity of dimethyl sulfite as a function of temperature

no detectable change in density, i.e., agreement was within 0.2%. Correspondence between the measurements of viscosity is shown in Table I. It is to be noted that there is a small but possibly significant increase in viscosity of the purified material compared to the as-received solvent.

**Dimethyl sulfite- $\text{CF}_3\text{SO}_3\text{Na}$  mixture.**—Density, kinematic viscosity, and ionic conductance were determined for mixtures of dimethyl sulfite and sodium trifluoromethane sulfonate in the concentration range 0.0098 up to 0.20 mole/kg solution for the temperature range  $30^\circ\text{--}80^\circ\text{C}$ .

Figure 3 shows variation of density as a function of concentration,  $m$  (in moles of  $\text{CF}_3\text{SO}_3\text{Na}$ /kg solution), and temperature (in  $^\circ\text{C}$ ). The linear variation of density at constant temperature, represented by the equation  $d = d_0 + \psi m$  where  $d_0$  is the density of dimethyl sulfite and  $\psi$  is the density increment, was found to be valid. The density increment  $\psi$  was  $(10.0 \pm 0.5) \times 10^{-2}$  and was constant within the temperature range studied.

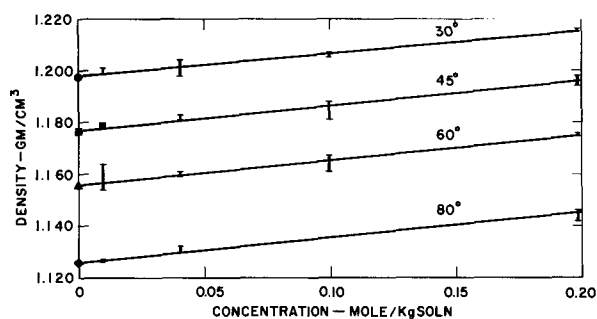
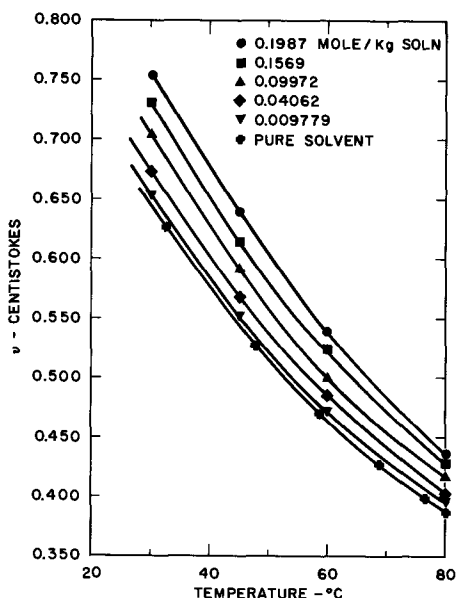
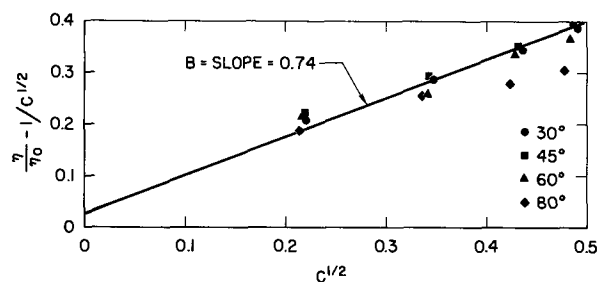
Figure 4 shows variation of kinematic viscosity  $\nu$  (in centistokes) as a function of temperature and concentration. Applicability of the Jones-Dole equation (6)

$$\frac{\eta}{\eta_0} - 1/C^{1/2} = A + BC^{1/2} \quad [1]$$

was examined where  $\eta_0$  is the real viscosity of the solvent in centipoises,  $\eta$  is the real viscosity of the electrolyte solution in centipoises at concentration  $C$  (in moles  $\text{CF}_3\text{SO}_3\text{Na}$ /liter), and  $A$  and  $B$  are the viscosity coefficients which are specific to a particular electrolyte-solvent system (7). Figure 5 shows the  $\eta/\eta_0 - 1/C^{1/2}$  vs.  $C^{1/2}$  plot. It should be noted that a 0.3% experimental error in  $\eta$  gives as much as 12% error in  $\eta/\eta_0 - 1/C^{1/2}$  at  $C = 0.04$ . The lower the concentration the greater the error in  $\eta/\eta_0 - 1/C^{1/2}$  for a constant experimental error in the measurement. A best fit straight-line as shown in Fig. 5 was drawn through the present data while taking into consideration that the intercept  $A$  of the line must lie within Falkenhagen's theoretical value (8), i.e., between 0.01 and 0.025. The straight line obtained in this manner had a slope of 0.74 which is the  $B$  viscosity coefficient. The  $B$  coefficient in dimethyl sulfite- $\text{CF}_3\text{SO}_3\text{Na}$  mixtures appears to be independent of temperature with perhaps a slight decrease at  $60^\circ$  and  $80^\circ\text{C}$ . This indicates that the ion-solvent interaction in the mixtures is only slightly affected by the thermal motion of the molecules. This finding is in contrast to the  $B$  coefficients found in  $\text{LiClO}_4$ -tetramethylene sulfoxide mixtures (2) which were decreasing functions of temperature

Table I. Correspondence between measurements of viscosity

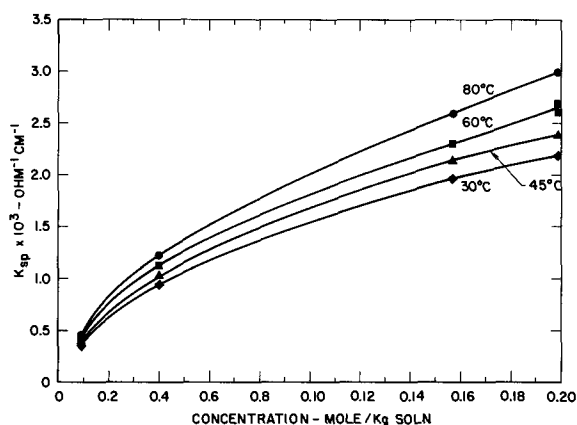
T, °C	Viscosity in centistokes		
	Eastman grade	Purified	% Deviation
30	0.645	0.652	1.07
45	0.543	0.552	1.63
60	0.465	0.478	2.72

Fig. 3. Density of  $\text{CF}_3\text{SO}_3\text{Na}$ -dimethyl sulfite mixturesFig. 4. Kinematic viscosity of  $\text{CF}_3\text{SO}_3\text{Na}$ -dimethyl sulfite mixtures.Fig. 5.  $\eta/\eta_0 - 1/C^{1/2}$  vs.  $C^{1/2}$  plot for  $\text{CF}_3\text{SO}_3\text{Na}$ -dimethyl sulfite mixtures.

indicating a decrease in the effective ionic volume with temperature. The  $B$  coefficient as determined for  $\text{CF}_3\text{SO}_3\text{Na}$  salt should be split into its respective ionic  $B$  coefficients for  $\text{Na}^+$  and  $\text{CF}_3\text{SO}_3^-$  ions in order to have a more meaningful interpretation. This was not done due to lack of individual mobility data of these ions in the medium studied. The apparent energy of activation for viscous flow in the mixtures was calculated from a  $\log \eta$  vs.  $1/T$  plot. The value was constant at  $2.44 \pm 0.04$  kcal/mole for the temperature and concentration range studied.

Specific conductance of dimethyl sulfite- $\text{CF}_3\text{SO}_3\text{Na}$  mixtures was determined and plotted as shown in Fig. 6. The specific conductance increased monotonically and seemed to approach some maximum value at about the saturation concentration, i.e., about 0.4 mole/kg solution at room temperature.

As a final check on the effects of impurities on dimethyl sulfite behavior, selected values of specific conductance were obtained for 0.11 mole/kg solution

Fig. 6. Specific conductance of  $\text{CF}_3\text{SO}_3\text{Na}$ -dimethyl sulfite mixtures.

$\text{NaCF}_3\text{SO}_3$  in purified dimethyl sulfite. Comparisons are shown in Table II.

The maximum specific conductance, measured in this work,  $3 \times 10^{-3}$  mho/cm, was obtained at a concentration 0.1987 mole/kg solution at  $80^\circ\text{C}$ . Using  $\text{LiClO}_4$  as the solute, a conductivity of  $10^{-2}$  mho/cm was measured for a concentration of 1.3 mole/kg of solution. Equivalent conductances,  $\Lambda$ , for the dimethyl sulfite mixtures are tabulated in Table III. A plot of  $\eta_0/\Lambda\eta$  vs.  $C\Lambda\eta/\eta_0$  is shown in Fig. 7. A straight-line is obtained for data at  $30^\circ\text{C}$  indicating the validity of the equation (2)

$$\frac{1}{\Lambda} \frac{\eta_0}{\eta} = \frac{1}{\Lambda_0} + \frac{1}{K_{\text{eq}}\Lambda_0^2} \frac{C\Lambda\eta}{\eta_0}$$

Negative deviations from straight-lines at higher concentration and at higher temperature indicate that the viscosity correction,  $\eta/\eta_0$ , is not sufficient to account for the variation of conductance with temperature at higher concentrations. Since the plots appear valid at low concentration where linear behavior is observed, extrapolation of the straight-lines to  $C = 0$  yields  $1/\Lambda_0$  as the intercepts on the ordinate for each temperature. From the slope of the straight-line (slope =  $1/\Lambda_0^2 K_{\text{eq}}$ ), the equilibrium dissociation constant,  $K_{\text{eq}}$ , for the ionization reaction  $\text{CF}_3\text{SO}_3\text{Na} \rightleftharpoons \text{CF}_3\text{SO}_3^- + \text{Na}^+$  was obtained for each temperature. The values of equivalent conductance at infinite dilution,  $\Lambda_0$ , and the equilibrium dissociation constant,  $K_{\text{eq}}$ , are tabulated in Table IV. It is seen from Table IV that the equilibrium dissociation constant,  $K_{\text{eq}}$ , for  $\text{CF}_3\text{SO}_3\text{Na}$  salt in dimethyl sulfite is considerably lower than for  $\text{LiClO}_4$  in a  $\text{LiClO}_4$ -tetramethylene sulfoxide mixture (2). This is expected since the dielectric constant of dimethyl sulfite is  $\epsilon_{23.3^\circ} = 22.5$  compared to  $\epsilon_{23.3^\circ} = 42.5$  for tetramethylene sulfoxide. Using the definition  $\alpha = \Lambda\eta/\Lambda_0\eta_0$ , where  $\alpha$  is interpreted as the fraction of ion-

Table II. Comparison of effects of impurities

$T, ^\circ\text{C}$	Specific conductance of solution		
	Eastman grade solvent	Purified solvent	% Deviation
30	$1.630 \times 10^{-3}$	$1.671 \times 10^{-3}$	2.45
45	$1.775 \times 10^{-3}$	$1.781 \times 10^{-3}$	0.34
60	$1.905 \times 10^{-3}$	$1.875 \times 10^{-3}$	-1.60

Table III. Equivalent conductance of  $\text{CF}_3\text{SO}_3\text{Na}$ -dimethyl sulfite mixtures

$T = 30^\circ$		$T = 45^\circ$		$T = 60^\circ$		$T = 80^\circ$	
$10^\circ\text{C}$	$\Lambda$	$10^\circ\text{C}$	$\Lambda$	$10^\circ\text{C}$	$\Lambda$	$10^\circ\text{C}$	$\Lambda$
1.172	30.675	1.1526	34.066	1.130	39.579	1.102	42.865
4.881	19.494	4.796	21.497	4.709	24.187	4.588	26.763
19.043	10.403	18.709	11.476	18.368	12.500	17.905	14.471
24.140	9.043	23.767	10.056	23.357	11.303	22.761	13.242

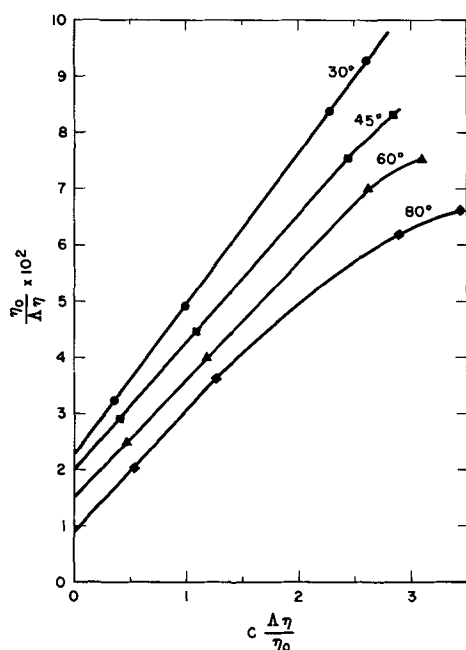


Fig. 7.  $\eta_0/\Delta\eta$  vs.  $C\Delta\eta/\eta_0$  plots for  $\text{CF}_3\text{SO}_3\text{Na}$ -dimethyl sulfite mixtures.

ization,  $\alpha$  is found to be 0.708 and 0.245 at 30°C for concentrations of 0.009779 mole/kg solution and 0.1987 mole/kg solution, respectively, in this mixture. This indicates that the  $\text{CF}_3\text{SO}_3\text{Na}$  salt behaves as a weak electrolyte in dimethyl sulfite. The values of  $\Lambda_0$  as tabulated in Table IV varied from 44  $\text{cm}^2/\text{ohm}$  equivalent at 30°C to 112  $\text{cm}^2/\text{ohm}$  equivalent at 80°C. The values reported here must be taken as approximate, since such an extrapolation is often misleading in weak electrolyte systems. It is, therefore, possible that  $\Lambda_0$  values are greater than reported here.

The Walden product,  $\Delta\eta$ , is shown as a function of temperature in Fig. 8. The Walden product decreases exponentially as a function of concentration indicating the typical behavior of a weak electrolyte solution. The plot cannot satisfactorily be extrapolated to obtain the Walden product,  $\Lambda_0\eta_0$ , at infinite dilution. However, the  $\Lambda_0\eta_0$  values were calculated from values of  $\Lambda_0$  obtained by extrapolation in Fig. 7 and tabulated in Table IV and the experimental value  $\eta_0$  of dimethyl sulfite. The Walden product,  $\Lambda_0\eta_0$ , at infinite dilution vs. temperature is plotted in Fig. 9. The  $\Lambda_0\eta_0$  product appeared to remain constant at lower temperature and increased when temperature was raised above 60°C. This positive temperature coefficient of the  $\Lambda_0\eta_0$  product for the salt means that the average Stokes ionic radius (9) decreases as a function of temperature. Strictly speaking only ionic Walden products  $\lambda_{o+}\eta_0$  or  $\lambda_{o-}\eta_0$  are meaningful, but this requires accurate data of individual ionic mobilities  $\lambda_{o+}$  and  $\lambda_{o-}$ . Decrease of Stokes ionic radii at temperatures above 60°C also means the decrease of specific interaction between the ion and the solvent molecule, *i.e.*, decrease of solvation number at these temperatures. This in turn means that the  $B$  viscosity coefficient must decrease at these temperatures since the  $B$  viscosity coefficient is related to the effective molar ionic volume (2). Decrease of the  $B$  viscosity coefficient is indeed observed for dimethyl sulfite- $\text{CF}_3\text{SO}_3\text{Na}$  mixtures at temperatures between

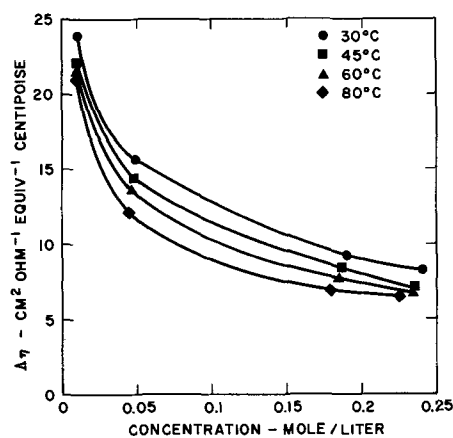


Fig. 8. Walden product,  $\Delta\eta$ , for  $\text{CF}_3\text{SO}_3\text{Na}$ -dimethyl sulfite mixtures.

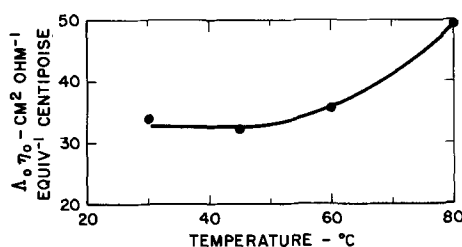


Fig. 9. Temperature dependence of Walden product,  $\Lambda_0\eta_0$ , at infinite dilution for  $\text{CF}_3\text{SO}_3\text{Na}$ -dimethyl sulfite mixtures.

60° and 80° (see Fig. 5). Similar behavior, *i.e.*,  $(\partial\Lambda_0\eta_0)/\partial T \propto \partial T/\partial B$  has been observed in other non-aqueous media (10). Apparent activation energy for ionic conduction was calculated from the slope of  $\log K_{sp}$  vs.  $1/T$  plot for dimethyl sulfite- $\text{CF}_3\text{SO}_3\text{Na}$  mixtures. The value was found to be constant at  $0.66 \pm 0.002$  kcal/mole for all concentrations. The ratio of activation energy for ionic conductance and for viscous flow in the mixtures was  $\xi = E_K/E_\eta = 0.27$  at 0.04 mole/kg solution.

**Battery tests.**—Four battery couples were tested in dimethyl sulfite-lithium perchlorate solutions. They were built in the discharged state and then charged as described in the Apparatus and Equipment section. All the cells accepted charge and delivered small currents at rather large voltages. The coulombic or charge efficiencies (coulombs in during charge divided by coulombs out to complete discharge) varied between 30 and 70%. Open-circuit voltages of between 3 and just over 4v were observed. These voltages were stable and the cells would return to these voltages after brief discharge periods.

These results must be considered preliminary in nature. However, they offer two important conclusions regarding dimethyl sulfite-lithium perchlorate solutions. Potentially useful secondary battery reactions can be carried out in this solution yielding high voltages and promising charge efficiencies. The discharge curves in each case were quite flat. Since the open-circuit voltages of over 4v could be maintained for periods of many minutes (up to 30 min for example), this solution has at least short term stability to oxidation or reduction over a wide potential range of interest for construction of high energy, secondary batteries. It has already been established that dimethyl sulfite is stable toward lithium (12). Thus, its stability to oxidation is also established.

#### Acknowledgment

The assistance of Mr. Allen Dodge and Mr. Avinoam Hershkowitz in performing the experiments is gratefully acknowledged. Financial support for this work has been provided by the U.S. Army Mobility Equipment Research and Development Center, Fort Belvoir,

Table IV.  $\Lambda_0$  and  $K_{eq}$  for  $\text{CF}_3\text{SO}_3\text{Na}$  Na-dimethyl sulfite mixtures

T, °C	$\Lambda_0$	$K_{eq}$
30	43.96	$1.95 \times 10^{-2}$
45	50.00	$1.78 \times 10^{-2}$
60	66.23	$1.10 \times 10^{-2}$
80	112.36	$3.76 \times 10^{-3}$

Virginia, and through an initiation grant from NASA Grant No. Nsg 237-62.

Manuscript submitted March 12, 1968; revised manuscript received ca. June 10, 1968.

Any discussion of this paper will appear in a Discussion Section to be published in the June 1969 JOURNAL.

#### NOMENCLATURE

$A, B$	Viscosity coefficients, (mole/liter) <sup>-1/2</sup> and (mole/liter) <sup>-1</sup> respectively
$C$	Molar concentration, mole/liter
$d_0$	Density of solvent, g/cm <sup>3</sup>
$d$	Density of solution, g/cm <sup>3</sup> , at molal concentration $m$
$E_K$	Molar activation energy for ionic conduction, kcal/mole
$E_\eta$	Molar activation energy for viscous flow, kcal/mole
$K_{eq}$	Equilibrium dissociation constant
$K_{sp}$	Specific ionic conductance, mho/cm
$m$	Molal concentration, mole/kg solution
$T$	Absolute temperature, °K
$\alpha$	Fraction of ionization
$\epsilon$	Dielectric constant of solvent
$\eta_0$	Real viscosity of solvent, centipoises
$\eta$	Real viscosity of solution, centipoises, at molar concentration $C$
$\Lambda_0$	Limiting equivalent conductance of electrolyte, cm <sup>2</sup> /ohm equivalent
$\Lambda$	Equivalent conductance of electrolyte, cm <sup>2</sup> /ohm equivalent
$\lambda_0^+, \lambda_0^-$	Limiting ionic mobilities, cm <sup>2</sup> /ohm equivalent
$\nu$	Kinematic viscosity, centistokes

$\xi$  Ratio of molar activation energy for ionic conduction and for viscous flow,  $\xi = E_K/E_\eta$

$\psi$  Density increment

#### REFERENCES

1. Raymond Jasinski, "High-Energy Batteries," Plenum Press, New York (1967).
2. E. D'Orsay, N. P. Yao, and D. N. Bennion, Being considered for publication.
3. D. N. Bennion, N. P. Yao and E. D'Orsay, "Non-Aqueous Electrolyte Systems, Interim Report No. 2," Contract DA-44-009-1661(T) (UCLA Engineering Report No. 67-52) September 1967.
4. T. Gramstad and R. N. Haszeldine, *J. Chem. Soc., London*, **1956**, 173.
5. L. P. Kyrides, *J. Am. Chem. Soc.*, **66**, 1006 (1944).
6. G. Jones and M. Dole, *J. Am. Chem. Soc.*, **51**, 2950 (1929).
7. R. H. Stokes and R. Mills, "Viscosity of Electrolytes and Related Properties," Vol. 3. International Encyclopedia of Physical Chemistry and Chemical Physics, Pergamon Press, New York (1965).
8. H. S. Harned and B. B. Owen, "The Physical Chemistry of Electrolytic Solutions," 3rd ed., p. 240, Reinhold Publishing Corp., New York (1958).
9. R. A. Robinson and R. H. Stokes, "Electrolyte Solutions," 2nd ed., chap. 6, Butterworths, London (1959).
10. G. P. Cunningham, D. F. Evans, and R. L. Kay, *J. Phys. Chem.*, **70**, 3998 (1966).
11. M. Eisenberg, Paper presented at the Santa Clara Valley Symposium, February 1967.
12. D. P. Boden *et al.*, Contract DA-28-043-AMC-01394, Final Report, June 1966.
13. A. I. Vogel and D. M. Cowan, *J. Chem. Soc.*, **1943**, 16.

## Cathodic Reduction Mechanism of MnOOH to Mn(OH)<sub>2</sub> in Alkaline Electrolyte

A. Kozawa\* and J. F. Yeager\*

Union Carbide Corporation, Consumer Products Division, Research Laboratory, Cleveland, Ohio

#### ABSTRACT

The cathodic reduction process of MnOOH, which is produced from  $\gamma$ -MnO<sub>2</sub> or  $\beta$ -MnO<sub>2</sub> by electrochemical reduction, was studied in 9M KOH with various particle sizes of the original  $\gamma$ -MnO<sub>2</sub> and various depths of discharge. The polarization of MnOOH produced from electrolytic  $\gamma$ -MnO<sub>2</sub> is small, less than 60 mv, until a certain current density is reached. Above the current density, a limiting current is reached and polarization increases sharply. There are two possible reduction mechanisms for the process from MnOOH to Mn(OH)<sub>2</sub>, i.e.: (i) reduction through Mn(III) ion dissolved in the electrolyte, and (ii) reduction of MnOOH directly to Mn(OH)<sub>2</sub> in solid state. It was concluded that most of the discharge current is attributed to the dissolved Mn(III) ion mechanism.

In previous publications (1-4) concerning the discharge process of MnO<sub>2</sub> in alkaline electrolyte, some discharge behavior of MnOOH, which is equivalent to MnO<sub>1.5</sub> (or Mn<sub>2</sub>O<sub>3</sub>), has been described. However, those investigations have been done mainly to study the discharge process from MnO<sub>2</sub> to MnOOH, i.e., the first step shown in Fig. 1 which gives a schematic summary of previously observed discharge curves for  $\gamma$ - and  $\beta$ -MnO<sub>2</sub>.

The purpose of the present study was to obtain more detailed polarization characteristics of the second step (see Fig. 1) and to determine the discharge mechanism of the second-step process from MnOOH to Mn(OH)<sub>2</sub>. The normal discharge curve of  $\gamma$ -MnO<sub>2</sub> or  $\beta$ -MnO<sub>2</sub> consists of two steps as shown in Fig. 1, although

multistep discharge curves are obtained under certain conditions (5). The discharge mechanism of the major part of the first step very likely involves solid state discharge, namely the proton-electron mechanism as discussed previously (1-4). On the other hand, it had not been determined whether the discharge mechanism of the second step involved a solid state discharge [direct reduction of MnOOH to Mn(OH)<sub>2</sub>] or discharge through dissolved Mn(III) ion, although some evidence in favor of the latter mechanism was presented by Kozawa and Yeager (1). Steps involved in these two possible mechanisms are given in Fig. 2. The solubility of Mn(III) and Mn(II) ions in 5-13M KOH has been determined (6).

In this investigation, MnOOH was first produced by electroreduction of  $\gamma$ -MnO<sub>2</sub> or  $\beta$ -MnO<sub>2</sub> in 9M KOH, and

\* Electrochemical Society Active Member.



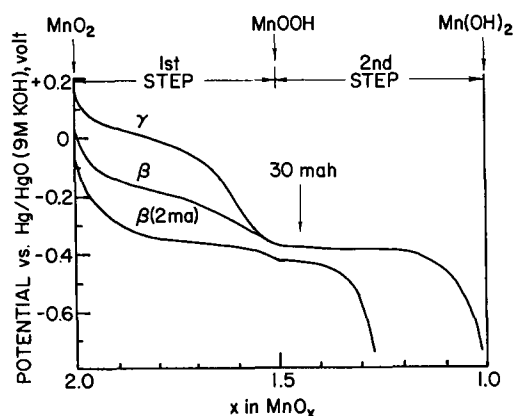


Fig. 1. Schematic discharge curves of  $\gamma$ - $\text{MnO}_2$  and  $\beta$ - $\text{MnO}_2$ . Curve  $\gamma$ : discharge curve of  $\gamma$ - $\text{MnO}_2$  at 1-2 ma/100 mg, curve  $\beta$ : discharge curve of  $\beta$ - $\text{MnO}_2$  at 0.3 ma/100 mg, curve  $\beta$  (2 ma): discharge curve of  $\beta$ - $\text{MnO}_2$  at 2 ma/100 mg.

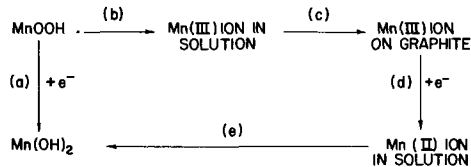


Fig. 2. Steps involved in the two possible discharge mechanisms: (i) direct solid state reduction mechanism, (a), and (ii) reduction through dissolved species, (b), (c), (d), and (e), where (b): dissolution of Mn(III) ion from  $\text{MnOOH}$ , (c): diffusion of Mn(III) ion onto the graphite surface, (d): charge transfer step, and (e): precipitation of  $\text{Mn(OH)}_2$ .

subsequently the cathodic polarization was measured in the same electrolyte in the same cell under various conditions. The effect of particle size of the original manganese dioxide sample, and depth of discharge ( $\text{MnO}_{1.45}$ - $\text{MnO}_{1.2}$ ) was investigated. Based on the limiting current densities for three particle size samples (13, 70, and 200 $\mu$ ), the discharge mechanism has been determined to be the one which involves the Mn(III) species dissolved in the electrolyte.

### Experimental

**Discharge cell.**—The discharge cell used in the present work was the same as that in the previous work (3-5). One hundred milligrams of each  $\text{MnO}_2$  sample were mixed with 1.00g of battery grade graphite powder and 2.0g of porous coke. This mixture was ground in a glass mortar and transferred into the cell. Then 0.7 ml of 9M KOH was added to the mixture and blended thoroughly and the mixture was spread evenly over the bottom of the cell. Then three layers of separator paper and a perforated Lucite disk were placed on the mixture. The mixture was pressed at 380 kg/cm<sup>2</sup> (5000 psi) with a plastic rod. After removing the rod, a threaded Lucite plug was screwed down tightly. More electrolyte was added from the top. The counter electrode used during discharge was a platinum wire contained in a glass tube having a glass frit at the end [see Fig. 4 of ref (3)].

The graphite powder had a particle size distribution as follows: 20% by weight was less than 9 $\mu$ , 40% by weight was less than 15 $\mu$ , and 60% by weight was less than 23 $\mu$ . Under these packing conditions, the total electrolyte retained between the graphite, coke, and  $\text{MnO}_2$  particles was approximately 0.7 ml. The volume occupied by the  $\text{MnO}_2$  sample in the mixture was only a few per cent.

**Preparation of  $\text{MnOOH}$ .**—In order to produce  $\text{MnOOH}$  by electrochemical reduction from  $\gamma$ - $\text{MnO}_2$ , the  $\text{MnO}_2$  sample packed in the cell was discharged at a constant current (1.00 or 2.00 ma) continuously at 23°C for 30 ma-hr. After this reduction, the oxide

should be approximately  $\text{MnO}_{1.45}$  (see Fig. 1); namely, the system should be composed of 90%  $\text{MnOOH}$  and 10%  $\text{Mn(OH)}_2$ . At this discharge stage, the circuit was kept open at least overnight in order to obtain the open circuit voltage (OCV). The OCV was usually  $-0.385 \pm 0.005\text{v}$  vs. Hg/HgO (9M KOH) in the case of  $\gamma$ - $\text{MnO}_2$  samples.

**Polarization measurement.**—Polarization was measured by passing a constant current for 5 min and then leaving the circuit open for the next 5 min. Immediately after the open circuit period, another constant current which was greater than the previous current was passed for 5 min and again the circuit was kept open for the next 5 min. This was repeated for the following currents: 0.1, 0.3, 1.0, 3.0, 10.0, 20.0, and 30.0 ma. Figure 3 shows a typical example of such a series of measurements: the curves show recorded closed circuit voltage (CCV) not corrected for IR-drop.

At the end of the 5 min discharge, the CCV (IR-free) was measured by interrupting the current for 1 or 2 sec at a fast chart speed of the recorder (Sargent MR recorder). The potential difference between the CCV (IR-free) and the initial OCV ( $-0.385 \pm 0.005\text{v}$ ) was taken as the polarization at each current. The details and errors associated with CCV (IR-free) measurements were described previously (3, 4).

**Samples.**—The five  $\text{MnO}_2$  samples used in this investigation are designated as follows:  $\gamma$ - $\text{MnO}_2$ ,  $\beta$ - $\text{MnO}_2$ (III),  $\gamma$ - $\text{MnO}_2$ (13 $\mu$ ),  $\gamma$ - $\text{MnO}_2$ (70 $\mu$ ), and  $\gamma$ - $\text{MnO}_2$ (200 $\mu$ ). The  $\gamma$ - $\text{MnO}_2$  was a typical electrolytic  $\text{MnO}_2$  for battery use, and the  $\beta$ - $\text{MnO}_2$ (III) was prepared from the  $\gamma$ - $\text{MnO}_2$  by heating at 400°C in air for 10 days and subsequently washing with  $\text{H}_2\text{SO}_4$  solution. The chemical and physical properties of these two samples [ $\gamma$ - $\text{MnO}_2$ , and  $\beta$ - $\text{MnO}_2$ (III)] have been published previously (3). The other three samples were prepared from a single batch of an electrolytic deposit of  $\gamma$ - $\text{MnO}_2$  simply by sieving at different stages of grinding. The particle size (diameter of the particle) shown in the brackets is an average value. The range of particle size was as follows:  $\gamma$ - $\text{MnO}_2$ (13 $\mu$ ) was from 2 to 38 $\mu$ ,  $\gamma$ - $\text{MnO}_2$ (70 $\mu$ ) was in a range of 50-100 $\mu$ , and  $\gamma$ - $\text{MnO}_2$ (200 $\mu$ ) was in a range of 150-300 $\mu$ . Chemical analysis of the three samples gave a  $\text{MnO}_2$  content 87.5  $\pm$  0.5% and the BET surface area was approximately 39 m<sup>2</sup>/g regardless of the particle size. This is understandable since the large surface area of electrolytic  $\text{MnO}_2$  is due to presence of fine pores of approximately 50Å in diameter (3), and grinding to finer particles (5  $\sim$  20 $\mu$ ) does not materially influence the surface area or the  $x$  value in  $\text{MnO}_x$ . The  $\gamma$ - $\text{MnO}_2$  had an average particle size of 15 $\mu$ , and the particle size distribution is very similar to that of the  $\gamma$ - $\text{MnO}_2$  (13 $\mu$ ). The  $\beta$ -

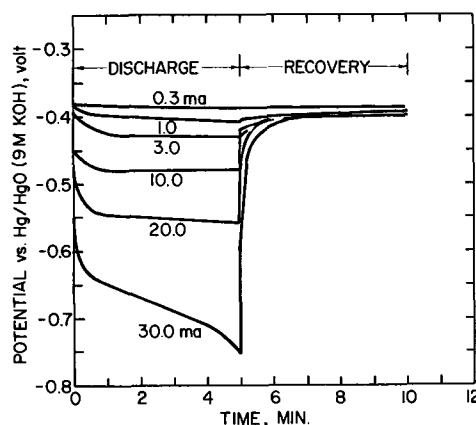


Fig. 3. Potential during constant current discharge and subsequent open circuit period. The numbers on the curves indicate constant currents passed for 5 min. This was measured with cells containing 100 mg of  $\gamma$ - $\text{MnO}_2$  at the 30 ma-hr discharge stage (90%  $\text{MnOOH}$  and 10%  $\text{Mn(OH)}_2$ ).

MnO<sub>2</sub>(III) was essentially the same in particle size distribution as the  $\gamma$ -MnO<sub>2</sub>.

### Results

Figure 3 and Fig. 5 show the potential changes during the polarization measurements at two different depths of discharge: 30 ma-hr ( $\approx$  MnO<sub>1.45</sub>) and 43 ma-hr ( $\approx$  MnO<sub>1.22</sub>), respectively. At 30 ma-hr (Fig. 3), the potential on the passage of constant current reaches a steady value in a minute or so except for 30 ma discharge; whereas, at 43 ma-hr (Fig. 5) the potential tends to decrease without showing a steady potential except at very low currents (0.3 and 1.0 ma). Above a certain current (for example, 30 ma in the case of Fig. 3 and 10 ma in the case of Fig. 5) a steady potential is not obtained during the 5 min discharge, indicating that the limiting current value has been exceeded. This will be discussed later.

As seen in Fig. 3 and 5, on open circuit, the potential returns to OCV, within experimental error, regardless of the depth of the discharge. However, the recovery rate of the deep discharged system (Fig. 5) is much slower than that of the slightly discharged system (Fig. 3).

Figures 4 and 6 show the polarization curves based on the CCV (IR-free) data at the end of 5 min discharge at each current. Curve (a) in Fig. 4 and curve (d) in Fig. 6 correspond to the measurements shown in Fig. 3 and Fig. 5, respectively. All the polarization curves shown in Fig. 4 and 6 have a similar general shape; i.e., up to a certain current, the curves (curves

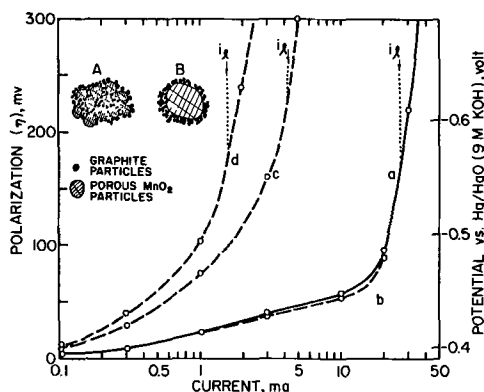


Fig. 4. Effect of particle size on polarization curve of MnO<sub>1.45</sub> derived from  $\gamma$ -MnO<sub>2</sub>. These polarization curves were taken with cells originally containing 100 mg of the manganese dioxide samples listed below, at the 30 ma-hr discharge stage (90% MnOOH and 10% Mn(OH)<sub>2</sub>). Curve a:  $\gamma$ -MnO<sub>2</sub>, curve b:  $\gamma$ -MnO<sub>2</sub>(13 $\mu$ ), curve c:  $\gamma$ -MnO<sub>2</sub>(70 $\mu$ ), curve d:  $\gamma$ -MnO<sub>2</sub>(200 $\mu$ ). See text for explanation of the schematic models shown in this figure.

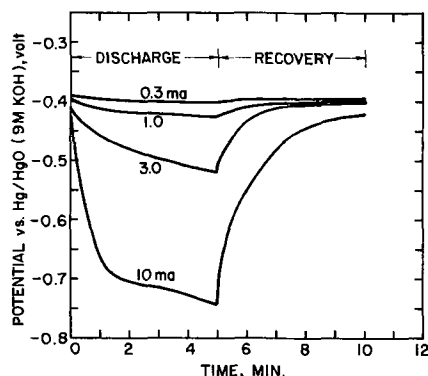


Fig. 5. Potential during constant current discharge and subsequent open circuit period. The numbers on the curves indicate the discharge current. This was measured with cells containing 100 mg of  $\gamma$ -MnO<sub>2</sub> at the 43 ma-hr discharge stage (44% MnOOH and 56% Mn(OH)<sub>2</sub>).

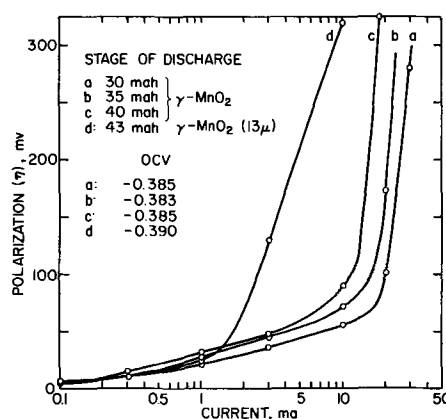


Fig. 6. Effect of the depth of discharge on the polarization curves

a, b in Fig. 4; a, b, c in Fig. 6) show a straight line portion with a slope of 30-33 mv per decade. Above a certain current, in every case a limiting current is reached and polarization increases sharply.

Figure 4 shows the effect of particle size of the original manganese dioxide. The limiting current decreases with increasing particle size of the original manganese dioxide sample. Curve (a) and curve (b) in Fig. 4 are almost identical. This is not surprising, because the particle sizes of the two samples is almost the same as pointed out earlier. The schematic models (A and B) for the fine and coarse MnO<sub>2</sub> samples packed with graphite particles are shown in Fig. 4. These will be discussed later.

Figure 6 shows the effects of discharge depth. The limiting current value decreases with increasing depth of discharge, although the general shape of the polarization curve remains the same up to 40 ma-hr. Also, the OCV's at various discharge depths remain almost constant as shown in Fig. 6.

Figure 7 shows a typical polarization curve of MnO<sub>1.45</sub> derived from  $\beta$ -MnO<sub>2</sub>(III) at 2 ma constant current discharge. The curve shows two steps; one up to 3 ma and the other from 3 ma to the limiting current, 27 ma. It should be noted that the open circuit potential (-0.315v) is much different (see the right side potential scale in Fig. 7) from those shown in Fig. 6, and also that the limiting current value is approximately the same as that of curves (a) and (b) for the  $\gamma$ -MnO<sub>2</sub> sample shown in Fig. 4.

### Discussion

Before discussing the details on the discharge mechanism of the second step (see Fig. 1) in which MnOOH is reduced electrochemically to Mn(OH)<sub>2</sub>, let us consider a few principal aspects of the electroreduction of metal oxides or other solid battery active materials.

When one solid phase (e.g., MnOOH, PbSO<sub>4</sub>, etc.) is electrochemically reduced to another solid phase (e.g.,

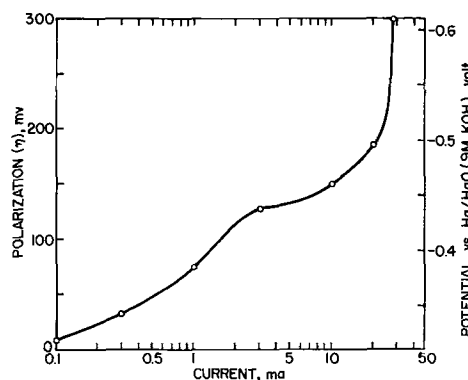


Fig. 7. Polarization curve of MnO<sub>1.45</sub> (30 ma-hr discharge) derived from  $\beta$ -MnO<sub>2</sub> at 2 ma discharge. This curve was measured after 103 hr storage at the 30 ma-hr discharge stage.

Mn(OH)<sub>2</sub>, Pb, etc.) at unit activity (absence of solid solution formation), the OCV of the system should remain constant as long as both phases [for example, MnOOH and Mn(OH)<sub>2</sub>, or PbSO<sub>4</sub> and Pb] co-exist, regardless of both the ratio of amounts of higher to lower valency material and the potential generating mechanism [e.g., potential arising directly from the solid system such as MnOOH-Mn(OH)<sub>2</sub>, or from a dissolved species such as the saturated Mn(III) ion-Mn(II) ion system]. This is a basic thermodynamic requirement as discussed previously (2). Therefore, the open circuit potential measurement itself should have no value in differentiating between the two discharge mechanisms shown in Fig. 2. Such a mechanism study must be based on kinetic behavior in the process.

When the solubility of the solid active material is in the order of 10<sup>-5</sup> mole/liter or higher, one must consider in addition to a solid state reduction mechanism, a mechanism in which a dissolved species is reduced on the surface of graphite or some other conductive network. The discharge current could now either be attributed entirely to one of the two mechanisms or apportioned between both.

Another important factor which must be taken into account is the electrical conductivity of the active material. If the solid active materials involved in the discharge [MnOOH and Mn(OH)<sub>2</sub> in the case shown in Fig. 2] are good electrical conductors, a dissolved Mn(III) ion can be reduced on the MnOOH surface instead of on graphite. This is equivalent to reduction of a surface Mn(III) atom to the Mn(II) state, and one cannot meaningfully distinguish between the two mechanisms. If the solid active materials involved are very poor conductors, the discharge current must be attributed only to the dissolved species mechanism. If the solid active materials have intermediate electrical conductivity, the true situation is rather complicated. The part which one mechanism plays in determining the total current should depend on the conductivity, solubility, and surface area as well as the current density.

Let us discuss now the details of the electrochemical reduction process of MnOOH. During this discussion we shall keep the schematic model (Fig. 4) in mind. We tentatively assume that the electrical conductivity of the MnOOH-Mn(OH)<sub>2</sub> system is very poor and that the MnOOH particles are surrounded by graphite particles in the present system as shown schematically in Fig. 4. Based on these assumptions and the solubilities of Mn(III) and Mn(II) in 9M KOH [4.4 × 10<sup>-3</sup>M for Mn(III) ion, and 0.4 × 10<sup>-3</sup>M for Mn(II)] as reported previously (6), the authors would like to prove here from the limiting current data for different particle sizes (Fig. 4) that the discharge current in the second step (Fig. 1) can be attributed essentially to the dissolved species mechanism.

Let us consider first the nature of the limiting current from the standpoint of the steps involved in the dissolved species mechanism of Fig. 2; b: dissolution of Mn(II), c: diffusion of Mn(III) ion, to the graphite surface, d: discharge of the Mn(III) ion, and e: precipitation of Mn(OH)<sub>2</sub>. The limiting current cannot be attributed to the charge transfer step because of the low polarization at the current densities below the limiting current density. The limiting current is not likely to be attributed to the diffusion process, because the MnOOH particles are in intimate contact with fine graphite particles and the diffusion path must be extremely short. Therefore, the limiting current under this situation is likely to be a measure of the dissolution rate of Mn(III) ion from the MnOOH.

With the highly porous oxide used, Mn(III) ion dissolution from all the fine pores which are filled with 9M KOH might contribute to the discharge current, but there should be very little influence on the limiting current value. The Mn(III) ion dissolved in the electrolyte in the fine pores has to diffuse some distance (depending on the particle size) in order to discharge

on the graphite surface. Therefore, the limiting current value will be determined essentially by the apparent surface area of the oxide. Therefore, if the average particle size is decreased by grinding the coarse manganese dioxide particles, the apparent surface area per unit weight should increase. This is shown schematically as systems A and B in Fig. 4. The relation between the total apparent surface area, *S<sub>a</sub>*, and the particle size (radius, *r*) is given by the following equation

$$S_a = \left[ \left( \frac{W}{d} \right) \div \left( \frac{4\pi r^3}{3} \right) \right] \times 4\pi r^2 = \frac{3W}{d} \frac{1}{r}$$

where *W* is the weight of sample, *d* the density of the oxide, and *r* the radius of the particle.

The limiting current value, *i<sub>l</sub>*, should be proportional to 1/*r*, since *S<sub>a</sub>* ∝ *i<sub>l</sub>*, or *i<sub>l</sub>* · *r* = constant should be held.

On the other hand, if the solid particle has a fair or good electrical conductivity and the discharge proceeds entirely or partly through a solid state mechanism; namely, the charge transfer reaction takes place at the entire solid-solution interface, the limiting current will be proportional to the true surface area. In such a case, the particle size should not be influential as long as the total true surface area remains the same regardless of the particle size. The present samples of different particle sizes have the same true surface area (39 m<sup>2</sup>/g).

If the real situation is a mixture of the two mechanisms in a certain proportion, *i<sub>l</sub>* · *r* = constant will not be true. Let us test the experimentally observed *i<sub>l</sub>* values for the relation. Table I shows the results in which there is a reasonably good constancy for the product, *r* · *i<sub>l</sub>*. This means the observed *i<sub>l</sub>* values for such a wide range of particle size can be well explained by the dissolved species mechanism.

The dissolved species mechanism was previously proposed based on some experimental evidence (1); namely, discharge during the second step was possible only at high KOH concentrations, or at low KOH concentrations with added triethanol amine (TEA). Both the high KOH concentration and the addition of TEA increase the dissolved Mn(III) ion concentration in KOH electrolyte. The limiting current data obtained in this study for different particle size samples and the discussion provided above support the dissolved species mechanism.

Two additional facts which lend further support to the present conclusion should be mentioned here. The first point concerns whether a system containing Mn(III) and Mn(II) ions in 9M KOH has a redox potential around -0.385v vs. Hg/HgO (9M KOH). This was experimentally investigated with a dropping mercury electrode and also with a platinum electrode. The half wave potential of the Mn(III)-Mn(II) system in 9M KOH was found to be -0.40v at a platinum electrode [Fig. 8 of ref. (6)] and -0.395v as a mean value of the anodic and the cathodic wave of the polarogram [Fig. 8 of ref. (1)].

The second point concerns whether or not the graphite surface is really responsible for the reduction reaction. In order to check this point, the amount of graphite mixed with 100 mg MnO<sub>2</sub> samples was varied from 0.1-1.0g without using coke. The limiting currents in these cells were measured with a potentiostat. The results (Fig. 8) show that the limiting current is pro-

Table I. Limiting current values (Fig. 4) and the product, *r* · *i<sub>l</sub>*

	<i>i<sub>l</sub></i> * (ma)	<i>r</i> · <i>i<sub>l</sub></i> **
γ-MnO <sub>2</sub> (13μ ± 3)	26 ± 3	348
γ-MnO <sub>2</sub> (70μ ± 10)	4.2 ± 0.5	294
γ-MnO <sub>2</sub> (200μ ± 20)	1.5 ± 0.2	300

\* *i<sub>l</sub>* (= limiting current) per 100 mg of sample MnO<sub>2</sub>.

\*\* *r* in μ and *i<sub>l</sub>* in ma.

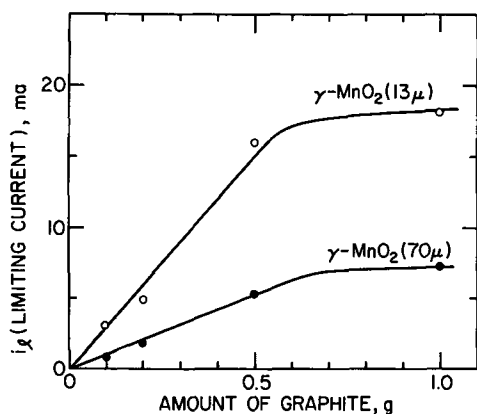


Fig. 8. Effect of amount of graphite mixed with 100 mg of  $\gamma$ -MnO samples (no coke was used in these experiments). The limiting currents were measured at 30 ma-hr discharge by a potentiostat 6 min after applying a constant potential which is 350 mv negative relative to the OCV [ $-0.385 \pm 0.005$ v vs. Hg/HgO (9M KOH)].

portional to the amount of graphite used up to a certain amount. This result is additional evidence in support of the schematic model (A in Fig. 4) of this powder packed system and shows that the graphite particle surrounding the MnO<sub>2</sub> particle is responsible for the electrochemical reaction [Mn(III) ion + e<sup>-</sup> → Mn(II) ion].

The two-step polarization curve seen in Fig. 7 can be explained as follows. As can be seen in the 2 ma discharge curve ( $\beta$ -MnO<sub>2</sub>) of Fig. 1, the potential during the early stage of discharge decreases to the point where the second step discharge reaction (MnOOH → Mn(OH)<sub>2</sub>) occurs before the reduction of tetravalent to trivalent oxide is completed. Therefore, at the 30 ma-hr discharge stage, the system contains Mn(IV)

oxide, Mn(III) oxide and Mn(OH)<sub>2</sub>. Under these conditions, the OCV should be determined by the Mn(IV) oxide instead of the Mn(III)-Mn(II) system (observed OCV:  $-0.315$ v) and the first step in the polarization curve (Fig. 7) is probably a discharge of the remaining Mn(IV) oxide. The second step in the polarization curve seems to be the discharge of dissolved Mn(III) ion. This is substantiated by the observed limiting current value for  $\beta$ -MnO<sub>2</sub>(III), 28 ma, which is close to that from  $\gamma$ -MnO<sub>2</sub>. Since the  $\beta$ -MnO<sub>2</sub>(III) and the  $\gamma$ -MnO<sub>2</sub> have almost the same particle size distribution, the  $i_L$  values for the two samples should be the same. It is worth noting that the undischarged Mn(IV) oxide does not appear to react with Mn(OH)<sub>2</sub> in 9M KOH on standing at 23°C over a long period (e.g., 103 hr).

#### Acknowledgment

The authors wish to thank Dr. R. A. Powers and Mrs. H. M. Joseph for suggestions in the preparation of the manuscripts and also to Mr. W. L. Adams for his experimental assistance.

Manuscript submitted Mar. 22, 1968; revised manuscript received ca. June 17, 1968.

Any discussion of this paper will appear in a Discussion Section to be published in the June 1969 JOURNAL.

#### REFERENCES

1. A. Kozawa and J. F. Yeager, *This Journal*, **112**, 959 (1965).
2. A. Kozawa and R. A. Powers, *ibid.*, **113**, 870 (1966).
3. A. Kozawa and R. A. Powers, *Electrochem. Technology*, **5**, 535 (1967).
4. A. Kozawa and R. A. Powers, *This Journal*, **115**, 122 (1968).
5. A. Kozawa and R. A. Powers, Abstract of the 35th Meeting of the Electrochemical Society of Japan, Paper B 105, p. B 7 (1968).
6. A. Kozawa, T. Kalnoki-kis, and J. F. Yeager, *This Journal*, **113**, 405 (1966).

## Structure Effects of Many-Membered Polymethyleneimine on Corrosion Inhibition

Kunitsugu Aramaki and Norman Hackerman\*

Department of Chemistry, The University of Texas at Austin, Austin, Texas

#### ABSTRACT

Corrosion rates of pure iron in HCl solution with and without corrosion inhibitors were determined by polarization measurements, volumetric measurements of evolved hydrogen, and weight loss measurements. C<sub>5</sub> and C<sub>8</sub> to C<sub>14</sub> polymethyleneimines and C<sub>6</sub> to C<sub>14</sub> symmetric secondary amines were tested as the inhibitor. Basicity values and relative molecular areas of these inhibitors were also determined. A comparison of the inhibition effectiveness within these two series indicates that the inhibition effect of the medium-sized cyclic imines (C<sub>9</sub> to C<sub>12</sub>) is closely related to the angle of the C-N-C bond in their molecules and thus to strain in the ring.

Some of the effective factors in the molecular structure of cyclic polymethyleneimines containing four to ten methylene groups on their corrosion inhibition of iron or steel in acid solution have been studied (1, 2). It was clearly established that polymethyleneimines having eight to ten methylene groups had a markedly higher inhibition efficiency than those of secondary amines containing the same number of groups. It was suggested (2) that this higher efficiency was closely related to strain in the ring of the imine molecule, since the strain of the polymethylene ring becomes maximum at the ten-membered ring (3). Further, it

was indicated that the enhanced inhibition could be attributed to improved adsorption. The larger C-N-C angle, due to greater ring strain, provides sp<sup>2</sup> hybrid orbital geometry in the nitrogen atom, giving rise to a  $\pi$ -electron bonding possibility between nitrogen and metal (2, 4).

In order to confirm these relationships with more cyclic imines, especially some beyond C<sub>10</sub> in which the strain does not exist, two groups of experiments were carried out. The first was a comparative study of inhibition effectiveness within the series of polymethyleneimines and within the series of symmetric secondary amines. These differ in structure only by the

\* Electrochemical Society Active Member.

presence of a ring closing bond and of two hydrogen atoms. Polymethyleneimines,<sup>1</sup> represented by the general formula  $(\overline{\text{CH}_2})_n\text{NH}$  and containing five and eight to fourteen methylene groups, were tested as corrosion inhibitors. Symmetric secondary amines,<sup>1</sup>  $(\text{C}_{n/2}\text{H}_{n+1})_2\text{NH}$ , where  $n$  is 6, 8, 10, 12, or 14, were also used.

In the second group of experiments, the inhibition efficiencies of cyclic compounds with nine methylene groups were measured and compared with that of  $\text{C}_9$  imine. These compounds were 1,2,3,4-tetrahydroquinoline, 1,2,3,4-tetrahydroisoquinoline and *cis*- and *trans*-decahydroquinoline.

Three kinds of corrosion rate measurements of pure iron wire in 6.1M HCl solution at 30°C were made with several concentrations of the inhibitors. The rates were determined by polarization measurement, volumetric measurement of evolved hydrogen, and weight loss measurement of the wire.

Basicity values of the inhibitors and approximate areas of metal surface which each inhibitor molecule effectively covered in the adsorbed position were determined.

### Experimental

**Corrosion inhibitors.**—Cyclic imines containing from nine to fourteen methylene groups were synthesized from the corresponding dibasic acids as starting materials. Cycloketone isooximes were obtained through the Schmidt reaction (5) with cycloketones (6) derived from cycloketonealcohols. The latter were produced through acyloin condensation (7) with methyl esters of the dibasic acids. The cycloketone isooximes were reduced with lithium aluminum hydride to cyclic imines (8). These products were repeatedly purified by fractional distillation or by recrystallization. Absence of impurities was shown by infrared spectra.

Piperidine, octamethyleneimine, dipropylamine, dibutylamine, dipentylamine, dihexylamine, diheptylamine, *trans*-decahydroquinoline, 1,2,3,4-tetrahydroquinoline, and 1,2,3,4-tetrahydroisoquinoline were obtained as high-grade commercial reagents and carefully purified by distillation before use. *Trans*-decahydroquinoline was further purified by recrystallization of its hydrochloride derivative (9). *Cis*-decahydroquinoline, obtained as the mixture of *cis*- and *trans*-isomers, was isolated and purified by recrystallization of its hydrochloride derivative (9).

Inhibitor solutions were prepared by dissolving a known weight of the inhibitors in an appropriate volume of constant boiling (107°C) HCl solution which was obtained by diluting the reagent grade solution (2).

**Polarization measurements.**—Pure iron wire (99.5%, Mallinckrodt analytical reagent grade, 0.36 mm diameter) was used. The wire was fixed at an end of a glass tubing with a Teflon joint and then cut to a length giving a calculated surface area of 0.25 cm<sup>2</sup> to provide an electrode assembly. This was washed with pentane, dipped in phosphoric acid (1:3), carefully rinsed with distilled water and then with acetone, and dried in a vacuum desiccator. Electrical contact was made by means of mercury inside the tubing of the electrode assembly.

A small glass cell in which the anode and cathode compartments were separated by fritted glass was used for these measurements. Coiled platinum wire was used as a counter electrode. The polarization current was supplied by a 90v battery and a series of variable resistances and determined with a Keithley electrometer. The potential of the test electrode was measured by using a saturated calomel electrode and a Keithley electrometer. In all runs the HCl solution was de-aerated by passing nitrogen gas through it for long periods.

<sup>1</sup>The term cyclic imine is used for polymethyleneimine in this study as are  $\text{C}_n$  imine and amine; for example,  $\text{C}_{10}$  imine for decamethyleneimine and  $\text{C}_{10}$  amine for dipentylamine.

Each whole polarization run was completed in 15 min before the surface area of the test electrode became small enough to affect the results. Several runs were made, both with and without the inhibitor in solution at each of the concentrations.

**Weight loss and hydrogen evolution measurements.**—Four iron wires were mounted through small holes in a Teflon disk with a glass rod hanger and cut into 5.0 cm lengths. This test wire assembly was washed with pentane, dipped into phosphoric acid (1:3) for about 15 sec, washed thoroughly with distilled water, cleaned with acetone, dried in vacuum, and then weighed. Thirty milliliters of the inhibitor solution was placed in a small flask equipped with a glass rod hook and a graduated gas buret, and the assembly was immersed in this solution at 30°C. From information obtained in a few trial experiments, the volume of the solution was adjusted to give a quantity of HCl large enough so that the  $\text{H}^+$  consumption would be less than 1% of  $\text{H}^+$  in the solution. These experiments were done without deaeration.

Hydrogen evolved from the iron wire in the solution was measured with the graduated gas buret. At the end of a given period, the test assembly was removed from the flask quickly, washed with a large volume of water, rinsed thoroughly with acetone, dried in vacuum, and weighed. Corrosion rates were calculated both from the volume of hydrogen evolved and from the loss in weight of the iron wire.

To estimate the approximate area of metal surface which the inhibitor molecule would effectively cover in the adsorbed position, relative areas were determined with molecular models. Stuart-Briegleb models of each inhibitor were arranged on a plane in a position corresponding to the possible configuration of the molecule adsorbed on the metal surface by formation of the coordinated bond between the metal and its nitrogen atom. Therefore, the bonding geometry of the nitrogen atom was based on that of the  $\text{sp}^3$  hybrid orbitals. The metal-nitrogen bond was assumed to be perpendicular to the metal surface. Thus, the arranged model was projected on the plane and the distance from the metal-nitrogen bond to the most extreme portion of the molecule was measured on the chart. The effective area covered by the molecule was calculated as the area of the circle with this distance as a radius. This simply assumes that the molecule is free to rotate on the metal-nitrogen bond as an axis. The area of piperidine with the ring placed parallel to the metal surface was also determined. The ratio of the area of each inhibitor to this piperidine area is defined as the relative molecular area. Since there are many possible configurations, the maximum and minimum relative molecular area for each of the inhibitors was determined to provide limits.

In order to compare the adsorption abilities of these inhibitors,  $\text{pK}_a$  values were determined by titration with  $\text{HClO}_4$  in 50% diethyleneglycol-water solution at 30°C. The pH of the solution was followed with a glass electrode and a Beckman Model H pH meter.

### Results

Polarization curves showed well-defined Tafel regions extending over more than a decade on the current axis. The slopes were high but consistent. The corrosion current,  $i_{\text{corr}}$ , and the corrosion potential were given by the intersection of extrapolated anodic and cathodic Tafel lines. Good reproducibility for  $i_{\text{corr}}$  was obtained with less than  $\pm 4\%$ .

Corrosion currents are shown as a function of inhibitor concentration in Fig. 1 for cyclic imines, in Fig. 2 for secondary amines, and in Fig. 3 for several  $\text{C}_9$  cyclic compounds, including the  $\text{C}_9$  imine. Concentrations of the  $\text{C}_{13}$  and  $\text{C}_{14}$  imines and  $\text{C}_{12}$  and  $\text{C}_{14}$  amines are limited by their solubility in the solution. For the secondary amines,  $i_{\text{corr}}$  decreases regularly with increase in number of carbons and irregularly for the cyclic imines. Thus,  $i_{\text{corr}}$  for  $\text{C}_{10}$  imine is smaller

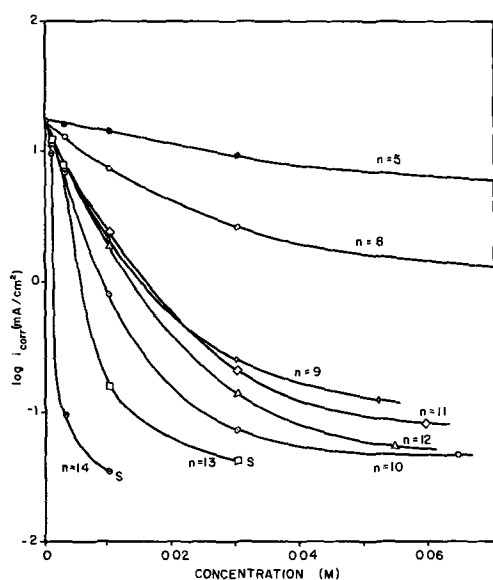


Fig. 1. Effect of cyclic imines  $[(CH_2)_nNH]$  on corrosion current. S = saturation; n = carbon number.

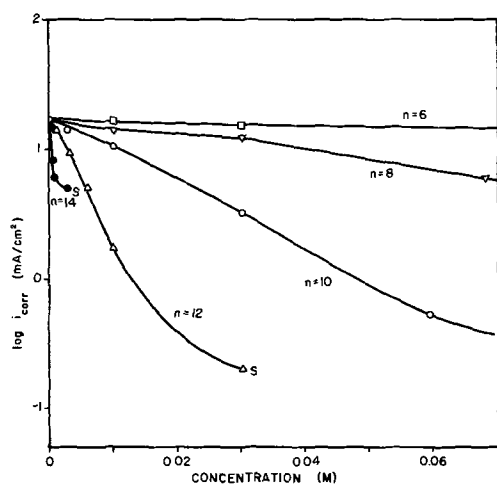


Fig. 2. Effect of secondary amines  $[(C_{n/2}H_{n+1})_2NH]$  on corrosion current. S = saturation; n = carbon number.

than for  $C_{11}$  and  $C_{12}$  imines. Also, Fig. 3 shows much lower corrosion currents for the  $C_9$  imine than for any of the other four  $C_9$  inhibitors. These measurements were also obtained by hydrogen evolution and weight loss, and the data were in essential agreement insofar as their general dependency was concerned.

Hydrogen evolution rates increased with time for about 20 min after the corrosion reaction had begun and then decreased gradually. Satisfactory reproducibility could not be obtained for the initial 20-min period or after some 120 min, deviation being more than  $\pm 5\%$ . Consequently, the rates of hydrogen evolution were measured by using the average slopes of  $H_2$  volume vs. time curves between 30 and 120 min after the test wires were immersed in the solution. The data were reproducible to  $\pm 4\%$ .

There was no effect due to oxygen as shown by measurements with the system thoroughly deaerated with nitrogen gas.

The hydrogen evolution rate data show the comparative inhibitive effects for each of the inhibitors to be the same as that shown by polarization measurement. In fact, inhibition efficiencies were the same for each compound by all three experimental methods used.

Weight loss measurements were made along with the hydrogen evolution measurements, so the im-

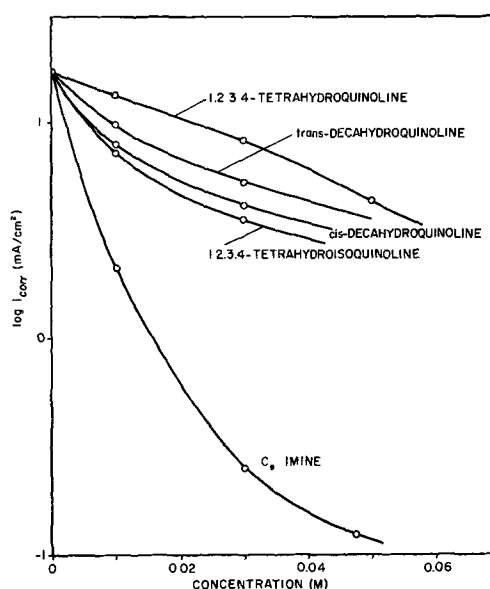


Fig. 3. Effect of  $C_9$  cyclic compounds on corrosion current

ersion time was 120 min. Reproducibility was good, again with a maximum deviation of  $\pm 4\%$ .

The data from each type of experiment were self-consistent with the electrochemical method giving high rates, but as already stated with the degree of inhibition being the same by all three methods. The inhibition effectiveness increases with the carbon number of the inhibitor for both series, the exception being that the  $C_{10}$  imine is more effective than the  $C_{11}$  or  $C_{12}$  imine.

For the  $C_9$  cyclic compounds, the inhibition order observed was tetrahydroisoquinoline > *cis*-decahydroquinoline > *trans*-decahydroquinoline > tetrahydroquinoline, but with the  $C_9$  imine notably more effective than the other four.

Molecular areas are shown in Fig. 4 for the cyclic imines and in Fig. 5 for the secondary amines. The maximum and minimum values shown arise from the different molecular configurations. Although the actual configuration on the metal surface is not known, the value must be between their limits.

The relative molecular areas were determined in duplicate and these values were within  $\pm 2.5\%$  of the average. Maximum and minimum values of  $C_5$  to  $C_9$  imine differ little since a lack of steric flexibility in their molecular structures restricts the configuration

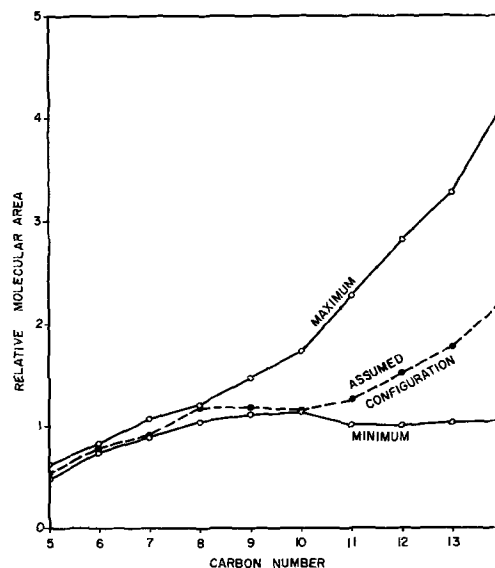


Fig. 4. Relative molecular area of cyclic imines

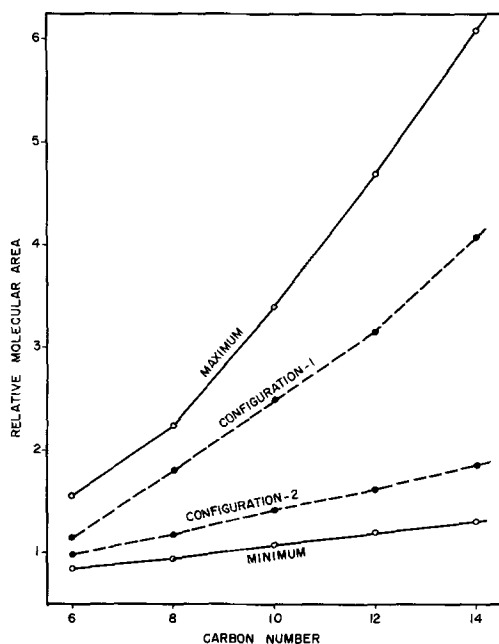


Fig. 5. Relative molecular area of secondary amines

of the imine molecules adsorbed on metal surface. For the imine series  $C_{10}$  and higher, however, there are large differences since the structures are more flexible. The differences are even greater in the case of the secondary amines. Hence, simple areal comparison is not suitable.

In order to compare these areas effectively, reasonable configurations must be assumed. These were chosen as follows: analogous configurations to those of cycloparaffin derivatives represented by Dunitz and Prelog (10) for the series of the cyclic imines containing less than twelve members and configurations involving less transannular interaction of hydrogen atoms for the cyclic imines with more than thirteen members. Configurational detail for the  $C_{11}$  imine is available (11).

The secondary amines have many "reasonable" configurations due to flexible deformation of their alkyl radicals, but two series of configurations were assumed. One, configuration-1, is of the type in which all of the methylene groups in alkyl radicals keep a staggered form as shown in Fig. 6A and the other, configuration-2, is the same except for an eclipsed form at the 3 and 4 position as shown in Fig. 6B. The former is an extended form and the latter a compacted one more like that of the cyclic imine. The relative molecular areas of these configurations were determined and are also given in Fig. 4 and 5, respectively.

The maximum and minimum relative molecular areas of the  $C_9$  cyclic compounds, as well as those of  $C_9$  imine, are listed in Table I. From the molecular geom-

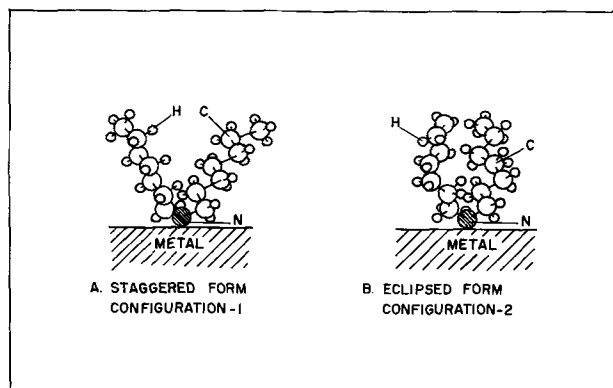


Fig. 6. Configurations of secondary amines

Table I. Relative molecular area and  $pK_a$  values of  $C_9$  cyclic compounds

Compounds	Relative molecular area	$pK_a$
<chem>C1CN(C)CC1</chem> 1,2,3,4-Tetrahydroquinoline	1.73-2.09	4.87
<chem>C1CN(C)C(C)C1</chem> 1,2,3,4-Tetrahydroisoquinoline	1.23-2.22	9.32
<chem>C1CN(C)CC1</chem> <i>cis</i> -Decahydroquinoline	1.33-1.56	10.41
<chem>C1CN(C)CC1</chem> <i>trans</i> -Decahydroquinoline	1.49-1.75	10.47
<chem>C1CN(C)CC1</chem> $C_9$ imine	1.11-1.48	9.86

etry it is likely that for tetrahydroquinoline and *cis*- and *trans*-decahydroquinoline adsorption via the nitrogen atom requires the hydrocarbon parts to be nearly parallel to the metal surface, while the tetrahydroisoquinoline can be placed either parallel or perpendicular to the surface. Consequently, the minimum relative molecular areas of the first three are larger than that of the last one. The relative molecular area of the  $C_9$  imine is similar to or smaller than that of the other four.

The study of the arrangement of these molecular models on the metal plane suggested an effect of steric hindrance by hydrogen atoms bonded to carbon atoms adjacent to nitrogen on the adsorption of nitrogen atoms in tetrahydroquinoline, *cis*-decahydroquinoline and especially in *trans*-decahydroquinoline. This effect may decrease their inhibition effectiveness.

The  $pK_a$  values, measured in duplicate for each of the inhibitors, were reproducible to within  $\pm 1.5\%$  of the average. These are shown in Fig. 7. The data for the series of the cyclic imines agree with those given in a previous paper (2) and correspond well to those measured by Ruzicka, Kobelt, Häfliger, and Prelog (8). However, the values for the series of the secondary amines are inconsistent with those reported earlier (2) but correspond to others (12, 13).

From these results it is apparent that the electron donating propensities for these two series are nearly equal, and that the  $pK_a$  value for the series of the cyclic imines reaches a minimum at  $C_{10}$ . The basic strengths of the  $C_9$  cyclic compounds are also shown in Table I together with those of the  $C_9$  imine.

### Discussion

To compare the corrosion rates measured by the three different methods more easily, all were converted to mdd. The corrosion rates of iron wire in uninhibited 6.1M HCl solution at  $30^\circ C$  are 43,600 mdd by polarization ( $R_1$ ), 15,380 mdd by gas evolution ( $R_v$ ),

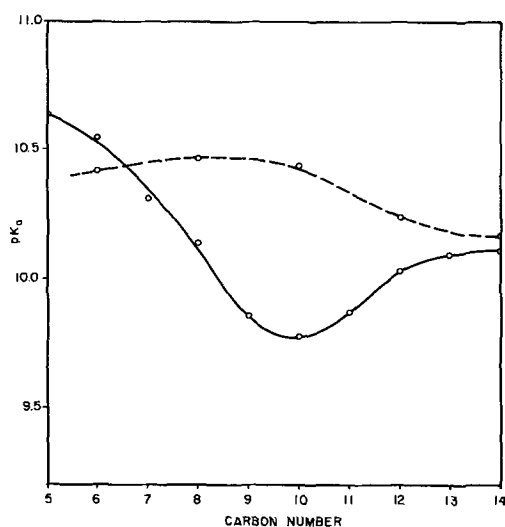


Fig. 7.  $pK_a$  values of cyclic imines and secondary amines. Cyclic imines, —; secondary amines, - - - -.

and 14,450 mdd by weight loss ( $R_w$ ). The reason for this disagreement will not be discussed here since the inhibition efficiency is in good agreement with each method.

Two corrosion inhibitor concentrations were selected as typical of high and low inhibition effectiveness, 0.001 and 0.01M. For most of the inhibitors the effectiveness was markedly greater at the higher concentrations; for example, rates of 11,700 mdd for  $C_{10}$  imine and 12,750 mdd for  $C_{12}$  amine at 0.001M, but 921 mdd and 1540 mdd at 0.01M. The corrosion rates by all three means are plotted in logarithmic scale in Fig. 8 and 9 (for convenience) as a function of carbon number of the inhibitor.

Inhibition efficiencies, defined as  $100 [(R_0 - R)/R_0] \%$  where  $R_0$  is the uninhibited rate and  $R$  the inhibited rate, were calculated with each of the three kinds of measurements. Inhibition efficiencies for a given inhibitor and concentration agree with each other with differences less than  $\pm 5\%$  at concentrations in excess of 0.003M. Consequently, the trend of the three curves derived from the three corrosion measurements for each of the inhibitor series are comparable at 0.01M as

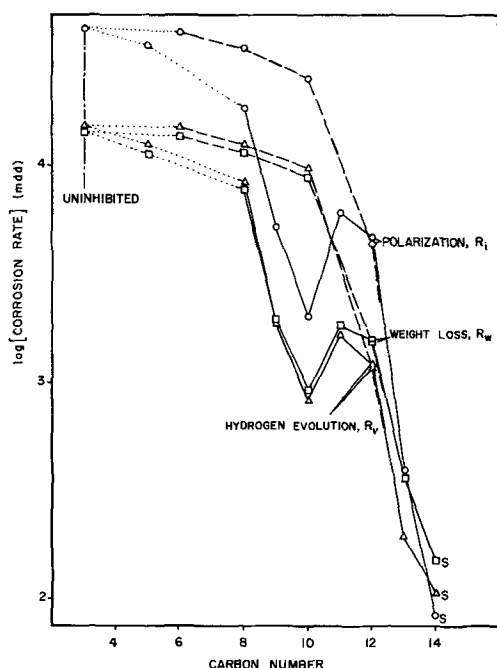


Fig. 8. Corrosion rates at the concentration of 0.01M. Cyclic imines, —; secondary amines, - - - -; S = saturation.

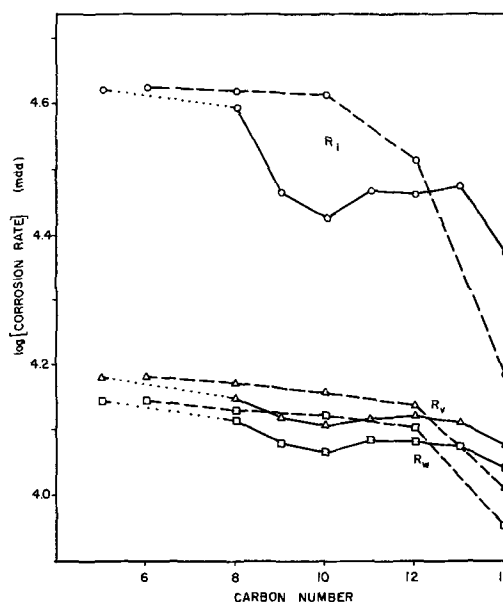


Fig. 9. Corrosion rates at the concentration of 0.001M. Cyclic imines, —; secondary amines, - - - -.

shown in Fig. 8. However, at 0.001M all of the inhibition efficiencies derived from  $R_1$  are larger than those from  $R_v$  and  $R_w$ . This disagreement may be attributed to the high Tafel slopes in the uninhibited system: the cathodic Tafel slope,  $b_c$ , being 0.127 and the anodic,  $b_a$ , 0.082 v/log  $i$ . This is probably due to the shape of the electrode because the normal Tafel slopes ( $b_c$ , 0.068;  $b_a$ , 0.053 v/log  $i$ ) and the corrosion current corresponding to the corrosion rate determined by the hydrogen evolution measurement were found in the experiments by using a pure iron rod (3.0 mm diameter). However, no further amplification was tried. Nonetheless, the trend of the corrosion rates derived from the three kinds of experiments was similar even at 0.001M as shown in Fig. 9. Therefore, all of the corrosion inhibition experiments are discussed by using the corrosion current as a typical corrosion rate. Both Fig. 8 and Fig. 9 show a minimum in corrosion rate at  $C_{10}$  for the cyclic imines, but none for the secondary amines.

An irregularity is found in the melting points for  $C_{10}$  to  $C_{13}$  imine; they are less than  $25^\circ\text{C}$  for  $C_{10}$  and  $C_{12}$  imine,  $41^\circ\text{C}$  for  $C_{11}$  imine,  $50^\circ\text{C}$  for  $C_{13}$  imine, and  $53^\circ\text{C}$  for  $C_{14}$  imine. Molecular association, which results in the high melting point, may also account for decrease of inhibition effectiveness (14). However, association of  $C_{11}$  imine was not detected at 0.1M in carbon tetrachloride using infrared spectra.

To estimate the effect of the area of metal surface covered with the inhibitor on the corrosion rate,  $\log i_{\text{corr}}$  values were plotted at 0.001M inhibitor vs. relative molecular areas of the assumed configurations for the two series of inhibitors (Fig. 10). A simple curve can be drawn through all of the points for the secondary amines in configuration-1, but not through all of them for the cyclic imines. A remarkable irregularity of  $i_{\text{corr}}$  values for the cyclic imines is found between nine and twelve carbons.

A curve similar in form to that for the secondary amine series is drawn through the points for  $C_5$  and  $C_{14}$  imine (Fig. 10). This curve is assumed to be that for a series of cyclic imines which are free from ring strain because six and fifteen membered rings are almost free from the ring strain (3) and all of the secondary amines are free of the strain.

Deviations of each point for the cyclic imines from this curve were measured on the graph and plotted vs. carbon number in Fig. 11. This deviation,  $\Delta \log i_{\text{corr}}$ , then means the decrease of  $\log i_{\text{corr}}$  due to the imine



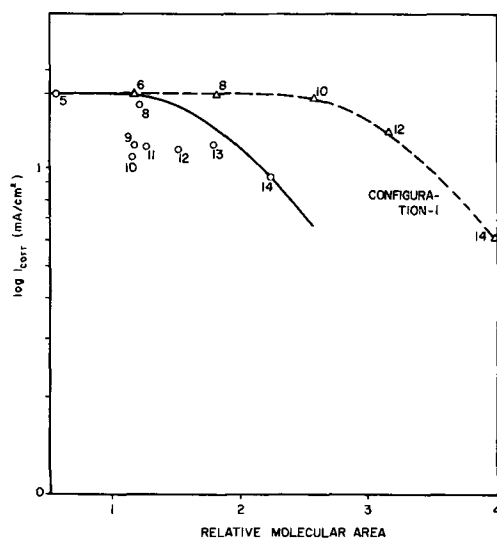


Fig. 10.  $\log i_{\text{corr}}$  vs. relative molecular area at the concentration 0.001M. Cyclic imines, —; secondary amines, - - - -; number indicates the carbon number.

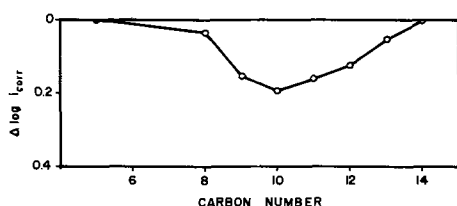


Fig. 11.  $\Delta \log i_{\text{corr}}$  vs. carbon number at the concentration 0.001M

strain. Notable differences appear for nine to twelve carbons with maximum effect at ten.

Figure 12 shows the  $\log i_{\text{corr}}$  vs. relative molecular area curves for the series of cyclic imines and secondary amines in their configurations described above at 0.01M concentration. As before (Fig. 10), there is the same irregularity for the cyclic imine series. A curve for the strain-free cyclic imines could not be obtained since  $i_{\text{corr}}$  for  $C_{14}$  imine and  $C_{14}$  amine could not be determined at 0.01M due to solubility limitation. This curve may be assumed to resemble that for secondary amines in configuration-2. As can be seen in Fig. 13,  $\Delta \log i_{\text{corr}}$  for the cyclic imines reaches a maximum at ten carbons. The  $\Delta \log i_{\text{corr}}$  derived from  $R_v$  or  $R_w$  also agreed with these results.

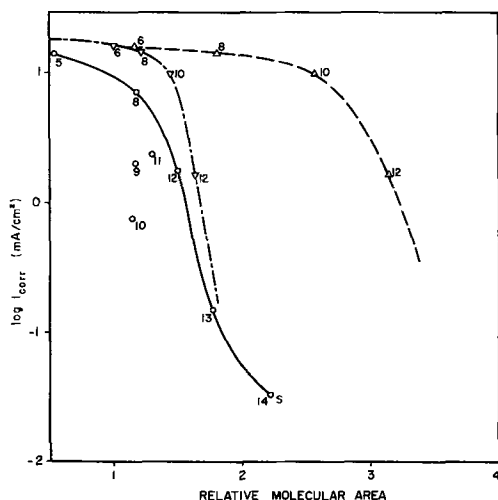


Fig. 12.  $\log i_{\text{corr}}$  vs. relative molecular area at the concentration 0.01M. Cyclic imines, —; secondary amines (configuration-1), - - - -, (configuration-2), - · - · - ·; S = saturation; number indicates the carbon number.

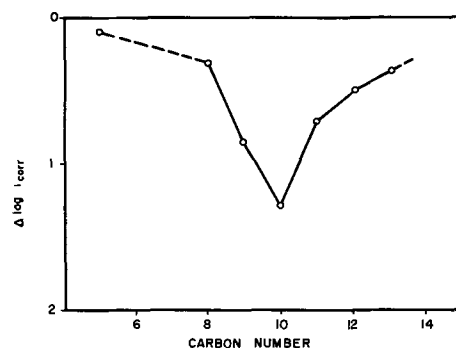


Fig. 13.  $\Delta \log i_{\text{corr}}$  vs. carbon number at the concentration 0.01M.

The  $\Delta \log i_{\text{corr}}$  vs. number of carbons parallels that for  $pK_a$  (Fig. 7). Thus, both of these properties of the cyclic imines as well as many of those reported by Prelog (15) may be due to the same effect of molecular structure.

As compared to  $C_5$  imine, the difference in equilibrium constants and rate constants between  $C_{10}$  and  $C_6$  cyclic compounds appear to be due to strain (16). The strain causes the angle of the C-N-C bond in the  $C_{10}$  imine to be larger than in the other. Data on the angles are not available for the whole series. The ones chosen here were assumed on the basis of C-C-C bond angle in cycloparaffin derivatives as determined by x-ray diffraction (17). This assumption is justified by comparison of the angle of the C-N-C bond in azacyclododecane ( $C_{11}$  imine) hydrochloride (11).

The angle of C-N-C bond in the  $C_5$  imine ring is about  $112^\circ$  (18) and is not too different from the bond angle of  $109^\circ 18'$  in the theoretical  $sp^3$  hybrid orbital geometry. Since  $C_5$  imine reacts with proton to form the stable ammonium ion without change of the geometry in the nitrogen atom, as shown in Fig. 14A, the equilibrium of this reversible reaction shifts toward the right side in acid solutions.

The C-N-C bond angle in the  $C_{10}$  imine is believed to be near  $120^\circ$ , which represents  $sp^2$  hybrid orbital geometry in the nitrogen atom. When the reaction of  $C_{10}$  imine with proton occurs to form the ammonium ion, the  $sp^2$  geometry in the nitrogen atom must change to the deformed  $sp^3$  geometry which is less stable than that in the piperidinium ion. Consequently, the equilibrium of this reaction for  $C_{10}$  imine shifts to the left side, resulting in a lower  $pK_a$  value. Thus, the relationship between  $pK_a$  and  $\Delta \log i_{\text{corr}}$  may be said to depend on the angle of C-N-C bond. In other words, the inhibition efficiency of the cyclic imines containing from nine to twelve methylene groups is related to the angle of C-N-C bond.

To verify this, the inhibition effectiveness of the four  $C_9$  cyclic compounds was compared with that of  $C_9$  imine taking their relative molecular areas and  $pK_a$  values into account. All the results in the three kinds

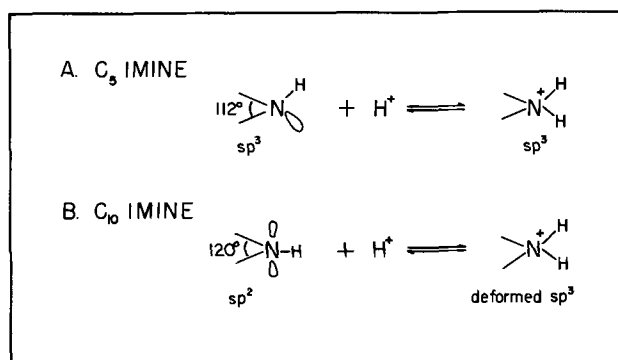


Fig. 14. Geometry of nitrogen atom in cyclic imines reacting with proton.

of measurements show the order of their inhibition effectiveness as tetrahydroquinoline < *trans*-decahydroquinoline < *cis*-decahydroquinoline < tetrahydroisoquinoline << C<sub>9</sub> imine.

As the pK<sub>a</sub> value of tetrahydroquinoline is much lower than the others, the low adsorbability on metal results in lower inhibition effectiveness. The order of the effectiveness among *trans*- and *cis*-decahydroquinoline and tetrahydroisoquinoline may be attributed to the configuration of their molecules adsorbed on metal surface. Hydrogen atoms near nitrogen atoms interfere with the adsorption of the nitrogen in decahydroquinoline, especially in the *trans*-isomer, by their steric hindrance (19). Tetrahydroisoquinoline is a better inhibitor than decahydroquinoline because there is less steric hindrance. However, in comparison, C<sub>9</sub> imine is an excellent corrosion inhibitor. The relative molecular areas of C<sub>9</sub> imine are similar to or smaller than those of the others and the pK<sub>a</sub> of C<sub>9</sub> imine lies between those of the other compounds. Thus, the strain in the ring must be the reason for the difference since there is strain only in the C<sub>9</sub> imine.

### Conclusion

From these results, it is concluded that the angle of the C-N-C bond, which is closely related to the strain in the ring of cyclic imines containing from nine to twelve methylene groups, is important in the corrosion inhibition effectiveness of these compounds. But there is no firm basis for explaining how the angle of the C-N-C bond or the strain in the ring of medium-sized cyclic imines affects the inhibition. Hackerman, Hurd, and Annand (2) believe that it can be attributed to an improved metal-nitrogen bond formed by chemisorption. This bond arises from the greater possibility for  $\pi$ -electron bond formation of the unshared pair of electrons due to the sp<sup>2</sup> hybrid orbital geometry of its nitrogen atoms (4). From generalization on addition reactions to a double bond, the sp<sup>2</sup> geometry of its nitrogen atom should be changed to the sp<sup>3</sup> geometry to form the metal-nitrogen bond by chemisorption. The strong adsorption of the medium-sized cyclic imine cannot be attributed to formation of the unstable, deformed sp<sup>3</sup> geometry. The formation of stable metal-nitrogen bond in which the sp<sup>2</sup> geometry remains in the nitrogen atom may be required to explain strong adsorption.

It can also be assumed that the higher energy associated with strained bonds in the medium-sized ring promotes a reaction for opening the ring, resulting in polymerization of the cyclic imine. The polymerized compound is expected to favor the inhibition effect (20). There is no evidence to confirm the polymerization of the cyclic imine adsorbed on iron surface in acid solution. But formation of resinous matter during distillation of the medium-sized cyclic imine suggests this probability. Further work is required to confirm this suggestion. Corrosion inhibition study on quaternary ammonium compounds of N-substituted derivatives of the medium-sized cyclic imines would be applicable.

### Acknowledgments

The authors are grateful to The Robert A. Welch Foundation of Houston, Texas, and to the Office of Naval Research under Contract NONR 375(15) for financial support of this work. They also wish to express their appreciation to Dr. J. S. Payne, Jr. of TRACOR, Inc. for his advice on synthesis of the cyclic imines.

Manuscript submitted April 4, 1968; revised manuscript received June 14, 1968. This paper was presented in part at the Chicago Meeting, Oct. 15-19, 1967, as Paper 74.

Any discussion of this paper will appear in a Discussion Section to be published in the June 1969 JOURNAL.

### REFERENCES

1. H. F. Finley and N. Hackerman, *This Journal*, **107**, 259 (1960).
2. N. Hackerman, R. M. Hurd, and R. R. Annand, *Corrosion*, **18**, 37t (1962).
3. S. Kaarsemaker and J. Coops, *Rec. Trav. chim. Pay-Bas*, **71**, 261 (1952); J. Coops, H. van Kamp, W. A. Lambregts, J. Visser, and H. Dekker, *ibid.*, **79**, 1226 (1960).
4. N. Hackerman and R. M. Hurd, "First International Congress on Metallic Corrosion," p. 166, Butterworths, London, 1962.
5. H. Wolff, "Organic Reactions," Vol. 3, p. 307, John Wiley & Sons, Inc., New York (1946).
6. A. C. Cope, J. W. Barthel, and R. D. Smith, "Organic Syntheses," Collective Vol. 4, p. 218, John Wiley & Sons, Inc., New York (1963).
7. N. L. Allinger, "Organic Syntheses," Collective Vol. 4, p. 840, John Wiley & Sons, Inc., New York (1963).
8. L. Ruzicka, M. Kobelt, O. Häfliger and V. Prelog, *Helv. chim. Acta*, **32**, 544 (1949).
9. W. Hüchel and F. Stepf, *Ann.*, **453**, 172 (1927).
10. J. D. Dunitz and V. Prelog, *Angew. Chem.*, **72**, 896 (1960).
11. J. D. Dunitz and H. P. Weber, *Helv. chim. Acta*, **47**, 1138 (1964).
12. E. T. Barrous, B. M. C. Hargraves, J. E. Page, J. C. L. Resuggan, and F. A. Robinson, *J. Chem. Soc.*, **1947**, 197.
13. D. D. Perrin, "Dissociation Constants of Organic Bases in Aqueous Solution," p. 13, Butterworths, London (1965).
14. K. Aramaki and S. Fujii, *Corrosion Engineering*, **14**, 542 (1965).
15. V. Prelog, *J. Chem. Soc.*, **1950**, 420.
16. J. Sicher, "Progress in Stereochemistry," Vol. 3, p. 202, Butterworths, New York (1962).
17. J. D. Dunitz, *et al.*, *Helv. chim. Acta*, **43**, 3, 18, 760 (1960); *ibid.*, **44**, 2027, 2033 (1961); *ibid.*, **45**, 951 (1964); *ibid.*, **48**, 1441, 1450 (1965); *ibid.*, **49**, 2492, 2502, 2505 (1966).
18. P. C. Rérat, *Acta Cryst.*, **13**, 72 (1960).
19. S. Fujii and K. Aramaki, *Comptes Rendus du Symposium Européen sur les Inhibiteurs de Corrosion*, p. 215, Università Degli Studi di Ferrara, 1961.
20. R. R. Annand, R. M. Hurd, and N. Hackerman, *This Journal*, **112**, 134, 144 (1962).

# Electrochemical Oxidation of Adenine: Reaction Products and Mechanisms

Glenn Dryhurst<sup>1</sup> and Philip J. Elving\*

Department of Chemistry, University of Michigan, Ann Arbor, Michigan

## ABSTRACT

The electrochemical oxidation of adenine (6-aminopurine), which gives a single well-defined voltammetric wave at the pyrolytic graphite electrode (PGE), was investigated by macroscale controlled electrode potential at the PGE in aqueous 1M acetic acid solution (pH 2.3) with exhaustive isolation, identification, and determination of reaction products and intermediates. The electrochemical oxidation of adenine appears to follow initially the same path as the enzymatic oxidation, but further oxidation and fragmentation of the purine ring system occur. Thus, adenine is oxidized in a process involving a total of 6 electrons per adenine molecule to give as the primary product a dicarbonium ion intermediate, which, being unstable, undergoes a further series of reactions: (a) electrochemical oxidation to parabanic acid (some of which is further hydrolyzed to oxaluric acid), urea, carbon dioxide, and ammonia; (b) electrochemical reduction to give ultimately 4-aminopurpuric acid, carbon dioxide, and ammonia; and (c) hydrolysis to allantoin, carbon dioxide, and ammonia.

Adenine (6-aminopurine)<sup>2</sup> is one of the two principal purines found in nucleic acid and, in the form of adenosine triphosphate (ATP), plays an important role in many metabolic processes. Because of the experimental similarities between conditions in the two heterogeneous oxidation processes based on enzymes and electrochemistry (1, 2), the electrochemical oxidation of adenine was investigated.

Few studies of the chemical oxidation of purines have been reported apart from those on uric acid (2,6,8-trihydropurine). Oxidation of adenine with an aqueous manganese dioxide suspension at 100° gives urea and biuret (3). Irradiation of aqueous adenine solutions gives 4,6-diamino-5-formamidopyrimidine and 8-hydroxy-6-amino-purine as the main products (4).

The enzymatic and biological oxidations of adenine have been more extensively examined and are covered in part in the reviews by Lister (5) and Robins (6). Adenine is directly oxidized *in vivo* to 2,8-dihydroxyadenine (7). Intravenously injected adenine is partially converted to uric acid, probably via 4-amino-5-imidazole-carboxamide ribotide (8). Oxidation by the enzyme xanthine oxidase gives 8-hydroxyadenine as an intermediate in the formation of 2,8-dihydroxyadenine (9). The main oxidative pathway with mammalian xanthine oxidase was shown to depend on the position of the oxygen atom first introduced (10); the first attack on purine, for example, occurs at position 6; hypoxanthine (6-hydroxy-purine) is then further attacked at position 2; however, positions 2 and 8 appear to be closely related and oxidation at one of these positions leads to attack of the other in the next step; thus, purine would be oxidized finally to uric acid. Oxidation of adenine with xanthine oxidase has been applied to the analytical determination of adenine (11). Adenine is also oxidized in various plants, *e.g.*, allantoin and allantoinic acid are the main products in silver maple leaves (12).

Investigation of the mechanism of the electrochemical oxidation of the purines is limited to two reports. Fichter and Kern (13) studied the oxidation of theophylline, theobromine, and caffeine under conditions

of constant current electrolysis; anode potentials were not specified and the probable occurrence of oxygen evolution with concomitant chemical oxidation makes the relevance of this work in relation to recent studies at controlled potential difficult to assess. Struck and Elving (2) found that uric acid was oxidized at controlled potential at the graphite electrode in 1M acetic acid, initially in a 2e process to a primary short-lived dicarbonium ion intermediate, which could undergo three simultaneous transformations: (a) hydrolysis to an allantoin precursor, (b) hydrolysis to alloxan and urea, and (c) further electrolytic oxidation and hydrolysis leading to parabanic acid and urea; each mole of uric acid produced on electrolysis 0.25 mole CO<sub>2</sub>, 0.25 mole of allantoin precursor, 0.75 mole urea, 0.3 mole parabanic acid, and 0.3 mole alloxan. The authors concluded that the electrochemical oxidation of uric acid resembles the enzymatic oxidation more closely than the chemical.

The present study of the electrochemical oxidation of adenine at controlled electrode potential at the pyrolytic graphite electrode (PGE) indicates a mechanism whereby adenine is oxidized in an over-all 6e process to a primary intermediate dicarbonium ion of the same type as that postulated for uric acid (2), but which is more complicated in terms of the further electrolytic and chemical steps involved. The electrochemical oxidation appears, thus, to follow initially the same path as enzymatic oxidation, but with subsequent further oxidation and fragmentation.

## Results and Discussion

The single well formed anodic voltammetric peak or wave shown by adenine (I) at the stationary PGE in aqueous solution between pH 0 and 11 in suitable background media is very close to background discharge in alkaline media, where it tends to be smaller than at lower pH (14, 15). Below pH 3, the discharge of certain background electrolytes masks the anodic wave; thus, no peak is observed in chloride background between pH 1 and 3, although a well formed peak is seen in 1M acetic acid (pH 2.3) and at low pH in sulphate buffers. The reaction was, accordingly, studied in detail in acetate background at pH 4.7 (buffered acetate solution) and 2.3 (1M acetic acid); the latter solvent is of particular value because of the favorable positive potential range that it affords and its ready removal by lyophilization (freeze-drying).

Voltammetric studies were supplemented by coulometry and exhaustive electrolysis at large electrodes. The detailed examination of the changes in the com-

\* Electrochemical Society Active Member.

<sup>1</sup> Present address: Department of Chemistry, University of Oklahoma, Norman, Oklahoma.

<sup>2</sup> Commonly accepted structural formulas of the principal compounds discussed are given in Fig 2; allowance must be made for alteration due to keto-enol and acid-base equilibria. Roman numerals cited in parentheses in the text refer to the structural formulas presented in Fig. 2. The *Chemical Abstracts* numbering system is used.

position of an adenine solution during electrolytic oxidation at a fixed anode potential allowed identification and quantitative determination of the ultimate products as well as characterization of probable intermediate species.

**Stability studies.**—Because of the possible decomposition of some of the expected products from the electrolytic oxidation of adenine, the stability of parabanic acid (V), oxaluric acid (VI), and alloxan (2,4,5,6-tetraoxypyrimidine) in 1M acetic acid and in pH 4.7 acetate buffer solutions was investigated; concentrations of the compounds were measured polarographically.

Parabanic acid (V) is fairly stable in 1M HOAc with some slow hydrolysis to oxaluric acid (VI); at pH 4.7, a 2 mM parabanic acid solution is completely hydrolyzed to oxaluric acid in six days.

Oxaluric acid is stable in both media for several days as evidenced by the constancy of the polarographic limiting current.

When alloxan was examined in 1M HOAc under electrolysis conditions, *i.e.*, at a potential of 1.3v, a 9.6 mM solution decreased in concentration to 4.6 mM after 164 hr, although the parabanic acid wave which appeared was only equivalent to a mM concentration. This discrepancy indicates the formation of other products, *e.g.*, alloxanic acid. Subsequent work showed that in 1M HOAc alloxan partially decomposes to parabanic acid in the absence of an applied potential. The instability of alloxan at low pH may explain Sartori and Liberti's (16) observation of a polarographic wave for alloxan  $E_{1/2} = -0.7v$ , which Struck and Elving (17) could not find; since the pH of the solution in which alloxan is stored affects its stability, the former authors probably observed a wave due to parabanic acid rather than to alloxan. The apparent nonstoichiometry of the alloxan to parabanic acid conversion is further evidenced by the large decrease in the alloxan limiting current on bubbling air through pH 4.0 acetate solution, when no parabanic acid was noted (17).

#### Voltammetry

Adenine (I) gives a well defined anodic voltammetric peak at the stationary PGE in 1M acetic acid (Fig. 1) and pH 4.7 acetate buffer. The peak potentials,  $E_p$ , of 1.30 and 1.14v, respectively, for 1mM adenine solution indicate the difficulty with which it is oxidized.  $E_p$  shifts to more positive potential at higher adenine concentration; thus, in 1M HOAc a 20 mM adenine solution gives an  $E_p > 1.5v$ .

Adenine gives a peak current,  $i_p$ , at the 1 mM level with a current density of  $2.4 \mu a/mM/mm^2$ , which, by comparison to earlier studies (18), suggests the involvement of about 4e per adenine molecule. However, adenine or its electrolysis product(s) are apparently adsorbed at the PGE (14,15), which results in exponential  $i_p$ -C curves even at scan rates as low as 3 mv/sec. On cyclic voltammetry at the PGE,  $E_p$  shifts 51 mv/pH unit more negative at a scan rate of

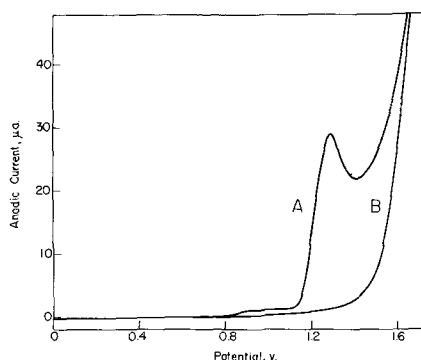


Fig. 1. Voltammogram of 1 mM adenine (A) in 1M acetic acid solution (background alone: B) at a stationary graphite electrode.

0.06 v/sec and 56 mv/pH unit at 0.6 v/sec, indicating that the numbers of protons and of electrons involved in the rate-determining step of the oxidation are the same. These shifts agree with that observed for  $E_p$  on normal voltammetry (*cf. supra*); assuming linear dependence in the region of measurement (pH 2.3 and 4.7)

$$E_p = 1.45 - 0.067 \text{ pH} \quad [1]$$

#### Macroscale Electrolysis

**Coulometry.**—At both pH 2.3 and 4.7, coulometry at appropriate controlled potential shows that 5.6-5.8 electrons ( $\pm 5-10$  relative per cent) are involved in the over-all oxidation (Table I). Electrolysis of 1 mM adenine solution usually takes about 2 days to reach completion; this is indicative of a very slow intermediate step in the oxidation, deposition of an insoluble reaction product, film formation on the electrode surface, or a combination of these phenomena. Cyclic voltammetry of adenine indicates that the current reaches a limiting value at about 1 mM (14); this, the behavior of adenine on alternating current polarography (14) and the deposit of a film on the electrode on macroscale electrolysis (*cf. below*) support the presence of adsorption and slow chemical intermediate step (or steps) in the over-all process.

**Preparative electrolysis.**—Exhaustive electrolysis of adenine solutions at fixed anodic potential allowed the preparation of sufficiently large amounts of products to permit their isolation, identification, characterization, and quantitative determination. A variety of isolation and measurement approaches, including lyophilization, ion-exchange, paper and thin layer chromatography, polarography, spectrophotometry, and other physical and chemical phenomena showed that urea, parabanic acid (V), oxaluric acid (VI), ammonia, 4-aminopurpuric acid (IX), and possibly one of the group of allantoin (X), uroxanic acid or alloxanic acid, were present in the electrolyzed solution.

On completion of the electrolyses, the working electrode was colored bright red, green, and blue, showing flow lines in the direction of stirring. The colored material could be extracted into dilute ammonia to give a yellow-green solution, which showed no sharp spectral peaks, although general absorption occurred at lower wavelengths; the extract showed no polarographic activity. Consequently, the colored electrode surface film differs chemically from the principal products isolated or identified in the electrolysis solution.

The procedures used and results obtained in examining electrolyzed solutions are given in the Experimental section. Certain important results identifying the principal products are summarized in the following sections.

**Polarographic behavior of electrolyzed solution.**—After exhaustive electrolysis of 1 mM adenine in 1M HOAc solution, polarography at the dropping mercury electrode (DME) shows two waves with  $E_{1/2}$  of  $-0.69$  and  $-1.12v$ . When the pH is adjusted to 5.1 by addition of pH 8 McIlvaine buffer, three waves appear with  $E_{1/2}$  of  $-0.80$ ,  $-1.07$ , and  $-1.42v$ . The first and largest wave is due to parabanic acid as

Table I. Coulometric determination of the number of electrons involved in the electrochemical oxidation of adenine<sup>a</sup>

Adenine concentration, mM	Applied potential, v	$n^d$
0.2 <sup>b</sup>	1.16	5.6
1.0 <sup>b</sup>	1.16	5.8
2.0 <sup>b</sup>	1.16	5.6
1.0 <sup>c</sup>	1.24	5.7

<sup>a</sup> All runs were corrected for background current.

<sup>b</sup> Acetate buffer: pH 4.7.

<sup>c</sup> 1M acetic acid background: pH 2.3.

<sup>d</sup> Average value of duplicate determinations.

Table II. Comparison of polarographic behavior of parabanic and oxaluric acids with products of electrolytic oxidation of adenine<sup>a</sup>

pH	— $E_{1/2}$ for wave indicated <sup>f</sup>				
	Parabanic acid, v		Oxaluric acid, v	Oxidation of product of adenine, v	
	I	II	I	I	II
2.2 <sup>b</sup>	0.68		1.12	0.69	1.12
3.6 <sup>c</sup>	0.75		1.32	0.74	1.32
4.6 <sup>c</sup>	0.77	1.36 <sup>c</sup>	1.36		
4.9 <sup>d</sup>	0.83		1.42	0.82	1.46
7.9 <sup>d</sup>	1.03	1.62	1.64	1.03	1.61

<sup>a</sup> Electrolysis of 1 mM adenine in 1M acetic acid.

<sup>b</sup> 1M acetic acid.

<sup>c</sup> Acetate background.

<sup>d</sup> Mixed acetate-McIlvaine background.

<sup>e</sup> After allowing parabanic acid to stand for a few hours in pH 4.6 acetate background.

<sup>f</sup> A blank indicates that no wave was observed.

shown by its pH-dependence and tendency to hydrolyze to oxaluric acid at low pH (Table II). The second wave is the split parabanic acid wave observed in mixed buffers, which is attributed to reduction of free acid and anion with the anion giving the postwave (19) and to complexation of part of the parabanic acid with phosphate (20). The most negative wave is due to oxaluric acid as evidenced by its pH-dependence (Table II); a mechanism for this reduction has been proposed (21). The parabanic acid wave in the polarographed sample of the electrolyzed HOAc solution corresponds to a concentration of approximately 0.3 mM; that of oxaluric acid to approximately 0.1 mM.

Oxaluric acid arises as a hydrolysis product of parabanic acid rather than as a direct oxidation product from adenine; as previously noted, parabanic acid is moderately rapidly hydrolyzed even at pH 4.7. Throughout the polarographic examination of dilute electrolysis solutions, no substantial evidence for the presence of alloxan was found.

**Lyophilization of oxidation products.**—Lyophilization of the solution after electrolysis of 2 millimoles of adenine gives initially a pale buff colored residue, which almost immediately turns bright violet-red even while still under vacuum; this same material was obtained on lyophilization of the product of electrolysis of 0.1 millimole of adenine. The residue is extremely hygroscopic and readily water soluble to give a bright red solution of pH 2.2-2.3 with  $\lambda_{\max}$  at 510 m $\mu$  (identical to visible spectrum of murexide) and with no absorption peaks in the ultraviolet but with increasing general absorption over the range of 400-270 m $\mu$  with strong absorption; such behavior indicates a system containing multiple double bonds (murexide shows two characteristic ultraviolet absorption peaks). The red color of the aqueous solution is stable for many days. Polarography shows the presence of comparable concentrations of parabanic and oxaluric acids. Attempts to isolate the red-producing product, e.g., by solvent extraction and ion exchange, were unsuccessful and usually resulted in the disappearance of the red color.

The red material had a number of characteristic reactions (cf. Experimental section), which, when combined with its hygroscopic nature and instability on basic ion-exchange columns and with subsequently discussed analytical data, indicate that it is 4-aminopurpuric acid (IX), which has all of the physical and chemical properties of the red electrolysis product (22).

Paper and thin layer chromatography indicate that urea is the most characteristic product. Minor products identified by these techniques are uroxanic acid and one or more of the group of allantoin, allantoic acid, and oxaluric acid (cf. Experimental).

The high acidity of the electrolysis product is due to the presence of oxaluric acid,  $pK_a$  5-5.3 (19,21),

parabanic acid,  $pK_a$  6.1 (23), and, possibly, small quantities of either uroxanic or alloxanic acid.

### Material Balance

In view of the complexity of the reaction as indicated by the variety of products identified, the rates of disappearance of reactant and of appearance of certain products and the analytical composition of the final mixture were determined; this approach was helpful in developing a reaction scheme which would identify the primary oxidation product, which had to be a short-lived species and whose subsequent reactions would lead to the ultimate products. As electrolysis proceeds, the ratio of adenine electrolyzed to urea and ammonia liberated, which is initially 1:0.4:1.5 (Table III), changes to 1:0.3:1.65 at completion of electrolysis. The final electrolysis solution contains, on the basis of each mole of adenine oxidized, 0.3 mole urea, 0.3 mole parabanic acid, 0.1 mole allantoin, 1.65 mole of ammonia, 0.1 mole of oxaluric acid, and traces of uroxanic acid; more accurately, the sum of the parabanic and oxaluric acids produced is about 0.4 mole/mole of adenine with the ratio depending on the actual electrolysis time.

The figures cited for urea, parabanic and oxaluric acids, and allantoin, account for 0.5 mole of adenine per mole of adenine electrolytically oxidized. Additional fission of adenine occurs to give 0.6 mole of  $NH_3$  above that expected for complete deamination of each mole of adenine at position 6.

It is not possible to account satisfactorily for the other 0.5 mole of adenine by assuming that alloxan and 4,5-diamino-2,6-dihydropyrimidine are produced, since this requires liberation of 0.25 mole urea above that measured, although these two compounds have been shown to condense to give 4-aminopurpuric acid (22). A more satisfactory hypothesis is that the postulated dicarbonium ion intermediate (cf. next section) reacts to give 5-amino-2,4,6-trihydropyrimidine and 4-amino-2,5,6-trihydropyrimidine, which condense to 4-aminopurpuric acid; this route involves the liberation of 0.5 mole  $NH_3$  and no further urea formation.

### Mechanism

The characteristic ultraviolet absorption spectrum of adenine ( $\lambda_{\max} = 263 m\mu$  in 1M HOAc) is due mainly to the  $-C(4)=C(5)-C(6)=N(1)$ -chromophoric group (24,25). Consequently, disappearance of this peak after electrolysis indicates that the  $-C(4)=C(5)-$  bond is oxidized.

Removal of six electrons from adenine suggests that the process proceeds initially (Fig. 2A) by sequential two-electron, two-proton oxidations to 2-hydroxyadenine (II) and then rapidly to 2,8-dihydroxyadenine (III) [these processes are presumably of the type suggested by Bergmann and Dikstein (10) for enzymatic purine oxidation]. The latter compound is similar to uric acid except for the presence of an amino group in place of an hydroxyl group at the 6-position. Further removal of two electrons results in oxidation

Table III. Course of controlled potential electrolysis of adenine<sup>a</sup>

Run	Time, hr	Adenine electrolyzed, mole-%	Urea present, mole-%	Urea: adenine ratio <sup>b</sup>	$NH_3$ present, mole-%	$NH_3$ : adenine ratio
1	20	55	23	0.42		
	32	69	28	0.40		
	45	83	30	0.36		
	70	100	31	0.31	180 [162] <sup>c</sup>	1.80 [1.62] <sup>c</sup>
2	22	78			119	1.53
	33	100			156	1.56
	47	100			163	1.63

<sup>a</sup> Electrolysis of 1 mM adenine in 1M acetic acid.

<sup>b</sup> Mechanism postulated in text assumes molar ratios of 0.4 for urea production and of 1.5 for  $NH_3$  production; the former ratio will decrease and the latter increase on hydrolysis of 1 mole of urea to 2 moles of  $NH_3$ .

<sup>c</sup> Corrected for hydrolysis of 9% urea.

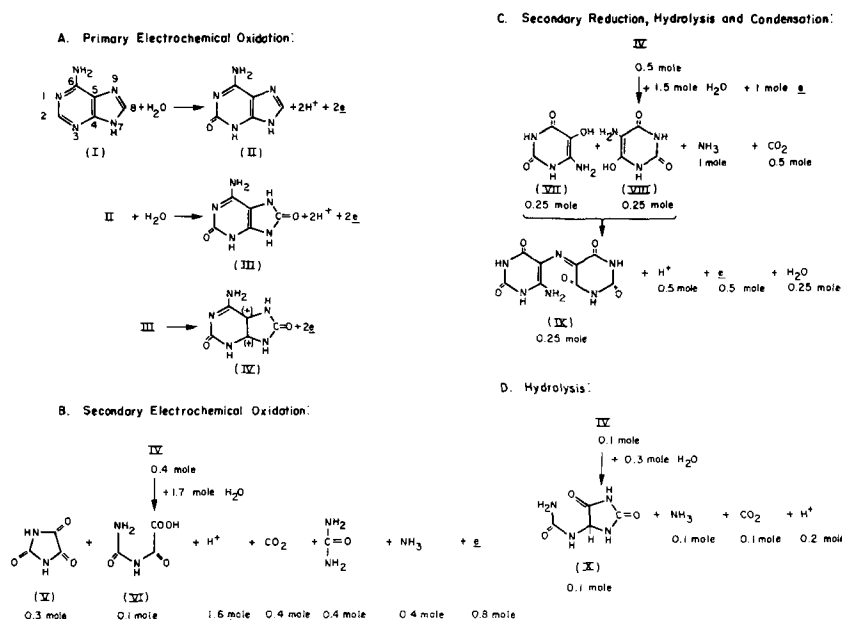


Fig. 2. Proposed pathways for electrochemical oxidation of adenine in 1M acetic acid solution and subsequent transformations. The molar quantities refer to the amount involved per mole of adenine (I) converted to the dicarbonium ion (IV). Other compounds listed are as follows: II, 2-hydroxyadenine; III, 2,8-dihydroxyadenine; V, parabanic acid; VI, oxaluric acid; VII, 4-amino-2,5,6-trihydroxypyrimidine; VIII, 5-amino-2,4,5-trihydroxypyrimidine; IX, 4-aminopurpuric acid; X, allantoin.

of the 4,5 double bond and formation of a dicarbonium ion (IV) of the same type as that postulated for the electrochemical oxidation of uric acid (2).

Continuation of oxidation to the dicarbonium ion stage, as soon as the electrolytic oxidation of adenine is initiated, is due to the fact that the ease of oxidation of purines generally increases with the number of hydroxyl groups on the molecule, *e.g.*,  $E_{p/2}$  for oxidation of the hydroxypurines at pH 3.7 are 1.14v for 6-hydroxypurine (hypoxanthine), 0.84v for 2,6-dihydroxypurine (xanthine) and 0.45v for 2,6,8-trihydroxypurine (uric acid) (26). Thus, 2-hydroxy- and 2,8-dihydroxyadenine are probably more easily oxidized electrolytically than adenine itself and consequently are unstable in respect to oxidation at the potential at which adenine is oxidized.

There is no evidence for deamination of 2,8-dihydroxyadenine under the reaction conditions; indeed, this highly insoluble compound (27) may possibly deposit on the electrode surface, causing the apparent voltammetric involvement of  $4e$  rather than of  $6e$  and the effects associated with the previously mentioned adsorbed layer. The yellow color noted on occasion during the electrolysis of fairly concentrated adenine solutions may have been due to 2,8-dihydroxyadenine (27).

The present investigation does not supply direct evidence for any other intermediate such as the symmetrical intermediate postulated for both the enzymatic (28-30) and electrolytic (2) oxidation of uric acid. However, since allantoin (X) is produced in the oxidation of adenine and since allantoin arises in uric acid oxidation via a symmetrical intermediate (31), a small quantity of such an intermediate may be produced.

Following the primary electrochemical oxidation to the dicarbonium ion (Fig. 2A), the nature and ratio of the products ultimately produced indicate that at least three further distinct chemical and electrolytic reactions occur. First, further electrochemical oxidation of the dicarbonium ion (VI) leads to parabanic and oxaluric acids, urea, and ammonia (Fig. 2B; the postulated amounts produced per mole of adenine electrolytically oxidized are noted).

Analytical data and the formation of 4-aminopurpuric acid (IX) indicate that some of the primary oxidation product is reduced to 4-amino-2,5,6-trihydroxy-(VII) and 5-amino-2,4,6-trihydroxypyrimidine (VIII) (Fig. 2C), which subsequently condense to form 4-aminopurpuric acid; such a series of reactions involves the liberation of 1 mole  $\text{NH}_3$  and consumption of  $1e$  per 0.5 mole of dicarbonium ion reduced. The

electrochemical reduction could occur at the counter electrode.

Formation of allantoin (X) results from acid hydrolysis of the dicarbonium ion, liberating  $\text{NH}_3$  and  $\text{CO}_2$  (Fig. 2D).

Summation of the molar quantities given in Fig. 2 shows that the postulated mechanism predicts that 1 mole adenine should yield 0.4 mole urea, 1.5 mole  $\text{NH}_3$ , 0.35-0.4 mole of parabanic and oxaluric acids (usually 0.3 mole parabanic and 0.1 mole oxaluric), 0.1 mole allantoin, 1 mole  $\text{CO}_2$ , and 0.25 mole 4-aminopurpuric acid with an over-all consumption of  $6.3e$ . These predicted products agree with the experimental data (*cf.* Material Balance), especially if allowance is made for the hydrolysis of urea during the long electrolysis, *e.g.*, *cf.* Table III and composition of final electrolysis solution. The mechanism does not preclude other reactions but merely indicates the predominant routes under the experimental conditions employed.

### Experimental

**Chemicals.**—Oxaluric acid, potassium alloxanate, and uroxic acid were prepared following Struck (32); uramil was prepared according to Koppel and Robins (33). Other chemicals were obtained from the sources listed: adenine (Nutritional Biochemicals); murexide, alloxan, allantoin, *p*-dimethylaminobenzaldehyde, phenylhydrazine hydrochloride, 2,3-butanedione monoxime, and sodium dithionite (Eastman); acetic acid, butanol, and ammonium chloride (Mallinckrodt); allantoinic acid (K & K Laboratories); parabanic acid (Mann); barbituric acid (Aldrich); urea (J. T. Baker); Dowex 2-X8 and 50W-X8 (Dow).

Two solvent systems were used in paper and thin layer chromatography: 1-BuOH-HOAc- $\text{H}_2\text{O}$  (12:3:5) and iso-PrOH- $\text{NH}_3$ - $\text{H}_2\text{O}$  (10:5:1). Ehrlich's reagent (10% w/v *p*-dimethylaminobenzaldehyde in concentrated HCl) (34) was used undiluted with acetone. Bromocresol green was prepared according to Smith (34).

Ion-exchange columns were prepared from Dowex 2-X8 (50-100 mesh) converted to the hydroxyl form by washing with 1M NaOH until the effluent was free of chloride ion, and then with water until the effluent was neutral to litmus. Dowex 50W-X8 (50-100 mesh) was used after being washed several times with distilled water.

Buffer solutions, prepared from analytical grade chemicals, had an ionic strength of 0.5M. Argon used for deoxygenation was equilibrated with water; no other purification was necessary.

**Apparatus.**—Polarograms were recorded on a Sargent Model XXI Polarograph, using a water-jacketed

H-cell maintained at  $25^\circ \pm 0.2^\circ\text{C}$ , which contained a saturated calomel reference electrode (SCE) in one leg. All potentials quoted are *vs.* SCE at  $25^\circ\text{C}$ . The dropping mercury electrode had normal *m* and *t* values.

Graphite indicating electrodes were prepared from General Electric pyrolytic graphite; 4-mm rods were sealed into 6-mm (OD) soft glass tubes with epoxy resin (Hysol Corporation Epoxy-Patch). The electrode was resurfaced before each voltammogram by polishing on a silicon carbide paper (600 grade, Carborundum Company) mounted on a rotating disk. For coulometry and macroscale electrolysis, 3-in. by 0.75-in. plates of pyrolytic graphite were used (1/32-1/8 in. thick); after each run, these electrodes were carefully washed and resurfaced by polishing with silicon carbide paper.

The most satisfactory of the various electrolysis cells used for coulometry was a large two-compartment cell; diffusion between compartments was minimized by a medium porosity fritted disk and a 1-in. KCl-saturated agar plug. The counter electrode was a cylindrical platinum gauze ( $1 \times 3$  in.). The working electrode consisted of five graphite plates connected together and mounted into a rubber stopper. The reference electrode was a Beckman calomel electrode. Stirring was done magnetically, using a Teflon-coated stirring bar.

The large single compartment cell generally used for macroscale electrolysis was fitted with a rubber stopper into which six graphite plates were mounted; three plates served as counter electrodes and three as working electrodes. In order to minimize KCl diffusion into the cell, the latter was connected to a large calomel electrode by a salt bridge made from a length of 3-mm nylon tubing plugged at the cell end with Corning Vycor Thirsty glass.

In preliminary studies and for coulometry, the anode potential was controlled by a Fisher controlled potential "Electro-Analyzer"; in macroscale electrolysis, where the IR drop was large, a unit with higher voltage output (maximum of about 100v and 40 ma), based on operational amplifier circuits (35), was used.

Current integration during coulometry utilized a Dymec Model DY-2210 voltage-to-frequency converter and a Hewlett-Packard Model 521-AR electronic counter; current flowing through the working electrode was measured in terms of the voltage drop across a 1-ohm resistor. The time of electrolysis was recorded with an Industrial Timer Corporation Model CMO elapse time counter.

The pH was measured with a Beckman Model G pH meter. Infrared spectra were obtained with a Perkin-Elmer Infracord spectrophotometer using Nujol mulls and KCl or KBr pellets prepared with a Wilks Mini Press. Ultraviolet spectra were recorded on a Beckman Model DB spectrophotometer, using 1-cm stoppered quartz cells. Melting points were obtained with a Fisher-Johns apparatus. Lyophilization was accomplished using a Cenco-Hyvac-7 vacuum pump; cooling traps contained 2-propanol-dry ice; the lyophilization vessel was usually a 1-liter round-bottom distillation flask, on whose walls the solutions were shell frozen.

Paper chromatography (ascending) utilized Whatman No. 1 filter paper cut into strips. Eastman Chromagram Type K 301R (silica gel) thin layer sheets were used.

**Coulometry.**—A measured volume of appropriate background solution was electrolyzed for several hours in the working electrode compartment until the current integrator gave a constant count per unit time (background counting rate). The integrator was reset and 0.02-0.1 millimole of adenine was introduced without altering the stirring; the applied potential, integrator, and timer were then set in operation simultaneously, and electrolysis was continued until the counting rate decayed to background or a low, con-

stant level. Completion of electrolysis was always confirmed by the disappearance of the characteristic adenine absorption peak at  $263\text{ m}\mu$ . Subtraction of the product of background counting rate and time required for electrolysis from the total count gave the counts proportional to the electron flow involved in the adenine oxidation.

**Macroscale electrolysis.**—As an indication of the long electrolysis time required, *e.g.*, complete electrolysis of 100 ml of 20-30 mM adenine solutions in 1M HOAc usually took 3-5 weeks, 20-30 mM uric acid solutions were completely electrolyzed (2) in about the same time required to electrolyze 0.2-2 mM adenine solutions, even though a larger electrode area was utilized in the present study; however, it should be pointed out that spectroscopic type graphite was employed in the earlier study and pyrolytic graphite in the present study. Consequently, 5-10 mM adenine solutions were generally employed; exhaustive electrolysis at 1.4v usually took 1-2 weeks. At times, development of a pale yellow color was noted after some time during electrolysis; however, it disappeared near completion of the electrolysis.

Use of separate counter and working electrode compartments in the electrolysis cell allowed movement of reactant and products into the former compartment. In addition, considerable quantities of KCl diffused from the salt bridges and reference electrode compartment into the other compartments contaminating the products; it was not possible to remove the KCl, *e.g.*, by ion-exchange or solvent extraction, without markedly altering the nature of the products. Accordingly, the working and counter electrodes were often housed in the same compartment.

**Paper and thin layer chromatography.**—With the exception of urea, which was spotted as a solution (1 mg/ml), all reference compounds were applied as very small crystals and were dissolved by repeated addition of water via a small loop of platinum wire, which deposited about  $5\ \mu\text{l}$  of water. Because of the high KCl content of the solid product obtained on lyophilization, it was usually necessary to load the spot heavily by repeated addition of crystals, which were also sequentially dissolved. Ascending development was used with two spots per strip, which was immersed in the solvent to a depth of about 0.6 cm; development for paper usually took about 12 hr. Reagents were applied by spraying, identification being based on parallel behavior of reference and unknown on the same chromatogram. When solvents containing acetic acid were used on paper, followed by application of bromocresol green reagent, the steaming technique recommended by Struck and Elving (2) was employed, although on no occasion was thoroughly satisfactory removal of acetic acid obtained.

Urea was identified as a major product with Ehrlich's reagent;  $R_f$  values for two solvent systems were identical on both supports to authentic urea, *e.g.*,  $R_f = 0.54$  on paper and 0.52 on silica gel thin layer plates with a BuOH-HOAc-H<sub>2</sub>O solvent.

Two other less intense spots, detected with Ehrlich's reagent on paper chromatograms using BuOH-HOAc-H<sub>2</sub>O solvent, have  $R_f$  values of 0.19 and 0.28. Of the probable reaction products, the former corresponds to uroxic acid ( $R_f$ , 0.19) and the latter to allantoin ( $R_f$ , 0.27), allantoic acid ( $R_f$ , 0.29) or oxaluric acid ( $R_f$ , 0.29). Spraying similar papers with bromocresol green reagent after very prolonged steaming to remove acetic acid (2) gave rather ill-defined results, although the presence of oxaluric acid was indicated.

**Ion-exchange isolation and identification of urea.**—Chromatography indicated that urea was a principal oxidation product; since many of the other products appeared to be acidic, isolation of the urea was attempted.

The lyophilized product from electrolysis of 1.0 millimole adenine, which contained at least an equal



quantity of KCl, was dissolved in 50 ml water and was passed through a Dowex 2-X8 column (hydroxide form); the column was washed with water until the total eluate was 150 ml. Lyophilization of the latter gave a fluffy white, strongly basic product, which was predominantly KOH formed by exchange of chloride. This product was dissolved in 20 ml water and passed through a column of Dowex 50W-X8 resin (strongly acid, hydrogen form), which was washed with water to a total volume of 125 ml; lyophilization of this eluate gave no solid material. The acid column was then washed with 50 ml 1M HOAc; lyophilization of this eluate gave a white fluffy material, mp 128°C, whose infrared spectrum was identical to that of authentic urea. Urea apparently forms a fairly weakly bound adduct on the acid resin, probably of the same type as urea oxalate and nitrate. Because of the high KCl concentration in the product, no estimate of the yield of urea was made.

The total acidic components of the product, retained on the basic column, was eluted with 125 ml 1M HCl; lyophilization gave a small quantity of a yellow deliquescent product, which could not be identified, *e.g.*, on dissolution in a very small volume of water no precipitate appeared on standing although oxaluric acid was undoubtedly present. It is probable that, because of the minute amounts of product used, the solubility of oxaluric acid was never exceeded.

Attempts to isolate allantoin by the methods of Struck and Elving (2) were unsuccessful, although subsequent analytical data showed the presence of allantoin. The lower initial concentrations of adenine, the relatively lower proportion of allantoin produced and the presence of considerable quantities of KCl would explain the failure to isolate allantoin.

*Characterization of 4-aminopurpuric acid.*—The residue obtained on lyophilization of an electrolyzed solution gave, as described, a bright red solution in water, whose color has been ascribed to the presence of 4-aminopurpuric acid on the basis of evidence which included a number of very characteristic reactions shown by the red material when in admixture with the other electrolytic products; in particular, it is red-violet and hygroscopic, and, on treatment with hot dilute HCl or NaOH, gives bisalloxazine, which is pale yellow, melts above 300°C, and is stable to nitric acid evaporation. Specific separation and confirmatory identification of 4-aminopurpuric acid was not possible because of its general instability and because of the small quantities of electrolysis product. Some of the experiments just summarized were as follows:

1. Addition of 1M HOAc gave initially a bright red solution, which decolorized in about 15-20 min. Polarography of such a solution showed that, immediately on addition of the red product, a small but distinct wave ( $E_{1/2} = -0.06v$ ) appeared, which decreased in height as the intensity of the red color diminished; murexide (ammonium purpurate) under the same conditions behaves identically. The wave at  $-0.06v$  is probably due to small quantities of alloxan (16,19), which appears to decompose, apparently to products other than parabanic acid; after 60 min, a murexide solution showed no wave at  $-0.7v$  which could be attributed to parabanic acid.

2. After dissolution in 1M HOAc and decolorization, the original red product is recovered on lyophilization, even if the solution is allowed to stand for a few days. Thus, the decolorization process in acetic acid is reversible.

3. Heating a solution of the oxidation products in 1M HOAc with nitric acid or treatment with sodium nitrite and nitric acid in the cold and then boiling to remove nitrogen oxides results in a significant increase in the parabanic acid wave; parabanic acid itself is partially oxidized to polarographically inactive products under the same conditions.

4. Treatment of the red product with 1M NaOH gives initially a blue-violet solution, which slowly

turns yellow. The yellow color is stable for many days.

5. Treatment of the product with hot 20% hydrochloric acid gives a yellow solution; after standing for some time, a small quantity of pale yellow crystals are produced. Evaporating this solution (without removing any crystals that may have formed) to dryness results in a yellow-brown residue which is stable to temperatures above 250°C, treatment of this residue with 1:1 HNO<sub>3</sub> gives a bright yellow solution, whose evaporation to dryness gives a small quantity of pale yellow crystals which do not melt below 300°C. The former yellow-brown product gives a deep yellow solution on 1M Na<sub>2</sub>CO<sub>3</sub>; cooling for several days at 10°C did not produce any precipitate.

The behavior just summarized indicates that the product is similar in some respects to murexide, *e.g.*, it decomposes to a very small extent to alloxan in 1M HOAc; however, spectra suggest that, even though multiple double bonds may be present, the product is not murexide. Bathochromic shifts in acid and alkaline solution are similar to those observed with murexide. The product is at least partially oxidizable to parabanic acid, probably via alloxan. The reversible color reaction in 1M HOAc suggests that the red material may decompose to simpler products in dilute solution, which recombine on concentration (lyophilization), although protonation and accompanying equilibria may be involved.

*Analytical examination of course of electrolysis.*—The solution electrolyzed at 1.3v, which originally was 100 ml of 1 mM adenine in 1M acetic acid, was analyzed during the course of electrolysis as described in the following sections. This volume of solution was insufficient to allow removal of several aliquots for polarographic determination of parabanic and oxaluric acids, thus, these compounds were only determined at the completion of electrolysis.

*Determination of residual adenine.*—A 1.00-ml sample of electrolysis solution was withdrawn and diluted with 1M HOAc (from 1:20 dilution at the beginning of the electrolysis to 1:5 dilution at the end). The adenine concentration was calculated from its ultraviolet absorption:  $\epsilon = 1.274 \times 10^4$  at 263 m $\mu$ .

*Determination of urea.*—Urea was determined by a modification of Rosenthal's method (36). One milliliter of electrolysis solution was diluted in a 70-ml test tube to exactly 5.00 ml with water; 3.00 ml As(V) solution (10 ml concentrated HCl saturated with As<sub>2</sub>O<sub>5</sub> and then diluted to 35 ml with HCl), 1.00 ml 2,3-butanedione monoxime (2.5% w/v in 5% HOAc) and 1:00 ml water were added. The tube was placed in boiling water for 30 min and then cooled for 3 min; the absorbance at 480 m $\mu$  was measured, using a water blank carried through the entire procedure. For each measurement, a calibration curve was prepared, using control samples of 10, 20, 30, 40, and 50  $\mu$ g urea per 5 ml water. Interference by allantoin was corrected for by carrying known concentrations of allantoin through the procedure and correcting on the basis of a subsequent allantoin determination (*vide infra*), as recommended (2).

*Determination of ammonia.*—Since addition of Nessler's reagent to a portion of the electrolyzed solution gave a bright yellow precipitate and no precipitate was produced with any of the expected organic products at the concentration levels anticipated, ammonia was measured by the Nessler method, following King and Faulconer (37). Nessler reagent was prepared by slowly adding a saturated mercuric chloride solution to a solution of 50g KI in 35 ml cold water until a slight precipitate of red mercuric iodide persisted. Then, 400 ml of clarified 9M NaOH was added and the resultant solution diluted to one liter with water. After standing at room temperature for 24 hr, the clear supernatant liquid was decanted and was ready for use.



A 1.00-ml sample of electrolysis solution was placed in a 70-ml test tube, followed by addition, while swirling, of 8.00 ml water and 1.00 ml Nessler reagent; after 5 min, the absorbance at 400 m $\mu$  was measured. Often at the end of an electrolysis the 1.00-ml sample aliquot was appropriately diluted with water and a 1.00-ml aliquot of the resultant solution run through the procedure.

A blank carried through the Nesslerization and photometry consisted of an aliquot of 1M HOAc, which had been left open to the atmosphere in order to compensate for the effect of ammoniacal fumes. A calibration curve was prepared by diluting aliquots of a stock solution (10 mg NH<sub>4</sub>Cl/1000 ml water) so that the weight of NH<sub>3</sub> in the final solution was 5 to 30  $\mu$ g.

Formation of an orange-yellow precipitate on addition of Nessler's reagent to the test solution indicates that the latter is too concentrated in ammonia or that the swirling during addition of reagent was insufficient; such samples were discarded.

**Determination of allantoin.**—Allantoin (or allantoin precursor) (2) was determined by a modified Young and Conway procedure (38). Because of the poor sensitivity of the latter procedure and the low yield of allantoin, the analysis was only run at the completion of an electrolysis. A 5.00-ml aliquot of electrolysis solution was transferred to a 70-ml test tube, 1.5 ml 5M NaOH added, and the solution heated on a boiling water bath for 7 min, after which the tube was rapidly cooled in ice and acidified with 2.0 ml 5M HCl. Then, 1.0 ml phenylhydrazine hydrochloride solution (40 mg/30 ml H<sub>2</sub>O) was added, the tube placed in boiling water for exactly 2 min and then cooled in ice-salt mixture ( $-10^{\circ}\text{C}$ ) for a few minutes, and 1.00 ml potassium ferricyanide (100 mg/30 ml H<sub>2</sub>O) added. The solution was thoroughly mixed and allowed to stand at room temperature for 40 min, when the absorbance at 515 m $\mu$  was measured. In order to correct for uroxic acid (or alloxanic acid), one 5-ml aliquot of test solution was not treated with NaOH but rather with 3.0 ml H<sub>2</sub>O and, after heating for 7 min, with 0.5 ml 5M HCl; the procedure was finished as usual.

Calibration curves were prepared with allantoin or allantoic acid solutions, which were 0.005 to 0.15 mM with respect to the initial 5-ml aliquot.

**Determination of parabanic and oxaluric acids.**—Parabanic acid was determined at the completion of the electrolysis by transferring about 20 ml of the electrolysis solution to the polarographic cell, deaerating, running a polarogram between 0 and  $-1.4\text{v}$ , and comparing the height of the wave at  $-0.7\text{v}$  with a calibration curve prepared from authentic parabanic acid.

Oxaluric acid was determined at the completion of an electrolysis in the same way, using the height of the wave at  $-1.12\text{v}$ .

#### Acknowledgments

The authors thank the National Science Foundation and the Institute of Science and Technology of The University of Michigan, which helped support the work described.

Manuscript submitted April 1, 1968; revised manuscript received June 25, 1968.

Any discussion of this paper will appear in a Discussion Section to be published in the June 1969 JOURNAL.

#### REFERENCES

1. P. J. Elving, *Ann. N. Y. Acad. Sci.*, Accepted for publication.
2. W. A. Struck and P. J. Elving, *Biochemistry*, **4**, 1343 (1965).
3. A. S. Jones, R. T. Walker, and A. R. Williamson, *J. Chem. Soc.*, 6033 (1963).
4. C. A. Ponnaperuma, R. M. Lemmon, and M. Calvin, *Radiation Research*, **18**, 540 (1963).
5. J. H. Lister, "Advances in Heterocyclic Chemistry," Vol. 6, p. 1, A. R. Katritzky and A. J. Boulton, Editors, Academic Press, New York (1966).
6. R. K. Robins, "Heterocyclic Compounds," Vol. 8, p. 162, R. C. Elderfield, Editor, John Wiley & Sons, New York (1967).
7. A. Bendich, G. G. Brown, F. S. Philips, and J. B. Thiersch, *J. Biol. Chem.*, **183**, 267 (1960).
8. J. B. Wyngaarden, J. E. Seegmiller, L. Laster, and A. E. Blair, *Metabolism, Clin. and Expt.*, **8**, 455 (1959).
9. J. B. Wyngaarden and J. T. Dunn, *Arch. Biochem. Biophys.*, **70**, 150 (1957).
10. F. Bergmann and S. Dikstein, *J. Biol. Chem.*, **223**, 765 (1956).
11. H. Klenow, *Biochem. J.*, **50**, 404 (1952).
12. R. L. Barnes, *Nature*, **184**, 1944 (1959).
13. Fr. Fichter and W. Kern, *Helv. Chim. Acta.*, **9**, 429 (1926).
14. G. Dryhurst and P. J. Elving, In preparation for publication (1968).
15. D. L. Smith and P. J. Elving, *Anal. Chem.*, **34**, 930 (1962).
16. G. Sartori and A. Liberti, *Ric. Sci. Suppl.*, **16**, 313 (1946).
17. W. A. Struck and P. J. Elving, *J. Am. Chem. Soc.*, **86**, 1229 (1964).
18. G. Dryhurst and P. J. Elving, *Anal. Chem.*, **39**, 606 (1967).
19. V. Hladik, *Sb. Mezinarod Polyarog. Sjezdu Praze, 1st Congr.*, Pt. 1, 686 (1951).
20. W. A. Struck and P. J. Elving, *Anal. Chem.*, **36**, 1374 (1964).
21. G. Dryhurst and P. J. Elving, *ibid.*, **40**, 492 (1968).
22. H. Wieland, A. Tarttar, and R. Purrmann, *Ann.*, **545**, 209 (1940).
23. G. Kortum, W. Vogel, and K. Andrussov, "Dissociation Constants of Organic Acids in Aqueous Solutions," Butterworths, London (1961).
24. F. Bergmann and S. Dikstein, *Biochem. J.*, **77**, 691 (1955).
25. L. F. Cavalieri, A. Bendich, J. F. Tinker, and G. B. Brown, *J. Am. Chem. Soc.*, **70**, 3875 (1948).
26. P. J. Elving, W. A. Struck, and D. L. Smith, *Mises Point Chim. Anal. Org. Pharm. Bromatol.*, **14**, 141 (1965).
27. E. Fischer, *Ber.*, **30**, 2226 (1897).
28. E. S. Canallekis and P. P. Cohen, *J. Biol. Chem.*, **213**, 385 (1955).
29. K. G. Paul and Y. Avi-Dor, *Acta Chem. Scand.*, **8**, 637 (1954).
30. G. Soberon and P. P. Cohen, *Arch. Biochem. Biophys.*, **103**, 331 (1963).
31. L. F. Cavalieri and G. B. Brown, *J. Am. Chem. Soc.*, **70**, 1242 (1948).
32. W. A. Struck, Ph.D. Dissertation, University of Michigan (1963).
33. H. C. Koppel and R. K. Robins, *J. Am. Chem. Soc.*, **80**, 2751 (1958).
34. I. Smith, "Chromatographic and Electrophoretic Techniques," 2nd Ed., Vol. I. Interscience Publishers, New York (1960).
35. W. M. Schwarz and I. Shain, *Anal. Chem.*, **35**, 1770 (1963).
36. H. L. Rosenthal, *ibid.*, **27**, 1980 (1955).
37. R. W. King and W. B. N. Faulconer, *ibid.*, **28**, 255 (1956).
38. E. G. Young and C. F. Conway, *J. Biol. Chem.*, **142**, 839 (1942).

# The Standard Free Energy of Formation of $UI_3$ from EMF Measurements on a Solid Electrolyte Galvanic Cell

J. O. Tveekrem and M. S. Chandrasekharaiah<sup>1</sup>

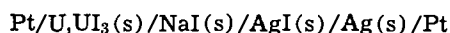
Brookhaven National Laboratory, Associated Universities, Inc., Upton, New York

## ABSTRACT

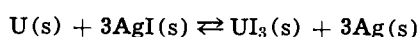
The first known experimental measurements of the  $\Delta F^\circ_f$  of  $UI_3$  are described. The emf of the solid electrolyte galvanic cell, Pt/ $U, UI_3(s)$ / $NaI(s)$ / $AgI(s)$ / $Ag(s)$ /Pt, was measured over the temperature range of 220°-370°C. The  $\Delta F$  values of the cell reaction  $U(s) + 3AgI(s) \rightleftharpoons UI_3(s) + 3Ag(s)$ , derived from the emf data from six cells, were combined with the  $\Delta F^\circ_f$  values of AgI to obtain the  $\Delta F^\circ_f$  of  $UI_3$ . This resulted in a value of  $-98.8 \pm 0.4$  kcal/mole at 370°C, which was 6.7 kcal/mole more positive than previously published estimated values.

The uranium iodides have been shown to be significant species in studies of fission products released from simulated reactor fuel meltdowns (1). In investigations of this nature, accurate thermodynamic values of the various chemical species are often necessary. In the case of the uranium iodides, the only values available are based on estimates rather than experimental data.

We have employed the technique of emf measurements on a solid electrolyte galvanic cell to obtain the standard free energy of formation of  $UI_3$ . The general technique has been thoroughly discussed by Kiukkola and Wagner (2). The cell utilized for these experiments was



The over-all cell reaction on passing three Faradays is



The free energy change of this reaction is given by the expression  $\Delta F = -3F\mathcal{E}$  where  $\mathcal{E}$  is the cell emf in volts and  $F = 23.06$  kcal/volt equivalent. The free energy can also be written

$$\Delta F_{\text{cell}} = \Delta F^\circ_f UI_3 - 3\Delta F^\circ_f AgI$$

Therefore, by combining the known standard free energy of formation of AgI (3) with the measured free energy change of the cell reaction, the standard free energy of formation of  $UI_3$  may be obtained.

The NaI serves as an auxiliary electrolyte and forms a chemically inert conducting bridge between the two sides of the cell. The auxiliary electrolyte must exhibit purely ionic conduction and preferably have a common anion with the other cell constituents. The stoichiometric alkali iodides meet these requirements (4, 5). An additional prerequisite is the lack of solid solution or compound formation between the auxiliary electrolyte and the adjacent phases in order to eliminate the possibility of appreciable junction potentials. This eliminated LiI, which forms a solid solution with AgI, and KI, which forms a congruently melting compound,  $KAg_3I_4$ , with AgI. No compound formation occurs between NaI and AgI, but a eutectic is formed at 384°C (6). This eutectic establishes the maximum temperature limit at which the cell can be operated. No literature data were available on compound formation between NaI and  $UI_3$ . To check on this possibility, x-ray diffraction analysis was applied to two types of sample: (i) a powdered mixture of the two salts which had been heated at 400°C for 24 hr and

(ii) samples of the material at the NaI/ $UI_3$  interface of two of the cells which had been operated for three months. None of the samples showed any compound formation between NaI and  $UI_3$ .

The ideal stoichiometric alkali halides are ionic conductors but do exhibit some electronic conduction if they contain excess alkali metal or halogen (4). The ionic conduction is predominantly via the cations until temperatures approaching their melting points are attained. No literature data were available on the electronic conductivity of NaI as a function of chemical potential, but conservative estimates based on the behavior of other alkali halides indicated that it should be completely negligible in this system. NaI has an ionic conductivity of  $10^{-8}$  to  $10^{-6}$  ohm<sup>-1</sup>cm<sup>-1</sup> in the temperature range of our experiments (7). The AgI is also an ionic conductor, conducting via the silver ions, with a very high conductivity of 1.7 to 2.2 ohms<sup>-1</sup>cm<sup>-1</sup> in this temperature range (8, 9).

The uranium and  $UI_3$  were intimately mixed to hasten the equilibration of any subhalide formation and thus eliminate any mixed potentials that might conceivably occur. Corbett *et al.* (10) have studied the U,  $UI_3$  system and found a solubility of 5.7% U in  $UI_3$  in the liquid state. The solubility of U in solid  $UI_3$  is undoubtedly much lower than this, as is true in the alkali halides and alkaline earth halides. Therefore, no appreciable stoichiometry change in the  $UI_3$  is anticipated, and the system is thermodynamically well defined. X-ray diffraction spectra of U- $UI_3$  pellets from two cells which had been operated for three months showed only uranium and  $UI_3$  patterns, indicating that no appreciable subhalide formation occurred in the cells.

## Experimental

$UI_3$  was prepared by a method similar to that described by Gregory (11). Uranium turnings which had been deoxidized by washing in dilute nitric acid were heated under vacuum in a quartz tube at 550°C. Iodine from a reservoir at room temperature ( $\approx 23^\circ\text{C}$ ) was pumped across the hot uranium, and  $UI_3$  was condensed immediately downstream where the temperature was maintained at 400°C by a second furnace. Approximately 48 hr of heating was required to prepare 30g of  $UI_3$ . The quartz tube was then sealed off under vacuum at both ends and transferred to a dry box for subsequent removal of the  $UI_3$ .

There was generally a slight amount of  $UI_4$  and some  $UO_2$  from reaction with the quartz, present in the  $UI_3$ . The crude product was purified by heating it under vacuum to 600°C in a linear temperature gradient Marshall furnace. This decomposed the  $UI_4$  to

<sup>1</sup> Present address: Atomic Energy Establishment, Trombay, Bombay, India.

UI<sub>3</sub> and distilled the UI<sub>3</sub> away from the UO<sub>2</sub>. The final product analyzed as UI<sub>3.0</sub>.

All operations involving the handling of UI<sub>3</sub> were performed under an argon atmosphere in a dry box because of the high reactivity of UI<sub>3</sub> with moisture. Uranium filings and powdered UI<sub>3</sub> were intimately mixed in U/UI<sub>3</sub> mole ratios of 5:1 for the earlier cells and 15:1 for the last three cells. The mixture was pelleted in a hand-operated hydraulic press inside the dry box. Powdered AgI (Fisher Scientific Company) was pelleted in the same manner. Single crystal NaI (Harshaw Chemical Company) was used.

The cell design is shown in Fig. 1. A platinum wafer with a platinum wire welded to one side of it was wrapped first with platinum foil and then with silver foil. The AgI pellet, NaI crystal and U, UI<sub>3</sub> pellet were stacked consecutively above the Ag foil. A tantalum wafer was placed between the U, UI<sub>3</sub> pellet and the upper platinum electrode to prevent possible alloying of the uranium and platinum. The entire assembly was held tightly together by a spring loaded quartz retainer.

A Pt/Pt-10% Rh thermocouple was located several millimeters from the center of the cell constituents, and its leads were sealed through the top of the cell container with Apiezon W wax. The platinum lead-in wires were brought to the top of the container and clasped with spring clips attached to tungsten wires which were sealed through the Pyrex top. The top of the cell container was sealed to the Pyrex body with Apiezon W wax.

The cell assembly was evacuated to  $<10^{-5}$  Torr at 200°C to thoroughly degas it, argon was introduced to a pressure of 500 Torr and the cell temperature adjusted to 370°C. The readings of the emf and temperature were made with a L&N K-3 potentiometer.

The argon used in the dry box was dried by passing it through a bed of Linde 5A molecular sieve. The argon which was introduced into the cell during a run was purified by passing it first through a furnace containing calcium chips at 600°C, then through a bed of Ascarite and finally through a bed of Linde 5A molecular sieve.

### Results and Discussion

The emf of the cell was followed as a function of time at constant temperature until a constant value

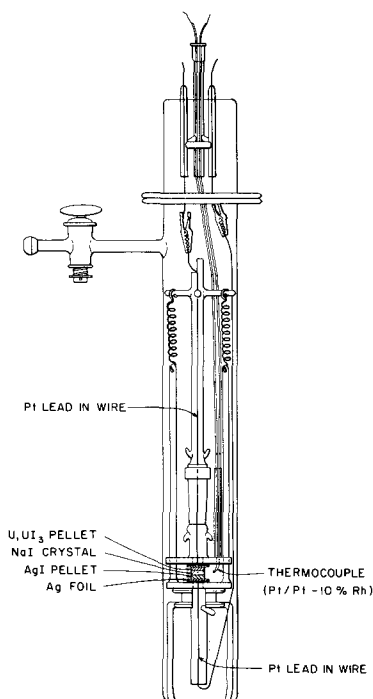


Fig. 1. Solid electrolytic cell

was maintained for two or three days. This emf was then considered to be the equilibrium value at that temperature. In general, when a cell was started, the emf would rise to within 0.05v of its equilibrium value during the first 24 hr and then require an average of three weeks to attain the final emf. Subsequent measurements at different cell temperatures required only one or two days to reach equilibrium. Measurements were continued on a cell until its emf rapidly decreased over a period of a few days. The operating time of individual cells varied widely, ranging from several weeks to four or five months.

The long equilibration time of the cell was not surprising since all the components were solids well below their melting points. Thus diffusion coefficients were orders of magnitude lower than in cells involving liquids. The U and UI<sub>3</sub> powders were intimately mixed to speed up the equilibration, but the diffusion was still quite slow. The cell emf deteriorated when the Ag<sup>+</sup> had diffused through the NaI and reached the UI<sub>3</sub>. This process required a longer time than the U-UI<sub>3</sub> equilibration because its path length was much longer. Meaningful emf data were obtained after the equilibration of U-UI<sub>3</sub> and before the Ag<sup>+</sup> diffused to the UI<sub>3</sub>.

The standard free energy of formation values for UI<sub>3</sub> obtained from six cells over the temperature range of 220°-370°C are plotted in Fig. 2. The average value of  $\Delta F_f^\circ$  at 370°C was -98.8 kcal/mole.

MacWood (12) obtained the standard heats of formation of the uranium halides from calorimetric measurements of several reactions in 12N HCl solvents containing either 10% FeCl<sub>3</sub> or saturated I<sub>2</sub>. He then estimated heat capacities and obtained the standard free energies as a function of temperature. Brewer, Bromley, Gilles, and Lofgren (13) used MacWood's heat of formation for UI<sub>3</sub> and slightly different heat capacity estimates to obtain the standard free energy as a function of temperature. The estimates of the free energy given by Brewer *et al.* and MacWood are also shown in Fig. 2 as a function of temperature.

Egan *et al.* (14) measured the standard free energy of formation of UCl<sub>3</sub> by a solid electrolyte galvanic cell technique over the temperature range of 400°-600°C and found it to be 10 kcal/mole more positive than those listed by Brewer *et al.* They obtained the same entropy change; therefore, it would seem that the major discrepancy lies in the heat of formation of UCl<sub>3</sub>. MacWood's calculation of the heat of formation

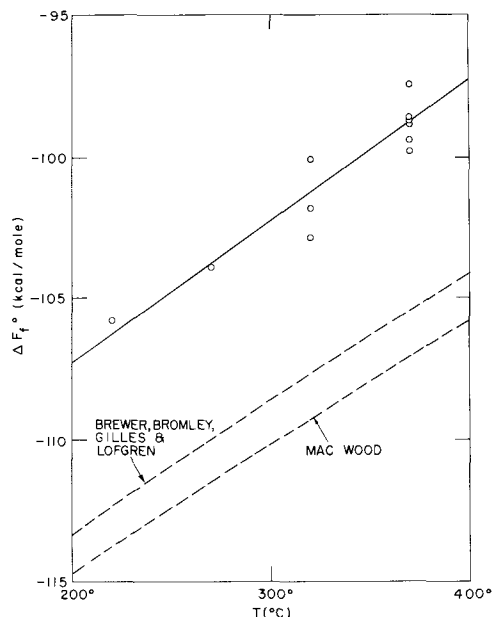


Fig. 2. Standard free energy of formation of UI<sub>3</sub> as a function of temperature.

of  $UI_3$  included his value for the heat of formation of  $UCl_3$ . Thus it would be expected, as a first approximation, that the heat of formation of  $UI_3$  would also be 10 kcal more positive than MacWood's value. Our results indicate a value  $\approx 6.7$  kcal/mole more positive.

The accuracy of our results for the  $\Delta F^\circ_f$  of  $UI_3$  involves not only the accuracy of the measured cell emf but also that of the literature value of  $\Delta F^\circ_f$  of  $AgI$  employed in the calculations. The recent compilation by Hamer, Malmberg, and Rubin (3) contains the best available thermochemically determined values in the form of the emf of the theoretical formation cell  $Ag/AgI/I_2(g)$  over the temperature range 25°-1500°C. There are, in addition, three papers (15-17) in the literature where the emf on the cell  $Ag/AgI/I_2(g),C$  has been determined experimentally. Reinhold measured the emf over the temperature range of 145°-350°C, obtained values  $\approx 100$  mv higher than those of Hamer *et al.*, and found a positive rather than negative temperature coefficient. Czepinski determined the emf over the temperature range 320°-740°C and obtained values  $\approx 35$  mv lower than those listed by Hamer *et al.*, but with approximately the same temperature coefficient. Sternberg *et al.* measured the emf over the temperature range 580°-650°C and obtained values 15 mv lower than those of Hamer *et al.* and also with approximately the same temperature coefficient.

This discrepancy between the thermochemically and electrochemically determined values prompted us to also make some emf measurements on the cell  $Ag/AgI/I_2(g),C$ . Our preliminary data agree within 5 mv with the values given by Hamer *et al.* over the temperature range 200°-400°C but with a slightly different temperature coefficient. This  $Ag/AgI/I_2(g),C$  cell will be further studied and fully reported at a later date, but the preliminary data convinced us to employ the values given by Hamer *et al.* in arriving at the  $\Delta F^\circ_f$  of  $UI_3$  reported herein.

The final emf values of the cells were constant to  $\pm 1$  mv, corresponding to  $\pm 0.07$  kcal/mole. The  $AgI$  data appear to be accurate to within  $\pm 5$  mv or  $\pm 0.35$  kcal/3 moles. Therefore, individual values from a given cell should be accurate to  $\pm 0.36$  kcal/mole. Calculation of the standard deviation of the mean value of the data at 370°C gives  $\pm 0.33$  kcal/mole. Thus, the  $\Delta F^\circ_f$  of  $UI_3$  at 370°C is  $-98.8 \pm 0.4$  kcal/mole.

#### Acknowledgments

The authors are deeply indebted to Dr. J. J. Egan and Dr. J. D. Van Norman for many helpful and stimu-

lating discussions. The aid of Dr. J. T. Clarke in arriving at the final cell design and his constant encouragement throughout the program is greatly appreciated. They are also extremely grateful for the valuable services of Mr. R. Watson, who carried out much of the experimental work. This work was performed under the auspices of the United States Atomic Energy Commission.

Manuscript submitted May 6, 1968; revised manuscript received June 19, 1968.

Any discussion of this paper will appear in a Discussion Section to be published in the June 1969 JOURNAL.

#### REFERENCES

1. A. W. Castleman, Jr. and I. N. Tang, *Proc. of the Conf. on Safety, Fuels and Core Design in Large Fast Power Reactors, ANL-7120*, pp. 848-54, Oct. 11-14, 1965.
2. K. Kiuokkola and C. Wagner, *This Journal*, **104**, 308 (1957).
3. W. J. Hamer, M. S. Malmberg, and B. Rubin, *ibid.*, **112**, 750 (1965).
4. R. W. Pohl, *Proc. Phys. Soc.*, **49**, (extra part), 3 (1937).
5. C. Wagner, "International Committee of Electrochemical Thermodynamics and Kinetics, Proceedings of the 7th Meeting Lindau, 1955," p. 361, Butterworth Publications, Ltd., London (1957).
6. G. Burley and H. E. Kissinger, *J. Research Natl. Bur. Standards*, **64A**, 403 (1960).
7. W. Lehfelddt, *Z. Physik*, **85**, 717 (1933).
8. C. Tubandt and F. Lorenz, *Z. Phys. Chem.*, **87**, 513 (1914).
9. C. Tubandt, *Handbuch der Experimentalphysik*, **12**, 383 (1932).
10. J. D. Corbett, R. J. Clark, and T. F. Munday, *J. Inorg. Nucl. Chem.*, **25**, 1287 (1963).
11. N. W. Gregory, Paper #54, "Chemistry of Uranium, Collected Papers," J. J. Katz and E. Rabinowitch, Editors, TID-5290 (1958).
12. G. E. MacWood, Paper #58, *ibid.*
13. L. Brewer, L. A. Bromley, P. W. Gilles, and N. L. Lofgren, Paper #33, *ibid.*
14. J. J. Egan, W. McCoy, and J. Bracker, "Thermodynamics of Nuclear Materials," p. 163, Int. Atomic Energy Agency, Vienna (1962).
15. V. Czepinski, *Z. Anorg. Chem.*, **19**, 208 (1899).
16. H. Reinhold, *Z. Elektrochem.*, **40**, 361 (1934).
17. S. Sternberg, I. Adorian, and I. Galasiu, *J. Chim. Phys.*, **62**, 63 (1965).

# Behavior of Tin Oxide Semiconducting Electrodes Under Conditions of Linear Potential Scan

H. A. Laitinen,\* C. A. Vincent,<sup>1</sup> and T. M. Bednarski<sup>2</sup>

University of Illinois, Urbana, Illinois

## ABSTRACT

Linear sweep voltammetric studies of thin layer semiconducting tin oxide layers on glass substrates revealed three regions of electrochemical interest. In the anodic region, oxygen or chlorine evolution occurs without disruption of the surface. In the intermediate region of potentials, cathodic-anodic processes attributable to charging and discharging of positive surface states occur. The charging-discharging process is most pronounced in the presence of high concentrations of hydrogen ions and chloride ions and is closely related to the specific adsorption of chloride ion. In the cathodic region, hydrogen ion discharge is accompanied by a disruption of the tin oxide layer, which is reduced to metallic tin.

This investigation describes the charging and discharging of the double layer on the semiconductor side of the semiconductor-solution interface under conditions of linear potential scan. Also included is a brief study of the cathodic decomposition of the tin oxide electrode to metallic tin.

While pure polycrystalline tin oxide is an insulator, the addition of certain electron donating species can render the material into a broad-band n-type semiconductor. These doped or unstoichiometric tin oxides with free carrier densities of approximately  $10^{19}$   $\text{cm}^{-3}$  are ideally suited for use as indicator electrodes in electrochemical investigations.

Thin semiconducting tin oxide films on glass or quartz substrates have been used as indicator electrodes for potentiometry (1), coulometry, and amperometry (2, 3). Kuwana and co-workers (4, 5) have taken advantage of the transparent nature of the tin oxide film electrodes in the visible region of the spectrum to directly observe electroactive species at the electrode-solution interface using internal reflection spectroscopy.

The literature also contains several papers describing the electrical and optical properties of stannic oxide-based semiconductors (6-13). The physical properties of this material have been described in detail, and several mechanisms of electron conduction have been proposed.

## Experimental

Glasses coated with semiconducting tin oxide were used as indicating electrodes for all the electrochemical studies included in this investigation. These antimony or fluoride doped tin oxides were manufactured by Corning Glass Company and obtained through F. J. Gray Company. The thickness of the tin oxide coating was determined by measuring the maxima and minima of interference fringes in visible light. Knowing the refractive index,  $\mu$ , of the tin oxide coating and the difference between successive maxima measured in wave numbers, the thickness can be obtained from the following equation according to Tolansky (14)

$$t = \frac{1}{2\mu \Delta\nu} \quad [1]$$

where  $t$  is the thickness in Angstroms and  $\Delta\nu$  the difference between successive maxima. The refractive index was taken as two (9), and the thickness of the tin oxide film was found to be between 6,000 and 10,000 Å depending on the sample. The specific resistivity calculated from a-c and d-c bridge mea-

surements was approximately  $6 \times 10^{-4}$  ohm cm. X-ray diffraction patterns indicated the material to be microcrystalline with a mean particle size of  $\sim 10$  m $\mu$  in diameter. Electron microscopic investigations indicated a homogeneous and compact surface free of any repeatable surface structure or grain boundaries.

To insure a clean and reproducible electrode surface, either of two pretreatment procedures was employed. The  $\text{SnO}_2$  coated glasses were either steam cleaned for 1 hr followed by drying at  $110^\circ\text{C}$  or washed with absolute ethanol followed by thorough washing in distilled water. When an electrode was subjected to either procedure, reproducible electrochemical characteristics were observed. If the electrode surface was subjected to either oxidizing or reducing media in the pretreatment procedure irreproducible electrochemical characteristics were noted. Although pre-electrolysis was used in some of the preliminary work, it was found later that preparation of solutions using doubly distilled water gave equally reproducible results.

Contact to the  $\text{SnO}_2$  surface was made by a specially designed silver ring. It is important that the metal-semiconductor contact be especially good, so that the contact impedance on the metal-semiconductor interface be negligible. Using the pressure contact shown in Fig. 1, the measured series capacitive reactance at a frequency of 1 kHz was  $\leq 10^{-4}$  ohm, and the resistive series component was negligible.

The cell consisted of cone-shaped Pyrex glass vessel with an optically flat surface at the narrow end. The  $\text{SnO}_2$  coated glass was then mounted *via* a Teflon

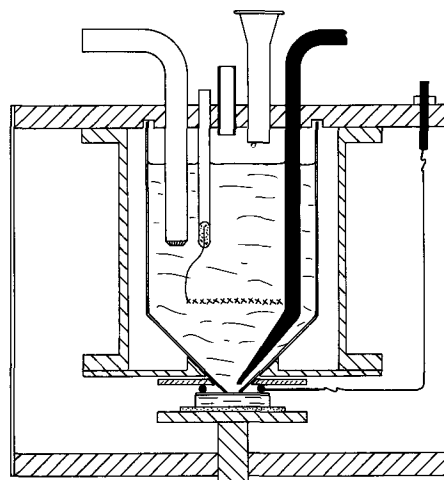


Fig. 1. Electrolysis cell assembly

\* Electrochemical Society Active Member.  
<sup>1</sup> Present address: University of St. Andrews, St. Andrews, Scotland.  
<sup>2</sup> Present address: Hercules, Inc., Wilmington, Delaware.

washer to the optically flat surface and tightly assembled to insure a leakproof seal. The electrode area was taken to be the same as the geometric area of the washer opening. This was also verified by electrochemically decomposing the  $\text{SnO}_2$  surface in contact with the solution and measuring the area of the decomposed surface analytically. Areas computed in the above manners were found to correspond within experimental error. The cell was then mounted in a brass cylinder attached to a Teflon block which served as a cell top. The entire assembly was then placed in a lighttight brass container which could be thermostatted if desired.

A saturated calomel electrode (SCE) was used as the reference electrode. This was connected to the electrolysis cell by means of a salt bridge containing the cell solution. The counter electrode consisted of either a large area platinum foil electrode or a platinum mesh electrode.

Prepurified nitrogen which had also passed through a vanadous scrubbing train and a presaturator containing the cell solution was used to obtain oxygen-free solutions. A nitrogen atmosphere was also maintained above the solution while electrochemical measurements were being taken.

All voltammetric studies were carried out using conventional operational amplifier circuitry with Philbrick vacuum tube units. A Beckman pH meter with appropriate electrodes was used to measure the hydrogen ion activity.

### Results

The electrochemical behavior of tin oxide semiconducting electrodes in aqueous HCl solution under conditions of linear potential scan is shown in Fig. 2. The current-potential dependence can be conveniently divided into three separate regions; namely, the anodic decomposition region, the charging region, and the cathodic decomposition region. For reasons of clarity and ease in presentation each region will be discussed separately.

The anodic potential limit is attributed to either oxygen or chlorine evolution depending on the supporting electrolyte. In chlorine free solutions the anodic decomposition potential was pH dependent, increasing approximately 31 mv per pH unit in the anodic direction for  $1 < \text{pH} < 13$ .

The charging region was characterized by well-formed peaks having reproducible peak currents and potentials at slow scan rates. Qualitatively, the peak definition was enhanced by increasing the hydrogen ion activity, increasing the concentration of chloride ion, and by slowing the scanning rate (but not below 0.05 v/min). A more detailed reproduction of the peaks obtained in 2M HCl is shown in Fig. 3. The peaks are symmetrical in shape, indicative of an exhaustive surface electrolysis or charging process

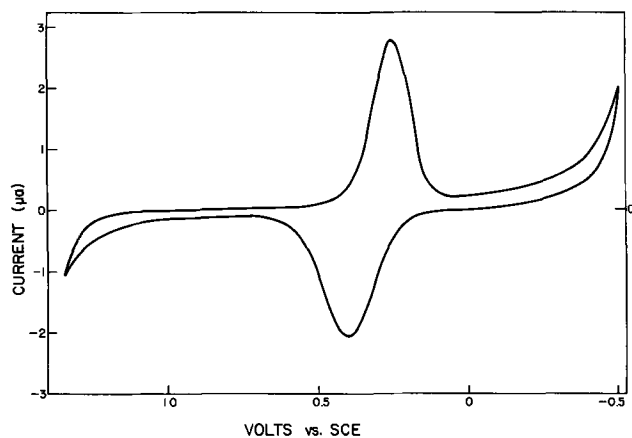


Fig. 2. Current-voltage behavior in 2M HCl. Scan rate was 0.2 v/min; electrode area is 0.135  $\text{cm}^2$ .

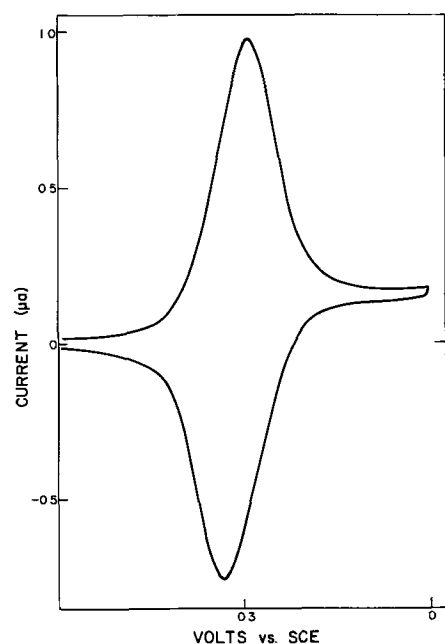


Fig. 3. Current-voltage curve in 2M HCl. Rate of scan was 0.05 v/min.

rather than the oxidation or reduction of a soluble species diffusing to or from the electrode surface.

In Table I are listed the peak currents and potentials obtained in 0.1 and 2.0M HCl. Only after the tin oxide electrode remained in contact with the solution for periods of time  $> 6$  hr were reproducible values of peak currents and potentials obtained. The quantity ( $E_{pa} - E_{pc}$ ) increased with increasing scan rate indicating a slow electrochemical process. Even at a scan rate of 0.05 v/min the anodic and cathodic peak potentials are not quite coincident in 2M HCl and even more removed in 0.1M HCl. The peak currents in the more concentrated HCl solution were approximately 7X those observed in the more dilute acid. Analysis showed that the peak currents were not proportional to either the square root of scan rate or directly to the scan rate. The peak currents obtained in 2M HCl after the electrode remained in contact with the solution for prolonged periods of time were the same as in 12M HCl. This is indicative of a saturation-type phenomenon occurring at the tin oxide electrode. Also included in Table I are the number of coulombs consumed in the electrolysis. These quantities were measured by analytically determining the area under the current-potential peak with a planimeter and converting the potential axis to a time basis. The peak areas were independent of scan rate, although at the faster scan rates the peaks were not well defined and the measurements were correspondingly less accurate. The number of coulombs consumed in the process were approximately 5X greater in the 2M acid than in the 0.1M acid.

Table I. Comparison of peak currents and potentials at various scan rates in 2M and 0.1M HCl

Scan rate v/min	2M HCl				0.1M HCl			
	$i_{pc}^{(1)}$ $\mu\text{A}$	$i_{pa}$ $\mu\text{A}$	$E_{pc}^{(2)}$ , v	$E_{pa}$ , v	$i_{pc}^{(1)}$ $\mu\text{A}$	$i_{pa}$ $\mu\text{A}$	$E_{pc}$ , v	$E_{pa}$ , v
0.05	0.85 <sup>(4)</sup>	0.79	+0.295	+0.332	0.13 <sup>(3)</sup>	0.13	+0.285	+0.318
0.1	1.60	1.45	+0.290	+0.350	0.27	0.25	+0.27	+0.34
0.2	2.60	2.15	+0.250	+0.395	0.45	0.41	+0.25	+0.38
1.0	4.80	4.20	+0.225	+0.435	1.90	1.64	+0.13	+0.49
2.0	8.05	6.75	+0.164	+0.475	2.55	2.50	+0.01	+0.58

<sup>(1)</sup> Area of electrode was 0.135  $\text{cm}^2$ .

<sup>(2)</sup> Potentials vs. SCE.

<sup>(3)</sup> Area under cathodic peak equivalent to  $1.73 \times 10^{-4}$  coul/cm<sup>2</sup>.

<sup>(4)</sup> Area under cathodic peak equivalent to  $8.82 \times 10^{-4}$  coul/cm<sup>2</sup>.

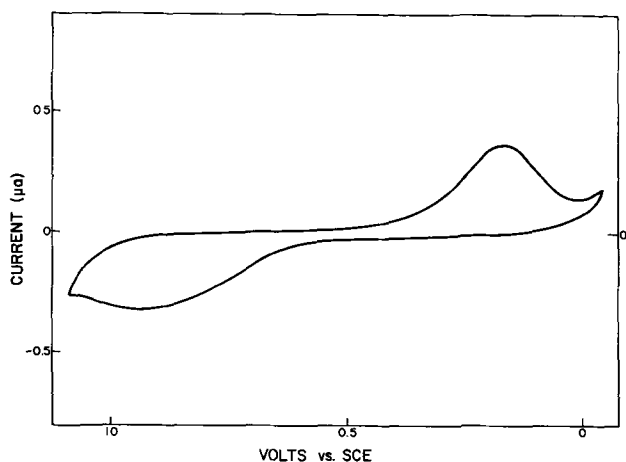


Fig. 4. Current-voltage curve in  $2M$   $HClO_4$ . Scan rate  $0.05$  v/min.

To differentiate the effect of hydrogen ion and chloride ion a number of experiments were carried out in  $2M$   $HClO_4$ . A typical current-potential curve obtained in this medium is shown in Fig. 4. The peaks are poorly developed in comparison to  $2M$   $HCl$ , and the separation of the anodic and cathodic peak potentials is greater.

Evidence for the specific adsorption of chloride ion on the tin oxide electrode was obtained from the following sequence of experiments. After normal linear scan voltammograms were obtained in  $2M$   $HCl$  the hydrochloric acid solution was removed, and the intact cell assembly was thoroughly washed with distilled water. Two molar perchloric acid was then added to the cell and the electrochemical behavior described in Fig. 5 was observed. Initially, peaks similar to those obtained in  $2M$   $HCl$  were observed. After various periods of standing, the peaks became broader and the peak potentials diverged. Curves 2, 3, and 4 in Fig. 5 were obtained after 2.5, 4.6, and 9.5 hr of standing, respectively. The peaks finally became very broad, and the peak separation in curve 4 became  $0.76$  v.

In another series of experiments after normal voltammograms were obtained in  $2M$   $HCl$ , the cell was thoroughly washed and a  $2M$   $HClO_4$  solution added. The electrode was then maintained at a potential anodic to the chlorine evolution potential for 2 min with a stream of nitrogen flowing through the cell. Linear sweep voltammograms then obtained were similar to curve 4 in Fig. 5, indicating that a short anodization completely removes the adsorbed chloride. To obtain a rough estimate as to the amount of specifically adsorbed chloride ions at the tin oxide

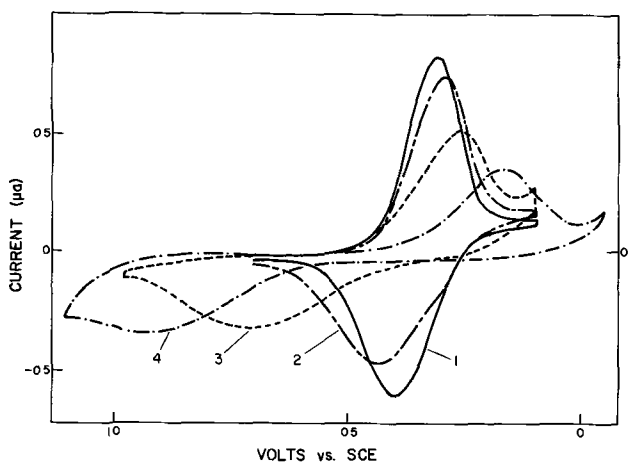


Fig. 5. Variation of current-voltage behavior with time in  $2M$   $HClO_4$  of an electrode which had been soaked in  $2M$   $HCl$ . Curve 1, 0.5 hr; curve 2, 2.5 hr; curve 3, 4.6 hr; curve 4, 9.5 hr.

electrode the following experiment was performed. After normal current-voltage curves were obtained in  $2M$   $HCl$ , the cell was thoroughly washed and an acetic acid-sodium acetate buffer of pH 4.03 was added. The potential applied to the indicator electrode was then scanned in an anodic direction, and a small hump due to the oxidation of chloride ions was observed. From the area under the current-voltage curve the number of coulombs in the oxidation could be determined. This corresponded to approximately the same number of coulombs as represented by the peak areas in  $2M$  hydrochloric acid. Because of the difficulty in determining the exact area of the chloride oxidation hump superimposed on the solvent decomposition current, quantitative evaluation was not possible.

Current-voltage curves obtained in solutions of higher pH in the absence of chloride ions were poorly defined and the peaks much smaller in magnitude and area. The peak definition was improved by adding varying amounts of  $LiCl$ , to a given buffer system; however, the quality of the peaks never approached those obtained in solutions when both hydrogen and chloride ions were present in concentrations  $> 1M$ .

The cathodic decomposition region is characterized by either the reduction of hydrogen ions from the solution or the solid-state reduction of the tin oxide layer to metallic tin or both concomitantly.

If a tin oxide semiconducting electrode is maintained at a constant potential of  $-0.75$  v vs. SCE in  $1M$   $HCl$ , the thin tin oxide layer is completely reduced to metallic tin. Metallic tin was positively identified by placing the reduced material in contact with mercury for a few days and then employing the resulting amalgam as the anode of an electrolysis cell. Stripping peak potentials obtained in this manner were then compared with those obtained from a tin amalgam of known composition and were found to agree within 5 mv. Qualitative observations of a partially decomposed tin oxide electrode with a binocular microscope at 50X magnification indicated the presence of square shaped crystals which could be indicative of  $\alpha$  gray tin which crystallizes in the cubic system (15).

In slow linear voltage sweep experiments with a cathodic limit of  $-0.7$  v, the return anodic sweep produces both sharp and broad anodic peaks, as shown in Fig. 6. The peak potential at approximately  $-0.5$  v vs. SCE varied linearly with pH at a rate of 58 mv per pH unit. The difference between the peak and half-peak potentials was 28 mv. The rather broad anodic peak with a peak potential of approximately  $0.5$  v vs. SCE in  $0.1M$   $HCl$  exhibited little measurable change with pH. A similarly shaped peak with a peak potential of  $+0.5$  v vs. SCE was obtained when

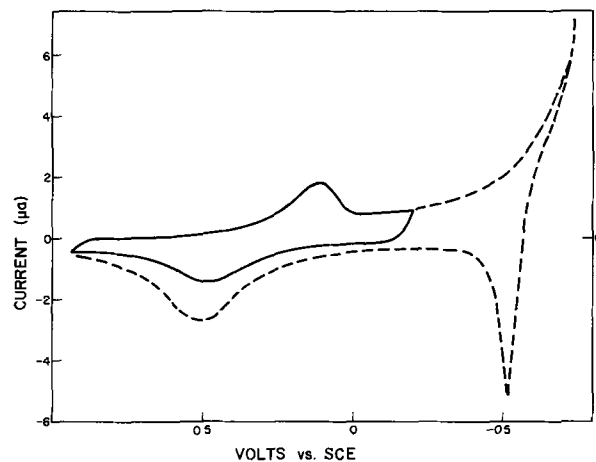


Fig. 6. Current-voltage curves in  $0.1M$   $HCl$  showing the behavior after the tin oxide electrode was subjected to an extreme cathodic potential. Scan rate is  $1.0$  v/min; electrode area is  $0.135$   $cm^2$ .

$\text{SnCl}_2 \cdot 2\text{H}_2\text{O}$  was added to a 0.1M HCl solution. This peak is attributed to the oxidation of a soluble Sn (II) species to Sn (IV). The cathodic decomposition potential of both Sn (II) and Sn (IV) in 0.1M HCl occurred at approximately  $-0.45\text{v}$  which is approximately 0.35v more anodic than the solid  $\text{SnO}_2$  reduction. The sharp peak at  $-0.54\text{v}$  vs. SCE is attributed to the oxidation of metallic tin from an inert  $\text{SnO}_2$  electrode to a Sn (II) species in solution. When the direction of scan is immediately reversed after the anodic peak had been transversed a cathodic reduction peak was obtained with  $E_p = -0.575\text{v}$  vs. SCE and the quantity  $(E_p - E_{p2}) = 0.025\text{v}$ . A similar peak with the identical peak potential was obtained when  $\text{SnCl}_2 \cdot 2\text{H}_2\text{O}$  is added to solution.

Recent investigations by Kirkov (16) have indicated that when the electrode is maintained at potentials considerably anodic to those described above for relatively long periods of time in acid solutions (ca.  $-0.3\text{v}$  for 24 hr in 0.1N HCl) metallic tin is also produced. He attributes this to the formation of chemisorbed hydrogen atoms from the reduction of hydrogen ions in solution, which then slowly reduces the tin oxide layer. Thus, it appears that both processes can be occurring simultaneously at the cathodic decomposition potential. Whether metallic tin is produced by direct electrochemical reduction of the tin oxide at more negative potentials, or whether the process always proceeds through chemisorbed hydrogen atoms cannot be determined from the present experiments.

### Discussion

The symmetrical current-voltage peaks obtained under conditions of linear potential scan are attributed to the reduction and subsequent oxidation of surface tin species. Similar anodic-cathodic curves have been observed by Rouse and Weininger (17) for lithium-doped nickel oxide single crystals.

A situation of this type in which both the oxidized and reduced species are immobile would be analogous to the exhaustive electrolysis of thin layers of solutions. Recently, Hubbard and Anson (18) have derived the current-voltage expressions expected for the electrolysis of thin layers using linear sweep voltammetry, assuming that the concentrations of the soluble electroactive species could be described by the Nernst equation. It is expected that similar expressions would apply for the solid-state electrolysis of immobile species under linear potential scan.

Assuming the concentrations of the immobile species can be expressed by a Nernst-type relationship, and the reduction is independent of the diffusion of electrons through the space charge region, the cathodic current can be described by the following equation

$$i = n^2 A v C_{\text{ox}}^0 \frac{F^2}{RT} \frac{\exp \frac{nF}{RT} (E^0 - E)}{[\exp nF/RT (E^0 - E) + 1]^2} \quad [2]$$

where  $n$  is the number of electrons transferred,  $A$  the electrode area in  $\text{cm}^2$ ,  $v$  the rate of scan in volts/sec,  $C_{\text{ox}}^0$  the initial concentration in moles/ $\text{cm}^2$ ,  $E^0$  the formal potential of the immobile species, and the remaining symbols having their usual significance.

A graphical representation of  $i = f(E)$  would be bell-shaped and symmetrical about the peak potential  $E^0$ . The peak current,  $i_p$ , at  $E = E^0$  would be given by the following expression

$$i_p = \frac{n^2 C_{\text{ox}}^0 A v F^2}{4 RT} \quad [3]$$

Equation [3] can also be written in terms of the number of coulombs consumed in the Faradaic process to give Eq. [4].

$$i_p = \frac{n^2 v Q F}{4 RT} \quad [4]$$

where  $Q$  is the number of coulombs determined by graphical integration of the current-voltage curve.

To test the applicability of Eq. [4], the ratio  $i_p/n^2$  was determined for the current-voltage curve shown in Fig. 3. Obtaining  $Q$  by graphical integration of the current-voltage curve and knowing the rate of scan and the experimentally measured  $i_p$ , the calculated number of electrons transferred is 1.05. This is indicative of a Faradaic process involving one electron.

If the Faradaic process indeed corresponds to the reversible transfer of one electron, a cathodic current-voltage curve should correspond to the following equation

$$E = E^0 - \frac{0.059}{n} \log \frac{Q_E}{Q_{\text{total}}} \quad [5]$$

where  $Q_E$  is the number of coulombs consumed up to a potential  $E$  and  $Q_{\text{total}}$  the total number of coulombs under the cathodic current-voltage curve. Plotting  $E$  vs.  $\log Q_E/Q_{\text{total}}$  for the current-voltage curve shown in Fig. 3 a straight line was obtained with a slope of 0.061v. This is consistent with the postulation of a reversible one-electron surface reaction.

It is apparent from Eq. [2] that, under conditions of cyclic potential scan, the peak potentials of both waves should be identical if the reaction is free from kinetic complications. As is shown in Table I at the slowest scan rate, 0.05 v/min, the experimentally determined anodic and cathodic peak potentials are not identical but differ by 37 mv. This separation becomes more pronounced as the scan rate increases and the  $n$ -values calculated from the ratio  $i_p/n^2$  decrease to less than unity. The reason for this apparent irreversibility does not appear to be caused by the diffusion of electrons through the space charge region. With a specific resistivity of approximately  $6 \times 10^{-4}$  ohm cm, the number of carriers/ $\text{cm}^3$  in a tin oxide semiconductor is only one or two orders of magnitude less than of a metal and equivalent to that present in a strong electrolyte of one-tenth molar concentration. Instead, the observed behavior appears to be dependent on the rate of the surface recombination.

If the observed behavior is due to the oxidation or reduction of surface tin species, the number of coulombs under the current-voltage peak should be a reflection of the number of tin atoms at the electrode-solution interface. Assuming that one electron is transferred to each tin atom the number of available sites  $2M$  HCl calculated from the data reported in Table I is  $5.5 \times 10^{15}$  sites/ $\text{cm}^2$ . If one takes a mean surface layer of approximately  $3\text{\AA}$  and a roughness factor of unity, the number of tin atoms available at the electrode-solution interface is approximately  $1 \times 10^{15}$ . This value is five times smaller than that found experimentally so either a roughness factor of one is unrealistic or more than a monolayer of tin atoms is involved, or both.

As shown in the results section, the presence of chloride ion is necessary for the attainment of well-defined peaks. Evidence for the specific adsorption and desorption of chloride was presented and the number of coulombs consumed in the Faradaic process attributable to the peak behavior was found to be approximately equivalent to one electron per adsorbed chloride ion.

Based on this evidence, it is suggested that the observed peak behavior is due to the charging and discharging of positive surface states, i.e., tin atoms, caused by a dipole type interaction with the adsorbed chloride ions. Because of this induced positive charge, surface tin atoms now become traps or holes and can accept electrons from the bulk of the semiconductor but still retain a stable rutile configuration. This would be chemically equivalent to a change in the oxidation states of the surface tin atoms, and a Nernst-type relationship would apply. The number of surface states would be a function of the bulk chloride



ion concentration and would expect to increase in the manner reported in Table I.

The appearance of peaks in chloride free solutions can also be attributed to the charging and discharging of surface states. In this instance, positive surface states result from the protonation of surface oxide ions and in this sense become part of the semiconductor material in contrast to the chloride ion behavior. As shown in Fig. 4, the oxidation and reduction of the surface tin atoms containing protonated oxide ions does not proceed as reversibly as those formed by the dipole interaction.

The cathodic decomposition region is attributed to the reduction of the  $\text{SnO}_2$  matrix to metallic tin proceeding from the solid-solution interface into the bulk of the semiconductor. No separate peaks were obtained for the stepwise reduction of  $\text{SnO}_2$  through a Sn (II) intermediate using linear potential scan. However, when  $\text{SnCl}_2$  was present in solution, a definite peak with  $E_p = -0.575\text{v vs. SCE}$  was obtained.

On subsequent oxidation of the reduced  $\text{SnO}_2$  matrix, two peaks are obtained. The peak observed at  $-0.5\text{v vs. SCE}$  is attributed to the oxidation of tin metal to divalent tin. Since the peak potential shifts 58 mv per pH unit, the product of the electrode reaction must contain the equivalent of two hydrogen ions per tin atom. The exact composition of the divalent tin species was not determined. The broad anodic peak shown in Fig. 6 with a peak potential of  $+0.5\text{v vs. SCE}$  is attributed to the irreversible oxidation of a soluble divalent tin species to a soluble quadrivalent tin species. A similar peak with the corresponding peak potential was obtained when  $\text{SnCl}_2$  was added to the solution.

The specific adsorption of chloride and hydrogen ions play a decisive role in determining the steady state potential on open circuit. The open-circuit behavior will be described in a forthcoming publication.

### Acknowledgment

This research was supported by the National Science Foundation, under Grant NSF G-3489. Many valuable discussions with Professor P. Kirkov (University of Skopje) are gratefully acknowledged.

Manuscript received March 22, 1968.

Any discussion of this paper will appear in a Discussion Section to be published in the June 1969 JOURNAL.

### REFERENCES

1. W. Cooper, *Nature*, **194**, 569 (1962).
2. V. Y. Dubrovinskii and V. Kumok, *Zhur. Analit. Khim.*, **19**, (9), 1159 (1964).
3. A. M. Titova, *Zhur. Fiz. Khim.*, **34**, 1692 (1958).
4. T. Kuwana, R. K. Dovington, and D. W. Leedy, *Anal. Chem.*, **36**, 2023 (1964).
5. W. N. Hansen, T. Kuwana, and R. A. Osteryoung, *ibid.*, **38**, 1810 (1966).
6. E. E. Kohnke, *Phys. Chem. Solids*, **23**, 1557 (1962).
7. L. D. Loch, *This Journal*, **110**, 1081 (1963).
8. A. Fisher, *Z. Naturforsch.*, **9a**, 508 (1954).
9. T. Arai, *J. Phys. Soc. Japan*, **15**, 916 (1960).
10. K. Ishiguro, T. Sasaki, T. Arai, and I. Imai, *ibid.*, **13**, 296 (1958).
11. H. Koch, *Phys. Status Solici*, **3**, 1619 (1963).
12. I. Imai, *J. Phys. Soc. Japan*, **15**, 937 (1960).
13. R. E. Aitchison, *Aust. J. App. Sci.*, **5**, 10 (1954).
14. S. Tolansky, "Multiple-beam Interferometry of Surfaces and Films," Clarendon Press, New York (1948).
15. H. E. Swanson, E. Tatge, and R. F. Fuyat, National Bureau of Standards (U.S.) Circ. No. 539, I, 24, and II, 12, (1953).
16. P. Kirkov and H. A. Laitinen, Unpublished experiments.
17. T. O. Rouse and J. L. Weininger, *This Journal*, **113**, 184 (1966).
18. A. T. Hubbard and F. C. Anson, *Anal. Chem.*, **38**, 58 (1966).

## Cyclic Chronopotentiometry. Systems Involving Kinetic Complications

Harvey B. Herman\*

Department of Chemistry, University of Georgia, Athens, Georgia

and Allen J. Bard\*

Department of Chemistry, The University of Texas, Austin, Texas

### ABSTRACT

The extension of cyclic chronopotentiometry to systems involving kinetic complications, including preceding, following, and catalytic reactions and combinations of these is described and tables are given which can be employed in a determination of the rate constants of these reactions. A general digital computer program is presented which allows calculation for any reaction scheme which conforms to the treatment of Ashley and Reilley. Experimental results for the electroreduction of p-nitrosophenol, an ECE-reaction, and the reduction of titanium (IV) in the presence of hydroxylamine, a catalytic reaction, are presented.

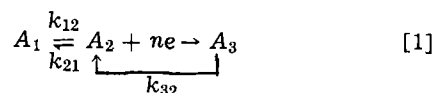
The technique of cyclic chronopotentiometry (CC) in which the applied current is successively reversed at each transition and the relative transition times determined, has been applied to simple diffusion controlled reactions (1), multicomponent systems (2), and electrode reactions with following chemical reactions (3). We recently discussed the application of CC to the study of electrode reaction mechanisms (4) and suggested qualitative guides for using CC as a diagnostic

aid. We present here a discussion of the methods for solving for the transition time ratios in CC for a number of different reaction schemes involving preceding, following, and intervening chemical reactions and give tables which can be employed in a determination of the rate constants of these reactions. A digital computer program is also described which can be used to determine the relative transition times for any reaction scheme amenable to the treatment of Ashley and Reilley (5).

\* Electrochemical Society Active Member.

## Theoretical Treatment

One approach which can be employed to compute tables of relative transition times for the different cases involves treatment of each possible reaction scheme separately. Concurrent chemical reactions require additional terms added to Fick's diffusion law. Thus, for the process



the following partial differential equations hold

$$\frac{\partial C_1}{\partial t} = D \frac{\partial^2 C_1}{\partial x^2} - k_{12}C_1 + k_{21}C_2 \quad [2]$$

$$\frac{\partial C_2}{\partial t} = D \frac{\partial^2 C_2}{\partial x^2} + k_{12}C_1 - k_{21}C_2 + k_{32}C_3 \quad [3]$$

$$\frac{\partial C_3}{\partial t} = D \frac{\partial^2 C_3}{\partial x^2} - k_{32}C_3 \quad [4]$$

assuming all diffusion coefficients are equal.  $C_n$  is the concentration of the  $A_n$  species and the other symbols have their usual meanings. The above system of partial differential equations can be solved by making suitable substitutions, namely  $\theta = C_1 + C_2 + C_3$ , which gives

$$\frac{\partial \theta}{\partial t} = D \frac{\partial^2 \theta}{\partial x^2} \quad [5]$$

$\gamma = C_3$  which gives

$$\frac{\partial \gamma}{\partial t} = D \frac{\partial^2 \gamma}{\partial x^2} - k\gamma \quad [6]$$

and  $\delta = C_3 + AC_2 + BC_1$ , which gives for proper choice of  $A$  and  $B$

$$\frac{\partial \delta}{\partial t} = D \frac{\partial^2 \delta}{\partial x^2} - k\delta \quad [7]$$

Further details concerning the solution of these equations are given by Hung, Delmastro, and Smith (6). Their results for the convolution integral will be used here. For example their solution for the concentrations of  $A_2$  and  $A_3$  for the above case (their equations 78, 79, 109-114 and  $k_{CY} = 0$ ) is the following

$$C_2 = C_2^0 - [nFA(D\pi)^{1/2}]^{-1}$$

$$\left[ L_1 \int_0^t e^{-k_{32}\lambda} i(t-\lambda) \lambda^{-1/2} d\lambda - L_2 \int_0^t e^{-(k_{12}+k_{21})\lambda} i(t-\lambda) \lambda^{-1/2} d\lambda \right] \quad [8]$$

$$C_3 = [nFA(D\pi)^{1/2}]^{-1} \int_0^t e^{-k_{32}\lambda} i(t-\lambda) \lambda^{-1/2} d\lambda \quad [9]$$

where

$$L_1 = \frac{k_{12} - k_{32}}{k_{12} + k_{21} - k_{32}} \text{ and } L_2 = \frac{k_{21}}{k_{12} + k_{21} - k_{32}}$$

Substitution of constant current boundary conditions and proper use of the step function theorem allows solution for the CC transition time ratios. The procedure is quite similar to the method used in earlier papers in this series where the computer programs were published (1-3).

In this case the computer program would generate the following equation for the third transition time

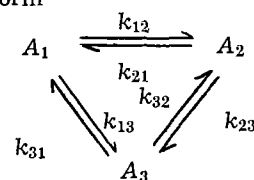
$$f(x) = k_{21}(k_{12} + k_{21})^{-1/2} [erf(\{(k_{12} + k_{21})x\}^{1/2})] + (k_{12} - k_{32})(k_{32})^{-1/2} [erf(\{k_{32}x\}^{1/2})] \quad [10]$$

and

$$f(\tau_1) = f(\tau_1 + \tau_2 + \tau_3) - Rf(\tau_2 + \tau_3) + Rf(\tau_3) \quad [11]$$

where  $\tau_1$  is one,  $erf(x) = 2\pi^{-1/2} \int_0^x e^{-\tau^2} d\tau$ ,  $R = (i_{Red} + i_{ox})/i_{Red}$  and  $\tau_2$  is calculated in the previous step from an equation representing  $A_2$ . The above nonlinear equation is solved using a standard numerical technique, e.g., the Newton-Raphsen method. Successive approximations are generated from evaluations of the function and its derivative. Occasionally this method does not converge and it is necessary to use our previous "brute force" method (1) which is quite a bit slower. While this approach works well and extensive tables of transition time ratios can be prepared in a comparatively short time using a digital computer, certain statements in the program have to be drastically modified each time a different mechanism is considered. Most of the theoretical calculations reported here were done using the above method and the convolution integrals reported by Hung, Delmastro, and Smith (6).

Recently Ashley and Reilly (5) showed how electrochemical systems coupled only by first order chemical reactions could be treated in a general way and general equations formulated. They considered subsystems of the form



and obtained the following equation for the concentration of the species in the Laplace transform plane

$$\bar{C}_n = \bar{C}_n^0 - D^{-1/2} \sum_g \sum_h \bar{i}_g K_{fgh} (s + \chi_h)^{-1/2} \quad [13]$$

where  $K_{fgh}$  and  $\chi_h$  are constants, which are determined by the rate constants of the coupled reactions in [12]. This equation is derived using substitutions such as those described before and applying matrix algebraic methods. The values of  $K_{fgh}$  and  $\chi_h$  in terms of the rate constants are given in (5). Inverse transformation of [13] gives the desired convolution integral. This is particularly easy for chronopotentiometry, because the fluxes of the components are constant.

The computer program discussed before was modified to treat the more general case embodied by Eq. [13]. A FORTRAN subroutine was written which evaluated the constants  $K_{fgh}$  and  $\chi_h$  and FORTRAN function subprograms were used to evaluate the summation and its derivative. The Newton-Raphsen method could then be used to solve for the individual transition time ratios. As expected, both methods gave the same results for selected systems. However, the general method is by far the more convenient. It is just necessary to label the species in a subsystem, decide which are oxidized or reduced and what values should be picked for the rate constants and the program does the rest. The only programming changes which are necessary when different reaction schemes are considered involve only input and output. A listing of this program for the system in Eq. [12] is available to interested readers and can easily be adapted to other mechanisms.

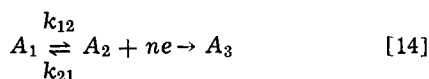
## Theoretical Results

The characteristics of each mechanism are treated separately. The mechanisms that are discussed include reversible chemical reactions preceding, following, and in parallel (catalytic), with the electrode process proper, as well as mixtures of each. The convolution integrals have been tabulated by Smith and co-workers (6) and will not be repeated. The familiar ECE case and its extension is also discussed. For all of the cases described we assume an initial reduction, equal diffusion coefficients for all species, and equal current densities for reduction and oxidation.

Table I. Relative transition times for cyclic chronopotentiometry with a preceding chemical reaction

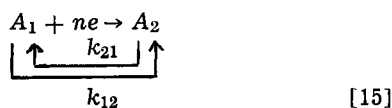
n	$A_1 \xrightleftharpoons[k_{21}]{k_{12}} A_2 + ne \rightarrow A_3$									
	$a_n$									
	$k_{12} \tau_1 = 0.5$	0.5	0.5	1.0	1.0	1.0	2.0	2.0	2.0	2.0
	$k_{21} \tau_1 = 0.5$	1.0	2.0	0.5	1.0	2.0	0.5	1.0	2.0	2.0
1	1.000	1.000	1.000	1.000	1.000	1.000	1.000	1.000	1.000	1.000
2	0.333	0.333	0.333	0.333	0.333	0.333	0.333	0.333	0.333	0.333
3	0.684	0.733	0.750	0.641	0.665	0.670	0.606	0.614	0.614	0.614
4	0.392	0.411	0.417	0.375	0.385	0.387	0.362	0.365	0.365	0.365
5	0.670	0.721	0.725	0.607	0.631	0.633	0.565	0.573	0.573	0.573
6	0.428	0.455	0.458	0.397	0.410	0.411	0.376	0.380	0.380	0.380
7	0.663	0.713	0.711	0.590	0.614	0.615	0.545	0.553	0.553	0.553
8	0.452	0.483	0.483	0.411	0.426	0.426	0.385	0.389	0.389	0.390
9	0.659	0.707	0.702	0.579	0.603	0.604	0.533	0.541	0.542	0.542
10	0.469	0.502	0.500	0.420	0.436	0.437	0.391	0.396	0.396	0.397

Preceding chemical reaction.—



Relative transition times ( $a_n = \tau_n/\tau_1$ ) for this case for different values of  $k_{12}$  and  $k_{21}$  are given in Table I. Note that in this case the second relative transition time ( $a_2$ ) is not affected by the chemical reaction, but  $a_3$  becomes larger than in the diffusion controlled case. In most cases the odd relative transition time decreases as in the diffusion case, but if the rate of the reverse reaction ( $k_{21}\tau_1$ ) is large, increases may be observed. If both values of the rate constant are quite large the diffusion controlled situation is approached again. This is true of many of the reversible mechanisms. A preceding chemical reaction can be positively differentiated from a catalytic type mechanism in which  $\tau_3$  may be larger than diffusion by its diffusion controlled value of  $a_2$  (1/3). In some of the reversible cases a steady state value for the relative transition times may be attained which can be used to calculate the rate constants, although convection might interfere with this measurement.

Parallel (catalytic) reversible reaction.—



The case of CC involving an irreversible catalytic reaction has been treated previously (3); we extend the work here to include a reversible reaction (Table II). Since  $A_1$  and  $A_2$  are in equilibrium before the application of the constant current, it is possible for the

Table II. Relative transition times for cyclic chronopotentiometry with a parallel (catalytic) reaction

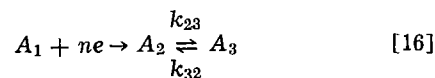
n	$A_1 + ne \rightarrow A_2$				
	$a_n$				
	$k_{12} \tau_1 = 0.5$	0.5	1.0 <sup>a</sup>	0.0	0.0
	$k_{21} \tau_1 = 0.5$	1.0	1.0	0.5	1.0
1	1.000	1.000	1.000	1.000	1.000
2	1.414	0.370	1.273	0.227	0.167
3	1.408	1.035	1.272	0.634	0.673
4	1.409	0.370	1.272	0.232	0.169
5	1.409	1.033	1.272	0.609	0.658
6	1.409	0.370	1.272	0.233	0.169
7	1.409	1.033	1.272	0.600	0.655
8	1.409	0.370	1.272	0.234	0.169
9	1.409	1.033	1.272	0.597	0.654
10	1.409	0.370	1.272	0.234	0.169

<sup>a</sup> No reverse transition is observed for  $k_{12} \tau_1 = 1.0$  and  $k_{21} \tau_1 = 0.5$ .

second transition time to be larger than the first. Any reaction involving a reversible catalytic system can be identified by the fact that an equilibrium amount of reduced form is present. Initial oxidations can confirm this presence. The second transition time may be lower than the diffusion controlled value but the third is higher than would be expected from an irreversible catalytic or kinetic mechanism calculated for the same rate constant. Interestingly we have found empirically that no second transition can be calculated for values of the rate constants when

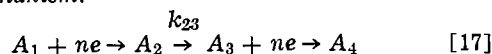
$$(k_{12}/k_{21}) \operatorname{erf} \{ (k_{12} \tau_1)^{1/2} \} \geq 1$$

Following reversible reaction.—



This case, treated previously for an irreversible following reaction [3], is characterized (Table III) by a second relative transition time which is smaller than 0.333. The even relative transition times calculated assuming this mechanism do not decay as fast as those found for an irreversible following reaction. No initial concentration of  $A_2$  would normally be observed with this system.

ECE mechanism.—



This reaction sequence is fundamentally different from the general sequence of Eq. [12], and cannot be treated by modification of the general computer program for a three component subsystem. The ECE mechanism under consideration here is the one in which  $A_3$  is reduced at potentials considerably less cathodic than those required to reduce  $A_1$ , so that on current reversal where  $A_2$  is oxidized,  $A_3$  continues to reduce. The treatment involves evaluating the cur-

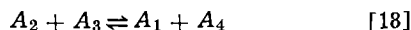
Table III. Relative transition times for cyclic chronopotentiometry with a following reaction

n	$A_1 + ne \rightarrow A_2 \xrightleftharpoons[k_{32}]{k_{23}} A_3$					
	$a_n$					
	$k_{23} \tau_1 = 0.5$	1.0	0.5	1.0	0.5	1.0
	$k_{32} \tau_1 = 0.0$	0.0	0.5	0.5	1.0	1.0
1	1.000	1.000	1.000	1.000	1.000	1.000
2	0.227	0.167	0.244	0.188	0.258	0.207
3	0.463	0.384	0.484	0.413	0.501	0.438
4	0.200	0.138	0.233	0.171	0.258	0.201
5	0.373	0.292	0.412	0.336	0.441	0.373
6	0.180	0.120	0.226	0.162	0.259	0.198
7	0.321	0.243	0.375	0.298	0.412	0.342
8	0.165	0.108	0.222	0.156	0.260	0.197
9	0.285	0.211	0.351	0.274	0.394	0.323
10	0.153	0.099	0.218	0.152	0.261	0.196

rent transforms of  $A_1$  and  $A_2$  by the method described in detail in a previous paper (7). The relative transition times are determined in the same manner as before, after inverse transformation of the concentration response (Table IV).

Several recent communications have discussed methods of treating the ECE mechanism [see ref. (7-10) and references contained therein]. An ECE reaction is indicated when another electrode couple appears at potentials less cathodic than those of the main reduction wave. The third transition time, although smaller than that observed in a diffusion controlled reaction, is not as small as that of an irreversible following reaction.

Hawley and Feldberg (8) recently pointed out that for the ECE mechanism treated above, the following additional reaction should be considered

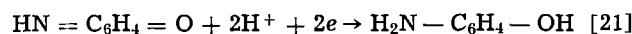
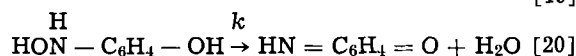
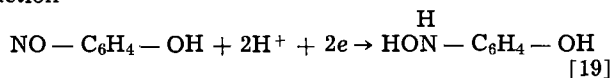


A preliminary investigation of relative transition times taking account of this reaction shows only very small differences with transition times in Table IV, so that CC is probably not useful in gauging the importance of [18] in a proposed ECE mechanism.

*Mixtures of the above cases.*—A large number of possible reaction schemes can result from the simultaneous occurrence of preceding, parallel, and following reactions. Some typical cases are shown in Table V. In general these more complicated cases are suggested when relative transition time trends similar to the simpler cases are observed, but a good fit to these simpler cases cannot be obtained with a given set of rate constants. However, as more complicated schemes are invoked to explain a reaction, more and more adjustable parameters (rate constants) are included and a better fit to the experimental data is expected. CC has the advantage over cyclic voltammetry that the rate constants of the electron transfer reactions do not enter into the consideration, but CC is probably more sensitive to adsorption of reactants, products, and intermediates. Certainly elucidation of a reaction mechanism requires that other electrochemical techniques, such as polarography and coulometry, and analysis of reaction products and intermediates, also be undertaken.

### Experimental Results

*Electroreduction of p-nitrosophenol.*—The electroreduction of p-nitrosophenol has been studied by various workers (7, 10, 11) using a variety of techniques and has been shown to follow the general ECE reaction scheme. The following reactions are given for the reaction

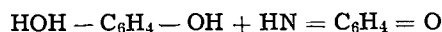


A comparison of experimental results for the relative transition times in CC with calculated ones are

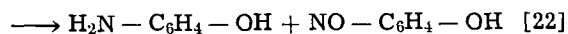
Table IV. Relative transition times for cyclic chronopotentiometry with ECE mechanism

$n$	$k_{23}$	$k_{21}$				
		$A_1 + ne \rightarrow A_2$	$A_2 \rightarrow A_3$	$A_3 + ne \rightarrow A_4$	$a_n$	
	$\tau_1 = 0$	0.2	0.4	0.6	0.8	1.0
1	1.000	1.000	1.000	1.000	1.000	1.000
2	0.333	0.241	0.182	0.142	0.114	0.093
3	0.588	0.542	0.494	0.447	0.403	0.362
4	0.355	0.228	0.161	0.120	0.094	0.078
5	0.546	0.471	0.406	0.352	0.306	0.269
6	0.366	0.215	0.145	0.106	0.082	0.066
7	0.525	0.427	0.353	0.297	0.254	0.220
8	0.373	0.203	0.133	0.096	0.074	0.060
9	0.513	0.394	0.315	0.260	0.220	0.190
10	0.378	0.192	0.123	0.089	0.068	0.055

given in Table VI. We also considered the possibility of the following reaction occurring in the reaction sequence, after the suggestion of Hawley and Feldberg (8)



fast



If the rate of Eq. [22] is assumed fast, calculated results assuming the sequence Eq. [19], [20], [22] fit the experimental data just as well as with an assumed ECE mechanism. The rate constant for Eq. [20] by either mechanism is about the same. This finding is in agreement with that for chronoamperometry (8) where it was found that for small values of  $kt$  (or in CC, small values of  $k\tau_1$ ) both mechanisms give almost the same working curves. Note that it is relatively easy to differentiate the ECE mechanism from other common possibilities with the use of cyclic chronopotentiometry. The decrease in the second relative transition time could be explained by a simple catalytic or kinetic mechanism. The 3rd transition time (and subsequent ones) serves to differentiate among these mechanisms.

*Electroreduction of titanium (IV)—hydroxylamine system.*—The reaction of electrochemically generated titanium (III) with hydroxylamine has been studied by several groups (3, 12-14). In a previous study in this series (3) we used this reaction as an example of a simple catalytic reaction scheme, i.e.



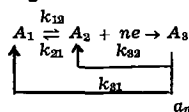
Some discrepancy was found between the theoretical calculations and the experimental results for that system. The experiments were done under conditions where the pseudo first-order rate constant ( $kC_Y$ ) had to be low because of the limitations imposed by the use of mechanical relays for switching. Because the hydroxylamine concentration had to be kept small, the ratio of hydroxylamine to titanium (IV) was only about 25 to 1. This may not have been a sufficient excess of reactant to maintain true pseudo first-order conditions. The experiments were repeated here using the electronic switching apparatus previously described (15) and ratios of hydroxylamine to titanium (IV) of 200 to 1. The relative transition times found under these conditions are in much better agreement with the simple catalytic mechanism than those given before (Table VII). The rate constant calculated from this data is also in good agreement with that reported by Christie and Lauer (12) at the concentration ratio. Further studies on this system to determine the range of pseudo first-order conditions is presently under investigation by one of us (HBH). Since this system does not give very well-defined complete chronopotentiograms, cyclic chronopotentiometry would probably not be the method of choice in an experimental study. Poor forward transitions are usually found for catalytic systems so that a method such as current reversal chronopotentiometry, which does not require going through a first transition, would be more suitable.

### Conclusion

Cyclic chronopotentiometry does appear to have some real advantages for study of complicated reactions over other techniques. Since the general solution for coupled chemical reactions in a three component subsystem has appeared (3), the method presented here can be used to prepare tables of transition times ratios for the systems discussed and many other possible reaction schemes. No assumptions are required about the rates of electron transfer, which complicate considerations in other techniques, such as cyclic volt-

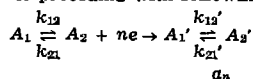
Table V. Relative transition times for cyclic chronopotentiometry for several reaction schemes

1. Reversible preceding with irreversible catalytic reaction



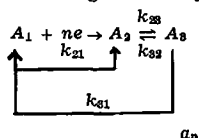
$n$	$k_{31} \tau_1 =$	—	—	—	—	—	—	—	0.5	1.0
	$k_{12} \tau_1 = 0.5$	0.5	1.0	1.0	0.5	1.0	1.0	1.0	0.5	1.0
	$k_{21} \tau_1 = 0.5$	1.0	1.0	0.5	0.5	1.0	0.5	0.5	0.5	1.0
	$k_{32} \tau_1 = 0.5$	0.5	0.5	0.5	1.0	1.0	1.0	1.0	0.5	1.0
1	1.000	1.000	1.000	1.000	1.000	1.000	1.000	1.000	1.000	1.000
2	0.227	0.227	0.227	0.227	0.167	0.167	0.167	0.167	0.167	0.105
3	0.777	0.881	0.748	0.708	0.673	0.867	0.785	0.673	0.673	0.737
4	0.254	0.268	0.250	0.244	0.169	0.182	0.177	0.169	0.169	0.105
5	0.805	0.931	0.739	0.698	0.658	0.889	0.796	0.658	0.658	0.733
6	0.267	0.286	0.257	0.250	0.169	0.186	0.180	0.169	0.169	0.105
7	0.823	0.952	0.735	0.693	0.655	0.895	0.801	0.655	0.655	0.732
8	0.274	0.294	0.260	0.252	0.169	0.187	0.181	0.169	0.169	0.105
9	0.833	0.960	0.734	0.692	0.654	0.896	0.803	0.654	0.654	0.732
10	0.277	0.297	0.261	0.253	0.169	0.187	0.181	0.169	0.169	0.105

2. Reversible preceding with following reaction



$n$	$k_{21}' \tau_1 =$	—	—	—	—	—	—	—	0.5	1.0
	$k_{12} \tau_1 = 0.5$	0.5	1.0	1.0	0.5	0.5	1.0	1.0	0.5	1.0
	$k_{21} \tau_1 = 0.5$	1.0	1.0	0.5	0.5	1.0	1.0	0.5	0.5	1.0
	$k_{12}' \tau_1 = 0.5$	0.5	0.5	0.5	1.0	1.0	1.0	1.0	0.5	1.0
1	1.000	1.000	1.000	1.000	1.000	1.000	1.000	1.000	1.000	1.000
2	0.227	0.227	0.227	0.227	0.167	0.167	0.167	0.167	0.244	0.207
3	0.555	0.611	0.547	0.517	0.468	0.527	0.469	0.436	0.577	0.522
4	0.218	0.228	0.217	0.211	0.149	0.155	0.149	0.145	0.256	0.219
5	0.477	0.536	0.460	0.430	0.380	0.438	0.373	0.342	0.524	0.462
6	0.206	0.220	0.202	0.195	0.136	0.145	0.135	0.130	0.264	0.227
7	0.427	0.484	0.405	0.376	0.330	0.384	0.319	0.290	0.495	0.431
8	0.195	0.210	0.190	0.182	0.127	0.136	0.124	0.119	0.269	0.232
9	0.389	0.444	0.366	0.338	0.296	0.347	0.282	0.256	0.476	0.413
10	0.185	0.200	0.179	0.170	0.119	0.129	0.116	0.110	0.274	0.237

3. Reversible following with catalytic reaction



$n$	$k_{31} \tau_1 =$	—	—	—	—	—	—	—	0.5	1.0
	$k_{23} \tau_1 = 0.5$	0.5	1.0	1.0	0.5	0.5	1.0	1.0	0.5	1.0
	$k_{32} \tau_1 = 0.5$	1.0	1.0	0.5	0.5	1.0	1.0	0.5	0.5	1.0
	$k_{21} \tau_1 = 0.5$	0.5	0.5	0.5	1.0	1.0	1.0	1.0	0.5	1.0
1	1.000	1.000	1.000	1.000	1.000	1.000	1.000	1.000	1.000	1.000
2	0.177	0.143	0.155	0.185	0.136	0.122	0.141	0.176	0.176	0.118
3	0.497	0.414	0.445	0.520	0.500	0.445	0.530	0.549	0.549	0.563
4	0.168	0.131	0.149	0.182	0.129	0.117	0.138	0.171	0.171	0.116
5	0.430	0.341	0.385	0.468	0.434	0.389	0.481	0.505	0.505	0.537
6	0.162	0.124	0.146	0.180	0.125	0.114	0.136	0.168	0.168	0.116
7	0.396	0.305	0.358	0.445	0.402	0.365	0.461	0.487	0.487	0.530
8	0.158	0.120	0.144	0.179	0.122	0.113	0.135	0.167	0.167	0.115
9	0.376	0.284	0.343	0.432	0.382	0.351	0.450	0.479	0.479	0.528
10	0.156	0.117	0.144	0.179	0.121	0.113	0.135	0.166	0.166	0.115

ammety. The data for CC can be interpreted without knowing the applied current, electrode area, diffusion coefficient, or concentration. It is sufficient to measure the relative transition time ratios and the first transition time in order to calculate the chemical rate constants, if the mechanism is known. If the mechanism is not known, CC can be used as a diagnostic tool to eliminate all but a few plausible reactions.

Cyclic chronopotentiometry does appear to have some real disadvantages. The effect of double layer charging and of adsorption of electroactive species has been ignored. Both tend to reduce the fraction of the current (ideally one) which goes to the faradaic reaction. Ordinary CC can be improved by the addition of derivative readout and some work along these lines has been reported (16).

Experimental

The operational amplifier apparatus previously described (15) was used for cyclic chronopotentiometry.

The p-nitrosophenol was purified according to the directions of Alberts and Shain (11). Fischer purified titanium tetrachloride was used as-received. The potential-time curves were recorded on a Tektronix 564 storage oscilloscope and photographed with a Tektronix C27 oscilloscope camera equipped with a Polaroid back.

Acknowledgment

The support of the Robert A. Welch Foundation is gratefully acknowledged. The authors are indebted to Henry N. Blount for assistance in the experimental measurements.

Manuscript received June 7, 1968.

Any discussion of this paper will appear in a Discussion Section to be published in the June 1969 JOURNAL.

Table VI. Experimental and theoretical relative transition times for electroreduction of p-nitrosophenol<sup>a</sup>

n	a <sub>n</sub>	
	Experimental	Theoretical
1. $\tau_1 = 1.34$ sec. Theoretical calculated for $k\tau_1 = 0.56$ ( $k = 0.42$ sec <sup>-1</sup> )		
1	1.000	1.000
2	0.149	0.149
3	0.449	0.457
4	0.136	0.127
5	0.372	0.362
6	0.121	0.112
2. $\tau_1 = 0.655$ sec. Theoretical calculated for $k\tau_1 = 0.26$ ( $k = 0.40$ sec <sup>-1</sup> )		
1	1.000	1.000
2	0.220	0.220
3	0.527	0.528
4	0.198	0.204
5	0.458	0.450
6	0.186	0.189

<sup>a</sup> Solution contained 1.0 mM p-nitrosophenol in a buffer of 1.0M acetic acid, 1.0M sodium acetate, and 1.0M potassium nitrate (20% v/v) ethanol). Hanging mercury drop electrode employed.

## REFERENCES

- H. B. Herman and A. J. Bard, *Anal. Chem.*, **35**, 1121 (1963).
- Ibid.*, **36**, 971 (1964).
- Ibid.*, p. 510.
- A. J. Bard and H. B. Herman, "Polarography—1964," p. 373.
- J. W. Ashley and C. N. Reilley, *J. Electroanal. Chem.*, **7**, 253 (1964).
- H. L. Hung, J. R. Delmastro, and D. E. Smith, *ibid.*, **2**, 1 (1964).
- H. B. Herman and A. J. Bard, *J. Phys. Chem.*, **70**, 396 (1966).
- M. D. Hawley and S. W. Feldberg, *ibid.*, p. 3459.
- R. S. Nicholson and I. Shain, *Anal. Chem.*, **37**, 178 (1965).

Table VII. Experimental and theoretical relative transition times for electroreduction of titanium (IV) in the absence and presence of hydroxylamine<sup>a</sup>

n	a <sub>n</sub>	
	Experimental	Theoretical
1. No hydroxylamine; $i_0 = 0.43$ ma/cm <sup>2</sup> ; $\tau_1 = 180$ msec		
1	1.00	1.00
2	0.34	0.33
3	0.62	0.59
4	0.34	0.36
5	0.58	0.55
6	0.36	0.37
2. 0.20M hydroxylamine; $i_0 = 0.74$ ma/cm <sup>2</sup> ; $\tau_1 = 86$ msec. Theoretical calculated for $kC\tau_1 = 0.70$ ( $k = 40$ l-mole <sup>-1</sup> -sec <sup>-1</sup> ) <sup>b</sup>		
1	1.00	1.00
2	0.20	0.20
3	0.67	0.65
4	0.24	0.20
5	0.66	0.63
6	0.23	0.20

<sup>a</sup> Solution contained 1.0 mM titanium (IV) and 0.20M H<sub>2</sub>C<sub>2</sub>O<sub>4</sub>. Hanging mercury drop electrode employed.

<sup>b</sup> Compare to  $k = 37$  (ref. (12)),  $k = 45$  (polarography), and  $k = 33$  (from first transition time) l-mole<sup>-1</sup>-sec<sup>-1</sup>.

- R. S. Nicholson, J. M. Wilson, and M. L. Olmstead, *ibid.*, **38**, 542 (1966).
- G. S. Alberts and I. Shain, *ibid.*, **35**, 1859 (1963).
- J. H. Christie and G. Lauer, *ibid.*, **36**, 2037 (1964).
- P. Delahay, C. Mattax, and T. Berzins, *J. Am. Chem. Soc.*, **76**, 5319 (1954).
- O. Fischer, O. Dracka, and E. Fischerova, *Collection Czech. Chem. Commun.*, **26**, 1505 (1961).
- H. B. Herman and A. J. Bard, *Anal. Chem.*, **37**, 590 (1965).
- P. E. Sturrock, *J. Electroanal. Chem.*, **8**, 425 (1964).

## A D-C Pulsed Bridge for Differential Capacity Measurements

G. M. Schmid\*

Department of Chemistry, University of Florida, Gainesville, Florida

## ABSTRACT

A d-c pulsed bridge is described for the measurement of the differential capacity,  $C_d$ , and parallel resistance,  $R_p$ , of the electrical double layer and the electrolyte resistance,  $R_e$ . The bridge consists of a d-c pulse generator, a suitable electrochemical cell, a comparison arm made up of a (variable) capacitor and a resistance box in parallel, and a resistance box in series, and an oscilloscope as null detector. Conditions of imbalance are detected separately for  $C_d$ ,  $R_p$ , and  $R_e$ . Operating on 100  $\mu$ sec pulses of about 10 ma, repetition rate 10 pulses/sec, and using a dummy circuit instead of an electrochemical cell, capacities  $< 3 \mu$ F can be measured with a precision of  $< 1$  p.p.t. Determinations of  $R_p$  and  $R_e$  are much less precise. For a "real" cell, Au in 1M HClO<sub>4</sub>, in the region 0.0 to 1.4v vs. SCE, the bridge can be balanced for capacities  $< 3 \mu$ F to  $\pm 0.01 \mu$ F and gives results in substantial agreement with, but of higher precision than, those obtained with short single d-c pulses.

Measurements of the differential capacity of electrode/electrolyte systems are usually made on conventional alternating current (a-c) bridges at frequencies  $< 100$  kHz. At ideally, or nearly ideally, polarizable interfaces this method is precise (to 0.1% or better), accurate, and entirely satisfactory, as shown by the pioneering work of Grahame (1). However, in the presence of a charge transfer reaction, and/or a charge

transfer adsorption reaction, the capacities measured are very large, are dominated by the charge transfer kinetics, and do not represent the "true" ionic double layer differential capacity (2). Also, on solid electrodes a frequency dispersion is observed, probably caused by the roughness of the electrode surface (3, 4). To obtain the ionic double layer capacity, without faradaic and frequency dispersion interference, measurements with frequencies in the MHz range are necessary, such

\* Electrochemical Society Active Member.

as those made on a transformer bridge by Lorenz (5). The interfacial impedance is then very small, typically  $< 0.01$  ohm, and precise and accurate measurements are difficult to make.

Differential capacities can also be obtained with voltage step (6) or direct current (d-c) pulse techniques (7, 8). In these methods the voltage or the current across an electrode is, at time zero, suddenly and abruptly stepped to a new value. The resulting current-time, or voltage-time, curve is observed, the slope of the curve being indicative of the capacity. It is easy to show in a Fourier analysis that the time necessary for observation represents half a cycle of an "equivalent" base frequency. Theoretically, extrapolating the current (or voltage)-time curves to zero time and measuring the slope at that point is equivalent to an a-c measurement at infinite frequency. In practice, reading a slope at one point is not possible and instrument rise times have to be considered as well, so that a minimum time span of  $0.1\text{--}1 \mu\text{sec}$  is needed to obtain meaningful data. Still, such measurements have an equivalent frequency of  $5\text{--}0.5$  MHz, are therefore relatively free of faradaic interference and are much easier to make than those on a-c bridges. Unfortunately, however, at such short times the current (or voltage)-time curves have to be displayed on oscilloscopes and the measurement suffers from the usual  $\pm 3\%$  error in the linearity of the scope amplifiers, unless extensive efforts at calibration are made.

Work on solid electrode/electrolyte interfaces has traditionally been plagued by irreproducibility. Therefore, even with their inherent  $\pm 3\%$  inaccuracy, voltage step and current pulse methods were quite useful in the study of such systems. Recently, however, work on at least one solid electrode, platinum, has become quite reproducible (9, 10), so much so that these methods can no longer be used because of their limitation in accuracy.

In the present paper a bridge type arrangement is proposed for the measurement of the differential capacity and parallel resistance operating on short ( $< 100 \mu\text{sec}$ ) repetitive (about 10 pulses/sec) d-c pulses. The bridge in its present form works at equivalent frequencies of only about 5 kHz and should therefore be used only for ideally or nearly ideally polarizable electrodes. However, we believe that extension to higher equivalent frequencies is possible. The bridge is comparable in accuracy to a conventional a-c bridge but still retains the advantages of a single d-c pulse differential capacity measurement.

#### Basic Circuit

The proposed bridge operates briefly as follows: A current pulse is divided into two equal parts, one of which flows through the cell, the other through a (variable) cell circuit analog. The potential-time function caused by the current passing through the cell is compared to that caused by the current through the cell circuit analog. If cell circuit and cell circuit analog are electrically equivalent the two potential-time curves are identical and their difference is zero at all times, thus indicating the bridge balance point.

The cell arm of the bridge (Fig. 1) consists of a voltage dropping resistor,  $R_d$ , and the electrolytic cell, represented here by the ionic differential capacity,  $C_d$ , and parallel resistor,  $R_p$ , of the test electrode, and the resistance of the electrolyte,  $R_e$ . The polarizing electrode is grounded and is assumed to be of very large area as compared to the test electrode so that it does not contribute to the electric characteristic of the cell. The second arm of the bridge is made up of a voltage dropping resistor,  $R_d'$ , identical to  $R_d$ , and a cell circuit analog of a variable capacitor,  $C_d'$ , and the variable resistors,  $R_p'$  and  $R_e'$ . A short rise time ( $< 0.1 \mu\text{sec}$ ) d-c pulse,  $i$ , is fed into point A, passes through a variable current regulator,  $R_r$ , and is divided at point B. The flow of current in the two arms of the bridge causes a potential to appear at C and at C'. These po-

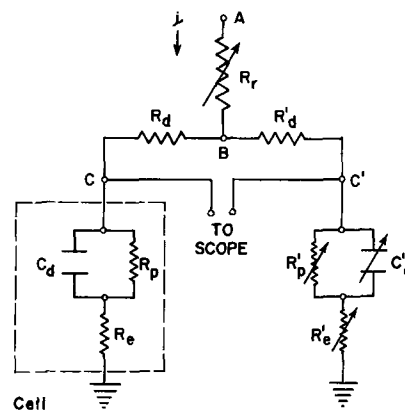


Fig. 1. Schematic bridge circuit diagram.  $R_r$ ,  $R_d$ ,  $R_d'$ , voltage dropping resistors;  $C$ ,  $C'$ , potential take-off points; cell circuit, consisting of  $C_d$ , ionic double layer capacitance,  $R_p$ , parallel resistance,  $R_e$ , electrolyte resistance; cell circuit analog consisting of  $C_d'$ ,  $R_p'$ , and  $R_e'$ .

tentials are fed into the differential input of an oscilloscope (triggered by the pulse) and their difference is displayed on the screen.

Three separate adjustments,  $C_d'$ ,  $R_p'$ , and  $R_e'$  have to be made to achieve bridge balance. This is facilitated by the following considerations:

1.  $C_d = C_d'$ ,  $R_p = R_p'$ ,  $R_e \neq R_e'$

The potential-time function developed by the pulse across  $C_d - R_p$  and  $C_d' - R_p'$  will be identical. The  $iR_e$  drop due to  $R_e$  will be different from that due to  $R_e'$  but will be constant and independent of time. The difference signal observed on the scope will show an "instantaneous" jump of the rest spot on the screen followed by a horizontal trace (Fig. 2a).

2.  $C_d \neq C_d'$ ,  $R_p = R_p'$ ,  $R_e = R_e'$

Circuit analysis shows that the potential across  $C_d - R_p$  for charging with a constant current,  $i$ , as a function of time from beginning of charging,  $t$ , is given by

$$E = i R_p [1 - \exp(-t/R_p C_d)] \quad [1]$$

The difference signal,  $\Delta E = E - E'$  ( $E'$  across  $C_d' - R_p'$ ), appearing on the scope can be written

$$\Delta E = i R_p [\exp(-t/R_p C_d') - \exp(-t/R_p C_d)] \quad [2]$$

For any time  $t$ , the slope of this curve is

$$\begin{aligned} d(\Delta E)/dt \\ = (i/C_d) \exp(-t/R_p C_d) - (i/C_d') \exp(-t/R_p C_d') \end{aligned} \quad [3]$$

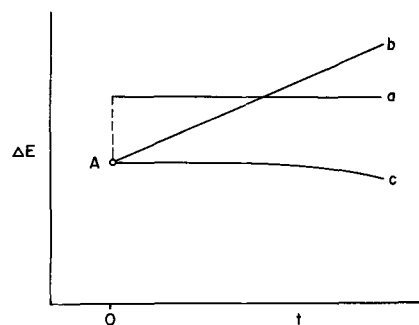


Fig. 2. Schematic oscilloscope traces expected for

- a:  $C_d = C_d'$ ,  $R_p = R_p'$ ,  $R_e \neq R_e'$  (case 1)
- b:  $C_d < C_d'$ ,  $R_p = R_p'$ ,  $R_e = R_e'$  (case 2)
- c:  $C_d = C_d'$ ,  $R_p < R_p'$ ,  $R_e = R_e'$  (case 3)

A: cathode ray beam rest spot.

and, at  $t = 0$

$$[d(\Delta E)/dt]_{t=0} = i(1/C_d - 1/C_d') \quad [4]$$

For  $t \ll R_p C_d'$ ,  $t \ll R_p C_d'$ , Eq. [2] can be linearized to

$$\Delta E = i(1/C_d - 1/C_d') t, t \ll R_p C_d, t \ll R_p C_d' \quad [5]$$

Thus, for short times,  $\Delta E$  is linear with time, the slope of the difference potential-time curve,  $d(\Delta E)/dt$ , is constant, starting at  $t = 0$  with a finite value (Eq. [4]). The slope is positive for  $C_d' > C_d$ , negative for  $C_d' < C_d$  ( $i > 0$ ) (Fig. 2b).

$$3. C_d = C_d', R_p \neq R_p', R_e = R_e'$$

For this case, the difference signal is given by (see Eq. [1])

$$\Delta E = i(R_p - R_p') + i [R_p' \exp(-t/R_p' C_d) - R_p \exp(-t/R_p C_d)] \quad [6]$$

and, for any time,  $t$

$$d(\Delta E)/dt = (i/C_d) [\exp(-t/R_p C_d) - \exp(-t/R_p' C_d)] \quad [7]$$

$$\text{For } t = 0, [d(\Delta E)/dt]_{t=0} = 0$$

At short times,  $t \ll R_p C_d$ ,  $t \ll R_p' C_d$ , after linearizing

$$E_{t \rightarrow 0} = 0 \quad [8]$$

i.e., for short times the slope of the  $\Delta E$  vs.  $t$  curve is zero, independent of  $t$ . Thus, for this condition, the oscilloscope trace will start from the rest point tangentially to the time axis. For longer times, Eq. [7], the slope will be  $> 0$  for  $R_p > R_p'$ ,  $< 0$  for  $R_p' > R_p$  ( $i > 0$ ) (Fig. 2c).

The difference between the two potential-time functions across  $C_d - R_p - R_e$  and  $C_d' - R_p' - R_e'$  will be zero only if all the circuit elements in the two bridge arms are individually identical. Using criteria 1 to 3 various conditions of unbalance can be detected and corrected.

Repetitive current pulses are needed to balance the bridge. It is assumed that repetition rate and pulse amplitude are selected such that the cell is not noticeably displaced from its equilibrium or its steady state.

As seen from the discussion of criteria 1 to 3 above, for short pulses, differences in capacity are much more readily detected than differences in parallel and series resistance. This is confirmed experimentally (see below). Therefore, in what follows, emphasis is placed on the measurement of the ionic differential capacity.

### Test Results

The comparison arm of the bridge consisted of a parallel combination of a General Radio (GR) Type 1424-A Standard Polystyrene Decade Capacitor,  $1 \mu F$  per step, and a GR Type 1412-BC Decade Capacitor representing  $C_d'$ , a GR Type 1432-J Decade Resistor serving as  $R_p'$ , and a GR Type 1432-K Decade Resistor making up  $R_e'$ . This gave a range of  $\sim 50$  pF to  $11.111100 \mu F$  in 100 pF steps and a Vernier dial with 1 pF divisions, nominal accuracy  $\pm 0.25\%$  for the  $1 \mu F$  steps,  $\pm 1.0\%$  for steps  $< 1 \mu F$  (at 1 kHz), for the capacity, a range for  $R_p'$  of 1-11,110 ohms in 1 ohm steps, nominal accuracy  $\pm 0.025\%$  for settings above 100 ohms/step, and a range of 0.1-1111 ohms, same accuracy, for  $R_e'$ . Current pulses were supplied to the bridge by a GR Type 1398-A Pulse Generator. No attempt was made to minimize induction and this necessitated the use of rather long pulses of 100  $\mu sec$  duration. A repetition rate of 10 pulses/sec was found satisfactory. The pulses were dropped through two ( $R_d$  and  $R_d'$ ) GR Type 500-M resistors, 5 kohm  $\pm 0.025\%$ . Pulse current was approximately 10 ma. The difference signal was observed on a Tektronix Type RM35A oscilloscope with a Tektronix Type 1A7 plug-

in unit. The scope was normally operated at 500  $\mu v/cm$  and 10  $\mu sec/cm$ .

The bridge was tested using for  $C_d$  commercial capacitors, nominal 2.0, 1.0, 0.33, 0.25, and 0.1  $\mu F$ , for  $R_p$  resistors (carbon type) nominal 47, 330, 1k, 10k, 110k, 1M, and 10 Mohms, for  $R_e$  resistors (carbon type) nominal 27, 150, and 910 ohms, in various combinations. The components were measured on a GR Type 1608-A Impedance Bridge of 1 kHz to 0.1%. Values of  $R_p > 100$  k-ohm could not be measured on the pulsed bridge with any kind of accuracy. The decade box serving as  $R_p'$  was then replaced by a resistor equal in nominal value to  $R_p$  and no further attempt was made to balance the bridge for  $R_p$ . For each combination  $C_d - R_p - R_e$  the bridge was balanced for  $C_d$  20 times. Results for two capacitors are given in Table I. The balance was checked for  $R_p < 100$  k-ohm and  $R_e$  periodically, precision generally being within a few per cent. Representative values are included in Table I.

It is seen that generally the agreement between the  $C_d$  value obtained on the pulsed bridge and that measured on the 1608-A is within  $< 1\%$ , often around 0.2%, and this is well within the accuracy of the capacitors used in the pulsed bridge. The internal consistency of the pulsed bridge is excellent, the standard deviation being usually  $< 1$  p.p.t., often 0.1 p.p.t.

While working with the pulsed bridge some interaction was observed between  $C_d$  and  $R_p$ . At a given  $C_d$ , the smaller  $R_p$ , the more difficult it becomes to obtain a precise balance for  $C_d$  (see Table I). Evidently, the time constant  $R_p C_d$  becomes too small to achieve the condition  $t \ll R_p C_d$  (Eq. [5] and [8]) within the times accessible to the equipment used ( $R_p$  also appears as a factor in Eq. [2]). Also, the bridge loses precision rapidly for  $C_d > 3 \mu F$ . This limitation could possibly be removed by using larger pulse currents, but this was not tried.

### Application

The pulsed bridge was used to measure the capacity of a gold electrode in 1M HClO<sub>4</sub> in the range 0.0 to +1.4v vs. a saturated calomel electrode (SCE). This system is (nearly) ideally polarizable over the lower part of this potential region, faradaic processes are absent, and measurements at low frequencies (5 kHz) should be satisfactory. At the more anodic potentials adsorbed "oxygen" and/or an oxide film is formed. Nevertheless, the pulsed bridge in its present form gives results in substantial agreement with fast single pulse measurements (see below).

The gold electrode was made from gold wire (Engelhard Industries, Fine Gold) by melting the tip of the wire to a bead using a hydrogen flame. The bead, ap-

Table I. Test results of pulsed bridge

Test capacitor:	$C_d = 0.941 \pm 0.001 \mu F$ (at 1 kHz)			Test capacitor: $C_d = 0.3373 \pm 0.0003 \mu F$ (at 1 kHz)			
$C_d^*$ $\mu F$	$\pm$ Standard deviation** p.p.t.	$R_p$ , ohms	$R_e^*$ , ohms	$C_d^*$ $\mu F$	$\pm$ Standard deviation** p.p.t.	$R_p$ , ohms	$R_e^*$ , ohms
0.946	1.0	45.3*	29	0.340	3.5	45.2*	29
0.943	0.7		164	0.333	12.0	46.1*	163
0.953	1.1		948	0.335	9.0	45.5*	946
0.9394	0.5	992*	28.8	0.33641	0.09	990*	28.9
0.9367	0.3	957*	163.3	0.3361	0.3		163.6
0.941	1.1	1001*	947.4	0.3364	0.7		947.8
0.9361	0.3	6470*	163.4	0.3360	0.0	8650*	163.8
0.9400	0.1	100 k***	29	0.33686	0.1	100 k***	29.0
0.9396	0.1		163.7	0.3368	0.0		164.2
0.9392	0.1		948.2	0.3365	0.3		949.2
0.9392	0.1	1 M***	163.7	0.33647	0.1	1 M***	164.1
0.9397	0.1	10 M***	28.7	0.3369	0.0	10 M***	28.8
0.9390	0.1		163.7	0.33653	0.1		163.6
0.9406	0.1		947.2	0.33684	0.03		947.4

\* Measured on pulsed bridge; average of 20 determinations.

\*\* Based on 20 determinations.

\*\*\* Nominal values.



proximately 0.075 cm<sup>2</sup> in apparent area, was mounted in a Teflon holder, washed in hot chromic acid cleaning solution, degreased with acetone, and thoroughly rinsed with triple distilled water. The latter was distilled once from alkaline permanganate in Pyrex and twice more in a quartz still. Solutions, 1M HClO<sub>4</sub>, were made up from B and A reagent grade 70% HClO<sub>4</sub> and triple distilled water. They were treated for a minimum of 12 hr with activated charcoal purified according to Barker. Helium was passed through for at least 2 hr prior to, and during, a run. The all Pyrex cell was of conventional design. It contained a large area platinum wire gauze electrode concentric to the gold test electrode, and two SCE's, each separated from the main compartment by a closed stopcock.

The gold electrode was polarized with a Sensitive Research Instrument Corporation Type PV potentiometer through one of the SCE's. Potentials were measured with respect to the other SCE (connected to the test electrode through a Haber-Luggin Capillary) with a Keithley Type 660 Differential Voltmeter. They are reported with respect to SCE. The pulsed bridge was connected to the test electrode and the grounded platinum wire gauze. The pulse generator was protected from the polarizing circuit with a 1N270 diode. The comparison arm of the bridge was not isolated from the polarizing circuit. This arm provides an external connection for the cell Au/1M HClO<sub>4</sub>/Pt through  $R_d$ ,  $R_d'$ ,  $R_p'$ , and  $R_e'$ . Thus, special care is necessary during current-potential measurements. (They were not made in this study.) All connections were removed from the cell during open circuit rest periods. A schematic circuit diagram is shown in Fig. 3.

Before each experiment, the test electrode was treated briefly and alternately in situ at -0.3 and +1.4v, always ending with -0.3v. Capacities were then measured as a function of potential in 100 mv steps, starting at 0.0v. The bridge could be balanced in all cases to  $\pm 0.01 \mu\text{F}$  or to  $\pm 0.3$  to 1% ( $\pm 0.13 \mu\text{F}$ /apparent cm<sup>2</sup>). The potential was changed every 10 min, this being sufficient time for the capacity to reach a steady state. Spot checks showed no change in capacity after 10 min for up to 2 hr. After 1.4v had been reached, the electrical equipment was disconnected and the cell left at open circuit overnight. The capacity determinations were repeated the next day.

The results of three such experiments, i.e., six determinations, are shown in Table II together with the standard deviation for each potential. Reproducibility is acceptable, the average standard deviation being  $\pm 6\%$ . The reproducibility within an experiment (two

Table II. Differential capacity of gold in 1M HClO<sub>4</sub>

Potential v. vs. SCE	Capacity $\mu\text{F}/\text{apparent cm}^2$	$\pm$ Standard deviation in %*
0.0	43.7	5.2
0.1	40.3	6.2
0.2	41.8	8.5
0.3	39.4	4.2
0.4	33.8	5.6
0.5	29.4	5.1
0.6	28.2	4.5
0.7	33.2	6.0
0.8	40.6	5.6
0.9	40.8	6.8
1.0	37.6	5.2
1.1	34.5	8.5
1.2	33.1	6.0
1.3	35.1	6.4
1.4	35.4	7.3

\* Average of six measurements.

subsequent determinations > 12 hr apart, same bead, same solution) can be much better. The three experiments had individual average deviations (not shown) of  $\pm 2.4$ ,  $\pm 3.8$ , and  $\pm 6.2\%$ .

Between -0.3 and -0.1v the capacity decreases from > 10  $\mu\text{F}$  at -0.3v for a bead 0.075 cm<sup>2</sup> in apparent area. This large capacity is not found in a (short) single pulse measurement (11, 12). The pulsed bridge in its present form uses 100  $\mu\text{sec}$  pulses. In an a-c measurement this would correspond to a base frequency of 5 kHz. In the region of beginning hydrogen evolution (< -0.2v) a faradaic impedance is expected for such a measuring frequency (2) and its influence is indeed observed with the pulsed bridge.

Comparison of the data in Table II with those obtained previously with a single pulse method (11) shows that the previous capacity minimum at 0.9-1.0v is shifted to 0.6v, the previous maximum at 1.2-1.3v to 0.8-0.9v. This seems to be due to a difference in pre-treatment, the previous (planar) electrodes having been etched in aqua regia, the present ones (beads) melted in a hydrogen flame. Beads etched in aqua regia showed a capacity minimum at 0.8v and a maximum at 1.0v in better agreement with previous data (the maximum is less pronounced).

It is thus evident that the pulsed bridge gives results in substantial agreement with, and of higher precision than, a single pulse capacity measurement.

#### Acknowledgment

This research was sponsored by AFOSR (SRC)-OAR, USAF, Grant No. AF-AFOSR-1034-66. The author gratefully acknowledges this support.

Manuscript received June 14, 1968.

Any discussion of this paper will appear in a Discussion Section to be published in the June 1969 JOURNAL.

#### REFERENCES

- D. C. Grahame, *Chem. Revs.*, **41**, 441 (1947).
- E. g., B. E. Conway and E. Gileadi, *Trans. Faraday Soc.*, **58**, 2493 (1962).
- T. I. Borisova, B. V. Ershler, and A. N. Frumkin, *Zhur. Fiz. Khim.*, **22**, 925 (1948).
- R. DeLevie, *Electrochim. Acta*, **10**, 113 (1965).
- W. Lorenz, *Z. Physik. Chem. (NF)*, **26**, 424 (1960).
- H. A. Laitinen and D. K. Roe, *Coll. Czech. Chem. Comm.*, **25**, 3065 (1960).
- J. S. Riney, G. M. Schmid, and Norman Hackerman, *Rev. Sci. Instr.*, **32**, 588 (1961).
- L. Ramaley and C. G. Enke, *This Journal*, **112**, 943 (1965).
- S. Schuldiner and T. B. Warner, *J. Phys. Chem.*, **68**, 1223 (1964).
- T. B. Warner and S. Schuldiner, *This Journal*, **111**, 992 (1964).
- G. M. Schmid and Norman Hackerman, *ibid.*, **110**, 440 (1963).
- G. M. Schmid, *Electrochim. Acta*, **12**, 449 (1967).

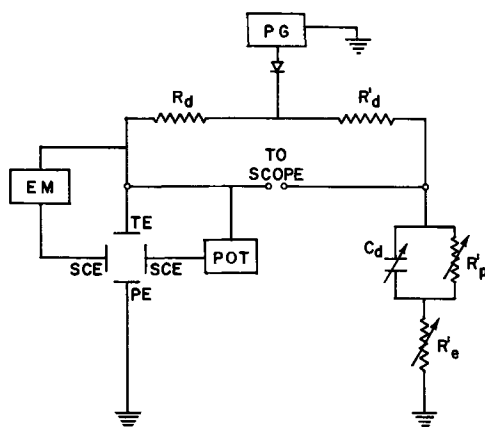


Fig. 3. Schematic circuit diagram. TE, gold electrode; PE, Pt wire gauze; SCE, saturated calomel electrode;  $R_d$ ,  $C_d$ ,  $R_p$ ,  $R_e$ , comparison bridge arm; PG, pulse generator; EM, Keithley differential voltmeter; POT, polarizing potentiometer.



## The Growth of Aluminum Oxide Films on Copper-Aluminum Alloys

S. R. J. Saunders and M. J. Pryor

Metals Research Laboratories, Olin Mathieson Chemical Corporation, New Haven, Connecticut

Pure aluminum oxidizes at temperatures above 300°C to form thin films of "amorphous"  $\gamma$ -Al<sub>2</sub>O<sub>3</sub> by parabolic kinetics (1). Despite the fact that at 450°C and above roughly cylindrical crystals of  $\gamma$ -Al<sub>2</sub>O<sub>3</sub> nucleate and grow at the amorphous oxide-metal interface they do not affect the continued growth of the amorphous film. The temperature sensitivity of the parabolic growth of amorphous aluminum oxide films is high, and recent work suggests a value of around 54 kcal/mole for the activation energy.

Habraken *et al.* (2) recently reported a low activation energy of from 8-12 kcal/mole for the growth of complex oxide films including an aluminum oxide layer on a copper-7% Al alloy and on a copper-5% Al-5% Sn alloy. Since the over-all oxidation process of the copper-aluminum alloys is likely controlled by the film of aluminum oxide such a wide divergence of activation energy is puzzling. Accordingly, in the present work we have studied the growth kinetics of aluminum oxide films formed upon a copper 3% aluminum, 2% silicon alloy. Kinetics of growth of the aluminum oxide film have been studied independently of the presence of overlaying oxides of copper so as to permit a more ready comparison of the activation energies for the formation of alumina on copper-aluminum alloys with that of the formation of similar films on pure aluminum.

The copper-aluminum-silicon alloy specimens were polished in a solution of equal parts of concentrated nitric, sulfuric, and acetic acids, washed in water and methanol. They were heated for varying periods of up to 30 min at 450°, 600°, and 740°C. A uniform layer of  $\gamma$ -Al<sub>2</sub>O<sub>3</sub> is formed at temperatures above 300°C. This layer is overlaid by films of CuO and Cu<sub>2</sub>O. The maximum temperature (740°C) was low enough to prevent the formation of cupric aluminate. The soluble copper oxides were removed by dissolution in 2% (vol) sulfuric acid at room temperature. Separate studies showed that the underlying  $\gamma$ -Al<sub>2</sub>O<sub>3</sub> resists attack by this acid for prolonged periods. Weight loss permitted determination of the quantities of copper oxides removed. The residual films were identified as  $\gamma$ -Al<sub>2</sub>O<sub>3</sub> by reflection electron diffraction. The thickness and electrical properties of the aluminum oxide films were measured using a capacitance-loss technique described by one of the authors in earlier publications (3, 4).

The results of aluminum oxide thickness determinations as a function of time and temperature are shown in Fig. 1. The formation of  $\gamma$ -Al<sub>2</sub>O<sub>3</sub> obeys simple parabolic kinetics to periods of up to 30 min. An activation energy of 19.1 kcal is obtained from an Arrhenius plot of these data (Fig. 2); this value is approximately one-third of the activation energy obtained previously for the parabolic oxidation of aluminum which is also depicted in the same figure. Table I shows the relative amounts of copper and aluminum oxides formed in a fixed time at the three temperatures. It may be seen that the proportion of copper oxides decreases as the temperature increases. Therefore the over-all oxidation process of the Cu-3% Al-2% Si alloy has a lower temperature sensitivity and

a lower activation energy than that measured for the formation of  $\gamma$ -Al<sub>2</sub>O<sub>3</sub> alone on the copper alloy. This is consistent with the observations of Habraken for somewhat similar copper alloys.

It is of interest to consider why the temperature sensitivity of the parabolic formation of  $\gamma$ -Al<sub>2</sub>O<sub>3</sub> on the Cu-3% Al-2% Si alloy should be so much lower than that of the formation of a structurally similar film on pure aluminum. A significant clue is provided by a plot of parallel a-c resistance at 1000 cps *vs.* thickness of the thermal oxide films formed both on pure aluminum (1) and on the copper-aluminum-silicon alloys (Fig. 3). It is clear from Fig. 3 that very thin aluminum oxide films on the copper alloy have lower resistivity than those on pure aluminum, whereas the reverse is true at higher thicknesses.

The foregoing data can be rationalized on the basis of a change in composition, defect structure, and ionic resistance of the  $\gamma$ -Al<sub>2</sub>O<sub>3</sub> film formed on the copper alloy. Because the aluminum oxide film must be permeable not only to the outward diffusion of aluminum but also copper ions it must surely contain a certain number of this latter species. Since at higher temperatures and longer times than those reported in this work, cupric aluminate will also form as an oxidation product, the amount of copper ions retained in the aluminum oxide films will increase with increasing temperature at constant time. This factor will produce much more variability in the defect structure and conductivity of the aluminum oxide films formed on the copper alloy than that which occurs when the substrate is pure aluminum.

There must be a strong tendency for the copper ions present in the aluminum oxide to associate with the substantial proportion of cation vacancies that exist in stoichiometric  $\gamma$ -Al<sub>2</sub>O<sub>3</sub>. These cation vacancies should represent the preferred paths for the outward

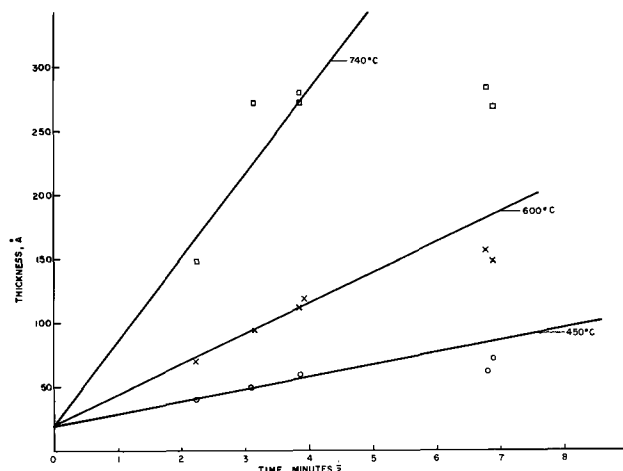


Fig. 1. Relationship between oxide thickness and the square root of time for the growth of aluminum oxide on copper 3% aluminum, 2% silicon at 450°, 600°, and 740°C.

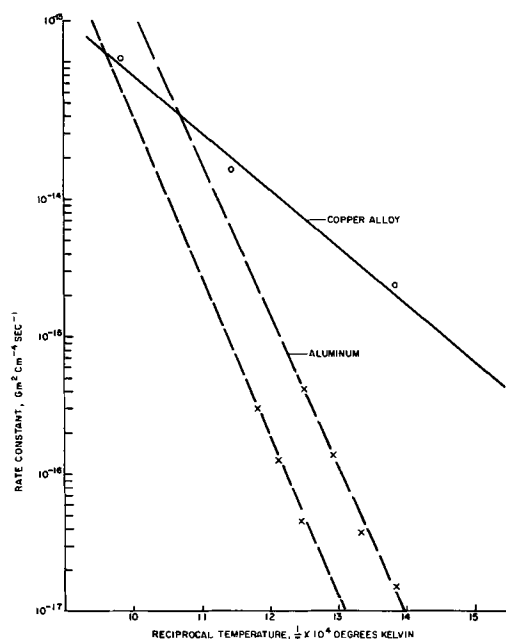


Fig. 2. Arrhenius plot of the logarithm of the rate constant for the formation of aluminum oxide on aluminum and copper, 3% aluminum, 2% silicon vs. the reciprocal of the temperature.

diffusion of both aluminum and copper ions. As more copper ions are introduced into the  $\gamma$ - $\text{Al}_2\text{O}_3$  structure by raising the oxidation temperature the number of diffusion paths must simultaneously decrease. This must in turn result in a reduced temperature sensitivity for the formation of the copper-doped aluminum oxide film. The fact that cation vacancies are preferred sites of diffusion for both aluminum and copper ions also results in a reduction of the proportion of copper oxides formed with increasing temperature, thereby making the activation energy for the total oxidation process even less than that for the formation of the copper-doped aluminum oxide itself.

The above interpretation is directly supported by calculation of the value of  $A$  the exponential constant in the Arrhenius equation (below) using the activation energies derived from Fig. 2.

$$R = Ae^{-Q/RT}$$

where  $R$  is the rate constant and the remaining symbols are conventional. Although many different interpretations of the significance of the value of  $A$  exist for heterogeneous reactions most emphasis has been placed on interpretations relating  $A$  to the number of active sites. Three values of  $A$  were calculated from Fig. 2, two for the formation of  $\gamma$ - $\text{Al}_2\text{O}_3$  on aluminum (above and below  $525^\circ\text{C}$ ) and one for the formation of copper doped  $\gamma$ - $\text{Al}_2\text{O}_3$  on the copper-aluminum-silicon alloy. These are given below in Table II.

The very low values of  $A$  for the formation of copper doped  $\gamma$ - $\text{Al}_2\text{O}_3$  on the copper alloy compared

Table I. Oxide composition on copper-aluminum-silicon alloy

	450°C, %	600°C, %	740°C, %
w/o $\text{Al}_2\text{O}_3$	10.5	21.0	35.5
w/o $\text{Cu}_2\text{O}$	89.5	79.0	64.5

Table II. Pre-exponential constant  $A$

$\gamma$ - $\text{Al}_2\text{O}_3$ on aluminum	$2.37 \times 10^{-1} \text{ g}^2 \text{ cm}^{-4} \text{ sec}^{-1}$	(below $525^\circ\text{C}$ )
	$2.26 \times 10^{-2} \text{ g}^2 \text{ cm}^{-4} \text{ sec}^{-1}$	(above $525^\circ\text{C}$ )
$\gamma$ - $\text{Al}_2\text{O}_3$ on copper alloy	$1.20 \times 10^{-9} \text{ g}^2 \text{ cm}^{-4} \text{ sec}^{-1}$	

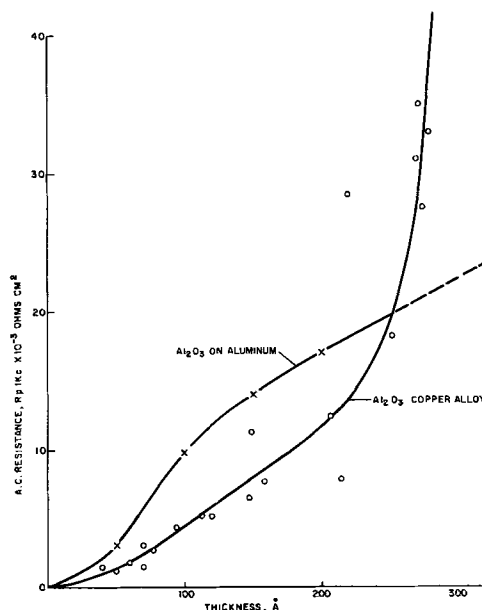


Fig. 3. Relationship between the a-c resistance and the thickness of thermally formed aluminum oxide on aluminum and copper, 3% aluminum and 2% silicon.

with either value for the formation of  $\gamma$ - $\text{Al}_2\text{O}_3$  on aluminum strongly suggests a considerable reduction in the number of cation vacancies as diffusion paths in the former structure, i.e., consistent with the defect structure-temperature relationship described earlier.

The variation of defect structure of the  $\gamma$ - $\text{Al}_2\text{O}_3$  film formed on the copper-aluminum-silicon alloy in which more copper ions fill cation vacancies in the  $\gamma$ - $\text{Al}_2\text{O}_3$  as the temperature is raised appears to account for the observed kinetics (Fig. 1) as well as for their reduced temperature dependence (Fig. 2). However, the a-c resistance vs. thickness curves (Fig. 3) deserve brief amplification. The measurement of a-c resistance at 1 kc is generally acknowledged to sense both electronic and ionic relaxation effects. At high thickness (high temperature) the resistivity of copper-doped  $\gamma$ - $\text{Al}_2\text{O}_3$  is around two times higher than that of  $\gamma$ - $\text{Al}_2\text{O}_3$  formed on aluminum. This appears to be primarily an ionic resistance effect due to filling of the cation vacancies by copper ions. However, at low thicknesses (and temperature) a reversal in resistivity is observed despite the fact the  $\gamma$ - $\text{Al}_2\text{O}_3$  formed on the copper alloy must contain some (but a smaller number) of copper ions. However, as copper ions occupy the cation vacancies additional electrons must be added to the structure for electrical neutrality. Accordingly, at low thicknesses and modest copper substitution the primary effect is the enhancement of a n-type structure showing higher electronic conductivity. As substitution is increased (by increasing temperature) the electronic conductivity must continue to rise, but the reduction of the number of cation sites becomes so pronounced so as to overwhelm electronic effects and thereby limit growth rate.

### Acknowledgments

The authors wish to thank the Brass Division of the Olin Mathieson Chemical Corporation for their support of this work and for their permission to publish the results.

Manuscript received June 6, 1968.

Any discussion of this paper will appear in a Discussion Section to be published in the June 1969 JOURNAL.

### REFERENCES

1. A. F. Beck, M. A. Heine, E. J. Caule, and M. J. Pryor, *Corrosion Sci.*, **7**, 1, 1967.
2. C. Rogister, A. Davin, D. Coutsouradis, and L.

Habraken, "Development of Stainless Copper Alloys for Architectural Purposes" Centre National de Recherches Metallurgiques, (Non Ferrous Division), Liege, Belgium, NF 5/67-Cu15 March, 1967.

3. M. A. Heine and M. J. Pryor, *This Journal*, **110**, 1205 (1963).
4. M. A. Heine, D. S. Keir, and M. J. Pryor, *ibid.*, **112**, 24 (1965).

## Pulsed Electrolysis of Wet Hydrogen Fluoride

J. A. Donohue and A. Zletz

Research and Development Department, American Oil Company, Whiting, Indiana

Although preparative electrolyses are usually carried out at a constant applied potential, recent work has shown that a pulsed potential can be used to advantage in varying the types of products formed (1) and in improving the operation of fuel cells (2). Our studies of the production of oxygen difluoride by electrolysis of wet hydrogen fluoride with a nickel/nickel fluoride anode likewise showed that periodic interruption of the voltage is advantageous (3). We have now improved our experimental and analytical techniques and have observed how the yields are affected by the water and potassium fluoride concentrations of the electrolyte as well as by the applied voltage. Our results reemphasize the importance of voltage interruption in maximizing oxygen difluoride and reducing ozone and oxygen, the other major products at the anode. In addition, we have found that continuous electrolysis of wet hydrogen fluoride is a potentially good method for producing ozone.

Although much work has been done on the preparation of ozone by electrolysis of aqueous acids (4), it has been reported that only sulfuric and perchloric acids give reasonable yields, and only platinum and its alloys are suitable anode materials (5). With respect to aqueous hydrogen fluoride, some investigators suggest that only small amounts of ozone are produced (6-8), and one claims that none is formed (9).

Of necessity, comments on the mechanism of any electrolysis in hydrogen fluoride have been pessimistic (10) or highly speculative (11), mainly because product analyses have been incomplete or the results have not been reproducible. Since our results largely avoid such obstacles, they provide a less speculative basis for predicting mechanism.

### Experimental

With the exception of some recent improvements, the electrolysis cell and analytical equipment (g.c. for determination of the gaseous products and infrared for water in the electrolyte) have already been described (3,12). The infrared cells are now made by flattening and polishing Kel-F tubing. These did not fog in wet hydrogen fluoride so the usual absorbance *vs.* concentration calibration can now be used. Modifications in the electrolysis cell include the introduction of the helium flush gas through a Kel-F gas dispersion disk below the electrodes to ensure better mixing of the electrolyte and removal of the product gases. Also, the anodes are smaller, ranging from 2.5 to 7.5 cm<sup>2</sup>. Both electrodes were untreated 20 gauge nickel sheet with about ¼ in. spacing between cathodes and the anode. A satisfactory Hg/Hg<sub>2</sub>F<sub>2</sub> reference electrode was not developed until late in this work and was used here only for the study of the anode voltage. Details of its construction will be given later (13).

Except during interruption, the applied voltage is constant during an entire run. Changing the voltage during a run will generally result in changing, non-reproducible yields. The applied voltage is adjusted manually at the power supply to maintain a pre-

determined value, which is displayed on a vacuum-tube voltmeter attached to the electrodes. Voltage decrease during interruption was not controlled, but cell potential generally fell to about 2.8v. However, no effect on product yields was noted when the voltage decrease was deliberately adjusted to within  $\pm 1v$  of the usual decrease, i.e., from 1.8 to 3.8v.

The electrolyte was prepared from Matheson anhydrous hydrogen fluoride (99.9%), reagent grade potassium fluoride, and distilled water. Its initial water concentration was 0.1-0.2 m/o (mole per cent) as determined by Karl Fischer titration. The same electrolyte was used in many experiments, since expended hydrogen fluoride and water were replaced. The electrolyte temperature was generally not controlled and usually warmed slightly above bath temperature (0°C) due to iR heating and circulation to infrared cell. This was acceptable at 1.0 m/o KF since temperature studies showed little effect on yield between 0° and 12°C. However, at higher KF concentrations there were appreciable yield variation at higher temperatures. Thus in this case the electrolyte temperature was held constant.

Runs generally were carried out for 4 to 5 hr at selected voltages, electrolyte concentrations, and interruption schedules. Gaseous products were analyzed at 10- to 20-min intervals. The electrolyte was analyzed for water before and after a run, and water was added during a run to maintain the desired concentration.

Two variables associated with interruption are frequency and duration. Frequency was not studied extensively, but preliminary results showed that one interruption every 2 min allowed optimum oxygen difluoride yields and stable current densities. Duration was ordinarily 1 sec, but sometimes was increased to prevent a drop in oxygen difluoride yields when other variables were changed.

### Results and Discussion

Figure 1 compares typical continuous and interrupted runs. Since there is always an induction period of about 2 hr, during which yields and current density change rapidly, comparisons among runs are best made with yields measured during the 4th hr (180-240 min). In a typical continuous run, oxygen difluoride yields pass through a maximum while ozone and oxygen yields continue to increase. However, these yields are not reproducible. By contrast, after the induction period, the interrupted runs show higher oxygen difluoride and lower ozone and oxygen yields, all of which are constant. As shown by the shaded areas in Fig. 1, interrupted runs are reproducible despite considerable variation in current density.

These product distributions doubtless reflect different reactions occurring at the anode-electrolyte interface. As continuous electrolysis gives changing product distributions, it presumably causes a continuously changing anode interface. Conversely, as properly timed pulsed electrolysis leads to stable product distributions, a steady state must develop at the interface. This particular steady state also results in greater fluorination of the substrate, water. Thus we predict that pulsed electrolysis of other

substrates in hydrogen fluoride should lead to improved yields of fluorine compounds.

To improve our understanding of the interruption technique and reactions at the interface we made studies of the reaction parameters. Some phenomena that occur at very low water concentrations are illustrated in Fig. 2. In a continuous run started at 0.1 m/o water, the yields of oxygen and oxygen difluoride are both less than 5%; with a dry electrolyte the rest of the current presumably goes to form fluorine or corrosion products (3). When the water concentration is increased at 2 hr to 0.26 m/o but voltage is not interrupted, oxygen yield jumps to 22%, oxygen difluoride increased to only 9-10%, and no ozone is yet detected. But a shift at 4 hr to interrupted operation at this same water concentration causes the oxygen difluoride yield to jump to 45%; ozone definitely becomes a product, and oxygen yield decreases slightly.

We postulate that the products formed at 2-4 hr primarily result from fluorine reacting chemically with the water and so preventing it from reaching the anode. This reaction produces only small amounts of oxygen difluoride and little, if any, ozone (14). Under such conditions, interruption is necessary to permit water to react at the anode interface. Then, since water has a lower oxidation potential (15), it is electrochemically decomposed before fluoride ion (fluorine precursor), and so leads to a sequence of reactions that produce ozone and higher oxygen difluoride yields.

At higher water concentrations, interruptions have a different function. If the only function were to allow water to reach the anode, shorter interruptions suffice at higher water concentrations. But as Fig. 3 shows, the opposite is true, longer interruptions are required to maintain oxygen difluoride yields. Since the decrease in oxygen difluoride at shorter interruptions is balanced by an increase in ozone, the decomposition products of water apparently are reacting with each other to form ozone rather than with some fluorine species to form oxygen difluoride. Consequently, interruption must also prevent a buildup of the decomposition products of water at the anode.

As shown in Fig. 3, during continuous electrolysis the 4th-hr ozone yield exceeds 30%, which is comparable to the best reported for electrolysis of other

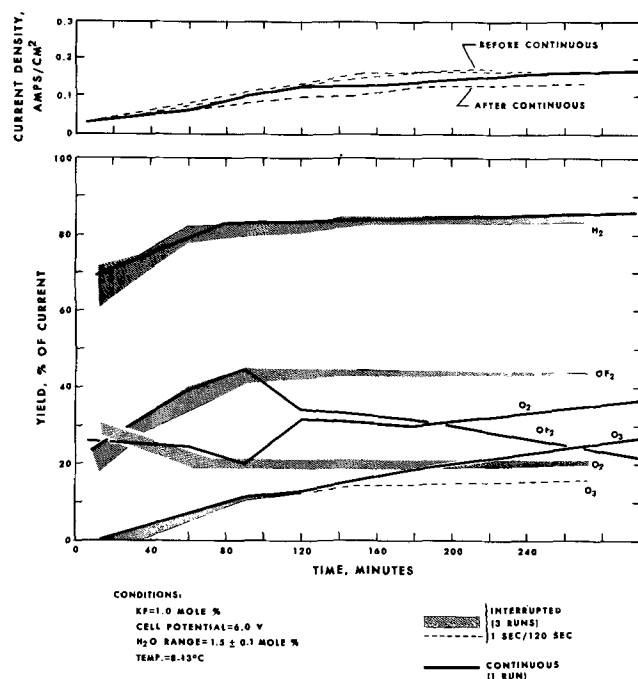


Fig. 1. Continuous vs. interrupted operation at constant cell potential.

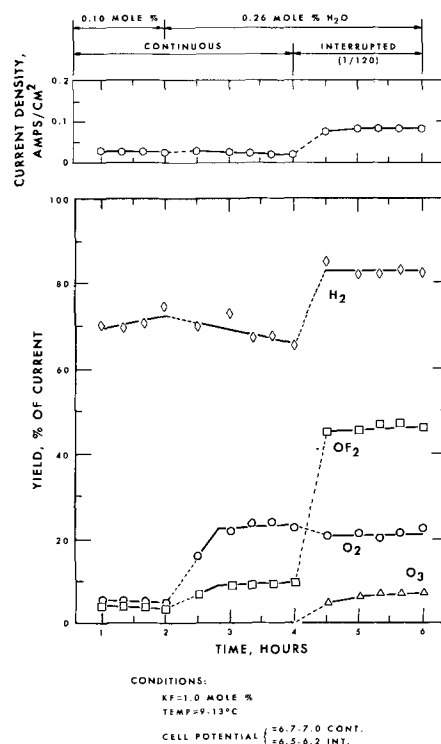


Fig. 2. Interruption effect

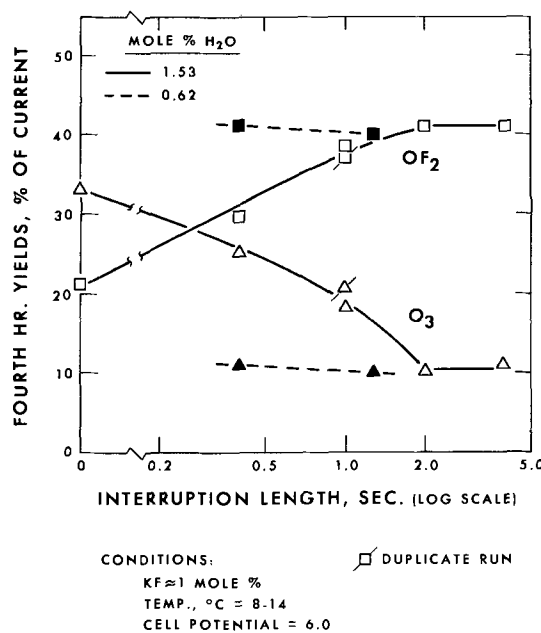


Fig. 3. Effect of interruption length

aqueous acids on platinum anodes (5) and much greater than previous (6-9) aqueous hydrogen fluoride yields. Despite the erratic yields, continuous operation may therefore have some potential for ozone synthesis.

In our experiments to date no combination of water concentration or interruption schedule produced oxygen difluoride yields exceeding 45%. Thus, while decomposition of water is the initial electrochemical reaction, oxygen difluoride yields also appeared to be limited by the availability of some reactive fluorine species. The possible fluorine species here include fluoride ion, fluorine atom, free fluorine molecules, hydrogen fluoride, and the nickel fluoride anode. The data in Fig. 2 exclude free fluorine as an important species, and the concentration of the solvent, hydrogen fluoride, is so high that its availability should not be limiting.

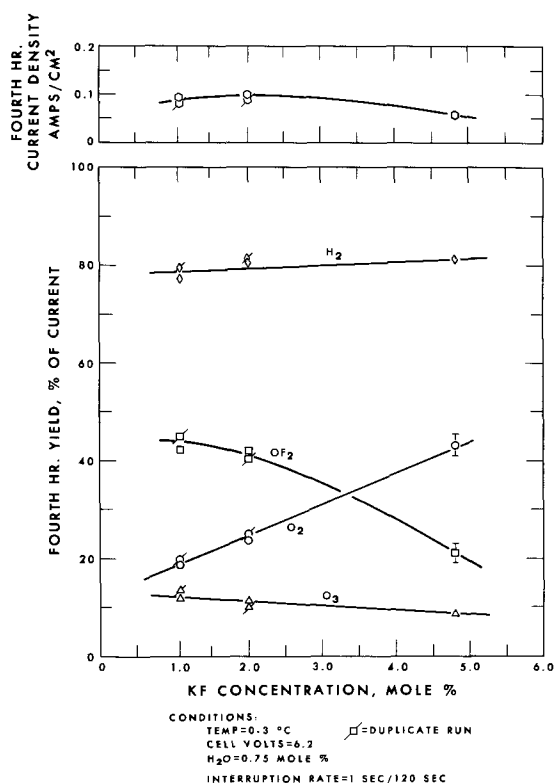
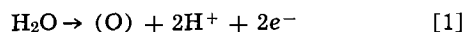


Fig. 4. Effect of KF concentration on yield

Figure 4 shows the results of increasing the concentration of the fluoride ion to determine whether it was the limiting species. However, the oxygen difluoride yield dropped with oxygen now showing a compensating increase. At the highest potassium fluoride concentration 4th-hr yields are not even constant (the range is denoted by the T marks). Increasing the interruption to 5 sec improves the oxygen difluoride yield, but only to 30%, while current density decreases. While this evidence does not exclude fluoride ion from some participation, it is certain that the availability of fluoride ion is not limiting oxygen difluoride yields and probable that fluoride ion is not a major source of fluorine in oxygen difluoride.

If fluorine atom is the limiting species, its concentration should be increased at higher voltages. But in Fig. 5 the oxygen difluoride yield shows no change over a 0.6v range of anode potential. At higher potentials (5.4v) the 4th-hr oxygen difluoride yield was less than 40% and decreased with time. Thus it is improbable that any electrochemical intermediate from fluoride ion discharge, as fluorine atom, is an important source. Since ozone yield does increase at higher potential, this indicates that it is more closely related to the initial electrochemical reaction than is oxygen difluoride.

Thus we believe that the remaining possibility, the nickel fluoride anode, is the source of fluorine and we propose the following sequence as a plausible outline of the mechanism. First



We favor oxygen atom as the decomposition product of water because ozone, which usually requires oxygen atoms for its formation, and oxygen difluoride appear to have a common intermediate (see Fig. 3). Next, the oxygen atoms react with the nickel fluoride anode



However, the resulting anode material, possibly an oxyfluoride, must be very unstable in hydrogen flu-

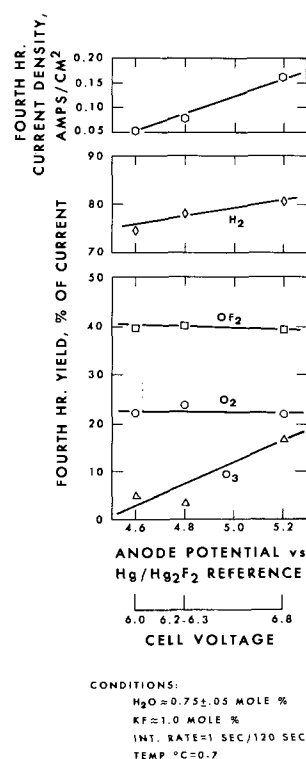
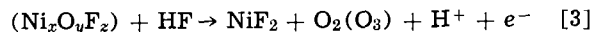


Fig. 5. Voltage effects

oride and, consequently, it reacts to regenerate nickel fluoride



During continuous electrolysis at high water levels, the oxyfluoride layers build up and so cause a drop in oxygen difluoride yield. Interruption permits reaction [3] to remove such layers and restore the oxygen difluoride yield. Also such oxyfluoride layers can explain the apparent 45% limit on oxygen difluoride yields if the oxygen atoms in it are not available for oxygen difluoride but can only go to oxygen or ozone.

### Acknowledgments

This work was supported by the Advanced Research Projects Agency through the U.S. Army Research Office-Durham under contract DA-31-124-ARO (D)-78. The authors thank R. R. Hopkins for his help in developing the infrared analysis, and J. Markovich for assisting with the experimental work.

Manuscript submitted May 20, 1968; revised manuscript received ca. July 10, 1968.

Any discussion of this paper will appear in a Discussion Section to be published in the June 1969 JOURNAL.

### REFERENCES

1. F. Goodridge, *New Scientist*, p. 98, 4/8/65.
2. J. O'M. Bockris, B. J. Piersma, E. Gileadi, and B. D. Cahan, *J. Electroanal. Chem.*, **7**, 487 (1964).
3. J. A. Donohue, T. D. Nevitt, and A. Zletz, *Advan. Chem. Ser.* **54**, 192 (1966).
4. Gmelins Handbook of Inorganic Chemistry, Sys. No. 3, Part 4, 1082 (1960).
5. J. D. Seader, and C. W. Tobias, *Ind. Eng. Chem.*, **44**, 2207 (1952).
6. H. Emeleus, *J. Chem. Soc.*, **1942**, 441.
7. E. Briner and R. Tolum, *Helv. Chem. Acta*, **31**, Part 2, 172 (1948).
8. A. Engelbrecht and E. Nachbaur, *Monatsh. Chem.*, **90**, 367 (1959).
9. Gmelins Handbook of Inorganic Chemistry, Fluorine Supplement, Sys. No. 5, 222 (1959).
10. J. H. Simons, *Fluorine Chem.*, **5**, 41 (1964).
11. J. Burdon and J. C. Tatlow, *Advan. Fluorine Chem.*, **1**, 160, (1960).

12. J. A. Donohue and F. S. Jones, *Anal. Chem.*, **38**, 1858 (1966).  
 13. J. A. Donohue, A. Zletz, and R. J. Flannery, *This Journal*, **115**, 1042 (1968).  
 14. G. Cady, XVII International Congress of Pure and

- Applied Chemistry, Inorganic Chemistry, **1**, 205, Munich (1959).  
 15. W. M. Latimer, "Oxidation Potentials," Prentice Hall, Inc., Englewood Cliffs, N. J. (1952).

## The Nickel/Nickel Fluoride Anode in Wet Hydrogen Fluoride The Conductive Nature of the Nickel Fluoride Film

J. A. Donohue, A. Zletz, and R. J. Flannery\*

Research and Development Department, American Oil Company, Whiting, Indiana

From our studies of the electrolysis of wet hydrogen fluoride with a nickel/nickel fluoride anode, we have tentatively concluded that oxygen difluoride, a principal product, is formed by a reaction involving fluorine derived from the anode (1). But to test this conclusion, we need a clearer understanding of the electrochemistry of the nickel/nickel fluoride system. In the presence of fluorine at high temperatures, nickel forms a nickel fluoride coating that limits further attack; the mechanism is well understood (2). Apparently, such coatings also catalyze reactions of fluorine (3). However, much less is known about the nickel fluoride formed in wet hydrogen fluoride or its behavior during electrolysis.

Appreciable amounts of nickel fluoride are lost from the anodes in fluorine cells (4), in the electrolytic drying of hydrogen fluoride (5), and often in the electrochemical fluorination of organic compounds (6). Conversely, in wet hydrogen fluoride, the nickel fluoride undergoes passivation so that losses are minimized (7, 8). The passivation is not due to water decreasing the solubility of nickel fluoride (8, 9), and the mechanism has yet to be identified.

To learn more about the effects of electrolysis on nickel fluoride, we obtained potential decay curves and measured the weight losses of nickel/nickel fluoride anodes that had been exposed to known pretreatments and electrolysis conditions in wet hydrogen fluoride. We also examined replicas of the anode surfaces with an electron microscope.

### Experimental

Most of our equipment and procedures have been described (1, 7). Consequently, only new developments and details specific to this work are discussed here. These include addition of a reference electrode to the electrolysis cell, as shown in Fig. 1, and an electrical system for automatic potentiostatic control of electrolysis, as shown in Fig. 2.

Weight loss and electron microscope studies were carried out with preweighed anodes that had been exposed to known conditions of electrolysis during previous experiments (1, 7). After these experiments, the anodes were removed from the cell, rinsed with hydrogen fluoride to remove potassium fluoride, dried at reduced pressure, and weighed. An equivalent weight of 29.4g ( $\text{Ni}^{+2}$ )/faraday was assumed, and weight loss was calculated as a percentage of the current passed during electrolysis. For the electron microscope studies, carbon replicas of the anode surfaces were obtained by a standard technique (10). The replicas were dried, "shadowed" at a low angle with gold-platinum, and observed on an RCA type EMU electron microscope.

The mercury/mercurous fluoride reference electrode (11) is an order of magnitude more stable than other alternatives for use in anhydrous hydrogen fluoride

(12), and we found it remains stable even when water and dissolved electrolysis products are present. However, because mercury decomposes ozone (13a) and oxygen difluoride (14), we avoided yield losses by placing the reference electrode outside the main cell (Fig. 1). Otherwise, the construction differs from the former design (12) only in that a porous plug and a valve were added to restrict diffusion. Except the nickel wire contact, all parts in contact with the electrolyte are of Teflon. Mercurous fluoride for the electrode was prepared from mercurous nitrate by Henne's method (15); the mercury was reagent grade, used as received. The reference was used at 0°C.

Rather than placing the opening of the salt bridge close to the anode, where bubbles could block the opening and cause a high resistance in the reference circuit, it was necessary to position the opening beside the sparger, approximately 1 in. from the anode. Because this distance was much greater than the 1/4-in. separation between the anode and the cathode, the IR drop in the electrolyte was included in the potentials measured during electrolysis.

For the potential decay studies, the upper limit of the potentiostat current prevented the use of anodes any larger than 2.5 cm<sup>2</sup> in area. Moreover, a break-in period was required in which the voltage was slowly increased so that the current would not exceed that limit. Otherwise, operation of the electrolysis cell was not appreciably different from previous work (1). First, the electrolyte (hydrogen fluoride containing 1 m/o (mole per cent) potassium fluoride and 0.75 m/o water) was pre-electrolyzed with an auxiliary anode until clear and colorless. Next, the test anode was placed in the cell for the break-in period, during which the nickel fluoride coating appeared to build up to some optimum thickness (8) and then stopped growing. (This coating also appeared to be thinner

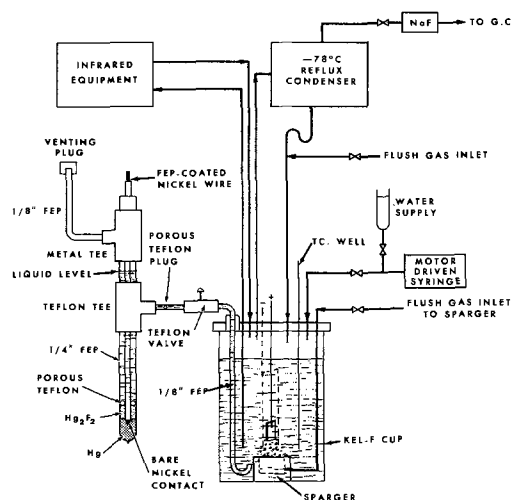


Fig. 1. Electrolysis cell

\* Electrochemical Society Active Member.

Key words: passivation by water, mechanism of passivation, conductivity of nickel fluoride, pulsed electrolysis, mercury/mercurous fluoride reference electrode.

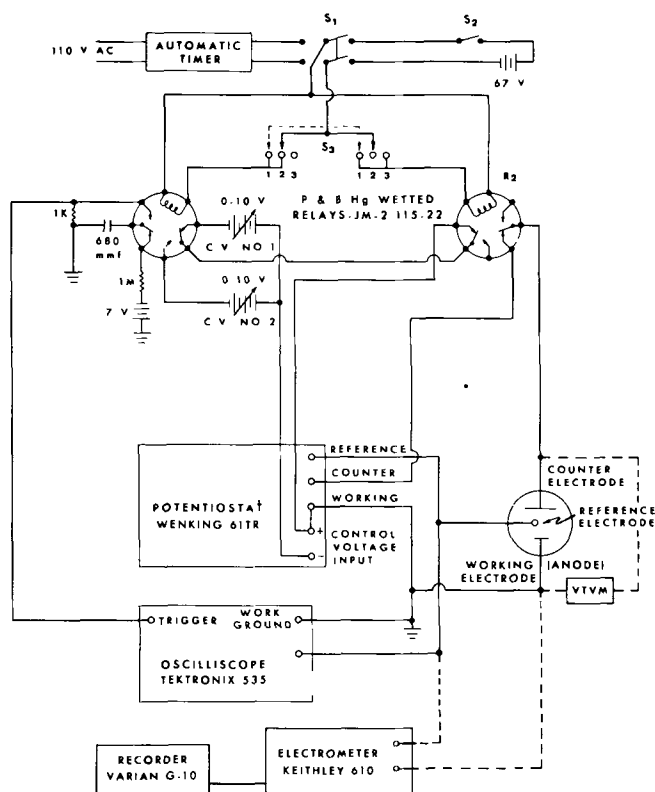


Fig. 2. Electrical equipment schematic

and more adherent than those produced without the gradual increase in voltage). Finally, the ohmic polarization ( $\eta_R$ ) was measured as a function of current density by potential decay techniques.

As diagrammed in Fig. 2, pulsed electrolysis was obtained from the potentiostat using an a-c timer, relay  $R_1$ , and control voltages set by CV 1 and CV 2. CV 2 allowed control of the voltage during pulsing, but was set to simulate previous uncontrolled work (1, 7). Since  $\eta_R$  decays rapidly ( $<1$  msec), it was recorded during the regular pulses; but the potentiostatic control had to be broken or only the potentiostat response was found. Thus, when a decay curve was to be obtained, a relay  $R-2$  was used to disconnect the potentiostat and allow normal decay during the pulse. Also, because the a.c. of the timer produced noise on the oscilloscope, the relays and scope trigger were operated manually on d-c current to observe decays. When the potential decay was observed for more than 1 sec, the regular electrolysis pulses were not long enough, and only one decay could be obtained per electrolysis run. To prevent rapid decay, the anode connection to the potentiostat was also broken. An electrometer and recorder were used to observe the longer decay processes.

### Results and Discussion

Our anode weight loss data are summarized in Table I. Of the principal electrolysis conditions studied, water concentration appears the most significant in producing a stable (passivated) anode. Appreciable weight losses were noted only when water concentration was less than 0.2 m/o. And contrary to our previous report (7), pulsed operation did not prevent such losses.

Changes in anodic voltage between 4.6 and 5.4v caused only negligible losses. However, at higher voltage (6.0v), at least a 2% loss has been observed (8) regardless of the water concentration. Thus, complete passivation apparently is maintained only if the anode voltage is less than 5.4v. Our experience suggests that about 5.0v anodic (6.2 for total cell voltage) is optimum for our system, but this may not hold for substrates other than water.

Table I. Anode weight losses

Electrolysis variables also studied	m/o H <sub>2</sub> O	Faradays cm <sup>2</sup>	Weight loss calculated as % current
Continuous operation	$<0.2$	0.013	5.0
Continuous operation	0.4-1.5	0.056	None**
Pulsed operation	$<0.2$	0.004	3.9
Pulsed operation	1.55	0.456	None**
Pulsed operation plus			
Anodic voltage* (4.8-5.4v)	0.75	0.074	$<0.01$
Anodic voltage† (4.6-5.2v) and temp. (2°-12°C)	0.75	0.098	$<0.05$
KF (2%) and temp. (2°-16°C)	0.075	0.055	None**
KF (5%) and temp. (2°-16°C)	0.75-1.5	0.035	None**

\* Total cell voltage 6.0-6.6v.

† Total cell voltage 6.0-6.8v.

\*\* Or very slight gain due to NiF<sub>2</sub> formation.

On the basis of our early yield data (7) at more than 0.2 m/o water, passivation was assumed (8) to persist after water was reacted away. However, recent yield data (1) at less than 0.1 m/o water now show low current efficiency for water-based products. Therefore, some small traces of water probably persist so long as there is any passivation.

Figure 3 compares electron micrographs of (A) a replica of one of our "passivated" anodes and (B) a nickel fluoride coating produced from the high-temperature reaction of nickel with fluorine. The latter coating, although polycrystalline, is hard without any cracks and is probably only one crystal layer thick (16). In contrast, the replicas of the anode has black areas caused by an adherent, soft, spongy nickel fluoride, whose presence was confirmed by electron diffraction analysis. The irregularly shaped lines in the remainder of the replica may indicate small pores or single crystal boundaries. From these observations we assume that the passivated nickel fluoride is soft, amorphous, or microcrystalline, and probably porous. However, it is unlikely that the porosity extends to the nickel support because the electrolyte would then be able to attack the nickel and probably cause further weight losses. Unfortunately, photomicroscopy was not very useful because the nickel fluoride was too soft to be polished, but a film thickness of 1-5 $\mu$  was found.

Our electrochemical measurements are summarized in Fig. 4 and 5. The ohmic polarization ( $\eta_R$ ) measured as a function of current density was found to obey Ohm's law, as shown in Fig. 4, and similar linear plots were obtained during the induction period of the electrolysis where current density changes with time at constant voltage. These results negate our earlier assumption (7) because, if ohmic resistance is constant, it cannot account for these changes in current density.

The very small value of  $\eta_R$  is significant; the 0.3-0.4v is only 5% of the total cell voltage ( $\sim 6.2$ v) at



Fig. 3. Electron micrographs of nickel fluoride surfaces. A, nickel fluoride by electrolysis in wet HF; B, nickel fluoride from Ni and F<sub>2</sub> at high temperature.



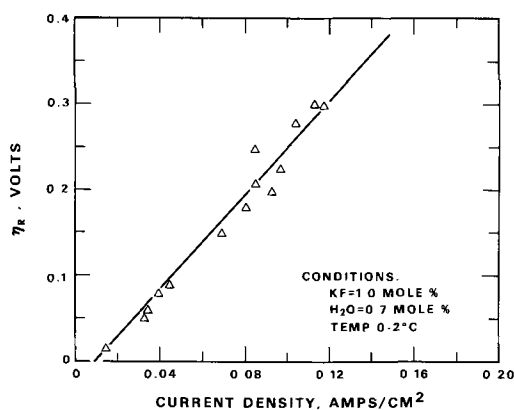


Fig. 4. Ohmic polarization

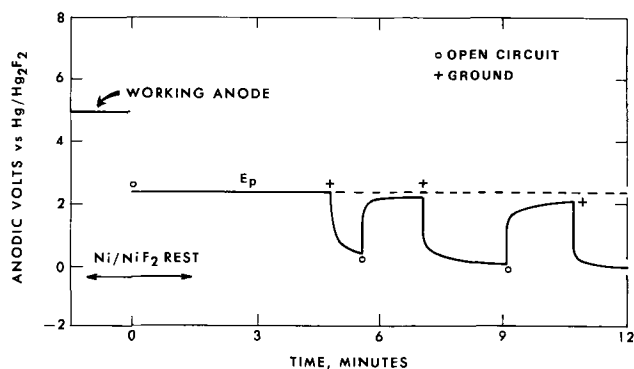


Fig. 5. Potential decay with intermittent short

normal operating conditions. Since  $\eta_R$  includes the IR drop in the electrolyte, which is estimated to be at least a few tenths of a volt, little if any ohmic polarization can be attributed to nickel fluoride. By contrast, the nickel anodes in a dry fluorine cell show very high ohmic polarization (17). Thus, the passivating substrate water also dramatically reduces the ohmic polarization of nickel fluoride. These phenomena may be related, at least on the basis of one theory (18) which holds that passivation occurs when a coating becomes electronically conducting. This prevents ion transport through the film, i.e., film growth.

As shown in Fig. 5, an indication of how conductivity may develop was obtained from additional potential decay studies. When the anode voltage was allowed to decay on open circuit, it fell rapidly ( $<1$  sec) to a stable potential plateau ( $E_p$ ) 2.5-3.0v more anodic than the rest potential of nickel/nickel fluoride. When an anode at  $E_p$  was grounded, the voltage decayed rapidly toward the expected rest potential. Then it recovered toward  $E_p$  when returned to open circuit if the grounded period was not long. Thus, we conclude that the anode is in an oxidized state as an electrode in a battery. Further, by analogy with the nickel oxide battery electrode (19), we assume that the accumulation of higher valent nickel ( $Ni^{+3}$  or  $Ni^{+4}$ ) species is the cause.

By integrating the current during grounding over the time to reach the expected rest potential, we were able to estimate the concentration of higher valent nickel species in the coating. As Table II shows,

Table II. Coulometry of  $E_p$ 

Total charge passed during electrolysis, coulombs	Charge in $NiF_3$ recovered on grounding, coulombs	% of Charge recovered
0.06	0.00062	0.97
0.78	0.0024	0.31
7.7	0.006	0.09

the charge in the coating decreases from 1 to 0.1% of the total charge as the total charge is increased. This percentage should be low since up to 90% of the total charge is accounted for as volatile products (1,7) of the electrolysis.

The concentration of higher valent nickel that would account for this charge in the coating was calculated to be from 0.1 to 1.0%. Semiconductors of good conductivity are obtained from nickel oxide doped with lithium oxide in this same concentration range. The conductivity of doped nickel oxide is thought to arise from higher valent nickel caused by the presence of the lithium cations in the host oxide (20). Therefore, we predict similar processes will be possible in anodic nickel fluoride.

That  $E_p$  is indeed a nickel fluoride bulk rather than a surface effect is shown by the fact that hydrogen bubbled over an anode at  $E_p$  will not cause a change in potential. Also, adsorption of soluble electrolysis products does not affect the potential of a resting anode during electrolysis on a different anode. Therefore, the products are not responsible for maintaining  $E_p$ .

We conclude that water passivates the nickel/nickel fluoride anode by making the nickel fluoride conducting, probably by stabilizing the formation of higher valent nickel species. This proposal is supported by the observation that water is required to stabilize the high valent nickel species in nickel oxide (13b). However, the water-dependent phase changes of nickel fluoride (9) and the amorphous or microcrystalline nature of anodic nickel fluoride should also affect conductivity.

We believe these studies have indicated the conditions required to produce a passivated nickel/nickel fluoride anode and hence should permit further progress toward identifying the mechanisms in the formation of oxygen difluoride and other products during the electrolysis of hydrogen fluoride. However, any electrochemical approach will require a better understanding of conductivity in nickel fluoride. Such an understanding should lead to anodes with permanently high conductivity, possibly even from metals that generally have nonconducting films (12), and also to improved electrolysis of the more difficult substrates such as ammonia (12) or hydrocarbons (6).

#### Acknowledgment

This work was supported by the Advanced Research Projects Agency through the U. S. Army Research Office—Durham; under contract DA-31-124ARO (D)-78. The authors are indebted to the late J. N. Markovich for assistance with the experimental work, to B. L. Meyers for the electron micrographs, and to G. Aronowitz for helpful discussions and suggestions.

Manuscript submitted May 20, 1968; revised manuscript received ca. July 10, 1968.

Any discussion of this paper will appear in a Discussion Section to be published in the June 1969 JOURNAL.

#### REFERENCES

- J. A. Donohue and A. Zletz, *This Journal*, **115**, 1039 (1968).
- R. L. Jarry, J. Fisher, and W. H. Gunther, *ibid.*, **110**, 346 (1963).
- B. G. Baker and P. G. Fox, *Nature*, **204**, 466 (1964).
- G. H. Cady, "Fluorine Chemistry," Vol. I, p. 301, Academic Press, New York (1950).
- H. H. Rodgers, S. Evans, and J. H. Johnson, *This Journal*, **111**, 701 (1964).
- J. Burdon and J. C. Tatlow, "Advances in Fluorine Chemistry," Vol. I, p. 129, Butterworth, London (1960).
- J. A. Donohue, T. D. Nevitt, and A. Zletz, *Advan. Chem. Ser.*, No. 54, 192 (1966).
- N. Hackerman, E. S. Snively, and L. D. Fiel, *Electrochim. Acta*, **12**, 535 (1967).
- A. F. Clifford and A. C. Tulumello, *J. Chem. Eng. Data*, **8**, 425 (1963).

10. D. E. Bradley, "Replica and Shadowing Techniques," in "Techniques for Electron Microscopy," Desmond Kay, Editor, Blackwell Scientific Publications, Oxford (1961).
11. G. G. Koerber and T. DeVries, *J. Am. Chem. Soc.*, **74**, 5008 (1952).
12. R. M. Hurd and E. S. Snavely, "Metal and Metal Fluoride Electrode Systems in Anhydrous Hydrogen Fluoride," ARPA Propellant Contractors Synthesis Conference, IIT Research Institute, Chicago, April 13-15, 1964.
13. N. V. Sedgwick, "Chemical Elements and Their Compounds," Vol. II, (a) p. 862, (b) p. 1449, Clarendon Press, Oxford (1950).
14. A. G. Streng, *Chem. Rev.*, **63**, 611 (1963).
15. A. L. Henne and M. W. Renoll, *J. Am. Chem. Soc.*, **60**, 1060 (1938).
16. C. F. Hale, E. J. Barber, H. A. Bernhardt, and K. E. Rapp, "High Temperature Corrosion of Some Metals and Ceramics in Fluorinating Atmospheres," AEC Report No. K-1459, Union Carbide Nuclear Co., U. S. Government Contract No. W7405, eng. 26, 9/30/60.
17. A. J. Arvia and J. Bebczuk de Cusminsky, *Trans. Faraday Soc.*, **58**, 1019 (1962).
18. J. O'M. Bockris, A. K. N. Reddy, and B. Rao, *This Journal*, **113**, 1133 (1966).
19. B. E. Conway and P. L. Bourgault, *Can J. Chem.*, **37**, 292 (1959).
20. N. B. Hannay, Editor, "Semiconductors," p. 622, Reinhold Publishing Co., New York, (1959).

## Kinetics of the Reaction between Lithium Hydride and Liquid Ammonia at $-78^{\circ}\text{C}$

Irving Warshawsky

*Lewis Research Center, National Aeronautics and Space Administration, Cleveland, Ohio*

Although the quantitative reaction between an alkali hydride and liquid ammonia to form the corresponding alkali amide and hydrogen has been known for many years (1), neither the reaction rate nor the mechanism has been reported. The purpose of this study is to elucidate the kinetics of the reaction between lithium hydride and liquid ammonia at  $-78^{\circ}\text{C}$ .

Experimental procedures were similar to those employed in previous work (2). A small amount of powdered, reagent grade lithium hydride was introduced into an ampoule on the vacuum line, and the system was evacuated for several days at  $<10^{-6}$  mm Hg. Next, liquid ammonia, which had been dried over sodium, was distilled into the ampoule containing the hydride and cooled to liquid nitrogen temperature. The volume of liquid ammonia was 3.00 cc at  $-78^{\circ}\text{C}$  in every case.

The rate of the reaction,  $\text{LiH}_{(s)} + \text{NH}_{3(l)} \xrightarrow{-78^{\circ}\text{C}}$

$\text{LiNH}_{2(s)} + \text{H}_{2(g)}$  was followed by measuring the pressure of hydrogen evolved. At convenient time intervals, pressure readings were taken by means of a calibrated McLeod gauge. In the range of interest, the error in reading the McLeod gauge was estimated to be less than 3%. During a pressure measurement, the dry ice-acetone bath (used to hold the ampoule at  $-78^{\circ}\text{C}$ ) was replaced with a liquid nitrogen bath, usually for about 1 hr, with the rest of the system ( $1.741$ ) at room temperature. The hydrogen was then pumped out of the system, and the liquid nitrogen bath replaced once more by the dry ice-acetone bath. This manipulation introduced an error of approximately 4 min in the time span between pressure measurements, causing an error of 3% in the worst cases.

The data are plotted as  $\log P_{\text{H}_2}$  vs.  $\log t$  in Fig. 1. For convenience, the region prior to the break in the slope of the curve is called region A, and that following, region B. In region A, the equation  $P=Ct^n$  may be used to represent the data, where  $P$  is the pressure of hydrogen evolved in microns of mercury,  $t$ , the time in hours, and  $n$  and  $C$  constants. In region B, there is a large increase in the rate of reaction which takes place after approximately 5% of the hydride has reacted. The constants were determined by a least square fit of the experimental points. The data for region A is summarized in Table I. It is apparent that the reaction rate is effectively parabolic, i.e.,  $n=0.5$ .

Assuming a linear relationship between surface area and weight of lithium hydride, Table I shows that the expected proportionality between the rate constant  $C$  and the amount of lithium hydride is lacking. This

may be attributed partly to data variation and partly to a surface area variation. For instance, the presence of impurities at the surface, such as hydroxide, might cause a variation in the surface area from run to run. However, the inherent difficulty of reproducing the same surface area from run to run for a given amount of material has been noted in kinetic studies of the oxidation of copper (3) and uranium dioxide (4), respectively.

In tarnishing reactions, it is customary to assume that parabolic kinetics are due to a rate-determining step which is diffusion-controlled. Further, the assumption is made that the diffusion process takes place in a nonporous film which separates the reactants (5, 6). If a similar set of assumptions is made here for region A, where  $n$  is approximately 0.5, it may be envisaged that the highly insoluble reaction product, lithium amide (7), forms a nonporous film which separates the reactants, lithium hydride and liquid ammonia, and which increases in thickness as the reaction proceeds.

One may speculate that once the reaction is underway, its continuation necessitates a chemisorption process in which ammonia dissociates at the lithium amide-liquid ammonia interface into a proton and an amide ion. Thus, given a source of protons and also given a sink for their removal at the lithium hydride-lithium amide interface (via the reaction with hydride ions), conditions are created favoring the transport of protons through the amide film. As a con-

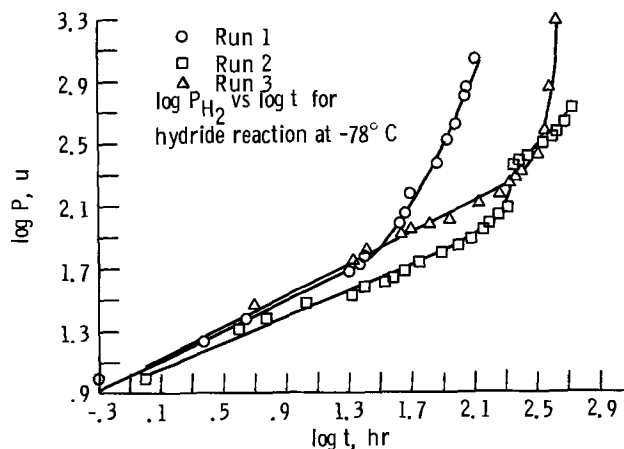


Fig. 1.

Table I. Constants of the kinetic equation

Run	Moles of LiH initially present $\times 10^4$	$n$	$C$
1	4.50	$0.54 \pm 0.04$	$11.6 \pm 0.5$
2	1.52	$0.41 \pm 0.01$	$10.5 \pm 0.2$
3	4.55	$0.49 \pm 0.01$	$12.2 \pm 0.2$

sequence, a charge imbalance created by hydrogen formation favors the migration of lithium ions from the lithium hydride-lithium amide interface to the lithium amide-liquid ammonia interface, leading to the formation of lithium amide at the latter interface. A transport process must also be assumed for the passage of hydrogen molecules through the amide film, leading to hydrogen evolution. Further, it may be suggested that the continued growth of the amide film may, at some critical film thickness, lead to the film breaking away (8), causing an increase in the rate of reaction by exposing new hydride surface to the liquid ammonia. Film breakaway may possibly

account for the abrupt change in the kinetic behavior in going from A to region B.

Manuscript received July 1, 1968.

Any discussion of this paper will appear in a Discussion Section to be published in the June 1969 JOURNAL.

## REFERENCES

- H. H. Sisler, "Chemistry in Non-Aqueous Solvents," p. 46, Reinhold Publishing Corp., New York (1961).
- I. Warshawsky, *J. Catalysis*, **3**, 291 (1964).
- W. E. Campbell and U. B. Thomas, *Trans. Electrochem. Soc.*, **91**, 632 (1947).
- P. Blackburn, J. Weissbart, and E. Gulbrandsen, *J. Phys. Chem.*, **62**, 902 (1958).
- N. F. Mott and R. W. Gurney, "Electronic Processes in Ionic Crystals," p. 249, Oxford Press, N. J. (1948).
- U. R. Evans, *Trans. Electrochem. Soc.*, **83**, 335 (1943).
- H. H. Sisler, "Chemistry in Non-Aqueous Solvents," p. 30, Reinhold Publishing Corp., New York (1961).
- U. R. Evans, "The Corrosion and Oxidation of Metals," p. 855, and comment by Wanklyn, p. 857, Arnold Publishing, London (1960).

# Brief Communication



## Electrochemical Painting of Titanium

Roberto Piontelli\* and Pietro Pedferri

*Institute of Chemical Physics, Electrochemistry and Metallurgy, Polytechnic of Milan, Milan, Italy*

The large variety of titanium oxides, obtainable by electrochemical passivation of the metal in various conditions, is well known. Furthermore, a wide range of modifications of the surface oxide may be obtained by operating with alternating or pulsating current, with various baths and working conditions. These modifications correspond as a rule to those obtainable with d.c., as far as the appearance and probably the composition and structure are concerned.

With applied voltages of 50 Hz, the substitution of the natural oxide by colored passivating layers requires that the current density exceed a roughly critical value, which, however, depends also on bath composition, temperature, and initial surface conditions. By plunging titanium or some of its alloys in a liquid already containing a counter electrode, an alternating voltage<sup>1</sup> being applied between them, the modifications of the metal surface region which comes into contact with the liquid depend on the instantaneous sign and value of the applied voltage. The influence of this value appears to be nearly discontinuous.

We may obtain, therefore, a succession of typical stripes, whose number on a given area is proportional to the product of the frequency (Hz) of the alternating current and the time (sec) required for the immersion of this area in the liquid. These stripes (see Fig. 1) are due to the alternation along the metal surface of regions in which the formed layers are different in color, thickness, electrical conductivity, porosity, adhesion, and resistance to chemical or electrochemical attack. Previous observations on oxide films formed on tantalum with alternating potential are due to Vermilyea (1).

\* Electrochemical Society Active Member.

<sup>1</sup> Of course, connecting the cell with a source of symmetric a.c., also, as a rule, has the result that the effective circulating current is strongly deformed due to the sudden changes of internal equivalent resistance, involving corresponding abrupt voltage changes.

In the case of titanium the appearance is largely influenced by the following factors: initial surface conditions, bath composition, characteristics of the electrical supply, temperature, etc.

As typical conditions under which these effects may be observed we may quote the following:

- aqueous solution of HCl 18% (by weight); room temperature; applied voltage: symmetric a.c. at 50 Hz and 5000/8000 amp/m<sup>2</sup>;
- ibid.*, the cell being supplied by both a source of a.c. (50 Hz;  $E_{eff} = 7v$ ) and one of d.c. (anodic voltage  $E_d = 8v$ , so that the titanium for most of the time is the anode);
- ibid.*, with  $E_{eff} = 7v$ ;  $E_d = 10.5v$ ;
- aqueous solution of NaOH 400 g/l; room temperature; applied voltage: symmetric a.c. at 50 Hz and 5000/10,000 amp/m<sup>2</sup>.

To obtain the effects above, the specimens may be utilized either with that surface condition which obtains following an exposure of many days to the atmosphere (at room temperature), or that derived from HF pickling, followed by boiling (for 15 min or more) in aerated water.

Those regions of the surface eventually wet at the moment of immersion become coated by a more conducting layer in a basic bath and by a less conducting layer in an acid bath.

Especially suggestive effects may be obtained when the electrolytic solution comes in contact with the metal surface by partially displacing a nonconducting liquid (Fig. 2).

The form of the figures then depends on the following circumstances:

- the conditions of the relative motion of the titanium surface (dry or on the other hand wetted with a nonconducting liquid) with respect to the electrolytic solution;

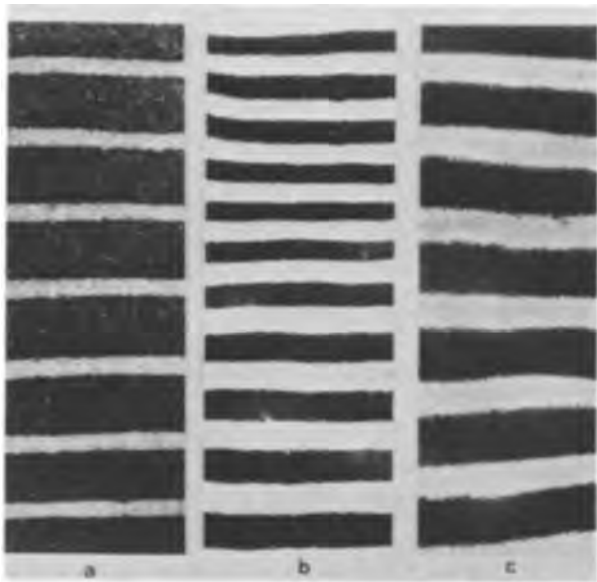


Fig. 1. Stripes obtained by vertical immersion of a Ti plate in aqueous HCl solution (18% by weight), at room temperature: (a) with alternating voltage; (b) and (c) with alternating voltage superimposed on d-c. voltage. Magnification 1X.

2. the inclination of the titanium surface with respect to the free surface of the liquid;
3. the boundary conditions;
4. the presence of obstacles;
5. the properties of the liquid phases (viscosity, surface tension and also their mixing-or reaction rate);
6. properties of the surface (microgeometry);
7. relationships between the surface and liquids (wettability, adhesion, and so on).

As possible applications of the results above one may consider the possibilities:

1. of fixing on the titanium surface, at definite time intervals, a line, which defines where the metal encounters an electrolytic solution, the frequency of this reproduction being coincident with the one of the applied a.c.;
2. of making conducting or insulating regions on a surface previously wetted with an electrolytic solution or with water, thus allowing selective metallizing of the surface by electroplating, following previously assigned drawings;
3. of fixing in the form of "isochronous lines" the three-phase boundary line formed by a foreign liquid

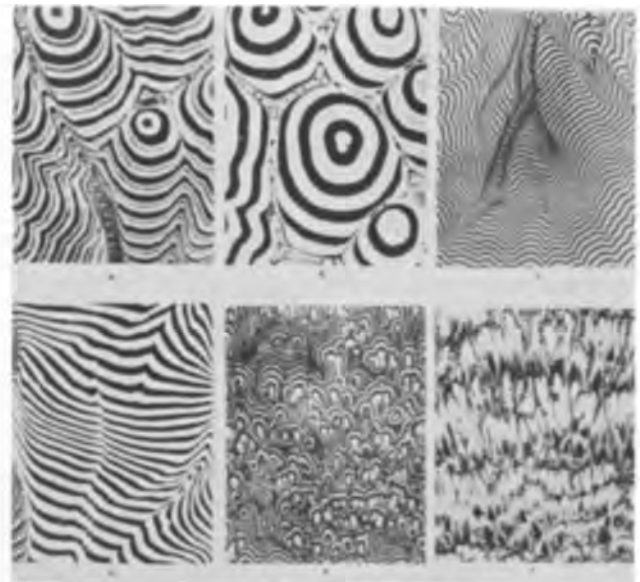


Fig. 2. Oxide film patterns formed at room temperature on titanium plates plunged horizontally into aqueous HCl solution (18% by weight) with alternating voltage superimposed on a d-c anodic voltage. The unique effects are obtained by partial displacement of previously applied wetting films of the following non-conducting liquids: (a) chloroform; (b) and (d) benzene; (c) and (e) acetic anhydride; (f) acetone; (a) (c) (d) figures formed on the upper face of the plate; (b) (e) (f) figures formed on the lower face. Magnification 0.5X.

coming into contact with an electrolytic solution on a titanium surface;

4. by differentiation from this map, the field of the advancement speed of the boundary line may also be deduced.

The details of the experimental work carried out in this laboratory on this matter are given in papers in print (2).

Manuscript submitted Feb. 23, 1968; revised manuscript received April 3, 1968.

Any discussion of this paper will appear in a Discussion Section to be published in the June 1969 JOURNAL.

#### REFERENCES

1. D. A. Vermilyea, *This Journal*, **111**, 883 (1964).
2. R. Piontelli and P. Pedferri, *Rend. Acc. Naz. Lincei*, to be published; *Electrochim. Metallorum*, to be published.

# Current Density-Anodic Potential Curves of Single Crystal GaAs at Low Currents in KOH

M. E. Straumanis,\* J. P. Krumme, and W. J. James\*

Graduate Center for Materials Research,  
Departments of Metallurgical Engineering and Chemistry, at The University of Missouri-Rolla, Missouri

## ABSTRACT

Single p-type, GaAs crystals of high purity, Zn doped, were used to determine whether or not the inverse octahedral {111} faces show potential differences and various rates of anodic dissolution. The Ga{111}, As{111}, {110}, and {100} faces, were polished, etched, and etch-polished with concentrated  $\text{H}_2\text{SO}_4 + \text{H}_2\text{O}_2$ , and immersed in 1N KOH. The Ga{111} faces were found to be the most noble with respect to rest and anodic dissolution potentials. The potential difference between the inverse {111} faces was as large as 0.14v for the rest and 0.123v for the dissolution potentials. The 4 anodic polarization curves gave nearly parallel Tafel lines, with a slope of  $66.0 \pm 1 \text{ mv}/\log i$ , up to current densities of  $0.5 \text{ ma}/\text{cm}^2$ . The rate of anodic dissolution of the As{111} faces was 69 X as high as the inverse Ga{111}. The activation energies of dissolution of all 4 faces were equal within experimental limits:  $16.7 \pm 0.7 \text{ kcal mole}^{-1}$ . It is concluded that the slow step in the dissolution of GaAs is a one electron discharge with subsequent steps leading to the formation of  $\text{Ga}(\text{OH})_3$  to provide a protective coating not readily soluble in KOH. From this point of view all observed phenomena can be explained in a qualitative manner.

Crystals without a symmetry center are polar; the polarity shows up through differences in chemical and physical behavior of the inverse planes of the respective crystals. The cubic III-V semiconductor compounds of diamond-type structure belong to this class, of which the best known are GaAs and InSb. Their polarity is displayed by the behavior of the inverse octahedral planes III{111} and V{111}, e.g., GaAs by Ga{111} and As{111}.

Reaction of III-V semiconductors in various media, with or without applied current have been studied by Gatos *et al.* (1), Pleskov (2), Gerischer (3, 4), Harvey (5), Brummer (6), Arthur (7), and others (8). They found that the various crystal planes react differently in aqueous media, such that the III{111} and V{111} inverse planes can be distinguished by the formation of specific etch patterns (1, 3, 8). The distinction can also be made from etching rates (1) from the inclination of etch tunnels produced by an anodic current on the GaAs octahedral planes (the tunnels run perpendicularly to As{111} and at an angle of  $20^\circ$  to Ga{111}) (8), and from LEED patterns (9). Furthermore, the two inverse planes exhibit different activation energies of oxygen desorption (as  $\text{Ga}_2\text{O}$ ):  $54 \pm 4$  from the Ga{111} and  $42 \pm 4$  kcal/mole from the As<111> face. Since there is little transfer of charges over the valence bridges (9, 10-13), the Ga atoms on the III{111} side retain their 3-valence electrons, while the As atoms on the inverse side retain 5. All this suggests that the two planes should also develop potential differences in electrolytes.

However, in this respect there are major disagreements. Gatos *et al.* reported that group III{111} planes exhibit more noble electrode potentials than group V{111} surfaces: for instance InSb inverse octahedral planes show a potential difference of 75 and more mv (1). Harvey (5) does not insist on a difference, but examination of his data (Fig. 2-3) reveals that the anodic potentials on Ga{111} are more noble than on As{111} at least up to current densities of  $50 \text{ ma}\cdot\text{cm}^{-2}$ . Conversely, Gerischer finds no difference either in dissolution rates or in the current density-potential curves.

Evidently the measurements have not been made under strictly identical conditions. The intention of the present investigation was, therefore, to use high-purity

GaAs crystals and to try to get an answer regarding the potentials exhibited in 1N KOH by the inverse 111-faces of GaAs, and also by the 110 and 100 planes.

## Materials and Preparation of the Electrodes

The single GaAs crystals were obtained from the Monsanto Company (St. Louis, Missouri), grown by the gradient-freeze technique. They were of the p-type containing Zn (<0.5 ppm) as a dopant. The impurity level was less than 1 ppm. The carrier concentration was  $\sim 1.6 \times 10^{16} \text{ cm}^{-3}$ , mobility  $\sim 250 \text{ cm}^2 \cdot \text{volt}^{-1} \cdot \text{sec}^{-1}$ , resistivity  $\sim 2 \text{ ohm}\cdot\text{cm}$ , and etch pit density  $\sim 800 \text{ cm}^{-2}$ . The disks (14-18 mm in diameter, 2-3 mm thick), were cut from the single crystal rod with a wire-blade slicer using a SiC slurry.

The orientation was determined from Laue back reflection patterns and the respective surface planes were adjusted within  $\pm 0.5^\circ$  of the desired orientation by successive grinding of the disks at a certain angle on fine SiC paper wetted with water and rechecking of the new direction with the Laue technique.

The damaged surface layer was removed from each crystal wafer by chemical etching for about 5 min with an aqueous mixture of 1HF (conc.): 1 $\text{H}_2\text{O}_2$  (30%): 2 $\text{H}_2\text{O}$  (by volume). After this operation the polarity of the {111} planes could be determined by comparing the etch patterns with those published in the literature (1, 3, 8).

Scratches, if present, were removed mechanically by polishing on cotton cloth with SiC slurry (600 mesh). Then a chemical polisher 3 $\text{H}_2\text{SO}_4$  (conc.): 1 $\text{H}_2\text{O}_2$  (30%) was used, which removed all remaining surface irregularities. The polisher has a high viscosity, provides a slow etch rate, and is not as sensitive to concentration changes as is CP4 etchant (mixture of HF,  $\text{HNO}_3$ , and  $\text{CH}_3\text{COOH}$ ). After this treatment the wafers were immediately transferred into dilute HF to prevent precipitation of a surface film, traces of which could be completely removed by dipping the samples into an aqueous solution of EDTA. Finally the wafers were rinsed in water and dried with alcohol. The whole procedure was repeated before any new series of potential measurements. The wafers then had a mirrorlike appearance (Fig. 1). To insure good electrical contact, one side of the wafer (less suited for potential measurements) was vacuum sputtered with Ag at room temperature, so that the impurity

\* Electrochemical Society Active Member.



Fig. 1. GaAs wafer in a Teflon holder (electrode)

level of the wafer could not be affected by the very slowly diffusing Ag. The contact with the circuit was achieved by Pt foil pressed to the wafer in a Teflon electrode holder (Fig. 1). A section through the holder is shown in Fig. 2. Teflon does not dissolve in the electrolyte (1N KOH) and repels water. The pressure of the screw cap against the wafer was equalized by the use of an O-ring below the Pt foil. Several runs were made on the same sample at current densities below  $0.5 \text{ ma} \cdot \text{cm}^{-2}$  where no surface disintegration of the electrode occurred (8). The potential determining anodic reactions are represented by Eq. [1] and [2]. As the exchange current could only be very small, it was not considered.

Then the electrode was placed in the cell and the potential measurements were made of the GaAs electrode against a 1N calomel reference in a  $\text{N}_2$  atmosphere at constant temperatures. Temperatures of  $4^\circ$  and  $21^\circ\text{C}$  were selected for the measurements of activation energies. The exposed GaAs surface was between  $1.2$  and  $1.4 \text{ cm}^2$ . The electrolyte was vigorously agitated employing a special stirrer and by bubbling  $\text{N}_2$  through the electrolyte. The influence of stirring rate on the potentials was not determined.

The d-c power was supplied and the potential controlled by an Anatrol potentiostat. Both power and potential were recorded on a 2-channel recorder on calibrated strip charts.

The chemicals used were all of reagent grade, and the nitrogen was prepurified. The electrolyte (1N aqueous KOH, 1600 ml) was pre-electrolyzed prior to each run using two Pt electrodes at  $180 \text{ ma}$  ( $\sim 60 \text{ ma/cm}^2$ ) over a period of 8 hr. Only traces of Pt could pass into solution and these would not affect the anodic dissolution of GaAs.

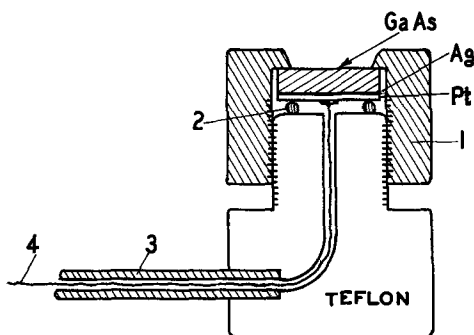


Fig. 2. GaAs electrode cross section: 1, Teflon screw cap; 2, O-ring; 3, Teflon tube (screwed in); 4, lead wire.

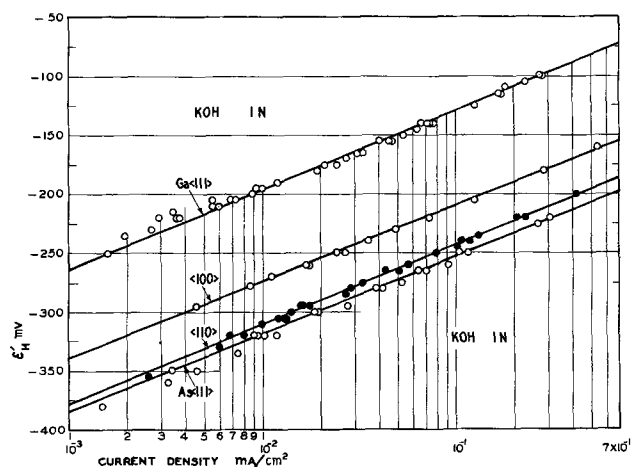


Fig. 3. Anodic dissolution potentials  $E'_H$  of GaAs vs. log of current density  $i$  of the planes Ga{111}, As{111}, {110}, and {100}. Hydrogen scale;  $4^\circ\text{C}$ .

### Results

Plots of anodic potential vs. the log of current density were linear for all the planes investigated (Ga{111}, As{111}, {110} and {100}). All had nearly the same slope, as shown by Fig. 3. The potential measurements for the various planes were highly reproducible. Rest potentials were not as reproducible:  $-402 \pm 40 \text{ mv}$  was obtained for As{111} and  $-262 \pm 40 \text{ mv}$  for Ga{111}. The  $\Delta E'/\Delta \log i$  values for the four planes in the sequence listed above are: 66.7, 65.6, 67.4, and  $64.8 \text{ mv}/\log i$ . They, therefore agree with the values of previous measurements, which usually were between 70 to  $95 \text{ mv}$  at room temperature (3). In acidic solutions (1N  $\text{H}_2\text{SO}_4$ ) they are lower, e.g.,  $62 \text{ mv}$  (5).

The fact that the slope  $\text{mv}/\log i$  on all 4 faces is the same within the limits of error, indicates that the rate-determining step is the same for all the planes subjected to anodic dissolution. The average value of  $66.1 \text{ mv}$  also suggests that a one-electron charge transfer is involved in the rate-determining step, similarly as for Ge (14, 15).

The activation energies (apparent) were calculated from the Arrhenius equation from the rates of dissolution (current density) at two temperatures ( $4^\circ$  and  $\sim 21^\circ\text{C}$ ), with all other factors remaining unchanged. The values are given in Table I.

Although the measurements were made with two or three GaAs crystals and the planes were etched-polished before each run, the activation energies differ only within the limits of error and, thus, are equal for all crystallographic planes. This result again suggests that the mechanism of dissolution (rds) must be the same on all the crystal faces.

However, Fig. 3 shows that appreciable differences in dissolution potentials do exist. While those exhibited by the As{111} and {110} planes may agree within the limits of error, the largest differences are found between Ga{111} and As{111}, ranging up to

Table I. Activation energies (apparent) of dissolution of various planes of GaAs in 1N KOH at temperatures of  $4.0^\circ$  and  $\sim 21^\circ\text{C}$  in  $\text{kcal mole}^{-1}$

Plane	Activation energies, $\text{kcal mole}^{-1}$	Average	Max. $\pm$ error
Ga {111}	15.8, 16.8, (19.6*), 17.3	16.6	0.8
As {111}	16.6, 16.9, 17.3	16.9	0.4
{110}	17.0, 16.05, 15.8, 16.3, 17.05	16.4	0.6
{100}	15.6, 16.8, 17.3	16.7	0.8
		Average 16.7	$\pm 0.7$

\* Excluded.

0.123v, which is in good agreement with 0.14v, the difference between the rest potentials. The III{111} plane exhibits thereby a more noble dissolution potential than the V{111} plane in agreement with the statements of Gatos *et al.* (1). The potentials of the {100} plane lie in between those of the {111} planes.

It is also apparent from Fig. 3, that the reaction rates on As{111} are highest. For instance, at an anodic potential of -250 mv (hydrogen scale) the rate of reaction on As{111} is about 69 times faster than on Ga{111}, since the current densities developed (16) are  $1.1 \times 10^{-1}$  and  $1.6 \times 10^{-3}$  ma, respectively.

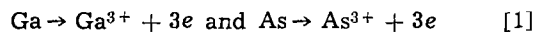
### Discussion

The first important question to be answered is: why are there differences in the rest and dissolution potentials on various faces of the single GaAs crystal, especially between the inverse {111} planes? GaAs, contrary to Ge (14, 15), has a noncentrosymmetric lattice. On etching such a crystal more Ga atoms will be present on one {111} plane whereas on the inverse side more As atoms will be present. This behavior is a consequence of the differential number of valence electrons (3 and 5) of the Ga and As atoms involved. While the bulk of the GaAs structure is, of course, neutral with no charge transfer across the four tetrahedral valence bridges (9-13), a difference in polarity should manifest itself on the outer planes, especially on the inverse {111}, where predominantly either Ga or As atoms are present. This situation causes a considerable difference in the chemical behavior and in the strength of bonding of the surface atoms. In fact, Arthur (7), has shown from O-desorption measurements that the gas is covering both inverse {111} planes; however, the binding state on the Ga{111} is stronger than on the inverse As side. Thus, Ga atoms are the active adsorption centers for O and the latter can be removed from the planes only as Ga<sub>2</sub>O (7). There was also evidence for an additional, weaker binding state on As{111} (7). Consequently, the sticking probability of O on clean As{111} faces is greater although the bonding is weaker than on Ga{111} faces, which agrees qualitatively with the LEED measurements (9).

However, oxygen may affect the potential of an anode in two or three ways. Taking, as an example, a metal in which O can be dissolved (formation of a solid solution) the free energy of the metal becomes less negative and its potential more noble (17). The same is also achieved by the development of oxides on the surface, presumably because of a mixed potential (18) formation and/or because of a reduction of the effective surface area. The more adherent and less permeable the oxide layer, the more noble is the potential of the metal. Passivation may eventually occur. Removal of the oxide layer must then result in activation of the metal. This behavior was confirmed by Beck and Gerischer, measuring rest potentials of semiconducting Ge in 0.1N NaOH in the presence of air or N<sub>2</sub>: in air the potential was considerably more noble (by 393 and more mv) than in N<sub>2</sub> (14). The reversibility of the change from a more noble potential to a less noble and *vice versa* indicated that the oxygen adsorbed on centrosymmetric Ge was rather loosely bound.

It is not known that GaAs dissolves O; therefore, only surface oxides are of importance with respect to surface charges. Since GaAs is noncentrosymmetric, the largest difference in surface arrangement of the Ga and As atoms occurs on the inverse {111} faces. Hence, the adsorption ability of O or of other species of ions such as OH<sup>-</sup> (in the electrolyte) by the two faces is not equal. Furthermore, the strength of bonding is influenced by the atomic species. According to Arthur (7) the bonding of O is stronger on Ga{111}, and it should exhibit a more noble potential than the inverse face in aqueous electrolytes. Such a behavior was actually observed not only in air but also in

a N<sub>2</sub>-atmosphere. In our study a difference of 0.14v for the rest potentials (3.23 kcal) between the two inverse faces was obtained. Therefore, different adsorption products must have been formed on the inverse faces. Figure 4 shows a 110-plane, perpendicular to both 111-planes of the GaAs lattice. On anodic dissolution both atomic species go into solution as trivalent ions (3, 5)



the 3e being absorbed by the cathode of the d-c source. The reaction of the Ga and As ions with OH<sup>-</sup> of the KOH-solution results in colloidal Ga(OH)<sub>3</sub> and soluble As(OH)<sub>3</sub> or HAsO<sub>2</sub> (+ H<sub>2</sub>O), which is quickly neutralized by the basic solution to form KAsO<sub>2</sub>. However, since the dissolution of Ga(OH)<sub>3</sub>



is slower and the rate decreases with aging of the colloidal hydroxide, the white hydroxide will be adsorbed by the Ga{111} face. The OH<sup>-</sup> might also react directly with the Ga surface atoms, since the Ga bonds are saturated by the bulk of the crystal and the positive charge of the Ga<sup>3+</sup> is on the {111} surface. Ga(OH)<sub>3</sub> adsorption is suggested by the fine, very thin white films observed on GaAs crystals especially on the {110} faces after 3 to 4 hr of anodic dissolution at higher current densities (~ 1 ma·cm<sup>-2</sup>). The adherence of the oxide is surely not equal on all the GaAs planes. It is expected that it will be strongest on Ga{111}, although the layer may be thinner than on the {110} face. Thus, even in a neutral gas atmosphere there is a protective layer on Ga{111} (less developed on As{111}) causing a potential difference between the two, the former being more positive. It is impossible at this time to give other than a qualitative characterization of the surface layers. Nevertheless, the layers explain the decreased rate of anodic dissolution of Ga{111} (Fig. 3).

The inverse side is attacked faster because of easy dissolution of As(OH)<sub>3</sub> in KOH. However, the closely adjacent layer of Ga-atoms (Fig. 4) dissolves also, as the Ga(OH)<sub>3</sub> formed, evidently cannot adhere to the next As row of atoms and, hence slowly dissolves in KOH according to Eq. [2] (formation of gallates). The next As-Ga layer is then attacked in the same way, starting from the dissolving Ga atoms and continuing at higher current densities into the depth of the crystal frequently along etch tunnels perpendicular to the As{111} plane (8). Thus the Ga and As atoms have to go into solution in pairs in accord with the premise of Gerischer (3).

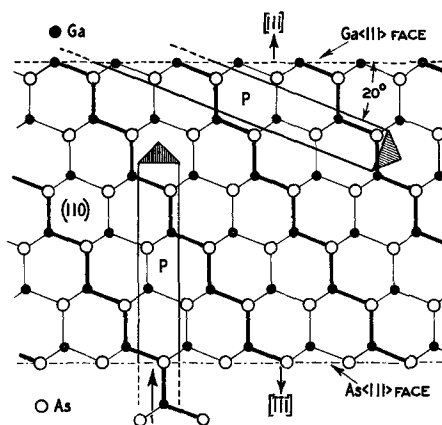


Fig. 4. GaAs{110}-face being in the plane of the page. Both {111}-faces are normal to it. P, primary etch tunnels. The chemical bonds, symbolized by heavy lines, lie in the {110} plane. The arrows represent the direction of the etch tunnels lying in the same plane as the heavy lines (8).



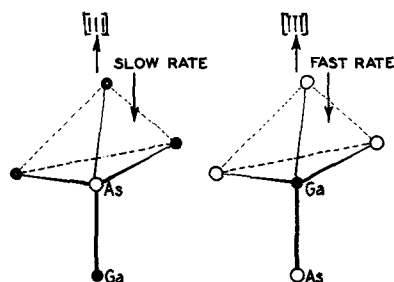


Fig. 5. Various rates of dissolution of Ga atoms on inverse {111} faces.

The Ga{111}-face is partially protected by the slowly dissolving  $\text{Ga}(\text{OH})_3$  film. Where the latter disappears (reaction [2]) the adjacent As atom also dissolves readily. However, this atom is in the {110} plane at an angle of  $20^\circ$  to the Ga{111}. Therefore, at higher current densities this direction may be that of the etch tunnels (Fig. 4) continuing from Ga to As into the depth of the crystal, which actually was observed (8). Consequently, different etch patterns should be produced on the inverse {111}-planes, in agreement with the photomicrographs (8). The dissolution rates on other crystallographic planes must lie between those found for Ga{111} and As{111} (Fig. 3).

The slope of all the  $\text{mv}/\log i$  lines is the same (Fig. 3) and there is no difference in the activation energies (Table I). The conclusion is, therefore, that the rate-determining step must be the same on all the crystallographic planes. The Ga atoms are those which, because of the reasons mentioned, will remain on any of the dissolving GaAs planes, although starting from the As{111} they will dissolve faster than from the Ga{111} side. Therefore, the dissolution of the complex  $\text{Ga-Ga}(\text{OH})_3$  which represents the  $\text{Ga}(\text{OH})_3$  adsorbed by Ga atoms, should be involved in the over-all mechanism. Depending on where the Ga atoms are in the planes (on faces, corners, or edges of the steps developed during dissolution) and how they are followed by As atoms (Fig. 5), different rates of dissolution on various planes will be developed, although the rate-determining reaction will be the same. The value of the dissolution potential appears then to be dependent on the extent of surface coverage and solubility of the  $\text{Ga}(\text{OH})_3$ .

Therefore, it is expected, that every III-V semiconductor will behave differently during etching and anodic dissolution, depending on the chemical behavior of the atoms in the respective electrolytes.

#### Acknowledgment

The authors thank the Office of Naval Research for sponsoring the project on dissolution of semiconductors, and the Monsanto Company, St. Louis, especially Mr. J. B. McNeely of the Central Research Department of the company for donation of the GaAs crystals. Thanks are also due to Dr. J. W. Johnson of the Graduate Center for Materials Research for helpful discussions. This paper is Contribution No. 36 from the Graduate Center for Materials Research.

Manuscript submitted April 19, 1968; revised manuscript received ca. May 21, 1968. This paper was presented at the Montreal Meeting, Oct. 6-11, 1968, as Paper 426.

Any discussion of this paper will appear in a Discussion Section to be published in the June 1969 JOURNAL.

#### REFERENCES

1. e.g., H. C. Gatos and M. C. Lavine, *This Journal*, **107**, 427, 433 (1960).
2. H. W. Pleskow, *Dokl. Akad. Nauk USSR*, **143**, 1399 (1962).
3. H. Gerischer, *Z. Elektrochem.*, **69**, 578 (1965).
4. H. Gerischer, *Z. physik. Chem. N. F.*, **49**, 112 (1966).
5. W. W. Harvey, *This Journal*, **114**, 472 (1967).
6. K. D. N. Brummer, *ibid.*, **114**, 1274 (1967).
7. J. R. Arthur, *J. Appl. Phys.*, **38**, 4023 (1967).
8. J. P. Krumme and M. E. Straumanis, *Trans. AIME*, **239**, 395 (1967).
9. A. U. MacRae, *Surface Sci.*, **4**, 247 (1966).
10. H. Kimmel, *Z. Naturf.*, **20a**, 359 (1965).
11. C. C. Wang and L. H. Spinar, *J. Phys. Chem. Solids*, **24**, 953 (1963).
12. I. I. DeMarco and R. I. Weiss, *Phys. Letters*, **13**, 209 (1964).
13. O. G. Folberth, in H. Welker, "International Conference on Semiconductor Physics," p. 889, Academic Press, New York (1961).
14. F. Beck and H. Gerischer, *Z. Elektrochem.*, **63**, 500, 503, 943 (1959).
15. P. J. Boddy, *This Journal*, **111**, 1136 (1964).
16. K. J. Vetter, *Z. Elektrochem.*, **59**, 596 (1955).
17. W. J. James, W. G. Custead, and M. E. Straumanis, *Corros. Sci.*, **2**, 237, 246, 252 (1962).
18. K. J. Vetter in H. Fischer, K. Haufler and W. Wiederholt "Passivierende Filme und Deckschichten," p. 249, Springer, Berlin (1956).

## Structural Changes During the Anodizing and Sealing of Anodic Aluminas: Intermediate and Far Infrared Analysis

G. A. Dorsey, Jr.

Department of Metallurgical Research, Kaiser Aluminum & Chemical Corporation, Spokane, Washington

#### ABSTRACT

The longer wavelength far infrared absorptions of anodic coatings are attributed to  $\text{Al-O-Al}$  or  $\text{Al-O}^{\cdot}\text{Al}$  linkages.

Absorption band shifts are found to coincide with changes in anodizing conditions, and these shifts appear to be caused by changes in alumina cross-linking. The effects of anodizing time and current density are examined, as are the effects of sealing; the latter also influencing alumina cross-linking. Apparently, during the formation of these films, there is a relatively short period during which an appreciable quantity of barrier layer converts into the form of the porous layer. Sealing yields a similar conversion.

The intermediate infrared region of from 4000 to  $\sim 400$  wavenumbers has been widely used for the examination of aluminas. For example, Frederickson (1) characterized the stretch and bend modes for a

number of mineralogical aluminas while Fichter (2) did some earlier work with anodic aluminas. Our own work (3), again with mineralogical aluminas, was used to derive the following correlation chart for the infrared absorptions of hydrous and anhydrous aluminas.



Alumina bond type	Infrared absorption frequency range (wavenumbers)	Interpretation
AlO $\leftrightarrow$ H (stretch)	3660-2940 $\text{cm}^{-1}$	Bands in this region indicate the presence of water; either free, adsorbed, or combined as hydroxide.
Al $\leftrightarrow$ O (stretch)	1696-1345 $\text{cm}^{-1}$	Monohydrate and anhydrous aluminas may show varying amounts of double bond character. The presence of this bond type indicates a potentially adsorptive or reactive material.
Al $\leftrightarrow$ OH (bend)	1162-900 $\text{cm}^{-1}$	Aluminum hydroxides are indicated by an absorption in this region. Monohydrates are characterized by a band near 1070 $\text{cm}^{-1}$ while trihydrates show bands near, or below, 1025 $\text{cm}^{-1}$ .
Al $\leftrightarrow$ OAl (stretch)	Below 900 $\text{cm}^{-1}$	Bands in this region indicate a high degree of cross-linking; intense bands in this region are often associated with an absence of Al=O bonds. As the degree of cross-linking, i.e., polymer weight, increases, the bond absorption frequency will shift to progressively lower values.

It was also found that the IR absorption of the anodic barrier layer could always be distinguished from IR absorptions due to other structural features within the same film, e.g., absorptions due to the porous layer (4). Deuteration experiments indicated that the anodic barrier layer, from aqueous electrolytes, appeared to be a cyclic trihydrate which underwent certain structural changes during the course of film formation (5). But it was difficult to correlate these changes with those occurring in the porous layer portion of these films. The most reliable indicator for the various anodic porous layers would be the Al—O— $\overset{\text{H}}{\text{H}}$

Al (or Al—O $\rightarrow$ Al) linkage (5). However, IR absorptions of this bond type begin only near the lower wave number limit of the instrument then available to us. Further, the band placement of this linkage shifts rapidly, for progressively thicker films, into the still longer wavelength (lower wavenumber) region of the far infrared.

The far infrared region is a comparatively new one for commercially available instrumentation, and aluminas have not been thoroughly explored with it. Kolesova (6) examined alpha alumina (corundum), alpha trihydrate (gibbsite), and sodium aluminate in the KBr region down to  $\sim 400$  wavenumbers as did Marshall (7), again for alpha alumina. This and our own work, however, indicate that the far infrared spectrum of aluminas is indeed useful in their analysis, often providing the only pertinent IR data that can be used to differentiate between various anhydrous alumina phases.

Alumina absorption in the far infrared appears to be due to Al—O—Al and Al—O $\rightarrow$ Al stretch modes. These occur below 900  $\text{cm}^{-1}$  and are especially pertinent for the investigation of alumina properties relating to cross-linking (polymer weight). Two aluminas of the same type might be expected to have different chemical properties if one were high in polymer weight while the other had a lower, less highly cross-linked, mass. So too, might the properties of various anodic aluminas vary as a function of porous layer cross-linking. Earlier work (5) has shown that the anodic barrier layer, by itself, produces no absorption in the far IR region and does not interfere with porous-layer measurements.

### Experimental

**Anodic aluminas.**—Cleaned alloy KS32 aluminum sheets (alloy 1100 clad with 1100) were used as the

substrate material for the samples prepared. A 1.7M (15 w/o [weight per cent]) sulfuric acid electrolyte was employed, with lead cathodes, at 25°C. Anodizing current densities of 1.3 and 2.6 amp/dm<sup>2</sup> were used with various anodizing times that ranged from 1 to 30 min.

After anodizing, the panels were cut in half and one half of each was sealed in pH 5.5 boiling distilled water while the other half was left unsealed.

**Infrared analysis.**—The samples were examined over the 4000-600  $\text{cm}^{-1}$  range of the Beckman IR-7, as before (3), using a reflectance attachment set at 45° angle of incidence. The far IR data were obtained using a Beckman IR-11 over the 600-35  $\text{cm}^{-1}$  range, but with the reflectance attachment set at 20° angle of incidence. This lower angle was necessary to avoid ATR effects that appear to originate at the barrier-porous interface, when higher reflectance angles are employed in the far IR region. With both instruments, double beam spectra were obtained *vs.* a front-surfaced aluminized mirror which was mounted the same as the sample.

Quantitative determinations were made using a weight method of graphical integration, while band center measurements were made using ordinate scale expansion.

The far IR data were further treated to include the effects of polymer weight (molecular mass) on the placement of an absorption band (wavenumber at maximum absorbance). An alumina with a high mass (highly cross-linked) would have absorption bands at longer wavelengths (lower wavenumbers) than an identical alumina with a lower mass (3). Taking this into account, an empirical relationship was used to differentiate between the same amounts of aluminas of different polymer weights. This relationship can be expressed as:

$$\text{Amount of cross-linking} = \frac{A_{\text{Al-O-Al}}}{\frac{\nu_{\text{Al-O-Al}}}{900}}$$

where:  $A_{\text{Al-O-Al}}$  is band absorbance,  $\nu_{\text{Al-O-Al}}$  is wavenumber of band peak, and 900 is the upper limit for Al—O—Al or Al—O $\rightarrow$ Al stretch vibrations.

### Results and Discussion

**Anodizing mechanisms.**—Figure 1 shows the effects of anodizing time, current density, and sealing on the amount of porous-layer cross-linking. Note that the level portion of each curve, which is established shortly after anodizing begins, breaks suddenly upward. The break occurs after about 10 min anodizing time, for the 1.3 amp/dm<sup>2</sup> coating, and 5 min anodizing time for the 2.6 amp/dm<sup>2</sup> film. Since the number of cou-

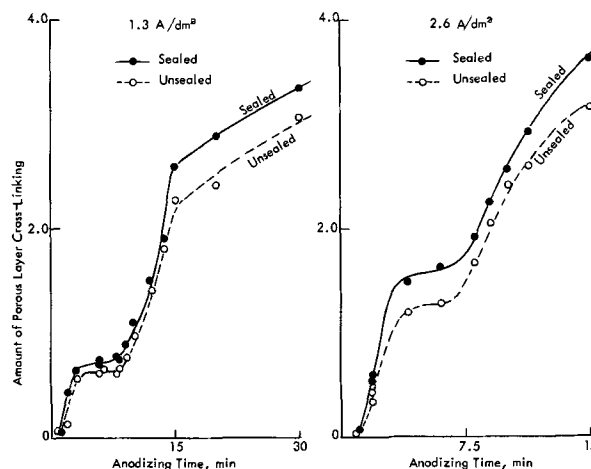


Fig. 1. Amount of porous-layer cross linking

lombs applied during anodizing (at either 1.3 or 2.6 amp/dm<sup>2</sup>) is increasing at a constant rate, the anodic alumina may be forming first one structure and then another. Clearly, the rapid growth of the porous layer accounts for much of this alumina, after the first 14 min of 1.3 amp/dm<sup>2</sup> anodizing (after 7 min of 2.6 amp/dm<sup>2</sup> anodizing). Prior to that, the apparently lower growth rate of the porous layer would imply an alumina distribution between this and other structures. After 20 min at 1.3 amp/dm<sup>2</sup> (10 min at 2.6 amp/dm<sup>2</sup>) the amount of porous-layer cross-linking again changes: it ceases to increase as rapidly, implying another such structural redistribution.

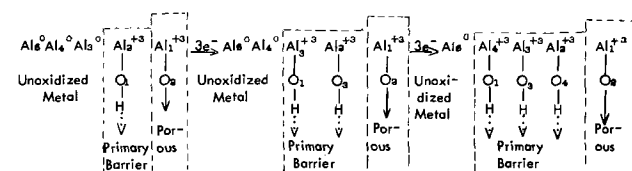
Intermediate range IR data indicated that the amount of incorporated sulfate (1325 cm<sup>-1</sup> band) showed the same trend as did the porous-layer cross-linking. This is reasonable, since the incorporated sulfate content of the porous layer is essentially constant: ~13 w/o. Thus, the apparent changes in porous layer growth rate cannot be accounted for by assuming new sulfate structures. And the amount of structural Al = O remained small and fairly constant, with respect to anodizing time, disappearing almost entirely during sealing. Since the amount of porous layer Al = O did not change during anodizing, this would imply that the apparent changes in porous layer growth rate were due to structural features apart from the porous layer, rather than due to a structural redistribution within that layer. Changes within the barrier layer itself should therefore be examined (Fig. 2).

The amount of barrier layer, identified as primary phase barrier layer, from its band position (5), remains relatively constant for the first 5 min at 1.3 amp/dm<sup>2</sup> anodizing. During this same period, the amount of porous layer increases. Next, the amount of barrier layer increases rapidly with further anodizing time, while the amount of porous-layer cross-linking levels off. But a key feature, here, is an apparent occurrence that took place after the first 10 min of 1.3 amp/dm<sup>2</sup> anodizing, or after the first 5 min of 2.6 amp/dm<sup>2</sup> anodizing. The amount of barrier layer decreases rapidly at this point, while the amount of porous layer increases. Further, as indicated by the band position of the barrier-layer absorption (Fig. 3), it appears that the primary phase barrier layer has been transformed into the secondary phase barrier layer (5).

Based on these data, something resembling the following processes might have taken place:

1. The bare aluminum is oxidized, and the oxidized metal distributes itself between the primary-phase barrier and porous-layer structures.

2. Later, after about 5 min anodizing at 1.3 amp/dm<sup>2</sup>, the oxidized aluminum stays largely in the form of the primary phase barrier layer (925 wavenumber band). Further oxidation of the metal substrate appears to lead mainly to the formation of more primary phase barrier layer.



Newly oxidized aluminum could be expected, under the driving force of the impressed voltage, to capture an oxygen (hydroxide ion) from the layer above it and thus enter the barrier-layer structure. A net

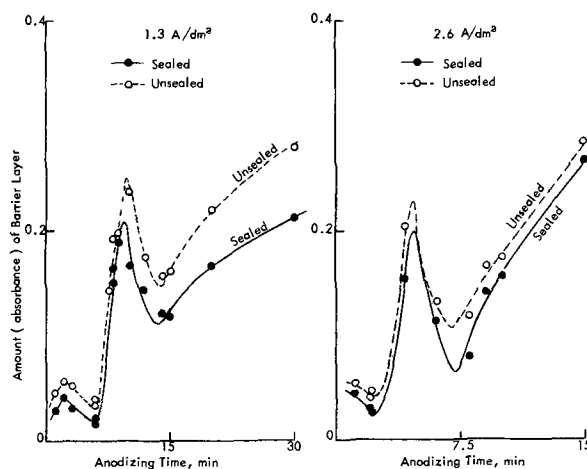


Fig. 2. Amount of barrier layer

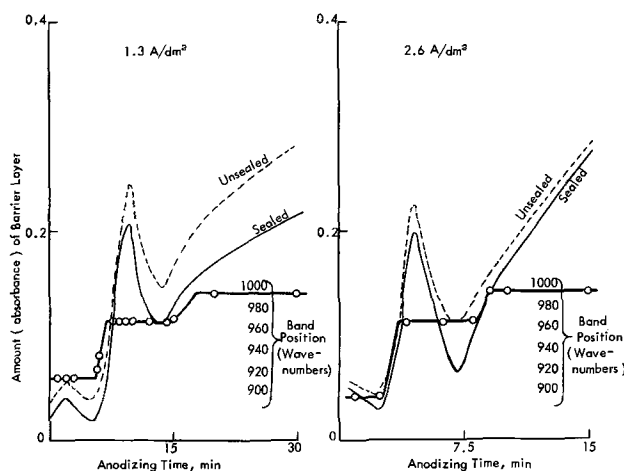
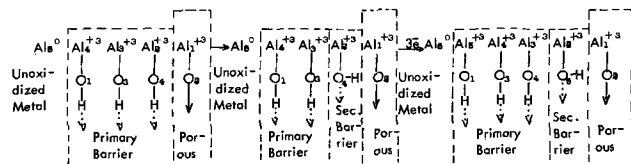


Fig. 3. Barrier layer data also showing band position (sealing did not produce a detectable change in band positions).

transfer of oxygen might then be accomplished if the surface portion of the barrier layer, now oxygen deficient, replenishes its oxygen (hydroxide) from the aqueous electrolyte.

3. Still later, after about 10 min anodizing at 1.3 amp/dm<sup>2</sup>, the already oxidized aluminum in the primary phase barrier structure is apparently transformed into the secondary phase barrier-layer structure (975-1000 wavenumber band). This transformation might be expected to occur at the outer surface of the barrier layer, perhaps due to the dissolving action of the electrolyte, here, due to the sulfate anion.



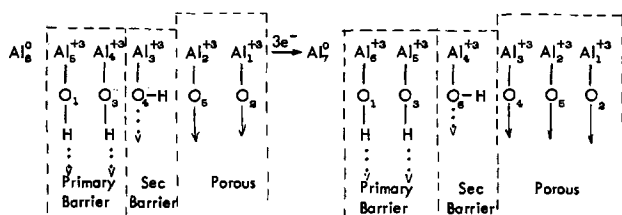
Note that the linkages in the primary and secondary phase barrier layers are represented as being somewhat different. The primary phase barrier layer may be strongly hydrogen bonded (viz., Al—O—H···O—Al bonds) whereas the secondary phase barrier layer may be composed of a mixture of hydrogen bonds and mu-

hydroxy linkages (viz., Al—O···Al).

4. Simultaneous with the transformation of primary-to-secondary phase barrier layers, there seems to be an additional transformation of the secondary phase into the porous layer structure. The rate of primary-to-secondary transformation apparently is somewhat

greater than the secondary-to-porous transformation. Therefore, while a portion of the barrier layer still remains, an appreciable amount of barrier layer appears to be in the form of the secondary phase.

Aluminum ions, created at the metal surface, migrate through the primary phase structure, being drawn out by the impressed voltage. Perhaps now, however, the new oxide layer forms at the primary-secondary barrier interface or somewhere within the secondary phase. The lower-polymer-weight secondary barrier phase would probably be a more open structure and therefore somewhat permeable to the electrolyte. This could mean that, while the coating thickness is continuously increasing, the voltage required to maintain a fixed current density would be relatively constant. The decreased voltage drop across the primary phase (due to the formation of less primary phase) might be offset by the combined (but lower) resistance of the secondary barrier phase and porous layer.



(Note that porous layer oxide is "dead" oxide. There is no migration of metal ions or hydroxide in the porous layer.)

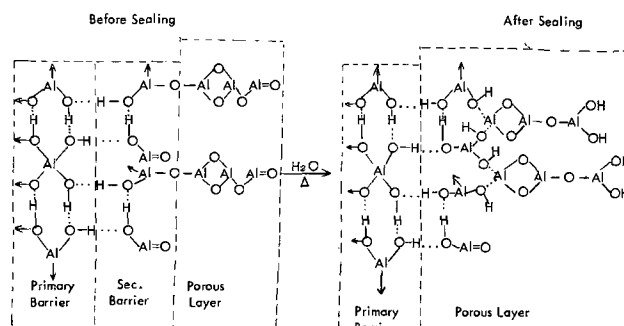
Much work has been done [ref. (8) through (13)] to determine the nature of the migrating species during anodizing. The general conclusion is that both aluminum and oxygen (as in the hydroxide ion) are the migrating species during the early stages of anodizing (which fits with our model previously described) with anion transport predominating.

**Sealing mechanisms.**—Note (Fig. 2) that sealing appears to have decreased the amount of barrier layer. This finding is in keeping with the earlier observations of Hunter and Fowle (14) who noted that sealing lowered the electrical resistance of the anodic coating. Their observation regarding the barrier layer was based on the fair assumption that most of the resistance of the coating is across the barrier layer.

The effect of sealing is also apparent in Fig. 1, showing porous layer cross-linking. Sealing uniformly increased the amount of cross-linking. Furthermore, we know that sealing improves the protectiveness of anodic oxide films. After sealing, the films are more resistant to chemical attack.

Since sealing decreased the amount of barrier layer but increased that of the porous layer, we are led to speculate that at least one important effect of sealing lies in a structural change at the interface between the barrier and porous layers. The upper portion of the barrier layer (secondary phase) may be transformed into the porous layer structure and thereby

cause an increase in the amount of porous layer cross-linking. Perhaps this is accomplished by a structural incorporation joining the individual alumina fibrils of the porous layer at their base. Schematically, this might be represented as follows.



Conventionally, the effects of sealing are measured by observations regarding the changed nature of the porous layer surface (dye rejection, etc.). Certainly, the outer surface of the porous layer is changed, structurally hydrated, by the sealing process. However, it may be that a more important change is that which has taken place at the barrier layer-porous layer interface.

### Acknowledgment

The author wishes to thank the Kaiser Aluminum & Chemical Corporation for its support of this work and for its permission to publish these results.

Manuscript submitted April 2, 1968; revised manuscript received ca. June 21, 1968. This paper was presented at the Dallas Meeting, May 7-12, 1967, as Paper 47.

Any discussion of this paper will appear in a Discussion Section to be published in the June 1969 JOURNAL.

### REFERENCES

1. L. D. Frederickson, Jr., *Anal. Chem.*, **26**, 1883 (1954).
2. R. F. Fichter, *Helv. Phys. Acta*, **19**, 21 (1946).
3. G. A. Dorsey, Jr., *This Journal*, **113**, 169 (1966).
4. G. A. Dorsey, Jr., *ibid.*, **113**, 172 (1966).
5. G. A. Dorsey, Jr., *ibid.*, **113**, 284 (1966).
6. V. A. Kolesova, *Optika i Spektroskopiia*, **6**, 20 (1959).
7. R. Marshall and S. S. Mitra, *J. Chem. Phys.*, **43**, 2893 (1965).
8. J. E. Lewis and R. C. Plumb, *This Journal*, **105**, 496 (1958).
9. G. Amsel and D. Samuel, *J. Phys. Chem. Solids*, **23**, 1707 (1962).
10. J. A. Davies, J. P. S. Pringle, R. L. Graham, and F. Brown, *This Journal*, **109**, 999 (1962).
11. J. A. Davies and B. J. Domeij, *ibid.*, **110**, 849 (1963).
12. J. A. Davies, B. J. Domeij, J. P. S. Pringle, and F. Brown, *ibid.*, **112**, 675 (1965).
13. H. Akahori, *J. Electronmicroscopy*, **10**, 175 (1961).
14. M. S. Hunter and P. Fowle, *This Journal*, **101**, 481 (1954).

# Effluent Gas Detection and Infrared Data for Anodic Alumina Films

G. A. Dorsey, Jr.

Kaiser Aluminum & Chemical Corporation, Department of Metallurgical Research, Spokane, Washington

## ABSTRACT

A simple technique is described for the measurement of volatile components evolved from thin films during baking. This technique is applied to measurements of water liberated from anodic alumina barrier-layer coatings, prepared in boric acid and ammonium tartrate electrolytes, and from the composite films produced in sulfuric acid electrolytes. When correlated with infrared data, these measurements appear to strengthen some earlier speculations regarding anodic oxide structures and transformations.

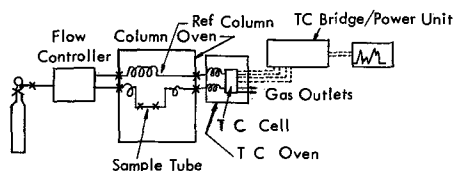
The infrared analysis of hydrate structures is frequently accompanied by thermogravimetric data, so that sample weight changes may be correlated with structural changes. Many papers have dealt with aluminum oxides using these techniques. But while infrared has been used in the analysis of anodic alumina films, similar thermogravimetric or related data have not been available.

Since infrared data led us to propose that hydroxide structures are produced during barrier-layer formation in aqueous electrolytes (1), we sought to re-examine this interpretation using thermal analysis. Unfortunately, a thermobalance is not suited to the measurement of the small quantities of water that might be evolved from these thin films. The anodic films cannot be isolated from aluminum substrates without jeopardizing the integrity of their water contents; for example, boiling methanol-iodine solution is commonly used to isolate these films. Weighing error generally precludes good thermogravimetric data when these films remain on their comparatively massive substrates.

Therefore, a new technique was developed for the thermal analysis of these thin films.

## Experimental

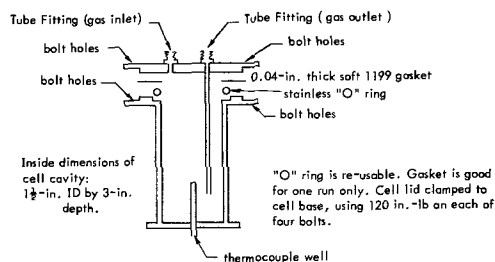
**Effluent gas detection (EGD) apparatus.**—A gas chromatograph, if one is available, will provide all the necessary instrumentation needed for these measurements. We used a Varian Aerograph Model 1525B, although any instrument should prove satisfactory if the column oven is large and accessible. Lacking a gas chromatograph, the necessary elements are: (a) an oven which can be heated to  $\sim 400^\circ\text{C}$ , or above, at a rate of  $\sim 15^\circ\text{C}/\text{min}$ , (b) a dual gas flow controller, and a regulated supply of helium, (c) a thermal conductivity detector (TC cell) with associated power supply, wheatstone bridge, and separate constant temperature oven, (d) a strip chart recorder, preferably equipped with a Disc Integrator (Disc Instruments, Inc.), and (e) associated tube fittings and stainless steel columns (diagram a).



The analysis is begun by stabilizing the TC oven to some preselected temperature, usually about  $30^\circ\text{C}$  above the maximum temperature to be reached by the column oven. The sample is then loaded into a short length of stainless tubing ( $\frac{3}{8}$ -in. OD), and this is joined to the gas inlet and outlet (TC side) fittings of the main sample column. Helium flow is then adjusted

to  $\sim 65$  ml/min through reference and sample columns, via a bubble flowmeter temporarily attached at the TC gas outlet. After allowing a few minutes to purge all air from the system, the TC bridge circuit may be turned on and adjusted (it should always be turned off before breaking connections at the end of a run, and when the system has not been thoroughly purged with helium). Starting at room temperature, the column oven heating is begun while the sample temperature is monitored with a thermocouple attached to the sample tube. As heating begins to liberate volatile components from the sample, the recorder tracing will be deflected in accordance with the quantity of gas liberated (Fig. 1), which may be recorded as a function of sample temperature. Once calibrated, the area under the deflection curve provides a direct measure of the quantity of volatile components liberated. The components themselves may be identified either by foreknowledge of the sample or by trapping the components, as they emerge in the TC outlet gas stream, for identification by other techniques.

We used a somewhat different arrangement for thin film analysis. Instead of tubing to contain the sample, a stainless steel cell was employed (diagram b). The



cell cavity easily contained 600 to 800  $\text{cm}^2$  of anodized foil, or thin sheet, so that the quantity of volatiles evolved (in this case, water) were relatively large. The O-ring and aluminum gasket combination provided a leaktight assembly throughout the baking cycle.

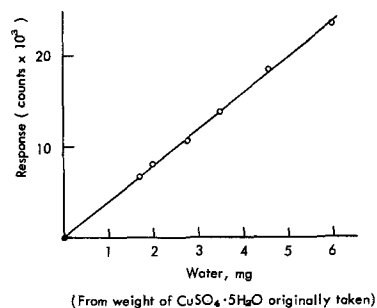


Fig. 1. Calibration curve for effluent gas detection method using copper sulfate pentahydrate (AR grade standard).

Key words: anodic aluminas, hydration, gas chromatograph, IR.

The heating rate of the cell, along with that of the column oven, is shown in Fig. 2. A calibration curve, for water, is shown in Fig. 1. The response, in counts  $\times 10^3$ , shown in Fig. 1 was taken from the readout of a Disc Integrator mounted on the recorder.

The effluent from some of the anodized samples (400-v boric acid films and 15-min sulfuric acid coatings) was trapped in nujol at the TC outlet and subsequently identified, by IR, as water. No detectable water was found in a similar trapping of carrier gas during a blank run.

**Anodized samples.**—Cleaned alloy 1199 aluminum foil was used as the substrate material for the samples. The following electrolytes were employed, prepared with distilled water: 0.2M ammonium tartrate at pH 5.5, 2.0M boric acid, and 0.3M sulfuric acid. The barrier-layer electrolytes (tartrate and borate) were operated at 90°C, with a current density of 0.32 amp/dm<sup>2</sup>, to the desired final voltage, after which the current was allowed to decay to  $\sim 0.02$  amp/dm<sup>2</sup>. The sulfuric acid-anodized films were prepared at 30°C, with a current density of 1.08 amp/dm<sup>2</sup>, and with the various anodizing times indicated in the Results section. None of these samples was sealed.

The coatings were rinsed thoroughly after anodizing and were dried at room temperature and humidity before proceeding further. Surprisingly, long periods of storage time before analysis (up to 60 hr) produced no measurable effects in the EGD data, when compared with duplicate films analyzed within 1 hr of preparation.

**Infrared analysis.**—The sulfuric acid-anodized samples were examined over the 4000-to-600 cm<sup>-1</sup> range of a Beckman IR-7 instrument operated in double-beam mode. As before (1), 45° specular reflectance attachments were used. The IR data were obtained both before and after the EGD bake.

The amount of barrier layer present was taken from the absorbance of the 900-to-1000 cm<sup>-1</sup> band. The amount of porous layer was based on the absorbance of the 1325 cm<sup>-1</sup> Al=O band (2); actually, this is probably an Al=O  $\leftarrow$  S band associated with structurally incorporated sulfate. We did not use far infrared here since, for thin films, this 1325 cm<sup>-1</sup> band provides as reliable a measure of porous layer quantity as does the far infrared Al—O—Al stretch. This may be seen by comparing the data shown in Fig. 6 with those given in ref. (3).

## Results and Discussion

Figure 3 shows Effluent Gas Detection (EGD) data obtained for barrier-layer oxides formed at various voltages (100 through 400v) for which the 14Å/v relationship should apply. Note the linear correspondence between the forming voltage and the micrograms of water evolved per square centimeter of sample area. Note, also, that these data were independent of the type of barrier-layer electrolyte employed: boric acid

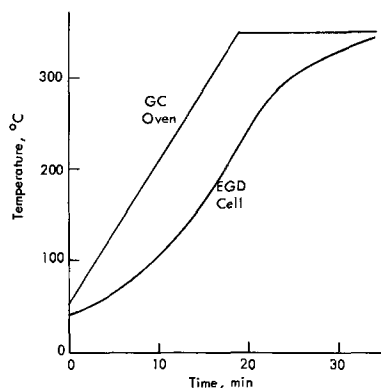


Fig. 2. Heating rate of effluent gas detection cell in gas chromatograph oven.

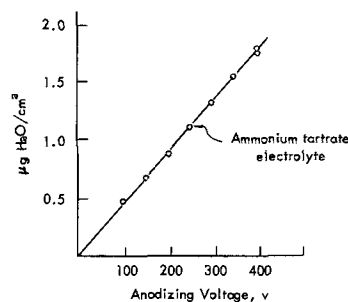


Fig. 3. Micrograms water (per cm<sup>2</sup>) evolved from boric-acid-anodized barrier-layer films plotted vs. forming voltage (350°C maximum cell temperature).

or ammonium tartrate. However, these data were obtained by heating only up to  $\sim 350^\circ\text{C}$ . Two partially resolved water peaks were thus obtained, near 120° and 170°C, but there are indications (Fig. 4) that another, probably larger, water liberation peak lies above 400°C. Since we are now unable to work in this upper temperature range, total hydrate contents could not be determined. However, even these limited data have proven useful.

Figure 5 shows similar EGD data obtained for unsealed films prepared in the 0.3M sulfuric acid electrolyte. Although most of these films contained porous layers as well as barrier layers, the EGD data (water liberation temperatures) for these films were not materially different from those obtained with the pure barrier-layer films formed in boric acid or ammonium tartrate. Furthermore, there was no detectable hydrate in the porous-layer portion of these unsealed films (the absence of 3400, 1640, or 1020 cm<sup>-1</sup> absorption bands in the IR data indicated that there was no physically adsorbed or structural hydroxide). These two observations allow us to propose that at least some of the effluent water came from the barrier-layer portion of these films.

Infrared data (Fig. 6) for these same films show that some correlation exists between the EGD data and the amount of barrier layer present. The quantity of effluent water was linear with respect to the amount of barrier layer (IR absorbance) for the first 4 min of

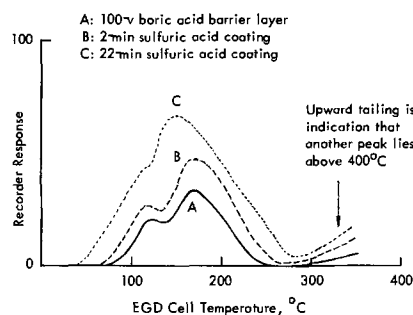


Fig. 4. Typical EGD curves of sulfuric-acid-anodized films. Recorder response vs. cell temperature.

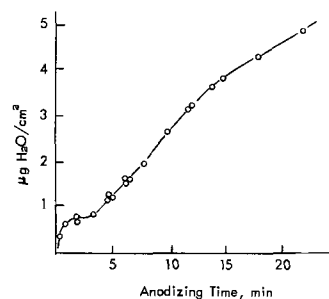


Fig. 5. Micrograms water (per cm<sup>2</sup>) evolved from films formed in 0.3M sulfuric acid at 1.08 amp/dm<sup>2</sup> and 30°C plotted vs. anodizing time.

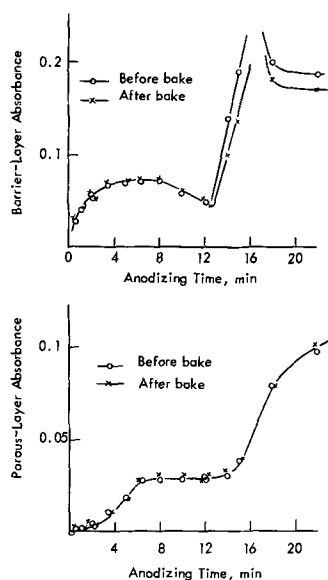


Fig. 6. Infrared data showing effect of baking on amounts of barrier and porous layers formed in sulfuric acid electrolyte.

anodizing time. But, from 4 to 14 min, the amount of effluent water increased while the amount of barrier layer remained relatively constant. However, there was an apparent change taking place within the barrier layer during this same period. The placement of the barrier-layer IR band center (Fig. 7) shifted from 920 to 980  $\text{cm}^{-1}$ ; this suggests a decrease in polymer weight of the barrier layer as anodizing progressed from 4 to 14 min.

We reported such a change earlier and termed it a transformation from primary to secondary barrier phases. It would probably be accompanied by an increase in the percentage of water released from the barrier layer at these temperatures. When heated to  $\sim 350^\circ\text{C}$ , the less polymerized secondary barrier phase might be expected to release proportionally more of its structural water than the more highly polymerized primary barrier phase. For these same films, there was also a minor confirming trend in the EGD peak placement: the major liberation temperature shifted from  $170^\circ\text{C}$ , for thin films, to  $\sim 150^\circ\text{C}$  for the thick films (see Fig. 4).

Infrared data for these films were obtained both before and after the EGD bake. But the IR data obtained after baking are subject to question. We found that baking to  $\sim 350^\circ\text{C}$  rendered these films highly reactive toward readsorption of water. After being baked under helium and cooled to room temperature, the purge was broken for 5 min. The purge was then resumed, and the EGD run was repeated. Most of the samples thus

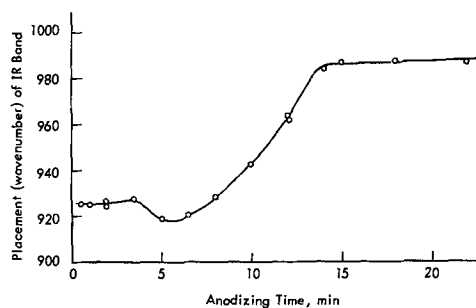


Fig. 7. Infrared data showing placement of barrier-layer absorption band center plotted as a function of anodizing time in sulfuric acid electrolyte.

treated regained 30-50% of their original water during this brief interruption of purge, and apparently regained their original structure: liberation peaks were again observed at  $120^\circ$  and  $170^\circ\text{C}$ , not at  $80^\circ$ -to- $100^\circ\text{C}$  as is the case for nonstructural water. When repetitive determinations were made with similar samples, but without interrupting the purge, no further water liberation took place once the sample had been baked to equilibrium at  $350^\circ\text{C}$ .

Since the IR analysis re-exposed each sample, after EGD bake, to atmospheric humidity, we should not expect too much difference in the IR spectra of these films before and after baking. Indeed, there was very little difference (Fig. 6). The amount of barrier layer was unaltered by baking, but only for those films prepared by anodizing for less than 14 min in sulfuric acid. After 14 min of anodizing, there was a noticeable decrease in the amount of barrier layer present after baking. This would seem to indicate that the secondary barrier phase, discussed earlier (1), was less subject to rehydration than the primary barrier phase which predominates in the first few minutes of anodizing. Baking did not appear to alter the amount of porous layer in any of these same films.

#### Acknowledgment

The author wishes to thank the Kaiser Aluminum & Chemical Corporation for its support of this work and for its permission to publish these results.

Manuscript submitted April 2, 1968; revised manuscript received *ca.* June 21, 1968. This paper was presented at the Boston Meeting, May 5-9, 1968, as Paper 19.

Any discussion of this paper will appear in a Discussion Section to be published in the June 1969 JOURNAL.

#### REFERENCES

1. G. A. Dorsey, Jr., *This Journal*, **113**, 284 (1966).
2. G. A. Dorsey, Jr., *ibid.*, **113**, 169 (1966).
3. G. A. Dorsey, Jr., *ibid.*, **115**, 1053 (1968).

# Preparation and Luminescence of Selected $\text{Eu}^{3+}$ -Activated Rare Earth-Oxygen-Sulfur Compounds

James W. Haynes and Jesse J. Brown, Jr.\*<sup>1</sup>

Chemical and Metallurgical Division, Sylvania Electric Products Inc., Towanda, Pennsylvania

## ABSTRACT

The hydrated sulfate, sulfate, oxysulfate, and oxysulfide compounds of yttrium, lanthanum, gadolinium, and lutetium were prepared using precipitation techniques and controlled atmosphere high temperature heat treatments. The temperature stability range in air for each compound was investigated by DTA and TGA methods. X-ray diffraction powder data are presented for the fourteen compounds isolated. The only compounds that showed significant  $\text{Eu}^{3+}$ -activated luminescence were the oxysulfates and oxysulfides.  $\text{Y}_2\text{O}_2\text{S}:\text{Eu}$ , the most efficient phosphor examined, is as bright as  $\text{YVO}_4:\text{Eu}$  and distinctly more "red." Luminescence data are presented and discussed.

The luminescence of  $\text{Eu}^{3+}$ -activated rare earth compounds has been a subject of considerable interest for a number of years, primarily, because of the use of certain of these materials in the preparation of color television screens. Recent interest throughout the industry has involved compounds arising from rare earth-oxygen-sulfur combinations.

In the present investigation the preparation, characterization, and luminescence of fourteen  $\text{Eu}^{3+}$ -activated rare earth sulfate, oxysulfate, and oxysulfide compounds are described. Of the rare earth elements, those which have been found to be most useful as host lattice cations for impurity activation are the ones with  $4f^0$ ,  $4f^7$ , or  $4f^{14}$  electronic configurations. These are lanthanum, gadolinium, and lutetium; yttrium, because of its close similarity to lanthanum, was also studied.

### Related Literature

Wendlandt and co-workers (1-3) investigated the thermal decomposition of the rare earth sulfates using differential thermal analysis (DTA) and thermogravimetric analysis (TGA) techniques. The hydrated sulfates, mainly octa-hydrates, were crystallized from solutions at room temperature. The thermal decomposition in air was found to follow the scheme: rare earth hydrated sulfate,  $\text{R}_2(\text{SO}_4)_3 \cdot x\text{H}_2\text{O} \xrightarrow{\text{I}}$  anhydrous rare earth sulfate,  $\text{R}_2(\text{SO}_4)_2 \xrightarrow{\text{II}}$  rare earth oxysulfate,  $\text{R}_2\text{O}_2\text{SO}_4 \xrightarrow{\text{III}}$  rare earth sesquioxide,  $\text{R}_2\text{O}_3$ .

The temperature ranges over which each of these reactions take place for the yttrium, lanthanum, gadolinium, and lutetium compounds are summarized in Table I.

The stable rare earth oxysulfide compounds,  $\text{R}_2\text{O}_2\text{S}$ , have been prepared by several methods. Eastman *et al.* (4) and others (5, 6) have prepared  $\text{Ce}_2\text{O}_2\text{S}$  by passing sulfur vapor or  $\text{H}_2\text{S}$  over  $\text{CeO}_2$  at  $1200^\circ$  and  $1300^\circ\text{C}$ . Surgutskii and Serebrennikov (7) prepared most of the rare earth oxysulfides by heating the appropriate anhydrous rare earth sulfate in a CO atmosphere above  $600^\circ\text{C}$ . Pitha, Smith, and Ward (8) prepared  $\text{La}_2\text{O}_2\text{S}$  by heating  $\text{La}_2(\text{SO}_4)_3$  to form  $\text{La}_2\text{O}_2\text{SO}_4$ , followed by reduction in a hydrogen atmosphere. It was also found that  $\text{La}_2\text{O}_2\text{S}$  was an ultraviolet excited phosphor when activated by lead-indium or lead-europium ions.

### Chemicals and Equipment

High purity, 99.99+%, rare earth oxides were used as starting materials. Semiquantitative spectrographic analyses of each oxide were obtained to assure that other rare earth impurities were not present above trace levels.

\* Electrochemical Society Active Member.

<sup>1</sup> Present address: Department of Metals and Ceramic Engineering, Virginia Polytechnic Institute, Blacksburg, Virginia 24061.

High-temperature heat treatments in air were carried out in an electrical resistance heated box furnace. Controlled atmosphere ( $\text{H}_2$ ,  $\text{H}_2\text{S}$ , and/or  $\text{N}_2$ ) heat treatments were performed in electrical resistance heated fused silica tube furnaces. Samples were normally heated in fused silica containers.

A Norelco x-ray diffractometer employing  $\text{CuK}\alpha$  radiation, operating at 40 kv and 15 ma was used and a goniometer scanning rate of  $1^\circ\text{-}2\theta/\text{min}$  was used.

Differential thermal analysis (DTA) data were obtained using a Model 12BC2 apparatus manufactured by Robert L. Stone Company, Austin, Texas. Thermogravimetric analysis (TGA) data were obtained using a Stanton Thermobalance, distributed by the Burrell Corporation, Pittsburgh, Pennsylvania. Both DTA and TGA data were normally obtained using a heating rate of  $10^\circ\text{C}/\text{min}$ .

All fluorescence excitation and emission spectra and peak height measurements were obtained with a Perkin-Elmer spectrofluorimeter as previously described (9). Cathodoluminescent spectra were obtained using a demountable cathode ray tube operating at 12 kv anode potential and 6  $\mu\text{amp}$  beam current over a standard scan TV raster of 1 in.<sup>2</sup> area. Brightnesses under these conditions were measured with an eye-corrected Weston foot-lambert meter.

## Experimental Results

**Preparation and identification of compounds.**—All compounds isolated in this study were routinely identified by x-ray diffraction powder methods. Since most of these data are not readily available in the literature, they are listed here in Table II.

**Hydrated sulfate compounds.**—Yttrium, lanthanum, gadolinium, and lutetium hydrated sulfates were prepared by precipitation techniques. The respective rare earth oxide was dissolved in concentrated nitric acid and the solution was diluted by addition of an equal volume of water, then a solution of sulfuric acid (enough to give approximately 10% excess sulfate ion over that required to form the stoichiometric rare earth sulfate) was added slowly. The solution was allowed to cool to room temperature and the rare earth hydrated sulfate was precipitated by adding a 200% (by volume) excess of methanol. After digesting for

Table I. Decomposition temperature ranges for the hydrated sulfate compounds of Y, La, Gd, and Lu

Starting material	Reaction range ( $^\circ\text{C}$ )		
	I	II	III
$\text{Y}_2(\text{SO}_4)_3 \cdot 8\text{H}_2\text{O}$	70-195	920-1124	1124-1248
$\text{La}_2(\text{SO}_4)_3 \cdot 9\text{H}_2\text{O}$	50-265	890-1096	>1400
$\text{Gd}_2(\text{SO}_4)_3 \cdot 8\text{H}_2\text{O}$	110-260	858-1014	1163-1300
$\text{Lu}_2(\text{SO}_4)_3 \cdot 8\text{H}_2\text{O}$	100-220	Unstable	Completed by 1144

about 45 min, the precipitate was filtered and washed twice; once with a 1:1 solution of H<sub>2</sub>O and methanol and once with pure methanol. The precipitate was allowed to dry thoroughly on the suction filter.

*Anhydrous sulfate compounds.*—The thermal decomposition in air of the four rare earth hydrated sulfates

Table II. X-ray diffraction powder data for the hydrated sulfate, sulfite, oxysulfate, and oxysulfide of Y, La, Gd, and Lu

La <sub>2</sub> (SO <sub>4</sub> ) <sub>3</sub> · 6H <sub>2</sub> O		Y <sub>2</sub> (SO <sub>4</sub> ) <sub>3</sub> · 8H <sub>2</sub> O		Gd <sub>2</sub> (SO <sub>4</sub> ) <sub>3</sub> · 8H <sub>2</sub> O		Lu <sub>2</sub> (SO <sub>4</sub> ) <sub>3</sub> · 8H <sub>2</sub> O	
d (Å)	I/I <sub>0</sub>	d (Å)	I/I <sub>0</sub>	d (Å)	I/I <sub>0</sub>	d (Å)	I/I <sub>0</sub>
7.98	100	9.02	14	—	—	8.84	32
7.02	49	7.56	5	—	—	7.43	8
5.98	4	6.75	48	6.77	13	—	—
5.68	4	6.60	75	6.60	77	6.53	74
5.24	88	5.94	100	5.96	100	5.90	95
5.11	82	5.53	82	5.57	7	5.47	27
4.83	27	5.21	14	5.23	13	5.15	65
4.61	18	5.12	4	—	—	—	—
4.51	40	4.77	56	4.79	33	4.71	79
4.26	30	4.48	53	4.48	68	4.43	80
4.13	19	4.13	12	4.13	23	4.07	26
4.07	43	4.04	5	—	—	—	—
3.76	13	3.96	4	—	—	3.86	3
3.50	22	3.75	56	3.76	23	3.70	75
3.42	54	3.67	75	3.69	77	3.64	80
3.29	82	3.64	34	3.64	20	3.60	45
3.25	74	3.42	39	3.42	10	3.40	54
3.20	98	3.40	45	3.40	29	3.36	75
3.13	88	3.35	63	3.38	44	3.31	75
3.06	5	3.30	7	3.31	3	—	—
2.97	25	3.20	37	3.22	4	3.17	11
2.94	11	3.12	28	3.14	16	3.08	55
2.86	34	2.98	94	3.01	35	2.94	100
2.79	32	2.95	86	2.97	40	—	—
2.73	19	2.92	40	2.94	16	—	—
2.72	29	2.91	40	2.92	15	2.88	76
2.64	57	2.85	2	—	—	—	—
2.62	64	2.82	10	2.84	7	2.79	8
2.58	21	2.77	5	2.79	6	2.73	12
2.55	40	—	—	2.76	5	—	—
2.51	5	2.68	30	2.69	17	2.65	53
2.44	4	2.62	42	2.63	35	2.60	68
2.41	4	—	—	—	—	2.54	23
2.35	12	2.54	5	2.54	4	2.51	24
2.30	19	2.50	19	2.50	26	2.47	68
2.25	42	2.48	19	2.49	38	2.46	47
2.24	40	2.46	11	2.46	10	2.44	20
2.18	18	2.42	2	—	—	—	—
2.16	10	2.41	2	—	—	—	—
2.12	14	2.37	17	2.39	13	2.36	32
2.09	24	2.35	9	2.36	5	2.33	24
2.06	6	—	—	—	—	2.27	4
2.04	44	2.28	16	2.27	11	2.24	27
2.02	33	Other ref.	—	Other ref.	—	Other ref.	—
Other ref.	—	—	—	—	—	—	—

La <sub>2</sub> (SO <sub>4</sub> ) <sub>3</sub>		Y <sub>2</sub> (SO <sub>4</sub> ) <sub>3</sub>		Gd <sub>2</sub> (SO <sub>4</sub> ) <sub>3</sub>		Lu <sub>2</sub> (SO <sub>4</sub> ) <sub>3</sub>	
d (Å)	I/I <sub>0</sub>	d (Å)	I/I <sub>0</sub>	d (Å)	I/I <sub>0</sub>	d (Å)	I/I <sub>0</sub>
9.02	6	6.46	13	6.51	15	6.41	51
7.62	6	6.03	10	—	—	—	—
7.43	10	5.84	34	5.90	10	—	—
6.49	80	4.90	19	—	—	—	—
5.94	5	4.55	100	4.61	100	4.52	97
5.20	93	4.09	52	4.15	10	4.02	5
5.01	17	3.90	61	3.93	38	3.86	62
4.89	13	3.76	43	3.83	7	3.75	5
4.43	100	3.64	11	3.59	7	—	—
4.25	3	3.53	43	—	—	3.52	4
4.05	6	—	—	—	—	3.42	11
3.88	3	3.31	78	3.36	24	—	—
3.73	6	3.25	34	3.27	27	—	—
3.54	80	3.20	47	3.24	40	3.20	89
3.46	42	3.11	40	3.15	13	3.11	8
3.41	40	—	—	—	—	3.02	13
3.03	79	2.98	30	—	—	2.93	10
2.91	42	2.92	25	—	—	2.87	67
2.83	55	—	—	2.86	21	—	—
2.72	8	2.75	39	2.79	5	—	—
2.60	13	2.62	58	2.67	33	2.61	100
2.47	32	2.56	11	—	—	2.55	10
2.25	13	2.46	4	—	—	—	—
2.18	30	2.39	3	—	—	2.36	2
2.15	28	2.32	17	—	—	—	—
2.12	14	2.26	25	2.30	17	2.25	28
2.08	13	2.17	19	—	—	2.14	13
2.03	3	2.11	11	—	—	2.08	5
1.99	6	2.08	22	—	—	—	—
Other ref.	—	2.04	21	2.05	13	2.02	65
—	—	Other ref.	—	Other ref.	—	Other ref.	—

La <sub>2</sub> O <sub>2</sub> S		Y <sub>2</sub> O <sub>2</sub> S		Gd <sub>2</sub> O <sub>2</sub> S		Lu <sub>2</sub> O <sub>2</sub> S	
d (Å)	I/I <sub>0</sub>	d (Å)	I/I <sub>0</sub> , %	d (Å)	I/I <sub>0</sub> , %	d (Å)	I/I <sub>0</sub> , %
6.91	6	6.55	32	6.66	22	6.51	30
3.49	54	3.27	98	3.34	91	3.24	100
3.46	69	2.93	100	2.99	100	2.88	100
3.12	100	2.78	8	—	—	—	—
2.46	71	2.74	6	—	—	—	—
2.30	15	2.32	98	2.36	87	2.28	92
2.02	74	2.19	83	2.22	29	2.16	51
1.92	57	1.89	98	1.93	92	1.85	92
Other ref.	—	1.82	97	1.85	87	1.79	89
—	—	Other ref.	—	Other ref.	—	Other ref.	—

La <sub>2</sub> O <sub>2</sub> SO <sub>4</sub>		Gd <sub>2</sub> O <sub>2</sub> SO <sub>4</sub>	
d (Å)	I/I <sub>0</sub>	d (Å)	I/I <sub>0</sub>
7.49	5	6.53	35
6.86	52	3.99	23
4.09	34	3.88	17
4.01	30	3.01	100
3.42	9	2.96	100
3.11	100	2.92	100
2.99	85	2.66	13
2.74	14	2.20	17
2.30	19	2.19	20
2.29	53	2.17	48
2.25	40	2.09	22
2.14	30	2.03	28
2.09	39	1.99	15
2.05	24	1.89	9
2.00	16	Other ref.	—
1.89	12	—	—
1.86	8	—	—
1.81	80	—	—
Other ref.	—	—	—

were examined by DTA and TGA methods. Although these results are in part repetitious of a previous study by Wendlandt *et al.* (1-3) their relevance to the luminescence results discussed in a later section justifies their appearance here (Fig. 1 and Table III). Because of variations in heating rates and purity of starting materials, small variations are expected and observed between the reaction temperatures observed in this investigation and those by Wendlandt *et al.* In addition, Wendlandt and co-workers found 9 waters of hydration for the lanthanum sulfate compound whereas the present study indicated only 6. This discrepancy may originate from the different methods of preparation employed.

Anhydrous rare earth sulfate compounds suitable for x-ray diffraction studies were prepared by igniting the hydrates at 600°C for 4 hr.

*Oxysulfate compounds.*—In view of the DTA and TGA data, decomposition of the rare earth sulfate compounds occurs in two steps: first, two molecular-equivalents of SO<sub>3</sub> are expelled, and then at a higher temperature, the final SO<sub>3</sub> is released. The temperature range separating these two steps was found to vary a great deal depending on the rare earth cation involved. The oxysulfate phases of yttrium and lutetium are either unstable or stable over such a limited temperature range that it was impossible to prepare them in the pure state. The oxysulfate compounds of lanthanum and gadolinium were prepared by heating the corresponding sulfate at 1100°C for several hours. La<sub>2</sub>O<sub>2</sub>SO<sub>4</sub> is stable from 1025° to 1275°C and Gd<sub>2</sub>O<sub>2</sub>SO<sub>4</sub> from 990° to 1125°C. The weight loss data contained in Table III along with x-ray diffraction data were used to identify the formation of these compounds.

*Oxysulfide compounds.*—The oxysulfide compounds of yttrium, lanthanum, and gadolinium were successfully prepared by heating the respective oxysulfate compounds at 1000°C for 2 hr in an inert atmosphere which contained a few per cent by volume of H<sub>2</sub> and H<sub>2</sub>S.

Identification of the oxysulfide compounds was carried out by observing the weight loss resulting from the decomposition of the oxysulfide compound to the sesquioxide as shown in Fig. 2 and Table IV. On heating the oxysulfide compounds in air they initially gain weight in the range of 500°-600°C. This results from the oxidation to the oxysulfate compound which, on further heating, decomposes to the oxide. Since these two reactions occur simultaneously for the yttrium and lutetium compounds it was necessary to follow the net weight loss instead of the stepwise weight change.

Several other methods were used successfully to prepare the oxysulfide compounds. Gassing the oxide with a H<sub>2</sub>S-N<sub>2</sub> mixture at high temperatures was found to be successful for preparing oxysulfide phosphors. This was the method used to prepare Y<sub>2</sub>O<sub>2</sub>S:Eu, the most efficient phosphor found in this investigation. The optimum conditions for the preparation of this phosphor consisted of a 1½ hr heat treatment at 1200°C in a 72% N<sub>2</sub>-28% H<sub>2</sub>S gas mixture (by volume). Although pure Y<sub>2</sub>O<sub>2</sub>S could be prepared over a wide



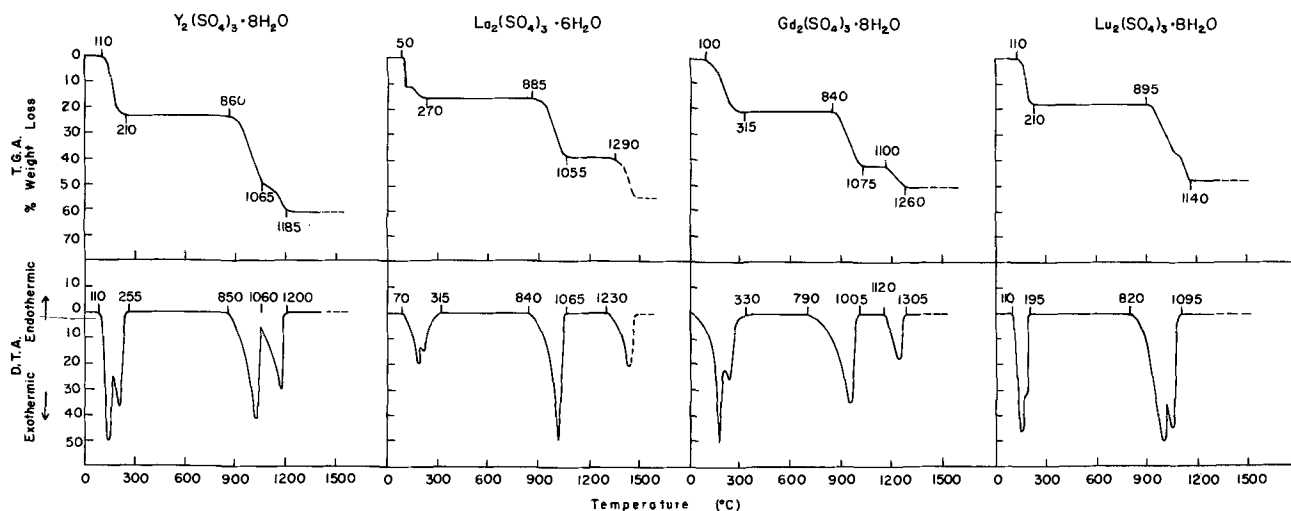


Fig. 1. TGA and DTA curves of the hydrated sulfates of yttrium, lanthanum, gadolinium, and lutetium.

range of temperatures, times, and atmospheres, the above conditions provided the brightest phosphor. Although some interdependence exists between these three variables, it was generally observed that below 800°C and at H<sub>2</sub>S concentrations below 10% incomplete reaction occurred. Above 38%, at all temperatures examined, a dark brown colored product developed on the exposed areas of the sample. Presumably this material was Y<sub>2</sub>S<sub>3</sub>.

Another method of preparation involved blending of rare earth oxide with excess (NH<sub>4</sub>)<sub>2</sub>SO<sub>4</sub> and heat treating the mixture between 600° and 900°C for 2 hr in an H<sub>2</sub> atmosphere. Several per cent H<sub>2</sub>S gas (by volume) added to the atmosphere insured the formation of the appropriate rare earth oxysulfide compound.

**Luminescence studies.**—All of the stable yttrium, lanthanum, gadolinium, and lutetium sulfate, oxysulfate, and oxysulfide compounds previously described were activated by co-precipitating Eu<sup>3+</sup> in the starting material and systematically examined for photo- and cathodoluminescence. The extent of examination varied from phosphor to phosphor depending on the promise each showed after preliminary experiments.

1. Sulfate compounds—The hydrous and anhydrous rare earth sulfate compounds are poor host matrices for Eu<sup>3+</sup>-activated luminescence. Both La<sub>2</sub>(SO<sub>4</sub>)<sub>3</sub>·Eu and Gd<sub>2</sub>(SO<sub>4</sub>)<sub>3</sub>·Eu showed weak red luminescence when prepared by igniting the hydrates at 600°C for 6 hr. The remainder of the rare earth sulfates were inert.

2. Oxysulfate compounds—La<sub>2</sub>O<sub>2</sub>SO<sub>4</sub> and Gd<sub>2</sub>O<sub>2</sub>SO<sub>4</sub>, the only oxysulfate compounds examined that were stable in air, provided mediocre red-emitting Eu<sup>3+</sup>-activated phosphors. Figure 3 shows the excitation and emission spectra for these two preparations. The most intense emission for both phosphors is approximately one third as intense as that of the commercial phosphor YVO<sub>4</sub>:Eu under 253.7 nm excitation. Neither phosphor displayed significant luminescence under cathode-ray excitation.

3. Oxysulfide compounds—Of the three groups of rare earth-oxygen-sulfur compounds investigated the oxysulfides consistently provided the most efficient Eu<sup>3+</sup>-activated luminescence. Three of these phosphors, Y<sub>2</sub>O<sub>2</sub>S:Eu, La<sub>2</sub>O<sub>2</sub>S:Eu, and Gd<sub>2</sub>O<sub>2</sub>S:Eu were examined in depth and the experimental data are included in Table V.

Lu<sub>2</sub>O<sub>2</sub>S:Eu was only briefly studied because of the high cost of lutetium.

The excitation and emission spectral energy distribution of the four rare earth oxysulfide phosphors are shown in Fig. 4. All of these preparations contained 5.0 m/o (mole per cent) Eu<sub>2</sub>O<sub>2</sub>S in crystalline solution with the host matrix. For all practical purposes the cathodoluminescent spectra are identical with those obtained using ultraviolet excitation.

As is the case with most families of rare earth compounds, the crystal structures of the oxysulfides are sufficiently similar to one another that only minor variations exist in the luminescent spectra. The major

Table III. Thermogravimetric data for the decomposition of the hydrated rare earth sulfates of Y, La, Gd, and Lu in air

Chemical reaction	Reaction temperature range (°C)	Theoretical	% Weight loss	Experimental
$Y_2(SO_4)_3 \cdot 8H_2O \xrightarrow{\Delta} Y_2(SO_4)_3 + 8H_2O \uparrow$	110-210	23.6		23.5
$Y_2(SO_4)_3 \xrightarrow{\Delta} Y_2O_2SO_4 + 2SO_3 \uparrow$	860->1065	34.4		33.2
$Y_2O_2SO_4 \xrightarrow{\Delta} Y_2O_3 + SO_3 \uparrow$	<1065-1185	26.2		25.7
$La_2(SO_4)_3 \cdot 6H_2O \xrightarrow{\Delta} La_2(SO_4)_3 + 6H_2O \uparrow$	50-270	16.0		16.7
$La_2(SO_4)_3 \xrightarrow{\Delta} La_2O_2SO_4 + 2SO_3 \uparrow$	885-1055	28.3		27.9
$La_2O_2SO_4 \xrightarrow{\Delta} La_2O_3 + SO_3 \uparrow$	1290->1400	19.7		—
$Gd_2(SO_4)_3 \cdot 8H_2O \xrightarrow{\Delta} Gd_2(SO_4)_3 + 8H_2O \uparrow$	100-315	19.3		20.9
$Gd_2(SO_4)_3 \xrightarrow{\Delta} Gd_2O_2SO_4 + 2SO_3 \uparrow$	840-1075	26.6		25.5
$Gd_2O_2SO_4 \xrightarrow{\Delta} Gd_2O_3 + SO_3 \uparrow$	1100-1260	18.1		15.2
$Lu_2(SO_4)_3 \cdot 8H_2O \xrightarrow{\Delta} Lu_2(SO_4)_3 + 8H_2O \uparrow$	110-210	18.4		18.2
$Lu_2(SO_4)_3 \xrightarrow{\Delta} Lu_2O_2SO_4 + 2SO_3 \uparrow$	895->1100	25.1	} 37.6 }	} 36.3 }
$Lu_2O_2SO_4 \xrightarrow{\Delta} Lu_2O_3 + SO_3 \uparrow$	<1100-1140	16.8		

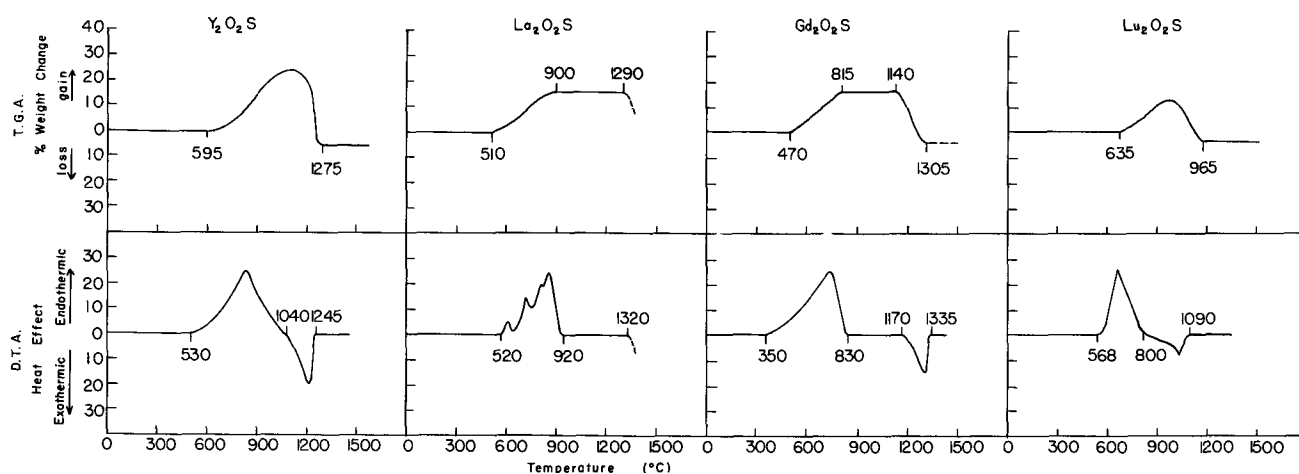


Fig. 2. TGA and DTA curves of the oxysulfide compounds of yttrium, lanthanum, gadolinium, and lutetium.

emission of all four phosphors arises from  ${}^5D_0 \rightarrow {}^7F_2$  transition of the  $\text{Eu}^{3+}$  ion. Less intense emissions arising from  ${}^5D_0 \rightarrow {}^7F_1$ ,  ${}^5D_0 \rightarrow {}^7F_4$ , and other transitions are also evident.

The excitation spectra of all four  $(\text{RE})_2\text{O}_2\text{S}:\text{Eu}$  phosphors show two broad bands which vary in relative intensity depending on the chemical composition of the host matrix.

A. Yttrium oxysulfide—The effect of activator concentration on cathodoluminescent brightness and color (chromaticity coordinates  $x$  and  $y$ ) is shown in Fig. 5. The brightness initially shows a rapid increase, reaching a maximum near 0.5 m/o  $\text{Eu}^{3+}$ . Between 0.5 and 4.0%  $\text{Eu}^{3+}$  the brightness decreases rapidly to a plateau (it should be noted that the brightness decrease in this region is partly due to the decrease in  $x$  chromaticity coordinate and partly to concentration quenching). The plateau extends from approximately 4 to 7 m/o  $\text{Eu}^{3+}$  and is followed by another region of rapidly decreasing brightness. As indicated by the two top curves in Fig. 5, the emission color of  $\text{Y}_2\text{O}_2\text{S}:\text{Eu}$  changes rapidly below 4 m/o Eu. At low activator concentrations (below 4 m/o) the emission is distinctly more orange and the total eye-corrected light output high. At high activator concentrations (above 4 m/o) the emission color is more red and does not change appreciably with activator concentration. In order to more fully understand the peculiar shape of the activator quenching curve of  $\text{Y}_2\text{O}_2\text{S}:\text{Eu}$ , the entire series of samples were examined carefully using a programmed slit spectrofluorimeter (9).

Figure 7 shows the marked difference in the emission spectrum of a sample containing 5 m/o  $\text{Eu}_2\text{O}_3\text{S}$  (top curve) compared with a sample containing 0.5

m/o activator. Numerous low wavelength emission lines become prevalent at low activator concentrations. Careful intensity measurements of each emission line, or in some cases, groups of lines, as activator concentration varied, resulted in the two curves shown in Fig. 6. All emissions occurring below about 600 nm followed curve A. The intensity of the "red"  ${}^5D_0 \rightarrow {}^7F_1$  emissions varies with activator concentration as shown by curve B of Fig. 6. This is a typical activator concentration vs. brightness curve for  $\text{Eu}^{3+}$ -activated phosphors.

By making the most reasonable energy level term assignment from analogy to the work of Brecher *et al.* (10), the groups of observed emissions were identified as shown in Fig. 7. The intensities of all of the transitions arising from  ${}^5D_1$  or  ${}^5D_2$  excited energy levels varied with europium concentration according to curve A in Fig. 6; those originating from  ${}^5D_0$  levels followed curve B.

B. Lanthanum oxysulfide— $\text{La}_2\text{O}_2\text{S}:\text{Eu}$  was prepared in a similar manner to that of  $\text{Y}_2\text{O}_2\text{S}:\text{Eu}$ . The optimum conditions for phosphor preparation were found to be a heat treatment at  $1260^\circ\text{C}$  for  $1\frac{1}{2}$  hr using a 90%  $\text{N}_2$ -10%  $\text{H}_2\text{S}$  (by volume) atmosphere. The lanthanum compound is much more sensitive to the atmosphere composition; formation of a dark skin, presumably  $\text{La}_2\text{S}_3$ , occurred at  $\text{H}_2\text{S}$  concentrations as low as 20%.

The effect of activator concentration on the cathodoluminescent brightness and color of  $\text{La}_2\text{O}_2\text{S}:\text{Eu}$  are shown in Fig. 8. The effect of low activator levels is very similar to that noted for  $\text{Y}_2\text{O}_2\text{S}:\text{Eu}$  as evidenced

Table IV. Thermogravimetric data for the decomposition of the rare earth oxysulfides of Y, La, Gd, and Lu in air

Chemical reaction	Reaction temperature range ( $^\circ\text{C}$ )	% Weight loss	
		Theoretical	Experimental
$\text{Y}_2\text{O}_2\text{S} + 2\text{O}_2 \xrightarrow{\Delta} \text{Y}_2\text{O}_2\text{SO}_4$	595->950	(26.5)	(24.2)
$\text{Y}_2\text{O}_2\text{SO}_4 \xrightarrow{\Delta} \text{Y}_2\text{O}_3 + \text{SO}_3 \uparrow$	<950-1095	26.2	29.3
Net weight loss		6.6	5.1
$\text{La}_2\text{O}_2\text{S} + 2\text{O}_2 \xrightarrow{\Delta} \text{La}_2\text{O}_2\text{SO}_4$	510-910	(18.7)	(16.5)
$\text{La}_2\text{O}_2\text{SO}_4 \xrightarrow{\Delta} \text{La}_2\text{O}_3 + \text{SO}_3 \uparrow$	1295->1400	19.7	No data
Net weight loss		4.7	—
$\text{Gd}_2\text{O}_2\text{S} + 2\text{O}_2 \xrightarrow{\Delta} \text{Gd}_2\text{O}_2\text{SO}_4$	470-815	(16.9)	(16.0)
$\text{Gd}_2\text{O}_2\text{SO}_4 \xrightarrow{\Delta} \text{Gd}_2\text{O}_3 + \text{SO}_3 \uparrow$	1140-1305	18.1	17.6
Net weight loss		4.3	4.3
$\text{Lu}_2\text{O}_2\text{S} + 2\text{O}_2 \xrightarrow{\Delta} \text{Lu}_2\text{O}_2\text{SO}_4$	635->850	(15.5)	(12.5)
$\text{Lu}_2\text{O}_2\text{SO}_4 \xrightarrow{\Delta} \text{Lu}_2\text{O}_3 + \text{SO}_3 \uparrow$	<850-965	16.8	14.0
Net weight loss		3.9	2.9

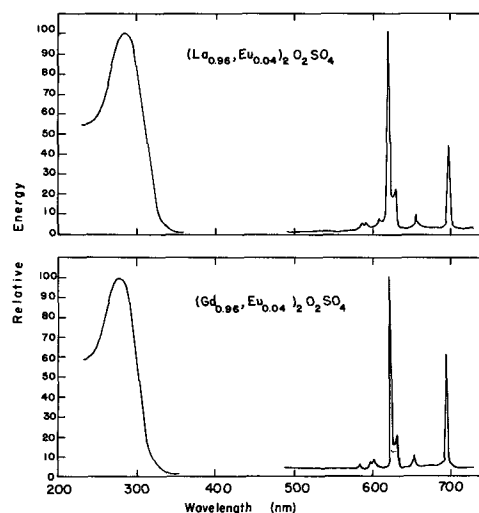


Fig. 3. Excitation and emission spectra of  $\text{Eu}^{3+}$ -activated  $\text{La}_2\text{O}_2\text{SO}_4$  and  $\text{Gd}_2\text{O}_2\text{SO}_4$ .

Table V. Experimental data used to optimize the cathodoluminescence of  $\text{Eu}^{3+}$ -activated  $\text{Y}_2\text{O}_2\text{S}$ ,  $\text{La}_2\text{O}_2\text{S}$ , and  $\text{Gd}_2\text{O}_2\text{S}$ 

Sample No.	Composition	Heat treatment Temp ( $^{\circ}\text{C}$ ) Time (hr)	Atmosphere (SCFH)*		Brightness ( $\times 10^4$ ) $\text{YVO}_4:\text{Eu}$	Chromaticity coordinates		Remarks
			$\text{H}_2\text{S}$	$\text{N}_2$		x	y	
1	$(\text{Y}_{0.97}, \text{Eu}_{0.03})_2\text{O}_2\text{S}$	815/1 $\frac{1}{2}$	2	18	88	0.663	0.337	$\text{Y}_2\text{O}_3$ present
2		815/1 $\frac{1}{2}$	4	18	71	0.669	0.331	$\text{Y}_2\text{O}_3$ present
3		815/1 $\frac{1}{2}$	7	18	61	0.674	0.326	$\text{Y}_2\text{O}_3$ present
4		815/1 $\frac{1}{2}$	12	18	63	0.676	0.324	
5		875/1 $\frac{1}{2}$	7	18	60	0.675	0.325	
6		930/1 $\frac{1}{2}$	7	18	64	0.676	0.324	
7		980/1 $\frac{1}{2}$	7	18	83	0.679	0.322	
8		1040/1 $\frac{1}{2}$	7	18	84	0.676	0.324	
9		1095/1 $\frac{1}{2}$	7	18	89	0.677	0.323	
10		1150/1 $\frac{1}{2}$	7	18	93	0.679	0.321	
11		1205/1 $\frac{1}{2}$	7	18	95	0.680	0.320	
12		1205/1 $\frac{1}{2}$	2	18	109	0.672	0.328	$\text{Y}_2\text{O}_3$ present
13		1205/1 $\frac{1}{2}$	4	18	101	0.676	0.324	
14		1205/1 $\frac{1}{2}$	12	18	90	0.679	0.321	
15	$(\text{Y}_{0.995}, \text{Eu}_{0.005})_2\text{O}_2\text{S}$	1205/1 $\frac{1}{2}$	7	18	192	0.520	0.431	
16	$(\text{Y}_{0.90}, \text{Eu}_{0.10})_2\text{O}_2\text{S}$				183	0.581	0.405	
17	$(\text{Y}_{0.85}, \text{Eu}_{0.15})_2\text{O}_2\text{S}$				140	0.650	0.350	
18	$(\text{Y}_{0.87}, \text{Eu}_{0.13})_2\text{O}_2\text{S}$				105	0.672	0.328	
19	$(\text{Y}_{0.86}, \text{Eu}_{0.14})_2\text{O}_2\text{S}$				100	0.677	0.323	
20	$(\text{Y}_{0.93}, \text{Eu}_{0.07})_2\text{O}_2\text{S}$				89	0.680	0.320	
21	$(\text{Y}_{0.91}, \text{Eu}_{0.09})_2\text{O}_2\text{S}$				87	0.679	0.321	
22	$(\text{Y}_{0.90}, \text{Eu}_{0.10})_2\text{O}_2\text{S}$				45	0.681	0.319	
23	$(\text{Y}_{0.85}, \text{Eu}_{0.15})_2\text{O}_2\text{S}$				12	0.680	0.320	
24	$(\text{La}_{0.95}, \text{Eu}_{0.05})_2\text{O}_2\text{S}$	815/1 $\frac{1}{2}$	2	18	60	0.626	0.374	
25		815/1 $\frac{1}{2}$	4	18	—	—	—	Dark body color
26		815/1 $\frac{1}{2}$	7	18	—	—	—	Dark body color
27		1040/1 $\frac{1}{2}$	2	18	81	0.628	0.371	
28		1095/1 $\frac{1}{2}$	2	18	72	0.633	0.367	
29		1150/1 $\frac{1}{2}$	2	18	88	0.634	0.366	
30		1205/1 $\frac{1}{2}$	2	18	92	0.628	0.372	
31		1260/1 $\frac{1}{2}$	2	18	90	0.633	0.367	
32		1260/1 $\frac{1}{2}$	1	18	71	0.623	0.377	
33		1260/1 $\frac{1}{2}$	0.1	18	37	0.630	0.370	
34	$(\text{La}_{0.99}, \text{Eu}_{0.01})_2\text{O}_2\text{S}$	1205/1 $\frac{1}{2}$	2	18	85	0.562	0.435	
35	$(\text{La}_{0.97}, \text{Eu}_{0.03})_2\text{O}_2\text{S}$				88	0.606	0.394	
36	$(\text{La}_{0.95}, \text{Eu}_{0.05})_2\text{O}_2\text{S}$				63	0.623	0.377	
37	$(\text{La}_{0.90}, \text{Eu}_{0.10})_2\text{O}_2\text{S}$				33	0.659	0.341	
38	$(\text{La}_{0.85}, \text{Eu}_{0.15})_2\text{O}_2\text{S}$				10	0.674	0.326	
39	$(\text{La}_{0.80}, \text{Eu}_{0.20})_2\text{O}_2\text{S}$				6	0.670	0.330	
40	$(\text{Gd}_{0.95}, \text{Eu}_{0.05})_2\text{O}_2\text{S}$	815/1 $\frac{1}{2}$	2	18	43	0.677	0.323	
41		815/1 $\frac{1}{2}$	4	18	40	0.678	0.322	
42		815/1 $\frac{1}{2}$	7	18	38	0.680	0.320	
43		815/1 $\frac{1}{2}$	12	18	29	0.679	0.321	
44		875/1 $\frac{1}{2}$	7	18	45	0.679	0.321	
45		935/1 $\frac{1}{2}$	7	18	53	0.678	0.322	
46		990/1 $\frac{1}{2}$	7	18	57	0.679	0.321	
47		1040/1 $\frac{1}{2}$	2	18	62	0.681	0.319	
48		1095/1 $\frac{1}{2}$	2	18	66	0.679	0.321	
49		1150/1 $\frac{1}{2}$	2	18	64	0.679	0.321	
50		1205/1 $\frac{1}{2}$	2	18	67	0.679	0.321	
51		1260/1 $\frac{1}{2}$	2	18	70	0.679	0.321	
52		1260/1 $\frac{1}{2}$	1	18	78	0.674	0.326	
53		1260/1 $\frac{1}{2}$	4	18	73	0.679	0.321	
54		1260/1 $\frac{1}{2}$	0.1	18	121	0.660	0.340	$\text{Gd}_2\text{O}_3$ present
55	$(\text{Gd}_{0.97}, \text{Eu}_{0.03})_2\text{O}_2\text{S}$	1260/1 $\frac{1}{2}$	1.5	18	155	0.651	0.350	
56	$(\text{Gd}_{0.97}, \text{Eu}_{0.03})_2\text{O}_2\text{S}$				146	0.661	0.340	
57	$(\text{Gd}_{0.95}, \text{Eu}_{0.05})_2\text{O}_2\text{S}$				118	0.665	0.335	
58	$(\text{Gd}_{0.90}, \text{Eu}_{0.10})_2\text{O}_2\text{S}$				81	0.664	0.336	
59	$(\text{Gd}_{0.85}, \text{Eu}_{0.15})_2\text{O}_2\text{S}$				30	0.664	0.336	
60	$(\text{Gd}_{0.80}, \text{Eu}_{0.20})_2\text{O}_2\text{S}$				11	0.658	0.342	
61	$\text{YVO}_4:\text{Eu}$ Standard Sylvania Phosphor				100	0.673	0.328	

\* Standard cubic feet per hour.

by the top two curves in Fig. 8. The brightness curve for  $\text{La}_2\text{O}_2\text{S}:\text{Eu}$  apparently changes slope similar to  $\text{Y}_2\text{O}_2\text{S}:\text{Eu}$  in the 5–10 m/o  $\text{Eu}^{3+}$  region. ( $\text{La}_2\text{O}_2\text{S}:\text{Eu}$  was not investigated in as much detail over this activator range as was  $\text{Y}_2\text{O}_2\text{S}:\text{Eu}$ ; consequently, this portion of the curve in Fig. 8 is shown by a dashed line to indicate this uncertainty.) The lanthanum compound could not be prepared nearly as bright or as "red" as the analogous yttrium compound.

C. Gadolinium oxysulfide— $\text{Gd}_2\text{O}_2\text{S}:\text{Eu}$  was found to parallel  $\text{Y}_2\text{O}_2\text{S}:\text{Eu}$  and  $\text{La}_2\text{O}_2\text{S}:\text{Eu}$  in brightness, color, and variation of luminescent properties with activator concentration (Fig. 9).  $\text{Gd}_2\text{O}_2\text{S}:\text{Eu}$ , optimized for brightness at constant europium concentration, was prepared by firing at  $1260^{\circ}\text{C}$  for  $1\frac{1}{2}$  hr in a 90%  $\text{N}_2$ -10%  $\text{H}_2\text{S}$  (by volume) atmosphere.

D. Lutetium oxysulfide—Only one sample of  $\text{Lu}_2\text{O}_2\text{S}:\text{Eu}$  was prepared because of the difficulty and high cost involved in obtaining a pure lutetium compound to use as a starting material. From qualitative visual examinations of a sample prepared at  $1200^{\circ}\text{C}$  for  $1\frac{1}{2}$  hr in a 90%  $\text{N}_2$ -10%  $\text{H}_2\text{S}$  atmosphere, it appears that this phosphor is as bright as  $\text{Y}_2\text{O}_2\text{S}:\text{Eu}$  and equally "red."

## Discussion of Results

Throughout this investigation it was noted that the behaviors of the yttrium compounds more nearly approximate those of the compounds of the heavy rare earth elements, viz., gadolinium and lutetium, than the corresponding light rare earth compounds.

From the x-ray powder data, within a given family, apparent isostructural relationships exist between the yttrium, gadolinium, and lutetium compounds. The d-spacings for the yttrium compounds typically lie intermediate between those of the corresponding gadolinium and lutetium compounds. Lanthanum oxysulfide is apparently isostructural with the yttrium, gadolinium, and lutetium analogues, while the hydrated sulfate, sulfate, and oxysulfate show distinctly different x-ray reflections, indicating significant structural differences.

The DTA and TGA data also reflect this over-all trend. For example, the temperature stability range of the oxysulfate compounds is largest for lanthanum and decreases in the order gadolinium, yttrium, lutetium. It is interesting to note the differences between the excitation and emission spectra of the oxysulfate (Fig. 3) and oxysulfide (Fig. 4) phosphors.

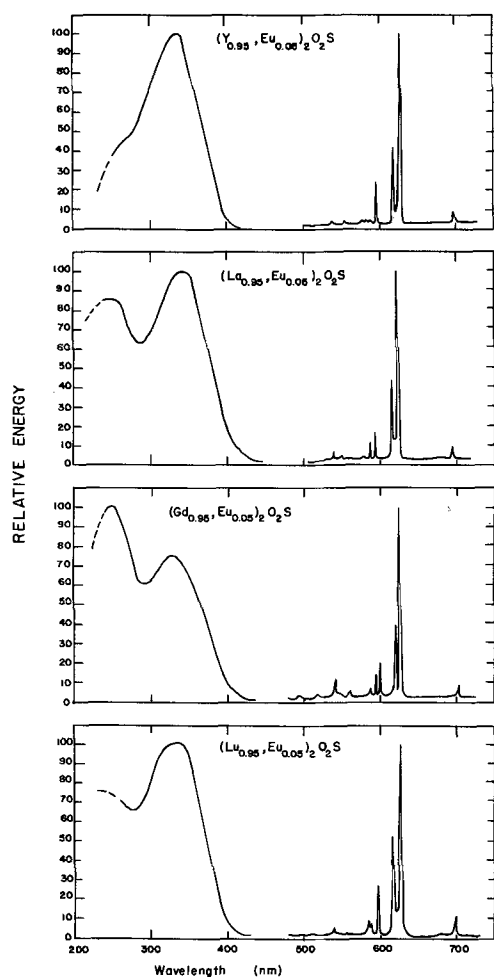


Fig. 4. Excitation and emission spectra of the  $\text{Eu}^{3+}$ -activated oxysulfide compounds of yttrium, lanthanum, gadolinium, and lutetium.

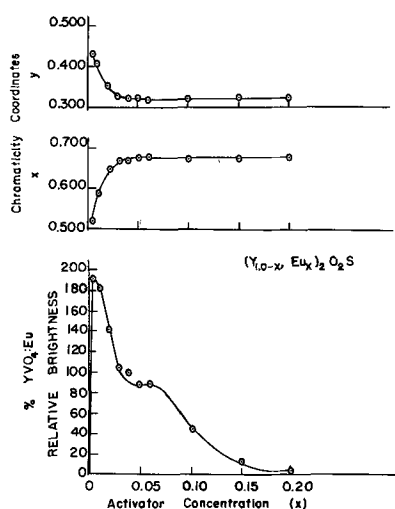


Fig. 5. Effect of activator concentration on cathodoluminescence brightness and chromaticity coordinates for  $\text{Y}_2\text{O}_2\text{S}:\text{Eu}$ .

The single excitation band of the oxysulfate phosphors can be assumed to arise from some type of  $(\text{RE})^{3+}-\text{O}^{2-}$  absorption. Presumably absorptions involving the  $(\text{SO}_4)^{2-}$  ions lie outside the energy range examined. On the other hand, the oxysulfide compounds show two distinct excitation bands. This implies  $(\text{RE})^{3+}-\text{S}^{2-}$  as well as  $(\text{RE})^{3+}-\text{O}^{2-}$  absorptions.

There are also marked differences between the emission spectra of the oxysulfate and oxysulfide compounds, most notably in the relative intensities of the

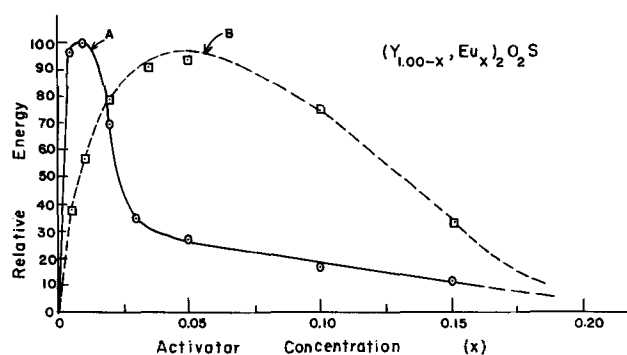


Fig. 6. Illustration of two types of activator concentration-brightness curves observed for  $\text{Eu}^{3+}$  emissions in  $\text{Y}_2\text{O}_2\text{S}:\text{Eu}$ .

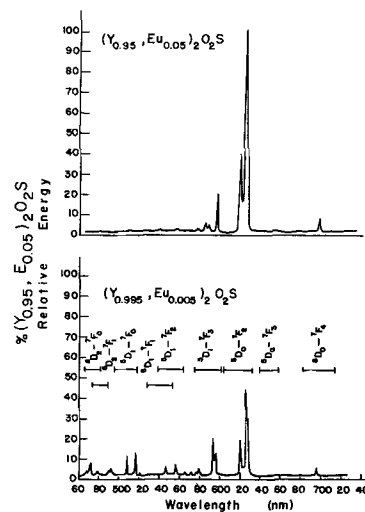


Fig. 7. Photoluminescence emission spectra of  $(\text{Y}_{0.95}, \text{Eu}_{0.05})_2\text{O}_2\text{S}$  and  $(\text{Y}_{0.995}, \text{Eu}_{0.005})_2\text{O}_2\text{S}$ .

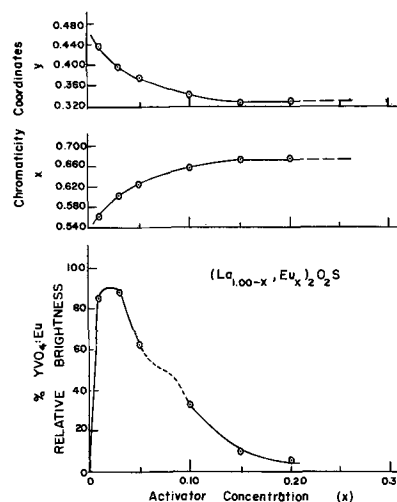


Fig. 8. Effect of activator concentration on cathodoluminescence brightness and chromaticity coordinates for  $\text{La}_2\text{O}_2\text{S}:\text{Eu}$ .

emission lines. These variations may result from structural differences which affect the activator site symmetry. For example, a strict center of symmetry makes the  ${}^5\text{D}_0-{}^7\text{F}_2$  transition forbidden. This may be the case with the oxysulfate phosphors.

On the other hand, Blasse *et al.* (11, 12) have noticed drastic changes in the relative intensities of various  $\text{Eu}^{3+}$  transitions resulting from chemical changes in the first coordination sphere of the activator ion. The substitution of S for  $(\text{SO}_4)^{2-}$  as we go from the oxysulfate to the oxysulfide matrix probably introduces severe changes in the neighborhood of the  $\text{Eu}^{3+}$  activator in addition to structural changes. Undoubtedly,

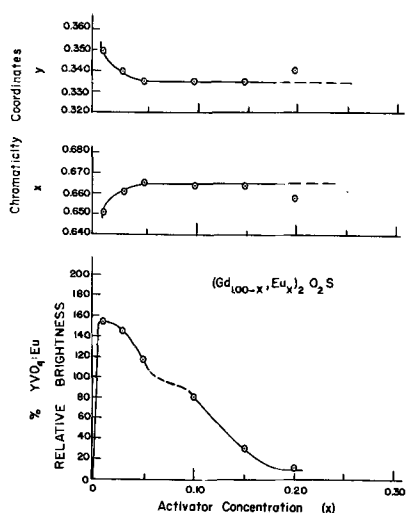


Fig. 9. Effect of activator concentration on cathodoluminescence brightness and chromaticity coordinates for  $Gd_2O_2S:Eu$ .

both the site symmetry and the chemical constitution of the ligands are responsible to varying degrees for these different emission spectra.

### Summary

Four families of Y, La, Gd, and Lu oxygen-sulfur compounds were studied and characterized. These families are  $R_2(SO_4)_3 \cdot n H_2O$ ,  $R_2(SO_4)_3$ ,  $R_2O_2(SO_4)$ , and  $R_2O_2S$ .

A. The rare earth hydrated sulfates were prepared by precipitation. In air these compounds begin decomposing to the anhydrous sulfates upon heating above  $100^\circ C$ . They do not provide efficient phosphors when activated by  $Eu^{3+}$ .

B. The rare earth sulfate compounds are stable in air up to near  $900^\circ C$  where they begin to decompose to the oxysulfate or the oxide. These compounds do not provide good  $Eu^{3+}$ -activated phosphors.

C. Only the oxysulfate compounds of lanthanum and gadolinium were found to be stable in air. They both exist over a relatively narrow temperature range, and at high temperatures decompose to the oxide. Yttrium and lutetium sulfates apparently decompose directly to the oxide without a stable intermediate oxysulfate phase. When activated by  $Eu^{3+}$ , both lanthanum and gadolinium oxysulfate exhibit the characteristic red  $Eu^{3+}$  luminescence. This emission is about 30% as bright as that of  $YVO_4:Eu$  under 253.7 nm excitation.

Both compounds are nearly inert when excited by cathode rays.

D. Heating the rare earth oxide, sulfate, or oxysulfate in a  $N_2-H_2S-H_2$  atmosphere at  $900^\circ-1100^\circ C$  will form the oxysulfide compound. The required temperature and atmosphere varies depending on the starting compound. All of the oxysulfide compounds are efficient  $Eu^{3+}$ -activated phosphors. The color and brightness of each compound is dependent on activator concentration. Low activator levels introduce low wavelength emission lines which become quenched as the activator level increases. The oxysulfide of yttrium is the most efficient phosphor with an emission which is characteristically more saturated and brighter than that of  $YVO_4:Eu$ .

### Acknowledgments

Messrs. O. Bullock, J. Looney, and J. Cook assisted with the sample preparation. Cathodoluminescent measurements were made by Mr. W. Persun. Numerous discussions with Mr. D. T. Palumbo and Dr. S. Z. Toma are greatly appreciated.

Manuscript submitted Jan. 10, 1968; revised manuscript received June 3, 1968.

Any discussion of this paper will appear in a Discussion Section to be published in the June 1969 JOURNAL.

### REFERENCES

1. W. W. Wendlandt, *J. Inorg. Nucl. Chem.*, **7**, 51 (1958).
2. W. W. Wendlandt and T. D. George, *ibid.*, **19**, 245 (1961).
3. W. W. Wendlandt and M. W. Nathans, *ibid.*, **24**, 869 (1962).
4. E. D. Eastman, L. Brewer, L. A. Bromley, P. W. Gilles, and N. L. Lofgren, *J. Am. Chem. Soc.*, **73**, 3896 (1951).
5. M. J. Flahaut and M. M. Guittard, *Compt. rend.*, No. 241, 1775 (1955).
6. G. Collin and J. Loriers, *ibid.*, **260** (19) (Groupe 8), 5043 (1965).
7. V. P. Surgutskii and V. V. Screbrennikov, *Zh. Neorgan. Khim.*, **9**, 786 (1964).
8. J. J. Pitha, A. L. Smith, and R. Ward, *J. Am. Chem. Soc.*, **69**, 1870 (1947).
9. W. Slavin, R. W. Mooney, and D. T. Palumbo, *J. Opt. Soc. Am.*, **51**, 93 (1961).
10. C. Brecher, H. Samelson, A. Limpichi, R. Riley, and T. Peters, *Tech. Memorandum 300.14 GT&E Laboratory, Bayside, N. Y.*, Aug. 25, 1966.
11. G. Blasse, A. Brill, and W. C. E. Nieuwpoort, *J. Phys. Chem. Solids*, Int. Conf. on Luminescence, Budapest 1966.
12. G. Blasse and A. Brill, *This Journal*, **114**, 250 (1967).

# Photoluminescent Efficiency of Phosphors with Electronic Transitions in Localized Centers

G. Blasse and A. Brill

Philips Research Laboratories, N. V. Philips' Gloeilampenfabrieken, Eindhoven-Netherlands

## ABSTRACT

No general theory exists that can predict the efficiency of phosphors with electronic transitions in localized centers. In this paper a survey and discussion are given of the correlation between fluorescent properties and chemical properties, like composition and structure. Points of discussion are (a) choice of the activator together with concentration quenching and critical concentration for this phenomenon, (b) influence of the host lattice on the photoluminescence efficiency for direct excitation of the activator, and (c) energy transfer between fluorescent centers. These considerations are illustrated by a large number of experimental examples.

In this paper we shall restrict ourselves to luminescence involving electronic transitions in simple, localized centers. Chemically this means that we shall deal mainly with the so-called oxygen-dominated phosphors. At the moment no general theory exists that can predict whether a phosphor of this type is efficient or not (1).

In our research of the last three years we have tried to contribute to the solution of this problem by studying the fluorescent properties as a function of crystal structure and chemical composition. Such an approach has been very successful in the case of other physical properties, for example, the magnetic and electrical properties of transition metal oxides. We have indeed found a number of correlations between structure and composition on the one hand and fluorescent properties on the other hand, part of which could be explained. In this paper we will survey and discuss the observed correlations.

In the group of phosphors under consideration two types of phosphors can be distinguished: (a) those in which the exciting radiation is absorbed by the luminescent center consisting of an activator and its immediate surroundings and where this absorption is followed by emission from the same center (called A); (b) those in which the absorption takes place outside the luminescent center. The absorbing center may be a host-lattice group or an intentionally added ion (usually called sensitizer, S). We shall not make a distinction between these two types of centers and will denote both centers (or sensitizers) by S. The absorption can be followed by energy transfer from S to S and finally from S to A. Emission can occur also from S itself.

In  $\text{Sb}^{3+}$ - and  $\text{Mn}^{2+}$ -coactivated calciumhalophosphate with blue  $\text{Sb}^{3+}$  and yellow  $\text{Mn}^{2+}$  emission the  $\text{Sb}^{3+}$  ion acts as a sensitizer (S) for  $\text{Mn}^{2+}$  (A). Simultaneously  $\text{Sb}^{3+}$  plays the role of activator for the blue emission. A given ion can play different roles in different host lattices: in  $\text{EuAl}_3\text{B}_4\text{O}_{12}$ -Cr, for example,  $\text{Eu}^{3+} = \text{S}$  (and  $\text{Cr}^{3+} = \text{A}$ ), but in  $\text{YVO}_4$ -Eu, on the other hand  $\text{Eu}^{3+} = \text{A}$  (and vanadate = S).

In later sections we shall first deal with the choice of the activator: which elements in which valency state can be used to give efficient phosphors? In this connection concentration quenching will also be dealt with. A second problem that will be treated is why the efficiency of the fluorescence of a certain activator varies strongly with the host lattice for the case that the exciting radiation is absorbed by the activator centers (phosphors of type a). Later sections discuss energy transfer between centers. This determines the efficiency of phosphors of the type b. The influence of the surroundings on the position of the energy levels of the fluorescent centers is considered later. This is

especially important for the efficiency of the energy transfer.

## Choice of the Activator

The question "which elements give efficient fluorescence?" is the first problem one encounters when one tries to predict the efficiency of phosphors. Recently we have given an empirical criterion to answer this question (2). It is based on the well-known assumption that it is necessary for efficient fluorescence from an isolated center that the configuration coordinate curve of the excited state is situated within the curve of the ground state (see Fig. 1A). Seitz (3) stated that no fluorescence can be expected if the equilibrium distance of the configuration coordinate curve of the fluorescent state is outside the curve of the ground state (Fig. 1C). Dexter *et al.* (4) have shown that even under less extreme conditions the excitation energy can be lost by radiationless transitions, *viz.*, if the system passes the intersection of the extrapolated curves of the fluorescent and the ground state after the excitation process (see Fig. 1B). If this is not the case, efficient fluorescence may be expected. This fluorescence will be quenched at higher temperature (Seitz-Mott).

It is immediately clear from Fig. 1 that the difference between the values of the equilibrium distance of the ground and excited state ( $\Delta r$ ) must play an important role. Unfortunately no values of  $\Delta r$  are known in the literature. It is possible, however, to obtain a rough measure of  $\Delta r$  from the set of radii corresponding to the principal maximum in the radial wave functions for atoms and ions given by Waber and Cromer (5). The difference between the sum of these radii for the ground and excited state of the constituents of the fluorescent center is considered as a measure of  $\Delta r$ .

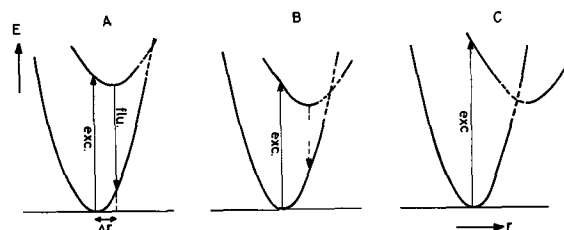


Fig. 1. Configuration coordinate diagram of the ground state and the fluorescent state (schematically). A, Excitation results in efficient fluorescence, the intersection of the two states being high above the excited vibrational levels of the excited state. B, Excitation results in inefficient fluorescence, since the excitation energy can be lost radiationlessly via the intersection of the two states. C, Excitation does not result in fluorescence, since all the excitation energy returns radiationlessly to the ground state.

Table I. Excitation transitions of some fluorescent centers in oxides and the orbital radii (Å) involved

Ion	Excitation transition <sup>a</sup>	Largest outer orbital radius connected with			Difference ( $\Delta r$ )	
		The ground state		The excited state		
Nb <sup>5+</sup>	2p <sub>0<sup>2</sup></sub> → 4d	4p (Nb)	0.59	4d (Nb)	0.75	0.16
W <sup>6+</sup>	2p <sub>0<sup>2</sup></sub> → 5d	5p (W)	0.58	5d (W)	0.75	0.17
Sn <sup>4+</sup>	4d → 5s, 5p	4d (Sn)	0.46	5s (Sn)	1.03 <sup>b</sup>	0.57
Sb <sup>5+</sup>	4d → 5s, 5p	4d (Sb)	0.44	5s (Sb)	0.97 <sup>b</sup>	0.53
Sn <sup>2+</sup>	5s → 5p	5s (Sn)	1.03	5p (Sn)	1.24	0.21
Sb <sup>3+</sup>	5s → 5p	5s (Sb)	0.97	5p (Sb)	1.16	0.19
Pb <sup>2+</sup>	6s → 6p	6s (Pb)	1.01	6p (Pb)	1.21	0.20
Ce <sup>3+</sup>	4f → 5d	5p (Ce)	0.82	5d (Ce)	~1.07	0.25
Eu <sup>2+</sup>	4f → 5d	5p (Eu)	0.74	5d (Eu)	~0.98	0.24
Eu <sup>3+</sup>	2p <sub>0<sup>2</sup></sub> → 4f	5p (Eu)	0.74	5p (Eu)	0.74	0
Mn <sup>2+</sup> , Mn <sup>4+</sup>	3d → 3d	3d (Mn)	0.39	3d (Mn)	0.39	0

<sup>a</sup> See e.g., ref. (36). Orbitals with subscripts relate to the O<sup>2-</sup> ions, orbitals without subscript to the metal ions.

<sup>b</sup> Values for the orbital radius of 5p are even larger than those for 5s.

The agreement is good for those cases where a comparison is possible between these values and the values used in configuration coordinate diagrams derived from experimental results (2). Table I gives some values of  $\Delta r$  derived from the Waber and Cromer radii. Consider, for example, the Sb<sup>5+</sup> ion. The excitation and fluorescence transition is 4d → 5s (or 5p). The outer orbital of the ground state is 4d (maximum at 0.44Å) and of the excited state 5s (maximum at 0.97Å). Their difference (~0.5Å) is considered as a measure of  $\Delta r$ . For further details the reader is referred to the original paper.

It seems to be a necessary, but not a sufficient, condition for efficient fluorescence that  $\Delta r$  is about 0.3Å or less. This is the case for the higher-charged transition metal ions without d-electrons (like V<sup>5+</sup>, W<sup>6+</sup>), the ions with ns<sup>2</sup>-configuration (Sn<sup>2+</sup>, Pb<sup>2+</sup>, etc), the rare earths ions and also for manganese and chromium. For the latter two elements the orbitals involved are the same for the ground and excited state, so that  $\Delta r$  is zero in first approximation. By applying this criterion it is possible to select possible fluorescent centers from the periodic table. This selection coincides with the selection that could be made before from experience:  $\Delta r = 0$  for manganese and trivalent europium, which elements give efficient temperature-persistent phosphors when used as activators in various materials. CaWO<sub>4</sub> and MgWO<sub>4</sub> are well-known efficient phosphors, while materials activated with Sn<sup>2+</sup>, Ce<sup>3+</sup>, and Pb<sup>2+</sup> can also show high efficiencies. For these activators  $\Delta r$  is 0.2Å.

Even if we have successfully selected the activator, efficient emission is not guaranteed on excitation in the activator, because in practice we are not dealing with isolated centers. In many cases there are restrictions on the concentration of the activator. Usually the quantum efficiency at room temperature decreases with increasing concentration. This phenomenon is known as concentration quenching. The amount of activator for which it starts is usually called the critical concentration. This concentration is very low in the case of uranium fluorescence in oxides (~0.1%). Usually it is somewhat higher, 1-5%, for example, for Bi<sup>3+</sup>. In other cases, however, no concentration quenching is observed at all (CaWO<sub>4</sub>, CaNb<sub>2</sub>O<sub>6</sub>). In Table II the critical concentration is given for a number of systems together with the Stokes shift of the fluorescence. Note that in first approximation the critical concentration increases, if the Stokes shift increases (6). The rare earth ions with line emissions are not considered here, since it is difficult to define the Stokes shift of their fluorescence. Since concentration quenching strongly depends on the probability of energy transfer between the fluorescent centers, the discussion of the relation given in Table II is deferred to the section on Phosphors with Very High Sensitizer Concentration.

Table II. Critical concentration ( $x_{crit.}$ ) and Stokes shift of the fluorescence of some systems

Composition	$x_{crit.}$	Stokes shift, 10 <sup>3</sup> cm <sup>-1</sup>
Li <sub>3+1/4x</sub> Nb <sub>1-5/4x</sub> U <sup>0+x</sup> O <sub>4</sub>	~0.001	1
Y <sub>1-x</sub> Bi <sub>x</sub> Al <sub>3</sub> B <sub>4</sub> O <sub>12</sub>	~0.005	2
Y <sub>1-x</sub> Bi <sub>x</sub> OCl	0.05	5
Sr <sub>3-3x</sub> Eu <sup>2+3x</sup> MgSi <sub>2</sub> O <sub>8</sub>	0.01	1.5
Y <sub>3-3x</sub> Ce <sup>3+3x</sup> Al <sub>3</sub> O <sub>12</sub>	0.04	4
Mg <sub>3</sub> Sn <sub>1-x</sub> Ti <sub>x</sub> O <sub>4</sub>	0.05	8
YP <sub>1-x</sub> V <sub>x</sub> O <sub>4</sub>	0.25	12
Ba <sub>2</sub> TiSi <sub>2</sub> O <sub>8</sub>	a	18
CaNb <sub>2</sub> O <sub>6</sub>	a	17
CaWO <sub>4</sub>	a	17

<sup>a</sup> No concentration quenching.

Nevertheless we may remark here that concentration quenching also plays a role in the group of transition metal ions without d electrons (Ti<sup>4+</sup>, V<sup>5+</sup>, Nb<sup>5+</sup>, W<sup>6+</sup>, etc.), a fact which has been overlooked up till now [see e.g., (7)]. Usually the absence of fluorescence at room temperature in compounds of the transition metal ions without d-electrons is ascribed to thermal quenching (i.e., a low activation energy). Undoubtedly this is the case for molybdates, because the isolated molybdate group does not fluoresce efficiently at room temperature. However, in the case of the vanadate or titanate group, concentration (and not thermal) quenching explains the absence of fluorescence at room temperature in the majority of the compounds of these groups (6).

#### Influence of the Host Lattice

If we have selected an efficient fluorescent center, a second and even more difficult problem arises, namely, the choice of the host lattice. In this section we restrict ourselves to those cases in which only the activator itself is directly excited, i.e. transfer through the host lattice and from the host lattice to the activator does not play a role (phosphors of type a). It is well known that a given center fluoresces efficiently only in a restricted number of host lattices. We recall two examples of fluorescent centers, viz., Eu<sup>3+</sup> and the niobate group. At room temperature Y<sub>2</sub>O<sub>3</sub>-Eu has a maximum quantum efficiency  $q = 75\%$  in the uv region, YAl<sub>3</sub>B<sub>4</sub>O<sub>12</sub>-Eu has  $q = 35\%$  and LaAlO<sub>3</sub>-Eu has  $q = 10\%$  [excitation is always in the Eu<sup>3+</sup>-center only (8)]. The compounds Li<sub>3</sub>NbO<sub>4</sub> and CaNb<sub>2</sub>O<sub>6</sub> fluoresce efficiently at room temperature, but LiNbO<sub>3</sub> and SrNb<sub>2</sub>O<sub>6</sub> do not do so (9, 10).

A relation between the efficiency of phosphors of this type and their chemical properties has been found. In his paper on the fluorescence of niobates Wachtel (9) puts forward a possible relation between the position of the absorption edge and the quenching temperature of the fluorescence of the niobates. We have shown that this relation holds not only for niobates, but also for other compounds.

In the case of the fluorescence of the octahedral niobate center (2, 10) it was found that, if the position of the first absorption band moves to longer wavelengths, the quenching temperature of the fluorescence decreases (see Table III). It is possible to account for the dependence of the position of the absorption band on the host lattice. The absorption (and emission)

Table III. Some data on fluorescent niobates

Compound	Absorption edge, cm <sup>-1</sup>	Quenching temperature, °K	Anion potential <sup>a</sup>
Li <sub>3</sub> NbO <sub>4</sub>	41,600	500	2-1/3
MgNb <sub>2</sub> O <sub>6</sub>	37,000	350	2-1/6
LiZnNbO <sub>4</sub>	36,800	350	2-1/9
LiNbO <sub>3</sub>	35,100	200	2
La <sub>2</sub> LiNbO <sub>6</sub>	33,300	~100	—
Nb <sub>2</sub> O <sub>5</sub>	27,000	<100	—

<sup>a</sup> See text.

transition involves a charge-transfer process in which an electron is transferred from the  $O^{2-}$  ions to the central  $Nb^{5+}$  ion. The higher the potential field from the cations at the  $O^{2-}$  site is, the more energy is needed for the electron transfer, so that the absorption band will be at shorter wavelengths. A qualitative measure of this potential field is given by using Pauling's electrostatic valence rule (11): if the sum of the electrostatic bond strengths from cation to anion is larger than 2, the potential field at the anion site is relatively large. This value gives indeed a rough measure of the quenching temperature.

The relations between the position of the absorption edge and the quenching temperature of the fluorescence could be accounted for even quantitatively by assuming that the  $NbO_6$  octahedron can be considered as a more or less isolated group (2). Configuration coordinate curves with a fixed shape and a fixed difference between the equilibrium distances were used. Only the vertical energy shift between the two curves is assumed to vary (Fig. 2). The relation can already be inferred from this figure on visual inspection. For excitation into curve 1 the excitation energy can be dissipated radiationlessly via the intersection point P. If the excited state moves to higher energies, this does not happen any more for the curves above curve 2. The higher the curve of the excited state, the higher the activation energy  $E_A$ .

It can be shown that a relation of this type exists also for centers with similar electron configuration as the niobates (titanates, molybdates, tungstates). A strict requirement is that the central metal ion is in six-coordination (Table IV). If, however, ions of this type are in four-coordination, the relation is no longer valid (Table IV). There is a tendency toward higher quenching temperatures, if the bonding between the tetrahedral groups becomes stronger. To illustrate this for the tetrahedral tungstate group:  $CaWO_4$  has a higher quenching temperature than  $SrWO_4$  and  $BaWO_4$ ,  $Li_2WO_4$  higher than  $Na_2WO_4$ . More examples are given in ref. (10).

It is remarkable that a relation between the position of the absorption band and the quenching temperature of the fluorescence (and therefore also the quantum efficiency at room temperature) has also

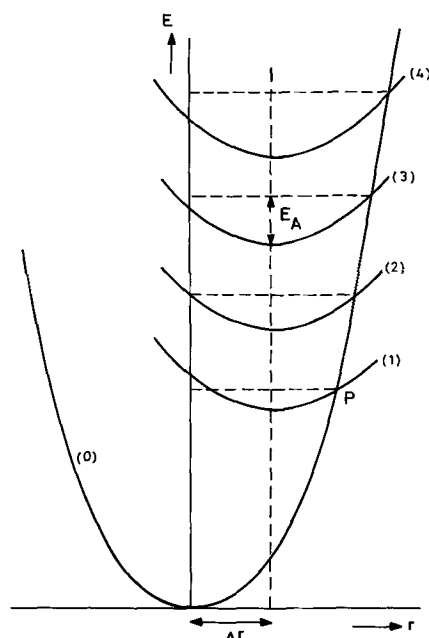


Fig. 2. Illustration of the relation between the position of the absorption (excitation) band and the quenching temperature of the fluorescence. The shape of the excited curve and the difference between the equilibrium distance of the ground and excited state remains fixed.

Table IV. Absorption edge and quenching temperature of the fluorescence of tungstates

Compound	Fluorescent center	Absorption edge, $cm^{-1}$	Quenching temperature, $^{\circ}K$
$\beta$ - $MgWO_4$	$WO_6$	34,200	475
$Ca_2WO_6$	$WO_6$	33,200	300
$Y_2WO_6$	$WO_6$	32,300	240
$Ba_3Gd_3WO_9$	$WO_6$	30,800	100
$CaWO_4$	$WO_4$	40,600	450
$Li_2WO_4$	$WO_4$	35,700	300
$BaWO_4$	$WO_4$	42,500	<100
$Na_2WO_4$	$WO_4$	45,400	<100

been observed for two centers completely different from the niobate group, viz., the  $Eu^{3+}$  center in oxides [in this case the charge-transfer absorption of the center is considered and not the  $4f - 4f$  absorptions (8, 12)] and the  $UO_6$  center (especially in the rocksalt lattice) (13). It seems probable that the explanation in these cases is similar to that for the octahedral niobate fluorescence. The quenching temperature and efficiency of the fluorescence of  $Ce^{3+}$  in oxides, however, can again be related to the size and charge of the cations of the host lattice (14). The fluorescence of  $Bi^{3+}$  was also investigated, but no apparent correlation between efficiency and other properties could be detected (15).

No doubt much more work has still to be done in order to obtain a better understanding of the dependence of the fluorescence efficiency on the host lattice.

#### General Discussion of Energy Transfer

Due to the work of Förster (16) and especially Dexter (17) the process of energy transfer in solids is nowadays reasonably well understood. This section reviews the theory briefly.

Neglecting energy transfer by movement of charge carriers, there remain two different mechanisms for energy transfer from a sensitizer S to an activator A, viz. (i) radiative transfer by emission by S and reabsorption by A, and (ii) nonradiative transfer associated with resonance between absorber (S) and emitter (A).

The probability of radiative transfer depends on how efficiently the A fluorescence is excited by the S emission. It requires a significant overlap of the emission region of S and the absorption region of A and an appreciable intensity of absorption of A. Especially in view of the latter requirement, radiative transfer does not often occur in inorganic systems.

Only two types of nonradiative transfer seem to be of importance, namely, those by electric multipole interactions and those by exchange interaction. The probability of nonradiative energy transfer by electric multipole-multipole interaction ( $P_{SA}^m$ ) is proportional to the reciprocal of the radiative decay time of S ( $\tau_S$ ), the absorption band area of A ( $Q_A$ ), the energy overlap between the emission band of S and the absorption band of A ( $E_{SA}$ ) and the reciprocal of a certain power of the distance between S and A ( $R_{SA}$ ), so that

$$P_{SA}^m \sim \frac{Q_A \cdot E_{SA}}{\tau_S \cdot R_{SA}^n} = g_{SA} \cdot E_{SA} \quad [1]$$

Here  $n = 6$  for electric dipole-dipole interaction and  $n = 8$  for electric dipole-quadrupole interaction. If  $P_{SA} \tau_S = 1$  (i.e., the transfer probability equals the probability of radiative decay), Eq. [1] can be solved for the critical distance  $R_0$ .

In the case of transfer by exchange the probability of nonradiative energy transfer ( $P_{SA}^e$ ) is proportional to  $E_{SA}$  and a function of the wave function overlap of the S and A electrons involved in the exchange interaction ( $f_{SA}$ )

$$P_{SA}^e \sim f_{SA} \cdot E_{SA} \quad [2]$$

$P_{SA}^m$  therefore depends on the optical strength of the transitions involved, whereas  $P_{SA}^e$  does not. Trans-



fer by exchange is restricted to nearest neighbors. Transfer by multipole interactions can be of importance even over distances of 20-30 Å.

From [1] and [2] we see that the probabilities of transfer  $P_{SA}$  for the two processes are determined by two factors, one which they have in common, viz., the energy overlap ( $E_{SA}$ ) and the other indicating the strength of the interaction between S and A (the functions  $f$  or  $g$ ).

In the next sections we shall deal first with phosphors that are excited in the host lattice (this is equivalent with a very high sensitizer concentration). Usually energy travels through the lattice and is finally transferred to the activator (next section). Afterward we shall discuss phosphors with a low sensitizer concentration. Here the sensitizer is an intentionally added foreign ion. We may stress, however, that there is no principal difference in the physical treatment of these two types of sensitized phosphors. The activator concentration of sensitized phosphors is always assumed to be low.

#### Phosphors with Very High Sensitizer Concentration (i.e., Host Lattice Excitation)

For high S and low A concentration one of the two following conditions must be fulfilled to have efficient A fluorescence on excitation into S. (a) The SA transfer takes place over large distances (of the order of magnitude of the separation between the activators in the crystal). Transfer through the host lattice (SS transfer) is not needed in that case. This situation is, however, not often realized in inorganic materials. (b) The SA transfer occurs only over short distances, and excitation of S has to be followed by several SS transfers (transfer through the host lattice) before finally the SA transfer occurs, resulting in the characteristic A fluorescence.

*Transfer through lattice plays no role.*—Let us first consider case (a) or long-distance transfer from S to A. Transfer by exchange interaction can be ruled out here, since transfer of this type is restricted to distances of a few angstrom units. Transfer can take place by multipole interaction which can be efficient for the case of overlapping reasonably allowed electric-dipole transitions. However, radiative transfer can also be expected in such a case. Two examples, where long-distance transfer from S to A occurs, may be mentioned, viz.,  $\text{Li}_3\text{NbO}_4\text{-Cr}$  (S = niobate group; A =  $\text{Cr}^{3+}$ ) and  $\text{EuAl}_3\text{B}_4\text{O}_{12}\text{-Cr}$  (S =  $\text{Eu}^{3+}$ , A =  $\text{Cr}^{3+}$ ).

The niobate emission of  $\text{Li}_3\text{NbO}_4$  (peaking at 370 nm) is quenched by very small amounts of  $\text{Cr}^{3+}$  ions (18). The addition of  $\text{Cr}^{3+}$  to  $\text{Li}_3\text{NbO}_4$  causes a strong absorption band at about 380 nm which is due to a charge-transfer process in the chromium-niobate center. This means that the emission is completely overlapped by this absorption (Fig. 3). Because the optical strength of both bands is strong, nonradiative

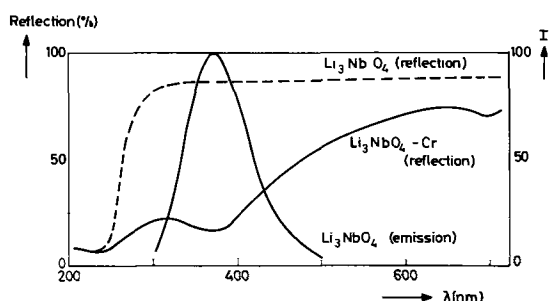


Fig. 3. Diffuse reflection spectra of  $\text{Li}_3\text{NbO}_4$  and  $\text{Li}_3\text{NbO}_4\text{-Cr}$  and spectral energy distribution of the emission of  $\text{Li}_3\text{NbO}_4$  (254 nm excitation). For the emission the relative radiant power per constant wavelength interval (I) is plotted in arbitrary units. Note the large overlap of the emission of  $\text{Li}_3\text{NbO}_4$  and the extra absorption of  $\text{Li}_3\text{NbO}_4\text{-Cr}$ .

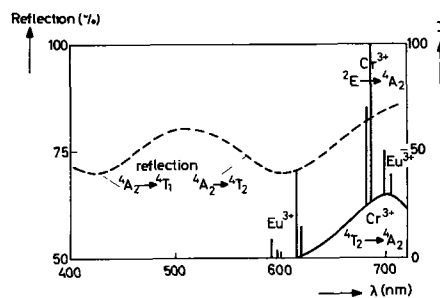


Fig. 4. Diffuse reflection spectrum (broken line) and spectral energy distribution of the emission of  $\text{EuAl}_3\text{B}_4\text{O}_{12}\text{-Cr}$  (254 nm excitation). Note the large overlap of the  ${}^5\text{D}_0\text{-}{}^7\text{F}_1$  and  ${}^5\text{D}_0\text{-}{}^7\text{F}_2$  emission of the  $\text{Eu}^{3+}$  ion and the  ${}^4\text{A}_2 \rightarrow {}^4\text{T}_2$  absorption of  $\text{Cr}^{3+}$  in the region around 600 nm.

as well as radiative transfer from niobate to  $\text{Cr}^{3+}$  occurs followed by  $\text{Cr}^{3+}$  emission (in the infrared). The same phenomenon occurs for  $\text{CaWO}_4\text{-Cr}$  (18).

The efficient red  $\text{Eu}^{3+}$  emission of  $\text{EuAl}_3\text{B}_4\text{O}_{12}$  is quenched by small amounts of  $\text{Cr}^{3+}$  ions (substituted for  $\text{Al}^{3+}$ ) (19). The exciting energy (e.g., 254 nm radiation) is absorbed mainly by the  $\text{Eu}^{3+}$  centers, but the emission consists, for the greater part, of a broad band and narrow line emission characteristic for  $\text{Cr}^{3+}$ . Since the SS transfer (from  $\text{Eu}^{3+}$  to  $\text{Eu}^{3+}$ ) can be neglected, no energy overlap being present, SA transfer (from  $\text{Eu}^{3+}$  to  $\text{Cr}^{3+}$ ) must be very efficient. Indeed the  $\text{Eu}^{3+}$  emission (mainly at 615 nm) overlaps the  $\text{Cr}^{3+}$  absorption in this compound ( ${}^4\text{A}_2 \rightarrow {}^4\text{T}_2$  absorption band at 590 nm) very well (Fig. 4). The critical distance for this transfer was experimentally determined as 14 Å and estimated theoretically at 17 Å. This is in fact a large distance for energy transfer in inorganic materials. The average Cr-Cr distance is of the same order of magnitude.

*Transfer through lattice plays an important role.*—Usually SA transfer occurs only over short distances. This means that SS transfer must also be involved in order to obtain efficient fluorescence from A. For efficient SS transfer it is necessary that the emission of S overlaps the absorption of S (energy overlap) and that there is a certain interaction between the S centers (either by exchange or by electric multipole interaction).

Although there is no difference in principle in the treatment of transfer through the lattice (SS transfer) and transfer from the lattice to the activator (SA transfer), in practice differences occur due to the fact that in SS transfer we are dealing with identical centers and in SA transfer with different centers. Consider, for example, transfer from a host lattice group (usually a broad band emitter) to a trivalent rare earth ion (usually a weak narrow band absorber). Nearly always the energy overlap condition is fulfilled due to the fact that the broad band emission extends over such a broad spectral region that it overlaps always one or more narrow absorption bands of the rare earth ion. Here the strength of the interaction is often the dominating factor which determines the transfer probability.

We will now illustrate these considerations of energy transfer by some examples. These examples have been selected in such a way that only one or two of the factors influencing the energy transfer processes are varied, whereas the other factors remain constant.

*Concentration quenching (energy overlap condition varied).*—It is possible to obtain information on the efficiency of the transfer through the lattice (SS transfer) from a study of concentration quenching. In this section it will be shown that the efficiency of this transfer is mainly determined by the energy overlap condition ( $E_{SS}$ ). The critical concentration for concentration quenching can be related to the efficiency of the SS transfer.

To explain concentration quenching at room temperature it was assumed by Dexter and Schulman (20) that the main factor in this process is the presence of particular quenching centers ("energy sinks") in the crystal lattice (e.g., imperfections, surface states, or impurities). The absorbed excitation energy is lost radiationlessly at these sinks during the migration through the lattice, so that the critical concentration depends on the probability of the transfer through the lattice: suppose the probability of this transfer is low, then the energy cannot escape to a quenching center and the quantum efficiency is high even at high concentrations (as a matter of fact, thermal quenching can still occur because this is a property of the isolated center). On the other hand, if the probability of the transfer is high, the excitation energy can be lost at an energy sink even for low center concentrations.

This condition for concentration quenching is illustrated by Table II. The energy overlap can be roughly estimated from the Stokes shift of the fluorescence, although of course the width of the bands also plays a role, broad bands having a larger overlap than narrow bands. From Table II we see: (A) The absence of concentration quenching in  $\text{CaWO}_4$  and  $\text{CaNb}_2\text{O}_6$ , where every host lattice group is a center, agrees with the large Stokes shift of the emission. This implies that the overlap of the emission and absorption bands is small. This holds in general for tungstates and niobates (see Fig. 5a). (B) In the system  $\text{YP}_{1-x}\text{V}_x\text{O}_4$  concentration quenching of the vanadate emission occurs for  $x > 0.25$ . The Stokes shift is smaller and  $E_{SS}$  therefore larger than for tungstates and niobates (Fig. 5b). The fluorescence of  $\text{YVO}_4$  is concentration-quenched at room temperature. We have to decrease the concentration of the vanadate groups by nonabsorbing phosphate groups to obtain efficient vanadate emission at room temperature. This means that the average distance between the vanadate groups increases, so that the interaction strength between these groups decreases. Consequently the probability for the vanadate-vanadate transfer becomes lower (see General Discussion of Energy Transfer). (C) Well-known fluorescent centers like  $\text{Bi}^{3+}$ ,  $\text{Ce}^{3+}$ , and  $\text{Eu}^{2+}$  show concentration quenching at still lower concentrations. Due to the smaller Stokes shift of the emission the energy overlap is larger (Fig. 5c). (D) For one and the same activator the Stokes shift may be different. The smaller the Stokes shift, the larger the energy overlap, the higher the transfer probability and the lower the critical concentration for concentration quenching.

This consideration does not take into account the variation of the factors  $f$  and  $g$  in the interaction between the centers. Obviously these factors are not dominating the variation of the transfer probability, although they will explain deviations from the correlation between critical concentration and Stokes shift. For ions like  $\text{Ce}^{3+}$ ,  $\text{Bi}^{3+}$ , or  $\text{Eu}^{2+}$ , for example, the emission and absorption transitions are practically allowed electric dipole transitions, so that the electric dipole-dipole interaction must be strong. For tungstates and niobates, however, this interaction is weaker. It is usually assumed that the interaction in this case is of the exchange type (17).

In general, however, the critical concentration of concentration quenching can be used as a measure of the probability of transfer through the lattice. This transfer probability increases in the sequence: tungstates (or niobates), vanadates,  $\text{Ce}^{3+}$  (or  $\text{Bi}^{3+}$ ,  $\text{Eu}^{2+}$ ). Since energy overlap clearly plays a dominant role in transfer through the host lattice, host lattice emission is only to be expected, if the Stokes shift is large. *Tungstate-molybdate systems (energy overlap conditions varied).*—Also in this example only the energy overlap will be varied. It is a well-known phenomenon that the fluorescence of tungstates at room temperature is quenched by partial replacement of tungsten by

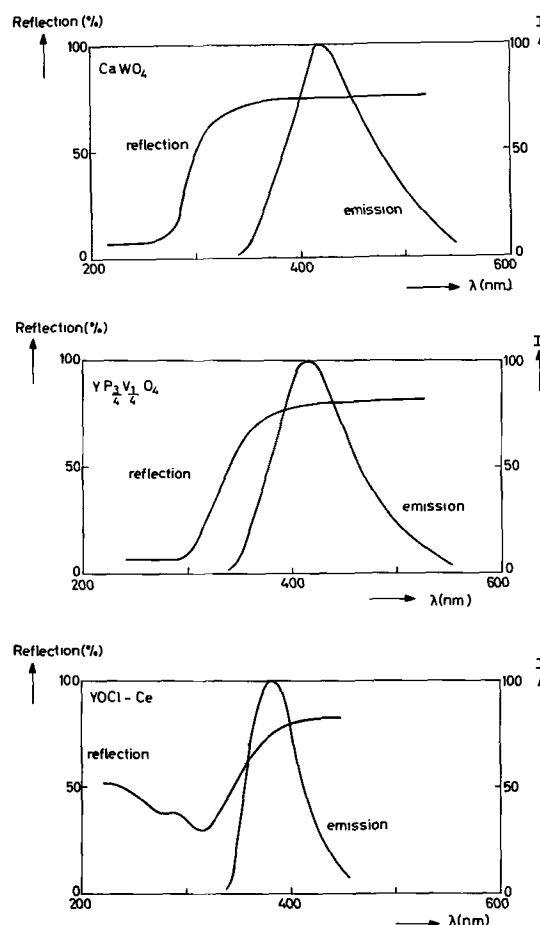


Fig. 5. Diffuse reflection spectra and spectral energy distribution of the emission (254 nm excitation) of a,  $\text{CaWO}_4$ ; b,  $\text{YP}_{0.75}\text{V}_{0.25}\text{O}_4$ ; c,  $\text{YOC1-Ce}$ . The three figures are on the same scale. Note the increase of the overlap of emission and absorption in the sequence a, b, c.

molybdenum (7, 21). At low temperatures mainly molybdenum emission is observed, if the tungstate group is excited. We investigated this phenomenon for the system  $\text{Y}_2\text{W}_{1-x}\text{Mo}_x\text{O}_6$  (22). The probability of energy transfer in this case varies in good approximation only with the energy overlap, since the interaction between tungstate groups and between molybdate groups mutually and between the tungstate and the molybdate group will not be strongly different. The shape of the bands involved being roughly equal, the difference between the position of the absorption edge and the emission band gives a good measure of the energy overlap. For the system  $\text{Y}_2\text{W}_{1-x}\text{Mo}_x\text{O}_6$  these values are given in Table V (compare also Fig. 6). Judging from these values the transfer probability should decrease in the sequence  $\text{WO}_4 \rightarrow \text{MoO}_4$ ,  $\text{WO}_4 \rightarrow \text{WO}_4$ ,  $\text{MoO}_4 \rightarrow \text{MoO}_4$ ,  $\text{MoO}_4 \rightarrow \text{WO}_4$ . An inspection of Fig. 6 even indicates that the two latter transfers have a negligible probability. This explains the experimental results mentioned above. If a tungstate group is excited, the excitation energy will travel through the lattice until a molybdate group is reached,

Table V. Position of the emission band and absorption edge ( $\text{cm}^{-1}$ ) of the molybdate and tungstate group in  $\text{Y}_2\text{W}_{1-x}\text{Mo}_x\text{O}_6$ , in relation to the transfer probability between these groups

Transfer from	Transfer to	Emission band	Absorption edge	Difference
Mo	Mo	14,300	28,600	14,300
W	W	21,300	32,300	11,000
W	Mo	21,300	28,600	7,300
Mo	W	14,300	32,300	18,000

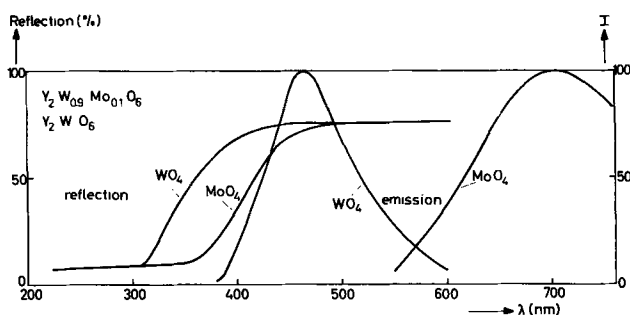


Fig. 6. Diffuse reflection spectra and spectral energy distribution of the emission of the tungstate and molybdate group in  $Y_2WO_6$ -Mo. The molybdate emission is excited by 365 nm, the tungstate emission of undoped  $Y_2WO_6$  by 254 nm. Note the decrease of the overlap of the emission and absorption bands in the sequence  $WO_4 \rightarrow MoO_4$ ,  $WO_4 \rightarrow WO_3$ ,  $MoO_4 \rightarrow MoO_4$ ,  $MoO_4 \rightarrow WO_4$ . The latter two have even a negligible overlap.

to which the excitation energy is transferred. It must be kept in mind that the molybdate emission is thermally quenched at room temperature.

An exception to this behavior is formed by  $Y_2SiW_{1-x}Mo_xO_8$  (23). At liquid nitrogen temperature this compound gives mainly tungstate emission, if the tungstate group is excited, and molybdate emission, if the molybdate group is excited. The positions of the emission and absorption bands in this system are similar to those given in Table V. The reason that no energy transfer occurs in this system must therefore be a vanishing interaction between the centers.  $Y_2SiWO_8$  has the same crystal structure as  $CaWO_4$ , but the  $Si^{4+}$  and  $W^{6+}$  ions occupy the tungstate sites of scheelite ( $CaWO_4$ ) in an ordered way, so that the distance between the tungstate groups in  $Y_2SiWO_8$  is indeed larger than in  $CaWO_4$ . Consequently the interaction strength will be less.

**$Eu^{3+}$ -activated  $Ln_2WO_6$  ( $P_{SS}$  constant,  $P_{SA}$  varied).**—In this section we will deal with systems where  $P_{SS}$  (transfer through the lattice) is constant and where  $P_{SA}$  (lattice to activator transfer) varies. Moreover the energy overlap term  $E_{SA}$  remains constant, so that only the interaction term  $f_{SA}$  is varied. It is an intriguing problem to explain why  $Y_2WO_6$ -Eu is an efficient red phosphor, whereas  $Gd_2WO_6$ -Eu has a medium efficiency (22, 24). First the efficiency of SS transfer should be considered.

Energy can be transferred through the host lattice in both cases, albeit the efficiency of this transfer will not be very high (see above). Since it has been shown that the efficiency of the  $Eu^{3+}$  emission of these tungstates for excitation into the narrow 4f levels of the activator itself is near to 100% (25), the difference between the efficiencies of the  $Eu^{3+}$  emission of  $Y_2WO_6$ -Eu and  $Gd_2WO_6$ -Eu for excitation of the tungstate groups must be ascribed to a difference in the SA (tungstate- $Eu^{3+}$ ) transfer probability. Since the energy overlap condition is fulfilled (the tungstate emission overlaps some  $Eu^{3+}$  levels), this difference must be due to the strength of the interaction. In view of the analogy between both compounds, electric multipole-multipole interaction can be excluded, since that would not depend so strongly on the crystal structure. Estimations indicate in fact that for this case transfer by exchange interaction has an order of magnitude higher probability than transfer by electric multipole interactions (22).

A necessary condition for exchange interaction is that the wavefunctions of the centers involved overlap each other. Therefore this type of energy transfer is comparable to the magnetic interaction between paramagnetic ions in insulators, the so-called superexchange (26). Superexchange is known to be strongly dependent on the angle between the paramagnetic ions and the intermediary oxygen ions. In the ferrites,

for example, the  $Fe^{3+}-O^{2-}-Fe^{3+}$  angle is about  $135^\circ$  giving rise to strong interaction, whereas in  $ZnFe_2O_4$  with  $Fe^{3+}-O^{2-}-Fe^{3+}$  angle  $90^\circ$  the interaction is very weak. In  $Ba_2GdNbO_6$  magnetic superexchange in the configuration  $Gd-O-Nb-O-Gd$  proves a certain 4f electron density on the intermediary niobate group (27). Also in  $GdPO_4$  magnetic interactions between  $Gd^{3+}$  ions using the phosphate group as an intermediary play a role (28). The latter compounds bring us back to rare earth activated oxides. Energy transfer from a tungstate group to  $Eu^{3+}$  by exchange interaction is possible, if also here the 4f electrons of the  $Eu^{3+}$  ion have a certain density at the tungstate group. This means that the angle  $W-O-Eu$  in  $Y_2WO_6$ -Eu and  $Gd_2WO_6$ -Eu ( $Eu^{3+}$  replaces  $Y^{3+}$  and  $Gd^{3+}$ , respectively) will determine the transfer efficiency. For  $Y_2WO_6$  this angle is about  $180^\circ$ ; for  $Gd_2WO_6$  it is about  $90^\circ$ . This then must be the explanation why the SA transfer is much more efficient in  $Y_2WO_6$ -Eu than in  $Gd_2WO_6$ -Eu. For low  $Eu^{3+}$  concentrations (say less than 1%) the efficiency of the  $Eu^{3+}$  emission on excitation into the tungstate group of  $Y_2WO_6$ -Eu is low. This must be ascribed to the relatively low probability of SS transfer (see also below).

The hypothesis that the transfer from lattice to rare earth ion is determined by the angle between the rare earth ion, the oxygen ion, and the cation at the center of the uv absorbing group has been confirmed for many other phosphors (6), e.g.,  $Y_6WO_{12}$ -Eu (low efficiency, angle  $100^\circ$ ),  $YVO_4$ -Eu (high efficiency, angle  $170^\circ$ ) and  $Gd_2Ti_2O_7$ -Eu (low efficiency, angle  $100^\circ$ ).

**The system  $YP_{1-x}V_xO_4$ -Eu ( $P_{SS}$  varied,  $P_{SA}$  constant).**—In the section on concentration quenching it was shown that in the system  $YP_{1-x}V_xO_4$  the probability of vanadate-vanadate transfer decreases by diluting the vanadate groups by nonabsorbing phosphate groups. In the system  $YP_{1-x}V_xO_4$ -Eu,  $P_{SS}$  varies with  $x$  (because the interaction depends on the distance) and  $P_{SA}$  is in first approximation constant. This is the reverse of the situation in the preceding section, where  $P_{SA}$  was varied and  $P_{SS}$  remained constant.

$YVO_4$ -Eu is known to be a very efficient phosphor even for very low  $Eu^{3+}$  concentrations (29). The host lattice emission of  $YVO_4$  is quenched for the greater part at room temperature (30). In the system  $YP_{1-x}V_xO_4$ , however, efficient vanadate fluorescence is observed, which shows concentration quenching for  $x > 0.25$  (6, 31). In this connection it is conspicuous that in the system  $YP_{1-x}V_xO_4$ - $Eu^{3+}$  the quantum efficiency of the  $Eu^{3+}$  emission remains constant in the region  $0.2 < x \leq 1$ , but decreases strongly for lower vanadium content (32). All these facts can be explained from the foregoing.

The low efficiency of the fluorescence of  $YVO_4$  at room temperature is due to concentration quenching. We conclude therefore that  $YVO_4$  is a compound in which the efficiency for transfer through the host lattice is high. This explains, on the one hand, the concentration quenching in this system (efficient transport of excitation energy to killer sites). On the other hand, it explains also the high efficiency of rare earth activated vanadates even for low activator concentration (efficient transport of excitation energy to the activator), because also the conditions for an efficient SA transfer are satisfied: the vanadate emission overlaps some rare earth absorption levels and the  $Y-O-V$  angle is  $\sim 170^\circ$ .

By diluting the vanadium concentration with phosphorus the efficiency of SS transfer will decrease due to the increasing vanadium-vanadium distance. This explains why at a certain critical vanadium concentration the effect of concentration quenching disappears (*viz.*, 25% vanadium). For this concentration the efficiency of SS transfer becomes so low that the excitation energy cannot travel through the lattice over large distances. This means also that we can no longer expect that all of the exciting quanta reach the  $Eu^{3+}$  ions. It is indeed a fact that the concentration region

Table VI. Survey of energy transfer considerations (for g, f and E, see section on General Discussion of Energy Transfer); ++ = large, + = medium, - = small

Phosphor (act. conc. 1 a/o)	SS transfer		SA transfer		Efficiency of A fluorescence for excitation into S	
	Interaction ( $g_{SS}$ and/or $f_{SS}$ )	Energy overlap ( $E_{SS}$ )	Interaction ( $g_{SA}$ and/or $f_{SA}$ )	Energy overlap ( $E_{SA}$ )	Predicted	Experimental
$\text{Li}_3\text{NbO}_4\text{-Cr}$	+	+	++	++	++	++
$\text{EuAl}_3\text{B}_4\text{O}_{19}\text{-Cr}$	+	-	++	++	++	++
$\text{Y}_2\text{WO}_6\text{-Mo}$	+	+	+	++	+	+
$\text{Y}_2\text{SiWO}_6\text{-Mo}$	-	+	-	++	-	-
$\text{Y}_2\text{WO}_6\text{-Eu}$	+	-	+	++	+	+
$\text{Y}_2\text{MoO}_6\text{-Eu}$	+	-	-	++	-	-
$\text{Gd}_2\text{WO}_6\text{-Eu}$	+	+	-	++	-	-
$\text{YNbO}_4\text{-Eu}$	+	+	+	++	+	+
$\text{YNbO}_4\text{-Tb}$	+	+	-	++	+	+
$\text{YVO}_4\text{-Eu}$	+	++	+	++	++	++
$\text{YF}_{0.9}\text{V}_{0.1}\text{O}_4\text{-Eu}$	-	++	-	++	+	+
$\text{Ba}_2\text{GdNbO}_6\text{-Eu}$	-	+	+	++	-	-

in the system  $\text{YP}_{1-x}\text{V}_x\text{O}_4\text{-Eu}$  where the  $\text{Eu}^{3+}$  quantum efficiency decreases is the same region in the unactivated system where concentration quenching is absent.

The present considerations are summarized in Table VI. We conclude that the agreement between prediction and experiment is good, albeit qualitative.

*Rare earth activated  $\text{YNbO}_4$  (a quantitative calculation).*—Finally we will treat one special case in a more quantitative way. We will show that the quantum efficiency of the red  $\text{Eu}^{3+}$  emission and the blue niobate emission of  $\text{YNbO}_4\text{-Eu}$  can be calculated, if one assumes that the transfer through the host lattice is restricted on the average to one niobate-niobate step.

In  $\text{YNbO}_4$  the energy transfer through the lattice cannot be efficient due to the poor overlap of the emission and absorption band (see Fig. 7). It is therefore interesting to see how high the efficiencies of rare earth activated  $\text{YNbO}_4$  phosphors are. In Fig. 8 we have plotted the quantum efficiency of the niobate emission and the quantum efficiency of the  $\text{Eu}^{3+}$  and  $\text{Tb}^{3+}$  emission for  $\text{YNbO}_4\text{-Eu}$  and  $\text{YNbO}_4\text{-Tb}$  (32). Note that even for high rare earth concentrations (15%) the niobate emission is not completely quenched. A complication arises from the fact that for such high activator concentrations the occurrence of concentration quenching of the rare earth emission

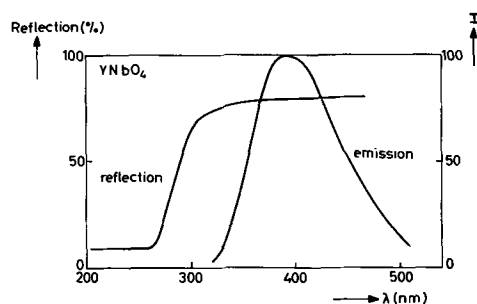


Fig. 7. Diffuse reflection spectrum and spectral energy distribution of the emission of  $\text{YNbO}_4$  (254 nm excitation).

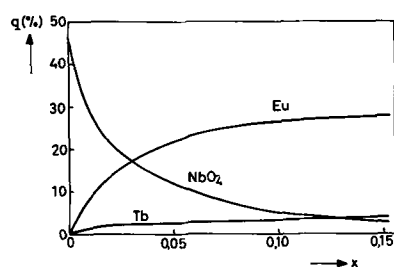


Fig. 8. Quantum efficiency of the niobate, europium, and terbium emission of phosphors  $\text{Y}_{1-x}\text{Eu}_x\text{NbO}_4$  and  $\text{Y}_{1-x}\text{Tb}_x\text{NbO}_4$  (250-270 nm excitation).

cannot be excluded. The sum of the niobate and rare earth quantum efficiency remains roughly constant for  $\text{YNbO}_4\text{-Eu}$ , but decreases for  $\text{YNbO}_4\text{-Tb}$ . It is therefore concluded that in  $\text{YNbO}_4\text{-Eu}$  the SS transfer is not very efficient, whereas the SA transfer is reasonably efficient. This agrees with the arguments given above, because the energy overlap in the case of the SS transfer is poor (Fig. 7) and the Nb-O-Y angle (of importance for SA transfer) is roughly  $130^\circ$ .

We tried to carry out a more quantitative calculation based on this simple model. Let us assume that the probability of SS transfer in the case of  $\text{YNbO}_4\text{-Eu}$  is 0% and that of SA transfer from the  $\text{NbO}_4$  group to an  $\text{Eu}^{3+}$  ion on the nearest Y-sites is 100% and that of transfer to all other  $\text{Eu}^{3+}$  ions 0%. Each  $\text{NbO}_4$  group has eight nearest Y sites. This means that, if a quantum is absorbed by a niobate group, the probability of niobate emission is  $(1-x)^8$  and the probability of europium emission  $1 - (1-x)^8$ . Here  $x$  is the  $\text{Eu}^{3+}$  concentration as defined by the formula of the sample  $\text{Y}_{1-x}\text{Eu}_x\text{NbO}_4$ . Another possibility is to assume that the SS transfer is not completely negligible and that on the average the excited niobate group transfers its energy to one of the four nearest niobate groups. If the restrictions on the SA transfer remain the same as above, the absorbed excitation quantum can then be transferred to 22 Y-sites (either directly or after one niobate-niobate transfer). The probability of niobate emission is now  $(1-x)^{22}$ . Loss of excitation energy by nonradiative transitions is neglected. For  $\text{Eu}^{3+}$  this has been proved to be correct by excitation into the narrow  $\text{Eu}^{3+}$  levels (25), and for the niobate group this is a good approximation, since the quenching range of the niobate fluorescence is in the region  $400^\circ\text{-}500^\circ\text{K}$  (33).

Table VII compares the results for these two models with the experimental results. To make the comparison easier the experimental quantum efficiencies are corrected in such a way that their sum is taken as 100%. It is seen that the model without SS transfer is too simple. The decrease of the efficiency of the niobate emission with increasing  $\text{Eu}^{3+}$  concentration is not rapid enough. The model which allows for one-step SS transfer gives surprisingly good agreement with the experimental results. For  $x = 0.15$  the theoretical

Table VII. Quantum efficiencies of niobate and  $\text{Eu}^{3+}$  emission of  $\text{Y}_{1-x}\text{Eu}_x\text{NbO}_4$  for excitation of the niobate group

x	Experimental <sup>a</sup>		Model I <sup>b</sup>		Model II <sup>c</sup>	
	$\text{NbO}_4$	$\text{Eu}^{3+}$	$\text{NbO}_4$	$\text{Eu}^{3+}$	$\text{NbO}_4$	$\text{Eu}^{3+}$
0	100	0	100	0	100	0
0.005	90	10	96	4	89	11
0.015	67	33	88	12	67	33
0.06	30	70	61	39	26	74
0.15	10	90	27	73	2.5	97.5

<sup>a</sup> Sum of the two efficiencies is always put at 100.

<sup>b</sup> No SS transfer.

<sup>c</sup> Not more than one SS transfer step allowed.

$\text{Eu}^{3+}$  efficiency is too high. This may be ascribed to concentration quenching.

Although we may conclude that our ideas on transfer from host lattice to rare earth ion are always valid for  $\text{Eu}^{3+}$ ,  $\text{Sm}^{3+}$ ,  $\text{Dy}^{3+}$  (and probably for other ions, but this has not been studied), the results for  $\text{YNbO}_4\text{-Tb}$  cannot be accounted for in such a simple way (34). In  $\text{YNbO}_4\text{-Tb}$  the niobate fluorescence is quenched in a similar way as in  $\text{YNbO}_4\text{-Eu}$ , but the efficiency of the  $\text{Tb}^{3+}$  emission is always very low. This is even more pronounced in, e.g.,  $\text{YVO}_4\text{-Tb}$  and  $\text{Y}_2\text{WO}_6\text{-Tb}$  which do not emit any  $\text{Tb}^{3+}$  fluorescence on host lattice excitation. We have shown that, if the absorption edge of the host lattice moves to shorter wavelengths, the  $\text{Tb}^{3+}$  output becomes higher:  $\text{YNbO}_4\text{-Tb}^{3+}$  shows at least some emission and  $\text{YPO}_4\text{-Tb}^{3+}$  is rather efficient (see Table VIII). Elsewhere we have given a possible explanation for this phenomenon (34, 35): in the case of exchange-regulated energy transfer from S to A the state  $\text{S}^+ + \text{A}^-$  (or  $\text{S}^- + \text{A}^+$ ) must have a much higher energy than the state S (excited) + A. If this is not the case, there is no reason why simultaneously the excited electron should be transferred from S to A and another electron back from A to S. There is no doubt that, e.g., in  $\text{YVO}_4\text{-Tb}$ , the energy of the excited state  $\text{Tb}^{3+}\text{-O}^{2-}\text{-V}^{5+}$  is near to that of the state  $\text{Tb}^{4+}\text{-O}^{2-}\text{-V}^{4+}$  in view of the low fourth ionization potential of terbium (in the ground state the configuration must be  $\text{Tb}^{3+}\text{-O}^{2-}\text{-V}^{5+}$  in view of the white body color of the sample).

#### Low Sensitizer Concentration

The example of  $\text{YP}_{1-x}\text{V}_x\text{O}_4\text{-Eu}$  in the preceding section shows that there is no essential difference between the case of high S concentration (host lattice excitation) and low S concentration (usually called sensitizer excitation). Well-known examples of sensitizers are  $\text{Sb}^{3+}$  (calcium halophosphates!),  $\text{Ce}^{3+}$ , and  $\text{Bi}^{3+}$ . The SS transfer between these ions is expected to be very efficient, since the energy overlap is large and the interaction strong (see above). The critical concentration for concentration quenching is therefore always low (Table II). These sensitizers cannot be used in high concentrations, because then the SS transfer probability would be much larger than the SA transfer probability, so that the energy travels "easily" through the lattice from S to S until a killer site is reached. We illustrate our considerations with some examples taken from a study on transfer from  $\text{Ce}^{3+}$ ,  $\text{Bi}^{3+}$ , and  $\text{Sb}^{3+}$  to  $\text{Sm}^{3+}$ ,  $\text{Eu}^{3+}$ ,  $\text{Tb}^{3+}$ , and  $\text{Dy}^{3+}$  in nonabsorbing yttrium compounds (35).

First we consider phosphors  $\text{YOCl} : \text{Bi}^{3+}$ ,  $\text{Ln}^{3+}$  ( $\text{Ln} = \text{Sm}, \text{Eu}, \text{Tb}, \text{Dy}$ ). The sensitizer  $\text{S} (= \text{Bi}^{3+})$  is the same for all cases, but the activator  $\text{Ln}^{3+}$  is varied, i.e.,  $P_{SS}$  is constant, but  $P_{SA}$  is varied. The efficiency of the  $\text{Ln}^{3+}$  emission for excitation into  $\text{Bi}^{3+}$  decreases in the sequence  $\text{Eu}^{3+}$ ,  $\text{Sm}^{3+}$  and  $\text{Dy}^{3+}$ ,  $\text{Tb}^{3+}$ . This must be ascribed to a variation of the SA transfer probability, since the SS transfer probability is equal for the four cases. It can be shown that the energy overlap of the S emission and A absorption is roughly equal for the four  $\text{Ln}^{3+}$  ions. Therefore the variation of the total transfer efficiency must be ascribed to a

variation of the interaction strength between S and A. For electric multipole interaction the SA transfer probability is expected to increase in the sequence  $\text{Tb}^{3+}$ ,  $\text{Eu}^{3+}$ ,  $\text{Dy}^{3+}$ ,  $\text{Sm}^{3+}$ , because the oscillator strength of the absorption bands in the region of the  $\text{Bi}^{3+}$  emission increases in this sequence. This does not agree with the experimental results. For exchange interaction the SA transfer probability is expected to increase in the sequence  $\text{Tb}^{3+}$ ,  $\text{Dy}^{3+}$ ,  $\text{Sm}^{3+}$ ,  $\text{Eu}^{3+}$ , because the energy necessary to promote an electron from  $\text{O}^{2-}$  to the 4f orbitals of the rare earth ion decreases in this series, i.e., the wave function admixture increases. This again proves that energy transfer from a sensitizer to a rare earth ion occurs generally by exchange interaction.

Now we will compare the efficiency of the  $\text{Eu}^{3+}$ -fluorescence of  $\text{YOCl-Bi}$ ,  $\text{Eu}$  and  $\text{YAl}_3\text{B}_4\text{O}_{12}\text{-Bi}$ ,  $\text{Eu}$  for excitation into the  $\text{Bi}^{3+}$  absorption band. Here the same S and A ions are introduced in different host lattices to study the influence of the host lattice on  $P_{SS}$  and  $P_{SA}$ . Figure 9 shows that the SS transfer probability is much higher in the borate than in the oxychloride due to the larger energy overlap. This is one reason why  $\text{YAl}_3\text{B}_4\text{O}_{12}\text{-Bi}$ ,  $\text{Eu}$  shows a much higher total transfer efficiency from  $\text{Bi}^{3+}$  to  $\text{Eu}^{3+}$  than  $\text{YOCl-Bi}$ ,  $\text{Eu}$ . There is still another reason. The SA transfer in the oxychloride is exchange-regulated (see above) and therefore of medium efficiency. In  $\text{YAl}_3\text{B}_4\text{O}_{12}\text{-Bi}$ ,  $\text{Eu}$ , however, the  $\text{Bi}^{3+}$  emission band overlaps the  $\text{Eu}^{3+}$  charge-transfer band. Both bands have a high oscillator strength, so that efficient transfer by electric multipole interaction can be expected (Fig. 10). This is the second reason why  $\text{YAl}_3\text{B}_4\text{O}_{12}\text{-Bi}$ ,  $\text{Eu}$  has a higher transfer efficiency than  $\text{YOCl-Bi}$ ,  $\text{Eu}$ . This example illustrates how the choice of the host lattice can influence energy transfer efficiencies, because the energy levels are also influenced.

It is remarkable that energy transfer from  $\text{Ce}^{3+}$  to  $\text{Eu}^{3+}$  is absent in many lattices, for example in  $\text{YOCl-Ce}$ ,  $\text{Eu}$ . The interaction between  $\text{Ce}^{3+}$  and  $\text{Eu}^{3+}$  in this case is expected to be of the exchange type, since the broad  $\text{Ce}^{3+}$  emission overlaps several narrow  $\text{Eu}^{3+}$  absorption levels. This absence of energy transfer can

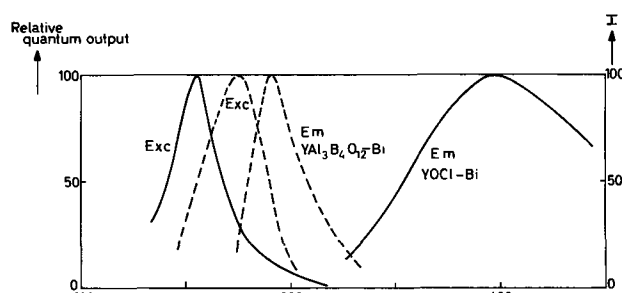


Fig. 9. Excitation spectra (Exc) and spectral energy distribution of the emission (Em) of  $\text{YOCl-Bi}$  and  $\text{YAl}_3\text{B}_4\text{O}_{12}\text{-Bi}$  (254 nm excitation). Note the larger overlap of the two spectra in the case of  $\text{YAl}_3\text{B}_4\text{O}_{12}\text{-Bi}$ .

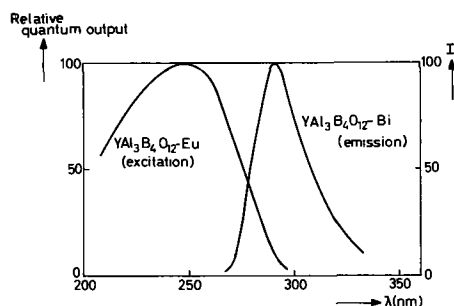


Fig. 10. Excitation spectrum of the emission of  $\text{YAl}_3\text{B}_4\text{O}_{12}\text{-Eu}$  and spectral energy distribution of the emission of  $\text{YAl}_3\text{B}_4\text{O}_{12}\text{-Eu}$  (254 nm excitation).

Table VIII. Host lattice absorption edge and efficiency of energy transfer from lattice to rare earth activator for some  $\text{Eu}^{3+}$ - and  $\text{Tb}^{3+}$ -activated phosphors

Host lattice	Host lattice absorption edge, nm	Efficiency*	
		$\text{Eu}^{3+}$	$\text{Tb}^{3+}$
$\text{YVO}_4$	320	+	+
$\text{Gd}_2\text{WO}_6$	310	+	-
$\text{Y}_2\text{WO}_6$	300	+	-
$\text{YNbO}_4$	260	+	+
$\text{YPO}_4$	~200	+	+

\* + + high, + low, - zero.

also be ascribed to the fact that the state  $Ce^{4+} + Eu^{2+}$  will not have a much higher energy than that of the state  $Ce^{3+}$  (excited) +  $Eu^{3+}$ , so that the probability of exchange-regulated transfer is decreased. As a matter of fact this is not true for  $Ce^{3+}$ ,  $Tb^{3+}$  and  $Ce^{3+}$ ,  $Dy^{3+}$  for which cases energy transfer was observed. In  $LaOCl-Ce, Eu$ , however, the emission of  $Ce^{3+}$  overlaps the charge transfer absorption band of  $Eu^{3+}$  giving rise to strong electric multipole interaction. Indeed transfer from  $Ce^{3+}$  to  $Eu^{3+}$  was observed for this case. The energy overlap for SS transfer is roughly equal for both oxychlorides.

#### Position of Energy Levels

From the previous section on energy transfer it follows that it is important to know how the position of absorption and emission bands is influenced by the host lattice. As a matter of fact this also influences the emission color of the phosphor and its absorption strength at certain wavelengths, important for the use of the phosphors in fluorescent lamps and in phosphor-coated high-pressure mercury vapor discharge lamps. Jørgensen (36) has done much work on the dependence of the position of absorption bands on the surroundings of the absorbing center. In our work we have in general followed his approach. The shift of the charge-transfer absorption band of  $Eu^{3+}$  in oxides was related to the potential field at the site of the  $O^{2-}$  anions (see above). The same can be done for the absorption (and emission) bands of niobates with  $NbO_6$  octahedra. The case of  $Ce^{3+}$  and  $Tb^{3+}$  is more complicated than that of  $Eu^{3+}$ . The shift of the broad band absorption and emission of  $Ce^{3+}$ -activated oxides will be given as an example (14).

The  $Ce^{3+}$  ion has  $4f^1$  configuration. The lowest excited state is the 5d level which is split by the crystal field. The position of the lowest absorption and emission level of the  $Ce^{3+}$  ion in solids is therefore determined by the energy difference  $4f - 5d$  in the solid and by crystal field effects. The energy difference between the 4f and 5d level is strongly influenced by the surroundings: it amounts to  $51,000\text{ cm}^{-1}$  for the free ion,  $48,000\text{ cm}^{-1}$  in fluorides and about  $33,000\text{ cm}^{-1}$  in oxides [nephelauxetic effect (36)]. The influence of crystal-field splitting is shown in Fig. 11, where the energy levels of  $Ce^{3+}$  in  $YAl_3B_4O_{12}$  (trigonal prismatic surroundings) and in  $Y_3Al_5O_{12}$  (distorted cubic surroundings) are given. The emission of the former is situated in the ultraviolet, that of the latter consists of a band in the green and a weaker band in the ultraviolet. Note the exceptional case of  $Y_3Al_5O_{12}-Ce$ : there is also emission from the next to the lowest

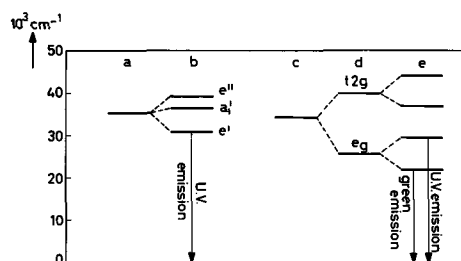


Fig. 11. Crystal field effects on the excited 5d level of  $Ce^{3+}$  in solids: a, center of gravity of the 5d level of  $Ce^{3+}$  in  $YAl_3B_4O_{12}$  (the free ion level is at  $51,000\text{ cm}^{-1}$ ); b, crystal field components of the 5d level of  $Ce^{3+}$  in  $YAl_3B_4O_{12}$  (trigonal prismatic coordination); c, center of gravity of the 5d levels of  $Ce^{3+}$  in  $Y_3Al_5O_{12}$ ; d, cubic crystal field components of the 5d level of  $Ce^{3+}$  in  $Y_3Al_5O_{12}$  (lower-symmetrical splittings neglected); e, crystal field components of the 5d level of  $Ce^{3+}$  in  $Y_3Al_5O_{12}$  (distorted cubic coordination). Emission has been observed from the two lower levels.

level; the emission from the lowest level is at extremely long wavelengths (usually  $Ce^{3+}$  emits in the ultraviolet or blue). How important the large crystal field splitting is, becomes clear by replacing  $Al^{3+}$  in  $Y_3Al_5O_{12}-Ce$  by  $Ga^{3+}$ . The crystal field splitting becomes smaller and the absorption and emission shift to the ultraviolet ( $Y_3Al_5O_{12}-Ce$  has a yellow body color, whereas  $Y_3Ga_5O_{12}-Ce$  is nearly white).

#### Acknowledgment

The authors express their sincere thanks to Dr. H. A. Klasens for his interest and constructive criticism during this work.

Manuscript received May 7, 1968. This paper was presented at the Boston Meeting, May 5-9, 1968, as Paper 28.

Any discussion of this paper will appear in a Discussion Section to be published in the June 1969 JOURNAL.

#### REFERENCES

1. See, for example, "Luminescence of Inorganic Solids," Chap. 5, P. Goldberg, Editor, Academic Press, New York (1966).
2. G. Blasse, *J. Chem. Phys.*, **48**, 3108 (1968).
3. F. Seitz, *Trans. Faraday Soc.*, **35**, 74 (1939).
4. D. L. Dexter, C. C. Klick, and G. A. Russell, *Phys. Rev.*, **100**, 603 (1955).
5. J. T. Waber and D. T. Cromer, *J. Chem. Phys.*, **42**, 4116 (1965).
6. G. Blasse, Philips Research Repts., **23**, 344 (1968).
7. F. A. Kröger, "Some Aspects of the Luminescence of Solids," Chap. 2, Elsevier, Amsterdam-New York (1948).
8. G. Blasse, *J. Chem. Phys.*, **45**, 2356 (1966).
9. A. Wachtel, *This Journal*, **111**, 534 (1964).
10. G. Blasse and A. Bril, *Z. Phys. Chem. N. F.*, **57**, 187 (1968).
11. L. Pauling, "The Nature of the Chemical Bond," Oxford University Press (1952).
12. G. Blasse and J. de Vries, *This Journal*, **114**, 875 (1967).
13. G. Blasse, *ibid.*, **115**, 738 (1968).
14. G. Blasse and A. Bril, *J. Chem. Phys.*, **47**, 5139 (1967).
15. G. Blasse and A. Bril, *ibid.*, **48**, 217 (1968).
16. T. Förster, *Ann. Phys. Leipzig*, **2**, 55 (1948).
17. D. L. Dexter, *J. Chem. Phys.*, **21**, 836 (1953).
18. G. Blasse *J. Inorg. & Nuclear Chem.*, **29**, 1817 (1967).
19. G. Blasse and A. Bril, *Physica Stat. Sol.*, **20**, 551 (1967).
20. D. L. Dexter and J. H. Schulman, *J. Chem. Phys.*, **22**, 1063 (1954).
21. F. A. Kröger, *Philips Research Repts.*, **2**, 177 (1947).
22. G. Blasse and A. Bril, *J. Chem. Phys.*, **45**, 2350 (1966).
23. G. Blasse, *J. Inorg. & Nuclear Chem.*, in press.
24. H. J. Borchardt, *J. Chem. Phys.*, **39**, 504 (1963).
25. A. Bril, G. Blasse, and J. A. A. Bertens, *This Journal*, **115**, 395 (1968).
26. P. W. Anderson, in "Magnetism," Vol. 1, p. 25, G. T. Rado and H. Suhl, Editors, Academic Press Inc., New York (1963).
27. G. Blasse, *Philips Research Repts.*, **20**, 327 (1965).
28. F. F. Y. Wang, *Phys. Stat. Sol.*, **14**, 193 (1966).
29. L. G. Van Uitert, R. C. Linares, R. R. Soden, and A. A. Ballman, *J. Chem. Phys.*, **36**, 702 (1962).
30. F. C. Palilla, A. K. Levine, and M. Rinkevics, *This Journal*, **112**, 776 (1965).
31. M. A. Aja, *ibid.*, **114**, 367 (1967).
32. W. L. Wanmaker, A. Bril, J. W. ter Vrugt, and J. Broos, *Philips Research Repts.*, **21**, 270 (1966).
33. W. L. Wanmaker, Private communication.
34. G. Blasse and A. Bril, *Philips Research Repts.*, **22**, 481 (1967).
35. G. Blasse and A. Bril, *J. Chem. Phys.*, **47**, 1920 (1967).
36. C. K. Jørgensen, "Absorption Spectra and Chemical Bonding in Complexes," Pergamon Press, London, New York (1962).

# Alkaline Earth Halophosphate Phosphors Activated by Divalent Europium

F. C. Palilla\* and B. E. O'Reilly

The Bayside Laboratory, research center of  
General Telephone & Electronics Laboratories Incorporated, Bayside, New York

## ABSTRACT

A new class of phosphors is described based on alkaline earth halophosphates possessing spodosite and apatite structures as host matrices for lanthanide ion activators. The materials are presented in terms of the formulations used for their synthesis; these formulations have pronounced effects on efficiency and spectral properties of the final compositions. Divalent europium is the principal activator considered.

The alkaline earth halophosphates were discovered as efficient ultraviolet stimulable luminescent materials in 1942 by McKeag and Ranby (1). Their adoption by the lighting industry in England and the United States for use in fluorescent lamps immediately established them as an important class of compounds (2-5). Since then, these halophosphates have been the subject of intensive theoretical and experimental investigations. An extensive literature has accumulated over the past twenty years which has recently been surveyed, in part, by Johnson (6).

$\text{Ca}_5(\text{PO}_4)_3(\text{Cl}, \text{F}) : \text{Sb}^{3+}, \text{Mn}^{2+}$  remains the principal fluorescent lamp phosphor, but no really useful cathode-ray halophosphate phosphor has been reported previously. This paper describes the preparation of alkaline earth halophosphates activated by divalent europium and the high luminescent response of these materials to both uv and cathode-ray excitation.

Divalent europium, as an activator, has been extensively studied, particularly in fluorite structures. The use of  $\text{Eu}^{2+}$  in such structures was the subject of a recent review by Feofilov (7). Freed and Katcoff (8) and Butement (9) have reported on the fluorescence spectrum of  $\text{Eu}^{2+}$  in the  $\text{EuCl}_2\text{-SrCl}_2$  system, and Reinfeld and Glasner (10) have extended the studies to alkali halide crystals. The structureless emission bands observed are attributed to  $4f \leftarrow 5d$  transitions. This result is confirmed by the sensitivity of the emission to the crystalline environment, as described by Jenkins and McKeag (11) in silicates and by McClure and Kiss (12) in several cubic crystals. More recent work by Palilla *et al.* on alkaline earth aluminates supports this view (13).

Most of the reported investigations utilizing divalent europium as an activator have been concerned with the emission under ultraviolet excitation. Nazarova (14) reported on the blue-violet cathodoluminescence of strontium meta-, pyro-, and orthophosphates activated with  $\text{Eu}^{2+}$ , and Levshin *et al.* (15) described in detail the cathode-ray response of  $\text{Sr}_3(\text{PO}_4)_2 : \text{Eu}$  as a function of excitation conditions.

This paper describes an investigation of the ultraviolet and cathode-ray-excited fluorescence from  $\text{Eu}^{2+}$  in alkaline earth halophosphates as a function of preparation conditions and formulation. In particular, it discusses single, binary and ternary alkaline earth halophosphates, activated by  $\text{Eu}^{2+}$ , which possess both spodosite and apatite structures.

## Experimental

The alkaline earth halophosphates were formulated according to  $w\text{M}_{3(1-x)}(\text{PO}_4)_2 \cdot y\text{M}'_{(1-x)}\text{Cl}_2 : \text{Eu}_x^{2+}$  or, approximately  $w\text{M}_3(\text{PO}_4)_2 \cdot y\text{M}'\text{Cl}_2 : \text{Eu}^{2+}$  where M and M' are Ca, Ba, Sr or combinations of the three, the ratio of  $y$  to  $w$  varied between 1 and 3. The source of the  $\text{M}_{3(1-x)}(\text{PO}_4)_2$  component can be the corre-

sponding orthophosphate itself, the salt  $\text{MHPO}_4$ , or appropriate mixtures of  $\text{MCO}_3 + (\text{NH}_4)_2\text{HPO}_4$ . The activator concentration  $x$  can be between 0.0025 and 0.10 gram-atom per gram atom of the host cation (M + M'). The starting ingredients were mixed and then fired in a molybdenum crucible at temperatures above  $1000^\circ\text{C}$ . The firings were generally performed under a reducing  $\text{H}_2$  atmosphere for several hours. No beneficial effects were observed when the  $\text{Cl}^-$  was completely or partially replaced by other halogens.

The procedures for the measurements of cathodoluminescent response, spectra and CIE color coordinates have been described by Avella *et al.* (16). Measurements of selected phosphors were also performed in 5-in. monochrome cathode-ray tubes fabricated by conventional techniques. To evaluate their potential commercial utility, the phosphors were incorporated in 40-w and 15-w fluorescent lamps fabricated by the usual production procedures.

The spodosite and apatite halophosphates are generally represented by the formulas  $\text{M}_2\text{PO}_4\text{X}$  and  $\text{M}_{10}(\text{PO}_4)_6\text{X}_2$  or  $\text{M}_5(\text{PO}_4)_3\text{X}$  where M = one or more alkaline earth elements and X is a halide other than  $\text{I}^-$ . These formulas can also be written as  $\text{M}_3(\text{PO}_4)_2 \cdot \text{MX}_2$  and  $3\text{M}_3(\text{PO}_4)_2 \cdot \text{MX}_2$ , respectively, corresponding to  $y/w$  ratios of 1/1 and 1/3. The conventional syntheses involve formulations close to the stoichiometric requirements. However, in order to emphasize the significant effect on fluorescence properties of the use of excess halide in the preparations, which corresponds to an initial  $y/w$  ratio of 1/3, the materials described herein will be discussed and presented in terms of their formulation. These formulations are such that the amount of alkaline earth halide used is in excess of that required for the formation of the spodosite or apatite composition, *e.g.*,  $y/w \cong 1$ . The excess halide is subsequently removed by water washing after the reaction at elevated temperatures is completed. Of the compounds so formed, the spodosite compound is obtained only in the case where M and M' = Ca and the preparation temperature is about  $1000^\circ\text{C}$ . In all other cases, *i.e.*, where M or M' is predominantly Ba or Sr, an apatite structure is obtained corresponding to the composition  $3(\text{M}, \text{M}')_3(\text{PO}_4)_2 \cdot (\text{M}, \text{M}')\text{X}_2$ .

## Results and Discussion

In the preparation of the alkaline earth halophosphates, no difficulties were experienced in the incorporation of divalent europium as activator. The substitution of  $\text{Eu}^{2+}$  (ionic radius 1.12Å) for  $\text{Ca}^{2+}$  (0.99Å) and  $\text{Sr}^{2+}$  (1.13Å) is facilitated by the similarity in ionic radii. Indeed, europium shows a tendency to assume the divalent state during substitution for  $\text{Ca}^{2+}$  or  $\text{Sr}^{2+}$  even when the syntheses are performed in air instead of  $\text{H}_2$ . The divalent state of europium is indicated by the band character of the emissions observed and by the absence of narrow emission lines in the

\* Electrochemical Society Active Member.



red spectral region typical of trivalent europium. In the preparation of the  $\text{Ba}^{2+}$  (1.35Å) compounds, divalent europium easily substitutes for this cation despite the large difference in ionic radii when the synthesis is performed in a  $\text{H}_2$  atmosphere. When synthesized in air, the Ba compounds contain both divalent and trivalent europium. This suggests that when the ionic radii are not nearly equal, there is competition between the valence which europium would normally prefer to assume in air and the valence which leads to easy substitution because no charge compensation is required. Attempts were made to prepare the Mg analogs, but the smaller ionic size of  $\text{Mg}^{2+}$  (0.65Å) prevents effective  $\text{Eu}^{2+}$  incorporation. Only when  $\text{Mg}^{2+}$  is part of a binary and ternary system can the  $\text{Eu}^{2+}$  be accommodated by the host matrix.

The alkaline earth phosphates, prepared as above, provide a series of phosphors with predominant emissions in the blue to green spectral regions. In general, when M and M' are the same cation, a narrow-band, symmetrical spectral energy distribution is obtained under cathode-ray excitation with peaks at 454 nm for the Ca compound, 446 nm for the Sr compound, and 447 nm for the Ba compound. These are shown in Fig. 1 together with the spectral distribution from  $\text{ZnS:Ag}$  for comparisons. The bandwidths of these unary  $\text{M} = \text{M}'$  compounds are narrow relative to that of  $\text{ZnS:Ag}$ . Some binary and ternary compounds, instead, yield an unsymmetrical spectrum skewed toward the longer wavelength region. This is especially pronounced for the compound formulated as  $\text{Sr}_3(\text{PO}_4)_2 \cdot 2\text{BaCl}_2:\text{Eu}$  (Fig. 1). The ternary formulation  $\text{Ba}_3(\text{PO}_4)_2 \cdot 2(\text{Ca}_{0.335}\text{Sr}_{0.665})\text{Cl}_2:\text{Eu}$  (Fig. 1) demonstrates a pronounced emission shift to longer wavelengths which sometimes occurs with cationic mixing. The consequences of unsymmetrical distributions and the effects of bandwidths on the color coordinates of the spectral emissions is discussed later.

$\text{Sr}_3(\text{PO}_4)_2 \cdot 2\text{SrCl}_2:\text{Eu}$  was used to illustrate the effect of activator concentration in the alkaline earth halophosphates. Table I presents the cathode-ray response and color coordinates of members of this system as functions of  $\text{Eu}^{2+}$  concentration. Maximum response is obtained with 0.02 gram atom of  $\text{Eu}^{2+}$  per gram atom of  $\text{M} + \text{M}'$ . With increasing  $\text{Eu}^{2+}$  concentration, the x coordinate is essentially unaffected, but the changes in y coordinate indicate a gradual but slight shift in spectral peak position toward longer wavelengths.

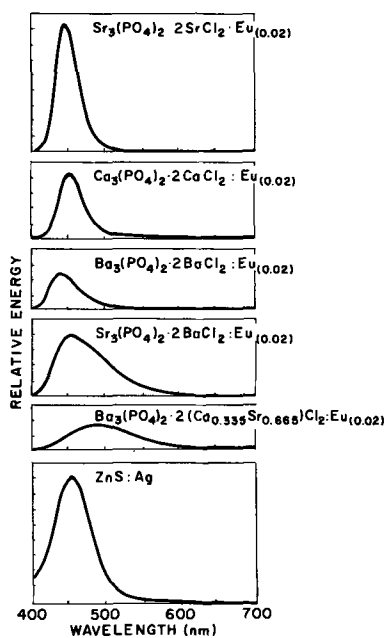


Fig. 1. Emission spectra of alkaline earth halophosphates activated by divalent europium and comparison with  $\text{ZnS:Ag}$ .

Table I. Effect of  $\text{Eu}^{2+}$  concentration on performance characteristics

	Relative luminosity	C.I.E. color coordinates	
		x	y
$\text{Sr}_{2.90}(\text{PO}_4)_2 \cdot 2\text{Sr}_{0.9975}\text{Cl}_2:\text{Eu}^{2+0.0025}$	59.5	0.154	0.028
$\text{Sr}_{2.065}(\text{PO}_4)_2 \cdot 2\text{Sr}_{0.993}\text{Cl}_2:\text{Eu}^{2+0.005}$	73.5	0.153	0.028
$\text{Sr}_{2.07}(\text{PO}_4)_2 \cdot 2\text{Sr}_{0.98}\text{Cl}_2:\text{Eu}^{2+0.01}$	93.0	0.153	0.028
$\text{Sr}_{2.01}(\text{PO}_4)_2 \cdot 2\text{Sr}_{0.98}\text{Cl}_2:\text{Eu}^{2+0.02}$	100.0	0.152	0.031
$\text{Sr}_{2.91}(\text{PO}_4)_2 \cdot 2\text{Sr}_{0.97}\text{Cl}_2:\text{Eu}^{2+0.08}$	93.0	0.152	0.033
$\text{Sr}_{2.85}(\text{PO}_4)_2 \cdot 2\text{Sr}_{0.95}\text{Cl}_2:\text{Eu}^{2+0.05}$	79.0	0.153	0.039
$\text{Sr}_{2.70}(\text{PO}_4)_2 \cdot 2\text{Sr}_{0.90}\text{Cl}_2:\text{Eu}^{2+0.10}$	63.0	0.157	0.061

To examine the effect of the excess alkaline earth chloride used in the synthesis, several series of phosphors were formulated in which the ratio of  $\text{MCl}_2$  to  $\text{M}_3(\text{PO}_4)_2$  ranged from 1 to 3. The relative cathode-ray and uv performances of representative systems are tabulated in Table II. For cathodoluminescence evaluation, the samples in groups (a) and (b) have been compared with the commercially available, silver-activated zinc sulfide. Under short-uv excitation (2537Å) the samples listed in group (a) are fairly saturated blue-emitting phosphors and have been compared with the standard short uv responsive tin-activated strontium pyrophosphate ( $\text{Sr}_2\text{P}_2\text{O}_7:\text{Sn}$ ). The phosphors of group (b) have broad emissions extending into the green region of the visible spectrum and therefore have been compared with the efficient green-emitting phosphor manganese-activated zinc silicate. The calcium halophosphate samples in group (a) best exemplify the effect of the phosphate-to-halide ratio on  $\text{Eu}^{2+}$  emission intensity. The 1:1 ratio yields an inefficient material which, according to its x-ray spectrum, consists of two major phases,  $3\text{Ca}_3(\text{PO}_4)_2 \cdot \text{CaCl}_2$  and  $\beta\text{-Ca}_3(\text{PO}_4)_2$ . The 2:1 and 3:1 formulations both yield  $3\text{Ca}_3(\text{PO}_4)_2 \cdot \text{CaCl}_2$  as the only phase. The products from these formulations are significantly more efficient than the product from the 1:1 formulation. It appears that once the stoichiometric requirements for formation of the apatite structure are satisfied, any additional halide serves to enhance fluxing and leads to more perfect and larger crystallite sizes. Figure 2 presents photomicrographs of the crystallites obtained in the calcium halophosphate series. The effect of excess  $\text{CaCl}_2$  on the particle size is clearly demonstrated.

A series of divalent europium-activated halophosphates were synthesized to examine changes in emission character, under cathode-ray excitation, brought about by cationic mixing. In this series, the phosphors are the result of the formulation  $\text{M}_3(\text{PO}_4)_2 \cdot 2\text{M}'\text{Cl}_2:\text{Eu}(0.02)$  where M is either strontium, calcium, or barium and where M' can be the same as M or a combination of any two alkaline earths. It was found that the most saturated emissions are obtained when M' is identical with M and when Ba is not a major component of either M or M'. When M' represents Ba or a cationic combination that includes Ba, desaturation of the blue emission color takes place. These findings are

Table II. Effect of excess halide on performance characteristics

Composition	Relative luminosity	
	Cathode-ray excitation	Ultraviolet excitation
(a)	( $\text{ZnS:Ag} = 100$ )	( $\text{Sr}_2\text{P}_2\text{O}_7:\text{Sn} = 100$ )
$\text{Ca}_{2.97}(\text{PO}_4)_2 \cdot 1\text{Ca}_{0.99}\text{Cl}_2:\text{Eu}^{2+0.01}$	6.0	11.9
$\text{Ca}_{2.97}(\text{PO}_4)_2 \cdot 2\text{Ca}_{0.99}\text{Cl}_2:\text{Eu}^{2+0.01}$	46.0	47.5
$\text{Ca}_{2.97}(\text{PO}_4)_2 \cdot 3\text{Ca}_{0.99}\text{Cl}_2:\text{Eu}^{2+0.01}$	39.0	41.3
$\text{Sr}_{2.91}(\text{PO}_4)_2 \cdot 1\text{Sr}_{0.98}\text{Cl}_2:\text{Eu}^{2+0.02}$	16.2	13.1
$\text{Sr}_{2.91}(\text{PO}_4)_2 \cdot 2\text{Sr}_{0.98}\text{Cl}_2:\text{Eu}^{2+0.02}$	28.0	30.0
$\text{Sr}_{2.91}(\text{PO}_4)_2 \cdot 3\text{Sr}_{0.98}\text{Cl}_2:\text{Eu}^{2+0.02}$	31.4	32.5
$\text{Sr}_{2.91}(\text{PO}_4)_2 \cdot 2\text{Ca}_{0.97}\text{Cl}_2:\text{Eu}^{2+0.03}$	100.0	96.2
$\text{Sr}_{2.91}(\text{PO}_4)_2 \cdot 3\text{Ca}_{0.97}\text{Cl}_2:\text{Eu}^{2+0.03}$	70.0	87.5
(b)	( $\text{ZnS:Ag} = 100$ )	( $\text{ZnSiO}_4:\text{Mn} = 100$ )
$\text{Ba}_{2.97}(\text{PO}_4)_2 \cdot 2\text{Ca}_{0.99}\text{Cl}_2:\text{Eu}^{2+0.01}$	86.0	65.0
$\text{Ba}_{2.97}(\text{PO}_4)_2 \cdot 3\text{Ca}_{0.99}\text{Cl}_2:\text{Eu}^{2+0.01}$	139.0	51.3
$\text{Ba}_{2.91}(\text{PO}_4)_2 \cdot 2\text{Ca}_{0.97}\text{Cl}_2:\text{Eu}^{2+0.03}$	120.0	75.0
$\text{Ba}_{2.91}(\text{PO}_4)_2 \cdot 3\text{Ca}_{0.97}\text{Cl}_2:\text{Eu}^{2+0.03}$	160.0	66.2



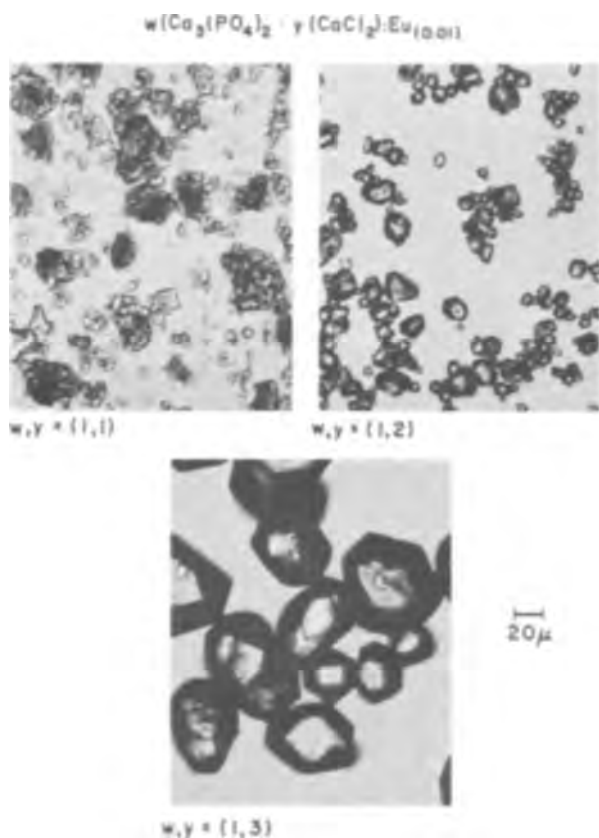


Fig. 2. Crystallite size vs. ratio of phosphate to halide used in formulation.

presented in graphic form in Fig. 3 to 5 in terms of the computed C.I.E. color coordinates of the emissions.

Thus, the formulations which contain Ba as part of a binary or ternary system appear less satisfactory as replacements for ZnS:Ag in television applications than those formulations which do not contain Ba. Although the desaturation which occurs with Ba is accompanied by an increase in luminosity, the requirement for increased efficiency as desaturation proceeds, in order to maintain color balance with the red and green primaries, increases at a faster rate than the luminosity increase (17). In addition, the loss in color gamut obtainable in combination with the red and green primaries is relatively great.

The saturated emissions from the unary compounds ( $M = M'$ ) and from the Ca-Sr binaries are acceptable. These compounds all have color coordinates close to those of the ZnS:Ag primary ( $x = 0.145, y = 0.052$ ). Indeed, the strontium unary compound has a lower  $y$  ( $x = 0.152, y = 0.032$ ) so that the output from this more saturated emission need only be about 70% of that of the sulfide to perform as well in color balancing; in addition, its use would result in an increase of about 11% in color area when combined with the currently used green and red primaries (18).

These latter materials now yield 30% or more of the levels of efficiency attainable in conventional shadow mask tubes, and for this reason the emission intensities are compared in this paper with ZnS:Ag under cathode-ray excitation at low current densities.<sup>1</sup> However, with increasing current densities, the efficiency of these materials remains unchanged, while the efficiency of ZnS:Ag decreases drastically.

Figure 3 presents the chromaticity data obtained for the strontium halophosphate group of phosphors. It may be noted, particularly in 3a and 3b, that the  $x$  coordinate remains relatively constant while the  $y$  coordinate changes as a function of composition. Figure

<sup>1</sup> The results reported herein were taken at 10 kv and at about  $0.5 \mu\text{a}/\text{cm}^2$ .

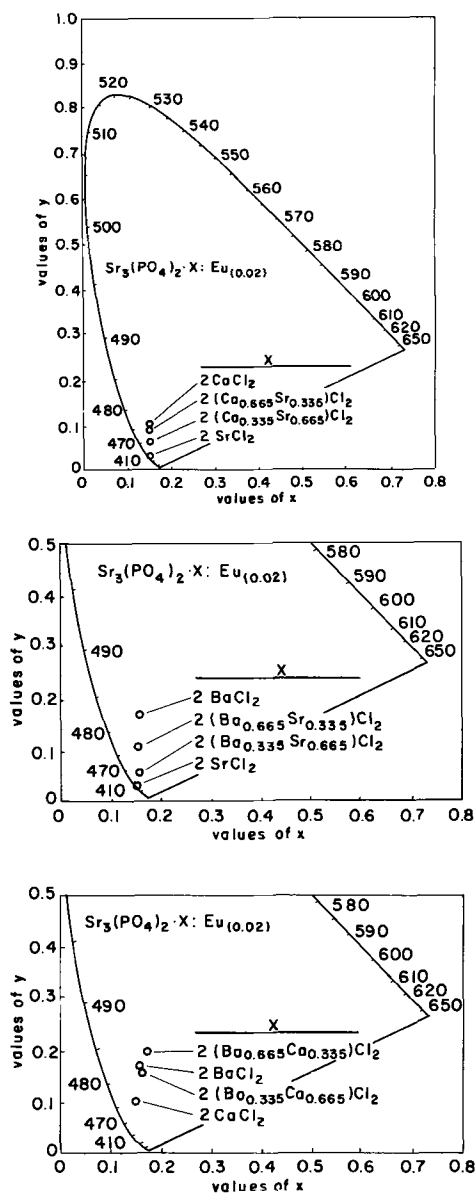


Fig. 3. Color coordinates from  $\text{Sr}_3(\text{PO}_4)_2 \cdot X \cdot \text{Eu}(0.02)$  where (a) (top)  $X = 2(\text{Ca}_{1-z}\text{Sr}_z)\text{Cl}_2$ , (b) (center)  $X = 2(\text{Ba}_{1-z}\text{Sr}_z)\text{Cl}_2$ , and (c) (bottom)  $X = 2(\text{Ba}_{1-z}\text{Ca}_z)\text{Cl}_2$ .

4 presents the corresponding data for the calcium analogs. This figure shows that in the phosphor group  $\text{Ca}_3(\text{PO}_4)_2 \cdot M'\text{Cl}_2 \cdot \text{Eu}(0.02)$ , the compositions where  $M'$  corresponds to a single alkaline earth halide have  $y$  coordinates which bracket those of compositions where the alkaline earth halide is mixed. This was generally true with the strontium compounds with one exception (Fig. 3c). Here again the unary compound ( $M = M'$ ) yields the most saturated phosphor of the group. In Fig. 5, the data for the barium analogs are presented. In contrast to the calcium and strontium series, the barium analogs give color coordinates which are unpredictable functions of cationic formulation. The only similarity to the previous series remains the greater saturation of the emission when  $M$  and  $M'$  are the same, in this case Ba. A possible explanation for this behavior, and for the one exception noted in Fig. 3c, may lie in the nature of the formation of the various apatites. The  $M_3(\text{PO}_4)_2$  component of the formulations described herein represents the larger part of the resulting phosphor  $(M, M')_5(\text{PO}_4)_3\text{Cl} \cdot \text{Eu}$ . Nonetheless, complex reactions are undoubtedly taking place during the formation of the final product from the halide and phosphate ingredients. These involve the ease of formation of the calcium, strontium, and barium apatites, the source of these cations, the variable effects on cell

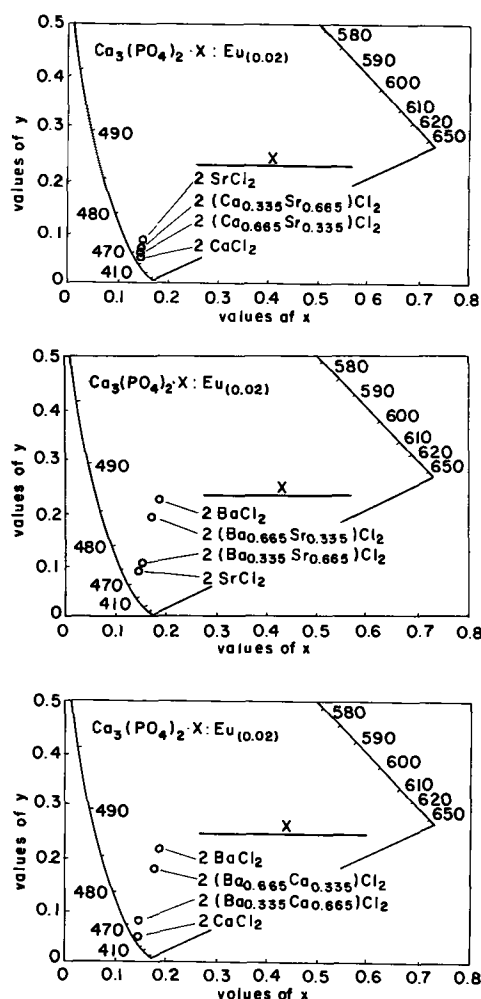


Fig. 4. Color coordinates from  $\text{Ca}_3(\text{PO}_4)_2 \cdot X:\text{Eu}(0.02)$  where (a) (top)  $X = 2(\text{Ca}_{1-z}\text{Sr}_z)\text{Cl}_2$ , (b) (center)  $X = 2(\text{Ba}_{1-z}\text{Sr}_z)\text{Cl}_2$ , and (c) (bottom)  $X = 2(\text{Ba}_{1-z}\text{Ca}_z)\text{Cl}_2$ .

dimensions with cationic species (19), and the degree to which each cation can accommodate the  $\text{Eu}^{2+}$ .

In order to clarify some of these factors, additional series of materials were prepared in which the amount of alkaline earth cation available from the halide component was equal to that available from the phosphate component of the formulation. In this way, it was found analytically that, in the formation of the final composition, preferential incorporation of the alkaline earth cation increased in the order barium, strontium and calcium. In these series, the ratio of  $\text{M}_3(\text{PO}_4)_2$  to  $\text{M}'\text{Cl}_2$  was 1/3. The europium concentration was formulated at 0.02 gram atom per gram atom of alkaline earth.<sup>2</sup> The cathode-ray brightness and color coordinates from these products follow the general trends which had been observed with the 1/2 formulations. Table III presents the formulations and the ratio of alkaline earth constituents analytically found in the final compositions.

From the  $\text{Ba}_3(\text{PO}_4)_2 \cdot \text{M}'\text{Cl}_2$  series it becomes obvious that, when the halide does not contain  $\text{BaCl}_2$ , the barium from the phosphate component is preferentially displaced by calcium and/or strontium. Even where  $\text{BaCl}_2$  is a constituent of the halide component, calcium and/or strontium are again incorporated into the final product to greater extent than the barium.

<sup>2</sup> The  $\text{Eu}^{2+}$  concentrations in the final products were found to reflect differences in the equilibrium distribution between the halophosphate formed and the excess halide subsequently removed. The final  $\text{Eu}^{2+}$  concentration in the unary Sr compounds was close to 0.02 indicating a 1:1 distribution while the  $\text{Eu}^{2+}$  concentrations in the unary Ca and Ba compounds were close to 0.01 and 0.03, respectively. The binary and ternary compositions contained intermediate concentrations. These variations in final  $\text{Eu}^{2+}$  concentrations would have little effect on emission efficiencies and colors (see Table I).

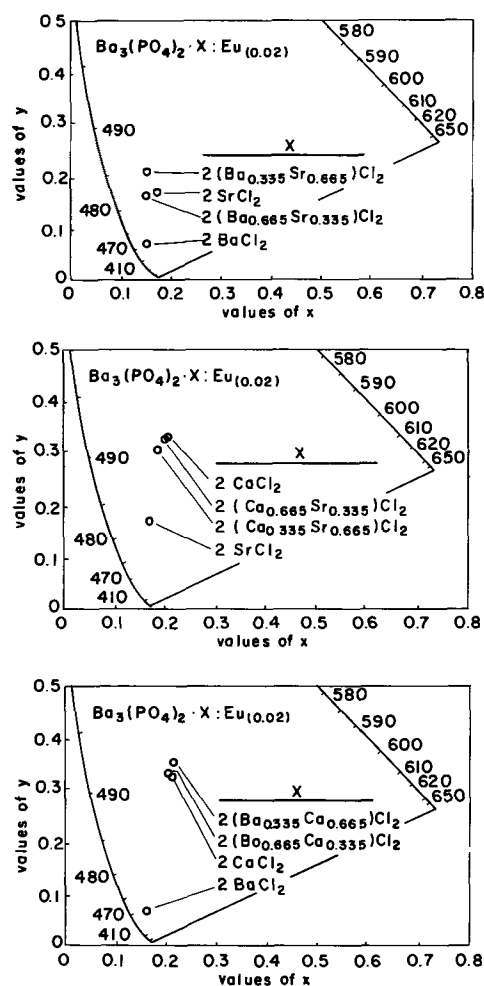


Fig. 5. Color coordinates from  $\text{Ba}_3(\text{PO}_4)_2 \cdot X:\text{Eu}(0.02)$  where (a) (top)  $X = 2(\text{Ba}_{1-z}\text{Sr}_z)\text{Cl}_2$ , (b) (center)  $X = 2(\text{Ca}_{1-z}\text{Sr}_z)\text{Cl}_2$ , (c) (bottom)  $X = 2(\text{Ba}_{1-z}\text{Ca}_z)\text{Cl}_2$ .

In the  $\text{M}_3(\text{PO}_4)_2 \cdot \text{M}'\text{Cl}_2$  series in which  $\text{M} = \text{Ca}$  or  $\text{Sr}$ , where the entire halide is  $\text{BaCl}_2$ , an additional two moles of the barium are not incorporated with the three moles of calcium or strontium from the phosphate component to give a final composition of  $(\text{M}_3\text{Ba}_2)(\text{PO}_4)_3\text{Cl}$ , where  $\text{M} = \text{Ca}$  or  $\text{Sr}$ . Instead, a smaller proportion of the  $\text{BaCl}_2$  component is utilized

Table III. Final compositions from  $\text{M}_3(\text{PO}_4)_2 \cdot 3\text{M}'\text{Cl}_2$  formulations

Formulation	Ba	Sr	Ca
$\text{Ba}_3(\text{PO}_4)_2 \cdot 3\text{SrCl}_2$	1.63	3.77	—
$\text{Ba}_3(\text{PO}_4)_2 \cdot 3\text{CaCl}_2$	1.75	—	3.25
$\text{Ba}_3(\text{PO}_4)_2 \cdot 2\text{SrCl}_2 \cdot 1\text{CaCl}_2$	1.94	2.00	1.06
$\text{Ba}_3(\text{PO}_4)_2 \cdot 1\text{SrCl}_2 \cdot 2\text{CaCl}_2$	1.78	1.03	2.19
$\text{Ba}_3(\text{PO}_4)_2 \cdot 3\text{BaCl}_2$	5.00	—	—
$\text{Ba}_3(\text{PO}_4)_2 \cdot 2\text{SrCl}_2 \cdot 1\text{BaCl}_2$	2.79	2.21	—
$\text{Ba}_3(\text{PO}_4)_2 \cdot 1\text{SrCl}_2 \cdot 2\text{BaCl}_2$	3.86	1.14	—
$\text{Ba}_3(\text{PO}_4)_2 \cdot 2\text{CaCl}_2 \cdot 1\text{BaCl}_2$	2.70	—	2.30
$\text{Ba}_3(\text{PO}_4)_2 \cdot 2\text{BaCl}_2 \cdot 1\text{CaCl}_2$	3.83	—	1.17
$\text{Ca}_3(\text{PO}_4)_2 \cdot 3\text{SrCl}_2$	—	1.95	3.05
$\text{Ca}_3(\text{PO}_4)_2 \cdot 3\text{CaCl}_2$	—	—	5.00
$\text{Ca}_3(\text{PO}_4)_2 \cdot 2\text{SrCl}_2 \cdot 1\text{CaCl}_2$	—	1.11	3.89
$\text{Ca}_3(\text{PO}_4)_2 \cdot 1\text{SrCl}_2 \cdot 2\text{CaCl}_2$	—	0.40	4.60
$\text{Ca}_3(\text{PO}_4)_2 \cdot 3\text{BaCl}_2$	1.32	—	3.68
$\text{Ca}_3(\text{PO}_4)_2 \cdot 2\text{SrCl}_2 \cdot 1\text{BaCl}_2$	0.10	1.64	3.26
$\text{Ca}_3(\text{PO}_4)_2 \cdot 1\text{SrCl}_2 \cdot 2\text{BaCl}_2$	0.39	1.03	3.51
$\text{Ca}_3(\text{PO}_4)_2 \cdot 2\text{CaCl}_2 \cdot 1\text{BaCl}_2$	0.02	—	4.98
$\text{Ca}_3(\text{PO}_4)_2 \cdot 1\text{CaCl}_2 \cdot 2\text{BaCl}_2$	0.34	—	4.66
$\text{Sr}_3(\text{PO}_4)_2 \cdot 3\text{CaCl}_2$	—	2.02	2.98
$\text{Sr}_3(\text{PO}_4)_2 \cdot 2\text{SrCl}_2 \cdot 1\text{CaCl}_2$	—	3.91	1.09
$\text{Sr}_3(\text{PO}_4)_2 \cdot 1\text{SrCl}_2 \cdot 2\text{CaCl}_2$	—	3.01	1.99
$\text{Sr}_3(\text{PO}_4)_2 \cdot 3\text{BaCl}_2$	1.64	—	3.36
$\text{Sr}_3(\text{PO}_4)_2 \cdot 2\text{SrCl}_2 \cdot 1\text{BaCl}_2$	0.30	4.70	—
$\text{Sr}_3(\text{PO}_4)_2 \cdot 2\text{BaCl}_2 \cdot 1\text{SrCl}_2$	0.84	4.16	—
$\text{Sr}_3(\text{PO}_4)_2 \cdot 2\text{CaCl}_2 \cdot 1\text{BaCl}_2$	0.17	2.73	2.10
$\text{Sr}_3(\text{PO}_4)_2 \cdot 1\text{CaCl}_2 \cdot 2\text{BaCl}_2$	0.81	3.07	1.12
$\text{Sr}_3(\text{PO}_4)_2 \cdot 3\text{SrCl}_2$	—	5.00	—

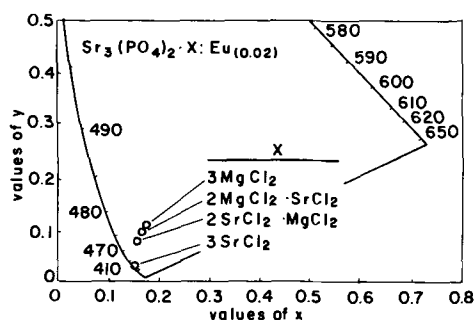


Fig. 6. Color coordinates from  $\text{Sr}_3(\text{PO}_4)_2 \cdot X \cdot \text{Eu}(0.02)$  where  $X = 3(\text{Sr}_{1-z}\text{Mg}_z)\text{Cl}_2$ .

to yield a final product in which the Ca (or Sr) to Ba ratio is greater than 3/2.

To a lesser extent, calcium is more easily accommodated in the final product than is strontium. Therefore, from the formulations  $\text{Sr}_3(\text{PO}_4)_2 \cdot 3\text{CaCl}_2$  and  $\text{Ca}_3(\text{PO}_4)_2 \cdot 3\text{SrCl}_2$ , products result which are close to  $(\text{Ca}_3\text{Sr}_2)(\text{PO}_4)_3\text{Cl}$ . Also, in those series in which  $\text{Ca}_3(\text{PO}_4)_2$  or  $\text{Sr}_3(\text{PO}_4)_2$  are reacted with both  $\text{CaCl}_2$  and  $\text{SrCl}_2$  as the halides, the calcium is preferentially utilized in the formation of the final product.

A detailed examination of all these complex interactions is beyond the scope of this paper. The results are included here to illustrate the various effects on emission characteristics. In general, while the effects on emission colors are reasonably predictable when only calcium and strontium are involved, the predictability is considerably reduced when barium is a constituent of a binary or ternary combination.

It has been mentioned previously that the formulation in which M and M' are both Mg results in an inefficient luminescent product. However, Mg may be a constituent in a binary or ternary system. A series of compounds formulated according to  $\text{Sr}_3(\text{PO}_4)_2 \cdot M'\text{Cl}_2 \cdot \text{Eu}(0.02)$  was prepared in which Mg was a constituent of the halide component. The chromaticity relationships among the products so obtained are given in Fig. 6. The behavior here resembles that of the Ca-Sr binary systems.

Selected members of the described families of phosphors were prepared with rare earth ions other than  $\text{Eu}^{2+}$  as activators. It was found that holmium did not yield noticeable luminescence, and thulium, erbium, samarium, gadolinium, and praseodymium were inefficient. However, the luminescence from dysprosium, ytterbium, cerium, and terbium under cathode-ray excitation was found to be within a useful range. The dysprosium and terbium emissions are typical of the trivalent species and yield line emissions in the yellow and green spectral regions, respectively. The emission from  $\text{Ce}^{3+}$  consists of two broad emissions in the blue and uv spectral regions. Ytterbium yields a band emission in the yellow spectral region which is attributable to its divalent state. The ytterbium is particularly interesting because the transitions probably involve valence electrons and therefore its emission, like that of  $\text{Eu}^{2+}$ , should also be sensitive to structural changes. Table IV summarizes the relative brightness and emission colors from  $\text{Sr}_3(\text{PO}_4)_2 \cdot 2\text{CaCl}_2$  formulations activated by the more effective rare earth ions.

Table IV. Emission properties of rare earth ions in the Sr-Ca binary

$\text{Sr}_{2.97}(\text{PO}_4)_2 \cdot 2\text{Ca}_{0.99}\text{Cl}_2 \cdot \text{A}_{0.01}$	Relative luminosity	Color
A		
$\text{Eu}^{2+}$	100.0	Blue
$\text{Dy}^{3+}$	97.0	Off-white
$\text{Yb}^{2+}$	33.0	Yellow
$\text{Ce}^{3+}$	11.0	Blue*
$\text{Tb}^{3+}$	33.0	Green

\*  $\text{Ce}^{3+}$  also exhibits a broad emission in the uv region.

It had been mentioned earlier that from formulations where  $M = M' = \text{Ca}^{2+}$ , a chlorospodiosite structure results when the synthesis is carried out at about  $1000^\circ\text{C}$ . The product here corresponds to  $\text{Ca}_3(\text{PO}_4)_2 \cdot \text{CaCl}_2 \cdot \text{Eu}$ . The emission of this compound is slightly more saturated than that of the chlorapatite  $3\text{Ca}_3(\text{PO}_4)_2 \cdot \text{CaCl}_2 \cdot \text{Eu}$ . The calculated color coordinates for the former are  $x = 0.147$ ,  $y = 0.046$ , and  $x = 0.144$ ,  $y = 0.053$  for the latter. The efficiencies are, however, comparable.

So far this paper has been concerned principally with the performance of these phosphors under cathode-ray excitation. The materials also respond efficiently to ultraviolet excitation. Figure 7 presents the excitation spectra of the phosphors whose emission curves are given in Fig. 1. The excitation curves are all characterized by a peak at 375 nm, attributable to effective absorption by  $\text{Eu}^{2+}$ . However, the curves are also unusually broad, indicating appreciable response throughout the entire uv region. Consequently, the utility of these materials in light applications is suggested. Figure 8 presents the excitation spectra of the spodiosite composition and, for comparison, a commercial halophosphate.

Several of the phosphors were tested in 15w fluorescent lamps and compared with a standard commercial phosphor  $\text{Sr}_2\text{P}_2\text{O}_7 \cdot \text{Sn}$  used for blue color correction. The comparison is presented in Table V. The Ba-Sr

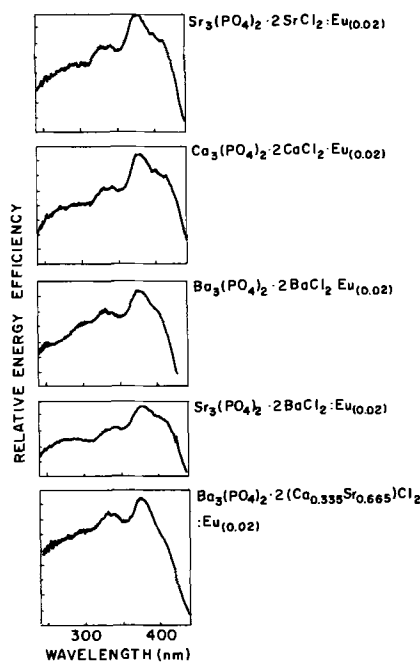


Fig. 7. Excitation spectra of alkaline earth halophosphates activated by divalent europium.

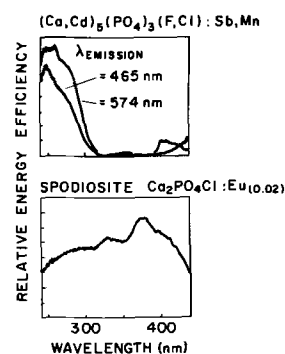


Fig. 8. Excitation spectra of calcium chlorospodiosite activated by divalent europium, and comparison with commercial  $(\text{Ca,Cd})(\text{PO}_4)_3(\text{F,Cl})\text{:Sb,Mn}$  for the Sb (465 nm) and Mn (574 nm) emissions.

Table V. Lamp performance of some alkaline earth halophosphates activated by  $\text{Eu}^{2+}$ 

Composition	Brightness in lumens			
	Initial	100 hr	500 hr	1700 hr
$\text{Sr}_2\text{P}_2\text{O}_7:\text{Sn}$ (Standard)	1477	1361	1300	1240
$\text{Ba}_{2.97}(\text{PO}_4)_2 \cdot 2\text{Sr}_{0.99}\text{Cl}_2:\text{Eu}^{2+0.01}$	1510	1461	1404	1290
$\text{Sr}_{2.94}(\text{PO}_4)_2 \cdot 2\text{Sr}_{0.9}\text{Cl}_2:\text{Eu}^{2+0.02}$	499	478	472	449
$\text{Sr}_{2.91}(\text{PO}_4)_2 \cdot 2\text{Ca}_{0.97}\text{Cl}_2:\text{Eu}^{2+0.03}$	915	878	869	830

binary is equivalent in emission color to that from  $\text{Sr}_2\text{P}_2\text{O}_7:\text{Sn}$  and its lumen output compares favorably with that from  $\text{Sr}_2\text{P}_2\text{O}_7:\text{Sn}$ . The unary Sr compounds and the Ca-Sr binary are less bright than  $\text{Sr}_2\text{P}_2\text{O}_7:\text{Sn}$ , but are more saturated in color. The same considerations apply here as in color television with regard to combining light of various colors to give a derived color. Therefore, a more saturated blue need not be as efficient as a less saturated blue to effect proper color balance. For this reason the  $\text{Sr}_{2.91}(\text{PO}_4)_2 \cdot 2\text{Ca}_{0.97}\text{Cl}_2:\text{Eu}^{2+0.03}$  sample of Table V, in effect, would probably be more useful than the Ba-Sr sample listed. The three phosphors listed in Table V show exceptional maintenance characteristics (rate of decrease of emission intensity with operational lifetime).

#### Acknowledgments

The authors wish to thank D. Bracco for his encouragement in this work, G. Gashurov for helpful discussions on structural details, C. Wiggins for the spectral data, W. Shelby for chemical analyses, and K. Butler of Sylvania Lighting Products Division for lamp evaluations. The authors also appreciate the critical review of this manuscript by S. Natansohn, F. Avella, and R. Amster.

Manuscript submitted April 19, 1968; revised manuscript received June 12, 1968.

Any discussion of this paper will appear in a Discussion Section to be published in the June 1969 JOURNAL.

#### REFERENCES

1. A. H. McKeag and P. W. Ranby, Brit. Pat. No. 578, 192 (1942).
2. A. H. McKeag and P. W. Ranby, *Ind. Chem.*, **23**, 513, 597 (1947).
3. H. G. Jenkins, A. H. McKeag, and P. W. Ranby, *J. (and Trans.) Electrochem. Soc.*, **96**, 1 (1949).
4. R. Nagy, R. W. Wollentin, and C. K. Lui, *ibid.*, **95**, 187 (1949).
5. K. H. Butler, *Illum. Eng.*, **44**, 267 (1949).
6. P. D. Johnson, "Luminescence of Inorg. Solids," P. Goldberg, Editor, Chap. 5, Academic Press, New York (1966).
7. P. P. Feofilov, *Acta Physica Polonica*, **26**, 331 (1964).
8. S. Freed and S. Katcoff, *Physica*, **14**, 17 (1948).
9. F. D. S. Butement, *Trans. Faraday Soc.*, **44**, 617 (1948).
10. R. Reisfeld and A. Glasner, *J. Opt. Soc. Amer.*, **54**, 331 (1964).
11. H. G. Jenkins and A. H. McKeag, *This Journal*, **97**, 415 (1950).
12. D. S. McClure and Z. Kiss, *J. Chem. Physics*, **39**, 3251 (1963).
13. F. C. Palilla, A. K. Levine, and M. Tomkus, *This Journal*, **115**, 642 (1968).
14. V. P. Nazarova, *Bull. Acad. Sci. USSR Phys. Ser.*, **25**, 322 (1961).
15. V. L. Levshin et al., *Trans. P. N. Lebedev Physics Institute*, **23**, "Soviet Researches on Luminescence," D. V. Skobel'tsyn, Editor; English Translation, Chap. 3, Consultants Bureau, New York (1964).
16. F. J. Avella, O. J. Sovers, and C. S. Wiggins, *This Journal*, **114**, 613 (1967).
17. O. J. Sovers and L. J. Bodi, *J. Opt. Soc. Amer.*, **55**, 1643 (1965).
18. F. C. Palilla, *Electrochem. Technol.*, **6**, 39 (1968).
19. R. W. Mooney and M. A. Aia, *Chem. Rev.*, **61**, 433 (1961).

## Crystal Growth and Electrical Properties of Potassium-Strontium and Potassium-Lead Niobates Containing Lanthanum

D. F. O'Kane, G. Burns, B. A. Scott, and E. A. Giess

IBM Watson Research Center, Yorktown Heights, New York

#### ABSTRACT

Crystal growth conditions are described for compositions from the  $\text{KNbO}_3\text{-SrNb}_2\text{O}_6\text{-LaNb}_3\text{O}_9$  and  $\text{KNbO}_3\text{-PbNb}_2\text{O}_6\text{-LaNb}_3\text{O}_9$  ternary systems. Typical compositions examined were the tetragonal tungsten bronze structures of  $(\text{KNbO}_3)_{45}(\text{SrNb}_2\text{O}_6)_{55}$  containing 3, 6, 9, and 18 w/o (weight per cent)  $\text{LaNb}_3\text{O}_9$ ,  $\text{KPb}_2\text{Nb}_5\text{O}_{15}$  with 3 w/o  $\text{LaNb}_3\text{O}_9$ , and  $(\text{KPb}_2\text{Nb}_5\text{O}_{15})_x\text{-}(\text{K}_2\text{LaNb}_5\text{O}_{15})_{1-x}$  where  $x = 0.4$  and  $0.6$ . The dielectric constant has been determined as a function of temperature for each composition.

We were interested in examining one method of altering the temperature dependence of the dielectric constant,  $\epsilon$ , of ferroelectric compositions with high dielectric and electrooptic constants. The dielectric constant is directly proportional to the electrooptic coefficient,  $r$  (1-3). Therefore, by broadening the peak in the  $\epsilon$  vs. temperature curve, it should be possible to raise  $r$  and also reduce the temperature sensitivity of  $r$ .

It has been reported that  $\text{La}_2\text{O}_3$  caused a lowering of the Curie temperature and a broadening of the peak in the  $\epsilon$  vs. temperature curve for ceramic compositions from the  $\text{Pb}_x\text{Ba}_{1-x}\text{Nb}_2\text{O}_6$  system (4). We studied the effect of lanthanum on the dielectric properties of the

tungsten bronze structures from the binary systems of  $\text{KNbO}_3\text{-SrNb}_2\text{O}_6$  and  $\text{KNbO}_3\text{-PbNb}_2\text{O}_6$ . Compositions from these binary systems were selected on the basis of their high room temperature dielectric constants and the large electrooptic coefficient reported for the composition  $\text{KSr}_2\text{Nb}_5\text{O}_{15}$  (5) from the  $\text{KNbO}_3\text{-SrNb}_2\text{O}_6$  binary system. The space group of  $\text{KSr}_2\text{Nb}_5\text{O}_{15}$  is probably  $\text{C}^{2}_{4v}\text{-P4bm}$  (6).

Lanthanum has an ionic radius larger than other rare earths and close to the radii of potassium, strontium, and lead. The niobate form was selected since  $\text{LaNb}_3\text{O}_9$  has a tetragonal structure (7) and could be expected in low concentrations to form a solid solution with

$\text{KNbO}_3$ - $\text{SrNb}_2\text{O}_6$  compositions and  $\text{KPb}_2\text{Nb}_5\text{O}_{15}$ . The composition  $\text{K}_2\text{LaNb}_5\text{O}_{15}$  was also used for the La addition since it has a tetragonal bronze structure (8) and also could be expected to form a solid solution with  $\text{KPb}_2\text{Nb}_5\text{O}_{15}$ .

Figures 1 and 2 show the ternary diagrams which are composed of the binary systems:  $\text{KNbO}_3$ - $\text{SrNb}_2\text{O}_6$ ,  $\text{KNbO}_3$ - $\text{LaNb}_3\text{O}_9$ ;  $\text{SrNb}_2\text{O}_6$ - $\text{LaNb}_3\text{O}_9$ ; and  $\text{KNbO}_3$ - $\text{PbNb}_2\text{O}_6$ . The phase diagram for the  $\text{KNbO}_3$ - $\text{SrNb}_2\text{O}_6$  system has been reported (6) to have a single-phase tetragonal bronze-type structure between 25 and 65 m/o (mole per cent)  $\text{KNbO}_3$ . The maximum melting composition occurs near 33%  $\text{KNbO}_3$ . In the  $\text{KNbO}_3$ - $\text{LaNb}_3\text{O}_9$  system, the composition  $\text{K}_2\text{LaNb}_5\text{O}_{15}$  has been reported (8) to be a tetragonal tungsten bronze-type structure. No other data are available. In the  $\text{SrNb}_2\text{O}_6$ - $\text{LaNb}_3\text{O}_9$  system there are no data. The  $\text{KNbO}_3$ - $\text{PbNb}_2\text{O}_6$  system has been examined (9);  $\text{KNbO}_3$  is soluble in  $\text{PbNb}_2\text{O}_6$  up to at least 50 m/o. The orthorhombic tungsten bronze  $\text{KPb}_2\text{Nb}_5\text{O}_{15}$  is contained in this region of solid solution.

### Experimental Procedures

The starting materials used were  $\text{PbO}$ ,  $\text{K}_2\text{CO}_3$ ,  $\text{SrCO}_3$ ,  $\text{Nb}_2\text{O}_5$  from the Johnson-Matthey Company, Grade I, with 10 ppm impurities, except for  $\text{Nb}_2\text{O}_5$  which contained less than 0.03 w/o Ta and  $\text{La}_2\text{O}_3$  (Linsay chemical, 99.997%). Differential thermal analysis was used to establish the freezing points of the various compositions. Two-gram powder samples of the various compositions were prepared by annealing about  $200^\circ\text{C}$  below the melting point. The reacted powders were loaded in platinum capsules containing a thermocouple well in the bottom. The sample and

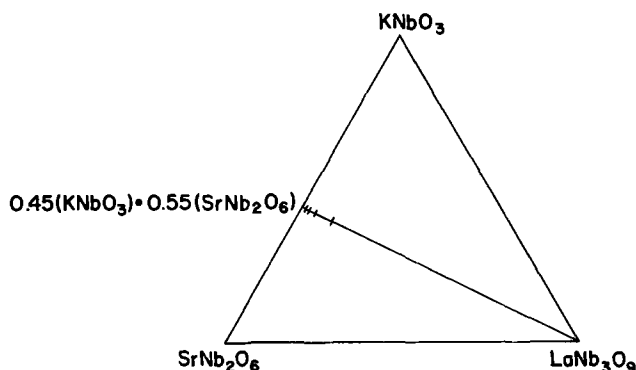


Fig. 1.  $\text{KNbO}_3$ - $\text{SrNb}_2\text{O}_6$ - $\text{LaNb}_3\text{O}_9$  ternary system. Crystals were grown at the compositions indicated.

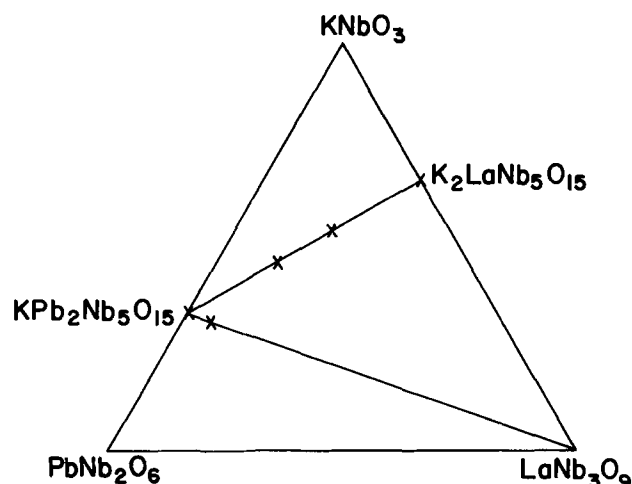


Fig. 2.  $\text{KNbO}_3$ - $\text{PbNb}_2\text{O}_6$ - $\text{LaNb}_3\text{O}_9$  ternary system. Crystals were grown at compositions indicated by  $x$ .

alumina reference material were heated and cooled at  $5^\circ\text{C}/\text{min}$ .

Each composition was prepared by heating stoichiometric quantities of the starting materials to  $1350$ - $1500^\circ\text{C}$  in a 100 cc platinum crucible. A Czochralski type crystal puller, Fig. 3, was used to obtain single crystals. A 23 kw RF generator supplied power to melt the charge in the platinum crucible. The output from the Pt-Pt, 10% Rh thermocouple under the platinum crucible was filtered to remove the RF pick-up before entering a L&N C.A.T. controller. Oxygen was passed into the system at 0.3 l/min to avoid reduction of the crystals and the resulting discoloration. Crystal growth was started with a seed crystal mounted on a shaft. Pull rates were approximately 10 mm/hr. The system was usually cooled at  $5^\circ\text{C}/\text{hr}$  to  $300^\circ\text{C}$  below the melting point and then at  $15^\circ\text{C}/\text{hr}$  to room temperature by moving the set-point potentiometer of the controller with a synchronous motor and gear train. In many cases, crystals were obtained from the frozen melt in addition to the pulled material. Crystals containing  $\text{KNbO}_3$ - $\text{SrNb}_2\text{O}_6$  had a tendency to grow along the  $c$ -axis in the crystal puller. During the growth of these compositions, the crystals were very sensitive to small changes in the melt temperature and to the temperature gradient above the melt surface. Compositions containing lead were the most volatile above their melting points. However, vapor loss was not a serious problem.

Crystal growth of  $0.45 \text{KNbO}_3 \cdot 0.55 \text{SrNb}_2\text{O}_6$  is more difficult than  $\text{KSr}_2\text{Nb}_5\text{O}_{15}$  which is to be expected since the phase diagram shows a larger difference in the melt and solid compositions at  $0.45 \text{KNbO}_3 \cdot 0.55 \text{SrNb}_2\text{O}_6$ . Slower growth rates are required to maintain equilibrium conditions.  $\text{KSr}_2\text{Nb}_5\text{O}_{15}$  would have been a better choice for the  $\text{LaNb}_3\text{O}_9$  doping since it is closer to the maximum melting point in the  $\text{KNbO}_3$ - $\text{SrNb}_2\text{O}_6$  diagram and the melt composition is almost the same composition as the crystals pulled from the melt. However, this information was not known when the  $\text{LaNb}_3\text{O}_9$  doping was started. Single crystals of  $0.45 \text{KNbO}_3 \cdot 0.55 \text{SrNb}_2\text{O}_6$  containing 3, 6, 9, and 18 w/o  $\text{LaNb}_3\text{O}_9$  for x-ray and dielectric measurements were grown by slowly cooling 400g melts of each composition in a platinum crucible.

Single crystals of  $x \text{KPb}_2\text{Nb}_5\text{O}_{15} \cdot (1-x) \text{K}_2\text{LaNb}_5\text{O}_{15}$ , where  $x = 0.4, 0.6$ , were grown after x-ray analyses indicated that the tetragonal tungsten bronze structure of  $\text{K}_2\text{LaNb}_5\text{O}_{15}$  is retained when  $\text{KPb}_2\text{Nb}_5\text{O}_{15}$  is added in concentrations up to 60 m/o. The composition  $\text{KPb}_2\text{Nb}_5\text{O}_{15}$  with 3 w/o  $\text{LaNb}_3\text{O}_9$  was one of the easiest single crystals to grow from the melt. However,

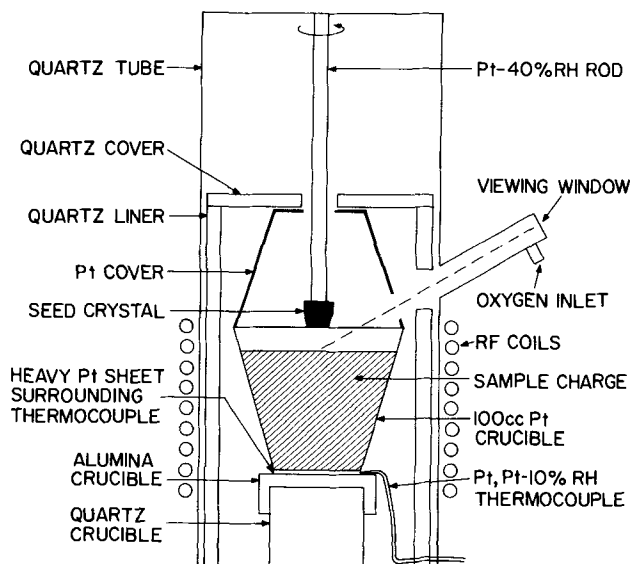


Fig. 3. Crystal puller.

Table I. Freezing points of some ternary compositions

Compositions	Temp. °C
(KNbO <sub>3</sub> ) <sub>45</sub> (SrNb <sub>2</sub> O <sub>6</sub> ) <sub>55</sub>	1460
(KNbO <sub>3</sub> ) <sub>45</sub> (SrNb <sub>2</sub> O <sub>6</sub> ) <sub>55</sub> with 18 w/o LaNb <sub>3</sub> O <sub>9</sub>	1480
KPb <sub>2</sub> Nb <sub>5</sub> O <sub>15</sub>	1325
(KPb <sub>2</sub> Nb <sub>5</sub> O <sub>15</sub> ) <sub>60</sub> (K <sub>2</sub> LaNb <sub>5</sub> O <sub>15</sub> ) <sub>40</sub>	1405
(KPb <sub>2</sub> Nb <sub>5</sub> O <sub>15</sub> ) <sub>40</sub> (K <sub>2</sub> LaNb <sub>5</sub> O <sub>15</sub> ) <sub>60</sub>	1432
K <sub>2</sub> LaNb <sub>5</sub> O <sub>15</sub>	1441

the material had a tendency to crack during cooling and lead oxide was lost from the melt during growth.

The KNbO<sub>3</sub>-SrNb<sub>2</sub>O<sub>6</sub> compositions were easily poled by applying an electric field of 20,000 v/cm along the c-axis at room temperature. Hysteresis loops can be observed even at room temperature. The crystals containing KPb<sub>2</sub>Nb<sub>5</sub>O<sub>15</sub> had an electric field of 20,000 v/cm applied along the a-axis while slowly cooling through the ferroelectric transition temperature. Hysteresis loops were not observed for these compositions.

The small signal dielectric constants were measured on poled, oriented, single crystals at 10<sup>4</sup> Hz. The temperature was measured continuously from room temperature to a point above the Curie temperature with various applied electric fields.

### Results

The crystal compositions investigated, (KNbO<sub>3</sub>)<sub>45</sub>-(SrNb<sub>2</sub>O<sub>6</sub>)<sub>55</sub> with 3, 6, 9, and 18 w/o LaNb<sub>3</sub>O<sub>9</sub>, KPb<sub>2</sub>Nb<sub>5</sub>O<sub>15</sub> with 3 w/o LaNb<sub>3</sub>O<sub>9</sub>, and  $x$  KPb<sub>2</sub>Nb<sub>5</sub>O<sub>15</sub> · (1 -  $x$ ) K<sub>2</sub>LaNb<sub>5</sub>O<sub>15</sub>, where  $x = 0.4$  and  $0.6$ , are shown as they appear in the respective ternary systems in Fig. 1 and 2. Single crystals of each of these compositions were obtained either by pulling or by slowly cooling a 400g melt. The compositions containing lead were more easily pulled in single crystalline form although they often cracked near 500°C during the slow cooling cycle. Freezing point data are contained in Table I.

Attempts to grow single crystals of K<sub>2</sub>LaNb<sub>5</sub>O<sub>15</sub> (mp 1441°C) were not successful; two liquid phases were present. On freezing, two phases were found with tetragonal bronze structures. The predominant phase had lattice parameters of  $a_0 = 12.58\text{Å}$  and  $c_0 = 3.930\text{Å}$  and the small amount of second phase (< 5%) had  $a_0 = 12.59\text{Å}$  and  $c_0 = 3.985\text{Å}$ . These data are different from the values of  $a_0 = 17.70\text{Å}$  and  $c_0 = 7.82\text{Å}$  reported for a ceramic sample by Krainik (8), who used a different unit cell which is equivalent to  $a_0 = 12.52\text{Å}$  and  $c_0 = 3.91\text{Å}$ . The two cells differ by factors of  $\sqrt{2}$  in the  $a_0$  direction and 2 in the  $c_0$  direction. Chemical analyses showed that the predominant phase corresponded closely to the starting composition. The second phase had approximately 0.1 w/o La and  $12.4 \pm 0.4$  w/o K. This suggested that the second phase may be from the K<sub>2</sub>O-Nb<sub>2</sub>O<sub>5</sub> phase diagram. Assuming this to be the case, 12.4 w/o K corresponds to (K<sub>2</sub>O)<sub>33</sub>(Nb<sub>2</sub>O<sub>5</sub>)<sub>67</sub> or K<sub>2</sub>Nb<sub>4</sub>O<sub>11</sub>. The phase diagram reported by Reisman (10) shows compounds at 25, 40, and 50 m/o K<sub>2</sub>O. The 25 and 40 m/o compositions would con-

tain 8.77 and 15.86 w/o K, respectively. The analytical result for the second phase is midway between these two values. The structure of the (K<sub>2</sub>O)<sub>40</sub>(Nb<sub>2</sub>O<sub>5</sub>)<sub>60</sub> is tetragonal bronze type (11) with  $a_0 = 12.525\text{Å}$  and  $c_0 = 3.763\text{Å}$ . However, there are significant differences between this structure and the second phase material in the x-ray patterns. It is not known what effect small concentrations of La (about 0.1 w/o) have on K<sub>2</sub>O-Nb<sub>2</sub>O<sub>5</sub> compositions.

The effects of the LaNb<sub>3</sub>O<sub>9</sub> addition on the lattice parameters of 0.45 KNbO<sub>3</sub> · 0.55 SrNb<sub>2</sub>O<sub>6</sub> are shown in Table II. The  $c_0$  parameter is lowered from 3.941Å to 3.919Å by 9 w/o LaNb<sub>3</sub>O<sub>9</sub>. No change is observed between the 9 and 18 w/o LaNb<sub>3</sub>O<sub>9</sub>.

The structural effects of the LaNb<sub>3</sub>O<sub>9</sub> can be examined by considering the cation sites available in 0.45 KNbO<sub>3</sub> · 0.55 SrNb<sub>2</sub>O<sub>6</sub>. There are 10 possible cation (A<sup>+</sup>, A<sup>2+</sup>) sites available in the tungsten bronze-type structure. These are: two  $\alpha$  sites which have 12 oxygen ions coordinating the site; four  $\beta$  sites with 15 oxygen ions; and four  $\gamma$  sites with 9 oxygen ions. Giess *et al.* (6) have discussed the atomic distributions in compositions from the KNbO<sub>3</sub>-SrNb<sub>2</sub>O<sub>6</sub> system. In the 0.45 KNbO<sub>3</sub> · 0.55 SrNb<sub>2</sub>O<sub>6</sub> composition, the  $\alpha$  and  $\beta$  sites probably are filled along with 0.45 of the four  $\gamma$  sites. As LaNb<sub>3</sub>O<sub>9</sub> is added to the structure, the  $\gamma$  sites probably become vacant at a concentration of 15.1 w/o or 8.26 m/o.

Giess *et al.* (6) have reported on the lattice parameters for  $x$  KNbO<sub>3</sub> · (1 -  $x$ ) SrNb<sub>2</sub>O<sub>6</sub> between  $x = 0.65$  and  $0.25$ . The  $c_0$  parameter decreases from 3.952 to 3.936Å as the SrNb<sub>2</sub>O<sub>6</sub> concentration is increased. The largest observed value of  $c_0$  (3.952Å) occurs at  $x = 0.65$  and may correspond to completely filled  $\alpha$  and  $\beta$  sites and to 1.4 of the four  $\gamma$  sites being filled. At  $x = 0.33$ , KSr<sub>2</sub>Nb<sub>5</sub>O<sub>15</sub>, the  $\gamma$  sites are thought to be empty; further decreases in  $x$  could cause an emptying of the  $\alpha$  or  $\beta$  sites. This decrease in the  $c_0$  parameter with the reduction in the number of occupied  $\gamma$  sites may be similar to that obtained by LaNb<sub>3</sub>O<sub>9</sub> additions to 0.45 KNbO<sub>3</sub> · 0.55 SrNb<sub>2</sub>O<sub>6</sub>.

A large electrooptic coefficient is usually associated with a large dielectric constant (1-3). This is true for KSr<sub>2</sub>Nb<sub>5</sub>O<sub>15</sub> [0.33 KNbO<sub>3</sub> · 0.67 SrNb<sub>2</sub>O<sub>6</sub>] which has an electrooptic coefficient of  $r_{11} = 1.3 \times 10^{-8}$  cm/v and a half-wave voltage of 500v (5) while the dielectric constant on poled single crystals is 430 at room temperature.

Dielectric measurements on compositions from the single phase region (25 to 65 m/o KNbO<sub>3</sub>) of the KNbO<sub>3</sub>-SrNb<sub>2</sub>O<sub>6</sub> system show no significant variation in ferroelectric transition temperature or dielectric constant (5). A room temperature dielectric constant,  $\epsilon_{RT}$ , of 430 and a peak dielectric constant,  $\epsilon_p$ , of 14,000 at the ferroelectric transition temperature,  $T_0$ , of 156°C are typical of both KSr<sub>2</sub>Nb<sub>5</sub>O<sub>15</sub> and 0.45 KNbO<sub>3</sub> · 0.55 SrNb<sub>2</sub>O<sub>6</sub>.

Addition of 3, 6, and 9 w/o LaNb<sub>3</sub>O<sub>9</sub> causes a progressive increase in  $\epsilon_{RT}$  to 5300 and a decline in  $\epsilon_p$  to 5740. The  $\epsilon$  vs.  $T$  data taken along the c-axis for the 3 and 9 w/o LaNb<sub>3</sub>O<sub>9</sub> crystals are shown in Fig. 4 and 5.

Table II. Lattice parameter data

Composition	Unit cell	No. of cation sites filled by K + Sr	No. of cation sites filled by K + Sr + La	Lattice parameters	
				$a_0$ , Å (±0.02) *	$c_0$ , Å (±0.006) *
<b>Single Crystals</b>					
0.45KNbO <sub>3</sub> · 0.55SrNb <sub>2</sub> O <sub>6</sub>	K <sub>2.90</sub> Sr <sub>3.55</sub> Nb <sub>10</sub> O <sub>30</sub>	6.45	6.45	12.46	3.941
+ 3 w/o LaNb <sub>3</sub> O <sub>9</sub>	K <sub>2.85</sub> Sr <sub>3.44</sub> La <sub>0.10</sub> Nb <sub>10</sub> O <sub>30</sub>	6.26	6.36	12.46	3.941
+ 6 w/o LaNb <sub>3</sub> O <sub>9</sub>	K <sub>2.73</sub> Sr <sub>3.34</sub> La <sub>0.20</sub> Nb <sub>10</sub> O <sub>30</sub>	6.07	6.27	12.47	3.932
+ 9 w/o LaNb <sub>3</sub> O <sub>9</sub>	K <sub>2.64</sub> Sr <sub>3.28</sub> La <sub>0.30</sub> Nb <sub>10</sub> O <sub>30</sub>	5.87	6.17	12.46	3.919
+ 18 w/o LaNb <sub>3</sub> O <sub>9</sub>	K <sub>2.36</sub> Sr <sub>2.02</sub> La <sub>0.56</sub> Nb <sub>10</sub> O <sub>30</sub>	5.31	5.90	12.48	3.919
<b>Ceramic samples (ref. 4)</b>					
0.65KNbO <sub>3</sub> · 0.35SrNb <sub>2</sub> O <sub>6</sub>	K <sub>1.61</sub> Sr <sub>3.56</sub> Nb <sub>10</sub> O <sub>30</sub>	7.40	—	12.48	3.952
KSr <sub>2</sub> Nb <sub>5</sub> O <sub>15</sub>	K <sub>2</sub> Sr <sub>4</sub> Nb <sub>10</sub> O <sub>30</sub>	6.00	—	12.47	3.942
0.25KNbO <sub>3</sub> · 0.75SrNb <sub>2</sub> O <sub>6</sub>	K <sub>1.43</sub> Sr <sub>4.26</sub> Nb <sub>10</sub> O <sub>30</sub>	5.72	—	12.46	3.936

\* Three times the standard deviation.

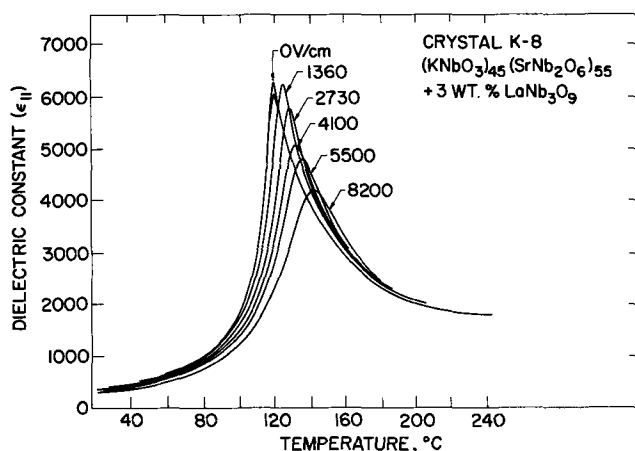


Fig. 4. Dielectric constant vs. temperature as a function of applied electric field for 0.45  $\text{KNbO}_3 \cdot 0.55 \text{SrNb}_2\text{O}_6 + 3 \text{ w/o LaNb}_3\text{O}_9$  single crystal.

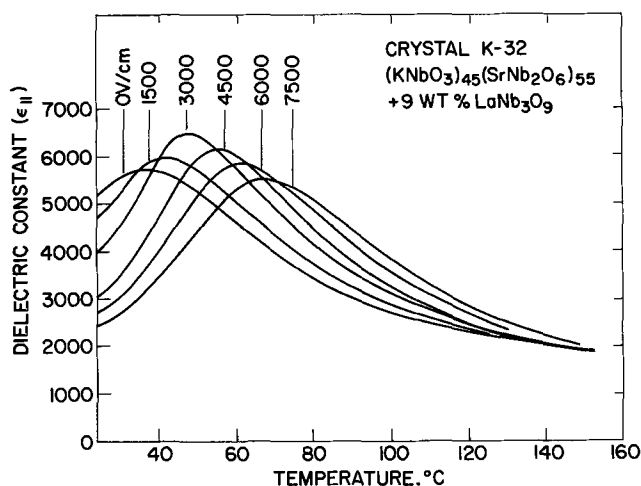


Fig. 5. Dielectric constant vs. temperature as a function of applied electric field for 0.45  $\text{KNbO}_3 \cdot 0.55 \text{SrNb}_2\text{O}_6 + 9 \text{ w/o LaNb}_3\text{O}_9$  single crystal.

Also,  $T_0$  is reduced to 37°C. Further addition of  $\text{LaNb}_3\text{O}_9$  lowers both  $\epsilon_{RT}$  and  $\epsilon_p$ , and  $T_0$  is below room temperature (9°C) for the crystal containing 18 w/o  $\text{LaNb}_3\text{O}_9$  (Table III).

The addition of 3 w/o  $\text{LaNb}_3\text{O}_9$  to  $\text{KPb}_2\text{Nb}_5\text{O}_{15}$  lowered  $T_0$  from 449° to 416°C; however, no broadening was observed in the  $\epsilon$  vs.  $T$  curves. The room temperature dielectric constant was increased from 332 to 442 by the  $\text{LaNb}_3\text{O}_9$  addition. Data on ceramic samples from the  $x \text{KPb}_2\text{Nb}_5\text{O}_{15} \cdot (1-x) \text{LaNb}_3\text{O}_9$  system show a reduction in  $T_0$  to 203°C when  $x = 0.6$ , and an increase in  $\epsilon_{RT}$  and a decrease in  $\epsilon_p$ . A ceramic sample of  $\text{K}_2\text{LaNb}_5\text{O}_{15}$  had values of  $T_0 = -120^\circ\text{C}$ ,  $\epsilon_{RT} = 500$ , and  $\epsilon_p = 1400$ . Polarization vs. electric field measurements along the  $c$ -axis showed no hysteresis loops in single crystals of the main phase in frozen melts of  $\text{K}_2\text{LaNb}_5\text{O}_{15}$ .

The effect of  $\text{K}_2\text{LaNb}_5\text{O}_{15}$  additions to  $\text{KSr}_2\text{Nb}_5\text{O}_{15}$  was examined with ceramic samples. The  $T_0$  was lowered from 156° to 141°C by the addition of 20 m/o  $\text{K}_2\text{LaNb}_5\text{O}_{15}$ , and  $\epsilon_{RT}$  increased while  $\epsilon_p$  decreased. The

Table III. Dielectric properties of single crystalline potassium-strontium and potassium-lead niobates containing  $\text{LaNb}_3\text{O}_9$

Composition	$\epsilon_{RT}$	$\epsilon_p$	$T_0, ^\circ\text{C}$
$\text{KSr}_2\text{Nb}_5\text{O}_{15}$ (11)	430	14,000	156
$(\text{KNbO}_3)_{45}(\text{SrNb}_2\text{O}_6)_{55}$	430	14,000	156
+ 3 w/o $\text{LaNb}_3\text{O}_9$	380	6,285	119
+ 6 w/o $\text{LaNb}_3\text{O}_9$	1,650	7,500	59
+ 9 w/o $\text{LaNb}_3\text{O}_9$	5,300	5,740	37
+ 18 w/o $\text{LaNb}_3\text{O}_9$	2,800	2,900	9
$\text{KPb}_2\text{Nb}_5\text{O}_{15}$	332	27,600	449
+ 3 w/o $\text{LaNb}_3\text{O}_9$	442	21,400	416
$\text{K}_2\text{LaNb}_5\text{O}_{15}$ (ceramic)	500	1,400	-120
$(\text{KPb}_2\text{Nb}_5\text{O}_{15})_{40}(\text{K}_2\text{LaNb}_5\text{O}_{15})_{60}$	1,143	—	—
$(\text{KPb}_2\text{Nb}_5\text{O}_{15})_{60}(\text{K}_2\text{LaNb}_5\text{O}_{15})_{40}$	1,630	1,700	—

use of low concentration of  $\text{LaNb}_3\text{O}_9$  rather than  $\text{K}_2\text{LaNb}_5\text{O}_{15}$  proved to be more effective in changing the  $T_0$  of compositions from the  $\text{KNbO}_3$ - $\text{SrNb}_2\text{O}_6$  system.

### Summary

Single crystals were grown from compositions contained in the ternary systems of  $\text{KNbO}_3$ - $\text{SrNb}_2\text{O}_6$ - $\text{LaNb}_3\text{O}_9$  and  $\text{KNbO}_3$ - $\text{PbNb}_2\text{O}_6$ - $\text{LaNb}_3\text{O}_9$ . Crystals from the former system were the more difficult to grow.

$\text{K}_2\text{LaNb}_5\text{O}_{15}$  was found to contain less than 5% of a second phase. This second phase had a composition close to  $\text{K}_2\text{Nb}_4\text{O}_{11}$  with approximately 0.1 w/o La.

The addition of  $\text{LaNb}_3\text{O}_9$  to 0.45  $\text{KNbO}_3 \cdot 0.55 \text{SrNb}_2\text{O}_6$  caused an increase in the number of vacant cation sites in the tetragonal tungsten bronze structure and a lowering of the lattice parameter,  $c_0$ . Also, the  $\text{LaNb}_3\text{O}_9$  results in higher  $\epsilon_{RT}$  and lower  $\epsilon_p$  and  $T_0$ . The ferroelectric transition also becomes less sharp.

### Acknowledgment

The authors would like to thank K. H. Nichols, B. A. Jenkins, and R. M. Potemski for their technical assistance and Dr. W. Reuter for the chemical analyses. Work on this paper was partially supported by Army Research Office, Durham, North Carolina, under contract DA-31-124-ARO-D-205.

Manuscript submitted May 2, 1968; revised manuscript received June 3, 1968. This paper was presented at the Boston Meeting, May 5-9, 1968, as Paper 108.

Any discussion of this paper will appear in a Discussion Section to be published in the June 1969 JOURNAL.

### REFERENCES

1. R. C. Miller, *Appl. Phys. Letters*, **5**, 17 (1964).
2. C. G. B. Garrett and F. N. H. Robinson, *IEEE J. of Quantum Elect.*, **QE-2**, 328 (1966).
3. S. K. Kurtz and F. N. H. Robinson, *Appl. Phys. Letters*, **10**, 62 (1967).
4. A. A. Anan'eva and M. A. Ugryumova, *Soviet Physics-Acoustics*, **10**, 227 (1965).
5. E. A. Giess, G. Burns, D. F. O'Kane, and A. W. Smith, *Appl. Phys. Letters*, **11**, 233 (1967).
6. E. A. Giess, B. A. Scott, D. F. O'Kane, and G. Burns, Submitted to the *J. Am. Ceram. Soc.*
7. R. W. G. Wyckoff, "Crystal Structures," Vol. 2, Interscience Publishers, New York (1964).
8. N. N. Krainik, V. A. Isupov, M. F. Bryzhina, and A. I. Agranovskaya, *Soviet Physics, Crystallography*, **9**, 281 (1964).
9. E. C. Subbarao and G. Shirane, *J. Chem. Phys.*, **32**, 1346 (1960).
10. A. Reisman and F. Holtzberg, *J. Am. Chem. Soc.*, **77**, 2117 (1955).
11. C. D. Whiston and A. J. Smith, *Acta Cryst.*, **19**, 169 (1965).

# Measurement of Epitaxial Doping Density vs. Depth

D. R. Decker

Bell Telephone Laboratories, Inc., Reading, Pennsylvania

## ABSTRACT

The determination of doping density *vs.* depth from capacitance-voltage measurements on diffused diodes in epitaxial material is derived for the general case. These calculations extend the useful range of the capacitance-voltage technique and allow profiling of epitaxial doping in depth through the use of deep-diffusion test diodes. Experimental comparison of the deep-diffusion and shallow-diffusion characterization techniques shows that the deep-diffusion technique extends the depth capability of capacitance-voltage measurements with accuracy comparable to the shallow-junction measurements (5-15%).

The use of epitaxial material for microwave devices requires a more complete characterization on this type of material than has been common in the past. Especially needed is a simple technique for determining the distribution of the doping impurity within the epitaxial film. This need arises for several types of devices operated under reverse bias, where the exact nature of the impurity profiles determines such device characteristics as capacitance and series resistance as functions of voltage, the reverse recovery and transition times, and the avalanche breakdown voltage (1, 2).

The profile that will be measured by any capacitance technique based on a diffused junction is a combination of the profiles produced by both the growth of the film and the diffusion of impurities into it. The advantage of the shallow junction is that it can generally be made abrupt with a very high concentration on the diffused side. Hence, the effects of the diffusion profile can be ignored. However, it is often desirable to be able to calculate impurity profiles from capacitance voltage measurements of diodes with junctions that are relatively deep compared to this approximation. For a deep-diffusion technique to work the diffusion profile must be known and subtracted from the measurement. The error involved in the uncorrected impurity density is to first order proportional to the ratio of the unknown density to the density of diffused impurities at the edge of the depletion layer. Thus, it is desirable to include corrections for the diffused impurities if it is not certain that their density is at least 10 or 20 times that of the unknown impurities.

A technique is described which gives the information needed for device design and is also compatible with standard epitaxial material evaluation techniques. The accuracy of the technique is comparable to the accuracy of present techniques for measuring the surface doping density of epitaxial layers, and the technique allows doping density measurements to be extended in depth through the use of deep-junction diffused diodes.

### Discussion of the Shallow-Junction, Capacitance-Voltage, Doping Density Measuring Technique

One standard technique for measuring epitaxial film doping density involves the fabrication of shallow-junction, diffused, mesa diodes (3, 4). The shallow diffusion is used so that the asymmetrical-junction capacitance-voltage law is a good approximation to the reverse biased junction behavior. This gives the following relationship (see Appendix I) between the film doping density and the diode capacitance  $C$ , diode area  $A$ , and bias voltage  $V$

$$N = \frac{C^3}{q\epsilon A^2 \left( \frac{dC}{dV} \right)} \quad [1]$$

The measurement involves an accurate determination of  $A$  and measurement of capacitance at two slightly different reverse bias voltages. The capaci-

tance is taken as the average of the two readings and is also used to calculate the depletion-layer width using the following formula

$$w = \frac{\epsilon A}{C} \quad [2]$$

The depth at which the doping density is thus determined is to a good approximation

$$d = x_j + w = x_j + \frac{\epsilon A}{C} \quad [3]$$

where  $x_j$  is the depth of the metallurgical junction.

The doping density of an epitaxial layer can be profiled in depth using a shallow-diffusion and making the differential capacitance measurements at many reverse bias voltages up to the breakdown voltage of the test diode.

This technique has the following two disadvantages:

1. Differential capacitance measurements made at large reverse bias voltages are subject to substantial measurement error due to the decrease of the change in capacitance,  $dC$ , with voltage (see section on accuracy).

2. The depth at which the test diode breaks down by avalanching may be shallower than the depth of interest, thus preventing further measurement.

The second limitation listed above is the most serious since it precludes obtaining the necessary information by use of the shallow-diffusion technique. The maximum measurement depth for this technique may be calculated from shallow-junction avalanche-breakdown curves. Devices whose characteristics are dependent on the impurity profile in the region inaccessible to the shallow-junction measurement should be characterized by a technique with greater depth capability.

### Evaluation of Doping Density in Depth by Combining a Deep Diffusion with the Differential Capacitance Technique

For an arbitrary impurity profile on each side of a p-n junction the relationship between doping densities, capacitance, and voltage is as follows (see Appendix I and Fig. 1)

$$\frac{1}{N_A(x_1)} + \frac{1}{N_D(x_2)} = \frac{1}{N_T(w)} \quad [4]$$

where  $N_S$  = surface concentration of the diffusant;  $N_0$  = substrate doping level;  $N_A(x_1)$  and  $N_D(x_2)$  are the net impurity densities at the edges of the depletion layer;  $x_e$  = epitaxial layer thickness;  $x_1$  = p-type edge of depletion region;  $x_2$  = n-type edge of depletion region;  $w = x_2 - x_1 = \epsilon A/C$  = width of depletion region.

$$N_T = \frac{C^3}{q\epsilon A^2 \frac{dC}{dV}}$$

(the effective doping density as determined from the C-V relationship) [5]



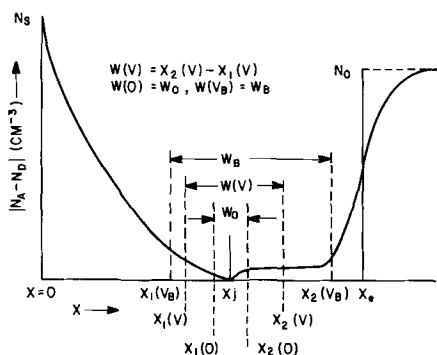


Fig. 1. Depletion layer spreading vs. bias

Also

$$N_D(x_2) = \frac{N_A(x_1)N_T(w)}{N_A(x_1) - N_T(w)} \quad [6]$$

The quantity  $N_T$ , which is a function of capacitance and voltage and has the units of impurity density ( $\text{cm}^{-3}$ ), has been defined for mathematical convenience. However, it will be seen that  $N_T$  is closely related to the individual impurity densities  $N_A$  and  $N_D$ , thus substantiating the concept of  $N_T$  being an effective impurity density.

It is seen that [6] reduces to [1] for the case that  $N_A(x_1) \gg N_D(x_2)$ . Therefore we can compare the true value given by [6] with the value that would be obtained using the asymmetrical-junction approximation.

$$N_D(x_2) = \frac{N_T(w)}{\left[1 - \frac{N_T(w)}{N_A(x_1)}\right]} > N_T(w)$$

also  $x_2 = x_1 + w < x_j + w$  since  $x_1 < x_j$ . Therefore, application of the asymmetrical-junction approximation to the general case leads to the erroneous result that the calculated impurity density is less than the actual density and that the calculated depth of the measurement is greater than the actual depth of measurement. The error in impurity density and the error in depth are both in such a direction as to shift the calculated distribution to lower densities and to greater depths than are actually measured. It is necessary to calculate the actual depth  $x_2$  and to correct the doping density according to Eq. [6] in order to obtain an accurate interpretation of the measurement.

The exact calculation of doping density and depth using the C-V technique with a deep junction requires determination of  $x_1$ ,  $x_2$ ,  $N_A(x_1)$  as functions of  $w$ . With the knowledge of  $x_1(w)$ ,  $x_2(w)$ , and  $N_A(x_1)$  it is simply a matter of substitution in Eq. [6] to find the desired impurity profile. However, the relationship between the depletion layer edges,  $x_1$  and  $x_2$ , and the total width,  $w$ , depends on the total integrated space charge through the charge conservation equation.

$$\int_{x_1}^{x_j} d\xi N_A(\xi) = \int_{x_j}^{x_2} d\xi N_D(\xi) \quad [7]$$

Therefore, an accurate knowledge of  $N_A(x)$  is necessary for an accurate determination of  $x_1(w)$  and  $x_2(w)$ . The relationship between  $x_1(w)$  and the measured quantities  $C$  and  $V$  is derived in Appendix II and yields the following result

$$\int_{x_1}^{x_j} d\xi N_A(\xi) = \int_0^w d\eta N_T(\eta) \quad [8]$$

This relation equates the total charge in one side of the depletion layer to the integral of the effective charge density,  $N_T(w)$ , from zero depletion layer width to the width  $w$  corresponding to  $x_1$ . Obviously, the right-hand side of Eq. [8] is also equal to the in-

tegrated donor density from Eq. [7], and this equality would be used if an unknown acceptor concentration was to be determined, e.g., a diffusion profile.

The right-hand side of Eq. [8] can be determined by a piecewise integration of the measured values of  $N_T$  vs. total depletion layer width. Since the integrals include the part of the depletion region that is swept at zero applied bias, it is necessary to make some approximation for the contribution of this region to the integral (this is analogous to calculating the built-in voltage of the junction). The approximation used in this work is that of an ideal graded junction for this region since the net compensated impurity density very near the metallurgical junction will closely approximate this distribution. Any error involved in this approximation will have a negligible effect on the doping density calculation for points moderately far removed from this area since the net impurity charge near the junction is quite small in comparison to the total depletion layer charge. Equation [8] is rather difficult to solve for  $x_1$ ; however, solution by computer is straightforward. Therefore, for a particular value of  $w$  it is possible to determine  $x_1$  from Eq. [8], to substitute  $x_1$  and  $w$  in Eq. [6] to find  $N_D$ , and finally to add  $x_1$  and  $w$  to obtain  $x_2$ .

#### Discussion of Accuracy

The accuracy involved in the calculation of  $N_T$  and  $N_A$  from capacitance-voltage data involves rather lengthy calculation which will be omitted here. The applicable results which are useful are

$$SN_T = \sqrt{9\left(\frac{\Delta C}{C}\right)^2 + 2\left(\frac{SC}{C_2 - C_1}\right)^2 + 4\left(\frac{\Delta A}{A}\right)^2} \quad [9]$$

and

$$SN_A = \frac{1}{2} \sqrt{\left(\frac{\Delta C}{C}\right)^2 + \frac{1}{2}\left(\frac{SC}{C}\right)^2 + \left(\frac{\Delta A}{A}\right)^2} \quad [10]$$

where  $SN_T$  and  $SN_A$  are the standard deviations from the actual values of these quantities,  $\Delta C$  is the capacitance calibration error (fixed),  $SC$  is the standard deviation of the repeatability of the capacitance measurement,  $C_1$  and  $C_2$  are the two values of capacitance chosen for calculating  $dC/dV$ ,  $C$  is the average value of  $C_1$  and  $C_2$ , and  $\Delta A$  is the error in measuring the junction area.

Equation [10] gives only the error in  $N_A$  that results from the measurement and calculation, not including the error inherent in assuming a specific profile for the diffused impurities. Typical values calculated for  $SN_T$  and  $SN_A$ , respectively, are 10-15% and  $< 1\%$ . Therefore, the error in  $N_A$  resulting from calculation is much smaller than the error in  $N_T$ , and any significant error in  $N_A$  is a result of deviations from the assumed diffusion profile.

The accuracy of calculation of  $N_D$  for the deep-diffused junction can now be discussed. Equation [6] can be rewritten as follows

$$N_D(x_2) = \left[1 + \frac{N_T(w)}{N_A(x_1) - N_T(w)}\right] N_T(w) = (1 + \alpha) N_T(w)$$

$$\text{with } \alpha = \frac{N_T(w)}{N_A(x_1) - N_T(w)} = \frac{N_D(x_2)}{N_A(x_1)} \quad [11]$$

Equation [4] can be used to derive the relationship between errors in  $N_A(x_1)$ ,  $N_T(w)$ , and the calculated values of  $N_D(x_2)$ . The normalized differential error is given by the following expression

$$\delta N_D = \frac{dN_D}{N_D} = N_D \left( \frac{dN_T}{N_T^2} - \frac{dN_A}{N_A^2} \right) \quad [12]$$

The normalized error is not independent of concentration. Equation [12] may be rewritten entirely in terms of  $N_A(x_1)$  and  $N_T(w)$  and their normalized

errors as follows

$$\delta N_D = \frac{N_A \delta N_T - N_T \delta N_A}{N_A - N_T} \quad [13]$$

From Eq. [13], it may be seen that for  $N_A \gg N_T$  the error in  $N_D$  is determined by the error in  $N_T$ . This is in accord with the asymmetrical-junction case.

It has been shown that the error in  $N_A(x_1)$  resulting from measurement errors is typically much less than the error in  $N_T$  (see Eq. [9] and [10]). Therefore, the error in  $N_A(x_1)$  is almost entirely the result of the inaccuracy inherent in the assumption of a specific profile for the diffused impurities. This error is not correlated with the error in  $N_T$ . Therefore, it is convenient to rewrite Eq. [13] in the following form

$$\delta N_D = (1 + \alpha) \delta N_T - \alpha \delta N_A \quad [14]$$

From Eq. [14], it is seen that the per cent error in  $N_D$  increases as the factor  $\alpha$  increases. From Eq. [11],  $\alpha$  is equal to the ratio of  $N_D(x_2)$  to  $N_A(x_1)$ . For the diffused junctions considered here  $N_A(x_1)$  remains greater than  $N_D(x_2)$ , and  $\alpha$  remains less than 1. Only if the impurity profile on the unknown side of the junction is steeper than the profile on the known side of the junction will  $\alpha$  be greater than 1. Therefore, for most cases, the error in  $N_D$  will be between 1 and 2 times the error in  $N_T$ . The statistical error in  $N_D$  can be written as follows, assuming that  $\delta N_T$  and  $\delta N_A$  are not correlated

$$SN_D = (1 + \alpha) \sqrt{\delta N_T^2 + \left(\frac{\alpha}{1 + \alpha}\right)^2 \delta N_A^2} \quad [15]$$

Equation [15] has been written so as to emphasize the major dependency of the error on  $\delta N_T$  (for  $\alpha < 1$ ).

**Experimental**

Figures 2 through 8 show plots of donor density vs. depth for diffused mesa diodes on epitaxial silicon slices as determined by three different methods. Shown for each slice on the same plot are:

1. The plot of concentration vs. depth using a shallow-diffused junction and the asymmetrical-junction approximation. These plots are extended as deep as

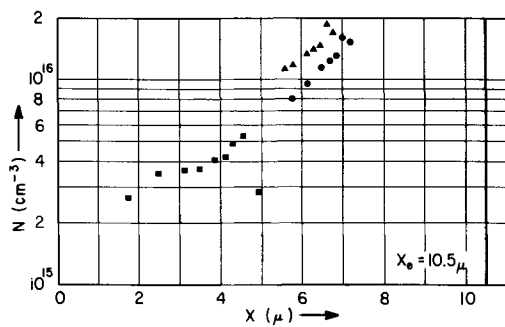


Fig. 2. Donor density vs. depth, slice 1283-3. ■  $x_j = 0.7\mu$  plot of  $N_T$ ; ●  $x_j = 5.2\mu$  plot of  $N_T$ ; ▲  $x_j = 5.2\mu$  plot of  $N_D$ . These symbols apply to Fig. 2 to 8.

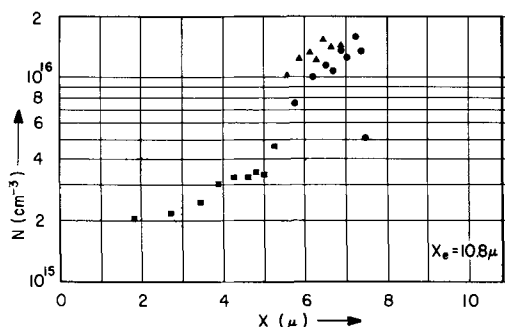


Fig. 3. Donor density vs. depth, slice 1283-4

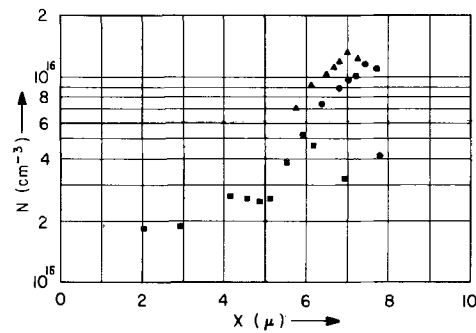


Fig. 4. Donor density vs. depth, slice 1283-6

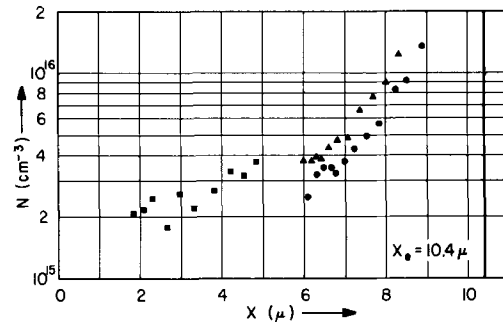


Fig. 5. Donor density vs. depth, slice 1310-2

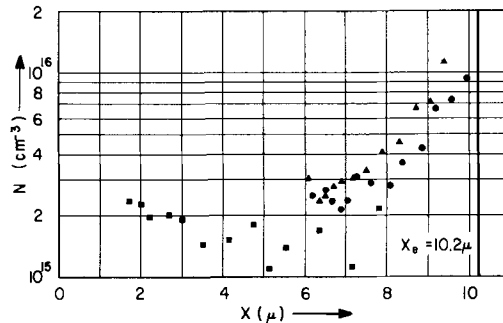


Fig. 6. Donor density vs. depth, slice 1310-3

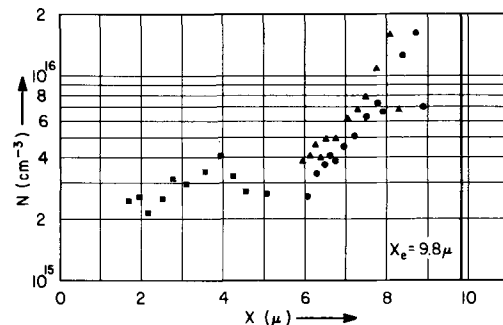


Fig. 7. Donor density vs. depth, slice 1310-4

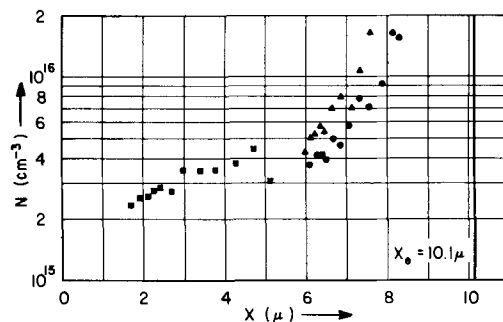


Fig. 8. Donor density vs. depth, slice 1310-5

the breakdown voltage of the test diode will permit.

2. A plot of concentration *vs.* depth for a deep-diffused junction ( $5.2\mu$ ) calculated from the asymmetrical-junction approximation. (This is actually a plot of  $N_T$  *vs.*  $x_j + w$ ).

3. A plot of concentration *vs.* depth for a deep-diffused junction using the same *C-V* data as in 2 above but calculating  $N_D$  and  $x_2$  using the method described.

#### Discussion of Experimental Results

The first aspect of the experimental results that merits discussion is the shallow-junction-generated profile, its accuracy and range of usefulness. It will be noted that all the concentration data points have a variation ranging from  $\pm 0\%$  to  $\pm$  about 15% (with the exclusion of the reading made at the highest bias voltage) from a smooth curve that could be drawn through the points. The typical variation is about  $\pm 8-10\%$  substantiating the error calculations previously discussed. Also noted is a tendency for the last point (highest bias voltage) to be quite out of line with the other points generally indicating a much lower doping density. This effect is mostly attributable to the small value of  $dC/dV$  in this range causing a large error in the measurement of  $dC$ . (Several other factors such as high leakage conductance or changes of depletion layer geometry with bias may cause measurement errors at large bias voltages. These effects must be minimized as much as possible to obtain good data in this region.) Therefore, the asymmetrical-junction technique is typically  $\pm 10\%$  accurate with the exclusion of the last data point.

The extension of the shallow-junction measurements is seen to give readings as deep as  $4.7$  to  $7.8\mu$  depending on the specific doping profile being measured. However, there is in general no guarantee of how deep the measurement can be extended. Nevertheless, the extended shallow-junction measurements are useful for resistivities greater than 1 ohm-cm and layer thicknesses less than  $7\mu$ . However, a deeper measurement is required to be able to predict junction characteristics such as capacitance *vs.* bias or series resistance or breakdown voltage for thicker or more heavily doped layers.

Turning our attention to the deep-diffused-measurement portion of Fig. 2 to 8 several features may be mentioned:

1. Smooth curves drawn through the deep-diffused asymmetrical-junction-calculated points and the shallow-diffused asymmetrical-junction-calculated points do not line up within the limits of accuracy discussed. In most cases, the deep-diffused points give lower values of doping density.

2. Excepting Fig. 3 and 4 the corrected deep-diffusion points line up acceptably well with the results of the shallow-junction points. Since the deep junction and shallow-junction are on different diodes there is a possibility of the curves being shifted up or down due to a difference in the error of measurement of the area on the two test units.

3. The corrected points always give larger values of doping density than the values of  $N_T$ . However, when the background doping density is low the correction is small (*e.g.*, Fig. 6 and 7).

4. The deep-diffused points exhibit about the same degree of fluctuation as do the shallow-diffused points, and in one case (Fig. 7), have the same tendency for deviation of the deepest point.

5. The uncorrected points always indicate a deeper measurement than the corrected points. In Fig. 6 this is so exaggerated that the last uncorrected measurement indicates a density of  $9 \times 10^{15}/\text{cm}^3$  only  $0.2\mu$  from the substrate interface. The substrate doping is greater than  $10^{19}/\text{cm}^3$ .

The details discussed above indicate that the corrected, deep-diffused measurement gives values that line up with and extend the range of the shallow-

diffused measurements. The error of this type of measurement is seen to be comparable to the error of the shallow-junction technique under the conditions considered.

Some mention of the correction for out-diffusion from the substrate should be made here. For the substrate doping levels (As,  $3 \times 10^{19}/\text{cm}^3$ ) and diffusion times and temperatures involved here, the distance of out-diffusion to a level of  $1 \times 10^{15}/\text{cm}^3$  additional donor atoms, amounts to less than  $1.5\mu$  assuming a step distribution at the interface initially. Since the initial profile is not a step distribution, but is probably close to that of a complementary error function, the resultant shift from the initial distribution is less than  $1.5\mu$ . The initial distribution may be estimated by assuming that both distributions are complementary error function and calculating the movement corresponding to the diffusion time and then subtracting this from the measured values to obtain the initial distribution. However, in many instances it is not necessary, or even desirable to find the initial distribution since the impurity distribution of the test diode will be close to that of the device to be made from the material under evaluation.

#### Conclusion

The general capacitance-voltage relationships for arbitrary impurity profiles on either side of a p-n junction have been discussed with their application to the measurement of unknown impurity profiles in mind. A technique of measurement using deep-diffused junctions has been described which allows measurement of epitaxial layer doping density in depth. The deep-diffusion technique allows measurement of impurity concentration without the necessity of any prior assumption of an asymmetrical junction.

The doping density profiles of a number of slices have been calculated for both shallow-diffused junctions and deep-diffused junctions using both the asymmetrical-junction approximation and a general calculation technique. These profiles exhibit the erroneous results obtained for deep diffusions using the asymmetrical-junction calculation. The fluctuations of the points and the error of measurement have been discussed for the curves exhibited. The correction for out-diffusion, if it is desirable to make such a correction, has been outlined.

The error of measurement of the effective doping profile,  $N_T$ , has been discussed and it has been shown that for a typical epitaxial measurement ( $0 < \alpha < 1$ ) using the technique outlined here the error is mostly determined by this error in  $N_T$  (according to Eq. [15]). It has been shown that a major source of error in  $N_T$  is the measurement of  $dC$ . Therefore, the accuracy of either technique can be improved significantly by the use of a capacitance bridge with better than  $\pm 0.1\%$  accuracy.

This measurement technique is very useful in the characterization of epitaxial material for devices that require thick epitaxial layers or where the low resistivity limits the depth of measurement. The technique is especially useful for devices whose operation is dependent on the exact shape of the doping profile throughout the entire active region, *e.g.*, varactor diodes, "punch-through" diodes, and IMPATT devices.

Manuscript submitted July 24, 1967; revised manuscript received April 3, 1968. This paper was presented at the Dallas Meeting, May 7-12, 1967, as Paper 96.

Any discussion of this paper will appear in a Discussion Section to be published in the June 1969 JOURNAL.

#### APPENDIX I

##### The Diode Capacitance-Voltage Law

Assuming that the charge due to free carriers within the depletion layer is negligible, the following equations govern the variation of depletion layer capacitance with voltage (refer to Fig. 1 for nomenclature).

$N_A$  and  $N_D$  are net acceptor concentration and net donor concentration, respectively.

$$\frac{d^2V}{dx^2} = -\frac{q[-N_A(x) + N_D(x)]}{\epsilon} \quad (\text{Poisson's equation}) \quad [\text{A1}]$$

$$\int_{x_1}^{x_2} [N_A(x) - N_D(x)] dx = 0 \quad (\text{charge conservation}) \quad [\text{A2}]$$

$$C = \frac{\epsilon A}{x_2 - x_1} \quad [\text{A3}]$$

Taking the derivative of [A2] with respect to  $x_1$  or  $x_2$  yields:

$$N_D(x_2) dx_2 = -N_A(x_1) dx_1 \quad [\text{A4}]$$

In order to find how the variation of capacitance with voltage is affected by the impurity concentrations at the edges of the depletion layer, consider the following derivative:

$$\frac{dC}{dV} = \frac{-C^2}{\epsilon A} \left[ \frac{1}{dV/dx_2} - \frac{1}{dV/dx_1} \right] \quad [\text{A5}]$$

We can now calculate  $dV/dx_2$  and  $dV/dx_1$  from the integral formula for  $V(x_1, x_2)$  which is obtained by a double integration of Eq. [A1]. The result of this differentiation using Leibnitz's rule (5), is the following two equations.

$$dV/dx_2 = q/\epsilon(x_2 - x_1) N_D(x_2) \quad [\text{A6}]$$

$$dV/dx_1 = -q/\epsilon(x_2 - x_1) N_A(x_1) \quad [\text{A7}]$$

Substitution of  $dV/dx_2$  and  $dV/dx_1$  into the formula for  $dC/dV$  yields the final result.

$$\frac{1}{N_A(x_1)} + \frac{1}{N_D(x_2)} + \frac{1}{\frac{C^3}{q\epsilon A^2 (dC/dV)}} = 0 \quad [\text{A8}]$$

It is convenient to write Eq. [A8] in the form

$$\frac{1}{N_A(x_1)} + \frac{1}{N_D(x_2)} = \frac{1}{N_T(w)} \quad [\text{A9}]$$

$$\text{with } N_T(w) \equiv \frac{C^3}{q\epsilon A^2 (dC/dV)}$$

(this reverses the voltage convention) [A10]

In this form it is readily apparent that for an abrupt-junction ( $N_A(x_1) \gg N_D(x_2)$ )

$$N_T(w) = \frac{N_A(x_1) N_D(x_2)}{N_A(x_1) + N_D(x_2)} \approx N_D(x_2) \quad [\text{A11}]$$

This is the approximation normally used in calculating doping density from C-V measurements on shallow-junction diodes.

#### APPENDIX II

##### Calculation of $N_D(x_2)$ and $x_2(w)$ from C-V Measurements

The relationships that will be used in the calculation are

$$N_D(x_2) = \frac{N_A(x_1) N_T(w)}{N_A(x_1) - N_T(w)} \quad [\text{B1}]$$

$$\int_{x_1}^{x_j} dy N_A(y) = \int_{x_j}^{x_2} dz N_D(z) \quad [\text{B2}]$$

The first step in the solution of the problem is to find  $x_1$  as a function of the depletion layer width  $w$ . This can be accomplished by noting that Eq. [A4] is true for all values of  $z$  inside the integral of Eq. [B2]. Therefore, Eq. [B2] can be rewritten in terms of  $\eta$  and  $N_T(\eta)$  instead of  $dz$  and  $N_D(z)$  as follows

$$dz = \frac{dz}{d\eta} d\eta = \frac{dz}{dz - dy} d\eta$$

but, from Eq. [A4]

$$dy = \frac{-N_D(z)}{N_A(y)} dz$$

therefore,

$$dz = \frac{dz d\eta}{dz + \frac{N_D(z)}{N_A(y)} dz} = \frac{N_A(y)}{N_A(y) + N_D(z)} d\eta$$

this can also be written

$$dz = \frac{N_T(\eta)}{N_D(z)} d\eta$$

Therefore, Eq. [B2] becomes

$$\int_{x_1}^{x_j} dy N_A(y) = \int_0^w d\eta N_T(\eta) \quad [\text{B3}]$$

This is the basic equation that is needed, since it relates the unknown  $x_1$  to the known functions  $N_A$  and  $N_T$  and the measured variable  $w$ . When  $x_1$  is found,  $N_A(x_1)$  is obtained by direct substitution, and  $N_D(x_2)$  is calculated using Eq. [B1]. It should be noted that  $N_T(w)$  must be integrated, and, therefore, a range of C-V measurements must be made up to the bias voltage required to obtain the desired measurement depth.

It is easily shown from Eq. [5] that the following identity is true (since  $dw = \epsilon A dC/C^2$ )

$$dw N_T(w) = \frac{CdV}{qA} \quad [\text{B4}]$$

Equation [B4] may be understood as stating a relationship between the applied charge increment per unit area and the depletion layer widening. Substitution of [B4] into [B3] yields the physical insight that the charge stored in one side of the depletion layer at any voltage equals the integral of the charge transferred during charging of the reverse bias junction capacitance.

#### REFERENCES

1. T. P. Lee, *IEEE Trans. Electron Devices*, **ED-13**, [12] pp. 881-896 (1966).
2. T. P. Lee, *ibid.*, **ED-12**, [8], pp. 457-470 (1965).
3. J. Hildebrand and R. D. Gold, *RCA Rev.*, June 1960.
4. I. Amron, *Electrochem. Technol.*, **2**, 327 (1964).
5. See, for example, J. Hildebrand, "Advanced Calculus for Applications," p. 360, Prentice Hall, Inc., Englewood Cliffs, N. J. (1962).
6. Yardley Beers, "Introduction to the Theory of Error," Addison-Wesley Publishing Co., Inc., New York (1957).



## Optical and Electrical Properties of SiC Films Prepared in a Microwave Discharge

O. A. Weinreich and A. Ribner

*The Bayside Laboratory, research center of  
General Telephone & Electronics Laboratories, Bayside, New York*

Microwave induced chemical reactions have been investigated increasingly in recent years (1). Relatively few reports, however, describe formation of films in microwave discharges. With this technique, films may be obtained at low temperatures by direct reaction of the plasma with the substrate, or by deposition of the products formed by the reaction of gaseous compounds in the discharge tube. Examples of the first kind are oxidation of silicon and gallium arsenide in an oxygen plasma. Oxidation in this case occurs at unexpectedly low temperatures (300°C for the oxidation of Si and 70°C for the oxidation of GaAs) (2, 3).

It has recently been reported that oxide films have been formed from the gas phase in a microwave plasma (4). These films were formed by the decomposition of gaseous organometallic compounds. In our Laboratory, films of several refractories have been formed from gaseous components by microwave induced reactions at low temperature. For example, we have prepared boron nitride from diborane and nitrogen, boron carbide from diborane and methane, silicon nitride from silane and nitrogen, and silicon carbide from silane and methane. This note describes the formation of the silicon carbide films and presents the results of a brief investigation of their optical and electrical properties.

### Equipment for Film Preparation

The experimental arrangement used in the preparation of the silicon carbide films is shown in Fig. 1. The microwave generator (MG) consists of a magnetron capable of delivering power up to 1 kw at a frequency of 2.54 GHz. Tuning is accomplished by a standard impedance transformer (E-H tuner T). The power toward the discharge tube is measured as the difference between forward and reflected power using the directional coupler (D<sub>1</sub>), attenuators A<sub>1</sub> and A<sub>2</sub> and power meters P<sub>f</sub> and P<sub>r</sub>. The microwave power is partly absorbed and partly transmitted by the discharge tube (DT), inserted into the wave guide (W) parallel to the E field. The transmitted power is measured using a second directional coupler (D<sub>2</sub>), attenuator (A<sub>3</sub>), and power meter P<sub>tr</sub>. The transmitted power is absorbed by a matched load (L). At the early stage of this investigation absolute power measurements were not made because the discharge tubes were initially placed in an open-ended tapered wave guide. With this arrangement transmitted power could not be determined. However, specific samples, the properties of which are described below, were prepared using the set up shown in Fig. 1, and for these the absorbed power in the discharge is given. Generally speaking, one advantage of film preparation in microwave discharges lies in the practicability of measuring and controlling the power absorbed in the discharge by applying standard microwave techniques.

The substrates are polished disks of either 14 ohm-cm p-type silicon or fused quartz. They are placed

on the silicon sample holder (SH) which can be moved vertically in the discharge tube and rotated during deposition by using a rotary Seal (RS). The temperature of the sample holder is measured with thermocouple (TC). Quartz discharge tubes of 0.5-1 in. in diameter were used. Before the gas mixture is admitted, the system is evacuated with a diffusion pump until the pressure measured by the ion gauge (IG) near the sample is in the 10<sup>-6</sup> Torr range. The gas is then admitted through the leak valve (LV) and the pumping speed is adjusted such that a pressure of 2 Torr is read with gauge (G).

### Film Preparation

Films were prepared in the equipment described above from a gas mixture of 90 m/o (mole per cent) He, 5 m/o SiH<sub>4</sub>, and 5 m/o CH<sub>4</sub> at a total pressure of 2 Torr. Flow rates varied from 5 to 20 Torr-liters/min. The substrates were heated by the plasma discharge itself without the use of external sources. A temperature range from 40° to 400°C was covered by varying the absorbed microwave density from a few tenths to about 4 w/cm<sup>2</sup>.

The location of the substrate in the plasma turned out to be an important factor in determining the deposition rate and the nature of the film. Slight variations in substrate position was sufficient to mask any effect of flow rates in the range investigated. Growth rates were varied from 50 to 500 Å/min by varying the position of the substrate in the plasma. Generally, growth rates were higher when the sample was outside the glow region. A dependence of the growth rate upon position in the plasma was also observed by Ligenza for the oxidation of Si in oxygen (2). When the sample was in the glow region, the growth was greatest in the center and usually a ring pattern of interference colors was obtained. This is believed to be related to the distribution of the electric field in the wave guide. Films formed outside the glow region were more uniform in thickness. The growth rates of the films were estimated during deposition from the interference colors. Color charts for SiO<sub>2</sub> on Si were used (5). Since equal colors indicate equal optical paths, the observed color gives the SiC film

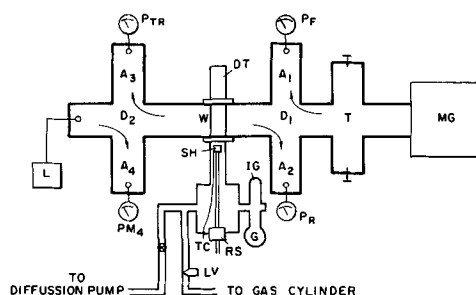


Fig. 1. Schematic representation of experimental equipment

thickness

$$d(\text{SiC}) = \frac{n(\text{SiO}_2)}{n(\text{SiC})} \cdot d(\text{SiO}_2)$$

where  $d$  is the thickness and  $n$  the refractive index. At substrate temperatures up to about 400°C the films obtained had a glassy structure, and therefore electron diffraction could not be used for identification. However, the following experimental results strongly indicate that the deposited films are SiC:

1. An intense absorption peak at 12.6 $\mu$  coincides with the fundamental lattice absorption reported by Spitzer and co-workers (6) for crystalline SiC films prepared by a reaction of Si with CH<sub>4</sub> at 1300°C. Figure 2 shows the infrared spectrum of one of the glassy films together with the absorption curve of Spitzer and co-workers.

2. The bandgap of the glassy SiC films on quartz substrates obtained from the short wavelength cut off of the transmission spectrum in the visible region was found to be 2.5 eV. This value falls between the values reported for  $\beta$  SiC (2.2 eV) and  $\alpha$  SiC (2.86 eV) (7).

3. The deposited films are inert with respect to acids such as HF, HNO<sub>3</sub>, HF-HNO<sub>3</sub> mixtures, etc. This is the chemical behavior to be expected from SiC.

#### Electrical and Optical Properties

To determine the refractive index, the films were deposited on quartz substrates with a step, and the Abeles Brewster angle method was used (3). Values for  $n$  varied from 1.8 to 2.3 depending on the position of the sample in the plasma. The bulk refractive index of SiC is 2.6 (8). Films with low values of  $n$  were always obtained when the sample was placed at the edge of the glow region or further away where no glow was observed. When the samples were placed near the waveguide in the region of glow, films with higher  $n$  values were formed, although in a less reproducible manner. It was found that the temperature of the sample was not responsible for change of the refractive index in the range from 40° to 400°C.

Breakdown strength measurements of the films made at 60 Hz gave an average value of 3 x 10<sup>8</sup> v/cm. These measurements were made with SiC films on 14 ohm-cm silicon wafers 17 mm in diameter and 20 mils thick. The back side was gold plated, and 16-mil diameter Al dots were evaporated onto the SiC film.

Samples having high resistivity, breakdown strength, and refractive index were obtained with a power absorbed by the plasma of 3 w/cm<sup>2</sup>, flow rates of 5 Torr liters/min, and sample temperatures of 380°C during deposition. An I-V curve for a typical sample is shown in Fig. 3. The d-c voltage is applied between the gold-

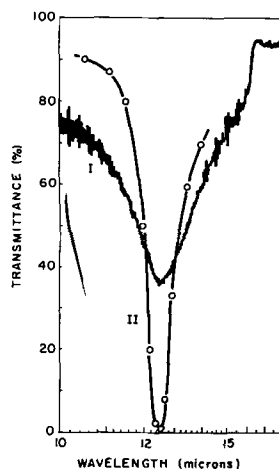


Fig. 2. Infrared transmission of SiC. Curve I, film prepared in microwave plasma; curve II, polycrystalline SiC reported by Spitzer and co-workers.

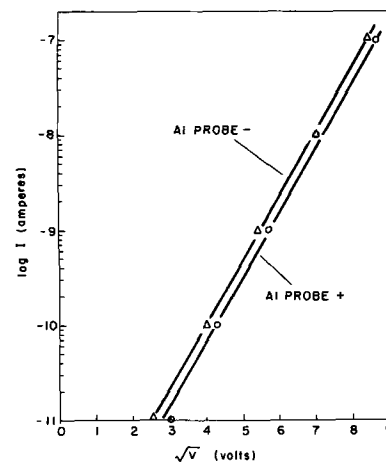


Fig. 3. Current-voltage characteristic of SiC film

plated side of the Si disk and the aluminum dots as described for the breakdown measurements. When  $\log I$  is plotted against  $\sqrt{V}$ , straight lines are obtained regardless of polarity. This field-dependent conductivity may be due to Schottky emission or the Poole-Frenkel mechanism (9), both of which predict  $\log I$  to be proportional to  $\sqrt{V}$ . Further work is needed to determine the actual conduction mechanism. The thickness of the SiC film of this particular sample was 1600Å and uniform in the center over a circular region of about 6 mm in diameter. The resistivity of this SiC film was of the order of 10<sup>13</sup> ohm-cm at a field strength of 5 x 10<sup>5</sup> v/cm and about 10<sup>11</sup> ohm-cm at 4 x 10<sup>6</sup> v/cm. The relatively high resistivity at low field strength may be due to submicroscopic grain structure rather than high purity. It has been reported in the literature that the resistivity of SiC increased 7 orders of magnitude when the compound was changed from bulk to granular form (10). The relative permittivity at 1 kHz was 3.9.

Since the SiC layers have reasonably high resistivity and breakdown values, the films were evaluated for use as dielectrics for insulated-gate field-effect devices. Measurement of capacitance at 1 kHz as a function of d-c bias yielded an interface charge density as low as 5 x 10<sup>11</sup>, at the flat-band point, lower than for silicon nitride. At fields up to 1.3 x 10<sup>6</sup> v/cm room temperature instabilities were negligible, i.e., less than  $\pm 0.2$ v. However, the slopes of the C(V) curves were only 35% of the theoretical maximum, indicating a relatively high density of fast surface states. This slope is comparable to that obtained for pyrolytically grown glassy silicon nitride films.

#### Summary and Conclusion

The feasibility of preparing refractory films at low temperatures from gaseous compounds in microwave plasmas has been demonstrated. Some properties of SiC films obtained by this method are disclosed. Many questions concerning film formation in microwave discharges such as influence of gas mixture, pressure, temperature and power, await further work to be answered.

#### Acknowledgment

The authors wish to express their thanks to C. F. Tufts for taking and evaluating the electron diffraction patterns and to E. Goldman for analyzing the C(V) curves. They also wish to thank R. Summergrad for reading the manuscript and for his many helpful suggestions.

Manuscript submitted April 23, 1968; revised manuscript received July 15, 1968.

Any discussion of this paper will appear in a Discussion Section to be published in the June 1969 JOURNAL.

## REFERENCES

1. Chemical Processing in a Microwave Discharge, R. F. Baddour and P. H. Dundas, MIT Dept. of Chemical Engineering, I. L. P. Preprint No. 755 (over 50 references).
2. I. R. Ligenza, *J. Appl. Phys.*, **36**, 733 (1965).
3. O. Weinreich, *ibid.*, **37**, 2924 (1966).
4. D. R. Secrist and J. D. Mackenzie, *This Journal*, **113**, 914 (1966).
5. W. A. Pliskin and E. E. Conrad, *IBM J. Res. & Dev.*, **8**, 43 (1964).
6. "Infrared Properties of Silicon Carbide," by W. G. Spitzer, D. A. Kleinman, C. J. Frosch, and D. J. Walsh, in "Silicon Carbide," p. 361, Pergamon Press, New York (1960).
7. *Ibid.*, "Intrinsic Optical Absorption in Single Crystal Silicon Carbide," by H. R. Philipp and E. A. Taft., p. 366.
8. R. M. Potter and C. A. Cusano, *This Journal*, **114**, 848 (1967).
9. D. R. Lamb, "Electrical Conduction Mechanisms in Thin Insulating Films," Methuen and Co., Ltd., London (1967).
10. "Resistivity of Granular Silicon Carbide—Impurity and Crystal Structure Dependence," by Paul Carrol, in "Silicon Carbide," *op. cit.*, p. 341.

## Direct Nitridation of Silicon Substrates

R. G. Frieser\*<sup>1</sup>

Sprague Electric Company, North Adams, Massachusetts

Thin, continuous films of silicon nitride have been of considerable interest in the last few years because of their dielectric properties and their considerable inertness toward chemicals. Bulk silicon nitride, of course, has been a commonly available material for quite some time. It is manufactured by standard metallurgical techniques, based on reacting finely divided silicon powder with nitrogen at elevated temperatures (1). This fact appears to bear out the simple statement found in many current textbooks, namely, that silicon nitride can be produced by the direct combination of the elements at temperatures above 1300°C (2-5). This statement, although correct as far as it goes, ignores the great importance which the role of physical subdivision of the silicon plays in this reaction.

Oxide films of varying thickness can easily be formed either by direct oxidation of silicon surfaces, large surfaces as well as powders, or by a chemical vapor deposition process. Direct oxidation yields the more uniform oxide.

With respect to nitrides, excellent results in this laboratory as well as in others have been obtained by CVD reaction of a silicon hydride or halide with ammonia. Since more uniform and more desirable properties are obtained for the oxide by direct oxidation, direct nitridation of silicon surfaces has been attempted. Although the free energy of formation of silicon nitride becomes less negative as the reaction temperature increases, at ~ 1300°C  $\Delta F$  is still about 45 kcal/mole. It appears therefore reasonable that direct nitridation should be feasible. Indeed, Knopp and Stickler reported thin, noncontinuous films of silicon nitride when heating silicon wafers in argon containing small percentages of oxygen and nitrogen (6). In their work, no efforts were made to remove the native film of oxide on the silicon surfaces prior to reaction with nitrogen. On the other hand, Gregor (7) states that: "Silicon nitride films cannot be grown on a silicon substrate by thermal nitridation either in nitrogen or anhydrous ammonia."

In our laboratory, early attempts by Sprague and by Saxena (8) led to the conclusion that direct nitridation is possible, but very hard to control. These experiments were made at 1250°C employing low nitrogen flow rates (1 l/min). Film formation rates were very slow (~ 500 Å/16 hr) and their refractive index varies from 2.0 to 2.4.

A more comprehensive look at direct nitridation seemed warranted in order to reconcile the different claims in the literature and to investigate whether film qualities achieved by chemical vapor deposition could be approached. Such a film grown directly

would also permit the study of the electrical properties without the interference of an underlying oxide film.

The experiments described here were performed in a commercial (Pittsburgh Material and Chemical Company) upright, 8-slice epitaxial rotating reactor. The substrates were silica sol-polished silicon wafers oriented in the <111> or <100> plane, having resistivities of 1.0, 4.0, and 10 ohm-cm, both p- and n-type. The substrates were placed in the reactor without any pretreatment. After a 2-min H<sub>2</sub> flush at room temperature, the substrates were heated in H<sub>2</sub> at 1250°C for 10 min and then HCl etched (10% HCl in 24 l/min H<sub>2</sub>) at 1250°C for 5 min. This treatment removed oxides and silicon by removing ~ a 25μ layer from the top surface. At this stage the surface did not exhibit any surface structure. After a 2-min H<sub>2</sub> flush and as soon as the substrate reached the requisite temperature, nitrogen was introduced in the reactor directly from the plant lines (containing no more than 1-2 ppm of H<sub>2</sub>O) for direct nitridation of silicon surfaces. Holding the above conditions constant, the following parameters were varied: the nitrogen flow rate (10-30 l/min), the deposition time (1 min-2 hr) and the deposition temperature (1150°-1375°C). The effect on the film properties of uv illumination during growth was also examined.

Under these conditions, the following results were observed:

1. Films were neither uniform nor continuous. The growth pattern was a function of the reactor geometry. Final films were approximately concentric with and covered only the central portion of the substrate. Increasing either the growth time (up to 2 hr), growth temperature, or N<sub>2</sub> flow rate, only increased the diameter of the growth area. Inspection of the grown films under the microscope showed that the films were highly faulted and faceted. Furthermore, the density of the nucleation was not uniform but greatest at the central portion. No obvious reason other than reactor geometry seemed to be apparent. It was noted, too, that these films showed either isolated growth or domains growing into each other (Fig. 1). Even after 6 hr of growth, individual nucleation sites could still be distinguished under a microscope, showing crystalline-looking structures which had not fused. No further increase in the diameter of the grown film was noted after 2 hr (up to 6 hr) of reaction time. Nor did these 6-hr films appear to be more continuous or thicker than the 2-hr films.
2. The films did not appear to be attacked by either concentrated (48%) HF or by a solution of 5 parts (48%) HF plus 95 parts HNO<sub>3</sub>.

\* Electrochemical Society Active Member.

<sup>1</sup> Present address: IBM Corporation, East Fishkill Facility, Hopewell Junction, New York 12533.



Fig. 1. Photomicrograph of the surface of a nitrided silicon wafer. Magnification ca. 330X.

3. Infrared transmission spectroscopy showed sharp absorption peaks at 11.0, 12.2, and 21.3 $\mu$ ; this is indicative of  $\text{Si}_3\text{N}_4$  (Fig. 2). No absorption was noted at 9, 13, or 23 $\mu$ ; this could be interpreted as an absence of Si-O bonds. Comparison of absorption peak heights of several runs indicated little change in the film thickness as a function of deposition time. A film of 1725 $\text{\AA}$  had a refractive index of 2.44 as determined by the ellipsometric technique. This higher value may be due to a high silicon content; it was not further investigated. Film thickness measurements were very difficult to make because of the unevenness of the films and were attempted only on a few samples.
4. The physical appearance of the films was dark, but transparent with some interference colors. Reflection electron diffraction studies indicated that the films were polycrystalline (Fig. 3). The d-spacings (Table I) calculated from these films matched those of alpha and beta  $\text{Si}_3\text{N}_4$ . This would indicate that the films are a mixture of both forms. Since the beta-form is the usual high-temperature form, some rearrangement on cooling may have occurred. These results differ in this respect from data published recently (9).
5. The n-type substrates used in this experiment showed consistently more extensive growth

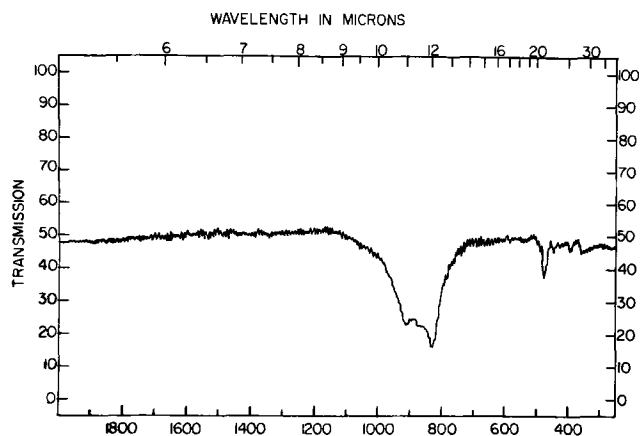


Fig. 2. Infrared transmission curve of a nitrided silicon under from 5 to 40 $\mu$ .

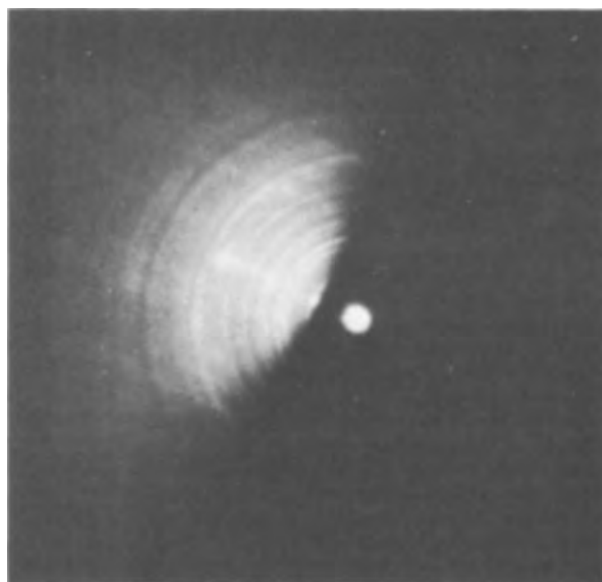


Fig. 3. Reflection electron diffraction picture of Cu nitrided silicon wafer. Magnification ca. 2X.

- (larger diameter) spots than p-type silicon, with all other parameters being equal. No effect of substrate orientation, (111) vs. (100), was noted.
6. No growth at all was obtained at 1150°C, and very little at 1250°C.
7. "Best" results were obtained at 1375°C with a  $\text{N}_2$  flow of 10 l/min. Decreasing the flow rate decreased the total growth area. Larger flow rates resulted in films which were too uneven for electrical measurements.
8. Omission of the HCl etch in situ did change the appearance, although not the character of the films. The Si wafers used in this experiment did not exhibit any surface structure. The extent of growth was about the same, the films if anything were thinner and not continuous, but in place of the "circular" growth about the nucleation sites, nucleation followed the crystallographic 110 directions in the (111) plane, reflecting the triangular pattern of that plane. This may indicate that the flow pattern of the HCl etch determined nucleation pattern of the substrates and therefore, the observed growth pattern.
9. Illumination of the substrates with a mercury vapor lamp during film growth possibly increased the size of the growth area slightly but not significantly. This experiment was performed for one reason; an orientation effect of uv illumination on the silicon surface was noted during low-temperature deposition of silicon on silicon (10).
10. An attempt was made to characterize electrically a 1725 $\text{\AA}$  thick film. Extremely low breakdowns frustrated this attempt.
11. The addition of  $\text{H}_2$  to the  $\text{N}_2$  decreased the size of the deposition area, with all other parameters being equal.

Table I. Comparison of observed d-spacing (electron diffraction) with x-ray values reported\* for  $\alpha$ - and  $\beta$ - $\text{Si}_3\text{N}_4$

Observed, A	$\alpha$ - $\text{Si}_3\text{N}_4$ , A	$\beta$ - $\text{Si}_3\text{N}_4$ , A
4.18	—	—
2.82	2.82	—
2.59	2.60	—
2.30	2.32	2.31
2.15	2.16	2.18
1.86	1.86	—
1.62	1.64	—
1.46	—	1.46
1.34	—	1.34

\* ASTM Index of Powder Diffraction File.



This work indicates that the growth of silicon nitride by direct nitridation is self-limiting. One has to assume that diffusion of N or Si through the nitride film is so slow at the deposition temperatures investigated that it is practically nonexistent. Similar results were obtained by Clark (12) of our laboratory. Using a glow discharge to produce atomic nitrogen, he found it impossible to diffuse nitrogen into Si to any extent at 1200°C, but in all cases formed a thin silicon nitride layer, which effectively stopped any nitrogen diffusion. It appears then that silicon nitride can be produced from the elements as stated in the literature, in a practical sense, only if silicon is present as a powder. Thus, if useful silicon nitride films are the objective one appears to be limited to chemical vapor deposition techniques.

#### Acknowledgment

The author is grateful to Dr. B. Hardeman for providing the electron diffraction data; to Dr. F. Hielscher for advice and electrical evaluation; to Dr. M. Ghezzi for the ellipsometric measurements; and to Mr. C. Debussy for assistance in the experimental part. This work was benefitted also from discussion with Drs. J. J. Casey and A. N. Saxena.

Manuscript submitted April 5, 1968; revised manuscript received ca. July 19, 1968.

Any discussion of this paper will appear in a Discussion Section to be published in the June 1969 JOURNAL.

#### REFERENCES

1. R. E. Kirk and D. F. Othmer, "Encyclopedia of Chemical Technology," Vol. 13, p. 823, Interscience Publishers, New York (1954).
2. P. J. Durrant and B. Durrant, "Introduction to Advanced Inorganic Chemistry," p. 604, John Wiley & Sons, Inc., New York (1962).
3. R. T. Sanderson, "Chemical Periodicity," p. 203, Reinhold Publishing Corp., New York (1962).
4. R. B. Heslop and P. L. Robinson, "Inorganic Chemistry," p. 29, Elsevier Publishing Co., New York (1960).
5. R. E. Kirk and D. F. Othmer, "Encyclopedia of Chemical Technology," Vol. 12, p. 370, Interscience Publishers, New York (1954).
6. A. N. Knopp and R. Stickler, *Electrochem. Technol.*, **3**, 84 (1965).
7. L. V. Gregor, Interim Report, Air Force Avionics, AF 33(615) - 5386, 15 November 1966.
8. A. N. Saxena, Private communications.
9. K. Okada, H. Sakane, and Y. Sugioka, *J. Phys. Soc. Japan*, **23**, 655 (1967).
10. R. G. Frieser, *This Journal*, **115**, 401 (1968).
11. A. Clark, Private communication.

## Brief Communications



### Deposition of New Binary Oxide Thin Films by the Pyrolytic Decomposition of Trimethylsiloxy-Aluminum-Isopropoxide ( $\text{Me}_3\text{SiO})_n\text{Al}(\text{O}^i\text{Pr})_{3-n}$ )

Yasuaki Nakaido and Satoshi Toyoshima

Department of Applied Chemistry, Faculty of Technology, Gunma University, Kiryu-shi, Japan

Thin films of metal oxide have previously been obtained by the pyrolytic decomposition of metal alkoxides in the vapor phase (1-5). Mixtures of two different kinds of alkoxides have also been used (6). The present paper describes the deposition of binary metal oxide films by the vapor phase pyrolysis of trimethylsiloxy-aluminum-diisopropoxide at temperatures in the range 300°-800°C with nitrogen gas as carrier. By using a compound in which the Al-O-Si bonds already exist, binary oxide films were obtained, a considerable proportion of the initial Al-O-Si bonds not being broken.

The starting material  $\text{Me}_3\text{SiOAl}(\text{O}^i\text{Pr})_2$  (7) was prepared by the method of transesterification between trimethylacetoxysilane and aluminum triisopropoxide in 1:1 molar ratio in cyclohexane solution. The apparatus consisted of an evaporator vessel, a resistance furnace 30 cm in length and a quartz reactor tube 3 cm in diameter. (111) silicon slices to be coated were placed on a quartz substrate holder. The reactor had a uniform hot zone about 20 cm long. A 360 l/hr flow of nitrogen was introduced to purge the reactor before the power was turned on. When the substrate reached

the operating temperature, 20 l/hr of nitrogen were passed through the sample in an evaporator at 150°C, and the sample gas was introduced into the reactor and pyrolyzed for a set period.

The thickness of the films was measured by interferometry. The films attained a maximum thickness of 4 $\mu$  without cracking.

The relation between the deposition rate and furnace temperature is shown in Fig. 1. Up to 600°C increasing furnace temperature decreased the rate of deposition; above 600°C increasing furnace temperature increased the rate.

The films were clear, almost transparent, and hard. No crystalline state was detected in the x-ray photographs of films deposited up to 500°C, but the films deposited at 600°, 700°, and 800°C gave distinct Debye-Scherrer rings. The lattice spacings of the oxide films are given in Table I, in which the spacings are compared with those of Kyanite (triclinic crystal of  $\text{Al}_2\text{O}_3 \cdot \text{SiO}_2$ ). Crystal phases of  $\text{Al}_2\text{O}_3$  or  $\text{SiO}_2$  alone were not detected. Analysis of films deposited at 800°C are Al, 33.9%, Si, 16.7%; calculated values for  $\text{Al}_2\text{O}_3 \cdot \text{SiO}_2$  are : Al, 33.3%, Si, 17.3%.

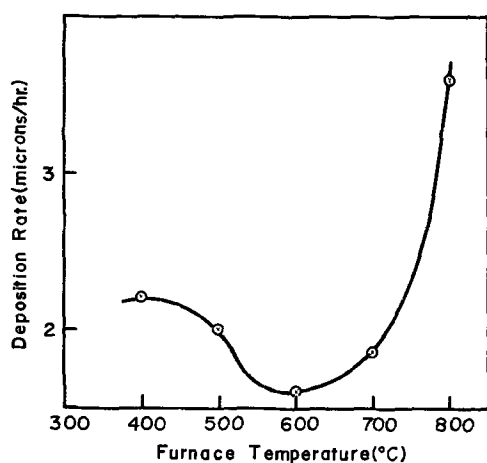


Fig. 1. Relation between deposition rate and furnace temperature

#### Acknowledgment

The author wishes to thank the Central Research Laboratory, Hitachi Ltd. for supplies and Dr. S. Otani for many helpful discussions.

Manuscript submitted May 17, 1968; revised manuscript received June 21, 1968.

Any discussion of this paper will appear in a Discussion Section to be published in the June 1969 JOURNAL.

Table I. Spacings obtained from the deposit film at 800°C compared to those of Kyanite\*

Deposit film		Kyanite	
d (kx)	Int.	d (kx)	Int. I/I <sub>1</sub>
3.22	S	3.35	65
3.13	S	3.18	100
1.96	W	1.962	55
1.93	S	1.935	50
1.67	W	1.676	9
1.65	S	1.650	3
1.37	W	1.377	75
1.26	M		
1.16	W		
1.12	S		
1.05	W		
0.965	M		
0.922	M		
0.861	M		
0.855	M		

\* ASTM X-ray Powder Diffraction Data Card No. 11-46.

#### REFERENCES

1. E. L. Jordan, *This Journal*, **108**, 478 (1961).
2. J. Klerer, *ibid.*, **108**, 1070 (1961).
3. J. Klerer, *ibid.*, **112**, 503 (1965).
4. S. Sakurai, S. Watabe, and A. Morio, *Rev. Electric Communication Lab.*, **11**, 178 (1963).
5. J. A. Aboaf, *This Journal*, **114**, 948 (1967).
6. F. C. Eversteijn, *Philips Research Repts.*, **21**, 379 (1966).
7. Y. Nakaido, *Kogyo Kagaku Zasshi*, **67**, 236 (1964).
8. ASTM X-ray Powder Diffraction Data Card No. 11-46.

## Crystallographic Character of the $\text{Sr}_{2-x}\text{Mg}_x\text{P}_2\text{O}_7$ System

Crispin Calvo

Institute for Materials Research, McMaster University, Hamilton, Ontario, Canada

Single crystals in the  $\text{Sr}_2\text{P}_2\text{O}_7$ - $\text{Mg}_2\text{P}_2\text{O}_7$  system have been prepared in conjunction with crystallographic (1) and electron spin resonance (2) studies of  $\alpha\text{Ca}_2\text{P}_2\text{O}_7$  and  $\alpha\text{Sr}_2\text{P}_2\text{O}_7$ . The structures of these compounds, although closely related, are nevertheless not the same.  $\alpha\text{Sr}_2\text{P}_2\text{O}_7$  is orthorhombic with space group  $\text{Pbnm}$  (2) and lattice parameters  $a = 13.1054\text{\AA}$ ,  $b = 8.9104\text{\AA}$ ,  $c = 5.4035\text{\AA}$  (3), while  $\alpha\text{Ca}_2\text{P}_2\text{O}_7$  has the monoclinic space group  $\text{P2}_1/\text{n}$  and lattice parameters  $a = 12.66\text{\AA}$ ,  $b = 8.542\text{\AA}$ ,  $c = 5.315\text{\AA}$ ,  $\beta = 90.3^\circ$  (1). The cations are coordinated to eight oxygen ions in the former compound and to seven in the latter one, but beyond this the structural differences are small. Since the space group of  $\alpha\text{Ca}_2\text{P}_2\text{O}_7$  is a subgroup of that of  $\alpha\text{Sr}_2\text{P}_2\text{O}_7$  and their difference transforms as one irreducible representation of the space group of the  $\alpha\text{Sr}_2\text{P}_2\text{O}_7$ , it appears possible that a reversible transformation relates the two structures (2). Further, the EPR data (2) were consistent with preferred solubility of  $\text{Mn}^{2+}$  in only one cation site. In an attempt to resolve the site of preferred solubility for  $\text{Mn}^{2+}$ ,  $\text{SrMnP}_2\text{O}_7$  was prepared. When this phase was found to be triclinic, emphasis was then directed toward the  $\text{Sr}_2\text{P}_2\text{O}_7$ - $\text{Mg}_2\text{P}_2\text{O}_7$  system.  $\text{SrMgP}_2\text{O}_7$  was prepared and found to have the  $\alpha\text{Ca}_2\text{P}_2\text{O}_7$  structure. The results of a study of the single crystal diffraction patterns are reported here. These results suggested that the transformation from the  $\alpha\text{Sr}_2\text{P}_2\text{O}_7$  to the  $\alpha\text{Ca}_2\text{P}_2\text{O}_7$  should be found as the composition is varied in the  $\text{Sr}_2\text{P}_2\text{O}_7$ - $\text{Mg}_2\text{P}_2\text{O}_7$  system.

In contrast to these results, Hoffman (4) reported no solid solution in the  $\text{Sr}_2\text{P}_2\text{O}_7$  and  $\text{SrMg}_2\text{P}_2\text{O}_7$  sys-

tem. Wanamaker and ter Vrugt (5) suggested a similarity between the powder pattern of  $\text{SrMgP}_2\text{O}_7$  and  $\text{BaMgP}_2\text{O}_7$ . However, the latter has the same triclinic structure as  $\text{SrMnP}_2\text{O}_7$ .

#### Experiments

$\text{Sr}_{2-x}\text{Mg}_x\text{P}_2\text{O}_7$  single crystals were prepared having compositions specified by  $x = 1/16, 1/8, 1/4, 1/2$ , and 1. Strontium nitrate and magnesium acetate were dissolved in distilled water and mixed with an aqueous solution of  $(\text{NH}_4)_2\text{HPO}_4$ . The precipitate was washed several times with distilled water, dried, and heated to 800°C. The sample was then transferred to a Vycor container, melted, and cooled slowly across its melting temperature. The sample's temperature was quenched to room temperature from about 1000°C to prevent the  $\alpha$  to  $\beta$  transformation.

Single crystals were examined at room temperature to determine unit cell sizes and symmetry. In addition, the density of  $\text{SrMgP}_2\text{O}_7$  was measured and used together with the accurately determined lattice parameters to check the composition. These lattice parameters were determined from films calibrated with reflections from a synthetic rutile ( $\text{TiO}_2$ ) sample whose lattice parameters were taken as  $a = 4.9529(5)\text{\AA}$  and  $c = 2.9591(3)\text{\AA}$  (6). These crystal data are recorded in Table I.

The intensity of about 500 reflections was estimated in order to establish the site of preferred occupancy for the  $\text{Sr}^{2+}$  ion. The intensity of the reflections of the type  $hnl$   $n = 0, 1, 2$  and  $mkl$   $m = 0, 1$  were estimated visually;  $\text{MoK}\alpha$  radiation was used to record the former data and  $\text{CuK}\alpha$  the latter. The data were corrected for Lorentz, polarization, and absorption effects.

Key words: pyrophosphate  $\text{SrMg}$ , phase transition, structure.

Table I. Crystal data for SrMgP<sub>2</sub>O<sub>7</sub>

$a$	= 12.59 (10) Å
$b$	= 8.293 (8) Å
$c$	= 5.260 (5) Å
$\beta$	= 91.0 (2)°
Extinctions:	hOl h + 1 odd OkO k odd
Density exp.	3.41 g/cm <sup>3</sup>
calc.	3.46 g/cm <sup>3</sup>

These data were compared to calculate intensity based on various fractional occupancy of Sr and Mg in the available cation sites. The final atomic parameters obtained in the refinement of the structure of  $\alpha$ -Ca<sub>2</sub>P<sub>2</sub>O<sub>7</sub> (1) were used as trial input parameters.

#### Results and Discussion

The Sr<sup>2+</sup> ion preferentially dissolves into cation site 1. This was anticipated on crystallographic grounds since this site cannot easily distort to accommodate a small cation. This cation site is bonded to oxygen atoms from opposite ends of the anion and therefore for the new environment to collapse about a small cation the P-O-P angle must change substantially from the value of 130.7° found in  $\alpha$ -Sr<sub>2</sub>P<sub>2</sub>O<sub>7</sub>. Since the anion has an eclipsed configuration and the shared oxygen atoms are on the trans side of the molecule, a smaller cation would demand a decrease in the P-O-P

angle of the anion. This angle, however, is already near the lowest value reported for a pyrophosphate.

It appears that at room temperature a phase boundary separating the  $\alpha$ -Sr<sub>2</sub>P<sub>2</sub>O<sub>7</sub>-like phase and  $\alpha$ -Ca<sub>2</sub>P<sub>2</sub>O<sub>7</sub>-like phase occurs at a composition of about 10 m/o (mole per cent). Mg<sub>2</sub>P<sub>2</sub>O<sub>7</sub> in Sr<sub>2</sub>P<sub>2</sub>O<sub>7</sub>. The space group of Sr<sub>15/8</sub>Mg<sub>1/8</sub>P<sub>2</sub>O<sub>7</sub> is the orthorhombic Pnbn while that of Sr<sub>7/4</sub>Mg<sub>1/4</sub>P<sub>2</sub>O<sub>7</sub> is the monoclinic P2<sub>1</sub>/n. These results suggest a continuous solid solution when the samples are prepared from the melt. This possible phase boundary is under investigation.

#### Acknowledgment

This research is supported by a grant from the Defence Research Board of Canada.

Manuscript received July 15, 1968.

Any discussion of this paper will appear in a Discussion Section to be published in the June 1969 JOURNAL.

#### REFERENCES

1. C. Calvo, *Inorganic Chem.*, **7**, 1345, (1968).
2. C. Calvo, K. Y. Leung, and C. V. Stager, *J. Chem. Phys.* (1968).
3. L. Hagman, I. Jansson, and C. Magneli, Preprint.
4. M. V. Hoffman, *This Journal*, **115**, 560 (1968).
5. W. L. Wanamaker and J. W. ter Vrugt, *Philips Research Repts.*, **22**, 355 (1967).
6. D. T. Cromer and K. Herrington, *J. Am. Chem. Soc.*, **77**, 4708 (1955).

## Relation Between Solid-State Cohesion of Metal Fluorides and the Electrochemical Behavior of Metals in Hydrogen Fluoride

Ashok K. Vijh\*

Research and Development Laboratories, Sprague Electric Company, North Adams, Massachusetts

Hackerman, Snavely, and Fiel (1) have recently reported some investigations on the anodic behavior of 23 materials in 0.01M NaF solutions made in high-purity anhydrous hydrogen fluoride (AHF). They classified the dissolution (anodic and/or on open circuit) tendency of these materials as follows:

**Class I: rapid corrosion.**—antimony; bismuth; cadmium; molybdenum; silver; zirconium diboride; thallium; tungsten; carbon (pyrolytic); tantalum.

**Class II: low corrosion.**—aluminum; chromium; cobalt; Hastelloy-F; iron; magnesium; titanium; zinc; zirconium.

**Class III: passive.**—Monel; platinum; nickel.

Hackerman *et al.* also attempted to relate the three types of aforementioned behavior of these materials to some of their fundamental properties, *e.g.*, solubility of the respective metal fluorides and Pilling-Bedworth ratios. Such correlations, however, were demonstrated not to exist.

Here, an attempt has been made to correlate the anodic behavior of these materials in AHF with those fundamental properties which of their fluorides characterize their general stability in the solid state, *e.g.*, melting points (and hence lattice energies and percentage ionic character) (2), heats of formation per equivalent ( $\Delta H_f/eq$ ), heats of atomization per equivalent ( $\Delta H_a/eq$ ), and a large variety of other properties which are derived from these quantities (2-4).

In the discussions to follow, only 20 elemental substances will be considered since relevant data, it is

believed, are not available for the three nonelemental substances, *i.e.*, Hastelloy-F, ZrB<sub>2</sub>, and Monel, which were also studied by Hackerman *et al.*

In Fig. 1, the fluorides of these substances have been arranged in order of their melting points. The data shown refer to the fluorides for which melting points are readily available in the Handbook (5); these, presumably are, in general, the stablest fluorides of the corresponding metals. It is clear that the higher the melting point (and hence the higher the lattice energy) (2) of a metal fluoride, the lower is the corrosion tendency of the corresponding metal in AHF. The classification into three classes on the basis of melting points coincides with the three types of corrosion behavior reported by Hackerman *et al.*; the only exception is CdF<sub>2</sub>.

In Fig. 2, two classifications have been attempted. In the first classification these materials have been arranged in order of the  $-\Delta H_f/eq$  values for the corresponding fluorides. The three groups may again be delineated except for a slight "buffer" region in which some metals of class I and II overlap. The data were calculated from the values of heats of formation per mole for the corresponding fluorides as obtained from ref. (5) and (6). It may be noted that the higher (exothermic) the  $\Delta H_f/eq$  for a metal fluoride, the lower the tendency for the corresponding metal to corrode in AHF.

In the second classification in Fig. 2, these materials have been arranged in order of the  $\Delta H_a/eq$  of the corresponding fluorides. Heats of atomization per mole for a metal fluoride MF may be obtained by algebraic addition of heat of formation per mole for MF, heat

\* Electrochemical Society Active Member.

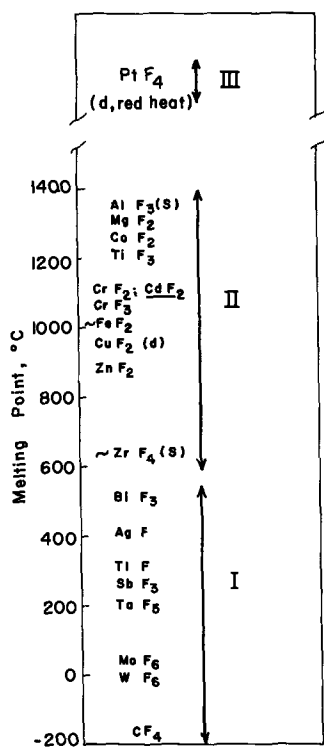


Fig. 1. Twenty metal fluorides arranged in order of their melting points; (s) and (d) mean sublimes and decomposes, respectively; no data available for  $\text{NiF}_2$ ; I, II, and III refer to the classification of Hackerman *et al.* on anodization behavior in AHF of the corresponding metals, in ref. (1).

of sublimation per mole for Metal M, and half the heat of dissociation per mole of  $\text{F}_2$  (4, 7). To obtain  $\Delta H_f/\text{eq}$  from  $\Delta H_f/\text{mole}$  is, of course, quite straightforward; e.g.,  $\Delta H_f/\text{eq}$  for  $\text{AlF}_3$  is  $(1/3) \times \Delta H_f/\text{mole}$ . The thermodynamic data used in the computation of  $\Delta H_f/\text{eq}$  have been obtained from ref. (5) and (6). It may be mentioned that it is immaterial as to which particular fluoride of a given metal may be used in the foregoing computations, since the values used are in per equivalent (and hence "normalized") and not in per mole. Taking several fluorides of a given metal gives the values of  $\Delta H_f/\text{mole}$  and  $\Delta H_a/\text{mole}$ , which are quite different; however  $\Delta H_f/\text{eq}$  or  $\Delta H_a/\text{eq}$  values for various fluorides of a given metal are approximately the same. Another rather obvious point may also be emphasized here; the only valid procedure in the types of arguments presented here is to use values of various quantities as per equivalent, *i.e.*, neither as per mole, nor as per atom but as per atom equivalent (2,4).

From the preceding discussion, it is clear that lower corrosion tendency of materials in AHF is observed in cases which tend to have fluorides with: (a) high melting point and hence high lattice energies and percentage ionic character (2); (b) high (exothermic)  $\Delta H_f/\text{eq}$ ; (c) high  $\Delta H_a/\text{eq}$ .

On dissolution, bonds between constituents of an ionic crystal are broken and a collapse of the lattice occurs (3). An increase in the energy needed to breakdown the lattice, *i.e.*, lattice energy (*cf.* melting point) would increase the tendency of the lattice to resist corrosion, either on open circuit or for a given value of the field at lattice-electrolyte interface. This conclusion is clearly supported by Fig. 1 here.

Again with increasing lattice energy (*cf.* Fig. 1) and increasing heat of formation (Fig. 2), heats of hydration, solution, fusion, and evaporation increase; also increase bond energies, the heats of activation for formation of ionic vacancies, band gaps, dielectric strength (*i.e.*, ability to sustain high fields), activation energies for the creation of dislocations and other physical "faults," specific heats and a variety of other

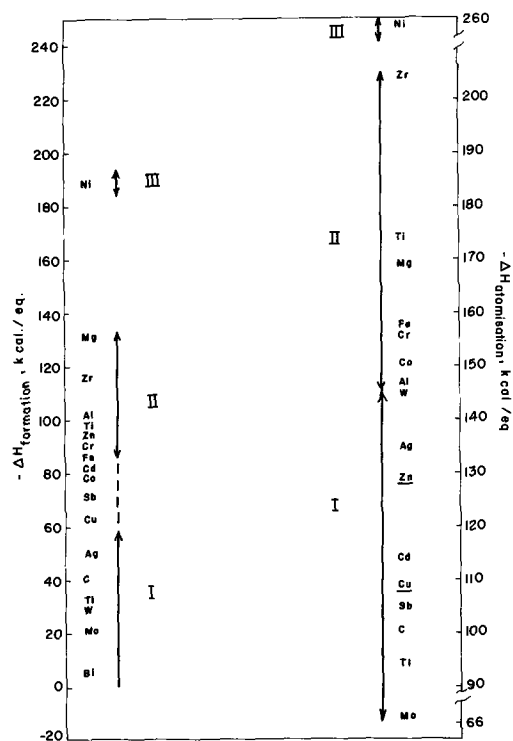


Fig. 2. (left) Eighteen substances arranged in order of  $-\Delta H_f/\text{eq}$  of their respective fluorides; I, II, and III refer to the classification of Hackerman *et al.* (1); slight "buffer" zone where classes I and II overlap has been shown by the dotted line; data for  $\text{PtF}_4$  and  $\text{TaF}_5$  not available. (right) Seventeen substances arranged in order of  $\Delta H_a/\text{eq}$  of their respective fluorides; relevant data not available for the case of Bi, Pt, and Ta; I, II, and III correspond to the classification of Hackerman *et al.* (1); two exceptions (Zn, Cu) may be noted.

related properties (3,4). In short, higher lattice energies (*cf.* Fig. 1) and heats of formation (Fig. 2) increase the magnitude of those properties which signify the general stability, in the solid state, of materials (3,4); hence, probably, the lower corrosion tendencies in Fig. 1 and 2 with increasing melting points and  $\Delta H_f/\text{eq}$ , respectively.

The heat of atomization emphasizes the covalent aspects of the bonding in these materials (fluorides), since almost all ionic crystals are at least partially covalent. If the spin correlation stabilization energies, which are usually small, are ignored, heat of atomization per equivalent is approximately equal to the average bond energy [not bond dissociation energy for a particular bond (8)]. Hence higher bond energies in metal fluorides indicate relatively high resistance to corrosion of the corresponding metals in AHF.

From the preceding discussion, it may be concluded that, roughly, in the case of those metals which do not corrode relatively readily in AHF (either open circuit or on anodization), the corresponding fluorides are held together rather strongly in the solid state. It is important, however, to qualify this statement by adding that in a given specific case of anodization of a metal in AHF (or in any solution, for that matter), electrochemical factors and the associated overpotentials at the metal-electrolyte (or metal-fluoride-electrolyte) interface may indeed be of paramount importance in the determination of the anodic behavior. It may also be remarked that the type of approaches outlined here yield only approximate trends and not exact predictions of anodization behavior of metals.

A tacit assumption involved in the foregoing arguments is that the corrosion of a metal proceeds via formation of a fluoride film on the metal. From our knowledge of the corrosion behavior of metals in general (9), it seems that this assumption is entirely valid in a great majority of cases (9). Irrespective of

the mechanism of corrosion, the relation between solid-state cohesion of metal fluorides and the anodization behavior of the corresponding metals in AHF (Fig. 1 and 2) is still quite persuasive.

Manuscript received July 12, 1968.

Any discussion of this paper will appear in a Discussion Section to be published in the June 1969 JOURNAL.

#### REFERENCES

1. N. Hackerman, E. S. Snavely, Jr., and L. D. Fiel, *Corrosion Sci.*, **7**, 39 (1967).
2. R. T. Sanderson, "Chemical Periodicity," Reinhold Publishing Corp., New York (1960).
3. A. A. Vorob'ev, *Russ. Chem. Rev.*, **36**, 440 (1967), English Translation by Consultants Bureau; idem., in "Chemical Bonds in Semiconductors and Solids," N. N. Sirota, Editor, Consultants Bureau, New York (1967); also see other papers in the latter book.
4. A. K. Vijn, *J. Phys. Chem. Solids*, to be published, *This Journal*, To be published.
5. "Handbook of Chemistry and Physics," The Chemical Rubber Co., Cleveland (1966).
6. F. Rossini *et al.*, Selected Values of Chemical Thermodynamic Properties, U. S. Gov't. Printing Office, Washington, D. C.
7. See for example, E. A. Moelwyn-Hughes, "Physical Chemistry," 2nd revised ed., Pergamon Press, New York (1961).
8. L. Pauling, "The Nature of the Chemical Bond," Cornell University Press (1960).
9. T. P. Hoar in "Modern Aspects of Electrochemistry," Vol. 2, J. O'M. Bockris, Editor, Butterworths, London (1959).

# Galvanic Monitoring of Battery Gases

P. A. Hersch\*

Gould-National Batteries, Inc., Minneapolis, Minnesota

## ABSTRACT

The rates of evolution of oxygen and hydrogen from a battery can be transduced continuously to an electric current for recording. A stream of nitrogen carries the evolved gases into a self-attenuating system with a galvanic-coulometric cell selectively activated by oxygen. Oxygen from the battery is monitored directly; hydrogen by a difference method invoking continuous combustion. The method may be used for studying charge acceptance, formation efficiency and, omitting attenuation, for determining self-discharge, corrosion rate, and other battery-related data.

In nearly all aqueous electrochemical systems the imposition of sufficiently extreme potentials or currents results in the evolution of oxygen at the anode and of hydrogen at the cathode. The same two gases are also products in the spontaneous decomposition of oxidizers and in the self-discharge of battery fuels. Measuring the rate of gassing along with the electrochemical and other variables is thus often desirable when studying electrodes and their depolarizers. The rate of gassing is of special interest in mixed processes such as occur at secondary battery electrodes towards the end of charging, when not all the electricity supplied is accepted for storage and coulombs are used up in the evolution of battery gases.

Simple collection methods for the gases and subsequent analysis with Orsats and gas chromatographs have been employed variously. Figure 1 shows a volumetric system combining an oil drop displacement flowmeter for low gassing rates with a two-stage soap bubble flowmeter for medium and fast rates. The travel time of the drop or soap bubble between a start and a finish mark gives the total rate of gassing. A one-quarter turn of the four-way stopcock permits a reversal of the drop movement. Although this primitive apparatus does not separate oxygen from hydrogen it nevertheless provides useful information. The gassing pattern of a battery on constant current charging and overcharging may be compared with the theoretical pattern of Fig. 2. A plot of gassing rate (ml gas/amp min) vs. charge (amp-hr) displays, ideally, a first plateau at a gassing rate of either 3.73 ml O<sub>2</sub>/amp min or 7.45 ml H<sub>2</sub>/amp min (at 20°C, 1 atm), according to whether the anode or the cathode is first in reaching saturation with charge. Following this, there is a second plateau at 11.2 ml gas/amp min when both electrodes are saturated. The distance on the abscissa between the onset of the two steps represents the excess ampere hour-capacity of the one electrode over the other. Similarly shaped curves appear on overdischarge. Failure in reaching the plateau and distortion of the theoretical pattern indicate the occurrence of gas recombination or reabsorption, frequently when the rate of charge is low.

The objective of this present work was primarily the continuous, separate monitoring of oxygen and hydrogen evolved singly or simultaneously in a battery, by a technique that expresses at any instant the individual rates of evolution of the two gases, in terms of an electrical quantity. To this end, a stream of nitrogen is sent through the head space of the battery, carrying the evolved gases to a measuring system. Specific detectors could be used, based on paramagnetism for oxygen and on thermal conductivity for hydrogen, but the more recently perfected galvanic method (1), based on electroabsorption of gases, is more genuinely fitted to the purpose of monitoring

\* Electrochemical Society Active Member.

Key words: batteries, charge acceptance, coulometry of gases, galvanic monitoring, gases, gassing, hydrogen, oxygen, rate of evolution.

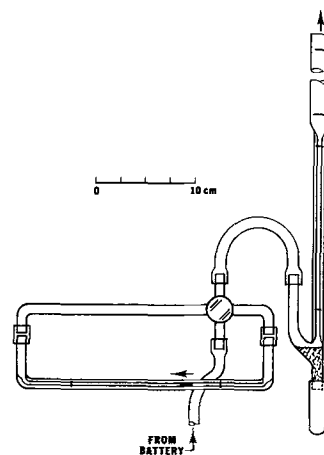


Fig. 1. Volumetry of slow and fast gassing

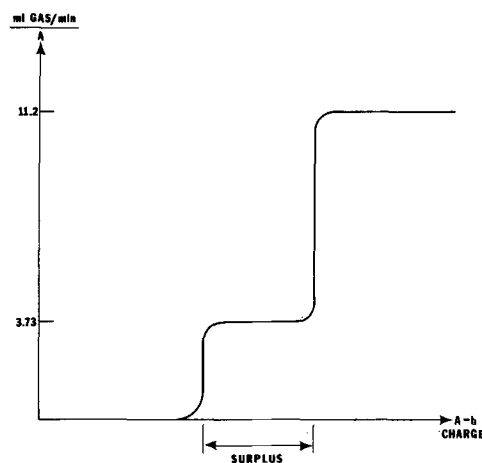


Fig. 2. Gassing behavior of a battery with surplus negative capacity

electroevolved gases; it is also simpler, selective and far more sensitive.

## Principle

In the case of oxygen measurement a stream of nitrogen carries the evolved oxygen into a galvanic system that absorbs it and thereby reproduces that part of the charging current that gives rise to the oxygen.

The oxygen sensor is essentially a primary battery with a base metal anode and an inert, partially gas-exposed, oxygen-absorbing cathode. Such cells have been proposed as analyzers since about 1930. The older cells were of limited use because they transduced only a small and variable portion of the oxygen delivered to them into electricity. Stability was poor

and linearity of response uncertain. Recent developments, borrowing from fuel cell technology, overcome these limitations, and an output close to the theoretical maximum for complete conversion of oxygen to hydroxyl ion is attained.

For monitoring the hydrogen, an analogous cell may be applicable, employing a partly gas-exposed, hydrogen-absorbing anode, as used in fuel cells, and a solid oxidizer cathode. A hydrogen sensor based on the system gas/Pt/HCl + KCl/Hg<sub>2</sub>Cl<sub>2</sub>, with the same geometry as one of the earlier galvanic sensors for oxygen, has been described (2). The system gas/Pt/H<sub>2</sub>SO<sub>4</sub>/Cu<sup>II</sup> is also practicable. However, the output of cells with platinum anodes in response to hydrogen is variable and sensitive to poisons, in contrast to the oxygen sensors based on silver or graphite cathodes. Moreover, while most oxygen-reducing cathodes are indifferent to hydrogen, the hydrogen-oxidizing anodes of platinum are not at all indifferent to oxygen. They tend to combine the two gases locally, giving a measurable galvanic response only to the excess of one gas over the other. With a cell of this kind one must remove all oxygen by a selective absorbent before hydrogen can be determined.

The procedure followed in this work, while also requiring a selective absorbent for oxygen, avoids a separate sensor for hydrogen. The nitrogen stream, stripped of all oxygen in the absorber, receives a constant proportion of oxygen in a microelectrolyzer, then passes a catalyst bed where all the hydrogen burns up, consuming part of the added oxygen. The oxygen left over is carried to the oxygen sensor. Hydrogen is thus signalled in coulometric terms by the extent to which a base line, representing the oxygen generated in the microelectrolyzer, is depressed as a result of the combustion. Oxygen absorber, microelectrolyzer, and catalyst form the "combustion segment" of the apparatus. The segment is bypassed when oxygen, not hydrogen, is of interest.

A uniquely suitable selective absorbent for oxygen is a bed of granular manganous oxide, made from the dioxide by reduction with hydrogen at about 400°C (3). The lower oxide removes all traces of oxygen at room temperature without absorbing hydrogen or catalyzing the hydrogen/oxygen reaction. The absorbent is self-indicating, changing from pale green to brown, with a sharp boundary between the virgin and used-up zones. Most popular absorbents for oxygen are based on copper. Among these, the "BTS catalyst" has been especially developed for action at room temperature (4). However, this material cannot be recommended for the present purpose since it retains and releases some hydrogen.

The galvanic sensor operates properly only on traces of oxygen. In order to measure the large rates of evolution of battery gases, very drastic dilution is essential. This has been achieved reliably by a special continuous sampling technique that needs no auxiliary diluent gas and does not delay response.

### Apparatus

**Sampling system.**—The carrier gas stream, prepurified tank nitrogen, adjusted to a flow rate  $F = 100$  ml/min, passes through a rotameter and along a wet paper wick to pick up moisture (Fig. 3). The wick is fed with water saturated with NaCl. At  $P_1$  the gas stream splits into two branches. The partial stream  $f$ , routed through a MnO absorber and flow restrictor  $R_2$ , flows to the analysis portion of the train. The other partial stream,  $F - f$ , traverses the head space of the battery under test and the head space of a calibrating electrolyzer, receiving  $\phi$  ml/min of electrode gases from either the battery or the calibrator. Nearly all of the mixture  $F - f + \phi$  discharges through  $R_1$  into the atmosphere. A minute portion  $\alpha(F - f + \phi)$  only flows through  $R_3$ , joining  $f$  at  $P_2$ . Thus, only the aliquot  $\alpha\phi$  of the battery gases reaches the analysis portion of the train.

The three flow restrictors are best made from stainless steel syringe needle tubing and are seated in silicone rubber plugs. The relationship  $R_1 < R_2 \ll R_3$  should hold. Typically,  $R_2$  is a 10 cm long, 22 gauge capillary (internal diameter  $D_2 = 0.394$  mm). Upon passing 50 ml N<sub>2</sub>/min through this capillary, a pressure head of about 26 cm H<sub>2</sub>O is established. When choosing appropriate lengths ( $L$ , cm) and gauge numbers (internal diameter  $D$ , mm) for the restrictors, one may use the formula

$$R = 0.00123 L D^{-4} \text{ cm H}_2\text{O}/(\text{ml N}_2/\text{min}) \text{ at } 20^\circ\text{C} \quad [1]$$

This approximation is derived from Poiseuille's law and applies to the present situation, where the pressure drop across the restrictors is small compared with the pressures at their entrance and exit.

Restrictor  $R_3$  may be of the same gauge and length as  $R_2$  but rendered far more restrictive by inserting a stainless steel wire into the bore.

The attenuation factor  $\alpha$  is largely determined by the ratio of flow resistances  $R_1 : R_3$ , and the splitting ratio  $f : (F + \phi)$  by the ratio  $R_1 : R_2$ . More precisely, the relationships are

$$\alpha = \frac{R_1}{R_3} \cdot \frac{1}{1 + \frac{r}{R_2} + \frac{R_1 + r}{R_3}} \quad [2]$$

$$\frac{f}{F + \phi} = \frac{R_1}{R_2} \cdot \frac{1}{1 + \frac{R_1 + r}{R_2} + \frac{R_1 + r}{R_3}} \quad [3]$$

where  $r$  is the flow resistance of the analytical part of the train.

These two equations may be derived by equating (a) the pressure drops (= flow rate flow resistance) along the path  $P_1$ -battery-electrolyzer- $R_3$ - $P_2$  with the pressure drop along  $P_1$ -MnO- $R_2$ - $P_2$  and (b) the pressure drop along  $P_1$ -battery-electrolyzer- $R_1$ -atmosphere with that along  $P_1$ -MnO- $R_2$ -analysis parts-atmosphere. The pressure drops in the battery and electrolyzer head spaces may be assumed to be zero and that within the MnO bed considered part of  $R_2$ .

**Calibrating electrolyzer.**—This, a "dummy battery" that accepts no charge, serves to determine the over-all attenuation factors ( $\alpha\eta$  for O<sub>2</sub>,  $\epsilon\alpha\eta$  for H<sub>2</sub>; see Table I), the combustion efficiency ( $\epsilon$ ), and, from time to time, the constancy of these factors. The electrolyzer (Fig. 3, lower right) is made from a 100 ml measuring cylinder and employs Ni-wire electrodes in aqueous KOH

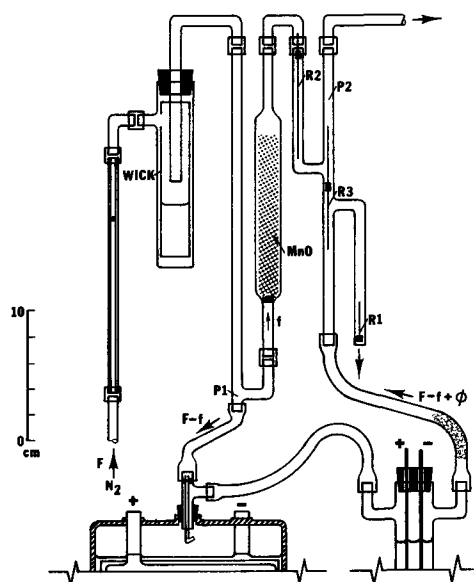


Fig. 3. Sampling system and calibrating electrolyzer

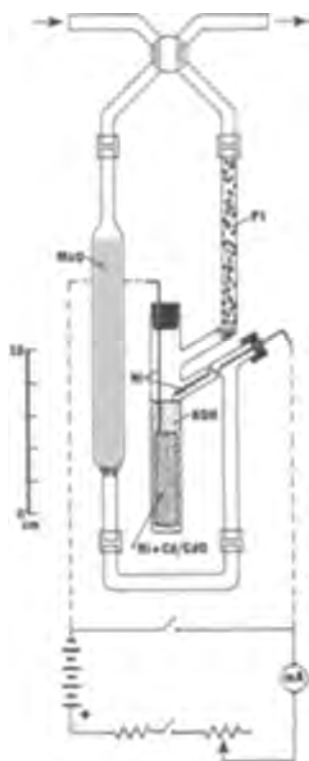


Fig. 4. Segment for hydrogen measurement

(5N). A wad of glass wool prevents liquid spray from reaching the restrictor  $R_3$ .

**Combustion segment.**—The segment (Fig. 4) follows in series to the sampling system and is bridged by a four-way stopcock permitting insertion or exclusion of the three components: MnO tube, microelectrolyzer, and catalyst.

The MnO tube is of the same type as the one in the sampling system.

The microelectrolyzer evolving  $O_2$  must not evolve any  $H_2$ . Its cathode is a Ni-screen carrying  $Cd(OH)_2$ , and the cathodic process is  $Cd^{++} \rightarrow Cd$ . The screen is a portion of the negative of a Ni/Cd battery in its discharged or partly discharged state and is formed into a scroll. A useful size is 5 x 6 cm, with up to about 1 amp-hr "worth" of  $Cd^{II}$ . The electrode is rejuvenable *in situ* by reverse current, resulting in reoxidation  $Cd \rightarrow Cd^{++}$ . The electrolyte is aqueous KOH (5N). The anode is the barely immersed tip of a thin Ni-wire carried as an extension by a thicker Ni-wire. The anode area is thus kept to a minimum and oxygen bubbles can grow to a small size only. The bubbles, barely visible, emerge in quick succession, ensuring a noise-free base line.

The microelectrolyzer is energized by a 12v battery in series with a milliamperemeter, a limiting resistor, variable resistors for coarse and fine adjustment, and an interrupter switch. A shunting switch, when closed, permits setting the current; it should also be closed when the combustion segment is bypassed for measurement of  $O_2$  evolution.

The combustion catalyst is 0.5 w/o Pt/ $Al_2O_3$  (about 40  $\frac{1}{8}$ -in. cylindrical pellets, from Engelhard Industries, Inc., Newark, New Jersey). The catalyst works at room temperature, despite the high dilution of the  $O_2$  and  $H_2$  it combines, and despite the brevity of contact time, 1-2 sec. If calibration as scheduled in Table I shows incomplete efficiency ( $\epsilon < 1$ ) the catalyst should be reconditioned by taking it to about 70°C, using heating tape, while passing  $N_2$  carrying some 5 ma "worth" of  $H_2$  generated in the microelectrolyzer with reverse current. After about 5 min the  $H_2$  generation is discontinued, but warming in the  $N_2$  stream

continued for another 5 min. Thereafter, an efficiency check at room temperature should show  $\epsilon \approx 1$ .

**Oxygen sensor.**—The principle and construction of the coulometric sensor have been described and illustrated elsewhere (1). The preferred embodiment is a sandwich structure: gas-exposed porous silver or graphite cathode/porous plastic sheet imbibed with 5N KOH/ negative from a Ni/Cd battery, in its virgin or charged state, as anode. The volume of electrolyte applied must be substantially smaller than the aggregate pore volume of the porous materials so that much of the cathode remains unflooded. A double sandwich structure is recommended, with a central stainless steel blade carrying one set of the three layers on either face. The two external (cathode) layers may each be 15 cm long and 20 mm wide. The housing may be a glass or stainless steel tube 18 cm long and with a 25 mm internal diameter.

This cell should be connected in series with a load resistor not greater than 100 ohm (preferably 10 ohm or less); the current, in terms of the potential difference across the resistor, is followed by a millivolt recorder. Its response to a step change of  $O_2$ -concentration (e.g.,  $O_2$  from the microelectrolyzer) should be 90% complete within 1 min. A high internal or load resistance would stretch the response time.

The element, once wet with electrolyte, must not be exposed to air, except for brief periods. Otherwise the cell may dry out and anode capacity will be wasted. Shorting in air may drain as much as 200-500 ma. When isolated from air and gas flow while on circuit electrically, the cell consumes all  $O_2$  from its gas space and the current decays to a few microamperes or less, except if there are leaks or unpurged pockets of air. After the initial assembly or after extended exposure of the cell to air or to  $O_2$ -rich gas the decay to low background takes 1-2 hr; after only brief ingress of oxygen, a few minutes. When nitrogen flows through the cell, coming from a manganous oxide column, through ducts connected end to end with a few Tygon sleeves, a residual current  $i_0$  below 10  $\mu a$  is attainable, but a higher one may be tolerated. The residual current does not fluctuate and drifts very little.

The volume and concentration of the KOH solution tends to adjust itself to the relative humidity of the gas stream. Moderate changes of relative humidity do not affect the performance.

The service life of the element is limited only by the amount of accessible metallic cadmium in the two anode strips. Two strips of common commercial negative material 15 cm long and 20 mm wide contain an amount of Cd equivalent to 2 amp-hr. Even discounting nonaccessible Cd and the Cd oxidized before use, the material should last for several weeks of continuous operation at levels of output on the order of 1-2 ma. Spent anodes may be "recharged." This may be done *in situ* if the cathode is of graphite. If it is of silver, the element should be submerged in 5N KOH solution and a third electrode, of a material more inert than silver, should be used as anode during the charging process. A nickel wire helix, surrounding the electrode bundle, serves the purpose.

The response to  $X$  volumes  $O_2$  per million volumes of gas in a stream of  $F$  ml/min (measured at  $\theta^\circ C$  and  $P$  Torr) conforms to the equation

$$i - i_0 = 0.268 \eta F X \cdot \left[ 1 - \frac{\theta - 20}{293} - \frac{760 - P}{760} \right] \mu a \quad [4]$$

where  $i_0$  is the residual current, with  $X = 0$ . The factor 0.268 derives from Faraday's law. The coulometric yield  $\eta$  should be within a few per cent of unity, at least when  $F \leq 100$  ml/min and the drain  $i < 2$  ma. The yield may be determined by passing  $j$  ma through the microelectrolyzer, which is done anyway when establishing the  $O_2$  supply for  $H_2$  measure-



Table I. Summary of Procedure

	Battery charge current input, ma	Macro-electrolyzer input, ma	Combustion segment	Micro-electrolyzer input, ma	O <sub>2</sub> sensor output, ma	Calculated ratios
<i>Determination of:</i>						
Background $i_0$	0	0	in or out	0	$i_0 = 0.02$	
Over-all attenuation factor for O <sub>2</sub> , $\alpha\eta$	0	$I_c = 2000$	out	0	$i_c = 1.21$	$\alpha\eta = (i_c - i_0)/I_c = 0.595 \cdot 10^{-3}$
Anodic gassing ratio $\rho$ at time $t$	$I = 2000$	0	out	0	$i(t) = 0.32$	$\rho(t) = \frac{i - i_0}{\alpha\eta I} = 0.15$
Base line $i_1$	0	0	in	$j = 2.00$	$i_1 = 1.94$	$\eta = (i_1 - i_0)/j = 0.96$
Over-all attenuation factor for H <sub>2</sub> , $\epsilon\alpha'\eta$	0	$I_c' = 2000$	in	$j = 2.00$	$i_c' = 0.78$	$\epsilon\alpha'\eta = (i_1 - i_c')/I_c' = 0.58 \cdot 10^{-3}$
Check on catalyst efficiency, $\epsilon$						$\epsilon \approx \frac{i_1 - i_c'}{i_c - i_0} \cdot \frac{I_c}{I_c'} = 0.97$
Cathodic gassing ratio $\rho'$ at time $t$	$I = 2000$	0	in	$j = 2.00$	$i'(t) = 1.30$	$\rho'(t) = \frac{i_1 - i'}{\epsilon\alpha'\eta I} = 0.55$

ment. One obtains, then,  $\eta = (i - i_0)/j$ , independently of  $F$ . Another check is to pass prepurified, but still O<sub>2</sub>-carrying, nitrogen from a tank, measuring  $i - i_0$  at two different flow rates. In this check, since  $X$  is constant,  $i - i_0$  should change in proportion to the change in  $F$ . (Transients, always occurring when the flow rate changes, should be ignored.)

### Procedure

Table I lists generally and by way of a numerical example the steps necessary to establish the oxygen flux  $\rho I$ , or the hydrogen flux,  $\rho' I$ , that results from a charging current  $I$ . The "gassing ratios,"  $\rho$  and  $\rho'$ , rise from zero and approach unity as a sigmoid function of charging time. Where there is recombination or reabsorption of gas,  $\rho$  and  $\rho'$  stay below unity and represent less than the proportion of current rejected by the battery electrodes. It is desirable for a battery to produce a steep slope of the two sigmoid curves.

Figure 5 reproduces a recording of the oxygen evolution rate from an 8 amp-hr Planté cell charged at  $I = 2$  amp. The terminal voltage was plotted manually. The steep rise of the voltage coincided with the beginning of oxygen evolution. However, the plateau of voltage was reached at a time when the gassing rate was still rising. The recorder trace is jagged because of the erratic release of the oxygen bubbles. The order of hold-up time of the major bubbles may be judged from the width of the small indentations of the curve. The over-all attenuation factor was  $\alpha\eta = 5.0 \cdot 10^{-4}$ . The gassing ratio  $\rho$  approached the value 1.0, showing absence of recombination and reabsorption of oxygen.

Figure 6 shows the recording of the hydrogen evolution rate during another charging of the same

battery, at the same current. Owing to excess negative capacity, gassing set in later than in the case of oxygen, at a time when the voltage was already on its way up. The voltage plateau was again reached earlier than the gassing plateau. The over-all attenuation factor was  $\epsilon\alpha'\eta = 5.0 \cdot 10^{-4}$ , the same as  $\alpha\eta$  in the run of Fig. 5. (This is not generally the case, since  $\epsilon$  may be less than unity, and  $\alpha'$  less than  $\alpha$ .) The gassing ratio  $\rho'$  approached 1.0, again showing that no gas has recombined or been reabsorbed.

Curves from sealed batteries, which for the purpose of measurement of gassing rates have to be unsealed, do not in general represent the events as they occur under service conditions when recombination and reabsorption take place. Flushing the head space of such batteries interferes with these processes. Accessories to the present system are being considered for the examination of sealed batteries through intermittent withdrawal or by means of a continuous bleed of gas from the head space, to be transferred to a carrier gas that does not sweep through the battery case.

*Simultaneous recording of O<sub>2</sub> and H<sub>2</sub> from a battery.*—The gas stream issuing from the sampling stream may be split to feed two analyzing branches, one, without catalyst, for O<sub>2</sub>, the other, with catalyst, for H<sub>2</sub>. It seems more practical to alternate instead between the two modes, jumping from the rising sigmoid curve for O<sub>2</sub> to the declining one for H<sub>2</sub>, and back following each curve for an interval of, say, 10 min before each change. The combustion segment and the microelectrolyzer current must be switched in and out at the same moment. It is also possible to design a routing system in which the combustion segment, instead of being bypassed, is made to succeed the

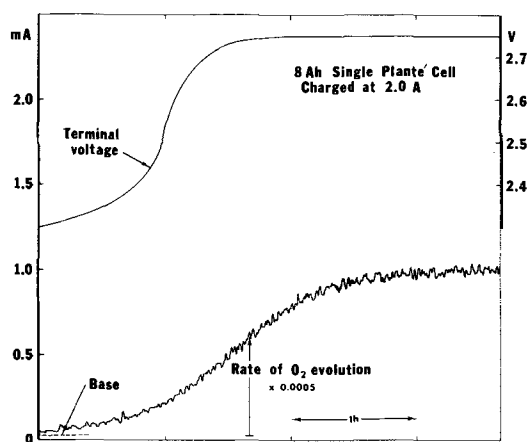


Fig. 5. Charge of positive

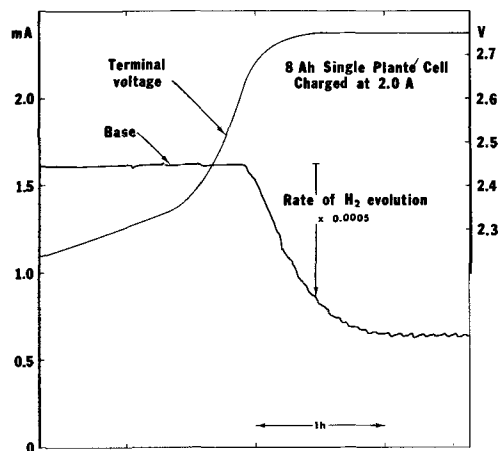


Fig. 6. Charge of negative

sensor in the  $O_2$  mode, but precedes it in the  $H_2$  mode. In this case the microelectrolyzer may be left in operation continuously.

**Transients.**—A step-change of charging current from  $I$  to  $I^*$  causes a transient excursion of the recorder trace before a new sensor output,  $i^*$ , is reached. This transient has nothing to do with the battery itself. Following a step in the total gassing rate, from  $\phi = 3.73 (\rho + 2\rho') I$  to  $\phi^* = 3.73 (\rho + 2\rho') I^*$  ml/min, the gas flow into the sensor changes immediately, but carrier gas with the changed oxygen concentration reaches the sensor only after a time interval. This interval depends on the volume of the ducts between the electrolytic source of oxygen and the sensor. Ignoring  $i_0$ , the transition of  $i$  is from  $\alpha\eta\rho I$  through  $\alpha\eta\rho IZ$  to  $\alpha\eta\rho I^*$ , with  $Z = (F - f + \phi^*) / (F - f + \phi)$ . There is no transient when the step is from  $I = 0$  to  $I^* > 0$ , but there is one when switching from  $I > 0$  to  $I^* = 0$ . Because  $Z$  is a function of both  $\rho$  and  $\rho'$ , the amplitude of the excursion of the oxygen trace is affected by the rate of evolution of both oxygen and hydrogen.

The hydrogen trace  $i'$  goes even through a double transient, depending on the duct volumes between the microelectrolyzer and the sensor and that between the source of electrolytic hydrogen and the microelectrolyzer. A sudden rise of  $I$  to  $I^*$  causes first a sharp rise of  $i'$ , then a mild fall, followed by a further fall. A step-down of charging current causes the opposite moves. The changes in output  $i'$  are from  $i_1 - \epsilon\alpha'\eta\rho'I$  through  $(i_1 - \epsilon\alpha'\eta\rho'I)Z$  through  $i_1 - \epsilon\alpha'\eta\rho'IZ$  to  $i_1 - \epsilon\alpha'\eta\rho'I^*$ .

**Related applications.**—The gradual decline of charge acceptance of a battery may be determined during formation, the battery's first cycle.

The galvanic technique may be used to advantage in determining slow evolution rates of hydrogen from self-discharging negatives of secondary, or anodes of primary, cells. The accidental or deliberate release of gases from incompletely sealed batteries may be measured. The loss of oxygen from silver oxide cathodes or the catalytic evolution of hydrogen from hydrazine anodes may be studied.

When the gas evolves very slowly, the attenuation system and the large electrolyzer should be omitted, while retaining the humidifier and combustion segment with its microelectrolyzer. The combustion efficiency ( $\epsilon$ ) can then be determined by placing two nickel wire electrodes in the microelectrolyzer, in addition to the submerged Cd/Cd<sup>II</sup> electrode. Using two electrolytic circuits, with the Cd/Cd<sup>II</sup> electrode in common, an oxygen flux  $j$  is produced at one nickel wire and a hydrogen flux  $j'$  at the other. First, with

$j' = 0$ , one obtains an oxygen base line  $i_1 = i_0 + \eta j$ ; then, injecting hydrogen, with  $0 < j' < j$ , one obtains a depressed level  $i' = i_1 - \epsilon\eta j'$ ; hence

$$\eta = \frac{i_1 - i_0}{j}; \quad \epsilon = \frac{i_1' - i_1}{i_1 - i_0} \cdot \frac{j}{j'}$$

The formulas for charge acceptance are still valid, but with  $\alpha = 1$  and the "input" current  $I$  representing the rate of the spurious spontaneous gassing under observation. Where the gas evolution stems from local galvanic action,  $I$  is the invisible action current, rendered visible. The method supersedes the writer's earlier galvanic procedure for measuring rates of metallic corrosion of the hydrogen evolution type (5).

The present technique may be applied in studies of gas evolution overvoltage and also of the thermal dissociation of oxides (PbO<sub>2</sub>, AgO, Ag<sub>2</sub>O, etc.) at temperatures too low for thermogravimetry to be applicable. The efficiency of oxygen/hydrogen combination catalysts under various conditions, and the effect of activating treatments given these catalysts, may be assessed using variants of the described procedures.

Applications for monitoring the fast or slow evolution of oxygen and hydrogen exist in chemical and biochemical systems. With appropriate catalysts, or with combustion at a sufficiently elevated temperature, the rates of emanation of most organic gases and vapors from liquid and solid systems could also be determined.

#### Acknowledgment

The author has to thank Chester Ling, Walter Maas, John Stewart, and Darrel Untereker for their assistance in various phases of this work.

Manuscript submitted May 10, 1968; revised manuscript received ca. July 23, 1968. This paper was presented at the Chicago Meeting, Oct. 15-19, 1967, as Paper 45.

Any discussion of this paper will appear in a Discussion Section to be published in the June 1969 JOURNAL.

#### REFERENCES

1. P. A. Hersch, "Galvanic Analysis" in "Advances in Analytical Chemistry and Instrumentation," Vol. 3, pp. 183-249, John Wiley & Sons, Inc., New York (1964). U.S. Pat. 3,223,597, Dec. 14, 1965.
2. H. J. Frey and R. C. Voter, (to E. I. duPont de Nemours and Co.) U.S. Pat. 3,003,932 (1961).
3. P. A. F. White and S. E. Smith, "Inert Atmospheres," Butterworths, London (1962).
4. M. Schütze, *Angew. Chem.*, **70**, 697 (1958).
5. P. A. Hersch, Proc. Internat. Symposium on Microchemistry, Birmingham, England 1958, pp. 141-150, Pergamon Press (1959).

# The Electric Resistivity of AgO

Aladar Tvarusko\*<sup>1</sup>

Research Center, ESB, Inc., Yardley, Pennsylvania

## ABSTRACT

The electric resistivity,  $\rho$ , of powder AgO samples, made by the chemical oxidation of AgNO<sub>3</sub>, was measured *in situ* up to 10 kbar.  $\rho$  increased linearly with decreasing AgO content of the samples (>70%). 63 AgO samples of 98.4% mean AgO content had a mean  $\rho$  of 59.3 ohm cm at 2.1 kbar. When Mg, Ca, Cd, In, Si, Y, Pd, Ni, or Co was added (as compounds) during the preparation of AgO,  $\rho$  of the sample increased. The addition of Hg, Ge, Sn, Pb, As, Sb, or Bi had a beneficial effect on  $\rho$  of AgO samples. Pb increased the length of the higher voltage plateau of AgO-Zn cells during discharge whereas Hg had no influence.

Silver oxide is extensively used in packaged power sources because it yields cells of high voltage and capacity per unit weight or volume. The capacity and discharge rate of these cells is greatly influenced by the electric resistivity of the silver oxide.

Silver belongs to group IB of the Periodic Table and may have three oxidation states, I, II, and III. The common valence of silver is +1, and Ag<sub>2</sub>O is its corresponding oxide. Ag<sub>2</sub>O has a high electric resistivity (1, 2) and 10<sup>8</sup> ohm cm (3) and 7.10<sup>8</sup> ohm cm (at 4.3 kbar) (4) were measured. Fortin and Weichman (2) found a band gap of 1.5 eV for Ag<sub>2</sub>O.

The trivalent silver compounds are unstable unless stabilized by coordination with suitable species (5, 6); the existence of the corresponding oxide, Ag<sub>2</sub>O<sub>3</sub>, has not yet been proven conclusively.

The divalent silver oxide, commonly designated as AgO, was found to be a silver (I)—silver (III) oxide (5, 7) with a considerable covalent bond and with no divalent silver present. The AgO formula will be used to describe the aforementioned silver oxide in this work.

The resistivity of AgO is much lower than that of Ag<sub>2</sub>O and the following values were found for AgO: 10 ohm cm at 20°C (3), 14.3 ohm cm  $\pm$  15% at 20°C and 12.16 kbar (8), 0.012 ohm cm (9), 5000 ohm cm at 4.3 kbar (4). These values form three distinctly different groups.

Yoshizawa and Takehara (10) found that the presence of Pb, Sn, In, Ti, Au, and Cu in the silver electrode had a marked influence on its charge and discharge. They claim that the lattice defects in Ag<sub>2</sub>O or AgO increase due to the addition of metals of higher valency than Ag<sup>+</sup> or Ag<sup>2+</sup>, and therefore the electric conductivity will increase. This is to be expected because the conductivity,  $\sigma$ , of a material is given by the product of the charge carrier concentration,  $n$ , their charge,  $e$ , and their mobility,  $\mu$ , [*e.g.*, (11)].

$$\sigma = ne\mu = \rho^{-1} \quad [1]$$

Yoshizawa and Takehara, however, did not measure the resistivity,  $\rho$ . According to Cahan (12, 4) silver plumbate forms in an alkaline electrolyte when lead or a compound of it is added to the active material of a silver electrode; the resistivity of silver plumbate is said to be approx. 3 x 10<sup>-3</sup> ohm cm.

The resistivity of AgO is studied in this work. The investigated variables are: pressure, time, AgO content of AgO samples, coprecipitated impurities in AgO, and AgO content in physical mixtures of Ag<sub>2</sub>O — AgO and AgO — HgO.

## Experimental

The AgO samples were made by the chemical oxidation of aqueous AgNO<sub>3</sub> solution in alkaline medium

by K<sub>2</sub>S<sub>2</sub>O<sub>8</sub> as described by Hammer and Kleinberg (13). "Baker Analyzed" reagents of the J. T. Baker Chemical Company were used for the synthesis. The AgO sample was dried in a vacuum oven at 60°  $\pm$  1°C for 16 hr and subsequently stored in an amber glass bottle with a ground joint. The sample was exposed to the ambient as little as possible. The active oxygen content of the various AgO samples was determined iodometrically and is expressed as AgO content. Commercially available battery-grade Ag<sub>2</sub>O (Ames Chemical Work, Inc., Glens Falls, New York) and reagent-grade red HgO (Merck and Company) were used. The various reagent-grade additives were incorporated into AgO during its preparation. The metal nitrate salt was added to the aqueous AgNO<sub>3</sub> solution before its addition to the alkaline K<sub>2</sub>S<sub>2</sub>O<sub>8</sub> reaction medium. Some of the impurities had to be added to AgNO<sub>3</sub> solutions as anions or mixed with alkaline K<sub>2</sub>S<sub>2</sub>O<sub>8</sub> medium before the AgNO<sub>3</sub> addition.

The electric resistivity of the powder sample was measured under pressure (*in situ*) in the measuring cell by a Keithley Milliohmmer, Model 503 (for samples of R < 1 kohm) or a Keithley Electrometer, Model 610 (for R > 1 kohm). The output of the aforementioned instruments was recorded on a recorder of adequate rise time and variable strip chart speed.

A Carver Laboratory Press, Model B was used for the compression of the sample. The measuring cell consisted of a flat Stellite base plate and rod which fitted a steel-jacketed insulating cylinder. The insulating material (Black XX-79 molded rod of The Budd Polychem Division, Newark, Delaware) had 5-6 x 10<sup>9</sup> ohm surface resistance (between ½ in. electrodes at ¼ in. basic). The steel-jacketed cylinder was firmly and flatly held to the base plate by a contoured steel plate, placed over its top, with the help of two strong embedded steel rods and wing nuts. Two similar measuring cells were used: (a) 5.0 cm<sup>2</sup> pellet area, used up to 2.1 kbar; the thickness of the pellet was measured, after its careful removal from the cell, by a micrometer caliper; (b) 1.0 cm<sup>2</sup> active area, used up to 10.6 kbar; the thickness of the sample during compression was measured *in situ* by an indicating micrometer caliper; naturally, the solidly attached resting arms for the caliper shoes were electrically insulated from the Stellite base plate and rod by polyethylene screws and spacers. The electric leads of the measuring instruments were connected to copper sheets (1 x 2 x 0.3 cm), firmly screwed to the base plate and rod, respectively.

At least two separate measurements were made on each dried sample (5000 and 2000g for up to 2.1 and 10.6 kbar pressures, respectively) at an ambient temperature of 25°  $\pm$  2°C. The sample was evenly distributed in the assembled, clean, and dry measuring cell, and the rod was slowly lowered into the cylinder. The assembled cell was placed into the press between two insulating layers consisting of Bakelite and pressed

\* Electrochemical Society Active Member.

<sup>1</sup> Present address: Engineering Research Center, Western Electric Co., Inc., Princeton, New Jersey 08540.

mica sheets. The pressure on the sample was first slowly raised and after selecting the proper resistance range on the instrument, rapidly ( $\sim 5$  sec) increased to the maximum pressure, unless otherwise mentioned. The resistance of the empty measuring cell was around 1m ohm and was neglected because it was less than 0.1% of the smallest measured resistance value.

### Results and Discussion

$\rho$  as a function of pressure and time.—In order to measure the resistivity of silver oxides, the powder samples had to be compacted. Figure 1 shows  $\log \rho$  of two AgO samples as a function of pressure. The resistivity of both samples decreased very rapidly at lower pressures as the AgO powder was compressed into shiny, brittle pellets. The apparent density of AgO samples at 2.1 kbar was calculated from the linear plot of sample weight and pellet thickness to be around 70% of that given in the literature. Thus, it can be safely assumed that the initial rapid decrease of  $\rho$  is due to the increased compaction of the sample. The initial decrease is reproducible in both measuring cells.

$\log \rho$  decreased linearly with pressure after its initial rapid decrease regardless of the AgO content of the sample.  $\rho$  should decrease with pressure because both  $\mu$  and  $n$  in Eq. [1] depend on pressure, in addition to temperature (14). The mobility increases to some degree with pressure, but the carrier production is the controlling factor in the resistivity of semiconductors. The carrier production is usually an activated process which is dominated by an exponential term containing the energy gap (14). An approximately linear decrease of the energy gap could possibly explain the aforementioned linear decrease of  $\log \rho$  with pressure.

Figure 1 shows that the resistivity of AgO samples increases with decreasing AgO content; this will be discussed later. The transition to the linear decrease of  $\log \rho$  shifts toward higher pressures with decreasing AgO content. Furthermore, the slope of the regression lines [fitted by the least square method (Fig. 1)] decreases with decreasing AgO content. The high resistivity of Ag<sub>2</sub>O, present in a sample of low AgO content, seems to be the controlling factor behind all these observations.

In order to compare the resistivity of AgO with the published values,  $\rho$  was extrapolated to the 12.16 kbar pressure of Neiding and Kazarnovskii (8) using the regression line equation (Fig. 1, 99.0%); the calculated 14.6 ohm cm compares very favorably with their 14.3 ohm cm  $\pm 15\%$ . Jones and Thirsk (9) obtained 0.012 ohm cm by extrapolation to  $1/P = 0$  pressure from a series of measurements up to 0.7 kbar. Replotting the  $\rho$  values of Fig. 1 (99.0% AgO) as a function  $1/P$ , the following regression lines were obtained: (a)  $\rho = 36.8 + 6.15 \times 10^4 1/P$  up to 2100 bar, coefficient of correlation,  $R = 0.998$ , and (b)  $\rho = 13.4 + 0.56 \times 10^4 1/P$  up to 10,600 bar,  $R = 0.998$ . The intercepts of these regres-

sion lines are approximately 3 orders of magnitude larger. The extrapolations to  $1/P = 0$ , i.e., extremely high pressures from measurements up to 700 bar, cannot be justified because of the possibility of a sharp discontinuity in the  $\rho - P$  curve at higher pressures (14).

It was observed that  $\rho$  of both silver oxides changed with time after a specified constant pressure was reached. The resistivity behavior of the two silver oxides was opposite and  $\rho$  of AgO increased whereas  $\rho$  of Ag<sub>2</sub>O decreased with time. The largest change occurred within the first minute of the measurement (10% increase for AgO and 3X decrease for Ag<sub>2</sub>O) and certain constant  $\rho$  values were approached asymptotically at the end of an hour long measurement (additional 10% increase for AgO and 1.8X decrease for Ag<sub>2</sub>O in 59 min). The time required to reach a constant  $\rho$  decreased with decreasing AgO content of AgO samples or AgO — Ag<sub>2</sub>O physical mixtures; the transition between the aforementioned opposite  $\rho$ -time behaviors occurred at 10 and 5% Ag<sub>2</sub>O contents ( $\rho$  remained constant right from the beginning). In view of the time dependence of  $\rho$ , the pressure was uniformly raised in approx. 5 sec to the final value. The  $\rho$  values reported here represent  $\rho$  right after the specified pressure was reached. The asymptotic value of  $\rho$  could be equally or perhaps more significant than the reproducible  $\rho$  values reported in this paper; the later ones were preferred because of the speed ( $< 1$  min vs. 1 hr) and ease of measurement (maintenance of constant pressure over long period is not required). No efforts were made to elucidate the time dependence of  $\rho$ , which may be due to several factors (e.g. development of contacts between some of the particles, temperature rise due to compression, carrier concentration and mobility changes, etc).

$\rho$  as a function of AgO content.—X-ray diffraction analysis revealed that AgO samples of inherently low AgO content contained only AgO and Ag<sub>2</sub>O. During the discharge of AgO in alkaline batteries Ag<sub>2</sub>O forms. In view of the high resistivity of Ag<sub>2</sub>O, the resistivity of AgO samples and the active materials of battery plates should be influenced by the amount of Ag<sub>2</sub>O present. It can be seen in Fig. 2 that resistivity of AgO samples increases with decreasing AgO content. The regression line represents 122 samples, and the coefficient of correlation is low ( $R = 0.859$ ). The large solid circles represent the resistivity of AgO — Ag<sub>2</sub>O physical mixtures prepared by the thorough mixing of AgO (98.2%) and commercially available battery-grade Ag<sub>2</sub>O (Ames Chemical Work, Inc.). The close agreement of  $\rho$  with the other data support the x-ray evidence that an AgO sample of inherently low AgO content is a physical mixture of AgO and Ag<sub>2</sub>O. Ball-milling did not influence the resistivity of the physical mixtures. The influence of the high resistivity of Ag<sub>2</sub>O

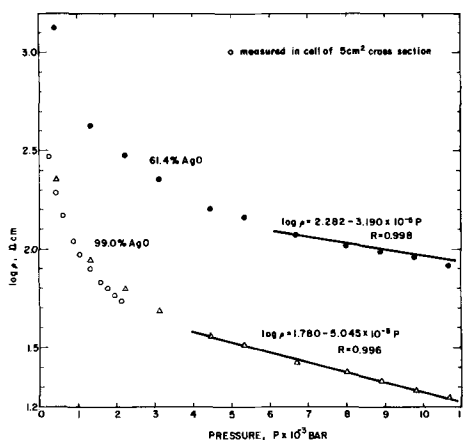


Fig. 1. Resistivity of AgO samples as a function of pressure

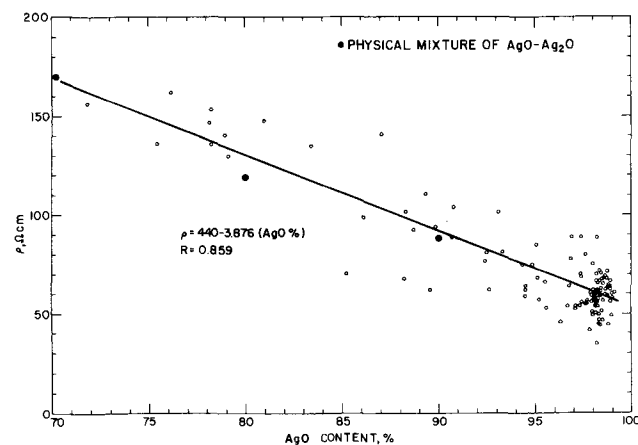


Fig. 2. Resistivity of chemically prepared AgO samples and physical mixtures of AgO — Ag<sub>2</sub>O as a function of AgO content.

on the resistivity of AgO — Ag<sub>2</sub>O physical mixtures became more apparent below 50% AgO and dominant below 20% AgO.

Table I shows the mean resistivity at 2.1 kbar and related statistical data of AgO samples at arbitrarily chosen AgO content levels. The majority of the usable ( $\geq 95.0\%$ ) AgO samples had an AgO content  $\geq 98.0\%$ . It can be seen that  $\bar{\rho}$  decreases with increasing mean AgO content according to  $\bar{\rho} = 435 - 3.819 (\text{AgO}\%)$  ( $R = 0.975$ ) which is similar to the regression line equation in Fig. 2. In view of the similarity of  $\rho$  values of Table I and Fig. 1 at 2.1 kbar (99.0% AgO) and resistivity behavior of AgO samples with pressure, it can be safely assumed that the  $\bar{\rho}$  values extrapolated to 12 kbar are comparable to the 14.3 ohm cm of Neiding and Kazarnovskii (8).

*Effect of inorganic additives.*—According to Yoshizawa and Takehara (10), the resistivity of AgO should decrease with the addition of metals of higher valency than I or II [this really should be I and III (5, 7)]. An investigation was undertaken to determine the effect of various impurities on the resistivity of chemically prepared AgO samples. Some elements are not suited for addition (inert gases, radioactive elements, etc), whereas salts of others were not available in commercial quantity, at the time, or have no effect (alkali metal ions are present during preparation). The investigated elements, in salt form, were added first at one concentration level, 1000 parts by weight per million parts of silver used for the preparation of AgO, i.e., 1000 ppm(Ag).

Results are presented in Tables II and III for the nontransition and transition elements, respectively. The transition elements in their broader definition (15) include also the coinage metals (Cu, Ag, Au) which have partly filled d or f shells in any of their commonly occurring oxidation states.

The AgO content should not decrease due to the addition of the aforementioned small amount of impurity unless the impurity is detrimental. The AgO contents of the samples with added nontransition elements vary slightly, but all are  $\geq 96.0\%$ . The samples made in the presence of transition elements have, in general,

Table I. Mean resistivity and related statistical data of AgO samples at 2.1 kbar

AgO content, %	No. of samples	Mean		Standard deviation	
		AgO content, %	$\rho$ , ohm cm	AgO content, %	$\rho$ , ohm cm
$\geq 95.0$	89	97.98	60.44	0.96	9.99
$\geq 98.0$	63	98.40	59.31	0.45	8.43
$\geq 99.0$	5	99.02	56.41	0.06	4.84

Table II. Effect of nontransition element impurities (added as compounds) on the AgO content and electric resistivity of AgO samples

Periodic Table group	Additive, 1000 ppm (Ag)	AgO content, %	$\rho$ , ohm cm at 2.1 kbar
—	—	$\geq 98.0$	$\bar{\rho} = 59.3$
II A	Be	97.5	56.7
	Mg	97.4	87.7
	Ca	98.2	103
	Sr	97.8	50.7
	Ba	97.4	50.4
II B	Zn	98.4	57.5
	Cd	97.7	346
	Hg	97.5	9.12
III	Al	98.5	54.5
	In	97.1	125
	Tl	96.0	64.3
IV	Si	97.8	78.9
	Ge	98.3	38.2
	Sn	97.2	10.7
	Pb	98.5	6.94
	As	98.3	43.8
V	Sb	96.8	23.1
	Bi	98.4	51.2
VI	Se	97.6	58.1
	Te	98.2	68.8

Table III. Effect of transition element impurities (added as compounds) on the AgO content and electric resistivity of AgO samples

Transition element	Additive, 1000 ppm (Ag)	AgO content, %	$\rho$ , ohm cm at 2.1 kbar	
First series	—	$\geq 98.0$	$\bar{\rho} = 59.3$	
	V	96.0	58.5	
	Cr	97.7	63.0	
	Mn	95.3	62.6	
	Fe	96.0	36.2	
	Co	37.7	416,000	
	Ni	38.0	34,500	
	Cu	97.3	68.2	
	Second series	Y	96.5	104
		Zr	88.0	33.4
Mo		98.5	40.8	
Pd		97.3	86.4	
Ta		92.2	59.4	
Third series	W	98.5	53.4	
	Ce	95.7	61.3	
	Pr	96.9	38.3	
Lanthanides	Eu	97.5	57.6	
	Th	96.7	58.7	
Actinides	—	—	—	

slightly lower AgO contents. Low AgO contents ( $\sim 90\%$ ) were obtained in the presence of Zr and Ta, and Co and Ni drastically reduced the AgO content to 38%. This AgO content shows up in the high resistivity of the two, latter mentioned samples. The addition of Mg, Ca, Cd, In, Si, Y, and Pd resulted in AgO samples of higher resistivity whereas Hg, Ge, Sn, Pb, As, Sb, and Bi (mainly at larger concentrations) yielded samples of lower resistivity. The resistivity of AgO samples with group IV elements seems to decrease with increasing atomic number. It is interesting to note that all beneficial additives have a IV and V valence (in their oxidized state) with the exception of Hg. Tables II and III show that In and Cu increased the resistivity of chemically precipitated AgO samples in contradiction with Yoshizawa and Takehara (10); in the case of Pb and Sn, however, the results of the present study support their claim.

$\rho$  as a function of additive concentration.—In view of the aforesaid beneficial and detrimental effects of the additives, it was of interest to determine the effect of additive concentration. The quantity of NaOH and K<sub>2</sub>S<sub>2</sub>O<sub>8</sub> was maintained constant (13) in these experiments, but the amount of AgNO<sub>3</sub> was decreased at higher additive concentrations to keep the reaction product to about 72g. Metal nitrates were preferentially added to the AgNO<sub>3</sub> solution, but Na<sub>2</sub>SnO<sub>3</sub>, GeO<sub>2</sub>, Na<sub>2</sub>SiO<sub>3</sub>, Na<sub>2</sub>HAsO<sub>4</sub>, Sb<sub>2</sub>O<sub>3</sub>, H<sub>2</sub>SeO<sub>3</sub>, and Na<sub>2</sub>TeO<sub>3</sub> were added to the alkaline K<sub>2</sub>S<sub>2</sub>O<sub>8</sub> medium.

Figure 3 shows the resistivity of AgO as a function of additive concentration. This concentration represents the metal content used in the preparation of AgO and does not necessarily correspond to the added metal content of the sample. It can be seen that the resistivity of the samples varies over 7 orders of magnitude, and the  $\rho$ -concentration curves form three distinct groups.

Ni, Cd, Mg, Be, and Te detrimentally affected the resistivity. Ni and Co (Table III) were detrimental already at very small concentrations and samples of low AgO contents were obtained. This can be seen very clearly in Fig. 4 which shows the AgO content of the samples as a function of the additive concentration. V up to  $2 \times 10^5$  ppm(Ag) concentration, did not influence the resistivity and the AgO content of the samples. It is very likely that soluble meta-vanadates formed on the addition of V<sub>2</sub>O<sub>5</sub> to the alkaline persulfate which were subsequently washed out from the AgO precipitate. Cr and Mn [1000 ppm(Ag)] did not influence the aforementioned properties to any significant degree because they were oxidized to soluble chromate and permanganate, respectively, by the alkaline persulfate as judged by the yellowish and red-wine colored mother liquors obtained.

Cd, which was found to replace Ag<sup>++</sup> (16), increased  $\rho$  already at small concentrations without detrimentally

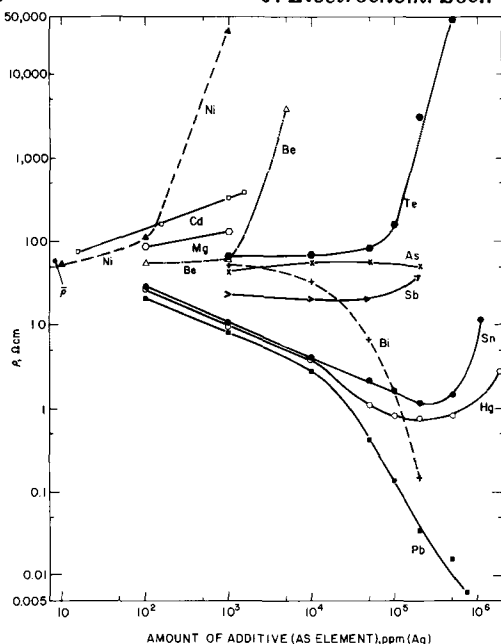


Fig. 3. Resistivity of AgO samples with additives which were intentionally added in various amounts during their preparation.

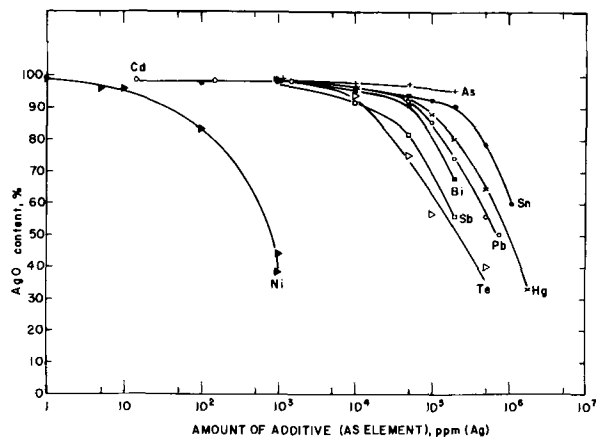


Fig. 4. AgO content of AgO samples as a function of additive concentration.

affecting the AgO content. At higher additive concentrations the AgO content of the samples, in general, decreased because the amount of silver nitrate used was decreased; the decrease of the AgO content is larger if the additive is detrimental (Fig. 4). Cadmium hydroxide was detected by x-ray diffraction in samples of higher Cd content.

The resistivity was slightly increased by the addition of Mg and Be in the  $10^3$  to  $10^4$  ppm(Ag) range; Be above this concentration increased  $\rho$  considerably. X-ray diffraction patterns of AgO samples with higher Be additions showed AgO present along with unidentified peaks.

The oxidation of  $\text{Ag}^+$  in the presence of  $\text{TeO}_2$  and NaOH by  $\text{K}_2\text{S}_2\text{O}_8$  yields a tellurate complex (5, 6, 15) with stabilized trivalent silver. The resistivity of samples with Te increased slowly up to  $10^5$  ppm(Ag) and rapidly above this concentration. X-ray diffraction patterns revealed the presence of AgO and a Te compound (not listed in ASTM file) in samples with  $10^4$  to  $2 \times 10^5$  ppm(Ag) Te added. Samples containing  $5 \times 10^5$  ppm(Ag) or more Te gave an x-ray diffraction pattern which had no AgO peaks and was different from the aforementioned pattern. No effort was made to identify these compounds.

AgO samples with 1000 ppm(Ag) Fe, Zr, Mo, Pr, Ge, As, or Sb have resistivities between 20 to 45 ohm cm. These additives form a transition between the detri-

mental and beneficial additives. Only As and Sb were studied as a function of concentration. In the case of As,  $\rho$  remained almost unchanged up to  $2 \times 10^5$  ppm(Ag) As concentration (52.1 ohm cm) and the AgO content decreased only to 95.3%. This and the obtained yields show that little or no As was incorporated into the AgO sample. When Sb or Bi were added, the product yield was greater than the anticipated yield for AgO. X-ray diffraction patterns showed AgO present as well as unidentified peaks in the aforementioned two series of samples. No values in the ASTM file corresponded to these peaks, and no attempt was made to identify these and other unknown compounds by analytical methods.

The resistivity of Sb-containing AgO samples changes little as a function of concentration. In contrast, the resistivity of samples with more than 1000 ppm(Ag) Bi, decreased rapidly to 0.148 ohm cm at  $2 \times 10^5$  ppm(Ag) in spite of a concomitant AgO content decrease.

Pb, Sn, and Hg markedly decreased the resistivity already at  $10^2$  ppm(Ag) concentration (Fig. 3). In the presence of Pb,  $\rho$  steadily decreased whereas  $\rho$  went through a minimum in the presence of Sn and Hg. Figure 5 shows  $\rho$  as a function of additive content which was determined by chemical analysis and is expressed in gram atomic weight (GAW) of elemental additive per gram atomic weight of silver present in the sample. The behavior of  $\rho$  is similar to that shown in Fig. 3. The comparison of the tin content of the AgO samples,  $c$ , with the amount of tin added during their preparation,  $c_a$ , however, revealed that much (82-92%) of tin added did not precipitate with the product; the  $c/c_a$  ratio decreased with increasing  $c_a$ . X-ray diffraction patterns of AgO samples containing tin at high concentrations showed the presence of  $\text{Ag}_2\text{O}$  which could account for the increase of  $\rho$ .

In view of the similarity of the structural dimensions of AgO ( $a_o = 5.85\text{\AA}$ ,  $b_o = 3.47\text{\AA}$ ,  $c_o = 5.49\text{\AA}$ ,  $\beta = 107^\circ 30'$ ) and HgO ( $a_o = 6.60\text{\AA}$ ,  $c_o = 3.52\text{\AA}$ ,  $b_o = 5.52\text{\AA}$ ,  $\beta = 90^\circ$ ), it is expected that  $\text{Hg}^{++}$  can replace some of the silver ions in the lattice, and influence the properties of the resulting AgO. The x-ray pattern of AgO was gradually distorted with increasing Hg content until it became identical with the HgO pattern at  $1.86 \times 10^6$  ppm(Ag) Hg indicating the replacement of Ag by Hg in the lattice.

The resistivities of physical mixtures of HgO and AgO (ball-milled) were also measured and are shown

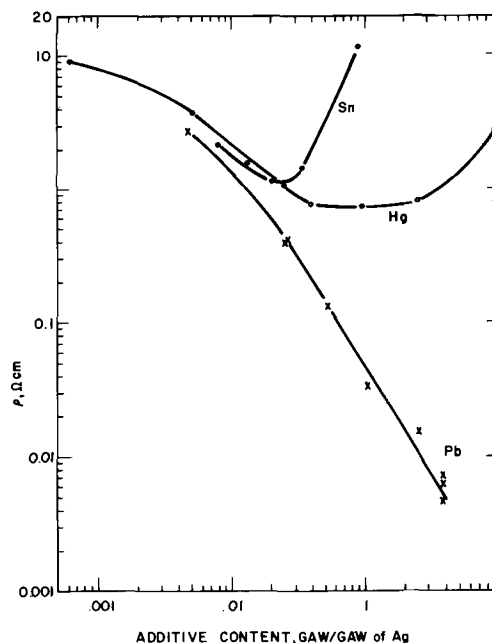


Fig. 5. Resistivity of AgO samples as a function of their additive content.

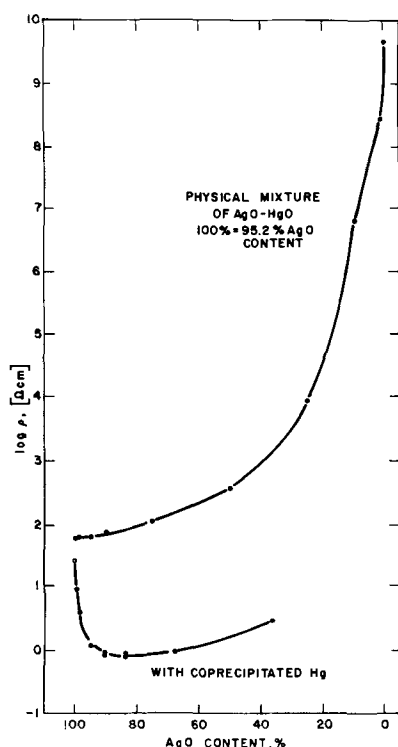


Fig. 6. Resistivity of physical mixtures of AgO—HgO and AgO samples with coprecipitated Hg.

in Fig. 6. It can be clearly seen that  $\rho$  increased in the physical mixtures steadily with increasing HgO content due to the very high resistivity of HgO. In contrast, the resistivity of the coprecipitated oxides decreased to a minimum and then increased with increasing Hg content (expressed as HgO content in Fig. 6). This supports the x-ray evidence for the incorporation of Hg in the lattice.

The resistivity of AgO samples continuously decreased with increasing elemental Pb content (Fig. 5) in the investigated range in contrast to samples containing Sn and Hg. Seemingly, the low resistivity of PbO<sub>2</sub> [as low as  $4 \times 10^{-5}$  ohm cm (17)] and high resistivity of tin oxides [ $\cong 10^4$  ohm cm (3)] and HgO (Fig. 6) could explain the aforementioned behavior. The lowest measured resistivities correspond to samples for which Pb was added in a ratio of the silver plumbate formula, Ag<sub>5</sub>Pb<sub>2</sub>O<sub>6</sub>. This was hydrothermally synthesized by Byström and Evers (18) from a mixture of Ag<sub>2</sub>O and PbO<sub>2</sub>, and its chemical essay is shown in Table IV. It can be seen that the experimental values of Byström and Evers agree well with the calculated percentages. In our case (average of 3 samples), the Ag and Pb contents are slightly lower but the available oxygen is approximately 3X larger than the calculated values for Ag<sub>5</sub>Pb<sub>2</sub>O<sub>6</sub>. The latter implies that some of the silver atoms are present in higher than monovalent state; the Pb atoms are said to be in tetravalent state (18). The x-ray diffraction patterns of these AgO samples showed an increase of the pattern of Ag<sub>5</sub>Pb<sub>2</sub>O<sub>6</sub>. It is, however, possible that the samples with various Pb contents form a mixed oxide phase of varying composition.

Table IV. Chemical analyses of AgO samples with Pb added in the ratio of formula Ag<sub>5</sub>Pb<sub>2</sub>O<sub>6</sub>

Content, %	Calculated for Ag <sub>5</sub> Pb <sub>2</sub> O <sub>6</sub>	Experimental	
		Byström and Evers (18)	Present study
Ag	51.39	51.0 ± 0.5	50.4 ± 0.5
Pb	39.44	39.0 ± 0.5	37.5 ± 0.45
Available O (peroxide)	2.29	2.32 ± 0.02	6.50 ± 0.09

Table V. Influence of Hg, Pb, Sn, and Ge in binary mixtures on the resistivity of AgO samples

Hg	Elements added, ppm (Ag)		Ge	AgO content, %	$\rho$ , ohm cm
	Pb	Sn			
1000	—	—	—	97.5	9.12
500	500	—	—	98.0	5.58
500	—	500	—	98.2	7.87
500	—	—	500	97.5	10.7
—	1000	—	—	98.5	6.95
—	500	—	500	98.4	7.41

*Influence of additives in binary mixtures.*—It was of interest to see the influence of two jointly added beneficial additives on the resistivity of AgO samples. Table V shows the effect of Hg, Pb, Sn, and Ge in mixtures of equal weight ratios. When part of Hg was replaced by Pb or Sn,  $\rho$  decreased, but increased with Ge. When half of Pb was replaced by Hg,  $\rho$  slightly decreased, and the replacement by Sn or Ge had no effect or slightly increased the resistivity. Thus, it can be said that the nature of the additives and their concentration affect the resistivity of AgO samples regardless whether they are used alone or in mixtures.

*Discharge of AgO-Zn cells with additives.*—Cahan *et al.* (4, 12) showed that the addition of PbO to the AgO in the cathode mix enhances the discharge of AgO at its higher voltage plateau. Therefore, it was of interest to discharge these AgO samples in cells (Ray-O-Vac 675 size). Figure 7 shows the discharge voltage of cells with various amounts of Pb added to the AgO during its preparation; cells were discharged continuously at 770 ohms (ca. 2 ma). It can be seen that the length of the higher voltage plateau, *i.e.*, the capacity to 1.6v, increases and the lower voltage plateau, concomitantly decreases and eventually disappears with the increasing amount of Pb added. The cell capacity decreased when the amount of Pb is increased from  $5 \times 10^4$  to  $10^5$  ppm (Ag). The optimum Pb amount seems to be between  $10^4$  and  $5 \times 10^4$  ppm (Ag). In view of the resistivity decrease of AgO samples with Pb content (Fig. 5), it was of no surprise that the flash amperage of the cell increased about three times (0.12-0.42 amp) and the cell impedance (at 60 Hz) decreased (14.7-4.6 ohms) with increasing Pb content [up to  $10^5$  ppm (Ag)].

Figure 8 compares the discharge voltages of cells containing AgO with  $5 \times 10^4$  ppm (Ag) coprecipitated Pb and 5% admixed PbO, respectively. It is obvious that the cells with PbO are superior to those containing AgO with coprecipitated Pb. The flash amperage and the impedance (60 Hz) of cells with admixed PbO were superior (0.56 amp, 2.6 ohms) to those with coprecipitated Pb (0.33 amp, 4.5 ohms). The improvement seems to be caused by a surface coating of a Pb-Ag compound [likely silver plumbate (12)] formed slowly in contact with alkaline electrolyte.

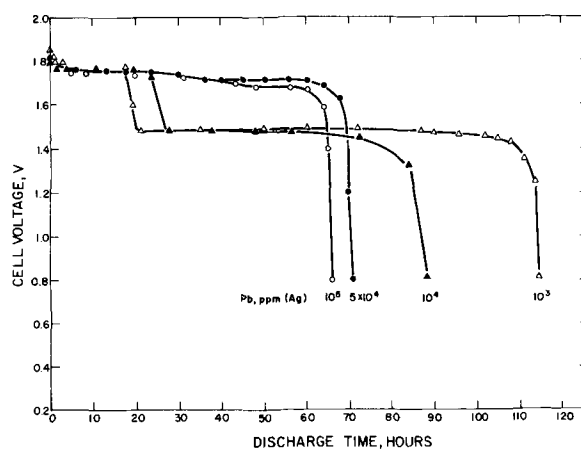


Fig. 7. Discharge voltage of AgO—Zn cells (Ray-O-Vac 675 size, discharged continuously at 770 ohms, ca. 2 ma) with various amounts of Pb added to AgO during its preparation.

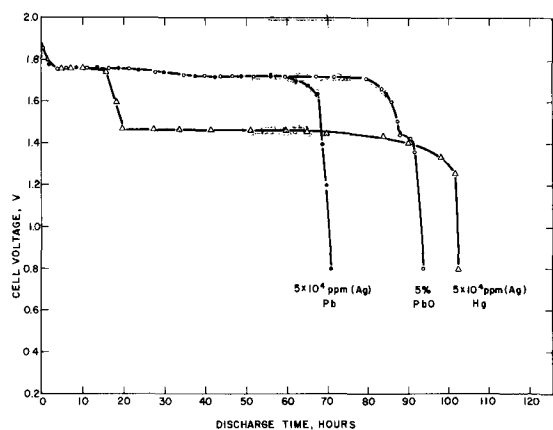


Fig. 8. Discharge voltage of AgO—Zn cells (Ray-O-Vac 675 size, discharged continuously at 770 ohms, ca. 2 ma) with AgO containing coprecipitated Pb, Hg, or admixed PbO.

It was shown earlier (Fig. 3, 5) that the resistivity of AgO samples containing Hg up to  $5 \times 10^4$  ppm(Ag) concentrations is only slightly higher than  $\rho$  of AgO samples with Pb. Figure 8 clearly shows that cells made with AgO containing  $5 \times 10^4$  ppm(Ag) Hg are inferior to cells with Pb added by either method and in any amount. This shows that the low resistivity of AgO samples alone is not sufficient to obtain a large capacity at the higher voltage plateau of AgO. No attempt was made to elucidate the cause of the aforementioned phenomena.

### Summary

The electric resistivity of powder AgO samples was measured *in situ* up to 10 kbar. The AgO samples were made by chemical oxidation of  $\text{AgNO}_3$  (13) in the absence or presence of intentionally added metal additives (as compounds). Log  $\rho$  was found to decrease linearly with pressure after its initial rapid decrease at lower pressures regardless of the AgO content of samples (Fig. 1). The resistivity of AgO samples increased linearly with decreasing AgO content (> 70%). 63 AgO samples of 98.4% mean AgO content had a mean resistivity of 59.3 ohm cm at 2.1 kbar.  $\rho$  is 14.6 ohm cm at 12 kbar which compares very favorably with 14.3 ohm cm  $\pm$  15% of Neiding and Kazarnovskii (8).

The AgO content of samples made in the presence of 1000 ppm(Ag) elemental additive (1000 ppm parts Ag) did not change noticeably with the exception of Zr, Ta (90%) and Co, Ni (38%). The addition of Mg, Ca, Cd, In, Si, Y, Pd, Ni, or Co yielded AgO samples of higher resistivity whereas the addition of Hg, Ge, Sn, Pb, As, Sb, or Bi (mainly at higher concentrations) gave samples of lower resistivity than the mean AgO resistivity. The resistivity of samples continuously decreased with increasing Pb and Bi concentration. In the presence of increasing Sn and Hg contents  $\rho$  first decreased, then went through a minimum and increased

rapidly. All the beneficial additives have four and five valence in their oxidized state with the exception of Hg. The nature of the additives and their concentration affect the resistivity of AgO samples regardless whether they are used alone or in mixture.

The continuous discharge of AgO samples in Ray-O-Vac 675 size cells at 770 ohms (ca. 2 ma) showed that the length of higher voltage plateau increased with increasing Pb content of the sample. Cells with admixed PbO were found to be superior to those with coprecipitated Pb. Cells with Hg were inferior to those with Pb in any amount.

### Acknowledgment

The author wishes to thank Dr. R. A. Schaefer for permission to publish this paper and Messrs. C. J. Venuto and H. Wilson for the x-ray and analytical data.

Manuscript submitted May 15, 1968; revised manuscript received ca. July 15, 1968. This paper was presented at the Montreal Meeting, Oct. 6-11, 1968, as Paper 371.

Any discussion of this paper will appear in a Discussion Section to be published in the June 1969 JOURNAL.

### REFERENCES

1. P. Weidenthaler, *Collec. Czechoslov. Chem. Commun.*, **26**, 2587 (1961).
2. E. Fortin and F. L. Weichman, *Phys. Stat. Sol.*, **5**, 515 (1964).
3. M. LeBlanc and H. Sachse, *Physik. Z.*, **32**, 887 (1931).
4. B. D. Cahan, J. B. Ockerman, R. F. Amlie, and P. Rüetschi, *This Journal*, **107**, 725 (1960).
5. J. A. McMillan, *Chem. Revs.*, **62**, 65 (1962).
6. Priyadarajan Ray and Debabrata Sen, "Chemistry of Bi- and Tripositive Silver," National Institute of Sciences of India, Monograph, New Delhi (1960).
7. V. Scatturin, P. L. Bellon, and A. J. Salkind, *This Journal*, **108**, 819 (1961).
8. A. B. Neiding and I. A. Kazarnovskii, *Doklady Akad. Nauk SSSR*, **78**, 713 (1951).
9. P. Jones and H. R. Thirsk, *Trans. Faraday Soc.*, **50**, 732 (1954).
10. S. Yoshizawa and Z. Takehara, *J. Electrochem. Soc. Japan*, **31**, 91 (1963).
11. S. P. Mitoff, *Prog. Ceramic Soc.*, **4**, 217 (1966).
12. B. D. Cahan, U. S. Pat. 3,017,448, Jan. 16, 1962.
13. R. N. Hammer and J. Kleinberg, "Inorganic Syntheses," Vol. IV., p. 12, McGraw-Hill Book Co., New York (1953).
14. H. G. Drickamer in "Solid State Physics," Vol. 17, F. Seitz and D. Turnbull, Editors, Academic Press, New York (1965).
15. F. A. Cotton and G. Wilkinson, "Advanced Inorganic Chemistry," Interscience Publishers, New York (1962).
16. J. Selbin and M. Usategui, *J. Inorg. Nucl. Chem.*, **20**, 91 (1961).
17. "The Encyclopedia of Electrochemistry", C. A. Hampel, Editor, p. 763, Rheinhold Publishing Co., New York (1964).
18. A. Byström and L. Evers, *Acta. Chem. Scan.*, **4**, 613 (1950).



# The Active Iron Electrode

## II. Anion Adsorption and Its Effects on the Iron Dissolution and Hydrogen Evolution Reactions

Eugene J. Kelly\*

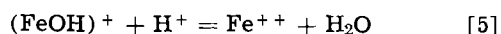
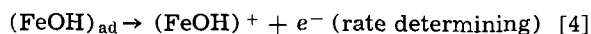
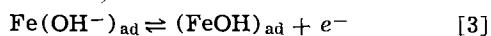
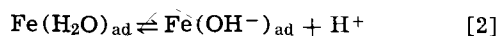
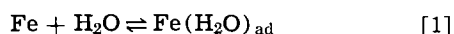
Chemistry Division, Oak Ridge National Laboratory, Oak Ridge, Tennessee

### ABSTRACT

The kinetics of adsorption/desorption of an anion inhibitor on zone-refined iron in the active state and the effects of the adsorbed inhibitor on the iron dissolution and hydrogen evolution reactions have been determined by means of quantitative analyses of "instantaneous," transient, and steady-state anodic and cathodic electrochemical polarization data. The mechanism proposed for iron dissolution in the inhibited system involves formation of an electrochemically active surface intermediate from the adsorbed anion and  $(\text{FeOH})_{\text{ad}}$ . On the other hand, the adsorbed anion accelerates the hydrogen evolution reaction, and this is attributed to a  $\psi$ -effect, i.e., to a double-layer effect and to a simultaneous diminution in the standard chemical free energy of activation for proton discharge. Of particular interest with regard to the hydrogen evolution reaction is the fact that, at constant solution composition,  $(\partial \log i_c / \partial E)_\theta = 1/S$ , where  $S$  is a constant the magnitude of which is a function of  $\theta$  and, consequently, the measurement of which enables the indirect evaluation of  $\theta$ .

A comparative study has been made of the electrochemical behavior of the active iron electrode in typical inhibiting and noninhibiting media. The purpose of the investigation was to examine the changes produced in the kinetics and mechanistics of a non-inhibited system as a result of specific adsorption of an anion inhibitor. Such information is not only essential to the understanding of corrosion inhibition, but is also relevant to the interpretation of kinetic data for other electrode processes involving adsorption.

The first paper in this series (1) reported on the iron dissolution and hydrogen evolution reactions for zone-refined iron in hydrogen-saturated, acidic sulfate solutions (hereafter referred to as the noninhibited system). It was shown that the steady-state iron dissolution reaction is characterized by an anodic Tafel slope of  $(2/3)(2.303 RT/F)$ , i.e., 40 mv/decade, and a first order dependency on the hydroxyl ion activity. These results were interpreted in terms of the following mechanism, which takes formal account



of the simultaneous coverage of the electrode surface by adsorbed water molecules, hydroxyl ions, and the surface intermediate,  $(\text{FeOH})_{\text{ad}}$ . The kinetic description of this mechanism is given by Eq. [6]-[9], in which

$$i_a/F = \bar{k}_3\theta_2 - \bar{k}_{-3}\theta_3 + \bar{k}_4\theta_3 \quad [6]$$

$$\beta d\theta_1/dt = \bar{k}_1(1 - \theta_T) - \bar{k}_{-1}\theta_1 - \bar{k}_2\theta_1 + \bar{k}_{-2}a_{(\text{H}^+)}\theta_2 \quad [7]$$

$$\beta d\theta_2/dt = \bar{k}_2\theta_1 - \bar{k}_{-2}a_{(\text{H}^+)}\theta_2 - \bar{k}_3\theta_2 + \bar{k}_{-3}\theta_3 \quad [8]$$

$$\beta d\theta_3/dt = \bar{k}_3\theta_2 - \bar{k}_{-3}\theta_3 - \bar{k}_4\theta_3 \quad [9]$$

$i_a$  is the net anodic current density,  $\bar{k}_j$  are electrochemical rate constants, and  $\theta_1$ ,  $\theta_2$ , and  $\theta_3$  represent the fractions of the total possible adsorption sites occupied by  $\text{Fe}(\text{H}_2\text{O})_{\text{ad}}$ ,  $\text{Fe}(\text{OH}^-)_{\text{ad}}$ , and  $(\text{FeOH})_{\text{ad}}$ , respectively, i.e.,

$$\begin{aligned} [\text{Fe}(\text{H}_2\text{O})_{\text{ad}}] &= \beta\theta_1, & [\text{Fe}(\text{OH}^-)_{\text{ad}}] &= \beta\theta_2, \\ [(\text{FeOH})_{\text{ad}}] &= \beta\theta_3 \end{aligned}$$

where the surface concentrations are expressed in mole/cm<sup>2</sup>, and  $\beta$  is a proportionality constant. The total fraction of sites occupied,  $\theta_T$ , is equal to  $(\theta_1 + \theta_2 + \theta_3)$ , and the other symbols have their conventional significance. It was shown that Eq. [6]-[9] reduce to the steady-state solution,

$$i_{a,\infty} = 2Fk_4 \frac{k_3k_2}{k_{-3}k_{-2}a_{(\text{H}^+)}} \left( \frac{k_1}{k_1 + k_{-1}} \right) \exp(3FE/2RT) \quad [10]$$

where  $E$  is the potential of the iron electrode relative to a reference electrode. Equation [10] fully describes the experimental results. The conditions leading to Eq. [10] are  $\bar{k}_{-3} \gg \bar{k}_4$ ,  $\bar{k}_{-2} a_{(\text{H}^+)} \gg \bar{k}_3/\bar{k}_{-3}$ , and  $\bar{k}_{-2} a_{(\text{H}^+)}$ ,  $(\bar{k}_1 + \bar{k}_{-1}) \gg \bar{k}_2 \{ \bar{k}_1 [1 + (\bar{k}_3/\bar{k}_{-3})] + \bar{k}_3\bar{k}_4/\bar{k}_{-3} \}$ . The latter condition means that  $1 \gg (\theta_2 + \theta_3)$  and, consequently, if  $\theta_T \approx 1$ , then  $\theta_1 \approx 1$ , i.e.,  $\bar{k}_1/(\bar{k}_1 + \bar{k}_{-1}) \approx 1$ .

The rate-determining step in the hydrogen evolution reaction on zone-refined iron in the noninhibited system has been shown to be slow proton discharge (1),  $\text{H}^+ + e^- \rightarrow \text{H}_{\text{ad}}$ , with a corresponding steady-state cathodic Tafel slope of  $-120$  mv/decade, i.e.,  $-2(2.303 RT/F)$ , and a first order dependency on the proton activity in solution, i.e.,

$$i_{c,\infty} = k_c a_{(\text{H}^+)} \exp(-FE/2RT) \quad [11]$$

where  $i_{c,\infty}$  is the absolute value of the steady-state current density corresponding to the hydrogen evolution reaction. Evidence favoring removal of  $\text{H}_{\text{ad}}$  via fast electrochemical desorption,  $\text{H}^+ + \text{H}_{\text{ad}} + e^- \rightarrow \text{H}_2$ , for zone-refined iron, and via catalytic desorption,  $2\text{H}_{\text{ad}} \rightarrow \text{H}_2$ , for Armco iron was discussed in detail.

The mechanisms described above serve as the experimental and mechanistic base for the analysis of the electrochemical behavior of the active iron electrode in an inhibited system. The present paper reports on the results obtained for the iron dissolution and hydrogen evolution reactions on zone-refined iron in hydrogen-saturated sodium benzoate solutions (hereafter referred to as the inhibited system). Transient and steady-state potentiostatic polarization data are analyzed and related to the adsorption/desorption kinetics and the potential-dependent steady-state adsorption isotherm for the benzoate anion; to the changes introduced into the iron dissolution mechanism, Eq. [1]-[5], as a result of the adsorbed inhibitor; and, of particular interest, to the double-

\* Electrochemical Society Active Member.  
<sup>1</sup> Operated by Union Carbide Corporation for the U. S. Atomic Energy Commission.

layer effect of the anion on the proton discharge reaction.

In many respects, the benzoate anion is an ideal anion for the studies described herein. It possesses no redox properties of its own under the conditions employed here. Its buffering action extends the current density region of activation control for the hydrogen evolution reaction, at a given pH, and enables the study of potentiostatic current/time transients over long periods of time without pH change. It may be obtained in a state of high purity and may easily be further purified by recrystallization. Its one relatively minor drawback arises from the relative insolubility of benzoic acid, coupled with an ionization constant of  $6.30 \times 10^{-5}$ . If one insists on excluding other ions as an inert electrolyte while maintaining a reasonably high ionic strength in order to suppress the potential drop in the diffuse part of the double layer, then these factors restrict the studies to the pH region in the vicinity of 5.0.

### Experimental

The experimental apparatus and techniques, as well as the composition of the zone-refined iron, have been described elsewhere in detail (1) and, therefore, only a brief resume is given here. In order to preclude contamination problems, the entire cell assembly was made of Pyrex glass and Teflon, and was so designed that essential operations, such as the addition of hydrogen-saturated pre-electrolyzed solutions, could be accomplished without opening the apparatus to the atmosphere. This latter feature was of particular importance in view of the extreme sensitivity of the iron/benzoate system to oxygen. Similarly, the pronounced effect of temperature variations on the inhibited system, in contrast to the noninhibited system, added significance to the maintenance of a constant solution temperature,  $25.00^\circ \pm 0.02^\circ\text{C}$ .

Sodium benzoate solutions were prepared from reagent grade materials, benzoic acid (recrystallized) and sodium hydroxide, and triply distilled water, and were pre-electrolyzed at an iron cathode. The saturated calomel electrode and the counter electrode were located in separate compartments from the test electrode, and a continuous stream of hydrogen was maintained throughout the assembly at all times. The hydrogen source was a Matheson generator which produces ultrapure gas via diffusion of electrolytically generated hydrogen through a palladium membrane. Additional stirring in the test compartment was achieved with a Teflon-coated magnetic stirrer.

Potentials were measured with a high impedance Beckman Research Model pH meter and recorded with a 10 mv Brown recorder. An O.R.N.L. Model Q-2003 Potentiostat was employed, the currents being measured via the potential drop across precision resistors.

### Results

In order to acquaint the reader with various aspects of a rather complex system, a Tafel diagram of typical data is shown in Fig. 1. If an electrode, initially in a steady state at the corrosion potential,  $E_{\text{corr}}$ , is subjected to "fast" anodic or cathodic polarization, the curves marked  $i_{a,1}$  and  $i_{c,1}$ , respectively, are obtained.<sup>2</sup> These anodic and cathodic curves exhibit Tafel behavior, the slopes of the Tafel lines being 59 and  $-88$  mv/decade, respectively. The extrapolated Tafel lines intersect at  $E_{\text{corr}}$  and, thereby, locate the corrosion current density,  $i_{\text{corr}}$ .

If the potential is held constant at some point along  $i_{c,1}$ , one observes a potentiostatic current/time transient,  $i_{c,t}$ , in which the current decreases from its initial value on  $i_{c,1}$  to a steady-state value on  $i_{c,\infty}$ . A subsequent fast cathodic polarization then yields a new Tafel line,  $i_{c,2}$ , having a more negative slope than  $i_{c,1}$ . In fact, at any point along  $i_{c,t}$ , a fast cathodic po-

larization yields a Tafel line having a slope lying between those of  $i_{c,1}$  and  $i_{c,2}$ . At sufficiently negative potentials,  $i_{c,\infty}$  approaches a limiting Tafel line,  $i_H$ , which has the same slope as that observed for proton discharge in the noninhibiting system, i.e.,  $-2$  ( $2.303 RT/F$ ) mv/decade. If an electrode is initially in a polarized steady state, for example, at the intersection of  $i_{c,3}$  and  $i_{c,\infty}$ , and the potential is changed to a less negative cathodic value, the initial current, lying along  $i_{c,3}$ , will be less than the steady-state current and, consequently, one observes a potentiostatic current/time transient in which the absolute value of the cathodic current increases with time.

If, at some point along  $i_{a,1}$ , the potential is fixed, an anodic current/time transient is observed, in which the current increases from its initial value to the steady-state value on  $i_{a,\infty}$ , as shown, for example, by the vertical line,  $i_{a,t}$ . A subsequent fast anodic polarization results in a new Tafel line,  $i_{a,2}$ , which is parallel to  $i_{a,1}$ , the Tafel slope being  $2.303 RT/F$  or 59 mv/decade. If the potential is then fixed at a less anodic value than that associated with  $i_{a,t}$ , the current decreases with time from its initial value on  $i_{a,2}$  to the steady-state value on  $i_{a,\infty}$ . It should be noted that the steady-state anodic polarization curve does not exhibit Tafel behavior. By the application of arbitrary time intervals, one may obviously generate the polarization hysteresis loops, both anodic and cathodic, so frequently mentioned in the corrosion literature. In the following sections, the system just described is treated in a quantitative fashion.

**Hydrogen evolution reaction.**—In the inhibited system illustrated in Fig. 1, the cathodic current density, at constant solution composition, is a function not of just the electrode potential, as in the case of the noninhibited sulfate system, but also of the surface activity of the adsorbed inhibitor, i.e.

$$\ln i_c = f(\eta, \theta) \quad [12]$$

where  $\eta$  is the electrode polarization relative to the steady-state corrosion potential at constant solution composition, and  $\theta$  represents the fraction of the electrode surface occupied by the adsorbed inhibitor. At sufficiently negative potentials, the benzoate anion is completely desorbed and, consequently,  $i_{c,\infty} = i_H$ , i.e.,  $i_H$  is the cathodic current density corresponding to  $\theta = 0$ . The total differential of  $\ln i_c$  is given by Eq. [13]

$$d \ln i_c = \left( \frac{\partial \ln i_c}{\partial \eta} \right)_\theta d\eta + \left( \frac{\partial \ln i_c}{\partial \theta} \right)_\theta d\theta \quad [13]$$

where, in the most general case, both  $(\partial \ln i_c / \partial \eta)_\theta$  and

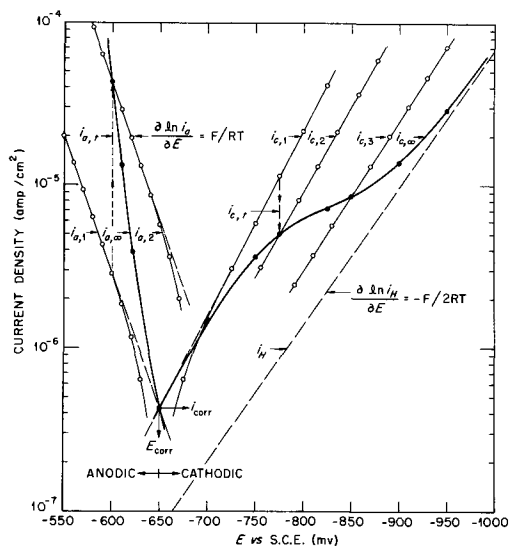


Fig. 1. Polarization of iron in 0.10M ( $\text{C}_6\text{H}_5\text{COOH} + \text{C}_6\text{H}_5\text{COONa}$ ); pH = 5.00;  $T = 25^\circ\text{C}$ .

<sup>2</sup> "Fast" here meaning on the order of a few seconds, as determined by the response time of the recorder ( $\sim 3$  sec full scale). In the noninhibited system, true steady states are attained within this time interval.

$(\partial \ln i_c / \partial \theta)_\eta$  may be functions of both  $\eta$  and  $\theta$ . In the present case, however,  $(\partial \ln i_c / \partial \eta)_\theta$  is a constant, the magnitude of which is a function of  $\theta$  only, i.e.,

$$\left( \frac{\partial \ln i_c}{\partial \eta} \right)_\theta = \frac{2.303}{S} \quad [14]$$

where  $S$ , a function of  $\theta$  only, represents the slope of a cathodic Tafel line resulting from a "fast" polarization, for which  $\theta$  remains essentially constant. As illustrated by the sequence of Tafel lines,  $(i_{c,1}, i_{c,2}, \dots, i_H)$  in Fig. 1,  $S$  becomes increasingly negative as  $\theta$  decreases, and ultimately attains the value of  $-2$  ( $2.303 RT/F$ ), i.e.,  $-118.24$  mv/decade, when  $\theta = 0$ . As  $\theta$  increases to its maximum value,  $\theta_m$ ,  $S$  approaches a limiting value of  $-88$  mv/decade. In Fig. 2, a "fast" cathodic Tafel line obtained for an electrode initially in a steady state at  $E = -0.800$  v vs. SCE is shown for the purpose of demonstrating the precision with which values of  $S$  may be determined. Since  $\partial(\partial \ln i_c / \partial \eta)_\theta / \partial \theta$  must equal  $\partial(\partial \ln i_c / \partial \theta)_\eta / \partial \eta$ , the result expressed by Eq. [14] enables one to write Eq. [15]

$$\left( \frac{\partial \ln i_c}{\partial \theta} \right)_\eta = -\frac{2.303}{S^2} \left( \frac{dS}{d\theta} \right) \eta + h(\theta) \quad [15]$$

where  $h(\theta)$ , i.e.,  $(\partial \ln i_c / \partial \theta)_\eta=0$ , is a potential-independent term for which the dependency on  $\theta$  remains to be considered below. If the expressions for the partial derivatives given by Eq. [14] and [15] are substituted into Eq. [13] integration of the latter leads to Eq. [16]

$$i_c = i_{c,\eta=0} \exp(2.303 \eta / S) \quad [16]$$

where  $i_{c,\eta=0}$  is equal to  $i_{H,\eta=0} \exp[\int_0^\theta h(\theta) d\theta]$ . Since  $i_H = i_{H,\eta=0} \exp(-F\eta/2RT)$ , Eq. [16] may be divided by  $i_H$  to obtain Eq. [17]

$$\frac{i_c}{i_H} = \left( \frac{i_c}{i_H} \right)_{\eta=0} \exp[2.303 (S + 118.24) \eta / 118.24 S] \quad [17]$$

Let the functional dependencies of  $(i_c/i_H)_{\eta=0}$  and  $S$  on  $\theta$  be represented by Eq. [18] and [19], respectively,

$$(i_c/i_H)_{\eta=0} = \exp(a\theta/\theta_m) \quad [18]$$

and

$$S = -118.24/[1 + b(\theta/\theta_m)] \quad [19]$$

where  $a$  and  $b$  are constants, the latter of which is equal to  $0.34363$  since  $S = -88$  mv/decade when  $\theta = \theta_m$ . The significance of Eq. [18] and [19] will be

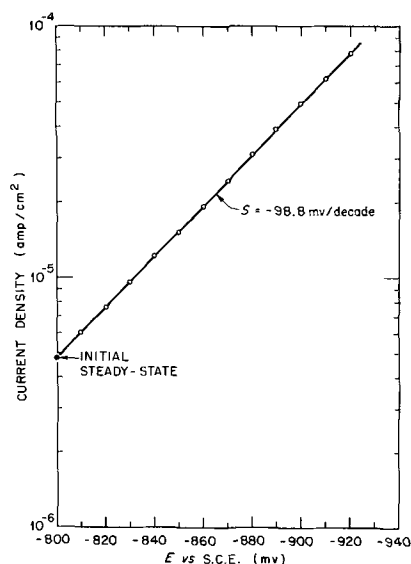


Fig. 2. "Fast" cathodic Tafel line for an electrode initially in a polarized steady state at  $E = -0.800$  v vs. SCE;  $0.10M$  ( $C_6H_5COOH + C_6H_5COONa$ );  $pH = 5.00$ ;  $T = 25^\circ C$ .

considered in the Discussion section, but it should be noted here that Eq. [18] identifies  $h(\theta)$  as a constant rather than as a function of  $\theta$ , i.e.,  $h(\theta) = a/\theta_m$ . If Eq. [19] is solved for  $\theta/\theta_m$  in terms of  $S$  and the results substituted into Eq. [18], the latter may be written in the form given by Eq. [20]

$$\log(i_c)_{\eta=0} = \log(i_H)_{\eta=0} - (S + 118.24) a/2.303 b S \quad [20]$$

However, according to Eq. [16]

$$\log(i_c)_{\eta=0} = \log i_c - \eta/S \quad [21]$$

and, therefore, one may subtract Eq. [21] from Eq. [20] to obtain Eq. [22]

$$\log i_c - (\eta/S) = \log(i_H)_{\eta=0} - (S + 118.24) a/2.303 b S \quad [22]$$

which shows that a plot of  $[\log i_c - (\eta/S)]$  vs.  $(S + 118.24)/S$  should result in a straight line having a slope of  $-(a/2.303 b)$ . Any set of corresponding  $i_c$ ,  $\eta$ , and  $S$  values may be used in testing Eq. [22]. For example, one might use values of  $S_x$  corresponding to points along the steady-state curve,  $i_{c,ss}$ , in Fig. 1. A test of data obtained in this manner is shown by the dashed curve in Fig. 3. Another convenient method is to determine the values of  $S$  corresponding to instantaneous values of  $i_c$  during a potentiostatic current/time transient by superimposing short potentiostatic pulses. Data obtained by this method are shown by the solid curve in Fig. 3. The linearity of the resulting curves provides confirmation of the validity of Eq. [22].

In view of the fact that  $S$  is a function of  $\theta$  only, one may determine the potential dependency of the steady-state coverage,  $\theta_{ss}$ , from the measured potential dependency of  $S_x$  and the relationship between  $S$  and  $\theta$ , i.e., Eq. [19]. In Fig. 4, measured values of  $S_x$  are plotted against  $\eta$ . If the steady-state coverage obeys a potential-dependent Langmuir type adsorption isotherm, i.e.,

$$(\theta_{ss}/\theta_m) = 1/[1 + K \exp(j\eta)] \quad [23]$$

then, according to Eq. [19]

$$S_x = -118.24/\{1 + 0.34363/[1 + K \exp(j\eta)]\} \quad [24]$$

This equation was used to calculate the solid curve shown in Fig. 4, where close agreement between the measured and calculated results is observed. The corresponding values of  $\theta_{ss}/\theta_m$  are plotted against  $\eta$  in Fig. 5. By means of Eq. [18] and [19], Eq. [17] may be written in terms of either  $\theta/\theta_m$  and  $\eta$  or  $S$  and  $\eta$ , i.e.,

$$i_c/i_H = \exp\{[a - (2.303 b\eta/118.24)](\theta/\theta_m)\} \quad [25]$$

or

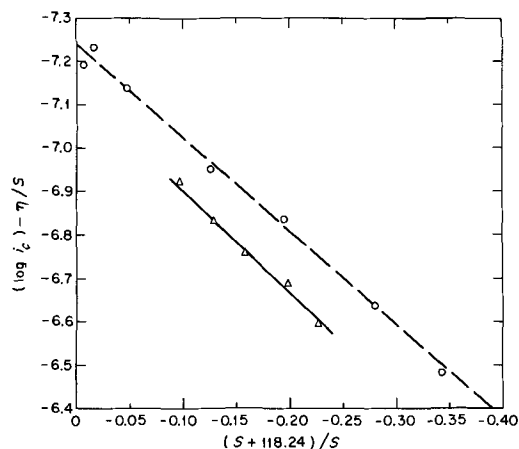


Fig. 3. Test of Eq. [22]: dashed line --  $i_{c,ss}$ ,  $S_{st}$ , and  $\eta$  values taken from Fig. 4 and 6; solid line —  $i_t$ ,  $S_t$  and  $\eta$  values observed during potentiostatic current/time transient at  $\eta = -200$  mv.  $0.10M$  ( $C_6H_5COOH + C_6H_5COONa$ );  $pH = 5.00$ ;  $T = 25^\circ C$ .

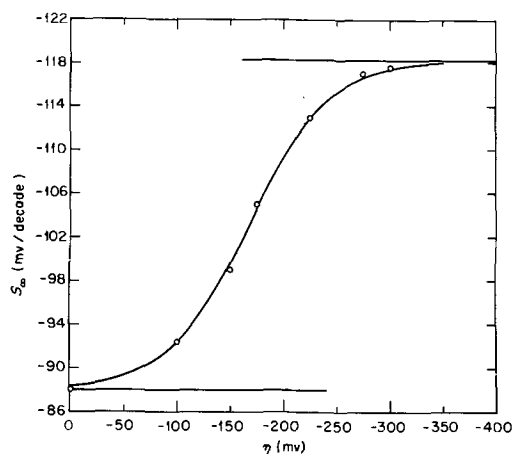


Fig. 4. Effect of potential on  $S_w$ . Solid curve calculated by means of Eq. [24]. 0.10M ( $C_6H_5COOH + C_6H_5COONa$ ); pH = 5.00,  $T = 25^\circ C$ .

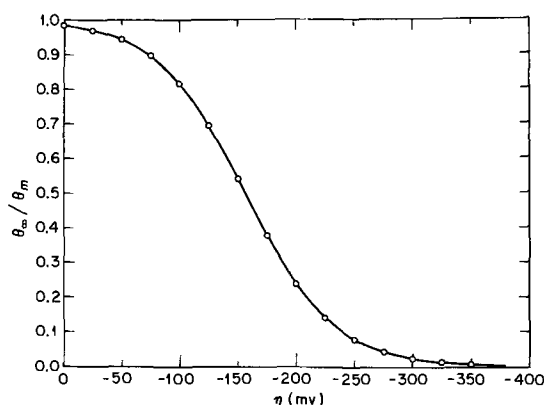


Fig. 5. Effect of potential on the steady-state coverage of the adsorbed inhibitor: curve calculated by means of Eq. [23], using the values of  $K$  and  $j$  corresponding to the solid curve of Fig. 4.

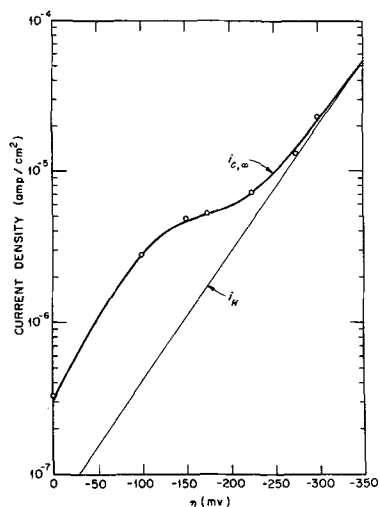


Fig. 6. Steady-state cathodic polarization curve for iron in 0.10M ( $C_6H_5COOH + C_6H_5COONa$ ); pH = 5.00,  $T = 25^\circ C$ . Solid curve calculated by means of either Eq. [25] with values of  $(\theta_w/\theta_m)$  and  $a$  taken from Fig. 5 and 3, respectively, or Eq. [26] with values of  $S$  and  $a$  taken from Fig. 4 and 3, respectively.

$$i_c/i_H = \exp \left\{ - \left[ \frac{a}{b} \right] - 2.303\eta/118.24 \right\} \left[ \frac{S + 118.24}{S} \right] \quad [26]$$

One may calculate the steady-state polarization curve using the values of  $\theta_w/\theta_m$  shown in Fig. 5 in Eq. [25], or by using the values of  $S_w$  shown in Fig. 4 in Eq. [26]. The results are shown in Fig. 6, where good

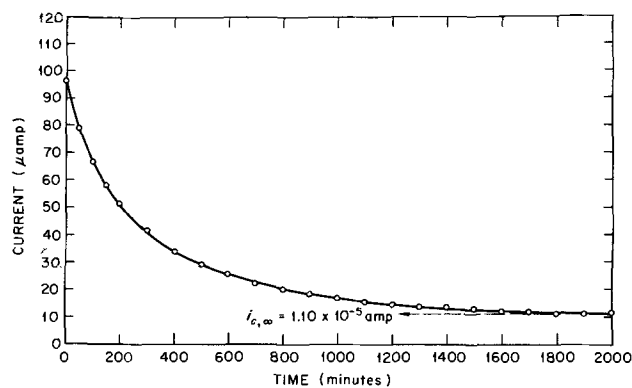


Fig. 7. Typical cathodic potentiostatic current/time transient. 0.10M ( $C_6H_5COOH + C_6H_5COONa$ ); pH = 4.88;  $T = 25^\circ C$ ; electrode apparent area = 1.346  $cm^2$ ;  $\eta = -210$  mv.

agreement between the experimental and calculated results is observed. Since the set of observed  $i_c$ ,  $\eta$ , and  $S$  values satisfies Eq. [26], it follows that it satisfies Eq. [22], and this is shown by the dashed curve in Fig. 3.

A typical potentiostatic current/time transient is shown in Fig. 7. The analysis of such a transient proceeds from Eq. [25], according to which one may write

$$\ln \left\{ \frac{\ln(i_c/i_{c,\infty})}{\ln(i_{c,0}/i_{c,\infty})} \right\} = \ln \left[ \frac{(\theta - \theta_\infty)}{(\theta_0 - \theta_\infty)} \right] \quad [27]$$

where the subscript zero refers to initial values, i.e., to values at  $t = 0$ . If the net rate at which the anion is adsorbed may be described by an equation of the form

$$(\partial\theta/\partial t)_\eta = \bar{k}_a a_{(Bz^-)} (\theta_m - \theta) - \bar{k}_d \theta \quad [28]$$

where  $a_{(Bz^-)}$  represents the constant solution activity of the benzoate anion, and  $\bar{k}_a$  and  $\bar{k}_d$  are potential dependent adsorption and desorption rate constants, respectively, then the relationship between  $\theta$  and  $t$ , obtained by integration of Eq. [28] under the potentiostatic condition, is given by Eq. [29]

$$\theta = \theta_\infty - (\theta_\infty - \theta_0) \exp \left[ - (\bar{k}_a a_{(Bz^-)} + \bar{k}_d) t \right] \quad [29]$$

The use of Eq. [29] in conjunction with Eq. [27] leads to the desired working equation

$$\log \log (i_c/i_{c,\infty})_\eta = - (\bar{k}_a a_{(Bz^-)} + \bar{k}_d) t / 2.303 + \log \log (i_{c,0}/i_{c,\infty}) \quad [30]$$

according to which a plot of  $\log \log (i_c/i_{c,\infty})$  vs.  $t$  should result in a straight line having a slope,  $\tau$ , equal to  $-(\bar{k}_a a_{(Bz^-)} + \bar{k}_d) / 2.303$ . As shown in Fig. 8, the transient depicted in Fig. 7 conforms to Eq. [30].

In the steady-state case,  $(\partial\theta/\partial t)_\eta = 0$ , Eq. [28] may be solved for  $\theta_\infty$

$$\theta_\infty/\theta_m = 1 / \left[ 1 + \frac{\bar{k}_d/\bar{k}_a a_{(Bz^-)}}{\exp(-\gamma F\eta/RT)} \right] \quad [31]$$

This expression for  $\theta_\infty$  is identical to that written earlier, Eq. [23], with  $(\bar{k}_d/\bar{k}_a a_{(Bz^-)}) = K$  and  $-\gamma F/RT = j$ . In writing Eq. [31], use was made of the identities,  $\bar{k}_a = k_a \exp(\epsilon\gamma F\eta/RT)$  and  $\bar{k}_d = k_d \exp[-(1-\epsilon)\gamma F\eta/RT]$ , where  $k_a$  and  $k_d$  are the chemical rate constants,  $\epsilon$  is the symmetry factor, and  $\gamma (< 1)$  may be regarded as the ratio of the Galvani potential difference between the initial and final states to the Galvani potential difference between the metal and the initial state (2). Since  $\tau$  is equal to  $-(\bar{k}_a a_{(Bz^-)} + \bar{k}_d) / 2.303$ ,  $|\tau|$  is a minimum when  $\bar{k}_a a_{(Bz^-)} / \bar{k}_d = (1-\epsilon)/\epsilon$ . It is apparent from Eq. [31] that if  $\epsilon = (1-\epsilon)$ , the minimum in  $|\tau|$ ,  $|\tau^*|$ , occurs at  $\theta_\infty/\theta_m = 1/2$  and, designating the corresponding polarization by  $\eta^*$ , one may write Eq. [32]

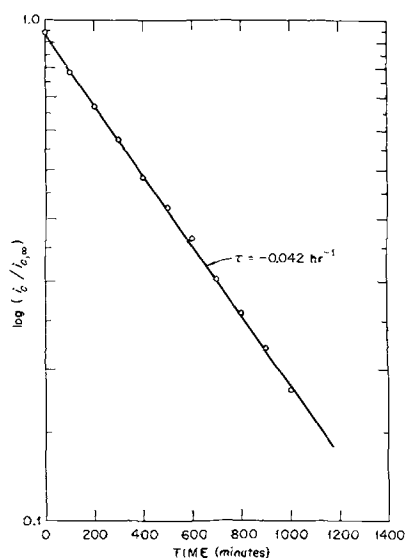


Fig. 8. Analysis of cathodic potentiostatic current/time transient. Test of Eq. [30] using the data shown in Fig. 7.

$$\tau/\tau^* = \cosh [\epsilon\gamma F(\eta - \eta^*)/RT] \quad [32]$$

which shows that  $\tau/\tau^*$  depends only on  $|\eta - \eta^*|$ . In Fig. 9, experimental values of  $\tau$  are plotted against  $\eta$ . The solid curve was calculated by means of Eq. [32], and a reasonable agreement between the experimental and calculated results is observed. In the calculation of the solid curve,  $\epsilon$  was assumed equal to 0.5, and the values of  $\eta^*$  and  $\gamma$  were taken from Fig. 5 via Eq. [31].

The order of the proton discharge reaction with respect to hydrogen ion activity was determined by measuring the cathodic current at various pH values while maintaining a constant potential sufficiently negative to eliminate interference from the anodic process. The electrode was initially in a steady state at the selected potential, and the pH was varied by the addition of deoxygenated NaOH solution. The results are shown in Fig. 10 and correspond to a reaction order,  $-(\partial \log i_c/\partial \text{pH})_{E,\theta}$ , equal to unity, just as in the noninhibited system.

**Iron dissolution reaction.**—From a diagnostic viewpoint, the most important observation relating to the dissolution of iron in the presence of the adsorbed inhibitor is expressed by Eq. [33]

$$(\partial \log i_a/\partial E)_{\theta,\text{pH}} = F/2.303 RT \quad [33]$$

which states that anodic polarization at constant pH and  $\theta$ , i.e., fast anodic polarization, results in a transitory Tafel line having a slope of 59 mv/decade. This result, described in connection with Fig. 1, is to be contrasted to that observed in the noninhibited system

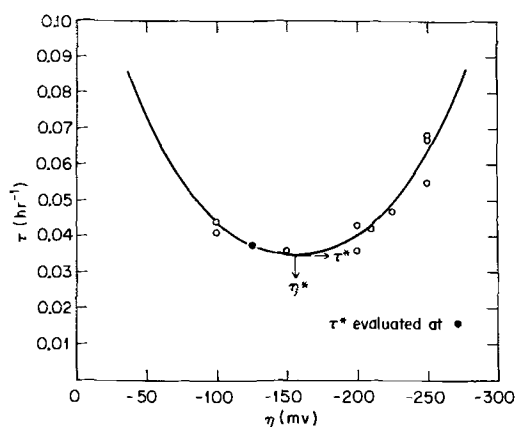


Fig. 9. Effect of potential on  $\tau$ . Test of Eq. [32] with  $\gamma$  and  $\eta^*$  taken from Fig. 5 via Eq. [31].

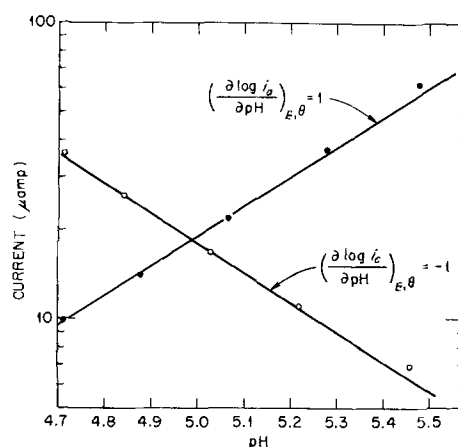


Fig. 10. Determination of the orders of the anodic (solid circles) and cathodic (open circles) reactions with respect to proton activity in 0.10M ( $\text{C}_6\text{H}_5\text{COOH} + \text{C}_6\text{H}_5\text{COONa}$ ) at 25°C. Anodic and cathodic data obtained at  $E = -620$  mv vs. SCE and  $E = -850$  mv vs. SCE, respectively. Electrode area = 2.86  $\text{cm}^2$ .

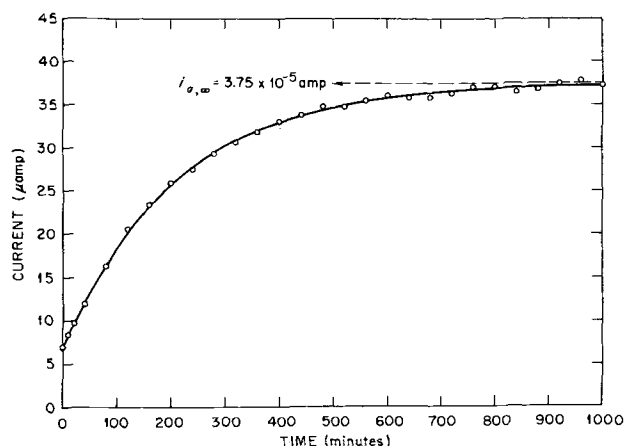


Fig. 11. Typical anodic potentiostatic current/time transient. 0.10M ( $\text{C}_6\text{H}_5\text{COOH} + \text{C}_6\text{H}_5\text{COONa}$ ); pH = 4.87;  $T = 25^\circ\text{C}$ ; electrode apparent area = 1.346  $\text{cm}^2$ ;  $E = -630$  mv vs. SCE.

for which a comparable rate of polarization results in a true steady-state Tafel line having a slope of (2/3) ( $2.303 RT/F$ ). Tafel behavior is not exhibited by the steady-state polarization curve for the inhibited system.<sup>3</sup>

A typical anodic potentiostatic current/time transient is shown in Fig. 11. In Fig. 12, a plot of  $\log(i_{a,\infty} - i_a)$  vs.  $t$  is shown for this transient, and one may conclude that  $[\partial \log(i_{a,\infty} - i_a)/\partial t]_{\eta}$  is essentially constant. The significance of this result is examined in the Discussion section.

An evaluation of the order of the iron dissolution reaction with respect to the hydroxyl ion activity,  $(\partial \log i_a/\partial \text{pH})_{E,\theta}$ , was accomplished by the rapid addition of deoxygenated NaOH solution under potentiostatic conditions. The potential was sufficiently positive to eliminate interference from the hydrogen evolution reaction. The results are shown in Fig. 10. The straight line was drawn with a unit slope, i.e.,  $(\partial \log i_a/\partial \text{pH})_{E,\theta} = 1$ , corresponding to a first order dependency on the hydroxyl ion activity.

### Discussion

Adsorption of the benzoate ion is accompanied by marked changes in the kinetics and/or mechanistics of both the iron dissolution and hydrogen evolution reactions. As indicated by the results described in the preceding section, the effect of the adsorbed anion on

<sup>3</sup> Actually, the degree of reproducibility of the steady-state anodic curve precludes a statement regarding the sign of  $d^2 i_{a,\infty}/dE^2$ .

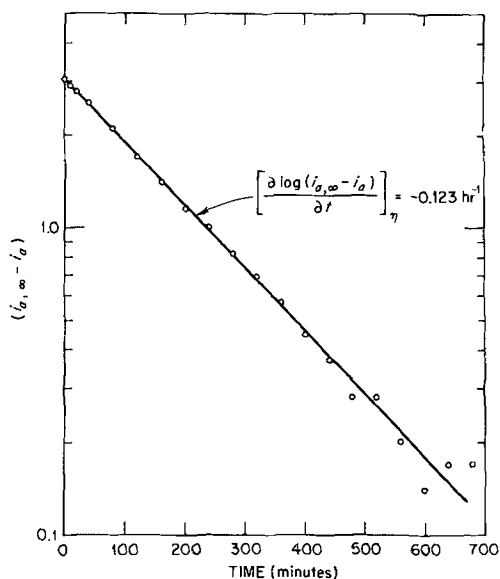


Fig. 12. Analysis of anodic potentiostatic current/time transient. Test of Eq. [71] using the data shown in Fig. 11.

the hydrogen evolution reaction is fundamentally different in character from that on the iron dissolution reaction and, consequently, in the following discussion, the two reactions are dealt with separately.

**Hydrogen evolution reaction.**—If absolute rate theory is applied in the usual fashion to the rate-determining proton discharge reaction, the resultant expression for the absolute value of the corresponding current density,  $i_c$ , is given by Eq. [34]

$$\ln i_c = \ln k - (\alpha F/RT)E - [(1 - \alpha)F/RT]\psi + \ln a_{(H^+)}, \quad [34]$$

where  $E$  is the previously defined potential,  $\psi$  is the Galvani potential difference between the pre-electrode plane and the bulk of solution,  $\alpha$  is the symmetry factor which, ideally, is equal to  $1/2$ , and  $a_{(H^+)}$  is the proton activity in the bulk of solution (2, 3). The differential of  $\ln i_c$ , at constant solution composition, is given by Eq. [35]

$$d \ln i_c = d \ln k - (\alpha F/RT)d\eta - [(1 - \alpha)F/RT]d\psi \quad [35]$$

Since  $\psi = f(\eta, \theta)$ ,  $d\psi$  is given by Eq. [36]

$$d\psi = (\partial\psi/\partial\eta)_{\theta} d\eta + (\partial\psi/\partial\theta)_{\eta} d\theta \quad [36]$$

which, when substituted into Eq. [35], leads to Eq. [37]

$$d \ln i_c = -[\alpha + (1 - \alpha)(\partial\psi/\partial\eta)_{\theta}](F/RT) d\eta + [(d \ln k/d\theta) - (1 - \alpha)(F/RT)(\partial\psi/\partial\theta)_{\eta}] d\theta \quad [37]$$

It should be noted that  $\alpha$  is regarded as being a true constant,  $\alpha = 1/2$ , independent of  $\theta$ , i.e., the symmetry of the activation barrier is retained in the presence of the adsorbed anion. On the other hand, although potential-independent,  $k$  is considered a function of  $\theta$  because  $k$  represents the quantity,  $k'(\kappa/\gamma^{\ddagger}) \exp(-\Delta\mu^{\ddagger,0}/RT)$ , where  $\kappa$  is the transmission coefficient,  $\gamma^{\ddagger}$  is the activity coefficient of the activated complex,  $k'$  is a constant, and  $\Delta\mu^{\ddagger,0}$  is the standard chemical free energy of activation. The quantity,  $\Delta\mu^{\ddagger,0}$ , in particular, must be regarded as a possible function of  $\theta$ .

According to Eq. [37],  $(\partial \ln i_c/\partial\eta)_{\theta}$  and  $(\partial \ln i_c/\partial\theta)_{\eta}$  are given by Eq. [38] and [39]

$$(\partial \ln i_c/\partial\eta)_{\theta} = -[\alpha + (1 - \alpha)(\partial\psi/\partial\eta)_{\theta}](F/RT) \quad [38]$$

and

$$(\partial \ln i_c/\partial\theta)_{\eta} = [(d \ln k/d\theta) - (1 - \alpha)(F/RT)(\partial\psi/\partial\theta)_{\eta}] \quad [39]$$

If one equates the values of  $(\partial \ln i_c/\partial\eta)_{\theta}$  given by Eq. [14] and [38], one obtains Eq. [40]

$$(\partial\psi/\partial\eta)_{\theta} = -[2.303 RT/(1 - \alpha)FS] - \alpha/(1 - \alpha) \quad [40]$$

which shows that  $(\partial\psi/\partial\eta)_{\theta}$  is a constant, the magnitude of which is a function of  $S$  and, therefore, of  $\theta$ . With  $\alpha = 1/2$ , Eq. [40] becomes

$$(\partial\psi/\partial\eta)_{\theta} = -(118.24 + S)/S \quad [41]$$

where, as usual,  $S$  is expressed in mv/decade. The explicit dependence of  $(\partial\psi/\partial\eta)_{\theta}$  on  $\theta$  is obtained from Eq. [19] and [41], and is given by Eq. [42]

$$(\partial\psi/\partial\eta)_{\theta} = b\theta/\theta_m \quad [42]$$

The significance of Eq. [40]-[42] will be discussed below. First, however, it should be observed that since  $\partial(\partial\psi/\partial\eta)_{\theta}/\partial\theta$  is equal to  $\partial(\partial\psi/\partial\theta)_{\eta}/\partial\eta$ , Eq. [42] enables one to write Eq. [43]

$$(\partial\psi/\partial\theta)_{\eta} = b\eta/\theta_m + g(\theta) \quad [43]$$

where  $g(\theta)$ , although independent of  $\eta$ , must for the moment be considered a possible function of  $\theta$ . If the value of  $(\partial\psi/\partial\theta)_{\eta}$  given by Eq. [43] is substituted into Eq. [39], one obtains Eq. [44]

$$(\partial \ln i_c/\partial\theta)_{\eta} = (d \ln k/d\theta) - (2.303 b\eta/118.24 \theta_m) - 2.303 g(\theta)/118.24 \quad [44]$$

On the basis of Eq. [16] and [19], one may write

$$(\partial \ln i_c/\partial\theta)_{\eta} = (\partial \ln i_c/\partial\theta)_{\eta=0} - 2.303 b\eta/118.24 \theta_m \quad [45]$$

which, when subtracted from Eq. [44], shows that

$$(\partial \ln i_c/\partial\theta)_{\eta=0} = (d \ln k/d\theta) - 2.303 g(\theta)/118.24 \quad [46]$$

However, according to Eq. [18],  $(\partial \ln i_c/\partial\theta)_{\eta=0}$  is a constant, i.e.,

$$(\partial \ln i_c/\partial\theta)_{\eta=0} = a/\theta_m \quad [47]$$

and, therefore, if  $d \ln k/d\theta$  is a constant, then  $g(\theta)$

must be a constant and *vice versa*. If  $\Delta\mu^{\ddagger,0}$  is a linear function of  $\theta$ , which is an entirely reasonable expectation, then  $d \ln k/d\theta$  should be a constant, provided  $(\kappa/\gamma^{\ddagger})$  is independent of  $\theta$ . If  $d \ln k/d\theta$  may be expressed by Eq. [48]

$$d \ln k/d\theta = A \quad [48]$$

where  $A$  is a constant, then, according to Eq. [46], [47], and [48],  $g(\theta)$  is given by Eq. [49]

$$g(\theta) = g = 118.24 \left( \frac{a}{\theta_m} - A \right) / 2.303 \quad [49]$$

and, therefore, Eq. [43] becomes simply

$$(\partial\psi/\partial\theta)_{\eta} = (b/\theta_m)\eta + g \quad [50]$$

i.e.,  $(\partial\psi/\partial\theta)_{\eta}$  is independent of  $\theta$ . To complete the analysis, the significance of the expressions obtained for  $(\partial\psi/\partial\theta)_{\eta}$  and  $(\partial\psi/\partial\eta)_{\theta}$  must now be examined.

One may divide  $\psi$  into two parts, i.e.,

$$\psi = \psi^i + \psi^o \quad [51]$$

where  $\psi^i$  is the Galvani potential difference between the pre-electrode plane and the outer Helmholtz plane, and  $\psi^o$  is the Galvani potential difference between the outer Helmholtz plane and the bulk of solution. In the absence of specifically adsorbed ions, one may identify  $\psi$  with  $\psi^o$  and, using conventional double-layer equations, interpret changes in the polarization data arising from changes in  $\psi^o$  (4). In the present case, however, Eq. [41] shows that  $(\partial\psi/\partial\eta)_{\theta}$  attains a maximum value of approximately  $1/3$ , corresponding to  $S = -88$  mv/decade, and the large value clearly identifies  $\psi$  with  $\psi^i$  rather than with  $\psi^o$ . The insignificant role of  $\psi^o$  in this system may be attributed to the use of a relatively high ionic strength, coupled with the fact that the potential region of in-

terest lies several hundred millivolts negative to the point of zero charge for iron (5). It should be noted that the observed value of  $S$  corresponding to  $\theta = 0$  is just that expected if, and only if,  $(\partial\psi^\circ/\partial\eta)_{\theta=0} = 0$ . One may conclude that specific adsorption of the anion is accompanied by a displacement of the pre-electrode plane from the outer Helmholtz plane toward the metal, the symmetry factor remaining equal to 1/2. If, in accordance with the concepts advanced by Grahame (6), one may regard the potential gradient in the inner region of the double-layer as essentially constant, then, identifying  $\psi^i$  with  $\psi$ , one may write Eq. [52]

$$\psi = (x/L) \Delta\phi \quad [52]$$

where  $\Delta\phi$  is the Galvani potential difference between the metal and the bulk of solution,  $x$  is the distance between the outer Helmholtz plane and the pre-electrode plane, and  $L$  is the distance from the outer Helmholtz plane to the electrode surface. The ratio,  $(x/L)$ , is a function of  $\theta$  only. Since  $(d\Delta\phi/d\eta) = 1$ , differentiation of Eq. [52] with respect to  $\eta$  leads to Eq. [53]

$$(\partial\psi/\partial\eta)_\theta = (x/L) \quad [53]$$

i.e.,  $(\partial\psi/\partial\eta)_\theta$  is a constant, the magnitude of which is a function of  $\theta$ . This is precisely the result expressed by Eq. [40] and [42] and, comparing Eq. [42] and [53], one finds that  $(x/L)$  may be related to  $\theta$  by Eq. [54]

$$(x/L) = b\theta/\theta_m \quad [54]$$

According to Eq. [54],  $d(x/L)/d\theta = b/\theta_m$  and, since  $(\partial\Delta\phi/\partial\theta)_\eta = 0$ , differentiation of Eq. [52] with respect to  $\theta$  results in Eq. [55]

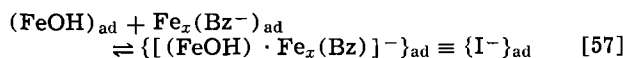
$$(\partial\psi/\partial\theta)_\eta = (b/\theta_m) \Delta\phi \quad [55]$$

which, by means of the identity,  $\Delta\phi = \eta + \Delta E$ , where  $\Delta E$  is a constant equal to  $(E_{\text{corr}} - E_{\Delta\phi=0})$ , converts Eq. [55] into Eq. [56]

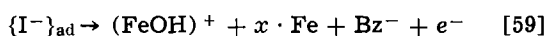
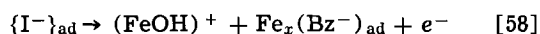
$$(\partial\psi/\partial\theta)_\eta = (b/\theta_m) \eta + (b/\theta_m) \Delta E \quad [56]$$

Again, this result is in accord with that expressed by Eq. [50] and, consequently, also serves to confirm Eq. [48]. Finally, at constant  $E$  and  $\theta$ ,  $\psi$  and  $k$  are constant and, therefore, according to Eq. [34],  $(\partial \log i_c/\partial \text{pH})_{E,\theta} = -1$ . This agrees with the results shown in Fig. 10.

**Iron dissolution reaction<sup>4</sup>.**—If the only effect of the adsorbed inhibitor on the iron dissolution reaction were to decrease the area available to the normal reaction scheme, Eq. [1]-[5], then  $(\partial \log i_a/\partial E)_\theta$  would retain the value observed for the noninhibited system, i.e.,  $(3/2)(F/2.303 RT)$ . However, as shown in Fig. 1 and expressed by Eq. [33],  $(\partial \log i_a/\partial E)_\theta$  is equal to  $(F/2.303 RT)$  and, consequently, one must conclude that the role of the adsorbed inhibitor cannot be adequately analyzed on the basis of a simple coverage concept alone. It is postulated that, once on the surface, the adsorbed benzoate anion interacts with the surface intermediate,  $(\text{FeOH})_{\text{ad}}$ , to form a surface complex,  $\{\text{I}^-\}_{\text{ad}}$ , as represented by Eq. [57]



where  $\text{Bz}^-$  represents the benzoate anion. The complex is oxidized according to the reactions represented by Eq. [58] and [59]



<sup>4</sup>The mechanism described here in detail, one involving a surface complex,  $\{\text{I}^-\}_{\text{ad}}$ , formed by  $(\text{FeOH})_{\text{ad}}$  and the inhibitor, was developed in a series of earlier publications (7,8). In particular, Eq. [65] may be found in ref. (7), and Eq. [57], [58], [59], [65], [69], and [71] in ref. (8). The mechanism, including the equations, was presented at the Buffalo Meeting of the Society, Oct. 10, 1965. With the preceding in mind, the author wishes to call to the attention of the reader two more recent articles (9, 10) by authors in attendance at the Buffalo presentation.

The latter reaction, Eq. [59], results in a desorption of the inhibitor, and is analogous to the "electrochemical" desorption of iodide from iron (11). This faradaic desorption of the inhibitor, together with the normal nonfaradaic adsorption/desorption reactions of the benzoate anion, determines the magnitude of  $\theta_R$ , i.e.,  $[\theta_4 + \lambda\theta_5/(\lambda + 1)]$ , where  $\theta_4$  and  $\theta_5$  are defined by the equations

$$[\text{Fe}_x(\text{Bz}^-)_{\text{ad}}] = \beta\theta_4/\lambda \quad \text{and} \quad [\{\text{I}^-\}_{\text{ad}}] = \beta\theta_5/(\lambda + 1)$$

in which the concentrations of the adsorbed benzoate anion and complex are expressed in moles/cm<sup>2</sup>, and  $\beta$  retains its earlier definition (see Eq. [6]-[9]). The symbol,  $\lambda$ , represents the number of H<sub>2</sub>O-type adsorption sites occupied by a benzoate anion. Studies relating to the adsorption of benzoate and other aromatics on mercury have shown that the aromatic ring is  $\pi$ -bonded to the metal, the plane of the ring being parallel to the metal surface (12), and one may assume this to be the case for iron.

During the short time interval required to establish the "fast" anodic Tafel lines defined by Eq. [33],  $\theta_R$  remains essentially constant while, for each potential, the system attains a pseudo steady-state corresponding to the fixed value of  $\theta_R$ . The kinetic description of the inhibited system, for constant  $\theta_R$ , is given by Eq. [60]-[64]

$$i_a/F = \bar{k}_3\theta_2 - \bar{k}_{-3}\theta_3 + \bar{k}_4\theta_3 + \bar{k}_{58}\theta_5 \quad [60]$$

$$\beta d\theta_1/dt = \bar{k}_1(1 - \theta_T) - \bar{k}_{-1}\theta_1 - \bar{k}_2\theta_1 + \bar{k}_{-2}a_{(\text{H}^+)}\theta_2 \quad [61]$$

$$\beta d\theta_2/dt = \bar{k}_2\theta_1 - \bar{k}_{-2}a_{(\text{H}^+)}\theta_2 - \bar{k}_3\theta_2 + \bar{k}_{-3}\theta_3 \quad [62]$$

$$\beta d\theta_3/dt = \bar{k}_3\theta_2 - \bar{k}_{-3}\theta_3 - \bar{k}_4\theta_3 - \bar{k}_{57}\theta_3\theta_4 + \bar{k}_{-57}\theta_5 \quad [63]$$

$$(\beta/\lambda) d\theta_4/dt = [-\beta/(\lambda + 1)] d\theta_5/dt \\ = -\bar{k}_{57}\theta_3\theta_4 + \bar{k}_{-57}\theta_5 + \bar{k}_{58}\theta_5 \quad [64]$$

where  $\theta_T$  is equal to  $\sum\theta_j$  ( $j = 1 \rightarrow 5$ ), and the other symbols retain their earlier definitions. It should be noted that if  $\theta_R = 0$ , this system of equations reduces to Eq. [6]-[9] and, consequently, describes the normal noninhibited system. The pseudosteady-state solution obtained from Eq. [60]-[64] by setting the coverage-time derivatives equal to zero, solving the resulting equations for  $\theta_j$ , and using the results to eliminate  $\theta_j$  from Eq. [60], is given by Eq. [65]

$$i_a/F = 2k_4 \frac{k_3k_2k_1(1 - \theta_R)}{k_{-3}k_{-2}a_{(\text{H}^+)}(k_1 + k_{-1})} \exp(3FE/2RT) \\ + 2k_{57} \frac{k_3k_2k_1\theta_R(1 - \theta_R)}{k_{-3}k_{-2}a_{(\text{H}^+)}(k_1 + k_{-1})} \exp(FE/RT) \quad [65]$$

In addition to the conditions imposed in the derivation of Eq. [10], the derivation of Eq. [65] requires only that  $\bar{k}_{58}/\bar{k}_{-57} \gg 1$ ,  $\bar{k}_{58}/\bar{k}_{57}\theta_3 \gg 1$ , and  $\bar{k}_{-3} + \bar{k}_4 + (\bar{k}_{57}\theta_4/\bar{k}_{-57}) \approx \bar{k}_{-3}$ . The latter two conditions correspond to  $\theta_3 \approx \bar{k}_3\theta_2/\bar{k}_{-3}$  and  $\theta_4/\theta_5 \gg 1$ , respectively. In Eq. [65],  $\theta_1 = k_1(1 - \theta_R)/(k_1 + k_{-1})$  and since, as in the noninhibited system,  $\theta_1 \gg (\theta_2 + \theta_3)$  and  $\theta_T \approx 1$ ,  $\theta_1 \approx (1 - \theta_R)$ , i.e.,  $k_1/(k_1 + k_{-1}) \approx 1$ , a fact which may be used to simplify Eq. [65]. For convenience sake, Eq. [65] may be written in an abbreviated form

$$i_a = i_{a,\theta_R=0}(1 - \theta_R) + i_a^* \quad [66]$$

where  $i_{a,\theta_R=0}(1 - \theta_R)$  and  $i_a^*$  represent the first and second expressions, respectively, on the right-hand side of Eq. [65]. If  $\theta_R = 0$ ,  $i_a^*$  vanishes and Eq. [66] reduces to Eq. [10], i.e.,  $i_{a,\theta_R=0}$  corresponds to the steady-state current density of the noninhibited system, and  $i_{a,\theta_R=0}(1 - \theta_R)$  corresponds to the same current density, reduced by the simple coverage factor,  $(1 - \theta_R)$ . According to Eq. [65], if one took into account only this simple coverage effect and omitted  $i_a^*$ , then, as previously mentioned, the slope of the fast ( $\theta_R = \text{constant}$ ) anodic Tafel lines would be

(3/2)(F/2.303 RT) instead of the observed slope of F/2.303 RT. The observed value results from the fact that, with  $\theta_R \approx 1$ ,  $i_a^* \gg i_{a,\theta_R=0} (1 - \theta_R)$ , i.e.,  $i_a \approx i_a^*$  and therefore, according to Eq. [65]

$$\left( \frac{\partial \log i_a}{\partial E} \right)_{\theta_R, pH} = \left( \frac{\partial \log i_a^*}{\partial E} \right)_{\theta_R, pH} = F/2.303 RT \quad [67]$$

which is in agreement with Eq. [33]. Again, according to Eq. [65], if  $i_a \approx i_a^*$ , then

$$\left( \frac{\partial \log i_a}{\partial pH} \right)_{\theta_R, E} = \left( \frac{\partial \log i_a^*}{\partial pH} \right)_{\theta_R, E} = 1 \quad [68]$$

Subject to the conditions imposed in the derivation of Eq. [65], the variation of  $\theta_R$  with time is given by Eq. [69]

$$(\beta/\lambda) (d\theta_R/dt) = \frac{\bar{k}_{ad} a_{(Bz^-)} (1 - \theta_R)}{-\bar{k}_{des} \theta_R - \bar{M} \theta_R (1 - \theta_R)} \quad [69]$$

where the first two expressions on the right side correspond to the nonfaradaic adsorption and desorption reactions, respectively, and the last term to the faradaic desorption process. The quantity,  $\bar{k}_{59} \bar{k}_{57} \bar{k}_{3} \bar{k}_{2} / \bar{k}_{58} \bar{k}_{-3} \bar{k}_{-2} a_{(H^+)}$ , is represented by  $\bar{M}$ . During the potentiostatic current/time transients,  $\theta_R$  remains nearly equal to unity and, therefore, although  $(1 - \theta_R)$  changes significantly,  $\theta_R$  may be considered virtually constant. Consequently, according to Eq. [65], since  $i_a \approx i_a^*$ , one may write Eq. [70]

$$i_a = \bar{\omega} (1 - \theta_R) \quad [70]$$

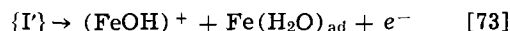
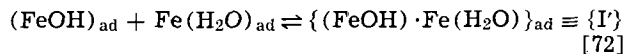
where  $\bar{\omega}$ , i.e.,  $2F (\bar{k}_{58} / \bar{k}_{59}) \bar{M} \theta_R$ , is regarded as being a constant. At constant potential and solution composition, integration of Eq. [69], followed by the substitution of  $i_a$  for  $\theta_R$  in accordance with Eq. [70], leads to Eq. [71]

$$\ln[(i_{a,x} - i_a)/(i_{a,\infty} - i_{a,0})] [(1 + P i_{a,0})/(1 + P i_a)] = -(\lambda/\beta) Q_x [\bar{k}_{des} + \bar{M} (1 - \theta_x)]^2 t \quad [71]$$

where  $P = \bar{M} (1 - \theta_x) / \bar{k}_{des} \bar{\omega}$  and  $Q_x = \bar{k}_{ad} a_{(Bz^-)} / \theta_x [\bar{k}_{des} + \bar{M} (1 - \theta_x)] = 1/(1 - \theta_x)$ . According to Fig. 12,  $[\partial \log (i_{a,x} - i_a)/\partial t]_\eta$  is virtually constant and, consequently,  $|\partial \ln (i_{a,x} - i_a)/\partial t|_\eta \gg |\partial \ln (1 + P i_a)/\partial t|_\eta$ , i.e.,  $2 + (1/P i_a) \gg i_{a,x}/i_a$ . This condition may also be expressed by the inequality,  $2 + [v_{des, nf, x} / v_{des, f, x} (1 - \theta)] \gg i_{a,x}/i_a$ , where  $v_{des, nf, x}$  and  $v_{des, f, x}$  represent the steady-state rates of the nonfaradaic and faradaic desorption processes, respectively. In view of the magnitudes attained by  $i_{a,x}/i_a$ , one may conclude that  $v_{des, nf, x} \gg v_{des, f, x} (1 - \theta)$ , a result which is true only because  $(1 - \theta) \ll 1$ . When an electrode, initially in a steady-state, is potentiostatically polarized at a more positive potential, the increase in  $i_a$  with time results from a decrease in  $\theta$ . If only the nonfaradaic adsorption/desorption reactions are considered, then, according to Eq. [31] or Fig. 5,  $\theta$  could only increase, not decrease, in such an experiment and, therefore, although  $v_{des, nf, x} \gg v_{des, f, x} (1 - \theta)$ ,  $v_{des, f, x}$  must be of sufficient magnitude to produce the decrease in  $\theta$ , i.e., to insure that  $d\theta_x/dE$  is negative. If  $d\theta/dt$  of Eq. [69] is set equal to zero and the result differentiated with respect to  $\eta$ , one finds that  $d\theta_x/dE$  is negative only if  $v_{des, f, x} (1 - \epsilon\gamma)/\gamma > v_{des, nf, x}$ . Since  $\epsilon\gamma \approx 1/3$ , the condition is entirely compatible with the previous condition,  $v_{des, nf, x} \gg v_{des, f, x} (1 - \theta)$ . It must be emphasized that  $d\theta_x/dE$  is negative in a potential region considerably negative to the point of zero charge for iron (5), i.e., negative to the potential at which one would expect maximum adsorption of the benzoate anion (the potential of maximum adsorption being positive to the potential of zero charge) if  $v_{des, f, x} = 0$ . Under proper conditions, at sufficiently positive potentials, complete faradaic desorption of the inhibitor occurs, and the system then obeys Eq. [10], the equation for

the noninhibited system. This has been observed in (0.01M benzoic acid + 0.10M Na<sub>2</sub>SO<sub>4</sub>) at pH values near 1. At higher pH values, one observes the "potentials of unpolarizability" previously described by Cartledge and Heusler (11).

In the preceding discussion, the anodic polarization data were interpreted on the basis of Eq. [66], with  $i_a \approx i_a^*$ , i.e.,  $i_a^* \gg i_{a,\theta_R=0} (1 - \theta_R)$ . This condition requires only that  $k_{57}\theta_R \gg \bar{k}_4$ . However, there is an alternative explanation which merits brief consideration. If to the reaction system represented by Eq. [1]-[5] there are added the reactions represented by Eq. [72] and [73]



reactions analogous to those represented by Eq. [57] and [58], then, proceeding as in the derivation of Eq. [10], one finds that, if  $k_{73}(k_{72}/k_{-72})\theta_1 \gg k_4$ , i.e., if the added reactions represent the principal mode by which  $(\text{FeOH})_{ad}$  is oxidized to  $(\text{FeOH})^+$ , then Eq. [10] is changed only to the extent of replacing  $k_4\theta_1$  by  $k_{73}(k_{72}/k_{-72})\theta_1^2$ . The effects of potential and pH on the steady-state current density remain unchanged and, as a result, provide no means of distinguishing between the two alternative representations of the noninhibited system. However, for the inhibited system,  $i_a^*$  remains unchanged and Eq. [66] must be replaced by Eq. [74]

$$i_a = i_{a,\theta_R=0} (1 - \theta_R)^2 + i_a^* \quad [74]$$

Consequently, in order that  $i_a \approx i_a^*$ , it is required only that  $k_{57}\theta_R \gg \bar{k}_{73}(k_{72}/k_{-72})(1 - \theta_R)$ , a condition which, since  $(1 - \theta_R) \ll 1$ , might appear to be more readily attainable than the previous condition,  $k_{57}\theta_R \gg \bar{k}_4$ .

### Summary

The complex electrochemical polarization behavior manifested by the active iron electrode in the presence of an adsorbed inhibitor has been analyzed in terms of the changes introduced into the mechanistic and kinetics of the iron dissolution and hydrogen evolution reactions in a noninhibited system as a consequence of the adsorbed inhibitor.

Specific adsorption of the inhibitor results in a reduction in the rate of the normal iron dissolution reaction via a simple coverage effect and, in addition, introduces a mechanistic change in which the adsorbed inhibitor interacts with the surface intermediate,  $(\text{FeOH})_{ad}$ , to form a surface complex. One mode of oxidation of the complex results in a faradaic desorption of the inhibitor and, as a consequence,  $(d\theta_x/dE)$  is negative in a potential region in which, in the absence of the faradaic or electrochemical desorption reaction, it would be positive. The proposed mechanism is consistent with the experimental observations:  $(\partial \log i_a/\partial E)_{\theta, pH} = F/2.303 RT$ ,  $(\partial \log i_a/\partial pH)_{E, \theta} = 1$ , and  $[\partial \log (i_{a,x} - i_a)/\partial t]_\eta = \text{constant}$ .

The adsorbed benzoate anion accelerates the rate of the proton discharge reaction and this has been shown to result from a  $\psi$ -effect, i.e., a double-layer effect, and a simultaneous diminution of the standard chemical free energy of activation for proton discharge. Of particular significance is the fact that, at constant solution composition,  $(\partial \log i_c/\partial E)_\theta = 1/S$ , where  $S$  is a constant the magnitude of which is a function of  $\theta$ , i.e., of the benzoate coverage. Using measured values of  $S_x$  together with the experimentally established relationship between  $S$  and  $\theta$ , it has been demonstrated that the steady-state coverage obeys a potential-dependent Langmuir adsorption equation. The variation of  $S$  with  $\theta$  was shown to result from the dependence of  $S$  on  $(\partial \psi/\partial \eta)_\theta$  which, in turn, was shown to be a linear function of  $\theta$ . The linear dependence of  $(\partial \psi/\partial \eta)_\theta$  on  $\theta$  was interpreted in terms of



the displacement of the pre-electrode plane from the outer Helmholtz plane toward the metal, the displacement being proportional to  $\theta$ . Similarly, on the basis of the experimental evaluation of  $(\partial \log i_c / \partial \theta)_\eta$  and the derived relationship between this variable and the variables,  $(\partial \psi / \partial \theta)_\eta$  and  $(d \ln k / d\theta)$ , it was established that the standard free energy of activation for proton discharge is a linear function of  $\theta$ , and that  $(\partial \psi / \partial \theta)_\eta$  is proportional to  $\eta$ . The hydrogen evolution reaction was shown to be first order in proton activity, i.e.,  $(\partial \log i_c / \partial \text{pH})_{E,\theta} = -1$ . In addition to the "instantaneous" and steady-state current/potential data, potentiostatic cathodic current/time transients were quantitatively analyzed on the basis of an appropriate potential-dependent adsorption/desorption rate equation and the established relationship between  $i_c$  and  $\theta$ .

The results of this investigation demonstrate the feasibility of analyzing the complex data characteristic of inhibited systems and provide further insight into the mechanisms of corrosion and corrosion inhibition.

#### Acknowledgment

During the course of this investigation, the author has had the advantage of numerous helpful discussions with Dr. G. H. Cartledge and wishes to acknowledge his continued encouragement and support.

Manuscript submitted May 13, 1968; revised manuscript received July 15, 1968.

Any discussion of this paper will appear in a Discussion Section to be published in the June 1969 JOURNAL.

#### REFERENCES

1. E. J. Kelly, *This Journal*, **112**, 124 (1965).
2. A. N. Frumkin, "Advances in Electrochemistry and Electrochemical Engineering," Vol. 1, pp. 65-121 P. Delahay, Editor, Interscience Publishers, Inc., New York, (1961).
3. B. E. Conway, "Theory and Principles of Electrode Processes," The Ronald Press Company, New York (1965).
4. R. Parsons, "Advances in Electrochemistry and Electrochemical Engineering," Vol. 1, pp. 1-64, P. Delahay, Editor, Interscience Publishers, Inc., New York (1961).
5. W. J. Lorenz and G. Eichkorn, *Ber. Bunsenges. Physik. Chem.*, **70**, 99 (1966).
6. D. C. Grahame, *Z. Elektrochem.*, **62**, 264 (1958).
7. E. J. Kelly, *Chem. Div. Ann. Prog. Rept. June 20, 1964*, ORNL-3679, p. 84.
8. E. J. Kelly, *Chem. Div. Ann. Prog. Rept. May 20, 1966*, ORNL-3994, p. 88.
9. F. M. Donahue, A. Akiyama, and K. Nobe, *This Journal*, **114**, 1006 (1967).
10. F. M. Donahue and K. Nobe, *ibid.*, **114**, 1012 (1967).
11. K. E. Heusler and G. H. Cartledge, *ibid.*, **108**, 732 (1961).
12. E. Blomgren, J. O'M. Bockris, and C. Jesch, *J. Phys. Chem.*, **65**, 2000 (1961).

## A Microstructural Study of the Reactivity of Cobalt Surfaces at Elevated Temperatures

R. Taggart, D. H. Polonis, and N. E. Dodds

*Division of Metallurgical Engineering, University of Washington, Seattle, Washington*

#### ABSTRACT

High-temperature metallographic techniques have been used to study the reactivity of cobalt surfaces at temperatures up to 1200°C and oxygen partial pressures in the range  $10^{-3}$  to  $10^{-7}$  Torr. The processes of thermal etching, faceting, and oxide particle formation can be controlled by adjusting the conditions of temperature and oxygen partial pressure. The faceting reaction is accompanied by sublimation and can be reversed in favor of either oxidation or thermal etching by changing the temperature and pressure. Oxide particles form with a density and morphology dependent on the orientation of the metal matrix. Dissolution of the particles on heating from 900°C has been attributed to the change in oxygen solubility in the cobalt matrix.

In the present work the formation of facets and oxide nuclei on cobalt surfaces has been investigated by means of direct observation of the microstructure during exposure to elevated temperatures under conditions of controlled oxygen partial pressure.

Previous investigations (1-10) of the oxidation of cobalt surfaces have revealed the formation of CoO layers at temperatures above 900°C and under oxygen pressures that varied between 0.005 and 1 atm. At temperatures below 900°C, the oxide  $\text{Co}_3\text{O}_4$  has also been reported, but it is unstable at higher temperatures and dissociates in favor of CoO.

Zettlemoyer *et al.* (11) and other investigators (1, 5, 12) have attributed the initial deviation from the parabolic rate law to adsorption, chemisorption, and phase boundary reactions. There has been an apparent disregard for the temperature dependence of oxygen solubility in cobalt and its potential effect on the very early stages of oxidation. Mathematical models to describe the initial oxidation process have been based on the concept of diffusion controlled thickening of

continuous oxide layers. Consideration has not been given in the case of cobalt to the discontinuous nature of the oxidation process as has been reported for copper and other metals (13, 14).

#### Experimental Methods

Polished and etched surfaces of 99.9% purity cobalt were examined at temperatures up to 1200°C in a Reichert hot stage metallograph. By means of a variable leak valve it was possible to control the oxygen partial pressure over the range  $10^{-3}$  to  $10^{-7}$  Torr, while the total pressure of oxygen and nitrogen in the chamber was in the range  $10^{-2}$  to  $10^{-6}$  Torr. The specimen temperature was determined by means of a chromel-alumel thermocouple spot welded on the polished surface.

#### Experimental Results

Three distinct microstructural processes have been identified during the exposure of cobalt surfaces to an oxidizing environment at temperatures above 500°C.

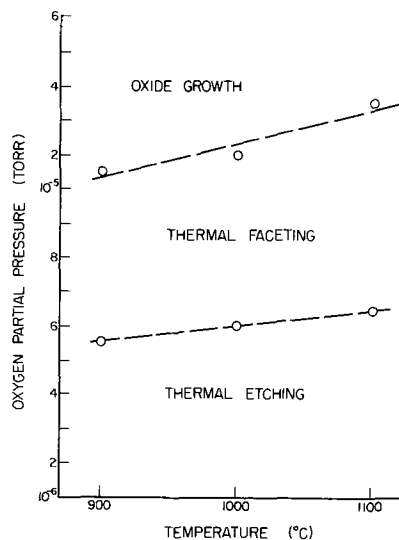


Fig. 1. Dependence of surface reactions on the temperature and pressure conditions.

The observations are summarized in Fig. 1 from which it can be deduced whether thermal etching, faceting, or oxidation should predominate, depending on the temperature and pressure conditions. Hot stage microscopy observations have shown that these stages may overlap and that the formation of oxide nuclei and thermal facets can be reversed. Although the available thermodynamic data for CoO suggests that this compound should be stable at the total pressures used in the present study, the oxide nuclei were observed to contract and, in some cases, to completely disappear at oxygen partial pressures below  $10^{-5}$  Torr.

*Thermal etching and faceting.*—Cobalt specimens that were heated for several hours above  $1000^{\circ}\text{C}$  in a vacuum of less than  $5 \times 10^{-6}$  Torr exhibited grain boundary grooving due to thermal etching, while at the same time all other features were eliminated from the grain surface. In accordance with the definition of a thermal facet by Moore (15), Fig. 2 shows the facets that developed on a cobalt surface after holding for several minutes at temperatures exceeding  $900^{\circ}\text{C}$  and pressures below  $10^{-5}$  Torr. The nucleation rate and the morphology of the facets varied with the orientation of the surface, the oxygen partial pressure, and the holding temperature. In general, the nucleation of facets occurred preferentially at oxide particle interfaces and at grain boundaries (see Fig. 3a and 3b). Figures 4a-4c illustrate the reversibility of facet formation at  $1000^{\circ}\text{C}$  when the oxygen

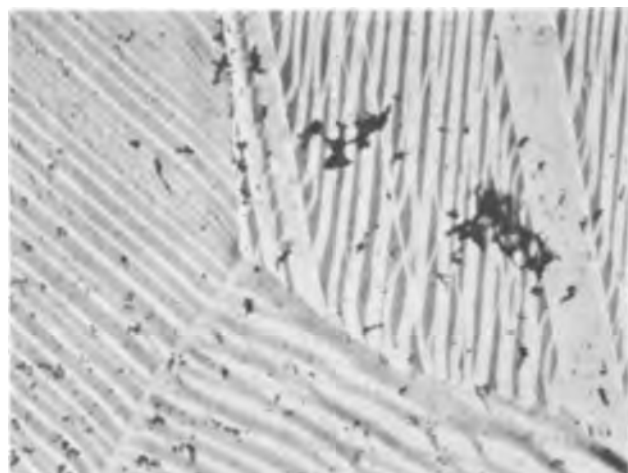


Fig. 2. Thermal facets developed at  $1000^{\circ}\text{C}$  and  $10^{-5}$  Torr oxygen partial pressure showing orientation dependence across twinned region. Electron micrograph, replica. Magnification ca. 2800X.

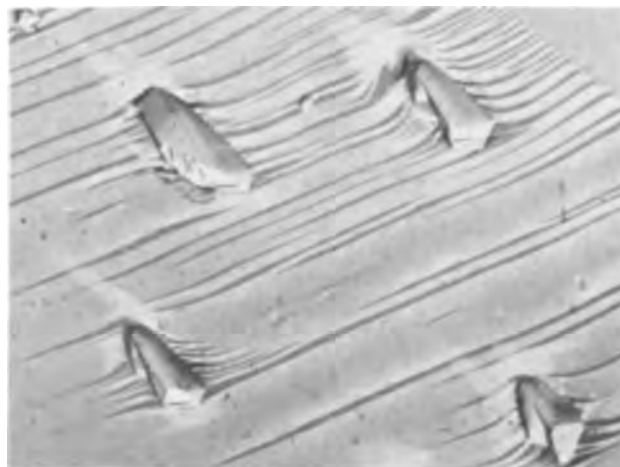


Fig. 3a. Preferential facet formation at pre-existing oxide particles. Electron micrograph, replica. Magnification ca. 6400X.

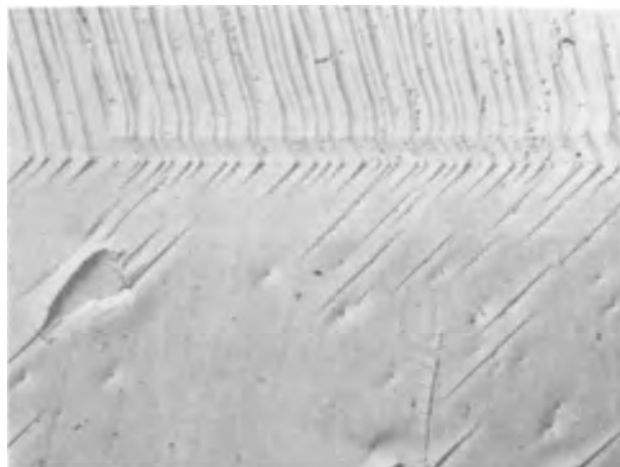


Fig. 3b. Cooperative facet formation across a grain boundary. Electron micrograph replica. Magnification ca. 2000X.

pressure was raised from  $8 \times 10^{-6}$  to  $1.2 \times 10^{-5}$  and then lowered to  $4.2 \times 10^{-6}$  Torr.

*Oxidation.*—The growth of discrete and discontinuous oxide particles characterized the initial stages of the oxidation of cobalt surfaces at  $900^{\circ}\text{C}$  and oxygen partial pressures of approximately  $2 \times 10^{-5}$  Torr. As shown in Fig. 5a-5c, the particles generally exhibited regular geometric shapes that were uniform within a given grain, suggesting an orientation relationship with the underlying matrix. During continued oxidation, the number of particles remained unchanged, but they eventually impinged to produce a uniform surface layer.

After oxide particles started to form on the surface, the reaction could be reversed by lowering the partial pressure or by raising the temperature. Figures 6a-6d show oxide reversion under constant temperature and varying pressure conditions. Dissolution of the oxide particles was followed by thermal faceting during prolonged holding at temperature. The facets developed preferentially at sites occupied by oxide particles resisting dissolution (see Fig. 3a) and, when oxidation conditions were restored, the facets were difficult to remove. The subsequent reoxidation of the surface resulted in particle formation at the pre-existing sites.

### Discussion of Results

*Thermal faceting.*—The observations of the present study point clearly to the heterogeneous nature of facet nucleation and its dependence on the oxidizing power of the atmosphere. Facet formation is favored at oxide particle interfaces, as shown in Fig. 3a and at grain boundaries, as shown in Fig. 3b. It is not



Fig. 4. Sequence of hot stage photomicrographs showing the growth and dissolution of thermal facets as a function of oxygen partial pressure at 1000°C. Optical micrograph. Fig. 4a, 3 min at  $1.2 \times 10^{-5}$  Torr. Magnification ca. 700X.

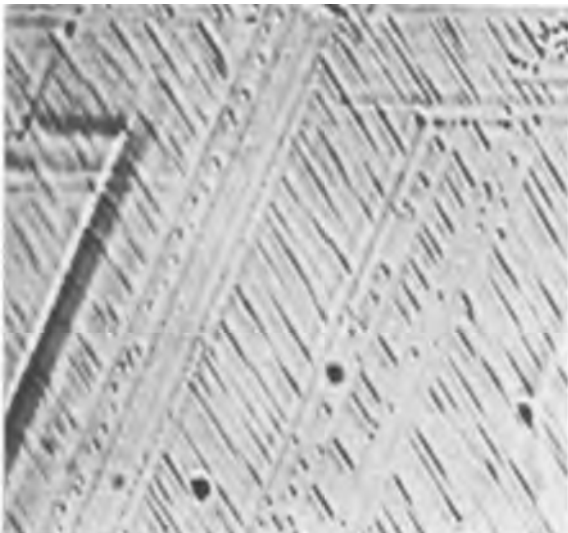


Fig. 4b. 8 min at  $1.2 \times 10^{-5}$  Torr

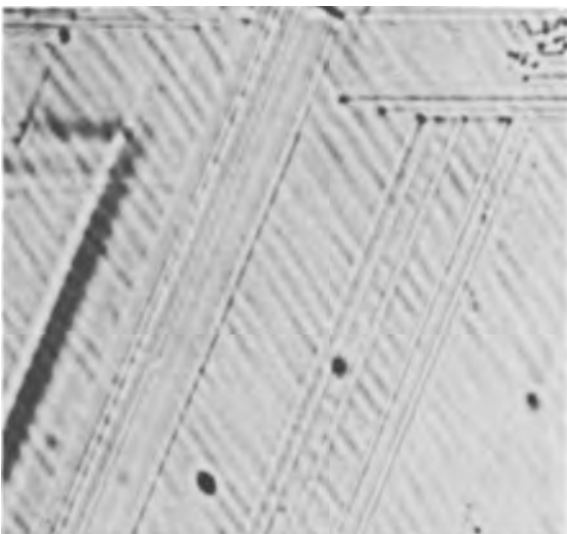


Fig. 4c. 22 min at  $4.2 \times 10^{-6}$  Torr

possible on the basis of the present work to define the relative contributions of surface diffusion and evaporation to the kinetics of facet formation on cobalt. However, it is apparent that oxygen assumes

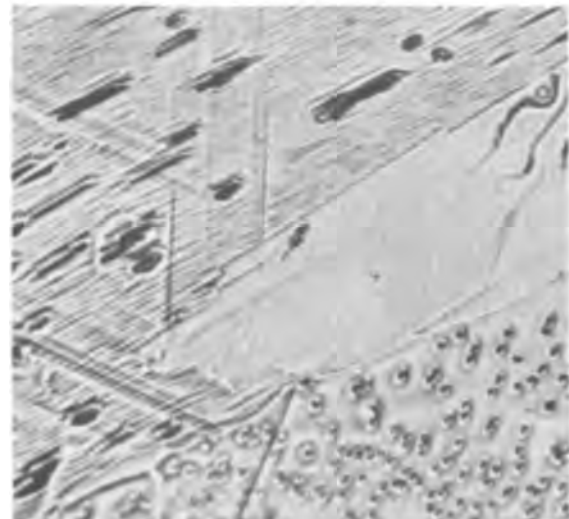
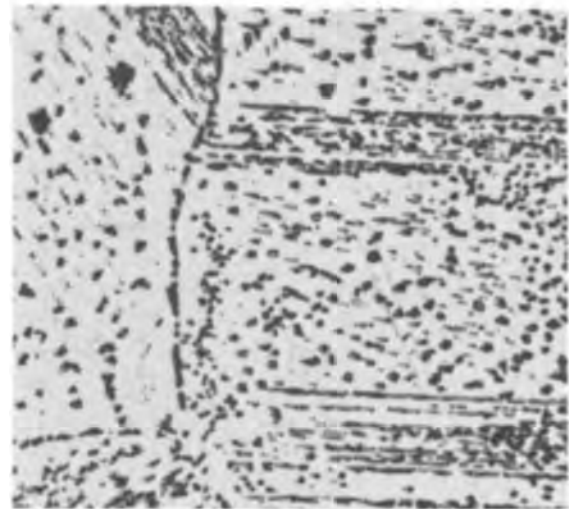
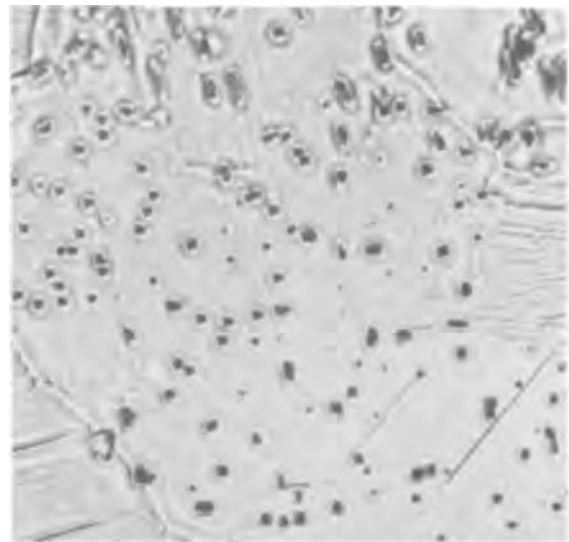


Fig. 5. Oxide formation combined with facet dissolution at 1000°C and oxygen partial pressure of  $2 \times 10^{-5}$  Torr showing the dependence of oxide morphology on the substrate orientation. Optical micrograph. Fig. 5a, top; Fig. 5b, center; Fig. 5c, bottom. Magnification 700X.

an important role in controlling the evaporation process that is involved in faceting. The observations support a proposed model based on the selective adsorption of oxygen on low index planes while evaporation occurs from a particular set of high index planes (15). This argument is substantiated by the fact that the dissolution of facets on reducing the oxygen pressure,

or by raising the temperature, required an incubation period before any visible changes occurred. At  $4.2 \times 10^{-6}$  Torr, 20 min elapsed prior to any visible change in the facet structure, but as shown in Fig. 4c, the facets became diffuse after 22 min, whereas after 26 min it was observed that surface relief was almost completely eliminated. From a kinetic viewpoint, the

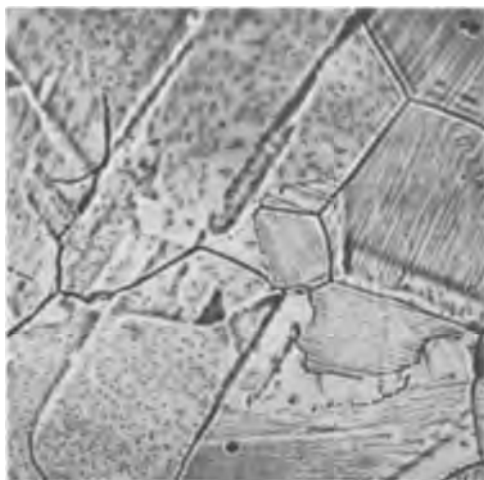


Fig. 6. Sequence of hot stage photomicrographs showing the growth and dissolution of oxide particles and the initiation of faceting. Fig. 6a. Oxidized at  $1000^\circ\text{C}$  and  $2 \times 10^{-5}$  Torr. Magnification ca. 315X.

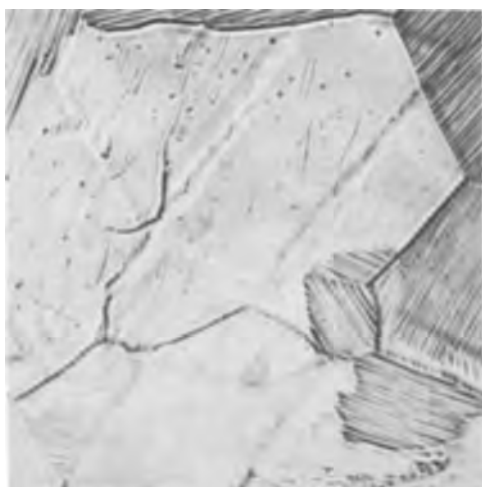


Fig. 6b. Held at  $1100^\circ\text{C}$  for 8 min at  $10^{-5}$  Torr (oxide particles have dissolved and facets begin to form).

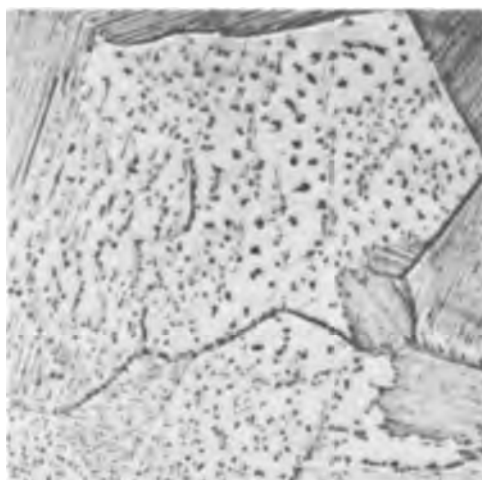


Fig. 6c. Re-oxidized at  $800^\circ\text{C}$  and  $4 \times 10^{-5}$  Torr

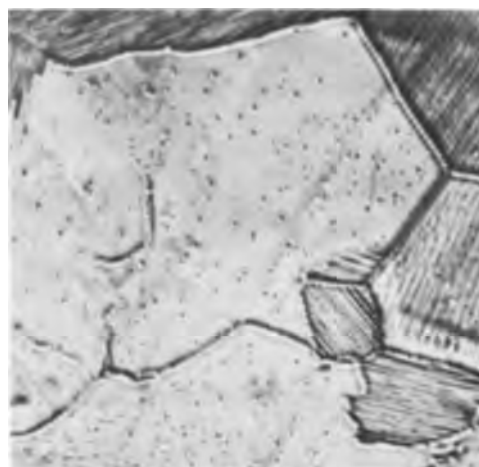


Fig. 6d. Held at  $1100^\circ\text{C}$  for 15 min (oxide particles again dissolve)

relative rates of metal evaporation and oxygen adsorption should determine for a given temperature whether thermal etching, faceting, or oxide formation will proceed on cobalt surfaces under a given set of oxygen partial pressure conditions. Thermal etching should occur when the evaporation rate exceeds the rate of oxygen adsorption, whereas faceting will be favored when these rates are approximately equal. When the oxygen pressure is sufficient for oxygen deposition to prevail, then the process of oxide formation should predominate.

In order to determine the time necessary for the adsorption of oxygen, it is essential to evaluate the rate of incidence of oxygen molecules on the surface for a particular set of temperature and pressure conditions. From kinetic theory (16) it may be deduced that  $N$ , the rate of incidence of gas molecules, of molecular weight  $M$  is given by

$$N = 3.513 \times 10^{22} (\text{Pmm}) (MT)^{-1/2} \text{ molecules/cm}^2\text{-sec} \quad [1]$$

For oxygen where the molecular weight is 32

$$N = 6.21 \times 10^{21} (\text{Pmm}) (T)^{-1/2} \quad [2]$$

On the basis of a value of  $3.64 \times 10^{-8}$  cm for the diameter of the oxygen molecule there are  $7.56 \times 10^{14}$  molecules/cm<sup>2</sup> for an adsorbed monolayer. The deposition time  $t$  for a monolayer of oxygen is then given by

$$t = \frac{7.56 \times 10^{14}}{N} \text{ sec/monolayer} \quad [3]$$

This relationship is plotted in Fig. 7 where it can be seen that the minimum time required for the

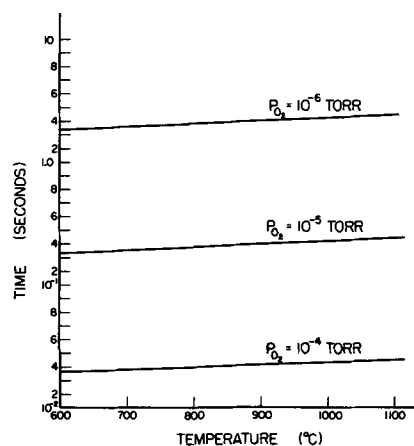


Fig. 7. Effect of temperature and oxygen partial pressure on the minimum time required for the formation of an oxygen monolayer.

formation of an adsorbed monolayer is strongly pressure dependent, but only slightly affected by temperature changes at constant pressure over the ranges of interest in the present work. The predominance of thermal etching at  $10^{-6}$  Torr can therefore be attributed to the relatively long incubation time necessary to establish the adsorbed monolayer that will inhibit the evaporation of cobalt atoms. On the other hand, at oxygen pressures of  $10^{-4}$  Torr an adsorbed layer can form almost instantaneously over the entire temperature range of the present experiments, resulting in conditions favoring oxide particle nucleation.

According to Fig. 7, raising the temperature of cobalt from  $900^{\circ}$  to  $1100^{\circ}\text{C}$  at  $10^{-5}$  Torr should not affect significantly the rate of impingement of oxygen molecules on the surface. Thermodynamic data for the compound CoO indicate that an existing oxide should continue to grow when the temperature is raised. The fact that the oxide particles disappear on heating under these conditions, requires an examination of the oxide stability in terms of the effect of temperature on the solubility of oxygen in the substrate.

*Kinetics of oxidation.*—For oxide thicknesses less than  $10,000\text{\AA}$  Reti reported (5) that the rate of oxidation is less than that predicted from the rate of cation vacancy diffusion through a homogeneous CoO layer. The results of the present research lend support to the contention of Reti (5) that the early stages of cobalt oxidation are controlled by the growth of small discrete nuclei of CoO. Rhead (17) assumes a concentration gradient at the edge of a radially growing cylinder of oxide and applies a surface diffusion coefficient in place of the bulk diffusivity in the diffusion equation. An important aspect of this analysis was the conclusion that the diffusion mechanism accounting for the growth of the particles may not be very different from either the surface diffusion of the metal or the surface transport of both metal and oxygen.

The observations of the oxidation of cobalt in the present study parallel the results of Lawless and Mitchell (18) who suggested that competition between the rate of the solution of oxygen in copper and the rate of formation of an oxide layer determined their rates for the nucleation and growth of oxide particles. The results of the present research suggest that Rhead's diffusion analysis is an oversimplification of the mechanism of oxidation as it occurs in cobalt. The incubation period observed during the initial stages of the oxidation of cobalt depends on both the temperature and the oxygen partial pressure and is a strong indication of the presence of a chemisorbed layer that exists when the underlying substrate of cobalt has satisfied local oxygen solubility requirements. The existence of such a stable layer is substantiated further by the fact that it was difficult to initiate the smoothing of an already faceted surface. When the partial pressure of the oxygen was reduced or when the temperature was raised, the localized oxidation reaction was reversed, and the oxide particles tended to disappear. This observation may be explained on the basis of the solubility of oxygen in the underlying cobalt metal (19) which increases up to  $800^{\circ}\text{C}$ , then decreases from  $800^{\circ}$ - $950^{\circ}\text{C}$ , and increases again at higher temperatures. Further evidence of the effect of oxygen solubility is provided by the fact that specimens oxidized at  $900^{\circ}\text{C}$  exhibited oxide particle dissolution when the temperature was raised to  $1100^{\circ}\text{C}$ . When the specimens were held for several minutes at the higher temperature, the oxide particles reappeared; this was taken as an indication that the solubility requirements had been satisfied and the necessary chemisorbed layer had been re-established.

The surface reactions under these conditions can therefore be attributed to the maintenance of a chemisorbed monolayer of oxygen established on a thin and highly defective layer of CoO. The thickness of this layer depends on the oxygen partial pressure

and the ambient temperature. Diffusion of oxygen from this thin film will establish an oxygen concentration gradient in the underlying cobalt matrix. Thus, the incubation period can be accounted for satisfactorily as the time during which the predominant reaction process is the solution of oxygen in the cobalt substrate. In accordance with the model proposed by Lawless and Mitchell for copper (18) the formation of cobalt oxide particles will occur when the process of cation diffusion through the thin film predominates over the diffusion of oxygen into the substrate. Under these conditions it is questionable to assume, as postulated by Rhead (17), that a surface diffusion coefficient will describe the transport process necessary to promote the radial growth of the particles. A more realistic model should consider cation diffusion through the stable chemisorbed layer that is maintained by a continuous reaction between oxygen and cobalt. In order to develop a meaningful quantitative description of the kinetics of particle growth, it is necessary to identify whether the surface transport of oxygen or the bulk diffusion of cations is rate controlling. In the oxidation experiments of the present study, the oxygen partial pressure is sufficient to provide a continuous supply of oxygen molecules to the surface. Under these conditions, the important unit processes leading to the migration of the oxide-metal interface and the radial growth of oxide particles should be the transport of cations through the thin surface layer followed by combination with the available adsorbed oxygen. The rate of radial growth will then be determined by the rate at which cobalt ions and oxygen can combine in the region immediately ahead of the oxide particle interface. It is obvious that a parabolic law cannot describe the kinetics of the oxide particle growth because layer thickening is not a significant factor until the radially growing particles impinge. The development of meaningful equations to describe particle growth is not possible unless the relative contributions of the separate diffusion processes are identified with certainty.

This work was supported by the National Science Foundation under NSF Grant GP-2367.

Manuscript submitted Jan 29, 1968; revised manuscript received ca. July 10, 1968.

Any discussion of this paper will appear in a Discussion Section to be published in the June 1969 JOURNAL.

#### REFERENCES

1. E. A. Gulbransen and K. Andrew, *This Journal*, **98**, 241 (1951).
2. R. E. Carter and F. D. Richardson, *Trans. AIME*, **7**, 336 (1955).
3. C. A. Phalnikar, E. B. Evans, and W. M. Baldwin, Jr., *This Journal*, **103**, 429 (1956).
4. H. G. Feller, *Z. Metallkunde*, **54**, 560 (1963).
5. A. R. Reti, *This Journal*, **112**, 967 (1965).
6. G. C. Wood, I. G. Wright, and J. M. Ferguson, *Corros. Sci.*, **5**, 645 (1965).
7. J. Kruger, A. Melin, and H. Winterhagen, *Cobalt*, **33**, 176 (1966).
8. O. Kubaschewski and B. E. Hopkins, "Oxidation of Metals and Alloys," 2nd ed., p. 240, Butterworth, London (1962).
9. Karl Hauffe, "Oxidation of Metals," p. 193, Plenum Press, New York (1965).
10. D. W. Bridges, J. P. Baur, and W. M. Fassell, *This Journal*, **103**, 614 (1956).
11. A. C. Zettlemyer, Y. F. Yu, J. J. Chessick, and F. H. Healey, *J. Phys. Chem.*, **61**, 1319 (1957).
12. F. S. Pettit and J. B. Wagner, Jr., *Acta Met.*, **12**, 41 (1964).
13. K. R. Lawless, "Energetics in Metallurgical Phenomena, I," W. Mueller, Editor, Gordon and Breach Science Publishers, Inc., New York (1965).
14. K. R. Lawless and D. F. Mitchell, *Memoires Scientifiques, Rev. Met.*, **62**, 27 (1965).
15. A. J. W. Moore, "Metal Surfaces," p. 155, American Soc. for Metals, Cleveland, Ohio (1963).
16. T. B. Wade, Tech. Report No. 3, Nonr 1228 (32)

- Project No. 039-086, Jan. 1967.  
 17. G. E. Rhead, *Trans. Faraday Society*, **61**, 797 (1965).  
 18. K. R. Lawless and D. F. Mitchell, Technical Report to the Office of Naval Research, Contract

- Nonr 474 (11), Report No. MS-3531-102-66U, (1966).  
 19. A. U. Seybolt and C. H. Mathewson, *Trans. AIME*, **117**, 156 (1935).

## Potentiostatic Current-Potential Measurements on Iron and Platinum Electrodes in High-Purity Closed Alkaline Systems

Clarence M. Shepherd\* and Sigmund Schuldiner\*

Naval Research Laboratory, Washington, D. C.

### ABSTRACT

Potentiostatic polarization curves were determined for Fe, Pt, and combinations of Fe and Pt electrodes in NaOH and LiOH solutions saturated with helium. With the high-purity, gas-tight system used, the level of reactable impurities was reduced to about  $10^{-6}$  ppm. Under these conditions the primary reactions are, depending on potential, the oxidation or reduction of  $\text{OH}^-$  and water. Iron does not significantly corrode or show a decrease in reaction rate with an increase in potential (passivate). Iron with its surface layer acts like an inert noble metal similar to platinum. Chloride ion causes extensive iron corrosion and completely changes the potentiostatic polarization behavior and does cause typical passive behavior. Under high-purity conditions, iron is an excellent catalyst for the hydrogen oxidation reaction; the presence of chloride ion, however, almost completely destroys the catalytic properties of Fe for this reaction. Unreactable and unremovable impurities such as carbonate, silicate, sulfate, etc., apparently do not have major effects on the polarization behavior of Fe. The major anion,  $\text{OH}^-$ , appears to dominate the inert anion effects.

Innumerable studies of the "passive" behavior of iron have been reported in the literature. Potentiostatic, steady-state investigations previously carried out on platinum electrodes, under conditions where the rates of the electrode reactions were very slow, have shown that under such conditions reactable impurities can play a dominant role (1). It therefore seemed reasonable that, in order to carry out meaningful electrochemical studies of the behavior of an iron electrode under conditions in which the electrode processes occurred at very slow rates, impurities which can react or otherwise affect reaction rates in a primary way would have to be minimized.

To carry out such an investigation the high-purity, gas-tight electrochemical system developed at this Laboratory (2) was used. In order to keep the iron electrode as inert as possible to corrosion, alkaline solutions were used.

A detailed explanation of the meaning of impurities should be made. By careful cleaning and aging of electrochemical cells and associated systems, the impurity level in solution can be kept low depending on the purity of the materials put into the cell. Further purification is possible by pre-electrolysis. Pre-electrolysis will remove species that deposit on an electrode which can then be removed from the cell. In addition, certain species, in particular organic materials, can be removed by electrochemical oxidation or reduction. If the electrochemical system is a tightly closed one, then a level of impurities which can be removed by electrochemical means can be reached and maintained which is limited by the rate of introduction of such impurities into the cell through leaks into the system or via materials (such as gases) which are introduced into the cell. Hence, the tighter the system, the more extensive the pre-electrolytic purification, and the better the purification of materials added during a run, then the lower the level of such impurities will be.

There always are, however, certain impurities which by our present technology are virtually impossible to remove below a certain level. For example, the elec-

trode material itself always contains impurities. At the present time it is virtually impossible to reduce these to a level much below 1 ppm. If the electrode is a solid, at room temperature, the rate of diffusion of such impurities from the bulk of the electrode to the surface may be slow enough so that during a run their rate of arrival will be insignificant. Also, under the proper conditions, such impurities may react and be removed as the run is being made. Depending on the net rate of the particular reaction being studied, the effect due to impurity reaction, may or may not be significant. In addition catalytic poisoning effects are possible.

Other possible sources of unremovable impurities in the electrolyte are the solvent, chemicals which compose the solute, and solution of species from the cell walls. The amounts of such unremovable species may be maintained at a low level, but their complete removal is not, as yet, possible. The best one can hope for is that such impurities have secondary effects only on the electrode processes under investigation. In short, one can with present techniques reduce the level of reactable impurities to very low quantities ( $10^{-12}$  to  $10^{-13}$  parts) and maintain these levels for long periods of time in a properly closed system (1, 2). Unremovable impurities should be maintained at as low a level as possible by careful purification and selection of materials and by adsorption on large areas of inert materials. It should always be kept in mind, however, that any such adsorbents, no matter how inert they are, also do contribute impurities to the system. The really important consideration concerning unremovable impurities is how they affect the electrode process being studied.

### Experimental

The high-purity closed electrochemical system and the experimental conditions were essentially the same as previously used (1, 2). Before each run, the cell was cleaned with hot concentrated nitric acid and rinsed by continually distilling triply distilled water into it for at least 24 hr; finally, about 100 ml of water

\* Electrochemical Society Active Member.



was distilled into the cell and cooled. The highest purity sodium hydroxide solutions (designated NaOH) were prepared by breaking in two a capsule of sodium metal (99.95% with < 55 ppm heavy metals, with the major unremovable impurities being potassium, iron, calcium, silicon, magnesium, and carbon, sealed under argon) and introducing the two halves into the cell under an atmosphere of purified helium. The two halves of the capsule were placed so the open ends were at the bottom of the cell. Thus as sodium metal dissolved, the hydrogen gas generated filled the capsule ends and regulated the introduction of water into the capsule. This allowed a rather slow solution of sodium metal.

Less pure sodium hydroxide solutions were prepared using a reagent grade sodium hydroxide (97.4%) pellets (designated NaOH pellets). The major unremovable impurities were  $\text{Na}_2\text{CO}_3$  (0.64%), NaCl (0.003%), and silicate (0.01%). Lithium hydroxide solutions were prepared using lithium metal from two sources (99.99 and 99.92%). The unremovable impurities were primarily potassium, sodium, chloride, calcium, silicon, aluminum, and iron.

The working electrodes were Fe wires (fabricated from 3 pass electron beam zone refined iron with less than 4 ppm metallic impurities, 20 mil diameter, geometric area about  $0.7 \text{ cm}^2$ ); a similar Fe wire with about 1 cm of 3 mil Pt wire spot welded to the Fe wire and wound around its tip (designated Fe  $\gg$  Pt electrode); and a Pt wire (99.99%, 20 mil diameter, geometric area =  $0.65 \text{ cm}^2$ ). Each of these electrodes were connected to Pt leads and sealed off in lead-free soft glass tubes. The counter electrode was a large Pt gauze electrode. The reference electrodes were in an arm off the main cell compartment and were a calibrated (*vs.* Pt/ $\text{H}_2$  in the same solution) miniature glass electrode and a Pd wire charged with hydrogen to a potential of about 50 mv positive to a hydrogen electrode in the same solution. This Pd-H wire electrode was used as the potentiostatic reference.

Each solution was pre-electrolyzed for several days in a helium saturated solution using a Pt pre-electrolysis cathode which was then removed from the cell. The purified helium flow was then replaced with a flow of hydrogen which was purified by passing through heated Pd-Ag tubes. The Pt wire, Pt gauze and Pd wire potentials were then determined against the glass electrode. After the Pt/ $\text{H}_2$  electrodes reached their equilibrium values and the Pd wire was 50 mv positive to the Pt/ $\text{H}_2$  potentials, an Fe wire (or Fe  $\gg$  Pt), cleaned in 1M  $\text{H}_2\text{SO}_4$  and rinsed with triply distilled water, was introduced into the cell under an anodic applied potential as the working electrode in the potentiostat circuit. The glass reference electrode continuously monitored the potential on the Fe working electrode via a Keithley 610B Electrometer. Current flow under potentiostatic conditions was determined with a Keithley 601 Electrometer and recorded.

A point was determined on the potentiostatic polarization curve by holding the working electrode at a constant potential [calculated and recorded in reference to the normal hydrogen electrode (NHE)] until a constant current was reached. The time required to reach steady state varied from minutes to days depending on the potential and potential sequence. The potential was then increased and the new steady-state current determined. This was continued until the potential was well into the oxygen generation region after which the potential was made less noble in similar constant current steps until the potential was well into the hydrogen generation region. Stepwise potential increases in the noble direction followed until a full potential cycle was achieved. The cycling continued until the current readings for consecutive cycles were consistent in value. These are the values given in the figures. It was found that several cycles over a period of several weeks were required before consistent polarization curves were attained. We believe that the inconsistencies in the initial cycles

were due to traces of reactable impurities (primarily organic) which were slowly removed by oxidation. The temperature was  $25^\circ \pm 2^\circ\text{C}$ , and the flow rate of gas was normally 40 ml/min.

### Characteristic Impurity Effects

During the pretreatment period when the potentiostatic current density *vs.* potential points varied considerably from cycle to cycle, certain characteristic behavior was observed which reflected decreases of reactable impurity levels in solution, from the electrode surfaces, and in the uppermost layers of the working electrode. In addition certain slow changes in the state of the working electrode surface undoubtedly occurred. We are not, as yet, in a position to specify, or even to speculate on, the species on the surface of the iron electrode and the changes which occur as the potential is varied. However, under the high-purity conditions which were maintained after the pretreatment purification, the surface states were consistently reproducible. The iron electrode itself underwent no visible change from the beginning to the end of a run (and some lasted for several months). The appearance of the iron did not indicate significant corrosion. Analysis of the solution at the end of a three month run gave about  $0.1 \mu\text{g}$  in the 50 ml of solution in the cell. Evidently the trace of iron which may come from the Fe electrode is so small that the anodic currents determined under potentiostatic conditions were primarily due to  $\text{OH}^-$  and water oxidation rather than to Fe oxidation.

Figure 1 represents typical current density changes with time due to a change in the working electrode potential. These show characteristic impurity behavior. Curve A, Fig. 1, typifies the smooth current *vs.* time behavior found after the pretreatment cycle purification. Curve B, is a synthesis which illustrates some of the abnormalities that may be caused by impurities found in a newly prepared electrolyte. Irregularities may occur such as those shown at point 1 or false trends such as those found in the neighborhood of point 2.

Oscillations similar to point 3 may occur and tend to extend over the full length of the curve. Over fairly long intervals their frequency and amplitude are roughly constant. Oscillations may occur from one every few seconds to one every few minutes and may be so large that they obscure the base curve and make it difficult or impossible to determine the final reading for the constant current value. Oscillations of this type have been induced in the pure Fe/NaOH system by the addition of small amounts of  $\text{O}_2$  or  $\text{Cl}^-$ .

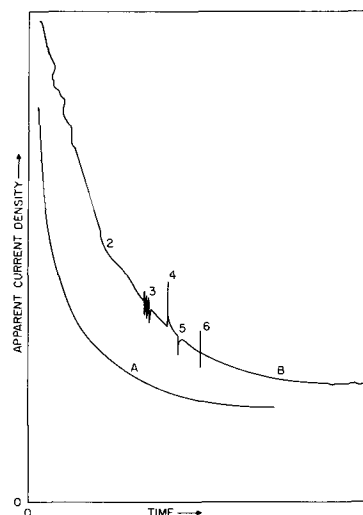


Fig. 1. Typical current density changes with time following potential change: curve A, electrochemically purified system; curve B, types of abnormalities caused by impurities, No. 1-6 are explained in the text.

Impurities can cause sharp breaks in the current *vs.* time curve such as shown at points 4, 5, and 6 of curve B, Fig. 1. Such changes in current generally occur quite rapidly and then return fairly slowly to the normal rate. Impurities that are reactable can contribute to the net current and can either sharply increase or decrease its value depending on whether they are oxidized or reduced.

For the purest Fe/NaOH system, at anodic currents, the number of coulombs that are passed from the start of the current-time curve until constant current, are approximately constant and roughly equal to a fraction of a monolayer (2 electron reaction). This value is less for small potential steps and at potential settings which give relatively low current densities and appreciably higher for large potential steps and at potentials which give high current densities. In comparing curve B to A in Fig. 1, it can be seen that the presence of reactable impurities increases the current at any given time and increases the time required for the current to become constant. Hence, when reactable impurities are present, the total number of coulombs which flow can be much larger.

Another important characteristic of reactable impurities in solution is the stirring effect. The pure Fe/NaOH system under helium flow was essentially independent of stirring rate (40-1000 ml He/min) except at the lowest current densities ( $10^{-9}$  amp/cm<sup>2</sup>). Reactable impurities gave substantial current differences at the highest stirring rate. The direction of such a current change depended on whether the current at slow He flow was anodic or cathodic and whether the impurity was being oxidized or reduced. Each of the effects shown in Fig. 1, curve B, have been induced by addition of impurities, such as Cl<sup>-</sup> to a pure Fe/NaOH system.

Previous work (1) has shown that it is possible to estimate the amount of oxidizable or reducible impurities present in a purified system. This is done by introducing known trace amounts of hydrogen or oxygen to the helium flowing into the cell and observing the minimum amount required to change the steady-state current density at a sensitive (very low steady-state current density) set potential. Such measurements have been made for the systems investigated in this work, and it was shown that under the conditions which data were taken the minimum levels of oxygen or hydrogen to which the system was sensitive was approximately  $10^{-6}$  ppm.

In addition to reactable impurities, which have been reduced to insignificant values in this work, the question of the effects of unremovable impurities must be considered. In the system used, one immediately becomes concerned with the presence of such impurities which dissolve from the Pyrex glass cell. These would primarily consist of silicate, borate, aluminate, sulfate, phosphate, and chloride. Our first reaction was to avoid alkali-glass contact in the cell by use of a Teflon coating or use of a noble metal cell. However, on consideration of the total unremovable impurity problem it was soon realized that this would be an essentially useless complication. This is because similar amounts of the same impurities would remain in any cell. The level of such impurities is determined primarily by the unremovable impurities in the water, chemicals (Na, Li, NaOH) used to form the solution, the electrodes, and the impurities which come from the atmosphere (dust, etc.) which are virtually impossible to avoid in the assembly of any system. These impurities cannot be satisfactorily removed at the present time or even be reduced to levels which are significantly less than monolayer quantities.

In any case, the best we can do at present is to determine, as well as possible, if such unremovable impurities do affect the electrode reactions of interest in a primary way. Using 99.95% sodium metal, 97.4% NaOH pellets, 99.99 and 99.92% lithium metal in the preparation of solutions, we could compare data taken

with each solution after the pretreatment purification procedures on each. The amounts of unremovable impurities varied considerably from solution to solution, but in all cases there undoubtedly were sufficient amounts of any of these impurities to form multiple monolayers if they deposited on the electrode surfaces. The actual data showed some significant differences which will be discussed later, but the over-all current density *vs.* potential curve shapes and characteristics were fundamentally the same. It was felt that most of the unremovable impurities, such as, silicates, borates, phosphates, sulfates, etc., would have little effect since adsorption of hydroxide would predominate in potential regions where the net charge on the electrode was positive. This is verified by the work of Pryor and Cohen (3) who showed that nonoxidizing anions had corrosion inhibiting effects very similar to hydroxyl ion in the presence of air and that in the absence of air nonoxidizing anions do not inhibit iron corrosion. The most likely unremovable anion which may have important effects on electrode processes is chloride ion (and other halides) and most of the differences found for the varying purity of solutions used in this work can be reasonably laid primarily to the differences in chloride ion content. This was at the highest value for the sodium hydroxide pellets (0.003%), and this solution did give the widest variation in results from the purest solution studied. Work was done in which chloride additions (0.2%) did cause large differences in behavior and actual visual corrosion of the iron. This is reported below.

### Experimental Results

Figure 2 shows the potentiostatic polarization curves obtained in electrolyte prepared using 99.95% sodium metal which then underwent extensive pre-electrolysis. In all the figures, the symbol  $\Delta$  represents a steady-state current density made at a set potential that was higher than the potential of the previous reading (increasingly noble potential sequence). Conversely, the symbol  $\nabla$  indicates that the potential sequence was decreasingly noble.

Curve AEF (Fig. 2) represents the increasing potential sequence data found when the initial potential was negative to, or at  $-0.17$ v. The decreasing potential sequence starting at potentials positive to  $0.76$ v (point E) gave data on curve FCA. If, on the decreasing potential sequence FCA, the potential was taken to point B ( $0.04$ v) and then a sequence of more noble potentials were applied, curve BDF was obtained. If, on the increasing potential sequence, AEF, the most noble potential applied was  $0.76$ v (point E) and the potential was subsequently decreased, the data points fell on curve EDDBA.

In any segment where the arrow indicates the direction of change of the potential sequence, a reversal in potential gave a reading on that segment. For example; in a segment such as AE which shows what happens when the potential is increased stepwise from point A to point E, any decrease from a point in

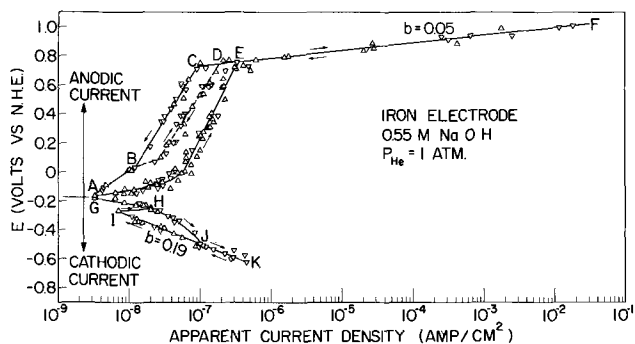


Fig. 2. Fe potentiostatic polarization curves in 0.55M NaOH:  $\Delta$  increasing potential sequence;  $\nabla$  decreasing potential sequence; letters A-K are explained in the text.



AE which does not take the potential below point A, will give a reading which is still on the segment AE. This is indicated by  $\Delta$  and data points for each curve segment in Fig. 2.

At point A and above the currents are anodic, while at point G and below they are cathodic. As the potential is made more cathodic below point G, the readings followed curve GHJK. Making the potential more noble in the region JK gave data points which followed curve KJHG.

The results shown in Fig. 2 were obtained for 0.55M NaOH (13.4 pH). Runs were made also at 0.30 (13.2 pH), 0.13 (12.9 pH), and 0.067 (12.7 pH) M concentrations. Such variations in concentration had little effect on the data shown, except for the segment CF. In this potential region, a decrease in alkali concentration resulted in a linear segment parallel to CF with the current densities being generally smaller as the solution was more dilute. Similar results were found with LiOH and other NaOH solutions.

The experiments depicted in Fig. 2 were repeated in a 0.2M NaOH (13.1 pH) solution prepared from a different batch of high-purity sodium from the same supplier. The results are shown in Fig. 3 which includes data from Thomas and Nurse (5) taken in 0.1M NaOH. Figure 4 shows the results which were obtained from a 0.58M NaOH electrolyte prepared from a reagent grade NaOH (NaOH pellets).

A 0.85M LiOH solution was prepared from high-purity metallic lithium (99.92%). The potentiostatic polarization curve is shown in Fig. 5. When this solution was diluted to 0.34M LiOH, the change in this curve was negligible except in the linear  $b = 0.04$  region where the curve ran about 0.06v higher.

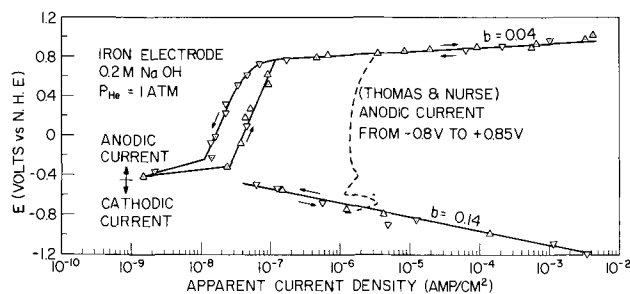


Fig. 3. Fe potentiostatic polarization curves in 0.2M NaOH. See Fig. 2 for meaning of symbols. Data from Thomas and Nurse (5),

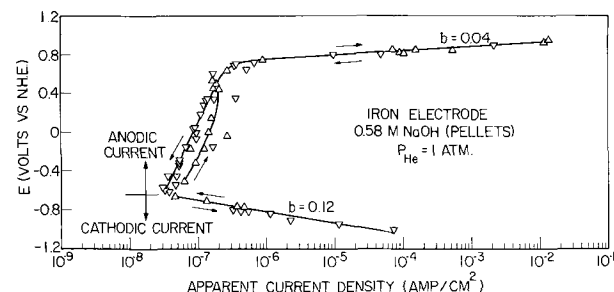


Fig. 4. Fe potentiostatic polarization curves in 0.58M NaOH (pellets). See Fig. 2 for meaning of symbols.

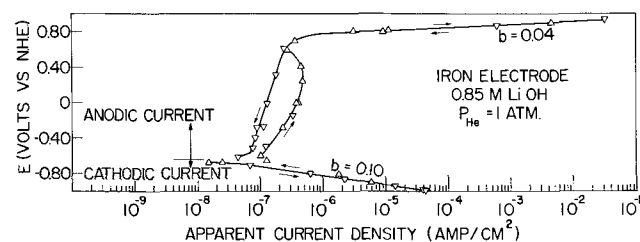


Fig. 5. Fe potentiostatic polarization curves in 0.85M LiOH. See Fig. 2 for meaning of symbols.

A 0.28M LiOH solution was prepared from another pure lithium (99.99%) sample which contained about one fifth the amount of unreactable impurities as the lithium used in Fig. 5. The results were very similar. The current densities were slightly lower, the hysteresis loop was narrower, and the change-over from anodic to cathodic current occurred at about 0.55 instead of 0.64v.

### Discussion

There are a number of differences in the results shown in Fig. 2 to 5. Most of them are small and can probably be attributed to the presence of different unremovable impurity levels. The important fact here is that in every case in which the reactable impurities have been reduced to the very low levels represented by these data, the iron behaves as an inert or noble electrode. The current densities are very small and in the anodic region primarily represent the oxidation of  $\text{OH}^-$  and possibly  $\text{H}_2\text{O}$  to oxygen, whereas in the cathodic region, the primary reaction is the reduction of water to hydrogen. The electrodes showed no corrosion or etching either visibly or under low-power microscopic examination. The iron remained bright and shiny throughout the runs without any visible discoloration.

The electrolyte used in obtaining the data in Fig. 4 was prepared from reagent grade NaOH pellets and had by far the highest level of unremovable impurities. The sodium carbonate content was 65 ppm, which was at least one order of magnitude higher than that in the other Fe/NaOH systems. The data shown in Fig. 2 are believed to be for the purest system. In going from Fig. 2 to Fig. 3 and finally to Fig. 4, it can be seen that the anodic hysteresis loop becomes much narrower. In going from Fig. 2 to 4, it can be seen that the current density decreases slightly over the major part of the hysteresis loop and the change-over potential from anodic to cathodic current decreases. These differences may be related to the level of unremovable impurities.

It is interesting to note that the width of the hysteresis loop, shape of the curves, current densities, and change-over potential from anodic to cathodic current did not vary appreciably when the electrolyte used to obtain Fig. 2 was diluted in four steps from 0.55 to 0.067M NaOH or when the LiOH used for Fig. 3 was diluted from 0.85 to 0.34M. If the differences observed in Fig. 2-4 are caused by impurities, it is not the variations in level of impurity that is important but rather the type of impurity or possibly the ratio of impurity to  $\text{OH}^-$ .

In the case of LiOH the impurity differences in the two samples of metallic lithium used were not as great as for the sodium hydroxide solutions. For LiOH the narrower hysteresis loop was obtained with the solution made from the purer sample. The differences in  $\text{Li}^+$  and  $\text{Na}^+$  are not great enough to conclude that there is a cation effect. Here again the small differences in behavior are most likely due to the differences in specific unremovable species rather than the net amounts of the total amount of unremovable impurities.

The potentiostatic polarization curve for a platinum electrode in 0.2M NaOH is given in Fig. 6. Compared to the Fe electrode data (Fig. 2 to 5) the general electrode behavior for Pt and Fe in alkaline solution are quite similar. Both metals are essentially inert electrode materials on which  $\text{OH}^-$  and water can be either slowly oxidized to oxygen or reduced to hydrogen depending on the set potential. The anodic hysteresis effect found on platinum in acid solution (1) was attributed to the dermasorption of oxygen atoms at high positive potentials. Similarly it is believed that the hysteresis found on Pt (Fig. 6) in alkaline solution is due also to dermasorbed oxygen atoms. The anodic hysteresis found for Fe electrodes (Fig. 2 to 5) can be attributed to the formation of an iron oxidelike species in the uppermost layers of iron. There is certainly no formation of an extensive bulk iron oxide on the surface

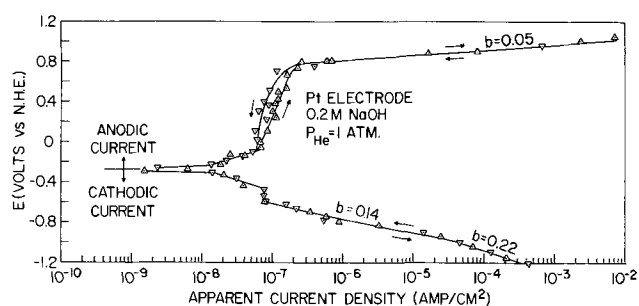


Fig. 6. Pt potentiostatic polarization curves in 0.2M NaOH. See Fig. 2 for meaning of symbols.

although a thin film of iron oxide is undoubtedly present (6). The exact nature of the species on the iron surface, its interactions at the metal/solution interface, are not known and further work is required to clarify these very important points.

A question arises as to whether the platinum counter electrode does contribute Pt which contaminates the Fe electrodes investigated. It has been shown (4) that a pure Fe electrode operating under the conditions described in this paper is a far better catalyst for the hydrogen oxidation reaction than a Pt electrode. A small piece of Pt attached to an Fe wire electrode actually reduced the activity of the iron for the hydrogen oxidation reaction and gave a very different potentiostatic polarization relation (4). This demonstrated that the contamination of Fe with Pt did not occur in our system.

Potentiostatic current density vs. potential curves were determined for an Fe  $\gg$  Pt and an Fe = Pt (an Fe wire shorted outside the cell to an equal size Pt wire) electrode in helium-saturated 0.2M NaOH. The results are shown in Fig. 7 and 8. Comparing Fig. 7 and 8 with those for pure iron and platinum (Fig. 2 to 6) show a number of minor differences which indicate that the contamination of an Fe electrode with Pt would have slight effects only. The

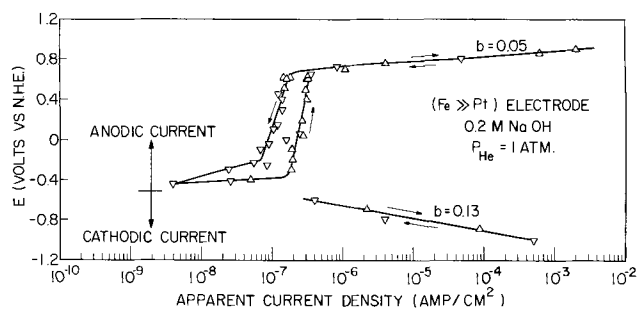


Fig. 7. Fe  $\gg$  Pt potentiostatic polarization curves in 0.2M NaOH. See Fig. 2 for meaning of symbols.

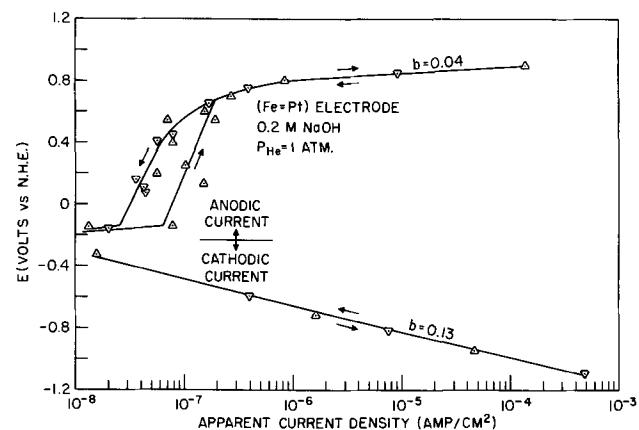


Fig. 8. Fe = Pt potentiostatic polarization curves in 0.2M NaOH. See Fig. 2 for meaning of symbols.

important thing to note is that in each of these cases each electrode is inert and that no appreciable corrosion is taking place. (A small amount of a light brown corrosion product was found only for the Fe  $\gg$  Pt electrode at the juncture of the two metals.) Moreover in each of these cases the current densities have generally the same small values and the polarization curves have essentially the same shapes.

The major removable trace impurities whose presence may affect potentiostatic polarization curves are oxygen, hydrogen, organic species, and metals. The initial pre-electrolysis in the high-purity closed system used has reduced the level of metallic impurities to at least their level in the electrode material itself. In fact, such impurities at the electrode surface are probably much less than in the bulk of the electrode metal itself. The other impurities were removed by the repeated oxidation or reduction procedure used. The levels of these impurities (other than the amounts of hydrogen or oxygen generated at the applied potentials) were found to be less than  $10^{-6}$  ppm as calculated on the basis of the hydrogen oxidation or oxygen reduction currents required to change the residual current density at a potential near the change-over from net cathodic to net anodic reactions (1). Since the steady-state currents for many inert electrodes, such as iron, are so small in their inactive potential region, they can be completely eclipsed by the electrode reactions due to oxidizable or reducible trace impurities.

To study the effect of an impurity which is unremovable but still may alter electrode behavior, experiments were run in which chloride ion was deliberately added (as NaCl). Figure 9 shows the change in steady-state polarization behavior which the iron electrode underwent upon the addition of 0.2%  $\text{Cl}^-$  to 0.2M NaOH. The Fe electrode with this  $\text{Cl}^-$  addition was covered with a heavy dark brown corrosion film which formed during polarization. The open triangles represent anodic current, and the solid triangles represent cathodic currents. The leftmost broken line indicates the variation which occurred between cycles so that there is no clear hysteresis at potentials above 0.3v. For the decreasing potential sequence at potentials above 0.8v, the current density remains fairly constant, and the activation at  $-0.1$ v was not observed. Thus, there is a large hysteresis loop in which the current density for the increasing potential curve is more than an order of magnitude higher than it is for the decreasing potential curve.

As the potential decreased, the current went from anodic to cathodic at about  $-0.25$ v. When the potential was increased, the current went from cathodic to anodic at about  $-0.65$ v. This large difference in change-over potentials observed in the presence of  $\text{Cl}^-$  is in marked contrast to the purer systems (Fig.

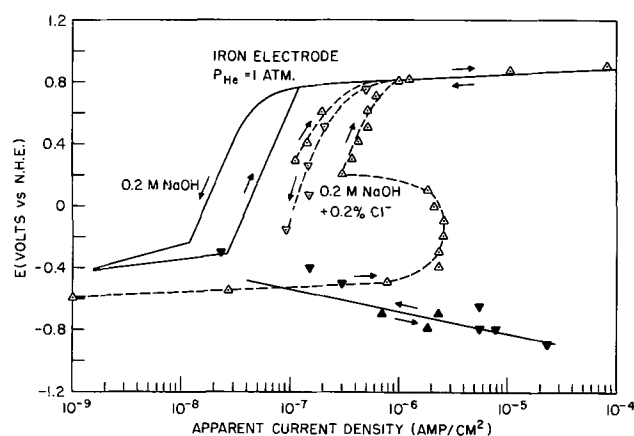


Fig. 9. Effect of addition of 0.2% chloride ion on Fe potentiostatic polarization curves in 0.2M NaOH:  $\Delta$  anodic current, increasing potential;  $\nabla$  anodic current, decreasing potential;  $\blacktriangle$  cathodic current, increasing potential;  $\blacktriangledown$  cathodic current, decreasing potential.

2-5), where in any given system the change-over from anodic to cathodic currents and from cathodic to anodic occurred at essentially the same potential.

After the run the electrode remained at open circuit for about a week in the electrolyte while bubbling hydrogen through it. During this time the dark brown oxide film disappeared leaving a shiny but extensively pitted wire. The steady-state open-circuit potential in this hydrogen-saturated solution was  $-0.682\text{v}$ . In the absence of added chloride ion, the Fe wire electrode potential was at the equilibrium hydrogen potential of  $-0.78\text{v}$  (4).

On the increasing potential sequence shown in Fig. 9, the Fe electrode does undergo normal passive behavior, the potential of highest activity for iron corrosion being about  $-0.1\text{v}$ . An attempt was made to duplicate the results of Thomas and Nurse (5) shown in Fig. 3. Their data were taken 5 min after a change in potential. Using a similar technique of taking readings 5 min after a change in potential in the chloride containing NaOH, the results shown in Fig. 10 were obtained. Under these conditions passivity behavior similar to that found by Thomas and Nurse was observed.

It has been shown that the high-purity Fe/NaOH system very effectively oxidizes hydrogen (4). The potentiostatic polarization curve for this system is shown by the broken line in Fig. 11. The curve for the identical system to which 0.2%  $\text{Cl}^-$  was added is shown as a solid line. The variations of the increasing and decreasing potential data about this solid line are small, which is in sharp contrast to the large variations obtained in an inert helium atmosphere (Fig. 9). This indicates that the fraction of the current density in the  $\text{Cl}^-$  contaminated solution which represents corrosion is much less than the fraction that represents oxidation of hydrogen. In the high-purity system, the

current density is so high that it must be essentially all due to hydrogen oxidation.

Chloride contamination makes iron an extremely poor catalyst for the hydrogen oxidation reaction. First, the iron is no longer a reversible hydrogen electrode and even at very low current densities, the polarization potential required for hydrogen oxidation is over  $0.2\text{v}$  above the reversible hydrogen potential. Second, at comparable potentials the chloride-free NaOH oxidizes hydrogen about  $10^3$  times faster. In terms of fuel cell operation, which would be at low polarization potentials, the chloride-free system is infinitely better.

Another important consequence of the data shown in Fig. 11 is that the passivation (reversal of  $dE/d\log i$ ) of the hydrogen oxidation reaction which occurs in the pure NaOH at about  $-0.3\text{v}$  is essentially nonexistent in the chloride contaminated NaOH. This confirms the hypothesis (7) that passivation can be caused by a reduction in the active electrode area, but is primarily due to a poisoning of catalytically active sites which cause large changes in the heat of activation for the hydrogen oxidation reaction on the electrode surface. On an iron electrode in alkali solution, chloride ion and the resultant corrosion products induced by its presence so completely retard the hydrogen oxidation reaction that the catalytic properties of the electrode are virtually nonexistent and therefore further adsorption of anions at more noble potentials does not cause significant active area changes or passivation of the hydrogen oxidation reaction. In the chloride-free NaOH, the passivation of the hydrogen oxidation is rather small and is most likely primarily an effect of reduction in active electrode area due to anion adsorption (4).

## Conclusions

In the high-purity alkaline solutions used, iron does not significantly corrode or show passive behavior [defined (7) as a condition in which the net reaction rate decreases with an increase in potential] over a wide range of concentrations and potentials. Iron acts like an inert noble metal similar to platinum rather than as a "passivated" metal. Depending on potential the primary reactions are the oxidation or reduction of  $\text{OH}^-$  and water. This does not mean that the iron electrodes used do not have species other than iron atoms on their surfaces. The species on the surface of the iron have not been determined by us; however, Foley *et al.* (6) have found a  $\gamma\text{-Fe}_2\text{O}_3$ ,  $\text{Fe}_3\text{O}_4$  film on passive iron in alkaline solution. Hysteresis effects were observed on decreasing the potential sequence after high noble potentials were applied. This caused a reduction in  $\text{OH}^-$  oxidation rates which are likely caused by changes in the surface layers on the iron.

Iron in the high-purity, closed system is an excellent catalyst for the electrochemical oxidation of hydrogen, being appreciably superior to Pt (4). Chloride ion causes extensive iron corrosion, completely changes the potentiostatic polarization relation, and does show passive behavior. Chloride ion virtually destroys the catalytic properties of the Fe electrode for the hydrogen oxidation reaction.

The presence of reactable impurities was shown to change strongly the electrochemical behavior of iron in alkali solution. The high-purity, closed electrochemical system successfully eliminated the major effects of such impurities.

Even though there were some variations among the high-purity Fe-alkaline systems investigated, each system had approximately the same shape curves and the same low activity for both water oxidation or reduction except at extremes in anodic or cathodic potentials, respectively.

The variations in behavior for the various Fe/alkaline systems studied may be largely due to the unremovable impurities. Probably the most important of these would be halide ions. Such impurities as carbonate, silicate, sulfate, etc., which are unre-

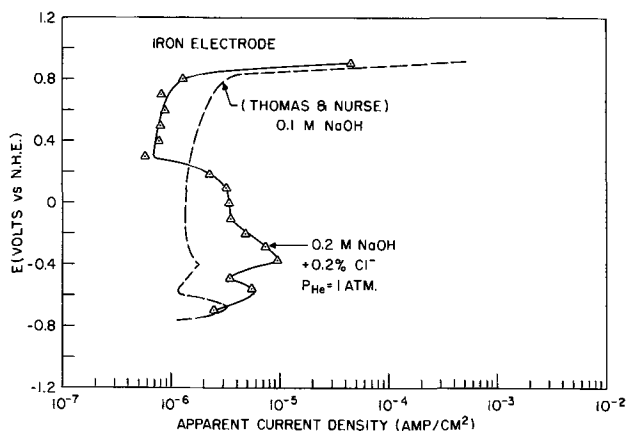


Fig. 10. Comparison of Fe (chloride contaminated) potentiostatic polarization curves with results of Thomas and Nurse (5). Data points taken 5 min after each potential setting.  $\Delta$  increasing potential sequence.

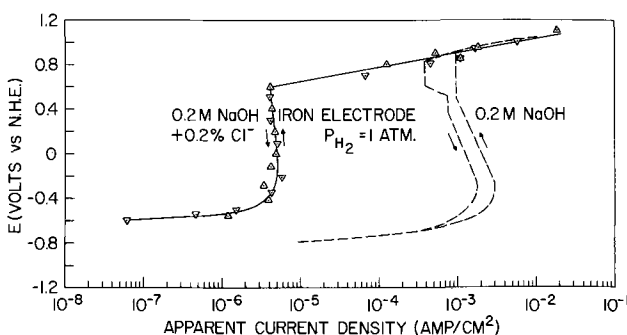


Fig. 11. Rates of hydrogen oxidation on potentiostated Fe in 0.2M NaOH and the effects of chloride ion contamination. See Fig. 2 for meaning of symbols.

movable may have caused minor differences in various runs. However, it is felt that the effects of the major anion,  $\text{OH}^-$ , would override those of other trace inert anions.

### Acknowledgment

This research was supported by the Advanced Research Projects Agency of the Department of Defense as part of the ARPA Coupling Program on Stress-Corrosion Cracking (ARPA Order 878).

Manuscript submitted April 19, 1968; revised manuscript received July 11, 1968. This paper was presented at the Montreal Meeting, Oct. 6-11, 1968, as Paper 390.

Any discussion of this paper will appear in a Discussion Section to be published in the June 1969 JOURNAL.

### REFERENCES

1. S. Schuldiner, T. B. Warner, and B. J. Piersma, *This Journal*, **114**, 343 (1967).
2. S. Schuldiner, B. J. Piersma, and T. B. Warner, *ibid.*, **113**, 573 (1966).
3. M. J. Pryor and M. Cohen, *ibid.*, **100**, 203 (1953).
4. S. Schuldiner and C. M. Shepherd, *ibid.*, **115**, 916 (1968).
5. J. Thomas and T. Nurse, *Brit. Corrosion J.*, **2**, 13 (1967).
6. C. L. Foley, J. Kruger, and C. J. Bechtoldt, *This Journal*, **114**, 994 (1967).
7. S. Schuldiner, *ibid.*, **115**, 897 (1968).

## Anodic Polarization of Austenitic Stainless Steels in Chloride Media

A. P. Bond\* and E. A. Lizlovs

Research Laboratory, Climax Molybdenum Company of Michigan, Ann Arbor, Michigan

### ABSTRACT

Potentiodynamic polarization experiments were performed in 0.1N hydrochloric acid and in 1N sodium chloride with austenitic alloys containing 18 to 20% Cr, 13 to 39% Ni, 0 to 5% Mo, and balance Fe. The pitting potentials varied consistently with alloy content and correlated well with the results of exposure tests in 0.33M ferric chloride. Increasing the molybdenum and nickel contents increased the resistance to pitting; however, decreasing the carbon and nitrogen contents also increased the resistance to pitting. Critical current densities for passivity decreased sharply at all nickel levels with increases in the molybdenum content.

One of the most important contributions of molybdenum alloying additions to stainless steels is the resulting increase in the resistance to pitting corrosion. Although this behavior has been known for a long time, very little quantitative information is available. Recent work on potentiodynamic determination of pitting potentials (1-6) suggests that this technique should be very useful in determining the relative pitting resistances of various alloys.

A study was undertaken to learn whether or not the concept of a pitting potential is valid and useful in characterizing the resistance to pitting corrosion of molybdenum-containing stainless steels. Once the utility of the technique was established the next step was to determine in detail how variations in molybdenum content affect the resistance of various stainless steels to pitting in environments containing chlorides. In achieving this goal, it seemed desirable to use stainless steels of widely differing nickel contents so that possible nickel-molybdenum interactions could be detected.

### Procedures

Two series of austenitic stainless steels, one containing about 13% nickel and the other 39% nickel, were induction-melted in an argon atmosphere and cast in air. Each series was prepared using the split heat technique. In this technique, the base composition is melted and part of the melt is cast into an ingot. To the balance of the melt, the required molybdenum addition is made and the next ingot is cast. This process is repeated until a series of the desired compositions is cast. By this procedure, the residual and impurity elements, which were intended to be in the range commonly present in commercial stainless steels, were held essentially constant within each series.

Three high-purity alloys were also prepared as separate heats by melting and casting in vacuum.

The compositions of all alloys produced for this investigation are shown in Table I.

The ingots were hot-forged and hot-rolled to a thickness of 0.76 cm and then cold-rolled to 0.38 cm. The 13% nickel steels were annealed at 1120°C for 1 hr and water-quenched. The 39% nickel steels and the high-purity alloys were annealed at 1150°C for 1 hr and water-quenched.

The electrodes for the potentiodynamic studies were mounted in acrylic plastic with a single exposed surface parallel to the rolling plane. Electrical contact was made by soft soldering a nickel wire to the back of the electrode. Soldering was accomplished quickly (about 5 sec) to minimize heat input, although no metallurgical changes would be expected even if the test surface of the electrode were heated to the melting point of the solder (190°C) for a few seconds. Contact between the solder or lead wire and the electrolyte

Table I. Compositions of alloys studied

Cr, %	Ni, %	Mo, %	Mn, %	Si, %	C, %	N, %
High-nickel austenitic series						
19.97	39.09	0.025	1.21	0.46	0.056	0.040
NA <sup>a</sup>	NA	0.97	NA	NA	NA	NA
NA	NA	3.03	NA	NA	NA	NA
20.01	39.13	4.85	NA	NA	NA	0.039
Low-nickel austenitic series						
17.67	13.57	1.99	1.84	0.45	0.025	0.030
NA	NA	2.45	NA	NA	NA	NA
NA	NA	2.93	NA	NA	NA	NA
NA	NA	3.37	NA	NA	NA	NA
17.60	13.56	3.89	1.72	0.53	0.027	0.033
High-purity austenitic series						
17.86	16.13	0.067	—	0.09	0.002	0.010
18.01	16.25	2.48	—	0.08	0.003	0.012
18.07	16.17	4.99	—	0.09	0.004	0.012

\* Electrochemical Society Active Member.

<sup>a</sup> NA = not analyzed, but in the range of the series.

was excluded by the plastic and a glass tube. The exposed surface ( $0.5 \times 0.6$  cm) was polished using standard metallographic techniques, ending with the distilled water slurry of  $0.3\mu$  alumina. For the pitting potential measurements, the electrode was masked with electroplater's tape (Scotch 470) except for a circular area 0.3 cm in diameter.

The potentiodynamic scanning experiments were performed using standard equipment and techniques. The platinum auxiliary electrode was isolated from the test solution by means of a glass frit. The solutions used were argon-saturated 0.1N HCl and 1.0M NaCl. All potential measurements were made using a saturated calomel reference electrode. Work reported in the literature (3,4,6) indicates that pitting potentials measured on stainless steels are quite dependent on experimental procedure. To minimize the effects of the prior history of the electrodes, the potential scans were started with  $-0.7$ v in the active region. By scanning into the passive potential region, the passive film was formed *in situ* under reproducible conditions. Scanning rates in most tests were 600 mv/hr up to potentials of about 0.2-0.3v less noble than the expected pitting potential. At this potential, the scanning rate was decreased to 60 mv/hr. In a few tests, this procedure was varied to determine the effect of change in scanning rate on the observed pitting potential.

Exposure tests were performed in 0.33M  $\text{FeCl}_3$  dissolved in 0.01N HCl. This medium gave a chloride ion concentration equal to that in the 1.0M NaCl medium used in the polarization measurements. Test coupons,  $2.5 \times 3.8 \times 0.3$  cm, were suspended in the unstirred solution by means of a glass rod through a 0.64-cm hole in each specimen. In all experiments, the temperature was  $24^\circ \pm 1^\circ\text{C}$ .

## Results

**Measurements in 0.1N HCl.**—The initial anodic polarization measurements in 0.1N HCl disclosed that crevice corrosion occurred at the interface between the metal and the plastic mount. Masking the electrode surface with electroplaters tape usually eliminated this crevice corrosion. These effects are illustrated in Fig. 1. Microscopic examination of the electrodes after the runs depicted in Fig. 1 showed that neither electrode was pitted, confirming that the rise in current for the unmasked electrode starting at about 0.1v was due to crevice attack and the rise in current at potentials above 0.8 for the masked electrode was the start of the normal transpassive region.

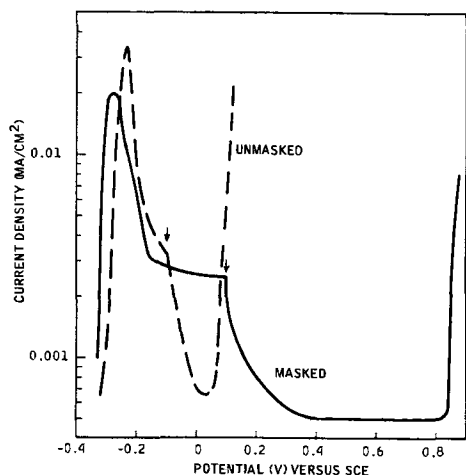


Fig. 1. Polarization curves obtained on masked and unmasked electrodes for the 17.6% Cr-13.6% Ni-2.45% Mo austenitic stainless steel in argon-saturated 0.1N hydrochloric acid. The potential was scanned from negative toward positive. The arrows indicate the potential at which the scanning rate was decreased from 600 to 60 mv/hr.

Since crevice corrosion on the unmasked electrodes did not occur until potentials much more noble than the primary passivation potential were reached, unmasked electrodes were used to determine the critical current density and primary passivation potential. The unmasked electrodes also allowed more precise determination of electrode area than did the masked electrodes.

The critical current densities (maximum anodic current density reached in the active region) and primary passivation potentials (potential at which the critical current density is reached) measured are shown in Fig. 2 and 3 and Table II. Examination of the data for both series of austenitic alloys reveals that increases in molybdenum content decreased the critical current density for passivation. This behavior is especially evident in the steels containing 39% nickel and in the high-purity alloys because these alloys cover a wider range of molybdenum contents. Comparison of the data for the three series of alloys, at roughly the same molybdenum contents, shows that the critical currents are in the same range.

The changes in molybdenum content within the range studied in the 13.5% nickel alloys had no effect on the primary passivation potentials ( $E_{pp}$ ), which were close to  $-0.26$ v. No pronounced variation of passivation potential with molybdenum content was

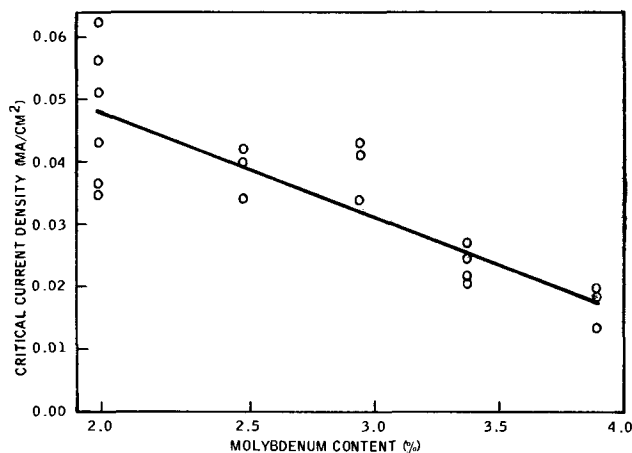


Fig. 2. Critical current densities obtained from potentiodynamic scans at 600 mv/hr in argon-saturated 0.1N hydrochloric acid on the 16.6% Cr-13.5% Ni steels.

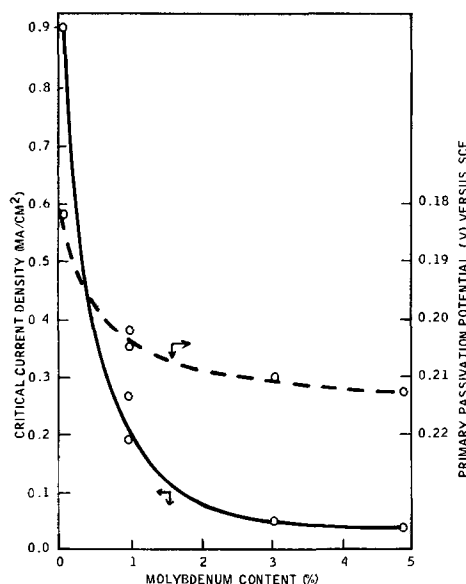


Fig. 3. Critical current densities and primary passivation potentials obtained from potentiodynamic scans at 600 mv/hr in argon-saturated 0.1N hydrochloric acid on the 20% Cr-39% Ni steels.

Table II. Primary passivation potentials ( $E_{pp}$ ) and critical current densities ( $I_{cr}$ ) for the 18% Cr-16% Ni high-purity alloys obtained from potentiodynamic polarization scans at 600 mv/hr in argon-saturated HCl

Molybdenum content, %	0.1N HCl		1.0N HCl	
	$I_{cr}$ , ma/cm <sup>2</sup>	$E_{pp}$ , v vs. SCE	$I_{cr}$ , ma/cm <sup>2</sup>	$E_{pp}$ , v vs. SCE
0.067	0.42	-0.265	— <sup>a</sup>	— <sup>a</sup>
2.48	0.050	-0.279	1.7	-0.250
4.99	0.012	-0.250	0.33	-0.275

<sup>a</sup> No passivation occurred for these steels in 1N HCl.

found in the high-purity series. In the 39% nickel series, increasing molybdenum did shift  $E_{pp}$  slightly in the active direction. On the other hand, comparison of the 39% nickel series with the 13.5% nickel series suggests that increasing nickel content shifted  $E_{pp}$  in the noble direction.

Because of the interference of crevice corrosion at the interface between the metal and the plastic mount, these electrodes could not be used to obtain pitting potentials. Figure 4 shows a typical potentiodynamic scanning curve obtained on a masked electrode in 0.1N HCl for a metal susceptible to pitting corrosion. Note that the decrease in scanning rate at 0.1v leads to a sharp drop in the passive current measured. The pitting potential is taken as the potential at which the passive current rises sharply. Microscopic examination revealed that pits were visible after this sharp rise in current and were not present when the electrode was examined before the current rise. Crevice corrosion, in addition to the normal pitting corrosion, was frequently initiated under the tape mask after the onset of pitting. For this reason the magnitude of the corrosion current after the onset of pitting was not a reliable indicator of the degree of pitting corrosion. In a few tests, only crevice corrosion was observed, and no true pits appeared on the free electrode surface. The data from these tests were therefore rejected. No potential scan was continued more than 20 mv beyond the potential at which passivity broke down, even if the breakdown was due only to crevice corrosion.

Most alloys studied were quite resistant to pitting in 0.1N HCl (Table III). None of the high-purity alloys exhibited a pitting potential less noble than

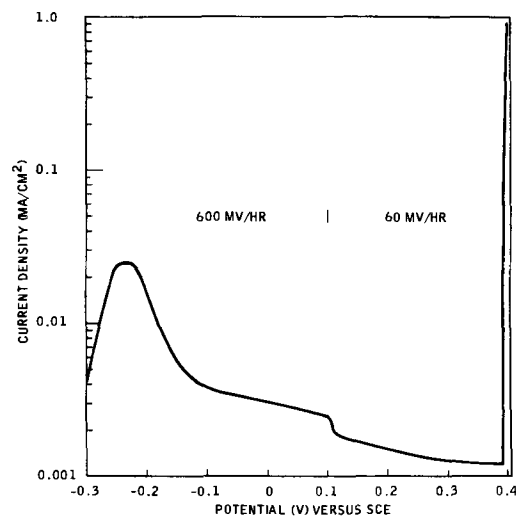


Fig. 4. Polarization curve obtained for 17.6% Cr-13.6% Ni-1.99% Mo austenitic stainless steel in argon-saturated 0.1N hydrochloric acid. The scanning rate was 600 mv/hr from -0.3 to 0.1v; it was decreased to 60 mv/hr from 0.1v to the pitting potential.

Table III. Pitting potentials obtained from potentiodynamic polarization scans in argon-saturated 0.1N HCl

Cr	Nominal composition, % Ni	Mo	Pitting potential, <sup>a</sup> v vs. SCE
High-nickel series			
20	39	0.0	0.64
20	39	1	NP <sup>b</sup>
20	39	3	NP
20	39	5	NP
Low-nickel series			
18	14	2	0.39
18	14	2.5	NP
18	14	3	NP
18	14	3.5	NP
18	14	4	NP
High-purity series			
18	16	0	NP
18	16	2.5	NP
18	16	5	NP

<sup>a</sup> Average of two or more runs.

<sup>b</sup> NP = no pitting up to 0.8v.

0.8v. Only the 39% nickel steel without molybdenum and the 13% nickel steel with 2% molybdenum displayed pitting potentials less noble than the transpassive range. Small increases in molybdenum content of the two susceptible alloys displaced the pitting potential beyond 0.8v. In addition, increasing the nickel content from 13.5 to 39% also increased the resistance to pitting corrosion.

*Measurements in 1M NaCl.*—An experimental program similar to that performed in 0.1N HCl was undertaken in 1.0M NaCl. The literature reports that increasing the chloride ion concentration increases the pitting susceptibility of stainless steels, but changing the pH from 1 to 7 does not affect pitting potentials (6). However, this increase in pH did suppress the critical current for passivity to such an extent that it could not be precisely measured on many of the steels tested. For this reason, the currents and potentials corresponding to the active-passive transition are not reported.

In contrast to the behavior observed in 0.1N HCl, in 1M NaCl many specimens showed current blips at potentials lower than those at which continuous pitting occurred. Microscopic examinations of electrodes on which momentary current increases had occurred showed some very small pits. Thus, these current blips appear to correspond to the initiation of a pit that then repassivates almost immediately. The pits thus formed are quite small and do not grow. A similar phenomenon has been described by Schwenk (2).

To check the significance of these current blips, some specimens were subjected to the usual potential scan until well-defined current pulses were obtained. At this point the scan was stopped, and the specimen was held at a constant potential while the current was recorded. The current pulses continued, becoming less frequent and smaller until they died away completely in a few hours. Holding electrodes at constant potentials, above those at which repassivating pits formed, for at least 24 hr did not cause a pit to propagate in any case. It is possible that these repassivating pits are associated with extremely small regions of considerable composition differences from the bulk composition and that after these regions are removed the pits are too small to propagate at the potential in question. Since this type of repassivating pit did not always occur on a given electrode and was never observed to lead to a propagating pit if the potential scan was stopped, the potential at which pits not only initiated, but continued to grow was taken as the most important pitting potential.

To determine the influence of scanning rate on these measurements, the 13.5% nickel steel containing 2.9% molybdenum was studied at various scanning rates in 1.0M NaCl. The results (Table IV) indicate that the pitting potentials tend to shift in the noble direction

Table IV. Pitting potentials obtained at various scanning rates on the 17.6% Cr-13.5% Ni-2.93% Mo alloy in 1.0M sodium chloride

Scanning rate, mv/hr	Repassivating pitting potential, v vs. SCE	Pitting potential, v vs. SCE
2000	0.29	0.43
600	0.32	0.47
600 from -0.7 to +0.3v then 60	0.29	0.525
600 from -0.7 to +0.3v then 20	0.31	0.495

as the scanning rate is decreased. The actual polarization curves obtained at the highest and lowest scanning rates (Fig. 5 and 6) indicate that scanning rate affects several aspects of the measurements. The higher scanning rate gives rise to a higher active anodic dissolution peak, which is shifted toward more noble potentials. As expected, the faster the scan, the higher the passive current. As the pitting potential is approached, the current blips corresponding to repassivating pits are much larger and more numerous at the faster scan. The potential at which the growth of stable pits begins is much more sharply defined at the lower scan rate and occurs at more noble potentials.

The results of the pitting potential measurements on the 13 and 39% nickel steels are shown in Fig. 7. The results obtained on the 13.5% nickel austenitic steels confirm that 1.0M NaCl is indeed a more severe pitting electrolyte than 0.1N HCl. It is also clear that increasing molybdenum content up to at least 3.5% improves pitting resistance of these alloys. However, at 3.9% molybdenum the pitting potential was tending toward lower values.

The anomalous behavior of the 3.9% molybdenum steel may be related to its microstructure. Delta ferrite is present in the alloys containing over 2.9% molybdenum, with the 3.9% molybdenum alloy containing an appreciable amount. It has been reported by others (7) that delta ferrite is detrimental to resistance to pitting corrosion. All the 39% nickel alloys were completely austenitic.

The results on the 39% nickel alloys were very similar to those obtained in 0.1N HCl, i.e., 1% molybdenum was sufficient to prevent stable pit growth at potentials below the transpassive region. Thus, even 1M NaCl is not a severe enough test medium to differentiate the behavior of the 1, 3, and 5% molybdenum alloys.

The behavior of the high-purity alloys in 1M NaCl was almost identical to that in 0.1N HCl. The molybdenum-free alloy showed a greater tendency toward pitting at potentials just below the onset of transpassivity (0.79v). The alloys containing 2.5 and 5% molybdenum were not pitted on scanning to 0.8v. Thus, the superior resistance of the high-purity alloys to pitting corrosion is even more evident in 1M NaCl than it was in 0.1N HCl.

The appearance of typical electrodes after exceeding the pitting potential is shown in Fig. 8.

Exposure tests in  $FeCl_3$ —Simple exposure tests were performed in 0.33M  $FeCl_3$  at pH 2. These results may be expected to be comparable with the pitting potential measurements in 1N NaCl despite the pH difference, since pH changes between 1 and 7 have little effect in NaCl solutions (6). The redox potential of this solution, as measured at a platinum electrode, was 0.540v vs. SCE. As can be seen from Table V, a rather sharp transition exists between compositions that undergo severe pitting corrosion and those that are highly resistant. These results agree quite well with the pitting potential data obtained in 1M NaCl, especially when account is taken of the fact that polarization effects would cause the potential at the local anodes of the corroding specimens to be somewhat less noble than that measured on the platinum electrode. It must be remembered that the pitting potential measurements were made on electrodes containing only the surface parallel to the rolling plane.

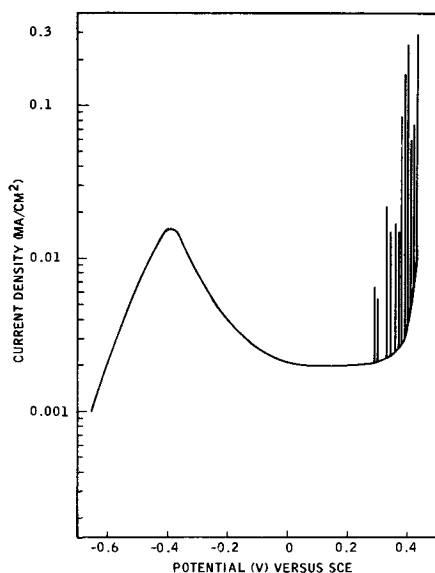


Fig. 5. Anodic polarization curves obtained on a masked electrode for the 17.6% Cr-13.6% Ni-2.93% Mo austenitic stainless steel in argon-saturated 1.0M sodium chloride. The scanning rate was 2000 mv/hr in the positive direction.

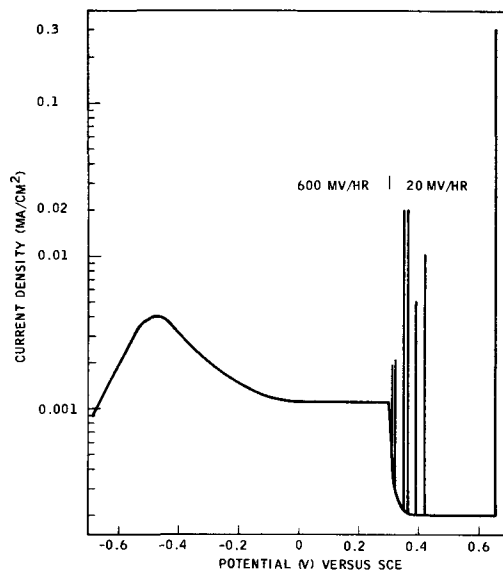


Fig. 6. Anodic polarization curves obtained on a masked electrode for the 17.6% Cr-13.6% Ni-2.93% Mo stainless steel in argon-saturated 1.0M sodium chloride. The scanning rate was 600 mv/hr up to 0.3v and thereafter, 20 mv/hr.

The appearance of typical electrodes after exceeding the pitting potential is shown in Fig. 8.

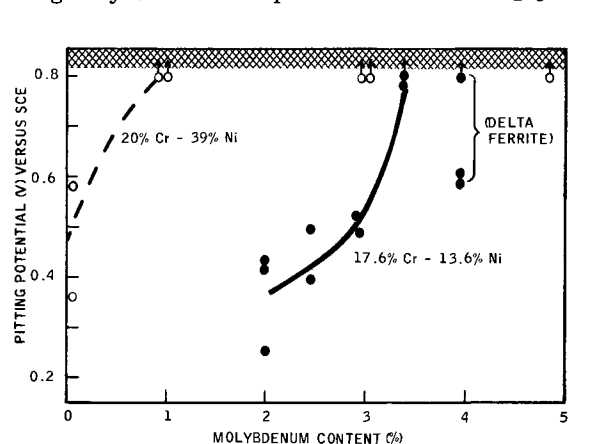


Fig. 7. Pitting potentials obtained from potentiodynamic polarization scans in argon-saturated 1.0M sodium chloride.

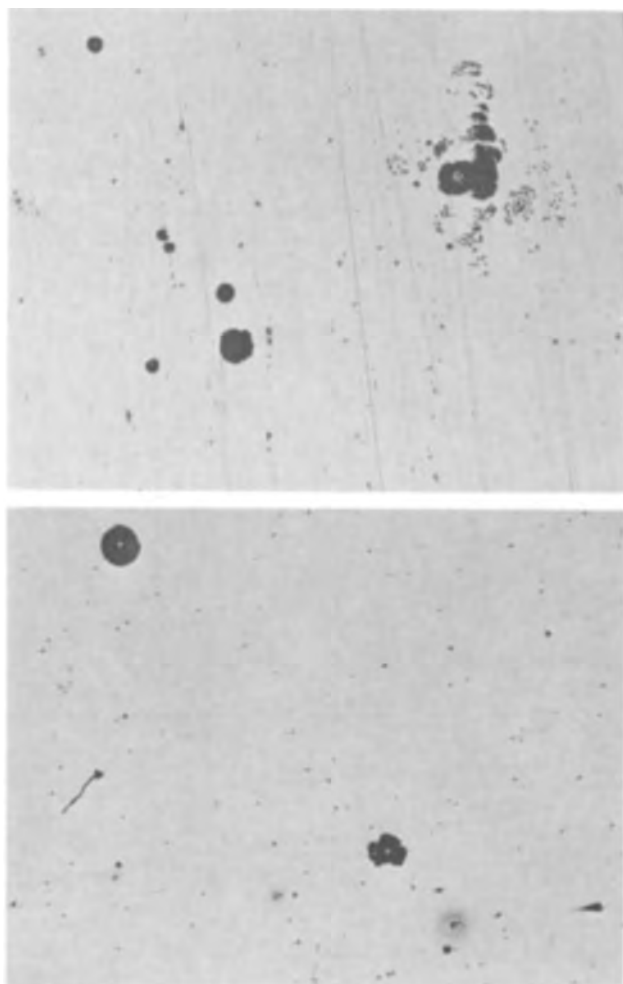


Fig. 8. Pits on representative electrodes after scanning beyond the pitting potential in argon-saturated 1M sodium chloride at 24°C, X100. (a) (top) 17.6% Cr-13.5% Ni-2.93% Mo stainless steel; (b) (bottom) 20% Cr-39% Ni stainless steel.

It is well-known that edges in stainless steels, *i.e.*, planes perpendicular to the rolling plane, are often more susceptible to pitting than is the rolling plane (2). Thus, the coupons that yielded only edge pitting in the exposure tests should be considered to correspond to no pitting up to a potential of about 0.5v in the controlled potential measurements.

### Discussion

These results show that the potentiodynamic scanning technique can give useful information about the relative pitting resistances of stainless steels. However, it is also clear that the details of experimental procedure must be carefully controlled. In particular, scanning rate was found to have a considerable influence on the results obtained. The avoidance of crevice corrosion was also found to be essential for obtaining any information on pitting potentials.

Table V. Results of exposure of austenitic steels to 0.33M ferric chloride at pH 2 for 3 days

Nominal Cr	Nominal composition, %		Weight loss in 3 days, mg/dm <sup>2</sup>	Remarks
	Ni	Mo		
17.6	13.5	1.99	703	General pitting
		2.45	828	General pitting
		2.93	173	Edge pitting
		3.37	77	One edge pit
		3.89	3	No visible attack
20	39	0.025	663	General pitting
		0.97	176	Pits at suspension hole
		3.03	40	Small edge pits
		4.85	8	No visible attack

The results of the effects of different scanning rates are at variance with results reported in the literature for molybdenum-free stainless steel (4,6). It has been reported that faster scans give more noble pitting potentials, but the opposite was found in this work on molybdenum-containing alloys. The observation made in the present studies can be rationalized by assuming that the passive film thickens with time, at a potential in the passive range. Thus the passive film would be thicker the slower the speed of scanning. As the film thickness increases, a larger fraction of the potential difference between metal and solution would be expected to occur within the film and thus not be available at the film-solution interface to assist in the entry of chloride ions into the film.

It has been found previously that for some stainless steel the passive film increases in stability, probably as a result of increasing thickness, as time at a given potential in the passive range increases (8). The effect was observed to be somewhat more pronounced for alloys with molybdenum than for those without molybdenum, perhaps indicating that passive film thickening is more important when molybdenum is present in the alloys. A similar effect was reported by Streicher (9), who found that passivation of type 316 after pickling and before undergoing a pitting test had a much larger beneficial effect than did a similar treatment of type 304. This reasoning is highly speculative, but may, at least in part, account for the contradiction between results from this work and those reported by others.

Even if absolute values of the pitting potential are open to question, it appears that relative pitting potentials provide useful information. In the two series of austenitic alloys investigated, increasing molybdenum content consistently increased the pitting potential except in the 13.5% nickel alloy of highest molybdenum content. Here the occurrence of ferrite as a second phase is promoted by higher molybdenum content and complicates the situation by introducing differences in composition, that is, the delta ferrite would be enriched in chromium and molybdenum and depleted in nickel (10). In all other steels, the beneficial effect of increasing molybdenum content on the pitting potential was clearly revealed even when the increments were as small as ½%. That these variations in pitting potential are significant was confirmed by the good correlation obtained with the results of exposure tests in FeCl<sub>3</sub>. Of course, since pitting potentials are dependent on test conditions and prior history of the specimen, agreement between pitting potentials and exposure results would only be expected when specimen treatment and exposure conditions were very similar in the two tests. Otherwise, only a relative correlation would be anticipated.

Pitting potential measurements clearly indicate the importance of minor constituents in these alloys. The high-purity alloys were much more resistant to pitting than were the alloys containing the usual levels of residual elements. The carbon and nitrogen contents are probably the most significant in this connection. Formation of chromium and molybdenum carbides and nitrides would deplete the matrix immediately surrounding the precipitates of chromium and molybdenum. Any depleted area would be more susceptible to pitting because of differences in composition; the discontinuities associated with an exposed particle of precipitate may also create favorable sites for initiation of pits. The work of Streicher (9) suggests that carbon is more effective than nitrogen in this regard. He found that large nitrogen additions reduced pitting. However, in some cases this was because the nitrogen addition produced a wholly austenitic steel and in no case did he study a steel with nitrogen as low as the high-purity steels considered in this work.

On the other hand, the high-purity alloys had about the same critical current densities for passivity as the impure steels of similar molybdenum content. It would be expected that small areas depleted in chromium



or molybdenum would make only a small contribution to the over-all current required to produce passivity.

The results of the critical current density and primary passivation potential determinations in 0.1N HCl agreed well with previous measurements in sulfuric acid on similar alloys, i.e., molybdenum decreases the critical current density required to produce passivity and to a lesser extent shifts the primary passivation potential to more active potentials (8). Nickel had little effect on critical current density, but did shift the primary passivation potential in the noble direction. Thus, molybdenum facilitates the attainment of the passive state for these alloys in 0.1N HCl, but nickel does not. These effects, however, are less significant than are the changes in pitting potential with alloy content as far as over-all corrosion behavior is concerned.

It should be kept in mind that even the most highly alloyed steels tested were not immune to crevice corrosion in chloride media even though their resistance to pitting was very high. Thus, crevice corrosion, although related to pitting, appears to be more difficult to avoid by means of alloy additions than is pitting.

### Conclusions

Potentiodynamic scanning in chloride electrolytes yields pitting potentials that vary consistently with alloy composition and that correlate well with exposure tests in FeCl<sub>3</sub> solution.

Resistance to pitting increases with increasing molybdenum content in 17.6% Cr—13.5% Ni or 20%

Cr—39% Ni austenitic stainless steels. Changes in molybdenum content as small as ½% have a significant effect on pitting potentials.

The pitting resistance of austenitic stainless steels increases when the nickel content is raised from 13.5 to 39%.

High-purity austenitic alloys are more resistant to pitting than are steels containing appreciable amounts of carbon and nitrogen.

Manuscript submitted April 15, 1968; revised manuscript received ca. July 16, 1968. This paper was presented at the Chicago Meeting, Oct. 15-19, 1967, as Paper 59.

Any discussion of this paper will appear in a Discussion Section to be published in the June 1969 JOURNAL.

### REFERENCES

1. J. M. Kolotyrkin, *Corrosion*, **19**, 261t (1963).
2. W. Schwenk, *ibid.*, **20**, 129t (1964).
3. W. Schwenk, *Corrosion Sci.*, **5**, 245 (1965).
4. G. Herbsleb, *Werkstoffe und Korrosion*, **16**, 929 (1965); **17**, 649 (1966).
5. V. Hospadaruk and J. V. Petrocelli, *This Journal*, **113**, 878 (1966).
6. H. P. Leckie and H. H. Uhlig, *ibid.*, **113**, 1262 (1966).
7. S. P. Odar and H. A. Smith, Discussion, *Trans. AIME*, **135**, 526 (1939).
8. E. A. Lizlovs, *Corrosion*, **22**, 297t (1966).
9. M. A. Streicher, *This Journal*, **103**, 375 (1956).
10. H. T. Shirley, *J. Iron Steel Inst.*, **174**, 242 (1953).

## Polarographic and Coulometric Studies of Compounds Related to 1,8-Dinitronaphthalene

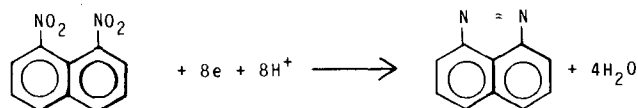
George M. LoPresti,<sup>1</sup> Suei-rong Huang, and Anthony A. Reidlinger\*

Chemistry Department, Long Island University,  
The Brooklyn Center, Zeckendorf Campus, Brooklyn, New York

### ABSTRACT

The polarographic reductions of 1,8-dinitronaphthalene, 5,6-dinitroacenaphthene, 3,4-dinitroacenaphthenequinone, and 4,5-dinitronaphthalic anhydride, were studied in buffered solutions at four different pH values. The relative wave heights of the multiple waves could be interpreted reasonably in terms of certain electron changes. A semi-empirical equation was derived to confirm certain electron changes in the polarographic reductions. These electron changes were also checked by coulometric measurements on electrolyses run at controlled potentials. Results indicated that in all but one instance there was agreement between the values for the electron changes obtained in the parallel analyses. The one exception was 3,4-dinitroacenaphthenequinone.

In general, the polarographic reduction of a polynitro aromatic compound proceeds in a stepwise manner, and the first step corresponds to a four-electron change. This has been interpreted as corresponding to the reduction of one of the nitro groups to an hydroxylamino group. In a study of the polarographic reductions of the ten dinitronaphthalenes (1), the 1,8-isomer was the only compound that did not exhibit this characteristic behavior. Instead it gave an initial wave that corresponded to either an eight or ten-electron change depending on the acidity of the solution. It was suggested that this might be due to the formation of the ring compound 1,8-naphthopyrazole.



Thus far large-scale electrolyses of 1,8-dinitronaphthalene at controlled potentials have not yielded a product identifiable as perinaphthopyrazole, but have instead yielded very high-melting, highly colored materials which appear to be polymeric.

Grimshaw and Rea (2) have recently reported that the electroreduction of 1-acetylnaphthalene did not yield the expected pinacol in base, but gave an unexpected product due to coupling in the 4-position.

In the present investigation several 4,5-disubstituted 1,8-dinitronaphthalenes were prepared, and their

\* Electrochemical Society Active Member.

<sup>1</sup> Present Address: Atlantic Richfield Oil Company, Philadelphia, Pennsylvania 19100.

Table I. Polarographic constants of 1,8-dinitronaphthalene and its related compounds<sup>a</sup>

pH Constants	2.1			6.4			9.3			11.0		
	$E_{1/2}$	$I_d$		$E_{1/2}$	$I_d$		$E_{1/2}$	$I_d$		$E_{1/2}$	$I_d$	
1,8-Dinitronaphthalene	-0.28	11.9		-0.50	7.5		-0.65	8.6		-0.77	10.0	
	-0.76	13.1		?			?			?		
5,6-Dinitroacenaphthene	-0.26	11.9		-0.48	9.3		-0.70	9.0		-0.79	9.3	
	-0.52	13.1		-0.97	12.1		?			-1.29	12.4	
3,4-Dinitroacenaphthene-quinone	-0.21	10.0		-0.42	9.4		-0.59	9.3		-0.82	12.1	
	?			?			?			?		
4,5-Dinitro-naphthalic-anhydride	-0.17	8.4		-0.47	6.9		-0.63	8.1		-0.72	7.6	
	?			?			-1.40	11.0		?		

<sup>a</sup> Values of  $E_{1/2}$  are in volts vs. saturated calomel electrode. Values of  $I_d$  are diffusion current constants.

polarographic behaviors determined in an attempt to elucidate the nature of the reduction process. Blocking the 4 and 5 positions would prevent coupling in these positions and might lead to the large-scale electrolytic preparation of the pyrazole ring system.<sup>2</sup>

### Experimental

**Nitro compounds.**—1,8-Dinitronaphthalene was prepared by the method of Hodgson and Walker (3), mp 172.0°–172.5° (lit. 172°). 5,6-Dinitroacenaphthene was prepared by the method of Sachs and Mosebach (4), mp 221°–224° (lit. 220°–224°). 3,4-Dinitroacenaphthenequinone was prepared by the method of Rowe and Davies (5), mp decomposes above 300° (lit. decomposes above 300°). 4,5-Dinitro-naphthalic anhydride was prepared by the oxidation of 5,6-dinitroacenaphthene, using the method of White and Elderfield (6), mp decomposes above 310° (lit. decomposes at 310°).

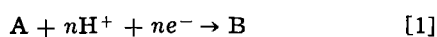
**Polarographic and coulometric procedure.**—The polarographic and constant-potential coulometric studies were carried out with the same equipment, in the same manner, and in the same buffers as described by Boyd *et al.* (7). A drop-time of mercury from the dropping electrode capillary was 4.0 sec, and the drop weight was 9.5 mg.

### Results

Polarographic data are given in Tables I and II.

#### Analysis of Data

The electrolytic reduction of an organic compound at the surface of a dropping mercury electrode is often an irreversible one. The chemical reaction can be written as



<sup>2</sup> Preliminary investigations have suggested that the product obtained from the coulometric analysis of 4,5-dinitroacenaphthene is the dihydro derivative of the pyrazole. However, because of the low solubility of the dinitro compound, complications arise in scaling-up the reaction. Reductions of the compound at lower acidities appear to be complicated by chemical reactions within the solutions. Similarly reductions of the other dinitro compounds are not simple. Work on the larger scale reductions is currently in progress and will be reported at a future date.

Table II. Constant potential reduction of 1,8-dinitronaphthalene and its related compounds

Compound	pH	$E_r$ vs. SCE <sup>a</sup>	$n$ (Coulom.) <sup>b</sup>	$n$ (Polarog.) <sup>c</sup>
1,8-Dinitro-naphthalene	2.1	-0.45	10.28	10
		-0.85	11.67	12
5,6-Dinitro-acenaphthene	2.1	-0.45	10.37	10
		-0.85	11.71	12
3,4-Dinitro-acenaphthene-quinone	2.1	-0.40	12.18	8 <sup>d</sup>
4,5-Dinitro-naphthalic-anhydride	2.1	-0.50	7.20	7
	6.4	-0.80	8.30	8

<sup>a</sup>  $E_r$  is the potential of the Cathode (vs. SCE) at which the reduction was carried out.

<sup>b</sup>  $n$  is the number of electrons involved in the reduction.

<sup>c</sup> Estimated to the nearest integral number of electrons from the wave heights of the polarographic curves.

<sup>d</sup> The difference between the coulometric  $n$  value and the polarographic  $n$  value is probably due to the fact that the macro reduction is complicated by reactions of nitro reduction intermediates with the carbonyl groups which are present.

where A is an organic compound, and B is the product. The rate constant  $k$  at a certain electrode potential  $E$ , and at 25°C, can be expressed as (8)

$$k = k_0 \exp(-2.303 \beta E n / 0.0591) \quad [2]$$

where  $E$  is the potential in volts referred to the normal hydrogen electrode;  $k_0$  is the value of  $k$  when  $E = 0$ ;  $n$  is the number of electrons transferred in Eq. [1]; and  $\beta$  is a parameter which is characteristic of the electrode reaction for given conditions of the electrolysis. The value of  $\beta$  ranges between 0 and 1 for many electrode reactions. The  $k$  value, according to the kinetic study of Eq. [1], depends on the height of energy barrier to be overcome by molecule, or ion A, and  $H^+$ . A schematic drawing of the reaction path is shown in Fig. 1. Therefore one can postulate a reaction



where  $M^+$  is the intermediate product at the height of potential energy-reaction path curve. The reaction rate  $k$  can also be expressed in another form

$$k = \frac{KT}{h} \cdot \left( \frac{f_{M^+}}{f_A \cdot f_{nH^+}} \right) \cdot \exp\left(\frac{-U}{RT}\right) \quad [4]$$

where  $K$  = Boltzmann's constant

$h$  = Plank's constant

$T$  = absolute temperature

$f$ 's = partition function for each component

$U$  = energy barrier to be overcome by reactants A and  $H^+$

Combining Eq. [2] and [4], one obtains

$$k_0 \exp(-2.303 \cdot \beta \cdot E n / 0.0591)$$

$$= \frac{KT}{h} \left( \frac{f_{M^+}}{f_A \cdot f_{nH^+}} \right) \exp\left(-\frac{U}{RT}\right) \quad [5]$$

Taking the natural logarithm on both sides of Eq. [5], rearranging and setting  $\beta$  equal to 1, gives

$$E = \alpha - 0.0591(pH) + \frac{1}{(n)23.06 \times 10^3} (\Delta E_0) \quad [6]$$

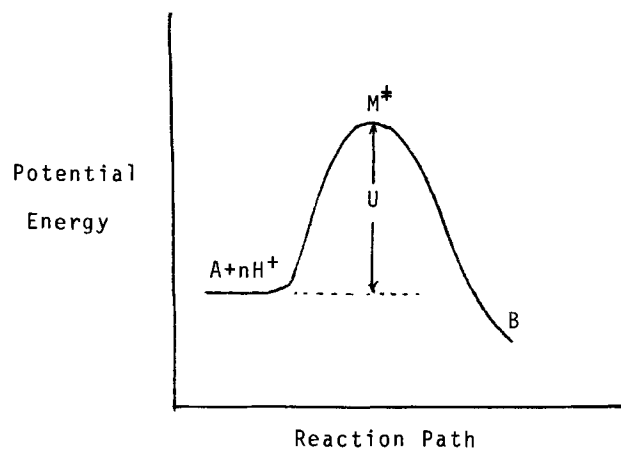


Fig. 1. Reaction path for the reaction  $A + nH^+ + ne^- \rightarrow B$

with

$$(H^+) \cong f_{H^+} \cdot \exp(-E_{H^+}^0/RT) \quad [7]$$

where

 $\alpha =$ 

$$\left\{ -\frac{0.0591}{(n)2.303} \ln \left[ \left( \frac{KT}{h} \right) \frac{f_{M^{\ddagger}}}{f_A} e^{-(nE_{H^+}^0/RT)} \right] + \frac{0.0591}{(n)2.303} \ln k_0 \right\} \quad [8]$$

$E_{H^+}^0 =$  ground state energy of  $H^+$  per mole and  $\Delta E_0 =$  difference in energy between reactant A and  $M^{\ddagger}$  per mole, and always is positive.

If the reactant A undergoes ring formation by the electrolytic reduction to form product B, then, as the first approximation, the following substitutions can be made;  $E$  is substituted by the half-wave potential,  $E_{1/2}$ , and  $\Delta E_0$  is replaced by the difference in resonance energies between molecules A and B,  $\Delta E_R$ . Equation [6] then yields

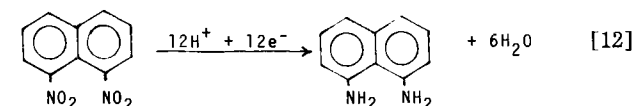
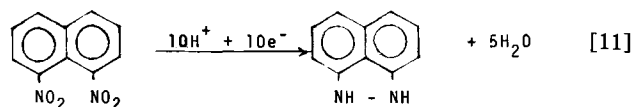
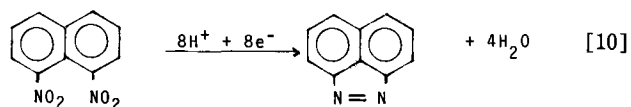
$$E_{1/2} = \alpha' - 0.0591 (pH) + \frac{1}{(n)23.06 \times 10^3} (\Delta E_R) \text{ volt} \quad [9]$$

where  $\alpha'$  is a constant related to  $\alpha$  but containing terms arising from the fact that an irreversible polarographic  $E_{1/2}$  depends on concentration polarization as well as the kinetics of electron transfer. The units for  $\Delta E_R$  are cal/mole. A similar attempt to relate half-wave potential to the resonance energy difference had been made by Hoijsink (9) and Evans (10).

For a particular set of values;  $E_{1/2}$ , pH, and  $\Delta E_R$ ,  $\alpha'$  can be evaluated. Similar aromatic compounds containing nitro groups yield a constant value for  $\alpha'$ . Furthermore, a particular aromatic compound, as previously mentioned, which can undergo several different polarographic reductions by the same intermediate path will also yield the same constant value for  $\alpha'$ .

### Discussion

The polarographic reductions of 1,8-dinitronaphthalene at the surface of dropping mercury electrode are assumed to be



Values of  $\alpha'$  for given sets of  $E_{1/2}$ ,  $n$ , pH, and  $\Delta E_R$  have been calculated and are listed in Table III.

Similarly, the polarographic reductions of 5,6-dinitroacenaphthene are proposed as follows

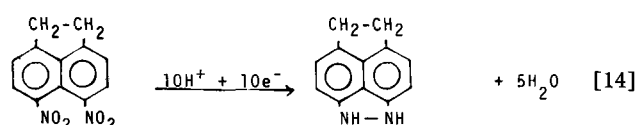
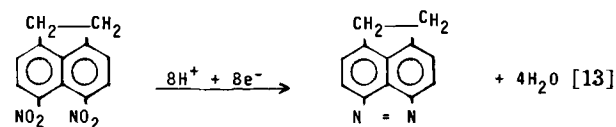
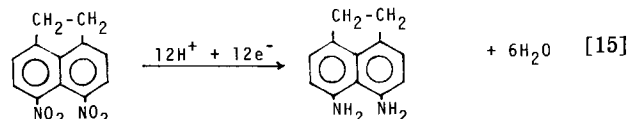


Table III. Polarographic reduction of 1,8-dinitronaphthalene<sup>a</sup>

$E_{1/2}$	$n$	pH	$\Delta E_R$	$\alpha'$	Type of reaction
-0.28	10	2.1	48.3	-0.365	[11]
-0.50	8	6.4	43.7	-0.359	[10]
-0.65	8	9.3	43.7	-0.337	[10]
-0.77	8	11.0	43.7	-0.357	[10]

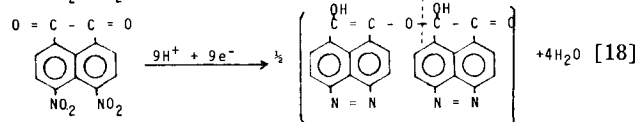
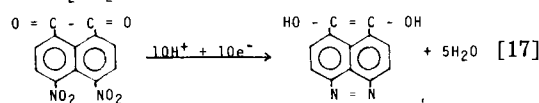
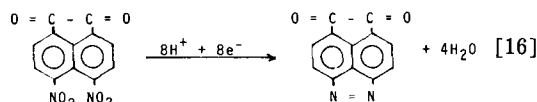
<sup>a</sup> The values of  $E_{1/2}$  are in volts vs. saturated calomel electrode.  $n$  is the number of electrons involved in the reduction. The values of  $\Delta E_R$  are in kcal/mole. The resonance energy has been obtained from the molecular orbital calculations. The values of  $\alpha'$  are in volts.



Some values of  $\alpha'$  have been computed and listed in Table IV. The numerical values of  $\alpha'$  for the reduction of 5,6-dinitroacenaphthene are close to those of 1,8-dinitronaphthalene. This indicates that both compounds undergo the same types of reductions as shown in Eq. [10] through [15]. The average value for  $\alpha'$  is  $-0.36 \pm 0.02$ v. Substituting the average value for  $\alpha'$ , the half-wave potential for the reduction of 1,8-dinitronaphthalene and 5,6-dinitroacenaphthene can be expressed semiempirically by Eq. [9].

$$E_{1/2} = -0.36 - 0.0591 (pH) + \frac{\Delta E_R}{(n)23.06 \times 10^3} \quad [9']$$

Polarographic reductions of more complex aromatic compounds containing nitro groups, such as 3,4-dinitroacenaphthenequinone and 4,5-dinitronaphthalic anhydride, also lend themselves to the same analysis. The polarographic reductions are shown in the following equations



Using Eq. [9], values of  $\alpha'$  have been calculated for reactions [16] through [18] and are  $-0.32$ ,  $-0.29$ , and  $-0.31$ , respectively.

It may be seen from the preceding discussion that these calculated  $\alpha'$  values exhibit some deviations from a constant value of  $-0.36$ . Two possible explanations for this deviation are suggested. First, several different intermediate paths may exist for a given polarographic reduction. Second, any delocalization of  $\pi$  electrons in the  $O=C-C=O$  skeleton has not been

taken into account in the calculation of the resonance

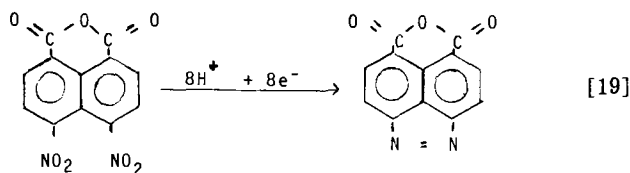
Table IV. Polarographic reduction of 5,6-dinitroacenaphthene<sup>a</sup>

$E_{1/2}$	$n$	pH	$\Delta E_R$	$\alpha'$	Type of reaction
-0.26	10	2.1	48.3	-0.345	(14)
-0.48	10	6.4	48.3	-0.321	(14)
-0.70	8	9.3	43.7	-0.388	(13)
-0.79	8	11.0	43.7	-0.377	(13)
-0.52	12	2.1	0.000	-0.396	(15)

<sup>a</sup> See footnote a, Table III.

energy. Evans (10) has shown that this delocalization effect is small but not negligible.

The values obtained from the polarographic reductions of 4,5-dinitronaphthalic anhydride in nearly neutral solutions indicate that the reduction process is similar to that of the other compounds.



The  $\alpha'$  value for the reaction indicated in [19] is  $-0.33\text{v}$ . The reductions in acid are probably influenced by interaction of the anhydride with the acid while at higher pH values interaction of the anhydride with the nucleophiles present in solution is likely.

#### Acknowledgment

The authors wish to thank Dr. Stewart Karp for his many helpful and enlightening discussions.

Manuscript submitted April 11, 1968; revised manuscript received July 12, 1968.

Any discussion of this paper will appear in a Discussion Section to be published in the June 1969 JOURNAL.

#### REFERENCES

1. R. N. Boyd and A. A. Reidlinger, *This Journal*, **107**, 611 (1960).
2. J. Grimshaw and E. J. F. Rea, *J. Chem. Soc.*, C **1967**, (24) 2628.
3. H. H. Hodgson and J. Walker, *ibid.*, **1933**, 1346.
4. F. Sachs and G. Mosebach, *Ber.*, **44**, 2852 (1911).
5. F. M. Rowe and J. H. S. Davies, *J. Chem. Soc.*, **1920**, 1350.
6. S. L. Wythe and R. C. Elderfield, *J. Org. Chem.*, **19**, 683 (1954).
7. R. N. Boyd, A. A. Reidlinger, and M. J. Sher, *This Journal*, **107**, 302 (1960).
8. P. Delahay, "Instrumental Analysis," 3rd ed., p. 82 MacMillan Co., New York (1963).
9. G. J. Hoijsink, *Rec. Trav. Chim.*, **74**, 1525 (1955).
10. M. G. Evans, *Trans. Faraday Soc.*, **42**, 113 (1946).

## Thermodynamic Properties of Bismuth Trifluoride

Daniel Cubicciotti\*

Stanford Research Institute, Menlo Park, California

#### ABSTRACT

Thermodynamic properties were determined for bismuth trifluoride that had been dried by heating in a stream of hydrogen fluoride. The melting point was found to be  $649^\circ\text{C}$ . The thermodynamic functions of the gaseous molecule were calculated from estimates of the molecular geometry and vibration frequencies. Heat capacities were measured for the solid and liquid, and the heat (5.16 kcal) and entropy of fusion (5.6 eu) were obtained.

The vapor pressure over the solid was measured by a transpiration method. The vapor pressure of  $\text{BiF}_3$  over the solid is given by

$$\log p(\text{mm}) = -\frac{9753}{T} + 11.72$$

An equation for the vapor pressure over the liquid was derived and the boiling point calculated to be  $900^\circ\text{C}$ . The enthalpy of sublimation (48.1 kcal/mole) and the entropy of sublimation (46.6 eu) at  $298^\circ\text{K}$  were derived from the vapor pressures.

The enthalpy of formation of bismuth trifluoride ( $-215$  kcal/mole) was determined by solution calorimetry. The enthalpy of atomization of bismuth trifluoride gas (273 kcal/mole) was calculated from the enthalpy of formation. The derived bismuth-fluorine bond energy is compared with those of the other group VA halides.

There is little information in the literature about the properties of bismuth trifluoride ( $\text{BiF}_3$ ). It can be precipitated from aqueous solutions and is apparently stable in air at room temperature; however, at elevated temperatures it is hydrolyzed by moisture in the air with the formation of oxyfluorides and oxide. Even at  $200^\circ\text{--}300^\circ\text{C}$ , a sample in air will lose weight, presumably by hydrolysis. Therefore, a pure sample cannot readily be obtained by drying in air. This hydrolysis is probably the reason for some erroneous reports in the literature. [For example, a transition at  $220^\circ\text{C}$  has been reported (1), based on a change in x-ray structure after prolonged heating in air. Since no thermal arrests were observed by us when the solid was heated in a sealed platinum capsule, the structural change observed in air may have been due to the formation of oxyfluoride during heating. The melting point given in the literature (2) is about  $120^\circ\text{C}$  higher than the value reported below, and the difference may be as-

cribed to oxygen in the sample.] The crystal structure (3, 4) is like that of yttrium trifluoride, and therefore is more ionic than the other halides of bismuth. The melting and boiling points, as well as other properties reported below, are in keeping with its ionic nature.

#### Experimental Methods and Results

*Preparation and analysis.*—The bismuth trifluoride used in this work was made by precipitation from a solution of Baker and Adamson reagent-grade bismuth oxide in nitric acid with hydrofluoric acid in Teflon ware. Samples were analyzed for bismuth gravimetrically as bismuth phosphate by the method given by Hillebrand *et al.* (5) except that a prior treatment was made to remove fluorine from the solution. About 0.1g boric acid was added, and the sample was taken twice to dryness. Material that had been dried in air for several hours at  $200^\circ$  to  $300^\circ\text{C}$  gave analyses for bismuth from 78.7 to 78.9%. A batch heated in air at  $500^\circ\text{C}$  for several hours showed 85.4% Bi. The calcu-

\* Electrochemical Society Active Member.

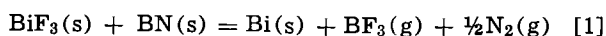
lated value for BiF<sub>3</sub> is 78.57% Bi. Samples with higher bismuth content were presumed to contain oxygen as the oxide or oxyfluoride. (Theoretical for Bi<sub>2</sub>O<sub>3</sub> is 89.7% and for BiOF is 85.7% Bi.) Therefore, heating in air converts the sample to oxide, as already observed by Aurivillius (6).

As a means of purification from oxide, one sample was distilled in a platinum retort in a stream of nitrogen. The distillation proceeded at a reasonable rate above about 850°C. Analysis of the distillate showed 78.57 ± 0.05% Bi in good agreement with the theoretical percentage for BiF<sub>3</sub>. Since the distillation procedure was slow, another purification treatment was tried. A sample of air-dried BiF<sub>3</sub> was heated in a stream of dry hydrogen fluoride in a platinum container for about 2 hr at 500°C. Four analyses of the product gave 78.59 ± 0.05% bismuth. This material was used for all the studies reported below. It was a fine, grayish powder.

**Melting point.**—The melting point was determined by a cooling curve method. A 12g sample of BiF<sub>3</sub> was placed in a cp platinum tube (3/8 in. OD x 5 mil wall x 3 in. long) whose ends were crimped-closed and platinum-soldered. A Pt-10% Rh thermocouple was wired tightly to the outside of the middle of the tube. The thermocouple had been checked against an NBS calibrated couple as well as against the melting point of sodium chloride from a cooling curve in a similar platinum container. The thermocouple was within 0.3°C of standard tables (6) in the range of 600°-800°C and within 0.5°C of the melting point (7) of sodium chloride (800°C). The cooling curves showed a melting break at 649° ± 2°C. After several cooling curves had been run, the platinum container was found to be brittle. Analysis gave 78.74% Bi, indicating no serious change in the salt.

Von Wartenberg (2) reports a melting point of from 725° to 730°C observed on a sample in a platinum boat in a stream of hydrogen fluoride. Unfortunately, an analysis of the sample was not given. It is possible that the values are high because of oxide in the sample. It is also possible that the thermometer, which was not described, was in error because of attack by the hydrogen fluoride stream.

The results of Darnell and McCollum (8) on the melting point at high pressures, extrapolated to one atmosphere, indicate a value of about 760°C. However, these authors used a boron nitride container. We have found that when BiF<sub>3</sub> is melted in boron nitride in an atmosphere of N<sub>2</sub>, it turns black and corrodes the container. This corrosion is in accord with the fact that the reaction



has a zero enthalpy change at room temperature (9) and a large positive standard entropy change and therefore a negative standard free energy change at elevated temperatures.

**Thermodynamic functions for BiF<sub>3</sub> gas.**—The molecular geometry and vibration frequencies for BiF<sub>3</sub> have not been determined; however, sufficient information on related molecules is available so that the molecular constants can be estimated reliably enough for the purpose of calculating thermodynamic properties. The geometries of the molecules PF<sub>3</sub>, PCl<sub>3</sub>, AsF<sub>3</sub>, AsCl<sub>3</sub>, and BiCl<sub>3</sub> have been reported (10). These are all pyramidal molecules with halogen-M-halogen angles of about 100°; therefore, that angle was assumed to be 100° in the BiF<sub>3</sub> molecule as well. The internuclear distance was assumed to be 2.0Å, i.e., 0.48 smaller than that in BiCl<sub>3</sub> because the internuclear distance in AsF<sub>3</sub> is 0.45 smaller than in AsCl<sub>3</sub>. The vibration frequencies of this type of molecule have been reviewed by Manley and Williams (11). For the fundamental frequencies, the ratio of the value for AsF<sub>3</sub> to that for AsCl<sub>3</sub> is 1.75; therefore, for the present calculation the four fundamental vibration frequencies of BiF<sub>3</sub> were assumed to

Table I. Thermodynamic functions calculated for BiF<sub>3</sub> gas

Temp, °K	$H^\circ_T - H^\circ_0$ kcal/mole	$S^\circ_T$ , eu	$(G^\circ_T - H^\circ_{298})$
			T Eu
298.2	3.96	75.92	75.92
400	5.79	81.17	76.60
500	7.66	85.36	77.95
600	9.57	88.82	79.47
700	11.50	91.80	81.02
800	13.44	94.40	82.54
900	15.39	96.69	83.98
1000	17.35	98.73	85.34
1250	22.27	103.11	88.46

be 1.75 times the values observed for BiCl<sub>3</sub>. The vibration frequencies used were: 505, 230, 425, and 175 cm<sup>-1</sup>, the last two being doubly degenerate. Electronic contributions to the entropy were assumed to be negligible. The thermodynamic functions calculated from these estimated molecular constants are given in Table I.

**Thermodynamic functions for the condensed phases.**—Enthalpy measurements above 298° to about 1000°K were measured in a drop calorimeter by the same method as described earlier (12, 13). The sample of about 10g of BiF<sub>3</sub> was placed in a platinum test tube and the end sealed by crimping and platinum soldering. Two different samples were used, and the results were in a good agreement. After the measurements were made, it was found that the platinum container was brittle and cracked open easily. Analysis of one of the BiF<sub>3</sub> samples which had been melted in the platinum container gave 78.74% Bi, indicating little change in the sample.

The observed data are given in Table II, expressed per mole of BiF<sub>3</sub> (266 g/mole). The data for the solid were fitted by a least squares method to a polynomial in powers of temperature ( $T$ ). The resultant analytical expression for the enthalpy increments ( $H_T - H_{298}$ ) is

$$(H_T - H_{298}) \pm 0.09 \text{ kcal/mole (solid BiF}_3) = \\ -6.72 + 2.499 \times 10^{-2}T - 1.192 \times 10^{-5}T^2 \\ + 1.438 \times 10^{-8}T^3. \quad [2]$$

The deviations of the experimentally observed points from this expression are also given in Table II. The standard deviation for all the points was ± 90 cal/mole. For the liquid, enthalpy increments were ob-

Table II. Measured enthalpy increments and deviations from analytical equations for solid and liquid BiF<sub>3</sub>

Temp, °K	$H_T - H_{298}$ measured, kcal/mole	Deviation, observed minus calculated cal/mole
362.2	1.49	37
362.6	1.53	70
364.1	1.55	56
427.5	2.88	-34
433.1	2.98	-62
477.9	4.13	55
482.2	4.14	-34
517.3	4.88	-135
523.5	5.11	-53
553.8	5.94	26
572.5	6.51	13
701.2	9.91	70
706.4	10.11	47
709.7	10.18	21
755.7	11.50	-70
758.9	11.67	17
843.5	14.57	59
849.9	14.67	-73
905.6	16.65	-170
911.4	17.23	183
912.7	17.09	-7
Melting point 922°K		
945.9	23.60	-88
949.7	23.89	39
967.4	24.73	99
979.7	25.14	-30
997.9	25.98	1
1008.2	26.41	-21

tained only over a 60° range, and since the results seemed linear in temperature, they were fitted to a linear expression by least squares. The result is

$$(H_T - H_{298}) \pm 0.07 \text{ kcal/mole (liquid BiF}_3) = -18.05 + 4.412 \times 10^{-2} T \quad [3]$$

The deviations of the experimental data from the equation are also given in Table II. The standard deviation was 70 cal/mole.

The enthalpy of fusion derived from the difference of the two analytical expressions at 922°K is  $5.16 \pm 0.15$  kcal/mole. This leads to an entropy of fusion of  $5.60 \pm 0.2$  entropy units. This value is substantially smaller than those of the other bismuth halides [BiCl<sub>3</sub>, 11.3 eu (14); BiBr<sub>3</sub>, 10.1 eu (15); BiI<sub>3</sub>, 13.7 eu (16)]. There is not much information on entropies of fusion available for comparison; however, for the calcium halides, the entropy of fusion (17) of the fluoride is substantially smaller than those of the chloride or bromide; barium fluoride (17) also has a substantially smaller entropy of fusion than its bromide or iodide. On the other hand, that of arsenious fluoride is about the same as its chloride or bromide. The melting points of these arsenious halides are below room temperature and indicate, together with their crystal structures (3), that they are molecular substances. The melting points and crystal structures of the bismuth halides indicate they are more ionic and should therefore behave more like the calcium and barium halides.

From the analytical expressions given above, enthalpy increments were calculated at even temperatures and at the melting point. Entropy increments were calculated from the derived heat capacity expressions and the heat of fusion. Free-energy function increments were also obtained. The results are compiled in Table III.

**Vapor pressures.**—The vapor pressure of BiF<sub>3</sub> was determined by the transpiration method with N<sub>2</sub> as carrier gas described in earlier reports from this laboratory (18). The cell and sample collectors were made of cp platinum. A first set of determinations was made on BiF<sub>3</sub> that had been heated in air to dry it. Analysis of that material showed 79.2% Bi, indicating that there was some oxide impurity. After it was apparent that BiF<sub>3</sub> was converted to an oxyfluoride during heating in air, a sample was prepared as described above by heating in a hydrogen fluoride stream.

Vapor pressures were measured for both samples over a temperature range for the solid. The data obtained for the two samples are shown in Fig. 1. The sample containing oxide shows a lower vapor pressure with a somewhat larger enthalpy of vaporization. If it is assumed that the vapor species are the same (BiF<sub>3</sub>) in both cases, the lower vapor pressures of the oxide-containing sample are in accord with a lower activity of BiF<sub>3</sub> and the larger enthalpy of vaporization implies that there is a (small) enthalpy solution of solid BiF<sub>3</sub> in the oxide-containing sample. The line drawn through the upper set of points represents the

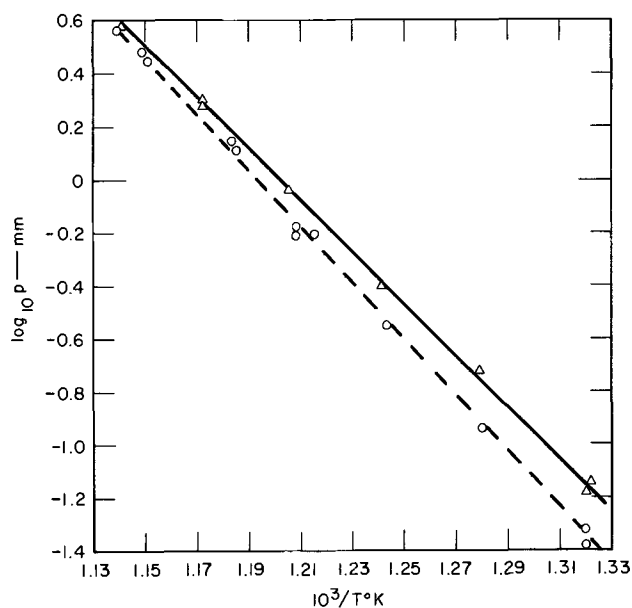


Fig. 1. Vapor pressure of bismuth trifluoride: upper curve, "pure BiF<sub>3</sub>"; lower curve, BiF<sub>3</sub> containing oxide.

vapor pressure of the sample considered to be pure BiF<sub>3</sub>. The experimental results are given in Table IV. The equation for the line drawn through these points is

$$\log_{10} p (\text{mm, for solid BiF}_3) = -\frac{9,753}{T} + 11.72 \quad [4]$$

To obtain the best value for the enthalpy of sublimation, a sigma plot treatment of the data was made. The method used has been described earlier (19). The free-energy function increment data used were those given in Tables II and III. A least squares treatment of the experimental data for the sample of pure BiF<sub>3</sub> gave  $\Delta H^\circ$  (sublimation, 298°K) =  $48.1 \pm 0.6$  kcal/mole and  $\Delta S^\circ$  (sublimation, 298°K) =  $46.6 \pm 0.8$  eu.

An equation for the vapor pressure of the liquid can be derived from the enthalpy of sublimation; the vapor pressure at the melting point ( $1.8 \times 10^{-2}$  atm, as calculated from Eq. [4]) and the thermal data for the gas and the liquid are given in Tables I and III. The resulting equation for the vapor pressure over the liquid is

$$\log_{10} p \text{ atm} = \frac{-13,102}{T} - 12.3 \log T + 48.928 \quad [5]$$

The boiling point of the liquid calculated from Eq. [5] is  $1173^\circ \pm 10^\circ \text{K}$ .

A mass spectrometer examination was made of the vapors evolved from a sample of BiF<sub>3</sub>. A small platinum Knudsen cell was used to contain the sample. The geometry of the system was such that a part of the gas emitted by the cell drifted directly into the ionization

Table III. Thermal data for solid and liquid BiF<sub>3</sub>

(Calculated from Eq. [2] and [3])

Temp, °K	Enthalpy increments $H^\circ_T - H^\circ_{298}$ , kcal/mole	Entropy increments $S^\circ_T - S^\circ_{298}$ , eu	Free-energy function increments		Absolute entropies $S^\circ_T$ , eu	Free-energy function $\left(\frac{G^\circ_T - H^\circ_{298}}{T}\right)$ , eu
			$\left(\frac{G^\circ_T - H^\circ_{298}}{T}\right)$ , eu	$\left(\frac{G^\circ_{298} - H^\circ_{298}}{298}\right)$ , eu		
298.2	0	0	0	0	29.3	29.3
400	2.29	6.45	0.71	0.71	35.8	30.01
500	4.60	11.59	2.39	2.39	40.9	31.69
600	7.09	16.13	4.30	4.30	45.4	33.60
700	9.87	20.40	6.30	6.30	49.7	35.60
800	13.01	24.59	8.33	8.33	53.9	37.63
900	16.61	28.81	10.36	10.36	58.1	39.66
922 (s)	17.47	29.76	10.81	10.81	59.1	40.11
922 (l)	22.63	35.36	10.81	10.81	64.7	40.11
1000	26.07	38.95	12.88	12.88	68.3	42.18
1100	30.48	43.15	15.44	15.44	72.5	44.74

Table IV. Results of transpiration vapor pressure measurements on pure BiF<sub>3</sub>

Temp, °K	BiF <sub>3</sub> collected, mg	N <sub>2</sub> passed, moles	Duration, min	Vapor pressure BiF <sub>3</sub> , mm
756.7	7.7	0.303	1375	0.073
757.7	63.9	2.76	5529	0.066
781.7	31.9	0.480	977	0.191
806.1	182.3	1.312	1415	0.398
829.8	185.9	0.575	1165	0.93
853.2	118.2	0.168	339	2.02
853.5	142.4	0.214	972	1.90
876.7	59.9	0.045	196	3.81

chamber of the mass spectrometer. The mass spectrometer was an Aero Vac Model 610-611 (Aero Vac Corporation, Troy, New York), which is a magnetic deflection type with an electron multiplier detector. The magnetic field applied during these experiments was great enough that mass numbers as large as 800 would be detectable. The ion fragments observed attributable to BiF<sub>3</sub> were BiF<sub>3</sub><sup>+</sup>, BiF<sub>2</sub><sup>+</sup>, BiF<sup>+</sup>, and Bi<sup>+</sup>, with relative intensities of approximately 2, 10, 1, and 5, respectively. No masses greater than 266 (BiF<sub>3</sub><sup>+</sup>) were observed. The vapors were examined over a range of cell temperatures from about 475° to 575°C. It was concluded that the only vapor species was BiF<sub>3</sub>, and no polymers were formed. Thus, the molecular weight of the gas observed in the transpiration experiments was taken to be 266.

The absolute entropy of gaseous BiF<sub>3</sub> at 298°K calculated from the estimated molecular constant data discussed above is 75.92 eu. Therefore, the absolute entropy of the solid at 298°K, obtained from the sublimation entropy, is 29.3 ± 1 eu. This is substantially in agreement with the value one would estimate by applying Latimer's rules (20), namely 28 eu. With this value for the absolute entropy for the solid, the free-energy functions and entropies can be evaluated as functions of temperature. These values are given in the last two columns of Table III.

**Enthalpy of Formation of BiF<sub>3</sub>.**—The enthalpy of formation of BiF<sub>3</sub> was determined by solution calorimetry in the same solvent used earlier in this laboratory (21, 22). The scheme of measurement involved determination of the individual enthalpies of solution of the following substances; BiF<sub>3</sub>, KF·2H<sub>2</sub>O (Baker and Adamson reagent grade) and KBr (Mallinckrodt, analytical reagent) plus the enthalpies of solution of Bi and Br<sub>2</sub> already reported. The results obtained and their standard error are given in the last column of Table V. The measurements were all made at solution temperatures of 295° ± 2°K. Because the precision of the results is only about 1%, it is presumed that they are the same as 298°K values within experimental error. Proper algebraic addition of the reactions and enthalpies of Table V results in the reaction

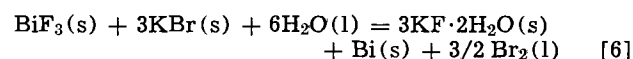


Table V. Enthalpies of Solution

Reaction	Sample weights, g	No. of determinations	ΔH <sub>298</sub> , kcal/mole
(Solvent = 200 cc 2N HBr + 2.0 cc Br <sub>2</sub> )			
BiF <sub>3</sub> (s) + solvent = Bi <sup>3+</sup> + 3F <sup>-</sup> (in solution)	0.5	4	- 3.90 ± 0.04
KF·2H <sub>2</sub> O + solvent = K <sup>+</sup> + F <sup>-</sup> + 2H <sub>2</sub> O (in solution)	0.5	4	+ 3.86 ± 0.04
KF·2H <sub>2</sub> O + solvent (containing 0.4g Bi <sub>2</sub> O <sub>3</sub> ) = K <sup>+</sup> + F <sup>-</sup> + 2H <sub>2</sub> O (in solution)	0.5	4	+ 3.88 ± 0.02
KBr + solvent = K <sup>+</sup> + Br <sup>-</sup> (in solution)	0.6	3	+ 4.63 ± 0.03
Bi(s) + 3/2 Br <sub>2</sub> (in solvent) = Bi <sup>3+</sup> + 3Br <sup>-</sup> (in solution)	}	[ref. (21) and (22)]	-72.6 ± 0.3
Br <sub>2</sub> (l) + solvent = Br <sub>2</sub> (in solution)			- 2.79 ± 0.02

with an enthalpy change of ΔH<sub>298</sub> = + 75.2 ± 0.6 kcal. This value can be combined with the following enthalpies of formation in kcal/mole given in Circular 500: KBr(s) (-93.73), H<sub>2</sub>O(-68.32), KF·2H<sub>2</sub>O (-277.0). The enthalpy of formation at 298°K of solid BiF<sub>3</sub> so derived is -215.1 kcal/mole. An uncertainty of about ±3 would give a reasonable estimate of the reliability of the result. This value is in essential agreement with the value of -212.0 ± 10 derived by Kubaschewski et al. (17) from the results of Jellinek (23).

## Discussion

**Bond energies.**—The information reported above can be used to evaluate the enthalpy of atomization of gaseous BiF<sub>3</sub>. This calculation is given in Table VI. The bond energy of a trihalide can be taken to be one third of the enthalpy of atomization of the gaseous trihalides at 298°K (26). The bond energies of most of the group VA trihalides can be evaluated from data now available. The values are given in Table VII.

There seems to be some regularities in the values, especially for the chlorides and bromides and iodides. The differences are about 2 to 3, - 1 to 2, and 5 to 7 for P - As, As - Sb, and Sb - Bi, respectively.

The bond energies of the fluorides from phosphorus to bismuth show a steady relatively large (26 kcal) drop as compared to the other halides which show a small drop (8-10 kcal) with a small alternation of values at antimony. This difference in the behavior of the fluorides from the other halides may be due to a smaller degree of binding of the d orbitals on the group V element with the lone pair electrons on fluorine as compared with the other halogens.

The ratio of the enthalpy of vaporization to the bond energy of a substance is a measure of the relative strengths of intermolecular and intramolecular binding. Small values of the ratio are indicative of small intermolecular energies compared to bond energies and arise from "molecular" substances, while large values are expected for "ionic" and "giant molecule" compounds. Values of this ratio for the group VA trihalides are given in Table VIII. There is a distinct trend in the values that increase with atomic weight

Table VI. Atomization enthalpy of BiF<sub>3</sub>

Reaction	ΔH <sub>298</sub> (kcal/mole)
Bi(s) + 3/2 F <sub>2</sub> (g) = BiF <sub>3</sub> (s)	-215.1 ± 3
Bi(s) = Bi(g)	49.5(24)
1/2 F <sub>2</sub> (g) = F(g)	18.9 ± 1(25)
BiF <sub>3</sub> (s) = BiF <sub>3</sub> (g)	48.1 ± 0.6
BiF <sub>3</sub> (g) = Bi(g) + 3 F(g)	273.2 ± 5

Table VII. Bond energies of group VA trihalides\*

	(1/3 enthalpy of atomization, in kcal at 298°K, of gaseous trihalide)				
	N	P	As	Sb	Bi
F	66.8	120.5	116.0	(107)**	91.1
Cl	(46)**	77.0	73.8	75	66.7
Br	—	62.8	61	62.9	55.9
I	—	(50)**	47.0**	47.6**	42.3

\* Enthalpies of formation of gaseous trihalides were taken from ref. (27), except values in parentheses, bismuth values, and for NF<sub>3</sub> from ref. (28) and PF<sub>3</sub> from ref. (29).

\*\* The enthalpy of formation of the solid or liquid was obtained from ref. (27), and the enthalpy of vaporization of sublimation was: for NCl<sub>3</sub>—estimated; for PI<sub>3</sub> and SbF<sub>3</sub>, ref. (30), AsI<sub>3</sub>, ref. (31), and SbI<sub>3</sub>, ref. (16) and (33). The enthalpies of atomization of the bismuth trihalides have been evaluated in ref. (32), (21), and (22), respectively, for the chloride, bromide, and iodide. The enthalpies of formation of all the monatomic gases except P were taken from ref. (27), the value for P from NBS Circular 500.

Note: The values in parentheses all involve an estimate in the enthalpy of sublimation and so have an uncertainty of about 2 kcal. The uncertainty in the other values is less than 1 kcal. The values for phosphorus compounds all include the enthalpy of formation of atomic P (75 kcal), which may be subject to revision.

Table VIII. Ratio of enthalpy of vaporization at the boiling point to bond energy (at 298°K) for group VA trihalides\*

	F	Cl	Br	I
P	(0.03)	0.09	0.15 <sup>1</sup>	0.21
As	0.061	0.068	0.12 <sup>1</sup>	0.22
Sb	---	0.14	0.23	0.36
Bi	0.34	0.26	0.34	0.43

\* Data from ref. (17), except PF<sub>3</sub> for which the enthalpy of vaporization was estimated from the boiling point (172°K), and the bismuth halides for which the enthalpies of vaporization were taken from earlier work in this laboratory.

of either the central atom or the halogen, with the exception of BiF<sub>3</sub>. To the left and above the dashed line in Table VIII, the compounds in the condensed states are molecular (3). The iodides all have layer lattices. The values of this ratio for the bismuth halides are relatively large and comparable to those found in the alkali halides. (Lithium halide values are: 0.38, 0.32, 0.35, and 0.49 for F, Cl, Br, and I; while sodium values are 0.47, 0.42, 0.44, and 0.53.) The ionic nature (3) of crystalline BiF<sub>3</sub> is in keeping with the relatively large value of this ratio, as well as other properties, including its crystal structure, lattice energy, and high melting point. In contrast, crystalline SbF<sub>3</sub> has a molecular structure. It would be valuable to have information on its vaporization properties to evaluate the energy ratio for comparison with bismuth fluoride.

**Electronegativity of bismuth.**—Allred (34) has considered the electronegativities of the elements as derived from thermochemical data as well as other methods. He points out that the value for bismuth has been based on only one measurement, namely, the enthalpy of formation of BiCl<sub>3</sub>. The enthalpies of formation of the other trihalides are now available and can be combined with Allred's values for the average electronegativities of the halogens [ref. (34), Table III] via Allred's Eq. 2 and 3 to yield electronegativities for bismuth of: 2.22, 2.02, 1.99, and 1.94 from the fluoride, chloride, bromide, and iodide, respectively. Corresponding values for antimony are 2.22, 2.01, 2.00, and 2.02. Values from the fluoride, chloride, and bromide for antimony are within 0.01 unit of the respective bismuth values.

Allred and Hensley (35) have considered the electronegativity differences for antimony and bismuth on several scales based on various properties and concluded that the value for bismuth should be larger than that for antimony. This conclusion seemed to be based mainly on NMR proton resonance of the protons on trimethyl bismuth and antimony in dilute solutions in 2,2 dimethyl propane. (However, the relatively large concentration effect that they observed with bismuth and antimony compared to nitrogen, phosphorus, and antimony implies that the chemical shift of the proton resonance depends on solution effects, and these effects may not be eliminated by extrapolation to infinite dilution.) Because the electronegativities of antimony and bismuth derived from the thermochemistry of their halides are now known to be the same, the NMR evidence indicating them to be different should be reexamined.

The equality of the thermochemical electronegativities of antimony and bismuth indicates that their bond energies with a given other element differ by the same amount from their bond energies in the elemental crystal. (Ideally, electronegativities are based on the single bond energies which are not known for these elements; therefore, the electronegativities are based on the bond energies in the crystalline elements.) The energies of the bonds of antimony and bismuth with another element are quite different, as indicated in Table VII. Not only do the bond energies of antimony and bismuth differ for a given halogen, but the difference for the fluoride is substantially larger than

for the other halides. The variation with halogen is compensated for by a difference in the enthalpies of sublimation, so that the electronegativities derived from enthalpies of formation of the solids do not show a variation.

### Acknowledgment

The author is indebted to Dr. H. Eding, who obtained the enthalpy increment data; to Mr. W. E. Robbins, who made many of the experimental measurements; and to Dr. Ward N. Hubbard of Argonne National Laboratory, for information on heats of formation.

This work was made possible by the support of the Research Division, U. S. Atomic Energy Commission, under Contract No. AT(04-3)-106.

Manuscript submitted April 29, 1968; revised manuscript received ca. July 8, 1968.

Any discussion of this paper will appear in a Discussion Section to be published in the June 1969 JOURNAL.

### REFERENCES

1. F. Hund and R. Fricke, *Z. anorg. u. allgem. Chem.*, **258**, 198 (1949).
2. H. von Wartenberg, *ibid.*, **244**, 337 (1940).
3. A. F. Wells, "Structural Inorganic Chemistry," 3rd ed., pp. 342, 664, Oxford University Press, England (1962).
4. B. Aurivillius, *Acta Chem. Scand.*, **9**, 1906 (1955).
5. W. F. Hillebrand, G. E. F. Lundell, H. A. Bright, and J. I. Hoffman, "Applied Inorganic Analysis," 2nd ed., p. 236, J. Wiley & Sons, Inc., New York (1953).
6. H. Shenker, J. I. Lauritzen, R. J. Corruccini, and S. T. Lonberger, "Reference Tables for Thermo-couples," Natl. Bur. Std. Circ. 561, April 27, 1955.
7. A. S. Dworkin and M. A. Bredig, *J. Phys. Chem.*, **64**, 269 (1960).
8. A. J. Darnell and W. A. McCollum, *ibid.*, **72**, 1327 (1968).
9. JANAF Thermochemical Tables, Dow Chemical Co., Midland, Mich. Sept. 30, 1967.
10. L. E. Sutton, "Tables of Interatomic Distances," Special Publ. No. 11, The Chemical Society, London, 1958.
11. T. R. Manley and D. A. Williams, *Spectrochem. Acta*, **21**, 1467 (1965).
12. H. Eding and D. Cubicciotti, *J. Chem. Eng. Data*, **9**, 524 (1964).
13. D. Cubicciotti and H. Eding, *ibid.*, **10**, 343 (1965).
14. D. Cubicciotti, H. Eding, F. Keneshea, and J. W. Johnson, *J. Phys. Chem.*, **70**, 2389 (1966).
15. D. Cubicciotti and H. Eding, *J. Chem. Eng. Data*, **12**, 548 (1967).
16. D. Cubicciotti and H. Eding, *J. Phys. Chem.*, **69**, 3621 (1965).
17. O. Kubaschewski, E. L. Evans, and C. B. Alcock, "Metallurgical Thermochemistry," 4th ed., p. 310, Pergamon Press Ltd., London, (1967).
18. F. J. Keneshea and D. Cubicciotti, *J. Phys. Chem.*, **96**, 3910 (1965).
19. D. Cubicciotti, *ibid.*, **70**, 2410 (1966).
20. W. M. Latimer, "Oxidation Potentials," 2nd ed., Appendix III, Prentice-Hall, Inc., Englewood Cliffs, N. J. (1952).
21. D. Cubicciotti, *Inorg. Chem.*, **7**, 208 (1968).
22. D. Cubicciotti, *ibid.*, **7**, 211 (1968).
23. H. H. G. Jellinek, *Trans. Faraday Soc.*, **40**, 1 (1944).
24. R. Hultgren, R. L. Orr, P. D. Anderson, and K. K. Kelley, "Thermodynamic Properties of Metals and Alloys," p. 51, J. Wiley & Sons, Inc., New York (1963).
25. K. S. Pitzer and L. Brewer, revision of G. N. Lewis and M. Randall, "Thermodynamics," p. 672, McGraw-Hill Book Co., New York (1961).
26. T. L. Cottrell, "The Strengths of Chemical Bonds," 2nd ed., p. 103, Butterworths Scientific Publications, London (1958).
27. D. D. Wagman, W. H. Evans, I. Halow, V. B. Parker, S. M. Bailey, and R. H. Schumm, Natl. Bur. Stds. Tech. Note 270-1, Oct. 1, 1965.
28. L. C. Walker, *J. Phys. Chem.*, **71**, 361 (1967).
29. Private communication from Dr. Ward M. Hubbard, Argonne National Laboratory of unpublished measurements by E. Rudzitis, E. H. Van Deventer, and W. N. Hubbard.



30. L. Brewer *et al.*, "The Chemistry and Metallurgy of Miscellaneous Materials, Thermodynamics," p. 220, McGraw-Hill Book Co., New York (1950).
31. D. Cubicciotti and H. Eding, *J. Phys. Chem.*, **69**, 2743 (1965).
32. D. Cubicciotti, *ibid.*, **71**, 3066 (1967).
33. D. Cubicciotti, Unpublished measurements show the enthalpy of formation of SbI<sub>3</sub> to be  $-27.9 \pm 0.6$  kcal/mole.
34. A. L. Allred, *J. Inorg. Nucl. Chem.*, **17**, 215 (1961).
35. A. L. Allred and A. C. Hensley, Jr., *ibid.*, **17**, 43 (1961).

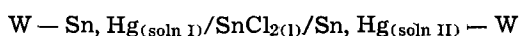
## EMF Measurements on Dilute Solutions of Tin in Mercury with a Structural Interpretation of the Calculated Activities

Guy R. B. Elliott\*

University of California, Los Alamos Scientific Laboratory, Los Alamos, New Mexico

### ABSTRACT

Emf measurements with H-cells of the type



were made with high precision for compositions from 0.001 to 0.128 mole fraction of tin at 520° to 570°K. The results show a constant change of emf with temperature for any one composition, but the constants relating change of emf to change of temperature are different at different compositions. The interrelationships of the constants suggests a structural interpretation as follows: For the most dilute solutions, the tin atoms randomly occupy any atomic positions in the solution, and Henry's law is followed closely. As the concentration is increased (*e.g.*, above 0.01 mole fraction Sn for 525°K) the Sn loses a third of its entropy of mixing, quite possibly by moving into sheets within which the tin atom positions are two dimensionally random.

As a continuation of experimental tests of solution and thermodynamic theory (1-11) the system Hg-Sn with tin as the solute was measured by EMF using a technique similar to that used with tin as the solvent (5, 12).<sup>1</sup>

### Experimental Procedures

**Material purification.**—Water was removed from reagent grade SnCl<sub>2</sub> · 2H<sub>2</sub>O by fusion under rough vacuum. Three distillations under vacuum (0.01-0.1 μ beyond the cold trap), *in situ*, with each side arm plus tailings sealed off and removed after each step, served to purify the SnCl<sub>2</sub>. The first distillation removed oxides, the second (after boiling with tin) removed hydroxides and reactive halides, and the third was for safety. (In Fig. 1 the side arms are not drawn full size and the first arm has been removed.)

Reagent grade tin was melted under vacuum and washed by boiling with SnCl<sub>2</sub> to remove reactive materials, then cast into rods which were flamed to bring any trapped electrolyte to the surface. The cold Pyrex was broken off, and the tin was washed with water. These smooth and shining rods were cut up with clean diagonal cutters, examined by microscope for possible iron pickup (none found), weighed, and loaded into the argon-filled arms of the H-cell.

Triple distilled mercury, boiled under vacuum, was scavenged of oxide and electrochemically important impurities by boiling under an argon atmosphere with molten SnCl<sub>2</sub>. After cooling, the last SnCl<sub>2(s)</sub> scum was removed by pressure filtration through a glass frit. This mercury (container weighed before and after) was poured through a long funnel into the legs of the argon-filled H-cell.

Argon was cleaned by condensing it in an N<sub>2(l)</sub> cold trap, boiling it gently to flush out volatiles, then warming the trap gently by lowering the Dewar until

enough argon had vaporized. The tungsten electrodes were made clean and shiny by electrolysis (0-15 VAC) in concentrated NaOH, then water wash, and drying by touching a tissue. Each cell, used only once and clean from annealing, was outgassed and filled with argon before the chemicals were added.

**Furnace and measuring equipment.**—These have been described elsewhere (5). The only change was the use of a new proportional temperature controller designed by Rexroth and Pacheco of this laboratory (report in preparation).

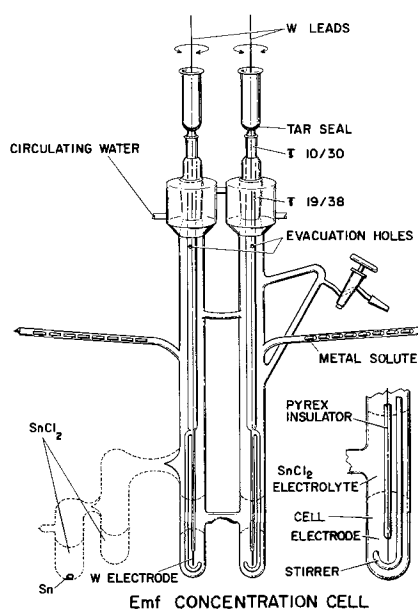


Fig. 1. Stirred H cell. Tubes drawn oversize below standard taper joints. Evacuation holes are only into stirrers.

\* Electrochemical Society Active Member.

<sup>1</sup>In Ref. 5 an error in the Dundee plot in Fig. 4 should be corrected. At 0.094 mole fraction of gold, the point should have been plotted at 1.20 rather than 1.19 for the ordinate.

**Operation of the cell.**—With mercury in the cell legs and the system evacuated, the mercury was gently flamed to remove gases. Then  $\text{SnCl}_2$  was added by its final distillation. About  $\frac{1}{2}$  atm of argon was added (to prevent boiling of the mercury), and the cock was closed. The cell was placed in the hot furnace. After stirring, a piece of tin was added to each leg. The system was stirred intermittently and heated, normally, overnight.

When a cell could be stirred with almost negligible effect on the voltage and then it returned in a few minutes to the original voltage, the system was accepted as being at equilibrium. This condition was achieved in about an hour after adding tin if the stirring was frequent, but 2 hr or more elapsed between additions. For temperature changes at a single composition, some measurements were taken about  $\frac{1}{2}$  hr apart, but most were taken more slowly.

(Commercial models of the cell are available through Los Alamos Thermodynamic Equipment, Santa Fe, New Mexico.)

### Results

The results of measurements on three runs are listed in Table I. These are low-temperature data taken to emphasize the change of emf with composition. The results from run I, points 25-28, were established from extrapolation or interpolation of data at different temperatures. (See Uncertainty of the Results for the comparison of run I with runs II and III.)

Table II shows the temperature dependence of the emf at various compositions for run I and run IV. Two measurements at 0.003989 mole fraction tin in run I are not reported because they involved reversing the potentiometer leads, and their accuracy is questionable; rough constants for these measurements are indicated by question marks in later plots.

### Uncertainty of the Results

The precision is shown by Fig. 2-5. If, in Fig. 3, the scatter is ascribed to compositional error, point 25 is off the line by an amount equal to about 1% of the

tin mole fraction. The curve could be moved to apportion the error between it and points 33 and 34. That would raise the scatter at points 33 and 34 to about 0.4%, or more than shown by the other points. As discussed below there is reason to be somewhat dubious of the composition at point 25 from Run I.

**Composition.**—The materials added as weighed by TCX balance are probably not in error by 0.1%. One or more of the following compositional uncertainties would seem to be the source of the additional uncertainty. (A) As shown by Fig. 4, diffusion of tin from leg to leg through the electrolyte, or removal of mercury through the salt and to the vapor is trivial during a set of measurements at high temperatures or for long periods at 525°K. However, some error of this type may have occurred in runs I and IV on standing at high temperatures before the measurements at any composition were started. (B) Although the linearity of the data argues against an extensive trapping of  $\text{SnCl}_2$  in the solid tin, it might have occurred in a piece or two. (C) If the tin scrubbing did not destroy all the  $\text{Sn}(\text{OH})_2$ , or if the argon contained traces of oxygen, variable amounts from run to run would have destroyed different fractions of the first tin pieces added and especially the first compositions might be detectably wrong. (D) Although the indications are that the solubility of tin in  $\text{SnCl}_2$  is low (15, 16, also 5), the results are not definitive and the corrections might not really be trivial. (E) The differences in stability reported for mercury and tin chlorides (17) would not allow for a significant displacement reaction (18) of mercury with  $\text{SnCl}_2$ . Gross error in these reported stabilities seems unlikely. (F) It is very doubtful if correction is necessary for any compositional errors resulting from impurities in the small amount of tin or in the vaporized mercury. (G) To correct, if necessary, for the solubility of  $\text{SnCl}_2$  in the mercury, its solubility was estimated both at room temperature and at  $\sim 520^\circ\text{K}$  by the following procedure. Mercury, saturated with  $\text{SnCl}_2$  and cooled to just below the  $\text{SnCl}_2$  freezing point, was decanted from the solid and cooled. The barely visible traces

Table I. Tin in mercury concentration cell emf data at  $\sim 525^\circ\text{K}$  (W—Hg,  $\text{Sn}_{(\text{soln})}/\text{SnCl}_{2(1)}/\text{Hg}$ ,  $\text{Sn}_{(\text{soln})}$ —W)

Point No.	Mercury, g	Tin added, g	Tin mole fraction, $N_{\text{Sn}}$	Temp, °K	Emf reading, <sup>a</sup> mv	$\frac{N_{\text{Sn}}}{N_{\text{Hg}}}$	$\log a_{\text{Sn}} + \text{constant}^b$	$\log \gamma_{\text{Sn}} + \text{constant}^c$	Emf/T, mv/°K
Run I									
Rt. leg									
Lt. leg	52.00206	0.34783	0.011178						
25	51.75026	0.43460	0.013994	523.4	4.326	0.014193	0.08333		
26		0.53254	0.030617	523.4	14.790	0.031584	0.28489		
27		0.65756	0.050385	523.4	20.156	0.053059	0.38826		
28		1.20570	0.084613	523.4	24.692	0.092434	0.47563		
Run II									
Rt. leg	63.73318	0.03796	0.0010056						
Lt. leg									
29	62.20571	0.06398	0.0017352	524.7	12.014	0.0017382	0.23085	2.99150	0.02290
30		0.04603	0.0029799	524.7	23.540	0.0029888	0.45232	2.97811	0.04486
31		0.10599	0.0058342	525.0	37.156	0.0058684	0.71354	2.94756	0.07077
32		0.11520	0.0089180	524.8	45.129	0.0089982	0.86699	2.91672	0.08599
33		0.13795	0.012586	525.3	51.164	0.012746	0.98199	2.88211	0.09740
34		0.15368	0.016640	525.3	55.699	0.016921	1.06903	2.84788	0.10603
35		0.38819	0.026734	525.7	62.452	0.027468	1.19773	2.77067	0.11880
36		0.59438	0.041793	525.6	67.651	0.043616	1.29769	2.67658	0.12871
37		0.60327	0.056609	525.5	70.674	0.060006	1.35593	2.60305	0.13449
38		0.67061	0.072550	525.4	72.837	0.078226	1.39770	2.53706	0.13663
Run III									
Rt. leg	71.04504	0.05362	0.0012739						
Lt. leg									
39	71.87960	0.06095	0.0014310	522.7	2.497	0.0014331	0.04816	2.89253	0.00478
40		0.06097	0.0028584	524.7	17.331	0.0028666	0.33302	2.87690	0.03303
41		0.07745	0.0046657	524.6	27.406	0.0046876	0.52671	2.85782	0.05224
42		0.09297	0.0068266	524.6	34.858	0.0068735	0.66992	2.83575	0.06645
43		0.09931	0.0091245	524.8	40.230	0.0092085	0.77287	2.81271	0.07666
44		0.11905	0.011865	524.1	44.794	0.012008	0.86170	2.78748	0.08547

<sup>a</sup> For Run I, obtain emf at 523.4°K from data at other temperatures as listed in Table II.

<sup>b</sup> Calculate from  $(10.08211) \left( \frac{e_{\text{obs.}}}{T^\circ\text{K}} \right) = \log a_{\text{Sn}} + \text{constant}$ . To plot all data on one graph, add 0.9444 to run I data, and add 0.0990 to run III data.

<sup>c</sup> Subtract  $\log N_{\text{Sn}}$  to get  $\log \gamma_{\text{Sn}} + \text{constant}$ . To plot runs II and III on one graph, subtract 2.0104 from run II data, and subtract 1.9090 from run III data.

Table II. Tin in mercury concentration cell data showing the effect of temperature

Point No.	Hg, g	Addition of Sn, g	Tin mole fraction	$\log N_{Sn}$	Emf, mv	T°K
Rt. leg 2nd day <sup>a</sup> Run I	52.00206	0.34783	0.011178	$\bar{2}.04836$		
Lt. leg 3rd day	51.75026	0.43460	0.013994	$\bar{2}.14594$	4.326	523.4
2					4.720	567.8
3		0.53254	0.030617	$\bar{2}.48597$	16.196	567.8
4					16.210	568.4
5					16.048	563.5
6					15.737	553.4
4th day						
7					14.945	528.4
8					14.922	527.8
9		0.65756	0.050385	$\bar{2}.70230$	20.329	527.1
10					20.807	537.5
11					20.846	538.4
12					21.039	542.6
5th day						
13					20.305	526.5
14		1.20570	0.084613	$\bar{2}.92744$	24.866	526.1
15					25.260	532.7
16					25.872	542.7
6th day						
17					27.272	566.3
18					27.315	566.9
19		0.74961	0.104676	$\bar{1}.01984$	29.356	568.8
7th day						
20					27.896	546.4
21					27.890	546.2
8th day						
22					26.465	524.9
23		0.89545	0.127520	$\bar{1}.10558$	27.900	524.4
10th day						
24					31.229	570.7
Run IV						
Rt. leg 5th day	51.93798	0.38461	0.01236	$\bar{2}.09203$		
45	46.46215	2.14828	0.07248	$\bar{2}.86021$	24.316	570.1
46					24.321	570.2
47					24.368	571.1
48					24.265	569.1
6th day						
49					23.436	553.4
50					23.428	553.2
51					23.417	553.1
52					23.057	546.2
53					22.914	543.6
54					22.721	540.0
55					22.423	534.3
56					22.419	534.0
57					22.284	531.7
58					22.280	531.5
7th day						
59					22.163	529.1
60					22.061	527.4
61					21.919	524.7
18th day <sup>b</sup> 62					21.994	525.9

<sup>a</sup> Cell had had a preliminary heating with stirring for four days, then was cooled and later reheated.

<sup>b</sup> Cell had been taken out of furnace and returned to furnace on 7th day.

of  $\text{SnCl}_2$  which showed after cooling were dissolved in water and precipitated with  $\text{AgNO}_3$ . This gave the difference in solubility between 520°K and room temperature. The solubility of  $\text{SnCl}_2$  in mercury at room temperature was estimated by aqueous extraction of  $\text{SnCl}_2$  from mercury by vigorous shaking. The solubility of the  $\text{SnCl}_2$  in mercury at either temperature is <5 ppm.

**Emf.**—There was nothing erratic about the emf readings and nothing to indicate high resistance films, electrochemically active impurities, or irreversibility. The K-2 potentiometer was calibrated by A. N. Shopp of our laboratory. Allowing for the larger emf values and different potentiometer scales used, the precision is in line with earlier results (5). Also the grounded Faraday cages around the cell had already been tested and found adequate (5).

Probably associated with small temperature gradients top-to-bottom in the cell, stirring altered the voltage as much as 0.002 mv. This is consistent with anticipated thermocell effects [see ref. (12)] of 0.6 mv/°K plus a temperature gradient of around 0.003°K. Isopestic balance results indicate this uniformity of temperature is bettered by nesting copper cylinders under more ideal conditions. The long-term stability

of emf was acceptable, as in Fig. 4 the values before and after 15 days were about 0.012 mv (~0.05%) off the line.

Possible spurious emf values from thermocouple effects at the copper-tungsten room temperature junctions were tested by moving the connection clamps. No effect was observed. (The W leads were ~25 cm, i.e., longer than in Fig. 1.)

**Temperature.**—For the runs where temperature was varied, the effects of temperature gradients can best be evaluated from the scatter of the data. This scatter from linearity amounts to only a few microvolts: if ascribed to a discrepancy between the thermocouple temperature and the alloy temperature, it amounts to about 0.06°K for the average temperature error; if ascribed to thermocell effects caused by temperature gradients between the cell legs, as discussed in the previous section, the corresponding gradients would be about 0.01°K.

Experience with Pt/Pt-10%Rh thermocouples, as used in these experiments and in isopiestic balance experiments, has demonstrated that thermocouple strains after the thermocouple wires were checked would not change the absolute temperature as much as 0.7°K; furthermore, if such an error did exist, it has been shown that the error would appear essentially equally in all readings. The thermocouple hot junction was taped to the Pyrex just outside the active electrode-electrolyte interface.

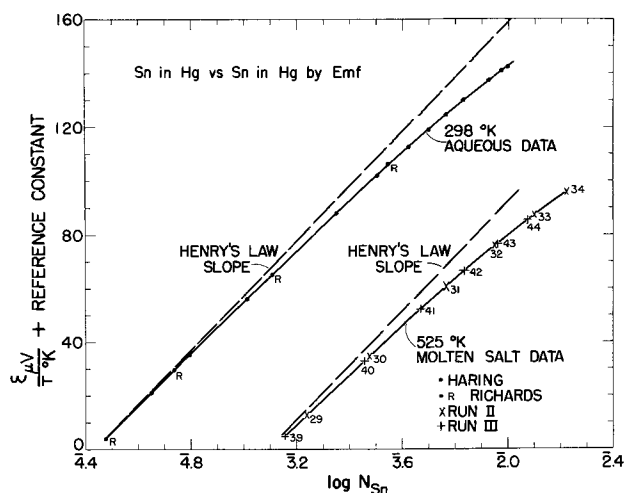


Fig. 2. Deviations from Henry's law slopes for runs II and III. Other data from Haring and White (13) and Richards and Wilson (14). The logarithms listed have a negative characteristic and positive mantissa. These indicate the concentrations of the changed electrode; the reference electrode differences are eliminated by the reference constant.  $\epsilon$  in microvolts is plotted.

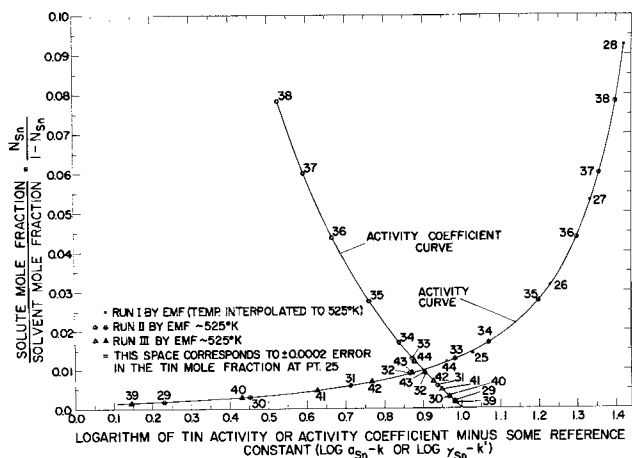


Fig. 3. Data for Duhem integration at 525°K

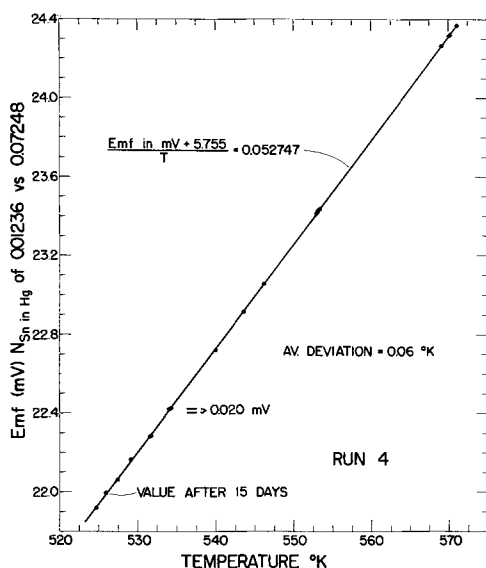


Fig. 4. Run IV data showing the effect of temperature for  $N_{\text{Sn}} = 0.01236$  vs.  $N_{\text{Sn}} = 0.07248$ .

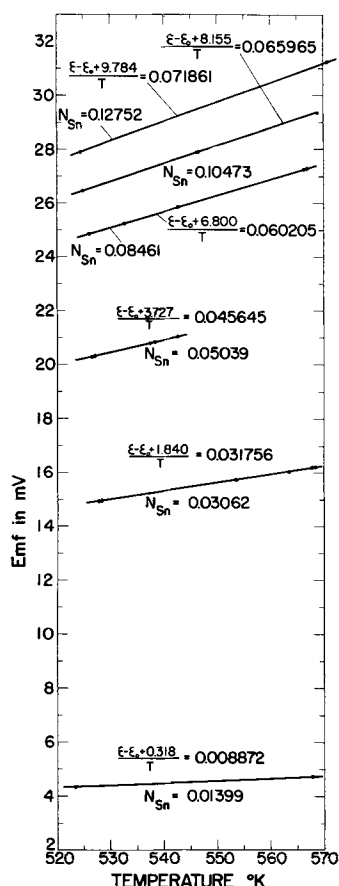


Fig. 5. Data for run I showing the effect of temperature at various compositions. Equation form  $(\epsilon - \epsilon_0 + A) T = B$ .

**Checks of the over-all accuracy.**—The aqueous measurements (13, 14) may be compared with the molten salt measurements as in Fig. 2. Their close similarity of form is consistent with Kleppa's conclusion (19) that the heat of alloy mixing shows no trend with temperature. It suggests that all three groups of measurements are truly indicating the solution behavior.<sup>2</sup>

<sup>2</sup> Two other groups of emf measurements on Hg-Sn should be mentioned. Van Heteren (20) had results in general agreement with these, but his lack of precision and different reference electrodes make an exact comparison difficult. Petot-Ervas *et al.* (21) have also recently reported measurements on emf cells using electrodes of tin and tin in mercury. They used water, glycerine, and ZnCl<sub>2</sub>-LiCl-KCl eutectic as solvents for the SnCl<sub>2</sub>. There is satisfactory agreement among the various measurements except for somewhat anomalous temperature coefficients with the eutectic solvent.

The data relating emf to temperature may be checked against those from Kozin and Nigmatova (22) who used a glycerine solvent for the electrolyte up to 513°K. Although their paper was criticized for theoretical mistakes (23), the experimental results appear to be valid though not of high precision.

From the results shown in Fig. 5,  $d(\epsilon - \epsilon_0)/dT = 0.045645$  mv/°K at  $N_{\text{Sn}} = 0.05039$ , and  $0.008872$  mv/°K at  $N_{\text{Sn}} = 0.01399$ . The difference is  $0.03677 \pm 0.00018$  mv/°K. Kozin and Nigmatova find a difference of  $0.038 \pm 0.009$  mv/°K (corrected value because of a slightly different composition range). All of the uncertainties have been evaluated from the data;  $\pm 1.5$  mv has been used for Kozin and Nigmatova and  $\pm 0.005$  mv for this work, *i.e.*, slightly less than the maximum apparent scatter.

Similarly for the change of emf with composition using the results of run II,  $d(\epsilon - \epsilon_0) (1/T)/d \log N = 0.06042 \pm 0.00003$  mv per mole fraction unit in the range 0.056609 to 0.008918 mole fraction of tin. Kozin and Nigmatova show the value  $0.060 \pm 0.006$  for the range 0.05 to 0.01 mole fraction of tin.

## Discussion

*Emf vs. mole fraction.*—Because

$$\frac{\epsilon - \epsilon_0}{T} = - \frac{R}{nF} \ln \frac{\gamma N}{\gamma_0 N_0} \quad [1]$$

then for Henry's law ( $\gamma = \text{constant}$ )

$$\frac{\epsilon - \epsilon_0}{T} - \left( \frac{2.303 R}{2F} \right) \log N_0 = - \left( \frac{2.303 R}{2F} \right) \log N \quad [2]$$

and this gives the reference slopes on Fig. 2. Empirical constants (Table I) have been used to correct for the reference electrode potential differences.

Since the aqueous data in Fig. 2 were largely rejected in a comparative analysis (24), some comments should be made. The curvature shown by the measurements is not consistent with regular solution theory [ref. (24), p. 15] which apparently has been used [ref. (24), p. 785] to give a rather unsatisfactory description of the mercury vapor pressure data (25). [Other vapor pressure data (26) are in general agreement with, but are less precise than, those taken earlier (25).] Consistent with regular solution theory but not consistent with the data, two lines of different slope were used to represent the different sets of concordant aqueous emf results (Fig. 2, 13, 14) and a third intermediate line representing a third and much less precise group of data (20) was used to calculate dilute solution mercury activities [ref. (24), pp. 785, 789]. This treatment would now appear to have been in error. (Structural phenomena are discussed in the next section; Duhem integrations are then described.)

*Emf vs. temperature with interpretation.*—The constants applied in Fig. 5 are interrelated as shown in Fig. 6 and 7. In the region 0.01–0.08 mole fraction of tin, a single equation consistent with the relationships in Fig. 6 and 7 can be used to describe the data roughly, but not within their apparent precision. Using volts here,

$$\frac{\epsilon - \epsilon_0 - \alpha + 0.0916 N_{\text{Sn}}}{T} = \left( \frac{2}{3} \right) \frac{R}{nF} \ln \frac{N_{\text{Sn}}}{N_{\text{Sn}^0}} \quad [3]$$

with  $\alpha$  from  $0.0916 N_{\text{Sn}^0}$  of the reference electrode.

The constants from the temperature dependent relationships can be checked against the more precise run II as in Fig. 8. This plot shows that the relationship holds well here also to about 0.01 mole fraction where a change of behavior occurs and Eq. [2] fits the lower concentration data acceptably.

After considering a number of postulates, the following is the only one I have reached which seems to be consistent with the data.

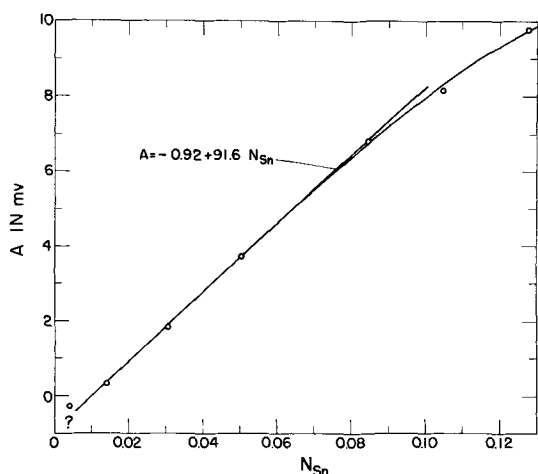


Fig. 6. Variation with composition of the temperature dependent terms, A, in Fig. 5.

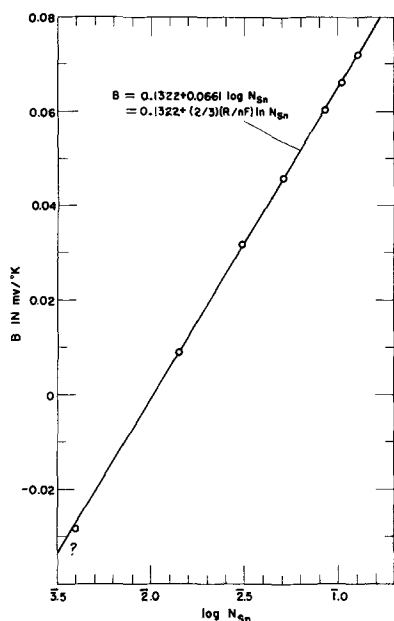


Fig. 7. Variation with log composition of the temperature independent terms, B, in Fig. 5.

The enthalpy changes for the cell reaction,  $-nFd[(\epsilon - \epsilon_0)/T]/d(1/T)$ , are indeed constant as observed less clearly by Kleppa calorimetrically (19). At about 0.1 mole fraction of tin, a deviation from the relationship (Fig. 6) occurs. It might be abrupt, although this is not clear either from the emf work or from the calorimetry. [Note that Kleppa's values from 0.1-0.4 mole fraction of tin in his Fig. 3 do all lie on a straight line of different slope from those for 0.02 to 0.1 mole fraction. Equations are given for other calorimetric measurements (27) but the data are not presented.] The linear enthalpy equation region suggests that these added tin atoms enter essentially equivalent sites, gradually changing the environment and bonding energy.

The 2/3 with the entropy term is unusual. Replacing  $n = 2$  by  $n = 3$  seems unacceptable: water (13, 14), glycerine (22), and pyridine (20) solvents, as well as the pure  $\text{SnCl}_2$  melt, produce comparable results so stray Sn(III) in the electrolyte and in contact with Sn(O) appears most unlikely; furthermore, using Sn(II) for melts of  $\text{SnCl}_{2(1)}$  (5) or with  $\text{SnCl}_2\text{-LiCl-KCl}$  (28) leads to Raoult's law behavior for solvent tin.

The only acceptable place for the 2/3 seems to be as  $(2/3) R \ln N_{\text{Sn}}$  or  $R \ln (N_{\text{Sn}})^{2/3}$  for the entropy of

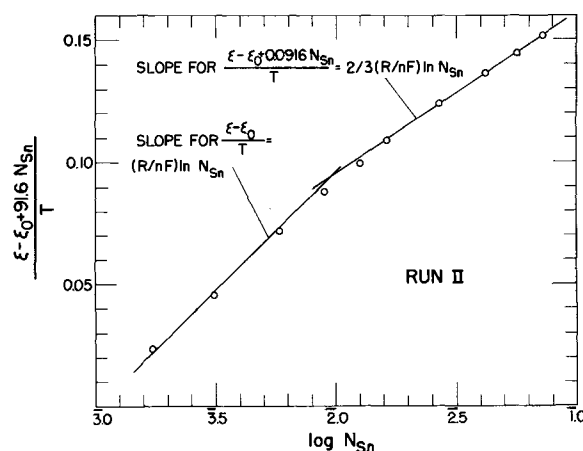


Fig. 8. Temperature-composition equation applied to run II. Ordinate uses mv.

dilution, i.e., 2/3 the normal limiting value. The enthalpy linearity seems to rule out usual association, e.g., to  $\text{Sn}_2$  and  $\text{Sn}_3$ . Peculiar rotational or vibrational effects would not seem to lead to an almost exact 2/3 as shown by Fig. 7. Long chains of tin would apparently not give this behavior [see ref (29), p. 293]. Perhaps the metallic resonance and metallic bond strengths for the mercury solvent are less disturbed if the tin atoms arrange randomly in planes or sheets rather than randomly through the whole solution volume. [See a similar discussion regarding ordered solid defects (2b). Certainly the sheets cannot be large, since the alloy is fluid; a densely packed finely divided powder might provide a fair instantaneous analogy.] Fairly widely separated planes without significant edge effects would not contribute much randomness, and  $(2/3) R \ln N_{\text{Sn}}$  would be expected to be approximated closely. Then (for 523°K) at 0.01 mole fraction of tin (Fig. 8) the randomizing forces overcome the ordering forces, the whole solution becomes available to the solute, and Henry's law is either obeyed or approached closely. The data are not clear on how abruptly the change occurs.

*The Duhem integrations.*—In connection with the thermodynamic questions (1-11), the Duhem integration is very important. For the present experiments, a constant reference electrode composition was used on one side of the cell, and the changes of emf with changes of the other electrode composition may be used to calculate the changes in activity of the tin. Thus, even though the Henry's law constant cannot be obtained from the data, a Duhem integration can be carried out to predict the variation of the mercury activity with composition.

The required data are presented in Table I and Fig. 3. Either activity or activity coefficient can be used. (Arbitrary constants have been added to superimpose the runs.) From the activity coefficient equation

$$\int_{N_{20}}^{N_2} \frac{d \log \gamma_1}{dN_2} = - \int_{N_{20}}^{N_2} \frac{N_2}{N_1} \frac{d \log \gamma_2}{dN_2} \quad [4]$$

the area under the curve in Fig. 3 according to thermodynamic theory gives the change in the mercury activity coefficient with mole fraction. No extrapolation to infinite dilution is necessary to perform this integration: Knowing the mercury activity at any point fixes the activities all along the curve. However, for convenience, the short extrapolation to infinite dilution was performed in order to fix the mercury activity from its pure solvent value. The predicted mercury activities are plotted in Fig. 9, out to 0.09 mole fraction of tin for comparison with some vapor pressure measurement being carried out by Dr. D. R. Conant of our laboratory. Just where one chooses to switch from  $(2/3) R \ln N_{\text{Sn}}$  to  $R \ln N_{\text{Sn}}$  for the entropy

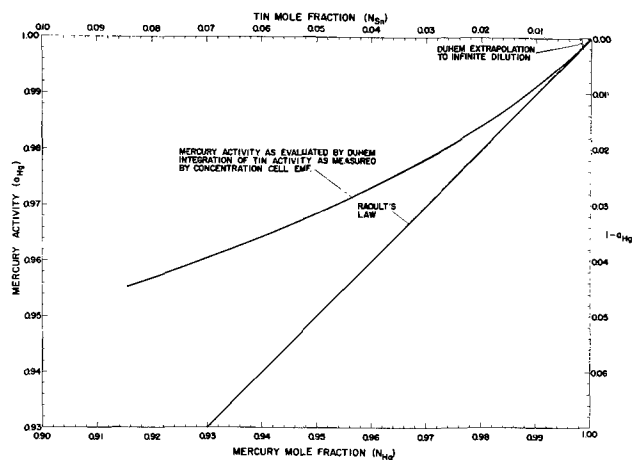


Fig. 9. Duhem integration of tin emf data at 525°K to predict the mercury activity-mole fraction relationships.

partial makes little difference to the value of the integral. Other errors in this extrapolation also may be expected to have only a very small effect on the shape of the curve in Fig. 9, e.g., if the mercury activity at the most dilute tin concentration measured were truly not at  $\sim 0.999$  but were even at  $\sim 0.900$ , the activity would drop only  $\sim 10\%$  less fast than is shown, since

$$(d \ln a_1/dN_1) = (1/a_1) (da_1/dN_1)$$

Likewise the uncertainty in the data leads to only a very small uncertainty in the Duhem integration—considering the reproducibility of the data, the fractional error in the area under the curve must necessarily be very small.

By extrapolating the temperature dependent equations to 595°K, a Duhem integration to 0.12752 mole fraction of tin can be carried out. This is shown in Fig. 10 along with the more precise earlier vapor pressure data (25). [The other vapor data (26) are comparable but less precise.]

The differences are systematic (each vapor pressure point represents several readings); the vapor pressure data lie some 10% closer to Raoult's law than the emf-Duhem prediction. Whether the differences are significant is not clear.

The published enthalpy data from solution calorimetry (19) are for a lower temperature. These agree approximately with the earlier emf data (22). Other enthalpy of mixing equations (no data, however) are given for 523°K (27). The present emf data offer no information on the total enthalpy of mixing, but only on its changes. The changes of slope in the  $\Delta \bar{H}_{Sn}$  for

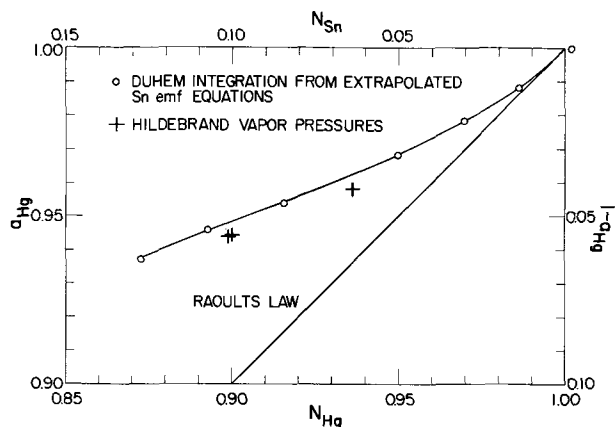


Fig. 10. Duhem integration at 595°K using emf data extrapolated about 30°K. Vapor pressures from Hildebrand, Foster, and Beebe (25) at 595°K.

the present emf data (Fig. 6), and  $\Delta \bar{H}_{Sn}$  from calorimetry appear at about the same composition ( $\sim 0.1$  mole fraction of tin). However, the line used by Kleppa in his Fig. 3 to describe  $\Delta \bar{H}_{Sn}$  corresponds to a change of 560 cal/mole in  $\Delta \bar{H}_{Sn}$  in the range 0.01-0.1 mole fraction of tin. The Wittig and Scheidt equation value changes 241 cal/mole in this range. For the emf the value is 380 cal/mole. The published calorimetric data scatter enough, however, so that a thermodynamically consistent line could be used without forcing the data greatly; no measure of the equation uncertainty is given.

### Acknowledgments

This work is part of a program to measure both emf and vapor pressure for Hg-Sn solutions. The vapor pressure measurements are being carried out by Dr. D. R. Conant, and we have been in close contact during the course of the present work. The author has also had many valuable discussions with Dr. C. E. Holley regarding these problems.

This work was done under the auspices of the U. S. Atomic Energy Commission.

Manuscript submitted Nov. 10, 1967; revised manuscript received July 18, 1968.

Any discussion of this paper will appear in a Discussion Section to be published in the June 1969 JOURNAL.

### REFERENCES

- G. R. B. Elliott and J. F. Lemons, *J. Phys. Chem.*, **64**, 137 (1960).
- G. R. B. Elliott and J. F. Lemons, in *Advances in Chemistry Series*, No. 39, R. F. Gould, Editor, American Chemical Society, Washington, D. C., 1963, a, pp. 144-52, b, pp. 153-69.
- G. R. B. Elliott, J. F. Lemons, and H. S. Swofford, Jr., Los Alamos Scientific Lab. Report, LA-2997 (July 1964).
- G. R. B. Elliott, J. F. Lemons, and H. S. Swofford, Jr., *J. Phys. Chem.*, **69**, 933 (1965).
- G. R. B. Elliott and J. F. Lemons, *This Journal*, **114**, 935 (1967) (see footnote 1).
- H. S. Swofford, Jr. and G. R. B. Elliott, Los Alamos Scientific Laboratory Report LA-3657 (October 1965).
- G. R. B. Elliott, C. C. Herrick, J. F. Lemons, and P. C. Nordine, Los Alamos Scientific Laboratory Report, LA-3526 (March 1966).
- H. S. Swofford, Jr. and G. R. B. Elliott, *Inorg. Chem.*, **7**, 666 (1968).
- G. R. B. Elliott, D. R. Conant, H. S. Swofford, Jr., and B. L. Houseman, "Solution Structure as Indicated by Precise Thermodynamic Measurements" Third International Symposium on High Temperature Technology, Asilomar, California, Sept. 1968, Paper 28, Ed. D. D. Cubicciotti, IUPAC Supplement, in press.
- D. R. Conant and G. R. B. Elliott, *J. Chem. Eng. Data*, **13**, 354 (1968).
- G. R. B. Elliott, Los Alamos Scientific Lab. Report, LA-3891 (1968), in press.
- G. R. B. Elliott and J. F. Lemons, Los Alamos Scientific Laboratory Report, LA-3733, 1967.
- M. M. Haring and J. C. White, *Trans. Electrochem. Soc.*, **73**, 211 (1938).
- T. W. Richards and J. H. Wilson, *Carnegie Inst. Wash. Pub.*, **118**, 27 (1909). Results reported in ref. (13) above.
- J. D. Corbett and S. von Winbush, *J. Am. Chem. Soc.*, **77**, 3964 (1955).
- A. A. Kolotii, *Sb. Tr. Tsent. Nauchn.-Issled. Inst. Chernoi Met.*, **34**, 34 (1963).
- L. Brewer, L. A. Bromley, P. W. Gilles, and N. L. Lofgren, Paper 6 in *National Nuclear Energy Series*, Vol. 19B, L. L. Quill Editor, McGraw-Hill Book Co., Inc., New York (1950).
- C. Wagner and A. Werner, *This Journal*, **110**, 326 (1963).
- O. J. Kleppa, *Acta Met.*, **8**, 435 (1960).
- W. J. van Heteren, *Z. anorg. Chem.*, **42**, 129 (1904).
- G. Petot-Ervas, P. Desré, and E. Bonnier, *Bull. Soc. Chim. France*, 1261 (1967).
- L. F. Kozin and R. Sh. Nigmatova, *Russ. J. Inorg. Chem.*, **8**, 1338 (1963).

23. V. F. Sergeeva and A. I. Zebreva, *ibid.*, **10**, 1067 (1965).
24. R. Hultgren, R. L. Orr, P. D. Anderson, and K. K. Kelley, "Selected Values of Thermodynamic Properties of Metals and Alloys," p. 785, John Wiley & Sons, Inc., New York (1963).
25. J. H. Hildebrand, A. H. Foster, and C. W. Beebe, *J. Am. Chem. Soc.*, **42**, 545 (1920).
26. G. C. Suydan and L. C. Tao, *J. Chem. Engr. Data*, **8**, 537 (1963).
27. F. E. Wittig and P. Scheidt, *Naturw.*, **11**, 250 (1960).
28. J. A. Yanko, A. E. Drake, and F. Hovorka, *Trans. Electrochem. Soc.*, **89**, 357 (1946).
29. K. S. Pitzer and L. Brewer, Revision of G. N. Lewis and M. Randall, "Thermodynamics," McGraw-Hill Book Co., Inc., New York (1961).

## Analysis and Application of the Thermoelectric Microprobe

J. S. Armijo

Stanford Research Institute, Menlo Park, California

### ABSTRACT

A microprobe technique has been developed and used for measuring thermoelectric profiles across Fe-Ni and Cu-Ni diffusion couples. Analysis of the technique permits calculation of the absolute thermoelectric power spectrum. Data are highly reproducible and are in good agreement with previous studies when probe loads of 3g or less are used. Resolution of the thermoelectric microprobe is found to compare favorably with the resolution of the electron microprobe.

The most widely used technique for studying the thermoelectric properties of alloy systems consists of preparing wire specimens of desired compositions, placing them in a temperature gradient, and measuring the thermal emf's produced by the alloys with respect to a reference metal.

The chief disadvantage of the technique is that one specimen must be prepared for each composition of interest. Consequently many specimens must be prepared and tested if the thermoelectric spectrum is to be studied in detail. Furthermore, absolute values of the measured thermoelectric properties can be incorrect if the alloys are not homogeneous. Another disadvantage is that the technique cannot be used for brittle phases which cannot be formed into wires.

A number of studies have been reported in which probe techniques have been used to make thermoelectric measurements on a microscale. In most of these studies (1-5) the experimental emphasis was on the use of thermoelectric effects to measure other physical properties. For example, probe techniques have been used extensively to measure the thicknesses of diffused p-n junctions in semiconductors. In these studies only the signs of the thermal emf's were of interest, since a change in sign during a probe traverse indicated a change from hole to electron conduction and thus defined the junction. The magnitudes of the thermal emf's produced in these studies were not reported and were not used to calculate thermoelectric properties. In 1959 Strug and Panchenko (6) described an improved thermoelectric probe that could be used to make measurements of the magnitudes of the thermal emf's generated at the contact point. This device consisted of a heated tungsten probe mounted on a microhardness testing machine. By using a fine enough tip, these authors found it possible to measure thermal emf differences between phases in alloys of a complex microstructure and between different compositions of binary alloys. The technique, however, was not analyzed in detail, and only qualitative values of thermoelectric properties were obtained.

A similar device was described by Westbrook, Seybolt, and Peat (7). These authors used the technique to detect evidence of solute segregation in NiGa and Pb bicrystals that were doped with oxygen and tin, respectively. In these experiments, pronounced ther-

moelectric minima were observed at grain boundaries. Efforts to calibrate the thermal emf with a series of specimens of homogeneous composition were unsuccessful. Further, the effects of experimental variables such as temperature and load on the probe were not determined. The technique therefore remained qualitative in nature.

The present studies were initiated with the objective of measuring quantitative thermoelectric spectra of Fe-Ni and Cu-Ni alloys with the thermoelectric microprobe.

### Experimental

The thermoelectric microprobe used in these studies was similar in design to those described previously (1-7). However, a number of significant changes were made in the design and operation of the probe to eliminate some of the problems encountered with the previous devices.

The probe itself was a tungsten rod approximately 6.5 cm in length and 0.6 mm in diameter. Efforts were made to maintain a high length to width ratio in order to maintain the cold junction at or very near room temperature. The probe tip was first roughly sharpened on a diamond grinding wheel, and then sealed into a close fitting alumina tube with epoxy cement. Uniform epoxy distribution was assured by submerging the assembled probe and insulator in the liquid epoxy and then evacuating all trapped gases. The probe was then removed from the bell jar and cleaned; the epoxy was allowed to harden for approximately 24 hr. The probe was then manually polished to a sharp point by using progressively finer diamond abrasives on standard metallographic polishing wheels. The electrolytic technique that Westbrook *et al.* (7) used to sharpen their probes was found to produce undesirably fragile probe tips. Probes made by mechanical polishing, however, were very strong, and did not lose their shape in normal experimental use.

The probe was then prepared for electrical connection by carefully abrading the end to remove surface contamination and expose a fresh metal surface. The probe was placed in a vacuum bell jar, masked where necessary, and coated with a thin layer of copper by vacuum deposition. The contact end was then covered



Fig. 1. Experimental arrangement showing microprobe, specimen, thermocouple, and specimen heating bath. Insert shows profile of mechanically polished probe tip.

with a thicker ( $\sim 0.1$  mm) copper layer by electropolating in a sulfuric acid-copper sulfate solution. With this procedure it was always possible to obtain a low contact resistance by normal soldering techniques. Efforts to copper plate directly to tungsten and efforts to solder directly to a thin vacuum-deposited copper were unsuccessful.

The probe was then mounted in a holder designed to fit a standard microhardness machine.<sup>1</sup> The design was such that the thermoelectric probe was located in the normal position of the diamond indenter. Consequently the normal precision of the microhardness machine with respect to position and load was maintained. The differences in weight between the thermoelectric microprobe and the diamond indenter were readily compensated for with normal load adjustments of the machine.

The placement of the probe in the microhardness machine is shown in Fig. 1. Also shown on the loading beam is a 2-g weight for load adjustment. Electrical connection to the probe was achieved by soldering a fine copper wire ( $\sim 0.025$  mm in diameter) to the copper-plated end. This connection provided good contact, and the effect of the wire on the motion of the loading mechanism was minimal.

Specimens studied in these experiments were binary diffusion couples of Fe-Ni and Cu-Ni. Specimens were prepared by clamping flat, polished pieces of high-purity materials (99.999 Cu, 99.95 Fe, 99.95 Ni) and annealing them in vacuum. The Fe-Ni couple was annealed at  $1300^{\circ}\text{C}$  for 4 hr and the Cu-Ni couple was annealed at  $1000^{\circ}\text{C}$  for 4 hr. Approximately 1 hr was required to cool the specimens to room temperature.

Electrical connection was made to each specimen by spot welding insulated wires of identical material, i.e., Fe to Fe, Cu to Cu, etc. Specimens were carefully mounted in epoxy cylinders to insure that the diffusion plane was normal to the surface. Metallographic polishing procedures were used to prepare the test surfaces.

For most measurements, only freshly polished (final vibratory polish with  $0.1\mu$  alumina slurry) specimens were used. Mounted specimens were placed in a standard holder that kept the plane of polish perpendicular to the probe axis. The holder was inserted

into a Plexiglas cylinder (see Fig. 1) and firmly wedged in place to avoid movement of the specimen during the experiment. The Plexiglas cylinder was then filled with silicone oil, and the oil was heated with electrically insulated, sheathed thermocouple wire. During each measurement, the oil temperature was measured with a fine Pt/Pt-13% Rh thermocouple or a calibrated thermometer. The procedure of heating the specimen rather than the probe was the most significant difference between these experiments and previous experiments (1-7). Heating of the specimen in the oil bath improved the thermal stability of the system and retarded the oxidation of the specimen during the experiment.

Heater current was supplied by a stabilized d-c power supply. Thermoelectric potential measurements were made with a high impedance electronic microvoltmeter which amplified the signal to a recording potentiometer. Manual measurement of thermal emf's also were made with a high precision potentiometer. Potentiometric measurements agreed within  $\pm 0.5\%$  with those obtained with the microvoltmeter-recorder arrangement. Therefore the microvoltmeter-recorder system was used throughout these measurements because of its speed and convenience.

The measurement procedures were closely followed in each test to minimize scatter. Freshly polished and mounted specimens were placed in the oil bath, and the bath was rapidly heated to the desired temperature. The heater current was then reset to a predetermined value which would hold the bath at the desired temperature. Approximately 2 hr were allowed for the bath temperature to reach a steady-state value. During this time the area of the specimen to be traversed was chosen and aligned with the indenter. Throughout each measurement, both the specimen and the probe tip were immersed  $\sim 7$  mm below the surface of the oil bath (the probe rested  $\sim 1$  mm above the specimen when not in contact).

When steady state had been reached, the probe was released and allowed to contact the specimen. After the thermal emf was recorded, the specimen temperature was recorded, and the specimen was moved for the next indentation. The specimen was removed from the solution after the electrical measurements were completed, and the location of each indentation was determined. Indentation positions were measured with respect to a reference interface for the Fe-Ni specimen and with respect to a line of Kirkendall porosity for the Cu-Ni specimen. These optical measurements (at magnifications of 500 to 750 times) were reproducible to  $\pm 2\mu$  with two different observers.

Several measurements of the thermoelectric spectra of the Fe-Ni and Cu-Ni diffusion couples were made. The effects of both temperature and load on the probe were evaluated for the Fe-Ni alloys only.

Chemical composition gradients in the specimens were determined by the use of an electron microprobe. Corrections for fluorescence and absorption were made by the use of internal standards.

## Results

In all measurements reported here, the oil temperature (as measured by the platinum/platinum-rhodium thermocouple) remained within  $\pm 0.25^{\circ}\text{C}$  of its reported value. The measured thermal emf was found to rise rapidly to its maximum value and remain constant within  $\pm 2\mu\text{v}$  during each measurement. The rise and stability of the specimen emf was almost identical to that of the thermocouple. This behavior was different from that observed by Westbrook *et al.* (7) who found a rapid initial rise in emf, then a slow steady rise to a value 15-20% higher than the initial value. This did not occur in the present studies, because the probe tip and the specimen surface were very nearly at the same temperature before contact.

The emf data and the indentation positions plotted together resulted in the thermoelectric spectrum at

<sup>1</sup> Wilson-Tukon Microhardness Tester Model MO.



the measurement temperature for each binary alloy system studied. The Fe-Ni spectrum was complex, while the Ni-Cu spectrum was simple. Results for these two systems will be described separately.

**Fe-Ni system.**—The thermoelectric spectrum for the Fe-Ni system was measured at various temperatures over the range 45°–80°C. The two measurements in Fig. 2 show that the thermoelectric spectrum of the Fe-Ni system is quite complex in this temperature range. The characteristics of this spectrum are as follows. First, there is a plateau on the pure Fe portion of the specimen, then a sharp peak (called peak I), followed by a minimum and then by a broad peak (peak II) and finally by a plateau on the pure Ni part of the specimen. These data were representative of the thermoelectric properties of small regions of the specimen. As Fig. 3 shows, the probe contact areas were small ellipses 1.5–2 $\mu$  wide and 3–4 $\mu$  long. Further metallographic examination of the specimen (Fig. 4) showed that the thermoelectric traverse had passed across a complex interface consisting of three zones. Zone I ( $\sim 8\mu$  wide) was a dark colored phase immediately adjacent to the iron. Zone II ( $\sim 10.5\mu$  wide) was a light gray phase adjacent to zone I. Between zones I and II and possibly within zone II there was evidence of an acicular phase. Zone III ( $\sim 170\mu$  wide) was a lighter color than zone II and extended from across the reference interface into the pure nickel part of the diffusion couple. On the basis of the measured composition profile and the Fe-Ni phase diagram (8), the various bands were identified as follows: zones I and II were, respectively, the Fe-rich and Ni-rich portions of the two phase ( $\alpha + \gamma$ ) field. The acicular structure in zone I is coarse martensite and the dark gray color of zone II is due to the presence of fine martensite. Zone III is simply iron-doped  $\gamma$ -Ni. Careful analysis of the data points from Fig. 2 and 3 showed that peak I occurred within the nickel-doped  $\alpha$ -iron, zones I and II. The minimum and peak II occurred entirely within zone III. Comparison of the thermoelectric profile with the composition profile (Fig. 2) shows that small composition changes were readily detected with the thermoelectric microprobe. The resolution of this instrument compares favorably with the resolution of the electron microprobe used for the composition profile measurement.

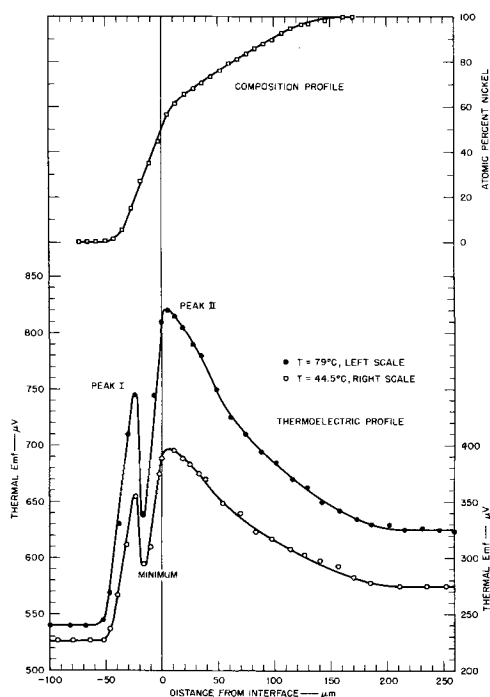


Fig. 2. Thermoelectric and composition profiles for Fe-Ni diffusion couple.

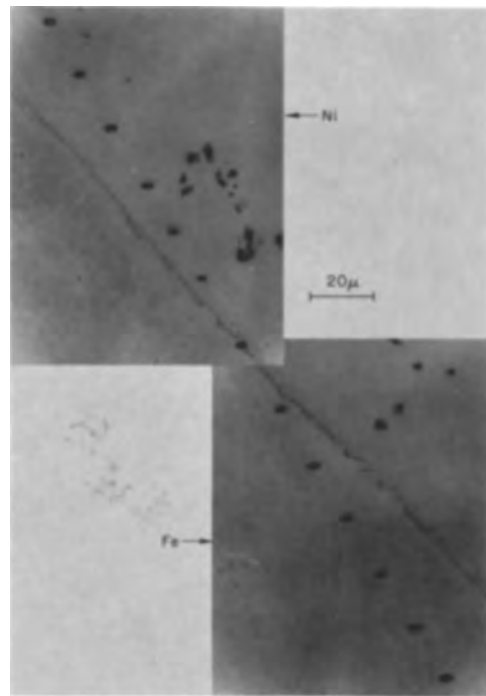


Fig. 3. Indentations produced by probe traverse across Fe-Ni diffusion couple using a 2-g load.

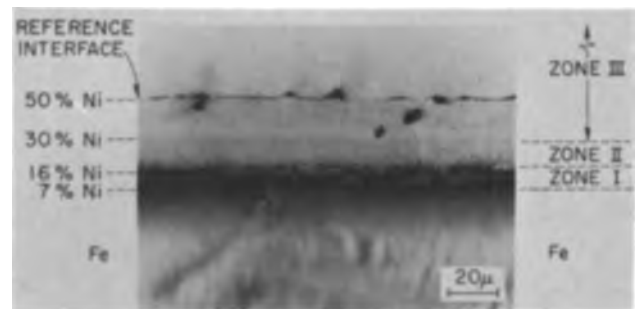


Fig. 4. Structural features of diffusion zone in the FeNi specimen

Changes in bath temperature resulted in changes in magnitude of the various thermal emfs (Fig. 2), but no change in the shapes of the curves. Increases in the load on the probe (Fig. 5) resulted in decreases in the thermal emfs of peaks I and II and an increase in the thermal emf of the minimum. Progressive shifts in the peak positions were also observed. As Fig. 5 shows, the shape of the thermoelectric spectrum could still be resolved even when the probe load was large. The effect of probe load on the apparent composition of the peaks and the minimum is shown in Fig. 6. Loads up to 3g produce no appreciable shift in composition, but

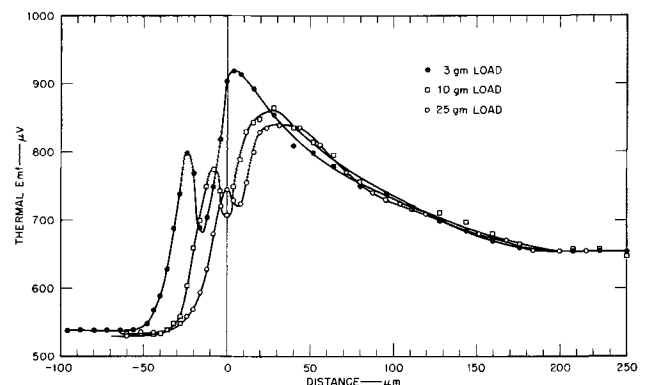


Fig. 5. Effect of probe load on thermoelectric profiles of Fe-Ni diffusion couple.

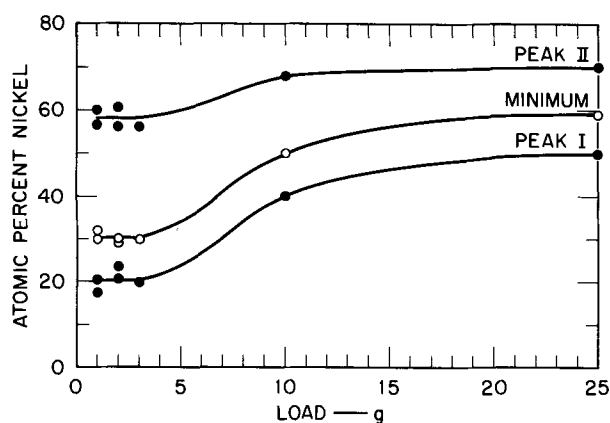


Fig. 6. Effect of probe load on measured composition of Fe-Ni diffusion couple.

further increases in load produce appreciable shifts. As will be shown later, loads from 1 to 3g yield essentially the same thermoelectric power spectrum for the Fe-Ni system; higher loads (10g or more) yield meaningless results.

**Cu-Ni system.**—The measured thermoelectric and composition profiles for the Cu-Ni specimen are shown in Fig. 7. As with the Fe-Ni data, the resolution of the thermoelectric microprobe was equivalent to the resolution of the electron microprobe. Small compositional changes ( $\sim 1\%$ ) were readily detected with the thermoelectric microprobe. Differences in the two thermoelectric profiles of Fig. 7 resulted from slightly different experimental conditions.

### Analysis and Discussion

It is evident that the high spatial and potential resolution of the thermoelectric microprobe makes it a useful tool for detailed qualitative studies of alloy systems. However, an analysis of the system is necessary before quantitative thermoelectric properties can be determined from the measured data. Consider the experimental arrangement shown in Fig. 8. Before the tungsten probe makes contact, the specimen surface is kept at a uniform temperature  $T_2$  by the hot oil bath. The cold ends of the tungsten probe and the electrical contact wire (in this example the contact wire is Fe) are at room temperature  $T_1$ . When the probe contacts the specimen, the local metal surface is cooled to a temperature  $T_3^x$  where  $x$  represents the metal com-

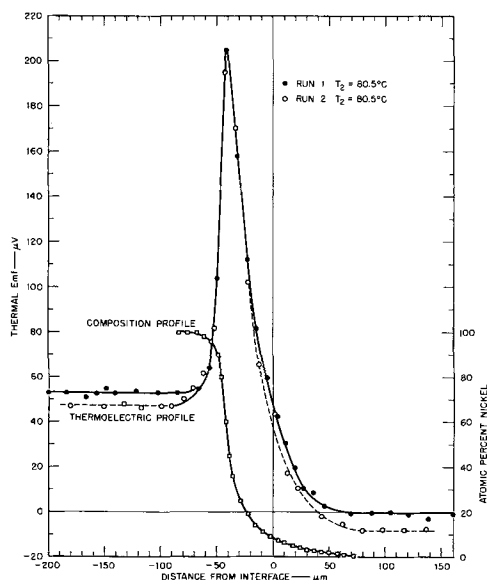


Fig. 7. Thermoelectric and composition profiles for Cu-Ni diffusion couple.

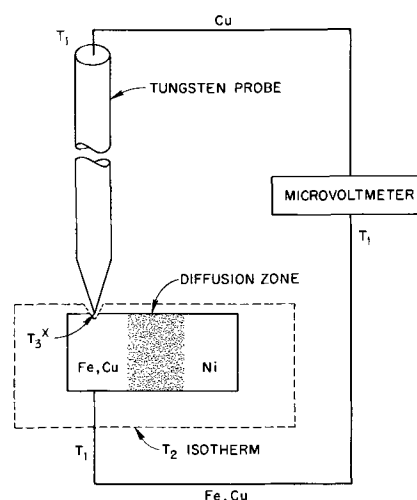


Fig. 8. Schematic of microprobe assembly

position of the contact point. The thermal emf produced when the probe makes contact on pure iron is given by

$$\Delta E_{Fe} = \int_{T_1}^{T_2} S_{Fe} dT + \int_{T_2}^{T_3^{Fe}} S_{Fe} dT + \int_{T_3^{Fe}}^{T_1} S_W dT \quad [1]$$

where  $\Delta E_{Fe}$  is thermal emf on the iron side of the diffusion couple, and  $S_{Fe}$ ,  $S_W$  are absolute thermoelectric powers of Fe and W, respectively. The thermal emf produced when the probe makes contact on pure nickel is

$$\Delta E_{Ni} = \int_{T_1}^{T_2} S_{Fe} dT + \int_{T_2}^{T_3^{Ni}} S_{Ni} dT + \int_{T_3^{Ni}}^{T_1} S_W dT \quad [2]$$

Substituting the identities

$$(T_1 - T_3^{Fe}) = (T_1 - T_2) + (T_2 - T_3^{Fe}) \quad [3]$$

$$(T_1 - T_3^{Ni}) = (T_1 - T_2) + (T_2 - T_3^{Ni}) \quad [4]$$

into Eq. [1] and [2] and subtracting [1] from [2] yields

$$\begin{aligned} (\Delta E_{Ni} - \Delta E_{Fe}) = & \int_{T_2}^{T_3^{Ni}} (S_{Ni} - S_W) dT \\ & - \int_{T_2}^{T_3^{Fe}} (S_{Fe} - S_W) dT \quad [5] \end{aligned}$$

Similarly, when the probe makes contact on an alloy of composition  $x$ ,

$$\begin{aligned} (\Delta E_x - \Delta E_{Fe}) = & \int_{T_2}^{T_3^x} (S_x - S_W) dT \\ & - \int_{T_2}^{T_3^{Fe}} (S_{Fe} - S_W) dT \quad [6] \end{aligned}$$

where  $S_x$  is the absolute thermoelectric power of an alloy of composition  $x$ .

During a given experiment, the values of  $\Delta E_{Fe}$ ,  $\Delta E_{Ni}$ ,  $\Delta E_x$ ,  $T_1$ , and  $T_2$  are measured. The values of  $T_3^{Fe}$  and  $T_3^{Ni}$  at the junction between the probe and the specimen can be calculated from Eq. [1] and [2] by using measured data and literature values of the thermoelectric powers of the pure elements. The values of  $T_3^x$  for alloys of intermediate composition, however, cannot readily be determined. Therefore, it is necessary to develop relations among  $T_3^{Fe}$ ,  $T_3^{Ni}$ , and  $T_3^x$ . A rigorous analytical determination of these relations will, in general, require the solution to a complex heat flow problem defined by the experimental conditions shown in Fig. 8. However, reasonable relations can be determined in the following manner. When the

probe contacts the metal surface it removes heat in proportion to the reciprocal of the thermal conductivity of the metal at the point of contact. Therefore the steady-state temperature gradient at the contact point can be written as

$$(T_2 - T_3^x) = \gamma/K_x \quad [7]$$

where  $K_x$  is the thermal conductivity of an alloy of composition  $x$ , and  $\gamma$  is a proportionality constant. The larger the value of  $K_x$ , the smaller will be the local temperature gradient. Assuming that the proportionality constant  $\gamma$  is the same for all alloy compositions,<sup>2</sup> one can write the relations required for the evaluations of Eq. [5] and [6]

$$(T_2 - T_3^{\text{Ni}})K_{\text{Ni}} = (T_2 - T_3^{\text{Fe}})K_{\text{Fe}} = (T_2 - T_3^x)K_x \quad [8]$$

The magnitude of the temperature gradient when the probe contacts the pure iron side of the couple can then be determined by substituting [8] into [5], which yields

$$(T_2 - T_3^{\text{Fe}}) = (\Delta E_{\text{Ni}} - \Delta E_{\text{Fe}}) / [(\bar{S}_{\text{Fe}} - \bar{S}_W) - \frac{K_{\text{Fe}}}{K_{\text{Ni}}} (\bar{S}_{\text{Ni}} - \bar{S}_W)] \quad [9]$$

where  $\bar{S}_{\text{Fe}}$ ,  $\bar{S}_{\text{Ni}}$ , and  $\bar{S}_W$  are the average thermoelectric powers of Fe, Ni, and W over the temperature range  $T_3^{\text{Fe}}$  to  $T_2$ .

Substituting [8] and [9] into [6] and simplifying yields the average thermoelectric power of the alloy of composition  $x$  over the temperature range  $(T_2 - T_3^x)$

$$\bar{S}_x = \bar{S}_W + \frac{K_x}{K_{\text{Fe}}} (\bar{S}_{\text{Fe}} - \bar{S}_W) \left( 1 - \frac{(\Delta E_x - \Delta E_{\text{Fe}})}{(\Delta E_{\text{Ni}} - \Delta E_{\text{Fe}})} \right) + \frac{K_x}{K_{\text{Ni}}} \left( \frac{\Delta E_x - \Delta E_{\text{Fe}}}{\Delta E_{\text{Ni}} - \Delta E_{\text{Fe}}} \right) (\bar{S}_{\text{Ni}} - \bar{S}_W) \quad [10]$$

It will be shown later that the temperature gradient at the tip of the probe is generally small enough ( $2^\circ$ - $5^\circ\text{C}$ ) that, for all practical purposes, Eq. [10] yields the value  $S_x$  rather than  $\bar{S}_x$  at temperature  $T_2$ . Equations analogous to [9] and [10] can be developed for the Ni-Cu system.

The thermoelectric power spectra were calculated for Fe-Ni and Cu-Ni alloys by using Eq. [10] and the thermal emf data of Fig. 2 and 6. Literature data (9, 10) were available for thermal conductivities of all elements and alloys at the temperature of interest. Literature values (11) of the thermoelectric powers of iron, nickel, copper, and tungsten with respect to various reference metals were converted to absolute thermoelectric powers (12, 13) by using values of the absolute thermoelectric power of platinum determined by Nystrom (14). Equations for the absolute thermoelectric powers used in this paper were

$$S_W = 4.4 + 0.38 \times 10^{-2}T$$

$$S_{\text{Ni}} = 13.52 - 8.38 \times 10^{-2}T + 5.7 \times 10^{-5}T^2$$

$$S_{\text{Fe}} = 19.46 - 6.00 \times 10^{-2}T - 26.75 \times 10^{-5}T^2$$

$$S_{\text{Cu}} = 5.57 - 1.81 \times 10^{-2}T$$

where  $T$  is given in  $^\circ\text{C}$  and  $S$  is in  $\mu\text{V}/^\circ\text{C}$ .

As Fig. 9 and 10 show, the thermoelectric power spectra of both the Fe-Ni and Cu-Ni specimens determined with the thermoelectric microprobe were in general agreement with data determined by conventional methods. The Fe-Ni data measured with the probe were in excellent agreement with Ingersoll's (15) data up to a composition of 35 a/o nickel. At

<sup>2</sup>It should be noted that  $\gamma$  will include a geometric term which will vary with the depth of penetration of the probe. For large differences in hardness of the materials studied,  $\gamma$  will not be the same and consequently will produce errors in measurement. The magnitude of error, however, cannot be estimated until the heat flow problem is solved.

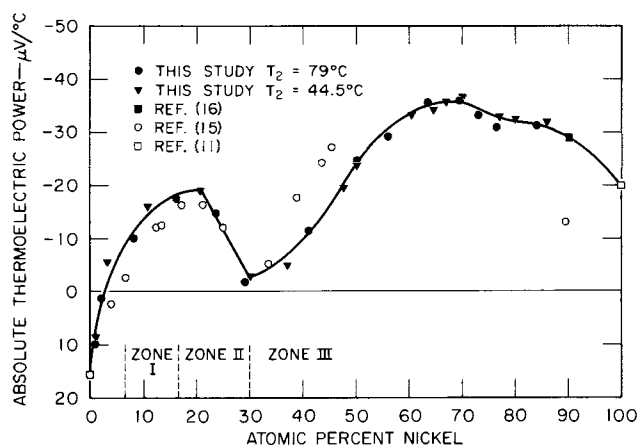


Fig. 9. Thermoelectric power spectrum of Fe-Ni alloys

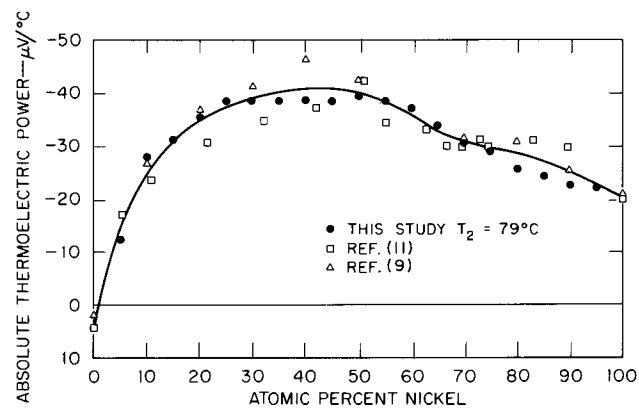


Fig. 10. Thermoelectric power spectrum of Cu-Ni alloys

higher nickel concentrations there were significant deviations. It should be noted that Ingersoll reported that the measured values of the thermoelectric powers in his study were dependent on the specimen dimensions. The only explanation for this effect would be inhomogeneity of the alloy. The agreement of the microprobe data with Rohn's (16) datum, and the absolute thermoelectric power of pure nickel suggest that Ingersoll's earlier data may not be correct at the higher nickel concentrations.

The effects of probe load and specimen temperature on the absolute thermoelectric powers of the characteristic emf maxima and minima of the Fe-Ni binary alloy system are listed in Table I and shown graphically in Fig. 11. As shown in Table I the temperature gradients calculated when the probe tip contacts the nickel side of the diffusion couple range from  $1.4^\circ$  to  $3.5^\circ\text{C}$ . In general, the gradient is lower for lower values of  $T_2$ . However, the temperature gradient can be varied at a given value of  $T_2$  by simply raising or lowering the oil bath level. This is what was done in run No. 3 of Table I. As Fig. 11 shows, the thermoelectric power spectrum of the Fe-Ni specimen is essentially independent of loads up to 3g. At higher loads, the thermoelectric powers are not correct. This loss of resolution at higher loads results from the increasing size of the probe contact area, and not from pressure effects on the thermal emf. Bridgman's (17) data on the effects of pressure gradients on the thermal emf indicate the maximum possible pressure-induced emf with the thermoelectric probe would be less than  $1 \mu\text{V}$ .

### Summary and Conclusions

The thermoelectric microprobe has been used for quantitative measurements of the absolute thermoelectric power spectra of Fe-Ni and Cu-Ni alloys. These spectra, measured from single Fe-Ni and Cu-Ni diffusion-couple specimens, were in good agreement with

Table I. Summary of measured thermoelectric properties of Fe-Ni alloys

Run No.	Load, g	$T_2, ^\circ\text{C}$	$(T_2 - T_3^{\text{Ni}}), ^\circ\text{C}$	Peak I		Minimum		Peak II	
				a/o Ni	$\bar{S}, \mu\text{V}/^\circ\text{C}$	a/o Ni	$\bar{S}, \mu\text{V}/^\circ\text{C}$	a/o Ni	$\bar{S}, \mu\text{V}/^\circ\text{C}$
1	1	70.5	2.8	17.5	-22.1	32	-1.8	57	-29.7
2	1	70.5	2.8	20.5	-22.5	30	-1.5	60	-31.9
3	2	79	2.4	23.5	-14.7	29	-1.7	56	-29.2
4	2	44.5	1.4	20.5	-18.7	30	-2.9	61	-33.1
5	3	79	3.5	20.0	-19.4	30	-1.9	56	-25.9
6	10	79	3.5	40	-7.4	50	-5.9	68	-30.1
7	25	79	3.5	50	-8.5	59	-10.0	70	-29.1

spectra determined by conventional techniques that require multiple specimens. In order to obtain quantitative thermoelectric properties from the measured emf data, one must know the composition and thermal conductivity profiles of the alloy system being studied, and the thermoelectric power of the pure elements in the system. Further, probe loads must be held below some low value (3g or less for the systems studied here) to obtain quantitative data. Use of higher load results in severe distortion of the measured thermoelectric power spectrum.

Because of its good spatial and potential resolution, the thermoelectric microprobe should be useful for diffusion studies, alloy phase analysis, grain boundary studies, and of course thermoelectric property measurements. In this latter application it is evident that

the probe technique would be particularly useful for rapid qualitative measurements of binary alloy systems and of brittle materials that are difficult to form into conventional wire specimens.

Manuscript submitted June 19, 1968; revised manuscript received July 29, 1968.

Any discussion of this paper will appear in a Discussion Section to be published in the June 1969 JOURNAL.

#### REFERENCES

1. B. K. Boltaks and V. P. Zhuze, *Zhur. Tekh. Fiz.*, **18**, 1459 (1948).
2. V. N. Novogradskii and I. G. Fadikov, *Phys. Met. Met.*, **7**, 99 (1959-1960).
3. C. S. Fuller, *Phys. Rev.*, **86**, 136 (1952).
4. W. L. Bond and F. M. Smits, *Bell Syst. Tech. J.*, **35**, 1209 (1956).
5. K. F. Holme and J. E. Kemp, *J. Phys. Chem. Solids*, **10**, 335 (1959).
6. E. M. Strug and E. V. Panchenko, *Nauchnye Doklady Vysshei Shkoly-Metallurgiya*, **2**, 252 (1959).
7. J. H. Westbrook, A. U. Seybolt, and A. J. Peat, *This Journal*, **111**, 888 (1965).
8. M. Hansen, "Constitution of Binary Alloys," p. 679, McGraw-Hill Book Co., New York (1958).
9. C. J. Smithells, "Metals Reference Book," Vol. II, p. 695, Butterworths (1962).
10. "International Critical Tables," Vol. V, pp. 120, 224, 225, E. W. Washburn, Editor, McGraw-Hill Book Co., New York (1929).
11. "International Critical Tables," Vol. VI, pp. 212, 218, 220, E. W. Washburn, Editor, McGraw-Hill Book Co., New York (1929).
12. D. K. C. MacDonald, "Thermoelectricity: An Introduction to the Principles," John Wiley & Sons, Inc., New York (1962).
13. T. P. Wang, C. D. Starr, and N. Brown, *Acta Met.*, **14**, 649 (1966).
14. J. Nyström, *Arkiv, Mat. Astr. Fys.*, **34A**, 1 (1948).
15. L. R. Ingersoll, *Phys. Rev.*, **16**, 126 (1920).
16. W. Rohn, *Z. Metall.*, **16**, 297 (1924).
17. P. W. B. Bridgman, *Proc. Am. Acad., Arts and Sci.*, **53**, 269 (1918).

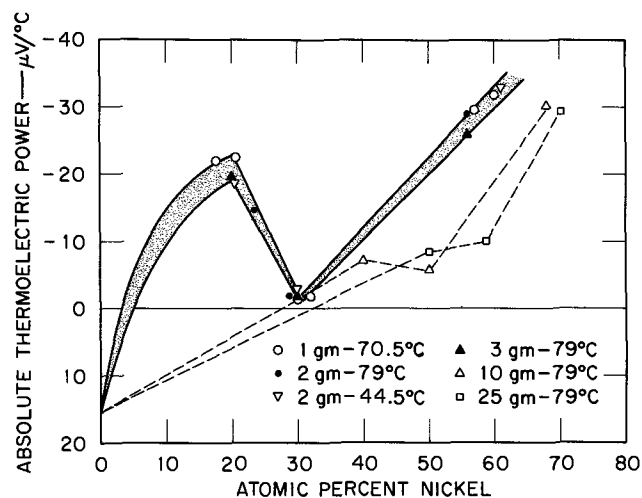


Fig. 11. Effect of probe load on the thermoelectric power spectrum of Fe-Ni alloys.

# A Chronocoulometric Study of the Adsorption of Anthraquinone Monosulfonate on Mercury

Fred C. Anson and Barry Epstein<sup>1</sup>

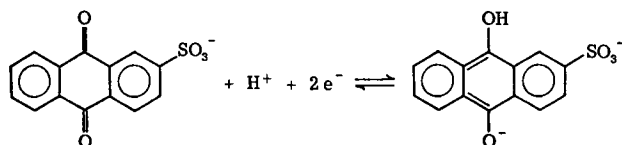
Gates and Crellin Laboratories of Chemistry, California Institute of Technology, Pasadena, California

## ABSTRACT

The quantity of anthraquinone monosulfonate (AQS) anions specifically adsorbed on mercury electrodes has been determined by chronocoulometry in fluoride, thiocyanate, nitrate, and p-toluene sulfonate electrolytes. In all electrolytes but fluoride competitive adsorption of AQS and the supporting electrolyte anion occurred. The adsorption produced very little change in the charge on the mercury or, therefore, on the amount of specifically adsorbed anions from the supporting electrolytes. The adsorbed anthraquinone monosulfonate anions produced large changes in the potential at the outer Helmholtz plane which were detected by the resulting changes in the rates of two irreversible electrode reactions.

The ability of the chronocoulometric technique to yield precise values for the surface concentrations of adsorbed reactants has been documented almost entirely with inorganic adsorbents (1-9). The present study was undertaken to test the technique with a simple organic redox couple and to examine the extent to which the composition of specifically adsorbed supporting electrolytes influences the adsorption of organic reactants.

Anthraquinone monosulfonate (AQS) was chosen for our experiments because Gill and Stonehill (10) and Furman and Stone (11) had established polarographically that the reduction of AQS in buffered aqueous solutions (*ca.* pH = 9) is a simple, reversible 2-electron reduction to give the monoprotonated quinol.



The semiquinone equilibrium constant is small in this pH range and no splitting of the wave is observed unless the pH is raised significantly or the dielectric constant of the solution is lowered. The polarographic  $E_{1/2}$  for AQS reduction has been reported as  $-0.55$  v. SCE (pH 8.69  $\rightarrow$  9.00) (10, 11) but no indication of adsorption in the form of pre- or postwaves has been reported.

In preliminary linear sweep voltametric experiments, the reduction peak for AQS was observed at  $-560$  mv vs. SCE (pH 8.9 buffer) as expected, but the peak current was unusually sharp and decayed much more rapidly than expected for typical diffusion controlled reactions. This behavior was strongly indicative of extensive adsorption (12, 13) so a quantitative chronocoulometric investigation was carried out.

The adsorption of aromatic compounds on mercury electrodes has been extensively investigated by electrocapillary experiments (14-18). The recent review by Frumkin (19) gives a full account of most earlier work. The general features which these previous studies have shown to characterize aromatic adsorption include: (i) substantial adsorption on both sides of the point of zero charge; (ii) flat orientation of the aromatic rings on the electrode surface which facilitates strong electronic interaction between the pi-electrons and the electrode surface so long as the latter bears a positive charge; (iii) increasing surface activity with increased number of aromatic rings; (iv) relatively small dependence of the adsorption on po-

tential (and therefore on charge), especially at positive charges on the electrode. Anthraquinone monosulfonate appears to follow this general pattern.

## Experimental

Double potential-step chronocoulometry (3, 20) was employed with the aid of the previously described digital data acquisition and analysis system (21). The electrode potential was stepped from various initial values,  $E_i$ , to  $-1400$  mv vs. SCE where drop time experiments with a dropping mercury electrode showed that no significant adsorption of the electrode reaction product occurred. A much less negative potential, *e.g.*,  $-800$  mv, would have sufficed to assure that the reaction remained diffusion controlled, but the appropriate double layer charging correction would have been more difficult to obtain because of extensive adsorption of the electrode reaction product. Positive feedback to the input of the potentiostat was employed to improve the potentiostatic compensation for solution resistance (22).

The electronic charge density of the mercury electrodes was determined as before (9) by measuring the charge flowing into dropping mercury electrodes (23). This procedure, in which the digital data acquisition and analysis system was again employed, gave a value for the electronic charge on the electrode,  $q^m$ , of  $-17.5 \pm 0.5$   $\mu\text{C}/\text{cm}^2$  in 0.5F NaNO<sub>3</sub>, 0.01F Na<sub>2</sub>B<sub>4</sub>O<sub>7</sub> at  $-1400$  mv vs. SCE. This agrees excellently with Graham's value of  $-17.6$   $\mu\text{C}/\text{cm}^2$  for 0.5F NaF at the same potential (24). The electrode's charge at each of the initial potentials was similarly measured in the pure supporting electrolyte solutions. In the presence of the reactant, sodium anthraquinone sulfonate, the values of  $q^m$  at the initial potentials were usually determined from the known value at  $-1400$  mv and values of the change in double layer charge obtained from analysis of the double potential step chronocoulometric data (9, 20). In some cases, the resulting values of  $q^m$  at  $E_i$  were compared with values obtained by means of d.m.e. experiments conducted in the presence of reactant and excellent agreement was observed.

The hanging mercury drop electrode employed was the standard commercially available type (Brinkmann Instruments), but the two internal sealing gaskets were replaced by Neoprene or silicone rubber gaskets to produce better seals and eliminate occasional leakage of air into the electrode reservoir. To avoid the frequently encountered high resistance between the mercury drop and the electrical contact on the mercury reservoir housing the plastic chamber at the top of the capillary was partially filled with mercury and fitted with a platinum wire which al-

<sup>1</sup> Present address: Gulf General Atomic, La Jolla, California.

lowed good contact to be made with the plunger [cf. Wopschall and Shain (25)].

The capillary for the electrode was treated with a 10% HF solution for a few seconds then rinsed with water and dried prior to an application of "Desicote" (Beckman Instruments). This pretreatment improved the precision of the results apparently because it kept the mercury column from flexing during large potential excursions with consequent variations in the electrode area.

The sodium salt of anthraquinone-2-sulfonic acid was obtained commercially and recrystallized three times from water. According to Beilstein (26) the salt recrystallizes as the monohydrate. This was confirmed by drying the salt for 19 hr at 120°C which produced the loss of 1.00 moles of water per mole of salt. Confirmation of purity was also established by comparison of ultraviolet absorptivities with literature values (27). The agreement was within 1%. The recrystallized monohydrate salt was used to prepare all of the AQS solutions. Sample solutions were prepared by weighing solid AQS into a volumetric flask, adding an aliquot of concentrated supporting electrolyte solution and diluting to volume.

Sodium fluoride, sodium thiocyanate, and sodium-p-toluene sulfonate were recrystallized at least twice from water. Other chemicals were reagent grade and were used without further purification. Water was triply distilled, the second distillation coming from alkaline permanganate solution. All solutions were buffered at pH = 8.9 with 0.01F Na<sub>2</sub>B<sub>4</sub>O<sub>7</sub>.

Prepurified nitrogen gas for deaerating solutions, was repurified by passing it over copper turnings at 450°C and then through a cold trap at dry ice-acetone temperature. The solution was stirred for 30 sec after the creation of each new mercury drop electrode to assure the attainment of adsorption equilibrium.

### Results and Discussion

The primary data resulting from chronocoulometric experiments are the amounts of adsorbed reactant as a function of bulk reactant concentration, initial electrode potential, and supporting electrolyte composition. The simplest cases are those in which there is little or no specific adsorption of the ions comprising the supporting electrolyte. Sodium fluoride supporting electrolytes were employed for this purpose.

**Adsorption from fluoride electrolyte.**—Table I contains a typical set of data obtained with 0.5F NaF supporting electrolyte of pH 8.9 (0.01F Na<sub>2</sub>B<sub>4</sub>O<sub>7</sub>). (In this and the following tables the values of  $q^m$  are for the supporting electrolyte containing AQS at the specified concentrations.) The data are quite insensitive to the concentration of NaF or even of AQS down to 0.02 mF. The main points of interest are the virtual absence of any potential dependence of the adsorption

and the very small values of  $\Delta q^m$ , the changes in the charge on the electrode, produced by the adsorption. The coverage of the electrode by the AQS in this solution is quite substantial; geometrical calculation of the amount of AQS required to produce a monolayer of flatly adsorbed molecules leads to values ranging from  $1.5\text{--}2.1 \times 10^{-10}$  moles/cm<sup>2</sup> depending on the closeness of the two-dimensional packing. The virtual absence of a dependence on the AQS concentration in the data in Table I suggests that the electrode surface is essentially saturated with AQS in these fluoride solutions.

**Adsorption from thiocyanate electrolytes.**—Table II contains data obtained with sodium thiocyanate supporting electrolytes in order to examine the effect of strong anionic adsorption on the adsorption of AQS. The much smaller adsorption of the AQS and the much greater potential dependence of its adsorption are clearly evident. A remarkable feature is the very small changes in the electronic charge on the electrode produced by the adsorption of AQS. The strong adsorption of thiocyanate ions in the pure electrolyte makes the charge on the electrode much greater in thiocyanate than in fluoride solutions. The decrease (usually) in this charge produced by the adsorption of AQS is much smaller than the charge difference between pure fluoride and thiocyanate solutions which clearly shows that very little if any of the adsorbed thiocyanate is desorbed by the AQS adsorption. However, there certainly is a strong antagonistic interaction between the adsorbed thiocyanate and AQS as is evidenced in the large dependence of the AQS adsorption upon thiocyanate concentration and potential. The magnitude of the potential dependence of the adsorption of AQS in thiocyanate solutions seems too great to be attributable to direct interactions between the adsorbed AQS and the electrode because of the very much smaller potential dependence observed in fluoride solutions (Table I). It appears, therefore, that the chief effect of the adsorption of thiocyanate is to interfere with the compactness of the AQS layer by interposition. [Damaskin has explained the effect of halide ions on butanol adsorption in the same way (28).] For example, at -300 mv in 0.1F NaSCN solution 21.5  $\mu\text{C}/\text{cm}^2$  of thiocyanate is adsorbed (29). This corresponds to about 15% of the maximum possible (hexagonally closest packed) coverage with thiocyanate ions (30) and allows a separation of about 8Å between thiocyanate ions. Addition of 0.10 mF AQS leads to about one-half of the electrode's surface being covered with AQS molecules without appreciable loss of the adsorbed thiocyanate ions which are presumably scattered throughout the AQS layer.

An alternative possibility is that the thiocyanate ions are adsorbed "on top of" the adsorbed AQS. This

Table I. Adsorption of AQS from fluoride electrolytes

$E_i$ , mv vs. SCE	0.5F NaF, <sup>a</sup> 0.01F Na <sub>2</sub> B <sub>4</sub> O <sub>7</sub> , pH 8.9		
	$q^m$ , $\mu\text{C}/\text{cm}^2$	$\Gamma_{\text{AQS}}$ , moles/cm <sup>2</sup> $\times 10^{10}$	$\Delta q^m$ , $\mu\text{C}/\text{cm}^2$
	0.10 mF AQS		
0	10.7 $\pm$ 0.6	1.63 $\pm$ 0.03	-1.7 $\pm$ 0.6
-100	8.2	1.67	-1.1
-200	6.1	1.68	-0.2
-300	3.5	1.70	+0.1
-400	0.7	1.70	0
	0.02 mF AQS <sup>b</sup>		
0	8.5 $\pm$ 2	1.2 $\pm$ 0.10	—
-100	5.6	1.3	—
-200	3.0	1.3	—
-300	0	1.4	—
-400	-0.9	1.3	—

<sup>a</sup> The values of  $\Gamma_{\text{AQS}}$  remained essentially unchanged in 0.1F NaF.

<sup>b</sup> These data were obtained without the digital data acquisition system and are therefore less precise.

Table II. Adsorption of AQS from thiocyanate electrolytes

$E_i$ , mv vs. SCE	$q^m$ , $\mu\text{C}/\text{cm}^2$	$\Gamma_{\text{AQS}}$ , moles/cm <sup>2</sup> $\times 10^{10}$	$\Delta q^m$ , $\mu\text{C}/\text{cm}^2$
	0.1F NaSCN, 0.10 mF AQS		
-200	16.0 $\pm$ 0.6	0.75 $\pm$ 0.03	-0.7 $\pm$ 0.6
-300	12.0	1.00	+0.3
-400	8.3	1.15	+0.8
	0.5F NaSCN, 0.01 mF AQS		
-200	19.2	0.11	-0.9
-300	13.2	0.21	-1.0
-400	8.8	0.465	-1.1
	0.5F NaSCN, 0.10 mF AQS		
-200	18.7	0.285	-1.4
-300	13.5	0.698	-0.7
-400	9.6	0.955	-0.3
	1.0F NaSCN, 0.10 mF AQS		
-200	21.2	0.072	-0.6
-300	14.4	0.358	-0.6
-400	10.0	0.698	-0.4

All solutions were buffered at pH 8.9 with 0.01F Na<sub>2</sub>B<sub>4</sub>O<sub>7</sub>.

Table III. Adsorption of AQS from nitrate electrolytes

AQS conc.:	0.01 mF			0.02 mF			0.05 mF			0.10 mF			0.20 mF			0.50 mF		
	$E_t$ , mv vs. SCE	$q_m$ , $\mu\text{C}/\text{cm}^2 \times 10^{10}$	$\Gamma_{\text{AQS}}$ , mole/ $\text{cm}^2 \times 10^{10}$	$\Delta q_m$ , $\mu\text{C}/\text{cm}^2$	$q_m$ , $\mu\text{C}/\text{cm}^2 \times 10^{10}$	$\Gamma_{\text{AQS}}$ , mole/ $\text{cm}^2 \times 10^{10}$	$\Delta q_m$ , $\mu\text{C}/\text{cm}^2$	$q_m$ , $\mu\text{C}/\text{cm}^2 \times 10^{10}$	$\Gamma_{\text{AQS}}$ , mole/ $\text{cm}^2 \times 10^{10}$	$\Delta q_m$ , $\mu\text{C}/\text{cm}^2$	$q_m$ , $\mu\text{C}/\text{cm}^2 \times 10^{10}$	$\Gamma_{\text{AQS}}$ , mole/ $\text{cm}^2 \times 10^{10}$	$\Delta q_m$ , $\mu\text{C}/\text{cm}^2$	$q_m$ , $\mu\text{C}/\text{cm}^2 \times 10^{10}$	$\Gamma_{\text{AQS}}$ , mole/ $\text{cm}^2 \times 10^{10}$	$\Delta q_m$ , $\mu\text{C}/\text{cm}^2$	$q_m$ , $\mu\text{C}/\text{cm}^2 \times 10^{10}$	$\Gamma_{\text{AQS}}$ , mole/ $\text{cm}^2 \times 10^{10}$
0.1F NaNO <sub>3</sub>																		
0	12.2	1.13	-0.7	12.3	1.23	-0.6	12.1	1.31	-0.8	12.0	1.40	-0.9	10.0	1.52	-2.9	8.0	1.70	-4.9
-100	10.1	1.20	-0.1	10.2	1.27	0	10.1	1.35	-0.1	9.9	1.42	-0.3	8.3	1.53	-1.9	6.0	1.71	-4.2
-200	7.8	1.24	+0.3	8.2	1.30	+0.7	8.1	1.37	+0.6	7.5	1.45	0	6.6	1.52	-0.9	4.4	1.69	-3.1
-300	5.6	1.26	+0.8	5.7	1.34	+0.9	5.7	1.40	+0.9	5.5	1.47	+0.7	4.7	1.53	-0.1	4.9	1.68	+0.1
-400	2.8	1.30	+0.9	2.8	1.38	+0.9	2.7	1.44	+0.8	2.8	1.50	+0.9	2.8	1.52	+0.9	0.9	1.68	-1.0
0.5F NaNO <sub>3</sub>																		
0	13.1	1.01	-0.8	13.2	1.07	-0.7	13.1	1.20	-0.8	11.6	1.39	-2.3	10.6	1.56	-3.3	7.5	1.80	-6.9
-100	10.8	1.12	-0.4	10.9	1.18	-0.3	11.2	1.29	0	9.1	1.47	-2.1	8.3	1.63	-2.9	5.9	1.80	-5.3
-200	8.5	1.20	-0.4	8.8	1.28	-0.1	8.9	1.35	0	7.5	1.48	-1.4	6.6	1.63	-2.3	5.2	1.75	-3.7
-300	6.3	1.27	0	6.2	1.31	-0.1	6.1	1.39	-0.2	6.1	1.54	-0.2	5.1	1.64	-1.2	3.9	1.68	-2.4
-400	3.2	1.31	0	3.4	1.33	+0.2	3.2	1.46	0	3.1	1.53	-0.1	3.2	1.61	0	2.8	1.69	-0.4
1.0F NaNO <sub>3</sub>																		
0	14.1	0.81	-0.1	13.3	0.93	-0.9	13.7	1.10	-0.5	12.6	1.24	-1.6	13.9	1.41	-0.3	11.2	1.79	-3.0
-100	11.3	1.02	+0.4	11.3	1.10	+0.4	11.3	1.24	+0.4	10.8	1.36	-0.1	10.9	1.52	0	5.8	1.81	-5.1
-200	8.8	1.16	-0.4	8.8	1.18	-0.4	9.1	1.31	-0.1	8.8	1.41	-0.4	8.0	1.59	-1.2	4.2	1.83	-5.0
-300	6.6	1.21	+0.2	6.5	1.25	+0.1	6.5	1.37	+0.1	6.4	1.46	0	4.5	1.68	-1.9	3.5	1.78	-2.9
-400	3.9	1.24	+0.2	3.8	1.31	+0.1	3.7	1.43	0	3.5	1.51	-0.2	1.5	1.75	-1.2	2.3	1.75	-1.4

All solutions were buffered at pH 8.9 with 0.01F Na<sub>2</sub>B<sub>4</sub>O<sub>7</sub>.

seems unlikely because one might then expect the adsorption of AQS to diminish the amount of adsorbed thiocyanate rather than *vice versa*, as observed.

Another possible explanation is that strong specific adsorption of anions "salts-out" the AQS from the electrode surface back into the bulk of the solution. This possibility has been discussed by Conway and Barradas in the case of aromatic amine adsorption (17).

*Adsorption from nitrate electrolytes.*—Table III contains extensive data obtained with sodium nitrate supporting electrolytes. The general features of the data are understandable on the basis of the data for fluoride and thiocyanate electrolytes. Nitrate ion is much less strongly adsorbed than thiocyanate so that the AQS adsorption shows smaller potential and nitrate concentration dependences than are observed in thiocyanate. Nevertheless, these dependences are clearly present in the nitrate electrolytes under conditions where they are absent in fluoride electrolyte. The charge changes produced by AQS adsorption in nitrate are also very small and indicate that little or none of the adsorbed nitrate is desorbed by the adsorption of AQS. This feature is somewhat more surprising with nitrate than it was for thiocyanate because of the generally weaker adsorption of nitrate. However, the nitrate coverages are much smaller and it may be that only a small perturbation of the adsorbed array of nitrate ions is produced by the adsorption of even a 0.7-0.8 monolayer of AQS.

At the highest concentration of AQS (0.5 mF) an anomaly appears in that the charge on the electrode appears to fall below the value in pure fluoride solutions even though comparable AQS adsorption in fluoride electrolyte has almost no effect on the electrode's charge. It seems likely that the values for  $q^m$  obtained in this experiment in nitrate media are erroneously small, possibly because at the highest concentration of AQS the product of the electrode reaction is not completely desorbed at -1400 mv and so depresses the measured double layer charge.

The data for nitrate show an apparent reversal in the dependence of the adsorption upon nitrate concentration. At low concentrations of AQS the adsorption decreases as the nitrate concentration increases presumably for the same reasons that were discussed in the case of thiocyanate electrolytes. At the highest concentration of AQS its adsorption appears to increase slightly with the nitrate concentration. This may be a reflection of a "salting out" of the organic compound from the solution as its ionic strength increases; the equilibrium solubility of AQS is only about 1.0 mF in 1F NaNO<sub>3</sub>.

*Mixed adsorption from p-toluene sulfonate electrolyte.*—The adsorption of p-toluene sulfonate anions (PTS) on mercury has been studied by Parry and Parsons (31). Higher concentrations of PTS are required to produce adsorption comparable to that displayed by AQS but in other respects these two aromatic sulfonates behave similarly. In particular, the adsorptions of both AQS and PTS show a very small potential dependence at positively charged electrodes. With high concentrations at negatively charged electrodes PTS adsorption displays a greater potential dependence which Parry and Parsons have attributed to a change from a flat orientation of the molecules on the electrode surface to a more perpendicular orientation.

Table IV contains data obtained with solutions containing both PTS (as supporting electrolyte) and AQS. A definite potential dependence of the AQS adsorption is apparent which contrasts with the behavior of either anion when present alone at the same concentrations. This behavior may result because the much more strongly adsorbing AQS forces the adsorbed PTS to convert to the perpendicular orientation at less negative potentials than are required in pure solutions of PTS.

*Effect of adsorbed AQS on electrode reactions.*—Having established that mercury electrodes in solutions of AQS are coated with almost a monolayer of adsorbed AQS it was of interest to investigate how other electrode reactions are affected by the adsorbed AQS. Two likely effects could be anticipated: The adsorbed organic compound might simply block off a major fraction of the electrode area thus decreasing the rate of other electrode reactions. In addition, a rather large double layer effect due to the adsorbed AQS seemed likely because it is an anion which is extensively adsorbed without much change in the electronic charge on the electrode (see Table I-III). This means that the potential at the outer Helmholtz

Table IV. Adsorption of AQS from p-toluene sulfonate (PTS) electrolyte

$E_t$ , mv vs. SCE	0.5F NaPTS, 0.01F Na <sub>2</sub> B <sub>4</sub> O <sub>7</sub> , pH 8.9		
	$q^m$ , $\mu\text{C}/\text{cm}^2$	$\Gamma_{\text{AQS}}$ , moles/ $\text{cm}^2 \times 10^{10}$	$\Delta q_m$ , $\mu\text{C}/\text{cm}^2$
0.10 mF AQS			
0	13.9	0.17 ± 0.03	0 ± 0.6
-100	11.7	0.29	0
-200	9.6	0.43	0
-300	7.2	0.56	+0.5
-400	4.7	0.61	+0.8

plane,  $\phi_2$ , must become much more negative when AQS is adsorbed.

To test these expectations, the reductions of  $\text{Co}(\text{NH}_3)_6^{+3}$  and  $\text{CrO}_4^{-2}$  were examined polarographically in a supporting electrolyte consisting of 0.1F  $\text{NaNO}_3$  and 0.01F  $\text{Na}_2\text{B}_4\text{O}_7$  (pH 8.9) in the absence and presence of 0.1 mF AQS. No evidence for any blocking of the electrode surface was observed and it seems likely that these electrode reactions are able to proceed via the flatly adsorbed AQS molecules about as well as on the uncoated mercury surface.

By contrast, the double layer effects observed were quite large. The half-wave potential for  $\text{Co}(\text{NH}_3)_6^{+3}$  reduction shifted from  $-0.24$  to  $-0.15\text{v}$  vs. SCE and that for  $\text{CrO}_4^{-2}$  reduction shifted from  $-0.31$  to  $< -0.55\text{v}$  vs. SCE upon addition of 0.1 mF AQS. Quantitative correlation with theoretical diffuse layer calculations of the changes in the  $\phi_2$ -potentials needed to account for the observed shifts in half-wave potentials, such as those recently employed in cadmium-iodide solutions (9), were not attempted in this case because of the time dependence of the amount of adsorbed AQS at the d.m.e. Nevertheless, the qualitative behavior is entirely in accord with the idea that AQS adsorption leads to a large change in the potential,  $\phi_2$ , at the outer Helmholtz plane. These results make it clear that the sulfonate group which carries the negative charge in the AQS molecule is not coordinated with a sodium or hydrogen ion in the adsorbed state, an interpretation which seemed possible on the basis of the very small changes in  $q^m$  which the adsorption of AQS produces.

To rule out the possibility that the observed behavior of AQS was, for some reason, atypical, the polarographic experiments with  $\text{Co}(\text{NH}_3)_6^{+3}$  and  $\text{CrO}_4^{-2}$  were repeated with 0.1M sodium p-toluene sulfonate as supporting electrolyte because Parry and Parsons (31) have shown that this organic anion is adsorbed to about the same extent in 0.1F solutions as is AQS in 0.1 mF solutions. The shifts in half-wave potentials were very similar to those in the case of AQS: for  $\text{Co}(\text{NH}_3)_6^{+3}$   $E_{1/2} = -0.17$ ; for  $\text{CrO}_4^{-2}$   $E_{1/2} = -0.48\text{v}$  vs. SCE.

It thus appears that the adsorptions of both AQS anions and p-toluene sulfonate anions affect other electrode reactions only indirectly by means of the changes in the  $\phi_2$ -potential produced by the anion adsorption. This behavior adds support to the assumption that the AQS molecules are adsorbed flatly on the electrode with the sulfonate group protruding no further than the compact layer.

#### Acknowledgment

This work was supported in part by the National Science Foundation and by the Army Research Office (Durham). Roger Abel contributed invaluablely to the programming and maintenance of the digital data acquisition system.

Manuscript submitted June 21, 1968; revised manuscript received July 19, 1968.

Any discussion of this paper will appear in a Discussion Section to be published in the June 1969 JOURNAL.

#### REFERENCES

1. J. H. Christie, G. Lauer, R. A. Osteryoung, and F. C. Anson, *Anal. Chem.*, **35**, 1979 (1963).
2. F. C. Anson, *ibid.*, **36**, 932 (1964).
3. F. C. Anson, *ibid.*, **38**, 54 (1966).
4. R. W. Murray and D. J. Gross, *ibid.*, **38**, 392 (1966).
5. G. W. O'Dom and R. W. Murray, *ibid.*, **39**, 51 (1967).
6. F. C. Anson and D. A. Payne, *J. Electroanal. Chem.*, **13**, 35 (1967).
7. F. C. Anson, J. H. Christie, and R. A. Osteryoung, *ibid.*, **13**, 343 (1967).
8. G. W. O'Dom and R. W. Murray, *ibid.*, **16**, 327 (1968).
9. F. C. Anson and D. Barclay, *Anal. Chem.*, **40**, 000 (1968).
10. R. Gill and H. I. Stonehill, *J. Chem. Soc.*, **1952**, 1845.
11. N. H. Furman and K. G. Stone, *J. Am. Chem. Soc.*, **70**, 3055 (1948).
12. S. Poffa and E. Vianello, *J. Electroanal. Chem.*, **15**, 405 (1967).
13. A. G. Voloshin, *Elektrokhimiya*, **3**, 924 (1967).
14. M. A. Gerovich and G. F. Rybalschenko, *Z. Fiz. Khim.*, **32**, 109 (1958); *Doklady Akad. Nauk. SSSR*, **86**, 543 (1954); **105**, 1278 (1955).
15. M. A. Gerovich, "Soviet Electrochemistry," Vol. 1, p. 34, Consultants Bureau, New York (1961).
16. E. Blomgren, J. O'M. Bockris, and C. Jesch, *J. Phys. Chem.*, **65**, 2000 (1961).
17. B. E. Conway and R. G. Barradas, *Electrochim. Acta*, **5**, 319, 349 (1961).
18. B. E. Conway, R. G. Barradas, P. G. Hamilton, and J. M. Parry, *J. Electroanal. Chem.*, **10**, 485 (1965).
19. A. N. Frumkin in "Modern Aspects of Electrochemistry, No. 3," Chap. 3, J. O'M. Bockris and B. E. Conway, Editors, Butterworths Publications, London (1964).
20. J. H. Christie, R. A. Osteryoung, and F. C. Anson, *J. Electroanal. Chem.*, **13**, 236 (1967).
21. G. Lauer, R. Abel, and F. C. Anson, *Anal. Chem.*, **39**, 765 (1967).
22. G. Lauer and R. A. Osteryoung, *ibid.*, **38**, 1106 (1966).
23. G. Lauer and R. A. Osteryoung, *ibid.*, **39**, 1866 (1967).
24. C. D. Russel, *J. Electroanal. Chem.*, **6**, 486 (1963). Note correction from SCE to NCE actually reported.
25. R. H. Wopschall and I. Shain, *Anal. Chem.*, **39**, 1527 (1967).
26. F. K. Beilstein, *Hanbuch der Organischen Chemie*, Vol. 11, p. 337, J. Springer, Berlin (1918).
27. K. Marcali, *Anal. Chem.*, **27**, 1586 (1955).
28. B. B. Damaskin, A. A. Survila, and L. E. Rybalka, *Elektrokhimiya*, **3**, 927 (1967).
29. H. Wroblowa, Z. Kovac, and J. O'M. Bockris, *Trans. Faraday Soc.*, **61**, 1573 (1965).
30. R. Parsons and P. C. Symons, *ibid.*, **64**, 1077 (1968).
31. J. M. Parry and R. Parsons, *This Journal*, **113**, 992 (1966).



# Anodic Oxidation Pathways of Carbazoles

## I. Carbazole and N-Substituted Derivatives

J. F. Ambrose and R. F. Nelson

*Department of Chemistry, Sacramento State College, Sacramento, California*

### ABSTRACT

Electrochemical and spectroscopic techniques have been employed in elucidating the anodic oxidation pathways of carbazole and several N-substituted derivatives. For carbazole and the N-alkyl or N-aryl derivatives, ring-ring coupling is the predominant decay pathway of the carbazole cations; the coupling rates are extremely rapid. N-N coupling is observed initially for carbazole, but in long-time electrolysis it is of little consequence. The oxidation products have been synthesized by chemical means and compared with the species formed electrochemically by matching of cyclic polarograms and visible absorption spectra. Molecular orbital calculations give a qualitative picture of active sites with regard to follow-up coupling reactions in the carbazole series. N-vinyl, N-acetyl, N-benzoyl, and N-nitroso carbazole were investigated briefly but found to be extremely complicated.

The area of anodic oxidations of heterocyclic molecules has received little attention in the past. A great deal of work on electrochemical reductions of these molecules is well documented (1); this makes the paucity of data on oxidations even more surprising. In contrast to electrochemical studies, a good deal of work on chemical oxidations of heterocyclics, in general, and carbazoles, in particular, has been published. It is not an uncommon situation when chemical and electrochemical oxidation pathways do not coincide, so the study of substituted carbazoles by electrochemical means was undertaken in order to compare these data with those from chemical oxidation studies. A number of differences and similarities were found and are reported herein.

Background material on the chemical oxidation work is extensive and merits mention. The first significant work was carried out independently by groups under Branch (2, 3) and Tucker (4). Branch and co-workers employed silver oxide as an oxidant and obtained two products, one of which was suspected as being 9,9'-dicarbazyl.<sup>1</sup> With permanganate in acetone, Tucker obtained a mixture of three products, designated A, B, and C. By synthesis of several possible dicarbazyls, the 3,3' (5), 9,9' (6), 1,1' (7) and 3,9' (8) isomers, it was determined that dicarbazyl A was in fact 9,9'-dicarbazyl. None of the other isomers could be identified as B or C. Subsequent work has shown that dicarbazyl B is really a tricarbazyl (9). Compound C had defied identification until just recently. It was, in fact, found to be several polymeric carbazole species whose structures were inferred from spectroscopic data (10).

Tucker also demonstrated that the oxidizing medium can affect the product distribution markedly; in an acetic acid/sulfuric acid mixture with dichromate present, only 3,3'-dicarbazyl was obtained (11). N-alkylated carbazoles also gave the respective 9,9'-dialkyl-3,3'-dicarbazyls (11). With the sulfuric acid absent, carbazole was oxidized to 9,9'-dicarbazyl (6). It is apparent from all these data that the coupling products formed depend markedly on solvent and ox-

idizing agents. A more definitive study along these lines has recently been published (12). It has been our experience that quite often electrochemical oxidations are somewhat more selective than their chemical counterparts, and it was hoped that this would be the case for the carbazoles. This hope was, in the main, confirmed. The formation of 3,3'-dicarbazyls is the predominant pathway by far; all others, with one notable exception, are undetectable.

Standard electrochemical and spectrophotometric techniques were employed to study the electrode processes and associated chemical reactions in these systems. These techniques have been amply reviewed, and it is assumed that the reader is familiar with them. The coupling rates are very rapid and radical stabilities are quite low, so the mechanisms could not be completely elucidated. However, a rather clear picture of the oxidation pathways of simple carbazoles has emerged; this, combined with further work now in progress on ring-substituted carbazoles, will hopefully yield a general interpretation of the electronic distribution and anodic oxidation pathways of these molecules.

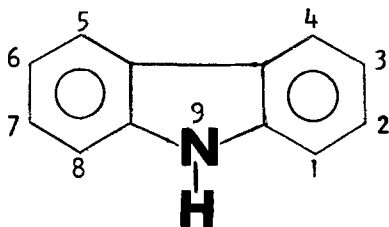
### Experimental Section

The procedures for purification of solvent (acetonitrile, denoted hereafter as MeCN) and supporting electrolyte (tetraethylammonium perchlorate, TEAP), as well as the electrodes and cell employed, have been discussed elsewhere (13). The multipurpose electrochemical instrument used for cyclic voltammetry, chronoamperometry, and chronopotentiometry incorporates solid-state circuitry into the basic Booman-Deford design. Moseley 7035B X-Y and 7101B strip chart recorders were used in conjunction with this instrument.

For rotating disk voltammetry, an apparatus employing a synchronous motor and gears was employed. This afforded a range of rotation rates between 580 and 3000 rpm with an accuracy of better than 0.5%. Rotation rates were checked on each run with a Strobotac unit. The electrode was constructed according to the recipe of Marcoux and Adams (14).

Controlled potential electrolyses were carried out with a Wenking 61RH fast-rise potentiostat using a large platinum gauze as the working electrode and a carbon rod as the auxiliary. They were separated by a medium porosity frit in a cell designed for fairly rapid electrolysis. In experiments designed to obtain "n-values," the electrolysis time was typically 8-10 min. For large-scale work, the duration of electrolysis was in the neighborhood of 1 hr. In the n-value experiments, the amount of current passed was determined by taking the output of the potentiostat and

<sup>1</sup>The numbering system for the molecules discussed herein is shown below.



recording current *vs.* time on the strip-chart recorder. The number of coulombs passed was obtained by the area under the current-time curve. These results were reliable to  $\pm 3-4\%$ .

Visible absorption spectra were obtained with a custom-made optical cell (Precision Glass Products, Oreland, Pennsylvania) which was positioned within the cavity of a Cary Model 14 spectrometer. The cell has a thin quartz window with a platinum gauze fitting into it; the light beam of the spectrometer passes through this window, thus ensuring sufficient electrolysis in the light path. The cell operates in a three-electrode configuration in conjunction with the Wenking potentiostat. The auxiliary electrode was spatially removed (3 cm) from the working electrode to avoid mixing of electrolysis products. To insure that colored species were not formed at the auxiliary electrode, a saturated calomel electrode (SCE) was employed. The reference SCE was positioned as close to the gauze as possible, usually about 1-2 mm away.

Infrared spectra were recorded with a Perkin-Elmer 337 Grating infrared Spectrometer. Carbazoles and dicarbazyls show the usual bands for substituted ring compounds. Of particular diagnostic value are the out-of-plane bending bands. Carbazole, 9,9'-dicarbazyl and the N-substituted carbazoles all show the band due to ortho disubstitution at  $750\text{ cm}^{-1}$ . In addition, 3,3'-dicarbazyl and the N,N'-substituted-3,3'-dicarbazyls show bands due to 1:2:4 trisubstitution at 800 and  $880\text{ cm}^{-1}$ . N-phenylcarbazole and 9,9'-diphenyl-3,3'-dicarbazyl also gave a band due to monosubstitution at  $700\text{ cm}^{-1}$ . N-substituents all show the appropriate stretching bands. Products mentioned in the text were characterized by their infrared spectra according to these diagnostic bands.

Products from large-scale controlled potential electrolyses were isolated by stripping off the acetonitrile and extracting the residue with a nonpolar organic solvent to obtain the desired product or by extracting the TEAP with water, leaving the organic residue. The much higher solubilities of carbazoles over dicarbazyls in ethanol afforded separation of starting materials. In some cases, the dicarbazyl perchlorate salts precipitated out of solution during electrolysis. These were collected and washed with large volumes of benzene and ethanol.

Carbazole was obtained commercially from Aldrich and Southern Dyestuff and purified by sublimation followed by crystallization from boiling acetic acid, washing in water, and drying to give mp  $246^{\circ}-247^{\circ}$ .

9-Methylcarbazole was prepared by adding 0.12 mole of sodium metal to 0.10 mole of carbazole in 500 ml of toluene; the mixture was boiled for 15 min to remove water and refluxed for 48 hr. The resulting white precipitate was separated from the solvent and unreacted sodium and dissolved in 300 ml of dry acetone. Methyl iodide (0.20 mole) was added and the whole refluxed for 1 hr. The mixture was treated with a water-benzene solution and the benzene phase chromatographed on basic alumina. On addition of heptane to the eluent, 9-methylcarbazole was obtained in nearly quantitative yield. It was then chromatographed on alumina with benzene and recrystallized from benzene-ethanol, mp  $91^{\circ}$ .

9-Ethylcarbazole was obtained from Southern Dyestuff and purified by chromatographing with benzene on neutral alumina to give mp  $68^{\circ}-69^{\circ}$ .

9-Isopropylcarbazole (Eastman Chemical Company, mp  $118^{\circ}-119^{\circ}$ ), 9-phenylcarbazole (K & K Laboratories, mp  $94^{\circ}-95^{\circ}$ ) and 9-vinylcarbazole (K & K Laboratories, mp  $91^{\circ}-94^{\circ}$ ) were used directly without further purification.

9-Nitrocarbazole was prepared by the method of Eikhman *et al.* (15) to give mp  $81^{\circ}$ .

9-acetylcarbazole (mp  $78^{\circ}-79^{\circ}$ ) and 9-benzoylcarbazole (mp  $98^{\circ}-99^{\circ}$ ) were prepared by the method of Berlin (16).

9,9'-Dicarbazyl was synthesized by the method of Perkin and Tucker (4), mp  $226^{\circ}-227^{\circ}$ .

3,3'-Dicarbazyl was unambiguously synthesized by the method of Tucker (5) and purified by sublimation to give mp  $375^{\circ} \pm 3^{\circ}$  (measured by comparison with indicating liquid supplied by the Tempil Corporation). Sublimation was observed to take place above  $350^{\circ}$ .

9,9'-Dimethyl-3,3'-dicarbazyl (mp  $201^{\circ}-203^{\circ}$ ) and 9,9'-diethyl-3,3'-dicarbazyl (mp  $189^{\circ}-190^{\circ}$ ) were prepared by the method of Wieland (17).

## Results and Discussion

**Carbazole.**—The electrochemical oxidation of carbazole, the parent molecule, will be discussed first in some detail. The various N-substituted derivatives will then be mentioned. Table I summarizes the electrochemical data for the molecules studied. Data for the first oxidation process of 5,10-dihydro-5,10-dimethylphenazine (DMPZ) are included in order to compare the carbazole data with a reversible one-electron system (18). Electrochemical data are not tabulated for the nitroso, acetyl, benzoyl, and vinyl derivatives because of the poorly defined curves obtained. The data varied so badly that it was not felt justifiable to present them.

Carbazole is oxidized at a potential of *ca.*  $+1.2\text{v}$  *vs.* SCE, presumably to the cation radical which is quite unstable. Due to this high degree of instability, there is no direct electrochemical or spectroscopic evidence for the cation radical. A previous report had cited stabilization of the carbazole cation radical as carbazole $^{+\cdot}-\text{BF}_4^{-}$  (18), but recent work indicates that it was probably the dicarbazyl radical being observed (19). Also, electrochemical oxidation of carbazole in the presence of tetrabutylammonium  $\text{BF}_4$  showed the system to be totally irreversible (20). However, substituted carbazoles, where the nitrogen and the 3- and 6- ring positions are blocked with substituents, are electrochemically reversible (21). The electrochemical one-electron reversibility of a carbazole with the active coupling sites blocked with substituents infers similar behavior for carbazole itself. The characteristics of these systems are very much like those of triphenylamines (13), which are structurally similar to carbazole, so it is felt that the proposal of the cation radical as the initial intermediate is not unwarranted. This highly reactive cation radical then couples either with another cation radical or with a parent molecule to form, initially, two kinds of dicarbazyls. These coupling reactions involve the loss of two protons per dicarbazyl formed (or one proton per carbazole nucleus); it cannot be determined whether the protons are lost before or after coupling. Of the two dicarbazyls formed, the 3,3'

Table I. Electrochemical characteristics of carbazoles

	$E_p/2^a$	$i_p/v^{1/2}c^b$	$it^{1/2}/c^c$	$it^{1/2}/c^d$	' $n$ -value' <sup>e</sup>
R = H	+1.16	66-75 <sup>f</sup>	120	230	2.5-2.8
Me	1.10	69	106	196	1.96
Et	1.12	70	107	194	2.01
Iso-pro	1.14	68	111	202	2.01
$\text{C}_6\text{H}_5$	1.21	66	103	190	2.08
NO	1.76 <sup>g</sup>				
COMe	1.64 <sup>g</sup>				
$\text{COC}_6\text{H}_5$	1.60 <sup>g</sup>				
$\text{CHCH}_3$	1.08 <sup>g</sup>				
DMPZ		36	51	94	

<sup>a</sup> In volts *vs.* SCE, measured at a scan rate of 4.8 v/min.

<sup>b</sup> Peak current data from linear scan polarograms; scan rate varied from 2.0-25.0 v/min.

<sup>c</sup> Chronoamperometric data from current-time curves, average values.

<sup>d</sup> Chronopotentiometric data from voltage-time curves, average values from runs at varying current densities.

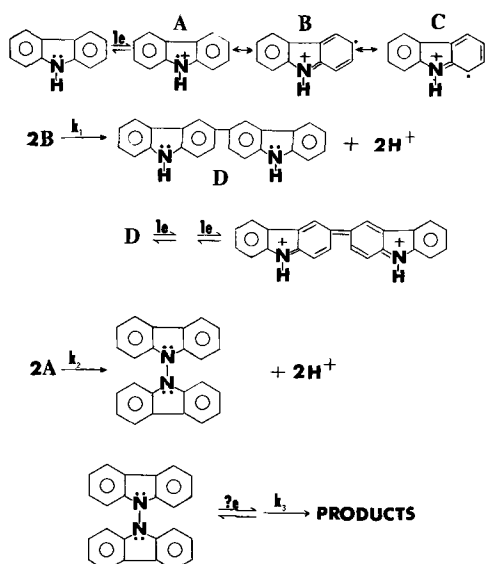
<sup>e</sup> Number of electrons transferred over-all as determined by controlled potential electrolysis of  $1.0 \times 10^{-3}\text{M}$  solutions of carbazoles in MeCN/0.1F TEAP

<sup>f</sup> Increases slowly with decreasing scan rate.

<sup>g</sup> Poorly defined wave.

isomer is the predominant product. This species is more easily oxidized than carbazole, so at the applied potential the dicarbazyl undergoes two successive reversible one-electron redox steps to yield the quinoidal dication. This species is relatively unstable in the presence of carbazole and further slow follow-up reactions occur. Another dicarbazyl, the 9,9' isomer, is formed in small amounts and does not oxidize electrochemically until far anodic potentials, and its oxidation pathway is not known. The general reaction scheme is given below.

A fair amount of evidence is available for the proposed oxidation pathway. The oxidation of carbazole has all the characteristics of a classical ECE mechanism, where each electrochemical step involves one electron per parent molecule. The peak current for the primary oxidation wave is just about twice that of a reversible one-electron process, as seen in Table I by comparison with DMPZ. Had the primary oxidation been a two-electron process, the peak current would have been about 2.83 times that of DMPZ (22, 23). There is also a steady anodic shift of  $E_{p/2}$  with increasing scan rate (about 60 mv per 10-fold increase), indicative of an ECE system (22). A decrease in  $ip/v^{1/2}C$  with increasing  $v$  is not observed because in the carbazole system the coupling reaction is very rapid. Due to the fact that the coupling reactions are so rapid, and the primary oxidation wave is a mixture of ECE and EC processes, little could be ascertained regarding the kinetics of the system. Attempts were made to determine just an approximate coupling rate via potentiostatic and rotating disk measurements, but these experiments were uniformly unsuccessful. In both cases, at the upper limit of measurement available, the current for carbazole oxidation could not be diminished substantially below two electrons. The coupling reactions are indeed quite rapid; calculations from rotating disk polarograms at 3000 rpm, using a diffusion coefficient of  $2.0 \times 10^{-5}$  cm<sup>2</sup>/sec (that of DMPZ determined from linear scan voltammetry, chronoamperometry, chronopotentiometry, and rotating disk voltammetry), set a lower limit of  $k$  at  $3 \times 10^7$  l. moles<sup>-1</sup> sec<sup>-1</sup>.



Structures A, B, and C in the above scheme are the most important resonance forms for the carbazole radical cation. Electron densities represented by the squares of the atomic orbital coefficients ( $c^2$ ) from simple HMO theory show that the reactive sites are the 1, 3, 6, 8, and 9 positions. The 3, 6, and 9 positions should be readily available as coupling sites; the 1 and 8 carbons are somewhat sterically hindered

due to the rather rigid structure of carbazole. Therefore, the formation of 1,1'-dicarbazyl from resonance form C seems unlikely and in fact, has not been observed.

Figure 1 gives a qualitative picture of the carbazole system in MeCN. The initial oxidation wave at +1.2v vs. SCE is followed by another anodic peak at  $\pm 1.8$ v which appears to be due to a small amount of 9,9'-dicarbazyl. Figure 2 is a cyclic polarogram of an authentic sample of 9,9'-dicarbazyl; one sees that the far anodic wave matches up nicely with the second oxidation peak in the carbazole system. Figure 2 also shows a small wave at +1.45v which appears to be missing in the carbazole system. However, this is a relatively small peak and is probably just "buried" in the trailing portion of the primary oxidation wave of carbazole. In fact, if one enhances the current sensitivity so that the primary oxidation peak grinds off scale, and scans very slowly, this buried peak is seen clearly, although it is not as well defined as in Fig. 2.

The direction of scan is reversed at +2.0v, and on cycling back, cathodic peaks are observed in the region from +1.2 to +0.8v. These compare reasonably well with an authentic sample of 3,3'-dicarbazyl (Fig. 1B). The cathodic wave at +0.1v corresponds to reduction of protons released in the coupling reactions. On the second anodic-going scan, oxidation of the

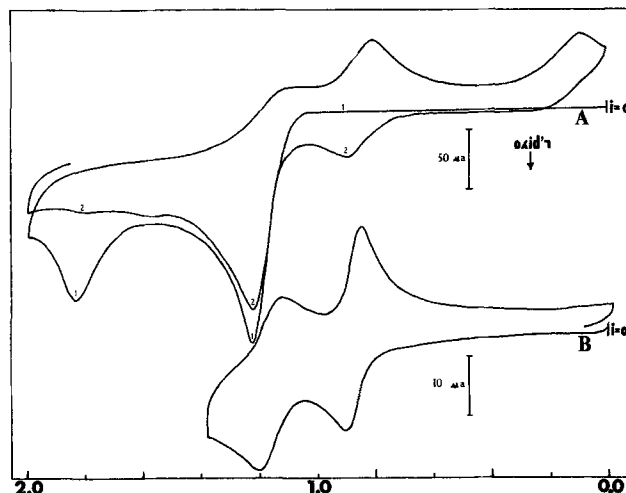


Fig. 1A. Cyclic polarogram of  $2.0 \times 10^{-3}$ M carbazole in MeCN/0.1M TEAP; scan rate is 4.8 v/min on a Pt button electrode. B, Cyclic polarogram of saturated solution (approximately  $1 \times 10^{-4}$ M.) of 3,3'-dicarbazyl in MeCN/0.1M TEAP; scan rate is 4.8 v/min on a Pt button electrode. For both, abscissa is in volts vs. SCE.

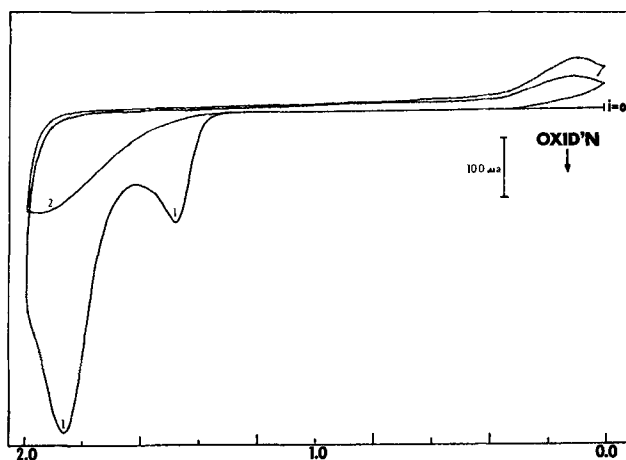


Fig. 2. Cyclic polarogram of  $1.0 \times 10^{-3}$ M 9,9'-dicarbazyl in MeCN/0.1M TEAP; scan rate is 4.8 v/min on a Pt button electrode. Abscissa is volts vs. SCE.

3,3'-dicarbazyl is seen, but there is essentially no oxidation of 9,9'-dicarbazyl. From Fig. 2 it is seen that there is a similar type of behavior for the authentic 9,9'-dicarbazyl, but what actually occurs is not known at this time.

The cyclic polarogram of Fig. 1 shows the carbazole system as being relatively uncomplicated, *i.e.*, a straightforward ECE. However, chronoamperometric and chronopotentiometric data show that somewhat more than two electrons are consumed per carbazole molecule (Table I). The *n*-value determination also varies from 2.5-2.8, the larger value being at longer electrolysis time. Even in a 5-min electrolysis, though, one obtains about 2.5 electrons per carbazole and a steady-state current is obtained on the tail of the current-time curve. This all points to a slow follow-up reaction in the dicarbazyl system. The reaction is apparently between carbazole and dicarbazyl because an *n*-value of 1.92 was obtained for 3,3'-dicarbazyl. The absence of similar behavior in the *N*-substituted derivatives suggests that the unsubstituted nitrogens of the carbazole and/or dicarbazyl are involved. This would lead to products of the type characterized by Waters by chemical oxidation of carbazole (10).

The initial, but not continued, formation of 9,9'-dicarbazyl in the carbazole system appears to be contingent upon a low proton concentration in the area around the electrode. After a few seconds of electrolysis, a rather large number of protons accumulate in the vicinity of the electrode surface, and further formation of the 9,9'-dicarbazyl is inhibited. In fact, addition of  $H_2SO_4$  to a carbazole solution suppresses the 9,9'-dicarbazyl wave, and addition of pyridine (to act as a proton scavenger) enhances it considerably. These phenomena have also been observed in the chemical oxidation work (10, 11). Further studies are now being carried out to determine whether these acid-base effects are general for nonaqueous electrochemical oxidations.

Since peak assignments are by no means conclusive by themselves in studies of this type, another method of identification of products was deemed necessary. *In situ* electrolysis in a Cary spectrometer shows absorption maxima at about 380 and 760  $m\mu$  for both carbazole and 3,3'-dicarbazyl, as shown in Fig. 3. The shorter wavelength band probably corresponds to the dicarbazyl cation radical (by comparison with benzi-

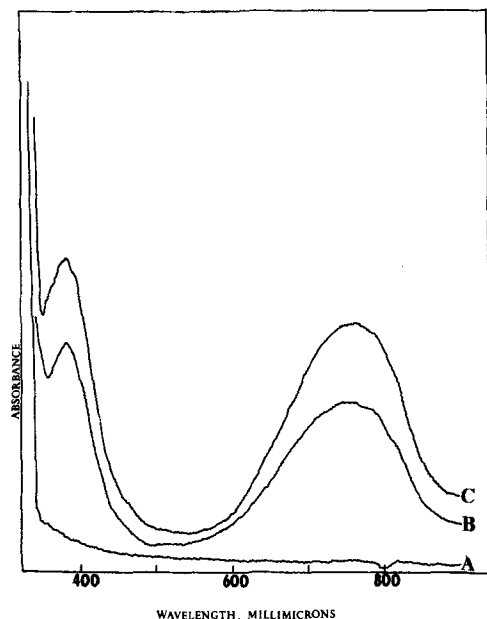


Fig. 3. Visible absorption spectra obtained by *in situ* electrolysis in a Cary 14 spectrometer: A, background scan; B, saturated solution (approximately  $1 \times 10^{-4}M$ ) of 3,3'-dicarbazyl electrolyzed at  $+1.3v$ ; C,  $1.0 \times 10^{-3}M$  carbazole electrolyzed at  $+1.3v$ .

dines of similar structure (12) and spectra obtained by *in situ* electrolysis at the foot of the first oxidation wave of 3,3'-dicarbazyl) and the other band appears to be due to the 3,3'-dicarbazyl dication and/or a dicarbazyl perchlorate salt that forms, presumably from the highly conjugated dication.

The 9,9'-dicarbazyl could not be detected at all spectrophotometrically due to the fact that electrolysis of an authentic sample produces only a weak band with  $\lambda_{max} = 425\mu$ . In the carbazole system, this band would be smothered by the 3,3'-dicarbazyl cation peak, which exhibits an intense absorbance in the same region.

Electron paramagnetic resonance (epr) was also employed in order to determine that 3,3'-dicarbazyl was the principal electrolysis product. *In situ* electrolysis in the cavity of a Varian E-3 epr spectrometer of both carbazole and 3,3'-dicarbazyl resulted in identical single-line spectra of the same shape and width.

Controlled potential electrolysis of carbazole in MeCN produced only 3,3'-dicarbazyl and the perchlorate salt; infrared spectra of electrolysis products revealed no detectable amount of 9,9'-dicarbazyl or any other product. Interestingly, in the presence of pyridine, only 9,9'-dicarbazyl is formed.

*N*-substituted carbazoles.—A series of *N*-substituted carbazoles was also studied and found to behave in a similar manner to carbazole. *N*-ethyl and *N*-methyl carbazole were investigated in some detail; the *N*-isopropyl and *N*-phenyl derivatives appeared to follow the same reaction pathway. Figure 4 shows the cyclic polarogram for oxidation of *N*-ethylcarbazole. Here, formation of 9,9'-dicarbazyl cannot occur, so only the 9,9'-diethyl-3,3'-dicarbazyl is seen. The cyclic polarogram of an authentic sample of the dicarbazyl matches up nicely (polarogram B), as do the visible absorption spectra (Fig. 5). The formation of dicarbazyl is quantitative, as shown by reverse-current chronopotentiometry (RCC) with unequal current densities. If  $i_r = 0.414i_f$  and  $n_f$ , the number of electrons involved in the forward (oxidation here) process, is two while  $n_r$ , the *n*-value for the reverse process, is one, a ratio of  $\tau_f/\tau_r$  of 2.34 should be obtained (24). In fact, at a number of different current density ratios, a quotient of transition times between 2.3 and 2.4 was obtained for *N*-ethyl carbazole, as well as for the methyl, isopropyl, and phenyl analogs.

These *N*-substituted carbazoles form dicarbazyls that are extremely stable, so they are pure ECE systems. The stability of the dicarbazyls is attested to by the *n*-values in Table I; all are two electrons,

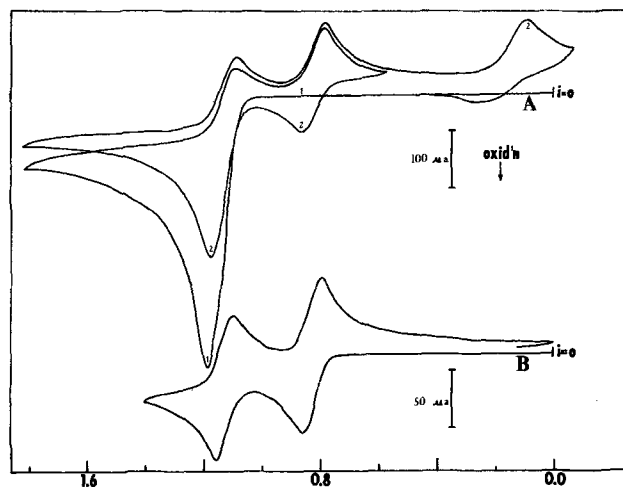


Fig. 4A. Cyclic polarogram of  $2.0 \times 10^{-3}M$  *N*-ethylcarbazole in MeCN/0.1M TEAP; scan rate is 9.7 v/min on a Pt button electrode. B, Cyclic polarogram of  $1.0 \times 10^{-3}M$  9,9'-diethyl-3,3'-dicarbazyl in MeCN/0.1M TEAP; scan rate is 4.8 v/min on a Pt button electrode. For both, abscissa is volts vs. SCE.

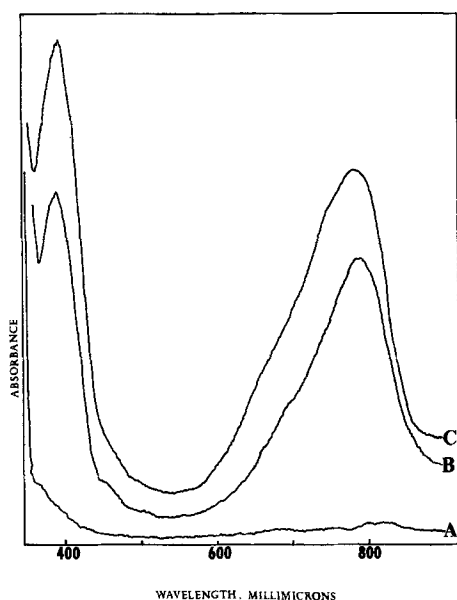


Fig. 5. Visible absorption spectra obtained by *in situ* electrolysis in the Cary 14 spectrometer. A, background scan; B,  $1.0 \times 10^{-3}$  M N-ethylcarbazole electrolyzed at +1.2v; C,  $5.0 \times 10^{-4}$  M, 9,9'-diethyl-3,3'-dicarbazyl electrolyzed at +1.2v.

within experimental error. The quantitative aspect of these systems is further illustrated in Fig. 6. The cyclic polarogram is that of a solution of N-ethylcarbazole that has been exhaustively electrolyzed at +1.4v vs. SCE. The scan is initiated in the cathodic direction; a large wave due to reduction of protons is first encountered. The peak current corresponds to 1.11 millimoles of protons per millimole of N-ethylcarbazole by comparison with a picric acid calibration curve (25). This is consistent with the proposed mechanism. In addition, the dicarbazyl waves shown on the anodic-going scan have peak currents whose magnitude indicate a concentration just half that of the parent carbazole, within experimental error. Since the coupling reaction is bimolecular, this is to be expected.

Electrochemical and spectroscopic data for the methyl, isopropyl, and phenyl derivatives are identical to the N-ethylcarbazole data. The 9,9'-dimethyl-3,3'-dicarbazyl was synthesized also and compared with the electrochemical oxidation product from N-methylcarbazole.

Table II summarizes the spectral data characterizing the various 3,3'-dicarbazyls. The shorter wavelength bands,  $\lambda_1$ , were generally much sharper and the other

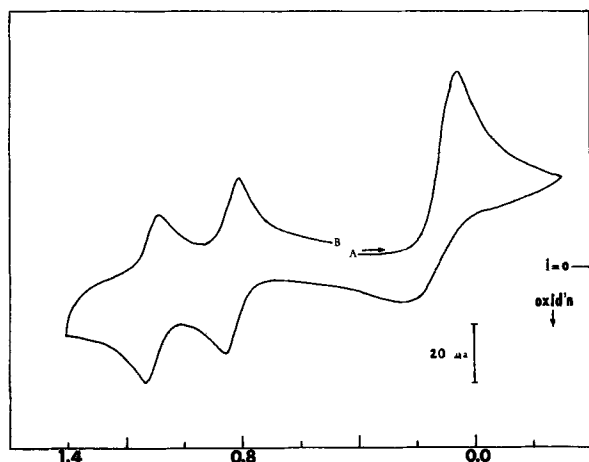
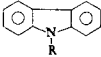


Fig. 6. Cyclic polarogram of  $1.0 \times 10^{-3}$  M N-ethylcarbazole solution following exhaustive electrolysis at +1.4v vs. SCE; scan rate is 4.0 v/min on a Pt button electrode; abscissa is volts vs. SCE; scan is initiated at A, ends at B.

Table II. Summary of spectral data

 R	Dicarbazyl Absorption bands	
	$\lambda_1$ , millimicrons	$\lambda_2$ , millimicrons
R = H	382	760
Me	390	780
-CH <sub>2</sub> -Me	383	795
-CH(Me) <sub>2</sub>	427	812
-C <sub>6</sub> H <sub>5</sub>	411	800

group,  $\lambda_2$ , was characterized by broadness and ill-defined shoulders toward the blue.

The N-phenyl derivative is of some interest from an HMO viewpoint. If it is assumed that the molecule were planar (no twist of the phenyl ring), the electron density ( $c^2$ ) is greater at the *para* position on the N-phenyl ring (0.096) than at the 3-position in the carbazole nucleus (0.074). However, with a moderate twist of about 20°-25°, the electron density is considerably greater in the carbazole portion of the molecule, and one would now expect to obtain a 3,3'-dicarbazyl upon electrochemical oxidation of N-phenylcarbazole. A fair degree of twisting is really to be expected because of steric crowding of the phenyl ring with the 1- and 8-position protons and, in fact, isolation of the electrolysis product from a controlled-potential oxidation of N-phenyl carbazole and analysis of its infrared spectrum shows that 9,9'-diphenyl-3,3'-dicarbazyl is the electrolysis product.

The remaining N-substituted carbazoles, *viz.*, N-acetyl-, N-benzoyl-, N-nitroso-, and N-vinylcarbazole, all exhibit complex electrochemical behavior. It may well be that the N-substituents are taking part in the chemical reactions following the initial electron transfers. Their electrochemical data are listed in Table I, but no serious attempts were made to characterize their anodic oxidation pathways. Each appears to be a formidable problem in itself!

#### Acknowledgment

Special thanks are due to Southern Dyestuff Company for the donation of several carbazoles and to Dr. S. H. Tucker for helpful suggestions and encouragement. Technical assistance from Dr. P. Maitland and S. Creason are appreciated. Financial support through a Frederick Gardner Cottrell Research Corporation grant and PRF Grant No. 1039-G3 are also gratefully acknowledged.

Manuscript received July 8, 1968.

Any discussion of this paper will appear in a Discussion section to be published in the June 1969 JOURNAL.

#### REFERENCES

- J. Volke, in "Physical Methods in Heterocyclic Chemistry," Vol. 1, Chap. 6, A. R. Katritzky, Editor, Academic Press, New York (1963).
- G. E. K. Branch and J. F. Smith, *J. Am. Chem. Soc.*, **42**, 2405 (1920).
- G. E. K. Branch and W. W. Hall, *ibid.*, **46**, 438 (1924).
- W. H. Perkin, Jr., and S. F. Tucker, *J. Chem. Soc.* **1921**, 216.
- S. H. Tucker, *ibid.*, **1926**, 3033.
- J. McLintock and S. H. Tucker, *ibid.*, **1927**, 1214.
- T. F. Macrae and S. H. Tucker, *ibid.*, **1933**, 1520.
- M. C. Nelmes and S. H. Tucker, *ibid.*, **1933**, 1523.
- B. Robinson, *Nature*, **210**, 520 (1966).
- W. A. Waters and J. E. White, *J. Chem. Soc. (C)* **1968**, 740.
- P. Maitland and S. H. Tucker, *ibid.*, **1927**, 1388.
- M. Kuroki, *Yuki Gosei Kagaku Kyokai Shi*, **23**, 447 (1965); *C.A.*, **63**, 4238 (1965).
- a, E. T. Seo *et al.*, *J. Am. Chem. Soc.*, **88**, 3498 (1966); b, R. F. Nelson, Ph.D. Thesis, Kansas University, 1966.
- L. S. Marcoux and R. N. Adams, *Anal. Chem.*, **39**, 1898 (1967).
- R. K. Eikhman *et al.*, *Org. Chem. Ind. (U.S.S.R.)*, **6**, 93 (1939); *C.A.*, **33**, 7297 (1939).

16. A. A. Berlin, *J. Gen. Chem. (U.S.S.R.)*, **14**, 438 (1944).
17. H. Wieland, *Ber.*, **46**, 3296 (1913).
18. R. F. Nelson, D. W. Leedy, E. T. Seo, and R. N. Adams, *Z. Anal. Chem.*, **224**, 184 (1967).
- 18a. A. Ledwith and M. Sambhi, *Chem. Commun.*, **1965**, 64.
19. D. H. Iles and A. Ledwith, *ibid.*, **1968**, 498.
20. Referee's observation.
21. J. F. Ambrose and R. F. Nelson, Unpublished data.
22. R. S. Nicholson and I. Shain, *Anal. Chem.*
23. R. F. Nelson, *J. Electroanal. Chem.*, in press.
24. P. Delahay, "New Instrumental Methods in Electrochemistry," p. 195, Interscience Publishers, Inc., New York (1954).
25. R. F. Nelson and R. N. Adams, *J. Electroanal. Chem.*, **16**, 439 (1968).

## Electrochemical Behavior of H<sub>2</sub>O in Nonaqueous Electrolyte

Brian Burrows\* and Susan Kirkland

Tyco Laboratories, Inc., Waltham, Massachusetts

### ABSTRACT

The electrochemical behavior of trace quantities of water (1-30 mM) in LiClO<sub>4</sub>-propylene carbonate solutions was studied *via* chronopotentiometric and cyclic voltammetric techniques. It was observed that, with platinum electrodes, the chronopotentiometric constant increased with increasing current density up to a constant limiting value at high current densities. Analysis of the cyclic voltammetric results showed analogous behavior. The reaction product of H<sub>2</sub>O reduction was inferred to be a porous, insoluble film of LiOH. This layer apparently acts to block part of the electrode surface thereby increasing the effective current density, decreasing  $\tau$  and hence  $i\tau^{1/2}$ . From the concentration dependence of  $i\tau^{1/2}$  and of  $i_p/v^{1/2}$  it was further inferred that strong complexes were formed between water and Li<sup>+</sup> ion which decreased the activity coefficient of H<sub>2</sub>O. Current reversal subsequent to the reduction step showed an oxidation step which may be associated with an adsorbed film of atomic hydrogen on the platinum surface.

The present interest in high energy density batteries based on lithium anodes has generated much activity in the area of aprotic organic solvents, particularly in the use of propylene carbonate (4-methyldioxolone-2) as a solvent medium. Little work pertaining to electrode reactions in this medium has been reported in the open literature (1), due, in part, to the unavailability of solvent with sufficient purity. Recent improvements in purification have reduced the major impurity content to less than 2 ppm H<sub>2</sub>O and  $\leq$  12 ppm propylene glycol (2). The behavior of these substances on smooth electrodes can now be studied with reasonable precision.

Water is a particularly ubiquitous impurity in aprotic organic solvents; hence its behavior is a matter of interest in relation to any electrochemical investigation in these media. In this paper we present the results of chronopotentiometric and cyclic voltammetric investigations in a PC/LiClO<sub>4</sub> solution containing H<sub>2</sub>O. The concentration of H<sub>2</sub>O was varied over the range 10<sup>-3</sup> to 3 x 10<sup>-2</sup>M, *i.e.*, from 20 to 500 ppm. Dey (3) has published a report on the electrochemical behavior of H<sub>2</sub>O in the same solution but at higher concentrations.

### Experimental

The cell, contained inside a recirculating argon-atmosphere dry box (Vacuum Atmosphere Corporation) was operated at 28° ± 0.2°C.

Chronopotentiograms were recorded on an X-Y recorder (Houston Omnigraphic, model HR-98T). A unity-gain follower, constructed from an operational amplifier (Philbrick, type P65AU), was used in the potential measuring circuit to avoid undue loading of the reference electrode-working electrode cell. A constant-current power source (Electronic Measurements, model C623) supplied the current at voltages up to 400v. A toggle switch was adequate to switch in the constant current, since transition times less than 0.5 sec were not measured.

The cyclic voltammograms were recorded on the same X-Y recorder. The cathode follower described above was used to increase the effective input impedance of the recorder. A triangular waveform from a function generator (Exact Electronics, Inc., type 255) was fed into the input of a Wenking potentiostat (type 61RS) to give a potentiostatic *i-v* curve.

The electrochemical cell had three compartments with the middle (working electrode) compartment separated from the reference electrode compartment by a Luggin capillary and separated from the counter electrode compartment by a fritted glass junction.

The reference electrode used in all the experiments was based on the Li/Li<sup>+</sup> couple. This was formed by simply immersing a Li rod in the PC/LiClO<sub>4</sub> solution (4). A Pt foil was used as the counter electrode. The working electrode for the cyclic voltammetric scans was made up from 0.05 cm diameter Pt wire sealed into Pyrex. Lengths of wire up to 1 cm were left exposed. The working electrode for the chronopotentiometric experiments was a Beckman No. 39723 Pt disk electrode (0.204 cm<sup>2</sup>) mounted horizontally in the working electrode compartment just above the Luggin capillary. The electrode was polished with alumina powder on a lapping wheel before use. Before each measurement it was also necessary to clean the electrode by dipping it into conc. HNO<sub>3</sub>, followed by washes in distilled H<sub>2</sub>O and in acetone. When the electrode was not cleaned after each measurement of transition time or current-peak height, irreproducible and poorly defined curves were recorded.

The solutions of LiClO<sub>4</sub> in PC were made up from distilled PC (2) and anhydrous LiClO<sub>4</sub> (K & K Laboratories, Inc.) and then dried by passing twice over ground Linde 4A Molecular Sieves. Flame photometric analysis showed a negligible loss of Li<sup>+</sup> as a result of ion exchange processes with the sieves. After two passes the transition time corresponding to H<sub>2</sub>O (or glycol) was not detectable. However, some water (or glycol) was detected by the more sensitive cyclic voltammetric technique (see below).

\* Electrochemical Society Active Member.

Portions of this dried PC/LiClO<sub>4</sub> solution were taken and the required concentration of H<sub>2</sub>O added with a syringe. Alternatively, some of the solutions low in H<sub>2</sub>O were made up by a dilution procedure from a solution containing 1000 ppm H<sub>2</sub>O. The results were identical to those obtained in solutions prepared by direct addition.

### Results and Discussion

**Background current.**—The potential at which water was reduced was determined from cyclic voltammograms of the appropriate solutions. An *i-v* trace showing the background current in a PC/LiClO<sub>4</sub> (1M) solution which had been dried over molecular sieves is shown in Fig. 1. The broad reduction peak at +1.4v vs. Li/Li<sup>+</sup> was observed to be diffusion controlled, dependent on solute, and independent of solvent. For example, when Et<sub>4</sub>NClO<sub>4</sub> was used as the supporting electrolyte, no peak was observed. It was present, however, in tetrahydrofuran containing LiClO<sub>4</sub> as supporting electrolyte. The peak was identified as being due to the reduction of residual H<sub>2</sub>O (and/or glycol), since additions of either H<sub>2</sub>O or glycol caused the peak to increase in height. The inhibition of the reduction of H<sub>2</sub>O in Et<sub>4</sub>NClO<sub>4</sub> solution is presumably due to an adsorption effect associated with the Et<sub>4</sub>N<sup>+</sup> cation. In aqueous solution several examples of strong adsorption of Et<sub>4</sub>N<sup>+</sup> ions, with concomitant inhibition of electrode reductions, have been reported (5, 6).

The reduction peak at +0.4v had similar properties to that of the peak at +1.4v; however, it could not be identified with any of the impurities present in the PC (e.g., H<sub>2</sub>O or glycol). The peak was also observed in THF/LiClO<sub>4</sub> solution. Assuming that the peak was caused by an impurity such as another alkali metal cation (present in LiClO<sub>4</sub>), an attempt was made to remove this impurity by electrolysis. A large surface area Pt black electrode (geom. area 4 cm<sup>2</sup>) was held at +0.4v for 30 min in PC/LiClO<sub>4</sub> solution. During this time considerable current flowed (50 ma). A subsequent *i-v* trace showed no change in the peak height. A Hg pool electrode (area approx. 4 cm<sup>2</sup>) which was stirred and held at +0.4v for 30 min also gave rise to considerable current (50 ma). In time this current decreased to near zero. A subsequent cyclic voltammogram showed no change in the peak height on the Pt probe. Cyclic voltammograms on nickel electrodes showed a broad peak at +0.4v, but on gold the peak was observed at +0.2v.

The implication then is that the solvent or impurities in the solvent are not responsible for this peak. Rather only LiClO<sub>4</sub> and platinum are involved. More specifically the peak at +0.4v vs. Li/Li<sup>+</sup> appeared to be due to Li<sup>+</sup> ion reduction at the Pt electrode surface, resulting, presumably, in the formation of a Li-Pt alloy. Further evidence in support of this

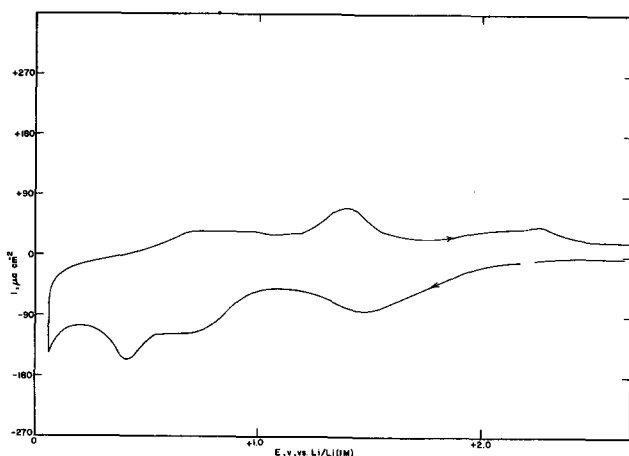


Fig. 1. Background *i-v* scan in 1M LiClO<sub>4</sub>/PC solution, dried over 4A molecular sieves. Scan rate 80 mv sec<sup>-1</sup>.

conclusion was obtained from an experiment where Pt black electrodes, which had been held at +0.4v, subsequently gassed vigorously when immersed in H<sub>2</sub>O. Similar conclusions regarding Li-Pt alloy formation have been reached from studies on the anodic-cathodic efficiencies of the Li/Li<sup>+</sup> ion reaction on Pt substrates (7).

**Cyclic voltammetry.**—A typical cyclic voltammogram in PC/LiClO<sub>4</sub>(1M) solution containing H<sub>2</sub>O is shown in Fig. 2. The H<sub>2</sub>O reduction peak is well defined and a reverse (oxidation) peak is also apparent. The relationship between peak current and voltage scan rate under linear diffusion conditions is given by (8)

$$i_p = KD^{1/2} C v^{1/2} \quad [1]$$

where  $i_p$  is in amp cm<sup>-2</sup>,  $D$  is the diffusion coefficient in cm<sup>2</sup> sec<sup>-1</sup>,  $C$  is the bulk concentration of electroactive species in moles cm<sup>-3</sup>,  $v$  is in volts sec<sup>-1</sup>, and  $K$  is a proportionality constant which depends on the nature of the electrode process and of the products of the reaction.  $i_p/v^{1/2}$  should be a constant independent of  $v^{1/2}$  for a given  $C$  provided that no mechanistic complications are present. Plots of  $i_p/v^{1/2}$  vs.  $v^{1/2}$  for a number of different H<sub>2</sub>O concentrations are shown in Fig. 3. This increase of  $i_p/v^{1/2}$  with  $v^{1/2}$  up to a constant limiting value will be discussed below in the context of the chronopotentiometric results. The use of a cylindrical electrode meant that the diffusion conditions were not exactly linear. This did not, however, affect the qualitative agreement of the results with the chronopotentiometric observations (see below).

The limiting values of  $i_p/v^{1/2}$  plotted vs.  $C_{H_2O}$  gave a graph with two linear portions (Fig. 4) analogous to Fig. 6 obtained from the galvanostatic experiments. The data were in general, less reproducible than the results obtained using the chronopotentiometric technique. However, apparent concentrations of water down to a few ppm could be detected at sweep rates of  $>0.8$  v sec<sup>-1</sup>.

**Chronopotentiometry.**—The Sand equation is applicable strictly only to conditions of one-dimensional, semi-infinite linear diffusion. Bard (9), in comparing shielded and unshielded planar electrodes, has observed that the chronopotentiometric constant increased at long values of the transition times in the case of unshielded electrodes due to convective effects

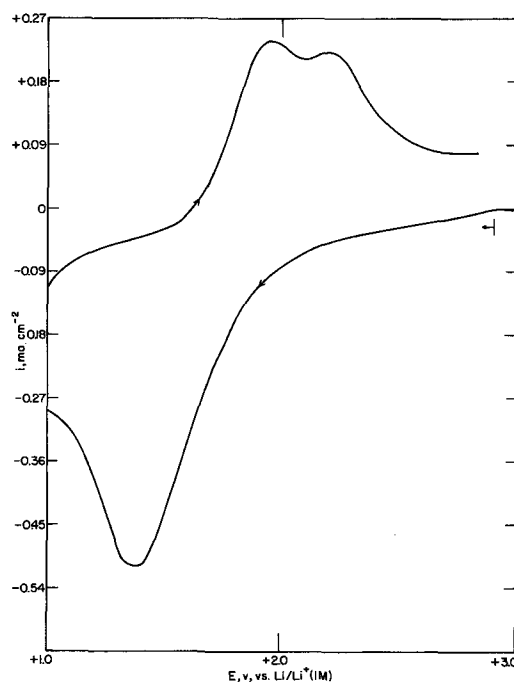


Fig. 2. Cyclic voltammogram in 1M LiClO<sub>4</sub>/PC solution containing 100 ppm H<sub>2</sub>O. Scan rate 320 mv sec<sup>-1</sup>.

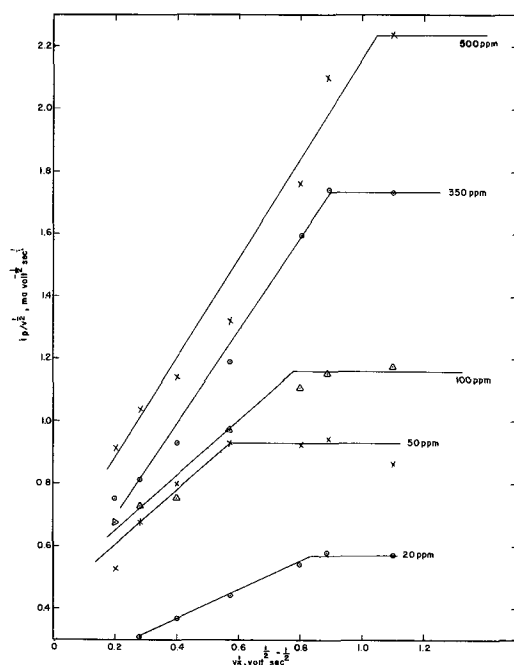


Fig. 3. Plot of  $i_p/v^{1/2}$  vs.  $v^{1/2}$  for  $H_2O$  reduction in 1M  $LiClO_4/PC$  solutions.

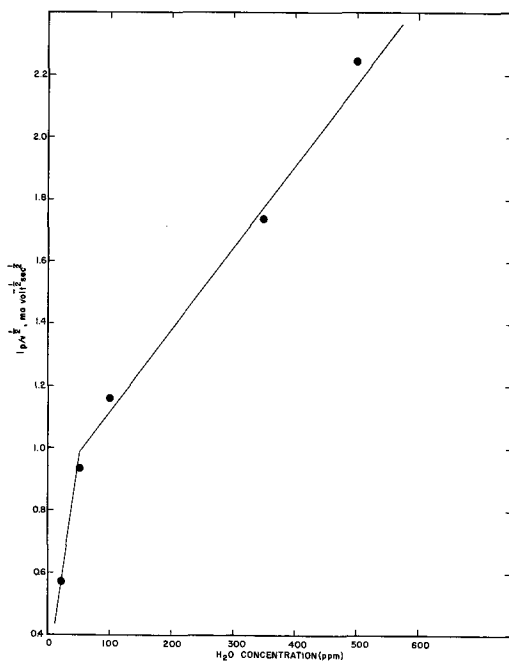


Fig. 4. Plot of limiting  $i_p/v^{1/2}$  values vs.  $H_2O$  concentrations in 1M  $LiClO_4/PC$  solution.

and spherical contributions to diffusion. Lingane (10) subsequently showed that the chronopotentiometric constant experimentally obtained with unshielded, circular, planar electrodes satisfied the equation

$$\frac{i\tau^{1/2}}{C} = \frac{nF\tau^{1/2}D^{1/2}}{2} \left[ 1 + 0.98 \left( \frac{D\tau}{r^2} \right)^{1/2} \right] \quad [2]$$

where the symbols have their usual meaning. Then for there to be an error of <5% in the values of  $i\tau^{1/2}/C$ , the following requirement applies

$$0.98 \left( \frac{D\tau}{r^2} \right)^{1/2} < 0.05$$

This condition ( $\tau$  must be less than 16 sec) was met by the measurements.

A typical chronopotentiogram is shown in Fig. 7. Dey (3), working with higher water concentration, reported that the galvanostatic transient for  $H_2O$  reduction had three distinct plateaus. In the present case these were not observed; however, two plateaus were apparent in the 500 ppm solution.

The significant feature of the chronopotentiometric results as summarized in the  $i\tau^{1/2}$  vs.  $i$  plot (Fig. 5) is the increase of  $i\tau^{1/2}$  with increasing current density up to a constant limiting value. This behavior is unusual and is the reverse of that which occurs when a kinetic step precedes the electrochemical step. An increase of  $i\tau^{1/2}$  with increase of current density can, of course, occur when the reduction of the electroactive species is complicated by the concomitant reduction of an adsorbed film of the species on the electrode (11). This effect, however, becomes more pronounced as the current density increases, whereas in the present case the  $i\tau^{1/2}$  values became constant at the shorter times. Thus electrolysis of an adsorbed film cannot be the explanation here.

A possible interpretation of the observed behavior can be given in terms of changing electrode area. Thus as  $H_2O$  is reduced,  $LiOH$  precipitates on the electrode surface (see below for evidence of  $LiOH$  formation). This layer of  $LiOH$  then blocks some portion of the surface, resulting in a decrease in active electrode surface area. As the surface area is decreased, the effective current density will increase and  $\tau$  will decrease. The decrease in  $\tau$  is apparently large enough to make  $i\tau^{1/2}$  smaller than it would be if there were no blocking effect by  $LiOH$ . At longer times (i.e., lower  $i$ ), the blocking effect would be more pronounced, as observed. A similar explanation holds for the cyclic voltammetric results (see Fig. 3).

Evidence for the formation of  $LiOH$  was the appearance of a violet-pink coloration on the surface after immersing an electrode at which  $H_2O$  had been reduced in phenolphthalein solution. Dey (3) used this same criterion for the formation of  $LiOH$  but reported the development of a blue coloration. The same violet-pink coloration was also observed when some drops of phenolphthalein were added to a  $PC/LiClO_4$  solution in contact with added  $LiOH$ . However, it should be noted that the coloration was only observed at the surface of the solid  $LiOH$  and not in the solution. This further indicates the low solubility of  $LiOH$ .

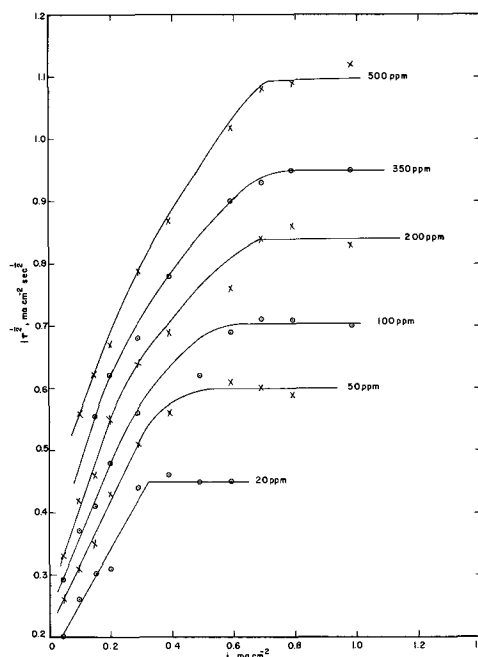


Fig. 5. Plot of  $i\tau^{1/2}$  vs.  $i$  for  $H_2O$  reduction in 1M  $LiClO_4/PC$  solution.



The above explanation can be put on a more quantitative basis. Consider the solution containing 100 ppm H<sub>2</sub>O as an example. For this solution the lowest  $i\tau^{1/2}$  point in Fig. 5 corresponds to  $i = 0.10 \text{ ma cm}^{-2}$ ,  $\tau^{1/2} = 3.7 \text{ sec}^{1/2}$ , and  $i\tau = 1.35 \text{ mc cm}^{-2}$ . The limiting  $i\tau^{1/2}$  value at high  $i$  is  $0.70 \text{ ma cm}^{-2} \text{ sec}^{1/2}$ . Hence the real current density corresponding to  $\tau^{1/2} = 3.7 \text{ sec}$  is at least  $0.70/3.7 = 0.19 \text{ ma cm}^{-2}$  which is double that of the apparent current density. This implies that half of the electrode surface is blocked by precipitated LiOH. A monolayer of LiOH would correspond to about  $0.2 \text{ mc cm}^{-2}$  of charge. The observed charge was  $1.35 \text{ mc cm}^{-2}$ . Thus there is more than enough LiOH available to block half the surface. The fact that not all of the surface was blocked suggests that either the film precipitate is porous or that not all of the LiOH is precipitated on the surface of the electrode.

The above explanation is to some extent supported by the results of H<sub>2</sub>O reduction (conc. 100 ppm) in THF/LiClO<sub>4</sub> solution (Table I). In this solvent LiOH is apparently more soluble so that a blocking effect should not be as pronounced. Indeed  $i\tau^{1/2}$  is relatively constant. Evidence for the relatively higher solubility of LiOH in THF as compared to PC was adduced from conductivity measurements. The ratio of the conductivity of THF equilibrated with LiOH compared to pure THF was approximately double the ratio obtained when PC was used as the solvent. The lower viscosity of THF-LiClO<sub>4</sub> (1M) solutions (1.02 centistokes at 25°C) compared with PC-LiClO<sub>4</sub> (1M) solution (6.01 centistokes at 25°C) would also encourage the dispersion of LiOH away from the electrode surface through convective effects. This lower viscosity, which implies a larger diffusion coefficient, would also explain the larger  $i\tau^{1/2}$  value obtained for a concentration of 100 ppm H<sub>2</sub>O in THF solution as compared with the same concentration in the PC solution.

It was next necessary to account for the actual magnitudes of  $i\tau^{1/2}$  in PC. The Sand equation was therefore used to calculate theoretical values. Assuming that  $D = 10^{-5} \text{ cm}^2 \text{ sec}^{-1}$ ,  $n = 2$ , and  $C = 10^{-3} \text{ M}$  (where any major complications from LiOH formation should be minimal), the  $i\tau^{1/2}$  product is given by

$$i\tau^{1/2} = \frac{nFD^{1/2}\pi^{1/2}C}{2}$$

$$= 9.65 \times 10^4 \times \pi^{1/2} \times (10^{-5})^{1/2} \times 10^{-3} \quad [3]$$

$$\text{i.e., } i\tau^{1/2} = 0.5 \text{ ma cm}^{-2} \text{ sec}^{1/2}.$$

Referring to Fig. 5, it can be seen that this value is in good agreement with observed values at concentrations near  $10^{-3} \text{ M}$ . However, for a tenfold increase in concentration to  $10^{-2} \text{ M}$  (i.e., 180 ppm) the  $i\tau^{1/2}$  product should increase to  $5.0 \text{ ma cm}^{-2} \text{ sec}^{1/2}$ . The observed value for 200 ppm H<sub>2</sub>O was only of the order of  $0.8 \text{ ma cm}^{-2} \text{ sec}^{1/2}$ . Thus as the concentration of added H<sub>2</sub>O is increased, the H<sub>2</sub>O available for electrochemical reduction (i.e., its activity) appears to decrease.

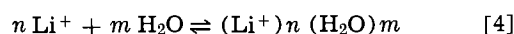
To explain this effect it seems reasonable to suppose that there is a strong attraction between the added H<sub>2</sub>O and Li<sup>+</sup> ions in the electrolyte. The extent of this attraction presumably increases with increasing H<sub>2</sub>O concentration as H<sub>2</sub>O is then more able to

compete with PC molecules for the Li<sup>+</sup> ions. The net result of this attraction would be to form clusters of hydrated Li<sup>+</sup> ions and to decrease the concentration of free, unassociated H<sub>2</sub>O molecules, i.e., to decrease the activity coefficient of H<sub>2</sub>O.

This explanation is consistent with the data shown in Fig. 6, a plot of  $i\tau^{1/2}$  vs. concentration of added water. There are two separate linear sections of the curve, implying two forms of water, i.e., different interactions of water with lithium ions. The cyclic voltammetric results behaved analogously. Thus a plot of  $i_p/v^{1/2}$  vs. H<sub>2</sub>O concentration (see Fig. 4) also had two linear portions.

To confirm this apparent interaction of H<sub>2</sub>O with Li<sup>+</sup> ions rather than with the solvent, the  $i\tau^{1/2}$  behavior of H<sub>2</sub>O in an 0.1M LiClO<sub>4</sub> solution in PC was investigated. The  $i\tau^{1/2}$  vs.  $i$  curves were similar in shape to those observed in 1M LiClO<sub>4</sub> solutions; the limiting  $i\tau^{1/2}$  values observed at high current densities are plotted in Fig. 6.

At low H<sub>2</sub>O concentrations (<50 ppm) there is no significant difference in the  $i\tau^{1/2}$  values in 0.1M and 1M LiClO<sub>4</sub> solutions. Thus H<sub>2</sub>O is not in equilibrium with a lithium ion complex at these concentration levels, or rather if an equilibrium does exist it does not affect the electrochemical availability of H<sub>2</sub>O for reduction. Alternatively, there could be some association of H<sub>2</sub>O with the solvent at these low H<sub>2</sub>O concentrations which again does not affect the availability of H<sub>2</sub>O molecules for electrochemical reduction. This agrees with results of the calculation of  $i\tau^{1/2}$  from Eq. [3]. At higher H<sub>2</sub>O concentrations, however, the  $i\tau^{1/2}$  values in 0.1M LiClO<sub>4</sub> solutions were significantly higher than those in 1M LiClO<sub>4</sub>. Presumably this indicates that H<sub>2</sub>O is interacting with Li<sup>+</sup> ions in the 0.1M LiClO<sub>4</sub> solution to a lesser extent than in the 1.0M LiClO<sub>4</sub> solution. Furthermore the fact that at higher H<sub>2</sub>O concentrations the  $i\tau^{1/2}$  vs. concentration plots are parallel suggests that the same equilibrium is involved at the two LiClO<sub>4</sub> concentrations. This equilibrium is presumably of the form



Using mass balances and the equilibrium expression for a 1:1 complex of Li<sup>+</sup> and H<sub>2</sub>O as represented in [4] it can be shown that  $i\tau^{1/2} \propto C_{\text{H}_2\text{O}}/(K C_{\text{Li}^+} + 1)$ , where  $C_{\text{H}_2\text{O}}$  and  $C_{\text{Li}^+}$  are analytical concentrations of

Table I. Results of chronopotentiometric analysis for the reduction of H<sub>2</sub>O (100 ppm) in THF/LiClO<sub>4</sub> (1M) solution

$i \text{ ma cm}^{-2}$	$\tau \text{ sec}$	$\tau^{1/2} \text{ sec}^{1/2}$	$i\tau^{1/2} \text{ ma cm}^{-2} \text{ sec}^{1/2}$
1.08	0.68	0.83	0.90
0.98	0.90	0.95	0.93
0.79	1.50	1.23	0.97
0.59	2.39	1.55	0.92
0.38	6.06	2.46	0.99
0.29	11.46	3.29	0.95

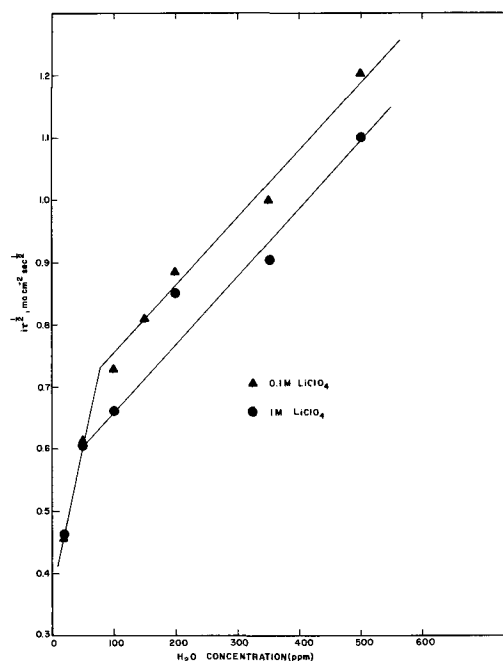


Fig. 6. Plot of limiting  $i\tau^{1/2}$  values vs. H<sub>2</sub>O concentration in 0.1M and 1.0M LiClO<sub>4</sub>/PC solutions.

$\text{H}_2\text{O}$  and  $\text{Li}^+$  and  $K$  is the equilibrium constant. Thus for a given  $C_{\text{H}_2\text{O}}$ , decreasing  $C_{\text{Li}^+}$  will have the effect of increasing  $i\tau^{1/2}$  as was observed.

Interpretation of NMR data obtained from experiments in other aprotic organic solvents (*viz.*, dimethylformamide and acetonitrile) lends support to the existence of the above equilibrium. For example, Craig and Richards (12) observed that proton chemical shifts remained constant as the DMF concentration was increased in  $\text{H}_2\text{O}$ -DMF mixtures containing  $\text{LiCl}$ . They concluded that most of the  $\text{H}_2\text{O}$  molecules in the system were directly involved in  $\text{Li}^+$  ion hydration. Another group (13) interpreted the effect of  $\text{H}_2\text{O}$  on  $\text{Li}^+$  ion shifts in  $\text{H}_2\text{O}$ -AN mixtures containing  $\text{LiClO}_4$  to indicate preferential solvation of  $\text{Li}^+$  ions by  $\text{H}_2\text{O}$  as opposed to AN.

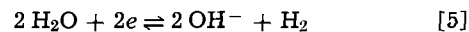
Dey (3) has investigated the electrochemical behavior of  $\text{H}_2\text{O}$  in  $\text{PC-LiClO}_4$  (1M) at concentrations substantially higher than those investigated here. His conclusions were generally similar to those reported here, namely, that  $\text{H}_2\text{O}$  exists as a complex with  $\text{Li}^+$  ions in  $\text{PC/LiClO}_4$  solution.

The results of the present chronopotentiometric investigation, as summarized in Fig. 6, can be considered a calibration curve for the quantitative analysis of  $\text{H}_2\text{O}$  in  $\text{PC-LiClO}_4$  solutions. The reproducibility of the method was estimated to be  $\pm 0.4$  in the limiting  $i\tau^{1/2}$  values. This is not sufficiently reproducible however for the method to give more than an approximate estimate of  $\text{H}_2\text{O}$  concentration.

A well-formed transition time was observed when the current was switched from cathodic to anodic. An example is shown in Fig. 7. The behavior of this transition time was as follows. It was found that the ratio of the reduction and oxidation transition times was about 2:1 at the smaller concentration and higher at the larger concentration range ( $\sim 4:1$ ). The ratio is in proportion to the amount of charge passed in the reduction process. The ratio was also found to be smaller at the shorter times (corresponding to the smaller amount of charge passed in the reduction) and larger at the longer times for any given concentration.

The charge associated with the reverse process for a given concentration was  $\sim 0.35$  mc/cm<sup>2</sup> at high current densities and  $\sim 0.45$  mc/cm<sup>2</sup> at the lower current densities. Furthermore, for a given concentration of  $\text{H}_2\text{O}$  the transition time for the reverse process did not

change significantly on stirring, whereas the forward transition time did. These observations imply that the reverse (oxidation) process is associated with an adsorbed layer of a reduction product on the surface of the electrode. The reduction process presumably is



in which adsorbed hydrogen atoms are reduction intermediates (14).

It has been estimated (15) that the oxidation of a monolayer of adsorbed hydrogen on a smooth polycrystalline Pt surface in aqueous solution consumes 0.21 mc/cm<sup>2</sup> of charge. This is of the same order as the 0.35-0.45 mc/cm<sup>2</sup> observed in these experiments.

### Summary

From the background *i-v* scans in propylene carbonate- $\text{LiClO}_4$  solutions, a reduction peak due to  $\text{H}_2\text{O}$  was identified at +1.4v vs.  $\text{Li/Li}^+$  (1M). The reduction peak at +0.4v is apparently due to the formation of a Li-Pt alloy.

The electrochemical behavior of trace quantities of water (1-30 millimolar) was investigated in detail *via* chronopotentiometry and cyclic voltammetry. It was observed that the chronopotentiometric constant increased with increasing current density up to a constant limiting value at high current densities. Analysis of the cyclic voltammetric results showed analogous behavior. These data can be interpreted in terms of a porous, insoluble film of  $\text{LiOH}$  formed by the reduction of water. This layer apparently acts to block part of the electrode surface thereby increasing the effective current density, decreasing  $\tau$  and hence  $i\tau^{1/2}$ .

From the concentration dependence of  $i\tau^{1/2}$  and of  $i_p/v^{1/2}$  it was further inferred that strong complexes were formed between water and  $\text{Li}^+$  ion which decreased the activity coefficient of  $\text{H}_2\text{O}$ . Current reversal subsequent to the reduction step showed an oxidation step which may be associated with an adsorbed film of atomic hydrogen on the platinum surface.

### Acknowledgments

The authors wish to thank both Dr. Raymond Jasinski for his helpful discussions and suggestions and Miss Susan Carroll for providing the distilled solvent. This work was carried out under Contract N00019-67-C-0680 for U. S. Navy Air Systems Command.

Manuscript submitted Feb. 12, 1968; revised manuscript received June 28, 1968. This paper was presented at the Boston Meeting, May 5-19, 1968, as Paper 206.

Any discussion of this paper will appear in a Discussion Section to be published in the June 1969 JOURNAL.

### REFERENCES

1. R. Jasinski, *J. Electroanal. Chem.*, **15**, 89 (1967).
2. R. Jasinski and S. Kirkland, *Anal. Chem.*, **39**, 1663 (1967).
3. A. N. Dey, *This Journal*, **114**, 823 (1967).
4. B. Burrows and R. Jasinski, *ibid.*, **115**, 365 (1968).
5. A. N. Frumkin and P. Delahay, "Advances in Electrochemistry and Electrochemical Engineering," Vol. 1, p. 95, Interscience, Inc., New York (1961).
6. K. M. Joshi, W. Mehl, and R. Parsons, "Trans. Symp. Electrode Processes," E. Yeager, Editor, John Wiley & Sons, New York (1961).
7. T. Reddy, Unpublished data, May (1967).
8. P. Delahay, "New Instrumental Methods in Electrochemistry," p. 119, Interscience, New York (1964).
9. A. J. Bard, *Anal. Chem.*, **33**, 11 (1961).
10. P. J. Lingane, *ibid.*, **36**, 1723 (1964).
11. A. J. Bard, *ibid.*, **35**, 340 (1963).
12. R. A. Craig and R. E. Richards, *Trans. Faraday Soc.*, **59**, 1972 (1963).

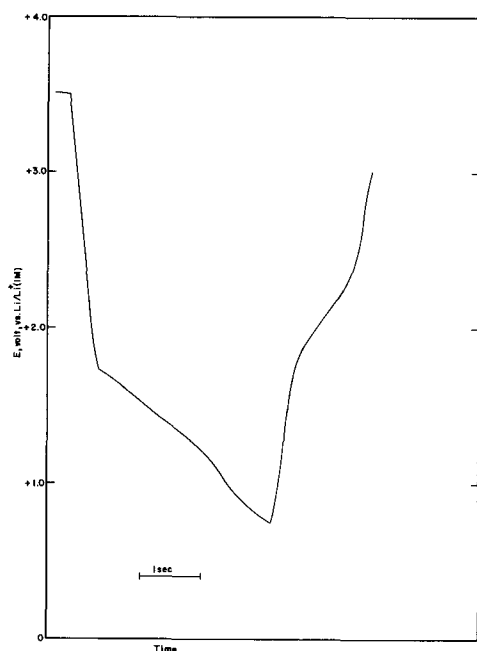


Fig. 7. Current-reversal chronopotentiogram in 1M  $\text{LiClO}_4/\text{PC}$  solution containing 200 ppm  $\text{H}_2\text{O}$ . Current density  $0.59$  ma cm<sup>-2</sup>.

13. G. A. Maciel *et al.*, *Inorg. Chem.* **5**, 554 (1966).  
 14. A. N. Frumkin, in P. Delahay, "Advances in Electrochemistry and Electrochemical Engineering,"

- Vol. 3, Interscience, New York (1963).  
 15. S. B. Brummer and J. I. Ford, *J. Phys. Chem.*, **69**, 1355 (1965).

# Technical Notes



## Further Studies on the Double Layer Capacitance of Zinc in KOH Solutions

T. P. Dirkse\*

Calvin College, Grand Rapids, Michigan

In a recent report dealing with the double layer capacitance (dlc) of zinc electrodes in KOH solutions (1), it was suggested that the lowering of this dlc may be related to improved cycle life of zinc electrodes, especially in silver-zinc batteries. Amalgamation, *e.g.*, which improves the cycle life of zinc electrodes, also brings about a reduction in the double layer capacitance. This work has been continued and further results are reported here. Furthermore, a recent report on the cycle life of silver-zinc cells (2) has made further comparisons possible.

### Experimental

The cell and general procedure was the same as that reported earlier (1). The method used to measure the dlc was the one described by McMullen and Hackerman (3). All measurements were made at room temperature, which was about 25°C.

### Results and Discussion

The first comparison that was made had to do with the effect of the purity of the zinc electrode. Two samples of zinc were used: one had a purity of 99.91% with lead the major impurity and about 0.01% iron; the other had a purity of 99.999%. These samples were compared in both 20% and 30% KOH, Fig. 1 and 2. The lower purity zinc does have a slightly lower dlc, and this seems more pronounced as the potential of the electrode becomes anodic. The following results were all obtained using only the higher purity zinc.

The effect of KOH concentration is shown on Fig. 3. The variation with changing KOH concentration is slightly different from that reported earlier (1), and it is believed that this may partly be due to the higher purity zinc used in this work.

Reference (2) contains results for the cycle life of silver-zinc cells which were cycled in a prescribed manner, the discharge portion of which is referred to as a 60% depth of discharge. Each cycle consisted of a 35-min discharge at 0.36 amp/in<sup>2</sup> followed by an 85-min charge at constant cell voltage which was regulated to provide about 2 or 3% overcharge.

Various surfactant materials were added to the zinc electrodes, and their effect on cycle life was noted. The cells did not fail because of shorting but because of a loss of negative capacity, *i.e.*, the zinc electrodes were no longer able to deliver the desired capacity during the prescribed discharge time. Samples of several of these additives were made available to us and these materials were added to 40% KOH in an

amount equal to 0.1% by weight. The dlc of the zinc electrode was then measured in each of these solutions.

The results obtained by using a series of Emulphogenes are shown on Fig. 4. These substances lowered the dlc of the zinc but by different amounts.

The effects of other additives are shown on Fig. 5. The effect of methacrylic acid in lowering the dlc of zinc was less in 30% KOH than in 40% KOH, and it had no effect on the dlc in 20% KOH. However, its solubility appeared to be greater in 20% than in 40% KOH.

Figure 6 illustrates the comparison between the effect of these additives in lowering the dlc of zinc and their effect in extending the cycle life of silver-zinc cells (2). The correlation, so far as it goes, is

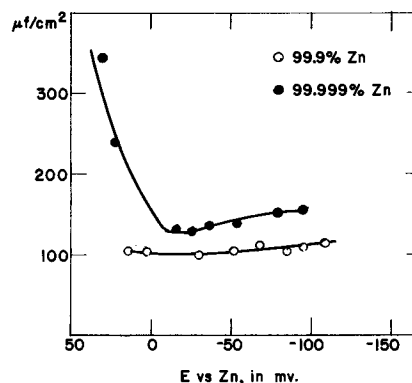


Fig. 1. Double layer capacitance of zinc in 30% KOH

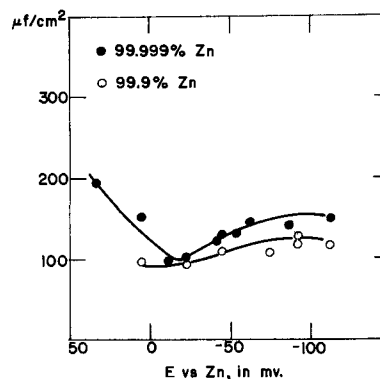


Fig. 2. Double layer capacitance of zinc in 20% KOH

\* Electrochemical Society Life Member.

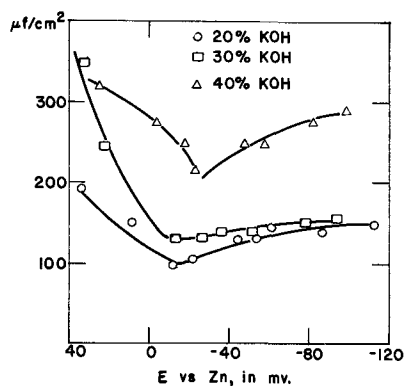


Fig. 3. Double layer capacitance of zinc at room temperature

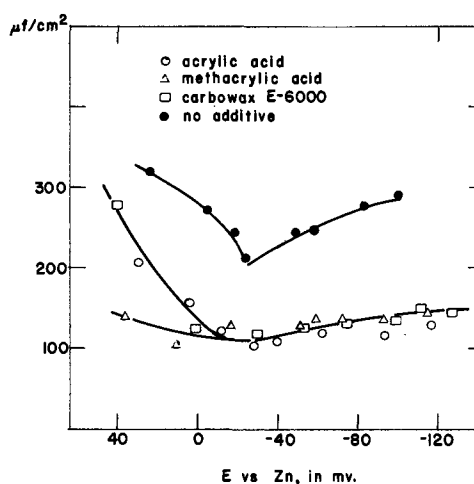


Fig. 5. Change in double layer capacitance of zinc due to additives in the 40% KOH electrolyte.

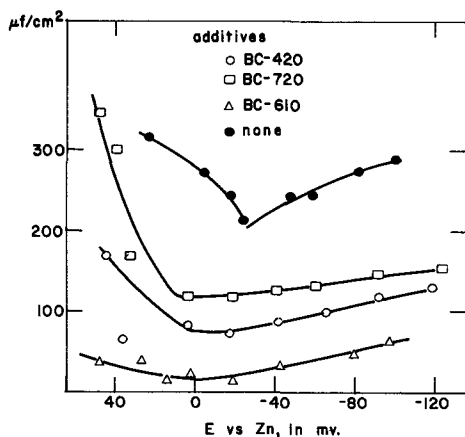


Fig. 4. Effect of some surfactants on the double layer capacitance of zinc in 40% KOH.

reasonably good. The dlc values on Fig. 6 are those at 0 mv on Fig. 4 and 5.

### Conclusions

The results reported here seem to provide added evidence for the suggestion made earlier (1) that additives which lower the dlc of a zinc electrode in KOH solutions also extend the cycle life of silver-zinc cells. Such additives, of course, must also be able to withstand the oxidation-reduction environment existing in such cycling cells. No evidence has been obtained to contradict the earlier suggestion that the effectiveness of these additives is due to their adsorption on the zinc electrode.

### Acknowledgment

This work was made possible by a research grant from the General Electric Company.

Manuscript submitted July 5, 1968; revised manuscript received Aug. 8, 1968.

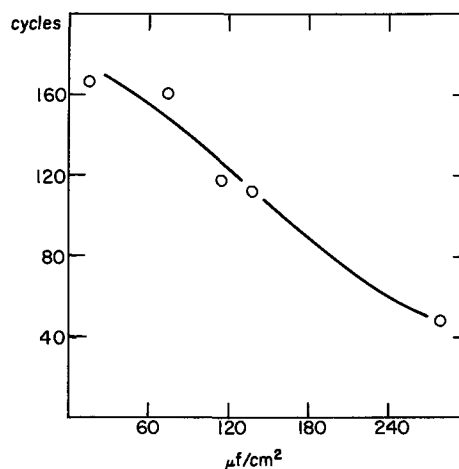


Fig. 6. Relationship of the double layer capacitance of zinc to the cycle life of silver-zinc cells, ref. (2).

Any discussion of this paper will appear in a Discussion Section to be published in the June 1969 JOURNAL.

### REFERENCES

1. T. P. Dirkse and R. Shoemaker, *This Journal*, **115**, 784 (1968).
2. J. J. Lander and J. A. Keralla, "Silver-zinc Electrodes and Separator Research," Report AFAPL-TR-67-107, 31 Aug. 1967, Contract AF 33-(615)-3487, Delco-Remy, Anderson, Ind.
3. J. J. McMullen and N. Hackerman, *This Journal*, **106**, 341 (1959).

## The Reaction of Aluminum with Molten Cryolite

R. J. Snow\*\* and B. J. Welch\*

School of Chemical Technology, University of New South Wales, Kensington, New South Wales, Australia

In this study we have found further information supporting the formation of Na(1,2) as the predominant reducing species when Al reacts with a  $\text{Na}_3\text{AlF}_6$  melt. The Na so formed has been found to enhance the volatilization of NaF from the melt suggesting that the Na exists as a  $\text{Na}_2^+$  cation in the melt and vaporizes as  $\text{Na}_2\text{F}$ . This is consistent with both

Grjotheim's (3) observation that Na is not formed as gas bubbles at the melt-metal interface and the proposal of Thonstad (4) for the solvolysis equilibrium.

This investigation involved simultaneously determining the change in weight of aluminum, weight of cryolite, and the NaF/ $\text{AlF}_3$  weight ratio of the melt. Subsequently each of the weight losses have been correlated with the ratio change for a fixed starting weight of melt. This approach differs from most of the

\*\* Electrochemical Society Student Associate Member.  
\* Electrochemical Society Active Member.

earlier studies which were of kinetic nature and usually neglected the changes induced on the melt by the solvolysis reaction. Being essentially a material balance it has the advantage that time can be eliminated as a dependent parameter thus removing end errors inherent in high temperature kinetic studies. Errors due to small temperature fluctuations are also minimized for the same reason.

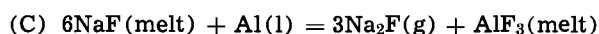
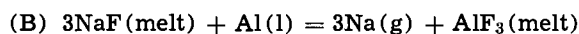
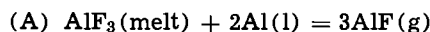
### Experimental

The reacting melt and metal were contained in a graphite crucible which was sheathed in an Inconel envelope and purified argon was passed over the crucible at a steady rate. The mixture was heated to 1020°C in a fixed zone of a resistance furnace and held at temperature for varying times. The melts were then quenched and physically separated so that weight changes of each could be determined. The NaF-to- $\text{AlF}_3$  weight ratio of resulting salt sample was then determined by pyrotitrations. For all measurements reproducible conditions of temperature and gas flow rate were employed. The results for starting reacting mixtures of 2g Al + 45g  $\text{Na}_3\text{AlF}_6$  are represented in Fig. 1 and 2.

The data presented have been corrected for changes resulting from vaporization of the melt ( $\text{NaAlF}_4$ ) in the absence of aluminum for the actual experimental melt composition range. In this way the experimental curves represent changes due only to the melt-metal reaction. (Because the ratio of NaF to  $\text{AlF}_3$  continually changes due to both the reaction and the vaporization processes, the correction curve for vaporization in absence of Al was determined for various weight ratios of NaF to  $\text{AlF}_3$ . The actual correction applied to the individual measurements was obtained by integrating the curve for the rate of vaporization between the initial and final compositions for the reaction period.) A small correction (0.02g) was also made for the residual dissolved metal in the melt at the end of the reaction. Because the degree of saturation of the melt was not known the correction applied was one half the saturation solubility of Al in pure cryolite (5). Possible errors due to this correction are less than the experimental accuracy of weight changes which are  $\pm 0.1\text{g}$ . The melt NaF-to- $\text{AlF}_3$  ratio was determined with an accuracy of  $\pm 0.02$  (wt/wt).

### Discussion

The experimental curves have been compared with the curves that would correspond to loss according to each of the following over-all solution and vaporization reactions:



That is, the reducing species escaping from the melt would be  $\text{AlF}$ , Na, or  $\text{Na}_2\text{F}$ .

$\text{AlF}$  formation has been established by studies of the reaction between Al and  $\text{AlF}_3$  (6) while the proposals for formation of Na (1) and  $\text{Na}_2\text{F}$  (4) have been mentioned earlier. Diffusion calculations (7) from reoxidation kinetics (8) show that it is unlikely that Al forms a pyrosol in the fused salt while the above three are the only other solvolysis products probable. Although aluminum could undergo a side reaction by reacting with graphite to form aluminum carbide, tests on the crucibles used showed that this did not occur to a measurable extent during the duration of the experiments.

From the results shown in Fig. 1 (ratio change as a function of salt loss) the curve shows closest agreement with the theoretical curve for  $\text{Na}_2\text{F}$  loss.

In Fig. 2 we find the experimental curve agrees with a second escape mechanism, namely, evolution of Na. While the two curves are conflicting they show clearly that the metal loss cannot be as  $\text{AlF}$  alone.

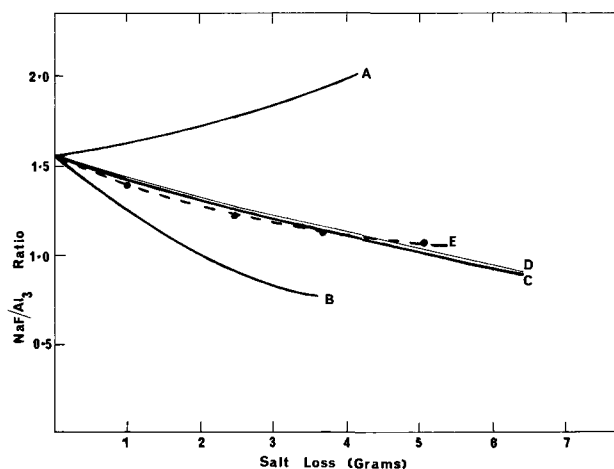


Fig. 1. Change in NaF/ $\text{AlF}_3$  weight ratio as a function of salt loss: A, theoretical curve for vaporization of  $\text{AlF}$ ; B, theoretical curve for vaporization of Na; C, theoretical curve for vaporization of  $\text{Na}_2\text{F}$ ; D, theoretical curve for vaporization of 30%  $\text{AlF}$  and 70%  $\text{Na}_2\text{F}$ ; E, corrected experimental curve.

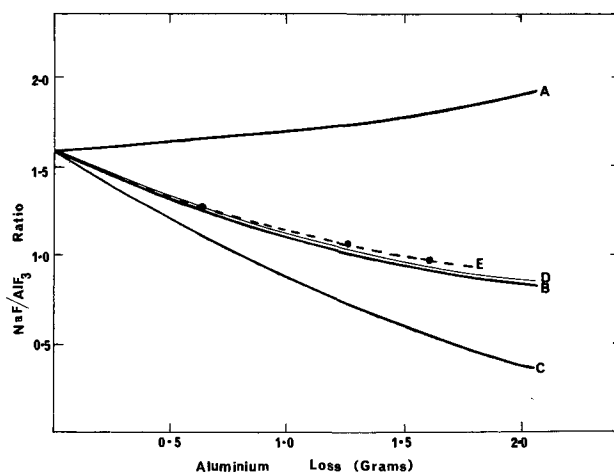
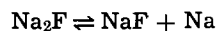


Fig. 2. Change in NaF/ $\text{AlF}_3$  weight ratio as a function of Al loss: A, theoretical curve for vaporization of  $\text{AlF}$ ; B, theoretical curve for vaporization of Na; C, theoretical curve for vaporization of  $\text{Na}_2\text{F}$ ; D, theoretical curve for vaporization of 30%  $\text{AlF}$  and 70%  $\text{Na}_2\text{F}$ ; E, corrected experimental curve.

In an attempt to resolve the discrepancy between the two correlations, various combinations of two simultaneously vaporizing species have been tried. Agreement for both experimental curves is obtained only if the metal loss is attributed to both  $\text{AlF}$  and  $\text{Na}_2\text{F}$  in the proportions of approximately 30%  $\text{AlF}$  to 70%  $\text{Na}_2\text{F}$ . The theoretical curves (D) for this composition are also included on the diagrams.

This explanation is consistent with Haupin's findings (2) and also the equilibrium proposed by Thonstad (4). That the Na volatilizes as  $\text{Na}_2\text{F}$  is supported by our finding that the melt becomes more volatile in the presence of Al, and when the condensate is examined by x-ray diffraction it is found that there has been a considerable increase in NaF content.

This would result in dissociation according to the scheme



which would have to favor the right-hand side as the temperature is reduced. Such an explanation would be consistent with Stokes and Franks (1) vapor studies.

To check our findings additional experiments have been carried out using different initial proportions of Al to the cryolite. Although the rate of reaction changed with the different proportions, in all cases

the data were consistent with the experimental curves of Fig. 1 and 2. This supports the suggested proportions of volatilizing species.

Manuscript submitted March 27, 1968; revised manuscript received ca. July 9, 1968.

Any discussion of this paper will appear in a Discussion Section to be published in the June 1969 JOURNAL.

#### REFERENCES

1. J. J. Stokes, Jr., and W. B. Frank in "Extractive Metallurgy of Aluminum," G. Gerard, Editor,

Vol. 2, p. 3, Interscience Publishers, Inc., New York (1963).

2. W. E. Haupin, *This Journal*, **107**, 232 (1960).

3. K. Grjotheim, *Kgl. Norske Videnskab. Selskabs, Skrifter* No. 5 (1956).

4. J. Thonstad, *This Journal*, **111**, 959 (1964).

5. J. W. Tomlinson, Private communications.

6. W. P. Witt and R. F. Barrow, *Trans. Faraday Soc.*, **55**, 730 (1959).

7. W. B. Frank, *This Journal*, **112**, 649 (1965).

8. S. Gjerstad and B. J. Welch, *ibid.*, **111**, 976 (1964).

## The Diffusion Coefficients of Hypochlorite, Hypochlorous Acid, and Chlorine in Aqueous Media by Chronopotentiometry

M. S. Chao\*

The Dow Chemical Company, Midland, Michigan

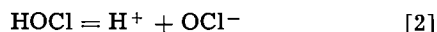
In describing the hydrodynamic conditions of the manufacture of chlorate, the diffusion coefficients of its precursors, hypochlorite and hypochlorous acid, will be expected to be important factors. A search of the literature shows that no such data have been reported. Chemically, hypochlorite and hypochlorous acid are related to chlorine through hydrolysis. The published diffusion coefficient of chlorine has been inconsistent and limited in temperature range (1-3). Therefore, it seems logical that the diffusion coefficients of these three species be studied as a group. Besides, the inclusion of values on chlorine will be of use to the related electrochemical process other than chlorate manufacture, such as the production of chlorine.

The present investigation utilized chronopotentiometry to determine the diffusion coefficients. In this instance the Sand equation is applicable

$$D^{1/2} = \frac{2 i \tau^{1/2}}{\pi^{1/2} n F A C} \quad [1]$$

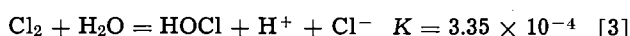
where  $D$  is the diffusion coefficient ( $\text{cm}^2/\text{sec}$ ),  $\tau$  the transition time (sec),  $C$  the concentration ( $\text{mol}/\text{cm}^3$ ) of the electroactive species in the bulk,  $i$  the electrolysis current (amp),  $F$  the Faraday,  $A$  the electrode area ( $\text{cm}^2$ ), and  $n$  the number of Faradays per molar unit of reaction (4). For the reduction processes used in the present study,  $n$  is equal to 2 for chlorine and hypochlorite (5), and is presumably the same for hypochlorous acid.

The dissociation constant of hypochlorous acid



has been cited in Mellor as between  $3 \times 10^{-8}$  and  $4 \times 10^{-8}$  (6). By choosing buffers of proper pH: phosphate (pH 6.10) or carbonate (pH 10.0) either hypochlorous or hypochlorite will be the predominant species.

The hydrolysis of chlorine is governed by the following equilibria with  $K$ 's at 25°



By using a solution 0.975*N* in  $\text{HClO}_4$  and 0.025*N* in  $\text{HCl}$ , the ratio of  $\text{HOCl}$  and  $\text{Cl}_3^-$  to  $\text{Cl}_2$  is approximately 1% (7). It is assumed that at higher temperature the composition of the solution does not change significantly.

\* Electrochemical Society Active Member.  
Key words: chlorine, chronopotentiometry, diffusion coefficient, diffusivity, hypochlorite, hypochlorous acid.

#### Experimental

The electrolysis cell was a 300 ml beakless beaker with a Teflon cover, into which the electrodes and a thermometer were inserted. The working electrode was a shielded platinum disk electrode according to Bard (8). Its geometrical area as calibrated with a  $\text{Fe}^{+3}$  solution by chronopotentiometry (9) was  $0.268 \text{ cm}^2$ , in good agreement with the  $0.267 \text{ cm}^2$  measured by photomicrography. The counter electrode, a spectrographic graphite rod, was enclosed in a glass frit of medium porosity. The reference electrode consisted of a salt bridge and a commercial saturated calomel electrode. The cell was thermostated to  $0.1^\circ\text{C}$ .

The constant current was derived from the +300v output of a Heathkit Operational Amplifier Manifold and a series of dropping resistors. An L&N pH meter (Model 7401) connected to a Sargent Model SR recorder with a chart speed of 12 in./min recorded the chronopotentiograms.

Chlorine of purity 99.8% was obtained from the Dow Chemical Company. Chloride-free lithium hypochlorite, the source for hypochlorite or hypochlorous acid, was prepared from reagent chemicals by W. G. Moore of this laboratory. All the rest of the chemicals were reagent grade. The phosphate and carbonate buffers, as well as the  $\text{HClO}_4 - \text{HCl}$  mixture, all had an ionic strength of unity.

The concentration of the electroactive species was analyzed by the usual KI-thiosulfate titration in acetic acid medium. The viscosity of the solution was determined with a modified Ostwald viscometer.

#### Results and Discussion

Typical chronopotentiograms of hypochlorite, hypochlorous acid, and chlorine are shown in Fig. 1. The transition times were determined by Kuwana's method (10). The  $i\tau^{1/2}$  products remained constant over a 2-3-fold change in current density, indicating the processes are diffusion controlled. Following the reduction of the soluble species, the surface oxides of platinum were also reduced. Because of the complex natures of these oxides, no attempt was made to study them.

The diffusion coefficients of hypochlorite and hypochlorous acid are shown in Fig. 2. Allowing for convection and other uncertainties the precision is estimated at 2-5%. The linear relationship between  $\log D$  ( $\text{cm}^2/\text{sec}$ ) and the reciprocal absolute temperature can be represented by an equation of the form

$$\log D = -a \times 10^3 \times \frac{1}{T} - b \quad [5]$$

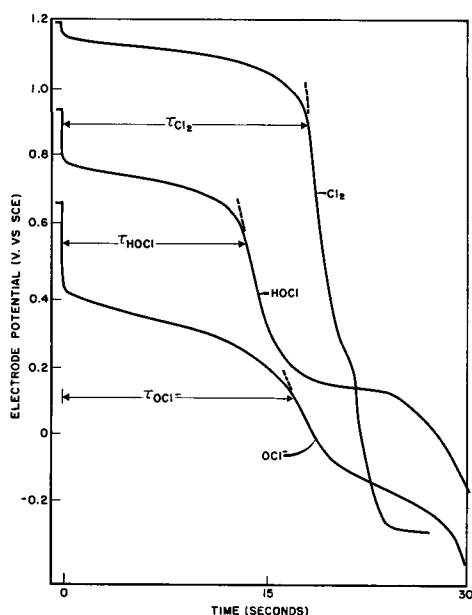


Fig. 1. Typical chronopotentiograms of hypochlorite, hypochlorous acid, and chlorine.

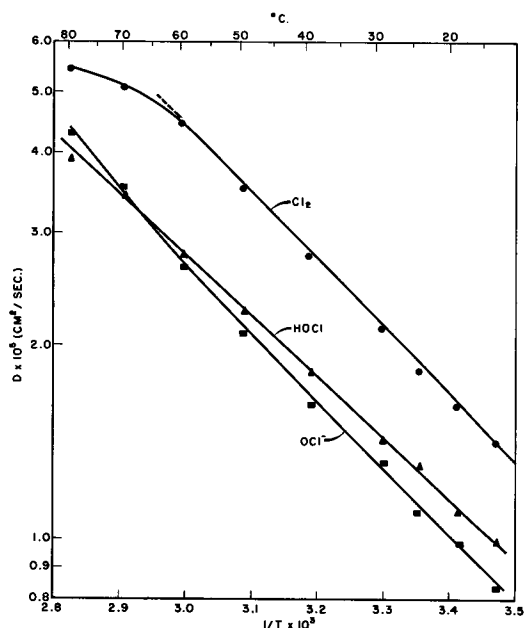


Fig. 2. Diffusion coefficients of hypochlorite, hypochlorous acid, and chlorine.

for hypochlorite,  $a = 1.06$  and  $b = 1.40$ ; for hypochlorous acid,  $a = 0.945$  and  $b = 1.72$ .

The diffusion coefficient of chlorine is also shown in Fig. 2. The volatility of chlorine may be one major source of error. The precision is estimated at 5% for values below 60°C and 10% above that. Compared with the data by other workers (Fig. 3), the present values are generally higher by a few per cent. The low value of Hüfner at 16°C, determined in 1897, was cited by the International Critical Tables as "too low" (1). The low value of Vivian and Peaceman (2) was determined in HCl, formation of  $\text{Cl}_3^-$  according to Eq. [4] may have taken place to some extent. It is of interest to note that the diffusion coefficient of hypochlorous acid is about 25% of that of chlorine. Therefore, failure on the part of the earlier workers to suppress the hydrolysis may lead to a lower value. However, considering the variety of techniques used by different workers, the agreement can be considered satisfactory.

The straight line portion (between 15° and 60°C) of the  $\log D$  vs.  $1/T$  plot may again be represented by

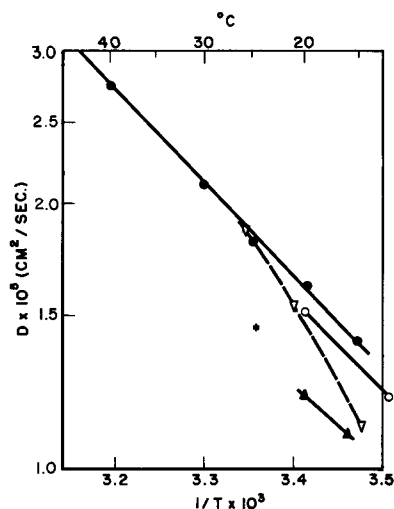


Fig. 3. Diffusion coefficient of chlorine by various workers: ● present study; ○ Euler (1897); ▲ Hüfner (1897); \* Vivian and Peaceman (1956); ▽ Davidson and Cullen (1957).

Eq. [5] with  $a = 1.09$  and  $b = 1.08$ .

The activation energy for diffusion may be estimated according to the following equation.

$$D = A \exp(-E/RT) \quad [6]$$

where  $A$  is a constant. The value of  $E$  is 4.9 kcal/mole for hypochlorite, 4.3 kcal/mole for hypochlorous acid, and 5.1 kcal/mole for chlorine.

According to the Stokes-Einstein law (11) the product of the viscosity ( $\eta$ ) and the diffusion coefficient ( $D$ ) is constant for spherical uncharged particles. As shown in Fig. 4, the  $D\eta$  product approaches a constant value in solutions of ionic strength greater than 1.5. The  $D\eta$  product at unit ionic strength is within 10% of those for a large range of concentrations. Therefore, approximate values of the diffusion coefficient in

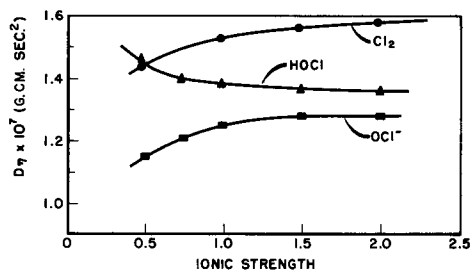


Fig. 4. Viscosity-diffusion coefficient products at 25°C as a function of ionic strength.

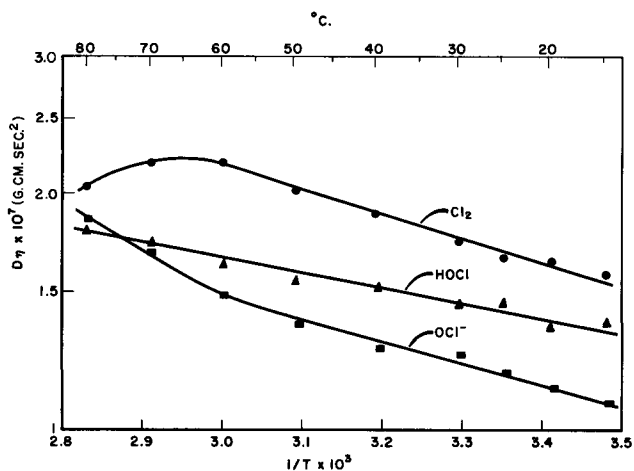


Fig. 5. Viscosity-diffusion coefficient products at unit ionic strength as a function of temperature.

various media may be calculated from the  $D\eta$  product at unit ionic strength, provided the viscosity of the medium has been determined. The data in Fig. 5 may be used for this purpose.

Manuscript submitted May 8, 1968; revised manuscript received ca. Aug. 1, 1968.

Any discussion of this paper will appear in a Discussion Section to be published in the June 1969 JOURNAL.

#### REFERENCES

1. International Critical Tables, Vol. V, p. 63, McGraw-Hill Book Co., New York (1928).
2. J. E. Vivian and D. W. Peaceman, *A. I. Ch. E. Journal*, **2**, 437 (1956).
3. J. E. Davidson and E. J. Cullen, *Trans. Inst. Chem. Engrs.*, **35**, 51 (1957).
4. J. J. Lingane, "Electroanalytical Chemistry," 2nd ed., p. 620, Interscience Publishers, New York (1958).
5. L. Meites, "Polarographic Techniques," 2nd ed., pp. 618-9, Interscience Publishers, New York (1965).
6. "Mellor's Comprehensive Treatise on Inorganic and Theoretical Chemistry," Suppl. II, p. 544, Longmans, Green & Co., New York (1956).
7. G. Zimmerman and F. C. Strong, *J. Am. Chem. Soc.*, **79**, 2063 (1957).
8. A. J. Bard, *Anal. Chem.*, **33**, 11 (1961).
9. S. Bruckenstein and T. O. Rouse, *ibid.*, **36**, 2039 (1964).
10. C. D. Russel and J. M. Peterson, *J. Electroanal. Chem.*, **5**, 467 (1963).
11. R. A. Robinson and R. H. Stokes, "Electrolyte Solutions," 2nd ed., p. 12, Butterworths, London (1959).



# On the Effect of Ultraviolet and X-ray Irradiation of Phosphors

George T. Bauer

Research Laboratories, Xerox Corporation, Rochester, New York

## ABSTRACT

The effect of long term ultraviolet and x-ray irradiation on the luminous efficiency, reflectance, and glow curves of several inorganic phosphors were measured. It was found that the decrease of their luminous efficiency caused by irradiation was always accompanied with an increased absorption in the uv and in the visible regions of the spectra. The depreciation of x-rayed phosphors could in most cases partially, and in several phosphors fully, be interpreted in terms of the absorbing effect of centers produced by the irradiation. However, in phosphate types and in magnesium germanate phosphors an additional process contributes to their depreciation. This process is related to the appearance of new peaks on their glow curves. The observed wavelength dependence of the loss in luminous efficiency was measured for several phosphors and in each case could be attributed to color center absorption. The x-ray and uv irradiation resulted qualitatively in the same type of changes in the measured optical data.

It has long been known that the luminescent intensity of phosphors decreases as a result of long term excitation. The depreciation appears for every form of the excitation (i.e., uv, x-rays, cathode rays, or electroluminescence) and often causes a serious problem in certain practical applications. Certain physical and chemical changes caused by uv irradiation of phosphors have been well discussed in the literature (1). A relatively new finding is that in phosphate base materials (2), in activated phosphate phosphors (3, 4), and single crystals (5), color centers are produced when irradiated by x-rays or uv. Some of these centers could be identified from different optical, epr, and ENDOR (6) studies on single crystals. It is believed that one of the main causes of the depreciation of the phosphors is the absorption by color centers of both a part of the exciting energy and a part of the light emitted by the luminescence centers (4).

The relation between color center formation and depreciation has up to now been studied chiefly on phosphate-type phosphors while relatively little data are available for other phosphors. In this work we study certain optical changes which accompany the depreciation of phosphors when irradiated by uv or x-rays. One of the main purposes of the study has been to determine more quantitatively how the absorption of color centers produced by irradiation influence the efficiency of the photoluminescence of the phosphor, and to separate the different processes which result in depreciation. All but one of the phosphors studied were commercial products (Table I).

## Experimental Methods

Previous studies (1, 3, 4) have shown that the luminous efficiency reflectance and glow curves of a number of powder phosphors change on uv or x-ray irradiation. We have completed measurements of these changes on the phosphors listed in Table I. The measurement of the wavelength dependence of relative luminous efficiency of the irradiated phosphors has also provided useful information.

The uv irradiation of the phosphors was carried out in a closed box in nitrogen or air using a low-pressure mercury discharge lamp with a dynasil quartz envelope as radiation source. In the spectral distribution of the lamp, the 2537Å mercury resonance line is dominant; however, a portion of the 1849Å radiation is also passed through the envelope. The phosphor layers were 2 mm thick and were placed in a brass substrate close to the lamp. The intensity of radiation at the surface of the phosphor measured

for 1849 + 2537Å wavelength was  $5000 \mu\text{wcm}^{-2}$ . For studying the effect of x-rays, the samples were irradiated in a Phillips apparatus by 50 keV, 40 ma tungsten x-rays.

The diffuse reflectance measurements were made using a Spex No. 1700-II Czerny-Turner spectrometer with a Sylvania DE350 deuterium lamp as radiation source. For measurement of the reflectance in the visible region, suitable Corning uv absorbing, visible transmitting filters were placed in front of the lamp in order to avoid the excitation of the phosphors. A thick magnesium oxide layer was used as standard.

The plaque brightness of the excited phosphors was measured using a Gamma photometer with an RCA 931A photomultiplier as sensor. The phosphors were excited by a low-pressure mercury discharge lamp through two 2-mm thick Corning U.G. 5 filters. A 2-mm thick Corning CS3-71 filter was set before the photomultiplier to absorb the uv radiation reflected from the phosphor surface. The measurements were relative: the plaque brightnesses of the irradiated samples were compared to those of the unirradiated ones. Because the spectral distribution of the luminescence of the phosphors was found to be not significantly affected by the irradiation, the spectral response of the multiplier-filter combination did not play a role in the measurements. A Hilger Watts Grating monochromator D292 with a deuterium lamp as radiation source was used to measure the excitation spectra. The thermoluminescence measurements were carried out from 25° to 400°C using a special furnace with a heating rate of  $0.5^\circ\text{C sec}^{-1}$ . For the detection of the emitted light of the phosphors, an RCA IP21 photomultiplier Corning CS3-71 filter combination has been used.

## Results

*Effect of irradiation on the diffuse reflectance of phosphor layers.*—The following three series of diffuse reflectance measurements were carried out: (a) after 100 hr of uv irradiation in nitrogen atmosphere; (b) after 16 hr x-raying; and (c) after 16 hr x-ray plus thermal bleaching the phosphors for 1 hr at 400°C. Figures 1 and 2 show the ratio of the diffuse reflectance  $R_i(\lambda)$  of the irradiated phosphors to that of unirradiated samples,  $R(\lambda)$ . This type of representation could indicate the appearance of narrow absorption bands in the irradiated samples (4). It should be noted that the penetration depth of the x-rays is significantly higher than that of the 1849-2537Å radiation. Thus, the reflectance data of x-rayed samples

Table I. Relative luminous efficiency of various irradiated phosphors excited at 2537Å

Activator	Source	Li/L After 100 hr uv irradiation	Li/L After 16 hr x-raying	Li/L After 16 hr x-raying + 1 hr bleaching at 400°C	m	m <sub>0</sub>	
Calcium halophosphate (cool white)	Mn, Sb	Xerox	0.85	0.55	0.91	0.63	0.84
Barium titanium phosphate	Sn	Sylvania	0.97	0.50	0.98	0.6	0.87
Strontium pyrophosphate	Sn	Sylvania	0.91	0.48	0.85	0.63	0.88
Strontium magnesium phosphate	Sn	Westinghouse	0.95	0.63	0.99	0.71	0.94
Calcium tungstate	Pb	Westinghouse	0.96	0.83	1.0	0.86	0.88
Magnesium fluorogermanate	Mn	Westinghouse	0.88	0.74	1.0	0.74	0.9
Zinc silicate	Mn, Pb, As	Westinghouse	0.78	0.89	0.93	0.94	0.93
Calcium silicate	Mn, Pb	Westinghouse	0.86	0.68	0.97	0.76	0.85
Cadmium borate	Mn	Westinghouse	0.94	0.94	1.0	0.94	0.95

cannot be directly compared to that of the uv irradiated ones.

Figures 1 and 2 show that, in most cases, the reflectance of the phosphors was decreased (*i.e.*, the absorbance increased) due to the x-ray or uv irradiation. The reflectance of the barium titanium phosphate showed no changes when irradiated by uv and the effect was very small in the case of calcium tungstate. Generally, wide absorption bands are introduced by the irradiation showing some structure in certain cases. The change in the reflectance (except in magnesium germanate) is greater in the uv than in the visible part of the spectrum. The absorption bands of the x-rayed samples partially or completely disappeared after heating for 1 hr at 400°C. Bleaching was more complete for the visible than for the uv reflectance.

*Effect of radiation on the luminous efficiency of the phosphors.*—The relative luminous efficiency of the phosphors can be determined from the relative plaque brightness and from their reflectance at the wavelength of the excitation. Let the plaque brightness of

the unirradiated and irradiated samples be  $I$  and  $I_i$ , respectively. Then the relative luminous efficiency of the irradiated sample with respect to the unirradiated is (7)

$$\frac{L_i}{L} = \frac{I_i}{I} \cdot \frac{1 - R(\lambda)}{1 - R_i(\lambda)} \quad [1]$$

Measurements were made using the above described mercury discharge lamp for excitation after (a) 100 hr uv irradiation, (b) 16 hr x-raying, (c) 16 hr x-raying and bleaching at 400°C for 1 hr. Because the greatest part of the uv energy was emitted by the lamp at 2537Å, the reflectance measured at this wavelength was applied for the calculations. The results are shown in Table I. Comparing the results to those of the reflectance measurements (Fig. 1 and 2), it can be seen that the depreciation of phosphors is always associated with an increase in their absorbance. After thermal bleaching which results in the recovery of the luminous efficiency of the phosphors (Table I), the absorption bands also become weak.

The relative luminous efficiency of the x-ray or uv irradiated phosphor was found to be dependent on the wavelength of the excitation. This wavelength dependence was measured for five phosphors after 16 hr x-ray irradiation. Results are shown in Fig. 3 and 4.

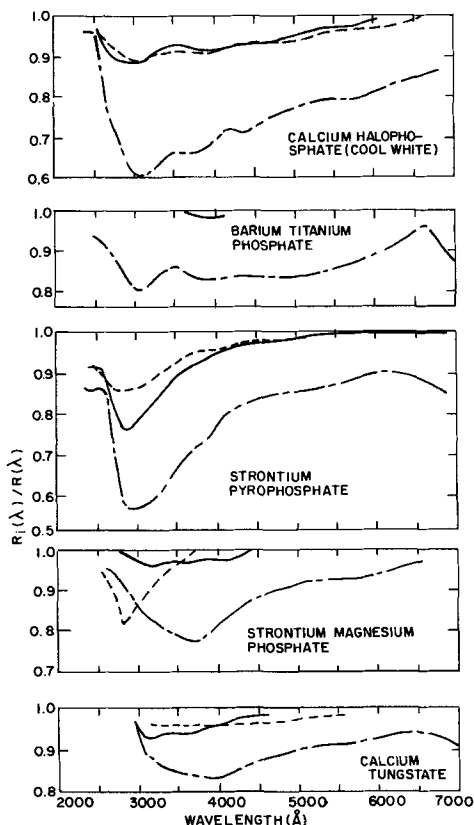


Fig. 1. Relative diffuse reflectance of irradiated phosphors compared with the unirradiated samples: — after 16 hr x-ray irradiation; — — after 16 hr x-ray irradiation and 1 hr bleaching at 400°C; - · - after 100 hr uv irradiation.

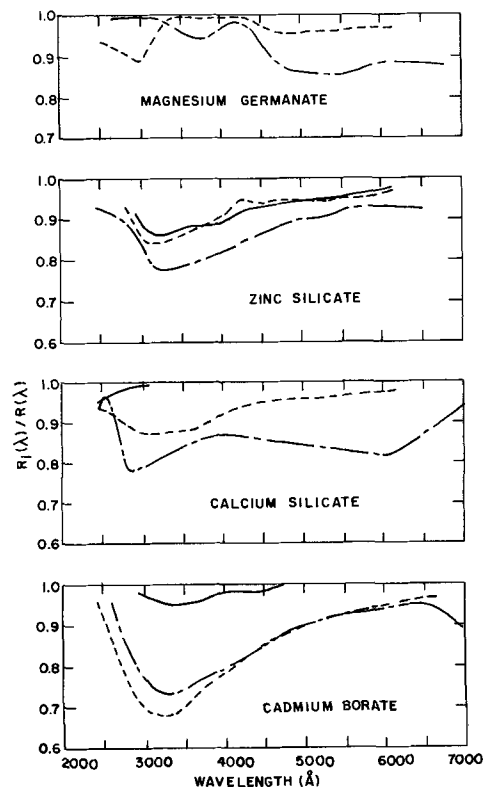


Fig. 2. Same as Fig. 1

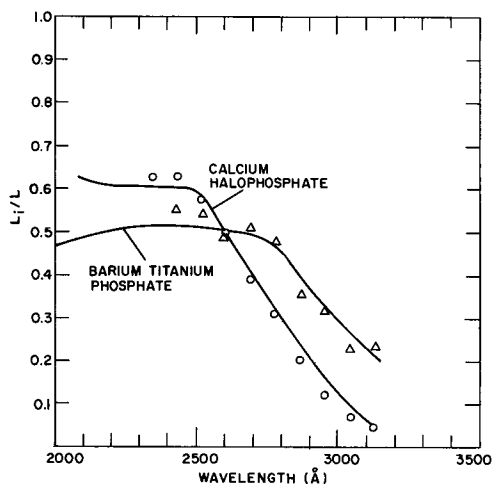


Fig. 3. Wavelength dependence of the relative luminous efficiency of irradiated phosphors compared with the unirradiated samples. Lines indicate measured quantities; points are calculated values based on Eq. [4] with  $m$  parameters shown in Table I.

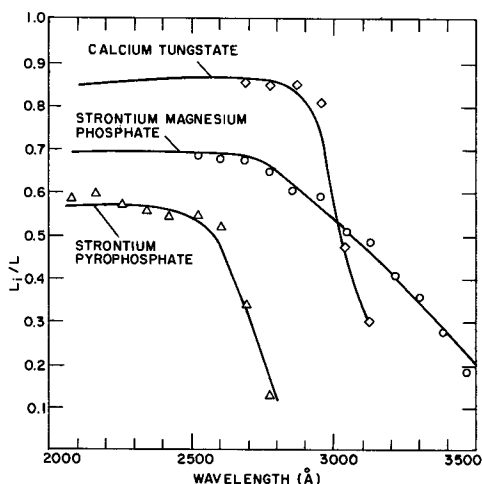


Fig. 4. Same as Fig. 3

**Thermoluminescence.**—The following three series of measurements were carried out: (a) after 10-min uv irradiation in the above described chamber in air, (b) after 100-hr uv irradiation in nitrogen atmosphere, and (c) after 2 hr of x-ray irradiation. Figures 5, 6d and 6f show that in phosphate-based phosphors and magnesium germanate, new glow peaks, not present after 10 min of uv irradiation, appear due to the long term uv or x-ray irradiation. The glow curves of the x-rayed and uv irradiated phosphors are very similar. In calcium tungstate and in cadmium borate, similar glow curves were observed after 10 min and after 100 hr uv irradiation. These glow curves differ chiefly in their intensities. However, the glow curves of the x-rayed samples of these phosphors were somewhat different. In silicates, there were no new glow peaks induced by the long term uv or x-ray irradiation (Fig. 7).

#### Calculation of Effect of Absorption of Color Centers on the Luminous Efficiency of Phosphors

The measurements indicate that in the x-rayed phosphors a part of the exciting uv energy and of the emitted light is absorbed in color centers induced by the irradiation. When discussing this effect quantitatively, we assume that the activator concentration in the high efficiency phosphors studied is small, i.e., far from the level where concentration quenching (8) becomes important. It is further assumed that the phosphors contain only a negligible quantity of im-

purities. A part of the exciting radiation is absorbed in the activator centers having concentration  $C$  and average capture cross section  $\sigma(\lambda)$ . Another part is absorbed in color centers with concentration  $C_i$  and average capture cross section of  $\sigma_i(\lambda)$ . The exciting uv energy absorbed in the activators of the x-ray treated phosphors is converted into light energy which leaves the phosphor layer with an efficiency of  $m_a$ . In the untreated phosphors this efficiency is  $m_o$ . We assume that the color centers either give rise to radiationless transitions or they emit the absorbed energy outside of the phosphor's emission band. Let  $a_i(\lambda)$  be the absorption coefficient of the x-ray treated, and  $a(\lambda)$  that of the untreated phosphor, and let  $m_a/m_o = m$ . Then the relative luminous efficiency of the irradiated phosphor layer is

$$\frac{L_i}{L} = m \frac{C \cdot \sigma(\lambda)}{C \cdot \sigma(\lambda) + C_i \sigma_i(\lambda)} = m \cdot \frac{a(\lambda)}{a_i(\lambda)} \quad [2]$$

The absorption coefficient of phosphors can be calculated to a good approximation from the diffuse reflectance of their quasi infinite thick layer (9)

$$a(\lambda) = \frac{1}{l} \frac{\alpha(\lambda)}{1 - \alpha(\lambda)} \cdot \frac{[1 - R(\lambda)]^2}{R(\lambda)} \quad [3]$$

where  $\alpha(\lambda)$  is the Fresnel reflection and  $l$  is the average particle size. Since the penetration depth of x-rays is considerably larger than that of optical rays, the absorption coefficient of the x-rayed phosphor layers may be considered as homogeneous from the viewpoint of absorption measurements. From Eq. [2] and [3]

$$\frac{L_i}{L} = m \cdot \frac{R_i(\lambda) [1 - R(\lambda)]^2}{R(\lambda) [1 - R_i(\lambda)]^2} \quad [4]$$

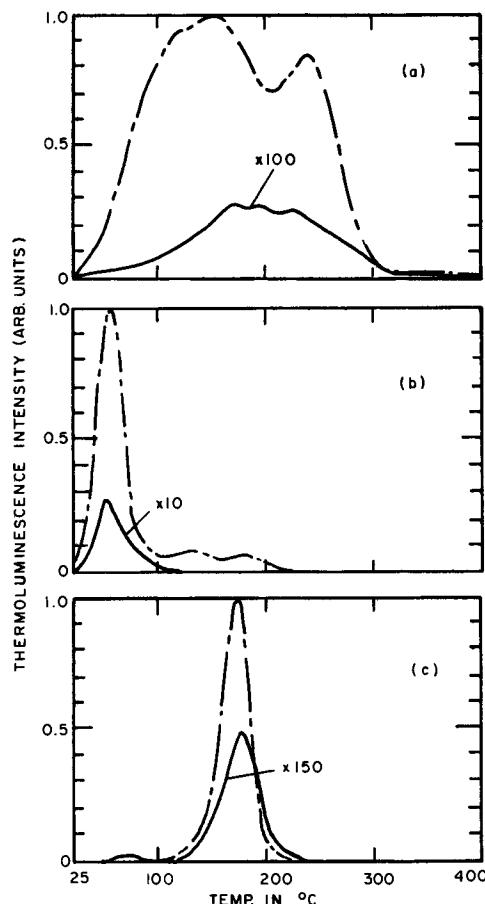


Fig. 5. Glow curves of phosphors: --- after 10 min uv irradiation; — after 100 hr uv irradiation; - · - after 2 hr x-ray irradiation. (a) calcium halophosphate, (b) barium titanium phosphate, (c) strontium pyrophosphate.

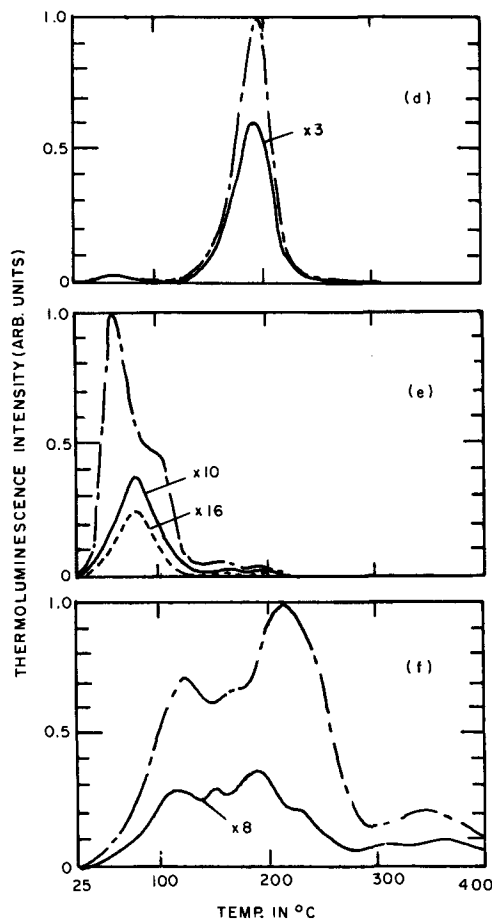


Fig. 6. Glow curves of phosphors: (d) strontium magnesium phosphate, (e) calcium tungstate, (f) magnesium fluorogermanate.

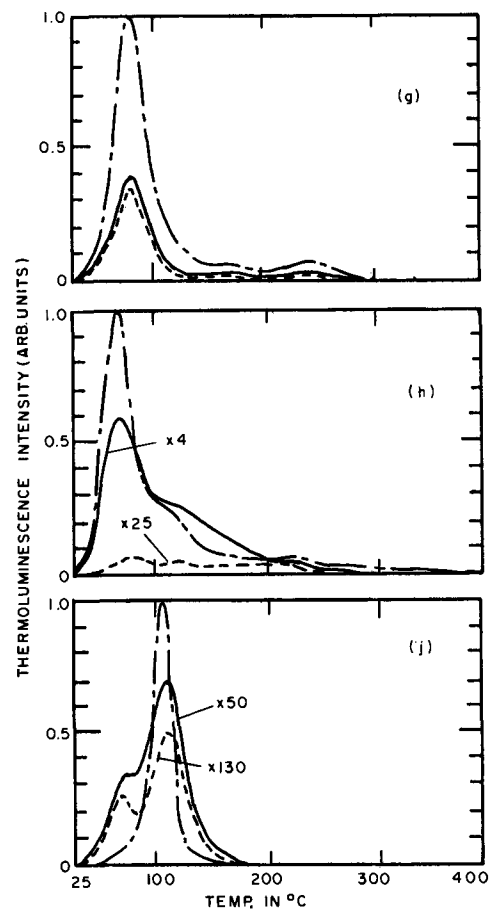


Fig. 7. Glow curves of phosphors: (g) zinc silicate, (h) calcium silicate, (j) cadmium borate.

The luminous efficiency and diffuse reflectance measurements permitted a determination of  $m$  by means of Eq. [4]. Values of  $Li/L$  calculated from the reflectance data and the  $m$  values given in Table I are compared to the measured luminous efficiency curves in Fig. 3 and 4. Very reasonable fits are obtained. In the cases of the magnesium fluorogermanate, cadmium borate, and the silicate phosphors the luminous efficiency was measured only at  $\lambda = 2537\text{\AA}$  excitation and these results were used for determination of  $m$ .

Since the value of  $m$  was found to be less than unity for all of the phosphors studied, then it must follow that the activators in the irradiated phosphors convert the absorbed energy into the output light leaving the layer with less efficiency than before the irradiation. This could be attributed either to the self-absorption of the emitted light in the phosphor layer or to a decrease of the intrinsic efficiency of the luminescent centers.

In order to estimate the loss in the layer due to the self-absorption, we assume on the basis of the reflectance measurements and Eq. [3] that the exciting uv radiation is absorbed in a thin layer of the phosphors. The absorption of this layer at the wavelength of the emission range of the phosphors is practically negligible since  $l \cdot a(\lambda)$  is small. One half of the  $S_i$  luminescent light flux produced in the excited layer leaves the layer in the direction of the source of the excitation (Fig. 8) while the other half leaves in the opposite direction. Taking into account the reflections shown on Fig. 8, the total luminescent light flux leaving the phosphor in the direction of the source of excitation is

$$G_i = \frac{S_i}{2} \frac{1 + R_i(\lambda_v)(2t - 1)}{1 - R_i(\lambda_v)(1 - t)} \quad [5]$$

where  $R_i(\lambda_v)$  is the average reflectance of the x-rayed quasi-infinite thick phosphor layer in its emission

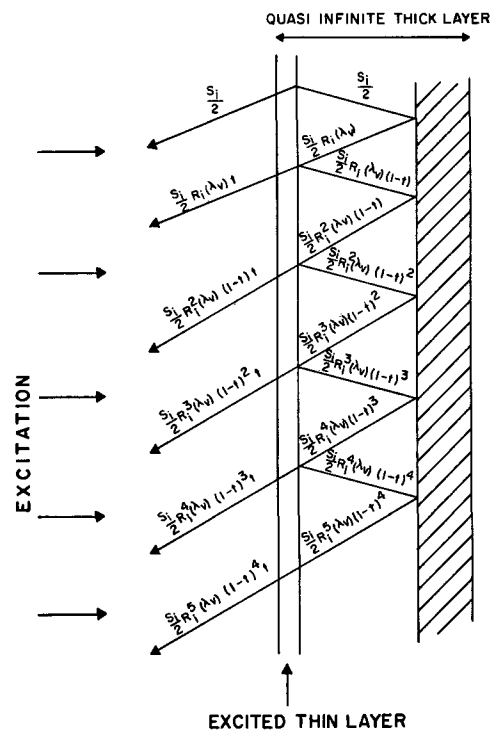


Fig. 8. Model for the calculation of the loss caused by the self-absorption of the emitted light within the phosphor layer.

range and  $t$  is the transmittance of the excited thin layer in the same range. Calculating only the effect of self-absorption it is assumed that the  $S_i$  luminescent light flux produced in the excited thin layer is the same in the irradiated and in the unirradiated phos-

phors. Comparing the  $G_i$  light flux emitted from the x-rayed phosphor to the  $G$  light flux emitted from the untreated one (from Eq. [5])

$$m_v = \frac{G_i}{G} = \frac{1 - R(\lambda_v)(1-t) + R_i(\lambda_v)(2t-1) - R(\lambda_v)R_i(\lambda_v)(2t-1)(1-t)}{1 - R_i(\lambda_v)(1-t) + R(\lambda_v)(2t-1) - R(\lambda_v)R_i(\lambda_v)(2t-1)(1-t)} \quad [6]$$

where  $m_v$  is the value of  $m$  obtained by assuming that the decrease in emission efficiency is due only to the irradiation-induced self-absorption of visible light. As an initial estimate,  $t$  could be taken equal to the transmittance of a layer having a thickness of average particle size (10); however,  $t$  also depends on the type of phosphors and on the method of their preparation. Table I shows the value of  $m_v$  calculated from Eq. [6].  $t = 0.6$  was chosen in the calculations and the values of  $R(\lambda)$  and  $R_i(\lambda)$  were taken at the emission maxima of the phosphors.

Within experimental error, the values of  $m$  and  $m_v$  were found equal for calcium tungstate, zinc silicate, and cadmium borate and for the thermally bleached calcium halophosphate and strontium pyrophosphate phosphors. However, significant differences between  $m$  and  $m_v$  were found in phosphate type and magnesium germanate phosphors. The dependence of the relative luminous efficiency of the x-rayed calcium tungstate phosphor layer on the  $\lambda$  excitation wavelength from Eq. [4] and [6] noting that  $m \approx m_v$  is

$$\frac{L_i}{L} = \frac{R_i(\lambda)[1 - R(\lambda)]^2}{R(\lambda)[1 - R_i(\lambda)]^2} \cdot \frac{1 - R(\lambda_v)(1-t) + R_i(\lambda_v)(2t-1) - R(\lambda_v)R_i(\lambda_v)(2t-1)(1-t)}{1 - R_i(\lambda_v)(1-t) + R(\lambda_v)(2t-1) - R(\lambda_v)R_i(\lambda_v)(2t-1)(1-t)} \quad [7]$$

This equation is also valid for zinc silicate and cadmium borate at least at  $\lambda = 2537\text{\AA}$  excitation and for the thermally bleached calcium halophosphate and strontium pyrophosphate.

### Discussion

According to the measurements on all of the phosphors studied in this work, color centers induced by x-ray irradiation appear to absorb both a part of the exciting uv radiation and a part of the light emitted by the luminescent centers.

Based on the results obtained on single crystals (5, 6), the enhanced absorption in irradiated phosphate type phosphors has been attributed to color centers (3). In our work, the observed increased absorption and the thermal bleachability of the absorption bands also indicate that color centers are formed by the irradiation in the phosphors investigated. The absorption by these centers results in a decreased luminous efficiency in the phosphors. When the excitation occurs at  $2537\text{\AA}$ , the term  $a(\lambda)/a_i(\lambda)$  in Eq. [2] was found to be larger than  $m$  for every phosphor studied. This means that the absorption of the exciting radiation by the color centers results in an efficiency drop smaller than the self-absorption and other processes produce. Exciting the phosphors at longer wavelength in the tail of the excitation band, causes the ratio  $a(\lambda)/a_i(\lambda)$  to become smaller (Fig. 3 and 4). Thus, the absorption of the exciting energy by the color centers make a significantly higher contribution to the whole efficiency loss. While the term  $a(\lambda)/a_i(\lambda)$  does not depend on the structure of the phosphor layer,  $m_v$  is a function of  $R(\lambda_v)$  and  $R_i(\lambda_v)$  [6] which are dependent on the grain size [3].

In the cases of phosphate and magnesium germanate phosphors, the depreciation cannot be completely explained by the direct absorption of color centers. For these phosphors the value of  $m$  was found to be significantly smaller than  $m_v$ . This indicates that the intrinsic efficiency of the luminescent centers are affected by x-ray irradiation. On the glow curves of these phosphors, new peaks appear due to the long

term x-ray or ultraviolet irradiation (Fig. 5, 6d, 6f) indicating interaction between luminescent and color centers. This interaction and its role in the deprecia-

tion of phosphors is not yet perfectly understood (3). A part of the energy absorbed in luminescent centers can probably be transferred to deep traps (11) caused by irradiation which give rise to radiationless transitions (12) or to emission at different wavelengths than that of the luminescent centers.

Ultraviolet irradiation for 100 hr causes very similar, but in most cases, smaller changes in the luminous efficiency, reflectance spectrum, and glow curve of the phosphors than 16 hr of x-ray irradiation. Both forms of irradiation cause basically the same effects. However, the method of absorption analysis used in this study for x-rayed phosphor layers could not be applied to uv irradiated samples. Thus, the role of different effects of irradiation on the depreciation could not be separated quantitatively.

The depreciation of phosphors is one of the limiting factors of the lifetime of luminescent light sources. In this paper, we have taken the decrease in luminous efficiency as a measure of phosphor depreciation. However, independent of their efficiency, a decrease in

the visible reflectance of phosphors due to uv irradiation may also result in a decreased light output in certain types of lamps. In the case of aperture lamps (13) a 1% decrease of the visible reflectance of the coating could cause a 4-8% decrease in lumen radiated through their aperture.

Manuscript received June 17, 1968.

Any discussion of this paper will appear in a Discussion Section to be published in the June 1969 JOURNAL.

### REFERENCES

1. N. T. Gordon, F. Seitz, and F. Quinlan, *J. Chem. Phys.*, **7**, 4 (1939); G. Meister and R. Nagy, *J. Opt. Soc. Am.*, **36**, 696 (1946); **37**, 403 (1947); H. C. Froelich, *J. Appl. Phys.*, **17**, 573 (1946); H. C. Froelich, *J. Opt. Soc. Am.*, **37**, 308 (1947); G. Kressin, *Abhandlungen der Osram-Gesellschaft*, **7**, 235 (1958).
2. L. Suchow, *This Journal*, **108**, 847 (1961).
3. J. H. Singleton and L. Suchow, *ibid.*, **110**, 36 (1963).
4. E. F. Apple, *ibid.*, **110**, 374 (1963).
5. P. D. Johnson, *J. Appl. Phys.*, **32**, 127 (1961).
6. B. Segall, G. W. Ludwig, H. H. Woodbury, and P. D. Johnson, *Phys. Rev.*, **128**, 76 (1962); R. K. Swank, **135A**, 266 (1964); W. W. Piper, L. C. Kravitz, and R. K. Swank, **138A**, 1802 (1965).
7. A. Brill, "Luminescence of Organic and Inorganic Materials," p. 479, H. P. Kallmann and G. M. Spruch, Editors, John Wiley & Sons, Inc., New York (1962); G. T. Bauer, *Acta Phys. Hung.*, **11**, 225 (1960).
8. P. D. Johnson and F. E. Williams, *J. Chem. Phys.*, **18**, 1477 (1950); P. D. Johnson, *J. Opt. Soc. Am.*, **51**, 1235 (1961).
9. V. V. Antonov-Romanovskii, *Zh. Eksperim. I Teoret. Fiz.*, **26**, 459 (1954); I. Masuda, *J. Phys. Soc. Japan*, **16**, 105 (1961); I. Masuda, *Oyobutsuri*, **28**, 147 (1959).
10. G. T. Bauer, *Acta Phys. Hung.*, **16**, 333 (1964).
11. L. E. Vrenken, T. H. De Vette, and R. W. Van Der Wolf, *Illumin. Eng.*, 59 (1964).
12. D. Curie, "Luminescence in Crystals," Methuen and Co., Ltd., London (1963).
13. D. E. Spencer and L. L. Montgomery, *J. Opt. Soc. Am.*, **51**, 727 (1961).

# Fluorescence of $\text{Eu}^{2+}$ -Activated Phases in Binary Alkaline Earth Orthosilicate Systems

Thomas L. Barry\*

*Sylvania Lighting Center, Sylvania Electric Products Inc., Danvers, Massachusetts*

## ABSTRACT

The dependence of the emission spectra on compositional variations has been studied in binary alkaline earth orthosilicate systems activated by divalent europium. Isotherms at 1200°C were run in the systems (i)  $\text{Ba}_2\text{SiO}_4$ - $\text{Sr}_2\text{SiO}_4$ , (ii)  $\text{Ca}_2\text{SiO}_4$ - $\text{Sr}_2\text{SiO}_4$ , and (iii)  $\text{Ca}_2\text{SiO}_4$ - $\text{Ba}_2\text{SiO}_4$ . Phosphors produced in the  $\text{Ba}_2\text{SiO}_4$ - $\text{Sr}_2\text{SiO}_4$  system were considerably more efficient than those in either of the other two systems and consequently were studied in much greater detail. A complete series of crystalline solutions exist between the end-members at 1200°C. The corresponding emission spectra vary in a fairly continuous manner from 505 nm for the pure barium end-member to 575 nm for the pure strontium end-member. X-ray diffraction data revealed complete crystalline solution between  $\beta$ - $\text{Ca}_2\text{SiO}_4$  and  $\text{Sr}_2\text{SiO}_4$  at 1200°C. However, the low level of brightness and the pronounced asymmetry of the emission peaks rendered this system less amenable to a detailed investigation. Emission spectra indicated the formation of an intermediate compound in the  $\text{Ca}_2\text{SiO}_4$ - $\text{Ba}_2\text{SiO}_4$  system. The existence of this compound,  $\text{Ba}_5\text{Ca}_3\text{Si}_4\text{O}_{16}$ , was verified by x-ray diffraction. The emission spectrum of this compound peaks at a considerably lower wavelength (~490 nm) than those of its bounding compositions. The two later systems were further complicated due to the polymorphism of  $\text{Ca}_2\text{SiO}_4$ . Frequently the  $\text{Ca}_2\text{SiO}_4$  phase was partially converted from  $\beta$ - $\text{Ca}_2\text{SiO}_4$  to  $\gamma$ - $\text{Ca}_2\text{SiO}_4$ .

This work was undertaken in an attempt to study the variation in emission spectra with composition in binary systems exhibiting complete crystalline solution between both end-members. Systems involving the alkaline earth ions were chosen because of the similarity in size between them and divalent europium; also the strongly divalent nature of these ions should favor the incorporation of europium in the divalent state and render it more stable to subsequent treatment. The ionic radii (Ahrens' values) (1) for the ions  $\text{Ca}^{2+}$ ,  $\text{Sr}^{2+}$ ,  $\text{Ba}^{2+}$ , and  $\text{Eu}^{2+}$  are 0.99, 1.12, 1.34, and 1.12Å, respectively.

Previous studies of divalent europium activation in alkaline earth orthosilicates have been carried out by McKeag and Ranby (2), and Jenkins and McKeag (3). These studies were limited almost exclusively to compositions involving only one alkaline earth ion. Both mention that studies involving combinations of the alkaline earth ions can be used, but these were not investigated fully because of the limited amount and expense of europium compounds at the time. The patent by McKeag and Ranby is more extensive in this area yet lists only nine such compositions. Only the emission colors of these prepared samples are given as complete spectral energy distribution data were not obtained.

A complete series of crystalline solutions between  $\text{Ca}_2\text{SiO}_4$  and  $\text{Ba}_2\text{SiO}_4$  has been reported by Toropov and Kononov (4). They likewise report complete crystalline solution between  $\beta$ - $\text{Ca}_2\text{SiO}_4$  and  $\text{Sr}_2\text{SiO}_4$  (5). An intermediate compound in the  $\text{Ca}_2\text{SiO}_4$ - $\text{Ba}_2\text{SiO}_4$  system ( $5\text{BaO} \cdot 3\text{CaO} \cdot 4\text{SiO}_2$ ) was reported by Nadachowski and Gyrlicki (6). They showed only limited solubility in  $\text{Ca}_2\text{SiO}_4$  and in the intermediate compound  $\text{Ba}_5\text{Ca}_3\text{Si}_4\text{O}_{16}$ . No previous phase equilibrium data were found on the  $\text{Ba}_2\text{SiO}_4$ - $\text{Sr}_2\text{SiO}_4$  system.

## Experimental

*Starting materials and blend preparation.*—The raw materials employed in this study consisted of luminescent grade alkaline earth carbonates and silicic acid. The other chemicals, europium oxide, and ammonium

\* Electrochemical Society Active Member.

Key words: phosphors alk earth silicates, luminescence alk earth silicates, emission spectra, europium ( $2+$ ) activation, fluorescence europium ( $2+$ ), temperature dependence, equilibrium subsolidus.

chloride were commercial reagent grade materials. The europium oxide was at least 99.9% pure (analyses given by American Potash and Chemical Corporation). The silicic acid was assayed so that the quantities weighed could be compensated for sorbed water.

Sample blends were prepared by dry blending the desired amounts of the constituents in a Model 8000 Spex Mixer/Mill for 15 min. A small amount of glass beads (easily removed after blending by screening) were incorporated in each blend of facilitate mixing.

*Firing procedure.*—The blended samples were pre-fired in alumina boats at 600°C to initiate decomposition of the carbonates and possible reaction with the ammonium chloride flux. The samples were then placed in a silica tube flushed with nitrogen and inserted into a global furnace at 1200°C. At this time the gas flow was adjusted to yield a mixture of 4 volumes of nitrogen to 1 volume of hydrogen. Firing temperatures between 1100° and 1300°C, and firing times of 2 to 12 hr were employed. The most frequent combination was 4 hr at 1200°C. On completion of the firing the silica tube is removed from the furnace, and the sample is allowed to cool close to room temperature with continued flow of the reducing atmosphere.

*Identification and characterization of products.*—X-ray diffraction techniques, using a Norelco diffractometer with filtered  $\text{CuK}_\alpha$  radiation, were employed for phase identification. Fluorescent properties (the excitation spectra and the spectral energy distribution curves) were determined on all samples using methods previously described by Eby (7).

## Results and Discussion

*The  $\text{Ba}_2\text{SiO}_4$ - $\text{Sr}_2\text{SiO}_4$  system.*—An isotherm run at 1200°C in which the composition was varied every 10 m/o (mole per cent) showed complete crystalline solution between these two compounds at this temperature. The x-ray diffraction patterns showed all preparations to result in a single phase material. All of the activator concentrations within the limits employed in this study, 0.005 to 0.10 atom fraction europium, produced efficient phosphors. A constant value of 0.02 was used in this system and in the systems to follow.

The incorporation of a small amount of ammonium chloride in the initial blend greatly accelerates the attainment of equilibrium in the finished sample. The crystallinity of the product is also greatly enhanced due to the fluxing action of the ammonium chloride. This is immediately obvious when the x-ray diffraction patterns of fluxed and unfluxed samples are compared. A more pronounced body color is also characteristic of the well-crystallized samples. The flux concentration used was about 0.25 mole/mole of matrix. Wet chemical analysis showed only a 0.13 w/o (weight per cent)  $\text{Cl}^-$  retained after firing which was water soluble and an additional 0.04 w/o on total analysis. Thus confirming that the ammonium chloride served as a flux and any residual could be substantially removed by water washing.

Differences in hydration properties of these materials were observed on washing to remove the residual chloride. The fluorescence of a sample of

$\text{Ba}_2\text{SiO}_4:\text{Eu}_{0.02}^{2+}$  is almost completely destroyed by

water washing, while  $\text{Sr}_2\text{SiO}_4:\text{Eu}_{0.02}^{2+}$  is unaffected by washing. Crystalline solutions containing 50 and 75 m/o  $\text{Sr}_2\text{SiO}_4$  were likewise unaffected by washing. If the crystalline solution contains more than 10 m/o  $\text{Sr}_2\text{SiO}_4$ , then water washing is not detrimental to the fluorescence of the resultant phosphor.

The fluorescent data for 2537Å excitation on the divalent europium activated crystalline solution series prepared are given in Table I. In the table the wavelength given is that of the peak position of the emission spectra,  $W_{h/2}$  is the width at half-height in nanometers, and the intensity factor is the product of the peak height (relative energy units), the scale factor, and the width at half-height. The intensity factors are for a particular set of samples and are given in order to compare luminous output within the series and subsequent series given in later sections of the paper. The reflectivity at 254 nm of all the samples in this series are within the range of 10-20% and are thus all good absorbers and potentially efficient phosphors. Although the reflectivity does contribute, the intensity factors even for one particular composition, are affected more by the method of synthesis.

The data in Table I show a fairly continuous shift in emission wavelength from 505 nm for the pure barium end-member to 575 nm for pure strontium end-member. This continuous shift in wavelength with composition of the crystalline solution is depicted in Fig. 1. Thus, by choosing the proper composition any emission wavelength between 505 nm ( $\text{Ba}_2\text{SiO}_4:\text{Eu}_{0.02}^{2+}$ )

and 575 nm ( $\text{Sr}_2\text{SiO}_4:\text{Eu}_{0.02}^{2+}$ ) may be obtained. These data show the very marked sensitivity of emission from divalent europium to the matrix composition in this system. The excitation spectrum of  $\text{BaSrSiO}_4:\text{Eu}_{0.02}^{2+}$ , determined on equipment designed by Eby (7), which corrects for instrumental effects and records excitation spectra in terms of relative efficiency, is given in Fig. 2. The excitation spectra of other mem-

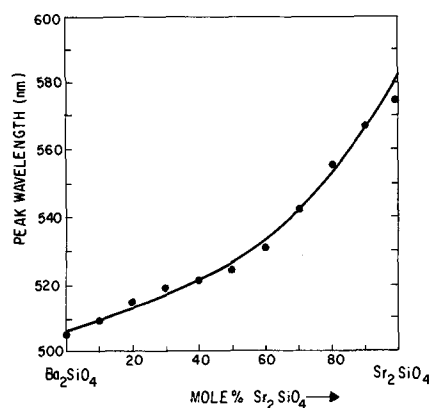


Fig. 1. Peak wavelength for 2537Å excitation vs. composition for crystalline solutions in the  $\text{Ba}_2\text{SiO}_4\text{-Sr}_2\text{SiO}_4$  system.

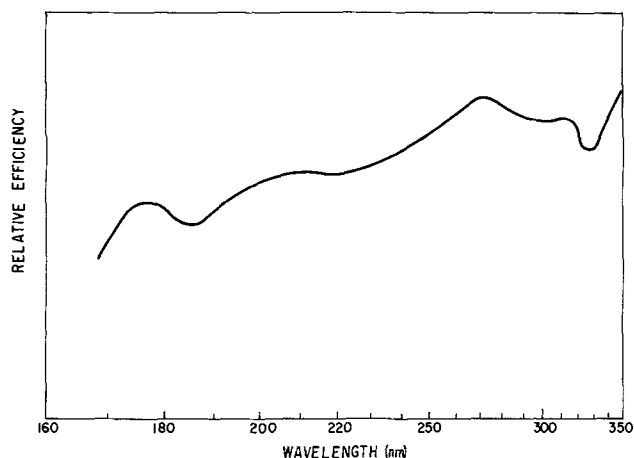


Fig. 2. Excitation spectrum of  $\text{BaSrSiO}_4:\text{Eu}_{0.02}^{2+}$  corrected for instrumental variables (for 525 nm emission).

bers of this series are very similar to the curve given. The interpretation of such a curve for a divalent europium activated phosphor has recently been fully discussed by Palilla *et al.* (8).

Emission curves of four of these samples are given in Fig. 3. Curves are given for the two end-members and two intermediate crystalline solutions. The curves demonstrate the variation in emission wavelength possible, as well as the broadening of the emission spectra with increasing strontium concentration in the crystalline solution phase. The distinct broadening is still present when these curves are plotted on a frequency scale (rather than wavelength). On a frequency basis the width at half-height varies from  $22 \times 10^3 \text{ cm}^{-1}$  ( $\text{Ba}_2\text{SiO}_4:\text{Eu}_{0.02}^{2+}$ ) to  $32 \times 10^3 \text{ cm}^{-1}$

Table I. Fluorescent data on compositions in the  $\text{Ba}_2\text{SiO}_4\text{-Sr}_2\text{SiO}_4$  system

Mole per cent $\text{Ba}_2\text{SiO}_4$	Mole per cent $\text{Sr}_2\text{SiO}_4$	$\lambda$ Peak nm	$W_{h/2}$ nm	Int. factor Arbitrary units
100	0	505	60	74.9
90	10	510	63	71.1
80	20	515	67	70.4
70	30	519	68	80.0
60	40	521	70	73.9
50	50	524	72	68.3
40	60	531	84	67.5
30	70	543	93	63.6
20	80	556	102	61.2
10	90	568	106	62.3
0	100	575	106	61.7

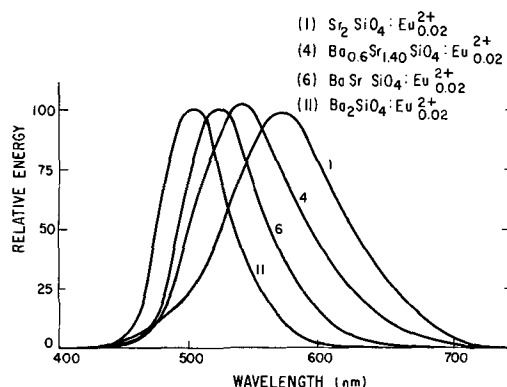


Fig. 3. Spectral energy distribution curves of the end-member phases and two intermediate crystalline solution phases in the  $\text{Ba}_2\text{SiO}_4\text{-Sr}_2\text{SiO}_4$  system (2537Å excitation).

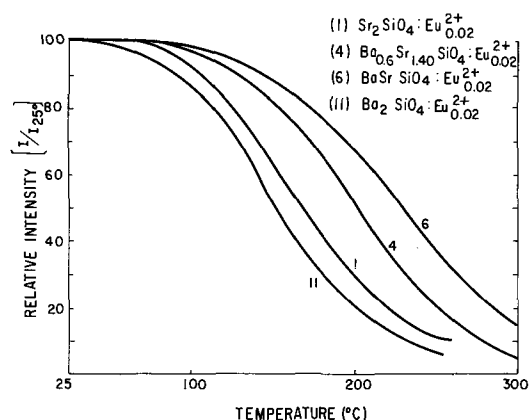


Fig. 4. Temperature dependence curves of the end-member phases and two crystalline solution phases in the  $\text{Ba}_2\text{SiO}_4$ - $\text{Sr}_2\text{SiO}_4$  system (2537Å excitation).

( $\text{Sr}_2\text{SiO}_4:\text{Eu}_{0.02}^{2+}$ ). Curves showing the temperature dependency of these same four samples are given in Fig. 4. These curves show the temperature dependence of the crystalline solution phases to be better than that of either pure end-member. The temperature stability

of the  $\text{BaSrSiO}_4:\text{Eu}_{0.02}^{2+}$  crystalline solution phase prepared in this study is considerably better than that of the corresponding preparation by Jenkins and McKeag (3). A drop of less than 5% was observed in the present work at 100°C, while they reported a drop of 20%. This is believed to be due to the enhanced crystallinity of the samples in this study.

No significant difference in the brightness of a given fluorescent composition was observed between samples in which allowance for the activator concentration was made by removal of a corresponding concentration of a large alkaline earth ion, and when the activator was added in excess of the stoichiometric amounts of alkaline earth ions.

It was also noted in this study that europium could be incorporated in  $\text{Ba}_2\text{SiO}_4$  in the divalent state even when the firing was carried out in pure nitrogen. This was not true for  $\text{Sr}_2\text{SiO}_4$ . Here a reducing atmosphere was required in order that the europium be incorporated in the divalent state. This is somewhat surprising in that the two compounds  $\text{Ba}_2\text{SiO}_4$  and  $\text{Sr}_2\text{SiO}_4$  possess isotypic structures (9) ( $\text{K}_2\text{SO}_4$ -type with space group  $\text{P}_{\text{nam}}$ ), and the ionic radii of strontium and divalent europium are identical (Ahrens' value 1.12Å) while divalent barium is larger (1.34Å).

**Lamp test data.**—Several tests were run on compositions in the  $\text{Ba}_2\text{SiO}_4$ - $\text{Sr}_2\text{SiO}_4$  system in standard 40w fluorescent lamps. Data on four compositions are given in Table II.

The ( $x, y$ ) values are the chromaticity coordinates of the phosphors in lamps. The 1:1 composition

$\text{BaSrSiO}_4:\text{Eu}_{0.02}^{2+}$  has been tested for long-term maintenance. After 1775 hr of burning, it maintained 95.3% of its initial value. The low lumen values for the

$\text{Ba}_2\text{SiO}_4:\text{Eu}_{0.02}^{2+}$  show it to be more sensitive than the other compositions to the processing necessary for incorporation into fluorescent lamps; also, the detrimental effect of residual chloride which could not be removed because of hydration problems.

Table II. Lamp test data

Composition	$x$	$y$	Lumens		% Maint.
			16 Hr	100 Hr	
$\text{Ba}_2\text{SiO}_4:\text{Eu}_{0.02}^{2+}$	0.198	0.579	1586	1447	91.2%
$\text{BaSrSiO}_4:\text{Eu}_{0.02}^{2+}$	0.272	0.630	3735	3614	96.8
$\text{Ba}_{0.5}\text{Sr}_{1.5}\text{SiO}_4:\text{Eu}_{0.02}^{2+}$	0.360	0.543	3664	3466	94.6
$\text{Sr}_2\text{SiO}_4:\text{Eu}_{0.02}^{2+}$	0.432	0.482	2797	2735	97.8

Table III. Fluorescent data on compositions in the  $\text{Ca}_2\text{SiO}_4$ - $\text{Sr}_2\text{SiO}_4$  system

$\text{Ca}_2\text{SiO}_4$	Mole % $\text{Sr}_2\text{SiO}_4$	$\lambda$ Peak nm	$W_{h/2}$ nm	Int. factor Arbitrary units
100	0	510	100	20.4
90	10	543	150	23.9
80	20	538	170	30.8
70	30	574	190	36.5
60	40	589	172	31.8
50	50	598	148	34.9
40	60	591	128	28.2
30	70	592	120	47.1
20	80	590	114	44.7
10	90	583	108	47.5
0	100	575	110	48.4

**The  $\text{Sr}_2\text{SiO}_4$ - $\text{Ca}_2\text{SiO}_4$  system.**—The 1200°C isotherm through this system showed complete crystalline solution to exist between  $\text{Sr}_2\text{SiO}_4$  and  $\beta$ - $\text{Ca}_2\text{SiO}_4$ . The intensity of fluorescence from these samples was considerably less than that in the previous system discussed, as seen by comparison of intensity factors with those of Table I. The data obtained on the divalent europium activated crystalline solutions prepared are given in Table III.

The terms in Table III are the same as those in Table I. The widths of the emission peaks in this system are considerably broader than those in the previous system and are decidedly asymmetric, possibly indicative of emission from divalent europium in two different crystallographic sites in the structure. The broadness of the peaks contributes very heavily to the total output from these samples since the peak heights are relatively low. This system was not studied at length due to the difficulties in attaining equilibrium, the polymorphism of  $\text{Ca}_2\text{SiO}_4$ , and the low luminous level of the initial phosphor samples prepared.

**The  $\text{Ca}_2\text{SiO}_4$ - $\text{Ba}_2\text{SiO}_4$  system.**—Much of what has been said about difficulties in the previous system applies here. The fluorescent data on the divalent europium activated compositions prepared in this system are given in Table IV.

The fluorescence data in this table show large inconsistencies in these samples. However, due to the low level of fluorescence of all compositions in this system, no attempt to reconcile the data was made. The only noteworthy feature is the formation of an intermediate compound in this system. The formation of the compound was indicated in the emission data obtained and was verified by x-ray diffraction data. The large shift in the emission spectra for the 30 m/o  $\text{Ca}_2\text{SiO}_4$ -70 m/o  $\text{Ba}_2\text{SiO}_4$  composition over that of adjacent compositions indicated such an occurrence in this compositional region. A review of the literature showed disagreement over the appearance of a compound in this system. However, the compound  $\text{Ba}_5\text{Ca}_3\text{Si}_4\text{O}_{16}$  had been reported by Nadachowski and Grylicki (6), and the data here tend to corroborate this composition.

### Summary

1. Complete crystalline solubility was detected in 1200°C subsolidus isotherms in the systems  $\text{Ba}_2\text{SiO}_4$ -

Table IV. Fluorescent data on compositions in the  $\text{Ca}_2\text{SiO}_4$ - $\text{Ba}_2\text{SiO}_4$  system

$\text{Ca}_2\text{SiO}_4$	Mole % $\text{Ba}_2\text{SiO}_4$	$\lambda$ Peak mn	$W_{h/2}$ mn	Int. factor Arbitrary units
100	0	508	108	27.2
90	10	546	144	20.9
80	20	534	144	9.1
70	30	540	140	10.1
60	40	525	132	17.4
50	50	523	136	25.1
40	60	522	140	37.5
30	70	491	138	53.0
20	80	532	84	47.0
10	90	527	78	38.1
0	100	510	66	39.5



$\text{Sr}_2\text{SiO}_4$  and  $\text{Ca}_2\text{SiO}_4$ - $\text{Sr}_2\text{SiO}_4$ . Emission spectra indicated the formation of an intermediate compound ( $\text{Ba}_5\text{Ca}_3\text{Si}_4\text{O}_{16}$ ) in the  $\text{Ca}_2\text{SiO}_4$ - $\text{Ba}_2\text{SiO}_4$  system. The existence of this compound was confirmed by x-ray diffraction studies.

2. The fluxing action of the  $\text{NH}_4\text{Cl}$ , which greatly enhances the crystallinity of the samples, brings the fluorescence, due to 2537Å excitation, to a level where it can be considered for application in fluorescent lamps. Also, extremely good maintenance is characteristic of the well-crystallized materials.

3. Fluorescent properties of some crystalline solutions, such as intensity of emission and temperature dependency, have been shown to be enhanced over those of the end-member phases.

4. Crystalline solutions in the  $\text{Ba}_2\text{SiO}_4$ - $\text{Sr}_2\text{SiO}_4$  system activated by divalent europium have been shown to produce phosphors potentially useful in fluorescent lamp applications. Divalent europium activated phosphors in both the  $\text{Sr}_2\text{SiO}_4$ - $\text{Ca}_2\text{SiO}_4$  and  $\text{Ca}_2\text{SiO}_4$ - $\text{Ba}_2\text{SiO}_4$  systems are much less efficient and seemingly unimportant commercially.

#### Acknowledgment

The author gratefully acknowledges the encouragement and advice given by Dr. K. H. Butler and Dr. M. J. B. Thomas throughout this study. Sample prepara-

tion and spectral determinations were carried out with the assistance of Mr. A. Rudis, and x-ray diffraction data collected by Miss M. Skeadas.

Manuscript submitted May 22, 1968; revised manuscript received July 11, 1968. This paper was presented at the Boston Meeting, May 5-9, 1968, as Paper 55.

Any discussion of this paper will appear in a Discussion Section to be published in the June 1969 JOURNAL.

#### REFERENCES

1. L. H. Ahrens, *Geochim. Cosmochim. Acta*, **2**, 155 (1952).
2. A. H. McKeag and P. W. Ranby, British Pat. 544, 160, Aug. 27, 1940.
3. H. G. Jenkins and A. H. McKeag, *This Journal*, **97**, 415 (1950).
4. N. A. Toropov and P. F. Kononov, *C. R. Acad. Sci. USSR*, **20**, 663 (1938), *C. A.*, **33**, 3651 (1939).
5. N. A. Toropov and P. F. Kononov, *C. R. Acad. Sci. USSR*, **40**, 155 (1943), *C. A.*, **38**, 6153 (1944).
6. F. Nadachowski and M. Grylicki, *Silikat. Tech.*, **10**, 79 (1959).
7. J. E. Eby, Paper presented at the Toronto Meeting, May 3-7, 1964, Paper 27.
8. F. C. Palilla, A. K. Levine, and M. R. Tomkus, *This Journal*, **115**, 642 (1968).
9. O'Daniel and Tscheischwili, *Z. Krist.*, **104**, 348 (1942).

## The Defect Structure of GaP Crystals Grown from Gallium Solutions, Vapor Phase and Liquid Phase Epitaxial Deposition

Robert H. Saul

*Bell Telephone Laboratories, Incorporated, Murray Hill, New Jersey*

#### ABSTRACT

The defect structure of GaP crystals grown from gallium solutions, vapor phase and liquid phase epitaxial deposition is described. Etchants have been used to demarcate emergent dislocations, stacking faults, and p-n and n-n<sup>+</sup> junctions. Crystals grown from gallium solutions are inhomogeneous with respect to defect structure and contain substantial dislocation-free regions. Evidence is cited which indicates that some dislocations are introduced during growth whereas others are apparently generated at high stress regions during cooling. It is demonstrated that vapor phase epitaxial deposition on GaP substrates is capable of yielding nearly dislocation-free crystals containing no stacking faults. The high density of defects observed in crystals grown on GaAs substrates is attributed to the heteroepitaxial mode of growth, in particular, the difference in thermal contraction of the growth layer and substrate on cooling from the growth temperature. GaP diodes fabricated by liquid-phase epitaxy, in contrast to those formed by vapor-phase epitaxy, do not contain interfacial dislocations at the growth-substrate interface, i.e., p-n junction.

The electrical and optical properties of semiconductors are highly dependent on the dislocation structure in these crystals (1). For example, laser emission and the improved laser efficiency of GaAs diodes after annealing has been correlated with dislocations located in the vicinity of the p-n junction (2, 3). Although there has been considerable interest in GaP for electrooptic devices, the defect structure in these crystals has not been studied in detail probably because of the lack of a reliable etchant for revealing dislocations. Solutions of aqua regia or halogen saturated methanol have been used (4); however, there is little evidence supporting the correlation of etch pits and individual dislocations, and it has been found that the density of etch pits may be reproducible only after annealing (5). This article reports several etchants which (i) reveal dislocations and stacking faults, (ii) can be used for nonselective chemical polishing, and (iii) delineate p-n and n-n<sup>+</sup> junctions in GaP

crystals. Etch pits not associated with dislocations are also reported. The defect structure of crystals grown by techniques which are currently being used for luminescent diodes is then described and some evidence which elucidates the sources of dislocations is provided.

#### Experimental

Crystals of GaP were grown by the slow cooling of saturated gallium solutions (6), vapor phase (7, 8) and liquid phase (9) epitaxial deposition. All crystals were polished, terminating with 0.1μ diamond paste, on either the Ga{111} or P{111} face.<sup>1</sup> Several crystals were subsequently chemically polished to remove the damaged surface layer which resulted in the elimination of certain nondislocation etch pits (described below). The etchants which were found to be most

<sup>1</sup> The Ga{111} and P{111} face designate the octahedral planes terminating with gallium or phosphorus atoms, respectively.

Table I. Etchants for gallium phosphide

Etchant	Reference	Comments
1. 10 ml H <sub>2</sub> O, 40 mg AgNO <sub>3</sub> , 5g CrO <sub>3</sub> , 8 ml HF at 75°C	(10)	Ga{111}, P{111}: dislocations, stacking faults (15-60 min); delineates p-n and n-n <sup>+</sup> junctions (1-5 min)
2. 8 ml H <sub>2</sub> O, 10 mg AgNO <sub>3</sub> , 6 ml HNO <sub>3</sub> , 4 ml HF at 60°C	(11)	Ga{111}, P{111}: dislocations, stacking faults (1-3 min)
3. 50 ml H <sub>2</sub> O, 6g KOH, 4g K <sub>3</sub> Fe (CN) <sub>6</sub> at 100°C	(12)	Ga{111}: dislocations (1-2 min); P{111}: polish (20-25 μ/hr)
4. 10 ml H <sub>2</sub> O, 10 ml HCl, 5 ml HNO <sub>3</sub> at 45°-50°C	—	Ga{111}: general pitting; P{111}: polish (2-5 μ/min)

reliable are listed in Table I and represent slight departures from those cited previously for GaAs and Ge. The higher temperatures and changes in the composition of the etchants are required to retard precipitates which tend to accumulate on the etched surfaces. The preparation of etchant 4 is rather critical, and the prescribed order should be followed. Moreover, if the color of the solution is dark yellow (NO<sub>2</sub> evolution), the etching rate is too rapid and selective etching of incipient scratches occurs. Experience has shown that the evolution of NO<sub>2</sub> is indicative of either the etchant temperature being too high, excessive HNO<sub>3</sub>, or contamination of the containing vessel. A clear to pale yellow color assures the nonselective attack required for polishing.

### Results and Discussion

*Revelation of dislocations.*—In establishing the correspondence of etch pits produced by etchants 1 and 2 to the site of emergent dislocations, it was demonstrated that (i) etch pits follow continuous lines as they are etched progressively deeper into the crystal,<sup>2</sup> (ii) the density of pits is markedly increased by deformation, and (iii) there is a 1:1 correspondence of etch pits on opposite {111} faces of a thinned crystal. Etchant 1 demarcates dislocations inclined to the surface by etch pit trails as in Fig. 1a and reveals dislocations nearly parallel to {111} surfaces as in Fig. 1b.

*Polarity of dislocations.*—Since etchant 3 has been shown (13) to reveal dislocations on the Ga{111} face, it is of interest to compare the etch figure derived by this etchant with that produced by etchant 1. Figures 2a and 2b were obtained after immersion in etchant 1 followed by immersion in etchant 3, respectively. While all pits produced by etchant 1 correspond to dislocations it is clear that not all dislocations are revealed by this etchant. Haasen (14) has pointed out that incomplete electron orbitals of either all group III atoms or all group V atoms are associated with dislocations in III-V compounds having the zinc blende structure. Moreover, there is experimental evidence suggesting that an etchant may reveal only one type of dislocation (15). Thus it is plausible that the difference between the etch figures derived by etchants 1 and 3 is a consequence of the polarity of dislocations. Although etchants 1 and 2 reveal dislocations on all octahedral faces, the density of etch pits on the P{111} face is generally higher (by as much as a factor of 7) than on the Ga{111} face. These observations have been confirmed in crystals of uniform dislocation density (verified by etching angle-lapped surfaces) and provides additional evidence for the selective etching of only one type of dislocation.

*Revelation of stacking faults.*—Figure 3 illustrates the linear etch grooves frequently observed in (vapor phase) epitaxially deposited GaP crystals after immersion in etchants 1 and 2. Since the etch grooves on

a {111} surface lie along <110> directions and frequently terminate with a dislocation etch pit, they are believed to be the etch traces of stacking faults. Pits which are coincident with the etch grooves, as in Fig. 3, may be indicative of impurity segregation at stacking faults.

*Nondislocation etch pits.*—Figure 4a depicts the irregularly shaped pits obtained on a Ga{111} face after immersion in etchant 1 for 15 min. Etching for an additional 30 min tends to obscure these pits and reveals additional pits not unlike the dislocation etch pits found on the P{111} face (see Fig. 4b). After chemically removing ~10μ, the crystal was re-etched (see Fig. 4c). The one to one correspondence of pits in Fig. 4b and 4c indicates that the pits formed after prolonged etching correspond to emergent dislocations. In light of the observation that the extent of surface damage resulting from mechanical abrasion is generally greater for the group III surface compared to the group V surface (16), it is likely that the irregular shaped pits observed on the Ga{111} face are a manifestation of surface damage. This interpretation for the origin of these pits is substantiated by the appearance of identical nondislocation pits on the P{111} face when the polishing cloth was contaminated and the elimination of these pits by prior chemical polishing. It is believed that these pits have previously been attributed to dislocations [cf Fig. 5 of Ref. (17)].

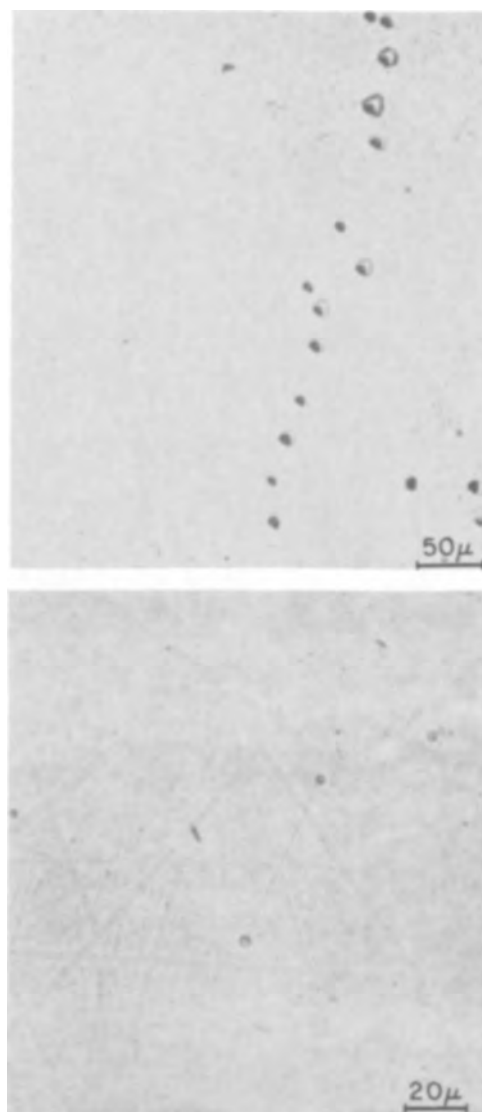


Fig. 1. Etch pits corresponding to dislocations inclined to the surface (a) (top) and a dislocation nearly parallel to the surface (b) (bottom).

<sup>2</sup> This was accomplished by correlating etch pits obtained prior to and subsequent to chemical polishing that obscures previous pits.

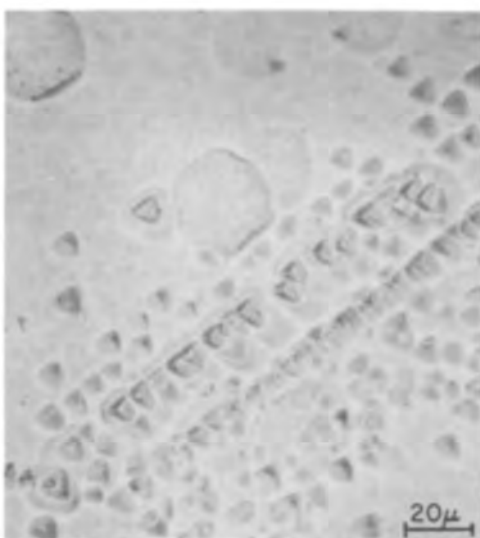
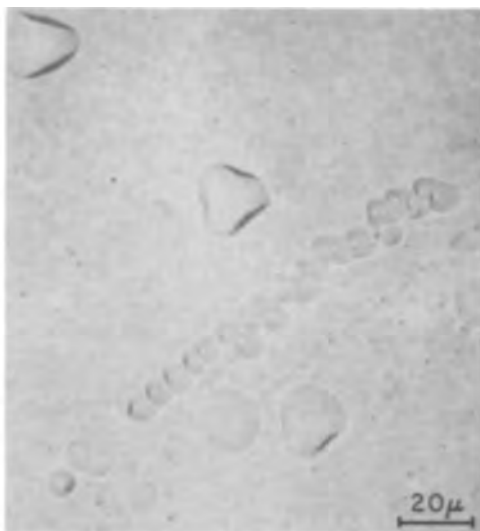


Fig. 2. Etch pits on the Ga{111} face after immersion in etchant 1 (a) (top) followed by immersion in etchant 3 (b) (bottom).

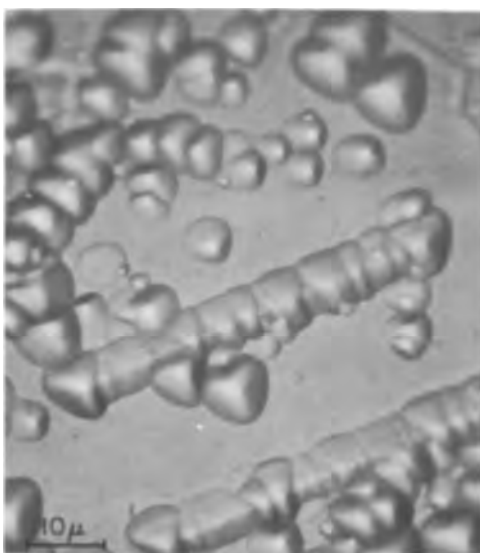


Fig. 3. Stacking fault traces and dislocation etch pits in an epitaxially deposited crystal.

Nondislocation etch pits are also revealed by warm aqua regia which has been reported to reveal dislocations (5). A solution-grown crystal was immersed in aqua regia for short periods until distinct pits appeared on the P{111} face; continued etching did

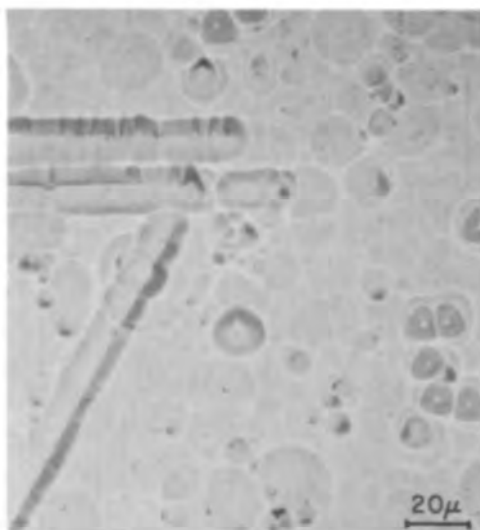
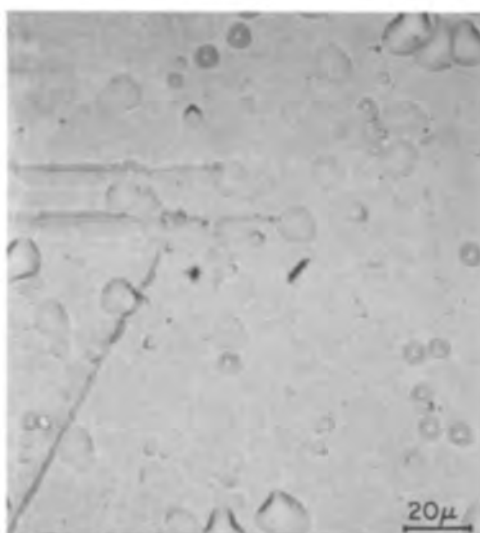
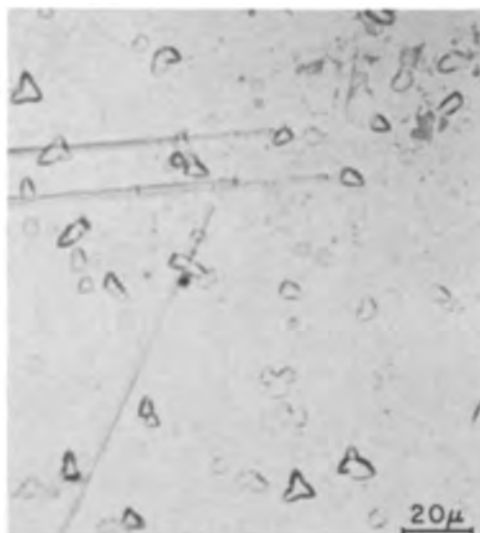


Fig. 4. Etch pits on the Ga{111} face after immersion in etchant 1 for 15 min (a) (top) and 45 min (b) (center). Same area after removing 10 μm and re-etching (c) (bottom).

not increase the number of these pits appreciably. The crystal was then immersed in etchant 1 (which has been shown to reveal dislocations) in an attempt to correlate the pits produced by aqua regia with dislocations. The large pits in Fig. 5 were produced by aqua regia and the small dark pits correspond to emergent dislocations. Although aqua regia does reveal some dislocations (center of figure), not all pits

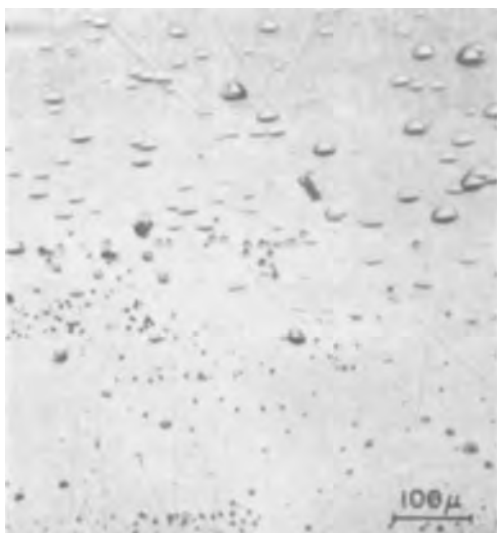


Fig. 5. Etch pits on the P{111} face after immersion in aqua regia (large pits) and etchant 1 (small dark pits).

are associated with dislocations (top of figure). Unfortunately, a visual distinction between these two types of pits cannot be readily made. Moreover, many dislocations are not revealed by aqua regia (bottom of figure). Thus aqua regia is considered to be unsuitable for revealing dislocations in GaP.

For several crystals, minute pits (less than  $1\mu$  in diameter) have been observed in addition to the dislocation etch pits revealed by etchant 1. Further etching does not enlarge these pits and, in fact, completely changes their arrangement. Since the depth of these pits is  $\sim 1-2\mu$ , it is tempting to speculate that these pits are due to impurity and/or vacancy clusters. In this connection, it is noteworthy that pits of this type have been observed in Ge crystals where they have been correlated to oxygen content (18). Anticipating that the minute etch pits observed in GaP might be attributable to oxygen, a correlation of oxygen concentration and pit density was sought.

Crystals of GaP were grown from gallium solutions containing 0.07 m/o (mole per cent) Zn and varying amounts of  $Ga_2O_3$  up to 0.04 m/o. (The addition of  $Ga_2O_3$  is presumed to increase the oxygen concentration in the crystals.) To avoid erroneous etch figures due to contamination or surface damage, approximately  $30\mu$  was removed by chemical polishing. Crystals were immersed in etchant 1 for 30 min which resulted in the dissolution of  $3.3\mu$ . Although pits differed in size, ranging from 0.1 to  $1\mu$ , all pits were counted irrespective of size. No systematic variation of pit size was observed. The measured pit density was consistently in the range  $0.3-6.7 \times 10^5 \text{ cm}^{-2}$ . No systematic variation of pit density with added  $Ga_2O_3$  was found. Moreover, the pit density varied by as much as an order of magnitude for a given specimen, and thus it is doubtful that the pits represent an intrinsic property of the crystal. The origin of the pits is tentatively ascribed to precipitates formed during etching.

*Delineation of p-n and n-n<sup>+</sup> junctions.*—In the course of etching GaP crystals of varying dopant level, the rate of attack of etchant 1 was found to depend on the net carrier concentration, the etching rate being highest in lightly doped n-type material and lowest in p-type material. The difference in etching rates results in a step at p-n and n-n<sup>+</sup> junctions on angle-lapped surfaces, thus sharply delineating these boundaries. The step height is a function of etching time, but has been determined by interferometry to be less than  $0.1\mu$  in height. An etching time of less than 3 min is usually used since the demarcation becomes diffuse after prolonged etching. Etch pits which appear after prolonged etching

are larger in the more rapidly attacked layer. Etchant 2, on the other hand, is insensitive to doping level: junctions are not delineated and etch pits are practically the same size.

*Dislocations in solution-grown GaP.*—Crystals grown from saturated gallium solutions (6) have inhomogeneous dislocation morphologies: most crystals contain large areas which are dislocation free, small areas of uniform dislocation density ( $\sim 10^4 \text{ cm}^{-2}$ ), and localized areas of very high dislocation density ( $>10^6 \text{ cm}^{-2}$ ) at high stress regions typically at voids (as in Fig. 6a) or channels (as in Fig. 6b). Such regions are believed to correspond to gallium which was entrapped as a consequence of the dendritic nature of growth and constitutional supercooling. More rarely, crystals have a high dislocation density distributed homogeneously. In one case, substantial polygonization at the periphery of a platelet was evident (see Fig. 7) implying that these dislocations were introduced at high temperatures. The location of the polygonized walls at the edge of the crystal is particularly significant. Platelet growth is believed to occur over the temperature range  $1150^\circ-900^\circ\text{C}$ , the periphery presumably freezing at the lower temperatures. It is doubtful that self-diffusion near  $900^\circ\text{C}$  ( $T/T_m = 0.67$ ) is sufficient to account for the extensive polygonization;

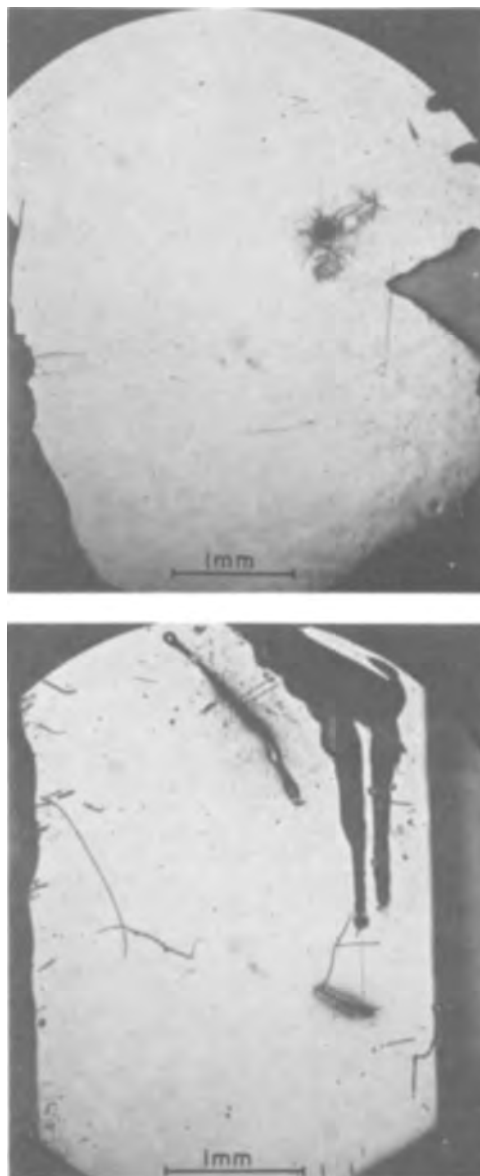


Fig. 6. Dislocation etch pits in solution-grown GaP crystals showing a high density of dislocations at a void (a) (top) and channel (b) (bottom).

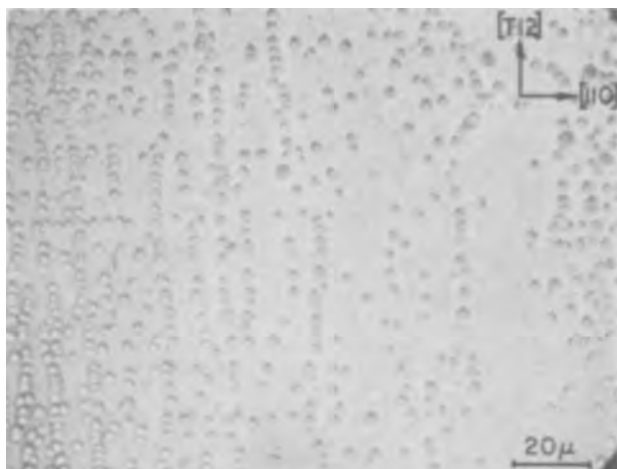


Fig. 7. Polygonized walls near the periphery of a solution-grown GaP crystal.

hence, crystal growth is apparently complete at a substantially higher temperature. Since these crystals are strain free, as evidenced by the lack of birefringence, it is believed that the perfection is due to the lack of physical constraint (which can cause large strains upon cooling) imposed by the molten gallium.

**Dislocations and stacking faults in vapor-grown GaP.**—Crystals grown by vapor-phase epitaxial deposition onto {111} oriented GaAs substrates (7,8) consistently contain a rather uniform distribution of dislocations in the range  $2 \times 10^5$ – $2 \times 10^6$   $\text{cm}^{-2}$  (compared to  $3 \times 10^4$   $\text{cm}^{-2}$  in the substrate), considerable strain and frequently stacking faults. In an attempt to determine if the gross defect structure can be ascribed to the growth conditions *per se* (deposition rate, thermal gradient, substrate preparation, etc.), crystals were grown on dislocation-free (solution grown) GaP substrates. Figure 8 is a contiguous series of photomicrographs of an angle lapped surface showing the defect structure of such a crystal. The substrate remains nearly dislocation free, and the growth layer is free of stacking faults and contains dislocations fewer than  $10^2$   $\text{cm}^{-2}$  albeit a high dislocation density appears at the substrate-growth interface. (The shallow, noncrystallographic pits which appear in the figure are the result of surface damage and are not to be confused with dislocation etch pits.) Another crystal contained stacking faults and dislocations; however, the density of these defects was nevertheless several orders of magnitude lower than for crystals grown on GaAs substrates. A high density of dislocations was also coincident with the substrate-growth interface. Where an inadvertent air leak into the growth chamber resulted in contamination and excessive growth rates, a very high density of stacking faults and dislocations was evident at the substrate-growth interface. The dislocation density decreased with distance from this interface to a final value of  $6 \times 10^4$   $\text{cm}^{-2}$ . In most cases the overgrowth or peripheral deposit is highly faulted and is demarcated by interfacial dislocations ( $\sim 3 \times 10^3$   $\text{cm}^{-1}$ ).

The above observations indicate that the gross defect structure which typifies crystals grown on GaAs substrates is not ascribable to the growth conditions,



Fig. 8. Etched angle-lapped surface of a GaP crystal (left) grown by vapor deposition on a nearly dislocation-free GaP substrate (right). The high density of etch pits is coincident with the substrate-growth interface.

and it is concluded that the heteroepitaxial structure, i.e., the discontinuity in lattice parameter at the substrate-growth interface and the difference in thermal contraction of GaP and GaAs on cooling from the growth temperature, gives rise to the observed structure.

The lattice mismatch of  $\sim 4\%$  at the growth temperature may be accommodated by three sets of interfacial dislocations aligned along  $\langle 211 \rangle$  directions, each set containing a linear density of  $\sim 9 \times 10^6$   $\text{cm}^{-1}$ . The occurrence of a mixed crystal region, i.e.,  $\text{GaP}_x\text{As}_{1-x}$ , could substantially lower the density of interfacial dislocations by reducing the magnitude of the local internal stresses. Examination of GaP crystals after removal of the GaAs seed has not revealed any interfacial dislocations, presumably because the material containing them has been removed by lapping or etching. (Dislocations are present at the original growth interface even in the case of deposition on GaP as noted above.) On the other hand, dislocations resulting from the "bending" of the growth layer on cooling would tend to be distributed throughout the bulk as observed. The strain birefringence of a GaP layer grown with a partially converted seed (to give a  $\text{GaP}_x\text{As}_{1-x}$  transition region) clearly shows a substantial residual bending stress (19). Since this bending stress vanishes on removal of the GaAs seed, leaving a much smaller random strain (19), the curvature of the stripped GaP crystal provides a measure of the plastic deformation which occurred at high temperatures in order to relieve the concomitant bending stress. Assuming that plastic deformation does not occur below  $600^\circ\text{C}$  and that the difference in thermal expansion coefficients of GaP and GaAs near the growth temperature is approximately equal to that at room temperature, the maximum residual radius of curvature of a typical GaP crystal which was grown at  $1100^\circ\text{C}$  (7) is computed to be 65 cm. The minimum density of dislocations which is compatible with this curvature is  $\sim 3 \times 10^5$   $\text{cm}^{-2}$ ; however, owing to the interaction of dislocations on congruent slip planes (the neutral plane is of the {111} type and hence at least three slip systems are activated) and the lack of annihilation of excess dislocations, the dislocation density could be up to an order of magnitude higher. Thus, one could conceivably account for the observed dislocation density in terms of thermally induced strains alone. The fact that stripped crystals frequently exhibit a radius of curvature of  $\lesssim 20$  cm and that a rather complex strain pattern is evident in crystals which were grown without deliberate seed conversion (19) indicates that the observed defect structure involves other sources as well.

Figure 9a shows a rather uniform distribution of dislocations aligned along congruent slip planes in a vapor-grown crystal. Comparison of this figure with Fig. 9b, which corresponds to the same area after  $\sim 10\mu$  was chemically removed, reveals the detailed rearrangements of etch pits corresponding to the circuitous path of dislocations caused by mutual interactions and dislocation reactions. Figure 9c, which represents a different area of the same crystal, shows several etch pits which can be followed to a depth in excess of  $30\mu$ ; these pits appear in the center of the halos or remnants of prior etching. The fact that the corresponding dislocations are practically straight over such a large distance suggests that they were present prior to the "forest" of dislocations. It is thus speculated that the straight dislocations were present at the growth temperature and subsequently locked by impurity segregation; the forest dislocations were then generated on cooling. The more rapid growth rate of etch pits associated with the straight dislocations ( $\sim 2X$  faster than for the forest dislocations) implies greater impurity segregation and thus lends support to this view.

In an earlier study, Gershenzon and Mikulyak (4) reported that, in vapor-grown GaP crystals, the re-



Fig. 9. Dislocation etch pits in a vapor-grown GaP crystal (a) (top); same area after  $10\mu$  was removed by chemical polishing and followed by subsequent etching to reveal dislocations (b) (center); dislocation etch pits in a different area of the same crystal (c) (bottom).

gions of minimum strain birefringence lie along specific crystallographic directions, and from deformation experiments they concluded that the strain minima correspond to traces of active slip planes. We find that for crystals grown by halogen transport (8) the regions of minimum strain birefringence lie along

$\langle 110 \rangle$  and  $\langle 211 \rangle$  directions which could correspond to the traces of congruent  $\{111\}$  and  $\{110\}$  slip planes, respectively. While subsequent etching indicates that dislocations tend to be aligned along  $\langle 110 \rangle$  slip traces, there is not a lower density of active slip planes in the regions of maximum birefringence as would be anticipated from the findings of Gershenzon and Mikulyak. Rather, there is a coincidence of stacking fault traces with these regions. There is not, however, a 1:1 correspondence between the strain pattern in the bulk and stacking fault traces on the viewed surface.

Comparison of the stacking fault morphologies on the substrate and growth faces of a  $\sim 150\mu$  thick crystal reveals that (i) many of the faults propagate through the growth layer, (ii) the density of faults is lower on the growth face, and (iii) not all fault traces on the growth face can be correlated to fault traces on the substrate face. These observations imply that, whereas most faults originate at the substrate-growth interfaces, many faults are generated within the deposited layer perhaps providing a mechanism of stress relief.

*Dislocations and stacking faults in GaP grown by liquid phase epitaxy.*—Crystals grown by liquid phase epitaxy (tipping) (9) have fewer defects than the GaP substrates on which they are grown. For example, a dislocation density of  $2 \times 10^6 \text{ cm}^{-2}$  is reduced by a factor of about 3 in a depth of less than  $5\mu$  as in Fig. 10. In contrast, the temperature gradient zone-melting or travelling solvent method reduces the dislocation density from an initial value of  $8 \times 10^4 \text{ cm}^{-2}$  by a factor of 8 over a depth of  $\sim 10^3\mu$  in GaAs crystals (20). The stacking fault density is not reduced in the tipped layer, i.e., faulted regions propagate into the tipped layer as in Fig. 11. Layers grown on dislocation-free (solution-grown) substrates contain no stacking faults and are essentially dislocation free. In this case dislocations tend to be isolated (straight or as half loops) or aligned along slip traces at voids.

It has been shown above that dislocations consistently appear at the original growth interface in crystals grown by vapor phase epitaxy. These dislocations may arise from the discontinuity in lattice parameter associated with differences in doping levels of the substrate and deposited layers. If this were the case, dislocations should also be observed in comparable tipped layers. Indeed, interfacial dislocations (ascribed to lattice mismatch) and precipitates have been observed in GaAs p-n junctions fabricated by vapor deposition as well as tipping (2). Dislocations and precipitates (electrically inactive species) confined to

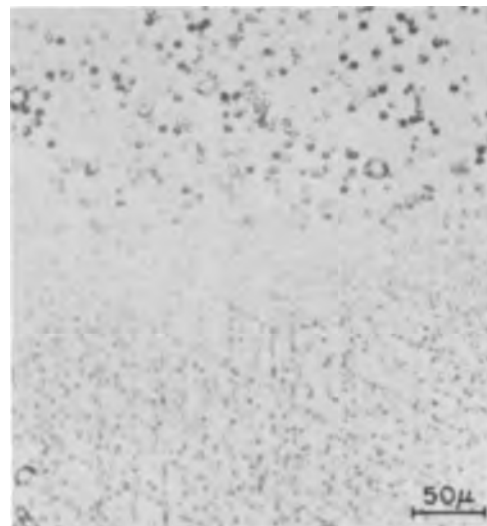


Fig. 10. Dislocation etch pits in a angle-lapped ( $3^\circ$ ) GaP crystal containing a p-n junction which was fabricated by tipping a Te-doped n layer (top) onto a vapor-grown Zn-doped p layer (bottom).



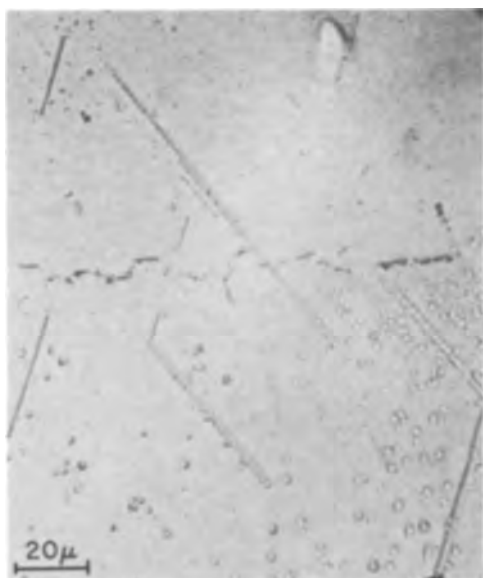


Fig. 11. Trace of a stacking fault in the substrate (bottom) which propagated into the tipped layer (top).

the junction region may have important consequences with regard to electrooptic properties; hence, GaP diodes fabricated by tipping have been carefully examined for these defects. Etching of angle-lapped samples has revealed no dislocations or precipitates in the vicinity of the junction plane in as-grown and annealed (8 hr at 600°C) diodes fabricated from dislocation-free substrates. Both etchants 1 and 2 were used since it was thought that, for the former, etch pits at the junction may be obscured by the difference in etching rates of the p- and n-regions.

Assuming that there are no concentration gradients except in the p-n transition region, the density of dislocations  $\rho$  in the transition region is given by (21)

$$\rho = \frac{1}{a^2} \sum_{i=n,p} \frac{\partial a}{\partial c_i} \frac{\partial c_i}{\partial x} \quad [1]$$

where  $a$  denotes the lattice parameter,  $c_p$  and  $c_n$  denote the respective concentration of p-dopant and n-dopant, and  $\partial c_i / \partial x$  denotes the concentration gradient in the transition region. Accordingly, the dislocation density is not directly a function of  $c_n - c_p$ , but depends on the concentration gradient of both donor and acceptor species in the transition region. Thus the presence or absence of interfacial dislocations depends upon the concentration gradients established during the fabrication of the diodes. The lack of interfacial dislocations as described above is apparently due to the lack of steep concentration gradients in these diodes.

### Conclusions

The large dislocation free areas (40-80% of a crystal) found in GaP crystals grown from gallium solution indicates that this method potentially offers a means of growing near-perfect crystals; however,

better control of the growth conditions is required to eliminate gallium occlusions and the probable inhomogeneous dopant distribution. The high density of dislocations and stacking faults present in crystals grown by vapor phase epitaxial deposition on GaAs substrates appears not to be due to the method of growth but rather the presence of a heteroepitaxial structure, in particular, the difference in thermal contraction of GaP and GaAs on cooling from the growth temperature. Liquid phase epitaxy is advantageous for GaP diode fabrication since, in contrast to vapor phase epitaxy, no dislocations are introduced at the substrate-growth interface (p-n junction), at least for diodes fabricated on dislocation free substrates.

### Acknowledgment

The author is indebted to L. Derick, L. C. Luther, and M. Kowalchik for supplying the crystals and to F. A. Trumbore and helpful comments. The author extends thanks to F. K. Reinhart for stimulating discussions about his unpublished work on the residual strain patterns in vapor-grown GaP.

Manuscript submitted March 18, 1968; revised manuscript received June 17, 1968. This paper was presented at the Boston Meeting, May 5-9, 1968, as Recent News Paper 291.

Any discussion of this paper will appear in a Discussion Section to be published in the June 1969 JOURNAL.

### REFERENCES

1. See, for example, W. Bardsley, "Progress in Semiconductors," Vol. 4, p. 155, A. F. Gibson, F. A. Kroger and R. E. Burgess, Editors, John Wiley & Sons, Inc., New York (1960).
2. M. A. Abrahams and C. J. Buiocchi, *J. Appl. Phys.*, **37**, 1973 (1966).
3. R. O. Carlson, *ibid.*, **38**, 661 (1967).
4. M. Gershenson and R. M. Mikulyak, *ibid.*, **35**, 2132 (1964).
5. R. A. Logan, H. G. White, and F. A. Trumbore, *ibid.*, **38**, 2500 (1967).
6. D. G. Thomas, M. Gershenson, and F. A. Trumbore, *Phys. Rev.*, **133**, A269 (1964).
7. C. J. Frosch, *This Journal*, **111**, 180 (1964).
8. G. S. Kamath and D. Bowman, *ibid.*, **114**, 192 (1967).
9. H. Nelson, *RCA Rev.*, **24**, 603 (1963).
10. M. S. Abrahams and C. J. Buiocchi, *J. Appl. Phys.*, **36**, 2855 (1965).
11. J. L. Richards and A. J. Crocker, *ibid.*, **31**, 611 (1960).
12. W. Reissler, *Z. Angew. Phys.*, **12**, 433 (1960).
13. M. I. Val'kovskaya and Yu. S. Boyanskaya, *Sov. Phys.-Sol. State*, **8**, 1976 (1967).
14. P. Haasen, *Acta Met.*, **5**, 598 (1957).
15. J. D. Venables and R. M. Broudy, *J. Appl. Phys.*, **29**, 1025 (1958).
16. H. C. Gatos, M. C. Lavine, and E. P. Warekois, *This Journal*, **108**, 645 (1961).
17. M. M. Cohen and F. D. Bedard, *J. Appl. Phys.*, **39**, 75 (1968).
18. J. R. Dale and J. C. Brice, *Sol. State Electron.*, **3**, 105 (1961).
19. F. K. Reinhart, Private communication.
20. M. Weinstein, H. E. LaBelle, and A. I. Mlavsky, *J. Appl. Phys.*, **37**, 2913 (1966).
21. See, for example J. Friedel, "Dislocations," p. 204, Addison-Wesley Co., Inc., Reading, Mass. (1964).

# A Method for Determining Sodium Content of Semiconductor Processing Materials

Bernard Yurash\* and Bruce E. Deal\*

*Fairchild Semiconductor Research and Development Laboratory, Palo Alto, California*

## ABSTRACT

A refined flame spectrophotometric method has been used to analyze and control sodium content in materials associated with the processing of semiconductor devices. Several examples of materials analyzed are presented which include water oxidation ambients, quartz oxidation tubes, various organic and inorganic solvents, and sedimented glasses. Very good correlations are obtained between sodium content of these materials and corresponding electrical stability of MOS structures. The method is relatively inexpensive and simple to use, with a detection limit in water of 0.05 ppb sodium.

Attention has been focused on ion transport phenomena and the effect of alkali ions, particularly sodium, on the behavior of surface sensitive, semiconductor devices (1, 2). Especially sensitive to such contamination are metal-oxide-semiconductor (MOS) structures, but any type of passivated device can be affected by the migration of ions through the passivating oxide layer. Every processing step during the fabrication of these devices is a potential source of contamination. Thus, any materials used in the fabrication are suspect in regard to such ions as sodium. These materials include water, etchants, organic and inorganic solvents, diffusion sources, furnace tubes and boats, gaseous ambients, metals used as field plates or interconnections, and encapsulation materials. A method of analysis for sodium in these processing materials and the control (and minimization) of such sodium would be considered an important requirement for producing electrically stable devices.

Analyses of sodium in silicon and silicon dioxide using neutron activation or mass spectrography have been reported by a number of investigators (3-7). However, many laboratories do not have this type of equipment. Therefore, a method of sodium analysis which makes use of a flame spectrophotometer, a common laboratory tool, has been refined for determining sodium content at low levels. As a result, we have been able to analyze and control sodium content of various materials employed during the fabrication of semiconductor devices. The results have provided very good agreement with corresponding data obtained by other methods of analysis. A brief description of the flame photometric method of sodium analysis will be given along with procedures for preparing various types of samples. Several examples are presented showing the comparison of sodium content obtained by this method and that indicated by MOS C-V analysis (8).

## Method

A literature search revealed several reports describing the analysis of sodium in aqueous media in the low parts per billion concentration by flame photometric techniques (9-11). It was obvious that instrumental conditions and sample treatment were critical and had to be strictly controlled for accurate results.

The instrument chosen for this investigation was the Beckman Model DU spectrophotometer. This instrument as delivered did not prove satisfactory, so modifications were made. The photomultiplier tube was specially selected for electronic stability. A medium-bore, oxyhydrogen burner was used. The pressure controller supplied with the instrument did not give reproducible settings at low pressures, yet re-

producible pressures and flow rates of the gases to the burner are required for stability of the flame. A flowmeter with needle valve control was installed in the hydrogen gas line to assure gas flow stability. Optimum oxygen and hydrogen flow rates and pressures depend on the individual instrument and must be determined empirically.

Ambient air drawn into the burner housing also affects signal stability at low sodium concentrations. A filtered air supply plenum chamber for the burner housing was constructed according to Rice (11). Existing Fiberglas acoustic absorber pads inside the burner housing were covered with thin Teflon sheets. A light proof tunnel was installed between the burner housing and the entrance slit to cut down on stray light. All instrument housing joints at the sample compartment end were covered with black plastic tape to eliminate light leaks, and a Teflon-covered, aluminum sheet was made to seal the floor of the burner chamber. During sample aspiration, the sample insertion opening was closed with a small removable panel. In later work, a sharp cut optical filter was added to the optical path in the cell holder compartment just before the photomultiplier shutter to eliminate stray light below 510 m $\mu$ . This addition improved the stability of the signal with very little loss of sensitivity. The flame exhaust guard was placed in a sheet metal duct or exhaust flue to prevent dust particles from falling into the burner housing during an analysis.

In the preparation of the standard calibration curve, two types of standards have been used: a sodium fluoride, reagent-grade material dried, weighed, and carefully diluted to known volumes; and a commercially available aqueous sodium chloride solution of known concentration diluted carefully to provide working standards. All dilutions are carried out using calibrated polyethylene graduated cylinders and pipets because Pyrex volumetric flasks and pipets contribute significant sodium to standards in the part per billion range. Polyethylene bottles in which standards are kept are wrapped in aluminum foil to prevent transport of sodium from the hands through the wall during handling.

The instrument is carefully tuned to the sodium emission line using one of the sodium standards, and then the slide wire % T (per cent transmittance) dial set at 10% T for the "zero" content water from a high-purity water machine. Standards are then run and % T vs. sodium content plotted.

For aspiration into the flame, 5 ml plastic disposable beakers are used which have been soaked for 5 min in the high-purity water machine. Stainless steel Teflon tipped tongs are used to manipulate the small beakers because we have found that merely touching them with the fingers introduces detectable amounts of sodium. Water from the bottle containing the so-

\* Electrochemical Society Active Members.



dium standard is poured into the clean 5 ml beaker, and this in turn is placed in the sample positioning device of the flame photometer. After the sample holder lever is actuated to bring the sample to the aspirator tube, a small panel is placed to cover the sample insertion opening to exclude unfiltered air. Null meter oscillations are pronounced at low signal levels and high instrument sensitivity settings, but with practice an experienced operator can obtain reproducible results and duplicate his calibration curves repeatedly. Our experience has been that with standards or samples which are not affected by environmental conditions, including sampling techniques and accidental contamination, etc., the standard deviation in the range 1-100 ppb is  $\pm 0.4$  ppb. Calibration curves of two ranges of sodium concentration are shown in Fig. 1.

An independent cross check of our standard calibration curve in the part per billion range was obtained by an isotope dilution analysis performed by Aerojet General Nucleonics of San Ramon, California. A sample of radioactive aqueous sodium chloride provided by Oak Ridge National Laboratories was analyzed by Aerojet General and then by us on our flame photometer when the material was safe to handle. Agreement was very good, as shown in Fig. 2.

High-purity water is especially important in the preparation of calibration curves at low sodium levels because one needs to approach zero content sodium for establishing the best signal to noise ratio for sub-nanogram quantities. The standard addition technique does not work well if one is unsure of the absolute concentrations of standard solutions. The source of our high-purity water for preparation of standards, reagents, and for washing samples, plastic beakers, and storage bottles is a water treatment machine as described by Koontz and Sullivan (12). This machine continuously recirculates water in a covered system through filters and ion-exchange resins to provide water very near to theoretical purity.

An excellent discussion of the production of large quantities of high-purity water is found in a report by Simon and Calmon (13). Although they report that the total electrolyte specification may be  $< 20$  ppb as NaCl, it is claimed that a typical loop inlet of a large factory size recirculating deionized water system shows no sodium. Our actual analyses indicate about 0.5 ppb in a properly operating system, with only 0.05 ppb of sodium in the water of the

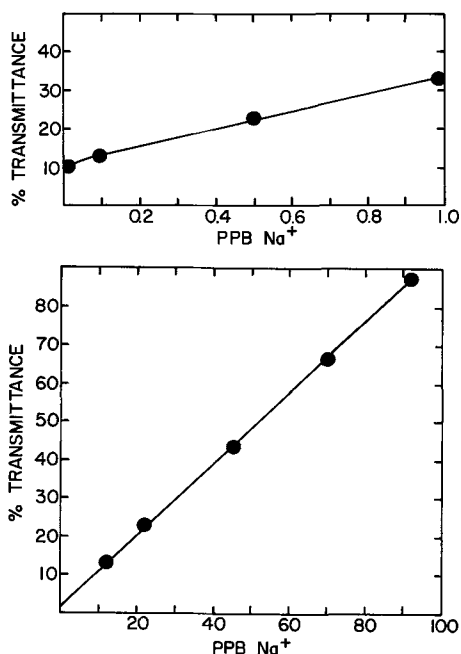


Fig. 1. Flame photometric calibration curves for two ranges of sodium ion concentration.

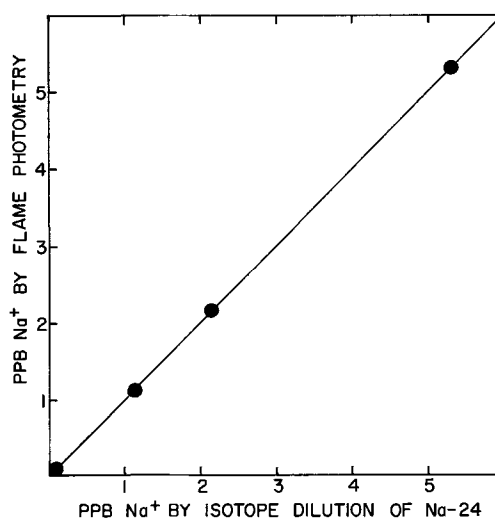


Fig. 2. Agreement between two methods of analysis for aqueous samples of NaCl.

small closed system used for the preparation of standards. If we take a water sample of 0.5 ml, in volume, we find our detection limit to be 0.025 nanogram of sodium.

### Procedure

Sample preparation is extremely important in all stages of the analysis for sodium. This has also been observed by Osborne *et al.* (4) in their activation analysis and by Yon *et al.* (6), who mention finding fractional parts per million levels of sodium in the nitric acid and water used in their work. We have found that surface contamination of samples and sample containers by the ambient laboratory environment and by ordinary handling during an analysis is so variable and at times so severe that a wash or pretreatment in the high-purity recirculating water machine is required before acceptable reproducibility of bulk values could be obtained. Avoidance of contamination is practiced by minimizing open exposure of the samples, reagents, equipment, and containers.

Following is a brief description of methods used to collect or prepare for analysis various types of materials associated with semiconductor device processing.

**Water.**—For our studies of the sodium content of water taken from wet oxidation furnaces, special precautions have to be taken. All equipment is made of quartz, including the furnace tube, the inlet boiling flask, (Pyrex flasks were used initially), and the outlet condenser and receiver. Samples of condensate collected in the receiver after a wet oxidation of silicon are transferred to a prewashed, aluminum foil covered, polyethylene bottle. This is taken to the analytical laboratory where it is introduced into the flame photometer in the same manner as described in the preparation of the calibration curve. A calibration curve is run each day that an analysis is performed (see Fig. 1). The emissivity or % T value found for the sample is compared with the calibration curve to determine the concentration of sodium in the sample. The standard deviation for a given sample collected in the above manner has been found to be  $\pm 1.6$  ppb.

**Quartz.**—Samples of quartz furnace tubes have been analyzed by etching the surface with hydrofluoric acid, soaking the specimen in the reservoir of the water machine for 30 min, and then dissolving a known amount of sample in hydrofluoric acid in a platinum crucible. The sample is taken to dryness on a hot plate, and the residue taken up in a known amount of water for aspiration into the flame of the burner. For optimum results, the hydrofluoric acid should be prepared by gaseous diffusion of anhydrous

hydrogen fluoride into high-purity water using Teflon tubing and vessels.

An independent check of our procedure was obtained by a neutron activation analysis of synthetic  $\text{SiO}_2$  grains prepared from silicon tetrachloride. The activation analysis by the General Atomic Division of General Dynamics Corp. showed  $3.29 \pm 0.03$  ppm and our flame photometric analysis yielded  $3.3 \pm 0.5$  ppm.

**Solvents.**—Analysis of solvents presents a slightly different problem because of enhancement or suppression effects by the solvent in the flame. A known volume is evaporated in a clean platinum dish and the residue taken up in high-purity water for aspiration into the flame. Here again, extreme care must be exercised to prevent contamination from the ambient and skin contact. All manipulations are performed with clean Teflon-tipped tongs, and the platinum crucibles are kept partially covered with platinum lids during the evaporation.

**Glasses.**—Most glasses used in semiconductor processing have appreciable sodium; therefore, reagent grade acids may be used in their dissolution. Reagent blanks must, of course, be run to eliminate the sodium contribution by the reagents. Sample treatment and handling is similar to the quartz analysis described above.

**MOS C-V Analysis.**—Briefly, the procedure for measuring effects of contamination on MOS (metal-oxide-semiconductor) structures using the capacitance-voltage method of analysis (1) is as follows. The MOS capacitor is prepared by thermally oxidizing single crystal silicon (approximately 1 ohm-cm resistivity) to  $0.2\mu$ . The silicon is generally lapped, cleaned, and chemically polished before oxidation. Metal field plates (usually aluminum) are deposited on the oxide surface in diameters ranging from 125 to  $750\mu$  diameter. Aluminum is also deposited on the back side of the silicon where the oxide has been removed. The sample is then annealed at  $550^\circ\text{C}$  in  $\text{N}_2$  for 2 min to assure backside ohmic contact and to minimize fast surface state density. At this point, the devices may be tested to determine prior processing effects, or may be subjected to further processing steps.

Stress tests themselves are accomplished by first plotting the C-V characteristics of the MOS capacitor. The initial curve is translated along the voltage axis from the theoretical case reflecting the fixed surface state charge  $Q_{ss}$ , the work function difference  $\phi_{ms}$ , and possibly some impurity ions  $Q_o$  in the bulk of the oxide. The devices are then subjected to low positive bias (5v) at  $300^\circ\text{C}$  for 2 min and the C-V curve again plotted. The mobile ions move to the silicon and cause the silicon surface to become more n-type. The C-V curve moves in the negative direction. The device is then stressed with a negative bias at  $300^\circ\text{C}$ , and the ions are drawn to the metal field plate. The total mobile ion content is now a function of the voltage difference of the C-V plots after positive and negative stress, as is shown in Fig. 3. Generally, the mobile ions will be on the oxide surface or in the oxide very close to the field plate. Thus, a measure of  $Q_o$  is obtained by a comparison of the initial C-V curve and that after positive bias stress.

#### Examples

The importance of controlling and minimizing impurity ion content, *i.e.*, sodium ions, during semiconductor device fabrication was emphasized in the Introduction. It was pointed out that each processing step is a potential source of sodium. The method of sodium analysis described above has been successfully used for a majority of the materials associated with the processing of semiconductor devices. In many such cases, a direct correlation has been obtained between the sodium content of the particular processing material and device electrical characteristics. In partic-

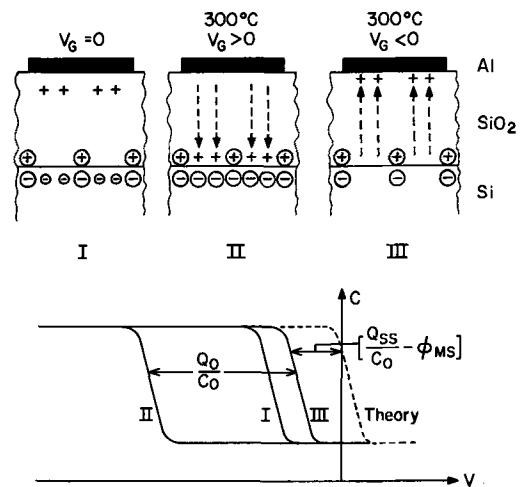


Fig. 3. Method for determining impurity ion concentration  $Q_o$  in MOS structure by capacitance-voltage method. Case I represents initial condition; case II is after positive bias stress test; and case III is after negative bias stress test.

ular, a measure of the latter has been obtained using the MOS capacitance-voltage method of analysis, since this type of measurement, in turn, has been directly correlated with actual device stability (2, 14, 15).

Listed below are several examples which demonstrate the use of this method of analysis for determining sodium content of materials employed in conjunction with semiconductor processing. In some of these cases, corresponding electrical stability data as obtained using MOS structures are also presented. Thus, the degree of correlation between the two analysis methods may be ascertained.

**Water**—Water is used in two important ways during the fabrication of semiconductor devices. One is as a rinse after treatment of the device structure and related materials in inorganic and organic solvents. This case will be discussed later in the Solvent section.

The other use of water is during thermal oxidation of silicon, which can be carried out either in dry oxygen or oxygen (or inert gas) bubbled through water. The latter, called wet oxygen, provides a much more rapid oxidation rate (16). The sodium content of the water carried into the oxidation tube will be very important in regards to the resulting oxide purity. Furthermore, any additional sodium picked up by this wet ambient in the gas lines or the quartz tube will also contribute to the oxide contamination. For this reason, experiments were conducted to relate the sodium content of the water used in thermal oxidation, before entering and after leaving the oxidation tube, and electrical stability of MOS structures oxidized at the same time. The tube was transparent, commercial-grade fused quartz (see Quartz section below).

Table I lists typical sodium content of deionized water collected at various stages of thermal oxidation of silicon. Two important facts can be noted from these data. First, while the initially high-purity water

Table I. Sodium concentration in various water samples used for silicon oxidation

Collection point of water	Na <sup>+</sup> content, ppb
From line (deionized water)	<1
Pyrex bubbler	300-500
Quartz* bubbler	10-50
Distillate from either bubbler	<10
Through quartz ox. tube, $1200^\circ\text{C}$	10-40
Through quartz ox. tube, $920^\circ\text{C}$	5-15

\* Transparent commercial-grade fused quartz.

Table II. Relationship of contamination  $Q_o/q$  in thermal oxides and sodium content of water collected from exit of oxidation tube during oxidation

Oxidation temp, °C	MOS drift, $Q_o/q$ , cm <sup>-2</sup>	Na <sup>+</sup> content in water, ppb
1200	$5 \times 10^{11}$	35
920	$2 \times 10^{11}$	12

can be contaminated by the flask, a fairly efficient distillation occurs. Second, a distinct difference in sodium content can be obtained between the water passing through the quartz oxidation tube at 920° and 1200°C, the latter being appreciably greater at any given time.

Corresponding instability data for MOS structures are listed for specific cases in Table II, along with Na<sup>+</sup> content of water collected after passing through the oxidation tube. The oxides were prepared at the two temperatures by oxidizing with O<sub>2</sub> bubbling through 95°C water for the times required to produce 0.2 $\mu$  layers [4¼ min at 1200°C, 45 min at 920°C (16)]. The  $Q_o/q$  values (in number of charges per cm<sup>2</sup>) were obtained by measuring the voltage displacement of capacitance-voltage plots of MOS structures after stressing at  $\pm 50$  v/ $\mu$  for 3 min at 300°C (1).

These results show a direct relationship between the contamination in the oxides as measured by MOS stress tests and the sodium analysis of the water collected from the end of the quartz tube. It is proposed that the greater amount of contamination obtained during the 1200°C oxidations in the case of these experiments was due to a faster etch rate of the quartz by the wet ambient. Thus, more of the sodium contained in the quartz was incorporated in the oxide during its formation. The amount of sodium coming from the water should actually be less at 1200°C, since the oxidation time for a given oxide thickness is much less than at 920°C while the flow rates were the same. Additional experiments which involved placing the silicon samples at 920°C ahead or behind a 1200°C region in the tube also confirmed that more contamination was coming from the quartz at 1200°C.

An interesting result obtained during these experiments was a profile of sodium in the wet oxides. This was obtained by MOS C-V stress measurements of oxides before and after etching off thin layers of the oxide in dilute hydrofluoric acid.<sup>1</sup> The data for the oxides prepared at the two temperatures are listed in Table III.

The results in Table III show first the total difference in  $Q_o/q$  for the two temperatures. They also show that at 1200°C, the contamination extends deeper into the 0.2 $\mu$  oxide, and 200Å must be etched off to remove it. At 920°C, the contamination is contained in the outer 50Å. In both cases, the sodium remains in the outer portion of the oxide due to the proposed field during thermal oxidation (16). Similar findings have been reported for experiments in which neutron activation analysis has been employed (4, 6, 7).

Two other effects were established during experiments relating drift of MOS structures and sodium analysis of water. One was that, if silicon slices were stacked one on top of another, the inside oxides pro-

<sup>1</sup> 1 part conc (49%) HF, 10 parts deionized H<sub>2</sub>O.

Table III. Profile of mobile ion concentration in 0.2 $\mu$  wet thermal oxides obtained by MOS stress tests

Oxidation temp, °C	SiO <sub>2</sub> removed, Å	Contamination $Q_o/q$ , cm <sup>-2</sup>
920	0	$1.9 \times 10^{11}$
920	50	$< 0.1 \times 10^{11}$
920	100	$< 0.1 \times 10^{11}$
1200	0	$4.5 \times 10^{11}$
1200	50	$2.6 \times 10^{11}$
1200	100	$1.2 \times 10^{11}$
1200	150	$0.5 \times 10^{11}$
1200	200	$< 0.1 \times 10^{11}$
1200	600	$< 0.1 \times 10^{11}$

duced in these sandwich arrangements were found to be relatively free from ion drift, i.e., sodium. Thus, it appears that, while the same thickness oxide can be produced on a "masked" or blocked surface, the sodium apparently does not contaminate this oxide.

The second effect noted was that caused by subsequent treatment of contaminated, wet oxides in dry O<sub>2</sub>, N<sub>2</sub>, and argon. It was found that a subsequent 15-min treatment at 1200°C of a 0.2 $\mu$ , 1200°C wet oxide in either argon or nitrogen would eliminate more than 90% of the contamination. On the other hand, 80 min in dry O<sub>2</sub> at the same temperature would remove only 75% of the sodium. These findings agree with data reported by Schmidt (17).

**Quartz.**—Since the analyses described above indicated that the quartz tube, boat, and other items used for high-temperature oxidations could contribute sodium to the oxide (especially in a wet ambient), the sodium content in quartz was determined. Three different "grades" of fused silica or quartz were checked. As expected, the optical grade quartz from two sources contains in the order of 1 ppb sodium. The commercial grade of transparent fused quartz contains about 1 ppm, while the translucent, commercial grade contains 15 ppm or more sodium. The use of the low sodium, optical grade quartz would obviously result in a minimum amount of sodium contamination. However, its use would depend on weighing its high cost against the actual stability requirements for the devices being processed. In any case, rigid conditions of cleanliness still must be maintained both in precleaning of quartz tube, boat, and in the oxidation process itself.

**Solvents.**—Various liquids including organic solvents, inorganic acids, and water are used for rinsing, cleaning, and etching device structures throughout the fabrication of semiconductor devices. As a result these solvents are a very likely source of ionic contamination. Experiments have therefore been carried out to relate MOS electrical stability to sodium in solvents as measured by the flame photometric method.

One experiment involved relating MOS stability to some of the standard sodium solutions used for calibration purposes (see Fig. 1). Oxidized silicon samples were rinsed in solutions containing 11, 46, and 92 ppb sodium as well as in deionized water (0.5 ppb sodium). For each of the four solutions, one sample was blown dry in N<sub>2</sub> after rinsing, while the solution on another was allowed to evaporate in a laminar flow hood. Aluminum dots were then evaporated on the treated oxides and the total impurity concentration  $Q_o$  was determined by MOS stress measurements. Results are plotted in Fig. 4.

Reproducibility for the "blow-dry-in-N<sub>2</sub>" case was about  $\pm 20\%$ . The spread was larger where the solution was evaporated as would be expected. However, average values of  $Q_o$  still provide good linear relationships with sodium content for both cases. The total contamination for those samples where the solution was evaporated is a little over ten times that of the rinse and N<sub>2</sub>-dry set. The thickness of the aqueous film was calculated from the  $Q_o/q$  values to be about 10 $\mu$  for the samples where the solution was evaporated, assuming all sodium remained on the oxide surface.

For the purpose of relating sodium content of other solvents to MOS stability, standard 0.2 $\mu$  thermal oxides were rinsed in the solvent being evaluated. In the case of organic solvents and water, they were allowed to dry, and aluminum dots were immediately deposited on the oxide surface. The acid treatments were followed by thorough DI water rinses and then air dried. Approximately 50Å of oxide was removed by the 1:10 HF:H<sub>2</sub>O treatment; in all other cases, no oxide was removed due to the solvent treatment. Typical results of these tests are given in Table IV where the concentration of mobile ions in the oxide,

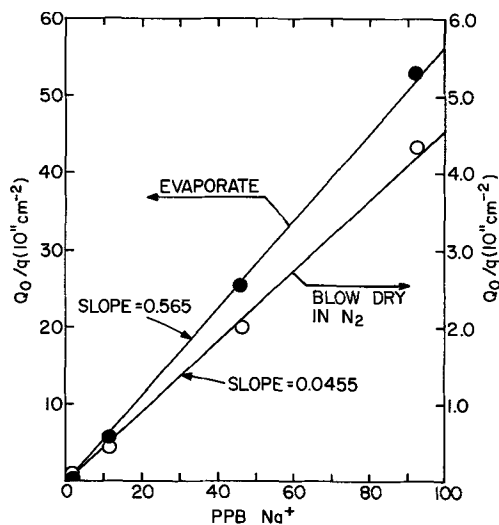


Fig. 4. Relationship between sodium content in standard solution used to rinse oxidized silicon samples and ionic contamination  $Q_o/q$  measured by stress tests of subsequently prepared MOS capacitors.

$Q_o/q$ , as measured by MOS temperature stress tests, and sodium content of the solvent are tabulated.

Representative samples of three classes of solvents, water, inorganic acids, and organic compounds, are included in Table IV. In each case solvents with low and higher sodium contents provide corresponding low and higher amounts of MOS drift. This same correlation has been found for a variety of other solvents, the total amount of contamination varying from lot-to-lot.

An interesting comparison may be made between the data obtained for tap water and the results of Fig. 4. The slope of the relationship of the "blow-dry-in- $N_2$ " case of Fig. 4 is 0.0455. If the ratio of  $Q_o/q$  to sodium content of the tap water listed in Table IV is calculated, it turns out to be 0.049. This means the tap water values would fit an extrapolated curve in Fig. 4 very well, even at the much higher sodium content value.

An additional experiment was carried out, the results of which support the data in Table IV. A number of clean MOS structures were prepared with small diameter ( $250\mu$ ) aluminum field plates. After annealing at  $550^\circ C$  in  $N_2$  and dicing, the measured drift was less than 0.1v. The dice were then rinsed in various solvents and stressed at  $300^\circ C$ . Although the resulting C-V curves were now distorted, the average amounts of drift were in the same order for various solvents as those treated with the solvents prior to metallization. Typical curves are shown in Fig. 5. For these structures, the contamination was believed to be due to some ionic species diffusing in from the edge of the field plate under the applied field. The source of the ions was therefore assumed to be the solvents used to rinse the devices.

Gregor (18) and Hofstein (19) have also studied the effect of organic solvents on MOS stability. Gregor's results for a series of organic solvents show the general effect that the more basic the solvent,

Table IV. Relationship of contamination  $Q_o/q$  in thermal oxides and sodium content of various solvents used to treat oxide surface prior to metallization

Solvent	MOS drift $Q_o/q$ , $cm^{-2}$	Na <sup>+</sup> content, ppb
DI water	$<1 \times 10^{10}$	0.4
Tap water	$>6 \times 10^{12}$	1300
Trichloroethylene	$<1 \times 10^{10}$	0.1-1.0
Acetone	$5-15 \times 10^{11}$	10-50
1:10 HF acid + DI water	$<1 \times 10^{10}$	1.5
Sulfuric acid + DI water	$2-5 \times 10^{11}$	40

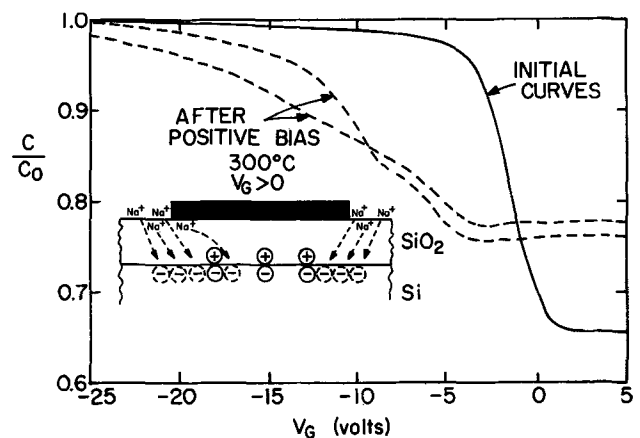


Fig. 5. Example of "edge-effect" in MOS stress test. Distorted C-V plot results from impurity ions, i.e.,  $Na^+$ , migrating under field at elevated temperature from edge of metal field plate.

the more adverse effect on MOS stability. Thus, he and Hofstein both propose some reaction between the metal (aluminum) and the treated oxide to release an active positive species such as hydrogen. However, the correlation obtained in the present work between sodium content of the organic solvents and MOS instability would suggest that the more active solvents might dissolve more sodium and thus would lead to increased contamination of the oxides.

**Glasses.**—Sodium content in glasses deposited by sedimentation techniques on device structures has been successfully analyzed and controlled by the flame photometric method (20). These glasses, based on  $PbO$ ,  $B_2O_3$ ,  $Al_2O_3$ ,  $SiO_2$  combinations, have been reproducibly prepared with sodium content below 10 ppm. This amount of sodium will still permit considerable drift of MOS structures (21).

An effort was made to compare the sodium analysis obtained on bulk material (glass frit) with a thin film ( $2.0\mu$ ) deposited on silicon slices. The latter is approaching the limit of the analysis since the expected sodium content of the solution used to dissolve the glass film would be in the low parts per billion range. The results are shown in Table V for two glasses of different purity. It can be noted that the relative sodium contents between the two glasses are the same for the bulk and film, although the absolute values for the film are lower. This is possibly due to an error in background and lower accuracy obtained in the film analysis, or leaching during the sedimentation process.

Attempts have also been made to determine sodium content in thermal oxides and vapor-deposited oxides. However, all analyses result in about the same value, 1 ppm. The MOS drifts vary over a wide range and should correspond to  $Na^+$  contents of less than 1 ppb to 1 ppm for the samples analyzed. As was the case with the glass determinations, 1 ppm in the oxide film actually corresponds to 1 ppb in the HF solution in which the film was dissolved. Thus, the resulting value of sodium content may or may not be significant when the very small weight of oxide being analyzed is considered. Efforts are being made to increase the sensitivity of sodium by the flame photometric technique so that dielectric films (in the 0.1- $1.0\mu$  thickness range) on silicon can be analyzed.<sup>2</sup>

### Conclusions

By suitable refinement, the flame spectrophotometer can be used to analyze and control sodium in semi-

<sup>2</sup> Donega et al. (22) have just reported in a Recent News Paper at the Boston Meeting of the Society that they have used the flame spectrophotometric method to determine sodium content of thermal oxides on silicon. Their detection limit for sodium in thermal oxides was the equivalent of  $8 \times 10^{11}$  Na atoms/ $cm^2$ . For oxide films in the thickness range of 0.1 to  $1.0\mu$ , this detection limit agrees with our findings above. The oxides analyzed by Donega, however, contained considerably more sodium, i.e., 10-100 ppm, than those analyzed in this investigation, i.e.,  $<1$  ppm.

Table V. Sodium content of sedimented glass frit and film

Batch No.	Bulk frit	2.0 $\mu$ Film
285	41 $\pm$ 2 ppm	23 $\pm$ 5 ppm
286	12 $\pm$ 2 ppm	8 $\pm$ 3 ppm

conductor processing materials. With a sufficient amount of sample, it is thus possible to measure sodium concentration down to 1 ppb or less, a value necessary for fabricating electrically stable, surface sensitive devices such as MOS transistors. Such processing materials as water used for oxidation, quartz tubes and accessories, solvents used for cleaning semiconductor devices, and glasses used for passivating device surfaces have been successfully analyzed for sodium content. In turn, it has been shown that a good correlation exists between the sodium content in these materials and resulting device stability as determined by MOS capacitance-voltage techniques. This correlation has been obtained even for cases where ionic species other than sodium have been postulated to be the cause of the instability, such as the treatment of oxide surfaces with various solvents.

This method of sodium analysis is relatively inexpensive, as well as easy and rapid to carry out when compared with such techniques as neutron activation analysis, mass spectrometry, and the like. By taking reasonable precautions, reproducible and accurate results can be obtained with minimum difficulty. One of the most important factors in this type of analysis is the use of high-purity water, both in establishing a "zero" sodium content reference point for the analyses and in obtaining minimum contamination during device processing. Sodium content of specially purified deionized water used as standards for these analyses has consistently been in the 0.05 ppb range, while the deionized water used on a larger scale for semiconductor processing has been shown to contain approximately 0.5 ppb sodium.

#### Acknowledgment

The authors wish to acknowledge the preliminary development involving the flame photometric method carried out by K. E. Lemons and G. Bobos. R. Ceynowa conducted most of the flame analyses reported in this paper, and M. Sklar conducted the MOS sample preparation and analyses. Finally, the authors wish

to thank Dr. Harry Sello for helpful advice and encouragement during the course of this work.

Manuscript received June 10, 1968.

Any discussion of this paper will appear in a Discussion Section to be published in the June 1969 JOURNAL.

#### REFERENCES

1. E. H. Snow, A. S. Grove, B. E. Deal, and C. T. Sah, *J. Appl. Phys.*, **36**, 1664 (1965).
2. E. H. Snow and B. E. Deal, *Trans. Met. Soc. AIME*, **242**, 512 (1968).
3. Associated Electric Industries, England, Private communication.
4. J. F. Osborne, G. B. Larrabee, and V. Harrap, *Anal. Chem.*, **39**, 1144 (1967).
5. G. Lunde, *Solid-State Tech.*, **11-1**, 32 (1968).
6. E. Yon, W. H. Ko, and A. B. Kuper, *IEEE Trans. Electron Devices*, **ED-13**, 276 (1966).
7. T. M. Buck, F. G. Allen, J. V. Dalton, and J. D. Struthers, *This Journal*, **114**, 862 (1967).
8. A. S. Grove, B. E. Deal, E. H. Snow, and C. T. Sah, *Solid-State Electronics*, **8**, 145 (1965).
9. F. W. J. Garton, J. L. Waddingham, P. C. Wildy, H. M. Davis, and S. J. Hawkins, U.K. Atomic Energy Authority Research Group Report AERE-R-4141 (1962).
10. H. A. Bloomer, D. D. Trammell, and F. C. Rector, *J. Lab. Clin. Med.*, **61**, 692 (1963).
11. J. K. Rice, Tech. Bull. No. 68, Cyrus Wm. Rice & Co., Pittsburgh, Pa.
12. D. E. Koontz and M. V. Sullivan, ASTM Special Tech. Publ. No. 246, p. 1 (1958).
13. G. P. Simon and C. Calmon, *Solid-State Tech.*, **11-2**, 21 (1968).
14. S. R. Hofstein, *Solid-State Electronics*, **10**, 657 (1967).
15. *IBM J. Research Dev.*, **8**, (1964), entire issue.
16. B. E. Deal and A. S. Grove, *J. Appl. Phys.*, **36**, 3770 (1965).
17. R. Schmidt, Paper presented at the Philadelphia Meeting of the Society, Oct. 9-13, 1966, Electronics Semiconductor RN-11.
18. L. V. Gregor, Paper presented at the Cleveland Meeting of the Society, May 1-6, 1966, Paper 12.
19. S. R. Hofstein, *IEEE Trans. Electron Devices*, **ED-14**, 749 (1967).
20. M. E. Dumesnil and R. Hewitt, To be published.
21. E. H. Snow and M. E. Dumesnil, *J. Appl. Phys.*, **37**, 2123 (1966).
22. H. M. Donega, J. E. Barry, and T. E. Burgess, Paper presented at the Boston Meeting of the Society, May 5-9, 1968, RN-306.

# A Theoretical Model of the Three-Point Probe Breakdown Technique

P. A. Schumann, Jr.\*

IBM Components Division, East Fishkill Laboratory, Hopewell Junction, New York

## ABSTRACT

A review is presented of available data for the three-point probe for silicon which indicate that the technique as commonly practiced is greatly influenced by thermal considerations. From the data an empirical model is developed involving the concept of constant power at breakdown. The voltage is accounted for by a combination of a spreading resistance and a contact or barrier voltage. Breakdowns are shown to exist in both forward and reverse directions, and the model is applied to both. The model is shown to be self-consistent, if reasonable values of the radius of contact and measured power are used. This model is used to explain the slope of the calibration curve, effects of layer thickness on breakdown voltage, and the effects of pressure on breakdown voltage. A simple explanation for the turnover or breakdown voltage is proposed, based on the intrinsic temperature, and it is shown that this temperature is achieved under the probe for the current levels commonly used.

The three-point probe (1-7) is a well-known instrument for the measurement of  $n/n^+$  or  $p/p^+$  semiconductor epitaxial structures. It has been most widely used for silicon, but has also been applied to germanium (6) and gallium arsenide (5). Other modifications of the technique (7) involving fewer point contacts and substituting broad area contacts have also been used. In all these studies, it has been assumed that the point-metal semiconductor contact can be treated as a step pn junction (2, 4) or a Schottky barrier diode (7). Very little mention is made of the forward characteristics, although some curves are shown (2). Primarily, the authors have been occupied with the effects of various factors on the reverse characteristics. There are many effects which would indicate that a junction theory is not applicable to the three-point probe as commonly used in the 0.1 to 1.0 ohm-cm resistivity range. A model is proposed herein which minimizes any junction or barrier effects and stresses the thermal conditions under which the measurement is performed.

The important factors which must be explained by any model are:

1. The slope of the calibration curve
2. The fact that n- and p-type semiconductors for the same impurity concentration yield different breakdown voltages
3. The high level of current needed to achieve breakdown
4. The effects of pressure which are different for epitaxial and bulk samples
5. The effect of duty cycle on the breakdown voltage
6. The effects of temperature on the breakdown voltage
7. The effects of epitaxial layer thickness on breakdown voltage
8. The fact that the power at breakdown is a constant and is different on epitaxial and bulk samples
9. The melting or near melting of the semiconductor material under the probe.

The calibration curve, which is necessary because the technique is empirical, has been determined by all the authors referenced above for various materials. The curves are summarized in Table I for the resistivity range 0.1 to 1.0 ohm-cm, which will be the restricted range of interest for this paper. The reason for this restriction is that the data at low resistivity are not

always reliable and the calibration curve bends above 1 ohm-cm. Over the 0.1-1.0 ohm-cm range, the calibration curve can be represented by a simple function

$$V = A\rho^B \quad [1]$$

The slope of the  $\log V - \log \rho$  curve varies, depends on the author, but the average is 0.54. This is much too low for a step junction. Miller (8) has a value of  $-0.66$  for the dependence of breakdown voltage on impurity concentration. If the assumption is made that, for this range the impurity concentration is inversely proportional to the resistivity, the dependence on resistivity should be 0.66.

It was shown in an earlier report (4) that the breakdown voltage was not the same for n- and p-type silicon of the same concentration. Compared with Miller's data, the three-point probe gave higher breakdowns for low resistivity material and lower breakdowns for high resistivity material, with the break point being about 1 ohm-cm. A true pn junction might differ from Miller's curve because of the size of the point contact (9, 10), but both p and n material should be the same.

Very high current levels are required to achieve breakdowns for the three-point probe. Current levels range from 20 to 100 ma, depending on the resistivity and type of probe.

The effects of pressure on three-point breakdown voltage have been studied by several authors (4, 6). It has been found that an increase in point loading decreases the breakdown voltage for both bulk and epitaxial material, but the decrease is greater for the epitaxial material. This decrease was also less for high resistivity material.

Duty cycle plays an important role in determining the breakdown voltage. As the duty cycle is decreased the breakdown voltage increases (6-11). It has been

Table I. Slope of  $\log V - \log \rho$  calibration curves

Material	Type	B	Source
Si	N	0.57	Gardner, Hallenback, and Schumann (1)
Si	N	0.59	Gardner, Hallenback, and Schumann (1)
Si	N	0.54	Gardner and Schumann (4)
Si	N	0.51	Brownson (2)
Si	N	0.55	Allen, Clevenger, and Gupta (6)
Si	P	0.67	Allen, Clevenger, and Gupta (6)
Ge	P	0.31	Allen, Clevenger, and Gupta (6)
Ge	N	0.50	Allen, Clevenger, and Gupta (6)
Average		0.54	

\* Electrochemical Society Active Member.

shown (11) that the breakdown voltage continues to increase even if the pulsewidth is decreased to 0.1  $\mu\text{sec}$  holding the repetition rate constant at 15 Hz.

Ambient temperature effects have not been discussed in much detail, but recent work (7, 11) has shown that an increase in temperature decreases the breakdown voltage, contrary to the results expected from a junction. Frank (7) explains this decrease in terms of a Schottky barrier diode and a change in the mobility with temperature.

It has been noted that decreasing epitaxial layer thickness decreases the breakdown voltage for certain ranges of thickness and resistivity (2-4, 6). It has generally been assumed that this is due to depletion width limiting, which Shields (12) has worked out in detail for a  $p/n/n^+$  structure. Comparisons between this model and experimental data for the three-point probe (4, 6) have been successful for the most part. The original model proposed by Brownson (2) is in error as he does not account for any change in voltage once the depletion region has reached the substrate. These comparisons are clouded, however, because the change in resistivity from the substrate to the surface of the layer is not a step function. For the layer resistivities and thicknesses where depletion width limiting should occur, the profile should be most graded, i.e. nonstep function. Also the surface resistivity will increase with an increase in thickness in this region just because of the shape of the profile.

Data presented in this paper show that the power, product of voltage and current, at breakdown is nearly a constant. It is also shown that this power will be higher for epitaxial  $n/n^+$  layers than for non-epitaxial wafers of the same resistivity and will be a function of layer thickness. There is no correspondence to this effect for a pn junction.

Photographs in another report (11) indicate that rather severe melting of the semiconductor can occur under the forward and reverse biased points if the electrical measurement is not made properly. This indicates a very high rise in temperature under the point even under ideal conditions.

#### Basic Considerations

Beginning with the statement that the power at breakdown is a constant and is different on epitaxial and bulk samples, we can make use of the simple equations for the spreading resistance (13-15) of a point contact for this configuration to propose a simple model.

The spreading resistance voltage of a flat circular contact of radius  $a$  in a three-point probe configuration is given by

$$V = \frac{I\rho}{4a} K \quad [2]$$

where  $V$  = spreading resistance voltage in volts,  $I$  = current in amperes,  $\rho$  = resistivity in ohm-cm,  $a$  = radius of contact in centimeters, and  $K$  = dimensionless correction factor.

The dimensionless correction factor is a function of geometry and resistivity structure of the sample and is discussed in detail elsewhere (15).

It is known that the breakdown voltage and resistivity can be related in a simple fashion, Eq. [1], where  $A$  and  $B$  are empirically determined constants having the units of volts/(ohm-cm) $^{1/B}$  and of a pure number, respectively. Combining [1] and [2] and solving for the current results in

$$I = \frac{4a A\rho^{B-1}}{K} \quad [3]$$

Solving for the power

$$P = VI = \frac{4a A^2\rho^{2B-1}}{K} \quad [4]$$

In order for the power to be independent of the resistivity,  $2B - 1 = 0$  or  $B = \frac{1}{2}$ . The actual average

value obtained in Table I was 0.54, which suggests that the power should be independent of resistivity. Note that the dimensionless correction factor appears in the denominator. For bulk material,  $K = 1$  and no effect is noted. However, for an  $n/n^+$  epitaxial structure,  $K$  is a positive number less than one, which would increase the power and would be a function of layer thickness, as stated in item 8. The equation is also interesting because there is no mention of forward or reverse biased conditions. A detailed study of forward characteristics showed that breakdowns do occur in both directions. Figures 1 and 2 are representative samples of both forward and reverse characteristics for  $n$ - and  $p$ -type silicon. The breakdowns in the forward direction were measured by taking the reading in the same fashion as for the reverse, i.e., ignoring the fact that it is supposed to be a forward. The reverse characteristics remained relatively unchanged throughout this process, provided the sample did not heat up too much. Both forward and reverse could be held simultaneously in breakdown with no drift. These measurements were made on chemically polished wafers with an a-c system (2, 3).

The forward and reverse breakdown voltage levels and the shape of the characteristics were almost the same. However, there was a consistent difference with the reverse level being higher than the forward. The linearity of the curve right out to the breakdown was better for  $n$ -type than for  $p$ -type.

#### Empirical Model

Because the forward and reverse breakdown levels are not the same, the simple model must be altered somewhat. If it is assumed that there is a contact or barrier resistance in the reverse direction which is not present in the forward direction, a better empirical

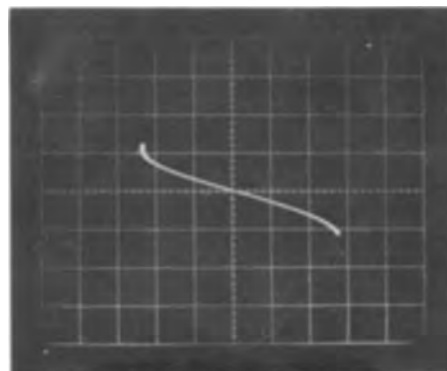


Fig. 1. Three-point probe I-V characteristics for a 0.233 ohm-cm  $n$ -type sample. Current is recorded vertically (50 ma/cm) and voltage horizontally (10 v/cm).

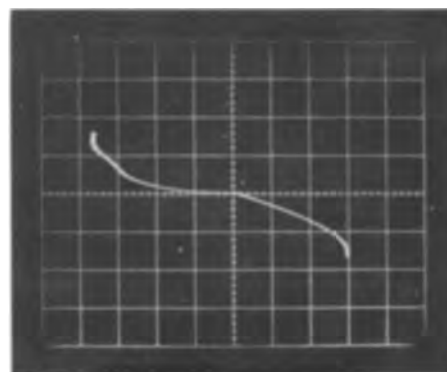


Fig. 2. Three-point probe I-V characteristics for a 0.206 ohm-cm  $p$ -type sample. Current is recorded vertically (50 ma/cm) and voltage horizontally (5 v/cm).

model can be developed. This contact resistance is due to the metal-semiconductor contact but will not be discussed here. Introducing the subscripts R for reverse, F for forward, and C for contact, the voltages and currents at breakdown are related by

$$V_F = \frac{I_F \rho}{4a} K \quad [5]$$

$$V_R = \frac{I_R \rho}{4a} K + V_C \quad [6]$$

The powers become

$$P_F = \frac{4a A_F^2 \rho^2 B_F^{-1}}{K} \quad [7]$$

$$P_R = \frac{4a A_R^2}{K} \left[ 1 - \frac{V_C}{V_R} \right] \rho^{2B_R-1} \quad [8]$$

Assuming that these are independent of resistivity,  $B_R = B_F = \frac{1}{2}$ , and solving for the breakdown voltages

$$V_F = \sqrt{\frac{\rho K P_F}{4a}} \quad [9]$$

$$V_R = \sqrt{\frac{\rho K P_R}{4a} + \frac{V_C^2}{4}} + \frac{V_C}{2} \quad [10]$$

Using the known relationships for  $V_F$  and  $V_R$  on resistivity,  $V_C$  may be calculated

$$V_C = A_R \left[ 1 - \frac{P_R A_F^2}{P_F A_R^2} \right] \rho^{0.5} \quad [11]$$

or

$$V_C = A_C \rho^{0.5} \quad [12]$$

An assumption is being made here that is not necessarily valid. By forcing the power to be a constant, as determined experimentally,  $V_C$  is forced into a square-root dependence on resistivity. A study of Eq. [8] will show that  $B_R$  can have values different from  $\frac{1}{2}$  still maintaining constant power as long as  $V_C$  varies in an appropriate manner. Also the power is not quite constant. All of this could result in a different dependence of  $V_C$  on resistivity, but the data or the model are not considered good enough to warrant this detail.

The equations may also be solved for the current dependence, resulting in

$$I_F = C_F \rho^{-0.5} \quad [13]$$

$$I_R = C_R \rho^{-0.5} \quad [14]$$

or

$$I_F = \frac{4a A_F}{K} \rho^{-0.5} \quad [15]$$

$$I_R = \frac{4a (A_R - A_C)}{K} \rho^{-0.5} \quad [16]$$

#### Comparison with Experiment

These basic equations can then be fitted to the data as obtained. The data used for this comparison were taken from measurements on n- and p-type chemically polished silicon wafers. The samples had resistivities between 0.1 and 1.2 ohm-cm. The probe was a modified Dumas P4-85, as described in an earlier report (4), operated at a loading of 35g per point. Using an a-c system (2) and oscilloscope display, five measurements were made for each point. The standard deviation was calculated and included on the graph. The variation in the data is high in most cases because of variations in both the material and the probe.

Figures 3 and 4 show the power obtained as the product of the voltage and current at breakdown as a function of resistivity for n-type silicon. To use the model for calculation, the effective radius of contact must be known. Figure 5 shows the radius of contact

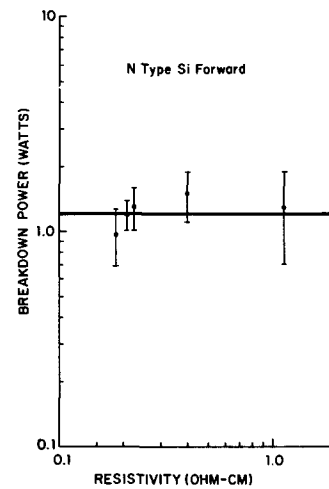


Fig. 3. Forward breakdown power as a function of resistivity for n-type silicon.

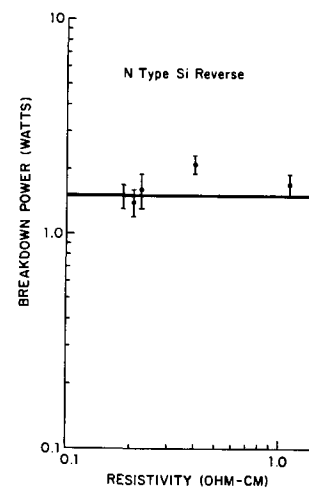


Fig. 4. Reverse breakdown power as a function of resistivity for n-type silicon.

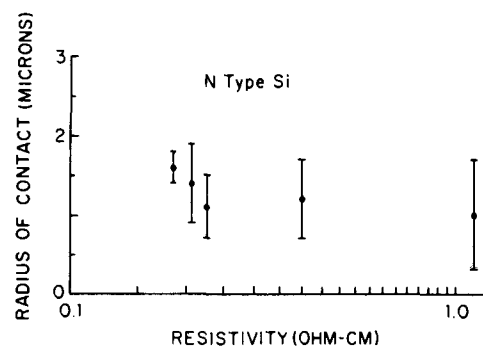


Fig. 5. Radius of contact calculated from spreading resistance at low levels for n-type silicon for this probe.

obtained from Eq. [2] and measurements of the current at 10 mv on the same samples, using the same probe at the same loading, as a function of resistivity. For n-type silicon over this range, the radius of contact is nearly constant. This has been reported earlier for the spreading resistance measurement (15, 16) and is confirmed here. The average radii of contacts are  $1.3 \pm 0.2\mu$  and  $2.4 \pm 1.2\mu$  for n- and p-type, respectively. The approximation of constant radius is better for n-type and is within experimental error. Using these values for the radii of contact and the  $A_F$  and  $A_R$  determined experimentally results in the solid curves shown in Fig. 3 and 4. Table II shows the comparison between the experimental averages and those obtained by the model.



Table II. Comparison of experimental averages and those obtained by model

Type	Current flow	Power, watts		Voltage				C	Current		Contact voltage $A_C$ model
		Average	Model	A	Model	B	Model		Current	Model	
N	F	1.3	1.2	44	47	0.45	0.50	$26 \times 10^{-3}$	$24 \times 10^{-3}$	0	
N	R	1.7	1.5	66	65	0.51	0.50	$26 \times 10^{-3}$	$23 \times 10^{-3}$	21	
P	F	1.1	0.9	29	31	0.47	0.50	$31 \times 10^{-3}$	$30 \times 10^{-3}$	0	
P	R	0.9	0.9	45	47	0.49	0.50	$20 \times 10^{-3}$	$19 \times 10^{-3}$	27	

A and B are constants from Eq. [1].  
C is a constant from Eq. [13].  
 $A_C$  is a constant from Eq. [12].

Figure 6 and 7 are plots of the breakdown voltage as a function of resistivity for n-type silicon. The solid line in each case is a least squares fit of Eq. [9] and [10] to the data. Table II shows the validity of this approximation by comparing the values of the constants obtained from fitting Eq. [1] to the data.

The current dependence on resistivity is shown in Fig. 8 and 9, and the results of the current dependence are summarized in Table II. A least squares fit of Eq. [13] and [14] yields results comparable to the model as calculated from Eq. [15] and [16]. Table II also shows the values of the constant  $A_C$  obtained from the model and experimental data using Eq. [11].

A comparison between the reverse power levels obtained on bulk and epitaxial layers is shown in Table III. The correction factors were obtained from previously published results on the spreading resistance (15).

Equation [10] can be studied in more detail to explain some of the additional phenomena observed with the three-point probe. It is clear that since  $V_C$  has a square-root dependence on resistivity, so does  $V_R$ . The correction factor  $K$  appears in the numerator, so as  $K$  decreases, so does the breakdown voltage.

For an  $n/n^+$  structure,  $K$  is always a positive number less than one and becomes small for a fixed radius of contact as the layer thickness is decreased. A representative graph is shown in Fig. 10. Thus the dependence on layer thickness discussed in statement 7 can be explained at least qualitatively by the change in the spreading resistance correction factors. This same argument can be used to describe the dependence of the breakdown voltage on pressure. For a bulk sample,  $K = 1$  and a change in the loading will change the radius of contact. An increase in load will increase the  $a$  and thus decrease the breakdown voltage. For  $n/n^+$  epitaxial material, this will also be true but, in addition,  $K$  will be decreasing (Fig. 10). The effects of increasing pressure will be more pronounced on epitaxial material than on bulk.

#### Theoretical Basis for Model

Since much of the data presented here and in other papers would indicate that thermal effects play a dominant role in determining the characteristics of point contact breakdown as commonly measured with the three-point probe, it does not seem unreasonable that the predominate effect is thermal and that the

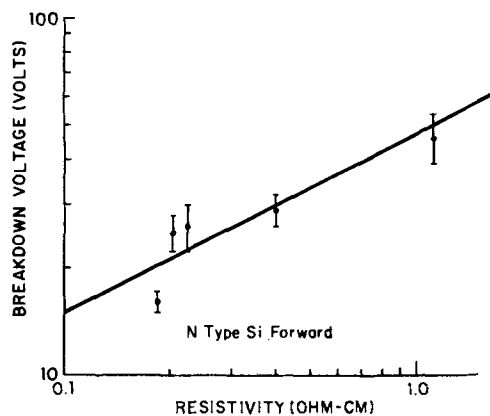


Fig. 6. Forward breakdown voltage as a function of resistivity for n-type silicon.

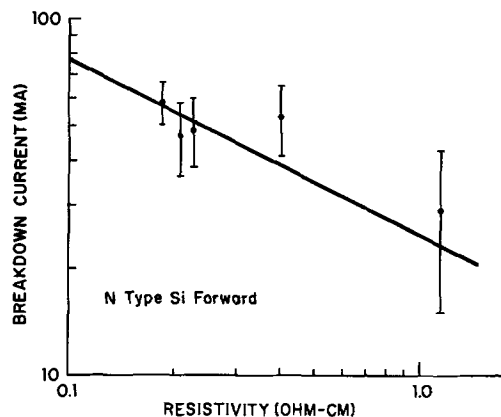


Fig. 8. Forward breakdown current as a function of resistivity for n-type silicon.

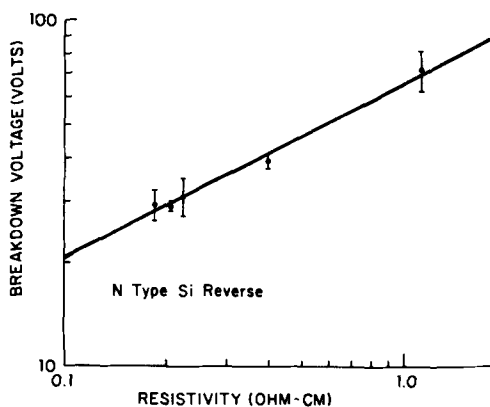


Fig. 7. Reverse breakdown voltage as a function of resistivity for n-type silicon.

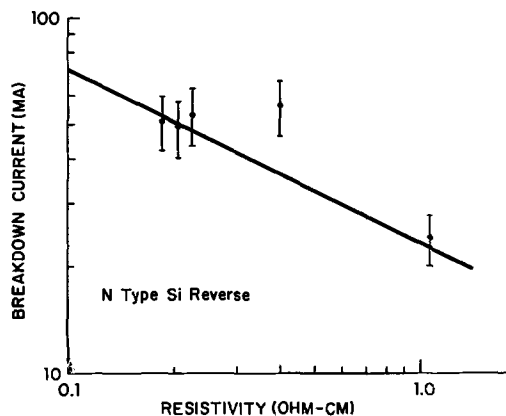


Fig. 9. Reverse breakdown current as a function of resistivity for n-type silicon.

Table III. Comparison of power levels in bulk and epitaxial layers

	Experi- mental power, watts	Layer thick- ness, $\mu$	$a, \mu$	$H_1$	$K$	Model power, watts
Bulk n-type	1.8	$\infty$	1.3	$\infty$	1	—
Epitaxial n/n+	2.1	5	1.3	3.8	0.88	2.05

three-point probe measures the intrinsic temperature of the semiconductor. The intrinsic temperature for the purpose of this discussion will be defined as the temperature above room temperature at which the resistivity is a maximum. For silicon, this is shown in Fig. 11. The curve was obtained from data by Hoffman, Reuschel, and Rupprecht (17), Putley and Mitchell (18), and Morin and Maita (19). The data on individual samples shown only for visualization were obtained from Gardner (20).

Analogous to the spreading resistance equation is the equation for heat flow (21)

$$T = \frac{Q}{4\lambda r_o} \quad [17]$$

where  $T$  is the temperature in degrees,  $Q$  is the heat input in watts,  $\lambda$  is thermal conductivity in watts/cm °K, and  $r_o$  is the radius of contact of heat source. This is the steady-state temperature, and its application in this case is certainly open to question. First, it is not clear that we are in a steady-state condition. And, second, the power is not all generated at the contact; it is generated in a rather complicated manner throughout the material.

The temperature under the contact  $T_C$  is the sum of this temperature and the ambient temperature  $T_o$ .

$$T_C = T + T_o \quad [18]$$

The amount of power generated should be the heat input in Eq. [17]. The fact that the heat is not all generated at the contact can be accounted for by letting  $r_o > a$ .

$$T_C = T_o + \frac{P}{4\lambda r_o} \quad [19]$$

Solving for the power

$$P = 4\lambda r_o (T_C - T_o) \quad [20]$$

For the power to be constant,  $\lambda (T_C - T_o)$  must be a constant. If  $T_C$  is the intrinsic temperature, it must

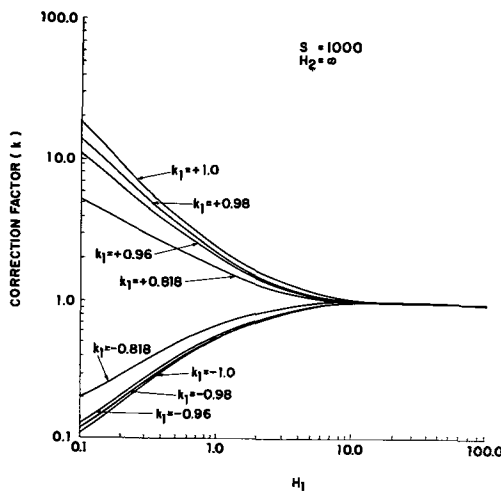


Fig. 10. Spreading resistance correction factor,  $K$ , as a function of  $H_1 =$  layer thickness/radius of contact for  $S = 1000 =$  probe spacing/radius of contact;  $H_2 = \infty =$  substrate thickness/radius of contact; and various values of  $k_1$  where  $k_1 = (\rho_2 - \rho_1)/(\rho_2 + \rho_1)$  with  $\rho_1 =$  layer resistivity, and  $\rho_2 =$  substrate resistivity.

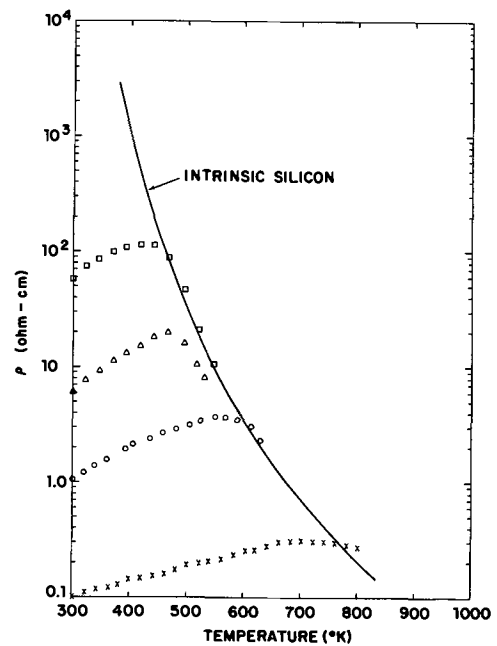


Fig. 11. Resistivity as a function of absolute temperature for several silicon samples.

vary with resistivity as indicated in Fig. 11. However,  $\lambda$  also varies with temperature almost as the inverse, and the product remains relatively constant, as indicated in Fig. 12. The range for the intrinsic temperature for this resistivity range falls between 550° and 750°K. (The average  $\lambda T$  for this temperature range is  $445 \pm 35$  w/cm.) The thermal conductivity data were taken from Glassbrenner and Slack (22) for high-resistivity silicon. The effect of doping on the high-temperature portion of the thermal conductivity curve probably is not significant.

Another simple model can be built to examine the time dependence of the temperature increase. If it is assumed that all the power is dissipated uniformly, with a hemisphere of radius  $r_o$  and with no chance for heat conduction to occur, the temperature rise becomes

$$\frac{\Delta T}{\Delta t} = \frac{P}{vCd} \quad [21]$$

where  $P$  is the power dissipated,  $v$  is the volume,  $C$  is the specific heat, and  $d$  is the density. Using a specific heat of 0.2 cal/g °K for silicon, this equation becomes

$$\frac{\Delta T}{\Delta t} = \frac{3P}{2\pi r_o^3 Cd} = \frac{250 P \times 10^9}{r_o^3} \text{ °K/sec} \quad [22]$$

where  $P$  is in watts and  $r_o$  is in microns. For the

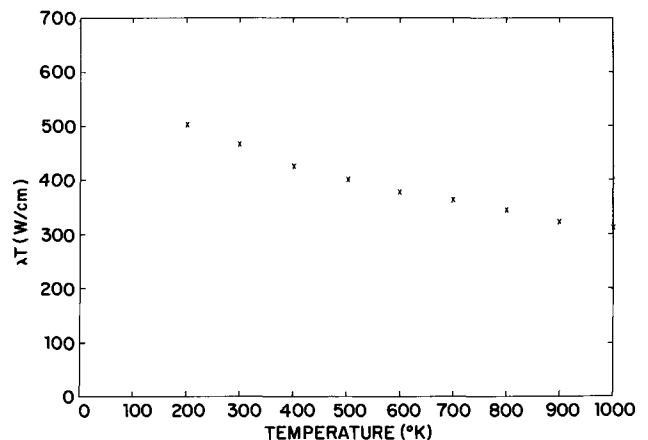


Fig. 12. The product of thermal conductivity and absolute temperature as a function of absolute temperature for silicon.

p-type silicon studied here,  $r_0 \approx 6\mu$  and  $P \approx 1w$

$$\frac{\Delta T}{\Delta t} \approx 1.16 \times 10^9 \text{ }^\circ\text{K/sec} \quad [23]$$

In an earlier work (11), use of pulse techniques showed that it took approximately a microsecond to reach thermal breakdown. For 1  $\mu\text{sec}$  in this model,  $\Delta T \approx 1200^\circ\text{K}$ , which is the right order of magnitude for thermal effects to become important and even destructive breakdown to occur. The same paper pointed out that approximately 3  $\mu\text{sec}$  must elapse before the silicon is melted. The heat of fusion of silicon is about 431 cal/g. Using the same volume as above, an energy of  $1.9 \times 10^{-6}$  w sec is needed to melt the volume of a hemisphere of radius  $r_0$ . Thus if 3  $\mu\text{sec}$  are needed to melt the silicon, a power of about 0.6w must be expended to accomplish this. The remaining 0.4w must be used to bring the sample up in temperature, so that the temperature rise would be about  $1400^\circ\text{K}$ , which when added to the  $300^\circ\text{K}$  ambient is about the melting point.

The same type of time dependence, although on a larger time scale, was observed by Agatsuma (23) for point contacts.

### Discussion

Of the many approximations and assumptions made in this model, the most important are:

1. The radius of contact as determined by the spreading resistance is the true electrical radius of contact.
2. The effects of pressure on the resistivity are ignored.
3. The resistivity used in the model calculations is the resistivity of the sample at room temperature.
4. No account is made of charge accumulation and barrier effects in the model. These are all combined into the  $V_C$  term.

The approximations made in trying to justify the model theoretically are perhaps even larger. The two cases considered are certainly the two extremes of heating. The first steady-state approximation will only be good for long times, and the rate of temperature calculation will only be good for the first few microseconds of heating. Both of these, however, still have the following major assumptions in common:

1. The thermal conductivity or heat capacity is independent of doping level.
2. The power is generated uniformly within a radius  $r_0$ .

There are still some factors the theoretical model does not explain. The most important is that the voltage at forward breakdown should be the same for n- and p-type silicon as predicted by Eq. [5]. It is probable that the effective radius of contact determined from spreading resistance is not the true electrical radius of contact. The calibration curve used for spreading resistance measurements would indicate that it is not (14-16). However, as yet there is no good means to separate the true spreading resistance from the contact resistance. The use of this radius probably also masks the other assumptions made in the model or the effects cancel each other out to allow such good fit. This error does not really become apparent until the thermal effects are considered.

The simple spreading-resistance model does not rule out the possibility that other phenomena could cause avalanche breakdown or that the breakdown could be a Zener effect. The maximum field under a planar contact occurs at the silicon-contact interface and is given by

$$E = \frac{I\rho}{\pi a^2} \quad [24]$$

or, written another way,

$$E = \frac{4V}{\pi a} \quad [25]$$

For Zener breakdown, field would be a constant, i.e., there would exist a critical field, so that, if  $a = \text{constant}$ , breakdown voltage must be constant. Thus the two concepts are not compatible.

Avalanche breakdown can occur because of a current constriction, and several papers have been written (24-28) describing the concept and measurement of the negative resistance. It is not the purpose to go into detail here of these theories and observations but to state that in all cases these effects were connected with a current saturation. The charge carriers reach a maximum velocity which is independent of the applied field. Although the fields due to the spreading resistance contact are extremely high, of the order of  $10^6$  v/cm, no current saturation effects were observed. Also, the experimenters searching for the avalanche effect had to use low duty cycles in order to observe their effects and avoid heating.

It is also possible that a straightforward avalanche effect may be occurring due to the high fields present. This would also seem improbable, because a simple model for a hemispherical contact based on a single ionization rate of the formula  $E = \theta e^{-\phi/E}$ , yields the following relationship between parameters

$$a = \frac{V}{2\phi} \ln \frac{\theta a V}{4\phi} \quad [26]$$

Since  $a, \theta$ , and  $\phi$  are constants, Eq. [30] would indicate that the breakdown voltage should be a constant. This, of course, is due to the simple way that the voltage and current are related in the spreading resistance.

Another effect observed in this laboratory (29) is that the point contact will oscillate. This oscillation can sometimes be audible, i.e., the point is vibrating. This has also been observed as current oscillations. Similar results have been reported for other point contacts (29, 30-32). A model for this effect described by Gundjian (33, 34) is based on the spreading-resistance field and the electrostrictive property of the semiconductor. The conditions for oscillations are very complex and probably explain why the effect is not always observed. Several times during the measurements presented in this paper, the audible oscillation was observed.

It is also possible that the self-heating model proposed by Hunter (35-37) and expanded on by others (38-39) for point contact diodes is applicable. This model is based on similar arguments of self-heating and the fact that an isothermal saturation current is never observed. It does not discuss the forward characteristic and is only qualitatively able to describe the breakdown phenomenon. In either case it is still a thermal phenomenon.

Henisch (38) discusses similar heating effects for point-contact diodes and compares various models of the turnover voltage. He presents data which show that the contact temperature is a constant at the breakdown or turnover voltage for a given sample as a function of ambient temperature. He implies that this may be attributed to the onset of intrinsic conduction.

The empirical model of the three-point probe as commonly used points to the spreading resistance as being the principal manner in which the voltage is built up. From this evidence and the fact that breakdowns occur in both forward and reverse biased directions, it would appear that the only reasonable explanation of the breakdown is a heating effect. In normal use this heating effect increases the temperature to the intrinsic temperature, but in extreme cases it can melt the semiconductor.

### Acknowledgment

The author would like to thank Miss Lucy A. Pietrogallo, Mr. M. R. Poponiak, Mr. C. P. Schneider, and Mr. A. Dupnock for the experimental data presented and Dr. E. E. Gardner and Mr. J. F. Hallenback, Jr., for many helpful discussions of this problem.

Manuscript submitted Feb. 20, 1968; revised manuscript received Aug. 1, 1968.

Any discussion of this paper will appear in a Discussion Section to be published in the June 1969 JOURNAL.

### REFERENCES

- E. E. Gardner, J. H. Hallenback, Jr., and P. A. Schumann, Jr., *Solid-State Electron.*, **6**, 311 (1963).
- J. Brownson, *This Journal*, **111**, 919 (1964).
- P. J. H. Dobbs and F. S. Kovacs, *Semicond. Prod.*, **7**, 28 (1964).
- E. E. Gardner and P. A. Schumann, Jr., *Solid-State Electron.*, **8**, 165 (1965).
- M. H. Norwood, *This Journal*, **112**, 875 (1965).
- C. C. Allen, L. H. Clevenger, and D. C. Gupta, *ibid.*, **113**, 508 (1966).
- H. Frank, *Phys. Stat. Sol.*, **18**, 401 (1966).
- S. L. Miller, *Phys. Rev.*, **105**, 1246 (1957).
- H. L. Armstrong, E. D. Metz, and I. Weiman, *IRE, Trans. Elec. Dev.*, **3**, 86 (1956).
- J. Shields, *J. Electron. Control*, **4**, 58 (1958).
- P. A. Schumann, Jr., J. F. Hallenback, Jr., M. R. Poponiak, and C. P. Schneider, To be published.
- J. Shields, *J. Electron. Control*, **4**, 544 (1958).
- R. Holm, "Electric Contacts Handbook," Springer-Verlag, Berlin (1958).
- A. G. Mazur and D. H. Dickey, *This Journal*, **113**, 255 (1966).
- E. E. Gardner, P. A. Schumann, Jr., and E. F. Gorey, Paper presented at the Philadelphia Meeting of The Society, Oct. 10-14, 1966, as Paper 139; "Measurement Techniques for Thin Films," B. Schwartz and N. Schwartz, Editors, p. 258, Electrochemical Society (1967).
- A. H. Tong and M. R. Poponiak, Late news paper presented at the Chicago Meeting of the Society, Oct. 15-18, 1967.
- A. Hoffman, K. Reuschel, and H. Rupprecht, *J. Phys. Chem. Solids*, **11**, 284 (1959).
- E. H. Putley and W. H. Mitchell, *Proc. Phys. Soc. (London)*, **72**, 193 (1958).
- F. J. Morin and J. P. Maita, *Phys. Rev.*, **96**, 28 (1954).
- E. E. Gardner, Unpublished data.
- H. S. Carslaw and J. C. Jaeger, "The Conduction of Heat in Solids," 2nd ed., p. 216, Oxford Clarendon Press (1962).
- C. J. Glassbrenner and G. A. Slack, *Phys. Rev.*, **134**, A1058 (1964).
- T. Agatsuma, *Proc. IEEE*, **54**, 1206 (1966).
- J. B. Gunn, *Proc. Phys. Soc. (London)*, **67B**, 575 (1954).
- J. B. Arthur, A. F. Gibson, and J. B. Gunn, *ibid.*, **69B**, 697 (1956).
- J. B. Gunn, *ibid.*, **69B**, 781 (1956).
- M. C. Steele, K. Ando, and M. A. Lampert, *J. Phys. Soc. Japan*, **17**, 1729 (1962).
- K. Ando, M. C. Steele, and M. A. Lampert, *ibid.*, **18**, 591 (1963).
- J. F. Hallenback, Jr., Unpublished data.
- M. Cardona and W. Ruppel, *J. Appl. Phys.*, **31**, 1826 (1960).
- M. Kikuchi, *J. Phys. Soc. Japan*, **17**, 240 (1962).
- B. S. Muravskii, *Sov. Phys.—Solid State*, **4**, 1820 (1963).
- A. A. Gundjian, *Solid State Commun.*, **3**, 279 (1965).
- A. A. Gundjian, *IEEE Trans. Electron. Dev.*, **ED13**, 866 (1966).
- L. P. Hunter, "Handbook of Semiconductor Electronics," 2nd ed., pp. 3-21, McGraw-Hill Book Co., New York (1962).
- L. P. Hunter, *Phys. Rev.*, **79**, 151 (1951).
- A. I. Bennett and L. P. Hunter, *ibid.*, **79**, 152 (1951).
- H. K. Henisch, "Rectifying Semiconductor Contacts," pp. 260, 312, Oxford University Press (1957).
- R. E. Burgess, *Proc. Phys. Soc. (London)*, **68B**, 908 (1955).

## Technical Notes



### The Cathodoluminescence Spectra and Coordination of $Mn^{2+}$ , $Fe^{3+}$ , and $Cr^{3+}$ in $\beta LiAl_5O_8$

P. M. Jaffe\*

Zenith Radio Corporation, Chicago, Illinois

Manganese activated phosphors may show essentially three different emissions: a red or a green band which is broad and structureless or a narrow structured red band. The broad band emissions are believed to be due to  $Mn^{2+}$  and the structured narrow band emission to  $Mn^{4+}$  (1-3). Linwood and Weyl have postulated that the green band emission is due to  $Mn^{2+}$  in tetrahedral coordination in the host lattice and the red band emission to octahedral coordination (4).

Recently, Hummel and Sarver have reported on the luminescence of the isoelectronic  $Fe^{3+}$  and  $Mn^{2+}$  ions in the normal spinel  $MgAl_2O_4$  (5). They found that activation by Mn resulted only in a green emission and by Fe in both a green and a red emission. The two green emissions had the same peak wavelengths and

half-widths. Based on the ideas mentioned above, Hummel and Sarver concluded from these data that the Mn was 4 coordinated and the Fe was both 4 and 6 coordinated in  $MgAl_2O_4$ .<sup>1</sup>

The high-temperature ( $\alpha$ ) form of  $LiAl_5O_8$  also forms a spinel (6) while the low-temperature ( $\beta$ ) form is more ordered (7). The  $\alpha$  form has the inverse spinel structure with 8 Al in tetrahedral sites and 4 Li plus 12 Al in octahedral sites. In the spinel-like  $\beta$  form, we may still consider the structure to be made up of a cubic close-packed oxygen lattice which contains both octahedral and tetrahedral holes. However, the exact relationship and location of the Li and Al ions is not known. In the inverse  $LiFe_5O_8$  spinel, the high-temperature form has the octahedrally coordi-

\* Electrochemical Society Active Member.

<sup>1</sup> In a spinel, the cations may only occupy the octahedral and tetrahedral holes that are present in the close-packed oxygen lattice.

nated Li and Fe randomly orientated; in the low-temperature form they are ordered (6).

From Hummel and Sarver's work plus the fact that  $\text{Fe}^{3+}$  prefers tetrahedral coordination (8, 9), one would expect the emission from  $\text{Fe}^{3+}$  activated  $\text{LiAl}_5\text{O}_8$  to be mainly green at low  $\text{Fe}^{3+}$  concentrations. However, Mochel (10), in his paper on air-fired  $\text{LiAl}_5\text{O}_8:\text{Fe}^{3+}$ , reports the photoluminescent spectrum to consist of only a red and a blue band.<sup>2</sup> There is evidence, to be published at a later date, which indicates that this blue emission is due either to host emission or to an impurity.

In this study I have prepared  $\beta\text{LiAl}_5\text{O}_8$  and tried to incorporate individually the two pairs of isoelectronic ions  $\text{Mn}^{2+}$ ,  $\text{Fe}^{3+}$  and  $\text{Cr}^{3+}$ ,  $\text{Mn}^{4+}$ . The goal was to try to correlate the cathodoluminescent emission with the respective activator coordination. However, no information can be obtained on the relative occupancy of these sites. The reason is that the intensity of emission from a site need not be directly proportional to its population.

Phosphors were prepared from reagent grade  $\text{Al}(\text{OH})_3$ ,  $\text{Li}_2\text{CO}_3$ ,  $\text{FeSO}_4$ ,  $\text{CrO}_3$ , and  $\text{MnSO}_4$  by firing at  $1200^\circ\text{C}$  for 2 hr. The firing atmospheres were  $\text{N}_2$ ,  $\text{O}_2$ , and 3:1  $\text{H}_2$ - $\text{N}_2$ . The stoichiometry of the phosphors was based on  $\text{LiAl}_{5-x}\text{Fe}_{5x}\text{O}_8$  where  $x$  was 0.002 [0.2 a/o (atomic per cent)]. Emission spectra were obtained in a demountable cathode-ray tube operated at 25 kv using a  $\frac{1}{4}$  meter Jarrel-Ash monochromator equipped with  $100\mu$  slits and a 7326 photomultiplier. All spectra were corrected for the detector response and monochromator errors. All measurements were made at room temperature.

#### Mn Activation

Firing in  $\text{N}_2$ ,  $\text{O}_2$ , or  $\text{H}_2$ - $\text{N}_2$  results in phosphors having essentially the same green band emission spectra, Fig. 1. There is no sign of structure or of a red band. The half-width of the emission, 30 nm, and the emission peak, 520 nm, are about the same as those obtained with  $\text{MgAl}_2\text{O}_4:\text{Mn}$  and  $\text{ZnAl}_2\text{O}_4:\text{Mn}$  (5).

The lack of a structured red emission in the Mn activated  $\text{LiAl}_5\text{O}_8$  phosphors indicates that no  $\text{Mn}^{4+}$  is present. Because the Mn emission in  $\text{LiAl}_5\text{O}_8$  is similar to that of  $\text{Mn}^{2+}$  in  $\text{ZnAl}_2\text{O}_4$  and  $\text{MgAl}_2\text{O}_4$ , we may assume that Mn has the same valency and coordination in these three hosts, namely, divalent and in tetrahedral coordination.

#### Fe Activation

The spectra of samples fired in  $\text{N}_2$  and  $\text{O}_2$  were essentially the same, consisting of a strong red band and a very weak green band peaking around 660 and 520 nm, respectively, Fig. 2. The  $\text{N}_2$ - $\text{H}_2$  fired samples showed a slight broadening of the red emission band, a slightly stronger green emission, and a new band in the IR.<sup>3</sup> Another phosphor containing 0.01 a/o Fe and fired in air showed a slightly stronger green emission than the air-fired sample containing 0.2 a/o Fe. Cooling to liquid nitrogen temperature had no effect on the intensities of the two emission bands.

The bulk of the Fe in  $\text{LiAl}_5\text{O}_8$  is most likely trivalent. It is present mainly in octahedral coordination, as indicated by the red emission, in spite of the known preference of  $\text{Fe}^{3+}$  for tetrahedral coordination (8, 9). Some  $\text{Fe}^{3+}$  is also present in tetrahedral coordination as evidenced by the weak green emission. The low intensity of the green emission is not due to concentration quenching since it increased only slightly when the Fe concentration was decreased to 0.01 a/o. There is no temperature quenching of the green emission since cooling had no effect on its intensity. Firing in  $\text{N}_2 + \text{H}_2$  may result in the formation of some divalent Fe as indicated by the appearance of the new near IR band. Gergely has found that Fe, presumably divalent, in ZnS causes an emission in the near IR (11). This is

<sup>2</sup> R. H. Datta has also investigated the photoluminescence of this system, *Bull. Am. Ceramic Soc.*, 44, #4 (1965), Abstract 26-B-65.  
<sup>3</sup> The spectrum of this IR emission was not determined.

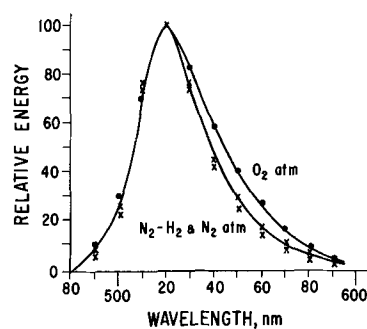


Fig. 1. Emission spectra of  $\beta\text{LiAl}_5\text{O}_8:\text{Mn}$  fired in  $\text{N}_2$ ,  $\text{O}_2$ , and  $\text{N}_2$ - $\text{H}_2$  atmospheres.

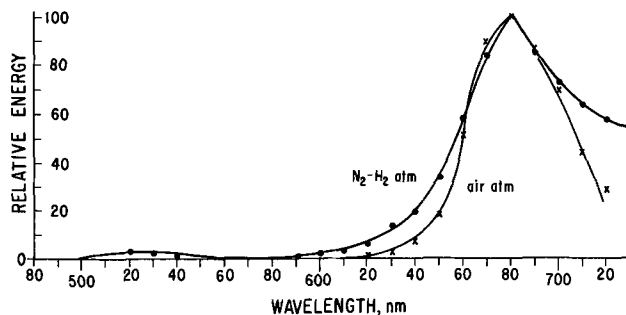


Fig. 2. Emission spectra of  $\beta\text{LiAl}_5\text{O}_8:\text{Fe}$  fired in  $\text{N}_2$ - $\text{H}_2$  and air atmospheres.

different from the emission due to  $\text{Fe}^{3+}$  in ZnS (12) which is in the visible, peak wavelength about 660 nm (13).

#### Cr Activation

The emission spectra from  $\text{N}_2 + \text{H}_2$  and  $\text{O}_2$  fired samples are shown in Fig. 3. The emission is characterized by a weak broad band with three main superimposed lines which are invariant with firing atmosphere.

The spectra of the Cr activated  $\text{LiAl}_5\text{O}_8$  phosphors is typical of that expected for  $\text{Cr}^{3+}$  in octahedral coordination (6, 14). However, comparing these spectra with those of  $\text{Cr}^{3+}$  in  $\text{Al}_2\text{O}_3$  and  $\text{MgAl}_2\text{O}_4$  shows that the main line at 718 nm is shifted to longer wavelengths by approximately 23 and 30 nm, respectively (14). This shift might be due to a slight "loosening" of the close packed oxygens, resulting in a slightly larger octahedral hole. This has the effect of decreasing the Dq value for Cr which would result in a shift of the spectrum to lower frequencies (longer wavelengths) (9, 15).

#### Acknowledgment

The author wishes to thank Miss K. Wolejko for her aid in sample preparation, Mr. Larry Flemming for obtaining the emission spectra, and Dr. Gerda Arai for the x-ray diffraction analysis.

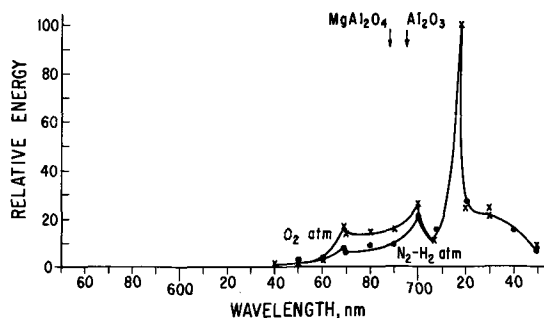


Fig. 3. Emission spectra of  $\beta\text{LiAl}_5\text{O}_8:\text{Cr}$  fired in  $\text{N}_2$ - $\text{H}_2$  and  $\text{O}_2$  atmospheres. The arrows indicate the position of the main emission line of  $\text{MgAl}_2\text{O}_4:\text{Cr}$  and  $\text{Al}_2\text{O}_3:\text{Cr}$ .

Manuscript submitted June 7, 1968; revised manuscript received July 22, 1968. This paper was presented at the Boston Meeting, May 5-9, 1968, as Paper 31.

Any discussion of this paper will appear in a Discussion Section to be published in the June 1969 JOURNAL.

## REFERENCES

1. H. W. Leverenz, "Luminescence of Solids," John Wiley & Sons, Inc., New York (1950).
2. F. A. Kroger, "Some Aspects of the Luminescence of Solids," Elsevier Publishing Co., New York (1948).
3. C. C. Klick, *Brit. J. Appl. Phys.*, Supp. #3, p. S74 (1954).
4. S. Linwood and W. Weyl, *J. Opt. Soc. Am.*, **32**, 443 (1942).
5. F. Hummel and J. Sarver, *This Journal*, **111**, 252 (1964).
6. H. F. Wells, "Structural Inorganic Chemistry," 3rd ed., Oxford, London (1962).
7. R. Datta and R. Roy, *J. Am. Ceram. Soc.*, **46**, 388 (1963).
8. G. Blasse, Philips Research Supplements #3 (1964).
9. L. Orgel, "An Introduction to Transition-Metal Chemistry," pp. 77-78, Methuen, London (1960).
10. V. D. Mochel, *This Journal*, **113**, 398 (1966).
11. G. Gergely, *J. Phys. et Rad.*, **17**, 679 (1956).
12. R. Title, *Bull. Am. Phys. Soc.*, Series 2, **7**, 88 (1962).
13. P. M. Jaffe and E. Banks, *This Journal*, **111**, 52 (1964).
14. R. H. Arlett, *J. Am. Ceram. Soc.*, **45**, 523 (1962).
15. L. Orgel, *Nature*, **179**, 1348 (1957).

## Thermoluminescence of Sintered Alumina

Charles R. Whitworth and Ivan B. Cutler

University of Utah, Salt Lake City, Utah

Thermoluminescence might be defined as the emission of light from a substance when it is warmed, usually at a constant rate, after having been subjected to some type of exciting radiation at a relatively low temperature. The data are most often presented in the form of a glow curve, which is a plot of emitted radiation intensity *vs.* temperature.

Several contributions occur in the literature concerning the use of manganese as a luminescent activator in alumina-based compounds (1). Kelley and Laubitz (2) used thermoluminescence to study the defect structure of pure and slightly doped alumina. Rieke and Daniels (3) obtained a rough correlation between the area under a glow curve and the amount of a given phase present. Atlas and Firestone (4) presented a correlation between various added impurities and the glow peaks they produced. The present work is concerned with the effects of additions of manganese oxide (up to 5600 ppm) and sodium. The manganese concentration is presented as ppm manganese because its valence state in the samples is unknown.

The samples used in this study were prepared from high-purity ( $\text{SiO}_2 < 0.0015\%$ ,  $\text{Fe}_2\text{O}_3 < 0.001\%$ ,  $\text{TiO}_2 < 0.001\%$ ,  $\text{P}_2\text{O}_5 < 0.001\%$ ,  $\text{Na}_2\text{O} < 0.003\%$ ) alpha alumina designated R-13 as supplied by AIAG (Aluminum-Industrie-Aktien-Gesellschaft). A major problem encountered in preparing homogeneous samples was the inadvertent introduction of  $\text{Na}_2\text{O}$  resulting in a tendency towards exaggerated grain growth producing grains as large as 1 mm. To minimize this problem, all handling was done in plastic containers. The alumina was doped with manganese by suspending it in a solution of 99.99% manganese metal in reagent grade  $\text{HNO}_3$ , then precipitating  $\text{Mn}(\text{OH})_2$  with  $\text{NH}_4\text{OH}$ . The resulting slurry was vigorously agitated for 15 min then dried and calcined at  $800^\circ\text{C}$  for 12 hr. The alumina for sample (13) was prepared by the hydrothermal oxidation of 99.999% aluminum metal. Disks (1 mm thick  $\times$  22 mm diameter) were pressed at 15,000 psig and each was surrounded with material of like composition to prevent excessive evaporation of the manganese additions at higher temperatures during sintering. Two series of disks were pressed: one series was fired in air, the other in an atmosphere containing sodium vapor. A small crucible containing the disks was placed inside a larger crucible and surrounded by alumina doped with 1000 ppm  $\text{Na}_2\text{CO}_3$ . Each series of disks was separately fired at  $1650^\circ\text{C}$  for 2 hr, and the products were polished on a 600

grit diamond lap to make their surfaces uniform. The manganese concentration of each fired disk was determined by x-ray fluorescence: all were then cut into squares (4.5 mm square  $\times$  0.5 mm thick) to give equal radiating surfaces. The squares were cleaned by boiling them in HCl for 30 min, followed by a rinse in distilled water; they were then heated to  $1000^\circ\text{C}$  to remove any water that might contribute to thermoluminescence (3). After calcining, the samples were placed in small plastic vials and activated with the radiation from a cobalt-60 source (145,000 roentgens). It was later determined that irradiation with 50 kv x-rays from a platinum tube was adequate to activate this type of alumina.

The apparatus was basically a light-tight box with a housing for a photomultiplier tube mounted on the top. The sample holder was mounted in an inset in a movable rod that slid horizontally through two holes in opposite sides of the box. Electrical and thermocouple leads were fed into the box through this sliding rod. The rod extended completely through the box and was long enough to keep the seal light-tight during removal of the sample holder section. This arrangement prevented exposure of the activated photomultiplier tube to the direct light of the room, preserving its sensitivity. The sample holder, which also served as the heater, was a strip of stainless steel cut in the shape of a dogbone so that heating was confined to the narrow section of the strip where the sample was placed. The iron-constantan thermocouple was in physical contact with the bottom of the heating strip. Because of its location, the thermocouple indicated a higher temperature than that of the radiating surface of the sample. For more accurate work, a second thermocouple temporarily placed at the radiating surface, might be used to calibrate the thermocouple touching the heater. Although it was not convenient to use an exact linear heating rate, the rate was the same for all samples; consistency was achieved by attaching a small motor to the variac controlling the voltage to the heating strip.

An EMI 9558B photomultiplier tube was used to measure the radiation emitted by the sample as it was heated. The photomultiplier tube was powered by a Kepco Inc. model ABC 1500M voltage regulated supply, and the activating voltage was nominally 1200v. The outputs from the thermocouple and the photomultiplier tube were recorded by a model 135 Mosley Autograph to produce the glow curves. The temperature was calibrated with the output from an L&N 8691 mv potentiometer.

Key words: alumina, manganese, sodium, thermoluminescence.

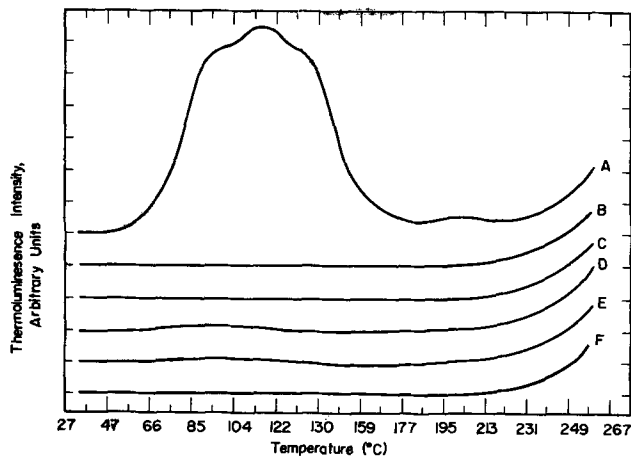


Fig. 1. Glow curves of samples fired in a sodium-free atmosphere. Each curve was started at 0 intensity, ppm Mn: (A) 0; (B) 710; (C) 1080; (D) 2310; (E) 3690; (F) 6740.

In practice, the sample, mounted on the heating strip, was positioned 3 in. below the photomultiplier tube by adjusting the sliding rod. The sample was then heated to 250°C at an approximate rate of 100°C/min. Since no allowance was made for the temperature of the radiating surface lagging behind that of the heater, the temperatures of the measured glow peaks are somewhat high. This error was not considered to be significant inasmuch as comparative results rather than absolute values were the objective.

In Fig. 1, glow curves are shown for a series of samples, sintered in a sodium-free atmosphere. The only sample exhibiting any glow peaks is the undoped R-13 alumina (curve 1). The addition of manganese appears to suppress the thermoluminescence characteristic of the untreated alumina. It was supposed that the peak shown in Fig. 1 might be caused by sodium; therefore, additional sodium was introduced into the alumina to prevent complete suppression by low concentrations of manganese. Different sodium concentrations were obtained by firing in atmospheres having different vapor pressures of sodium, and it was found that the sodium induced thermoluminescence reached a maximum for concentrations  $1000 < \text{Na}$ . The low thermoluminescence exhibited by the hydrothermally produced alumina reflects its low sodium content. The rise in intensity at 250°C is the beginning of a background radiation and was verified by making a run without a sample on the heater.

Apparatus was designed to accommodate Control-Data, sharp-cut-off filters between the sample and the photomultiplier tube. A series of these filters were used in an attempt to determine the wavelength distribution of the light corresponding to each peak. Since Rieke and Daniels noted that the radiation emitted from their alumina samples was light blue to blue green, filters in the orange to red region were selected to maximize absorption. The results were inconclusive: the only effect noticed was a reduc-

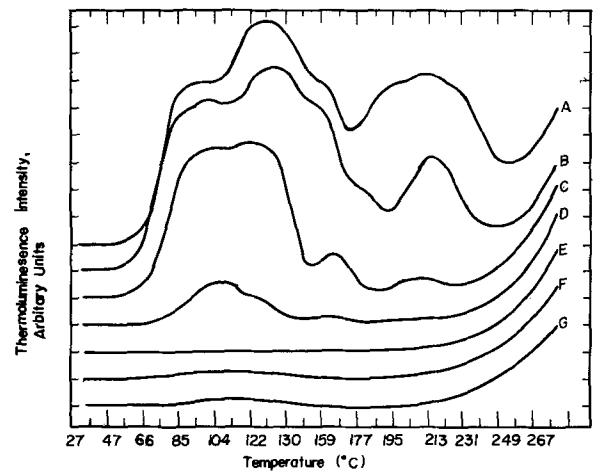


Fig. 2. Glow curves of samples fired in a sodium atmosphere. Each curve was started at 0 intensity, ppm Mn: (A) 0; (B) 430; (C) 1370; (D) 1950; (E) 2735; (F) 5630; (G) pure hydrothermally produced alumina.

tion of the height of the major peaks, particularly near 104°C. Since this effect occurred with all of the filters used, the absorption is probably caused by the silicate structure of the glass rather than by the colorants.

Several conclusions can now be drawn:

1. The addition of manganese decreases the thermoluminescence of alumina across the entire glow curve. Manganese thereby acts as a poison for this process rather than as a fluorescence activator as is usually the case.
2. The introduction of sodium (by firing in an atmosphere containing sodium vapor) increases the thermoluminescence of alumina, and introduces a new peak near 210°C. With sodium additions, a higher concentration of manganese is required to suppress the thermoluminescence completely.
3. The hydrothermally produced alumina contains less sodium than R-13, which is reported to contain 30 ppm.

#### Acknowledgment

The authors gratefully acknowledge the financial support of the National Science Foundation through grant GP-3138.

Manuscript submitted Aug. 31, 1967; revised manuscript received Aug. 15, 1968.

Any discussion of this paper will appear in a Discussion Section to be published in the June 1969 JOURNAL.

#### REFERENCES

1. F. A. Kroger, "Some Aspects of the Luminescence of Solids," p. 82, Elsevier, Amsterdam (1948).
2. P. J. Kelley and M. J. Laubitz, *J. Am. Ceram. Soc.*, **50**, 540 (1967).
3. J. K. Rieke and Farrington Daniels, *J. Phys. Chem.*, **61**, 629 (1957).
4. L. M. Atlas and R. F. Firestone, *J. Am. Ceram. Soc.*, **43**, 476 (1960).



## A Low-Temperature Nonpreferential Gaseous Etchant for Silicon

T. L. Chu\*<sup>1</sup>

*Electronic Sciences Center, Southern Methodist University, Dallas, Texas*

The cleanliness and perfection of the surface of silicon substrates are important in many device fabrication processes, such as epitaxial growth, preparation of MIS (metal-insulator-semiconductor) structures, etc. For example, foreign impurity particles and defects on the substrate surface have been shown to cause structural defects in epitaxial silicon and high interface charge densities in MIS structures (1, 2). Since clean surfaces cannot be readily prepared and maintained by conventional techniques, silicon substrates are frequently etched *in situ* prior to the deposition process. Anhydrous hydrogen chloride and water vapor have been used as *in situ* etchants for silicon with varying degrees of success (3-5). However, high substrate temperatures, 1150°C or above, are required in both cases to obtain structureless surfaces. In searching for a nonpreferential gaseous etchant effective for silicon at lower temperatures, hydrogen sulfide at low partial pressures in a hydrogen atmosphere has been found to be satisfactory. Some preliminary results on the etching of silicon by hydrogen sulfide are reported in this communication.

The reaction between silicon and hydrogen sulfide at high temperatures is similar to that between silicon and water vapor (4). The reaction product is silicon disulfide; however in the presence of excess silicon, silicon disulfide further reacts with silicon to form the volatile monosulfide. The chemical reactions and the associated standard free energy changes (kcal/mole) in the temperature range 298°-1100°K (6), are as follows

	$\Delta G^{\circ}_{298^{\circ}\text{K}}$	$\Delta G^{\circ}_{500^{\circ}\text{K}}$	$\Delta G^{\circ}_{800^{\circ}\text{K}}$	$\Delta G^{\circ}_{1000^{\circ}\text{K}}$
$\text{Si (s)} + 2\text{H}_2\text{S (g)} =$				
$\text{SiS}_2\text{ (s)} + 2\text{H}_2\text{ (g)}$	-26.0	-21.5	-15.9	-10.9
$\text{Si (s)} + \text{SiS}_2\text{ (s)} =$				
$2\text{SiS (g)}$	51.1	33.9	9.2	-14.9

Both reactions are thermochemically feasible at temperatures above 1000°K. In fact, the reaction between silicon and silicon disulfide has been found to take place readily to completion under vacuum at 850°C (7). Thus, at low partial pressures of hydrogen sulfide and at temperatures above 1000°K, silicon is oxidized to the volatile silicon monosulfide. Because of the fav-

orable thermochemical and kinetic factors, the etching of silicon by hydrogen sulfide can be achieved at temperatures considerably below that required by the use of water vapor.

Mixtures of hydrogen and hydrogen sulfides containing up to 0.5% hydrogen sulfide were used in the etching of silicon in a flow system. The silicon substrates were n-type, 10-40 ohm-cm, and had main faces of {111} orientation. The substrates, mechanically lapped and chemically polished in the usual manner, were supported on a silicon-coated graphite susceptor in a fused silica reaction tube, and the susceptor was heated externally by an rf generator. During the etching process, the flow rate of hydrogen was 20 l/min, and the substrate temperature was varied in the range of 850°-1050°C. Depending on the experimental conditions, silicon was removed from the substrate surface at a rate of up to about 3  $\mu$ /min. Optical microscope examinations indicate that the resulting surface obtained at etching temperatures higher than about 950°C is clean and structureless, and is similar to the original surface in appearance. Thus, hydrogen sulfide at low partial pressures in a hydrogen atmosphere is a nonpreferential etchant for silicon at relatively low temperatures. Details of this etching process will be discussed in a subsequent publication.

Manuscript received March 5, 1968. Publication was deferred at the authors request of April 17, 1968.

Any discussion of this paper will appear in a Discussion Section to be published in the December 1968 JOURNAL.

### REFERENCES

1. T. L. Chu and J. R. Gavaler, in "Metallurgy of Advanced Electronic Materials," G. E. Brock, Editor, P. 209, (Metallurgical Society Conferences, vol. 19), Interscience, New York (1963).
2. T. L. Chu, G. A. Gruber, and J. R. Szedon, *Trans. Met. Soc. AIME*, **242**, 532 (1968).
3. G. A. Lang and T. Stavish, *RCA Rev.*, **24**, 488 (1963).
4. T. L. Chu and R. L. Tallman, *This Journal*, **111**, 1306 (1964).
5. T. L. Chu, G. A. Gruber, and R. Stickler, *ibid.*, **113**, 156 (1966).
6. JANAF Interim Thermochemical Tables, Dow Chemical Co., Midland, Mich., Dec. 1960.
7. W. C. Schaub and W. J. Bernard, *J. Am. Chem. Soc.*, **77**, 904 (1955).

\* Electrochemical Society Active Member.

<sup>1</sup>Major portion of this work was done while the author was associated with Westinghouse Research Laboratories, Pittsburgh, Pennsylvania.



# A Semi-Empirical Mathematical Model for Predicting the EMF of Small Silver Chloride-Magnesium Cells

Duane W. Faletti and Michael A. Gackstetter

*Applied Physics Laboratory, University of Washington, Seattle, Washington*

## ABSTRACT

A method has been developed for predicting the emf of small silver chloride-magnesium cells, under a constant current load, as a function of current density, temperature, electrolyte composition, and degree of exhaustion. Over a current density range of 0.116 ascm to 0.527 ascm, and a temperature range of 4°-65°C, this method gives excellent agreement with experimental emf-time traces, to a cutoff voltage of 0.75v. This technique promises to provide the foundation for a new design method for AgCl-Mg sea water-activated batteries.

The Applied Physics Laboratory of the University of Washington is engaged in an effort to develop improved design methods for high-drain water-activated magnesium-silver chloride batteries which are less dependent on prototype testing than the design methods now available. A Semi-Empirical Mathematical Model (SEMM) is presented here which promises to be the foundation for the new design methods.

A brief description of the reactions involved in this type of battery and their method of construction is given in an earlier paper (1). In another paper (2), the authors give information on the composition and electrical conductivity of the characteristic electrolytes.

High drain AgCl-Mg batteries are characterized by temporal and spatial variations in current density, temperature, electrolyte composition, and degree of expenditure. In order to develop an improved quantitative design method for AgCl-Mg sea water batteries based on numerical analysis, a method of predicting the emf of small AgCl-Mg cells over the range of operating conditions found in full-size batteries is required. The results of a program developing and verifying such a method for the case of constant current discharges are presented here. This method not only promises to be useful for the design of small high-drain cells and batteries, but represents an important step toward the ultimate goal of computer design of large high-drain AgCl-Mg water-activated batteries.

### Semi-Empirical Mathematical Model

SEMM predicts discharge characteristics of a AgCl-Mg cell by dividing the discharge into three regions (Fig. 1). In region No. 1 of Fig. 1, the mathematical model, Eq. [8], is followed. In region No. 2 a phenomenon termed the Mid-Run Voltage Anomaly (MRVA) occurs under certain operating conditions. In region No. 3 of Fig. 1 the voltage decay caused by exhaustion of the AgCl occurs. All cells discharged in this study were cathode limited.

Figure 2 delineates the basis for the mathematical model of a typical cell in a high-drain AgCl-Mg battery. In this type of battery [see ref. (1)], electronic contact to the cathode is achieved by pressing a sheet of metal, generally silver, against the back of the silver chloride cathode. The contact resistance between the electronic conductor and the cathode is designated  $R_1$ . Since silver chloride is a poor conductor, AgCl cathodes for large high-drain batteries are prepared by perforating them with holes 0.0825 cm in diameter and located 0.635 cm apart. After perforation, the silver chloride is treated by an appropriate reducing solution to give a very thin layer of silver over the entire surface of the cathode. This process, which reduces only a small fraction of the silver chloride

(~1.0%), results in an acceptably low, but unknown, resistance  $R_2$ .  $R_2$  decreases as the discharge progresses because of the additional silver formed on the cathode by the electrochemical reduction of silver chloride. An additional contact resistance,  $R_3$ , exists between the back of the magnesium anode and the conducting metal sheet (generally silver).

Two additional resistances occur in the AgCl-Mg cell during discharge:  $R_s$ , which is the resistance of the electrolyte retained in the sponge silver (a term applied to the exhausted portion of the silver chloride cathode), and  $R_e$ , the resistance of the electrolyte in the space between the electrodes.

Note that the following model is based on the assumption of uniform conditions over the entire cell. Because of this assumption, the cross-sectional area of the cells studied was made as small as mechanical practicality permitted.

To account for the role of area in the contact resistances  $R_1$ ,  $R_2$ , and  $R_3$ , specific contact resistances  $R_1'$ ,  $R_2'$ , and  $R_3'$  are defined and used as follows

$$\begin{aligned} R_1 &= R_1'/A \\ R_2 &= R_2'/A \\ R_3 &= R_3'/A \end{aligned} \quad [1]$$

where  $A$  is the cell area. Similarly,  $R_s$  and  $R_e$  are given by

$$\begin{aligned} R_s &= \rho_s(X/A) \\ R_e &= L(K \cdot A) \end{aligned} \quad [2]$$

where  $X$  is the depth of the sponge silver layer,  $L$  is the electrode separation distance,  $K$  is the electrical conductivity of the electrolyte in the gap sep-

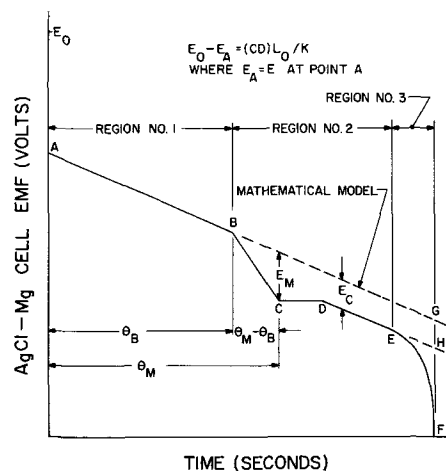


Fig. 1. Generalized discharge characteristics of a silver chloride-magnesium cell under constant current load.

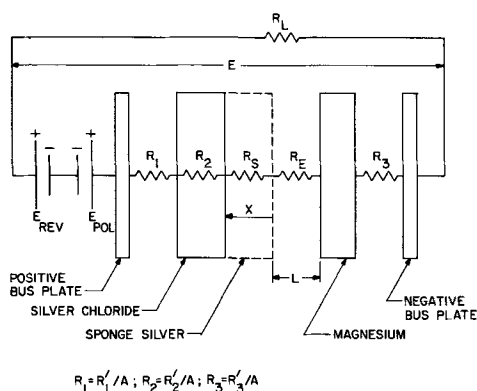


Fig. 2. Electrical analog of a magnesium-silver chloride cell.

arating the electrodes and  $\rho_s$  is the specific resistance of the sponge silver-electrolyte matrix (not the specific resistance of the electrolyte filling the voids in the sponge silver).

Based on the circuit depicted in Fig. 2,  $E$ , the emf of a small AgCl-Mg cell, is given by

$$E = E_{\text{rev}} - E_{\text{pol}} - (CD) (R_1' + R_2' + R_3' + \rho_s X + L/K) \quad [3]$$

where  $E_{\text{rev}}$  is the thermodynamically reversible emf of the AgCl-Mg couple,  $E_{\text{pol}}$  is the total emf loss from polarization at both electrodes and  $CD$  is the current density,  $I/A$ .

Let  $X_0$  be the initial sponge silver thickness (formed by the chemical reduction described above),  $L_0$  be the initial electrode separation distance and  $\eta$  be the anode efficiency defined as the ratio of the predicted (from Faraday's law) anode weight loss to the observed weight loss.  $X$  and  $L$  at time  $t$  are then given by (assuming cell discharge begins at time  $t = 0$ )

$$X = X_0 + W_c \lambda / (d_c F) = X_0 + (2.67 \cdot 10^{-4}) \lambda \quad [4]$$

$$L = L_0 + W_a \lambda / (\eta d_a F) = L_0 + (7.24 \cdot 10^{-5}) (\lambda / \eta) \quad [5]$$

where  $W_c$ ,  $W_a$  = equivalent weights of the AgCl cathode (143.3 g/equiv) and Mg anode (12.16 g/equiv), respectively,  $d_c$ ,  $d_a$  = densities of the AgCl cathode (5.56 g/cm<sup>3</sup>) and Mg anode (1.74 g/cm<sup>3</sup>), respectively,  $F$  = Faraday's constant,  $9.65 \times 10^4$  C/equiv, and  $\lambda = \int_0^t (CD) dt$ .

It should be noted that the equivalent weight of pure magnesium, 12.16 g/equiv, was used for  $W_a$ , whereas the AZ61 alloy (nominal composition: 6% Al, 1% Zn, 0.2% Mn, and 92.8% Mg) used for anode material has a nominal equivalent weight of 12.63 g/equiv. However, since the same value of  $W_a$  used in Eq. [5] was used for calculating the anode efficiency, the variation in the composition of AZ61 alloy is the only source of error. The range of composition allowed by present specifications is not considered significant. Substituting Eq. [4] and [5] into Eq. [3], the following relationship for  $E$  results

$$E = E_{\text{rev}} - E_{\text{pol}} - (CD) (R_1' + R_2' + R_3') - CD (\rho_s X_0 + L_0/K) - (CD) \{2.67 \rho_s + 0.724 / (\eta \cdot K)\} (10^{-4}) \lambda \quad [6]$$

At this point it is worthwhile to introduce the term  $E_0$ , defined as the emf of a silver chloride-magnesium cell with an interelectrode separation,  $L$ , of zero at time zero (hence  $L_0 = 0.0$ ,  $X = X_0$ ,  $\lambda = 0.0$ ).

$$E_0 = E_{\text{rev}} - E_{\text{pol}} - (CD) (R_1' + R_2' + R_3') - (CD) (\rho_s X_0) \quad [7]$$

Since magnesium is a highly irreversible electrode in aqueous solutions, the magnitude of  $E_{\text{pol}}$  is on the order of 1v and is a function of temperature, electrolyte composition, and current density.  $R_1'$  and  $R_3'$  are functions of the pressure used to compress the com-

ponents of the cell together and the cleanliness of the contact surfaces. Also,  $X_0$  and  $R_2'$  (at  $\lambda = 0$ ) are functions of the technique used to reduce the silver chloride surface. Combining Eq. [6] and [7]

$$E = E_0 - (CD) \{L_0/K + 10^{-4} [2.67 \rho_s + 0.724 / (\eta \cdot K)] (\lambda)\} \quad [8]$$

Equation [8] makes clear the importance of considering the voltage loss across the sponge silver matrix, determined by  $\rho_s$ , as well as the voltage loss across the gap separating the electrodes determined by  $K$ . It will be shown later that, under most conditions likely to be encountered by a AgCl-Mg water-activated battery,  $\rho_s$  is approximately 10-20 ohm-cm,  $\eta$  is approximately 0.7 and, from ref. (2),  $K$  is approximately 0.02 to 0.25 mho/cm. Hence, the magnitude of the terms  $2.67 \rho_s$  and  $0.724 / (\eta \cdot K)$  will be in the range of 25-55 and 4-50, respectively. Thus the two sources of voltage losses are roughly equivalent.

An examination of Eq. [8] reveals that the emf of a silver chloride-magnesium cell is a function of three empirically determined variables  $E_0$ ,  $\rho_s$ , and  $\eta$ . If  $CD$  and  $K$  are held constant, and if  $E_0$ ,  $\rho_s$ , and  $\eta$  do not change with time, Eq. [8] predicts a linear time-voltage trace. However, two significant nonlinearities were observed. The first of these resulted from a poorly understood phenomenon, the Mid-Run Voltage Anomaly (MRVA); the second was the expected drop in voltage on exhaustion of the silver chloride cathode.

The MRVA has been successfully described with the help of several quantities (Fig. 1) which have been empirically related to electrolyte composition and operating conditions (see Presentation of Results).

The voltage correction required to account for the nonlinearity due to cathode exhaustion was empirically determined as a function of the remaining cathode capacity.

Given the electrolyte composition, operating temperature, and current density, the following procedure is used to predict the voltage output *vs.* time of a small AgCl-Mg cell undergoing a constant current discharge. From ref. (2), determine the electrolyte conductivity,  $K$ , and, from the correlations given later in this paper, determine  $\rho_s$ ,  $\eta$ ,  $E_0$ ,  $\theta_B$ ,  $E_M$ ,  $\theta_M$ , and  $E_C$ . Then, referring to Fig. 1, use Eq. [8] to establish the straight line A-G. Point B is found on this line at time  $\theta_B$ , and point C is found by dropping  $E_M$  volts below the line at time  $\theta_M$ . A straight line parallel to and  $E_C$  volts below line A-G is drawn, and its intersection with a horizontal line drawn through point C locates point D. Finally, to the line A-B-C-D-H, the necessary correction for cathode exhaustion is applied as the remaining cathode capacity (determined from the elapsed discharge time, the current density, the thickness of the silver chloride cathode, and Faraday's law) diminishes, typically yielding a curve similar to E-F of Fig. 1. The emf-time trace is then given by curve A-B-C-D-E-F (solid line).

Although the discussion has been limited to the case of small cells at constant current, this method offers promise of use in the design of full size batteries by applying numerical techniques with the aid of computers.

The results obtained in predicting the emf of small silver chloride-magnesium cells by this semi-empirical mathematical model are presented in the body of this paper.

### Apparatus

The apparatus consisted of (a) an electrolyte flow system, (b) the cell assembly, (c) a device for maintaining a known stacking pressure on the cell assembly, and (d) a constant current electrical system with related electrical measuring equipment.

*Electrolyte flow system.*—The electrolyte flow system provided a constant flow of electrolyte at a constant temperature to the cell during discharge. Motive

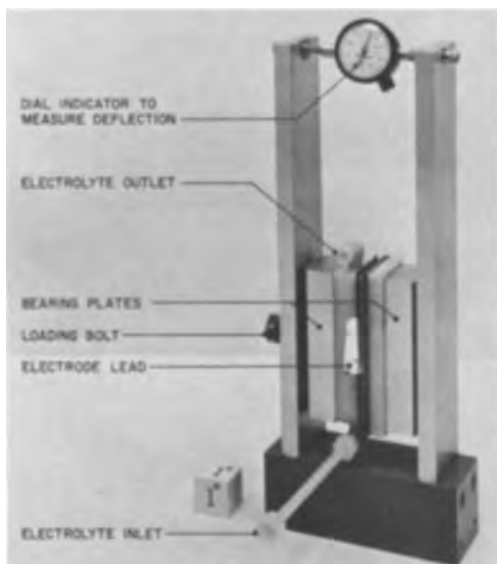


Fig. 3. Device for applying compressive load—cell assembly in place.

force for the flow was provided by displacement from a reservoir by pressurized nitrogen. The requisite cooling and/or heating was provided by stainless steel tubing wrapped with electrical heating tape or coiled in an ice bath. Valving was provided for bypassing the cell. Electrolyte temperatures entering and leaving the cell were measured with copper-constantan thermocouples accurate to about  $\pm 0.1^\circ\text{C}$ . All components in contact with the electrolyte were constructed of inert plastics, glass, and/or stainless steel to minimize electrolyte contamination.

#### Device for compressive loading of the cell assembly.

—Since  $R_1$  and  $R_3$  (Fig. 2) are functions of the stacking pressure, it was necessary to design a device capable of applying to the cell assembly reproducible compressive loads, independent of operating conditions. This device is shown in Fig. 3. A known stacking force was applied to the cell assembly by turning the loading bolt until a given reading was obtained on the dial indicator. Transverse stresses were minimized by the use of ball bearings between the cantilever beams and the bearing plates. The relationship between the compressive force and the dial reading was determined to an accuracy of  $\pm 5\%$  by a calibrated load machine.

**Cell assembly.**—An exploded view of the cell assembly is shown in Fig. 4. Both the AZ61 magnesium alloy anodes and the silver chloride cathodes were  $0.953 \pm 0.003$  cm wide by  $3.385 \pm 0.003$  cm long.

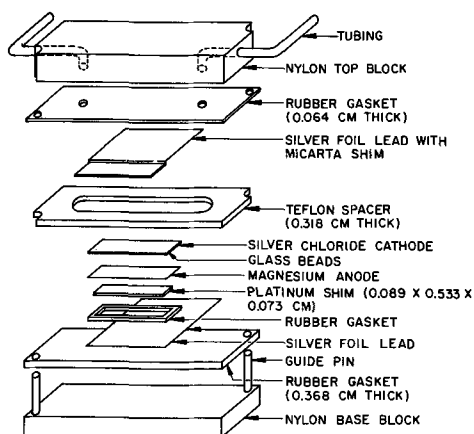


Fig. 4. Exploded view of cell assembly

The total thickness of the micarta shim used in the positive bus plate assembly, the silver foil sheets used for the positive and negative leads, the platinum shim, the anode, and the cathode exceeded the thickness of the Teflon spacer by approximately 0.008 cm. A 0.363 cm thick rubber gasket ensured only negligible variations in stacking pressure across the entire cell assembly.

Electrical contact was made to the magnesium anodes in large AgCl-Mg batteries by laying 0.0025 cm sheets of silver foil on the back sides of the anodes and cementing the sheets to the anode around the periphery. This method did not give reproducible results with small cells, possibly because of surface contamination with cement or vapors from the cement. To avoid this a platinum shim with a watertight gasket was used instead. This technique gave acceptable results.

**Electrical system and instrumentation.**—All discharges were made under conditions of constant (within  $\pm 0.3\%$ ) cell current which were achieved by a constant current power supply and a series connected resistance. Current measurements were made to  $\pm 0.3\%$  accuracy with a reference ammeter.

Cell voltages were recorded on an X-Y recorder and, together with the thermocouple outputs, on a 12-channel strip chart recorder. Both recorders were referenced at 1-min intervals against a standard mercury cell.

**Conductivity equipment.**—The equipment used in determining the conductivities of the electrolytes was identical to that described in ref. (2).

#### Procedure

**Preparation of electrolytes.**—Electrolytes were prepared by adding up to 70g of magnesium chloride per liter to artificial sea water electrolytes whose chlorinities were  $4.5^{0/00}$ ,  $9.00^{0/00}$ , and  $19.00^{0/00}$ . The term "added  $\text{MgCl}_2$  [see ref. (2) for procedural details], which will be used henceforth and denoted by the symbol, CM, is defined as the grams of  $\text{MgCl}_2$  added per liter of sea water at  $25^\circ\text{C}$ . The composition of a given electrolyte will be given by "chlorinity-added  $\text{MgCl}_2$ " (for example 4.5-23.0).

**Preparation of electrodes.**—All anodes were fabricated from one batch of AZ61A alloy. Silver chloride from five batches was used. Two of these batches have nominal thicknesses of  $0.0520 \pm 0.0030$  cm and  $0.0546 \pm 0.0030$  cm and are both referred to herein as "thick" or 0.053 cm silver chloride. The remaining three batches had nominal thicknesses of  $0.0381 \pm 0.0030$  cm and are referred to as "thin" or 0.038 cm silver chloride.

The silver chloride, which was received in the perforated and reduced condition, was cut into approximately  $4.45 \times 2.54$  cm pieces and then beaded prior to being cut to its final dimensions. Beading of the thick (batches D and E) and thin (batches A, B, and C) silver chloride was accomplished with 0.045 and 0.059 cm thick micarta guides, respectively. Each guide had holes of slightly larger diameter than the glass beads located on 0.318 cm centers. Beads of a narrow range of diameters, 0.076–0.084 cm, were placed in the holes in the micarta guides and then driven into the silver chloride with a vise and two hardened steel blocks. The bead height was determined for each cathode by subtracting the thickness of the silver chloride sheet from the thickness of the beaded silver chloride cathode. Generally, the total variation in bead height on an individual cathode was less than 0.0018 cm and the interelectrode separation was in the range of 0.0404–0.0440 cm and 0.0500–0.0546 cm for the thick and thin batches of silver chloride, respectively.

The surface of the magnesium anode was cleaned by sanding both sides followed by an acetone rinse. Immediately after cleaning (always within  $\frac{1}{2}$  hr),

the cells were assembled and the discharge carried out.

**Discharge procedure.**—The nominal flow rates varied from 70 to 100 ml/min with variations of  $\pm 10\%$  occurring during the discharges. The flow rates were sufficiently high that the cell emf was, for all practical purposes, not affected by flow rate.

All discharges reported herein were conducted at a compression loading of 50 psi.

Power supply operation and the electrolyte flow rate and temperature were stabilized with the current and electrolyte bypassing the cell. At this point the electrolyte flow was switched to the cell. As soon as the outlet temperature had stabilized, electrical discharge of the cell was initiated. The inlet temperature of the electrolyte was held constant to within  $\pm 0.1^\circ\text{C}$  except in the case of a few discharges in which temperature variations up to  $\pm 0.3^\circ\text{C}$  occurred.

When the battery emf fell to the cutoff voltage (usually 0.0v), the discharge was stopped and the cell disassembled as quickly as possible. The post-run magnesium weight was determined by the two techniques given in ref. (1). The first technique includes washing and mechanical cleaning with a nylon brush; the second includes a 30-60 sec dip in a 30% (by weight) solution of  $\text{CrO}_3$  in water (in some of the early discharges this technique was not used). The anode efficiency was calculated from the post-run anode weight as in ref. (1).

All calculations were based on the average of the inlet and the effluent temperatures. During passage of the electrolyte through the cell assembly, its temperatures dropped by about  $2.5^\circ$  at  $65^\circ\text{C}$ ,  $1^\circ$  at  $45^\circ\text{C}$ , and increased by about  $0.4^\circ$  at  $25^\circ\text{C}$ , and about  $2^\circ$  at  $5^\circ\text{C}$ . Hence the temperature rise or fall across the cell assembly was the largest contributor to the uncertainty of the estimate of the operating temperature.

### Presentation of Results

A condensation of the results of this study is presented in Fig. 5 through 10 and in Tables I through III. A more complete summary of the results, including the time-voltage traces of all the discharges appropriate to this study, is found in ref. (3).

### Discussion of Results

**Experimental reproducibility.**—Let the term "discharge pair" refer to two discharges made under identical conditions with cathodes and anodes fabricated from the same batches of silver chloride and magnesium. The term "agreement" is then defined as the percentage of the average elapsed discharge time at a voltage cutoff of 0.75v (the elapsed discharge times at cutoff for the individual discharges of a discharge pair generally agreed to within 4%) over which the individual cell voltages of the discharge pair agreed to within a given voltage tolerance.

Of the 34 possible discharge pairs (from this study), the agreement was at least 93% for all but two with a voltage tolerance of 0.05v and at least 75% for all but four with a voltage tolerance of 0.03v.

$E_0$ .— $E_0$  was approximated by the equation

$$E_0 = E' + 0.129 (0.271 - CD) \quad [9]$$

Values of  $E'$  (which are best estimates of  $E_0$  at a current density of 0.271 ascm) are given in Table I. Evidence supporting the use of Eq. [9] is presented in Fig. 5. A substantial part of the data scatter of Fig. 5 is attributable to errors arising from uncertainties of the electrode separation. For example, an error in the electrode separation of 0.001 cm could give rise to errors in  $E_0$  up to 0.02v. Another important source of scatter in both  $E_0$  and  $\rho_s$  is associated with determining the best linear fit to the experimental voltage traces. Despite the scatter, it is apparent that the

Table I.  $E'$ , the values of  $E_0$  at 0.271 ascm

Average temperature, $^\circ\text{C}$	CM g/liter				
	0.0	11.5	23.0	37.5	70.0
5.0	1.381	1.392	1.397	(1.400)*	(1.403)
12.4	1.395	1.407	1.413	(1.417)	(1.420)
25.0	1.420	1.434	1.443	1.449	(1.453)
29.9	(1.433)	1.449	(1.460)	1.466	1.472
34.8	(1.448)	(1.466)	(1.478)	1.486	(1.494)
44.2	1.476	1.500	1.517	1.530	1.539
54.6	(1.495)	(1.524)	(1.541)	1.555	1.565
64.8	(1.502)	(1.529)	(1.546)	1.560	1.570

\* Values in parentheses are interpolated or extrapolated values.

linear correction for the effect of current density in Eq. [9] improves the prediction of  $E_0$ .

Examination of Eq. [7] shows several ways in which a dependence of  $E_0$  on current density can arise. Since tests showed that reducing the stacking pressure from 65 to 10 psi did not affect  $E_0$ , it is likely that the contact resistances  $R_1$  and  $R_3$  were too small to be responsible for the current density dependence of  $E_0$ . This dependence probably arises from increased electrode polarization through  $R_s$  (at time equal to zero), and  $R_2'$  might contribute to the current density dependence. The temperature and magnesium chloride content of the electrolyte can affect  $E_0$  by changing  $E_{\text{pol}}$  and/or  $E_{\text{rev}}$  as well as affecting  $E_0$  by increasing or decreasing the magnitude of the IR drop across  $X_p$ .

The hydrogen released by the AZ61 during discharge decreases the effective conductivity of the electrolyte. However, calculations (assuming uniform dispersion of the hydrogen) show that this would account for only 12% of the dependency of  $E'$  on current density. Hydrogen evolution could account for the decrease in  $E'$  with current density if the gas were dispersed in the electrolyte in such a manner that its effect on the internal resistance of the cell was increased (e.g., by forming a film on the anode).

**Anode efficiency.**—Figure 6 gives anode efficiencies of AZ61 magnesium alloy [ $\text{CrO}_3$  cleaning method, see

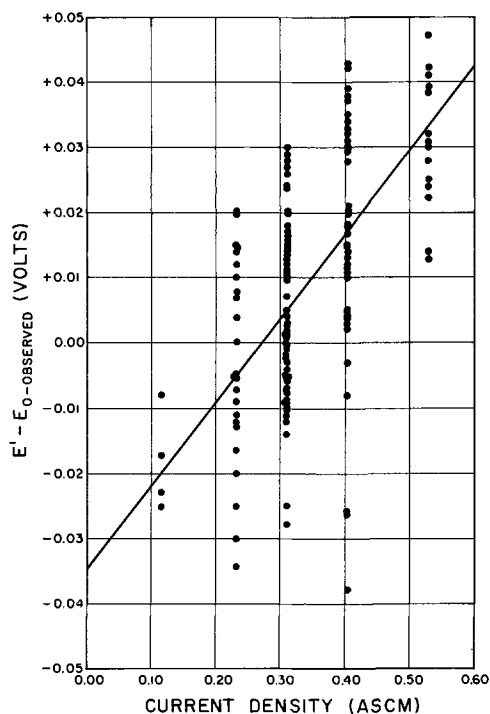


Fig. 5. Effect of current density on the differences between values of  $E'$  from Table I and experimental values of  $E_0$ . The solid line gives the values of  $E_0 - E'$  predicted by Eq. [9].

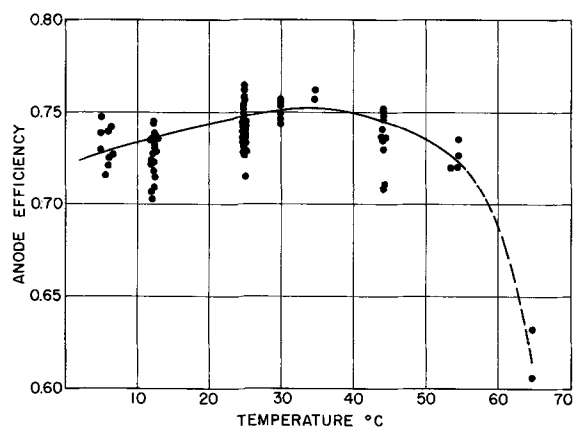


Fig. 6. Anode efficiencies determined by the chromate cleaning method.

ref. (1)]. Evidence of a large drop in anode efficiency of high temperature is given by the two data points at 65°C. However, the results obtained at 65°C must be used with some caution because there is much more clogging at this temperature, which made it difficult to obtain reliable anode efficiency data (all anode efficiencies obtained for discharges exhibiting clogging were presumed unreliable), and the strong effect that the type of cleaning method used had on the value of anode efficiency obtained (see the discussion immediately below).

The values of anode efficiency obtained with the  $\text{CrO}_3$  cleaning method were, for temperatures of 45°C and below, 1 to 3% less than those obtained with the mechanical cleaning method. In the two discharges at 65°C where anode efficiencies were determined by both methods, the  $\text{CrO}_3$  cleaning method gave values of anode efficiency 9.3 and 10.4% lower than the anode efficiencies obtained by the mechanical cleaning method. No comparative values between mechanical and  $\text{CrO}_3$  cleaning were obtained at 55°C.

$\rho_s$ .—Figure 7 presents values of  $\rho_s$  as a function of temperature and current density. The experimentally determined values of  $\rho_s$  exhibited scatter which was large when compared to the effects of current density for values of current density of 0.232 ascm and above, primarily because of the sensitivity of the value of  $\rho_s$  obtained to the value of the slope of the "best line" drawn through the emf-time trace. In spite of this, current density was retained as a parameter since better results were obtained when this was done. More will be said about this in the Simplifications of the SEMM.

Empirical equations for  $\rho_s$  ( $CD \geq 0.116$  ascm) were developed; they are as follows:

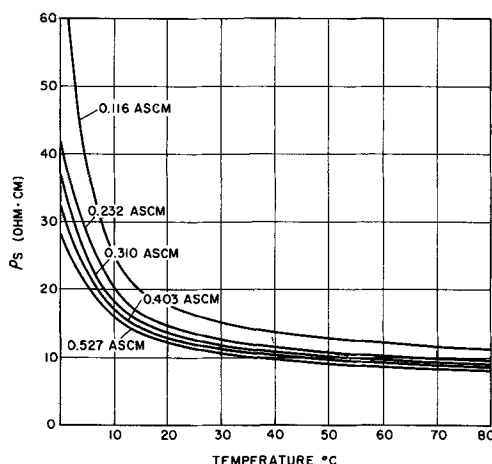


Fig. 7.  $\rho_s$  as a function of temperature and current density.

for  $T < 12.5^\circ\text{C}$

$$\rho_s = (0.1062 CD^{0.176} + 0.002667T - 0.0598)^{-1} \quad [10a]$$

for  $T \geq 12.5^\circ\text{C}$

$$\rho_s = (41.05)/[1.388(\ln T + 0.6162)CD^{0.176} - 1.088] \quad [10b]$$

It is noteworthy that six cases of negative  $\rho_s$  values were observed at temperatures equal to or less than 25°C. Negative values of  $\rho_s$  arise when the observed value of  $dE/d\theta$  is less than that portion of the calculated value of  $dE/d\theta$  arising from the increasing electrode separation associated with the dissolution of magnesium. Three of the above cases of negative  $\rho_s$  are associated with electrolyte 4.5-0.0 (*i.e.*, 4.5% salinity 0.0 g/liter of added  $\text{MgCl}_2$ ), two with electrolyte 4.5-11.5 and one with electrolyte 9.0-11.5. Negative values of  $\rho_s$  cannot be attributed to the low conductivities of the electrolytes since positive values of  $\rho_s$  were obtained in many discharges with electrolytes of much lower conductivity (*e.g.*, the discharges made at 5°C). A comparison of identical discharges indicates that this behavior may be batch sensitive (*e.g.*, under identical conditions  $\rho_s$  for batch A ranged from -1.8 to -5.7 ohm-cm while  $\rho_s$  for batch C ranged from +13.3 to +16.4 ohm-cm).

*Mid-run voltage anomaly (MRVA).*—The nonlinearity of the MRVA region is taken into account by the quantities  $\theta_M$ ,  $E_M$ ,  $E_C$ , and  $(\theta_M - \theta_B)$ , used in accordance with the procedure given in the SEMM section.<sup>1</sup>

The location of  $\theta_M$  is given by the empirically determined equation

$$(CD)^{2\theta_M} = (4.27 CHL - 4.05)(10^{-4}) \exp [4.29 \cdot CHL^{-0.1363}(T + 273.2 - N \cdot CHL/5) \cdot 10^{-2}] \quad [12]$$

where  $N$  is equal to 0.0 for 0.053 cm thick silver chloride and to 1.0 for 0.038 cm thick silver chloride. Figures 8 and 9 compare Eq. [12] with the experimental data.

The relation

$$\theta_M - \theta_B = 23.3/CD \quad [13]$$

was used to determine  $\theta_B$  once  $\theta_M$  was determined.

The dependence of the magnitude of  $E_M$  on temperature is adequately described by the following empirical relation

$$E_M = \max \{0; (CD)[52.0 + 2.0(CM)^{0.5} - 1.6T](10^{-2})\} \quad [14]$$

The relation

$$E_C = 0.6E_M \quad [15]$$

gives adequate results.

*Effect of the silver chloride batch on the MRVA.*—Using thin silver chloride results in considerable batch-to-batch variations in the extent and location of the MRVA. No such variation was observed with thick silver chloride, although the possibility of batch-to-batch variations cannot be ruled out because only two batches were tested. Work is now underway to determine the cause of these variations. Evidence that the heat-treatment history of the silver chloride plays a role has been discovered. It must be emphasized that the use of  $N = 0.0$  for the thick silver chloride and  $N = 1.0$  for the thin silver chloride in Eq. [12] is based on experience gained with these few batches of  $\text{AgCl}$ . Furthermore, in the absence of experimental data, any extrapolation of  $N$  for thicknesses of  $\text{AgCl}$  lying outside of this range of thickness is not recommended. In short, the limiting factor in predicting the MRVA is the batch-to-batch variation in the cathode behavior of the silver chloride. A quantitative study of this variability will be difficult because the process methods used for producing cathode-grade rolled sil-

<sup>1</sup> Equations [12] through [15] apply only over the range of temperatures and chlorinities studied.

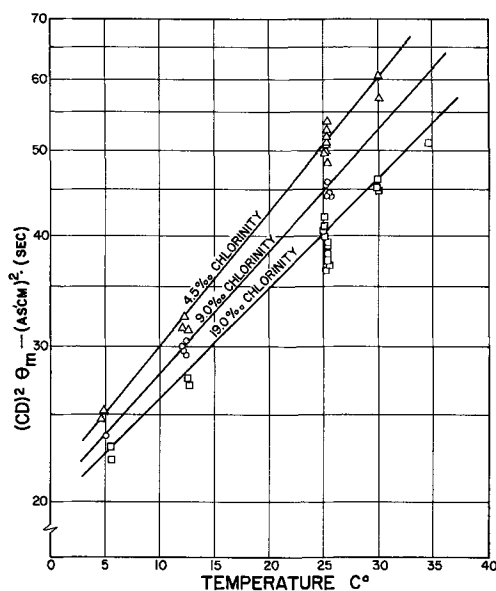


Fig. 8. Comparison of experimental values of  $(CD)^2\theta_M$  with those predicted by Eq. [12] for the case of 0.053 cm thick silver chloride. The symbols designate electrolytes of the following chlorinities:  $\triangle$  4.5%/ $\infty$ ,  $\circ$  9.0%/ $\infty$ , and  $\square$  19.0%/ $\infty$ .

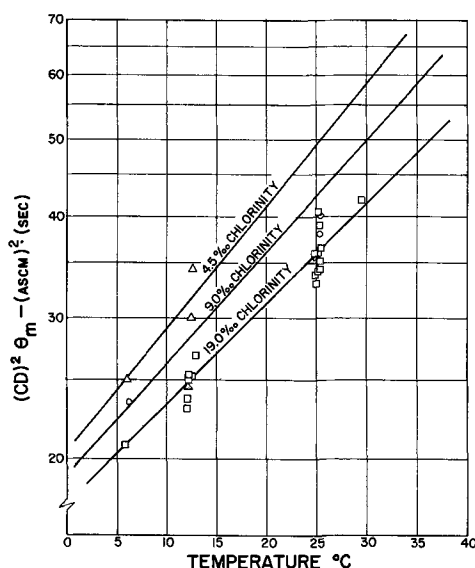


Fig. 9. Comparison of experimental values of  $(CD)^2\theta_M$  with those predicted by Eq. [12] for the case of 0.038 cm thick silver chloride. The symbols designate electrolytes of the following chlorinities:  $\triangle$  4.5%/ $\infty$ ,  $\circ$  9.0%/ $\infty$ , and  $\square$  19.0%/ $\infty$ .

ver chloride sheets are protected by manufacturer's rights.

**Voltage corrections for cathode exhaustion.**—A set of experimental discharges was selected for which the only apparent deviation from the linear voltage-time trace predicted by Eq. [8] was that owing to cathode exhaustion, i.e., for which no MRVA was observed. For each of these discharges, the voltage deviation from linearity was plotted vs. the remaining cathode capacity (calculated on the basis of 100% cathode efficiency) to obtain a curve of best fit as shown by the eight representative discharges in Fig. 10. The values of voltage corrections used to account for cathode exhaustion (as illustrated by region No. 3 of Fig. 1) were taken from this curve.

**Accuracy of the SEMM.**—It is necessary to define some quantity that will provide a measure of the degree of agreement between the model predictions and the experimental results. The quantity chosen for

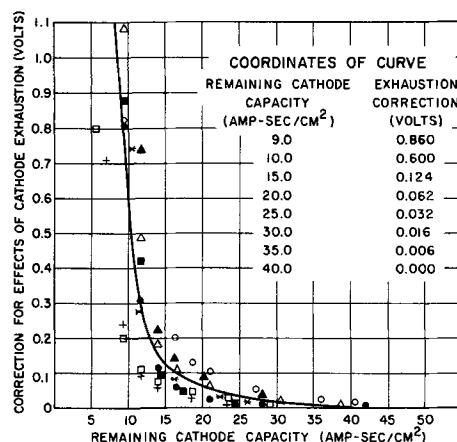


Fig. 10. Comparison of the cathode exhaustion correction to those calculated from the emf's of several cathode limited discharges (high temperature and high electrolyte conductivity).

this purpose, henceforth called "agreement," was the per cent of "the duration of discharge to  $E_{co}$ " during which the experimental and predicted emf's agreed to within a given voltage tolerance. The duration of discharge to  $E_{co}$  is defined as the time, measured from the start of the discharge, at which the emf predicted by the semi-empirical model dropped to the cutoff voltage.

In typical battery design, the thickness (hence the amount of silver chloride) is controlled to about  $\pm 5\%$ . Other important dimensions, such as the electrode spacing, are held to about the same tolerance. Furthermore, large high-drain batteries are generally designed with an electrode spacing of 0.059 cm because smaller spacings increase the danger of electrical shorts and of the cells becoming clogged with reaction products. When these considerations are taken into account, a reasonable criterion is that the predicted and observed emf's of a cell with an electrode spacing of 0.059 cm agree to within 0.05v for 90% or more of the duration of the discharge to a cutoff voltage of 0.75v.

The model was tested against 108 discharges using the thick silver chloride and 39 discharges using thin silver chloride. Satisfactory agreement, as defined above, was obtained for 107 and 29 of these discharges, using thick and thin silver chloride, respectively. The discharge conditions of temperature, chlorinity, magnesium chloride concentration, and current density for which satisfactory agreement was obtained are given in Table II. Table III lists all discharges in which the agreement fell below 90% (11 out of a total of 147 discharges). Two of these discharges failed to pass because of errors in  $E_0$ .

The remaining discharges which, significantly, were from the same batch of thin silver chloride, fall into two groups. The first of these exhibited a phenomenon in which the slope of the time-voltage trace,  $dE/d\theta$ , suddenly decreased at some period during the discharge. If values of  $\rho_s$  are calculated for this region of decreased  $dE/d\theta$ , negative values of  $\rho_s$  often resulted (see the discussion of  $\rho_s$ ). The cause for this phenomenon is not known at present. Inspection of all the discharges indicates, however, that it is negligible at either 19%/ $\infty$  chlorinity or at temperatures above 30°C. The two discharges which appear on Table III used thin silver chloride cathodes from a batch which was characterized by an extremely early onset of the change in the  $dE/d\theta$  compared to discharges made with other batches of silver chloride.

The use of the agreement as defined in this paper somewhat obscures the magnitude of this effect, since, because of space considerations, the duration of the discharge was based on the time at which the emf predicted by the model dropped to 0.75v. If the agreement is based on the time at which the observed emf

Table II. Discharge conditions for which satisfactory\* agreement was obtained

Nominal temp, °C	Chlorinity, ‰	C <sub>M</sub> , g/liter	CD, ascm				
			0.116	0.232	0.310	0.403	0.527
Group I. Thick silver chloride							
5.0	9.0	23.0			x†		
5.0	19.0	0		x	(2)	x	
5.0	19.0	11.5			(2)		
5.0	19.0	23.0			x		
11.5	4.5	23.0			x	x	
11.5	9.0	11.5		x	x		
11.5	19.0	0		x	x		
11.5	19.0	11.5			x	(2)	x
11.5	19.0	23.0					x
25.0	4.5	0	x				
25.0	4.5	11.5	x		(5)		
25.0	4.5	23.0			x		(2)
25.0	4.5	37.5			(2)	x	
25.0	9.0	0	x				
25.0	9.0	11.5			x		
25.0	9.0	23.0			x	(2)	x
25.0	19.0	0	x	(2)	(5)	x	x
25.0	19.0	11.5			x	x	x
25.0	19.0	23.0		x	x	(5)	
25.0	19.0	37.5		x	x		x
30.0	4.5	37.5				x	
30.0	4.5	70.0			x		
30.0	19.0	11.5			(2)	(2)	
30.0	19.0	37.5				x	
35.0	19.0	37.5			x	x	
45.0	4.5	11.5			x		
45.0	4.5	23.0			x		
45.0	4.5	37.5			x		x
45.0	4.5	70.0					x
45.0	9.0	0		(2)	x	(2)	
45.0	19.0	0		x	x	x	
45.0	19.0	11.5			(2)		
45.0	19.0	23.0		x	x	x	
45.0	19.0	37.5		x	(2)	x	x
45.0	19.0	70.0		x	x	x	x
55.0	4.5	37.5					x
55.0	4.5	70.0					x
55.0	19.0	37.5					x
55.0	19.0	70.0					x
65.0	4.5	70.0		x	x	x	
65.0	19.0	37.5		x			
65.0	19.0	70.0		x	x		
Group II. Thin silver chloride							
5.0	4.5	23.0			x		
5.0	9.0	23.0			x		
5.0	19.0	0		x			
11.5	4.5	11.5		(2)			
11.5	4.5	23.0			x		
11.5	19.0	0		x	x		
11.5	19.0	11.5			x	x	
25.0	4.5	11.5			(2)		
25.0	9.0	23.0				x	(2)
25.0	19.0	0		(2)	x	(3)	
25.0	19.0	23.0				(2)	
25.0	19.0	37.5			x	(2)	
45.0	4.5	11.5			x		
45.0	4.5	37.5					x
45.0	19.0	37.5		x			

\* 90% or better agreement with voltage tolerance of 0.05v and  $E_{co} = 0.75v$ .

† An "x" means a single discharge; an "(n)" means n discharges.

falls to 0.75v (adjusted to an electrode spacing of 0.059 cm), (a) agreement values of 49 and 54% are obtained for discharges number 199 and 205, respectively, and (b) the value of  $E_{co}$  at which 90% agreement is reached becomes 0.83v for both discharges. It should be noted, however, that this source of error is not as serious as first appears, since (a) it leads to an underestimation of the voltage, which would lead to conservative battery designs, and (b) it is not important unless operating voltages of 0.83v or less are contemplated. Studies are underway to obtain more information about the causes of the decrease in  $dE/d\theta$ .

The discharges in group III on Table III failed to agree because of: (a) abrupt voltage decays which occurred earlier than predicted by Fig. 10 and (b) atypical MRVA behavior for one batch of thin silver chloride which was characterized by large observed values of  $E_M$  and low observed values of  $\theta_M$  (early onset of the MRVA). This gave rise, in some cases, to a serious lack of agreement between the model and the observed emf. The lack of agreement of the discharges shown in group III of Table III was due mainly to the early onset of MRVA for the one batch

of silver chloride with, in general, about one-third of the error due to an early voltage decay.

Of the other two batches of thin silver chloride studied, one followed the MRVA predictions reasonably well, i.e., Eq. [12], [13], [14], and [15]; the other lay almost midway between the predictions of the MRVA for the thick and the thin silver chloride as good results were obtained when either  $N = 0.0$  or 1.0 was used in Eq. [12].

Note that all but five of the discharges in Table III agree at the 90% level if  $E_{co}$  is raised to 0.85v, and all but two agree at the 90% level at an  $E_{co}$  of 0.92v.

In summary, the primary cause for failure to reach agreement was the variations between the batches of silver chloride which gave rise to the variations in the MRVA. In spite of this only 2 out of 147 discharges failed to agree at the 90% level for electrode spacings commonly used in sea water-activated silver chloride batteries when an  $E_{co}$  of 0.92 is used. SEMM is now being extended to the more general case of discharges where changes in current density, electrolyte composition, and operating temperature occur.

The extension of this model to include the use of alternate anodes, e.g., zinc, appears to be straightforward; some work with zinc has been done at this Laboratory.

### Simplifications to the SEMM

The model presented herein was developed with the objective of predicting the voltage of a silver chloride AZ61 magnesium alloy water-activated battery to within 0.05v (preferably 0.03v) to a cutoff voltage (based on the SEMM) of 0.75v. Several simplifications to the SEMM can be made if higher cutoff voltages, lower per cent agreements or greater error tolerances can be accepted. The following comments should be used as guidelines only as parameters such as geometry, electrolyte composition, etc., affect the loss of accuracy for a given simplification.

If a value of anode efficiency of 0.73 is used, the degradation in accuracy will be about 0.005v for temperatures under 60°C. At 65°C an error of about 0.03v will occur under some operating conditions. It bears mention that the effect of anode efficiency on the temperature distribution in a large battery may be very important since the secondary reactions (which lead to the observed anode efficiencies) are an important source of heat.

The correction for the effect of current density on  $E_0$  (Eq. [9]) can be neglected if the voltage tolerance is increased to 0.08v.

Similarly, for current densities of 0.23 and above, the values of  $\rho_s$  presented for 0.310 ascm can be used if the voltage tolerance is increased to 0.08v (though in most cases, 90% agreement will still be achieved with the 0.05v tolerance). A more detailed error analysis should be carried out before attempting any similar type simplification below 0.23 ascm.

Since the cathode exhaustion corrections (Fig. 10) exceed 0.05v at the value of remaining cathode capacity equal to about 15% of the total capacity of the "thin" silver chloride, some sort of correction of this type appears necessary in most cases. Alterations to the corrections presented on Fig. 10 suitable for specific design problems can be developed as needed.

In most cases the corrections for the MRVA can be neglected above 35°C with little loss in accuracy; however they are very important over the temperature range of 10°-28°C. (Below 10°C the main effects of the MRVA generally occur after the voltage has fallen below 0.75v; hence generally little accuracy loss will occur if they are neglected.) Between 10° and 28°C the MRVA effects often occur when the emf is still high and, if the MRVA corrections are neglected, serious losses in agreement will occur unless the cutoff voltage is raised to about 1.0-1.05v for an adiabatically operated battery. An error analysis is strongly recommended before attempting

Table III. Discharges with less than 90% agreement (0.05v error tolerance) with Model  
Calculations based on an 0.059 cm electrode spacing and a 0.75v cut-off

Discharge No.	Chlorinity, ‰	CM, g/liter	Current density, ascm	Temp, °C	% Agreement $E_{co} = 0.75v$ , %	$E_{co}$ giving 90% agreement, v	Time to 0.75v, min	Time to $E_{co}$ 90% agreement, min
Group I.* Reason for lack of agreement: incorrect values of $E_0$ predicted by Eq. [7]								
208	19.0	11.5	0.232	5.0	86	0.81	7.05	6.50
174	19.0	0.0	0.403	25.0	89	0.76	3.85	3.80
Group II.† Reason for lack of agreement: decrease in $dE/d\theta$								
199	4.5	11.5	0.310	25.0	78	0.83	3.60	3.10
205	4.5	11.5	0.310	25.0	81	0.77	4.35	3.90
Group III.‡ Reason for lack of agreement: atypical MRVA behavior and early voltage decay								
139	19.0	37.5	0.403	25.0	87	0.87	5.40	5.03
169	19.0	23.0	0.403	25.0	81	0.85	5.20	4.55
171	19.0	11.5	0.403	29.9	87	0.85	4.85	4.50
206	19.0	11.5	0.232	12.0	72	1.01	9.05	6.20
207	19.0	11.5	0.232	12.0	77	0.89	9.15	6.70
213	19.0	37.5	0.403	25.0	80	0.92	5.20	4.70
214	19.0	37.5	0.403	25.0	71	1.03	5.35	3.10

\* Discharge No. 208 with thick AgCl, No. 174 with thin.

† All discharges used same batch of thin AgCl.

any simplifications to the MRVA corrections as the agreement obtained is highly sensitive to electrolyte composition and electrode separation.

### Conclusions

A semi-empirical mathematical model for predicting the emf of small silver chloride AZ61 magnesium alloy cells, discharged under a constant current load, has thus been developed. Excellent agreement was obtained over a range of current densities of 0.116-0.527 ascm from 5° to 65°C. The range of chlorinities and magnesium chloride concentrations studied was more than adequate to allow safe extrapolation to any set of electrolyte conditions likely to be encountered in a large, high-drain water activated AgCl-Mg battery.

Two deviations from the linear time-voltage trace predicted by the equivalent circuit on which the mathematical model was based were (a) the expected voltage decay which occurs on exhaustion of the cathode and (b) the MRVA, a drop in voltage which occurs prior to exhaustion of the cathode under some operating conditions. These have been predicted reasonably well by empirically developed corrections (hence the term semi-empirical mathematical model), but room for improvement exists. The MRVA was found to be dependent on the batch of silver chloride used and, under some operating conditions, an early voltage decay took place prior to the exhaustion of the silver chloride cathode. Another source of error was a very slowly decaying voltage trace which caused the model to predict low values of emf. All three of these problem areas are under study, especially the batch-to-batch variations in the MRVA. Since errors arising from batch-to-batch variations in silver chloride were the most important, the accuracy of the model is primarily limited by the reproducibility of the cathode grade silver chloride presently available.

Studies are also underway to determine the adequacy of the model for discharges where changes in current density, temperature, and electrolyte composition occur; the results to date appear promising.

### Acknowledgment

Dr. William R. Davis, Assistant Director of the Applied Physics Laboratory, and staff, Mr. William Felton, Mr. Rodney Lipp, and Mr. Robert Van Valkenburgh contributed to the success of this effort. Their contributions are gratefully acknowledged.

This work was supported by the Bureau of Naval Weapons, U.S. Department of the Navy, under Contract NOW 65-0207-d.

Manuscript submitted Nov. 17, 1967; revised manuscript received Aug. 16, 1968.

Any discussion of this paper will appear in a Discussion Section to be published in the June 1969 JOURNAL.

### REFERENCES

1. D. W. Faletti and L. F. Nelson, *Electrochem. Technol.*, **3**, 98 (1965).
2. D. W. Faletti and M. A. Gackstetter, *This Journal*, **114**, 299 (1967).
3. D. W. Faletti and M. A. Gackstetter, Applied Physics Lab., University of Washington report, APL-UW 6816 dtd 1 April 1968; Defense Documents Center, DDC-TC 831619L, Alexandria, Va.

### NOMENCLATURE

- A Electrode area, cm<sup>2</sup>  
 CD Current density, amp/cm<sup>2</sup>  
 CHL Chlorinity, ppt  
 CM Grams of MgCl<sub>2</sub> per liter of sea water at 25°C  
 d<sub>a</sub> Density of magnesium anode, g/cm<sup>3</sup>  
 d<sub>c</sub> Density of silver chloride cathode, g/cm<sup>3</sup>  
 E Cell emf, v  
 E' Quantity equal to the emf of a AgCl-Mg cell with zero electrode separation (or, equivalently, zero electrolyte IR drop) at time equal to zero when under a 0.271 ascm current density, v  
 E<sub>c</sub> Empirical correction subtracted from the value of E provided by Eq. [15] from point D to point H of Fig. 1, v  
 E<sub>co</sub> Cutoff voltage, v  
 E<sub>M</sub> Maximum MRVA correction, and predicted by Eq. [14], subtracted from the value of E at time equal to  $\theta_M$ , v  
 E<sub>0</sub> Same as E' but true for any specified current density, v  
 E<sub>pol</sub> Total loss of emf due to polarization at time equal to zero, v  
 E<sub>rev</sub> Reversible emf of the AgCl-Mg, v  
 F Faraday's constant, 96,500 C/equiv  
 I Current, amp  
 K Electrical conductivity of the electrolyte, mho/cm  
 L Electrode separation, the separation between the cathode and anode of a cell, cm  
 L<sub>0</sub> Value of L at time equal zero, cm  
 N Parameter used in Eq. [12], equal to 1.0 for 0.038 cm thick AgCl; equal to 0.0 for 0.053 cm thick AgCl  
 R<sub>1</sub> Contact resistance between the positive bus plate and the silver chloride cathode, ohms  
 R<sub>1</sub>' Specific contact resistance between positive bus plate and the cathode, ohm-cm<sup>2</sup>  
 R<sub>2</sub> Resistance of the silver on the surface of the silver chloride cathode; that formed chemically prior to the discharge, and the sponge silver formed during the discharge, ohms  
 R<sub>2</sub>' Specific resistance of the silver coating the cathode, ohm-cm<sup>2</sup>  
 R<sub>3</sub> Contact resistance between the AZ61 magnesium anode and the negative bus plate, ohms  
 R<sub>3</sub>' Specific contact resistance between the AZ61 magnesium anode and the negative bus plate, ohm-cm<sup>2</sup>  
 W<sub>a</sub> Equivalent weight of magnesium anode, g/equiv.



$W_c$	Equivalent weight of silver chloride cathode, g/equiv.	$\theta$	Time, sec
$X$	Thickness of the layer of sponge silver, cm	$\theta_B$	Time at which the voltage effects of the MRVA begin, sec
$X_0$	Thickness of the layer of sponge silver at the initiation of discharge, cm	$\theta_M$	Time at which the greatest voltage effects of the MRVA occur, sec
$\eta$	Anode efficiency; the ratio of the weight loss predicted by Faraday's law, to the observed anode weight loss, dimensionless	$\rho_s$	Specific resistivity of the electrolyte-sponge silver matrix, ohm-cm

## Electrocatalysts for the Direct Electrochemical Oxidation of n-Octane in Fuel Cells

Elton J. Cairns\*<sup>1</sup> and John Paynter\*

General Electric Research and Development Center, Schenectady, New York

### ABSTRACT

Until very recently, the direct oxidation of hydrocarbons in fuel cells required high loadings of platinum in the anodes, making such fuel cells prohibitively expensive. This paper describes some progress toward acceptably low loadings of high-activity platinum electrocatalysts for the direct anodic oxidation of liquid n-octane. The activity of both supported and unsupported platinum, prepared in various ways, has been compared to that of commercial platinum black. Investigations of carbon substrates of widely varying specific areas showed that an increase in the specific area of the substrate yields a corresponding increase in electrocatalyst activity, up to at least 200 m<sup>2</sup>/g. Certain preparations of platinum on a carbon support show activities of six to eighteen times that obtained from commercial platinum black. No current or voltage cycling has been encountered when 36 m/o hydrofluoric acid at 105°C has been used as the electrolyte, in contrast to the behavior with other acidic electrolytes.

The direct anodic oxidation of saturated hydrocarbons at practical current densities (tens to hundreds of ma/cm<sup>2</sup>) has been possible only since 1963 (1-14). In general, it has been found necessary to employ platinum electrocatalysts, strong acid electrolytes, and temperatures above about 100°C in order to obtain reasonable reaction rates. Even when these elevated temperatures and acidic electrolytes were used, it was still required (until just recently) that relatively large amounts of platinum be used in the electrodes in the range of 40-200 mg/cm<sup>2</sup>. The electrolytes which have been found useful with hydrocarbon fuels are dilute sulfuric acid (3N, 95°C) (7), phosphoric acid (1, 2, 4, 5, 8-10, 13), cesium fluoride-hydrofluoric acid mixtures (3, 6, 11, 12), and hydrofluoric acid (6, 12, 14). The saturated hydrocarbon fuels which have shown the greatest reactivity in fuel cells have been ethane (12, 14-17), propane (12, 14-17), and butane (12, 14, 16, 17), and consequently these have been the most frequently studied.

Even though the anodic oxidation of propane at current densities in excess of 500 ma/cm<sup>2</sup> has been achieved at temperatures as low as 105°C (14), this performance was obtained with an anode containing 102 mg Pt/cm<sup>2</sup>. This platinum loading and those used in similar investigations were too high to make hydrocarbon fuel cells commercially feasible. Consequently, there has been a continuing effort to decrease the platinum content of fuel-cell anodes for use with hydrocarbons, without a proportional decrease in anode performance. The achievement of a tenfold increase in current per unit weight of platinum (above that obtained with commercial Pt black) at an anode potential of 0.4v vs. r.h.e. and at a loading of about 10 mg Pt/cm<sup>2</sup> has been reported for a graphite-supported electrocatalyst when used with propane at 105°C in an HF electrolyte (14).

Because liquid hydrocarbon fuels are more convenient to handle and are more readily available than the gaseous fuels, the investigations of more effective use of platinum in hydrocarbon fuel cell anodes were extended to include n-octane (bp 125.7°C) as a representative hydrocarbon fuel which is a liquid in the fuel chamber of the cell at operating temperature (105°C). The use of higher activity forms of unsupported platinum and platinum supported on both graphitic and nongraphitic carbon powders has been investigated. Carbon is particularly attractive for use as an electrocatalyst support because it is one of the few materials which is inexpensive in high-area form, electronically conducting, and resistant to corrosion by hot strong acids under the electrochemical conditions found at hydrocarbon anodes. The employment of platinoid elements other than platinum (9, 14) and of platinoid-element alloys (9, 13, 18) has been found to be an unrewarding approach and was not pursued in this work.

### Experimental

The electrolyte used in this investigation was the HF-H<sub>2</sub>O maximum-boiling azeotrope (36 m/o HF), which boils at 112°C (20, 21) and has a resistivity of 1.8 ohm-cm (20). The azeotrope was chosen because its composition will remain uniform and constant in the pores of the electrodes. The fluoride anion is not expected to adsorb on the platinum (22, 23) thereby leaving a maximum fraction of the electrocatalyst surface available for adsorption, surface reaction, and oxidation of fuel (24, 25). Access of the fuel to this surface is facilitated by the relatively high solubility of hydrocarbons in HF-H<sub>2</sub>O solution (26). These advantages contribute to the high performance on hydrocarbons which can be obtained with this electrolyte at relatively low temperatures (105°C). This feature is of importance in minimizing the sintering of highly active electrocatalysts which has been found to occur in other acids at higher temperature (19).

\* Electrochemical Society Active Member.

<sup>1</sup> Present address: Argonne National Laboratory, 9700 South Cass Avenue, Argonne, Illinois 60439.

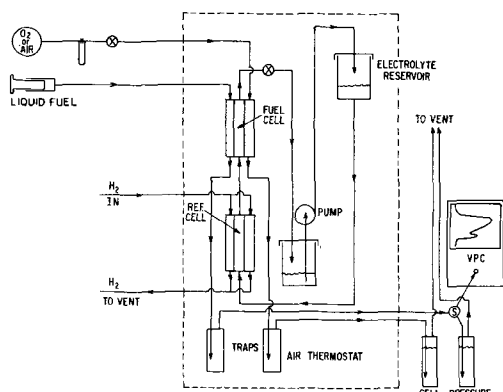


Fig. 1. Schematic diagram of fuel-cell apparatus

The HF-H<sub>2</sub>O azeotrope was prepared from Baker and Adamson reagent grade 48 w/o (weight per cent) hydrofluoric acid, containing less than 20 ppm impurities, and from quartz-redistilled water.

All of the apparatus which came into contact with the electrolyte was made of polytetrafluoroethylene (PTFE) in order to prevent any contamination of the electrolyte by dissolved materials. The PTFE gas compartments were circular, 3 mm deep, and had an area of 11.38 cm<sup>2</sup>; the PTFE electrolyte compartment was the same size. The thin, PTFE-bonded electrodes were held in place between the gas compartments and the electrolyte compartment by means of Monel end plates and bolts. The cell was assembled as shown in Fig. 1 of ref. (12). No gaskets were necessary because the PTFE surfaces formed leak-tight seals against one another.

The assembled fuel cell and an identical cell containing two reversible hydrogen reference electrodes (PTFE-bonded Pt black) were mounted in the apparatus shown schematically in Fig. 1. The forced-convection air thermostat maintained the apparatus at 105°C. This temperature was chosen in order to maximize the reaction rate of the hydrocarbon fuel, while maintaining the proper water vapor pressure in order to avoid the (thermodynamically) possible deposition of carbon (or carbon-rich residue) from the fuel onto the electrocatalyst surface (27-30). The oxidant, electrolytic grade oxygen, 99.6 m/o minimum purity, was metered to the cathode through a needle valve and was monitored by means of a capillary-tube flowmeter. The Phillips research grade 99.85 m/o minimum purity<sup>2</sup> n-octane liquid fuel was fed to the anode by means of a constant-speed (0.01%) syringe drive. The gas streams leaving the cell passed through PTFE traps to remove any liquids and then to water bubblers which provided a seal from the atmosphere. The exit streams could be sampled and analyzed by a vapor phase chromatograph as desired.

The electrolyte flowed by gravity from an upper PTFE reservoir to the cells, passing upward through them and into a lower reservoir, to be returned to its starting point by an all-PTFE bellows pump. The flow rate was 2-3 cell volumes per minute and was controlled by the electrolyte head.

The electrodes were all of the thin (0.15-0.38 mm) PTFE-bonded type, containing a 45-mesh platinum screen as a current collector. A thin, porous PTFE film (~ 0.3 mg/cm<sup>2</sup>) was bonded to the fuel (or oxidant) side of the electrode in order to maintain hydrostatic stability. The structure of the electrodes was similar to that of other PTFE-bonded electrodes (14, 31), but the preparation methods were modified as necessary to accommodate the specific characteristics of the electrocatalyst materials. In general, the electrocatalysts prepared by the authors were maintained in an oxidized form during electrode fabrication in order to

prevent sintering of the very small (< 100Å) platinum crystallites. The oxidized form of platinum was maintained during the KOH dissolution of the aluminum foil backing by holding the electrode potential above that required for oxygen evolution in the KOH stripping bath; the hydrogen was evolved from a remote counter electrode. In most cases, the platinum was gently reduced to the elemental form by electrochemical and/or chemical methods after the electrode was mounted in the fuel cell apparatus.

Both unsupported and supported forms of high-area platinum were used as electrocatalysts. The support materials were various forms of carbon black, both graphitic and nongraphitic.

The unsupported platinum was of two types: commercial platinum black (~ 20 m<sup>2</sup>/g), which served as a standard of comparison, and Adams catalyst (14, 32-38) (PtO<sub>2</sub> · H<sub>2</sub>O), which was fabricated into electrodes and subsequently reduced *in situ* to form a high-area platinum black.

The supported electrocatalysts were prepared by the deposition of a platinum salt onto the carbon surface from a solution of platinum diammine dinitrite (J. Bishop & Co.) in 50 w/o nitric acid, followed by roasting in air to obtain an oxidized form of the supported platinum. The concentration of the platinum salt in solution was determined by the weight per cent Pt/C desired and by the amount of solvent required to give a thick slurry with the substrate (2-3 ml/g C). As a guide in selecting appropriate thermal decomposition and oxidation temperatures, a thermogravimetric analysis was performed on the material obtained from the evaporation of a solution of platinum diammine dinitrite in 50 w/o nitric acid. The results indicated that a minimum temperature for the thermal-oxidative transformation of the salt to platinum dioxide would be above 160°C, probably near 200°C. Higher temperatures may be of interest because of their possible effect on the specific activity of the resultant electrocatalyst. Table I and Fig. 2 summarize the preparation conditions for some of the supported electrocatalysts that were used in this work.

A few commercially available carbon-supported platinum catalysts were also evaluated. No detailed information was available from the suppliers concerning the preparation methods, but it is believed that platinum salts were deposited from solution and were then reduced by a gas such as hydrogen.

Some properties of the carbon supports investigated are summarized in Table II. Half of the carbons tested were graphitic; half were nongraphitic. The material obtained from American Cyanamid Company served as the substrate in earlier propane investigations (14), and the n-octane results reported below can be compared directly to the earlier propane results.

The electrical measurements of electrocatalyst performance were obtained with the aid of a 60 Hz modified Kordes-Marko interrupter (39, 40), yielding the potentials of the anode *vs.* the H<sub>2</sub> reference electrode ( $E_{a-r}$ ), the cathode *vs.* the H<sub>2</sub> reference electrode ( $E_{c-r}$ ), and the anode *vs.* the cathode ( $E_{a-c}$ ), all on a resistance-free basis. The use of a frequency of interruption as low as 60 Hz can lead to high values of  $E_{c-r}$  and  $E_{a-c}$  and low values of  $E_{a-r}$  under some conditions at low platinum loadings (41). The magnitude of this error was found to be less than 2% of the values of the readings under the conditions used in the investigations reported here.

All of the results reported below are on a resistance-free basis unless specified otherwise. The reference electrode was always reversible hydrogen in the same electrolyte (36 m/o HF) at the same temperature (105°C). The current-voltage data were taken at steady state, which was usually achieved within 5 min after changing the current. In general, the current was increased in a stepwise manner, starting from open circuit. The resistance-included cell voltages ( $E_{cell}$ ) can be estimated from the resistance-free ( $E_{a-c}$ ) val-

<sup>2</sup> The principal impurities were 0.13 m/o isononanes and 0.02 m/o isooctanes.

Table I. Time-temperature programs for carbon-supported electrocatalysts

Catalyst preparation No.	w/o Pt per lamination	Zone A		Zone B		Zone C		Zone D		Zone E	
		T <sub>1</sub> , °C	τ <sub>1</sub> , min	T <sub>2</sub> , °C	τ <sub>2</sub> , min	T <sub>3</sub> , °C	τ <sub>3</sub> , min	T <sub>4</sub> , °C	τ <sub>4</sub> , min	T <sub>5</sub> , °C	τ <sub>5</sub> , min
*20	7	82	45	90	90	115	135	170	180	215	240
*21	5	82	45	90	90	115	135	170	210	—	—
#22, 30, 40, 50	10	82	45	100	105	150	165	200	240	—	—
†51, 60, 70, 80, 90	10	82	120	100	120	150	60	200	90	—	—

\* Decomposition performed on a hot plate open to the air.  
 # Decomposition performed in a tube furnace with flowing air.  
 † Decomposition performed in a forced-convection air thermostat.

Table II. Some properties of carbon powders

Catalyst Prep. No.	Type	Specific area, <sup>b</sup> m <sup>2</sup> /g	Average particle diameter, <sup>c</sup> Å		Volatile content, w/o	Source
			Before	After		
20-22	g <sup>a</sup>	11.4	~2500	~2500	0	American Cyanamid
30	g	68.4	350	350	0	Cabot Corporation
40	g	23.7	1000	1000	0	Cabot Corporation
50, 51	g	212	140	140	0	Cabot Corporation
60	n	850	120	506	13	Cabot Corporation
70	n	42	410	591	1	Cabot Corporation
80	n	110	250	287	5	Cabot Corporation
90	n	380	160	163	5	Cabot Corporation

<sup>a</sup> g = graphitic, n = nongraphitic.

<sup>b</sup> Nitrogen adsorption method, before deposition of catalyst.

<sup>c</sup> Before and after heat-treatment during deposition of platinum on carbon surface. Determined by measurements on electron photomicrographs.

ues using the following equation

$$E_{\text{cell}} = E_{a-c} - i\rho l \quad [1]$$

where  $i$  is the current density,  $\rho$  is the resistivity of the electrolyte, 1.8 ohm-cm; and  $l$  is the interelectrode distance, 0.3 cm. The small resistance of the electrodes is ignored in Eq. [1].

### Results and Discussion

**Unsupported electrocatalysts.**—Commercially available platinum black with a surface area of 20 m<sup>2</sup>/g was adopted as a standard against which the results with other electrocatalysts were compared. It was previously shown that over the range 10-100 mg Pt/cm<sup>2</sup>, the current density for propane oxidation in 36 m/o HF (14) at a given overvoltage was directly proportional to the electrocatalyst loading. This same effect has been noted in general with other saturated hydrocarbon fuels and unsupported electrocatalysts (14). The direct proportionality between current density and electrocatalyst loading for platinum black forms the basis for electrocatalyst comparisons using as criteria the specific current (ma/mg Pt) and the effectiveness ratio  $\left( \frac{\text{ma/mg Pt in test catalyst}}{\text{ma/mg commercial Pt black}} \right)$ . The results presented below will serve to illustrate the calculation and use of the specific current and the effectiveness ratio.

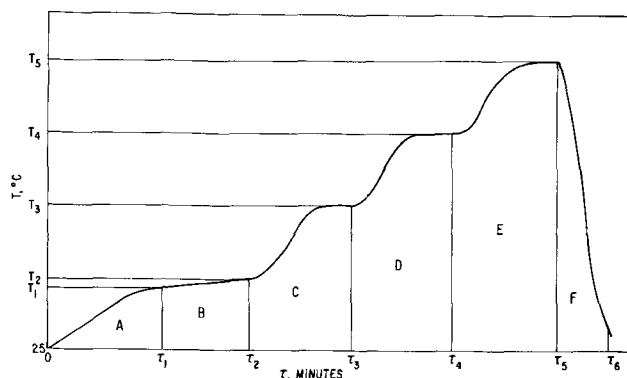


Fig. 2. Generalized time-temperature profile used for the preparation of carbon-supported platinum electrocatalysts.

The performance of liquid n-octane on commercial platinum black, at a loading of 25.8 mg Pt/cm<sup>2</sup> is shown in Fig. 3. These data are representative of those adopted as the standard of comparison, and correspond to 0.27 ma/mg Pt at  $E_{a-r} = 0.5v$ . By definition, the effectiveness ratio for platinum black is unity. The curve showing the resistance-free voltage difference between the anode and cathode,  $E_{a-c}$ , was obtained using an average of the results from several standard cathodes containing commercial platinum black at a loading of 51 mg Pt/cm<sup>2</sup>. This use of a standard cathode current density-voltage curve allows comparisons to be made among anodes on the basis of either the anode data alone or on the basis of cell performance (e.g., mw/cm<sup>2</sup> at a given  $E_{a-c}$ ).

The performance of an anode containing 10.2 mg Pt/cm<sup>2</sup> reduced from Adams catalyst is also shown in Fig. 3. Note that for anode potentials below 0.56v, the electrode prepared from PtO<sub>2</sub> · H<sub>2</sub>O yielded higher current densities than the electrode of commercial Pt black, even though the Pt loading was much higher for the commercial Pt black electrode. The specific current (designated  $i^*$ ) for the Pt black electrode at  $E_{a-r} = 0.5v$  was 0.27 ma/mg Pt, while that for the electrode made from PtO<sub>2</sub> · H<sub>2</sub>O was 0.90 ma/mg Pt.

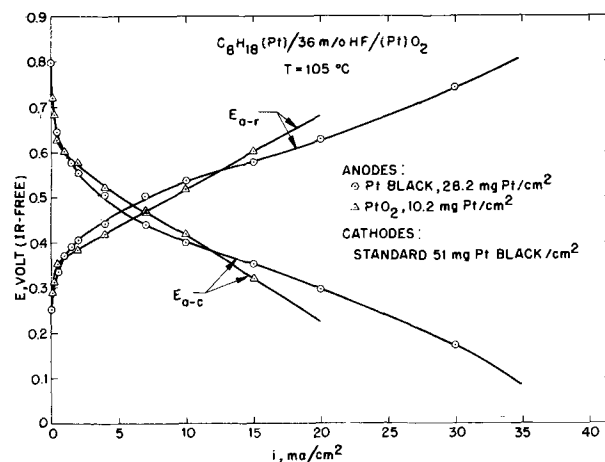


Fig. 3. Current density-voltage curves for n-octane on two unsupported platinum electrocatalysts.

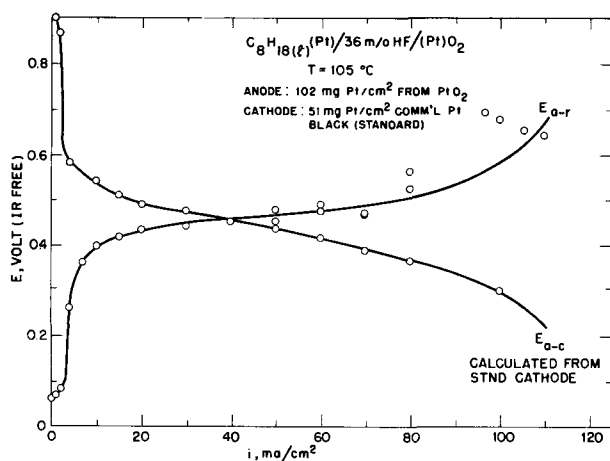


Fig. 4. Current density-voltage curve for n-octane on platinum black prepared from the reduction of Adams catalyst.

The quotient of specific currents yields an effectiveness ratio of 3.3 for the Adams catalyst electrode at  $E_{a-r} = 0.5v$ . This means that at any given Pt content, the n-octane current density at  $E_{a-r} = 0.5v$  for an electrode made from Adams catalyst will be 3.3 times that for an electrode made from commercial Pt black, providing that the effectiveness ratio is constant, as was found for propane on various electrocatalysts (14). This represents a reduction of a factor of 3.3 in the platinum requirement (in the anode) for a given amount of power.

The encouraging results with Adams catalyst at low Pt loadings led to further work at high loadings, in an attempt to verify the constancy of the effectiveness ratio over a wide range of loadings found for this catalyst when used for propane oxidation (14). Figure 4 shows the current density-voltage curves for a cell with an anode containing 102 mg Pt/cm<sup>2</sup> from Adams catalyst. Current densities in excess of 100 ma/cm<sup>2</sup> were obtained at (resistance-free) cell potentials near 0.3v. This represents a performance well into the practical range, but still with impractical platinum loadings. The specific current at  $E_{a-r} = 0.5v$  was 0.78 ma/mg Pt, corresponding to an effectiveness ratio of 2.9 (vs. 3.3 at 10.2 mg Pt/cm<sup>2</sup>). The effectiveness ratio was almost the same as that for the 10.2 mg Pt/cm<sup>2</sup> electrode, verifying the previous observation of constant specific current over a wide range of loadings for unsupported electrocatalysts when used with propane (14). It is interesting to observe that the same effectiveness ratio of 3 was found for commercial Adams catalyst when used for gaseous propane (14), which may hint at a similarity in the rate-determining steps

for the over-all anodic oxidation of propane and octane. The results obtained with the unsupported electrocatalysts are summarized in the first three rows of Table III.

**Supported electrocatalysts.**—The improvement in electrocatalytic activity of platinum when prepared from an oxidized form such as Adams catalyst, and the improvements obtained in earlier work with propane when carbon electrocatalyst supports were used (14) led to an attempt to combine the two types of activity enhancement. Two kinds of finely divided carbons were investigated as platinum supports: graphitized and ungraphitized carbons. In general, the graphitic carbons have lower electrical resistivity, lower volatiles content, and are easier to fabricate into electrodes. The graphitic carbon obtained from American Cyanamid was investigated first and was used for the development of electrode preparation procedures. Some of the characteristics of this carbon are given in Table II; additional information can be found in ref. (14) and (42).

A number of electrodes were prepared using electrocatalysts supported on the graphitic powder from American Cyanamid (11.4 m<sup>2</sup>/g). The electrocatalysts were prepared as described in the experimental section above, using various ratios of platinum to carbon. In addition, two electrocatalysts supplied by American Cyanamid using the same support were tested (10 w/o Pt/C and 50 w/o Pt/C). The results of the experiments using the American Cyanamid graphitic carbon support are summarized in Table III in the rows labeled Preps 20 to 22, and CYAN. In the case of CYAN (improved), the results in Table III are the best from a group of twelve electrodes; in the cases of Preps 20-22, the results are from single electrodes. The electrode Prep 20, 28 w/o Pt/C showed the best performance, and the best of the CYAN 50 w/o Pt/C electrodes was next best. The voltage-specific current curves for these two electrocatalysts are shown in Fig. 5. The Prep 20, 28 w/o Pt/C shows the highest currents per unit weight of platinum, while the CYAN 50 w/o Pt/C and the Pt from Adams catalyst show very similar performances. The effectiveness ratio of Prep 20, 28 w/o Pt/C was 18.5 at  $E_{a-r} = 0.4v$  and 6.0 at  $E_{a-r} = 0.5v$ , indicating that the greatest improvements in specific current are evident at the lower anode overvoltages. The lower effectiveness ratios and specific currents for Prep 20 — 42 w/o Pt/C (shown in Table III) were probably caused by the fact that zone E of Table I was eliminated in the preparation of this electrocatalyst, as an experiment on the effect of the final roasting temperature on activity. Evidently, temperatures of at least 200°C result in higher activity electrocatalysts than those roasted at lower temperatures.

Table III. n-Octane performance  
C<sub>8</sub>H<sub>18</sub> (l) (Cat)/36 m/o HF/(Pt)O<sub>2</sub>, 105°C

Electrode identity	Catalyst <sup>a</sup>	Loading, mg Pt/cm <sup>2</sup>	$i_{E_{a-r}=0.4v}$ , ma/cm <sup>2</sup>	$i^*_{E_{a-r}=0.4v}$ , ma/mg	Eff. ratio <sub>0.4v</sub>	$i_{E_{a-r}=0.5v}$ , ma/cm <sup>2</sup>	$i^*_{E_{a-r}=0.5v}$ , ma/mg	Eff. ratio <sub>0.5v</sub>	Specific <sup>c</sup> area of substrate, m <sup>2</sup> /g
Comm'l	Pt Black	25.8	1.8	0.07	1.0	7.0	0.27	1.0	—
Comm'l	PtO <sub>2</sub>	102	11	0.11	1.6	80	0.78	2.9	—
Comm'l	PtO <sub>2</sub> + B <sub>2</sub> C	10.2	2.9	0.29	4.1	9.0	0.90	3.3	—
Prep 20	28 w/o Pt/C <sub>g</sub>	9.2	12	1.30	18.5	15.0	1.63	6.0	11.4
Prep 20	42 w/o Pt/C <sub>g</sub>	17.7	5.4	0.31	4.4	12.2	0.69	2.6	11.4
Prep 21	50 w/o Pt/C <sub>g</sub>	22.1	4.7	0.21	3.0	12.8	0.58	2.1	11.4
Prep 22	30 w/o Pt/C <sub>g</sub>	9.9	1.5	0.15	2.1	3.9	0.39	1.4	11.4
Prep 30	30 w/o Pt/C <sub>g</sub>	11.9	2.2	0.19	2.7	6.7	0.56	2.1	68.4
Prep 40	30 w/o Pt/C <sub>g</sub>	16.9	2.1	0.12	1.7	5.7	0.34	1.3	23.7
Prep 50	30 w/o Pt/C <sub>g</sub>	13.1	3.6	0.28	4.0	8.3	0.64	2.4	212
Prep 51 <sup>b</sup>	30 w/o Pt/C <sub>g</sub>	10.3	4.7	0.46	6.6	14.3	1.39	5.1	212
Prep 60 <sup>b</sup>	30 w/o Pt/C	13.5	2.7	0.20	2.9	5.2	0.39	1.4	850
Prep 70 <sup>b</sup>	30 w/o Pt/C	12.0	2.0	0.17	2.4	4.3	0.36	1.3	42
Prep 80 <sup>b</sup>	30 w/o Pt/C	15.0	5.4	0.36	5.1	11.1	0.74	2.7	110
Prep 90 <sup>b</sup>	30 w/o Pt/C	14.4	6.8	0.47	6.7	15.1	1.05	3.9	380
CYAN	10% Pt/C <sub>g</sub>	2.2	0.06	0.03	0.43	0.55	0.25	0.93	11.4
CYAN (IMPROVED)	50% Pt/C <sub>g</sub>	24.8	8.8	0.35	5.0	19.5	0.79	2.9	11.4

<sup>a</sup> The subscript g indicates graphitic carbon. The carbon was graphitized by heat treatment at 2700°C for 2 hr in an inert atmosphere.

<sup>b</sup> The results for these electrocatalysts represent an average of two or three cells each.

<sup>c</sup> Before deposition of electrocatalyst.

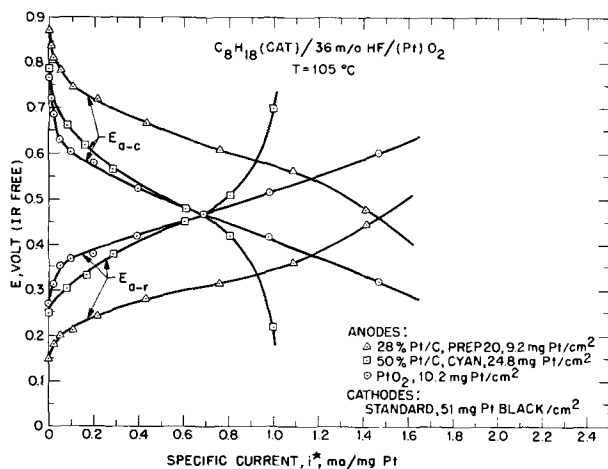


Fig. 5. Voltage-specific current curves for n-octane on two graphite-supported platinum electrocatalysts compared to the results using Pt from  $\text{PtO}_2 \cdot \text{H}_2\text{O}$ .

After completing the study of various platinum-to-carbon ratios (10-50 w/o) on the  $11.4 \text{ m}^2/\text{g}$  graphite, an investigation was made concerning the effect of increasing the graphite specific surface area on electrocatalyst activity. The higher specific area graphites were obtained from the Cabot Corporation and had specific areas of 23.7, 68.4, and  $212 \text{ m}^2/\text{g}$ . A group of four electrocatalysts was prepared starting with a sample of each of the graphitic carbons listed in Table II, and making use of the same platinum deposition techniques for all. All of the electrodes were prepared in the same way and tested in the same apparatus. These electrodes are designated as Preps 22, 30, 40 and 50 in Table III. All had a nominal 30 w/o Pt/C electrocatalyst, with Pt loadings in the range 10-17  $\text{mg}/\text{cm}^2$ .

The specific currents for the oxidation of liquid n-octane at anode vs. reference potentials of 0.4 and 0.5 v are shown in Fig. 6 as a function of the specific surface area of the graphitic carbon substrate. The specific current increases with substrate specific area, but at a rate lower than direct proportionality. The specific current approximately doubles for an increase from  $11.4$  to  $212 \text{ m}^2/\text{g}$ . A search for still higher specific area graphites was not fruitful, but did lead to the investigation of nongraphitic carbons, which are available in higher specific area forms.

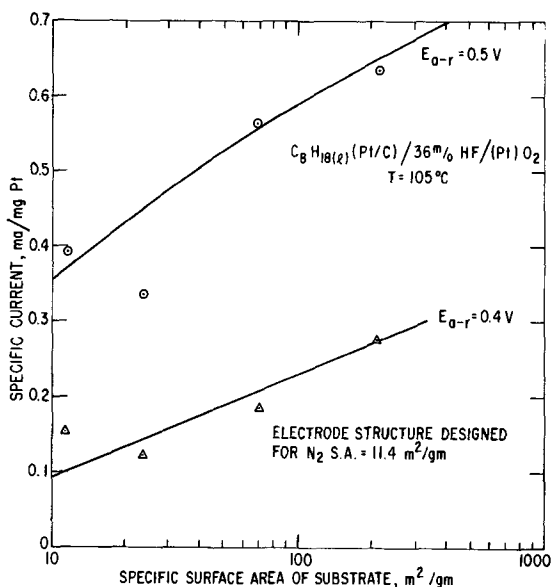


Fig. 6. Specific current for n-octane oxidation on graphite-supported platinum, as a function of the specific area of the graphite.

Four nongraphitic carbon blacks (Cabot Corporation), having specific areas of 42, 110, 380, and  $850 \text{ m}^2/\text{g}$ , were used as substrates in the preparation of electrocatalysts. Some modification of preparation procedures was necessary because of the tendency of the nongraphitic carbon substrates to oxidize rapidly in air when heated above  $200^\circ\text{C}$  in the presence of platinum compounds deposited on the carbon surface. Because of the necessity of modifying the electrocatalyst preparation procedures, this group of electrodes also contained one prepared using an electrocatalyst supported on a graphitized substrate ( $212 \text{ m}^2/\text{g}$ ) for comparison. One other change from previous procedures was the use of a slower *in situ* reduction of the platinum oxides. These electrodes are designated as Preps 51, 60, 70, 80, and 90 in Table III. All had a nominal 30 w/o Pt/C electrocatalyst, with Pt loadings in the range 10-15  $\text{mg}/\text{cm}^2$ .

In relation to the tendency of the carbon-supported electrocatalysts to oxidize in air when heated, it was suspected that some changes in the electrocatalysts might take place even in the absence of gross effects visible to the unaided eye. In order to investigate this possibility, the electrocatalysts (after deposition of Pt) were examined by means of an electron microscope, and it was found that in some cases there was a significant increase in electrocatalyst particle size as a result of the platinum deposition procedures. The extent of particle size increase (sintering) was related to the volatiles content of the carbon (Table II). Note in Table II that for Prep 60, which had 13% volatiles, the mean carbon particle size increased from 120 to  $506 \text{ \AA}$ , while the other substrates with lower volatile contents sintered to a much smaller extent. It was found that the increase in particle size (decrease in specific area) was accompanied by a weight loss which was equal to the volatiles content calculated from the values listed in Table II. Evidently, the volatiles were catalytically oxidized on the Pt crystallites. The heat of combustion raised the local temperature sufficiently to cause sintering of the substrate, and probably also of the platinum crystallites.

Because of the loss of specific surface of the substrate during the electrocatalyst preparation procedure, it was necessary to correlate the n-octane anode performance with the particle size after activation, rather than specific area before activation. The average particle diameters in column 5 of Table II were used in the preparation of Fig. 7. Note that the results for Prep 60 are similar to those for Prep 70 indicating that there would be no correlation of performance on the basis of specific areas before performance (see Table II), but the expected correlation is found on the basis of reciprocal substrate particle diameter after activa-

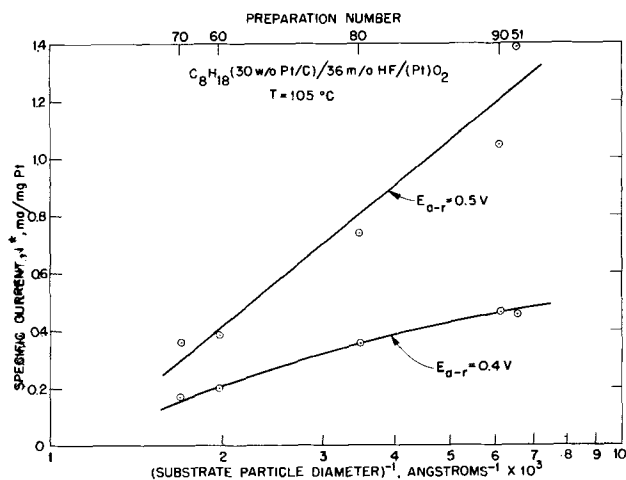


Fig. 7. Specific current for n-octane oxidation on carbon-supported platinum electrocatalysts as a function of reciprocal substrate particle diameter.

tion. (Note that reciprocal particle diameter is proportional to specific area.) The results in Fig. 7 show that increasing the specific area of the ungraphitized carbon substrate increases the specific current of n-octane, at least up to about 300 m<sup>2</sup>/g corresponding to a reciprocal particle diameter of  $6 \times 10^{-3} \text{ \AA}^{-1}$  (see Table II and Fig. 7), and that specific currents of about 1.4 ma/mg Pt can be obtained at  $E_{a-r} = 0.5\text{v}$  with the 212 m<sup>2</sup>/g graphitic support. Each data point in Fig. 7 is the average of results from two different anodes prepared in slightly different ways from the same electrocatalyst. The differences among pairs of results averaged about 10%. It is evident that Prep 51 yielded better results than Prep 50 (Table III), probably because of the slower *in situ* reduction of the Pt in Prep 51.

The correlation between specific current on n-octane and substrate specific surface area probably indicates a relationship between the specific current and the specific area of the platinum. (The specific surface area of the platinum could not be determined directly by either the chemisorption of hydrogen or by electron photomicrographs because of experimental difficulties with both approaches.) For a given weight fraction of platinum on carbon, the specific surface area of the platinum probably increases with increasing carbon specific surface area, because the larger carbon area allows more room for each platinum crystallite, and therefore larger distances between platinum crystallites are obtained. This condition makes it more difficult for the Pt crystallites to coalesce (or sinter together), and therefore the high specific area of the platinum is maintained due to the lower probability of sintering during the heat-treatment stages of electrocatalyst deposition and electrode preparation.

The voltage-specific current curves for the electrocatalysts supported on the two highest-area nongraphitic carbons (after Pt deposition, Preps 80 and 90) and on the highest-area graphitic carbon (Prep 51) are compared in Fig. 8. Prep 51 shows the highest performance of this group and is comparable to the performance level of Prep 20, 28 w/o Pt/C, Fig. 5. Probably a combination of the electrocatalyst preparation procedures used for Prep 20, 28 w/o Pt/C with the substrate of Prep 51 would result in a higher performance electrocatalyst at low overvoltages.

With respect to the use of carbon substrates with specific surface areas above 200 m<sup>2</sup>/g, it is suggested that the volatiles be removed by heating the substrate in vacuum before deposition of the platinum, increasing the probability that the high surface area of the carbon will be retained during subsequent heat-treatment. It may also be possible to use a gas mixture of lower oxygen content than that of air in the activation procedure, reducing the tendency to oxidize the re-

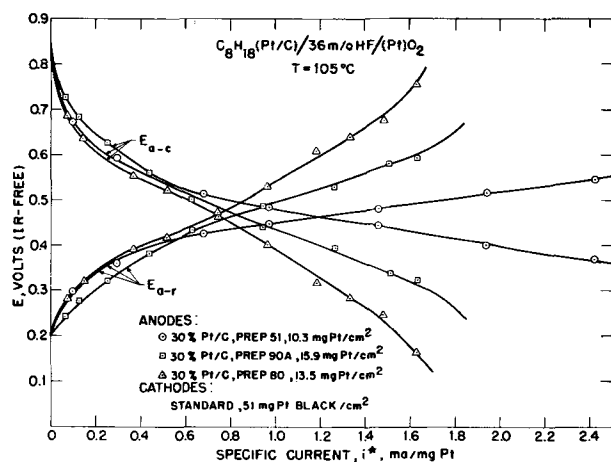


Fig. 8. Voltage-specific current curves for the two best nongraphitic carbon-supported platinum and a correspondingly prepared graphite-supported platinum.

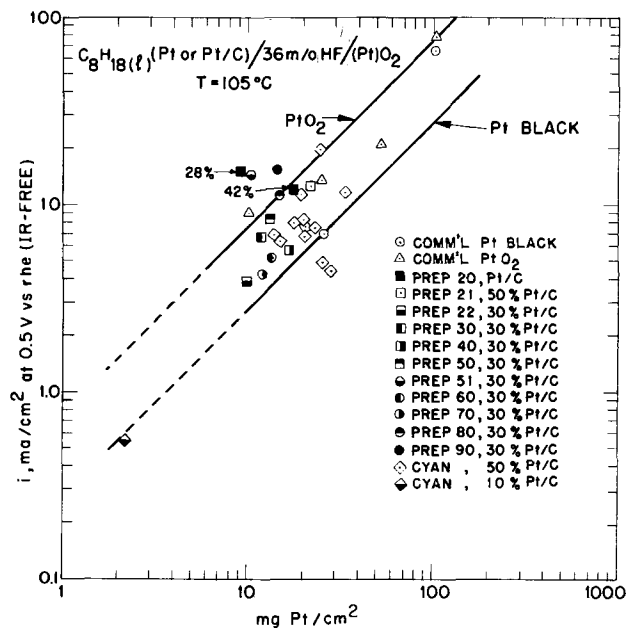


Fig. 9. Current density (at  $E_{a-r} = 0.5\text{v}$ )-platinum loading plot for all electrocatalysts tested on n-octane.

sidual volatiles and/or the substrate. Further work on optimization of electrode structures using high area substrates is likely to lead to improved performance, because the structures used in this work were optimized for the 11.4 m<sup>2</sup>/g graphite.

The results of all of the experiments reported here are summarized in Fig. 9 in terms of the n-octane oxidation current density at  $E_{a-r} = 0.5\text{v}$  as a function of platinum loading in the anode. The straight lines of unit slope indicate a constant specific current. Note that the line for Adams catalyst corresponds to an effectiveness ratio of about 3. There are not sufficient data for the various supported electrocatalysts to draw lines of constant preparation method for various loadings, etc. It can be seen from Fig. 9 that many of the supported electrocatalysts were not as active as platinum prepared from Adams catalyst, but 28 w/o Pt/C, Prep 20, and 30 w/o Pt/C, Prep 51, indicate that rather high activities can be obtained at platinum loadings near 10 mg Pt/cm<sup>2</sup>.

In this work with liquid n-octane using 36 m/o HF as the electrolyte, no voltage or current cycling has been observed under any conditions of operation. This is significant and in marked contrast to the cycling observed with saturated hydrocarbon fuels in other electrolytes such as sulfuric acid (7) and phosphoric acid (43-45).

### Conclusions

1. The use of platinum black obtained by the controlled *in situ* reduction of Adams catalyst provides an electrocatalyst with an activity for the anodic oxidation of liquid n-octane of about 3 times that of commercial platinum black, in agreement with a similar ratio found earlier for propane oxidation.
2. Carbon (both graphitic and nongraphitic) is an effective electrocatalyst support, providing a stable (in 37 m/o HF at 105°C) support for high-activity platinum. The activity of the carbon-supported electrocatalysts for liquid octane oxidation increases with increasing substrate specific surface area, up to at least 212 m<sup>2</sup>/g. This effect is probably due to the fact that the higher specific area substrates provide sufficient area for the very small Pt crystallites to exist without sintering together.
3. Certain carbon-supported electrocatalysts are effective in reducing the amount of platinum required for a given octane performance by factors

of 6 to 18. Further improvements are likely by use of higher specific area carbon substrates.

- No cycling of the cell current or potential has been observed with liquid octane under any conditions of operations.

#### Acknowledgment

It is a pleasure to thank E. J. McInerney and J. R. Morgan for their help with many of the experiments, Dr. E. L. Simons and Mrs. V. B. Hughes for their assistance in the thermogravimetric analysis, and Dr. W. T. Grubb for information concerning deposition of platinum salts. They are also grateful to W. G. Burbine and W. E. Campaigne of the Cabot Corporation for their generous cooperation in providing most of the support materials and to R. J. Haldeman and V. J. Cable of the American Cyanamid Company for samples of one of the supports and some of the electrocatalysts.

This work is a part of the program under contracts DA-44-099-AMC-479(T) and DA-44-009-ENG-4909, ARPA Order No. 247 with the U.S. Army Mobility Equipment Research and Development Laboratories, Fort Belvoir, Virginia, to develop a technology which will facilitate the design and fabrication of practical military fuel cell power plants for operation on ambient air and hydrocarbon fuels.

Manuscript submitted May 23, 1968; revised manuscript received Aug. 5, 1968. This paper was presented in part at the Philadelphia Meeting, Oct. 9-14, 1966, as Paper 8.

Any discussion of this paper will appear in a Discussion Section to be published in the June 1969 JOURNAL.

#### REFERENCES

- W. T. Grubb and L. W. Niedrach, *This Journal*, **110**, 1086 (1963).
- H. G. Oswin, A. J. Hartner, and F. Malaspina, *Nature*, **200**, 256 (1963).
- E. J. Cairns, G. J. Holm, Paper presented at the Washington, D. C. Meeting of the Society, Oct. 11-15, 1964, Paper No. 30; See Also *Extended Abstr. of the Battery Div.*, **9**, 75 (1964).
- R. Jasinski, J. Huff, S. Tomter, and L. Swette, *Ber. der. Bunsengesellschaft*, **68**, 400 (1964).
- W. T. Grubb and C. J. Michalske, *This Journal*, **111**, 1015 (1964).
- E. J. Cairns in "Hydrocarbon Fuel Cell Technology," B. S. Baker, Editor, Academic Press, New York (1965).
- H. Binder, A. Kohling, H. Krupp, K. Richter, and G. Sandstede, *This Journal*, **112**, 355 (1965).
- W. R. Epperly, in *Proc. 19th Ann. Power Sources Conf.*, PSC Publications Committee, Red Bank, N. J. (1965).
- O. J. Adhart, in *Proc. 19th Ann. Power Sources Conf.*, PSC Publications Committee, Red Bank, N. J. (1965).
- J. A. Shropshire, E. H. Okrent, and H. H. Horowitz, in "Hydrocarbon Fuel Cell Technology," B. S. Baker, Editor, Academic Press, New York (1965).
- E. J. Cairns, *Nature*, **210**, 161 (1966).
- E. J. Cairns, *This Journal*, **113**, 1200 (1966).
- O. J. Adhart and A. J. Hartner, in *Proc. 20th Ann. Power Sources Conf.*, PSC Publications Committee, Red Bank, N. J. (1966).
- E. J. Cairns and E. J. McInerney, *This Journal*, **114**, 980 (1967); See also *Extended Abstracts of the Industrial Electrolytics Div.*, **2**, 1 (1966).
- G. J. Young and R. B. Rozelle, in "Fuel Cells," Vol. 2, G. J. Young, Editor, Reinhold Publishing Co., New York (1963).
- W. T. Grubb and C. J. Michalske, in *Proc. 18th Ann. Power Sources Conf.*, PSC Publications Committee, Red Bank, N. J. (1964).
- E. J. Cairns, *Science*, **155**, 1245 (1967).
- L. W. Niedrach and D. W. McKee, in *Proc. 21st Ann. Power Sources Conf.*, PSC Publications Committee, Red Bank, N. J. (1967).
- O. J. Adhart and A. J. Hartner, *ibid.*
- E. J. Cairns, *Electrochem. Technol.*, **5**, 8 (1967).
- R. Vieweg, *Chem. Tech.*, **15**, 734 (1963).
- D. C. Grahame, *Chem. Rev.*, **41**, 441 (1947).
- A. N. Frumkin, in "Advances in Electrochemistry and Electrochemical Engineering," Vol. 3, P. Delahay, Editor, John Wiley & Sons, Inc., New York (1963).
- E. J. Cairns and A. M. Breitenstein, *This Journal*, **114**, 764 (1967).
- E. J. Cairns, A. M. Breitenstein, and A. J. Scarpellino, Paper presented at the Philadelphia Meeting of the Society, Oct. 9-14, 1966, as Paper 1; See also *Extended Abstracts of the Battery Div.*, **11**, 1 (1966); *This Journal*, **115**, 569 (1968).
- E. B. Butler, C. B. Miles, and C. S. Kuhn, Jr., *Ind. Eng. Chem.*, **38**, 147 (1946).
- E. J. Cairns, A. D. Tevebaugh, and G. J. Holm, *This Journal*, **110**, 1025 (1963).
- E. J. Cairns and A. D. Tevebaugh, *J. Chem. & Eng. Data*, **9**, 453 (1964).
- A. D. Tevebaugh and E. J. Cairns, *ibid.*, **10**, 359 (1965).
- H. A. Liebafsky and E. J. Cairns, "Fuel Cells and Fuel Batteries," John Wiley & Sons, Inc., New York (1968).
- L. W. Niedrach and H. R. Alford, *This Journal*, **112**, 117 (1965).
- R. Adams, V. Voorhees, and R. L. Shriner, "Organic Synthesis," Col. Vol. I, John Wiley & Sons, Inc., New York (1932).
- V. Voorhees and R. Adams, *J. Am. Chem. Soc.*, **44**, 1397 (1922).
- R. Adams and R. S. Shriner, *ibid.*, **45**, 2171 (1923).
- A. H. Cook and R. P. Linstead, *J. Chem. Soc.*, **1934**, 946.
- W. F. Bruce, *J. Am. Chem. Soc.*, **58**, 687 (1936).
- V. L. Frampton, J. D. Edwards, and H. R. Henze, *ibid.*, **73**, 4432 (1950).
- C. W. Keenan, B. W. Gisemann, and H. S. Smith, *ibid.*, **76**, 229 (1953).
- K. Kordesch and A. Marko, *This Journal*, **107**, 480 (1960).
- E. J. Cairns and A. D. Tevebaugh, Saturated Hydrocarbon Fuel Cell Program, Technical Summary Report No. 3, Part I, Task IV, Jan. 1-June 30, 1963, Contract No. DA-44-009-Eng-4909, ARPA Order No. 247, Project No. 8A72-13-001-506, USAERDL, Ft. Belvoir, Va.
- L. W. Niedrach and M. Tochner, *Electrochem. Technol.*, **5**, 270 (1967).
- R. G. Haldeman, W. P. Colman, S. H. Langer, and W. A. Barber in "Fuel Cell Systems," p. 113, R. F. Gould, Editor, Adv. in Chem. Series No. 47, Amer. Chem. Soc., Washington, D. C. (1965).
- E. R. White and H. J. R. Maget, in *Proc. 19th Ann. Power Sources Conf.*, PSC Publications Committee, Red Bank, N. J. (1965).
- R. P. Hamlen and E. J. Szymalak, *Electrochem. Technol.*, **4**, 172 (1966).
- E. H. Okrent and C. E. Heath, in Preprints of Papers Presented before the Division of Fuel Chemistry, Fuel Cell Symposium, Amer. Chem. Soc., Chicago, September 1967, **13**, 265 (1967).

# Electrochemical Oxidation of Fuels in Liquid Ammonia

M. H. Miles\* and P. M. Kellett

Naval Weapons Center Corona Laboratories, Corona, California

## ABSTRACT

Overvoltage measurements for the hydrogen and nitrogen evolution reactions in acid ( $\text{NH}_4\text{SCN}$ ) liquid ammonia on more than thirty electrode surfaces permit the evaluation of these surfaces as catalysts for the electrochemical oxidation of hydrogen and ammonia in this electrolyte, as well as yielding the electrostability regions available for fundamental electrochemical studies on these surfaces. Testing of various fuels on ten selected electrode surfaces in acid liquid ammonia showed that hydrazine could be oxidized on rhodium and platinum, 1,2-diphenylhydrazine is oxidizable on mercury, and borohydrides show activity on rhenium and platinum. Constant current oxidation in stirred acid ammonia solutions yields almost 4 electrons per molecule of hydrazine, 2 electrons per molecule of 1,2-diphenylhydrazine, and 2 to 3 electrons per molecule of potassium borohydride. The activation energies are about 15 kcal/mole for the oxidation of  $\text{KBH}_4$  on platinum and 5 kcal/mole for the oxidation of 1, 2-diphenylhydrazine on mercury. The rate of the oxidation of hydrazine on platinum in acid liquid ammonia solutions does not appear to follow the Arrhenius temperature dependence.

Most fuel cell research has been centered on systems using solid oxide, molten carbonate, or aqueous electrolytes (1, 2). Research data on low temperature fuel cell systems using nonaqueous electrolytes are limited (3). The high conductivities and solubilities attainable in liquid ammonia (4, 5) make this solvent attractive for fuel cells; therefore, fundamental investigations in liquid ammonia were begun.

## Experimental

Inorganic salt solutions of liquid ammonia were used in which the vapor pressure of  $\text{NH}_3$  at 25°C was below 1 atm (5, 6). These solutions were prepared by condensing anhydrous ammonia (Matheson Company, 99.99%) onto the vacuum-dried salt (Baker reagent grade). Most measurements were made in  $\text{NH}_4\text{SCN}$  solutions at 25°C. At this temperature the mole ratio of  $\text{NH}_3$  to  $\text{NH}_4\text{SCN}$  was 2.0 (8.5M  $\text{NH}_4\text{SCN}$ ). Other chemicals used include Fisher certified  $\text{N}_2\text{H}_4 \cdot \text{H}_2\text{SO}_4$  (99.7%), Metal Hydrides  $\text{KBH}_4$  (97+%), and Eastman practical hydrazobenzene washed with ligroine to remove azobenzene.

The electrochemical measurements were made in a glass cell in which the working and counter electrode compartments were separated by a glass frit. Most of the metals used for the working electrodes had purities of 99.9%. Electrical contacts to copper leads were made by spot welding, soldering, or with a mercury contact. The electrodes were sealed in glass tubing using Bipax<sup>1</sup> epoxy (BA-2112). A platinum counter electrode was always employed. The reference electrode used was Pb/saturated  $\text{PbNO}_3$  with two glass microcracks separating the reference electrode,  $\text{NH}_3\text{-LiNO}_3$  salt bridge, and solution. Due to the high impedance of this reference electrode (3M ohm), a unity-gain follower with input impedance of  $10^{12}$  ohms was constructed from an operational amplifier (Philbrick Researches, Inc., Type EP 25 AU) and used in the potential-measuring circuit.

The cyclic voltammetric curves were obtained using an electronic triangular wave generator to program a Wenking potentiostat (Model 63 TRS), and the i-v curves were recorded on an X-Y recorder. Most cyclic voltammograms were obtained using a scan rate of 125 mv/sec.

## Electrostability Results

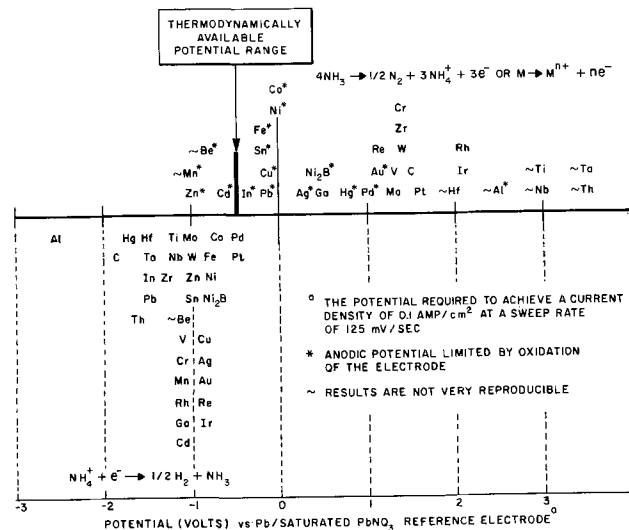
Thermodynamically, there is only a 0.04v potential difference at 25°C between the electrochemical reac-

tions where  $\text{NH}_3$  is reduced to  $\text{H}_2$  and oxidized to  $\text{N}_2$  (4). Kinetically, these reactions are slow on most electrode surfaces; therefore, a much larger potential range is available for electrochemical studies in this solvent.

Electrostability results for over thirty electrode surfaces in acid liquid ammonia solutions at 25.0°C are given in Table I. Oxidation is represented above the center line and reduction below the line. Except for pyrolytic graphite and nickel boride, these are all metallic surfaces. Four interesting observations can be made from Table I.

First, the potential region between the reduction of  $\text{NH}_4^+$  and the oxidation of  $\text{NH}_3$  or of the electrode surface defines the electrostability region for that surface in this electrolyte at 25°C. Electrochemical studies outside this region cannot readily be made. For example, Table I defines an electrostability region for Pt of -0.5 to +1.6v, for Mo of -1.0 to +1.3v, and for Hg of -1.7 to +0.8v, all with respect to the Pb/saturated  $\text{PbNO}_3$  reference electrode. The electrostability regions limited by the  $\text{H}_2$  and  $\text{N}_2$  evolution reactions are not very sensitive to the potential sweep rate, or to the ammonium (acid) salt used as long as its anion is not easily oxidized. Experiments at -35°C showed that the electrostability region is also independent of the acid salt concentration for concentrations above 0.1M. The

Table I. Electrostatic results from cyclic voltammetric experiments in  $\text{NH}_3\text{-NH}_4\text{SCN}$  at 25.0°C



\* Electrochemical Society Active Member.  
Key words: Ammonia, borohydrides, electrocatalysts, electrostability, fuels, hydrazine, hydrazobenzene, hydrogen, metals, oxidation.

<sup>1</sup> From Tra-Con, Inc., Medford, Massachusetts.



electrochemical stability region, of course, increases with decreasing temperature. For example, a 60°C drop in temperature gives about a 10% increase in the electrochemical stability region of Pt. Electrode oxidation rather than solvent oxidation is more likely to determine the anodic limit as the temperature or sweep rate increases.

Second, Table I shows which structural materials are useful in acid liquid ammonia fuel cells or batteries. The starred materials (limiting anodic potential due to electrode oxidation) which oxidize at low potentials should be avoided. For example, structural parts of Fe, Cu, or Ni will give corrosion problems in acid ammonia, while Al, Ti, and Ta are quite inert in this electrolyte.

Third, Table I enables one to evaluate the various electrode surfaces as catalysts for the oxidation of  $\text{NH}_3$ . Excluding the starred materials, the more negative in potential the listing of the materials above the line, the more effective they are in catalyzing the oxidation of  $\text{NH}_3$ . Therefore, from Table I, the best catalyst for  $\text{NH}_3$  oxidation is Ga, followed by Re, then V, and Mo. Even on Ga, however, the overvoltage for  $\text{NH}_3$  oxidation in acid ammonia is approximately 0.7v at 25°C, and improved electrocatalysts are needed before this fuel can be used effectively at ambient temperatures. At higher temperatures (150°C) in aqueous KOH solutions, ammonia is a useful fuel on platinum catalysts (7). Our results suggest that less expensive electrocatalysts (Ga, V, Mo) may be more effective than Pt for this oxidation of  $\text{NH}_3$ .

Fourth, the evaluation of the various electrode surfaces as catalysts for the oxidation of hydrogen in acid ammonia can be made indirectly from Table I. For the

general reaction  $R \rightleftharpoons 0 + ne$ , the equilibrium constant,

$K = k_f/k_b$ , is a thermodynamic quantity unchanged by catalysis; hence, a catalyst that increases  $k_f$  will also increase  $k_b$ . The electrochemical oxidation of hydrogen in acid ammonia,  $\frac{1}{2}\text{H}_2 + \text{NH}_3 \rightleftharpoons \text{NH}_4^+ + e^-$ , is the reverse of the hydrogen evolution reaction; hence, effective electrocatalysts for the reverse reaction will also be effective for the forward reaction. Therefore, the more positive in potential the listing of the materials below the line in Table I, the more effective they will be in catalyzing the electrochemical oxidation of hydrogen in acid liquid ammonia electrolytes. Of the electrocatalysts tested, Pt and Pd are the best for this reaction. The exchange current,  $i_0$ , determined both by Tafel and low overpotential methods (8), for the hydrogen reaction on Pt in acid ammonia is  $10^{-3}$  amp/geometrical  $\text{cm}^2$ , about the same as in aqueous solutions. This indicates that hydrogen as a fuel should be about as effective in acid ammonia as in aqueous solutions.

### Fuel Oxidation

The fuels investigated for possible electrochemical oxidation in acid liquid ammonia include methanol and several other organic molecules with hydroxyl groups, acetylene, potassium borohydride, hydrazine sulfate, and 1,2-diphenyl hydrazine, all of which are soluble in liquid ammonia. Each of these substances was tested for oxidation on ten electrode surfaces selected from various groups of the periodic table. Cyclic voltammetry is especially useful for such screening, and the results using this method are summarized in Table II. The results for the various electrode surfaces indicate that in liquid ammonia, as in aqueous electrolytes, platinum and other precious metals are the best catalytic surfaces.

The results for the various fuels in Table II suggest that inorganic fuels are more easily oxidized in liquid ammonia than carbonaceous fuels. No definite electrochemical oxidation of an organic substance was observed, although such reactions occur readily in aqueous solutions. From studies of the electrochemical oxidation of methanol on platinum in aqueous electrolytes,

Table II. Results from testing various fuel-electrode combinations for electrochemical oxidation in liquid  $\text{NH}_3\text{-NH}_4\text{SCN}$ . Positive results for fuel oxidation are indicated by "yes," negative results by "—," and questionable results by "Q." Carbon surface is pyrolytic graphite.

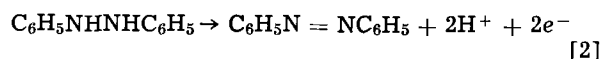
	Ti	Ta	W	Re	Rh	Pt	Pt-Ir	Au	Hg	C
Methanol	—	—	—	—	—	—	—	—	—	—
Ethanol	—	—	—	—	—	—	—	—	—	—
Cyclohexanol	—	—	—	—	—	Q	Q	Q	—	Q
Phenol	—	—	—	—	—	—	—	—	—	—
Ethylene glycol	—	—	—	—	—	—	—	—	—	—
Glucose	—	—	—	—	—	—	—	—	—	—
Acetylene	—	—	—	—	—	Q	—	—	—	—
$\text{C}_6\text{H}_5\text{NHNHC}_6\text{H}_5$	Q	—	—	Q	Q	—	Q	—	Yes	Q
$\text{N}_2\text{H}_4 \cdot \text{H}_2\text{SO}_4$	—	—	—	Q	Yes	Yes	Yes	Q	—	—
$\text{KBH}_4$	—	—	—	Yes	—	Yes	Yes	Q	—	—

Bagotzky and Vassilyev postulate that the slow step is the oxidation of carbon-containing chemisorbed residues by chemisorbed OH fragments produced from the solvent (9). If the reaction mechanism in liquid ammonia is analogous, it is reasonable that adsorbed  $\text{NH}_2$  species are not as effective oxidizing agents as adsorbed OH species; hence, the electrochemical oxidation of carbonaceous fuels would involve a higher energy barrier in liquid ammonia than in water. In general, the electrochemical oxidation of carbonaceous fuels will probably be kinetically most favorable in solvents containing fluorine, chlorine, or oxygen atoms. Other solvents such as liquid ammonia should be useful for fuels such as hydrazine, hydrogen, and metals since for these fuels the solvent is not directly involved in the oxidation reaction.

Figure 1 shows typical curves for constant current oxidation of  $\text{KBH}_4$ ,  $\text{N}_2\text{H}_4 \cdot \text{H}_2\text{SO}_4$ , and  $\text{C}_6\text{H}_5\text{NHNHC}_6\text{H}_5$  in stirred acid ammonia solutions. For the electrochemical oxidation of  $\text{KBH}_4$  and  $\text{N}_2\text{H}_4 \cdot \text{H}_2\text{SO}_4$ , platinum electrodes of about 50  $\text{cm}^2$  geometrical area were used, while 1,2-diphenylhydrazine was oxidized on a mercury pool of about 3  $\text{cm}^2$  area. The arithmetic means for these experiments are  $1.8 \pm 0.3$  electrons/molecule for  $\text{C}_6\text{H}_5\text{NHNHC}_6\text{H}_5$ ,  $2.4 \pm 0.4$  electrons/molecule for  $\text{KBH}_4$ , and  $3.7 \pm 0.2$  electrons/molecule for  $\text{N}_2\text{H}_4 \cdot \text{H}_2\text{SO}_4$ , where the limits are the 95% confidence interval within which the true population mean would lie, assuming only random errors. The net oxidation reaction for hydrazine in acid ammonia is therefore



and for 1,2-diphenylhydrazine



where  $\text{H}^+$  represents the ammoniated proton.

The net reaction for  $\text{KBH}_4$  is uncertain; however, hydrogen evolution is observed when  $\text{KBH}_4$  is added to acid liquid ammonia solutions, probably produced

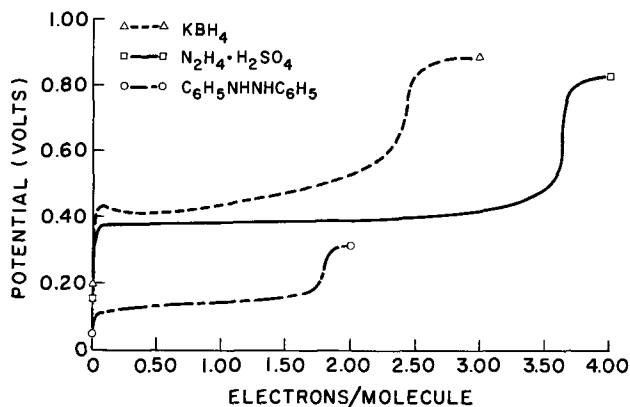


Fig. 1. Constant current oxidation of  $\text{KBH}_4$ ,  $\text{N}_2\text{H}_4 \cdot \text{H}_2\text{SO}_4$ , and  $\text{C}_6\text{H}_5\text{NHNHC}_6\text{H}_5$  in stirred  $\text{NH}_3\text{-NH}_4\text{SCN}$ .  $I = 1.00$  ma;  $T = 25.0^\circ\text{C}$ .

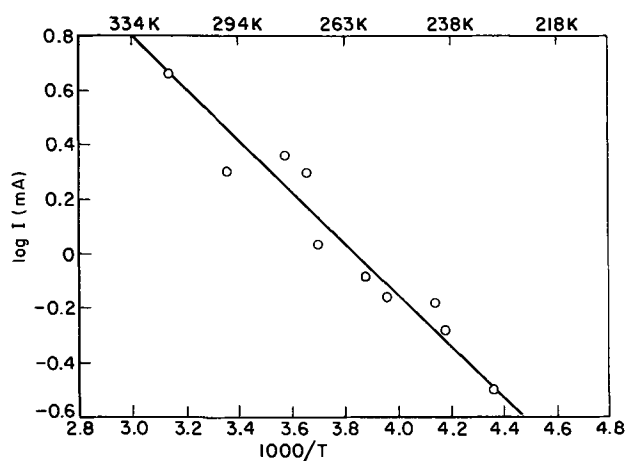


Fig. 2. Graph of  $\log I$  vs.  $1000/T$  for the electrochemical oxidation of 1,2-diphenylhydrazine on Hg in stirred  $\text{NH}_3\text{-NH}_4\text{SCN}$ .

by the reaction  $\text{NH}_4^+ + \text{BH}_4^- \rightarrow \text{BH}_3\cdot\text{NH}_3 + \text{H}_2$ . The electrochemical activity remains even after the hydrogen evolution has ceased, indicating that  $\text{BH}_3\cdot\text{NH}_3$  is the reactive substance. No hydrogen evolution and no electrochemical oxidation of  $\text{KBH}_4$  are observed in neutral ( $\text{NaSCN}$ ) liquid ammonia solutions.

#### Temperature Effect

Figure 2 shows the graph of  $\log I$  vs.  $1/T$  for the electrochemical oxidation of 0.02M 1,2-diphenylhydrazine on a 3 cm<sup>2</sup> mercury pool at approximately constant overpotential. The current  $I$  is that recorded 15 sec after beginning the oxidation at 0.1v overpotential in stirred acid ( $\text{NH}_4\text{SCN}$ ) ammonia solutions. From the slope of the line in Fig. 2, an Arrhenius activation energy of about 5 kcal/mole is calculated at this overpotential.

For the electrochemical oxidation of  $\text{KBH}_4$  on platinum, an approximate value of about 15 kcal/mole for the energy of activation was determined. The results, however, were not as reproducible as for the oxidation of 1,2-diphenylhydrazine. This high value for the activation energy reflects a need for great improvement in the catalysis of this reaction.

The rate of the electrochemical oxidation of hydrazine on platinum in acid liquid ammonia does not show the expected Arrhenius temperature dependence. In fact, the rate of the hydrazine oxidation reaction diminishes as the temperature increases. This behavior is not uncommon for heterogeneous reactions where

the rate-determining step involves reaction in the adsorbed state. This decrease in rate with increase in temperature is often the result of the unfavorable effect of temperature on the chemical adsorptions (10).

#### Summary

The main results of these experiments can be summarized by the following statements.

1. Electroactivity regions in acid liquid ammonia solutions for over thirty electrode surfaces are defined.
2. Carbonaceous fuels are difficult to oxidize in liquid ammonia.
3. For the electrochemical oxidation of  $\text{NH}_3$  and  $\text{KBH}_4$ , better electrocatalysts are needed.
4. Hydrogen and hydrazine show promise as fuels in liquid ammonia electrolytes and merit further study.

#### Acknowledgments

The authors wish to express their thanks to Dr. William S. Harris and Dr. Richard E. Panzer for many helpful discussions and suggestions.

Manuscript submitted June 24, 1968; revised manuscript received Aug. 20, 1968. This paper was presented at the Boston Meeting, May 5-9, 1968, as Paper 212.

Any discussion of this paper will appear in a Discussion Section to be published in the June 1969 JOURNAL.

#### REFERENCES

1. K. R. Williams, Editor, "An Introduction to Fuel Cells," Elsevier Publishing Co., New York (1966).
2. A. B. Hart and G. J. Womack, "Fuel Cells—Theory and Application," Chapman and Hall, London (1967).
3. L. G. Austin, "Fuel Cells—A Review of Government Sponsored Research, 1950-1964," p. 270, NASA Report SP-120, Washington, D. C. (1967).
4. W. J. Jolly and C. J. Hallada in T. C. Waddington, "Non-Aqueous Solvent Systems," Academic Press, New York (1965).
5. G. Jander, H. Spandau, and C. C. Addison, "Chemistry in Nonaqueous Ionizing Solvents. Vol. I, Chemistry in Anhydrous Liquid Ammonia. Part I, Anorganische und Allgemeine Chemie in Flüssigem Ammoniak," Interscience Publishers, John Wiley & Sons, Inc., New York (1966).
6. D. E. Sellers and G. W. Leonard, *Anal. Chem.*, **34**, 1457 (1962).
7. E. J. Cairns, E. L. Simons, and A. D. Tevebaugh, *Nature*, **217**, 780 (1968).
8. J. P. G. Farr, N. A. Hampson, and M. E. Williamson, *J. Electroanal. Chem.*, **13**, 462 (1967).
9. V. S. Bagotzky and Yu. B. Vassilyev, *Electrochim. Acta*, **12**, 1323 (1967).
10. M. Prettre, "Catalysis and Catalysts," pp. 24-26, Dover Publications, New York (1963).

# Changes in the Microstructure of a Sintered Silver Electrode after Repeated Cycling at a Low Current

C. P. Wales\* and A. C. Simon\*

Naval Research Laboratory, Washington, D. C.

## ABSTRACT

Cross sections of Ag electrodes were examined by optical microscopy. Most small particles present in an unused sintered Ag electrode were completely oxidized to AgO during the first charge, but electrode capacity then decreased markedly during the next few cycles at the 20-hr rate in 35% KOH. Slow discharges resulted in the formation of large granular Ag particles which did not oxidize as readily or extensively as small Ag particles. Voids were small and well distributed in the unused electrode, but with repeated cycling the voids became large as active material clumped. Grid corrosion occurred but did not impair performance.

Silver-zinc and silver-cadmium cells are important as high capacity power sources, but their full capabilities are not always realized, for reasons not fully understood. Cell capacity often decreases with use. Discharge performance appears to be influenced by the charging method and by conditions of the previous discharge. Since these cells are normally constructed with an excess of negative active material, performance is usually limited by the silver electrode. The present investigation was undertaken in the belief that changes in crystal morphology during the life of the silver electrode are related to changes in electrode performance. If a relationship can be established, it may be possible to determine and control the optimum structure for a given type of performance in order to improve the charge acceptance and capacity of the silver electrode.

Optical microscopy has been used successfully as a tool for solving problems connected with the lead-acid storage battery (1, 2). Special techniques were developed that have aided considerably in understanding the mechanisms of corrosion and crystallogeneses that occur in the lead-acid system (3, 4). Electron microscopy of replica films has been used to describe the surface and back side of silver electroplated on sheet platinum and then charged and discharged to various conditions while in alkaline solution (5). The present work used optical microscopy of cross sections of sintered silver electrodes manufactured for silver-zinc storage batteries and applies to conditions that can develop when such batteries are used.

Porous electrodes cannot be ground and polished successfully in preparation for microscopic examination unless the voids within the electrode are filled with a solid material. Since the techniques being used for the microscopic study of lead-acid batteries require heat for curing the plastic used in the impregnation of the electrode samples, the instability of the silver oxide electrode at elevated temperature indicated that difficulty might be experienced. Both Ag<sub>2</sub>O and AgO are known to decompose when heated and to have increasing rates of decomposition with increasing temperature (6). Since AgO, the more unstable of the two oxides, decomposes more rapidly when in alkaline solution (7) difficulty in washing the electrodes free from KOH electrolyte might also cause problems. In addition to decomposition of the silver oxides which might occur when the samples are heated, there might also be reaction between the silver oxides and the plastic, before the plastic hardened, or decomposition during the time before the sample is finally polished satisfactorily for ex-

amination. While these factors had to be considered in sample preparation, the difficulty was less than anticipated.

The products resulting from anodic oxidation of Ag electrodes and the cathodic reduction of silver oxide electrodes in alkaline solutions were identified previously by subjecting the electrodes to x-ray diffraction after removal from a cell (8) and by x-ray diffraction of an electrode in a cell which permitted x-ray examination simultaneously with electrochemical oxidation and reduction (9). These studies showed that during a charge the Ag was oxidized first to Ag<sub>2</sub>O and then to AgO, and that during a discharge AgO was reduced first to Ag<sub>2</sub>O and then to Ag. There was no evidence of a silver suboxide, an oxidation state higher than AgO, a solid solution, or an alloy of oxygen and silver. These x-ray diffraction studies have eased the problem of microscopic examination since only the three phases Ag, Ag<sub>2</sub>O, and AgO were expected to be present and needed to be identified.

The present report describes changes in the structure of an unused sintered silver electrode when the electrode was charged and discharged at a relatively low rate. The changes are illustrated mainly by showing differences in the form of silver present in discharged electrodes, but changes that occurred in the appearance of oxide formations are also given. The charge and discharge processes as such are not illustrated in detail here, but are the subject of later reports.

## Experimental Procedure

The silver electrodes used for the microscopic examination were all of the same size and type. The electrodes had been manufactured commercially for silver-zinc storage batteries that were designed to discharge at comparatively low rates, requiring at least 1 hr for a complete discharge. The electrodes were constructed in the customary way that the manufacturer used for small cells, but details of the process were considered proprietary. Electrode dimensions were 41.5 mm wide by 38.0 mm high by 0.8 mm thick. The electrodes consisted of sintered Ag particles with a grid of expanded sheet Ag. The grid was much closer to one surface of an electrode than to the other surface. The theoretical capacity of an electrode, based on the amount of sintered Ag present, was 2.9 amp-hr.

A piece of plastic 53 x 52 x 3.2 mm was made into a U-shape by cutting out a section 43 x 43 mm. This plastic U was wrapped with five layers of treated cellulose separator to slow the diffusion of soluble Ag species. The top of the plastic U was open so that an electrode could be removed and reinserted without unwrapping the separator when it was desired to cut a sample from the electrode. Two other sintered Ag electrodes of the same size were wrapped with the

\* Electrochemical Society Active Member.

Key words: silver electrode, silver oxides, storage batteries, microstructure.

cellulose separator and put on each side of a removable electrode. These two electrodes were connected in parallel and served as counter electrodes. Since the counter electrodes were being reduced at the same time as a test electrode was being oxidized, and *vice versa*, little gas was produced in a cell except at the end of charge and discharge. The electrodes fit loosely in a plastic cell, together with a reference electrode of Ag/Ag<sub>2</sub>O. The work was done at approximately 25°C in an excess of 35% KOH solution.

The removable electrodes were charged and discharged individually at the constant current which required 20 hr for a complete charge or a complete discharge. Since the capacity of a previously unused electrode gradually declined, progressively lower values of charge and discharge current were used during the first few cycles. Capacity declined more slowly after about 5 cycles and became relatively constant after 8 to 10 cycles. Samples approximately 19 x 21 mm were cut from a removable electrode at various times, for microscopic examination. The remainder of the electrode was then returned to the cell and placed within the separator as before. Current was lowered by an amount sufficient to compensate for the removal of each sample, so that current density on the remainder of the electrode was unchanged.

The cells described above were used to obtain 16 samples of Ag electrodes that had been cycled a low number of times before removing a portion of the electrode. Four samples of an electrode that had been cycled over 200 times were taken from a cell in which the test electrode had been wrapped directly with cellulose separator and which had only a single counter electrode. The test electrode in this cell had been given 217 complete charges to oxygen evolution followed by complete discharges before the first sample was removed for microscopic examination during cycle 218. Over half of the charges were done at the 20-hr current with the remainder taking from 20 to 30 hr. The first 137 discharges were at the 20-hr rate, then followed 45 discharges at the 1-hr rate, and the remainder of the discharges were again done at the 20-hr rate.

Each sample was handled separately to avoid delay in microscopic examination. After a sample was cut from an electrode, the sample was immediately washed in 4 to 6 changes of distilled water to remove the KOH solution and then dried in a vacuum for 1 hr. A dry sample was placed in a 38 mm diameter by 52 mm deep cavity in an aluminum mold and held upright by surrounding the sample with Lucite pellets. While under a vacuum, the sample was impregnated with an epoxy resin.<sup>1</sup> The impregnated sample was returned to atmospheric pressure and transferred to an oven at 40°C for 8 hr to cure the plastic. Although several liquid polyesters and epoxy resins have been tried as the impregnating plastic, none were wholly satisfactory. Liquid polyesters can be obtained which have low viscosity and form a clear, hard plastic when cured, but of the polyesters tried all reacted slowly with the silver oxides before the plastic hardened. If the electrode had only a thin layer of black Ag<sub>2</sub>O on its surface, sufficient reaction took place between the Ag<sub>2</sub>O and the polyester that the electrode surface usually lightened noticeably. Epoxy resins have the disadvantages of a higher viscosity which makes complete impregnation more difficult, and of being opaque after solidifying. Epoxy resins were used for an impregnation plastic, however, because they were less reactive with Ag<sub>2</sub>O and AgO.

After the plastic had cured, a cross section of the electrode sample was prepared. The sample was ground successively on 120, 240, 400, and 600 mesh silicon carbide abrasive papers and was finally wet polished using Geoscience 9 micron boron carbide<sup>2</sup>

on a lap of Buehler Texmet.<sup>3</sup> This was followed by dry polishing on a sponge rubber lap charged with Linde 0.3 $\mu$  Alumina powder.<sup>4</sup> The sample was then examined by optical microscopy and the appearance of significant areas recorded by photography.

### Results and Discussion

No noticeable decomposition of silver or its oxides was observed when they were entirely within the embedding plastic. Where exposed at the polished surface, however, the system changed slowly as metallic Ag tarnished and AgO was reduced to Ag<sub>2</sub>O, often with simultaneous oxidation of nearby metallic Ag to Ag<sub>2</sub>O. Ag<sub>2</sub>O was the most stable form. For most purposes these slowly occurring changes offered no difficulty, because several days were required for appreciable changes and observations could easily be completed within this time. If it was necessary to re-examine a sample that had changed at the exposed surface, the original appearance could again be restored by regrinding the sample with fine mesh silicon carbide papers and repolishing. Often repolishing alone was sufficient to restore the original appearance.

The three phases Ag, Ag<sub>2</sub>O, and AgO were quite distinct from one another and easily identified by the optical microscope. When observed under bright field vertical illumination in the manner used for most metallographic specimens, metallic Ag had practically specular reflectance. The reflectivity of the two oxides was considerably less than that of the Ag, but the oxides were readily differentiated since AgO was much brighter than Ag<sub>2</sub>O. In polarized light the Ag appeared much darker but was brighter than Ag<sub>2</sub>O or AgO, while the Ag<sub>2</sub>O was the darkest constituent. Neither Ag nor Ag<sub>2</sub>O exhibited polarization colors, but under polarized light and with an interference plate the AgO showed strong color variations from one grain to another. The Ag<sub>2</sub>O crystals were much smaller than the AgO crystals.

Individual crystals could not be observed at the relatively low magnification of 250X or less, but these low magnifications were useful because they revealed changes in aggregation that took place, the appearance and disappearance of large voids in the active material, evidence of uneven reaction rates, and other features of interest. At higher magnifications the true microstructure of the electrode could be observed. Provided that magnification was sufficient, individual crystals could be detected as well as changes in crystal form during oxidation and reduction. The highest magnification used in the present work was 1600X.

The appearance of an unused sintered Ag electrode is shown at low magnification in Fig. 1. This and all subsequent photographs are of cross sections through the electrode and, therefore, also show cross sections through individual crystals or other particles of which the electrode is composed. In the unused electrode the Ag was present in the wide range of sizes from approximately 0.5 to 100 $\mu$ , which many of the particles too small to be individually visible at 100X magnification. While the proportion of large to small particles varied considerably in different areas of an electrode, the general appearance of the structure remained fairly uniform. At higher magnification it can be seen that the major portion of the Ag particles were quite small (Fig. 2). Many of the small particles appeared to form agglomerates with a very definite outline about the same size as the large Ag particles. The agglomerates were quite porous and consisted of individual particles with considerable variation in size and shape. At the highest magnification used in the present work, the individual particles of Ag in an unused electrode could be seen more clearly (Fig. 3). Many of the particles had their smallest dimension in the range 1.5–2 $\mu$ . Most of the voids in the unused

<sup>1</sup> Castabond No. 121 with Hardener J, Rector Engineering and Plastics Company, 318 Randolph Place, N.E., Washington, D.C.

<sup>2</sup> Geoscience Instruments Corporation, 110 Beekman Street, New York, New York.

<sup>3</sup> Buehler Ltd., 2120 Greenwood Street, Evanston, Illinois.

<sup>4</sup> Crystal Products Department, Linde Company, 2065 U.S. Route 22, Union, New Jersey.

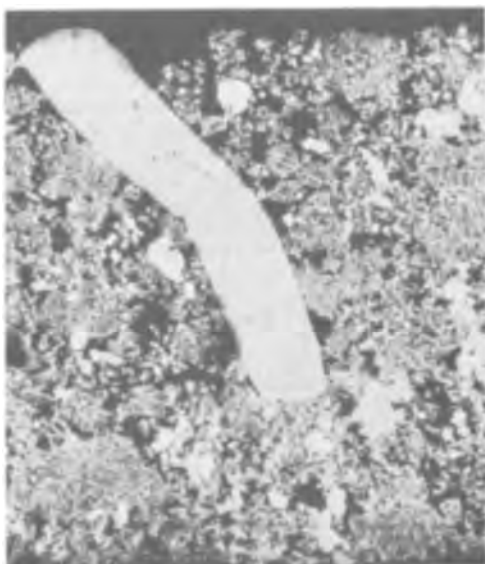


Fig. 1. Structure of a commercially prepared, sintered Ag electrode that had never been used. Electrode surfaces are at the top and bottom of the photograph. The large white area is a cross section of the grid, and the white particles are Ag active material. The dark background represents areas filled by the impregnation plastic and, therefore, areas that were void. The lines forming squares indicate  $238\mu$  separation. The original magnification before reproduction was 100X.

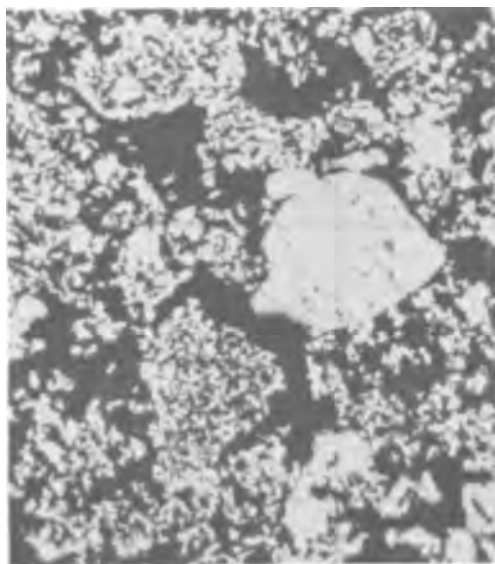


Fig. 2. Portion of the unused electrode of Fig. 1 at higher (400X) original magnification, showing that many Ag particles were quite small and some had clumped together into larger masses. The lines forming squares indicate  $60\mu$  separation.

electrode were quite small and well distributed among the smaller particles of Ag.

The electrode structure had changed markedly in particle size and porosity after the first charge to oxygen evolution and discharge back to metallic Ag using the 20-hr rate of current. A discharge was ended when potential fell to  $-300$  mv *vs.* the Ag/Ag<sub>2</sub>O reference electrode, a potential equivalent to an endpoint of 1.2-1.3v for a typical Ag-Zn cell. Over half of the Ag was present as larger granular particles at the end of the first discharge, although many small Ag particles were also present (Fig. 4). There was much variation in the electrode with some areas having many more small particles than other areas, so that

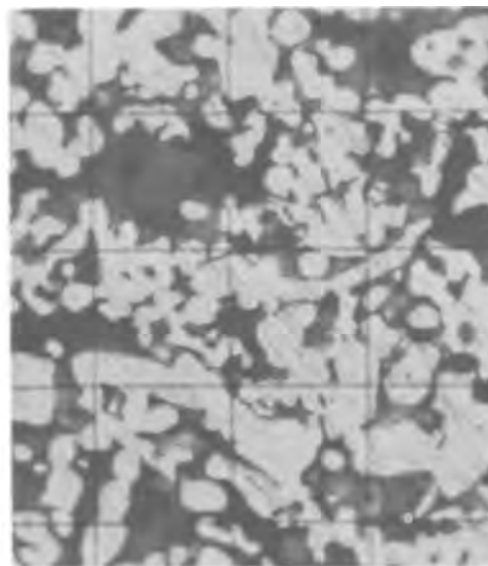


Fig. 3. Area of small Ag particles in the unused electrode of Fig. 1 and 2 at 1600X original magnification. The Ag particles were very irregularly shaped and had many sizes. The lines forming squares indicate  $15\mu$  separation in this and all other photographs that had an original magnification of 1600X before reproduction.

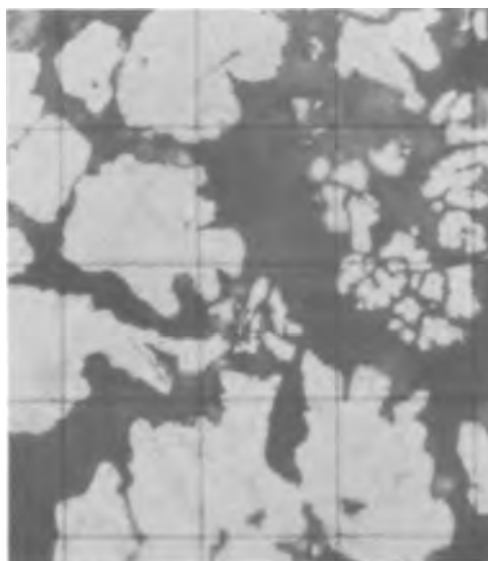


Fig. 4. Area of an electrode at the end of the first discharge. Many large Ag particles formed during the discharge at the 20-hr rate although small particles also formed. Compare with Fig. 3 at the same magnification.

no area could be specified as being truly typical of the entire electrode. Figure 4 gives an idea of the size range of the particles that formed during the first discharge. Many of the granular particles had convolutions on at least a portion of their surfaces. Although some small particles were still present, the small particles produced by electrolytic reduction did not resemble the small particles of the unused electrode (compare Fig. 3 and 4). The large particles found in the unused electrode (Fig. 1, 2) were still present, but none are included in the area shown in Fig. 4. Since a small amount of additional capacity could have been removed if the discharge had ended at a lower potential, no doubt traces of oxide still remained. Oxides could not be detected by optical microscopy after a slow discharge to the usual endpoint, however, nor by x-ray diffraction in earlier work (8,9).

During the second charge an electrode almost always accepted fewer ampere-hours before potential rose to oxygen evolution than during the initial charge of a sintered Ag electrode. Electrode capacity tended to decline for several cycles when the 20-hr discharge rate was used. In the initial cycle in 35% KOH, the capacity obtained was from 67 to 87% of the capacity theoretically possible from the sintered Ag, and was usually in the 70–80% range, averaging 75%. At the end of cycle 5 at the 20-hr rate, capacity was usually only 50–63% of the capacity theoretically possible, averaging 56%. By cycle 10 capacity of an electrode had become relatively constant somewhere in the range of 43–58% of the capacity theoretically possible, averaging 50%. Following this decrease to relatively constant values, capacity tended to increase irregularly. The increase was slow and only became evident when electrodes were cycled many times. In the period from cycle 70 to 120 the capacity had increased sufficiently that it usually averaged 55% of that theoretically possible.

During the first five cycles, while the electrode was losing capacity most rapidly, the Ag particles present at the end of the discharges noticeably changed in appearance. The greatest change occurred during the first discharge and has already been illustrated (Fig. 3 and 4). The Ag formed during the second discharge at the 20-hr rate had approximately the same range of particle sizes as the Ag formed during the first discharge, but more of the large, granular particles had clumped together (Fig. 5). The large particles residual from the unused electrode (lower left of Fig. 5) showed evidence of attack at their surfaces after two cycles. By the end of the fifth discharge most Ag active material was present as large, granular particles, and many particles had clumped together in agglomerates composed of several particles (Fig. 6). Increasingly large void spaces had formed between the agglomerates. The large particles residual from the unused electrode gradually decreased in size and number in the early cycles as a result of continued attack at their surfaces. Comparison of Fig. 1 and 6 shows that particle size became more uniform with repeated cycling at the 20-hr rate. The fine particles originally present had disappeared al-

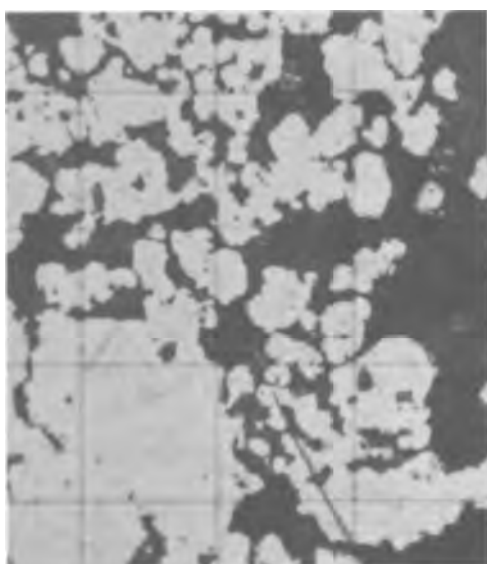


Fig. 5. Appearance of an electrode at the end of the second discharge. Although individual Ag particles had approximately the same size range as they did after the first discharge at the 20-hr rate, more particles had clumped together during the second discharge. Lines forming the squares indicate  $30\mu$  separation. The original magnification was 800X. Compare with Fig. 4 but note difference in magnification.

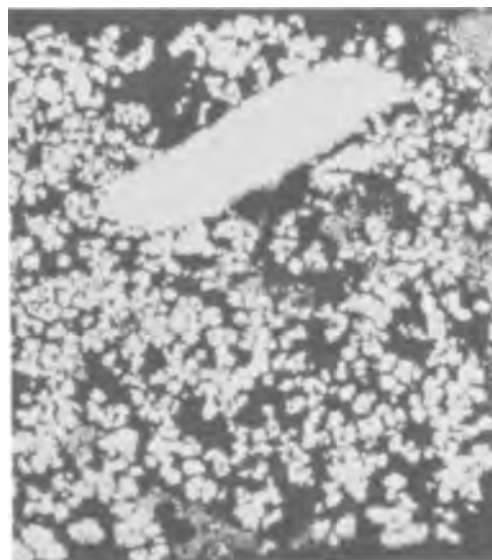


Fig. 6. Cross section including the grid at the end of the fifth discharge. Most Ag was present at large particles. Electrode surfaces are at the top and bottom of the photograph. Compare with Fig. 1 at the same magnification.

though some fine particles having a different appearance could be found.

The capacity loss was the direct result of the formation of large Ag particles in place of the small particles originally present in the electrode. Microscopic examination of Ag electrodes after a rapid discharge showed that small Ag particles formed when the discharge current was high (10). This finding agreed with the results of x-ray diffraction which showed that particle size varies inversely with current density (9). Since the discharges were done at a relatively low current density in the present work, conditions within the electrode promoted the formation of large Ag particles as the silver oxides were reduced. The majority of the active material was present as AgO at the end of a charge, although particles of Ag covered with oxide remained also. During discharge the AgO was reduced to Ag<sub>2</sub>O and the Ag<sub>2</sub>O reduced to Ag. Growth of Ag particles during a slow discharge is illustrated in Fig. 7 by an electrode that had been discharged at the 20-hr rate for approximately 13 hr. At this point the electrode was composed largely of Ag and Ag<sub>2</sub>O with a small amount of AgO still present. The Ag particle at the lower left in Fig. 7 has the angular, irregular outline that was characteristic of Ag particles that remained in an electrode at the end of a charge. This particle was separated from the electrolyte by a tight coating of Ag<sub>2</sub>O. Ag particles with access to the electrolyte increased in size as Ag<sub>2</sub>O disappeared from the immediate vicinity of the particles. The Ag particle shown in cross section at the upper center of Fig. 7 had the rounded, convoluted form typical of a particle produced by slow electrolytic reduction. Note that this particle retained its original angularity at the upper left where the Ag still contacted the Ag<sub>2</sub>O. The cavity that largely surrounded this growing particle illustrates the fact that metallic Ag occupies less volume than Ag<sub>2</sub>O and indicates that the oxide went into solution before it deposited as Ag during slow electrolytic reduction. The angular form of Ag shown at the lower left in Fig. 7 had entirely disappeared by the end of a discharge.

After the first few discharges at the 20-hr rate the appearance of the large granular Ag particles that were present in discharged electrodes did not change appreciably. An electrode discharged once at the 20-hr rate contained granular particles approximately the





Fig. 7. Ag particles in an electrode discharged 65% at the 20-hr rate. Ag was the lightest shade in the photograph,  $\text{Ag}_2\text{O}$  dark gray, and the impregnation plastic was black. Small patches of  $\text{AgO}$  remaining in the  $\text{Ag}_2\text{O}$  are shown as a gray shade intermediate between Ag and  $\text{Ag}_2\text{O}$ . Compare Ag particle newly formed by electrolytic reduction (upper) with Ag particle that had not oxidized completely in the previous charge (lower left). Original magnification 1600X.

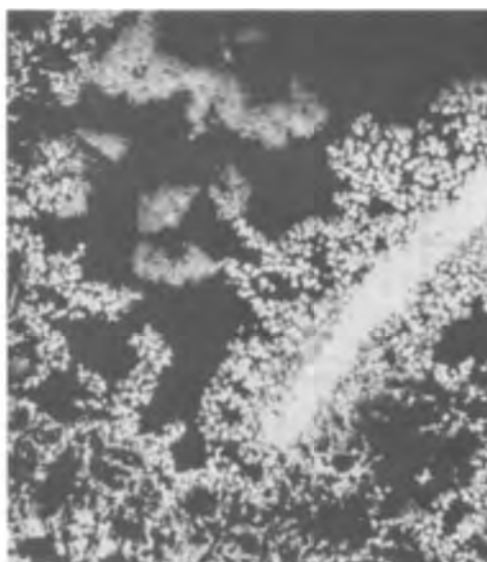


Fig. 9. Three forms of Ag present on discharged electrode after 218 cycles. Large granular particles are in the center and near the grid member at upper right. Fine dendritic particles are at the top center, while coarser dendritic particles are at the bottom. Compare with Fig. 1 and 6 at the same magnification.

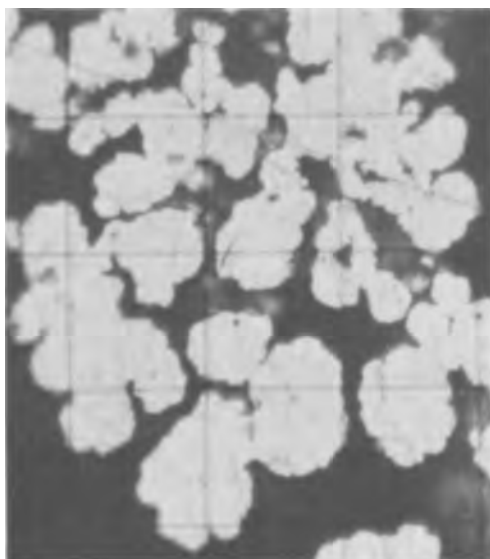


Fig. 8. Large granular Ag particles present in many areas of a discharged electrode after 218 cycles. Some particles were larger than those shown here. Compare with Fig. 4 at the same magnification.

same size as the large particles in an electrode cycled over 200 times (Fig. 8). This electrode had been discharged at the 20-hr rate for 172 times, including the previous 35 discharges, and contained Ag in three forms (Fig. 9). The large granular particles shown in Fig. 8 were joined in a network similar to what a dendritic growth would form, but it was also possible that the network resulted from individual crystals contacting one another while growing. Since the actual surfaces of the large particles contained many small, faceted crystals, it was also possible that much smaller crystals had aggregated to form these granular structures, but cross sections of the granular crystals did not indicate that the large particles were composed of many small crystals.

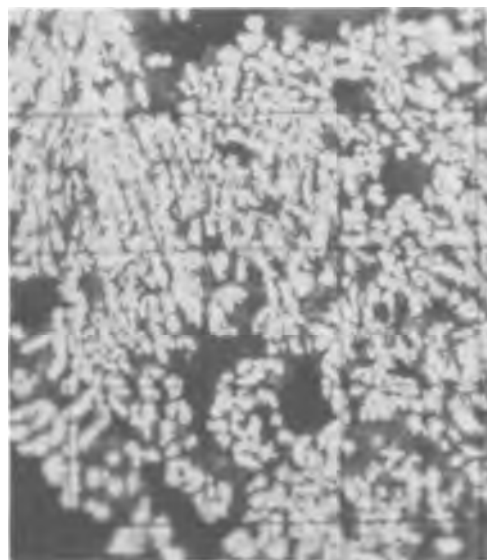


Fig. 10. Fine dendritic crystals of Ag present in many areas of the discharged electrode of Fig. 9. Original magnification 1600X.

In addition to large particles such as those shown at high magnification in Fig. 8, many areas contained small dendritic crystals that were closely packed (Fig. 9 and 10). Less common were the coarse dendritic crystals of Ag which were found in some areas of this electrode (Fig. 11). The coarse dendritic crystals had a definite tendency to assume rectilinear forms. In the discharged electrode that had been cycled 218 times, approximately one-sixth of the area consisted of these coarse dendritic Ag crystals and the remainder of the area was equally divided between the fine dendritic crystals and the large granular particles. Although this electrode previously had been discharged 45 times at the 1-hr rate and fine Ag particles had formed under these conditions, it was highly unlikely that any of these fine particles were still present after 35 consecutive discharges at the 20-hr rate, since many large Ag particles form after only a single slow discharge. Furthermore, small dendrites such as are shown in Fig. 10 were not found



Fig. 11. Coarse dendritic crystals of Ag present in some areas of the discharged electrode of Fig. 9. Angles of approximately 90 degrees were often present. Compare with Fig. 8 and 10 at the same magnification.

in a sample of the same electrode removed at the end of the previous charge. Remnants of both types of large particle were present at the end of the previous charge, with most remnants coming from the granular type illustrated in Fig. 8 and remnants from the coarse dendritic type illustrated in Fig. 11 being much less common. It was concluded that the small crystals of the type shown in Fig. 10 were newly nucleated during the discharge and originated in areas in which few if any Ag particles had remained at the end of the previous charge.

Few of the very small dendritic particles were coexistent with the larger particles in the discharged electrode. Discharged electrodes that had been cycled only a few times contained small dendritic particles, but not in large amounts. For example, after the fifth discharge at the 20-hr rate about 5% of the electrode area contained small particles that had dendritic characteristics (Fig. 6). These small Ag particles had a configuration more like those shown in Fig. 11 than those in Fig. 10 and were intermediate in size between the two types illustrated. These small particles were found at both the center and surface of an electrode.

The voids in the electrode had become significantly larger with repeated cycling. The change in void or pore size can be seen by comparing the compacted structure of the unused electrode (Fig. 1) to the structure with large voids obtained after five cycles (Fig. 6) and to the structure with larger voids obtained in over 200 cycles (Fig. 9). The electrode shown in Fig. 9 had increased in thickness by approximately 20% during the many cycles it had undergone in a loosely fitting cell case. The consequent increase in pore size may have been a factor in a greater proportion of Ag forming as small particles in this electrode than the proportion found in electrodes cycled a relatively low number of times. The large particles shown in Fig. 8 and 9 were not clumped together to the extent that particles had clumped in an electrode after five slow discharges (Fig. 6). An electrode with fewer large Ag particles, such as is shown in Fig. 9, should charge to a greater extent than an electrode composed mostly of large particles. This was probably the reason that capacity of electrodes cycled many times increased slowly after reaching a minimum value.

An electrode that was not completely discharged but in which a substantial amount of oxide remained would not have formed as many large Ag particles

during a discharge as an electrode discharged to 100% of available capacity. A partially discharged electrode, such as the one shown in Fig. 7, should oxidize more readily than electrodes with many large Ag particles, such as Fig. 4, 5, and 8. Fewer large particles being present is very likely to be the main reason for the well-known fact that silver batteries cycled at 50–75% depth of discharge have a better life than the same batteries cycled at 100% depth of discharge, the depth used in the present work.

Figures 1, 6, and 9 all include portions of the grid of expanded Ag sheet metal. The relative size of the grid section shown was not significant, since the apparent size depended both on the angle of sectioning and the location in the Ag sheet where the cut was made. Most of the grid sections were the length shown in Fig. 6, but many were twice this length as in Fig. 1 and 9. The smooth and regular outline of the grid section in the unused electrode (Fig. 1) had disappeared by the time that the electrode had been cycled five times. Grid corrosion as the result of penetrating attack during the first five cycles was evident from the roughened, irregular grid outline shown in Fig. 6. After an electrode had been cycled over 200 times the grid outline had become very irregular and the original cross section of the grid had been greatly reduced (Fig. 9). Although much grid corrosion had occurred, there was no evidence that the usefulness of the electrode had been particularly impaired by this corrosion.

Since electrodes examined in various states of charge and discharge did not indicate that reactions take place preferentially at the grids, at least at the low rates of charge and discharge used in the present work, many areas of the electrode must have been in good electrical contact with the grid even though in the photographs they do not appear to be in contact. Particles that appeared to be isolated reacted to the same extent as areas where the active material particles obviously touched each other. The connections for the particles must have been above or below the plane of the cross sections. Although only one side of the silver electrode faced the counter electrode in the cell that contained a single counter electrode instead of two, reactions were not limited to that one side nor was reaction on that side favored particularly when the electrode was charged or discharged. The similarity between the two surfaces of the silver electrode in this cell probably resulted from the high porosity of the electrode and from the relatively low current densities. Under the conditions used, adjacent areas of an electrode had more differences than there were between the two surfaces.

The size and distribution of the Ag particles present in an electrode at the beginning of a charge had a strong effect on oxide formation. X-ray diffraction studies (8, 9) have shown that, during a constant current charge in alkaline solution, the Ag is oxidized first to  $\text{Ag}_2\text{O}$  at a potential plateau that remains relatively constant at a value a little above the  $\text{Ag}/\text{Ag}_2\text{O}$  equilibrium. After most or all of the Ag has a coating of  $\text{Ag}_2\text{O}$ , potential rises sharply until it exceeds the  $\text{Ag}_2\text{O}/\text{AgO}$  equilibrium value. At the higher potential AgO begins to form and then potential decreases slightly from a maximum or peak to a second plateau. Much of the remaining Ag oxidizes to  $\text{Ag}_2\text{O}$  and then to AgO at this second potential plateau. Finally the potential rises to a third plateau and the main reaction becomes oxygen evolution. Figure 12 gives the appearance of a previously unused sintered Ag electrode after charging to the potential peak that begins the second potential plateau. Electrodes charged to this point contained only Ag and  $\text{Ag}_2\text{O}$ . Almost all of the Ag had been covered by  $\text{Ag}_2\text{O}$  crystals. Some Ag particles larger than those shown in Fig. 12 were also present (Fig. 1, 2). The large Ag particles tended to have thinner layers of  $\text{Ag}_2\text{O}$  on their surfaces than the small particles, but the unused electrode was largely composed of small particles. Samples removed



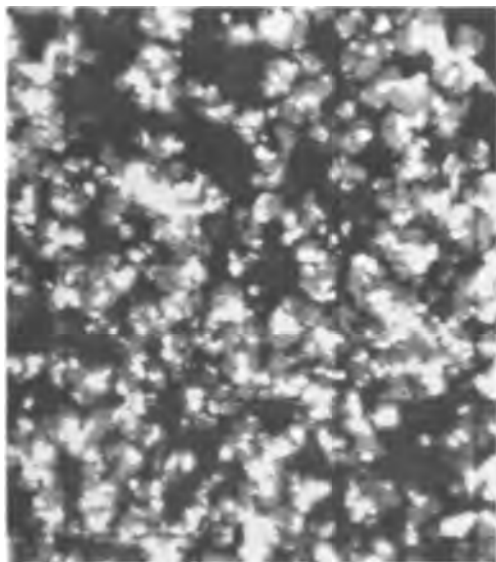


Fig. 12.  $\text{Ag}_2\text{O}$  that has formed on Ag during the first charge of a previously unused sintered Ag electrode. Electrode was charged to the potential peak that begins  $\text{Ag}_2\text{O}/\text{AgO}$  potential plateau. Ag was lightest shade in photograph,  $\text{Ag}_2\text{O}$  dark gray, and impregnation plastic appears as black. Compare with Fig. 3. Original magnification 1600X.

from electrodes charged part way to the potential peak indicated that small Ag particles were oxidized preferentially.

After an electrode had been charged and discharged several times at the 20-hr rate the Ag particles were present as large, granular particles and many had clumped together in agglomerates (Fig. 5 and 6). An electrode that had been cycled five times and had reached this condition is shown in Fig. 13 after being charged to the potential peak that precedes the second potential plateau. Much less  $\text{Ag}_2\text{O}$  was present on this electrode than was on the electrode shown in Fig. 12. The capacity which an electrode accepted before charge potential reached the peak that began the  $\text{Ag}_2\text{O}/\text{AgO}$  plateau decreased markedly during the first few cycles at the 20-rate. On the sixth charge this capacity was only one-third as large as on the first



Fig. 13.  $\text{Ag}_2\text{O}$  that formed on Ag during sixth charge when electrode was charged to the potential peak that begins  $\text{Ag}_2\text{O}/\text{AgO}$  potential plateau. Compare with Fig. 12 at the same magnification.

charge. The progressive decrease in the charge capacity accepted before reaching the potential peak was the result of the increase in size of the Ag particles that formed during the slow discharges. Figure 13 shows that the small particles had oxidized to a greater extent than the large particles. Although the large particles had convoluted surfaces which gave relatively large surface areas, only a small proportion of a large particle oxidized at the  $\text{Ag}/\text{Ag}_2\text{O}$  potential plateau despite the penetrating attack that had occurred on the surface of these particles. The large particles such as those shown in Fig. 13 did not oxidize extensively until charge potential rose to the  $\text{Ag}_2\text{O}/\text{AgO}$  plateau.

The appearance of an electrode after it was charged to oxygen evolution depended greatly on the size of Ag particles present before the charge began. At the end of the initial charge of a previously unused sintered silver electrode, most of the smaller Ag particles had disappeared while the larger particles had not been oxidized completely. Figure 14 illustrates, as well as one photograph can, the general appearance of an electrode at the end of the first charge. The size and distribution of the Ag particles varied from area to area. All of the remaining Ag particles were surrounded by a thin layer of  $\text{Ag}_2\text{O}$  with no clearly defined crystal structure. This  $\text{Ag}_2\text{O}$  was in turn surrounded by a more or less complete layer composed of relatively large AgO crystals which tended to have angular forms. Under polarized light it could be seen that what appears to be large AgO crystals in Fig. 14 actually consisted of several smaller crystals. Comparison of Fig. 14 to Fig. 3 and 12 shows that the AgO crystals tended to fill the voids originally present in the electrode. Complete oxidation of all Ag particles probably did not occur because AgO crystals blocked internal channels and formed tight coatings on the Ag, thus limiting access of the KOH solution to the Ag. No areas were found where  $\text{Ag}_2\text{O}$  and Ag alone were present at the end of a charge at the 20-hr rate.

A single discharge at the 20-hr rate resulted in sufficient change in Ag particle size that the appearance of the charged electrode at the second cycle had changed markedly. Many more large Ag particles remained at the end of the second charge than had

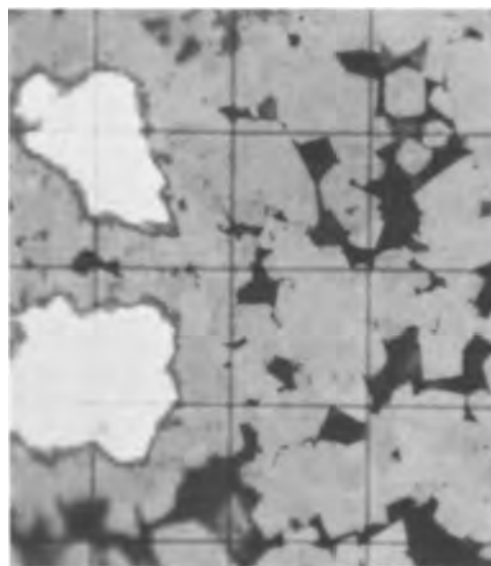


Fig. 14. Oxides present after oxygen evolution began at end of first charge of a sintered Ag electrode. At left are two Ag particles (lightest shade) that had not oxidized completely. Most of the electrode consisted of AgO crystals (medium gray). A thin layer of  $\text{Ag}_2\text{O}$  (dark gray) separated Ag from AgO. Impregnation plastic appears as black. Original magnification 1600X.

remained at the end of the first charge, and no large areas were found that consisted of AgO without Ag such as the area shown on the right half of Fig. 14. As the large clumps of AgO were reduced to Ag<sub>2</sub>O and then to Ag during discharge, Ag particles tended to form in groups with the result that large voids occurred adjacent to the particles. Changes continued to take place during the next few cycles at the 20-hr rate as the Ag particles clumped together into agglomerates. A typical view of the changes that have occurred after several cycles is shown in Fig. 15 for the sixth charge. The charged electrode had changed from a closely joined mass of AgO crystals with numerous small voids in the AgO (Fig. 14) to a structure of large voids and clumps of Ag surrounded by AgO, with very little porosity in the AgO (Fig. 15). Many of the Ag particles which remained at the end of the sixth charge were still joined where they had grown together during earlier discharges. Small particles also remained, but were less common. Every area of AgO crystals had formed as a dense but not very thick layer around the Ag. As always, a thin layer of Ag<sub>2</sub>O separated the Ag from the AgO. Oxides had formed on the surface of small voids within the large Ag particles. Presumably the small voids within the Ag had been formed when adjacent Ag particles grew together. On the first charge the growth of AgO had been much more extensive than the growth shown in Fig. 15 and gave the appearance of having attacked the Ag to a greater depth. More AgO formed on the first charge because a large portion of the Ag particles in the unused electrode was small. When Ag particles had grown larger after slow discharges, less oxidation was required to cover the large particles with an AgO layer that limited access of electrolyte to the Ag.

Additional cycles at the 20-hr rate gave comparatively little further change. The main difference between the electrode that had been cycled over 200 times and an electrode cycled five or six times was in the large voids that had formed with the additional cycling (Fig. 16) although there was also more variation in Ag particles from one area to another. Most areas resembled Fig. 15 or the left half of Fig. 14, depending on whether the area had been one of small or large Ag before the charge.

Only one type of silver electrode was used in the present investigation, since the purpose did not in-



Fig. 15. Electrode appearance after oxygen evolution began at end of sixth charge. The large Ag particles that had formed during slow discharges did not oxidize as extensively as the small Ag particles originally present. Compare with Fig. 14 at the same magnification.

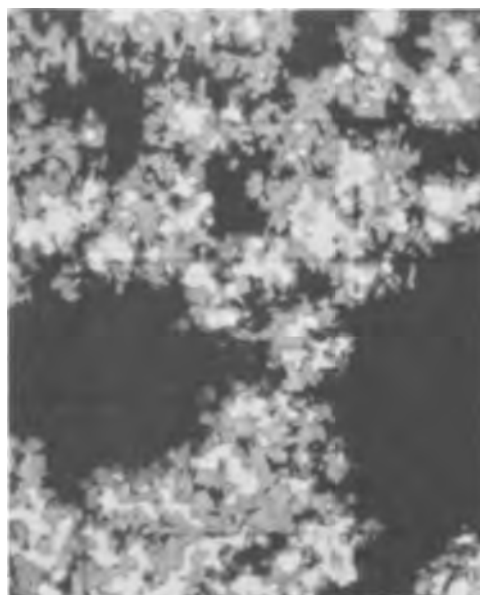


Fig. 16. Large voids present in electrode charged to oxygen evolution on cycle 218. Compare with Fig. 14 and 15 but note difference in magnification. Original magnification 400X.

clude studying effects of different initial electrode structures. The changes that occurred in the first few charge-discharge cycles suggested that small changes in the average size of the particles used in manufacturing Ag electrodes for secondary cells would only have an effect on capacity of the initial few cycles when the 20-hr rate was used for discharges, because of the tendency to form a limited size range of Ag particles as AgO was reduced during discharge. A large increase in starting particle size should be avoided because capacity would be decreased significantly as a result of the smaller surface area available for oxidation during charge.

### Summary

In an unused sintered Ag electrode particle sizes ranged from approximately 0.5–100 $\mu$ , with most particles having their smallest dimension in the range 1.5–2 $\mu$ . After the first charge to oxygen evolution and discharge back to Ag using the 20-hr current most Ag was present as large granular particles in the size range 10–25 $\mu$  although smaller and larger particles were also present. Electrode capacity decreased during the first five cycles as large granular particles of Ag formed and clumped together.

Capacity loss was the direct result of large Ag particles forming during slow discharges in place of the small particles originally present. After about five discharges at the 20-hr rate particle appearance did not change appreciably, and capacity gradually stopped decreasing. The large particles residual from the unused electrode gradually decreased in size and number because of continued attack at their surfaces. An electrode cycled over 200 times had many granular particles approximately the same size as those formed during the first discharge, although small dendritic Ag crystals were also common.

Most voids in the unused electrode were quite small and well distributed, but the voids became significantly larger with repeated cycling, and the electrode increased in thickness. The original cross section of the Ag grid greatly decreased as the result of penetrating attack in an electrode cycled over 200 times, but conductivity was still good.

Small Ag particles were oxidized more readily and more extensively than large particles. At the end of the first charge to oxygen evolution, most of the smaller Ag particles originally present had oxidized completely to AgO. A single discharge at the 20-hr rate resulted in sufficient particle size change that many more

large particles remained at the end of the second charge than at the end of the first. During the fifth charge an electrode accepted only three-fourths as much capacity as during the first charge, and only one-third as much Ag<sub>2</sub>O formed before potential rose and AgO began to form. The Ag particles that remained at the end of a charge were always surrounded by a thin layer of Ag<sub>2</sub>O with no clearly defined crystal structure. This Ag<sub>2</sub>O was surrounded by a layer of relatively large AgO crystals.

Manuscript submitted June 7, 1968; revised manuscript received July 20, 1968. This paper was presented at the Montreal Meeting, Oct. 6-11, 1968, as Paper 372.

Any discussion of this paper will appear in a Discussion Section to be published in the June 1969 JOURNAL.

## REFERENCES

1. A. C. Simon, *Electrochem. Technol.*, **1**, 82 (1963).
2. A. C. Simon and E. L. Jones, *This Journal*, **102**, 279 (1955).
3. A. C. Simon, *ibid.*, **114**, 1 (1967).
4. A. C. Simon, *ibid.*, **109**, 760 (1962).
5. S. Yoshizawa and Z. Takehara, *J. Electrochem. Soc. Japan*, **31**, 91 (1963).
6. J. A. Allen, *Australian J. Chem.*, **14**, 20 (1961); "Proc. First Australian Conf. Electrochem. Feb. 1963," p. 72, Pergamon Press, N. Y. (1965).
7. T. P. Dirkse and B. Wiers, *This Journal*, **106**, 284 (1959).
8. C. P. Wales and J. Burbank, *ibid.*, **106**, 885 (1959).
9. C. P. Wales and J. Burbank, *ibid.*, **112**, 13 (1965).
10. C. P. Wales and A. C. Simon, To be published.

## The Formation and Characterization of the Tetrahydroxyargentate (III) Ion in Alkaline Solution

G. L. Cohen\*<sup>1</sup> and G. Atkinson

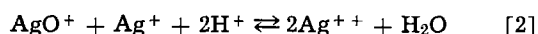
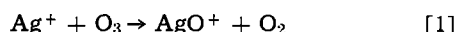
U. S. Naval Ordnance Laboratory, White Oak, Maryland, and  
Department of Chemistry, University of Maryland, College Park, Maryland, respectively

## ABSTRACT

When smooth silver metal is anodically oxidized in 12M KOH solution at 70 ma/cm<sup>2</sup>, a solution containing silver all in the +3 oxidation state results. The Ag (III) species was shown to be Ag(OH)<sub>4</sub><sup>-</sup> by a polarographic method involving the variation of half-wave potential with ligand concentration.

Except for complexes with periodate (1) or tellurate (2), the literature contains no direct evidence for the presence in alkaline solution of a species of silver with an oxidation state higher than one. Dirkse (3) postulated the presence of a species of silver (II) in basic solutions resulting from AgO dissolution. However, by measurement of the magnetic properties of such solutions, McMillan (4) showed that no silver (II) species was present. He postulated the existence of the species Ag(OH)<sub>4</sub><sup>-</sup>, but offered no direct proof for the existence of this ion. Yost (5) showed kinetic evidence for a transient Ag (III) species, formed during Ag (I) catalyzed persulfate oxidation of Cr (III) (5), ammonia (6), and VO<sup>++</sup> (7), and Carman (8) came to the same conclusion when he studied the auto-oxidation of (NH<sub>4</sub>)<sub>2</sub>S<sub>2</sub>O<sub>8</sub> in the presence of Ag (I). Other workers (9-11) have interpreted similar results in terms of Ag (II) and sulfate radical ion (SO<sub>4</sub><sup>-</sup>) intermediates, rather than a silver (III) species.

A series of papers by Noyes and co-workers (12-16) published between 1935 and 1937 described a detailed study of the chemistry of higher oxidation states of silver in acid solution. In the first of these (12), they showed that ozone oxidizes AgNO<sub>3</sub> in nitric acid solution to AgO<sup>+</sup>, which reacts with Ag<sup>+</sup> according to the following mechanism



They further showed (13) that the silver in the salt produced in the above reaction is almost all in the plus two oxidation state when the concentration of nitric acid is between 1 and 4M. This was demonstrated by titration with TiNO<sub>3</sub> which is oxidized by silver (II) but not by concentrated nitric acid. Dundon

and Gryder (17) studied the kinetics of this silver (II)-thallium (I) reaction. They reported that the oxidation to thallium (III) could occur by means of a mechanism involving silver (III) and equilibrium reaction [2], with direct oxidation of thallium (I) to thallium (III). They prefer, however, a mechanism involving two one-electron steps with thallium (II) and the NO<sub>3</sub><sup>-</sup> free radical as intermediates.

When AgO, which is a mixed oxide containing equimolar amounts of Ag (I) and Ag (III) (18), is dissolved in acid solution, the silver is found to be all in the plus two oxidation state (19). AgO is only slightly soluble in alkaline solution (20), but reacts, in the presence of a coordinating ligand such as periodate (21), to form a silver (III) complex stable in alkaline solution. This difference in behavior in acid and in alkali media is in agreement with Eq. [2], which shows that Ag (II) which is present in acid, disproportionates to Ag (I) and Ag (III) in alkaline solution.

This present research was initiated as part of an investigation of the chemistry and electrochemistry of higher oxidation states of silver in alkaline solution, especially in relation to the behavior of silver oxide as an alkaline battery cathode material. Casey and Moroz (22) reported the electrochemical formation of Ag<sub>2</sub>O<sub>3</sub> when sheet silver metal is electrically oxidized at 15 ma/cm<sup>2</sup> at -40°C in eutectic KOH-H<sub>2</sub>O. At higher temperature, or at lower current density, they found only AgO. Kazakevich, Yablokova, and Bagot'skii (23) demonstrated that Ag<sub>2</sub>O<sub>3</sub> was formed during asymmetric anodization of silver metal at relatively high current density. However, neither paper discusses the possibility of formation of a soluble silver (III) species. On the basis of preliminary results, Hills (24) suggested that a colored solution containing a species of silver in an oxidation state higher than plus one could be formed in concentrated potassium hydroxide solution by electrical oxidation of silver metal at high current density. He did not define the conditions for formation of this species nor did he know the oxi-

\* Electrochemical Society Active Member.

<sup>1</sup> Present address, Gillette Research Institute, Rockville, Maryland 20850.

dation state of silver which was present. The object of the research described herein was to prepare such a soluble species, ascertain the oxidation state of the silver contained in it, and determine the stoichiometry of the species.

### Experimental

**Chemicals.**—Potassium hydroxide solutions were prepared, except where otherwise indicated, from Baker Analyzed 45% potassium hydroxide solution which was analyzed by acidimetric titration and found to be 12.00M. The silver foil used was Handy and Harman sheet fine silver (1 mil thick), and the silver powder was Handy and Harman Silpowder 120. Potassium metal, 99.99% pure, was supplied by the United Mineral and Chemical Corporation. The metal was sealed under argon in specially made double-tipped glass ampoules containing 20g of potassium. All other chemicals used were Baker Analyzed reagents.

Water used in these experiments was redistilled from alkaline permanganate solution.

Potassium bis(periodato) argentate (III)  $[K_3H_4Ag(IO_6)_2 \cdot 3H_2O]$  was prepared as described by Cohen and Atkinson (21).

The saturated  $KIO_4$  solution used for colorimetric determinations was analyzed by iodimetric titration and found to be  $3 \times 10^{-2}M$ . (This solution is designated solution B.)

**Equipment used.**—The d-c power supply used for preparation of silver (III) solutions, was model 865B of Harrison Laboratories, Incorporated, and has a range from 0 to 0.6 amp and from 0 to 40v.

Polarographic measurements were made on a Metrohm Polarecord Model E261 with a rotating platinum microelectrode and a saturated calomel reference electrode. The glove box used was manufactured by the Kewaunee Scientific Equipment Corporation, and was modified so that electrical connections for polarography and electrolysis could be made from the interior without openings in the box.

Temperature for the polarographic runs was controlled by use of a Bronwill constant temperature circulator.

Spectra were measured on a Perkin-Elmer Model 202 uv-visible dual beam recording spectrophotometer. Absorptivity measurements for the colorimetric determinations of silver (III) were made on a Beckman Model DU spectrophotometer with photomultiplier and DU power supply attachments.

**Preparation of tetrahydroxyargentate (III) solutions.**—The silver (III) species was prepared by anodizing a silver electrode at a current density of 70 ma/cm<sup>2</sup> of smooth silver surface (apparent area) against a platinum strip in 45% KOH solution. A cell, such as is illustrated in Fig. 1, was used in order to separate the anode and cathode compartments.

The electrolysis was carried out until the solution in the compartment containing the silver anode had become yellow and contained a black suspension. In no case did the yellow color migrate through the U-tube into the compartment containing the platinum cathode. On completion of electrolysis, the solution in the anode compartment was filtered through a fine porosity fritted glass filter, yielding a clear yellow solution (solution A) and a black residue.

**Preparation of solutions for spectral measurements.**—Solutions for measurement of spectra of bis(periodato)argentate (III) were prepared as follows: 0.0120g of  $K_3H_4Ag(IO_6)_2 \cdot 3H_2O$  was added to a 25 ml volumetric flask. The solution was brought to volume with water and a 5 ml portion was rediluted to 50 ml with water, yielding a solution  $6.58 \times 10^{-5}M$  (solution 1). For measurement of spectrum of bis(periodato) argentate (III) formed from solution A, the following method was used. To 20 ml of solution B was added 5 ml of solution A, and the mixture diluted to 25 ml with water. A 5 ml aliquot was diluted to 50 ml with water (solution 2).

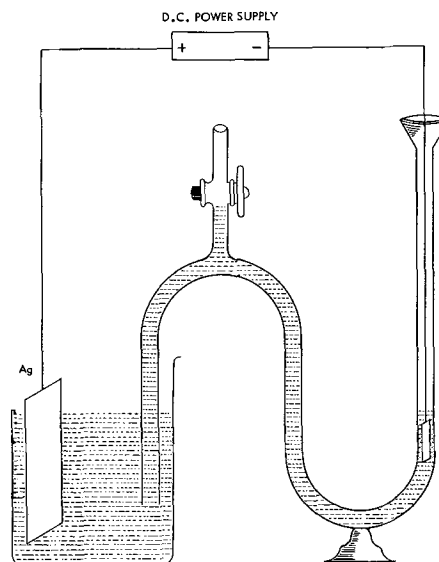


Fig. 1. Cell for silver (III) formation

Solutions for the measurement of spectra of diluted samples of solution A were prepared as shown in Table I. The required amount of 45% KOH solution was added to each volumetric flask, and the flask was filled to within 2 ml of volume with water. A 1 ml portion of solution A was added to each flask just before measurement of the spectrum, and the solution was brought to volume with water. A blank, consisting of a KOH solution of the same concentration as the solution whose spectrum was being studied was prepared in advance and used as a reference in the determination of the spectra of the silver (III) solutions. The exact concentration of silver (III) in solution A used for these spectral measurements was determined by a colorimetric method described below prior to each spectral measurement.

**Preparation of solutions for test of Beer's law for bis(periodato)argentate (III).**—To 15 ml of solution B in a 25 ml volumetric flask was added 0.0195g of  $K_3H_4Ag(IO_6)_2 \cdot 3H_2O$ . To this solution was added 5 ml of 45% KOH solution, and the solution brought to volume with solution B (solution 3). Into a 25 ml volumetric flask was placed 5 ml of 45% KOH solution, and the solution brought to volume with solution B (solution 4). Solutions 3 and 4 were mixed in 50 ml volumetric flasks as shown in Table II and the solutions brought to volume with water. The absorbance of each of the ten solutions was measured at 362 m $\mu$  using water as a reference. From these solutions, the absorptivity of the complex silver (III) salt was found to be constant over the range studied. Solutions prepared in the same manner as solution 2 were used to routinely determine the concentration of silver (III) in preparation of solution A.

**Gravimetric silver chloride analysis.**—Concentrated nitric acid was added dropwise to 150 ml of solution A contained in a 600 ml beaker in an ice bath until

Table I. Tetrahydroxyargentate (III) solutions for spectral measurements

Series 1 Solutions diluted to 100 ml with water (ml 45% KOH added)	Series 2 Solutions diluted to 50 ml with water (ml 45% KOH added)	Series 3 Solutions diluted to 25 ml with water (ml 45% KOH added)	[KOH] in final solution, M
3	1	0	0.48
7	3	1	0.96
11	5	2	1.44
15	7	3	1.92
19	9	4	2.40
Approximate concentration of Ag (III)			
$2.8 \times 10^{-5}M$	$5.6 \times 10^{-5}M$	$11.2 \times 10^{-5}M$	

Table II. Solutions for test of Beer's law in bis(periodato) argentate(III)

(Each solution diluted to 50 ml with water)		
ml Solution 3	ml Solution 4	Concentration of bis (periodato) argentate (III), M
0.5	4.5	$1.07 \times 10^{-5}$
1.0	4.0	$2.14 \times 10^{-5}$
1.5	3.5	$3.21 \times 10^{-5}$
2.0	3.0	$4.28 \times 10^{-5}$
2.5	2.5	$5.35 \times 10^{-5}$
3.0	2.0	$6.42 \times 10^{-5}$
3.5	1.5	$7.49 \times 10^{-5}$
4.0	1.0	$8.56 \times 10^{-5}$
4.5	0.5	$9.63 \times 10^{-5}$
5.0	0	$1.07 \times 10^{-4}$

the solution was clear and colorless. To this solution was added about 0.1 ml of concentrated HCl solution. The resultant AgCl precipitate was digested on a steam bath for 3 hr, and recovered by decanting most of the liquid and filtering the remainder of the hot solution through a fine porosity, fritted glass filter crucible. The hot filtrate and decantate, were combined and diluted with about 100 ml of water, whereupon further AgCl precipitated. This was digested for 3 hr on a steam bath and recovered in the same filter crucible used for the first AgCl precipitate. Further dilution yielded no additional AgCl. The precipitate was washed with  $10^{-3}M$  HCl and dried to constant weight. The validity of the method was demonstrated by dissolving silver nitrate in water and mixing the solution with 150 ml of 45% KOH solution so that the amount of silver in the solution was about the same as the amount of silver (III) in solution A. This suspension of silver (I) oxide in 45% KOH solution was treated in the manner described for solution A, and the gravimetric determination showed that all of the silver put in the solution was recovered as silver chloride.

**Redox method using silver metal.**—To 100 ml of solution A in a 250 ml beaker was added about 0.1g of silver metal powder weighed exactly. The mixture was set in the dark for 18 hr, after which time 1 drop of Sterox surfactant solution was added in order to facilitate washing of the silver metal powder from the beaker. The solution was filtered through a tared, fine porosity, fritted glass filter crucible and washed with about 50 ml of 1:20 ammonia solution. The solid silver metal remaining behind was dried to constant weight, and the amount of silver metal that had reacted with solution A was determined by difference.

**Polarographic analysis.**—A solution 1.0M in KOH was prepared by dilution of 20.82 ml of 45% KOH solution to 250 ml with freshly boiled distilled water. This solution was electrolytically oxygenated using two platinum electrodes with the cell shown in Fig. 1. Electrolysis at 0.5 amp was carried out for about 1.5 hr, and the solution in the anode compartment (solution 5) was used for polarography. To a 100 ml portion of solution 5 was added about 1g of  $Ag_2O$ , and the mixture was stirred for 3 hr, after which it was filtered through a fine porosity fritted glass filter, yielding a clear solution (solution 6). By diluting 20.9 ml of solution A to 250 ml with water, a silver (III) solution with the same concentration of KOH as solutions 5 and 6 was prepared (solution 7). Polarograms were recorded for solutions 5, 6, and 7 in the potential span between +0.5 and -0.5v vs. a saturated calomel electrode (SCE) using a rotating platinum microelectrode. The SCE was prepared using redistilled mercury and was separated from the solution by an agar gel- $KNO_3$  salt bridge.

**Concentration of silver (III).**—Solutions of KOH concentration 1.2, 3.0, and 6.0M were prepared by dilution of 45% KOH solution with freshly boiled distilled water. Silver metal was anodically oxidized in these solutions using the cell shown in Fig. 1. After

electrolysis for 1.5 hr at 71 ma/cm<sup>2</sup>, the solution in the anode compartment was filtered. The filtered solution was analyzed for silver (III) using a modified version of the colorimetric method, so that the concentration of KOH,  $KIO_4$ , and silver (III) in the solutions used for absorbance measurements was within the limits of Beer's law applicability.

**Identification of silver (III) species by polarography.**—Solution A was prepared in the glove box under  $CO_2$  free argon atmosphere using the cell shown in Fig. 1. A solution of 2.4M  $KNO_3$  was prepared by dissolving 121.3g of  $KNO_3$  in 500 ml of water. Solutions for polarographic runs at two different constant ionic strengths of 1.2 and 2.4M were prepared using 12.00M KOH solution, 2.4M  $KNO_3$  solution, and solution A, and polarograms were run at 27.2°C in the glove box on each solution immediately after its preparation. The rotating platinum microelectrode used was cleaned in concentrated nitric acid after each polarogram was recorded. The concentration of silver (III) in the solutions was determined by use of the colorimetric method on solution A.

**Preparation of carbonate free potassium hydroxide solution.**—Carbonate-free potassium hydroxide solutions were prepared in the glove box under an atmosphere of argon fed into the box through a cylinder containing Fisher "Indicarb"  $CO_2$  absorbant material. Argon was passed through the box constantly during all work in which it was used, and a positive pressure of argon was maintained in the box at all times.

Water for use in preparation of carbonate-free potassium hydroxide solution was prepared by boiling doubly distilled water under vacuum for 5 min, sealing the boiling container while still hot, and placing the container in the glove box. An ampoule containing 20g of potassium metal, a small heater made especially for the potassium ampoule, a 50 ml graduated cylinder, a propipette bulb, a fine porosity fritted glass filter crucible, a filter flask, the cell shown in Fig. 1 including a 15 ml beaker, and the apparatus shown in Fig. 2 along with a sufficient number of beakers, spatulas, and clamps were placed in the glove box, and the box was flushed with argon for 14 hr. After this time, the tips were broken off of the double tipped ampoule containing potassium, the ampoule was placed in the heater, and the potassium melted and collected in a beaker. Into the cell shown in Fig. 2 was placed 36 ml of water, and ice-cold water was circulated through the glass jacket for about 3 hr. The silver funnel tube was placed in the polyethylene cup, and small pieces of potassium metal were dropped into the water using a stainless steel spatula. The silver tube protected the polyethylene cup from the potassium metal, and the funnel prevented solution from splattering due to the violent reaction between water and potassium. After about 6 hr, the 20g of potassium had been added to the solution, yielding a solution which

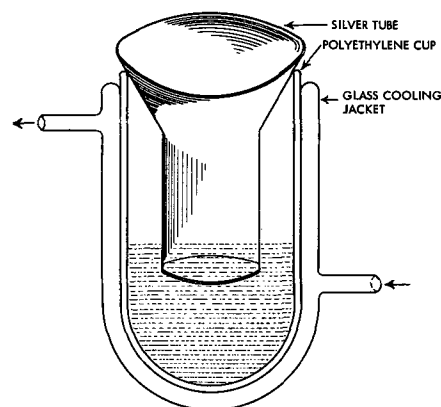


Fig. 2. Cup for preparation of carbonate-free KOH solution

was found, by acidimetric analysis, to be 11.7M KOH. About 35 ml of solution were produced (solution C).

The cell shown in Fig. 1 was filled with solution C, and electrolysis with silver metal was performed at about 0.5 amp for 45 min. The solution was filtered, and the concentration of silver (III) in the solution was determined colorimetrically. To a second preparation of solution C was added 0.02g of  $K_2CO_3$ , and electrolysis was performed as before. Electrolysis was also performed in the same manner using Baker Analyzed 45% KOH solution.

**Polarographic study of effect of carbonate on silver (III).**—The concentration of carbonate in Baker Analyzed 45% potassium hydroxide solution was estimated by adding known amounts of  $K_2CO_3$  to a series of 45% KOH solutions and measuring the absorptivity at 226  $m\mu$ , where  $CO_3^{2-}$  has a sharp absorbance peak, using freshly boiled water as a reference. A Perkin-Elmer Model 202 dual beam recording spectrophotometer with range-extending filters in the reference beam was used for these experiments.

Solutions of  $KNO_3$  and  $K_2CO_3$ , such that the total ionic strength was 1.0M, with the  $K_2CO_3$  concentration varying from 0.28M to 0, were prepared in the glove box. A series of solutions for polarographic study were prepared by mixing 5 ml of each of the above  $K_2CO_3$ - $KNO_3$  solutions with 5 ml of freshly prepared solution A in a 10 ml volumetric flask and diluting to volume with water, so that the final concentrations were as shown in Table III. Polarograms were run on each solution in the glove box at a constant temperature of 27.2°C in the potential span from +0.75 to -0.25v vs. SCE.

### Results

**Presence of silver (III).**—Solution A was a clear yellow solution, and, immediately after preparation, contained no colloidal matter, as evidenced by the lack of Tyndall light scattering in the solution. When some solution A was added to a saturated solution of potassium periodate, a deeper yellow colored solution resulted. This solution exhibited absorption maxima at 362 and 255  $m\mu$ , which corresponded with the spectrum previously reported by Cohen and Atkinson (21) and by Papalardo and Losi (25) for solutions of bis(periodato)argentate (III) salts. The maximum at 215  $m\mu$  previously reported for these salts may have been obscured by the presence of a strong absorption due to excess periodate at 221  $m\mu$  (26). Figure 3 shows a comparison of the spectrum of a solution of a bis(periodato)argentate (III) salt with a spectrum resulting from the reaction of solution A with periodate. This spectral comparison shows that a silver complex was formed when solution A was treated with a solution containing a ligand which stabilizes silver (III). This implied that silver (III) was present in solution A. By use of a colorimetric method, a wet chemical redox method, and polarographic method, all of the silver in solution A was shown to be in the plus three oxidation state.

**Demonstration of silver (III) as the only oxidation state of silver present.**—**Colorimetric method.**—Potassium bis(periodato)argentate (III) was prepared

Table III. Solutions for polarographic study of effect of carbonate on silver (III)

[KOH] = 6M in each solution [Silver (III)] = $1.06 \times 10^{-3}M$ in each solution Total ionic strength of each solution = 6.5M	
[ $K_2CO_3$ ] M	[ $KNO_3$ ] M
$3.1 \times 10^{-3}$	0.05
$4.7 \times 10^{-3}$	0.49
$19.8 \times 10^{-3}$	0.44
$86.4 \times 10^{-3}$	0.24
$169.7 \times 10^{-3}$	0

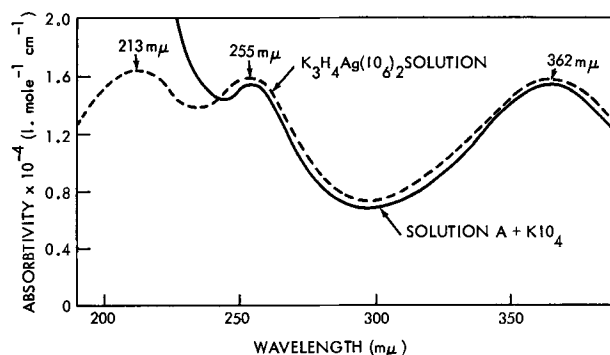


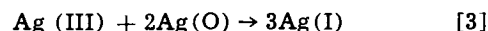
Fig. 3. Spectra of bis(periodato)argentate formed in two ways

by reaction of AgO with  $KIO_4$  in alkaline solution (21). This salt was found to obey Beer's law at 362  $m\mu$ , with a molar absorptivity of  $1.52 \pm 0.03 \times 10^4$  l mole<sup>-1</sup> cm<sup>-1</sup> when the total concentration of periodate was about  $2 \times 10^{-3}M$ , the concentration of hydroxide was about 0.25M, and the concentration of the silver salt was between  $10^{-5}M$  and  $10^{-4}M$ . All colorimetric measurements were made using solutions of the above concentrations. Thus, when some solution A was quantitatively diluted with periodate solution so that the final solution concentrations were as above, the concentrations of silver in solution A which reacted to form the complex could be determined. The total concentration of silver in solution A could be determined gravimetrically as chloride. For two typical preparations of solution A, the concentrations of silver found by each method were as follows:

	Gravimetric chloride M	Colorimetry M
Preparation 1	$3.16 \times 10^{-3}$	$3.21 \times 10^{-3}$
Preparation 2	$3.31 \times 10^{-3}$	$3.38 \times 10^{-3}$

The agreement between the methods of analysis showed that all of the silver in solution A reacted with the periodate to form the silver (III) complex compound.

**Redox method.**—The silver (III) present in AgO oxidizes silver metal to silver (I) oxide (27). Therefore, a silver (III) species present in solution might oxidize silver metal to silver (I) according to the general reaction



Assuming the stoichiometry of reaction [3], the amount of silver (III) present in solution A could be determined as previously described. The total concentration of silver was again determined by gravimetric analysis as chloride. The concentrations of silver found for two typical preparations of solution A were as follows:

	Gravimetric chloride M	Reaction with silver metal M
Preparation 3	$0.98 \times 10^{-3}$	$1.00 \times 10^{-3}$
Preparation 4	$1.02 \times 10^{-3}$	$1.04 \times 10^{-3}$

This agreement between these two analyses showed that all of the silver in solution A was in the form of silver (III).

The agreement of the gravimetric analysis with both the redox analysis and the colorimetric determination shows that the colorimetric method can be used to determine the amount of silver (III) present in solution A. This colorimetric method was used routinely for the determination of silver (III) concentration in subsequent work.

**Polarographic method.**—During the preparation of solution A, oxygen was evolved at the anode, and so the solution contained some dissolved oxygen. Silver (III) oxidizes  $NH_4OH$  to  $N_2$  and  $NO_3^-$  (28), and, there-



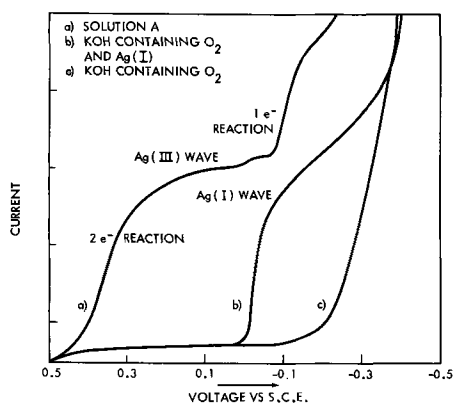


Fig. 4. Polarographic curves in 1M KOH solution

fore, might possibly oxidize  $N_2$  to  $NO_3^-$ . Thus, the following experiments were performed without passing  $N_2$  through the solutions to remove dissolved oxygen. In order to test whether the oxygen would affect the polarographic results, oxygen was dissolved in a potassium hydroxide solution by electrolysis using cell A with two platinum electrodes. Polarograms were run on solutions diluted with water so that the concentration of KOH was a constant 1.0M. Figure 4 shows a typical series of results. Curve c is a polarogram run on oxygenated KOH solution, and illustrates that the oxygen reduction wave will not interfere with the results. Curve b is a polarogram run on 1.0M KOH solution containing oxygen and silver (I), prepared by dissolving silver (I) oxide in it. There is one wave preceding the oxygen wave at about  $-0.1$  vs. SCE, which is close to the value reported by Amlie and Ruetschi (20) for the silver (I) half-wave potential. Curve a is a polarogram run on a diluted portion of solution A. Two waves are seen in this curve. The second is close to the potential of the silver (I) wave in curve b. The first wave, occurring at a more positive potential, is twice the height of the second. Thus, if the solution initially contained only one species which is polarographically reduced in the range of potential scanned, and the second wave is due to the one electron reduction of silver (I) to silver (0), then the first wave corresponds to a two-electron reduction process. This can be ascribed to the reduction of silver (III) to silver (I). These results support the chemical and colorimetric results showing that all of the silver in solution A is in the plus three oxidation state. The concentration of silver in the solution used for curve a was determined by the colorimetric method to be  $1.86 \times 10^{-4}M$ .

The wide potential span of the silver (III) reduction wave (from about  $+0.46v$  to about  $0.15v$  vs. SCE) indicates that the reduction of silver (III) to silver (I) at the rotating platinum electrode is irreversible.

**Spectra.**—Solution A is a clear yellow solution and exhibits one absorption maximum in the ultraviolet region of the spectrum shown in Fig. 5. For the range

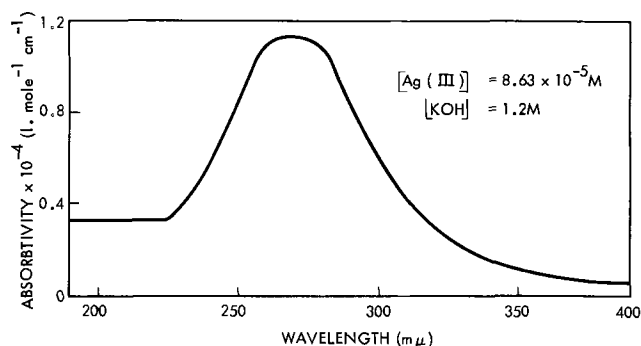


Fig. 5. Spectrum of silver (III) solution

of hydroxide and silver (III) concentrations studied, the wavelength of maximum absorption remains constant at  $271 m\mu$ , with a molar absorptivity of  $1.17 \pm 0.08 \times 10^4 l \text{ mole}^{-1} \text{ cm}^{-1}$ .

**Effect of carbonate on silver (III) species.**—An extrapolation of a plot of concentration of carbonate added to Baker Analyzed 45% potassium hydroxide solution vs. absorptivity at  $226 m\mu$  showed that the 45% KOH solution used for this experiment had a concentration of about  $6.2 \times 10^{-3} M K_2CO_3$ . Since this concentration is of the same order of magnitude as that of the silver (III) formed electrolytically, a series of experiments was performed to determine if the carbonate was coordinated with the silver (III) in solution. Preliminary experiments, performed with no control of atmosphere, had indicated that the addition of potassium carbonate to potassium hydroxide solution changed the amount of silver (III) formed. However, since potassium hydroxide solution absorbs carbon dioxide from the air, with conversion to carbonate ion, the concentration of carbonate in these preliminary experiments was not known. Carbonate was shown to have no direct effect on the silver (III) by use of carbonate free potassium hydroxide solution, and not to be coordinated with silver (III) by a polarographic method.

**Use of Carbonate-free potassium hydroxide solution.**—The same amount of silver (III) (about  $3 \times 10^{-3} M$ ), as determined by the colorimetric method, was electrolytically formed in carbonate-free potassium hydroxide solution (prepared by direct reaction of potassium metal with water) as in Baker Analyzed potassium hydroxide solutions containing carbonate. This indicated that carbonate is not necessary for formation of the silver (III) species.

**Polarographic resolution of carbonate problem.**—Crow and Westwood (29) describe a polarographic method for the study of complex ions in solution. The method is based on the shift in half-wave potential with changing concentration of coordinating ligand, while keeping total ionic strength constant. If the half-wave potential does not change, then the component of the solution whose concentration was varied is not a ligand. To investigate whether carbonate acts as a coordinating ligand with silver (III), six solutions in which the concentration of carbonate was varied from  $6.2 \times 10^{-3}M$  to  $1.7 \times 10^{-1}M$  were prepared. This work was carried out in the  $CO_2$  free argon atmosphere. The concentration of KOH was kept constant at 6M, and the total ionic strength was kept constant at 6.2M by use of potassium nitrate. The polarographic half-wave potential determined by a least squares fitting method did not vary for the six concentrations of carbonate studied. The half-wave potential was found to be  $+0.191 \pm 0.005v$  vs. SCE. This experiment showed that the carbonate was not a ligand which coordinates with silver (III) in the solutions studied. Similar results were obtained for 3 and 1.2M potassium hydroxide solutions.

All of the following experiments using potassium hydroxide solution were performed under  $CO_2$  free argon atmosphere.

**Concentration of silver (III).**—The variation of the concentration of silver with concentration of hydroxide ion is compared with the saturation concentration of silver (I) oxide reported by Amlie and Ruetschi (20) in Fig. 6. These results show that the concentration of the silver (III) species formed electrolytically increases with increasing hydroxide concentration, as opposed to the silver (I) species, dissolved in alkaline solution by mechanical shaking of silver (I) oxide, whose concentration reaches a maximum at about 6M KOH and then decreases at higher concentrations.

**Identification of tetrahydroxyargentate (III) species.**—The polarographic method for the study of complex

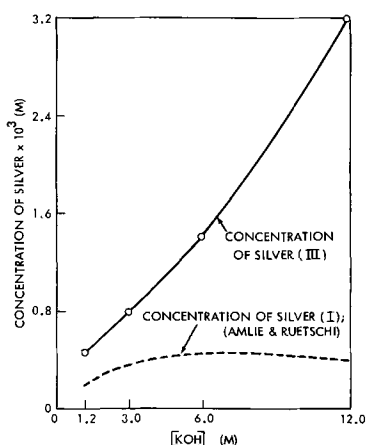


Fig. 6. Variation of concentration of silver with concentration of KOH.

ions in solution described by Crow and Westwood (29) was used to identify the silver (III) hydroxy species formed by electrolytic oxidation of silver metal in potassium hydroxide electrolyte.

A series of solutions with constant concentration of silver (III) and constant ionic strength maintained with  $\text{KNO}_3$ , but varying concentrations of potassium hydroxide was prepared, and a polarogram taken on each solution immediately after its preparation. The polarographic data was fitted by a least-squares method to the Heyrovsky equation for irreversible reactions

$$i = i_1 / [1 + \exp(\alpha n F (E - E_{1/2}) / RT)] \quad [4]$$

where:

- $i$  = current
- $i_1$  = polarographic limiting current
- $\alpha$  = measure of irreversibility
- $n$  = number of electrons per mole involved in the polarographic reaction
- $F$  = Faraday's constant
- $E$  = potential
- $E_{1/2}$  = polarographic half-wave potential
- $R$  = ideal gas constant
- $T$  = absolute temperature.

Experiments run at two different constant ionic strengths, 1.2 and 2.4M with the concentration of KOH ranging from 0.12 to 2.4M, gave the same results. Table IV shows the values of half-wave potential,  $E_{1/2}$ , and  $\alpha n$  found from the least squares curve fit. Values of  $\alpha$  were calculated assuming that the polarographic wave being studied represents a two-electron reaction, the reduction of silver (III) to silver (I) according to Eq. [5].

Table IV. Results of curve fit of polarographic data

[OH <sup>-</sup> ] M	$E_{1/2}$ , v vs. SCE	$\alpha n$	$\alpha$
(a) Total ionic strength = 1.2M, [Ag(III)] = $5.8 \times 10^{-3}$ M			
0.12	0.4273	1.234	0.617
0.24	0.3927	1.204	0.602
0.48	0.3698	1.198	0.599
0.60	0.3629	1.226	0.613
0.72	0.3413	1.246	0.623
0.96	0.3317	1.208	0.604
1.20	0.3140	1.190	0.595
(b) Total ionic strength = 2.4M, [Ag(III)] = $1.15 \times 10^{-4}$ M			
0.24	0.3977	1.228	0.614
0.48	0.3610	1.184	0.592
0.96	0.3435	1.238	0.619
1.20	0.3220	1.228	0.614
1.44	0.3180	1.232	0.616
1.92	0.3136	1.206	0.603
2.40	0.2977	1.240	0.620
		$1.218 \pm 0.018$	$0.609 \pm 0.009$

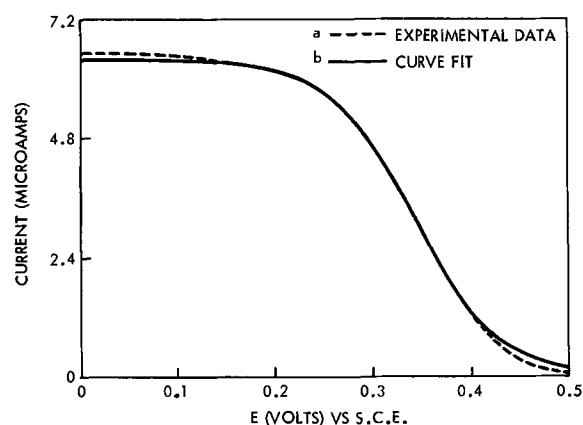
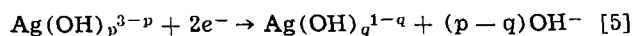


Fig. 7. Polarographic wave for silver (III)



$\alpha$  was found to be constant throughout the series of concentrations studied, and was determined to be  $0.609 \pm 0.009$ .

Figure 7 is an example of a typical polarographic run, and shows a comparison of the experimental data with a least-squares curve fit. Curve a is the experimental polarogram, and curve b was constructed using the values of  $E_{1/2}$ ,  $\alpha n$  and  $i_1$  determined by the least-squares curve fit.

Figure 8 is a plot of the half-wave potential of the silver (III) ion against the logarithm of the concentration of hydroxide ion, for the two ionic strengths used. The linearity of the data indicates that only one complex species is present in the solutions under study. The number of ligands is determined from the slope of the line, which is defined by

$$\frac{\Delta E_{1/2}}{\Delta \log C_{\text{OH}^-}} = \frac{-(p-q)2.303 RT}{\alpha n F} \quad [6]$$

where  $p$  and  $q$  are the ligand numbers shown in Eq. [5]. The slope was calculated by a least squares fit of the data and found to be  $-0.09975$ . The experiments were run at  $27.2^\circ\text{C}$ , and using the value of  $\alpha n$  shown in Table III,  $(p-q)$ , the difference in ligand number between the silver (I) and silver (III) species, was calculated to be  $2.041 \approx 2$ . Antikainen and co-workers (30) found that in 1.5M potassium hydroxide solutions, the silver (I) species present is  $\text{Ag}(\text{OH})_2^-$ , and they report that there is no evidence to show the presence of any other silver (I) species up to at least 5M KOH. Thus, the silver (III) species has a formula of  $\text{Ag}(\text{OH})_4^-$  based on the two ligand difference found from the slope in Fig. 8.

### Summary

When silver metal is electrolytically oxidized at about  $70 \text{ ma/cm}^2$  in potassium hydroxide solution, the silver (III) complex ion, tetrahydroxyargentate (III)

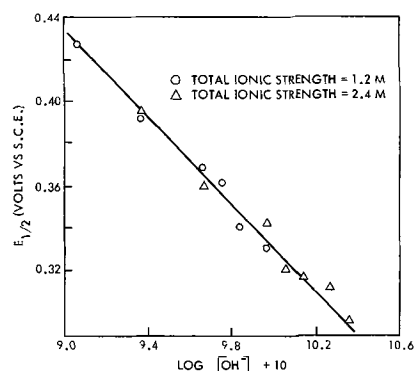


Fig. 8.  $E_{1/2}$  vs.  $\log [\text{OH}^-]$  for silver (III) at two total strengths



[Ag(OH)<sub>4</sub><sup>-</sup>] is formed. Solutions of the species are yellow, with an intense absorption band centered at 271 mμ ( $\epsilon = 1.17 \times 10^4$  l mole<sup>-1</sup> cm<sup>-1</sup>). The concentration of Ag(OH)<sub>4</sub><sup>-</sup> that can be formed increases with increasing KOH concentration between 1.2 and 12M. In 12M KOH solution, the concentration of Ag(OH)<sub>4</sub><sup>-</sup> is found to be  $3.2 \times 10^{-3}$ M, compared with  $0.39 \times 10^{-3}$ M reported for the silver (I) species Ag(OH)<sub>2</sub><sup>-</sup> in the same concentration of KOH. No evidence was found for coordination of silver (III) with carbonate.

Manuscript submitted May 21, 1968; revised manuscript received Aug. 9, 1968. This paper was presented at the Chicago Meeting, Oct. 15-19, 1967, as Paper 43. This paper was abstracted from a thesis submitted by one of the authors (G.L.C.) to the Faculty of the Graduate School of the University of Maryland in partial fulfillment of the requirements for the Ph.D. degree, 1967.

Any discussion of this paper will appear in a Discussion Section to be published in the June 1969 JOURNAL.

#### REFERENCES

1. L. Malatesta, *Gazz. Chim. Ital.*, **71**, 467 (1941).
2. L. Malatesta, *ibid.*, **71**, 580 (1941).
3. T. P. Dirkse and B. Wiers, *This Journal*, **106**, 284 (1959).
4. J. A. McMillan, *Nature*, **195**, 594 (1962).
5. D. M. Yost, *J. Am. Chem. Soc.*, **48**, 152 (1926).
6. D. M. Yost, *ibid.*, **48**, 374 (1926).
7. D. M. Yost and W. H. Claussen, *ibid.*, **53**, 3349 (1931).
8. P. C. Carman, *Trans. Faraday Soc.*, **30**, 566 (1934).
9. A. Malaguti, *Annal. Chim. (Rome)*, **41**, 241 (1955).
10. C. E. H. Bawn and D. Margerison, *Trans. Faraday Soc.*, **51**, 925 (1955).
11. A. J. Kalb and T. L. Allen, *J. Am. Chem. Soc.*, **86**, 5107 (1964).
12. A. A. Noyes, J. L. Hoard, and K. S. Pitzer, *ibid.*, **57**, 1221 (1935).
13. A. A. Noyes, K. S. Pitzer, and C. L. Dunn, *ibid.*, **57**, 1229 (1935).
14. A. A. Noyes and A. Kossiakoff, *ibid.*, **57**, 1238 (1935).
15. A. A. Noyes, C. D. Coryell, F. Stitt, and A. Kossiakoff, *ibid.*, **59**, 1316 (1937).
16. A. A. Noyes, D. DeVault, C. D. Coryell, and T. J. Deahl, *ibid.*, **59**, 1326 (1937).
17. R. W. Dundon and J. W. Gryder, *Inorg. Chem.*, **5**, 986 (1966).
18. V. Scatturin, P. L. Bellon, and A. J. Salkind, *This Journal*, **108**, 819 (1961).
19. J. A. McMillan and B. Smaller, *J. Chem. Phys.*, **35**, 1698 (1961).
20. R. F. Amlie and P. Ruetschi, *This Journal*, **108**, 813 (1961).
21. G. L. Cohen and G. Atkinson, *Inorg. Chem.*, **3**, 1741 (1964).
22. E. J. Casey and W. J. Moroz, *Can. J. Chem.*, **43**, 1199 (1965).
23. G. Z. Kazakevich, I. E. Yablokova, and V. S. Bagotskii, *Soviet Electrochem.*, **2**, 969 (1966).
24. S. Hills, Private communication.
25. R. Pappalardo and S. Losi, *Annal. Chim. (Rome)*, **54**, 156 (1964).
26. C. E. Crouthamel, H. V. Meek, D. S. Martin, and C. V. Banks, *J. Am. Chem. Soc.*, **71**, 3031 (1949).
27. R. D. Wagner, "A Method for the Analysis of the Silver Oxide Cathode," NOLTR 64-214, U. S. Naval Ordnance Laboratory, White Oak, Md. (1965).
28. W. F. Pickering, *Aust. J. Chem.*, **16**, 969 (1963).
29. D. R. Crow and J. V. Westwood, *Quart. Rev.*, **19**, 57 (1965).
30. P. J. Antikainen, S. Heitanen, and L. G. Sillen, *Acta. Chem. Scand.*, **14**, 95 (1960).

## Galvanostatic Transients in Passive Iron

J. H. Bartlett\* and J. R. Hudson

Department of Physics, University of Alabama, University, Alabama

#### ABSTRACT

Galvanostatic transients have been recorded for iron passive in 2N H<sub>2</sub>SO<sub>4</sub>. Comparison with the Dewald theory of anodic oxidation is made and this theory is found to be inapplicable because (i) space charge effects are important and (ii) the zero-field current varies much more rapidly than the theory predicts. Both overshoot and undershoot decay exponentially. (The overshoot disappears if the constant current is applied at a late stage of an open-circuit break.)

The nature and behavior of the layer (s) on passive iron are matters which still require experimental work and theoretical analysis. Even though both electrical (1) and optical (2) experiments have led to the conclusion that there is a layer, usually many atoms thick, on the surface of passive iron, the detailed mechanism of how ions move through this layer remains to be elucidated.

If we could explain quantitatively all the transient phenomena which occur, then we could be confident that we know what is actually happening. Such phenomena are the galvanostatic transients (potential vs. time at constant current), (ii) the potentiostatic transients (current vs. time at constant potential), (iii) optical transients (ellipsometric data vs. time), and (iv) the possible photoconduction due to irradiation by uv light.

The anodic passivation of iron shows features which are common to oxidation of tantalum and other metals. In particular, the galvanostatic oxidation curves for

iron in neutral solution and for tantalum (in general) look very much alike. Consequently, if we can devise an acceptable theory of anodic oxidation for any one metal, the chances are that it will have a great measure of validity for other metals.

The present work is concerned mainly with the presentation of further results on galvanostatic transients in iron and with the phenomenon of overshoot. New evidence is adduced which indicates that space charge effects are of importance.

#### Experimental Equipment and Procedures

Iron anodes were prepared from single crystals of pure iron purchased from Research Crystals, Inc., Richmond, Virginia. These crystals which came as rods 0.3 in. in diameter and 2 to 3 in. long were machined to form cylinders 0.20 in. in diameter and 0.20 in. high. A 1/16 in. hole was drilled through the axis to allow passage of a 1/16 in. steel rod which was used to make electrical contact with the sample and to hold the anode assembly together, as shown in Fig. 1. Teflon

\* Electrochemical Society Active Member.

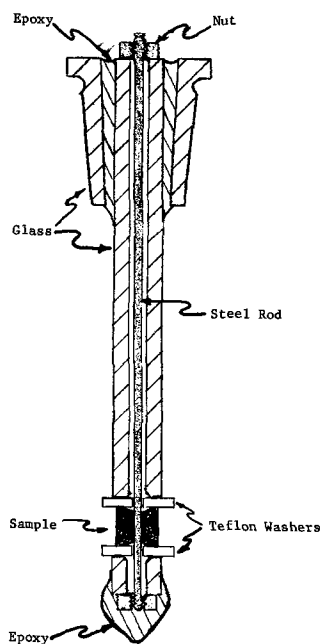


Fig. 1. Anode assembly

gaskets were used between the ends of the sample and the glass tubes, as shown. This was to prevent leakage of electrolyte around the edges of the sample and therefore changes of the surface area of the anode. The glass tube cap at the bottom of the assembly consists of a steel nut completely sealed from the electrolyte by many layers of epoxy. This cap is checked often for any leakage current by assembling the anode without a sample and testing it in the electrolyte for any current which might be leaking around or through the epoxy. The pressure on the gaskets is applied by adjusting the nut at the top of the assembly. This type of anode construction gave leak-tight anodes which have remained in continuous use for 15 days before leakage currents developed either at the edges of the sample or in the epoxy. Such leakage currents can be recognized by an increase in the steady-state current, which in a typical anode might increase from 9 to  $9.5 \mu\text{a}/\text{cm}^2$  in an hour while the current had been holding constant at  $9 \mu\text{a}/\text{cm}^2$  for days. The anode area exposed to the electrolyte was  $0.81 \text{ cm}^2$ . A design similar to this was first used by Feller and Osterwald (3).

The cell in which the anode was used consisted of a five neck-jacketed 500 ml flask equipped with standard tapered joints so that any neck being used could be sealed off. A reversible hydrogen electrode made from a square of platinized platinum foil, of approximately  $3 \text{ cm}^2$  surface area, was used at the cathode. A 0.1N mercurous sulfate electrode was used as a reference electrode for all potential measurements. The sulfate electrode was used so as to exclude the chlorine ion found in the calomel electrode.

To remove oxygen and other dissolved gases as well as to provide a stirring action, hydrogen gas was bubbled continuously through the electrolyte. It was introduced through a fritted glass diffusion tube at a rate of about  $5 \text{ cm}^3/\text{min}$  and allowed to escape through a tube submerged in water.

The electrolyte used was prepared from distilled water which had been subsequently passed through a Barnsted 8902 mixed bed demineralizer. The sulfuric acid used was of reagent grade. Unless otherwise noted data were taken in a  $2N \text{ H}_2\text{SO}_4$  electrolyte.

The circuit layout for all electrical measurements is shown schematically in Fig. 2. The potentiostat consists of a 25-ohm 10-turn Helipot in parallel with a bank of twelve 2v Willard rechargeable wet cells wired to produce 4v. The equivalent resistance of the potentiostat is approximately 10 ohms. A potentiostat

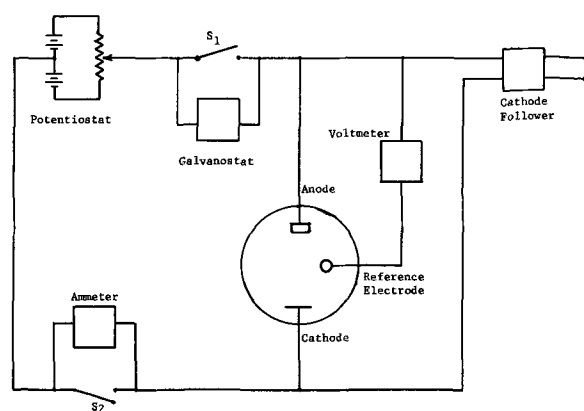


Fig. 2. Schematic circuit

of this type must be used with a reversible electrode as it does not directly control the anode reference potential.

The galvanostat consists of a variable resistor in series with a 180v battery bank. This arrangement holds the current constant within 0.5% for all transients of interest. Switching from potentiostatic conditions to galvanostatic conditions is accomplished by shorting out the galvanostat with switch  $S_1$ .

Potential measurements were made with a Keithley d-c VTVM Model 200B with an input impedance of more than  $10^{14}$  ohms. The current was measured with a Keithley Micro-Microammeter Model 414. This was removed from the circuit by closing switch  $S_2$ . Potential variations were recorded on a Sanborn Chart Recorder Model 7700 with a 8803A low level preamplifier capable of recording  $1 \mu\text{v}/\text{mm}$ . The rise time of the recorder was 20 msec for the potential variations which we recorded. Since this time is much shorter than the observed times (of the order of seconds) to the potential maximum, our plots show the potentials after all the transients have died out. A battery operated cathode follower with a bandwidth of over 100 kc was used to isolate the cell from the recording equipment. The follower used a 6F5 with a grid current of less than  $10^{-9}$  amp. The noise level at the recorder pen was about  $50 \mu\text{v}$ . This equipment was first assembled and used by Ord and Bartlett at the University of Illinois.

To take a series of measurements the equipment is turned on and allowed to stabilize. The anode is first passivated in a fresh acid solution and then transferred to the cell through which hydrogen has been bubbled for at least 12 hr. The potential is set at zero, with respect to the reference electrode, to allow the layer to be reduced to its smallest thickness. After about 1 hr the current has reached a constant value of about  $50 \mu\text{a}$ . The potential at which a measurement is to be taken is then set and the current is allowed to reach the steady-state value. After the measurement is taken new conditions are set and the anode again allowed to reach the steady-state. The time between measurements taken this way is from about 30-60 min. All voltages referred to in this paper are potential differences between the anode and the mercurous sulfate reference electrode.

### Dewald Theory of Transients

*Galvanostatic transients.*—With the anode initially passive and the constant steady-state current flowing, we may switch to a lower or a higher constant current. In the former case, the potential decreases rapidly to a plateau sloping downward and the anode eventually goes active. Figure 3 shows an example of this where the new applied current equals zero. If the applied current is greater than the steady-state value, one observes a rapid increase in the potential followed by a much slower exponential change in the opposite direction to a minimum, then the assumption

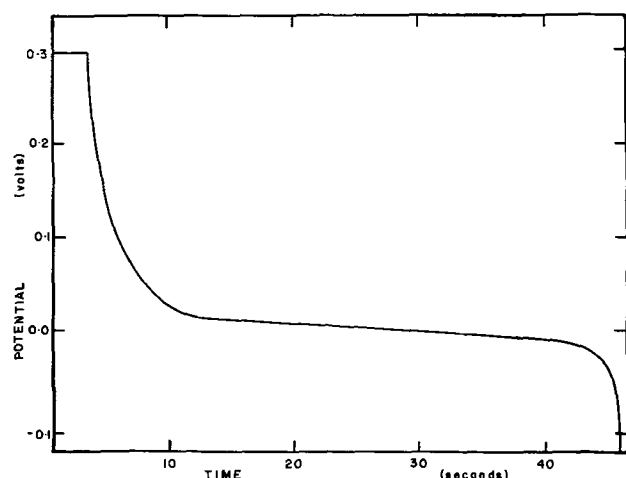


Fig. 3. Open-circuit break, potential vs. time

of a linear rise representing layer growth. This rise of the potential to a maximum and the subsequent decay to the final state will be defined as overshoot. If at some point along this transient the current is switched back to the steady-state value, the potential decreases rapidly, passes through a minimum and then increases to a new steady-state value. This decrease of the potential to a minimum and the subsequent increase to the steady-state value will be defined as undershoot. Figure 4 shows both an overshoot and undershoot transient, and particular values of  $V$  are labelled by appropriate symbols.

Originally, Cabrera and Mott (4) had assumed (A) that there is a high electric field present in the layer, (B) the layer is a uniform lattice, and (C) that only one type of ion is mobile and moves by jumps from one interstitial position to the next. On this basis, they obtained the following relation for the current at any point in the layer

$$i = q\mu_0 n e^{\beta E} \quad [1]$$

where  $q$  is the charge on the ion,  $\beta = aq/kT$ , with  $k =$  Boltzmann's constant,  $T =$  absolute temperature, and  $a$  the "jump distance,"  $2a$  is the distance between successive interstitial positions,  $\mu_0 = 2a\nu e^{-aU/kT}$ ,  $\nu$  is the vibrational frequency of the ion,  $U$  is the activation energy for motion between interstitial positions in the absence of the electric field,  $E$  is the electric field,  $n$  is the concentration of mobile ions.

Furthermore, using Poisson's equation and the equation of continuity one can derive the following relation between the internal current,  $i$  the external cur-

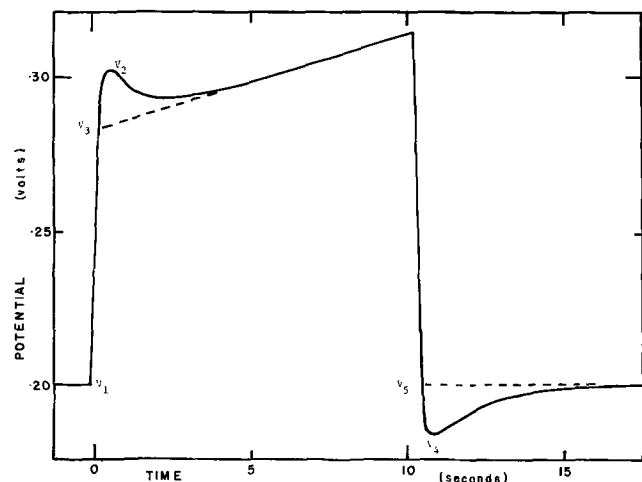


Fig. 4. Galvanostatic transient, potential vs. time. (Overshoot occurs when the current is suddenly raised to a new constant value, and undershoot when the current is suddenly reduced to its initial steady-state value).

rent,  $I$  and the electric field

$$\frac{\partial E}{\partial t} \Big|_z = \frac{1}{KK_0} (I - i) \quad [2]$$

where  $K$  is the dielectric constant of the film,  $K_0$  is the permittivity of free space, and  $z$  is the distance normal to the metal surface.

Dewald (5, 6) made the additional assumptions (D) that the field is constant across the layer and (E) that Frenkel defects are created in the layer at the rate

$$\frac{dn_+}{dt} = (N_0 - m)\nu e^{-[W - E\lambda q]/kT} \quad [3]$$

where  $N_0$  is the concentration of lattice sites,  $m$  is the vacancy concentration,  $W$  is the activation energy for the creation of an ion-vacancy pair,  $\lambda$  is the distance from the equilibrium position to the maximum in the potential energy diagram of an ion around a lattice site.

The rate of annihilation of the carriers is

$$\frac{dn_-}{dt} = \frac{-i\sigma m}{q} = \frac{dm_-}{dt} \quad [4]$$

where  $\sigma$  is the cross section for ion capture by a vacancy. The net rate of change of the vacancy concentration with time is then

$$\frac{dm}{dt} = (N_0 - m)\nu e^{-[W - E\lambda q]/kT} - \frac{i\sigma m}{q} \quad [5]$$

For simplicity, the electric field is assumed to be uniform across the layer. Making the above substitutions for  $\mu_0$  and  $\beta$  and combining Eq. [1], [2], and [5] we have

$$\frac{dE}{dt} = \frac{1}{KK_0} (I - 2nq\nu e^{-[U - Ea q]/kT}) \quad [6]$$

$$\frac{dn}{dt} = N_0\nu e^{-[W - E\lambda q]/kT} - 2\sigma a\nu n^2 e^{-[U - Ea q]/kT} \quad [7]$$

For a galvanostatic transient, where the ratio of the applied current to the steady-state current is  $p$ , we may write Eq. [6] and [7] in dimensionless form as

$$\frac{dy}{dx} = p - Ze^y \quad [8]$$

$$\frac{dZ}{dx} = B[e^{\alpha y} - Z^2 e^y] \quad [9]$$

where  $x = \frac{I_0 t}{KK_0} \frac{qa}{kT}$ ,  $y = (E - E_0)aq/kt$ ,  $Z = n/n_0$ ,

$\alpha = \lambda/a$ ,  $B = \sigma kTKK_0/aq^2$ ,  $I_0$  is the initial current density,  $E_0$  is the initial electric field,  $n_0$  is the initial carrier concentration.

A reasonably good first-order solution of Eq. [8] and [9] is possible for values of  $B$  less than about 0.01. This will be the case if, as we expect, the cross section  $\sigma$  is of the order of atomic dimensions. In this case  $Z$  will hardly change at all in the initial stages of the transient, while initially  $y$  will change rapidly. Subsequently as  $y$  increases,  $dy/dx$  will decrease, eventually going through zero. From then on  $y$  can change only slowly as  $Z$  changes. For values of  $x$  beyond the maximum in  $y$  we may then approximate  $y$ , using Eq. [8], as

$$e^y \approx p/Z \quad [10]$$

If this is substituted in [9], we have

$$(dZ^{\alpha+1}/dx) + p(\alpha + 1)B(Z^{\alpha+1} - p^{\alpha-1}) = 0 \quad [11]$$

The quantity  $Z^{\alpha+1}$  approaches  $p^{\alpha-1}$  as  $t \rightarrow \infty$ , and the decay constant is  $p(\alpha + 1)B$ . In fact, the equation for  $Z^{\alpha+1}$  is

$$Z^{\alpha+1} = p^{\alpha-1} - (p^{\alpha-1} - 1)e^{-p(\alpha+1)Bx} \quad [12]$$

So, if  $p > 0$ ,  $Z$  increases from unity to the value  $p^{(\alpha-1)/(\alpha+1)}$ . According to Dewald, "when  $y$  is at its maximum, the value of  $p(\alpha + 1)Bx$  is considerably less than unity and so can be set equal to zero." In this case,  $Z$  will not have changed much from its original value of unity and so, from Eq. [10]

$$y_{\max} = \ln p \quad [13]$$

In general

$$y = y_{\max} - \ln Z \quad [14]$$

If in [12] we make the approximation  $\ln(1 + A) = A$ , then from [14] we have

$$y = (2/\alpha + 1) \ln p + [1/(\alpha + 1)](1 - p^{1-\alpha})e^{-p(\alpha+1)Bx} \quad [15]$$

**Comparison with Experiment**

*Initial jump.*—From assumption (D), the potential drop across the layer is  $V = ED$ , where  $D$  is the thickness. From Eq. [13]

$$(E - E_0)_{t=0} = (kT/eq) \ln(I/I_0) \\ V_2 - V_1 = (\Delta V)_{t=0} = (kT/eq)D \ln(I/I_0) \quad [16]$$

Experimentally, as seen in Fig. 5, one obtains proportionality with  $\ln p$ , with  $D$  fixed.

However, according to Eq. [16],  $V_2 - V_1$  should be equal to zero when the thickness is zero, which according to Ord and Bartlett (2) is when  $V = -0.055v$ . Figure 6 shows the results obtained by applying different current densities to an anode in the steady state at different passive potentials. These results are very reproducible, and the points shown are averages of many individual results. If the curves for the various current ratios are extrapolated back to the lower voltage axis, they do not have a common zero intercept, as is predicted by Dewald.

There are perhaps two reasons for the discrepancy between theory and experiment, based on work by Ord and Bartlett (1). [They expressed the current (when transient effects have died out) as

$$i = i_0 \exp(v/v_0),$$

where  $v$  is the potential difference across the layer and  $i_0$  and  $v_0$  are parameters determined from experiment. Comparison with Eq. [1] shows that the quantity  $v/v_0$  is proportional to the field  $E$ , while the coefficient  $i_0$ , which we can call the zero-field current (because  $i$  would equal  $i_0$  if  $E$  were equal to zero), is proportional to the concentration  $n$ .] The first reason is that, while the layer thickness cannot have changed appreciably when the potential maximum is reached, the parameter  $v_0$  of Ord and Bartlett has changed markedly [see Fig. 11, ref. (1)]. The consequence is that the field does not have the value  $v/D$ , i.e., the field across the activation barrier does not equal the average field across the layer and so there must exist a space charge. The second reason is that the zero-field current  $i_0$  has also changed significantly by the time the maximum is reached [see Fig. 12, ref. (1)], so that the mobile ion concentration  $n$  would also have to change by the same percentage, whereas Dewald assumed this change to be negligible. Our re-

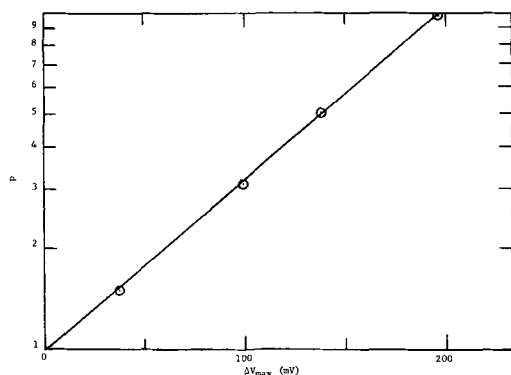


Fig. 5. Current ratio vs. initial jump of potential

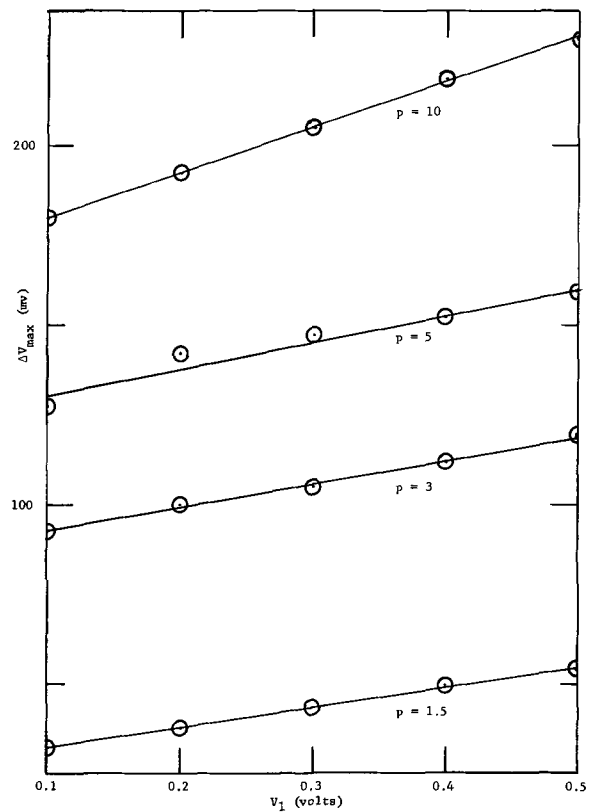


Fig. 6. Initial jump of potential vs. initial potential

sults therefore call into question the correctness of the Frenkel defect mechanism of Eq. [9].

*Overshoot decay.*—A further test of the Dewald theory is accounting for the shape of the overshoot decay (from the potential maximum to the minimum). The data are somewhat difficult to reproduce, but if the same anode is used all the time, the results can be duplicated within 10%. An enlarged view of the overshoot decay is shown in Fig. 7. A semilog plot of this curve shows it to be exponential to the point A with an asymptote about 10 mv down from the maximum. It seems reasonable to assume that the point A, where the potential deviates from an exponential, is where the layer starts to grow. To test this hypothesis the linear rise following the minimum is extrapolated back to the point B directly below A. The potential at B corresponds to the asymptotic value of the exponential prior to A. Now starting at A the linear voltage curve,  $V_B$ , is subtracted from the recorded potential curve. This results in  $V_A$  which turns out to be a continuation of the exponential down to A. This would seem to verify the fact that the actual potential curve is the sum of two curves, one representing the

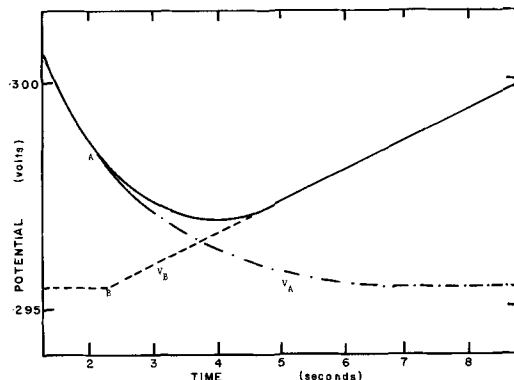


Fig. 7. Section of galvanostatic curve showing overshoot decay and layer growth, potential vs. time.

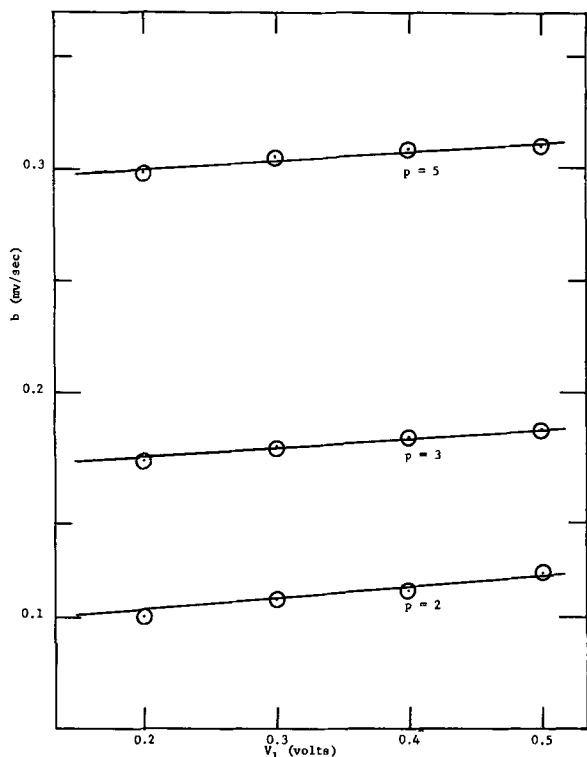


Fig. 8. Overshoot decay constant vs. initial potential

growth of the layer and the other an exponential decay of the potential with time, which may be represented by the equation

$$V - V_f = Ae^{-bt} \quad [17]$$

The value of  $A$  was found to be 13 mv for all current ratios and values of the passive potential.

The exponent  $b$ , if it is compared with Dewald's theory, should be equal to  $-pBx(1 + \alpha)$ , i.e., proportional to the current ratio but independent of thickness. Experiment does show a proportionality to  $p$ ,

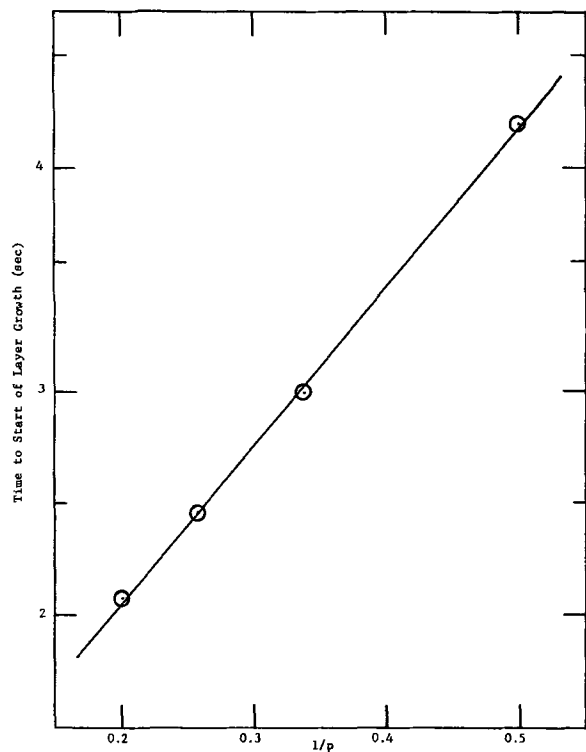


Fig. 9. Time to start of layer growth vs. current ratio

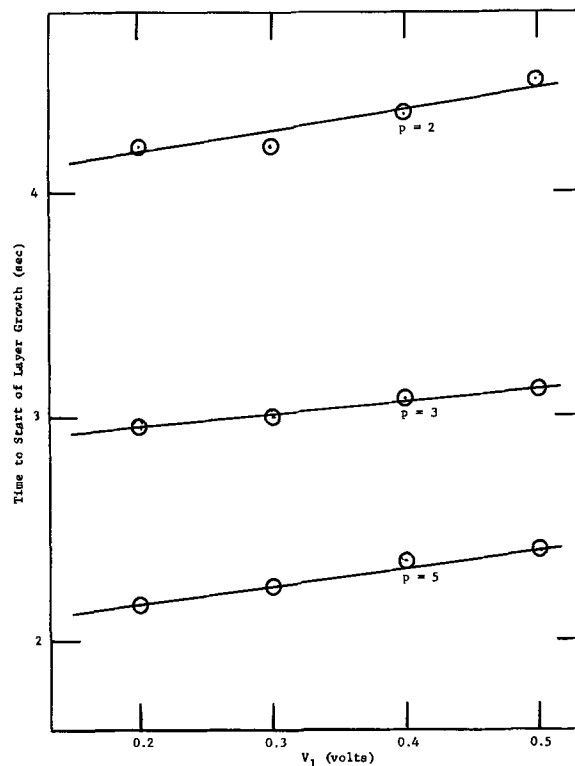


Fig. 10. Time to start of layer growth vs. initial potential

but a linear increase with  $V$  and hence with thickness (see Fig. 8).

The time before the layer growth starts was found to be inversely proportional to the current ratio, as shown in Fig. 9, and the dependence on the thickness is shown in Fig. 10.

It may be mentioned that the undershoot behaves in the same general way as the overshoot, except that there is little if any complication due to layer growth. The rapid drop is at first capacitive and the total amount to the minimum is in accordance with a relation similar to Eq. [16]. The rise from the minimum approaches exponentially the final value, in the manner given by

$$V_s - V = Ce^{-bt}$$

The decay constant  $b$  was found to depend on the initial passive potential and hence on the layer thickness.

Finally, overshoot can be observed to vanish if one applies a constant current at a late stage of an open-circuit break. In Fig. 11 the lower curve shows how the potential changes with time if the anode is ini-

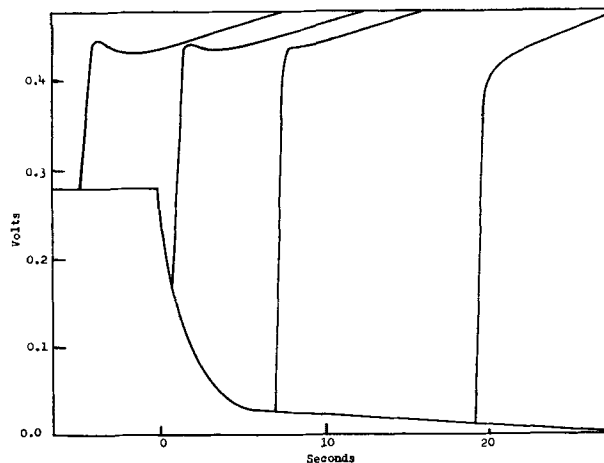


Fig. 11. Galvanostatic curves for constant current applied at various phases of an open-circuit break.

tially passive and the circuit is interrupted. The other curves show the change when the same constant current, greater than that in the steady state, is applied. The right-hand curve shows no overshoot. This may be due to the relative absence of charge carriers in the layer at the time the circuit is again closed.

*Validity of the Dewald theory.*—As we have shown, experiments with galvanostatic transients in iron are not in accord with the predictions of Dewald (*loc.cit.*). This may be due (i) to the existence of space charge and (ii) to the fact that the zero-field current, and hence the mobile ion concentration, changes very appreciably during the rise to the voltage maximum.

Furthermore, it is not known for iron that just one kind of ion moves, but in other systems (tantalum, niobium, aluminum, tungsten) for which we do have evidence (7), it has been shown that both metal and oxygen ions are mobile, and so the Dewald theory would have to be modified for them. These systems are not strictly comparable to iron, because they are irreducible and iron is reducible, but the charging curves are very similar in character.

The Dewald theory has also been questioned by Dignam (8) on the basis of his experiments with tantalum.

### Acknowledgment

This research was supported in part by the Office of Naval Research, Contract N0014-66-CO200 and in part by the National Aeronautical and Space Administration, Grant NsG 381.

Manuscript submitted Jan. 8, 1968; revised manuscript received Aug. 8, 1968. This paper was presented at the Philadelphia Meeting, Oct. 9-14, 1966, as Paper 84.

Any discussion of this paper will appear in a Discussion Section to be published in the June 1969 JOURNAL.

### REFERENCES

1. J. L. Ord and J. H. Bartlett, *This Journal*, **112**, 160 (1965).
2. J. L. Ord and D. J. DeSmet, *ibid.*, **113**, 1258 (1966).
3. H. G. Feller and J. Osterwald, *ibid.*, **111**, 119 (1964).
4. N. Cabrera and N. F. Mott, *Rept. Phys. Soc. of Prog. Phys.*, **12**, 163 (1948-49).
5. J. F. Dewald, *This Journal*, **102**, 1 (1955).
6. J. F. Dewald, *J. Phys. Chem. Solids*, **2**, 56 (1957).
7. J. A. Davies *et al.*, *This Journal*, **112**, 675 (1965).
8. M. J. Dignam and P. J. Ryan, *Can. J. Chem.*, **41**, 3108 (1963).

## Field Ion Microscopy Study of the Formation of Oxide Particles on Tungsten

S. S. Brenner and W. J. McVeagh

*Edgar C. Bain Laboratory for Fundamental Research,  
United States Steel Corporation, Research Center, Monroeville, Pennsylvania*

### ABSTRACT

The induction period for the formation of oxide particles on tungsten was found to be inversely proportional to  $(p_{O_2})^{0.8}$  and exponentially related to  $1/T$  indicating an activation energy of  $21 \pm 2$  kcal/mole. The particles appear to be irregularly shaped, and their distribution is crystallographically nearly homogeneous. It is proposed that the length of the induction period is determined primarily by the rate of penetration of oxygen into the tungsten lattice.

The formation of isolated oxide particles preceding the growth of a continuous film has been observed on a number of metal surfaces which are exposed to a mildly oxidizing environment. Indeed this phenomenon may be common to all metals. Reviews of this subject and summaries of the experimental results can be found in ref. (1-5).

Oxide particle formation has also been observed on tungsten surfaces by one of us (6) (S.S.B.) using field ion microscopy (FIM) and by Rausch and Moazed (7) and Rausch (8) using field emission microscopy (FEM). These studies have shown that in common with other gas-metal systems there is an induction period associated with the appearance of particles of the reaction product. The present paper is an extension of the earlier FIM work and discusses in particular the temperature and pressure dependence of this induction period.

### Experimental

*Apparatus.*—A Müller field ion microscope using helium as the imaging gas and operated at 77°K was used in this investigation. It deviated from the standard design by the use of copper-gasketed stainless steel flanges as shown in Fig. 1. The residual gas pressure in the vacuum system after bakeout and prior to the oxidation experiments was less than  $1 \times 10^{-9}$  Torr. Oxygen was introduced into the system either by diffusion through a heated silver tube or from a bottle of spectroscopically pure gas. Care was taken to minimize the production of CO at the pressure gauges either by using thermocouple gauges or by intermit-

tently using thoria-coated ion gauges operated at low emission currents.

The field emitter was heated by thermal conduction from the supporting wire loop (Fig. 1), and its temperature was determined from the resistivity change of a small section of the loop in contact with the spot-welded specimen. For short heating periods a temperature pulser with a rise time of about 0.2 sec was used.

*Procedure.*—Prior to each oxidation experiment the tungsten tip was field evaporated, after which the potential was reduced to ground level and the oxygen pressure was adjusted to the desired level between  $10^{-6}$  and 1 Torr. Since this adjustment required at least 10 min it is certain (9) that the surface of the field emitter became covered with adsorbed oxygen. After heating in oxygen, the specimen was cooled rapidly, and the oxygen pressure was reduced to less than  $10^{-7}$  Torr before the tip was examined by removing in succession monatomic layers of metal using pulsed field evaporation. When the heat-treatment produced significant amounts of oxide, the specimen was flashed for a short period above 1200°C to vaporize the oxide prior to the next experiment. It must be emphasized that during the oxidation treatment the applied potential was always zero.

### Results

*Structural observations-oxygen adsorption.*—A clean field-evaporated tungsten surface is shown in the micrograph of Fig. 2a. The adsorption of oxygen caused the appearance of many randomly distributed ioniza-

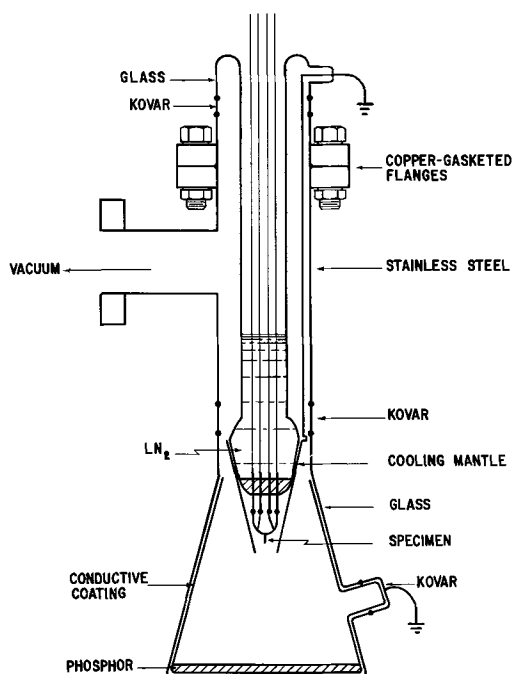


Fig. 1. Müller field ion microscope using copper-gasketed flanges

tion centers (Fig. 2b). Whether these ionization centers represent the chemisorbed oxygen atoms or displaced tungsten atoms is still a matter of conjecture (10-12). The effects of oxygen adsorption could be eliminated (Fig. 2c) by the field evaporation of one to two (110) layers (2.2-4.5Å) at the apex of the tip. If after an oxidation treatment the perfect surface was restored by the removal of no more than 2 atomic layers of tungsten, it was assumed that only chemisorption and not oxidation has occurred.

**Oxide formation.**—Oxidation manifested itself in two ways: (i) by the appearance of dark regions in the ion images and (ii) if the oxidation treatment was more severe, by a decrease in the radius of curvature,  $r$ , of the field emitter. The dark regions have previously been interpreted (6) to be the images of the depressions or holes left by oxide particles that were evaporated by the imaging field (Fig. 3). The decrease in the radius of curvature is believed to be due to the formation and subsequent field-evaporation of a more continuous (although not necessarily compact) oxide layer. When the thickness of the oxide layer is only a

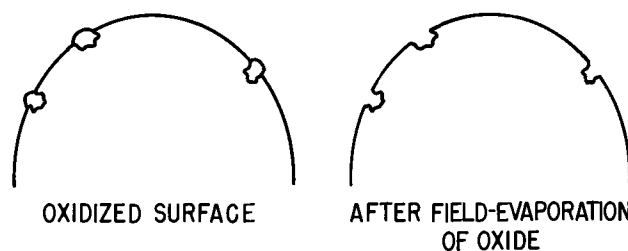


Fig. 3. Formation of surface holes caused by the field-evaporation of oxide particles.

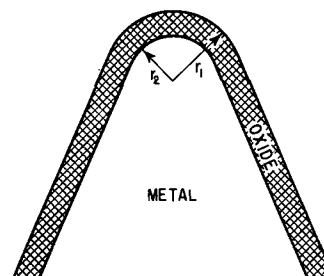


Fig. 4. Decrease of radius of curvature of field-emitter caused by the formation of a continuous oxide film and its subsequent removal by field-evaporation.

fraction of  $r_1$ , the change in  $r$  equals the depth of metal oxidized (Fig. 4).

**Shape and distribution of oxide particles.**—A typical example of a tungsten surface after heating for 10 min at 960°K in  $10^{-4}$  Torr oxygen is shown in the sequence of photographs in Fig. 5. When the imaging potential was first applied, the ion image contained many dark areas and some bright spots due to adsorbed gas atoms or displaced substrate atoms (Fig. 5a). As the voltage was raised, many of the bright spots disappeared and the edges of the (110) planes became visible. Field evaporation of three (110) planes (Fig. 5c) removed most of the dark areas, except for some isolated regions, such as indicated by the arrows. The deepest of the remaining holes persisted to a depth of about 20Å. In other experiments holes were observed up to 30Å in depth. In addition to the deeper holes the oxidation and subsequent field evaporation also caused the formation of many shallow fissures and depressions less than 7Å deep and extending more than 100Å over the surface (Fig. 5b).

It is evident from these micrographs (Fig. 5) that the shape of the holes, i.e., the oxide particles, is highly

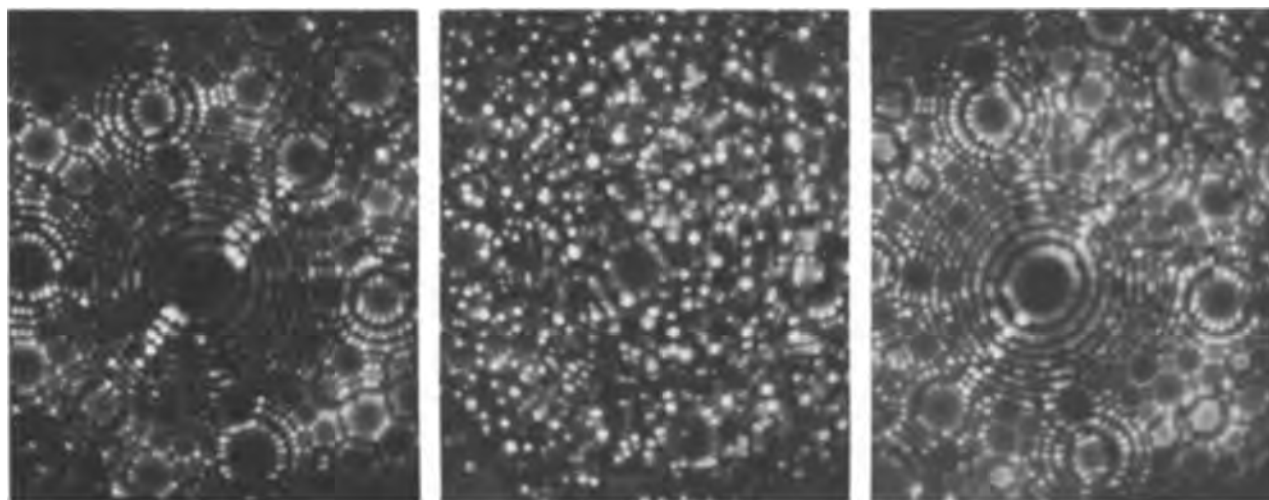


Fig. 2. Effect of chemisorption of oxygen on field-evaporated tungsten surface. Tip exposed to  $8 \times 10^{-3}$  Torr  $O_2$  for 19 hr at 500°K: a (left) clean surface; b (center) after adsorption; c (right) after removal of 4.5Å of metal.

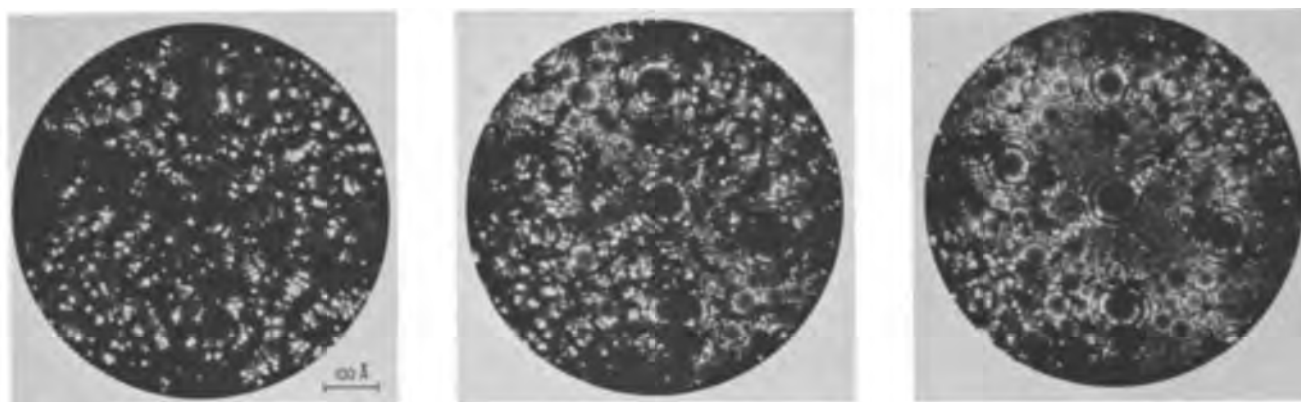


Fig. 5. Corrosion of tungsten surface exposed to  $10^{-4}$  Torr oxygen at  $960^\circ\text{K}$  for 10 min.  $\Delta h$  refers to the depth of field evaporation: left,  $\Delta h = 0$ ; center,  $\Delta h = 2.2\text{\AA}$ ; right,  $\Delta h = 6.7\text{\AA}$ .

irregular, possibly on account of preferential field evaporation at the sides of the holes (oxide-metal interface). Because of the irregular shape it was difficult to assess the total number of particles per unit area. The number of deeper holes on the projected surface area was usually of the order of ten, giving a particle density of approximately  $10^{11}/\text{cm}^2$ . The incidence of holes appeared to be slightly greater at the (110) steps and near the  $\langle 112 \rangle$  poles; however, no strong crystallographic preference was found. Since the low-index planes normally appear dark in the ion images, the incidence on these planes could not be determined. Particles did not appear to form preferentially at grain boundaries, although some of the particles in contact with boundaries were unusually large.

**Pressure and temperature dependence of oxide formation.**—Oxide particles were observed only after an induction period,  $t_i$ , which is both pressure and temperature dependent. The magnitude of  $t_i$  was determined from a series of experiments in which the temperature and pressure were held constant and the time was varied. The shortest time necessary to give a definite indication of oxide formation (the criterion for this was stated earlier) was taken as  $t_i$ . In Fig. 6  $t_i$  is plotted as a function of pressure at  $1000^\circ\text{K}$ ; the uncertainty in  $t_i$  is indicated by the spread between the pairs of closed and open circles, which represent minimum time to detect oxidation and the maximum time at which no oxidation was observed, respectively. The data are represented by

$$t_i = 0.16 p^{-0.8} (1000^\circ\text{K}; p \text{ in Torr})$$

Less complete data at  $650^\circ$  and  $700^\circ\text{K}$  indicate a similar pressure dependence for oxygen pressures in the range from 0.01 to 100 Torr.<sup>1</sup>

The temperature dependence of  $t_i$  was determined in a similar manner and is shown in Fig. 7 for  $p$  equal to  $10^{-4}$  and 1 Torr. At both pressures the data can be represented reasonably well by an Arrhenius-type equation yielding an activation energy of  $21 \pm 2$  kcal/mole. At the pressure of 1 Torr a temperature correction was applied to account for the heat loss due to gas conduction. This correction only shifted the intercept of the  $\log t_i - 1/T$  plot, but did not appreciably affect its slope.

**Oxide film formation.**—In some experiments the oxidation was allowed to proceed until a continuous film was formed resulting in a decrease in the radius of curvature of the field emitter. The radius of curvature,  $r$ , may be calculated from the number of steps between two planes of known orientation (13). The minimum detectable value of  $\Delta r$  is about  $20\text{\AA}$ . A typical example of the decrease in radius of curvature with oxidation is shown in Fig. 8 in which the average radius of curva-

ture,  $r$ , decreased from  $360$  to  $200\text{\AA}$ . The apparent shift of the grain boundary is due to the recession of the apex and the change of the intersection of the boundary with the surface.

In Fig. 9  $\Delta r$  is shown as a function of time at  $700^\circ\text{K}$  and  $1.2 \times 10^{-2}$  Torr oxygen. The linear relationship indicates that the rate of oxidation is constant at least up to a depth of  $180\text{\AA}$  and suggests that the film is still porous at that thickness.

### Discussion

The results of this study show that the induction period for the formation of oxide particles on tungsten is related to temperature and pressure in a manner similar to that for other metals such as iron (14), copper (15-17), and tantalum (18). The greater the oxygen pressure and the higher the temperature the shorter is the induction period,  $t_i$ . Contrary to an earlier publication by one of us (6) (S.S.B.), there is no evidence for a critical pressure associated with the formation of oxide particles; the magnitude of  $t_i$  depends only on kinetic factors.

Values of  $t_i$  obtained in this study are appreciably greater than those observed by Rausch (8) using FEM. The reason for this is uncertain but may be a result of the larger (20 to 50 times) surface areas that are observed with the field-emission microscope.

Despite the numerous publications on oxide initiation it is still uncertain what process takes place and what the state of the surface is during the induction period. Several investigators (1, 15, 19) have concluded that a continuous, randomly oriented oxide film first forms on the metal, and then oriented oxide particles nucleate and grow within or from this primary oxide layer. However, Lawless (4) concluded from careful reflection electron diffraction studies made on copper

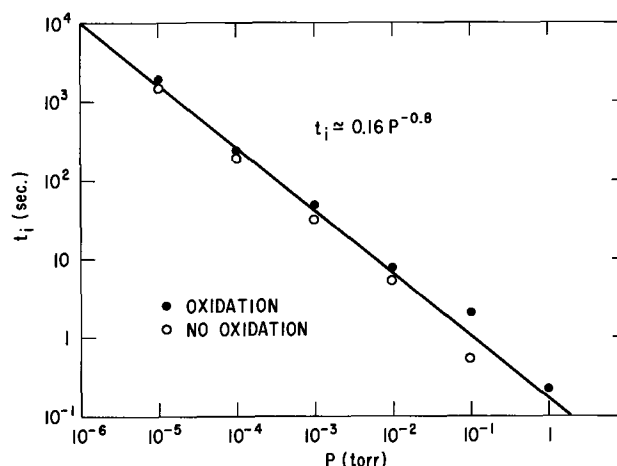


Fig. 6. Oxygen pressure dependence of the induction period at  $1000^\circ\text{K}$ .

<sup>1</sup> The dissociation pressure of  $\text{WO}_2$  at  $1000^\circ\text{K}$  is about  $10^{-15}$  Torr (33). Hence all experiments were performed under conditions far from equilibrium.



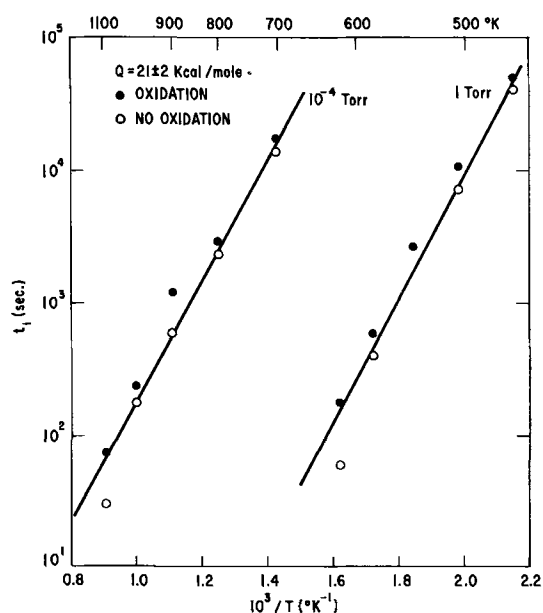


Fig. 7. Temperature dependence of the induction period at  $10^{-4}$  and 1 Torr oxygen.

that during the induction period not more than  $10\text{\AA}$  of oxide is present on the metal surface. Lawless, as well as Mitchell (17) and Van Der Schrick (16), concluded that the most likely process occurring during the induction period of copper is the dissolution of oxygen into the subsurface layer to form a supersaturated metal-oxygen solution. At a sufficiently large supersaturation, precipitation of oxide particles occurs. A similar explanation was given by Kofstad (18) for the nucleation of tantalum suboxide platelets. In this case it could be shown that the concentration of oxygen in solution in the metal near the surface was considerably larger than the solubility of oxygen in the presence of  $Ta_2O_5$ .

Within the limits of detection ( $\sim 20\text{\AA}$ ) the results of this study show that a continuous thin film of oxide was not present during the induction period, and it is also suggested that the induction period is associated with the solution of oxygen into the surface layer of the metal. The solution occurs by the penetration of oxygen atoms from the adsorbed layer into the first few lattice planes. Deeper penetration of the dissolved oxygen into the bulk of the metal is prevented by the low thermal diffusivity of the gas atoms in the metal. The metal-oxygen solution layer at the surface corresponds to the "rearranged" or "reconstructed" surfaces postulated by some (20-24) to explain low energy electron diffraction (LEED) results.

The penetration of oxygen into tungsten was observed by Zingerman and Ishchuk (25) in a series of experiments involving work function measurements. Penetration was observed at temperatures as low as  $850^\circ\text{K}$ . At  $1040^\circ\text{K}$  oxygen penetration occurred over a period of at least 10 min when the surface was exposed to a beam of oxygen the intensity of which was equivalent to a pressure of about  $3 \times 10^{-9}$  Torr. The number of injected atoms was estimated to correspond to about two monolayers of adsorbed atoms.

Neither the temperature dependence nor the pressure dependence of the rate of oxygen penetration was determined by Zingerman and Ishchuk. It is therefore not possible to confirm at this time whether the controlling step of the formation of oxide particles on tungsten is indeed the rate of oxygen penetration from the chemisorbed layer into the metal lattice.

If oxygen penetration is the controlling step then its pressure dependence differs from that of normal gas-metal diffusion where a  $p^{0.5}$  dependence is expected for a diatomic gas. The  $p^{0.8}$  dependence found in this study is not understood but it is nearly equal to the  $p^{0.7}$  dependence found by Singleton (26) for the rate of interaction of oxygen with tungsten filaments at  $1250^\circ\text{K}$  in which a similar process may proceed oxidation.

Neither the rate of penetration of oxygen atoms into metals nor the concentration of injected atoms just below the surface can be obtained from the bulk properties of the gas-metal system. With nickel, Roberts and Wells (27) reported that oxygen penetration occurs at temperatures below  $300^\circ\text{K}$  with an activation energy of only 2 to 15 kcal/mole depending on the amount of injected oxygen. Delchar and Tompkins (28) proposed that the incorporation of oxygen into the nickel lattice is facilitated by the electrical double layer at the surface. The activation energy for incorporation is decreased by  $\frac{1}{2} qV$  where  $q$  is the virtual charge of the adatom and  $V$  the potential difference across the double layer. They concluded that  $q$  is equal to  $0.3e$  where  $e$  is the electronic charge. To reconcile the large difference between the calculated and measured rates of incorporation they assumed that a large negative activation entropy accompanies the incorporation process. They suggested that this entropy term may be indicative of a cooperative phenomena in which the atoms on the surface undergo a concerted movement which enlarges the aperture through which the adatom can pass.

The penetration of chemisorbed oxygen at  $298^\circ\text{K}$  into metals other than nickel, such as copper, iron, chromium, and molybdenum was reported by Quinn and Roberts (29), and the anomalous surface solution rate compared to normal gas diffusion appears to be general in nature.

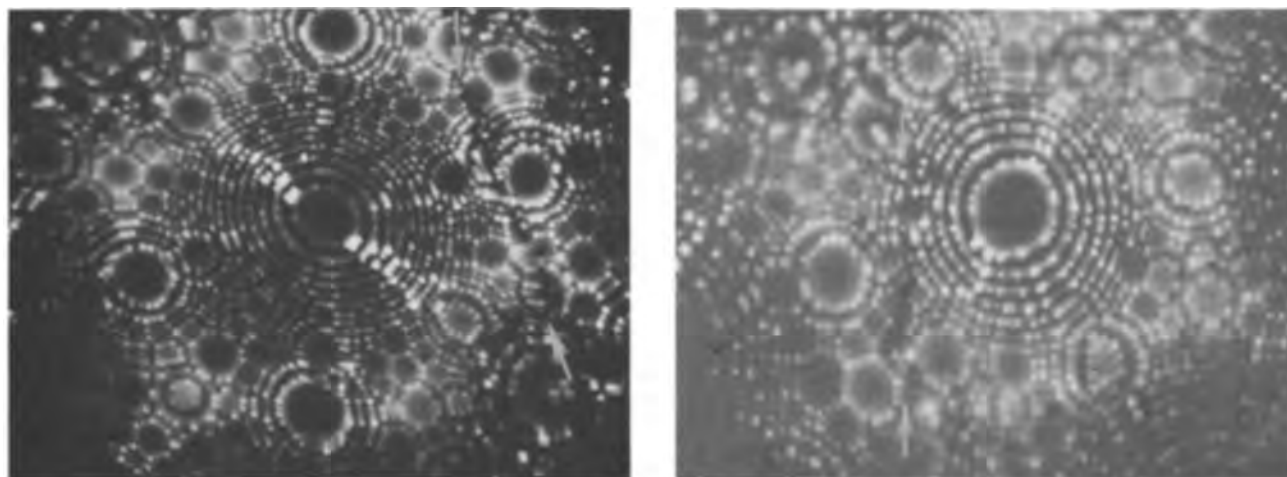


Fig. 8. Reduction in radius of curvature due to oxide film formation. Apparent shift of boundary is caused by recession of apex of tip, 15 hr at  $650^\circ\text{K}$  in  $1.5 \times 10^{-2}$  Torr oxygen. Left, before  $r \approx 360\text{\AA}$ ; right,  $r \approx 200\text{\AA}$ .

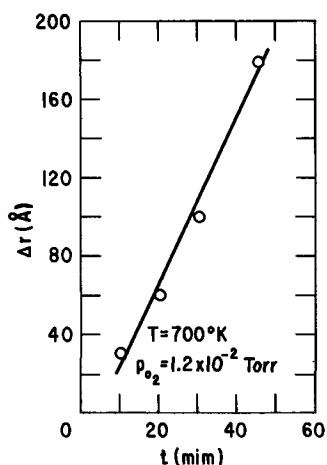


Fig. 9. Decrease of radius of curvature due to field-evaporation of oxide film formed on tungsten emitter at 700°K and  $1.2 \times 10^{-2}$  Torr oxygen.

While it appears reasonable to conclude that the length of the induction period preceding the observation of oxide particles on tungsten is determined by the rate of penetration of chemisorbed oxygen into the metal lattice, it is recognized that other explanations may be equally valid. For instance the rate-controlling step may be the nucleation process itself, i.e., the formation of the distinct oxide phase and the formation of the metal-oxide interface (30). The induction period may also be associated with the time to form a sufficiently large number of nuclei ( $> 10^{10}/\text{cm}^2$ ) or with the time necessary to cause sufficient thickening of the nuclei ( $> 5\text{\AA}$ ) to be discernible in the ion microscope. The rate of oxide growth may therefore determine the length of the induction period. The data now available do not make it possible to choose conclusively between these processes.

**Morphology and density of oxide particles.**—The shape of the oxide particles during their early stage of growth cannot be determined unambiguously by FIM because of possible field-evaporation effects. The ion micrographs suggest that the particle shapes are quite irregular. Polygonally shaped oxide particles have been reported but usually of much larger dimensions and their shapes are the result of their prolonged growth. Irregularly shaped oxide particles have been observed (31) on copper especially on high-index planes during the very early stages of corrosion. The growth of oxide particles on metals has been discussed by Rheed (32). It is obvious that the lateral growth rate of the particles will be considerably greater than their rate of thickening since the latter must occur by bulk diffusion or metal-oxide interface diffusion, while the former depends mostly on surface diffusion. Our observation of shallow fissures and depressions on oxidized tungsten surfaces indicates rapid lateral growth which is consistent with this prediction. However, the fact that the rate of metal consumption was still constant after the corrosion of 180Å of metal at 700°K and  $1.2 \times 10^{-2}$  Torr  $\text{O}_2$  suggests that the lateral growth was still incomplete at this stage.

The concentration of oxide particles formed on some metals (3, 4) is a function of crystal orientation. The absence of such an effect in this study may be due to one or more of the following factors: (i) the number of particles that were observed was too small to determine their statistical distribution; (ii) particles on the low-index planes such as {100}, {110} and {112} are not observable; and (iii) the field-evaporated surfaces are highly stepped surfaces on which epitaxial growth would be difficult. The use of field emitters of smaller curvatures which would allow viewing larger areas would be helpful in studies of particle concentration.

## Summary

The initial oxidation of tungsten occurs by the formation of oxide particles which field evaporate on the application of the imaging voltage in FIM, leaving behind holes in the surface. Oxide particles are observed after a induction period which is inversely proportional to the 0.8 power of the oxygen pressure. The activation energy associated with their appearance is  $21 \pm 2$  kcal/mole, independent of the oxygen pressure. No strong crystallographic effects were observed in the particle density. The results of the study are consistent with the hypothesis that the induction period is associated with the penetration of oxygen into the metal lattice to form a supersaturated metal-oxygen solution from which oxide nuclei precipitate.

## Acknowledgment

The authors are grateful to Mr. H. G. Grendon of this laboratory for his very able assistance in constructing and maintaining the experimental equipment.

Manuscript received June 19, 1968.

Any discussion of this paper will appear in a Discussion Section to be published in the June 1969 JOURNAL.

## REFERENCES

- J. Benard, "L'Oxydation des Metaux," Gauthier-Villars (1962).
- J. Bernard, *Korrosion*, **18**, 23 (1966).
- P. Kofstad, "High Temperature Oxidation of Metals," John Wiley & Sons, Inc., New York (1966).
- K. Lawless in "Energetics in Metallurgical Phenomena," 6th ed., p. 345, Wm.M. Mueller, Editor, Gordon and Breach Science Publishers, Inc., New York (1965).
- H. H. Uhlig, *Corrosion Sci.*, **7**, 325 (1967).
- S. S. Brenner in "High Temperature, High Resolution Metallography," H. I. Aaronson and G. S. Ansell, Editors, Gordon and Breach Science Publishers, Inc., New York (1967).
- D. W. Rausch and K. L. Moazed in "Oxidation of Tungsten and Other Refractory Metals," P. L. Faust, Editor, Technical Documentary Report No. ML-TDR-64-162, Air Force Materials Laboratory.
- D. W. Rausch, "Initial Oxidation of Tungsten and Tantalum," Ph.D. Thesis, The Ohio State University, 1965.
- I. Langmuir and D. S. Villars, *J. Am. Chem. Soc.*, **53**, 486 (1931).
- G. Ehrlich, *Discussions Faraday Soc.*, **41**, 7 (1966).
- A. A. Holscher and W. M. H. Sachtler, *ibid.*, **41**, 29 (1966).
- A. A. Holscher, "Adsorption Studies with the Field-Emission and Field-Ion Microscope," Thesis, Leiden University, 1967.
- M. Drechsler and P. Wolf, "Fourth International Conference on Electron Microscopy," 325 (1958).
- J. Bardolle and J. Benard, *Rev. Met.*, **49**, 613 (1952).
- F. Grönlund, *J. Chim. Phys.*, **53**, 660 (1956).
- G. Van Der Schrick, Ph.D. Thesis, University Libre de Bruxelles, 1960.
- D. F. Mitchell, Ph.D. Thesis, University of Virginia, 1965.
- P. Kofstad, *J. Inst. Metals*, **90**, 253 (1961-2).
- E. W. Gulbransen, W. R. McMillan, and K. F. Andrews, *Trans. AIME*, **200**, 1027 (1954).
- D. Brennan, D. O. Hayward, and B. M. W. Trapnell, *Proc. Roy. Soc. London*, **A256**, 81 (1960).
- L. H. Germer, *Ann. N. Y. Acad. Sci.*, **101**, 599 (1963).
- H. E. Farnsworth, *Adv. Catalysis*, **15**, 31 (1964).
- J. W. May, *Ind. Eng. Chem.*, **57**, 18 (1965).
- L. H. Germer and J. W. May, *Surface Sci.*, **4**, 452 (1966).
- Ya. P. Zingerman and V. A. Ishchuk, *Soviet Physics-Solid State*, **6**, 904 (1964); **7**, 173 (1965); **8**, 2394 (1967); **9**, 623 (1967).
- J. H. Singleton, *J. Chem. Phys.*, **45**, 2819 (1966).
- M. W. Roberts and B. R. Wells, *Trans. Faraday Soc.*, **62**, 1608 (1962).
- T. Delchar and F. C. Tompkins, "The Structure of Surfaces," p. 165, H. M. Davies and K. R. Lawless, Editors, North Holland Publishing Co. (1967).

29. C. M. Quinn and M. W. Roberts, *Trans. Faraday Soc.*, **61**, 1775 (1964).  
 30. J. P. Hirth and K. L. Moazed in "Symposium on Fundamental Phenomena in Materials Sciences," 3, Boston, 1965, Plenum Press, New York (1966).

31. K. Lawless, Private communication.  
 32. G. E. Rheed, *Trans. Faraday Soc.*, **61**, 797 (1965).  
 33. O. Kubaschewski and B. E. Hopkins, "Oxidation of Metals and Alloys," p. 10, Butterworths, London (1962).

# Technical Note



## The Thermodynamic Interaction between Zinc and Indium in Dilute Solution in Molten Lead

H. W. Slager, J. V. Gluck, and R. D. Pehlke

Boeing Company, Seattle, Washington, Tecumseh Products Research Laboratories, Ann Arbor, Michigan, and Department of Chemical and Metallurgical Engineering, University of Michigan, Ann Arbor, Michigan, respectively

A study has been conducted on the effect of small additions of indium on the thermodynamic activity of zinc in dilute solution in molten lead at 550°C. The present work is a continuation of an investigation of various third element interactions on zinc dissolved in lead (1-3). A previous investigation had considered the same third element interactions with zinc dissolved in molten bismuth (4). Although the lead-zinc binary system has been studied several times, and a number of lead-zinc-j ternary systems have also been investigated, there appears to be no previously reported thermodynamic studies in the literature on any region of the lead-zinc-indium system.

The experiments were conducted in high-temperature galvanic cells represented as follows:

Zn (pure reference standard)	Zn <sup>++</sup> (as 1.5 m/o ZnCl <sub>2</sub> ) in LiCl-KCl eutectic (fused salt electrolyte)	Zn + In in Pb (molten alloy)
------------------------------------	--	---------------------------------

The experimental apparatus, a multi-electrode system employing alumina refractories and contained in a Vycor tube under a helium atmosphere, has been described previously (1, 5), as have been the experimental procedures and precautions (2, 4, 5), and the methods of data reduction (4, 5). Experimental measurements were made over a temperature range of 450°-650°C. The linear dependence of the electromotive force (emf) on temperature was verified by statistical techniques of regression. The 90% confidence limit for the emf at 550°C was 0.17 mv on the average over the composition range investigated.

The experimental results summarized in Table I include the interpolated emf at 550°C and the temperature dependence of emf. A previous correlation of the results from 28 binary electrodes had shown that up to 0.0375 mole fraction zinc, the limiting activity coefficient of zinc in lead is given by the relation (1, 2)

$$\log \gamma^{\circ} \text{Zn} = \frac{1215}{T \cdot K} - 0.418 \quad [1]$$

The expected emf's and temperature dependence were calculated from this correlation and are compared with the present results in Table I for the measurements made on binary electrodes. Since the effect of the indium addition was to decrease the cell potential, the activity and activity coefficient of zinc were increased and thus the interaction is a positive one. A plot showing the effect of the indium addition on the activity coefficient of zinc is presented in Fig. 1 for alloys where the zinc content was fixed at 0.015

or 0.025 mole fraction. The relation is linear to 0.05 mole fraction indium and does not depend on the zinc concentration. This indicates that the influence of indium is substantially confined to a first-order effect. The slope of the relation yields Wagner's first-order interaction parameter at 550°C (6)

$$(\text{in Pb}) \left( \frac{\partial \ln \gamma_{\text{Zn}}}{\partial X_{\text{In}}} \right)_{\substack{X_{\text{In}}=0 \\ X_{\text{Zn}} < 0.025}} = \frac{\text{In}}{\epsilon_{\text{Zn}}} \cong + 2.7 \pm 0.3 \quad [2]$$

The temperature dependence of the effect is slight and the parameter decreases with increasing temperature. The temperature dependence is approximately expressed by the relation

$$\frac{\text{In}}{\epsilon_{\text{Zn}}} \cong \frac{490 \pm 160}{T \cdot K} + 2.1 \quad [3]$$

In both the sign and magnitude of the interaction, the effect of indium on the activity of zinc was similar in bismuth as a solvent [at 550°C  $\frac{\text{In}}{\epsilon_{\text{Zn}}} = + 2.2$  (in Bi)] (4).

Experimental measurements were also made on alloys where zinc was fixed at 0.0375 or 0.050 mole fraction. The same quantitative effect of the indium addition was observed; however, an anomalous and apparently reproducible effect caused the emf's of all the electrodes, both binary and ternary, in those cells to be shifted uniformly several millivolts higher. This effect cannot be explained by displacement reactions because the emf is shifted in the opposite direction (7). The quantitative values of the zinc-indium interaction in these cells was identical to that reported above for the more dilute solution. Further work is

Table I. Experimental results at 550°C

$X_{\text{Zn}} =$	$X_{\text{In}} = 0$		0.015		0.025		0.0375		0.050	
	Emf	$\frac{\partial E}{\partial T}$	Emf	$\frac{\partial E}{\partial T}$	Emf	$\frac{\partial E}{\partial T}$	Emf	$\frac{\partial E}{\partial T}$	Emf	$\frac{\partial E}{\partial T}$
0.015	64.19	0.237	62.26	0.211	60.87	0.213	60.47	0.206	59.29	0.198
	63.74	0.211								
	*62.57	0.222								
0.025	45.79	0.199	43.63	0.196	43.35	0.196	42.80	0.193	40.71	0.190
	45.91	0.195	43.84	0.195						
	*44.41	0.200								

\* Values from correlation of 28 previous binary electrodes. Composition in mole-fraction, weighed-in basis. Emf, mv;  $\partial E/\partial T$ , mv/°C.

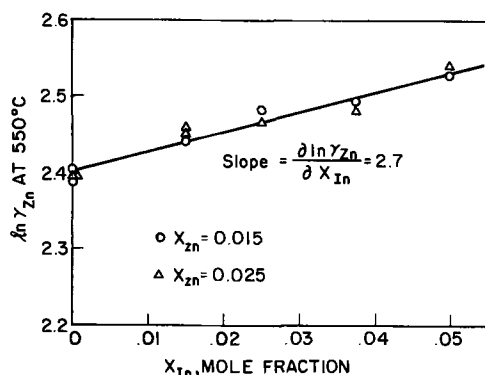


Fig. 1. Effect of indium on the activity coefficient of zinc in dilute solution in molten lead at 550°C.

warranted to clarify the thermodynamic behavior in this system.

Since the data in Table I suggest a decreasing trend in the emf-*vs.*-temperature slope with increasing indium content, there might be a detectable entropy

interaction in this system (8). Such an effect would have to be confirmed by additional free energy measurements and by calorimetry to establish the enthalpy interactions, if any.

Manuscript submitted July 1, 1968; revised manuscript received Aug. 3, 1968.

Any discussion of this paper will appear in a Discussion Section to be published in the June 1969 JOURNAL.

#### REFERENCES

1. R. D. Pehlke, K. Okajima, and T. L. Moore, *This Journal*, **114**, 800 (1967).
2. R. D. Pehlke and K. Okajima, *Trans. Met. Soc. AIME*, **239**, 1351 (1967).
3. K. Okajima and R. D. Pehlke, *J. Japan Inst. Met.*, **29**, 961 (1965).
4. J. V. Gluck and R. D. Pehlke, *Trans. Met. Soc. AIME*, **239**, 36 (1967).
5. J. V. Gluck and R. D. Pehlke, *ibid.*, **233**, 233 (1965).
6. C. Wagner, "Thermodynamics of Alloys," p. 51, Addison-Wesley, Cambridge, Mass., (1952).
7. C. Wagner and A. Werner, *This Journal*, **110**, 326 (1963).
8. C. H. P. Lupis and J. F. Elliott, *Trans. Met. Soc. AIME*, **233**, 829 (1965).

## DISCUSSION SECTION



This Discussion Section includes discussion of papers appearing in the *Journal of The Electrochemical Society*, Vol. 114, No. 8 and 9 (August and September), and Vol. 115, No. 2, 4, and 5 (February, April, and May).

### Overpotential-Time Variation for Galvanostatic Charging with Potential Dependent Capacitance

Leonard Nanis and Philippe Javet, (pp. 810-812, Vol. 114, No. 8)

**S. K. Rangarajan**<sup>1</sup>: We offer the following comments pertaining to the validity of the equations used and the correctness of the solutions given by the authors: (A) Whereas it is true that the "total" current  $J_T$  is the algebraic sum of the "Faradaic" current  $J_F$  and the "charging" current  $J_C$ , care should be exercised to ensure consistency of sign-conventions while stating the dependence of  $J_C$  and  $J_F$  on  $\eta$  explicitly.

For example, if the convention " $\eta$ : positive when cathodic;  $\eta$ : potential of the electrolyte/electrode" is chosen

$$J_F = J_o \left[ \exp\left(\frac{-\alpha ZF\eta}{RT}\right) - \exp\left(\frac{(1-\alpha)ZF\eta}{RT}\right) \right] \quad [1]$$

but

$$J_C = -C \frac{d\eta}{dt}, \quad (C: \text{positive}) \quad [2]$$

and not

$$J_C = +C \frac{d\eta}{dt} \quad [3]$$

as used by the authors. The equation to be solved is therefore

$$J_T = J_o \left[ \exp\left(\frac{-\alpha ZF\eta}{RT}\right) - 1 \right] - C \frac{d\eta}{dt} \quad [4]$$

(for the case  $\alpha \approx 1$ ) and not Eq. [5] of the authors.

There have been other instances<sup>2</sup> where such an incorrect equation is quoted. Four forms of expressing

<sup>1</sup> Central Electrochemical Research Institute, Karaikudi-3, S. Rly, India.

<sup>2</sup> J. O'M. Bockris and A. Damjanovic, "Modern Aspects of Electrochemistry," Vol. 3, J. O'M. Bockris and B. E. Conway, Editors, p. 233, Eq. [6], Butterworths, London (1964); A. D. Graves, G. J. Hills, and D. Inman, "Advances in Electrochemistry," Vol. IV, P. Delahay, Editor, p. 116, Eq. [34] and [35], Interscience Publishers (1966).

$J_f - \eta$  relationship are possible<sup>3,4</sup> depending on the convention chosen. The sign to be adopted for  $C \frac{d\eta}{dt}$  is also dependent on this. A working rule can be that the sign of  $C \frac{d\eta}{dt}$  is the same as the sign of  $(\partial J_f / \partial \eta)$ :

(B) To explain how the authors are able to compare their solution favorably with that of Karasyk, it should be pointed out that their results (Eq. [6], p. 811) is not the solution of their equation (Eq. [5], p. 811) but is a solution of the corrected equation! As a matter of fact, the solution of Nanis and Javet's equation turns out to be

$$\eta = \frac{RT}{\alpha ZF} \ln \left[ \frac{\exp\left[\frac{\alpha ZF(J_o + J_T)t}{RTC}\right] + \frac{J_o}{J_T}}{1 + J_o/J_T} \right] \quad [5]$$

(Note the behavior of  $\eta$  with  $t \rightarrow \infty$ ). The proper  $\eta - t$  is, of course, that given by Karasyk. (C) Equation [10] of the authors is also to be modified as

$$\begin{aligned} & C_o b \eta + C_1 b \eta^2 + \ln(1 - I e^{-b\eta}) \\ & \cdot (C_o + 2C_1 \eta) - C_o \ln(1 - I) \\ & + \frac{2C_1}{b} [L_2(I) - L_2(I e^{-b\eta})] = -\frac{\alpha ZF(J_o + J_T)t}{RT}; \alpha \approx 1 \end{aligned} \quad [6]$$

where

$$L_2(Z) = \sum_{n=1}^{\infty} Z^n / n^2 \quad [7]$$

is Euler's dilogarithm.

We hasten to add that Eq. [6] is a solution of the corrected equation, *viz.*, Eq. [4] given above, and not the equation purported to be solved by the authors.

The extension to the condition  $\alpha \neq 1$  is direct.

<sup>3</sup> S. K. Rangarajan and K. S. G. Doss, *Electrochem. Acta.*, **7**, 201 (1962). A misprint in the definitions of  $C_{21}$  and  $C_{22}$  is to be corrected. Read under  $C_{21}$ ,  $C_{22}$  columns in Table I "net current taken as positive when anodic."

<sup>4</sup> S. K. Rangarajan and K. S. G. Doss, *Bull. of Nat. Inst. Sci. (India)*, **29**, 120 (1961)

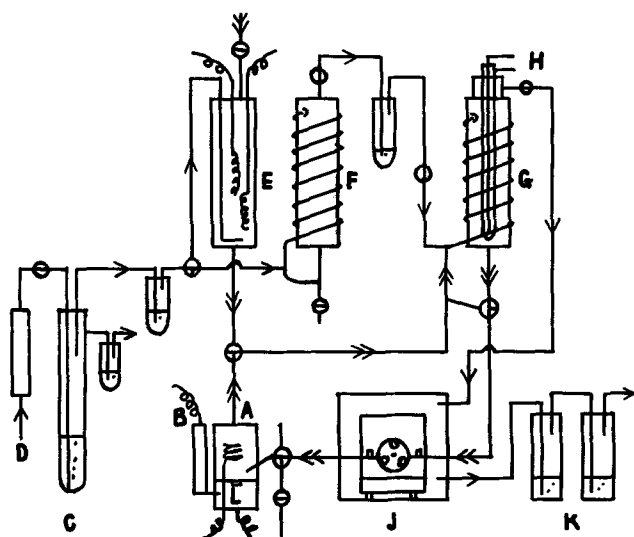


Fig. 2. Diagram of the apparatus used to study the anodic oxidation of methanol in deaerated acid solution which incorporates the specimen holder shown in Fig. 1: A, polarization cell; B, reference electrode; C, mercury safety valve; D, nitrogen deoxygenator; E, preelectrolysis cell(s); F, nitrogen gas scrubber; G, electrolyte scrubber; H, heat exchanger; J, enclosed flow inducer; K, seals to atmosphere; L, specimen holder; < gas flow; << electrolyte flow.

and out of the cell to the gas scrubbers. Diffusion of any generated gases to the specimen was thereby made more difficult.

Figure 2 shows a typical arrangement utilizing these holders. In this particular figure the apparatus was built to study the anodic oxidation of methanol in deaerated, acid solutions. While one holder was in use in the apparatus another was being cleaned, and assembled ready for the next specimen.

**W. D. France, Jr.<sup>8</sup>:** The author appreciates the interest E. W. Brooman has shown in our specimen holder for precise polarization measurements on metal sheets and foils. However, several comments regarding the design that Brooman is publishing in this discussion section are pertinent. Apparently his assembly leaks around the specimen when the Teflon deforms at this interface since a silicone rubber gasket (F) is placed behind the specimen (E). Unfortunately such solution leakage causes crevice effects and can result in erroneous data.<sup>8</sup> We avoided this problem by using polycarbonate and a replaceable Teflon gasket in front of the specimen. Also, unlike our published design, the holder suggested by Brooman provides a horizontal cavity that will accumulate corrosion products on the specimen. Such an occurrence becomes rather critical here due to the proximity of the capillary orifice (D) for potential measurement and control. Additional advantages of our holder include rapid and effective assembly and accommodation in conventional polarization cells, such as the one proposed by Greene,<sup>9</sup> which is available commercially<sup>10</sup> and is used in many electrochemistry and corrosion laboratories.<sup>11</sup> Although the versatility of Brooman's alternative design is somewhat limited, we have found the miniaturization of the electrochemical cell interesting and are pleased that features of our specimen holder were an integral part of this assembly.

<sup>8</sup> N. D. Greene, W. D. France, Jr., and B. E. Wilde, *Corrosion*, 21, 275 (1965).

<sup>9</sup> N. D. Greene, "Experimental Electrode Kinetics," Rensselaer Polytechnic Institute, Troy, N. Y. (1965).

<sup>10</sup> Available from Corning Glass Works.

<sup>11</sup> "The Reproducibility of Potentiostatic and Potentiodynamic Anodic Polarization Measurements," June 29, 1967, Report of ASTM G-1/XI Task Group 2, W. D. France, Jr., Chairman.

## Adherence and Porosity in Ion Plated Gold

C. F. Schroeder and J. E. McDonald  
(pp. 889-892, Vol. 114, No. 9)

**John L. Miles<sup>12</sup>:** The name of "ion plating" given to the process developed by Mattox<sup>13-17</sup> seems to me to be somewhat misleading. Electroplating could reasonably be called ion plating since only positively charged current carriers are plated out. However, taking the figures from footnote 17 we see that this is far from being the case in "ion plating." The rate of deposition of gold is  $2 \mu/\text{min}$  at a current density of  $0.5 \text{ ma}/\text{cm}^2$ . With the liberal assumption that half of this current is carried by gold ions Faraday's law shows that only 1% of the deposited gold atoms are ionized. The calculated amount of charged gold reaching the cathode cannot be increased by assuming the formation of ionic dimers, since the  $\text{Au}_2$  content of gold vapor has been shown to be about 0.1%.<sup>18</sup>

Thus, although the good adherence of deposited films results from ion bombardment, the excellent throwing power of the method is virtually independent of the presence of ions. These points were readily demonstrated by performing an ion plating experiment in argon with the workpiece unconnected to the cathode and not in the cathode dark space of the glow discharge. It is clearly the scattering of the gold atoms due to their short mean free path in the argon environment rather than electrostatic attraction which causes fairly uniform coatings to form on irregularly shaped workpieces. "Scatter plating" would seem to be a more logical and less misleading name for this process. (Support for this work by Greenfield Components Corporation is gratefully acknowledged.)

**Donald M. Mattox<sup>19</sup>:** The authors of the referenced paper have asked me to reply to the letter expressing criticism of the term "ion plating." I must confess that the name ion plating for this process began as a colloquialism, but since everything must be called something it has gradually gained some acceptance as a name, at least on an informal basis. The name is generally applied to a process in which the substrate is being bombarded by a flux of high energy ions sufficient to cause appreciable sputtering both before and during the actual deposition. The necessary flux depends on the substrate material, gas discharge conditions, and contamination in the system.

It is felt that the principal benefits obtained by the ion plating process are: (a) the ability to sputter clean the surface and maintain it "clean" until the first monolayer of film material is formed; (b) provide a high energy flux to the substrate surface thus enhancing diffusion, chemical reaction, etc., and (c) alter the surface and interfacial structure and thus change the interaction mechanisms and rates. The principal useful result seems to be obtaining good adherence in systems where other techniques do not work because of barrier layers, insoluble materials, etc.

I agree that the actual ionization of gold atoms is probably of little consequence, but I don't think that the term "ion plating" is any more misleading than most other terms applied to deposition techniques. As a matter of fact, most names for deposition techniques seem to apply to the environment, i.e., vacuum deposition, plasma spraying, chemical vapor deposition, rather than what actually happens to the depositing material.

As to the throwing power of the ion plating process, I am inclined to think that an entrainment mechanism

<sup>12</sup> Arthur D. Little, Inc., Acorn Park, Cambridge, Mass.

<sup>13</sup> D. M. Mattox, Reprint SC DR 281 63, Sandia Corp. (1963).

<sup>14</sup> D. Mattox, *Electrochem. Tech.*, 2, 295 (1963).

<sup>15</sup> D. M. Mattox, U. S. Pat. 3,329,601.

<sup>16</sup> T. Spalvins, et al., NASA Tech Note TND 3707.

<sup>17</sup> C. F. Schroeder, et al., *This Journal*, 114, 889 (1967).

<sup>18</sup> M. Ackerman, et al., *J. Chem. Phys.*, 33, 1784 (1960).

<sup>19</sup> Ceramics and Surface Physics Division, Sandia Corp., Sandia Base, Albuquerque N. M.

in the gas discharge is more important than the scattering. If one does the deposition in a gas atmosphere without the discharge, one obtains a finely divided particulate deposit which has little structural integrity and obtains a lower deposition efficiency than is obtained with the gas discharge present.

In summary I would like to say that since the process has some defining characteristics, however nebulous they may be, it does deserve a name and that "ion plating" is as good as any and more lyrical than most.

### Investigations of Electrocrystallization at Silver Electrodes

W. M. Krebs and D. K. Roe (pp. 892-899, Vol. 114, No. 9)

**D. J. Astley and J. H. Harrison**<sup>20</sup>: In the paper by Krebs and Roe the authors postulated that the formation of nuclei weakly bound to the underlying substrate may be involved in the electrocrystallization of Ag on an Ag single crystal. The experiment consisted of sweeping the potential anodic from the reversible potential then cathodic and anodic again. Figure 4 of their paper shows an anodic current peak corresponding to the dissolution of the nuclei before the main anodic dissolution of the substrate.

However, Budewski *et al.*<sup>21</sup> were unable to find evidence for nucleation on crystals which had a large number of dislocations. It did occur to us that it might be possible to reproduce the sweep curves of Krebs and Roe by a qualitative argument as follows. In a potentiostatic sweep experiment starting from a stationary cathodic current an anodic current peak would be observed before the main dissolution if the rate of change of  $C^0$ , the  $Ag^+$  concentration at the surface, outstripped the supply of material by diffusion from the bulk of solution, Fig. 1a, 1b, and 1c. To test this hypothesis sweep curves for the metal deposition case were calculated assuming the Nernst equation between the silver ions at the interface and the metal which has an activity ( ) = 1 because of the large number of lattice building positions, and solving

$$\frac{\partial C}{\partial t} = D \left( \frac{\partial^2 C}{\partial x^2} \right) \quad \dots [1]$$

with the appropriate conditions:

$$\begin{aligned} C^0 &= C^* \exp[-zF(\eta_i + wt)/RT]; \\ x &= \delta, \quad C = C^*; \\ i &= 2FAD(\partial C/\partial x)_{x=0} \end{aligned}$$

where  $C^*$  is the bulk silver concentration and the other symbols are usual,  $\eta$  positive for cathodic overpotential. This was solved by a finite difference method<sup>22</sup> by digital computation. The theoretical curves are shown in Fig. 2. These have been calculated by starting at  $t = 0$  with a stationary anodic current, and sweeping cathodic and back again, which essentially reproduces the Krebs and Roe experiment. The curves have some interesting features. The expected peaks only show as small inflections on the anodic going current. At sweeps slower than  $10 \text{ mv sec}^{-1}$  (not shown in Fig. 2) the anodic and cathodic going currents between  $\eta = +10$  and  $-20$  mv superimpose without hysteresis, and the currents are fairly linear with potential (or time) and pass through the point  $\eta = 0$ .

Experimental and calculated data is shown in Fig. 3 for an electropolished Ag single crystal in  $0.01M \text{ Ag}(\text{ClO}_4)$  in  $1M \text{ HClO}_4$  at  $100 \text{ mv sec}^{-1}$  sweep rate with gas bubbling to maintain a Nernst diffusion layer. The fit of the two curves is reasonable. At slow sweeps the curves superimpose without any sign of a

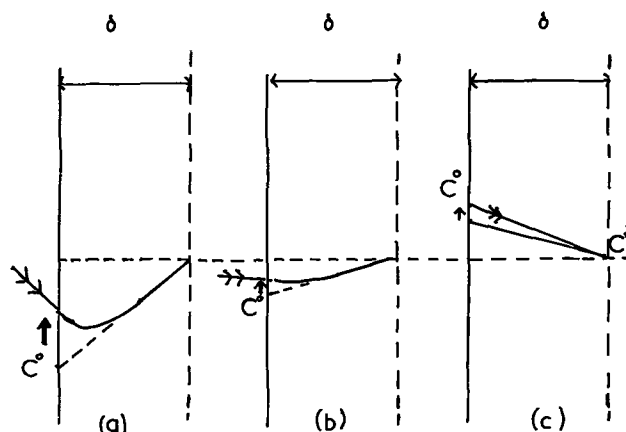


Fig. 1. Scheme of surface concentration-gradient variation for sweep conditions.

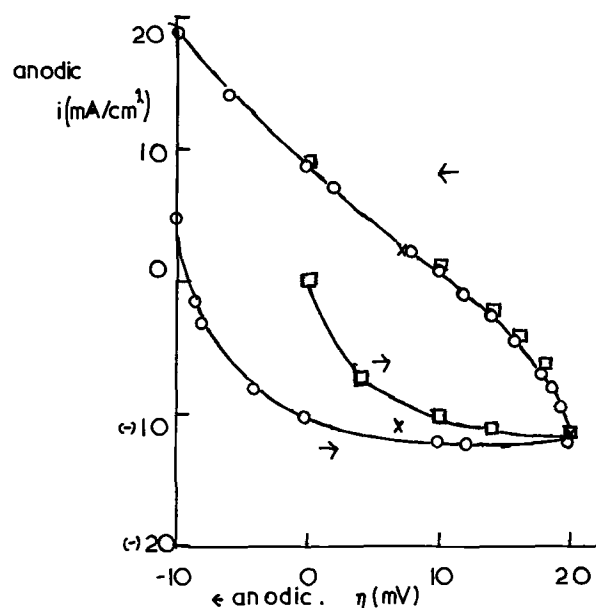


Fig. 2. Computed  $i-\eta$  plot.  $C^* = 0.01M$ ;  $\delta = 0.001 \text{ cm}$ ;  $1 \text{ v/sec}$ .  $n = 50$  (O,  $\square$ );  $n = 10$  (X).  $n$ , the number of iteration steps along the X axis.

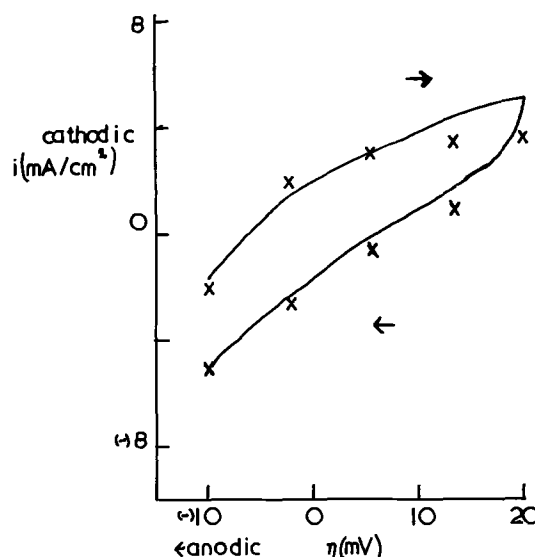


Fig. 3.  $0.01M \text{ AgClO}_4/1M \text{ HClO}_4$  single Ag crystal.  $i$  vs.  $\eta$  for  $100 \text{ mv/sec}$ . X—computed values for  $n = 10$ ,  $\delta = 0.00216 \text{ cm}$  (from current at an anodic polarization of  $10 \text{ mv}$ ).

<sup>20</sup> Department of Physical Chemistry, University of Newcastle upon Tyne, Newcastle upon Tyne, NE 1, 7RU, England.

<sup>21</sup> E. Budewski, W. Bostanoff, T. Vitanoff, Z. Stoinoff, A. Kotz-ewa, and R. Kaischew, *Phys. Stat. Sol.*, 13, 577 (1966).

<sup>22</sup> A. D. Booth, "Numerical Methods," p. 114, Butterworths (1955).

maximum. The essential difference between our measurements and those of Krebs and Roe is that their cell arrangement consisted of a spherical Ag single crystal (formed by melting) in contact with a small drop of the  $\text{Ag}^+$  solution. It would seem to us that this arrangement is liable to changes in contact angle and consequently electrode area with change in potential.

A comparison of the calculated curves with the data of Krebs and Roe shows that, assuming  $\delta = 10^{-3}$  cm, their currents are very much lower (by more than a factor of 10) in the cathodic region and it is clear that the anodic region is very much passivated. It would seem that two possibilities could explain this behavior; either the surface has few dislocations in it or the active sites at dislocations have become blocked by adsorption of impurities. It seems unlikely that few dislocations could be achieved by melting. In any case dissolution at dislocations to form etch pits and the reverse process on deposition would only affect the above theory by making the curves increase more steeply with time during the anodic sweep with no maximum. The second possibility would require nucleation during the cathodic sweep.

At low sweep rates the currents should in any case pass through the  $i$ - $\eta$  origin. Our electrodes behave exactly as a reversible system. It must be concluded that the surfaces of Krebs and Roe were not typical. It seems likely that their surfaces were severely inhibited.

**W. Michael Krebs<sup>23</sup> and David K. Roe<sup>24</sup>:** It has been shown previously that under certain conditions, silver, freshly deposited on a silver substrate, appears to be more labile than the substrate. This was clearly revealed by a series of cyclic current-voltage curves in which anodic peaks appeared following cathodic polarization, but not before. Furthermore, the charge represented by the anodic peaks was found to agree quantitatively with the amount of silver deposited during the immediately preceding cathodic scan. These measurements were made using a probe technique to form a bridge of electrolyte between bulk electrolyte, containing the silver reference-counter electrode, and selected areas on a spherical silver single crystal, as has been described in the paper under discussion. The measurements under discussion were carried out on stepped regions surrounding the (111) facets. Astley and Harrison have attempted to explain the anodic stripping peak phenomenon in terms of the  $\text{Ag}^+$  concentration profile resulting from the cathodic-anodic sequence. Their calculations, however, are based on stirred solution resulting in a Nernst diffusion layer of constant thickness. This is at variance with our experimental conditions in which stirring was not employed nor even possible due to the unusual cell configuration.

The fact that their calculations predict no hysteresis at low scan rates is sufficient to discount such a hypothesis. In addition, a simple consideration of the time intervals involved in our measurements at low scan rates (0.1-10 mv/sec) is sufficient to demonstrate the inapplicability of a mechanism which necessarily assumes large and sharp concentration gradients.

It is rather surprising that Astley and Harrison make a point of comparing current densities, noting that those observed by us are a power of ten lower than theirs, since one of the main points of our work is that deposition on the stepped regions does not proceed in a layer-like fashion, but that it commences at active sites on the step edges giving rise to the hemispherical or mound-shaped deposits revealed in Fig. 3a, b, of the discussed paper. The actual active electrode area is, therefore, very much smaller than electrolyte contact area in the initial stages of depo-

sition, and is continually changing. This is true for both the cathodic process and the anodic process, although substrate removal does contribute increasingly as the potential becomes more anodic. It is this assumption of constantly changing electrode area which is essential to the derivations presented in the paper under discussion, and the evidence for mound-like discontinuous growth is clearly shown in the photomicrographs.

The derivations do not include any reference to simultaneous substrate removal, thus making it unnecessary to define the activity of the deposit with respect to the substrate. It would be difficult to incorporate such a parameter in the derivation since an *a priori* assignment of deposit activity, and its variation with coverage, would have to be made. It was, therefore, decided that the least ambiguous method of attack was to treat the deposit alone, thus assuming the electrochemical behavior of the substrate to be unchanged. In comparing calculated with experimental curves, the substrate contribution was subtracted out of the latter using the initial anodic curve (before any deposition). This initial anodic curve could be reproduced fairly well by repeating the anodic scan after stripping off the deposit.

Budewski *et al.*,<sup>25</sup> have shown that nearly dislocation free (111) facets of silver can be prepared by growing the crystal electrolytically. We claim the same perfection for our thermally prepared (111) facets. Similar measurements made exclusively on these facets, to be presented in a future paper, reveal that up to 60 mv overvoltage is required before deposition commences, indicating a pronounced paucity of growth sites. In addition, double layer capacity measurements yield values which are consistent with those obtained by other workers<sup>26</sup> suggesting that both their surfaces and ours were either equally clean or equally contaminated. The fact that the faces of the steps are parallel to the facet, and possibly of the same perfection, could explain deposition being preferentially restricted to the edges of these steps.

The reproducibility of cyclic current voltage curves exhibiting stripping behavior furnishes additional evidence that contamination is of minimal importance, if any at all. In addition, the much more favorable electrode area/electrolyte volume, noted in the original paper, tends to decrease accordingly the susceptibility of the system to impurities.

Cyclic curves which were obtained on random areas of the silver crystals, areas on which faceting was not present, showed no hysteresis. These regions undoubtedly consist of micro steps, which were, however, not observable and approximate a polycrystalline specimen. Indeed, there was little difference between curves obtained on random areas of single crystal samples and those measured on polycrystalline specimens of silver. This is the behavior expected for a surface containing many growth sites.

### Effect of Hydrogen Absorbed by Electrode and Electrolyte on Hydrogen Coverage

D. J. BenDaniel and F. G. Will (pp. 909-915, Vol. 114, No. 9; pp. 1271-1272, Vol. 114, No. 12); S. Schuldiner (pp. 916-917, Vol. 114, No. 9)

**G. Dubpernell<sup>27</sup>:** The continued insistence on a small and functional solubility of hydrogen in platinum at room temperature seems something of a travesty on the ever increasing need to convert electrochemistry from an art to a science. Some facts which should be considered more seriously than in the past are listed below.

1. The solubility determinations at high temperatures clearly show that there is no appreciable solu-

<sup>25</sup> E. Budewski, V. Bostanov, T. Vitanov, Z. Stoinov, A. Kotseva, and R. Kaischew, *Electrochim. Acta.*, 11, 1967 (1966).

<sup>26</sup> L. Ramaley and C. G. Enke, *This Journal*, 112, 947 (1965).

<sup>27</sup> 13366 Wales Ave., Huntington Woods, Mich.

<sup>23</sup> Present address: Instrumentation Laboratory, Lexington, Mass.

<sup>24</sup> Present address: Oregon Graduate Center, Portland, Oregon.



bility at room temperature. Thus Sieverts and Jurisch [BenDaniel and Will's ref. (7)] determined the relatively small solubility of hydrogen in platinum at temperatures of 827°-1342°C. A determination of the solubility at 409°C was considered uncertain because of its smallness. Efforts to determine a solubility at room temperature were fruitless, and Sieverts and Jurisch concluded that "compact platinum does not dissolve any measurable quantity of hydrogen at room temperature."

Sieverts and Jurisch plotted their results for the solubility of hydrogen in platinum in such a way that they showed a zero solubility at 800°C. Schuldiner's ref. (8) (D. P. Smith, "Hydrogen in Metals," 1948) replots the Sieverts and Jurisch data in such a way as to indicate zero solubility at 600° or 400°C (p. 35). If the five best measurements made by Sieverts and Jurisch are plotted on a logarithmic scale they give a reasonably good straight line plot which can easily be extrapolated from 800°C down to room temperature. Such an extrapolation would seem to indicate a solubility at room temperature of about  $28 \times 10^{-10}$  grams of hydrogen per gram of platinum ( $3 \times 10^{-8}$  moles  $H_2/cm^3$  Pt) if this figure has any meaning. In their discussion, BenDaniel and Will give much lower figures, but do not make clear their method of extrapolation.

2. BenDaniel and Will's ref. (8) (the Smithell's book of 1937) contains a description on p. 148 of an experiment by Berry based on the fact that platinum will not absorb any electrolytic hydrogen evolved on it in 5% sulfuric acid solution at 6 ma/cm<sup>2</sup>.

3. BenDaniel and Will give five references (9-13) to the older work on the solubility and diffusion coefficient of electrolytic hydrogen through platinum membranes near room temperature. A comprehensive survey of such work on the permeability of metal membranes was made in 1933<sup>28</sup>, including these five references and many others. It was concluded from this survey and the experimental work done that ". . . electromotively active hydrogen and oxygen do not diffuse through solid metals."

4. Schuldiner [ref. (3)] points out that several workers have found that hydrogen does not diffuse through platinum membranes if they are clean or if the sulfuric acid electrolyte used is pure. If hydrogen has any solubility in platinum at room temperature it should certainly be evident under these conditions. Since the lack of any diffusion or solubility under these conditions is accepted, there can hardly be diffusion under other conditions unless they include damage to the membrane.

5. Schuldiner [ref. (8)] refers to Professor D. P. Smith's book on the extremely low solubility at 400°C, and yet fails to consider the solubility at room temperature as essentially zero. Professor Smith discusses cathodic occlusion by platinum on pp. 79-80 and concludes: "Nearly all indications point to a real, but extremely small, occlusion at ordinary temperatures and to the probability that this is purely rift occlusion unaccompanied by any appreciable solubility in the undisturbed lattice."

Again in a personal communication in 1949 Professor Smith said: "We certainly seem to be in agreement as to the lack of solubility, in the sense of interstitial distribution of hydrogen, in the lattices of platinum and other metals which absorb hydrogen endothermically, and the view that hydrogen (and oxygen) pass through these metals by way of some sort of crevice; although I may perhaps go farther than you would care to accompany me in considering the crevices ("rifts") something else than mere accidental defects in the lattice."

Surely the theory of the hydrogen electrode behavior can be developed on the basis of the physical

and chemical surface properties of the metal, without insisting on some solubility of hydrogen in the lattice at room temperature.

**F. G. Will and D. J. BenDaniel:** While Dr. Dubpernell does not dispute that hydrogen is slightly soluble in platinum at elevated temperatures (i.e., between 827° and 1342°C), he maintains that the solubility at room temperature is "essentially zero." In fact, Dr. Dubpernell<sup>29</sup> restates his conclusion from an earlier literature survey and his own work on platinum and palladium that "electromotively active hydrogen and oxygen do not diffuse through solid metals."

This view is particularly surprising with respect to the permeation of electrolytically evolved hydrogen through palladium. The solubility and diffusivity of hydrogen in this metal are so large, even at temperatures below 100°C, that they have been established beyond doubt by a large number of investigators [compare ref. (14-18), (20, 21) of our rebuttal].<sup>30</sup>

Since the permeation rates of hydrogen through platinum are about 4 orders of magnitude smaller than through palladium, it is understandable that relatively few investigators have been able to establish unambiguously the diffusion of hydrogen through platinum. For the purpose of our discussion here, we may disregard older work on the subject [earlier ref. (11) and (20-23) in our rebuttal] and only consider the recent findings of Vetter [earlier ref. (12)] and Gileadi *et al.* [earlier ref. (13)].

Certainly, there is some disagreement with respect to the exact magnitude of solubility ( $10^{-5}$  moles  $H_2/cm^3$  Pt at 25°C vs.  $2 \cdot 10^{-6}$  moles/cm<sup>3</sup> at 70°) and diffusivity ( $3 \cdot 10^{-8}$  cm<sup>2</sup>/sec at 25°C vs.  $10^{-18}$  cm<sup>2</sup>/sec at 70°). However, in permeation studies such disagreement is not uncommon, due to the difficulties in producing similar states of the surface and the metal texture. Most strikingly, both investigators find that (a) the steady-state permeation rates are inversely proportional to the thickness of the platinum foils and (b) the half-rise times of the permeation transients are proportional to the square of the thickness. This behavior is typical for a diffusion process, and it is difficult for us to see how it can be interpreted on any other reasonable basis.

We will now comment on some remaining specific points of Dr. Dubpernell.

1. With regard to our method of extrapolation, we plotted Sieverts' original data [earlier ref. (27)] in the usual semi-log plot, i.e., the logarithm of the solubility against 1/T, and extrapolated the resulting straight line (between 1033 and 1342°C) to 25°C. Thus, we arrived at a solubility of  $4 \cdot 10^{-17}$  moles  $H_2/cm^3$  Pt. This extremely low value was discarded for the purpose of our analysis. Parenthetically, Dr. Dubpernell, in extrapolating Sieverts' data, finds a value which is 9 orders of magnitude higher than ours. This might be due to an error in his conversion of the unit mgH<sub>2</sub>/100 gPt, as used by Sieverts, into moles  $H_2/cm^3$  Pt.

2. Berry<sup>31</sup> merely measured the occlusion of hydrogen by Pd-Au alloys by forming the difference in the amounts of hydrogen evolved by the same current from a Pd-Au cathode and a Pt cathode. He did not concern himself with H<sub>2</sub> absorption by Pt. The volumes occluded by the alloys were found to range from 5 to 150 cm<sup>3</sup>H<sub>2</sub>/g alloy. The corresponding volume absorbed by Pt is only 0.01 cm<sup>3</sup>H<sub>2</sub>/g Pt (based on Vetter's solubility data which we used in our analysis). Hence, Berry's implicit assumption that the absorption of H<sub>2</sub> by Pt can be neglected in his experiments is fully justified. But this assumption can hardly be interpreted as a "fact that platinum will not absorb any electrolytic hydrogen."

<sup>28</sup> G. Dubpernell, "The Mechanism of the Penetration of Electrolytic Polarization Through Thin Metal Sheets," Dissertation, University of Michigan, 1933; A. L. Ferguson and G. Dubpernell, *Trans. Electrochem. Soc.*, **64**, 221 (1933).

<sup>29</sup> A. L. Ferguson and G. Dubpernell, *Trans. Electrochem. Soc.*, **64**, 221 (1933).

<sup>30</sup> F. G. Will and D. J. BenDaniel, *This Journal*, **114**, 1271 (1967).

<sup>31</sup> A. J. Berry, *J. Chem. Soc.*, **99**, 463 (1911).



Point 3 of the discussion has already been answered, points 4 and 5 are not addressed to us.

Finally, with regard to Dr. Dubpernell's concluding remark, we state that our analysis, based on diffusion of hydrogen into platinum, leads to a quantitative interpretation of recent transient measurements on platinum by Schuldiner and Warner [earlier ref. (25)]. Surely, we welcome any alternate quantitative interpretation of those experimental findings.

### Two Remarks on the Resistive Contribution to Overpotential

Benson R. Sundheim (pp. 158-160, Vol. 115, No. 2)

**R. Piontelli**<sup>32</sup>: This paper recalls very opportunely the attention of the experimental electrochemists to the existence and importance of the systematic errors involved in overvoltage measurements by means of the Luggin-Haber capillary.

This matter has been dealt with in great detail in a large number of papers from this laboratory.<sup>33</sup>

The experiments carried out to prove the theoretical conclusions have fully confirmed the quantitative importance of the systematic errors introduced when the screen-effect is exasperated, the Luggin-Haber capillary being very near or pressed against the electrode surface.

Our research work has led also to the realization of arrangements, suitable for reducing the systematic errors to a very acceptable minimum.

The principle of these arrangements is recalled in Fig. 1. in which also the traces on the drawing plane of the equipotential surfaces<sup>34</sup>, together with the ones of the current lines, are represented.

The problem of eliminating the "resistive contribution," without introducing "shielding effects" has found, therefore, practical solutions.

According to the practice of this Laboratory (for more than 18 years), in all of the cases in which the electrode material must be treated by a careful policy, the "side-channel capillary" (Fig. 1a) is especially suitable. On a regular surface this capillary leads to a very efficient shielding of the underlying surface, while reducing the resistive contribution to that of just a solution layer of (10/40)  $\mu$ .

The only restriction in the application of this device concerns the cases in which the electrode surface undergoes strong passivation phenomena, by formation of covering layers.

In these cases, the eventual intervention of "crevice effects" must be taken into account.

In view of the strong equivalent resistance of the layers themselves, and of the improved throwing power of the anodic process, however, one may then

<sup>32</sup> Institute of Electrochemistry, Physical Chemistry and Metallurgy, Milan Polytechnic, Milan, Italy.

<sup>33</sup> R. Piontelli, *Gazz. Chim. Ital.*, **83**, 357, 370, (1953); *Z. Elektrochem.*, **59**, 778 (1955); *Trans. Inst. Metal Finishing*, **31**, 51 (1954); *This Journal*, **103**, 356 (1955); *ibid.*, **105**, 752 (1958); *Corrosion*, **9**, 115 (1953). R. Piontelli, et al., C.R. 2nd Meeting CITCE (1950) p. 379; *Gazz. Chim. Ital.*, **80**, 596 (1950); *Z. Elektrochem.*, **56**, 86 (1952); *ibid.*, **58**, 54, 86 (1954); *Ricerca Scientifica*, **26**, 838 (1956). See also: K. J. Vetter, "Electrochemical Kinetics," p. 393 and 407, Academic Press (1967).

<sup>34</sup> Experimentally determined on models. Also the essentially "operative meaning" of these equipotential surfaces is discussed in the above mentioned papers.

simply displace the probe from the electrode surface in the order of 1 to 2 mm, neglecting or correcting the ohmic drop contribution to the measured overvoltage.

The parasitic capacitive effect, involved by very quick measurements, may be reasonably reduced by using a double wall probe.

In many cases also an arrangement of the type indicated in Fig. 1c may correspond to practical requirements.<sup>35</sup>

Of course, the extremely short time-constant of the resistive contribution to the overvoltage allows its correction or direct compensation<sup>36</sup>, a route which we too are following in the overvoltage measurements on liquid metal electrodes, especially in melts<sup>37</sup>, when the arrangements above cannot be applied.

In the very numerous cases in which the so-called "classical techniques" for measuring the overvoltages are still the most reliable, exhaustive, and adequate in giving information on practical problems, the cell geometry and thus the capillary form and placement deserve the most careful attention by the experimental electrochemist.

The compatibility of these requirements with those of a careful prepurification of the solution and eventually of the electrode surface preparation has been attained in some cell types realized here.<sup>38</sup>

### Influence of Thin Noble Metal Films on Zirconium Oxidation

A. Fiegna and P. Weisgerber (pp. 369-371, Vol. 115, No. 4)

**B. Cox**<sup>39</sup>: Fiegna and Weisgerber show ignorance not only of previous work on the effect of evaporated metal contacts on the oxidation of zirconium, but also of previous studies of the oxidation of zirconium in water vapor. Although experiments in water vapor are not numerous, there are at least two sources of directly comparable data<sup>40,41</sup> and a further two studies at higher temperatures.<sup>42,43</sup> However, whilst they may perhaps be forgiven for failing to locate these references, they should have been aware of the previous instances where enhanced oxidation of zirconium resulted from contact with noble metals<sup>44-46</sup> since this is the primary subject of their study.

In this respect their results agree with previous studies<sup>46</sup> which showed no enhancement of the oxidation rate in oxygen for thin gold films, but a large increase in oxidation rate for thicker films. The reasons for this discrepancy may become evident if we consider the possible explanations of the phenomenon.

<sup>35</sup> For the application to a potentiostatic measurement see the exhaustive work: M. Pepersack, C. Capel, R. Boute, and C. Decroly, *Electrochim. Acta.*, **10**, 479 (1965).

<sup>36</sup> See Vetter, *loc. cit.*

<sup>37</sup> R. Piontelli, *Annals of the New York Academy of Sciences*, **79**, 1025 (1960).

<sup>38</sup> R. Piontelli, et al., *Rend. Acc. Lincei VIII*, **25**, 431 (1958); in E. Yeager, "Trans. Symposium on Electrode Processes," p. 67, John Wiley & Sons, Inc., New York (1961); *Electrochim. Metall.*, **1**, 5 (1966).

<sup>39</sup> Atomic Energy of Canada Ltd., Chalk River, Ont., Canada.

<sup>40</sup> M. W. Mallett, et al., *This Journal*, **104**, 349 (1957).

<sup>41</sup> B. Cox, UKAEA Reports, AERE-R4348 and R4458 (1963).

<sup>42</sup> R. E. Westerman, *This Journal*, **111**, 140 (1964).

<sup>43</sup> T. Maekawa and J. Kai, *J. Jap. Inst. Metals*, **24**, 581 (1960).

<sup>44</sup> D. H. Bradhurst, J. E. Draley, and C. J. Van Druenen, *This Journal*, **112**, 1171 (1965).

<sup>45</sup> S. B. Dalgaard, Atomic Energy of Canada Report, AECL-2006 (1964).

<sup>46</sup> J. Levitan, J. E. Draley, and C. J. Van Druenen, US Report ANL-7252 (1966).

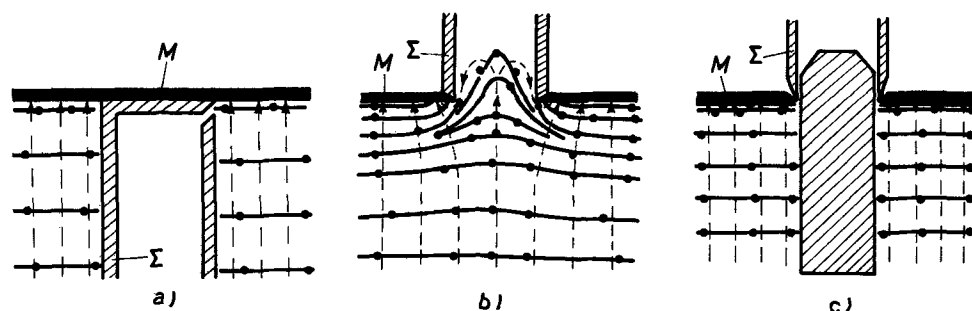
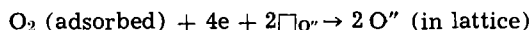


Fig. 1. M = electrode material;  $\Sigma$  = capillary; heavy full lines = traces of the equipotential surfaces; interrupted lines = current lines; (a) side channel capillary; (b) back capillary; and (c) back capillary occluded.

The explanations offered by the authors make the *a priori* assumption that only transport of oxygen through the oxide is important in the oxidation of zirconium. Thus, they ignore the reverse electronic current and the effect which a conducting surface layer might have on it. Recent evidence<sup>47</sup> has shown that the electronic current flows at only a few sites in the oxide ( $\sim 10^2/\text{cm}^2$ ) on zirconium. These sites have been tentatively related to local segregation of impurities, by analogy with Zircaloy-2, where the  $\sim 10^4$  sites/ $\text{cm}^2$  for electronic conduction have been positively identified with the sites of second phase particles resulting from the alloying additions. Since iron is generally the most prominent transition metal impurity in crystal-bar zirconium, this metal is possibly the source of the conducting impurities in this case too.

The ionic transport process is, by comparison, far more uniform, although it proceeds by the transport of oxygen ions through the poorly crystalline (or amorphous) matrix between the monoclinic  $\text{ZrO}_2$  crystallites.<sup>48,49</sup> Recent studies have shown that when  $\text{O}^{17}$  is diffused into an oxide formed in  $\text{O}^{16}$  saturation is not attained at the oxide-gas interface.<sup>48</sup> Thus, the process occurring at this interface is apparently slow compared with the inward diffusion of oxygen. The over-all process occurring at this interface in oxygen is given by



Thus the presence of not only oxygen vacancies but also electrons is required at the points of oxygen entry (i.e., oxide crystallite boundaries).

Since the electrons are transported through the oxide film at a relatively few flaws they must reach the reaction site by surface diffusion. This surface diffusion may be the slow step which results in the failure to maintain equilibrium at the outer oxide interface. Any process which speeded up surface diffusion would permit the fraction of mobile oxygen atoms at the surface to approach saturation. The oxygen concentration at the inner interface will be set independently by the conditions of equilibrium at this interface, and, therefore, an increase in the boundary concentration of mobile oxygen at the outer interface will result in an increase in the diffusion of oxygen ions through the oxide, and hence an increase of the oxidation rate.

However, this explanation predicts that any metal film continuous enough to give good surface conductivity would result in an increase in the oxidation rate. This was not found by the authors for either silver or gold contacts in oxygen, and possibly not in water vapor either since their oxidation rate for the uncoated specimen is apparently a factor of two lower than would be expected.<sup>40,41</sup> Draley *et al.*, did observe enhanced attack with thick, but not thin, gold contacts<sup>44,46</sup> in line with the above prediction. The significant feature of the gold contacts used by Fiegna and Weisgerber is probably the thickness,  $\sim 300\text{\AA}$ , compared with contacts  $\sim 6400\text{\AA}$  thick which gave enhanced oxidation at Argonne National Laboratory.

In addition to the observation by Fiegna and Weisgerber of diffusion of gold into growing zirconia films, earlier work by Dalgaard which demonstrated physical welding of gold probes onto growing zirconia films<sup>45</sup> gave positive evidence for this phenomenon. Thus it is possible that following diffusion of the thin gold films into the oxide there was insufficient change in surface conduction to result in an increase in the oxidation rate. This could be checked by varying the initial thickness of evaporated metal. The increase effected by the platinum contact in oxygen may result

from a greater surface conductivity during oxidation in this instance.

The difference between the apparent behavior of metallic contacts in oxygen and water vapor may result from an error in the curve for the uncoated zirconium specimens in water vapor. Other studies<sup>40,41</sup> predict a weight gain about twice as high in water vapor, and indicate little difference between the oxidation curves for oxygen and water vapor at low pressures.<sup>41-43</sup> The authors do not indicate whether the curves they report were repeated, or what was the reproducibility of their results in water vapor.

**A. Fiegna and P. Weisgerber:** Our oxidations in oxygen and in water vapor were made several times and final weight gains never differed more than 10%.

But it is a common experience with oxidation of pure metals that deviations of a factor of 2 and more are to be expected, if factors as the purity grade of the reactants, the method of specimen and surface preparation, or temperature gradients in the reaction zone are not standardized.

Because of the important influence of these conditions, it seems unduly to conclude errors in our experiments because they differ by a factor of 2 from data found elsewhere. Moreover, the data Cox cited were found not only under different experimental conditions as mentioned but also with different parameters as temperature, vapor pressure, and reaction time so that additional uncertainties have to be taken into account which result from errors of the rather complex extrapolations.

As final conclusion it is to say that our experimental data from oxidation of gold and silver coated zirconium in oxygen do not fulfill the prediction derived from the theory of Cox, that increased reaction rates result from increased surface conductivity of electrons.

### The Standard Potential of the Silver-Silver Chloride Electrode in N-N Dimethylacetamide at 25°C

B. Scrosati, G. Pecci, and G. Pistoia  
(pp. 506-507, Vol. 115, No. 5)

**Robert S. Alwitt<sup>50</sup>:** The authors claim to have determined  $E^\circ$  for the  $\text{AgCl}/\text{Ag}$  electrode in dimethylacetamide (DMA) by using the same classical techniques that have proved so successful when working with protic solvents such as water, alcohols, formamide<sup>51</sup>, and N-methylacetamide.<sup>52</sup> However, dipolar aprotic solvents, such as DMA, have some properties very different from protic solvents<sup>53</sup> and the same experimental techniques cannot necessarily be applied. The two factors that require the closest attention are indicated below.

1. Hydrogen chloride is a weak acid in aprotic solvents. For example, the  $\text{pK}_a$  of  $\text{HCl}$  at 25°C is 3.55 in dimethylformamide (DMF) and 8.94 in acetonitrile.<sup>53</sup> The authors treat their data as if  $\text{HCl}$  were completely dissociated in DMA solutions. Did they verify this by independent measurements?

2. Silver chloride is soluble in DMF to the extent of about 0.01g/100g DMF<sup>54</sup>, and is quite soluble in other aprotic solvents in the presence of excess chloride.<sup>55</sup> It is obviously undesirable to use a  $\text{AgCl}/\text{Ag}$  reference electrode in solutions in which  $\text{AgCl}$  has appreciable solubility. Did the authors find that  $\text{AgCl}$  was insoluble in solutions of  $\text{HCl}$  in DMA?

<sup>50</sup> Research and Development Laboratories, Sprague Electric Co., North Adams, Mass.

<sup>51</sup> R. K. Agawari and B. Nayak, *J. Phys. Chem.*, **70**, 2568 (1966).

<sup>52</sup> L. R. Dawson, R. C. Sheridan, and H. C. Eckstrom, *J. Phys. Chem.*, **65**, 1829 (1961); L. R. Dawson, W. H. Zuber, Jr., H. C. Eckstrom, *J. Phys. Chem.*, **69**, 1335 (1965).

<sup>53</sup> A. J. Parker, *Quarterly Rev.*, **16**, 163 (1962).

<sup>54</sup> "DuPont DMF" Technical Bulletin, E. I. du Pont de Nemours & Co., Industrial and Biochemicals Dept., Wilmington, Delaware.

<sup>55</sup> I. M. Koltoff and T. B. Reddy, *Inorg. Chem.*, **1**, 189 (1962); W. H. Smyrl and C. W. Tobias, *This Journal*, **113**, 754 (1966); J. N. Butler, D. R. Cogley, and W. Zurosky, *This Journal*, **115**, 445 (1968).

<sup>47</sup> N. Ramasubramanian, Atomic Energy of Canada Report, AECL-3082 (1968).

<sup>48</sup> B. Cox and J. P. Pemsler, *J. Nucl. Mat.*, to be published.

<sup>49</sup> R. A. Ploc, Atomic Energy of Canada Report, AECL-2794 (1967).

The authors report a slope of  $-0.640$  for a plot of  $E'$  vs.  $m_{\text{HCl}}$ . This is a considerably larger slope than is usually obtained for such a plot. For the same cell as used by the authors, but with other solvents, this slope has been reported as  $-0.08$  with water<sup>56</sup>,  $-0.05$  with formamide<sup>51</sup>, and  $-0.03$  with N-methylacetamide<sup>52</sup>. A plot of  $E'$  vs.  $m$  is used to make essentially second-order corrections to the value of  $E^\circ$ , and would be

<sup>56</sup> R. A. Robinson and R. H. Stokes, "Electrolyte Solutions," 2nd Ed., p. 192, Butterworths, London (1959).

expected to have a small slope. We suggest that the factors discussed above contribute to the large slope that was obtained.

This seems a suitable place to report an observation made in our laboratory when trying to measure pH in DMF solutions. We found that general purpose glass electrodes (0-11 pH range) did not behave reversibly in DMF solutions. An E2 glass electrode recommended for alkaline conditions (Coleman 3-424) was found to be reversible, as demonstrated by a response of 59 mv per decade change in hydrogen ion concentration.

# Electropolymer Studies

## II. Electrical Conductivity of a Polystyrene Sulfonic Acid Membrane

Charles S. Fadley<sup>1</sup> and Richard A. Wallace<sup>2</sup>

Department of Chemical Engineering and Sea Water Conversion Laboratory,  
University of California at Berkeley, Berkeley, California

### ABSTRACT

The electrical conductivity of an ion exchange membrane containing polystyrenesulfonic acid was studied as a function of two primary variables: temperature and extent of water absorption. The conductivity of dry membrane obeys an Arrhenius relation in the range of  $28^\circ < T < 55^\circ\text{C}$  with an activation energy of approximately 1 ev. A semi-empirical equation was derived to predict the variation of conductivity with water absorption. This equation gives a good description of the data over a range of 7 orders of magnitude ( $10^{-8} < \sigma < 10^{-1} \text{ ohm}^{-1}\text{-cm}^{-1}$ ). The net volume change accompanying water absorption was also measured and its behavior can be qualitatively correlated to that of conductivity.

The study of electrical conductivity and other transport properties in polar polymers has long been of interest. Early studies on the conductivity of textile fibers (1-4) have been extended by now to a variety of biological polymers (5, 6). In these experiments, the nature of the charge carriers is often a major question, and the role of absorbed water is very important. The development of ion exchange materials has led to a consideration of similar problems in these highly ionic polymers (7). Conductivity and diffusion coefficient studies have been made on bead and rod samples of these polymers (8-11) and also on ion exchange membranes containing them (12-15). In addition, the important role of water in the transport and selectivity properties of such materials gave rise to some rather thorough investigations into the thermodynamics of the water absorption process for cross-linked polystyrenesulfonic acid (16-19). However, the exact details of the transport processes are still not totally understood (7, 20).

We report here an experimental and theoretical study of the electrical conductivity of a polystyrenesulfonic acid ion exchange membrane. The membrane was not immersed in solution, as in most previous investigations, but was exposed to varying partial pressures of water vapor. The extent of water absorption was varied from complete dryness to saturation, a broader range than has previously been studied with regard to ion exchange membranes. The effects of temperature, applied voltage, and duration of current flow were also investigated.

A theoretical analysis was made in order to predict the effect of water absorption on conductivity. Several treatments of this kind have been made previously. Among them are attempts to correlate changes in conductivity with the dielectric constant (3, 5, 14), gaps in water pathways for conduction (4), and the viscosity of "pore" fluid (4, 9). Only the first approach is reasonable for describing an ion exchange membrane over broad ranges of water absorption, and it requires a knowledge of both the dielectric constant and a somewhat indefinite polarization radius about the charge carriers in order to predict conductivity. We have therefore tried a new approach which makes use of the theory of absolute reaction rates (21). The conduction and absorption processes are linked via the free energy of absorption, and the semi-empirical equations so derived are in reasonably good agreement with experimental results.

**Key words:** Absorption of water, activation energy, electrical conductivity, free energy of absorption, free energy of activation, ion exchanging substances, membrane, sulfonated styrene polymers, sulfuric acid, conductivity volume.

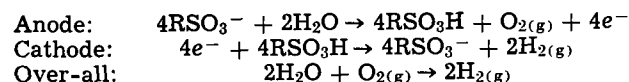
<sup>1</sup>Present address: Lawrence Radiation Laboratory and Department of Chemistry, University of California, Berkeley.

<sup>2</sup>Present address: Polymer Research Institute and Department of Chemical Engineering, Polytechnic Institute of Brooklyn, Brooklyn, New York.

As a further aid in understanding the relationship between conduction and water absorption, we have measured the net volume change for absorption. This quantity is qualitatively correlated with conduction via a hydration sphere model.

The ion exchange membrane selected for study consisted of approximately 25% by weight of polystyrenesulfonic acid (PSA) supported in a matrix of polyethylene. We assume that the effects of the polyethylene matrix on conductivity are only indirect (separating adjacent PSA molecules or reducing the effective dielectric constant, for example) in view of its very low conductivity in the pure state (approximately  $10^8$  less than the smallest membrane conductivity measured). Therefore, the conduction mechanism will be primarily related to properties of the PSA molecule.

The electrode reactions that are believed to occur in water-saturated cross-linked PSA are (8):



In the absolutely dry membrane (if such a state can be achieved without degradation) these reactions would be impossible. Although other electrode reactions could take place involving the oxidation of the  $\text{RSO}_3^-$  group (22), they also involve water. Therefore, at least a very small amount of water seems essential for sustained ionic conduction, and we have investigated both voltage and time variation of conductivity in order to verify this mechanism of conduction in the "dry" state obtained with our experimental conditions.

### Theory

We wish to derive an equation predicting the variation of specific conductivity with water absorption. As the indicator of water absorption, we use the moles of water absorbed per equivalent of PSA in the membrane ( $n$ ). The theory of absolute reaction rates (21) will be used to derive this equation, although it is probable that several other formalisms could be used to arrive at the same final result.

The basic "reaction" involved in conduction is assumed to be the passage of a hydrogen ion over an energy barrier between two more stable points in the membrane separated by some distance,  $\lambda$ . The rigorous application of reaction rate theory would thus require a knowledge of the statistical distribution of all possible types of ion movement (that is, a knowledge of the activation energy and jump distance for each type of motion and its relative frequency of occurrence). Such an exact treatment would automatically include abnormal hydrogen ion transport (by Grotthuss conduction). However, such knowledge is

not available for the complex polymer-water mixture under study, and we choose to use effective activation energies and jump distances to describe the motion of hydrogen ions along or between PSA molecules.

Abnormal transport thus remains as a separate problem which arises only at higher extents of water absorption. Abnormal transport in aqueous solutions has been analyzed using the theory of absolute reaction rates (23), and the results obtained for  $\sigma$  differ significantly from the assumptions above only in that a specific jump distance and free energy of activation are involved, these being connected with the reaction transferring a hydrogen ion from one water molecule to the next. We neglect abnormal conduction in the remainder of this derivation, since it cannot occur for  $n < \sim 1$  and does not occur for most cations other than  $H^+$ . It must, of course, be considered in comparing experiment and theory for the membrane at hand, however.

If we now make use of the approximate validity of the Nernst-Einstein equation relating conductivity and self-diffusion coefficient (13), reaction rate theory gives as a final result

$$\sigma = [(cq^2\lambda^2)/h] \exp[-\Delta F^\ddagger/RT] \quad [1]$$

where:  $\sigma$  = specific conductivity ( $\text{ohm}^{-1} \text{cm}^{-1}$ ),  $c$  = concentration of charge carriers ( $\text{cm}^{-3}$ ),  $q$  = electronic charge (C),  $\lambda$  = effective jump distance (cm),  $h$  = Planck's constant (J-s),  $\Delta F^\ddagger$  = effective free energy of activation (cal/mole),  $R$  = gas constant (cal/mole-°K),  $T$  = temperature (°K).

The experimental activation energy, ( $E_x$ ), can now be determined in the standard way as

$$E_x = -R \partial \ln \sigma / \partial (1/T) \quad [2]$$

This gives

$$E_x = \Delta H^\ddagger \cong \Delta E^\ddagger \quad [3]$$

where:  $\Delta H^\ddagger$  = effective enthalpy of activation (cal/mole),  $\Delta E^\ddagger$  = effective internal energy of activation (cal/mole).

Thus we arrive at an Arrhenius expression for conductivity

$$\sigma = \sigma_o \exp[-E_x/RT] \quad [4]$$

where

$$\sigma_o = [(cq^2\lambda^2)/h] \exp[\Delta S^\ddagger/R] \quad [5]$$

$\Delta S^\ddagger$  = effective entropy of activation (cal/mole - °K).

The only parameters in Eq. [1] which will be significantly affected by water absorption are  $c$  and  $\Delta F^\ddagger$ . The PSA molecule is a very rigid structure (24), and therefore the jump distance along the molecule will be little changed by absorption of water. The contribution of jumps between molecules to the conductivity is difficult to estimate, but one can make a rough calculation of the change in this jump distance as water is absorbed. The average of this distance should be roughly proportional to  $1/(c)^{1/3}$ . Since our results indicate that this latter quantity changes by only a factor of 2 in going from very dry to completely saturated membrane (whereas conductivity changes by a factor of  $10^7$ ) we will assume  $\lambda$  to be constant.

The variation of  $c$  with water absorption is due simply to the expansion of the membrane as water enters the polymer matrix. The effect of this expansion on  $\sigma$  can be termed a dilution affect.

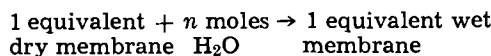
The qualitative variation of  $\Delta F^\ddagger$  with water absorption can be deduced by using the dry membrane as a reference state and considering the changes which take place upon absorbing an average of  $n$  molecules of water per each sulfonic acid group. Let  $\sigma_D$  and  $\Delta F_D^\ddagger$  refer to the dry state. In this state the effective free energy of activation should be a maximum, since any water absorption results in partial or complete ionization of the sulfonic acid groups, thereby lowering the energy barrier for hydrogen ion motion. It has, in fact, been shown that all water molecules absorbed by cross-linked PSA in the early stages of absorption ( $0 < n < 4$ ) are attached to the hydrogen

ion in an ordered chain structure or hydration sphere (18).

A quantitative prediction of the dependence of  $\Delta F^\ddagger$  on  $n$  is rather difficult to make but a reasonable assumption proves to be that

$$\Delta F^\ddagger = \Delta F_D^\ddagger + \beta \Delta F_A \quad [6]$$

where  $\beta$  = empirical constant ( $>0$ ),  $\Delta F_A$  = free energy change for the reaction:



Since  $\Delta F_A$  is in general negative this equation shows the proper reduction in  $\Delta F^\ddagger$  with increase of  $n$ . This assumption links thermodynamically the conduction and absorption processes and implies that both  $\Delta S^\ddagger$  and  $\Delta H^\ddagger$  are altered by water absorption, in contrast to an earlier hypothesis wherein  $\Delta H^\ddagger$  was assumed to be the quantity primarily affected (14).

Combining Eq. [1] and [6] gives

$$\sigma = [(cq^2\lambda^2)/h] \exp[-(\Delta F_D^\ddagger + \beta \Delta F_A)/RT] \quad [7]$$

or, since

$$\sigma_D = [(c_D q^2 \lambda^2)/h] \exp[-\Delta F_D^\ddagger/RT] \quad [8]$$

we can rewrite Eq. [7] as

$$\sigma = \sigma_D (c/c_D) \exp[-\beta \Delta F_A/RT] \quad [9]$$

The assumption of Eq. [6] can be verified qualitatively by a consideration of previous work on conductivity and water absorption of ion exchange materials containing sulfonic acid. It has been found (14) that for the range of water activity  $0.2 < a_{H_2O} < 1.0$ ,  $\ln \sigma$  is proportional to  $a_{H_2O}$ . Furthermore,  $\Delta F_A$  is approximately proportional to  $a_{H_2O}$  in this region [ $3 < n < n(\text{saturation})$ ] (16, 17). Combining these results shows that we can write  $\sigma \sim \exp[-\beta \Delta F_A/RT]$ .

Equation [9] may be used to predict the behavior of  $\sigma$  with  $n$  or  $T$ , provided we can estimate  $\beta$  empirically. Its applicability is illustrated by Fig. 1, where it has been used to fit conductivity data for sulfuric acid (25). The calculated curve is based on Eq. [9] with  $\beta = 0.48$  and experimental data for  $c/c_D$  (26) and  $\Delta F_A$  (27). The agreement is reasonably good, especially in view of the formation of a stable

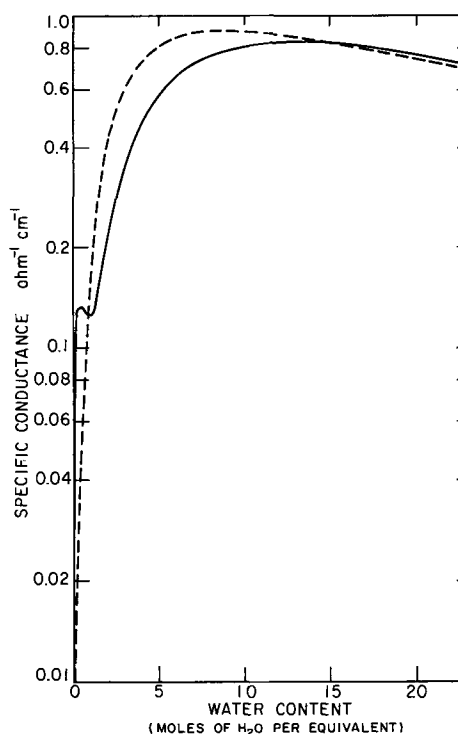


Fig. 1. Comparison of sulfuric acid conductivity from ref. (25) (solid line) to values calculated with our Eq. [9] (dotted line).

monohydrate ( $n = 1$ ), and the fact that conduction occurs not only by normal hydrogen ion transfer but also by anion transfer and Grotthuss conduction. To be sure, the theory is not strictly applicable as derived above, but it nevertheless fits the data reasonably well.

No data are available on  $\Delta F_A$  for the particular membrane material investigated here. However, a check of similar data for low cross-linkage (2% divinylbenzene) PSA ion exchange materials (17) [which reach the same approximate value of  $n$  (saturation)] shows that  $\Delta F_A(n)$  at constant  $T$  can be well approximated by

$$\Delta F_A = \Delta F_A^0 [1 - \exp(-n/n_0)] \quad [10]$$

where:  $\Delta F_A^0$  = asymptotic free energy of absorption at high  $n$  (cal/mole),  $n_0$  = empirical constant. The validity of this approximation is demonstrated in Fig. 2 where experimental values are compared to a curve calculated with Eq. [10] and the values  $\Delta F_A^0 = 6900$  cal,  $n_0 = 1.61$ . The difference between the two is never greater than 10% of  $\Delta F_A$  (exptl). We now assume that the same relationship can be used to describe  $\Delta F_A$  for the membrane and arrive at the following equation for  $\sigma$

$$\sigma = \sigma_D(c/c_D) \exp[-\beta\Delta F_A^0(1 - \exp(-n/n_0))/RT] \quad [11]$$

We thus have a relationship with essentially 2 empirical constants ( $\beta\Delta F_A^0$  and  $n_0$ ).

The form of Eq. [11] can be further justified from an empirical point of view by taking its logarithm for small  $n$

$$\ln \sigma = A - [(\beta\Delta F_A^0)/(RTn_0)]n \quad [12]$$

where  $A$  is a constant provided  $c/c_D$  is relatively constant in the region  $n \ll n_0$ . For low extents of water absorption, work on a variety of substances [biological polymers (5) and polyamide resins (15), for example] has shown that  $\ln \sigma$  is proportional to the weight per cent of water absorbed ( $m$ ). Since  $m$  is proportional to  $n$  for small  $n$ , this result is equivalent to Eq. [12].

Since the exponential term in Eq. [11] approaches a constant value at high  $n$ , conductivity should level off as  $n$  increases and, depending on the behavior of  $c/c_D$ , could perhaps exhibit a maximum. Such behavior has been observed for polymethacrylic ion exchangers (28) and proteins (5).

A further quantity that can be used to study the variation of conductivity with water absorption is the net volume change on mixing one equivalent of dry membrane with  $n$  moles of water ( $\Delta v_A$ ) divided by  $n$ . We denote this quantity by  $\Delta v$  so

$$\Delta v = \Delta v_A/n \quad [13]$$

$\Delta v$  is useful in that it can be used as a measure of how tightly absorbed water molecules are packed around hydrogen ions. A negative value indicates some kind

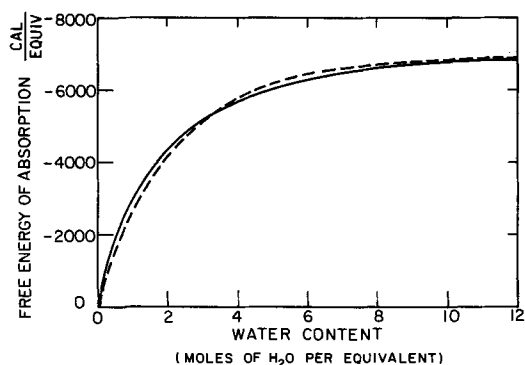


Fig. 2. Comparison of free energy of absorption data from ref. (17) (solid line) to values calculated with our Eq. [10] (dotted line).

of net ordering relative to liquid water and dry membrane. If  $\Delta v$  has a minimum, the  $n$  value at the minimum would represent approximately the number of water molecules which can be accommodated in an ordered, densely packed hydration sphere about the hydrogen ion. Above this  $n$ , absorbed water would tend to enhance the dilution effect as opposed to specifically interacting with hydrogen ions and increasing conductivity.

### Experimental

The membrane used in this investigation was type C-60 (American Machine and Foundry Company). Its composition has been described previously (see early paragraphs). The membrane was purified by five batchwise washings with deionized water. The final concentration of ionic impurities in the interstitial water within the membrane was estimated from the conductivity of the deionized water after the final washings and was found to be negligible.

Rectangular strips of membrane were then placed in various pre-equilibration enclosures, wherein they were brought to the desired temperature and extent of water absorption by either being suspended over saturated salt solutions (for  $n > 0$ ) or by being pumped down to a pressure of approximately 30  $\mu$ Hg at 55°C (for  $n \approx 0$ ).

With a stainless steel die, rectangular samples were cut from the above strips. All strips were cut with their conduction directions parallel to the same axis in the original membrane sheet to minimize anisotropy effects. Thus, all samples had exactly the same dimensions except for thickness, which varied with water absorption. The samples were 0.5 cm wide with a conductive length of 3.0 cm between electrodes.

The sample was then clamped at each end between two platinum-plated electrodes. The electrodes compressed about 0.5 cm<sup>2</sup> of membrane material at each end under constant pressure. The pressure developed between the electrodes was sufficient to compress samples of high water content to approximately half their original thickness, thereby indicating good electrical contact. Temperatures were measured at four points near the sample with thermocouples. The accuracy of these measurements was  $\pm 0.1^\circ\text{C}$ , and the differences among the four readings were never greater than  $0.2^\circ\text{C}$ .

A sample was then placed in the sample enclosure of Fig. 3, wherein it was maintained at essentially the same temperature and extent of water absorption as during pre-equilibration. Most conductivity measurements were made in this enclosure. The enclosure temperature was held constant to  $\pm 0.1^\circ\text{C}$  by means of a recirculating oil system. For measurements on dry membrane samples, valves 2, 3, and 4 were closed and valve 1 open. For other measurements, valves 2, 3, and 4 were open and valve 1 closed. In the latter cases, recirculating nitrogen gas was contacted with

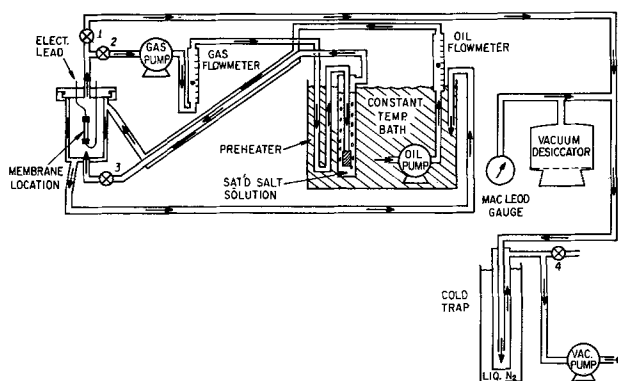


Fig. 3. System used for regulating temperature and water absorption.

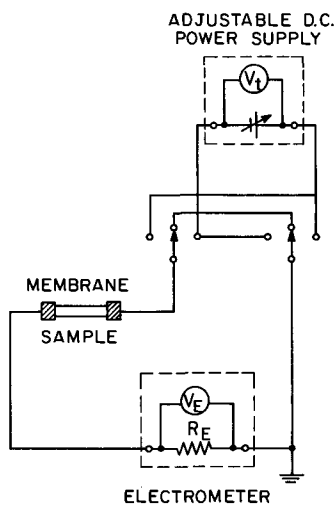


Fig. 4. Circuit for measurement of conductivity

the same saturated salt solution used in pre-equilibration and then passed over the sample.

Several measurements were also made with the sample outside the enclosure and under a burette which slowly dripped deionized water to ensure complete saturation.

The circuit used for measuring conductivity is shown in Fig. 4, where the operation of each unit is indicated in terms of its functional equivalents. With the control switch in its central position the electrometer could be used to measure any polarization voltage ( $V_{pol}$ ) generated within the sample by the passage of current. ( $V_{pol}$  decayed slowly with time, requiring 5-10 min to disappear. The left or right positions of the control switch applied plus or minus d-c voltages to the sample for conductivity measurements. In order to avoid long-term polarization of the sample, the voltage was reversed for each successive measurement. For a given value of the total voltage ( $V_t$ ), conductivity measurements were made in both directions and the average quoted as our final result. The deviation between the two measurements was always well within experimental error. The only electrical quantities measured were thus  $V_t$  and the electrometer voltage,  $V_E$ .  $R_E$  was a calibrated resistor variable in decade steps, thereby permitting calculation of the sample current  $I_s$ . The sample voltage  $V_s$  could be varied by varying  $V_t$ .

As the application of a d-c voltage to the sample will give rise to decaying capacitive currents, a check was made of the duration of such currents to ensure that they introduced no significant error in our conductivity measurements. The time constant calculated with an experimental value of 30 as the approximate static dielectric constant for dry membrane (29) is approximately  $10^{-4}$  sec. This value is small enough with respect to the measuring times involved ( $\geq 0.1$  sec) that we can neglect capacitive currents.

The time dependence of  $I_s$  is indicated in Fig. 5 for dry and wet membrane. Since the sample current decreased rapidly with time after the application of the voltage step, we have chosen to report conductivity values corresponding to the maximum values of  $I_s$  registered on the electrometer before the decrease began. This choice minimized any errors due to sample polarization as well as eliminating the effect of capacitive currents, as we have mentioned. Our choice of  $I_s$  value was checked by comparison to a-c measurements at 60 and 1000 Hz. For 10 saturated samples, the d-c, 60 Hz, and 1000 Hz conductivity values all agreed to within  $\pm 10\%$ . These results are consistent with previous comparisons of this type spanning the range d.c. to 500,000 Hz (8, 30). Inasmuch as the transient effects on conductivity should be largest for

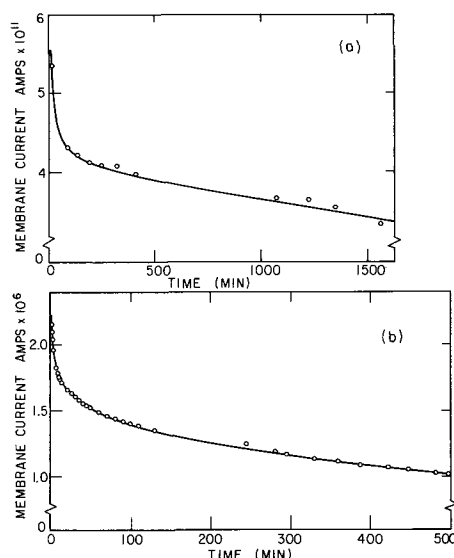


Fig. 5. Effect of an extended application of d-c voltage on the current passing through membrane samples.  $T = 28.3^\circ\text{C}$  for both cases. In (a) the sample was dry, in (b) it contained 7.02 moles of water per equivalent.

saturated samples, our measuring technique was quite adequate.

The times required to reach maximum current were less than 10 sec for dry measurements and less than 0.5 sec for wet measurements. The total time of voltage application was about 10 sec, at which time  $V_{pol}$  never exceeded 30 mv, a negligible value compared to  $V_s$  which was  $\geq 0.8\text{v}$  for all cases. Conductivities were calculated with the difference of sample voltage ( $V_s$ ) and decomposition voltage ( $V_D$ ) as the pertinent applied voltage. The decomposition voltage was defined in a standard way, as the intercept of a straight line through current-voltage data (8). Such a plot is shown in Fig. 6. The data at all extents of water absorption were quite well described by straight lines, so  $V_D$  could be unambiguously determined for all cases. Excluding any property variations from sample to sample, the reproducibility of our conductivity values should be  $\pm 10\%$ . The absolute accuracy is  $\pm 15\%$ .

In view of the fact that both heat transfer and mass transfer were taking place at the sample surfaces, the conductivity of a given sample changed with time after placement in the enclosure. Therefore, measurements were taken until the fractional change per hour in conductivity was less than 0.01 for dry measurements and 0.04 for wet measurements to ensure a stable system. The lower rate for dry samples provided for a closer approach to  $n = 0$ . Such mass transfer

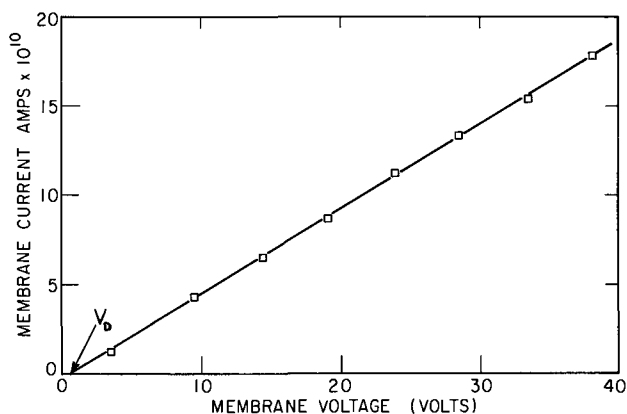


Fig. 6. Variation of sample current with voltage magnitude for a typical membrane sample ( $T = 28.3^\circ\text{C}$ , dry).

equilibrium was not essential for wet samples, since  $n$  was measured directly in these cases.

After electrical measurements were completed, the sample was removed from the enclosure and its thickness and weight were measured. Thicknesses varied from 0.023 to 0.031 cm and weights from 0.041 to 0.071g. The wet samples were then dried in the vacuum desiccator of Fig. 3 at a temperature of 55°C until their weight had stabilized. This weight was then used in calculating  $n$ . The exchange capacity of each sample was then measured by standard methods. From these measurements the density ( $\rho$ ),  $n$ ,  $c/c_D$  and  $\Delta v$  were easily obtained. The approximate accuracies of these measurements were:  $\rho \pm 0.05$  g/cc,  $n \pm 0.15$ ,  $c/c_D \pm 0.17$ ,  $\Delta v \pm 6.3$  cc.

A sample was tested at only one water absorption before being discarded.

### Results and Discussion

As mentioned previously, plots of  $V_s$  vs.  $I_s$  were linear for  $5 < V_s < 35$  V. The decomposition voltages obtained from these plots were not found to vary in any systematic way with  $n$ , but the accuracy of the  $V_D$  determinations was not particularly high. All values are contained within  $V_D = 0.77 \pm 0.58$  v.

The lack of systematic variation of  $V_D$  with  $n$  could indicate that the same electrode reactions are responsible for current flow in both wet and "dry" samples and also make it fairly certain that current flow is ionic even in such a "dry" membrane. The latter result is further verified by the rapid fall of current with time after voltage application as shown in Fig. 5(a).

Previous measurements of conductivity in water-immersed beads of cross-linked PSA have indicated  $V_D \approx 2.0$  v (8). A similar value was obtained in measurements on textile fibers (4). However, both these measurements were made at effectively very large times after application of a d-c voltage, which could explain the higher value. The systems studied were also sufficiently different from this membrane that no real contradiction exists.

Figure 7 presents the results of conductivity measurements at various temperatures. There is no systematic deviation of the data from straight lines. Least-square fits gave the  $E_x$  values of Table I. An increase of  $E_x$  with  $\rho$  is apparent, possibly due to the difficulty of obtaining membrane samples of identical residual water contents, especially under our moderate drying conditions (corresponding to  $a_{H_2O} \leq 10^{-3}$ ). The less dense samples would correspond to samples of higher residual water content and therefore lower  $E_x$ . A value of  $E_x = 0.99$  ev thus probably represents conduction in the driest state observed. This value is of the same order as those obtained from similar

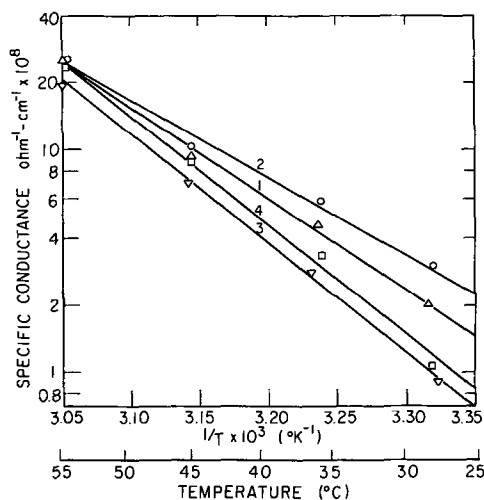


Fig. 7. Effect of temperature on the conductivity of dry membrane samples (see Table I).

Table I. Density and experimental activation energy values for four dry samples. Activation energies determined from Fig. 7

Sample No.	$\rho$ , g/cc	$E_x$ , cal	$E_x$ , ev
1	1.12	18,100	0.783
2	1.11	15,900	0.691
3	1.14	22,700	0.983
4	1.19	22,900	0.993

measurements on a variety of dry polar polymers: 1.3 ev for cytochrome C (1), 0.8-1.1 ev for sodium deoxyribonucleic acid (6), 1.0-1.4 ev for various textile fibers (4), and 2.5 ev for synthetic polyamides (15).

Figure 8 indicates the variation of  $c/c_D$  with  $n$ . As assumed in the derivation of Eq. [12],  $c/c_D$  is relatively constant for  $0 < n < 0.5$ .

Figure 9 shows the effect of water absorption on specific conductivity. The slight scatter of the data probably indicates some property variations from sample to sample, but not a sufficient amount to obscure the systematic variation of  $\sigma$  with  $n$ .

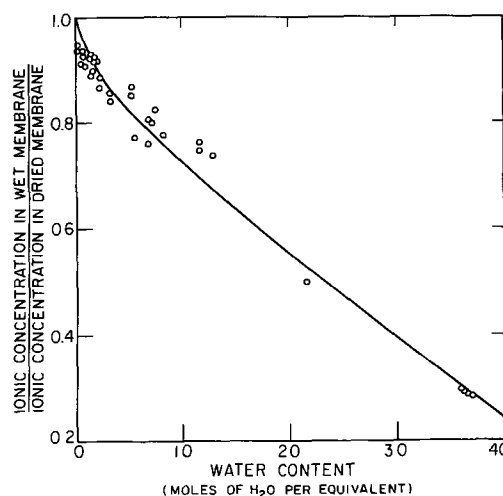


Fig. 8. Effect of water absorption on the ratio of wet ionic concentration to dry ionic concentration in the membrane.

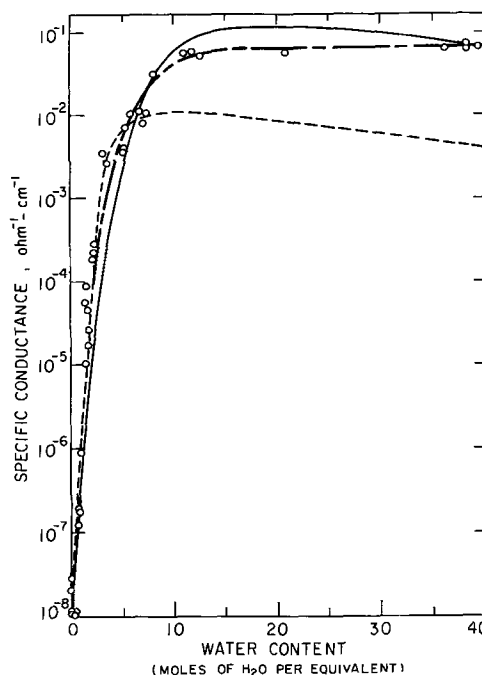


Fig. 9. Effect of water absorption on membrane conductivity ( $T = 28.3^\circ\text{C}$ ). One curve is through the data (— — —); the solid and dotted curves are calculated.



The calculated curves in Fig. 9 were obtained from Eq. [11] with  $c/c_D$  values from the curve of Fig. 6 and  $\sigma_D = 1.06 \times 10^{-8} \text{ ohm}^{-1}\text{-cm}^{-1}$ . The empirical constants used were:  $\beta\Delta F_A^\circ = 10,340 \text{ cal}$ ,  $n_o = 3.69$  for the solid curve, and  $\beta\Delta F_A^\circ = 8,515 \text{ cal}$ ,  $n_o = 1.61$  for the dotted curve. Two theoretical curves are shown to indicate the different types of agreement that can be obtained with this equation. The solid curve gives a reasonable description of the data over the entire range of  $n$ , but is off by as much as a factor of 10 in some places. The dotted curve, on the other hand, agrees much better with the data in the region  $0 < n < 5$ , and is too low by about a factor of 10 for  $n > 10$ . One possible explanation for this is that abnormal hydrogen ion conduction is fully operative for  $n > 5$ . Since our theory does not include abnormal conduction, it would be expected to agree well in the low  $n$  region and be too low in the high  $n$  region. The solid curve would then represent an attempt to extend the theory beyond its original assumptions, and the fact that this curve agrees fairly well with the data is somewhat fortuitous. In fact, measurements on sodium-form membranes of the same type investigated here give a better fit of theory to experiment, and a factor of 7 difference in conductivities at high  $n$  (31), indicating almost certainly that abnormal conduction occurs in the hydrogen form. These results disagree with a recent hypothesis that membrane inhomogeneity may seriously disrupt Grotthuss conduction chains (20). It is of further interest that the parameters  $\beta\Delta F_s^\circ$  and  $n_o$  used in calculating the dotted curve in Fig. 9 agree quite well with those used to fit the experimental data of Fig. 2 on low cross-linkage PSA. The fact that PSA of this cross-linkage (2% divinylbenzene) also reaches approximately the same  $n$  value on being saturated with water (17) further verifies the similarity between the two materials and indicates that  $\beta$  could be quite close to unity for the membrane.

If we consider the dotted curve in Fig. 9 to represent the conduction process exclusive of abnormal conduction, it is possible to check the variation of  $\Delta S^\ddagger$  with water absorption in an approximate way. Our dry conductivity measurements indicate a value of  $\lambda^2 \exp[\Delta S_D^\ddagger/R] = 3.06 \times 10^{-10}\text{-cm}^2$ . Sodium ion self-diffusion coefficient measurements on saturated PSA beads of 4% divinylbenzene cross-linkage give a value of  $\lambda^2 \exp[\Delta S^\ddagger/R] = 3.61 \times 10^{-16} \text{ cm}^2$  (11). As sodium and hydrogen ions move in quantitatively the same fashion if the effects of abnormal conduction are excluded (32), we might expect the value of  $\lambda^2 \exp[\Delta S^\ddagger/R]$  for dry PSA beads to be reasonably close to our value for dry membrane. The  $10^6$  factor between the two values quoted is quite probably due to changes in  $\Delta S^\ddagger$  with water absorption and related only partially to fundamental structural or ionic differences between the two materials. To estimate  $\lambda^2 \exp[\Delta S^\ddagger/R]$  for dry PSA, we extend our assumption in Eq. [6] to

$$\Delta S^\ddagger = \Delta S_D^\ddagger + \beta\Delta S_A \quad [14]$$

Assuming for this case also that  $\beta \approx 1$ , and using experimental data for  $\Delta S_A$  (17), we calculate that  $\lambda^2 \exp[\Delta S_D^\ddagger/R] = 5.03 \times 10^{-10} \text{ cm}^2$ . The excellent agreement of this number with our result for dry membrane is no doubt somewhat accidental, but nonetheless further justifies the use of equations such as [6] and [14]. An experimental study involving measurements of conductivity,  $E_x$  values over a range of  $n$ , and thermodynamic functions of absorption for the same material would be the only truly accurate test of these equations, however.

Conductivity measurements on membranes consisting of phenolsulfonic acid polymerization products (9) show some similarities to the present results. These studies were made on materials which would absorb far more water at saturation than the membrane studied in this work and all measurements were carried out in this high absorption region ( $n > 40$ ). It

was found that  $\sigma$  increased when  $n$  was decreased from very high values. This indicates some sort of maximum in conductivity, as there is little doubt that  $\sigma$  must decrease when  $n$  becomes very small. The higher saturation  $n$  values of the phenolsulfonic materials permit a much larger dilution effect than in the membrane, and thus the maximum in conductivity occurs. The results of these previous measurements also indicate abnormal hydrogen ion conduction, since the equivalent conductance of the hydrogen form is about 6.3 times that of the sodium form.

The variation of  $\Delta v$  with  $n$  is shown in Fig. 10. The general shape of the curve drawn through the experimental data agrees quite well with a curve calculated from more accurate experimental data on cross-linked PSA of 10% divinylbenzene content (16). It is to be expected that the minimum in  $\Delta v$  for this highly cross-linked PSA would be lower than the minimum for the membrane, since the cross-linkages inhibit motion of the PSA molecules relative to one another, thereby reducing the number of water molecules which can enter into an ordered structure about a hydrogen ion. The significance of the approximate minimum shown in the membrane curve is that it occurs at a value of  $n$  very close to the value where  $\sigma$  levels off. Absorbed water increases conductivity by specifically interacting with the hydrogen ion and thereby facilitating ionization. This interaction probably occurs up to a certain extent of hydration for each ion. Past this extent, absorbed water acts more to enhance the dilution effect and the conductivity levels off and may begin to decrease. These ideas are very qualitative and can be put on a quantitative basis only by considering equilibria between water molecules and the hydrogen ion, as has been done previously in the analysis of thermodynamic data (18, 19). One such calculation for hydrogen ions in water gives a hydration number of 7.3 (33) in fair agreement with the minimum in  $\Delta v$  and the levelling off point in  $\sigma$ . For  $n > 7$ , it should also be noted that water molecules could be specifically attracted to the  $-\text{SO}_3^-$  groups attached to the polymer chain. This interaction would probably be small, however, due to the small volume available between adjacent  $-\text{SO}_3^-$  groups along the polymer chain (24). Also, since the hydrogen ions should all be essentially dissociated by  $n \approx 7$ , this additional interaction should serve primarily to enhance the dilution effect.

### Conclusions

The voltage and time dependence of specific conductivity for this PSA-based membrane indicate a

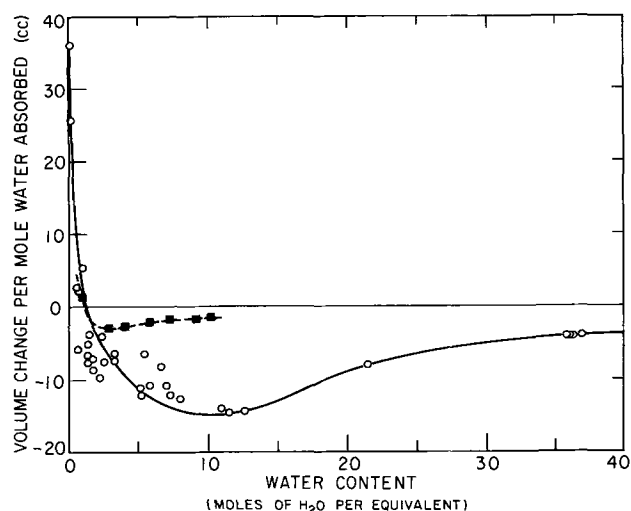


Fig. 10. Variation of the net volume change for absorption per mole of water absorbed with total water absorbed. The solid curve represents data taken in this investigation. The dotted curve was calculated with data from ref. (16).

similar mode of ionic conduction over the entire range of water absorption we have studied. The temperature dependence of conductivity for dry membrane is well-described by an Arrhenius relation between 25° and 55°C. The activation energy in this case is approximately 1 ev. The semi-empirical equations we have derived to relate conductivity and water absorption *via* the free energy of absorption give a reasonably good fit to the membrane data, and could be of use in describing a wide variety of ionically conducting polymers which absorb water. The net volume change for absorption per mole of water absorbed exhibits a minimum at approximately that extent of water absorption at which membrane conductivity levels off. This can be explained by the filling of hydration spheres about hydrogen ions.

### Acknowledgments

The authors wish to express their gratitude to the Office of Saline Water, United States Department of the Interior, for financial support. They also thank Mr. J. Ampaya for making the a-c conductivity measurements.

The results presented here are taken from a thesis by C. S. Fadley, submitted in partial fulfillment of the requirements for the M.S. degree at the University of California, Berkeley.

Manuscript submitted Feb. 26, 1968; revised manuscript received Aug. 15, 1968.

Any discussion of this paper will appear in a Discussion Section to be published in the June 1969 JOURNAL.

### SYMBOLS

$a_{H_2O}$	activity of water, dimensionless
$A, B, C$	constants in equations for $\ln \sigma$ , dimensionless
$c$	concentration of ionic charge carriers, $cc^{-1}$
$c_D$	concentration of ionic charge carriers in dry material, $cc^{-1}$
$E_x$	experimental activation energy, cal or ev
$h$	Planck's constant, $6.62 \times 10^{-24}$ J-s.
$I_s$	sample current, A
$m$	weight per cent of water absorbed, dimensionless
$n$	moles of water absorbed per mole of ionic charge carriers, dimensionless
$n_0$	empirical constant in equation for $\Delta F_A$ , dimensionless
$q$	electronic charge, C
$R$	gas constant, 1.99 cal/mole-°K
$R_E$	calibrated electrometer resistance, ohms
$T$	temperature, °K
$V_D$	decomposition voltage, $v$
$V_E$	electrometer voltage, $v$
$V_{pol}$	polarization voltage, $v$
$V_s$	voltage applied to sample, $v$
$V_t$	total voltage, $v$
$\beta$	empirical constant in conductivity equations, dimensionless
$\Delta E^\ddagger$	effective internal energy of activation, cal/mole
$\Delta F^\ddagger$	effective free energy of activation, cal/mole
$\Delta F_A$	free energy of absorption, cal/mole
$\Delta F_A^0$	empirical constant in free energy of absorption equation, cal/mole
$\Delta F_D^\ddagger$	effective free energy of activation for dry material, cal/mole
$\Delta H^\ddagger$	effective enthalpy of activation, cal/mole
$\Delta S^\ddagger$	effective entropy of activation, cal/mole-°K
$\Delta S_D^\ddagger$	effective entropy of activation for dry material, cal/mole-°K
$\Delta v_A$	net volume change for absorption, cc

$\Delta v$	net volume change for absorption per mole of water absorbed, cc
$\lambda$	effective jump distance, cm
$\rho$	density, g/cc
$\sigma$	specific conductivity, $ohm^{-1}cm^{-1}$
$\sigma_0$	constant in Arrhenius expression for conductivity, $ohm^{-1}cm^{-1}$
$\sigma_D$	specific conductivity of dry membrane, $ohm^{-1}cm^{-1}$

### REFERENCES

1. S. Baxter, *Trans. Faraday Soc.*, **39**, 207 (1943).
2. G. King, and J. A. Medley, *J. Coll. Sci.*, **4**, 1 (1949).
3. G. King, and J. A. Medley, *ibid.*, **4**, 9 (1949).
4. J. W. S. Hearle, *J. Textile Inst.*, **44**, T177 (1953).
5. B. Rosenberg, *J. Chem. Phys.*, **36**, 816 (1962); *Nature*, **193**, 364 (1962).
6. C. T. O'Konski, P. Moser, and M. Shirai, *Biopolymers*, Symposium No. 1, 479 (1962).
7. F. Helfferich, "Ion Exchange," Chap. 7 (A general review), McGraw-Hill Book Co., New York (1962).
8. K. S. Spiegler and C. D. Coryell, *Science*, **113**, 546 (1951); *J. Phys. Chem.*, **56**, 106 (1952).
9. A. O. Jakubovick, G. J. Hills, and J. A. Kitchener, *Trans. Faraday Soc.*, **55**, 1570 (1959).
10. A. E. Lagos, and J. A. Kitchener, *ibid.*, **56**, 1245 (1960).
11. G. E. Boyd, and B. A. Soldano, *J. Am. Chem. Soc.*, **75**, 6091 (1954).
12. W. Juda, N. W. Rosenberg, J. A. Marinsky, and A. A. Kasper, *ibid.*, **74**, 3736 (1952).
13. K. S. Spiegler, and C. D. Coryell, *J. Phys. Chem.*, **57**, 687 (1953).
14. W. T. Grubb, *ibid.*, **63**, 55 (1959).
15. L. -T. Yu, *J. Phys. (Paris)*, **24**, 677 (1963).
16. H. P. Gregor, B. R. Sundheim, K. M. Held, and M. H. Waxman, *J. Coll. Sci.*, **7**, 511 (1952).
17. B. R. Sundheim, M. H. Waxman, and H. P. Gregor, *J. Phys. Chem.*, **57**, 974 (1953).
18. E. Glueckauf and G. P. Kitt, *Proc. Roy. Soc. (London)*, **A228**, 322 (1955).
19. E. Glueckauf and G. P. Kitt, *Nature*, **171**, 1010 (1953).
20. M. Block and J. A. Kitchener, *This Journal* **113**, 947 (1966).
21. H. Eyring, K. J. Laidler, and S. Glasstone, "Theory of Rate Processes," McGraw-Hill Book Co., New York (1941).
22. M. J. Allen, "Organic Electrode Processes," Reinhold Publishing, New York (1958), pp. 29 and 139; M. Yokoyama, *Helv. Chim. Acta*, **12**, 756 (1929).
23. H. Eyring, *op cit.*, p. 559.
24. N. Grubhofer, *Makromol. Chem.*, **30**, 96 (1959).
25. J. E. Roughton, *J. Appl. Chem. (London)*, **1**, S141 (1951); K. Rosen, *Acta Chem. Scand.*, **9**, 1086 (1955); G. Hetherington, *J. Chem. Soc. (London)*, **1955**, 3300 (1955).
26. "Handbook of Chemistry," N. A. Lange, Editor, p. 1145, McGraw-Hill Book Co., New York (1961).
27. M. H. Waxman, B. R. Sundheim, and H. P. Gregor, *J. Phys. Chem.*, **57**, 969 (1953).
28. A. Despic and G. J. Hills, *Trans. Faraday Soc.*, **51**, 1266 (1955).
29. Z. Urban and R. A. Wallace, *This Journal*, **115**, 276 (1968).
30. J. H. B. George, C. Schlaikjer, A. D. Little, Inc., Quarterly Report to the Office of Saline Water (10/66-1/67), U. S. Dept. of the Interior, Washington, D. C.
31. R. A. Wallace *et al.*, Saline Water Conversion Report (1966), Office of Saline Water, U.S. Dept. of the Interior, Washington, D. C.
32. H. Eyring, *op cit.*, p. 562.
33. R. H. Stokes and R. A. Robinson, *J. Am. Chem. Soc.*, **70**, 1870 (1948).

# Luminescence of Divalent Europium in the BaO-MgO-P<sub>2</sub>O<sub>5</sub> System

Costas C. Lagos\*

Phosphor Research Laboratory, Sylvania Lighting Center, Danvers, Massachusetts

## ABSTRACT

The binary and ternary compounds in the BaO-MgO-P<sub>2</sub>O<sub>5</sub> system were activated with divalent europium and examined for luminescence under 2537 and 3650 Å excitation. Three compounds, Ba<sub>3</sub>(PO<sub>4</sub>)<sub>2</sub>, the low-temperature form of Ba<sub>3</sub>P<sub>4</sub>O<sub>13</sub>, and BaMgP<sub>2</sub>O<sub>7</sub> produced bright phosphors with blue emission. Many other compounds in the ternary system also fluoresced blue, but with reduced intensities.

Very little work has been previously reported on the luminescence of phosphates activated with divalent europium. In 1967, Wanmaker and ter Vrugt (1) reported on the uv and cathodo excitation of the divalent europium activated pyrophosphates of Ca, Sr, Ba, Zn, Cd, and Mg; Gorbacheva (2) in 1966 presented information on the uv excitation of the divalent europium activated orthophosphates of strontium and magnesium; and Nazarova (3) in 1961 published on the uv and cathodo excitation of the pyro-, meta-, and orthophosphates of strontium. To our knowledge no work has been reported on the divalent europium activation of compounds in either the BaO-P<sub>2</sub>O<sub>5</sub> or BaO-MgO-P<sub>2</sub>O<sub>5</sub> systems. Hoffman (4) in 1963 reported the use of europium as an activator in the BaO-MgO-P<sub>2</sub>O<sub>5</sub> system, but the europium was probably trivalent because only red emission was mentioned.

The primary interest of the present study was the development of phosphors for application in fluorescent or HPMV lamps. Compounds which did not show any emission under 2537 or 3650 Å excitation were not investigated further.

Some of the better phosphors in the BaO-MgO-P<sub>2</sub>O<sub>5</sub> system were bright enough for fluorescent lamp applications. These phosphors were: Ba<sub>3</sub>(PO<sub>4</sub>)<sub>2</sub>:Eu<sup>+2</sup>, the low-temperature form of Ba<sub>3</sub>P<sub>4</sub>O<sub>13</sub>:Eu<sup>+2</sup>, BaMg<sub>2</sub>(PO<sub>4</sub>)<sub>2</sub>:Eu<sup>+2</sup>, Ba<sub>2</sub>MgP<sub>4</sub>O<sub>13</sub>:Eu<sup>+2</sup>, and BaMgP<sub>2</sub>O<sub>7</sub>:Eu<sup>+2</sup>. All other compounds produced either no luminescence at all or very weak divalent or trivalent europium emissions.

## Experimental

The chemicals used in the preparation of the phosphors were luminescent grade BaHPO<sub>4</sub> and BaCO<sub>3</sub>, reagent grade (NH<sub>4</sub>)<sub>2</sub>HPO<sub>4</sub> and 3MgCO<sub>3</sub>·Mg(OH)<sub>2</sub>·3H<sub>2</sub>O, and 99.9% pure Eu<sub>2</sub>O<sub>3</sub>. Phosphor blends were prepared by dry mixing of the raw materials; no wet precipitations were made. Formulations were made up to stoichiometry and no deliberate excess of anion was used in any of the preparations. The ratio of activator-to-matrix cation in moles was 0.02 to 1, i.e., for every mole of total cation 0.02 moles of Eu were added as Eu<sub>2</sub>O<sub>3</sub>.

Firing of all blend mixtures was made in two steps: (i) a low-temperature pre firing usually for 3 hr at 700°C in a stagnant air atmosphere to prevent spewing and subsequent loss of material and also to allow the 3MgCO<sub>3</sub>·Mg(OH)<sub>2</sub>·3H<sub>2</sub>O and (NH<sub>4</sub>)<sub>2</sub>HPO<sub>4</sub> which have low decomposition temperatures to react more readily with the other raw materials; (ii) a final higher temperature firing in a 1% H<sub>2</sub>-99% N<sub>2</sub> reducing gas mixture flowing over the samples with the firing temperature depending on the compound that is being prepared. Between firings all samples were remixed by a thorough grinding with a mortar and pestle.

Spectral energy distribution curves were run on the luminescent phosphor samples using an emission spectral radiometer designed by Eby (5). The emission

band peak height intensities of the phosphor samples were compared to the emission band peak height intensity of the high brightness Zn<sub>2</sub>SiO<sub>4</sub>:Mn phosphor, which peaks at 527 nm and is used as a control for our radiometer. All phosphor emission intensities in this paper are expressed as peak height percentages of the peak height of the Zn<sub>2</sub>SiO<sub>4</sub>:Mn radiometer standard phosphor. This comparison is not an absolutely correct comparison in some cases because of wavelength-energy differences between the phosphor samples and the Zn<sub>2</sub>SiO<sub>4</sub>:Mn standard, but for the majority of the phosphors being discussed here this method is a great improvement over the use of a plaque tester where differences between narrow and wide emission band widths play a misleading role in brightness comparisons and evaluations. Half-height widths and peak height intensities of the emission bands of some well-known phosphors were measured on our radiometer and were also included here as references for the phosphors reported in this paper.

Finally, x-ray diffraction patterns were obtained on all fired samples using copper K $\alpha$ -radiation. The x-ray diffraction angle scan was varied from a 2 $\theta$  of 2° to a 2 $\theta$  of 60°, which was quite sufficient for proper identification of the compounds and polymorphs.

## Results and Summary

There were a total of fourteen compounds and polymorphs in the BaO-MgO-P<sub>2</sub>O<sub>5</sub> ternary system which were prepared with divalent europium as the activator. In order to simplify their presentation the compounds have been separated into four categories: (i) metaphosphates and gamma compound, (ii) tetraphosphates, (iii) pyrophosphates, and (iv) orthophosphates.

*Metaphosphates and gamma compound.*—Two metaphosphate compounds Mg(PO<sub>3</sub>)<sub>2</sub> (6) and Ba(PO<sub>3</sub>)<sub>2</sub> (7) and the  $\gamma$  compound which had the composition 6.3 BaO-1.0 MgO-2.7 P<sub>2</sub>O<sub>5</sub> (4) were tested with divalent europium as the activator. Of these three compounds only the barium metaphosphate showed any fluorescence which could be attributed to divalent europium. Figure 1 shows the emission curve for this phosphor under 2537 Å excitation. The emission band of the phosphor peaked at 375 nm with a half-height width of 31 nm and a peak height intensity only 5% of the peak height of the radiometer standard, Zn<sub>2</sub>SiO<sub>4</sub>:Mn. The uv emission of the Ba(PO<sub>3</sub>)<sub>2</sub>:Eu<sup>+2</sup> phosphor was quite low when compared to the reference phosphor BaSi<sub>2</sub>O<sub>5</sub>:Pb which peaked at 355 nm with a half-height width of 41 nm and was 205% of the Zn<sub>2</sub>SiO<sub>4</sub>:Mn standard. When visually observed under 2537 Å excitation, the Ba(PO<sub>3</sub>)<sub>2</sub>:Eu<sup>+2</sup> phosphor had a weak violet emission.

The other two compounds Mg(PO<sub>3</sub>)<sub>2</sub> and the  $\gamma$  compound (6.3 BaO-1.0 MgO-2.7 P<sub>2</sub>O<sub>5</sub>) were not activated by divalent europium. Under 2537 Å excitation the only emission that was observed was a weak red emission which, when examined with the spectral radiometer, was found to be the typical line emissions of trivalent europium.

\* Electrochemical Society Active Member.

Key words: luminescence, phosphors, 2537 excitation, 3650 excitation, Eu<sup>+2</sup> activation, barium phosphates, magnesium phosphates, barium magnesium phosphates, spectral energy distribution.

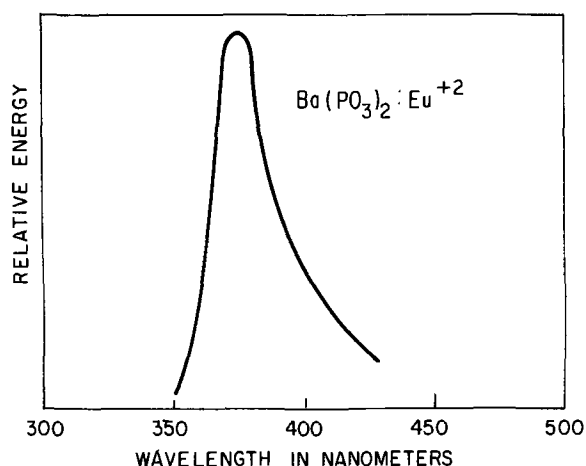


Fig. 1. Spectral energy distribution of the emission of  $\text{Ba}(\text{PO}_3)_2:\text{Eu}^{+2}$ ; 2537Å excitation

**Tetraphosphates.**—There are three tetraphosphate compounds that exist in the  $\text{BaO-MgO-P}_2\text{O}_5$  ternary system. These are the  $\text{Ba}_2\text{MgP}_4\text{O}_{13}$  (4) compound and the high- and low-temperature polymorphic forms of  $\text{Ba}_3\text{P}_4\text{O}_{13}$  (8) whose transition temperature is at 870°C.

Activation of the high- and low-temperature forms of  $\text{Ba}_3\text{P}_4\text{O}_{13}$  with divalent europium resulted in two interesting emission curves (Fig. 2). The high-temperature form of  $\text{Ba}_3\text{P}_4\text{O}_{13}:\text{Eu}^{+2}$  gave a very wide emission band of 197 nm half-height width with the band peak located at 575 nm. Because of this unusually wide emission curve the phosphor emitted a fairly bright yellow when observed under 2537Å excitation, but its emission band peak height intensity was only 7.4% of the  $\text{Zn}_2\text{SiO}_4:\text{Mn}$  radiometer standard and 38% of the reference phosphor  $\text{CaSiO}_3:\text{Pb, Mn}$  which peaked at 618 nm with a half-height width of 87 nm. The position of this wide emission band was also unusual in that it was located further towards the longer wavelengths than were the emission bands of practically all of the other divalent europium phosphors which were found in the  $\text{BaO-MgO-P}_2\text{O}_5$  system. Most of these other emission bands were located in the 400-450 nm region of the spectrum.

The low-temperature form of  $\text{Ba}_3\text{P}_4\text{O}_{13}$  also gave a very unusual emission curve with divalent europium (Fig. 2). Its emission band was located at 438 nm, and its intensity was 18% of the peak height intensity of the  $\text{Zn}_2\text{SiO}_4:\text{Mn}$  standard. The half-height width measurement was not too meaningful in this case because of the extreme asymmetry of the emission curve towards the long wavelength end of the spectrum. This asymmetry appeared to be caused by the presence of another less intense emission band in the vicinity of 500-510 nm, and this band plus the main

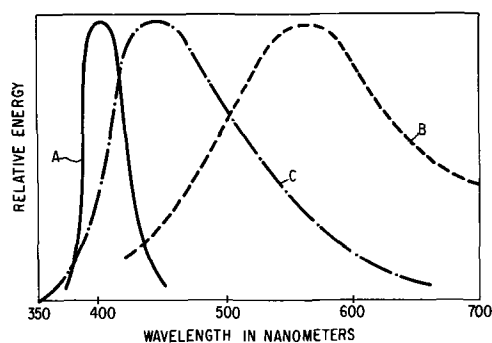


Fig. 2. Spectral energy distribution of the emission of:  $\text{Ba}_2\text{MgP}_4\text{O}_{13}:\text{Eu}^{+2}$ , curve A;  $\text{Ba}_3\text{P}_4\text{O}_{13}:\text{Eu}^{+2}$ , high-temperature form, curve B;  $\text{Ba}_3\text{P}_4\text{O}_{13}:\text{Eu}^{+2}$ , low-temperature form, curve C; 2537Å excitation

band at 438 nm combined to give a single wide curve with a long tail. X-ray diffraction data of this phosphor corresponded to the data of Harrison (8) for the low-temperature form of  $\text{Ba}_3\text{P}_4\text{O}_{13}$ , and there were no other extraneous phases present.

This double emission band curve might have been the result of divalent europium emission from two different cationic sites in the compound, but since no crystallographic structure determinations had been made on the compound, no definite conclusions could be drawn.

The wide emission curve of the low temperature  $\text{Ba}_3\text{P}_4\text{O}_{13}:\text{Eu}^{+2}$  material resulted in a phosphor which had a moderately bright blue-white emission when visually observed under 2537Å excitation. Plaque test brightness measurements were made on this phosphor and compared to similar measurements made on the well-known  $\text{Ca}_5\text{F}(\text{PO}_4)_3:\text{Sb}$  phosphor which had a wide emission band at 494 nm with a half-height width of 116 nm.

	Plaque		
	Red	Green	Blue
$\text{Ca}_5\text{F}(\text{PO}_4)_3:\text{Sb}$	100%	100%	100%
$\text{Ba}_3\text{P}_4\text{O}_{13}:\text{Eu}^{+2}$	105%	111%	125%

These data showed the divalent europium activated material to be slightly brighter and more blue than the  $\text{Ca}_5\text{F}(\text{PO}_4)_3:\text{Sb}$  phosphor which is used in fluorescent lamps for color correcting purposes. Use of the low temperature  $\text{Ba}_3\text{P}_4\text{O}_{13}:\text{Eu}^{+2}$  phosphor in place of  $\text{Ca}_5\text{F}(\text{PO}_4)_3:\text{Sb}$  in fluorescent lamp phosphor blends would subsequently yield more efficient fluorescent lamps.

Divalent europium activation of  $\text{Ba}_2\text{MgP}_4\text{O}_{13}$  resulted in a phosphor with an emission band at 403 nm and a half-height width of 28 nm with a peak height intensity of 59% of the  $\text{Zn}_2\text{SiO}_4:\text{Mn}$  standard (Fig. 2). This phosphor fluoresced a moderately bright deep violet when viewed under 2537Å excitation, and it was one of the brighter divalent europium activated phosphors in the  $\text{BaO-MgO-P}_2\text{O}_5$  system.

The emission properties of the barium magnesium tetraphosphate phosphor were radically different from those of either of the barium tetraphosphates. The emission band intensity of the magnesium containing phosphor was greatly increased by a factor of more than three over the low-temperature barium tetraphosphate phosphor and by a factor of more than six over the high-temperature barium tetraphosphate phosphor, while the band width of the magnesium containing material was decreased considerably by factors of one-fifth and one-seventh of the low- and high-temperature forms of barium tetraphosphate, respectively. Apparently, the replacement in the  $\text{Ba}_3\text{P}_4\text{O}_{13}$  compounds of even only one of the three of the larger ionic radius barium cations by the smaller magnesium cation to form the barium-magnesium compound changed the structures of the high and low barium tetraphosphates quite drastically so that there was no similarity at all between the magnesium containing and either of the nonmagnesium containing crystal structures and their subsequent emission properties.

**Pyrophosphates.**—Four pyrophosphates exist in the  $\text{BaO-MgO-P}_2\text{O}_5$  ternary system. These compounds are  $\text{Mg}_2\text{P}_2\text{O}_7$  (6),  $\text{BaMgP}_2\text{O}_7$  (4), and  $\text{Ba}_2\text{P}_2\text{O}_7$  (9), which exist in two polymorphic forms,  $\alpha$  which is the low temperature form, and  $\delta$  which is the high-temperature form. The  $\alpha$  to  $\delta$  transition temperature is at 790°C.

Here again, as it was previously in the case of the magnesium metaphosphate compound and the  $\gamma$  compound, it was not possible to reduce the trivalent europium to divalent europium in the  $\text{Mg}_2\text{P}_2\text{O}_7$  compound. With 2537Å excitation the only fluorescence that was observed in the europium activated  $\text{Mg}_2\text{P}_2\text{O}_7$  material was an extremely weak red fluorescence which on examination by the spectral radiometer was found to be the typical line emissions of plus three europium.

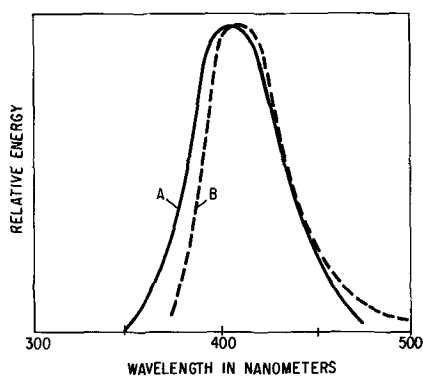


Fig. 3. Spectral energy distribution of the emission of:  $\text{BaMgP}_2\text{O}_7:\text{Eu}^{+2}$ , curve A;  $\text{Ba}_2\text{P}_2\text{O}_7:\text{Eu}^{+2}$ , curve B; 2537Å excitation

The  $\delta$ - $\text{Ba}_2\text{P}_2\text{O}_7$  compound was completely dead to 2537Å excitation while the  $\alpha$ - $\text{Ba}_2\text{P}_2\text{O}_7$  compound had a fair white-blue emission.  $\alpha$ - $\text{Ba}_2\text{P}_2\text{O}_7$  had an emission band which peaked at 406 nm with a peak height intensity 11.4% of the  $\text{Zn}_2\text{SiO}_4:\text{Mn}$  standard and a half-height width of 32 nm. Figure 3 shows the emission curve for this phosphor.

$\text{BaMgP}_2\text{O}_7:\text{Eu}^{+2}$  whose emission curve is also given in Fig. 3 was one of the brightest phosphors in the  $\text{BaO-MgO-P}_2\text{O}_5$  system. The phosphor appeared a brilliant deep violet when viewed under 2537Å excitation, and it had an emission peak at 402 nm with a half-height width of 45 nm and a peak height intensity 103% of the  $\text{Zn}_2\text{SiO}_4:\text{Mn}$  standard. When compared to the reference phosphor  $\text{CaWO}_4$  which peaked at 422 nm with a half-height width of 116 nm, the  $\text{BaMgP}_2\text{O}_7:\text{Eu}^{+2}$  phosphor was approximately three times as intense.

**Orthophosphates.**—There are four orthophosphate compounds in the  $\text{BaO-MgO-P}_2\text{O}_5$  ternary system:  $\text{Ba}_3(\text{PO}_4)_2$  (10),  $\text{Ba}_2\text{Mg}(\text{PO}_4)_2$  (4),  $\text{BaMg}_2(\text{PO}_4)_2$  (4), and  $\text{Mg}_3(\text{PO}_4)_2$  (6).

Table I lists the emission properties of the divalent europium activation of these compounds and Fig. 4 gives the spectral energy distribution curves. Two reference phosphors,  $\text{CaWO}_4$  and  $\text{CaSiO}_3:\text{Pb, Mn}$  were also included in the table for comparison purposes,  $\text{CaWO}_4$  for the experimental phosphors in the blue region of the spectrum and the  $\text{CaSiO}_3:\text{Pb, Mn}$  for the  $\text{Ba}_2\text{Mg}(\text{PO}_4)_2$  phosphor which peaked at 585 nm.

The  $\text{Ba}_3(\text{PO}_4)_2:\text{Eu}^{+2}$  phosphor was the brightest phosphor found in the  $\text{BaO-MgO-P}_2\text{O}_5$  system. It was 138.5% of the  $\text{Zn}_2\text{SiO}_4:\text{Mn}$  radiometer standard and over four times as intense as the  $\text{CaWO}_4$  reference phosphor.

Divalent europium activation of the  $\text{Ba}_2\text{Mg}(\text{PO}_4)_2$  compound resulted in a wide band emission phosphor whose spectral energy distribution curve was similar in width to the low-temperature  $\text{Ba}_3\text{P}_4\text{O}_{13}:\text{Eu}^{+2}$  phosphor and similar in width and emission to the high-temperature  $\text{Ba}_3\text{P}_4\text{O}_{13}:\text{Eu}^{+2}$  phosphor. The emission band peak height of  $\text{Ba}_2\text{Mg}(\text{PO}_4)_2:\text{Eu}^{+2}$  was only about half as intense as the  $\text{CaSiO}_3:\text{Pb, Mn}$  reference phosphor, but because of the extreme width of its emission band, the  $\text{Ba}_2\text{Mg}(\text{PO}_4)_2:\text{Eu}^{+2}$  phosphor ap-

Table I. Emission properties

Phosphor	Position, nm	Peak		Emission color under 2537
		½ Ht. width, nm	% of $\text{Zn}_2\text{SiO}_4:\text{Mn}$ , %	
$\text{Ba}_3(\text{PO}_4)_2:\text{Eu}^{+2}$	415	31	138.5	Exc. deep violet
$\text{Ba}_2\text{Mg}(\text{PO}_4)_2:\text{Eu}^{+2}$	585	148	8.5	Mod. lt. yel.
$\text{BaMg}_2(\text{PO}_4)_2:\text{Eu}^{+2}$	418	77	24.5	Mod. blue
$\text{Mg}_3(\text{PO}_4)_2:\text{Eu}^{+2}$	425	47	13.0	Mod. blue
$\text{CaSiO}_3:\text{Pb, Mn}$	618	87	19.3	Mod. red orange
$\text{CaWO}_4$	422	116	31.5	Mod. blue

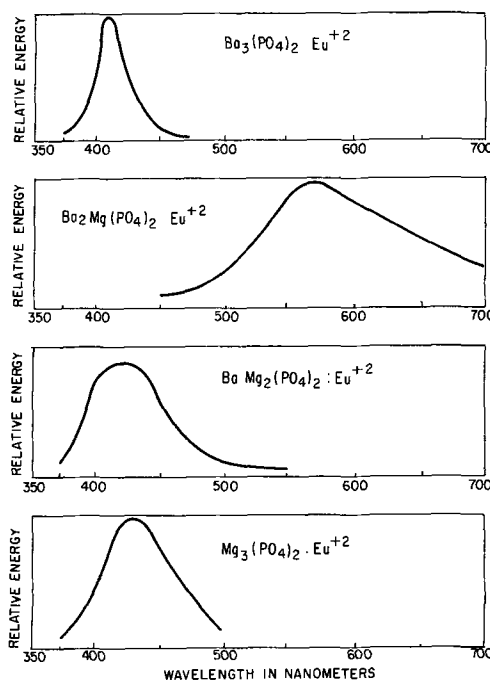


Fig. 4. Spectral energy distribution of the emission of  $\text{Ba}_3(\text{PO}_4)_2:\text{Eu}^{+2}$ ,  $\text{Ba}_2\text{Mg}(\text{PO}_4)_2:\text{Eu}^{+2}$ ,  $\text{BaMg}_2(\text{PO}_4)_2:\text{Eu}^{+2}$ , and  $\text{Mg}_3(\text{PO}_4)_2:\text{Eu}^{+2}$ ; 2537Å excitation.

peared a moderately bright yellow when visually observed under 2537Å excitation.

A phosphor with a half-height width of 77 nm and an emission peak at 418 nm was obtained with  $\text{BaMg}_2(\text{PO}_4)_2:\text{Eu}^{+2}$ . This phosphor was about three-fourths as intense as the  $\text{CaWO}_4$  reference phosphor and its emission band width half-height of 77 nm was wider than usual for a divalent europium activated phosphor with an emission in the near uv-blue region of the spectrum. All of the other phosphors in the  $\text{BaO-MgO-P}_2\text{O}_5$  system which peaked in this same region of the spectrum had considerably smaller emission band half-height widths varying from 31 to 47 nm.

The final member of the orthophosphate phosphor group was  $\text{Mg}_3(\text{PO}_4)_2:\text{Eu}^{+2}$ . Its intensity was less than half of the  $\text{CaWO}_4$  reference phosphor, and its emission band peak was located at 425 nm with a half-height width of 47 nm. Magnesium orthophosphate was the only pure magnesium containing compound which gave an emission with divalent europium activation. The other two magnesium compounds  $\text{Mg}(\text{PO}_3)$  and  $\text{Mg}_2\text{P}_2\text{O}_7$  which were discussed previously could not be activated with divalent europium but instead gave weak red emissions which were found to be trivalent europium line emissions.

All of the divalent europium activated phosphors in the  $\text{BaO-MgO-P}_2\text{O}_5$  system which fluoresced under 2537Å excitation were also found to fluoresce quite strongly under 3650Å excitation. Emission characteristics, such as band location and band width were found to be the same under 3650Å excitation as they were under 2537Å excitation.

The yellow luminescence of the  $\text{Ba}_2\text{Mg}(\text{PO}_4)_2:\text{Eu}^{+2}$  phosphor under 3650Å excitation was found to be reduced greatly when the phosphor was heated to 300°C, ruling out its applicability in high pressure mercury lamps. No other temperature-dependence studies were attempted.

Introduction of the divalent europium activated phosphors into fluorescent lamps posed no particular problems in lamp processing or lamp life. Normal lamp processing conditions were not severe enough to re-oxidize the europium from a valence of plus two to plus three and subsequently change the emission color and decrease the brightness of the phosphor. Table II compares the 40-w fluorescent lamp lumen-life data

Table II. Comparison of data

Phosphor	100 Hours			300 Hours	
	0 Hours lms	Lumens	% of 0 Hours	Lumens	% of 0 Hours
Ba <sub>3</sub> (PO <sub>4</sub> ) <sub>2</sub> :Eu <sup>+2</sup> Cool White Ca Halophosphate	310	300	96.8	294	94.8
	3299	3234	98.0	3148	95.4

obtained for the intense narrow emission band Ba<sub>3</sub>(PO<sub>4</sub>)<sub>2</sub>:Eu<sup>+2</sup> phosphor to similar data obtained for a typical cool-white halophosphate phosphor.

Because of the disparity in emission band widths between the phosphors, the total lumen output of the Ba<sub>3</sub>(PO<sub>4</sub>)<sub>2</sub>:Eu<sup>+2</sup> phosphor was understandably lower than that of the halophosphate phosphor, but the per cent of zero hour results were virtually the same for both phosphors at 100 hr and again at 300 hr.

A detailed examination and comparison of the emission bands of the various divalent europium activated phosphors which were found in the BaO-MgO-P<sub>2</sub>O<sub>5</sub> system indicated that the intensities and widths of the divalent europium emission bands of practically all of the phosphors in the system appeared to be a function of the emission band location in the visible spectrum. When the divalent europium emission band was located at the shorter wavelength end of the spectrum, the emission band was quite narrow and intense. On the other hand, when the emission band was located at the longer wavelength end of the spectrum, the band was quite wide and of fairly low intensity. Examples of the former were Ba<sub>3</sub>(PO<sub>4</sub>)<sub>2</sub>:Eu<sup>+2</sup>, BaMgP<sub>2</sub>O<sub>7</sub>:Eu<sup>+2</sup>, and Ba<sub>2</sub>MgP<sub>4</sub>O<sub>13</sub>:Eu<sup>+2</sup>, while examples of the latter were Ba<sub>2</sub>Mg(PO<sub>4</sub>)<sub>2</sub>:Eu<sup>+2</sup> and both the high- and low-temperature forms of Ba<sub>3</sub>P<sub>4</sub>O<sub>13</sub>:Eu<sup>+2</sup>.

The location of the divalent europium emission band in the spectrum is probably dependent on the coordination of the cations which the divalent europium is replacing in the crystal lattice and also on the crystal structure of the host compounds. Since the crystallographic structures of very few of the fourteen compounds and polymorphs in the BaO-MgO-P<sub>2</sub>O<sub>5</sub> system have been determined and since the determination of such crystal structures was not within the scope of this work, no conclusions could be drawn with regards to the effects of different crystal structures on the luminescence of the divalent europium ion.

The emission data obtained from the divalent europium activation of the fourteen compounds and polymorphs in the BaO-MgO-P<sub>2</sub>O<sub>5</sub> system are summarized in Table III. Data on three reference phosphors BaSi<sub>2</sub>O<sub>5</sub>:Pb, CaSiO<sub>3</sub>:Pb, Mn, and CaWO<sub>4</sub> are also included for comparative analyses.

#### Acknowledgments

The author wishes to thank Dr. K. H. Butler and M. J. B. Thomas for their valuable comments and

Table III. Summary of emission data

Phosphor	Peak Position	½ Height Width	Peak Ht. I % Zn <sub>2</sub> SiO <sub>4</sub> :Mn	Fluorescence under 2537A
Metaphosphates and gamma compound				
Mg(PO <sub>3</sub> ) <sub>2</sub>	Eu <sup>+3</sup> Line Emissions	—	—	Weak red
Ba(PO <sub>3</sub> ) <sub>2</sub>	375 nm	31 nm	5.0	Weak violet
6.3 BaO-1.0 MgO-2.7 P <sub>2</sub> O <sub>5</sub> (Gamma)	Eu <sup>+3</sup> Line Emissions	—	—	Weak red
Tetraphosphates				
Ba <sub>3</sub> P <sub>4</sub> O <sub>13</sub> (High T Form)	575 nm	197 nm	7.4	Fair lt. yel.
Ba <sub>3</sub> P <sub>4</sub> O <sub>13</sub> (Low T Form)	437	138	18.0	Mod. lt. blue
Ba <sub>2</sub> MgP <sub>4</sub> O <sub>13</sub>	403	28	59.0	Good deep violet
Pyrophosphates				
Mg <sub>2</sub> P <sub>2</sub> O <sub>7</sub>	Eu <sup>+3</sup> Line Emissions	—	—	Weak red
δ-Ba <sub>2</sub> P <sub>2</sub> O <sub>7</sub>	—	—	—	Dead
α-Ba <sub>2</sub> P <sub>2</sub> O <sub>7</sub>	406	32	11.4	Fair lt. blue
BaMgP <sub>2</sub> O <sub>7</sub>	402	45	103.0	Exc. deep violet
Orthophosphates				
Ba <sub>4</sub> (PO <sub>4</sub> ) <sub>2</sub>	415	31	138.5	Exc. deep violet
Ba <sub>2</sub> Mg(PO <sub>4</sub> ) <sub>2</sub>	585	148	8.5	Mod. lt. yel.
BaMg <sub>3</sub> (PO <sub>4</sub> ) <sub>2</sub>	418	77	24.5	Mod. blue
Mg <sub>2</sub> (PO <sub>4</sub> ) <sub>2</sub>	425	47	13.0	Mod. blue-violet
Reference Phosphors				
BaSi <sub>2</sub> O <sub>5</sub> :Pb	355	41	205.0	Weak violet
CaWO <sub>4</sub>	422	116	31.5	Mod. blue
CaSiO <sub>3</sub> :Pb, Mn	618	87	19.5	Mod. red or.

suggestions, and Mr. Allen Rudis and Miss Marion Skeadas for the spectral energy distribution and x-ray diffraction measurements.

Manuscript submitted May 23, 1968; revised manuscript received June 23, 1968. This paper was presented at the Boston Meeting, May 5-9, 1968, as Paper 58.

Any discussion of this paper will appear in a Discussion Section to be published in the June 1969 JOURNAL.

#### REFERENCES

- W. L. Wanmaker and J. W. ter Vrugt, Philips Research Repts., **22**, 355 (1967)
- N. A. Gorbacheva, *Bull. Acad. Sci. USSR*, **30**, 1586 (1966).
- V. P. Nazarova, *ibid.*, **25**, 322 (1961)
- M. V. Hoffman, *This Journal*, **110**, 1223 (1963)
- J. E. Eby, Paper presented at the Toronto Meeting of the Society, May 3-7, 1964, as Paper 27.
- Jozef Berak, *Roczniki Chem.*, **32**, 17 (1958); *C.A.*, **52**, 9836b.
- R. P. Langguth, R. K. Osterheld, and E. Karl Kroupa, *J. Phys. Chem.*, **60**, 1335 (1956); ASTM Powder Data File Card 9-46.
- D. E. Harrison, *This Journal*, **107**, 217 (1960).
- P. W. Ranby, D. H. Mash, and S. T. Henderson, *Brit. J. Appl. Phys. Supplement No. 4S-18*.
- W. H. Zachariasen, *Acta Cryst.*, **1**, 264 (1948); ASTM Powder Data File Card 4-0582.

# Fluorescence of Fe, Co, and Ni in Reduced Germanate Glass

C. Hirayama and F. E. Camp

Westinghouse Research Laboratories, Pittsburgh, Pennsylvania

## ABSTRACT

Red fluorescence has been observed in a reduced germanate glass doped with iron, cobalt, and nickel. The reduced, undoped glass also fluoresced in the red. There was a strong concentration dependence of the fluorescence intensity and quantum efficiency. The fluorescent center appears to be associated with oxygen vacancy in the host.

The fluorescence in glasses produced by certain transition metals and rare earth ions is well known. In nearly all cases the fluorescence in glass resembles that in a crystalline host where the activator is coordinated by oxygens. Not reported in the literature to date, however, is the fluorescence arising from an iron activator site in a glass; there is one mention (1) of a greenish fluorescence in a silicate glass, which probably arises from an impurity other than iron. The fluorescence of  $\text{Ni}^{2+}$  and  $\text{Co}^{2+}$  in glass is also relatively unknown. Fischer, in a patent (2), describes a red and orange fluorescence, respectively, for  $\text{Ni}^{2+}$  in glass.

Iron is generally known to be a killer of fluorescence at concentrations higher than about  $10^{-4}\text{M}$  in crystalline hosts. However, red fluorescence (3) from  $\text{Fe}^{3+}$  in  $\text{Al}_2\text{O}_3$ -containing phosphors, and red (4) and infrared (5) fluorescence from  $\text{Fe}^{2+}$  in ZnS have been reported. The fluorescence of  $\text{Co}^{2+}$  and  $\text{Ni}^{2+}$  in crystalline hosts has been observed in a few cases (6). Depending on the host, the former emits in the yellow or red, while  $\text{Ni}^{2+}$  emits in the yellow, red, or infrared. In all instances the activator concentration was very low.

This paper reports the observations of strong red fluorescence arising from  $\text{Fe}^{2+}$ ,  $\text{Ni}^{\text{I}}$  and  $\text{Co}^{\text{I}}$  in a germanate glass of composition  $66\text{GeO}_2 \cdot 17\text{K}_2\text{O} \cdot 17\text{BaO}$  prepared under strongly reducing conditions. The absorption and fluorescence are now reported, and a later report (7) will present the electron spin resonance (ESR) spectra which supports some of the conclusions herewith. Only a brief summary of the esr results is presented here.

## Experimental

**Preparation.**—The glasses of base composition  $66\text{GeO}_2 \cdot 17\text{K}_2\text{O} \cdot 17\text{BaO}$  were prepared in 50-g batches by fusing the ingredients at  $1250^\circ\text{C}$  in fused silica or in recrystallized alumina crucibles in a globar furnace. Although the properties of the glasses in both crucibles were the same, most of the samples were melted in alumina. Aside from the semiconductor grade of  $\text{GeO}_2$ , the chemicals were of reagent grade. For the oxidized samples, appropriate amounts of  $\text{GeO}_2$ ,  $\text{BaCO}_3$ ,  $\text{K}_2\text{CO}_3$ , and  $\text{Fe}(\text{NO}_3)_3 \cdot 9\text{H}_2\text{O}$  were mixed and fused for  $\frac{1}{2}$  to 1 hr in air in an open crucible. For the reduced glasses,  $\text{GeO}_2$ ,  $\text{Ba}(\text{Ac})_2 \cdot \text{H}_2\text{O}$ ,  $\text{KAc}$ , and  $\text{Fe}(\text{NH}_4)_2(\text{SO}_4)_2 \cdot 6\text{H}_2\text{O}$  were fused for  $\frac{1}{2}$  to 1 hr in a covered crucible. The dissociation of the acetate in the covered crucible was sufficient to maintain a strongly reducing atmosphere. The iron concentration varied from 0.0005 to 0.75 w/o (weight per cent) Fe. At the low concentrations the iron salt was dissolved in water and aliquots added to the mixture. The  $\text{Mn}^{2+}$  and  $\text{Ni}^{2+}$  were added as the acetates while  $\text{Co}^{2+}$  and  $\text{Cr}^{3+}$  were added as the nitrate. The latter four ions were added only in 0.01 w/o as the metal, in both reduced and oxidized glasses.

All samples were cast into disks, and annealed at  $500^\circ\text{C}$ . The samples were subsequently cut and prepared for the different measurements. The grinding

and polishing of the flat samples were made with butyl alcohol as the vehicle.

Two samples each from the oxidized and reduced glasses were analyzed for  $\text{BaO}$ ,  $\text{K}_2\text{O}$ , and  $\text{R}_2\text{O}_3$  (including  $\text{Al}_2\text{O}_3$  and  $\text{Fe}_2\text{O}_3$ ); the  $\text{GeO}_2$  content, because there is no accurate analytical method for Ge, was calculated as the difference.

**Measurements.**—The optical absorption, fluorescence and excitation spectra were obtained on polished samples of approximately 3.5 mm thickness. The visible and ultraviolet absorption spectra were obtained on a Cary model 14 spectrophotometer, and the infrared spectra were obtained on a Perkin-Elmer 521. Most of the fluorescence and excitation spectra were obtained on a Jarrel-Ash 0.5m grating spectrometer (the Excifluor). The fluorescence was corrected for spectral sensitivity on a liquid nitrogen-cooled Si detector. The excitation spectra were obtained by monochromatically exciting the fluorescence with a 900 W, Hanovia, xenon short-arc lamp, and corrected so that the excitation spectra were proportional to the fluorescence per incident photon rate. Fluorescence was also measured by exciting the sample with 365 nm radiation from a Beckmann DU spectrophotometer, then detecting the emitted light with appropriate photocells in the region 550–1000 nm. The latter measurements were made at room temperature and at  $77^\circ\text{K}$ .

Relative fluorescence brightness measurements were made with a Photo Research Spectra Brightness meter on powdered material. This plaque test was made on equal volumes of samples packed in a black-painted brass cup at a fixed, focused distance from the meter. The relative quantum efficiency measurements were made on quasi-infinitely thick layers of powder at room temperature. The samples were excited by 365 nm radiation, and the detection of emitted and reflected light was made with a silicon photodiode whose sensitivity was practically flat, within 10%, to 800 nm. Above the latter wave length, the sensitivity decreased fairly rapidly.

Electron spin resonance measurements were made on solid samples at  $77^\circ$  and at  $4.3^\circ\text{K}$  on a superheterodyne x-band spectrometer.

## Results

The glasses prepared in oxidizing atmosphere were all clear and possessed the color characteristic of the transition metal ion in glass (8). The reduced glasses were usually clear, with some bubbles in the quenched glass. The color of most of the latter glasses was slightly yellow. The Co- and Mn-containing glasses were colorless. The reduced glasses were readily soluble in water and were soft when samples were cut on a carborundum wheel. In contrast, the oxidized glasses were only slightly attacked by water during the grinding and polishing of samples.

Table I shows the analyses of four of the glasses prepared in both oxidizing and reducing atmospheres. The analyses are also compared with the nominal composition of the glass without addition of transition metal ion. The analytical molar ratio  $\text{BaO}/\text{K}_2\text{O}$  is 1.10

<sup>1</sup> Since the valence states of nickel and cobalt in our fluorescent glasses have not been established, we will refer to Co and Ni without specifying the valence.



Table I. Analyses of oxidized and reduced glasses and density

Sample	Melting condition	BaO	K <sub>2</sub> O	R <sub>2</sub> O <sub>3</sub>	Analysis, w/o *GeO <sub>(2-x)</sub>	x	% Fe added	Density
30-1	ox.	23.7	13.2	0.2	62.9		0.2	
33-6	ox.	24.0	13.5	-0.2	62.3		0	4.015
41-1	red.	26.9	14.5	0.3	58.3	1.16	0	3.855
41-2	red.	26.7	14.3	0.4	58.6	1.10	0.1	
Nominal		23.5	14.4	—	62.1			

\* By difference.

in the oxidized glasses, whereas this ratio is 1.14 in the reduced glasses. This increase in the ratio shows that at least 4.4% of K<sub>2</sub>O was lost in the melting process. The loss occurs in part by volatilization of K<sub>2</sub>O itself, and probably in part by the reduction and volatilization as potassium vapor.

From the standpoint of thermodynamic stability, the potassium and barium are most probably in their normal valence states. However, germanium has been known to occur in both tetra- and divalent states in GeO<sub>2</sub> glass (9). By assuming that no barium or germanium was lost in the glasses the value of  $x$  in GeO<sub>2-x</sub> was calculated, based on the Ge/Ba ratio. As shown in Table I, the value of  $x$  was about 1.1. This value is obviously too high in view of the absence of color in the undoped reduced glass. It could very well be that considerable germanium was volatilized as GeO since this species is known to have a high vapor pressure (10).

In one preparation, considerable metal globules were found in the quenched glass. The emission analysis showed the metal to be predominantly Ge, with little or no Ba or K. The glass samples on which spectroscopic and density measurements were made were free from metallic Ge, as shown by the absence of Ge esr absorption.

There was a significant decrease in density of the glass when prepared in a reducing atmosphere. The densities of two glasses are shown in Table I. Similar values were obtained for other glasses, and the ratio of density of the oxidized to the reduced glasses was around 1.04. With a loss of at least 10 w/o in the reduced glass, this ratio would be expected to be higher since the reduced glass should have a much lower density. This of course assumes that the structure of the glass is not changed. It may be inferred, therefore, that the glass structure is pulled in to a more compact one as the result of the loss of oxygen.

**Absorption spectra.**—The absorption spectra of the glasses containing Fe, Co, Ni, and Mn, and that with no added transition metal ion are shown in Fig. 1. The curves are normalized for approximately the same sample thickness. Curve 1, for the undoped glass which was prepared in oxidizing atmosphere, is typical for most glasses prepared from reagent grade

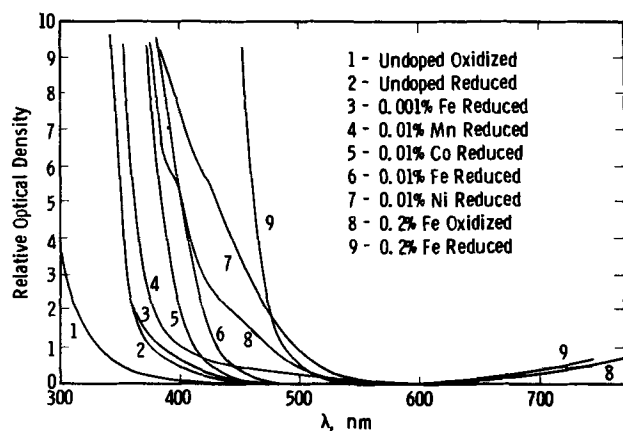


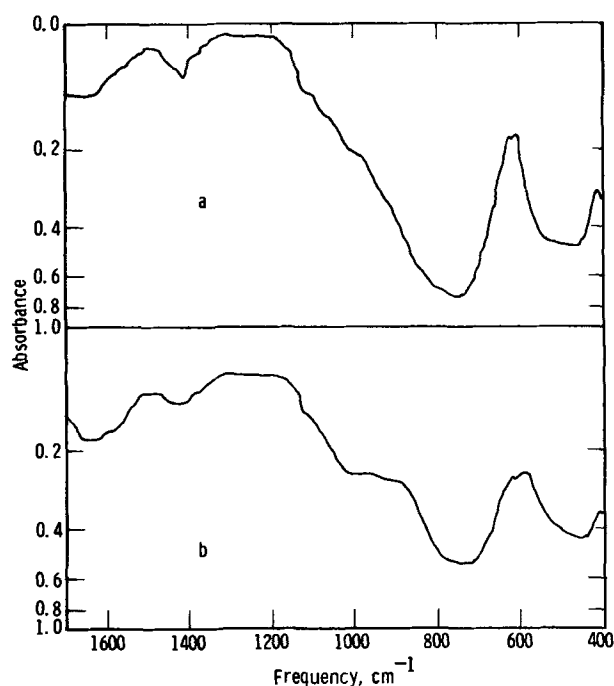
Fig. 1. Absorption spectra of glasses

materials melted in air. However, the reduced glass, curve 2, shows intrinsic absorption starting at about 50 nm longer wavelength. Curve 3, for the reduced glass containing 0.001% Fe, is almost identical to curve 2, except for a slightly stronger absorption at around 400 nm. This absorption could have been due to scattering since some of the samples contained more bubbles than others. The reduced glass containing 0.01% Co was colorless, as seen in curve 5. The oxidized glass containing 0.01% Co was a deep blue, typical of Co<sup>2+</sup> in glasses. Curve 7, for the reduced Ni-doped glass, has a shoulder at around 450 nm, and the cutoff is not as sharp as in the other reduced glasses. The oxidized glass containing 0.01% Ni<sup>2+</sup> was purple, while the reduced glass was a light yellow. The spectrum for the oxidized glass containing 0.2% Fe, curve 8, shows two shoulders which arise from the Fe<sup>3+</sup> absorption bands at around 435 and 385 nm. The reduced glass containing 0.2% Fe has a sharp cutoff near 500 nm. Both glasses containing 0.2% Fe show the broad, near infrared tail of the Fe<sup>2+</sup> absorption which has its maximum at 1000 nm.

There are large differences in the short wavelength region between glasses prepared in oxidizing and in reducing atmospheres. Strong absorption due to charge-transfer appears at considerably longer wavelength in the reduced glasses; the cutoff increases significantly with the transition metal ion concentration. It should be noted that Fe<sup>2+</sup> does not absorb between 300 and 600 nm.

The strong charge-transfer absorption in the reduced glasses must arise from a center associated with the divalent transition metal ion. The absence of visible absorption in the reduced 0.01% Co-containing glass is surprising in view of the intense color usually associated with this ion in glass.

Figure 2 shows the infrared absorption spectra of the reduced and oxidized glasses in which no transition metal ion was added. The spectra for reduced and oxidized glasses doped with transition metal ions were identical to the corresponding glasses shown in Fig. 2. The peaks for Ge-O-Ge antisymmetric stretching frequency in both glasses appear at about 750 cm<sup>-1</sup>. The latter frequency is lower than the 800 cm<sup>-1</sup> found for this peak in alkali germanate glasses (11). There is a flat region between 900 and 1000 cm<sup>-1</sup> in the reduced glasses, whereas the oxidized glasses show

Fig. 2. Infrared absorption spectra of glasses 66GeO<sub>2</sub>·17K<sub>2</sub>O·17BaO: (a) oxidized glass; (b) reduced glass.



only a slight shoulder at  $1000\text{ cm}^{-1}$ . Although the difference in infrared absorption shows some difference in the germanate glass structure, the exact origin of the broad, flat infrared absorption in the reduced glass is not known at present.

*esr.*—Certain results of the esr measurements are pertinent: (A) At  $4^\circ\text{K}$  the reduced glass with no added transition metal showed only a strong, highly symmetrical, sharp line of about 10 gauss width at  $g = 1.9975$ . This line was still present at  $77^\circ\text{K}$ . It saturated at low microwave powers at both temperatures. This sharp line was very similar to the resonance originating from oxygen vacancies in vitreous  $\text{GeO}_2$  (12). There was no resonance at  $g = 4.3$ , nor a broad resonance at  $g = 2$ . (B) At  $4^\circ\text{K}$  the reduced glass containing 0.1% Fe showed a weak, narrow line of about 0.9 gauss superimposed on a broad line centered at  $g = 2$ . The lines did not saturate even at the highest microwave power input. In addition to the  $g = 2$  resonance, there was a very weak absorption at  $g = 4.3$ , which was about 20 gauss wide. At  $77^\circ\text{K}$  all of the resonances disappeared, except a very weak absorption at  $g = 2$ , which was observed only at very high gain. (C) The oxidized glass containing 0.01% Fe, at  $4^\circ$  and at  $77^\circ\text{K}$ , showed resonances at  $g = 2$  and 4.3, the latter approximately 20 gauss wide, while the  $g = 2$  line was very broad. These resonances are typical of  $\text{Fe}^{3+}$  in glasses (13).

*Fluorescence.*—All of the above glasses prepared in silica and alumina crucibles in oxidizing atmosphere showed no fluorescence on excitation with 254 and 365 nm radiation. However, the glass prepared in a platinum crucible showed a weak pinkish-white fluorescence with 365 nm excitation. Addition of 0.1%  $\text{PtCl}_4$  to the glass prepared in a silica crucible also showed the same fluorescence.

When prepared under reducing atmosphere, the undoped glass had a weak orange-red fluorescence with 365 nm excitation. On adding increasing amounts of iron the fluorescence of the reduced glasses became stronger, up to 0.2% Fe. Beyond the latter, the fluorescent brightness started to decrease rapidly. The glasses doped with 0.01%  $\text{Mn}^{2+}$  and  $\text{Cr}^{3+}$  showed only a very weak orange-red fluorescence which was weaker than that of the undoped glass. The glasses containing Ni and Co showed strong red and yellow-orange fluorescence, respectively. Figure 3 shows the relative brightness of the emission of Fe-containing glasses at room temperature, as measured on powder samples with the Spectra Brightness meter. The meter has an S4 response, so that its sensitivity to the glass emission is very low.

The room temperature excitation and fluorescent spectra of the reduced glasses with no added transi-

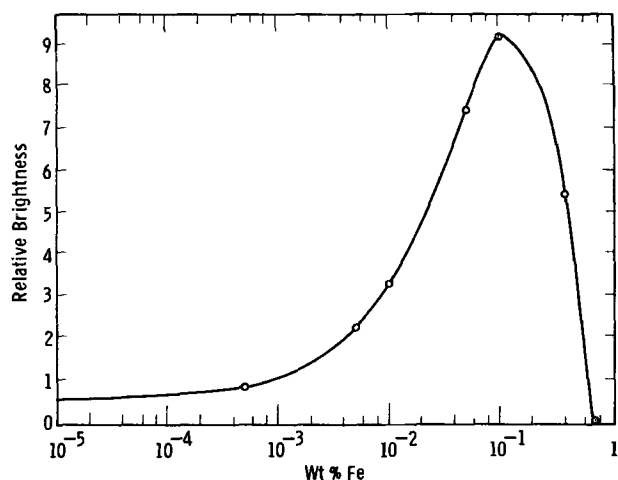


Fig. 3. Brightness dependence of reduced glass on Fe concentration; 0.01% Fe =  $4.1 \times 10^{18}$  ions/cc.

tion metal and those containing 0.01% of Fe, Co, and Ni are shown in Fig. 4-7, respectively. The excitation bands are all similar except for slight shifts in peak position and in the width. The Ni-doped glass has an excitation band almost twice that for the other three glasses. The excitation bands of all of the glasses have a tail that extends into the visible. In the Fe-doped glass, there is also a weak excitation band at 500 nm.

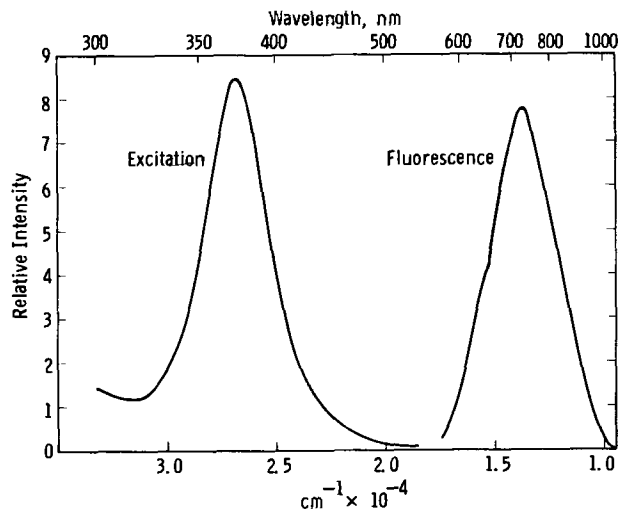


Fig. 4. Excitation and fluorescence spectra of undoped reduced glass.

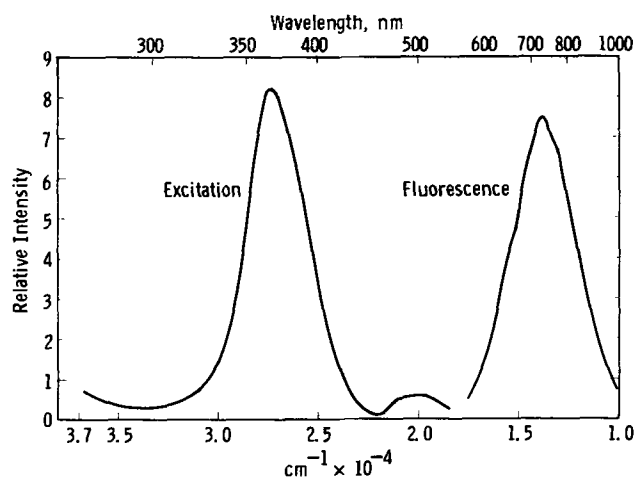


Fig. 5. Excitation and fluorescence spectra of reduced glass doped with 0.01% Fe.

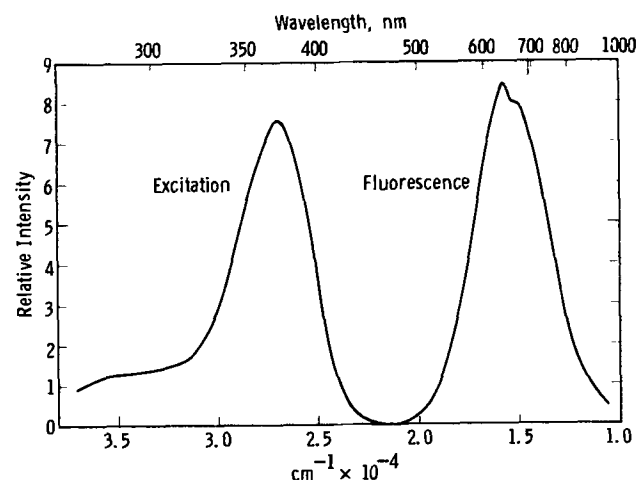


Fig. 6. Excitation and fluorescence spectra of reduced glass doped with 0.01% Co.

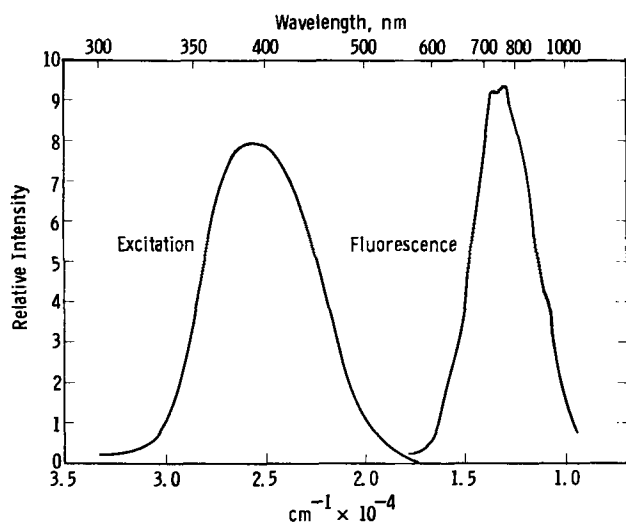


Fig. 7. Excitation and fluorescence spectra of reduced glass doped with 0.01% Ni.

The fluorescent bands are all very broad; those for the glasses doped with Fe and Ni, and the undoped glass are similar and occur between  $1.1$  and  $1.8 \times 10^4$   $\text{cm}^{-1}$ . The fluorescent band for the Co-doped glass is slightly broader than that in the other three glasses, and is shifted to shorter wavelength. The yellow-orange fluorescence of the latter glass results from the shift to the shorter wavelength. The shape of the fluorescent bands in all of the glasses suggests that the bands are composites of several components.

In iron-containing glasses, the fluorescent band at room temperature remained in the same wavelength region up to Fe concentration of 0.2%. At 0.4% Fe the band shifted to shorter wavelength by about 50 nm. At 77°K the fluorescent bands of glasses containing 0.1% and less Fe were shifted to longer wavelengths by 40–80 nm, while the shift at 0.4% Fe was only about 10 nm. The intensity of the fluorescence in the glasses doped with less than 0.1% Fe increased by three to fivefold at 77°K, whereas the increase was only about 50% above 0.1% Fe.

Table II records the relative quantum efficiency of some of the glasses. These values are probably low because of the decreased spectral sensitivity of the silicon photodetector. There is a strong dependence of the quantum efficiency on the iron content.

### Discussion

The strong red fluorescence from Fe, Ni, and Co in the germanate glasses appears to be associated with the highly reduced nature of the host. There was no fluorescence observed at these low activator concentrations in phosphate and silicate glasses prepared under similar reducing conditions. The weak orange-red fluorescence from the  $\text{Mn}^{2+}$  is typical for this ion in glasses; its fluorescent intensity in the reduced germanate at 0.01%  $\text{Mn}^{2+}$  was very low compared to the glasses doped with the other three activators. In fact, the fluorescent intensity of the Mn-doped glass was significantly lower than that in the undoped glass.

The germanate glass system is very complex, compared to the silicates, phosphates, and vitreous  $\text{GeO}_2$ , because of the existence of both four- and six-coordinated germanium. The structure of the reduced germanate glasses is further complicated by the appar-

ently large deficiency of oxygen. One could also state that there is apparently a mixture of  $\text{Ge}^{4+}$  and  $\text{Ge}^{2+}$ . The sharp esr absorption at  $g = 1.9975$  in the reduced, undoped glass is somewhat similar to that observed in irradiated vitreous  $\text{GeO}_2$  (12). In the latter, all of the Ge is four-coordinated. It has been suggested by Weeks and Purcell that an oxygen vacancy is created on irradiation with electrons or x-ray, and that an electron is trapped by a Ge atom, giving rise to the  $g = 1.9975$  resonance. When pure  $\text{GeO}_2$  is prepared under slightly reducing conditions, the glass has an absorption band at 244.5 nm (9). This absorption, also found in irradiated  $\text{GeO}_2$ , is attributed (12) to reduced (or oxygen-deficient) germanium oxide. The  $g = 1.9975$  resonance is associated with the oxygen deficient state of hexagonal and of pure, vitreous  $\text{GeO}_2$ . We did not observe the optical absorption at 244.5 nm because of the absorption edge at longer wavelengths.

As shown in Fig. 1, the absorption edge of the Fe-doped glasses has a strong dependence on the iron concentration. The excitation band, however, remains essentially in the same region as in Fig. 5. The concentration dependence was not studied on the Co and Ni-doped glasses. The shift in absorption edge to longer wavelength suggests that the increasing Fe concentration creates defect sites of progressively lower energy. Similar observations have been recently reported for  $\text{Fe}^{2+}$  doped fosterite (14). No electrical measurements have been made as yet, so it is not known if the iron-doped glass is photoconducting.

The exact nature of the fluorescent center in the reduced glasses is difficult to conjecture at present, but the centers seem to be of similar nature in the glasses doped with either Fe, Co, or Ni. The valence state of  $\text{Fe}^{2+}$  is established from the esr absorption of the reduced glass. The concentration of  $\text{Fe}^{3+}$  in the latter is extremely low, in view of the very weak absorption at  $g = 4.3$  observed only at 4°K. The exact valence states of the nickel and cobalt are not clearly established at present, although these ions are normally divalent in glasses. The extremely weak  $\text{Ni}^{2+}$  absorption and the absence of  $\text{Co}^{2+}$  absorption in these glasses cannot be explained in the absence of more definitive data, such as the magnetic properties.

The fluorescence in the  $\text{Fe}^{2+}$ -doped glasses has certain resemblances (3) to that in  $\text{Li}_2\text{O} \cdot 5\text{Al}_2\text{O}_3 \cdot \text{Fe}$ , where the fluorescent center is associated with  $\text{Fe}^{3+}$ . The excitation band in the aluminate is centered at around 300 nm, as compared to around 365 nm in the glass; the fluorescent band in both materials is located in approximately the same region. The excitation and fluorescent bands in the glass, although of the same shape, are broader than that for the  $\text{Fe}^{3+}$  in the aluminate. The optical and fluorescent bands in glasses are generally broader than in crystals, and there are often slight shifts in the wavelengths.

Ferrous ion acts as a hole trap in glasses (15), with the formation of  $\text{Fe}^{3+}$ . The  $\text{Fe}^{2+}$  fluorescence in ZnS has been attributed to the capture of a hole by the  $\text{Fe}^{2+}$ , with subsequent red emission of the excited  $\text{Fe}^{2+}$ -hole pair on returning to the ground state (4). In the absence of esr data on the excited Fe-doped glasses it is not possible to assign a similar mechanism to the  $\text{Fe}^{2+}$  fluorescence in the reduced glass. That the  $\text{Fe}^{2+}$  is an activator is clear from the strong concentration dependence of the fluorescence. The absence of fluorescence in the oxidized glasses conclusively shows that  $\text{Fe}^{3+}$  itself does not fluoresce in the glass. The  $\text{Fe}^{3+}$  in this instance may be occupying sites quite different than that of  $\text{Fe}^{2+}$  in the reduced glass.

The  $\text{Mn}^{2+}$  ion in a glass also acts as a hole trap (16). The decrease in fluorescence in the glass containing this ion may well be due to  $\text{Mn}^{2+}$ -hole pair formation, if this state returns to the ground state by a nonradiative process. The latter then would compete with the normal  $\text{Mn}^{2+}$  radiative process.

Any mechanism for the observed bright fluorescence in the Fe-, Co-, and Ni-doped, and suppressed fluores-

Table II. Relative quantum efficiency,  $\eta$ , of reduced glasses

Dopant	Concentration, %	$\eta$
Fe	0.01	0.13
Fe	0.1	0.41
Ni	0.01	0.11
Co	0.01	0.035

cence in the Mn-containing glasses, must be consistent and account for the phenomenon in all cases. If a metal ion-hole pair is the fluorescent center, the formation of the hole must also be explained. In the absence of more information, it is not possible at present to explain the fluorescent mechanism. The association of the  $\text{Fe}^{2+}$ , Co, and Ni with a defect center seems to be required for the fluorescent center.

The absence of visible absorption in the Co-doped, reduced glass must also be explained, since this seems to be required for the bright fluorescence from this glass. The  $\text{Co}^{2+}$  in four-coordination is blue, while the six-coordinated ion is pink. When the colorless, reduced glass was remelted in air, the blue color was obtained. The glass, like all of the remelted and oxidized glasses, was not fluorescent.

#### Acknowledgment

The authors thank W. Lehmann for some of the fluorescent measurements and for discussions; R. Perevuznik and N. T. Melamed for the excitation and fluorescence spectra; and G. R. Wagner for the esr measurements.

Manuscript received Aug. 9, 1968.

Any discussion of this paper will appear in a Discussion Section to be published in the June 1969 JOURNAL.

#### REFERENCES

1. P. Gilard, L. Dubrul, and D. Crespini, *Verre et Silicates inds.*, **9**, 253, 266 (1938).
2. G. Fischer, Neth. Pat. 55132.
3. V. D. Mochel, *This Journal*, **113**, 398 (1966).
4. P. M. Jaffe and E. Banks, *ibid.*, **111**, 52 (1964).
5. G. A. Slack and B. M. O'Meara, *Phys. Rev.*, **163**, 335 (1967).
6. F. A. Kroger "Some Aspects of the Luminescence of Solids," pp. 265, 275, Elsevier Publishing Co., New York (1948).
7. G. R. Wagner, To be reported.
8. W. A. Weyl, "Colored Glasses," 541 pp, Dawson's of Pall Mall, London, (1959).
9. V. Garino-Canina, *Compt. rend.*, **247**, 593 (1958); *ibid.*, **250**, 1815 (1960); A. J. Cohen and H. L. Smith, *J. Phys. Chem. Solids*, **7**, 301 (1958).
10. C. Hirayama, *J. Chem. Eng. Data*, **9**, 65 (1964).
11. M. K. Murthy and J. Aguayo, *J. Am. Ceram. Soc.*, **47**, 444 (1964).
12. R. A. Weeks and T. Purcell, *J. Chem. Phys.*, **43**, 483 (1965).
13. T. Castner, Jr., G. S. Newell, H. C. Holton, and C. P. Slichter, *ibid.*, **32**, 668 (1960).
14. T. J. Shankland, *Science*, **161**, 51 (1968).
15. R. F. Tucker, "Advances in Glass Technology," pp. 103-114, Plenum Press, Inc., New York (1962).
16. J. S. Stroud, J. W. H. Schreurs, and R. F. Tucker, in Proc. VII International Congress on Glass, Brussels, Belgium, June 28-July 3, 1965.

## Emission Spectra of Individual Phosphor Particles

Andre C. Boucharde\*

*Sylvania Electric Products Incorporated, Danvers, Massachusetts*

#### ABSTRACT

Measurement of the emission (350-750 nanometers) from single 5-50 $\mu$  particles of various phosphor systems under 2537 $\text{\AA}$  excitation has been achieved utilizing a modified fiber optic microspectroradiometer. The system greatly facilitates identification of phosphor components in blends often employed in fluorescent lamps and has enabled positive identification of most phosphors from their respective emission spectra. Minor secondary phases present in experimental phosphors, which had heretofore been impossible to verify with standard spectroradiometric equipment, have now become readily identifiable. Successive stages of phosphor activation of the system  $\text{Ca}_5(\text{X})(\text{PO}_4)_3:\text{Sb}^{+3}, \text{Mn}^{+2}$  have been explored with variations in spectral characteristics of particles occurring not only in different locations of the firing vessel, but among adjacent grains within a small volume. Particles from standard cool white fluorescent lamps have been found to exhibit slight variations in  $\text{Sb}^{+3}$  to  $\text{Mn}^{+2}$  emission ratios resulting in possible luminous efficiency losses. Brightness profile data across individual cool white phosphor grains, utilizing a 1.2 $\mu$  measurement probe area have indicated variations of the order of 10-15% difference across single grains. Brightness data from particle to particle have also indicated substantial differences.

#### Experimental

A schematic illustration of the equipment used in our experiments is shown in Fig. 1. The phosphor excitation source consisted of a Model 11 Sc-1L "Pen Ray" quartz, low-pressure Hg arc lamp. Maximum uv intensities for phosphor excitation were obtained in the apparatus by removing the substage of a standard petrographic microscope, and vertically mounting the Pen Ray lamp in as close a proximity to the microscope object slide as possible. The object slide consisted of a 1 in. x 2 in. x 3 mm 9863 Corning uv filter which served a twofold purpose of filtering the visible Hg lines from the exciting source as well as a mounting medium for the phosphor particles. All samples to be investigated were either dry mounted or immersed in high uv transmitting cp glycerin to the top surface of the filter.

\* Electrochemical Society Active Member.

Key words: Microspectroradiometer, spectral energy distribution, phosphor inhomogeneity, cool white halophosphate.

The visible light generated by the excited phosphor particle was brought to a focus in the image plane of the microscope eye lens, where a centrally located small fiber optic probe (5 $\mu$  measurement area) picked up and fed the light from the area to be measured into an external fiber optic light pipe coupled to a motorized Bausch and Lomb grating monochromator, 1350 grooves/mm with bandwidth of approximately 20 nm using a 1.34 mm exit slit. The dispersed light from the single particle was picked up at the exit slit of the monochromator and amplified by a 9558 A EMI photomultiplier tube with a built-in 4 sec time constant to obtain acceptable signal to noise properties. All spectral energy distribution (SED) measurements were automatically recorded on a standard x-y recorder, and scanning speeds of 20 nm/min were found necessary to obtain repeatable spectra. It was found that the sensitivity of the system was dependent on the optical transmission of the equipment as well

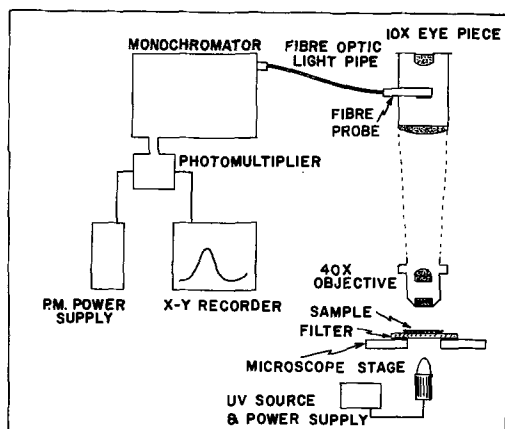


Fig. 1. Diagram of apparatus

as the quantum efficiency and spectral emission bandwidth of the particular phosphors under investigation.

### Applications and Results

This tool has been found useful in identifying phosphor components present in blend type fluorescent lamps, especially the deluxe types, employing up to six compositionally different phosphors. The identification of all these phosphor components by x-ray techniques or chemical analyses is tedious due to the percentage of components present, as well as the similarity in crystal structure of the particular phosphors. The use of the microspectroradiometer in conjunction with the uv microscope has facilitated the task of phosphor identification and yielded a good estimate (by count) of the percentage of the individual phosphors used in the particular blends. Identification techniques consisted of mounting the phosphor blend on the uv filter object slide, traversing the microscope stage until the probe measurement area coincided with the phosphor particle image, and recording the SED of the various color emitting particles. From a comparison of the SED spectra of the phosphor particles with SED spectra of standard phosphor systems, rapid identification of all particles present in a particular blend was obtained. As an example, Fig. 2 illustrates the SED of a deluxe type fluorescent lamp obtained from a standard radiometer. Figure 2A obtained from our experimental apparatus resolves the standard SED curve of Fig. 2 into the various emitting components.

Use for this instrument has been found in the field of new phosphor development. In many instances the instrument has yielded information virtually impossible to determine with standard spectroradiometric equipment. Minor extraneous phases, oftentimes giving rise to variations in the spectral emission of particles, are readily identifiable with this tool. The question of multiple emission band spectra, whether arising from nonequivalent sites, or from extraneous impurity phases can often be resolved with the use of this instrument. In Fig. 3 and 3A comparisons of the

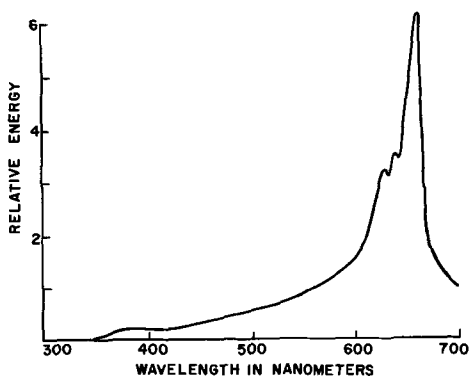


Fig. 2. Standard SED of deluxe fluorescent lamp

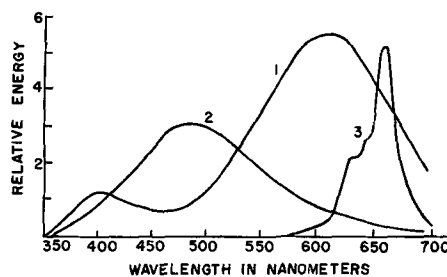


Fig. 2A. Single particle emission curves of deluxe fluorescent lamp. Curve 1, calcium strontium magnesium orthophosphate 30% by volume; curve 2, magnesium tungstate 10% by volume; curve 3, magnesium fluorogermanate 60% by volume.

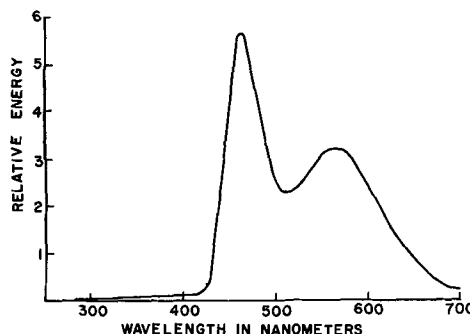


Fig. 3. Experimental phosphor standard SED measurement

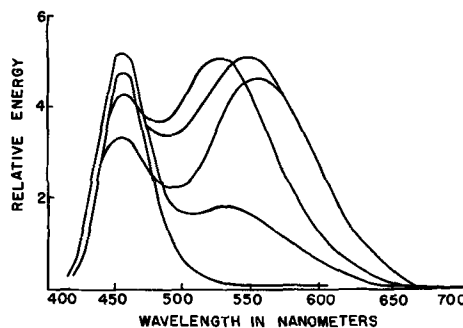


Fig. 3A. Single particle emission curves of experimental phosphor

SED of an experimental phosphor obtained from a standard *vs.* the experimental radiometer indicates that the SED curve of Fig. 3 was actually a composite of five closely overlapping emission bands. The spectra in Fig. 4 and 4A, also obtained from an experimental phosphor, similarly illustrate the usefulness of the single particle radiometer in separating various phases and substantiating the existence and locations of very weak emission bands.

The radiometer has been employed in the field of standard phosphor improvement also. Recent experiments were conducted on the successive stages of activation of the system  $\text{Ca}_5(\text{X})(\text{PO}_4)_3:\text{Sb}^{+3}, \text{Mn}^{+2}$  to determine if any spectral color changes occurred during the solid-state reaction of the many constituents used during the formation of the phosphor. Samples for investigation were prepared by formulating a standard 4500°K cool white halophosphate blend and mix-

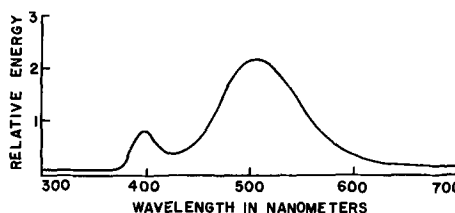


Fig. 4. Experimental phosphor standard SED measurement

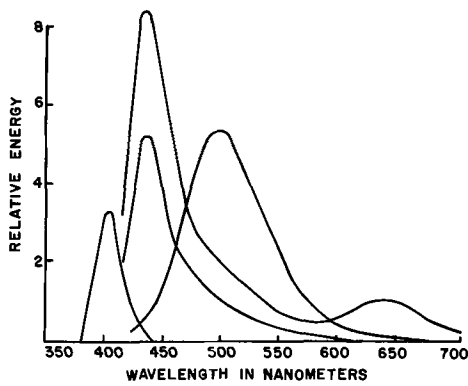


Fig. 4A. Single particle emission curves of experimental phosphor

ing all ingredients for 30 min in a Spex mixer mill. All samples were fired in 1 x 5 in. zircon boats at temperatures ranging from 1400° to 2200°F in 100°C-steps. Particular interest was devoted to the SED spectra of the underfired samples for indications of possible initial preferential diffusion of Sb, Mn, Cl, F into the apatite lattice. It was observed that variations, due to possible blending techniques and thermal gradients existing in the firing vessels, yielded too great a disparity in emission colors among particles to justify any conclusions as to diffusion mechanisms occurring during the activation processes. Not only were variations in spectral compositions found in various locations of the firing vessels, but differences occurred among adjacent phosphor particles within a small volume. Generally, the differences in color were attributed to variations in the ratio of the Sb to Mn emission bands.

To substantiate that the differences found in our experimental firings were present in larger production vessels, fired under more ideal conditions, a sample production fired vessel was broken into various sections and analyzed for spectral inhomogeneities. Although it was found that the emission spectra of the majority of particles were generally very similar, some large differences in the SED of individual grains were found in various locations of the firing vessel as illustrated in Fig. 5. It should be emphasized that these differences occurred in proportions no greater than ½% of the total phosphor volume in the vessel. The SED spectra only indicate some of the largest variations that might be found utilizing standard firing techniques.

Particles from cool white fluorescent lamps were very closely examined also for minor spectral variations. It was established that most particles possessed slight but significant variations in their Sb to Mn emissions band ratios. Figure 6 illustrates typical small SED variations obtained from particles present in cool white fluorescent lamps.

An investigation of the brightness of individual halophosphate grains was also conducted by removing the Bausch and Lomb monochromator from the optical

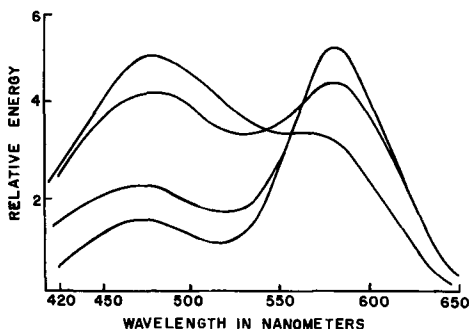


Fig. 5. Single particle emission curves obtained from cool white (4500°K) halophosphate production vessel.

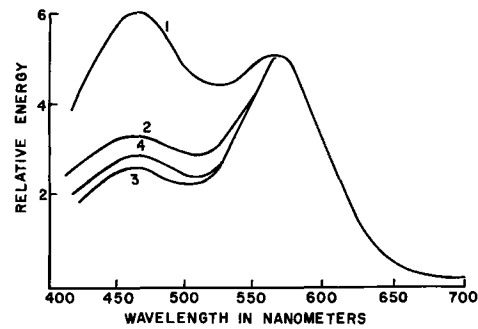


Fig. 6. Cool white 4500°K halophosphate lamp particle SED's vs. daylight halophosphate. Curve 1, 6500°K daylight halophosphate (average SED); curves 2 and 3, halo particles with slight SED variations; curve 4, 4500°K cool white halo (average SED).

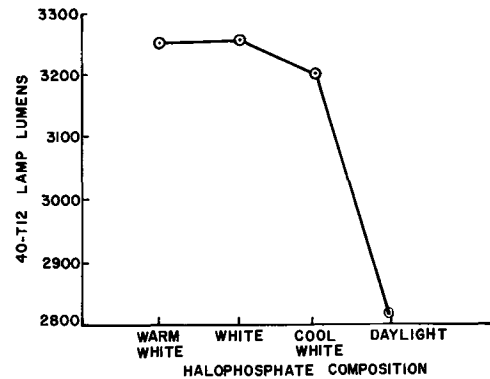


Fig. 7. Fluorescent lamp brightness as a function of halophosphate composition.

train and feeding the undispersed light from the single particles to the 9558 PM tube. This mode of operation enabled us to utilize probe measurement areas of 1.2 $\mu$ . Scans across individual grains and from particle to particle resulted in brightness differences of 10-15% in some cases.

### Discussion

The significance of the SED variations found among particles in cool white halophosphate lamps can be realized by an examination of Fig. 7 wherein the lumen output vs. color composition of four standard halophosphate phosphors are plotted. The rather abrupt drop in lumen output for the daylight lamps is a result of the shift in spectral character of this phosphor away from the peak of the eye sensitivity curve. Particles with SED's intermediate between cool white halo and daylight halo in the same lamp, which were found in our investigation and presented in Fig. 6, strongly indicate suspected luminosity losses occurring in cool white lamps due to these offcolored species. No quantitative data as to gains in lumens that would result by removal of these particles have been obtained to date.

The observed differences in brightness from particle to particle and across individual grains can be attributed to the varying uv scattering properties of the individual grains. Particles with irregular external morphologies and possible minor internal extraneous phases with slightly varying refractive indices, such as  $\beta$  calcium pyrophosphate may in fact internally scatter a greater proportion of the incident uv radiation thus giving rise to increased uv absorption of the individual particles.

### Acknowledgments

Grateful acknowledgment is made to Dr. John E. Eby of our Research Laboratories for his valuable

assistance in the designing of all the apparatus used in our investigation. The author is also indebted to Dr. Martha Thomas of our Laboratories for her valuable suggestions and help in interpreting all the collected data.

Manuscript submitted July 3, 1968; revised manuscript received Aug. 19, 1968. This paper was presented at the Boston Meeting, May 5-9, 1968, as Paper 42.

Any discussion of this paper will appear in a Discussion Section to be published in the June 1969 JOURNAL.

## The Effect of Heat-Treatment on Transistor Low Current Gain with Various Ambients and Contamination

A. A. Bergh<sup>\*.1</sup> and C. Y. Bartholomew

Bell Telephone Laboratories, Incorporated, Allentown, Pennsylvania

### ABSTRACT

In a planar transistor low current d-c gain is the most sensitive parameter to changes in the properties of the oxide-silicon interface. It is dominated by the nonideal base current,  $I_{BN}$ . In the transistors investigated here,  $I_{BN}$  is made up of a Sah-Noyce-Shockley recombination-generation current ( $I_{SNS}$ ) and a channel current ( $I_{CH}$ ). The two components can be separated by analyzing the temperature dependence of  $I_{BN}$ , making it possible to determine the failure mechanism of the transistor gain degradation.

In order to control gain degradation, a correlation was sought between the components of  $I_{BN}$  and physical processes affecting the Si-SiO<sub>2</sub> interface. This paper shows the effect of heat-treatment in various ambients on  $I_{BN}$ . Heat-treatment in hydrogen and water vapor improve the gain primarily by reducing the recombination-generation current. This improved gain corresponds to the state of a transistor completed by standard processing. The high transistor gain may be degraded by baking in dry inert gases or with sodium contamination. Baking in inert gases increases the recombination-generation component of  $I_{BN}$ . Hydrogen ambient accelerates, and water vapor impedes the migration of sodium through the oxide relative to dry inert gases. A model is presented to explain the effect of hydrogen on the diffusion of sodium in the oxide. Experiments with MOS capacitors are in good agreement with transistor results.

The understanding and control of the Si-SiO<sub>2</sub> interface strongly affects the performance of semiconductor devices. Changes in the surface state (1) and surface charge (1) densities influence both initial device characteristics and reliability. Physical measurements (2) and radioactive tracer experiments (3) have shown that the major source of the surface charges is the diffusion of alkali ions through the oxide to the Si-SiO<sub>2</sub> interface (1, 2). The surface states on the other hand are probably associated with lattice defects (4) and unsaturated silicon bonds (5) at the interface. It follows, therefore, that the surface charge density can be reduced by the control of impurities during processing, while the surface states can be affected by treatments altering the structure and the stoichiometry of the oxide, such as heat-treatments in various ambients.

The effects of sodium concentration and heat-treatment in various ambients have been evaluated on npn planar transistors by monitoring low current d-c gain ( $h_{FE}$ ). The following discussion is divided into three parts. (i) First, the correlation between the oxide-silicon interface and the low current gain is discussed. (ii) This is followed by the effect of sodium contamination and the heat-treatment in various ambients on  $h_{FE}$ , and on the flat band voltage on MOS capacitors. (iii) Finally, a mechanism is offered for the migration of sodium ions through the oxide to explain the effect of the ambient on the diffusion rate.

#### Low Current D-C Gain ( $h_{FE}$ )

Low current d-c gain ( $h_{FE}$ ) is the most sensitive device parameter under all aging conditions used in this experiment.  $h_{FE}$  is defined as

$$h_{FE} = I_C/I_B \quad [1]$$

\* Electrochemical Society Active Member.

<sup>1</sup> Present address: Bell Telephone Laboratories, Inc., Murray Hill, New Jersey.

where  $I_C$  and  $I_B$  are the collector and base currents, respectively. Both components of  $h_{FE}$  can usually be described by the formula

$$I = I^0 \exp(qV_{EB}/nkT) \quad [2]$$

where  $I^0$  and  $n$  are constants,  $V_{EB}$  is the emitter to base potential, and  $q$ ,  $k$ , and  $T$  have their usual meaning.  $I_C$  was unchanged in all aging experiments. Similar observation was reported by Reddi in a detailed study of the effect of surface properties on low current gain (6). Figure 1 depicts a typical  $I_B - I_C$  plot after the manner of Iwersen *et al.* (7).  $I_B$  is seen to consist of an "ideal" component,  $I_{BI}$ , ( $n = 1$ ), and a "nonideal" component,  $I_{BN}$  ( $n > 1$ ). All the chemical and thermal treatments discussed below affected only the nonideal component,  $I_{BN}$ , and hence the low current gain. The parameters characterizing  $I_{BN}$ , *i.e.*,  $I_{BN}^0$  and  $n$ , are readily determined from the  $I_B - I_C$  plot (Fig. 1).

The nonideal base current has two components closely related to fixed charge and surface state densities, respectively. They are the channel current and the recombination-generation current in the junction space charge region (7-9).

The theory of space-charge recombination-generation currents was developed by Sah, Noyce, and Shockley (8), and Sah (11), and recently extended by Evans and Landsberg (12) and by Morgan (13). The temperature dependence of this component,  $I_{SNS}$ , (after Sah, Noyce, and Shockley) is determined by the temperature dependence of the intrinsic carrier density,  $n_i$ . The activation energy,  $E_a$ , of  $I_{SNS}$  is then to a first approximation equal to one-half of the band gap energy, or 0.6 eV (11). A typical value of  $n$  for the  $I_{SNS}$  current is about 1.5 at room temperature as found in our experiment and reported elsewhere (7, 10).

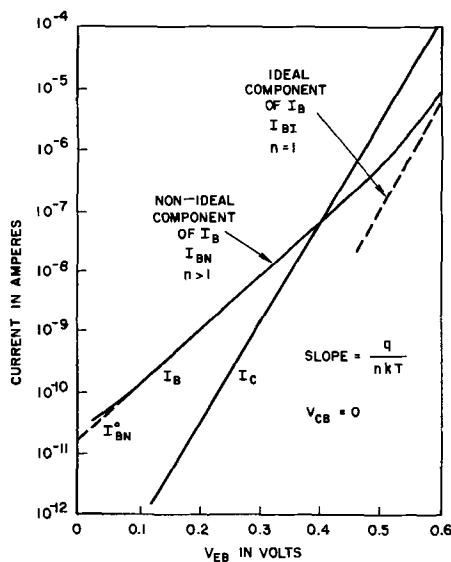


Fig. 1. Typical  $I_B - I_C$  curves

It is shown in the Appendix that the temperature dependence of the current in a channel can be described by the following equation

$$E_{a, ch} = \frac{E_g}{2} + 2 \left( 2.75 \frac{kT}{q} - |\phi_s| \right) \quad [3]$$

where  $E_g$  is the band gap energy and  $\phi_s$  is the surface potential. The activation energy,  $E_{a, ch}$  as a function of surface potential is plotted in Fig. 2. In general, the enhancement in surface inversion results in a monotonically decreasing activation energy below the value of  $E_g/2$ .

The variation of  $n$  with increasing channel current is discussed in ref. (9) and (10). Depending on the geometry of the junction and on the extent of the inversion,  $n$  increases to values significantly larger than 2. Values of  $n$  as high as 4.9 have been observed in our experiments.

A typical plot of  $I_{BN}^0$  vs.  $1/T$  is shown in Fig. 3. At elevated temperatures the recombination-generation current dominates while below room temperature the channel current becomes important. Typical values of the components of the nonideal base current for normal and degraded devices are given in Table I.

**Experimental**

*Description of the transistors.*—The experiments were carried out on an npn silicon planar transistor. A schematic diagram is shown in Fig. 4. The transistor has ring-dot geometry, and it is bonded to a TO-18 header. As indicated by the activation energy

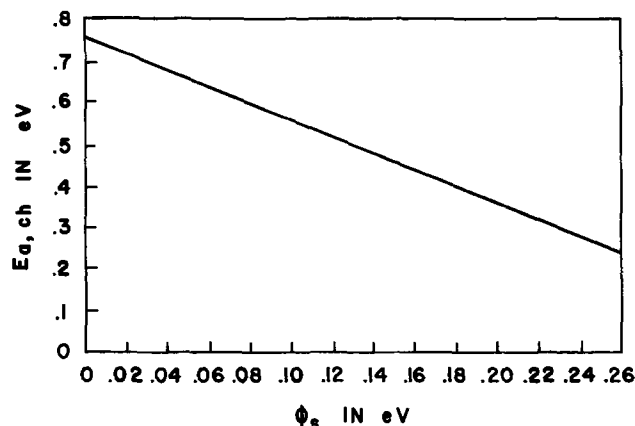


Fig. 2. Activation energy of the channel current,  $E_{a, ch}$  as a function of the surface potential,  $\phi_s$ .

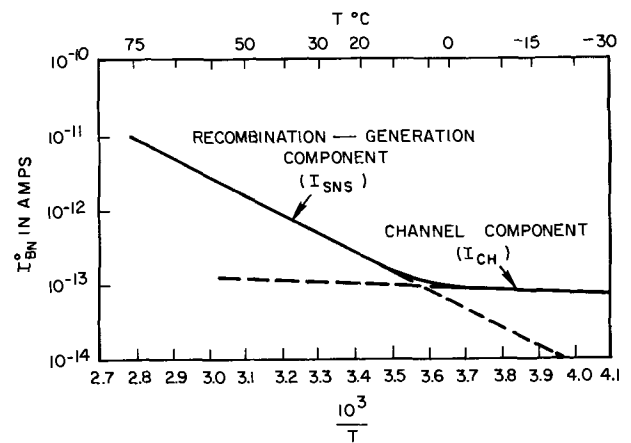


Fig. 3. Arrhenius plot of  $I_{BN}^0$

of  $I_{BN}$ , the units have a small built-in channel as prepared. The value of  $E_a$  is lower than the expected value for generation-recombination current due to a channel component (see Fig. 3).

In order to investigate the effect of this channel on the gain, special transistors were fabricated of the same design except for an aluminum field plate over the oxide of the emitter-base junction. The peak in the recombination-generation current as a function of field plate voltage, observed by Sah (10) and Reddi (14), was not seen on our units (Fig. 5), indicating that the surface was not entirely inverted. No evidence of such a peak was found in the ambient-bake experiment of the transistors used without field plates. All the treatments described below resulted in a monotonic change in gain.

*Contamination and heat-treatments.*—The transistors were cleaned in hot solvents, (trichloroethylene, acetone, alcohol) followed by a cascade rinse in low conductivity water and dried in filtered nitrogen. The clean units were split into two groups. One group was kept clean as control, and the units of the second group were contaminated by evaporating a 5 microliter drop of a 0.02M NaCl solution. Assuming a uniform sodium distribution over the entire header and wafer surface this corresponds to approximately  $5 \times 10^{16}$  sodium atoms/cm<sup>2</sup>. The sodium in fact was not uniformly distributed; small crystallites formed over the surface with a higher density of crystallites over the metal contacts. The sodium concentration over the SiO<sub>2</sub> was probably closer to  $5 \times 10^{15}$  atoms/cm<sup>2</sup>. Some of the experiments were later repeated with vacuum evaporated NaCl. The salt in this case formed a uniform layer over the entire surface, the gain degradation results, however, were similar with the two methods.

The transistor leads were welded to the ports of a specially built Vac-Ion station, and thus all transistors were exposed to the identical ambient. The vacuum station was flushed with high-purity gases at a rate of 1.5 l/min. The dry gases had a water vapor content of less than 1 ppm. The wet gases were saturated with water vapor at room temperature. The baking cycle lasted for 16 hr at 350°C.

Table I. Typical values of  $I_{BN}^0$ ,  $E_a$ , and  $n$  for the different components of  $I_{BN}$

$I_{BN}$ component	$I_{BN}^0$ , 300°K (amp)	$V_a$ (ev)	$n$
Recombination-generation	$10^{-13}$ - $10^{-12}$	0.7	1.5
Channel*	$10^{-10}$ - $10^{-5}$	0-0.6	2-4

\* Values depend on the degree of inversion and on the geometry of the junction. The values given here are typical for degraded devices.

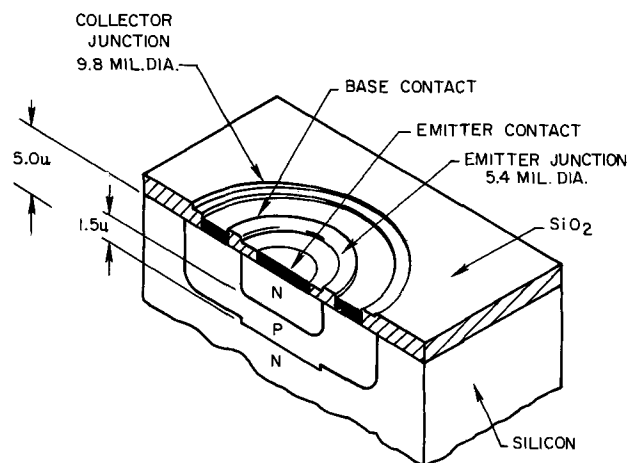
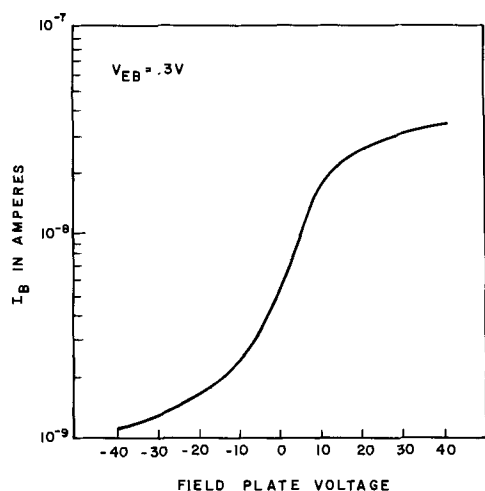


Fig. 4. Silicon planar transistor schematic diagram

Fig. 5.  $I_B$  as a function of field plate voltage. Field plate over the emitter junction of an npn planar transistor.

The transistor aging conditions were also applied for MOS capacitors. High resistivity p-type slices were oxidized to form approximately 1800Å of oxide, cleaned similar to the transistors and split into 3 pieces. One piece was sodium contaminated by NaCl evaporation and the other two pieces were kept clean. The sodium contaminated pieces and one of the clean pieces received a temperature-ambient treatment and the second clean piece was kept as a control. The heat-treatments in this case lasted for 2 hr at 450°C. Ten-mil diameter aluminum dots were then simultaneously evaporated over all three pieces to determine the flat band voltages.

### Results

A summary of the aging experiments is given in Table II. Not shown in the table are transistors with more than  $10^{17}$  atoms/cm<sup>2</sup> of evaporated sodium. The results can be listed as follows.

**Sodium contaminated transistors.**—(A) High (over  $10^{17}$  atoms/cm<sup>2</sup> concentration of sodium degrades the gain in all ambients under our aging conditions; (B) gain degradation occurs only in hydrogen ambient on transistors contaminated with  $\sim 10^{16}$  atoms of Na/cm<sup>2</sup>; (C) sodium contaminated units degraded in hydrogen or dry nitrogen at any sodium level can be partially recovered with water vapor (in N<sub>2</sub> or O<sub>2</sub>); (D) phosphorous glass reduces the gain degradation in hydrogen (Table III).

The different parameters of base current can be analyzed with the help of Table IV. Wet and dry forming gas showed identical results. Comparing the results of Table IV with the trends summarized in the

Table II. Changes in  $h_{FE}$  ( $I_C = 10^{-5}$  amp) after heating for 16 hr at 350°C (average of 3 transistors)

No. of experiments	Ambient	$h_{FE}$ , Final/ $h_{FE}$ , Initial	
		Cleaned	Na contaminated*
1	Dry N <sub>2</sub>	1.2	1.1
2	Dry O <sub>2</sub>	1.2	1.2
3	Wet N <sub>2</sub>	1.9	1.8
4	Wet O <sub>2</sub>	2.0	2.0
5	Dry FG	2.6	0.3
6	Wet FG	4.1	0.5
	Dry FG	2.6	0.5
7	Wet O <sub>2</sub>	2.8	1.7
		Dry FG	1.6
8	Wet N <sub>2</sub>	1.9	0.29

#### Remarks:

Typical  $h_{FE}$ , Initial  $\sim 15$ -20.

\* Approximately  $10^{16}$  atoms of Na/cm<sup>2</sup>.

FG: 10% H<sub>2</sub> in 90% N<sub>2</sub>.

7 and 8 are successive treatments on the same transistors.

Table III. Effect of phosphorous glass on the heat-treatment of Na contaminated transistors\*

( $h_{FE}$  at  $I_C = 10^{-5}$  A)

Ambient	No P-glass NaCl	P-glass Clean	P-glass NaCl
Wet N <sub>2</sub>	43	48	32
Dry FG	8	56	24
Wet N <sub>2</sub>	35	48	28

\* Consecutive bakings in each ambient for 16 hr at 350°C.

Table IV. Change in the base current parameters of sodium contaminated\* units after baking at 16 hr at 350°C

(Average of 3 transistors)

Ambient	Parameter	Initial	Final
Dry N <sub>2</sub>	$I_{BN}^0$	$1.0 \times 10^{-12}$	$1.6 \times 10^{-9}$
	$n$	1.53	2.3
	$E_a$	0.48	0.35
Dry FG	$I_{BN}^0$	$9.0 \times 10^{-13}$	$8.3 \times 10^{-9}$
	$n$	1.53	4.7
	$E_a$	0.50	0.07

\* Contamination level  $> 10^{17}$  atoms Na/cm<sup>2</sup>.

section on Low Current D-C Gain the following results are obtained. Sodium gives rise to a channel current, and the effect of sodium is enhanced by the presence of hydrogen.

**Sodium contaminated MOS capacitors.**—The above results were substantiated by the MOS capacitor experiments. Table V shows the results. A large shift occurred in the flat band voltage after heat-treatment in dry N<sub>2</sub> and dry FG. A smaller shift was observed in wet FG and no shift appeared in wet N<sub>2</sub>. Increasing the sodium concentration to higher levels or aging at higher temperatures results, however, in a large shift of flat band voltage in all ambients.

**Noncontaminated transistors.**—The results obtained with noncontaminated devices (Table II) can be summarized as follows:

Table V. Position of the flat band voltage on MOS capacitors after baking for 2 hr at 450°C before metal evaporation

Ambient	Flat band voltage			Thickness (Å)
	Not baked	Baked, clean	Baked, sodium contaminated	
Wet N <sub>2</sub>	5.0	5.0	4.0	1900
Wet FG	5.7	4.5	16.2	1870
Dry N <sub>2</sub>	5.2	4.5	20.0	1650
Dry FG	6.2	6.5	21.3	1950



1. Water vapor and hydrogen improve the gain during heat-treatment. Baking in dry inert gas has no appreciable effect.

2. Dry ambients other than hydrogen ( $N_2$ ,  $O_2$ , vacuum) degrade the gain previously improved in water vapor or hydrogen.

3. Both the improvement and the degradation of gain are reversible.

The relative change in the values of  $I_{BN}^0$  at various temperatures is listed in Table VI. The change becomes larger with increasing temperatures in both wet nitrogen and dry forming gas. This indicates that the major effect of the baking is the reduction of the recombination-generation component of the base current.

### Mechanism

There are numerous attempts in the literature to explain the MOS device results in terms of a physical model (4, 6, 16, 19-21). Some of the proposed mechanisms help to explain our results for noncontaminated transistors. None of the models accounts, however, for the observed effect of hydrogen on the migration of sodium through the oxide.

There is a controversy in the literature regarding the effect of hydrogen on the Si-SiO<sub>2</sub> interface. Some authors observe a decrease in fast states at the interface (4, 5, 16) or increase in low current gain (17) on annealing in hydrogen or water vapor. Contrary to these results an inversion layer has been reported external to the metal contact on a p-type MOS capacitor after heat-treatments in hydrogen (18, 19). Blum *et al.* (20) observed that forming gas baking turned the collector surface more n-type. Busen and Lindmayer (21) used this observation to support their hypothesis that H<sup>+</sup> might be the source of the fixed positive charge at the Si-SiO<sub>2</sub> interface.

Our results indicate that the effect of hydrogen depends on the contamination level of the device. On clean transistors hydrogen improves gain by reducing the generation-recombination current. This can be explained by the saturation of dangling silicon bonds close to the Si-SiO<sub>2</sub> interface through the formation of Si-H bonds (4, 5, 16).

On contaminated units hydrogen "activates" the sodium which in turn degrades the gain. It is very likely that the degradation attributed to hydrogen in earlier experiments (19-21) was in fact caused by sodium. In order to explain the "activation" of sodium by hydrogen let us examine some features of amorphous SiO<sub>2</sub>.

Sodium ions migrating to the Si-SiO<sub>2</sub> interface can induce a negative charge in the bulk silicon. We shall be concerned therefore with the degree of ionization of the sodium, and the migration of the ions through the oxide. In amorphous SiO<sub>2</sub> the adjacent silicon atoms are bridged by an oxygen atom. At defect sites or if silicon is replaced by a trivalent metal such as aluminum ( $Al^{3+}$ ), the oxygen is connected only to one silicon. The second valence of such a nonbridging oxygen is usually occupied by a monovalent species such as sodium or hydrogen. Another site for sodium in SiO<sub>2</sub> is at a normal interstitial position. Based on the differences in electronegativity between sodium and oxygen, the O-Na bond has approximately a 63% ionic character. This is a lower value than the almost

fully ionized sodium in an interstitial position. In addition, sodium ions attached to nonbridging oxygens occupy a lower energy level and have a lower mobility in the oxide than the interstitial ions. It can be expected, therefore, that sodium is more "active" in an interstitial position than in the O-Na bond.

The permeability of hydrogen through fused quartz has been thoroughly investigated (22) with close agreement on both permeability and activation energy data. Similar to sodium ions, hydrogen might occupy interstitial sites, or it can be accommodated in the form of isolated OH groups. The direct exchange of alkali and hydrogen has been demonstrated in high-temperature electrolysis (23). Alkali ions are removed from the anode and migrate to the cathode in vitreous silica. Infrared measurements showed that as sodium is removed from the anode it is replaced by hydrogen, present at Si-OH groups.

It follows that in the absence of hydrogen the alkali ions occupy low energy vacancy sites resulting in a low mobility. In the presence of hydrogen some of the alkali ions are forced into the high energy interstitial sites, thus increasing their ionic character and mobility. It should be noted that the pronounced effect of hydrogen is only present at moderate temperatures and sodium concentrations. At high temperatures the vacancy migration becomes appreciably fast, and at high sodium concentration the vacancy sites are saturated leaving a fraction of the sodium ions in interstitial position.

The improvement in gain during heat-treatment in water vapor on sodium contaminated devices previously degraded in hydrogen might be associated with vacancy formation by the water vapor. This can be accomplished by either facilitating the degassing of hydrogen from the oxide or by the formation of new vacancy sites (nonbridging oxygen).

### Discussion and Conclusion

Transistor low current d-c gain is dominated by the nonideal component of the base current. This in turn is made up of a Sah-Noyce-Shockley recombination current and a channel current. The two components can be separated by analyzing the temperature dependence of  $I_{BN}$ .

Hydrogen and water vapor bakes improve the gain primarily by reducing the recombination current. Baking with sodium contamination degrades gain; hydrogen accelerates the degradation and water vapor impedes it. Sodium baked transistors degrade by an increase in the channel component of  $I_{BN}$ .

It is suggested that hydrogen enhances sodium migration in SiO<sub>2</sub> by displacing Na from vacancy sites in the oxide; Na is forced into interstitial sites where it is more mobile and fully ionized.

The technique of analyzing  $I_{BN}$  as a function of temperature offers a means of investigating transistors which have degraded low current gain. Thus degradation mechanism may be identified on transistors from production rejects and on life test failures.

### Acknowledgment

Acknowledgment is made to N. Carthage for heat-treating the transistors and making electrical measurements, to B. J. Snyder for sample preparation and sodium contamination, and to J. H. Burchill for MOS measurements.

Manuscript received April 10, 1968; second revised manuscript received ca. Aug. 1, 1968. This paper was presented at the Philadelphia Meeting, Oct. 9-14, 1966, as a Late News Paper.

Any discussion of this paper will appear in a Discussion Section to be published in the June 1969 JOURNAL.

### APPENDIX

In this appendix, the following equation for the activation energy of a channel will be derived.

Table VI. Temperature dependence of the change in  $I_{BN}^0$  on heat-treatment

350°C, 16 hr, noncontaminated transistors

Ambient	Temp, °C	$I_{BN}^0$ Final/ $I_{BN}^0$ Initial
Wet N <sub>2</sub>	-15	0.90
	30	0.59
	75	0.24
Dry FG	-15	1.10
	30	0.56
	75	0.14

$$E_{a, ch} = \frac{E_g}{2} + 2 \left[ 2.75 \frac{kT}{q} - |\Phi_s| \right] \quad [A-1]$$

where  $E_g$  = band gap energy in ev.  $\Phi_s$  = surface potential in ev.  $E_{a, ch}$  = activation energy in ev, and  $q$ ,  $k$ , and  $T$  have their usual meanings.

The derivation is given for a p-type inversion layer on n-type layer on p-type material.

At pinch-off, the channel current is proportional to the square of the mobile charge density (24)

$$I_p = K \mu q^2 Q_p^2 \quad [A-2]$$

where  $\mu$  = mobility of the holes in the inversion layer.  $Q_p$  = mobile charge density in  $\text{cm}^{-2}$ .  $I_p$  = channel current in amperes.  $K$  = a constant. In terms of the Kingston-Neustadter theory (25)

$$Q_p = n_i L_D G(u_s, u_B) \quad [A-3]$$

where  $Q_p$  = mobile charge density in  $\text{cm}^{-2}$ .  $n_i$  = electron (or hole) density in intrinsic material,  $\text{cm}^{-3}$ .  $L_D$  = Intrinsic Debye length in cm.  $G(u_s, u_B)$  = a function defined by Kingston and Neustadter (25).  $u_B$  = Fermi level minus midgap potential for the bulk material in  $kT/q$  units.  $u_s$  = Fermi level minus midgap potential for the surface in  $kT/q$  units. For an accumulated surface,  $u_s$  is  $-$  for p-type and  $+$  for n-type material; for a depleted (or inverted) surface, the reverse relationship holds.

The activation energy of  $I_p$ ,  $E_{a, ch}$  is

$$E_{a, ch} = - \frac{k}{q} \frac{d}{d(1/T)} \ln I_p \quad [A-4]$$

The temperature dependence of quantities entering into Eq. [A-2] is given in Eq. [A-5] and [A-8] below.

$$n_i = CT^{3/2} \exp \left[ \frac{-qE_g}{2kT} \right] \quad [A-5]$$

where  $C$  = a constant.

$$L_D = \left[ \frac{\epsilon kT}{2q^2 n_i} \right] \quad [A-6]$$

where  $\epsilon$  = permittivity of silicon.

For the case where the mobility is dominated by the impurities in the silicon,

$$\mu \sim T^{3/2} \quad [A-7]$$

The function  $G(u_s, u_B)$  cannot be expressed in closed form, but has been accurately tabulated by Mattauch *et al.* (27). By a numerical analysis based on Mattauch's tables, it has been determined that to a good approximation

$$\frac{d}{d(1/T)} \ln G(u_s, u_B) = \frac{q}{k} |\Phi_s| \quad [A-8]$$

To a good approximation, this result is independent of  $u_B$ .

Then, using [A-2] to [A-8], after some manipulation, Eq. [A-1] results.

$$E_{a, ch} = \frac{E_g}{2} + 2 \left[ 2.75 \frac{kT}{q} - |\Phi_s| \right] \quad [A-9]$$

#### REFERENCES

1. For the definition of the expressions "surface state," and "surface change" see *e.g.*, E. H. Nicollian and A. Goetzberger, *Bell System Tech. J.*, **46** 1055 (1967).
2. E. H. Snow, A. S. Grove, B. E. Deal, and C. T. Sah, *J. Appl. Phys.*, **36**, 1664 (1965).
3. E. Yon, W. H. Ko, and A. B. Kuper, *Trans. IEEE*, **ED-13**, 276 (1966).
4. A. G. Revesz, *ibid.*, **ED-12**, 97 (1965).
5. P. Balk, Paper presented at the San Francisco Meeting of the Society, May 9-13, 1965, as Paper 109.
6. V. G. K. Reddi, *Solid State Electronics*, **10**, 305 (1967).
7. J. E. Iwersen, A. R. Bray, and J. J. Kleimack, *Trans. IRE*, **ED-9**, 474 (1962).
8. C. T. Sah, R. N. Noyce, and W. Shockley, *Proc. IRE*, **45**, 1228 (1957).
9. C. T. Sah, *ibid.*, **49**, 1623 (1961).
10. C. T. Sah, *ibid.*, **ED-9**, 94 (1962).
11. C. T. Sah, *ibid.*, **49**, 603 (1961).
12. D. A. Evans and P. T. Landsberg, *Solid-State Electronics*, **6**, 169 (1963).
13. T. N. Morgan, *Phys. Rev.*, **139**, A294 (1965).
14. V. G. K. Reddi, *Trans. IEEE*, **ED-13**, 381 (1966).
15. J. E. Thomas and D. R. Young, *IBM Jour.*, **8**, 368 (1964).
16. E. Kooi, *Trans. IEEE*, **ED-13**, 238 (1966).
17. M. N. Giuliano, R. M. McLouski, C. A. Leinkram, and E. W. Goins, *Proc. IEEE*, **35**, 712 (1964).
18. J. Olmstead, J. Scott, and P. Kuznetzoff, *ibid.*, **ED-12**, 104 (1965).
19. K. H. Zaininger and G. Warfield, *Proc. IEEE*, **52**, 972 (1964).
20. J. Blum, R. Warwick, H. M. Pollack, and M. Genser: Paper presented at Toronto Meeting of the Society, May, 3-7, 1964, as Paper 55.
21. K. M. Busen and J. Lindmayer, *Trans. AIME*, **233**, 536 (1965).
22. R. W. Lee, R. C. Frank, and D. E. Swets, *J. Chem. Phys.*, **36**, 1062 (1962).
23. G. Hetherington, K. H. Jack, and M. W. Ramsay, *Phys. Chem. Glasses*, **6**, 6 (1965).
24. J. T. Wallmark and H. Johnson, Editors, "Field-Effect Transistors," p. 232, Prentice-Hall, Englewood Cliffs, N. J. (1966).
25. R. H. Kingston and S. F. Neustadter, *J. Appl. Phys.*, **26**, 718 (1955).
26. A. B. Phillips, "Transistor Engineering," p. 66, McGraw-Hill Book Co., New York (1962).
27. R. J. Mattauch, R. W. Lade, and G. B. Hoadley, "Tables of  $F(u_s, u_B)$  and  $G(u_s, u_B)$  Functions for Semiconductor Surface Calculations," Dept. of Engineering Research, School of Engineering, North Carolina State University, Raleigh, N. C., Bulletin No. 80.

## Growth and Properties of Nb<sub>2</sub>O<sub>5</sub> Thin Film Capacitors

H. R. Brunner, F. P. Emmenegger,\* M. L. A. Robinson, and H. Röttschi

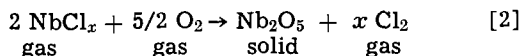
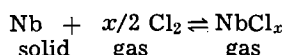
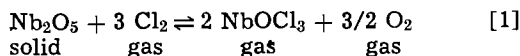
Laboratories RCA, Ltd., Zurich, Switzerland

The reduction in the area occupied by the capacitors in an integrated circuit by using a high permittivity material is a well established problem. Although many materials and methods of preparation (1) have been tried, the established insulators SiO<sub>2</sub> and Si<sub>3</sub>N<sub>4</sub> have yet to be seriously challenged, except for specialized purposes (2).

The present paper reports work in which halogen transport reactions, a technique powerful in the preparation of single crystals of new compounds and epitaxial layers (3), have been used for the first time to prepare thin oxide films. Films of Nb<sub>2</sub>O<sub>5</sub>, Ta<sub>2</sub>O<sub>5</sub>, TiO<sub>2</sub>, and ZrO<sub>2</sub> have been successfully prepared. Of these Nb<sub>2</sub>O<sub>5</sub> has been least studied, and an investigation into its potential as a thin film capacitor is reported here.

### Growth of Nb<sub>2</sub>O<sub>5</sub> Films in a Flow System

Nb<sub>2</sub>O<sub>5</sub> may be deposited by either of the following two reactions



$x = 2.33-5$  depending on temperature and chlorine pressure (4).

For the chemical deposition of Nb<sub>2</sub>O<sub>5</sub>, a low but manageable concentration of a gaseous niobium compound is needed. Reaction [2] goes completely to the right at all temperatures in question. In order to generate a low concentration of gaseous NbCl<sub>x</sub>, very low chlorine concentrations in an inert gas carrier stream would have to be monitored carefully and good, or at least reproducible, contact between chlorine and the niobium source would have to be ensured.

From the equilibrium constant of reaction [1] (5) it can be calculated that the equilibrium pressure of NbOCl<sub>3</sub> is around 0.3% of the chlorine pressure at around 850°C. Therefore low concentrations of the volatile niobium species NbOCl<sub>3</sub> can be generated by easy to control chlorine pressures, and sufficient contact between chlorine and niobium source is not critical.

Reaction [1] was therefore used to generate the volatile niobium species for the chemical deposition of Nb<sub>2</sub>O<sub>5</sub> films. Growth of Nb<sub>2</sub>O<sub>5</sub> films took place in the apparatus shown in Fig. 1. It consists of a system of quartz tubing heated by split ovens. Gas supply is through calibrated flow meters.

A gas mixture consisting of 3% Cl<sub>2</sub> and 97% argon was streamed at a flow rate of 100 cm<sup>3</sup>/min over a boat containing Nb<sub>2</sub>O<sub>5</sub> powder (Ciba optical quality 99.9%). After entering the deposition zone, the argon stream carrying the NbOCl<sub>3</sub> was mixed with pure oxygen flowing at a rate of 70 cm<sup>3</sup>/min. Reaction of the oxygen with the NbOCl<sub>3</sub> took place preferentially on the substrate and on the walls of the quartz tubing, generating a microcrystalline, well-adherent Nb<sub>2</sub>O<sub>5</sub> film.

Platinum foil or polished {111} wafers of n-type silicon (Sb, 0.01 ohm cm) were used as substrates. In some experiments the silicon was covered with a thin evaporated metal film or a cermet layer (see the next section). Usually four silicon substrates 10 x 5 x 1 mm were mounted on the quartz holder by a drop of sodium silicate solution. Useful growth rates of Nb<sub>2</sub>O<sub>5</sub> films were observed in the temperature range 700°-1100°C with source and deposition zone at the same temperature as measured by thermocouples I, III, and IV (Fig. 1).

Additional features (only used in the preliminary investigation of the Nb<sub>2</sub>O<sub>5</sub> film growth) of the growth apparatus are the possibility to add, through furnace II, a third component into the reaction chamber and to keep the substrate temperature below that of the reaction chamber by aircooling the substrate holder.

After preliminary evaluation of the uniformity of growth and film thickness measurement under the microscope, Nb<sub>2</sub>O<sub>5</sub> capacitors were completed by the following standard procedure. A matrix of top electrodes of aluminum, gold or, indium, 0.2 x 0.2 mm square and with 0.6 mm separation, was evaporated onto the film. The bottom electrode was provided by the silicon substrate, the back of which was sandblasted and completely covered with a thin film of Hg-In alloy. Samples were mounted between gold pressure contacts in a screened holder. Three terminal capacity and loss measurements were made between 20 Hz and 500 kHz, and 2 terminal measurements between 1 MHz and 100 MHz using standard laboratory equipment.

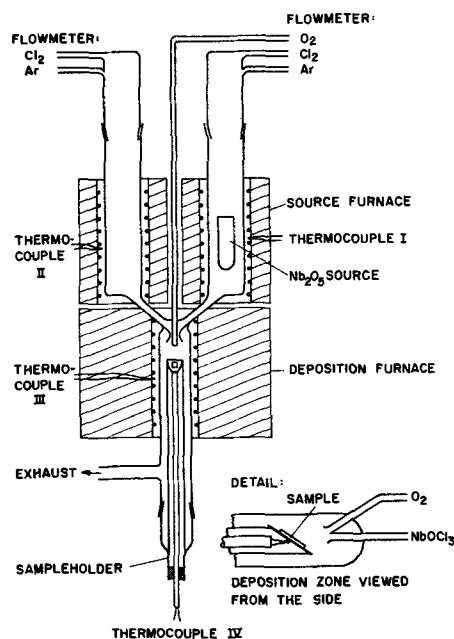


Fig. 1. Schematic drawing of the apparatus used for the chemical deposition of niobium oxide films.

\* Electrochemical Society Active Member.

Table I. Dielectric properties of Nb<sub>2</sub>O<sub>5</sub> films grown on various substrates

Sample No.	Substrate	Deposition temp, °C	Approx. thick-ness, $\mu$	Capacitance per unit area $\mu\text{F}/\text{mil}^2$	Loss factor ( $\tan \delta$ ) at 5 kHz	Breakdown voltage (volts d.c.)		Temperature coefficient of capacitance, ppm/°C
						Maximum value	Minimum value	
3	Pt foil	1000	26	$\epsilon = 100 \pm 10^*$	$0.06 \pm 0.02^\dagger$	>500	190	~500
4	Pt foil	1000	40	$\epsilon = 125 \pm 20^*$	$0.10 \pm 0.05^\dagger$	>500	80	~500
5	Pt foil	1000	10	$\epsilon = 70 \pm 20^*$	$0.03 \pm 0.02^\dagger$	>500	150	~500
27	Si	1000	5	$0.23 \pm 0.15$	$1.27 \pm 0.10$	~5	~2	Conductive above 100°C
31	Si/Fe	1000	0.5	$1.26 \pm 0.05$	$0.06 \pm 0.003$	5	2	3000
37	Si/Fe	900	0.12	$1.89 \pm 0.06$	$0.06 \pm 0.04$	20	5	3000
56	Si/Fe	850	0.1	$1.11 \pm 0.01$	$0.04 \pm 0.003$	35	4	3000
60	Clean Si	850	0.3	$0.65 \pm 0.07$	$0.010 \pm 0.003$	15	4	1000
61	Clean Si	850	0.4	$0.52 \pm 0.05$	$0.012 \pm 0.002$	32	8	1000
62	Clean Si	860	0.3	$0.80 \pm 0.05$	$0.04 \pm 0.01$	50	14	1000
63	Clean Si	860 + anneal	0.4	$0.50 \pm 0.05$	$0.03 \pm 0.01$	70	18	1000
84	Clean Si	850	0.2	$1.42 \pm 0.04$	$0.06 \pm 0.03$	38	7	1000

\* For these thicker films the low-frequency dielectric constant is given instead of the capacitance per unit area.

† The spread in the capacitance and loss factors represents the extreme values measured on a particular substrate.

### Properties of Nb<sub>2</sub>O<sub>5</sub> Films

Preliminary studies were made by growing thick (5-50 $\mu$ ) films on platinum foil (e.g., Table I, sample 3 to 5). These films were grown at temperatures of 900°-1000°C where the transport rate was highest, a typical rate being 10  $\mu$ /hr. The films were polycrystalline needles oriented with the needle axis perpendicular to the substrate, and were identified by x-ray analysis, as the H-modification of Nb<sub>2</sub>O<sub>5</sub>. As with crystals of this modification grown in a closed system (6), the dielectric properties were dominated by interfacial polarization effects. However, in contrast to the closed system, in which it was desired to produce large crystals, the polarization effects could be removed either by growing films at high oxygen pressures or by annealing in oxygen at 1000°C, which produces films with dielectric constant of  $100 \pm 20$ , with loss factors of 0.03 at 1 kHz and breakdown voltages of greater than  $5 \times 10^5$  v/cm. The value of the low-frequency dielectric constant is in good agreement with that deduced from measurements on bulk material (6).

Similar films grown on silicon, however, always showed interfacial polarization effects and high losses (Table I, sample 27). This was at first considered to be due to the incorporation of some silicon into the Nb<sub>2</sub>O<sub>5</sub> crystallites, similarly to B-modification Nb<sub>2</sub>O<sub>5</sub> crystals (7), but this was later disproved (see below). However, the polarization was greatly reduced by covering the silicon substrate with a thin evaporated metal film (Table I, samples 31, 37, 56) prior to deposition of the Nb<sub>2</sub>O<sub>5</sub>. 50-200Å of iron, chromium or titanium was found to be satisfactory. At the same time it was found that the presence of these metals, and particularly of iron, greatly improved the uniformity of nucleation of the Nb<sub>2</sub>O<sub>5</sub>. However, the frequency dependence of the capacity and loss tangent of films grown on thin iron films was complicated by a relaxation amounting to typically 10% in capacitance in the megahertz region arising from the presence of the thin iron oxide film under the Nb<sub>2</sub>O<sub>5</sub>.

Interfacial polarization effects were best eliminated, by using a rigorous cleaning procedure developed by Zaininger and co-workers (8) (Table I, sample 61, 62, 84), for the reduction of the number of surface states on silicon, especially those due to sodium. It was again noticeable that the uniformity of nucleation of the Nb<sub>2</sub>O<sub>5</sub> was greatly improved on silicon substrates which had been cleaned in this way. If a thin iron film (50-200Å) was evaporated onto such thoroughly cleaned silicon wafers, prior to the deposition of the Nb<sub>2</sub>O<sub>5</sub> layer, almost no further improvement of the uniformity of the Nb<sub>2</sub>O<sub>5</sub> layers could be detected on electron microscope photographs. Therefore the evaporation of the iron film was dispensed with.

The correlation of the removal of interfacial polarization effects with the great improvement in uniform-

ity of growth, and, in the case of the carefully cleaned silicon, with the reduction in the density of surface states is quite remarkable. Although much more experimental work is clearly necessary, this result may be of general significance.

Once the problem of interfacial polarization had been solved, it was found that the capacity per unit area on partially masked substrates together with frequency dependence and thickness dependence capacity measurements indicated the formation of about 100-200Å of SiO<sub>2</sub> under the Nb<sub>2</sub>O<sub>5</sub> films during growth. This SiO<sub>2</sub> layer always formed even when the temperature of the furnace was reduced to below 750°C where clean silicon is not easily oxidized in a dry atmosphere (9, 10). It is tentatively concluded that the oxidation is either catalyzed by the chlorine or by the niobate reaction products [compare ref. (8)].

The presence of the SiO<sub>2</sub> layer under any Nb<sub>2</sub>O<sub>5</sub> film grown by chlorine transport method is naturally very limiting. Capacities greater than that of the SiO<sub>2</sub> alone cannot be achieved without the use of an additional electrode between the SiO<sub>2</sub> and the Nb<sub>2</sub>O<sub>5</sub>. Unfortunately trials with a number of conductive substrates failed to reproduce the uniform quality of the Nb<sub>2</sub>O<sub>5</sub> films grown on silicon, so that some effort was directed into optimizing the uniformity of the Nb<sub>2</sub>O<sub>5</sub> films with rigorously cleaned silicon, as a substrate, using temperature and reaction rates as parameters. The best films produced showed no crystalline structure in magnifications up to 1000X, and the capacity per unit area was reproducible within  $\pm 10\%$ . Their frequency response shown in Fig. 2 is consistent with a composite dielectric of about 100Å of SiO<sub>2</sub> (dielectric constant ~5) and about 2000Å of H-modification Nb<sub>2</sub>O<sub>5</sub> [dielectric constant ~120 (6)].

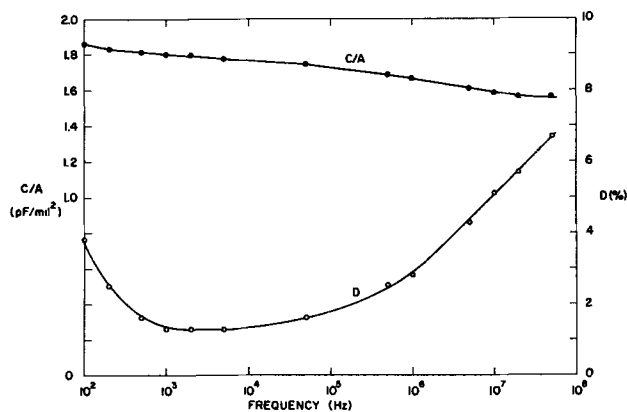


Fig. 2. Frequency dependence of the capacity and loss factor of an Nb<sub>2</sub>O<sub>5</sub> film grown on n-type silicon at 850°C. The top electrodes were evaporated gold, and the substrate formed the bottom electrode.

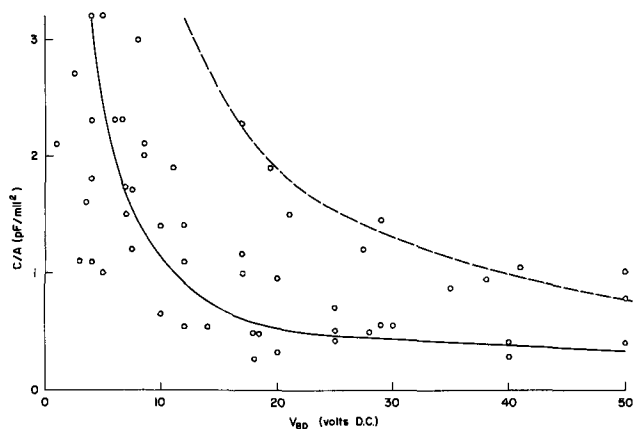


Fig. 3. Capacitance per unit area plotted against d-c breakdown voltage for niobium oxide capacitors on silicon. Each point is an average value of 5-10 measurements on a given sample. The dotted curve was calculated for Nb<sub>2</sub>O<sub>5</sub> layers using the following values for the breakdown voltage and the dielectric constant:  $V_B = 5 \cdot 10^5$  v/cm and  $\epsilon = 120$ . [see section on Properties of Nb<sub>2</sub>O<sub>5</sub> Films and ref. (6)] The solid curve shows what can be achieved at present using Si/SiO<sub>2</sub> capacitors.

However, as can be seen from Fig. 3 the relation between breakdown voltage and capacity per unit area value of most of the layers were more characteristic of SiO<sub>2</sub> than of Nb<sub>2</sub>O<sub>5</sub>, and it was suspected that this was due to the presence of large numbers of pinholes in the Nb<sub>2</sub>O<sub>5</sub> layers. This was eventually confirmed by growing Nb<sub>2</sub>O<sub>5</sub> on platinum/palladium cermet deposited on silicon as a base electrode. This cermet mixture retains its conductive properties, and its smoothness up to temperatures in excess of 1000°C and Nb<sub>2</sub>O<sub>5</sub> layers grown on it were optically very similar to those grown on silicon. Their breakdown voltages were much lower than for the layers grown on oxidized silicon, thus confirming the above hypothesis. Further confirmation was provided by electron microscope studies.

#### Discussion

High permittivity, low loss materials are necessarily crystalline (well ordered). Thus, if the present-day capacitor films are to be improved fundamentally, one should aim at the deposition of crystalline dielectrics.

Therefore an attempt has been made to deposit crystalline Nb<sub>2</sub>O<sub>5</sub>-films [Nb<sub>2</sub>O<sub>5</sub> is known to have outstanding dielectric properties, see ref. (6)] on silicon by chlorine transport. Metal oxides deposited by halogen transport will always tend to be crystalline because of the high deposition temperature which is required to achieve fast and complete reaction be-

tween metal halide (or oxyhalide) and oxygen. Only very few metals will form glassy, amorphous oxides at elevated temperatures.

In the case of Nb<sub>2</sub>O<sub>5</sub>-capacitors it was found that thin polycrystalline films suffered from low breakdown voltage. Low breakdown voltage will be difficult to overcome in polycrystalline thin films for the following reasons.

1. It is virtually impossible to achieve sufficiently dense packing of the individual crystallites to yield a pinhole-free film.

2. Impurities tend to collect at grain boundaries thereby creating regions of increased conductivity.

It is therefore concluded that only epitaxial films will have the desired high capacity and high breakdown voltage properties.

Crystallinity, the first of the two requirements for improved dielectric films, is easily fulfilled by depositing oxide films using the halogen transport method. Epitaxy, the second requirement, has not yet been achieved, but it is not completely unfeasible.

#### Acknowledgments

It is a pleasure to acknowledge the advice of Dr. R. Nitsche and Dr. W. J. Merz in carrying out this work. The authors should also like to thank E. R. Lewin for taking the electron microscope photographs, J. L. Vossen for supplying the cermet substrates, K. H. Zaininger for useful discussions on the preparation of silicon surfaces, and, last but not least, D. Richman for initiating the project.

Manuscript received July 1, 1968; revised manuscript received Aug. 2, 1968.

Any discussion of this paper will appear in a Discussion Section to be published in the June 1969 JOURNAL.

#### REFERENCES

1. See, for example, *Solid State Technol.*, **10**, No. 5 (May 1967).
2. For example, high-precision low-frequency film capacitors of HfO<sub>2</sub>; see F. Huber, W. Witt, and I. H. Pratt, Proc. 1967 Electronic Components Conference (USA), Washington D. C., May 1967, p. 66.
3. H. Schäfer, *Chemische Transportreaktionen*, Verlag Chemie, Weinheim, 1962.
4. H. Schäfer and H. G. Schnering, *Ang. Chem.*, **76**, 833 (1964).
5. H. Schäfer and F. Kahlenberg, *Z. anorg. u. allgem. Chem.*, **305**, 327 (1960).
6. F. P. Emmenegger and M. L. A. Robinson, *J. Phys. Chem. Solids*, **29**, 1673 (1968).
7. M. L. A. Robinson and H. Roetschi, *ibid.*, (1968) In press.
8. K. H. Zaininger, Private communication.
9. A. G. Revesz, *Phys. Stat. Solidi*, **19**, 193 (1967).
10. B. E. Deal and A. S. Grove, *J. Appl. Phys.*, **36**, 3770 (1965).

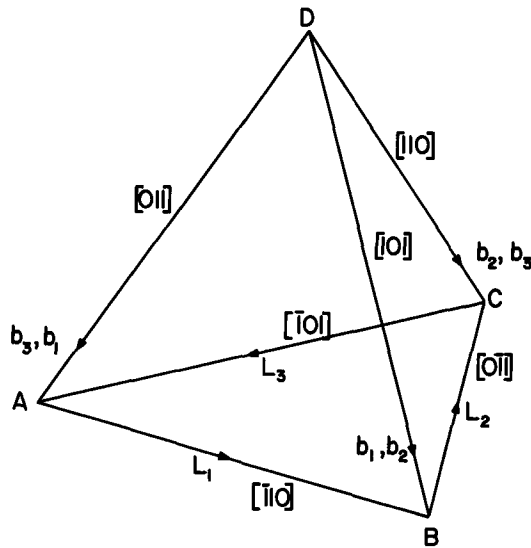


Fig. 1. The dislocation network generated by the diffusion of phosphorus into a (111) silicon surface.

Shockley<sup>6</sup> has shown that the elastic energy released by gliding a dislocation with a Burgers vector  $b$ , a distance  $r$  down the slip plane is

$$E_s = \sqrt{2}\mu[(1+\nu)/(1-\nu)]br e_o \quad [2]$$

where  $\mu$  is the shear modulus of elasticity,  $\nu$  is Poisson's ratio, and  $e_o$  is the elastic strain. In order to estimate  $E_g$  we need to consider in more detail the dislocation configurations which are generated by the diffusion of phosphorus in silicon.

The six slip systems which are usually observed<sup>5-7</sup> when phosphorus diffusion takes place into the (111) surface of a silicon crystal are illustrated schematically with a tetrahedron of {111} planes in Fig. 1. The plane ABC represents the crystal surface. Dislocations  $L_1$ ,  $L_2$ , and  $L_3$ , can lie along the directions AB, BC, and CA, respectively, with Burgers vectors  $b_1$ ,  $b_2$ , and  $b_3$ , respectively, of magnitude  $a/2$ , along the remaining  $\langle 110 \rangle$  directions, where  $a$  is the lattice constant. The corresponding glide planes are ABD, BCD, and CAD, respectively. Thus a dislocation line,  $L_1$ , along AB can have a Burgers vector,  $b_1$ , along either DA or DB, etc. The dislocation intersections which occur in this configuration and result in the formation of edge jogs have been described elsewhere.<sup>17</sup>

The energy dissipated by vacancy generation when a unit length of one of these dislocations containing  $p$  edge jogs glides a distance  $r$  down the slip plane has been previously<sup>2</sup> estimated as

$$E_g = 2\sqrt{2}rp E_v/\sqrt{3}a \quad [3]$$

where  $E_v$  is the energy of formation of a vacancy.

By substituting Eq. [2] and [3] into the criterion expressed by Eq. [1], it is seen that a dislocation will continue to glide only if it has a jog concentration

$$p \leq (\sqrt{3}ab\mu e_o/2E_v)[(1+\nu)/(1-\nu)] \quad [4]$$

This criterion can be used, as follows, to estimate the critical surface concentration at which the work hardening mechanism begins to operate. Then, as a test of the model, the result can be compared with the critical surface concentration observed by Duffy *et al.* at which the retarded diffusion phenomenon begins.

When a significant number of dislocations with jog concentrations near this value accumulate on an atomic plane the energy criterion expressed by Eq. [1] can continue to be satisfied by the formation of a network of dislocations which glide into the crystal simultaneously, thus substantially reducing the jog

concentration. It is possible, in this way, for relief of the diffusion-induced stress to continue by dislocation glide with a significantly reduced rate of vacancy generation, and a consequent reduction in the amount of anomalous diffusion. Thus, according to this interpretation, the two cases illustrated in Fig. 2 of the paper under discussion correspond to one surface concentration below the critical value and another above it. After the drive-in stage, the steeper curve, which corresponds to the higher dislocation density, exhibits the shallower phosphorus diffusion of the two, as would be expected from a reduction in the amount of anomalous diffusion due to the formation of the dislocation network.

We have previously established<sup>2</sup> that a dislocation which has moved from the crystal surface to a position at the front of the dislocation network during the diffusion of phosphorus from a constant surface concentration  $C_o$  would be likely to have a jog concentration of approximately

$$p = (1/\sqrt{3})(\beta/\alpha)C_o \quad [5]$$

where  $\beta$  is the solute lattice contraction coefficient, and  $\alpha$  is the component parallel to the crystal surface of the Burgers vector of the dislocations which are generated.

Substituting for  $p$  from Eq. [4], the condition that the jog concentration should be substantially reduced by the formation of a suitable dislocation network becomes

$$C_o \leq (3\alpha ab\mu e_o/2\beta E_v)[(1+\nu)/(1-\nu)] \quad [6]$$

By substituting suitable values in Eq. [6] it can be shown<sup>2</sup> that the critical surface concentration varies from  $1.2 \times 10^{21}$  atom/cm<sup>3</sup> at 1000°C to  $2.2 \times 10^{20}$  atom/cm<sup>3</sup> at 1250°C. These values are in good agreement with the value of about  $10^{21}$  atom/cm<sup>3</sup> at 970°C which is obtained from Fig. 2 of the paper.

Thus, to summarize, we consider that in the low phosphorus concentration range in which no dislocations are generated, the enhancement of the rate of phosphorus diffusion reported by Duffy, Barson and Schwuttke<sup>3</sup> is explicable in terms of field aided diffusion. At higher surface concentrations, on the basis of the present model, the dislocation density would be expected to increase with the surface concentration and produce anomalously fast diffusion. Ragged junctions would result from the localized enhanced diffusion produced by the glide of individual heavily jogged dislocations into the crystal. However, with surface concentrations in excess of the critical value, the movement of these dislocations would be prevented by the formation of the dislocation network. Thus, the formation of the dislocation network would simultaneously produce a reduction in the degree of anomalous diffusion and more uniform junctions. Thus, most of the observations can be adequately explained in terms of this model.

**M. C. Duffy, F. Barson, J. M. Fairfield, and G. H. Schwuttke:** We appreciate the comments of Dr. Parker; unfortunately his publications,<sup>19</sup> (in which he applied a generalized concept of Balluffi and Ruoff<sup>20</sup> to diffusion into single crystal diamond type lattices), were not available until after our revised manuscript was submitted. However, we do have a few clarifying comments.

It was not our purpose to explain completely the anomalous enhancement of diffusion at the intermediately high concentrations but only in so far as such explanations would help elucidate the retarded diffusion at the highest concentrations.<sup>21</sup> However, since this question has been opened, we suggest that a significant

<sup>19</sup> T. J. Parker, *J. Appl. Phys.*, **38**, 3475 (1967); *J. Appl. Phys.*, **38**, 3471 (1967); and *J. Appl. Phys.*, **39**, 2043 (1968).

<sup>20</sup> R. W. Balluffi and A. L. Ruoff, *J. Appl. Phys.*, **34**, 1634 (1963).

<sup>21</sup> M. C. Duffy, F. Barson, J. M. Fairfield, and G. H. Schwuttke, *This Journal*, **115**, 84 (1968).

mechanism of diffusion enhancement, in addition to the effects of field and lattice strain discussed above by Parker, is through an enhanced equilibrium vacancy concentration in the regions of high N-type doping (e.g., phosphorus) which is caused by the excess electrons through a mass action principle.<sup>22</sup> Incidentally, in our investigation the background concentration was less than the intrinsic value and does not enter explicitly into calculations of effective diffusion coefficients as influenced by built-in electric field.

At any rate, it is the possible strain enhancement that is of principle interest to explain the diffusion retardation. We suggested,<sup>21</sup> as one possible mechanism, that the formation of the small cell diffusion induced dislocation network [see Fig. 3 of ref. (21)] may well reduce the magnitude of the strain enhancement of diffusivity by rendering the dislocations individually less mobile. It is gratifying that Dr. Parker finds this suggestion to be quantitatively feasible through his proposed mechanism. However, we still feel that the suggestion is speculative owing to the following uncertainties: (a) the assumption of substitutional diffusion at these extremely high impurity concentrations and in the presence of precipitates is, at best, problematical; (b) the kinetics of the dislocation formation in our case are not steady state; thus, the quantitative applicability of Prussin's model is unjustified; and (c) there are vacancy sinks in addition to the crystal surface, for example in the formation of vacancy type dislocation loops; thus, there will be a vacancy annihilation rate of uncertain magnitude.

#### Impedance for Tunnel Exchange of Electrons Across the Annealed Ta/Ta<sub>2</sub>O<sub>5</sub> Interface

K. Lehovc (pp. 192-199, Vol. 115, No. 2)

**D. M. Smyth**<sup>23</sup>: Lehovc proposes to explain the impedance properties of heat-treated, anodized tantalum by means of a tunneling process across the Ta-Ta<sub>2</sub>O<sub>5</sub> interface. The essential difference between this mechanism and the previously proposed exponential conductivity gradient<sup>24,25</sup> is in the spatial distribution of the controlling process within the oxide. The conductivity model assumes that there is an effective dielectric thickness which is obtained from the observed equivalent series capacitance and the parallel plate equation; the rest of the oxide thickness is effectively short-circuited. The short-circuited region generally amounts to a few hundred angstroms (18% of the total thickness) for samples heat-treated in air. The tunneling model, on the other hand, implies that the active region is confined to the oxide within a few tens of angstroms of the Ta-Ta<sub>2</sub>O<sub>5</sub> interface (about 1% of the oxide thickness). Since both models can explain the basic experimental observations, it is important to search for experiments which might distinguish between them. I would like to describe two experiments which give an indication of how far the dielectric losses extend into the oxide.

First, when anodized tantalum is heat-treated in vacuum, subsequent capacitance measurements made near room temperature behave as if the oxide film were completely short-circuited. The question is, is this a true electronic short-circuit, or does it merely indicate extremely high dielectric losses, perhaps still located near the Ta-Ta<sub>2</sub>O<sub>5</sub> interface? To answer this question, we have heated a tantalum sample, anodized to 75v, in vacuum at 450° and then applied several small Ni dots (~ 0.2 cm<sup>2</sup>) to the lower half of the sample by electroless deposition. All five electrode dots became d-c short-circuits when 1-2v were applied (Ta<sup>+</sup>). This means either that the oxide film was conducting throughout, or that it was badly damaged by

the heat-treatment. In order to disprove the latter, the same sample was reheated at 400° in air and Ni dots were then applied to the upper half. One dot broke down at about 25v; the other four supported maximum voltages between 75 and 80v. Apparently most of the oxide had been restored to an insulating condition as expected from the conductivity model.

The only difference between the vacuum-heated samples and the air-heated samples is the ambient atmosphere during heat-treatment. When the heating is done in vacuum, it appears that both the vacuum and the tantalum are sufficiently good reducing agents to render the oxide sufficiently conducting to affect its dielectric properties. There is no reason to expect the tantalum to react any differently when the heating atmosphere is changed to air. The only difference is that the oxide at the air interface is more highly oxidized and hence less conducting. It is reasonable to expect a steep conductivity gradient to result from such a change in oxygen activity across these thin films.

The other experiment involves the behavior of tantalum samples anodized in concentrated H<sub>3</sub>PO<sub>4</sub> solutions. It is well established that the resulting oxide film consists of an outer portion which contains large amounts of phosphorus, and a portion next to the metal which contains no phosphorus. In the case of anodization in 85% H<sub>3</sub>PO<sub>4</sub> (~ 14.7M) the phosphorus-free region makes up about a third of the total thickness.<sup>26</sup> When such a sample is heat-treated in air, the dielectric properties are in accord with a conductivity gradient which has split into two parts: a shallow, inner gradient, and a steep outer gradient. By stepwise dissolution of the oxide of a sample anodized 75v in a H<sub>3</sub>PO<sub>4</sub> solution containing P<sup>32</sup>, the boundary between the two conductivity gradients has been identified with the boundary between the phosphorus-containing and phosphorus-free oxide.<sup>27</sup> In fact, as the oxide was chemically thinned, the residual radioactivity went to zero simultaneously with the reciprocal series capacitance, a measure of the effective dielectric thickness. Thus the remaining 500Å of phosphorus-free oxide was an effective short-circuit. The interference color of the sample at this point was consistent with such a thickness. The splitting of the conductivity profile into two slopes for these cases has been attributed to a proposed difference in the mobility of oxygen in the phosphorus-free and phosphorus-containing layers during the heat-treatment.<sup>27</sup> This proposal has subsequently been confirmed by Pawel.<sup>28</sup>

It should be stressed that the times and temperatures of heat-treatment are similar for all of these samples, and that the environment at the Ta-Ta<sub>2</sub>O<sub>5</sub> interface is exactly the same for all cases.

These two experimental observations indicate that the region of high dielectric losses in the heat-treated, anodic oxide film on tantalum can extend across hundreds, and even thousands, of angstroms of the oxide film. Such an extension is in accord with the model of a conductivity gradient, and these observations are readily accommodated by this model. It is difficult to see how they can be explained by the tunneling model. Lehovc proposes that the model of a conductivity profile may indeed be the correct one for the two cases described here, whereas the tunneling model might be valid for "ordinary annealed Ta/Ta<sub>2</sub>O<sub>5</sub> structures." Keeping in mind that there is a continuous and gradual change of dielectric properties with the ambient oxygen pressure during heat-treatment and with the H<sub>3</sub>PO<sub>4</sub> concentration in the anodization electrolyte, it seems unnecessary to invoke a new theory which can explain only one end of a range of properties when an existing model is compatible with all of the observations.

<sup>22</sup> M. F. Millea, *J. Phys. Chem. Solids*, **27**, 315 (1966).

<sup>23</sup> Research and Development, Sprague Electric Co., North Adams, Mass.

<sup>24</sup> D. M. Smyth, G. A. Shirn, and T. B. Tripp, *This Journal*, **110**, 1271 (1963).

<sup>25</sup> *Idem*, *ibid.*, **111**, 1331 (1964).

<sup>26</sup> J. J. Randall, Jr., W. J. Bernard, and R. R. Wilkinson, *Electrochim. Acta.*, **10**, 183 (1965).

<sup>27</sup> D. M. Smyth, T. B. Tripp, and G. A. Shirn, *This Journal*, **113**, 100 (1966).

<sup>28</sup> R. E. Pawel, *This Journal*, **114**, 1222 (1967).

**K. Lehovec:** D. Smyth discusses two extreme cases of annealed Ta/Ta<sub>2</sub>O<sub>5</sub> samples where dielectric losses arise from conduction, namely (i) Ta/Ta<sub>2</sub>O<sub>5</sub> annealed in a reducing ambient (i.e., vacuum) resulting in a reduction of the entire oxide film, and (ii) Ta<sub>2</sub>O<sub>5</sub> films grown anodically in a concentrated phosphoric acid solution and annealed in air, resulting in reduction of the phosphorus-free inner oxide region. As already mentioned in my paper, I agree with Smyth on the applicability of the conductivity model to the dielectric losses in these two extreme cases.

Smyth points out that in the case of ordinary (i.e., not phosphorus-rich) anodic oxide samples annealed in an oxidizing atmosphere such as air "a steep conductivity gradient results from the change in oxygen activity across these thin films." It seems to me that the steepness of this gradient, i.e., whether the significantly reduced oxide extends over a few tens of angstroms or over a few hundreds of angstroms will determine whether the tunnel model or the conductivity model applies. I do not know of any past experiments which clarify this point.

A theoretical distinction between the two models is not possible without understanding the mechanism of oxygen transport from an oxidizing ambient to the tantalum during the anneal. My attempt<sup>29</sup> to interpret available experimental data to provide a model leading to an exponential oxygen vacancy distribution such as postulated by Smyth *et al.*, was less than fully successful. Therefore, I searched for another interpretation of Smyth's impedance measurements resulting in the tunneling model. This does not rule out, of course, the possibility that a mechanism leading to an exponential vacancy distribution may yet be found, e.g., by a suitable dependence of oxygen vacancy diffusion constant on concentration. Incidentally, the tunnel model proposed by me postulates an inverse-square dependence of the receptor concentration on the position in the oxide adjacent to the tantalum interface in order to provide an exponential conductivity profile and the observed Schottky plot; the

<sup>29</sup> K. Lehovec, *This Journal*, 115, 520 (1968).

origin of this space dependence has not been accounted for either.

In the case of the heavily doped phosphorus-containing samples, there appears to be a discontinuity in the oxygen transport through the oxide at the boundary between the phosphorus-containing outer region and the phosphorus-free inner region. In such a case, the oxidizing ambient atmosphere and the reducing tantalum metal may indeed cause a nearly homogeneous reduction of the inner region, with an abrupt change to a very nearly stoichiometric outer region. However, I would be hesitant to generalize this behavior of an extremely phosphorus-rich sample to "normal" films, where such a pronounced oxygen transport barrier may not be present in the outer film region.

Smyth sees in the gradual change of the "conductivity profile" with phosphorus content an indication of the same underlying mechanism. It is conceivable, however, that two different mechanisms, conduction losses in case of phosphorus-rich oxides and interface tunneling losses in case of phosphorus-free oxide, are superimposed with a gradual transition arising from the relative weights of these two contributions, these weights varying with phosphorus concentration in the forming electrolyte.

In summary, I question the generalization of the two extreme cases discussed by Smyth to the structures on which the measurements analyzed by me have been made. I believe that a clarification should be sought along the following lines: (a) an understanding of the oxygen transport during anneal in an oxidizing atmosphere; (b) electrical measurements on samples of oxide thickness of about 100Å or less, and (c) more extensive measurements of Schottky plots as function of temperature, and of the associated time lags.

In conclusion, I would like to point out again that the tunneling model has been offered by me as a possible alternative for the conduction model. In my opinion, the evidence existing at present does not permit a clear-cut rejection of one or the other of these two models, except in certain extreme cases.





### Polymers: Their Structure and Dielectric Properties

C. A. Buehler

3M Company, Saint Paul, Minnesota

#### ABSTRACT

Polymers, with their high molecular weight and great lengths *vs.* relatively small diameters, tend to have very complex physical and dielectric properties. The dielectric properties, like the mechanical properties, are dependent on the mobility of their constituent parts and are therefore quite sensitive to both temperature and frequency. The effects of glass transition temperature, melting point, impurities, and atomic structure on the dielectric properties are discussed with specific examples from the literature. Conduction and breakdown are covered rather briefly with emphasis on the need for fundamental structural studies in this area.

Polymers may be simply defined as very high viscosity liquids or solids of intermediate or high molecular weight (1). They are made by the chemical union of large numbers of small molecules (monomers) to form a macromolecule. Two general methods of preparing these materials may be described (see Fig. 1). Addition polymerization makes use of unsaturated compounds as monomers and involves their combination without rearrangement of the atoms in the structure. It is normally a fast chain reaction occurring *via* activated free radical or ionic intermediates. Monomeric units add rapidly one after another to a growing chain, and interaction between such chains either does not occur or results in the cessation of growth of one or both chains. On the other hand, condensation polymerization is normally a stepwise, relatively slow reaction. It is best described as a growth process which usually involves the splitting off of a small molecule. Molecules of any size may interact to yield larger molecules capable of further reaction to yield still bigger molecules.

Polymers which are commercially useful usually have molecular weights which vary from 10,000 to 1,000,000. The ultimate molecular weight in one single molecule is actually the result of a series of random events. This usually results in a distribution of molecular weights in a given sample, as shown in Fig. 2 (2). Several methods of describing the molecular weights of a polymer are also illustrated in this figure [for further information on these methods consult Billmeyer (1)]. The most unusual characteristic of these macromolecules is their unique structure. Take for example polymethylene, which has  $-\text{CH}_2-$  units connected together to form a chain 40,000Å long and a diameter of only 4.9Å. A good analogy (3) would be a snarled clothesline 150 ft long and 3/16 in. in diameter. With so many possible conformations available to it, what usually results is a jumbled mass (see Fig. 3) (4). It has been possible to describe mathematically the conformations of such a molecule. If one calculates (3) the end to end distance in the same clothesline analogy, assuming free rotation about bonds, only 1½ ft would separate the two ends (in

solution or melt). An increase in the length of the hypothetical clothesline to almost 1¼ miles increases the end to end distance to only 10-15 ft. Of course, there is not complete free rotation about bonds, but calculations such as this form the foundation for a basic understanding of polymer molecules.

Nonpolymeric materials that form simple crystals usually have a well-defined crystalline melting point. Above this temperature the material is liquid, and the molecular structure does not have a well-defined space lattice. In such a liquid state there is not complete randomness as in a gas; however, there is a lack of any long range order. Below the crystallization temperature we find the well-defined spatial geometry of the crystalline state. Some polymer structures, as we have just discussed, also exhibit this kind of behavior. As long as the polymer molecules have a repetitive pattern and they can move into a regular conformation, the material can become crystalline below a given temperature.

However, crystallization in polymers usually requires a high degree of symmetry (see Fig. 4) as found in materials such as polyethylene, polytetrafluoroethylene, polyvinylidene fluoride, and polyvinylidene chloride. These materials all have a regular structure, and they also possess a high degree of symmetry. They crystallize readily; in fact, polyethylene is so prone to crystallization that it cannot be obtained completely in the amorphous form even with shock cooling of a thin film in liquid air.

Addition polymers of the  $(\text{CH}_2-\text{CHX})_x$  type are most often prepared in the amorphous condition, for

REVIEW  
SECTION

Key words: dielectric, polymer, dielectric/constant.

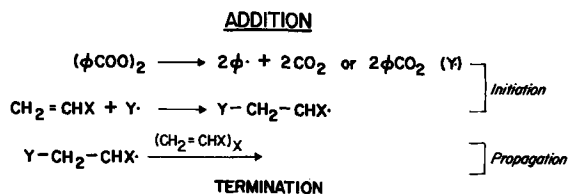
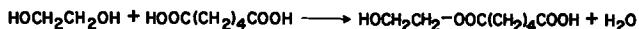
**CONDENSATION**

Fig. 1. General methods of preparing organic polymers

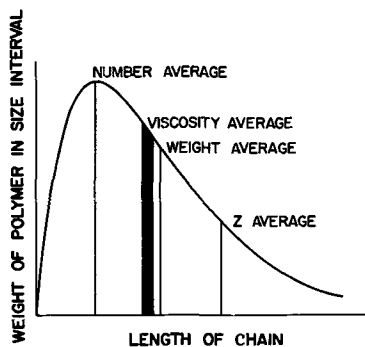


Fig. 2. Distribution of molecular weights in a typical polymer (2)

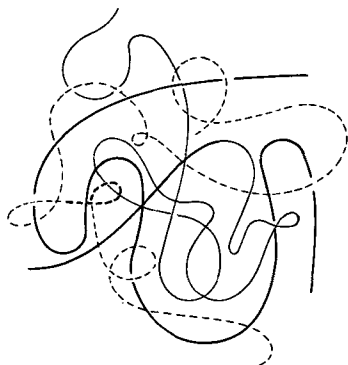


Fig. 3. Schematic drawing of the random molecular state of an amorphous polymer, showing the entanglement of three molecules (4).

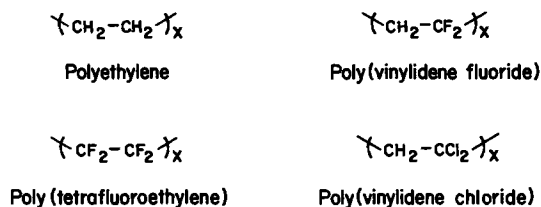


Fig. 4. Atomic structure of some crystalline polymers

although they are composed of chemically identical repeating units, they are in general sterically irregular. Thus, the CH-X groups will be found to occur along the chain randomly in the d- or l-configuration. Such geometric irregularities prevent crystallization unless the X is very small, as is the case in polyvinyl fluoride. However, polymers of the  $(\text{CH}_2\text{CHX})_x$  type are not always found to be sterically irregular. Under certain conditions it is possible to control the ionic or free radical polymerization so that the chains have all one configuration or regularly alternating d- and l-configurations (see Fig. 5). However, more often than not, the structures of polymers tend to be amorphous in character. In the cooling of such polymers there is no sudden rearrangement of the molecules, as in crystallization, but rather a steady loss of mobility

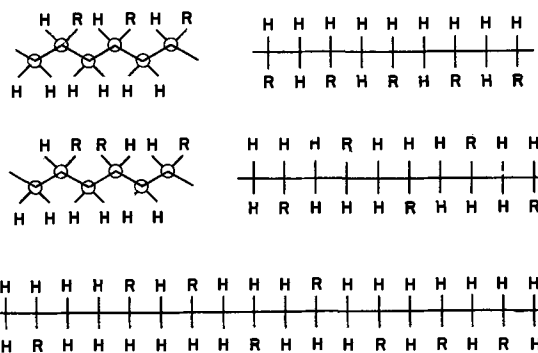


Fig. 5. Monosubstituted ethylenic polymers in three potential configurations, top to bottom, isotactic, syndiotactic and atactic.

until there is no longer fluid resistance to molecular motion. The resistance to motion becomes so high that the material is solid-like in every sense of the word. This transition (1), commonly called Tg (glass transition temperature), is in a thermodynamic sense like a second order transition in that the energy, heat content, volume, and entropy plus many other properties show a discontinuity in slope when plotted vs. temperature (see Fig. 6). However, the analogy to thermodynamic quantities can be misleading since no phase transition is involved.

Since the transition (5) is not sharp, the Tg is generally taken as the mid-point of the temperature interval over which the discontinuity takes place. It is generally believed that at the glass transition temperature all large-scale backbone chain motion ceases, and the long range conformation at this point becomes fixed for all lower temperatures.

The mechanical properties of polymers are directly determined by the molecular mobility of the constituent groups (5); crystallinity is important only in a secondary sense. A material in which all groups are rigidly fixed is brittle irrespective of whether it is crystalline, glassy, or both. In order, therefore, to estimate the effect of temperature (including "room temperature") on the mechanical and the dielectric properties of a proposed or existing polymer, it is very important to have an understanding of the fundamental molecular motions of polymers and how they are influenced by temperature and frequency.

The close relationship between the mechanical and electrical properties of polymers is linked basically to the close association of both properties to their fundamental molecular motions. Although the source of dielectric properties (dielectric constant,  $\epsilon'$  and loss,  $\epsilon''$ ) is electronic, atomic, orientational, and ionic polarizations (see Fig. 7), the major contribution in most polymers is obviously from the latter two polarizations. The ability of dipoles to orient in an applied field is directly dependent on their fundamental mobility as a function of temperature and frequency. Therefore the dielectric properties are closely related to the fundamental motions of the polymer structure. (An excellent treatise on the

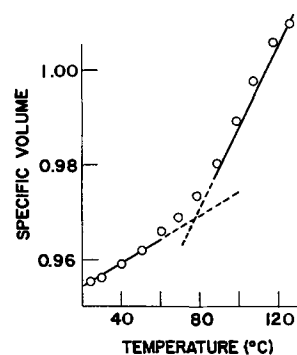


Fig. 6. Volume-temperature curve of polystyrene

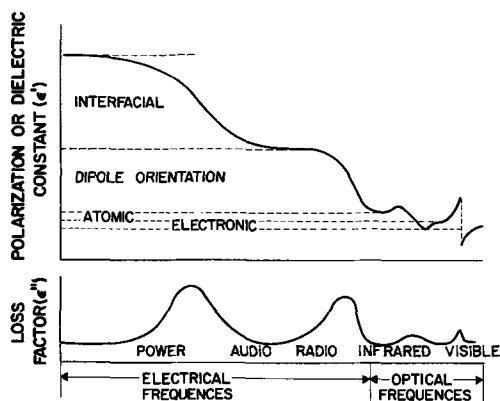


Fig. 7. Schematic representation of a hypothetical insulation having all four kinds of polarization showing the effects of frequency on the dielectric properties,  $\epsilon'$  and  $\epsilon''$ .

mechanical and dielectric effects in polymers was recently published by McCrum *et al.* (6) and should be consulted for a more detailed examination of these properties.)

Debye (7)<sup>1</sup> originally suggested that the high dielectric constant of such compounds as water and alcohols is caused by permanent dipoles in the molecules themselves since the square of the index of refraction (due to electronic polarization) in water, for example, is only 1.77, while the dielectric constant, measured at radio frequencies, is 78. In a simple liquid such as glycerol (8) the effect of temperature and frequency on the dielectric properties is illustrated (see Fig. 8). In the case of polymers in the amorphous state, which is often described as a very viscous liquid, the result is a broadening of the loss peak due to the multiple set of relaxation times rather than a single relaxation (see Fig. 9) (9). Polymers through their multiple transitions, as we discussed earlier, serve to complicate the situation further. This is not to say simple molecules do not have such transitions, but because of the complexity introduced by the mere size of the polymer molecule it is imperative that each transition be separated and examined.

In nonpolar polymers (10) the ideal case is fairly straight-forward (see Fig. 10). As the temperature is increased, the dielectric constant or permittivity ( $\epsilon'$ ) decreases slowly because of the decrease in density and its effect on the number of dipoles per unit volume. There is a sharp jog in the curve at the melting point because of the further decrease in density in the liquid state. One might expect a similar jog at the glass transition. Within the range of radio frequencies, no loss maximum should develop since no permanent dipoles are present. Interfacial polarization [see ref. (7) for further details] may be observed if impurities were present, especially at the low frequencies. Polyethylene may be classified as a nonpolar polymer although a small dielectric loss ( $\tan \delta \sim 10^{-4}$ ) has been generally reported. It has been shown quite conclusively that most, if not all, of this loss is due to the presence of extraneous dipoles (11), most probably carbonyl groups introduced through accidental oxidation during preparation of the polymer. The dielectric properties at low frequency (see Fig. 11) (12) require very careful measurements since the loss is extremely low. Fairly evident is the change in loss tangent ( $\tan \delta = \epsilon''/\epsilon'$ ) as the material proceeds through melting point ( $T_M$ ) around 100°C along with loss maxima at 0° and -80°C. The two low-temperature maxima have been labeled as  $\alpha$  (0°C) and  $\gamma$  (-80°C) loss regions. The fundamental source of these loss maxima is still questionable, especially the one at 0°C. The  $\gamma$  loss is generally associated with

<sup>1</sup> It should be noted that the dipolar molecules show only a slight preferential orientation in the field direction. Debye pointed out at a full field intensity of 1 v/cm the effect equals alignment of one dipole moment in 5,000,000 in the field direction; this fractional orientation would suffice to produce a dielectric constant of 80.

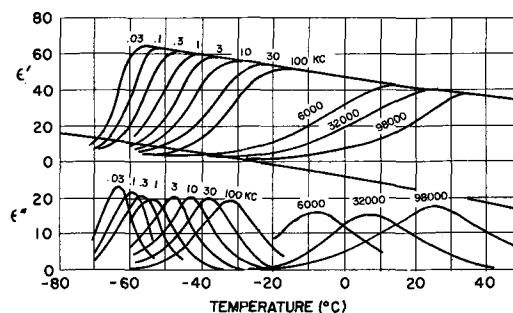


Fig. 8. Temperature dependence of dielectric constant and loss factor for glycerol (8).

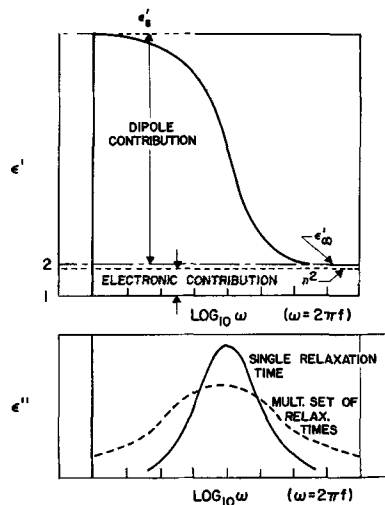


Fig. 9. Effect of frequency on the dielectric constant,  $\epsilon'$  and loss index,  $\epsilon''$ , for polar polymers (9).

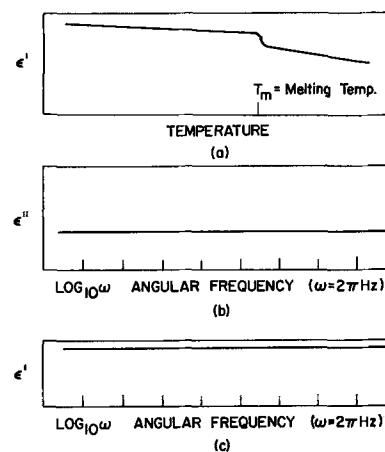


Fig. 10. Dielectric behavior of ideal nonpolar materials (10)

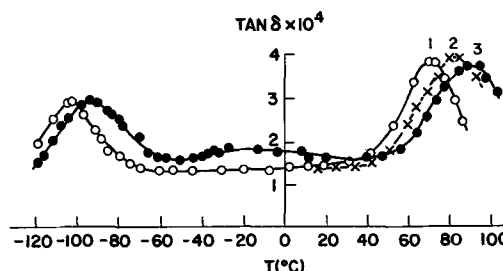


Fig. 11. Dielectric loss tangent ( $\tan \delta = \epsilon''/\epsilon'$ ) of linear polyethylene as a function of temperature: curves 1, 2, and 3 at frequencies 1, 5, and 10 Hz (12).

a local relaxation mode of the main chain in the solid state of the polymer involving movement of a few monomer units. The  $\alpha$  process has been associated with the glass transition.

The results with polyethylene are substantiated with other nonpolar polymers such as polyisobutylene (11) and polytetrafluoroethylene (11). In the latter case, this material has come closest to showing the ideal behavior predicted for nonpolar polymers probably because of greater purity during preparation. However, even in this case where the loss is extremely low, it has been possible, via very low-frequency, low-temperature measurements, to detect transitions in the crystalline phase. Since the loss is extremely low, there is little effect on the dielectric properties other than to slightly lower the dielectric constant due to a decrease in density.

In the case of polar materials, the situation is far more complex, yet the dielectric properties are much easier to measure, because the dipoles produce substantial changes as they go through various stages of mobility. Inspection of the ideal cases serves to simplify our discussion (Fig. 12 a+b) (10).

At high temperature thermal energy agitates the dipoles so violently that the electric field has relatively less effect on them. As temperature decreases,  $\epsilon'_s$  (static dielectric constant) increases until structural changes such as crystallization or the glass transition decreases the influence of the electric field. In crystalline polymers, unlike simple frozen liquids or glassy polymers, dipoles which are partially immobile at lower temperature tend to be freed as the temperature is increased (Fig. 12a, Case IIa). These dipoles are easily influenced by electric field, the increasing mobility with increasing temperature is usually so high that it overcomes the opposite effect of increased thermal agitation so that  $\epsilon'_s$  increases as the temperature increases. A similar effect occurs with rigid glassy polymers (Fig. 12b, Case IIIb) with stiffly attached dipoles. On the other hand, in some highly imperfect crystalline lattices, rather symmetrical dipoles may have considerable freedom so that  $\epsilon'_s$  follow Case Ia. In glassy polymers with rotatable side groups, such as polymethylmethacrylate, the main structure may become glassy, but still considerable freedom may exist in the side groups.

Polymethylmethacrylate (PMMA) has been studied rather extensively with regard to both its dielectric and mechanical properties by a large number of researchers. One of the most thorough pieces of work was published by Deutsch and co-workers (13). Two transitions were observed and at 1000 Hz, the  $\alpha$  and  $\beta$  transitions were at 120° and 50°C, respectively (see Fig. 13) (13). The  $\alpha$  transition we have defined earlier while the  $\beta$  transition has been associated with the relaxation process associated with the polar side groups. An important additional piece of information from another source (14) about the nature of the  $\alpha$  transition concerns the effect of addition of a plasticizer. At a given frequency of measurement, the addition of up to 25% by weight of dibutyl phthalate caused a decrease in the temperature of the  $\alpha$  loss

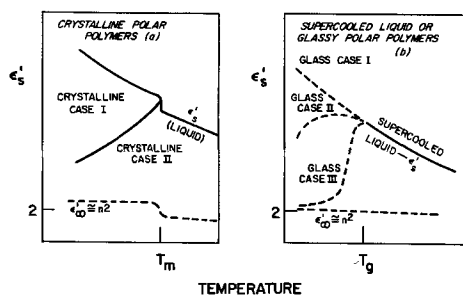


Fig. 12. Effect of temperature on the static (low frequency) dielectric constant of polar compounds (dotted curves are for high-frequency dielectric constant for comparison) (10).

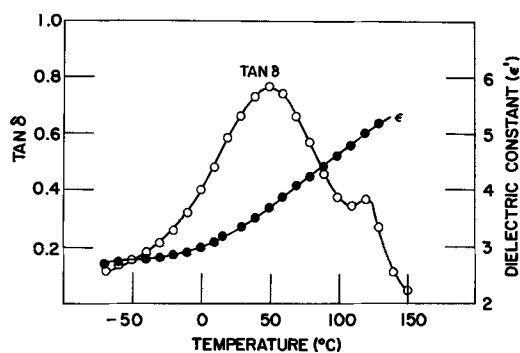


Fig. 13. Dielectric properties of PMMA (log freq. = 1.9) (13)

maximum by about 30°C, while little if any effect was noted in the case of the  $\beta$  loss maximum. The same effect has been verified in other polymers both through electrical and other measurements. PMMA also exhibits a  $\gamma$  loss region (11), but we will not discuss it here.

Polystyrene (atactic) represents the case where a rigidly attached dipole is joined to the main chain. This material is an outstanding insulating material and has found wide use in the electrical industry. Polystyrene is generally considered to have only one dispersion region, which would be consistent with the expected behavior of one-phase polymer without independently orientable polar side groups (see Fig. 14).

In the case of crystalline polymers, a most interesting case is that of poly(chlorotrifluoroethylene). Its properties are in many respects similar to polytetrafluoroethylene, but the presence of a small permanent dipole gives rise to dielectric loss and dispersion. Also, the substitution of a chlorine atom gives a point of possible stereoisomerism which, apparently because of the close similarity in size of the chlorine and fluorine atoms, does not prevent crystallization but does result in a much less highly ordered crystal. While high molecular weight PCTFE has a crystalline mp at about 220°C, one sample of fractionated "Fluorolube" with a molecular weight of 980 had a melting point of 22°C. This low molecular weight material, which had a 10 Hz dielectric constant of 3 at 40°C above its melting point, was found to have a dielectric constant of almost 6 below the crystalline melting point, at about -10°C (see Fig. 15) (15). These and other results were interpreted as indicating rotation of the polar molecules within the crystalline phase, as has so often been observed in organic solids. In this case, an enhanced dipole moment on freezing results from alignment of the neighboring dipoles on each molecule in the crystalline phase, whereas the dipoles tend to adopt a lower energy configuration involving partial cancellation of these dipoles in the liquid state. The same effect has been observed in high molecular weight material but not to such a high degree.

The area of "microstructure" and how it is related to the dielectric properties of materials is large in itself, and it would be impossible to discuss this area in detail here. However, two recent reports (16, 17) illustrate a different approach and represent an attempt to understand dielectric properties

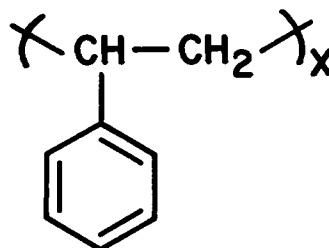


Fig. 14. Polystyrene ( $T_g = 79^\circ - 80^\circ\text{C}$ )

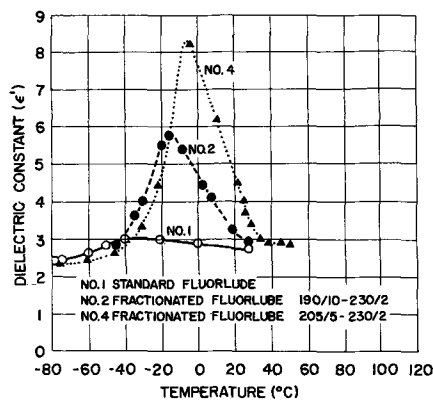


Fig. 15. Dependence on dielectric constant of temperature at 10 kc. Liquid fluororubane samples 1, 2, and 3 (15).

vs. structure with a specific objective in mind; synthesis of higher dielectric constant materials (see Fig. 16).

By comparing the dielectric constants of a given series of fluorinated polymers at the same frequency and at temperatures equally above their  $T_g$ 's, it is possible to see a distinct effect of the stereochemical size of the dipole on the dielectric constant. Studies such as this and those discussed earlier should bring the day closer when the polymer scientist will be able to synthesize materials based on a specified list of desired dielectric properties.

Conspicuous by their absence in this discussion are two other areas properly classed under the title "dielectric properties of polymers", i.e., conduction and breakdown. There are two reasons for this, one being the rather obvious choice of the author who feels that more detailed explanation of a particular area is of greater benefit than a cursory attempt to cover all areas. The second reason is a shortage of fundamental structural work on both conductance and breakdown in insulating dielectrics. One reason for this lack of structural data is that practical breakdown, whether in thin films or thicker sections, tends to be governed by factors such as electrode geometry, testing procedures, physical integrity of the sample, etc., rather than a molecular structural one (18). As for conduction, suffice it to say that there have been only a few papers which have dealt with truly pure materials and they have been most interesting (19). However, the problem of impurities as sources of charge carriers continues to leave this field in a state of uncertainty. This problem as to the nature of the charge carrier ultimately questions much of the data on the effects of crystallinity, polarity, crosslinking, etc., on conduction from a structural viewpoint.

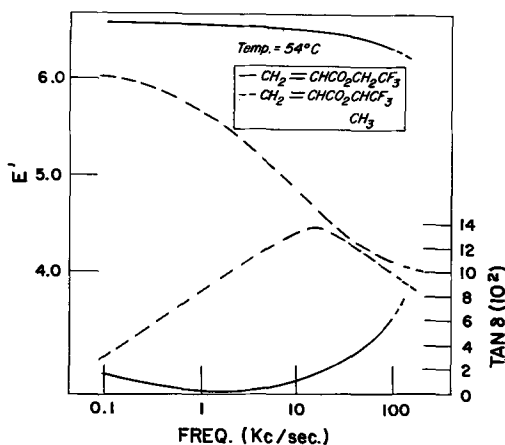


Fig. 16. Dielectric constant and  $\tan \delta$  of various fluorocarbon polymers based on monomers shown (17).

In conclusion, the development of the theory of the dielectric properties of polymers is an area of considerable interest and activity. Further information on some of the areas listed below should be very interesting as well as contributing significantly to the field of dielectric properties of polymers (20).

1. What effect do dipoles in the backbone itself have on the dielectric properties, particularly in  $\alpha$  dispersion region?

2. The influence of crosslinking is insufficiently known. It should, according to theory, have much more influence on the  $\alpha$  than on the  $\beta$  transition.

3. With the recent availability of stereoregular polymers, many interesting questions should be answerable, such as testing the theory relating the distribution of relaxation times for the  $\beta$  band to microscopical heterogeneity, and the entropy of activation to a destruction of local order.

4. A class of polymers in which there is a considerable and increasing degree of interest is that in which the polymer chain is conjugated and the possibility of appreciable conductivity exists. Theoretical and experimental dielectric studies on these polymers, both in the solid state and in solution, are needed as a basis for understanding their microscopic electrical and electronic properties.

5. Are there other transitions in polymers as one approaches the point where all molecular motion ceases?

Manuscript submitted Mar. 28, 1968; revised manuscript received May 16, 1968. This paper was presented at the Boston Meeting, May 5-9, 1968, as Abstract 4.

#### REFERENCES

1. F. W. Billmeyer, Jr., "Textbook of Polymer Science," Interscience Publishers, New York (1962).
2. W. M. D. Bryant, *J. Polymer Sci.*, **56**, 277 (1962).
3. B. Wunderlich, *Ind. Eng. Chem.*, **56**, 18 (1964).
4. A. T. Di Benedetto, "The Structure and Properties of Materials," pp. 218 and 227, McGraw Hill Book Co., New York (1967).
5. W. A. Lee, Royal Aircraft Establishment, Publication No. CPM8, Ministry of Aviation, London W. C. 2, 1964.
6. N. G. McCrum, B. E. Read, and G. Williams, "Anelastic and Dielectric Effects in Polymeric Solids," John Wiley & Sons, London (1967).
7. C. P. Smyth, "Dielectric Constant and Molecular Structure," p. 38, The Chemical Catalog Co., New York (1931).
8. S. O. Morgan and W. A. Yager, *Ind. Eng. Chem.* **32**, 1519 (1940).
9. K. N. Mathes, in "Engineering Design for Plastics," E. Baer, Editor, Chap. 7, Reinhold Publishing Corp., New York (1964).
10. J. Hoffman, "The Mechanical and Electrical Properties of Polymers," in *I.R.E. Trans. (Component Parts)*, June, 1957, ref. 9, p. 536.
11. A. J. Curtis, "The Dielectric Properties of Polymeric Systems," in "Progress in Dielectrics," Vol. 2, J. B. Birks, Editor, p. 38, John Wiley & Sons, Inc., New York (1960).
12. G. P. Mikhailov, S. P. Kabin and T. A. Krylova, *Zhur. Tekh. Frz.*, **27**, 2050 (1957), ref. 11, p. 39.
13. K. Deutsch, E. A. W. Hoff and W. Reddish, *J. Polymer Sci.*, **13**, 565 (1954).
14. G. P. Mackhailov, T. I. Borisova, and D. A. Dmitrochenko, *Zhur. Tekh. Fiz.*, **26**, 1924 (1956), ref. 11, p. 46.
15. S. I. Reynolds, V. G. Thomas, A. H. Sharbaugh, and R. M. Fuoss, *J. Am. Chem. Soc.*, **73**, 3714 (1952).
16. H. Sorkin, H. W. Graessley, J. A. Manson, and J. H. Zufall, *Natl. Acad. Sci., Natl. Res. Council, Publ.* 1238, 34 (1964).
17. P. H. Schertler, "Dielectric Properties of Some Poly (Fluoroalkyl-acrylates), Paper presented at the Conf. on Electrical Insulation and Dielectric Phenomena, Nat. Res. Council, 1967.
18. J. J. O'Dwyer, "The Theory of Dielectric Breakdown of Solids," Oxford (1964).
19. C. A. Buehler, "High Polymeric Materials" in

"Digest of Literature on Dielectrics," D. W. Swan, Editor, Vol. 29, p. 273, National Academy of Sciences, Publication #1461, Washington, D. C. (1965).

20. L. de Brouckere, in "Unsolved Problems in Polymer Science," National Academy of Sciences, Publication #995, p. 172, Washington, D. C., (1962).

## Internal Photoemission as a Tool for the Study of Insulators

Alvin M. Goodman

RCA Laboratories, Princeton, New Jersey

### ABSTRACT

Photoemission of electrons or holes from a conducting electrode into an adjoining insulator can be used to determine information about the energy-band relationships at the interface between the conductor and the insulator and about carrier transport in the insulator. The basic theory of the measurement techniques is discussed, and some experiments employing these techniques (using silicon dioxide as the insulator) are described.

If one is interested in the study<sup>1</sup> of insulators he is quickly struck by the following realization: Many of the most interesting electronic properties may be investigated only by making the insulator somewhat conducting. The principal objective of this paper is to describe (i) a method for introducing controlled conductivity into a normally insulating medium and (ii) what may be learned from concomitant electrical measurements.

The major process considered is that of *internal photoemission*, i.e., the photoemission of mobile electrons or holes into an insulator from an adjacent conducting medium. As a preliminary, however, some of the basic aspects of external photoemission (photoemission into vacuum) from metals and semiconductors are briefly reviewed. The treatment of internal photoemission considers first, the possible internal photoemission processes. This is followed by a description of a number of experiments in which these processes occur and what can be learned from them about the electronic transport properties of insulators and about the properties of interfaces between insulators and noninsulators (metals and semiconductors).

The scope of this paper is somewhat narrower than that which would be desirable for a complete discussion of internal photoemission.<sup>2</sup> The emphasis in what follows is directed principally toward the study of insulators; this is somewhat different from the usual studies involving photoemission in which the major concern is with the properties of the photoemitting electrode.

### External Photoemission

**Metals.**—The process of photoelectric emission into vacuum or, more simply, external photoemission is illustrated in Fig. 1 which shows a simplified model of an energy band diagram in the vicinity of a metal-vacuum interface. The electron energy is plotted against distance perpendicular to the interface. A photon impinges on the metal surface and is absorbed in the metal giving its energy  $h\nu$  to an electron; the electron then has sufficient energy to surmount the

potential barrier at the metal surface and enter the vacuum. The energy difference  $e\phi$  between the Fermi level  $E_F$  and the vacuum level is called the work function or, more particularly, the *vacuum value of the work function* to distinguish it from an effective value which will be considered shortly in connection with internal photoemission.

In the analysis of the photoemission of electrons from metals, Fowler (1, 2) assumed that (i) the metal can be represented by the Sommerfeld free electron model (one simple conduction band with a single effective mass), (ii) the photoemission is independent of the depth at which the photon is absorbed, and (iii) the yield (electrons emitted per absorbed photon—a number less than one) is proportional to the density of electrons within the metal which have thermal velocity components  $v_x$  normal to the emitting surface such that  $1/2 mv_x^2 + h\nu > e\phi$ . He found that for a given photon flux, the photoemitted current is given to a good approximation by  $I = AT^2 f(x)$  where  $x = (h\nu - e\phi)/kT$ ,  $A$  is a constant,  $k$  is Boltzmann's constant,  $T$  is absolute temperature, and

$$f(x) = e^x - \frac{e^{2x}}{2^2} + \frac{e^{3x}}{3^2} - \dots \quad x < 0$$

$$f(x) = \frac{\pi^2}{6} + \frac{x^2}{2} \left( e^{-x} - \frac{e^{-2x}}{2^2} + \frac{e^{-3x}}{3^2} - \dots \right) \quad x > 0$$

One can think of  $h\nu_0 = e\phi$  as a "threshold energy" and  $x$  as the amount by which the energy of an incoming photon exceeds the threshold energy measured in units of thermal energy  $kT$ . It is helpful to make two observations about Fowler's result: First,  $I \propto f(x)$  for constant temperature  $T$ , and second, for large  $x$  (say  $x \geq 8$ ), only one term in  $f(x)$  is important, the

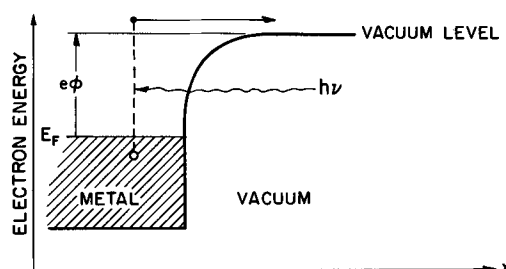


Fig. 1. Photoelectric emission into vacuum

<sup>1</sup> Much of the recent interest in the properties of insulators, particularly thin films, has been engendered by the technological importance of insulating layers in MIS (metal-insulator-semiconductor) charge controlled devices.

<sup>2</sup> There are other aspects of internal photoemission which, although important, are not covered in this paper. Among these are the use of internal photoemission in the study of barrier heights at metal-semiconductor contacts and at semiconductor heterojunctions, and in the study of hot electrons and holes in metals. A more general treatment including an historical background of "Injection by Internal Photoemission" by Richard Williams will appear as a chapter in a forthcoming volume of the series "Physics of III-V Compounds."

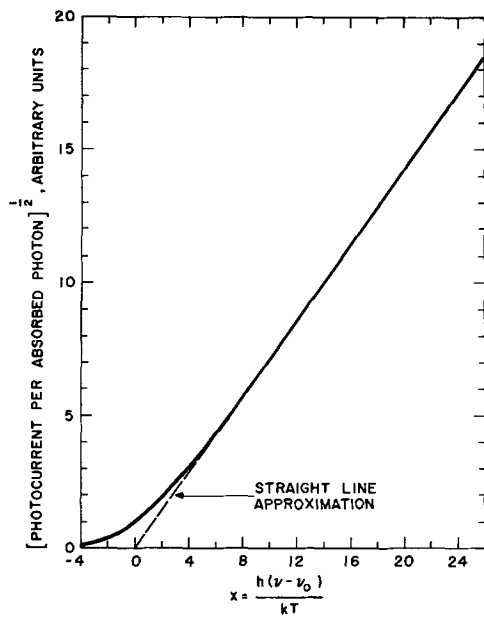


Fig. 2. Square root of the yield [or  $f(x)$ ] vs. photon energy above threshold.

$x^2$  term. Thus, if one plots the value of the square root of  $f(x)$  vs.  $x$ , a straight line is obtained for large  $x$ .

In Fig. 2, the square root of  $f(x)$  is plotted against  $x$ . The curvature at the bottom of the plot is due to the spread in the occupation probability of the electron energy states near the Fermi level in the metal due to finite temperature; the curved portion is sometimes referred to as a "thermal tail." In practice, in order to evaluate the threshold energy, one would plot the square root of the experimentally determined values of the photocurrent per photon, against  $x$  and extrapolate the best straight line through the data points to an intersection with the  $x$ -axis.

**Semiconductors.**—The foregoing discussion of photoemission applies only to metals. The considerably more complex theory of photoemission from semiconductors has been treated by Kane (3). He found that for a "real" semiconductor (like silicon) it was necessary to consider a variety of photoelectron production and scattering mechanisms. He concluded that the yield (electrons emitted per photon absorbed) may vary as the  $p$  power of photon energy above the threshold, where  $p$  may have the value 1, 3/2, 2, or 5/2 depending on the excitation and scattering mechanisms involved. In addition, more than one mechanism may be involved in the same energy range, complicating matters still further. If there is a space charge layer in the semiconductor adjacent to the emitting surface, this may also significantly affect the energy dependence of the yield curve.

In Kane's work it was assumed that the semiconductor was at  $0^\circ\text{K}$  and that the photoemitted electrons originated from the valence band and/or filled surface states. The expected effect of finite temperature would be in some cases to produce a "thermal tail" on the curve of  $(\text{yield})^{1/p}$  vs.  $x$  such as that found by Fowler in the case of photoemission from metals.

It is also possible to treat the case of photoemission from a narrow band of filled levels, e.g., a somewhat degenerate conduction band. In this case it can be shown that to a good approximation, the yield should increase linearly with photon energy above threshold (4).

An example of photoemission from tungsten and silicon from the work of Gobeli and Allen (5) is shown in Fig. 3. In each case the square root of the yield is plotted against photon energy. It is clear that for both tungsten and heavily doped p-type silicon an excellent straight line dependence is obtained allow-

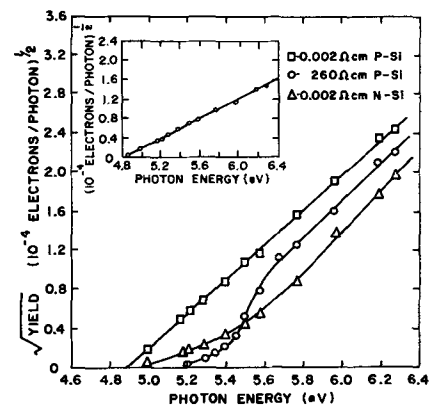


Fig. 3. Square root of the yield vs. photon energy for tungsten and silicon [from ref. (5)].

ing the unambiguous evaluation of a threshold energy. The heavily doped n-type silicon exhibits a straight line dependence of photon energies far above threshold with a large tail at lower energy values. The tail is due to photoemission from filled surface states while an extrapolation of the straight line portion would give the threshold for photoemission from the valence band. The high resistivity silicon presents a much more complicated situation to analyze; the experimentally determined yield is due to a combination of three mechanisms each having a different energy dependence and each being dominant in a different energy range.

This brief look at photoemission into vacuum may be summarized in a crude way by saying that although it is possible for the results to be rather complicated, it is also possible to arrange an experiment that gives results which are simple to analyze, e.g., photoemission from metals or heavily doped silicon. Looking ahead for a moment to the design of an experiment involving internal photoemission, it is advantageous to bear in mind those electrodes from which the electron emission yield dependence on photon energy is a relatively simple one.

### Internal Photoemission

**Possible processes.**—In Fig. 4 the electron energy is plotted vs. distance normal to an interface for 6 dif-

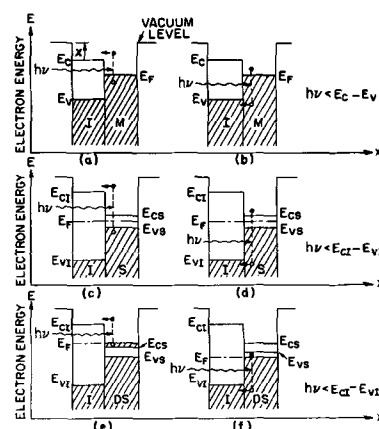


Fig. 4. Some internal photoemission processes: (a) electrons from a metal into an insulator conduction band; (b) holes from a metal into an insulator valence band; (c) electrons from a semiconductor valence band into an insulator conduction band; (d) holes from a semiconductor conduction band into an insulator valence band; (e) electrons from a degenerate n-type semiconductor conduction band into an insulator conduction band; (f) holes from a degenerate p-type semiconductor valence band into an insulator valence band. The symbols I, M, S, and DS in the figure denote, respectively, insulator, metal, semiconductor, and degenerate semiconductor.

ferent examples of the internal photoemission process. In Fig. 4 (a) is illustrated the photoemission of an electron from a metal into an insulator. A photon is absorbed in the metal transferring its energy to an electron which is then able to enter the insulator conduction band. Note that the threshold energy for this process  $e\phi_T$  is, according to this simple model (6), the vacuum value of the metal work function  $e\phi_M$  minus the electron affinity,  $\chi$ .

$$e\phi_T = e\phi_M - \chi \quad [1]$$

We may think of  $e\phi_T$  as an effective work function for internal photoemission i.e., as a work function of the metal with respect to the insulator conduction band.

In Fig. 4 (b) the process of "hole emission" from a metal into an insulator is shown. Here an electron receives the photon energy and undergoes a transition to a previously unoccupied state in the conduction band, leaving a deep hole, which may then enter the insulator valence band.

In Fig. 4 (c) an electron is photoemitted from the valence band of a semiconductor to the conduction band of an insulator. In Fig. 4 (d) a hole is photoemitted from the conduction band of a semiconductor to the valence band of an insulator. If the semiconductor is degenerate, two other processes are possible; the photoemission of an electron from the conduction band of the degenerate n-type semiconductor as shown in Fig. 4 (e) and the photoemission of a hole from the valence band of a degenerate p-type semiconductor as shown in Fig. 4 (f).

Although it is obvious, it may be worth mentioning that the internal hole photoemission processes (b), (d), and (f) have no vacuum analogues.

All of the internal photoemission processes discussed thus far have been "volume" processes. It is, in principle at least, possible to have photoemission of holes or electrons from internal surface states at a semiconductor-insulator interface.

**Experiments.**—The experiments to be described in this section (7-13) have been carried out mainly on layers of  $\text{SiO}_2$  which were fabricated by thermal oxidation of silicon in steam. The experimental techniques, however, should be applicable quite generally to the study of insulators.

A typical experimental arrangement is shown in Fig. 5. The silicon dioxide layer (of several microns thickness) is sandwiched between a degenerate silicon base wafer and a semitransparent evaporated metal counterelectrode. The metal is positively biased with respect to the silicon so that electrons photoemitted into the oxide from the silicon will drift through the oxide toward the metal counterelectrode. The electrometer measures the resultant current flow in the external circuit.

The corresponding energy band diagram is shown in Fig. 6. The diagram is qualitatively correct but quantitatively somewhat out of scale.

The plot of photocurrent versus photon energy shown in Fig. 7 is a typical one. The undulations in

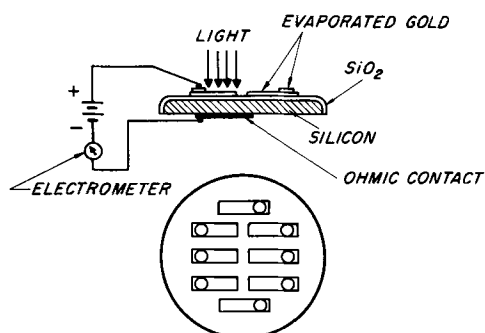


Fig. 5. Schematic circuit diagram and construction drawing of sample.

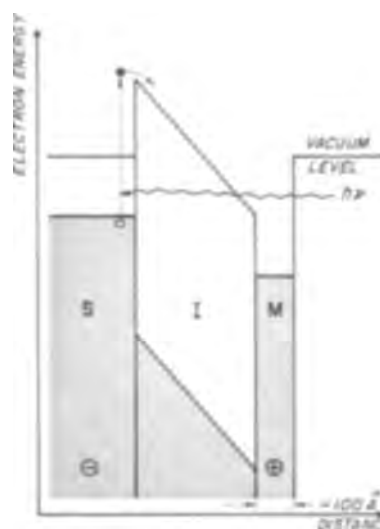


Fig. 6. Energy band diagram of a metal-insulator-semiconductor sandwich with bias voltage applied (metal  $\oplus$ ).

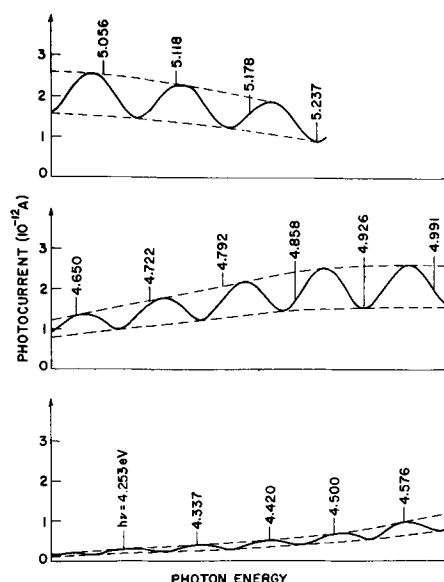


Fig. 7. Photocurrent vs. photon energy for a silicon-silicon dioxide-gold sandwich with positive bias applied to the gold.

the photocurrent are due to the silicon-oxide-metal sandwich structure acting as an optical interferometer. It is easy to show (9) that the thickness  $l$  of the oxide layer can be computed from the formula

$$l = Mhc/2n(E_{N+M} - E_N) \quad [2]$$

where  $h$  is Planck's constant,  $c$  is the velocity of light in vacuum,  $n$  is the index of refraction, and  $E_N$  and  $E_{N+M}$  are the photon energies corresponding to the photocurrent peaks when the layer is  $N$  and  $N+M$  half-wavelengths thick, respectively. Thus, the oxide thickness value falls out of the internal photoemission measurement as a "bonus."

If an envelope of the photocurrent is normalized with respect to the photon flux, the yield curve is obtained, and this may be analyzed to obtain a threshold value. This will be done shortly but first consider the effect of reversing the bias voltage as shown in Fig. 8. Here the field is in the opposite direction and electrons photoemitted from the metal will drift through the oxide toward the silicon. A spectral distribution of the photocurrent similar to but not identical with that in Fig. 7 is obtained.

In Fig. 9 the square root of each of the yield curves obtained from the photocurrent envelopes is plotted against photon energy. The threshold value obtained



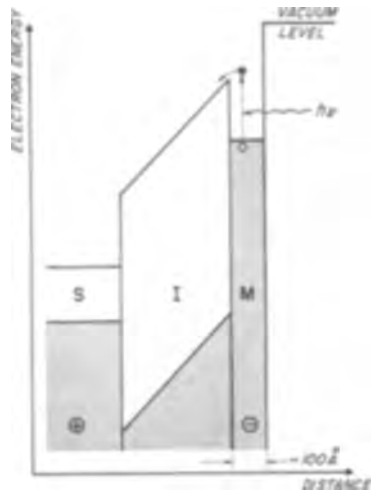


Fig. 8. Energy band diagram of a metal-insulator-semiconductor sandwich with bias voltage applied (metal  $\ominus$ ).

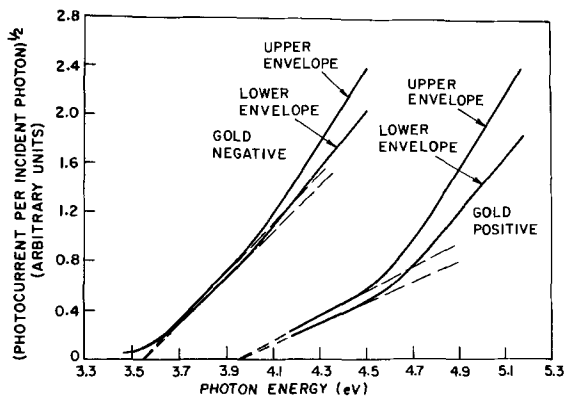


Fig. 9. Envelopes of (photocurrent per incident photon)<sup>1/2</sup> vs. photon energy for a silicon-silicon dioxide-gold sandwich.

with the gold negative is associated with the energy difference between the conduction band in the oxide and the Fermi level in the metal at the metal-SiO<sub>2</sub> interface (8, 9). The threshold energy with the silicon negative is associated with the energy difference between the conduction band in the oxide and the valence band in the silicon at the silicon-SiO<sub>2</sub> interface (7, 8). In a similar manner, the threshold energy for photoemission of electrons into SiO<sub>2</sub> from a variety of metals may be determined as shown in Fig. 10. If the threshold energies are plotted against the metal work functions, the value of the electron affinity  $\chi$

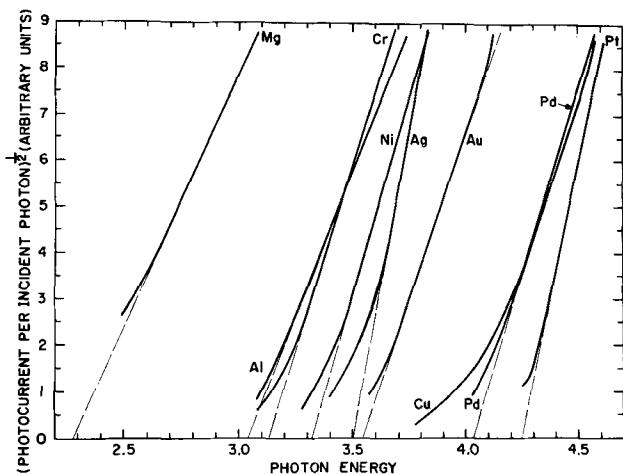


Fig. 10. Envelopes of (photocurrent per incident photon)<sup>1/2</sup> vs. photon energy for nine metals.

may be determined from Eq. [1] and it turns out to be 1.0 eV for silicon dioxide (9).

It is important in experiments of this type to ask the following question: Are the observed currents due to the photoemission of holes or electrons? In the work on SiO<sub>2</sub> the answer was obtained from the observation that the threshold energy was dependent upon which metal was used for the counterelectrode *only when the metal was negative*; thus it was known that in this case the carriers came from the metal and that the carriers photoemitted from the metal must have been electrons. When the metal was positive the threshold energy was independent of which metal was used and the carriers must have been coming from the silicon which was negative and were therefore electrons.

In order to unambiguously observe hole emission into silicon dioxide it was necessary to suppress the electron emission from the negative electrode. This was accomplished by using water as the negative electrode as shown in Fig. 11. Since water is quite transparent in the ultraviolet region of the spectrum for photon energies less than 6 eV, the photon energy cannot be transferred to the electrons in the water and no electrons can be photoemitted from the water. When the electron emission was suppressed in this way, a new and higher threshold energy was obtained corresponding to the photoemission of holes from silicon into silicon dioxide (10). This threshold energy is interpreted as the energy difference between the silicon conduction band and the oxide valence band at the silicon-SiO<sub>2</sub> interface.

At an abrupt interface between a metal and an insulator the photoemission threshold energy is a function of the voltage applied across the insulator because an electron (or hole) in the insulator near the interface is acted on by two forces, one due to the field in the insulator and the other due to the image charge induced in the metal. This is illustrated in Fig. 12. The resultant lowering of the work function (Schottky effect) is according to simple electrostatic theory

$$\Delta\phi = \frac{1}{2} (eE/\pi K\epsilon_0)^{1/2} \quad [3]$$

where  $E$  is the electric field in the insulator,  $e$  is the magnitude of the electronic charge,  $\epsilon_0$  is the permittivity of free space, and  $K$  is the effective image force relative dielectric constant. A similar description can be given for an abrupt interface between a semiconductor and an insulator. In Fig. 13 the decrease in the photoelectric threshold energy is plotted against the square root of the electric field strength in the insulator at 8 different points for each of 3 samples. The theoretical Schottky effect is indicated by the three straight lines, each corresponding to a particular value

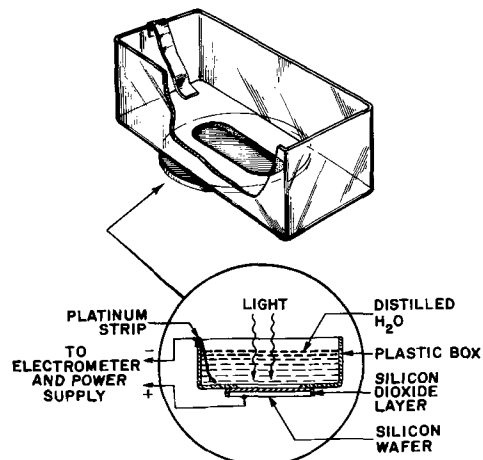


Fig. 11. Silicon-silicon dioxide-water cell for photoelectric measurements.

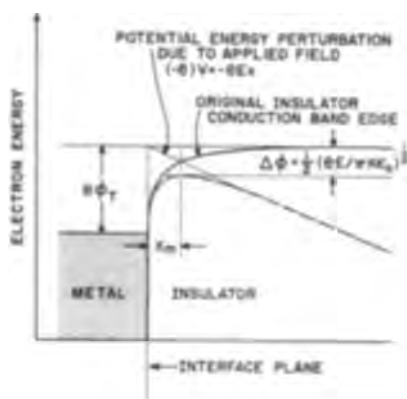
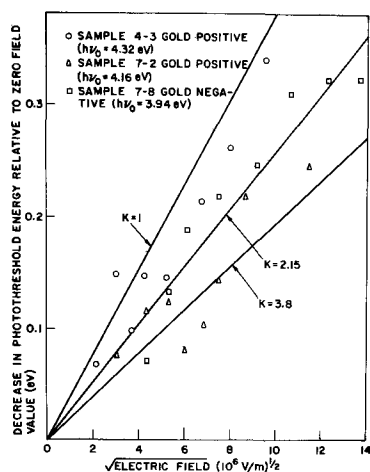
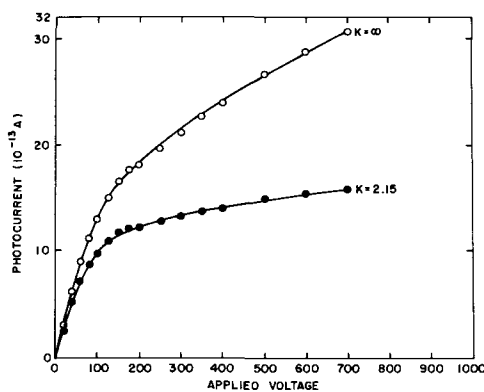


Fig. 12. Schottky effect at a metal-insulator interface

Fig. 13. Decrease in phototreshold energy vs. (electric field)<sup>1/2</sup>

of  $K$ . The value  $K = 1$  would be correct for emission into a vacuum and the value  $K = 3.8$  is the low-frequency relative dielectric constant for silicon dioxide. The value  $K = 2.15$  corresponds to the average of the slopes of the best straight-line fits for each sample. Presumably the photoemitted carrier passes through the potential maximum in too short a time for the low-frequency dielectric constant to be a valid parameter for describing the polarization of the oxide. Similar measurements (but with less scatter in the results) were subsequently carried out by Mead *et al.* (11) who inferred from their data the value  $K = 2.1$ .

The shift in the photoemission threshold energy with electric field has been used by Williams to observe the presence and drift of positive ions in silicon dioxide layers (12). There were two steps in the experiment. First, the oxide layer to be studied was incorporated into a sandwich structure as shown in Fig. 5. The threshold energy for photoemission of electrons from the p-type silicon into the silicon dioxide at a particular value of applied voltage was then determined. The second step was to heat the sample (to 200°C) with a positive voltage applied to the gold counter electrode. The sample was then cooled to room temperature (maintaining the applied field). The threshold energy for electron photoemission was then redetermined under the original conditions; it was found to have lowered dramatically. The mechanism responsible for the threshold shift was the redistribution of positive ion impurities in the oxide. These ions became more mobile due to the rise in temperature and drifted under the influence of the applied field, accumulating in the oxide near the silicon-SiO<sub>2</sub> interface. This produced a strong electric field in the oxide adjacent to the interface lowering the photoemissive threshold by Schottky effect and possibly by inverting the silicon at the surface from p-type to degenerate n-type giving

Fig. 14. Photocurrent vs. applied voltage. ○ -raw data (uncorrected), ● -corrected values using  $K = 2.15$ .

rise to photoemission from the silicon conduction band as well as the valence band. Thus, internal photoemission can be a useful tool for the detection of mobile ionic impurities in insulators.

If, for a given photon energy, the photocurrent is measured as a function of voltage across the sample, a curve is obtained which rises steeply at first, then bends toward the voltage axis but continues to rise at a decreasing rate. A typical set of data is shown in Fig. 14. The upper set of points (open circles) is the raw data. The current rises with increasing sample voltage for two reasons: (i) the increasing field lowers the energy threshold for photoemission by Schottky effect (as discussed previously) and thus, causes an increase in the current photoemitted into the oxide, and (ii) the mean drift range (or Schubweg) of the carriers in the oxide increases directly with the electric field enhancing the photocurrent measured in the external circuit. It is possible to separate the two effects if the form of one of them is known. Here the photocurrent has been corrected to eliminate the Schottky effect assuming that the yield is proportional to the square of the photon energy above the threshold and an effective value for the image force relative dielectric constant  $K = 2.15$ . These are the filled in circles.

The mean drift range (or Schubweg)  $w$  is the average distance that the carriers drift in the electric field before they are captured, *i.e.*, immobilized due to trapping or recombination. Thus

$$w_{\pm} = \mu_{\pm} E \tau_{\pm} = \mu_{\pm} \tau_{\pm} V/l \quad [4]$$

where  $\mu$  is the mobility (subscript + for holes and - for electrons),  $V$  is the applied voltage,  $l$  is the oxide thickness, and  $\tau$  is the mean time an electron spends in the oxide conduction band (or a hole spends in the valence band) before immobilization by deep trapping. If  $V_0$  is defined as that value of  $V$  at which  $w = l$ , then the theoretical form of the corrected photocurrent  $I$  vs. the applied voltage  $V$  should be

$$I/I_0 = (V/V_0) (1 - e^{-V/V_0}) \quad [5]$$

where

$$V_0 = l^2/\mu\tau \quad [6]$$

and  $I_0$  is the photoemitted current in the absence of Schottky effect.

The experimental data for electron emission for three samples are shown in Fig. 15 fitted to the theoretical curve by adjusting  $I_0$  and  $V_0$ . The results of this type of experiment indicate that  $\mu_{-}\tau_{-} \sim 10^{-9}$  cm<sup>2</sup>/v for electrons and  $\mu_{+}\tau_{+} \sim 10^{-10}$  cm<sup>2</sup>/v for holes.

Williams has used internal photoemission to study in some detail the transport and trapping properties of electrons in SiO<sub>2</sub> layers (7). By applying only a weak drift field in the oxide he found that most of the photoemitted electrons could be trapped rather than drifted entirely through the oxide. He then illumi-

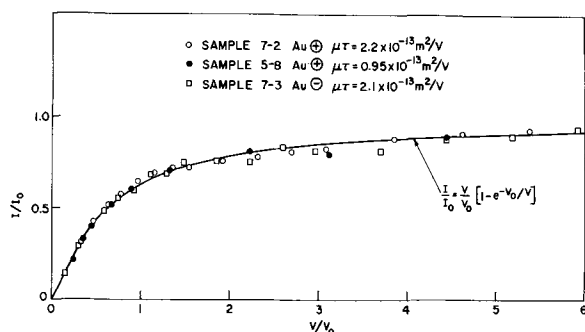


Fig. 15. Normalized photocurrent vs. normalized voltage

nated the sample with light of photon energy less than the photoemission threshold value releasing the trapped electrons. By measuring the released charge he determined that the trap density was  $\sim 3 \times 10^{14}/\text{cm}^3$ , a remarkably low number for a noncrystalline material. By measuring the spectral response of the charge release process he found a threshold value of 2.0 eV indicating that this was the minimum depth of the traps below the oxide conduction band in his samples. By studying the kinetics of the trapping process, he was able to determine a value for the capture cross section of the traps,  $S = 1.3 \times 10^{-12} \text{ cm}^2$ . This was then used to estimate a mobility value. The value was either 17 or 34  $\text{cm}^2/\text{v-sec}$  depending on whether the trapping center was doubly or singly charged. The actual charge on the trapping center is not known, leaving an ambiguity in the mobility of a factor of two. Nevertheless, the fact that the mobility is of the order of or greater than 10  $\text{cm}^2/\text{v-sec}$  indicated that another, more direct mobility measurement might be made and, in fact, inspired the development of a modified Hall measurement particularly suited for use with insulator films (13).

A cross-sectional view of the experimental Hall effect arrangement is shown in Fig. 16. The metal counter electrodes are opaque and define the light pattern on the photoemitting silicon surface. If the potentials applied to the counter electrodes are equal and the incoming light is of normal incidence, the circuit is balanced when there is no magnetic field applied, and the electron paths follow the electric field lines as shown. If a magnetic field is applied normal to the plane of the figure, the electron paths will be altered and the currents to the two counter electrodes will no longer be balanced; more current will flow to one than to the other. The difference between the counter electrode currents can then be quantitatively related to the mobility of the electrons in the oxide. The average value for the mobility of electrons in  $\text{SiO}_2$  determined in this way was  $\sim 29 \text{ cm}^2/\text{v-sec}$ . This value is in good agreement with the estimate previously obtained by Williams from trapping studies.

Although the emphasis in this discussion has been on  $\text{SiO}_2$ , the experimental techniques described and others employing internal photoemission as the basic tool have been and are being used to investigate other insulators. Among these are the oxides of aluminum, niobium, tantalum, and titanium, as well as some organic materials such as anthracene and tetracene. Also, internal photoemission has been used to investigate the properties of diamond, silicon carbide, silicon, germanium, and many of the III-V, II-VI, and I-VII compounds. Whether some of these materials should be considered insulators or semiconductors is of course a moot point which need not concern us here.

There are, of course, other experiments in which internal photoemission has been used as an investigative tool. Although a complete discussion of them is beyond the scope of this paper, there are two which

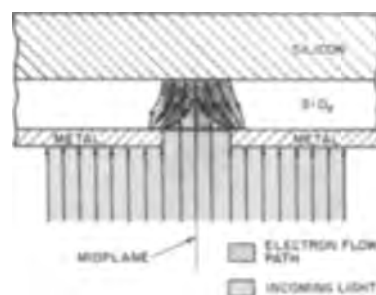


Fig. 16. Cross-sectional sketch of sample geometry and electron paths for a Hall-effect electron mobility measurement in a silicon dioxide layer. The magnetic field, when applied, is normal to the plane of the figure.

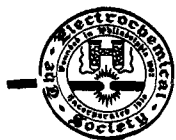
should at least be mentioned because it seems likely that more use will be made of them in the future. One is the work of Williams and Dresner (14) who utilized the spectral variation of internal photoemission to obtain information about the structure of the multiple narrow energy bands in an organic insulator, anthracene. The second is a study of the variation of electron photoemission from Al into thin (40-100 Å)  $\text{Al}_2\text{O}_3$  films with photon energy and electric field. Work on this subject has been described by several groups (15-18). Their results were interpreted in terms of the effective work function at the interface and the mean free path for electrons in the  $\text{Al}_2\text{O}_3$  conduction band. There is considerable disagreement in the results. For example, Schuermeyer *et al.* interpreted their results in terms of an electron-phonon scattering mechanism and thereby inferred a mean free path of 10 Å. On the other hand, Ludwig and Korneffel obtained data which could be interpreted only in terms of a much longer mean free path. Some or all of the discrepancies may of course be due to differences in the  $\text{Al}_2\text{O}_3$  layers. Despite the apparent disagreement in results, the techniques employed show promise for use in the study of other very thin insulating films.

In summary, a number of experimental techniques have been described in which internal photoemission can be used as a very effective tool for the study of insulator properties.

Manuscript received June 17, 1968. This paper was presented at the Boston Meeting, May 5-9 1968, as Paper 11.

#### REFERENCES

1. R. H. Fowler, *Phys. Rev.*, **38**, 45 (1931).
2. A. L. Hughes and L. A. DuBridge, "Photoelectric Phenomena," McGraw Hill Book Co., New York (1932).
3. E. O. Kane, *Phys. Rev.*, **127**, 131 (1962).
4. A. M. Goodman, *ibid.*, **152**, 785 (1966).
5. G. W. Gobeli and F. G. Allen, *ibid.*, **127**, 141 (1962).
6. N. F. Mott and R. W. Gurney, "Electronic Processes in Ionic Crystals," 2nd ed., Oxford, Clarendon Press, London (1948).
7. R. Williams, *Phys. Rev.*, **140**, A569 (1965).
8. A. M. Goodman, *ibid.*, **144**, 588 (1966).
9. A. M. Goodman and J. J. O'Neill, Jr., *J. Appl. Phys.*, **37**, 3580 (1966).
10. A. M. Goodman, *Phys. Rev.*, **152**, 780 (1966).
11. C. A. Mead, E. H. Snow, and B. E. Deal, *Appl. Phys. Letters*, **9**, 53 (1966).
12. R. Williams, *J. Appl. Phys.*, **37**, 1491 (1966).
13. A. M. Goodman, *Phys. Rev.*, **164**, 1145 (1967).
14. R. Williams and J. Dresner, *J. Chem. Phys.*, **46**, 2133 (1967).
15. A. I. Braunstein, M. Braunstein, and G. S. Picus, *Phys. Rev. Letters*, **15**, 956 (1965).
16. K. W. Shepard, *J. Appl. Phys.*, **36**, 796 (1965).
17. W. Ludwig and B. Korneffel, *Phys. Stat. Sol.*, **24**, K137 (1967).
18. F. L. Schuermeyer, C. R. Young, and J. M. Blasingame, *J. Appl. Phys.*, **39**, 1791 (1968).



### Alkali Metal Ion Sources

Julius Perel

*Electro-Optical Systems, Inc., Pasadena, California*

#### ABSTRACT

The development of alkali metal ion sources has been greatly accelerated in the past decade because of the interest in these ions in basic research and more important because of cesium ion engine development for space propulsion. Three techniques used to generate alkali metal ions are described. The porous tungsten surface ionization source, highly developed for electric propulsion, has generated ion beams of over 1 amp of cesium and is being used to produce other alkali metal ions. The electron bombardment engine, or low-pressure discharge source, has produced high currents of  $\text{Cs}^+$ ,  $\text{Na}^+$ , and  $\text{Hg}^+$  and is used to generate other ions. The liquid metal hydrodynamic spray technique, also studied as an electric propulsion thruster, is used to produce high current densities from a very small source and generates some molecular ions. The operational levels of the various engines and their modification for use as laboratory ion sources are described.

*Brief survey.*—Alkali metal ion source technology has been greatly advanced in order to use high-velocity ions to produce thrust from ion engines for manipulating and propelling space and orbital vehicles. The aims in the development of ion engines which do not differ greatly from those in developing ion sources are examined in this report with the emphasis placed on the generation of alkali metal ions and the description of ion engines and their features as ion sources.

The two most used methods of generating ions for ion engines are surface ionization and electron impact ionization. Efficient surface ionization is applicable for elements having low ionization potentials such as the alkali metals. The technique of ionization by electron impact in a gaseous discharge is applicable for producing a wide range of ion species including molecular ions. A third method, discussed in this report, is the generation of charged particles from the surface of a liquid by the application of high electric fields. Heavy charged particles are generally produced from organic liquids while ions are generally produced from liquid metals, with the alkali metals being particularly suitable using this latter method.

The alkali metals comprise a family of elements each of which have a single electron in the outer or valence shell. The ease with which the single outer electron can be removed to form an ion is indicated by the low first ionization potentials which are listed in Table I. The second ionization potentials are higher than the first by factors ranging from 15 to 5 going from Li to Cs. Therefore singly ionized alkali metals can be generated without producing an appreciable number of doubly ionized species in a low voltage discharge. In addition the first ionization potentials are somewhat less than refractory metal work functions and/or surface work functions increased by adsorbed layers of  $\text{O}_2$ , a condition required for efficient surface ionization.

Table I also contains the atomic number, atomic weight, and melting points of the alkali metals. Cs and Rb are highly reactive and must be handled under an inert atmosphere. The others can be stored in oil or kerosene and can be handled in air under relatively dry conditions with inert atmosphere handling recommended.

*Ion engine and ion source characteristics.*—An ion engine is characterized in terms of parameters such as thrust, power, weight, efficiency, etc. Since an engine is designed to operate on a space vehicle, the emphasized features include reliability, long life, and low power consumption. Laboratory lifetime tests have shown that engines can operate reliably for thousands of hours with little degradation in performance.

Ion engine accelerating voltages are usually limited to several kilovolts because of mission considerations and to minimize breakdown problems. With these constraints in voltage the desired currents and thrust levels are obtained by using large ion emission areas and multibeam electrode systems. Accel-decel electrode configurations are typically used with ions generated by an ionizer at +3 kv, an accel electrode at -1 to -8 kv, and possibly a decel electrode at ground potential. The accel serves as an electron trap to prevent electrons in the ion beam from backstreaming to the ionizing region and sometimes to increase the

REVIEW  
SECTION

Table I. The Alkali Metals

Element	Atomic No.	Atomic weight, amu	Melting point, °C	Ionization potential, ev
Lithium	3	6.94	186	5.39
Sodium	11	22.99	97.7	5.14
Potassium	19	39.1	63	4.34
Rubidium	37	85.48	39	4.18
Cesium	55	132.91	28	3.89

engine perveance in order to extract high beam currents.

In space both current neutralization and beam space charge neutralization, required to obtain thrust, are achieved by electron emission. Emitted electron currents must be equal to the ion beam current to prevent excessive charging of the spacecraft. A large rise in the potential of a spacecraft with respect to the ambient potential degrades the ion emission energy and could ultimately result in beam turn-around with loss of thrust. Beam space charge causes the ions in the beam to diverge and could also result in a degradation of thrust. Thus, the electrons neutralize the ion beam, which results in a highly ionized, low-density plasma ( $\approx 10^9$  particles/cm<sup>3</sup>). Electrons are obtained from a separate source located near the ion engine, with emission regulated by the positive potential of the ion beam.

Parameters which characterize an ion engine as a thruster system are examined in terms of ion source operational parameters. The thrust ( $F$ ) produced by an ion engine is the force required to accelerate a beam of particles to a velocity ( $v$ ) and is given by

$$F = \dot{m}v \quad [1]$$

where  $\dot{m}$  is the ion beam mass flow rate. The mass flow rate in terms of the ion beam current ( $i$ ) is given by

$$\dot{m} = \frac{m}{e} i \quad [2]$$

where  $m$  is the ion mass and  $e$  is the charge, and  $e/m$  is the particle charge-to-mass ratio.

In terms of measurable operating parameters, the thrust is given by

$$F = (2m/e)^{1/2} i V^{1/2} \quad [3]$$

where  $V$  is the accelerating voltage and  $eV = mv^2/2$ .

Equation [3] shows the advantage, in achieving greater thrust, of using particles having a low charge-to-mass ratio such as Cs and Hg, which are  $7.21 \times 10^5$  and  $4.77 \times 10^5$  coulombs/kg, respectively. Even lower charge-to-mass ratios are achieved by generating heavy particles from a liquid using the electrohydrodynamic technique. Small ion engines have been developed that produce a few micropounds of thrust, with large ones producing thrusts up to a few tenths of a pound. For example, at an accelerating voltage of 4 kv, a Cs ion engine requires an ion beam current of 42 ma to produce 1 mlb (0.454g) of thrust.

Another term used to characterize the operation of an ion engine is the specific impulse ( $I_{sp}$ ), defined as the ratio of thrust to propellant weight flow rate ( $\dot{M}g$ ) and given by

$$I_{sp} = \dot{m}v/\dot{M}g \quad [4]$$

The term  $\dot{M}$  is the total mass flow rate and is equal to the ion mass flow rate plus the neutral particle flow rate, with  $g$  being the gravitational acceleration at the surface of the earth. This latter term is a constant independent of operating environment such as space and is used to relate the engine operation to the weight of the propellant as part of the payload for liftoff from the earth. The parameters discussed above are sufficiently interdependent so that a change in one affects the others. Optimization is made by trade-off considerations. For example, the propellant weight

and power available, determined by mission requirements, can be used to select an ion engine type and its operating levels.

Another important parameter is the mass utilization efficiency ( $\eta$ ), given by  $m/\dot{M}$ . When  $\eta \approx 1$ , as in the case for surface ionization engines, the specific impulse is proportional to the ion exhaust velocity. Using the operating parameters for the thruster example given above, the specific impulse is approximately 8000 sec, and about 4 lb of propellant is required for continuous operation during 1 year with a total impulse of  $3 \times 10^4$  lb-sec.

Mass utilization efficiencies generally range from 85% to nearly 100%. This efficiency is high enough in terms of propellant usage, but low neutral fractions ( $1 - \eta$ ) are required for long-life ion engines, since the emission of neutral particles contributes to the erosion of ion engine electrodes, which can severely limit the lifetime. A slow ion, generated in the inter-electrode region by a charge transfer collision between a fast ion and a slow atom, is likely to impinge on an electrode and produce sputtering. This removes electrode material, weakening the electrode, and the sputtered material may form harmful deposits on sensitive surfaces such as insulators, ionizers, and cathodes.

#### Surface Ionization Sources

*Fundamentals of surface ionization.*—The surface ionization process of ion generation depends primarily on the difference between the work function of the surface and the ionization potential of the atoms to be ionized. The process can be illustrated by considering the metal to be a potential well filled with electrons up to an energy level called the Fermi level. The potential difference between the Fermi level and the space just outside the metal is the energy that is required to remove an electron from the metal and is known as the work function of the metal ( $\Phi$ ). The energy required to remove an electron from an atom is known as the ionization potential ( $I$ ).

When the work function of the metal is greater than the ionization potential of an atom located at the metal surface (i.e.,  $\Phi > I$ ), the most loosely bound atomic electron has a high probability of transferring to the metal so that the particle is desorbed from the surface as an ion. The ratio of the number of ions ( $n_p$ ) to the number of atoms ( $n_a$ ) desorbed is given quantitatively by the Saha-Langmuir equation (1) which may be expressed as

$$\frac{n_p}{n_a} = \left( \frac{w_p}{w_a} \right) \exp [(\Phi - I)/kT] \quad [5]$$

where the weighting factor for each state ( $w$ ) is equal to  $2J + 1$ , with  $J$  being the inner quantum number (or total angular momentum) of the ion or atom, and  $T$  the temperature.

For alkali metal atoms  $J = 1/2$ , while for alkali metal ions  $J = 0$  so that  $w_p/w_a = 1/2$  and Eq. [5] reduces to

$$\frac{n_p}{n_a} = \frac{1}{2} \exp \left( \frac{\Phi - I}{kT} \right) \quad [6]$$

The ionization potentials of the alkali metals are well defined and are given in Table I. The work function of a metal is not so well ordered and depends on the conditions at the surface of the metal. The work function of "clean" tungsten is about 4.6 ev, but the presence of adsorbed atoms on the surface can increase or decrease the work function depending on the characteristics of the composite surface produced. The adsorption of alkali metal atoms on a tungsten surface tends to decrease the effective work function, the amount of decrease depending on the concentration of alkali atoms on the surface. This concentration is defined in terms of the fraction of a monolayer coverage ( $\theta$ ), where a monolayer on tungsten is about  $4.5 \times 10^{14}$  atoms/cm<sup>2</sup>. The effective work function of

tungsten decreases very rapidly as the coverage exceeds a few per cent of a monolayer so that the ratio of ions to atoms desorbed from the composite surface decreases greatly with small changes in coverage. The coverage is therefore quite critical, and it is necessary to control it by controlling temperature and/or the rate at which alkali metal atoms are supplied to the surface.

The effect of coverage on ion and atom emission rates from solid tungsten with cesium atoms supplied to the surface is shown in Fig. 1. The ion emission rate increases nearly linearly up to a coverage of about 1% of a monolayer with only a small increase in the atom emission rate. As the coverage increases, the effective work function of the surface decreases, with a decrease in ion emission occurring above a 2% coverage. Here an instability occurs. As the coverage increases, the ion emission rate decreases, further increasing the coverage, and so on. Thus, the emission mode changes from point a to point b, and the ion emission drops sharply. Surface ionization is inefficient at coverages above point a. With increasing temperatures the curves increase appreciably toward high emission rates, and the peak near point a shifts only slightly toward higher coverage.

Efficient and stable ion emission is obtained at or below 1% of a monolayer. In this coverage region, the mean time that a particle remains on the surface before desorption is approximately 100 times longer for the emission of an atom than an ion. The ion desorption time,  $\tau_i$ , decreases with increasing surface temperature ( $T$ ) and is given by

$$\tau_i = \tau_0 \exp(Q/kT) \quad [7]$$

where  $Q$  is the energy required to desorb an ion, and  $\tau_0$  is the extrapolated desorption time at  $T^{-1} = 0$ .

In this low coverage region the emitted ion current density,  $j$ , as a function of coverage,  $N$  in atoms/cm<sup>2</sup> is given by

$$j = eN/\tau_i \quad [8]$$

where  $e$  is the charge of the ion and the  $\tau_i$  dependence on the temperature is given by Eq. [7]. To determine an approximate ion emission upper limit, the value of  $N$  at 1% of a monolayer is about  $4.5 \times 10^{12}$  particles/cm<sup>2</sup>. Desorption measurements extrapolated to 1400°K show the ion desorption time ranging from  $2 \times 10^{-5}$  to  $10^{-4}$  sec with variations probably due to surface contamination (2, 3). Using Eq. [8] to find  $j/e$ , the

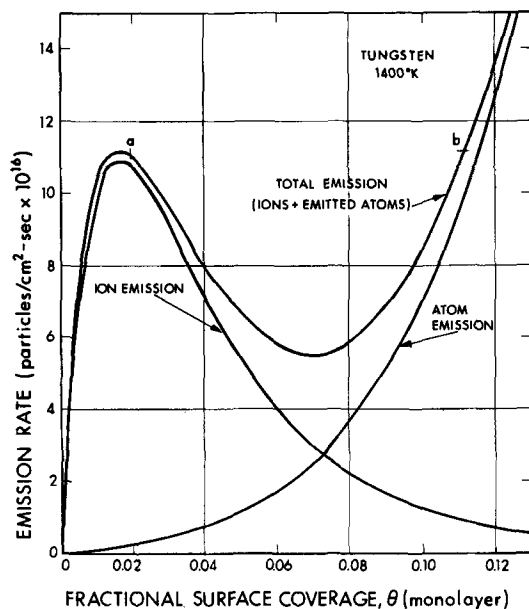


Fig. 1. Cesium ion and atom emission from a tungsten surface as a function of the surface coverage in fraction of a monolayer. The region of stable and efficient ion emission operation is below 0.02 of a monolayer.

upper limit ion emission rate at this temperature ranges from  $4.5 \times 10^{16}$  to  $2.25 \times 10^{15}$  ions/cm<sup>2</sup>-sec, which is consistent with the curve of Fig. 1.

In the operation of a surface ionization source, currents, voltages, and temperatures are first determined for stable and efficient modes. Consider a flow of Cs atoms onto a tungsten surface whose temperature is controllable. A sufficiently high voltage is applied between the ionizer and an ion collector to assure emission-limited current flow. At a fixed atom impingement rate  $\mu_1$  (atoms/cm<sup>2</sup>-sec), the temperature of the ionizer is decreased from a very high value. Figure 2 illustrates a typical ion emission current variation with the surface temperature. The ion current density does not vary appreciably with temperatures down to a value  $T_1$ . In this plateau region where the emission is stable, the ion current is approximately equal to the atom flow rate and the coverage is below about 1%. At the knee of a given curve for a temperature  $T_1$ , the coverage corresponds to the peak near point a in Fig. 1. With further lowering of the temperature, the ion current decreases sharply and the atom emission rate increases corresponding to operation at point b in Fig. 1. Reversing the process and increasing the temperature from a low value gives a very similar emission curve except that the knee is shifted toward a higher temperature. The hysteresis occurs because the change from high to low coverage operation requires higher temperatures to desorb sufficient atoms. At a higher atom flow rate,  $\mu_2$ , the  $T_1$  knee shifts toward a higher temperature ( $T_2$ ) as illustrated in Fig. 2. The lower temperature knee ( $T_1$ ) is the lowest temperature at which efficient surface ionization occurs for a given beam current density. The position of the knee can be estimated at each current density using Eq. [8] and desorption time data. Adsorbed contaminants such as O<sub>2</sub> or C can affect the position of the knees and/or the ionization efficiency.

An adsorbed layer of O<sub>2</sub> increases the work function of most refractory metals. The work function of tungsten can be increased to values over 6 eV with a stable layer of O<sub>2</sub>. Thus, oxygenating a hot tungsten surface makes it possible to efficiently produce ions from atoms whose ionization potentials are below 6 eV and somewhat less efficiently for those slightly above this value. This includes all of the alkali metals, indium, gallium, and several other elements which are not reactive with hot tungsten.

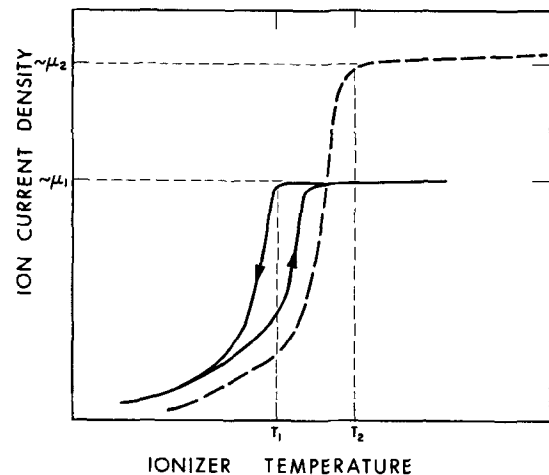


Fig. 2. Ion emission current density versus ionizer temperature for two atom impingement rates  $\mu_1$  and  $\mu_2$ . At an atom impingement  $\mu_1$  a hysteresis loop occurs between the decreasing and increasing temperature cycles. The knee of the curve at  $T_1$  is the lowest temperature for stable and efficient operation. The dashed curve shows the change with a higher atom impingement rate with  $T_2$  being the lowest stable and efficient operating temperature at  $\mu_2$ .

**Types of surface ionization sources.**—A surface ionization source is designed and operated according to the principles discussed in the section on Fundamentals of surface ionization and by Worlock (4). The ionizer temperature and the vapor feed rate are selected to maintain an adsorbed Cs coverage near 1% of a monolayer with the ion current emission limited.

Front feed techniques, in which an atom beam impinges on a heated solid refractory surface to produce ions, were found to be inadequate for ion engines because the ion beam interaction with the atoms caused excessive electrode erosion and other problems. A porous tungsten ionizer was introduced to avoid this troublesome interaction between the two beams (5).

The porous tungsten ionizer is made from slabs of sintered tungsten granules which are cut to shape and brazed into a crucible manifold. Cs vapor is distributed by the manifold to the rear of the porous tungsten, operated at about 1100°C. The vapor percolates through the hot ionizer and ions are formed at the surface and in the pores. Ionizers made of granules of different sizes and shapes have been fabricated and tested in an effort to obtain low neutral fraction and high performance at low power (6, 7).

In some cases ion generation was found to occur predominantly in the pores (8, 9) and resulted in ion current densities in excess of those obtained from a solid tungsten surface. Other refractory metals and alloys have also been investigated to find higher ionization efficiencies (10).

Figure 3 shows a typical surface ionization engine configuration with a zero-gravity feed system. The delivery rate is controlled by the feed rate heater, which determines the vapor pressure at the porous ionizer. The sastrugi ionizer shown in the diagram is a large slab of porous tungsten machine-ground to form spherical concavities. This shape was found to optimize focusing of the ion beam for the current densities and voltages of an operating ion engine (11-13). The ionizer is operated at positive voltages from 2 to 4 kv which determine the kinetic energy of the ions (i.e., exhaust velocity). The accel electrode is maintained at several kilovolts negative and the decel at ground potential. Individual beams are formed in the electrode region which merge to a single large beam several cm downstream. Figure 3 also shows a neutralizer which emits electrons into the ion beam to assure beam neutrality and to prevent charging of a spacecraft. Tests in vacuum chambers do not require neutralizers, since sufficient electrons for ion beam

neutralization are provided by secondary emission from ion impingement on the ion beam collector.

The reservoir and feed system shown in Fig. 3 are capable of operating on earth or under zero-gravity conditions. The reservoir is heated to above the Cs melting point, and the liquid Cs wets the radial fins which converge toward the porous rod. Since surface tension forces tend to minimize a surface area, the liquid flows toward the rod. It fills the porous rod for the same reason and is vaporized from the end by heat from the feed rate control heater. This type of feed system is used to supply Cs for the electron bombardment ion engine and for the discharge type neutralizer, both discussed in the section on Electron bombardment ion engines.

To provide a low neutral fraction and assure that the ion current is controlled by the feed rate, ion engines are operated in an emission-limited, although near a space-charge-limited mode. Design criteria stemming from analysis of space-charge-limited operation provide a good approximation for discussion.

Space-charge-limited current density ( $j$ ) given by the Child-Langmuir equation, can be written as

$$j = \frac{PV^{3/2}}{d^2} \quad [9]$$

where  $d$  is the distance between ionizer and accel electrode and  $P$  is the perveance in units of  $A/V^{3/2}$ . The perveance is proportional to the square root of the ion charge-to-mass ratio.

To avoid low fields at the beam axis near the ionizer, the aspect ratio, or ratio of  $d$  to the beam aperture diameter, is limited to values equal to or greater than one. For  $Cs^+$ , a perveance of about  $5 \times 10^{-9} A/V^{3/2}$  is a practical value for the extraction and acceleration of stable beams using circular apertures. Choosing an emission surface area equal to  $d^2$ , the current that can be obtained through a single aperture at 4 kv is about 1 ma (from Eq. [9]). At an emission current density of 2 ma/cm<sup>2</sup> the emission area is limited to about 0.5 cm<sup>2</sup> with an electrode spacing of about 0.8 cm. To achieve higher currents a multi-aperture electrode system is used to form up to several hundred beams. To obtain multiple ionizing surfaces, a single crucible is made with many porous tungsten ionizer buttons or a large-area porous tungsten slab is machined to form separate concave emitting surfaces as in the sastrugi ionizer shown in Fig. 3. To obtain a higher current through each aperture, an accel-decel electrode system is used, since the extracted current may be space-charge-limited by the potential between ionizer and ground potential. By applying a high negative voltage to the accel electrode, the extraction field is increased without increasing the net energy of the ions in the beam. Nevertheless beam focusing is affected by the accel potential.

Surface ionization engine emission current densities are typically below 5 ma/cm<sup>2</sup>, with total beam currents determined by the emission area. A single-beam microthruster generates about 1 ma, providing several  $\mu$ lb of thrust (14). A large-area engine tested at EOS produced 3.8 amp of beam current to provide about 0.1 lb of thrust. Many engines have been developed to fill the gap between these two.

Single-beam  $Cs^+$  sources have been developed to study emission characteristics and for application studies of ion beam interaction phenomena. Special ionizers composed of tungsten spherical powder were used to produce current densities up to 80 ma/cm<sup>2</sup> for an ionizer temperature just above 1200°C (15). Charge transfer collisions, ion sputtering, secondary electron emission, and ion implantation studies were conducted using porous tungsten ion sources to generate  $Cs^+$ ,  $Rb^+$ , and  $K^+$  (16-19). Modification of this type source was made to permit high-temperature operation ( $> 1200^\circ C$ ), and an  $O_2$  spray on the ionizer was introduced so that ion beams of the rest of the

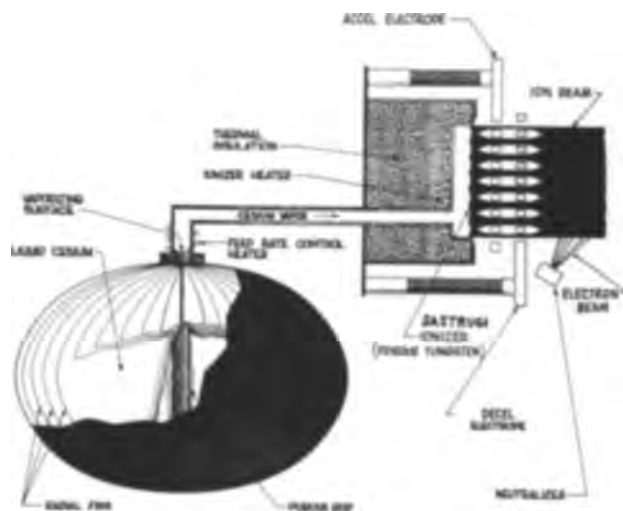


Fig. 3. Schematic of a multibeam surface ionization engine with zero-gravity feed system. Ions emitted from hot porous tungsten surface are accelerated by the electrodes to form individual ion beams. These beams merge downstream into a single large beam which is neutralized by the introduction of electrons.



alkali metals and other species could be generated (20, 21). Total currents of about 0.3 ma of  $\text{Li}^+$  were obtained from a 0.475-in.-diameter porous tungsten ionizer operated at a temperature of  $1200^\circ\text{C}$  and with an  $\text{O}_2$  impingement rate of about  $10^{15}$  particles/cm<sup>2</sup>-sec. This source was operated up to about 20 kv with little change in the current above 3 kv. A special source was constructed and operated with reservoir and ionizer at  $> 1200^\circ\text{C}$  to generate the required vapor pressure and ionize indium (22). Up to 0.5 ma of  $\text{In}^+$  was obtained with the current being feedrate limited.

#### Low-Pressure Discharge Sources

**Fundamentals of ion generation.**—A discharge source used to produce ion beams is applicable for those species which can be introduced as gas or vapor. Ions, generated by electron bombardment, are extracted from the discharge and accelerated to produce an ion beam. When the vapor is composed of a single atomic specie, such as in the case of the alkali metals, the number of singly charged ions can be enhanced and the fraction of emitted multiply charged ions can be minimized by optimizing the discharge mode.

To sustain a gaseous discharge, electrons are emitted from a cathode into a gas and accelerated to the anode by the application of an electric field. Electrons collide with the gas atoms and some of these collisions result in ionization of the atom. The electron removed from the atom will also be accelerated and will participate in further ionization processes. Ions are accelerated toward the cathode, and the current flow through the discharge is carried by both electrons and ions. Because of their much lower mass, the current flow of electrons will greatly exceed that of the ions.

The probability that an electron will collide with and ionize an atom depends on the product of the atom density, the electron path length through the gas, and the ionization collision cross section. This cross section, the effective physical area presented by the atom to the oncoming electron, depends on the electron energy (23). The ionization cross sections of atoms have several distinct features. Thresholds (or onset energies) occur at the ionization potential with cross sections rising rapidly to a maximum at an electron energy about five times the ionization potential, then slowly decreasing with increasing energy. Thus, as an electron is accelerated toward the anode in a gas discharge the probability that the electron undergoes an ionizing collision is affected by the gas density and the electric field. To sustain the discharge, the field and gas density must be such that the energy gained between collisions is high enough for ionization to occur. This is enhanced by increasing the field and/or increasing the mean free path (average path length between collisions) by decreasing the gas density. The number of collisions at a given gas density can be increased by lengthening the total path traversed by each electron, using a magnetic field which causes the electron to spiral and be constrained from reaching the anode. Thus, a discharge can be operated at an optimum condition for producing desired current densities by varying gas pressure, applied discharge voltage, magnetic field, etc.

Because the electrons travel more rapidly than the ions, the region where the ions are generated tends to become more positive than it would be due to the electric field between cathode and anode. Electrons escape rapidly enough to increase the potential of this region to somewhat above that of the anode, forming a nearly field-free plasma region. Because the plasma region is at a somewhat higher potential than the anode, it also constrains the electron flow to the anode. This is a self-regulating process, since an excessive loss of electrons increases the potential of the plasma region, which in turn further constrains the electron loss to the anode.

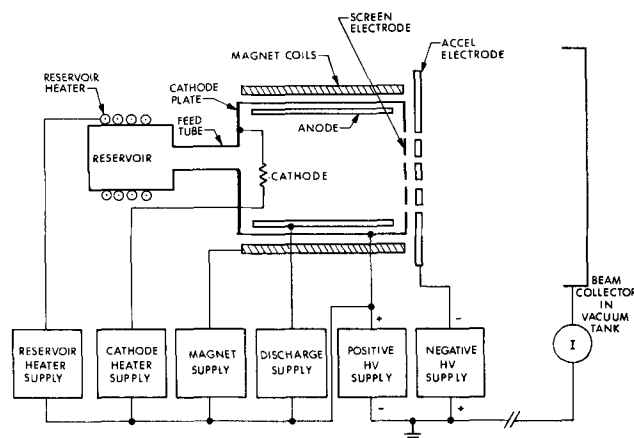


Fig. 4. Schematic diagram of low pressure discharge ion source with associated power supplies.

Ions are extracted out of the edge of the plasma through a region called the plasma sheath. Figure 4 illustrates schematically a typical low-pressure discharge source. The cathode in the discharge chamber is electrically connected to the enclosing cylinder, and the cylindrical anode is contained within the chamber. The magnetic field is coaxial with the cylinders. The screen electrode at the cathode potential aids in forming the plasma sheath from which the ions are extracted. Since the accel electrode is negative by several kilovolts with respect to the screen, positive ions are accelerated and electrons are retarded. Thus, the plasma sheath shape or the meniscus at the screen aperture is affected by the ion current extracted.

The meniscus is determined by the plasma ion density, the aperture configuration, and the field between the screen and accel electrodes. Good focusing of the ion beam occurs when the meniscus is concave. This general shape and the formation of the ion beam using an accel-decel electrode system are essentially the same as described in the section on Types of surface ionization sources for the surface ionization source.

**Electron bombardment ion engines.**—In the electron bombardment ion engine, a low-pressure discharge is used to generate ions which are extracted and accelerated to produce a beam. This type of engine differs from the surface ionization engine only in the means of ionization, the rest of the features being nearly the same. Bombardment engines have been developed to use Cs or Hg as the propellant, with some differences in components and operating modes to accommodate the particular vapor used. Both these elements provide the heavy ions desired for propulsion. The discharges are optimized to provide a predominance of singly charged ions with a minimum of emitted neutral atoms. Cs shows some advantage over Hg because of its lower ionization potential and higher ratio of second to first ionization potentials.

An electron bombardment ion engine (Fig. 4) is composed of a reservoir for propellant storage, a feed system, a discharge chamber for producing ions, and an ion acceleration electrode system. The reservoir containing the propellant in liquid form can be either the laboratory type or the zero-gravity type discussed in the above mentioned. The vapor is generally delivered to the discharge at or through the cathode, depending on the type of cathode used. The gas pressure, in a typical Cs discharge operating between 7 and 15v, is maintained between  $10^{-4}$  and  $10^{-3}$  Torr to provide an extracted ion current density of between 1 and 10 ma/cm<sup>2</sup>. The axial magnetic field, generally near  $10^{-3}$  Wb/m<sup>2</sup>, maintains the electrons in a long spiraling trajectory to increase the probability of ionization collisions. As the electrons collide and lose



energy, they tend to drift toward the anode, where they are lost from the discharge. Ions are also lost from the discharge when they strike a surface and re-enter the discharge as atoms. Ions, atoms, and electrons drift toward the screen electrode, where the electrons are repelled, the ions are extracted by the electrode field, and the neutral atoms escape. A beam collector located at the end of the vacuum chamber is used to measure the ion beam current and absorb the beam energy. To enhance the emission of ions over that of atoms, diverging magnetic fields have been used to increase the flow of charged particles toward the screen (24). This tends to decrease the neutral fraction and/or the discharge power by increasing the ionization efficiency.

Mass utilization efficiencies of 85-95% have been achieved with these engines. Beam currents, obtained by using a broad-area source having many apertures, up to 1A of  $\text{Cs}^+$  and 10A of Hg, have been produced by bombardment engines.

Because a large portion of the discharge power is generally consumed in heating the cathode, attention was given to the development of low-power cathodes. As a result, several types of cathodes have been developed and used with bombardment engines. Refractory wire and oxide-coated filaments were used initially with Cs and are still used with Hg. In the early Cs engines the vapor was directed toward the cathode, the adsorbed Cs coating decreasing the electron emission work function. This lowers the cathode operating temperature with a net saving of power. In the Hg engine the vapor flow is directed away from the cathode because the adsorbed Hg coating increases the filament work function. A further improvement in cathodes was made by using an autocathode, wherein Cs vapor is fed through a refractory metal cathode which is heated by ion bombardment from the discharge (24). The discharge is operated at low voltages (6-8v) so that ion sputtering of the cathode is negligibly small. This cathode is operable only over a limited range of discharge modes suitable for an ion engine stabilized by an electronic control system.

Another electron source known as the discharge cathode or discharge neutralizer is capable of emitting very large electron currents (25, 26). Cesium vapor is fed into a small enclosed chamber heated to about 600°C. The cesiated surface at this temperature is capable of emitting high electron current densities. An aperture approximately 0.02 cm in diameter allows particles to escape from the chamber. When a relatively low electric field is applied outside the chamber aperture, a discharge strikes and the plasma is emitted. Electron currents of several amps are readily drawn from this device with electron-to-atom (and electron-to-ion) emission ratios in the range of several hundred to one. When used as a cathode this discharge electron emitter is regulated to introduce Cs vapor,  $\text{Cs}^+$ , and electrons at rates required for the main chamber discharge. When it is used to neutralize the ion beam outside the ion engine, a plasma bridge to the ion beam is formed, resulting in good coupling with only a few volts potential difference between the beam and neutralizer.

Electron bombardment ion engines have been developed to produce ion beams of from 1 ma to 1 amp. A series of Cs microthrusters was developed, the smallest having a single beam aperture, to operate efficiently in the range from 10 to 100  $\mu\text{lb}$  of thrust (26). Other engines generating hundreds of ma of beam current have been developed in investigating cathode types, discharge modes, and electrodes to increase performance efficiency (27). Large Hg engines with source diameters up to 50 cm produce up to several amps of beam current (28). Cs engines have been life-tested for over 8000 hr of continuous operation and terminated only because the propellant was exhausted (29).

A 1-amp beam of  $\text{Na}^+$  was produced at EOS by an ion engine modified to operate at somewhat higher temperatures. The source was operated with 4 kv applied to the ionizer and about 1 kv to the accel electrode. The multibeam electrode system contained over 500 apertures and was heated to about 300°C to prevent condensation and thereby obtain stable operation. Other species such as Kr, Ar,  $\text{N}_2$ , and  $\text{H}_2$  (30) in addition to others not reported, have been used with standard ion engines.

#### Electrohydrodynamic Ion Source

Investigations conducted to generate heavy charged particles having charge-to-mass ratios a factor of approximately 100 below that of  $\text{Cs}^+$  are aimed at developing a thruster which operates at a specific impulse of about 1000 sec. This type of thruster can produce a higher thrust per unit power than the two types of ion engines described above, but it requires higher mass flow rates.

Heavy charged particles are generated by the application of intense electric fields at the surface of a conducting liquid (31-33). The intense electric field is achieved at nominal voltages (2-10 kv) by using high-curvature particle emitters such as capillary needles. Organic fluids such as glycerol, doped with salts or acids, have been used to produce charged particles over a wide range of charge-to-mass ratios up to  $10^5$  C/kg. Since the charged particle beam contains a distribution of charge-to-mass ratios, time-of-flight (TOF) techniques in addition to current and voltage measurements are employed to determine thruster operational parameters. Alkali metals used as the liquid produce ions predominately at high-current densities (32).

The state of the art in this field is not as advanced as those of the surface ionization and electron bombardment ion engines. For this reason generalizations are not drawn from the limited data available.

The experimental arrangement for charged particle generation and testing is shown in Fig. 5. Fluid flow to the tip of a capillary needle emitter is controlled by a pressure feed system. High voltage (2-10 kv) is applied to the emitter with an extractor electrode maintained at several hundred volts negative. The extractor aids in forming the electric field at the needle tip and prevents electrons in the particle beam from backstreaming to the emitter. It is important to prevent backstreaming electrons from impinging upon the emitter because they cause excessive emitter heating and also errors in measuring emitter ion current. A shielded collector is provided to measure part of the beam current and determine the charge-to-mass distribution using TOF analysis. The emitter potential is brought to ground by means of the shorting switch,

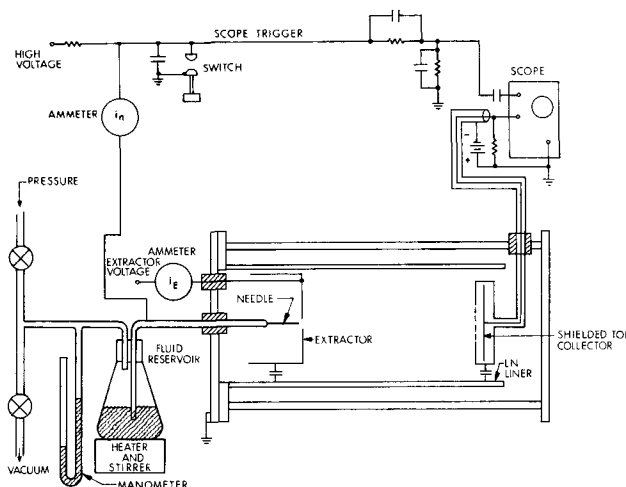


Fig. 5. Schematic diagram of electrohydrodynamic ion source experiments showing the arrangement for measuring time of flight.

and the subsequent current decay is observed on the oscilloscope. This provides the beam particle velocity distribution, from which the charge-to-mass ratio distribution can be obtained. Emitter tips are fabricated from capillary tubing made of stainless steel, platinum, or tungsten ranging in size from  $2.5 \times 10^{-3}$  to  $2 \times 10^{-2}$  cm ID and from  $7.5 \times 10^{-3}$  to  $4.5 \times 10^{-2}$  cm OD. The tips are tapered by grinding to provide a narrow, rounded rim.

The interaction between the conductive liquid and the metal surface at the emitter tip under high field conditions results in the electrohydrodynamic emission of charged particles. The electric fields at the emitter tips are somewhat below  $10^6$  v/cm, which is insufficient to extract charged particles or ions by field emission. Instabilities can occur at the liquid surface which is under tension because of high field and opposing surface tension forces. As the liquid develops a surface protuberance, the electrical force at the peak increases with the distance from the average surface level. This can grow into a liquid spike with dimensions one or two orders of magnitudes below those of the emitter. With the effective electric field at these spikes greater than  $10^7$  v/cm, ions can be extracted by field emission. The space charge of the emitted ions lowers the field at the spike to either limit the current flow or allow the spike to collapse to be regenerated a short time later. Conductivity, surface tension, and emitter tip size determine the applied voltage required to produce emission and also the average size of the particles emitted. Ions are generated from liquid alkali metals because of their high conductivities, high surface tension, and good wetting properties. No positive feed system pressure was required in the cesium tests, with only sufficient pressure applied initially to fill the feed system lines. The liquid metal then replenished itself at the needle tip by self-sustaining capillary and surface tension forces.

Needle currents of  $270 \mu\text{a}$  at 4.4 kv were obtained using a  $2.5 \times 10^{-3}$  cm needle, and  $200 \mu\text{a}$  at 4.03 kv using the  $10^{-2}$  cm ID needle with a 0.16 cm extractor aperture. In all of the tests the charged particle beam consisted almost wholly of  $\text{Cs}^+$  ions. Figure 6 shows two TOF traces showing  $\text{Cs}^+$ ,  $\text{Cs}^{+2}$ , and  $\text{Cs}^{+3}$  at 4.03 kv and  $\text{Cs}^+$  alone at 7.8 kv. No attempt was made to focus the beam, with the result that only a few per cent of the ions impinged upon the collector. Onset of spraying occurred at about 0.9 kv for the  $2.5 \times 10^{-3}$  cm ID needle.

In conjunction with the spraying of cesium ions, the neutral cesium yield was measured directly with neutral cesium detector used for similar measurements with ion engines. The measurements show that the neutral fraction of the total mass flow rate varied from less than 1.8 to 3.8% for the case where the emitter temperature was between  $100^\circ$ - $200^\circ\text{C}$ . Above  $200^\circ\text{C}$  the neutral fraction was nearly 100%, and the cesium

spray from the emitter showed a visible glow. At the lower temperatures the spray was not visible, indicating a correlation of the neutral yield with the visible spray. The transition between the two operating conditions was abrupt and showed considerable hysteresis. The glow indicates the presence of a discharge which heats the emitter tip, evaporating copious quantities of neutral cesium.

### Acknowledgment

The author wishes to thank H. L. Daley for the aid and criticism he provided in the course of writing this paper.

Manuscript submitted June 17, 1968; revised manuscript received September 6, 1968. This paper was presented at the Boston Meeting, May 5-9, 1968, as Paper 170B.

### NOMENCLATURE

$F$	= thrust, newtons
$\dot{m}$	= ion mass flow rate, kgm/sec
$v$	= velocity, m/sec
$e$	= charge of ion, $1.6 \times 10^{-19}$ coul
$m$	= mass of ion, kgm
$i$	= ion beam current, amperes
$V$	= accelerating potential, volts
$I_{sp}$	= specific impulse, sec
$\dot{M}$	= total mass flow rate, kgm/sec
$g$	= acceleration due to gravity, $9.8 \text{ m/sec}^2$
$\eta$	= mass utilization efficiency
$\Phi$	= surface work function, ev
$I$	= atomic ionization potential, ev
$n_a$	= atom emission rate, atoms/cm <sup>2</sup> -sec
$n_p$	= ion emission rate, ions/cm <sup>2</sup> -sec
$w_a$	= atom weighting factor, $2J + 1$
$w_p$	= ion weighting factor, $2J + 1$
$J$	= total angular momentum of ion or atom
$k$	= Boltzmann constant $1.38 \times 10^{-23} \text{ J/}^\circ\text{K}$ or $8.63 \times 10^{-5} \text{ ev/}^\circ\text{K}$
$T$	= temperature, $^\circ\text{K}$
$\tau_i$	= ion desorption time, sec
$\tau_o$	= ion desorption time extrapolated to $T^{-1} = 0$ , sec
$Q$	= ion desorption energy, ev
$J$	= ion current density, amperes/cm <sup>2</sup>
$N$	= adsorbed atom surface coverage atoms/cm <sup>2</sup>
$\theta$	= surface coverage fraction of a monolayer
$\mu$	= atom flow rate, atom/cm <sup>2</sup> -sec

### REFERENCES

1. J. B. Taylor and I. Langmuir, *Phys. Rev.*, **44**, 423 (1923).
2. J. Perel, R. H. Vernon, and H. L. Daley, *J. Appl. Phys.*, **36**, 2157 (1965).
3. M. D. Scheer and J. Fine, *J. Chem. Phys.*, **37**, 107 (1962).
4. R. M. Worlock, "The Surface Ionization Ion Engine," "First International Conf. on Electron and Ion Beam Science and Technology," p. 853, R. Bakish, Editor, John Wiley & Sons, Inc., New York (1964).
5. A. T. Forrester and R. C. Speiser, *Astronautics*, **4**, (1959).
6. G. Kuskevics and B. L. Thompson, *AIAA J.*, **2**, 284 (1964).
7. M. LaChance, G. Kuskevics, and B. Thompson, *ibid.*, **3**, 1498 (1965).
8. A. T. Forrester, *J. Chem. Phys.*, **42**, 972 (1965).
9. T. R. Bates and A. T. Forrester, *J. Appl. Phys.*, **38**, 1956 (1967).
10. O. K. Husmann, *ibid.*, **37**, 4662 (1966).
11. S. L. Eilenberg, W. Seitz, and E. Caplinger, *AIAA J.*, **3**, 866 (1965).
12. S. L. Eilenberg, E. Caplinger, H. L. Daley, J. Perel, and W. Seitz, *J. Spacecraft and Rockets*, **2**, 982 (1965).
13. W. S. Seitz and S. L. Eilenberg, *J. Appl. Phys.*, **38**, 276 (1967).
14. R. M. Worlock, P. Ramirez, Jr., M. P. Ernstene, and W. E. Beasley, Jr., "A Contact Ion Micro-thruster System," AIAA Paper 67-80, New York (1967).\*
15. G. Kuskevics and B. Thompson, *Rev. Sci. Instru.*, **37**, 710 (1966).
16. J. Perel, R. H. Vernon, and H. L. Daley, *Phys. Rev.*, **138**, A937 (1965).

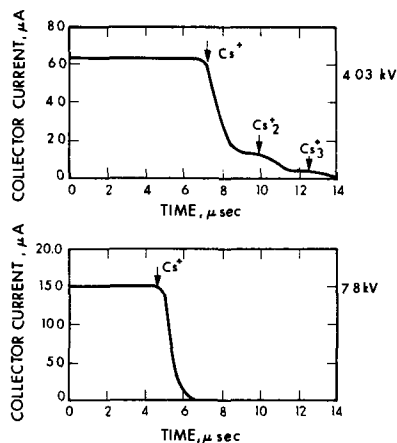


Fig. 6. Time-of-flight data from cesium tests

17. J. Perel, R. H. Vernon, and H. L. Daley, "Measurement of  $K^+$ -Rb Charge Transfer Cross Sections," IVth International Conference on Physics of Electronic and Atomic Collisions," p. 336, Quebec, Aug. 1965, Science Bookcrafters, Inc., Hastings-on-Hudson, N. Y.
18. H. L. Daley and J. Perel, *AIAA J.*, **5**, 113, (1967) (AIAA Paper 62-203, 5th Electric Propulsion Conf., San Diego, California, March 1966).\*
19. D. B. Medved, J. Perel, H. L. Daley, and G. P. Rolik, *Nuclear Instr. and Methods*, **38**, 175 (1965) (Proceedings of Electro-Magnetic Isotope Separators Conf., Holland, 1965).
20. J. Perel and A. Y. Yahiku, "Oscillations in Total Cross Sections of  $Rb^+$ ,  $K^+$ ,  $Na^+$  and  $K$  Charge Transfer," p. 400, Fifth Int. Conf. on the Phys. of Elect. and Atomic Collisions—Leningrad, July 1967, Publishing House "Nauka" Leningrad.
21. J. Perel and H. L. Daley, " $Li^+$  and  $Na^+$  Source," To be published.
22. H. L. Daley, J. Perel, and R. H. Vernon, *Rev. Sci. Instr.*, **37**, 473 (1966).
23. R. H. McFarland and J. D. Kinney, *Phys. Rev.*, **137**, A1058 (1965).
24. G. Sohl, G. C. Reid, and R. C. Speiser, *J. Spacecraft and Rockets*, **3**, 1093 (1966).
25. M. P. Ernstene, E. L. James, G. W. Purmal, R. M. Worlock, and A. T. Forrester, *J. Spacecraft and Rockets*, **3**, 744 (1966).
26. G. Sohl, V. V. Fosnight, S. J. Goldner, and R. C. Speiser, *J. Spacecraft and Rockets*, **4**, 1180 (1967).
27. G. Sohl, K. Wood, T. R. Dillon, and R. Vernon, "Performance of a Cesium Bombardment Ion Engine with a Self-Rectifying Discharge and Automatic Controls," AIAA Paper 67-666, Colorado Springs, Colo., (1967).\*
28. P. D. Reader, "Experimental Performance of a 50-cm Electron Bombardment Ion Rocket," AIAA Paper 64-689, Toronto, (1964)\* and NASA TMX-52042 (1964).
29. V. V. Fosnight, G. Sohl, S. J. Goldner, and R. C. Speiser, "Cesium Ion Engine System Life Test Results," *J. Spacecraft and Rockets*, To be published.
30. P. D. Reader, "The Operation of an Electron Bombardment Ion Source with Various Gases," *First Inter. Conf. Electron and Ion Beam Science and Technology*, p. 925, R. Bakish, Editor, J. Wiley & Sons, Inc., New York (1964).
31. C. Hendricks, "Classical Physics in Modern Space Propulsion: Heavy Particle Beam Formation by Electrical Spraying of Liquids," *First Inter. Conf. Electron and Ion Beam Science and Technology*, p. 915, R. Bakish, Editor, J. Wiley & Sons, Inc., New York (1966).
32. J. Perel, T. Bates, J. Mahoney, R. D. Moore, and A. Y. Yahiku, "Research on a Charge Particle Bipolar Thruster," AIAA Paper 67-728, Colorado Springs, Colo. (1967).\*
33. J. C. Beynon, E. Cohen, D. S. Goldin, M. N. Huberman, R. W. Kidd, and S. Zafran, "Present Status of Colloid Microthruster Technology," AIAA Paper No. 67-531, Colorado Springs, Colo. (Sept. 1967).\*
34. J. Perel, R. H. Vernon, and H. L. Daley, "Ion and Atom Angular Distributions from a Multibeam Cesium Ion Engine," AIAA Paper 64-696, Philadelphia, Pa. (Aug. 1964).\*

## BIBLIOGRAPHY

- A. R. Brewer, M. R. Currie, and R. C. Knechtli, "Ionic and Plasma Propulsion for Space Vehicles," *Proc. Inst. Radio Engrs.*, **49**, 1789 (1961).
- A. T. Forrester and J. M. Teem, "Advances in Electrostatic Propulsion," *Astronautic*, **6**, 34 (1961).
- "Progress in Astronautics and Rocketry: Electrostatic Propulsion," p. 5, D. B. Langmuir, E. Stuhlinger, and J. M. Sellen, Jr., Editors, Academic Press, New York (1961).
- "Progress in Astronautics and Rocketry: Electric Propulsion Development," p. 9, E. Stuhlinger, Editor, Academic Press, New York (1963).
- A. T. Forrester and S. L. Eilenberg, "Ion Rockets," *International Sci. and Tech.* (January 1964).
- E. Stuhlinger, "Ion Propulsion for Space Flight," McGraw-Hill, New York (1964).
- G. R. Brewer, "Physical Electronics Phenomena in Ion Propulsion Engines," *IEEE Spectrum*, **2**, 65 (1965).
- M. P. Ernstene, "Progress and Prospects of Electric Propulsion," AIAA Paper 66-830, Boston (1966).\*
- W. R. Mickelsen, "Auxiliary and Primary Electric Propulsion, Present and Future," *J. Spacecraft and Rockets*, **4**, 1409 (1967).
- "Ion Propulsion," A. T. Forrester and G. Kuskevics, Editors, AIAA Selected Preprints, Vol III, (1968).\*
- R. M. Worlock, "The Surface Ionization Ion Engine," p. 853, *First International Conference on Electron and Ion Beam Science and Technology*, R. Bakish, Editor, John Wiley & Sons, Inc., New York (1964).

\* AIAA preprints can be obtained from American Institute of Aeronautics and Astronautics, 1290 6th Ave., New York, N. Y. 10019.

\* AIAA preprints can be obtained from American Institute of Aeronautics and Astronautics, 1290 6th Ave., New York, N. Y. 10019.